LHC OPERATION AT HIGHER ENERGY AND LUMINOSITY

G. Papotti, CERN, Geneva, Switzerland

Abstract

The Large Hadron Collider (LHC) at CERN (Geneva) was commissioned and operated in the years 2009-2013 up to a beam energy of 4 TeV. A peak luminosity of $0.77 \cdot 10^{34}\,\mathrm{cm}^{-2}\mathrm{s}^{-1}$ was reached and an integrated luminosity of around 29 fb^{-1} was delivered to both ATLAS and CMS. This performance allowed the discovery of a scalar boson. The LHC is presently in a shutdown phase dedicated to consolidation and maintenance that will allow the restart of beam operation in early 2015 at an increased beam energy of 6.5 to 7 TeV. Maximum acceptable pileup, effectiveness of electron-cloud scrubbing, and fast loss events are some of the issues that will shape the choice of operational parameters, cycle setup, and the commissioning strategy. The baseline choices and options for the restart after the shutdown are presented. In addition the roadmap for future performance upgrades is sketched.

INTRODUCTION

The Large Hadron Collider (LHC) at CERN is a 27 km long circular accelerator and collider based on superconducting two-in-one magnets and designed for a beam energy of 7 TeV [1]. It features 8 straight sections: 4 Interaction Points (IPs) are reserved for accelerator equipment and 4 house particle physics experiments. IP3 and 7 are dedicated to the collimation system, IP4 houses the RF system and most of the beam instrumentation, IP6 the beam dump system. IP1 and 5 contain ATLAS and CMS, the high luminosity experiments, while IP2 and 8 accommodate ALICE and LHCb, together with beam injection.

Initial commissioning with beam was re-started at the end of 2009, and first collisions at 3.5 TeV were achieved on 30 March 2010. The decision to limit the energy to 3.5 TeV was taken in order to reduce the risk of repeating events similar to the 2008 incident, when a highly resistive splice combined with a non-continuity in the copper stabilizer caused localized over-heating and an accidental release of the 600 MJ that were stored in the sector. After two years of successful running at 3.5 TeV with no accidental beam-induced quench at high energy, the decision was taken to run at 4 TeV per beam (in 2012 and 2013) until the start of the first Long Shutdown (LS1) during which the machine is being consolidated to run safely at 7 TeV.

The few weeks in 2009 and the year 2010 were dedicated to gaining the first operational experience. Initially, operation was with "pilot" bunch intensity (few 10^9 ppb), to commission the first squeeze. In June 2010 the bunch intensity was increased to "nominal" ($\approx 10^{11}$ ppb) and the summer was a period of steady running at $\approx$1 MJ to gain experience with intense beams and Machine Protection. In September the injection of bunch trains was commissioned (150 ns bunch spacing) and by mid-October the yearly target of an instantaneous luminosity of $10^{32}\,\mathrm{cm}^{-2}\mathrm{s}^{-1}$ was achieved.

Operation in 2011 started with 75 ns beams, and 50 ns beams were used only after a scrubbing run. With 50 ns beams, the number of bunches was slowly increased to 1380, then luminosity production was improved by reducing the transverse emittance, by squeezing further (from beta star 1.5 m to 1 m) and finally by gently increasing the bunch intensity. Squeezing to 0.6 m in 2012 allowed the production rates to increase even further and the year culminated with the discovery of the Higgs boson on 4 July 2012. The main machine and beam parameters are recalled in Table 1 for 2010-2012 and for the Design Report [1] for comparison. Operation with lead ions was also very successful [2, 3], but is not discussed here.

LONG SHUTDOWN 1

In the morning of 16 February 2013 the last LHC beam of run 1 was dumped and the LS1 started. The duration of the LS1 is planned to be approximately 20 months, and first beam is supposed to be back in the LHC in early 2015. This is to be compared to the winter shutdowns of 2010, 2011, 2012, that were as short as a couple of months and during which only fundamental maintenance was carried out.

The LS1 [4] firstly addresses the need to consolidate the interconnections between the LHC main magnets (soldered joints of two superconducting cables, splices, stabilized by a copper bus bar) to allow the LHC to operate at the nominal centre-of-mass energy of 14 TeV. It additionally targets consolidation activities to guarantee reliable operation of the LHC and its injectors until the next long shutdown (presently foreseen for 2018). Quality controls are performed on the splices and, in case of failure, the splices are remade. Consolidation activities include also the installation of shunts to improve electrical continuity and insulation boxes that provide mechanical restraints in addition to dielectric strength.

At the time of writing, the shutdown activities are progressing well. The consolidation activities spread across most of the machine, with hte interconnections being opened in sectors 12 and 23 being opened, the electrical

Copyright © 2013 CC-BY-3.0 and by the respective authors

Table 1: Main Beam and Machine Parameters for Design Peport, 2010, 2011, 2012 and Options for 2015

Parameter	2010	2011	2012	Nominal	2015 (50 ns)	2015 (25 ns)
collision energy [TeV]	3.5	3.5	4	7	6.5	6.5
N_b [10^{11} ppb]	1.2	1.45	1.6	1.15	1.6	1.15
k	368	1380	1380	2808	1260	2508
bunch spacing	150	75/50	50	25	50	25
stored energy [MJ]	25	112	140	362	210	300
tr. emittance [μrad]	2.4	2.4	2.5	3.75	1.6	1.9
beta star (β^*) [m]	3.5	1.5, 1	0.6	0.55	0.4	0.5
L [$\mathrm{cm}^{-2}\mathrm{s}^{-1}$]	$2 \cdot 10^{32}$	$3.5 \cdot 10^{33}$	$7.7 \cdot 10^{33}$	$1 \cdot 10^{34}$	$2 \cdot 10^{34}$	$1.5 \cdot 10^{34}$
pile-up μ	8	17	38	26	120	44

quality of the old splices being tested in sector 81, shunts and insulation boxes being installed in sectors 67 and 78. The activities in sector 56, the first to be opened, are completed apart from few non-conformities, and the first vacuum leak tests gave positive results.

The activities have so far accumulated a delay of 3 weeks with respect to the initial schedule. This can be traced back to a few causes: a few technical issues (which are being solved), the summer vacation period and the consequent slow down of activities, and the fact that more splices than expected are to be redone (15% was expected, while 30% failed the quality tests so far, on 40% of the machine). A few bad surprises were also discovered, e.g. damaged bellows in the cryogenic system and in the electrical feed boxes, for which the repair is under study.

PREPARATION FOR RESTART

At the end of the shutdown activities a number of tests are performed on a sector by sector basis: electrical quality assurance tests are performed at room temperature, followed by flushing and cool down to cryogenic temperatures, further electrical quality tests and a full campaign of powering tests.

The hardware commissioning powering tests verify correct behaviour of the superconducting circuits and the associated protection systems, and are currently foreseen for the second half of 2014. All circuits but the main ones are tested up to the 7 TeV equivalent current values. Concerning the main circuits, the current baseline is to train them to 6.55 TeV (for which about 100 quenches are expected to be needed [5]), to allow to initially operate at 6.5 TeV beam energy.

In parallel to the powering campaigns, the other accelerator systems are also tested in "dry runs", so to verify the equipment control from the central control room (e.g. beam dump, RF, injection kickers, etc.). Also, in parallel to the end of the powering tests, a "sector test" with beam is foreseen for the end of 2014. It plans the injection of beam from point 8 to point 7 to the dump in point 6. It requires the readiness of sectors 67 and 78 and many other systems, and allows verifying system-wide integration and pre-commissioning many key procedures.

Finally, a global machine checkout takes place, in which the integration of all systems is verified, including interlocking functionality. The goal is to run the machine through the full cycle without beam.

BEAM COMMISSIONING

The LHC commissioning with beam starts after a successful machine cold checkout. The breakdown of the beam commissioning into phases to build the nominal cycle is rather standard. Traditionally, the first injections are used to "thread" the beam around the machine: with the smallest intensity detectable by the beam position monitors, the trajectory is corrected one sector at a time, and the beam stopped on collimators. When a closed orbit is established, the setup of the RF system can start, allowing to capture the beam. Injection of a bunch of nominal intensity is used to record a flat orbit reference and setup primary collimators, beam instrumentation, transverse damper, etc.

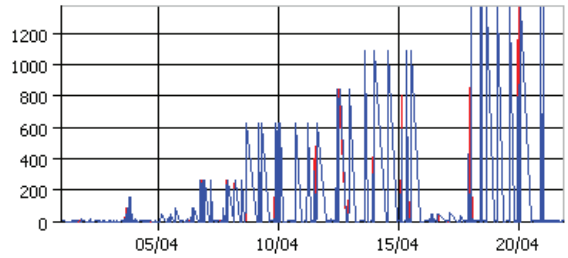
The first energy ramp and beta star squeeze require the commissioning of orbit, tune and radial feedback, then optic measurements and corrections are also performed. Then, crossing and separation bumps are added throughout the cycle, allowing further measurements of aperture and beta star. Finally, collisions are established in all interaction points and RF cogging is performed to align the collision in the center of the experiments. Note that the protection by the collimators is verified by performing controlled tests of losses at injection, flat top, after squeeze and in collisions.

A total of about 2 months in the beginning of 2015 is required for completing these steps, including testing thoroughly all machine protection systems. While in this initial phase everything is performed with at most 2-3 nominal bunches in the machine, the injection of many bunches at a time (bunch trains) and the increase of intensity in the machine is performed in steps, i.e. "intensity ramp-up".

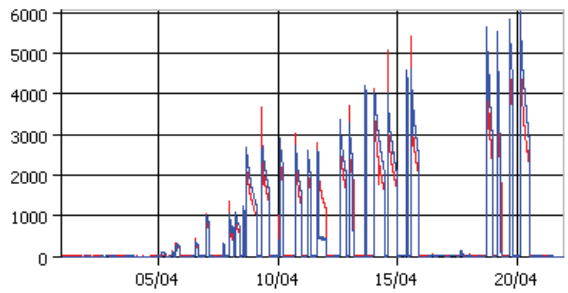
Intensity Ramp-up

The intensity increase from few nominal bunches to a full machine is staged in steps. Some fills with limited number of bunches allow verification of the nominal cy-

Copyright © 2013 CC-BY-3.0 and by the respective authors



(a) Number of bunches per fill in April 2012.



(b) Luminosity per fill in April 2012 [10^{30} cm^{-2}s^{-1}].

Figure 1: Intensity ramp-up in April 2012.

cle and the procedures, e.g. scaling of losses. Fills with more bunches allow approaching intensity (or luminosity) related problems slowly, e.g. effects on vacuum or heating of machine components. This procedure took about one month in April 2012 and it was divided in 7 steps: 2-3 fills and 4-6 hours each with 48, 84, 264 and 624 bunches for cycle validation, and 3 fills for a total of at least 20 hours with 840, 1092, 1380 bunches for intensity-related problems. The resulting number of bunches and luminosity are shown in Figure 1.

For the restart in 2015, the uncertainty on the duration of the intensity ramp-up is dominated by the effectiveness of electron-cloud scrubbing.

OPEN QUESTIONS

Three effects that are expected to shape beam commissioning in 2015 are recalled next: electron cloud effects and their scrubbing, the so-called Unidentified Falling Objects (UFOs) and beam stability. Additionally the issue of radiation effects on electronic components is included.

Electron-cloud and Scrubbing

The operation of an accelerator with closely spaced proton bunches can give rise to local accumulations of electrons inside the vacuum chamber depending on beam structure and properties of the chamber (e.g. the Secondary Electron Yield, SEY). In particular if the SEY is higher than a threshold value, an avalanche effect can take place and cause vacuum pressure rise, increased heat load on the cryogenic system, increased beam emittance, and single and multi bunch instabilities.

Electron cloud effects were observed in the LHC as soon as bunch trains were injected, with 150, 75, 50 and 25 ns bunch spacing. Scrubbing runs took place in 2011 and 2012 as dedicated periods during which the electron cloud generation is enhanced so to "clean" the vacuum chamber walls, and thus decrease the SEY and effectively improve beam quality for physics operation. Additionally, Machine Development time was allocated for electron cloud studies for 25 ns beams. In particular, in December 2012, a short run was dedicated to study 25 ns beams to assess the evolution of the SEY and other possible differences compared to 50 ns beams [6]. After an initial improvement of heat load and beam lifetime, a sharp slow down of the scrubbing process was observed in the studies at 450 GeV (see Figure 2). This lead to the conclusion that, at restart in 2015, at least one week of scrubbing will be required for 50 ns running, an additional week for 25 ns running, and that coexistence with electron cloud will be probably inevitable in the first part of the physics run (so that physics will be performed with degraded beam parameters). The understanding of the observations and underlying physical phenomena is progressing well at the moment of writing, and this could impact positively on the above statements.

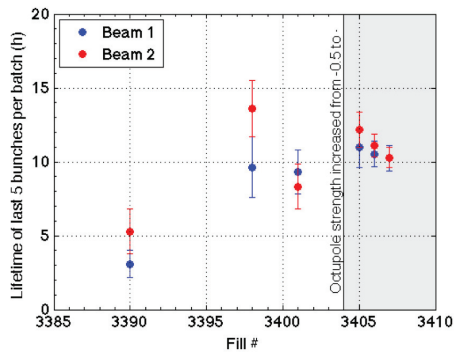


Figure 2: Single beam lifetime during the December 2012 scrubbing run.

Unidentified Falling Objects

UFOs are micrometer size dust particles that, when interacting with the beam, produce fast beam losses (approximate duration of about 10 turns). Such events were observed since 2010 and caused a non negligible number of beam aborts (about 5% of the total number of dumps above injection energy, or ≈20 dumps/year).

The occurrence of such events has been thoroughly studied [7]. There is evidence for a "scrubbing" effect over the course of 2011 and 2012, e.g. the rates in 2011 decreased from 10 to 2 events/hour. There is also evidence for deconditioning after periods without beam as technical stops, e.g. an increase of a factor 2.5 after the 2011-12 winter stop. Because of this, an increase in rates is expected after LS1. Additionally, during the 25 ns studies, UFO rates increased by a factor 10 at 4 TeV. This, combined with the

Copyright © 2013 CC-BY-3.0 and by the respective authors

energy dependence of UFOs, indicate that they might be a major source of beam dumps (extrapolations indicate over 100 dumps per year). In a very pessimistic scenario they might impose to start with 50 ns beams, or at a lower beam energy.

Beam Stability

Many instabilities were observed during run 1, in all phases of the operational cycle, and many different countermeasures have been deployed to cure them (see for example [8]). Transverse instabilities caused emittance blow up at injection (2010 and 2011) and were cured by increasing the octupole strength for increased Landau damping. "Dancing bunches" (longitudinal dipolar and quadrupolar motion) are observed at high energy for low longitudinal emittance, and are cured by controlled emittance blow up by phase noise since 2010. Lack of Landau damping was also observed in 2012 for beams colliding only in LHCb, and was solved by changing the filling scheme to have additional collisions in ATLAS and CMS for these bunches so to increase the tune spread by the beam-beam interaction. A transverse instability was reproducibly observed at the end of squeeze in 2012 and caused mostly emittance increase: it was not fully understood, but it could be mitigated by high chromaticity and high transverse damper gain.

Beam instabilities are expected also at 6.5-7 TeV and will shape many operational choices. The option to collide the beam already during the squeeze is being considered to profit from Landau damping by head-on beam-beam force. The amount of opening of collimator jaws is still under discussion as it compromises between cleaning efficiency and machine impedance. The high setting of chromaticity and transverse gain will be kept if needed, the efficiency of the octupoles might be limited by the available hardware current and the small emittance.

Radiation to Electronics

The Radiation To Electronics project (R2E) aims at limiting the Single Event Effects so to reduce the R2E induced beam dumps and the impact on machine availability [9]. A thorough analysis allows identifying which beam dumps are likely to be caused by radiation effects, correlate them with radiation levels in the tunnel and integrated luminosity. The systems that were the most sensitive in 2012 operation were the Quench Protection System and an auxiliary power supply of 600 A Power Converters, followed by cryogenics and vacuum equipment.

R2E mitigation actions consist of equipment relocation from critical to safer areas or addition of shielding to reduce the exposure to radiation, and equipment upgrades or redesign to improve radiation hardness. These measures already improved the number of dumps from 12 dumps/fb^{-1} in 2011 to 3 in 2012, and a major campaign during the LS1 aims at reducing the rate further to 0.5 dumps/fb^{-1}.

EXPECTED PEAK PERFORMANCE

The main machine and beam parameters for 2015 operation are shown in Table 1. With a baseline beta star of 40 cm, peak luminosities of 1.5 to 2 $\cdot$ 10^{34} are within reach with 25 ns and 50 ns beams. The excessive pile-up that characterizes the 50 ns beams makes 25 ns the preferred choice for having cleaner physics events. Electron cloud scrubbing might be slow or impose initial physics operation with degraded beam parameters, but would be an investment until LS2 (2018).

Conversely, 50 ns beams are the fallback plan in case in of insurmountable problems with 25 ns beams, e.g. electron cloud or UFOs. The higher brightness that can be provided by the LHC injectors for the 50 ns beams allows achieving higher luminosity with less stored energy in the machine, but would impose the need for luminosity leveling at ATLAS and CMS.

UPGRADES

The present LHC will reach the end of its usefulness in the early 2020s, when the running time necessary to halve the statistical error in the measurements will be more than 10 years, making a substantial increase in luminosity necessary to maintain scientific progress. At the same time, the triplet and cleaning insertion magnets will reach the end of their lifetime due to radiation, and the limit of cooling and cryogenics systems will be reached (at $\approx$ 1.75 $\cdot$ 10^{34} cm^{-2}s^{-1}. A novel machine configuration, called High Luminosity LHC (HL-LHC), will be installed during the LS3 to overcome these limitations.

High Luminosity LHC

The High Luminosity LHC (HL-LHC, [10]) is an approved project aiming at obtaining 3000 fb^{-1} within ten-twelve years of operation. This translates to the goal of an integrated luminosity of 250 fb^{-1} per year, i.e. about ten times the present LHC, which can achieved with peak luminosities of 5 $\cdot$ 10^{34} cm^{-2}s^{-1} , leveled down from higher, "virtual" luminosities.

These specifications require a number of equipment upgrades. Large aperture magnets are needed for the IP quadrupoles to accommodate for very low beta star. Crab cavities are also needed to profit from the small beta star despite the large crossing angle. Additional dispersion suppressor collimators remove cleaning bottlenecks, but require the use of high field dipoles to free up space longitudinally to allow their installation. Additional cryogenics plants for P1, P4, P5 will provide the same cooling power in all arcs. The use of new, super-conducting links (300-700 m long) allow power converters to be moved to surface, effectively reducing radiation-induced risks and increase availability (critical aspect when working with leveled luminosities). Additionally, an upgrade of the LHC Injector Chain is foreseen that will help both beam brightness and

Copyright © 2013 CC-BY-3.0 and by the respective authors

availability, and an upgrade of the high-luminosity experiments will allow them to cope with higher pile-up density (i.e. 140 events per crossing).

Options for the Farther Future

The HL-LHC will also reach the end of its lifetime after 10-12 years of operation, i.e. in the mid-2030's. For the LHC, the lead time was about 25 years, so that similarly the design phase of a new accelerator should start now for it to be operational few years after the end of HL-LHC. A number of new designs are being studied at present at CERN, to take advantage of the existing accelerator complex and infrastructure.

Studies aiming at very high field magnets (16-20 Tesla) are ongoing [11], and would allow a High Energy LHC [12] to be installed in the LHC tunnel, that could reach center of mass energies of 26-33 TeV. With similar, high field magnets, and a tunnel with larger circumference (84-104 km), a Very High Energy LHC could be installed with center of mass energies of 100 TeV (see for example [13]).

Similarly to the LEP/LHC experience, where the same tunnel was reused for two different machines, lepton-proton collisions could be explored in the LHC tunnel with LHeC [14], or e+e- in the 84-104 km tunnel with TLEP [15.

CONCLUSIONS

The LHC is presently in a shutdown phase and operation with beam resume in early 2015 at a higher beam energy, the present baseline is 6.5 TeV. The use of 25 ns beams is imposed by the need to limit the pile-up and provide clean physics events to the experiments, but might bring other important issues along, as degraded beam parameters due to electron cloud effects or impaired machine availability due to excessive UFO rates. Work is already ongoing to prepare the High Luminosity upgrade of the LHC, that is supposed to start operating in about 10 years, and studies are taking place to devise what the next circular accelerator might look like.

ACKNOWLEDGEMENTS

The author would like to acknowledge the whole LHC team whose work was summarized in this paper, in particular G. Arduini, T. Baer, V. Kain, W. Herr, G. Iadarola, E. Metral, M. Pojer, L. Rossi, G. Rumolo, G. Spiezia, L.Tavian, J. P. Tock, F. Zimmermann. Additionally, a special mention goes to M. Lamont and J. Wenninger.

REFERENCES

[1] O. S. Brüning, P. Collier, P. Lebrun, S. Myers, R. Ostojic, J. Poole, P. Proudlock, "LHC Design Report", CERN-2004-003-V-1.

[2] J. Jowett et al., "First run of the LHC as a heavy-ion collider", Proceedings of the 2nd International Particle Accelerator Conference (IPAC11), San Sebastian, Spain, 4-9 September 2011, TUPZ016.

[3] J. Jowett et al., "Proton-nucleus collisions in the LHC", Proceedings of the 4th International Particle Accelerator Conference (IPAC13), Shanghai, China, 12-17 May 2013, MOODB201.

[4] F. Bordry et al., "The First Long Shutdown (LS1) for the LHC", Proceedings of the 4th International Particle Accelerator Conference (IPAC13), Shanghai, China, 12-17 May 2013, MOZB202.

[5] E. Todesco et al., "Energy of the LHC after the 2013-2014 shutdown", Proceedings of the Chamonix 2012 Workshop on LHC Performance, Chamonix, 6-10 February 2012.

[6] G. Iadarola et al., "Electron cloud and scrubbing in 2012 in the LHC", Proceedings of the LHC Beam Operation workshop, Evian, 17-20 December 2012.

[7] T. Baer et al., "UFOs: observations, statistics and extrapolations", Proceedings of the LHC Beam Operation workshop, Evian, 17-20 December 2012.

[8] E. Metral et al., "Review of the instabilities observed during the 2012 run and actions taken", Proceedings of the LHC Beam Operation workshop, Evian, 17-20 December 2012.

[9] G. Spiezia et al.,"R2E - experience and outlook", Proceedings of the LHC Beam Operation workshop, Evian, 17-20 December 2012.

[10] L. Rossi, O. Brüning, "High Luminosity Large Hadron Collider A description for the European Strategy Preparatory Group", CERN-ATS-2012-236.

[11] P. Ferracin, "Review of Superconducting Magnet (LTS and HTS) Developments for Accelerator Applications", these proceedings, FRYAB1.

[12] O. Brüning et al., "High Energy LHC Document prepared for the European HEP strategy update", CERN-ATS-2012-236.

[13] O. Dominguez, F. Zimmermann, "Beam parameters and luminosity lifetime evolution for an 80-km VHE-LHCVHE", Proceedings of the 4th International Particle Accelerator Conference (IPAC13), Shanghai, China, 12-17 May 2013, TUPFI042.

[14] O. Brüning et al, "Overview of the LHeC Design Study at CERN", Proceedings of the 4th International Particle Accelerator Conference (IPAC13), Shanghai, China, 12-17 May 2013, MOZB201.

[15] M. Koratzinos et al., "TLEP: a high performance circular e+e- collider to study the Higgs boson", Proceedings of the 4th International Particle Accelerator Conference (IPAC13), Shanghai, China, 12-17 May 2013, TUPME040.

Copyright © 2013 CC-BY-3.0 and by the respective authors

THE CLIC PROJECT - STATUS AND PROSPECTS*

E. Adli†, University of Oslo, Norway
On behalf of the CLIC/CTF3 collaboration

Abstract

Following the feasibility demonstration of the novel CLIC technology and the publication in 2012 of a CLIC Conceptual Design Report for a Multi-TeV Linear Collider to be built in stages, a new phase towards a technical design is being launched by a global collaboration of volunteer institutes. This paper reviews the status and plans of the CLIC study outlining the developments planned for the next project phase.

INTRODUCTION

The CLIC project is a study for a Multi-TeV e+ e- collider based on normal-conducting X band technology, and a Two-Beam Acceleration scheme in order to provide compressed rf pulses for the main accelerating structures with high efficiency. The compressed rf pulses allow the main charge to be accelerated at a very high loaded gradient of 100 MV/m, in short pulses of 156 ns. CLIC completed the CDR in 2012 [1] and the project is currently in a project preparation phase where further optimization, system tests and detailed design of the machine will take place. In addition, the CLIC project has started collaborations for the use of CLIC X band technology in compact free electron lasers and medical applications.

The CLIC project is linked to the European Strategy Particle Physics priorities related to the Energy Frontier. The LHC may discover Beyond Standard Model physics when operation starts at full energy in 2015, and, depending on the findings, higher-energy hadrons as part of LHC energy upgrades or a high energy e+ e- collider might be the best option to access the new physics. The CLIC work in this period is also integrated under the Linear Collider collaboration, where the ILC technology provides an option for an early exploration of the Higgs sector in particular, while CLIC remains the only option for a Multi-TeV e+ e- collider. Wherever possible, shared activities for ILC and CLIC are being coordinated.

This paper will discuss the main conclusions of the Conceptual Design Report and highlight key activities foreseen in the project period from 2012 to 2018, which we will refer to as the "next period".

CONCEPTUAL DESIGN REPORT

The CLIC conceptual design report (CDR) was completed in 2012, and documents a proof of principle of all aspects related to the Two-Beam Acceleration scheme, both by comprehensive simulation studies of all parts of the machine and by a detailed experimental program in the CLIC

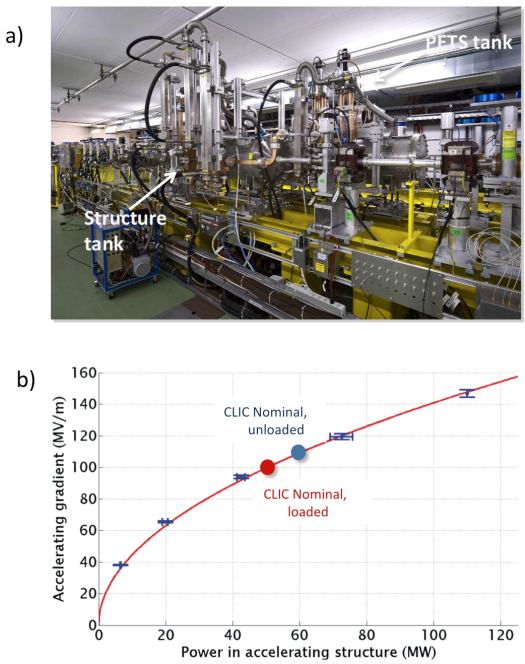


Figure 1: a) The Two-Beam Test Stand at the CLIC Test Facility. b) Experimental results of two-beam acceleration, up to and beyond the nominal CLIC gradient.

Test Facility 3 at CERN [2]. Figure 1 shows a) the CLIC Test Facility Two-Beam Test Stand and b) data points for the achieved two-beam accelerating gradient as function of input power to the X band accelerating structure. Drive beam generation has been verified and the achieved gradient is up to and beyond the CLIC target of 100 MV/m. Furthermore, ongoing rf based tests of the main linac structure gradient are close to or on target for all parameters (gradient, pulse length and breakdown rate), and Figure 2 shows a summary of the latest results. Uncertainty from beam loading will be tested in the current next period. Studies of the deceleration versus power production shows good consistency [3]. Concerning emittance generation, the CLIC damping ring has similar specification to an ambitious light source, and no show stoppers were identified for generation of the ultra low emittances. Concerning emittance preservation, the alignment system principle has been demonstrated, the stabilization system have been developed and benchmarked and integrated simulations of emittance preservation in the main linac meet or exceed the luminosity targets.

STAGING AND OPTIMIZATION

The Two-Beam Acceleration scheme is particularly suited for energy staging of the machine; once the drive

* This work is supported by the Research Council of Norway.
† Erik.Adli@fys.uio.no

Copyright © 2013 CC-BY-3.0 and by the respective authors

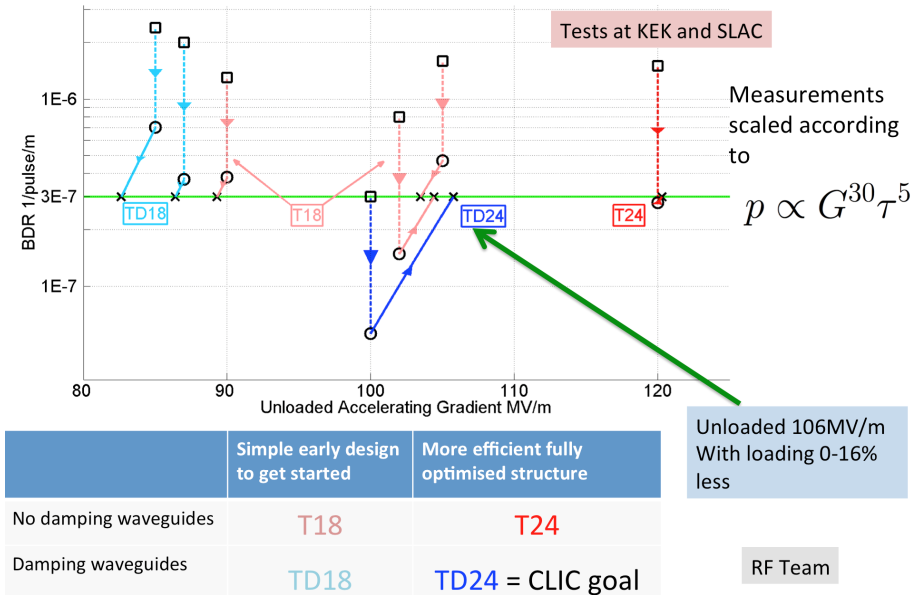


Figure 2: Structure test results, where gradients are scaled to the CLIC allowed breakdown rate of 3×10^{-7}. A fully optimized CLIC structure with damping waveguides have recently reached an unloaded gradient of 106 MV/m.

beam complex is constructed, rf power for additional lengths of the main linac can be provided simply by increasing the drive beam length in the drive beam accelerator. No upgrades are needed for the drive beam complex, and once the drive beam complex has been constructed, the addition cost per GeV of center of mass energy is favorable to klystron based alternatives. Furthermore, lower energy machines can run most of the time during the construction of the next stage. A consistent three stage implementation scenario has been defined. Schedules, cost and power are being developed, although the energies of the individual stages will be determined by LHC physics results. The minimum center of mass energy being considered is about 375 GeV, which will allow precision studies of the Higgs and the Top quark. Figure 3 illustrates an example of the various stages of a CLIC machine.

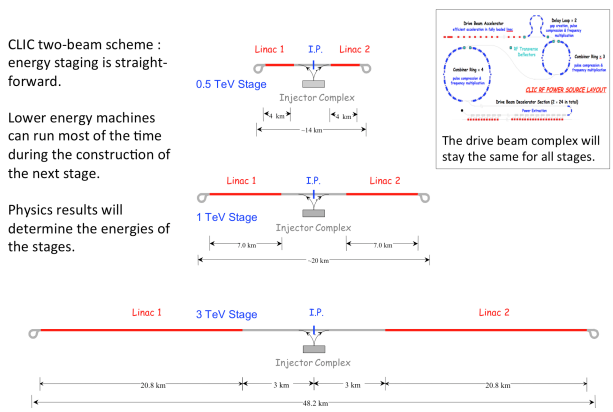


Figure 3: Example of CLIC energy stages. The center of mass energy can be increased without modifications to the drive beam accelerator complex. The actual energy of each stage will be guided by LHC physics results.

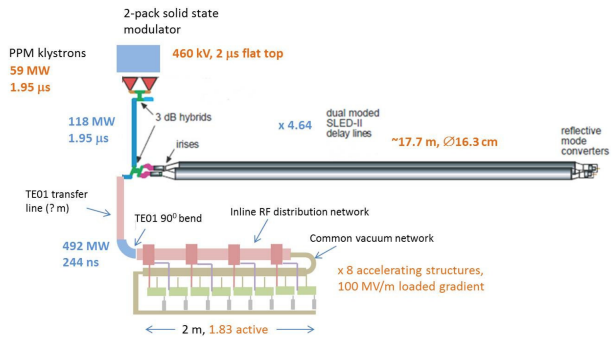


Figure 4: A rf unit for a klystron based CLIC. Two 60 MW klystrons can power 8 CLIC accelerating structures at a gradient of 100 MV/m.

The CLIC machine is currently being re-optimized for the lowest energy stage (375 GeV). The optimization includes overall design and system optimization, technical parameters for all systems, cost, power/energy optimization, scheduling and site studies. Examples of areas which can give increased machine power efficiency are the use of permanent magnets for the drive beam, and studies of high-efficiency L-band multi-beam klystrons for the drive beam acceleration. The goal is to push the tube efficiency towards 80%, and increase the drive beam klystron power output.

As part of the preparation for an optimal implementation strategy, a 500 GeV CLIC where the main linac are powered by klystrons (as opposed to a drive beam) has been studied in detail [4]. 4,400 klystrons would be required for a 500 GeV machine and a simple cost study indicated a comparable cost as for a drive beam-based CLIC linac. The luminosity is comparable to that of the drive-beam based design. The pulse length is the same as for the drive-beam

Copyright © 2013 CC-BY-3.0 and by the respective authors

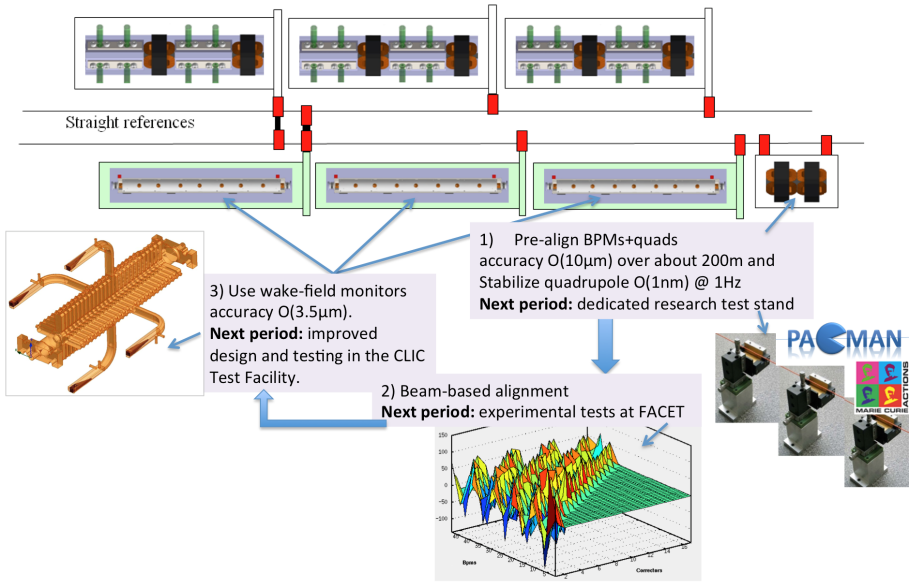


Figure 5: Three areas where main alignment and stabilization will be further studied in the next period: 1) development of an automatic alignment and stabilization test stand, 2) experimental tests of beam-based alignment at FACET, 3) experimental tests of wakefield monitors.

design. The drive beam design has the advantage of a comparably lower cost per additional GeV. Figure 4 shows one rf unit for a klystron-based CLIC, where a compressed rf pulse from two 60 MW klystrons powers 8 CLIC accelerating structures.

LUMINOSITY AND ALIGNMENT

In order to reach the target luminosity of 10^{34} $/\mathrm{cm}^2/\mathrm{s}$ CLIC requires a normalized vertical emittance of 20 nm at the interaction point, and a maximum emittance growth of 10 nm in the main linacs. Robust emittance preservation in the main linac is foreseen to be achieved using beam-based alignment and integrating wakefield monitors on the structures. In the next period, the two topics will be addressed experimentally. The 2 km FACET linac test facility at SLAC [5] now provides a unique opportunity to test beam-based alignment for linear colliders experimentally, and a proof of principle of the dispersion free correction algorithm as planned for CLIC has recently been experimentally demonstrated [6]. The experiments have shown that an automatic global correction scheme can successfully control the dispersion and reduce the emittance over 500 m of linac. Wakefield monitors are currently being developed, with the aim of providing the required resolution of 3.5 um with a robust and economical design. The monitors will be tested in CTF3 to ensure that the target precision can be reached [7]. Figure 5 illustrates the CLIC alignment techniques and some of the developments foreseen in the next period.

In addition, the machine components in the main linac and the beam delivery system must be pre-aligned at a 10 um level, and the final doublet quadrupoles must be stabilized to a sub nm level. Proof of principles of both pre-alignment and stabilization has been demonstrated with the CDR, and in the next period a sizable research project funding ten PhD student grants, "PACMAN", has been approved [8]. The technical goal of the program is to develop very high accuracy metrology and alignment tools and integrate them in a single automatic alignment test stand.

CLIC TEST FACILITY

The CLIC Test Facility 3 (CTF3) has demonstrated drive beam generation and two-beam acceleration in the CDR period. CTF3 is planned to be operated up to the end of 2016 to address further system tests and perform more detailed studies. The facility has recently demonstrated drive beam combination by a factor four with the nominal emittance of 150 um in both planes, and the current stability of the drive beam has earlier been demonstrated to better than the CLIC requirements of $\Delta I/I = 7.5 \times 10^{-4}$ [9]. The final step of a full demonstration of the CTF3 drive beam generation is stable factor 8 combination. The progress has been impeded the last year by technical problems with the traveling wave tubes required for the sub-harmonic bunching, required for delay loop operation. A fast phase feedforward system has been designed to correct the drive beam phase profile and jitter, with the aim of demonstrating the CLIC drive beam phase requirements [10]; the first kickers and amplifiers are to be installed in 2013. As a prototype of a CLIC injector, a 1 GHz klystron test stand to test a drive beam accelerating structure at full power is planned, including a gun and a sub-harmonic buncher [11].

In the two-beam test stand, new structures will be conditioned with drive beam rf and the breakdown rates measured. Kicks imparted to the beam during breakdown events will be measured and characterized, and the precision of the CLIC wakefield monitors will be measured. A dogleg halfway down the linac allows the drive beam to

Copyright © 2013 CC-BY-3.0 and by the respective authors

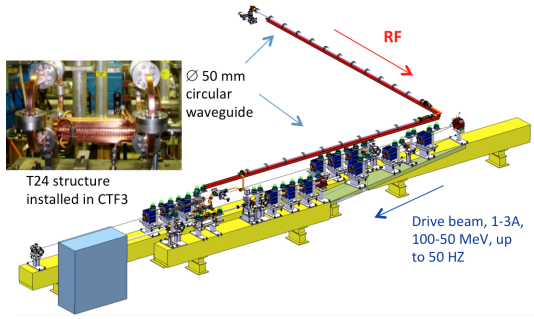


Figure 6: A new beam loading test facility: a 1 A CTF3 beam and X-band rf power will be simultaneously delivered to an accelerating structure.

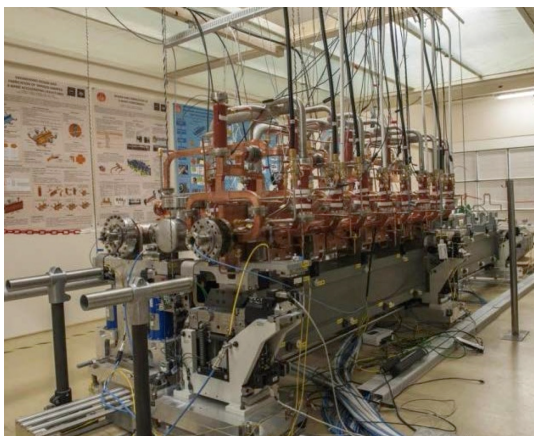


Figure 7: The first prototype of the CLIC two-beam module has been completed, and is undergoing thermo-mechanical validation.

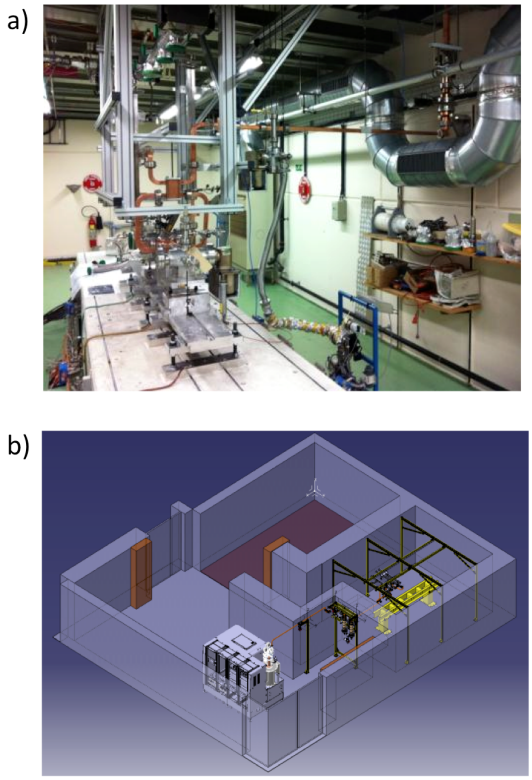


Figure 8: a) a new X-Band test facility, with a SLAC-provided 12 GHz klystron. b) Planned X-Band test facilities will include commercially acquired tubes from CPI and Toshiba. In total these facilities will provide X-band power for testing up to 8 accelerating structures simultaneously.

be directed to a test accelerating structure. Using this to deliver a 1 A beam from the linac, simultaneously as it is filled with the nominal X-band rf power [12], breakdown rates in the accelerating structure can be tested with beam loading and compared to operation without beam loading. Figure 6 shows the sketch of the planned beam loading test facility.

Finally, full prototypes of the CLIC two-beam modules are being constructed and tested [13]. Two modules will be build for laboratory system integration tests and thermo-mechanical validation. Figure 7 shows a picture of the first of the laboratory modules, completed and installed at CERN. The first tests results are promising and in line with simulations [14]. A similar two-beam module is currently under fabrication for installation in CTF3, fully equipped with X-band structures and components. The power extraction structures will provide the nominal power for the accelerating structures, thus giving a complete system test of a full CLIC main linac module with rf and beams.

X-BAND TECHNOLOGY

In the coming project period, the CLIC project will see a significant increase in X-band structure test capacity. One 12 GHz klystron based X-band test stand ("XBOX 1") has been operating at CERN for a year [12], allowing 12 GHz structure to be tested at 50 Hz. This test stand uses a scaled version of the XL4 klystron tube developed for the NLC, provided by SLAC. With the use of a SLED1-type pulse compressor output power of up to 100 MW can be provided in pulses of 250 ns, sufficient to power two CLIC accelerating structures at nominal power and pulse length. A second test area ("XBOX2") is under construction and planned to be commissioned by end 2014. A SLAC XL5-type tube will be commercially procured from CPI, and will provide XBOX2 similar capabilities as XBOX1. A cluster of four 6 MW tubes from Toshiba ("XBOX3") is planned to be commissioned by the end of 2015 and will give additional test capabilities. In total we estimate that more than 40 accelerating structures will be tested in these facilities by 2017. Figure 8 shows the XBOX test facilities.

The basic high gradient structure research will continue in the next period, including further development of the understanding of rf breakdown from first principles by theoretical studies, and multi-scale simulation studies. Modeling and simulations efforts for understanding the formation of vacuum arcs in breakdowns are being pursued [15], and the simulation results will be benchmarked against experiments at the DC spark test stand at CERN [16].

Two CLIC X-band technology application projects have recently been started. The first is use of CLIC X-band structures for compact FELs in the few GeV range. An

Copyright © 2013 CC-BY-3.0 and by the respective authors

early collaboration with Turkey has been followed by a recent initiative where countries or institutes can collaborate with CLIC on common CDR work for a FEL based on CLIC X-band technology [17]. Institutes from 5 different countries have already shown interest. Example parameters for an X-band FEL are an electron energy of 6 GeV and a charge of 250 pC, as proposed in [18], however, different institutes could pick different parameters. Collaborators may profit from the planned X-band test facilities at CERN, thus reducing the risk of starting a new project. For CLIC, development and eventually operation of GeV level e- linacs with high gradient X-band structures will provide an increased technology maturity for the X-band technology. A second project studies the potential for technology transfer of CLIC high-gradient research to 3 GHz high gradient structures for proton therapy, where a main goal is to increase the effective gradient in proton therapy linac structures to about 50 MV/m (a factor of two with respect to the state of the art).

CONCLUSIONS

The CLIC project has demonstrated the two-beam acceleration proof of principle, documented in the comprehensive Conceptual Design Report completed in 2012. In the next period up to 2018, the CLIC study will continue a number of technical studies on power and cost optimization, system tests including full CLIC module tests with rf and beam and experimental verifications of methods to preserve nm emittances. New X-band test facilities are being constructed and will greatly increase the capacity for 12 GHz rf testing. Finally, projects for the use of CLIC X-band technology in high-gradient FELs and CLIC high-gradient research technology transfer have been initiated with a potential outcome of increased technology maturity of a linear collider X-band technology.

ACKNOWLEDGMENTS

This paper is written based on input from the entire CLIC collaboration. In particular we acknowledge in-depth discussions with Walter Wuensch, Daniel Schulte, Igor Syratchev and Steinar Stapnes. This work is supported by the Research Council of Norway.

REFERENCES

[1] M. Aicheler et al., A Multi-TeV Linear Collider Based 434 on CLIC Technology: CLIC Conceptual Design Report.

[2] G. Geschonke et al., CTF3 Design Report No. CERN-PS-2002-008 (RF), 2002.

[3] R.L. Lillestol, S. Doebert, M. Olvegaard and E. Adli, in Proceedings of IPAC'13, TUPWA046 (2013).

[4] D. Schulte et al., in Proceedings of IPAC'13, TUPME049 (2013).

[5] http://facet.slac.stanford.edu

[6] A. Latina et al., submitted to Phys. Rev. ST-AB.

[7] F. Peauger et al., in Proceedings of LINAC'10, TUP098 (2010).

[8] http://pacman.web.cern.ch/pacman/

[9] A. Dubrovskiy et al., In Proceedings of LINAC'12, MOPB032 (2012).

[10] P.K. Skowronski et al., in Proceedings of IPAC'13, WEOBB203 (2013).

[11] H. Shaker et al., in Proceedings of IPAC'13, TUPME052 (2013).

[12] J. Kovermann et al., CERN-ATS-131

[13] D. Gudkov et al., in Proceedings of IPAC'13, WEPFI055 (2013).

[14] F. Rossi et al., in Proceedings of IPAC'13, WEPFI056 (2013).

[15] H. Timko et al., Contrib. Plasma Phys. 51 (2011) 5 .

[16] N. Shipman et al., in Proceedings of IPAC'12, THPPC027 (2012).

[17] http://indico.cern.ch/conferenceTimeTable.py?confId=270450

[18] C. Adolphsen et al., in Proceedings of LINAC'10, TUP015 (2010).

Copyright © 2013 CC-BY-3.0 and by the respective authors

COLLIDERS – "QUO VADIS?" : PAST 20 YEARS, NEXT 20 YEARS, AND BEYOND*

V.Shiltsev#, Fermilab, Batavia, IL 60510, USA

Abstract

Particle colliders for high-energy physics have been in the forefront of scientific discoveries for more than half a century. The accelerator technology of the colliders has progressed immensely, while the beam energy, luminosity, facility size, and cost have grown by several orders of magnitude. The method of colliding beams has not fully exhausted its potential but has slowed down considerably in its progress. This paper briefly reviews the colliding beam method and the history of colliders, discusses the development of the method over the last two decades in detail, and examines near-term collider projects that are currently under development. The paper concludes with an attempt to look beyond the current horizon and to find what paradigm changes are necessary for breakthroughs in the field.

PAST AND PRESENT COLLIDERS

It is estimated that in the post-1938 era, accelerator science has influenced almost 1/3 of physicists and physics studies and on average contributed to physics Nobel Prize-winning research every 2.9 years [1]. Colliding beam facilities which produce high-energy collisions (interactions) between particles of approximately oppositely directed beams did pave the way for progress since the 1960's. Discussion in this section mainly follows recent publication [2].

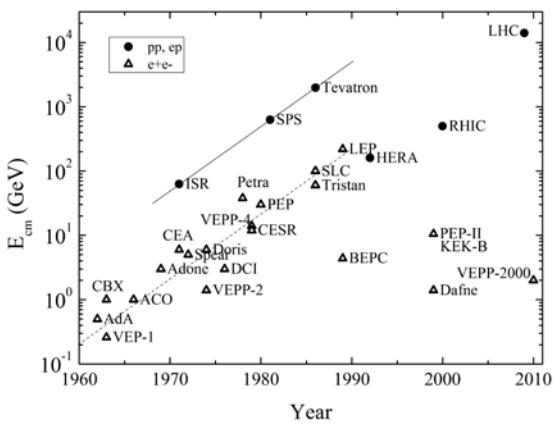


Figure 1: Colliders over the decades (after [2]).

Twenty nine colliders reached operational stage between the late 50's and now. The energy of colliders has been increasing over the years as demonstrated in Fig. 1. There, the triangles represent maximum CM energy and the start of operation for lepton (usually, *e+e-*) colliders and full circles are for hadron (protons, antiprotons, ions, proton-electron) colliders. One can see that until the early 1990's, the CM energy on average increased by a factor of 10 every decade and, notably, the hadron colliders were 10-20 times more powerful. Since then, following the demands of high energy physics, the paths of the colliders diverged to reach record high energies in the particle reaction. The Large Hadron Collider (LHC) was built at CERN, while new *e+e-* colliders called "particle factories" were focused on detail exploration of phenomena at much lower energies. Over the last 50 years, the luminosity of the colliders has improved by more than 6 orders of magnitude and reached record high values of over 10^{34}cm^{-2}s^{-1}. At such luminosity, one can expect to produce, e.g., 100 events over one year of operation (about 10^7 s) if the reaction cross section is 1 picobarn (pb)=10^{-39} cm^2.

Table 1: Past, Present and Possible Future Colliders; hadron colliders are in **bold**, lepton colliders in *Italic*, facilities under construction or in decisive design and planning stage are listed in parenthesis (…)

	early 1990's	early 2010's	2030's
Europe	**HERA, (LHC)** *LEP (Dafne)*	**LHC** (*Super-B,* **HL-LHC, LHeC,** *ENC*)	**HE-LHE** *CLIC?*
Russia	*VEPP2, VEPP4* (**UNK**, *VLEPP*)	*VEPP2000, VEPP-4M* (**NICA**, *Tau-C*)	**NICA** ? *Higgs Factory* ?
US	**Tevatron**, (**SSC**) *SLC, CESR,*(*PEPII*)	**RHIC** (*e***RHIC**, *ELIC*)	*Muon Collider* ? *PWLA/DLA* ?
Asia	*Tristan, BEPC* (*KEK-B*)	*BEPC* (*Super-KEKB*)	*ILC* ? *Higgs Factory* ?
Total	9 (7)	5 (9)	1 + ?

At the same time, the number of the facilities in operation has dropped from 9 to 5, as indicated in Table 1 which lists all operational colliders as of the early 1990's and now (early 2010's) and accounts for the projects under construction or under serious consideration at this time (in parenthesis).

NEXT TWO DECADES

There are several colliders currently under construction or at the design stage and which, therefore, have good prospects of becoming operational and deliver results in the next 20 years. Schematically they can be categorized by as follows:

Energy Frontier: the LHC luminosity upgrade project HL-LHC [3] to quintuple the performance of the energy frontier machine by mid-2020's to $5\cdot10^{34}$cm^{-2}s^{-1} with luminosity leveling at 14 TeV c.m. energy in proton-

*Fermi Research Alliance, LLC operates Fermilab under contract No. DE-AC02-07CH11359 with the U.S. Department of Energy
#shiltsev@fnal.gov

Copyright © 2013 CC-BY-3.0 and by the respective authors

proton collisions; the LHC energy upgrade to ~33 TeV cme will require development 20T dipoles [4].

Low-Energy Hadron Collders: like, e.g., Nuclotron-based Ion Collider fAcility (NICA) currently under construction at JINR (Dubna, Russia) [5] which will allow for the study of ion-ion (Au^{+79}) and ion-proton collisions in the energy range of 1-4.5 GeV/amu with average luminosity of 10^{27} cm^{-2} s^{-1} and also polarized proton-proton (5-12.6 GeV) and deuteron-deuteron (2-5.8 GeV/amu) collisions.

Electron-Hadron Colliders: such as LHeC [6], in which polarized electrons of 60 GeV to possibly 140 GeV collide with LHC protons of 7000 GeV with design luminosity of about 10^{33} cm^{-2}s^{-1}; eRHIC at BNL (polarized nuclear beam to 100 GeV/nucleon and polarized protons upto 250 GeV colliding with 20-30 GeV ERL-accelerated polarized electrons, the luminosity varies from 10^{33} cm^{-2}s^{-1} to 10^{34} cm^{-2}s^{-1}) [7] and Electron-Ion Collider (ELIC) at JLab (30-7 GeV polarized electrons and 30 to 150 GeV storage ring for ions, high luminosities of ~$5\cdot10^{33}$ cm^{-2}s^{-1} to 10^{35} cm^{-2}s^{-1} require continuous electron cooling) [8]; and electron-nucleon collider ENC at FAIR (GSI, Darmstadt, Germany) utilizing the 15 GeV antiproton high-energy storage ring HESR for polarized *p* and *d* beams, with the addition of a polarized *e*- 3.3 GeV storage ring with peak luminosities in the range of 10^{32} to 10^{33}cm^{-2}s^{-1} [9].

Electron-Positron Factories: such as asymmetric $e+e-$ Super-B factory in KEK [10] with beam energies of about 4 GeV and 7 GeV and with a design luminosity approaching 10^{36} cm^{-2} s^{-1}; and Tau-Charm factory in Novosibirsk [11] which calls for c.m. collision energy variable from 3 GeV to 4.5 GeV (from J/psi resonances to charm barions) and luminosity in excess of 10^{35} cm^{-2} s^{-1}.

Higgs Factories: *e+e-* coliders with an optimal $E_{cm} \sim m_H$ + (110±10) GeV ~250 GeV can be either ring-based as, e.g., TLEP [12] or be based on the ILC-type linear collider [13]; their issues and challenges are discussed in [14]. A possible alternative can be a $\mu+\mu-$ collider with factor of two lower c.m. energy $E_{cm}\sim m_H$ which would have advantageously large cross section some $(m_\mu/m_e)^2\sim$40,000 times higher than for *e+e-*, and significantly smaller c.m.e. spread $\delta E_{cm}/E_{cm}\sim$ 0.01-0.003% (compared to ~0.2% for the *e+e-* factories) [15].

Energy Frontier Lepton Colliders: if - as presently believed - a multi-TeV lepton collider will be needed to follow the LHC discoveries, then the most viable options currently under consideration are e+e− linear colliders ILC and CLIC [16] or μ+μ− Muon Collider [15] – see Table 2. Each of these options has its own advantages and issues [17].

FAR FUTURE COLLIDERS

The forecast on the far future of colliders beyond, say, the 2030's, will require several things: understanding of the available resources, the desired science reach, and on the possibilities. As of today, the world's particle physics research budget is some 3B$. Assuming that it will not change by much in the future (in todays' dollars) and that not more than 1/3 of the budget can be dedicated to construction of the next energy frontier collider, one can estimate the cost of an affordable future facility to be about or less then 10B$ (in current prices). Other desired features of such flagship could be: it ideally should not exceed 10 or few 10's of km in length, it should stay under *O*(100MW) of AC wall power consumption, and, of course, it would be great if its energy reach significantly (> ×10) exceeds that of the LHC.

Table 2: Comparison of Lepton Collider Alternatives

	ILC	CLIC	MC
c.m.e., TeV	0.5	3	1.5-4
dE/E, rms	~2%	>5%	~0.1%
L, cm^{-2}s^{-1}	$2\cdot10^{34}$	$2\cdot10^{34}$ *	$(1\text{-}4)\cdot10^{34}$
Feasibility	2007	2012	~2016
Techn.design	2013	2016	~2020
# elements	38,000	260,000	10,000
Σ length, km	36	~60	14-20
AC pwr,MW	230	580	~170-220

*peak luminosity within 1% c.m. energy spread

The cost estimates of the modern colliders are quite complicated, but an attempt to analyse known costs of 15 large accelerators (SSC, RHIC, VLHC, ILC, B-Factories, FNAL MI, NLC, SNS, LHC, XFEL, FAIR, ESS, CLIC, SPL, NuFactory) has resulted in a phenomenological cost model [18] that matches the actual costs (in terms of *TPC*, the Total Project Cost, widely used in the US DOE accounting) within approximately ±30% :

$$TPC = \alpha\left(\frac{L}{10km}\right)^{1/2} + \beta\left(\frac{E}{1TeV}\right)^{1/2} + \gamma\left(\frac{P}{100MW}\right)^{1/2}$$

where, *L* is the total length of the tunnel, *E* is cm energy, *P* is total site AC power for the facility; and technology dependent coefficients are α=2B$, β=1B$ for NC magnets, 3B$ for SC magnets, and ≈10B$ for NC/SC RF, γ=2B$ - see Fig.2.

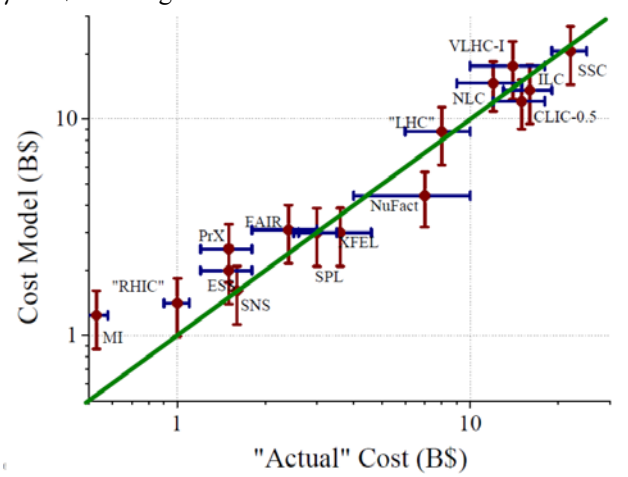


Figure 2: Phenomenological cost model vs actual cost for large accelerator facilities.

Copyright © 2013 CC-BY-3.0 and by the respective authors

The model predicts that if currently available technologies are employed, then only Higgs factories or a few-TeV Muon Collider can potentially meet the desired cost requirement. If the costs of civil construction and power infrastructure are not changed, i.e., α and γ are as of today, then future 100 TeV, 10 km and 100MW collider should be based on technology that guarantees cost of the accelerator components of about 6B$, i.e., the coefficient β< 0.6B$, that is two times cheaper than for modern NC magnets. Are there now or can we think of such technologies?

ARE THERE WAYS TO THE FUTURE?

To the date, the community thinking was more about fast acceleration to get to the energies of interest within a smaller footprint, rather than explicitly about the cost. The opportunities for high energy colliders under active discussion now are :

Acceleration in Dielectric Structures: direct beam excitation of wakefields in dielectric structures allows accelerating gradients of ~100 MV/m and ~1 GV/m at the microwave $O(10)$ GHz and THz ranges [19]. Conceptually, a DWA-based linear collider would consist of a large number of ~100 GeV modules (stages) with some ~0.3 GeV/m gradient each driven by a separate ~1 GeV high intensity electron beam. Even without going into difficulties associated with staging, cost and power considerations, it is hard to imagine that more than 3 TeV c.m. energy DWA facility can fit within in a 10 km site. Further increase of the gradient to ~1-3 GV/m is thought to be possible in μm scale dielectric structures driven by lasers operating in optical or near-infrared regime [20, 21].

Acceleration in Plasma: generation of the PWA gradients on the order of 30-100 GV/m by beams or lasers in plasma densities of n_0=10^{17}-10^{18} cm^{-3} have been already demonstrated in small scale (few cm to a meter) experiments [22, 23]. Laser-PWA collider would operate at relatively low densities n_0~10^{17}cm^{-3} and energy gain per ~2m stage of 10 GeV and average gradient ~5TeV/km, while a beam-PWA collider design needs a conventional high power 25 GeV electron drive beam accelerator and many (dozens to hundreds, depending on the final energy) 1-m long plasma cells with an average geometric accelerating gradient ~0.25 TeV/km. Without going into the luminosity considerations [24] and just projecting such gradients further one can think of an ultimate ~10 TeV e+e- collider within 10 km footprint.

More than an order of magnitude reduction of the cost of accelerator components in such colliders is predicted to be needed in order to fit under the expected TPC limit [18]. In addition, due to radiation in the focusing channel and beamstrahlung at IPs acceleration of electrons is limited to only few TeV. Heavier particles are required.

Acceleration in Crystal Channels: field gradients of upto 100 GeV/cm or 10 TV/m are possible in solids due to high density of charge carriers n_0~$10^{22\text{-}23}$ cm^{-3}. Muons, which do not interact with nuclei, would the particles of choice. X-ray lasers can efficiently excite solid plasma and accelerate muons inside a crystal channel waveguide [25], though ultimate acceleration gradients ~10TeV/m might require relativistic intensities, exceeding those conceivable for X-ray sources as of today. Side injection of powerful x-ray pulses into continuous fiber of 0.1 – 10 km long fiber allows to avoid multiple staging issues intrinsic to other methods and reach 10-1000 TeV collider energies – see Fig.3.

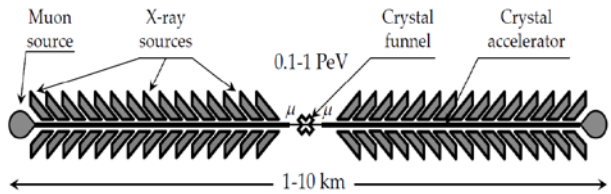


Figure 3: Layout of linear X-ray crystal muon collider [2].

It is not possible to even guess-timate the cost of such unproven acceleration method. One can only foresee that a quest for 100-1000 TeV energies will come at the price of the expected luminosities and will require at least three paradigm shifts [2]: 1) development of the new economical technology for ultrahigh acceleration gradients ~0.1-10 TeV/m in sub-nm structures (crystal fibers); 2) acceleration of heavier particles, preferably, muons; and 3) new approaches to HEP at such energies research with luminosities limited to ~$10^{30\text{-}32}$ cm^{-2}s^{-1}.

REFERENCES

[1] E. Haussecker, A.W.Chao, *Phys.Persp.* **13** 146 (2011).
[2] V.Shiltsev, *Phys. Uspekhy* **55** 965–976 (2012).
[3] L.Rossi, in Proc. IPAC 2011 (Spain), p.908.
[4] HE-LHC, Preprint CERN-2011-003 (2011).
[5] G.Trubnikov, et al., in Proc. 2010 RuPAC, p.14.
[6] M.Klein, in Proc. IPAC 2011 (Spain), p.908.
[7] V.Ptitsyn, et al. in Proc. IPAC 2011(Spain), p.3726.
[8] S.Ahmed, et al., in Proc. PAC'11 (New York), p.2306.
[9] A.Lehrach, et al., *J.Phys.:Conf.Ser.***295** 012156 (2011).
[10] T.Abe, et al., arxiv:1011.0352.
[11] E.Levichev, *Phys.Part.Nucl. Lett.* **5** 554 (2008).
[12] Koratzinos, M. et al. arXiv:1305. 6498 (2013).
[13] *ILC TDR*, FERMILAB-TM-2554 (2013).
[14] S.Henderson, Proc. NA-PAC'13, MOXAP1(2013).
[15] S.Geer, Annu.Rev.Nucl.Part.Sci. **59**, p.347 (2009).
[16] J.P.Delahaye, *Mod. Phys. Lett. A* **26** 2997 (2011).
[17] V.Shiltsev, *Mod. Phys. Lett. A* **25** 567 (2010).
[18] V.Shiltsev, in Proc. "Pre-Snowmass Workshop on Frontier Capabilities " (U.Chicago, Feb 25-26, 2013).
[19] W.Gai, *AIP Conf. Proc.* **1086** 3 (2008).
[20] G. Travish, et al, *AIP Conf. Proc.* **1086**, pp. 502–507.
[21] E.Peralta, et al, *Nature,* doi:10.1038/nature12664 (2013).
[22] C.Schroeder, et al *PRSTAB* **13** 1013014 (2010).
[23] A.Seryi, *Nucl. Instr. Meth A* **623** 23 (2010).
[24] V.Lebedev, S.Nagaitsev, PRSTAB **16** (2013).
[25] T.Tajima, M.Cavenago *PRL* **59** 1440 (1987).

Copyright © 2013 CC-BY-3.0 and by the respective authors

STATUS OF THE ELECTRON-POSITRON COLLIDER VEPP-2000 *

A. Romanov, D. Berkaev, A. Kasaev, I. Koop, A. Kyrpotin, A. Lysenko, E. Perevedentsev, V. Prosvetov, Yu. Rogovsky, A. Senchenko, P. Shatunov, Yu. Shatunov, D. Shwartz, A. Skrinsky, I. Zemlyansky, Yu. Zharinov
BINP SB RAS and Novosibirsk State University, Russia

Abstract

VEPP-2000 began high energy physics experiments in the end of 2010 and finished its third experimental season in July of 2013. The last season was dedicated to the energy range of 160-510 MeV per beam. Compton back-scattering based energy measurements were used for the regular energy calibration of the VEPP-2000 together with resonance depolarization and NMR based methods. The concept of the round colliding beams lattice along with the precise orbit and lattice correction yielded the high peak luminosity of $1.2\times10^{31}cm^{-2}s^{-1}$ at 505 MeV with average luminosity of $0.9 \times 10^{31}cm^{-2}s^{-1}$ per run. The total beam-beam tune shift up to 0.174 was achieved in the runs at 392.5 MeV. This corresponds to beam-beam parameter $\xi = 0.125$ per one interaction point. The injection system is currently being upgraded to allow for the injection of particles at the top energy of VEPP-2000 collider and to eliminate the present lack of positrons.

COLLIDER OVERVIEW

VEPP-2000 collider was designed for the refinement of the cross section of the e^+e^- annihilation to hadrons in the energy range $0.4 \div 2$ GeV [1]. The lattice design was aimed to fulfill the conditions of round colliding beams [2], which promised higher luminosity performance because of an additional integral of motion.

The main proposed collider parameters are given in Table 1. VEPP-2000 was designed for one-by-one bunch operation with two functional interaction points. The ring consists of four 90 degree achromatic bends with four straight sections (Fig. 1). Two of the straight sections are occupied by the CMD-3 and SND detectors along with final focus superconducting solenoids, the third is used for injection, and the RF cavity is placed in the fourth.

The focusing system consists of six quadrupole families, three focusing and three defocussing, and four final focus configurable solenoids. Three sextupole families are available for the chromaticity correction. All sextupoles have additional coils that form skew-quadrupole fields to correct the coupling. Due to dense element placement, the orbit steering fields are generated by additional coils in main dipoles and quadrupoles resulting in 20 horizontal and 16 vertical correctors.

The beam diagnostics system consists of 4 electrostatic pickups that are capable of taking turn-by-turn data; 16

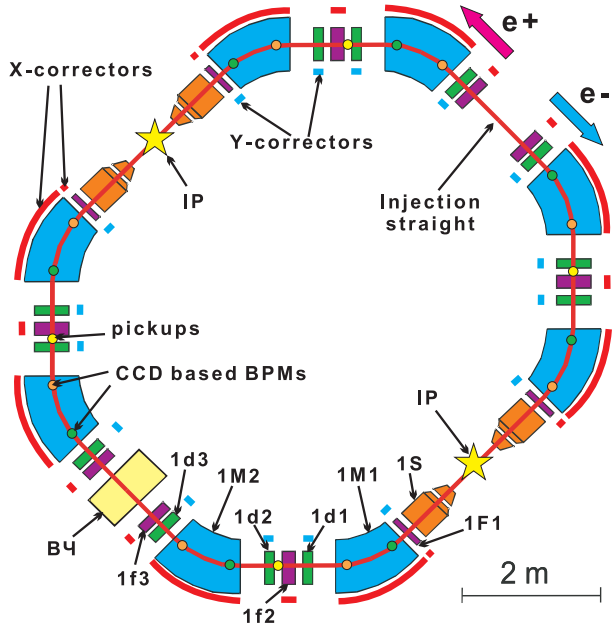


Figure 1: VEPP-2000 layout.

Table 1: VEPP-2000 Parameters at 900 MeV

Circumference, m	C	24.388
RF frequency, MHz	f_0	172
RF voltage, kV	V	100
RF harmonic number	q	14
Momentum compaction	α	0.036
Transverse emmitances, $cm \cdot rad$	ϵ_x, ϵ_y	$2.2 \cdot 10^{-5}$
Betatron tunes	ν_x, ν_y	4.1, 2.1
Twiss β at IP, cm	β_x, β_y	6.3
Particles/bunch	e^-, e^+	$1.0 \cdot 10^{11}$
Tune shifts	ξ_x, ξ_y	0.075
Luminosity/IP, $cm^{-2} \cdot s^{-1}$	L_{max}	$1.0 \cdot 10^{32}$

CCD cameras that take beam images using synchrotron light; two photomultipliers for bunch current measurements; one DCCT for measurements of full circulating current; two phi-dissectors [3] that give information about the longitudinal distributions of particles in both bunches.

The first beam was injected to the VEPP-2000 in the end of 2007 without final focus solenoids. This special "warm" configuration of lattice was used to test all vital systems of the collider. After installation of the final focus solenoids, the first luminosity runs were done in 2010. These runs were done only with SND detector, while the CMD-3 de-

* Work supported by the Ministry of Education and Science of the Russian Federation

Copyright © 2013 CC-BY-3.0 and by the respective authors

tector and its solenoidal field were off. The CMD-3 field of 8-13 kGs breaks the lattice symmetry with greater influence at lower energies.

ENERGY CALIBRATION

The requirement for the precise measurement of the hadron creation cross sections applies strict constraints on the precision of the energy measurement tools. The relative uncertainty of the beam energy should be within $\Delta E/E \leq 10^{-4}$. VEPP-2000 has a number of tools to solve this complex task.

The most precise absolute method is based on resonant depolarization of the beam [4]. The series of spin resonances of the experimental ring leaves only several energy points that could be used for this method, also non-ideal orbit inside the final focus solenoids affects the measurements in unpredictable way. Therefore the main goal of the resonant depolarization method is to calibrate and test faster techniques using special lattice without solenoid fields. The other, even longer, absolute method of energy calibration is measuring the cross sections of the well-known resonances, for example, of ϕ and ω mesons.

The fastest and the least precise method is based on power supplies readings and a complex calibration model. It gives the precision of about 1 MeV and is used for the preliminary energy adjustments. Another fast method is based on readings from the NMR probes installed in each main dipole. The data from the NMR should be calibrated and combined with readings from steering magnets located inside the achromatic bends to give the energy measurement. These measurements have very low statistical jitter of about $0.2 \cdot 10^{-4}$ but the systematic errors are still quite big $\sim 10^{-3}$.

The main energy measurement tool is based on the Compton backscattering [5]. The laser beam interacts with the electron bunch inside the main dipole and the germanium calorimeter detects spectra of the reflected photons. The short interaction length results in lower flux in comparison to the regular configurations where the interaction occurs in the straight section, but it also produces a non-trivial energy distribution of these photons that is used to compensate low statistics. Figure 2 shows the typical edge of the backscattered photons.

In January 2013, a detailed comparison of Compton, NMR and depolarization methods of energy measurements was done. During these tests the precise calibration coefficients for NMR based method have been worked out (Fig. 3).

LATTICE AND CLOSED ORBIT CORRECTION

Fast and reliable closed orbit and lattice correction algorithms are extremely important for successful operation of the VEPP-2000 because of regular energy change in very wide range.

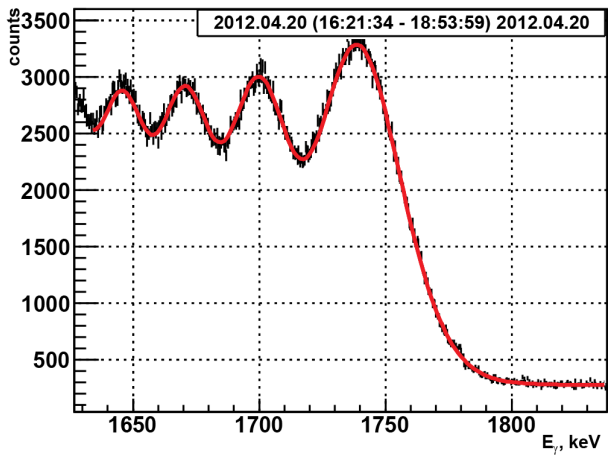


Figure 2: Compton backscattering spectrum at VEPP-2000. Reconstructed energy is $E = 993.662 \pm 0.016 MeV$.

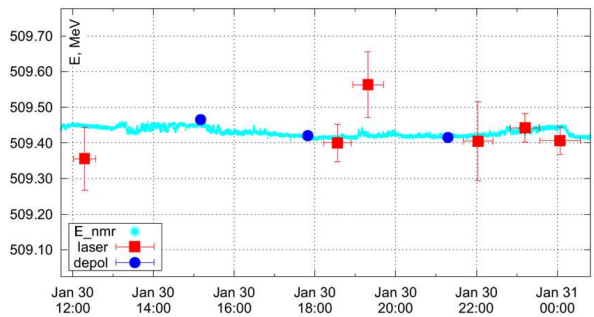


Figure 3: Comparison of three different method of energy measurements: blue circles – resonance depolarization; red squares Compton backscattering; light-blue curve – calibrated NMR.

The main task of the orbit correction in VEPP-2000 is to set the closed orbit as close to magnetic axes of elements as possible. After the best orbit is achieved, one can save and store ideal positions of the beam at locations of the BPMs and use them for future orbit corrections.

To correct the lattice of VEPP-2000, a program was written to implement expanded LOCO algorithms [6–8]. First, a model that best describes the experimental data is found. Second, based on this model, the corrections can be found that fix supposed distortions. The first task is usually performed by minimizing χ^2:

$$\chi^2 = \sum_i \frac{(M_{\mathrm{mod},i} - M_{\mathrm{mes},i})^2}{\sigma_i^2} = \sum_i V_i^2 \qquad (1)$$

where $M_{\mathrm{exp},i}$ and $M_{\mathrm{mod},i}$ are the experimental and theoretical sets of data points; σ_i is precision of corresponding measurement. If the model has the set of parameters p_j, then one can linearize the dependence $V_i(p_j)$:

$$\Delta V_i(\Delta p_j) \simeq \sum_j \frac{\partial V_i}{\partial p_j} \Delta p_j = -V_i, \qquad (2)$$

Copyright © 2013 CC-BY-3.0 and by the respective authors

Inverting the Eq. 2 with help of singular value decomposition (SVD) one can find the variation of the model parameters to reduce χ^2:

$$\Delta p_j = \sum_i \left(\frac{\partial V_i}{\partial p_j} \right) \Big|^{-1}_{SVD} (-V_i) \,. \qquad (3)$$

Several iteration are needed because of nonlinear dependence of the model on the parameters.

Before the last season, one of the main drawbacks of the full lattice correction procedure was required time of 2-3 hours. During the shutdown in the summer of 2012, the replacement of the old CCD cameras with the new ones was performed. Additionally, the image treating software was rewritten so the overall time required for the correction decreased to 40-50 minutes.

LUMINOSITY PERFORMANCE

Last season started with unexpectedly small dynamic aperture in the collider ring. Investigations revealed that it was reduced by strongly nonlinear dipole correctors. Due to dense element placement, most steering magnets are located in the quadrupoles and create significant sextupole fields. To fix huge initial distortion of the uncorrected closed orbit, the superconducting final focus solenoids were slightly moved. This hardware orbit correction in combination with of other tuning tools allowed to reach very good results during the last season.

VEPP-2000 team steadily increases the luminosity production rate over the whole running period. Recently the careful lattice tuning with and the bunch length control resulted in world largest beam-beam parameter $\xi = 0.125$ per one IP that corresponds to the observed tune difference between frequencies of the π and σ modes of $\Delta\nu = 0.174$. This outstanding result was obtained during regular runs in the strong-strong regime at the energy level of $E = 392.5$ MeV per bunch.

Figure 4 illustrates comparison of the predicted luminosity and the one obtained in the best runs. Blue dashed line illustrates the case of constant lattice scaling with energy:

$$\beta^* = const;\ \epsilon \propto \gamma^2;\ L \propto \gamma^4. \qquad (4)$$

The final focus solenoids could provide lower β^* at energies lower than 1000 MeV. Red dashed lines in Figure 4 represent the luminosity dependence in the case of variable final focus strength, so that:

$$\beta^* \propto \gamma;\ \epsilon \propto \gamma;\ L \propto \gamma^2. \qquad (5)$$

Finally, there is another trick to boost the luminosity at lower energies. The final focus solenoids have complex inner structure with longitudinal and radial sectioning. At lower energies, it is possible to switch the current supplies to move the effective center of the final focus closer to the interaction point. Three solid lines on Fig. 4 illustrate the predicted limit of luminosity for three different configurations of the final focus fields. The tests of this approach revealed a dramatic decrease of dynamic aperture, probably because of increased influence of the solenoid fringe fields.

During the last season, VEPP-2000 collected data at energies down to 160 MeV per beam that is the world record for modern electron-positron colliders.

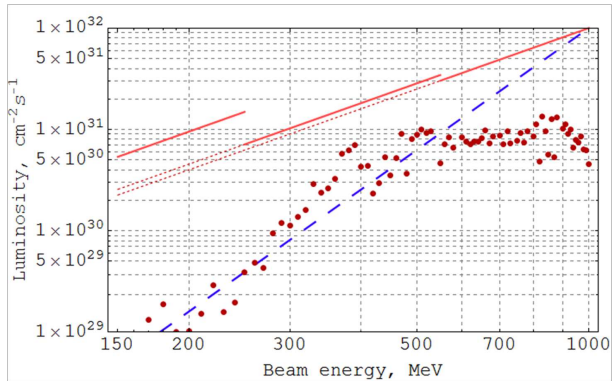


Figure 4: Luminosity dependence on energy. Lines – theoretical estimations; dots – performance in best runs over the entire VEPP-2000 operation time.

Figure 5 illustrates luminosity integrals in different energy ranges over the entire VEPP-2000 operation time. The last season was dedicated to the low energy range, but despite this the total integral is of the same order of magnitude as in the previous seasons aimed at higher energies.

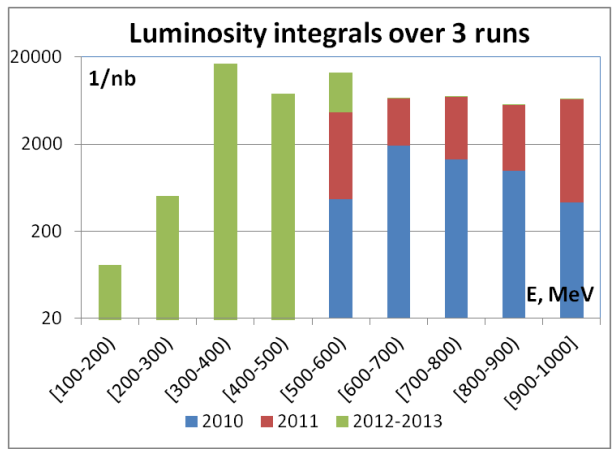


Figure 5: Luminosity integrals collected by SND in different energy ranges over the entire VEPP-2000 operation time.

LUMINOSITY MONITORING

There are a number of theoretical and empirical considerations regarding lattice configuration depending on the energy [8], but the last step of the final tuning is almost always unique and done manually. To optimixe the luminosity performance, the operator should fine tune parameters such as beta-functions at the IPs, closed orbit position, betatron tunes, chromaticity, betatron coupling and others.

Copyright © 2013 CC-BY-3.0 and by the respective authors

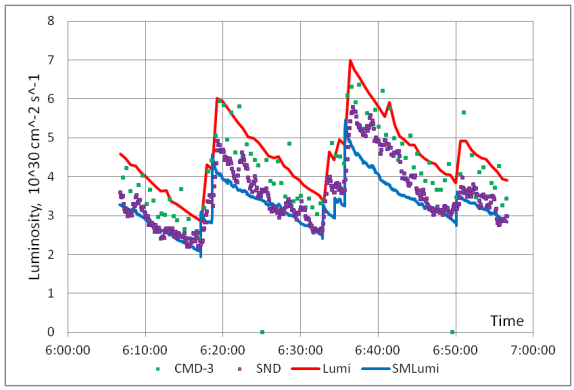


Figure 6: Comparison of the luminosity values from different measurements: green dots – CMD-3, purple dots – SND, red and blue lines – estimation methods.

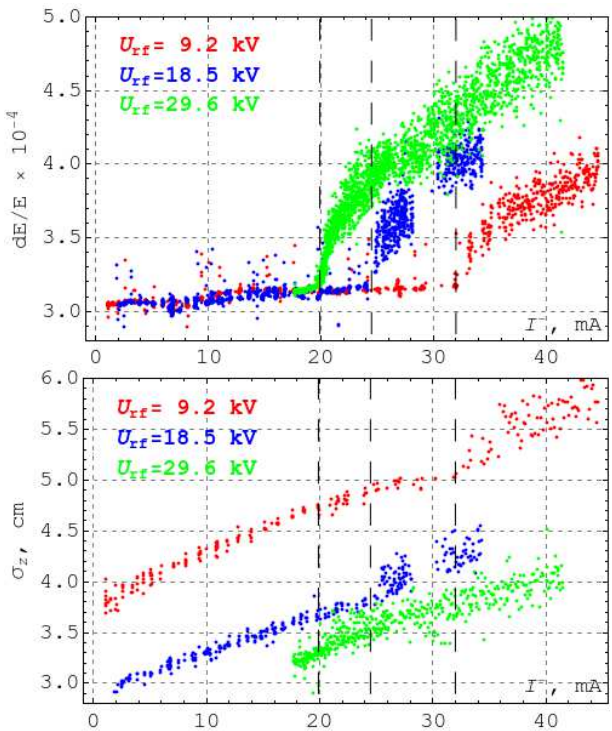


Figure 7: Correlation of the current dependence of the extracted energy spread and the measured bunch length.

To help the operator with this task both detectors provide luminosity measurements. Unfortunately, the time needed for one data point is too long and, in addition, at low energies statistics become to poor. To overcome these limitations, two luminosity estimation methods were developed based on machine diagnostics [9].

Both presented methods of luminosity estimation assume that the accurate optics model of the real accelerator ring is available. If there are no focusing perturbations in the lattice other than those caused by the collisions, and thus located at the IP, one can use known transport matrices to evaluate the beam sizes at the IPs from the beam size measurements by CCDs.

The first method was implemented in the software called "LumiMeter" and is based on the fitting of the emitances and effective beta functions for e^- and e^+ bunches and both IPs. The second method was implemented in Java code called "SMLumiMeter" and is based on fitting of the set of second moments for both bunches.

Bunch lengthening

At the end of the last experimental season, the e^- and e^+ phi-dissectors were installed at VEPP-2000, that can measure bunch length with the precision of about 2 mm [3]. The bunch length measurements combined with energy spread estimations produced by "SMLumiMeter" revealed the presence of microwave instability that could be controlled by RF voltage (Fig. 7).

UPGRADE STATUS

Starting from the first experimental season it became obvious that old injection complex strongly limits the operation of the VEPP-2000 at high energies. Last season also demonstrated insufficient positron production range at lower energies when the beam lifetime in the collider goes down.

To overcome the listed difficulties, a deep upgrade of the injection system was started in July 2013 at VEPP-2000. Booster BEP will be modified to be able to cover the full energy range of VEPP-2000. In the new configuration, particles will be transported to the BEP from the VEPP-5 injection system by about 200 meters channel. Table 2 shows comparison of the old and new injection systems. Figure 9 illustrates VEPP-2000 facility after upgrade.

Table 2: Comparison of the Old and New Injection Facilities

e^+ production rate, e^+/sec	2×10^7	3×10^8
e^- production rate	10^9	1×10^11
Max booster energy, MeV	825	1000
Booster accum. energy, MeV	125	500
Max pulses rate, Hz	0.7	12.5

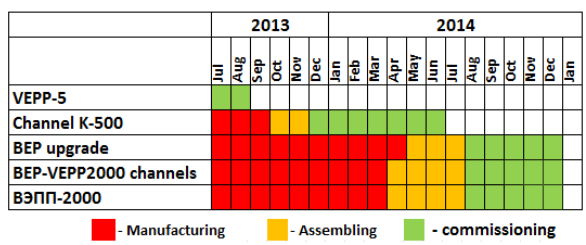


Figure 8: VEPP-2000 upgrade schedule.

In general, there are five major parts of the started upgrade. First of all VEPP-5 injection system should be fully commissioned and become a reliable source of high quality beams. Next, some elements of new channel K-500

Copyright © 2013 CC-BY-3.0 and by the respective authors

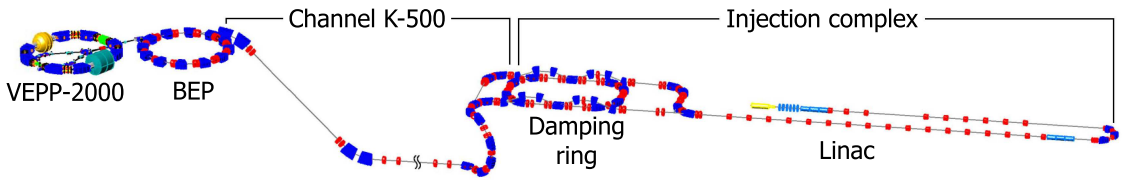


Figure 9: Layout of the facilities related to the VEPP-2000 collider after upgrade.

should be manufactured, installed and tested. The third part is aimed at booster BEP upgrade. Some subsystems of VEPP-2000 will be modified for better beam control. In addition, the old transport lines between BEP and VEPP-2000 were designed for the old BEP energy and, therefore, must be significantly modified. Figure 8 illustrates a timetable for the listed activities.

Due to funding limitations it was decided to upgrade the BEP booster rather than to build a completely new ring. The main dipoles and quadrupoles will be manufactured by reshaping existing yokes. The preserved bending radius and cross section of conductors apply extreme requirements to the design. At 1GeV, it will be possible to operate BEP only in rapid-cycling mode with fast ramping up and down with top guiding field almost 26 kGs. The first prototype of the upgraded main dipole was recently tested and demonstrated all necessary parameters (Fig. 10). Quadrupole prototype manufacturing is in progress. The vacuum chamber will be also re-shaped by compressing and milling the old one.

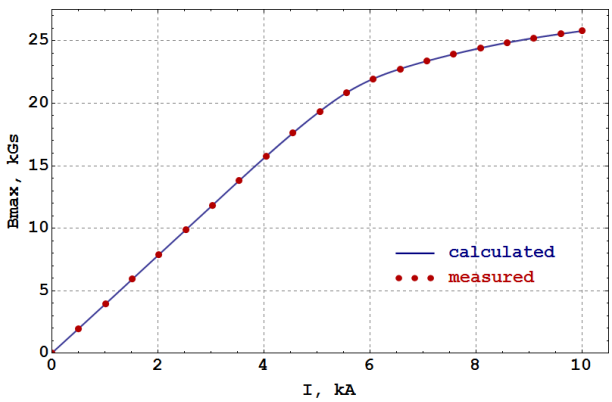


Figure 10: Comparison of the calculated and measured magnetic field vs current for the upgraded BEP dipole.

CONCLUSION

Correction techniques from precise magnet alignment to versatile beam-based algorithms, as well as bunch length adjustments and manual fine tuning, based on computer control, allowed to reach the limits of the VEPP-2000. It became obvious that main limitations come from the obsolete injection facility, therefore its upgrade will be necessary for the long term, high luminosity performance of the VEPP-2000. The long shutdown for the serious upgrade was stared in July of 2013.

Among the main VEPP-2000 achievements over the past years are:

- The total integral in the energy range $160 \div 1000$MeV is about $64pb^{-1}$.
- The world record of the beam-beam parameter $\xi = 0.125$ obtained during the regular run.
- Data collection in lowest energy range for the e^+e^- colliders down to 160 MeV per bunch.

REFERENCES

[1] Yu. Shatunov et al., Project of a New Electron-Positron Collider VEPP-2000, in: Proc. 7th European Particle Accelerator Conf. (EPAC 2000), Vienna, Austria, 439-441.

[2] V. Danilov et al., The Concept of Round Colliding Beams. In Proc of the EPAC 1996, Sitges, vol. 2, p.1149.

[3] E. Zinin, PhD Thesis, Budker Institute of Nuclear Physics, Novosibirsk, 1984 (in Russian).

[4] Yu. Shatunov, A. Skrinsky, Phys.Lett. B198, p.302, (1987).

[5] E. Abakumova et al., Backscattering of Laser Radiation on Ultra-Relativistic Electrons in Transverse Magnetic Field: Evidence of Photon Interference in a MeV Scale, Phys. Rev. Lett. **110**, 140402(2013).

[6] J. Safranek. Experimental Determination of Storage Ring Optics Using Orbit Response Measurements, Nucl. Instr. and Meth. A388, (1997) p. 27.

[7] *V. Sajaev, V. Lebedev, V. Nagaslaev, A. Valishev*. in Proc. of PAC'05, Knoxville, Tennessee, 3662-3664, 2005.

[8] A. Romanov et al., "Round Beam Lattice Correction using Response Matrix at VEPP-2000," Conf. Proc. IPAC2010 (2010) THPE014.

[9] A. Romanov et al., Luminosity estimation and beam phase space analysis at VEPP-2000, These Proc. WEPBA04.

Copyright © 2013 CC-BY-3.0 and by the respective authors

PERSPECTIVES AND CHALLENGES FOR DIFFRACTION-LIMITED STORAGE RING LIGHT SOURCES*

R. Hettel, SLAC NAL, Menlo Park, CA 94025, USA
M. Borland, ANL, Argonne, IL 60439, USA

Abstract

This paper provides an overview of the scientific motivation for developing diffraction limited storage ring (DLSR) light sources, reviews the main R&D challenges associated with DLSR implementation and summarizes the worldwide effort presently in progress to build a new generation of very low emittance rings.

INTRODUCTION

Synchrotron radiation from storage rings is the dominant source of high brightness photons from the infrared to hard X-rays, serving a multitude of scientific applications. Recently X-ray free electron lasers (FELs) have emerged, offering orders-of-magnitude higher peak brightness in ultra-short pulses. FELs offer nearly complete transverse coherence and energy bandwidth that will approach the transform-limit with seeding. Both ring- and FEL-based sources will play a vital role as they offer complementary beam properties, with rings providing low peak brightness with high average brightness and pulse repetition rate, which does not over-excite or damage samples as FELs do [1]. Another complementary capability for some storage ring sources is the production of high repetition rate (MHz), picosecond pulses for probing materials dynamics on the >10 ps timescale.

There are scientific applications and experimental methods that would greatly benefit from ring-based sources having much higher average brightness and transverse coherence. These include nanometer imaging applications; X-ray correlation spectroscopy and spectroscopic nanoprobes; and diffraction microscopy, holography and ptychography [2]. These applications will benefit from X-ray sources with average spectral brightness exceeding ~10^{22} photons/s/mm^2/mrad^2/0.1% BW and significantly higher coherent photon flux than presently available. This can best be provided only by reducing the electron beam emittance well below the present-day standard of nanometer-radians, towards the diffraction limit for X-ray beams.

WHAT IS A DLSR?

Diffraction-Limited Photon Emittance

While diffraction is typically associated with the divergence of a photon beam as it passes through a limiting aperture, it can be shown by solving the electric field wave equation that diffraction also occurs for a transverse spatially restricted photon beam, such as a Gaussian laser beam [3]. The transverse size and divergence of the electric field are related by a Fourier transform and the observed radiation intensity pattern, proportional to the square of electric field strength, satisfies the following:

$$\sigma_r(\lambda)\,\sigma'_r(\lambda) = \frac{\lambda}{4\pi} = \varepsilon_r(\lambda) \qquad (1)$$

where $\sigma_r(\lambda)$ and $\sigma'_r(\lambda)$ are the rms size and divergence, respectively, and $\varepsilon_r(\lambda)$ is the diffraction-limited emittance for a Gaussian photon beam having wavelength λ.

Extensive calculations of the radiation emitted by an undulator having N periods and length L have been carried out by several authors [3,4]. They reveal transverse beam size and divergence profiles that are only approximately Gaussian, so that the transform-limited value for the radiation emittance in (1) does not hold exactly. The rms size and divergence associated with the Gaussian fits to the calculated patterns are [4]

$$\sigma_r(\lambda) \approx 1.9\frac{\sqrt{2\lambda L}}{4\pi} \qquad \sigma'_r(\lambda) \approx \sqrt{\frac{\lambda}{2L}} \qquad (2)$$

and thus

$$\sigma_r(\lambda)\,\sigma'_r(\lambda) \approx \frac{\lambda}{2\pi} = \varepsilon_r(\lambda)\ . \qquad (3)$$

It should be noted that the factor of 1.9 for $\sigma_r(\lambda)$ in (2) is missing in [3]. This is not a serious issue – in fact, several other values can be derived depending on calculation and fitting assumptions. For the remainder of this paper, $\lambda/4\pi$ will be used since that value is commonly used by the synchrotron radiation community.

Diffraction-Limited Electron Emittance

A hypothetical filament of electrons having essentially no transverse size or divergence ("single electron" dimensions) passing through an undulator would emit radiation having the dimensions and emittance given in (2) and (3). A real electron beam has transverse size and divergence, which must be convolved with the single-electron photon parameters to determine the photon beam properties. Assuming Gaussian profiles, total horizontal or vertical emittance $\Sigma_{x,y}$ is given by

$$\Sigma_{x,y}(\lambda) = \varepsilon_r(\lambda) \oplus \varepsilon_{x,y}(e-) = \sqrt{\sigma_r{}^2(\lambda) + \sigma_{x,y}{}^2(e-)}\sqrt{\sigma'_r{}^2(\lambda) + \sigma'_{x,y}{}^2(e-)} \qquad (4)$$

where $\oplus$ denotes convolution, and $\sigma_{x,y}(e-)$ and $\sigma'_{x,y}(e-)$ are electron size and divergence, respectively, given by

$$\sigma_{x,y}(e-) = \sqrt{\beta_{x,y}\varepsilon_{x,y}(e-)} \quad \sigma'_{x,y}(e-) = \sqrt{\varepsilon_{x,y}(e-)/\beta_{x,y}} \qquad (5)$$

at the waist of the electron beam (and assuming zero dispersion). Total emittance is minimized when photon

†Work supported in part by Department of Energy Contract DE-AC02-76SF00515 and Office of Basic Energy Sciences, Division of Chemical Sciences

Copyright © 2013 CC-BY-3.0 and by the respective authors

and electron phase space orientations are matched, i.e.

$$\sigma_{x,y}(e\text{-})/\sigma'_{x,y}(e\text{-}) = \sigma_r(\lambda)/\sigma'_r(\lambda) \Rightarrow \beta_{x,y} = L/2\pi \quad (6)$$

(Fig. 1). This result assumes $\varepsilon_r = \lambda/4\pi$ and imposes a demanding requirement, e.g., $\beta = 0.6$ m for $L = 4$ m, a difficult value to achieve in the horizontal plane when using accumulation-based injection. Relaxing β_x to ~10 m can increase effective emittance by a factor of ~2 for emittances near the diffraction limit. This condition is less difficult if actual $\varepsilon_r = \lambda/2\pi$; then $\beta_x = L/\pi$. An optimization of beta functions that depends on undulator and electron beam properties is required in real designs.

From the above it can be inferred that a diffraction-limited emittance is reached when $\varepsilon_{x,y}(e\text{-}) << \varepsilon_r(\lambda)$. However it is conventional to say a ring is diffraction-limited when $\varepsilon_{x,y}(e\text{-}) = \varepsilon_r(\lambda)$. The diffraction-limited emittance for 1-Å X-rays (~12 keV) is 8 pm-rad, far below the nm-rad horizontal emittances for present-day storage ring light sources. However, vertical emittances at or below this scale are routinely reached in present machines by reducing vertical dispersion and coupling.

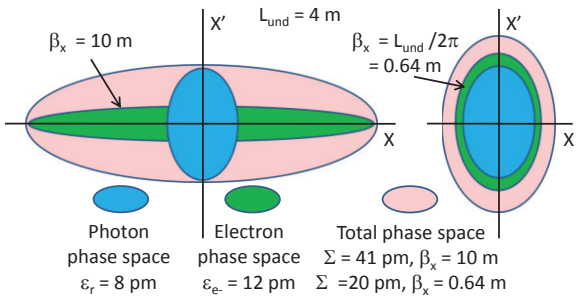


Figure 1: Total emittance (pink) is minimized when electron (green) and photon (blue) phase space ellipse orientations are matched. $\varepsilon_r = \lambda/4\pi$ is assumed.

Brightness and Coherence

The average brightness for a photon beam having wavelength λ is defined as the photon density in 6-dimensional phase space at that wavelength:

$$B(\lambda) = \frac{N_{ph}(\lambda)}{4\pi^2 \Sigma_x(\lambda)\cdot\Sigma_x(\lambda)\cdot(s\cdot\%\,BW)} \quad (7)$$

Closely related to brightness is the fraction f_{coh} of photons that are transversely coherent in each plane:

$$f_{coh-x,y}(\lambda) = \frac{\varepsilon_r(\lambda)}{\Sigma_{x,y}(\lambda)} \quad (8)$$

$$f_{coh-tot}(\lambda) = f_{coh-x}(\lambda)\cdot f_{coh-y}(\lambda)$$

When $e_x(e\text{-}) = e_r(\lambda)$, the horizontal coherence is 50%. If both horizontal and vertical electron emittances are at the diffraction limit, the total coherent fraction is 25%. Horizontal coherent fraction as a function of electron emittance for different wavelengths is shown in Fig. 2.

From (7) it is evident that brightness can be increased either by reducing emittance in the denominator, or by increasing photon flux ($N_{ph}(\lambda)/s$) in the numerator. The latter can be achieved by increasing the stored beam current and through the use of longer or higher-performance undulators. Nevertheless, while X-ray users are interested in high coherent flux, achieving it by increasing coherent fraction is more desirable since this reduces the amount of "unusable" incoherent flux and mitigates issues associated with high heat loads.

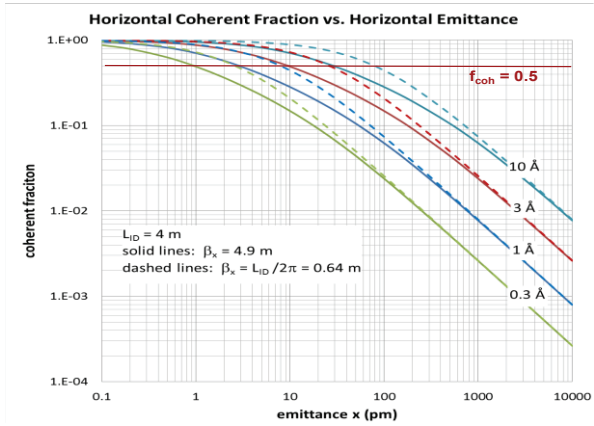


Figure 2: Horizontal coherent fraction versus emittance for various X-ray wavelengths. Dashed curves indicate the gain coherence for 4-m undulators when β_x is reduced from 4.9 m to 0.64 m (= $L/2\pi$).

The brightness and coherent fraction for various existing, imminent and potential future storage ring light sources are shown in Fig. 3. While these parameters will be increased ten-fold in the 0.1 to 10 keV range by sources now in construction, an even greater increase in that spectral range, and an enhancement of 2 or more orders of magnitude in the 10 to 100-keV range should be achieved by converting existing high energy rings (ESRF, SPring-8, APS) to lattices with emittances in the 60-150

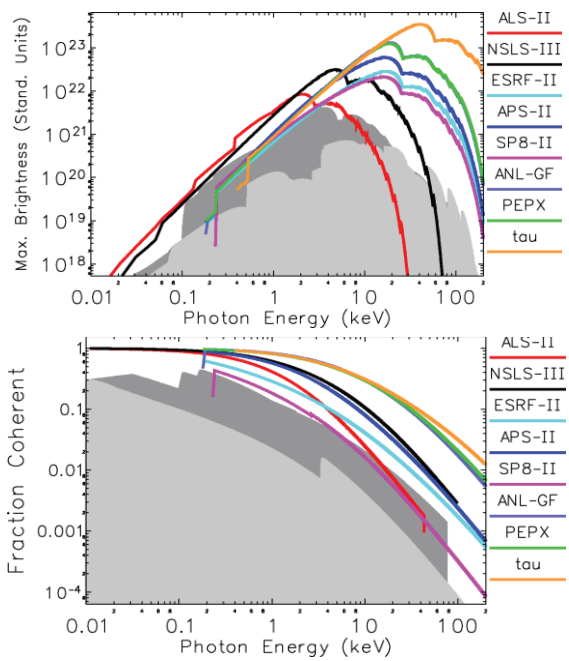


Figure 3: Brightness and coherence for present day storage rings (light gray), rings in construction (MAX-IV, NSLS-II, dark gray) and future rings (colored curves). Ring parameters given in Table 1.

Copyright © 2013 CC-BY-3.0 and by the respective authors

pm-rad range. Large circumference green-field machines having emittances of 1 to 10 pm-rad (e.g. PEP-X [5], TauUSR [6]) would approach maximal brightness and coherent fraction for hard X-rays.

Reducing Emittance

The natural electron emittance ε_0 is given by [7]

$$\varepsilon_0(e-) = F(\nu,\ cell)\frac{E^2}{(N_d N_s)^3} \propto \frac{E^2}{C^3} \qquad (9)$$

where F(ν,cell) is a function of the betatron tune and cell type, E is the electron beam energy, N_d is the number of dipoles in a given sector, N_s is the number of sectors (and straights) in the ring, and C is ring circumference. The C^{-3} scaling is valid only when the cell type is fixed. Stated simplistically, ring emittance for a given electron energy is reduced by increasing the total number of dipoles in the ring and by increasing focusing between dipoles to maintain low dispersion. Horizontal and vertical emittances are set by the coupling factor κ:

$$\varepsilon_x(e\text{-}) = \frac{1}{1+\kappa}\varepsilon_0(e-) \qquad \varepsilon_y(e\text{-}) = \frac{\kappa}{1+\kappa}\varepsilon_0(e-) \qquad (10)$$

Present-day rings have $\kappa < 0.1$. As ε_0 is reduced towards the diffraction limit, it is reasonable to set $\kappa = \sim 1$, enabling operation with a quasi-round beam that is beneficial to users. This increases Touschek lifetime and combats emittance growth caused by intra-beam scattering (IBS) in the very small electron bunch volumes.

Emittance can also be reduced by introducing more damping to combat radiation- and IBS-induced emittance growth. This can be accomplished using high-field damping wigglers (DW) and is effective if the energy loss per turn U_W in the wigglers is greater than the energy loss per turn U_0 in the dipole magnets, in which case

$$\frac{\varepsilon_W}{\varepsilon_0} \approx \frac{1}{1+U_W/U_0} \qquad (11)$$

The dipole field strength for large rings can be low (~0.5 T), making damping wigglers a practical way to reduce emittance by a factor of 2-3.

A third way to reduce horizontal emittance is to increase the horizontal damping partition J_x by a factor of two or so by passing the beam through magnets having a combination of positive dipole and defocusing gradient fields, e.g., gradient dipoles, Robinson wiggler [8], or by orbit offset in quadrupoles [9]. This method increases horizontal damping at the expense of longitudinal damping, reducing emittance while increasing the energy spread. Once gradient dipoles are used in the lattice, the other two methods do not add a significant benefit.

DLSR Properties

Given the discussion above, the properties of DLSRs can be summarized as follows:

- Brightness and coherence are as high as possible for a given beam current.
- Beam sizes and divergences are small in both transverse dimensions (microns and microradians).
- High coherence and small size allows beams to be focused to very small sizes – "nano-focusing" not achievable with present day sources, .
- High coherence preserves X-ray wavefront phase uniformity, enhancing coherent imaging techniques by providing high coherent flux with minimal need for aperturing slits, etc.
- "Round" beams are possible with the appropriate adjustment of coupling, betatron functions and vertical dispersion, enabling optimal use of H-V symmetric x-ray optics, circular zone plates, etc.
- Large circumference for multi-GeV rings allows reaching the diffraction limit for hard X-rays.
- Damping wigglers can be used to combat IBS, reduce emittance and increase lifetime.

As noted below the strong focusing lattices needed to reach a minimum emittance have small dynamic aperture (DA), potentially inadequate for normal beam accumulation using off-axis injection. In this case, an additional property for some designs is the need for on-axis "swap-out" injection [10] where stored electron bunches are completely replaced with new incoming bunches. Such lattice designs also tend to have a low momentum compaction factor, resulting 5-10 ps rms natural bunch lengths in some cases for rings having ~500-MHz RF systems, a factor of ~3 lower than present-day sources. In these cases, bunch lengthening RF cavities are needed to increase lifetime and reduce IBS.

CHALLENGES AND SOLUTIONS

The science case for high coherence storage rings has gained sufficient momentum to motivate existing facilities (e.g., ESRF, SPring-8, and APS) to develop plans to replace their lattices with ultra-low emittance designs. These lattices will increase brightness and coherent fraction by orders of magnitude, reaching diffraction limited horizontal emittances for few-keV X-rays. To reach the diffraction limit and maximal brightness for hard X-rays (<10 pm-rad), new machines with large circumference (~1.5 km for ~5-GeV electrons) will be required. The challenges and technological solutions related to these designs are discussed below.

Fundamental Challenges

The main path to reducing emittance in a storage ring is to increase the number of dipoles while limiting dispersive orbit amplitudes using many strong quadrupoles. These quadrupoles introduce chromatic aberrations that must be corrected with strong sextupoles, which in turn introduce higher order aberrations that must be corrected in order to achieve adequate dynamic and momentum aperture (MA). Without sufficient MA and DA, beam lifetime will be reduced, increasing beam loss, and off-axis injection becomes difficult, if not impossible.

The ~2-fold stronger quadrupoles and ~10-fold stronger sextupoles required by these rings, necessitates bore radii 2-3 times smaller than today's light sources. Small magnet bores imply small-aperture vacuum chambers in both transverse dimensions, reducing vacuum system

Copyright © 2013 CC-BY-3.0 and by the respective authors

conductance, and increasing issues with synchrotron radiation power absorption. Furthermore, the impedance from small aperture chambers exacerbates single- and mutli-bunch beam instabilities.

Challenges for DLSRs have been discussed in several workshops, including [11-13] and others.

DLSR Technology

Multi-bend achromat (MBA) lattices having more than 3 dipoles per sector has been envisioned as a way to increase the number of dipoles while providing many insertion device straight sections beginning with 4BAs in the early 1990s [14], an early 7BA lattice for the Swiss Light Source [15] and a 7BA, 3-GeV lattice reaching 0.5-nm-rad emittance with a 400-m circumference [16] (Fig. 4). Still, the challenges associated with compact magnets and small-bore vacuum chambers were daunting enough at the time to prohibit construction of such a machine.

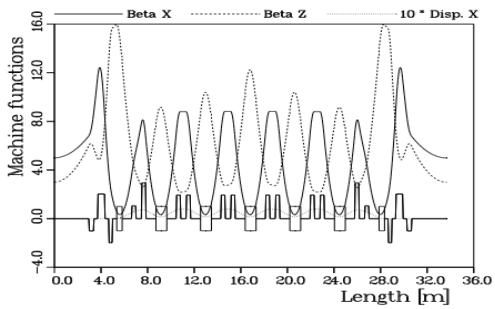


Figure 4: 7BA lattice [16].

Compact magnet and vacuum chamber technology for DLSRs has now been developed, primarily by MAX-Lab in Sweden, enabling construction of MAX-IV, the first 7BA light source [17]. MAX-IV will have a 2.6-cm diameter, primarily round copper vacuum chamber with shallow antechambers where needed to extract the X-ray beams (Fig. 5). To achieve sufficient vacuum pumping the chambers will be NEG-coated, using CERN technology already exploited in nearly 1/3 of the vacuum chambers at Soleil. NEG-coated chambers are now used routinely for small-gap insertion devices (IDs) in many light sources.

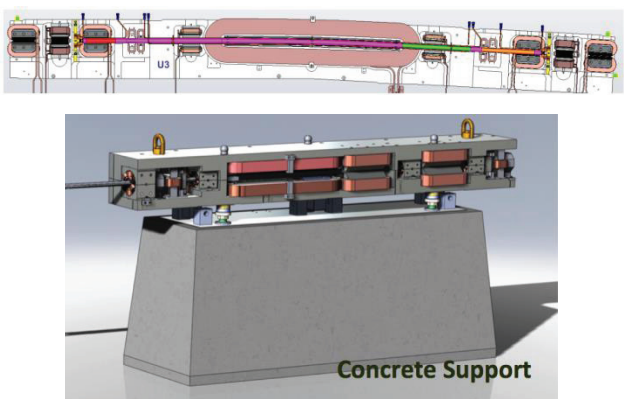


Figure 5: MAX-IV machined magnet block and vacuum chamber (top); a different style magnet block assembly on its concrete support (bottom).

MAX-IV magnets are machined from single blocks of iron, each containing a dipole and adjacent multipoles; the gradient dipole poles are machined directly from the block, while the highly precise multipole poles are machined separately and bolted in place, giving alignment precision on the order of 10 μm. The blocks are mounted on elevated concrete blocks, eliminating both support girders and individual magnet supports (Fig. 5). A magnet measurement system employing rotating coils, Hall probe sensors and precise alignment technology has been developed. The technology has been tested, first by constructing similar combined function magnets for the 700-MeV MAX-III ring in 2008, and then by testing the NEG-coated vacuum chamber system in one area in the 1.5-GeV MAX-II ring. Other DLSR designs use independent magnets having high alignment tolerances.

Accelerator physics methods and modeling tools for storage ring design have advanced appreciably over the last two decades, driven by the design of high-luminosity colliders, low-emittance damping rings, and enhanced light sources. Tools include symplectic tracking methods to accurately determine DA and MA, tracking-based lattice optimization codes and methods (e.g. multi-objective genetic algorithms, frequency map analysis, etc.) and analytical methods (e.g Lie algebra, amplitude dependent tune shift and resonance driving term minimization). These methods have been benchmarked on real machines with beam-based lattice calibration tools (e.g. LOCO [18]) and parameter measurement techniques.

Other relevant advances include: success of top-up injection in accommodating short beam lifetime; advances in electron and photon beam diagnostics, allowing precise characterization and correction of the ring, as well as stabilization of the beam to the sub-micron and sub-microradian level; development of fast high-voltage stripline kickers for the ILC effort, supporting on-axis injection with closely-spaced bunches; advances in electronics, from power supply stability to the speed of digital processors used for orbit feedback; development of highly stable solid state RF power sources; high performance undulator development (including superconducting); and coherence-preserving X-ray optics being developed for FELs.

DLSR Design Optimization

The optimization of parameters for any storage ring is a complex process that can only be briefly addressed here. In the case of DLSRs, the scientific community is likely to be a mixture of users seeking high brightness and coherence and those whose experiments are flux- rather than brightness-limited, leading to tension between reducing emittance and increasing stored current – an optimization that impacts facility cost since it is generally less expensive to increase current than it is to build an ultra-low emittance ring. As mentioned, it is possible to get high coherent flux with a high current, low coherent fraction ring. As seen in Fig. 2 there is a diminishing return in coherent fraction for decreasing emittance that must be weighed in the optimization.

Copyright © 2013 CC-BY-3.0 and by the respective authors

Another consideration is the electron energy needed to fulfil spectral requirements. Higher energy, larger circumference rings (e.g. 6 GeV or more) will produce higher brightness hard X-rays, but competing brightness (within an order of magnitude) can be achieved with less expensive, lower energy, smaller circumference rings (e.g. 3-4 GeV) using harmonics from high performance undulators. Another factor is that ring energy can be optimized to minimize emittance growth due to IBS for a given beam current; for ~1-km rings, the optimal energy from this standpoint is ~4-5 GeV, while it is 5-6 GeV for 2-km rings. However the gain in hard X-ray emission at higher energy can lead to higher brightness, even if emittance is degraded. There is thus a trade-off between spectrum, emittance, circumference and cost.

A final comment on design optimization concerns the number, length and spacing of straight sections. Designers must decide whether long straight sections will be used for two IDs in a chicane, as opposed to providing more short straight sections holding single IDs. The spacing between straight sections, lattice bending radius, and thus the angle between adjacent photon beam lines, ultimately determines the length of X-ray beam lines and the amount of expensive experimental floor space needed for them. Experimental halls for very large rings can become overly expensive unless ID straights are spaced for efficient beam line alignment. In some cases this could lead to a hybrid lattice design for very large rings where beam line straight sections are consolidated in specific arcs having optimal spacing using one lattice type, while another minimal emittance lattice type is used elsewhere [19].

Table 1: Parameters for some low-emittance rings. (IC/IP/ID = in construction, planning, development; DW = damping wiggler.)

Facility	E(GeV) / I(A)	C (m)	ε_0 (pm)	Features
NSLS-II	3/0.5	792	600	DBA, DW, IC
MAX-IV	3/0.5	528	250	7BA, 100 MHz RF, IC
Sirius	3/0.5	518	280	5BA, superbend, IC
ESRF	6/0.2	844	150	7BA w/dispersion bumps, long. grad., IP
APS	6/0.2	1104	60	ESRF style, swap-out, IP
SPring-8	6/0.2	1436	280	QBA, ID
ALS	1.9/0.5	200	100	9BA, superbend insert, swap-out, IP
SLS	2.4/0.5	288	250	Pre-conceptual design
BAPS (Beijing)	5/0.2	1500	30-50	Pre-conceptual design
SLAC	6/0.2	2.2	10	7BA, 90m DW, conceptual design
TauUSR	9/0.2	6280	3	7BA, DW, pre-conceptual design

A summary of low emittance rings and future DLSRs being considered for the future is given in Table 1.

SUMMARY AND OUTLOOK

Storage ring light source technology has reached the stage where construction of a new generation of sub-nm-emittance rings is feasible. Machines having horizontal emittances as low as 0.25 nm-rad are now in construction, and several others having sub-100-pm emittances are in planning stages. Longer range plans envision rings having sub-10-pm emittances – machines whose technology will build on that developed for rings to be built in the next several years and which may require R&D in accelerator technology [12]. The longer range future for DLSRs might include enhanced capabilities, such as ring-based high repetition rate, low peak power FELs [20] and short bunch operation that offer beam properties complementary to linac-based FELs while serving a larger number of simultaneous users. The "MBA generation" is an exciting time for light source designers.

ACKNOWLEDGMENTS

The authors are grateful for the contributions from a large number of colleagues for the information in this paper, including R. Bartolini, Y.Cai, L. Emery, M. Eriksson, W. Guo, Z. Huang, S. Leeman, L. Lin, L. Nadolski, D. Robin, Q. Qing, P. Raimondi, C. Steier, A. Streun, H. Tanaka and many others.

REFERENCES

[1] ANL, BNL, LBNL, SLACNAL, "Science and Technology of Future Light Sources - A White Paper," SLAC R-917, 2008.
[2] "Workshop on Science at the Hard X-ray Diffraction Limit," XDL 2011, Cornell, June 2011.
[3] K. J. Kim, AIP 184, vol. 1, 1989.
[4] P. Elleaume, "Wigglers, Undulators and their Applications," Taylor and Francis, New York, 2003.
[5] Y. Cai et al., private communication.
[6] M. Borland, IPAC12, 1683 (2012).
[7] J. Murphy, BNL-42333, 1996.
[8] K. Robinson, Phys. Rev. 111(2), 1958.
[9] M. Borland, PAC11, 2339 (2011).
[10] L. Emery, et al., PAC03, 256 (2003).
[11] M. Bei et al., NIM A, 662, p 518 (2010).
[12] R. Hettel, Q. Qin, Report on the 2012 Beijing Workshop on R&D for USRs, SLAC-PUB-15379.
[13] Low Emittance Ring Workshop, Oxford, 2013, www.physics.ox.ac.uk/lowemittance13/index.asp
[14] D. Einfeld et al., NIMA 335(3), 1993.
[15] W. Joho et al., EPAC94, London, 627 (1994).
[16] D. Einfeld et al., PAC '95, Dallas, 177 (1995).
[17] "MAX-IV Detailed Design Report," https://www.maxlab.lu.se/node/1136, 2010.
[18] J. Safranek, NIMA 388(21), 1997.
[19] M-H Wang et al., NIMA 649(1), 2011.
[20] Y. Ding et al., IPAC13, Shanghai, 2286 (2013).

Copyright © 2013 CC-BY-3.0 and by the respective authors

Contribution not yet Received or QAed

Copyright © 2013 CC-BY-3.0 and by the respective authors

ULTRA-LOW EMITTANCE UPGRADE OPTIONS FOR THE DIAMOND LIGHT SOURCE

R. Bartolini[1,2], N. Hammond[2], J. Kay[2], T. Pulampong[1] and R.P. Walker[2]
[1]John Adams Institute, University of Oxford, UK
[2]Diamond Light Source, Oxfordshire, UK

Abstract

Many synchrotron radiation facilities are studying lattice upgrades in order to lower the natural emittance and hence increase the radiation brilliance and transverse coherence. While large circumference rings are favoured for reaching ultra small emittance, recent advances in design and optimisation tools allow also medium size rings to reach emittances down to the some 100s of pm region, with workable lattices. Diamond is investigating a novel design whereby low emittance is conjugated with doubling of the capacity of the ring, based on a double-double bend achromat (DDBA) cell. Plans for the installation of one or more low emittance cells will be presented. This will serve as a prototype for a possible full phased upgrade of the storage ring in the longer term.

INTRODUCTION

The Diamond Light Source is actively pursuing a research programme for the development of an ultra-low emittance upgrade of the storage ring in order to achieve emittances in the range of 270 pm and below [1,2] which would improve the present emittance by a factor 10 or more. This emittance will allow the facility to remain competitive with the next generation high brightness light sources by substantially increasing the brilliance and the transverse coherence of the synchrotron radiation.

Accelerator physics studies have shown that lattices based on Multiple Bend Achromats (MBAs) can produce appealing emittance even with medium size rings such as the 561.6 m of the Diamond storage ring. The Diamond lattice upgrade is constrained by the requirement of maintaining the tunnel geometry and the position of the beamlines. The possibility of phasing the upgrade on a cell-by-cell basis to avoid long shutdowns was also considered in the studies. Reusing as much hardware as possible was considered, however it turned out that the magnets of the present lattice are not adequate for a reduced emittance lattice and so new magnet designs are now developed. Other technical subsystems are also under design, notably vacuum and diagnostics, while the RF system [3] and the power supplies will be reused. In this report we present the advances on the accelerator physics design.

MBAs have been proposed in the early '90s as a promising lattice design that allows reducing the emittance towards the diffraction limit [4] in the hard X-ray region. We therefore investigated the possibility of replacing our DBA lattice with an MBA. Various options were analysed starting with a very aggressive 7BA design with 45 pm emittance but with a very small dynamic aperture. More relaxed lattices 5BA and 4BA produced slightly larger emittance, 150 pm and 270 pm respectively. These values are in any case meeting the 10-fold emittance reduction target. In the analysis of the 4BA lattice it transpired that the 4BA cell can be split in two, inserting a new straight section in the middle of the cell. We later found that a similar concept was proposed in [5]. In this way the lattice strongly resembles again a DBA, despite the fact that the outer and inner dipoles in the cell have different lengths, and was therefore named "Double Double Bend Achromat" (DDBA). The additional straight section in the middle of the cell allows doubling the capacity of the present Diamond ring for Insertion Devices (IDs), while still maintaining a very small horizontal emittance.

The possibility of introducing an additional straight section has triggered the study of the installation of one or more such DDBA cells into the present Diamond lattice. The VMX [6] and the DIAD [7] beamlines have expressed strong interest in utilising a DDBA cell located in cell 2 and cell 11 respectively. A third modification of the lattice in cell 20 would allow the installation of a third harmonic cavity for bunch lengthening which will support the increase in the operational current to 500 mA and is in line with the potential phased upgrade of the full lattice.

The installation of the DDBA cells in the present lattice will provide the opportunity of testing many critical areas of a possible full upgrade of the machine. In particular it has kick-started the necessary R&D on several technical subsystems such as magnets, vacuum, diagnostics and the engineering integration of the subsystems.

MBA LATTICE STUDIES

The first options investigated to replace the existing DBA was a 7BA lattice, providing an emittance of 45 pm. The basic cell, shown in Fig. 1, is built on gradient dipoles with 0.45 T and 30 T/m quadrupole component and 90 cm length. The larger number of dipoles is accommodated by slightly reducing the lengths of straight sections. The natural chromaticity of this lattice is very high and requires strong sextupoles for correction. A dispersion bump is created between dipole 1 and 2 and symmetrically between dipole 6 and 7 to locate the chromatic sextupoles and reduce their required strength. The lack of a proper phase advance (π or 3π usually) between the chromatic sextupoles in the cell prevents the cancellation of the geometric driving terms. The phase advance was matched to complete 2π within one super period (4 cells). Most of the resonance driving terms (RDTs) can be cancelled in one super period in this way

Copyright © 2013 CC-BY-3.0 and by the respective authors

[8]. However, higher order terms are still large, difficult to compensate and the resulting dynamic aperture is only ± 1mm. With such a small dynamic aperture, off-axis injection is excluded and a major reconsideration of the injector system would be required. Furthermore the effect of intra-beam scattering quickly blows up the emittance for beam currents under consideration: at 300 mA in 900 bunches and 10% coupling, the emittance is double to 90 pm. Given the constraints on the geometry and layout of the beamlines, we do not have the flexibility to install damping wigglers to compensate for this effect. It was therefore decided not to pursue this option further for the moment.

A similar design based on a 5BA providing an emittance of 156 pm also showed similar, albeit mitigated, difficulties: the dynamic aperture is only ±3 mm. The layout of the optics function in the cell for these two options is shown in Fig. 1. The main parameters of the two lattices are reported in Tab. 1.

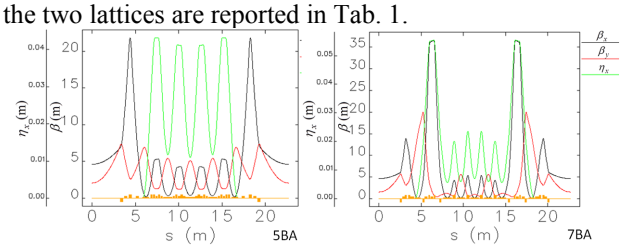


Figure 1: Optics functions for 5BA and 7BA lattices.

Table 1: Parameters for 5BA and 7BA Lattices

Parameters	5BA	7BA
Circumference [m]	561.6	561.6
Emittance [pm.rad]	156	45.7
Tune Point [Q_x / Q_y]	53.66/ 28.87	75.42/52.17
Chromaticity(ξ_x / ξ_y)	-130 / -50	-348/ -119
Length of straights [m]	9.5 / 6.5	8.0 / 5.0
Momentum compaction	1.30e-04	7.98e-05

THE DDBA LATTICE

Given the above difficulties, more relaxed optics were then considered. The usual 4BA cell, based on standard TME cells and matching cells, has been modified to accommodate an additional straight section in the middle of the cell, in the so called DDBA cell shown in Fig. 2. In this way the number of straight sections per cell is doubled. Table 2 reports the main parameters of the DDBA lattice and a comparison with the present lattice design.

The length of the additional middle straight section is a parameter of the optimisation and it turned out that a good matching can be achieved only up to 3.4 m. This length is sufficient to install one of the existing 2m in-vacuum ID and leaves sufficient space for flanges, BPMs, bellows and correctors. The excellent control of the optic functions in this straight allows the use of narrow gap ~5mm IDs without any detrimental effect on emittance and gas lifetime.

Table 2: Parameters for Existing DBA and DDBA Lattices

Parameters	Existing DBA	DDBA lattice
Energy [GeV]	3.0	3.0
Circumference [m]	561.6	561.0
Emittance [pm.rad]	2750	276
Tune Point [Q_x / Q_y]	27.20/ 13.37	50.76/18.36
Chromaticity(ξ_x / ξ_y)	-80.4 / -35.6	-128/ -94
Length of straights [m]	11.3 / 8.3	9.1- 6.7 / 3.4
Mom. compaction	1.66e-04	1.02e-04

The combined function dipoles play an important role in making the cell compact as almost all the vertical focussing is provided by the gradient in such dipoles. The maximum gradient of all quadrupoles and combined function dipoles was limited at 55 T/m and 15 T/m respectively. The dipole at the edge of the cell is shorter than the middle dipole by the factor of $3^{1/3}$ in order to minimise the contribution to the beam emittance and matching to zero dispersion in the straight section [9]. To achieve a more efficient chromaticity correction, we introduced a dispersion bump between dipoles 1 and 2 and dipoles 3 and 4. Chromatic sextupoles are introduced in these locations.

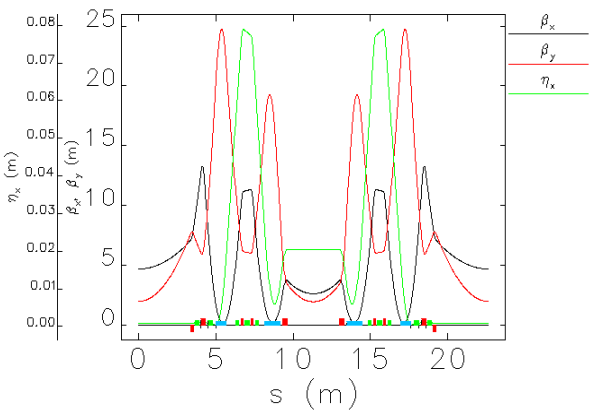


Figure 2: Optics functions for the DDBA cell.

The dynamic aperture and the momentum aperture were further optimised with a Multi-Objective Genetic Algorithm (MOGA) implemented in elegant [10], using the 10 sextupole families in the ring. The dynamic aperture is about ± 5 mm while the momentum aperture exceeds ±2 % everywhere in the ring and corresponds to a Touschek lifetime of 2.2 h. While the dynamic aperture is still too small for off-axis injection we believe that a more thorough search for the optimal phase advance per cell and using more sextupole families can improve the dynamic aperture to values compatible with our off axis-injection that currently produces a residual oscillation of 8.3 mm. This work will be the subject of forthcoming investigation. More details on the nonlinear dynamics optimisation can be found in ref. [1]. Alternative injection schemes in small dynamic apertures are under investigation [11].

Copyright © 2013 CC-BY-3.0 and by the respective authors

IMPLEMENTATION OF ONE DDBA CELL

The DDBA cell opens the possibility of adding new straight sections to the ring and therefore accommodating new beamlines. This opportunity was used to modify the layout of the VMX beamline [6] by implementing one DDBA cell in the present cell 2 of the lattice. The VMX beamline was originally designed with two branches which were served by one in-vacuum ID and one short ex-vacuum ID respectively. With the DDBA cell, both branches can be served by 2m in-vacuum IDs with a considerably better performance. The modified lattice is shown in Fig. 3.

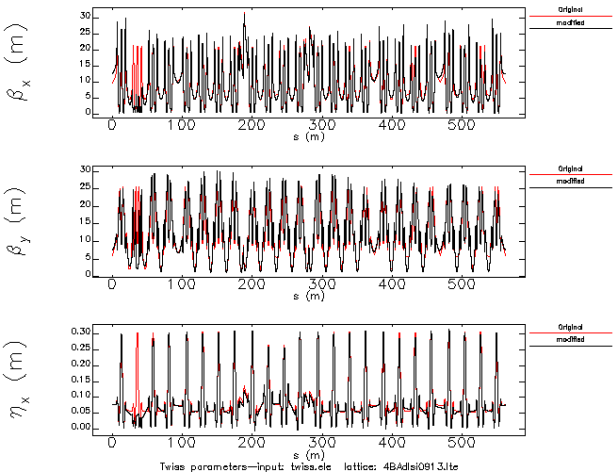


Figure 3: Optics functions with cell 2 upgraded to a DDBA cell.

The optimisation of the beam dynamics with MOGA showed that the insertion of the DDBA can be made almost transparent, as the dynamic aperture and Touschek lifetime of the ring are restored to the values of the original lattice. Figure 4 shows the DA of ±15 mm and the corresponding frequency map. The computed Touschek lifetime is 27h compared to the 29h of the original lattice.

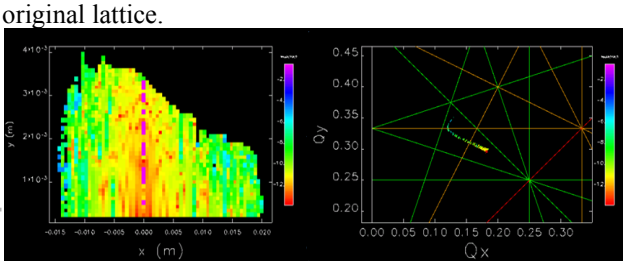


Figure 4: Dynamic aperture and frequency map for the Diamond lattice with one DDBA cell.

TWO AND MORE DDBA CELLS

In following studies, cell 11 was altered to a DDBA cell in correspondence of the DIAD beamline [7]. A new set of extensive numerical simulation was set up to optimize the dynamic aperture and the Touschek lifetime. Also in this case MOGA was used to set the values of ten existing sextupole families as parameters and the sextupoles in the new cell 11. A marginal readjustment of the sextupoles in the DDBA cell2 was required. The result presently achieved shows that the dynamic aperture is still about ±15 mm. The Touschek lifetime is 18h, that is a reduction to 62% of the existing value of the Touschek lifetime. We believe that, while already very promising, these values can still be improved to make also the second cell installation transparent to the operation of the existing ring.

Consequently we have started the analysis of a third DDBA cell. While this exercise is driven by the requirement to install a third harmonic cavity for bunch lengthening, it is also in line with the concept of a phased upgrade of the full ring and serves to prove the flexibility of our lattice. The lattice functions were matched as reported in Figure 5. The study of nonlinear beam dynamics will be carried out in the near future.

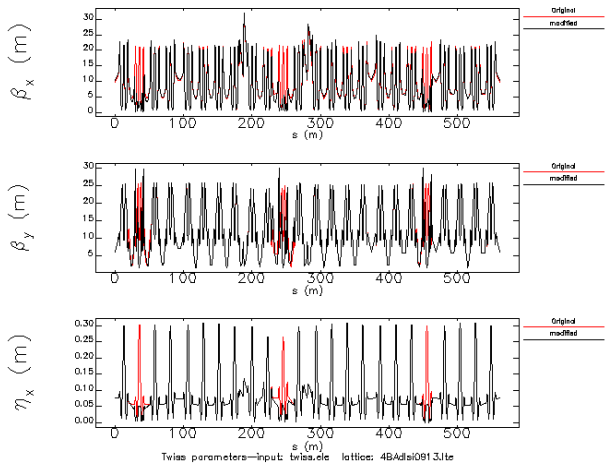


Figure 5: Optics functions with three cells upgraded to a DDBA (cell 2, cell 11 and cell 20).

CONCLUSION

Several MBA lattice options are considered for a possible low emittance upgrade of the Diamond storage ring. Lattices based on 7BA cells promise very small emittance, but their optimisation appears to be challenging. A modified 4BA lattice providing small beam emittance and doubling the number of beamlines appears to be a strong candidate for the upgrade of Diamond. The beam dynamics optimisation of one and two DDBA cells in the present lattice has shown that their installation will not compromise the operation of the ring, while providing substantial benefits for the corresponding beamlines. The implementation of a third DDBA cell is under investigation.

REFERENCES

[1] R. Bartolini et al., Proceedings of the IPAC13, 237, (2013).
[2] R. Bartolini et al., Proceedings of the IPAC13, 240, (2013).
[3] C. Christou et al., Proceedings of the IPAC13, 243, (2013).
[4] D. Einfeld et al., NIM **A335**, 402, (1993).
[5] M.H. Wang et al., Rev. Sc. Inst., **78**, 055109, (2007).
[6] T. Sorensen et al., VMX CDR, DLS 2012.
[7] M. Drakopoulos et al., DIAD CDR, DLS 2010.
[8] J. Bengtsson,. SLS-TME-TA-1997-0009, SLS note, (1997).
[9] S.Y. Lee, Phys. Rev. **E 54**, 1940, (1996).
[10] M. Borland, elegant, APS LS-287, (2000).
[11] T. Pulampong et al, Proceedings of IPAC13, 2268, (2013).

Copyright © 2013 CC-BY-3.0 and by the respective authors

ANALYSIS OF TRANSVERSE INSTABILITIES OBSERVED AT J-PARC MR AND THEIR SUPPRESSION USING FEEDBACK SYSTEMS

Y. H. Chin, KEK/Sokendai, Tsukuba, Japan

Abstract

This paper presents an analysis of head-tail instabilities observed at the J-PARC MR (Main Ring) and their suppression using feedback systems. Instabilities were mainly observed at low energies. About 30% of particles are lost due to the instabilities if the feed-back system is turned off at the beam power of 120kW. Both horizontal and vertical instabilities were observed. Measurements of the horizontal oscillations initially suggested the excitation of higher-order head-tail modes during the injection. An analysis unveils that a dipole mode has a temporal appearance of higher-order head-tail modes if the chromaticity is sufficiently large. The development of instabilities in the presence of a large chromaticity should be considered for conditions beyond the Sacherer's text book case.

INTRODUCTION

J-PARC consists of three proton accelerators: a 400 MeV linear accelerator (currently operating at 180 MeV), a 3 GeV Rapid-Cycling Synchrotron (RCS) and a 50 GeV (currently 30 GeV) Main Ring (MR). The main parameters of the MR are summarized in Table 1.

Table 1: Main Parameters of the MR Ring

Circumference	1568 m
Injection Energy	3 GeV
Extraction Energy	30 GeV
Repetition Period	3 sec
RF Frequency	1.67-1.72 MHz
Number of bunches	8
Synchrotron tune	0.002-0.0001
Betatron tune	22.4, 20.77

In the normal operation mode, over 90% of the protons accelerated in the RCS are directed to the muon and neutron production targets in the Materials and Life Science Experimental Facility (MLF). The remaining protons are transported to the MR for further acceleration before being extracted via one of two (fast and slow) MR extraction ports.

The MR impedance is dominated by the transverse resistive-wall impedance of the stain-less steel chamber and the horizontal kicker impedance [1]. The kicker impedance has sharp peaks at about 1MHz and 10MHz. It is almost halved after four injection kickers were replaced by parasitic-impedance-free new models with HOM dampers (we still use five old-type kickers). The transverse resistive-wall impedance is exceptionally high, since the first betatron unstable line appears at around 40kHz on the vertical plane where the skin-depth is comparable to the wall thickness and the transverse impedance is proportional to the inverse of the frequency, not the square root of the frequency [2]. The beam instability evaluation before the commissioning of MR predicted that beam instabilities would start to hurt beam operation from the beam power of 100-200kW. Although the necessity of a damper system has been recognized, actual development has been delayed due to financial constraints. After the commissioning of MR started, the careful inventory of the existing hardware revealed that we already have some key components necessary to compose the damper system: several unused Stripline Position Monitors (SPM), and the exciters for tune measurements that can be exploited as damper kickers. It was found that only remaining component to be developed is a signal processing circuit to filter and process SPM data and then to produce kick signals. The whole project costs only less that 100k USD.

Figure 1 sketches the transverse (narrow-band) bunch-by-bunch feedback system. The beam position signals are sampled at an RF frequency times 64 rate (108.8MHz at 3GeV). The signal processing and digital filtering circuits consist of two LLRF4 boards with four 14-bit ADCs and two 14-bit DACs. They extract the betatron oscillation signals using 8-tap FIR filters. Its system integration and firmware development including EPICS interface was done by the Dimtel Inc. The kick signals are sent to the stripline damper kickers through the power amplifiers (two 500W/ 10kHz-250MHz ones for the horizontal plane and two 1kW/100kHz-8MHz ones for the vertical plane) to provide a single kick per bunch per passage for the both directions.

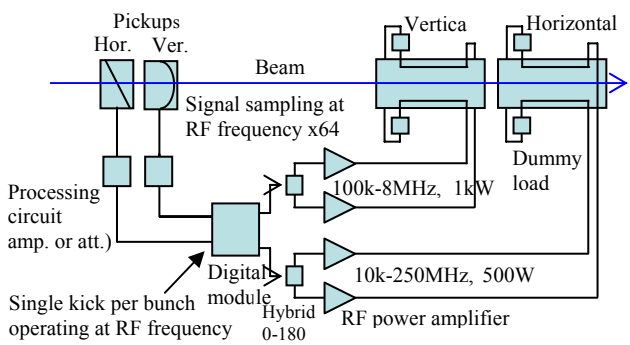


Figure 1: Schematic view of the transverse bunch-by-bunch feedback system (narrow-band).

Figures 2 (a) and (b) show the beam oscillation signals from the SPM recorded at a 500MHz sampling rate for the first 128ms period that covers the injection of the last batch of bunches from RCS (K4) and the onset of acceleration (P2) where all instabilities take place. The top figure (a) shows the signals with the feedback (FB) off, while the bottom figure (b) shows one with the FB on.

Copyright © 2013 CC-BY-3.0 and by the respective authors

The strong vertical oscillations are visible just after the onset of acceleration when the FB is turned off. The large horizontal oscillation can be also seen just after the injection of the last batch of bunches. They are strongly damped when the FB is tuned on. The DCCT monitor shows that the particle losses at the injection and at the onset of acceleration are about 500W and 4,800W, respectively, which are far larger than the collimator tolerance (400W). They are reduced to 100W and 25W, respectively, when the FB is turned on. Figures 3 (a) and (b) show the beam intensity measured by the DCCT monitors without and with FB, respectively. It can be seen that almost 30% of particles are lost due to the beam instabilities when FB is turned off. The FB is now indispensable in daily operation of MR.

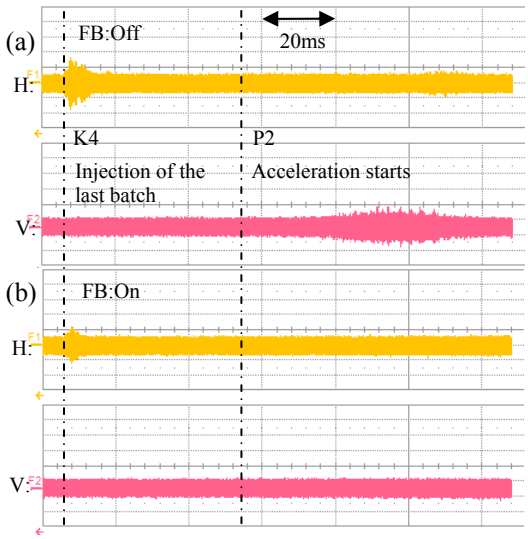


Figure 2: The beam oscillation signals from SPM for the first 128ms (a) when FB is turned off and (b) when FB is turned on.

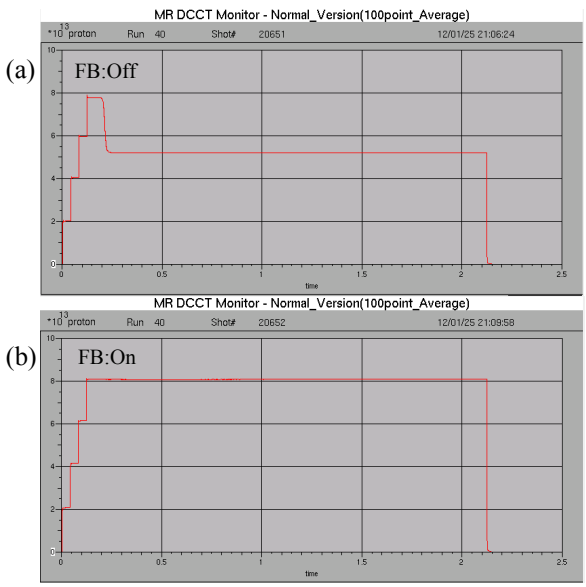


Figure 3: The beam intensity measured by the DCCT monitors (a) when FB is turned off and (b) when FB is turned on.

HEAD-TAIL INSTABILITY THEORY

Let us revisit the Sacherer's head-tail instability theory [3]. The chromaticity is defined by

$$\xi = \frac{d\omega_\beta}{\omega_\beta} / \delta \ , \tag{1}$$

where ω_β is the angular betatron frequency and $\delta = \Delta p / p$ is the relative momentum deviation. In other words, the betatron frequency depends on the momentum deviation as

$$\omega_\beta(\delta) = \omega_{\beta 0}(1 + \xi\delta) \cdot \tag{2}$$

When a particle moves along the ring, the accumulated betatron phase advance is given by

$$\phi_\beta(s) = \int \omega_\beta(\delta) \frac{ds}{\beta c} = \omega_{\beta 0}\left(\frac{s}{\beta c} - \frac{\xi}{\eta}\tau\right) , \tag{3}$$
$$\equiv \omega_{\beta 0} \frac{s}{\beta c} - \omega_\xi \tau$$

where τ is the arrival time difference of the particle at the position s (positive toward the head of bunch), βc is the velocity of the particle, and η is the slippage factor. Thus, the betatron phase advance varies linearly along the bunch and attains its minimum (maximum) at the head (tail) of the bunch.

To investigate how the difference of phase advance between the head and the tail of the bunch varies over one synchrotron oscillation period, we have developed the four particle model in the synchrotron phase space, as illustrated in Fig. 4. We assume that the arrival time is oscillating as

$$\tau = \hat{\tau} \cos(2\pi \nu_s k) \, , \tag{4}$$

where ν_s is the synchrotron oscillation tune and k is the revolution turn. We also assume that the chromaticity is negative and the ring is operated below the transition energy ($\eta < 0$). Thus particles move clockwise in synchrotron phase space.

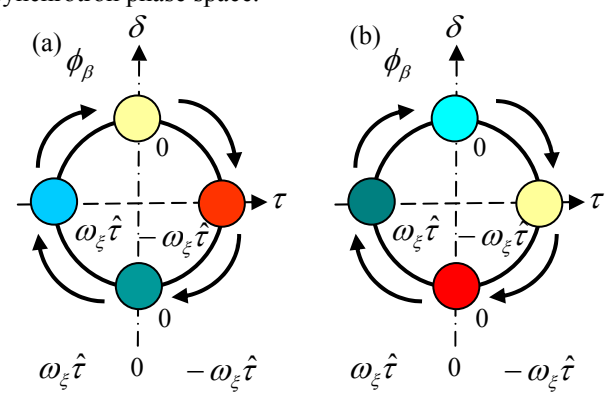


Figure 4: (a) The initial phase advance setting of the four particles. (b)The phase advance after a quarter period of the full synchrotron oscillation.

In principle, the betatron phase advance slows down (quickens up) by $\omega_\xi \hat{\tau}$ for every quarter period of synchrotron oscillation as the particle moves forward

Copyright © 2013 CC-BY-3.0 and by the respective authors

(backward) along the synchrotron orbit, respectively. As can be seen in Fig.4, the initial phase relationship along the bunch is preserved after the quarter period of synchrotron oscillation. One can quickly check that the phase pattern remains stationary over the full period of the synchrotron oscillation. In other words, the difference of the phase advance between the head and the tail of the bunch is constant, and we denote this constant as χ:

$$\chi = \phi_{\beta Tail} - \phi_{\beta Head} = 2\omega_\xi \hat{\tau} = 2\frac{\xi}{\eta}\omega_{\beta 0}\hat{\tau} = \text{constant}. \quad (5)$$

Let us assume that the dipole moment observed at a single point in the ring has the following standing wave pattern:

$$p_m(t) = \begin{cases} \cos(m+1)\pi\dfrac{t}{\tau_L} & m = 0,2,4,... \\ \sin(m+1)\pi\dfrac{t}{\tau_L} & m = 1,3,5,... \end{cases}, \quad (6)$$

where $\tau_L = 2\hat{\tau}$ is the total bunch length. The transverse pick-up signal observed at that point on the k-th revolution turn is given by

$$I_m(t) \propto p_m(t)\exp(i\omega_\xi t + i2\pi k\nu_{\beta 0}), \quad (7)$$

where $\nu_{\beta 0}$ is the betatron tune. The effect of the travelling-wave component $\exp(i\omega_\xi t + i2\pi k\nu_{\beta 0})$ over the standing-wave dipole moment $p_m(t)$ is to shift the bunch spectrum by ω_ξ. Figure 5 shows an example where the transverse resistive-wall impedance and the narrow-band kicker impedance are shown as impedance examples. The spectra are drawn for the head-tail modes 0 and 1 with positive phase difference χ. In this example, the mode 0 is stabilized, while the mode 1 becomes unstable by the transverse resistive-wall impedance at low frequency.

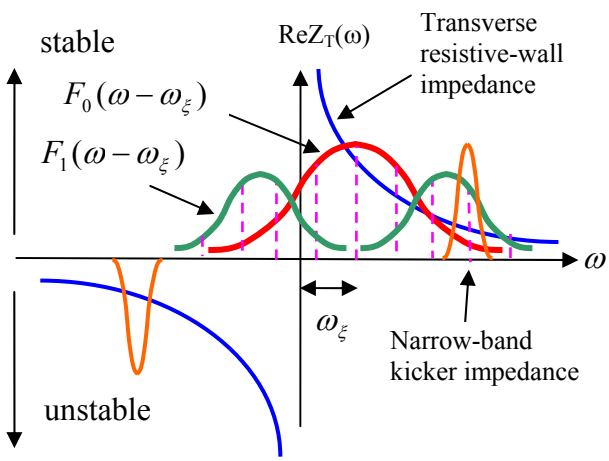


Figure 5: An example of the bunch spectrum shift by non-zero chromaticity.

The shift of the left peak of the bunch spectrum of the mode 1 means that a part of the mode now oscillates slowly. The head and the tail of the bunch will move almost in phase, not out of phase, to synchronize with the low frequency impedance. On the other hand, the shift of the right peak of the mode 1 bunch spectrum implies that this part of the mode now oscillates faster. In summary, the mode m=1 is degenerated at zero chromaticity, but it now splits to slower and faster oscillating parts by non-zero chromaticity. These split modes are equally excited due to the standing-wave condition of head-tail modes, and thus they always have a node at the centre just like the m=1 mode at zero chromaticity.

BEAM SIGNAL MEASUREMENT AT MR

We have made several beam studies to investigate beam oscillation signals from the SPM in more depth. The studies were done with 8 bunches with the beam power of 120-140kW. The typical chromaticity pattern is shown in Fig. 6.

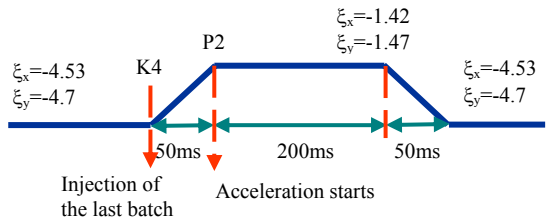


Figure 6: The typical chromaticity pattern.

Vertical Instability at the Onset of Acceleration

The vertical instability at the onset of acceleration (see Fig. 2(a)) is a text book case of the head-tail instability: it starts with a noise with the right phase relationship as shown in Fig.4 and then grows. Let us estimate head-tail modes that could be excited at the onset of acceleration by the MR transverse impedances. The phase difference χ is 4.4 for the chromaticity $\xi = -1.45$, the total bunch length of $\tau_L = 2\hat{\tau} = 150ns$ and the slippage factor of 0.058. That leads to the excitation of the m=0 or m=1 mode by the low frequency transverse resistive-wall impedance. The 10MHz kicker impedance can produce $\chi = 13.8$ and thus the m=3 mode is likely to be excited. Figures 7 show the maximum amplitude of the vertical oscillation when the FB is turned off (left) and is turned on (right), respectively.

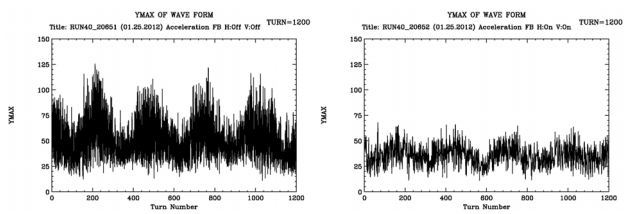


Figure 7: The time evolution of the maximum amplitude of vertical oscillation for the FB off (left) and on (right).

From these figures, the growth time can be estimated as about 1.2ms. The huge damping effect by the FB is recognizable in the right figure of Fig. 7. Figure 8 shows the vertical oscillation signals superimposed on 10 consecutive turns (when FB is tuned off). No node is visible, suggesting that the vertical oscillation is just a

Copyright © 2013 CC-BY-3.0 and by the respective authors

dipole mode. The BBU approach for the growth time estimate delivers the growth time of 1.5ms, in a reasonable agreement with the measurement of 1.2ms [4].

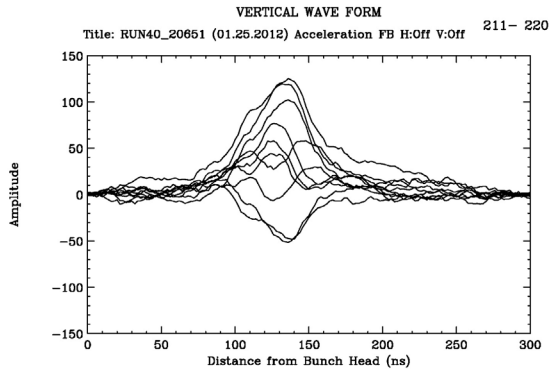


Figure 8: The vertical oscillation signals superimposed on 10 consecutive turns when FB is turned off.

Horizontal Instability at the Injection

The horizontal instabilities during the injection evolve from very different initial conditions compared to conventional head-tail instabilities. They start, not from noise, but from a large transverse displacement due to injection errors or ones by kicks by the mismatching field of the kicker magnets. There is no betatron phase difference along the bunch at the moment of the injection or the kicks by the mismatching field. Nevertheless, if we still apply the Sacherer's text book analysis to this case, the head count of head-tail modes that could be excited at 140kW is the m=3 mode by the low frequency resistive-wall impedance and the m=6 mode by the 10MHz kicker impedance. Figures 9 show the time evolution of the maximum amplitude of horizontal oscillation of the first bunch at the injection of the last batch when the FB is turned off (left) and on (right), respectively. Figures 10 show the measured horizontal oscillations of the same bunch for the FB on (left) and FB off (right) at the 1st (top), 250-th (middle) and 501-th (bottom) turns, respectively.

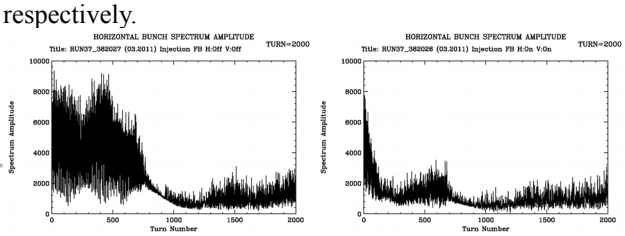


Figure 9: The time evolution of the maximum amplitude of horizontal oscillation of the first bunch at the injection of the last batch (K4) for the FB off (left) and on (right), respectively.

One can see that main growing mode with the FB off is the dipole mode and it is very quickly and effectively damped by the FB system. However, complex intra-bunch oscillations occasionally emerge and fade out. It looks like that a lower-order head-tail mode appears first and then it is transmuted into higher-order modes (m=6 or 7), and then transmuted back to the lower-order mode again after one full synchrotron oscillation period (~500 turns).

No large particle loss has been observed associated with these intra-bunch oscillations at present. However, if they are indeed head-tail modes excited by the 10MHz kicker impedance, it is likely that they will impose a significant limit on the beam power in future, since the present narrow-band FB system is ineffective to damp such intra-bunch oscillations. To defuse such possibility, first we started to develop a broadband intra-bunch feedback system based on the iGp12 module [5]. At the same time, we made more in-depth investigation of the measured intra-bunch oscillations to find their true identity.

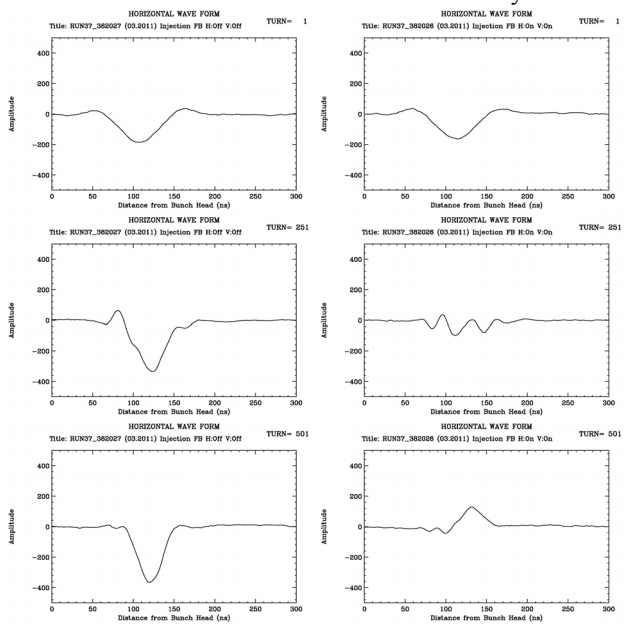


Figure 10: The measured horizontal oscillations of the first bunch at the injection of the last batch (K4) for the FB off (left) and FB on (right) at the 1st (top), 250-th (middle) and 501-th (bottom) turns, respectively.

The iGp12 digital signal processing module is widely used in electron rings. It is operated at the rate of RF frequency times 64 and replaces the present narrowband digital module shown in Fig. 1, which is operating at just the RF frequency. It divides each RF bucket into 64 segments (bins) and acts on each bin as if it is a small bunch (bunch-let) in a narrowband mode.

Let us take a closer look at the horizontal oscillations signals to see if they are forming envelops, one of signatures of head-tail modes. Figures 11 show the horizontal oscillation signals superimposed on 10 consecutive turns starting from 251-th turn. No clear node is visible in the both cases with and without active FB.

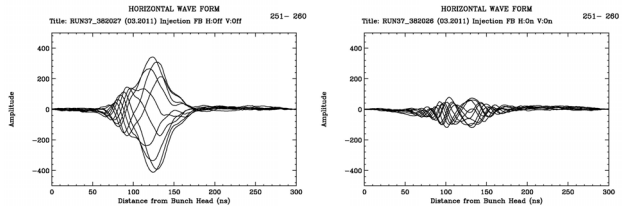


Figure 11: The horizontal oscillation signals superimposed on 10 consecutive turns starting 251-th turn for the FB off (left) and the FB on (right), respectively.

Copyright © 2013 CC-BY-3.0 and by the respective authors

One possible explanation is that the kicker 10MHz impedance is not strong enough to sustain higher-order head-tail modes alive for long period of time. Another possible explanation is that the simple application of Sacherer' text book analysis is inadequate in the present case.

Let us re-investigate how the betatron phase difference between the head and the tail of a bunch evolves over a full synchrotron oscillation period using the four particle model again (see Fig. 12). All the particles have the same betatron phase at the beginning. At every a quarter period of the full synchrotron oscillation, the phase difference between the head and the tail increases by $2\omega_\xi\hat{\tau}$ till the half of the synchrotron oscillation. Then, the phase difference starts to decrease and come back to zero at the full synchrotron oscillation (namely, the picture next to (d) comes back to (a)). More detailed analysis shows that the phase difference oscillates like

$$\chi = \phi_{\beta Tail} = \phi_{\beta Head} = \frac{\xi}{\eta}\omega_{\beta 0}\tau_L \cdot (1-\cos(2\pi\nu_s k)). \qquad (8)$$

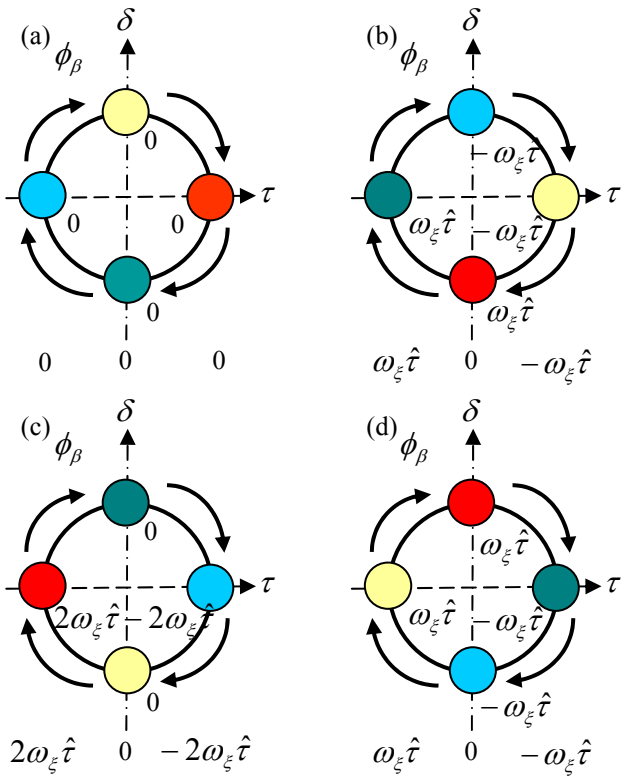


Figure 12: (a) The initial zero phase difference. (b-d) Change in phase advance after every quarter period of the full synchrotron oscillation. After (d), the phase difference comes back to (a).

Let us see how a simple dipole mode changes its oscillation appearance when the phase difference between the head and the tail oscillates as specified in Eq. (8). Figures 13 show the simulated horizontal oscillations and their superposition on 10 consecutive turns at the 1st (top), 251-th (middle) and 501-th (bottom) turns, respectively. They are strikingly similar to the right figures of Figs. 10 and Figs. 11. We also analysed the frequency spectra of the horizontal oscillation signals and found that the low frequency signal (lower than ~5MHz) is dominant and there is no clear peak at higher frequency. These results demonstrate that a simple dipole mode can create a temporal deceptive appearance of higher-order head-tail modes, when the betatron phase difference between the head and the tail of the bunch is oscillating as in Eq. (8).

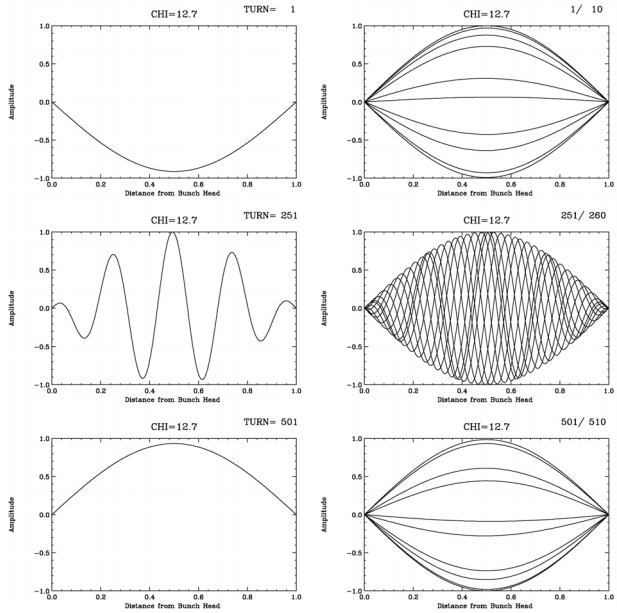


Figure 13: The simulated horizontal oscillations and their superposition on 10 consecutive turns at the 1st (top), 251-th (middle) and 501-th (bottom) turns, respectively.

SUMMARY

The present (narrowband) bunch-by-bunch feedback system is found to be quite effective to suppress transverse beam instabilities at MR, allowing the beam power to reach 230kW with only particle losses of 400W. The initial analysis of the horizontal instabilities during the injection raised concern over the excitation of higher-order head-tail modes. However, the detailed analysis revealed that a simple dipole oscillation can be deceived as higher-order head-tail modes, when a bunch starts to oscillate from a large transverse displacement. The new broadband intra-bunch feedback system is under testing.

REFERENCES

[1] Y.H. Chin et al., "Impedance and Beam Instability Issues at J-PARC Rings", HB2008, Nashville, August 2008, WGA01, p.40 (2008).
[2] A. Burov and V. Levedev., "Transverse Resistive-Wall Impedance for Multi-Layer Round Chambers," EPAC'02, Paris, June 2002, p. 1452 (2002).
[3] F.J Sacherer, "Transverse Bunched Beam Instabilities", CERN/PS/BR76-21 (1976).
[4] Y. Shobuda, private communications.
[5] O. A. Konstantinova, et al., "Bunch by Bunch Intra-Bunch Feedback System for Curing Transverse Beam Instabilities at the J-PARC MR", IPAC13, Shanghai, May 2013, TUPWA009, p.1739 (2013).

Copyright © 2013 CC-BY-3.0 and by the respective authors

TRANSVERSE IMPEDANCE AND TRANSVERSE INSTABILITIES IN THE FERMILAB BOOSTER*

A. Macridin, J. Amundson, P. Spentzouris, V. Lebedev, T. Zolkin Fermilab, Batavia, IL 60510, USA

Abstract

The Fermilab Booster is characterized by large space charge and large wake fields, leading to beam loss and instabilities at high intensity. Using the Synergia simulation package with a realistic lattice model and realistic wake functions we investigate the coherent tune shift and the instabilities at injection energy. We calculate the wake functions in the laminated magnets and find them to be four orders of magnitude larger than the wakes in the metallic straight sections. We find a large decrease of the vertical tune shift and a small increase of the horizontal tune shift with intensity, in good agreement with experiment. In agreement with measurements, we find that a large chromaticity is required to avoid a horizontal instability. The instability is caused by short-range bunch-bunch interaction and is due to the large coupling between the horizontal wake function and large lattice beta function at the locations of the focusing magnets.

INTRODUCTION

The Fermilab Booster [1] is a 40-year-old machine which provides protons for the Fermilab Main Injector. It runs at an intensity of 4.5×10^{12} protons per batch, which is about two times larger than the originally designed intensity. The machine shows beam loss and instabilities at high intensity. For machine improvements required by the demand of future Fermilab programs for high intensity beams, it is essential to have a good understanding of these instabilities.

The particular thing about the Booster is the presence of the dipole-quadrupole combined-function focusing (F) and defocusing (D) magnets, which cover about 60% of the machine length. The rest of the machine is made by straight metallic beam pipe sections. Since there is no beam pipe in the combined-functions magnets, the beam is exposed directly to the magnets' laminations. A consequence of the presence of bare laminations is the formation of very large wake fields. Since the machine runs at low energy (injection E/final $E = 0.4GeV/8GeV$), the space charge is also strong. The presence of both large wakes and space charge effects together with complex single-particle optics makes any attempt of analytical treatment very difficult.

*This work was performed at Fermilab, operated by Fermi Research Alliance, LLC under Contract No. De-AC02-07CH11359 with the United States Department of Energy. It was also supported by the ComPASS project, funded through the Scientific Discovery through Advanced Computing program in the DOE Office of High Energy Physics. We also used resources of the Argonne Leadership Computing Facility at Argonne National Laboratory, which is supported by the Office of Science of the U.S. Department of Energy under contract DE-AC02-06CH11357.

We address these effects by using Synergia [2], a state of the art simulation package developed at Fermilab. We perform single- and multibunch simulations at the injection energy. Since the RF sets the number of buckets in the Booster to 84, a full machine simulations requires simulations with 84 bunches.

In order to properly take into account the wake fields, we calculate the wake functions in the laminated magnets. We find that the wake functions in the laminated magnets have a non-metallic behavior and are four orders of magnitude larger than the wakes in the metallic pipe section.

The measurements of the coherent tune shift show a large negative shift for the vertical tune and a small positive shift for the horizontal tune [3, 4]. Close to injection, the beam is horizontally unstable unless the machine runs with a large horizontal chromaticity [5]. The result of our simulations are in good agreement with experiment. We find that the instability is due to short range bunch-bunch interactions. The instability is caused by the large value of the coupling between the lattice horizontal beta function and the horizontal wake at the location of the F magnets.

SYNERGIA CODE

Synergia [2] is a simulation package for beam dynamics in accelerators developed at Fermilab. It can address single-particle optics by using direct symplectic integration through the lattice elements or/and by using arbitrary-order polynomial maps. Collective effects are incorporated by employing the split-operator method [6]. A variety of space-charge solvers (such as 3D Poisson solvers with different boundary conditions, 2.5D solversand semi-analytical 2D solvers) can be used with Synergia. Synergia can accommodate arbitrary wake functions by reading them from external files.

In our Booster simulations, in order to account for the large nonlinear lattice effects, we used direct symplectic integration for particle propagation. Space charge was addressed by using three different 3D Poisson solvers with appropriate boundary conditions for the F magnets, D magnets and straight sections, respectively. We used different wake functions for the F and the D magnets. The wake functions for the laminated magnets were calculated separately, as is described in the next section.

WAKE AND IMPEDANCE

The electromagnetic field created by a particle moving through the accelerator induces currents in the vacuum chamber walls. The field created by these currents will affect a trailing particle. This effect can be addressed by a

Copyright © 2013 CC-BY-3.0 and by the respective authors

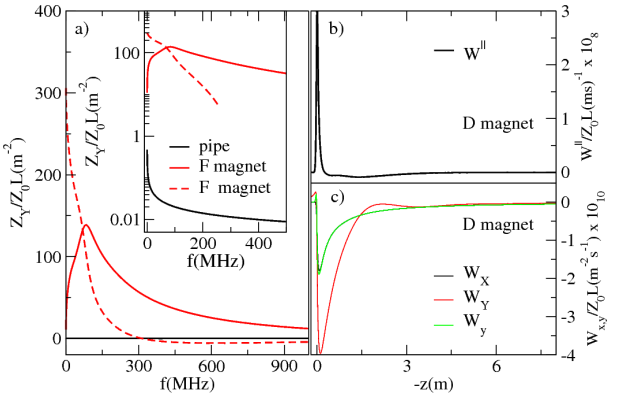


Figure 1: a) The vertical impedance caused by the source displacement in the F magnet ($ReZ_Y(\omega)$ -solid line, $Im(Z_Y(\omega)$ -dashed line) and in the pipe section. (See inset for the plot using a logarithmic scale). The impedance in the laminated magnets is four orders of magnitude larger than in the pipe. b) Longitudinal wake in the D magnet. c) Transverse horizontal and vertical wakes in the D magnet. The vertical wake caused by the source displacement (red) is about two times larger than the corresponding horizontal one (black). Due to nonultrarelativistic effects, the wakes are nonzero up to a small distance ($\approx 0.1m$) in front of the source particle.

simple formalism [7],

$$\beta c \Delta p_z = -qQW^{||}(z) \quad (1)$$

$$\beta c \Delta p_x = -qQ\left(W_X(z)X + W_x(z)x\right) \quad (2)$$

$$\beta c \Delta p_y = -qQ\left(W_Y(z)Y + W_y(z)y\right). \quad (3)$$

Here Q, X, Y (q, x, y) represent the charge and horizontal and vertical displacements of the source (witness) particle. The momentum of a witness particle going through a lattice element is kicked with a term proportional to a wake function which depends only on the distance, z, between the source and the witness particle. Only the terms up to the first order in the particles displacements are considered. Note that for highly symmetric chambers, such as circular or rectangular, and in the ultrarelativistic limit, the terms proportional to the witness particle displacement are zero. For a flat chamber like the one we use to model the Booster magnets, $W_X = -W_x$ due to the horizontal translational symmetry.

For a realistic simulation it is important to have an accurate estimate of the wake functions. Calculation of the wakes requires solving the electromagnetic problem for the vacuum chamber. This is usually done in the frequency domain. The impedance, which is related to the wake function via a Fourier transform is proportional to the force acting on the witness particle. The solution is dependent on the chamber geometry and on the boundary conditions for the electromagnetic field at the vacuum chamber walls.

Due to the exposure of the laminations, the impedance and wakes are orders of magnitude larger in the combined-function magnets than in the metallic pipes. The ultrarelativistic impedance calculation in the laminated structures is presented in [8], while the nonultrarelativistic effects for flat chambers are addressed in [9]. In Fig. 1 a) we show the vertical impedance Z_Y in the F magnet and compare it with the straight section vertical impedance. While the straight section impedance shows the conventional (i.e. metallic) $\omega^{-0.5}$ behavior in the frequency domain of interest, the real part of the F magnet impedance shows a broad peak around $80MHz$ and is four orders of magnitude larger. In Fig. 1 b) and c) we show the longitudinal and transverse wakes in the D magnet. The vertical wake W_Y is about two times larger the corresponding horizontal wake, W_X, while the vertical wake caused by the witness particle displacement W_y is close to the corresponding horizontal wake W_x. (They are equal in the ultrarelativistic limit). Note that due to the nonultrarelativistic effects, the wakes are nonzero up to a small distance ($\approx 0.1m$) in front of the source particle.

SIMULATION RESULTS

To ensure agreement between the lattice model and the real lattice the parameters of the dipole and quadrupole correctors were determined using Orbit Response Measurement fitting [10]. We performed single- and multi-bunch simulations up to 2000 turns at the injection energy $(0.4GeV)$.

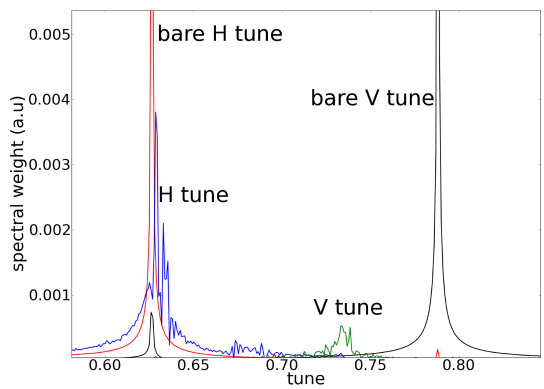


Figure 2: Fourier transform of the beam centroid horizontal and vertical displacements at intensity 4×10^{10} p per bunch for the full machine (84 bunches). When the collective effects are neglected (red and black), the spectral weight exhibits sharp peaks for frequencies corresponding to the bare tunes. The spectral weight shows small positive horizontal (blue) and large negative vertical (green) tune shifts when the collective effects are present. Note the wide spectral features when the collective effects are included.

The coherent tune was determined by Fourier transforming the beam centroid displacement as a function of the trajectory length. The spectral analysis is shown in Fig. 2. When no collective effects are included, the spectrum shows sharp peaks at frequencies corresponding to

Copyright © 2013 CC-BY-3.0 and by the respective authors

the bare tunes. With the collective effects taken into account, the spectral weight shows small positive horizontal and large negative vertical tune shifts. Aside from that, the spectral features are broad, indicating the evidence of an interaction between multiple modes.

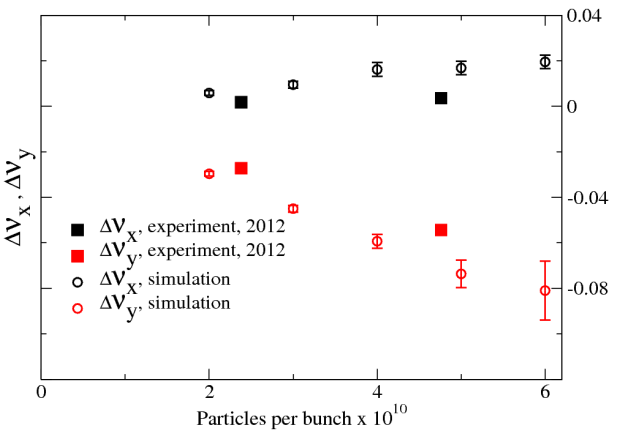


Figure 3: Comparison of the calculated coherent tune shifts for a full machine at injection with measurements. The simulation shows a slightly larger tune shift.

A comparison of the simulated coherent tune shift at injection with measurements [4] is shown in Fig. 3. As in the experiment, the simulations show a large decrease of the vertical tune and a small increase of the horizontal tune with increasing intensity. Our simulation shows a slightly larger tune shift ($\approx 10\%-15\%$) than the experiment. However, note the large error bar of the simulated tune shift which increases with increasing the intensity. The error bar is a consequence of the difficulty to uniquely determine the tune for a wide spectral feature.

Single-bunch simulations (not shown) suggest that, regarding beam loss, it is most favorable to have small values of chromaticity, $\frac{\omega_{\xi x}}{\beta c}, \frac{\omega_{\xi y}}{\beta c} \leq 2\pi \times 0.023 m^{-1}$. An increase of chromaticity results in an increase of the bunch transverse spatial dimensions. More particles hit the vacuum chamber walls and the beam loss is larger.

However, full machine (i.e. 84 bunch) simulations find that the beam is horizontally unstable for small horizontal chromaticity. The beam centroid horizontal displacement versus the turn number is shown in Fig.4 for different values of the horizontal chromaticity. This behavior is in very good agreement with the experiment [5]. In order to stabilize the beam, a large horizontal chromaticity, $\frac{\omega_{\xi x}}{\beta c} = 2\pi \times 0.091 m^{-1}$ [11] (which corresponds to $\xi_x = -19$ in Ref. [5]), should be chosen.

Simulations with a smaller number of bunches, occupying subsequent buckets also exhibit horizontal instability. In Fig. 5 the horizontal centroid displacement for different bunches in a 14-bunch train is shown. The instability is more pronounced for the bunches traveling at the end of the train. This result indicates that the instability is caused by short-range bunch-bunch interaction rather than by coupling to a resonant mode.

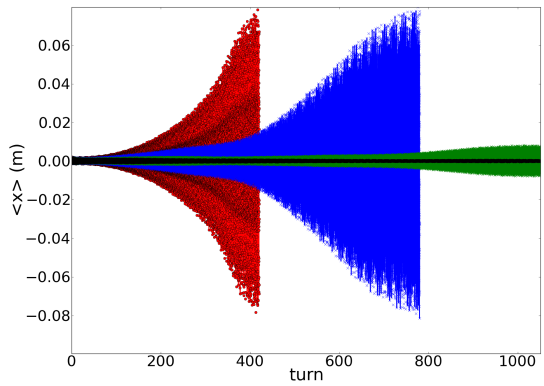


Figure 4: Full machine simulation. Beam centroid horizontal displacement at BPMs location versus turn number for different horizontal chromaticities, $\frac{\omega_{\xi x}}{\beta c} = 2\pi \times 0.023 m^{-1}$ (red), $\frac{\omega_{\xi x}}{\beta c} = 2\pi \times 0.046 m^{-1}$ (blue), $\frac{\omega_{\xi x}}{\beta c} = 2\pi \times 0.069 m^{-1}$ (green) and $\frac{\omega_{\xi x}}{\beta c} = 2\pi \times 0.091 m^{-1}$ (black). The vertical chromaticity is kept constant, $\frac{\omega_{\xi y}}{\beta c} = 2\pi \times 0.023 m^{-1}$. The intensity is 5×10^{10} p per bunch (i.e. 4.2×10^{12} p per batch). The beam shows horizontal instability unless a large horizontal chromaticity is considered, similar to the experiment [5]. In our units, the chromaticity is $\frac{\omega_{\xi x}}{\beta c} = 2\pi \times 0.091 m^{-1}$, which stabilizes the beam, corresponding to $\xi_x = -19$ in Ref. [5].

In order to understand the contribution of the different wake terms to the instability we performed simulations with modified wakes. First, we turned direct space charge [12] off in our simulations. The instability is still present, but the growth rate is smaller. Next, we ran simulations with the wake function terms (see Eqs. 1, 2, 3) modified. The instability growth rate is influenced very little by the multiplication of the longitudinal wake, $W^{||}$, or of the transverse wakes caused by the displacement of the witness particle, W_x and W_y, with a factor of two or by neglecting them (not shown). We also find that the vertical wake W_Y caused by the source displacement, has little contribution to the instability. This can be seen from Fig. 6, where the number of particles and centroid horizontal displacement are shown for both the original wakes and for enhanced W_Y. Nevertheless, we find that the instability is very sensitive to the horizontal wake W_X, as illustrated in Fig. 6. An increase of W_X by a factor of 1.5 strongly enhances the instability.

Considering that the vertical wake in the laminated magnets is about two times larger than the horizontal wake (remember Fig. 1 -c), it might seem counter intuitive that the system is prone to horizontal instability and not to vertical instability. However, note that the momentum kick is proportional to the wake coupled to the displacement. In a rough approximation, the instability growth rate should be proportional to the average over the machine length of the lattice beta function multiplied by the wake. Taking into

Copyright © 2013 CC-BY-3.0 and by the respective authors

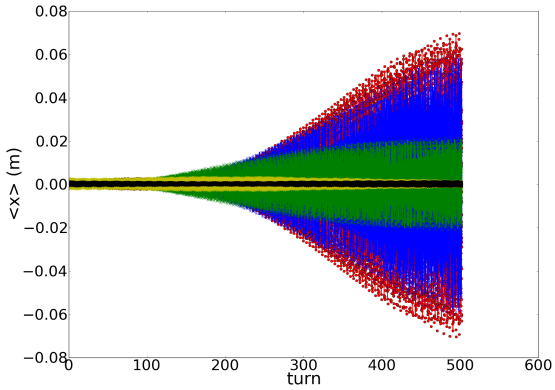


Figure 5: 14 bunch simulation with subsequent buckets occupied. $\frac{\omega_{\xi x}}{\beta c}, \frac{\omega_{\xi y}}{\beta c} = 2\pi \times 0.023 m^{-1}$. The intensity is 5×10^{10} p per bunch. The bunch centroid horizontal displacements versus turn number. $14^{\mathtt{th}}$ (red, the last bunch), $13^{\mathtt{th}}$ (blue), $9^{\mathtt{th}}$ (green), $4^{\mathtt{th}}$ (yellow), $1^{\mathtt{st}}$ (black, the leading bunch). The motion of the trailing bunches is unstable. The instability is caused by short-range bunch-bunch interaction rather than by a coupling to a resonant element.

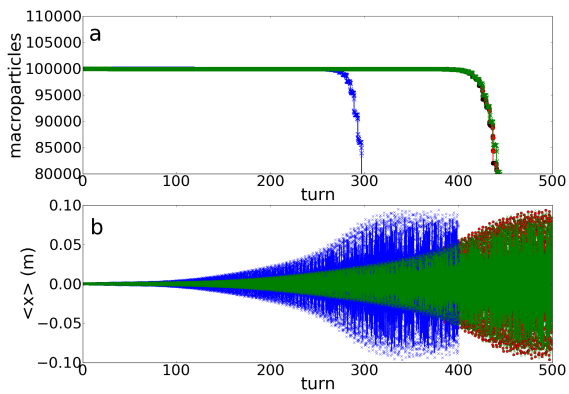


Figure 6: The number of macroparticles a) and beam centroid horizontal displacement b) versus turn number for different values of the wake functions. $\frac{\omega_{\xi x}}{\beta c}, \frac{\omega_{\xi y}}{\beta c} = 2\pi \times 0.023 m^{-1}$. The intensity is 5×10^{10} p per bunch. The direct space charge [12] is turned off. The instability is present for unmodified wakes (the ones corresponding to the real machine, red) and is very little affected by the increase of the vertical wake. (W_Y increased two times shown with green). However it is strongly enhanced by the increase of the horizontal wake caused by the source particle. (W_X increased 1.5 times shown with blue).

account that the average horizontal beta over the F magnets length is about 3.5 times larger than the corresponding average vertical beta ($< \beta_x >_F = 27.75$, $< \beta_y >_F = 8.15$), while the averages over the D magnets are of similar magnitude ($< \beta_x >_D = 12.78$, $< \beta_y >_D = 16.78$), one can conclude that the instability is caused by the large horizontal beta wake coupling at the location of the F magnets.

CONCLUSIONS

Experimental measurements show the presence of large wake fields and horizontal beam instability in the Fermilab Booster. We calculate the wakes in the laminated magnets and find them to be four order of magnitude larger than in the metallic straight section. Using Synergia we ran single- and multibunch simulations with a realistic lattice model, space charge and wake fields. The simulated coherent tune shift and the instability behavior are in good agreement with experiment. We find that the horizontal instability is caused by short-range bunch-bunch interaction rather than by a coupling to a resonant element. The instability is due to the large coupling between the horizontal wake and the horizontal lattice beta function at the location of the F magnets.

ACKNOWLEDGMENT

We want to thank M. McAteer, Y. Alexahin and W. Pellico for their contribution to this work.

REFERENCES

[1] Booster Rookie Book, Fermilab, http://www-bdnew.fnal.gov/operations/rookie_books/rbooks.html

[2] Synergia simulation package, https://cdcvs.fnal.gov/redmine/projects/synergia2

[3] D. McCarron, "Measurement and simulations of intensity-dependent effects in the Fermilab Booster Synchrotron" PhD Thesis, FERMILAB-THESIS-2010-50, (2010).

[4] Y. Alexahin, private communication.

[5] Y. Alexahin et al., "Observation of Instabilities of Coherent Transverse Oscillations in the Fermilab Booster", FERMILAB-CONF-12-219-AD-APC, IPAC-2012-WEPPR085.

[6] H. Yoshida, "Construction of high order symplectic integrators", Phys. Let. A, vol. 150, No. 57, pp. 262-268, (1990).

[7] A. Chao, "Physics of Collective Beam Instabilities in High Energy Accelerators", Jhon Wiley & Sons, NY, (1993).

[8] A. Macridin et al, "Coupling impedance and wake functions for laminated structures with an application to the Fermilab Booster", Phys. Rev. ST Accel. Beams 14, 061003 (2011).

[9] A. Macridin et al, "Nonperturbative algorithm for the resistive wall impedance of general cross-section beam pipes", FERMILAB-PUB-13-390-CD.

[10] Meghan McAteer, private communication.

[11] We define the chromaticity as $\omega_\xi = \omega_0 \frac{\xi}{\eta}$, where ω_0 is the revolution angular frequency, $\eta = \frac{p \delta \nu}{\delta p}$ and η is the slippage factor.

[12] By direct space-charge we mean the effect of the electromagnetic field created in a perfect conductor beam pipe. It is the result of the space-charge 3D Poisson solver with closed boundary conditions. The remaining effects of the electromagnetic field are included in the wake functions.

Copyright © 2013 CC-BY-3.0 and by the respective authors

THE JLAB 12 GEV ENERGY UPGRADE OF CEBAF *

Leigh Harwood (for the JLab 12 GeV project team)
Thomas Jefferson National Accelerator Facility, Newport News, VA 23606 USA

Abstract

CEBAF at Jefferson Lab was a 5-pass, recirculating cw electron linac operating at ~6 GeV and devoted to basic research in nuclear physics. The 12 GeV Upgrade is a major project, sponsored by the DOE Office of Nuclear Physics, that is expanding its research capabilities substantially by doubling the maximum energy and adding major new experimental apparatus. The Upgrade is illustrated in Figure 1 includes: doubling the accelerating voltages of the linacs by adding 10 new high-performance cryomodules; the requisite expansion of the 2K cryogenics plant and rf power systems to support these cryomodules; upgrading the beam transport system from 6 to 12 GeV through extensive re-use and/or modification of existing hardware; and the addition of one recirculation arc, a new experimental area, and the beamline to it; and the construction of major new experimental equipment for the GPD, high-xBjorken, and hybrid meson programs. The accelerator upgrade is essentially complete and the construction of the new experimental apparatus is well underway. This paper provides some details about the accelerator upgrade.

OVERVIEW

Scientific Motivation

In the 20+ years since the original design parameters of CEBAF were defined the understanding of the behavior of strongly interacting matter has evolved significantly, and important new classes of experimental questions have been identified that can be addressed optimally by a CEBAF-type accelerator at higher energy. The original design of the facility, coupled with developments in superconducting RF technology, makes it feasible to triple the initial design value of CEBAF's beam energy to 12 GeV in a cost-effective manner, providing a new research tool capable of addressing the science.

The science motivating the 12 GeV Upgrade includes breakthrough programs that will be launched in four main areas (they are described in detail in [1]):

- Discovering the quark structure of nuclei
- Probe potential new physics through high precision tests of the Standard Model using precision, parity-violating electron scattering experiments.

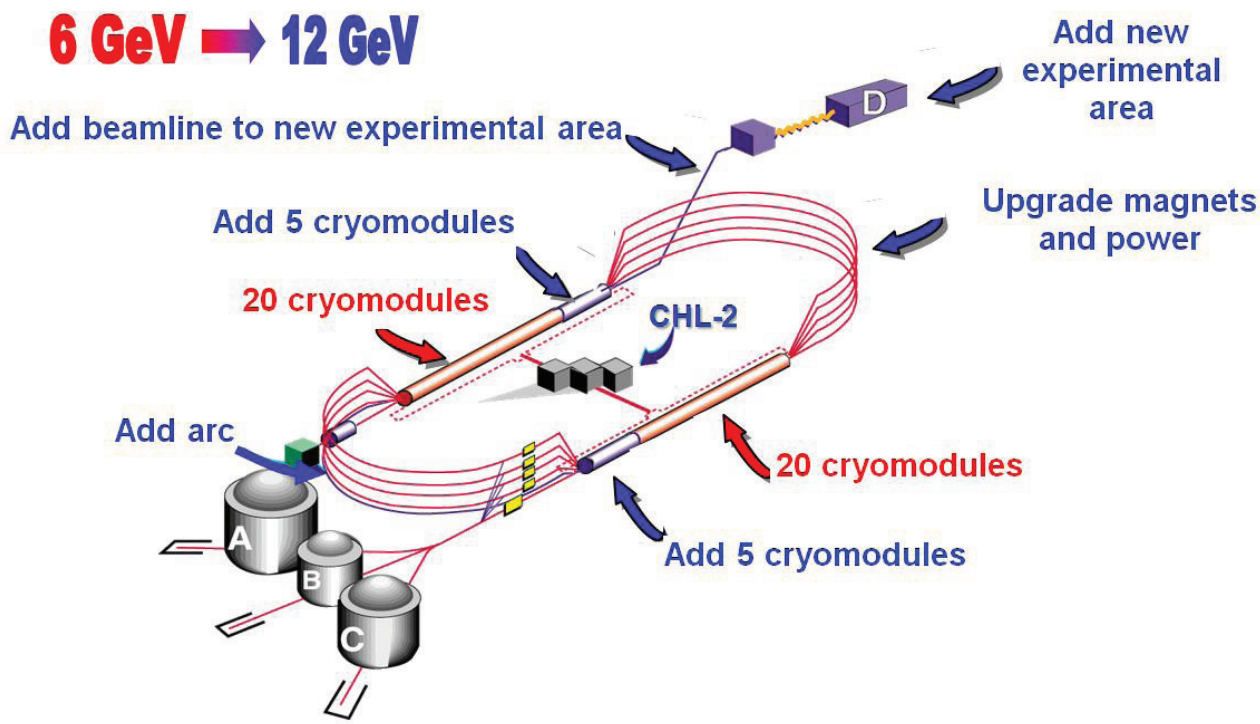


Figure 1: Changes to CEBAF.

* This work was supported by the U.S. Department of Energy Contract Number DE-AC05-06OR23177 under which Jefferson Science Associates, LLC operates Jefferson Lab

Copyright © 2013 CC-BY-3.0 and by the respective authors

- Explore the physical origins of quark confinement (GlueX experiment): A potential explanation, supported by lattice QCD calculations, is that quark confinement stems from the formation of a string-like "flux tube" between quarks. This conclusion (and proposed mechanisms of flux tube formation) can be tested by determining the spectrum of the gluonic excitations of mesons (referred to as "hybrid" mesons)

Base Requirements

The exotic meson spectroscopy program needs 9 GeV polarized photons for optimal production of the hybrid mesons and distinguishing them from the other meson excited states. Coherent bremsstrahlung, obtained by passing a high quality, cw beam of 12 GeV electrons through a crystal radiator, is the ideal source of these photons. Similar electron beam energies are nearly ideal for the other research programs outlined above.

CEBAF, which had originally been built to operate at 4 GeV, had been incrementally upgraded to 6GeV. Thus, to reach 12 GeV a net of 6 GV of acceleration had to be added. A new experimental area (for the hybrid meson program) has been added on the opposite end of the accelerator from three existing end stations, so the beam reaching it will transit one linac once more than beams for the existing end stations

12 GeV could have been achieved by increasing the linac capabilities or increasing the number of passes. An analysis determined that it would be more cost effective to increase the linac capabilities than to reconfigure (rebuild) the beam transport system for additional passes. Therefore, the 0.6 GV linacs have been upgraded to 1.1 GV. The hybrid meson studies need < 5 μA; the other programs need much larger beam currents. The original beam power limit of 1 MW has been retained.

The original beam transport system supported 5 pass beam at 6 GeV to the existing end stations. It has been modified to deliver 11 GeV beam to those halls and beam transport must be added to deliver the full 12 GeV beam to the photon radiator target for the new end station, including an additional recirculation arc.

BEAM PHYSICS

Beam Breakup

Beam breakup (BBU) driven by high-order modes (HOM) in the cavities must always be addressed when using srf cavities even if the beam current in the cavities, < 1 mA in this case, is not exceptional on the scale of storage rings. As was done for 4 GeV CEBAF, a BBU analysis was done [2] to set limits on the Q's of the HOM's. An impedance budget of $(R/Q)Qk < 2.4x10^{10}\ \Omega/m$ for transverse HOM's and $(R/Q)Q < 6.5x10^{11}$ for longitudinal modes came out of the study. The simulated cavities did not always meet those budgets when evaluated as single cavities because of longitudinal mode asymmetries and the presence of HOM dampers on only one end of the cavity. However, when evaluated as an assembled string, the fundamental power coupler on the adjacent cavity coupled out the asymmetric modes. The cavities on the ends of the cryomodule do not have that benefit so dampers were added in the waveguides for those cavities.

Emittance, Energy Spread, and Halo

Emittance growth from synchrotron radiation of the electrons in dispersive sections of the beam transport was not a limitation to meeting the 1 nm-rad specification for CEBAF at 4 GeV. For the Upgrade, cost containment drove a desire to forego extensive modifications to the existing optics. A so-called "double-bend achromat" lattice was adopted [3] for the higher-energy passes as it reduced the emittance growth relative to the original lattice without requiring reconfiguration of the beamline components. The resulting beam characteristics are summarized in Table 1. These values are consistent with the needs of the proposed research programs. Tracking calculations which included errors (misalignment, mispowering, field nonlinearities, etc) were carried out [4]. With all errors included in the model, the study found that the emittance and energy spread specifications will be met with some margin.

The hybrid meson experiment needs a very low beam halo to prevent unacceptable backgrounds. Particle-tracking calculations with multiple seeds for misalignment, mis-steering, field nonlinearities, and mispowering have shown [5] that the halo requirement for commissioning and early years of operation will be met.

Table 1: Beam Properties at 6 and 12 GeV

	6 GeV	12 GeV
Transverse emittance at Halls A, B, & C	$\varepsilon_x=\varepsilon_y=$ 1 nm-rad	ε_x=7 nm-rad ε_y=1 nm-rad
Transverse emittance at Hall D	NA	ε_x=10 nm-rad ε_y=2 nm-rad
δE/E at Halls A, B, & C	0.01%	0.02%

ACCELERATION

SRF

The additional 0.5 GV/linac is achieved by having added five new 100 MV cryomodules to each linac. Each cryomodule has eight 7-cell cavities. While only 17.5 MV/m is required for the cryomodule to reach 100 MV, the goal was set at 19.2 MV/m (on average for the ensemble in a linac) to deal with the likelihood (based on our operations experience with CEBAF) that some cavities might be off-line. The existing linacs could operate at the 5 pass equivalent of 5.6 GeV if none of the margin is needed for off-nominal conditions in the cryomodules.

Typically, the performance specification for cavities is stated as a Q0 at a particular gradient. We chose to keep with the parameters determined by the overall system. For 12 GeV we used a dynamic heat requirement rather

Copyright © 2013 CC-BY-3.0 and by the respective authors

than a Q0. After taking into account the load from the waveguides, the heat budget for dynamic load of each cavity was 29 W.

The cavity and cryomodule designs have undergone some evolution since the start of the design process. There had been a number of challenges that needed to be addressed during that evolution:

- RF windows: One of the developmental cryomodules used a single RF window on each cavity. It had some unexplained window failures. Those failures led to contamination of the cryomodule and seriously reduced performance. The incremental cost savings of using a single window did not offset the long term risk, so we returned to using both primary and secondary rf windows between the cavity and the external waveguide. All ten of the new cryomodules use the double-window configuration.
- Tuner: A new, less-expensive "rock crusher" tuner concept was developed for another of the developmental cryomodules. During testing some problems were experienced with the mechanical robustness of the tuner. Subsequent to that, SNS had some problems with their cryogenic motors. The original scissor-jack design was reworked for cost reduction. That design improved reliability with little cost impact, so it was used for all of the new cryomodules. It has the additional advantage that the motor and piezo-electric element are at room temperature, thus simplifying any required maintenance.
- Microphonics: During testing of the initial new cryomodules it was found that the cavity-tuner assembly was less stiff than those in previous JLab cryomodules with the result that their sensitivity to mechanical vibrations was much higher than had been seen in any of JLab's previous designs. It was determined that a number of factors (cell shape, lack of inter-cell stiffening rings, lack of bellows between the cavities, and a tuner-to-cavity interface that wasn't very stiff) were contributing factors. Finite element analysis indicated that a significant improvement in the overall stiffness could be achieved by a redesign of some of the tuner cavity interface components. That new design was implemented on the fourth cryomodule to be completed. The seven cryomodules with that change have ~2x lower microphonics than the three that were completed prior to the change.

All ten new cryomodules have been fabricated, tested, and installed. Nine have re-tested after installation. The performance goals have been met. The tenth cryomodule will be tested in October. A summary of the achieved voltages is given in Table 2.. Additional information can be found in the paper by John Hogan at this conference [6]

Table 2: Cryomodule Performance

Cryomodule	In-tunnel performance
#1	104 MV
#2	110 MV
#3	118 MV
#4	105 MV
#5	109 MV
#6	108 MV
#7	108 MV
#8	Testing in progress
#9	108 MV
#10	109 MV

RF

Each cavity is energized by its own klystron. In a 2001 overall system design initiative, the required saturated output power for the klystrons was based on the following criteria: 1) ≤450 μA of beam transiting the cavity (limited by 1 MW total beam power limit), 2) Qext is off-optimum by ≤30%, 3) maximum detuning ≤25 Hz of (4 Hz is 2x the tuner resolution and 21 Hz was 6σ of the measured microphonics spectrum on the original cavities), 4) some cavities would be able to operate at 21 MV/m (10% above the mean of the population but within the range that had been seen in early testing of prototype cavities) and stay within the cryogenic budget, 5) losses in the waveguides, and 6) add 10% so that the klystron would still have gain. The result of the calculation was 12.8 kW per cavity. In 2006 a study was performed to determine the cost-effectiveness of powering mutiple cavities with a single klystron. It was found that cost reduction was possible but only at the expense of failing to meet the phase and amplitude control goals. This option was not adopted and 12 GeV Upgrade uses one klystron per cavity. [7] Eighty 13 kW klystrons have been installed (one per cavity). Since the original klystron performance was established, cavity characteristics and waveguide losses have changed. The current de-tuning budget (static plus microphonics) with the 13kW klystrons is now 35Hz.

A new rf control module was developed using digital technology. Important control issues that were addressed were:

- Phase and amplitude control must meet the following specifications: 1) Amplitude noise <0.01% and 2) Phase noise < 0.2°
- The system has multi-valued resonance detuning curves resulting from the cavities' high fields and the accompanying high external Q (>2x107 for 12 GeV), as illustrated in Figure 2.

The new system has been completely installed and used to operate all of the installed new cryomodules including delivering beam at full system performance goals. [8]

Integrated RF-cryomodule Performance

Two of the new cryomodules were operating in the south linac during the 2011-2012 final nuclear physics run prior to shutting down to do the bulk of the upgrades. As

Copyright © 2013 CC-BY-3.0 and by the respective authors

the focus of that run was acquiring data for the nuclear physics experiments, the digital control algorithms could be optimized in only one of the two cryomodules. That one was able to deliver the targeted 108 MV with the full beam loading planned for the 12 GeV era. The nuclear physics experiment was a particularly precise measurement that required high quality beam. The users reported no change in beam quality.

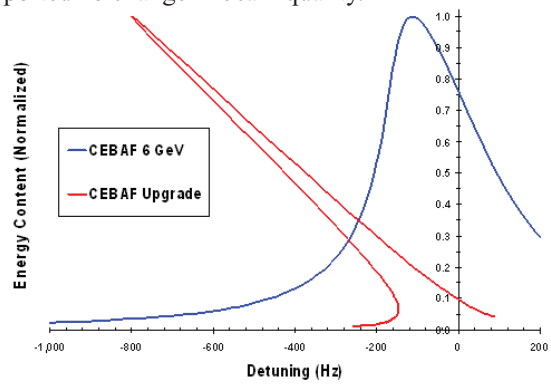


Figure 2: Detuning curves for 6 and 12 GeV.

As mentioned earlier, the cavities in the string were more mechanically coupled and "softer" than previous versions. As a result, if one cavity tripped off, then the others on that end of the cryomodule tripped as the field in the first one collapsed, thereby eliminating the Lorentz forces on that cavity which, in turn, pushed on the other cavities and took their resonant frequency outside the control band and they tripped also. Automated recovery of tripped cavities is still under development. For the 2012 run, a workaround was developed in which the cavities that don't trip are shifted to SEL mode and thus can stay energized; recovery is then simply turning on the resonance control then shifting back to phase and amplitude control once the cavity that tripped has been brought back up to full field.

Cryogenics

The original 2K helium plant was operating at its full capacity; any additional load, such as the new cryomodules, required an expansion. JLab had an unused 2K coldbox identical to the primary 2K coldbox. A plan was established to combine that 2K coldbox with a new 4.5K coldbox plus requisite new warm compressors to get a plant with maximum capacity of ~5kW at 2K. That new hardware has been fabricated, installed and successfully tested. [9] As the new 4.5K coldbox uses the JLab-patented "Ganni cycle", the power consumption of the new 4.5K plant is 30% less than that of the similarly sized original plant. Connections between the 4.5K and 2K systems have been completed. Commissioning of the integrated new plant is about to start.

BEAMLINES

Upgrading Existing Beamlines

The existing beam transport system consists of ~400 dipoles (BxL $\geq$ 0.2T-m) and ~700 quads. Simply replacing their power supplies was not viable because, at the approximately doubled fields, saturation in the return iron would require excessively large power supplies and installation of a large refrigerated cooling-water system. Replacing the magnets is also cost prohibitive. Happily, another alternative was identified.

For the majority of the dipoles, i.e. those in the nine 180° arcs and in the beamlines to the existing end stations, the present "C" shape was changed to "H" profiles by adding bolted on iron plates. The magnets will be operated at ~2x the original currents. The saturation would have exceeded 50% without that change. With the change the maximum is 1%. However, the roughly doubled currents result in much hotter magnets. The temperature rise (above the cooling water supply temperature) is now as much as 38C.

The dipoles in the spreaders and recombiners (S/R), i.e. the sections of the beam transport system which separate the co-linear beams after they exit the linacs or combine them before re-injection into the linacs, are so closely spaced that the bolt-on iron option is often not viable. A combination of three approaches was used: 1) reshape the poles to reduce the flux, and thus the saturation, 2) add coil packs and accept some saturation, and 3) add iron, but in lesser amounts than in the 180° arcs.

All the reused magnets were refurbished to extend their lives. The refurbishment included: replacing all the elastomers with material suited to the new operating temperatures, installing new coil constraints, re-silvering the contacts for the buss cables, and installing Belleville washers to insure that the bolts stay tight.

A small number of new magnets were for the spreaders and recombiners. They were procured with a build-to-print contract. Principal among the new magnets were seven 3m-long septa, which are critical for separating the beams in the higher passes. Six new curved dipoles were also bought. All of the magnets have been fabricated, received, inspected, field mapped, and installed.

The quadrupole fields required for the Upgrade exceeded the original design specifications of the original magnets for ~20% of the population. Testing found satisfactory field quality if the units were pushed to the required field levels, even though there was saturation. That ~20% of the quadrupoles are receiving new power supplies (20A vs the original 10A). The remainder were left as is. In some locations increasing the power supplies did not bring the quad to the required field. New magnets were bought for those locations; all of the new quads get the 20A supplies. Most of the 240 new 20A supplies have been received and installed.

The original dipole strings were energized by 32 power supplies varying in size from 35kW up to 260 kW. Half have been reused for the Upgrade. The rest are being replaced by larger units with output power ratings ranging up to 1.1MW. The new supplies are being fabricated by a commercial firm. The first three units have been received and onsite testing is underway.

Copyright © 2013 CC-BY-3.0 and by the respective authors

New Beamlines

A new recirculation arc was needed to return the beam to the north linac for its final acceleration before going to the new Hall D. Arc 10 uses the double-bend achromat mentioned above. Thirty six new 4m-long dipoles and forty five new quadrupoles were purchased for Arc 10 and the Hall D beamline. New units of existing diagnostics designs had been planned for Arc 10 and for the beamline to Hall D. However, it became impossible to find components for the beam position monitor electronics needed for the beamline to Hall D due to parts obsolescence, so a new system using stripline bpm's was designed and has been installed on the new beamlines. The other diagnostics used the original designs.

Extraction

A key to the effectiveness of CEBAF's research program has been the ability to deliver beam to multiple halls simultaneously. This feature has been retained in the Upgrade. One or two of the three interleaved but independent 499 MHz bunch streams can be extracted at any of the five passes. Extraction is done through the use of properly phased 499 MHz horizontally deflecting copper cavities; the horizontal split is amplified by the downstream lattice and a septum. A second, stronger septum completes the separation into two separate beamlines, one going to the beam switchyard and the other entering the recirculation arcs. This is done on all five passes.

The field integrals of the magnets and rf kickers was doubled for the Upgrade. The rf kick was increased by a combination of running some cavities at higher fields and increasing the number of cavities. The magnet integrals were increased by reuse of longer magnets from other locations. The optics for all five passes are identical.

CONTROL AND SAFETY SYSTEMS

The control network has been extended to cover the beamline to Hall D and Hall D itself. No new technology was required.

All of the safety systems have been expanded to incorporate Hall D and the beamline to the associated tagger dump. Specifically we upgraded the Personnel Safety System (PSS), the Beam Envelop Limit System (BELS), and Machine Protection System (MPS). The MPS and BELS modifications were simple extensions of the present systems. A new engineering approach was developed for the PSS in order to be in compliance with present regulations.

CHALLENGES ALONG THE WAY

Aside from the usual changes in funding profile, the 12 GeV Upgrade accelerator systems encountered some procurement challenges because of market conditions.

When contracting for the components of the new 4.5K coldbox we were in competition with major natural gas and oil companies. Those firms use similar equipment as some we needed and thus use the same vendors as we needed for those components. In addition, the price for the carbon steel was elevated due to international market conditions. As a result, the 4.5K coldbox was rather more expensive than had been anticipated and was delivered later than anticipated. Similarly, the srf cavities cost more than expected because of the market price for high RRR niobium.

A rather different problem occurred with the contract for the large magnet supplies. The original vendor had a large US manufacturing arm and a smaller offshore design arm. Well into the contract, the design arm went bankrupt and the manufacturing arm was unable to fulfill the contract. A new higher-priced contract was placed with a new vendor. Considerable schedule delay was incurred in the process, too.

STATUS

The upgrade of the accelerator is essentially complete. The beamlines to the end stations are still to be completed. Commissioning of the accelerator is scheduled to begin in Novermber of this year.

SUMMARY

An exciting new range of scientific inquiry into the quark nature of nuclear matter will soon be opened by the availability of a 12 GeV cw electron beam at JLab. The needed upgrade of the CEBAF accelerator is nearly complete and commissioning is about to begin. The new research program could begin as early as 2014.

REFERENCES

[1] http://www.jlab.org/12GeV/
[2] Ilkyoung Shin, Thesis, University of Connecticut, (2013).
[3] S. Bogacz, JLab internal report TN-07-010.
[4] Y.Roblin, JLab internal report TN-08-042.
[5] A. Freyberger and Y. Roblin, JLab internal report TN-06-048.
[6] John Hogan,"Overview and Lessons Learned of the Jefferson Lab Cryomodule Production for the CEBAF 12GeV Upgrade", WEZAA2, NA-PAC'13.
[7] R. Nelson and A Kimber, CWRF-2012, "RF Power Upgrade at Jefferson Lab".
[8] Hovater et al., IPAC12, "Commissioning and Operation of the CEBAF 100MV Cryomodules", WEPPC.
[9] CEC/ICMC-2012 V, Ganni, et al., "Commissioning Status of Helium Refrigeration System at JLab for the 12 GeV Upgrade, V. Ganni, et al", 2EOrC4-01.

Copyright © 2013 CC-BY-3.0 and by the respective authors

FULL 3D STOCHASTIC COOLING AT RHIC*

K. Mernick#, M. Blaskiewicz, J.M. Brennan, BNL, Upton, NY 11973, USA

Abstract

Over the past several years, the installation of the full 3-dimensional stochastic cooling system in RHIC has been completed. The FY12 U-U and Cu-Au collider runs were the first to benefit from the full installation. In the U-U run, stochastic cooling improved the integrated luminosity by a factor of 5. This presentation provides an overview of the design of the stochastic cooling system and reviews the performance of the system during the FY12 heavy ion runs.

INTRODUCTION

Intra-beam scattering (IBS) is a primary cause of emittance growth of the heavy ion beams in the Relativistic Heavy Ion Collider (RHIC). A 3D bunched beam stochastic cooling system has been implemented to combat IBS and reduce the emittance of the beams. This system has been installed in stages over the past several years. The first operational use of stochastic cooling, in the longitudinal plane of the Yellow ring, began in 2007 [1,2]. The 2010 and 2011 collider runs had longitudinal and vertical cooling in both rings [3,4]. Commissioning of the horizontal cooling system in the 2012 run completed the full system.

SYSTEM DESIGN

The stochastic cooling system is essentially a wideband feedback damper. The momentum error of samples of particles within the bunch is measured and reduced via an applied kick. Longitudinal mixing randomizes the samples on subsequent turns and, over time, the emittance of the bunch is reduced. The time resolution of the samples and the resulting cooling rate are a function of the bandwidth of the system.

The layout of the fundamental components of the RHIC stochastic cooling systems is shown in Fig. 1. The longitudinal cooling pickups are located on either side of the 2 o'clock intersection region. The signals from these pickups are transmitted approximately 700m via microwave link to low-level electronics located near the kickers, which are in sector 4 for the Blue (clockwise) ring and sector 11 for the Yellow (counter-clockwise) ring. The longitudinal microwave links "cut the chord," transmitting the pickup signal across the center of the ring in the same direction the beam travels. This leaves only 200 ns for signal processing and cable delays. To minimize delay, the Blue ring electronics are located in the attic of the RF service building and cables are routed through a dedicated penetration to the tunnel. The Yellow ring electronics are located in a dedicated building on the berm above the tunnel.

*Work supported by Brookhaven Science Associates, LLC under Contract No. DE-AC02-98CH10886 with the U.S. Dept. of Energy.
#kmernick@bnl.gov

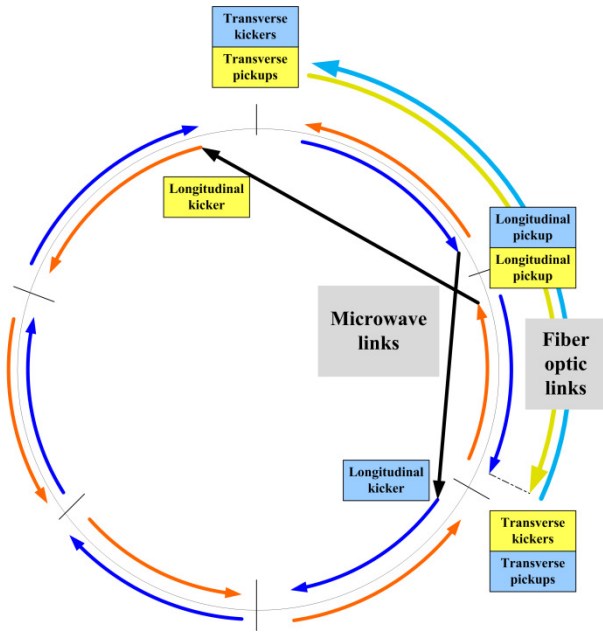


Figure 1: Locations of pickups and kickers (blue and yellow boxes), longitudinal system microwave links (black arrows), and transverse system fiber optic links (light blue and yellow arrows). The dark blue and orange arrows indicate the directions the beams travel.

In the Blue transverse system, signals from pickups in sector 3 are transmitted by fiber optic link to low-level electronics in the 12 o'clock service building, and from the electronics to the kickers in sector 12. The Yellow transverse system is the mirror-image of the Blue, with pickups in sector 12, electronics in a dedicated trailer outside the tunnel, and kickers in sector 3. The fiber optic link travels approximately 1/3 of the ring, while the beam travels 2/3 of the ring in the opposite direction.

Longitudinal Pickups

The longitudinal pickups measure fluctuations in the beam current as a function of the longitudinal position in the bunch. New longitudinal pickups have been designed and installed since the end of the 2012 run. These pickups consist of a keyhole-shaped vacuum chamber, shown in Fig. 2, with a 7 cm aperture round section and a 2 cm high rectangular section. During injection and ramping, the beam circulates in the large round section of the chamber. At top energy, the pickup chamber is moved, with pivoting double bellows on either side, to center the beam in the rectangular section. The small aperture cuts off the propagation of waveguide modes up to 9 GHz. The beam couples to top and bottom WRD-475 double-ridge waveguides parallel to the rectangular section through 8 mm by 6 mm slots. The top and bottom slots are offset in the beam direction, which improves the flatness of the pickup gain across the 6 to 9 GHz operating range.

Copyright © 2013 CC-BY-3.0 and by the respective authors

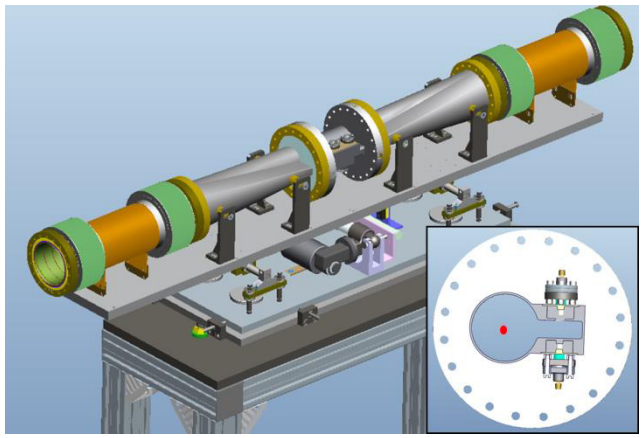


Figure 2: The longitudinal pickup vacuum chamber, drive assembly and stand (main figure) with a cross-sectional view of the active area of the pickup (inset). The red dot in the inset indicates the beam trajectory at injection and while ramping.

The pickup is driven by a DC motor coupled to the vacuum chamber through a gearbox that disengages when it reaches its maximum travel. This determines the in and out positions of the pickup without relying on precise control of the motors. Shape transition pieces provide a smooth transition from the 13 cm RHIC warm bore pipe to the keyhole cross-section. Along with custom RF shields for the welded bellows, these shape transitions minimize the impedance seen by the beam.

The new longitudinal pickup design was tested during the RHIC polarized proton run in 2013. The observed beam spectra are shown in Fig. 3. The response of the pickup across the 6 – 9 GHz band is much flatter than the previous version of the longitudinal pickups, which consisted of waveguides coupled to ceramic windows in a 7 cm round chamber.

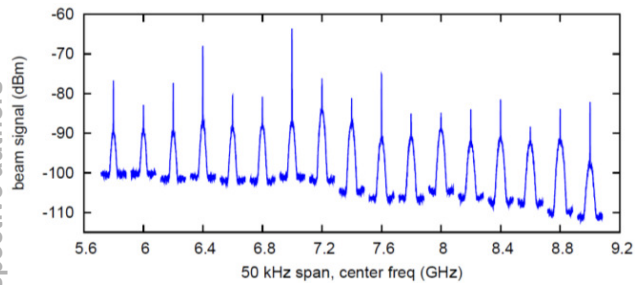


Figure 3: Beam spectra for polarized protons using the keyhole longitudinal pickup. The traces are centered at 5.8, 6.0, …, 9.0 GHz and each have a 50 kHz span.

Transverse Pickups

The transverse pickups measure the fluctuations in transverse position as a function of longitudinal position in the bunch. Each pickup contains two planar loop arrays, originally designed and built at Fermilab for stochastic cooling studies in the Tevatron [5], located above and below (for vertical) or inside and outside (for horizontal) the beam trajectory. The signals from the two pickup arrays must be subtracted with good common-mode rejection. Precision alignment and control of the positions of the two array plates are provided using linear

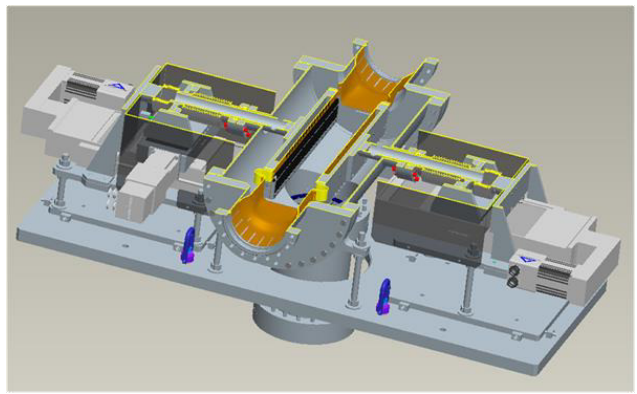


Figure 4: A cross-sectional view of the horizontal pickup vacuum chamber and assembly.

stages from Aerotech. The RF signals from the two plates are routed through matched coaxial cables and vacuum feedthroughs to an external hybrid. For additional fine-tuning of the common-mode rejection, one side has an additional linear stage to adjust the z-axis (beam direction) position of the pickup plate, and remotely adjustable trombones provide adjustable delay matching for the signals before the hybrid.

The design of the pickups, which is described in greater detail elsewhere in these proceedings [6], is nearly identical for the horizontal and vertical planes. The support plates and stands are modified to orient the pickup in the required plane. A cross-sectional view of the horizontally-mounted pickup is shown in Fig. 4.

Kickers

A novel feature of the RHIC stochastic cooling system is that the kickers are composed of an array of high Q resonant cavities. The RHIC beam is bunched with a bunching frequency of approximately 10 MHz and a bunch length of approximately 5 ns. Each kicker consists of 16 cavities, with resonant frequencies spaced by 200 MHz, the reciprocal of the bunch length, and bandwidths of 10 MHz. This allows a Fourier synthesis of the kick waveform to match the broadband signal for the 5 ns length of the bunch, and for the amplitude and phase of the signal to change bunch-by-bunch. This is illustrated schematically in Fig. 5.

In order to match the filling time of the cavities, the bunch signal at the pickup is periodically extended with a traversal filter, whose output is given by

$$y(t) = \sum_{k=0}^{15} u(t - k\tau)$$

with $\tau = 5.0$ ns. This filter is implemented with a series of coaxial cable delay lines, tuned with a resolution of 1 ps. There are no active components in these filters that could saturate and cause distortion. The traversal filter also serves to reduce the dynamic range of the signal before it is sent over either the fiber optic or microwave link.

The Fourier synthesis approach to creating the kick greatly reduces the required drive power. Each cavity is driven with a 40 W solid-state amplifier, and the kicker

Copyright © 2013 CC-BY-3.0 and by the respective authors

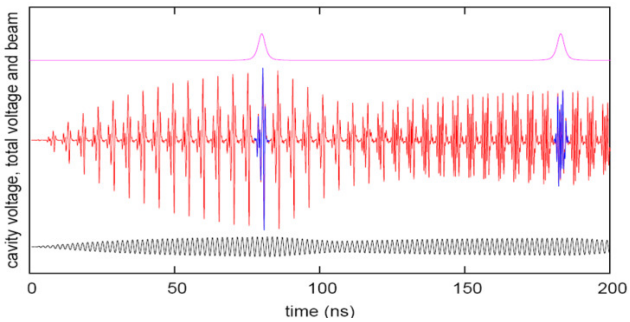


Figure 5: Schematic representation of the synthesis of the kicker waveform. The top trace indicates the time of arrival of two bunches at the kicker. The bottom trace indicates the voltage present on a single kicker cavity, and the middle trace indicates the sum of the voltage on the 16 cavities (red). The blue sections of the middle trace indicate the desired broadband kicker waveform.

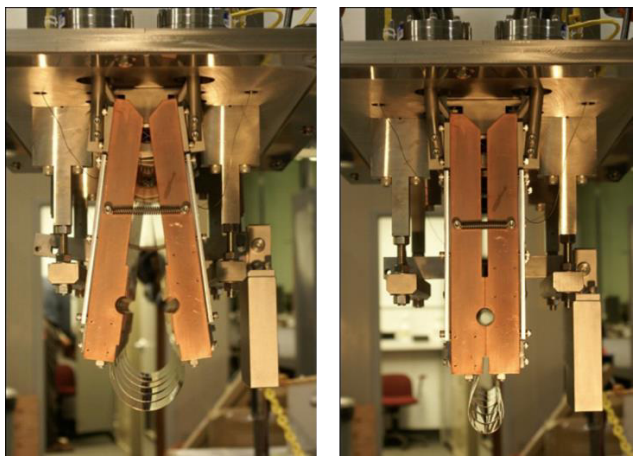


Figure 6: Photographs of the first Blue vertical kicker cavity assembly that used the scissor design, in the open position (left) and the closed position (right). The aperture in the closed position is 2 cm.

generates a kick of several kilovolts. The cost savings due to this method made the RHIC stochastic cooling system possible.

The RHIC stochastic cooling system presently uses three different mechanical designs for the kicker vacuum tanks. The longitudinal kickers are made from retrofitted vacuum tanks originally designed for the Tevatron [7]. Each kicker consists of three vacuum tanks, with either 5 or 6 cavities in each tank. The cavities in this design are split down the middle, allowing them to open to increase the available aperture during injection and acceleration. The cavity bodies are supported on a stainless steel strongback, which is rigidly attached to the drive mechanism. The linear bearings in these tanks have galled and seized on several occasions. Modifications made while refurbishing the kickers prior to the 2011 and 2012 runs have reduced the likelihood of these problems, but it is still a potential failure risk.

The vertical kicker in the Yellow ring was the first to be built in a vacuum vessel designed at BNL. This version of the kicker houses all 16 cavities in a single vacuum tank. This design required very delicate and time-consuming alignment adjustments during assembly, which made it impractical for production. The lessons learned working with this kicker and the Fermilab tanks led to a new design which has been used for all the subsequent kickers.

The vertical kicker in the Blue ring and the horizontal kickers in both rings use a scissor-like pivoting motion on a "flexi-hinge" to allow the cavities to open and close (see Fig. 6). This design has no sliding joints in vacuum. In the closed position, one cavity plate assembly rests against a hard stop and the linkage to the motor goes slack. The other half of the cavity assembly closes against the side supported by the hard stop and its motor linkage goes slack as well. This provides a repeatable closed position, while relaxing the requirements for precise motion control. Further detail on the mechanical design of these kickers is provided elsewhere in these proceedings [8].

During the present shutdown period, new longitudinal kickers are being fabricated using the scissor design. In addition to addressing the reliability concerns mentioned previously, the new longitudinal kickers have several enhancements. The 4-cell cavities in the existing kickers are being replaced by 6-cell cavities in the new kickers. With a higher R/Q, these cavities will provide a larger kick for the same input power. Power is now fed to the cavities through waveguides, rather than coaxial cable, and new coax-to-waveguide transition feedthroughs are used. These changes eliminate the Teflon dielectric in the vacuum chamber, allowing an increased bakeout temperature. The previous kickers all were designed with water cooling of the cavity bodies. The new longitudinal kickers will use radiant heaters to transfer heat to the cavities through glass vacuum windows. A control loop will monitor the cavity temperature and balance the radiant heat input with the RF losses in the cavities and conduction losses to the outside of the vacuum vessel to maintain a constant temperature. These kickers are expected to be completed and installed before the beginning of the 2014 heavy ion run.

Electronics

There are minimal RF electronics located in the RHIC tunnel at the pickups and kickers, but the majority of the electronics are housed outside the tunnel in service buildings. The electronics at the each pickup consist of a digitally-controlled step attenuator, several gain stages, the traversal filter, and low- and high-pass filters to match the system bandwidth and minimize the dynamic range of the signal. At each kicker, there are the 16 power amplifiers that drive the cavities, along with their DC power supplies and monitoring electronics. In addition, some motion control electronics – such as motors, linear potentiometers, limit switches, and resolvers – and PIN diode based beam loss monitors are also located at the pickups and kickers.

The transverse systems use the Photonics Systems PSI-1600 series fiber optic links to transmit the filtered pickup signal to the service buildings. In the longitudinal systems, the filtered pickup signal is used to amplitude

Copyright © 2013 CC-BY-3.0 and by the respective authors



Figure 7: The microwave link transmitter for the Yellow ring, above the pickup in sector 2, is shown in the foreground. The receiver and dedicated electronics trailer, above the kicker in sector 11, are shown in the distance and the inset.

modulate the carrier of a 70 GHz E-Band microwave link, built by HXI Millimeter Wave Products. The microwave link installation is shown in Fig. 7. A pilot tone is added to the pickup signal, transmitted over the link, and used to correct phase modulation introduced by the link [9].

A block diagram of the electronics for one of the transverse systems is shown in Fig. 8. The optical signal from the pickup is amplified using an Erbium-doped Fiber Amplifier (EDFA), and routed through a delay line to the fiber optic receiver. The length of the delay line is determined to make the signal propagation time from the pickup to kicker match the beam's travel time. The output from the fiber optic receiver is routed through a series of splitters, amplifiers, and band-pass filters with 100 MHz bandwidth to generate the 16 input signals that are sent to the kicker cavities. Each of these 16 signals is connected through an independent I/Q modulator, which is used to optimize the amplitude and phase of the open-loop response. In this way, each cooling system can be tuned as 16 independent feedback systems, and the required precision for matching the pickup to kicker delay is only on the order of a few nanoseconds.

In the longitudinal systems, the microwave link replaces the fiber optic link, and the received signal is filtered with a one-turn delay notch filter prior to the 16-way fanout. The notch filter differentiates the pickup signal, giving an output proportional to the momentum error. A block diagram of the notch filter is shown in Fig. 9. The response of the notch filter is measured by a network analyzer, and the delay is calculated with 0.1 ps resolution. A feedback system regulates the length of the 12.8 μs fiber optic delay line with a piezoelectric line stretcher that provides ±40 ps of adjustment. The entire fiber optic assembly is mounted in a digitally controlled thermal chamber, and a second feedback loop regulates the temperature to keep the delay correction within the range of the line stretcher.

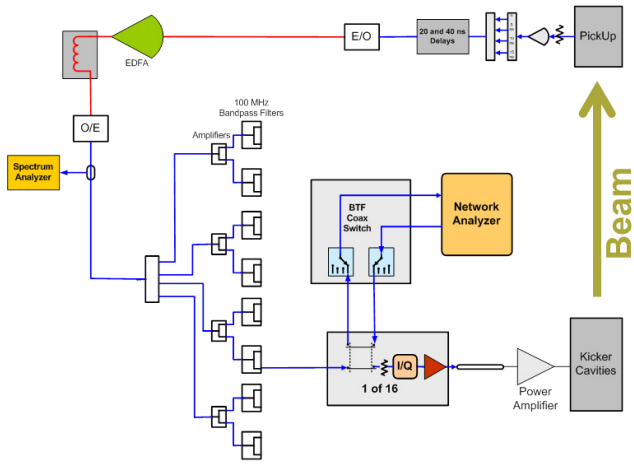


Figure 8: Electronics block diagram for one of the transverse systems. Red lines indicate fiber optic signal paths; blue lines indicate electrical signal paths.

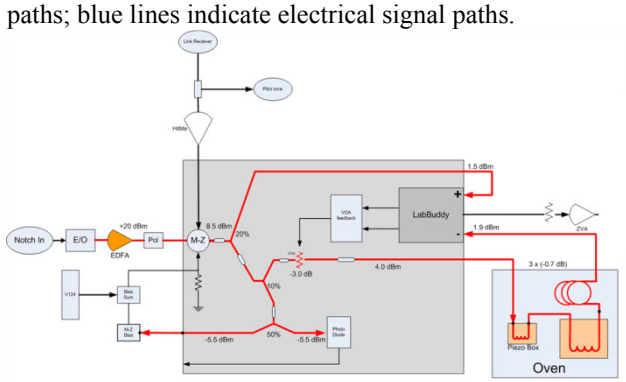


Figure 9: One-turn delay notch filter block diagram. The input from the microwave link is at the top. The block on the left labelled "Notch In" is for the network analyzer measurements. The output at the right of this diagram is connected to the input of the signal fanout.

Control and Operation

Transfer switches in the I/Q modulators and coax relay-based multiplexers allow measurement of the system transfer functions and real-time monitoring of signals while the system is operating. The gain and phase settings of the I/Q modules and the switch settings are sent on a locally broadcast serial "NIM link." This 10 Mbps, bi-phase mark encoded link is electrically identical, and functionally similar, to the RHIC Real Time Data Link [10], allowing common support hardware to be used.

Routine operation of the stochastic cooling systems is fully automated with the "tape" sequencer program. When beam has reached top energy, the sequencer sends commands to control system managers and accelerator device objects (ADOs) to start the cooling system. Several control system managers handle closing and opening of the pickups and kickers, and provide interlocks and alarms if beam loss monitor readings exceed a threshold. Once the pickups and kickers are in the operating positions, the sequencer enables the ADOs that control the low-level electronics.

The low-level software enables the electronics for one cavity at a time and measures the system open-loop

Copyright © 2013 CC-BY-3.0 and by the respective authors

transfer function. The I/Q modulator gain and phase are modified to minimize the error between the measured and reference transfer functions. The reference transfer function is stored during setup at the beginning of the run after manually optimizing the gain and phase while observing the amount and symmetry of signal suppression [11] in the Schottky spectrum. Once the system is running, the control software continues to automatically measure and correct the transfer functions approximately every 15 minutes. These periodic corrections compensate slow drifts of system delays and changes in the beam conditions.

FY12 RESULTS

In the 2012 heavy ion run, RHIC provided Uranium-Uranium collisions at 96.4 GeV/nucleon and Copper-Gold collisions at 100 GeV/nucleon [12].

Uranium-Uranium

The 2012 Uranium run was the first RHIC run with Uranium, as well as the first to use the EBIS source. The number of ions per bunch was approximately 3 x 10^8, significantly fewer than the 1 – 1.5 x 10^9 Gold ions per bunch in previous runs. This, along with the addition of horizontal cooling, was expected to increase the benefit provided by stochastic cooling.

In the 2011 Gold run, longitudinal and vertical stochastic cooling doubled integrated luminosity. For the 2012 Uranium run, stores with only longitudinal and vertical cooling yielded an improvement by a factor of 3.75. After the horizontal cooling was commissioned, stores with full 3D cooling showed a factor of 5 improvement in integrated luminosity [13]. Peak luminosity was tripled with 3D cooling, the first time in RHIC that the initial luminosity was not also the peak.

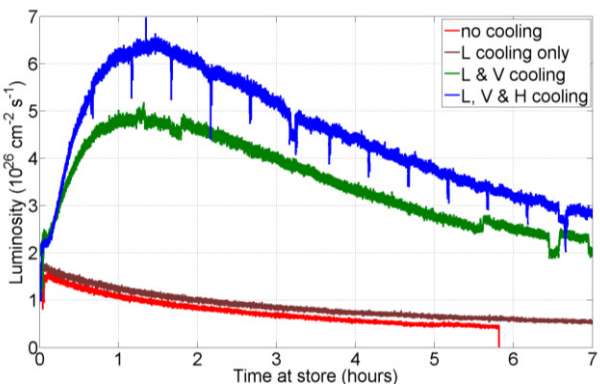


Figure 10: Effect of stochastic cooling on Uranium-Uranium luminosity.

Copper-Gold

The 2012 Copper-Gold run was the first in RHIC with this combination of ions. In addition, it was the first run with different ion species in the two rings with the transverse cooling systems available. Significant improvements in beam intensity were made throughout the run, mostly as a result of improvements at the EBIS source and tuning and introduction of additional bunch merges in the injectors. Ultimately, intensities of 4.0 x 10^9 Copper and 1.3 x 10^9 Gold ions per bunch were reached. Due to changing beam conditions, exact store-to-store comparisons are not possible. However, qualitatively, the benefit from stochastic cooling was clear.

The major operational challenge of the Copper-Gold run was managing the transverse emittance of the Gold beam. Due to the smaller number of ions per bunch, the cooling time for Gold was approximately 1/3 that for Copper. If both beams were cooled with the systems operating at peak performance, the Gold beam emittance was reduced to a much smaller value than the Copper beam. In this circumstance, the beam-beam interaction caused poor lifetime of the Copper beam [14]. To preserve the Copper beam, and maximize integrated luminosity, the transverse cooling for the Gold beam was slowed by turning off the horizontal cooling system and reducing the gain of the vertical system. More detail is available elsewhere in these proceedings [14].

ACKNOWLEDGMENT

We thank the members of the C-AD Accelerator Components & Instrumentation, Controls, Mechanical Systems, Operations, and RF groups for their work implementing these designs.

REFERENCES

[1] J.M. Brennan, M. Blaskiewicz, F. Severino, "Successful Bunched Beam Stochastic Cooling in RHIC," EPAC06, THPCH078.
[2] M. Blaskiewicz, J.M. Brennan, F. Severino, Phys Rev Lett. 100 174802 (2008).
[3] M. Blaskiewicz, J.M. Brennan, K. Mernick, Phys Rev Lett.105 094801 (2010).
[4] M. Blaskiewicz, et al., "Stochastic Cooling of a High Energy Collider," IPAC 2011, TUYA03.
[5] D. McGinnis, et al., "Design of 4-8 GHz Bunched Beam Stochastic Cooling Arrays for the Fermilab Tevatron," PAC1991.
[6] C.J. Liaw, et al., "Robust Mechanical Design for RHIC Transverse Stochastic Cooling Pickup," THPH008, NA-PAC'13.
[7] P. Hurh, et al., "The Mechanical Design of a Bunched Beam Stochastic Cooling Tank for the FNAL Tevatron," PAC1993.
[8] C.J. Liaw, et al., "Novel Mechanical Design for RHIC Transverse Stochastic Cooling Kicker," THPH007, NA-PAC'13.
[9] K. Mernick, et al., "Microwave Link Phase Compensation for Longitudinal Stochastic Cooling in RHIC," BIW10, TUPSM085.
[10] H. Hartmann, "The RHIC Real Time Data Link System," PAC97.
[11] D. Mohl, CERN 87-03, p500 (1987).
[12] Y. Luo, et al., "RHIC Performance for FY2012 Heavy Ion Run," IPAC2013, TUPFI082.
[13] J.M. Brennan, M. Blaskiewicz, K. Mernick, "Stochastic Cooling in RHIC," IPAC12, WEPPP082.
[14] Y. Luo, et al., "Burn-off Dominated Uranium and Asymmetric Copper-Gold Operation in RHIC," TUXA1, NA-PAC' 13.

Copyright © 2013 CC-BY-3.0 and by the respective authors

ARIEL ELECTRON LINAC

S. Koscielniak, F. Ames, R. Baartman, I. Bylinskii, Y.C. Chao, D. Dale, R. Dawson, I. Earle, K. Fong, E. Guetre, N. Kahn, A. Koveshnikov, R. Laxdal, F. Mammarella, L. Merminga, A.K. Mitra, T. Planche, Y.N. Rao, A. Trudel, V. Verzilov, D. Yosifov
TRIUMF*, 4004 Wesbrook Mall, Vancouver, B.C. Canada
D. Karlen, Victoria University, Victoria, B.C.

Abstract

The TRIUMF Advanced Rare Isotope Laboratory (ARIEL) phase I is funded since 2010 June by federal and BC provincial governments. ARIEL I comprises buildings and electron linac; the future phase II includes hot cells, target stations, mass separators and beam transport to ISAC experimental areas. The linac vault and He compressor building were completed 2012. The ARIEL targets building completion is 2013 August. With the exception of the 30 MeV accelerator cryomodule and second klystron and HV power supply, the linac major procurements are complete. This paper reports progress for the following systems: locally manufactured niobium 9-cell cavity, 300 keV electron gun, 4 K cryogenic plant and sub-atmospheric pumps, 290 kW cw klystron and 65 kV DC power supply. Status of the 10 MeV injector cryomodule assembly and beamlines construction will also be addressed.

CONVENTIONAL INFRASTRUCTURE

The ARIEL project, described in Refs. [1,2], is essentially a new front end for the existing ISAC I & II experimental complex. The project contains two new "drive beams" and two target stations to supplement those at ISAC. The conventional infrastructure consists of four main contracts: the ARIEL construction, demolition and excavation, the Stores building, and Badge building. The new Compressor Building forms part of the ARIEL package as does major renovation of the former Proton Hall that has segregated the Electron Hall (e-hall) area from the future BL4N protons vault.

The Stores and Badge building construction was completed in 2011. The e-hall and Compressor building occupancy were taken 2012 November 1st and December 1st respectively. The ARIEL building occupancy was taken 2013 September 1st; and the connecting tunnel was completed one month prior.

The ARIEL cooling water system which provides capacities of 3 MW each to the ARIEL building and e-linac, and 0.3 MW to the compressor building, was completed 2013 June 1st. The site electrical connections to the 5 MW utility feed are made through a 12.5 kV switchgear supplied by Siemens. This connection supplies up to 1.5 MW to klystrons, 0.5 MW emergency power, 1 MW to compressor building, and 2 MW to the ARIEL building. Switchgear was energized 2012 December. A rack farm for magnet power supplies, beam diagnostic and LLRF controls is now complete on the e-hall roof.

*TRIUMF is funded under a contribution agreement with the National Research Council of Canada.



Figure 1: ARIEL building, view south.

ELECTRON GUN

The thermionic gun provides 300 keV kinetic energy electron bunches with charge up to 16 pC at a repetition frequency of 650 MHz. Unique features of the gun are its inverted cathode/anode geometry to reduce dark current, and transmission of rf modulation via a ceramic waveguide through SF6 dielectric. An impedance network inside an HV shroud matches the waveguide to the gridded cathode. The waveguide was received 2012 September from Kyocera. The HV cage containing the Glassman 300 kV supply, isolation transformer and bias and heater supplies was completed 2013 March. The gun electrodes polishing and assembly to the ceramic was completed 2013 May. The SF6 vessel also was received and installed in May. The vessel internal corona domes and shroud were fabricated and installed in the SF6 vessel 2013 September. 200 kV High voltage was first applied in October and a breakdown encountered with the receptacle connecting to the conditioning resistor.

INJECTOR TEST FACILITY

The Injector test facility, under collaboration between TRIUMF and VECC of Kolkata, India, provides an ideal proving ground for e-linac design and operation strategies. It duplicates the e-linac up to the exit of the injector cryo-module with enhanced diagnostic capability. Commissioning this facility began Nov 2011 with a 100kV gun and low energy solenoid beam transport and continued to 2013 Feb. The primary objective is a complete 6D phase space characterisation of the 100 kV beam. The 99% longitudinal phase is ±18.8 deg at 650 MHz and $\Delta p/p \pm 3.7\times10^{-4}$. The measured transverse r.m.s. normalized emittance is 9.3 µm horizontal and

Copyright © 2013 CC-BY-3.0 and by the respective authors

9.5 µm vertical. Further, a transverse deflecting cavity and scintillator view screen in the momentum analysis stub was used to visualize longitudinal phase space rotation effected by the buncher cavity, and to calibrate and adjust the settings to those believed to be needed to match the beam to that of the injector cryomodule acceptance.

BEAM LINES

The beam transport sections after the Injector are: the EMBT "Merger" section; the EABT and EHAT before and after the accelerator cryomodule; the EHDT to a 100 kW beam dump; and the EHBT, which transports to the photo-fission targets, consists mainly of a periodic section consisting of six 90° FODO cells, each 4 m in length. The EMBT contains a 36° bend section, the EHDT, a 90-degree section, and the EHBT two doglegs and a bend section to target. All insertions are achromatic. After the Injector, the focusing is performed by magnetic quadrupoles. These are grouped in three classes: (i) weak, < 0.2 T; (ii) medium, < 0.5 T; (iii) strong, < 1.3 T. The weak and medium designs retain the same spherical [4] poles and yolks, but differ in their coils and cooling: air-cooled or chill-plates, respectively. The strong quads follow a conventional water-cooled design, and have cylindrical poles. Prototypes were received 2013 February from *Buckley Systems*, leading to shipments completed in August totaling 80 magnets.

Dipole procurements have followed a separate path using a variety of vendors and custom designs. The three EMBT dipoles were received 2013 July. The eight S34 bends used in EABD and final EHBT bends before the east and west target stations are in shipment from *Everson-Tesla*. The contract for three Y30 bends used in EHDT and the EHBT dogleg was awarded 2013 September. The final tender, for two vertical dipoles for the dogleg, will be let in November.

Beam Diagnostics

Initial beam threading will be facilitated by profile monitors equipped with scintillators and OTR screens. 17 camera boxes and actuator assemblies are now complete. Orbit correction will be performed with the backbone system of 56 four-button type position monitors. All parts are acquired, and assembly in progress. The BPM electronics, which operates in pulse and cw. modes, comprises three blocks: a commercial front-end to down convert the input 650 MHz signals to the IF frequency, a 14-bit ADC and a Spartan-6 FPGA for the digital signal demodulation and filtering. The electronics is currently in production phase. 26 units are needed for the e-hall by 2014 May; 3 are complete, 7 in assembly, and remainder on track.

CRYOMODULES AND CAVITIES

Due to heavy beam loading, five 9-cell cavities at 100 kW/cavity are required to reach the 0.5 MW beam power. The injector cryomodule (EINJ) contains a single 9-cell cavity, and is designed and constructed in collaboration with VECC. The accelerator cryomodules (EACA,B) each house two 9-cell cavities.

The cryomodule design [2] utilizes a box vessel with a top-loading cold mass. A 4 K phase separator, 4 K/2 K heat exchanger and Joule-Thomson expansion valve are installed within each module to produce 2 K liquid. The cold mass is suspended from the lid with mounting posts, struts and strong back; and is surrounded by a LN2-cooled copper box for thermal isolation. A 1 mm warm mu-metal shield is fastened to the inside of the vacuum vessel. The cold mass consists of the cavity hermetic unit, a cold mu metal layer and the tuner. The tuner cold part is the Jefferson lab style scissor type; and is actuated by warm rotary servo motor mounted on the lid. The hermetic unit includes the cavity(s), power couplers, rf pick-up(s), the warm-cold transitions with HOM damping material and warm isolation valves.

The 4 K/2 K cryo-insert has undergone cold testing since 2013 January. Measured: static load of 4 K (2 W) and 2 K (0.5 W) reservoirs. Measured: efficiency of 2 K conversion is 66% at 0.5 g/s mass flow. Measured: 4 K siphon circuit efficiency – extra heat load caused by convection in 4 K reservoir ~15-20 W. After modification, the siphon loop is well behaved with a static load of 1.6 W.

All sub-assemblies of the EINJ are fabricated, and many are assembled. The tank is complete, and the entire assembly that is suspended from the lid is the subject of a mock up to verify that there are no conflicts or interferences. During the final assembly, 2013 Nov., the Nb cavity will substitute a dummy used in the mock up.

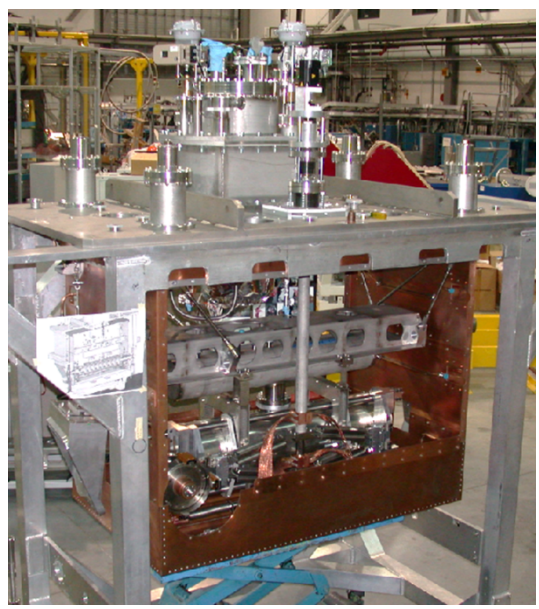


Figure 2: Injector cryomodule internal assembly.

Concerning the accelerator cryomodule, EACA, 95% of the design and detailing tasks are performed and fabrication is imminent. The lid is already received and the tank ordered.

The nine-cell 1.3 GHz elliptical cavity borrows the TESLA/ILC type inner cell geometry but uses modified

Copyright © 2013 CC-BY-3.0 and by the respective authors

end groups to accommodate the large power couplers and to mitigate HOMs. The HOM spectrum of the copper prototype has been measured [5] up to 4 GHz.

The first ARIEL cavity was received from *PAVAC Industries* of Richmond 2013 May 28. Subsequently, the cells were tuned to achieve field flatness, the cavity BCP etched, and cavity tested. No quenching or field emission was detected up to a field of 10 MV/m. The measured quality factor ($Q = 3\times10^9$) is not adequate, and the cavity has been sent for furnace degassing at FNAL. The second cavity is fabricated, tuned and etched, and ready for testing. The third cavity is in fabrication.

CRYOGENIC EQUIPMENT

In essence the cryogenics contains two components: a system responsible to deliver 4 K liquid He to a dewar; and a system to produce 2 K sub-atmospheric He inside the cryomodules. The first comprises a helium refrigerator-liquefier (HELIAL 2000 cold-box), and oil removal and gas management systems (OR/GMS), both delivered by *Air Liquide Advanced Technologies* (France) in 2013 March; and main and recovery compressors delivered by *Kaeser* in 2013 January; and 1000 litre dewar. Further, this system contains a helium gas storage tank fabricated locally, and variety of warm He piping completed 2013 September. All connections and services for this equipment are now complete. Presently, preparations are underway for the 4 K acceptance test in November.



Figure 3: Helium dewar (left) and 4 K coldbox (right).

Concerning the 2 K sub-atmospheric system, four pumps were delivered by *Busch* 2013 March and one successfully tested; the forward 4 K line to cryomodules is anticipated delivered October, the return line is recently tendered, the return heat exchanger is expected delivered in October; and the 4 K/2 K (in-cryomodule) insert is prototyped and installed in the Injector.

RADIO-FREQUENCY EQUIPMENT

The ARIEL project has procured two 290 kW klystrons from CPI, and two 600 kW HV supplies from *Ampegon/ Comark* (formerly *Thomson*). The first klystron was factory tested to 300 kW in 2013 January, and installed at TRIUMF [3] in June; and the 300 kW circulator and water-cooled loads added in September. The 65 kV power supply was factory tested in May and installed at TRIUMF 2013 August. All connections and services for this equipment are now complete. Presently, preparations are underway for the acceptance test in October. The second klystron and HV power supply will be delivered 2014 March.



Figure 4: klystron, circulator and loads.

The first klystron will initially be deployed to drive the injector cryomodule (EINJ) for a beam test starting 2014 May. After the second klystron is installed, the first will be switched to drive the accelerator cryomodule (EACA). In the ARIEL II phase of the project, the second klystron will drive the second cryomodule EACB, and a dedicated 150 kW RF source will be found for EINJ.

Power Coupler Conditioning Station

A routine procedure is now established: one week bakeout of warm window under N2 flow at 100 C. Four couplers have been conditioned at room temperature. 12.5 kW cw in traveling wave (TW) and 10 kW pulsed in standing wave (equivalent to 40 kW in TW) are achieved.

CONCLUSION

We are justified to report excellent progress across all areas: delivery and test of 1st ARIEL cavity; ARIEL building occupancy; imminent acceptance tests of Klystron & HVPS and 4 K Cryogenic Plant. The following milestones are anticipated: e-gun complete 2013 Nov; Injector Cryomodule complete 2013 Dec; beam test start at ISAC/VECC 2014 January; and Accelerator Cryomodule beam test 2014 Sept.

REFERENCES

[1] L. Merminga *et al*: "ARIEL: TRIUMF's Rare IsotopE Laboratory", WEOBA001, proc. IPAC 2011.
[2] S. Koscielniak *et al*: "ARIEL Superconducting Electron Linac", WE1A04, proc. of LINAC2012, Tel-Aviv, Israel.
[3] A. Mitra *et al*: Proc. of NA-PAC'13, WEPHO01.
[4] R. Baartman: Proc of NA-PAC'13, WEZBB1.
[5] P. Kolb *et al*: "Measuring the HOM Spectrum of the TRIUMF 9 Cell Cavity", proc. SRF2013, Paris.

Copyright © 2013 CC-BY-3.0 and by the respective authors

THE RHIC POLARIZED SOURCE UPGRADE

A. Zelenski, G. Atoian, J. Fite, D. Raparia, J. Ritter, D. Steski, BNL, Upton, NY USA
V. Klenov, V. Zubets , INR Moscow, Russia
V. Davydenko, A. Ivanov, A. Kolmogorov, BINP, Novosibirsk, Russia

Abstract

A novel polarization technique has been successfully implemented for the upgrade of the RHIC polarized H^- ion source to higher intensity and polarization. In this technique, a proton beam inside the high magnetic field solenoid is produced by ionization of the atomic hydrogen beam (from an external source) in the He-gas ionizer cell. Proton polarization is produced by the process of polarized electron capture from the optically-pumped Rb vapor. Polarized beam intensity produced in the source exceeds 4.0 mA. Strong space-charge effects cause significant beam losses in the LEBT (Low Energy Beam Transport, 35.0 keV beam energy) line. The LEBT was modified to reduce losses. As a result, 1.4 mA of polarized beam was transported to the RFQ and 0.7 mA was accelerated in linac to 200 MeV. A maximum polarization of 84% (in the 200 MeV polarimeter) was measured at 0.3 mA beam intensity and 80% polarization was measured at 0.5 mA. The upgraded source reliably delivered beam for the 2013 polarized run in RHIC at √S=510 GeV. This was a major factor contributing to the increase in RHIC polarization to over 60 % for colliding beams.

OPPIS UPGRADE WITH THE ATOMIC HYDROGEN BEAM INJECTOR

The polarized beam for the RHIC spin physics experimental program is produced in the Optically-Pumped Polarized H^- Ion Source (OPPIS) [1].

An Electron Cyclotron Resonance (ECR) ion source was used as the primary proton source in the old operational polarized source. The ECR source was operated in a high magnetic field. The proton beam produced in the ECR source had a comparatively low emission current density and high beam divergence.

In pulsed operation, suitable for application at high-energy accelerators and colliders, the ECR source limitations can be overcome by using a high brightness proton source outside the magnetic field instead of the ECR source. In this technique (which was implemented for the first time at INR, Moscow [2]), the proton beam is focussed and neutralized in a hydrogen cell producing the high brightness 6.0-8.0 keV atomic H° beam. The atomic H^0 beam is injected into the superconducting solenoid, where both the He ionizer cell and the optically-pumped Rb cell are situated in the 25-30 kG solenoid field. The solenoid field is produced by a new superconducting solenoid with a re-condensing cooling system. The injected H atoms are ionized in the He cell with 60-80% efficiency to form a low emittance intense proton beam and then enter the polarized Rb vapour cell (see Figure 1). The protons pick up polarized electrons from the Rb atoms to become a beam of electron-spin polarized H atoms (similar to the ECR based OPPIS). A negative bias of about 3.0-5.0 kV applied to the He cell decelerate the proton beam produced in the cell to the 3.0 keV beam energy, optimal for the charge– exchange collisions in the rubidium and sodium cells. This allows energy separation of the polarized hydrogen atoms produced after lower energy proton neutralization in Rb-vapour and residual hydrogen atoms of the primary beam.

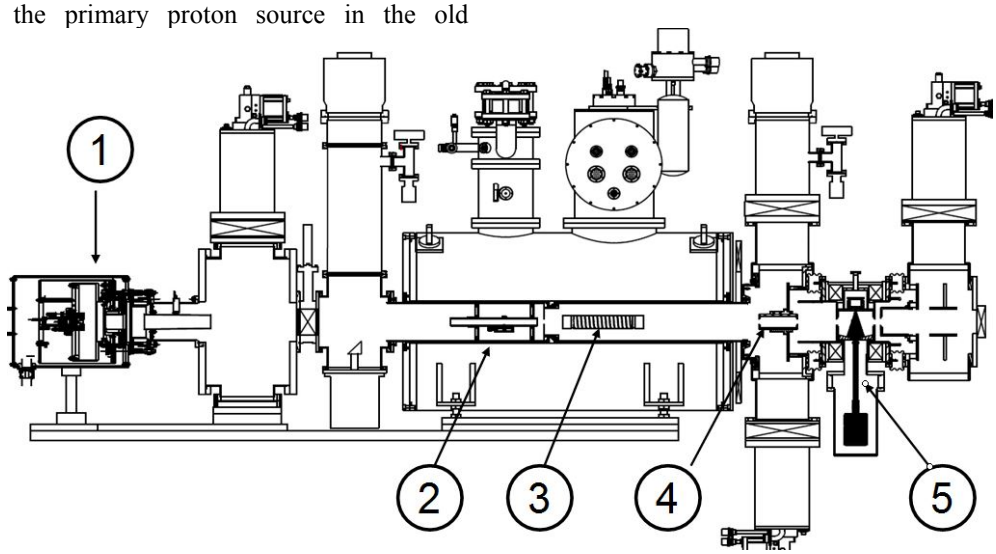


Figure 1: A new polarized source layout: 1–atomic hydrogen injector; 2–pulsed He –gaseous ionizer cell; 3–optically-pumped Rb-vapour cell; 4–Sona-transition; 5–Na-jet ionizer cell.

Copyright © 2013 CC-BY-3.0 and by the respective authors

Residual atomic H beam is converted to un-polarized H^- ion beam with lower yield (3-4% at 6.0-8.0 keV atomic beam energy). The H^- ion beam acceleration (by applying a pulsed -32 kV voltage to the ionizer cell) produces polarized H^- ions with beam energy of 35 keV and un-polarized beam with energy of 38-40 keV. Further suppression of un-polarized higher energy ion beam is produced by magnetic separation in the LEBT.

Atomic hydrogen beam currents of equivalent densities in excess of a 100 mA/cm^2 were obtained at the Na jet ionizer location (about 240 cm from the source) by using a high brightness fast atomic beam source which was developed in collaboration with BINP, Novosibirsk. Estimated polarized H^- ion beam current of about 5-10 mA is expected in this source after upgrade completion (assuming 50% ionization efficiency in He-cell and 50 % neutralization efficiency in the optically-pumped Rb-vapour cell). In feasibility studies of this technique (performed at TRIUMF) in excess of 10 mA polarized H^- and 50 mA proton beam intensities were demonstrated [3]. The beam losses during proton beam deceleration introduced additional losses. Higher polarization is also expected with the fast atomic beam source due to: a) elimination of neutralization in residual hydrogen; b) better Sona-transition efficiency for the smaller ~ 1.5 cm diameter beam; c) use of higher ionizer field (up to 3.0 kG). All these factors combined should increase polarization in the pulsed OPPIS to over 85%.

ATOMIC BEAM SOURCE DEVELOPMENT

In the atomic hydrogen beam source the primary proton beam is produced by a four-grid multi-aperture ion extraction optical system and neutralized in the H_2 gas cell downstream from the grids. A high-brightness atomic hydrogen beam was obtained in this injector by using a plasma emitter with a low transverse ion temperature (of about 0.2 eV), which is formed by plasma jet expansion from the arc plasma generator [4]. The multi-hole grids are spherically shaped to produce "geometrical" beam focusing. The grids are made of 0.4 mm thick molybdenum plates. Holes (0.8 mm diameter) in the plates were produced by photo-etching techniques. The hole array form a hexagonal structure with a step of 1.1 mm and outer diameter of 5.0 cm. The grids were shaped by re-crystallization under pressure at high temperature and were welded to stainless steel holders by a pulsed CO_2 laser. At an emission current density of 470 mA/cm^2, the angular divergence of the produced beam was measured to be ~ 10-12 mrad.

The focal length of the spherical ion extraction system was optimized for the OPPIS application, which is characterized by a long polarizing structure of the charge-exchange cells and small (2.0 cm diameter) Na-jet ionizer cell, which is located 240 cm from the source (see Figure 1). An optimal drift-space length of about 140 cm is required for convergence of the 5 cm (initial diameter) beam to 2.5 cm diameter He-ionizer cell. About 20% of the total beam intensity (~3.5 A) can be transported through the Na-jet cell acceptance by using the optimal extraction grid system with a focal length: $F \sim 200$ cm. Three spherical IOS were tested on the test-bench at BNL. The focusing lengths of IOS #1 and #3 were ~150 cm and for IOS#3 F~250 cm, which allowed study of optimal beam formation. IOS#2 produced about 500 mA equivalent atomic H beam within the 2.0 cm diameter Na-jet ionizer acceptance (at the distance 240 cm from the source) and 16 mA H^- ion beam current.

HELIUM IONIZER CELL. BEAM ENERGY SEPARATION

The He-ionizer cell is a 40 cm long stainless steel tube with an inside diameter 25.4 mm. A new fast "electro-dynamic" valve for He-gas injection to the cell was developed for operation in the 30 kG solenoid field. In this valve, a pulsed current of about 100 A is passed through the flexible springing plate (made of beryllium bronze foil with a thickness of 0.5 mm). The Lorentz force: $\mathbf{F} = eL\,[\,\mathbf{I}\times\mathbf{B}] = 15$ N for a L=5 cm long plate. The plate is fixed at one end and this force bends the plate and opens the small (0.5 mm diameter) hole which is sealed with a Viton O-ring. The pulsed current rise-time is ~ 50 μs and gas pressure rise time is about 100 μs

The proton beam produced in the He cell is decelerated from 6.0 keV to 2.5 keV by a negative potential of 3.5 keV applied to the cell. At the 2.5 keV beam energy, the H^- ion yield in the sodium ionizer cell is near maximum (~ 8.4%) and the polarized electron capture cross-section from Rb atoms is also near the maximum of ~ $0.8\cdot10^{-14}$ cm^2. The deceleration was produced by a precisely aligned (to reduce beam losses) three wire-grid system. A small negative bias was applied to the first grid at the cell entrance and second grid at the cell exit to trap electrons in the cell for space-charge compensation. Fine tuning of the grids voltages is required for the polarized beam current optimization and total current reduction of the He-cell pulsed power supply.

About 40% residual (which passed the He-cell without ionization) atomic beam component at 6.0 keV energy will pass through the deceleration system and Rb cell and be ionized in Na-cell producing H^- ion beam. The H^- ion yield at 6 keV is about 4%. This is a significant suppression in comparison with the main 2.5 keV beam, but it would be a strong polarization dilution unless further suppression is applied. The H^- ion beam acceleration produce polarized H^- ion beam with 35 keV beam energy and un-polarized beam with 38.5 keV energy. The un-polarized 38.5 keV beam component is well separated after the 24 degree bending magnet in the LEBT. In measurements of beam separation, the beam energy was varied by the accelerating voltage applied to the Na-jet ionizer cell. At 32.5 keV accelerating voltage (where the polarized beam component of 2.5 keV beam energy accelerated to 35.0 keV, optimal for injection into the RFQ) the transmission of residual 6.0 keV un-polarized beam component is strongly suppressed (to less than 2 % of polarized beam component).

Copyright © 2013 CC-BY-3.0 and by the respective authors

EXPERIMENTAL RESULTS

The beam polarization was measured in the precision absolute polarimeter at 200 MeV beam energy after the Linac [5]. The polarization and H^- beam current measurements (after acceleration to 200 MeV in the Linac) vs. Rb-vapor thickness is presented in Figure 2.

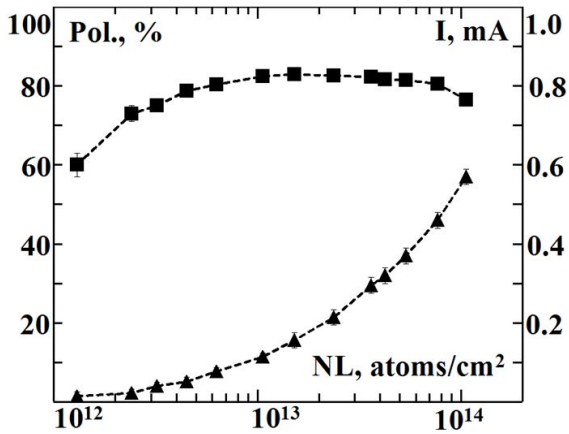


Figure 2: Polarization (squares at the left axis) and beam intensity (triangles- in mA at the right axis) vs. Rb-vapour thickness.

At low Rb-vapor densities, the residual (un-polarized) H^- ion beam current produced by neutralization in residual gas and incomplete energy separation is less than 0.01 mA. Therefore, the polarization dilution due to these factors does not exceed ~ 2%. There was observed some polarization drop at **NL** $\geq 10^{14}$ atoms/cm^2 (**N** ~ $3 \cdot 10^{13}$ atoms/ cm^3, Rb-cell length - **L**=30 cm). Depolarization due to "radiation trapping" is small (at this density Rb-vapor), but some polarization losses may occur due to reduced polarization near the cell walls. This limits the proton beam size and requires good matching between the beam and the Rb-cell diameter. These losses depend on atomic beam intensity and were reduced by laser tuning and atomic beam parameters optimization.

Polarized beam intensity produced in the source exceeds 4.0 mA. The H^- ion beam produced in the sodium-jet ionizer cell is accelerated to 35 keV. This energy increase is essential for the high intensity beam transport. Strong space-charge effects cause significant beam losses in the LEBT line. Basic limitations on the high-intensity polarized H^- ion beam production and transport were experimentally studied in charge-exchange collisions of the neutral atomic hydrogen beam in the Na-vapor-jet ionizer cell. The LEBT was modified to reduce losses and 1.4 mA of polarized beam (after energy separation in the bending magnet and after 6 m in LEBT) was transported to the RFQ and ~ 0.7 mA of beam was accelerated in the Linac to 200 MeV. This current can be further increased by increases in the atomic beam intensity and reduction of the beam losses in LEBT.

Electron depolarization due to spin-orbital interaction in exited (2S, 2P) states of hydrogen atoms should be suppressed by high magnetic field in the Rb-cell [6]. Polarization dependence on magnetic field in the Rb-cell is presented in Figure 3. At every field set-point, the Sona-transition field distribution was optimized by correction – coil tuning. The polarization saturation was observed at super-conducting solenoid fields ≥ 25 kG.

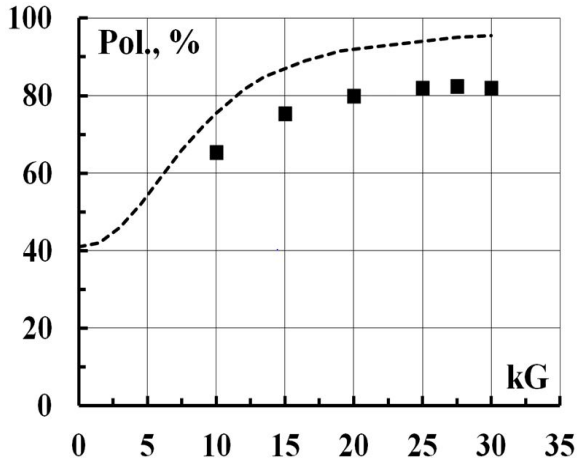


Figure 3: Squares-polarization vs. magnetic field in the Rb-cell. Dashed line–calculations [6].

SUMMARY

The performance of the new source in Run 13 is presented in Table 1 (Rb-cell thickness **NL**$\times 10^{13}$ atoms/cm^2. Linac pulse duration-300 μs. Booster input $\times 10^{11}$ ions/pulse):

Table 1: New Source Performance in Run 13

Rb-cell thickness, **NL**	3.6	5.3	7.6	10.6
Linac Current, μA	295	370	430	570
Booster Input $\times 10^{11}$	4.9	6.2	7.3	9.0
Pol. %, at 200 MeV	84	83	80.5	78

Very reliable operation and reduced maintenance time was demonstrated. In the first year of operation, the new source performance exceeded the old ECR-based source parameters. This was a major factor contributing to the polarization increase to about 60 % for the RHIC colliding beams.

REFERENCES

[1] A. Zelenski et al., ICIS 2001 Proc., Rev. Sci. Instr., **73** (2002) 888.
[2] A. Zelenski et al., NIM **245** (1986) 223.
[3] A. Zelenski et al., Hyperfine Interaction **127** (2000) 475.
[4] V.I. Davydenko, A.A. Ivanov, Rev. Sci. Instr. **72**, (2004) 1809.
[5] A. Zelenski et al., SPIN 2010 Conf. Proc., J. Phys. Conf. Ser. (2011) 295012132.
[6] E. Hinds et al., NIM **189** (1981) 599.

Copyright © 2013 CC-BY-3.0 and by the respective authors

FIRST COMMISSIONING EXPERIENCE WITH THE LINAC4 3 MEV FRONT-END AT CERN

J.B. Lallement, A. Akroh, G. Bellodi, J.F. Comblin, V.A. Dimov, E. Granemann Souza, J. Lettry, A.M. Lombardi, O. Midttun, E. Ovalle, U. Raich, F. Roncarolo, C. Rossi, J.L. Sanchez Alvarez, R. Scrivens, C.A. Valerio-Lizarraga, M. Vretenar, M. Yarmohammadi Satri
CERN, Geneva, Switzerland

Abstract

Linac4 is a normal-conducting 160 MeV H^- linear accelerator presently under construction at CERN. It will replace the present 50 MeV Linac2 as injector of the proton accelerator complex as part of a project to increase the LHC luminosity. The Linac front-end, composed of a 45 keV ion source, a Low Energy Beam Transport (LEBT), a 352.2 MHz Radio Frequency Quadrupole (RFQ) and a Medium Energy Beam Transport (MEBT) housing a beam chopper, have been commissioned at the 3 MeV test stand during the first half of 2013. The status of the installation and the results of the first commissioning stage are presented in this paper.

THE LINAC4 PROJECT

Linac4 is a new accelerator, first part of a project to improve the CERN proton accelerator chain [1]. The higher injection energy (160 MeV vs 50 MeV for Linac2) and the H^- charge exchange injection will make it possible to inject more intensity into the PS Booster. The 80 m long accelerator will be housed in a 101 m tunnel, 12 m underground. A view of the Linac in its tunnel is shown in Figure 1. It consists in a 45 keV RF ion source, a 2 magnetic solenoid LEBT; a 352.2 MHz RFQ accelerating the beam to 3 MeV; a MEBT housing a fast beam chopper; a 50 MeV Drift Tube Linac (DTL) composed of 3 tanks; a 100 MeV Coupled Cell Drift Tube Linac made of 7 modules of 3 coupled tanks and a Pi Mode Structure (PIMS) up to 160 MeV. The schematic layout is shown in Figure 2. The Linac will be connected by a 60 m transfer line to the present Linac2-PSB line. Figure 3 represents the integration of Linac4 in the PS complex. The linac positioning was also designed to be compatible with an extension to 5 GeV as part of the Superconducting Proton Linac (SPL) [2].

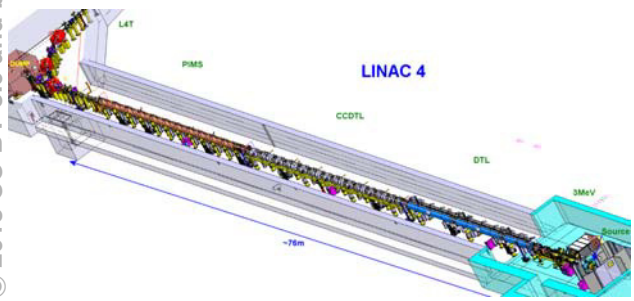


Figure 1: Linac4 in its tunnel.



Figure 2: Linac4 layout.

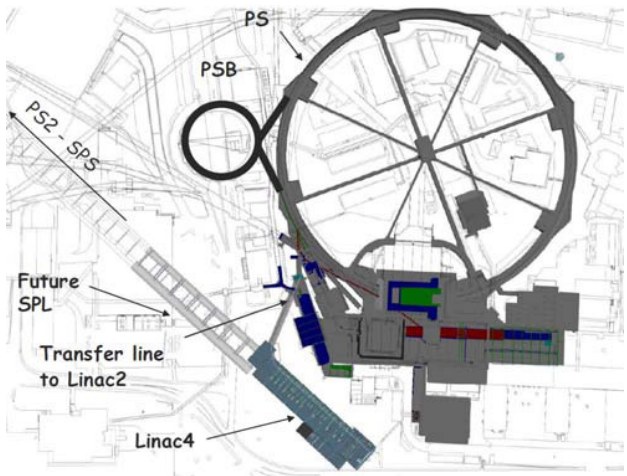


Figure 3: Linac4 integration in the CERN PS complex.

The Linac4 energy and repetition rate (160 MeV, 1.1 Hz) are defined by the PSB while the 352.2 MHz operation frequency is that of the LEP accelerator, from which a large inventory of RF equipment is recuperated. The design parameters are given in Table 1.

Table 1: Linac4 Design Parameters

Ion Species	H^-	
Length	77	m
Output Energy	160	MeV
Frequency	352.2	MHz
Repetition rate	1.1 (max. 2)	Hz
Pulse length	400 (max. 1200)	μs
Chopping factor	62	%
Source current	80	mA
Linac pulse current	40	mA

Copyright © 2013 CC-BY-3.0 and by the respective authors

5 COMMISSIONING STAGES

The commissioning of Linac4 is foreseen in 5 stages at the energies of 3, 12, 50, 105 and 160 MeV, corresponding to the commissioning of the different accelerating structures composing the accelerator [3]. At each stage a dedicated beam diagnostic bench will be temporarily installed.

A first pre-commissioning at 3 MeV was completed in June 2013 in a dedicated test stand before removal and installation of the RFQ and chopper line to the final location in the tunnel. From October 2013, beam commissioning in the tunnel will start with the aim of finishing the commissioning of the 3 MeV part. Once completed, the first tank of the DTL will be installed and the beam should reach an energy of 12 MeV in the first half of 2014. Beam commissioning and machine installation periods will then be interlaced until 2015: Tank 2 and 3 of the DTL to 50 MeV, the 7 CCDTL modules and the first PIMS cavity to 105 MeV and all the PIMS section up to 160 MeV. In order to set the transverse and longitudinal beam parameters, 2 movable diagnostic benches will be used in addition to the diagnostics permanently installed in the Linac. The first bench with an emittance meter and a spectrometer line will be used up to 12 MeV. The second one, with quadrupoles and transverse profile diagnostics (SEM-Grids) for emittance reconstruction with the forward method and with phase pick-ups (BPMs) for Time Of Flight (TOF), will be used at 50 and 105 MeV. This second diagnostic line can be seen in Figure 4. For the last stage, beam commissioning at 160 MeV, the diagnostics permanently installed in the straight line going to the main beam dump will be used.

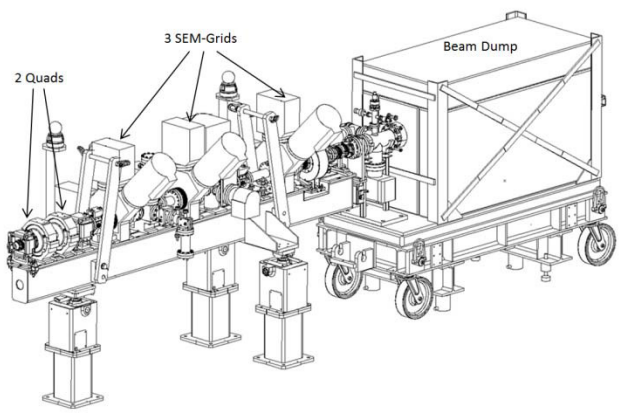


Figure 4: Technical drawing of the 50-105 MeV diagnostic bench attached to the commissioning beam dump.

THE 3 MEV TEST STAND

Experience with other linacs and dedicated beam dynamics studies show that the most difficult part to master is the low energy part, where the beam is strongly influenced by the space charge. This is also the part where there are 2 very critical devices defining the transverse and longitudinal beam characteristics, the ion source and the RFQ. Beam current, distribution and emittance from the source, space charge neutralization in the LEBT, capture and longitudinal emittance in the RFQ, matching and chopping efficiency in the MEBT are all parameters that define the quality of the beam delivered to the PSB. In order to have enough time to study and characterize the low energy beam, it was decided to have a dedicated test stand comprising the ion source, the LEBT, the RFQ, the chopper-line and a temporary diagnostic bench. The test stand was operational in the first half of 2013. Detailed results of the measurement campaign are given in the following paragraphs. A view of the 3 MeV test stand is shown in Figure 5.



Figure 5: View of the test stand.

In the top-left corner, the 45 keV ion source inside the high voltage cage and the RFQ, followed by the MEBT and the diagnostic bench. On the right, the RFQ klystron and wave guides.

Diagnostic Bench

In addition to the diagnostics permanently installed in the line, a temporary diagnostic bench was designed in order to fully characterize the beam at 3 MeV including:

- Beam Current Transformers (BCTs), for intensity measurements.
- Beam Position Monitors (BPMs) which determine the position of beam as well as its intensity.
- An emittance meter, consisting of a 200 µm slit producing a beamlet whose angular distribution is measured with a wire grid 3 m downstream.
- A spectrometer line to measure the beam energy spread.
- A Bunch Shape Monitor (BSM) [4], which provides a measurement of the longitudinal distribution in a micro bunch.
- A halo monitor [5] used to measure not only the transverse beam halo but also the remaining part of the incompletely chopped bunches (time resolved chopping efficiency).

Copyright © 2013 CC-BY-3.0 and by the respective authors

A detailed drawing of the 3 MeV diagnostic bench, straight line and spectrometer line, is shown in Figure 6.

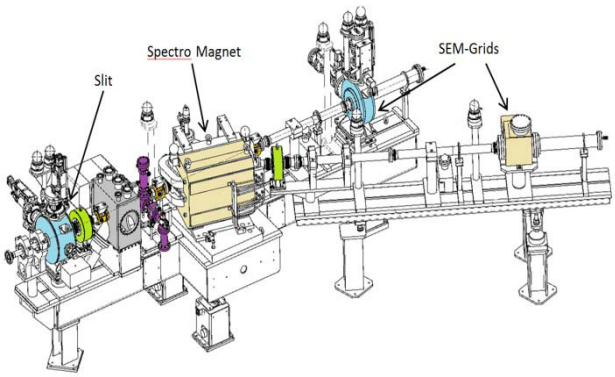


Figure 6: The 3 MeV diagnostic bench.

COMMISSIONING RESULTS

Source and LEBT

The Linac4 ion source consists of a plasma generator and a multi-electrode extraction system (Figure 7). During the commissioning, it was operated in a pulsed mode at 1.2 s interval, keeping the beam output as stable and reliable as possible. During 4 months it was running without any major problems. After typically 2 hours of warming up (stabilization time) it provided stable energy and H- beam current of 16 mA. The source used at the 3 MeV test stand is not the final source of Linac4; the new Cesiated source is presently under construction and test. An operating source with increased performances is due in June 2014.

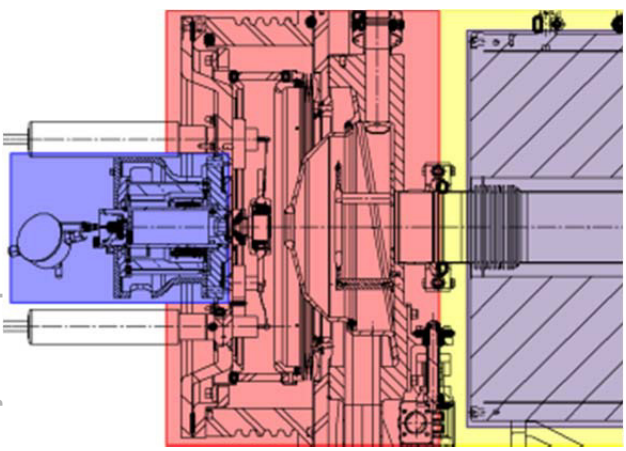


Figure 7: The ion source used at the test stand. Plasma generator (blue), front-end (red) and first part of the LEBT (yellow) including the first solenoid (purple).

The beam transverse emittance was measured with the LEBT emittance meter positioned after the first solenoid for different solenoid settings. These measurements were back-traced with the code Travel [6] to the output of the source, giving a realistic beam distribution further used for simulating the matching to the RFQ. We can see on Figure 8 five different measurements corresponding to different solenoid settings and the respective "back traced" source beam outputs which are all very similar. For the preparation of the RFQ commissioning (matching, transmission studies etc…), the superimposition of these 5 beams was taken as the source beam output distribution for the multiparticle tracking code. The measured RMS normalized transverse emittance out of the source is equal to 0.8 mm.mrad.

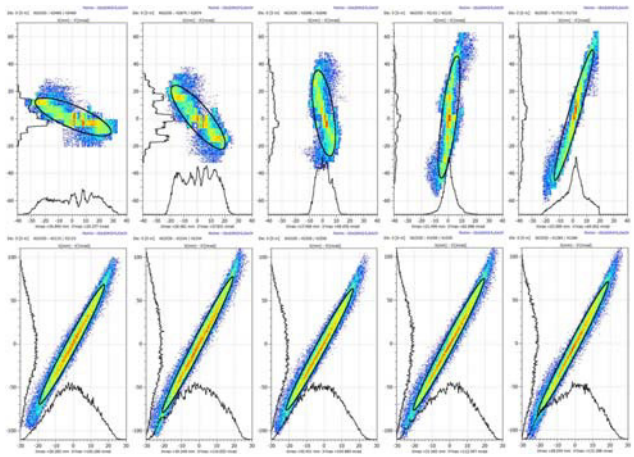


Figure 8: On the top, horizontal emittance measurement for 5 different solenoid settings; on the bottom, the 5 corresponding back-traced source output beam.

In the LEBT, the space charge compensation caused by the secondary particles created by ionization of the residual gas plays an important role in the beam dynamics. The evolution of the transverse emittance ellipse along the beam pulse has been measured for different residual pressures [7]. Figures 9a and 9b show the evolution of the transverse emittance and the Twiss parameter β along the pulse. The stabilization time of the space charge compensation is shorter for high residual gas pressure but the resulting emittance is then larger.

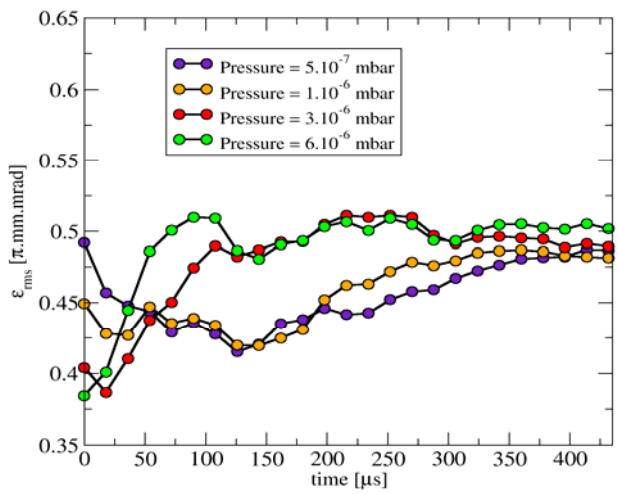


Figure 9a: Transverse emittance evolution along the beam pulse for different residual gas pressure.

Copyright © 2013 CC-BY-3.0 and by the respective authors

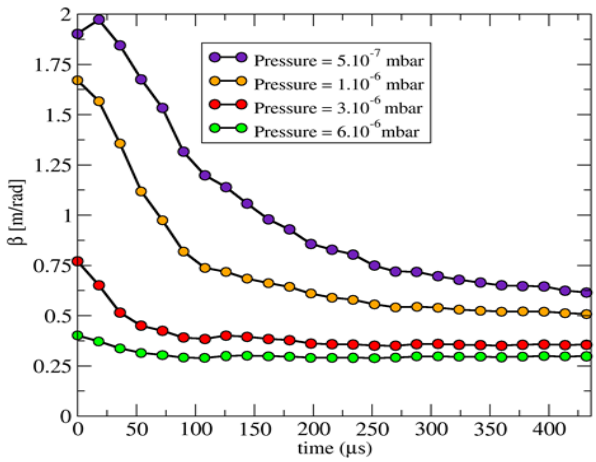


Figure 9b: Beta parameter evolution along the beam pulse for different residual gas pressure.

RFQ

The Linac4 RFQ was designed and manufactured at CERN [8]. The first H- ion beam was injected on March 13th 2013 and the first accelerated beam was observed at the RFQ output after 10 minutes of LEBT solenoids and steerer magnets fine tuning. The empirically optimised solenoid settings were within 3% of the one expected from simulations with Travel code, demonstrating the quality of the RFQ machining and of the LEBT modelling. The first 3 MeV BCT signal observed on that day is shown in Figure 10 (10 mA steady state H- beam current).

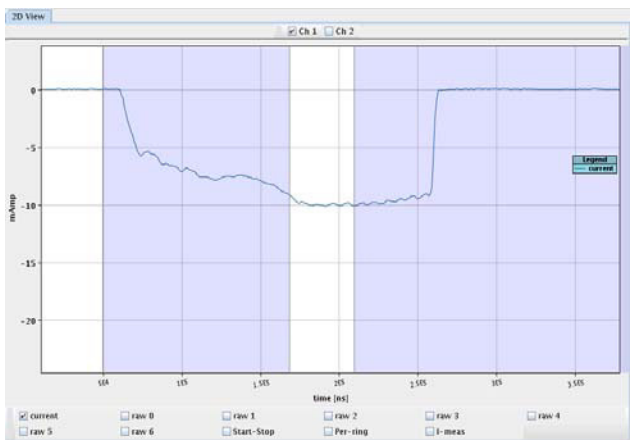


Figure 10: RFQ output beam current – 2013/03/13.

After retuning beam focusing and steering in the LEBT, the RFQ maximum transmission was reached, giving a 12 mA peak current at 3 MeV (75% transmission). The RFQ transmission was studied with Parmteq [9] and Toutatis [10] codes, taking into account the beam parameters measured in the LEBT. Given that the emittance from the source is larger than expected, 25% of the beam from the source is bound to be lost in the first centimetres of the RFQ. Figure 11 shows the comparison of the emittance measured in the LEBT and the RFQ acceptance.

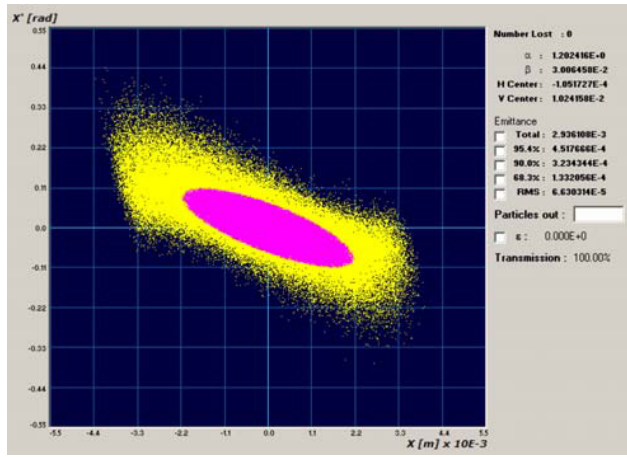


Figure 11: Comparison of measured emittance (yellow) and RFQ acceptance (pink).

Figure 12 shows a comparison of the simulated RFQ transmission (purple dots) and measured transmission for different gas pressure in the LEBT and RF power. It should be noted that the solenoids and steering magnets were optimized, for the case corresponding to 1.e-6 mbar pressure in the LEBT.

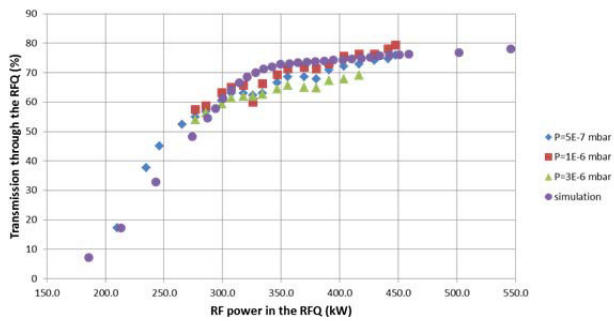


Figure 12: RFQ transmission vs power for different gas pressure in the LEBT.

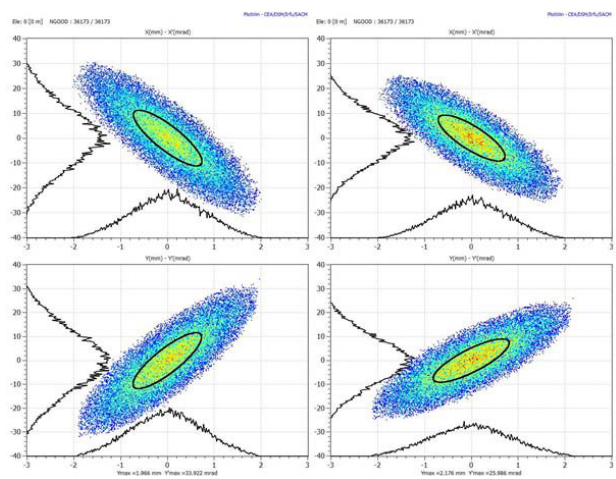


Figure 13: Beam distribution in the Horizontal (top) and vertical (bottom) phase planes at RFQ output; Left: expected from simulation, Right: reconstructed with the forward method.

Copyright © 2013 CC-BY-3.0 and by the respective authors

The transverse emittance was reconstructed after the RFQ with the so-called forward method [3]. The beam profile was measured for different test bench quadrupole settings and the corresponding emittance at the RFQ output computed with the Travel code taking the space charge effects into account. The reconstructed normalized emittance is equal to 0.32 and 0.34 mm.mrad in horizontal and vertical plane respectively compared to 0.36 and 0.37 mm.mrad expected from the simulations. The comparison of the reconstructed and expected phase space distribution is given in Figure 13.

Chopper-Line

The MEBT was installed after the RFQ commissioning was completed. It aims to match the beam to the DTL and modify the time structure of the pulse in order to reduce losses at the PSB injection. The fast chopper is based on an original "low-voltage" concept: the micro bunches that should not be injected in the PSB see a relatively low electric field, generated by two chopper plates. The resulting kick in the phase space is further transferred in the real space by a defocusing quadrupole located at 90° phase advance. The chopped bunches are then collected in a conical aperture beam dump. Figure 14 shows the comparison of the simulated and measured transmission of the chopper-line for chopper ON and OFF varying a MEBT quadrupole gradient. We can see a very good correspondence between simulation and measurements for chopper OFF. For the chopper ON, it turned out that the experimental results are better than simulations, indicating a chopper efficiency better than expected. This could be explained by a coverage factor of the field generated by the chopper higher than expected or by a transverse distribution more Gaussian than assumed in the simulations. The rise and fall time of the chopper is expected to be a few ns; a preliminary measurement with a fast BCT indicates that it is below 10 ns.

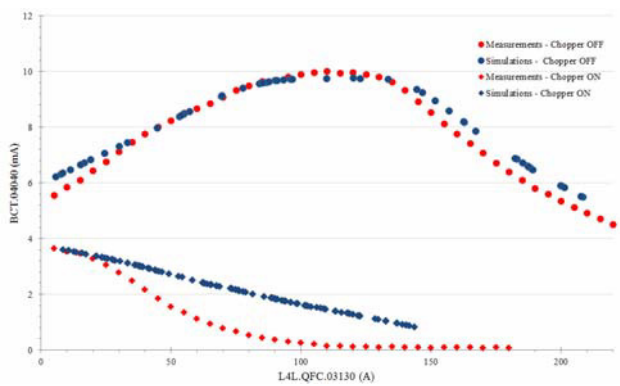


Figure 14: Measured and simulated transmission in the MEBT for chopper ON and OFF.

The longitudinal distribution of the beam was also reconstructed using a method equivalent to the 3 gradients method in the longitudinal plane. The beam phase spread was measured with a BSM for different settings of the second MEBT buncher cavity. As for the transverse plane, we applied the forward method to reconstruct the emittance ellipse in the Phi/E phase space at the output of the RFQ. The measured energy spread is equal to 22 keV RMS compared to the 21 keV expected from simulation.

The matching to the DTL, time resolved measurement with the halo monitor and comparison between TOF and spectrometer measurement will be studied once the line moved in the tunnel.

PROJECT STATUS AND SCHEDULE

The installation of general infrastructure and services is now completed in the Linac4 tunnel. After the successful measurement at the test stand, the 3 MeV line was installed and will be re-commissioned from October 2013. The DTL and CCDTL will be installed and commissioned in 2014, and the PIMS in 2015. A one year reliability run is foreseen in 2016 before the connection of the Linac to the PS Booster foreseen in 2017-18, during an extended stop of the LHC injector chain. Figure 15 shows a view of the Linac4 tunnel in September 2013.



Figure 15: Linac4 tunnel seen from the low energy side. In the foreground, the RFQ and the MEBT.

REFERENCES

[1] F. Gerigk, M. Vretenar (eds.), Linac4 Technical Design Report, CERN-AB-2006-084.
[2] M. Vretenar (ed.), Conceptual Design of the SPL, a high-power superconducting Linac at CERN, CERN 2000-012.
[3] JB. Lallement et al., Linac4 beam commissioning strategy, HB-2012, Beijing.
[4] AV. Feshenko, Methods and instrumentation for bunch shape monitor, PAC 2001, Chicago.
[5] K. Hanke, M. Hori, Design and construction of a Beam Shape and Halo Monitor for the CERN SPL, CERN AB-2005-033 OP.
[6] A. Perrin, JF. Amand, Travel v4.06 user manual, CERN, 2003.
[7] CA. Valerio-Lizarraga et al., Space charge compensation in the Linac4 Low Energy Beam Transport line with negative hydrogen ions, ICIS2013, Chiba.
[8] C. Rossi et al., The RadioFrequency Quadrupole accelerator for the Linac4, Linac08, Victoria.
[9] KR. Crandall, TP. Wangler, PARMTEQ-a beam-dynamics code for the RFQ linear accelerator, AIP, 1988.
[10] R. Duperrier et al., Toutatis, the CEA Saclay RFQ code, Linac2000.

Copyright © 2013 CC-BY-3.0 and by the respective authors

PROTON ACCELERATOR DEVELOPMENT IN CHINA

S.N. Fu, IHEP, Beijing 100049, China

Abstract

The China Spallation Neutron Source (CSNS) and the Chinese Accelerator Driven Systems (C-ADS) projects are both underway in China. The CSNS includes a 100 kW RCS accelerator and first beam on target is planned for 2017. The C-ADS project includes a high power superconducting linac with a low energy (25-50 MeV) initial stage by 2015 and higher power deployment later. In addition to these intense-beam proton accelerators, some other proton accelerators for various applications are also under construction or planned. In this paper, the plans, R&D and construction activities of these projects will be discussed.

INTRODUCTION

Proton accelerator becomes a new direction in Chinese accelerator community for its many important applications. It will be used for neutron source for neutron scattering applications, Accelerator Driven Subcritical system (ADS) for nuclear waste transmutation, proton therapy for cancer treatment, as well as the space radiation effects research. China Spallation Neutron Source started construction in 2011[1]. Its accelerator provides a proton beam of 100 kW power onto the target in the first phase, and then will be upgraded to 500 kW beam power in the second phase. And meanwhile, a small neutron source is under construction in Tsinghua University[2]. In 2010 a Chinese roadmap for long-term development of ADS was proposed by Chinese Academy of Sciences[3] and the first budget of about $260M has be allocated for an ADS test setup construction. This year, Chinese central government has approved two proton accelerator-based big-science projects in its five-year plan: ADS program and space radiation effect research program. These proton accelerator-related projects, no matter big or small, give a great chance to Chinese accelerator community to develop the cutting-edge high-technology of proton accelerator in China. This paper will present an overview of these projects at different stage, including their design, key technology R&D, construction and future plan.

CHINA SPALLATION NEUTRON SOURCE

The CSNS is designed to accelerate proton beam pulses to 1.6 GeV kinetic energy at 25 Hz repetition rate, striking a solid metal target to produce spallation neutrons. The accelerator provides a beam power of 100 kW on the target in the first phase. It will be upgraded to 500kW beam power at the same repetition rate and same output energy in the second phase. For this reason, the present design has reserved a long beam line in LRBT for superconducting spoke cavity installation for the linac energy upgrade in order to compensate for space-charge effect in the RCS when the beam current becomes 5-times higher. Table 1 lists the major parameters of the accelerator in the two phases.

Table1: CSNS Design Parameters

Project Phase	I	II
Beam Power on target [kW]	100	500
Proton energy [GeV]	1.6	1.6
Average beam current [μ A]	62.5	312.5
Pulse repetition rate [Hz]	25	25
Linac energy [MeV]	80	250
Linac type	DTL	+Spoke
Linac RF frequency [MHz]	324	324
Macropulse. ave current [mA]	15	40
Macropulse duty factor	1.0	1.7
RCS circumference [m]	228	228
RCS harmonic number	2	2
RCS Acceptance [πmm-mrad]	540	540
Target Material	Tungsten	Tungsten

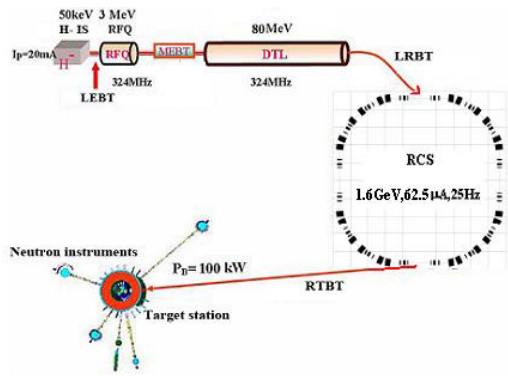


Figure 1: Schematics of the CSNS complex.

A schematic layout of CSNS phase-1 complex is shown in Figure 1. In the phase-1, an ion source produces a peak current of 25mA H^- beam. RFQ linac bunches and accelerates it to 3MeV. DTL linac raises the beam energy to 80MeV. After H^- beam is converted to proton beam via a stripping foil, RCS accumulates and accelerates the proton beam to 1.6GeV before extracting it to the target. 20 neutron channels are designed surrounding the target, but only 3 spectrometers will be built in the first phase due to limited budget.

The CSNS project started construction in September 2011 after the site land and the access road had been

Copyright © 2013 CC-BY-3.0 and by the respective authors

prepared by the local government. The architectures for the linac tunnel has been completed and klystron gallery are under construction. We plan to start installation of the front end of linac in November, 2013. The civil construction status is shown in Figure 2.



Figure 2: Civil construction status of CSNS project.

Front-end

Penning H^- surface source is chosen for CSNS. Based on prototype experience and some optimization in design, a new source for the project has been fabricated and set up at the laboratory of the Dongguan University of Technology for beam extraction test before the test hall is available, as shown in Figure 3.



Figure 3: CSNS H^- ion source in beam extraction test.

RFQ accelerates H^- beam from 50keV to 3MeV, with duty factor of 1.05%. A four-vane type RFQ at 324 MHz has total length of 3.62 m, composed of four technical modules. Two section cavities are resonantly coupled together with a coupling plate in between, as shown in Figure 4. The four module cavities are ready for assembly to form a whole cavity for field tuning. Two sets of 1000 *l*/s ion pumps and 500 *l*/s turbo-molecular pumps are designed for an order of 10^{-7} Torr dynamic vacuum pressure. Another set of backup pumps can be easily added. The RFQ cavity has been fabricated and is ready for assembly for field tuning measurement. Two sets of Burle 4616 Tetrode feed 530 kW total RF power to the RFQ through two coaxial power couplers. In the power test, each source reached 400 kW pulse power with pulse length of 700 μ s at 25 Hz, as shown in Figure 5.

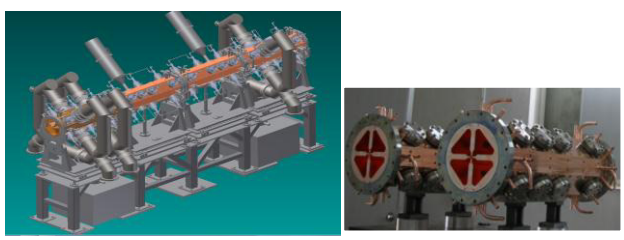


Figure 4: RFQ design and assembled cavity for field tuning.



Figure 5: RFQ power source and its output power in test.

The total length of MEBT is about 3 m, including 10 qaudrupole magnets, 2 bunchers, 12 steering magnets, as well as some beam diagnostics, including 8 BPM, 5 FCT, 4 BPrM, 3 BLM, 2 CT and EM. As the LEBT chopper has already reach a rise/fall time less than 17ns, we will not install the RF choppers in the MEBT in Phase-I, but leaves space for them for upgrade.

DTL Linac

The 324 MHz DTL accelerates the 3 MeV beam from the RFQ to 80 MeV. The DTL linac is composed of 4 tanks with a total length of 35 m. Each tank is about 9m long and assembled with three technical modules. Mass production of the tank and tube started in early 2012 and the first DTL tank has been fabricated. Figure 6 shows the fabricated tubes and tank. They will soon be assembled for field measurement and field tuning with slug tuners and coupling stems.



Figure 6: The fabricated drift tubes and tank.

The RF power source for DTL is 324 MHz klystron from CPI, with maximum output power of 3 MW. The adopted HVPS scheme is 400 Hz AC series resonance high voltage power supply. One power supply feeds the same voltage of 120 kV to two klystron cathodes through their m-anode modulators. We proposed such a new type of HVPS for klystron and demonstrated its feasibility with a 100 Hz prototype. Two sets of the power supply are under manufacture for CSNS DTL. Figure 7 shows the klystron and its HVPS under assembly.



Figure 7: 3MW klystron and its 120 kV HVPS under manufacture.

RCS

The RCS lattice consists of 48 quadrupoles and 24 dipole magnets, forming a four-fold ring with

Copyright © 2013 CC-BY-3.0 and by the respective authors

circumference of 227.92m. In the each super period, an 11m long drift space is left in a triplet cell. These four uninterrupted long straight sections are arranged with injection, extraction, RF acceleration and transverse collimation respectively. To reduce space charge effect, H^- beam from linac is stripped by a carbon foil and painted into a large phase space about 240 π mm-mrad in two transversal directions with 8 pulsed bump magnets. The maximum space charge tune shift is -0.28 in bunching stage. A two-stage collimator system with an acceptance of 350 π mm-mrad is utilized for removing halo particles.

The RCS AC dipole and quadrupole magnets is in mass production. The first dipole and quadrupole magnets in mass production have been produced(Figure 8). They have been continuously operated with full AC current of 877 A for 72 hours. The coils and cores of the magnets are robust enough, and no crack was found on their surfaces. The field of these two types of magnets has also been measured, and the results meet the specification. The magnet installation in the ring tunnel is foreseen in the middle of 2015 when the tunnel is available.

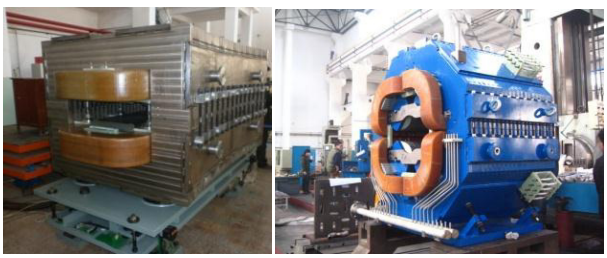


Figure 8: RCS dipole and quadrupole magnets in mass production.

The power supply for the magnets uses White resonant circuits to avoid the impact to the grid. Due to nonlinear feature of the magnet core, a pure sinusoid AC current from the power supply will result in a deformed sinusoid magnetic field with an unacceptable tracking error. To deal with this issue, high order harmonic current is injected into the power supply for compensating for the nonlinearity. The 24 dipole magnets are powered with one set of current supply and the 48 quadrupole magnets are powered with 5 sets of current supplies. All of these power supplies are under mass production.

The RCS has eight ferrite-loaded cavities for proton acceleration, of which seven cavities provide total 165 kV RF voltage with additional one as backup. The cavity resonant frequency shifts from 1.02 MHz to 2.44 MHz in 20 ms by a bias current supply. In the prototype RF system, the response bandwidth of the bias current supply has been improved up to 10 kHz by adding a small linear shunt modulator to the existing switching power supply. The resulted tracking error apparently reduced within the specification of ±0.2%. Based on the experience of high power operation of the RF system prototype, the design of the RF cavity structure has been optimized to ameliorate the cavity and RF transmitter performance. Manufacture of 8 sets of RF cavities and 500 kW transmitters has been in good progress. Figure 9 shows the fabricated cavity and its RF power source.



Figure 9: Ferrite-loaded RCS cavity and its RF power source in mass production.

Ceramic vacuum chambers are used in the RCS dipole and quadrupole magnets, injection bumps and extraction kickers to avoid the eddy current. The chamber size for dipole magnet is rather large with a length of 2.8 m and a cross-section of 135(V)×218(H) mm in inner diameter. All of these chambers have started mass production by a Germany vendor FRIATECH and domestic vendors. The inner surface of the chamber will be coated with TiN for low SEE. Figure 10 is the ceramic chamber for dipole magnet.



Figure 10: Ceramic chamber for dipole magnet.

The Beam Lines and Interface

The LRBT transports the H^- beam to the ring and it 47quadrupoles and 4 bending magnets. Some of the quadrupoles have been produced. A rebuncher is installed for reduction of the beam momentum spread. The injection stripping foil facility has been manufactured with 20 carbon foils on a rotating frame, as shown in Figure 11.

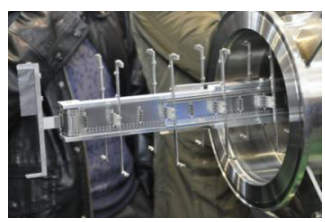


Figure 11: Stripping foil for H^- injection.

C-ADS CW PROTON LINAC

ADS in China is applied for nuclear waste transmutation, as a backup to the rapid nuclear power development. The accumulated waste is estimated to be more than 10k tons in 2020, and it will be doubled in 2030. ADS has been recognized as the best option for the nuclear waste final disposal. Roadmap of ADS development has been scheduled in four phases in China, as shown in Figure 12. In phase-I from 2011 to 2015, as R&D period, A 25-50 MeV linac will output a beam

Copyright © 2013 CC-BY-3.0 and by the respective authors

current of 10 mA in CW; phase-II will take a few years to increase the beam energy up to 250 MeV with superconducting spoke cavities and the accelerator will be coupled with a subcritical reactor to form an ADS research system. In Phase-III, until 2022, the beam energy will further rise to 0.6-1 GeV to drive a subcritical system of 100 MW thermal power. In phase-IV, more superconducting elliptical cavities will be added to the linac to raise beam energy up to 1.2-1.5 GeV until 2032, serving for a full-scale ADS demonstration facility.

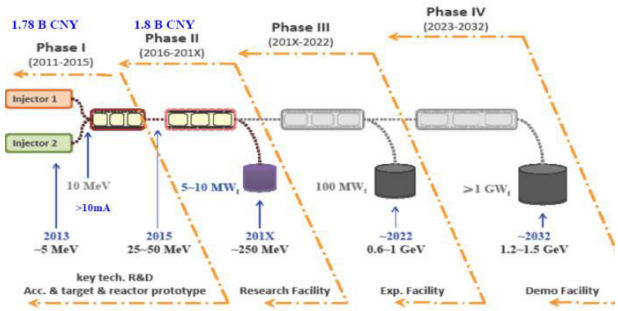


Figure 12: Roadmap for ADS development in China.

Linac Design

In the preliminary design a 1.5 GeV linac consists of two injectors, two spoke cavity sections and two elliptical cavity sections, as shown in Figure 13. In operation, only one injector runs and another is hot standby for a high reliability which is a key requirement for the target and reactor. To explore different technology at present, the two injectors have different design: the Injector-I is mainly composed with an ECR ion source, a 3.2 MeV room temperature RFQ at 325 MHz and superconducting spoke cavities at 325 MHz; while the Injector-II mainly consists of an ECR ion source, a 2.1 MeV room-temperature RFQ at 162.5 MHz and superconducting HWR cavities at 162.5 MHz. IHEP is in charge of the Injector-I, and IMP in charge of Injector-II.

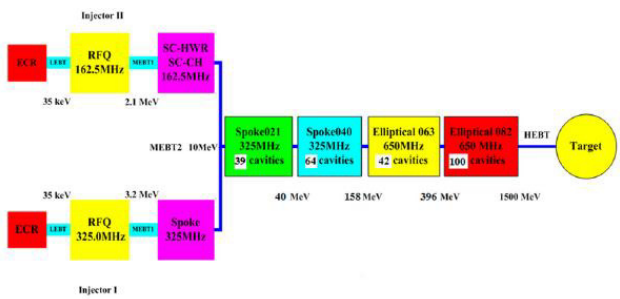


Figure 13: Layout of the C-ADS linac.

Key Technology R&D

Ion source An ECR ion source has been set up for beam extraction test at IMP, as shown in Figure 14(left). It can provide the RFQ with a CW proton beam of 25 mA at 35 KeV. This ion source together with LEBT will recently be installed in the tunnel at IHEP. At present the major work focus on the long-term operation stability of the ion source.

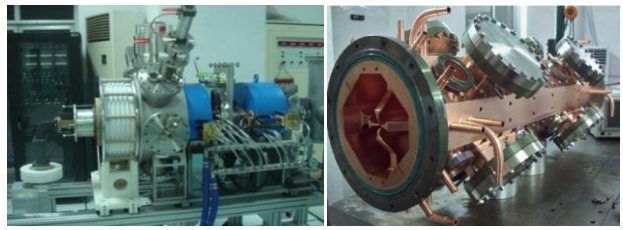


Figure 14: ECR ion source together with LEBT(left), and RFQ cavity(right) for Injector-I.

RFQ-I This four-vane type 325MHz RFQ will operate in CW mode at room temperature with RF power consumption about 273 kW. The full length of the vane is about 4.7m and maximum power density on the surface is 3.77 W/cm^2. Fabrication of the RFQ cavity is finished (Figure14) and RF measurement result shows that the design values have been achieved. Toshiba 600kW 325MHz CW klystron and 80 kV PSM power supply are adopted as the RF power source for the RFQ.

RFQ-II This four-vane type 162.5 MHz RFQ uses the PI-mode stabilizer for a wide mode separation between working quadrupole mode and the nearby modes. Fabrication of such a large cavity is not easy, and thus a short model cavity has been made for manufacture technology development, as shown in Figure 15.

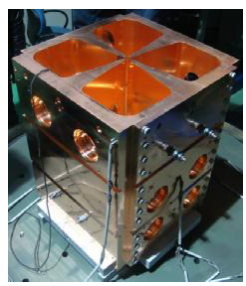


Figure 15：Short model cavity of 162.5 MHz RFQ for Injector-II.

Spoke012 This 325 MHz superconducting spoke cavity follows the 3.2 MeV RFQ-I. Two such low-β of 0.12 cavities has been fabricated. The horizontal test has been completed at 4K and Q_0 value reaches 2.2x10^8 at E=6.5 MV/m, as shown in Figure 16.

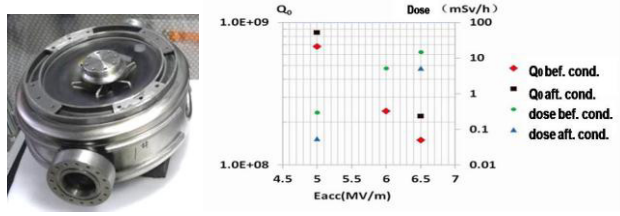


Figure 16: Spoke012 cavity and its horizontal test result for Injector-I.

HWR This 162.5 MHz superconducting cavity of β =0.1 follows 2.1 MeV RFQ-II. Two prototype cavities have been made (Figure 17) with measured Q_0=4.1x10^8 at 8.3 MV/m.

Copyright © 2013 CC-BY-3.0 and by the respective authors



Figure 17: Prototype QWR cavity with β =0.1 for Injector-II.

Spoke021 and elliptic cavity In addition to the low energy section, superconducting cavities for medium and high energy sections are also under development. At present, two 325 MHz spoke cavities of β = 0.21 and some 650 MHz elliptical cavities of β =0.82 are under development, as shown in Figure 18.



Figure 18: Prototype development of 325 MHz spoke cavities with β = 0.21 and some 650 MHz elliptical cavities with β =0.82, for main linc.

OTHER PROTON ACCELERATORS

Except for the two high intensity proton accelerators for CSNS and C-ADS, some other proton accelerators are also under construction or in planning.

CPHS Accelerator

The Compact Pulsed Hadron Source (CPHS) in Tsinghua University, is driven by a pulsed high-current proton linac with a beam duty factor of 3%. The accelerator consists of an ECR ion source, a LEBT, an RFQ, a DTL and a HEBT beam line. The linac accelerates the proton beam to 13MeV, and delivers it to a Beryllium target. Four neutron beam lines are planned in the CPHS project, among which two lines are being constructed for the SANS and Neutron Imaging.

The 325 MHz RFQ has a four-vane structure and accelerates protons from 50keV to 3MeV. The inter-vane voltage increases with the beam energy. The total length of the RFQ is greatly shortened with a high transmission rate. The coupling plates become unnecessary for the 3m-long RFQ. The RFQ are designed to be matched to the DTL directly without MEBT. The 13MeV DTL adopts Samarium-cobalt permanent magnets with a field gradient almost constant (84.6T/m) in lattice structure of FDFD, which ensures small envelop of the beam.

At present, the 3MeV RFQ has been installed for beam tuning (Figure 18). In March 2013, its output peak current of 44 mA was achieved and the transmission efficiency was 88% while the input peak current was 50 mA with 50 μs pulse length at 50 Hz. The following DTL is under fabrication.



Figure 19: CPHS linac under beam tuning.

First neutron beam was obtained in July, 2013 by 22 mA proton beam with pulse length of 80 μs at 50 Hz. The total estimated neutron flux is about 2.8×10^{10} n/s.

APTron Accelerator

The Advanced Proton Therapy Facility (APTron) is proton therapy machine serving as a hospital-based facility [4]. It will be built at Jiading district of Shanghai with the technical support from Shanghai Institute of Applied Physics, CAS. The accelerator consists of a 7 MeV linac injector, a 24.6m circumference synchrotron capable of accelerating protons up to 250MeV, two horizontal fixed beam line and an isocentric gantry beam line in phase I, and can be upgraded to 3 gantry beam lines in total in phase II. The 7-MeV injector is composed of a RFQ and a short DTL tank. A proton beam is extracted from the synchrotron in an energy range of 70~250MeV with proton particles of 8×10^{10}p/spill at a repetition frequency of 0.1~0.67 Hz. This project has been funded by the local government.

Proton Accelerator for Space Radiation Test

Space radiation effect study calls for a proton accelerator with a weak beam current and micro-size beam spot on sample. This accelerator consists of a tandem with terminal voltage of 6 MV and a synchrotron with output energy range from 10-300 MeV. Beam from the tandem and the synchrotron will be sent to several test stands. A preliminary design of the accelerator has been proposed by IHEP. And this project has been approved in principle by the central government and it is foreseen the project will start construction in a couple of years.

ACKNOWLEDGEMENTS

The author thanks Prof. X.L Guan, Prof. D.M Li and Chinese proton accelerator community for their providing the necessary information for this paper.

REFERENCES

[1] S.N. Fu, H.S. Chen, et al., Status of CSNS Project, IPAC2013, May, 2013, Shanghai.
[2] Guan Xialing, et al., Compact Pulse Hadron Source Status, Proceedings of HIAT 2012, Chicago, IL USA.
[3] Wenlong Zhan, ADS Program and Key Technology R&D in China, IPAC2013, May, 2013, Shanghai.
[4] J. Xu, et al., Radiation Calculations for Advanced Proton Therapy Facility, IPAC2013, May, 2013, Shanghai.

Copyright © 2013 CC-BY-3.0 and by the respective authors

ACCELERATOR-DRIVEN SUBCRITICAL FISSION TO DESTROY TRANSURANICS AND CLOSE THE NUCLEAR FUEL CYCLE*

S. Assadi, C. Collins, J. Comeaux, K. Damborsky, J. Kellams, F. Lu, P. McIntyre#, K. Melconian, N. Pogue, M. Salanne, A. Sattarov, E. Sooby, and P. Tsvetkov, Texas A&M University, College Station, TX 77845 USA

Abstract

A design for accelerator-driven subcritical fission in a molten salt core (ADAM) has been made for the purpose of destroying the transuranic elements in used nuclear fuel as fast as they are made in a conventional nuclear power plant. The oxide fuel is extracted from the used fuel assemblies into molten chloride salt using pyroprocessing, and the transuranic, uranium, and fission product salts are separated into three batches using electroseparation. The transuranic salt is then transferred to a subcritical core, with neutron gain 0.97. The core is driven by 800 MeV proton beams from a 12 mA CW strong-focusing cyclotron. The transuranics are destroyed and the fission heat is used to produce electric power. Simulations of many potential failure modes have been performed; the core cannot reach criticality in any failure-mode scenario considered. It operates as an energy amplifier with an energy gain ~5.5.

INTRODUCTION

Today nuclear power plants generate 20% of the electric power in the United States [1]. Until recently nuclear power comprised 20% of the grid in Germany and 30% in Japan, but Germany has moved to end their nuclear power production and Japan has idled their reactor fleet. Those decisions reflect a growing public concern about the safety of nuclear power. The meltdowns at Three Mile Island [2], Chernobyl [3], and Fukushima [4] underscore that this abundant source of energy can also produce extreme hazards.

The most enduring hazard of nuclear power is the large quantity of hazardous radioisotopes in used nuclear fuel (UNF). The most dangerous among those are transuranics (TRU, elements beyond uranium in the periodic table). The transuranics contained in the ~70,000 tons of UNF in the US have a radiotoxicity $>10^{13}$ Sv and half-lives of 10^5-10^6 years. The present accumulation of UNF also still contains about 1/3 of the entire US reserves of uranium. Long-term storage would pose the risk unto the generations of future release of immense radiotoxicity, and would sequester a major portion of available uranium resources. ADAM has been designed to offer an alternative: to destroy the transuranics, to recover the uranium for future use, and to produce 10x more energy than was produced in the first use of the fuel.

* Work supported by State of Texas and the Mitchell Foundation.
# mcintyre@physics.tamu.edu

ADAM OVERVIEW

ADS Core Neutronics

The individual ADS core must be sized to optimize the normalized burn rate $\dot{T}/T$; i.e. to minimize the TRU inventory required to sustain core operation. Figure 3 shows the energy dependence for neutron capture on ^{238}Uwhich breeds TRU) and for n-induced fission of the dominant TRU isotopes. The fission cross sections for most TRU isotopes are significant only for ultra-fast neutrons (>1 MeV). Optimization of fast spectrum for the ADAM core places strong constraints upon the core size and geometry and upon the fuel salt composition. The optimized core is shown in Figure 1, and its neutronics properties are summarized in Table 1. In its spectrum 20% of the neutrons have >1 MeV energy. It operates with a neutron gain k_{eff} = 0.97, produces 280 MW_{th}, and requires a 10 MW proton driver. The optimized burn rate is $\dot{T}/T = 5.6\%/year$, corresponding to a destruction time of 18 years.

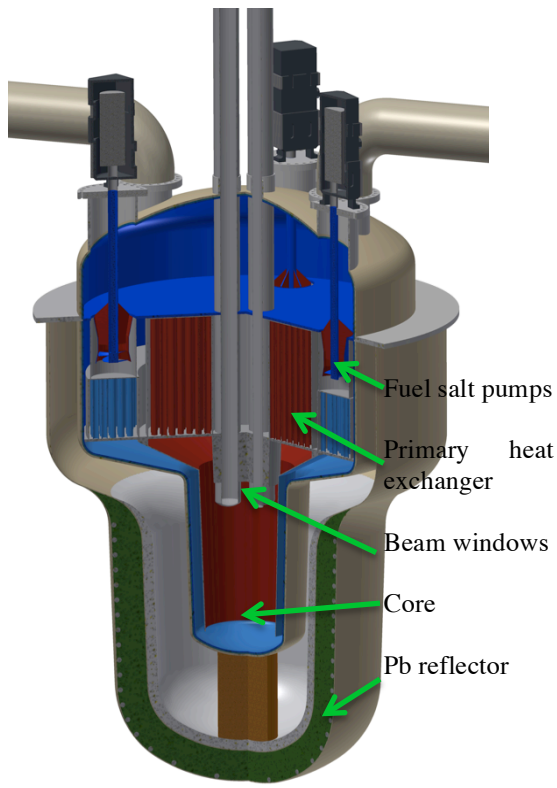


Figure 1: ADS molten salt core assembly.

Copyright © 2013 CC-BY-3.0 and by the respective authors

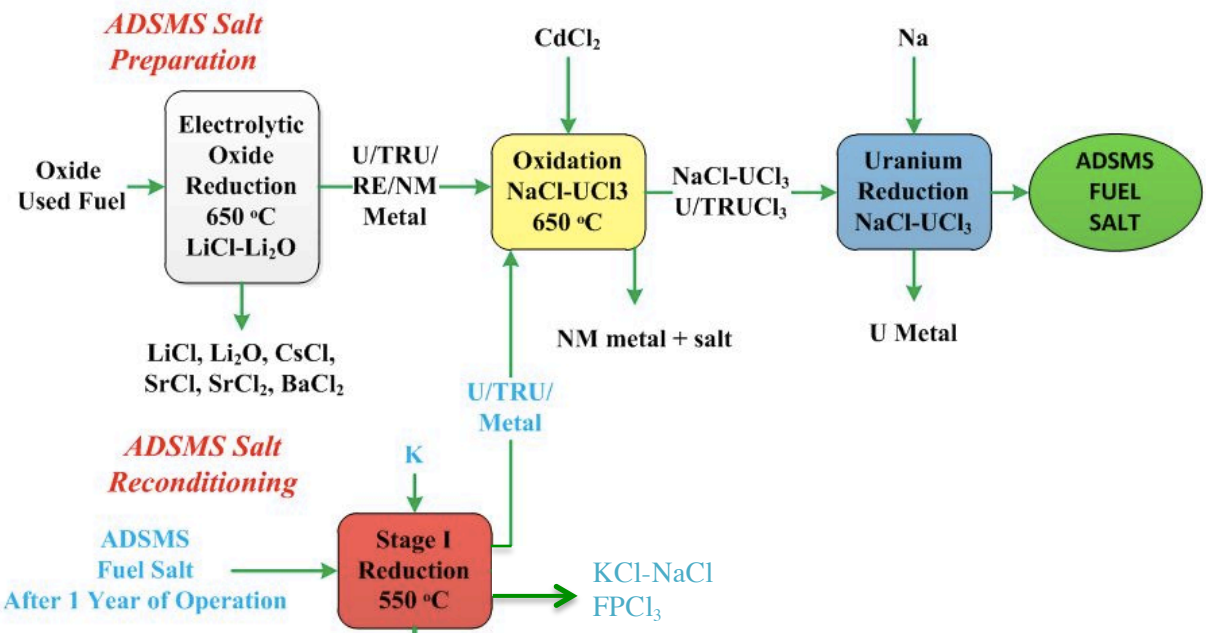


Figure 2: Pyroprocessing and electro-separation to prepare the fuel salt.

Fuel Salt Preparation and Reconditioning

The fuel salt for the ADAM core is a eutectic of $TRUCl_3$, UCl_3, and NaCl. It is prepared by a sequence of reduction and oxidation steps, shown in Figure 2. Fuel assemblies are chopped and crushed, and the oxide fuel is extracted from its Zircalloy cladding into molten salt (pyroprocessing [5]). Successive oxidation and reduction steps are used to plate out the uranium and to separate the remnant into separate batches of $TRUCl_3$ and $FPCl_3$ (FP = fission products). All of the steps of this electroprocessing have been developed into small-scale practice at ANL, INL, and KAERI [6].

The ADAM fuel salt contains as molar constituents $TRUCl_3$ (15.2%), UCl_3 (13.6%), NaCl (70%), and $FPCl_3$ (1.2%) [7]. The fuel salt has a melt temperature of 525 C and a boiling point of ~1500 C. The primary heat exchanger is integrated directly into the Ni vessel, and operates with an inlet temperature of 675 C and outlet temperature of 575 C.

As the ADAM core burns TRU its k_{eff} decreases. We modulate the proton beam power to maintain constant thermal power in the cores (increase the drive beam power from 8 MW to 10 MW) for a period of 3 months. At the end of 3 months we restore k_{eff} to its starting value by adding 90 kg of $TRUCl_3$. We can continue doing this for 5 years (20 cycles), at which time the fuel salt is transferred back to the electro-processing system, the accumulated $FPCl_3$ is removed, and the fuel salt is returned to the core vessel to begin another 5-year operating period.

Proton Driver

Each ADAM core requires a total of 12 mA of 800 MeV continuous proton drive beam. We have developed a design for a two-stage strong-focusing cyclotron (SFC) that can provide that performance [8]. The acceleration sequence is shown in Figure 5. It begins with acceleration of 100 mA CW to 6.5 MeV in the 350 MHz LEDA rf

Table 1: Main Parameters and TRU-burning Performance of ADAM Core compared to Fast Critical Reactor Designs

System	ADAM	SFR	GFR	LFR	
Net TRU Destruction	0.84	0.74	0.76	0.75	g/MW_t-day
System Power	**290**	**840**	**600**	**840**	**MW_t**
Outlet Temperature	665	510	850	560	C
Thermal Efficiency	44	38	45	43	%
Power Density	200	300	103	77	W/cc
TRU Inventory	**1733**	**2250**	**3420**	**4078**	**kg**
Fuel Volume Fraction		22	10	12	%
TRU Enrichment	53	44 - 56	57	46 - 59	% TRU/HM
Fuel Burnup	129.5	177	221	180	GWd/tHM

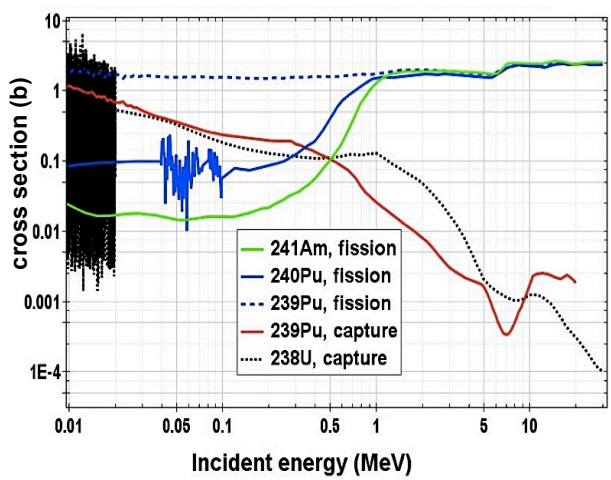


Figure 3: Energy dependence of cross sections for fission and capture by 238U and the dominant transuranics.

Copyright © 2013 CC-BY-3.0 and by the respective authors

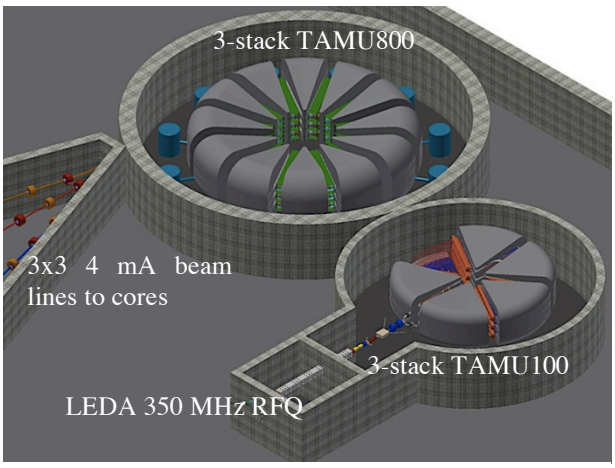


Figure 5: Acceleration chain for an ADAM site.

quadrupole (RFQ) [9]. The beam is then subharmonic-modulated, split into three 117 MHz beams, and passed through a sequence of 6-D collimators to yield three beams each with a normalized emittance < $1\pi10^{-6}$m and a phase width ±5°. The beams are then injected into a 3-stack of 100 MeV strong-focusing cyclotrons.

The world-record CW beam power for a proton accelerator is the PSI isochronous cyclotron [10]. It produces 2.2 mA CW at 590 MeV. Two issues pose the main limits to beam current in a cyclotron: the succeeding orbits overlap strongly so the defocusing action of space charge is exacerbated; and it has only weak focusing so that the betatron tunes migrate throughout acceleration and cross multiple resonances. We solved both of these problems in the SFC by incorporating two new elements: superconducting ¼-wave slot-geometry cavities that provide sufficient energy gain per turn to fully separate the orbits; and beam transport channels that provide alternating-gradient strong focusing to maintain constant betatron tunes throughout acceleration.

The details of the SFC design have been presented previously [8]. Three SFCs are configured as a flux-coupled stack, in which the dipole field for each SFC is created by

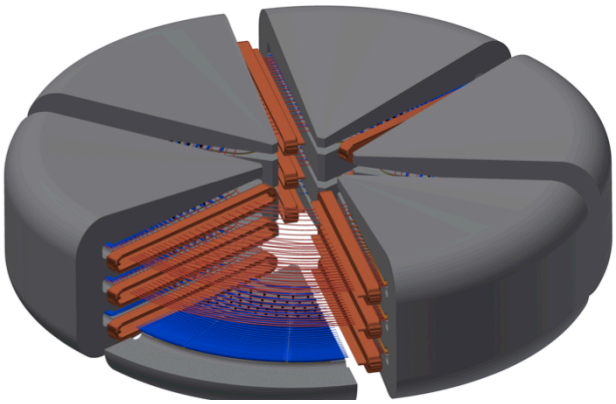


Figure 6: 3-stack of 100 MeV strong-focusing cyclotrons, with cutaway to show cavities, BTCs, and orbits.

a pair of cold-iron flux plates (Figure 4b) that are supported within a warm-iron flux return so that Lorentz forces on each flux plate cancel [11].

The superconducting cavity and beam transport channels are shown in Figure 6. The Nb superconducting cavity operates at 4.2 K and produces a ~2 MV acceleration. It is designed with fairly conservative surface field limits – 21 MV/m, 54 mT, and has provisions to suppress multipacting [12]. The rf power for each cavity is delivered to a linear array of input couplers, distributed along the upper and lower lobes of the cavity as shown in Figure 4a. Each coupler is driven by a solid-stage power source, and the linear array makes it possible to deliver input power in the same spatial distribution that is delivered to the circulating orbits of beam, so that beam loading does not drive transverse modes.

The beam transport channel (BTC) contains a single layer wire-wound Panofsky quadrupole winding and a window-frame dipole winding, both utilizing the superconductor MgB_2 which operates in the 15-20 K temperature range. An arc-shaped BTC is aligned along each equilibrium orbit in each sector as shown in Figure 4b, and is configured as an F-D doublet. The dipole winding is used to maintain precise isochronicity on all turns.

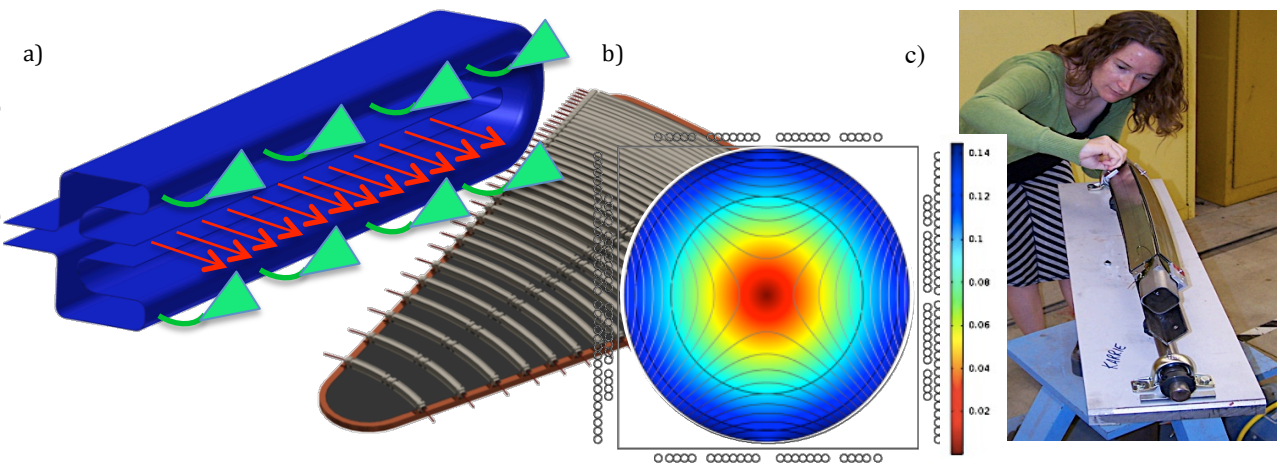


Figure 4: Innovations in the strong-focusing cyclotron: a) 117 MHz ¼-wave superconducting cavity with linear array of input couplers (green); b) beam transport channels on a flux plate; c) detail of the MgB_2 windings on a BTC and its quadrupole field distribution (max gradient 6 T/m).

Copyright © 2013 CC-BY-3.0 and by the respective authors

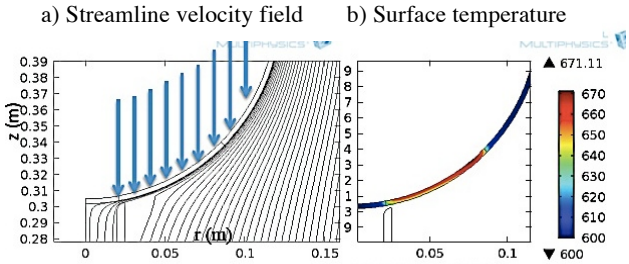


Figure 7: a) Molten salt flow on a proton beam window; b) Temperature profile on the window with 4 mA beam.

A companion paper [13] presents studies of the beam dynamics of the SFC for low-loss acceleration of high-current proton beam. We find that the elimination of overlapping orbits, the control of betatron tunes, and the suppression of transverse mode excitation by wake fields enables us to maintain stable acceleration of 12 mA CW through both SFCs to 800 MeV energy without beam breakup and with low loss for injection and extraction.

Delivery of 4 mA Proton Beam into Molten Salt

Each core requires a total of 12 mA drive beam. In order to operate within presently achieved beam window limits, we chop the proton beam after the RFQ to deliver ~10 μs bunch trains for acceleration, we split the 800 MeV bunch trains from each SFC to feed 3 transport lines, and we deliver the 3 bunch trains to 3 hemispherical Nb windows (Figure 1). The closed-circuit flow of molten salt in the core is channelled to deliver a chimney flow to cool each beam window, as simulated in **Error! Reference source not found.**.

Safety Considerations

The molten salt provides the spallation target and heat transfer medium for the beam windows, and it cannot be shocked by interruption of drive beam. All ADS designs that utilize a core based upon solid fuel pins have the problem that interruptions of drive beam (which happen every day at any extant accelerator) would thermally shock the fuel cladding which can lead to cracking.

All of the fuel salt is completely contained within the Ni core vessel and 5 shells of outer structure throughout a 5-year operating period. By contrast all previous core designs using molten salt pass the molten salt frequently through external circuits for reprocessing and re-conditioning, opening the risk of leaks.

The core vessel contains a removable inner vessel (in contact with the fuel salt) made from a single-piece of CVD Ni with no weld seam, which is resistant against molten salt corrosion. The Ni is much more robust against embrittlement from neutron damage in the ultra-fast spectrum of the ADAM core than it would be for a thermal spectrum. The CVD Ni vessel is encased in a spiral-wrap Hastelloy-N structure that provides mechanical support for the Ni can. An array of K vapor heat pipes is bonded to the outer surface of the Hastelloy shell and passively heat-sinks its surface to ~400 C during normal operation (consuming ~2 MW of heat) and during power and cooling failure modes. Maintaining the temperature of the Hastelloy at 400 C preserves its high tensile strength and toughness, which would be compromised if the Hastelloy operated at core temperature.

Many failure modes have been modeled, including loss of primary and/or secondary heat exchanger, loss of drive beam, loss of controls, and cracking of the core vessel. No failure mode studied can lead to leaking fuel salt beyond the multi-layer vessel, and no failure mode can produce criticality.

IMPLEMENTATION TO DESTROY TRANSURANICS

The ADAM core is sized to optimize the destruction of transuranics $\dot{T}/T$. Three ADAM cores are required to destroy TRU at the same rate that it is produced in a typical GW_e nuclear power plant. Figure 8 shows the site plan for an ADAM facility containing three cores and a 3-

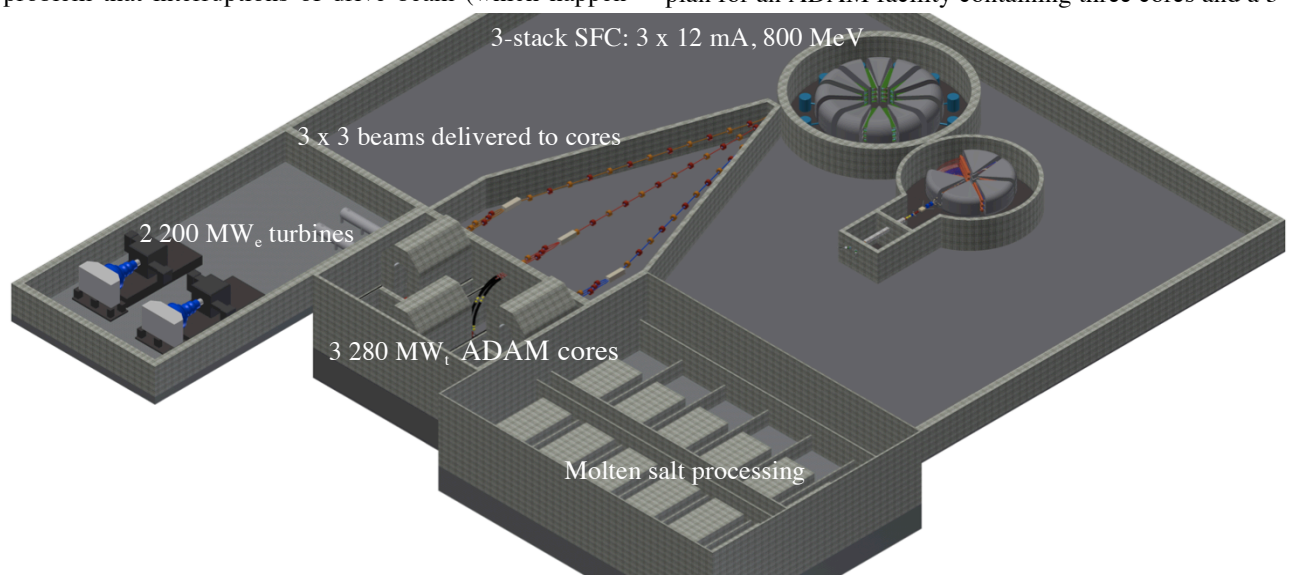


Figure 8: ADAM facility that destroys transuranics at the same rate they are produced by a GW_e nuclear power plant.

Copyright © 2013 CC-BY-3.0 and by the respective authors

stack SFC proton driver. It is appropriate in capacity to co-locate with an existing power plant, process its spent nuclear fuel, destroy the transuranics, recover the uranium, and generate uranium. The three ADAM units produce 3x290 MW_t of heat, which generates ~44%x870 = 380 MW_e. The SFC systems operate with ~50% efficiency, so it requires ~3x10MW/50% = 60 MW_e to operate the ADAM installation. The ADAM installation therefore is essentially an energy amplifier with a gain ~5.5. For as long as the adjoining GW_e power plant operates, its ADAM companion will generate ~320 MW_e of co-generated power to augment the plant's output while it destroys its hazardous waste.

Table 1 summarizes the performance parameters of the ADAM core, and compares them with the performance of several fast critical reactors that have been designed to destroy transuranics [14]: SFR is a sodium-cooled fast reactor; GFR is a high-temperature He gas-cooled fast reactor; and LFR is a molten lead-cooled fast reactor. Notably the ADAM core performs as well or better than any critical core design, and conveys the benefits for safe subcritical operation discussed above. ADAM provides a feasible candidate method to destroy the transuranics in used nuclear fuel and close the nuclear fuel cycle.

ACKNOWLEDGMENTS

We wish to thank Dan Barth (Friatech NA) for his help in designing molten salt pumps for the heat exchanger, and Jesse Johns (Texas A&M) for simulations of transient dynamics of the ADAM core. Michael Simpson (University of Utah) and Suprathorn Phongikaroon (Old Dominion University) are collaborating with us in developing the molten salt processing technology. Paul Madden (Oxford) and Matthieu Salanne (Université Pierre et Marie Curie) have collaborated with us in developing molecular dynamics models for the fuel salt. We wish to thank all members of the External Review of the ADAM project who conducted an in-depth review in January 2013: Ed Temple, Rick Baartman, Robert Hamm, Edward Hoffman, Pete Miller, Steve Myers, Bojan Petrovic, Gary Rochau, and Mark Williamson. It is a pleasure to acknowledge helpful discussions with Marvin Adams, Abe Clearfield, Richard Garwin, and Burton Richter.

REFERENCES

[1] World Nuclear Association, http://world-nuclear.org/info/inf01.html
[2] J.S. Walker, Three Mile Island: Nuclear Crisis in Perspective, University of California Press, 2004.
[3] L.R. Anspaugh, R.J. Catlin, and M. Goldman, 'The global impact of the Chernobyl reactor accident', Science **242**, 1514 (1988).
[4] IAEA Fukushima Daiichi Status Report, http://www.iaea.org/newscenter/focus/fukushima/.
[5] R.W. Benedict and H.F. McFarlane, 'Radwaste Management **5**, 5, 23 (1998).
[6] S.D. Herrmann *et al.*, 'Electrolytic reduction of spent nuclear oxide fuel as part of an integral process to separate and recover actinides from fission products', Separation Sci. and Technol. **41**,10, 1965 (2006).
[7] E. Sooby *et al.*, 'Candidate molten salt investigation for an accelerator driven subcritical core', J. Nucl. Mater. **440**, 1-3, 298 (2013).
[8] P. McIntyre *et al.*, 'Strong-focusing cyclotron for high-current applications', Proc. Int'l Particle Accelerator Conf., New Orleans, May 25-29, 2012.
[9] L.M. Young,'Operations of the LEDA resonant RFQ', Proc. 2001 Particle Accelerator Conf., p. 309 (2001).
[10] A. Adelmann *et al.*, 'On start-to-end simulation and modeling issues of the megawatt proton beam facility at PSI', 2005 Part. Accel. Conf., Knoxville, p. 3319.
[11] A. Sattarov *et al.*, 'Flux-coupled stacking of cyclotrons for a high-power ADS fission driver', Proc. Int'l Particle Accelerator Conf., New Orleans, May 25-29, 2012.
[12] N. Pogue *et al.*, 'Superconducting cavity for high-power cyclotrons', *ibid*.
[13] S. Assadi *et al.*, 'Nonlinear dynamics studies of high-intensity, high-brightness proton drivers', proceedings NA-PAC'13.
[14] R.N. Hill and T.A. Taiwo, 'Transmutation impacts of Generation-IV nuclear energy systems'. PHYSOR-2006, ANS Topical Meeting, Vancouver, Sept. 2006.

Copyright © 2013 CC-BY-3.0 and by the respective authors

THE ADVANCED SUPERCONDUCTING TEST ACCELERATOR (ASTA) AT FERMILAB*

P. Piot[1,2], V. Shiltsev[1], M. Church[1], P. Garbincius[1], E. Harms[1],
S. Henderson[1], J. Leibfritz[1], S. Nagaitsev[1]
[1] Fermi National Accelerator Laboratory, Batavia, IL 60510, USA
[2] Department of Physics and Northern Illinois Center for Accelerator & Detector Development, Northern Illinois University DeKalb, IL 60115, USA

Abstract

The Advanced Superconducting Test Accelerator (ASTA) currently in construction at Fermilab will enable a broad range of beam-based experiments to study fundamental limitations to beam intensity and to develop transformative approaches to particle-beam generation, acceleration and manipulation. ASTA incorporates a superconducting radiofrequency (SRF) linac coupled to a photoinjector and small-circumference storage ring capable of storing electrons or protons.This report describes the facility, its capabilities, and provide an overview of enabled research thrusts.

INTRODUCTION

The Advanced Superconducting Test Accelerator (ASTA) currently in construction at Fermilab will establish a unique resource for R&D towards Energy Frontier facilities and a test-bed for superconducting radiofrequency (SRF) accelerators and high-brightness beam applications. The unique features of ASTA include: (1) a high repetition-rate, (2) one of the highest peak and average brightness within the U.S., (3) a GeV-scale beam energy, (4) an extremely stable beam, (5) the availability of SRF and high-quality beams together, and (6) a storage ring capable of supporting a broad range of ring-based advanced beam dynamics experiments. These unique features will foster a broad program in advanced accelerator R&D which cannot be carried out elsewhere.

ACCELERATOR OVERVIEW

The backbone of the ASTA facility is a radio-frequency (RF) photoinjector coupled with 1.3-GHz superconducting accelerating cryomodules (CMs); see Fig. 1 [1]. The electron source consists of a 1-1/2 cell 1.3-GHz cylindrical-symmetric RF gun comprising a Cs_2Te photocathode illuminated by an ultraviolet (UV, $\lambda = 263$ nm) laser pulse obtained from frequency quadrupling of an amplified infrared IR pulse The photocathode drive laser produces a train of bunches repeated at 3 MHz within a 1-ms-duration macropulse.

The $\sim$ 5-MeV electron bunches exiting the RF gun are then accelerated with two SRF TESLA-type cavities (CAV1 and CAV2) to approximately 50 MeV. Downstream of this accelerating section the beamline includes quadrupole and steering dipole magnets, along with a four-bend magnetic compression chicane (BC1) [2]. The beamline also incorporates a round-to-flat-beam transformer (RTFB) capable of manipulating the beam to generate a high transverse-emittance ratio. In the early stages of operation, the bunches will be compressed in BC1. In this scenario the longitudinal phase space is strongly distorted and the achievable peak current limited to less than 3 kA. Eventually, a third-harmonic cavity (CAV39) operating at 3.9 GHz will be added enabling the generation of bunches with $\sim$ 10 kA peak currents by linearizing the longitudinal phase space. In addition CAV39 could also be used

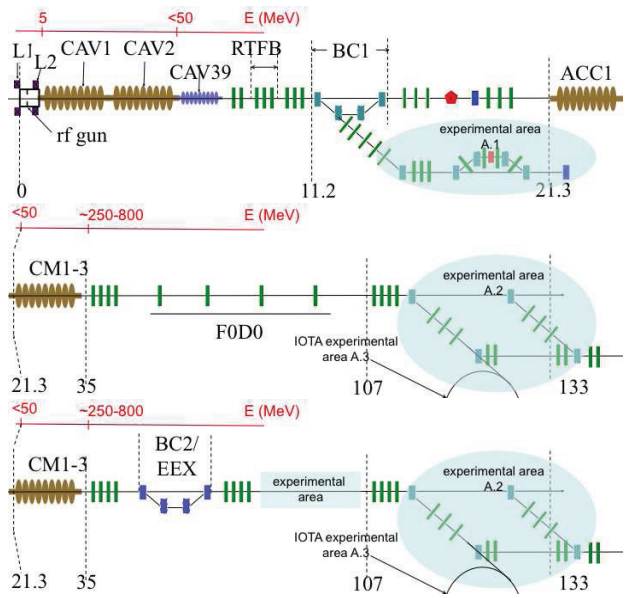


Figure 1: Overview of ASTA photoinjector (top); ASTA nominal high-energy transport beamline (middle) and modified high-energy transport beamline to accomodate a second-stage bunch compressor (bottom); "L1" "L2" stand for solenoids, "CAV1", "CAV2", and "CAV39" correspond to accelerating cavities, "CM1-3" to an ILC cryomodule string, "BC1" and "BC2/EEX" to bunch compressors, and "DL" to a dogleg beamline. "PEX" represents a possible reconfiguration of "BC2" to act as a transverse-to-longitudinal phase space exchanger.

* This work is supported by DOE contract DE-AC02-07CH11359 to the Fermi Research Alliance LLC

Copyright © 2013 CC-BY-3.0 and by the respective authors

to shape the current profile of the electron bunch [4]. The photoinjector was extensively simulated and optimized [3]. The photoinjector also includes an off-axis experimental beamline branching off at the second dipole of BC1 that will support beam physics experiments and diagnostics R&D.

The 50-MeV beam is injected into the SRF linac, which will eventually consist of three, 12-m long, TESLA/ILC-type CMs. Each CM includes eight 1.3-GHz nine-cell cavities. The first two cryomodules (CM1 and CM2) are a TESLA Type-III+ design, whereas the third (CM3), will be an ILC-Type IV design [5]. Together, these three CM constitute a complete ILC RF Unit. The SRF linac will be capable of generating a beam energy gain of $\sim$ 750 MeV. The installation of the cryomodules will be staged pending the completion of their construction. The first CM has already been installed in the ASTA Facility [6].

Downstream of the linac is the test beam line section, which consists of an array of multiple high-energy beam lines that transport the electron beam from the accelerating cryomodules to one of two beam dumps. In addition to testing the accelerator components, the intent of this facility is to also test the support systems required for a future SRF linac. The facility anticipated beam parameters appear in Table 1.

Table 1: Beam Parameters Expected at the ASTA Facility

parameter	nominal value	range
wnergy (A1) [MeV]	50	[5,50]
energy (A2) [MeV]	[250-800]	[50,820]
bunch charge Q [nC]	3.2	[0.02,20]
bunch freq. f_b [MHz]	3	see $^{(a)}$
macr. duration [ms] τ	1	≤ 1
macr. freq. f_{mac} [Hz]	5	[0.5, 1, 5]
num. bunch/macro. N_b	3000	[1,3000]$^{(b)}$
trans. emit$^{(b)}$ [μm]	$2.11Q^{0.69}$	[0.1, 100]
long. emit$^{(b)}$ [μm]	$30.05Q^{0.84}$	[5, 500]
peak current $\hat{I}$ $^{(c)}$	~ 3	≤ 10

$^{(a)}$ f_b and N_b are quoted for the nominal photocathode laser. Optical pulse stacking methods or field-emission sources could lead to smaller bunch separation within the rf macropulse.

$^{(b)}$ normalized rms values for an uncompressed beam. The scaling laws are obtained from Ref. [3] and correspond to an uncompressed case. Bunch compression results in larger horizontal emittances; see Ref. [2].

$^{(c)}$ the nominal value corresponds to a 3.2-nC compressed bunch without operation of CAV39. Higher values of $\hat{I}$ are possible with CAV39. For the uncompressed case, we have $I[\text{A}] \simeq 54.95Q[\text{nC}]^{-0.87}$.

During the first high energy beam operation and commissioning, only one CM will be installed allowing for the production of bunches with energies up to $\sim$ 300 MeV. Eventually, the second and third cryomodules will be installed in Stage II. Together, the three cryomodules plus the RF power systems will make up one complete ILC RF unit. During Stage II operation the beam energy will reach approximately 800 MeV. Beyond that stage several options are under consideration, including the installation of a 4th cryomodule downstream of a phase-space-manipulation beamline (either a simple magnetic bunch compressor or a phase space exchanger) [7, 8].

ASTA was designed with the provision for incorporating a small storage ring to enable a ring-based AARD program in advanced beam dynamics of relevance to both Intensity and Energy Frontier accelerators. The Integrable Optics Test Accelerator (IOTA) ring is 39 meters in circumference capable of storing 50 to 100-MeV electrons to explore, e.g, optical stochastic cooling methods [10] and integrable optics [11].

It is planned to expand capabilities for AARD in ASTA by the installation of the 2.5-MeV proton/H- RFQ accelerator which was previously used for High Intensity Neutrino Source (HINS) research at Fermilab [12]. That accelerator starts with a 50-keV, 40-mA proton (or H- ion) source followed by a 2-solenoid low-energy beam-transport line. The protons/ions are then accelerated by the pulsed 325-MHz RFQ to 2.5 MeV (with 1 ms pulse duration) prior to injection into IOTA.

USER OPPORTUNITIES

ASTA is intended to be operated as a scientific user facility for advanced accelerator research and development [13]. All the characteristics of a national user facility will be in evidence in the operation of ASTA and its user program. The facility is open to all interested potential users and the facility resources will be determined by merit review of the proposed work. The user program will be proposal-driven and peer-reviewed in order to ensure that the facility focuses on the highest quality research. Proposals will be evaluated by an external Program Committee (the ASTA Program Advisory Committee), consisting of internationally recognized scientists. Proposal evaluation will be carried out according to established merit review guidelines. We expect the first batch of proposal submitted as part of our proposal to DOE [14] will be reviewed during the fiscal year (FY) 2014.

Three experimental areas [A1, A2, and A3 (IOTA) in Fig. 1] will be available to users for installation of experiments. Area A1, situated in an off-axis beamline within the photoinjector, will provide electron bunches, possibly compressed, with energies up to 50 MeV. The current layout of the off-axis beamline includes a chicane-like transverse-to-longitudinal phase space exchanger, and provision for the installation of a short undulator for beam-laser interaction (e.g., to enable microbunching studies). The high-energy experimental area A2 consists of three parallel beamlines. Two of the beamlines are downstream of doglegs while one is inline with the ASTA linac. Experiments in the three user beamlines and IOTA could be ran simultaneously (switching the beam from one beamline to the other would only require minor optical-lattice adjustment). Fi-

Copyright © 2013 CC-BY-3.0 and by the respective authors

nally, the eventual availability of a H- source would allow IOTA to be operated independently of the ASTA electron-beam users. In addition, in order to accomodate additional experiments during the stage I, we are considering the installation of a chicane that could operate as a second-stage bunch compressor or transverse-to-longitudinal phase space exchanger (BC2/EEX in Fig. 1).

ANTICIPATED RESEARCH THRUSTS

In this Section we highlight expression of interests to perform experiments along the five main research thrusts enabled at ASTA.

Accelerator R&D for Particle Physics at the Intensity and Energy Frontiers

The combination of a state-of-the-art superconducting linear accelerator and a flexible storage ring enables a broad research program directed at the particle physics accelerators of the future.

The proposed research program includes at IOTA has expanded well beyond its initial goal to test non-linear, integrable, accelerator lattices, which have the potential to shift the paradigm of future circular accelerator design [15, 16, 17]. IOTA will also be used to explore optical-stochastic cooling [10]. The addition of an H^- source will also enable the investigation of integrable optics in presence of significant space charge effects. The H^- beam will also open the path to the study of space-charge compensation schemes in high-intensity circular accelerators [18]. IOTA will also support some fundamental Physics studies such as the measurement of the wave-function associated to a single electron using a method similar to an experiment previously attempted [19].

The availability of advanced phase space manipulations will also support the development and test of beam-driven acceleration methods, which would greatly benefit from shaped current profiles [21, 22, 23] to significantly increase the transformer ratio – the energy gain of the accelerated bunch over the energy loss of the driving bunch. When combined with the aforementioned round-to-flat beam transformation, this shaping technique could produce flat beams with tailored current profiles suitable for test of beam-driven acceleration methods based on, e g., slab dielectric-loaded waveguide (DLW) [24, 23], Other advanced acceleration techniques to be explored at ASTA include the acceleration and cooling of muon beams based on carbon-based crystal structures [25],

Finally, the high-power beam produced by the SRF linac will provide opportunities for high-energy Physics detector R&D. These include the high-power tests of target required for the Long-Baseline Neutrino Experiment (LBNE) and the generation of tagged-photon beams necessary to test components associated to the Project-X detectors.

Accelerator R&D for Future SRF Accelerators

High gradient, high-power SRF systems are critical for many accelerator facilities under planning for the needs of high-energy physics, basic energy sciences and other applications. ASTA offers a unique opportunity to explore most critical issues related to the SRF technology and beam dynamics in SRF cryomodules. The low injection energy ~ 50 MeV combined with achievable low emittance beams is well suited to explore beam dynamics effects and especially beam degradation due to the time-dependent field asymmetries introduced by the input and higher-order mode (HOM) couplers. The pulsed operation of SRF cavities at high-gradient while accelerating mA beam currents over long period of time has also relevance to the International Linear Collider program. Furthermore, the SRF linac will provide an experimental platform necessary to develop the required low-level RF controls for the Project-X pulsed linac [26]. Additionally, comprehensive beam-based measurements of long-range wakefield in SRF CMs are being planned using an upgraded version of the photocathode laser that would enable the production of charge-modulated bunch trains. Scanning the charge-modulation frequency and recording the HOM-induced beam displacements downstream of the cryomodule(s) under test would enable the characterization of HOMs over a continuous range of frequencies [27]. Finally, a precise characterization of the jitter and beam-based stabilization of the SRF module has been proposed. It relies on the measurement of the bunch relative time of flight downstream of a bunch compressor, bunch energy and on the detection of coherent synchrotron radiation. These measurements are fed to an algorithm and used to control the phase and amplitude of the SRF cryomodule(s) [28].

It was also pointed out that with adequate changes in the RF system, the ILC-type cryomodule installed at ASTA could in principle be operated in CW mode to perform tests relevant to the proposed next-generation CW light sources [30]. The maximum gradient attainable by the cavities is limited by the cryogenic system and HOM coupler. Cryogenic considerations indicate that the maximum gradient would be limited to $\sim 5-7$ MV/m. Likewise, the ILC-type input coupler design nominally used at ASTA would limit the average beam current to ≤ 1 mA [29].

Accelerator R&D for Novel Radiation Sources

High energy, high-peak and high-average brightness electron beams are crucial to the generation of high-brillance high-flux light sources with photo energies ranging from keVs to MeVs. The high average power and brightness of the ASTA electron beam has unmatched potential for development of several novel radiation-source concepts. Head-on collision of the electron bunch with an intense laser produces radiation with maximum up-shifted frequency $\omega \simeq 4\gamma_l^2\omega_L$ where γ_l is the bunch's Lorentz factor and ω_L the laser frequency. At ASTA, colliding the bunch with a 800-nm laser would provide γ rays with energies ranging from 1 to 20 MeV; see typical spectrum in Fig. 2 (left). If the laser repetition frequency matches the electron bunch frequency, an unprecedented γ-ray brilliance in excess of 10^{24}

Copyright © 2013 CC-BY-3.0 and by the respective authors

phot.mm^{-2}.mrad^{-2}.s^{-1}/(0.1%BW) could be attained [31]. The main technical challenge will be to develop a laser capable of producing Joule-level pulse energy with MHz repetition rate and will rely on a recirculating optical cavity [32, 33]. Such high-flux γ-ray source is foreseen to be extremely beneficial to the measurement of the cross section associated to the $^{12}C(\alpha,\gamma)^{16}O$ reaction which is crucial in nuclear astrophysics as it enters in the synthesis of many elements. Due to its low cross section, a precise measurement of this reaction using a nucleation process in a bubble chamber remains elusive with presently available γ-ray sources (as only a handful of events per year are expected). The potential availability of a high-flux γ-ray source at ASTA could result in significantly higher statistics (up to 200,000 events per year).

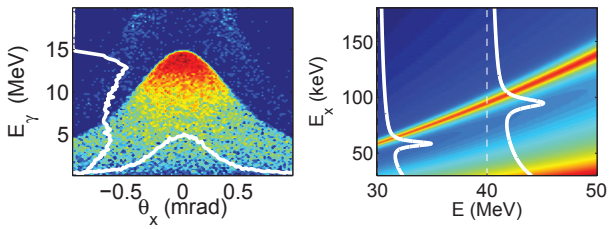


Figure 2: left: Spectral-angular distribution of γ rays produced by a 800-nm laser pulse backscattered on the ASTA 800-MeV beam (the density is plotted using a logarithmic color scale). right: X rays spectral yield as function of electron beam energy and photon energy for the $1 \rightarrow 0$ transition in (110) plane of diamond. Both CR and bremsstrahlung are considered in these calculations. The white traces are expected photon-energy spectrum for 30 and 40-MeV electrons

In the photoinjector area, it is foreseen to test a concept enabling the production of high-brilliance x rays by combining the low-emittance beam produced out of the photoinjector with channeling radiation (CR) [34]. The production of CR will occur downstream of the bunch compressor (BC1). Several crystal materials will be tested. Simulations using a $\sim$ 40 μm-thick diamond crystal indicate the production of x rays energy in the [10-150] keV range for the electron-beam energies available in the ASTA phtoinjector (15 to 50 MeV); see Fig. 2 (right).

Additionally, it was suggested that the available long stable bunch train could serve for a proof-of-principle experiment of an extreme-ultraviolet (EUV) FEL oscillator at 13.4 nm wavelength. Preliminary simulations indicate that saturation of the FEL process occurs after 300-350 passes [35]. Initial experiments could be conducted at low energy (250-300 MeV) and provide 120-nm FEL radiation.

Finally, the combination flat beams with long bunch train could support the test of micro-undulators [36]. These micro-undulators, made of laser-micromachined bulk rare-earth magnetic materials (SmCo and NdFeB), have magnetic fields with spatial period on the order of a few 100 μm. The associated undulator parameter is on the order of $K \sim 10^{-2}$ which results in a low photon yield $\sim \alpha K^2$ (where α is the fine-structure constant). Therefore the test and characterization of the associated undulator radiation would greatly benefit from the long bunch train available at ASTA.

Accelerator R&D for Stewardship and Applications

With its high energy, high brightness, high repetition rate, and the capability of emittance manipulations built-in to the facility design, ASTA is an ideal platform for exploring novel accelerator techniques of interest for very broad scientific community beyond high energy physics.

Some of the experiments include the development and test of subsystem and beam-manipulation scheme to improve the performance and decrease the cost of next-generation accelerator-based light sources. An example include the combination of the aforementioned phase-space manipulations to taylor the emittance partition within the three degrees of freedom to produce ultra-low emittance beams for future hard X-ray free-electron lasers [37].

Several proposals aim at developing techniques to "dechirp" the beam, i.e. to remove the residual correlated energy spread that generally subsists downstream of the final bunch compression stage in FEL drivers. The proposed dechirping methods include (i) the use of short-range wakefields impressed on the bunch as it passes in a dielectric [38, 39] or corrugated [40] passive structure, or (ii) the judicious arrangement of three transverse-deflecting cavities to produce a transfer matrix with a non-vanishing R_{56}. In addition using these passive structures to further control the longitudinal-phase-space nonlinearities could also be test at ASTA [41]. Demonstrating the compatibility of these techniques with high-repetition rate beam available at ASTA could lead to their inclusions in proposed CW FEL projects.

The flat-beam transformation available at ASTA could also support tests relevant to nuclear-physics accelerator R&D, e.g., to validate the concept of a fast beam-beam kicker [42] for the Medium-energy Electron-Ion Collider (MEIC) [43] being under design at Jefferson Laboratory.

Finally, the beam available at ASTA will foster the development and tests of advanced beam diagnostics relevant to, e.g., CW FELs or energy-recovery linacs. Some of these diagnostics especially those capable of measuring single-bunch parameters within the RF macropulse, will be crucial for optimizing the feedback system needed to stably operate the ASTA SRF cryomodule(s).

STATUS

The ASTA accelerator is currently under construction [44]: the electron source and associated subsystems were installed and are being commissioned; see Fig. 3. First electrons were produce in June 2013 from a temporary molybdenum cathode resulting in a 8-pC electron bunch. Typical operating parameters during the commis-

Copyright © 2013 CC-BY-3.0 and by the respective authors



Figure 3: Photographs of the RF gun assembly used to produce first electrons (left) and of the cryomodule CM1 installation (right).

sioning phase are 80 μs-long RF macropulse, 31.5 MV/m peak electric field on the cathode surface and $f_b = 1$ Hz repetition frequency. The measured beam's kinetic energy at the gun exit is $E_k = 3.24 \pm 0.1$ MeV.

In parallel the 50-MeV injector line is being assembled and we anticipate that 50-MeV electron bunches will be produced early in CY2014. Further acceleration in one CM is foreseen late in FY14, once the high-energy beamline assembly is completed.

A program advisory committee (PAC) was formed and the first ASTA users' and PAC meeting was held at Fermilab on July 23-24, 2013. The meeting had $\sim$ 80 attendees (about 2/3 were external to Fermilab) and led to 24 expressions of interest. Further details on this users' meeting can be found in Ref. [45].

REFERENCES

[1] M. Church (Editor), "Design of the ASTA facility", Fermilab report beams-doc 4212 (2011).

[2] C. R. Prokop, et al., Nucl. Instrum. Meth. A **719** 17 (2013).

[3] P. Piot, et al., Proc. IPAC10, 4316 (2010).

[4] P. Piot, et al., Phys. Rev. Lett. **108**, 034801 (2012).

[5] T. Arkan, et al., Proc. LINAC10, 599 (2010).

[6] T. Arkan, et al., Proc. NAPAC13, WEPAC29 (2013).

[7] Y.-E. Sun, et al., Phys. Rev. Lett. **105**, 234801 (2010).

[8] J. Ruan, et al., Phys. Rev. Lett. **106**, 244801 (2011).

[9] V. A. Lebedev, et al., Proc. HB2012, Beijing, China, in press (2012).

[10] V. A. Lebedev, et al., Proc. NAPAC13, TUODA2 (2013).

[11] V. Danilov, et al., Phys. Rev. ST Accel. Beams **13**, 084002 (2010).

[12] J. Steimel, et al., Proc. IPAC12, 3877 (2012).

[13] V. Shiltsev, et al., Proc. NAPAC13, MOPAC15 (2013).

[14] see proposal at http://asta.fnal.gov/ .

[15] S. Nagaitsev, et al., ArXiV:1301.7032 (2012).

[16] A. Valishev, et al., Proc. NAPAC13, MOOCB1 (2013).

[17] T. Zolkin, et al., Proc. NAPAC13, MOOCB2 (2013).

[18] M. Chung, et al., Proc. NAPAC13, TUOBB1 (2013).

[19] T. Shaftan, PhD thesis, BINP, Novosibirsk (1997) (in Russian).

[20] P. Piot, et al., Phys. Rev. ST Accel. Beams **14**, 022801 (2011).

[21] K. L. F. Bane, P. Chen, P. B. Wilson, report SLAC-PUB-3662 (1985).

[22] B. Jiang, Phys. Rev. ST Accel. Beams **15**, 011301 (2012)

[23] E. Simkov, et al., Proc. NAPAC13, TUPMA14 (2013).

[24] D. Mihalcea, et al., Phys. Rev. ST Accel. Beams **15**, 081304 (2012).

[25] Y.-M. Shin, et al, Proc. NAPAC13, MOPAC18 (2013).

[26] for information see http://projectx.fnal.gov/.

[27] S. Fartoukh, report CEA/DAPNIA/SEA-98-18, CEA Saclay (1998).

[28] F. Loehl et al, Phys. Rev. Lett. **104**, 144801 (2010).

[29] N. Solyak, private communication (2013).

[30] J. N. Corlett, Proc. NAPAC13, TUZb1 (2013).

[31] A. Murokh, private communication (2012).

[32] I. Jovanovic et al., Nucl. Instr. and Meth. A 578, 160 (2007)

[33] R. Tikhoplav, A. Ovodenko and I. Jovanovic, High-power pulse recirculation in a stable pseudo-confocal geometry, submitted for publication to Optics Letters (2012).

[34] C. A. Brau, et al., Synchr. Rad. News, 25 (1), 2012.

[35] A. Lumpkin et al., Proc. FEL13, MOPS051 (2013).

[36] O. D. Oniku, W. C. Patterson, A. Garraud, E. Shorman, P. Ryiz, D. P. Arnold, B. A. Peterson, F. Herrault, M. G. Allen, Presentation at the HBEB 2013 conference, Puerto Rico (2013).

[37] B Carlsten, et al., Phys. Rev. ST Accel. Beams **14**, 050706 (2011).

[38] M. Rosing and J. Simpson, Passive momentum spread reduction, the wakefield silencer, ANL Report WF-144 (1990).

[39] S. Antipov, et al., Phys. Rev. Lett. **108**, 144801 (2012).

[40] K. Bane and G. Stupakov, Nucl. Instr. Meth. A, **690**, 106-110 (2012).

[41] P. Craievich , Phys. Rev. ST Accel. Beams **13**, 034401 (2010).

[42] V. Shiltsev, Nucl. Instr. Meth. A **374**, 137 (1996).

[43] S. Ahmed, et al., Proc. IPAC12, 2014 (2012).

[44] J. Leibfritz, et al., Proc. IPAC12, 58 (2012).

[45] see https://indico.fnal.gov/conferenceDisplay.py?confId=6822.

Copyright © 2013 CC-BY-3.0 and by the respective authors

THE AWAKE PROTON-DRIVEN PLASMA WAKEFIELD ACCELERATION EXPERIMENT AT CERN

P. Muggli*, Max Planck Institute for Physics, Munich, Germany
for the AWAKE Collaboration

Abstract

We briefly outline the proposed AWAKE plasma wakefield accelerator (PWFA) experiment to be performed with the CERN SPS proton bunches. We focus on the experimental setup, allude to some of the physics involved and describe some of the measurements that are planned.

INTRODUCTION

A new high-gradient acceleration technique for electrons (e^-) and positrons (e^+) is required. Among those currently proposed and explored, plasma-based acceleration has led to the largest energy gain (>40 GeV) over a meter-scale distance [1]. However, producing with plasmas beams with parameters equal to or better than those produced by conventional, RF-based accelerators remains challenging. One of the challenges arises from the energy of the drive bunch that limits the energy gain of the witness bunch. Current short laser pulses or e^- bunches carry less than ∼100 J. Therefore, staging of a large number of plasma accelerator sections, with all the ensuing issues (alignment, timing, gradient dilution, etc.), is required to reach the desired energy (TeV range).

Proton (p^+) bunches available today, e.g. at CERN, carry much more energy than that carried by a future e^-/e^+ collider bunches: ∼1.6 kJ for 2×10^{10} particles at 500 GeV. With 10^{11} p^+, CERN SPS (400 GeV) and LHC (7 TeV) bunches carry 6.4 and 112 kJ, respectively. However, these bunches are long (σ_z ∼10 cm). For single-bunch operation at a plasma e^- density n_{e0} such that the electron plasma wave period $\lambda_{pe} = 2\pi c\left(\epsilon_0 m_e/n_{e0}e^2\right)^{1/2}$ matches the bunch length ($\lambda_{pe}\sim\sigma_z$, as in [1]) would result in a very low maximum accelerating field: $\leq E_{WB} = \left(2\pi m_e c^2/e\right)/\lambda_{pe} \cong 3.2\times10^9/\sigma_z(mm) \cong$32 MV/m in a plasma with $n_{e0}\sim10^{11}$ cm^{-3}. Short p^+ bunches (σ_z ∼0.1-1 mm) are thus necessary to reach fields higher than in RF cavities (>200 MeV/m).

P^+-DRIVEN PWFA

The potential for a p^+-bunch driven, plasma-based accelerator to produce a high energy e^- bunch was demonstrated in proof-of-principle simulations [2, 3]. An energy gain of ∼500 GeV in a plasma ∼500 m-long with a density of 6×10^{14} cm^{-3} with a σ_z ∼100 μm-long drive bunch was achieved. A train of short bunches can be produced out of a long bunch ($\sigma_z \gg \lambda_{pe}$) by the plasma itself through a transverse self-modulation instability (SMI) [4]. Thanks to the periodic focusing/defocusing fields of the initial wakefields, the SMI produces a train of $\sim\lambda_{pe}/2$-long bunches separated by $\sim\lambda_{pe}$ that can then resonantly drive the wakefields to large amplitudes. Interestingly, the amplitude of the wakefields is comparable the one that would be driven if all the charge were in a single short bunch. However, using the long bunch and the SMI to drive wakefields brings new challenges.

When the SMI grows from noise it needs a long plasma length to saturate. Also, the final relative phase of the wakefields is unknown and varies from event to event, which prevents the deterministic injection of the witness bunch into the accelerating and focusing phase of the wakefields. Over this long propagation distance the long bunch is subject to a competing, but asymmetric transverse instability, the hose instability (HI) [5]. The HI can break-up the bunch before the SMI can grow or before the witness bunch can gain large amounts of energy. Calculations and simulations indicate that the growth length of the SMI can be shortened, the phase of the wakefields determined and the occurrence of the HI mitigated by seeding the SMI with a signal of large amplitude [6] and known phase. They also indicate that in certain regimes the full bunch self modulation can effectively prevent the HI from developing over the acceleration region [7].

Even when seeded, the phase velocity of the SMI is slower than that of the drive and witness bunch during the growth phase of the SMI [8]. This leads to dephasing of the witness bunch with respect to the wakefields and to its loss through strong defocusing. The witness bunch must therefore be injected after the SMI has saturated and the bunch is fully self-modulated.

The SMI also grows along the bunch (convective instability) and the witness bunch must be injected many plasma periods behind the start of the wakefields ($\sim1\sigma_z \gg \lambda_{pe}$). Therefore the proper position within the drive bunch for the witness bunch to be focused and accelerated ($\sim\lambda_{pe}/4$) over a long distance is rather sensitive to plasma density variations since $\delta\lambda_{pe}/\lambda_{pe} = -\frac{1}{2}(\delta n_{e0}/n_{e0})$. When injecting the witness bunch $N\sim\sigma_z/\lambda_{pe}$ periods after the start of the wakefields the density uniformity requirements becomes $|\delta n_{e0}/n_{e0}| \leq (1/2N)$ (for a $\leq\lambda_{pe}/4$ phase shift). This requirement must be met over the plasma length, but only over the time scale of the interaction ($\sim\sigma_z/c$).

THE AWAKE EXPERIMENT

The AWAKE collaboration proposed an experiment to be performed at CERN to study the physics of self-modulation of long p^+ bunches in plasmas, to determine the potential of plasma-based accelerators driven by self-

* muggli@mpp.mpg.de

Copyright © 2013 CC-BY-3.0 and by the respective authors

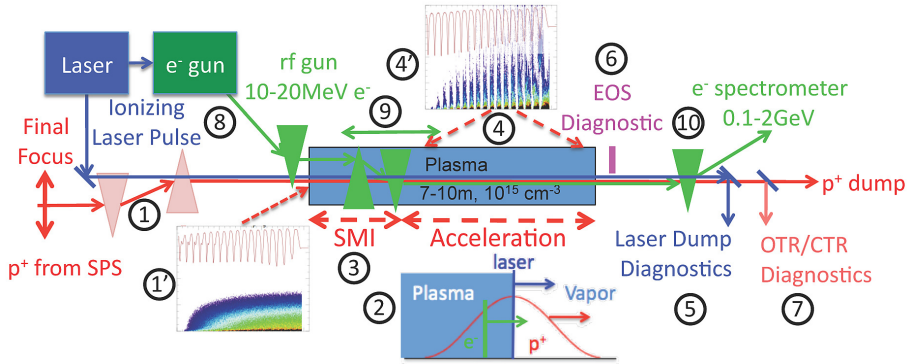


Figure 1: (1) p^+ bunch extracted from SPS. (1') p^+ bunch charge distribution when entering the plasma and transverse wakefields (red line). (2) Time sequence showing the p^+ and e^- bunch and the ionizing laser pulse. (3) Region of the plasma where self-modulation occurs. (4) Region of the plasma where acceleration occurs. (4') p^+ bunch charge distribution when exiting the plasma and transverse wakefields (red line). (5) Laser beam dump. (6-7) EOS and OTR-based p^+ bunch diagnostics. (8) e^- beam for injection into wakefields. (9) Dipole magnets to "side-inject" the witness e^-. (10) Magnetic energy spectrometer for the e^-. Note: the schematic is not to scale and a shorter e^- bunch is used for illustration in 1' and 4'.

modulated p^+ bunches and to explore the possibility of using short p^+ bunches to accelerate e^- to very high energies.

The baseline parameters for the AWAKE experiment using the p^+ bunches from the CERN SPS-CNGS beam line [9] are given in Table 1. A schematic of the experiment is shown in Fig. 1. Note that many standard beam line diagnostics are not shown (alignment screen, beam position monitors, toroids, etc.) [9]. The bunch is extracted from the SPS and transported to the CNGS beam line with an energy of 400 and up to 3×10^{11} p^+. It is focused to a rms radius σ_r^*=200 μm ($\beta^* \cong 5\ m$ $\beta^* \cong$5 m) near the entrance of a 10 m-long ($\sim 2\beta^*$) plasma. After the plasma the p^+ bunch free streams to the beam dump. The plasma density can be varied in the $10^{14} - 10^{15}$ cm^{-3} range to keep $k_{pe}\sigma_r^* \leq 1$ ($k_{pe} = 2\pi/\lambda_{pe}$) in order to avoid beam transverse filamentation [10]. The plasma is created by laser field-ionization of a rubidium (Rb) vapor. The vapor with a very uniform density is created in a Rb vapor source with a very uniform temperature [11]. The seeding of the SMI is insured by propagating the short ($\ll \lambda_{pe}$) laser pulse within the p^+ bunch itself [12] (see (2) on Fig. 1). Note that the interaction between the three beams (p^+, e^- and laser) is locally over after approximately one p^+ bunch length ($\sim$12 cm or $\sim$400 ps). Therefore the plasma once locally created by the laser pulse within the p^+ bunch needs to remain uniform only over that time scale. Long-term plasma evolution through diffusion, recombination, etc. common to most other sources is therefore avoided. Over the first few meters of plasma (typically $\sim$4) the SMI develops, saturates and the bunch becomes self-modulated (see (4') on Fig. 1).

The focus of the first experiments will be the study of the SMI. Simulations indicate that with the parameters of Table 1 the SMI does not develop unless seeded. The radial modulation of the p^+ bunch will be measured using various diagnostics. The p^+ bunch will emit incoherent optical transition radiation (OTR) when traversing a thin metal foil placed downstream from the plasma. The OTR light can be time resolved, for example with a streak camera, to directly measure the period of modulation through its intensity variations and perhaps to obtain information about the bunch transverse size. The modulation period and the depth of modulation can also be inferred from electro-optic (EO) measurements. Since there is a large number of modulation periods within the bunch ($\sim 100/\sigma_z$) EO measurements can be made in the frequency rather than in the time domain. EO measurement can either sample the coherent

Table 1: AWAKE Experiment Baseline Parameters

Parameter & Symbol	**Value**
p^+ bunch ...	
Population, N_b	3×10^{11}
Length (rms), σ_z	12 cm
Radius (rms), σ_r^*	200 μm
Energy, W_b	400 GeV
Normalized emittance, ϵ_N	3.6 mm mrad
Beta function, β^*	4.7 m
Plasma ...	
Density, n_{e0}	$7 \times 10^{14}\ cm^{-3}$
Wavelength, λ_{pe}	1.2 mm
Frequency, f_{pe}	239 GHz
Length, L_{plasma}	10 m
Density uniformity, $\delta n_{e0}/n_{e0}$	$\leq 0.25\%$
Relative ...	
Bunch density, n_b/n_{e0}	6×10^{-3}
Bunch length, $k_{pe}\sigma_z$	597
Bunch radius, $k_{pe}\sigma_r^*$	1
Plasma length, $k_{pe}L_{plasma}$	50,000
Plasma length, L_{plasma}/β^*	~ 2

Copyright © 2013 CC-BY-3.0 and by the respective authors

transition radiation (CTR) emitted by the p^+ bunch or the transverse CTR recently proposed [13]. Measurements of the CTR frequency using cut-off waveguides or heterodyne microwave systems (f_{pe}=239 GHz with n_{e0}) will be used to detect the occurrence of SMI and measure the frequency of the bunch self-modulation as a function of n_{e0}.

The wakefields themselves will be sampled by externally injecting e^-. These e^- will be produced by an RF photo-injector gun driven by a laser pulse derived from the ionization laser system [9]. This is necessary to be able to chose the injection position of the e^- bunch with respect to the p^+ bunch and to the wakefields (see (2) on Fig. 1), i.e., at their peak and in the accelerating and focusing phase. First injection experiments will use side-injection [14]. This method avoids splitting the plasma source in two, as necessary for on-axis injection thereby avoiding issues related to local plasma density non-uniformities and precise density adjustment between sources. Also, it can be realized with a long e^- bunch ($> \lambda_{pe}$) letting the wakefields trap a fraction of the incoming e^-. Simulations show that e^- with an energy of ∼15 MeV crossing the p^+ bunch path at an angle of a few mrad can be trapped when injected along the plasma after SMI saturation (>4 m). Bunches with energies larger than 2 GeV and an energy spread of a few % have been observed after the plasma in simulations with the parameters of Table 1. Note that inherently short (a few fs), high-current (kA) e^- bunches routinely produced by laser-driven plasma-based accelerators (LWFAs) could also be considered for injection.

Later experiments will use two plasmas for on-axis injection of the e^- bunch and accelerator physics experiments. The first source will be a laser-ionized alkali metal vapor source to preserve the SMI seeding ability. However, the second source, used exclusively for e^- acceleration in the wakefields resonantly driven by the modulated p^+ bunch can be of a different, simpler type. Discharge and helicon sources are possible candidates. These sources can be scaled to very long lengths, while the length of the laser-ionized source does not scale well. An interesting option afforded by the two-source scheme (but also with single vapor sources with two heating systems [11]) is the possibility of introducing a step in the plasma density. Simulations suggest that a step up of a few percent during the growth of the SMI can help mitigating the decrease in wake amplitude generally observed after SMI saturation [3]. This decrease is due to the continued evolution of the bunch train and wakefields structure and is most pronounced with positively charged bunches.

OUTLOOK

Using the SMI to produce a train of short bunches and resonantly drive wakefields to large amplitudes is an attractive method when single bunches with suitable properties are not available. However, with the SMI a large fraction of the long initial bunch (at least half) is defocused and does not contribute to the wakefields generation. Another fraction is excluded by the seeding mechanism chosen here. The long distance along the bunch it takes for the SMI to saturate forces the injection of the e^- many plasma periods into the wakefields. This in turn leads to a very tight requirement on the plasma density uniformity. Some of these issues can me mitigated, for example by compressing the bunch and thereby reducing its relative length ($k_{pe}\sigma_z$). Compressions by a factor of a few is possible in the SPS ring and will be explored [9] as a means of increasing wakefields and better understanding SMI physics. However, methods to produce short p^+ bunches (∼100 μm) will also be explored to reach the single-bunch non-resonant regime of PWFA excitation and circumvent the issues related to the use of SMI.

SUMMARY

The AWAKE plasma wakefield accelerator experiment is in its preparation phase. We described the high-level experimental set-up, some of the physics involved as well as planned and possible measurements that will be used to test the physics of the SMI and of the acceleration of externally injected e^- in the wakefields driven by the long p^+ bunch. These experiments are tentatively scheduled to start at the end of 2016. These will be the first p^+-driven PWFA experiments and will explore PWFA in a low density range with $\sim GV/m$ accelerating fields that can be sustained over many meters of plasma and potentially accelerate e^- to very large energies in a single (or a few) plasma section [2]. Operation at lower density decreases the accelerating gradient (∼1 vs. 100's GeV/m) and increases the plasma length for reaching a fixed final energy. However, operating with a larger accelerating structure ($\sim \lambda_{pe}^3 \propto n_e^{-3/2}$) simplifies the drive and witness bunch production as well as the spatial and temporal alignment of the two bunches. It also increases the beam beta function matched to the plasma focusing force ($\beta_{matched} \propto n_e^{-1/2}$ in the blow out regime) and makes it easier to capture the bunch exiting the plasma.

REFERENCES

[1] I. Blumenfeld *et al.*, Nature **445**, 741 (2007).
[2] A. Caldwell *et al.*, Nat. Phys., 363 (2009).
[3] K. Lotov *et al.*, Phys. Rev. ST-AB **13** 041301 (2010).
[4] N. Kumar *et al.*, Phys. Rev. Lett. **104** 255003 (2010).
[5] D. H. Whittum *et al.*, Phys. Rev. Lett. **67**, 991 (1991).
[6] K. V. Lotov*et al.*, Phys. Rev. ST-AB 16, 041301 (2013).
[7] J. Vieira *et al.*, to be submitted.
[8] C. B. Schroeder *et al.*, Phys. Rev. Lett. **107** 145002 (2011); A. Pukhov *et al.* Phys. Rev. Lett. **107** 145003 (2011).
[9] C. Bracco *et al.*, submitted to NIM A, August 2013.
[10] B. Allen *et al.*, Phys. Rev. Lett. **109**, 185007 (2012).
[11] E. Oz *et al.*, submitted to NIM A, August 2013.
[12] D. Gordon et al, PRE, 64 046404 (2001).
[13] A. Pukhov *et al.*, Phys. Rev. ST-AB 15, 111301 (2012).
[14] K. V. Lotov, J. Plasma Phys. 78(04), 455 (2012).

Copyright © 2013 CC-BY-3.0 and by the respective authors

BEAM-BEAM LIMIT IN AN INTEGRABLE SYSTEM*

A. Valishev#, S. Nagaitsev, FNAL, Batavia, IL 60510, USA
D. Shatilov, BINP, Novosibirsk, 630090, Russia
V. Danilov, ORNL, Oak Ridge, TN 37831, USA

Abstract

Round colliding beams have been proposed as a way to push the attainable beam-beam tune shift limit, and recent successful experiments at the VEPP-2000 collider at BINP demonstrated the viability of the concept. In a round-beam system the dynamical stability is improved by introducing an additional integral of motion, which effectively reduces the system from a two and a half dimensional to one and a half dimensional. In this report we discuss the possible further improvement through adding the second integral of motion and thus making the system fully integrable. We explore the ultimate beam-beam limit in such a system using numerical simulations taking into account various imperfections.

INTRODUCTION

The strong nonlinearity of transverse focusing force is inherent to beam-beam interaction and affects the stability of particle motion in the present circular colliders. The beam-beam kick localized in a short interaction length along the accelerator circumference represents a nonlinear and time-dependent excitation of the otherwise linear betatron motion in the rest of the machine. In such systems, a multitude of resonances lead to particle diffusion and to chaotic-bounded motion, which limits the attainable beam brightness and collider performance. The typical maximum value of beam-beam parameter ξ in such 'conventional' machines is about 0.05÷0.06 for electron colliders, and up to 0.03 for hadron colliders due to the absence of synchrotron radiation damping.

In an attempt to mitigate the beam-beam effect, Krishnagopal and Siemann [1] analyzed the effect of the strong bunch length σ_z on the magnitude of resonances with the use of canonical perturbation theory. They concluded that '…the finite longitudinal extent of the beam-beam interaction results in averaging of the betatron phase over the collision, which mitigates the destructive effects of resonances'. Conversely, the synchrotron oscillations of the test particle lead to a greater depth of modulation and enhance the effect of resonances. Since the lengths of the two colliding bunches are usually equal, an optimal length should exist at which the two effects are compensating one another. The ratio of the bunch length to the beta-function of the order of one was determined as viable.

In further work along this direction Y. Alexahin [2] and T.Sen [3] studied the effect of phase averaging on the Tevatron performance, and also predicted the optimal $\sigma_z/b^* \approx 1$.

The growing interest to integrable systems in mathematical physics motivated Danilov and Perevedentsev to investigate the application of these systems to accelerators and colliding beams in particular [4, 5]. In a round colliding beams system, the beam-beam interactions as well as the transport through accelerator lattice possess axial symmetry. This results in the existence of an additional integral of motion, the longitudinal component of the angular momentum. An important consequence of the additional integral of motion is the elimination of transverse coupling resonances.

In Ref. [5], a round colliding beam system is proposed, which has two integrals of motion. The full integrability is achieved through proper shaping of the longitudinal bunch density, which makes the system Hamiltonian time-independent. The line charge density λ in this case must be inversely proportional to the beta-function β: $\lambda(2s)=C/\beta(s)$. In the case of no external focusing in the interaction region, the beta-function is a quadratic function of the azimuth s, $\beta(s)= \beta^*+s^2/\beta^*$, and the proper 'ideal' longitudinal distribution is

$$\lambda(s) = \frac{C}{1+(s/2\beta^*)^2}.$$

An important property of the fully integrable system is that the exact shape of transverse density distribution is irrelevant and does not affect the stability. However, the complete integrability is valid only for the center particles in the weak bunch, and synchrotron oscillations introduce modulation that disturbs the system. Also, the longitudinal distribution in a typical collider is Gaussian. Numerous numerical simulations have been performed to explore the stability of the round colliding beam systems to these imperfections (see e.g. [6, 7]). More importantly, the experimental implementation of the concept at the VEPP-2000 collider (BINP, Novosibirsk), where the record-high value of ξ=0.25 was achieved (at $\sigma_z/\beta^*\approx1$), demonstrated its viability [8, 9].

This, and the recent progress in the development of nonlinear integrable systems [10] motivated us to re-visit the question of optimization of a round colliding beam system with the goal to achieve even higher beam-beam parameters. We use the Lifetrac weak-strong particle tracking code [11] to perform numerical simulations, and characterize the tracking data with the Frequency Map Analysis [12, 13].

*Fermi Research Alliance, LLC operates Fermilab under contract No. DE-AC02-07CH11359 with the U.S. Department of Energy.
#valishev@fnal.gov

Copyright © 2013 CC-BY-3.0 and by the respective authors

SIMULATION MODEL

The layout of the test lattice used in simulations is presented in Fig. 1. The machine consists of two main elements: a) a linear arc cell with axially symmetric focusing and phase advance of $\pi \times n$ (n is integer) in both planes; b) interaction region (IR), which is a drift space with length L and phase advance $2\pi Q_0$. The horizontal and vertical beta-functions in the IR are equal, with the minimum at the center of the drift. The well known relation between the phase advance and beta-function in a drift determines the value of the beta-function minimum β^*: $\pi Q_0 = \text{atan}(L/2\beta^*)$. The purpose of the arc cell is to match the beginning and the end of the IR lattice functions, otherwise being transparent – we consider dispersion and focusing chromaticity to be zero everywhere.

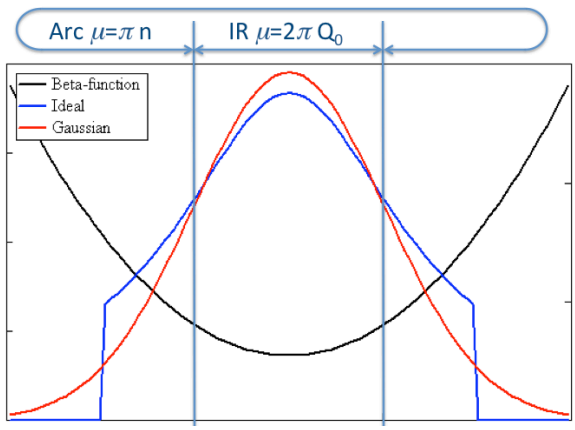


Figure 1: Schematic of the model lattice. Beta-function (black trace), ideal bunch density $\lambda=1/\beta$ (blue) and Gaussian density with $\sigma_z=\sqrt{2}\ \beta^*$ (red) as a function of azimuth. $Q_0=0.3$. Bunch length for the ideal case is $2\times L$ due to the counter-propagation of two beams.

Note that a significant difference between this model and the system proposed in [5] is that the betatron tune working point does not need to be close to integer or half-integer. Indeed, the betatron tune is $n/2+Q_0$, and Q_0 is determined by the ratio of β^* and L.

Next, we track a number of test particles with different initial conditions through the lattice with beam-beam interaction, and plot the tune variation along the trajectory as a color chart either in tune space (footprint) or in betatron amplitude space. The regions with significant tune variation represent either resonances or the chaotic motion.

RESULTS

For the synchronous particle in a weak bunch, in the case of ideal bunch density the system has two integrals of motion and the motion is infinitely stable for any value of beam-beam parameter. Figure 2 shows the tune footprint for $\xi=1$ (throughout this report the focusing beam-beam interaction with Gaussian transverse profile is used). The limited number of longitudinal slices of beam-beam interaction explains the existence of resonance lines. The motion also remains stable for $\xi=5$, 10.

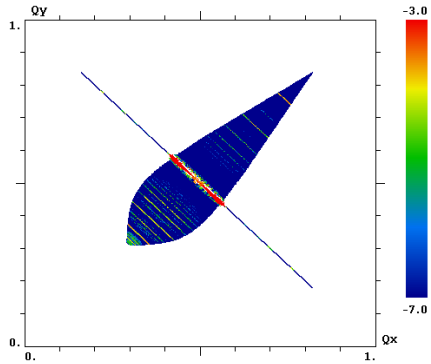


Figure 2: Tune footprint for the case of ideal bunch density $\lambda=1/\beta$, $Q_0=0.3$, and zero synchrotron amplitude. Beam-beam parameter $\xi=1$. Particles with betatron amplitudes up to 20 σ. The color represents tune jitter according to the scale on the right (log scale).

For the case of Gaussian longitudinal density, the integrability is lost and one can see the strong overlapping of resonances at $\xi=1$ (Fig. 3) but still no significant resonances at $\xi=0.5$ (Fig. 4). Note that in either case the large amplitude motion is stable, which could allow using such systems for purposes other than colliders, for example to create large betatron tune spread.

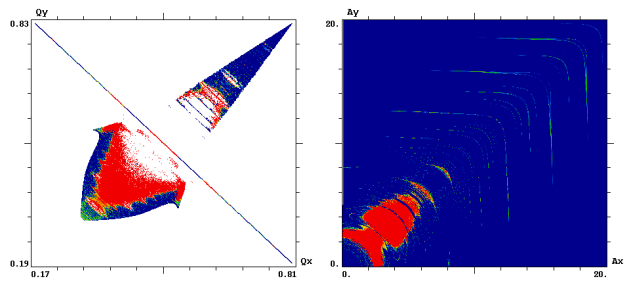


Figure 3: FMA plots for the case of Gaussian bunch density $\sigma_z=\sqrt{2}\ \beta^*$, $Q_0=0.3$, $\xi=1$, and zero synchrotron amplitude. Particles with betatron amplitudes up to 20 σ. Tune footprint (left), FMA in amplitude space (right).

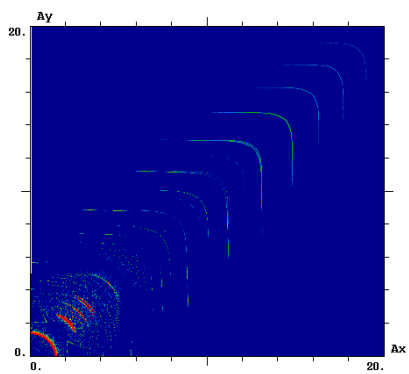


Figure 4: FMA for Gaussian bunch density $\sigma_z=\sqrt{2}\ \beta^*$, $Q_0=0.3$, and zero synchrotron amplitude. $\xi=0.5$.

Copyright © 2013 CC-BY-3.0 and by the respective authors

In the simulations for particles with non-zero synchrotron amplitude, we investigated the effect of the bunch length ratio for weak and strong bunch, and of the synchrotron tune. The variation of synchrotron tune does change the resonance configuration, emphasizing some betatron amplitudes more than the others, but does not reduce resonances in a large enough area. As one could expect, the shortening of weak bunch length has a profound effect on the system stability. Simulations suggest that beam-beam parameter of 0.5 could be sustained for the bunch length ratio of about 1/10 (Fig. 5).

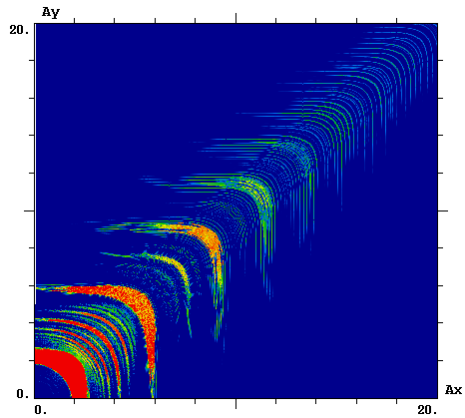


Figure 5: FMA for Gaussian bunch density $\sigma_z=\sqrt{2}\ \beta^*$, Q_0=0.3, ξ=0.5. Synchrotron amplitude 0.1 σ_z.

The results of multi-particle simulations for the VEPP-2000 lattice, taking into account the dynamic beta-function and emittance, synchrotron radiation damping and quantum excitation, are not very encouraging. We observe a reduction of the luminosity with the increase of σ_z/β^* ratio exceeding that expected from the hour-glass effect.

CONCLUSION

We confirmed that in a specially designed accelerator lattice, and by a careful shaping of the longitudinal profile of strong bunch, the value of beam-beam parameter exceeding one could be achieved for particles with zero synchrotron amplitude. The approach described in this report is advantageous with respect to the previously considered schemes because the machine betatron tune does not need to be close to integer or half-integer. This makes the scheme less sensitive to imperfections of the accelerator lattice.

For particles with non-zero synchrotron amplitude, the integrability is lost but their motion remains stable even at large amplitudes, although a significant emittance growth is induced by the overlapping resonances. Simulations predict that a scheme with the bunch length ratio between the weak and the strong bunch of about 1/10 may be feasible, which could be useful for asymmetric machines such as the electron-ion colliders.

A more rigorous study of the feasibility of the scheme in a real accelerator is in progress.

ACKNOWLEDGMENTS

The authors would like to thank E. Perevedentsev and D. Swartz for fruitful discussions.

REFERENCES

[1] S. Krishnagopal and R. Siemann, "Bunch-length effects in the beam-beam interaction", Phys. Rev. D 41, 2312 (1990)

[2] Y. Alexahin, "Excitation of the Synchro-Betatron Resonances by the Beam-Beam Interaction in the Tevatron Run II Lattice", FERMILAB-TM-2148 (2001)

[3] T. Sen, "The beam-beam interaction of finite length bunches in hadron colliders", FERMILAB-Pub-00/093-T (2000)

[4] V. Danilov, E. Perevedentsev, "Invariants for Nonlinear Accelerator Optics and Round Colliding Beams", Workshop on Beam-Beam effects, Dubna (1995)

[5] V. Danilov, E. Perevedentsev, "An Approach to Integrability in Round Colliding Beams", 14th Advanced ICFA Beam Dynamics Workshop, Frascati (1997); V.V. Danilov and E.A. Perevedentsev, "Two Examples of Integrable Systems with Round Beams", PAC97, Vancouver, Canada (1997)

[6] V.Danilov and V. Shiltsev, "Round Colliding Beams as a way to Integrability: Theory and Simulations for Tevatron", FERMILAB-FN-655 (1997)

[7] A. Valishev et al., "Strong-Strong Simulation of Beam-Beam Interaction for Round Beams", FPAB051, PAC'03, Portland, OR (2003).

[8] A. Romanov et al., "Status of the Electron-Positron Collider VEPP-2000", MOOAA2, NA-PAC'13.

[9] D. Shwartz et al., "Recent Beam-Beam Effects at VEPP-2000 and VEPP-4", BB2013, ICFA mini-workshop on beam-beam effects, March 18-22, CERN (2013)

[10] V. Danilov and S. Nagaitsev, Phys. Rev. ST Accel. Beams **13**, 084002 (2010)

[11] D. Shatilov et al., "Lifetrac Code for the Weak-Strong Simulation of the Beam-Beam Effects in Tevatron", TPAT084, PAC'05, Knoxville, TN, USA (2005)

[12] J. Laskar, Icarus 88, 266 (1990)

[13] D. Shatilov et al., "Application of frequency map analysis to beam-beam effects study in crab waist collision scheme", Phys. Rev. ST Accel. Beams **14**, 014001 (2011)

Copyright © 2013 CC-BY-3.0 and by the respective authors

A MODEL RING WITH EXACTLY SOLVABLE NONLINEAR MOTION

T. Zolkin*, The University of Chicago, Department of Physics, Chicago, IL 60637–1434, USA
Y. Kharkov, I. Morozov†, BINP SB RAS, Novosibirsk 630090, Russia
S. Nagaitsev‡, FNAL, Batavia, IL 60510–5011, USA

Abstract

Recently, a concept of nonlinear accelerator lattices with two analytic invariants has been proposed [1]. Based on further studies [2], the Integrable Optics Test Accelerator (IOTA) was designed and is being constructed at FNAL. Despite the clarity and transparency of the proposed idea, the detailed analysis of the beam motion remains quite complicated and should be understood better even for the case when no perturbations are taken into account. In this paper we will review one of the three proposed realizations of integrable optics, where the variables separation is possible in polar coordinates. This system allows for an exact analytical solution expressed in terms of elliptic integrals and Jacobi elliptic functions [3]. It gives the possibility to check numerical algorithms used for tracking and to perform more rigorous analysis of the motion in comparison with the "crude" analysis of the topology of the phase space. In addition we will discuss some difficulties associated with numerical simulations of such a comparatively complex dynamical system and will take a look at the possible perturbations for a model machine.

INTRODUCTION

Below we will consider the design of the accelerator lattice which includes nonlinear lens, while the transverse motion remains integrable. Several such systems possessing a second invariant of motion, which is quadratic in momentum, have been proposed in [1]. One of the possible realization is based on the application of a point-like magnetic quadrupole inserted into the center of a vacuum pipe. In this case, the motion allows the variables separation in polar coordinates and its analytical solution was described in [3]. Here, we will focus on the implementation of this idea and will design a model accelerator ring. For more details on dynamics in such a magnetic field one should consult the list of references.

ACCELERATOR LATTICE DESIGN

The particle dynamics in the magnetic field of point-like magnetic quadrupole is unusual in that there is no equilibrium orbit of motion; trapped particles are only in dynamical equilibrium, i.e. in constant motion in at least one degree of freedom. This feature is related to the presence of singularity at the origin. On the other hand, it means that under the action of friction force, let say caused by the synchrotron radiation, particles will fall towards the singularity and eventually will be lost on the inner aperture of the vacuum pipe, ρ_{in}. Thus, below we will consider the design of an accelerator ring for protons, so far as the damping of oscillations due to radiation effects is negligible for them.

* zolkin@uchicago.edu
† imorozov@fnal.gov
‡ nsergei@fnal.gov

Axially Symmetric Focusing

As it was described in [1], the concept of nonlinear integrable optics under consideration requires an axially symmetric focusing in the accelerator ring. A super-period of such a lattice can be realized as $\frac{F}{2}O\frac{F}{2}$ lattice, with a drift space of length L, where the nonlinear lens is located, and an optics insert (also so-called T-insert), which is equivalent to a thin axially symmetric lens with the focal length equal to $1/k$ (see Fig. 1).

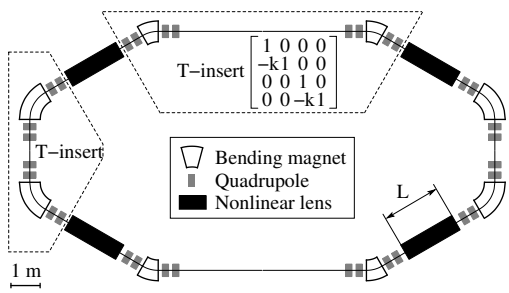


Figure 1: Schematic layout of the IOTA ring.

To study the transverse motion of the monochromatic beam the principal realization of the optics insert is not essential, and for all further simulations we will use a parameters designed for IOTA ring [2]. The dependence of the minimum and maximum of beta function in the drift space as well as betatron frequency as a function of the T-insert strength are show in Fig. 2. Main parameters of the ring are listed in Table 1.

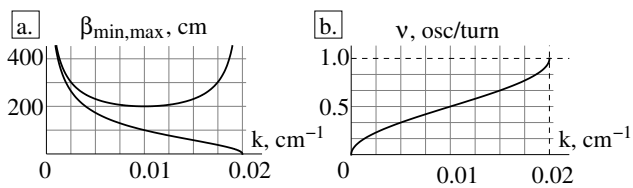


Figure 2: Minimum and maximum of beta-function (a.) and betatron frequency (b.) as a function of axially symmetric lens strength parameter, k.

Copyright © 2013 CC-BY-3.0 and by the respective authors

Table 1: IOTA ring parameters used in simulations and optimized for compatibility with nonlinear lens under consideration

Linear Lattice Parameters		
# of super-periods		4
# of nonlinear lenses		2
Circumference, Π	(m)	38.7
Bending dipole field, B	(T)	0.7
Drift space length, L	(cm)	200
T-insert strength parameter, k	(cm^{-1})	$\in (0; 0.02)$
Beam at the Injection		
Beam kinetic energy, $\mathcal{E}_{\rm kin}$	(MeV)	1.91
Beam momentum, $P_{\rm eq}$	(MeV/c)	60
Normalized emittance, $\epsilon^{\perp}_{\rm norm}$	(cm rad)	2×10^{-5}

Nonlinear Lens

The design of nonlinear lenses, corresponding to integrable potentials proposed at [1], brings in two major inevitable perturbations. They are associated with the special longitudinal dependence of the field, and, the physical realization of poles of the lens. The first condition is automatically satisfied due to invariance of the potential under the transformation to normalized coordinates and time, except the effect from the fringe fields. While the second one can not be realized without introducing the perturbation, since poles can not be placed at the same point in the space.

Point-like magnetic quadrupole can be approximated with four wires of diameter D, which are spaced very closely to each other at the vertices of a square, $\vec{R}_\alpha$, and numbered counter-clockwise from the corner located at $\vec{R}_1 = (b, 0)$ (see Fig. 3). "Dot" and "cross" symbols in the figure show the current direction: coming out and into the page (along the beam direction) respectively. In order to keep particles which are performing the libration ($0 < W < \mathsf{A}$), the vacuum chamber can be made of two nested half-cylinders of radii $\rho_{\rm in,out}$, forming a c-shape.

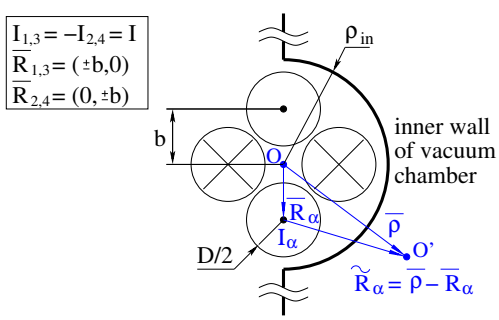


Figure 3: Schematic plot of the nonlinear lens geometry along with inner part of vacuum pipe. Points O and O' represents the origin of coordinates and the point inside the vacuum chamber where the field induced by the lens should be considered, $\vec{\rho} = \overline{OO'}$.

Indeed, in ordinary polar coordinates

$$\rho = \sqrt{x^2 + z^2}, \qquad \theta = \arctan(z/x),$$

the longitudinal component of the magnetic vector potential $\mathbf{A} = (0, A_s, 0)$ created by such a quadrupole structure can be easily calculated and expressed as a multipole series

$$\begin{aligned} A_s &= -\frac{\mu_0}{2\pi} \sum_{\alpha=1,2,3,4} I_\alpha \ln|\widetilde{R}_\alpha| \\ &= \frac{\mu_0 I}{\pi} \sum_{n=0}^{\infty} \left(\frac{b}{\rho}\right)^{2+4n} \frac{\cos[(2+4n)\theta]}{1+2n} \\ &= \frac{\mu_0 I}{\pi} \left(b^2 \frac{\cos 2\theta}{\rho^2} + \frac{b^6}{3} \frac{\cos 6\theta}{\rho^6} + O\left[\left(\frac{b}{\rho}\right)^{10}\right] \right), \end{aligned}$$

where μ_0 is a vacuum permeability. As one can see that first perturbing term corresponds to the dodecapole field which is significantly suppressed by 4 orders of magnitude in a smallness parameter (b/ρ). It shows that the drawing apart of wires does not create a strong perturbation since all additional terms are rapidly decay with the growth of ρ. The nonlinear potential in the Hamiltonian is related to A_s as

$$V(\rho, \theta) = \frac{U(r, \theta)}{\beta(s)} = \frac{\mathsf{A} \sin(2\theta + \varphi)}{\rho^2} = -\frac{eA_s}{P_{\rm eq}},$$

which gives the expression for the field amplitude:

$$\mathsf{A} = \frac{\mu_0 e I b^2}{\pi P_{\rm eq}}.$$

Due to a presence of the physical aperture, the following inequality should be satisfied

$$\frac{\rho^4_{\rm in}}{\beta^2(L/2)} < \mathsf{A} < \frac{\rho^4_{\rm out}}{\beta^2(L)}, \qquad (1)$$

in order to have a suitable admittance. Among the transverse geometrical parameters of the lens there is only one independent since we want to pack all wires as tightly as we can. Thus for a given current density in a wire, $\rho_I = 4I/\pi D^2$, the optimization of A becomes a problem of a single parameter variation. For example, the value of the diameter of a wire allows to approximate the wire displacement and the inner radius of vacuum pipe as

$$b \approx D/\sqrt{2}, \qquad \rho_{\rm in} \approx (1 + \sqrt{2})D/2.$$

Possible choice of A is presented in Fig. 4.

For simulations we considered 2 possible scenarios: lens with water cooling and the superconducting one. Parameters for both cases are listed in a Table 2. It is worth noting that the use of high current is limited from technical limitations, while the use of low current lens leads to the shrink of admittance, which can be compensated by decreasing the energy of a beam.

In order to study the monochromatic beam motion in a lattice with perturbations, we decided to use the Poincaré

Copyright © 2013 CC-BY-3.0 and by the respective authors

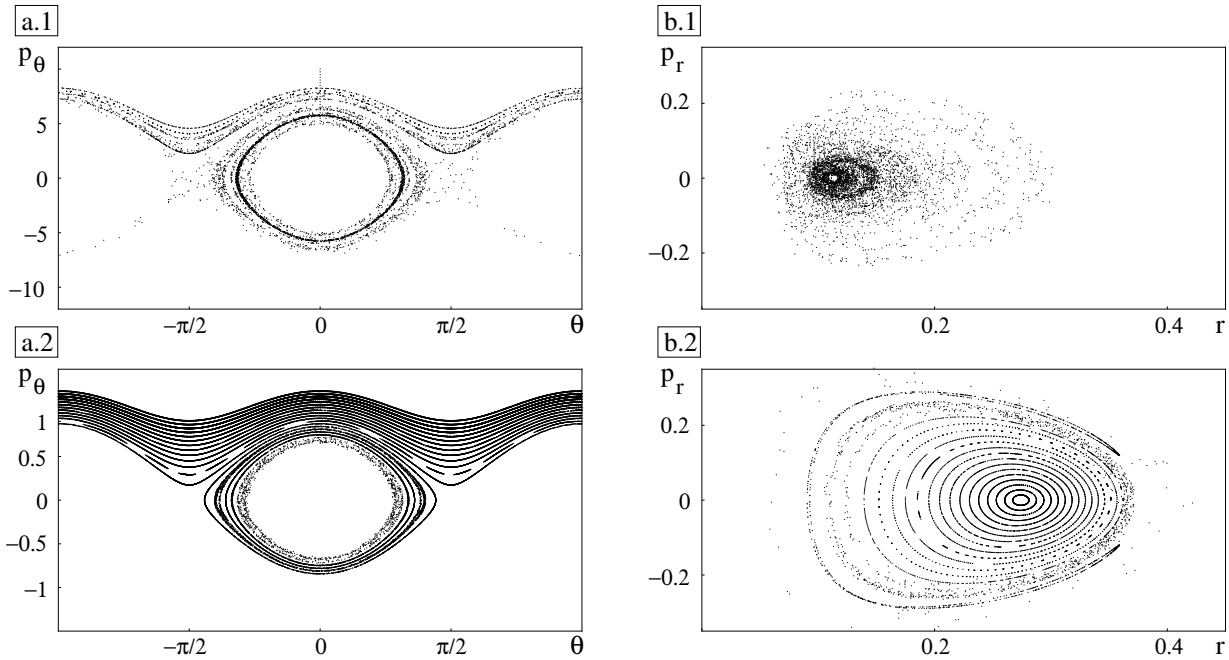


Figure 5: (a.1,2) and (b.1,2) show Poincaré surfaces of section for $[r = r_0, p_r = 0]$ and $[\theta, p_\theta = 0]$ respectively at the middle of nonlinear lens. Beam motion is simulated with nonlinear kick defined by 4 wires moved apart from each other. Linear lattice parameters are calculated for betatron frequency $\nu_{x,z} = 0.44$. Parameters of nonlinear lens are chosen in accordance to Fig. 4. Plots show presence of different types of cross sections in a phase space: (a,b.1) — strongly chaotic and (a,b.2) — close to integrable.

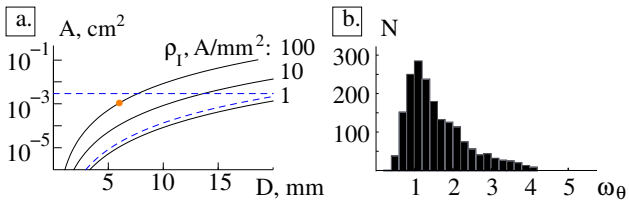


Figure 4: (a.) Nonlinear lens strength, A, dependence of the wire diameter, D, for a given values of the current density in logarithmic scale ($\rho_I = 10$ A/mm^2 requires water cooling of wires, while in order to keep $\rho_I = 100$ A/mm^2 lens should be superconducting). Blue dashed lines represent condition given by inequality from Eq. (1). Orange circle shows possible choice of A for superconducting scenario. (b.) Example of the distribution of angular frequencies in the beam filling the admittance, which determined by the choice on left figure.

surfaces of section in a phase space. A numerical example, when the perturbation of integrable optics caused by the moving apart wires in superconducting nonlinear lens, is presented in Fig. 5.

Table 2: Parameters of the nonlinear polar lens for two different values of current density: superconducting lens and the one with water cooling

	Supercond.	**Water Cooling**
Beam momentum P_{eq}, (MeV/c)	60	30
Diameter of the wire D, (mm)	6	7
Current density ρ_I, (A/mm^2)	100	10
Total current I, (A)	2827	385
Inner radius of pipe ρ_{in}, (cm)	0.85	1
Outer radius of pipe ρ_{out}, (cm)	4	4
Strength of lens A, (cm^2)	10.8×10^{-4}	4×10^{-4}

REFERENCES

[1] V. Danilov and S. Nagaitsev, "Nonlinear accelerator lattices with one and two analytic invariants," Phys. Rev. ST Accel. Beams **13**, 084002 (2010).

[2] P. Piot, V. Shiltsev, S. Nagaitsev, M. Church, P. Garbincius, S. Henderson and J. Leibfritz, "The Advanced Superconducting Test Accelerator (ASTA) at Fermilab: A User-Driven Facility Dedicated to Accelerator Science & Technology," arXiv:1304.0311 [physics.acc-ph].

[3] T. Zolkin, Y. Kharkov, I. Morozov and S. Nagaitsev, "Nonlinear Accelerator with Transverse Motion Integrable in Normalized Polar Coordinates," Conf. Proc. C **1205201**, 1116 (2012).

Copyright © 2013 CC-BY-3.0 and by the respective authors

NONPARAXIAL TRANSVERSE EFFECTS ON THE PROPAGATION OF NONLINEAR ELECTROMAGNETIC PULSES *

A. Bonatto†, UFPR Curitiba, UFRGS Porto Alegre, Brasil
S.R.Lopes, UFPR, Curitiba, Brasil
R.P. Nunes, R. Pakter, F.B. Rizzato, UFRGS, Porto Alegre, Brasil
C. Bonatto, UFPel, Pelotas, Brasil

Abstract

In the present analysis we study the weakly nonlinear interaction between trains of electromagnetic pulses and space-charge fields in laser-plasma systems. We direct the analysis to regimes evolving with the co-moving coordinate of the beam frame, but do not make any assumptions on paraxial or underdense approximate conditions. The model thus constructed allows us to investigate regimes where transverse and longitudinal length scales of the pulses are comparable. Resonant and nonresonant regimes of space-charge wave excitation are analyzed. In both cases, with aid of analytical estimates and numerical simulations, we examine how far trains of electromagnetic pulses can travel before being affected by the destructive transverse effects.

INTRODUCTION

The propagation of localized radiation pulses in plasmas has been the subject of continuous interest in a variety of areas, including nonlinear wave excitation [1, 2] and particle acceleration [3, 4, 5]. Pulses are formed as large amplitude electromagnetic waves undergo the process of modulational instability in the plasma, breaking up into a series of narrow quasi-isolated structures. This is a typical behavior in soliton turbulence [6] and in self modulated laser accelerators, once an option in laser acceleration, whose interest has been reignited recently [7].

Pioneering works [8, 9] have studied the self-consistent problem of electromagnetic pulses propagating in plasmas and the space-charge waves generated by this propagation in one dimensional models. These models, however, usually refers to nonparaxial solutions (where dependence of the field on transverse coordinates is completely neglected) or the opposite, the paraxial limit (where transverse effects dominate the dynamics). In several occasions, a laser beam reaches operational conditions where longitudinal and transverse sizes become similar in magnitude [10, 11]. Under these conditions, an accurate account of the dynamics should treat transverse and longitudinal effects on the same footing.

The objective of the present work is to perform an analysis of the nonlinear interaction of electromagnetic and space-charge without invoking 1D, paraxial, or approximate nonparaxial approaches [12, 13]. Our main interest will be to determine how the the transverse structure affects a train of solitons, typically formed after an initially injected pulse breaks up through self-modulation [14].

* Work supported by CNPq, Brasil, and AFOSR Grant FA9550-12-1-0438, USA.
† abonatto@if.ufrgs.br

THE MODEL

We can model this system with the following coupled equations for the laser field a and for the space-charge potential $\varphi \equiv v_g^2 n - a^2/2$,

$$\kappa \frac{\partial^2 a}{\partial \xi^2} = \delta a + \frac{1}{v_g^2}\varphi\, a + \frac{\kappa}{2v_g^2} a^3 - \nabla_\perp^2 a, \qquad (1)$$

$$\frac{\partial^2 \varphi}{\partial \xi^2} + \frac{1}{v_g^2}\varphi = -\frac{1}{2v_g^2} a^2 + \frac{1}{2}\nabla_\perp^2 a^2, \qquad (2)$$

derived in details in our previous work [15]. If the transverse structure is neglected, this set becomes similar to models analyzed in the past [9] and one can think of it as describing the coupled nonlinear dynamics of fields a and φ as a function of the co-moving coordinate ξ, which plays the role of time. With the transverse structure included, it describes the weakly nonlinear, spatio-temporal interaction of laser and space-charge field. Coordinate ξ can still be seen as time, and space is associated with the transverse structure itself. These Eqs. are solved numerically with the following initial conditions

$$a(0, x_\perp) = a_0\, e^{-\lambda x_\perp^2} \;\;,\;\; \partial a/\partial\xi|_{\xi=0} = 0 \qquad (3)$$

$$\varphi(0, x_\perp) = -a(0, x_\perp)^2/2 \;\;,\;\; \partial\varphi/\partial\xi|_{\xi=0} = 0 \qquad (4)$$

EVOLUTION OF THE TRAIN OF PULSES.

Examining Eqs. (1) and (2) together with the initial conditions we find that $(\delta/\kappa)^{-1/2}$ is the time scale for pulse formation along the propagation axis, $(\lambda/\kappa)^{-1/2}$ is the time scale for transverse effects. When $\lambda \ll \delta$, pulses are formed before being affected by transversal effects, and when the inequality reverses, one recognizes the typical instability associated with the transverse term, shown in a recent work to be of the form $a \sim e^{\lambda\xi^2/\kappa}$ [15]. Depending on the relative magnitude of the parameters δ and λ one thus may or may not observe pulses in the system.

In order to see how the electromagnetic pulses evolve as they move into the plasma, we will split the analysis into nonresonant and resonant regimes. Nonresonant regimes are the ones where the adiabatic approximation would remain valid throughout the entire dynamics, if the transverse derivatives were turned off. Resonant regimes, on the other hand, are the ones where adiabaticity is broken and proper plasma waves are excited, even in the absence of the transverse structure.

Copyright © 2013 CC-BY-3.0 and by the respective authors

Nonresonant Regimes

Nonresonant cases are those where the time scale for the dynamics is much longer than the plasma time scale scale. In our dimensionless system, this means that $1/v_g^2$ is sufficiently large that the the corresponding terms in Eq. (2) are much larger than the term with the ξ-derivative. In this case $\varphi = -a^2/2$ and one says that the φ field becomes enslaved to the field a, which allows to use Eq. (1) as a closed, governing equation (with transverse derivatives turned off) for field a in the adiabatic regime:

$$\kappa \frac{\partial^2 a}{\partial \xi^2} = \delta a - \frac{a^3}{2}. \qquad (5)$$

As Eq. (5) describes a nonlinear oscillator with stable equilibria at $a = \pm\sqrt{2\,\delta}$, each transverse coordinate $x_\perp$ the laser oscillates with a different, local nonlinear frequency $\Omega = \Omega(x_\perp)$. When the transverse derivatives are turned on, it is only a matter of the time ξ until the gradient of the phase $\Omega(x_\perp)\,\xi$ along $x_\perp$ monotonically grows to any desired value. As one turns the transverse term on, even if initially small, the associated transverse derivatives will eventually grow and affect the dynamics. In the nonresonant case we are investigating, a quick estimate can be made on the value of ξ where the transverse term is expected to become comparable with the terms already present in Eq. (5). We first observe that for noise-like initial conditions, the right-hand-side of the energy conserving Eq. (5) keeps oscillating within the region $\mathcal{R}$ bounded by the limits $-2\delta^{3/2} \le \mathcal{R} \le 2\delta^{3/2}(2/27)^{1/2}$. To obtain the estimate, we simply integrate Eq. (5) for all $x_\perp$'s using the initial profile provided by Eq. (3), calculate $\nabla_\perp^2 a$ with basis on the solution for a yielded by the very same Eq. (5), and take note of the earliest time where $\nabla_\perp^2 a$ cross the boundaries of $\mathcal{R}$.

Figure 1 displays the corresponding behavior. Once again we choose $\delta = 10^{-2}$, along with $v_g^2 = 0.2$ and $\lambda = 10^{-3}$. The upper and lower straight lines represent the boundaries of $\mathcal{R}$ and we can see how the magnitude of $\nabla_\perp^2 a$ grows in time. At $\xi \sim 35$ the transverse Laplacian reaches the boundaries of $\mathcal{R}$ at $\lambda^{1/2}x_\perp \sim 1$, and at this time one can expect to see the effects of the transverse derivatives on the pulse dynamics.

Let us then integrate the full space-time system formed by Eqs. (1) and (2) to make comparisons with the estimates in some instances. Results are displayed in Fig. 2.

Panel (a) of Fig. 2 represents the case with the transverse term turned off. We repeat the parameters used in Fig. 1: $\delta = 10^{-2}$, $v_g^2 = 0.2$ and $\lambda = 10^{-3}$. For the given initial conditions (3) and (4), the tridimensional plot displays the regular behavior of the corresponding nonlinear pulses. At each $x_\perp$ the laser oscillates, but with a steady phase slippage rate existing along this transverse axis. This is why one observes curved wave fronts as ξ grows.

Keeping the parameters of panel (a), in panel (b) of the same Fig. 2 the transverse term is turned on. We see that the train of pulses starts to develop sharp spikes before

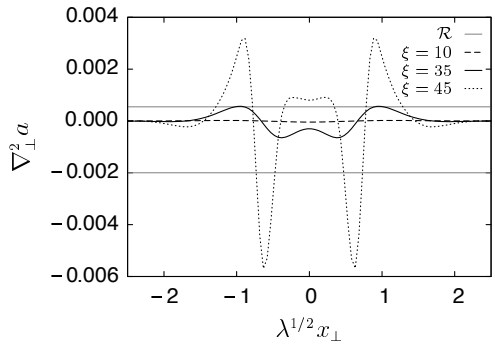


Figure 1: Magnitude of the transverse Laplacian as a function of $x_\perp$ and ξ. At $\xi = 35$ the Laplacian touches the boundary of region $\mathcal{R}$, which signals the instant where its corresponding effects become noticeable.

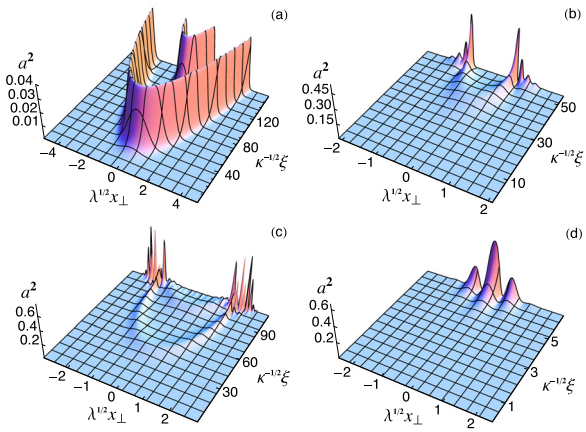


Figure 2: Space-time dynamics of the laser field in the nonresonant regime. In all cases we take $\delta = 10^{-2}$ and $v_g^2 = 0.2$. In panel (a) we consider $\lambda = 10^{-3}$ but keep the transverse Laplacian switched off. In the remaining panels the Laplacian is turned on with $\lambda = 10^{-3}$ in (b), $\lambda = 2.5 \times 10^{-4}$ in (c), and $\lambda = 10^{-1}$ in (d).

$\xi = 50$, which agrees with the previous estimates. The spikes arise from the action of the second derivatives along $x_\perp$, as can be seen again from Fig. 1, and shortly afterwards the space-time dynamics merges into a chaotic pattern. The chaotic pattern cannot be followed for long due to the fact that, in that stage, the fields grow to values beyond our weakly nonlinear approximation. However, the important information to be gathered here is on how far solitary pulses behave as such, before being affected by the transversal effects.

For sake of comparison, in panel (c) we also examine what happens when the initial beam width is extended, with a smaller λ given by $\lambda = 2.5\times10^{-4}$ (remaining parameters are kept with the same previous values). In that case our estimate indicates that, as expected, the transverse term takes longer to affect the pulse dynamics. The critical time ξ, once again obtained as the one where $\nabla_\perp^2 a$ escapes region

Copyright © 2013 CC-BY-3.0 and by the respective authors

$\mathcal{R}$, reads $\xi \sim 70$, which agrees with the curves displayed in the present Fig. 2 (c). The case with large values of λ, say $\lambda = 10^{-1}$ ($\gg \delta$), is also worthy of inspection, as done in Fig. 2(d). In this case the transverse term dominates the dynamics, generating the exponential growth commented earlier [15]. As a matter of fact, in this latter case of large λ, the maximum of $\nabla_\perp^2 a$, here located at $x_\perp = 0$, already starts off from a value beyond the boundaries of $\mathcal{R}$.

Resonant Regimes

Since with transverse derivatives neglected the system already displays a nonintegrable behavior in the resonant regime, the quasi-integrable estimates based on the reduced - and integrable - equation (5) becomes inaccurate. However, one can still be tempted to associate the time scale $(\delta/\kappa)^{-1/2}$ with the longitudinal dynamics, and the time scale $(\lambda/\kappa)^{-1/2}$ with the transverse term, as discussed previously. In panel (a) of Fig. 3 we take $v_g^2 = 0.9$ and $\delta = 10^{-2}$, along with $\lambda = 10^{-4}$. Here λ is much smaller than the mismatch δ and we are therefore under circumstances where pulses have time enough to be formed, even if in an irregular fashion. This is essentially what happens, as can be appreciated from the figure. In panel (b) we analyze the dynamics with the same set of control parameters, but with the transverse term switched off. A comparison between both panels allows us to realize that the presence of the transverse structure, even for λ as small as $\lambda = 10^{-4}$, already has a relatively noticeable effect on the dynamics of the laser amplitude a. In fact, the transverse term shortens somewhat the characteristic oscillatory time scale, what is expected from the larger transverse gradients associated with a chaotic case. The shortening of the time scales becomes gradually more pronounced as λ grows.

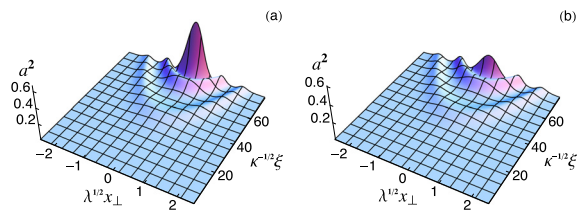


Figure 3: Space-time dynamics of the laser field in the resonant regime. In panel (a) we take $\delta = 10^{-2}$ and $v_g^2 = 0.9$, along with $\lambda = 10^{-4}$. Panel (b) is plotted for the same parameters, but with the transverse term switched off.

CONCLUSIONS

Space-charge waves are excited as the pulses travels into the plasma. Both resonant and nonresonant cases of space-charge plasma wave excitation were examined. In the nonresonant regime, accurate estimate of the transverse effects is possible. One can, for instance, predict, with relatively narrow margins of error, how far does a soliton train move into a plasma before being distorted.

In resonant cases estimates become less accurate due to the nonintegrability of the overall dynamics, but one can still produce reliable predictions on the wave pattern. In the case specifically studied here, the transverse scale $(\lambda/\kappa)^{-1/2}$ is sufficiently larger than the pulse length $(\delta/\kappa)^{-1/2}$ and localized structures can be observed before being affected by the transversal effects.

In general, the number of unperturbed pulses in a train can be roughly estimated as $(\delta/\lambda)^{1/2}$. Since the amplitude a_p of the pulses is proportional to $\delta^{1/2}$, one sees that the number of pulses in a train can be rewritten as $a_p\,\lambda^{-1/2}$. The factor $\lambda^{-1/2}$ itself is the transverse length measured in units of the plasma wavelength. If the laser beam is wide with $\lambda^{-1/2} \gg 1$ the number of pulses can still be appreciable even with a_p small. This is the case of a beam width $50\mu m$ and plasma wavelength $0.5\mu m$, which matches one of the cases studied in the text, where $\lambda = 10^{-4}$. In extreme cases where $\lambda^{-1/2} \sim 1$, only strong lasers can form pulses; otherwise, no pulses are formed as in the cases with $\lambda \sim 10^{-1}$ also investigated in the work.

The present analysis essentially adds transverse effects to the known one-dimensional behavior of train of planar pulses. As an overall conclusion, we see that transversal effects become already important even when the cross section of the radiation beam is relatively larger than the longitudinal pulse size.

REFERENCES

[1] P.K. Shukla, N.N. Rao, M.Y. Yu, and N.L. Tsintsadze, Phys. Letts. **138**, 1 (1986).

[2] D. Farina and S.V. Bulanov, Phys. Rev. Lett. **86**, 5289 (2001).

[3] T. Tajima and J.M. Dawson, Phys. Rev. Lett. **43**, 267 (1979).

[4] E. Esarey, B. Hafizi, R. Hubbard, and A. Ting, Phys. Rev. Lett. **80**, 5552 (1998).

[5] R. Bingham, Nature **424**, 258 (2003).

[6] P.A. Robinson and G.I. de Oliveira, Phys. Plasmas **6**, 3057 (1999).

[7] C. Kamperidis, C. Bellei, N. Bourgeois, M.C. Kaluza, K. Krushelnick, S.P.D. Mangles, J.R. Marques, S. R. Nagel, and Z. Najmudin, J. Plasma Phys. **78**, 433 (2012).

[8] V.A. Kozlov, A.G. Litvak, and E.V. Suvorov, Zh. Eksp. Teor. Fiz **76**, 148 (1979).

[9] U.A. Mofiz and U. de Angelis, J. Plasma Phys. **33**, 107 (1985).

[10] S.-C. Tang, H.-B. Jiang, Y. Liu, and Q.-H. Gong, Chin. Phys. Lett. **25**, 3268 (2008).

[11] E. Miura, *Electron acceleration using an ultra-short ultra-intense laser pulse* in *Femtosecond-scale optics.*, ed. by A. Andreev, ISBN: 978-953-307-769-7, 11 (2011).

[12] B.J. Duda and W.B. Mori, Phys. Rev. E **61**, 1925 (2000).

[13] E. Esarey, C.B. Schroeder, B.A. Shadwick, J.S. Wurtele, and W.P. Leemans, Phys. Rev. Lett. **84**, 3081 (2000).

[14] Lj. Hadžievski, M.S. Jovanović, M.M. Skorić, and K. Mima, Phys. Plasmas **9**, 2569 (2002).

[15] A. Bonatto, R. Pakter, F.B. Rizzato, and C. Bonatto, Laser. Part. Beams **30**, 583 (2012).

Copyright © 2013 CC-BY-3.0 and by the respective authors

ELECTRON AND POSITRON BUNCH SELF-MODULATION EXPERIMENTS AT SLAC-FACET*

P. Muggli†, O. Reimann, Max Planck Institute for Physics, Munich, Germany
N. Lopes, L. Silva, J. Vieira, Instituto Superior Tecnico, Lisbon
E. Adli, S. Gessner, M. Hogan, S. Li, M. Litos, SLAC, Menlo Park, California
C. Joshi, K. Marsh, W. Mori, N. Vafaei-Najafabadi UCLA, Los Angeles, California
Y. Fang, USC, Los Angeles, California

Abstract

We describe some of the measurements that will be performed to study the physics of the self-modulation instability of electron and positron bunches. These measurements will be performed at SLAC-FACET in the E209 experiment. The effect of the SMI on the drive bunch itself (electron or positron) will be studied. Differences between electron and positron bunches are expected since the wakefields are driven into the nonlinear regime.

INTRODUCTION

It was recently proposed to use the self-modulation instability (SMI) of long charged particle bunches in dense plasmas to drive large amplitude (∼1 GV/m) accelerating wakefields [1]. Using the SMI is a method to produce a train of short bunches out of long bunches available today. Long bunches are interesting for driving wakefields and possibly accelerating particles because they can cary large amounts of energy, between 6 and 110 kJ for the p^+ bunches produced by the CERN SPS or LHC with σ_z ≅10-12 cm. Short bunches are desirable because the maximum amplitude of the accelerating field scales as $E_{WB} = \left(2\pi m_e c^2/e\right)/\lambda_{pe}$ and wakefields are most efficiently driven by bunches with $\sigma_z \cong \lambda_{pe}$, therefore $E_{max} \propto 1/\sigma_z$. Since $\lambda_{pe} = 2\pi c/\omega_{pe} = 2\pi c/\left(n_{e0}e^2/\epsilon_0 m_e\right)^{1/2}$, shorter bunches also require larger plasma densities n_{e0}.

We proposed to use the long e^- and e^+ bunches the SLAC linac produced for early plasma wakefield accelerator (PWFA) experiments (σ_z ≅500-700 μm) [2, 3, 4] and the high density plasma available for current experiments n_{e0} ≅10^{16}-10^{17} cm^{-3} [5] to test some of the SMI physics [6].

Theory and simulations predict that as long as the wakefields are in the linear regime, the SMI of positively and negatively charged particle bunches are identical (all other parameters being the same). The wakefields are in the linear regime as long as $E_z \approx (\delta n_e/n_{e0})\, E_{WB} \ll E_{WB}$, i.e., the electron density perturbation δn_e that sustains the wakefields satisfies $\delta n_e \ll n_{e0}$. But the nonlinear wakefield regime with $\delta n_e \sim n_{e0}$ is interesting because the accelerating field can reach the wave breaking field amplitude. In this regime the wakefields become anharmonic and in general more favorable for propagation and acceleration of negatively charged bunches. This is due to the pure ion column (focusing for electrons, defocusing for positrons, for example) occupying most of the phase of the wakefields. This regime is often referred to as the blowout or bubble regime. While the wakefields driven by the (long) unmodulated bunch are in the linear regime ($\delta n_{e0} \cong n_{b0} \ll n_{e0}$, see Table 1), the self-modulation and the ensuing resonant wakefield excitation drives the wakefields into the nonlinear regime. As a result, different quantitative outcomes are expected when changing only the sign of the drive bunch charge.

With the beam and plasma parameters available at SLAC-FACET many of the physics aspects of the SMI, including the asymmetry between negatively and positively charged drive bunches can be studied [6]. We outline here some of the measurements currently planned in experiment tentatively scheduled for this Fall and beyond.

PLANNED MEASUREMENTS

The experiment aims at observing as many of the characteristics of the SMI as possible with the FACET infrastructure. The nominal parameters for the beam and plasma are given in Table 1. However, these parameters will be varied over as large a range as possible depending on the setup that will be available at the time of the experiments.

Table 1: E209 Experiment Parameters

Parameter & Symbol	Value
Bunch population, N_b	<2× 10^{10}
Length, σ_z	500 μm
Radius, σ_r	>30 μm
Density, n_{b0}	<2.8 × 10^{15} cm^{-3}
Energy, W_b	20 GeV
Plasma density, n_{e0}	1-30 × 10^{16} cm^{-3}
Wavelength, λ_{pe}	334-61 μm
Frequency, f_{pe}	0.9-5 THz
Length, L_{plasma}	1 m
Relative bunch density, n_b/n_{e0}	0.1-0.003
Bunch length, $k_{pe}\sigma_z$	3.5-51
Bunch radius, $k_{pe}\sigma_r$	0.6-3
Plasma length, $k_{pe}L_{plasma}$	19,000-103,000

*This work performed [in part] under DOE Contract DE-AC02-7600515
† muggli@mpp.mpg.de

Copyright © 2013 CC-BY-3.0 and by the respective authors

Energy Gain/Loss

The first evidence that SMI has occurred can be obtained by comparing the energy spectrum of the bunch downstream from the plasma location with and without plasma. Without plasma the energy spectrum is that of the incoming bunch, i.e., around 20 GeV and with a correlated energy spread on the order of 1%. The imaging magnetic spectrometer has an energy range from ~11 GeV to >60 GeV with sub-GeV resolution, reaching ~100 MeV for the nominal energy [7]. With the plasma, but without occurrence of SMI, the maximum energy gain and loss would be given by the longitudinal wakefields amplitude driven the long bunch multiplied by the plasma length. This amplitude can be calculated from 2D linear theory [8]. The longitudinal field amplitude far behind a symmetric Gaussian current profile distribution bunch with N particles is: $E_{\pm} \cong \frac{e}{4\pi\epsilon_0} N_b k_{pe}^2 e^{\frac{-k_{pe}^2\sigma_z^2}{2}}$, where $k_{pe} = 2\pi/\lambda_{pe}$. Note that this expression is valid for narrow bunches ($k_{pe}\sigma_r \ll 1$, σ_r the rms Gaussian bunch radius), and it overestimates the fields driven in the $k_{pe}\sigma_r \sim 1$ bunches of these experiments. With the parameters of Table 1 (n_{e0}=10^{16} cm^{-3}), this amplitude is ≅630 MV/m. Therefore, for the case of a 1 m-long plasma, the energy gain/loss would be less than 0.63 GeV, much lower than the one predicted by simulations when SMI occurs (>5 GeV both for electrons and positrons, see Fig. 5 in [6]). The wakefield amplitude and thus the energy gain are even smaller at larger plasma density (larger $k_{pe}\sigma_r$). Even the product of the post-saturation amplitude (>7 GV/m, see Fig. 3 in [6]) with a 1 m plasma length leads to multi-GeV gain and loss.

For these experiments the plasma will be created by laser-ionization of an alkaline metal vapor [9]. The laser pulse is focused to a line along the beam propagation axis by an axicon lens. The axicon maps the radial intensity of the laser pulse onto position along the line focus. Therefore, the plasma length can in principle be varied by changing the transverse size of the laser pulse on the axicon, for example by an iris. Variation of the plasma length could provide information about variations of the longitudinal wakefields along the plasma, or even, with short enough plasma length, about the growth of the SMI itself.

Note that since the energy gain and loss are much larger than the incoming energy content of the bunch, no evidence of the periodic structure of the wakefields is expected in the energy spectra. This is unlike what was observed in experiments at BNL-ATF with a 50 pC, 60 MeV electron bunch and a 2 cm-long plasma [10]. Note also that unlike in experiments planed for example at CERN, in these experiments the plasma length (~1 m) is much larger than the saturation length of the SMI (~5-10 cm). Also, the expected energy gain and loss can be comparable to the bunch incoming energy. Therefore, energy change by drive bunch particles is a suitable diagnostic for SMI occurrence.

Transverse Modulation

Of course, the SMI occurs because of the transverse wakefields. The observation of the effect of the longitudinal wakefields, although the goal of particle acceleration experiments, is only indirect evidence of SMI development. The longitudinally periodic modulation of the bunch density is the result of local focusing and defocusing. Transition radiation [11] is often used to characterize the time structure of charged particle bunches. While incoherent optical transition radiation (OTR) carries direct information about the bunch time structure it is difficult to measure in the plasma frequency range of these experiments (~1-5 THz). The information contained in the long wavelength, coherent range of transition radiation (or CTR) can be measured using interferometry. In this case the information is contained in the transverse, bunch radius dependent form factor. The effect of this bunch factor has been observed at lower energy at the FLASH facility [12]. While the effect of radial modulation tends to be suppressed for high-energy bunches that emit CTR essentially in the forward direction (peak angle at $\sim 1/\gamma$, γ the particles' relativistic factor), this effect has previously been observed at FACET [13].

Therefore, CTR interferometry should reveal the time structure of the bunch when SMI occurs. With a typical Mach-Zender interferometer arrangement, the periodicity is expected with a path length difference $\Delta z \cong \lambda_{pe}/2$. Note that the interferometer trace will be obtained from multiple SMI events with parameters as similar as possible. Although the amplitude of the modulation and its phase along the bunch may vary, its periodicity should remain essentially constant, as long as the plasma density is reproducible. The metal vapor is produced in a system with a long thermal time constant (minutes) [14]. The laser ionization is a threshold process rather insensitive to the small shot-to-shot laser intensity variations expected. These variations should therefore not impede the SMI period determination.

Seeding and Hose Instability

An important topic is that of the seeding of the SMI. The SMI can be seeded to reduce the plasma length for it to reach saturation at the same maximizing the length available for acceleration with a fixed plasma length. In addition, the seeding should allow for the fixing of the phase of the wakefields along the drive bunch. Without seeding, the SMI grows from noise and the phase of the SMI wakefield is random with respect to position along the bunch. The position of the seed (short laser pulse or particle bunch, ionizing laser pulse, sharp bunch leading edge) determines the wakefields starting point. A witness bunch to be accelerated can then be injected into the optimum accelerating and focusing phase of the wakefields once their zero is fixed.

Another important issue is the mitigation of the competing transverse hose instability (HI) [15]. This instability competes with SMI and could destroy the drive bunch before SMI or acceleration can occur. This effect has been

Copyright © 2013 CC-BY-3.0 and by the respective authors

illustrated for the case of a proton bunch in Ref. [16]. Calculations and simulations indicate that seeding the SMI allows it to win over the HI, at least under some circumstances and plasma length [6, 17].

A notch collimator method is available at FACET to produce a drive/witness bunch train for PWFA experiments [5, 18]. This method will be used to create a sharp (when compared to λ_{pe}) leading edge at various positions along the bunch. The effect of seeding on energy gain and hosing will be studied.

Varying Parameters

The development of the SMI and of the HI depend on the initial beam and plasma parameters. The effect of the bunch charge species, population, radius, as well as of the plasma density and length on all the above measurements will be studied in details.

SUMMARY

The E209 experiment was proposed to SLAC FACET to study the physics of SMI thanks to the available long ($\sim$500 μm) particle bunches (electron/positron), source of dense plasma (n_{e0}=10^{16}-10^{17} cm^{-3}), seeding mechanism (notch collimator) and diagnostics: large range, good resolution energy spectrometer, OTR, CTR, etc. The effects of SMI onto the drive bunch only will be measured, no particles will be injected in the wakefields to be accelerated. These experiments are scheduled for the Fall 2013 and beyond.

REFERENCES

[1] N. Kumar *et al.*, Phys. Rev. Lett. **104** 255003 (2010).

[2] B. E. Blue *et al.*, Phys. Rev. Lett. **90**, 214801 (2003).

[3] P. Muggli *et al.*, Phys. Rev. Lett. 93, 014802 (2004).

[4] M. J. Hogan *et al.*, Phys. Rev. Lett. 95, 054802 (2005).

[5] M.J. Hogan *et al.*, New J. Phys. **12**, 055030 (2010).

[6] J. Vieira *et al.*, Phys. Plasmas **19** 063105 (2012).

[7] E. Adli, private communication.

[8] P. Chen *et al.*, IEEE Trans. On Plasma Science, PS-15(2), 218 (1987).

[9] M. Litos *et al.*, NA-PAC 13.

[10] Y. Fang *et al.*, NA-PAC'13 and references therein.

[11] M. L. Ter-Mikaelian, High-Energy Electromagnetic Processes in Condensed Media (Wiley- Interscience, New-York, 1972).

[12] O. Grimm *et al.*, Proceedings of EPAC08, 1113 (2008).

[13] Z. Wu, private communication.

[14] P. Muggli *et al.*, IEEE Trans. on Plasma Science PS-27(3), 791 (1999).

[15] D. H. Whittum *et al.*, Phys. Rev. Lett. **67**, 991 (1991).

[16] K. V. Lotov *et al.*, Phys. Rev. ST Accel. Beams 16, 041301 (2013).

[17] J. Vieira *et al.*, to be published.

[18] M. Litos *et al.*, NA-PA'13.

Copyright © 2013 CC-BY-3.0 and by the respective authors

PHOTONIC CRYSTAL AS A PASSIVELY DRIVEN STRUCTURE TO BOOST BEAM ENERGY*

B.R. Poole#, LLNL, Livermore, CA 94550, USA
J.R. Harris, S.V. Milton, Colorado State University, Fort Collins, CO 80523, USA

Abstract

The use of electromagnetic structures to couple energy to a charged particle beam is well known. These structures are usually driven by an external source of electromagnetic energy and the structure distributes that energy in such a way as being favorable to accelerate charged particles. Photonic crystals which typically consist of periodic arrays of metal and/or dielectric structures spaced on a scale comparable to the wavelength of interest, have been investigated for use both as sources of microwave radiation and as particle accelerators. In this case we consider driving a photonic crystal structure using a repetitive sequence of charge bunches driven from a photo-injector to resonantly excite the structure to produce an acceleration field to accelerate a suitably-delayed witness bunch to high energy. We examine the generation of the acceleration field as well as spurious modes. The characteristics of the witness bunch are examined to determine the longitudinal dynamics of the bunch and the energy spectra.

INTRODUCTION

Periodic structures are commonly used in the accelerator community for particle accelerators and as slow wave structures for microwave sources. The use of an L-band RF source to drive an X-band linac structure consisting of a disk loaded waveguide to accelerate properly phased electron bunches has been described [1]. Periodic structures with alternative geometries may be considered for the same task. For example, a structure consisting of a waveguide with a periodic array of metal rings at two radii was demonstrated as a microwave source operating as a backward wave oscillator [2] and such configurations in principle could be used to add energy to the beam rather than extracting energy from it In this paper we consider several structures for use with an L-band source for passive acceleration including the disk loaded waveguide and two ring array geometries The dispersion properties of various structures are determined using the COMSOL MultiPhysics RF package eigenmode solver [3]. The 2-D PIC code OOPIC [4] is then used to examine the excitation of the X-band structure at the 9th harmonic of the 1.3 GHz L-band source. The effect of higher order modes (HOMs) are investigated as well as the dynamics of a witness bunch.

MODELING AND SIMULATIONS

Three X-band structures were considered in this paper. All the structures have the same π-mode resonance at 11.7 GHz, the 9th harmonic of the 1.3 GHz electron source by adjusting various geometric structure parameters. The only fixed parameter was the spatial periodicity d, to maintain the π-mode axial wavenumber $k_z = \pi/d$. The drive beam consisted of 6 MeV, 1.3 GHz Gaussian-like bunches with 100 A peak current, 10 ps FWHM, and 1.23 nC of charge per bunch with a bunch radius of 2 mm. The Fourier spectrum of the drive beam current is a comb of frequencies with 1.3 GHz spacing as shown in Fig. 1. The witness bunch is injected into the structure typically after 50-100 ns (65-130 drive pulses) during the accelerating phase of the fields established by the drive bunch.

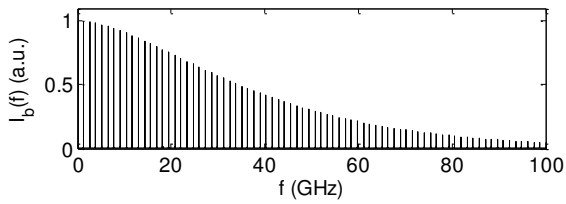


Figure 1: Beam current 1.3 GHz frequency comb.

Disk Loaded Waveguide

The first structure considered is the disk loaded waveguide shown in Fig. 2 with $R_0 = 1$ cm, $a = 0.3$ cm, $w = 0.2$ cm, and $d = 1.2$ cm.

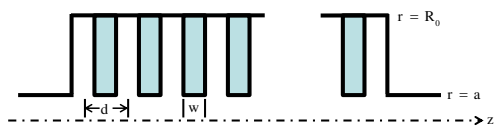


Figure 2: Disk loaded waveguide.

The TM_{0n} dispersion properties are shown in Fig. 3 and Fig.4 shows the axial electric field distribution for the 11.7 GHz π-mode.

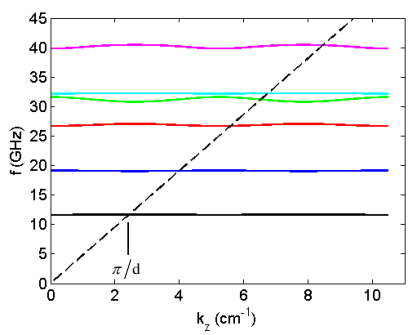


Figure 3: TM_{0n} modes of disk loaded waveguide.

The response of the structure to a single bunch was found using OOPIC to verify the various structure resonances. Figure 5 shows this response with resonances located at

* This work performed under the auspices of the U.S. Department of Energy by Lawrence Livermore National Laboratory under Contract DE-AC52-07NA27344
#poole1@llnl.gov

Copyright © 2013 CC-BY-3.0 and by the respective authors

the intersection of the structure modes with the beam mode, $\omega = k_z \beta c$.

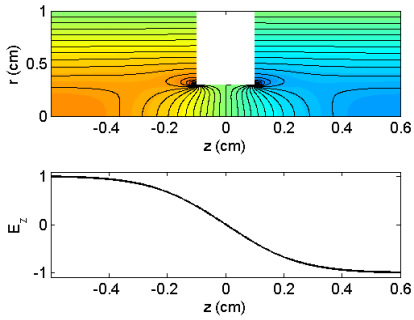


Figure 4: Axial electric field distribution at 11.7 GHz.

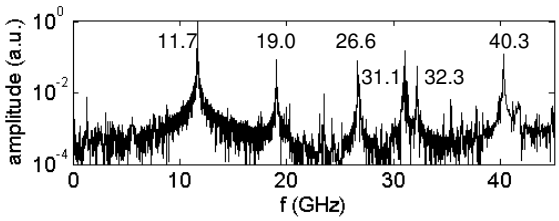


Figure 5: Single bunch response of disk loaded waveguide showing mode resonances.

A 1.3 GHz bunch sequence with the frequency comb spectra shown in Fig. 1 will resonantly excite the 9th harmonic 11.7 GHz π-mode in the linac structure. This field may then be used to accelerate a witness bunch to higher energy. Figure 6 shows a typical accelerating field greater than 1 MV/cm in the linac at 74.49 ns. The drive bunch has lost nearly 5 MeV of energy at this time.

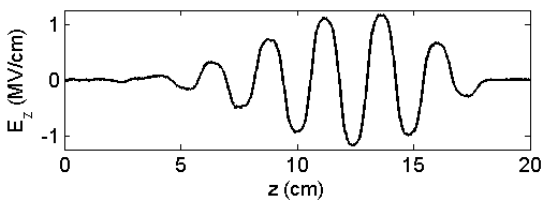


Figure 6: Acceleration field at 74.49 ns.

The evolution of the witness bunch energy distribution is shown in Fig. 7 and the evolution of the mean energy of both the drive and witness bunches shown in Fig.8. The maximum acceleration gradient is 1.2 MV/cm producing an energy boost of nearly 7 MeV for the witness bunch.

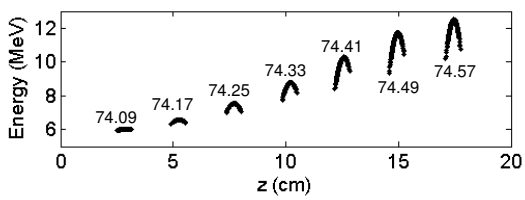


Figure 7: Snapshots of witness bunch energy distributions. The times indicated in the plot are in ns.

Note that the energy gain of the witness bunch benefits from the integrated energy stored in the linac structure accumulated from the previous drive bunches.

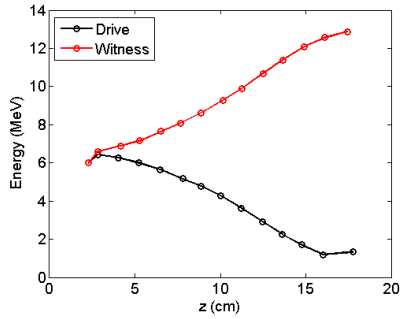


Figure 8: Mean energy of drive and witness bunches near the time of maximum acceleration gradient.

Single Ring Array

The single ring array consists of an axial array of circular rings, in this case with rectangular cross-section as shown in Fig. 9.

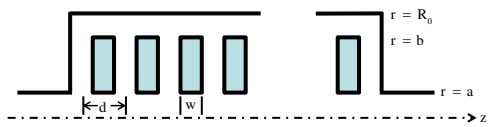


Figure 9: Single axial ring array loaded waveguide.

The structure dimensions are $R_0 = 1.475$ cm, $a = 0.3$ cm, $b = 1.1$ cm, $w = 0.2$ cm, and $d = 1.2$ cm. Figure 10 shows the TM_{0n} dispersion properties.

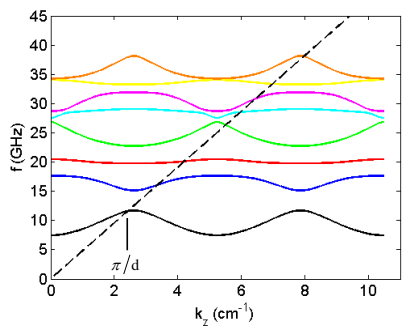


Figure 10: TM_{0n} modes of single ring array structure.

The dispersion curves in this structure exhibit much larger passbands compared to the disk loaded waveguide. There are also two additional modes for frequencies less than 40 GHz. This is due to increased coupling between the periodic cells and additional capacitance elements between the rings and the waveguide wall. Figure 11 shows the single bunch response for this structure which allows many additional discrete resonances in each of the modal passbands. It is easily seen in Fig. 11 that modes with larger passbands have more discrete resonances. The strength of these discrete resonances depends on the interaction with the bunch, the field distribution, as well as axial boundary conditions associated with the finite length periodic structure. Based on this spectral response, HOM's are expected to be more severe and tuning of the structure more difficult. Figure 12 shows the evolution of the drive and witness bunch mean energies showing an energy boost of only 4 MeV.

Copyright © 2013 CC-BY-3.0 and by the respective authors

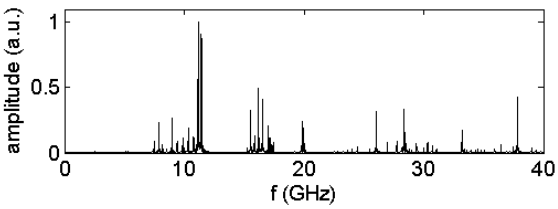


Figure 11: Single ring array single bunch response showing discrete resonances within each passband.

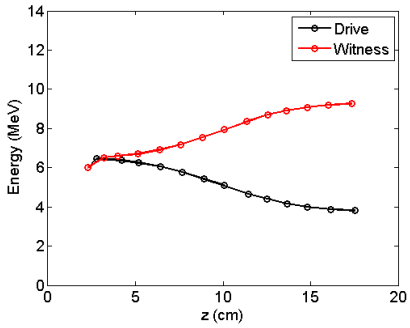


Figure 12: Mean energy of drive and witness bunches for single ring array structure.

Double Ring Array

The double ring array consists of two radial layers of an axial array of circular rings as shown in Fig. 13 with $R_0 = 1.73$ cm, $a_1 = 0.3$ cm, $b_1 = 0.7$ cm, $a_2 = 1$ cm, $b_2 = 1.4$ cm, $w = 0.3$ cm, and $d = 1.2$ cm.

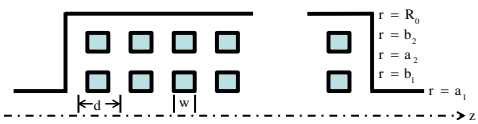


Figure 13: Double axial ring array loaded waveguide.

Figure 14 shows the TM_{0n} dispersion properties showing an additional mode for frequencies less than 30 GHz, and significantly wider passbands compared to the single array structure allowing for a significant number of discrete modes within each passband.

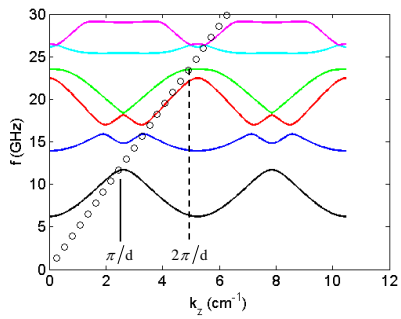


Figure 14: TM_{0n} modes of double ring array structure.

Also evident in Fig. 14 is the presence of a driven 2π-mode resonance for the 4th mode near 23.4 GHz at the 18th harmonic of the L-band source. This HOM competes with the 11.7 GHz π-mode and makes energy transfer to the witness bunch more difficult. To detune the 23.4 GHz resonance, the outer ring layer was moved radially inward by 1 mm moving the resonance upward by about 400 MHz. Simulations with the 1.3 GHz bunch sequence were run for both cases. Figure 15 shows typical spectra for both cases. It is easily seen, that both resonances appear in the original structure (Case A) with the 23.4 GHz resonance dominating and after shifting the outer rings the 23.4 GHz resonance is eliminated and the 11.7 GHz resonance become prominent (Case B). Figure 16 shows the energy evolution for both cases showing an energy boost of 1 MeV for Case A and 1.8 MeV for Case B.

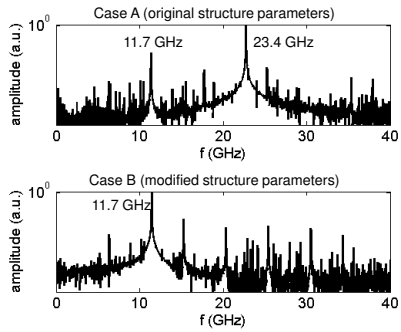


Figure 15: Double ring array response to 1.3 GHz bunch sequence showing effect of detuning 23.4 GHz mode.

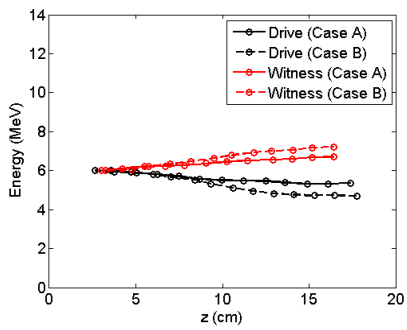


Figure 16: Mean energy of drive and witness bunches for double ring array structure.

CONCLUSION

X-band structures for passive acceleration were studied for their effectiveness in providing an energy boost to a 6 MeV witness bunch when driven with a 1.3 GHz 6 MeV bunch sequence. It was found that the disk loaded waveguide was able to boost the energy by 7 MeV while the open ring array structures provided more modest energy boosts. This is due to the open nature of the ring structures which reduce the electric field near the axis due to higher capacitance and the presence of HOM's.

REFERENCES

[1] S. Biedron et al, "Passively Driving X-band Structures to Achieve Higher Beam Energies," IPAC'13, Shanghai, May 2013, TUPEA075, (2013); http://www.JACoW.org

[2] D. Shiffler et al., IEEE Trans. On Plasma Sci. 38 (2010) 1462.

[3] COMSOL MultiPhysics is a product of COMSOL, Inc. Burlington, MA; http://www.comsol.com

[4] OOPIC is a product of Tech-X Corp., Boulder, CO; http://www.txcorp.com

Copyright © 2013 CC-BY-3.0 and by the respective authors

LONG TERM EVOLUTION OF PLASMA WAKEFIELDS*

A.A. Sahai†, T.C. Katsouleas,
Electrical Engineering, Duke University, Durham, NC, 27708 USA
Frank S. Tsung, Warren B. Mori
Physics and Astronomy, UCLA, Los Angeles, CA, 90095 USA

Abstract

We study the long-term evolution (LTE) of plasma wakefields over multiple plasma-electron periods and few plasma-ion periods, much less than a recombination time. The evolution and relaxation of such a wakefield-perturbed plasma over these timescales has important implications for the upper limits of repetition-rates in plasma colliders. Intense fields in relativistic lasers (or intense beams) create plasma wakefields (modes around ω_{pe}) by transferring energy to the plasma electrons. Charged-particle beams in the right phase may be accelerated with acceleration/focusing gradients of tens of GeV/m. However, wakefields leave behind a plasma not in equilibrium, with a relaxation time of multiple plasma-electron periods. Ion motion over ion timescales, caused by energy transfer from the driven plasma-electrons to the plasma-ions can create interesting plasma states. Eventually during LTE, the dynamics of plasma de-coheres (multiple modes through instability driven mixing), thermalizing into random motion (second law of thermodynamics), dissipating energy away from the wakefields. Wakefield-drivers interacting with such a relativistically hot-plasma lead to plasma wakefields that differ from the wakefields in a cold-plasma.

INTRODUCTION

Intense laser and particle beams interacting with plasma can force plasma electrons to relativistic energies. Under the appropriate plasma conditions, energy gained by the plasma electrons can be used to create short-lived coherent structures in the plasma. These structures (such as linear electron waves and bubble) have been extensively studied and employed as accelerating and focussing systems for charged-particle beams. The structures created in the plasma have spatio-temporal scales that are defined by the characteristic of the plasma. The spatial scales by the plasma skin-depth, $\frac{c}{\omega_{pe}}$ ($\omega_{pe} = \sqrt{4\pi e^2/m_e}\sqrt{n_e/\gamma_e}$). And the temporal scales by the plasma frequency, $\frac{1}{\omega_{pe}}$. It should be noted that the wakefield theory assumes fixed background ions. In addition to this, the plasma structures are used only over a few plasma electron periods. However, when these plasma structures evolve over time, ion-dynamics which occurs over ion-acoustic wave times $\frac{1}{\omega_{ia}}$ ($\omega_{ia} = \omega_{pe}\sqrt{m_e/M_i}$) becomes significant. For instance, in electron-proton plasma, $\omega_{pe} = 43\ \omega_{ia}$. If plasma density, $n_e = 10^{18}$, $\frac{1}{\omega_{pe}} \simeq 20fs$ and $\frac{1}{\omega_{ia}} \simeq 1ps$. These timescales are important to understand the upper limits of the repetition-rate (and hence luminosity) in a future plasma collider [1]. Also, highly relativistic plasmas are created in astrophysical entities such as Active Galactic Nuclei (AGN such as Centaurus-A (NGC-5128), M-87) and lab-based hot plasmas can better explain phenomenon such as the relativistic jets emanating from AGNs. These particle jets interact with surrounding gravitationally heated hot plasma and can exhibit phenomenon such as self-focussing, hosing and radiation generation.

The plasma wave is *coherent* under the cold-plasma approximation as seen from its dispersion characteristic, $\omega^2 = \omega_{pe}^2 + 3k^2v_{th}^2$ which under, $v_{phase} \gg v_{th}$ is excited over a narrow-band mode centered around ω_{pe}. However, if the plasma is thermally inhomogeneous or the electrons have a large thermal spread the plasma wave mode begins to lose its narrowband characteristic. When a plasma wave evolves in time, plasma spatial inhomogeneities, driver spatial non-uniformity and ion motion introduce a new set of frequencies into the plasma. With non-linearity and instability driven phase mixing between these modes, the plasma wave further de-coheres and equilibriates into random thermal motion. This increase in the entropy of the system follows from the second law of thermodynamics which makes the energy distribution equipartitioned between all possible modes of a system, driving it towards equilibrium.

In a future plasma collider, the need for high luminosity would require each plasma stage to be re-used within a finite interval (depending upon the drive bunch-train design). The fraction of drive-bunch energy coupled into the plasma that is absorbed by the accelerated-bunch has been shown to be $\simeq 50\%$ under optimal non-linear beam-loading which implies significant energy leftover in the accelerating plasma structure. Hence the next drive bunch would be affected by the thermalization of the wake from the previous pulses. In this paper we discuss the long-term evolution of a wake-perturbed plasma in terms of its temperature and density profile. We look at the electron momenta to determine if unabsorbed energy from a previous drive-bunch could heat the plasma to relativistic temperatures ($k_BT_e \simeq 0.5MeV$). We use simulations to estimate the plasma diffusion timescales. Past experimental work have imaged about 10 plasma periods behind the driver [2].

ENERGY IN A PLASMA WAVE

The planar electron plasma wave in 1-D can be denoted as $\vec{E}_{pw}(x) = \hat{x}\ E^0_{pw}\ e^{\mathbf{i}(\omega_{pe}t - k_{pe}x)}$. The force equation of the plasma wave acting on a single plasma electron is $m_e\frac{d\vec{v_e}}{dt} =$

* Work supported by the National Science Foundation under NSF-PHY-0936278 and the US Department of Energy under DE-SC0010012
† aakash.sahai@duke.edu

Copyright © 2013 CC-BY-3.0 and by the respective authors

$-e\vec{E}_{pw}$. Therefore, $\vec{v_e} = \frac{-eE^0_{pw}}{m_e}\int e^{\mathbf{i}(\omega_{pe}t-k_{pe}x)}\hat{x} = \frac{e\vec{E}_{pw}}{m_e\omega_{pe}}e^{\mathbf{i}\pi/2}$ and $|\vec{v_e}|/c = \frac{e|\vec{E}_{pw}|}{m_e c\omega_{pe}}$. From the electron velocity we can estimate the kinetic energy of the single electron in the plasma wave, $\mathcal{E}_k = \frac{1}{2}\left(\frac{e|\vec{E}_{pw}|}{m_e c\omega_{pe}}\right)^2 m_e c^2$. If all the plasma electrons are picked up by the plasma wave, we can estimate the kinetic energy density of the electrons in the plasma wave as $\mathcal{E}_k/unit\ volume = \frac{1}{2}\left(\frac{e|\vec{E}_{pw}|}{m_e c\omega_{pe}}\right)^2 m_e c^2\ n_e$. The field energy density in the plasma wave fields is $\mathcal{W}_f = \frac{|\vec{E}_{pw}|^2}{8\pi} = \left(\frac{e|\vec{E}_{pw}|}{m_e c\omega_{pe}}\right)^2 \frac{m_e^2c^2\omega_{pe}^2}{8\pi e^2}$. Using $\omega_{pe}^2 = \frac{4\pi n_e e^2}{m_e}$, we have $\mathcal{W}_f = \frac{1}{2}\frac{m_e\omega_{pe}^2}{4\pi n_e e^2}\left(\frac{e|\vec{E}_{pw}|}{m_e c\omega_{pe}}\right)^2 m_e c^2 n_e = \frac{1}{2}\left(\frac{e|\vec{E}_{pw}|}{m_e c\omega_{pe}}\right)^2 m_e c^2 n_e$. As $\mathcal{E}_k = \mathcal{W}_f$, there is an energy exchange between the kinetic energy of the oscillating electrons and the electric field of the wave.

If the beam-loading of the plasma wave by an accelerated beam is 50%, the energy leftover in the plasma can be estimated as $\mathcal{E}_{plasma}/unit\ volume = \frac{1}{2}\left(\frac{e|\vec{E}_{pw}|}{m_e c\omega_{pe}}\right)^2 m_e c^2\ n_e$. We study the density and temperature distribution of the plasma (electrons and ions) over $\simeq$ 10000 cycle of $\frac{1}{\omega_{pe}}$ and $\simeq$ 1000 cycle of $\frac{1}{\omega_{ia}}$.

SIMULATIONS OF LONG TERM EVOLUTION OF LASER DRIVEN WAKEFIELD

To study the LTE of a laser wakefield in the plasma, we use $2\frac{1}{2}D$ OSIRIS[3] PIC code with Eulerian specification of the plasma dynamics. We initialize the plasma density to $0.01n_c$ with background ions of $10m_p$ and pre-ionized singly-charged state. We have intentionally chosen a relatively high density plasma because $\omega_{pe} = \omega_0 \times \sqrt{n_e/n_c}$. We resolve and reference the real time in simulation to the laser period $2\pi/\omega_0$ thereby the dynamics within a single plasma cycle is simulated in just $\sqrt{n_c/n_e} = 10$ laser cycles. We discretize the space with 20 cells per skin-depth (c/ω_{pe}) in the longitudinal and 10 cells per c/ω_{pe} in the transverse direction. The simulation space size is chosen as 300 c/ω_{pe} x 600 c/ω_{pe}. We use absorbing boundary conditions for fields and particles of all species. The laser pulse is chosen to be a circularly polarized Gaussian pulse with normalized vector potential $a_0 = 4.0$ with pulse width of $10fs$.

From the simulations we observe that a plasma bubble is excited by the laser pulse, as seen in Fig. 1[a] at $264\frac{1}{\omega_{pe}}$. The ions are stationary as seen from the ion density in Fig. 2[a]. We observe that the bubble oscillates for about 20 plasma periods. The more the oscillations are delayed in time, the more the bubble's transverse size decreases and the electron sheath around the bubble curves with smaller radii towards the back of the bubble. We also observe at the end of the bubble oscillations that the density of electrons in the sheath around the bubble reduces and the electron density is modulated further away from the axis of the bubble in the transverse direction. Such a weak bubble with

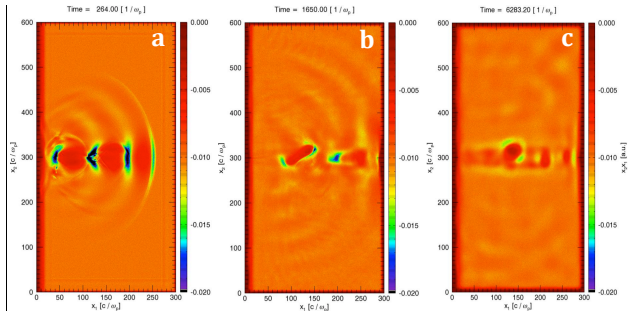


Figure 1: Laser wakefield LTE snapshots of **plasma electron density in real space** at times, t = **(a)** $264\frac{1}{\omega_{pe}}$ **(b)** $1650\frac{1}{\omega_{pe}}$ **(c)** $6283.20\frac{1}{\omega_{pe}}$.

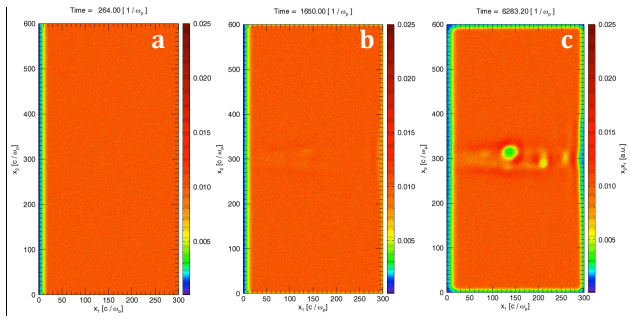


Figure 2: LTE snapshots of **plasma ion density in real space** at times, t = **(a)** $264\frac{1}{\omega_{pe}}$ **(b)** $1650\frac{1}{\omega_{pe}}$ **(c)** $6283.20\frac{1}{\omega_{pe}}$. We can observe onset of ion motion in **(b)**.

curved electron sheath may be observed around $200\frac{c}{\omega_{pe}}$ in Fig. 1[b].

At later times we also observe that neighboring plasma bubbles merge into each other and the electrons in the sheath execute motion around the merged ion cavity. The merged bubbles can be seen around $100\frac{c}{\omega_{pe}}$. The ion density at the same time as Fig. 1[b] is shown in Fig. 2[b]. From the ion density snapshot in Fig. 2[b] a feature can be observed in the background ions around $100\frac{c}{\omega_{pe}}$ which has shape similar to the merged bubble in electron density. The

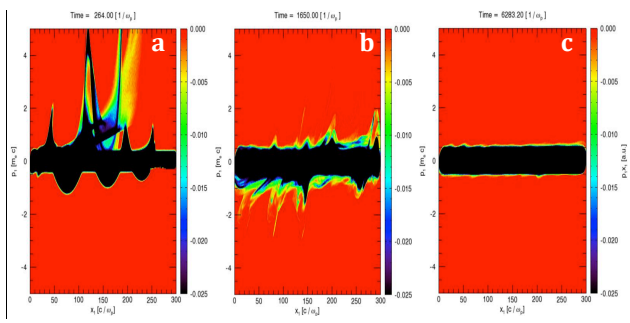


Figure 3: LTE snapshots of **electron longitudinal momentum phase space** along longitudinal dimension at times, t= **(a)** $264\frac{1}{\omega_{pe}}$, **(b)** $1650\frac{1}{\omega_{pe}}$, **(c)** $6283.20\frac{1}{\omega_{pe}}$.

Copyright © 2013 CC-BY-3.0 and by the respective authors

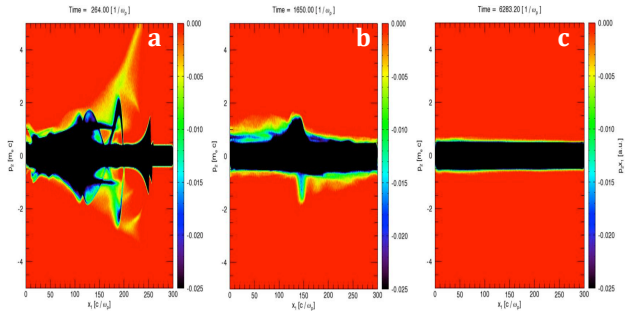


Figure 4: LTE snapshots of **electron transverse momentum phase space** along the longitudinal direction at times, t= **(a)** $264\frac{1}{\omega_{pe}}$ **(b)** $1650\frac{1}{\omega_{pe}}$ **(c)** $6283.20\frac{1}{\omega_{pe}}$.

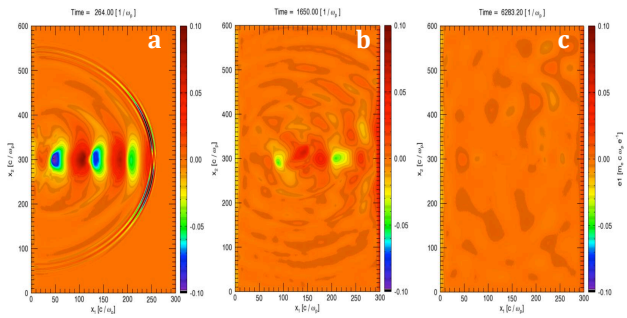


Figure 5: LTE snapshots of **longitudinal electric field in real space** along the longitudinal direction at times, t= **(a)** $264\frac{1}{\omega_{pe}}$ **(b)** $1650\frac{1}{\omega_{pe}}$ **(c)** $6283.20\frac{1}{\omega_{pe}}$.

ion motion occurs as expected at the ion acoustic timescales as the Fig. 2[b] is shown is around $10\frac{1}{\omega_{ia}}$. After the onset of ion motion we observe structures with very low phase velocities in comparison to the plasma wave, as seen in Fig. 1[c] and Fig. 2[c]. In Fig. 2[c] we see ion expansion away from the axis and an ion channel is seen.

In Fig. 3 and Fig. 4, we show the momentum phase spaces corresponding to the density snapshots. In Fig. 5 and Fig. 6, we show the fields in the real space corresponding to the density snapshots. It can be seen from the fields much after the short laser pulse ($10fs$ long) has passed by and the plasma wave has evolved and decayed there is still significant trapped electric field (Fig. 6[b] and Fig. 5[b]) in the merged bubble seen in the Fig.1[b]. This is the characteristic of a *caviton*. In the laser driven wake we can observe trapped laser radiation, however in beam driven case there is no driving radiation and hence the characteristic of beam-driven wake LTE differ from the laser-driven wake LTE.

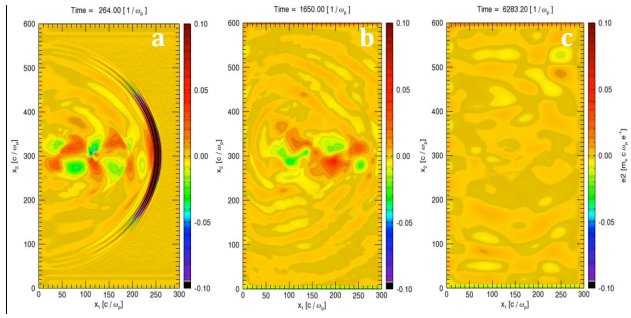


Figure 6: LTE snapshots of **transverse electric field in real space** along the longitudinal direction at times, t = **(a)** $264\frac{1}{\omega_{pe}}$ **(b)** $1650\frac{1}{\omega_{pe}}$ **(c)** $6283.20\frac{1}{\omega_{pe}}$.

REFERENCES

[1] A.A. Sahai, T.C. Katsouleas, et.al., Excitation of wakefields in a relativistically hot plasma created by dying non-linear plasma wakefields, AIP Conf. Proc. **1507**, pp. 618-622; doi:10.1063/1.4773768, SLAC-PUB-15367: http://www-public.slac.stanford.edu/scidoc/docMeta.aspx?slacPubNumber=SLAC-PUB-15367

[2] J. Marques, et al., Phys. Rev. Lett. 76 (1996), doi:10.1103/PhysRevLett.76.3566,
L. Gorbunov et al., Phys.Plasma 10 (2003), doi:10.1063/1.1559011,
A. Maksimchuk, et al., Phys. Plasma 15 (2008), doi:10.1063/1.2856373.

[3] R.A. Fonseca, V.K. Decyk, et al., OSIRIS, a three-dimensional fully relativistic particle in cell code for modeling plasma based accelerators. Lect. Note Comput. Sci. **2331**, 342-351 (2002). doi:10.1007/3-540-47789-6_36

Copyright © 2013 CC-BY-3.0 and by the respective authors

ANALYSIS OF HIGH REPETITION RATE EFFECTS IN DIELECTRIC WAKEFIELD ACCELERATORS*

Paul Schoessow#, Sergey P. Antipov, Chunguang Jing, Alexei Kanareykin, Stanley Zuo
Euclid Techlabs, 5900 Harper Rd 102, Solon, OH 44139, USA
John Gorham Power, Alexander Zholents, ANL, Argonne, IL 60439, USA

Abstract

Recently the question has arisen of whether dielectric charging might become a significant limiting effect on the performance of the DLAs (dielectric loaded accelerators), leading either to deflection of the beam by the static electric field generated, or to breakdown of the structure. In experiments to date this has not been problematic with appropriate choice of dielectric material. However, given the high repetition rate that would be required, the device would be subjected to essentially a dc bombardment from the beam halo and thus be vulnerable to these effects because there is no time between machine pulses for discharge of the dielectric. We have begun re-examining this problem, emphasizing the expected charging rate and charge distribution in a thin walled dielectric device and the physics of conductivity and discharge phenomena in a dielectric medium. Simulations of the charging process will be presented. We will review early work on beam-induced charging of dielectric structures and also results from deep charging of satellite components by cosmic rays. Ageing and induced conductivity under large radiation doses are also to be investigated.

IRRADIATION EFFECTS ON DLAS

The physical processes involved with the unwanted interception of beam electrons by a dielectric accelerating structure are complex and interacting:

- Asymmetric charging of the dielectric, leading to beam deflection;
- Breakdown (with structure damage). Although breakdown thresholds ~14 GV/m have been demonstrated for very short (<330 fs) pulses [1], maximum DC fields that can be supported are considerably lower;
- Changes in material properties with absorbed dose and repeated DC breakdowns;
- Dynamics of the charging/discharge process in the presence of high dose rates. Table 1 lists the characteristic discharge times for a number of dielectric materials used in DLAs, nearly all of which do not reflect the observed resistance to charging. This seems to suggest that other effects are compensating, for example ionization induced conductivity.

Charging effects were studied by the Argonne group as an incidental part of the first dielectric wakefield acceleration tests in 1988 [2]. In these experiments the charging originated from missteering of the drive beam through the dielectric structure. Transverse deflection of the beam through large angles by the induced DC field was sufficiently large as to deflect the beam outside the acceptance of the spectrometer focal plane detector. The initial tests used dielectric tubes made from plastics. Rexolite and Nylon dielectrics showed rather different behaviors under charging.

Table 1: Characteristic discharge times $\tau_c=\varepsilon/\sigma$ for commonly used dielectrics [6]. Here σ is the dc conductivity and ε is the (SI) permittivity.

Material	τ_c
Alumina	>0.78 s
Delrin ®	310 s
Kapton ®	3.5 d
Mylar ®	3.1 d
Polystyrene	37 min
Fused Quartz	>38 d
Borosilicate glass	0.41 s (variable) [7]
Teflon ®	2.1 d

Rexolite was found to charge until the beam was deflected and to hold its charge (and maintain the dc electrostatic field) for an extended time (~ 1 hr). No breakdowns were seen under the test conditions. Nylon would charge up and deflect the beam until breakdown occurred, snapping the beam back to its nominal undeflected position. The charge-discharge period was found to be ~ 30 s. It is worth noting that no permanent damage to the nylon structure was observed (based on repeated longitudinal wakefield measurements) despite being subjected to many charge-discharge cycles.

The rexolite structure was field-modified by depositing a thin layer of graphite powder on the interior surface of the tube. A thin conducting layer can short out the static field but be thin enough (<< 1 skin depth) to allow the rf fields of the structure to penetrate into the vacuum channel as before. It was determined that the graphite layer did in fact have the desired effect, although some trial and error was necessary to obtain a sufficiently thin layer. While use of graphite in this fashion is impractical for high energy acceleration, the principle of using an interior conductive coating was demonstrated. Ultimately the best approach was found to be tuning the beam through an electrically isolated aluminum tube in place of the dielectric, minimizing the intercepted beam current, and then swapping in the dielectric under test for the aluminum tube.

*Work supported by US Dept of Energy, SBIR Program
#paul.schoessow@euclidtechlabs.com

Copyright © 2013 CC-BY-3.0 and by the respective authors

Later AATF and AWA experiments used borosilicate glass as the dielectric [3]. This material exhibits a large temperature dependent electrical conductivity. Measurements on wakefield structures made of this material showed no detectable charging and no apparent degradation in the magnitude of the wakefield excitation. While borosilicate glass does indeed possess a short discharge time, fused quartz has a discharge time longer than 30 days, while repeated experiments at the AWA and elsewhere have not observed DC charging effects with this material.

Euclid and ANL have begun a systematic study of radiation effects in dielectric wakefield accelerators, with the goal of understanding both acute (charging, dose rate, electric field) and long term (material damage) effects. This project involves both experimental and computational aspects; here we focus on the status of the simulation effort.

COMPUTATIONAL APPROACH

A complete model of DLA irradiation effects needs to include

- characteristics of the halo (energy spectrum, angular distribution) either determined experimentally or from a simulation of the accelerator;
- interaction of the halo particles with the dielectric structure (spatial distribution of stopped charges and energy deposited in the dielectric);
- computation of the electric field in the dielectric from the trapped charge distribution using a self-consistent determination of the conductivity. This will give the dependence of the equilibrium electric field on the halo current.

Dielectric Irradiation by Halo Electrons

The Geant4 Monte-Carlo code [4] will be used to transport the halo electrons through the dielectric structure, simulating their electromagnetic interactions with the material and scoring the distribution of charges injected into the material. User-written C++ routines are used to code the geometry and material of the target structure, and a Tcl/Tk interface is used to input parameters to control the execution of the program. While originally designed for high energy physics applications, a number of authors ([5], e.g.) have used Geant4 for the study of dielectric charging in spacecraft.

We have begun looking at some test problems to study charging in dielectric structures. Fig. 1 shows a Geant4 simulation of 100 MeV electrons striking the interior of a quartz wakefield structure at glancing incidence to simulate beam halo. The user code we developed flags the location of each stopping electron and also the location where an effective positive charge is created (for example where an electron is removed by a Compton scattering event). In this way the distribution of charge internal to the dielectric induced by the halo is computed (Fig. 2-3). At the same time, the energy deposited in the dielectric and any induced temperature rise is also calculated. The charge and energy deposition results are then input to a field calculator.

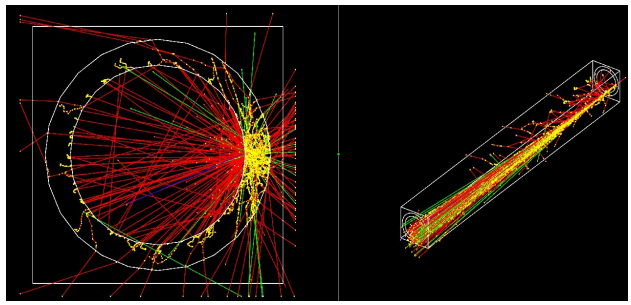


Figure 1: Geant4 simulation of 100 MeV electrons striking a quartz tube (0.35 mm inner radius, 0.45 mm outer radius, 10 mm long, 336 GHz fundamental TM_{01} mode) at glancing incidence to a point on the inner surface. The plots are a sum of 100 events. Red tracks: photons; green: e^+ and e^-. The yellow rectangles indicate the segmentation of the tracks.

This part of the simulation code will use the spatial dependence of the stopped charges from Geant4 and a Poisson solver to compute the dc field inside the dielectric. Using the electric field and the energy deposited in the dielectric, the conductivity can be determined as a function of position. Finally, the trapped charges can be updated using Ohm's law. The procedure is iterated to obtain the time dependence of the field and charges in the dielectric.

An assumption is made here that the quasistatic electric field and its effect on the conductivity are independent of the rf fields induced by the beam. If needed, rf effects could be incorporated through the use of a FDTD EM solver.

Dielectric Conductivity

There are a number of empirical relations used in the literature to parameterize the time, temperature and electric field and dose rate dependence [8-11] of the dielectric conductivity σ.

$$\sigma(t)= \frac{\sigma_1}{F(1+bt)} \qquad \text{(time)} \qquad (1)$$

$$\sigma(T)= \sigma_\infty \exp(-\frac{E_A}{kT}) \qquad \text{(temperature)} \qquad (2)$$

$$\sigma(E,T) = \frac{1}{3}\sigma(T)\times [2+\cosh(\frac{\beta_F E^{1/2}}{2kT})][\frac{2kT}{eE\delta}\sinh(\frac{eE\delta}{2kT})] \qquad \text{(electric field)} \qquad (3)$$

$$\sigma(\frac{dD}{dt})= \sigma_0 + k_p(\frac{dD}{dt})^\Delta \qquad \text{(Dose rate)} \qquad (4)$$

here $\beta_F = \sqrt{e^3/\pi\varepsilon}$, E is the electric field strength, and D is the absorbed radiation dose (rads). k_p and Δ are positive constants, with Δ in the range 0.6-1.0; these and the other free parameters in eq. (1)-(4) need to be determined

Copyright © 2013 CC-BY-3.0 and by the respective authors

experimentally. We note that the conductivity increases with increasing dose rate and electric field, leading to

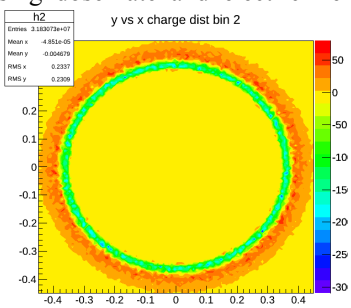


Figure 2: Trapped charge distribution in a 1 mm axial segment for 100 MeV electrons incident symmetrically around the circumference of the tube in Fig. 1. Note that regions with excess electrons and depleted in electrons both occur.

reduced discharge times of accumulated charge in an accelerator environment.

Modeling of Beam Halos

Machine parameters (rf, optics, vacuum) are input to a halo simulation code. (Alternatively, if sufficient data from the accelerator exists, they could be parameterized and input directly to the particle transport code.) The tracking code Placet [12] incorporating the halo simulator htgen [13] has been chosen as a reference to perform the machine simulation. The accelerator lattice and other parameters are input via Tcl/Tk scripts.

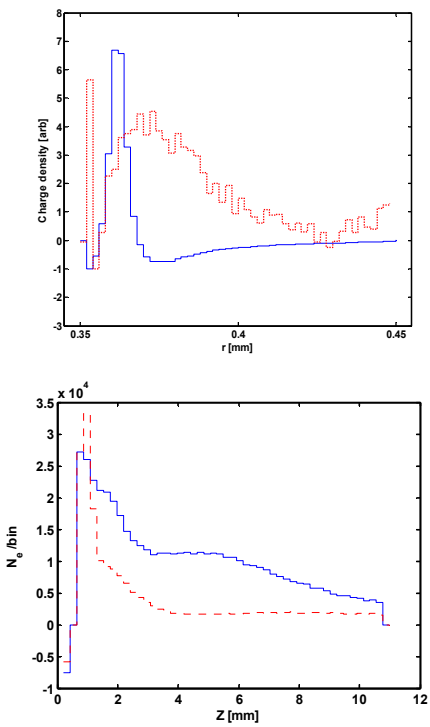


Figure 3: Trapped charge distribution as a function of (a) radial (b) axial position. in the geometry shown in Fig. 2. (Solid: 100 MeV e^-; dotted: 10 MeV e^-.)

Htgen models the effects of beam-gas scattering and bremsstrahlung from scraping on collimators and other beamline components, using the Placet components to model the beam and also transport the halo particles produced to the dielectric structure.

SUMMARY

We have begun investigating the effects of irradiation on dielectric wakefield structures. We consider developing a simulation code to calculate the interaction of halo electrons with DLA structures. Because of the more complex geometry the problem presents challenges not treated in previous analyses.

REFERENCES

[1] M. C. Thompson et al., "Breakdown Limits on Gigavolt-per-Meter Electron-Beam-Driven-Wakefields in Dielectric Structures," Phys. Rev. Lett. 100 (2008) 214801.

[2] W. Gai, P. Schoessow, B. Cole, R. Konecny, J. Norem, J. Rosenzweig, J. Simpson, "Experimental Demonstration of Wake Field Effects in Dielectric Structures," Phys. Rev. Lett. 61 (1988) 2756.

[3] P. Schoessow, M. E. Conde, W. Gai, R. Konecny, J. Power, and J. Simpson, "High power radio frequency generation by relativistic beams in dielectric structures," Journal of Applied Physics, 84(2),)15 July 1998) 663.

[4] http://geant4.web.cern.ch/geant4/

[5] C. Lemon et al., "A 3-D Model of the Internal Charging of Spacecraft Dielectric Materials," http://www.ngdc.noaa.gov/stp/satellite/anomaly/2010_sctc/docs/9-4_CLemon.pdf

[6] Henry B. Garrett and Albert C. Whittlesey, "Guide to Mitigating Spacecraft Charging Effects," JPL Space Science and Technology Series, June 2011.

[7] www.camglassblowing.co.uk/gproperties.htm; www.us.schott.com/borofloat/english/download/electric_volume.pdf

[8] B. L. Beers and V. W. Pine, "Electron Beam Charged Dielectrics--Internal Charge Distribution," Spacecraft Charging Technology (1980).

[9] S. T. Lai ed., *Spacecraft Charging*, Progress in Astronautics and Aeronautics Vol. 237, AIAA 2011, Ch. 7.

[10] J. F. Fowler, "X-Ray Induced Conductivity in Insulating Materials," Proc. R. Soc. Lond. A 236 1956; doi: 10.1098/rspa.1956.0149

[11] V. Adamec, J. H. Calderwood, "Electrical conduction in dielectrics at high fields," J. Phys. D: Appl. Phys. 8 (1975).

[12] D. Schulte et al., "The Tracking Code PLACET," EUROTeV-Memo-2005-xxx-1.

[13] I. Ahmed et al., "User Manual for the Halo and Tail generator HTGEN," EUROTeV-Memo-2008-003.

Copyright © 2013 CC-BY-3.0 and by the respective authors

ASTA AT FERMILAB: ACCELERATOR PHYSICS AND ACCELERATOR EDUCATION PROGRAMS AT THE MODERN ACCELERATOR R&D USERS FACILITY FOR HEP AND ACCELERATOR APPLICATIONS*

V. Shiltsev#, P. Piot, Fermilab, Batavia, IL 60510, USA

Abstract

We present the current and planned beam physics research program and accelerator education program at Advanced Superconducting Test Accelerator (ASTA) at Fermilab.

ASTA FACILITY

The Advanced Superconducting Test Accelerator (ASTA) at Fermilab will enable a broad range of beam-based experiments to study fundamental limitations to beam intensity and to develop transformative approaches to particle-beam generation, acceleration and manipulation. ASTA incorporates a superconducting radiofrequency (SRF) linac coupled to a photoinjector and small-circumference storage ring capable of storing electrons or protons. ASTA will establish a unique resource for R&D towards Energy Frontier facilities and a test-bed for SRF accelerators and high-brightness beam applications. The unique features of ASTA include: (1) a high repetition-rate, (2) one of the highest peak and average brightness within the U.S., (3) a GeV-scale beam energy, (4) an extremely stable beam, (5) the availability of SRF and high-quality beams together, and (6) a storage ring capable of supporting a broad range of ring-based advanced beam dynamics experiments. These unique features will foster a broad program in advanced accelerator R&D and accelerator education which cannot be carried out elsewhere. Several experiments and test can be carried out at ASTA simultaneously at three experimental areas – see Fig.1. Detail description of ASTA can be found elsewhere [1,2]

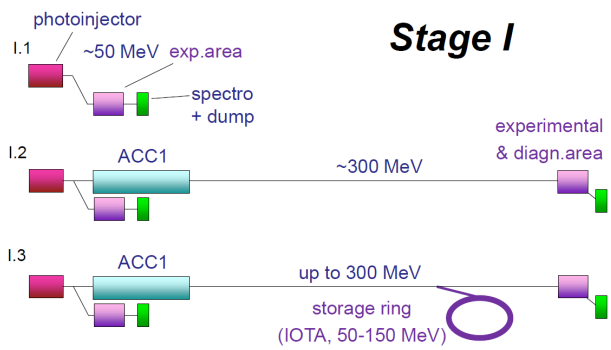


Figure 1: Schematics of ASTA (Stage I configuration).

*Fermi Research Alliance, LLC operates Fermilab under contract No. DE-AC02-07CH11359 with the U.S. Department of Energy
#shiltsev@fnal.gov

ASTA ACCELERATOR R&D THRUSTS

Accelerator R&D for Particle Physics at the Intensity and Energy Frontiers

The combination of a state-of-the-art superconducting linear accelerator and a flexible storage ring enables a broad research program directed at the particle physics accelerators of the future. The corresponding research program includes a number of proposals:

i) Test of non-linear, integrable, accelerator lattices (the Integrable Optics Test Accelerator) which have the potential to shift the paradigm of future circular accelerator design
ii) Test of space charge compensation in high intensity circular accelerators
iii) Advanced phase space manipulations
iv) Test of optical stochastic cooling
v) Flat-beam-driven dielectric-wakefield acceleration in slab structures
vi) Investigation of acceleration and cooling of carbon-based crystal structures for muon accelerators
vii) Measurement of the electron wave function size in a storage ring
viii) Studies of beam echo phenomena in a storage ring
ix) Development of a quadrupole pickup and study of the quadrupole mode dynamics in space-charge dominated beams
x) High power targetry studies for LBNE
xi) A tagged photon beam at ASTA for Detector R&D
xii) HEP applications of inverse Compton scattered photons.

It was specifically noted at the 2013 Community Summer Study ("Snowmass-2013" [2]) that there is obvious lack of accelerator test facilities where many burning accelerator science and technology issues of the Intensity Frontier (IF) accelerators [4] can be addressed. ASTA will provide this so-much needed platform for the IF accelerator R&D.

Accelerator R&D for Future SC RF Accelerators

High gradient, high power SC RF systems are critical for many accelerator facilities under planning for the needs of high-energy physics, basic energy sciences and other applications. ASTA offers a unique opportunity to explore the most critical issues related to SC RF technology and beam dynamics in SC RF cryomodules, such as:

Copyright © 2013 CC-BY-3.0 and by the respective authors

i) Demonstration of High Power High Gradient SRF Cryomodules with Intense Beams
ii) Demonstration of technology and beam parameters for the Project X pulsed linac
iii) Wakefield measurements in the SC RF cryomodules
iv) Demonstration of ultra-stable operation of SC RF cryomoduyles with beam-based feedback
v) Development and experimental test of neural network based control systems and optimization tools for SRF accelerators
vi) Exploration of CW mode of operation of the ILC-type SRF cryomodule

Accelerator R&D for Novel Radiation Sources

High energy (up to 1 GeV), high peak and average power and high brightness electron beams have tremendous potential for generation of high-brightness high energy photon beams spanning the range from keVs to dozens of MeV. The high average power and brightness of the ASTA electron beam has unmatched potential for development of several novel radiation source ideas, such as:

i) High brightness X-ray channeling as a compact x-ray radiation source
ii) Inverse Compton scattering gamma-ray source and its applications
iii) Demonstration of feasibility of an XUV FEL oscillator
iv) Production of narrow-band gamma-rays
v) Laser-induced microbunching studies with high micropulse-repetition rate electron beams

Accelerator R&D for Stewardship and Applications

With its high energy, high brightness, high repetition rate, and the capability of emittance manipulations built-in to the facility design, ASTA is an ideal platform for exploring novel accelerator techniques of interest for very broad scientific community beyond high energy physics. The proposed research program includes several proposals and expressions of interest for such explorations:

i) Demonstration of techniques to generate and manipulate ultra-low emittance beams for future hard X-ray free-electron lasers
ii) Beam energy dechirper using corrugated pipes
iii) Development and test of a beam-beam kicker
iv) Coherent diffraction radiation measurements of bunch length

All the proposals can be found in [1] and have been discussed by the Fermilab's Accelerator Advisory Committee (February 6-8, 2013). Later, all of them have been presented at the 1st ASTA User's Meeting and reviewed by the ASTA Program Advisory Committee (July 23-24, 2013).

ACCELERATOR EDUCATION OPPORTUNITIES AT ASTA, ASTA AND IARC

Accelerators have taken an increasingly important role in our Society and improving their performances, downsizing their footprints, or reducing their cost will be a long and challenging endeavour that will strongly rely on future generation of accelerator scientists. In addition, the multidisciplinary nature of Accelerator Science makes accelerators ideal platforms for student education over a vast range of topics.

New beam physics issues associated with future accelerators have emerged (single-bunch and multi-bunch collective effects in high brightness electron accelerators, simulations of large emittance beams in heavy ions and/or multi state charge accelerators) and more intricate accelerator physics tools capable of accounting for all these effects are being developed and need to be carefully validated at available facilities. Such models are mandatory to efficiently design and test the performance of these accelerators prior to their construction. Similarly, future accelerators will require the development of precise diagnostics and controls capable of measuring and/or correcting unprecedented beam parameters (sub-micrometer size, femtosecond duration, with high average current). Most of these topics will be explored to some extent at ASTA and could form the basis of research projects for PhD, Masters, or internships.

Interdisciplinary research projects involving the engineering discipline will also be possible at ASTA. Examples that come to mind are fabrication of state-of-the-art accelerator components requiring precision modeling, drafting and manufacturing. RF engineering R&D examples are ubiquitous in accelerator physics. Likewise, novel synchronization techniques and feedback systems will be needed, e.g. to insure that the accelerating fields in the superconducting linear accelerators are very stable.

Over the last decade the number of Educational Institutions that have taken on developing a curriculum in Accelerator Science has increased from a couple to about 10 [5]. None of these Universities currently operates a full-fledged accelerator complex and generally rely on facilities available at National Laboratories to carry most of their experiments. National laboratories have developed programs to foster partnership with Universities. Fermilab was actually the first laboratory to initiate such a selective program, which offers to financially support students to carry-out Accelerator-Science research at Fermilab's facilities [6]. This program – the Joint University - Fermilab Doctoral Program in Accelerator Physics and Technology – has graduated close to 40 students since its initiation in 1987. More than half of the program's graduates have remained in the field of Accelerator Science, and approximately one quarter of them are prominent scientists with leadership positions in national laboratories or universities.

Copyright © 2013 CC-BY-3.0 and by the respective authors

Fermilab also created prestigious fellowships to attract promising scientists to carry-out research in Accelerator Science: the Peoples fellowshipwas created in 2001 and the Bardeen-Engineering Leadership fellowship [7] was created in 2005. The John Bardeen Engineering Leadership Program is designed to provide entry-level opportunities for outstanding engineering graduates who are interested in working in a cutting edge research environment. Fermilab provides opportunities in the fields of electrical, electronics, radio frequency systems, power distribution, magnets, RF cavities, mechanical, materials science and cryogenic engineering. The Peoples Fellowship was created at Fermilab with the goal of attracting outstanding accelerator scientists early in their careers, both to enhance Fermilab's capabilities in accelerator science and related technologies, and to train and develop the accelerator scientists and technologists who will carry our field forward in the future. Together these fellowship programs have attracted and trained approximately 20 people within the last decade. Most of these fellows still carry-out research in Accelerator Science.

Finally, Fermilab has also been active in involving younger scientists (undergraduate students) through various summer programs. One of these programs, the Lee Teng Undergraduate Internship in Accelerator Science and Engineering established by Fermilab and Argonne, aims at attracting undergraduate students into the world of particle accelerator physics and technology. The selected students first attend a two-week general accelerator physics class at the summer US particle accelerator school thereby gaining a broad overview of Accelerator Science. They then work on a research project for the following weeks under the supervision of Fermilab and Argonne staff members. ASTA offers the possibility of significantly enhancing the Lee Teng program by incorporating a "hands-on" component to the students' summer research experience, making it a truly unique internship with the potential to attract future accelerator scientists at the critical undergraduate stage.

In addition to these laboratory-driven programs, Fermilab has also welcomed students from University groups carrying out research at Fermilab funded by grants to universities. Examples includes the development of photo-emission laser with University of Rochester, research on flat-beam generation with University of Chicago, or the investigation of beam-driven plasma wakefield acceleration with University of California, Los Angeles.

ASTA will be an excellent platform that could support and enhance the aforementioned education programs and support extramural research engaging students from Universities. Given the breath of the scientific program described in this proposal, we expect ASTA to provide support for topics of research in Advanced Accelerator R&D, laser science, beam diagnostics and synchronization, accelerator-based light source, superconducting RF system, and Beam Physics. Finally, some of the proposed topics could also foster research beyond Accelerator Science such as the utilization of single-cycle Terahertz pulses for solid-state Physics research or the use of X-rays for developing phase-contrast imaging (with possible spin-off to medical imaging).

ASTA will also offer a unique opportunities for the US Particle Accelerator School [8] sessions and classes. A number of hand-on, practical training laboratory sessions can use the ASTA accelerators – the photoinjector, the SRF cryomodule and the IOTA ring. Among them, those which were very popular in the past US PAS sessions:

a. Modern RF systems class
b. Beam Instrumentation Lab
c. Fundamentals of Accelerator Instrumentation
d. Beam Measurements and Diagnostics in Linacs and Rings
e. Beam Dynamics Experiments at the IOTA ring
f. Beam Measurements, Manipulation and Instrumentation in SRF Linac

Proximity of the Illinois Accelerator Research Center (IARC) at Fermilab [9] will make these classes attractive for the industrialists and technologists. At the IARC, scientists and engineers from Fermilab, Argonne and Illinois universities will work side by side with industrial partners to research and develop breakthroughs in accelerator science and translate them into applications for the nation's health, wealth and security. Besides a dedicated state-of-the-art facility that will house offices, technical and educational space to study cutting-edge accelerator technologies, it is anticipated that IARC's private industry partners will have access to the nearby ASTA facility to perform high power beam tests and collaborate with ASTA users from the US universities in training a new generation of scientists, engineers and technical staff in accelerator technology. These partnerships will make critical contributions to the technological and economic health of Illinois and the nation in general.

REFERENCES

[1] *ASTA Facility Proposal*, Fermilab-TM-2568 (2013).
[2] P. Piot, NA-PAC'13.
[3] *Snowmass-2013*, http://www.snowmass2013.org
[4] V. Shiltsev, et al, arXiv:1305.6917.
[5] W. Barletta, S. Chattopadhyay, A. Seryi, arXiv1203:3065.
[6] Fermilab Accelerator PhD Program, see at http://apc.fnal.gov/programs2/joint_university.shtml
[7] Fermilab Fellowships, see at http://www.fnal.gov/pub/forphysicists/fellowships
[8] US Particle Accelerator School, http://uspas.fnal.gov/
[9] Illinois Accelerator Research Center at Fermilab, see at http://iarc.fnal.gov/

Copyright © 2013 CC-BY-3.0 and by the respective authors

ISSUES AND R&D REQUIRED FOR THE INTENSITY FRONTIER ACCELERATORS*

V.Shiltsev#, S.Henderson, P.Hurh, I.Kourbanis, V.Lebedev, Fermilab, Batavia, IL 60510, USA

Abstract

Operation, upgrade and development of accelerators for Intensity Frontier face formidable challenges in order to satisfy both the near-term and long-term Particle Physics program. Here we discuss key issues and R&D required for the Intensity Frontier accelerators.

INTENSITY FRONTIER ACCELERATORS

The near-term program of HEP research at the Intensity Frontier continuing throughout this decade includes the long-baseline neutrino experiments and a muon program focused on precision/rare processes. It requires: a) double the beam power capability of the Booster; b) double the beam power capability of the Main Injector; and c) build-out the muon campus infrastructure and capability based on the 8 GeV proton source. The long-term needs of the Intensity Frontier community are expected to be based on the following experiments: a) long-baseline neutrino experiments to unravel neutrino sector, CP-violation, etc.; and b) rare and precision measurements of muons, kaons, neutrons to probe mass-scales beyond LHC.

Both types of experiments will require MW-class beams. The Project-X construction is expected to address these challenges [1]. The Project X represents a modern, flexible, Multi-MW proton accelerator (see Fig.1).

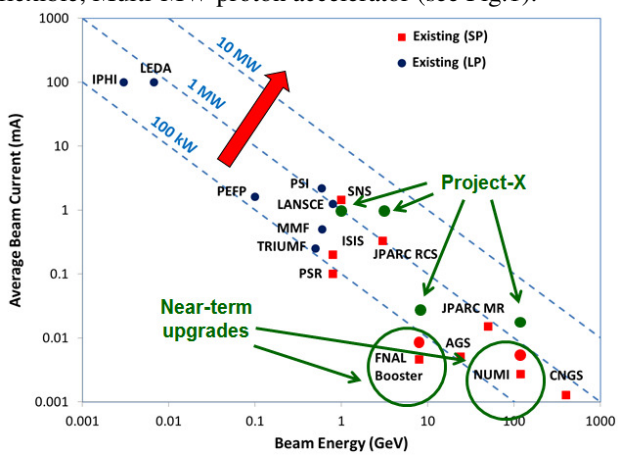


Figure 1: Accelerator beam power landscape.

High power hadron accelerators for the Intensity Frontier have two over-riding design constraints [2]:
Minimizing beam loss (typical beam loss requirements for a MW proton beam: < 1 Watt/m, or/and < 1×10^{-4} total beam loss), and
Proper beam structure (the required formats significantly vary from experiment to experiment – from a quasi-CW for rare particle decays to a single ~2-ns long bunch for MC/NF). The key challenges to satisfy these constrains include:

- Producing high current, high-quality and high brightness beams with required bunch structure;
- Accelerating high beam currents to high energy with (1) high-duty factors required for high resolution experiments and (2) very low duty factors for neutrino experiments;
- Running multiple experiments in parallel (quasi-simultaneously) required means for beam manipulations on the bunch-by-bunch base – see Fig.2;
- Transporting high power beams while maintaining beam loss at a level where routine maintenance is possible – see Fig.3;
- Acceleration of beams from keVs to GeVs preserving emittance and minimizing amplitude growth for large-amplitude particles ("beam halo");
- Low-loss extraction of the beams;
- Target systems capable of handling extreme power densities and extreme radiation environments – see Fig.4;
- A related challenge is producing intense, high-quality beams of secondary particles (muons, kaons, …).

ACCELERATOR R&D NEEDED

Below we outline the directions of the accelerator R&D needed to address the above challenges (we omit specific Project X R&D needs which are addressed elsewhere [3], and focus mostly on other important needs, especially, for the Fermilab's future intensity frontier program, which have not been articulated yet):

High Intensity beam sources: Radio-frequency quadrupoles (RFQs) are the injector technology of choice at present; the state of the art performance of 100 mA CW demonstrated at LANL/LEDA with 6.7 MeV output energy; is there an alternative technology which could compete with conventional technology?);

Beam dynamics issues with high intensity beams in existing accelerators (e-cloud, impedances/instabilities): RF systems (how to provide RF power for beam acceleration with many-fold higher beam current when the beam induced voltage greatly exceeds RF voltage?);

Space Charge issues (need to understand the Space Charge losses with the higher intensity slipped stacked bunches in MI and Recycler; the need collimators in

*Fermi Research Alliance, LLC operates Fermilab under contract No. DE-AC02-07CH11359 with the U.S. Department of Energy
#shiltsev@fnal.gov

Copyright © 2013 CC-BY-3.0 and by the respective authors

Recycler (?); realistic Space Charge MI simulations with predictive power that we can compare with data);

SYNERGIA simulations (to include all apertures and magnetic multipoles; compare with beam data);

Electron-Cloud (most effective coating and scrubbing; *in situ* SEY measurements, micro-wave measurements in the Main Injector);

Transition Crossing (evaluation need of a gamma-t jump in MI, transition crossing in Booster);

Injection issues (investigation of painting scenarios and other potential mitigation schemes - such as use of laser assisted stripping and R&D on rotating injection foil technology - Ultra Nano Crystalline Diamond (UNCD) technology, rotating graphene foil technology);

Loss Control (the need and design of the most efficient collimation schemes)

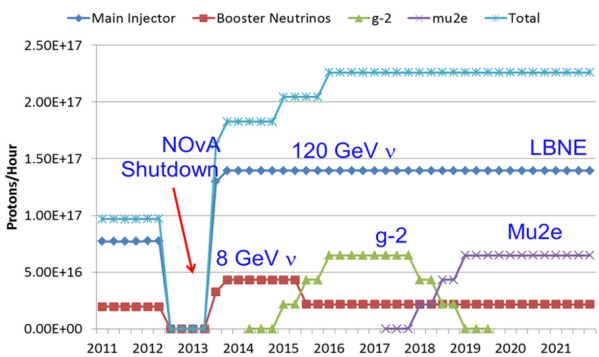


Figure 2: Fermilab's Proton Source proton flux ramp up expectations for the Intensity Frontier experiments.

Advanced simulation/modeling capabilities for high-intensity beams : We definitely will need to capitalize on the theoretical developments in beam physics theory and further develop the theory itself. Understanding the coherent instabilities is the corner-stone of the Intensity Frontier developments. Theory of coherent motion of coasting and bunched beams needs to be further studied in various approximations with several complimentary approaches.

Characterization of the loss mechanisms will have significant impact on the entire field of high-intensity accelerators – it is fundamental to loss minimization and control.

Development of a (flexible) beam dynamics framework with fully 3D PIC capabilities (eg on base of SYNERGIA) which will include space-charge & impedance capabilities, both single and multi-bunch effects, single-particle physics with full dynamics and which could run on on desktops, clusters and supercomputers.

Further development of Energy Deposition modeling tools (eg MARS) including: (1) updates related to recent developments in nuclear interaction model; (2) implementation of polarized particle transport and interaction, (3) recent developments of radiation damage models and transfer matrix algorithms in accelerator material-free regions; and (4) further enhancement of the geometry modules.

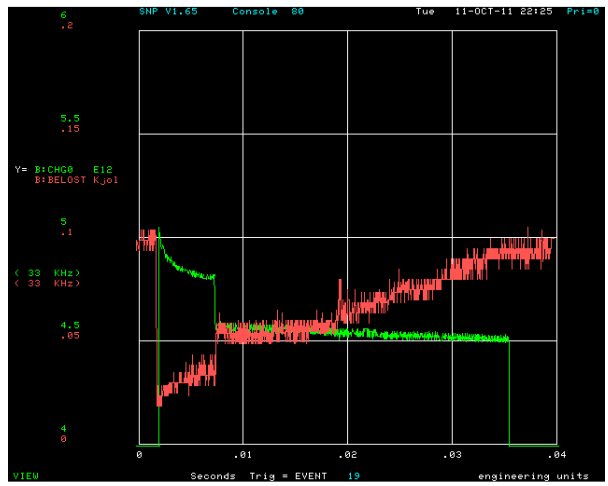


Figure 3: Losses in 8 GeV Fermilab Booster during its 15 Hz cycle occure at injection due to poorly captured beam, at the moment of notch creation (gap for extraction created with a kicker, particles lost in a gradient magnet). slow losses at high-energy (due to optics issues, RF variation), and losses at the transition energy (courtesy of Fermilab's Proton Improvement Plan team).

There is a need in a trustable weak-strong fully symplectic particle tracking codes with a comprehensive set of features for simulation of beam dynamics effects in electron and hadron storage rings, such as dynamics in integrable optics, in presence of space-charge forces and electron compensators, which could also do element-by-element tracking through machine lattice, incorporate FMA methods to assess particle diffusion, etc.

Transfer knowledge from theory and modeling to general R&D (support of the Intensity Frontier-related experiments in existing accelerators and beam test facilities, e.g., ASTA [4]) further into the projects.

Beam-stripping and beam-chopping with laser-based methods: The conventional approach to accumulating high proton intensities in a ring is to use multi-turn charge-exchange injection of H- beams, but it is very challenging to apply to >MW class beams, esp. CW beams. Novel laser stripping idea from *Danilov, et. al.* [5] has been demonstrated, but scaling to realistic accelerator parameters is needed. Laser chopping offers very attractive way to form the required beam current structures, and needs to be explored in realistic beam environment.

Targetry and collimation for Fermilab's future plans, delivery of 2MW beam power on the Long-Baseline Neutrino Experiment (LBNE) target, etc. [6, 7]:

Copyright © 2013 CC-BY-3.0 and by the respective authors

There is a need in enhanced modeling of beam energy deposition, secondary particle production and collection, radiation damage (DPA), transmutation products (gas production), and residual dose. Also required are advanced simulations of target material (non-linear) response using FEA codes including fracture and/or phase change; exploration/determination radiation damage effects in candidate target and collimator materials at accelerator target facility operating parameters (e.g., via the RaDIATE Collaboration: Radiation Damage In Accelerator Target Environments).Verification and benchmarking of the above mentioned simulation tools and material properties is needed through dedicated testing at beam facilities and autopsy of existing materials.



Figure 4: A downstream cooling water turn-around end of NuMI target NT-06 that failed after 4 month of operation at peak beam power of 340kW (toatl of 1.3e20 protons on target, 2011, courtesy J.Hylen, Fermilab)

One also needs to explore and compare high heat flux cooling methods through analysis and testing; to develop novel target and beam window concepts for use in proposed facilities; to develop target facility conceptual designs taking into account full life-cycle and radiation protection issues (remote handling, radioactive component disposal, tritium mitigation, etc.) and diagnostics for use in high radiation environments. We need to continue to engage in the high power targetry community to leverage the collaborative expertise and knowledge base to address the challenges of the High Intensity Frontier.

New ideas for clean slow extraction: Slow spills of high intensity beams are needed in particle physics, but beam loss limits intensity. Are there novel ways to cleanly achieve slow spills of high intensity beams? E.g., the resonant extraction - can it be extended to higher orders? Can crystals be used for high-power proton extraction or can electron beams be used to extract protons [8]? Are there other absolutely novel ideas which can employ lasers or high brightness electron beams?

Revolutionary ideas for Intensity Frontier accelerators: Integrable Optics [9] promises significant advance for low-loss operation of the IF facilities and must be tested at the IOTA ring at Fermilab's ASTA facility.

Space-charge compensation with either electron columns or electron lenses [10, 11] also has a promise of significant benefit for high intensity beams (due to improved emittance and loss control in high intensity beams) and also needs to be tested at the IOTA in ASTA [12].

Experimental Characterization and Understanding of High Intensity Beams and Underlying Dynamics (Advanced Instrumentation): reliable beam instrumentation is needed for precise halo (and emittance) measurements and connection to simulation in a reliable way. Novel diagnostics is required for in-depth understanding of intra-bunch and multi-bunch dynamics (position, modes, tunes, chromaticities, etc.).

One has to note that many of the above listed R&D thrusts are synergetic with the needs of the Accelerator Driven Systems (ADS) [13].

The facilities where the above listed R&D can/will be carried out include existing accelerators (Fermilab's Booster, Recycler and Main Injector) and the ASTA facility. Radiation damage studies for high power targetry may need dedicated facilities for required irradiations and examinations, such as BLIP at BNL for high energy proton irradiations or the proposed UK triple-beam facility, TRITON, for low energy ion irradiations. Verification studies for high power targetry will need dedicated areas at beam facilities capable of delivering intense beam pulses on heavily instrumented test samples, such as HiRadMat at CERN [14-16].

REFERENCES

[1] *Project X RDR*, FERMAIB-TM-2557 (2013)
[2] S. Henderson, in Proc. AAC'2012 (2012)
[3] S. Holmes, et al, arXiv:1305.3809 (2013)
[4] *ASTA Facility Proposal*, Fermilab-TM-2568 (2013)
[5] V. Danilov, et al, PRSTAB **10**, 053501 (2007)
[6] P. Hurh, et al, Proc. US-UK PASI (RAL, UK, 2013)
[7] P. Hurh, et al, Proc. IPAC'13, p.3484 (2013)
[8] V.Shiltsev, Proc.IPAC'12, p.517 (2012)
[9] V. Danilov, S. Nagaitsev, PRTSAB **13**, 084002 (2010)
[10] V.Shiltsev, Proc. IEEE PAC'07, p.1159 (2007)
[11] A.Burov, et al, Fermilab TM-2125 (2000)
[12] P.Piot, NA-PAC'13
[13] R.Raja, S.Mishra (eds.), Proc. *Workshop Applications of High Intensity Proton Accelerators* (World Scientific, 2010)
[14] P. Hurh, et al, Proc. IPAC'13, p.3487 (2013)
[15] S. Roberts, Proc. US-UK PASI (RAL, UK, 2013)
[16] A. Fabich, et al, Proc. IPAC'13, p.3415 (2013)

Copyright © 2013 CC-BY-3.0 and by the respective authors

RF-COMPONENTS EMBEDDED WITH PHOTONIC-BAND-GAP (PBG) AND FISHNET-METAMATERIAL STRUCTURES FOR HIGH FREQUENCY ACCELERATOR APPLICATION

[1]Sara Robak, [1]Daniel Boyden, and [1, 2]Young-Min Shin
[1]Department of Physics, Northern Illinois University, Dekalb, IL, 60115, USA
[2]Fermi National Accelerator Laboratory (FNAL), Batavia, IL 60510, USA

Abstract

In the development of high efficiency and high gradient RF-accelerators, RF waveguides and cavities have been designed with Photonic Band Gap (PBG) and fishnet-metamaterial structures. The designed structures are comprised of a periodically corrugated channel sandwiched between two photonic crystal slabs with alternating high to low dielectric constants and a multi-cell cavity-resonator designed with fishnet-metamaterial apertures. The structural designs of our interest are intended to only allow an operating-mode or -band within a narrow frequency range to propagate. The simulation analysis shows that trapped non-PBG modes are effectively suppressed down to ~ -14.3 dB/cm, while PBG modes propagated with ~2 dB of insertion loss, corresponding to ~1.14 dB/cm attenuation. The preliminary modeling analysis on the fishnet-embedded cavity shows noticeable improvement of Q-factor and field gradient of the operating mode (TM_{010}) compared to those of typical pillbox- or PBG-cavities. Fabrication of the Ka-band PBG-waveguide and S-band fishnet cavity structures is currently underway and they will be tested with a microwave test bench/8510C Network Analyzer and 5.5 MW S-band klystron. These structures can be applied to stable short-bunch formation and mono chromatic radiation in high frequency accelerators.

INTRODUCTION

Periodic conducting structures have been utilized as active slow wave media interacting with high energy electron beams in a wide range of applications from high gradient linear accelerators to coherent power radiation sources. The distorted dispersion relation of metallic lattices constitutes effective plasmonic modes with negative permittivity (epsilon-negative materials, $\varepsilon < 0$) [1 – 4]. The non-radiative waves have been widely used in microwave regimes as they can be readily guided in passive components or strongly excited by energy-momentum-coupling with kinetic electrons as an active medium [5]. The confined evanescent waves induce electron bunches when the current density exceeds thermo-dynamic divergence ($\propto f^{-2}$) [6]. This gives rise to a strong coherent electron-photon interaction that is commonly used for high intensity photon generation or high gradient RF acceleration. The spectral regime of the electronic RF devices has rapidly increased from microwave to near terahertz (near-THz) wave regime (0.1–1 THz) as device size can be significantly reduced proportional to the wavelength.

Energy conversion efficiency on the photon- emission or -absorption process is thus noticeably reduced as the optical cycle is decreased [7, 8] Recent trends in the development of THz electron beam devices have gradually transitioned to elliptical sheet beams from round ones as enlarging the beam width either increases radiation intensity or reduces beam current loading. Among various planar slow wave structures (SWSs) recently micro-channels with an asymmetrically aligned double grating array [9] were intensively studied for frequency-tunable coherent radiation source application as they have large instantaneous bandwidth of plasmonic modes that are strongly confined in the beam channel with small ohmic losses. However, this broad band characteristic can lead to unstable oscillation of abnormal modes, which possibly destabilize beam-wave interactions, and perturb normal electronic energy conversion. In particular, the structure becomes heavily overmoded (TE → TEM) as its aspect ratio between x-y transverse dimensions is increased to expand the beam-wave interactive area. It is thus certain that there is a limitation in increasing the aspect ratio of the sheet beam structure due to low-energy mode excitation. A substantial solution to the issue could be obtained from bandgap structures. This paper will present the band-selective planar waveguide combined with the photonic crystal slabs and fishnet-type metamaterial slab. The composite structure permits only non-radiative photonic-band-gap (PBG) modes [2–4] to propagate through the sub-wavelength micro-channel. Comparative numerical analysis and test results on the spectral response and field distribution will be discussed in detail.

PHOTONIC BAND GAP WAVEGUIDE

In principle, the lowest frequency (cutoff) of a rectangular TE-mode waveguide is determined by waveguide width, so TE modes become closer to TEM modes as the cutoff decreases. Figure 1 shows the 0^{th} order dispersion curves (m = 0) of TE- and TEM-waveguides. Normalized structural dimensions of the designed models are specified with $a_0/d_0 = 0.75$, $L_0/d_0 = 0.6$, $b_0/d_0 = 0.33$, and $h_0/d_0 = 1.674$, where d_0 is the grating period of a unit cell. The surface wall conductivity is defined with oxygen-free high-conductivity (OFHC) copper ($\sigma = 5.8 \times 10^8$ [$\Omega^{-1}m^{-1}$]). With an increase in the guide width, the entire eigenfrequencies of the fundamental band (grey solid → grey dashed) are lowered as the other dimensions remain consistent with the ones of the TE mode waveguide. In the 2^{nd} TEM waveguide (grey

Copyright © 2013 CC-BY-3.0 and by the respective authors

dashed line), the grating height (L_0) is shortened to keep the upper cutoff (stop-band) at the same frequency as the TM mode dispersion curve, which further extends the x-y dimensional aspect ratio. The passband of the 2nd TEM SWS (higher aspect ratio: black solid) thus tends to become even more heavily overmoded with larger phase and group velocities. As aforementioned, spatial harmonic components of lower frequency modes are readily coupled with low energy electrons, so that while haunting around in the structure, once excited, they are often self-amplified by phase-mismatching condition, which can cause strong perturbation to electron-photon coupling.

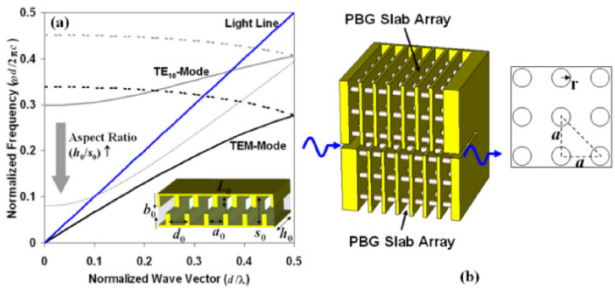


Figure 1: (a) Dispersion graph of the overmoded planar SWS. Inset is the schematic drawing of the staggered double grating arrayed waveguide with the dimensional parameters (TEM-mode) (b) 3D drawing of the PBG-slab-arrayed waveguide and unit cell of the designed PBG slab.

Embodiment of PBG elements in guided wave structures significantly reduces background noise level, including non-PBG modes, in the dynamic spectral range. In Fig. 1(b), the top and bottom gratings are replaced with the arrayed PBG slabs, which consist of alumina (Al_2O_3: ε_r = 9.4, tanδ = 0.0004) rods. In the crystal designed with the lattice constant of a/λ = 0.3 and filling ratio of r/a = 0.25, normalized global band-gap emerges at f (= $\omega d_0 /2\pi c$) = 0.25 –0.3. As depicted in Fig. 1(b), like an ordinary confined slow wave structure, electromagnetic (EM) waves bouncing back from the crystal lattices in the band-gap spectra that satisfy the Bragg condition propagate through the channel between the two PBG slab-arrays with strong field confinement. On the other hand, non-resonant eigenmodes outside the band gaps are freely radiated through the lattices, which are thereby strongly suppressed in the channel. Figure 2 shows dispersion curves, (a), of the TEM waveguide with the staggered vane arrays and transmission spectra of the photonic crystal slab, (b), and the PBG-slab embedded TEM waveguide, (c), with respect to two filing ratios, r/a = 0.2 and 0.3. In Fig. 3(b), the crystal slab arrays with r/a = 0.2 and 0.3 have three band gaps below the coalesced mode (upper cutoff) of the fundamental passband (a). Therefore, only the eigenmodes in the band gaps are allowed to propagate through the beam channel. Figure 3(c) shows an apparent emergence of three spectral bands with zero insertion loss which are exactly matched with the band gaps in Fig. 3(b). The background loss level of radiative non-PBG modes is about _45 dB that is low so as not to cause an abnormal beam-wave interaction. In Figs. 2(b) and 2(c), it is readily noticeable that the band-gap widths of r/a = 0.3 is only about half of widths of r/a = 0.2, which implies that increase of the rod size relative to the lattice constant leads to raising population density of guided photonic eigenstates with narrowing their intrinsic bandwidths. This indicates that the active spectral range and dispersion characteristics of confined waves are primarily determined by a lattice constant and a filling ratio of the photonic crystal filter rather than by the grating dimensions.

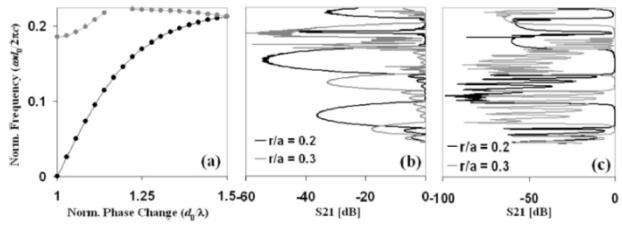


Figure 2: (a) 0_{th} order dispersion graph of TEM-mode SWS and transmission spectra of the PBG-slabs (b), and the PBG slab-arrayed SWS (c), of r/a = 0.2 (black) and 0.3 (grey).

The simulation models in Figures 2 and 3 are designed to be the ideal TEM-mode waveguide with the magnetic boundaries in the major transverse axis that appear impractical in actual application. The actual device model is thus designed with the oversized TE-mode waveguide that has an electric boundary. Figure 3(a) is the dispersion curves of the two slow waveguide structures embedded with the grating arrays (grey) and the photonic crystal slab arrays (red) that are procured by the finite-integral-technique (FIT) eigenmode solver.

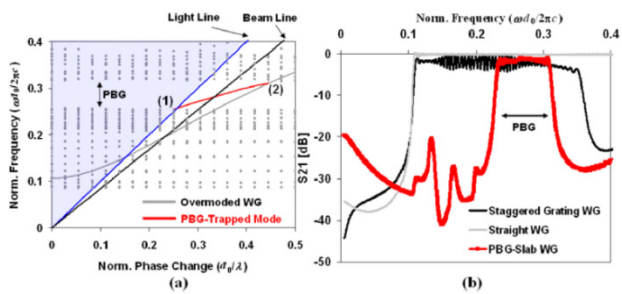


Figure 3: (a) 0_{th} order dispersion graphs (band-diagram) of the PBG-slab-arrayed SWS and TEM-mode SWS. (b) Transmission spectra (S21) of staggered grating waveguide, straight waveguide, and PBG-slab-arrayed waveguide.

The blue-shaded and white colored areas represent the photonic zone (far-field, $k < 2\pi/\lambda$) and plasmonic one (near-field, $k > 2\pi/\lambda$), respectively. The plotted points indicate all scattering modes corresponding to a phase change per period of the staggered corrugation. These unguided waves travel around and radiate in free space, and therefore have no interaction with the electron beam. In Fig. 3(b), the global band-gap noticeably emerges from f = 0.265 to f = 0.31 at either the photonic or plasmonic

Copyright © 2013 CC-BY-3.0 and by the respective authors

wave area. There is no other photon mode than interactive plasmon modes in the first forbidden band. The channel confined interaction modes disappear beyond the stop-band as they radiate to annihilate owing to the non-resonant matching condition with the crystal lattices. Note that the PBG-modes are considerably more dispersive than fundamental eigenmodes of the oversized waveguide (grey line). Figure 4 (a) shows a K-band test device machined and assembled with two PBG slabs. The reflection and transmission coefficients (S_{11} and S_{21}) are measured by a vector network analyzer (HP8510C), as shown in Fig. 4(b). The experimental data, well agreeing with simulation result, clearly show the PBG band in the transmission spectrum. The transmission spectrum of the PBG band is ~ 25 dB higher than that of the non-resonant band.

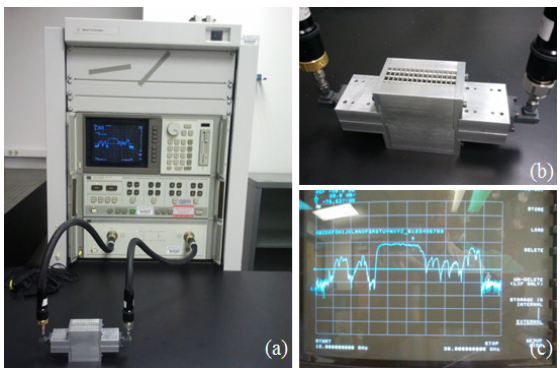
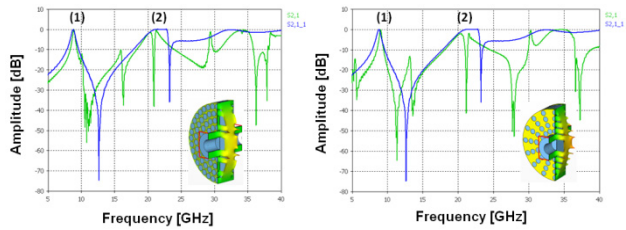


Figure 4: (a) Experiment setup with HP8510C vector network analyzer (b) K-band test device (c) transmission spectrum (S_{21}) of 12 – 38 GHz.

FISHNET-METAMATERIAL RF CAVITY

A higher frequency SRF cryomodule will make a great benefit that can save construction and operation costs, in addition to reduce a physical size of facility and to increase accelerating gradients. Also, operating at high frequency and low bunch charge reduces the risks of brightness degradation during beam transport. However, presence of higher-order-mode (HOMs) wakefields in the high-Q cavities possibly decreases RF energy conversion efficiency, plus inducing thermal heating. Especially, for high-duty-factor machines the heat is not easily extracted, which possible causes deformation or even quenching. The wakefields, normally proportional to a cube of the frequency, can significantly reduce luminosity and cause a beam breakup (BBU), which can severely destabilize acceleration and collision of beams in the long-pulse or CW mode operation. A fishnet structure [ref], consisting of the sandwiched metal-dielectric-metal layer [2 – 4], is one of the simplest double negative meta-materials with negative refractive indexes at resonances. The negative field response can efficiently remove HOMs from a beam interaction area over the broad spectral range. We designed two types of pillbox cavities with fishnet absorbers. Figure 5 shows the cavities strongly suppress a level of HOM wakefields down to - 30 ~ 40 dB in the transmission spectrum. Note that the accelerating mode becomes much narrower with the fishnet-embedded cavities. It is found that a small size cavity with the same physical dimensions with an accelerating mode (TM_{010}) cavity can be used to suppress or filter HOMs with the structure (over-sizing cavity volume is unnecessary). We also observed that implementing the structure in the cavity doubles Q-values (loaded Q, Q_L). It is expected that negative dispersion response of the novel RF component have potential to advance SRF technology and we will look into its field characteristics and thermal properties of HOMs by simulation and experimentation.



(a) (b)

Figure 5: Transmission spectrums of fishnet metamaterial RF cavities (a) type-1 and (b) type-2 ((1) TM010 and (2) HOM)

CONCLUSION

The staggered double PBG-slab arrays enable over-moded planar slow waveguides to induce monochromatic wave propagation of a single plasmonic mode within a narrow band-gap. This highly selective band filtering noticeably improves spectral purity of plasma-interactive evanescent waves in the over-moded slow waveguides, free from the instability problems. A fishnet meta-material absorber strongly suppresses HOM wakefields down to – 30 ~ 40 dB range in a high-Q RF cavity. The quasi-optical mode-filtering/damping/absorbing devices support efficient energy conversion, which can be utilized as a passive or active component for various optoelectronic and electron beam devices.

REFERENCES

[1] R. A. Shelby, et. al., Science 292(5514), 77–79 (2001).
[2] J. B. Pendry, Phys. Rev. Lett. 85, 3966 (2000).
[3] V. George and K. G. Balmain, Negative-Refraction Metamaterials: Fundamental Principles and Applications.
[4] R. W. Ziolkowski, Metamaterials: Physics and Engineering Explorations (Wiley, 2006).
[5] R. K. Parker, et. al., IEEE Trans. Microwave Theory Tech. 50, 835 (2002).
[6] K. Mizuno, J. Appl. Phys. 46(4), 1849 (1975).
[7] X.-C. Zhang, Phys. Med. Biol. 47, 3667 (2002).
[8] C. Sirtori, Nature (London) 417, 132–132 (2002).
[9] Y.-M. Shin et. al., Appl. Phys. Lett. 92, 091501 (2008).

Copyright © 2013 CC-BY-3.0 and by the respective authors

FEASIBILITY STUDY OF CHANNELING ACCELERATION EXPERIMENT AT THE FERMILAB ASTA FACILITY

[1, 3]Young-Min Shin, [2]Tao Xu, [3]Dean A. Still, and [3]Vladimir Shiltsev
[1]Department of Physics, Northern Illinois University, Dekalb, IL, 60115, USA
[2]Department of Chemistry, Northern Illinois University, Dekalb, IL, 60115, USA
[3]Fermi National Accelerator Laboratory (FNAL), Batavia, IL 60510, USA

Abstract

Crystal channeling technology has offered various opportunities in accelerator community with a viability of ultrahigh gradient (TV/m) acceleration for future HEP collider in Energy Frontier. The major challenge of the channeling acceleration is that ultimate acceleration gradients might require high power driver at hard x-ray regime (~ 40 keV), exceeding those conceivable for x-rays as of today, though x-ray lasers can efficiently excite solid plasma and accelerate particles inside a crystal channel. Moreover, only disposable crystal accelerators are possible at such high externally excited fields which would exceed the ionization thresholds destroying the atomic structure, so acceleration will take place only in a short time before full dissociation of the lattice. Carbon-based nanostructures have great potential with a wide range of flexibility and superior physical strength, which can be applied to channeling acceleration. This paper present beam-driven channeling acceleration concept with CNTs and discuss feasible experiments with the Advanced Superconducting Test Area (ASTA) in Fermilab and beyond.

INTRODUCTION

The cost models of the modern colliders are quite complicated, but one may safely assume that a future facility should not exceed a few tens of km in length and simultaneously require less than 10 to a few tens of MW of beam. To get to the energies of interest within the given footprint, fast particle acceleration is inevitable. Plasma-wakefield acceleration (PWA) has become of great interest because of the promise to offer extremely large acceleration gradients, on the order of E0 ≈ n01/2 [GeV/m], where n0 is the ambient electron number density (n0 [1018cm-3]), on the order of 30-100 GV/m at plasma densities of n0 = 1017 – 1018 cm-3.[1] The density of charge carriers (conduction electrons) in solids n0 = ~ 1020 – 1023 cm-3 is significantly higher than what was considered above in plasma, and correspondingly, wakefields of up to 100 GeV/cm or 10 TV/m are possible. In the solid plasma, as escaping from a driving field due to fast pitch-angle diffusion resulting from increased scattering rates, particles must be accelerated along major crystallographic directions. This is called "channeling acceleration". Normally, crystal channeling has been applied to high energy beam control such as collimation, bending, and refraction [2]. For high energy beam optics, carbon nanotubes (CNTs) have been considered for bending and collimation [3, 4] on account of the much wider range of flexibility, including superior physical strength, which also ideally fits with channeling acceleration. CNTs, composed of graphene sheets rolled into seamless hollow cylinders with diameters ranging from 1nm to about sub-micron, exhibit unique physical and chemical properties as a quasi-one dimensional material [5]. In principle, both straight and bent CNTs can effectively be used for high-energy particle channeling [6], provided the technological challenge of achieving an almost perfect alignment of CNTs with respect to the beam direction could be tackled effectively in the synthesis of samples.

Recently, Fermilab built the Advanced Superconducting Test Accelerator (ASTA) facility (50 MeV and several hundreds of MeV energy beams) that will enable a broad range of electron beam-based experiments to study fundamental limitations to beam intensity and to developing transformative approaches to particle-beam generation, acceleration and manipulation, which is ideally suited for the channeling acceleration experiment. We plan to detect a measurable energy gain from the electron bunches passing through CNTs. Successful demonstration of the experiment with this beam driven method will verify the viability of CNT channeling interaction for ultra-high gradient acceleration, which will also prove the feasibility of the laser-driven channeling acceleration. The experimental setup will be accommodated to a 50 MeV main stream beamline and high energy (50 – 300 MeV) beamline in our plan. In the research, beam energies and radiation spectra of CNT samples will be mainly characterized by beam tests at relativistic regimes.

CHANNELING ACCELERATION

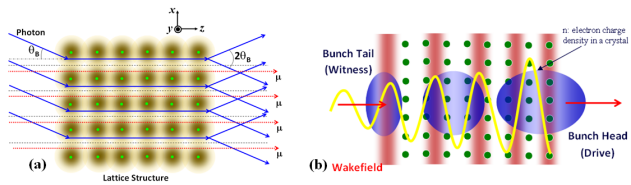


Figure 1: (a) Laser (x-ray) driven acceleration (muon, proton) (b) beam-driven acceleration (electron).

Wakefields in crystals can be excited by two sorts of driving sources: x-ray laser (Fig. 1(a)) or short electron bunch (Fig. 1(b)). With the x-ray pumping method [7], a crystal channel can hold > 1013 V/cm transverse and 109 V/cm longitudinal fields of diffracted traveling EM-waves at the Bragg diffraction condition ($\lambda/2b = \sin\theta B$), where b is the lattice constant and θB is the diffraction angle) However, to hold the ultimate gradients, the acceleration requires coherent hard x-rays ($\hbar\omega \approx 40$ keV) of ≥ 3 GW to compensate for radiation losses, which

Copyright © 2013 CC-BY-3.0 and by the respective authors

exceed those conceivable today. The x-ray driving method thus fits for heavy particles, e.g. muons and protons, which have relatively smaller radiation losses. For electrons, the beam-driven acceleration is more favorably applicable to channeling acceleration as the energy losses of a drive beam can be transformed into acceleration energy of a witness beam [8]. The highly intensive plasma interaction in a crystal channel induces thermal radiations and collisional impacts accompanied by a large amount of heat energy, which would exceed the ionization thresholds and may even destroy the atomic structure. Only disposable forms of crystals such as fibers or films can be used for channeling acceleration. Also, lattice structures of crystals have fixed atomic dimensions, which thereby have some limits in designing acceleration parameters to mitigate physical constraints in solid plasma channels. Carbon nanostructures have potential advantages over crystals for channeling acceleration such as wider channels (weaker de-channeling), broader beams (using nanotube ropes), wider acceptance angles (< 0.1 rad), 3D beam control over greater lengths, and in particular excellent thermal and mechanical strength, which are ideally fit to channeling acceleration and cooling applications, plus beam extraction, steering, and collimation. CNTs are comprised entirely of *sp*2 bonds, which are extremely stable and thermally and mechanically stronger than crystals, steels, and even diamonds (*sp*3 bond). Nanotubes thus have a higher probability of surviving in an extremely intense channeling, radiation, and acceleration environment.

Plasma frequencies of CNTs are normally in the THz range, which need a beam bunch duration within an order of microns for wakefield generation in the linear regime, an electron bunch in the pico-second range, which is readily obtained from conventional RF photoemission technique, would need to be either compressed down to an order of a femto-second or split into microbunches. It is well known that injecting a driver beam with multiple microbunches in a plasma channel improves field gradient, transformer ratio, and energy efficiency of plasma wakefield acceleration. With the multiple microbunches, phase matching conditions between a plasma wave and a modulated beam can be selectively tuned in order to maximize wakefield, transformer ratio, or energy efficiency.

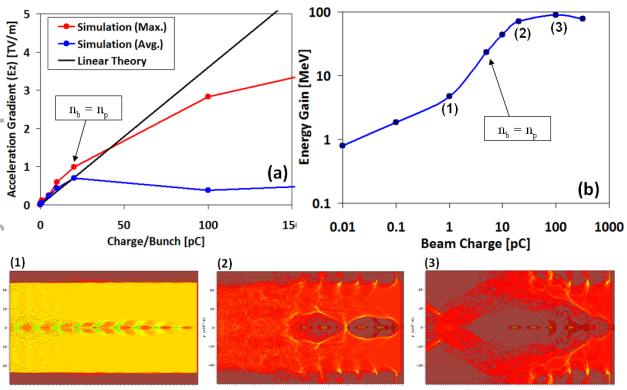


Figure 2: Channeling acceleration analysis, obtained from the linear wakefield theory and computer simulations: top - (a) acceleration gradients and (b) energy gain versus beam charge and bottom - spatial charge distributions of plasma and beam (1) 10 pC (2) 200 pC (3) 1 nC.

SIMULATION ANALYSIS

The basic pattern of channeling acceleration has been analyzed by theoretical model and computer simulation with the nominal ASTA beam parameters: bunch-to-bunch space = 10 μm, beam energy = 50 MeV, charge density of plasma channel = 10^{25} m^{-1}, bunch length = 2 ~ 3μm. Figure 2 shows summarized acceleration gradient and energy gain graphs with respect to beam charges, obtained from the 1D linear wakefield theory and plasma accelerating simulator (VORPAL). The simulation data agree well with the theoretical graph in the linear regime. This result clearly verifies that micro-spaced electron bunches gain energy up to ~ 70 MeV (~ 200 pC) along a 100 μm long channel, corresponding to a ~ 0.7 TeV/m acceleration gradient. The analysis indicates that further increase of the beam charge excessively blows out the ambient plasma charges in the channel ((3) of Fig. 3: bottom). It strongly pushes plasma waves out of phase-synchronization with the beam wave, which rather decreases the energy gain. The analyzed parameters will be implemented into the design process of the experimental setup. This kind of simulation method will be continuously used to analyze/design the beam-driven accelerator with various channeling conditions.

EXPERIEMNTAL LAYOUT

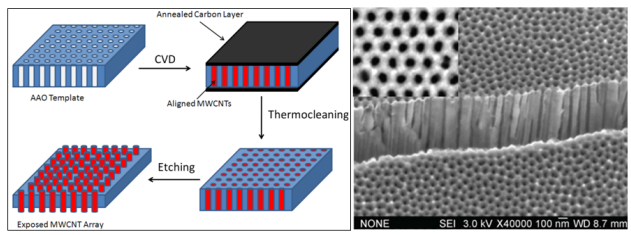


Figure 3: (a) Schematic diagram of an AAO template process (b) SEM image of an AAO film, inset is the enlarged SEM image.

Two kinds of channeling accelerator structures, crystals (silicon or diamond) and arrayed CNT bundles, will be manufactured and tested and compared in the first experiment. Crystal samples will be obtained by a similar fabrication technique used for silicon samples in channeling experiments in Tevatron of Fermilab: cleaved and cut silicon wafers [9]. The sample holder, used for the experiment, will also be re-used for crystal acceleration tests, but only with the straight section (no bending). A test device with a straight multi-wall CNT bundle will be prepared using an anodic aluminum oxide (AAO) template (Fig. 3(a)) [10]. We plan to test a 100 μm long, 200 nm wide CNT structure first, which may possibly be manufactured within 2 ~ 3 months. It is expected that these types of crystal channels induce plasmonic waves of $\lambda_p \leq \sim 10$ μm.

Copyright © 2013 CC-BY-3.0 and by the respective authors

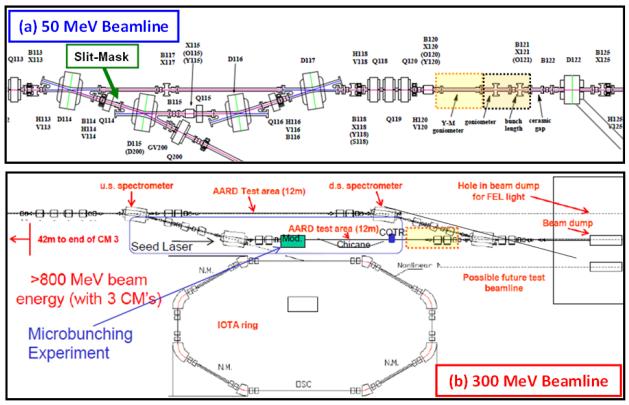


Figure 4: Prospective locations of experiment setup: 50 MeV beam line (top) and 300 MeV (bottom).

As we plan to conduct the 1st experiment at 50 MeV beamline of the Fermilab-ASTA, test equipment will be installed downstream of the capture cavity-2 (CC-2) and bunch compressor before the 1st cryomodule. Figure 4 shows the beam line drawing, describing the currently planned location of the proposed experiment. The boxed areas indicate prospective locations of the vacuum-compatible goniometer to be loaded with a test sample. While passing through the BC, the slit-mask placed in the BC will produce microbunch trains by imprinting the shadow of a periodic mask onto a bunch with a correlated energy spread. Once passing through a test device in the goniometer, beam energies will be measured by a spectrometer with a dipole magnet and yttrium aluminum garnet (YAG) screen positioned in the beamline toward a beam dump. A test with higher energy beams is also planned, so the experiment will be accommodated to the Development of a Compact Photo-injector with RF-Focusing Lens for Short Pulse Electron Source Application mainly consider the slit-mask technique, which is the simplest way to create multiple sub-ps micro-bunches [11], and an inverse free electron lasing technique. Currently, a laser-induced microbunching (LIM) scheme with the FEL undulator is proposed in the ASTA stewardship program, which is potentially employed to generate microbunches to the channeling acceleration test.

The proposed experimental scheme will need several positions to monitor bunch profiles and measure their spatiotemporal radiation patterns and energy spectra of accelerated beams. We measure the time pattern of a masked beam entering the dispersion-free region of the beam line using coherent transmission radiation (CTR) interferometry. The broadband transition radiation emitted by the electrons when entering a copper mirror placed after the dogleg, near the experimental region, is sent to a Martin-Puplett interferometer. After the energy-analyzed and collimated beam of electrons is transported through the bunch compressor into the experimental area, it is defocused by an asymmetrically split quadrupole triplet to give a low-divergence (nearly parallel) beam incident upon the crystal in its goniometer. A critical factor in performing channeling acceleration experiments is the divergence of the incident beam. Since the characteristic angle for the process is $1/\gamma$, an angular resolution at least an order of magnitude smaller is required in order to obtain data of sufficient precision to compare with the results of theoretical calculations; for $\gamma \sim 100$, a beam divergence larger than 1 mrad is inadequate. Moreover, the critical angle for channeling is a few mrad for electrons of a few tens of MeV, and varies as $\gamma^{-1/2}$; therefore, in order that a large fraction of the beam be channeled, a beam divergence ≤ 1 mrad is required. The experimental arrangement is used for obtaining a very-low-divergence beam, which is used as well for measurements of the transmission of electrons through crystals.

CONCLUSION

Despite the great potential of HEP colliders, excessively high driving energy and power requirements accompanied by the insufficient durability of crystal structures has removed channeling acceleration from primary consideration for high gradient (HG) accelerators. However, replacing crystals with nano-structures makes this possible by mitigating the power and energy requirements, with the advantage of improved physical strength. The fundamental mechanisms of plasmon excitation and photon-particle coupling of the nanotube can thus be studied at Fermilab-ASTA. Successful demonstration of all the simulations and experimental tests will open new opportunities for HG accelerator research efforts by merging nanotechnology and high energy physics. All of the new techniques and methods developed from heuristics will indeed be incorporated into existing technologies for current HEP collider R&D programs.

ACKNOWLEDGEMENT

We thank Alex Lumpkin for his suggestion on micro-bunching technique. We thank Philippe R. G. Piot for helpful discussion and support for the proposal and Chris Prokop for sharing his ASTA simulation design parameters.

REFERENCES

[1] W. Leemans, *ICFA Beam Dynamics Newsletter* **56** 10 (2011).
[2] P. Chen, R. Noble, *AIP Conf. Proc.* **398** 273 (1997).
[3] V. M. Biryukov, NIM *B* 234 (2005) 99–105.
[4] S. Bellucci, NIM B 234 (2005) 57–77.
[5] N. Hamada, et. al., Phys. Rev. Lett. 68 (1992) 1579.
[6] V. M. Bellucci, et. al., NIM B 202 (2003) 236.
[7] T. Tajima, and M. Cavenago, PRL 59, 1440 (1987).
[8] P. Chen and R. J. Noble, AIP. Conf. Proc. 156, 2122 (1987).
[9] http://accelconf.web.cern.ch/accelconf/IPAC10/talks/tuoamh03_talk.pdf
[10] H. Peng Xiang, L. Chang, S. Chao, and C. HuiMing, Chinese Science Bulletin 57, 187 (2012).
[11] P. Muggli, V. Yakimenko, M. Babzien, E. Kallos, and K. P. Kusche, PRL **101,** 054801 (2008).

Copyright © 2013 CC-BY-3.0 and by the respective authors

COMMISSIONING AND INITIAL EXPERIMENTS ON NDCX-II*

S. M. Lidia#, T. Schenkel##, W. G. Greenway, K. Murphy, T. Schenkel, C. D. Weis,
W. L. Waldron, Lawrence Berkeley National Laboratory, Berkeley, CA 94720, U.S.A.

Abstract

The Neutralized Drift Compression Experiment (NDCX-II) is a new induction accelerator facility designed to facilitate user experiments in high energy density laboratory physics, intense beam physics, and materials processing and testing with intense, pulsed ion beams. The facility has completed the initial commissioning phase of its injector, 27-cell solenoid transport lattice, induction accelerator modules and non-neutral pulse compression section. Space-charge-dominated Li^+ beams carrying 20-50 nC have been generated from the 133 kV pulsed, ~1.0 microsecond (FWHM), 65-mA injector, and compressed to 20-30 ns with 0.75-1.3 A peak currents and amplification factors of 10-20. We report results of non-neutral beam compression and transport studies to generate variable ion beam fluences on to solid targets. We also report on studies of dose rate effects in pulsed ion implantation and on the recombination dynamics of radiation-induced defects in semiconductors using the NDCX-II Li^+ beam.

INTRODUCTION

The NDCX-II facility [1, 2] was constructed between July 2009 and December 2012. Commissioning results of the source and injector systems has already been reported [3]. The induction accelerator modules with pulsed, 2-3 T solenoid magnet transport were added in several stages (5-cell, 11-cell, 27-cell) to facilitate the integration of diagnostic and controls systems [4].The 27-cell beamline configuration is shown in Fig. 1, with schematic representation indicating the position of the active induction cell modules, diagnostic cells, injector and end station. Each cell is instrumented with a pulse solenoid for transport.

The original complement of beam diagnostics for commissioning included a movable end station complemented with a Faraday cup, slit and slit-cup pairs, and scintillator viewable through downstream flange window. A pepper-pot mask and dedicated scintillator were added later, with the removal of the slit/slit-cup pairs. Other non-interceptive beam diagnostics included 6 capacitive plate beam position monitors at the diagnostic cell locations, solenoid current transformers, and accelerator cell voltage resistive monitors. This level of beam instrumentation was sufficient for initial beam transmission studies and beam quality measurements.

* This work is supported by the Director, Office of Science, Office of Fusion Energy Sciences, of the U.S. Department of Energy under Contract No. DE-AC02-05CH11231.

#smlidia@lbl.gov, ##T_Schenkel@LBL.gov

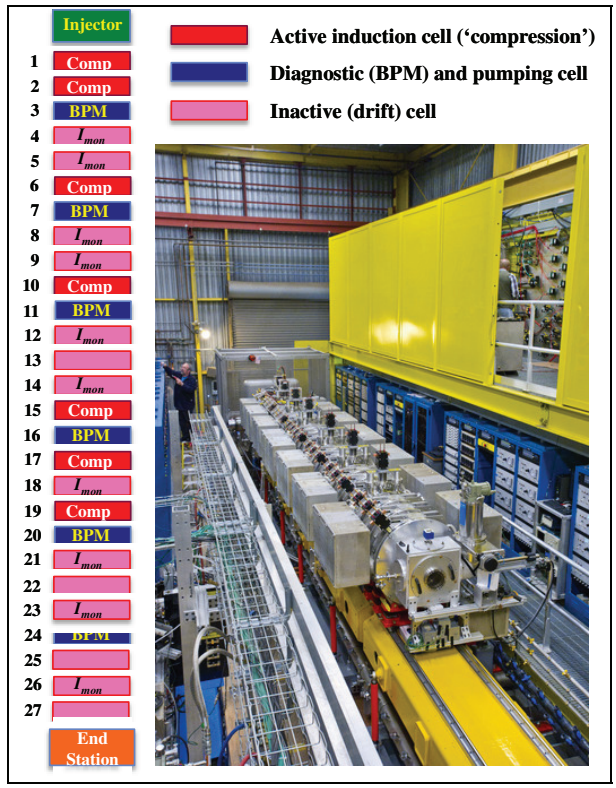


Figure 1: NDCX-II beamline and schematic.

ENHANCED DIAGNOSTICS AND COMMISSIONING STRATEGY

The modular beamline is built up from 21 identical induction cells and 6 diagnostic cells. For these commissioning exercises, only 7 of the induction cells are active, with the remaining inactive cells providing drift length for longitudinal compression. We utilized an additional 10 inactive cells as reciprocal inductive current monitors. The drive matching circuits for these cells were modified to provide a ~5Ω termination, and measured *L/R* response times were in the range of 1.6 – 2.2 µs.

These additional current diagnostics increased the spatial resolution of time-of-flight measurements along the beamline, and permitted determination of velocity and beam energy to within accepted error margins. Furthermore, interpolation of the beam arrival time and beam pulse duration to the active induction cell positions permits fine tuning of the accelerating voltage waveform amplitude and delay, enabling optimization of the bunch compression process and tailoring of the magnetic solenoid lattice.

Copyright © 2013 CC-BY-3.0 and by the respective authors

LONGITUDINAL COMPRESSION AND ACCELERATION

The 7 active induction cells function to impress a time-varying energy (or velocity) ramp on the beam and, with the additional drift lengths between them, to allow the beam to compress longitudinally with concurrent increase in the peak current. The injector and induction cell voltage waveforms are shown in Fig. 2 for a particular tune of delays and amplitudes.

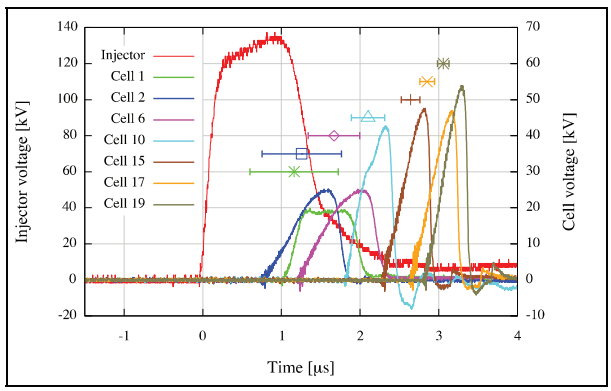


Figure 2: Injector and induction cell voltages. Interpolated beam arrival times and pulse durations are indicated.

Beam line charge density profiles and beam current profiles are measured with the BPMs and inductive current monitors, respectively. The current waveforms are shown in Fig. 3.

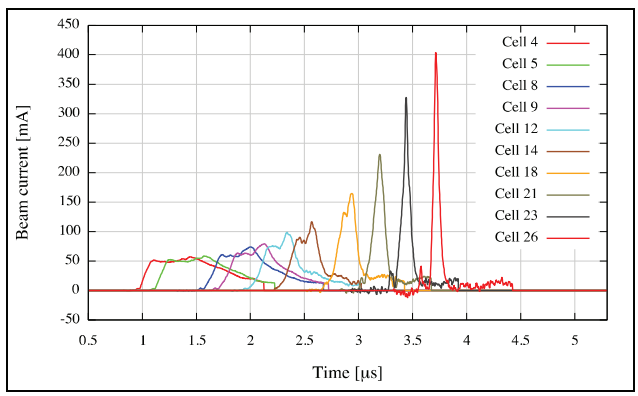


Figure 3: Evolution of beam current profile.

Time-of-flight calculations based on the arrival times of the pulse leading edge at the monitoring stations is used to generate a profile of the beam velocity and energy evolution through the machine. The peak current, average beam energy, and pulse duration (FWHM) are shown in Fig. 4.

BEAM TRANSPORT

Several classes of solenoid focusing lattice tunes were examined for beam matching and transmission in the drifting (i.e. not accelerator or compressed) case. Simple space-charge dominated envelope simulations were performed and are shown in Fig. 5.

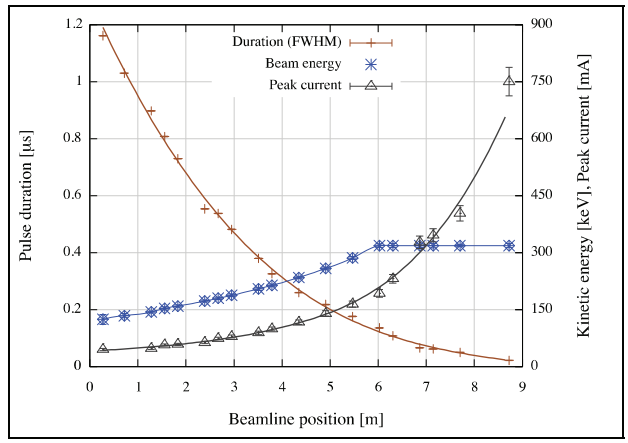


Figure 4: Evolution of longitudinal beam parameters.

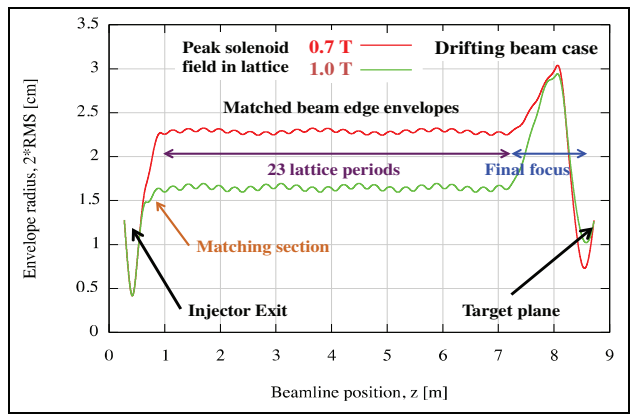


Figure 5: Solenoid transport tune classes for 135 keV, 65 mA drifting beam.

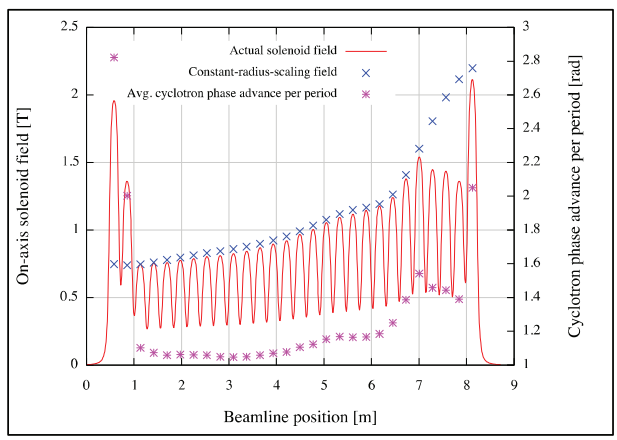


Figure 6: Solenoid field profile match to evolving beam current and energy.

These tune classes provide a basis for tuning the compressed pulse case. Using the field scaling $B^2 \sim I_{pk}/v_{avg}$, where I_{pk} and v_{avg} are the peak currents and average bunch velocity, respectively, we retune the solenoid field (Fig. 6) to maintain constant beam radius along the accelerator.

Copyright © 2013 CC-BY-3.0 and by the respective authors

BEAM EMITTANCE AND FLUENCE

At the target plane, a scintillator captures the beam transverse profile, while a pepper-pot is used to measure the 4D phase space distribution. The last solenoid is scanned to vary the beam envelope and convergence angle. The resultant variation in the radius, peak fluence, and emittances is shown in Fig. 7 for the compressed beam case (Table 1).

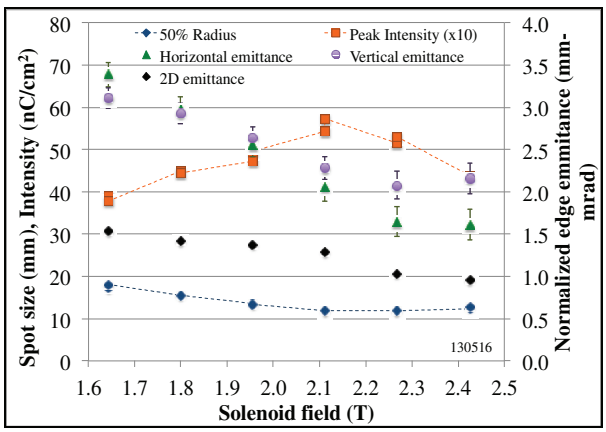


Figure 7: Peak intensity and emittances at target plane.

Table 1: Target Plane Beam Parameters

	Drifting	Compressed
Final energy (keV)	135	315
Peak current (mA)	65	760
Pulse length, FWHM (ns)	450	20
50% beam radius (mm)	5.1	11.8
Average fluence (mJ/cm^2)	3	0.84
Peak intensity (kW/cm^2)	8.8	88

INITIAL TARGET EXPERIMENTS

Intense, short ion beam pulses enable pump-probe type experiments to access the multi-scale (ps to many seconds) dynamics of radiation induced defects in materials [5, 6]. Using NDCX-II, we are conducting studies to examine the pulse length and peak fluence dependence on lattice defect generation and recovery in single crystal silicon and metals. First, we irradiated single crystal silicon (100) samples and performed *ex situ* SIMS (Secondary Ion Mass Spectrometry) analysis of Li ion depth profiles [5]. Here, damage built-up during ion implantation shots reduces the probability for ions to channel along high index crystal directions. When varying dose rates (~0.1 - 50 mA/cm^2) and pulse lengths (~20 - 500 ns), we saw evidence for defect recombination on a 100 ns time scale.

In the next series of experiments we utilize a thin (1-µm) single crystal silicon (100) membrane to intercept the beam. The membrane thickness is chosen to block the randomly scattered ions while allowing the channeled ion flux to pass. A fast Faraday cup (FFC) on the downstream side of the membrane is used to collect the transmitted ions with a time resolution of a few ns. The effect of pulse duration and peak fluence on transmitted beam is shown in Fig. 8. In the long pulse/lower fluence (137 keV, 640 ns, 6 nC) case, the transmitted flux profile reproduces the control case without the Si membrane, indicating low effective angles for the uncompressed beam. In the short pulse case (261 keV, 40 ns, 2.2 nC), the transmitted ion current profile deviates significantly from the control case. For the tuning conditions of this 40 ns shot, ions in the pulse peak are mostly absorbed in the membrane, indicating effective beam angles of a few degrees, while trailing ions later in the pulse transmit the membrane, indicating beam angles <1°. The critical angle for channeling of ~300 keV Li^+ ions in Si (100) is about 1°. Ion transmission tracking provides *in situ* feedback for tuning of effective beam angles. For the short pulse tune in Fig. 8, ions in the peak generate defects (vacancies and interstitials) and the disordered lattice is probed by ions that arrive later on channeling trajectories. For the relatively low dose rates present in the shots shown in Figure 8, we see no evidence for damage built-up. Dose rates will be increased 10 to 50 fold in experiments with shorter (~15 ns), more intense (~40 nC) pulses. Tuning of pump-probe type ion beam pulses shapes [6] and implementation of auxiliary diagnostics will enable unprecedented access to multi-scale defect dynamics in materials.

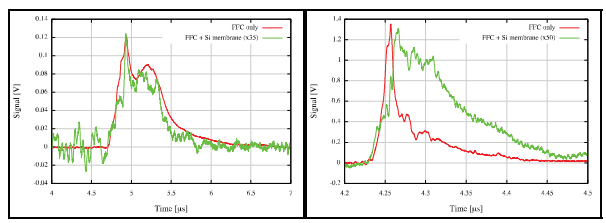


Figure 8: Current traces for a single 640 ns long (left) and 40 ns short pulse, (right), with (green) and without (red) Silicon membrane target in front of the FFC.

SUMMARY

We have implemented diagnostics and tuning techniques to produce a variety of target plane conditions on NDCX-II, with unneutralized pulse compression ratios of 10-20 for high perveance (~10^{-2}) beams. The measured beam quality matches numerical predictions. We present results from experiments that utilize the unique short pulse capabilities of NDCX-II.

REFERENCES

[1] A. Friedman et al., Phys. Plasmas 17 (2010) 056704.
[2] W.L. Waldron, NIM A (2013), in press. http://dx.doi.org/10.1016/j.nima.2013.05.063
[3] P.A. Seidl et al., PR-STAB 15 (2012) 040101.
[4] S. Lidia et al., IPAC 12 Proceedings, MOEPPB005.
[5] T. Schenkel et al., NIM B (2013), http://dx.doi.org/10.1016/j.nimb.2013.05.074
[6] A. Froideval et al., J. Nucl. Mater. 416 (2012) 242 .

Copyright © 2013 CC-BY-3.0 and by the respective authors

BETATRON X-RAYS FROM A LASER WAKEFIELD ACCELERATOR IN THE IONIZATION INDUCED TRAPPING REGIME *

F. Albert, B.B. Pollock, Y.-H. Chen, D. Alessi, J.E. Ralph, P.A. Michel, A. Pak,
LLNL, Livermore, CA 94550, USA
J. Shaw, K.A. Marsh, C.E. Clayton, C. Joshi, UCLA, CA 90095, USA
S.H. Glenzer, SLAC, Stanford, CA 94309, USA

Abstract

Betatron x-rays with multi-keV photon energies have been observed from a GeV-class laser-plasma accelerator. The experiment was performed using the 200 TW Callisto laser system at LLNL to produce and simultaneously observe GeV-class electron beams and keV Betatron x-rays. The laser was focused into various gas cells with sizes ranging from 3 to 10 mm, and containing mixed gases (He, N, CO2, Ar, Ne) to accelerate large amounts of charge in the ionization induced trapping regime. KeV betatron x-rays were observed for various concentrations of gases. Electron spectra were measured on large image plates with the two-screen method after being deflected by a large 0.42 Tesla magnet spectrometer.

INTRODUCTION

Laser Wakefield Acceleration (LWFA)[1] is one of the most notable applications of petawatt-class laser systems. Since the discovery that this mechanism can accelerate monoenergetic electron beams up to energies comparable to those obtained with conventional rf accelerators[2, 3, 4] but in a table-top setup, novel applications of these electron beams have been constantly increasing. Concurrently, x-ray sources such as synchrotrons, or more recently free-electrons lasers such as the Linac Coherent Light Source (LCLS)[5] continue to explore new properties of atoms, molecules, condensed matter, warm dense matter or plasmas. In this context, LWFA beams are very attractive to seed the next generation of light sources. Such beams can either be wiggled by an external periodic magnetic structure[6] or directly by the plasma in the wake of the laser pulse[7, 8] to produce keV x-rays. The latter example, the betatron x-ray source, first observed in a beam-driven plasma channel[9] is the subject of this work, and its mechanism can be described as follows: an ultrashort (femtosecond), ultraintense ($I > 10^{18}$ W/cm^2) laser pulse is focused under vacuum on the edge of a gas target. The gas is fully ionized to form a plasma. The laser ponderomotive force (proportional to the gradient of light intensity) plows the electrons of the plasma away from the strong light intensity regions. Because of the very short duration of the laser pulse, the heavier ions stay immobile and a bubble free of electrons is formed in the wake of the pulse. At the back of this bubble, some electrons are trapped, accelerated and wiggled by the electrical fields present in the plasma: these electrons emit the betatron x-rays. This source produces broadband, synchrotron-like radiation in the keV energy range[10, 11], within a source size of a few microns[12, 13], a divergence of less than 100 mrad[14], and a pulse duration of less than 100 fs[15]. Since betatron x-rays are directly related to the electrons emitting them, the source is also widely used as an electron beam diagnostic. The electron beam emittance and size can be deduced from the x-ray beam profile[14], spectrum[16] or source size[17], using various x-ray spectroscopy and imaging techniques. Traditionally, betatron x-rays are produced in the blowout regime of laser wakefield acceleration[18] using pure helium gas, where electrons are self-injected into the wake. This paper investigates the properties of betatron x-ray radiation produced in mixed gases.

BETATRON RADIATION MODELING

The motion of an electron accelerated along $\vec{u_z}$ with momentum $\vec{p}$ and position $\vec{r}$ in the wake of a laser pulse can be described by the Lorentz equation of motion:

$$\frac{d\vec{p}}{dt} = -m\omega_p^2 \frac{\vec{r}}{2} + \alpha \frac{mc\omega_p}{e}\vec{u_z}, \qquad (1)$$

where m is the electron rest mass, e the elementary charge, and $\omega_p = \sqrt{n_e e^2/m\epsilon_0}$ is the plasma frequency. Here, n_e is the electron density, and ϵ_0 the vacuum permittivity. In the blowout 3D nonlinear regime of laser wakefield acceleration [18], $\alpha = \frac{1}{2}\sqrt{a_0}$ is the normalized accelerating field, where a_0 is the laser normalized vector potential, typically around 2 for our experiments. Equation 1 can be solved by using a 4th order Runge-Kutta algorithm to obtain the single electron trajectories for given initial conditions and fields. The electron trajectory is used to calculate the intensity radiated by the particle per unit frequency ω and solid angle Ω [19]:

$$\frac{d^2I}{d\Omega d\omega} = \frac{e^2\omega^2}{4\pi c}\left|\int_{-\infty}^{\infty} \vec{n}\times(\vec{n}\times\beta)\, e^{i\omega(t-\frac{\vec{n}.\vec{r}}{c})}dt\right|^2, \qquad (2)$$

where $\vec{n}$ is the vector corresponding to the direction of observation, and $\beta = v/c$ the normalized electron velocity. The betatron x-ray beam profile is calculated by integrating Equation 2 over frequencies. Figure 1 shows an example of electron trajectory, with its corresponding betatron x-ray spectrum and beam profile. For this particular case, the parameters are $n_e = 10^{19}$ cm^{-3}, $\gamma = 200$, x_0=1 μm, $y_0 = 0$,

* This work was performed under the auspices of the U.S. Department of Energy under contract DE-AC52-07NA27344, and supported by the Laboratory Directed Research and Development (LDRD) Program under tracking code 13-LW-076.

Copyright © 2013 CC-BY-3.0 and by the respective authors

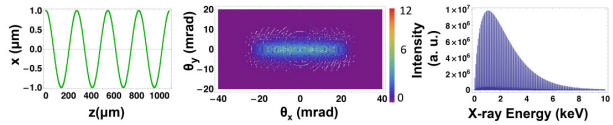


Figure 1: From left to right: example of an electron trajectory in the plasma, with the corresponding betatron spectrum observed on-axis and the x-ray beam profile.

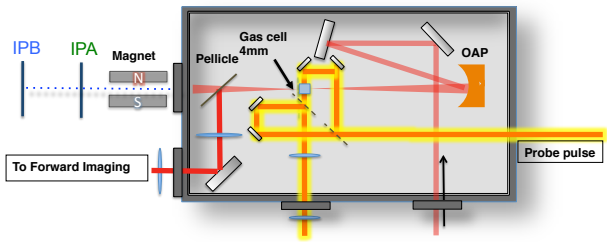


Figure 2: Experimental setup for betatron x-rays production and detection (see text for details).

and $\alpha = 0$. The trajectory was calculated using 3000 time steps (with each unit step $dt = 0.2c/\omega_p$). At each point of calculation of the trajectory, the spectrum and beam profile were calculated using frequency steps of 100 eV. For the chosen parameters, ω_c= 4.2 keV and $K \simeq 6$. The beam has a divergence of $1/\gamma$ and K/γ along the direction parallel and perpendicular to the plane of the oscillations, and the on-axis spectrum peaks at $\sim$ 2 keV. Although more computationally intensive, electrons trajectories obtained from PIC simulations can be post-processed using Equation 2 to calculate the spectrum and profile with a much better resolution[20].

EXPERIMENTAL SETUP

The experiments were conducted at the Jupiter Laser Facility (JLF) using the 200 TW Callisto laser system. Callisto can deliver up to 12 J in a 60 fs pulse (full width at half maximum, fwhm). The 13 cm diameter beam was focused by an off-axis parabola (f/8) onto the 500 μm entrance pinhole of a gas cell. The experimental setup is shown on Figure 2. The laser focal spot size w_0 was measured under vacuum at low power to be 12 μm. The back pinhole is 1 mm wide, and we have used different gas cell lengths (from 3 mm to 10 mm) as well as two-stage designs [21]. The cell was typically filled with He gas, but also with N, CO2, Ar and Ne. Electron densities ranging from 2×10^{18} cm^{-3} to 1.5×10^{19} cm^{-3} were measured for each shot with a 100 fs probe using interferometry in combination with an Abel-inversion code. The laser spot at the exit of the gas cell was imaged using a forward diagnostic, and spectrally resolved using grating and prism-based spectrometers. The electron beams were characterized using a two-screen spectrometer [22, 23]. This system provides an accurate measurement

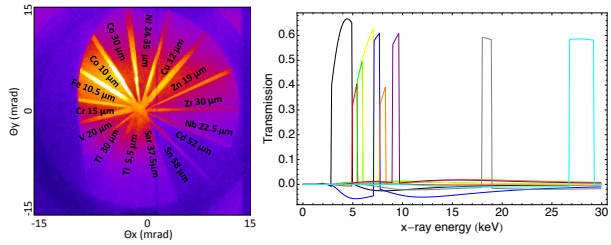


Figure 3: Betatron x-ray beam observed on IP$_a$ through the pie-shaped set of filters (left) and corresponding Ross filter pairs used to measure the spectrum (right). Each pair corresponds to the difference of signal observed through two specific filters. The nine pairs (and their respective mean energy E_n and bandwidth ΔE_n) are, from low to high x-ray energy: 5.5 μm Ti and 37.5 μm Saran (3.9 keV, 2 keV), 20 μm V and 30 μm Ti (5.2 keV, 0.45 keV), 15 μm Cr and 20 μm V (5.7 keV, 0.45 keV), 10.5 μm Fe and 15 μm Cr (6.5 keV, 1.05 keV), 10 μm Co and 15 μm Fe (7.4 keV, 0.53 keV), 24.35 μm Ni and 30 μm Co (8.3 keV, 0.52 keV), 19 μm Zn and 17.5 μm Cu (9.3 keV, 0.6 keV), 22.5 μm Nb and 30 μm Zn (18.5 keV, 0.9 keV), 58 μm Sn and 52 μm Cd (28 keV, 2.3 keV).

of the energy of the electrons, the vertical and horizontal angle that the electrons exit the plasma relative to the original laser axis, the divergence, and the electron charge. The electrons exiting the plasma are deflected in the vertical direction by a 21-cm-long, 0.42 Tesla dipole magnet. The electrons are detected by two successive image plates (IP$_a$ and IP$_b$) allowing for a unique solution to their energy and deflection, provided common spatial features can be identified on both image plates. Both the betatron x-ray beam profile and the x-ray spectrum were measured on the first image plate IP$_a$. At the vacuum/air interface, we used a 12 μm thick Al foil to block the 800 nm light from the laser as well as a 60 μm mylar window to hold vacuum. X-rays (profile or spectrum) are then measured on the image plate. To measure the x-ray spectrum from 1 keV to 30 keV, we used a set of Ross filter pairs, with transmission functions that provide narrow energy bands. The number of x-ray photons per unit energy is given by $N_{ph} = S_n/(T_n \Delta E_n)$, where S_n, T_n and ΔE_n are respectively the signal, transmission and bandwidth of a given energy band. Shown on Figure 3 is a typical x-ray beam observed on IP$_a$ through the pie-shaped sets of filters, as well as the energy bands used in the experiment.

RESULTS AND DISCUSSION

Betatron x-rays where observed in different gases. For the different profiles shown in Figure 4, observed on IP$_a$ through the filters, the x-rays where produced in a 4 mm gas cell containing mixed gases. Although these x-rays where produced in different gases, in order to make quantitative arguments it is important to note that they corre-

Copyright © 2013 CC-BY-3.0 and by the respective authors

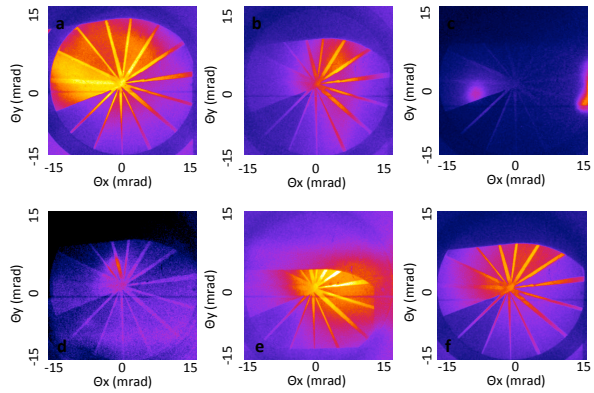


Figure 4: Betatron x-ray beam beam profiles observed on IP_a through the pie-shaped set of filters (see text for details). The gas composition for each shot was (from top left, clockwise): 100% He, 95% He and 5% Ar, 80% He and 20 % N2, 80% He and 20 % N2, 98% He and 2% Ar, 95% Ar and 5% He.

spond to different electron beam energies. The electron beam maximum energy (the largest contribution to the x-rays) is, for each of these shots: 234 MeV, 300 MeV, 385 MeV, 186 MeV, 280 MeV, 125 MeV (from top left, clockwise). Electron densities were in the 5×10^{18}- 1×10^{19} cm^{-3} range for each of these shots and $2 < a_0 < 2.5$. In some cases (Figure 4) the beam profile could be very well observed on both IP_a and IP_b with a 25% transmission from IP_a to IP_b. According to the theoretical and experimental response function and transmission curve of the image plates[24], it means that the beam contains a large amount of x-rays with energies above 20 keV. For this particular case, the electron beam peaked at $\sim$ 385 MeV, where most of the charge was located. Since the critical frequency scales with γ^2 and that in practical units, $\hbar\omega_c$[keV]=$5 \times 10^{-24} \times \gamma^2 n_e$[$cm^{-3}$]$r$[$\mu$m], it means that for $n_e = 10^{19}$ cm^{-3} and $\gamma = 750$, $r \simeq 0.7$ μm when the electrons reach their end energy. The drawback of using filter wedges in our experiments was the beam pointing jitter. As observed on Figure 4, the beam center location varies up to a few milliradians around the filter tips. Since the x-ray intensity and energy strongly depend on the angle of observation (Equation 2), making quantitative statements about the x-ray spectrum requires x-ray measurements be made at the same angular position with respect to the beam center.

CONCLUSION AND PERSPECTIVES

In conclusion we have observed betatron x-rays at energies beyond 20 keV in a collimated beam with <30 mrad divergence. X-rays have been observed in pure He, but also in He/N and He/Ar mixes, which opens several possibilities to improve and control the x-ray flux and spectrum of the source. By taking advantage of electron acceleration in the ionization-induced trapping regime, large amounts of charge can be trapped and produce bright betatron x-rays. Our preliminary measurements support betatron oscillations of $\sim$1 μm in the plasma, but also show that a simultaneous measurement of the x-ray beam profile and spectrum at a particular angle is necessary in order to make quantitative arguments about betatron x-rays production in this regime.

REFERENCES

[1] T.Tajima and J.M. Dawson *Phys. Rev. Lett.* **43**, 267–270 (1979).

[2] S. P. D. Mangles et al. *Nature* **431**, 535–538 (2004).

[3] C. G. R. Geddes et al. *Nature* **431**, 538–541 (2004).

[4] J. Faure et al. *Nature* **431**, 541–544 (2004).

[5] P. Emma et al. *Nat. Photon.* **4**, 641–647 (2010).

[6] M. Fuchs et al. *Nat. Phys.* **5**, 826–829 (2009).

[7] A. Rousse et al. *Phys. Rev. Lett.* **93**, 135005 (2004).

[8] S. Corde et al. *Rev. Mod. Phys.* **85**, 1–47 (2013).

[9] S. Wang et al. *Phys. Rev. Lett.* **88**, 135004 (2002).

[10] F. Albert et al. *Phys. Rev. E* **77**, 056402 (2008).

[11] S. Fourmaux et al. *New J. Phys.* **13**, 033017 (2011).

[12] R. C. Shah et al. *Phys. Rev. E* **74**, 045401(R) (2006).

[13] S. Kneip et al. *Nat. Phys.* **6**, 980–983 (2010).

[14] K. Ta Phuoc et al. *Phys. Rev, Lett* **97**, 225002 (2006).

[15] K. Ta Phuoc et al. *Phys. Plasmas* **14**, 080701 (2007).

[16] G. R. Plateau et al. *Phys. Rev. Lett.* **109**, 064802 (2012).

[17] S. Kneip et al. *Phys. Rev. ST Accel. Beams* **15**, 021302 (2012).

[18] W. Lu et al. *Phys. Rev. ST Acc. Beams* **10**, 061301 (2007).

[19] J.D. Jackson, [*Classical Electrodynamics*] (1998).

[20] J.L. Martins et al. *Proc. SPIE* **7359**, 73590V–1–73590V–8 (2009).

[21] B. B. Pollock et al. *Phys. Rev. Lett* **107**, 045001 (2011).

[22] B. B. Pollock et al. *Proceedings of PAC09, Vancouver, BC Canada*, 3035–3037 (2009).

[23] C. E. Clayton et al. *Phys. Rev. Lett* **105**, 105003 (2010).

[24] B. R. Maddox et al. *Rev. Sc. Instr.* **82**, 023111 (2011).

Copyright © 2013 CC-BY-3.0 and by the respective authors

PARTICLE-IN-CELL MODELING OF DIELECTRIC WAKEFIELD ACCELERATOR*

C.-K. Huang#, T. J. T. Kwan, D. Yu. Shchegolkov, and E. I. Simakov, Los Alamos National Laboratory, Los Alamos, NM 87545, USA

Abstract

We explore the potential of Dielectric Wakefield Accelerator (DWA) to achieve compact high gradient acceleration of high brightness beams required by an X-ray Free Electron Laser (FEL). Particle-In-Cell (PIC) simulations of a LANL DWA experimental design utilizing a double triangle beam current profile indicate accelerating field >100 MV/m and large transformer ratio are accessible while the longitudinal wakefield phase is insensitive to beam parameters and radial offset for fixed longitudinal profile. End-to-end simulation is developed, which allows us to validate and optimize future DWA experimental design.

INTRODUCTION

The pre-conceptual design for Matter-Radiation Interactions in Extremes (MaRIE) future signature facility at LANL calls for a 12 GeV electron linear accelerator for hard X-ray FEL production. MaRIE demands a high quality electron beam with the electron bunch charges of 0.1 to 1 nC, normalized RMS emittances of 0.1 to 1 mm, and RMS energy spreads of less than 0.1%. A major deficiency of the conventional accelerator technology is the accelerating gradient that is limited to a few tens of MV/m, which put a severe restraint on the cost and future upgrade of such facility.

The wakefield which causes the dominant energy spread in beams in conventional linacs can be used in carefully designed electromagnetic structures, specifically, dielectric loaded waveguides in this study, to generate extraordinary gradients and potentially small energy spreads for electron beam acceleration. In this paper we present simulation study to assess the characteristics of DWA and its potential applications in advance of experimental validation.

THEORY ON WAKEFIELD IN DWA

Figure 1 shows the schematic of the dielectric-lined metallic waveguide. Here we confine our study to a waveguide with cylindrical symmetric geometry. The theory of wakefield generation in a cylindrical dielectric waveguide is generally formulated in frequency domain and dated back at least to 1951 in Ref. [1], where Bessel's equation for the fields is solved with boundary matching conditions at the dielectric-vacuum interface. In general, the dielectric-lined waveguide supports infinite number of discrete Hybrid EM modes. The supported EM modes have low frequency cut-off determined by the geometric

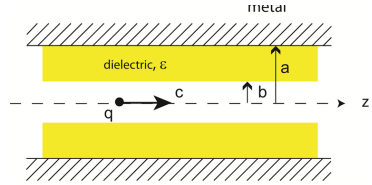


Figure 1: A schematic of the DWA consisting of a dielectric-lined metallic waveguide and an electron beam as the excitation source.

parameters of the waveguide and the dielectric constant ε of the liner materials.

However, for axial symmetric excitation (azimuthal mode number m=0), the TE and the TM modes are decoupled. For co-linear particle acceleration, the TM_{0n} modes are most useful for particle acceleration via the strong longitudinal electric field. While TE modes are detrimental to acceleration but can be used for beam deflection.

In Ref. [1], the dispersion of the TE, the TM and the HEM eigen modes are derived. Similar efforts are found in Ref. [2-4] for resonant modes driven by a moving particle. Here we adopt the notation used in Ref. [3] and summarize the key results relevant to our interests below:

(1) The conditional equation (dispersion relation) for modes with phase velocity $v_{ph} = \beta = v/c$,

$$C(s)=\frac{m^2sk^2}{a^2}\beta^2\left(\frac{\varepsilon-1}{1-\beta^2}\right)^2-s^3\left(\frac{kS_m'(sa)}{S_m(sa)}+\frac{sI_m'(ka)}{I_m(ka)}\right)\left(\frac{sI_m'(ka)}{I_m(ka)}+\frac{\varepsilon kR_m'(sa)}{R_m(sa)}\right)=0 \quad (1)$$

where $k^2=\omega^2(1-\beta^2)/v^2$, $s^2=\omega^2(\varepsilon\beta^2-1)/v^2$, $k_0=\omega/c$, and R_m, R'_m, S_m, S'_m are combinations of mth–order Bessel functions of the first and second kinds as defined in Eq. (35-38) in Ref. [3].

(2) The TM_{mn} longitudinal electric field for a single particle (Green's function),

$$E_{z,mn}(r,\theta,z-vt)=-8e\cos(m\theta)\cos\left(\frac{\omega}{v}(z-vt)\right)\times I_m(kr)I_m(kr_0)\times\frac{K_m(ka)}{I_m(ka)}\frac{T(s)}{sdC(s)/ds}\bigg|_{s=s_n} \quad (2)$$

where

$$T(s)=-\frac{m^2k^4\beta^2}{a^2}\left(\frac{\varepsilon-1}{1-\beta^2}\right)^2-s^2k^2\left(\frac{kS_m'(sa)}{S_m(sa)}+\frac{sI_m'(ka)}{I_m(ka)}\right)\times\left(\frac{sK_m'(ka)}{K_m(ka)}+\frac{\varepsilon kR_m'(sa)}{R_m(sa)}\right)$$

and s_n is the solution of Eq. (1).

To obtain the wakefield generated by a beam, one can convolve (sum) the single particle field from Eq. (2) with the beam profile. For smooth beams, this can be done

*Work supported by the LDRD program at LANL.
#huangck@lanl.gov

Copyright © 2013 CC-BY-3.0 and by the respective authors

with sufficient accuracy using the first few modes excited. However, this procedure will involve more modes if the beam profile has a large Fourier content. A more efficient method is the expansion of the fields into the orthonormal modes of the dielectric waveguide [5]. In addition, evanescence modes that co-move with the beam have to be taken into account for Gauss's law to be satisfied [6].

DWA PROTOTYPE EXPERIEMENT

We attempt to combine the concepts of the dielectric wakefield acceleration and the Emittance Exchanger (EEX) [7] in a unique way to experimentally demonstrate a high-brightness DWA with an acceleration gradient exceeding 100 MV/m and with less than 0.1% induced energy spread in the accelerated beam. The designed DWA parameters are listed in Table 1. ELEGANT simulation is used to track the beam through the beam line elements to the entrance of the DWA. More detail about the beam optics to produce the double triangle drive beam current profile and a witness beam can be found in Ref. [7]. Theoretical analysis [8] indicates that a double triangle drive beam can excite a wakefield with large (>2) transformer ratio.

Table 1: DWA Parameters

Parameter	Value
Inner/Outer radius b/*a*	0.57 mm / 0.662 mm
Dielectric constant ε	3.75
TM mode cutoff freq.	298 GHz
Drive/Witness beam charge	5 nC / 250 pC
Drive/Witness beam length	2.35 ps / 100 fs

PIC SIMULATION OF DWA

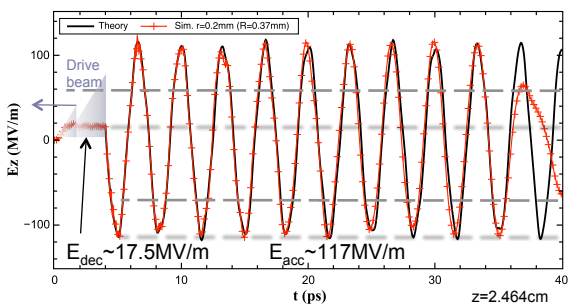


Figure 2: Comparison of theoretical prediction and MERLIN simulation result for the longitudinal wakefield driven by a double triangle beam.

We use PIC codes MERLIN [9] and LSP [10] to model the DWA in 2D cylindrical (r, z) and 3D (r, θ, z) geometries, respectively. We first conduct benchmark with analytic DWA theory presented in Ref. [3] using the same dielectric waveguide parameters defined in Table 1, but with a longer 4 ps, 5 nC, 100 MeV double-triangle beam of a temporal profile described by $f(t) = t$ for $0 \le t \le 0.85$ ps and $f(t) = t - 0.52$ (ps) for 0.85 ps $\le t \le$ 4 ps.

The MERLIN simulation uses stationary box of size 0.662 mm × 30 mm. The simulation box is divided into 133×6000 cells. The dielectric material is placed at 0.57 mm < r < 0.662 mm. The cell size is 0.00498 mm × 0.005 mm and the time step is 11.7 fs. The electron beam is injected from the boundary at z=0 mm. 1600 macro-particles per cell is used for the beam. Perfect Electric Conductor is used at the boundaries at z=0 mm and r = 0.662 mm. Transmitting boundary for particles and fields is used for the boundary at z=30 mm.

Benchmark Result

The longitudinal wakefield in the simulation and the analytical result based on the formalism described in previous section are compared in Fig. 2. The simulation lineout is taken at radius R=0.37 mm when the beam has propagated 2.464 cm into the DWA. Good agreement between the simulation and theoretical result is seen for the wakefield generated in the beam (the decelerating field) and behind (periodic accelerating and decelerating fields). Lineout on the axis shows similar agreement but is noisier. The deceleration field within the drive beam is nearly flat, which is a consequence of the double-triangle drive beam current profile and important for a high transformer ratio (in this particular example, E_{dec}≈17.5 MV/m and E_{acc}≈117 MV/m, leading to a transformer ratio of about 6.7). The difference at t >35 ps is due to the transient behavior of the wake excitation near the DWA entrance.

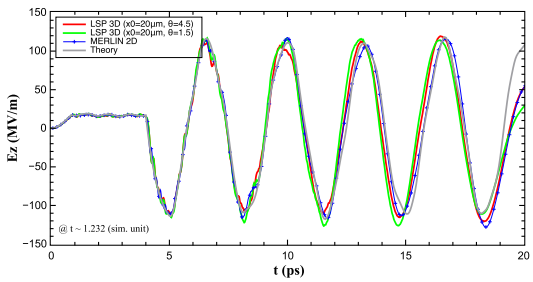


Figure 3: Comparison of the wakefield generated by on-axis beam (MERLIN) and off-axis beam (LSP, shifted by 20 μm at θ=0) at t=41 ps. The simulation lineouts are taken at R=0.04 cm and θ=1.5, 4.5.

When the transverse shape of drive beam is varied among a radial flat-top profile with radius of 0.2 mm (result shown in Fig. 2) and a Gaussian profile with spot size of 0.165 mm and 0.0825 mm respectively (not shown), the longitudinal dependence of the longitudinal wakefield shows little variation in overall shape but different noise levels (noisier for narrower beam). The former observation is consistent with Eq. (2) where the longitudinal and radial dependences are completely separate. On the other hand, higher longitudinal resolution simulation indicates that the noise is a numerical artifact, which mostly results from under-resolving the sharp edge of the double triangle beam.

Copyright © 2013 CC-BY-3.0 and by the respective authors

The wakefield of an off-axis beam in LSP simulation is compared to the MERLIN simulation and the theory in Fig. 3. The result shows that its longitudinal dependence is largely unaffected by the shift as the theory predicts.

End-to-End Simulation of DWA

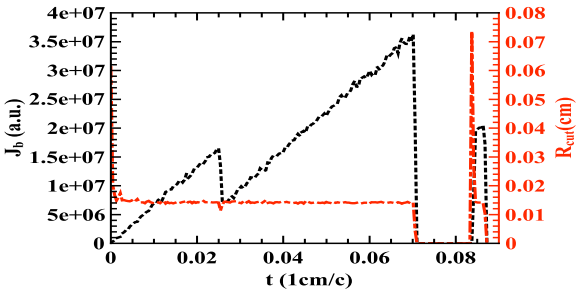


Figure 4: The on-axis beam current density (black) from the ELEGANT and the calculated cut-off radius (red) for the symmetrized Gaussian beam distribution.

Although our benchmark shows reasonable agreement between the DWA analytical theory and simulation, experiment conditions are often non-ideal, requiring more realistic simulation to validate the experimental observations and to optimize the design. It is important that this can be done in an end-to-end type simulation where beam particles are tracked through various beam-line elements and modeled self-consistently in the DWA. For this purpose, we started developing a link between the beam tracking code ELEGANT and the electromagnetic PIC codes. We have built such a prototype code for linking with the 2D cylindrical code MERLIN. The particles are taken from the ELEGANT simulation, resampled (described below) and injected into MERLIN simulation, while the transverse beam fields are first calculated in a quasi-static solver similar to Ref. [11] and subsequently imported into the MERLIN simulation as initial conditions. For relativistic beams, the beam fields are predominantly quasi-static fields and the longitudinal fields can be ignored, therefore a quasi-static solver would be sufficient (an advantage of this approach is the removal of the image charge at the DWA entrance in the simulation). Because of the cylindrical nature of the MERLIN code, we need to apply an extra step to slice and symmetrize the beam particle population (not necessary in 3D simulation). We assume the beam has a cylindrically symmetric Gaussian shape at the entrance of the DWA and calculate a cut-off radius according to the following formula for each slice,

$$Q(z) = 2\pi \int_0^{R_{cut}} \frac{J_{b0}(z)}{e} e^{-r^2/\sigma_r^2} r dr \qquad (3)$$

where $Q(z)$ and $J_{b0}(z)$ are the total charge and on axis longitudinal current density of the each beam slice from the ELEGANT data.

Figure 4 shows the calculated cut-off radius using this approach. Figure 5 shows the charge density of the beam injected into the MERLIN simulation and the longitudinal wakefield generated in the DWA.

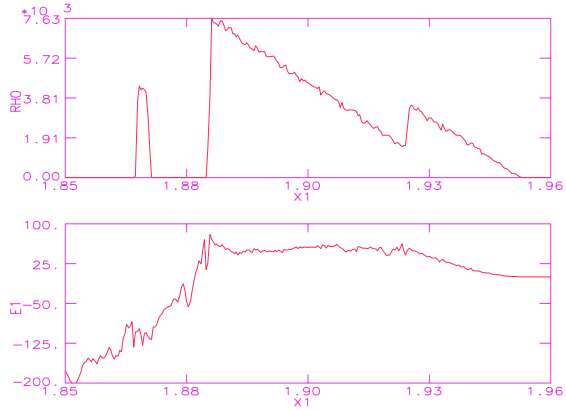


Figure 5: (Top) The on-axis beam charge density in an end-to-end simulation of DWA using MERLIN and input from ELEGANT and parameters in Table 1. Both drive and witness beams propagate to the left. (Bottom) The longitudinal wakefield generated (x_1 in cm and E_1 in MV/m). An accelerating field >100 MV/m together with a transformer ratio >3 are observed. The field noises are mostly due to the under-resolved sharp edge of the beam.

SUMMARY

We have carried out 2D and 3D PIC simulations of the DWA concept for potential application in high gradient compact accelerator. Simulations show good agreement with the analytic DWA theory for the accelerating field, the transformer ratio and the longitudinal dependence of the accelerating field with respect to the transverse beam shape and offset. End-to-end simulation shows that the LANL proof-of-principle DWA design can achieve an accelerating field >100MV/m and a transformer ratio >3.

REFERENCES

[1] G. Flesher et al., AIEE Transactions 70, 887 (1951).
[2] C. Chang et al., J. of Applied Phys. 41, 4493 (1970).
[3] M. Rosing et al., Phys. Rev. D, 42, 1829 (1990).
[4] K.-Y. Ng, Phys. Rev. D, 42, 1819 (1990).
[5] S. Y. Park et al., Phys. Rev. E, 62, 1266 (2000).
[6] C. Wang et al., Phys. Rev. ST-AB, 9, 031301 (2006).
[7] E. I. Simakov et al., "Shaping Electron Bunches For Ultra-Bright Electron Beam Acceleration In Dielectric Loaded Waveguides," TUPMA13, NA-PAC'13.
[8] K. L. F. Bane et al., IEEE Trans. on Nucl. Sci. 32, 3524 (1985).
[9] T. J. T. Kwan et al., in Monte Carlo Methods and Applications in Neutronics, Photonics, and Statistical Physics (New York: Springer-Verlag, 1985).
[10] T. Hughes et al., Phys. Rev. A, 464, 134 (2001).
[11] C. Huang et al., J. of Comp. Phys., 217, 658 (2006).

Copyright © 2013 CC-BY-3.0 and by the respective authors

BEAM PULSE SHAPING EXPERIMENTS FOR UNIFORM HIGH GRADIENT DIELECTRIC WAKEFIELD ACCELERATION*

D. Shchegolkov#, E.I. Simakov, Los Alamos National Laboratory, Los Alamos, NM 87545, USA
S. Antipov, Euclid TechLabs, Solon, OH 44139, USA
M. Fedurin, C. Swinson, Brookhaven National Laboratory, Upton, NY 11973, USA

Abstract

Dielectric wakefield accelerators (DWA) can produce high accelerating gradients and could possibly be used as afterburners for the accelerators of future free electron lasers (FELs) such as X-ray FEL of the proposed Matter-Radiation Interactions in Extremes (MaRIE) experimental facility at LANL [1]. With a double triangular drive bunch DWAs can produce a high transformer ratio. Also, by slightly customizing the time profile of the accelerated bunch it is possible to achieve high gradient uniformity along the accelerated bunch resulting in a low induced energy spread [2]. We plan to test a DWA which would incorporate all those benefits. The only way to produce the desired current profile of the main and drive bunches is to use current shaping with a beam mask. A variation of this technique is currently used at Accelerator Test Facility (ATF) at Brookhaven National Laboratory (BNL) which is available for outside users' experiments.

We report our recent beam shaping experiments at BNL for a transformer ratio test. We used a 58 MeV energy chirped electron beam and a single dogleg with a beam mask inserted in a region where the beam transverse size was dominated by the correlated energy chirp. Both measurement results and Elegant simulation data are presented.

INTRODUCTION

A demand for compact accelerators has recently resulted in an increased interest in dielectric wakefield accelerators (DWAs). The DWA is formed by one or several co-axial dielectric layers surrounded by metal cladding (Fig. 1) [3]. Wakefields in dielectric structures may reach gradients on the order of 10 GV/m [4] with 100 MV/m being demonstrated in multiple experiments [5]. They also have the remarkable property that the wakefield's axial electric field and the transverse electric field are transversely uniform and linear, respectively. This is due to the fact that the relativistic drive beam and the subsequent wakefield travel very nearly at the speed of light. If one can make the wakefield to be longitudinally constant along the bunch it will result in no induced energy spread within the bunch, leading to an extraordinary condition of preserving the main beam brightness while providing high gradient acceleration. We have realized that by a proper longitudinal customization of the accelerated beam the induced energy spread in a DWA can be made small enough (<0.1%) to satisfy tight requirements for X-ray free electron laser linac afterburner of the proposed Matter-Radiation Interactions in Extremes (MaRIE) facility at LANL [1, 2, 6].

An important characteristic of the wakefield acceleration is a transformer ratio (TR). It is the ratio of the peak accelerating gradient to the peak decelerating gradient experienced by the drive bunch, and thus it determines how long the drive bunch will be stable before some part of it decelerates to low energies. For a finite length longitudinally symmetric bunch the TR can never exceed 2 [7]. An enhanced TR can be achieved with a ramped beam or a ramp-profiled bunch train [7]. Recently a Double Triangular (DT) beam shape was proposed making possible high TRs with almost uniform drive bunch deceleration [8]. In the DT bunch the TR is approximately proportional to the beam length in wavelengths of the induced wakefield radiation and thus can be made very large.

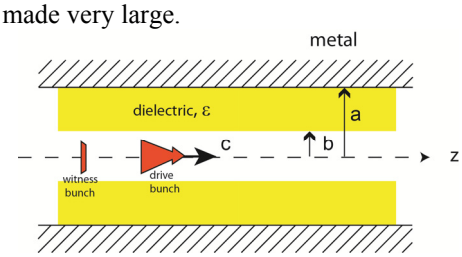


Figure 1: The schematic of a dielectric loaded waveguide with shaped electron bunches traveling on axis.

The main obstacle on the way to experimental demonstration of superior properties of the DWA with a DT drive beam is that the DT bunch shapes are difficult to produce in the submillimeter scale required for ~300 GHz DWAs using conventional methods based on direct beam current modulation. One of the actively popularized methods to shape the beam currents in such a small scale is based on an emittance exchanger technique [9]. It is easy to shape the transverse beam profile using a mask. The emittance exchanger allows to convert a transverse particle distribution into longitudinal. However this method is relatively new and not available at any user accelerator facility although it has already been verified at the Fermilab A0 Photoinjector [10]. A relatively simpler technique is used at Accelerator Test Facility (ATF) of BNL [11] which also allows current shaping on the required scale. It utilizes an energy chirped beam which is cut with a transverse beam mask placed inside of the beamline dispersive region where one transverse coordinate is linearly related to both the particle energy and arrival time.

We studied the possibility of using the ATF facility at BNL for demonstrating high gradient high transformer ratio operation of a DWA with a double triangular beam.

*Work supported by LDRD program at LANL
#d_shcheg@lanl.gov

Copyright © 2013 CC-BY-3.0 and by the respective authors

THE BEAMLINE SET-UP

The electron beam at the ATF is produced with an S-band RF photoinjector followed by an S-band linac. After the linac the beam can be directed to one of three different beamlines. For our experiment in May, 2013 we used the beamline #2. The system parameters relevant to the experiment are listed in Table 1. A linear energy chirp in time was produced by accelerating the beam off the crest of the RF wave.

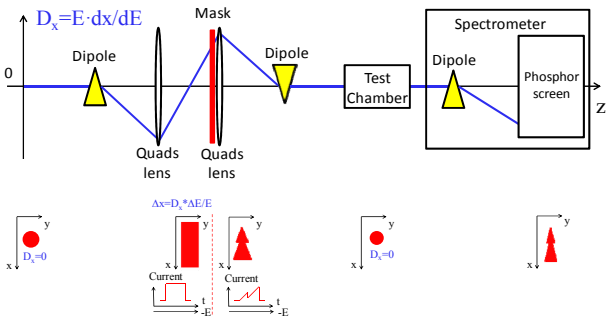


Figure 2: Principal of beam shaping: simplified scheme with only essential beamline elements pictured. Top plot shows dispersion evolution caused by the beamline elements. Bottom plots show particle distributions in different locations along the beamline.

Table 1: ATF Beamline #2 Beam Parameters.

Beam energy	58 MeV
Beam current	100 A
Pulse shape	Square
Pulse duration	5 ps
Repetition rate	1.5 Hz
Beam transverse profile	Gaussian
Normalized transverse emittances	≈ 2 mm*mrad
Typical energy chirp, ΔE/E	1.5%
Beamline dispersion, D_x	≈ 1 m

Figure 2 illustrates the principal of beam shaping employed at the ATF. Several quadrupole magnets are used inside of the dispersion region in the dogleg to minimize the beam x-beta function on the mask to make the beam size due to the dispersion strongly dominate over the beam size caused by a transverse emittance. The dogleg is followed by a zero dispersion region with a vacuum chamber where a DWA can be installed on a motorized mount. The last beamline element is a spectrometer. The spectrometer consists of a single dipole which produces dispersion, a phosphor coated metal screen and a high resolution camera. It also has a set of quadrupole magnets for minimizing the beam x-beta function on the screen. The brightness of pixels in the pictures from the camera is proportional to the density of electrons hitting the surface of the screen. There is also a number of pop-up phosphor screens with cameras along the beamline which are used to visualize the beam during a tuning of magnets process which had to be performed every day after the accelerator was warmed up. The beam parameters, including emittances, varied at the linac output quite substantially from day to day. Figure 3 shows the plots of the beam twiss parameters inside the whole beamline starting from the linac output with magnets' currents optimized in MAD-X [12] for beam shaping for some realistic set of initial beam parameters. At the top of Fig. 3 there is a scheme with all magnets, excluding weak dipole magnets used for fine beam steering, positioned along the beam path.

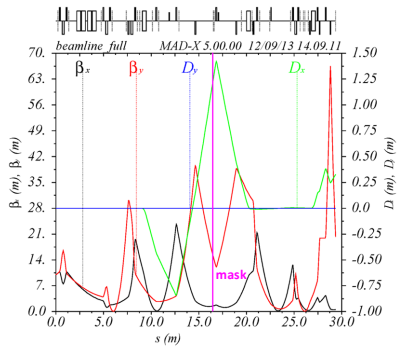


Figure 3: Twiss parameters as modeled in MAD-X vs the beam propagation distance with the mask location marked.

BEAM SHAPING EXPERIMENT

We used a mask on a motorized holder with three openings in the form of arrows, one of them being double triangular (Fig. 4). The mask was mounted on a motorized holder, its orientation corresponded to the tail of the arrows always irradiated by higher energy electrons.

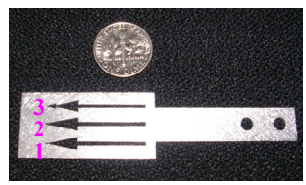


Figure 4: Aluminum mask used in the experiment.

Figures 5-7 show experimental results. The beam had a close to a Gaussian shape with no noticeable x-energy correlation left after the dogleg (Fig. 5). However the spectrometer revealed a strong energy spectrum distortion. Also, depending on the sign of the beam energy chirp the energy spectrum looked either stretched or compressed. The observed behavior was consistent with the coherent synchrotron radiation (CSR) effect making the beam tail lose more energy than the head (Fig. 6).

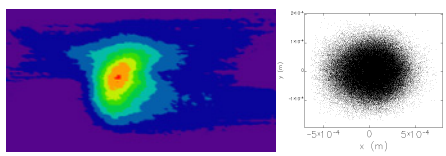


Figure 5: The beam in the test chamber: pictured with a camera using a phosphor screen (left), and simulated (right).

Copyright © 2013 CC-BY-3.0 and by the respective authors

Another evidence denoting the charge related effects was that a low charge bunch transmitted through the off beam center mask opening was reproduced on the spectrometer with minimal distortions (Fig. 7).

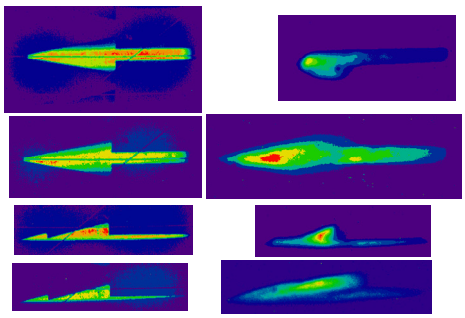


Figure 6: Left column: the beam profiles measured immediately after the mask. Right column: the beam profiles on the spectrometer, all at the same horizontal scale. Upper two rows are for a single triangular arrow mask, lower two rows are for a double triangular arrow mask (due to mechanical constraints only half of it was illuminated with the beam). For each mask the upper two pictures are for the arrow looking forward in the direction of propagation, and the lower two are for the backward arrow orientation.

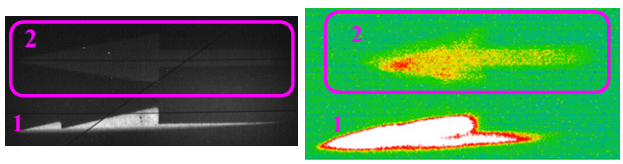


Figure 7: A low charge arrow #2 on the mask (left) is nicely reproduced on the spectrometer (right).

SIMULATIONS

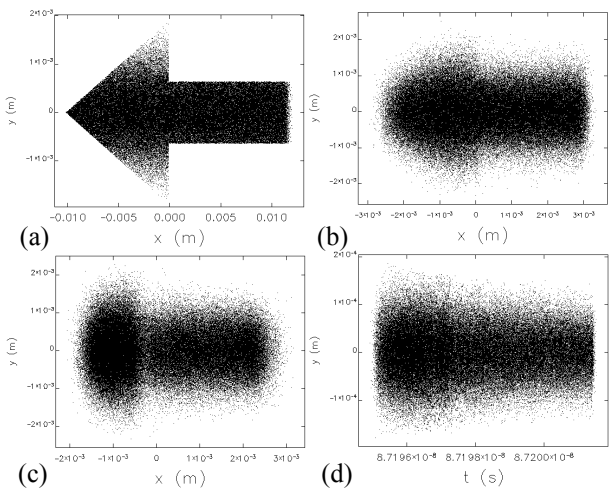


Figure 8: Simulated distribution of electrons in the beam: (a) immediately after the mask; (b) on the spectrometer obtained using the transfer matrix method; (c) on the spectrometer and (d) in the test chamber with account for the LSC effect in drift spaces & CSR in the dipole bends.

In order to confirm the nature of the effects observed in the experiment we performed simulations in Elegant [13]. We converted the MAD-X beamline model with parameters used to obtain the plot in Fig. 3 into Elegant format and wrote a script to incorporate the mask as an x-y filter element in Elegant. Elegant is a matrix code, for each beamline element it uses a transfer matrix in the form of tensors accounting for up to the 3rd order nonlinearities. It can also account for a longitudinal space charge (LSC) and coherent synchrotron radiation (CSR) by doing a specified number of kicks on the length of each beamline element. Figure 8 demonstrates the severity of the beam shape distortion inside the beamline for the initially 100 A beam. The beam energy spectrum looks different compared to its time profile (Fig. 8(c)-(d)).

CONCLUSION

We have carried out a beam shaping experiment at the ATF BNL user facility. We tried two different masks with single and double triangular shapes. For nominal current of 100 A we observed a strong CSR effect which considerably degraded the output beam energy spectrum. At the same time for a low charge beam the shaping seemed to work very well. A simple dipole-based spectrometer installed on the beamline was not helpful in characterizing the beam time profile. An RF deflecting cavity is needed to be able to resolve the beam shape in time. The deflecting cavity is going to be implemented on the beamline in the nearest future. Its addition will allow to acquire both the current shape and the energy spectrum of the beam needed for a DWA experiment with a double triangular beam. However simulations show that obtaining a perfect double triangular beam is challenging due to space charge related effects and beamline nonlinearities. Probably, some of these effects can be taken care of by customizing the mask shape.

REFERENCES

[1] http://marie.lanl.gov.
[2] E.I. Simakov, B.E. Carlsten, D. Shchegolkov, AIP Conf. Proc. 1507, pp. 634-638 (2012).
[3] W. Gai, et al, Phys. Rev. Lett., **61**, 2756 (1988).
[4] M.C. Thompson, et al, Phys. Rev. Lett., **100**, 214801 (2008).
[5] M.E. Conde, DOI: 10.1109/PAC.2007.4441323 (2007).
[6] This conference, paper TUPMA13 by E.I. Simakov.
[7] K. Bane, et al, IEEE Trans. Nucl. Sci. NS-32, 3524 (1985).
[8] B. Jiang, et al, Phys. Rev. ST Accel. Beams **15**, 011301 (2012).
[9] D. Xiang and A. Chao, 2011 PAC Proc, WEP044, New York, NY, USA (2011).
[10] J. Ruan, et al, Phys. Rev. Lett. 106, 244801 (2011).
[11] P. Muggli, et al**,** PRL 101, 054801 (2008).
[12] http://mad.web.cern.ch/mad/.
[13] M. Borland, Advanced Photon Source LS-287, September 2000.

Copyright © 2013 CC-BY-3.0 and by the respective authors

UPDATE ON FABRICATION AND TUNING OF THE PHOTONIC BAND GAP ACCELERATING STRUCTURE FOR THE WAKEFIELD EXPERIMENT*

Evgenya I. Simakov#, Sergey Arsenyev, Randall L. Edwards, Samuel Elson, Cynthia Heath, David Lizon, and William Romero, Los Alamos National Laboratory, Los Alamos, NM 87545, U.S.A.

Abstract

We designed an experiment to conduct a detailed investigation of higher order mode spectrum in a room-temperature traveling-wave photonic band gap (PBG) accelerating structure at 11.7 GHz. It has been long recognized that PBG structures have great potential in reducing long-range wakefields in accelerators. The first ever demonstration of acceleration in room-temperature PBG structures was conducted at MIT in 2005. Since then, the importance of that device has been recognized by many research institutions. However, the full experimental characterization of the wakefield spectrum in a beam test has not been performed to date. The Argonne Wakefield Accelerator (AWA) test facility at the Argonne National Laboratory represents a perfect site where this evaluation could be conducted with a single high charge electron bunch and with a train of bunches. We describe the design of the accelerating structure that will be tested at AWA in the near future. We also report the results of fabrication and tuning of PBG cells and the initial cold-testing of the traveling-wave accelerating structure. We discuss the plan for the wakefield experiment.

INTRODUCTION

The next generation of linear colliders with multi-hundred GeV to TeV beam energies pushes the frontiers of the current beam physics and technology with the goal of obtaining high luminosity of the beam and avoiding bunch to bunch beam breakup. Thus, the aaccelerating cavities for the future linear colliders must be selective with respect to the operating mode, and higher order mode (HOM) wakefields that affect the quality of the beam must be suppressed. Photonic Band Gap [1] (PBG) cavities have the unique potential to absorb all HOM power and greatly reduce wakefields. A PBG structure or simply, photonic crystal, represents a periodic lattice of macroscopic components (e.g., rods), metallic, dielectric or both. For accelerator applications, two-dimensional PBG resonators based on arrays of metal rods are commonly employed. The first ever demonstration of acceleration in a PBG resonator was conducted at Massachusetts Institute of Technology (MIT) in 2005 [2]. Since then, the importance of PBG structures for accelerators has been recognized by many research institutions worldwide.

*Work is supported by the U.S. Department of Energy (DOE) Office of Science Early Career Research Program.

#smirnova@lanl.gov

Two attempts to experimentally study wakefields in PBG accelerators were conducted to date, but were incomplete [3,4]. The MIT team [3] cold-tested the 6-cell PBG accelerator structure of [2] in a wide frequency range and recorded the wakefield spectrum. They also ran a beam test with a train of 200 picosecond electron bunches with the charge of 1-18 pC per bunch. Radiation was observed at the output port of the PBG structure and had a quadratic scaling with current at 17 GHz and at 34 GHz. However, with the MIT setup, observation of significant wakefield radiation into other important HOMs, such as a dipole mode was impossible. A more advanced test was conducted by a team at Argonne National Laboratory (ANL) [4]. They observed wakefields in a three-cell X-band standing wave PBG structure when driven by a single electron bunch with a charge up to 80 nC. Major monopole and dipole modes were identified in the collected signal. A variable delay low charge witness bunch following a high charge drive bunch was used to calibrate the gradient. However, this test was not the test of the actual traveling-wave PBG accelerator. At this point, the full experimental characterization of the wakefield spectrum in a traveling-wave PBG accelerator is overdue.

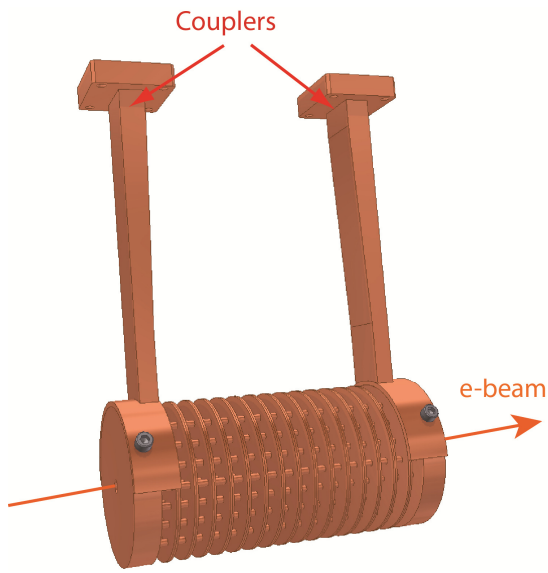


Figure 1: A 16-cell traveling-wave PBG accelerator structure with two waveguide couplers.

We have initiated a project at Los Alamos National Laboratory (LANL) to conduct the full experimental characterization of the wakefield spectrum of a traveling-wave PBG accelerator structure. We plan to put together an 11.7 GHz 2π/3-mode accelerating structure of 16 PBG

Copyright © 2013 CC-BY-3.0 and by the respective authors

cells, install it at the Argonne Wakefield Accelerator (AWA) facility and test it with a high charge (up to 100 nC) electron bunch (as shown in Figure 1) to record the full traveling-wave (TW) wakefield spectrum.

DESIGN OF 11.7 GHZ TW PBG ACCELERATOR

We designed a 16-cell traveling-wave 2π/3-mode PBG accelerator structure with characteristics similar to the 6-cell MIT PBG structure. The PBG accelerator was designed at the frequency of 11.7 GHz, which is 9 times the frequency of the AWA (1.3 GHz). The design of the traveling-wave cells was conducted with the CST Microwave Studio [5] and benchmarked with the HFSS [6]. The exact dimensions and the accelerator characteristics of the structure are summarized in Table 1. The structure has a slightly bigger beam opening and slightly larger group velocity than the scaled MIT structure to be more appropriate and attractive for higher current operations. We plan to have 14 traveling-wave and 2 coupler cells in the structure, 16 cells total.

Table 1: Dimensions and accelerator characteristics of the 11.7 GHz traveling-wave PBG accelerator.

Frequency	11.700 GHz
Phase shift per cell	2π/3
Q_w	5000
r_s	72.5 MΩ /m
$[r_s/Q]$	14.5 kΩ /m
Group velocity	0.015c
Gradient	15.4 √P[MW] MV/m
Rod radius, a (TW cell/coupler cell)	1.55 mm/1.54 mm
Lattice vector, b (TW cell/coupler cell)	10.33 mm/10.30 mm
a/b	0.150
Length of the cell	8.53 mm
Diameter of the iris	6.31 mm = 0.250 in
Thickness of the iris	1.90 mm = 0.075 in
OD of the cavity	76 mm = 3 in

The coupler cells were designed with the HFSS using a periodic voltage standing-wave ratio method. WR-90 waveguides were attached to the coupler cells, and three rods next to the waveguides were removed from the PBG structure to achieve critical coupling for the fundamental mode. The period and the diameters of the rods in the coupler cell differed slightly from the dimensions of the TW cell (Table 1) [7].

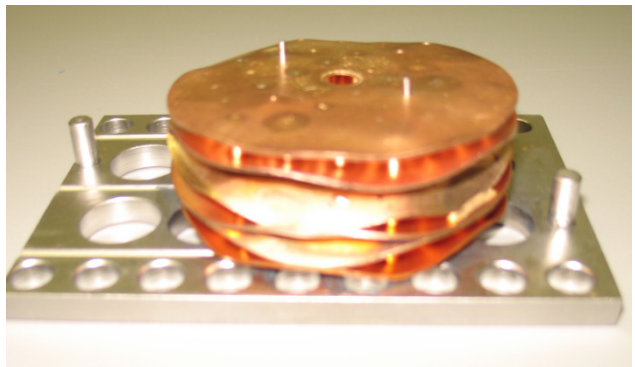


Figure 2: Photograph of the electroformed cells destroyed by brazing.

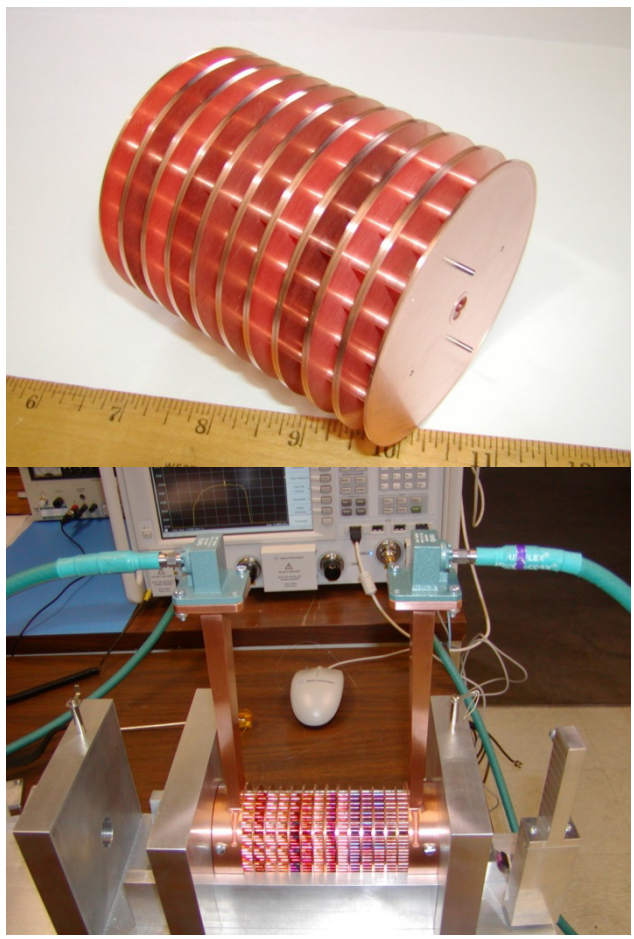


Figure 3: Photographs of the electroformed 11.7 GHz PBG cells and the assembled 16 cell PBG structure on a cold test bench.

FABRICATION AND COLD TESTS OF THE 16-CELL STRUCTURE

Three TW test cells were fabricated first in order to benchmark the tuning and brazing processes before

Copyright © 2013 CC-BY-3.0 and by the respective authors

fabricating and assembling the 16 cell structure [7]. The cells were electroformed by Custom Microwave, Inc. and then tuned at LANL with the same etching procedure as described in [7,8]. The cells were then brazed in a hydrogen furnace and this step was totally unsuccessful. The internal stresses in electroformed cells caused deformations in the structure and the cells were destroyed (Figure 2). The lesson learned was that the electroformed structures cannot be brazed and the future 16-cell structure will have to be bonded instead of brazed.

Next we fabricated PBG cells for the 16-cell structure. The total number of fabricated cells was 29, which included 25 TW cells and 4 coupling cells. The photographs of the several TW cells joined together and the assembled 16-cell PBG structure with waveguides are shown in Figure 3. The PBG cells were fabricated with small rings surrounding the beam holes which were elevated above the end surface and polished to mirror finish (Figure 3). This would ensure good electrical contact between the cells after bonding with non-conductive vacuum-compatible epoxy.

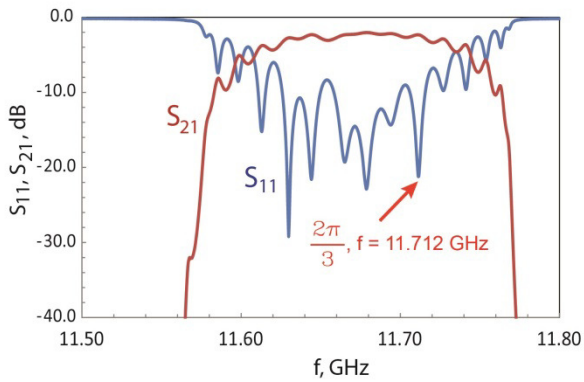


Figure 4: Transmission and reflection through the assembled 16 cell PBG structure.

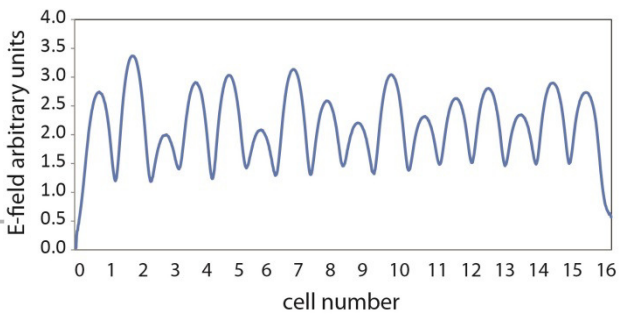


Figure 5: Bead pull field profile measurement in the 16 cell PBG structure.

The cells were tested with a network analyser and it was concluded that the frequencies of the end cells were close to the design value and the frequencies of TW cells were high. The frequencies of individual cells differed between each other all within 10 MHz frequency interval. This corresponded to approximately 0.1 thousand of an inch difference in the actual dimensions of cells. The two etching cycles were conducted to lower the frequencies of the TW cells following the procedures described in [7,8]. Each cycle removed 0.1 thousand of an inch or less off the diameter of each PBG rod. The frequencies of all PBG cells were equalized and lowered.

The transmission and reflection from the assembled PBG structure after the two etch cycles is shown in Figure 4. The $2\pi/3$-mode is the 6^{th} dip from the right on the reflection curve, at the frequency of 11.712 GHz. The reflection curve shows that the frequencies of TW cells were still higher than the target frequency and more etching cycles are needed.

The same conclusion can be made from the field profile measured with a bead pull method (Figure 5). The electric field in different cells of the structure differs slightly. The measurement of the phase shift between the cells confirms that the frequencies of the TW cells still need to be tuned down.

Another etching cycle is currently underway. Once the etching is complete, it will be followed by bonding.

CONCLUSION AND PLANS

We have planned an experiment to conduct a complete evaluation of the higher order mode wakefields in a room-temperature traveling-wave open photonic band gap accelerator structure at the frequency of 11.7 GHz. A 16-cell TW PBG accelerator structure was fabricated and is currently undergoing tuning. Once tuned, the cells will be bonded together. The structure will go on the Argonne Wakefield Accelerator beamline in 2014. We plan to drive the structure with a single 100 nC electron bunch first and look at the spectrum of the wakefields at the waveguide outputs and with antennas at the side of the structure. We might be able to conduct some experiments with a train of bunches and with a low charge witness bunch.

REFERENCES

[1] E. Yablonovitch. Phys. Rev. Lett., 258, p.2059, (1987).
[2] E.I. Smirnova, A.S. Kesar, I. Mastovsky, M.A. Shapiro, and R.J. Temkin, Phys. Rev. Lett. 95(7), p. 074801 (2005).
[3] R.A. Marsh, M.A. Shapiro, R.J. Temkin, E.I. Smirnova, J.F. DeFord., NIMA 618, 16 (2010).
[4] C. Jing, F. Gao, S. Antipov, Z. Yusof, M. Conde, J. G. Power, P. Xu, S. Zheng, H. Chen, C. Tang, and W. Gai, PR STAB 12, 121302 (2009).
[5] Microwave Studio, Computer Simulation Technology, www.cst.com.
[6] Ansys HFSS, Ansys Inc., www.ansys.com.
[7] Evgenya I. Simakov and Randall L. Edwards, Proceedings of IPAC Proceedings of 2012 International Particle Accelerator Conference, 2012, p. WEPPP033.
[8] E.I. Smirnova, I. Mastovsky, M.A. Shapiro, R.J. Temkin, L.M. Earley, R.L. Edwards, PR STAB 8(9), 091302 (2005).

Copyright © 2013 CC-BY-3.0 and by the respective authors

BEAM BRIGHTNESS BOOSTER WITH IONIZATION COOLING

V. Dudnikov#, R. Johnson, L. Vorobiev and C. Ankenbrandt, Muons, Inc. Batavia, IL, 60510 USA

Abstract

The brightness and intensity of a circulating proton beam can be increased up to the space charge limit by means of charge exchange injection or by electron cooling but cannot be increased above that limit. Significantly higher brightness can be produced by means of charge exchange injection with space charge compensation [1]. The brightness of the space charge compensated beam is limited at low level by development of the electron-proton (e-p) instability. Fortunately, e-p instability can be self-stabilized at a high beam density. By development of surface plasma sources (SPS) with cesiation and RFQ, H^- beam injectors were prepared with intensity ~0.1 A. We discuss possibilities for production of a "superintense" circulating beam with intensity and brightness far above the space charge limit. A beam brightness booster (BBB) for significant increase of accumulated beam brightness is discussed. Ionization cooling can be used for suppression of the beam brightness dilution. The superintense beam production can be simplified by development of a nonlinear nearly integrable focusing system with broad spread of betatron tunes and the broadband feedback system for e-p instability suppression [2].

INTRODUCTION

Charge Exchange Injection (CEI) was developed for increasing the circulating beam intensity and brightness above injected beam parameters by multiturn injection of beam into the same transverse phase space areas [3-5]. At that time the intensity of H^- beam from plasma source was below 5 mA with normalized emittance ~1 π mm mrad. The intensity of H^- beam from charge exchange sources was up to 15 mA, but the brightness B of this H^- beam was ~100 times less than the brightness of a primary proton beam because only 2% of the proton beam was converted into the H^- ions. In this situation the increase of the circulating beam brightness up to 100 times was necessary for reaching of the brightness of primary proton beam which can be used for one or several turn injection. The intensity and brightness of H^- ion beams were increased by orders of magnitude by adding a trace of cesium into gas discharges (cesiation effect) [6]. After development of surface plasma source (SPS) with cesiation, the H^- beam intensity was increased up to 0.1 A with emittance ~0.2 π mm mrad [7,8], so the brightness of injected beam approached the space charge limit of real accelerators such as the Fermilab Booster [9]. With such beam the further increase of circulating beam brightness is impossible, but CEI is routinely used to increase the circulating beam intensity by many orders of magnitude by injection into different parts of the transverse phase space (painting in the transverse phase space) [5, 9, 10]. Further increase of circulating beam brightness is possible by using multiturn CEI with space charge compensation by particles with opposite charge (electrons or negative ions) [1, 11, 12]

Unfortunately, such possibility is complicated by strong transverse two-beam instability driven by beam interaction with accumulated compensating particles in the circulating beam.

The strong instability with fast loss of a bunched beam was discovered at 1965 in a small scale proton storage ring (PSR) during development of charge exchange injection and was stabilized by feedback [3, 4, 5, 12, 13]. This instability was explained in [4] as an inverse variant of the strong transverse instability of circulating electron beam caused by the interaction with compensating ions (beam- ion instability) predicted in 1965 by B. Chirikov [14]. An analogue of this instability, electron-proton (e-p) instability with very low threshold was observed experimentally at the same time during accumulation of a coasting beam [1, 5, 11-13]. The e-p instability of coasting beam was in good agreement with theory [14, 15].

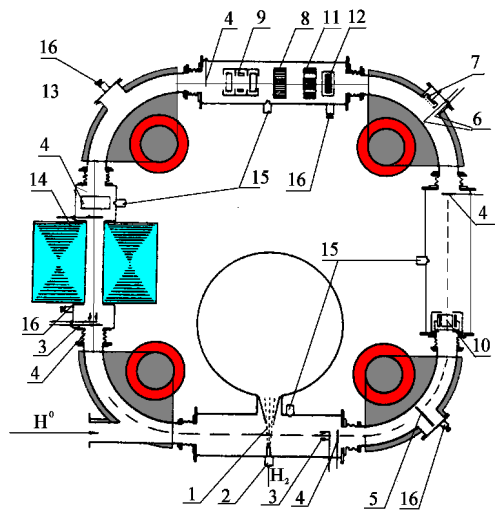


Figure 1: Schematic of storage ring with diagnostics and control. 1-stripping gas target; 2-gas pulser; 3-Faraday Cup; 4-Quartz screen; 5, 6-moving targets; 7-ion collectors; 8-current monitor; 9-Beam Position Monitor; 10-Quadrupole pick ups; 11-magnetic BPM; 12-beam loss monitor; 13-detector of secondary particle density; 14-inductor core; 15-gas pulses; 16-gas leaks.

Superintense circulating beam with intensity far above the space charge limit was produced in BINP in a simple race track ring [5,12,13,16] shown in Fig. 1.

#Vadim@muonsinc.com

Copyright © 2013 CC-BY-3.0 and by the respective authors

H^0 beam with current up to 8 mA, energy 1 MeV, produced by stripping of H^- beam, is injected by CEI with electron stripping in the supersonic hydrogen jet into race track with a bending radius 42 cm, magnetic field 3.5 kG, index n=0.2-0.7, straight sections 106 cm, aperture 4x6 cm^2, revolution frequency 1.86 MHz. An inductive core was used for compensation of the ionization energy loss of ~200 eV per turn, which produces some effects of an ionization cooling [3].

A superintense proton beam with intensity ~1 A corresponding to the calculated vertical betatron tune shift ΔQ=0.85x6 =5.1 with Q=0.85 was accumulated with e-p instability self-stabilization by fast accumulation of high circulating beam current and accumulation of plasma from residual gas ionization.

This self- stabilization of the transverse e-p instability in the PSR was explained by increasing the beam density and increasing the rate of secondary particle generation above a threshold level with fast decrease of the unstable wavelength λ below the transverse beam size *a*. (i.e. the sum of beam density n_b and ion density n_i is above a threshold level):

$$(n_b + n_i) > \beta^2 / 2\pi r_e a^2 \; ; (r_e = e^2/mc^2).$$

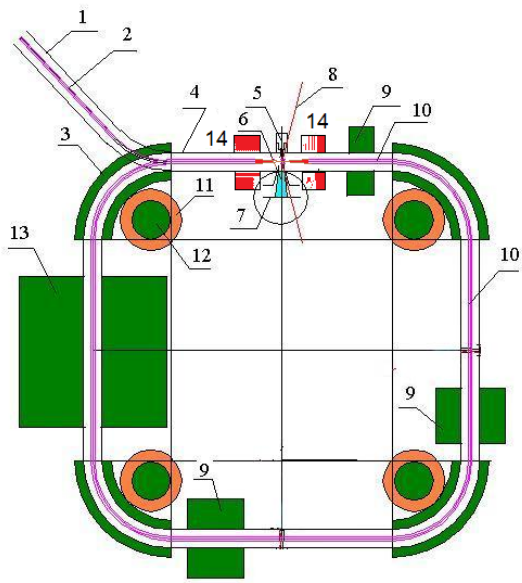


Figure 2: Schematic of BBB of circulating proton beam with thin targets accompanied by enhanced ionization cooling. 1- beam line for transportation of injecting H- beam; 2- injecting beam of H-; 3-bending magnets; 4- vacuum chamber of storage ring; 5- generator of supersonic jet- stripping, reaction target; 6- supersonic jet, stripping-reaction target; 7- pump-recirculate of target jet; 8- cone of resonant gamma rays; 9, 13- iron core for inductor for compensation of beam energy loss in first target; 10-circulating proton beam; 11- magnetic coil; 12- yoke of bending magnet; 14- magnetic lenses for beam focusing to the target.

In high current proton rings it is possible to reach this "Island of stability" by fast, concentrated charge exchange injection without painting and enhanced generation of secondary plasma as it was demonstrated in the small scale PSR at the BINP [5, 12, 13, 16]. The beam brightness loss through proton scattering and ionization loss straggling can be compensated by improved ionization cooling with beam focusing to the target by lenses (14) as shown in Fig. 2. As a prototype of magnetic system it is possible to use a round beam collier VEPP 2000 from BINP with a stron focusing of beams into the colliding point by strong solenoids [17].

The broad betatron tune and corresponding Landau damping are important for increasing the threshold of e-p instability [14,15]. This inference is supported by the increase of instability threshold with increase of bunching RF voltage, increasing of separatrix size and energy spread. With high RF voltage only the central (coherent) part of the beam is unstable and lost.

With a broad betatron tune spread it is possible to produce stable space charge compensated ion and electron beams because e-p instability (electron cloud effect, ion instability) should be suppressed by Landau damping [13, 14, 15].

We hope that production of superintense beam can be easier in BBB with a stable close to integrable nonlinear focusing lattice proposed in [2].

A possible design of such a storage ring is shown in Fig. 3. In design of the storage ring with nonlinear focusing it is good to have possibility for high brightness beam accumulation by charge exchange injection. For energy up to 10 MeV it is possible to use a supersonic gas jet as a stripping target as was done in the small scale proton storage ring in BINP [3-5]. An RFQ and small linac can be used as injector with H^- beam ~100 mA, 2-10 MeV.

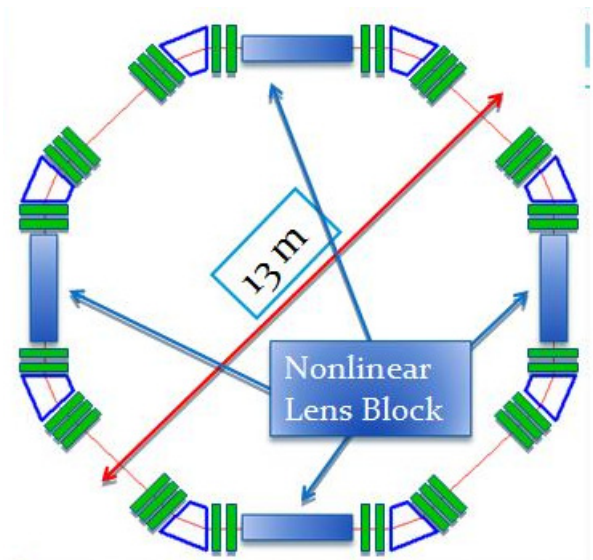


Figure 3: Schematic of storage ring with a nonlinear close to integrable focusing system from [2].

Copyright © 2013 CC-BY-3.0 and by the respective authors

Some other methods of space charge compensation were discussed in [9, 18].

A circulating proton beam ~10 or 100 A can be accumulated. Such a beam can be used for realization of resonance reaction induced by circulating ions in a thin internal target.

The plasma accumulation during accumulation of superintense beam was discussed in [11].

A comprehensive review of e-p instability in different accelerators and storage rings was presented in [19]. Theoretical estimation of self-stabilization is presented in [20]. Practical application of space charge neutralization in advanced ion implanters is considered in [21].

With the barrier bucket acceleration, tried at the AGS in the collaboration between KEK and BNL [21], it is possible to accelerate a long uniform bunch of ions without loss of space charge neutralization. Acceleration of compensating electrons should be suppressed by magnetic field as in [12, 16].

CONCLUSION

BBB with space charge neutralized superintense ion beams with intensity far above the space charge limit can be useful in an induction Linac with recirculation and for inertial fusion, neutron, antiproton, and muon generators, resonant reaction with internal targets, high power density physics, FFAG accelerators, and inductive synchrotrons.

It is very attractive to repeat an accumulation of superintense ion beam with modern high current injectors. High current density beam should be stable without secondary ions.

The barrier bucket acceleration [22] can be used for acceleration of the long uniform bunch of ions without loss of space charge neutralization.

Now from RFQ it is possible to have H- beam with current ~100 mA and Energy ~2-3 MeV.

This can be enough for accumulation of about 1 kA of circulating proton beam in a small storage ring with R~1m.

As a first step it is possible to conduct realistic simulations of superintense beam accumulation with enhanced ionization cooling. Simulation of the self stabilization of the e-p instability can become a basis for new advanced accelerators and storage rings with intensity far above the space charge limit (by many orders of magnitude). This opens the way for new applications of accelerator technology in high energy density physics and technology. With a high injection current and with nonlinear focusing it is possible to have e-p instability self stabilization without the high density secondary plasma.

The important tasks are the development of a physical model of electron multiplication, including ion generation, slow ion dynamics, ion/electron secondary emission, and gas desorption by ion and electron impact.

An important aspect of this work is the estimation of parameters and scales for physical processes, leading to the development of a mathematical model. It is necessary to verify the proposed physical model. The system of Vlasov equations is nonlinear, requiring the use of numerical methods to solve them. As the first step it is appropriate to perform 1D and 2D simulations and compare the results of simulation with available experimental data and published results of simulations based on other codes [1-5,11-21].

REFERENCES

[1] V. Dudnikov, in Proceedings of the Particle Accelerator Conference, Chicago, 2001 (IEEE, Piscataway, NJ, 2001).

[2] S. Nagaitsev, A. Valishev, V. Danilov, "Nonlinear optics as a path to high-intensity circular machines", Proceedings of HB2010, Morschach, Switzerland, THO1D01, 2010.

[3] G. Budker, G. Dimov, and V. Dudnikov, Sov. Atomic Energy 22, 384 (1967); G. Budker, G. Dimov, and V. Dudnikov, in Proceedings of the International Symposium on Electron and Positron Storage Rings, Saclay, France, 1966 (Saclay, Paris, 1966), Article No. VIII-6-1.

[4] V.Dudnikov, Production of Intense Circulating Proton Beam by Charge Exchange Injection Method, Ph. D. Thesis, Novosibirsk, INP, 1966 [published in 1, 3, 5, 7-12].

[5] M. Reiser, "Theory and design of charged particle beam", second edition, p. 565-570, Wiley-VCH, 2006.

[6] V. Dudnikov, The Method of Negative Ion Production, SU Author Certificate, C1.H01 3/04, No. 411542, Application, 10 March,1972.

[7] V. Dudnikov, Rev. Sci. Instrum. 63(4),2660 (1992).

[8] V. Dudnikov, Rev. Sci. Instrum. 73(2), 992 (2002).

[9] A.V. Burov, G.W. Foster, V.D. Shiltsev, "Space-Charge Compensation in Proton Boosters", PAC2001, RPAH023, Chicago, IL, USA, 2001.

[10] Dimov G.I.,"Use of hydrogen negative ions in particle accelerators" Rev. Sci. Instrum. 67, 3393-3404 (1996).

[11] V. Dudnikov. PAC05, Knoxville, 2005.

[12] Yu. Belchenko, G. Budker, G. Dimov, V. Dudnikov,et al., Proceedings of the Xth International Conference on Particle Accelerators, Protvino, 1977, v. 2, p. 287 (1977).

[13] G. Budker, G. Dimov, V. Dudnikov, and V. Shamovsky, in Proceedings of the International Conference on High Energy Accelerators, Cambridge, MA, 1967 (CEA, Cambridge, MA, 1967).

[14] B.V. Chirikov, Sov. At. Energy 19, 1149 (1965).

[15] D. Koshkarev and P. Zenkevich, Particle Accelerators, 3, 1-9 (1972).

[16] G.Dimov, V. Chupriyanov, Particle accelerators, 14, 155-184 (1984).

[17] I.Koop,Vepp-2000Project, http://arxiv.org/abs/physics/0106013

[18] M. Aiba1, M. Chanel1, U. Dorda1, et al., "Space-Charge Compensation Options for the LHC Injector Complex", PAC07, THPAN074, Albuquerque, NM, USA, 2007.

[19] F. Zimmermann, Phys. Rev. ST, 7, 124801 (2004).

[20] R. A. Bosch, Suppression of two-stream hose instabilities at wavelengths shorter than the beam's transverse size, Phys.Rev. ST, 6 (2003).

[21] Dudnikov V and Dudnikov A , Rev. Sci. Instrum., v.73 995 (2002).

[22] K. Takayama and J. Kishiro, Induction Synchrotron, Nucl. Instrum.Methods A:v. 451, p. 304-317 (2000).

Copyright © 2013 CC-BY-3.0 and by the respective authors

TRANSVERSE BEAM DYNAMICS IN PLASMA GUIDED LASER DRIVEN ACCELERATION

D. B. Cesar, P. Musumeci, UCLA *, PBPL, Los Angeles, CA 90095, USA

Abstract

An axially modulated plasma waveguide supports slow-wave laser modes suitable for direct laser acceleration. The channel studied here supports a gradient of 2 GeV/m driven by a 1 TW laser. The transverse beam dynamics are analyzed in the context of the envelope equation and simulated by particle tracing to demonstrate the feasibility of using a photogun as the electron source. External injection promises to take advantage of the precision offered by state-of-the-art RF photogun technology to increase shot-to-shot reproducibility.

INTRODUCTION

The acceleration of electrons directly by laser fields is an attractive design for a compact accelerator because of the large gradients lasers can provide. In particular, direct laser acceleration (DLA) requires less power than laser plasma wakefield acceleration (LWFA), which enables more compact designs. In order to take advantage of the high fields of the laser it is necessary to overcome the restrictions due to phase slippage implied by the Lawson-Woodward theorem [1]. The DLA scheme pursued here overcomes these limitations by guiding a high intensity pulse through a corrugated plasma channel [2]. Analogous to a conventional disk-loaded LINAC, the corrugations introduce slow wave components phase matched to the electron beam.

Corrugated plasma channels have been created in a laser-ionized plasma [3]. Gas clusters were ionized and then heated by a 100ps pulse focused to a line by an axicon. The corrugations considered for quasi-phase matching were created by using a ring diffraction grating to introduce radial modulations in the laser pulse. The axicon maps the radial intensity pattern to the axis, and uneven heating of the plasma leads to density modulations during the shock-wave expansion. The use of the heater pulse to shape the modulations offers control over the modulation parameters.

Here we propose fixing the modulation parameters to provide focusing for an emittance dominated beam. The transverse beam dynamics in an ideal channel are studied in the context of the envelope equation. A matched solution with asymptotically damped oscillations is calculated. The input beam to match the channel can be obtained from an RF photogun. This solution bypasses the problems LWFA experiments have faced with injecting bunches from the plasma into the accelerating field.

ANALYSIS

Following previous analysis [4], the density profile of the plasma channel used for Direct Laser Acceleration experiment can be approximately described as Eq.(1), with addition of a density ramp, $n_s(z)$ to be used for phase-matching throughout the accelerator [5].

Table 1: Channel Parameters

n_0	k_m	δ	w_{ch}	λ_0	a_0
$5 \cdot 10^{19}/\mathrm{cm}^3$	232200	.9	37 μm	800nm	.2

$$n(z) = n_0 \left[1 + \delta \sin\left(k_m z\right)\right] + n_0'' r^2/2 + n_s(z) \qquad (1)$$

The parabolic density channel supports TM guided modes of radially polarized waves. The lowest order solution is expanded into slow-wave components and the transverse forces due to the resonant and non-resonant components are studied and used as the basis for an envelope calculation. Channel parameters used throughout the paper are listed in table 1 and are chosen to be consistent with experiment [3]. The channel is taken to be 1.8cm long so that the length of the accelerating pulse does not limit acceleration [4]. A laser power of $a_0 = .20$ is chosen to correspond with the TW laser in construction at UCLA's Pegasus beamline.

Guided Modes

Since we want a longitudinal field component for acceleration, we seek the radially polarized component of the laser vector potential in the slowly varying envelope approximation: $A_\perp = \hat{A}_r e^{i(k_0 z - \omega_0 t)}$, with $\hat{A}_r$ satisfying:

$$\left[2ik_0\left(\frac{\partial}{\partial z} + \frac{1}{c}\frac{\partial}{\partial t}\right) + \nabla_\perp^2\right]\hat{A}_r = \frac{\omega_p^2}{c^2}\hat{A}_r$$

where $\omega_p^2 = \frac{ne^2}{m\epsilon_0}$. This can be solved using separation of variables and expanded into harmonics using the Jacobi-Anger expansion. Palastro [4] includes discussions of the assumptions behind this model. Ignoring time dependence in the laser envelope, the lowest order solution is written in the Columb gauge as:

$$\hat{A}_r = A_0 \frac{r}{w_{ch}} e^{\frac{-r^2}{w_{ch}^2}} \sum_{q=-\infty}^{+\infty} i^q J_q(\Psi) e^{i\left(-\Psi + (\delta k + q k_m)z - \frac{\int k_{ps}^2 dz}{2k_0}\right)} \qquad (2)$$

where:

- $w_{ch} = \left(\frac{8c^2}{\omega_{p0}''^2}\right)^{1/4}$
- $k_{ps}^2(z) = \frac{e^2 n_s(z)}{m\epsilon_0 c^2}$
- $\delta k = -\frac{1}{k_0}\left(\frac{\omega_{p0}}{2c^2} + \frac{4}{w_{ch}^2}\right)$
- $\Psi = \frac{\delta\omega_{p0}}{2c^2 k_0 k_m}$

The transverse potential peaks at $r = w_{ch}/\sqrt{2}$. For our parameters $\Psi \approx .5$ is small, so that the Bessel functions limit the relevant terms in Eq(2) to small q.

* dcesar@ucla.edu

Copyright © 2013 CC-BY-3.0 and by the respective authors

The axial component of the potential is given by $\vec{\nabla} \cdot \vec{E} = 0 \Rightarrow \vec{\nabla} \cdot \vec{A} = 0$. The magnetic field is given by $\vec{B} = \nabla \times \vec{A}$ and the electric field by $\vec{E} = -\frac{\partial}{\partial t}\vec{A}$. The phase velocity of an individual harmonic is calculated by taking the derivative of the exponent of Eq.(2). The optical scale dominates $\left(k_0 >> \delta_k, nk_m, \int k_{ps}^2 dz/k_0\right)$ such that phase matched particles would have acceleration given by $\gamma = \gamma_0 + \gamma' z$. This determines v_p and allows phase matching of the largest subluminal harmonic (q=1) by using a density ramp. The density ramp asymptotically approaches $\frac{m\epsilon_0 c^2}{e^2}\left(2k0(\delta k + qk_m)\right)$ from below and rises slowly compared to both the optical and modulation periods, but quickly compared to the length of the plasma channel. The condition to keep the total density positive is:

$$km > \frac{e^2}{m\epsilon_0 c^2 2k_0}\delta n_0 + \frac{4}{k_0 w_{ch}^2} - k_0\left(1 - \frac{1}{\sqrt{1 - 1/\gamma_0^2}}\right)$$

For the small values of ψ under consideration we have the relation $E_z \propto a_0 n_0 \delta / k_m w_{ch}$. This scaling helps determine acceptable values for the parameters used.

Transverse Force

The equations of motion for a particle in the channel described above are:

$$\ddot{x_i} = \frac{e}{m_e \gamma}\mathrm{Re}[\sum_{q=-\infty}^{+\infty} f_{i,q} e^{i(n-1)k_m v_p t}] + \text{c.c.}$$

where, for $r << w_{ch}$

$$f_{z,q} = \frac{m_e c \omega_0 a_0}{eK_q}\frac{1}{w_{ch}} J_q(\Psi) e^{i\phi + ik_m \xi(q-1) + i(\frac{\pi}{2}(q) - \Psi)}$$

$$f_{r,q} = f_{z,q} K_q r\left[1 - \frac{\beta_z}{\beta_q}\left(1 + \frac{8}{(K_q w_{ch})^2}\right)\right] e^{i\frac{3\pi}{2}}$$

where $K_q = \left(k_0 + \delta k + qk_m + k_{ps}^2/2k_0\right)$, $\xi \approx z - v_p t$, and ϕ is the phase. Since ξ and ϕ are constant due to the phase matching condition the f vary in time minimally, only through the K_q's dependence on $n_s(z(t))$. The $\frac{8}{(K_q w_{ch})^2}$ is due to the finite spot size of the laser.

Following the notation of [6] the motion is separated into a slowly varying secular motion and a fast (corrugation scale) motion. In solving for the rapid motion we have used $k_0 >> \delta_k, qk_m, \kappa(z)$ and neglected terms $\kappa(z)/k0$. Averaging over the fast motion yields the secular equation of motion:

$$R''(z) = \frac{-1}{\beta^2\gamma}\frac{\omega_0 a_0}{c}\frac{R}{w_{ch}} J_1(\Psi)\left(\frac{8}{(K_n w_{ch})^2}\right) e^{i\phi + i(\pi - \Psi)} \tag{3}$$

$$+\frac{a_0^2}{w_{ch}^2(n-1)^2}\left(\frac{K_1}{k_m}\right)^2 R\sum_{q\neq 1}$$

$$\frac{1}{\beta^2\gamma^2} J_q(\Psi)^2\left(-\frac{(q-1)k_m}{k_0} - \frac{8}{(K_q w_{ch})^2}\right)^2$$

$$+\mathcal{O}\left(\frac{k_0}{k_m\gamma^2}\right) + \mathcal{O}\left(J_q(\Psi) J_{2-q}(\Psi)\right)$$

The term outside the sum is due to the resonsant force. The terms in the sum are the ponderomotive force. For our parameters the terms in big O notation are small for $\gamma >> 6$ and q> 1. For $\gamma >> 30$ the resonant term dominates the pondermotive force. To study the propagation of an electron beam through the channel we consider the envelope equation in the emittiance dominated regime:

$$\sigma_r'' + \frac{(\beta\gamma)'}{\beta\gamma}\sigma_r' + k_r^2\sigma_r = \frac{\epsilon_{nr}^2}{(\beta\gamma)^2\sigma_r^3} \tag{4}$$

The pondermotive focusing term allows for a matched beam envelope:

$$\sigma_m \approx \left(\frac{\epsilon_{nr} w_{ch}}{\sqrt{2} a_0 J_0(\Psi)}\right)^{1/2}$$

Because $\sigma_r'(0) \neq 0$ the pondermotive force will cause spot size oscillations. In addition, the resonant term will add overfocusing as γ increases. The asymptotic behavoir of this system can be be easily interpreted as $\beta \to 1$ by writing $\sigma_r(z) = \sigma_m + \delta(z)$, where it is assumed $\delta(z) << \sigma_m$. Still approximating the particles' phases as constant, and changing variables to $\hat{z} = \gamma_0 + \gamma' z$ Eq.(4) becomes:

$$\delta'' + \frac{\delta'}{\hat{z}} + \frac{1}{\gamma'^2}\left(\frac{k_{\text{res}}^2}{\hat{z}} + \frac{4k_{\text{pond}}^2}{\hat{z}}\right) = -\frac{k_{\text{res}}^2\sigma_m}{\gamma'^2\hat{z}} \tag{5}$$

where k_{res}^2 is the focusing due to the resonant harmonic, k_{pond}^2 is the focusing due to the pondermotive forces, and primes denote derivatives with respect to $\hat{z}$. In the limit where $k_{\text{res}}^2\gamma >> k_{\text{pond}}^2$ the solution is a linear combination of $J_0(2k_{\text{res}}\sqrt{\hat{z}}/\gamma')$ and $Y_0(2k_{\text{res}}\sqrt{\hat{z}}/\gamma')$. For large z this represents damped oscillations with a growing period. When still in the regime $\beta \approx 1$, but $k_{\text{res}}^2\gamma \approx k_{\text{pond}}^2$ the solution can be shown to be oscillations formed from a combination of Bessel and Hypergeometric functions.

Table 2: Beam Parameters

	γ	Espread	ϵ_n	σ_r	Q
Initial	20	.2%	0.1 mm·mrad	2.6μm	1pC
Final	90	2.2%	0.3 mm·mrad	2.6μm	.64pC

Particle Tracking

The particle tracking code General Particle Tracer (GPT) was used to test the approximations made in determining the envelope behavior. The tracing is only as accurate as the input field, Eq.(2), as the tracer does not simulate the plasma. For simplicity the laser is still assumed to be much longer than the electron beam so that the overall pulse envelope can be ignored. The solver does calculate the small contribution from spacecharge fields, but it does not account for wakefields in the plasma.

Beam parameters before and after acceleration are listed in table 2. The input parameters are similar to those obtained in UCLA's Pegasus beamline, and the final parameters are for the accelerated electrons only. Further, the

Copyright © 2013 CC-BY-3.0 and by the respective authors

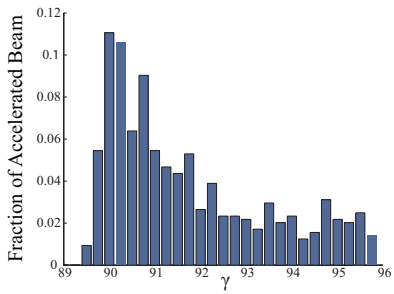


Figure 1: Energy spread of the accelerated bunch.

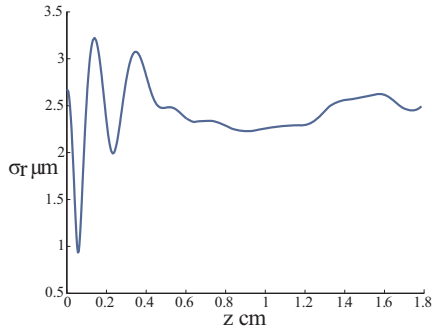


Figure 2: Envelope dynamics showing the spot size oscillations of the accelerated bunch.

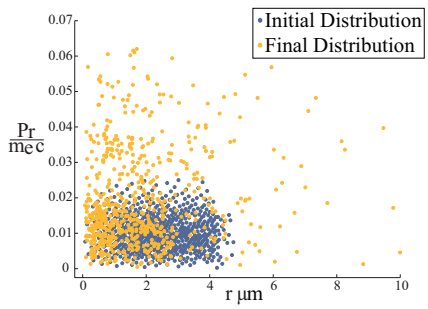


Figure 3: The inital and final phase space of the accelerated bunch. The growth in transverse momentum is due to betatron oscillations.

beam is assumed to have been previously microbunched into 20 optical length bins, with each box having a FWHM $\lambda_0/9$, as might be created by bunching in an undulator [7].

During the first millimeter of acceleration many of the particles far from the axis de-phase from the matched wave, slip into the defocusing region of the resonant harmonic, and are ejected from the channel. The remainder of the particles are accelerated with a linear gradient to $\gamma = 92$. A capture rate of as high as 64% was achieved by setting the initial phase at $\pi/6$. Because of the dephasing, the electrons fill the accelerating bucket and the final energy spread (Fig.1) is nearly 5%. The energy spread and capture rate are improved by reducing the dephasing. The capture rate is little improved by reducing the emmittance, as the dephasing is caused by betatron oscillations that are large enough to modulate γ and dephase the outer electrons. This effect would be reduced by increasing the channel width, but at the cost of the accelerating gradient. A more complex scheme may pursue a slowly changing channel width.

The envelope of a single bunch in the accelerated group of electrons is graphed in Fig.2. The beam has an input rms radius of 2.6μm, and then oscillates about the matched spot size. The oscillation magnitude is damped and the period is lengthening, consistent with the behavior predicted by the asymptotic solution to the envelope equation. The maximum spot size is 1/10 of the channel size, indicating that the forces remain linear, yet the normalized emittance triples. The increase in emittance is visually evident in the evolution of the transverse phase space (Fig.3) as an increase in the transverse momentum. Further increase in the transverse momentum is limited by dephasing due to coupling between the longitudinal and transverse momentum. Particles at the edge of the phase space are slowly dephase into the defocusing phase for arbitrarily large accelerators.

CONCLUSIONS

The transverse dynamics in an ideal corrugated waveguide have been studied and found to yield focusing forces suitable for matching a μm size beam. However, the large focusing and over-focusing forces contribute to the dephasing of electrons which leads to low capture rates, large energy spread, and emittance growth. Increasing the channel width decreases these effects and a tapered channel width may contribute to higher beam quality. Further analysis of the accelerator would benefit from modeling the plasma formation and beam-plasma interaction. Nonetheless, the analysis here suggests it would be possible to channel an externally injected beam in a proof of principle experiment.

ACKNOWLEDGMENT

U.S. DOE Grants No.DE-FG02-92ER40693, No.DEFG02-07ER46272

REFERENCES

[1] J.D. Lawson, IEEE Trans. Nucl. Sci. NS-26, 4217 (1979).

[2] B. D. Layer, A. York, T. M. Antonsen, S. Varma, Y.-H. Chen, and H. M. Milchberg Phys. Rev. Lett. 99, 035001 (2007).

[3] B.D. Layer, *Structured Plasma Waveguides and Deep EUV Generation Enabled by Intense Laser-Cluster Interactions*, (Digital Repository at University Of Mayland, 2012)

[4] J. P. Palastro, T.M. Antonsen, S. Morshed, A. G. York, and H.M. Milchberg, Phys. Rev. E77, 036405 (2008).

[5] Yoon, S. J. and Palastro, J. P. and Gordon, D. and Antonsen, T. M. and Milchberg, H. M., Phys. Rev. ST Accel. Beams 15 8 081305 (2012), 10.1103/PhysRevSTAB.15.081305

[6] B. Naranjo, A. Valloni, S. Putterman, and J.B. Rosenzweig, Phys. Rev. Lett. 109 (2012) 16 164803.

[7] L. V. Ho, P. Musumeci, "Modeling Space Charge In Optical Bunchers", NA-PAC 2013.

Copyright © 2013 CC-BY-3.0 and by the respective authors

APPLICATIONS FOR OPTICAL-SCALE DIELECTRIC LASER ACCELERATORS

R.J. England, Z. Huang, R. J. Noble, J. E. Spencer, Z. Wu
SLAC National Accelerator Laboratory, Menlo Park, CA 94025, USA
B. Montazeri, E. Peralta, K. Soong, Stanford University, Stanford, CA, USA
C. Lee, M. Qi, Purdue University, West Lafayette, IN, USA
L. Schacter, The Technion, Haifa, Israel

Abstract

Particle acceleration in dielectric laser-driven microstructures, recently demonstrated at SLAC, holds the promise of providing low-cost compact accelerators for a wide variety of uses. Laser-driven undulators based upon this concept could attain very short (mm to sub-mm) periods with multi-Tesla field strengths. And since dielectric laser accelerators operate optimally with optical-scale electron bunch formats, radiation production with high repetition rate (10s of MHz) attosecond-scale pulses is a natural combination. We present preliminary analysis of the harmonic field structure for a periodic undulator based on this concept.

INTRODUCTION

The increasingly prohibitive cost and size of modern accelerator facilities has prompted interest in a variety of schemes for accelerating particles at higher gradients than traditional metallic cavity accelerators can provide, rapid fabrication techniques, and more readily available energy sources. One of the most promising of these schemes is the use of dielectric near-field structures powered by an infrared (IR) laser to produce a confined accelerating mode. Since the size of the confining beam channel scales with the wavelength of the source, the apertures of such structures are at most a few microns in transverse size. As a result, particle beam confinement requires a new operating regime with beams of low charge (10-100 fC) and ultra-low normalized emittance (1-10 nm). The bunches should ideally be short compared to the optical wavelength (10-100 fs), must be spaced at the optical period of the laser (or an integer multiple thereof), and should come in bunch trains commensurate with typical solid state laser pulse lengths (10 fs - 1 ps). The decrease in luminosity due to such small bunch charges are compensated by the fact that solid state lasers permit repetition rates 3 orders of magnitude higher than typical microwave sources. The requisite dielectric structures can be fabricated with nanometer-level precision on silicon wafers using modern solid state fabrication methods, and the first experimental demonstration of high-gradient acceleration in such structures has been recently reported [1].

The DLA concept leverages well-established industrial fabrication capabilities and the commercial availability of tabletop lasers to reduce cost, while offering significantly higher accelerating gradients, and therefore a smaller footprint. Power estimates for the DLA scenario are comparable with convention RF technology, assuming that similar power efficiency (near 100%) for guided wave systems can be achieved, 40% wall plug laser efficiencies (feasible with solid state Thulium fiber laser systems), and 40% laser to electron beam coupling (consistent with published calculations).

This research has significant near and long-term applications for energy frontier science [2, 3]. Additional applications including radiation production for compact medical x-ray sources, university-scale free electron lasers, NMR security scanners, and food sterilization are beginning to be explored. A dielectric laser-driven deflector, operating on the same basic principles as recently demonstrated accelerator devices, was proposed by Plettner and Byer [4]. The scheme uses a pair of dielectric gratings excited transversely by a laser beam and separated by a gap of order the laser wavelength where a beam of electrons would travel. By changing the sign of the excitation between successive structures (e.g. by alternating the direction of illumination) an optically powered undulator could be constructed to create laser driven micro-undulators for production of attosecond-scale radiation pulses synchronized with the electron bunch.

As a next step in exploring this concept in more detail, the commercial electromagnetic finite element code HFSS 12.0 was used to obtain realistic field profiles along the axis of an electron beam propagating in a single stage of deflection (representing half of one undulator period). These fields are analyzed with respect to the injection phase of a test electron and the deflecting forces calculated to produce a single-period model of the proposed undulator concept.

BACKGROUND

The deflector design proposed in Ref. [4] consists of a pair of coplanar gratings with a pillar height g separated by a gap of width w. If the gratings are constructed of an optically transmissive material (such as glass) an electromagnetic mode can be excited in the gap region by transverse illumination of the structure with a monochromatic plane wave. The resultant confined mode is found to produce a net deflecting force transverse on a trajectory lying in the midplane between the two gratings at an angle $\pi - \alpha$ relative to the direction of the grating lines. Consquently

Copyright © 2013 CC-BY-3.0 and by the respective authors

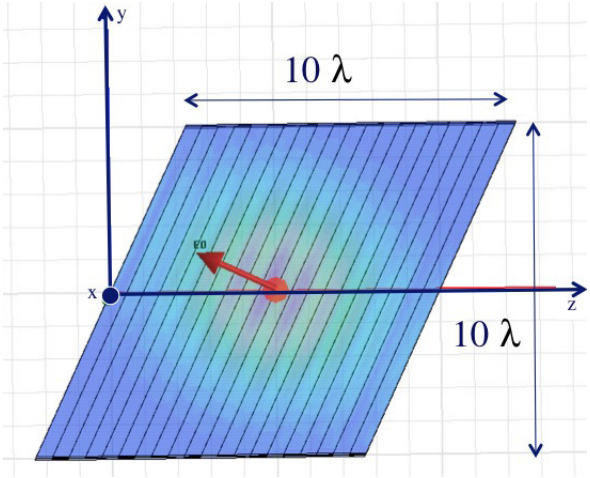


Figure 1: HFSS simulation geometry with superimposed color contour plot of the Gaussian excitation.

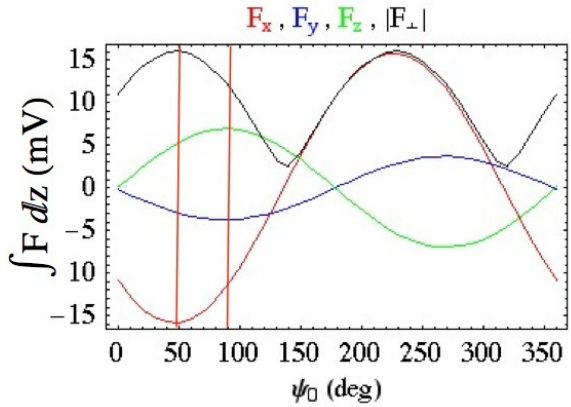


Figure 2: Computed force components as a function of particle injection phase, for an incident field E_0 = 1 V/m, integrated over half an undulator period (10λ).

by tilting the gratings at an angle α relative to the beam axis in the plane parallel to the grating surfaces a net transverse deflecting force can be imposed on a charged particle traveling between the gratings. The maximum amplitude of this deflection is found to be $F_\perp \approx qE_0 sin^2\alpha$, where E_0 is the electric field amplitude of the incident laser field and q is the particle charge, which occurs for the optimized geometrical values $w = 0.4\lambda$, $\alpha = 25°$, and $g = 0.85\lambda$. For a silicon dioxide structure with a 0.3 ps laser pulse, the corresponding peak surface electric field corresponding to the damage limit is $E_{pk} \approx 8.2$ GV/m, and the corresponding incident laser field is $E_0 = E_{pk}/3$, corresponding to an equivalent undulator magnetic deflection field $B_u = \mu_0 E_0/Z_0$ = 1.6 T.

It should be noted that the deflection has both x and y components and that there is also a significant z component of net accelerating force. To create an undulator from such structures, they can be staged, with successive stages of deflection illuminated from opposite sides so as to alternate the sign of the deflection force. Since the longitudinal extent of the deflecting force in each stage is determined by the transverse extent of the exciting laser field, in principle the period of such an undulator could be many times the laser wavelength.

SIMULATIONS

A single stage of the proposed deflector (half a period of the undulator) was simulated using the commercial electromagnetic finite element code HFSS 12.0. The computational volume includes the entire structure, with no symmetry planes, and absorbing boundary conditions on all exterior boundaries. The geometry is shown in Fig. 1. The model is excited by a Gaussian laser mode at normal incidence propagating in the negative x direction transverse to the planes of the gratings. The beam axis is taken to be the positive z direction, and the primary deflection component is in the x direction.

For the structure orientation and dimentions, we take the optimized values $\alpha = 25°$, $w = 0.4\lambda$, $g = 0.85\lambda$ as calculated in Ref. [4], with the excitation field polarized perpendicular to the lines of the gratings. The fields are then extracted along the z-axis and the integrated force on a speed of light particle is computed. The force components as a function of injection phase ψ_0 of the particle, for an incident laser field with an electric field amplitude $E_0 = 1$ V/m, are shown in Fig. 2. We see that the deflecting force $F_\perp$ is dominated by the x component. At $\psi_0 = 0$, the integrated force on the particle is entirely in the x direction, as the contributions from the other two components are zero. If the fields from the half-period are mirrored in z to produce a single undulator period, the results can be harmonically analyzed by a Fourier sine decomposition as

$$F_x(z) = \frac{a_0}{2} \sum_{n=1}^{\infty} [a_n \cos(n\pi x/L) + b_n \sin(n\pi x/L)] \quad (1)$$

The resulting harmonics at $\psi_0 = 0$ are found to have a mixture of harmonic contributions from both the cosine and sine terms. However, at an injection phase of 90°, $a_n = 0$, the accelerating (z) contribution is a maximum but the field harmonics are sinusoidal with dominant contributions at the first and third harmonics ($b_1 = 0.2E_0$, $b_3 = 0.05E_0$). The corresponding lowest-order deflection force is consistent with the analytical predictions of the prior section. The next significant harmonic contributions appear at $n = 18$ and higher, and correspond to the fast oscillation component related to the laser wavelength λ, as seen in the right-hand plot of Fig. 3. The first and third harmonic sinusoids are combined to produce the red curve superimposed upon the plot in Fig. 3. If the system is scaled to larger undulator periods (of order 100 λ), these components get pushed to higher n values and hence the undulator parameter contributions K_n from these higher harmonics become increasingly ignorable.

The significant third harmonic contribution, however, will contribute significantly to the radiation produced if

Copyright © 2013 CC-BY-3.0 and by the respective authors

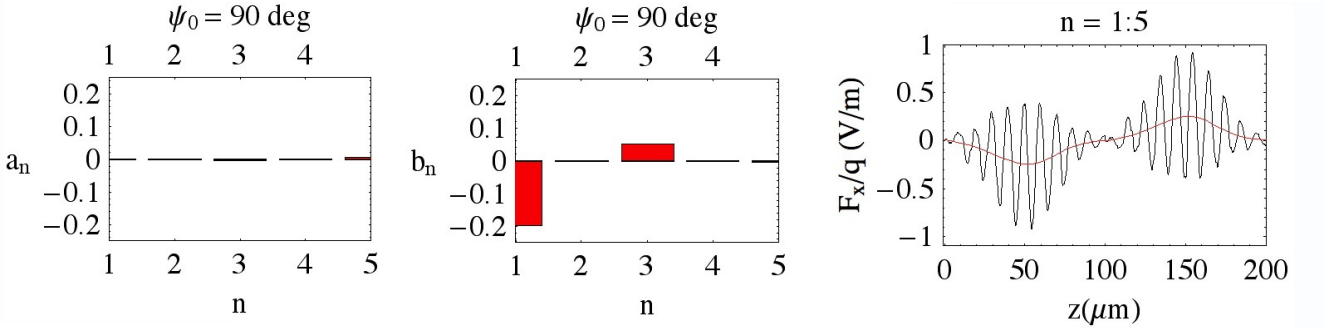


Figure 3: Harmonic analysis of a single undulator period for 90° injection phase, showing the cosine and sine harmonic terms and the dominant x force component (black curve) with superposition of the first 5 harmonics (red curve).

this device is used as an undulator for an optical-scale free electron laser. In traditional undulator designs, third harmonic field content occurs as a perturbative contribution due to the nonlinear motion of the electrons in the undulator field. However, the presence of significant inherent third harmonic has recently been studied as a mechanism to intentionally generate efficient third harmonics of the fundamental FEL radiation [5]. In addition, although we have here assumed a Gaussian laser mode for simplicity, the harmonics of the undulator fields may be manipulated (and the third harmonic contribution enhanced or reduced) by transverse shaping of the incident laser mode profile.

Unlike other electromagnetic undulator concepts, the undulator period in this scheme is set by the length of each deflection stage and can therefore be much larger than the driving wavelength. From simple 1D calculations, undulators based upon this concept could attain very short (mm to sub-mm) periods with multi-Tesla field strengths: an undulator with a 250 μm period driven by a 2 μm solid state laser would have a gain length of 4 cm and an X-ray photon energy of 10 keV when driven by a 500 MeV electron beam. Since DLA structures operate optimally with optical-scale electron bunch formats, high repetition rate (10s of MHz) attosecond-scale pulses are a natural combination.

CONCLUSIONS

The grating-based optical deflector concept presented previously by Pletter and Byer presents the possibility of creating a FEL undulator compatible with future laser-driven accelerators. We have simulated one period of such an undulator concept using an electromagnetic finite element code with a grating excited transversely by a Gaussian monochromatic mode. The axial fields extracted do show a significant integrated transverse deflecting force, as well as a net integrated acceleration, as predicted. However, while in Ref. [4], the ratio of these components is predicted to be $F_z/F_\perp \approx 2$, we find that the accelerating component is generally smaller than the deflecting force, and varies significantly with injection phase, an effect not previously noted. In addition, we find that for a Gaussian laser mode, the fields contain significant third harmonic content. The impact of these observations will be explored in future by analytical calculations as well as computational analysis using FEL codes. Prototype devices based on a modified version of the architecture reported in [1] are being developed for experimental testing at SLAC.

ACKNOWLEDGEMENTS

We thank William Fawley for helpful discussions. This work was supported by U.S. Department of Energy under Grants DE-AC02-76SF00515, DE-FG06-97ER41276 and by DARPA Grant N66001-11-1-4199.

REFERENCES

[1] E. A. Peralta and et al. Demonstration of electron acceleration in a laser-driven dielectric microstructure. *Nature, accepted for publication*, 2013.

[2] E. R. Colby, R. J. England, and R. J. Noble. A laser-driven linear collider: Sample machine parameters and configuration. In *2011 Particle Accelerator Conference Proceedings*, page 262, New York, NY, 2011.

[3] P. Bermel, R. L. Byer, E. R. Colby, B. M. Cowan, J. Dawson, R. J. England, R. J. Noble, M. Qi, and R. B. Yoder. 2011 Dielectric Laser Acceleration Workshop (DLA2011). *ICFA Beam Dynamics Newsletter*, 56:91–108, 2011.

[4] T. Plettner and R. L. Byer. Proposed dielectric microstructure laser-driven deflector. *Phys. Rev. ST-AB*, 11:030407, 2008.

[5] J. Qi-ka. The effect of undulator harmonic field on free-electron laser harmonic generation. In *Proceedings of the 2010 Free Electron Laser Conference in Malmo Sweden*, IEEE, 2010.

Copyright © 2013 CC-BY-3.0 and by the respective authors

MULTIBUNCH BEAM PHYSICS AT FACET*

S. J. Gessner†, E. Adli, K. L. F. Bane, F. J. Decker, Z. D. Farkas, R. K. Jobe, M. D. Litos, M. Ross
SLAC, Menlo Park, CA, 94025, USA
T. Katsouleas, A. A. Sahai, Duke ECE, Durham, NC, 27708, USA

Abstract

Plasma wakefield studies are normally conducted as single-shot experiments. Here, single-shot means that the plasma returns to its original state before the next bunch passes through the plasma. The time scale for the plasma to return to equilibrium is 10-100 ns, which is comparable to the bunch separation in proposed linear colliders. The SLAC linac typically delivers beam at a rate of 10 Hz to FACET, but can also be operated in a manner that delivers two electron bunches per RF pulse to FACET. We explore operating modes with beam separations as small 5.6 ns so that high repetition rate plasma wakefield acceleration can be studied at FACET.

INTRODUCTION

The SLAC linac provides electron bunches with total beam charge of 3.2 nC to FACET experiments. The beam originates at Sector 0 from a thermionic cathode gun, passes through the sub-harmonic buncher for longitudinal compression, is captured and accelerated in the Sector 1 s-band linac and sent to the North Damping Ring (NDR) for beam cooling. After the emittance is damped in the ring, the beam is extracted into the Sector 2 linac, accelerated to 20.35 GeV, and delivered to Sector 20 for final compression and focusing. An overview of the linac and associated systems is given in Fig. 1. Each system imposes its own constraints on the possible bunch parameters and inter bunch spacings.

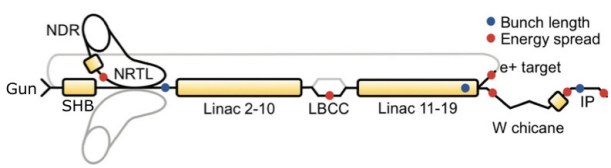


Figure 1: Overview of Linac with affected subsystems and diagnostics for multi-bunch operation.

BEAM GENERATION AND CAPTURE

Source

The electron source is a thermionic cathode driven by a multi-channel pulser. The pulser is a circuit with two planar triode amplifiers that couple into a common amplifier driving the cathode. The two triodes can be fired independently to produce electron pulses from the cathode with arbitrary separation in time. The gun can generate up to 27 nC of charge in a single pulse. We look to generate two pulses with 3.2 nC each. This can be achieved without changing the existing gun hardware [1].

Subharmonic Buncher

Immediately after the beam is generated it is captured in the sub-harmonic buncher (SHB). The SHB is operated at the $1/16^{th}$ sub-harmonic of the s-band linac. The bucket spacing for the SHB is 5.6 ns. The SHB bucket size sets the interbunch spacing in the rest of the machine. Without the SHB, most of the beam does not get captured in the linac and there is the potential for radiation damage in the injector. All of the interbunch spacings considered in this paper are multiples of 5.6 ns.

The longitudinally compressed bunches are captured in an s-band bucket at the start of Sector 1 and accelerated to 1.19 GeV before being sent to the NDR via the North Linac-to-Ring arc.

NORTH DAMPING RING

Kickers

A loaded ferrite kicker magnet with a flat-top of 30 ns kicks the bunches into the ring. This magnet was designed to have an extremely sharp rise and fall time, so as not to disturbed another bunch in the ring, which was typical during SLC operation. A second kicker magnet is located on the opposite side of the ring and is used to extract the bunches. This magnet is identical to the injection kicker except that it has a different pulse forming network that uses a Blumlein generator to produce an extremely flat pulse to the magnet [2]. The field in the magnet provides a uniform 7 mrad kick for more than 60 ns. The injection and extraction kickers set limits on the maximum separation between the two bunches. The maximum bunch spacing that is consistent with the NDR RF and SHB RF is 61.6 ns. The injection kicker would have to be equipped with a similar PFN as the extraction kicker to achieve this separation.

Instabilities

The NDR limits the bunch charge and separation in another manner due to single-bunch and coupled beam instabilities. The single bunch instability is a short range, microwave instability. With 3.2 nC per bunch, the ring is operated above the threshold for the instability. However, at this charge the instability is weak and does not degrade the bunch quality [3]. Note that having two 3.2 nC bunches

* Work supported by the U.S. Department of Energy under contract number DE-AC02-7600515.
† sgess@slac.stanford.edu

Copyright © 2013 CC-BY-3.0 and by the respective authors

in the ring instead of one has no effect on this instability because it is very short range.

On the other hand, a pi-mode instability arrises in the ring due to bunch coupling to HOMs in the RF cavities. The bunches exhibit both zero mode and pi-mode oscillations with respect to the ring RF. The zero mode oscillation is damped by synchrotron radiation but the pi-mode is not. To counteract this instability, a passive cavity was added to the ring in 1992 [4]. At the time, the cavity was tuned to 1062.4 MHz, just below the 125^{th} revolution harmonic to accommodate two bunches with a bunch separation $t_i = 61.6$ ns. The cavity has a movable plunger that can be adjusted to match the frequency of the pi-mode oscillation for each of the different bunch separations tested at FACET.

MAIN LINAC

The beam is extracted from the NDR and passes to the main linac via the North Ring-to-Linac arc. The bunches pass through a compressor cavity at the zero crossing of the RF and this imprints a linear chirp on the beam. The beam is compressed down to 500 μm bunch length by the R_{56} of the chicane and then captured in an s-band bucket in the linac. Once the bunches reach the linac, the trailing bunch is affected by longitudinal and transverse wakefields of the leading bunch. Those two effects are discussed below.

Beam Loading

The leading bunch absorbs energy as it passes through the accelerating cavities. This energy cannot be replaced with additional energy from the klystron if the inter bunch spacing is very short. This effect, called beam loading, results in the trailing bunch receiving less energy after passing through the cavity as compared to the leading bunch. The voltage drop induced in the cavity by the leading bunch is given by $V_w = 2eNL\kappa_z$ where eN is the bunch charge, L is the cavity length, and $\kappa_z = 20$ V/pc/m is the fundamental wakeloss factor for the SLAC s-band cavities. The trailing bunch sees the accelerating voltage reduced by this amount.

If the cavity phase is not zero (on crest), the trailing bunch also sees a different RF phase as compared to the leading bunch. The phase the trailing bunch sees is given by Eq. 1 and explained visually in Fig. 2.

$$\phi' = \tan^{-1}\left[\frac{V_{RF}\sin\phi}{V_{RF}\cos\phi - V_w}\right] \quad (1)$$

The phase shift effect is significant at FACET because each sector in the front half of the linac is phased differently. The chirping scheme depicted in Fig. 3 was designed to minimize the effect of wakefields on the beam at low energy while still achieving the necessary chirp for compression in the Sector 10 chicane. The phase in each sector is an integer multiple of the Decker Phase, which is usually about 10^o. This rather complicated chirping scheme means that the trailing bunch will we see a different phase relative to the leading bunch in Sectors 2 though 10. The resulting phase shifts are listed in Table 1.

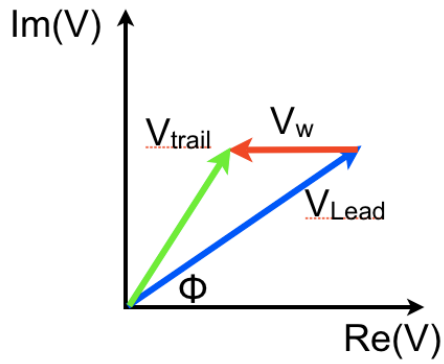


Figure 2: Phase diagram showing the RF voltage and phase difference seen by the trailing bunch.

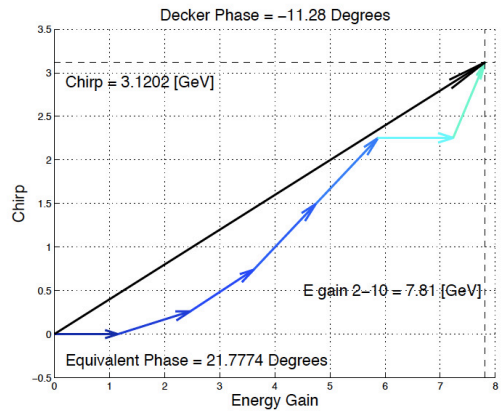


Figure 3: FACET front-end chirping scheme. Each phase arrow represents one sector and is an integer multiple of the Decker Phase.

Table 1: Sector by Sector Phase Shifts for a Decker Phase of 10^o. Note that Sectors LI07 and LI08 are omitted from the table since they are not powered.

Sect.	L [m]	$V_{RF}[GV]$	ϕ	V_w [MV]	$\Delta\phi$
LI02	75.5	1.59	0^o	9.66	0^o
LI03	96.0	1.85	10^o	12.3	0.066^o
LI04	84.0	1.72	20^o	10.8	0.12^o
LI05	97.4	1.88	30^o	12.5	0.19^o
LI06	97.4	1.88	30^o	12.5	0.19^o
LI09	97.4	1.88	0^o	12.5	0^o
LI10	67.0	1.44	50^o	8.57	0.26^o

Beam loading reduces the energy of the second bunch by 0.8% in Sectors 02-10 and 0.5% in Sectors 11-20, relative to the first bunch. This does not pose a problem because the full-width half-maximum energy apertures of the Sector 10 and Sector 20 chicanes are 5% and 4% respectively. The effective phase of the trailing bunch with respect to the

Copyright © 2013 CC-BY-3.0 and by the respective authors

leading bunch is 23.49^o compared to 23.38^o at the Sector 10 chicane. Although this effect seems small, it is amplified by the difference in compression that each bunch will see in the Sector 10 chicane, which leads to different wakefields in Sectors 11-20. Short-range longitudinal wakefields effectively chirp the extremely short beams, and therefore they will be compressed differently in the Sector 20 chicane. This extremely non-linear problem will be studied in simulation to determine the severity of the effect.

RF Pulse Compensation

For bunch separations larger 5.6 ns, RF pulse compensation can be used to correct for the beam loading effect. The SLEDed RF pulse fills the cavity over a period of several microseconds according to the parabolic form depicted in Fig. 4. Typically, the bunch is accelerated at the crest of the pulse. In order to accommodate multiple bunches per pulse, the bunches are instead accelerated on the rising slope of the pulse, with the leading bunch slightly lower on the slope and the trailing bunch slightly higher. For a bunch separation of 16.8 ns (three times the minimal separation), the effect of beam loading can be totally compensated [5].

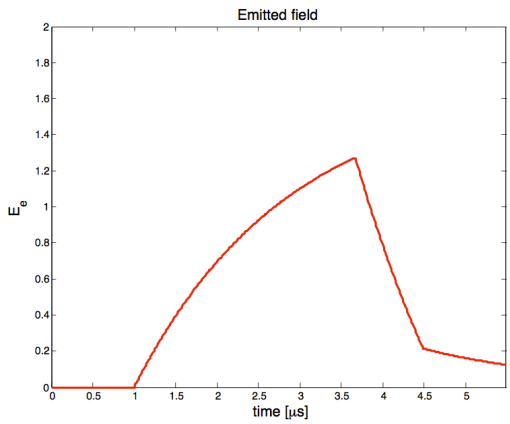


Figure 4: Temporal shape of the SLEDed pulse in the s-band cavity.

Transverse Wakefields

If the leading bunch is misaligned with respect to the RF cavities, the trailing bunch may see a significant transverse kick from the wakefields in the cavity. Fig. 5 shows that there is a minimum in the transverse wake strength at around 5 ns. For this reason, it is advantageous to choose the 5.6 ns bunch spacing for our first tests of multibunch operation. The size of the second envelope in Fig. 5 is indicative of the wake strength out to 60 ns, which is the largest bunch separation possible at FACET [6].

CONCLUSION AND OUTLOOK

The scientific merit for multibunch studies at FACET is very high considering the recent advances in plasma wakefield technology. It is critical to demonstrate that PWFA is stable and reproducible at high repetition rates before this technology can be used in light source or collider applications.

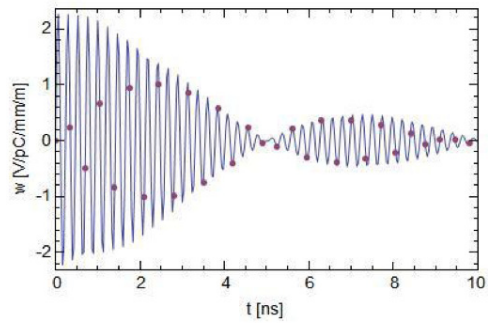


Figure 5: The time domain transverse wakefield in the SLAC s-band cavity.

Relatively few systems need to be modified in order to achieve in the multiple bunches at FACET. However, from an operations perspective, the multibunch mode is challenging because many diagnostics, including BPMs, cannot resolve the closely spaced bunches, and the timing windows are very tight for injection and extraction at the NDR. Some of these issues might be mute if the thermionic cathode is replaced by an LCLS-style photocathode. This has been proposed for FACET or FACET II. On the other hand, the phase shifts in the main linac are still an important issue, and would have to be dealt with for any high-charge, multibunch mode at FACET, regardless of the beam source.

REFERENCES

[1] M. J. Browne, J. E. Clendenin, P. L. Corredoura, R. K. Jobe, R. F. Koontz, and J. Sodja, "A Multi-Channel Pulser for the SLC Thermionic Electron Source", Particle Accelerator Conference, Vancouver, 1985. SLAC-PUB 3546.

[2] T. Mattison, R. Cassel, A. Donaldson, H. Fischer, and D. Gough, "Pulse Shape Adjustment for the SLC Damping Ring Kickers", Particle Accelerator Conference, San Francisco, 1991. SLAC-PUB 5461.

[3] K. Bane, et. al. "High-Intensity Single Bunch Instability Behavior In The New SLC Damping Ring Vacuum Chamber", Particle Accelerator Conference, Dallas, 1995. SLAC-PUB 6894.

[4] Y. Chao, P. Corredoura, A. Hill, P. Krejcik, T. Limberg, M. Minty, M. Nordby, F. Pedersen, H. Schwarz, W. Spence, P. Wilson, "Damping the Π-mode Instability in the SLC Damping Rings with a Passive Cavity", Particle Accelerator Conference, San Francisco, 1991. SLAC-PUB 5589.

[5] F. J. Decker, Z. D. Farkas, J. Turner. "High Current, Long Beam Pulse with SLED", Particle Accelerator Conference, New York, 1999. SLAC-PUB-8113.

[6] K. Bane. "Wakefield Calculations for the LCLS Multibunch Operation", International Particle Accelerator Conference, San Sebastein, 2011.

Copyright © 2013 CC-BY-3.0 and by the respective authors

SIMULATION OF POWER COUPLING AND WAKEFIELD IN PHOTONIC BANDGAP FIBERS FOR DIELECTRIC LASER ACCELERATION*

C.-K. Ng, R.J. England, A. Kwiatkowski, R.J. Noble, J.E. Spencer, SLAC, Menlo Park, U.S.A.

Abstract

A photonic bandgap (PBG) lattice in a dielectric fiber can provide high gradient acceleration in the optical regime, where the accelerating mode is obtained from the presence of a single defect in the lattice. In this paper, we will investigate two aspects of the PBG for acceleration. First, the excitation of the accelerating mode can be achieved by directing high-power lasers from free space. Simulation using ACE3P has demonstrated that, by appropriately shaping the end of the PBG fiber, power can be coupled into the fiber using a simple laser configuration. Second, the wakefield generated by the transit of a beam through a PBG fiber will be simulated. The radiation spectrum of the wakefield will be evaluated and corroborated with measurements from a commercial fiber.

INTRODUCTION

The photonic bandgap (PBG) structure proposed by Lin [1] has demonstrated the possibility of confining an accelerating mode in an energy bandgap existing in a periodic lattice of vacuum holes in a dielectric fiber with a central vacuum defect of larger diameter. High accelerating gradient can be achieved in such fibers in the optical regime using lasers for excitation of the accelerating mode. The mechanism of coupling power into the PBG fiber needs to be investigated to ensure efficient excitation of the accelerating mode. Previous studies have shown that a coupling scheme from free space by directly focusing laser pulses in a certain configuration into the fiber can excite the accelerating mode [2]. However, for best results the configuration requires an array of six laser beams arranged in a pattern that obeys the hexagonal symmetry of the Lin lattice. It is desirable to develop improved coupling schemes that can simplify the laser configuration by modification of the existing geometry. It will be shown in the next section that a simpler coupling scheme can be achieved by appropriately shaping the end of the PBG fiber.

While attempts to fabricate Lin-type PBG fibers that can support an accelerating mode are being explored, off-the-shelf telecom fibers are available in the commercial market place, providing samples that can be tested using high energy electron beams at the test facility at SLAC [3]. An example of these commercial fibers is the HC1060 fiber of NKT Photonics which supports the propagation of a telecom mode at the wavelength of 1060 nm. Although the HC1060 fiber does not support a strong TM-like accelerating mode, by measuring the radiated signal after the passage of an electron beam, it is possible to identify the modes that exist in the bandgap of the fiber. In order to corroborate with the measured radiation spectrum obtained from beam tests, simulations have been carried out using the 3D parallel electromagnetic code suite ACE3P [4] to model beam excitation in the HC1060 fiber to calculate wakefield effects and to compare with measurements.

* Work supported by the Department of Energy under Contract Number DE-AC02-76SF00515 and funds provided by Incom, Inc. through CRADA 383 from DOE STTR Grant DE-SC0007718.

POWER COUPLING IN LIN FIBER

The Lin PBG fiber consists of circular holes in a hexagonal lattice with spacing a between the centers of neighboring holes. The holes have a radius of $0.35a$. In order to introduce a defect in the lattice, one hole is replaced by another with a radius of $0.52a$. The material of the fiber has a dielectric constant of 2.13 for this glass at near IR wavelengths. A quarter of the model in the transverse plane is shown in Fig. 1, exhibiting a lattice with hexagonal symmetry and a central defect. The Lin PBG fiber supports a TM-like accelerating mode. For example, the wavelength of the defect mode is 2 μm for a = 2.61 μm. Using ACE3P's frequency domain eigensolver module Omega3P, the calculated longitudinal electric field pattern of the defect mode is shown in Fig. 1. It can be seen that a fairly uniform longitudinal electric field appears in the central circular hole and the field magnitude decays gradually at larger radial distances.

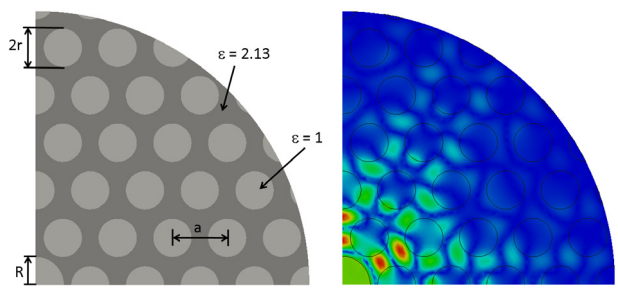


Figure 1: (Left) A quarter model of the Lin PBG fiber; (Right) The longitudinal component of the electric field of the defect mode in the Lin PBG fiber.

The study of power coupling from free space can be carried out through an inverse process by simulating the transmission and radiation of the accelerating mode through a slab of the fiber. The electric and magnetic field patterns calculated by Omega3P are loaded as an excitation at the incident port for ACE3P time domain simulation module T3P. The calculation has been reported in a previous work [2] and has shown that the radiation focuses in six hot spots, which observes the hexagonal symmetry of the Lin fiber. Figure 2 shows the model used in the simulation where a cylindrical slab of the fiber is placed in a hemisphere representing the free

Copyright © 2013 CC-BY-3.0 and by the respective authors

space. The power on the surface of the hemisphere exhibits the six-fold symmetry of the radiation pattern.

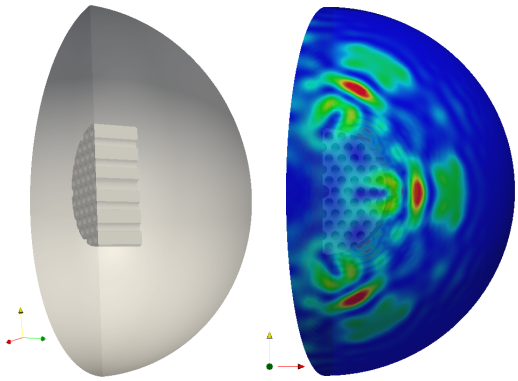


Figure 2: (Left) One half of the model for a cylindrical slab located in free space with the defect mode driven from the left end of the slab; (Right) Radiated power pattern in the forward hemisphere (after reflection at the symmetry plane in the front) with radius of 40λ.

Modification of the above scheme by cleaving the end of the fiber at a certain angle has shown that the far-field radiation pattern changes to a simpler pattern. A model with a cleaved angle of 45° is shown in Fig. 3. By varying the angle gradually, the far-field radiation pattern moves away from its six-fold symmetry without cleaving to focus into two well-defined spots in the upper hemisphere for the slab cleaved with an angle of 45° at the mode exit end. Figure 4 shows the comparison of the far-field radiation for the two cases with and without cleaving. The latter fiber geometry that produces the two hot radiated spots has the potential of simplifying the configuration of laser beams needed to excite the defect mode.

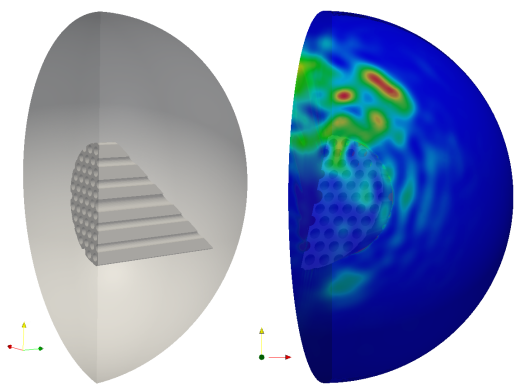


Figure 3: (Left) One half of the model for the Lin fiber slab cleaved at 45° at the exit end of the mode propagation; (Right) Radiated power pattern in the forward hemisphere (after reflection at the symmetry plane in the front) with radius 40λ.

WAKEFIELD IN HC1060 FIBER

The geometry of the commercial HC1060 fiber (KNT Photonics, Denmark) used for telecom was carefully modeled based upon scanning electron micrograph (SEM)

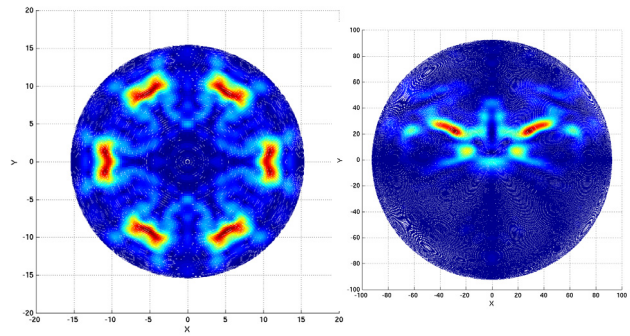


Figure 4: Far-field radiation pattern in the forward hemisphere with radius 80λ for (a) fiber without cleaving showing six-fold symmetry; (b) fiber cleaved at 45° showing two hot spots.

images taken at Stanford University. Figure 5 shows a recent SEM image of a HC1060 sample with ε = 2.13 that was used in the wakefield experiments. The core of the fiber is a circular region, which is the PBG lattice, surrounded by a cladding with a thickness about 2/3 of the diameter of the lattice region. The lattice has a central defect whose size is much bigger than the other lattice holes when compared with the Lin fiber in the previous section. The lattice holes are separated by dielectric vertices and webs whose dimensions are on the order of sub-microns. Simulation using R-Soft BandSolve shows that the web thickness determines the bandgap location with thicker web making lower bandgap frequency. The glass vertices determine the bandgap width, with more glass making wider bandgap. More detailed SEM measurements will be carried out to elucidate more accurately the vertices and web dimensions. For T3P simulation, the lattice period a 2.75 μm, the defect diameter 9.6 μm, the vertex size = 0.16a, and the web thickness = 0.036a have been used.

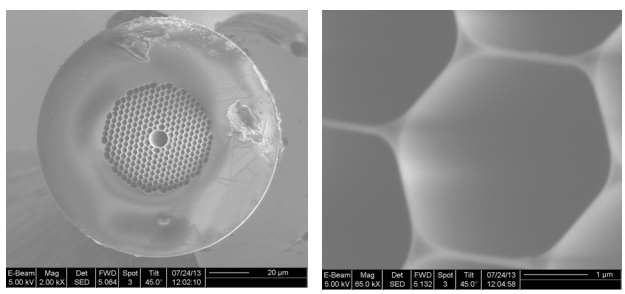


Figure 5: (Left) SEM image of a sample HC1060 commercial fiber; (Right) Close-up image showing the glass webs and vertices connecting the vacuum hexagonal-shape holes.

The T3P simulation of the HC1060 fiber assumes a perfect symmetry of the lattice, so that a 30° slice is sufficient to model the full geometry for the excitation of an axial beam. A Gaussian bunch of RMS σ = 0.3 μm enters from the left boundary and transits through the fiber with a length of 20a. The frequency content of the Gaussian bunch covers the bandgap frequency range as

Copyright © 2013 CC-BY-3.0 and by the respective authors

well as that contributed by mostly the cladding modes located near the edge of the fiber. Figure 6 shows a snapshot of the wakefield generated by the transiting beam. The trailing field inside the lattice indicates possible excitation of the fiber modes and the field in the cladding demonstrates Cerenkov radiation because of its higher dielectric constant. The simulated model has a shorter cladding width than that shown in the SEM image. This mostly affects the excitation of the cladding modes. The effect on the lattice modes is small. The radiation field is monitored as a function of time outside the HC1060 structure, from which the mode spectrum is obtained by the Fourier transform of the radiated signal.

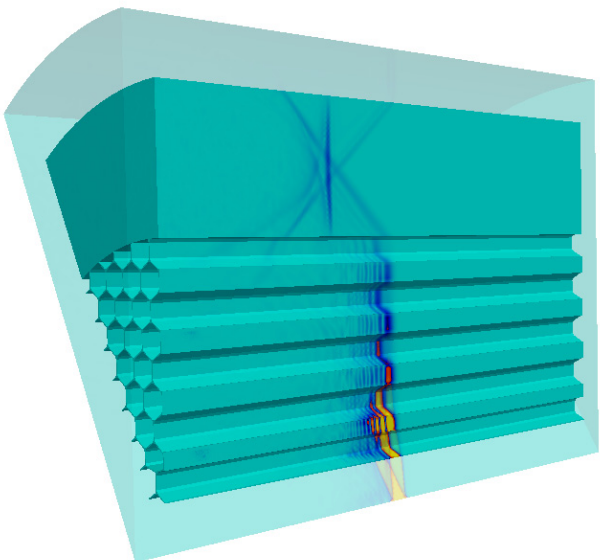


Figure 6: Snapshot of T3P simulation of beam transit through the HC1060 fiber enclosed in a vacuum region. The beam enters the structure from the left end and exits at the right.

Figure 7 shows the comparison of the radiated spectrum obtained by simulation and measurements. The spectrograph measurement in the experimental setup ranges from 550 nm to 1200 nm with 3 nm resolution step, which is comparable to the resolution of the time domain simulation. It can be seen that the simulated spectrum is in good qualitative agreement with measurements. It should be pointed out that modes of lower frequencies (or longer wavelengths) are also found in simulation. They are likely the modes generated in the cladding region of the HC1060 and will radiate away at short distances. The spectrograph measurement can be extended to the lower frequency region to determine whether the cladding modes still contribute to the signal measured at large distance from the beam excitation region.

The modes in the peaks of the spectrum can be identified by calculation in the frequency domain using Omega3P. Figure 8 shows some modes that are localized in the lattice without much field content in the cladding. In particular, a mode with significant longitudinal electric field component is found at 994 nm, which is just outside the bandgap calculated by BandSolve.

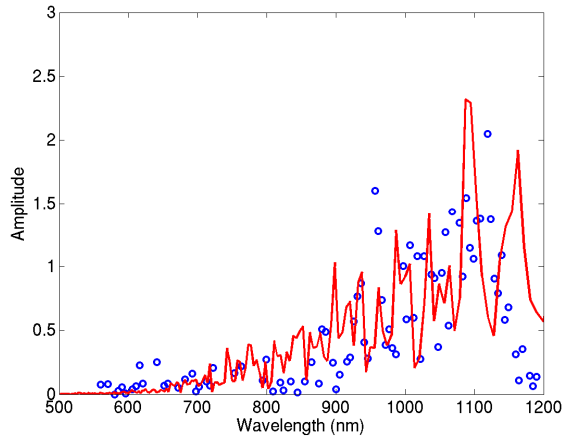


Figure 7: Comparison of simulation (red) and measurements (blue) for the radiation spectrum generated by a beam transit in the HC1060 fiber.

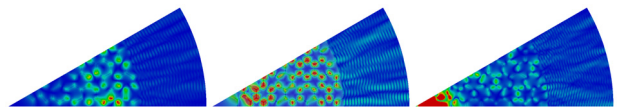


Figure 8: Field patterns of lattice modes in the HC1060 fiber. The wavelengths of these modes are 1150 nm, 1114 nm and 994 nm (from left to right).

SUMMARY

We have used the electromagnetic code suite ACE3P to simulate power coupling and wakefield in photonic bandgap fibers. A simple mechanism of coupling power into the Lin fiber for exciting the accelerating mode can be achieved by cleaving the fiber end at 45° where the laser pulses are directed as indicated in Fig. 4. For the HC1060 commercial fiber for telecom applications, simulation results corroborate well with wakefield experiments, showing that modes in the bandgap can be excited by the transit of a beam through the fiber.

ACKNOWLEDGEMENTS

This research used resources of the National Energy Research Scientific Computing Center, which is supported by the Office of Science of the U.S. Department of Energy under Contract No. DE-AC02-05CH11231.

REFERENCES

[1] X.E. Lin, Phys. Rev. ST Accel. Beams **4**, 051301 (2001).
[2] C.-K. Ng et al., Phys. Rev. ST Accel. Beams **13**, 121301 (2010).
[3] R.J. England et al., Experiment to Demonstrate Acceleration in Optical Photonic Bandgap Structures, Talk given at PAC 2011, March 28 – April 1, 2011, New York, USA.
[4] ACE3P electromagnetic simulation suite: https://confluence.slac.stanford.edu/display/AdvComp/Materials+for+cw11

Copyright © 2013 CC-BY-3.0 and by the respective authors

BEAM POSITION MONITOR FOR MICRO-ACCELERATORS*

K. Soong†, R.L. Byer, E.A. Peralta, Stanford University, Stanford, CA 94305, USA
R.J. England, Z. Wu, SLAC National Accelerator Laboratory, Menlo Park, CA 94025, USA

Abstract

Rapid progress in the development of laser technology and in the sophistication of semiconductor manufacturing has enabled the realization of the first dielectric laser-driven particle accelerator (DLA) on a chip [1]. Since the accelerating channel in DLA structures typically have dimensions in the sub-micron range, the ability to precisely control particle position within these structures will be critical for operation. A number of beam deflection and focusing schemes have been devised, but without the ability to measure the position of the particle beam to nanometer accuracy, these schemes will be extremely difficult to implement.

We present a new concept for a beam position monitor with the unique ability to map particle beam position to a measurable wavelength. Coupled with an optical spectrograph, this beam position monitor is capable of sub-nanometer resolution. We describe one possible design of this device, and present the current status of the structure fabrication and experimental demonstration.

INTRODUCTION

Recent success at SLAC and Stanford have demonstrated the proof-of-principle of the dielectric laser-driven accelerator (DLA) [1]. These dielectric accelerator structures are fabricated using commercially developed lithographic fabrication methods and can be mass produced on conventional dielectric wafers. The accelerator structures are powered using commercially available laser systems, rather than specialized klystrons, and can support peak electric fields well beyond those found in traditional accelerator components. Therefore, DLAs have the advantage of requiring a three-order of magnitude smaller footprint, while boasting significantly higher acceleration gradients than those achievable in traditional accelerator structures. With its inherent advantages, DLAs have the potential to revolutionize the concept of particle accelerators, moving the technology from expensive grand-scale machines to low cost printed microstructures. The applications of compact particle accelerators are numerous and extensive, spanning everything from radiation therapy to x-ray microscopy. While the recent proof-of-principle demonstration is a momentous occasion, the road to a complete particle accelerator-on-a-chip is still an arduous journey. A complete particle accelerator will require the staging of hundreds or thousands of individual dielectric accelerator microstructures, as well as beam focusing and beam deflecting elements – with submicron alignment tolerances. And although nanometer-class alignment of structures within a single wafer is inherent through well-established lithography methods, alignment from wafer-to-wafer does not have a corresponding process. For this reason, beam monitoring elements will necessarily be a critical component for DLA devices.

We present experimental demonstration towards a novel beam position monitor (BPM) which has the ability to map beam position to a measurable wavelength [2]. Coupled with a commercial optical spectrograph, this novel BPM device is capable of sub-nanometer resolution. Additionally, this BPM device can be easily fabricated alongside the DLA accelerator structures, using the same mass-producible lithographic processes; thereby ensuring nanometer-class alignment.

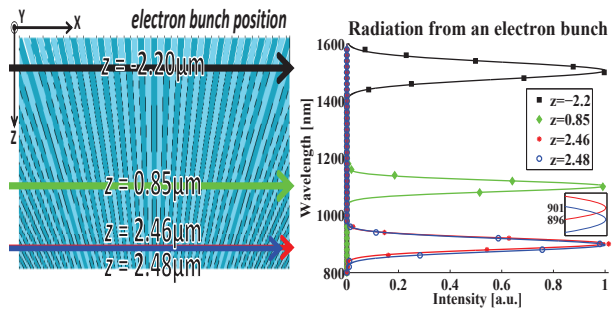


Figure 1: A top-down view of the grating BPM geometry (left), and the predicted normalized radiation spectrum from an electron bunch traversing the grating BPM at four unique positions (right). The markers on the plot represent simulation data, whereas the solid lines depict a Gaussian fit. The inset highlights the distinct radiation spectrum generated by two closely separated bunches.

The geometry of the proposed beam position monitor is shown in Fig. 1. The structure operates on the principles of an inverse-accelerator structure. If a grating accelerator structure can accelerate electrons with a laser pulse, then by reciprocity an electron beam traversing an unpowered grating structure will decelerate (slightly) and radiate. Based on the operating principles of the grating structure as an accelerator, we expect the generated wakefield radiation to be polarized in the direction of beam propagation. Additionally, from the phase-synchronicity condition ($\lambda_{laser} = \lambda_{grating}$), we expect a traversing electron beam to generate wakefield radiation with a center wavelength matching the observed structure periodicity. By varying the periodicity of the grating structure as a function of position, we create a structure which generates position-dependent

* Work supported by DOE (SLAC and LEAP), DARPA (AXiS), the Stanford Graduate Fellowship and the Robert Siemann Fellowship.
† kensoong@slac.stanford.edu

Copyright © 2013 CC-BY-3.0 and by the respective authors

radiation. We can then deduce the position of a traversing electron beam by simply observing the color of the radiation.

We have begun fabrication of a grating beam position monitor with a periodicity varying continuously from 800 nm to 1600 nm. A lithographic mask has be produced, and initial analysis of the exposure of resist on a fused silica wafer look promising, as shown in Fig. 2a. In anticipation of a complete grating BPM structure, we have begun beam-based experiments to demonstrate the proof-of-principle of the BPM device concept. In the following experiments, we verify the operating principles of the grating BPM using a single period grating structure as a stand-in, shown in Fig. 2b. Namely, we verify a polarization dependent radiation, as well as a geometry dependent radiation wavelength.

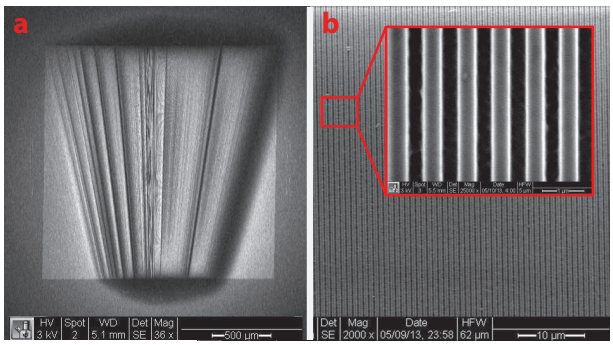


Figure 2: SEM images of (a) the in-progress grating BPM structure and (b) the uniform single period grating accelerator structure.

EXPERIMENT

The experiments were performed at the Next Linear Collider Test Accelerator (NLCTA) at SLAC. The NLCTA beamline is capable of generating a 60 MeV relativistic electron beam, with a bunch length of 130 μm and 5 pC of charge. This electron beam is then focused through a high-field strength permanent magnet quadrupole triplet, which produces a typical beam r.m.s. spot size of 30 x 30 μm^2 at the entrance of our test structure. The test structure itself is mounted on a four-axis stage, allowing for micrometer-precision control of the structure's vertical, horizontal, tip, and rotation with respect to the beam. The structure used in this experiment was the uniform binary dual grating structure optimized for the laser-driven acceleration experiments [1]. In this experiment, a drive laser source was not used to power the structure. Instead, a photomultiplier tube (PMT) was used to monitor the coupling port, along with either a polarizer or a spectrograph to filter the radiation. A simplified schematic is shown in Fig. 3.

In the first experiment, we monitored the strength of the radiation signal filtered by a polarizer. The physics of the grating accelerator predicts a strong wakefield polarization in the direction of the beam trajectory. In our experiment, this will manifest as a cosine-squared pattern in the wakefield intensity versus polarization. We find that our experimental results are in strong agreement with theory, as shown in Fig. 4. This agreement verifies that the nature of the radiation is an inverse-acceleration effect, rather than Cherenkov or optical transition radiation.

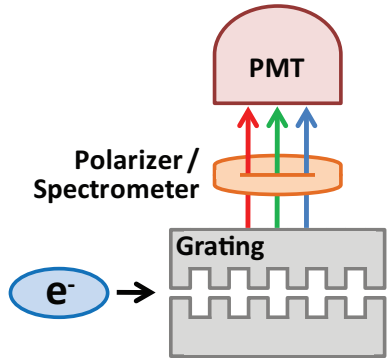


Figure 3: A simplified schematic of the primary components in the wakefield radiation experiment.

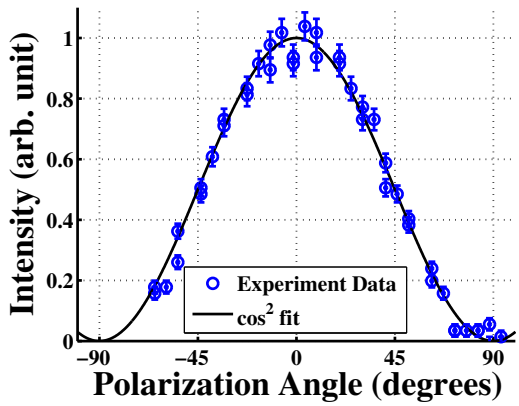


Figure 4: Experimental data (blue markers) showing highly polarized wakefield radiation, which is in strong agreement with theory (black line).

In the second experiment, we monitored the strength of the radiation signal filtered by an optical spectrograph (10 nm slit width). From the electron-laser phase synchronicity condition of the grating accelerator, we expect to observe wakefield radiation with a periodicity matching that of the grating accelerator. A wavelength versus intensity scan of the emitted wakefield radiation reveals a distinct peak in radiation near the design periodicity of the grating structure. We extract the wavelength peak and bandwidth by fitting the recorded wakefield spectrum with an asymmetric Gaussian, as shown in Fig. 5, where we find a center radiation wavelength at 782.5 $\pm$ 9.5 nm. This is in close agreement with the 800 nm design period of the grating structure. The wide bandwidth of the radiation signal is likely due to the 10 nm slit width of the spectrograph.

In the third and final experiment, we varied the rotation of the grating structure relative to the electron beam,

Copyright © 2013 CC-BY-3.0 and by the respective authors

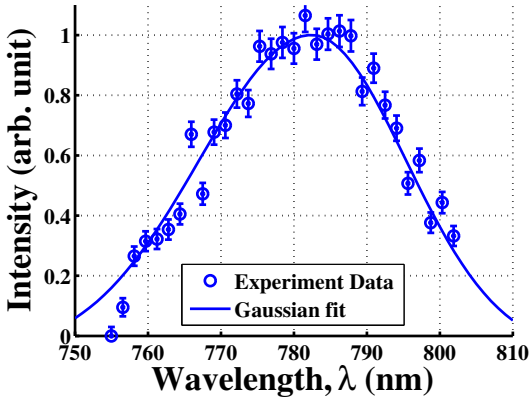


Figure 5: Spectrum of the wakefield radiation as measured by a spectrograph (blue markers). An asymmetric Gaussian fit (blue line) predicts the center wavelength at 782.5 nm with a bandwidth of 9.5 nm.

thereby effectively modifying the grating period observed by the electrons. For a grating structure rotated at an angle ϕ relative to the electron trajectory, the effective grating period λ_e is given by,

$$\lambda_e = \frac{\lambda_0}{\cos\phi} \tag{1}$$

where λ_0 is the nominal grating period. At each grating rotation position, we measured the wakefield spectrum using an optical spectrograph, in the same manner as the previously mentioned experiment. A comparison of the extracted peak wavelength for five unique rotation positions reveals the trend described by Eq. 1. This comparison is shown in Fig. 6.

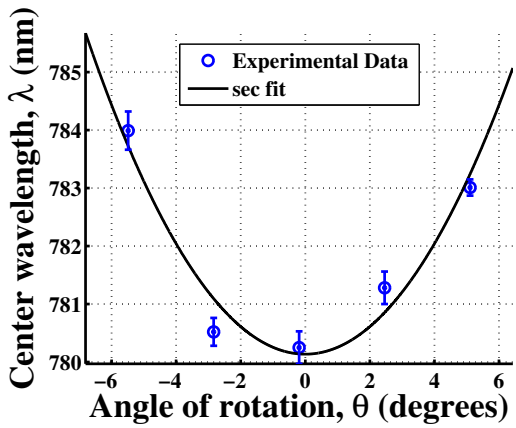


Figure 6: The observed center wavelength (blue markers) at five distinct grating rotation angles. A secant fit to the data (black line) verifies that the radiation wavelength is dependent on the structure geometry.

From these three experiments, we demonstrate the operating principles of the grating beam position monitor. We observed a wakefield radiation signal generated by the inverse-acceleration effect, we measured the spectrum of the wakefield radiation, and we show that the spectrum of the wakefield radiation signal is highly dependent on the geometry of the radiating structure. Future work include the complete fabrication of the continuously variable grating beam position monitor, as well as the beam testing of this device.

ACKNOWLEDGMENT

This work is funded by the Department of Energy (SLAC and LEAP), DARPA (AXiS), the Stanford Graduate Fellowship, and the Robert Siemann Fellowship.

REFERENCES

[1] E.A. Peralta, K. Soong, R.J. England, et al., "Demonstration of electron acceleration in a laser-driven dielectric microstructure," Nature, advance online publication, doi:10.1038/nature12664.

[2] K. Soong and R.L. Byer, Opt. Lett. v. 37 (2012) p. 975-977.

Copyright © 2013 CC-BY-3.0 and by the respective authors

SILICA ROD ARRAY FOR LASER DRIVEN PARTICLE ACCELERATION*

Z. Wu, J. England, R. Noble, SLAC, Menlo Park, CA 94025, USA
E. Peralta, K. Soong, Stanford University, Stanford, CA 94305, USA
M. Qi, Purdue University, West Lafayette, IN 47907, USA

Abstract

Here we describe a structure of double-row silica rods array for laser driven acceleration. Similar to the dual-layer rectangular grating structure, the periodic arrangement of the rods alongside the beam channel provides the necessary phase modulation of the electromagnetic fields, and therefore required phase synchronicity for laser acceleration of charged particles. Resonances among adjacent rods could enhance the near-fields in the gap region to achieve high gradient operation. Simulation has been carried out to optimize the structure dimensions for high accelerating gradient or high acceleration factor. Results show that acceleration factor up to 0.45 could be achieved from this rod array structure. One advantage of this structure is that all the rods are fabricated on one single substrate, therefore positioned and aligned with photolithographic level precision. Several prototype samples have been fabricated for potential laser acceleration experiments.

INTRODUCTION

To utilize the extraordinary electric field available from the state-of-the-art laser systems for charged particle acceleration has long been attractive in the advanced accelerator research. Laser driven dielectric accelerator structures possess advantages over conventional metallic RF structures in their miniaturized dimensions, greatly reduced manufacturing cost, larger breakdown threshold, and higher accelerating gradient [1]. Several resonant or waveguide based structures have been proposed theoretically [1-3]. Recently, near-Infrared laser induced electron energy modulation has been demonstrated for the first time on a fused silica near-field grating structure [4], with larger than 250 MV/m gradient observed.

The dual-layer rectangular grating structure [2] is advantageous for its structural simplicity and convenience of excitation (direct side illumination). However, on-chip power network of an integrated accelerator or accelerator-based light source usually employs a high-index-material waveguide sitting upon a planar low-index substrate, where laser light travels inside the waveguide parallel to the substrate. Side illumination then implies that grating teeth needs to stand up straight with respect to the chip substrate. Direct lithographic fabrication of these vertical teeth up to tens of micron tall is challenging. To vertically assemble a dual-layer, pre-bonded grating accelerator to the chip substrate also demands much fabrication and alignment effort.

*wzr@slac.stanford.edu Work supported by U.S. Department of Energy under Grants DE-AC02-76SF00515, DE-FG06-97ER41276 and by DARPA Grant N66001-11-1-4199.

Meanwhile, deep etching of silicon to form long cylinder array on a substrate has been demonstrated feasible. Oxidation process after etching is also demonstrated to transfer these rods to fused silica. This rod array may essentially serve as the phase-resetting dielectric mask just as well as the rectangular grating structure, but already integrated since it can share the same substrate with the on-chip waveguide network. This paper explores this possibility, by looking into achievable acceleration gradient from a silica rod array structure. Parametric study results of the structure dimensions will be shown, aiming for either optimal acceleration factor or large field enhancement. Following that will be an introduction to the manufacture of the structure.

DESIGN AND SIMULATION

Figure 1 below illustrates the proposed rod array accelerator structure. Two rows of dielectric rods with radius r and length l are laid on a substrate. The two lines are separated in the z direction by a gap width w, forming the electron accelerating channel. Rods across the gap have their centre positions aligned along the y direction. Within each row, the centre-to-centre periodicity between adjacent rods is p. Laser light is incident along the z direction to power this accelerator structure.

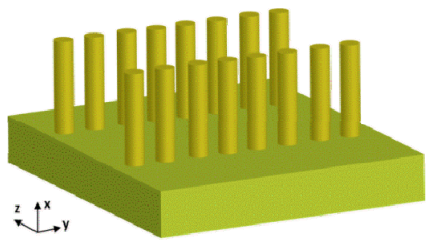


Figure 1: Layout of the rod array accelerator structure.

Silica Rod Array for Acceleration

The structure is modelled in Ansoft HFSS [5] to look for possible phase modulation for net acceleration gradient. Figure 2 shows the single-period structure simulated, with its geometrical parameters denoted on the schematic. Its y-direction periodicity is reflected by assigning master and slave boundary conditions to its left and right xz plane boundaries, with zero-degree phase delay. A plane wave excitation propagating towards the positive z direction is launched, with two perfect-matching-layer boundaries terminating the front and back xy planes to simulate infinite open spaces. The incident plane wave has its e-field polarized in the y direction, with magnitude of 1V/m. The top and bottom yz planes of the model are terminated by perfect magnetic boundary

Copyright © 2013 CC-BY-3.0 and by the respective authors

conditions, so that the rods (1 um long in the model) are effectively infinitely long in the x direction. The rods are made of silica with a dielectric constant of 2.40 and assumed no material loss. The periodicity p is set to 3 um, and so is the simulation wavelength. Note that the gap width $w = p/6$ is defined as the nearest rods edge distance along z, so that the centre-to-centre rod distance is $w+2r$ as marked in the figure. The rod radius is initially set to $0.456p$ in order for the plane wave to experience π extra phase shift per rod along its longest dielectric path in the z direction, so that the wave front can be recovered past the rods [2]. The inset in Fig. 2 plots the real part of the E_y component on the bottom yz surface. One can observe that the incident plane wave recovers its phase front well behind the rods. Also an enhanced field and modulated phase distribution occur in the gap between the rods, which are necessary for net acceleration after integration over one period.

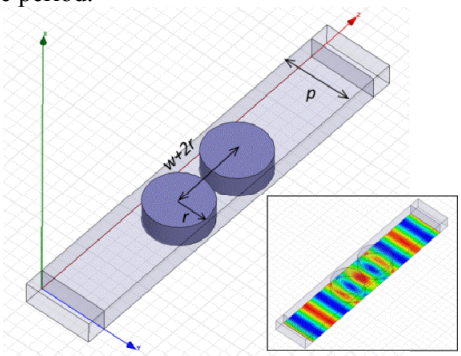


Figure 2: Simulation model of one period of the silica rod array accelerator structure. Inset is the colour map of its longitudinal y component with a plane-wave illumination.

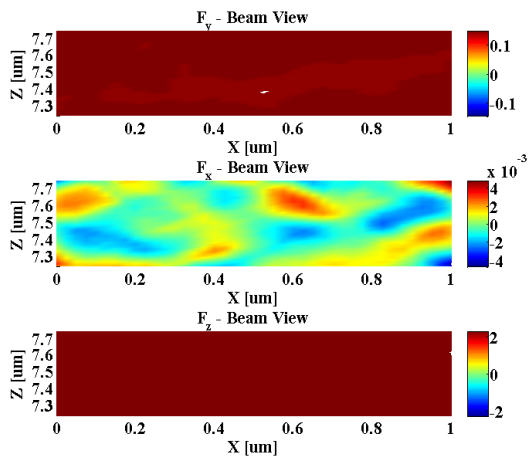


Figure 3: Integrated accelerating force F_y, and deflecting forces F_x and F_z over one rod array period, at a particle injection phase optimized for maximum F_y.

To evaluate the accelerating and deflecting forces a charged particle traversing the channel experiences, the three components E_x, E_y, and E_z in the gap region are sampled and exported. E_y at the centre of the xz cross-sectional area, offset by an extra phase Φ denoting the particle injection phase with respect to the optical phase, is then integrated over the y coordinate for one period to get $F_y(\Phi)$ as the integrated kick a particle of unit charge will encounter. Φ is then scanned over the 2π optical cycle to determine its optimal value to maximize the net acceleration F_y. E_x and E_z are then offset by this optimal injection phase, and integrated as the net deflecting kicks. Calculation results of the model in Fig. 2 are colour-mapped over the gap transverse area in Fig. 3 below. Net acceleration is indeed feasible, with quite uniform F_y of around 0.145 V/m over the whole cross-section of the channel. F_x is almost three orders of magnitude smaller, thus negligible. However, F_z is quite large – about 2.253 V/m over the transverse area, therefore this structure mainly deflects the particle in the z direction.

Elliptical Rods to Optimize Acceleration

From the inset of Fig. 2, it is clear that the dielectric path length along the longitudinal y direction needs to be further shortened to approach one half of the full sinusoidal cycle, so that ideal for maximum net acceleration [2]. With the z dimension size of the rods fixed still for the purpose of the wave front recovery, it implies that the rods need to be elliptically shaped, whose major axis radius R_z will be equal to $r = 0.456p$, and minor axis radius R_y being a variable.

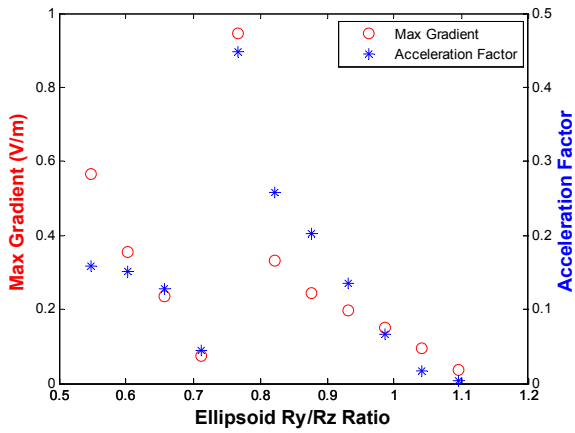


Figure 4: Maximum longitudinal gradient (red circle) and the corresponding acceleration factor (blue star), as the minor axis length of each rod in an elliptical rod array accelerator varies.

Parametric study of R_y (with $p/6$ gap width) has its results plotted in Fig. 4. The maximum gradient value is still the integrated acceleration gradient F_y at optimal injection phase. The acceleration factor (AF), as another important figure of merit (FOM) for dielectric laser acceleration, is defined as the acceleration gradient divided by the maximum e-field magnitude in the dielectric material. It measures the practical achievable gradient before the material breaks down at certain threshold field intensity. The plot shows coincident peaks of both FOMs at $R_y = 0.767R_z$, where the maximum gradient F_y is greatly improved, reaching 0.945 V/m. The optimal acceleration factor on the right ordinate is

Copyright © 2013 CC-BY-3.0 and by the respective authors

roughly 0.45. It is worth mentioning that in this case F_z is about 1.05 V/m and F_x remains negligible. Thus the longitudinal kick is of comparable magnitude with the deflection kick, also a great improvement over the circular rod array design.

Resonant Structure to Enhance Gradient

When doing the same parametric study of R_y, however with doubled gap width $w = p/3$, the elliptical rod array structure shows strong field resonance at $R_y = 0.658R_z$. In this case, with the same incident field magnitude of 1 V/m, the scattered fields from one rod and its adjacent rods interfere constructively, enhancing the longitudinal field in the middle of the gap up to 42 V/m from simulation. Figure 5 illustrates this sharp resonance, and the resultant extraordinary gradient of 17.9 V/m at the peak of the resonance. The inset figure depicts the colour map of the E_y component on the bottom surface of the model, much stronger in magnitude than the excitation plane wave. However, the inset also shows enhanced fields at spots inside the silica rods, normalizing the large gradient to mediocre AF values of 0.311 maximum and 0.267 at the resonance peak.

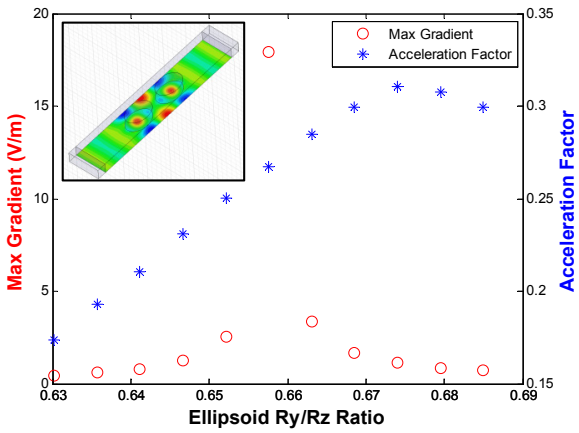


Figure 5: Maximum gradient (red circle) and the corresponding AF (blue star) of a resonant elliptical rod array design.

Despite the fact that its AF is not outstanding, with much smaller excitation field this resonant design could yield the same accelerating gradient as that of non-resonant designs. Therefore it could be operated at low laser power level. Also, at resonance the other two components E_x and E_z remain unenhanced, and the integrated deflecting kick F_z is only 1.8 V/m, almost one order of magnitude lower than the longitudinal kick. F_x is three orders of magnitude lower than F_y. This resonant design deflects charged particles much less, and uses laser energy more efficiently on acceleration.

FABRICATION

The adopted strategy to make this silica rod array structure is to first fabricate the rods in silicon and then convert the rods into silicon dioxide. It takes advantage of the available deep etch chemistry for silicon while avoiding the difficulty in fabricating high-aspect ratio silicon dioxide rods. A 600 nm thick negative tone resist, Hydrogen SilsesQuioxane (HSQ), was spun on a silicon wafer and subsequently exposed by an electron-beam lithography tool at 100 kV acceleration voltage. After development the pattern was transferred to silicon in a high-density plasma etching tool using chlorine chemistry. The etched depth was about 10 micrometers. The conversion into silica rods was achieved through wet oxidation at around 900 degree C.

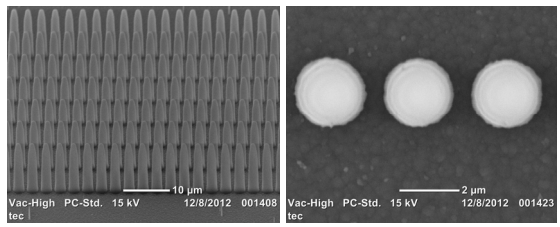


Figure 6: Side-view and top-view SEM images of a fabricated silica rod array structure.

SEM images of some prototype samples of a silica rod array structure are shown in Fig. 6. From the top view on the right, the circular shapes are well defined, and the centre-to-centre spacing of the rods is roughly 3 um. From the side view on the left, the rods have consistent heights of around 10 um. However, instead of a uniform cylinder, each rod exhibits a tapered down diameter along its long axis. A silicon-made rod array may provide net acceleration just as well, whose manufacture then avoids the oxidation process and may lead to better control on the rod cross-sectional uniformity. Fabrication of elliptical shaped rods array is also under exploration.

CONCLUSION

In this work, a new accelerator structure of double-row silica rod array is studied. Net acceleration is found achievable with circular shaped rods, and elliptical shaped rods improve its performance in terms of optimized acceleration factor and reduced deflecting forces. Acceleration factor as high as 0.45 can be realized with an ellipse aspect ratio of 0.767. Of certain dimensions the structure also exhibits strong longitudinal e-field enhancement in the accelerating channel, therefore useful for achieving large gradient with low laser power, and for suppressing beam deflection. Preliminary fabrication of a circular shaped rod array has been done. Samples appear promising, and show room to improve with respect to the uniformity of the rod cross-section, as well as possibility to fabricate elliptical shaped rods.

REFERENCES

[1] X. E. Lin, Phys. Rev. ST-AB 4 (2001) 051301.
[2] T. Plettner et al., Phys. Rev. ST-AB 9 (2006) 111301.
[3] B. M. Cowan, Phys. Rev. ST-AB 11 (2008) 011301.
[4] E. A. Peralta et al., Nature, in press, (2013).
[5] Ansoft HFSS, version 12.

Copyright © 2013 CC-BY-3.0 and by the respective authors

SPECTRAL BROADENING OF IONS ACCELERATED BY A RADIATION PRESSURE DRIVEN SHOCK *

N. Cook†, C.M. Maharjan, P. Shkolnikov, Stony Brook University, Stony Brook, NY 11790, USA
I. Pogorelsky, M.N. Polyanskiy, O. Tresca, BNL, Upton, NY 11973, USA
N.P. Dover, Z. Najmudin, Blackett Laboratory, Imperial College,
London SW7 2AZ, United Kingdom

Abstract

Laser driven ion acceleration has been the focus of considerable research efforts since multi-MeV energies were first demonstrated. Most experiments use solid state laser pulses focused onto thin foil targets. However, recent progress in CO_2 laser technology allows for the creation of intense pulses at lambda $\sim$10 μm. The longer wavelength permits the use of low density targets. In these conditions ion acceleration is primarily driven by a shock wave due to the radiation pressure of the laser. This acceleration mode has the advantage of producing narrow energy spectra while scaling well with laser intensity. New improvements to the CO_2 laser at the Accelerator Test Facility allow for the unique production of a single picoseconds-scale pulse with 1TW peak power. We report on the interaction of an intense CO_2 laser pulse with overdense hydrogen and helium gas jets. Using a two pulse optical probe, we are able to obtain real-time density profiles at different times during the interaction, allowing for the characterization of shock wave velocities and peak density conditions. Ion energy spectra are measured using a Thomson spectrometer and scintillating screen.

INTRODUCTION

Acceleration of protons by intense laser pulses has become an increasingly active area of study amongst nuclear, plasma, and accelerator physicists. Considerable progress has been made using thin foils as targets for high intensity lasers at optical wavelengths [1] [2] . These experiments utilize the highest intensity lasers to reach the highest proton energies, but at the expense of beam quality and energy spread.

An alternative is to use the radiation pressure of the laser to drive hole-boring or shock wave acceleration of ions from a low density target. The ponderomotive force of the laser can drive plasma electrons in an underdense plasma further into the target, forming a critical surface. For a cold electron population, hole-boring acceleration takes place. The plasma critical surface recedes at the hole-boring velocity, v_{HB}, reflecting ions at a velocity of $2v_{HB}$. Recent experiments with intense, circularly polarized, CO_2 laser pulses have demonstrated hole-boring acceleration by producing collimated bunches of protons with energies greater than 1 MeV and narrow energy spread [3] [4].

* Work supported by the United States Department of Energy, Grant DE-FG02-07ER41488.

† ncook@bnl.gov

In the case of a hot electron population, the strong charge separation at the critical surface launches a shockwave into the plasma, which reflects ions at nearly twice the shockwave velocity [5]. This mechanism requires a high electron temperature to reach high shock velocities. Collisionless shockwave acceleration has been shown to similarly produce quasi-monoenergetic proton beams [6].

Improvements to the CO_2 laser system at Brookhaven National Laboratory's Accelerator Test Facility have allowed for the production of ps-scale single pulses with TW peak power [7]. We report on the acceleration of protons using intense linearly polarized CO_2 pulses. With two pulse optical probing, we measure peak densities and shock wave velocities, while ion spectra are measured using a scintillator and Thomson spectrometer. Observed profiles correlate with 1D PIC simulations predicting declining shockwave velocity immediately following the laser plasma interaction (LPI).

EXPERIMENTAL METHOD

Utilizing a isotopic CO_2 mixture in a regenerative amplifier, we amplify a 10.2 μm CO_2 pulse centered on the R-branch of vibrational transitions. The pulse passes through a 10 bar amplifier resulting in a single 5 ps pulse providing a maximum of 1 TW power [7]. The pulse is then focused with an $f/3$ off-axis parabolic mirror to a focal spot of $w_0 = 50$ μm, providing a maximum on-target intensity of $I \sim 3 \times 10^{16} W cm^{-2}$ corresponding to $a_0 = 1.5$. The laser contrast is $> 10^5$ as measured by an infrared power meter.

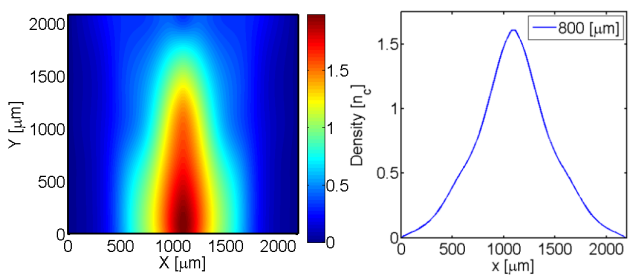


Figure 1: H_2 neutral density from a 1 mm nozzle at 15 bar backing pressure. Right, the density profile 800 μm above the nozzle.

We use 1 mm and 2 mm cylindrical nozzles to produce high density gas jets. Figure 1 shows the neutral density for H_2 gas with a backing pressure of 15 bar. A lineout is taken at 800 μm from the nozzle, showing a peak density

Copyright © 2013 CC-BY-3.0 and by the respective authors

of $1.5 \times 10^{19} cm^{-3}$ along the laser axis, with an underdense absorption region upstream of the laser focus. The critical density for a 10.2 μm laser is $1.06 \times 10^{19} cm^{-3}$.

A frequency-doubled 532 nm YAG pulse is split into two 14 ps probe channels for plasma diagnostics, as shown in Figure 2. Each pulse interacts with the plasma transverse to the laser axis, with a variable delay of 50 ps to several ns achievable between pulses. One beam is used for shadowgraphy; the resulting image provides highlights areas of rapidly changing density, due to the dependence on the 2nd-derivative of refractive index. The other is sent through a Mach-Zehnder interferometer, providing a density dependent fringe pattern.

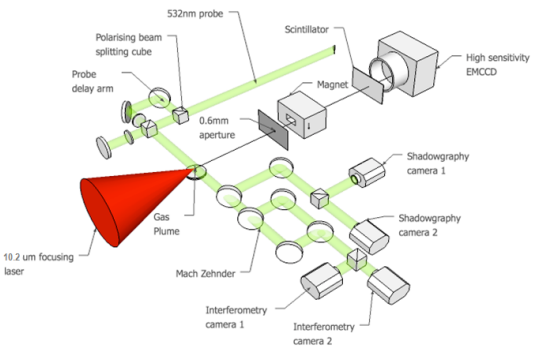


Figure 2: Optical probing arrangement.

The accelerated ion beam is filtered through a 600 μm pinhole before being dispersed by a Thomson spectrometer. The corresponding solid angle seen by the pinhole is 1.2×10^{-5} sr. The beam is dispersed according to momentum by a 5 cm magnet, while a 6.4 cm long electrode provides an adjustable electric field for displacing different ion charge states, if needed. The dispersed beam strikes a 0.5 mm thick sheet of BC-408 polyvinyl toluene (PVT) based scintillator. Photon yield calibrations have been performed using low energy protons at the Stony Brook Tandem Van de Graaf [8]. Scintillation light is imaged by a Princeton ProEM+ EMCCD camera.

PROTON ACCELERATION WITH NARROW ENERGY SPREAD

The ion beam profile is near Gaussian in both spectral and transverse directions, the latter of which is caused by passage of the beam through the pinhole along the laser axis. We can deduce the instrument function of the pinhole from this transverse spread, allowing us to calculate a true spectral profile of the beam. The obtained spectrum is shown in Figure 3. The central energy of the beam is measured at $\sim$ 1.6 MeV with a 12% FWHM energy spread. Using our calibrated BC-408 yields, we observe $\sim 8 \times 10^9$ protons/MeV/sr.

For this particular shot, the H_2 backing pressure is 12 bar, leading to peak neutral densities of $1.5 \times 10^{19} cm^{-3} \simeq 1.4$ n_c. We measure a laser pulse energy of 4.34 J on target, corresponding to $a_0 = 1.25$. The predicted hole-boring velocity at this intensity and density is $v_{hb} \approx 8 \times 10^6 ms^{-1}$, resulting in a kinetic energy of 1.3 MeV, less than the observed proton energies. We also measure the proton density using interferometry taken 132 ps after the beginning of the LPI. By performing an inverse Abel transform on the target's phase map, we obtain electron density profiles of the plasma, as shown in Figure 4.

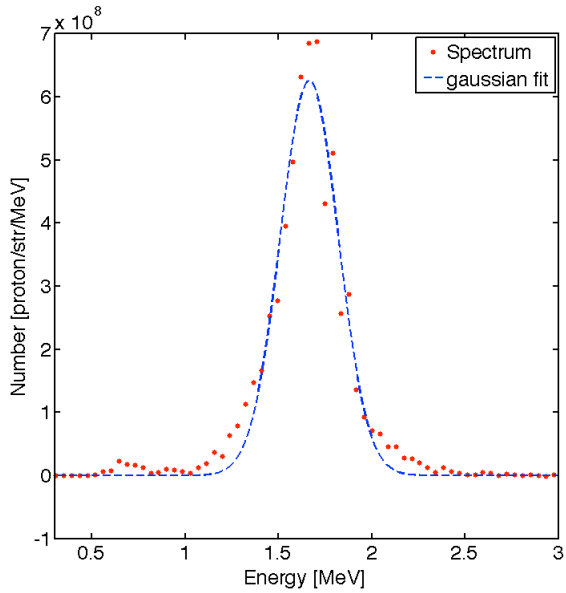


Figure 3: Proton energy spectrum shows a well defined peak at 1.6 MeV with a 12% FWHM energy spread.

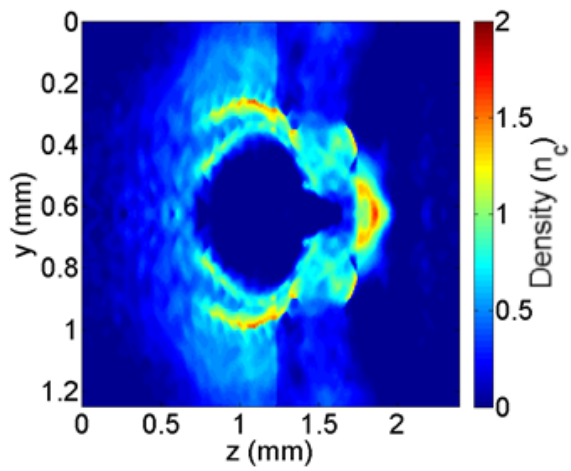


Figure 4: Time resolved interferometry reveals the plasma density distribution at 132 ps after the LPI begins. The laser travels left to right.

SHOCKWAVE VELOCITY EVOLUTION

We observed many instances of accelerated protons possessing a broad energy spectrum under the same experimental conditions as described above. Figure 5 shows a combined spectra of protons accelerated by similar laser intensities. Single shot outcomes are strongly sensitive to

Copyright © 2013 CC-BY-3.0 and by the respective authors

target conditions [9]. In particular, the laser pre-pulse has a significant effect on the ion spectrum by tailoring the density profile prior to the arrival of the main pulse. This effect will be discussed in detail in a future publication.

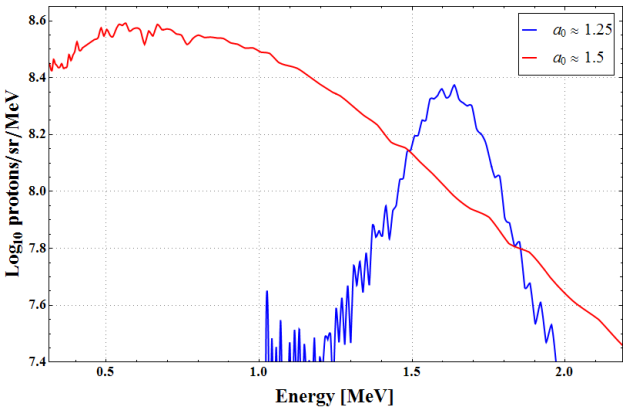


Figure 5: A comparison of measured proton spectra with listed laser intensities.

We performed 1D PIC simulations using EPOCH to investigate time dependence of shockwave velocity. Simulations were performed using 1300 cells at 100 particles per cell within a 500 μm simulation box. Figure 6 shows the proton density evolution through an infinite slab of cold plasma with density $2n_c$ after irradiation by a 1 TW pulse. Collisions are included in the simulation processes.

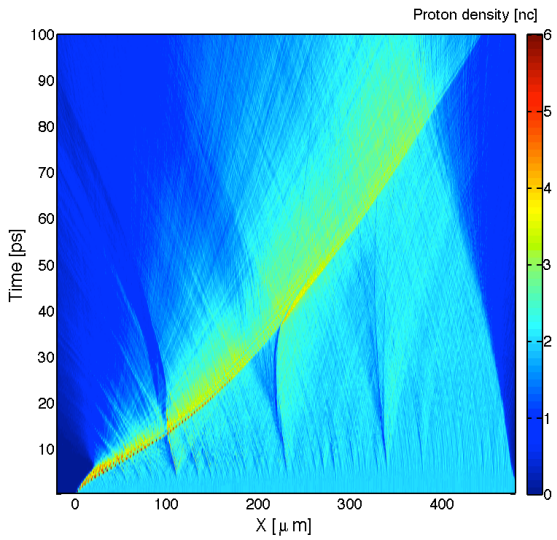


Figure 6: Particle density plotted from 1D PIC simulations.

These simulations show a clear decline in shockwave velocity beginning within the first few ps beyond the LPI. A significant reduction in peak ion density is also predicted by the simulation. The decay of the shockwave velocity modifies the accelerated proton spectra as protons are reflected at lower energies. The resultant spectra are highly dependant upon the duration in which ion reflection occurs. Energy spectra predicted by PIC simulations document the degradation of ion spectra with time and are shown in figure 7. A lengthened ion reflection period would suggest an increase in the total number of ions accelerated, which is consistent with observed spectra in figure 5.

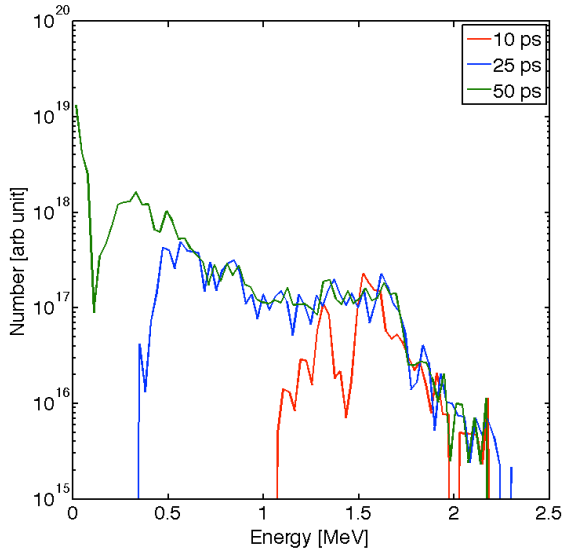


Figure 7: Simulated ion spectra extracted at different times after the LPI.

CONCLUSION

We have reported the production of high purity proton beams from the interaction of a single, linearly polarized 10.2 μm CO_2 pulse with near critical density Hydrogen gas. Peak proton energies correlate well with those predicted by radiation pressure models. Interferometry taken immediately following the LPI show the creation of a high density shock which propogates into the plasma. However, a broad swath of proton energy spectra are measured, providing evidence of rapid decline of shockwave velocities. These findings are corroborated by 1D PIC simulations with comparable experimental parameters. Our results emphasize the importance of target profile and LPI timeframe in accelerating ions with a narrow energy spread.

REFERENCES

[1] H. Daido et al. Rep. Prog. Phys. 75 (2012) 056401

[2] A. Macchi, M. Borghesi, & M. Passoni. Rev. Mod. Phys. 85 (2013) 751793

[3] C. Palmer et. al. Phys. Rev. Lett. 106 (2011) 014801.

[4] Najmudin et. al. Phys. Plasmas. 18 (2011) 056705.

[5] Pogorelsky et. al, "Ion acceleration by laser hole-boring into plasmas," AIP Conf. Proc. 1507, pp. 814-819

[6] Haberberger et al. Nat. Phys. 8 (2012) 9599.

[7] M.N. Polyanskiy, I. Pogorelsky, & V. Yakimenko. Optics Express, 19 (2011) 7717-7725.

[8] N. Cook, Dissertation, Stony Brook University. To Be Published.

[9] A. Macchi, A.S. Nindrayog, F. Pegoraro. Phys. Rev. E. 85(2012) 046402.

Copyright © 2013 CC-BY-3.0 and by the respective authors

A BETATRON-ANALYSIS TECHNIQUE FOR IDENTIFYING NARROWBAND TRAPPED CHARGE WITHIN A BROADBAND ENERGY TAIL IN PWFA EXPERIMENTS AT FACET*

Chris Clayton#, Weiming An, Chan Joshi, Kenneth Marsh, Warren Mori, Navid Vafaei- Najafabadi (UCLA, Los Angeles, California), Patric Muggli (MPI, Muenchen), Erik Adli, Christine Isabel Clarke, Sebastien Corde, Jean-Pierre Delahaye, Robert Joel England, Alan Stephen Fisher, Joel Frederico, Spencer Jake Gessner, Mark Hogan, Selina Zhao Li, Michael Dennis Litos, Dieter Walz, Ziran Wu (SLAC, Menlo Park, California), Wei Lu (TUB, Beijing)

Abstract

Plasma accelerators driven by ultra-relativistic electron beams have demonstrated greater than 50 GeV/m acceleration gradients over a distance of a meter [1] though the accelerated particles typically have had a 100% energy spread when a single drive bunch was used. However, it is known that by locally producing electrons via ionization within the beam-driven plasma wake, they can become trapped and accelerated so that high-energy, mono-energetic electron bunches can be produced [2]. Prior experiments and the associated simulations [3] suggested that, by augmenting the usual He buffer gas in the heat pipe oven plasma source [4] with a moderate ionization potential (IP) gas such as Ar or Ne, local injection can indeed occur. In a recent experiment associated with the E-200 plasma wakefield accelerator (PWFA) experiment at the Facility for Advanced Accelerator Experimental Tests (FACET) [5] at SLAC, the expected energy gain of these injected electrons (initially at rest) puts them within the energy range of the accelerated tail electrons of the FACET beam. We propose a technique to help identify bunchlets of electrons at the 10's of pC level arising from the ionization injection of Ar/Ne electrons that may otherwise be lost or overlooked as part of the discrete betatron-focusing maxima or the maxima inherent the chromaticity of the imaging electron spectrometer.

OBJECTIVES OF THE EXPERIMENT

For most applications of high-energy beams, narrow energy spreads are desired. By employing spatially localized ionization to produce and inject new electrons within the plasma wake, a PWFA can produce high-energy, mono-energetic electron "bunchlets".

When these bunchlets appear at the image plane of the imaging spectrometer, there are two other types of distinct features that may mask the bunchlets having only 10's of pC of charge. First is the fact that the highly chromatically aberrated electron imaging spectrometer has a very narrow energy range for which a stigmatic focus–a focus that is simultaneous focusing in x and in y (or energy) at the same spot–is located and thus there is always a "bright feature" in the spectrum due to this. Secondly, even with a broadband spectrometer, the electrons (both the FACET beam electrons and any injected electrons; i.e., the bunchlet) exit the plasma with an energy-dependent phase advance of their betatron envelope oscillations [6] that leads to an energy-dependent divergence of the electrons at the plasma exit. This fact also puts structure onto the final spectrum, as discussed below.

Let ζ_k represent the local (within the wake) longitudinal location of the k^{th} slice of the accelerated electrons. Suppose further that this k^{th} slice exits the plasma as a nearly parallel beam having undergone $N = N_k$ betatron oscillations. Due to the finite angular acceptance of the spectrometer coupled with the strong focusing force of the ion column within the wake in the blowout regime, and the finite bit-depth of the recording CCD cameras, this slice will appear relatively bright on the spectrometer. There will be another slice, the k+1$^{\text{th}}$ slice at a lower energy that has undergone $N = N_{k+1} = N_k + 1$ betatron oscillations and will likewise appear relatively bright at the spectrometer. In fact, for each final slice energy such that $N_{k,m} = N_k \pm m$ where $m = \pm1, \pm2$, etc., there will be a corresponding bright spot on the spectrometer. We call this series of spots the "betatron ladder". This ladder was clearly visible in the E-167 energy-doubling experiment of Ref. [1].

In the following Sections we will describe the experimental setup, derive the energy-locations of the betatron ladder, and finally suggest a strategy for identifying the bunchlets within the other structures appearing at the image plane of the spectrometer. Specifically, by placing the stigmatic focus on one "rung" of the ladder after another over a series of data aquistion runs, we can optimize our chances of observing accelerated bunchlets, especially if they lay between or straddle the rungs on the aforementioned betatron ladder.

* The work at UCLA was supported by DOE grant DE-FG02-92-ER40727 and NSF grant PHY-0936266. Work at SLAC was supported in part by Department of Energy contract DE-AC02-7600515.
#cclayton@ucla.edu

Copyright © 2013 CC-BY-3.0 and by the respective authors

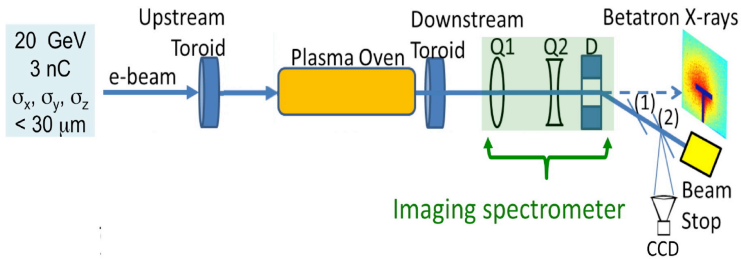


Figure 1: Schematic of portions of the E-200 experimental setup. A 20.35 GeV, 3 nC, compressed (σ_z ~ 30 μm) electron beam is focused ($\sigma_x = \sigma_y$ ~ 30 μm) near the entrance of a Li-vapor column contained in the plasma oven. Toroids measure the incoming and outgoing electron charge. Betatron X-rays excite a phosphor screen located behind 1 mm of copper; the emitted light is captured by a CCD camera (not shown). The imaging spectrometer (quadrapole doublet Q1 and Q2 plus dipole D), discussed further in the text, sends the electrons to the beam stop prior to which is the Cherenkov air gap. The gap is composed of the two Si wafers (1) and (2) which are in laboratory air, thus emitting a Cherenkov-light cone that is subsequently reflected by wafer (2) to a pair of CCD cameras (two cameras for a wide vertical or energy field of view).

EXPERIMENTAL SETUP

A rough schematic of the FACET setup for the E-200 experiments is shown in Fig. 1. The fully compressed FACET beam (σ_z ~ 30 μm) is focused to a nearly round spot of $\sigma_x = \sigma_y$ ~ 30 μm near the front edge of the Li vapor column which has a length of about 39 cm FWHM. The Li is contained in an oven at a temperature of nearly 1000°C, giving a Li neutral density of 2.5 x 10^{17}cm^{-3}. At each end of the oven is the buffer gas composed of He alone or He with an admixture of an intermediate IP gas such as Ar or Ne. This closed system is in pressure balance. The cooler buffer gas confines the Li by collisionally forcing the escaping Li atoms to the walls where a wick returns the (now liquid) Li back towards the oven's center. The length of the boundary region is about 10 cm on each side of the ~ 29 cm-long constant-density portion of the vapor column. The Li is easily field-ionized by the radial electric field of the (vacuum-size) FACET beam while the He is not. To obtain a mono-energetic beam from the accelerated ionization-injected electrons—the goal of this experiment—fine-tuning of the focal position of the FACET beam and the longitudinal distribution of the admixture is required. Ideally, the FACET beam would have a betatron pinch localized to where the flat-topped region of Li begins and where the availability of the admixture element nearly ends thus terminating injection.

The imaging spectrometer consists of a quadrapole doublet, a dispersing dipole magnet, a pair of Si wafers tilted at 45° to the beam, and two CCD cameras to record the Cherenkov light emitted in the air gap between the wafers and reflected to the lenses of the cameras. As mentioned before, the energy-bandwidth for which a stigmatic focus is obtained is very small.

Examples of the spectra recorded by the spectrometer cameras are shown for three different experimental conditions in Figs. 2(a)-(c). As can be seen especially in Fig. 2(b), the local brightness of the spectrum increases at an energy for which the spectrometer was set to produce a stigmatic focus. The magnification of the spatial imaging from the plasma exit to the Cherenkov air gap is about nine times larger in the *x*-direction than in the *y*- or energy-direction.

Figure 1(a) shows the aforementioned betatron ladder; the few bright spots beginning at ~ 24 GeV and up, as well as a rung near 17 GeV as evidenced by the bulge in this (purposely) saturated portion of the image. For this shot, the final focus quadrapoles were set to put the main interaction point waist about 20 cm upstream of the Li column, twice the β^*_x (= 10cm) of the vacuum waist. Since β^*_y = 100 cm, the beam had a larger *x*-size when it began to field-ionize the Li and hence the amplitude of the betatron oscillations was large in the *x*-direction. This allowed for a clear analysis of the betatron features that is discussed in the following Section.

BETATRON ANALYSIS

For a given plasma density, the number N_k of betatron oscillations experience by the k^{th} slice of the beam is related to the *initial* energy of the beam slice E_0 (which we will approximate as independent of ζ), the effective length L of the plasma and the *final* energy of that slice E_k ($z = L$).

Number of betatron envelope oscillations

A simple definition of N_k is the ratio of L to the betatron period for the k_{th} slice. The betatron period is given by [6] $\pi / k_\beta(\zeta_k, z) = \omega_p(z)/(\pi c)/\left(2\gamma(\zeta_k, z)\right)^{0.5}$. The general expression for N_k at the plasma exit is given by

$$N_k(\zeta_k)\big|_{z=L} = \int_0^L \frac{k_\beta(\zeta_k, z)}{\pi} dz = \frac{\omega_p}{\pi c\sqrt{2}} \int_0^L \gamma(\zeta_k, z)^{-\frac{1}{2}} dz = \frac{\omega_p}{\pi c\sqrt{2}} \int_0^L \left[\gamma_0 + \frac{eG(\zeta_k) z}{mc^2}\right]^{-\frac{1}{2}} dz \quad (1)$$

Copyright © 2013 CC-BY-3.0 and by the respective authors

where we have assumed a constant density along z and a non-evolving electric field of the wake $G(\zeta)$. The final form of Eq. (1) reduces to

$$N_k(\zeta_k)\big|_{z=L} \approx L\frac{\sqrt{2}\omega_p\left(mc^2\right)^{\frac{1}{2}}(\pi c)^{-1}}{E_k^{0.5}(\zeta_k)+E_0^{0.5}} \qquad (2)$$

where $E_k(\zeta_k)$ is again the *final* energy of the k_{th} slice.

Building the betatron ladder

As mentioned before, integer changes in N define the betatron ladder. Thus, taking $N_{k+1} - N_k = 1$ and solving for L we have

$$L = \frac{\pi c}{\sqrt{2}\omega_p\left(mc^2\right)^{0.5}}\left(\frac{1}{E_k^f(\zeta_k)^{0.5}+E_0^{0.5}}-\frac{1}{E_{k+1}^f(\zeta_{k+1})^{0.5}+E_0^{0.5}}\right)^{-1} \qquad (3)$$

where $E_{k+1} < E_k$. After substituting L from Eq. (3) into Eq. (2), and replacing N_k with $N_{k,m} = N_k \pm m$ ($m = \pm1, \pm2$, etc.) the expected energy-locations $E_{k,m}$ of all the other rungs on the betatron ladder are obtained. The dashed lines in Fig. 2 show this calculated ladder lying nicely on the experimentally identified locations of the betatron features.

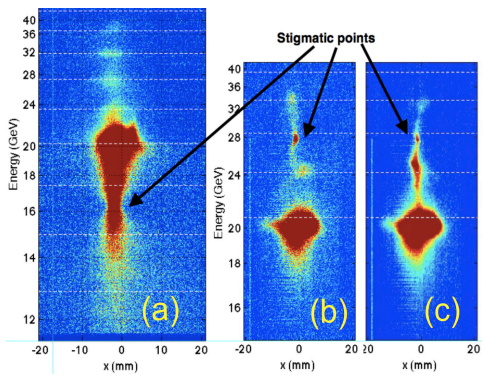


Figure 2: Three electron spectra with betatron ladders overlaid (white dashed lines, see text). (a) Buffer gas: He only, FACET waist 20 cm upstream of Li. (b) Buffer gas 50% He, 50% Ar, FACET waist 0 cm upstream of Li. (c) same as (b) but shot - by - shot difference: potential candidate shot.

The value of L is determined numerically by the measured energies of two of the rungs of the ladder; E_k and E_{k+1}. If there are multiple betatrons spots as in Fig. 2(a), one can take E_k and E_{k+2} while taking $N_k - N_{k+2} = 2$. The same value for L should obtain.

STRATEGY

To distinguish the ionization-injected and accelerated bunchlets from the other structures due to the betatron ladder as in Fig. 2(a) and the narrowband stigmatic focusing of the imaging spectrometer as seen in Fig. 2(b), it is best to place the stigmatic point on a rung of the ladder in order to reduce the complexity of the structred spectrum and thus make the identification of a bunchlet more obvious. Since the energy of the bunchlet is initially unknown, this process would be repeated over a series of data acquisition runs, each run with the stigmatic point dialed onto one of the ladder's rungs. In this way, charge that appears between rungs of the ladder or widely stradling them may possibly be attributable to the bunchlets.

It is important to note that, even if a bunchlet and accelerated FACET tail electrons in some longitudinal slice have the same energy, they will not have the same number of betatron oscillations since the initial energy $E_{0,\text{trapped}}$ of the trapped charge is zero. Thus, the bunchlets could very well be focused or badly defocused at any given output energy. This is why scanning the energy-imaging point is important.

A co-called "candidate shot" for a bunchlet is shown in Fig. 2(c) where there appears to be charge both away from the stigmatic point and straddling rungs the betatron ladder; i.e., it appears that this charge is a new feature not seen in Fig. 2(b).

Although a full analysis of existing data using this strategy has only now begun, looking forward to future runs at SLAC, the plasma length L at FACET is designed to be increased by several times over the current length. While this could in principle simply scale the bunchlet-identification issue to higher energies on the one hand, on the other hand, it may result in a much cleaner measurement of these bunclets. Simulations show that the bunchlet is trapped in the high-field spike at the back of the wakefield, giving it an inherent energy-gain advantage over the FACET tail electrons. Thus, the density of the plasma can dropped to depopulate the high-gradient portion of the wakefield of FACET-beam tail electrons, potentially isolating the ionization-injected and accelerated charge on the spectrometer screen.

REFERENCES

[1] Ian Blumenfeld et al., *Nature* **445**, 471 (2007).
[2] E. Oz et al., *Phys. Rev. Lett.* **98**, 084801 (2007).
[3] Navid Vafaei-Najafabadi et al, *submitted for publication*.
[4] P. Muggli et al., *IEEE Trans. Plasma Sci.* **27**, 791 (1999).
[5] M.J. Hogan et al., *New J. Phys.* **12**, 055030 (2010).
[6] C.E. Clayton et al., *Phys. Rev. Lett.* **88**, 154801 (2002).

Copyright © 2013 CC-BY-3.0 and by the respective authors

SELF AND IONIZATION-INJECTION IN LFWA FOR NEAR-TERM LASERS*

A.W. Davidson, W. Lu, M. Zheng, C. Joshi, L.O. Silva, J. Martins, R.A. Fonseca, W.B. Mori
UCLA, Los Angeles, CA 90024, USA

Abstract

In plasma based acceleration (PBA), the methods of injecting high quality electron bunches into the accelerating wakefield is of utmost importance for various applications, including next generation light sources and high energy colliders. Numerous simulations are being conducted in order to study various methods of injection and to optimize the beam parameters. Particle-In-Cell simulations using codes such as OSIRIS are used to model PBA. 3D simulations are possible in some cases but are computationally expensive. 2D simulations are computationally less expensive, but 2D simulations in cartesian coordinates only provide qualitative agreement and 2D simulations in cylindrical coordinates cannot model laser wakefield acceleration (LWFA) at all and cannot include important physics such as hosing and low mode azimuthal mode asymmetries for particle beam drivers (PWFA). Here we discuss one method for reducing the computational load of a 3D simulation into those comparable to a 2D simulation that can model LWFA and include hosing. It utilizes a truncated azimuthal mode expansion. We describe how this expansion has been included into the OSIRIS simulation framework and show preliminary results.

INTRODUCTION

Simulations have played an essential role in the development of plasma based acceleration from the seminal work of Tajima and Dawson to the very present. Simulations are used to model both laser wakefield acceleration (LWFA) and plasma wakefield acceleration (PWFA). These simulations have evolved from 1D simulations to demonstrate the feasibility of new ideas to full 3D simulations that model current experiments one to one and that model parameters out of reach of current experiments. Although 3D simulations are now possible they are still computational expensive, therefore, when simulating LWFA and PWFA using we often begin with a series of 2D simulations over a range of parameters. The parameters are either for an ongoing experiment, for a future experiment, or for understanding a new theory or concept. We then have to perform a few large-scale 3D simulations to determine in what manner and to what degree the 2D simulations replicate a more realistic result.

*This work was supported by DOE awards DE-FC02-07ER41500, DE-SC0008491, DE-FG02-92ER40727, and DE-SC0008316, and by NSF grants NSF PHY-0904039 and NSF PHY- 0936266. Simulations were carried out on the UCLA Hoffman 2 Cluster, and Dawson 2 Cluster.

DIFFERENCES IN 2D AND 3D SIMULATIONS

One topic that is receiving much theoretical, computational, and experimental attention is how to best inject electrons into a plasma wave wakefield. One concept is to use field ionization to create electrons inside the wake. An important question is how do the 2D simulation results compare to those from otherwise identical 3D simulations. When using a laser, it is not possible to use 2D azimuthally symmetric simulations as such simulations only allow radially polarized modes. Therefore, 2D cartesian geometry are used and in such simulations both structure of the wakefield and the evolution of the laser can be very different. We provide examples of the differences by showing results from a a series of 2D and 3D simulations that were performed to model experiments conducted using the Callisto laser at LLNL. These simulations highlight some of the differences we see and the importance of the including full 3D physics. In these simulations a linearly polarized, 60 fs laser was focused into an "Injection Section" that is composed of 99.5% He and 0.5% N. After the laser propagates 1.5 mm in the injection section, it enters an "Acceleration Section" composed entirely of He. The total plasma density is $n_p = 1 \times 10^{18}$ cm^{-3} aside from the 0.5 mm up ramp at the beginning. Simulations were conducted with a 100 TW and a 500 TW laser beam. The spot size was 20.0 μm for the 100 TW case, and 26.2μm for the 500 TW simulation.

As can be seen from Table 1, the peak energy of the trapped electrons can be significantly different between the 2D and 3D simulations. Another notable difference is that in the two 2D simulations, a comparable number of particles are trapped whereas in the 3D simulations 3.9 times more particles are trapped for the 500TW laser than for the 100TW laser. And in the 2D cartesian simulations only the charge per unit length that is trapped can be obtained. These differences illustrate that if one uses 2D simulations to optimize the process one can be led very far astray.

There is another notable qualitative difference in the 2D and 3D 500 TW simulation. If you look at the particle energy spectrums about 3 mm into the plasma (Figures 1 and 2), you see that there is a large, lower-energy peak exclusively in the 3D simulation. Although this peak eventually falls out, it dynamically affects the shape and the evolution of the wake. The 2D simulation fails to capture this process. Although not shown the evolution of the laser is also very different.

Copyright © 2013 CC-BY-3.0 and by the respective authors

Table 1: The Peak Energy, Charge, and Normalized Emittance of the Trapped Particles After the Laser Traverses 1.4 cm into the Plasma in the Two-Stage Injection-Acceleration Scheme

Simulation	E_n [GeV]	q	ϵ [π mm-mrad]
100TW (2D)	1.49	1.37 a.u.	13
100TW (3D)	1.14	19 pC	34
500TW (2D)	3.37	1.29 a.u.	107
500TW (3D)	3.07	72 pC	86

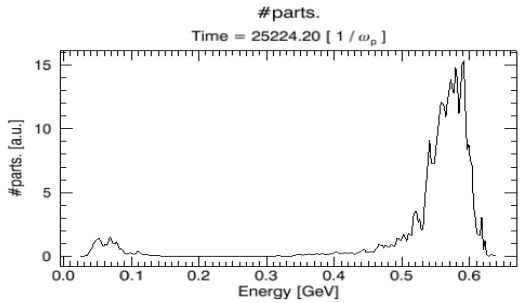


Figure 1: The spectrum of the trapped particle energies in the 2D, 500 TW simulation 3 mm into the plasma.

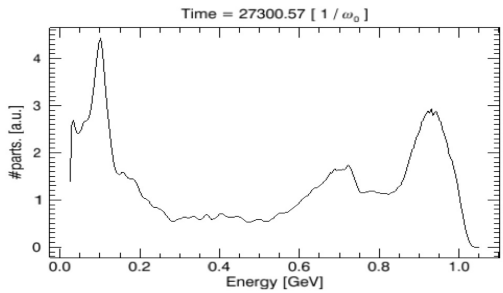


Figure 2: The spectrum of the trapped particle energies in the 3D, 500 TW simulation 3 mm into the plasma.

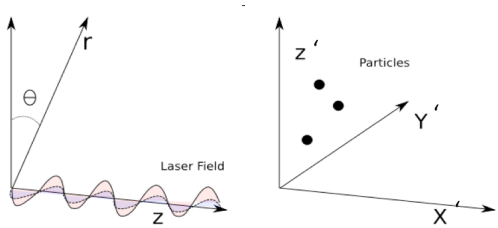


Figure 3: Coordinates of the cylindrical mode simulation.

AZIMUTHAL MODE EXPANSION

There are various possible ways to reduce the computational requirements for capturing the 3D physics including using boosted frames, the ponderomotive guiding center approximation, and the use of the quasi-static approximation. Another recent idea proposed by Lifshitz et al. [1] is to expand the electromagnetic fields into a truncated Fourier expansion along the poloidal direction in cylindrical coordinates. The idea is to provide key 3D physics for situations where only low mode azimuthal asymmetry exists (a linearly polarized laser can be described by the m=1 mode). Such simulations will have a similar computational load to 2D r-z simulations. Here we describe how this algorithm has been implemented into OSIRIS and present some preliminary results. We can keep an arbitrary number of m modes. As noted in [1] a linearly polarized laser propagating along x, as described in Figure 3, can be expressed in cylindrical coordinates as

$$\mathbf{E}(\mathbf{r},\mathbf{x},\theta,t) = E_y(r,x,t)(\cos(\theta)\hat{r} - \sin(\theta)\hat{\theta}) \quad (1)$$

$$\mathbf{B}(\mathbf{r},\mathbf{x},\theta,t) = B_z(r,x,t)(\sin(\theta)\hat{r} - \cos(\theta)\hat{\theta}), \quad (2)$$

which are first order terms in the expansion

$$\mathbf{F}(r,x,\theta) = \Re\left(\sum_{m=0} \hat{\mathbf{F}}^m(r,x)e^{-im\theta}\right),$$

where $\mathbf{F}$ is any vector field and the index m is the mode number. The zeroth order mode contains the cylindrically symmetric fields that are already incorporated in the 2D cylindrical coordinate simulation in the OSIRIS framework. Therefore, a linearly polarized laser can be modeled by only keeping the $m = 1$ mode. PWFA can be modeled in an r-z code, however, while very useful it is limited as it cannot include hosing or spot size asymmetries.

Algorithm

Therefore, as suggested above, the vector fields ($\mathbf{E}$, $\mathbf{B}$, and $\mathbf{J}$) are calculated as a series of modes truncated at a number specified at the input. Each mode is stored on a different 2D grid. Due to the linearity of the Maxwells equations they each evolve independently[1], according to Equations 3-8.

$$\frac{\partial \mathbf{B}_r^m}{\partial t} = \frac{im}{r}\mathbf{E}_x^m + \frac{\partial \mathbf{E}_\theta^m}{\partial x} \quad (3)$$

$$\frac{\partial \mathbf{B}_\theta^m}{\partial t} = -\frac{\partial \mathbf{E}_r^m}{\partial \mathbf{x}} + \frac{\partial \mathbf{E}_x^m}{\partial \mathbf{r}} \quad (4)$$

$$\frac{\partial \mathbf{B}_x^m}{\partial t} = -\frac{1}{r}\frac{\partial}{\partial r}(r\mathbf{E}_\theta^m) - \frac{im}{r}\mathbf{E}_r^m \quad (5)$$

$$\frac{\partial \mathbf{E}_r^m}{\partial t} = -\frac{im}{r}\mathbf{B}_x^m + \frac{\partial \mathbf{B}_\theta^m}{\partial x}\mathbf{J}_r^m \quad (6)$$

$$\frac{\partial \mathbf{E}_\theta^m}{\partial t} = \frac{\partial \mathbf{B}_r^m}{\partial \mathbf{x}} + \frac{\partial \mathbf{B}_x^m}{\partial \mathbf{r}} - \mathbf{J}_\theta^m \quad (7)$$

$$\frac{\partial \mathbf{E}_x^m}{\partial t} = \frac{1}{r}\frac{\partial}{\partial r}(r\mathbf{B}_\theta^m) - \frac{im}{r}\mathbf{B}_r^m - \mathbf{J}_x^m \quad (8)$$

The mode mixing occurs when there is a presence of macro-particles, which are followed in cartesian space (x, y, z, p_x, p_y, p_z) and pushed according to the Lorentz Force Law (Equation 9). This requires transforming the fields in cylindrical coordinates to cartesian coordinates before pushing the particles.

Copyright © 2013 CC-BY-3.0 and by the respective authors

$$\dot{\mathbf{P}} = q(\mathbf{E} + 1/cv \times \mathbf{B}) \qquad \dot{\mathbf{x}} = 1/(m\gamma)\mathbf{P} \quad (9)$$

The current density (or charge density) for each cylindrical modes at each r-z grid point i and j is obtained according to the equation

$$\rho_{ij}^{m} = \frac{1}{\pi} e^{im\theta} S_{ij} q/\Delta V,$$

where S_{ij} is the area-weighing coefficient (subject to the interpolation scheme), and $\Delta V = 2\pi r \Delta r \Delta x$. The cylindrical angle θ is calculated from the particle's x and y values. Looping over field evolution, particle advance, and charge deposition, we have a complete PIC algorithm.

Laser-Driven Field

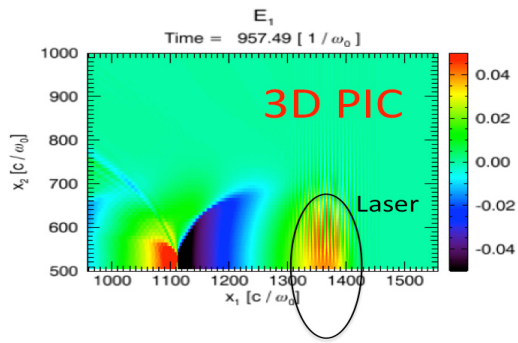


Figure 4: A full 3D PIC simulation of a laser propagating through a pre-ionized plasma. E_1 in units of $[m_e c\omega_o/e]$.

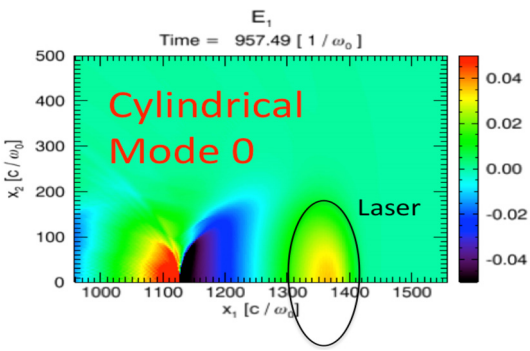


Figure 5: The 0th mode of the cylindrical mode simulation.

The above algorithm was implemented into the development version of OSIRIS, and tested using the parameters modeled after the LWFA simulation described by Lu et al [2]. Here a linearly polarized 200 TW,30 fs laser pulse is shot into a fully ionized $n = 1.5 \times 10^{18}$ cm^{-3} plasma, with a spot size of 19.5 μm. The computational window is of dimension $76.4 \times 127\mu\text{m}^3$, with the number of grid points 3000×256. Figures 5 and 6 show the E_1 field formed after the laser propagates 0.1 mm. A clear bubble is formed. In this simulation only the zeroth and first modes of the fields have been included.

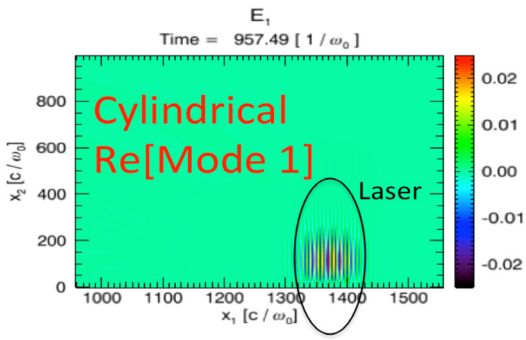


Figure 6: $\Re[E_1]$ of mode 1 of the cylindrical modes.

The full 3D PIC simulation is shown in Figure 4 for comparison (the plot is sliced in the middle for better comparison with the cylindrical simulations). Since in this simulation the wake is nearly perfectly cylindrical, it appears in the plot of the zeroth order mode of E_1 as shown in Figure 5. The oscillations in the real part of the first mode, however, are directly produced by the laser. You can see in the full 3D simulation that ordinarily these two modes of electric fields are solved together.

Since in this case the full 3D simulation requires another 256 grids along the third dimension, it is necessarily at least 256 times slower then the equivalent 2D simulation. With the cylindrical modes truncated at $m = 1$, we only need to solve three 2D grids (two for the real and imaginary parts of the 1st nonzero mode). By design this algorithm is magnitudes faster then the 3D simulation while capturing much of the 3-dimensionality of the laser-plasma interaction. It is the ideal tool for wakefield accelerators.

CONCLUSION

We have illustrated though simulations of a two stage ionization injection LWFA concept that there are both qualitative and quantitative differences between 2D and 3D simulations on injection and acceleration of electrons in LWFA stages. Because 3D simulations are often computationally intensive, it is important to be able to conduct simulations whose computational requirements is comparable to a 2D simulation, and yet includes the physics that makes the 2D simulations unreliable for accurate predictions. We describe how a new algorithm proposed by [1] has been successfully implemented into OSIRIS. This algorithm expands the EM fields into a truncated number of azimuthal mode numbers (often just 2). Preliminary results were also presented that show that using only 2 modes provides good agreement with full 3D simulations.

REFERENCES

[1] A. F. Lifshitz, X. Davone, etc., Journal of Computational Phys. 228 (2009) 1803

[2] W. Lu, M. Tzoufras, and C. Joshi, Phys. Rev. STAB. 10 (2007) 061301

Copyright © 2013 CC-BY-3.0 and by the respective authors

LASER-PLASMA INTERACTION STUDIES USING ABOVE CRITICAL DENSITY GAS JET PLASMAS AND A MULTI-TW CO_2 LASER*

C. Gong, S. Tochitsky, J. Pigeon, C. Joshi, Neptune Laboratory, Department of Electrical Engineering, University of California Los Angeles, CA, 90095, USA

Abstract

CO_2 laser-plasma interaction provides a unique parameter space for particle acceleration in a gas jet plasma taking place at a critical plasma density $n_{cr} \sim 10^{19}$ cm^{-3} and even at higher densities (3~10 n_{cr}) of 10μm radiation. Here we report the latest results of our study of electron acceleration in a wide range of plasma densities 1~10 n_{cr} using a multi-TW CO_2 laser system at the UCLA Neptune Laboratory. To gain insight into plasma density profile evolution during ~120 ps long CO_2 laser-plasma interaction, we used laser interferometry with two 1 ps, 532 nm probe pulses with variable delay of 5~120 ps. The knowledge of spatial distribution of accelerated electron beam transported through the overdense gas plasma is critically important for minimizing laser beam filamentation and for understanding influence of other laser-plasma instabilities. This should allow for optimization of CO_2 laser driven shock wave acceleration of low-divergence monoenergetic ion beams [1].

INTRODUCTION

The interaction of short high-intensity laser pulses with an overdense plasma can produce forward directed multi-MeV ions and electrons. Electrons heated/accelerated by the laser pulse can drag ions with them due to the space charge separation. Studying the spatial distribution of accelerated electrons can help to optimize the quality and yield of ion beams and is also important for understanding laser-plasma instabilities.

At the UCLA Neptune laboratory, a ~120 ps CO_2 laser train of 3ps pulses separated by 18ps with a peak intensity up to ~4×10^{16} W/cm^2 is used to study overdense laser plasma interaction in a helium gas jet. One of our goals is to optimize the ion acceleration by collisionless shock waves [1]. In order to gain an insight into the plasma density profile evolution during the CO_2 laser pulse train, a two-frame interferometry using 1ps, 532nm light has been developed. An adjustable temporal delay 5~120ps between pulses allows for optical probing of the laser/plasma interaction region. Through a careful analysis and comparison of the two-frame interferogram, the hole boring speed of the above critical density layer pushed by the radiation pressure along the laser propagation axis can be measured. Also, forward directed electron and ion beam is recorded on the LANEX phosphor screen to analyse its spatial distribution and divergence. A permanent magnetic dipole with ~600 Gauss magnetic field is placed before the LANEX phosphor screen to estimate the energy of particle beams.

*Work supported by DOE grant DE-FG02-92-ER40727, NSF grant PHY-0936266 at UCLA

EXPERIMENTAL SETUP

Target Chamber

The CO_2 Master Oscillator Power Amplifier system having a multi-terawatt peak power is used in the experiment. Due to a modulated gain spectrum of the CO_2 molecule, a ~3ps CO_2 laser seed pulse evolves into a ~120ps long pulse train after amplification. Each individual pulse within the pulse train preserves the original pulse width and is separated from the adjacent pulse by ~18ps.

The experimental arrangement in a target chamber is shown in Fig. 1.

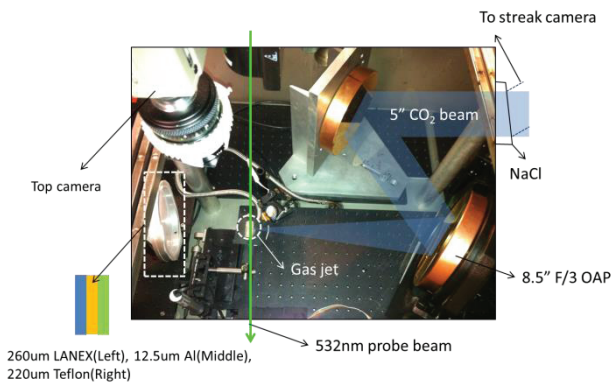


Figure 1: Experimental setup in the target chamber.

A 5" diameter CO_2 laser beam with an energy of ~60J is coupled into the target chamber through an 8" NaCl window mounted on a 4° wedged flange. The back reflection of the beam from the salt window is combined with a red diode laser beam in a CS_2 Kerr modulator. The red pulse modulated by the high intensity 10μm CO_2 laser is analysed by a Hamamatsu streak camera (Model: C5680-21) for the temporal structure measurement of the CO_2 pulse. The beam inside the chamber is focused in a 2mm diameter gas jet by an 8.5" F/3 off-axis parabolic mirror. Using an IR camera, we have characterized the spatial profile of the unamplified CO_2 laser beam by scanning along the laser axis (Z-scan) which is shown in Fig. 2. The measured spot size is w_o = 48μm. Using this spot size and an estimate of the energy contained in the most intense of the 3ps pulses (~20%) in the train of pulses, we estimate that a peak a_o of >1 can be achieved in these experiment. Here a_o is the normalized vector

Copyright © 2013 CC-BY-3.0 and by the respective authors

potential with a_o~1 corresponding to 10^{16} W/cm^2 for a CO_2 laser.

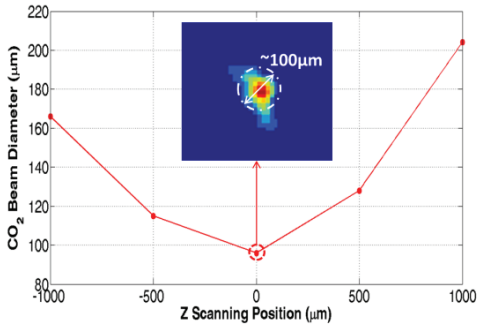


Figure 2: Spot size measurement of 10 μm CO_2 laser beam.

The laser beam interacts with a pulsed supersonic gas jet which allows for the peak plasma density around 0.1 to 10 times of the critical density for the 10μm light (10^{19} cm^{-3}).

As shown in Fig. 1, a detector consisting of a 260 μm LANEX phosphor screen (Left), 12.5 μm Al foil (Middle) and 220 μm Teflon (Right) layer is put 150mm away from the gas jet. The LANEX phosphor screen imaged by a COHU analog camera outside the target chamber is used to detect the forward directed electron beams with energy above 220keV. A permanent magnetic dipole (600 Gauss) capable of resolving energy in the range of 0.3-4 MeV is placed between the gas jet and the LANEX phosphor screen. A top COHU analog camera is installed to determine the focal position of the high power CO_2 beam relative to the center of the gas jet. A 1ps, 532nm, green probe with energy of ~20μJ is delivered to the interaction point (IP) for the two-frame interferometry and schlieren diagnostics.

Two-Frame Interferometry and Schlieren Diagnostics

The two-frame polarization based interferometry and schlieren optical scheme is depicted in Fig. 3.

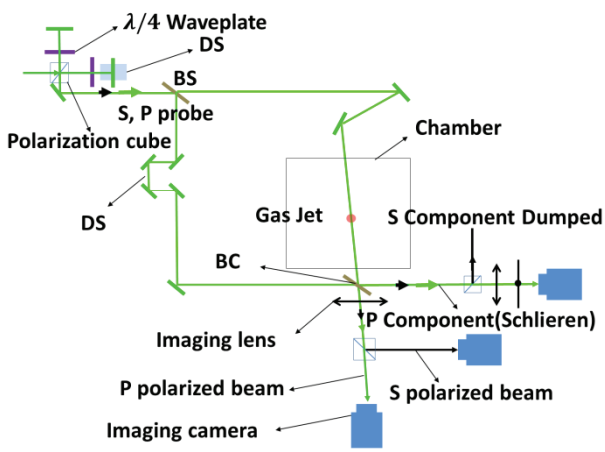


Figure 3: Schematic of the 1ps, 532nm two-frame interferometry and Schlieren diagnostics setup. Beam Splitter (BS), Delay Stage (DS), Beam Combiner (BC).

The 1ps, 532nm elliptically polarized probe beam enters the narrowband polarization cube and is separated into P (60%) and S (40%) components. This is a classical Michelson scheme in which an arbitrary delay can be introduced for the S polarized component. Then, each of them goes through a quarter wave plate twice and changes their polarization. A translational delay stage of the S probing arm is used to control the temporal delay relative to the P arm. The adjustable temporal range is 5~120ps with the P probe arriving at the IP earlier. After switching the polarization, P and S probes follow the same beam path and enter into the Mach-Zehnder interferometry system. Another narrow band polarization cube is placed behind BC to separate the polarized beams into two orthogonal directions. The imaging lens transfers the image plane of the plasma to the two CCD cameras. The measured spatial resolution of interferograms is ~20um. In addition to the interferometry, part of the beam probing the plasma is reflected off BC for a Schlieren diagnostic. The reflected beam contains P and S components and we use another polarization cube to select P component for the Schlieren image. A dark field schlieren technique [2] is used to analyse the plasma density gradient. A ~250um diameter ink dot deposited on a 2" transparent plastic disc is used as a beam stopper. The green probe passing through the plasma without refraction is attenuated by the dot by a factor of 10^5. The measured resolution of the schlieren images is ~40um.

EXPERIMENTAL RESULTS

At the Neptune laboratory, the 10um short pulse and the 532nm probe pulse are both produced using the same 1μm pulse [3], so inherently they are deterministically synchronized with each other. However, due to the different transport length, they arrive at the IP at different times and need to be temporally re-synchronized with a picosecond accuracy. Also as mentioned earlier, our structured CO_2 pulse train contains multiple ~3p micropulses separated by ~20ps. We are interested in observing the interaction between the overdense plasma and different micropulses in the pulse train and to learn how the plasma density profile will evolve temporally. To synchronize CO_2 laser pulse envelope and green probe with better than 20ps accuracy, a cross-correlation measurement in Si was used [4]. The probe timing of P arm is adjusted such that the probe pulse arrives approximately at the peak of the CO_2 pulse train. And the relative delay of the S arm can be changed using a delay stage in order to cover a chosen micro-pulse that arrives at a later time.

One of the most important mechanisms in laser overdense plasma interaction is hole boring or pushing of the density steepened plasma layer by radiation pressure of the laser field. Two frame interferometry allows for accurate measurement of the hole boring speed. For example, for interferogram shown in Fig. 4, we can extract this information by comparing how the overdense plasma layer is pushed by the radiation pressure at two different times.

Copyright © 2013 CC-BY-3.0 and by the respective authors

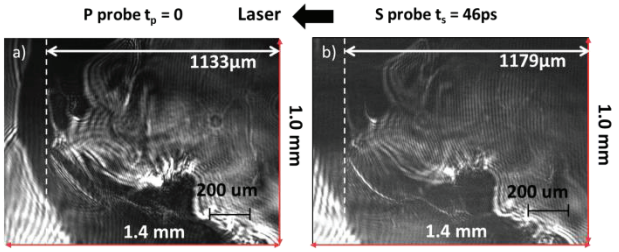


Figure 4: Two-frame interferogram at different times. a) shows P probe. b) shows S probe with 46ps delay. White dashed line shows the instantaneous position of the overdense plasma layer pushed by the radiation pressure.

For this shot our CO_2 laser beam is focused into a helium gas jet target and the laser intensity is above the ionization threshold of He^{2+} (~8.5×10^{15} W/cm^2). According to our neutral density calibration data of the gas jet, a backpressure of 1000psi corresponds to ~$6n_{cr}$ for a fully ionized He gas. Analysis of two interferograms of P and S arms (S is 46ps later) reveals that the pushed layer is moving forward with a hole boring velocity of 0.0037c (c is the speed of light).

Using the formula $\frac{v_h}{c} = [\frac{n_{cr}}{2n_{pe}}\frac{Zm}{M}\frac{I\lambda_L^2}{1.37\times10^{18}}]^{1/2}$ [5], where v_h is the hole boring velocity, n_{cr} the critical density for 10μm light, n_{pe} the plasma density and Z is the charge state of the ionized atoms, one can extract the laser intensity in the hole boring process which is 1.5×10^{16} W/cm^2. However, this formula assumes a constant radiation pressure and not directly applicable for the case of CO_2 laser 3ps pulses separated by 18ps. Thus, the intensity 1.5×10^{16} W/cm^2 corresponding to the measured v_h is a lower estimate of the laser intensity in the experiment.

Another shot, shown in Fig. 5, corresponds to the case when neutral density of the gas jet was reduced. We observed a nicely formed plasma channel. Analysis of the fringe shift in the interferogram gives us the plasma density in the channel of P probe time equal to 1×10^{18} cm^{-3} and S probe equal to 5×10^{17} cm^{-3}, which indicates a drop in plasma density over 46ps delay. Schlieren image in Fig. 5(c) shows a piled up plasma upstream of the plasma channel.

For this shot, a well-confined, beam-typed signal was detected on the LANEX screen with a divergence angle of 2°. Currently, we are studying the nature and energy of this forward directed beam.

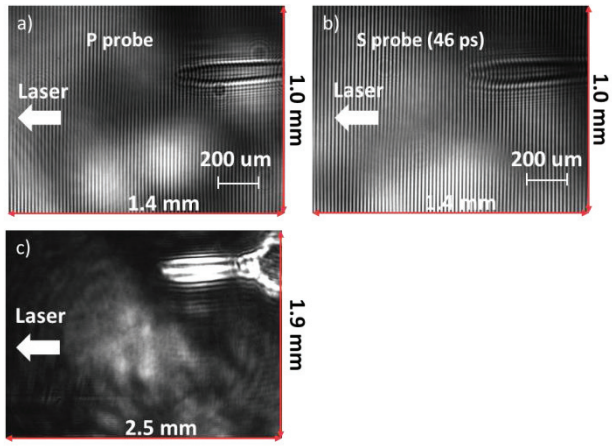


Figure 5: Two-frame interferogram and dark field schlieren images. a) Shows the channel formation as seen by P probing arm. b) Shows the channel expansion probed by S arm (46ps later). c) Shows the schlieren image for P polarized probe with a larger field of view.

CONCLUSION

In this paper, we describe the current status of the experiment being carried out in the Neptune laboratory at UCLA. Two-frame interferometry and dark field schlieren technique have been demonstrated to be very critical plasma interaction diagnostics. Hole boring velocity has been measured by comparing two interferogram images taken at different time. A channel guided propagation of laser light is observed at the underdense plasma condition and the corresponding signal on the LANEX phosphor screen requires further investigation.

REFERENCES

[1] Haberberger, et al. 2012 Collisionless shocks in a laser-produced plasma generate monoenergetic high-energy proton beams. Nat.Phys. 8, 95–99.
[2] G.S. Settles, *Schlieren and Shadowgraph Techniques* (Springer-Verlag, Berlin, 2001).
[3] D. Haberberger et al., Opt. Exp. 18, 17865 (2010).
[4] A.J. Alcock and P.B. Corkum, "Ultra-fast switching of infrared radiation by laser produced carriers in semiconductors," *Can. J. Phys*., vol. 57, p. 1280, 1979.
[5] S.C. Wilks, et al. "Absorption of Ultra-intense Laser Pulse", PRL, Vol. 69, Number 9.

Copyright © 2013 CC-BY-3.0 and by the respective authors

RESULTS OF THE SHORT PULSE DRIVEN LLNL/UCLA IFEL EXPERIMENT*

J.T. Moody, P. Musumeci
Department of Physics and Astronomy, UCLA, Los Angeles California, USA
G.G. Anderson, S.G. Anderson, S. Betts, S. Fisher, D. Gibson, A. Tremaine, and S. Wu
Lawrence Livermore National Laboratory, Livermore, California, USA

Abstract

The results of the LLNL/UCLA inverse free electron laser (IFEL) experiment are presented. A 500 mJ 120 fs Ti:Saph laser pulse interacts with a short electron beam in a planar undulator tapered both in magnetic field strength and period to accelerate the electron beam. The tapering of the undulator maintains resonant energy exchange between the laser and electron beam while the electron beam's energy increases. We observe an energy modulation from 77 MeV to 120 MeV. Through use of simulations that are consistent with the observed data, we report a peak acceleration gradient of at least 180 MeV/m.

INTRODUCTION

The growing expense of high energy electron accelerators has produced a demand for increasingly compact, high gradient accelerators than traditional rf accelerators. Because of breakdown which occurs at around 100 MeV/m for traditional rf structures, shorter wavelengths must be used to drive the acceleration. The inverse free electron laser (IFEL) [1] is a laser driven electron accelerating scheme that has the advantage of taking place in vacuum.

In this acceleration scheme, a high intensity laser copropagates with a relativistic electron beam through an undulator. As the electron beam oscillates in the periodic magnetic field, it's transverse velocity allows for coupling to the laser's transverse electric field. If the laser's frequency, electron beams energy, and the magnetic field's strength and period are set such that the electron beam slips one laser wavelength per undulator period, energy is maximally transferred between the laser and the electron beam. As the electron beam becomes accelerated by this period averaged effect, the undulator must be tapered in order to maintain the resonance condition and facilitate efficient energy exchange.

This concept was demonstrated at Neptune at UCLA [2], as well as STELLA at Brookhaven National Lab (BNL) [3]. Renewed interest in IFEL has allowed experiments to be performed at Lawrence Livermore National Lab and BNL. While BNL's Rubicon [4] focused on use of a helical undulator to give stronger coupling to a circularly polarized CO_2 laser at low rep rate (.05Hz), the LLNL IFEL Project focuses on exploiting the high repetition rate of TW class Titanium Sapphire laser systems (10 Hz) and achieving high gradient acceleration with a sub picosecond driving laser. This paper covers the preliminary results of the LLNL IFEL experiment.

THEORETICAL BACKGROUND

If we define a pondermotive phase as $\Psi = (k + k_w)z - \omega t - \Phi_G$, we can use this phase as the coordinate of an electron in the period averaged pondermotive field. Here k and k_w are the radiation wave number and undulator wave number, respectively, and ω is the radiation frequency, and Φ_G is the Guoy phase shift.The electron's conjugate momentum then can be described by γ, the electron's energy normalized by it's rest energy. The longitudinal equations of motion then can be described by:

$$\frac{d\gamma}{dz} = \frac{1}{2\gamma} k K_L K J J sin\Psi \tag{1}$$

$$\frac{d\Psi}{dz} = k_w - k\frac{1+\frac{K^2}{2}}{2\gamma^2} - \frac{1}{z_r(1+\frac{z}{z_r}^2)} \tag{2}$$

Where K_L is the radiation parameter equal to eE_0/kmc^2 and E_0 is the peak radiation electric field, m is the electron mass, and c is the speed of light. K is the undulator strength parameter and is equal to $eB_w/k_w mc^2$ and B_w is the peak undulator magnetic field. JJ is the coupling factor, which is a result of using a planar undulator. z_r is the Rayleigh range, and the final term in the pondermotive phase evolution is due to the Guoy phase shift.

If we allow the left hand side of Eq. 2 to go to zero, this gives the condition for which the pondermotive phase does not evolve. γ_r is then resonant electron's normalized energy. Plugging into Eq. 1 we have a description of evolution of a resonant particle as it is accelerated with a stationary phase. Expanding about the resonant phase,Ψ_r, we have a pondermotive potential that goes like $cos\Psi + \Psi sin(\Psi_r)$. This potential creates a stable accelerating bucket whose width in phase is dependent on the resonant phase. If the resonant phase is near zero, the bucket is wide and traps many particles at the cost of reduced accelerating gradient whereas if the resonant phase is near $\pi/2$ then the gradient is maximum but only a single point in phase space can be accelerated. If the laser intensity is not matched to the design, the injected electrons can fall out of the pondermotive bucket and resonant acceleration ceases. Non trapped particles interaction increases the energy spread of the non-captured distribution. Beyond the 1-D equations of motion, the particle tracking code cbeam [5] was used together with

* This work supported by US DOE Grant DE-FG02-92ER40693,Defense of Threat Reduction Agency award HDTRA1-10-1-0073 and University of California Office of the President award 09-LR-04-117055-MUSP.

Copyright © 2013 CC-BY-3.0 and by the respective authors

Parmela [6]and Elegant[7] to model the evolution of the electron beam in a start-to-end simulation. The results of the integration of the equations of motion in the pondermotive phase description matched the start-to-end simulation well.

EXPERIMENTAL DESCRIPTION

A layout of the interaction area can be seen in Fig 1. The electron beam approaches from the left of the diagram after being accelerated to injection energy and acquiring longitudinal chirp appropriate for compression. The electron beam is then compressed by the chicane and put on axis for the final focus quadrupole magnets that focus that electron beam at the center of the undulator to a spot size of 100 µm. The laser approaches from the right of the diagram and Spatial overlap between the electron beam and laser is achieved using DRZ fluorescent screens before and after the undulator, as well as a finger at the center of the undulator. Synchronicity to 2 ps between the electron beam and laser pulse is achieved by observing the optical transition radiation and laser in a streak camera. A micrometer on the delay arm on the interaction laser is then slowly scanned until electron beam modulation is observed. Experimental parameters can be seen in Table 1.

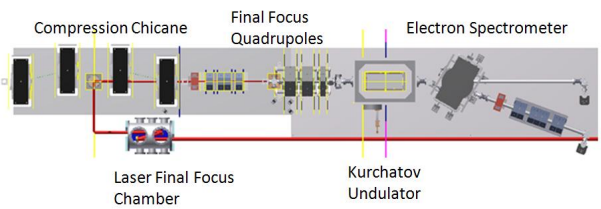


Figure 1: CAD Model of IFEL Interaction Region.

The LLNL BLDG 194 beamline consists of a SLAC/UCLA/BNL 1.6 Cell S-Band photogun, acceleration by three 3 m SLAC style accelerating sections, chirped for compression by a final accelerating section compressed through a chicane, and focused into the undulator. With the radius of 1 mm a 120 fs laser pulse applied to the cathode, the electron beam is produced in the photoinjector blowout regime, in which the electron beam expands nonlinearly into a near uniformly filled ellipsoid, helping to preserve transverse and longitudinal emittance during initial acceleration.

The KIAE-2p hybrid planar undulator was used in this experiment. Built by the Kurchatov Institute and originally designed for the UCLA Neptune IFEL experiment[2], the aggressively tapered undulator was designed for a 3.5 cm Rayleigh Range. It is nonlinearly tapered in both field strength and undulator period.

The Ti:Saph laser was purchased from Amplitude Technologies [8]. The laser consists of an SHG fiber oscillator, a regenerative amplifier 4 pass amplifier, and compressor. The spot size which is larger than the diffraction limited case, is a result of higher order modes acquired in the main amplifier, resulting in an M^2 value of approximately 1.3. The laser waist parameters shown in Table 1 were measured by attenuating it at low power and putting it directly into a CCD camera. The camera was moved along a linear stage and the Rayleigh range, minimum spot and a degree of astigmatism were measured.

Determination of energy modulation for the high gradient IFEL requires a broadband spectrometer. The spectrometer was made by placing a DRZ fluorescent pop-in within the tank of the dipole magnet. Such a broadband spectrometer has a nonlinear calibration, which was determined by sweeping the magnetic field for a fixed momentum electron beam and determining the various bend radii. A simple geometrical model was developed to ensure accuracy of the spectrometer. The method of calibration data was well matched with the model.

Table 1: IFEL Experimental Parameters

Beam Parameters	
Average Injection Energy	55-77 MeV
Charge	50 pC
Undulator Parameters	
K_0	0.2
K_f	2.8
λ_{w0}	1.5 cm
λ_{wf}	5.0 cm
L_w	50 cm
Laser Parameters	
λ	785 nm
τ	150 fs
Pulse Energy	500 mJ
z_r	12 cm
w_0	200 µm

EXPERIMENTAL RESULTS

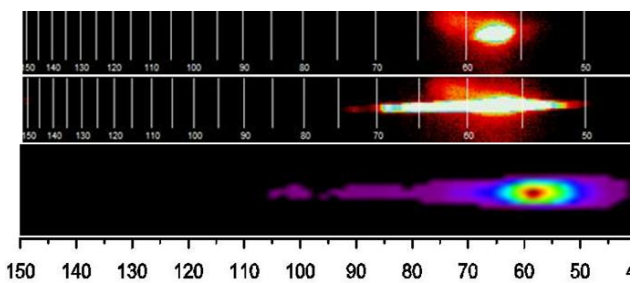


Figure 2: 57 MeV IFEL Interaction Results. a. Electron beam without laser. b. Electron beam with laser applied, IFEL interaction. c. 2D histogram binning of comparable simulation results. Horizontal Scale is Energy in MeV, measured data has nonlinear scaling.

We placed the waist of the laser approximately 2 cm upstream of the center of the undulator and used 57 MeV injection energy into the IFEL. Placing the waist further up-

Copyright © 2013 CC-BY-3.0 and by the respective authors

stream allows for capture earlier in the undulator at the cost of dropping off of the resonant energy curve faster. The energy modulation can be seen in Fig. 2. For both sets the images data has a nonlinear scale by nature of the spectrometer while the simulation data has a linear scale.

We then placed the waist at the center of the undulator and injected at 77 MeV, the highest energy our chicane compressor will allow, injecting into the undulator at above initial resonant energy. The results from this interaction can be seen on Fig. 3. In both cases simulations were run with the measured laser waist parameters. The simulation spectra matched the observed spectra fairly well, justifying the examination of the simulation data as acceleration occurs in the undulator.

Figure 4 shows the average energy evolution for the particles gaining the most energy in three simulations: the design case with a 3.5 cm Rayleigh range 100 µm laser waist is used, and the two cases for our measured waist parameters at the two observed energies. The lower bound energy cuts were 180, 110 and 70 MeV for the design, 77 and 57 MeV cases, respectively. The peak gradient of the 77 MeV injected energy curve shows a maximum gradient of 180 MeV/m. While the design curve shows resonant gain throughout the undulator, the 77 and 57 MeV cases show the electron beam accelerated up to a point where there is a sharp change in slope as the electrons fall out of the pondermotive bucket in the first half of the undulator. After the electrons fall out of the pondermotive bucket nonresonant energy modulation occurs to further increase the energy spread, showing mild gain based upon the selection of the highest energy particles.

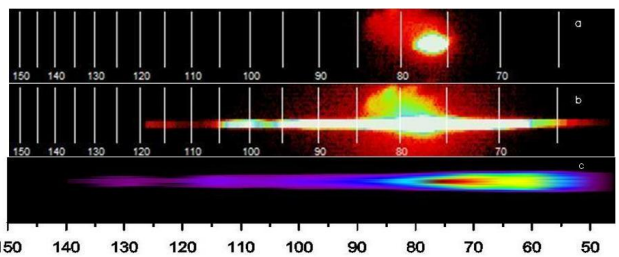


Figure 3: 77 MeV IFEL Interaction Results.a. Electron beam without laser. b. Electron beam with laser applied, IFEL interaction. c. 2D histogram binning of comparable simulation results. Horizontal Scale is Energy in MeV, measured data has nonlinear scaling.

CONCLUSION AND FURTHER STUDY

The IFEL interaction has been demonstrated and has produced high peak gradient acceleration (180 MeV/m) and a record maximum energy produced by the IFEL acceleration mechanism of 120 MeV. Further improvement of the laser waist should yield a higher gradient over the entire undulator with acceleration to the design energy. The short pulse nature of the Ti:Sapphire IFEL is planned to be investigated over the next few months with an electrooptic

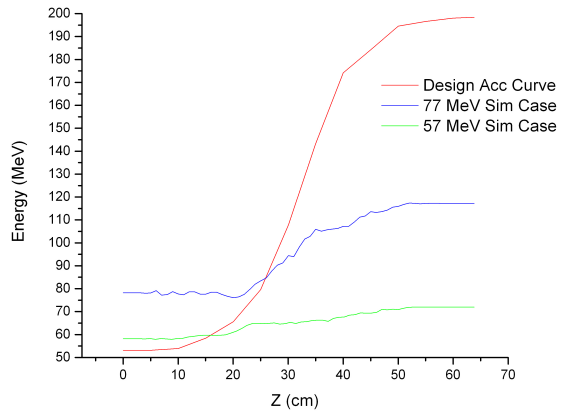


Figure 4: Acceleration curves for the design laser and injection at 50 MeV, The 57 MeV case, and the 77 MeV case.

sampling based time of arrival diagnostic discussed in previous work.[9]. The electrooptic sampling diagnostic will allow for relative time of arrival measurements to be correlated with the observed energy modulation so that the time of arrival jitter can be unfolded from the temporal overlap tolerance.

REFERENCES

[1] E.D. Courant, C. Pellegrini, and W. Zakowicz. High-energy inverse free electron laser accelerator. Physical Review A, 32:2813, 1985.

[2] P. Musumeci et al., High Energy Gain of Trapped Electrons in a Tapered, Diffraction-Dominated Inverse-Free-Electron Laser, Physical Review Letters, 94:154801, (20 April 2005).

[3] Kimura, W. D. et al., 2004b First demonstration of hightrapping efficiency and narrow energy spread in a laser-driven accelerator. Phys. Rev. Lett. 92, 054 801.

[4] J. Duris et al., High Energy Gain of Electrons in a High Gradient Helical Inverse Free Electron Laser PRL (submitted August 2013).

[5] S. Anderson et al., Proc of PAC2011 (2011).

[6] L.Young and J. Billen, The Particle Tracking Code PARMELA, PAC03 Proceedings, May 2003

[7] M. Borland, elegant: A Flexible SDDS-Compliant Code for Accelerator Simulation, Advanced Photon Source LS-287, September 2000.

[8] Amplitude Technologies: `www.amplitude-technologies.com/`

[9] J. Moody et al., Proc of IPAC 2012 (2012)

Copyright © 2013 CC-BY-3.0 and by the respective authors

DEVELOPMENT OF A HIGH-REPETITION RATE TW CO_2 LASER DRIVER FOR A COMPACT, VARIABLE SPECIES ION SOURCE

J. Pigeon, S. Tochitsky, C. Joshi, UCLA, Los Angeles, CA 90095, USA

Abstract

CO_2 laser-driven ion acceleration has been used to generate monoenergetic, MeV proton beams from a gas jet plasma. Use of a gas jet is advantageous because it offers interactions at a density around the critical plasma density for 10 μm pulses (10^{19} cm^{-3}) and can be run at a repetition rate of 1-100 Hz. This opens the possibility to create a variable species ion source easily switchable from protons to light ions (*e.g.* He, N and Ne). A TW class high repetition rate CO_2 laser driver is required for implementing such a source. At the UCLA Neptune Laboratory we have built a 1 Hz CO_2 laser system and demonstrated the amplification of 20 GW, 3 ps laser pulses. However, peak powers on the order of 0.2-1 TW are required for producing ~ MeV proton beams. Here we report progress on an ongoing project in which the peak power of our laser system will be increased by nonlinear chirping and broadening followed by pulse compression. We also discuss a possible strategy for generating 300 mJ, 300 fs CO_2 laser pulses for driving a 1 – 10 Hz laboratory ion source.

INTRODUCTION

There are applications in material science, radiation biology and medical physics [1] that would benefit from a MeV class, multiple species ion accelerator. The cost of such a machine, if built using conventional accelerator technology, is prohibitively expensive for most universities and hospitals. Laser driven ion acceleration (LDIA) may be one avenue for reducing this cost, either as a stand-alone accelerator or as an injector for a conventional accelerator.

Recent experiments have demonstrated monoenergetic, MeV ion acceleration from over-dense ($\omega_{plasma} \geq \omega_{Laser}$) laser plasma interactions (LPI) [2]. High power CO_2 lasers are an attractive candidate for LDIA because, at a wavelength of 10 μm, the critical plasma density can be achieved using a gas jet or cell. In contrast, the majority of high power lasers operate at wavelengths from 0.8 – 1 μm and must use solid targets to study over-dense LPI. Due to the potential ease in targetry, 10 μm drivers are the most technological option for a multi-species, laser driven ion accelerator.

CO_2 LDIA studies have been limited to single shot experiments even though optimization of the laser-plasma interaction may only be possible at a high repetition rate. Although gas jet technology can be scaled up to 100 Hz, experiments have suffered due to limitations in the repetition rate of the driver. At the UCLA Neptune Laboratory we have recently developed a 20 GW, 3 ps CO_2 laser system which operates at 1 Hz [3]. Peak power on the order of 0.2 TW is required for acceleration of ~ 3 MeV protons from a H_2 plasma. In this paper we investigate a method to increase the peak power of our system by using nonlinear chirping and broadening followed by compression. Further we propose a path to a 300 mJ, 300 fs CO_2 laser to be used as a 1 – 10 Hz driver for a compact, multi-species ion source.

STATUS OF THE 1 HZ, PICOSECOND CO_2 LASER SYSTEM

CO_2 lasers have some technological advantages that cannot be matched by solid state laser systems. The gas medium can withstand intensities up to the ionization threshold, $\geq 10^{12} \frac{W}{cm^2}$, which allows for direct amplification of short pulses. Further, gas discharge technology can be scaled in repetition rate and provides high wall plug efficiency. Despite these advantages, high peak power amplification in CO_2 is difficult due to the relatively narrow bandwidth present in gaseous media. Gas lasers typically provide a bandwidth of 3.5 GHz/atm such that, at 1 atm of pressure, a CO_2 laser can only produce pulse lengths greater than 1 ns. Unfortunately, pulse lengths on the order of picoseconds or less are necessary to reach the relativistic intensities required for LDIA.

At the UCLA Neptune Laboratory we achieve broad band CO_2 laser amplification by relying on two broadening mechanisms: pressure and field broadening. Figure (1) shows simulated gain spectrums of the CO_2 medium at 1, 10 and 25 atm of pressure. At 1 atm of pressure the gain spectrum consists of a family of 3.5 GHz, rovibrational lines.

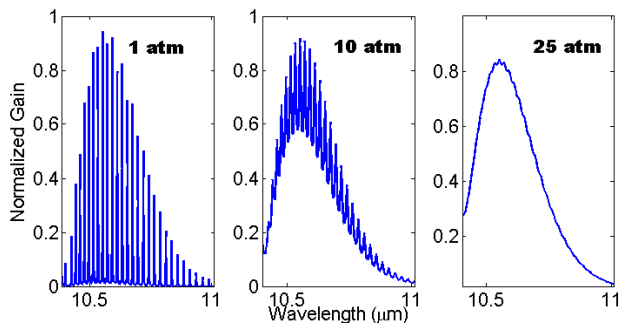


Figure 1: Simulations of the CO_2 gain medium at 1, 10 and 25 atm of pressure for the 10P branch.

At high pressures the collisional time becomes comparable to the radiative transition time which results in line broadening. At 25 atm of pressure the gain spectrum is a continuum across the entire 1.2 THz branch. In practice modules with 10 atm of pressure are used as it is difficult to obtain stable discharge at pressures greater than this. The presence of residual modulation in the gain

Copyright © 2013 CC-BY-3.0 and by the respective authors

spectrum at 10 atm results in the amplification of a pulse train as depicted in figure 2. The resulting pulse train consists of 5 – 7, 3 ps pulses separated by 18 ps.

After the pulse reaches intensities on the order of GW/cm^2 the lasing transition can be broadened by the field of the pulse itself. This broadening manifests in a way similar to the ac Stark effect and can be estimated by $\Delta\nu_{Field} \approx \mu\sqrt{I}$ where μ is the dipole moment in Debye and I is the peak intensity of the pulse. For CO_2 $\mu = 0.0275$ such that, at intensities of $10\frac{GW}{cm^2}$, a 1 atm amplifier has the bandwidth of a 10 atm machine [3]. The total broadening is the sum of the pressure and field dependent terms, $\Delta\nu_{Total} = \Delta\nu_{Pressure} + \Delta\nu_{Field}$.

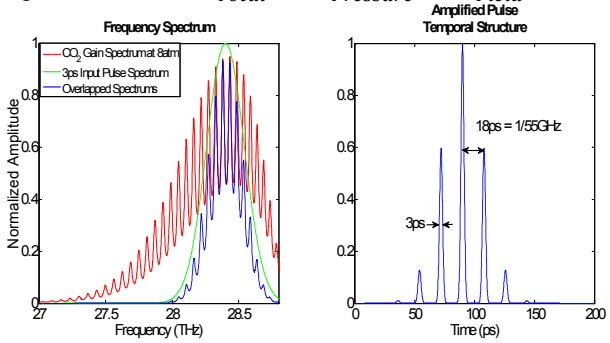


Figure 2: Simulations showing the production of a ps pulse train after amplification of a single ps pulse in a 10 atm CO_2 laser.

Figure 3 is a block diagram of the Neptune Laboratory's CO_2 master-oscillator power-amplifier chain where amplification is realized in two stages. In the first stage the pulse is amplified from nJ to mJ in two 8 atm CO_2 lasers where the pressure sustains the bandwidth for ps pulse amplification. The first module is used as a regenerative amplifier while the second module is used as double pass booster. In the second stage the seed is sent for final amplification in a 1 meter, 1 atm CO_2 laser where the field from the pulse sustains the bandwidth for final amplification.

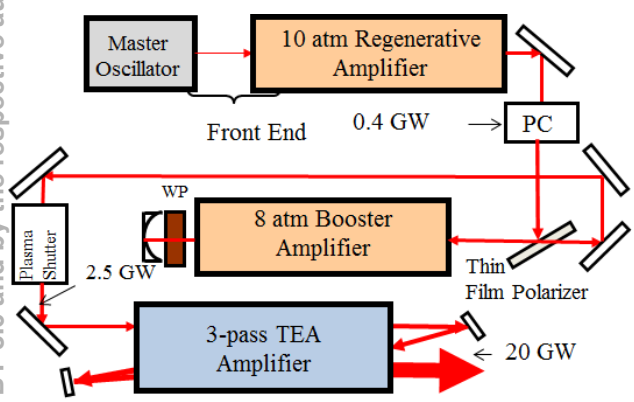


Figure 3: Block diagram of the Neptune Laboratory's high repetition rate system. The orange and blue blocks refer to amplifiers which use pressure and field broadening to sustain ps bandwidth, respectively.

Figure 4 is a plot of the temporal structure of our output pulse train as measured by a streak camera. As simulations predict, the pulse train consists of 3 ps pulses separated by 18 ps, a time scale related to the 55 GHz modulation in the gain spectrum.

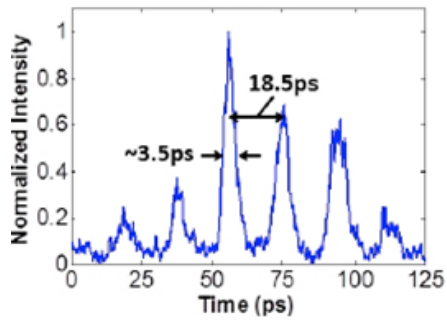


Figure 4: Temporal profile of the ps pulse train

As reported in [3] we extract 200 mJ out of our final amplifier which results in a peak power of 20 GW for the most intense pulse in the train. The amount of extracted energy is limited by saturation and could be increased if the 1 atm final amplifier was replaced by a larger aperture, 2 – 3 atm TE CO_2 module.

NONLINEAR SPECTRAL BROADENING IN A NOBLE GAS FILLED HOLLOW GLASS WAVEGUIDE

A peak power beyond one defined by the CO_2 bandwidth can be obtained via self-phase modulation in a nonlinear optical medium. Nonlinear spectral broadening and subsequent compression of guided waves is a technique which has been successful in the near-IR but has not been explored at 10 µm. Hollow glass waveguides (HGW) which are coated with Ag/AgI are commercially available and have been used in our laboratory to guide GW, 10 µm pulses with a throughput of 95% in the air [4].

Figure 5 illustrates our scheme to use a Xe filled HGW to broaden and chirp our pulses through self-phase modulation. After the HGW the pulses will be compressed via propagation through NaCl, a material with negative group velocity dispersion at 10 µm. The plots of figure 5 depict simulated time and frequency domain representations of our pulse train before and after the pulse compressor.

We have modelled this process by numerically solving the nonlinear Schrödinger equation [5] for our pulse parameters. We have assumed a waveguide radius of 500 µm which corresponds to a peak intensity of 6 TW/cm^2 when the beam is coupled into the EH_{11} mode of the waveguide. The pulse is broadened by a factor of 5 in 200 cm of Xe gas. The length of NaCl to compress the output pulse train was approximately 35 cm which results in 100 GW, 650 fs pulses on the output of the Brewster angled salt plate. Currently the set-up for pulse compression is being built.

Copyright © 2013 CC-BY-3.0 and by the respective authors

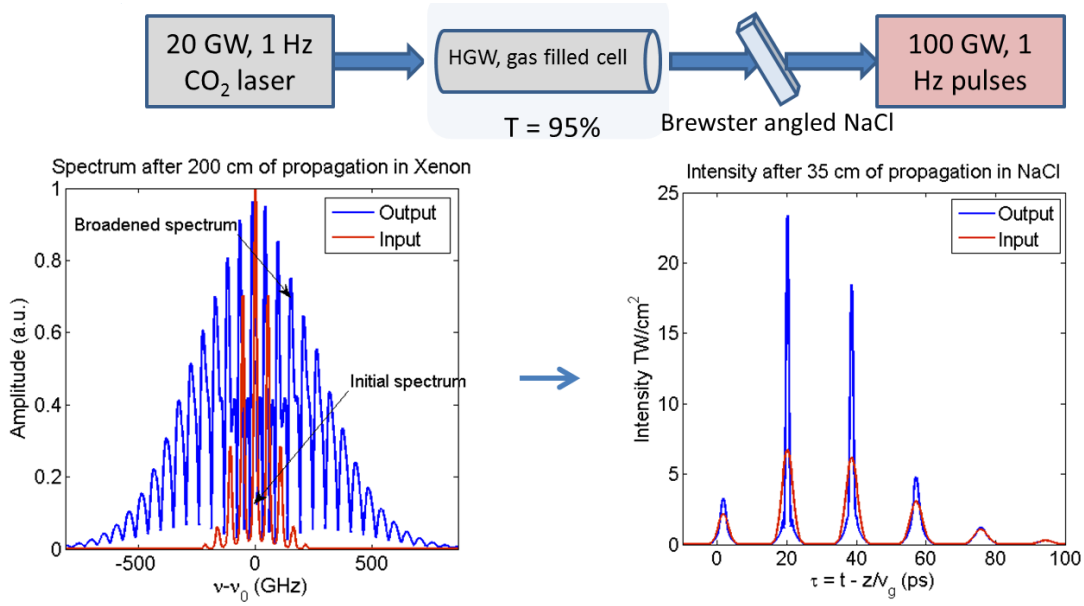


Figure 5: Top: Proposed set-up to use self-phase modulation followed by compression in NaCl to produce 100 GW CO_2 laser pulses. Bottom: Simulated frequency and time domain representations of our pulse train before and after the pulse compressor.

Based on this technique we envision the development of a 1 TW, 1-10 Hz CO_2 laser system by using the strategy described here. In order to extract the energy required to produce a TW class driver we must first replace the 1 atm final amplifier with a 100 cm length, 3 atm CO_2 laser. With this final amplifier we can extract 3 J of energy which can be sent through the same nonlinear pulse compressor of figure (5) to produce 300 fs, 300 mJ pulses.

CONCLUSION

We have presented the status of an on-going project to develop a 100 GW CO_2 laser driver for a variable species ion source at the UCLA Neptune Laboratory. If nonlinear broadening in 200 cm of a noble gas filled HGW followed by pulse compression is successful then we will scale the interaction to generate >0.1 TW CO_2 laser pulses. This power will be sufficient to study CO_2 LDIA with a gas jet target. The capability to study LDIA at a high repetition rate is critical for understanding and optimizing the laser plasma interactions responsible for ion acceleration. Such a system would be an ideal driver for a multi-species, MeV class ion accelerator.

ACKNOWLEDGMENT

This work was supported by U.S. Department of Energy grant DE-FG03-92ER40727 and National Science Foundation grant PHY-0936266.

REFERENCES

[1] DOE and NIH Summary Report, "Workshop on Ion Beam Therapy," Washington D.C., January 2013. http://science.energy.gov/~/ /media/hep/pdf/accelerator-rd-stewardship/Workshop_on_Ion_Beam_Therapy _Report_Final_R1.pdf

[2] D.J. Haberberger, et al., *Nature Phys.* **8** (2012) 95.

[3] S. Ya Tochitsky, J.J. Pigeon, D.J. Haberberger, C. Gong and C. Joshi, *Optics Express* **20**(13), (2012) 13762.

[4] G.P. Agrawal, *Nonlinear Fiber Optics*, 3rd ed. (San Diego: Academic, 2001).

[5] C. Sung, S. Ya Tochitsky and C. Joshi, *Eleventh AAC Workshop*, (2004) 512.

Copyright © 2013 CC-BY-3.0 and by the respective authors

TECHNIQUE FOR DETERMINING THE MAXIMUM ENERGY OF A DISPERSED ELECTRON BEAM FROM LASER WAKEFIELD ACCELERATORS*

J. Shaw#, N. Vafaei-Najafabadi, K.A. Marsh, C. Joshi, UCLA, Los Angeles CA 90024, USA

Abstract

We present a new curve-fitting method based on asymptotically fitting transverse size contributions to the measured electron spectrum that is capable of determining the maximum energy of a dispersed electron beam from a laser wakefield accelerator regardless of its transverse size. This method is applied to experimental spectra obtained in the characterization of a new injector stage to show that Direct Laser Acceleration may be an additional acceleration mechanism in laser wakefield accelerators where the laser pulse is long enough to overlap the trapped electrons.

INTRODUCTION

The energy of electron beams from an accelerator is typically measured by magnetically dispersing the electron beam onto a detector. Because the magnetic dispersion is highly nonlinear, the lower-energy charge generally experiences higher deflection and is well dispersed on the detector, whereas the higher-energy charge is deflected less and therefore is less dispersed. This small spatial separation leads to reduced resolution at higher energies and makes it challenging to accurately determine the maximum energy of an electron beam in the 10s to 100s of MeV energy range using a non-imaging but dispersive magnet. The issue of determining the maximum energy of an electron beam is further complicated when that beam has a large transverse size at the detection plane. In such a case, it is difficult to determine whether the signal at high energies on the detector is actually high-energy electrons or if it is an artifact of the transverse size of the beam. This proceedings describes a curve-fitting method to determine the maximum energy of an electron beam regardless of its transverse size.

EXPERIMENT

This curve-fitting method was developed to accurately characterize a newly-designed laser wakefield acceleration (LWFA) injector, which could produce ~100 MeV electron bunches in gas cells with lengths of 400 μm to 1100 μm [1, 2]. The Ti:Sapphire laser used to do this characterization had a pulse width of 45 fs FWHM and an a_0 of ~2. During the characterization, the injector was tested over a range of plasma densities from 8.1 x 10^{18} cm^{-3} to 2.5 x 10^{19} cm^{-3}. For these laser and plasma parameters, the LWFA is not operating in the ideal blowout regime [3]. Therefore, self-trapping of electrons in the wake will not occur without significant laser pulse evolution. To eliminate the need for laser pulse evolution and thus devote the length of the injector to acceleration, the ionization injection technique [4] was employed. As a result, the spectrum of the accelerated electrons was typically continuous with an exponentially decreasing tail as shown in Figure 1(a). To demonstrate that the injection stage was capable of producing ~100 MeV electrons as designed, it was critical to accurately measure the maximum energies of these electron beams even though they have exponentially decreasing tails. The method described here was found to converge on many real data sets and enabled us to determine the maximum energy of an electron beam regardless of its transverse size, its energy spread, or its exponentially decreasing tail.

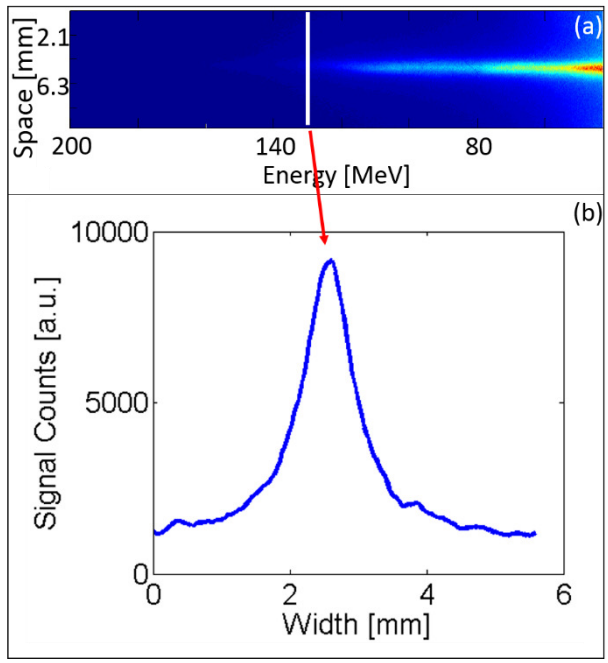


Figure 1: (a) Linearized electron spectrum showing the location of the transverse lineout taken at 130 MeV. (b) Typical raw transverse lineout of the electron spectrum taken at 130 MeV before being rotated and linearized.

DETAILS OF THE METHOD

The method separates out the transverse size contribution by comparing the signal in the dispersed plane to the signal in the transverse (undispersed) plane. In the dispersion plane, the lineout of the electron spectrum has the combined effects of energy dispersion and transverse size. The transverse lineout, however, only

*Work supported by: DE-AC52-07NA27344, DE-FG03-92ER40727, DE-FG02-92ER40727, NSF Grants No. PHY-0936266, DGE-0707424, PHY-0936266; DoD, Air Force Office of Scientific Research NDSEG Fellowship, 32 CFR 168a (Shaw).
#jshaw05@ucla.edu

Copyright © 2013 CC-BY-3.0 and by the respective authors

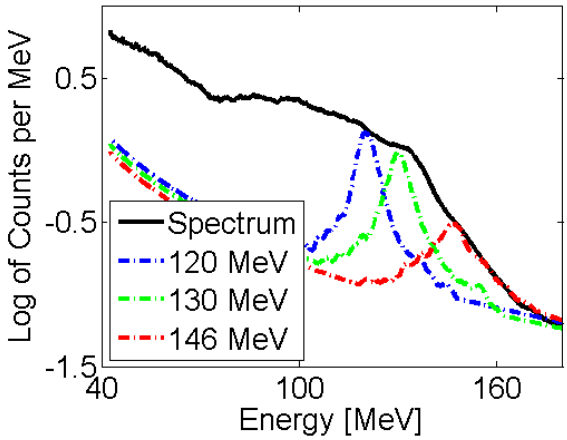


Figure 2: Process of comparing the rotated and linearized transverse lineouts (dashed lines) against the central lineout of the electron spectrum (solid black line). The converted transverse lineout at 146 MeV (red dashed curve) is asymptotic with the central lineout; therefore the maximum electron energy is 146 MeV.

shows the effects of the transverse size. Therefore, by comparing the transverse and longitudinal lineouts of the electron spectrum at a particular energy, it is possible to determine if the signal at that point is due to electrons of that energy or if the signal is from the transverse size contribution of lower-energy electrons.

To compare the transverse lineout of the signal at a particular energy to the actual spectrum, the transverse size contribution of the transverse lineout must first be converted into a dispersed signal. This process is best illustrated on an actual electron spectrum. The raw electron spectrum is first linearized as shown in Figure 1(a) to correct for the energy dispersion of the spectrometer. Based on the energy scale of this linearized spectrum (Figure 1(a)), the maximum electron energy appears to be between 110 MeV and 160 MeV. Therefore, transverse lineouts of the raw spectrum are taken for a series of energies between 110 MeV and 160 MeV. A typical transverse lineout is shown in Figure 1(b).

Each transverse lineout contains the transverse size contribution from the electrons at the energy where it was taken. Assuming that the transverse size effects are radially symmetric, this transverse lineout also includes the contributions of any lower-energy electrons whose transverse sizes are large enough to overlap the chosen energy. The selected transverse lineouts are rotated 90^0 to orient them in the dispersion plane. They are then linearized using the same process used to linearize the dispersed spectrum. Again, because the transverse lineout has no dispersion effects and therefore only accounts for the transverse size contribution, by rotating it into the dispersion plane and linearizing it, the transverse size contribution is converted into a linearized signal in the dispersion plane. This converted transverse lineout thus only shows the portion of the total signal at a given energy that is due to the transverse size. Each converted transverse lineout can then be compared to the central lineout of the actual dispersed signal as shown in Figure 2. In this figure, the solid black curve is the central lineout of the dispersed electron spectrum, and the blue, green, and red dashed curves are the converted transverse lineouts from 120 MeV, 130 MeV, and 146 MeV, respectively. If the tail of the longitudinal lineout has a greater magnitude than the tail of the converted transverse lineout, then the longitudinal signal cannot be caused by the transverse size of the energy of interest alone. There must be a contribution from higher-energy electrons. However, if the tail of the converted transverse lineout at a given energy has a higher signal, then the longitudinal signal at that energy can be attributed to the transverse size contributions of electrons at energies less than the energy being compared. Therefore, the comparison must be repeated with the transverse lineout at the next lowest energy.

To illustrate this comparison, in Figure 2, the tail of the blue curve (the transverse lineout at 120 MeV) is below the dispersed signal. Therefore, 120 MeV is not the maximum measured electron energy; there must be a contribution to the measured electron spectrum from higher-energy electrons. The tail of the red curve falls on the dispersed lineout. Therefore, the tail of the actual dispersed signal can be attributed to the transverse size contribution of the 146 MeV electrons. Therefore, 146 MeV is the maximum energy of this electron spectrum. Note that this method does not account for errors in the measurement of the maximum electron energy due to the electron bunch leaving the plasma at an angle relative to the laser axis. However, if this method is used with a two-screen spectrometer [5, 6], both the transverse size and the exit angle of the electron bunch can be taken into account when calculating the maximum electron energy.

EXPERIMENTAL FINDINGS

Using the curve-fitting method just described, the maximum energy of the electron beams produced in the characterization of the injector cell [1, 2] were determined. Figure 3 shows typical electron spectra obtained at low ($<1\text{x}10^{19}$ cm^{-3}) and high ($>2\text{x}10^{19}$ cm^{-3}) plasma densities.

The performance of LWFAs operating in the blowout regime ($a_0>2$) is commonly benchmarked against the scaling equation for the dephasing-length-limited energy gain [3]:

$$\Delta E \cong \frac{2}{3} mc^2 \frac{\omega_0^2}{\omega_p^2} a_0 \qquad (1)$$

where ω_0 is the frequency of the drive laser and ω_p is the plasma frequency. Equation 1 predicts a maximum energy gain of 126 MeV for the typical low-density shot (Figure 3(a)) and of 48 MeV for the typical high-density shot (Figure 3(b)). Though the parameters of the UCLA injector characterization are not rigorously in the blowout

Copyright © 2013 CC-BY-3.0 and by the respective authors

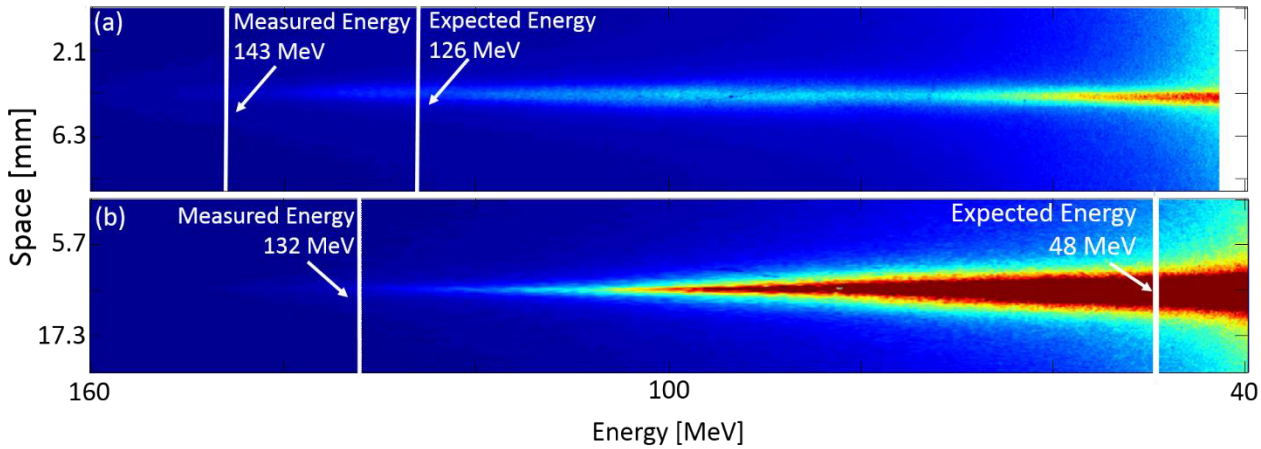


Figure 3: (a) Typical low-density electron spectrum. The cell length l_{cell} was 1100 μm, the plasma density n was 9.1 x 10^{18} cm^{-3}, and a_0 was 2.00. (b) Typical high-density spectrum. l_{cell} was 430 μm, n was 2.2 x 10^{19} cm^{-3}, and a_0 was 1.86.

regime, the measured energy for the low-density spectra agree relatively well with the energies predicted by Equation 1. However, for the typical high-density spectrum shown in Figure 3(b), there is a 175% difference between the maximum measured energy (132 MeV) and the energy predicted by Equation 1 (48 MeV).

DIRECT LASER ACCELERATION

Through a detailed study and a series of OSIRIS [7] particle-in-cell simulations (future publication), it was determined that the source of the additional energy gain produced in high plasma densities is Direct Laser Acceleration (DLA). In LWFAs, the electrons that are trapped in the wake therefore undergo betatron oscillations in response to the field of the ion column formed behind the drive laser. In the UCLA work, the laser had a fixed pulse length of 45 fs and an approximately constant a_0 of 2. Because the length of the bubble formed in LWFAs decreases for increasing plasma densities [3], when the injector was operating at low densities, only the tail of the 45-fs pulse overlapped the electrons trapped in the back of the first bubble, but when the injector ran at high densities, the bubble length was short enough that the higher-intensity portions of the 45-fs pulse overlapped the electrons trapped at the back of the bubble. When the pulse overlaps the trapped electrons that are oscillating in the ion column, the transverse field of the laser will increase the transverse momentum of the electrons that are at the correct phase. This increased transverse momentum can then be transformed into longitudinal momentum through the **v** x **B** force due to the magnetic field of the laser. This process of enhancing the transverse momentum of an electron and then converting that increase to longitudinal momentum is known as DLA [8]. DLA can lead to increased energy gain in LWFAs operating in a regime where the pulse overlaps the electrons trapped in the first bucket and is the source of the additional energy gain seen at UCLA when the injector was operating at high densities.

CONCLUSION

This proceedings details a newly-developed curve-fitting method for determining the maximum energy gain of a dispersed electron beam regardless of its transverse size. This method was applied to experimental work at UCLA to find that DLA is an additional acceleration mechanism at work in LWFAs where the laser pulse overlaps the trapped electrons.

REFERENCES

[1] J.L. Shaw et al., "100 MeV Injector Cell for a Staged Laser Wakefield Accelerator," AAC'12, Austin, June 2012, AIP Conf. Proc. **1507**, 728 (2012); http://www.proceedings.aip.org
[2] J.L. Shaw et al., "Characterization of Submillimeter-scale Gas Cells as Possible Injectors for Staged Laser Wakefield Acceleration," Master's Thesis (2013); http://www.library.ucla.edu
[3] W. Lu et al., Phys. Rev. ST Accel. Beams 10 (2007) 061301.
[4] A. Pak et al., Phys. Rev. Lett. 104 (2010) 025003.
[5] B. B. Pollock et al., "Two-Screen Method for Determining Electron Beam Energy and Deflection from Laser Wakefield Acceleration," PAC09, Vancouver, May 2009, WE6RFP101 (2009); http://www.JACoW.org
[6] C. E. Clayton et al., Phys. Rev. Lett. 105 (2010) 105003.
[7] Fonseca, R.A. et al., Lect. Notes Comput. Sci. 2331 (2002) 342.
[8] A. Pukhov, Rep. Prog. Phys. 66 (2003) 47.

Copyright © 2013 CC-BY-3.0 and by the respective authors

SUPPRESSION OF THE TRANSFORMER RATIO DUE TO DISTRIBUTED INJECTION OF ELECTRONS IN A PLASMA WAKEFIELD ACCELERATOR*

N. Vafaei-Najafabadi†, W. An, C.E. Clayton, C. Joshi, W. Lu‡, K.A. Marsh,
W.B. Mori, UCLA, Los Angeles, CA 90095, USA
E. Adli§, C.I. Clarke, S. Corde, J.-P. Delahaye, R.J. England, A.S. Fisher, J. Frederico, S.J. Gessner,
M.J. Hogan, S.Z. Li, M.D. Litos, D. Walz, Z. Wu, SLAC, Menlo Park, CA 94025, USA
P. Muggli, Max Planck Institute for Physics, Munich, Germany

Abstract

Evidence of beam loading due to distributed injection in Plasma Wakefield Accelerator experiments carried out at the FACET facility at SLAC during the year 2012 is presented. The source of the injected charge is tunnel ionization of Rb^+ inside the wake, which occurs along the length of the interaction at each minima of envelope betatron oscillation. Rb was used specifically to mitigate the problem of head erosion, which limited the energy gain in earlier experiments using Li that were carried out at FFTB in SLAC. In the present experiment however, electrons produced via secondary ionization of Rb were injected in the wake and led to a severe depletion of the accelerating wake, i.e. beam loading, which is observed as a reduction of mean, i.e. measured, transformer ratio. This "dark current" limitation on the maximum achievable accelerating gradient is also pertinent to other heavier ions that are potential candidates for high-gradient PWFA.

INTRODUCTION

A Plasma Wakefield Accelerator (PWFA) uses a short, dense, high current electron beam to drive a high amplitude wake [1], which can accelerate electrons with gradients that are orders of magnitude larger than the conventional accelerators [2]. When the beam density (n_b) is higher than the plasma density (n_p), the electron beam expels all of the plasma electrons locally and creates a blowout region, a structure of uniform ion density that accelerates and focuses electrons [3]. The FACET Facility at SLAC [4] is currently used for further research on PWFA.

Two particular physics problems that have to be addressed are the problems of head erosion [5] and ion motion [6]. Head erosion is a physical effect limiting the length of the acceleration. Briefly, if the plasma is generated by the beam via field ionization, as was the case in [2], the part of the beam that ionizes the medium into plasma is not in the blowout region and therefore continues to expand at a rate that is dependent on its emittance. The expansion then causes the ionization front to recede back in the frame of the beam. The rate of this "head erosion" effect is dependent on $1/\gamma$, ϵ_n, and $\mathrm{IP}^{1.73}$ [7], where ϵ_n is the normalized emittance and IP is the ionization potential of the element that is being ionized. Ion motion is a problem because it leads to distortion of the linear focusing force in the blowout regime, and it occurs for $n_b/n_p > m_i/m_e$.

Both of these problems can be addressed by switching Li (used previously [2]) to a higher Z element, such as Rb. With an ionization potential that is 23% smaller than Li, the application of the scaling equations for head erosion implies that the interaction length in Rb would be 40% longer, leading to a proportional increase in maximum achievable energy. Additionally, with an atomic mass of over 12 times larger than Li, Rb ions are an order of magnitude less mobile. On the other hand, the ionization potential of the second Li electron is so high (75.6 eV) that it is not exceeded during the experiment. This is not the case with Rb. The second ionization potential of Rb is 27.3 eV, which could be reached during the experiment. Here, we show that this secondary ionization of Rb is responsible for significantly reducing the energy gradient. The suppression of the accelerating gradient is diagnosed in this experiment by monitoring average transformer ratio $\langle T \rangle$, which can be measured in experiments as $\Delta W^+/\Delta W^- = \int E^+ dz / \int E^- dz$.

EXPERIMENTAL SETUP

The 3 nC, 20.35 GeV electron beam from the FACET facility at SLAC was focused on the rising edge of a column of Rb vapor at the neutral density of 2.7×10^{17} cm^{-3} in a heat pipe oven [8] (Fig. 1). Rb gas was contained in the oven using Ar as buffer. Therefore, the density of Ar rose as the density of Rb fell in such a way that the total pressure stayed the same. The bunch length of the beam was monitored for every shot using the integrated transition radiation signal, which was generated as the beam traversed a 1 μm thick Ti foil and was measured by a pyroelectric detector (pyro). This signal correlated with a THz Michelson interferometer (Fig. 1) and was the main diagnostic of the bunch length. Two absolutely calibrated toroids before and after

*The work at UCLA was supported by DOE grant DE-FG02-92-ER40727 and NSF grant PHY-0936266. The simulations were carried out on the Hoffman cluster at UCLA. Work at SLAC was supported by Department of Energy contract DE-AC02-7600515.

† navidvafa@ucla.edu
‡ Also at Tsinghua University, Beijing 100084, China
§ Also at Department of Physics, University of Oslo, 0316 Oslo, Norway

Copyright © 2013 CC-BY-3.0 and by the respective authors

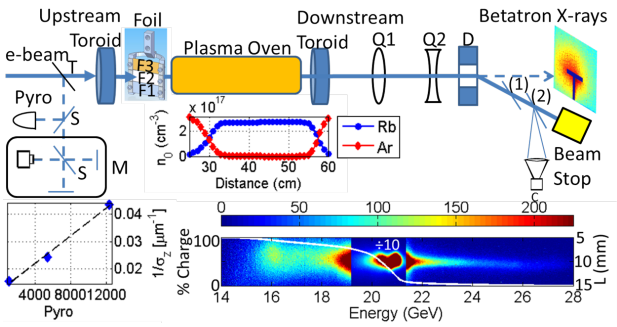


Figure 1: Experimental setup. The electron beam enters from the left. Transition radiation generated as the beam traverses the 1 μm Ti foil is observed simultaneously by a pyroelectric detector (Pyro) and a THz Michelson interferometer (M). Correlation of the two signals is shown beneath the setup. Foils can be inserted in the path of the beam before it enters the plasma oven to change its emittance from $\epsilon_{n0} = 250 \times 50\,\mu$m (see Table 1 for details). Underneath the schematic of the oven, the density profiles of neutral Rb and Ar are shown in blue circles and red diamonds, respectively. The quadrupole magnets Q1 and Q2 along with the dipole magnet D form the spectrometer. The Cherenkov radiation emitted between silicon wafers (1) and (2) is detected by camera C. An example of the energy spectrum with the white curve showing the integrated charge is shown below the camera C. The charge near 20.4 GeV observed not to lose any energy has been attenuated by a factor of 10. The Lanex screen, shielded by a 1mm copper foil, detects the betatron x-rays.

the plasma oven were used to monitor the incoming and outgoing charge. Excess charge generated during the interaction was calculated by subtracting the upstream toroid from the downstream one. To vary the beam emittance, a set of foils of various thicknesses and compositions (F1-F3, see Fig. 1 and Table 1) were placed in to path of the beam. An imaging spectrometer containing two quadrupole magnets and one dipole magnet are used to measure the energy spectrum of the beam after the plasma. After being dispersed by the dipole, the electrons traveled in air and generated Cherenkov radiation, which was imaged onto a 12 bit CCD. An example of such image is shown in Fig. 1. X-ray photons of 50-200 keV are observed using a Lanex film, which is shielded from low energy x-rays using a 1 mm copper mask [9].

Table 1: Composition, Thickness, and Emittance Contribution [10] of the Foils F1-F3 in Fig. 1

Foil	Thickness	Metal Composition	ϵ_n/ϵ_{n0}
F1	25.4 μm	71.15 Ag/28.1 Cu/0.75 Ni	1.2
F2	50.8 μm	25.57 Au/74.43 Cu	1.3
F3	38.1 μm	81.1 Au/16 Cu/2 Ni	1.4

METHODS AND ANALYSIS

The energy gain and energy loss are needed to calculate the average transformer ratio. To calculate these values, a plot of the integrated charge (white curve shown in spectrometer image in Fig. 1) is first produced by integrating the counts on the spectrometer image first in the non-dispersive dimension and then in the dispersive dimension. Energy gain and loss in this experiment are defined as the energies where this curve exceeds 2% and 98%, respectively. For example, in the spectrometer image shown in Fig. 1, the maximum energy is 24.4 GeV and minimum energy is 15.1 GeV, leading to values of 4 GeV and 5.3 GeV for energy gain (ΔW^+) and energy loss (ΔW^-), respectively.

From the same spectrometer image, it is clear that a significant portion of the charge has not moved from the initial energy. This portion of the beam is the unaffected charge and is dependent on where the ionization occurs in the frame of the beam. Modeling the ionization with the ADK model [11, 12], we can plot an ionization contour for the beam and calculate the amount of unaffected charge at a certain ionization contour based on the element and beam characteristics. This measurement can also be applied in reverse, inferring the initial size of the beam as it enters the plasma. The insertion of foils F1-F3 causes an increase in the beam size [13], reducing the beam density and field, leading to an increase in the unaffected charge for increasing foil number. Typical value of the unaffected charge as a function of total charge were 38% for the case of no foil, 43% for F1, 43% for F2 and 51% for F3. These values are for a pyro reading between 3000 and 6000 or $\sigma_z \sim 40\,\mu$m. Subtracting the unaffected charge from the total charge yields the amount of charge that participated in driving the wake and forming the accelerating structure.

Once the Rb vapor was ionized, the experiment quickly evolved into the blowout regime, where the electron beam traveled in a uniform ion column. The evolution of the electron beam in this ion cavity can be illustrated by the envelope evolution model [14]. If the initial beam radius is larger than the matched radius, given by $\sigma_r^2 = \epsilon_n(c/\omega_p)\sqrt{2/\gamma}$ [15], the envelope radius of the beam decreases in the up-ramp of the plasma and then oscillates along the entire length of the interaction. As the envelope of the beam oscillates, the electrons generate x-rays that will be observed by the x-ray diagnostic. To calculate the x-ray yield resulting only from the beam-plasma interaction, background data is obtained by sending the electron beam through neutral Ar. This yields a background emission region, which is independent of the plasma interaction, and is then selected and blocked in the experimental results. Furthermore, since the number of electrons participating in the oscillations varies from one experiment to another, the x-rays yield is normalized to the participating charge. In this manner, the x-ray yield per electron can be compared in different experiments.

The envelope oscillation of the beam has another signif-

Copyright © 2013 CC-BY-3.0 and by the respective authors

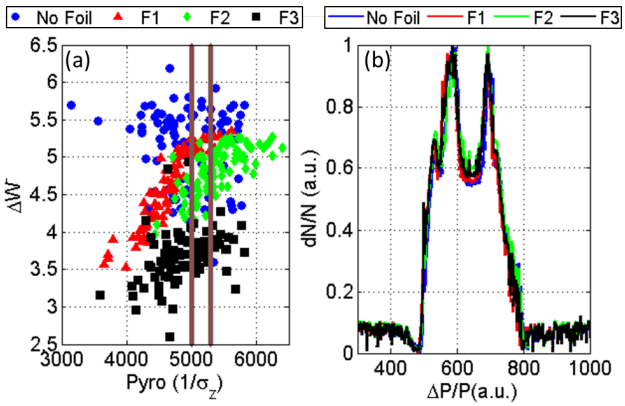


Figure 2: (a) Energy loss as a function of inverse bunch length ($\propto$ pyro). Data with 5000<pyro<5300 is marked. (b) Projection of phase space for data with 5000<pyro<5300. Current profiles are nearly identical.

icant consequence. As the envelope radius decreases, the radial electric field of the beam increases. For a participating charge of $N = 1.3 \times 10^{10}$ electrons, $\sigma_z = 40\,\mu$m and $\sigma_r^* = 3\,\mu$m, where σ_r^* represents the minimum value of the envelope radius, the electric field can be calculated from $E_r^{max} = 17.3\,\text{GV/m}(N/10^{10})(10\mu\text{m}/\sigma_r^*)(30\mu\text{m}/\sigma_z)$, which yields an E_r^{max} of 56 GV/m. The peak electric field strength required to ionize Rb^+ by 10% for the same σ_z is 53 GV/m. Therefore, Rb^+ electrons are ionized at the lowest point of the radius oscillation, released inside the wake, accelerated by the wake structure [14], and observed as excess charge on the toroids.

To minimize the effect that different current density profiles can have on the results, ΔW^-, ΔW^+, and excess charge data were filtered to a narrow range of pyro reading with nearly identical current densities (Fig. 2). This specific range of pyro (5000 <pyro< 5300) was selected because the data contained in this region spanned a large range of values. For instance, ΔW^- shown in Fig. 2(a) varied by more than a factor of 2. This variation allowed for meaningful study of the correlation between different parameters. The current density profiles were inferred from the projection of the electron beam's phase space, which is recorded on every shot. This projection is obtained using a vertical half period wiggler magnet, which reroutes electrons through two small bends [16]. The resulting radiation illuminates a scintillating crystal of YAG:Ce, which is imaged onto a CCD camera. These profiles confirm that experimental data points in the narrow range of pyro selected indeed have a beam current profile that is nearly identical to one another (Fig. 2(b)). Using this dataset selected for their similar current density profile, it is observed that excess charge is almost linearly correlated with both the x-ray yield and energy loss [17]. In other words, for every betatron oscillation contributing to x-ray yield, the excess charge increases as well. Furthermore, the correlation between excess charge and the energy loss strongly implies that this distributed trapping occurs over the length

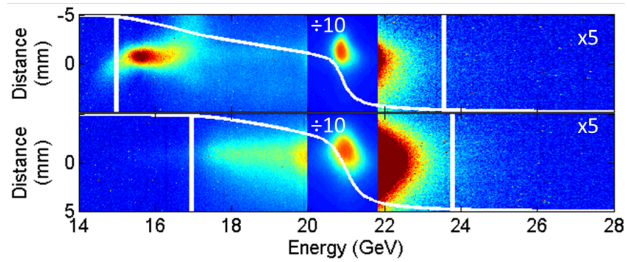


Figure 3: Electron energy spectra. Top: Excess charge was 770 pC and $\langle T \rangle = 0.6$. Bottom: Excess charge was 510 pC and $\langle T \rangle = 1.1$; Foil F3 was also inserted in the beam path. $\langle T \rangle$ decreases as the excess charge increases.

of the interaction. This distributed injection of charge in turn beam loads the wake, reducing the accelerating gradient and the transformer ratio. As stated earlier, this effect is observed in the experiment by measuring the average transformer ratio $\langle T \rangle$. The spectrum corresponding to the two data points with the highest and the lowest excess charge from the narrow range of pyro selected in Fig. 2 is shown in Fig. 3. It is evident that while the energy loss increases significantly, the energy gain is nearly the same between the two as the result of the heavy beam loading.

In summary, secondary ionization of heavy ion species in the blowout region is a significant limiting factor for the accelerating gradient in PWFA. In our experiment, Rb^+ ionization led to beam loading and a reduction in $\langle T \rangle$ by a factor of two. Other heavy elements considered as candidates to mitigate head erosion and ion motion in PWFA experiments may be limited in their accelerating gradient by the same effect.

REFERENCES

[1] P. Chen et al., Phys. Rev. Lett. 56 (1985) 693.
[2] I. Blumenfeld, et al., Nature 445 (2007) 741.
[3] W. Lu et al., Phys. Rev. Lett. 96 (2006) 165002.
[4] M. J. Hogan, et al., New J. Phys. 12 (2010) 055030.
[5] I. Blumenfeld, Ph.D. Thesis, Stanford University (2009)
[6] J. Rosenzweig et al., Phys Rev. Lett. 95 (2005) 195002
[7] M. Zhao, Ph.D. Thesis, UCLA (2008)
[8] P. Muggli, et al., IEEE T. Plasma. Sci. 27 (1999) 791.
[9] M. Litos and S. Corde, AAC'12, Austin, June 2012, p. 705.
[10] S. Li et al., AAC'12, Austin, June 2012, p. 1507.
[11] D. L. Bruhwiler et al., Phys. Plasmas 10 (2003) 2022.
[12] C. L. O'Connell et al., Phys. Rev. ST Accel. Beams 9 (2006) 101301.
[13] K. A. Marsh et al. NA-PAC'13, Pasadena, September 2013, TH0CA1
[14] E. Oz et al., Phys. Rev. Lett. 98 (2007) 084801.
[15] P. Muggli et al., Phys. Rev. Lett. 93 (2004) 014802.
[16] S. J. Gessner et al., IPAC'13, Shanghai, May 2013, TUPWA069, pp. 1865-1867
[17] Vafaei-Najafabadi, et al., submitted.

Copyright © 2013 CC-BY-3.0 and by the respective authors

SIMULATION OF LASER WAKEFIELD ACCELERATION IN THE LORENTZ BOOSTED FRAME WITH UPIC-EMMA

Peicheng Yu*, Viktor K. Decyk, Weiming An, Frank S. Tsung, Warren B. Mori, UCLA, CA 90024
Xinlu Xu, Wei Lu, Tsinghua University, Beijing 100084, China
Jorge Vieira, Ricardo A. Fonseca, Luis O. Silva, Instituto Superior Técnico, Lisbon, Portugal

Abstract

Simulating Laser wakefield acceleration (LWFA) in a Lorentz boosted frame in which the plasma drifts towards the laser with v_b can speedup the simulation by factors of γ_b^2, where γ_b is the Lorentz factor of the boosted frame. To eliminate the high frequency numerical instability induced by relativistic plasma drift in these simulations, we develop a fully parallelized, multi-dimensional, particle-in-cell code that uses a spectral solver to advance the Maxwell's equations. This new EM-PIC code is called UPIC-EMMA and it is based on the components of the UCLA PIC framework (UPIC). It is shown that using UPIC-EMMA, LWFA simulations in the boosted frames with large γ_b can be conducted without any notable numerical instability. We also benchmark the UPIC-EMMA results with OSIRIS in the lab frame, an EM-PIC code with a finite difference time domain (FDTD) Maxwell solver, and good agreements are found.

INTRODUCTION

Laser wakefield acceleration [1] offers the potential to construct compact accelerators that has a numerous potential applications, and the last ten years has seen an explosion of theoretical and experimental results. Due to the strong nonlinear effects in the laser plasma interaction involved, numerical simulations, in particular particle-in-cell (PIC) simulation, are critical in exploring the physics of LWFA. Recently, it was shown that by performing the simulation in an optimal Lorentz boosted frame with velocity v_b, the time and space scales to be resolved in a numerical simulation may be minimized [2, 3, 4]. The basic idea is that in the boosted frame the plasma length (the laser propagation distance) is Lorentz contracted while the plasma wake wavelength and laser pulse length are Lorentz expanded, which lead to savings of factors of $\gamma_b^2 = (1 - v_b^2/c^2)^{-1}$ as compared to a lab frame simulation using the so-called moving window [5].

However, in the boosted frame simulations noise from a numerical instability can be an issue. As discussed in [6, 7, 8, 9, 10], the noise results from a numerical Cerenkov instability induced by the plasma drifting with relativistic speeds on the grid. According to the dispersion relation this numerical instability is attributed to the coupling between the wave-particle resonances with EM modes (including aliased modes) in the numerical system. The pattern of the instability in Fourier space can be found at the intersections of the EM dispersion relation of the solver used in the simulation algorithm, and the wave-particle resonances [8, 9, 10].

In order to mitigate this instability, it is preferable to use an EM solver that eliminates the numerical instability at the main beam resonance [10]. When using a spectral solver that spatially advances the EM fields in Fourier space, its EM dispersion curve assures no instability pattern at the main beam resonance. In addition, the pattern at the first space aliasing beam mode is found to be located at high $|\vec{k}|$ values that are far away from the interested physics. For the spectral solver the numerical Cerenkov instability of the first aliased beam mode is located at a predicted pattern in $\vec{k}$ space so it can be conveniently eliminated by applying simple filters directly in $\vec{k}$ space.

We developed a fully parallelized three-dimensional electromagnetic spectral PIC code called UPIC-EMMA that was built using components of the UCLA PIC Framework called UPIC [11]. A spectral EM-PIC code has the same basic flow chart as a finite-difference-time-domain (FDTD) PIC code. In a spectral EM-PIC code both the charge and current are deposited on the mesh from the particles; the forces exerted on the particles are interpolated from the mesh points, and particles are advanced using the Lorentz forces. The main difference between the spectral PIC code and FDTD PIC code is the solver used to advance the electromagnetic field and that all field quantities, including the charge and current densities, are defined at the same locations on a cell (no Yee mesh [12] is needed). In a spectral PIC code the charge and current are directly deposited, and a strict charge conserving current deposit is not needed because Gauss's law is solved at each time step using the charge density.

There are no dispersion errors for light waves due to the grid (however there are errors from the finite time step). This is a significant advantage of the spectral solver, whereas a FDTD code describes the $[k]_i$ operator to $\mathcal{O}(k_i\Delta x_i)^3$, the spectral code has no errors in the finite $[\vec{k}]$ operator. In addition, when including time step errors, the numerical dispersion of a spectral PIC code is superluminal, while that of the FDTD code is sub-luminal. The more accurate and superluminal aspect of the EM dispersion relation provided by the spectral solver (together with the simple filters) is crucial for eliminating the numerical Cerenkov instability. This ensures no non-physical interaction between waves and particles in the first Brillouin zone for the spectral PIC code.

* tpc02@ucla.edu

Copyright © 2013 CC-BY-3.0 and by the respective authors

LAUNCHING LASER AND ELECTRON BEAM

To model LWFA stages including beam loading it is necessary to have an antenna and a cathode in the boosted frame. Next, we discuss how these are implemented in UPIC-EMMA.

Moving Antenna

As discussed in [3] and [13], the effective spot size of the laser increases by a factor of $\gamma_b^2(1+\beta_b)$ because the Rayleigh length of the laser contracts by γ_b and the pulse length expands by $\gamma_b(1+\beta_b)$. To prevent the need for using a simulation box with transverse size $\sim \gamma_b^2$ times that is needed in the lab frame, we utilize a thin slice of grids at the plasma boundary as an antenna to drive the laser pulse into the plasma. The antenna moves backward together with the plasma boundary in the boosted frame.

In the spectral code, the transverse and longitudinal components of the fields are solved for separately. Therefore, on the antenna we set ρ equal to zero so there are no longitudinal fields on it. When launching a laser from the antenna, we assign current (in the direction of the laser polarization direction) at every point inside the antenna such that $\vec{E}$ has the desired form and polarization. The other components and the magnetic field follow naturally from Maxwell equations. The antenna has a finite width of around $\lambda/2$ where λ is the wavelength of the laser in vacuum to eliminate any backward propagating signal. The current for generating the laser is added after the current is deposited for all the particles in the system is finished.

Beam Cathode

Similarly to the initialization of laser, when initializing a particle beam in the Lorentz boosted frame the effective β^* contracts, which greatly enhances the effective spot sizes of the beam. We implement a beam cathode in UPIC-EMMA which, similarly to the moving antenna for laser, launches beam particles from a thin slice moving together with the plasma boundary. The corresponding EM fields produced by the beam are likewise initialized within the slice. The beam cathode also enables UPIC-EMMA to be used to simulate loading a particle beam into a wake driven by a laser and simulate plasma wakefield acceleration (PWFA).

BENCHMARK WITH OSIRIS

To benchmark the boosted frame simulation results from UPIC-EMMA, we performed extensive simulations. Here we present simulations of a 1 GeV LWFA stage with both UPIC-EMMA in a boosted frame and OSIRIS [14] in the lab frame. OSIRIS uses a FDTD solver, e.g. Yee solver, to push the EM field. The parameters for the OSIRIS simulations are listed in table 1, and the results for the $a_0 = 8.0$ cases are shown in figure 1. From the plasma density plot and wakefield plot in the Lorentz boosted frame, we can see clean physical results with no evidence of the numerical Cerenkov instability. Good agreement for the on-axis wakefield is found between OSIRIS lab frame and UPIC-EMMA boosted frame simulation. More comparisons can be found in Ref. [15].

Table 1: Simulation Parameters for the Simulations Shown in Figure 1 and 2 – ω_0 is the Laser Frequency and k_0 is the Laser Wave Number in the Lab Frame

2D LWFA boosted frame simulation	
Plasma	
plasma column length L	0.9 cm
density n_0	2×10^{18} cm^{-3}
Laser	
pulse length τ	30 fs
norm. vector potential	$a_0 = 8.0$
pulse waist W	15 μm
Simulation	
grid size $(k_0\Delta x_1, k_0\Delta x_2)$	$(0.0982, 0.0982)$
time step $\omega_0\Delta t$	0.0225
number of grid in box	16384×512
boosted frame γ_b	14
particle shape	quadratic
3D PWFA lab frame simulation	
Plasma density n_0	5×10^{16} cm^{-3}
Beam	
pulse length τ	113.7 fs
spot size W	10 μm
beam energy	22.5 GeV

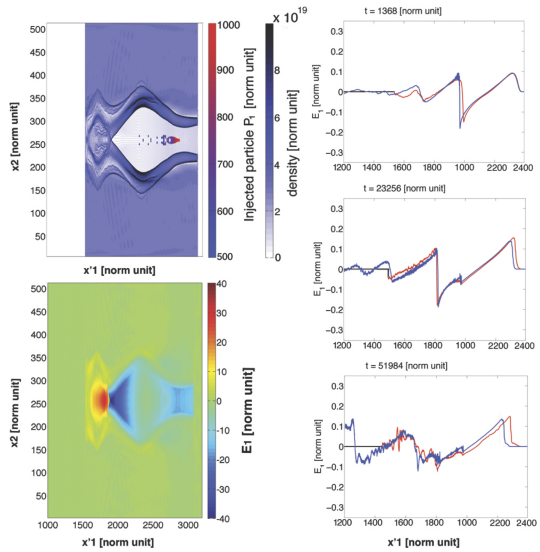


Figure 1: Highly nonlinear case at $a_0 = 8.0$. Left column shows the 2D plots of plasma electron density, and the corresponding E_1 at $t = 221$ [norm unit] in the boosted frame ($\gamma_b = 14$). The second column shows the on-axis E_1 comparison between OSIRIS lab frame, and UPIC-EMMA boosted frame simulation ($\gamma_b = 14$).

Copyright © 2013 CC-BY-3.0 and by the respective authors

BOUNDARY CONDITIONS

Currently, in UPIC-EMMA there are 3 types of EM boundary conditions (b.c.) available: (i) 3D periodic boundary; (ii) 3D conducting boundary; and (iii) mixing boundaries with conducting boundary in x_1 and x_2, and periodic boundary in x_3. The particles are specularly reflected from the conducting boundary. The conducting b.c. is particularly useful when modeling beam loading or PWFA. This is due to the fact that when all the three directions are periodic, the charge neutrality in the simulation box is enforced, while in the PWFA simulation the system is non-neutral because of the electron beam. To illustrate this issue we show UPIC-EMMA results from a lab frame simulation where only one driving particle beam is modeled (no trailing beam). In figure 2 we present the results of a 3D PWFA simulation in the lab frame, using 3D periodic b.c. (first row), and mixing b.c. (second row), and the comparison in the on-axis wakefields are shown in figure 2 (c) and (d). The QUICKPIC results are also shown in figure 2 (c). In figure 2 (d) we plot the transverse lineout of the wakefield in the bubble, to illustrate the differences in the wakefield due to the different b.c.

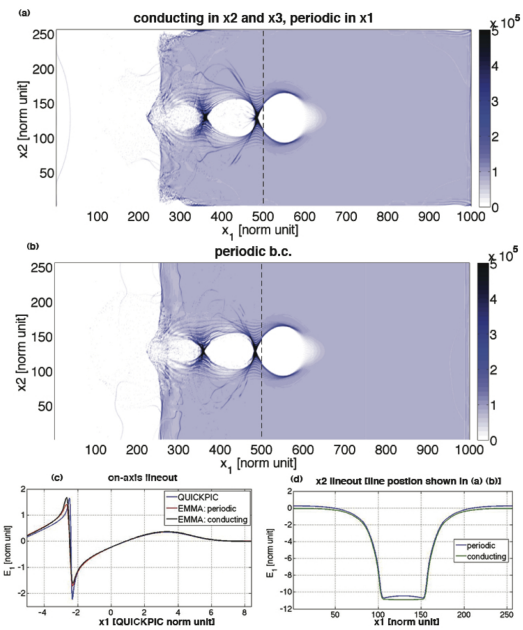


Figure 2: (a) and (b) show the 2D plasma density plot of a 3D PWFA lab frame simulation using the parameters shown in table 1. (a) uses the conducting b.c. in the transverse directions of the propagating driving beam, while (b) uses 3D periodic b.c. In (c) the on-axis wakefields are compared between the mixing b.c. and 3D periodic b.c., and also compared with the QUICKPIC results. In (d) we plot the transverse lineout of the wakefield in the bubble for the two types of b.c; the position of this cross section is shown in (a) and (b).

CONCLUSIONS

In this paper we briefly described a new simulation code called UPIC-EMMA that can model LWFA stages, including beam loading from an injected particle beam, at very high gammas γ_b. UPIC-EMMA uses a spectral solver to mitigate the numerical instability induced by the relativistic plasma drift. The spectral solver together with a band-pass filter conveniently mitigates the numerical instability.

We have also implemented a moving antenna to launch a laser and a moving cathode to launch a particle beam. The moving cathode allows beam loading as well as PWFA studies. The implementation of a mixing boundary condition is shown to give correct results for the wakes from the driving particle beams.

We presented details of LWFA parameters for simulating LFWA stages using UPIC-EMMA in the Lorentz boosted frame. The γ_b of the boosted frame is chosen such that the laser frequency is in the same order as the plasma frequency so neither of these two characteristic lengths are over-resolved. We compared the transformed boosted frame data in UPIC-EMMA with the lab frame data from OSIRIS, and good agreements are found.

This work is supported by DOE awards DE-FC02-07ER41500, DE-SC0008491, DE-FG02-92ER40727, and DE-SC0008316, and by NSF grants NSF PHY-0904039 and NSF PHY- 0936266, and by NSFC Grant 11175102, thousand young talents program. Simulations were carried out on the UCLA Hoffman 2 Cluster, and Dawson 2 Cluster.

REFERENCES

[1] T. Tajima, J. M. Dawson, Phys. Rev. Lett. 43, 267 (1979).
[2] J. -L. Vay, Phys. Rev. Lett. 98, 130405 (2007)
[3] S. F. Martins, R. A. Fonseca, L. O. Silva, W. Lu, W. B. Mori, Comp. Phys. Comm. 181, 869 (2010).
[4] J. -L. Vay, C. G. R. Geddes, E. Cormier-Michel, D. P. Grote, J. Comp. Phys. 230, 5908 (2011).
[5] C. D. Decker, W. B. Mori, Phys. Rev. Lett., Vol. 72, 490 (1994)
[6] B. B. Godfrey, J. Comp. Phys. 15, 504 (1974); B. B. Godfrey, J. Comp. Phys. 19, 58 (1975)
[7] K. Nagata, PhD thesis, Osaka University, 2008.
[8] P. Yu et.al, in Proc. 15th Advanced Accelerator Concepts Workshop, Austin, TX, 2012.
[9] B. B. Godfrey and J.-L. Vay, J. Comp. Phys., 248, 33-46 (2013)
[10] X. Xu, et. al., Comp. Phys. Comm., Vol. 184, 2503–2514 (2013)
[11] V. K. Decyk, Comp. Phys. Comm. 177, 95 (2007).
[12] K. Yee, IEEE Transactions on Antennas and Propagation, Vol. 14, 302 (1966)
[13] J.-L. Vay, C. G. R. Geddes, E. Cormier-Michel, D. P. Grote, arXiv:1009.2727v2
[14] R. A. Fonseca, et al., in: P.M.A. Sloot, et al. (Eds.), ICCS, in: LNCS, Vol. 2331, 2002, pp. 342–351.
[15] P. Yu et. al. in preparation.

Copyright © 2013 CC-BY-3.0 and by the respective authors

POSSIBILITY OF CONFIRMING SMI THROUGH ENERGY SPECTRUM WITH THE 1 nC ATF ELECTRON BUNCH

Y. Fang*, University of Southern California, Los Angeles, CA
P. Muggli, University of Southern California, Los Angeles, CA
and Max Planck Institute for Physics, Munich, Germany
W. Mori, University of California, Los Angeles, Los Angeles, CA

Abstract

In this paper, we demonstrate numerically the possibility of measuring the energy gain/loss experimentally to confirm the self-modulation instability (SMI) development with electron bunch parameter available at Accelerator Test Facility (ATF) of Brookhaven National Laboratory (BNL). The results also show that due to plasma wakefield dephasing during the SMI development, the actual energy gain/loss by drive bunch particles is lower than deduced from maximum accelerating fields. All the simulations are performed with the 2D-cylindrically symmetric partilcle-in-cell code OSIRIS [1].

INTRODUCTION

We have successfully demonstrated the excitation of multiple-periods plasma wakefields by a 50 pC bunch with square current profile available at the Accelerator Test Facility of Brookhaven National Laboratory (BNL-ATF) [2]. These wakefields act as the seed for self-modulation instability (SMI). The experimental data is in excellent agreement with the linear theory and OSIRIS-2D [1] simulation results. With this low 50 pC charge, the SMI does not grow within the 2 cm propagation distance in the plasma density range available in the experiment (10^{15}-10^{17} cm^{-3}), and therefore periodic energy modulation measurements were possible. However, simulations have shown that the SMI of the 1 nC bunch grows significantly and reaches saturation over the 2 cm propagation distance (see Fig. 1 b)). Note that for 1 nC bunch, the beam-plasma interaction is still in the linear regime of the PWFA for the plasma density range as indicated above, i.e., n_b/n_p <0.06. According to linear theory, the initial wakefield amplitude is 20 times higher for 1 nC bunch than that of 50 pC bunch, and this has been confirmed by previous simulations [3]. We here further analyze the simulation results of 1 nC bunch to examine the possibility of measuring the energy spectrum experimentally to confirm the development of SMI. As an example, we take the plasma density of $n_e = 4.85 \times 10^{15}$ cm^{-3} such that $L_{\rm beam}/\lambda_{pe} = 2$. It has been demonstrated that during the development of SMI, the plasma wave phase velocity becomes smaller than the beam velocity, resulting in dephasing between the bunch particles and the wakefields [4, 5]. The following results show that due to such dephasing, the actual energy gain/loss by drive bunch particles is $\approx 25\%$ lower than deduced from maximum accelerating field plots, i.e. assuming the wakefield on the particles do not dephase. However, the resulting energy gain is approximately 2.4 times larger than the case without SMI development. It is therefore still possible to confirm the SMI development through the measurement of resulting energy spectrum in the experiment.

ENERGY GAIN/LOSS

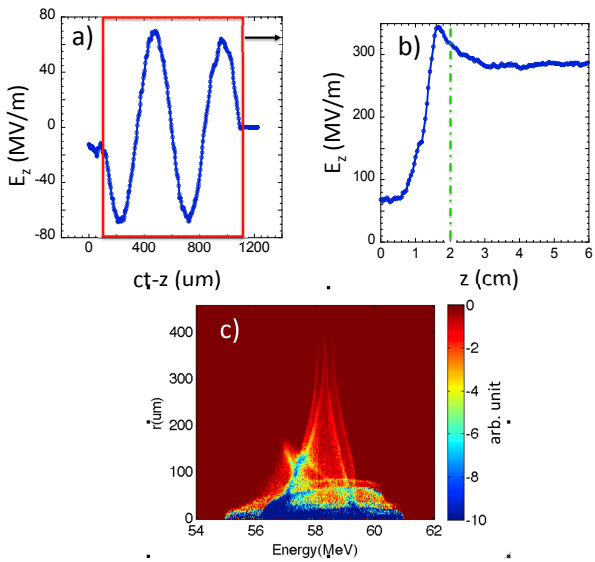


Figure 1: a) The longitudinal wakefield E_z on the axis ($r = 0$) at plasma entrance ($z = 0$) within the bunch. The red rectangle indicates position of the electron bunch. b) The evolution of maximum E_z on the axis ($r = 0$) along the propagation distance. The green line indicates the plasma length in the experiment. c) Electron bunch density in the r, E space, showing the energy spectrum of the beam at plasma exit ($z = 2$ cm). Results are obtained from OSIRIS 2D.

We first assume that there is no SMI growth during the 2 cm propagation for the 1 nC bunch, and therefore the energy gain/loss at the plasma exit can be estimated by multiplying the initial E_z amplitude (at $z = 0$) with 2 cm. Figure 1 a) shows the initial longitudinal wakefield E_z on the axis ($r = 0$) at the plasma entrance ($z = 0$) obtained from simulation, with an acceleration amplitude $E_{z0} \approx 67$ MV/m, which is within $\%5$ difference with the estimation of linear theory (≈ 64 MV/m). Therefore, assuming no SMI growth and hence no E_z amplitude evolution, the energy

* yunf@usc.edu

Copyright © 2013 CC-BY-3.0 and by the respective authors

gain/loss at the plasma entrance would be $\Delta E_{\mathrm{no-growth}} = E_{z0} \times 2$ cm$\approx$ 1.33 MeV. Figure 1 b) shows the evolution of maximum longitudinal field on the axis E_{zmax} along the propagation distance. The exponential growth and saturation of E_{zmax} indicate the development of SMI with the 1 n bunch. Since the SMI is a convective instability, the maximum E_z is expected to be at the back of the bunch, e.g. at the acceleration peak of the second wakefield bucket in this case. Assuming no dephasing of the plasma wave with respect to the square bunch during the propagation, the maximum energy gain can be estimated as the integral of E_{zmax} over the propagation distance, resulting in $\Delta E_{\mathrm{growth-integration}} \approx 3.52$ MeV. Figure 1 c) shows the energy spectrum of the electron bunch particles at the plasma exit, obtained from the OSIRIS-2D simulation. With the mean incoming energy of 58.35 MeV, the maximum energy gain is estimated as $\Delta E_{\mathrm{growth-spectrum}} \approx 60.98 - 58.35 = 2.63$ MeV, more than 2 times larger than the value obtained assuming no SMI growth. We hence conclude that it is experimentally possible to confirm the development of SMI through the measuring of the energy gain/loss at the plasma exit. It is also worth noting that the particles' actual maximum energy gain/loss $\Delta E_{\mathrm{growth-spectrum}}$ is 25% smaller than the integration of the maximum E_z result $\Delta E_{\mathrm{growth-integration}}$. This clearly indicates the occurrence of dephasing during the development of SMI, which will be further examined in the following section. Note that the conclusion also applies to energy loss, although the figures are not shown here.

DEPHASING OF THE WAKEFIELD

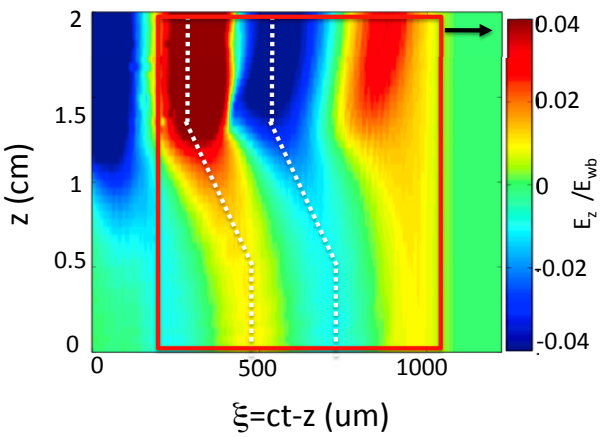


Figure 2: Evolution of the accelerating wakefield structure E_z within the bunch(es) along the propagation distance z. The red rectangle shows the longitudinal position of the bunch and the white dotted lines show the "trajectory" of the peak accelerating and decelerating field in the $z - \xi$ plane, respectively.

To confirm the dephasing of the plasma wave with respect to the electron bunch during the propagation, Fig. 2 shows the evolution of accelerating wakefield structure E_z. The phase velocity of the longitudinal plasma wave v_ϕ can be deduced from the slope of maximum E_z in the z and $\xi(= ct - z)$ plane (as shown schematically by the dotted line in Fig. 2), yielding $v_\phi = c \times (1 + \frac{1}{\delta z/\delta\xi})$ [6]. Consequently, a smaller negative slope ($\delta z/\delta\xi$) means a smaller phase velocity. Figure 3 d) shows the fitting to obtain the phase velocity. During the first 0.5 cm propagation, there is no significant growth of SMI (as can be observed in Fig. 1 b)) , and therefore the wakefield phase velocity is close to the beam velocity $v_b(\approx c)$. Between $z = 0.5 - 1.5$ cm, the beam density becomes modulated due to the periodic focusing/defocusing field and hence SMI develops, resulting in a lower wakfield phase velocity v_ϕ. Its value is estimated as 0.986 c according to Fig. 3 d). For $z = 1.5 - 2.0$ cm, the SMI saturates and the wake phase velocity almost reaches c again.

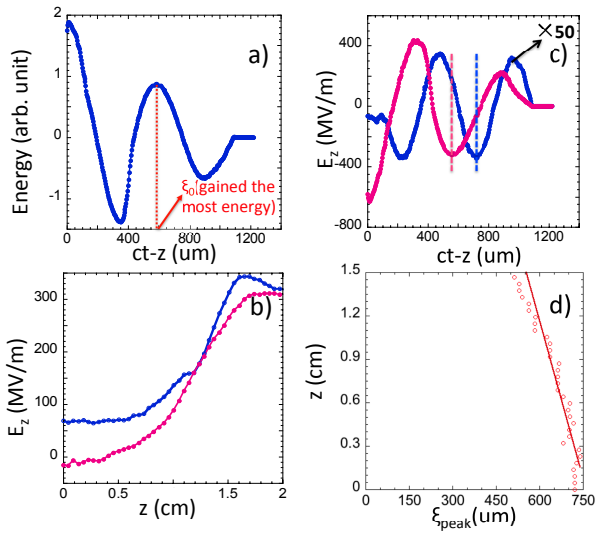


Figure 3: a) Energy gain/loss by particles along the bunch (ξ) after 2 cm plasma, obtained by integrating the acceleration field (as shown in Fig. 2 c)) over the propagation distance z. ξ_0 indicates the position in the bunch where particles gain the most energy; b) the accelerating field on the axis at position ξ_0 of the bunch ($E_z(\xi_0, r = 0)$) along the propagation distance z (red line) and the maximum E_z field on the axis along z (blue line); c) Longitudinal wakfield E_z on axis ($r = 0$) at plasma entrance $z = 0$ (blue line) and plasma exit $z = 2$ cm (red line). Note that E_z at $z = 0$ (blue line) is multiplied by 50 in order to make it visible on the same scale. The dotted lines show the accelerating peaks of the respective fields, and the distance between the two dotted lines directly shows the wakefield dephasing; d) the shifting of the position ξ of the peak accelerating field along the propagation distance z, and the fitted line is given as: $z(\mathrm{cm}) = 5.5467 - 0.0072932 \times \xi(\mathrm{cm})$, yielding $v_\phi = c \times (1 + \frac{1}{\delta z/\delta\xi}) \approx 0.986c$.

Figure 3 a) shows the energy gain of the beam particles along ξ, obtained by integrating the acceleration field in Fig. 2 over the propagation distance z, yielding the ap-

Copyright © 2013 CC-BY-3.0 and by the respective authors

proximate energy gain/loss of the bunch particles during the 2 cm propagation ($\int E_z dz \approx \sum E_z \Delta z$). We can therefore identify the ξ_0 position where the bunch particles gain the most energy. This is indicated by the dotted line in the Fig. 3 a). Figure 3 b) shows the evolution of the accelerating wakefield experienced by the the particles at ξ_0 (red curve), compared to the maximum accelerating wakefield (blue curve) along the bunch. The fact that the former amplitude is smaller than the later one explains the energy difference between the integration from maximum E_z and the actual energy spectrum of the particles at the plasma exit, as mentioned above. Fig. 3 c) shows the longitudinal field E_z on the axis along ξ at the plasma entrance $z = 0$ (blue line, $\times 50$) and at the plasma exit $z = 2$ cm (red line). The shift of the peak accelerating field between $z = 0$ and $z = 2$ cm clearly confirms the dephasing. It is worth noting that the dephasing occurs mostly over the first plasma period.

CONCLUSION

In conclusion, simulation results presented here demonstrated that the SMI grows significantly over the 2 cm propagation distance for 1 nC bunch at ATF with a plasma density such that $L_{beam} = 2\lambda_{pe}$. Due to dephasing between the bunch particles and the plasma wakefield, the actual energy gain is $\approx 25\%$ smaller than the integration of the maximum E_z over the propagation distance. However, the resulting energy gain is still approximately 2 times larger than the case without SMI development. It is therefore possible to confirm the SMI development through the measurement of resulting energy spectrum in the experiment.

REFERENCES

[1] R. A. Fonseca *et al.*, Lect. Notes Comp. Sci. vol. 2331, (Springer Berlin/Heidelberg, (2002).

[2] Y. Fang *et al.*, submitted to Phys. Rev. Lett. .

[3] Y. Fang. *et al.*, AIP Conf. Proc. 1507, pp. 559-564 (2012).

[4] A. Pukhov *et al.*, Phys. Rev. Lett. **107**, 145003 (2011).

[5] C. Schroeder *et al.*, Phys. Rev. Lett. **107**, 145001 (2011).

[6] J. Vieira *et al.*, Phys. Plasmas 19, 063105 (2012).

Copyright © 2013 CC-BY-3.0 and by the respective authors

CURRENT INDUCED IN VACUUM CHAMBER DURING NSLS-II BOOSTER RAMP*

S. Gurov#, V. Kiselev, S. Sinyatkin, BINP SB RAS, Novosibirsk, Russia

Abstract

Fields that arise in the booster magnets during a ramp induce currents in the vacuum chamber, including currents through the "ground". These induced currents produce magnetic fields, which influence the beam. Calculations and simulations for the NSLS-II booster are discussed.

INTRODUCTION

Budker Institute of Nuclear Physics has built the booster for NSLS-II. The booster has been designed [1, 2], produced [2], delivered, assembled and tested [3]. The booster is intended for continuous and reliable acceleration of electron beam from a minimum 170-MeV injection energy to a maximum energy of 3.15 GeV at an average beam current of 20 mA and a 2 Hz repetition rate.

The combined-function dipole magnets have magnetic fields with quadrupole and sextupole components. The basic parameters of the dipoles are given in Table 1.

Table 1: Specification of the Dipoles

Dipole parameters	BF	BD
Number	28	32
Effective magnetic length	1.24 m	1.30 m
Angle	3.2673°	8.3911°
Vertical gap	±14 mm	±13 mm
Field injection	0.03068 T	0.07516 T
Field extraction	0.46021 T	1.12734 T
Quadrupole K1, extraction	0.82 m^{-2}	-0.55509 m^{-2}
Sextupole K2, extraction	3.6 m^{-3}	-4.3 m^{-3}
Good field region	±12 x ±20 mm	
Field quality in the good field region, ΔB/B0	± $1\cdot10^{-3}$	

During a ramp, the fields arising in the booster magnets induce currents in the vacuum chamber, including currents through the "ground".

CURRENT THROUGH THE "GROUND"

The current through the "ground" is the total current I_{total} through the vacuum chamber:

$$I_{total} = \oint\!\!\iint \sigma E_z(r,\varphi,t)\,dS \qquad (1)$$

The integrating is done over the entire vacuum chamber cross-section with the conductivity σ.

The induced electric field can be found from the Maxwell-Faraday equation,

$$rot\vec{E} = -\frac{1}{c}\frac{\partial\vec{B}}{\partial t}, \qquad (2)$$

with $B_z = 0$ and $\frac{\partial\vec{E}}{\partial z} = 0$ taken into account.

We have the following equations:

$$\frac{1}{r}\frac{\partial E_z}{\partial\varphi} = -\frac{1}{c}\frac{\partial B_r}{\partial t} \quad \text{and} \quad \frac{\partial E_z}{\partial r} = \frac{1}{c}\frac{\partial B_\varphi}{\partial t} \qquad (3)$$

A magnet with symmetry in its median plane has the following magnetic field in the aperture:

$$B_r(r,\varphi,t) = \sum_{n=1}^{\infty} B_n(t)\cdot r^{n-1}\sin(n\varphi)$$
$$B_\varphi(r,\varphi,t) = \sum_{n=1}^{\infty} B_n(t)\cdot r^{n-1}\cos(n\varphi) \qquad (4)$$

As result,

$$E_z(r,\varphi,t) = E_{0z}(t) + \frac{1}{c}\sum_{n=1}^{\infty}\frac{\partial B_n(t)}{\partial t}\cdot\frac{r^n}{n}\cos(n\varphi) \qquad (5)$$

Here we get a component $E_{0z}(t)$, which is independent from the coordinates r and φ. This component depends on some external conditions.

If the vacuum chamber is isolated, I_{total}=0 and we get $E_{0z}(t)$ from Eq. (1) and Eq. (5).

If the vacuum chamber is grounded on the both sides of magnet, we can find $E_{0z}(t)$ in the following way. There is a field line that divides the magnetic field flow into two parts (see Fig. 1). This line crosses the magnet median plane at the point x_o. Let the circuit consist of the ground circuit and a line which is parallel to the beam axis and cross x_o. Then, the magnetic field flow through this circuit does not change during a ramp. Therefore, $E_z(r = x_o, \varphi = 0, t) = 0$, and from equation (4)

$$E_{0z}(t) = -\frac{1}{c}\sum_{n=1}^{\infty}\frac{\partial B_n(t)}{\partial t}\cdot\frac{x_0^n}{n}. \qquad (6)$$

#S.M.Gurov@inp.nsk.su

Copyright © 2013 CC-BY-3.0 and by the respective authors

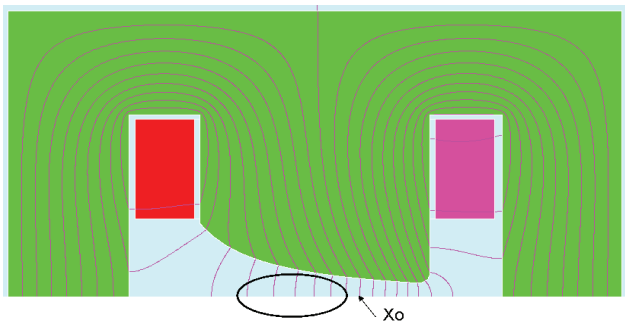


Figure 1: Magnetic field distribution in a BF dipole. The ellipse denotes the vacuum chamber. The "zero shift" is x_o = 30.7 mm for the BF dipole and x_o = 4.4 mm for the BD dipole.

If we neglect the effects related to the steel properties of the magnetic yoke,

$$B_n(t) = Bm_n \cdot f(t). \quad (6)$$

Here Bm_n is the field harmonics at the maximum magnet current and $f(t)$ is a function that describes the ramp of the magnets, such that $f(t) = 1$ at the maximum magnet current.

Consequently

$$E_{0z}(t) = -\frac{1}{c}\frac{\partial f(t)}{\partial t}\sum_{n=1}^{\infty} Bm_n \cdot \frac{x_0^{\,n}}{n}$$

or

$$E_{0z}(t) = -\frac{1}{c}\frac{\partial f(t)}{\partial t}\int_0^{x_0} Bm_y(x)dx \quad (7)$$

MAGNETIC FIELD

Since the current induced in the vacuum chamber has symmetry in the median plane, the induced magnetic field $Bc(t)$ in the vacuum chamber looks similar to that Eq. (4) with the field harmonics $Bc_n(t)$. This harmonics can be found in the following way. On the one hand, the magnetic field in the median plane is

$$Bc_y(x,t) = \sum_{n=1}^{\infty} Bc_n(t)\cdot x^{n-1}. \quad (8)$$

On the other hand,

$$Bc_y(x,t) = \frac{2}{c}\iint \frac{(r\cos\varphi - x)}{R^2}\cdot j(r,\varphi,t)\cdot r\,d\varphi\cdot dr \quad (9)$$

The integrating is done over the entire vacuum chamber cross-section; r is a function of φ; R is the distance from the current dI to x:

$$R^2(\varphi, x) = (r\cos\varphi - x)^2 + r^2\sin^2\varphi. \quad (10)$$

Since $\frac{x}{r} < 1$ in the vacuum chamber, we can use the following expression:

$$\frac{\cos\varphi - x/r}{(\cos\varphi - x/r)^2 + (\sin\varphi)^2} = \sum_{m=0}^{\infty}\left(\frac{x}{r}\right)^m \cos(m+1)\varphi \quad (11)$$

Therefore,

$$Bc_n(t) = \frac{2\sigma}{c}\iint \frac{E_z(r,\varphi,t)\cos(n\varphi)}{r^{n-1}}d\varphi\cdot dr \quad (12)$$

In case of round vacuum chamber, there is no induced magnetic field. In case of elliptical vacuum chamber, the main component of the induced field is a quadrupole harmonics.

SIMULATION

Dynamical effects arising during an energy ramp were simulated with the help of the computer code ANSYS for a stainless steel dipole vacuum chamber 1 mm thick with a 41×24 mm cross-section.

Simulated were the "through-ground" currents of the BD (see Fig. 3) and BF dipoles (see Fig. 4) during a ramp (see Fig. 2).

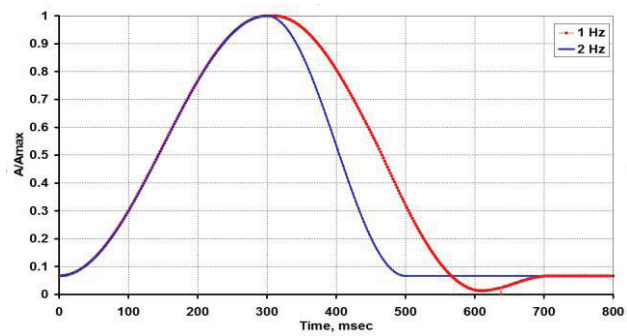


Figure 2: Dipole field ramp for 1 Hz and 2 Hz.

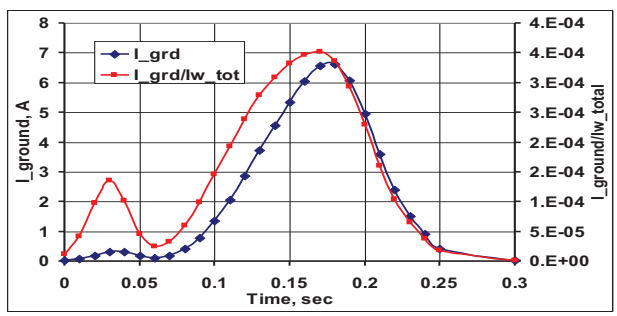


Figure 3: "Through-ground" current of the BD dipoles (red); the same normalized to the dipole current in Ampere-turns (blue).

Copyright © 2013 CC-BY-3.0 and by the respective authors

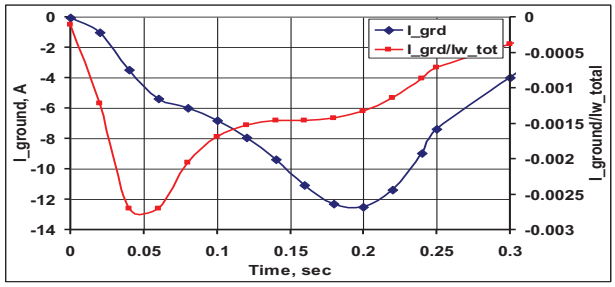


Figure 4: "Through-ground" current of BF dipoles (red); the same normalized to the dipole current in Ampere-turns (blue).

Figures 5 and 6, respectively, show the deviation of magnet parameters for the BD and BF magnets. The eddy current effect results in an equal relative deviation of the magnetic field and gradient magnitudes (Fig. 5 and Fig. 6, ΔB/B_eddy, ΔG/G_eddy). The eddy current in the vacuum chamber induces a strong sextupole component of the magnetic field (ΔS/S_eddy). The "through-ground" currents through the vacuum chamber induce an additional large gradient of the field (ΔG/G_eddy+ground) and give a small contribution to the field and sextupole strength (ΔB/B_eddy_ground, ΔG/G_eddy_ground).

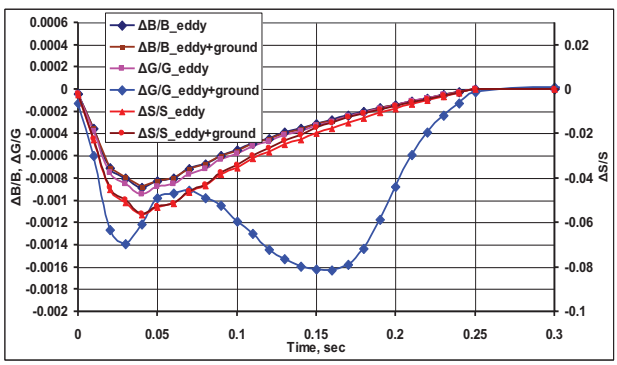


Figure 5: Deviation of the magnet parameters of the BD dipoles due to the eddy current effect.

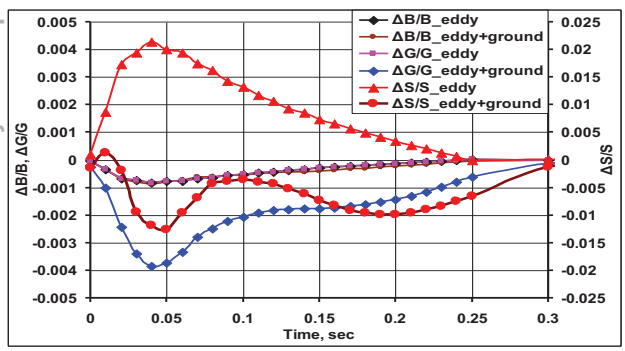


Figure 6: Deviation of the magnet parameters of the BF dipoles due to the eddy current effect.

MEASUREMENTS

The dipoles were measured with Hall probes at DC currents [4]. In addition, one BF dipole and one BD dipole were measured during a ramp with an assembly of long coils [5]. This coil assembly allows measuring integrated fields with and without the vacuum chamber.

When the vacuum chamber was grounded on both sides, the through-ground current (see Fig. 7) was measured with a current probe. This current produces the measured quadrupole and sextupole components (see Fig. 8).

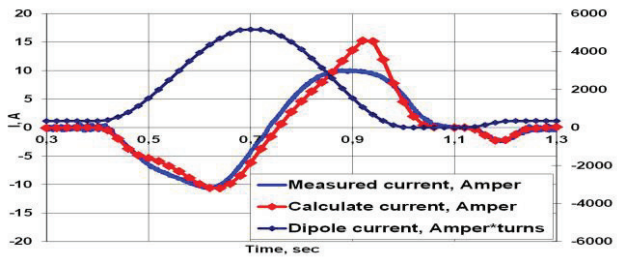


Figure 7: Through-ground current for the BF dipole. Calculated current (red); measured current (blue); dipole current in Ampere-turns (black).

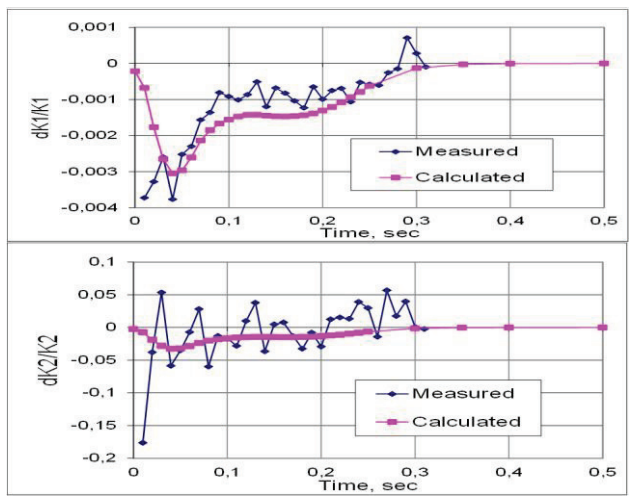


Figure 8: Influence of the vacuum chamber grounding on the quadrupole (top) and sextupole (bottom) field components of the BF dipole.

REFERENCES

[1] T.Shaftan et al., "NSLS-II Booster Design", NSLS-II Tech. note 0061 (2009).

[2] S.Gurov et al., "Status of NSLS-II booster," PAC'11, New-York, April 2011, WEP201, p. 1864 (2011).

[3] G.M.Wang et al., "NSLS-II Injector Integrating Testing," IPAC'13, Shanghai, May 2013, THPEA063, p. 3285 (2013); http://www.JACoW.org

[4] S.Sinyatkin et al., "Magnetic Measurement Results of NSLS-II Booster Dipole Magnets" IPAC'13, Shanghai, May 2013, THPME031; p. 3573 (2013).

[5] I.Okunev, et al., "Ramped Magnetic Measurement of NSLS-II Booster Dipoles", IPAC'13, Shanghai, May 2013, THPME031; p. 3576 (2013); http://www.JACoW.org

Copyright © 2013 CC-BY-3.0 and by the respective authors

SELF-CONSISTENT SIMULATIONS OF PASSIVE LANDAU CAVITY EFFECTS*

G. Bassi†, A. Blednykh, S. Krinsky, J. Rose, BNL, Upton, NY 11973-5000, USA.

Abstract

We discuss passive Landau cavity effects for arbitrary fill patterns. We present a new algorithm for the self-consistent calculation of the long-range multibunch interaction and implement it in the parallel OASIS code. As an application, we show numerical simulations with parameters of the passive Landau cavity system of the MAX-IV storage ring, which consists of normal conducting cavities. Together with with the uniform filling case, which is planned for nominal operations of the MAX-IV storage ring, we discuss the case with a gap in the fillings.

EQUATIONS OF MOTION

We assume M bunches, each with N electrons, circulating in a ring with circumference C and revolution period T_0. According to the steady state beam loading compensation scheme shown in Fig.1, for self-consistent simulations of passive Landau cavity effects, the dynamics of the particles in bunch m ($m = 0, .., M-1$), under the one-turn map approximation, is governed by (without radiation damping and quantum fluctuations)

$$\begin{aligned} \delta_{n+1} &= \delta_n \\ &+ \frac{e}{E_0}\Big[V_{gr}\cos\Psi\sin(\phi_s+\theta_L+\Psi-\omega_{rf}\tau_n) \\ &- V_m(\tau_n) - V_{rf}\sin\phi_{s0}\Big], \\ \tau_{n+1} &= \tau_n - \eta T_0\delta_{n+1}, \end{aligned} \tag{1}$$

where n is turn number, e the electron charge, δ is the relative energy deviation with respect to the nominal energy E_0, τ is arrival time and η the momentum compaction. Here V_{gr} (generator voltage) V_{rf} (rf voltage), ϕ_s (synchrotron phase), Ψ (detuning angle) and θ_L (load angle) are the parameters of the main cavity and $\sin\phi_{s0} = U_s/(eV_{rf})$, where U_s is the energy loss per turn. $V_m(\tau_n)$ is the collective voltage induced by the passages of the M bunches through the main and Landau cavities.

The self-consistent calculation of $V_m(\tau_n)$ for a narrow-band resonator wake can be done efficiently by computing averages, via a MonteCarlo integration, of trigonometric functions with respect to the "history" of the bunch densities [3]. For the case of an arbitrary long-range wakefield interaction, see [2], where the collective voltage is calculated via a Taylor series expansion. The algorithm is implemented in OASIS, a self-consistent parallel code for efficient simulations of instabilities driven by short and long-range wakefields [3], and allows the study of passive Landau cavity effects for normal conducting cavities. The case with superconducting cavities is at the moment computationally too expensive. However, we are planning to extend the capability of the algorithm to cover the superconducting case, since our ultimate goal is the study of the passive Landau cavity system of the NSLS-II storage ring, which is planned to operate with superconducting cavities. Notice that Eq.(1) provides Robinson damping of the 0 mode by properly detuning the main cavity. This is crucial vhenever the longitudinal radiation damping is not strong enough to suppress the Robinson instability induced by detuning the Landau cavity for bunch lengthening.

UNIFORM FILLINGS

As an application of our current algorithm, we study passive Landau cavity effects with parameters of the MAX-IV storage ring [1] (see Table 1), which will be operated with normal conducting cavities (see Table 2). In our simulations we include only the fundamental mode of the main and Landau cavity. The optimal bunch lengthening can be estimated by calculating the collective voltage induced by equally spaced stationary bunches [4]. According to the parameters of MAX-IV the optimal bunch lenghtening for uniform fillings is ≈ 200ps.

In Fig.2 we show self-consistent simulations of Eq.(1) with the OASIS code. OASIS is based on a Vlasov approach and implements a particle tracking method to solve the Vlasov equation, therefore uses $\mathcal{N}$ simulation or representive particles to sample the underlying phase space density, and its number is not necessarily related to the actual number of particles in the bunch N. The simulations of M bunches, each with $\mathcal{N}$ simulation particles, are done in parallel using M processors, by assigning $\mathcal{N}$ of each bunch to a single processor. Eq.(1) is integrated up to 300K turns. The parameters (per cavity) used to solve Eq.(1) are $V_{gr} = 0.495$MV, $\phi_s = 2.728$rad, $\Psi = -1.137$rad and $\theta_L = 0$. The detuning frequency of the Landau cavity is 47.53kHz and the number of simulation particles used is $\mathcal{N} = 100$K. In Fig.2 (left) we plot the bunch length of the bunch train after 300K turns. The red curve represents the numerical result with Landau cavities. The bunch length is roughly constant across the bunch train and approximately equal to 210ps. The curve in blue shows the nominal bunch length of 40ps without Landau cavities. In Fig.3 (top left) we plot the longitudinal density of the bunch train. We clearly see that for uniform fillings the Landau cavities induce roughly the same bunch lenghtening across the train without displacing the bunch centroid.

* Work supported by DOE contract DE-AC02-98CH10886
† gbassi@bnl.gov

Copyright © 2013 CC-BY-3.0 and by the respective authors

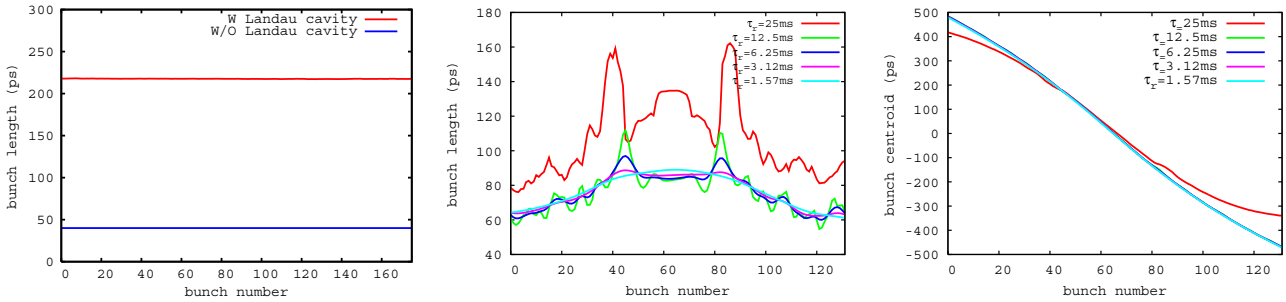


Figure 2: Numerical simulations with OASIS. The number of simulation particles used is $\mathcal{N} = 100$K. Bunch length vs bunch number after 300K turns for uniform fillings and maximum bunch length equal to 210ps (left) and for a gap of 44 bunches in the fillings and several values of the radiation damping time (center). Right: same as center for the bunch centroid.

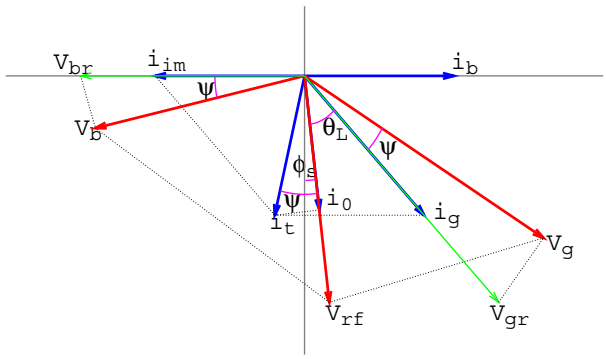


Figure 1: Phasor plot for steady state beam loading compensation according to Eq.(1). Per cavity (main) parameters: V_{gr} is the generator voltage, V_{rf} the rf voltage, ϕ_s the synchrotron phase, Ψ the detuning angle and θ_L the load angle.

Table 1: MAX-IV Storage Ring Parameters (Bare Lattice)

Parameter	Symbol	Value	Unit
Beam energy	E_0	3	GeV
Average current	I	500	mA
Number of bunches	M	176	
Harmonic number	h	176	
Circumference	C	528	m
Bunch length w/o HC	σ_τ	40	ps
Energy spread	σ_p	7.7×10^{-4}	
Energy loss per turn	U_s	364	keV
Momentum compaction	η	3.07×10^{-4}	
Long. radiation damping	τ_r	25	ms

NON-UNIFORM FILLINGS

We now discuss the case of a gap in the fillings. We assume 44 empty buckets and 132 filled buckets, with the same average current $I = 500$mA. The per cavity parameters used are $V_{gr} = 0.491$MV, $\phi_s = 2.729$rad, $\Psi = -1.139$rad and $\theta_L = 0$. The detuning frequency

Table 2: Main (4 Cavities) and Landau ($m = 3$) Cavity

Per cavity parameter	Symbol	Value	Unit
RF frequence (main)	ω_{rf}	$2\pi\times99.93$	MHz
RF frequency (Landau)	$m\omega_{rf}$	$2\pi\times299.793$	MHz
RF voltage (main)	V_{rf}	0.255	MV
Shunt impedance (main)	R_L	2.6	MΩ
Shunt impedance (Landau)	R_H	2.3644	MΩ
Quality factor (main)	Q_L	21000	
Quality factor (Landau)	Q_H	21000	

of the Landau cavity is 47.53kHz. The bunch centroid and bunch length vary accross the bunch train as shown in Fig.2 and Fig.3. For the nominal radiation damping $\tau_r = 25$ms we observe a dipole instability (as shown in Fig.4, center) as well as an increase of the bunch length vs bunch number, as shown also in Fig.2 (center) by the red curve. This instability is not present for smaller values of the radiation damping. We observe also that the bunch length shows two spikes around bunch number 40 and 85. These spikes weaken when reducing τ_r, disappearing at $\tau_r = 1.57$ms, as shown by the cyan curve in Fig.2 (center) and by the longitudinal density across the bunch train shown in Fig.3 (bottom right). We are investigating the nature of this effect. Notice that the bunch centroids for $\tau_r < 25$ms are roughly the same, as shown in Fig.2 (right). The numerical results discussed in this paper are preliminary and will be subject to further analysis.

REFERENCES

[1] M. Klein et al., Paper MOPWO003, proceedings of IPAC2013.

[2] G. Bassi et al., Paper TUPPP042, proceedings of IPAC2012.

[3] G. Bassi, in preparation.

[4] K.Y. Ng, "Physics of Intensity Dependent Beam Instabilities", Fermilab-FN-0713.

Copyright © 2013 CC-BY-3.0 and by the respective authors

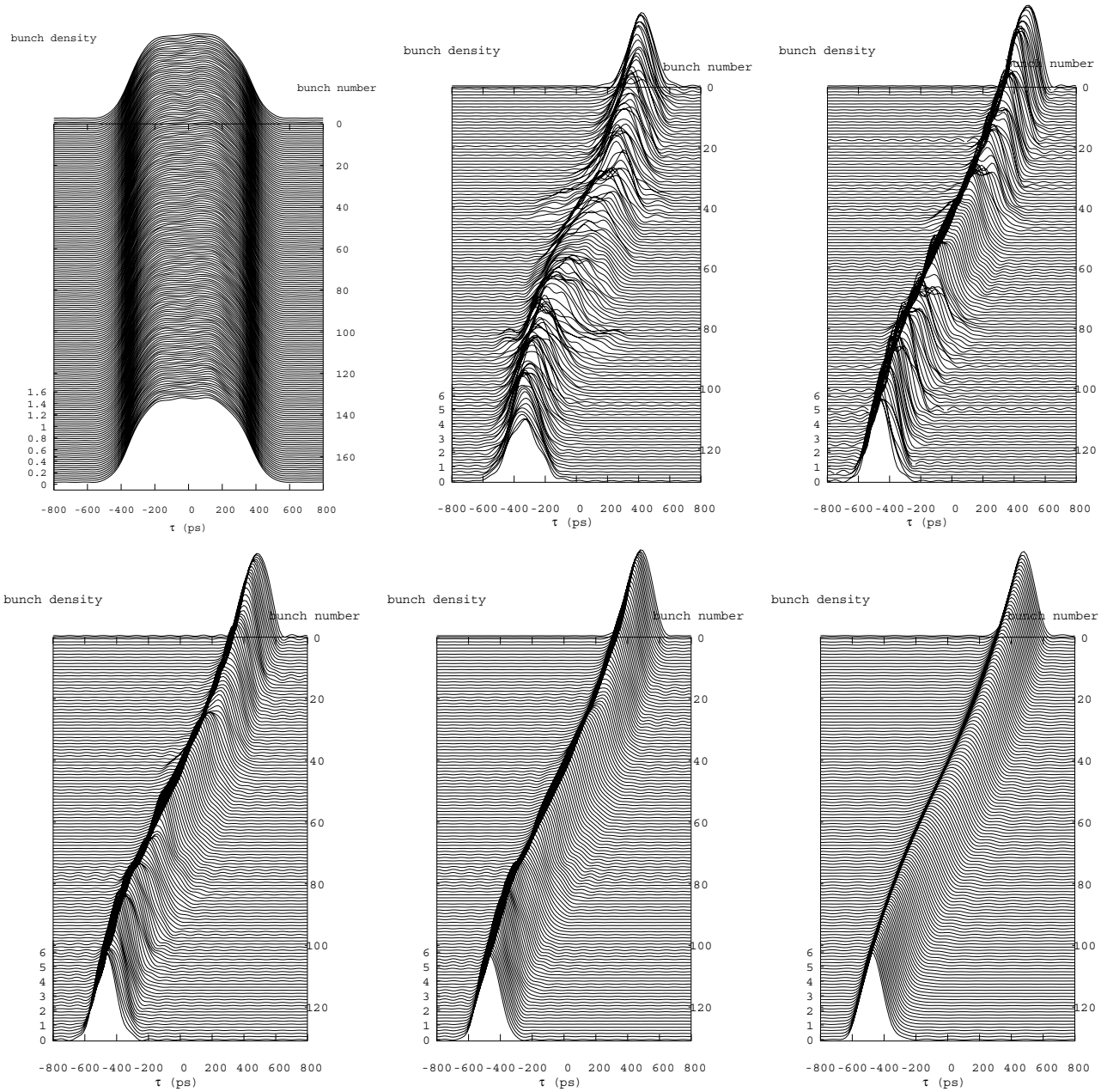


Figure 3: Bunch train after 300K turns for uniform fillings and maximum bunch length equal to 210ps (top left) and for a gap of 44 bunches in the fillings and radiation damping time τ_r=25ms (top center), τ_r=12.5ms (top right), τ_r=6.5ms (bottom left), τ_r=3.12ms (bottom center) and τ_r=1.57ms (bottom right).

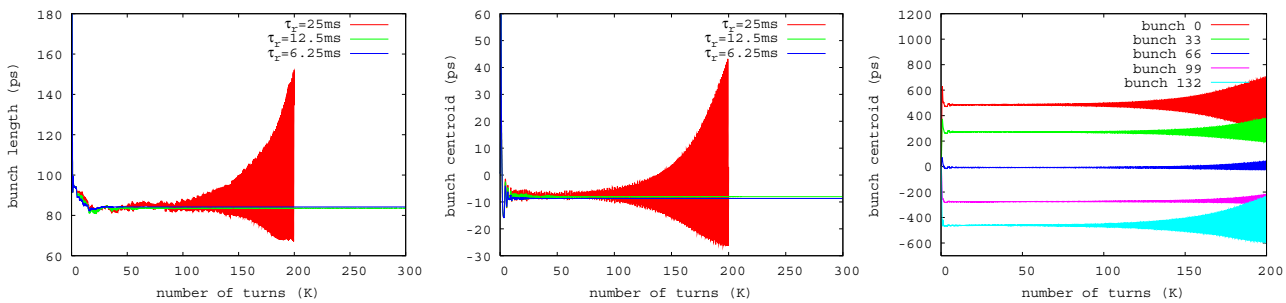


Figure 4: Time evolution of bunch length (left) and bunch centroid (center) for bunch number 66 and several values of τ_r, and time evolution of bunch centroids for τ_r=25ms (right).

Copyright © 2013 CC-BY-3.0 and by the respective authors

POLARIZATION PROFILE AND SPIN DYNAMICS SIMULATIONS IN THE AGS USING THE ZGOUBI CODE*

Y. Dutheil, L. Ahrens, H. Huang, F. Méot, V. Schoefer
BNL, Upton, Long Island, New York, USA

Abstract

Polarization transmission during the AGS acceleration cycle is critical for the RHIC polarized proton program.Thus drives a strong interest on the exploration of the polarization losses in the AGS. Intrinsic spin resonances are the main source of depolarization in the AGS. This results in the formation of a polarization profile since the strength of such depolarizing resonance depends on the Courant-Snyder invariant of each particle. The Zgoubi code and the AGS Zgoubi on-line model now allow exploration of the formation of the polarization profile during the acceleration cycle using multi-particle trackings with realistic beam and machine conditions. This paper introduces the specifics of these simulations and compares some of the latest simulated and experimental results.

INTRODUCTION

Acceleration of polarized protons in a synchrotron requires particular schemes to conserve the polarization. Two main types of depolarization resonances can reduce the overall polarization of the beam. The imperfection resonances are driven by vertical closed orbit distortions and occur when $Q_s = I$ with Q_s the spin tune and I an integer [1]. The intrinsic resonances are driven by the vertical betatron motion and occur when $Q_s = I \pm Q_y$ with Q_y the vertical tune.

The AGS uses two partial Siberian snakes to overcome the spin resonances [2], usually called *warm* and *cold* snakes. While in a regular synchrotron $Q_s = G\gamma$ (G is the anomalous gyromagnetic g-factor of the proton), the complex helical dipole fields of the Siberian snakes open forbidden bands in the spin tune around the integer values of $G\gamma$, the spin tune gap. The imperfection resonances are avoided since the integer values of Q_s are now forbidden. The vertical intrinsic resonances are overcome by keeping the vertical tune in the spin tune gap, typically around $Q_y = 8.98$.

Despite the use of Siberian snakes polarization losses are observed in the AGS and while the polarization profile at injection is negligible, measurements show significant profiles of polarization in both vertical and horizontal planes after the acceleration. We will present the main candidates that can explain the observed profiles then some simulation methods and results will be compared to measured polarization profiles.

* Work supported by Brookhaven Science Associates, LLC under Contract No. DE-AC02-98CH10886 with the U.S. Department of Energy.

Copyright © 2013 CC-BY-3.0 and by the respective authors

Sources of Polarization Profile

The strength of an intrinsic spin resonance depends on the *Courant-Snyder* invariant, hence the depolarization experienced by a particle across such a spin resonance also depends on the single particle emittance. The crossing of such resonance can result in the particles at larger amplitude being depolarized while the center of the beam remains polarized.

The injection in the AGS occurs at $G\gamma = 4.5$ and the vertical tune needs to be placed in the spin gap before the first vertical intrinsic resonance, around $G\gamma = 5$. Figure 1 shows the vertical tune crossing the spin tune around $G\gamma = 5$. Due to the strong optical distortions caused by the Siberian snakes it is not possible to push vertical tune high enough at low energy. We expect that the crossing of vertical intrinsic resonances in this region depolarizes part of the beam and induces a polarization profile in the vertical plane.

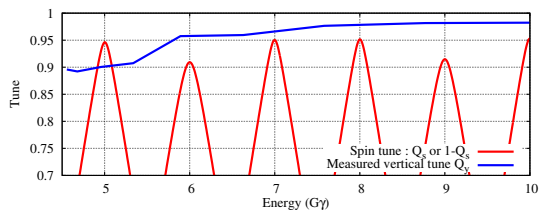


Figure 1: Fractional part of the vertical tune and spin tune at low energy.

While the partial Siberian snakes configuration avoid depolarizations caused by the imperfection and vertical intrinsic resonances, it can also induce depolarization through horizontal intrinsic resonances when $Q_s = I \pm Q_x$ with Q_x the horizontal tune. The stable spin direction is never perfectly vertical with partial snakes and therefore the non-zero horizontal component of the spin can resonate with the horizontal betatron tune. The strength of these resonances depends on the horizontal emittance and horizontal component of polarization. The crossing of these resonances builds up an horizontal polarization profile.

Other sources of depolarization can contribute to the polarization profile. For instance linear betatron coupling or high order partial snake resonances [3] can increase the polarization profile but will not be discussed here.

SIMULATIONS

Extensive development of the AGS Zgoubi on-line model provides a realistic model of the polarized proton

machine [4][5][6]. Measured currents of the power supplies along the acceleration cycle are used by the Zgoubi on-line model to generate corresponding optics of the AGS. The Siberian snakes were represented by 3-D OPERA field maps to exploit the precision of the stepwise ray-tracing code Zgoubi and achieve the high accuracy required for long term spin tracking.

Simulations Conditions

Due to the lack of a reliable field map to simulate the warm snake, a cold snake map has been scaled down to achieve the same snake angle as the warm snake and is used as the warm snake in this model. This provides a realistic spin dynamics and a better behavior of the beam dynamics at low energy. This is the solution adopted while a new field map of the warm snake is being developed.

Measurements are used to constrain the model and achieve realistic machine parameters. Modeled tunes have been modified around $G\gamma = 10$ and $G\gamma = 35$ to avoid resonant lines during the tracking but the modeled and measured tunes are very close elsewhere (Fig. 2). The measured chromaticity has been smoothed before being used to tweak the model in order to avoid fast variations of the chromaticity during the tracking.

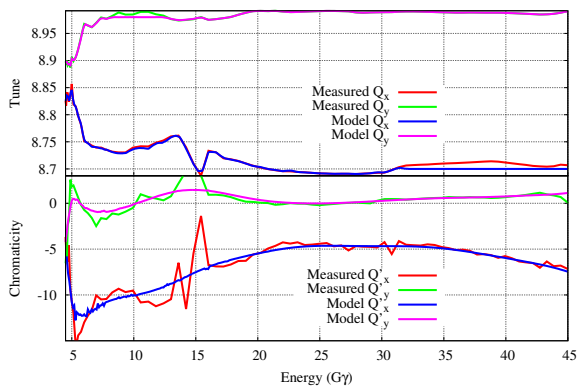


Figure 2: Comparison of tune and chromaticity used in the model and measured in the machine.

The simulations also include the tune jumps, used in the AGS to reduce the polarization losses across the horizontal intrinsic resonances [7].

No dipole error is added to the lattice, hence the modeled orbit coincides with the design orbit of the AGS. Longitudinal dynamics is naturally handled by the Zgoubi code. The model uses a single RF cavity and the synchrotron motion is determined by the characteristics of the lattice and the RF parameters. A harmonic number of $h = 8$ and a realistic RF voltage are used, synchronous phase is computed from measured acceleration rate. This results in a tracking of 150 000 turns to go from the injection energy $G\gamma = 4.5$ to the AGS flat-top at $G\gamma = 45.5$.

The beam is formed by 5000 particles picked in a 6D Gaussian distribution, cut at 3σ. The transverse emittances were chosen at $\epsilon_x^{N,95\%} = 10\,\pi$·mm·mrad and $\epsilon_y^{N,95\%} = 10\,\pi$·mm·mrad, values slightly lower than the measured values at extraction but still realistic. A longitudinal emittance of $\epsilon_l^{95\%} = 0.8$ eV·s is used, leading to a realistic bunch length of $l^{95\%} = 28$ ns at extraction. The spin of the particles is randomly chosen with the condition $\vec{S} \cdot \vec{n}_0 = 0.82$ with $\vec{S}$ the spin vector of the particle and $\vec{n}_0$ the stable spin direction, such that the initial polarization is realistic with 82 % without profile. These simulations require huge amount of computation power and are carried on the supercomputer of the NERSC but the tracking of a single particle on a single CPU for the full acceleration cycle takes one to two hours.

Beam Dynamics

In order to simulate the full AGS cycle the main challenge was to introduce the gamma transition optics and RF gymnastics. The gamma transition quadrupoles were naturally handled by the Zgoubi On-line model, the same way as the other magnets [4][5][6]. Figure 3 shows the behavior of the momentum spread across the transition region during a tracking of 1000 particles, with realistic momentum spread. Despite the perfectly timed jump of the synchronous phase, the transition induces a quadrupole oscillation of the beam but likely due to the non-linear momentum compaction factor of the lattice it is unavoidable.

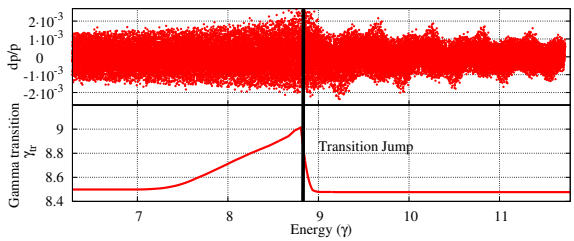


Figure 3: Momentum distribution of the particles and gamma transition of the lattice as a function of the energy around the gamma transition region.

The transverse emittance is estimated by using the variance of the particles coordinates after removing the effect of the chromatic orbit. Figure 4 shows important variations of the estimated emittance when particles are lost during the tracking. Some particles are lost during the transition around $G\gamma = 15$ but also at lower energy ($G\gamma = 6$) when the vertical tune is brought very close to the integer. Beam dynamics behavior is clearly smoother than using the warm snake map but losses during the tracking remains, likely due to the crossing of resonant lines.

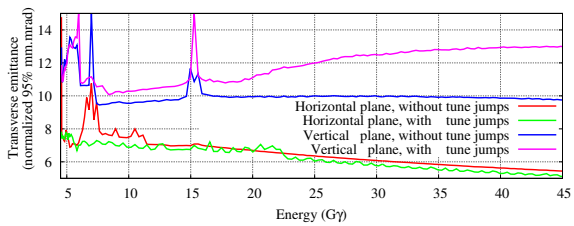


Figure 4: Evolution of the estimated emittances with or without tune jumps.

Copyright © 2013 CC-BY-3.0 and by the respective authors

POLARIZATION PROFILE

The polarization measurement in the AGS uses a thin carbon foil target plunged into the circulating beam. One of the operation modes moves the target across the beam during the measurement and determine the polarization of the beam as a function of the target position. Measured intensity and polarization as a function of the target position are fitted to a Gaussian function to extract σ_P and σ_I respectively the standard deviations of the polarization and beam intensity. Then the polarization profile is defined by P_{max} the maximum polarization at the center of the profile and $R = \sigma_I^2/\sigma_P^2$ to characterize the steepness of the profile.

Simulations and Measurements

The particles coordinates at the end of the tracking are transported to the location of the polarimeter and binned, along with the polarization. The top plot on figure 5 shows the binned beam profile in grey and the average polarization in each beam in blue. The polarization is fitted to a Gaussian and the number of particles in each beam is used as weight for the fit. The process is very similar to the measurements analysis and lead to a similar figures.

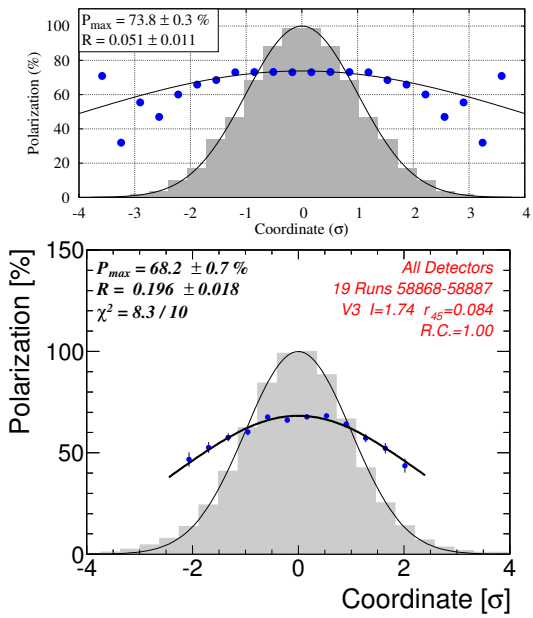


Figure 5: Polarization profile in the horizontal plane without tune jumps along with the beam profile for the simulation (top plot) and for a measurement (bottom plot).

Table 1 summarizes the simulation results and compares them to measured data. The simulated profiles are not as big as the measured ones but it is expected since the emittance used in the simulations is smaller than the usual emittance in the AGS. The simulated horizontal profile is greatly reduced when the tune jumps are used, which is expected and consistent with the measured data.

CONCLUSION

The Zgoubi on-line model provides variable and realistic optics of the polarized proton AGS for tracking. In addition, recent developments allow tracking with realistic longitudinal dynamics around the injection and transition regions.

Table 1: Polarization Profiles Simulated (Sim.) and Measured (Meas.), With or Without Tune Jumps (TJ)

	Horizontal	Vertical
No TJ Meas.	$P_{max} = 68.2 \pm 0.7\,\%$ R $= 0.196 \pm 0.018$	$P_{max} = 66.5 \pm 0.9\,\%$ R $= 0.190 \pm 0.022$
No TJ Sim.	$P_{max} = 73.8 \pm 0.3\,\%$ R $= 0.051 \pm 0.011$	$P_{max} = 72.2 \pm 0.2\,\%$ R $= 0.015 \pm 0.006$
TJ Meas.	$P_{max} = 73.8 \pm 0.6\,\%$ R $= 0.109 \pm 0.012$	$P_{max} = 71.6 \pm 0.7\,\%$ R $= 0.080 \pm 0.014$
TJ Sim.	$P_{max} = 76.3 \pm 0.1\,\%$ R $= 0.012 \pm 0.004$	$P_{max} = 77.3 \pm 0.2\,\%$ R $= 0.035 \pm 0.006$

The model of the AGS currently uses a replacement for the warm snake field map while a new warm snake map is being developed. While this model does not allow us to draw definite answers for now, it still provides good indications about depolarization sources. Polarization profiles and maximum polarization are not comparable to the measured values but the evolution of the profiles when the tune jumps are used is consistent with the measurements. More work is needed to refine the model in view of improved comparison with measured beam and polarization data.

The Zgoubi model of the AGS is a unique and extremely accurate tool to simulate the polarized proton acceleration in the AGS. Ongoing work based on the Zgoubi code aims to develop new and original schemes to reduce polarization losses at low energy using, for instance, the tune jumps.

ACKNOWLEDGMENT

This research used resources of the National Energy Research Scientific Computing Center, which is supported by the Office of Science of the U.S. Department of Energy under Contract No. DE-AC02-05CH11231.

REFERENCES

[1] A. W. Chao and M. Tigner, "Handbook of accelerator physics and engineering," Singapore (2006) p. 702.

[2] T. Roser *et al.*, EPAC-2004-TUPLT190.

[3] S. Y. Lee, Singapore (1997) p. 186.

[4] F. Méot *et al.*, "Modelling of the AGS Using Zgoubi - Status," Conf. Proc. C **110904** (2011) 1897.

[5] F. Méot *et al.*, "Modelling of the AGS Using Zgoubi - Status," Conf. Proc. C **1205201** (2012) 181.

[6] F. Méot *et al.*, "AGS Model in Zgoubi. RHIC Run 13 Polarization Modeling. Status," Conf. Proc. IPAC13.

[7] V. Schoefer *et al.*, "Increasing the AGS Beam Polarization with 80 Tune Jumps," Conf. Proc. C **1205201**, 1015 (2012).

Copyright © 2013 CC-BY-3.0 and by the respective authors

DESIGN OF THE INJECTION INTO THE 800 MeV/amu HIGH POWER CYCLOTRON*

M. Haj Tahar, Y. Dutheil, A. Morgan, F. Méot, N. Tsoupas
BNL, Upton, Long Island, New York, USA
L. Calabretta†, INFN/LNS, Catania, Italy; A. Calanna, MIT, Cambridge MA, USA

Abstract

We present the design of the injection into a separated sector cyclotron (SSC) aimed at the production of a high power beam of 800MeV/amu molecular H_2^+ for ADS-Reactor applications. To work out the beam line parameters and beam dynamics simulations, including the first accelerated turns, we used the ray-tracing code Zgoubi and the OPERA magnetic field map of the cyclotron sector. We simulated the injection path of the H_2^+ and evaluated radial injection scheme in order to evaluate the parameters so derived. The paper details and discusses various aspects of that design study and its outcomes.

INTRODUCTION

The present paper addresses an attempt to find an appropriate injection design for our SSC: the cyclotron complex consists of an injector cyclotron accelerating H_2^+ molecules from 50 KeV/amu up to 60 MeV/amu. The beam is then injected to our 6-sector cyclotron by means of electrostatic and magnetic elements, and accelerated up to 800 MeV/amu. In order to do so, 6 RF cavities, 4 single-gap and 2 double-gap are used, which are PSI-like. A plot of the OPERA magnetic field map in the median plane, for one sector is shown in Fig. 1. There are many considerations that explain the magnetic field shape [1]:

- The azimuthal variations show that the field is decreasing in the central region which ensures more focusing of the beam.
- The superconducting coils of each sector, which are wound around the hills, and the iron of the sector, produce the magnetic field that has to follow the γ(r) law in order to keep the isochronicity, where γ stands for the Lorentz factor.
- The isofield lines show that one edge of the sector has spiral shape while the other is quite straight: even though it is better to have spiral edges to increase the vertical focusing, the design of the magnet becomes problematic when it comes to using superconducting coils, because of the expansion radial force exerted from the inner region of the coil towards the outer radii. A superconducting magnet with a convex shape of the coil would be very difficult to build.

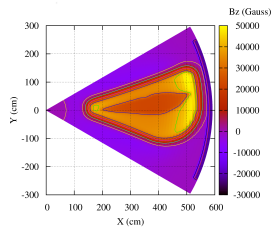


Figure 1: Plot of the z-component of the magnetic field in the median plane for one sector, with the isofield lines.

BEAM DYNAMICS AT INJECTION

Orbits at various energies from injection to nearby extraction are shown in Fig. 2. These orbits were obtained by Zgoubi [2] . It can be easily seen that the distance between consecutive turns (that have the same step size in energy) decreases quickly. In fact, the transverse separation of the turns is very important to consider in our design because it has to be maximized in order to allow clean injection. The step width per turn can be described by the formula [3]:

$$\frac{dR}{dn_t} = \frac{U_t}{m_0 c^2} \frac{R}{(\gamma^2 - 1)\gamma} \quad (1)$$

where U_t denotes the energy gain per turn. However, this assumes that the condition of isochronicity is perfectly satisified. It can be deduced from Eq. 1 that both the energy gain per turn and the injection radius should be made as big as possible in order to increase the step width per turn at injection as well. The transverse separation of the turns as a function of the kinetic energy is shown in Fig. 3.

The first orbit suitable for acceleration is the first closed orbit shown in Fig. 2. This orbit is very important to study in order to match the injected beam properly. Paraxial rays were generated around this orbit in order to compute the transfer matrix of the sector. From that, the betatron functions of the sector ensuring the 6-fold symmetry were computed. The beam envelope of the entire cyclotron was then obtained by multi-turn tracking of a set of particles generated around the eigen ellipse. Both axial and radial beam envelopes are shown in Fig. 4 and 5 respectively. All the results obtained here assume a H_2^+ beam energy of 60 MeV/amu and a normalized emittance of 13.5 π mm.mrad.

INJECTION LINE

The injection system needs to transport the beam from a point outside the cyclotron ring to the first orbit suitable for

* Work supported by Brookhaven Science Associates, LLC under Contract No. DE-AC02-98CH10886 with the U.S. Department of Energy.
† calabretta@lns.infn.it

Copyright © 2013 CC-BY-3.0 and by the respective authors

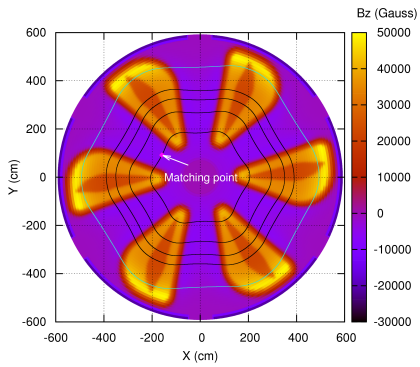


Figure 2: Plot of the closed orbits: the first closed orbit at injection which corresponds to an energy of 60 MeV/amu is shown in black, the next ones, still in black, correspond to a constant step size of energy of 80MeV/amu with respect to each other. The blue one however shows the closed orbit near the extraction, at 700 MeV/amu. The point marked with a pink color is the matching point inside the first closed orbit that will be used to match the beam properly.

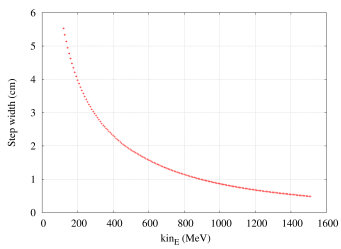


Figure 3: Plot of the transverse separation of the turns as a function of the kinetic energy: this result was obtained from tracking by searching for the closed orbits assuming a constant energy gain per turn of 4 MeV/amu.

acceleration. The main constraints of the design are:

- The beam has to match the equilibrium orbit at a reference azimuth that in our simulations is $\theta = 150°$. This position is referred to as the matching point (see Fig. 2): the beam machine functions (betatron functions) as well as the beam coordinates have to be matched at this point.
- The beam envelope has to be kept small along the injection trajectory: in our case, the maximum beam

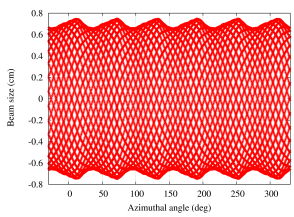


Figure 4: Axial beam envelope vs θ along the 1st closed orbit.

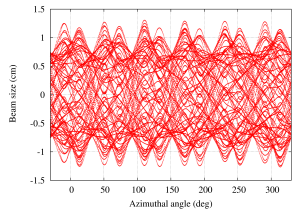


Figure 5: Radial beam envelope vs θ along the 1st closed orbit.

size allowed in both the vertical and horizontal plane is 4 cm in the region where 150 cm <R< 500 cm.

An easy and straightforward solution to the injection problem is to track backwards (≡ clockwise) starting from the matching point. So the field map had to be flipped. Then, to insert the injection elements, the magnetic field was recalculated by adding the equivalent magnetic field to, either electrostatic or magnetic devices. The solution obtained is shown in Fig. 6.

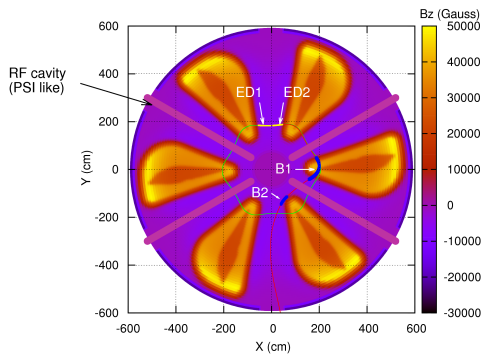


Figure 6: Layout of the injection system for the Superconducting Ring Cyclotron.

NB: The effect of the two RF cavities along the injection trajectory was neglected in the current study.

Electrostatic Deflectors (ED): Design Considerations

According to a design study of the RF cavities [4], it was shown that the voltage at injection should not exceed 500 kV for each single gap cavity instead of 1 MV. This implies that the step width was even smaller at injection. Taking this into account, as well as the radial dispersion of the beam, it was found that we have ≈ 1 cm available space (in the radial direction) at the location of the matching point. The choice then was to place an electrostatic deflection channel at this location. In fact, there are many reasons that explain this choice:

1. The small step size which is of about 1 cm here;

2. The neighbouring turns would not be affected by such a thin electrode while a magnetic element would need much more material to be placed between the turns;

Copyright © 2013 CC-BY-3.0 and by the respective authors

3. Avoid arcing problems by placing the septum in the free space between two magnets: for each material, there is a critical magnetic field beyond which the spark damage is severe [5]. The upper limit here is 60 kV/cm inside the drift.

4. The ED was divided into two pieces as shown in Fig. 7 in order for the electrodes to be tailored to the trajectory of the beam.

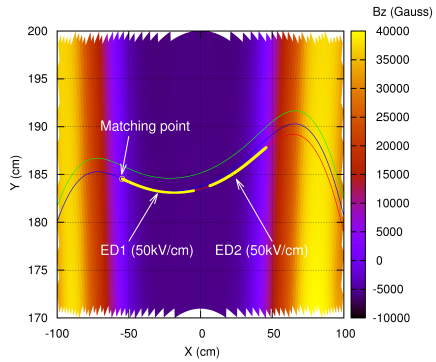


Figure 7: Plot of the beam trajectory inside the eletrostatic deflectors (red curve): the blue curve shows the first closed orbit (that has to be matched) while the green one represents the first accelerated orbit at the location of the septum.

Magnetic Channels (MC)

The choice then was to use two magnetic channels B1 and B2: B1 was placed inside the gap of the main magnet for two reasons:

1. It was preferred to avoid the RF cavity which will occupy most of the space inside the drift.

2. While tracking backwards, it was noticed that we gain at least 1 cm more at this location.

The next step was to focus the beam properly. For that, a gradient was applied to magnet B2. Figure 8 and Fig. 9 show the axial and radial beam envelope respectively. A conservative value of 0.68 kG/cm was found which ensures that the beam size does not exceed 4cm inside the pole gap.

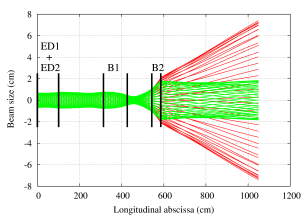


Figure 8: Axial beam envelope vs the longitudinal abscissa along the injection trajectory: the green and red curves show the result when a 0.68 kG/cm or 0 kG/cm gradient is applied to the magnet B2, respectively. The difference between the two envelopes is observed after dipole magnet B2.

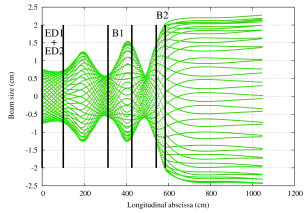


Figure 9: Radial beam envelope vs the longitudinal abscissa along the injection trajectory: there is almost no change in the beam envelope before and after applying the gradient to the dipole B2. However, the beam size exceeds 4 cm outside the pole gap which is fine especially that the radial inter-turn separation at the location of B2 is not limiting any more.

The specifications for the magnetic and electrostatic elements required are summarized in Table 1. It is important to point out that the solution proposed has the merit to avoid us using quadrupoles inside the cyclotron ring to focus the beam.

Table 1: Magnetic and Electrostatic Elements Required for the Proposed SRC Injection System

Element Label	Type	Strength	Effective Length
ED1	Electrostatic septum	50 kV/cm	0.55 m
ED2	Electrostatic septum	50 kV/cm	0.39 m
B1	Magnetic septum	9 kG	1.13 m
B2	Magnetic channel	18 kG	0.42 m

REFERENCES

[1] A.Calanna et al., A multi-megawatt ring cyclotron to search for CP violation in the neutrino sector, April 2011, e-Print: arXiv:1104.4985

[2] An all-purpose accelerator code, F. Méot, Brookhaven National Laboratory, ZGOUBI USERS' GUIDE

[3] Mike Seidel, Paul Scherrer Institute, *Cyclotrons for high-intensity beams* http://arxiv.org/abs/1302.1001

[4] L.Calabretta et al, *Preliminary Design Study of High-Power H2+ Cyclotrons For the Daeδalus Experiment* http://arxiv.org/pdf/1107.0652.pdf

[5] Smith.Bob H and Grunder. Hermann A, Berkeley, California, *Electrical Design Of Electrostatic Deflectors For Sector-Focused Cyclotrons* page 3-7

Copyright © 2013 CC-BY-3.0 and by the respective authors

ALGORITHMS FOR SELF-CONSISTENT SIMULATIONS OF BEAM-INDUCED PLASMA IN MUON COOLING DEVICES

R. Samulyak*, Stony Brook University, Stony Brook, NY and BNL, Upton, NY, USA
K. Yu, Stony Brook University, Stony Brook, NY, M. Chung, A. Tollestrup,
K. Yonehara, FNAL, Batavia, IL, R. D. Ryne, LBNL, Berkeley, CA, USA

Abstract

A code called SPACE for the simulation of beam-induced plasma in gas-filled RF cavities has been developed. The core code uses the particle-in-cell (PIC) method for the Maxwell equations coupled to the dynamics of particles. In the SPACE code, the electromagnetic PIC methods are coupled with probabilistic treatment of atomic physics processes. The aim of the project is to demonstrate the feasibility of the RF cavity with muon collider beams. The most critical part is investigating how intense muon beams influence the plasma dynamics. Initial phase of simulations demonstrating the plasma generation and its short time dynamics in the high pressure hydrogen filled RF test cell has been performed.

INTRODUCTION

A dense hydrogen gas filled RF cavity has been proposed for muon beam phase space cooling and acceleration. The aim of the simulation program is the development of mathematical and numerical models and parallel software for the simulation of processes occurring in gas-filled RF cavities. An important issue in high-pressure gas filled cavity is a RF power loading due to beam-induced plasma [1]. Incident particle beam interacts with dense hydrogen gas and causes significant ionization level. Due to high frequency of collisions with neutrals, electrons reach equilibrium within picosecond time scale and move with a slow drift velocity. The recombination processes occur on the millisecond time scale. In order to induce the three-body electron capture, electronegtive gas has been tested in the test cell. This is the most critical process in the final cooling stage and should be modeled accurately in simulations. Other important processes include the interaction between positive and negative ions and the interaction of the beam with wakefields. A parallel electromagnetic PIC code with atomic physics, called SPACE, has been developed at Stony Brook University / BNL. It implements new mathematical models and numerical algorithms for the interaction of high-energy proton and muon beams with neutral gas and plasmas.

NUMERICAL METHODS

PIC method for Maxwell's equations

The system of Maxwells equations is discretized using the finite difference time domain (FDTD) method on a staggered mesh [2] that achieves second order accuracy in space and time. Electric charges are represented by discrete macroparticles coupled with electromagnetic fields by the action of Lorentz forces and electric currents. When one solves Maxwells equations analytically, solving two equations describing the Faraday and Ampere laws is sufficient as the equations expressing the Gauss law and the divergence-free constraint for the magnetic field are invariants of motion. The numerical method of Yee [2] for electromagnetic fields in vacuum also preserves the divergence-free properties of the electric and magnetic fields. To deal with the last two equations in the presence of charges and currents, the rigorous charge conservation method was developed within the PIC framework in [3]. The method calculates electric currents along computational grid edges by solving a geometrical problem of sweeping the computational mesh by finite volumes associated with each macroparticle. By using this method, we find first a set of initial conditions consistent with the Maxwell equations by either solving the Poisson problem for the electric potential or by a superposition of electric fields and changes created by each particle. Then only the first two Maxwell equations and the Newton-Lorentz equation are solved numerically thus avoiding solving the Poisson problem at each time step.

A schematic of processes computed at each time step is depicted in Figure 1. We would like to note that the conservative Leapfrog time discretization scheme for the Newton-Lorentz equations of particle motion becomes implicit. We use the Boris scheme for the time update [4], which is a modification of the Leapfrog scheme resulting in an explicit and conservative scheme. We also implement modifications of the Boris scheme proposed in [5] for dealing with rapidly accelerating particles for which the relativistic factor is not constant.

For accurate simulations of electromagnetic fields in geometrically complex structures, we have implemented the embedded boundary method [6] in a stand-alone Maxwell equation solver. The coupling of algorithms for complex boundaries with the main electromagnetic PIC code will be performed in the next phase.

Code Structure and Properties

The code is developed in C++ utilizing the advantages of Objected-Oriented Programming. The code is composed of three major parts. The first part, the FieldSolver class, contains FDTD solvers of the Maxwell equations. The second part, the ParticleMover class, contains solvers for the Newton-Lorentz equation. This class also includes various physics models describing particle interactions and trans-

* roman.samulyak@stonybrook.edu

Copyright © 2013 CC-BY-3.0 and by the respective authors

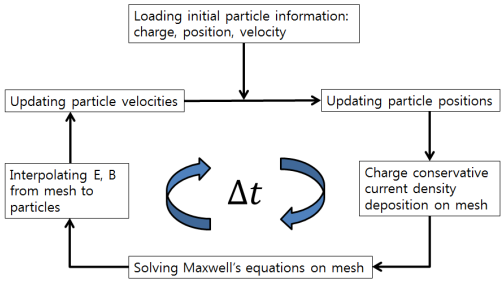


Figure 1: Interaction of muons with plasma in cooling absorbers. Negative (top) and positive (bottom) muons (red dots) interacting with ions (green) and electron (blue dots). Semi-transparent iso-surfaces represent electric field intensity.

formations by atomic physics processes. The code is capable of tracking numerous particle species. Finally, the third, TimeController class, controls the above classes and any miscellaneous classes such as classes performing the visualization of electromagnetic fields and particle data. The visualization is done using the visualization software called VisIt developed at LLNL for the remote parallel visualization on distributed memory supercomputers. Since the main classes of the code are connected via the interface classes, the code can easily be extended by implementing additional functions and physics models. For convenience of a new problem setup, the initialization routines use XML (eXtensible Markup Language).

Parallelization Methods

The electromagnetic PIC code is parallelized using a hybrid MPI / tread programming for distributed memory multicore supercomputers. The FieldSolver uses a three-dimensional domain decomposition for solving Maxwell's equations. The ParticleMover uses a decomposition of particles that is independent of the FieldSolver domain decomposition. Namely, particles in a parallel computing node can be distributed in the whole computational domain whereas Maxwell's equations are solved in a local domain of a parallel computing node. As the distribution of particles is usually very non-uniform in the space, such a decomposition maximizes the load balance.

In the electromagnetic-PIC code, computations performed by the ParticleMover are more time consuming compared to computations by the FieldSolver. The described parallel decompositions minimizes the CPU computing time but requires a large amount of communications between the FieldSolver and ParticleMover. We have adopted ideas from the sparse matrix storage to minimize the amount of communications and send field data to ParticleMover from only those computational cells that contain macroparticles.

Verification and Validation

The electromagnetic PIC code has undergone a V&V program and its accuracy and parallel scalability has been

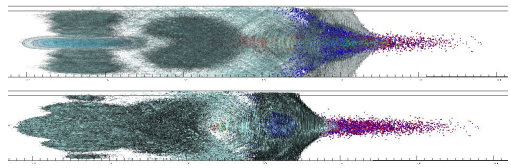


Figure 2: Example of simulation using SPACE code. Interaction of muons with preset plasma in cooling absorbers. Negative (top) and positive (bottom) muons (red dots) interacting with ions (green) and electron (blue dots). Semi-transparent iso-surfaces represent electric field intensity.

estimated. The FieldSolver has been verified using analytical solution for electromagnetic fields in a rectangular cavity. The FieldSolver achieves the second order accuracy and achieves close to linear weak scalability on thousands of processors. The embedded boundary solver has also been verified using analytical solutions for rectangular cavities initialized under some angle to the computational mesh. While the stair-case approximation of boundaries results in a zero-order accuracy, the use of the embedded boundary method restores the accuracy to the order of 1.4 1.5. The ParticleMover has been verified using space charge problems and problems with special distributions of particles.

ATOMIC PHYSICS EFFECTS

In this section, we describe the implementation of probabilistic models for atomic physics processes in gases under the influence of high energy particles and high gradient electromagnetic fields. As each macroparticle passes through the absorber, it ionizes the medium in real time by creating electron - ion pairs. The motion of ions and electrons is explicitly tracked, and their recombination and other atomic physics transformation are resolved as described below. The code supports the dynamics of multiple particle species.

Consider a high-energy particle entering an absorber medium. The energy loss of this particle by ionization can be described by the Bethe-Bloch formula [7]

$$\frac{dE}{ds} = 4\pi N_A r_e^2 m_e c^2 \rho \frac{Z}{A}\left(\frac{1}{\beta^2}\ln\frac{2m_e c^2\gamma^2\beta^2}{I} - 1 - \frac{\delta(\beta)}{2\beta^2}\right), \quad (1)$$

where N_A is the Avogadro number, ρ, A, and Z are the density, atomic weight and number of the absorbing material, and m_e and r_e are the mass and the classical radius of the electron. Numerically,

$$4\pi N_A r_e^2 m_e c^2 = 0.3071\, MeV cm^2/g.$$

The ionization constant I is approximately $16Z^{0.9}$eV, and δ is the density effect factor that arises from the screening of remote electrons by close electrons and results in a reduction of energy loss for higher energies.

Copyright © 2013 CC-BY-3.0 and by the respective authors

Implementation of Atomic Physics Processes

While various atomic physics transformations are supported in the code, we currently resolve the following processes that are most essential for the problem of interest:

$$p + H_2 \rightarrow p + H_2^+ + e^-, \quad (2)$$

$$H_2^+ + 2H_2 \rightarrow H_3^+ + H_2 + H, \quad (3)$$

$$H_3^+ + e^- \rightarrow 3H. \quad (4)$$

The implementation using macroparticles is as follows. The energy loss of each proton macroparticle is calculated by integration the Bethe-Bloch formula along the particle trajectory

$$\Delta E = N_p \int f(v) ds,$$

where $f(v)$ denotes the right hand side of the Bethe-Bloch formula and N_p is the number of real protons represented by one macroparticle. At each time step,

$$(int)\frac{\Delta E}{I N_H}$$

of ion – electron pairs are created along the proton macroparticle path by assigning them random direction velocities corresponding to their initial energy. Here N_H is the number of real H_2 molecules represented by one macroparticle. The initial time is recorded for each new ion and electron macroparticles and they are then tracked in the code. (int) stands for the rounding-off to integer as only integer number of ion-electron pairs can be created. The rounding-off error is saved and used in the next time step to satisfy the energy balance.

When the macroparticle of H_2^+ propagates the distance equal to the mean free path of the second atomic transformation (2.3), it is transformed into the H_3^+ ion. This simply requires changing the mass of the ion macroparticle and resetting its internal time in the data structure. As there is no need to track neutral particles, the molecule H_2 and atom H in (2.3) are ignored. The error due to the fact that the atomic weight of neutrals in the left and right sides of (2.3) differ by one atomic mass is negligible in terms of changing properties (density and pressure) inside of the RF cavity.

Finally, when the ion H_3^+ macroparticle propagates the distance equal to the mean free path of the transformation (2.4), it captures the closest electron and neutralizes into $3H$. In the code, the corresponding H_3^+ and e^- macroparticles are simply eliminated from data structures.

The interaction of electrons and ions with neutrals is modeled in the code using theory and available experimental data. For instance, electrons equilibrate on the picosecond time scale due to high frequency collisions with neutral molecules. The experimental measurements [8] suggest that the electron drift velocity in the conditions of the HPRF experiment is very low, 2.9×10^4 m/s.

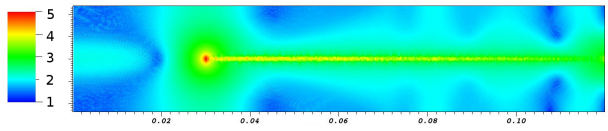


Figure 3: Logarithm of the electric field magnitude [log V/m] in the longitudinal slice of HPRF test cell during the propagation of the proton beam.

RESULTS AND DISCUSSION

We have performed simulations of the entrance of 200 MeV proton beam into the HPRF test cell filled with the hydrogen gas with the density of $10^{21}\ 1/cm^3$ at the pressure of 200 bar and the generation and short time scale dynamics of plasma. Each proton generates on the order of 1000 electron-ion pairs per 1 cm travel distance. Accelerated by the external field, electrons and ions practically instantaneously reach the equilibrium drift velocity defined by their collisions with neutral molecules. Unlike in simulations with preset initial distributions of positive and negative charges in vacuum shown in Figure 2, the self consistent simulation of the plasma formation and evolution in high density gas demonstrates very weak wake fields induced by the proton pulse. The 2D distribution of the magnitude of the electric field is shown in Figure 3.

CONCLUSIONS AND FUTURE WORK

We have developed a parallel electromagnetic code SPACE that combines the PIC method for particles with atomic physics. Simulations of the generation of plasma by the 200 MeV proton beam in the hydrogen filled RF test cell and the short time scale dynamics of plasma and induced wake fields have been performed. Simulations demonstrated insignificant strength of wake fields. In the future, we will perform simulations involving electronegative ions using the SPACE code. We will complete implementation of a multiscale approach in SPACE that allows simulations of both short (picosecond) and long (microsecond) time scale processes in plasma, and conclude on plasma effects in a practical RF cavity.

REFERENCES

[1] K. Yonehara et al., Proceedings of IPAC 2013, TUPFI059.

[2] K. Yee, IEEE Transactions on Antennas and Propagation, 14 (3) (1966) 302-307.

[3] J. Villasenor and O. Buneman, Comput. Phys. Commun. 69 (1992) 306-316.

[4] J. Boris, Proc. the 4th Conf. on Numerical Simulation of Plasmas (Washington DC, NRL) (1971) pp 3.67.

[5] J. L. Vay, Physics of Plasmas, 15 (2008), 056701.

[6] S. Dey, R. Mittra, IEEE Microwave and Guided Wave Letters, 7 (1997), 273-275.

[7] D. Neuffer, Nucl. Inst. & Methods in Phys. Research, A 532 (2004), 26 - 31.

[8] J.J. Lowke, Aust. J. Phys., 16 (1962), No. 1.

Copyright © 2013 CC-BY-3.0 and by the respective authors

MULTIPLE SCATTERING EFFECTS IN A STRONG MAGNETIC FIELD*

P. Snopok, J. Ellison, Illinois Institute of Technology, Chicago, IL 60616, USA
T. Roberts, Fermilab, Batavia, IL 6051, USA

Abstract

New computational tools are essential for accurate modeling and simulation of the next generation of muon-based accelerator experiments at the energy and intensity frontiers. There is a long list of crucial physics processes specific to muon accelerators that have not yet been implemented adequately. One of the long-standing entries on that list is multiple scattering in the presence of strong magnetic field. Earlier studies showed significant discrepancies depending on the models used and step sizes when stepping through the field. A liquid Hydrogen (LH2) absorber in a strong longitudinal magnetic field is analyzed using G4beamline to study and mitigate the effects of step size, and compared to a past study. The updated results and an algorithm to limit step size depending on the field strength are presented.

INTRODUCTION

Though accelerator simulation codes have been steadily improving over the years, there is still much room for improvement. Many single-particle processes and collective effects in vacuum and matter, such as space charge, beam-beam effects, plasma effects from ionized electrons and ions, etc. have not been studied thoroughly or implemented. In order to ensure proper accuracy of simulations, these effects have to be either deemed negligible or taken into account.

One of the processes that is a source of concern is multiple scattering in a strong magnetic field. In a paper by P. Lebrun [1] scattering of muons through a 32 cm length of LH2 is compared between a Moliere (GEANT3) model and a Discrete Scattering model for both a zero field and a several Tesla magnetic field arrangement, showing significant discrepancies, especially in the tails of the distributions. This paper attempts to recreate the simulations of Lebrun as best as possible in G4beamline [2] based off the GEANT4 package. Several problems presented themselves during the recreation, and a complete recreation was not possible, however we believe it to be accurate enough for our purposes. Since [1], the PDG value for the radiation length of LH2 has been updated. Attaining a perfect match to the magnetic field profile in [1] was also not possible. Overall, GEANT4 shows a much better agreement with a Discrete Scattering model studied by Lebrun.

Another issue is that scattering in a strong magnetic field as simulated in G4beamline will yield different results for different step sizes as shown in the first plot in Fig. 4. Consistent results are achieved at very small step sizes, so an algorithm is required that will reduce step size in matter according to the field strength, so that the performance of tracking of particles in vacuum or in a relatively weak magnetic field is not affected.

OVERVIEW OF ALGORITHMS

The main difference in multiple scattering algorithms between GEANT3 and GEANT4 (and as a result G4beamline) was the change from the Moliere formalism to Lewis theory. In GEANT3, Moliere theory was used. This has a few limitations [1, 3]:

- the angular deflection is small;
- the theory applies only in semi-infinite homogeneous media;
- the absorber is not a very low Z material, as the Thomas-Fermi model could be inaccurate here;
- there is no energy loss built into the theory.

GEANT4 is based on the more complete Lewis theory. Like Moliere theory, this simulates the scattering of a particle after a step, but Lewis Theory also computes the path length correction and the lateral displacement, along with the moments of spatial distribution as well [4].

WITHOUT MAGNETIC FIELD

The simulation presented in Lebrun's paper was recreated as close as possible using G4beamline 2.14. A pencil beam of 180 MeV/c muons are scattered through a 32 cm length of LH2 in and out of an intense magnetic field. The magnetic field comes from the 2 m long Alternate Solenoid cooling channel [5] which reaches a peak field of 15 T. The 32 cm length of LH2 begins where the field is at peak. Ref. [1] makes a comparison between a Discrete Scattering model for LH2 and the Moliere model used in GEANT3 at the time, while we compare these to the current G4beamline 2.14 based on the GEANT4 package. The step sizes of the simulations were discussed in [1] and are set to 4 mm in the Moliere results and G4beamline results, and to a micron in the Discrete Scattering results.

Table 1 shows the compared results for the case with no magnetic field. Extensive track cuts were made by insisting on an aperture cut of 2.5 cm and angle cut of 250 mrad and maximum $r \cdot \theta$ of 500 mm·mrad.

WITH MAGNETIC FIELD

In recreating the coils, the data from [5] was used and is summarized in Table 2. The Z offsets were adjusted to

* Work supported by DOE.

Copyright © 2013 CC-BY-3.0 and by the respective authors

Table 1: The Average and σ Values of the Distributions without Magnetic Field

Moments	Moliere (GEANT3)	Discrete Scatt.	G4beamline 2.14 (GEANT4)
$\langle r \rangle$ (mm)	3.43	2.87	3.02
σ_r (mm)	2.18	1.75	1.85
$\langle r' \rangle$ (mrad)	19.0	16.1	16.86
$\sigma_{r'}$ (mrad)	13.4	9.4	10.55
$\langle r \cdot r' \rangle$ (mm·mrad)	72.8	55.2	59.40
$\sigma_{r \cdot r'}$ (mm·mrad)	76.5	58.9	63.23

reflect the positions of the centers of the coils rather than their front faces. Actual current densities were calculated from the relative densities, scaled down by a constant factor. The constant factor was determined by trial and error, such that the maximum field in the configuration was 15 T, and found to be 1/1015.6. For symmetry and to alleviate fringe effects, five identical cells of coils were used. In Lebrun's work, the field decreases from its 15 T maximum to 10.9 T after 32 cm of LH2. It was found in our simulation that the field dropped to 11.2 T instead. That is consistent with a difference in radiation length of LH2 between the previous and current simulations. Figure 1 shows the arrangement of the simulation. Table 3 shows the comparison of the first and second moments in the case with magnetic field.

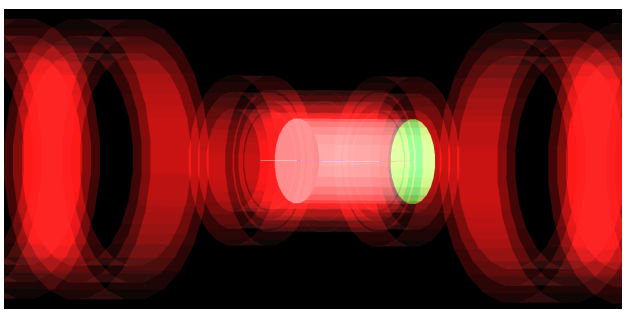


Figure 1: Arrangements of solenoids. The muon beam enters from the left. The 32 cm length of LH2 ends where the detector (green) is.

Figures 2 and 3 show the r and r' distributions, respectively, for the different models used. The data points were obtained using a digital graph analyzer for the points in [1]. It is argued in [1] that although the overall shape of the distributions is similar, the Moliere model did not simulate properly the tail end of the spectrum, while the Discrete Scattering model did. It is seen here that the current scattering model implemented in G4beamline 2.14 (based on GEANT4) follows the tail of the Discrete Scattering distributions much more closely than GEANT3.

EFFECTS OF STEP SIZE

As mentioned in the introduction, scattering in a strong magnetic field as simulated in G4beamline depends strongly on the tracking step size as per Fig. 4. Consistent

Table 2: List of Current Sheets for the 15 T Solenoid, as adjusted by R. Palmer. (Actual Current Density adjusted by a Factor of 1015.6.)

Z offset (m)	Length (m)	Radius (m)	Curr. dens. (unnormalized)	Curr. dens. (A/mm^2)
.075	.15	.1133333	-3639588	-3583.68
.075	.15	.14	-3639588	-3583.68
.075	.15	.1666667	-3639588	-3583.68
.2	.1	.12	-6629837	-6528.00
.2	.1	.16	-6629837	-6528.00
.2	.1	.2	-6629837	-6528.00
.6	.16	.25	-7587805	-7471.25
.6	.16	.29	-7587805	-7471.25
.6	.16	.33	-7587805	-7471.25
.9	.16	.25	7747188	7628.19
.9	.16	.29	7747188	7628.19
.9	.16	.33	7747188	7628.19
1.3	.1	.12	6292018	6195.37
1.3	.1	.16	6292018	6195.37
1.3	.1	.2	6292018	6195.37
1.425	.15	.1133333	3990090	3928.80
1.425	.15	.14	3990090	3928.80
1.425	.15	.1666667	3990090	3928.80

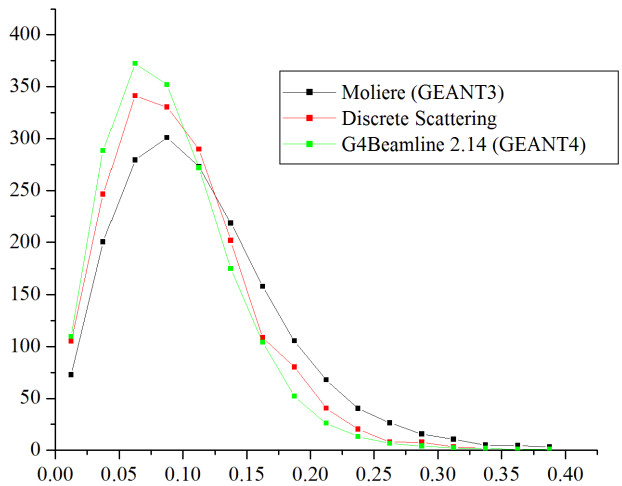


Figure 2: Comparison of the r distribution through different models. Data for the Moliere and Discrete Scattering models were taken from [1]. Our simulation matches the tail of the Discrete Scattering distribution much better than the older Moliere model, as suggested in [1] it should.

results are achieved at very small step sizes, so an algorithm is required that will automatically control step size in matter according to the field strength.

In a G4beamline simulation, a pencil muon beam with a momentum of 200 MeV was passed through 30 cm of LH2 in various uniform magnetic fields, and the beam widths were recorded. Ideally, there should be no variation in results from altering the step length used, but as the magnetic field was increased, it was found that a smaller step size was needed to maintain accuracy. The number of steps taken have a great impact on computing time, therefore it

Copyright © 2013 CC-BY-3.0 and by the respective authors

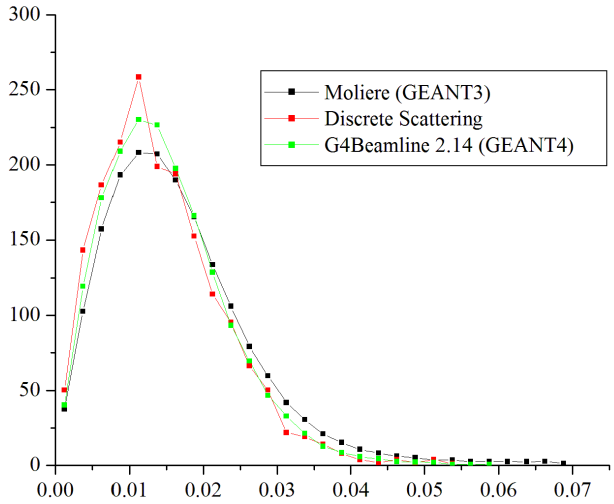


Figure 3: Comparison of the $r' = \theta$ distrubition through different models. Data for the Moliere and Discrete Scattering models were taken from [1]. Our simulation matches the tail of the Discrete Scattering distribution much better than the older Moliere model, as suggested in [1] it should.

Table 3: The Average and σ Values of the Distributions with Magnetic Field

Moments	Moliere (GEANT3)	Discrete Scatt.	G4beamline 2.14 (GEANT4)
$\langle r \rangle$ (mm)	1.18	0.99	0.927
σ_r (mm)	0.87	0.77	0.669
$\langle r' \rangle$ (mrad)	16.9	14.3	15.349
$\sigma_{r'}$ (mrad)	12.0	8.4	10.043
$\langle r \cdot r' \rangle$ (mm·mrad)	23.0	16.1	16.247
$\sigma_{r \cdot r'}$ (mm·mrad)	32.6	19.6	22.747

would be good to find an optimal way to balance accuracy and load.

To less than one percent difference of the value at a step size of one millimeter, it was found empirically that the step size should be scaled with magnetic field as $Step(\text{mm}) \leq 1/(0.004 * Field(\text{T}) + 0.01)$. The results before and after automatic step limiter is implemented are shown in Fig. 4. Similar simulations for Al, Be, LHe, Li and LiH show the same scaling. It was found that in addition, the step length should be shorter than one third the length of the material, to allow for at least 4 steps to take place. This allows for good accuracy with as little CPU time lost as possible.

Note that the step sizes obtained by using the limiting algorithm are consistent with those used for the purposes of comparison with Lebrun's work.

ACKNOWLEDGMENT

Authors would like to thank Paul Lebrun for fruitful discussions and for providing the relevant code decks of the original GEANT3 simulation.

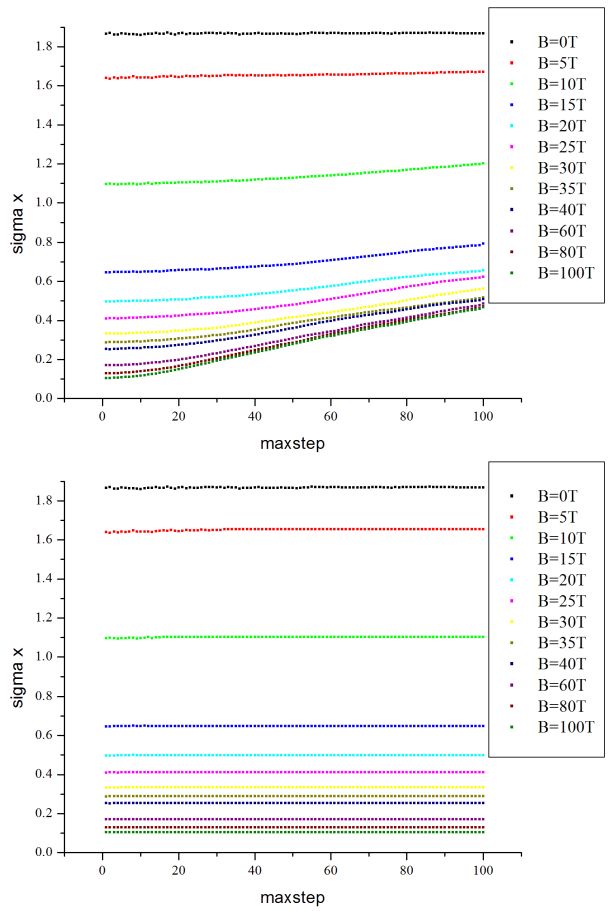


Figure 4: G4beamline results measuring the width of a 200 MeV muon pencil beam after passing through 30 cm of LH2 with 150k events before (top) and after (bottom) implementing a step limiter.

REFERENCES

[1] P. Lebrun, MuCool Note #30, http://nfmcc-docdb.fnal.gov/cgi-bin/ShowDocument?docid=30

[2] G4beamline, http://www.muonsinternal.com/muons3/G4beamline

[3] GEANT3 User Manual, http://wwwasdoc.web.cern.ch/wwwasdoc/pdfdir/geant.pdf

[4] GEANT4 User Manual, excerpt, http://geant4.cern.ch/G4UsersDocuments/UsersGuides/PhysicsReferenceManual/html/node34.html

[5] P. Lebrun, MuCool Note #33, http://nfmcc-docdb.fnal.gov/cgi-bin/ShowDocument?docid=33

Copyright © 2013 CC-BY-3.0 and by the respective authors

PROGRESS OF THE MATTER-DOMINATED MUON ACCELERATOR LATTICE SIMULATION TOOLS DEVELOPMENT FOR COSY INFINITY*

P. Snopok†, J. Kunz, Illinois Institute of Technology, Chicago, IL 60616, USA

Abstract

COSY Infinity is an arbitrary-order beam dynamics simulation and analysis code. It can determine high-order transfer maps of combinations of particle optical elements of arbitrary field configurations. For precision modeling, design, and optimization of next-generation muon beam facilities, its features make it the ideal code. The one component that needs to be included in COSY is the algorithm necessary to follow the distribution of charged particles through matter. Muon beams are tertiary production particles and high-intensity collection necessitates a large initial phase space volume. Therefore, accurate modeling of the dynamics and correction of aberrations is imperative. To study in detail some of the properties of particles passing through material, the transfer map approach alone is not sufficient. The interplay of beam optics and atomic processes must be studied by a hybrid transfer map–Monte-Carlo approach in which transfer map methods are used when there is no material in the accelerator channel, and Monte-Carlo methods when particles pass through material. Progress on the development of the hybrid algorithm is reported.

INTRODUCTION

Muon beams are tertiary production particles and high-intensity collection necessitates a large initial phase space volume. The resultant spray of muons must be collected, focused, and accelerated well within the muon lifetime (2.2 μs in the rest frame). The only technique fast enough to reduce the beam size within the muon lifetime is ionization cooling. Muons traverse a certain amount of material in order to lose energy in both longitudinal and transverse direction due to ionization. The energy is then restored in the longitudinal direction only, leading to an overall reduction in the transverse direction (cooling). In order to achieve cooling in the longitudinal direction, emittance exchange is used, usually involving wedge-shaped absorbers.

In order to carefully simulate the effect of the absorbers on the beam, one needs to take into account both deterministic and stochastic effects in the ionization energy loss. The deterministic effects in the form of the Bethe-Bloch formula with various theoretical and experimental corrections fit well into the transfer map methods approach, where the effect of the lattice on the particles is evaluated first by producing the so-called transfer map, and then applied to a given initial distribution of particles. The arbitrary-order simulation code COSY Infinity [1] is a key representative of the transfer map codes. COSY was chosen because of its built-in optomization tools, speed, its ability to produce high-order transfer maps, and its ability to control individual aberrations.

However, the stochastic effects are not easy to take into account in the framework of the transfer map paradigm. To compensate, we are interfacing COSY with select parts of another code, ICOOL [2], which was written specifically to study the ionization cooling of muon beams. The implementation of the stochastic effects due to various geometries and materials into COSY is reported with the most recent results.

CODE SELECTION PROCESS FOR STOCHASTIC PROCESSES

A variety of codes exists which would complement COSY. Initially, it was hoped that the implementation of a fragment separator into COSY that used a Monte-Carlo approach [3] could be repurposed; however, the libraries were heavily oriented towards electrons, protons, and heavy ions, with no muon data. Other codes that were considered included MUSIC [4], MARS [5], and GEANT4 [6], but were discarded either due to the code focusing on cosmic ray muons, difficulty in interfacing, or sheer bulk.

ICOOL was eventually chosen due to its modularity, compactness, and the fact that, like COSY, is written in FORTRAN. ICOOL's main purpose is to simulate particle-by-particle propogation through electromagnetic fields and matter, with roughly twenty built-in materials to call. The processes included are decays, delta rays, multiple scattering, energy loss, and straggling. Although built for muons, ICOOL can also keep track of other relevant particles such as electrons, pions, kaons, and protons. Additionally, ICOOL can either generate a beam with uniform or Gaussian distribution, or it can read particle information from an input file. This is advantageous since COSY also has a similar input/output file method, which makes direct comparison between the two codes simple.

INTERFACING DETAILS

While ICOOL has routines to calculate particles through, for example, an RF cavity, those were not used since there are corresponding routines in COSY that work faster since the transfer map is only calculated once and then applied to simultaneously to all particles. Therefore, only the routines that directly dealt with absorbers were interfaced. Currently, the following routines have been implemented into COSY: flat absorber (a cylindrical block of arbitrary thickness and radius), radially-symmetric wedge (where

* Work supported by the Department of Energy.
† psnopok@iit.edu

Copyright © 2013 CC-BY-3.0 and by the respective authors

the thickness of the wedge dz is given by the third order polynomial $dz = a_0 + a_1 r + a_2 r^2 + a_3 r^3$), and an arbitrary-order polynomial absorber (a symmetric or asymmetric absorber of order n such that thickness dz is given by $dz = a_{10}x + a_{01}y + a_{11}xy + \ldots + a_{nn}x^n y^n$). The polynomial absorber is of the most significance, as there exists a routine in COSY (WA) with similar functionality and could be used to account for the deterministic effects. This will further limit the use of the slow particle-by-particle tracking using ICOOL routines to only account for stochastic effects. The ultimate goal is to have COSY do the deterministic part, propagate the beam through a negative drift back to the beginning of the absorber again, and then call the stochastic ICOOL routines that would do multiple scattering and energy straggling for the particles without the loss of energy due to ionization.

As previously mentioned, both ICOOL and COSY are written in FORTRAN. Therefore, the initial task was to gather the relevant subroutines from ICOOL and compile them with COSY which would allow COSY to call ICOOL subroutines. Next, ICOOL and COSY had to exchange information about the same beam. For that, $(6 \times n)$ arrays were used, where the six columns held coordinates and n was the number of particles. When COSY runs its polynomial absorber subroutine it constructs a transfer map based on the absorber, runs the vector through the map (which includes the negative drift), and write the vector to a temporary file. ICOOL would then read this temporary file, run the particles through the stochastic processes, and write a second temporary file with the updated particles. In turn, COSY would read this new file, assign the particle coordinates back to the vector, and delete both of the temporary files. Observe that this process can have anything before or after the wedge, as well as repeat the wedge any number of times. Ultimately, those temporary files will be replaced by direct interaction of the codes.

Additionally, it was mentioned that ICOOL only has 20 materials through which to propagate particles. Its routines read strings, such as 'GHE' (gaseous helium), and then read its libraries to find parameters that match (i.e. Z-number, A-number, ionization potential, etc.). However, COSY takes the parameters themselves as arguments, and as such is not limited to a certain list of materials. To alleviate this, subroutines were placed in COSY and ICOOL such that any absorber routine could accept a string or vector argument for the "material" argument. If, for example, the polynomial absorber was given an argument 'LH' (liquid hydrogen), ICOOL would give the parameters to COSY from its library. If the argument given was a vector containing Z-number, A-number, ionization potential, etc. (as is customary in COSY routines), then ICOOL would read a dummy material named 'XXX' and associate it with the vector contents. In this manner, all relevent information that was needed by either program could be stored into one input variable and be read by both COSY and ICOOL subroutines.

In the interest of benchmarking, it should be noted that at this point it is possible to "turn on" the deterministic processes in ICOOL and run it by itself. Indeed, at this point it is possible to have any combination of (ICOOL, COSY) with (deterministic, stochastic), except for COSY+stochastic of course.

SIMULATION RESULTS

The following compares pure ICOOL and the COSY-ICOOL hybrid with one another. All simulations were done using a flat liquid hydrogen absorber of length 32 cm. The absorber is preceded and followed by a drift of 10 cm. The initial beam consists of 1000 muons with a mean momentum of 200 MeV/c. Beam parameters are summarized below in Table 1 for both initial and final distributions.

Table 1: Distribution Parameters and Simulation Results (Stochastics on)

Parameter	Initial	ICOOL	COSY-ICOOL
avg(x) (mm)	0.157	-1.673	-1.641
std(x) (mm)	96.71	100.24	100.36
avg(y) (mm)	1.817	1.165	1.097
std(y) (mm)	103.48	105.16	105.23
avg(p_x) (MeV/c)	-0.703	-0.641	-0.650
std(p_x) (MeV/c)	10.09	9.81	10.33
avg(p_y) (MeV/c)	-0.325	-0.187	-0.221
std(p_y) (MeV/c)	9.91	9.58	10.21
avg(p_z) (MeV/c)	200.0	188.6	188.6
std(p_z) (MeV/c)	0.0	0.96	0.98

It is clear from Table 1 that there is a good agreement between the two codes. The source of discrepancy is the stochastic treatment of multiple scattering as evidenced by Figs. 1–3. These plots were produced by a different simulation with a beam emanating from a single point with a 5% spread in momentum.

SUMMARY AND FUTURE DIRECTIONS

Interfacing of COSY and ICOOL was successful. It is now possible to simulate realistic matter-dominated lattices in COSY. However, further investigation is in order: the hybrid method has only been shown to work for simple absorber configurations; the interaction between the codes as well as the overall performance of the hybrid code can be optimized significantly; interaction with the end-user can be streamlined.

For the future, it is anticipated that COSY will make use of a one-time analysis of the absorber for faster simulations. When turning on stochastic processes, the simulation can easily take up to 400% longer, and in a realistic cooling channel a beam may have to pass through several absorbers of the same geometry. To that end, it has been proposed that when COSY encounters an absorber, it will propagate the beam through using both deterministic and stochastic processes as previously described. It will then produce a trans-

Copyright © 2013 CC-BY-3.0 and by the respective authors

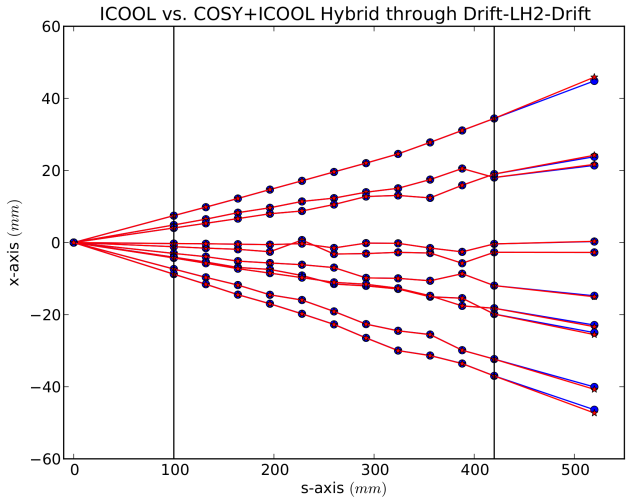


Figure 1: Comparison of individual trajectories. All particles start at the same point with a 5% momentum spread.

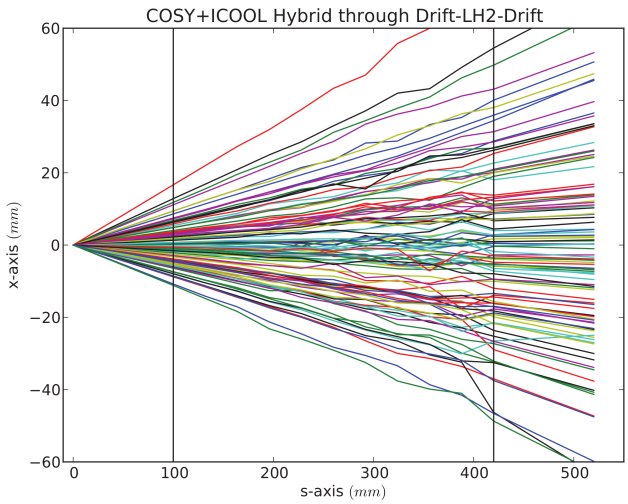


Figure 2: Particle tracks as calculated by the COSY-ICOOL tandem. All particles start at the same point with a 5% momentum spread.

fer map taking into account all the effects, which will then be re-used for future absorbers of the same geometry in the beamline. How this map depends on various properties of the beam will be determined and then approximated (i.e. if the map depends linearly on total momentum, etc.). Using this method would greatly reduce the computation time involved in realistic simulations of muons through matter.

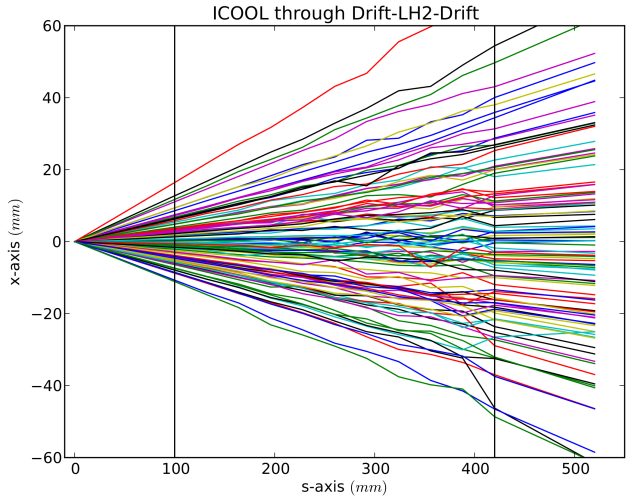


Figure 3: Particle tracks as calculated by pure ICOOL. All particles start at the same point with a 5% momentum spread.

REFERENCES

[1] COSY Infinity, http://bt.pa.msu.edu/index_cosy.htm.

[2] ICOOL, https://pubweb.bnl.gov/~fernow/icool/readme.html.

[3] L. Bandura, *Next-Generation Fragment Separators for Exotic Beams*, Ph.D. thesis, http://www.niu.edu/physics/_pdf/academic/grad/theses/bandura_thesis.pdf.

[4] V. Kudryavtsev, *Muon simulation codes MUSIC and MUSUN for underground physics*, http://arxiv.org/abs/0810.4635.

[5] N. Mokhov, *MARS: Intro/Manual*, http://www-ap.fnal.gov/MARS/intro_manual.htm.

[6] Geant4, http://geant4.cern.ch/

Copyright © 2013 CC-BY-3.0 and by the respective authors

SPACE CHARGE SIMULATION IN COSY USING FAST MULTIPOLE METHOD

B. Loseth*, M. Berz*, K. Makino*, H. Zhang*, P. Snopok**
* Michigan State University, East Lansing, MI 48824, USA
** Illinois Institute of Technology, Chicago, IL 60616, USA

Abstract

A method is presented that allows the computation of space charge effects of arbitrary and large distributions of particles in an efficient and accurate way based on a variant of the Fast Multipole Method (FMM). It relies on an automatic multigrid-based decomposition of charges in near and far regions and the use of high-order differential algebra methods to obtain decompositions of far fields that lead to an error that scales with a high power of the order. Given an ensemble of N particles, the method allows the computation of the self-fields of all particles on each other with a computational expense that scales as O(N). Using remainder-enhanced DA methods, it is also possible to obtain rigorous estimates of the errors of the methods. Furthermore, the method allows the computation of all high-order multipoles of the space charge fields that are necessary for the computation of high-order transfer maps and all resulting aberrations. This method has been implemented in COSY Infinity, and the progress of applying it to simulating the 6D cooling channel for the Muon Collider is reported.

FAST MULTIPOLE METHOD

The fast multipole method for the Coulomb interaction between many charged particles divides an arbitrary charge distribution into small boxes with a hierarchical structure. It then computes the multipole expansions and local expansions of charges far from the observer to achieve a computation efficiency that scales with the number of particles, N, and computational errors scaling with a high power of the differential algebra order. The FMM algorithm is especially suited for beam dynamic simulations because of the efficiency and low computational error compared to other spacecharge algorithms.

Other methods, such as the particle-particle interaction (PPI) and the particle in cell (PIC) method, while computationally efficient, incur excess error due to modeling and statistics. The PPI method uses macroparticles and assumes a particular distribution. The PIC method places the charge distribution onto a mesh, solves the Poisson equation on mesh points and interpolates between mesh points to find the field on each particle. Both of these methods suffer from an inability to precisely handle complicated charge distributions. This difficulty is overcome in the FMM by decomposing the charge distribution into boxes according to the charge density such that there are a pre-specified number of particles in each box to efficiently and accurately compute the multipole expansions.

FMM Algorithm

The principle of the FMM is to determine the potential of groups of source particles sufficiently far from the observer in terms of expansions in $1/r$, utilizing the fact that far away, high powers of $1/r$ become less significant. These multipole expansions can be translated and combined, and again locally expanded to determine the field on a group of nearby observer particles.

First, all of the charges are enclosed in a cube box called the zero-level box. A box is defined to be a parent box if the number of charges inside is larger than s, which we select. If a box is a parent box, it will be split into eight equal square boxes which are its child boxes and form a new level. If any of the child boxes have more than s charges, they will in turn be split into eight child boxes which form the next level. This process is iterated until no box has more than s charges. At each subdivision, we keep only the nonempty boxes, so the empty boxes are ignored by the subsequent field calculation.

Analytic Considerations

For a distribution of n particles of charge q_i located at $\mathbf{r_i}(x_i, y_i, z_i)$, the potential at a point $\mathbf{r}(x, y, z)$ can be expressed as

$$\phi = \sum_{i=1}^{n} \frac{d_r \cdot q_i}{\sqrt{1 + r_i^2 d_r^2 - 2x_i d_x - 2y_i d_y - 2z_i d_z}} \qquad (1)$$

with

$$d_x = \frac{x}{x^2+y^2+z^2} \quad d_y = \frac{y}{x^2+y^2+z^2}\ , \qquad (2)$$

$$d_z = \frac{z}{x^2+y^2+z^2} \quad d_r = \frac{1}{\sqrt{x^2+y^2+z^2}}\ . \qquad (3)$$

In COSY Infinity [1,2] we apply the DA techniques [3,4] to express ϕ as a DA vector by choosing d_x, d_y, and d_z as our DA variables. This DA vector is essentially the Taylor expansion of ϕ with respect to $1/d_x$, $1/d_y$, $1/d_z$, $1/d_r$, and can be translated into another multipole expansion at an arbitrary point and converted into a local expansion with a simple composition operation on the DA vector. Using the domain decomposition to determine near and far regions, the field in a box is computed using a combination of far multipole expansions and local expansions.

LINEAR COOLING CHANNEL IN COSY

The demonstration of muon ionization cooling is one of the key challenges for the Muon Accelerator Program

Copyright © 2013 CC-BY-3.0 and by the respective authors

hosted at Fermilab [5]. A linear cooling channel consists of solenoids, RF cavities, and wedge absorbers designed for the transverse cooling of a muon beam (Figure 1). Longitudinal emmitance is not reduced in this channel; slower particles lose more energy in absorbers than their faster counterparts, leading to an increase in longitudinal emittance. As the overall beam size is reduced, the density of particles is increased which leads to space charge effects becoming significant. Studying these space charge effects requires developing tools in COSY that are coherent with the FMM.

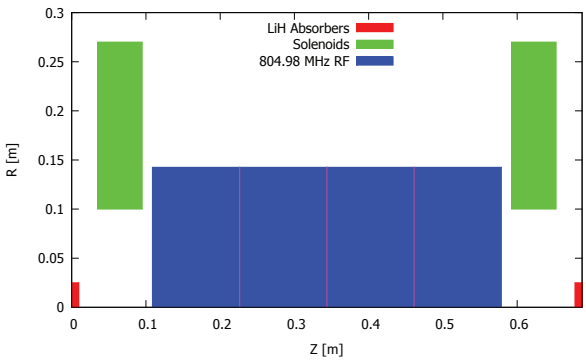


Figure 1: R vs. Z geometry of 1 cell.

Ionization Cooling

Muons are produced by sending proton bunches into a target in order to create pions, which in turn decay into muons. As a consequence of this production, the muons are quite 'hot' by having a large momentum spread. The beam must be cooled significantly, within the muon lifetime, in order ensure a high luminosity muon collider. Beam emittance is reduced via ionization cooling; the beam is strongly focused with magnetic fields and subsequently sent through an absorber material to reduce overall momentum. The beam regains longitudinal momentum in RF cavities, resulting in a net loss in perpendicular momentum and thus beam emittance [6].

Solenoids

The cooling channel is divided into 10 cells with two solenoids of opposite polarity per cell. These solenoids are placed on either side of the absorber wedges that divide the cells in order to increase transverse focusing at the absorber, which in turn minimizes the heating due to multiple scattering.

To implement these solenoids in COSY, a 2-dimensional fieldmap with sufficient range was produced using a Taylor Model based integrator. For a thick solenoid with uniform azimuthal current and finite length, the field at an arbitrary point in space $\mathbf{r}$ is given by the Biot-Savart Law

$$\mathbf{B} = \frac{\mu_0}{4\pi} \int \frac{(\mathbf{J}dV) \times (\mathbf{r} - \mathbf{r}')}{|\mathbf{r} - \mathbf{r}'|^3} \,. \qquad (4)$$

To perform this integral, the domain is subdivided into small cylindrical boxes centered at $\mathbf{r}'$, and the taylor model of the integrand is computed. If the remainder bound of this taylor model is larger than a predefined error bound, the box at $\mathbf{r}'$ is subdivided into 8 equal boxes and the taylor model is computed again for the child boxes. This process is repeated until the remainder bound criterion is met, and integrated over the entire domain of current. Integrating the domain in this manner is computationally efficient because the areas of the domain that are far from the observation point are not subdivided as finely, so less time is spent on the domain compared to a uniform domain decomposition.

To generate the field on a particle in the ring:

- The particles are translated, rotated, and tilted into the first solenoid's frame of reference
- Using linear interpolation between field map points, the magnetic field on each particle is determined in each direction
- The resulting magnetic field in the solenoid's frame is then tilted and rotated back into the global frame and added to the total field
- This process is repeated for each solenoid in the channel
- For this channel, the solenoids have no rotation or tilt, so a 2D fieldmap for an entire cell was produced to take advantage of the cylindrical symmetry

RF Cavities

Each cell in the ring contains four closely spaced RF cavities which fit inside the solenoids. Similar to the solenoids, a fieldmap is used to determine the electric and magnetic fields on the particles inside the cavity. The timing of the $\omega = 804.98$ MHz cavities is determined by the time the reference particle is tracked through the center of the cavity. In order to achieve the correct RF phase (φ_0) at the center of the cavity, the tuning process proceeds as follows:

- Stop the reference particle at the boundary of the cavity and create an identical tune particle
- make a crude guess of the offset time: $t_0 = RFlength/2v$
- propagate the tune particle to the center of the cavity using the crude offset time for the RF fields
- update the offset time: $t_0' = t + 0 + dt$, where $dt = (\varphi - \varphi_0)/\omega$
- reload the tune particle at the beginning of the cavity with the updated offset time
- exit the tuning loop once dt is sufficiently small

Absorber Wedges

The absorber wedges are placed at the boundary of each celll. The energy loss of a particle over a distance ds in the absorber is determined by the Bethe-Bloch formula

$$\frac{dE}{ds} = -K\rho\frac{Z}{A}\frac{z^2}{\beta^2}(log(\frac{2m_e c^2\beta^2\gamma^2 T_{max}}{I^2}) - 2\beta^2 - \delta), \qquad (5)$$

Copyright © 2013 CC-BY-3.0 and by the respective authors

for the parameters

- $K = 15.35375(MeV \cdot cm^3)/(m \cdot g)$,
- Z is the atomic number of the absorber material (LiH),
- A is the atomic mass of the absorber material,
- ρ is the density of the absorber material,
- I is the ionization potential in MeV,
- δ is the density correction parameter,

where the maximum kinetic energy transferred to a single electron in the absorber in a collision is

$$T_{max} = \frac{2m_e c^2 \beta^2 \gamma^2}{1 + 2\gamma m_e/m_\mu + (m_e/m_\mu)^2}. \quad (6)$$

SIMULATIONS IN COSY AND G4BEAMLINE

With all of the lattice elements previously discussed implemented in COSY, we proceeded to compare simulations of a 10-cell cooling channel in both COSY Infinity and G4beamline [7] with and without space charge effects. G4beamline is one of the de-facto codes for muon beam simulations and provides a space charge calculation algorithm and is useful to benchmark for the new COSY functionality. Stochastic effects and particle decays were turned off in both codes to ensure an accurate comparison; these processes are not yet implemented in COSY.

We start with the same beam of 1000 particles in both codes and compare the average orbit excursion, average momentum (Figure 2) and finally, transverse and longitudinal emittance (with and without spacecharge; Figures 3, 4). As mentioned previously, longitudinal cooling is not achieved in this linear channel; this region of the Bethe-Bloch function has a negative slope (ie slower particles lose more momentum). The behavior of the emittances is noticeably different between the codes although the form of the emittance graphs is similar.

Conclusions

In conclusion, we have gained a lot of insight into cooling channel simulations. We can simulate various lattice elements and compare meaningful figures between the codes with and without spacecharge. As this is a work in progress, some of the issues and differences evident during the cross-check with other codes are not resolved yet and require further investigation. There is still a lot of effort to be made on a detailed result comparison in order to obtain consistent results upon comparing the codes, as well as general improvment to efficiency and functionality in COSY.

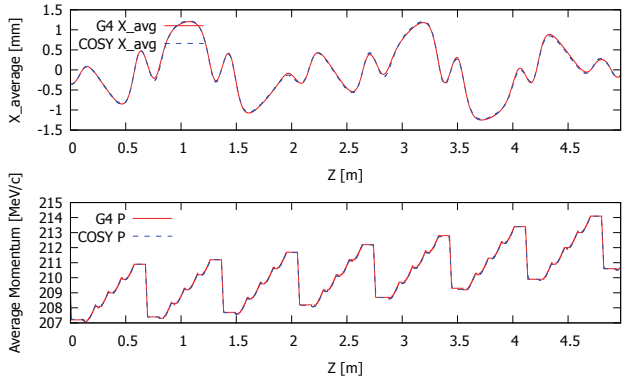


Figure 2: Average Momentum and X as a function of Z for the beam in G4beamline and COSY.

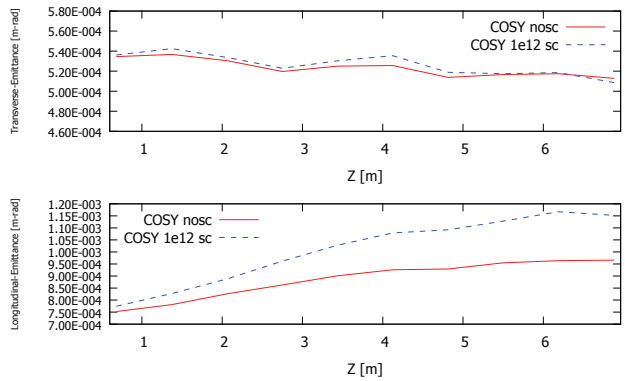


Figure 3: Transverse and Longitudinal beam emittance over 10 cells in COSY with and without space charge.

REFERENCES

[1] M. Berz and K. Makino. COSY INFINITY Version 9.1 Programmers Manual. Technical report, Dept. of Physics and Astronomy, Michigan State University, East Lansing, MI 48824, 2011. See also http://cosyinfinity.org

[2] M. Berz. "Modern Map Methods in Particle Beam Physics", Academic Press, San Diego, 1999. Also available at http://bt.pa.msu.edu/pub

[3] H. Zhang, Martin Berz, "The fast multipole method in the differential algebra framework", NIM A 645, pp. 338-344, 2011.

[4] H. Zhang, "The Fast Multipole Method in the Differential Algebra Framework for the Calculation of 3D Space Charge Fields", Ph.D Thesis, Michigan State University, 2011.

[5] Muon Accelerator Program; http://map.fnal.gov

[6] D. Neuffer, "Introduction to Muon Cooling", NIM A 532, p.26, 2004.

[7] G4beamline, http://public.muonsinc.com/Products/Software.aspx

Copyright © 2013 CC-BY-3.0 and by the respective authors

MITIGATION OF NUMERICAL NOISE FOR SPACE CHARGE CALCULATIONS IN TRACKING CODES

L.G. Vorobiev, C. Ankenbrandt, T.J. Roberts, Muons, Inc., Batavia, IL 60510, USA
F. Schmidt, CERN, Geneva, Switzerland

Abstract

Modern tracking codes have very stringent requirements concerning space charge calculations. They should combine speed of calculations, in order to track particles for many turns (e.g. the LHC injection chain), with numerical accuracy while maintaining symplecticity. Grid solvers and modified Green's function algorithms have been compared, and upgrades were suggested.

INTRODUCTION

Multiple-particle tracking allows for accurate space charge (SC) beam simulations and design. However, in the particle-in-cell (PIC) formalism [1], spatial non-physical grid effects may jeopardize the validity of modeling in accelerator rings and colliders, especially during multi-turn particle tracking. To remedy artificial grid noise, PIC codes increasingly use more macro-particles, denser grids, and more SC kicks per bunch, requiring massive parallelization. Even so, numerical errors persist. The split operator method itself (unlike the general PIC paradigm) decouples three-dimensional (3D) SC forces and dynamics, possibly resulting in additional errors and faulty estimates of instabilities, dynamic aperture, emittance growth, etc. Recent numerical experiments demonstrated artificial noise due to mesh effects and interpolation, leading to micro-scale beam instability [2].

The situation can be improved in two ways. First, we perfect the components of the PIC formalism itself. We will develop a grid density module, suppressing numerical noise to upgrade the accuracy of Poisson solvers. Secondly, we avoid spatial grids entirely, because despite precautions the grid-related noise will always persist. The known grid-free SC solvers are based on the classic Green's function or direct Vlasov solvers (we are aware only of axi-symmetric ones) [3], but they are too slow for multiple particle tracking in rings and work only in free space without boundaries. Instead, we introduce hybrid SC solvers based on "space-charge templates", which represent macro Green's functions for macro-elements [4-5], from which a large family of beam distributions can be built. These SC templates calculate the 3D self-forces of a beam in the presence of conducting boundaries.

There is a gap in terms of generality and performance between fast but over-simplified "frozen" models and standard PIC codes. The proposed hybrid SC solvers fill that gap: they are more flexible than "frozen" models and approach the accuracy of PICs while being much faster. Template-based solvers can simulate rather arbitrary beam distributions within conducting boundaries and may be parallelized, boosting their performance even further.

ACCURACY OF MULTIPLE-PARTICLE TRACKING BY PICS

The computational flows of multiple-particle tracking codes are similar, and our analyses of the accuracy and performance of their components have much in common.

PIC Computational Modules

Each macro-particle in a 3D beam has six phase space coordinates, and a step-by-step evolution of the ensemble of N macro-particles $\mathbf{X}=(x_1, x'_1, y_1, y'_1, z_1, z'_1,\ldots, x_N, x'_N, y_N, y'_N, z_N, z'_N)$ looks like the following:

$$\mathbf{X}_{\text{old}} \rightarrow \underbrace{\rho_{3D}}_{\text{Space}}, \underbrace{u_{3D}}_{\text{Charge}}, \underbrace{\mathbf{E}_{3D}}_{\text{module}} \rightarrow \left[\begin{array}{c}\text{Trajectory}\\ \text{Integrator}\end{array}\right] \rightarrow \mathbf{X}_{\text{new}} \quad (1).$$

Here the trajectories are integrated either by multi-step (2nd order leap-frog, or higher order) schemes, or symplectic maps, which are more customary for multi-turn modeling in the rings. These higher order maps take into account non-linearities of the lattice and SC forces, and they trace particles with any prescribed accuracy in the framework of the single particle approximation [6].

Contemporary Poisson solvers are able to derive nearly exact grid solutions by multi-grid techniques, assuming that the input, i.e. the grid density, is known exactly. The interpolation between grid nodes is also very accurate. Unfortunately, the grid density is evaluated only approximately, and moreover, it represents the main source of numerical noise in (1). We need to find remedies to manage this.

Space Charge Density on the Grid

The Cloud-In-Cell (CIC) technique was developed decades ago (see [1] and references therein). If a spatial grid has dimensions of $N_x \times N_y \times N_z$ and meshes $h_x \times h_y \times h_z$, then the macro-particle sizes are $\delta_{x,y,z}=\Delta \times h_{x,y,z}$ ($\Delta \geq 0.5$). A redistribution of elementary space charge among grid nodes must satisfy a conservation of space charge and should converge for higher order interpolations. A linear scheme is used in ORBIT, WARP, and Synergia codes. A quadratic interpolation is also possible.

Using finite clouds with bell-like shape functions is beyond linear/quadratic interpolation. One needs an infinite polynomial series to represent them. For example, Fig. 1 shows a family of one dimensional (1D) clouds:

$$S_2(\xi)=\frac{q}{2\Delta}, S_3(\xi)=\frac{3q}{4\Delta}\left[1-\frac{\xi^2}{\Delta^2}\right], S_4(\xi)=\frac{q}{2\Delta}\left[1+\cos\left(\frac{\pi\xi}{\Delta}\right)\right],$$

$$S_5(\xi)=\frac{q}{3\Delta}\left[1+\cos\left(\frac{\pi\xi}{\Delta}\right)\right]^2, S_6(\xi)=\frac{15q}{16\Delta}\left[1-\frac{\xi^2}{\Delta^2}\right]^2 \text{ for } |\xi| \leq \Delta.$$

Copyright © 2013 CC-BY-3.0 and by the respective authors

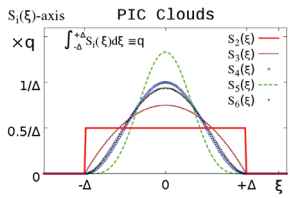


Figure 1: Macroparticle clouds in CIC scheme. All clouds have different ramps, but carry the same space charge "q".

As shown in [7], the integrals $\Phi_k=\int_a^\eta S_k(\xi)d\xi$ are:

$$\Phi_2(\eta,a)=q\frac{\eta-a}{2\Delta},\quad \Phi_3(\eta,a)=q\frac{3(\eta-a)}{4\Delta}-q\frac{\eta^3-a^3}{4\Delta^3},$$
$$\Phi_4(\eta,a)=q\frac{(\eta-a)}{2\Delta}-q\left(\sin\frac{\pi\eta}{\Delta}-\sin\frac{\pi a}{\Delta}\right)/2\pi\ ,$$

and so on for $\Phi_{5,6}(\eta\, q)$. In our algorithm, the choice of the cloud may vary from the beam center to the edges. Figs. 2 illustrate SC density of 10^5 macro-particles within 40cm×40cm boundary, N_x=N_y=128 and different sizes of macro-particles for the cloud $S_3(\xi)$.

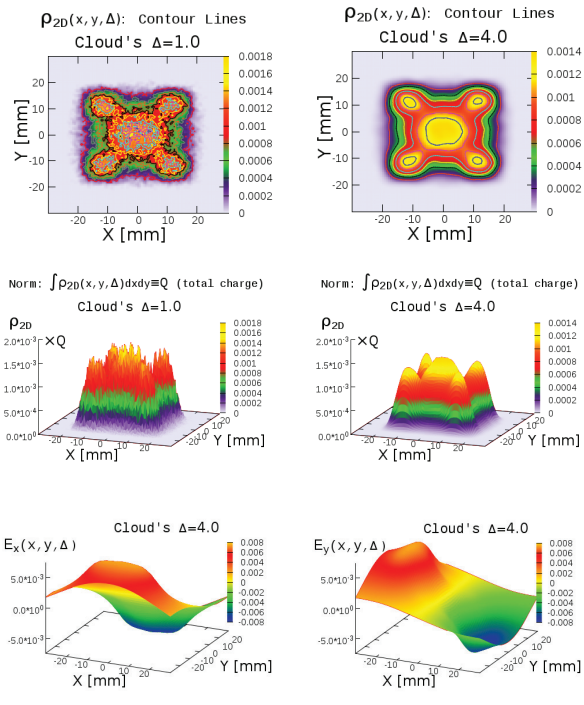


Figure 2: Contour plot (top), 3D space charge densities (middle) for Δ=1, 4; and corresponding fields $E_{x,y}$ (bottom) for Δ=4.

For Δ=1 and 4, contour lines and 3D plots are very different (~15%). The potentials, as integrals of densities differ by < 0.01%. The field differences drop from 3% to less than 0.01% for Δ=1 and 4 respectively [8].

SPACE CHARGE TEMPLATES

A concept of space charge templates was introduced in [5,9]. The templates are macro-elements reproducing an original beam; their fields are derived from the library of template fields via superposition. A family of beam distributions built by templates is rather general but always has elliptical cross-sections along "z". See Fig. 3.

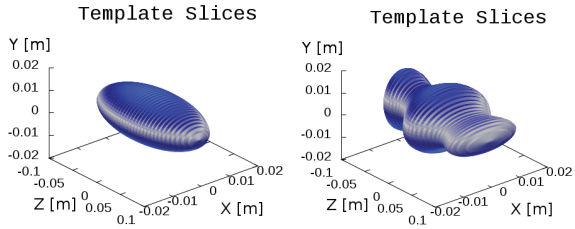


Figure 3: 3D beam bunches within a round cylindrical pipe of 4 cm in diameter (not shown). An ellipsoid 1cm×1cm×10cm (left) and an arbitrary 3D beam (right). Both bunches are "sliced" longitudinally by templates.

In earlier versions of space charge templates, the fields of a 3D beam were calculated, using a library of charged disks/slices with pre-assigned density distributions.

A more universal way to model a composite structure of real charge distributions is to use template-rings [10,8].

The 3D potential in free space $\Re$ is

$$u_{tmp}(\mathbf{x})=\iiint_{\Re}\rho(\tilde{\mathbf{x}})d\tilde{\mathbf{x}}\,/\left|\mathbf{x}-\tilde{\mathbf{x}}\right|.$$

For the particular case of a round ring of the outer radius R_{tmp} and the inner radius R_{tmp}-dR (dR_{tmp} stands for the thickness) with constant surface density σ_{tmp}, the potential becomes:

$$u_{tmp}(\mathbf{x})=2\pi\sigma_{tmp}\left[\sqrt{R_{tmp}^2+z^2}-\sqrt{(R_{tmp}-dR)^2+z^2}\right]\quad(2),$$

leading to analytical formulae for the longitudinal field on the axis [10]. We used this equation along with successive over-relaxation (SOR 3D) technique, which solves the Poisson equation with and without boundaries.

For illustration, the potentials of a positively charged disk of R=0.01 m, a negatively charged disk of R=0.007 m, a ring, as a superposition of these disks and a ring field are plotted in Fig. 4 (left). Template fields, representing a beam from right part of Fig. 3 are plotted in Fig. 4 (right).

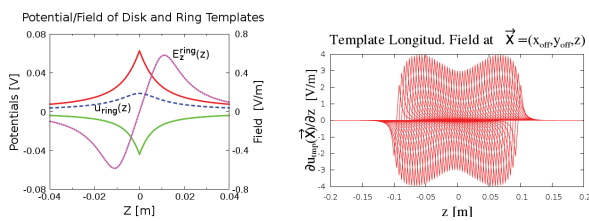


Figure 4: Potentials and a field of disks/ring in free space (left). Template potentials of a beam from right part of Fig. 3 (right).

We benchmarked the results for a 3D 1cm×1cm×10cm ellipsoid, carrying a uniformly distributed space charge of Q=10^{-11} C, placed into a conducting pipe of 4 cm in diameter. The results obtained for disk and for ring templates agreed very well. Figs. 5 shows the same potential and fields as in [11, p.407] at x_{off}=y_{off}=0, obtained by SOR 3D, for distributions from Figs. 3. For longer bunches with semiaxes 1cm×1cm×50cm, the field flattens in the middle and "ear-fields" appear at the edges.

Copyright © 2013 CC-BY-3.0 and by the respective authors

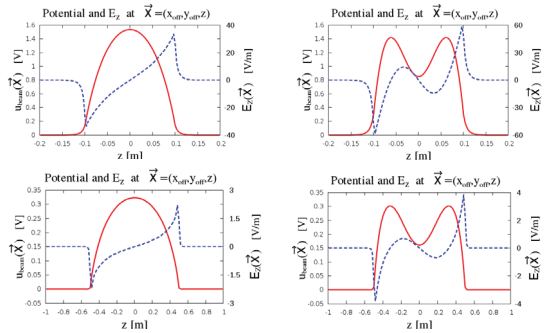


Figure 5: Potentials and fields of 3D ellipsoids with 1cm×1cm×10cm (top), and 1cm×1cm×50cm (bottom).

Fig. 5 suggests that non-linear behavior of longitudinal field becomes very strong due to image forces (in free space, a uniformly charged 3D ellipsoid has linear fields).

A Gaussian 3D beam of ellipsoidal shape in free space has an analytical form of $E_{x,y,z}$ fields (the so-called "frozen" SC model). The presence of a boundary changes them dramatically, limiting their applicability in tracking codes. We refer especially to the longitudinal field E_z, which is most affected by image forces.

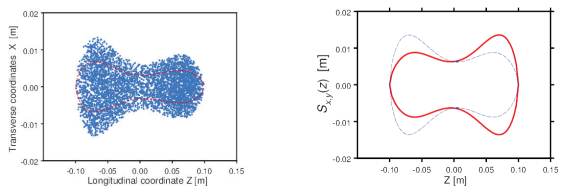


Figure 6: Transverse rms profiles $\langle x^2\rangle^{1/2}(z)$, $\langle y^2\rangle^{1/2}(z)$ (left) and shape functions $S_{x,y}(z)$, defining the template shell (right).

The number of templates for accurate space charge calculations is a free parameter. For a beam depicted in Figs. 3, one needs 15-20 templates. "Thick" slices may also be helpful to deal with very long bunches.

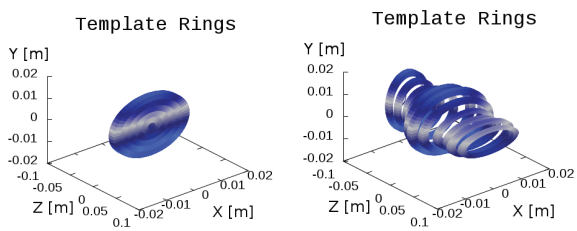


Figure 7: Disk templates (left), built from rings. Ring templates for the outer layer of beam bunch (right).

For a real 3D bunch consisting of macro-particles, Figs. 6 demonstrate the procedure to find shape functions $S_{x,y}(z)$, determining the shell containing all templates, and Fig. 7 illustrates how ring templates reproduce the beam.

Halo and Hollow Beams

For high-brightness accelerators (HL-LHC, ESS), beam loss control is critical, and generally must obey "the 1W/m rule" [12]. While losses may be less than 0.1%, the halo (from which most losses come) may contain a much larger fraction of a beam, and fields from halo particles can't be neglected. Numerical noise from halo particles in a regular grid-based PIC may well be unacceptable.

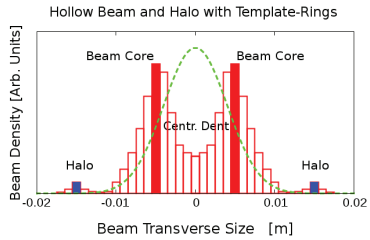


Figure 8: A transversal cross-section of an arbitrary "made-up" hollow beam with a halo, represented by a library of ring templates. An ideal Gaussian beam distribution is a dashed line.

Ring templates are quite appropriate for halo as well as hollow beam field calculations, as shown in Fig. 8. Having disk templates, a special distribution like that would be difficult to reproduce.

DISCUSSION

The goal of this paper is to evaluate accuracies of SC tracking codes for rings, to develop a strategy to suppress artificial numerical effects, and ultimately, to improve code performance. The errors in SC fields will always persist due to granularity of space charge distribution, and inaccuracies of grid density calculations will dominate other errors: a grid Poisson solver and field interpolation and of course those of higher order tracking engines.

A decrease of grid dimensions (larger meshes) damps density fluctuations. The same is valid for larger CIC clouds. However, these fluctuations may be physical, and such a brute force remedy simply eliminates them. A beam halo requires special treatment.

The split operator paradigm is valid for very long bunches (a coasting beam approximation, as in PSR, SNS). For shorter bunches, a more accurate approach is required, based on templates and hybrid technique [5,8].

ACKNOWLEDGEMENTS

The authors are grateful to L. Michelotti, N. Mokhov (FNAL) and A. Friedman (LLNL) for useful discussions.

REFERENCES

[1] R.W. Hockney, J.W. Eastwood: "*Computer Simulation Using Particles*", CRC Press (1988).
[2] SC13, CERN, Geneva (2013), F.Schmidt et al.
[3] F.Filbet et al., ICCSA 2002: 305-314.
[4] L.G.Vorobiev and R.C.York, ibid. 315-324.
[5] L.G.Vorobiev and R.C.York. Phys. Rev. ST Accel. Beams 3, 114201 (2000), EPAC 2002, p. 1679-1681 (2002).
[6] Leo Michelotti, et al. PAC 2005, pp. 988-990 (2005).
[7] L.G.Vorobiev and K.Hirata, KEK-Report 95-12 (1995).
[8] L.G.Vorobiev, Fermilab Beamdocs, docid=4340 (2013).
[9] L.G.Vorobiev and R.C.York, PAC 2003, p. 3533 (2003).
[10] L.G.Vorobiev, Fermilab-Pub-08-236-APC (2008).
[11] M.Reiser, "*Theory and Design of Charged Particle Beams*", John Wiley & Sons, New York (1994).
[12] N.V.Mokhov et al.: Fermilab-Conf-12-634-APC (2009).

Copyright © 2013 CC-BY-3.0 and by the respective authors

OPTIMIZATION OF THE MULTIPOLE TO LOCAL TRANSLATION OPERATOR IN THE ADAPTIVE FAST MULTIPOLE METHOD

S. Abeyratne[^], B. Erdelyi[*,^]
[^]Department of Physics, Northern Illinois University, DeKalb, IL 60115
*Physics Division, Argonne National Laboratory, Argonne, IL 60439

Abstract

The Fast Multipole Method (FMM) is an accurate and fast way to calculate potentials/fields created by a very large number of particles. The runtime of the FMM is significantly less than that of the pairwise calculation if the particle number, N, is sufficiently large. Two major parts in the FMM are the upward pass and the downward pass. The upward pass calculates multipole expansions and then performs multipole-to-multipole translations. The downward pass calculates multipole-to-local expansions and local-to-local expansions. The multipole-to-local translation in the downward pass is the most time consuming translation in the FMM. In order to make the FMM more efficient, we sought to minimize the time taken by the multipole-to-local translation. The promising and practical strategy to minimize the multipole-to-local translation time is to replace the 3D multipole-to-local translation with a 1D multipole-to-local translation in conjunction with rotations of the coordinate axes. In this paper we show how to perform the 1D multipole-to-local translation and the time comparisons between the two FMM variants.

INTRODUCTION

The traditional method to calculate the Coulomb interaction between charged particles is pairwise calculation. The computational power needed for this method is of the order $O(N^2)$ and it is not practical if the number of particles is very large. The FMM can reduce the computational power to $O(N)$.

The details of the two major components of the FMM, data structuring [1, 2] and calculation of the potential/field [3], are discussed in our previous papers. If the number of particle is large, the data structuring time scales linearly [2]. We have also shown that the total runtime, the addition of data structuring time and the time taken to calculate the potential, scales linearly with the number of particles, if the number is large enough [3].

The major components of runtime with optimized settings are the time taken by upward pass (~3%), the downward pass (~50%) and the direct calculation in the final summation (~47%). To decrease the runtime we need to decrease the downward pass time or the direct calculation time. As the direct calculation time solely depends on the optimum q (the parameter q has its usual meaning, the maximum number of sources allowed in the neighbourhood of a given target), it is no longer possible to reduce the direct calculation time. Hence, we focus on reducing the downward pass time. Further analysis showed that the multipole-to-local translation (M2L) used in the downward pass is the bottleneck. This paper places emphasis on the M2L operator and shows that the FMM runtime can be significantly reduced if the 3D M2L translation is replaced by the 1D M2L translation.

ALGORITHM

In the data structuring we create the C-forest (the collection of trees) and the D-tree (parent-child relations of all boxes which contain target particles) [1, 2] at the optimum q. Once the octree-type data structure is created we can implement the FMM proper to calculate the potentials/fields.

The FMM implementation consists of two key components, the upward pass and the downward pass [3]. The downward pass starts at level two and it has three steps. The first step is the M2L translation of the multipole expansions of the boxes in the interaction list of a particular box or leaf node, b. In the second step, we move to the next finer level and compute the local expansion of child nodes of b around their centers from the multipole expansions of the boxes in the interaction list of child nodes. In the third step, we re-expand the result in the first step to evaluate the contribution from the local expansion of the parent box and add that to the result obtained in the second step. In order to complete the downward pass the above three steps must be repeated until we reach the finest level.

After the upward pass and downward pass we move to the final summation [3]. In the second step of the final summation we calculate the potential at each target in b due to the sources in the neighbourhood of b. This is a pairwise calculation. We have noticed that the M2L translation in downward pass and direct calculation in final summation take a considerably longer amount of time compared to all the other operations in the FMM process. Since this pairwise calculation is unavoidable and we cannot reduce that time it becomes apparent that the FMM runtime can be further reduced by optimizing the M2L translation operator. At higher orders M2L translation takes more than 50% of the total FMM runtime.

In this translation, we perform a 3D M2L translation in all three directions, x, y and z. In 3D, the number of boxes in the interaction list varies from 27 to 189. Therefore, the M2L translation takes a longer time. If we rotate the coordinate system of the box with the multipole expansion to be translated in such a way that the z-axis of the box aligns with the line joining the centers of the box and the interaction list boxes, the 3D transformation of the M2L becomes a 1D transformation. Hence, the time taken

Copyright © 2013 CC-BY-3.0 and by the respective authors

for M2L translation can be considerably reduced as shown in Table 1 and 2.

1D M2L TRANSLATION

There are four coordinate systems involved in changing 3D M2L translation to 1D.

- Original multipole expansion in $(X, Y, Z)_{m,\,o}$
- Rotated multipole expansion in $(X, Y, Z)_{m,\,r}$
- Original local expansion in $(x, y, z)_{l,\,o}$
- Rotated local expansion in $(x, y, z)_{l,\,r}$,

where the subscripts *l*, *m*, *o*, and *r* denote local, multipole, original, and rotated, respectively.

The rotation about any arbitrary axis $\hat{\boldsymbol{\omega}}$ by an angle θ can be described by the matrix *R*,

$$R = \begin{pmatrix} t\omega_x^2 C & t\omega_x\omega_y - S\omega_z & t\omega_x\omega_z + S\omega_y \\ t\omega_x\omega_y + S\omega_z & t\omega_y^2 C & t\omega_y\omega_z - S\omega_x \\ t\omega_x\omega_z - S\omega_y & t\omega_y\omega_z + S\omega_x & t\omega_z^2 C \end{pmatrix}.$$

C, *S* and *t* denote cos θ, sin θ and (1- cos θ), respectively.

In order to make a 1D translation we need to rotate the coordinate system of the interaction list box such that the z axis lies along the line joining the center of an interaction list box and the center of a D-tree node, which is denoted by **r** (Fig. 1). In our implementation, we avoid this rotation if the z axis is already aligned with **r.** The unit vector along the axis of rotation, $\hat{\boldsymbol{\omega}}$, is then given by the cross product between **z** and **r**.

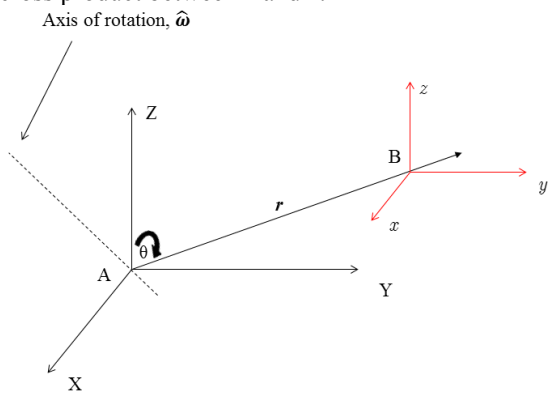


Figure 1: Rotation of the coordinate system.

If $\boldsymbol{r} = (\boldsymbol{r_x}, \boldsymbol{r_y}, \boldsymbol{r_z})$, $\hat{\boldsymbol{\omega}} = (\boldsymbol{\omega_x}, \boldsymbol{\omega_y}, \boldsymbol{\omega_z})$ and $\boldsymbol{z} =$ (0,0,1), then $\omega_x = -\frac{r_y}{r}$, $\omega_y = \frac{r_x}{r}$, $\omega_z = 0$.

Once the coordinate system is rotated, we transfer the multipole expansion into a local expansion. Finally, this rotated local expansion must be rotated back to the original coordinate system. This process is explained below.

The relationship between rotations can be given as follows:

$$\begin{pmatrix} X \\ Y \\ Z \end{pmatrix}_{m,r} = R \begin{pmatrix} X \\ Y \\ Z \end{pmatrix}_{m,o} \text{ and } \begin{pmatrix} x \\ y \\ z \end{pmatrix}_{l,r} = R \begin{pmatrix} x \\ y \\ z \end{pmatrix}_{l,o}.$$

The translation of the multipole expansion M_o to local expansion L_o can be expressed as a composition between M_o and M2L.

$$L_o \begin{pmatrix} x \\ y \\ z \end{pmatrix}_{l,o} = M_o \circ M2L_o \begin{pmatrix} x \\ y \\ z \end{pmatrix}_{l,o}.$$

Since *r* is the distance between the centers of the boxes (invariant under *R*), we can establish the following relationships:

$$\frac{1}{r^2} \begin{pmatrix} X \\ Y \\ Z \end{pmatrix}_{m,o} = M2L_o \begin{pmatrix} x \\ y \\ z \end{pmatrix}_{l,o};$$

Similarly, the new operator $M2L_n$ can be introduced as,

$$\frac{1}{r^2} \begin{pmatrix} X \\ Y \\ Z \end{pmatrix}_{m,r} = M2L_n \begin{pmatrix} x \\ y \\ z \end{pmatrix}_{l,r},$$

where the subscript *n* stands for *new*.

The two operators, $M2L_o$ and $M2L_n$, must give the same local expansion around centers of the nodes. Hence,

$$L_n \begin{pmatrix} x \\ y \\ z \end{pmatrix}_{l,o} = L_o \begin{pmatrix} x \\ y \\ z \end{pmatrix}_{l,o}.$$

By further simplification, it can be shown that

$$L = M \circ R^{-1} \circ M2L_o \circ R,$$

where $L_o = L_n = L$ and $M_o = M$. Since the rotation matrix is orthogonal $R^{-1} = R^T$.

PERFORMANCE ANALYSIS

The 3D M2L translation requires a dense function composition operator in three variables while the 1D M2L translation requires a sparse function composition operator in the variables *x* and *y* and a dense operator in *z*. The 3D translation is computationally more expensive compared to the 1D translation. Both translations are order-dependent and hence the difference in cost between these translations becomes order-dependent. The two rotations needed for the 1D translation are considered order-independent overhead. Empirically, we notice that the time saving by employing the 1D operator instead of 3D operator becomes significant around order five, independent of the type of distribution. Therefore, based on our results, it is clear that below order five 3D M2L translation is advantageous, while above order five 1D translation is advantageous, independent of the distribution (Figs. 2 and 3). In order to achieve high accuracy, it is essential to perform calculations at higher orders [3, 4].

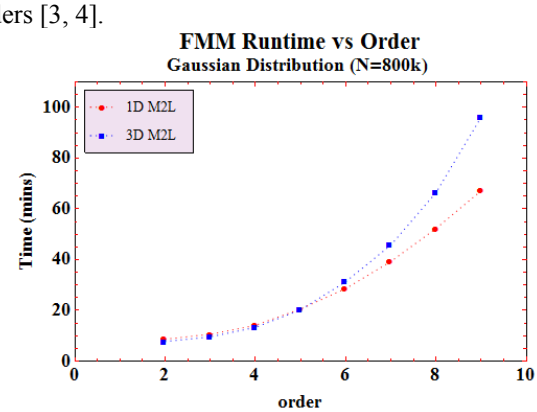


Figure 2: Runtime measured for normally distributed particles using 1D and 3D M2L operators.

Copyright © 2013 CC-BY-3.0 and by the respective authors

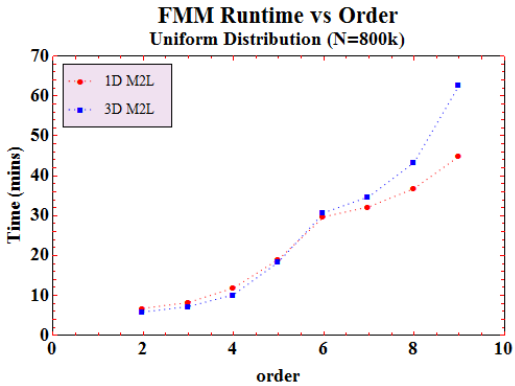


Figure 3: Runtime measured for uniformly distributed particles using 1D and 3D M2L operators.

Tables 1 and 2 summarize the runtime measured for normally and uniformly distributed particles, respectively, at different orders at optimum q (in each case identical sources and targets are used).

We studied the relationship between the FMM runtime (t) and the expansion order (p) in the region where the order is greater than five. For normally distributed particles (N=800k), t is proportional to the nth power of p and the value of n is 3.4 and 2.4 for 3D M2L and 1D M2L, respectively. For uniformly distributed particles (N=800k), the corresponding values are 7.2 and 5.5.

Table 1: Runtime measured for normally distributed particles using 1D and 3D M2L operators.

Order	Time(mins)	
	1D	3D
2	8.724	7.765
3	10.589	9.621
4	14.155	13.314
5	20.582	20.235
6	28.620	31.342
7	39.294	45.760
8	52.292	66.442
9	67.178	96.185

Table 2: Runtime measured for uniformly distributed particles using 1D and 3D M2L operators.

Order	Time(mins)	
	1D	3D
2	6.800	5.886
3	8.265	7.236
4	11.900	10.204
5	19.107	18.450
6	29.732	30.752
7	32.240	34.767
8	36.809	43.323
9	44.926	62.701

The runtimes are machine dependent. All the tests were run on a single core Intel® Core™ i5-2410M @ (2.30GHz) computer (no SSE). The machine had 8GB of RAM. The code for data structuring is written in C++ and compiled under Cygwin on Windows 7, and used the g++ compiler with optimization flags –O3 and –funroll-loops. The FMM is implemented in COSY Infinity [4].

SUMMARY

In this paper, we showed that the use of 1D M2L operator (for expansion orders greater than five) in the downward pass to calculate the potentials/fields reduces the overall FMM runtime in both normally and uniformly distributed particles. As shown in Table 3, when run at optimum q, 1D M2L operator saves the downward pass time by 40% for uniformly distributed particles and by 35% for normally distributed particles. Hence, the overall FMM runtime is reduced by 30% and 29% for normal and uniform distributions, respectively.

Table 3: Downward pass times at order 9 (N=800k).

Distribution	Dimension	Optimum q	Time (mins)
Uniform	1D	6000	9.40
	3D	6000	15.70
Normal	1D	12000	31.08
	3D	20000	47.75

ACKNOWLEDGMENT

This work was supported by the U.S. Department of Energy, Office of Nuclear Physics, under Contract No. DE-SC0005823.

REFERENCES

[1] Nail A. Gumerov and Ramani Duraiswami, “Fast Multipole Methods for the Helmholtz Equation in Three Dimensions,” Elsevier, 2004.

[2] S. Abeyratne, S.Manikonda and B. Erdelyi, “Optimal Fast Multipole Method Data Structures,” Conf. Proc. C1205201 (2012) 352-354.

[3] S. Abeyratne, S.Manikonda and B. Erdelyi, “A Novel Differential Algebraic Adaptive Fast Multipole Method,” Conf. Proc. (2013).

[4] H. Zhang and M. Berz, “The Fast Multipole Method in Differential Algebra Framework,” Nuclear Instruments and Methods A 645 (2011) 338.

Copyright © 2013 CC-BY-3.0 and by the respective authors

NUMERICAL INTEGRATOR FOR COULOMB COLLISIONS

A. Al Marzouk*, B. Erdelyi*,^
*Department of Physics, Northern Illinois University, DeKalb, IL 60115
^Physics Division, Argonne National Laboratory, Argonne, IL 60439

Abstract

The trajectories of protons interacting through Coulomb forces were computed using a numerical integrator based on Picard's iteration method. This is a variable order, adaptive integrator with dense output. We show different cases by varying some parameters such as the impact parameter, the relative velocity of the protons and the order of the differential algebraic (DA) vector. The accuracy of the trajectories was tested by changing the order of the DA vector while fixing the other parameters. The impact parameter between the protons and the velocity of the incident proton has the most impact on the trajectories. The maximum time step is determined by the radius of convergence of the expansions, while a fixed accuracy is attained by varying the order.

INTRODUCTION

Many physical phenomena involve N bodies (particles) interacting with one another by long range forces which decrease inversely as the square of the distance. Examples include the gravitational interaction among the stars in a galaxy, and the Coulomb forces between charges. Many particle systems have wide range of applications in different areas such as biophysics, chemistry, astrophysics [1], etc.

This work includes the two-body problem, in which two charges interact through Coulomb forces. Coulomb's law describes the force between two point charges by the following equation:

$$\overrightarrow{F} = \frac{1}{4\pi\varepsilon_o}\frac{q_1 q_2 \vec{r}}{|\vec{r}|^3},$$

where $\overrightarrow{F}$ is the force, q is the charge, $\vec{r}$ is the radial distance between the two charges, and ε_o is the permittivity of free space.

It is complicated to solve the N-body problem numerically due to the singularity of very close encounters where $|\vec{r}| \to 0$ (very strong interaction $\overrightarrow{F} \to \infty$), and the requirements of high precision with violently varying time steps that are necessary to reduce errors to acceptable levels.

We consider the interaction between two protons in two dimensions. The first proton is initially at rest, and the second proton is moving horizontally towards the first one with a specific vertical distance between them. According to Coulomb's law, the electrostatic force between two similar charges is repulsive.

The integrator has applications in electron cooling of heavy ion beams, and any other beam dynamics problem where individual collisions need to be resolved.

ALGORITHM

To compute the trajectories of both of the protons, we used a code developed by us via COSY INFINITY [2]. The code is a numerical integrator based on Picard's iteration method (see [3] for details). Picard's method uses the initial conditions of the system and gives a sequence of functions that converge to the solution. This method can compute completely algebraically the Maclaurin polynomial (Taylor series expansion of a function about zero).

In this program, the Maclaurin polynomial of the solution is represented by DA vectors. The DA vector is an array of elements that describe a multi-variable function when given its value and derivatives at a specific point [4]. The integrator order is equivalent to the DA order, and we can vary this order to the one that we want to truncate the Taylor series at. At each time step, the program evaluates the change of the radius between the particles and compares it with the one at the next time step. Whenever the convergence radius is exceeded, the program will display an error message.

The maximum velocity (β_{max}) used for the incident proton is 0.283. Different fractions of this velocity were used as well. The initial horizontal distance between the protons was varied from 10^{-15}-10^{-9} m. The impact parameter (vertical distance between the particles) was varied from 10^{-15}-10^{-11} m. It is possible to use larger distances (horizontal or vertical), but the strong interactions are localized within these distances. Hence, larger distances would result into very small changes in the positions of the protons that would be hard to see.

EXAMPLES

The parameters of the system will be denoted as follows: d = horizontal distance (m), b = vertical distance (m), δt = time interval ($1/c$ s), N = number of time steps, and the DA order was set to be 4 unless specified otherwise.

Example 1

The impact parameter and the moving proton's velocity are fixed at 10^{-15} m and 10% β_{max}, respectively. The other parameters are varied in two instances:

- The parameters are: d = 10^{-15} m, N =10^4, δt = 3.6 × 10^{-17} $1/c$ s. The trajectories are shown in Fig. 1.
- Fig. 2 shows the protons' paths with the parameters: d = 10^{-10} m, N = 5.5 × 10^4, δt = 10^{-13} $1/c$ s.

The resulted trajectories in this example are as one would expect due to the Coulomb's interaction.

Copyright © 2013 CC-BY-3.0 and by the respective authors

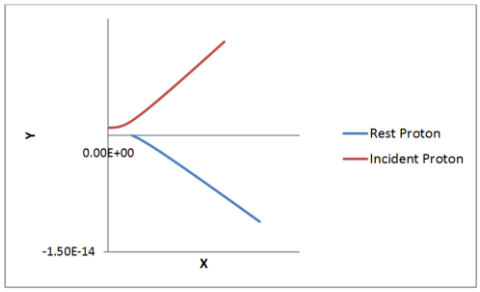


Figure 1: The paths of the protons from Ex. 1 where d = 10^{-15} m and the trajectories are as predicted by the Coulomb interaction.

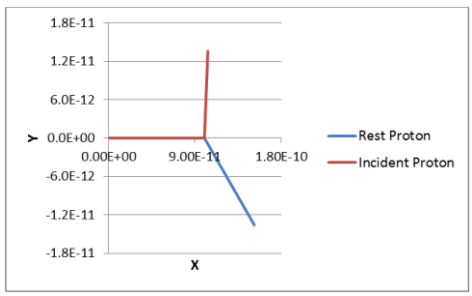


Figure 2: Ex. 1 paths of the protons when d is relatively large (10^{-10} m). The incident proton moves straight horizontally until very close to the rest proton where they start to interact.

Example 2

The horizontal distance is fixed at d = 10^{-12} m and the incident proton has high velocities in the two cases included here:

- The parameters are: b = 10^{-14} m, β = β_{max}, N = 5 × 10^4, δt = 3 ×10^{-16} 1/*c* s. In this case, the rest proton follows a parabolic path for a very short time, and then moves downward (see Fig. 3). This could be a result of the incident proton having a very high velocity such that it knocks the other proton down while its path deviates upward.

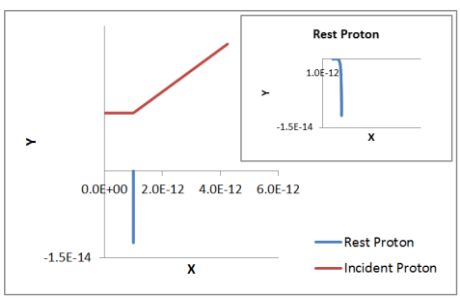


Figure 3: The rest proton moving downward when the moving proton has very high velocity (Ex. 2). The inset shows the parabolic path of the rest proton.

- In this example: b = 10^{-12} m, β = 50% β_{max}, N = 7 × 10^4, δt = 10^{-13} 1/c s. This is one of the cases in which the rest proton exhibited unexpected behavior. It moves downward for a very short interval, and then it starts to recoil and goes backward (as shown in Fig. 4). However, this behavior is very un-noticeable such that it appears like the proton is just going vertically down (as shown in Fig. 5).

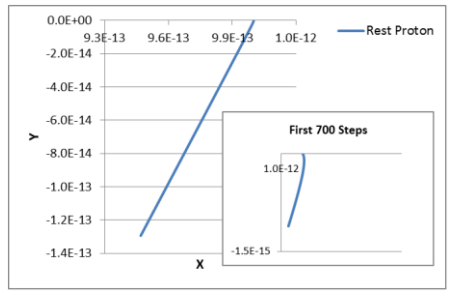


Figure 4: The path of the rest proton going backwards. In the small box, the first 700 steps shows the recoiling.

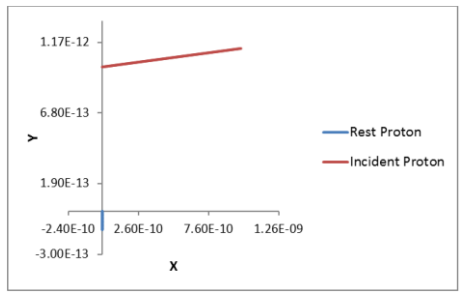


Figure 5: The proton at rest going downward with the un-noticeable recoiling when the moving proton has a relatively high velocity.

ACCURACY TESTS

To check the accuracy of the computed trajectories, we varied the order of the DA vector and the time interval in two ways, as described next.

Fixing the time interval

We used a small δt and different orders of the DA vector. If the trajectory of a low DA order is the same as the trajectory of a higher DA order, then the chosen time interval is sufficiently small to get accurate paths. The other parameters in this example are: d = 10^{-12} m, b = 10^{-13} m, β = 10% β_{max}, N = 6 × 10^4. Fig. 6 shows this accuracy for δt on the order of 10^{-15} 1/*c* s, in which the trajectory with the DA order of 4 is exactly the same as the one with the DA order of 20.

Changing the time interval

We used various time intervals with a specific order of the DA vector. We increased δt until the new trajectory diverges from the accurate one (with small δt) of the same order. We fixed the other parameters at: d = 10^{-12} m, b = 10^{-13} m, β = 10% β_{max}. The number of time steps was changed according to the change of δt.

Since the code we are using tests for errors of the radius of convergence, we include two cases:

Copyright © 2013 CC-BY-3.0 and by the respective authors

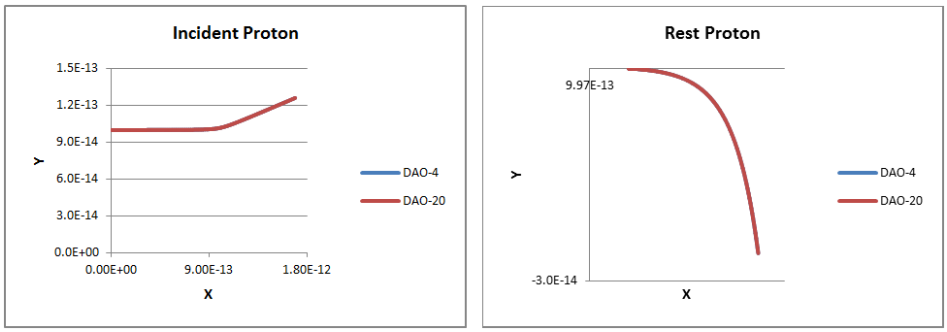


Figure 6: The accuracy test by fixing the time interval and varying the DA order. The paths of the incident proton and the rest proton are illustrated in the left and right pictures, respectively.

- δt is large, but not such that we get errors. Here are two examples with DA order = 4 and 20. In both examples, the trajectory of the moving proton was not affected by changing δt. Therefore, we show only the paths of the rest proton in Fig. 7. For DA order = 4, the paths with large δt start to diverge from the ones with small δt. For DA order = 20, both paths are almost the same.

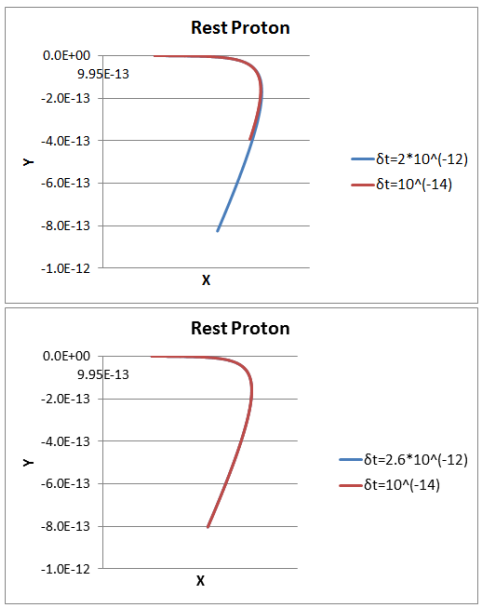


Figure 7: The paths of the rest proton with large δt (in blue), and with small δt (in red). The DA order is 4 in the top box, and 20 in the bottom one.

- Beyond the radius of convergence errors. The resulted trajectories are unphysical and inaccurate. It is hard to explain these results, and the only reason might be the errors of the radius of convergence. Fig. 8 is an example where the DA order is 18.

SUMMARY

Using a numerical integrator based on Picard's iteration method, we computed the trajectories of two protons interacting through the Coulomb force. Our main interest was in close encounters of the protons. We showed different examples by changing different parameters in the problem. The results are in agreement with the theory: to obtain certain accuracy most efficiently, a maximum step size is determined by the region of convergence, and the desired accuracy is achieved by increasing the DA order with the given maximum time step. Also, these results will enable us to automatically adjust the time step adaptively, as needed. More studies are needed to get better understanding of the results. A future work is to apply similar studies for the attracting case (proton-electron interaction).

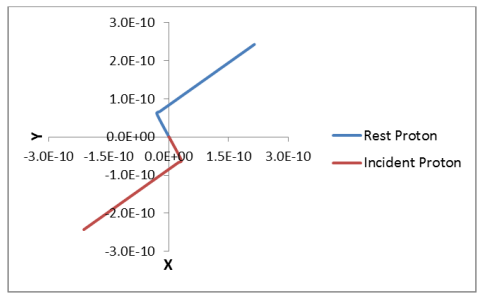


Figure 8: The unphysical results from having large time interval such we get radius of convergence errors.

ACKNOWLEDGMENT

This work was supported in part by the U.S. Department of Energy, Office of Nuclear Physics, under Contract No. DE-SC0008588 with Northern Illinois University.

REFERENCES

[1] G. Efstathiou, M. Davis, C. S. Frenk, and S. D. M. White, "Numerical Techniques for Large Cosmological N-Body Simulations," ApJS, 57:241, (1985).

[2] M. Berz and K. Makino, COSY Infinity Version 9, "Nuclear Instruments and Methods," A558 (2005) pp. 346-50.

[3] H. Schaumburg and B. Erdelyi, "A Picard Iteration Based Integrator," in these proceedings.

[4] M. Berz, "Differential Algebraic Description of Beam Dynamics to Very High Orders," Particle Accelerators, 24:109, (1989).

Copyright © 2013 CC-BY-3.0 and by the respective authors

STUDY AND COMPARISON OF THE METHOD OF MOMENTS AND THE SINGLE LEVEL FAST MULTIPOLE METHOD FOR 2D SPACE CHARGE TRACKING

Anthony Gee*[1] and Bela Erdelyi†[1,2]
[1]Physics Dept., NIU, DeKalb, IL, USA
[2]Physics Dept., ANL, Argonne, IL, USA

Abstract

Strong space charge is a significant impediment in charged particle beam physics, particularly at the high intensity frontier. For future applications, where particles must occupy the smallest region possible, quickly and accurately and efficient modeling space charge modeling is essential, for instance, to minimize the space charge contribution to beam dispersion. In this paper, we study and compare the performance for the method of moments (MoM) and the single-level fast multipole method (SLFMM) in 2D. The method of moments has been widely used to solve computational electromagnetic problems but assumes a series-expandable smooth distribution function, limiting its reliability in some cases. The fast multipole method was more recently developed and shows remarkable accuracy with difficult beam distributions. We demonstrate these methods using a simplified version of the University of Maryland electron ring (UMER). We present some multi-particle tracking results obtained using these methods. Future work will study the space charge inclusive transfer maps calculated from these methods.

INTRODUCTION

The general N body problem, although simple in principle, is computationally very challenging. The simplest method uses direct pair-wise interaction computations, where the complexity behaves like $O(N^2)$, and gives a machine precision solution for each pair. The mean field methods almost always involve some kind of numerical approximation. Two methods in particular were developed that approximate our solution to a significant degree of accuracy and reduce the scaling to $O(NlogN)$ or even $O(N)$ [1, 4, 5]. The method of moments (MoM) has been successfully used in several cases [1, 2]. As expected, it is most accurate for smooth unimodal distributions, where the relatively low order moments reliably approximate the distribution [4]. The fast multipole method (FMM), recently developed by Greengard and Rokhlin in 1987 [5], shows remarkable accuracy with arbitrary distributions, overcoming some weaknesses of the MoM. We are mainly interested in efficiently and accurately modeling the nonlinear effects present in a space charge dominant beam. The purpose of this paper is to evaluate and compare the MoM and FMM performance for a test case involving a simplified model of UMER.

* agee1@niu.edu
† erdelyi@anl.gov

IDEALIZED UMER

The University of Maryland electron storage ring has been designed and built specifically for the study of space charge dominated, high intensity beams in a localized, inexpensive setting. Some of the design specifications are shown in Table 1, with our specific settings in the lower section [3]. The design is such that the electron bunches fill the ring, allowing a quasi-2D approximation. We included only the main recirculation (RC) sections, each consisting of two equivalent FODO sections with a guiding dipole in the middle of each FODO section.

Table 1: The UMER Design Specifications are Listed in the Top Half and Our Relevant Simulation Conditions are in the Bottom Half

Circumference	11.52 m
Electron energy	10 keV
$\beta(=\frac{v}{c})$	0.2
Current	1–100 mA
Aperture	2.95 cm
Pulse Length	40 ns
Lap time	197 ns
Pulse repetition rate	60 Hz
Turns	30
Simulated current	6 mA
FODO period	0.32 m
# of FODO sections	36
Dipole bend	10°
Dipole effective length	3.82 cm
Quadrupole current	1.826 A
Quadrupole effective length	5.164 cm
Initial emittance (X,Y)	(5.28×10^{-8},4.94×10^{-8})
Integration region	5.25σ

RESULTS

MoM

Reference [1] explains the details of our implementation of the MoM and FMM. For the MoM, there are three separate orders to which we will refer. The space charge order (SO) is the order of computation for the space charge map. The map order is the order of computation for the regular transfer map or equivalently the order of the

Copyright © 2013 CC-BY-3.0 and by the respective authors

differential algebra vectors (DAO).The moment order (MO) is the order of the sample moments used to model the particle distribution. The main purpose for the development of the MoM was the ability to extract self-consistent transfer maps that include space charge. However, the same method can be used for tracking space charge dominated beams. On the other hand, it is not clear how accurate is the MoM for tracking. Therefore, we focus on tracking capabilities in this paper. We started with a spatially uniform, angularly Gaussian beam that almost fills the ring acceptance.

In principle, the map order and space charge order do not have to be equal. We performed a study on the effects of mismatched DAO and SO, up to $DAO = SO + 3$, with overall maximum order at 18. We also constrained the SO and MO to be equal. We first examined the final emittances of our 6 mA electron beam. Figure 1 shows our final emittances. We calculated the emittances in X and Y using the standard deviations in position and angle of the beam and plot the total emittance. The results show that high order space charge effects are important, as expected, while no other high order effects are present in the ring.

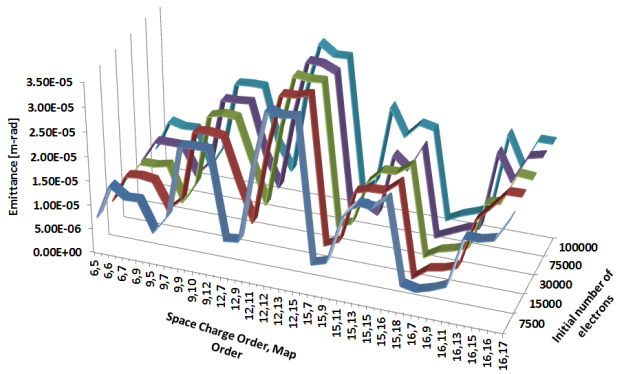


Figure 1: Comparison of Final Emittance [m-rad] vs. Space Charge Order, Map Order vs. N_p using the moment method for the UMER model.

In Figure 1, we compare the final total emittance with the space charge order, map order and number of particles, N_p. The emittance grows with map order and space charge order. The growth is mainly in the Y emittance. The variation in the plateau heights reflect the well-known fact about the optimal truncation order, i.e. best space charge order. As detailed in [1], there are two competing effects: increasing the space charge order improves the modeling of the distributions in the ideal case, but the finite number of particles introduce noise, which affect the sample moments that in turn decrease the accuracy due to the large condition number of the matrix that embodies the linear relationship between the moments and the coefficient set of the distribution function expansion. As shown in Table 2, the final emittances also reflect this slight instability of the moment method tracking, with optimal order seen around 12. The evolution of the particle distribution showed significant formation of halos and chaotic regions. The differences are minor between N_p. Our beam lifetimes showed similar behavior to the emittance, low survival at low map order, and approximately same survival once DAO equals SO. The timing results for the idealized UMER model are shown in Figure 2. We only show three representative order sets for each N_p.

Table 2: Averages and Standard Deviations of the Final Emittances at Plateau for SO 12, Sampling DAO 12,13,15 for $N_p = 7500, 15000, 30000, 75000, 100000$ After 30 Turns. Convergence is achieved in map order.

N_p	Average [m-rad]	σ
7500	3.399×10^{-5}	4.376×10^{-7}
15000	3.433×10^{-5}	5.79×10^{-7}
30000	3.420×10^{-5}	1.996×10^{-7}
75000	3.347×10^{-5}	7.651×10^{-7}
100000	3.308×10^{-5}	1.147×10^{-6}

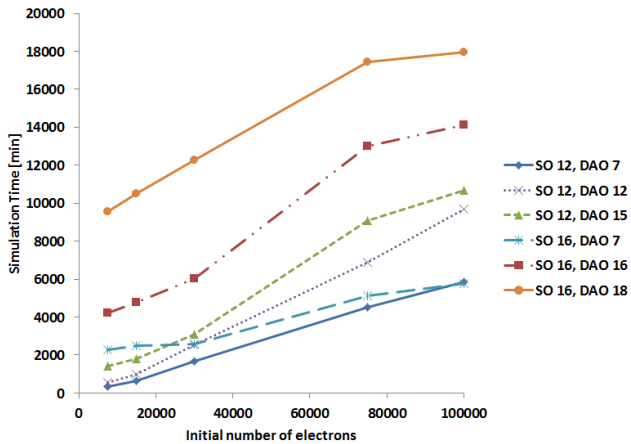


Figure 2: Comparison of Simulation time for 30 turns in mins using the moment method for the UMER model.

As shown in Figure 2, the simulation time exhibits roughly linear behavior. At low map, high space charge order, the number of particles decreases due to higher order space charge terms being truncated which would cancel strong lower order terms. This significantly decreases simulation time and leads to the kinks. Overall, we can achieve accurate results at high orders but expect unreliable predictions for low space charge order, showing the importance of higher order space charge terms.

FMM

Our implementation of the fast multipole method is one of the few using the differential algebraic framework. There are some key concepts to the FMM calculation worth noting here, but the full details may be found in a number of references [1, 5, 6]. We will refer to the number of boxes as N_{box}. The current box of interest, the nth box, will be designated our target box and all others will be designated sources. We use the single level FMM where we subdivide the space only once, into N_{box} equal size boxes. For the potential calculation, each nonempty source box is Taylor expanded with respect to the target box. Thus, the simulation time depends on N_{box}, N_p, SO, and the number of

Copyright © 2013 CC-BY-3.0 and by the respective authors

coefficients for the expansion in the FMM akin to the moment order, which we will call the FMM order (FO).

Due to time constraints, we decided to only run the FMM in tracking mode for 1 turn rather than 30 as for the MoM and at $N_p = 7500, 15000$ to compile the results in this paper. Preliminary tests showed the emittances from the FMM stabilize extremely quickly, usually within 1 turn, and the time per turn behaves consistently. Beam lifetime exhibits similar behavior, but we are hesitant to assume consistent lifetime for all FMM orders and N_p. For this study, our simulation has $N_{box} = 40^2$. A future study will test the dependence on N_{box}. Our results are shown in Figure 3 and Figure 4.

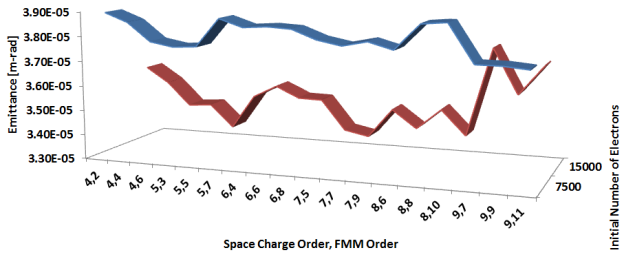


Figure 3: Final emittances [m-rad] after 1 turn vs. Space Charge Order, FMM Order using the fast multipole method.

Table 3: Averages and Standard Deviations of the Final Emit-tances at SO 9, Sampling FO 7,9,11, and $N_p = 7500$, 15000 After 1 Turn for the UMER Model Using the Fast Multipole Method

N_p	Average [m-rad]	σ
7500	3.746×10^{-5}	5.315×10^{-8}
15000	3.691×10^{-5}	9.185×10^{-7}

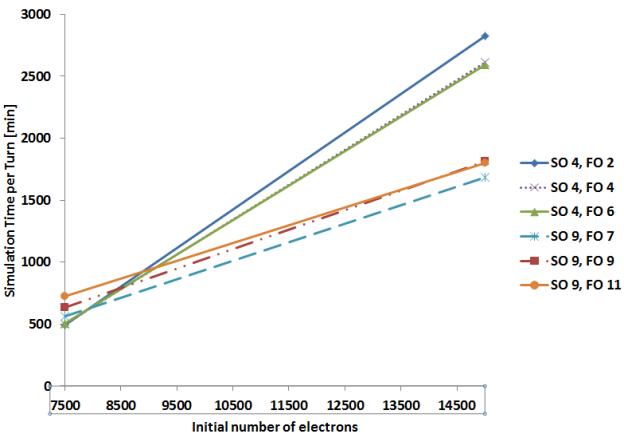


Figure 4: Simulation time per turn [mins] vs. initial number of electrons for select space charge orders, FMM orders using the fast multipole method.

In Figure 4, the simulation times per turn using the FMM tracking mode slightly depend on the orders. We reserve judgment on its N_p dependence at this time. In Figure 3, the final emittance after 1 turn for the idealized UMER model exhibits a small variation. Table 3 shows the averages and standard deviations for the final emittances at SO 9 as a function of FO for $N_p = 7500, 15000$. The relatively erratic emittance at SO 9, FO 7-11, $N_p = 15000$ is due to requiring more turns for the emittance to stabilize. The evolution of the distributions showed similar behavior to what was shown with the moment method, but the variation is no longer significant, thus it may be attributed to the chaotic nature of space charge.

CONCLUSIONS

Our study shows the various orders strongly affect our MoM results. Convergence in terms of moment and map order are achieved. There is no convergence in space charge order. Our optimum SO is 12 for SVD cutoff parameter of 1×10^{-12}. The MoM shows little dependence on N_p. From its emittances, The FMM shows slightly more dependence on N_p but stabilizes for large N_p.

Our FMM shows stable results. There is a hybrid mode implemented using FMM for tracking and MoM for map extraction but has not been studied thoroughly yet. More detailed comparisons will be forthcoming. We plan to optimize our FMM implementation for reduced runtime and further improve our MoM implementation.

ACKNOWLEDGMENTS

This work was supported in part by the U.S. Department of Energy, Office of High Energy Physics, under Contract No. DE-FG02-08ER41532,with Northern Illinois University.

REFERENCES

[1] E. Nissen. "Differential algebraic methods for space charge modeling and applications to the University of Maryland Electron Ring," Ph.D. Thesis, Northern Illinois University, (2011).

[2] B. Erdelyi et al., "An Accumulator/Pre-booster for the Medium-energy electron Ion Collider at JLab," PAC'11, NY, April 2011, WEP206, p. 1873 (2011).

[3] P.G. O'Shea, et al. "The University of Maryland Electron Ring (UMER)," PAC'01, Chicago, June 2001, TOAA008, p.159 (2001).

[4] W.C. Gibson. "The Method of Moments in Electromagnetics," (Florida: CRC, 2007), 272 pp.

[5] L. Greengard and V. Rokhlin, "A fast algorithm for particle simulations," *Journal of computational physics* 73.2 (1987), p. 325.

[6] Eric Darve, "The Fast Multipole Method: Numerical Implementation," Journal of Computational Physics, Volume 160, Issue 1, 1 May 2000, Pages 195-240, http://dx.doi.org/10.1006/jcph.2000.6451.

Copyright © 2013 CC-BY-3.0 and by the respective authors

A PICARD ITERATION BASED INTEGRATOR *

H. Schaumburg, NIU, DeKalb, IL 60119, USA
B. Erdelyi, NIU, DeKalb, IL 60119, USA

Abstract

Picard iteration is mainly used as a theoretical tool to establish the existence and uniqueness of a solution to an initial value problem. We have developed a method based on Picard iteration that computes the exact Taylor polynomial of the solution to arbitrary order. The method has been implemented in COSY INFINITY to numerically solve Coulomb interactions.

INTRODUCTION AND BACKGROUND

Picard iteration generates a sequence of functions $\phi_n(t)$ related to the solution of the initial value problem

$$\begin{cases} \mathbf{y}' = \mathbf{f}(t, \mathbf{y}) \\ \mathbf{y}(t_0) = \mathbf{y}_0 \end{cases}.$$

When $\mathbf{f}$ satisfies a local Lipschitz condition with respect to $\mathbf{y}$ on U, a connected open subset of $\mathbb{R}^{m+1}$ and $(t_0, \mathbf{y}_0) \in U$, the Picard iterates given by

$$\phi_0(t) = \mathbf{y}_0$$
$$\phi_n(t) = \mathbf{y}_0 + \int_{t_0}^{t} \mathbf{f}\left(s, \phi_{n-1}(s)\right) ds.$$

converge to a unique solution of the IVP up to the boundary of U [1]. In general, ϕ_n may converge slowly to the exact solution.

The Picard iteration based integrator described in this paper has three main advantages. The the integrator has arbitrary order, is time adaptive, and has dense output. Dense output refers to the integrator being able to take time steps of variable length without having to recompute previous steps. These advantages are intertwined to balance local truncation error with computational efficiency. When smaller time steps are required, the order can be reduced to maintain efficiency. When a larger time step is appropriate, the order can be increased to maintain lower local truncation error.

The advantages of the integrator make it well suited for modelling the motion of charged particles. The forces in Coulomb interactions are proportional to the inverse of the square of the distances between particles. There are situations such as when two particles with same signed charges are on a near collision course. If too large of a time step is taken, the large repulsive force between the particles as they move closer to one another may not be considered and the integrator will give physically unrealistic results. An integrator with dense output can avoid these errors.

* This work was supported in part by the U.S. Department of Energy, Office of Nuclear Physics, under Contract No. DE-SC0008588, and Office of High Energy Physics, under Contract No. DE-FG02-08ER41532, with Northern Illinois University.

THEORY BEHIND THE INTEGRATOR

First, we will introduce notation to write Taylor polynomials. When f has a Taylor series centered at a with nonzero radius of convergence, define the operator $\mathcal{T}_{t,a}^{n}$ acting on function f to be the degree n Taylor polynomial centered at a for f. That is

$$\mathcal{T}_{t,a}^{n}[f] = \sum_{k=0}^{n} f^{(k)}(a) \frac{(t-a)^k}{k!}.$$

Main Theorem Statement

The main theorem below supplies two Picard iteration based integrators with different compositions. From the initial Taylor polynomial $\mathcal{T}_{t,0}^{0}[\mathbf{z}(t)] = \mathbf{z}_0$, we can find the next Taylor polynomials using either recursive relationship below. After each iteration, the local truncation error drops by an order of magnitude. Algorithm 1 in the implementation and results section shows how to implement the first composition.

Theorem 1. *Let* $\mathbf{z}\,'(t) = \mathbf{f}(t)$ *and* $\mathbf{z}_0 = \mathbf{z}(0)$. *Suppose* $\mathbf{z}$ *has a Taylor series centered at* 0 *with nonzero radius of convergence* R *and* $t < R$, *then*

$$\mathcal{T}_{t,0}^{n}[\mathbf{z}(t)] = \mathbf{z}_0 + \int_0^t \mathcal{T}_{s,0}^{n-1}\left[\mathbf{f}\left(\mathcal{T}_{s,0}^{n-1}[\mathbf{z}(s)]\right)\right] ds$$
$$= \mathbf{z}_0 + \int_0^t \mathcal{T}_{s,0}^{n-1}\left[\mathcal{T}_{s,\mathbf{z}_0}^{n-1}[\mathbf{f}] \circ \mathcal{T}_{s,0}^{n-1}[\mathbf{z}(s)]\right] ds.$$

In order to prove theorem 1, we need two lemmas. In order to show the first lemma, we will need the Faà Di Bruno formula [2], which is a generalization of the chain rule.

Theorem 2 (Faà Di Bruno)**.** *If* g *and* f *are functions with a sufficient number of derivatives, then*

$$\frac{\mathrm{d}^m}{\mathrm{d}t^m} f(g(t)) = \sum \frac{m!}{\prod_{i=1}^{m} b_i!} f^{(k)}(g(t)) \prod_{i=1}^{m} \left(\frac{g^{(i)}(t)}{i!}\right)^{b_i}$$

where the sum is over all different solutions in nonnegative integers $b_1, \ldots, b_m$ *of* $b_1 + 2b_2 + \cdots + mb_m = m$ *and* $k \equiv b_1 + b_2 + \cdots + b_m$.

Let $S_{m,k}$ denote the nonnegative integer solutions of $b_1 + 2b_2 + \cdots + mb_m = m$ and $k \equiv b_1 + b_2 + \cdots + b_m$, and $T_{n,m,k}$ denote the nonnegative integer solutions of $b_1 + 2b_2 + \cdots + nb_n = m$ and $k \equiv b_1 + b_2 + \cdots + b_m$.

Copyright © 2013 CC-BY-3.0 and by the respective authors

Lemma 1. *Suppose g has a Taylor series centered at a and f has a Taylor series centered at $g(a)$ with nonzero radii of convergence. Then,*

$$\mathcal{T}^n_{t,a}[f \circ g] = \mathcal{T}^n_{t,a}\left[\mathcal{T}^n_{t,g(a)}[f] \circ \mathcal{T}^n_{t,a}[g]\right].$$

Proof $\mathcal{T}^n_{t,a}\left[\mathcal{T}^n_{t,g(a)}[f] \circ \mathcal{T}^n_{t,a}[g]\right]$ will be directly evaluated. The two things needed to start are

$$\mathcal{T}^n_{t,a}[g] = \sum_{k=0}^{n} g^{(k)}(a)\frac{(t-a)^k}{k!}$$

and

$$\mathcal{T}^n_{t,g(a)}[f] = \sum_{k=0}^{n} f^{(k)}(g(a))\frac{(t-g(a))^k}{k!}.$$

Plugging the first one into the second one, the following can be done:

$$\begin{aligned}
&\mathcal{T}^n_{t,g(a)}[f] \circ \mathcal{T}^n_{t,a}[g] = \sum_{k=0}^{n} f^{(k)}(g(a))\frac{(\mathcal{T}^n_{t,a}[g]-g(a))^k}{k!}\\
&= \sum_{k=0}^{n}\frac{f^{(k)}(g(a))}{k!}\left(\sum_{i=0}^{n} g^{(i)}(a)\frac{(t-a)^i}{i!} - g(a)\right)^k\\
&= \sum_{k=0}^{n}\frac{f^{(k)}(g(a))}{k!}\left(\sum_{i=1}^{n}\frac{g^{(i)}(a)}{i!}(t-a)^i\right)^k\\
&= \sum_{k=0}^{n}\frac{f^{(k)}(g(a))}{k!}\sum_{T_{n,m,k}}\frac{k!}{\prod_{i=1}^n b_i!}\prod_{i=1}^{n}\left(\frac{g^{(i)}(a)}{i!}(t-a)^i\right)^{b_i}\\
&= \sum_{k=0}^{n}\sum_{T_{n,m,k}}\frac{f^{(k)}(g(a))}{k!}\frac{k!}{\prod_{i=1}^n b_i!}\prod_{i=1}^{n}\left(\frac{g^{(i)}(a)}{i!}(t-a)^i\right)^{b_i}.
\end{aligned}$$

The fourth step is done using a combinatorial argument. Think of each $\frac{g^{(i)}(a)}{i!}(t-a)^i$ as a letter α_i. What is being counted by $\frac{k!}{b_1!\,b_2!\,b_3!\ldots b_n!}$ is the number of words with k letters that have b_1 letter α_1's, b_2 letter α_2's, $\ldots$, and b_n letter α_n's.

In $T_{n,m,k}$, $m = b_1 + 2b_2 + \cdots + nb_n$. It must be that $b_i = 0$ when $i > m$ for $i = 1, 2, \cdots, n$. In $\mathcal{T}^n_{t,a}\left[\mathcal{T}^n_{t,g(a)}[f] \circ \mathcal{T}^n_{t,a}[g]\right]$ each term has degree n or less, so $m \le n$. In this case, $T_{n,m,k} = S_{m,k}$, and we have

$$\begin{aligned}
&\mathcal{T}^n_{t,a}\left[\mathcal{T}^n_{t,g(a)}[f] \circ \mathcal{T}^n_{t,a}[g]\right]\\
&= \sum_{k=0}^{n}\sum_{S_{m,k}}\frac{(t-a)^m}{m!}\frac{m!}{\prod_{i=1}^m b_i!}f^{(k)}(g(a))\prod_{i=1}^{m}\left(\frac{g^{(i)}(a)}{i!}\right)^{b_i}\\
&= \sum_{m=0}^{n}\frac{(t-a)^m}{m!}\sum_{S_{m,k}}\frac{m!}{\prod_{i=1}^m b_i!}f^{(k)}(g(a))\prod_{i=1}^{m}\left(\frac{g^{(i)}(a)}{i!}\right)^{b_i}\\
&= \sum_{m=0}^{n}\frac{(t-a)^m}{m!}\frac{\mathrm{d}^m}{\mathrm{d}t^m}f(g(t))\\
&= \mathcal{T}^n_{t,a}[f \circ g].
\end{aligned}$$

□

Lemma 2. *Suppose g has a Taylor series centered at a and f has a Taylor series centered at $g(a)$ with nonzero radii of convergence. Then,*

$$\mathcal{T}^n_{t,a}\left[f(\mathcal{T}^n_{t,a}[g])\right] = \mathcal{T}^n_{t,a}[f \circ g].$$

Proof

$$\begin{aligned}
\mathcal{T}^n_{t,a}\left[f(\mathcal{T}^n_{t,a}[g])\right] &= \mathcal{T}^n_{t,a}\left[f \circ (\mathcal{T}^n_{t,a}[g])\right]\\
&= \mathcal{T}^n_{t,a}\left[\mathcal{T}^n_{t,(\mathcal{T}^n_{t,a}[g])(a)}[f] \circ \mathcal{T}^n_{t,a}\left[\mathcal{T}^n_{t,a}[g]\right]\right]\\
&= \mathcal{T}^n_{t,a}\left[\mathcal{T}^n_{t,g(a)}[f] \circ \mathcal{T}^n_{t,a}[g]\right]\\
&= \mathcal{T}^n_{t,a}\left[f \circ g\right]
\end{aligned}$$

The second line is from applying lemma 1. The third line can be seen noting that $\left(\mathcal{T}^n_{t,a}[g]\right)(a) = g^{(0)}(a) = g(a)$ and $\mathcal{T}^n_{t,a} \circ \mathcal{T}^n_{t,a} = \mathcal{T}^n_{t,a}$. □

We are now ready to prove theorem 1.

Proof From lemma 2,

$$\mathcal{T}^{n-1}_{s,0}\left[\mathbf{f}\left(\mathcal{T}^{n-1}_{s,0}[\mathbf{z}(s)]\right)\right] = \mathcal{T}^{n-1}_{s,0}\left[\mathbf{f}\left(\mathbf{z}(s)\right)\right].$$

This implies

$$\begin{aligned}
&\mathbf{z}_0 + \int_0^t \mathcal{T}^{n-1}_{s,0}\left[\mathbf{f}\left(\mathcal{T}^{n-1}_{s,0}[\mathbf{z}(s)]\right)\right]ds\\
&= \mathbf{z}_0 + \int_0^t \mathcal{T}^{n-1}_{s,0}\left[\mathbf{f}\left(\mathbf{v}(s)\right)\right]ds\\
&= \mathbf{z}_0 + \int_0^t \sum_{k=0}^{n-1}\frac{\mathrm{d}^k}{\mathrm{d}s^k}\left[\mathbf{f}\left(\mathbf{z}(s)\right)\right](0)\frac{(s)^k}{k!}ds\\
&= \mathbf{z}_0 + \sum_{k=0}^{n-1}\int_0^t \frac{\mathrm{d}^k}{\mathrm{d}s^k}\left[\mathbf{f}\left(\mathbf{z}(s)\right)\right](0)\frac{(s)^k}{k!}ds\\
&= \mathbf{z}_0 + \sum_{k=0}^{n-1}\frac{\mathrm{d}^k}{\mathrm{d}s^k}\left[\mathbf{f}\left(\mathbf{z}(s)\right)\right](0)\int_0^t \frac{(s)^k}{k!}ds\\
&= \mathbf{z}_0 + \sum_{k=0}^{n-1}\frac{\mathrm{d}^k}{\mathrm{d}t^k}\left[\mathbf{f}\left(\mathbf{z}(t)\right)\right](0)\frac{t^{k+1}}{(k+1)!}\\
&= \mathbf{z}_0 + \sum_{k=0}^{n-1}\mathbf{z}^{(k+1)}(0)\frac{t^{k+1}}{(k+1)!}\\
&= \sum_{k=0}^{n}\mathbf{z}^{(k)}(0)\frac{t^k}{k!}ds = \mathcal{T}^n_{t,0}[\mathbf{z}(t)].
\end{aligned}$$

From lemma 1,

$$\mathcal{T}^{n-1}_{s,0}\left[\mathbf{f}\left(\mathbf{z}(s)\right)\right] = \mathcal{T}^{n-1}_{s,0}\left[\mathcal{T}^{n-1}_{s,\mathbf{z}(0)}[\mathbf{f}] \circ \mathcal{T}^{n-1}_{s,0}[\mathbf{z}(s)]\right].$$

It follows then that

$$\begin{aligned}
\mathcal{T}^n_{t,0}[\mathbf{z}(t)] &= \mathbf{z}_0 + \int_0^t \mathcal{T}^{n-1}_{s,0}\left[\mathbf{f}\left(\mathcal{T}^{n-1}_{s,0}[\mathbf{z}(s)]\right)\right]ds\\
&= \mathbf{z}_0 + \int_0^t \mathcal{T}^{n-1}_{s,0}\left[\mathcal{T}^{n-1}_{s,\mathbf{z}_0}[\mathbf{f}] \circ \mathcal{T}^{n-1}_{s,0}[\mathbf{z}(s)]\right]ds.
\end{aligned}$$

□

Copyright © 2013 CC-BY-3.0 and by the respective authors

IMPLEMENTATION AND RESULTS

Implementation

The Picard iteration based integrator was implemented using COSY INFINITY. COSY has several unique data types including differential algebra (DA) vectors which were used to store the Taylor polynomials. Many operations on DA vectors are also efficiently coded into COSY such as polynomial multiplication and composition. Built in operations allow for computing the Taylor expansions of various functions to specified order [3].

Algorithm 1 below describes how to compute $\mathbf{z}(t)$ at the points $t = \frac{T}{N}, \frac{2T}{N}, \cdots, T$. Here, T is the total time interval under investigation with N time steps of length Δt. This algorithm uses the first composition in Theorem 1.

Algorithm 1 Picard Iteration Based Integrator

input $\mathbf{z}_0,\ \mathbf{f}(\mathbf{z},t)\ T,\ N,$ Tolerance
$\Delta t \leftarrow \frac{T}{N}$
$\hat{\mathbf{z}_0} \leftarrow \mathbf{z}_0$
for $i = 1 \rightarrow N$ **do**
  Compute the "best" smaller time step to use $\frac{\Delta t}{M}$, and an appropriate ORDER for the Taylor series that keeps the local truncation error $\mathcal{O}$(Tolerance).
  $\hat{t} \leftarrow \frac{\Delta t}{M}$
  for $j = 1 \rightarrow M$ **do**
    $\phi_0(t) \leftarrow \hat{\mathbf{z}}_0$
    for $k = 1 \rightarrow$ ORDER **do**
      $\phi_k(t) \leftarrow \hat{\mathbf{z}}_0 + \int_0^t \mathcal{T}_{s,0}^{k-1} \left[\mathbf{f}\left(\phi_{k-1}(s), s\right)\right] ds$
    end for
    $\hat{\mathbf{z}}_0 \leftarrow \phi_{\text{ORDER}}(\hat{t})$
      ▷ *The above is* $\mathbf{z}\left([i-1+j/M]\Delta t\right)$.
  end for
  Write $\hat{\mathbf{z}}_0$ ▷ *This is* $\mathbf{z}(i\Delta t)$.
end for

In the loop from $j = 1$ to $j = M$ the time scale for the initial value problem is shifted left when j increases so that the initial condition involves $t_0 = 0$.

$$\begin{cases} \mathbf{z}' = \mathbf{f}(t, \mathbf{z}) \\ \mathbf{z}(t_0) = \mathbf{z}_0 \end{cases} \rightarrow \begin{cases} \mathbf{z}' = \mathbf{f}(t - t_0, \mathbf{z}) \\ \mathbf{z}(0) = \mathbf{z}_0 \end{cases}$$

This matches the conditions for Theorem 1 and reduces the work of evaluating the definite integral by making the second indefinite integral evaluation 0.

Results

One test of the integrator was to consider a system with a proton following a circular orbit around another super massive particle with opposite charge. The momentum of the proton was set at $\frac{2\,m\,c}{3\times10^5}$ where m is the mass of a proton, and the mass of the massive particle was set at $10^{40}\ m$. Balancing the centrifugal and Coulomb forces, the radius of the orbit is approximately $0.512 \times 10^{-5} m$. For this test, the time step is fixed at around $\frac{0.24169}{c}$s. The theoretical trajectory and integrator computation for the four thousandth orbit are plotted in Fig. 1 as thick black semicircles and red circled points, respectively.

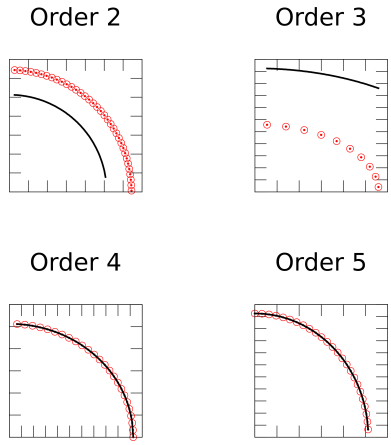


Figure 1: Orbiting Particle Trajectories at Different Orders

Additional details concerning the integrator's performance have been studied [4].

CONCLUSION

By utilizing the Picard iteration based integrator described, a wide class of functions can be integrated numerically. The integrator has the advantages of being variable order, being time adaptive, and having dense output. These advantages have been utilized in a successful implementation to solve Coulomb interactions using COSY INFINITY.

REFERENCES

[1] W. Walter, Ordinary Differential Equations, Springer-Verlag New York, Inc. 1998.

[2] W. P. Johnson, "The Curious History of Faà di Bruno's Formula," The American Mathematical Monthly 109:217-234, March 2002.

[3] K. Makino and M. Berz, "COSY INFINITY Version 9," Nuclear Instruments and Methods in Research Physics Section A, 558:345-350 December 2005.

[4] A. A. Marzouk, "Numerical Integrator for Coulomb Collisions," in these proceedings.

Copyright © 2013 CC-BY-3.0 and by the respective authors

A USER FRIENDLY, MODULAR SIMULATION TOOL FOR LASER-ELECTRON INTERACTIONS*

S. Seung, G. Andonian, M. A. Harrison, S. Wu (RadiaBeam, Santa Monica), T. Shaftan (BNL, Upton, Long Island, New York), D. L. Bruhwiler (University of Colorado at Boulder, CIPS)

Abstract

The code RadTrack was developed to accurately model observable beam parameters in real laboratory environments RadTrack is a fast, reliable computational application that can calculate radiation observables in complex interactions between realistic laser and electron beam distributions. The interaction between laser and electron beams is important in processes such as inverse Compton scattering and inverse free electron laser schemes. Modeling these interactions, RadTrack incorporates functions from Synchrotron Radiation Workshop (SRW) with full parsing support to capitalize on well-established radiation generation and propagation code available for start-to-end simulations, while expanding simulated radiation to x-ray regimes [1]. RadTrack is based on the Python environment, which uses a hierarchal module system and possesses built-in data types that will allow further expansions of the code. The code provides an intuitive visualization work canvas that emphasizes the users overall objective.

INTRODUCTION

RadTrack is designed to addresses a number of issues in the accelerator community, with special attention to the radiation properties for direct comparison to available diagnostics. To achieve this, the code emphasizes modularity, breaking down these issues into digestible pieces. The graphical user interface is built on a visualization canvas that easily generates and displays important information. The interface is intuitive for seamless management of start-to-end simulations, which incorporate several codes. The interface allows for simple parallelization for complex, memory demanding calculations. RadTrack was developed as a code that can calculate beam dynamics as well as emitted radiation processes, in a transparent, intuitive manner,.

Complete modelling of a beam from its inception to detection, requires a complicated string of start-to-end studies, employing a concatenation of various function-specific simulations to achieve a high degree of confidence in the final outcome. RadTrack is specifically designed to address start-to-end simulations by seamlessly stitching I/O from various codes and file formats.

The code, RadTrack, was originally developed as an extension to the radiation code QUINDI [2] to calculate the radiative effects of bending beam trajectories. QUINDI was developed for a specific problem and its results benchmarked to experiments at Brookhaven National Laboratory Accelerator Test Facility [3]. RadTrack makes use of QUINDI's particle tracker and radiation field solver, which are based on the Lorentz for and Lienerd-Wiechert potentials, respectively [4]. RadTrack is able to generate laser and electron beam distributions and pass these distributions through an extensive library of optics, magnets and diagnostics, in particular, the use of undulators is important to many laser electron interaction schemes, such as laser heating, laser slicing and sub-femtosecond temporal diagnostics. Figure 1 displays the work flow and modular philosophy of the code; this is advantageous for implementation of the functions, where multiple outputs of codes are parsed as inputs into subsequent codes.

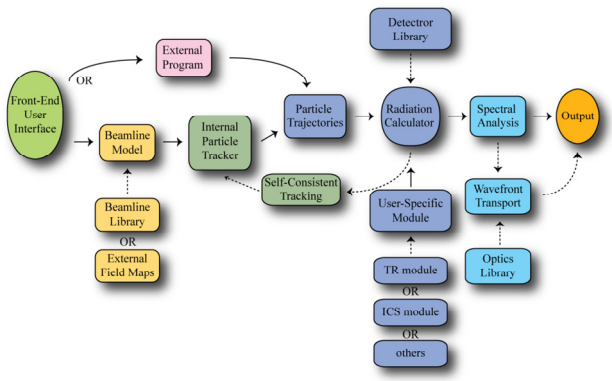


Figure 1: Work flow chart between physics modules, radiation modules, wave front propagator and various libraries.

LASER-ELECTRON INTERACTIONS

The motivation to develop a comprehensive software package that incorporates detailed beam dynamics calculations and radiation interactions has roots in many scientific cases prevalent throughout the advanced accelerator and light communities. Here are some laser electron interactions and their applications:

- The laser-heater is a laser-electron electron interaction in an undulator that increases the beam energy spread in a controllable way to reduce microbunching instability.
- The interaction between a relativistic electron beam and a high power laser induces an undulator-like radiation process that have the ability to produce short wavelength photons [5].
- The interaction between the laser and electron bunch is used to generate a beam energy modulation on the 100 femtosecond scale in storage rings.

* This work is supported by US DOE Grant No. DE-SC0006284.

Copyright © 2013 CC-BY-3.0 and by the respective authors

- Recent studies have explored the use of an advanced laser-electron interaction coupled inside an undulator, resonant at the laser wavelength, to achieve sub-femtosecond resolution on the electron beam longitudinal profile [6].
- The recent echo-enabled FEL projects reported from SLAC describe the energy modulation due to a laser in two undulators resonant at the laser frequency or harmonic [7]. The code Genesis can model this FEL experiment [8].

INPUT DATA VISUALIZATION

Laser and Particle Distribution

RadTrack incorporates an instinctive beam distribution panel. Initial beam parameters (used for the source particles) are defined and a 6-dimensional phase space distribution is generated. The user specified inputs include beam moments, correlations, various degrees of noise, and complex modulations or Courant-Snyder parameters. This panel also supports the importing of 6-dimensional particle distributions from external codes, such as ELEGANT [9]. Alteration of beam parameters is handled by textual input or sliders and buttons on the graphical displays, allowing for intuitive creation of particle distributions (such as rescaling of twiss parameters).

Generation of an initial laser distribution is handled in a similar manner, with interface analogues of the particle beam distribution panel. The inputs include wavelength, transverse profile, longitudinal profile, power, beam waist sizes and chirp factor.

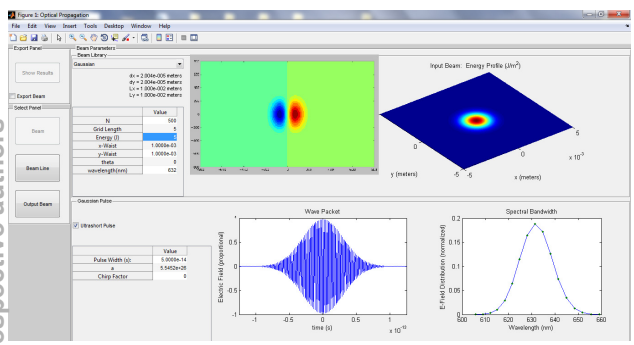


Figure 2: Laser beam generator I/O page from RadTrack, displaying a Gaussian profile, a simple MxN profile and temporal distribution

Beamline Constructor

The definition of the beamline lattice is addressed graphically in RadTrack. Beamline elements, such as drifts, bending magnets, quadrupoles, undulators, etc. are selectable and editable in a text dialog. The reference particle trajectory is calculated and plotted through the displayed beamline for immediate visualization (and error-checking). RadTrack allows for the placement of the detector for radiative processes at arbitrary locations, defined by beam offsets and rotations in the form of Euler angles. This allows for the modelling of bending radiation, such as synchrotron or edge radiation.

Generation of an optical beamline is also graphically generated in RadTrack, with panel analogues of the particle beamline lattice generator.

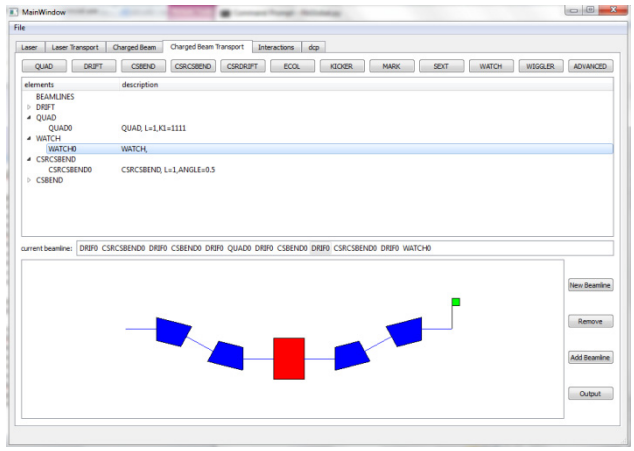


Figure 3: Beamline constructor written in Python with a streamlined interface and dynamic graphical previews.

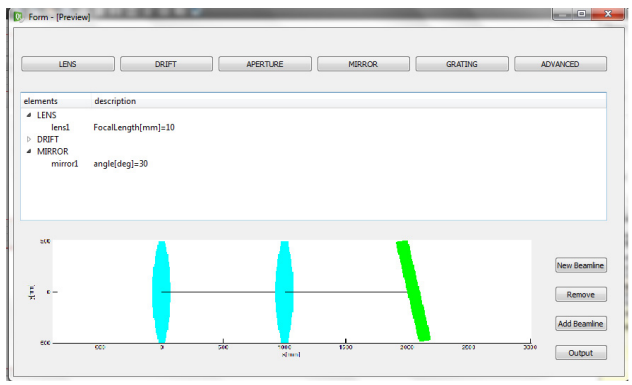


Figure 4: Optical beamline constructor

Originally written in MatLab, RadTrack has been slowly ported over to Python, offering more dynamic and streamlined controls. RadTrack is now equipped with very intuitive drag and drop abilities, where elements created by the user can be dragged from an organized list of available elements and dropped into a beamline. The graphics are also dynamic, as a graphical preview is generated when a user clicks on an element or beamline, and as a user creates a beamline. From there, a user can output a file that can be tuned as an ELEGANT input file or other external codes.

OUTPUT DATA VISUALIZATION

Added to RadTrack is the ability to view and explore data files generated from external code, such as ELEGANT, SRW, QUINDI, plain text files, etc... Parsers were written to identify simulation parameters, display

Copyright © 2013 CC-BY-3.0 and by the respective authors

the data in tables. Drop down menus allow the user to select which data sets to graph and RadTrack automatically labels the x and y axis. A toolbar is implemented to be able to zoom in, edit and save graphs. Very large files are broken down into pages and previewed in tables. Convenient functions allow RadTrack to identify filenames and current directories. Some mathematical functionality, such as Fourier transforms and running averages are able to be performed on desired data sets.

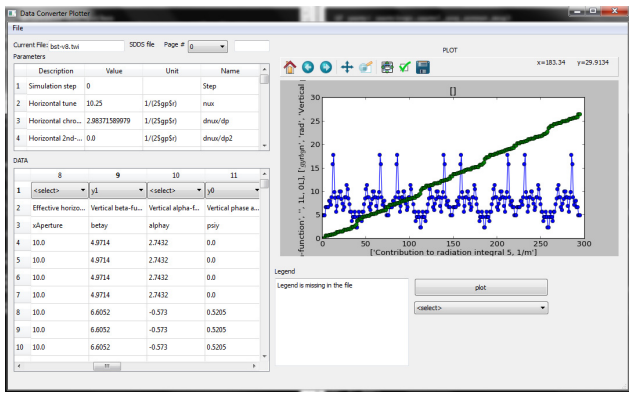


Figure 5: Viewing and plotting data from a self-describing data set (SDDS) [5] file, plotted is the horizontal beta function (blue) and the vertical phase advance (green).

CONCLUSION

RadTrack is a user-friendly tool used for the calculation of beam trajectories and emitted radiation of high brightness beams. The novel user-interface is accessible to a wide range of users and incorporates intuitive features such as the visualization of beam phase space densities and the graphical display of beamline lattice files in real time. It also incorporates a seamless method for start-to-end simulations and parallel extensions via the project management aide. Laser-electron interactions have myriad applications in Free Electron Lasers, ultrafast diagnostics, inverse Compton scattering, laser heating and slicing. One can easily see the convenience of being able to simulate all these processes and devices in a single easy to use interface.

REFERENCES

[1] O. Chubar, "Precise computation of electron beam radiation in non-uniform magnetic fields as tools for the beam diagnostics", Rev. Sci. Instrum. 66(2), 1872-1876 (1995).

[2] D. Schiller, et al., Proc. Particle Accelerator Conference 2007, Albuquerque, N.M., p. 3612 (2007).

[3] G. Andonian, et al., Phys. Rev. ST Accel. and Beams, vol.12, p.030701 (2009).

[4] J.D. Jackson, *Classical Electrodynamics*, Wiley, New York (1999).

[5] O'Shea, O. Williams, G. Andonian, S. Barber, Y. Sakai, J. Rosenzweig, I. Pogorelsky, M. Fedurin, K. Kusche, and V. Yakimenko, "Single shot diffraction of picosecond 8.7keV x-ray pulses," Phys. Rev. ST. Accel. Beams 15, 020702 (2012).

[6] G. Andonian, et al., Phys. Rev. ST Accel. and Beams, 14, 072802 (2011).

[7] D. Xiang, et al., Phys. Rev. Lett. 105, 114801 (2010).

[8] S. Reiche, "GENESIS 1.3: A fully 3D time dependent FEL simulation code," Nucl. Instrum. Methods Phys. Res. A 429, 243, 1999.

[9] M. Borland. "Elegant: A flexible sdds-compliant code for accelerator simulations," APS Technical Report, LS-287, (2000).

Copyright © 2013 CC-BY-3.0 and by the respective authors

MULTIPACTING SIMULATION OF ACCELERATOR CAVITIES USING ACE3P*

Lixin Ge, Kwok Ko, Zenghai Li, Cho-Kuen Ng and Liling Xiao
SLAC, Menlo Park, CA 94025, U.S.A

Abstract

ACE3P [1] is a 3D parallel finite element code suite for cavity design and optimization including electromagnetic, thermal and mechanical effects. Taking advantages of the power of computing on multi processors, ACE3P's particle tracking module Track3P allows efficient multipacting (MP) simulation by extensive scanning in field gradient and on cavity surface to identify the occurrences of MP activities. The output from Track3P simulation includes the determination of resonant trajectories and their locations, the calculation of electron impact energy on cavity surface, and the evaluation of the electron enhancement counter as a function of field gradient. The sensitivity of MP on secondary emission yield can be readily obtained through post processing. The basic capabilities of Track3P for MP simulation will be presented.

INTRODUCTION

Multipacting (MP) is an undesireable, resonant built-up of electrons inside RF structures. It can cause wall heating and high power breakdown of RF components, prolong processing time and limit the achievable design field gradient. While most of the soft MP barriers could be processed through RF, the presence of a hard MP barrier prevents a RF component from reaching its design power or field gradient level.

Much work has been done on MP studies to identify potential MP events and to mitigate MP activities. In recent years, with more computing power, full 3D simulation tools have been developed to investigate potential MP activities. High resolution EM field, correct representation of particle emission from curved surface, realistic SEY curve for surface material and comprehensive post-processing of particle data to identify MP events are the basic requirements for accurately simulation of MP. Furthermore, the use of high performance computing allows efficient MP simulation by making use of hundreds to thousands of CPU cores running in parallel, by which the speedup in computation time facilitates extensive parameter scans. Track3P, a 3D parallel particle tracking code, provides a MP simulation tool with these advanced modeling and computational features. It has been extensively benchmarked against experiments and applied to model and predict MP activities for the design of many accelerator cavities and RF components.

* The work was supported by the U.S. DOE contract DE-AC02-76SF00515 and used the resources of NERSC at LBNL under US DOE Contract No. DE-AC03-76SF00098.
[1]lge@slac.stanford.edu

MULTIPACTING SIMULATION USING ACE3P

ACE3P

ACE3P (Advanced Computational Electromagnetics 3D Parallel) is a comprehensive set of conformal, higher-order, parallel finite-element electromagnetic codes with two unique features. First, it is based on higher-order curved finite element method for high-fidelity modeling and improved solution accuracy. Second, it is implemented on massively parallel computers for increased memory (problem size) and speed. The six modules of ACE3P cover a wide range of simulation capabilities for accelerators: Omega3P for calculating cavity modes and damping, and S3P for transmission in open structures in frequency domain; T3P for calculating wakefields and transients in time domain; Track3P for MP and dark current studies using particle tracking; Pic3P for RF gun design with particle-in-cell (PIC) method; and TEM3P for multi-physics analysis including EM, thermal and mechanical effects.

Track3P Characteristics

Track3P provides accurate and efficient simulation for MP by tracking particle trajectories under the influence of RF fields or external static fields. The RF field in an accelerator structure is first solved by Omega3P or S3P, which calculates the EM field to high accuracy using higher-order basis functions (up to 6^{th} order), and then loaded into Track3P for particle tracking. In a similar manner, external static electric and magnetic fields can be read into the code as input field data. The high-fidelity geometry representation built in the finite-element method allows realistic modeling of particle emission on cavity wall. Track3P constructs the MP map by identifying resonant particle trajectories. With a realistic secondary electron yield (SEY) curve provided by experiments, Track3P can calculate the particle enhancement counter and locate MP regions. This is achieved using the versatile postprocssing tools that have been developed to identify the onset of MP through various parameter scans.

MP Module in Track3P

The following describes the procedure for modeling MP in Track3P. Electrons with specified kinetic energy and emission direction are launched from specific surfaces at different phases over a full RF period. The initial launched electrons follow the electromagnetic fields in the structure and eventually hit the boundary,

Copyright © 2013 CC-BY-3.0 and by the respective authors

where secondary electrons are emitted. The tracing of electrons will continue for a specified number of RF cycles, after which MP trajectories are determined and the MP types (order: # of RF cycles to return to the original site; point: # of sites on the wall) are identified. The necessary condition for MP is when the trajectory traced out by consecutive emissions is in resonance with the RF cycle. These particles impact on the surface at the same locations with the same impact energy. When the impact energy falls in the range with SEY greater than unity, the resonant trajectory is considered as a MP event. One can also estimate the strength (soft or hard) of the MP event by the value of the SEY.

TRACK3P SIMULATION CAPABILITIES

Track3P has been extensively benchmarked against theories and measurements [2-7]. In a typical MP run, Track3P generates a large amount of particle and field information data such as the position and momentum as a function of time and the history of particles in a resonant trajectory. Various diagnostics and postprocessing tools have been developed to provide simulation capabilities for modeling MP in realistic cavities for accelerator projects. The basic capabilities are as follows.

Determination of Resonant Trajectories

MP activities are due to the resonant built-up of electrons inside an RF structure. The first step to identify the occurrences of MP is the formation of resonant particle trajectories. Based on the resonant particle information, one can identify potential MP locations, types (order and points), and determine impact energies. Fig. 1 shows the locations of resonant particles in the HOM coupler of the SNS SRF cavity at the field level of 4.22 MV/m. The resonant particles are located at the coupler gap region. By drawing out one typical resonant trajectory, the MP type is found to be first order and two point, with impact energies 490 eV and 650 eV on the inner and outer walls of the gap, respectively [8].

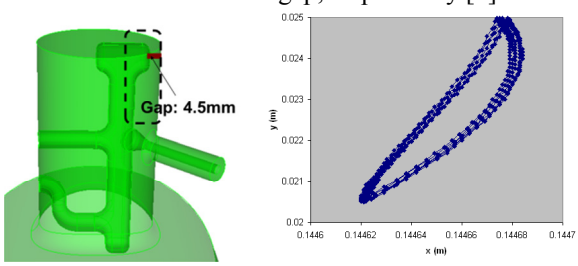


Figure 1: MP simulation of SNS HOM coupler. Left: Locations of particles with resonant trajectories; Right: A resonant trajectory at 4.22 MV/m field gradient.

Construction of MP Susceptible Zones

The main objective of MP simulation is to determine the field levels at which potential MP activities occur. In Track3P simulation, the tracking of particles will be carried out by scanning a range of field levels at a prescribed field step increment. Resonant particles are identified at each field level, and based on this information it is possible to construct potential MP zones. Fig. 2 shows the impact energy as a function of field level for the FRIB Quarter Wave Resonator (QWR) and the locations of the impact positions of resonant particles at all field levels [4]. A hard barrier MP band is found at low field levels from 800V to 7.5kV, with impact energies corresponding to SEY values near its peak. The simulation result agrees well with the high power test data which showed a processing barrier at 1.2kV ~ 7.2kV.

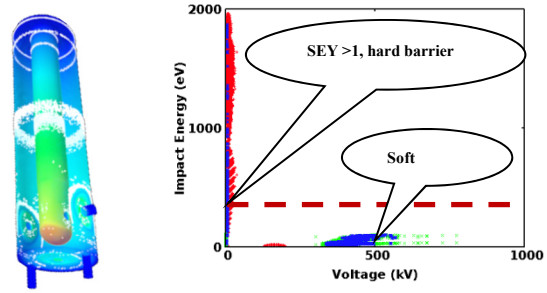


Figure 2: MP simulation for FRIB Quarter Wave Resonator. Left: Resonant particle impact positions at all field levels; Right: Impact energy vs. accelerating voltage for particles with resonant trajectories. Red color indicates resonant particles at the top region of cavity, and green at the middle and blue at the bottom.

Calculation of Enhancement Counter

One parameter to quantify MP is the enhancement counter, which is given by

$$\mathrm{ec} = \delta_1 * \delta_2 * \cdots \delta_m$$

where $\delta_1, \delta_2 \cdots \delta_m$ are the number of secondary electrons generated at the 1st, 2nd, … mth impacts determined by the SEY curve. Generally, when ec > 1, there will be potential MP activities. The larger the ec is, the harder the MP barrier. In Track3P simulation, the calculation of the enhancement counter is treated in postprocessing by applying the SEY on the impact energies of resonant particles, and thus one can use different SEY curves to estimate the effects of different surface material properties from a single computer run. Fig. 3 shows the MP simulation results for the MICE 201 MHz cavity [9]. Three enhancement counters are plotted using three different SEY curves [10]. Although the SEY curves have different magnitudes for the range of electron impact energies, the peak enhancement counter is found in the same region at the field levels of 2~4 MV/m. As a result, this MP event is believed to be a hard barrier.

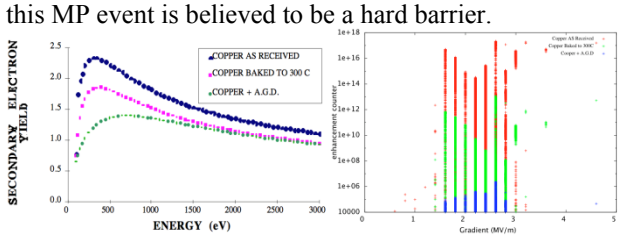


Figure 3: MP simulation for MICE 201 MHz cavity. Left: Three SEY curves; Right: Enhancement counters calculated using the three SEY curves.

Copyright © 2013 CC-BY-3.0 and by the respective authors

Effects of External Magnetic Field

In addition to loading Omega3P or S3P field, Track3P can load external magnetic field as input. This feature has been applied to improve the designs of the 805 MHz and 201 MHz Muon cooling cavities by studying external magnetic field effects [6]. Fig. 4 shows the location of resonant particle activities around the coupler iris of the prototype 805 MHz Muon cooling cavity without external magnetic field and with 3T solenoid magnetic field. It can be seen that MP activities appear at different locations of the coupling iris.

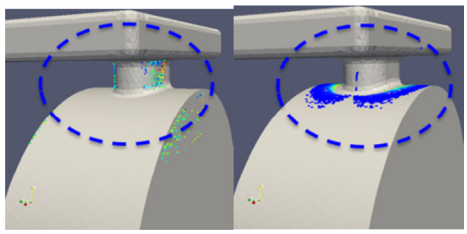


Figure 4: Resonant particle activities around coupler iris for the prototype 805 MHz Muon cooling cavity. Left is with 3T external magnetic field; Right is without external magnetic field.

Modeling of RF Window

The study of ceramic windows such as in couplers requires the implementation of emission on internal surface of the model [2]. Fig. 5 shows the simulation result for the TTFIII coupler with a ceramic window. A 2-point resonant trajectory occurs between the ceramic window and the inner conductor on the cold side of the coupler.

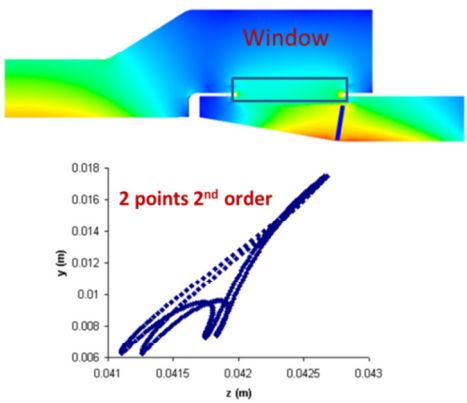


Figure 5: Resonant particle activities in the window region of the TTFIII coupler. Top: the electric field pattern; Bottom: a close-up of the resonant trajectory between the window and the metal wall.

Mitigation of Multipacting

Once MP activities are found in a cavity design, their effects can be mitigated by modifying the geometry where they occur [6]. In conjunction with Omega3P for calculating the RF fields, Track3P can evaluate MP effects at each iteration of the geometry change. For example, the original 805 MHz Muon cooling cavity suffered from severe gradient degradation and surface damage. Through simulation, a new design is achieved which significantly reduces the peak surface field by rounding the coupling slot and using an elliptical disk (see Fig. 6).

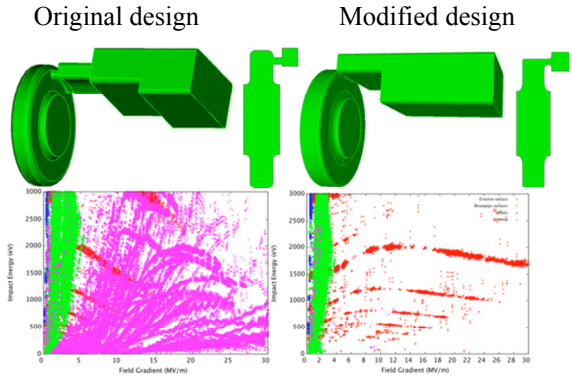


Figure 6: MP studies for 805 MHz Muon cooling cavity. MP locations: Windows (green); Disk rounding (blue); Coupling iris (magenta); Others (red).

SUMMARY

Track3P is the particle tracking module of the parallel finite-element code suite ACE3P and has been applied to study multipacting in accelerator cavities. Running on massively parallel computers, Track3P provides an efficient simulation tool in identifying multipacting barriers, locations and types of trajectories during the design or operation process of cavities. Track3P has been extensively used to study multipacting activities in many accelerator cavities and helps successfully mitigate multipacting effects and thus improve cavity designs.

REFERENCES

[1] K. Ko et al, "Advances in Parallel Computing Codes for Accelerator Science and Development," Proc. LINAC2010, Tsukuba, Japan, 2010.

[2] L. Ge et al., "Multipacting Simulations of TTF-III Power Coupler Components," Proc. PAC07, Albuquerque, New Mexico.

[3] L. Ge et al., "Multipacting Simulation and Analysis for the FRIB Superconducting Resonators Using Track3P," Proc. LINAC2010, Tsukuba, Japan, 2010.

[4] L. Ge et al., "Multipacting Simulations and Analysis for the FRIB β=0.085 Quarter Waver Resonators Using Track3P," Proc. IPAC12, New Orleans, LA, 2012.

[5] W. Xu et al., "Design, Simulations and Conditioning of 500 kW Fundamental Power Couplers for a SRF Gun," Phys. Rev. ST Accel. Beams 15 (2012) 072001.

[6] Z. Li et al., "RF Optimization and Analysis of the 805-MHz Cavity for the US MuCool Program Using ACE3P," Proc. AAC12, Austin, TX, USA. 2012.

[7] F. L. Krawczyk, "Status of Multipacting Simulation Capabilities for SCRF Applications," Proc. 10th workshop on RF Superconductivity, Tsukuba, Japan, 2001.

[8] Lixin Ge, "Multipacting simulation using parallel Code Track3P," Wakefest 2007.

[9] T. Luo et al., " Multipacting Simulation of MICE 201 MHz RF Cavity", Proc. IPAC2013, Shanghai, China 2013.

[10] D.R. Walters and Q. Ma, "Secondary electron yield of a thin film coating on the APS RF cavity tuners," Proc. PAC2001, (2001).

Copyright © 2013 CC-BY-3.0 and by the respective authors

INTER-BUNCH COMMUNICATION THROUGH CSR IN WHISPERING GALLERY MODES*

R. Warnock †, SLAC National Accelerator Laboratory, Menlo Park, CA, USA
J. Bergstrom, Canadian Light Source, Saskatoon, SK, Canada
M. Klein, Synchrotron SOLEIL, Gif-sur-Yvette, France

Abstract

Theory predicts that coherent synchrotron radiation (CSR) in electron storage rings should appear in whispering gallery modes, which are resonant modes of the vacuum chamber, characterized by their high frequencies and concentration near the outer wall of the chamber. Such modes produce an extended wake field behind a particle bunch, which can influence the CSR from a succeeding bunch in a train. We review experimental evidence for the resonances and for the inter-bunch communication. We then present a calculation based on coupled Vlasov-Fokker-Planck equations which confirms an effect seen experimentally, namely that increasing the charge in a leading bunch increases the radiation from a following bunch.

RESONANCES: THEORY AND EVIDENCE

Synchrotron radiation in electron accelerators is strongly affected by the metallic vacuum chamber surrounding the beam, as was already shown theoretically by Schwinger in 1945 [1]. In the parallel plate model of the chamber [1] there is an exponential suppression of radiation at wavelengths greater than $\lambda_0 \approx 2h(h/R)^{1/2}$, where h is the separation of infinite conducting plates, and R is the radius of the particle's circular trajectory lying in the midplane. The model is made more realistic by adding conducting side walls perpendicular to the plates, so that the beam moves in a circular torus of rectangular cross section, with width w and height h. For w of order h, the cutoff λ_0 is roughly the same as before, but a markedly different physical picture emerges.

Radiation to infinity is now forbidden, and radiation synchronous with the beam appears in resonant modes, sharply concentrated in frequency [2]. We call these *whispering gallery modes*, because of a close analog in acoustics [3]; similar phenomena are widely studied in RF engineering and optics. .

A theoretical spectrum of resonant modes is shown in Fig. 1, which is a plot of the real part of the radiation impedance $Z(k)$ for a beam centered in a circular torus with rectangular cross-section and resistive walls of conductivity σ [2]. The parameters correspond to those of the ANKA light source in Karlsruhe: $R = 5.559$m, $w = 6.8$cm, $h = 3.2$cm, $\sigma = 1.33 \cdot 10^6$ (SI units). The power spectrum of CSR is proportional to $ReZ(k)|\hat{\lambda}(k)|^2$, where $\hat{\lambda}(k)$ is the Fourier transform of the bunch profile.

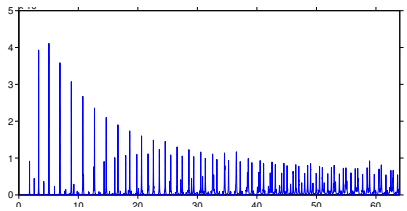


Figure 1: Re $Z(k)$ in ohms for ANKA parameters, vs. $k = 1/\lambda$ in cm^{-1}.

At ANKA and other light sources (CLS, BESSY, MLS, *et al.*) there are large flared vacuum chambers where the IR radiation is extracted, and these may alter the observed spectrum in comparison to that of the smooth toroidal model. The longitudinal electric field $E(s,t)$ may always be regarded as a function of the two independent variables $z = s - \beta ct$ and s. That leads to the concept of position dependent wake $\mathcal{W}(z,s)$. We define

$$\mathcal{W}(z,s) = E(s,t)\ ,\ \bar{\mathcal{W}}(z) = \frac{1}{C}\int_0^C \mathcal{W}(z,s)ds\ . \quad (1)$$

The average $\bar{\mathcal{W}}(z)$ over the circumference C is probably adequate to describe the bunch dynamics, since the synchrotron period is large compared to the revolution time. We suppose that $\bar{\mathcal{W}}$ can be approximated as the wake from the impedance of the smooth toroidal model, with central radius R equal to the bending radius of the dipoles.

Note that an interferometer at the position $s = s_{IR}$ of a flared IR chamber will see a field with time dependence given by $\mathcal{W}(z - \beta ct, s_{IR})$, in general different from the time dependence of $\bar{\mathcal{W}}(z - \beta ct)$. Specific theoretical modeling of fields in the flared chamber will be necessary to compare interferometer data with theory.

In an older ring, the NSLS-VUV at Brookhaven, the IR chamber is the same as in other dipoles, so the aforementioned difficulty is not so severe. Moreover, a power spectrum was measured at VUV in the bursting CSR mode, using a Michelson interferometer and also microwave techniques. In Ref.[4] a good fit of the model to experimental positions of spectral lines was shown. Zhou [5] did a similar fit including straight sections, but with less detailed discussion of low frequency lines. The straights induce a width of the lines, which could be part if not all of the explanation of experimental widths.

* Partial support at SLAC from U.S. Dept. of Energy contract DE-AC03-76SF00515; support at CLS from CFI, NSERC, NRC, The Canadian Institutes of Health Research, and the Government of Saskatchewan.
† warnock@slac.stanford.edu

Copyright © 2013 CC-BY-3.0 and by the respective authors

Spectra of CSR have been observed with high precision at the Canadian Light Source (CLS), by using an interferometer with resolution down to 0.001 cm^{-1}. The spectra show a remarkable stability with respect to changes in the machine setup and the structure of the IR beam line. Figure 2 compares a power spectrum (red) taken in the bursting mode of CSR with one bunch at 2.9 GeV, on 18/5/2010, with another (blue) taken in the continuous mode with 210 bunches at 1.5 GeV, on 30/1/2012. The latter was multiplied by a factor of 8 to aid comparison. Because of the large change in the beam one expects the positions of peaks to agree better than the relative heights, as is found, but even the relative heights show a lot of similarity between the two runs. We take this stability as a strong indication that the spectrum is determined primarily by the vacuum chamber and bends.

The form of the IR chamber at CLS is shown in Fig. 3. Equations to model fields in this structure are under study. As the crudest approximation we can try the simple toroidal model with an increased distance d from the beam to the outer wall. With $d = 33$cm the spacing of the dominant TE modes [2] is $\Delta k = \Delta(1/\lambda) = 0.073\mathrm{cm}^{-1}$, fitting the fine structure of the spectral data.

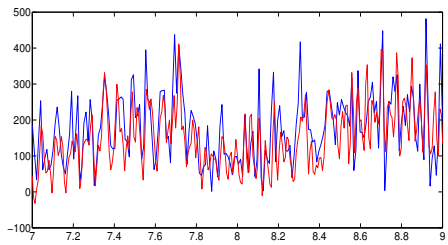


Figure 2: CLS spectra from two very different runs, power (a.u.) vs. k in cm^{-1}.

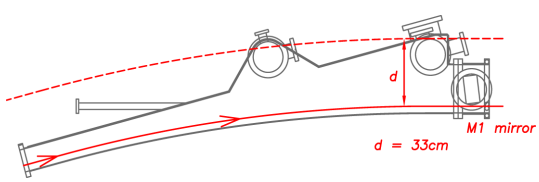


Figure 3: Vacuum chamber of CLS at dipole where IR is extracted

LONG RANGE WAKE FIELD: THEORY AND EVIDENCE

An impedance like that of Fig. 1 implies an appreciable wake field at long distances from the bunch, much greater than the bunch length. Fig. 4 shows the wake potential corresponding to Fig. 1, as a function of distance in centimeters, with the head of the bunch on the right. A feature of the model, if not of the real system, is that the wake wraps all the way around the ring, resulting in a precursor field in front of the bunch. If we try to model the wake field expected at the IR chamber of the CLS, using the effective beam-to-wall distance d as mentioned above, we get the rather different long-range wake pattern of Fig. 5.

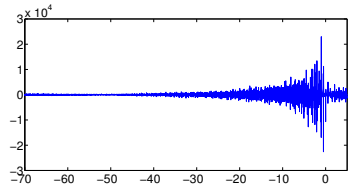


Figure 4: Wake potential $W(z)$ in V/pC from impedance of Fig. 1., vs. z in cm.

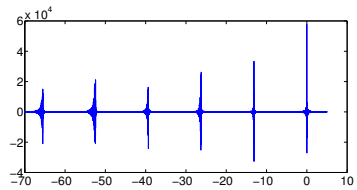


Figure 5: Wake potential for CLS model with $d = 33$cm.

Experiments which aspire to observe the wake field directly were carried out at the CLS, following an idea of S. Kramer to put a microwave horn and diode detector at a backward port (in the horizontal pipe seen in Fig. 3) in one of the two IR dipole chambers. The diode has a bandwidth of roughly 50-75 GHz, and receives signals traveling opposite to the direction of the beam, which might come from backward reflections off structures present in the chamber. Fig. 6 shows a typical oscilloscope trace of the diode signal. Labeling the prominent *downward* peaks from left to right as 1 to 4, we have a plausible explanation as follows: 1 and 2 are reflections from the first downstream obstacle in the flared chamber, a copper photon absorber (in second circle from right in Fig. 3), whereas 3 and 4 are from the next obstacle, a structure supporting the M1 pick-off mirror. The 1-3 separation corresponds closely to the separation of these obstacles. Peak 1 is seen as the prompt wake field from the bunch, while peak 2 is a delayed pulse in the wake field, about 13.5 cm behind the bunch; similarly for 3 and 4, coming from the later reflection. The point to emphasize is that the distance from bunch to delayed wake pulse is very close to the reciprocal of the average spacing of peaks in the power spectrum shown in Fig. 2, namely $\Delta k \approx 0.073\mathrm{cm}^{-1}$. Correspondingly, the distance between the center burst and the first side peak in the interferogram is 13.5cm, as is the spacing of peaks in the naive theory of Fig. 5.

The interpretation of the peaks in terms of reflections is given added weight by a second experiment in which the diode was moved to a "normal" dipole chamber. That resembles the special IR chamber, but lacks the pick-off mirror and has a slotted wall (centered slot of width 1 cm) between the beam and the large flared box. The analog of

Copyright © 2013 CC-BY-3.0 and by the respective authors

peaks 1-2 is seen, but that of 3-4 goes away, in accord with the absence of the mirror support structure.

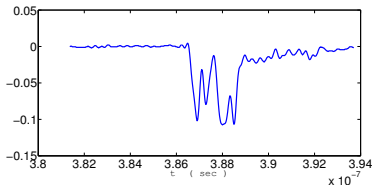


Figure 6: Signal (a.u.) from backward viewing diode at CLS vs. time in seconds.

Further evidence of a long range wake field comes from an experiment at ANKA by V. Judin [6] and collaborators. This observed THz radiation with a fast bolometer having sufficient time resolution to distinguish radiation from individual bunches. A large number of buckets were filled with known but varying amounts of charge. Bolometer signals from the various bunches were sorted into two groups: the blue group in which the preceding bunch in the fill has at least 10% less charge, and the red group in which the preceding bunch has at least 10% greater charge. The power signals were preponderantly greater for the red group, as is seen in the histogram of Fig. 7. The latter gives the distribution of red and blue signals relative to a curve which is a global fit to all the signals.

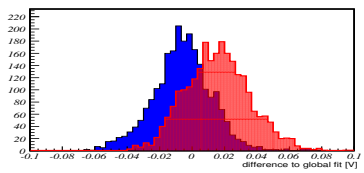


Figure 7: Radiation enhancement by higher charge in preceding bunch.

VLASOV-FOKKER-PLANCK (VFP) SIMULATION WITH TWO BUNCHES

We demonstrate the effect of the long range wake field from whispering gallery modes by solving a nonlinear VFP system for two bunches in two adjacent buckets, taking ANKA parameters for which the interbunch spacing is 60cm. The impedance is that of Fig. 1. We have two coupled VFP equations, each referring to the longitudinal phase space distribution for a bunch in its beam frame, but with a term in the wake field defined by the distribution of the other bunch. The equations are solved by the method of Ref.[7] , but with bi-cubic rather than bi-quadratic interpolation to update the distribution. The initial distributions are Haïssinski equilibria, which are highly unstable at the currents considered.

We plot the total coherent power (a.u.) radiated by each of the two bunches vs. time in synchrotron periods. There are $N_a = 1.14 \cdot 10^9$ particles (0.49mA)in bunch

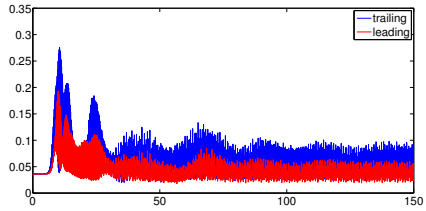


Figure 8: Power from two bunches with equal charges.

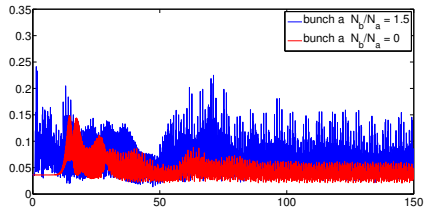


Figure 9: Power from trailing bunch (a), with and without leading bunch, which has 50% more charge.

(a), and an unperturbed bunch length for both bunches of $\sigma_z = 1.92$mm, typical for a low-α setup of ANKA used in CSR runs. For Fig. 8 we have $N_a = N_b$, but the power from the trailing bunch (blue) is consistently greater than that from the leading bunch (red). Fig. 9 shows the power from trailing bunch (a), without a leading bunch (red) and with a leading bunch having 50% more charge (blue). The strong enhancement due to the leading bunch is perhaps surprising in view of the seemingly small wake potential at 60cm shown in Fig. fig:wake, but is believed to be an authentic consequence of the model, evidently a feature of the unstable bunch dynamics at the large (but realistic) currents considered. Of course, the corresponding calculation with the parallel plate impedance shows no inter-bunch communication.

ACKNOWLEDGMENT

We thank S. Kramer, B. Billinghurst, V. Judin, and all the others who contributed to the experiments.

REFERENCES

[1] J. Schwinger, unpublished (1945), transcribed in LBL-39088 (1996) from Lawrence Berkeley Laboratory.

[2] R. Warnock and P. Morton, SLAC-PUB-4562 (1988), published in Part. Accel. **25**, 113 (1990).

[3] Lord Rayleigh, Phil. Mag. Ser. 6, **20**,1001-1004 (1910); **27**, 100-109 (1914).

[4] R. Warnock and J. Bergstrom, PAC 2011, paper WEP119.

[5] D. Zhou, IPAC 2012, paper MOOBBO3.

[6] Beam Dynamics Newsletter **57**, §3.13.5.2.

[7] R. Warnock and J. Ellison, Proc. 2nd ICFA Workshop on High Brightness Beams, 1999 (World Scientific, 2001), SLAC-PUB-8404.

Copyright © 2013 CC-BY-3.0 and by the respective authors

REVISED VIEW OF BASIC FEL EQUATIONS AND A NONLINEAR VLASOV DESCRIPTION*

R. Warnock †, SLAC National Accelerator Laboratory, Menlo Park, CA, USA

Abstract

The standard one-dimensional FEL equations are revised to incorporate a new approach to the wiggle average, in a context of continuous frequency. It has a firmer mathematical foundation, and leads to an interesting reformulation in the time domain. The equations are interpreted as a nonlinear Vlasov system for a continuous distribution function of ponderomotive angle and energy spread. Numerical solutions are illustrated.

VLASOV THEORY OF THE FEL

A linearized version of the Vlasov or Vlasov-Klimontovich equation is accepted as the natural mathematical framework for an analytic discussion of the basic mechanism of the FEL, at distances up to and including the exponential growth region. At greater distances along the undulator a nonlinear saturation comes into play, and to understand that regime one usually resorts to a simulation based on a limited number of representative particles. I explore an alternative approach, based on the full nonlinear Vlasov equation. The general advantage of nonlinear Vlasov over particle simulations is in reduction of modeling noise, but there may also be opportunities for analytic studies of the nonlinear equation. This approach requires a representation of the phase space distribution as a smooth function. To account for granularity from the finite particle number in the startup of the SASE process, I take the initial distribution to be noisy but smooth in the mathematical sense, namely a truncated formal Fourier series of a random discrete particle distribution.

REVISED TREATMENT OF BASIC FEL EQUATIONS

I first review a different treatment of basic FEL equations in one degree of freedom. I work with equations for general continuous frequency ν, and perform the wiggle average at general ν, not just at integers. Moreover, the averaging is now in a form that is justified by the mathematical theory of averaging of differential equations. The new equations suggest a more radical step, namely to reverse integration orders so as to pass from the frequency domain to the time domain (more exactly the domain of the ponderomotive angle). The kernel in the new scheme, analogous to a wake potential, has compact support and intriguing properties.

I consider planar electron motion in a planar undulator, with z and x being longitudinal and transverse position coordinates. A general representation of the transverse electric field is [1]

$$E_x(z,t) = \int_{-\infty}^{\infty} \hat{E}_x(\nu,z) e^{i\nu k_1(z-ct)} d\nu \ , \qquad (1)$$

assuming only that the field is smooth and decaying at infinity as a function of $\alpha = k_1(z-ct)$. Here $k_1 = 2\pi/\lambda_1$ is the wave number of the fundamental optical mode. A similar representation holds for the current density $J_x(z,t)$, in the sense of Fourier transforms of generalized functions if the source consists of point particles. A calculation invoking the wave equation and the slow variation approximation (dropping the second derivative), followed by the inverse FT with respect to α, yields the result

$$\frac{\partial \hat{E}_x(\nu,z)}{\partial z} = -\frac{Z_0}{2} \hat{J}_x(\nu,z) \ , \qquad (2)$$

with SI units, Z_0 being the impedance of free space.

To derive $\hat{J}_x$ assume a volume density of electrons

$$n_e(z,t) = -\frac{e}{\Sigma_\perp} \sum_{j=1}^{N} \delta(z - z_j(t)) \ , \qquad (3)$$

where $\Sigma_\perp$ is an average transverse area of the beam. Then by applying the formula for velocity v_x in the undulator one finds

$$J_x(z,t) \approx \frac{1}{\gamma_0} K \cos\zeta \ n_e(z,t) \ , \ \zeta = k_u z \ , \ \gamma = \gamma_0(1+\eta) \ , \qquad (4)$$

where $k_u = 2\pi/\lambda_u$ is the undulator wave number and the approximation is $|\eta| \ll 1$, used without comment henceforth. Now take the FT of J_x with respect to α, and for each j change the integration variable from α to u where $t = t_j(u)$, $z_j(t_j(u)) = u$. Next introduce the ponderomotive angle θ as a convenient phase space coordinate, namely

$$\theta = \alpha + \chi(\zeta) \ , \quad \chi(\zeta) = \zeta + \xi \sin 2\zeta \ , \quad \xi = \frac{1}{2 + 4/K^2} \ , \qquad (5)$$

and define

$$\theta_j(z) = \alpha_j(z) + \chi(\zeta) = k_1(z - ct_j(z)) + \chi(\zeta) \ . \qquad (6)$$

Then the FT of the current becomes

$$\hat{J}_x(\nu,z) = -\frac{ecNK}{\gamma_0 \Sigma_\perp \lambda_1} w(\zeta,\nu) < e^{-i\nu\theta(z)} > \ , \qquad (7)$$

$$w(\zeta,\nu) = \cos\zeta \ e^{i\nu\chi(\zeta)} \ , \qquad (8)$$

$$< e^{-i\nu\theta(z)} > = \frac{1}{N} \sum_{j=1}^{N} e^{-i\nu\theta_j(z)} \ . \qquad (9)$$

* Partially supported by U.S. Dept. of Energy contract DE-AC03-76SF00515

† warnock@slac.stanford.edu

Copyright © 2013 CC-BY-3.0 and by the respective authors

Now to make contact with Vlasov theory imagine a smooth phase space distribution function $f(\theta,\eta,z)$. It and its projection are normalized to 1:

$$\int d\theta \int f(\theta,\eta,z)d\eta = 1\ , \quad \rho(\theta,z) = \int f(\theta,\eta,z)d\eta\ . \tag{10}$$

The mean value of $\exp(-i\nu\theta(z))$ over the discrete distribution will be identified with the mean value at z over the continuous distribution, which is the Fourier transform of the bunch form:

$$\frac{1}{2\pi} < e^{-i\nu\theta(z)} >= \frac{1}{2\pi}\int e^{-i\nu\theta}\rho(\theta,z)d\theta = \hat{\rho}(\nu,z)\ . \tag{11}$$

Returning to Eq.(2) and using (7) and (11) the field is calculated merely by integrating with respect to z. Then the equations of motion for η and θ can be derived in a standard way, so that they take the form

$$\frac{d\eta}{dz} = -\kappa\int w^*(\zeta,\nu)e^{i\nu\theta}d\nu\int_0^z w(\zeta',\nu)\hat{\rho}(\nu,z')dz'\ , \tag{12}$$

$$\frac{d\theta}{dz} = 2k_u\eta\ , \tag{13}$$

where

$$\kappa = \frac{k_1 Z_0 (eK)^2 N}{2mc\gamma_0^3\Sigma_\perp}\ . \tag{14}$$

Eq.(12) is stated for the case of zero initial field in the integration of (2). Now the differential equations (12) and (13) are to be integrated, using the Vlasov equation to update the distribution function, hence updating $\hat{\rho}(\nu,z')$ through (10) and an FT , at each integration step dz. The Vlasov equation is

$$\frac{\partial f}{\partial z} + \frac{d\theta}{dz}\frac{\partial f}{\partial\theta} + \frac{d\eta}{dz}\frac{\partial f}{\partial\eta} = 0\ . \tag{15}$$

The update is done by the method of local characteristics, "local" referring to the procedure of holding the electric force constant over an integration step in z. Thus

$$f(\theta,\eta,z+dz) = f(\theta - d\theta_{E(z)}, \eta - d\eta_{E(z)}, z)\ , \tag{16}$$

the subscripts indicating an evaluation of coordinate increments with the field having its values at z.

It is usual to make use of the average of the "wiggle factor" w over one undulator period at integer ν, which is given by a Bessel function expression $[JJ]_q/2$ at odd $\nu = 2q+1$, and is zero at even ν [2] The average is used to replace w in ν-neighborhoods of integers which are, unfortunately, not well defined. One can avoid the ambiguity and proceed more naturally as follows, for arbitrary continuous ν. Change the independent variable from z to $\zeta = k_u z$ and integrate in steps $\Delta\zeta = 2\pi p$, that is in steps of p undulator periods with p an integer (in practice a small integer, say 1 to 5, proves to be satisfactory). During a step, $\hat{\rho}(\nu,\zeta')$ is regarded as constant, so comes out of the integral in (12).

Note that local integrals of w are a phase factor times a function $g_p(\nu)$:

$$\int_{\zeta_n}^{\zeta_{n+1}} w(\zeta,\nu)d\zeta = e^{in\nu\Delta\zeta}\ \Delta\zeta\ g_p(\nu)\ ,$$

$$g_p(\nu) = \int_0^{2\pi p}\cos u\ \exp\left[i\nu(u - 2\xi\sin 2u)\right]du\ . \tag{17}$$

Then putting $\zeta_n = n\Delta\zeta$, the differential equation for $\zeta\in[\zeta_n,\zeta_{n+1}]$ has the form

$$\frac{d\eta}{d\zeta} = -\frac{\kappa}{k_u^2}\int w^*(\zeta,\nu)e^{i\nu\theta}d\nu\Big[\hat{\rho}(\nu,\zeta_n)\int_{\zeta_n}^{\zeta} w(\zeta',\nu)d\zeta' + \Delta\zeta\ g_p(\nu)\sum_{m=0}^{n-1}\hat{\rho}(\nu,\zeta_m)e^{im\nu\Delta\zeta}\Big] \tag{18}$$

So far the integrals of w have arisen naturally, without invoking the concept of averaging. Finally, averaging is introduced by replacing the r.h.s. of the differential equation (18) by its average over the interval $[\zeta_n,\zeta_{n+1}]$. This local averaging of the vector field of an ODE gives an approximation with rigorous error bounds attributed to Eckhaus [3]. With the definition

$$h_p(\nu) = \frac{1}{(\Delta\zeta)^2}\int_0^{\Delta\zeta} w^*(v,\nu)\Big[\int_0^v w(u,\nu)du\Big]dv\ , \tag{19}$$

the averaged equation on the interval $[\zeta_n,\zeta_{n+1}]$ is

$$\frac{d\eta}{d\zeta} = -\frac{\Delta\zeta\ \kappa}{k_u^2}\int e^{i\nu\theta}d\nu\Big[h_p(\nu)\hat{\rho}(\nu,\zeta_n) + e^{-in\nu\Delta\zeta}|g_p(\nu)|^2\sum_{m=0}^{n-1}\hat{\rho}(\nu,\zeta_m)e^{im\nu\Delta\zeta}\Big] \tag{20}$$

I take (13) and (20) as the basis for the numerical work of the following. The functions $|g_p(\nu)|^2$ and $h_p(\nu)$ (divided by their values at $\nu = 1$) are plotted in Fig.1 for $p = 3$. The peaks get narrower with increasing p.

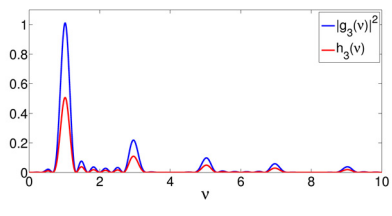


Figure 1: Functions appearing in Eq.20 (normalized)

A REFORMULATION IN THE θ DOMAIN

Introducing the definition (11) of $\hat{\rho}$ and reversing the order of integrations one can recast (20) in θ-space as

$$\frac{d\eta}{d\zeta} = -\frac{\kappa}{k_u^2}\int d\theta'\Big[T_p(\theta-\theta')\rho(\theta',\zeta_n) + \sum_{m=0}^{n-1}S_p(\theta-\theta'-\zeta_n+\zeta_m)\rho(\theta',\zeta_m)\Big]\ . \tag{21}$$

Copyright © 2013 CC-BY-3.0 and by the respective authors

The kernels S_p and T_p are

$$S_p(\theta) = p\int d\nu |g_p(\nu)|^2 e^{i\nu\theta}\ ,\ T_p(\theta) = p\int d\nu h_p(\nu) e^{i\nu\theta}\ . \tag{22}$$

These functions have compact support (vanish outside a finite interval) as can be seen from the Paley-Wiener theorem [4]. Also $T_p(\theta) = S_p(\theta)$ for $\theta > 0$ and is zero for $\theta < 0$. The graph of S_3 is shown in Fig.2.

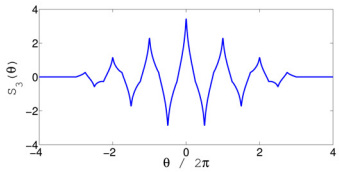


Figure 2: The kernel $S_p(\theta)$ for $p = 3$.

NUMERICAL VLASOV SOLUTIONS

To reduce the FEL equations to the simplest form, one assumes that the field and source are periodic in θ with period 2π, giving the so-called steady state case with identical motion in all buckets. More generally one can take a period $2\pi n_b$ of n_b buckets, and this can imitate the non-periodic case for large n_b. The following results are from a periodic code with arbitrary n_b, which represents f by its values on a grid, and implements the update (16) by bicubic interpolation to off-grid points. Parameters are for the LCLS: undulator parameter $K = 3.7$, Pierce parameter $\rho = 6 \cdot 10^{-4}$ (as defined in [1]). In terms of the normalized length $\bar{z} = 2\zeta\rho$ the gain length as given by linear theory is $1/\sqrt{3}$ ([1], §4.5.1).

I first take a single bucket, using a 400×400 grid in (θ, η)-space and $p = 1$ (integration step of one undulator period). The initial distribution is Gaussian in η with $\sigma = \rho$, times the truncated Fourier series of a random uniform distribution in θ of 50000 particles. There is no initial seed of the field. The calculation takes one minute on a single processor (2.3 GHz). Integration for 30 gain lengths gives the gain curve shown in Fig.3 (left). Fig.3 (right) shows the slope of the log of the power (blue) and the value $\sqrt{3}$ that this has in the linear theory (red). The linear prediction is good from about 5 to 12 gain lengths.

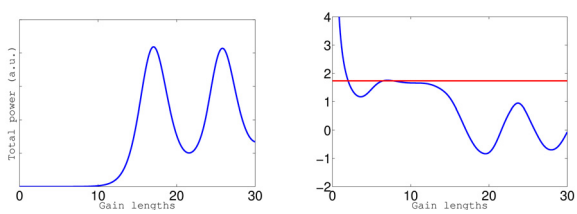


Figure 3: Left: power vs. number of gain lengths; Right: slope of log of power (blue) and its value in linear theory (red).

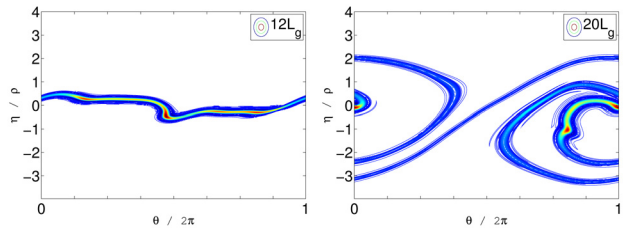


Figure 4: Phase space at 12 and 20 gain lengths.

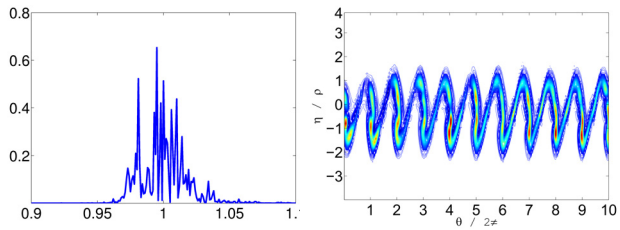


Figure 5: Field spectrum and phase space density, SASE model.

Fig.4 shows contour plots of phase space densities near the end of the exponential region and well into the saturation region.

To model the SASE mechanism one needs in principle a non-periodic θ dependence. To realize this numerically I take instead a long period of $n_b = 1000$ buckets, and also increase the Peirce parameter to $\rho = 0.01$, to decrease the computation time while still demonstrating the qualitative picture of SASE. I integrate to 8 gain lengths, at which point the coherence length $c\sigma_\tau$ is $4.8\lambda_1$ (by Eq.(4.155) in [1]), much less than the bunch length of $1000\lambda_1$; this should mean that the non-periodic case is well imitated. The frequency distribution in the field, $|\hat{E}_x(\nu)|^2$, appears near $\nu = 1$ as in Fig.5 (left). The expected number of spikes in a very crude estimate ([1], p.90) is $M \approx n_b\lambda_1/4c\sigma_\tau = 52$, not grossly different from what is seen. The phase space density in 10 adjacent buckets is shown in Fig.5 (right).

ACKNOWLEDGMENT

Conversations with G. Stupakov, Z. Huang, W. Fawley, R. Ruth, and J. Ellison were very helpful. The work was started at Gennady Stupakov's suggestion.

REFERENCES

[1] My introduction follows in part notes by K.-J. Kim, Z. Huang, and R. Lindberg, "Introduction to Free Electron Lasers", June, 2010.

[2] Z. Huang and K.-J. Kim, Phys. Rev. E **62**, 7295 (2000).

[3] J. A. Sanders, F. Verhulst, and J. Murdock, "Averaging Methods in Nonlinear Dynamical Systems", (Springer, 2007).

[4] R. E. A. C. Paley and N. Wiener, "Fourier Transforms in the Complex Domain", (AMS, 1934), p.12.

Copyright © 2013 CC-BY-3.0 and by the respective authors

MODELING LOCALIZED STATES AND BAND BENDING EFFECTS ON ELECTRON EMISSION ION FROM GaAs*

D. A. Dimitrov, C. Nieter, Y. Choi, Tech-X Corp., Boulder, CO 80303, USA
I. Ben-Zvi, J. Smedley, T. Rao, BNL, Upton, NY 11973, USA
I. Bazarov, S. Karkare, W. Schaff, CLASSE, Cornell University, Ithaca, NY 14853, USA

Abstract

High acceptor doping of GaAs and (Cs, O) surface coating leads to downward band bending terminating with effective negative electron affinity surface. The periodicity breaking at the surface together with the formed potential leads to one or more localized states in the band bending region together with effective Fermi level pinning. We report results on how to calculate the band bending potential, the Fermi level pinning, and localized states as functions of GaAs p-doping density, surface density of states, and temperature. We also consider how these surface properties affect electron emission.

INTRODUCTION

High-average current and high-brightness electron beams are needed in advanced applications such as ultra-high Free-Electron Lasers, electron cooling of hadron accelerators, and Energy-Recovery Linac light sources. Semiconductor cathodes, such as negative electron affinity GaAs-based cathodes, are known [1] to have good quantum efficiency (QE) (10% achieved experimentally), low thermal emittance with prompt response time [2], and are candidates to achieve high average current up to 100 mA.

However, how to design, fabricate, and reliably operate semiconductor cathodes at high average current (reaching 100 mA) still represents a major problem. Some of the most important effects to understand are related to surface space charge region, controlling the electron affinity and band bending as a function of surface properties and charge propagation to the surface [3, 4].

In addition to experiments, simulations provide a complementary way to efficiently explore relevant parameter sets. Moreover, they allow us to obtain data on properties that are currently not accessible through experiments or very difficult to measure. For example, the energy distribution of electrons inside the cathode material in the region of the emission surface is directly accessible in the simulations but very difficult to measure in experiments. Producing high fidelity simulations data of semiconductor cathode properties depends on accurate modeling of the surface space-charge region. Specifically, the calculation of the band bending region (BBR) energy profile, determination of Fermi level pinning (e.g. for GaAs cathodes), development of localized electron levels with emission from them, and how the electron affinity depends on these properties significantly affect electron emission.

Emission from localized states has been shown to contribute to the observed energy distribution of electrons from GaAs and one approach was proposed to explain it [3] that depends on specific properties of the potential across the GaAs-vacuum interface. Similar effects were considered for emission from diamond but the model developed was based on a different surface potential [5].

We have already done simulations with a surface band bending profile that uses a quadratic approximation [6]. Here, we provide a general approach for calculation of the band bending profile and the Fermi level pinning for GaAs.

BAND BENDING AND LOCALIZED STATES

The surface band bending arises as a consequence of the space charge region that develops as a result of the symmetry breaking and appearance of surface states. The electrostatic potential in the band bending region (BBR) is determined from the solution of the Poisson equation:

$$\nabla \cdot (\varepsilon \nabla \phi) = q \left(n\left[\phi\right] - p\left[\phi\right] + N_A^-\left[\phi\right] - N_D^+\left[\phi\right] \right), \quad (1)$$

where $\varepsilon(\mathbf{r})$ is the dielectric constant, q is the fundamental charge, n and p are the electron and hole densities in the conduction and valence band, respectively, N_A^- and N_D^+ are the densities of ionized acceptor and donor impurities when present. Generally, all charge densities are non-linear functions of the potential. When periodicity is preserved in the emission surface, the resulting non-linear Poisson equation is effectively one-dimensional. For p-doped GaAs, when the donor density can be neglected and the acceptors are fully ionized, it has the form:

$$\frac{d^2U(x)}{dx^2} = \frac{q^2}{\varepsilon k_B T}\left(N_A - \frac{2N_V}{\sqrt{\pi}} F_{1/2}\left(\eta_V - U(x)\right)\right), \quad (2)$$

where $\eta_V = (E_V - E_F)/k_BT$ (with E_V the valence band maximum in bulk and E_F the Fermi level, k_B the Boltzmann constant and T the lattice temperature), $U(x) = q\phi(x)/k_BT$, $N_V = 2\left(\frac{m_{dh}k_BT}{2\pi\hbar^2}\right)^{3/2}$ with m_{dh} a hole-related effective mass, and $F_{1/2}(x) = \int_0^\infty \frac{\sqrt{u}}{1+e^{u-x}}du$. The boundary conditions imposed on the 1D non-linear Poisson equation are determined from the requirement of zero

* The authors wish to acknowledge the support of the U.S. Department of Energy (DOE) and the National Science Foundation (NSF) under grants DOE DE-SC0006246, NSF DMR-0807731, and DOE DE-SC0003965.

Copyright © 2013 CC-BY-3.0 and by the respective authors

applied field in bulk:

$$\frac{dU}{dx}\left(x \to \infty\right) = 0,$$

and a given value at the semiconductor surface

$$U\left(x = 0\right) \equiv U_S \equiv q\phi_S / k_B T.$$

This 1D non-linear Poisson equation can be solved by a finite difference discretization and then using a Newton-Ralphson algorithm to find the roots of the resulting matrix equation.

In the case of non-degenerate semiconductors, $E_V + 3k_BT \leq E_F \leq E_C - 3k_BT$ where E_C is the minimum of the conduction band in bulk, the solution for the band bending potential can be expressed in the integral form:

$$\mathrm{sgn}\left(U_S\right) \int_{U(x)}^{U_S} \frac{du}{F\left(u,\, U_F\right)} = \frac{x}{L_D}, \qquad (3)$$

where

$$F\left(x, y\right) = \sqrt{e^y\left(e^{-x} + x - 1\right) + e^{-y}\left(e^x - x - 1\right)},$$

$U_F = \left(E_i - E_F\right)/k_BT$ with E_i the Fermi level for the intrinsic semiconductor (no ionized impurities), and $L_D = \sqrt{\frac{\varepsilon k_B T}{2q^2 n_i}}$ with n_i the conduction band electron density in the intrinsic case.

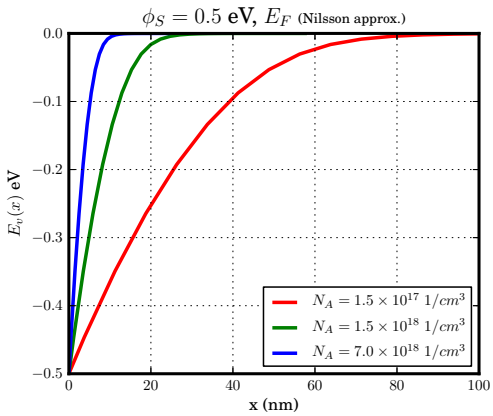


Figure 1: Calculated band bending energies as a function of acceptor doping for three different values. The band bending for $N_A = 7 \times 10^{18}$ cm^{-3} and $\phi_S = 0.5$ eV is in agreement with previously published data [3].

The value of the potential ϕ_S at the surface is determined from the requirement to satisfy charge neutrality. Since U_F is calculated from bulk properties as a function of temperature and bulk doping density, we can determine the band bending potential $U(x)$ by numerically solving Eq. (3). We have implemented a bisection algorithm to evaluate the integral in Eq. (3) and find its root for a given value of x. The value of $U(x)$ for the lower limit of the integral from the calculated root value represents the band bending potential at distance x from the GaAs surface. Results from the code are shown in Fig. 1 for three different acceptor doping densities and a pinned surface potential energy $q\phi_S = 0.5$ eV. The results demonstrate the importance to consider the nonlinear corrections since the band-bending profiles deviate from the initially assumed quadratic form. Moreover, we can now directly obtain the depth of the band bending potential in GaAs when varying the bulk acceptor density. Finally, the obtained band bending profile for $N_A = 7 \times 10^{18}\ cm^{-3}$ is in good agreement with previously published data [3].

For the results presented in Fig. 1, the Fermi level position was calculated from bulk properties using Nilsson's approximation (see [6] and references therein).

The value of the potential ϕ_S at the surface is determined from the requirement to satisfy charge neutrality. Moreover, at specific surface conditions for GaAs, the surface potential ϕ_S and the Fermi level are pinned. For

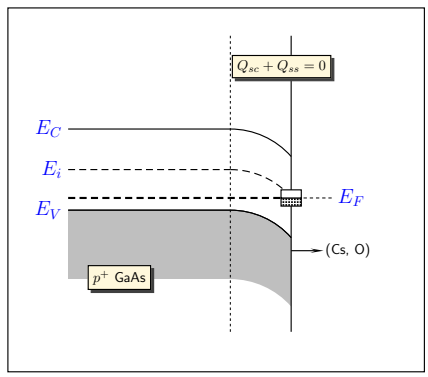


Figure 2: The Fermi pinning regime is reached when the band bending leads to overlap of the energy of the surface states (shown in the diagram with the partially filled rectangle) with the chemical potential E_F.

p-doped GaAs and downward band bending $\phi_S > 0$ at the surface and $\phi\left(x \to \infty\right) \to +0$ in bulk, the space-charge region is negatively charged since near the surface: $p\left(x\right) - N_A = p\left(x\right) - p_{bulk} < 0$. For this case, charge neutrality at the surface can be satisfied if there are surface donor states that are positively charged. The surface band bending ϕ_S is determined from the charge neutrality condition $Q_{ss}\left(\phi_S\right) + Q_{sc}\left(\phi_S\right) = 0$ where $Q_{ss}\left(\phi_S\right)$ is the total change density on surface states and $Q_{sc}\left(\phi_S\right)$ is the space-charge surface density $\left|Q_{sc}\left(\phi_S\right)\right| = \left|\varepsilon \frac{d\phi(x=0)}{dx}\right|$. For a given type of a surface donor state with density N_{sd}, Q_{ss} is determined from:

$$Q_{ss}\left(\phi_S\right) = qN_{sd}\left(1 - 1/\left(\exp\left(\beta\left(E_{sd} - E_F\right)\right) + 1\right)\right),$$

where E_{sd} is the energy of electrons on the surface state, determined by atomic properties and is at a given position (0.55 eV for GaAs) relative to the valence band maximum at the surface effectively making $E_{sd} - E_F$ a function of ϕ_S. The band bending potential determined from the charge neutrality condition is reached when $E_F \approx E_{sd}$

Copyright © 2013 CC-BY-3.0 and by the respective authors

as shown in Fig. 2. The plots in Fig. 3 indicate the onset of the Fermi level pinning for different N_A values and approaches to calculate E_F (the bottom right plot uses an exact numerical calculation for the Fermi level rather than the Nilsson approximation). From the plots at low bulk doping in Fig. 3, the Fermi level and ϕ_S are pinned for for $N_{sd} \geq 10^{12}$ cm^{-2} while for high doping, the pinning regime is reached for $N_{sd} \geq 10^{13}$ cm^{-2}. The Fermi level

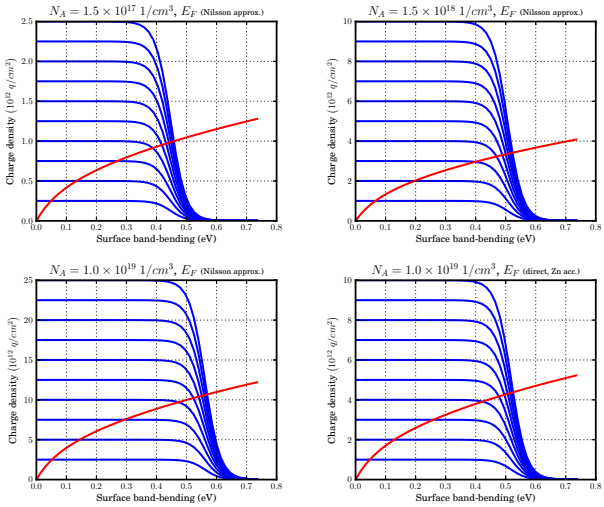


Figure 3: The intersection of each Q_{ss} curve (for a given surface state density N_{sd}) with the Q_{sc} curve for given doping concentration N_A determines the value of the surface band bending ϕ_S.

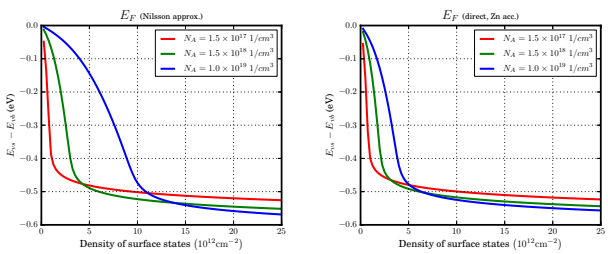


Figure 4: When the band bending leads to $E_F \approx E_{sd}$, the Fermi level at the surface changes only by $2.3k_BT$ per decade of surface state density. This is the regime of effective Fermi level pinning due to the small change of E_F with further increase of the surface density of states.

pinning regime is clearly revealed when we calculate ϕ_S as a function of the surface density of states for different bulk acceptor concentrations. Results from these calculations are shown in Fig. 4. In the pinning regime, the surface band bending ϕ_S changes little when further increasing the surface density of states N_{sd}. Note that the values for which the Fermi pinning regime starts, $N_{sd} \sim 10^{12}$ to 10^{13} cm^{-2} is still orders of magnitude smaller that the value 10^{15} cm^{-2} for the density of a complete monolayer of adatoms.

Finally, we briefly mention the importance of including emission from localized states that develop in the BBR. This effect was demonstrated in electron emission energy distribution data for GaAs [3]. The localized energy levels can be calculated by self-consistently solving the Schrödinger-Poisson equations in the BBR. We have prototyped an implementation to solve the Schrödinger-Poisson equations self-consistently and are currently investigating results from it with different emission surface potentials. Note, however, that depending on the boundary conditions imposed when solving the Schrödinger-Poisson equations, emission from quasi-stationary levels and electron lifetime on them has to be included in the calculations [3].

SUMMARY

We reported here results for calculation of the band bending region and pinning of the Fermi level in p-doped GaAs as a function of the acceptor doping concentration and the density of surface states. The results allow for accurate evaluation of the band bending in the surface space-charge region. The calculated band bending profiles can be used as input in codes to simulate charge transport and electron emission from semiconductor cathodes. Emission from localized states represents another important effect that is still to be properly integrated in photocathode simulations.

ACKNOWLEDGMENT

We are grateful to Dr. D. A. Orlov and Prof. A. S. Terekhov for providing additional information regarding their work [3].

REFERENCES

[1] D. H. Dowell, I. Bazarov, D. Dunham, K. Harkay, C. Hernandez-Garcia, R. Legg, H. Padmore, T. Rao, J. Smedley, and W. Wan. Cathode R&D for future light sources. *Nucl. Instr. Meth. Phys. Res. A*, 622:685–97, 2010.

[2] I. V. Bazarov *et al.* Thermal emittance and response time measurements of negative electron affinity photocathodes. *J. Appl. Phys.*, 103:054901–1/8, 2008.

[3] D. A. Orlov, V. E. Andreev, and A. S. Terekhov. Elastic and Inelastic Tunneling of Photoelectrons from the Dimensional Quantization Band at p^+-GaAs-(Cs, O) Interface into Vacuum. *JETP Lett.*, 71:151–4, 2000.

[4] E. Wang, I. Ben-Zvi, T. Rao, D. A. Dimitrov, X. Chang, Q. Wu, and T. Xin. Secondary-electron emission from hydrogen-terminated diamond: Experiments and model. *Phys. Rev. ST Accel. Beams*, 14:111301–7, 2011.

[5] L. Gan, E. Baskin, C. Saguy, and R. Kalish. Quantization of 2D Hole Gas in Conductive Hydrogenated Diamond Surfaces Observed by Electron Field Emission. *Phys. Rev. Lett.*, 96:196808–1/4, 2006.

[6] Siddharth Karkare, Dimitre Dimitrov, William Schaff, Luca Cultrera, Adam Bartnik, Xianghong Liu, Eric Sawyer, Teresa Esposito, and Ivan Bazarov. Monte carlo charge transport and photoemission from negative electron affinity gaas photocathodes. *Journal of Applied Physics*, 113(10):104904, 2013.

Copyright © 2013 CC-BY-3.0 and by the respective authors

INTEGRATED KINETIC AND PLASMA DIELECTRIC MODELS OF ELECTRON CLOUD BUILDUP AND TE WAVE TRANSMISSION *

S. A. Veitzer†, Tech-X Corporation, Boulder, CO, 80303 USA
P. H. Stoltz, Tech-X Corporation, Boulder, CO, 80303 USA
P. G. Lebrun, Fermilab, Batavia, IL, 60510 USA

Abstract

Buildup of electron plasmas in accelerator cavities poses a serious threat to performance for current and future accelerators. Traveling-wave rf diagnostics are an effective, non-destructive way to measure electron clouds, although determining the true cloud density from spectra is difficult due to the effects of reflections, non-uniform cloud density, and magnetic field effects. We model traveling-wave rf diagnostics of electron clouds by simulating spectra using both harmonically modulated plasma dielectric models, and dielectric models based on simulated electron cloud densities. We compare here the differences in computed side band spectra due to different magnetic field configurations for Main Injector parameters, and report on computational challenges inherent to numerical modeling of systems with large variances of spatial and temporal scales.

RF DIAGNOSTICS PROVIDE DIAGNOSTIC MEASUREMENT OF ELECTRON CLOUDS

Electron clouds have been identified as a potential performance-limiting element in both hadron and lepton accelerators [1]. Recently, methods for measuring electron cloud densities in a non-destructive manner have been developed. These methods rely on measurement of rf signals injected into the beam pipe, either at a frequency just below the cutoff frequency (resonant rf method) or above the cutoff frequency (traveling wave method). For traveling wave rf diagnostics, the presence of an electron cloud plasma in the beam pipe induces a phase shift due to changes in the dielectric properties of the medium in which the rf is traveling. The plasma dielectric strength is modulated at the revolution frequency as the plasma builds up during bunch passages, and dissipates during gaps in the bunch train. This is typically observed in experiments as side bands at the revolution frequency, with a height that is proportional (in the linear approximation) to the average plasma density. Magnetic field effects also come into play with these diagnostics in two ways. First, magnetic fields may excite a cyclotron resonance [2, 3] that increases the phase delay per unit length, and second, magnetic fields will affect the electron trajectories that will in turn change the spatial distribution of electrons in the beam pipe and hence the dielectric properties of the plasma. It has been observed in both experiments and in simulations that dipole fields tend to align electrons in vertical stripes [4, 5]. Recent studies indicate that quadrupole fields may be able to trap electron clouds thereby leading to negative effects on the lead bunch in a train [6].

* This work was performed under the auspices of the Department of Energy as part of the ComPASS SCiDAC-2 project (DE-FC02-07ER41499), and the SCiDAC-3 project (DE-SC0008920).

† veitzer@txcorp.com

SIMULATION RESULTS

We are developing numerical models that are appropriate for simulating electron clouds and rf diagnostics in the Main Injector at Fermilab, using the plasma simulation framework VSim [7]. In all of the simulations reported here, we use a circular cross section beam pipe with radius 7.46125 cm, and 50 cm long. We use a mesh with 48 computational cells in the longitudinal direction, and 16 cells in each of the transverse directions. We simplify the bunch train structure from that in the actual Main Injector by modeling one full revolution as a single continuous bunch train of 18.8 ns bunches of roughly 8 GeV protons. We artificially set one revolution time to $2.0\mu s$, including an abort gap of 0.4μ s during which time there are no beam bunches. This sets the modulation frequency to 500 kHz. The cutoff frequency for this beam pipe is 1.1774 GHz, and we drive rf above this frequency to model traveling wave diagnostics.

Kinetic PIC Simulations

We first perform detailed electrostatic Particle-In-Cell (PIC) simulations of electron cloud buildup using VSim. We start with a low-density, uniformly distributed, cold electron plasma in a circular beam pipe with radius 7.46 cm. We solve for the electric fields electrostatically given the overall charge distribution and subject to the appropriate boundary conditions; metallic boundaries on the beam pipe walls, and port boundaries on the open ends of the simulation domain. Port boundaries are a numerical filter model that effectively absorbs wave energy at a given phase velocity, preventing reflections from the boundary. We do not inject rf power in the kinetic simulations because we are focused on modeling cloud buildup here.

In buildup simulations we inject beam bunches with a spacing of 18.8 ns by specifying a time-dependent charge density that simulates the passage of proton beam bunches. Bunches cross the simulation domain for 1.2μs, followed by a 0.8μs abort gap, representing a single revolution. These times are chosen to demonstrate the physics of electron cloud buildup while maintaining numerical efficiency. In future simulations the actual Main Injector revolution period will be approached. Electrons that make up the plasma (cloud) are modeled as variable-weight kinetic par-

Copyright © 2013 CC-BY-3.0 and by the respective authors

ticles, and are pushed by electrostatic forces from other charges (space charge effects) and current sources (beam potential). Electrons are attracted to the potential of the beam as it passes and are accelerated across the beam pipe into the opposing wall. Electrons that are absorbed by the beam pipe walls emit low-energy secondary electrons according to the Furman-Pivi model [8]. These electrons are accelerated by subsequent bunches giving rise to a buildup of electrons, that saturates at a density that is about 0.7 times the linear beam density [9], where the cloud shields electrons from the beam potential.

In our buildup simulations we set the time step to be 18.86 ps in order to match the plasma dielectric simulations whose time steps are limited for numerical stability reasons (CFL condition), although we could relax this by a factor of at least 20 and just resolve the Debye length because these simulations are electrostatic. We save the 6D phase space for each particle at each time step. We then compute the charge density for the electron cloud from the particle positions and can subsequently use that density in plasma dielectric simulations over many revolution periods (see below).

Figure 1 shows the total energy of the cloud electrons as they build up. On average the energy follows the total number of electrons in the buildup and dissipation of the cloud. The inset shows fine-scale structure indicating bunch crossings. Spikes in the electron energy are due to a single bunch crossing, where the electrons are accelerated by the positively-charged bunch. Nearly all of this energy is lost when the (fast) electrons are absorbed by the walls. There is a short period of drift, capped off with a period where some (slow) electrons are absorbed by the walls that creates a reduction in the total energy that corresponds to a reduction in the total number of electrons.

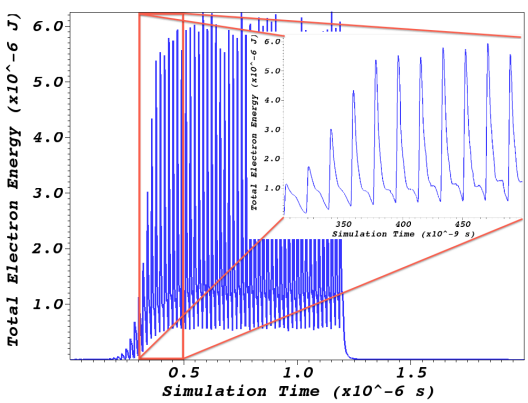


Figure 1: Total energy of the electron cloud as a function of simulation time. Bunch crossings punctuate the electron energy, which then relaxes as electrons are absorbed by the beam pipe walls.

Modulated Plasma Dielectric Simulations

We modulate the dielectric strength at a frequency of 500 kHz to match the kinetic buildup simulations, and simulate approximately 160 revolution periods with a time step of 18.86 ps, or approximately 16.78 million time steps. This corresponds to at least 550,000 rf periods, which is sufficient to resolve plasma-induced side bands. We use port boundaries to launch an rf wave into the simulation from the left boundary. This rf wave is then measured at the right end of the simulation after it has passed through the plasma dielectric.

In these simulations we model rf propagation through a plasma dielectric that is spatially uniform across the whole simulation domain, with an equivalent plasma density of 9.1×10^{12} electrons/m^3, corresponding to 8.0×10^{10} electrons at saturation during buildup in our kinetic PIC simulations. The dielectric tensor is modulated purely harmonically at 500 kHz, simulating the effects of dissipation of the cloud during gaps in the bunch train. Simulations such as these are much smoother than simulations where the plasma density at each time step is determined by particle positions from kinetic PIC simulations. They also serve to demonstrate the modeling capability of accurately generating synthetic spectra with side band structures, that can be directly compared to experimental results, and require numerical stability and accuracy over extremely long simulation times.

Figure 2 shows a portion of the synthetic spectrum for uniform, modulated plasma dielectric simulations. The left-hand plot shows the spectrum for a simulation run with rf at 50% above the cutoff frequency with no externally applied magnetic fields, and the right-hand plot is for a simulation driven at 5% above cutoff with a 0.06 T transverse dipole applied field, which is close to the cyclotron resonance. The spectrum is very smooth because the simulations plasma dielectric is spatially uniform, and the simulations are run for a long time which gives better frequency resolution. The first side band is readily seen at the modulation frequency and the height of the side band is dependent on the plasma dielectric constant, as expected.

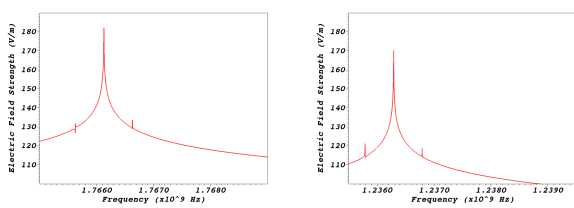


Figure 2: Synthetic spectra generated by harmonic modulation of plasma dielectric tensor. Left plot shows the spectrum with zero applied magnetic field, driven at 50% above the cutoff frequency. Right plot shows the spectrum with excitation of the extraordinary wave, near the cyclotron resonance with an applied dipole field of 0.06 T, and hence the upper hybrid resonance, driven at 5% above the cutoff frequency.

Copyright © 2013 CC-BY-3.0 and by the respective authors

The effect of externally applied magnetic fields on plasma-induced phase shifts in rf diagnostics has been documented [4, 5, 10]. Here we have performed simulations with different magnetic field orientations using the modulated plasma dielectric model. In Figure 2, the left-hand plot shows the spectrum for the case where there is zero magnetic field, as in a drift section. The right-hand plot shows the spectrum in the case where there is an applied dipole magnetic field with strength 0.06 T oriented in the transverse direction normal to the rf polarization. This orientation excites the upper hybrid resonance which modifies the side band strength. All other simulation parameters are the same between these simulations. Simulations in which an applied magnetic field is aligned parallel to the rf polarization do not show any enhancement in the side band strength.

Integrated Plasma Dielectric Simulations

For these simulations we implement a plasma dielectric model based on electron cloud densities derived from the kinetic simulations described above. For integrated plasma dielectric simulations we first convert particle positions from the buildup simulations into a 3-Dimensional density map that we use as input to our plasma dielectric model. We then perform plasma dielectric simulations for nearly 200 revolutions, changing the value of the dielectric tensor in each computational cell periodically according to the electron density in that cell. We repeat the electron densities determined in the corresponding kinetic buildup simulations every $2.0\mu s$, and sub-sample the electron positions, changing the corresponding plasma dielectric strength every 50 time steps for computational efficiency. We drive the rf at 2.2 times cutoff in these simulations.

Figure 3 shows a spectrum generated by converting electron cloud densities from the kinetic simulations into a 3-Dimensional field of dielectric strength over a single revolution period, and then repeating that pattern in a plasma dielectric simulation over 1,000,000 rf periods. The average density for these simulations is the same as the harmonically modulated plasma dielectric simulations discussed above. It may be expected that different fill patterns and modulation shape will affect the amplitudes of the side bands, as well as changing the power in higher-order side bands with respect to the first side band [11]. As can be seen in Figure (3), the first side band amplitude is somewhat larger in comparison to the harmonic modulation simulations. In addition, higher order side bands are observed, as is expected because the shape of the modulation of the electron density is more like a square wave than a purely harmonic signal. The spectrum overall is much coarser than the previous simulations, and there is more high-frequency noise. This is due to the discreteness of both the binning of electron positions to the computational grid, as well as undersampling effects.

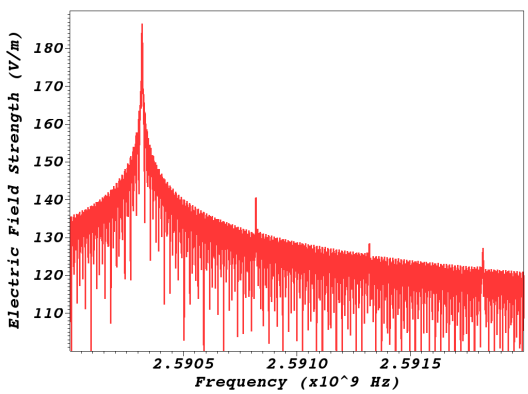


Figure 3: Simulated spectrum for integrated plasma dielectric model, where the 3-Dimensional electron densities from kinetic simulations determines the plasma dielectric strength.

REFERENCES

[1] F. Zimmerman, "Electron-Cloud Effects in Past and Future Machines - Walk Through 50 Years of Electron-Cloud Studies, *ECLOUD'12*, doi: 10.5170/CERN-2013-002.9, (2012).

[2] C. M. Celata, M. A. Furman, J.-L. Vay, J. W. Yu, "Electron Cyclotron Resonances In Electron Cloud Dynamics", *Proc. EPAC'08*, TUPP024, (2008).

[3] S. A. Veitzer, K. G. Sonnad, P. L. G. Lebrun, P. H. Stoltz, "Modeling Electron Cloud Buildup And Microwave Diagnostics Using Vorpal", *Proc. ECLOUD'10*, MOD04, (2010).

[4] S.A. Veitzer, P.H. Stoltz, K.G. Sonnad, and J.M. Byrd, "Modeling microwave transmission in electron clouds", *Proc. PAC'09*, (2009).

[5] S. De Santis, J. M. Byrd, J. Sikora, J. Calvey, J. Livezey, K. Hammond, "TE wave measurements of the electron cloud in a dipole magnetic field", *Proc. PAC'11*, (2011).

[6] M. G. Billing, J. Conway, E. E. Cowan, J. A. Crittenden, J. Lanzoni, Y. Li, C. S. Shill, J. P. Sikora, K. G. Sonnad, "Observation of Electron Trapping in a Positron Storage Ring", arXiv:1309.2625, and PRL (submitted), (2013).

[7] VSim, Powered by Vorpal; Empowered by Tech-X Corp.

[8] M. A. Furman and M. T. F. Pivi, "Probabilistic model for the simulation of secondary electron emission", Phys. Rev. ST Accel. Beams **5**, 124404 (2002).

[9] P. Lebrun et al., "Simulation of the Electron Cloud in the Fermilab Main Injector using Vorpal", *FERMILAB-PUB-11-228-APC-CD*, (2011).

[10] S. A. Veitzer, H. Stoltz, J. A. Crittenden, K. G. Sonnad, "3-Dimensional Modeling of Electron Clouds in Non-Uniform Magnetic Fields", *Proc. IPAC'12*, TUOAA01, (2012).

[11] S. De Santis, J. Sikora, M. Billing, M. Palmer, B. Carlson, "TE Wave Measurements of the Electron Cloud in the CESR-TA Ring", *Proc. IPAC'10*, MOPE088, (2010).

Copyright © 2013 CC-BY-3.0 and by the respective authors

CREATION OF GAMMA RADIATION USING ANNIHILATION OF CHANNELED POSITRONS IN CRYSTALS

Koryun B. Oganesyan*,
A.I.Alikhanyan National Science Lab, Yerevan, Armenia

Abstract

A possibility of channeling of low-energy ($5 \div 20\,Mev$) relativistic positrons with coaxial symmetry around separate crystal axes of negative ions in some types of crystals, is shown. The annihilation processes of positrons with medium electrons are investigated in details. The lifetime of a positron in the regime of channeling is estimated $10^{-6}\,sec$ which on a $10^9 \div 10^8$ is bigger than at usual cases.

INTRODUCTION

Studying of ways of generation of short-wave coherent radiation always was an essential problem of a science and was stimulated by its wide applied application. In work [1] one of the first the mechanism of radiation of relativistic electrons at their movement in periodic structures (see also [2]) was offered (later such types of structures have been named undulators). It at first sight imperceptible work later has essentially accelerated a process of creation of of modern devices the synchrophasotrons and the lasers on free electrons (see for example review [3]). In spite of the fact that the technology of generation of undulator radiation steadily is being developed and successes are obvious [4], however the problems also are obvious and they remain unresolved up to now. Let's note that the frequency of undulator radiation is being defined by length of its periodic element which in FELs and the undulators devices are macroscopic. Other defects of undulators their big sizes and used big energies of electrons. After opening of channeling of electrons (positrons) in crystals [5–7] and accompanying by its short-wave radiation [8] was appeared a hope to solve all the aforementioned problems. However these hopes up to now is justified only partially. In particular the problems of generation of short-wave radiation (x-ray) from less energetic electrons (of order a several Mev) on very small distances (of order a several micron) have been solved. Now a new problem arise. The point is that in the regime of channeling the particle (electrons and positrons) usually live very short time $\sim 10^{-14} \div 10^{-15}\,sec$. However this time is very short for conversion of a appreciable part of particle energy to energy of radiation. The short lifetime as well doesn't conduce to use of external factors for control by beam of channeling particles and to improving of spectral characteristics of radiation.

The quantum theory of channeling for electrons and positrons has been elaborated by many authors [8–10]. It is important to note that an electron in a crystal can commit both planar and axial channeling. At the same time only one type of real channeling for the positrons is known, the regime where a particle is localized between two adjacent planes. The possibility of axial channeling of positive particles has not been investigated, seriously up to now, because the crystallographic axes, irrespective of grade of crystal are been charged positively. However investigation of possibilities of axial channeling of positrons and, hence, the formation of metastable relativistic positron systems (PS) is a problem of utmost importance for a radiation physics.

In this work a role of different processes (scattering of positron on media electrons, the annihilation processes etc) in the expansion of energy levels of relativistic PS is analyzed and shown that PSs are metastable.

FORMATION OF RELATIVISTIC POSITRON SYSTEM (PS)

In previous work [11] we have shown, that if a low-energy relativistic positrons ($5 \div 20\,Mev$) are scattering under a small corners $\vartheta \le \vartheta_L$ (where ϑ_L is a Lindhard angle) on the axis $\langle 100 \rangle$ of chlorine ions Cl^- that they fall into regime of axial channeling. Moreover the motions of positrons concentrate between two cylinders that is very important from the point of view of movement stability. In particular, as was shown the effective $2D$ potential of channeling don't depend from temperature of media in a broad range of temperatures and has an order $-10\,eV$ depths of potential which is sufficient for formation a several quantum states of transverse motion. Recall that this type of effective potential can be in other crystals too. For example the effective potential of negatively charged ions O_2 axes often used in experiments of crystal SiO_2 is such.

In other words, the relativistic positrons in described regime of channeling don't interact with phonons subsystem. That means a main factor of de-channeling of particles in considered case is absent.

Taking into account the symmetry of effective potential for positrons around of the negative ions axis we can write the following analytical formula:

$$\begin{aligned} U_0(\rho) &= D_0(e^{-2\alpha\overline{\rho}} - 2e^{-\alpha\overline{\rho}}), \overline{\rho} = (\rho - \rho_0)/\rho_0, \\ \rho &= \sqrt{x^2 + y^2}, \end{aligned} \quad (1)$$

where the parameters for usual crystals are being found into intervals $D_0 = 5 \div 10eV$, $\alpha = 0.5 \div 0.8$ and $\rho_0 \sim 0.5d$, where d is a lattice constant.

* bsk@yerphi.am

Copyright © 2013 CC-BY-3.0 and by the respective authors

The full wavefunction of positron in the potential (1) in atomic units $\hbar = c = 1$ is being solved exactly and represented in [11] and [12]

PROCESSES LEADING TO DECAY OF POSITRON-SYSTEMS

After exception of major factor of dechanneling the three different processes still remain which lead to decay of PS:

a) The annihilation of positron with electron of media on one γ photon;

b) The annihilation of positron with electron of media on two γ photons;

c) The scattering of positron on electrons of media.

The main problem now is investigation of processes investment in lifetime of PS.

Decay PA on One and Two γ Photon

It is obvious that PS may be illustrated as a system, with total zero spin (like of parapositronium), because the skeleton of negatively charged ions axis does not possess spin and accordingly there are not spin-spin interaction between it and the positron. In other words the interaction between positron and the axis only is an electromagnetic. Another distinction between positronium and PS is a possibility of decay of the last on one γ photon. Recall that in this case the conservation laws of energy and momentum takes place in view of presence of media.

This process is being defined by matrix element of first order [13]:

$$\langle f|S^{(1)}|i\rangle = \frac{2\pi i e}{\sqrt{2\omega}} \int \Psi^*(\mathbf{r}) \hat{e} e^{-i\mathbf{qr}} \psi(\mathbf{r}) d^3r \cdot \delta(\varepsilon_p + \varepsilon_e - \omega), \quad (2)$$

where Ψ and ε_p are the wavefunction and the total energy of positron, $\psi(\mathbf{r})$ and ε_e designed the wavefunction and the energy of media's electron, $\mathbf{q}$-is the momentum of γ photon, ω-its frequency. Taking into account that the distribution of electrons in positive as well in negative ions is given by spherical model JMGR, we can write the wavefunction of electrons system in factorized form:

$$\psi(\mathbf{r}) \equiv \psi(\rho, z, \varphi) = \frac{1}{\sqrt{d}} e^{i\eta(z)z} \chi(\rho), \quad (3)$$

where $\eta(z)$ is a momentum of media electron in the point z, it is supposed that the random function $\eta(z)$ has a zero average value. This means that the statistical averaging of random term in (3) is equal to unit $\langle e^{i\eta z/\hbar}\rangle = 1$. In addition $\chi(\rho)$ Gaussian function which is normalized to unit:

$$\chi(\rho) = \frac{1}{(\pi)^{3/4}\rho_0} e^{-\bar{\rho}^2/2}. \quad (4)$$

For the effective differential cross-section of annihilation we can write the following expression:

$$d\sigma = \frac{e^2}{2(2\pi)^2\omega} \sum_{\nu_e \nu_p} |Q|^2 \delta(\varepsilon_p + \varepsilon_e - \omega)\omega^2 \, do_\gamma, \quad (5)$$

where $do_\gamma = \sin\vartheta d\vartheta d\varphi$ the solid angle element in which is situated a photon momentum, ν_e and ν_e are a summation indices of electron and positron spins in the initial state. However for the considered problem the orientation of electrons spin does not play important role and correspondingly later we will ignore the summation. In (5) the term Q in weakly relativistic case is being written in the kind:

$$Q = \int \Psi^*(\mathbf{r}) \mathbf{e}\hat{\mathbf{v}} \, e^{-i\mathbf{qr}} \psi(\mathbf{r}) d^3r, \quad \hat{\mathbf{v}} = \frac{1}{i\mu}\nabla_{\mathbf{r}}, \quad (6)$$

where $\hat{\mathbf{v}}$ is the operator of positron velocity, correspondingly $\mathbf{e}$ - describes the unit vector of photon polarization. The expression (6) may be transformed to the form:

$$Q = \frac{(2\pi)^3}{\mu} \int (\mathbf{ep}') \widehat{\Psi}^*(\mathbf{p}') \widehat{\psi}(\mathbf{q} - \mathbf{p}') \, d^3p',$$

where $\widehat{\Psi}^*(\mathbf{p}')$ and $\widehat{\psi}(\mathbf{q} - \mathbf{p}')$ are Fourier transforms of corresponding wavefunctions:

$$\widehat{\Psi}(\mathbf{p}') = \frac{1}{(2\pi)^3} \int \exp(-i\mathbf{p}'\mathbf{r}) \Psi(\mathbf{r}) d^3r,$$
$$\widehat{\psi}(\mathbf{q} - \mathbf{p}') = \frac{1}{(2\pi)^3} \int \exp[-i(\mathbf{q} - \mathbf{p}')\mathbf{r}] \psi(\mathbf{r}) d^3r. \quad (7)$$

In (7) $\mathbf{p}'$-designates the momentum of positron which in considered case in toto coincides with its p_z projection. Analyzing of expression for $\widehat{\psi}(\mathbf{q} - \mathbf{p}')$ shows that the transition amplitude is more probably if positron and photon momentums coincides i.e. $\mathbf{q} = \mathbf{p}'$. Using the equality $(\mathbf{ep}') = p' \sin\vartheta'$ and above mentioned conclusion the expression (7) we can write in the following kind (see Fig 2):

$$Q = \frac{(2\pi)^3}{\mu} \widehat{\psi}(0) \int p' \, \widehat{\Psi}^*(\mathbf{p}') \, \sin\vartheta' d^3p', \quad (8)$$

where $d^3p' = p'_\perp d\theta dp'_\perp dp'_z$.

The function $\widehat{\Psi}(\mathbf{p}')$ is being calculated simply:

$$\widehat{\Psi}(\mathbf{p}') = \frac{(-1)^m}{(2\pi)^2} \frac{e^{im\theta}}{\sqrt{d}} \delta(p_z - p'_z) \Theta_m(p'_\perp),$$
$$\Theta_m(p'_\perp) = \int_0^\infty \Phi(\rho, 0) J_m(p'_\perp \rho) \sqrt{\rho} \, d\rho. \quad (9)$$

The calculation of cross-section we will begin with averaging of expression (8) by the photon polarization. It is obviously when we rotate the polarization vector $\mathbf{e}$ around photon's momentum $\mathbf{q}$ on the angle π at this time as may be shown, the angle ϑ' respectively is being changed in the limits $\pi/2 - (\beta_q - \beta_{p'}) \le \vartheta' \le \pi/2 + (\beta_q - \beta_{p'})$, where

Copyright © 2013 CC-BY-3.0 and by the respective authors

$\beta_q = \arccos(q_z/q)$ and $\beta_{p'} = \arccos(p'_z/p')$. After integration by angle ϑ' in Eq. (8) it is easy to find:

$$Q = -\frac{2(2\pi)^3}{\mu}\widehat{\psi}(0)\int p'\,\widehat{\Psi}^*(\mathbf{p}')\,\sin(\beta_q-\beta_{p'})d^3p'. \quad (10)$$

Now substituting (9) into (10) and making the elementary calculations we find:

$$\begin{aligned} Q &= -\frac{2(2\pi)^2}{\mu d}\,\delta(p_z-q_z)\widehat{\psi}(0) \\ &\times \int_0^\infty \bar{p}\,\Theta_0(p'_\perp)\,\sin(\beta_q-\beta_{\bar{p}})p'_\perp dp'_\perp, \end{aligned} \quad (11)$$

where $\bar{p} = \sqrt{{p_z}^2 + {p'_\perp}^2}$, the δ- function shows the momentums conservation law on z- axis.

Finally let's analyze the amplitude Q forward which is more probable direction of PS decay on one γ photon, when in the PS doesn't rotate. In this case with high accuracy take place the following equalities $\beta_q = 0$, $\beta_{\bar{p}} = \arccos(p_z/\bar{p})$ and $m = 0$.

Using these equalities we can substantially simplify expression (11):

$$Q = \frac{2(2\pi)^{5/2}}{\mu d}\,\delta(p_z-q_z)\widehat{\psi}(0)p_z^{1/2}\int_0^\infty \Theta_0(p'_\perp){p'_\perp}^{3/2}dp'_\perp. \quad (12)$$

Now using the expression (12) and standard connection between amplitude and transition probability [13] for the one-photon decay of PS we can write the following assessment:

$$P_\gamma \sim 10^6 sec^{-1}. \quad (13)$$

Recall that for finding assessment (13) we used the parameters of crystal $CsCl$.

The probability of PA decay on two γ photons [13] is

$$P_{2\gamma} \sim 10^6 sec^{-1} \quad (14)$$

At scattering of positron on a media's electrons the amplitude of transition is being described by S-matrix element of second order, similar to process of two photons' decay.

CONCLUSION

The problem of creation of sources for the generation of short waves radiation is a problem of utmost importance. The experimental discovery of the phenomenon of channeling of relativistic charged particles in crystals has given a good hope for creation of compact devices for generation of powerful radiation in X-rays region. Despite the made big efforts these hopes for a long time were not justified. The point is that at the channeling arises difficultly solvable problem connected with the short length of de-channeling. The characteristic times of channeling in axial or planar regimes accordingly of order $10^{-14}sec$ and $10^{-15}sec$, that does not allow to increase the share of radiated energy and a fortiori to control process. As have shown our recent investigations this problem is being solved if we consider the channeling of positrons of energy $5 \div 20\,Mev$ in particular, in ionic crystals of type $CsCl$ along the chlorine ions axis $< 100 >$. In this case in crystal forms $2D$ relativistic positron-systems which with phonons subsystem of lattice practically are not interacting. All other types of influence on PS, collisions with electrons of media, the scattering on lattice discreteness etc, are perturbations of essentially small or similar to PS annihilation processes order. In other words in mentioned way with high probability it is possible to create of $2D$ relativistic PSs in media with the lifetimes bigger than $t \sim 10^{-6} \div 10^{-7}\,sec.$ This means that we solved the main problem on way of creation of nano-undulators which have very large lifetimes and by which we can control.

REFERENCES

[1] V. L. Ginzburg, Izv. AN SSSR, Ser. Fiz. **11** (2) 165 (1947).

[2] G. A. Schott, Electromagnetic Radiation and the Mechanical Reactions Arising from It (Cambridge: Univ. Press, 1912)

[3] G.N. Kulipanov, Usp. Fiz. Nauk **177** (4) 384 - 393 (2007).

[4] G. N. Kulipanov, A. N. Skrinskyd and N. A. Vinokurov, J. Synch. Rad. **5** 176 (1998).

[5] J. A. Davies, J. Friesen and J. D. McIntyre, Can. J. Chem., **38** 1526 (1960).

[6] M. T. Robinson and O. S. Oen, Appl. Phys. Lett., **2**, 30 (1963).

[7] J. Lindhard, Kgl. Dan. Viden. Sels. Mat. - Fys. Medd., **14**, 34 (1965).

[8] M. A. Kumakhov, Phys. Lett. Ser. A., **57**, 17 (1976).

[9] V. V. Beloshitsky and F. F. Komarov, Phys. Rep., **93**, 117 (1982)

[10] V. A. Bazylev and N. K. Zhevago, Sov. Phys. Usp., **25**, 565 (1982).

[11] A.I. Artemiev, M.V. Fedorov, A.S. Gevorkyan, N.Sh. Izmailyan, R.V. Karapetyan, K.B. Oganesyan, A.A. Akopyan, Yu.V. Rostovtsev, M.O. Scully, G. Kurizki, J. Mod. Optics, **56**, 18, 2148-2157, 2009,

[12] K.B. Oganesyan, Proceedings of FEL'13, MOPSO60, New York, 2013

[13] A. I. Akhiezer and V. B. Berestetskii, Quantum Electrodynamics, (in Russian), Moscow Nauka 1969, 623.

Copyright © 2013 CC-BY-3.0 and by the respective authors

HOW ACTS PLANE WIGGLER MAGNETIC FIELD INHOMOGENEITY ON THE SPONTANEOUS RADIATION AND THE GAIN

Koryun B. Oganesyan*, A.I. Alikhanyan National Science Lab, Yerevan, Armenia

Abstract

A relativistic electron motion in a transversally inhomogeneous magnetic field of a wiggler is shown to consist of fast (undulator) and slow (strophotron) components. By separating fast and slow motions and by averaging equations of motion over fast undulator oscillations, we find spectral intensity of strophotron spontaneous emission in such a system. By solving similarly equations of motion in the presence of an external light wave, we find the gain in a Free-Electron Laser based on the interaction of light with the strophotron mode of the electron motion. Both the strophotron gain and the corresponding intensity of spontaneous emission are shown to be well separated spectrally from the usual undulator parts.

INTRODUCTION

Usually FEL [1, 2] use the kinetic energy of relativistic electrons moving through a spatially modulated magnetic field(wiggler) to produce coherent radiation. The frequency of radiation is determined by the energy of electrons, the spatial period of magnetic field and the magnetic field strength of the wiggler. This permits tuning a FEL in a wide range unlike atomic or molecular lasers. In usual FEL magnetic field of wiggler is supposed to be uniform. But really the magnetic field is inhomogeneous in transverse direction(see for example [3]). It is important to take into account this inhomogeneity. This account leads to complex motion of electrons: fast undulator oscillations along the wiggler axis and slow strophotron motion [4] – [9] in transverse direction . In the next section we describe the equation of motion of electrons moving along the axis of the wiggler with transversal inhomogeneous magnetic field. In the Sec. III and IV we calculate the spectral distribution of spontaneous emission and the gain correspondingly.

EQUATIONS OF MOTION

The vector potential of undulator's magnetic field has a form [10]

$$\overrightarrow{A_W} = -\frac{H_0}{q_0}\cosh q_0 x \sin q_0 z \;\; \hat{j} \tag{1}$$

where H_0 is the strength of magnetic field and $q_0 = 2\pi/\lambda_0$, λ_0 - period of wiggler, $\hat{j}$ unit vector in y direction.

The change of energy is

$$\frac{d\varepsilon}{dt} = 0, \qquad \varepsilon = const \tag{2}$$

* bsk@yerphi.am

Further we consider paraxial approximation when

$$q_0 x < 1 \tag{3}$$

Taking into account (3) the magnetic field (1) becomes

$$H_x = H_0\left(1+\frac{q_0^2x^2}{2}\right)\cos q_0 z; H_y = 0;$$
$$H_z = -H_0 q_0 x \sin q_0 z \tag{4}$$

Then we can write equations of motion taking into account (2) ($p_{x,y,z} = v_{x,y,z}\varepsilon$)

$$\begin{aligned}
\ddot{x} &= -\left(\frac{eH_0}{\varepsilon}\right)^2 x\sin^2 q_0 z \\
\dot{y} &= \frac{eH_0}{\varepsilon q_0}\left(1+\frac{q_0^2x^2}{2}\right)\sin q_0 z \\
\ddot{z} &= -\frac{1}{2q_0}\left(\frac{eH_0}{\varepsilon}\right)^2 \sin 2q_0 z(1+q_0^2x^2)
\end{aligned} \tag{5}$$

After averaging first equation of Eq. (5) on period $2\pi/q_0$ and taking into account that $\overline{\sin^2 q_0 z} = 1/2$ we have

$$\ddot{x} + \Omega^2\, x = 0 \tag{6}$$

which has a solution

$$x = a_0\cos(\Omega t + \theta_0) \tag{7}$$

where

$$\begin{aligned}
\Omega &= \frac{eH_0}{\sqrt{2}\varepsilon}; \qquad a_0 = \sqrt{x_0^2+\frac{\alpha^2}{\Omega^2}}; \\
\cos\theta_0 &= \frac{x_0}{a_0}; \quad \sin\theta_0 = -\frac{\alpha/\Omega}{a_0}; \\
\theta_0 &= -\arctan\frac{\alpha}{x_0\Omega}
\end{aligned} \tag{8}$$

Averaging of the second equation of Eq. (5) gives

$$\ddot{z}^{(0)} = 0; \quad \dot{z}^{(0)} = v; \quad z^{(0)} = vt. \tag{9}$$

The solution of the second equation of Eq. (5) using Eq. (7) and Eq. (9) has a form

$$\begin{aligned}
\delta z &= -\frac{\Omega^2}{2q_0^2}t + \frac{\Omega^2}{4q_0^3}\sin 2q_0 t \\
&+ \frac{a_0^2\Omega^2}{16q_0}\sin\{2(q_0+\Omega)t + 2\theta_0\} \\
&+ \frac{a_0^2\Omega^2}{16q_0}\sin\{2(q_0-\Omega)t - 2\theta_0\}
\end{aligned} \tag{10}$$

Copyright © 2013 CC-BY-3.0 and by the respective authors

So, for z we have

$$\begin{aligned} z &= t\left(1-\frac{1}{2\gamma^2}-\frac{\Omega^2}{2q_0^2}\right)+\frac{\Omega^2}{4q_0^3}\sin 2q_0 t \\ &+ \frac{a_0^2\Omega^2}{16q_0}\sin\{2(q_0+\Omega)t+2\theta_0\} \\ &+ \frac{a_0^2\Omega^2}{16q_0}\sin\{2(q_0-\Omega)t-2\theta_0\} \end{aligned} \quad (11)$$

Here we take into account, that $1-v=\frac{1}{2\gamma^2}$, where $\gamma=\frac{E}{mc^2}$ is a relativistic factor, m- mass of electron, c- velocity of light and E- energy of electrons.

Limitations used in above consideration are

$$a_0 q_0 < 1; \quad \frac{\Omega}{q_0} < 1; \quad a_0\Omega_0 < 1 \quad (12)$$

In longitudinal direction(along axis z, wiggler's axis) electrons perform fast undulator oscillations, while in transverse direction they perform slow strophotron oscillations in one direction(x direction) and fast undulator oscillations in another direction(y direction).

SPONTANEOUS EMISSION

Now using the solutions for x Eq. (7), $\dot{y}$ Eq. (5) and z Eq. (11), we can find the spectral intensity of a spontaneous emission. The spectral intensity of emission in the z axis direction (wiggler's axis) is determined by the formula [11]

$$\frac{d\varepsilon}{d\omega do}=\frac{e^2\omega^2}{4\pi^2}\left|\int_0^T dt[\vec{n}\times\vec{v}]e^{i\omega(t-z)}\right|^2 \quad (13)$$

where do is an infinitely small solid angle in the z direction and T is electron traveling time through wiggler.

Using formulae [12]

$$e^{-iA\sin x}=\sum_{-\infty}^{\infty}J_n(A)e^{-inx} \quad (14)$$

with Bessel functions $J_n(A)$ we find

$$\begin{aligned} \frac{d\varepsilon}{d\omega do} &= \frac{e^2\omega^2\Omega^2T^2}{8\pi^2q_0^2} \\ &\times \sum_{n,m,k=-\infty}^{+\infty}\left[(I_{n+1,k,m}-I_{n,k,m})^2\frac{\sin^2 u_y}{u_y^2}\right. \\ &+ \left.\frac{a_0^2q_0^2}{2}(I_{n,k,m+1}-I_{n,k,m})^2\frac{\sin^2 u_x}{u_x^2}\right] \end{aligned} \quad (15)$$

where

$$\begin{aligned} u_y &= \frac{T}{2}\left[\omega\left(\frac{1}{2\gamma^2}+\frac{\Omega^2}{2q_0^2}\right)-(2n+1)q_0-2m\Omega\right] \\ u_x &= \frac{T}{2}\left[\omega\left(\frac{1}{2\gamma^2}+\frac{\Omega^2}{2q_0^2}\right)-2nq_0-(2m+1)\Omega\right] \\ I_{nkm} &= J_{n-k}(Z_1)J_{\frac{k+m}{2}}(Z_2)J_{\frac{k-m}{2}}(Z_2); \\ Z_1 &= \frac{\omega\Omega^2}{4q_0^3}; \quad Z_2=\frac{\omega a_0^2\Omega^2}{16q_0} \end{aligned} \quad (16)$$

Equation Eq. (15) describes the spectrum of emission consisting of a superposition of the spectral lines located at the combination frequencies of odd harmonics $(2n+1)\omega_{res,und}$ and even harmonics $2m\Omega_{res,st}$, and even harmonics $2n\omega_{res,und}$ and odd harmonics $(2m+1)\Omega_{res,st}$, $(m,n=0,1,2,...)$ where

$$\omega_{res,und}=\frac{2\gamma^2q_0}{1+\gamma^2\frac{\Omega^2}{q_0^2}}, \qquad \omega_{res,str}=\frac{2\gamma^2\Omega}{1+\gamma^2\frac{\Omega^2}{q_0^2}} \quad (17)$$

are resonance frequencies in undulator and strophotron correspondingly.

THE GAIN

The gain can be found from the above derived spectral intensity of a spontaneous emission (Eq. (15)) using Madey's theorem [13].

But in a derivation of these general relations between spontaneous and stimulated processes, some assumptions are used. They require a check in any new case. Therefore we prefer a direct derivation of the gain from equations of motion.

Now let electromagnetic wave propagates along z (wiggler axis) with vector potential

$$\overrightarrow{A_L}=-\frac{E_0}{\omega}\sin\omega(t-z)\left(\hat{i}\cos\alpha+\hat{j}\sin\alpha\right) \quad (18)$$

where ω is the frequency of electromagnetic wave and E_0 its electrical field strength, α is angle between x direction and vector of electric field strength of the propagating electromagnetic wave, $\hat{i}$ and $\hat{j}$ are the unit vectors in x and in y directions correspondingly.

The equations of electron motion in the wiggler (1) and electromagnetic (18) fields are

$$\begin{aligned} \frac{dp_x}{dt} &= -eH_0q_0xv_y\sin q_0z \\ &+ eE_0\cos\alpha(1-v_z)\cos\omega(t-z) \\ \frac{dp_y}{dt} &= eH_0\left[v_z\left(1+\frac{q_0^2x^2}{2}\right)\cos q_0z+q_0v_xx\sin q_0z\right] \\ &+ eE_0\sin\alpha(1+v_z)\cos\omega(t-z) \\ \frac{dp_z}{dt} &= -eH_0v_y\left(1+\frac{q_0^2x^2}{2}\right)\cos q_0z \\ &+ eE_0\cos\alpha\ v_x\cos\omega(t-z) \end{aligned} \quad (19)$$

and the rate of energy change is [11]

$$\frac{d\varepsilon}{dt}=e\overrightarrow{v}\overrightarrow{E}=eE_0(v_x\cos\alpha+v_y\sin\alpha)\cos\omega(t-z) \quad (20)$$

We are interesting in linear gain to find which is sufficient to obtain the first-order corrections $x^{(1)}(t)$, $y^{(1)}(t)$ and $z^{(1)}(t)$ to $x^{(0)}(t)$ Eq. (7), $y^{(0)}(t)$ Eq. (5) and $z^{(0)}(t)$ Eq. (11). These first-order corrections obey the equations(obtained from Eqs. (19))

Copyright © 2013 CC-BY-3.0 and by the respective authors

$$\begin{aligned}
\frac{dp_x^{(1)}}{dt} &= -\varepsilon_0\Omega^2 x^{(1)} \\
&+ eE_0\cos\alpha(1-v_z^{(0)})\cos\omega(t-z^{(0)}) \\
\frac{dp_y^{(1)}}{dt} &= eE_0\sin\alpha(1+v_z^{(0)})\cos\omega(t-z^{(0)}) \\
\frac{dp_z^{(1)}}{dt} &= eE_0\cos\alpha\ v_x^{(0)}\cos\omega(t-z^{(0)}) \qquad (21)
\end{aligned}$$

The linear (field-independent) gain is determined by the second order ($\propto E_0^2$),

$$\begin{aligned}
\frac{d\varepsilon}{dt} &= eE_0\left(v_x^{(1)}\cos\alpha + v_y^{(1)}\sin\alpha\right)\cos\omega(t-z^{(0)}) \\
&+ eE_0\omega\left(v_x^{(0)}\cos\alpha + v_y^{(0)}\sin\alpha\right)z^{(1)} \\
&\times \sin\omega(t-z^{(0)}) \qquad (22)
\end{aligned}$$

which is found from Eq. (20)

Now finding $x^{(1)}(t)$, $y^{(1)}(t)$ and $z^{(1)}(t)$ from Eqs. (21) and using $x^{(0)}(t)$ Eq. (7), $y^{(0)}(t)$ Eq. (5) and $z^{(0)}(t)$ Eq. (11) we obtain expression of electron emitted energy ($\Delta\varepsilon$) during time T and gain ($G = \frac{8\pi N_e}{E_0^2}\Delta\varepsilon$, N_e is electron beam concentration).

All these calculations are simple, although rather cumbersome. Here we present only the found result:

$$\begin{aligned}
G &= \frac{e^2\omega^2\Omega^2T^2}{8\pi^2q_0^2} \\
&\times \sum_{n,m,k=-\infty}^{+\infty}\Big[(I_{n+1,k,m}-I_{n,k,m})^2\sin^2\alpha \\
&\times \frac{d}{du_y}\frac{\sin^2 u_y}{u_y^2} + \frac{a_0^2q_0^2}{2}(I_{n,k,m+1}-I_{n,k,m})^2 \\
&\times \cos^2\alpha\ \frac{d}{du_x}\frac{\sin^2 u_x}{u_x^2}\Big] \qquad (23)
\end{aligned}$$

From Eq. (23) we conclude that maximum gain is achieved when vector of electromagnetic wave E_0 is directed in y direction ($\alpha = \pi/2$).

We calculate the spectral distribution of spontaneous emission and the gain of electrons moving in plane wiggler with inhomogeneous magnetic field. It is shown, that electrons do complex motion consisting of slow (strophotron) and fast (undulator) parts. We average the equations of motion over fast undulator part and obtain equations for connected motion. It is shown, that the account of inhomogeneity of the magnetic field leads to appearance of additional peaks in the spectral distribution of spontaneous radiation and the gain. Having much peaks and using the well-known mode-locking one can obtain ultrashort impulses.

REFERENCES

[1] C.A. Brau, "Free-Electron Lasers", Acadenmic, Boston, 1990.

[2] M.V. Fedorov, "Atomic and Free Electrons in a Strong Light Field", World Scientific, Singapore, 1997.

[3] K.B. Oganesyan, M.L. Petrossyan, "The magnetic fields of hellical wiggler", Yerevan 1981, YERPHI-475(18) - 81.

[4] M.V. Fedorov, E.A. Nersesov, K.B. Oganesyan, "Potential laser realization on relativistic strophotron-type free-electrons", Sov. JTP 56, 2402-2404 (1986).

[5] M.V. Fedorov, K.B. Oganesyan, "Classical theory of emission at high harmonics in the relativistic strophotron FEL", IEEE Journal of Quant. Electr. **21**, 1059-1068 (1985).

[6] D.F. Zaretsky, E.A. Nersesov, K.B. Oganesyan, M.V. Fedorov, "A laser utilizing free-electrons moving in transverse-gradient fields", Sov. Quant. Electronics, **13**, pp.685-692, (1986).

[7] K.B. Oganesyan, M.V. Fedorov, "Non-linear amplification theory in free-electron laser of the relativistic strophotron type", Sov. ZHTF, **57**, 2105-2114, (1987).

[8] M.V. Fedorov, K.B. Oganesyan, A.M. Prokhorov, "Free-electron laser based on the effect of channeling in an intense standing light-wave", Appl. Phys. Lett., **53**, 353-354 (1988).

[9] K.B. Oganesyan, A.M. Prokhorov, M.V. Fedorov, "Transverse channeling and free-electron laser on intense standing wave", Sov. ZHETF, **53**, 80-86, (1988); Sov. Phys. JETP **68**, 1342 (1988).

[10] E. Jerby, "The axial-velocity distribution function and the longitudinal susceptibility of an e-beam in a plannar wiggler FEL", NI and M in Physics A**27**, 457-466 (1988).

[11] L.D. Landau, E. M. Lifshits, "The classical theory of fields", New York, Academic, 1975.

[12] I.S. Gradstein and I.M. Ryzhik, "Tables of integrals, Series and Products", New York, Academic, 1966.

[13] J.M.J. Madey, "Relationship between mean radiated energy, mean squared radiated energy and spontaneous power spectrum in a free-electron laser", Nuovo Cimento, **50b**, 64-88, 1979.

Copyright © 2013 CC-BY-3.0 and by the respective authors

GENERATION OF INTENSIVE TRANSITION RADIATION IN MODULATED MEDIUM

Koryun B. Oganesyan*, A.I.Alikhanyan National Science Lab, Yerevan, Armenia

Abstract

The 3D spin-glass system in the external standing electromagnetic field is considered. It is shown on an example of amorphous quartz, under the influence of a standing microwave field, at its certain parameters, superlattice is created in the medium where difference in values of dielectric constants of neighboring layers can be up to third order. This superlattice exists during the nanosecond, however it is sufficient for using it as a radiator for generation of transition radiation by relativistic electrons.

INTRODUCTION

The formation and governing of periodically modulated refractive index in media is a most important problem of solid state physics and material science. First of all it is related to the possibility of developing compact UV or X-ray Free-Electron Lasers (FEL) based on emission of transition radiation (TR) (see for example [1]). Currently the following two problems are discussed intensely:

1. A gas-plasma medium with periodically varied ionization density [2–9],

2. A special periodical solid-state superlattice-like (SSL) structures composed of layers with different refraction indexes [10–20].

TR is generated due to the difference in frequency-dependent dielectric constants (permittivity functions) of adjacent layers (remember that the radiation power is proportional to $[\epsilon_1^R(w) - \epsilon_2^R(w)]^2$, where $\epsilon_{1;2}^R(w) = Re[\epsilon_{1;2}(w)]$) [21]. Therefore, the possibility of controlling this difference by means of an external field is highly important. In other words, the problem here is to construct a superlattice with difference in dielectric constants of neighboring domains having the form $[\epsilon_1^R(w,\mathbf{g}) - \epsilon_2^R(w,\mathbf{g})]^2$, where $\mathbf{g}$ describes the controlling parameters, $\epsilon_1(w,\mathbf{g})$ and $\epsilon_2(w,\mathbf{g})$ are dielectric permittivity functions in neighboring regions. According to theoretical and experimental studies, the periodical structures may be formed in condensed matter by means of external electromagnetic or acoustic fields [22–25].

This idea was recently realized in TR generation experiments [26]. In particular, it was shown that at the passage of a beam of 20 Mev electrons through amorphous silicon dioxide $a - SiO_2$ with a standing electromagnetic wave (of 10 GHz frequency) inside, anomalous high short-wave radiation was produced. Preliminary studies explain this high intensity radiation as a result of multiple passage of the electron beam through interfaces between regions with different permittivity functions. Theoretically the appearance of $1D$ superlattice order in random media is explained by the polarization of media due to the orientational relaxation of elastic dipoles in the direction of external electromagnetic field propagation [27].

So, the main objective of this work is a systematic investigation of relaxation processes and critical effects in $a - SiO_2$ compound type disordered $3D$ systems under the action of external electromagnetic field that forms a standing wave in the medium, and in particular, to prove the possibility of formation of $1D$ periodic superlattice of permittivity function in the scales of space-time periods of standing wave.

FORMULATION OF THE PROBLEM

The starting point in our discussion will be the Clausius-Mossotti relation for dielectric constant. It is known that in isotropic media (as well as in crystals of cubic symmetry) the dielectric constant is well described by the Clausius-Mossotti equation [28–30]:

$$\frac{\epsilon_s - 1}{\epsilon_s + 2} = \frac{4\pi}{3}\sum_m N_m^0 \alpha_m^0, \qquad (1)$$

where N_m^0 is the concentration of particles (electrons, atoms, ions, molecules) with given m types of polarizability and α_m^0 correspondingly are polarizability coefficients. It follows from this formula that the static dielectric constant ϵ_s depends on the polarizability properties of particles as well as on their topological order. In the external field the homogeneity and isotropy of the medium is often lost. Then, it is expected that the formula (1) will be applicable after slight generalization.

The object of our investigation are solid state dielectrics of the amorphous silicon dioxide $a-SiO_2$ type. According to numerical $ab\ initio$ simulations [31], the structure of this type compound may be well described by the model of $3D$ disordered spin system.

In particular the $3D$ spin system we can represent as a $3D$ lattice with the lattice's constant $d_0(T) = \{m_0/\rho_0(T)\}^{1/3}$, where m_0 is the molecule mass, ρ_0 is the density and T is the temperature. We will assume also, that in each cell of this lattice there are only one randomly distributed spin (roughly polarized molecule).

We will suppose that the media under the influence of external standing electromagnetic field the electrical part

* bsk@yerphi.am

Copyright © 2013 CC-BY-3.0 and by the respective authors

of which has a kind:

$$E(x; E_0, \Omega, \lambda_s, \varphi_0) = E(x; \mathbf{g}) = 2E_0 \sin(\varphi_0)\cos(kx), \quad (2)$$

where $\varphi_0 = \Omega t_0$ and t_0 are respectively the initial phase and time, Ω is a wave frequency, $k = 2\pi/\lambda_s$ and λ_s is the wavelength, the symbol $\mathbf{g}$ shows the parameters of standing wave (controlling parameters) $(E_0, \Omega, \lambda_s, \varphi_0)$.

Here follows a natural question, how does the dielectric constant change on the scale of wavelength period and in time interval $\Delta t \ll \Omega^{-1} \sim 10^{-9} sec$, when the relaxation time of molecular dipoles is $\tau \sim 10^{-11} \div 10^{-12} sec \ll \Omega^{-1}$. This question is important since the processes associated with the Cerenkov and transition radiation produced in media are much faster than the above time scale. Note, that the time, during which a relativistic electron passes the wavelength ($\lambda_s \sim 10^{-4} cm$) of standing wave and the formation times of transition or Cherenkov photons in this layer is less than $10^{-15} sec$. This time interval is essentially less than the time, during which the standing wave is steady-state. Since the wavelength is supposed to be much larger than the inter-dipole distance $\lambda_s \gg d_0$, the Clausius-Mossotti relation is still true. In this case the main problem is to calculate the polarizability coefficient related to orientation effects.

Taking into account the external field, one can express the polarization of matter at an arbitrary point as the macroscopic self-consistent relation:

$$\mathbf{P}(\mathbf{r}) = \sum_{\boldsymbol{l}} \mathbf{p}\,(\boldsymbol{l} - \mathbf{r}) = \sum_m n_m \alpha_m (\boldsymbol{l} - \mathbf{r}) \mathbf{E}_{loc}(\boldsymbol{l} - \mathbf{r}), \quad (3)$$

where $\boldsymbol{l} \equiv \boldsymbol{l}(l_x, l_y, l_z)$ is $3D$ lattice vector, $\mathbf{p}$ is respectively the dipole moment of molecule. The second equation in (3) contributes to the value of dipole moment (spin). Note, that the number of the carriers of given polarization type in an elementary cell is $n_m \sim (d_0(T))^{-3}$, α_m being coefficients of the polarizability of corresponding types with due regard for external field and $\mathbf{E}_{loc}$ is the local field, i.e. the effective field that induces the polarization at the site of an individual molecule. The contribution of each effect to the net dipole moment per molecule is linear, that is actually verified by experiments. Under the action of external field the polarization of different types arise in media. However, simple analyzes shows that the values of polarizability coefficients due to orientation effects essentially exceed the others.

Note that the coefficient of elastic orientational polarizability in amorphous media $\alpha_{dip}(\boldsymbol{l}-\mathbf{r})$ is a random function of cell location. This fact is due to random orientation of local field strengths $\mathbf{E}_{loc}(\boldsymbol{l} - \mathbf{r})$ with respect to the external field $\mathbf{E}(x; \mathbf{g})$. Therefore, all terms in the right side of (1) are basically known and well studied in literature (see, e.g., [28–30]) except from those connected with the orientation effects.

The orientation effects have a collective nature and are characterized by average value of random sum $\sum_{\boldsymbol{l}} \alpha_{dip}(\boldsymbol{l}-\mathbf{r})$ (sum of random coefficients of orientational polarizability).

Multiplying both sides of equation (3) on the field (2), we find:

$$\mathbf{P}(\mathbf{r}, \mathbf{g})\mathbf{E}(x, \mathbf{g}) = -\delta U(\mathbf{r}, \mathbf{g}) = \sum_m n_m \Big[\sum_{\boldsymbol{l}} \alpha_m(\boldsymbol{l} - \mathbf{r}) \mathbf{E}_{loc}(\boldsymbol{l} - \mathbf{r})\Big] \mathbf{E}(x; \mathbf{g}), \quad (4)$$

where $-\delta U(\mathbf{r}, \mathbf{g})$ describes the potential energy of amorphous matter in the external field. The statistical properties of media in the direction of wave propagation will be considered later.

Taking into account (4), one can obtain the following expression for the part of potential energy of $3D$ spin system which is related with the orientational effects of spins in the external field:

$$-\delta U_{dip}(\mathbf{r}, \mathbf{g}) = \sum_{\boldsymbol{l}} \alpha_{dip}(\boldsymbol{l} - \mathbf{r}) \mathbf{E}_{loc}(\boldsymbol{l} - \mathbf{r}) \mathbf{E}(x; \mathbf{g}). \quad (5)$$

Let us separate a layer with volume $V = L_x \times L_y \times L_z$ in the infinite crystal lattice, where $L_x \sim (\lambda_s) \gg d_0(T)$ and $(L_y, L_z) \to (\infty, \infty)$. It is easy to see that this volume is filled with the infinite number of steric spin-chains with length L_x.

An important problem is now to calculate the mean value of the interaction potential between the spin layer and the external field.

Formally the following expression may be written for that:

$$-\delta U_V(\mathbf{r}, \mathbf{g}) = -\sum_{\boldsymbol{l}_\perp} \delta U_{L_x}(\boldsymbol{l}_\perp | \mathbf{r}, \mathbf{g}), \boldsymbol{l}_\perp \equiv \boldsymbol{l}_\perp(l_x, l_y),$$
$$-\delta U_{L_x}(\boldsymbol{l}_\perp | \mathbf{r}, \mathbf{g}) = \sum_{l_x} \alpha_{dip}(\boldsymbol{l} - \mathbf{r}) \mathbf{E}_{loc}(\boldsymbol{l} - \mathbf{r}) \mathbf{E}(x; \mathbf{g}) \quad (6)$$

where $-\delta U_{L_x}(\boldsymbol{l}_\perp | \mathbf{r}, \mathbf{g})$ is the interaction potential between the $1D$ steric spin-chain and external field. We will drop out calculating part and go to conclusion.

CONCLUDING REMARKS

In the present article a new microscopic approach has been developed for studying the properties of stationary dielectric constant and permittivity function in dielectric media under the influence of external standing electromagnetic field. The approach consists of the following two general steps:

1. Generalization of the Clausius-Mossotti equation for dielectric constant in the external standing electromagnetic wave;

2. Generalization of the equation for dielectric permittivity function taking into account the previous results.

Mathematically the problem is solved as follows. The dielectric medium in the external electromagnetic field is

Copyright © 2013 CC-BY-3.0 and by the respective authors

modelled as a $3D$ spin glass system under the influence of external field. Note that all general changes of properties of media take place in the wavelength scale of external field space-time period. We have investigated in detail the layer of medium that consisted of disordered $1D$ spin-chains with the length of the order of external field's wavelength. Taking into account the fact that on infinite (x, y) plane the distribution of spin-chains is isotropic we can use the Birgoff ergodic hypothesis (see 6) and to reduce the initial $3D$ spin-glass problem on a two conditionally separated $1D$ problems. It means that we can investigate each $1D$ problem separately. However we must remember, that at the solution of the second $1D$ problem the parameters of a first $1D$ problem ought to be taken into account.

In the work we have constructed all formulas which are necessary to allow for the contribution of orientational effects at calculation of stationary and frequency-depending dielectric constants.

As was shown in result of catastrophe in *C-M* equation, in the region of short wave-length, the difference between permittivities of neighboring layers may be essentially big.

Last circumstance allows us in homogenous and the isotropic dielectrics of spin-glasses type, artificially to create a superlattice from different permittivitys the parameters of which it is possible to control by external fields and use this structure for generation of extremely intensive transition radiation.

REFERENCES

[1] V. V. Apollonov, A. I. Artemyev, M. V. Feodorov, E. A. Shapiro, Optic Express, **3**, 162 (1998).

[2] K. R. Chen, J. M. Dawson, Ion-ripple laser, Phys. Rev. Lett., **68**, 29 (1992).

[3] R. N. Agrawal, V. K. Trpathi, IEEE Trans. Plasma Scince, **23**, 788 (1995).

[4] K. Nakajima, M. Kando, T. Kawarkubo, T. Nakanishi, A. Ogata, Nuc. Inst. and Meth. Phys. Res., A **356**, 433 (1996).

[5] V. A. Bazylev, V. Goloviznin, M. M. Pitatelev, A. V. Tulupov, T. J. Schep, Nucl. Instr. and Meth. Phys. Res., A **358**, 433 (1995).

[6] N. I. Karbushev, Nucl. Instr and Meth. Phys. Res. A **358**, 437 (1995).

[7] M. V. Feodorov, E. A. Shapiro, Laser Physics **5**, 735 (1995)

[8] A. I. Artemev, M. V. Fedorov, J. K. McIver, E. A. Shapiro, IEEE J. Quantum Electron., **QE 27**, 2440 (1991).

[9] J. Zhang and Z. Ren, J. Phys. D: Appl; Phys. **33**, 1798 (2000).

[10] M. A. Piestrup, P. F. Finman, IEEE J. Quantum Electron. **QE 19**, 357 (1983).

[11] M. B. Reid, M. A. Piestrup, IEEE J. Quantum Electron. **QE 27**, 2440 (1991).

[12] G. Bekefi, J. S. Wurtele, I. H. Deutsch, Phys. Rev. A **34**, 1228 (1986).

[13] A. E. Kaplan, S. Datta, Appl. Phys. Lett. **44**, 661 (1984).

[14] M. S. Dubovikov, Phys. Rev. A **50**, 2068 (1994).

[15] C. S. Liu, V. K. Trpathi, IEEE Trans. Plasma Scince **23**, 459 (1995).

[16] C. I. Piencus, M. A. Piestrup, D. G. Boyers, Q. Li, J. L. Harris, X. K. Maruyams, D. M. Skopik, R. M. Silzer, H. S. Kaplan, Phys. Rev. A **43**, 2387 (1991).

[17] M. A. Piestrup, D.G. Boyers, C.I. Pincus, J. L. Harris, X. K. Maruyama, J. C. Bergstrom, H. S. Kaplan, R. M. Silzer, D. M. Skopik, Phys. Rev. A **43**, 3653 (1991).

[18] A. E. Kaplan, C. T. Law and P. L. Shkolnikov, Phys. Rev., E **52**, 6795 (1995).

[19] M.V. Fedorov, K. B. Oganesyan, and A. M. Prokhorov, Appl. Phys. Lett. **53**, 353 (1988).

[20] K.B. Oganesyan, A.M. Prokhorov, M.V. Fedorov, Sov. Phys. JETP **68**, 1342 (1988).

[21] V. L. Ginzburg and V. N. Tsitovich, Phys. Rep., **49**, 1 (1979).

[22] G. V. Morozov, D. W. L. Sprung and J. Martorell, J. Phys. D: Appl. Phys. **35**, 2091 (2002).

[23] A. S. Rasporin and H. L. Cui, Phys. Rev. B **68**, 045305 (2003).

[24] M. Shen and W. Cao, J. Phys. D: Appl. Phys. **33**, 1150 (2000).

[25] X. Zhang, et al., J. Phys. D: Appl. Phys. **35**, 1414 (2002).

[26] A. R. Mkrtchyan et al., Nanotechnologies in the area of physics, chemistry and biotechnology, Fifth ISTC SAC Seminar (St. Petersburg, Russia, 2002), 202.

[27] A. S. Gevorkyan and Chin-Kun Hu, Proceedings of the ISAAC Conf. on Analysis, Yerevan, Armenia, Eds by G. A. Barsegian et al, 164 (2004).

[28] Ch. Kittel, Introduction to Solid State Physics, J. Wiley and sons, Inc., New York, London, Sydney, Toronto, 1962.

[29] D. J. Griffith, Introduction to Electrodynamics, p.192 (Prentic Hall, New Jersy 1989).

[30] R. Becker, Electromagnetic Fields and Interactions, p. 95 (Dover, New York 1972).

[31] Y. Tu, J. Tersoff and G. Grinstein, Phys. Rev. Lett., **81**, 4899 (1998).

Copyright © 2013 CC-BY-3.0 and by the respective authors

ULTRA-LOW EMITTANCE LIGHT SOURCE WITH A TORUS-KNOT TYPE ACCUMULATOR RING

A. Miyamoto and S. Sasaki
HSRC; Hiroshima Synchrotron Radiation Center, Hiroshima University
2-313 Kagamiyama, Higashi-Hiroshima, Japan

Abstract

We proposed a torus knot type synchrotron radiation ring in that the beam orbit does not close in one turn but closes after multiple turns around the ring. This ring is capable to have many straight sections and it is advantageous to installation of many insertion devices. Currently, we are designing a new ring based on the shape of a (11, 3) torus knot for our future plan 'HiSOR-II.' This ring is mid-low energy light source ring with a beam energy of 700 MeV. It has eleven 3.6-m-long straight sections though the ring diameter is as compact as 15 m.

In late years, some compact light source rings achieved very low emittance of several tens of nmrad. However for the ring we propose, the emittance can be reached less than 10 nmrad when the multi-bend scheme is adopted to the arc section. With this ultra-low emittance, the size and divergence of electron beam is smaller than the diffraction limited light in lower energy part of VUV region, and it will be very useful for many synchrotron radiation users' experiments. Therefore we are designing this ultra-low emittance light source ring having innovatively odd shape.

INTRODUCTION

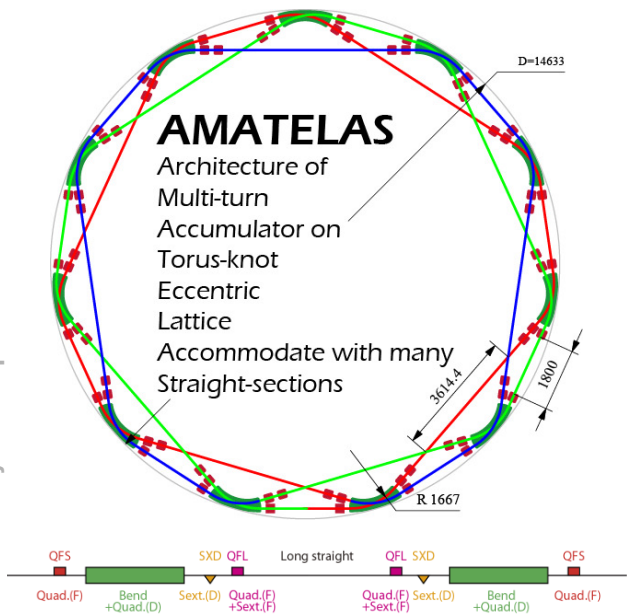


Figure 1: Schematic drawings of (11, 3) AMATELAS designed for HiSOR-II and the lattice of unit cell.

For small light source rings, it is very important to obtain a lot of straight sections in which we can install insertion devices, but it is difficult in reality because they are occupied by various magnets, RF systems or beam monitors. In this context we got a hint from the shape of the torus knot [1], and contrived the ring which had the orbit closed after multiple turns around the ring [2] and named it AMATELAS.

We are planning a new light source ring for our facility [3], therefore we are designing a new ring based on the shape of a (11, 3) torus knot for our future plan 'HiSOR-II' [4]. This ring has 11 long straight sections and we can place insertion devices efficiently by placing the elements such as quadrupole magnets near bending magnet, outside of the orbit crossing section. Furthermore, this ring has about 3 times longer closed orbit in comparison with the conventional ring, the diameter of this ring is as compact as 15 m, but its total orbit length is as long as 130 m. The AMATELAS ring designed for HiSOR-II and the lattice of unit cell are shown in Figure 1, and the main parameters of (11, 3) AMATELAS designed for HiSOR-II storage ring [5] is shown in Table 1, and beta or dispersion function of a unit cell is shown in Figure 2.

Table 1: The main parameters of (11, 3) AMATELAS for HiSOR-II storage ring

Perimeter	45.97 m
Orbit shape	(11,3) Torus knot
Perimeter	45.97 m
Orbit length	130.187 m
Beam energy	700 MeV
Straight sections	3.614 m ×11 1.728 m ×11
Betatron tune	(10.362, 7.807)
Natural emittance	17.9 nmrad
Chromaticity	(+1.0, +1.0)

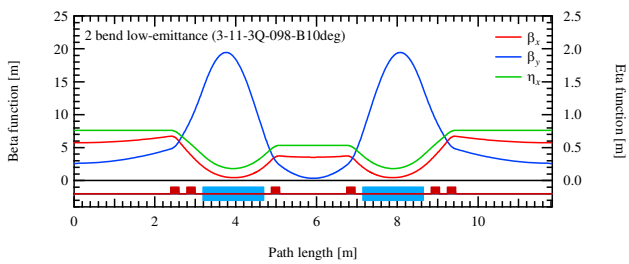


Figure 2: Optical function of (11, 3) AMATELAS for HiSOR-II storage ring.

Copyright © 2013 CC-BY-3.0 and by the respective authors

ULTRA-LOW EMITTANCE WITH MULTI-BEND LATTICE

In late years, some compact light source ring achieved ultra-low emittance of several tens of nmrad. For VUV light sources, it means that it obtains the diffraction limited light to achieve such a low emittance beam. Generally, the beam emittance to obtain the diffraction limited light is given as the following.

$$\varepsilon \leq \frac{\lambda}{4\pi}$$

If energy of the light from undulator is 10 eV, this equation shows that emittance should be less than about 10 nmrad. We judged emittance of this size to be possible by adopting the multi-bend lattice, and we started the design ultra-low emittance light source ring for HiSOR-II.

Multi-bend lattice

In the original lattice shown in Figure 1, it has two bending magnets in one unit cell. It is advantageous to lower emittance that the bend is divided into more bends, however, we decided to adopt the multi-bend lattice having 4 bending magnets for reasons of the geometric size of this ring. There are many variations to length of magnets or drift spaces between the magnets in lattices having 4 bends in one cell, but we notice that placement is not so much easy from necessity to place on a torus-knot shape.

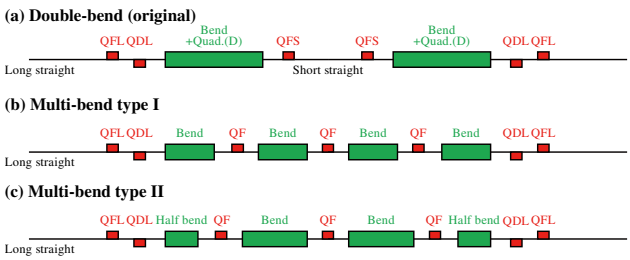


Figure 3: Multi-bend type cells compared with double-bend lattice. (a) is original double-bend lattice. (b) shows multi-bend lattice that all bends has equal length, and (c) is the other type that 2 bends at the end of arc have a half length.

The schematic draws of two types of the multi-bend lattices are shown in Figure 3. In this figure, (a) shows the original double-bend lattice, (b) and (c) are the multi-bend lattices. (b) shows the lattice that all bends has equal length. In another type (c), the length of two bends at the end of arc section is half of the ones in the central section.

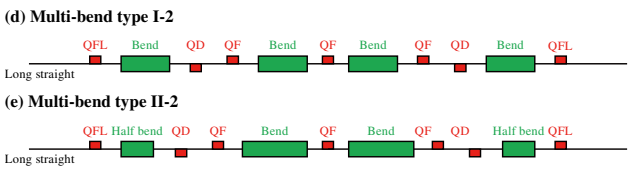


Figure 4: The modified lattices that the doublets are placed in the inside arc section.

In all lattices shown in Figure 3, quadrupole doublets are placed in the outside of arc section, but those doublets should be placed in the inside of arc to control the three parameters, β_x, β_y and η_x in a achromatic lattice better. These modified lattices from (b) and (c) in Figure 3 are shown in Figure 4.

Geometry

In original double-bend type lattice, beam orbit crosses in the bending magnets, but it is necessary to consider where it should cross in these multi-bend lattices. As for the simplest geometry, all magnets of arc section are placed in the outside of the crossing section, however actually it is impossible to have enough length. Therefore we consider some cases that the crossing section of the orbit is in the bending magnet of the edge of arc, in the specific quadrupole magnet and in the drift space.

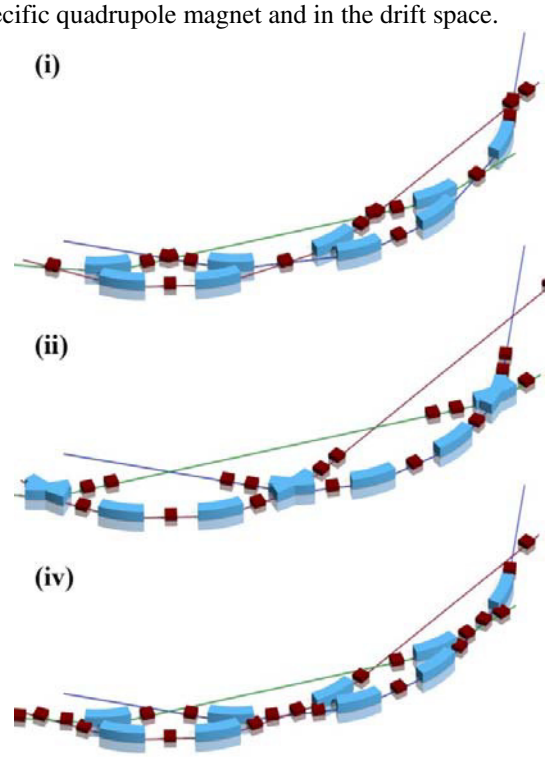


Figure 5: Geometries of multi-bend lattice type-I.

Figure 5 and Figure 6 show geometries in case of multi-bend lattice type-I and type-II. The crossing points of orbit are different in each geometries, it is placed in the singlet quadrupole in arc section in (i), in the bend of edge of arc in (ii), in the one of doublet quadrupole in (iii), in the drift space between the doublet in (iv). Because the crossing angle of the orbit is too small in Type-I (iii) and the magnets are not able to placed, it is not described in Figure 5

Copyright © 2013 CC-BY-3.0 and by the respective authors

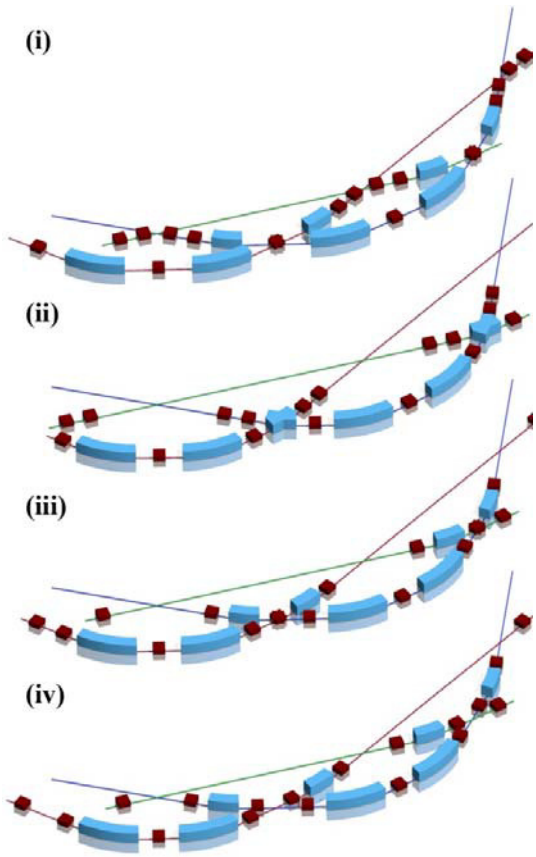


Figure 6: Geometries of multi-bend lattice type-II.

In these lattices, all bend has equal quadrupole force K=-1.8 [m^{-2}] except (iii) type that orbit crosses in bending magnet. Finally, the optical functions in the unit cell and natural emittance of each lattice are shown in Figure 7 and Figure 8.

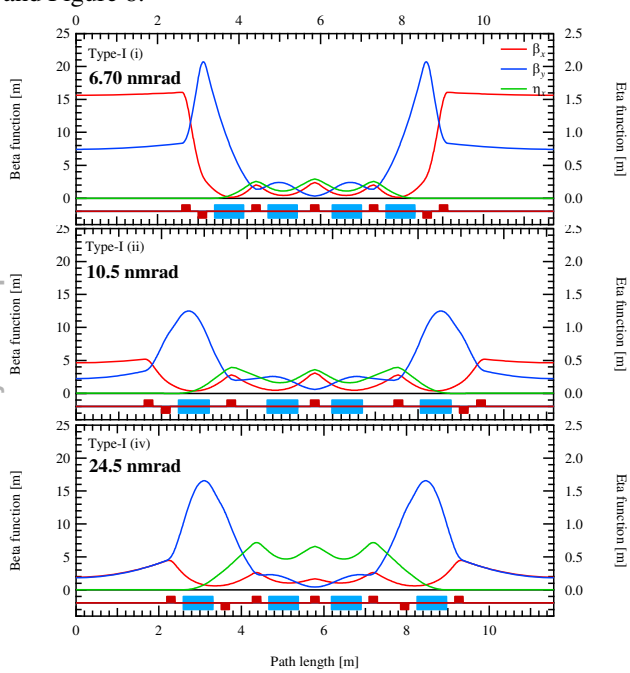


Figure 7: Optical functions of multi-bend lattice type-I.

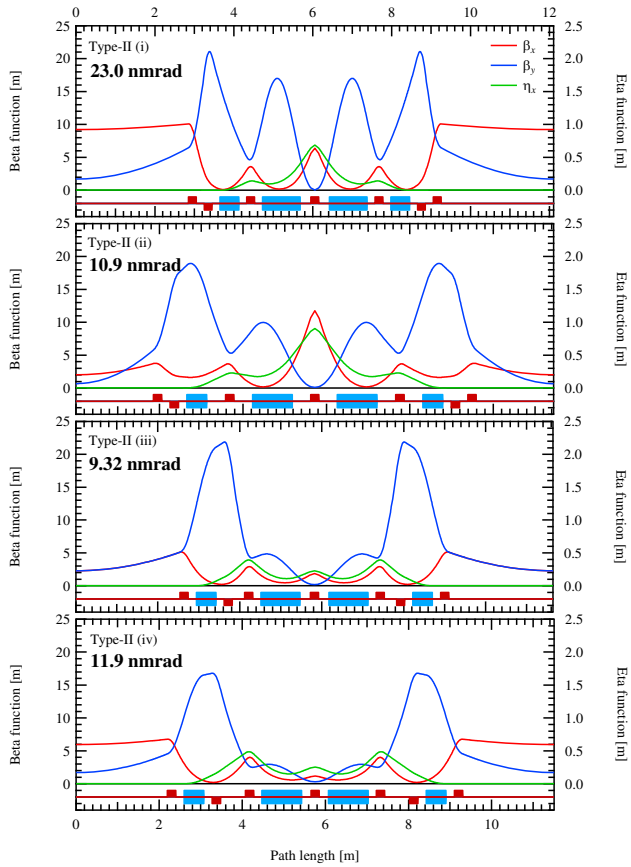


Figure 8: Optical functions of multi-bend lattice type-II.

SUMMERY

We are designing the light source ring based on the torus-knot shape as our future plan HiSOR-II. We can get smaller emittanc6e and may get diffraction limited light in the VUV region adopting a multi-bend lattice to this ring.

As a result of considering in various lattices in the linear dynamics, we were able to make the lattice that reached emittance less than 10 nmrad as our target. However, the geometric conditions by the torus-knot are severe, and it is necessary to consider about the effective chromaticity correction that does not reduce the dynamic aperture.

REFERENCES

[1] http://en.wikipedia.org/wiki/Torus_knot
[2] S. Sasaki and A. Miyamoto, Proc. of IPAC2011, San Sebastian, Spain, TUPO010, pp.1467-1469 (2011).
[3] A. Miyamoto, et. al., Proc. of IPAC'10, Kyoto, Japan, WEPEA029,.pp.2546-2548 (2010).
[4] A. Miyamoto and S. Sasaki, Proc. of IPAC2011, San Sebastian, Spain, TUPO009, pp.1464-1466 (2011).
[5] A. Miyamoto and S. Sasaki, Proc. of IPAC2012, New Orleans, Louisiana, USA TUPPP014, pp.1635-1637 (2012).

Copyright © 2013 CC-BY-3.0 and by the respective authors

COUPLING AND BRIGHTNESS CONSIDERATIONS FOR THE MAX IV 3 GeV STORAGE RING

S.C. Leemann*, M. Eriksson, MAX IV Laboratory, Lund University, SE-22100 Lund, Sweden

Abstract

It is often suggested that the emittance coupling of a storage ring should be adjusted to the so-called diffraction limit corresponding to the shortest wavelength of interest. For 1 Å radiation this leads to a typical requirement of 8 pm rad vertical emittance. In ultralow-emittance storage rings like the MAX IV 3 GeV storage ring this corresponds to a comparably large setting of the emittance coupling (2.5%). This approach, however, does not produce the brightest radiation and needs to be revisited taking into account that overall photon brightness depends on the emittances of the electron beam and the intrinsic photon beam. This paper summarizes an analytic approach to maximizing brightness as a function of emittance coupling while retaining sufficient lifetime. Instead of "meeting the diffraction limit", we further reduce the coupling, thus increasing both the brightness and transverse coherence of the emitted radiation. We derive that reducing the MAX IV 3 GeV storage ring's vertical emittance to 2 pm rad (0.6% coupling) will increase brightness and transverse coherence by almost a factor two while 10 h overall lifetime can still be achieved.

INTRODUCTION

The MAX IV facility will use a 3 GeV linac and two storage rings to deliver synchrotron radiation to a broad and international user community across a wide spectral range and covering different temporal scales [1, 2]. The MAX IV 3 GeV storage ring has been optimized [3, 4] for insertion devices (ID's) producing high-brightness x-rays. A typical scenario is radiation at 1 Å produced in an in-vacuum undulator of roughly 4 m magnetic length. The intrinsic photon beam (i.e. the photon beam emitted by a single electron) emerging from such an ID [5] has a diffraction-limited RMS source size given by $\sigma_r = \sqrt{2L\lambda}/4\pi$ and its central cone has an RMS width $\sigma_{r'} = \sqrt{\lambda/2L}$ where L is the magnetic length of the ID and λ the (fundamental) emitted wavelength. This leads to the often quoted emittance criterion for diffraction limited radiation $\varepsilon_r = \sigma_r\sigma_{r'} = \lambda/4\pi$, which calls for 8 pm rad for 1 Å radiation.

In existing 3rd generation light sources, where the equilibrium emittance $\varepsilon_0 = \varepsilon_x + \varepsilon_y$ is several orders of magnitude larger than 8 pm rad, the conventional approach is to adjust the emittance coupling $\kappa = \varepsilon_y/\varepsilon_x$ by e.g. skew quadrupoles so that $\varepsilon_y \approx \varepsilon_r$. For small values of coupling $\varepsilon_x = \varepsilon_0/(1+\kappa) \approx$ const. The Touschek lifetime then scales like $\sqrt{\kappa}$ and the emittance coupling is therefore usually set "at the diffraction limit" and not much lower in order not to reduce overall beam lifetime.

This treatment, however, neglects the actual radiation process in the ID[1]. The brightness of the emitted radiation depends on the overlap of electron beam *and* intrinsic photon beam in phase space. This overlap, assuming a dispersion-free straight, is calculated as [5]

$$\Sigma_{x,y} = \sqrt{\sigma_r^2 + \sigma_{x,y}^2} = \sqrt{\frac{2L\lambda}{(4\pi)^2} + \varepsilon_{x,y}\beta_{x,y}}, \quad (1)$$

$$\Sigma_{x',y'} = \sqrt{\sigma_{r'}^2 + \sigma_{x',y'}^2} = \sqrt{\frac{\lambda}{2L} + \frac{\varepsilon_{x,y}}{\beta_{x,y}}}, \quad (2)$$

where $\beta_{x,y}$ is the beta function in the ID and we have assumed $\alpha_{x,y} = 0$ so that $\gamma_{x,y} = 1/\beta_{x,y}$. The spectral brightness of the emitted radiation is the flux at a specific wavelength[2] emitted from within a specific volume of transverse phase space volume, i.e.

$$\mathcal{B}(\lambda) = \frac{\mathcal{F}(\lambda)}{(2\pi)^2\mathcal{E}_x\mathcal{E}_y},$$

where $\mathcal{E}_{x,y} = \Sigma_{x,y}\Sigma_{x',y'}$ describes the effective emittance, i.e. the emittance of the overlap between electron beam and intrinsic photon beam[3]. In a nutshell, this motivates the push for low-emittance rings running with large amounts of stored current and long undulators with short period lengths.

Finally, since the transversely coherent flux emitted at a specific wavelength λ is given by

$$\mathcal{F}_c(\lambda) = \mathcal{B}(\lambda)\left(\frac{\lambda}{2}\right)^2,$$

the coherent fraction of the emitted radiation can be expressed as

$$\begin{aligned} f_c(\lambda) &= \frac{\mathcal{F}_c(\lambda)}{\mathcal{F}(\lambda)} = \frac{(\lambda/4\pi)^2}{\mathcal{E}_x\mathcal{E}_y} \\ &= \frac{1}{\sqrt{1+(\frac{\sigma_x}{\sigma_r})^2}\sqrt{1+(\frac{\sigma_{x'}}{\sigma_{r'}})^2}} \times \\ &\quad \frac{1}{\sqrt{1+(\frac{\sigma_y}{\sigma_r})^2}\sqrt{1+(\frac{\sigma_{y'}}{\sigma_{r'}})^2}}. \end{aligned} \quad (3)$$

[1] This approach also entirely neglects the horizontal plane and tacitly accepts that ID radiation will, at best, be diffraction-limited in the vertical plane only. Diffraction-limited light sources, i.e. storage rings where the equilibrium emittance is so low that both transverse planes can be operated at or below the diffraction limit, present a solution to this problem and have recently become a topic of great interest [6, 7].

[2] This spectral flux $\mathcal{F}(\lambda)$ is conventionally defined as the number of photons emitted per second and per 0.1% BW ($\Delta\lambda/\lambda$). It is proportional to the stored current and the number of undulator periods.

[3] A noteworthy consequence is that intrinsic photon and electron emittances are added linearly, not quadratically.

* simon.leemann@maxlab.lu.se

Copyright © 2013 CC-BY-3.0 and by the respective authors

It is interesting to note here, that even if the electron beam were perfectly matched to the intrinsic photon beam in transverse phase space, the coherent fraction achieved in this way would be only 25%. Increasing the coherent fraction beyond this level requires diminishing the electron beam's transverse phase space volume with respect that of the intrinsic photon beam.

MATCHING OPTICS TO ID RADIATION

Low-emittance storage rings need to be matched locally to strong ID's to prevent beta beating and tune shifts away from the working point [8]. In addition to such matching, the optics of the ring also need to be matched globally to a specific type of ID and a certain wavelength of interest in order to achieve highest brightness radiation. In 3rd generation light sources the source of radiation is a sheet beam where the horizontal emittance is much larger than that of the emitted radiation, while the vertical emittance and optics are usually the focus of matching efforts[4].

A first attempt at matching could be made by calling for perfect matching of the vertical beta function to a specific ID

$$\beta_y \stackrel{!}{=} \beta_r = \frac{\sigma_r}{\sigma_{r'}} = \frac{L}{2\pi}, \qquad (4)$$

which turns out to be independent of wavelength. This, however, leads to very small beta functions in the ID's which, in connection with the narrow gaps (4 mm are typically assumed), quickly leads to acceptance and hence lifetime issues[5]. On the other hand, one can easily show that $\beta_y = L/2$ ensures maximum acceptance for a given ID and gap setting. In the MAX IV 3 GeV storage ring, assuming a typical in-vacuum undulator of 4 m magnetic length, this has led to a choice of $\beta_y = 2\,\mathrm{m}$ at the center of the long straight sections.

In terms of optics matching to the ID, this choice of β_y is a factor π too large and hence the overlap needs to be improved by appropriate choice of emittance coupling. Assuming the MAX IV 3 GeV storage ring is operated "at the diffraction limit" $\varepsilon_y = 8\,\mathrm{pm\,rad}$[6], inspection of Eqs. 1 and 2 reveals that for the typical in-vacuum undulator, in the vertical plane the angular overlap is dominated by the intrinsic photon beam, while the spatial mismatch is caused by the height of the electron beam in the ID. Figure 1 illustrates this situation: the horizontal mismatch between intrinsic photon beam and electron beam is very large while the vertical overlap can be considerably improved by choosing a reduced coupling.

[4] In addition, horizontal optics in straight sections are often also constrained by other requirements, e.g. large β_x required for injection.

[5] Note also, even if the vertical emittance is set at the diffraction limit and the vertical beta function is adjusted according to Eq. 4, the effective vertical emittance will still be twice the vertical intrinsic photon emittance according to Eqs. 1 and 2. This already indicates that a further reduction of vertical emittance pays off.

[6] Note this corresponds to $\kappa = 2.5\%$, a very relaxed requirement for emittance coupling compared to existing 3rd generation light sources. This is a consequence of the ultra-low emittance lattice of the MAX IV 3 GeV storage ring.

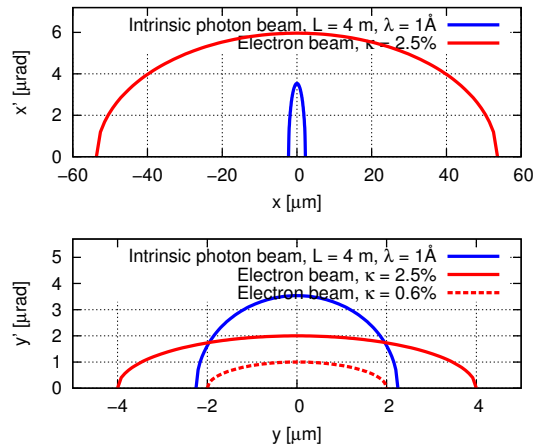


Figure 1: RMS beam size of the intrinsic photon and electron beam in phase space assuming 1 Å radiation emitted from a 4 m undulator installed in a long straight section of the MAX IV 3 GeV storage ring.

MAXIMIZING BRIGHTNESS AND COHERENCE

Since for very small values of coupling, $\mathcal{E}_x \approx \mathrm{const}$, as a consequence of $\varepsilon_x \approx \varepsilon_0 = \mathrm{const}$ (in the absence of IBS), the brightness scales as

$$\mathcal{B}(\lambda) \propto \frac{1}{\mathcal{E}_y} = \frac{1}{\Sigma_y \Sigma_{y'}},$$

and hence one can expect a substantial brightness increase by reducing the vertical electron emittance. The results of an exact calculation assuming two typical ID's are displayed in Fig. 2.

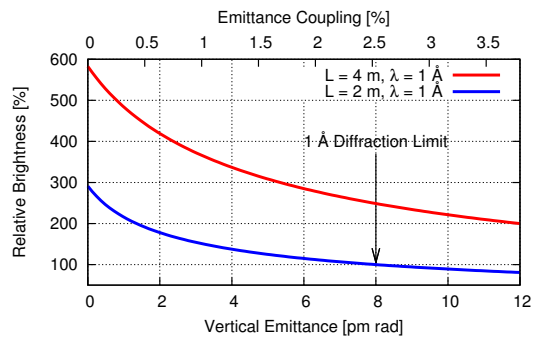


Figure 2: Brightness increase as emittance coupling is reduced for two ID's tuned to 1 Å. The brightness values have been normalized to that of the short ID operated at 8 pm rad. The effect of IBS has not been included.

Although 2 pm rad is a very low vertical emittance, it corresponds to 0.6% coupling which is comparable to presently operating light sources. Tracking studies for the MAX IV 3 GeV storage ring [4, 9] indicate roughly such a level of emittance coupling can be expected as a result of imperfections (magnet and alignment errors) as well as application of orbit correction and linear optics corrections.

Copyright © 2013 CC-BY-3.0 and by the respective authors

Tracking studies have also quantified the decrease of Touschek lifetime and the emittance increase caused by IBS at 500 mA as a result of operating at reduced coupling. These studies have shown that the increase of IBS blow-up can be counteracted by bunch lengthening using Landau cavities. Furthermore, although Touschek lifetime reduces by roughly 50% as a consequence of the coupling reduction, with bunch lengthening from Landau cavities operated at the third harmonic (leading to stretching by roughly a factor five over the natural bunch length [10]) it should remain around 25 h, sufficient to ensure overall lifetime around 10 h.

Figure 3 shows the spectral brightness for a 3.3 m long in-vacuum undulator operated in the MAX IV 3 GeV storage ring at 500 mA. The roughly two-fold brightness increase at wavelengths around 10 keV as a result of coupling reduction from the diffraction limit to 2 pm rad can be clearly recognized.

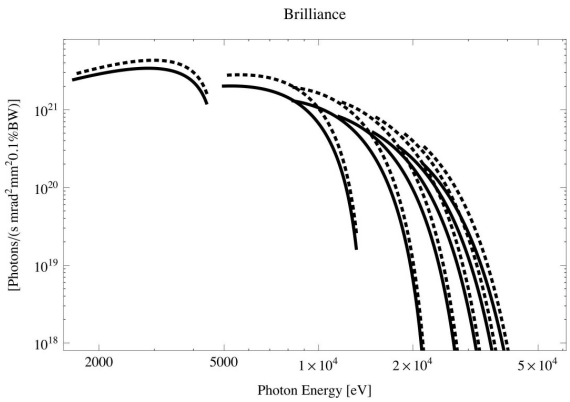


Figure 3: Spectral brightness at peak energy for a 3.3 m long in-vacuum undulator (18 mm period, 4 mm gap, 1.15 T effective field) installed in the MAX IV 3 GeV storage ring at 500 mA stored current for a vertical emittance of 8 pm rad (solid line) and 2 pm rad (dashed line) [7].

In addition to offering much higher brightness for x-rays, the reduced coupling also increases the transverse coherence of the emitted radiation. Figure 4 shows the degree of transverse coherence according to Eq. 3 for three undulators in the MAX IV 3 GeV storage ring tuned to three different wavelengths. Roughly a factor of two increase in coherence at 1 Å when going from the diffraction limit to 2 pm rad vertical emittance can be recognized. Note, however, that even for an ideal sheet beam no more than 2.1% transverse coherence can be achieved at 1 Å because of the mismatch in the horizontal plane (cf. Fig. 1, top). Higher levels of transverse coherence can be observed for softer radiation, albeit with a reduced dependence on emittance coupling since the overlap becomes dominated by the intrinsic photon beam's phase space volume.

CONCLUSIONS

We have demonstrated that setting the vertical emittance below the diffraction limit can lead to a substantial increase of brightness for x-rays. The emittance coupling in the MAX IV 3 GeV storage ring is expected to be close to the required 0.6% and can be adjusted using the skew quadrupoles in the lattice. Since the impact of this reduced coupling on lifetime and IBS emittance blow-up can be mitigated by the Landau cavities, we will be able to offer a vertical emittance of 2 pm rad to our hard x-ray users. Transverse coherence is also improved by this reduction in coupling. However, the horizontal mismatch persists and hence transverse coherence at 1 Å remains low. A fully diffraction-limited storage ring delivering round beams to ID's below the diffraction limit in both planes simultaneously presents a possible solution.

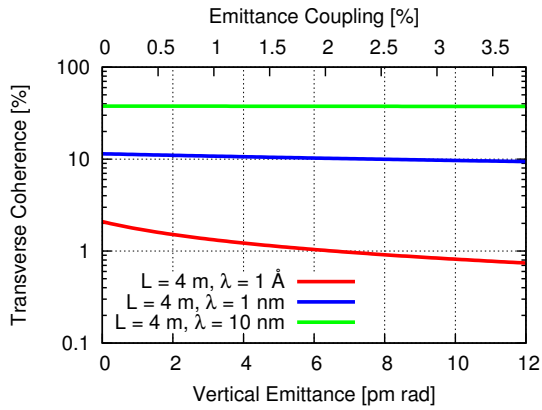


Figure 4: Degree of transverse coherence as a function of emittance coupling for radiation emitted at different wavelengths from ID's installed in a long straight section of the MAX IV 3 GeV storage ring.

REFERENCES

[1] MAX IV Detailed Design Report, available at http://www.maxlab.lu.se/node/1136.

[2] M. Eriksson et al., "The MAX IV Synchrotron Light Source", THPC058, IPAC 2011, San Sebastián, Spain.

[3] S.C. Leemann et al., Phys. Rev. ST Accel. Beams, **12**, 120701 (2009).

[4] S.C. Leemann, MAX-lab Internal Note 20121107, available at http://www.maxlab.lu.se/node/999.

[5] K.-J. Kim, Opt. Eng., Vol. **34**, No. 2, pp. 342-352 (1995).

[6] M. Borland, "Progress Towards Ultimate Storage Ring Light Sources", TUXB01, IPAC 2012, New Orleans, LA, USA.

[7] ICFA Beam Dynamics Newsletter, No. 57, April 2012, available at http://icfa-usa.jlab.org/archive/newsletter/icfa_bd_nl_57.pdf.

[8] E. Wallén, S.C. Leemann, "Strategy for Neutralizing the Impact of Insertion Devices on the MAX IV 3 GeV Storage Ring", TUP235, PAC'11, New York, NY, USA.

[9] S.C. Leemann, MAX-lab Internal Note 20130724, available at http://www.maxlab.lu.se/node/999.

[10] Å. Andersson et al., "The 100 MHz RF System for the MAX IV Storage Rings", MOPC051, IPAC 2011, San Sebastián, Spain.

Copyright © 2013 CC-BY-3.0 and by the respective authors

SIMULATION OF USING ORBIT BUMPS TO TEST SEXTUPOLE COMPENSATION FOR THE SHORT PULSE X-RAY SYSTEM AT THE ADVANCED PHOTON SOURCE *

M. Borland†, V. Sajaev, ANL, Argonne, IL 60439, USA

Abstract

As part of an ongoing upgrade of the Advanced Photon Source (APS), a Short Pulse X-ray (SPX) system is being developed based on two sets of crab cavities separated by 180 degrees vertical phase advance. Emittance growth due to incomplete cancellation of the kicks from the sets of cavities is a concern. Simulations predict that it can be controlled by adjustment of the sextupoles between the cavities. To test these predictions, we can use orbit bumps that reproduce the trajectories of individual particles through the sectors in question. We present results of simulations of such tests, showing the degree to which the emittance growth and other properties of the machine will differ for optimized and unoptimized sextupoles. We also show results of recent experimental tests.

INTRODUCTION

One of the challenges of operating the Short Pulse X-ray (SPX) facility [1, 2] will be preserving the small vertical size of the APS beam. Vertical emittance increase was predicted in early simulations of SPX [3]. It results mainly from additional coupling occurring due to large vertical trajectories in sextupoles between the SPX cavities [4]. This emittance increase is undesirable because it decreases the x-ray brightness seen by all users. It also increases the minimum x-ray pulse duration that SPX can deliver.

We also found that lifetime and injection efficiency were negatively affected by this strong local coupling through stronger excitation of nearby nonlinear resonances. We resolved these problems in simulation by optimizing the sextupoles between the SPX cavities so as to minimize the vertical emittance growth, while at the same time preserving injection efficiency and lifetime [5].

Owing to the expense and complexity of SPX, it is desirable to test as many aspects of the beam dynamics ahead of time. With deflecting cavities, every longitudinal slice of the beam travels on its own vertical trajectory. The amplitudes of those trajectories depend on the longitudinal position of the slice. Without deflecting cavities, we cannot recreate this behavior completely, but we can generate a real orbit bump using orbit correctors where the entire beam would go on a trajectory corresponding to some beam slice. We could thus verify that the effect of the orbit bump on coupling and nonlinear dynamics is reduced when properly optimized sextupoles are used.

* Work supported by the U.S. Department of Energy, Office of Science, under Contract No. DE-AC02-06CH11357.

† borland@aps.anl.gov

Any two vertical correctors bracketing a straight section can be used to produce a trajectory that exactly corresponds to a trajectory originating from a single vertical kick somewhere in the straight section. Using existing correctors powered at modest levels, we can simulate deflections equivalent to a cavity deflecting voltage of about 4 MV without loss of stored beam. Note that this is a very stringent test, not only because it exceeds the intended maximum deflection by a factor of two, but because with actual deflecting cavities, very few electrons experience deflections that are close to the maximum possible deflection, owing to the small 33° rms phase spread of the bunch.

LATTICE OPTIMIZATION

The lattices used for the simulations and experiments are mock-ups of the planned operational lattices. The latter will differ from today's lattice by long straight sections (LSS) in straight sections 1, 5, and 7, as well as a special insertion with reduced horizontal beam size (RHB) in straight section 20. Two of the LSSs (in straights 5 and 7) are associated with SPX, being required in order to make room for the cryomodules. The vertical phase advance between these straights (i.e., through sectors 6 and 7) is ideally 2π. The LSSs are mocked up by setting to zero certain magnets that would be removed to make an actual long straight.

The tests require two lattices: one in which the sextupoles in sectors 6 and 7 are optimized to minimize SPX emittance growth, and a second with normal sextupoles in those sectors. The first lattice was optimized using a direct genetic algorithm [6] with fictitious zero-length crab cavities located located 1.2 m downstream of the center of straight sections 5 and 7. The cavities were powered at 2-MV deflection strength during the optimization of dynamic aperture, lifetime, and vertical emittance growth. The optimization was very effective, giving a nominal lifetime of over 11 hours for 24 bunches, 100 mA, 1% coupling, and $\xi_x = \xi_y = 5$; dynamic acceptance of -15 mm; and emittance growth of less than 1 pm on a base of 35 pm.

The second lattice started from the first, but the sextupoles in sectors 5 and 7 were identical to those in sector 1, while the sextupoles in sectors 6 and 8 were identical to those in sector 2. This condition results from the fact that straight sections 1, 5, and 7 are all long straights. This optimization also worked well, but not as well as the previous one, which is perhaps not surprising given that it had fewer knobs with which to work. The lifetime was just under 10 hours, with dynamic acceptance beyond -15 mm.

Copyright © 2013 CC-BY-3.0 and by the respective authors

SIMULATION RESULTS

The purpose of the simulations is to determine whether we can realistically expect to measure differences between the two lattices. Lacking a calibrated model for these lattices, we used 500 random error ensembles, with realistic error levels, with the quadrupole tilt error level chosen to give a vertical emittance of about 10 pm. The vertical emittance was computed for each ensemble using the 6D equilibrium beam moments computation in `elegant` [7]. However, some ensembles gave much higher vertical emittance, so we selected those ensembles giving a vertical emittance of 10 to 15 pm for use in the remaining simulations. For the uncompensated lattice, we had 140 ensembles left, while for the compensated lattice we had 127.

For each ensemble, we performed simulations with bump amplitudes up to 4 MV equivalent. Figure 1 shows the Courant-Snyder invariant of the orbit outside the bump vs voltage for the two cases. Even for 4 MV equivalent, the error bars nearly overlap, indicating that bump leakage is not a reliable way to distinguish between the lattices.

The conclusion is more promising for the vertical emittance, as shown in Figure 2. Here we see that at the 2-MV level the two cases will be separated by a significant gap. Hence, we can expect to see a significant difference when we perform experiments.

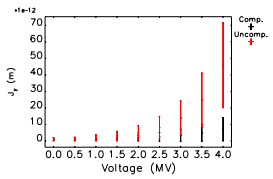


Figure 1: Courant-Snyder invariant vs equivalent deflecting voltage for lattices with and without compensated sextupoles, for many error ensembles.

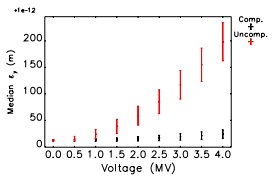


Figure 2: Median vertical emittance vs. equivalent deflecting voltage for lattices with and without compensated sextupoles, for many error ensembles.

We also simulated the dynamic acceptance (DA) and local momentum acceptance (LMA) [8], and computed the Touschek lifetime from the latter. These are to be seen from a different perspective, since we do not expect the configuration with compensated sextupoles to perform as well as the uncompensated case. The compensation is required to reduce the vertical emittance and is designed to have an acceptably small impact on nonlinear dynamics. In comparison to the last set of calculations, these are far more CPU intensive. Hence, we performed runs for only five values of voltage from 0 to 4 MV. In addition, for the LMA computations we used only 50 of the ensembles (subject to the same selection process described above).

For dynamic acceptance, we used all the available ensembles (subject to the vertical emittance limit described above). We tracked 400 turns using parallel `elegant` [9] with kick elements, rf, and lumped synchrotron radiation.

Figures 3 and 4 show the DA for the compensated and uncompensated cases. We see that up to 3 MV, the DA is maintained at nearly the level for the uncompensated case, dropping signicantly for both cases at 4 MV.

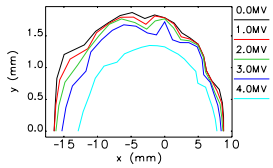


Figure 3: Median dynamic acceptance for case with compensated sextupoles as a function of equivalent deflecting voltage.

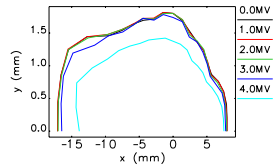


Figure 4: Median dynamic acceptance for case with uncompensated sextupoles as a function of equivalent deflecting voltage.

Simulations of the LMA show that the uncompensated case is significantly worse as the equivalent voltage is increased, which is not surprising [5]. However, when we compute the Touschek lifetime for each ensemble using `touschekLifetime` [10], including the inflated emittances computed above, we see that the lifetime is significantly longer for the uncompensated case, as seen in Figure 5. This is a result of the larger vertical emittance, and hence this measurement would add nothing new.

The momentum acceptance can be measured more directly by scanning the main rf voltage V_m. Figure 6 show the momentum acceptance as a function of equivalent deflecting voltage. The difference of more than 0.2% in momentum acceptance for an equivalent voltage of 3 MV corresponds to the difference between 8.2 and and 8.7 MV in V_m, which should be measurable.

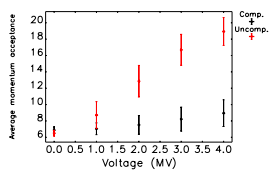


Figure 5: Touschek lifetime as a function of equivalent deflecting voltage for compensated and uncompensated sextupoles.

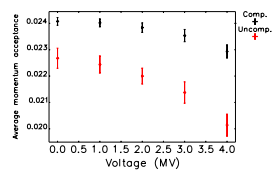


Figure 6: Average momentum acceptance as a function of equivalent deflecting voltage for compensated and uncompensated sextupoles.

EXPERIMENTAL RESULTS

The mock-up lattices desribed above were set up during storage ring studies, using the so-called "reference" orbit, which goes through the centers of magnets rather than accommodating user steering. Figure 7 shows the beta functions after the lattice setup was completed for the lattice with compensated sextupoles.

Copyright © 2013 CC-BY-3.0 and by the respective authors

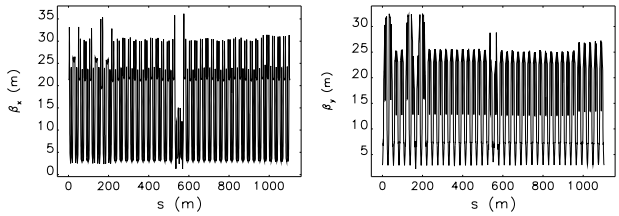


Figure 7: Beta functions of the lattice with compensated sextupoles as measured by the response matrix fit after optics correction.

We used pairs of A:V1 and B:V1 correctors bracketing straight sections 5 and 7 to generate the orbit bumps. The ideal corrector settings nearly closed orbit bumps, with maximum orbit distortion outside the bump of only 2% of the bump amplitude. To improve the bump closure further, we decided to change manually only the pair of correctors around straight section 5 while the other pair of correctors was controlled by orbit feedback.

According to the simulations presented above, the biggest distinction between the lattices shows up in the vertical emittance—and therefore beam size—dependence on the orbit bump amplitude. We performed scans of the bump amplitude for both sets of sextupoles and recorded the beam sizes. Figure 8 shows the dependence of the vertical beam size on the orbit bump amplitude, which is presented in the units of the equivalent deflecting voltage. This plot should be compared with Figure 2. As expected, the lattice with compensated sextupoles shows almost no beam size dependence on the deflecting voltage amplitude, while the lattice with uncompensated sextupoles shows strong dependence. This measurement has verified that the emittance growth can be controlled by optimizing sextupoles.

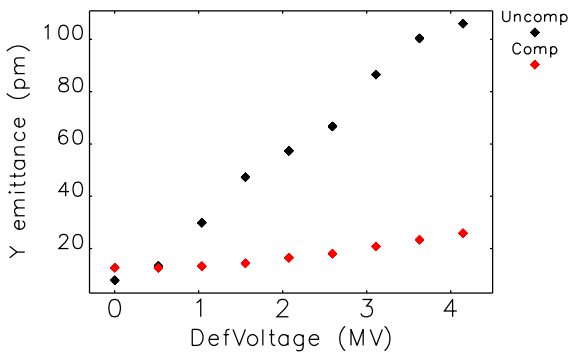


Figure 8: Measured vertical emittance dependence on the equivalent deflecting voltage for lattices with and without compensated sextupoles.

We also measured lifetime and injection efficiency as a function of the orbit bump amplitude. Figures 9 and 10 show the results. Simulations predict that for the lattice with compensated sextupoles the lifetime should not change significantly in the range of deflecting voltage up to 4 MV (see Figure 5). In our measurements, the lifetime stayed approximately constant for the orbit bumps corresponding to deflecting voltage in the range from -4 MV to +3 MV, which roughly corresponds to the predictions.

We have not directly measured the dynamic acceptance of the lattices. However, we have recorded injection efficiency, which can be used as a measure of the dynamic acceptance since our efficiency is defined mostly by the dynamic acceptance of the storage ring. The dynamic acceptance simulations show no big effect for voltages up to 3 MV and then a reduction for 4 MV (Figures 3 and 4). The measurements gave us good injection in the range of orbit bumps corresponding to voltages from -4 MV to +2.5 MV. This again roughly corresponds to simulations.

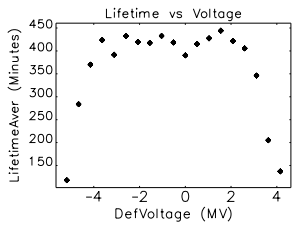


Figure 9: Lifetime as a function of the orbit bump amplitude presented in units of the deflecting voltage for compensated sextupoles.

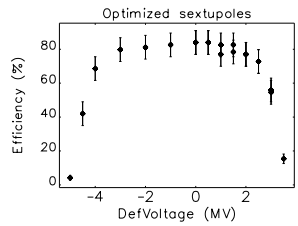


Figure 10: Injection efficiency as a function of the orbit bump amplitude for the compensated sextupoles.

CONCLUSIONS

We performed simulations and experiments to investigate whether use of closed orbit bumps is a valid way to simulate the sextupole compensation scheme for SPX. In simulation, we found that vertical emittance and, to a lesser extent, momenmtum aperture, should show a measurable difference between the two configurations. Experiments verified that the emittance growth is controlled by the compensating sextupoles.

REFERENCES

[1] A. Zholents, R. Heimann et al., NIM A 425, 385 (1999).

[2] A. Nassiri et al., IPAC 2012, 2292 (2012).

[3] M. Borland, PRSTAB 8(7), 074001 (2005).

[4] M. Borland and V. Sajaev, PAC 2005, 3886 (2005).

[5] APS Upgrade Preliminary Design Report (2012), Chapter 3.2.2.4.

[6] M. Borland, V. Sajaev et al., ANL/APS/LS-319, APS (2010).

[7] M. Borland, ANL/APS/LS-287 (2000).

[8] M. Belgrounne et al., PAC 2003, 896 (2003).

[9] Y. Wang, M. Borland et al., ICAP 2009, 355 (2009).

[10] A. Xiao and M. Borland, PAC 2007, 3453–3455 (2007).

Copyright © 2013 CC-BY-3.0 and by the respective authors

A SEVEN-BEND-ACHROMAT LATTICE AS A POTENTIAL UPGRADE FOR THE ADVANCED PHOTON SOURCE*

M. Borland†, V. Sajaev, Y.-P. Sun, ANL, Argonne, IL 60439, USA

Abstract

The Advanced Photon Source (APS) is a 7-GeV storage ring light source that has been in operation since 1996. In that time, the emittance has dropped from 8 nm to 3 nm. The increasing feasibility of multi-bend-achromat lattices (e.g., the MAX-IV project) promises the possibility of a much greater reduction in emittance. In this paper, we show the design of a symmetric seven-bend-achromat lattice, including linear optics, nonlinear dynamics optimization, magnet requirements, and performance with errors.

INTRODUCTION

There is now wide-spread interest in multi-bend achromat lattices as a means of achieving significantly lower emittance in light source storage rings. Notable efforts include the MAX-IV [1] and SIRIUS projects [2], which are under construction, as well as proposed upgrades for ESRF and SPring-8. A recent report of the Basic Energy Sciences Advisory Committee recommended re-examination of existing upgrade plans for US storage rings to explore the potential of such a lattice. Such work was already on-going at the Advanced Photon Source (APS), but has now taken on renewed urgency.

We have explored a number of lattice concepts, including designs similar to the one being built at MAX-IV. In this paper, we present a design based on the hybrid-multi-bend achromat (HMBA) concept proposed by ESRF [3].

LATTICE OPTIMIZATION

The HMBA lattice is distinguished from the MAX-IV-style lattice by having a dispersion bump between the outer pairs of dipoles, which also feature a longitudinal gradient. Sextupoles are located only in the dispersion bump, by virtue of which their strengths are dramatically reduced. In addition, the phase advance between pairs of sextupole centers in the two dispersion bumps for any sector is 3π and π for the horizontal and vertical planes, respectively.

We started with a lattice file provided by N. Carmignani of ESRF. The first step was to modify the angles for a 40-sector ring (ESRF has only 32 sectors) and perform some basic matching to get a stable lattice. This gave acceptable dynamic acceptance (DA) and local momentum acceptance (LMA), albeit in the absence of errors, and an emittance of about 80 pm at 6 GeV.

For further development, our goal was to reduce the emittance as far as possible, consistent with workable lifetime and sufficient injection aperture for on-axis, swap-out injection [4]. Toward this end, we performed a wide-ranging scan of the integer and fractional tunes that covered over 4000 possible working points with $\nu_x : (99, 109)$ and $\nu_y : (32, 39)$. For each target working point, we used `elegant` [5] to perform linear optics optimization to minimize the emittance, obtain relatively small < 3 m beta functions at the insertion devices (IDs), restrain the maximum beta functions below 20 m, ensure the correct phase advance between sextupoles, ensure the correct overall geometry, etc. In this process, essentially every parameter of the lattice was allowed to vary, including strengths, lengths, and positions of all elements.

Once matching was completed, we corrected the chromaticity to $+2$ in both planes, using a reflection- and translationally-symmetric sextupole distribution. We then used `Pelegant` [6] to perform tracking without errors to determine the maximum stable amplitudes for momentum and amplitude deviations, which involved evaluation of particle survival, crossing of integer and half-integer resonances, and diffusion rates. Figures 1 and 2 show maps of natural emittance and minimum LMA. Note that the latter is often limited at the high-dispersion point and may be smaller than indicated by the tunes vs momentum offset. Figures 3 and 4 show maps of the beta functions at the IDs, which would ideally both be 1.5 m to maximize brightness.

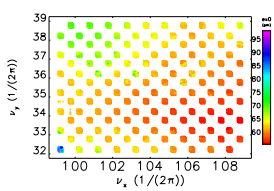


Figure 1: Map of natural emittance vs working point.

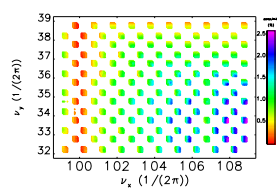


Figure 2: Map of minimum momentum acceptance vs working point.

Since not all parameters can be simultaneously optimized, we performed a non-dominated sort [7], which yielded a handful of superior solutions from which to choose. Dynamic acceptance (DA) and lifetime were optimized for several of these using a tracking-based multi-objective genetic algorithm (MOGA) [8]. This included fine adjustment of the working point and linear optics, as well as adjustment of individual sextupoles. Following ESRF, we organized the sextupoles into 12 families with

* Work supported by the U.S. Department of Energy, Office of Science, under Contract No. DE-AC02-06CH11357.

† borland@aps.anl.gov

Copyright © 2013 CC-BY-3.0 and by the respective authors

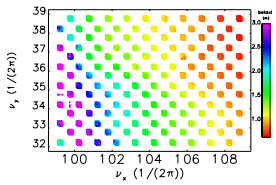


Figure 3: Map of $\beta_{x,ID}$ vs working point.

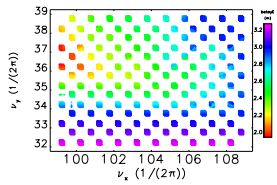


Figure 4: Map of $\beta_{y,ID}$ vs working point.

two-period translational symmetry. Figure 5 shows the lattice functions for the best configuration, while Table 1 lists lattice properties. Of particular note is the natural emittance, which is below 60 pm, and the rather small beta functions at the IDs in both planes. Quadrupole strengths are under 80 T/m, while sextupoles have $|B''| < 6.5kT/m^2$. In the remainder of this paper we present detailed results for this configuration.

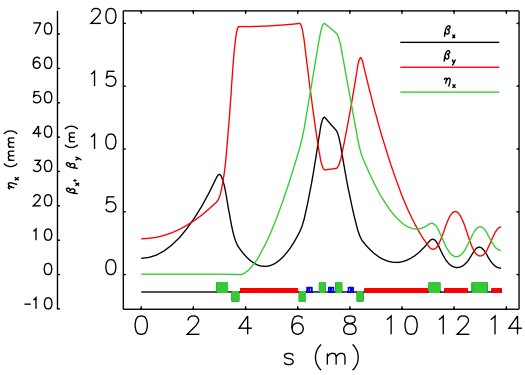


Figure 5: Lattice functions for a half cell, with the ID straight on the left.

Table 1: Parameters of the Optimized Lattice

$\nu_x = 105.45$	$\nu_y = 34.15$
$\epsilon_0 = 59$ pm	$\sigma_{\delta,0} = 0.094\%$
$U_0 = 2.1$ MeV/turn	$\alpha_c = 6 \times 10^{-5}$
Max. $\beta_x = 12.5$ m	Max. $\beta_y = 20$ m
Max. $\eta_x = 73$ mm	
$\beta_{x,ID} = 1.3$ m	$\beta_{y,ID} = 2.9$ m
$\tau_x = 13.5$ ms	$\tau_\delta = 15$ ms

NONLINEAR DYNAMICS

Figures 6 and 7 show the results of frequency map analysis (FMA). We see that the horizontal tune shift with amplitude is quite large. As we'll see below, the regions of the frequency map with no data (e.g., around x=0.5 mm) correspond not to particle loss, but to difficulty determining the tune of the particle when it starts near the $\nu_x = 0.5$ resonance. Detailed simulations with errors showed no particle loss resulting from this resonance. The momentum-dependent tunes and FMA are shown in Figures 8 and 9. Here again we see voids in the FMA resulting from particles with hard-to-determine tunes, not particle loss.

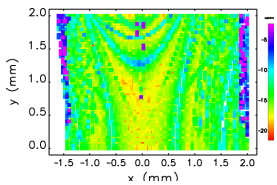


Figure 6: FMA in x-y space.

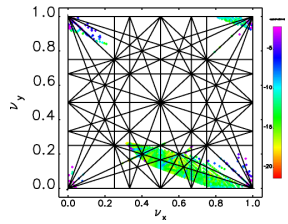


Figure 7: FMA in ν_x-ν_y space.

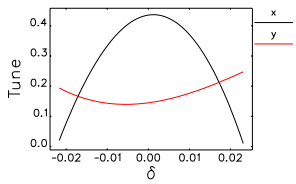


Figure 8: Tunes versus momentum offset.

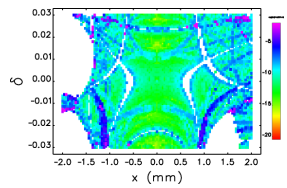


Figure 9: FMA in x-δ space.

For further evaluation, we need a set of error ensembles. We constructed these by first computing lattice functions and 6D equilibrium beam moments for 12,000 ensembles, then selecting those with beta beats between 7 and 10% and $\kappa = \epsilon_y/\epsilon_x : [0.1, 0.2]$. This resulted in 93 ensembles that represent possible machine instances with somewhat large uncorrected errors. We also added systematic multipoles to the quadrupoles and dipoles, at a level of 1% per multipole at a 10-mm radius. Performance with these large errors provides a stringent test of the robustness of the lattice.

DA simulations, shown in Figure 10, exhibit a dynamic aperture of $|x| > 1.3$ mm and $|y| > 1.7$ mm, more than adequate for on-axis injection given that the beam size from the booster will have $\sigma_x = 0.2$ mm and $\sigma_y = 0.3$ mm. The DA search algorithm included radiation damping and had a sufficiently small step size to ensure that the $\nu_x = 0.5$ resonance would not be stepped over. To further verify this, we tracked particles clustered around $x = 0.625$ mm, corresponding to a shift tune bracketing $\nu_x = 0.5$ for each of the 93 ensembles. In tracking for 1500 turns with damping and quantum excitation, no particles were lost, even though many were observed to move across the resonance. Evidently, the tune shift with amplitude is so large that this resonance is not harmful.

Local momentum aperture (LMA) was determined for the 93 ensembles, and is shown in Figure 11. The 10^{th} percentile aperture is over $\pm 2\%$, an acceptable result.

Again, owing to the voids in the FMA shown in Figure 9, we performed additional tracking to verify that the LMA search algorithm did not step over any aperture limits. This consisted of tracking 4100 turns (one longitudinal damping

Copyright © 2013 CC-BY-3.0 and by the respective authors

time) with an 91x91 grid of particles with $x : [-2, 2]$ mm and $\delta : [-4, 4]$ %. A 2-d histogram of the accepted particles for 16 error ensembles, shown in Figure 12, shows the expected region of stability for off-momentum particles.

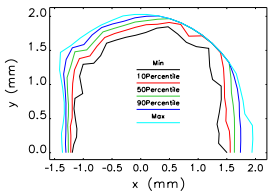


Figure 10: DA contours from 93 error ensembles.

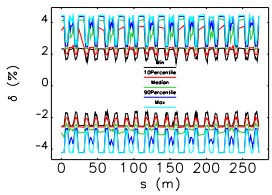


Figure 11: LMA for 93 ensembles, showing 25% of the ring.

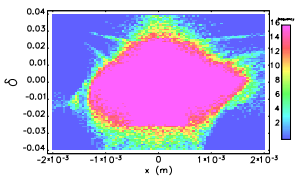


Figure 12: Grid of acceptance counts for 16 error ensembles.

INTRA-BEAM SCATTERING AND LIFETIME

We used `ibsEmittance` [9] to compute the effect of intrabeam scattering (IBS) for two bunch patterns at 200 mA, as a function of the emittance ratio, including a third-harmonic cavity that increases the rms bunch length to 20 mm. Figure 13 shows the effect on the horizontal emittance, which is fairly modest for $\kappa > 0.2$. The effects on energy spread are also modest.

Using the beam parameters from the IBS calculations, we computed the Touschek lifetime using `touscheckLifetime` [10] for the same two bunch patterns. This was done using the 93 LMA results described above, along with the ideal lattice functions. The results, shown in Figure 14, indicate that lifetime for $\kappa = 1$ is 40-60% longer than the lifetime for $\kappa = 0.2$. The gas-scattering lifetime was computed from the DA and the average beta functions listed above using the Toolkit for Accelerator Physics on Androids (TAPAs) [11]. The value is 32 hours, assuming a gas pressure of 2 nT and a gas mixture similar to that found in the APS today.

Since swap-out injection is envisioned, the required lifetime τ with N_b bunches is determined by the minimum possible bunch-swapping interval ΔT_s and the allowed droop $D = N_b \Delta T_s / \tau$ between swaps. With $N_b = 48$, $D = 0.1$, and $\Delta T_s \geq 5$ s, we need $\tau \geq 0.6$ h, which appears possible. For $N_b = 48$, the bunch charge is 15 nC, requiring a rather modest average current of 3.8 nA into the existing accumulator ring, assuming 80% overall efficiency. Accumulation of the required high-charge bunches is described in [12], while the swap-out injection scheme is described in [13].

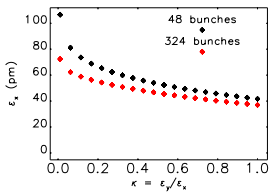


Figure 13: Effect of IBS on the horizontal emittance for 200 mA.

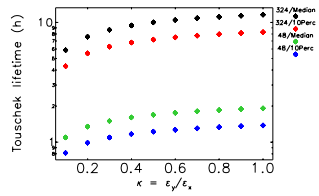


Figure 14: Median and 10^{th}-percentile Touschek lifetime for two bunch patterns.

CONCLUSIONS

A hybrid seven-bend achromat lattice has been developed that could replace the existing APS storage ring, providing a reduction in emittance from 3.1 nm to about 60 pm. Nonlinear dynamics was optimized using a tracking-based multi-objective algorithm, resulting in a design that appears workable for on-axis injection even in the presence of rather large errors. Intra-beam scattering does not have a dramatic effect for emittance ratios greater than about 0.2, even for 48 bunches in 200 mA. Lifetime appears to be workable with the existing APS injector.

ACKNOWLEDGMENTS

Parts of this work were performed using the Blues cluster at Argonne's Laboratory Computing Resource Center and the Mira cluster at Argonne's Advanced Leadership Computing Facility. Thanks to P. Raimondi, L. Farvacque, N. Carmignani, and others at ESRF for providing a copy of an earlier version of their lattice, which helped start this effort.

REFERENCES

[1] S. C. Leemann et al. *Physical Review ST Accel Beams*, 12:120701 (2009).

[2] L. Liu et al. *Proc. IPAC 13*, 1874 (2013).

[3] L. Farvacque et al. *Proc. of IPAC13*, 79 (2013).

[4] L. Emery et al. *Proc.of PAC 2003*, 256 (2003).

[5] M. Borland. ANL/APS/LS-287 (2000).

[6] Y. Wang et al. *ICAP 2009*, 355 (2009).

[7] K. Deb et al. *IEEE TEC*, 6:182 (2002).

[8] M. Borland et al. ANL/APS/LS-319, APS (2010).

[9] A. Xiao. *Proc. Linac 08*, 296–299 (2008).

[10] A. Xiao et al. *PAC 2007*, 3453–3455 (2007).

[11] M. Borland. *Proc. NA-PAC 13*. THPMA06, to be published.

[12] C.-Y. Yao et al. *Proc. NA-PAC 13*. TUPMA03, to be published.

[13] A. Xiao et al. *Proc. NA-PAC 13*. WEPSM13, to be published.

Copyright © 2013 CC-BY-3.0 and by the respective authors

VARIOUS CANTING SCHEMES FOR UTILIZING MORE THAN ONE INSERTION DEVICE IN AN INSERTION DEVICE STRAIGHT SECTION *

V. Sajaev†, G. Decker, L. Emery, ANL, Argonne, IL 60439, USA

Abstract

Presently, the APS utilizes one simple canting scheme for separation of radiation generated by two insertion devices (IDs) located in the same ID straight section. This scheme is based on triangular horizontal orbit bump with one corrector located between the IDs and orbit distortion limited to the ID straight section only. However, this scheme does not allow for switching between the upstream and downstream devices, nor does it allow for one beamline to accept the combined radiation of both devices. These capabilities are being requested for future APS Upgrade. In this paper, we describe more advanced canting schemes that allow for these capabilities, and also present test results. The main complication here is that the orbit distortion is required to go through the storage ring magnets thus generating optics errors, which have to be corrected.

INTRODUCTION

The Advanced Photon Source (APS) is a 7-GeV third-generation synchrotron light source that has been serving a wide variety of users since operations began in 1996. 34 straight sections are used for installation of insertion devices, and each straight section allows space for up to two 2.4-meter-long devices. Because of ever-increasing demand for beam time from experimenters, over time several straight sections were modified to double the beamline capacity. This was done by introducing so called dual-canted undulators [1]. In this configuration, a chicane is created with a trio of dipole magnets with an undulator in each leg as shown in Figure 1 (1-mrad dipoles used to separate dipole radiation from the ID radiation [2] are omitted for simplicity). The result is an angular separation between the x-ray beams that can be exploited downstream to create two independent beamlines from a single straight section.

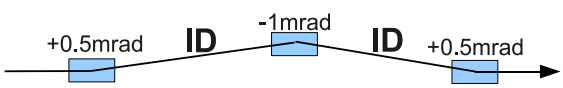


Figure 1: Canted ID straight section configuration presently used at the APS.

Since then, there have been a number of requests from user programs about the possibility of modifing this simple canting scheme to allow for better utilization of the insertion devices. The biggest problem with the present configuration is that the radiation from upstream and downstream devices cannot be switched between the two experimental stations. It is not a big issue presently because most of the insertion devices at the APS are similar to each other. But as more and more narrowly optimized devices are installed, the issue of switching the two photon beams can become more important. For example, the request to explore such a possibility already has come from the user group that plans to install one permanent magnet and one superconducting undulator in their straight section. In this paper, we will present several canting schemes and evaluate their performance from the accelerator physics point of view.

* Work supported by the U.S. Department of Energy, Office of Science, under Contract No. DE-AC02-06CH11357.

† sajaev@aps.anl.gov

SWITCHABLE CONFIGURATIONS

The most straightforward way to switch radiation of upstream and downstream undulators is just to flip the signs of the correctors that create the triangular orbit bump. The advantage of this approach is its simplicity and the fact that the orbit does not change outside of the ID straight section. This approach, however, has a major deficiency — the position of the radiation source will be shifted transversely by several mm after the switching, as shown in Figure 2. The shift will present challenges in both designing the beamline front end and the beamline optics. Therefore, it is desirable to create such an orbit bump that the source position does not change during the switch.

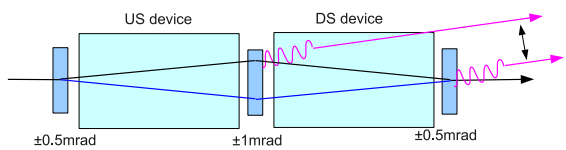


Figure 2: Diagram showing a position shift during ID switch in a triangular-bump configuration.

Symmetric Five-Corrector Bump (W-bump)

Using additional SR correctors outside of the ID straight section, we can make a bump such that source positions stay on the same line after the switch. Figure 3 illustrates the idea: when the beam travels along the trajectory shown in blue, the radiation of the upstream device goes into the inboard beamline; when the orbit is switched to the one shown in red, the downstream ID's radiation goes into the same inboard beamline. This configuration is strongly preferred by the users, but it presents difficulties for the storage ring operation – now the orbit will be changing outside of

Copyright © 2013 CC-BY-3.0 and by the respective authors

the straight section. Non-zero orbit through sextupoles will result in optics distortion that needs to be corrected.

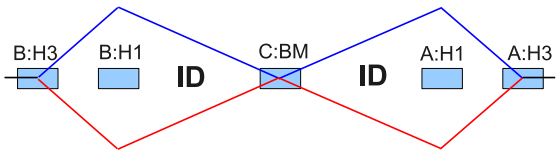


Figure 3: Five-kicker bump that allows photon beams to be sent from both undulators along the same line.

To generate this bump, we simultaneously matched orbit and beta functions using matching in `elegant` [3]. Two correctors on each side of the bump as shown on Figure 3 were used for orbit matching and eight quadrupoles around the straight section were used to match lattice functions. Figure 4 shows the resulting orbit and corresponding lattice functions for two sectors around the ID for no bump configuration and for positive and negative bumps. Lattice function changes are minimal and should not affect users.

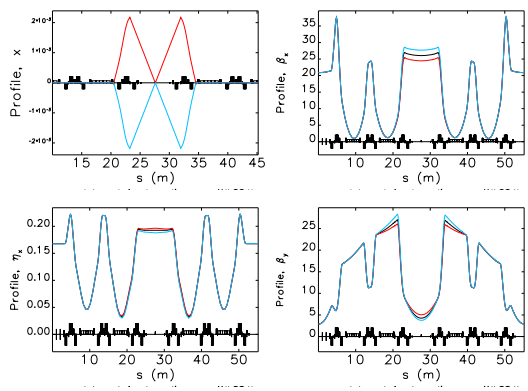


Figure 4: Lattice functions and orbit for two sectors around the ID straight section for W-bump. Starting from top left in clockwise order: orbit, horizontal beta function, vertical beta function, and horizontal dispersion. No bump, positive, and negative bumps are shown.

We also need to ensure that the nonlinear beam dynamics is not affected by this bump. Figures 5 and 6 show dynamic and local momentum apertures for no bump and for positive bump lattices. No effect on lifetime and injection efficiency is expected based on these simulations.

When combined with the 1-mrad bending angle required for the separation of the dipole and ID radiation, the strength of H1 correctors required to generate the orbit bump exceeds the limit. The easiest way to overcome this problem is to install additional correctors right next to the existing H1 correctors. However, this may shorten the length available for ID installation. Another approach is to involve more correctors in the creation of the orbit bump, but the upstream bending magnet radiation source can be slightly affected. From the storage ring operations point of view, however, all these configurations would work as good as the one presented here, and the choice is up to the user.

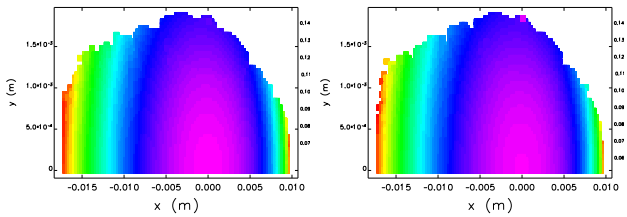


Figure 5: Dynamic aperture for the lattice without orbit bump (left) and with W-bump (right), color coding is horizontal tune.

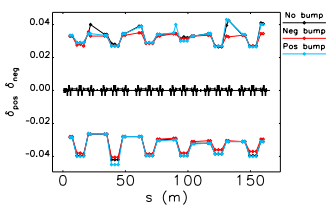


Figure 6: Local momentum aperture for lattice with W-bump.

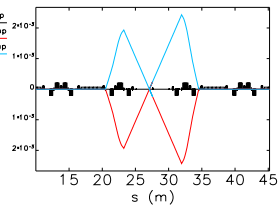


Figure 7: Orbit for W-bump with asymmetrically located central dipole.

One of the possible options for the APS Upgrade is introduction of several longer ID straight sections [4]. It is possible that insertion devices in a longer straight section would have different lengths. In that case, the central dipole does not have to be in the middle of the straight section. The same bump configuration would still work, as shown in Figure 7.

Antisymmetric Four-Corrector Bump

Another option possible in the W-bump configuration is sending the radiation of both devices down the same beamline. To do that, we just need to turn off the central dipole C:BM (Figure 3). Orbit and lattice functions for this bump are shown in Figure 8. Since beta function differences are almost invisible, we don't expect any effects on the nonlinear dynamics in this bump configuration.

Asymmetric Three-Corrector Bump

Recently, a user expressed interest in a configuration where most of the time the undulators will be used in an in-line configuration and only occasionally will the radiation be separated into two beamlines. The two configurations described above would completely satisfy this request. However, for simplicity of everyday operation it would be preferable to have the simplest possible in-line configuration — the straight non-canted configuration. This, however, would require the beamline front end to have an opening at 0 mrad angle relative to the line connecting closest to the ID dipoles. But the existing canted front-end design has only two openings at ± 0.5 mrad relative to that line. This design could still be used if the front end is moved by 0.5 mrad inboard. In the canted mode, this

Copyright © 2013 CC-BY-3.0 and by the respective authors

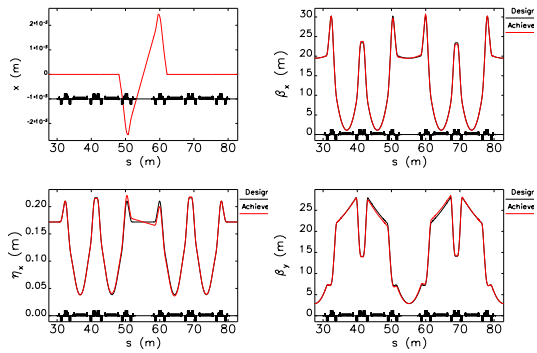


Figure 8: Lattice functions and orbit for two sectors around the ID straight section for an antisymmetric 4-corrector bump. No bump and negative bumps are shown. The order of the plot is the same as in Figure 4.

bump would start with C:BM magnet (see Figure 3). Orbit and lattice functions for this bump are shown in Figure 9.

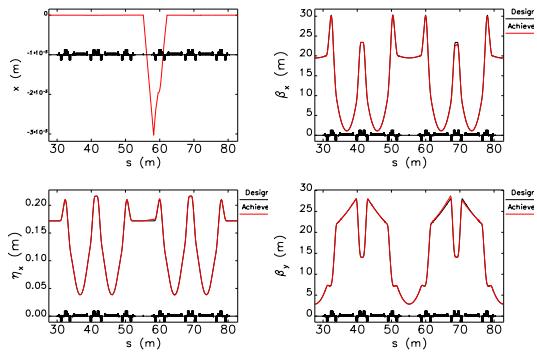


Figure 9: Lattice functions and orbit for two sectors around the ID straight section for an asymmetric 3-corrector bump. No bump and negative bumps are shown. The order of the plot is the same as in Figure 4.

LATTICE CORRECTION

For every case shown above, we first used matching in `elegant` to simultaneously create required orbit bump and adjust the quadrupoles to correct beta functions on the new orbit. For some cases, the matching turned out to be not an easy task and required clever choice and adjustment of varying parameters. This is a valid approach that we have used many times. However, in the real world we would probably just create a required orbit bump, then measure and correct beta functions. We might also change the quadrupoles to some pre-calculated values together with the orbit, but in the end we would still need to measure and correct beta functions.

We decided to test if we could skip beta function matching in the design of a canted lattice and just do optics correction on the new orbit. We wrote a script that performs two steps: runs `elegant` to match orbit bump and then runs our standard beta function correction program *calculateTwissCorrection* that uses SVD inversion of a beta function response matrix. Since the closed-orbit bump condition breaks after beta function correction, this two-step process is repeated for several iterations. The program is bump configuration-independent and can be used for different orbit bumps — it will only require a proper orbit-matching `elegant` file; the beta function correction part is universal. This process usually takes less time than direct matching, is easy to automate, and actually provides better corrected optics. Figures 8 and 9 actually show the results obtained this way.

OTHER ISSUES

To make it out of the vacuum chamber and into the beamline, the radiation would have to fit between the two absorbers that protect the vacuum chamber from dipole radiation and without touching them. Ray tracing shows that this condition is satisfied for all configurations discussed here. However, if the sign of the asymmetric 3-corrector bump is switched to the outboard, then the radiation of the downstream device will hit the wedge absorber W2. Therefore, this canting bump can only exist in the inboard configuration.

Another concern is the pollution of the x-ray BPM signal by the radiation from quadrupoles and sextupoles inside the orbit bump. We have calculated the magnetic fields that the electron beam will see along the canted orbit as a function of the orbit angle. We found that the strongest field encountered by the beam is in the central C:BM magnet, which is the same case as in the present triangular canting configuration.

There are some other issues that would need to be considered. For example, the good field region of the undulators would need to be about 5 mm wider to satisfy the field quality requirements on the switching orbit. Also, rf BPMs on the ID vacuum chamber would need to have an operational range of about ± 2 mm horizontally. This would require an increased distance between the BPM buttons.

CONCLUSIONS

We have simulated several orbit bump configurations that allow for dual-switchable undulator operation. For W-bump and for antisymmetric 4-corrector bump the required corrector strength exceeds the limit, but relatively easy solutions exist that slightly degrade the beamline performance. We have also shown that existing optics correction software can be used to recover lattice functions on the orbit bumps such that the nonlinear beam dynamics is only minimally affected.

REFERENCES

[1] P. Den Hartog, G. Decker et al., PAC'03, MPPB04 (2003).

[2] G. Decker, O. Singh et al., PAC 1999, WEA71, 2051 (1999).

[3] M. Borland, ANL/APS/LS-287 (2000).

[4] APS Upgrade Preliminary Design Report (2012).

Copyright © 2013 CC-BY-3.0 and by the respective authors

NEW CONSIDERATION FOR INSERTION-DEVICE DIPOLE-ERROR PERTURBATION REQUIREMENTS WHEN INCLUDING THE EFFECTS OF ORBIT FEEDBACK*

L. Emery†, V. Sajaev‡ and A. Xiao§, ANL, Argonne, IL 60439, USA

Abstract

For various reasons insertion devices (IDs) in storage ring light sources generally produce small dipole perturbations on the stored beam, which is usually compensated by orbit correction. Tougher orbit stability requirements for the Advanced Photon Source Upgrade (APS-U) project have led us to revisit the requirements of these magnetic-field errors. When including the effect of orbit correction (slow orbit feedback plus fast orbit feedback), we realized that the field-error requirements change from a limit in absolute values of magnetic-field error integrals to that of *rates of change* in magnetic-field error integrals. Some modeling of the combined effect of ramping the strength of an ID with orbit correction will be presented. This new thinking has the potential of greatly alleviating the tuning requirements of insertion devices of all types.

INTRODUCTION

In the early stages of APS operation, perturbations from insertion device (ID) field errors was studied intensively, resulting in a set of ID field specifications [1]. Since then, many IDs have been built, measured, and placed into operation at APS. Their properties and the achievable manufacturing limits are by now well known.

The first- and second-field integrals of an ID are not zero, and also, very importantly, vary with gap. To maintain the source-point during user operations, these perturbations must be held within some limits relative to an appropriate short-term "average reference" condition, which is not necessarily the same as the open-gap condition or starting conditions.

The undulators are slow-moving devices; the induced perturbation on the stored beam has a time scale of 1 seconds to 2 to 3 minutes. When a device gap is scanned repeatedly near their closed position, the period could be a few seconds to a few minutes, depending on the experimenter's data collection requirements. At the smallest gap position a significant beam perturbation could take place within 1 second. Thus the frequency range of interest is, say, 0.01 to 1 Hz, the lower limit selected to be approximately the reciprocal of two minutes.

Given that the stored beam can be subjected to perturbations from general sources of all frequencies, a general beam stability requirement for APS-U was recently re-established (see Table 1). Just like the original APS beam stability requirement, this requirement is meant as a guide for setting limits on individual sources of perturbation. One of the specifications sets limits on all sources in the frequency range 0.01 to 200 Hz (middle column in Table 1).

As discussed previously, conventional undulators are expected to produce perturbations within a tiny fraction of that frequency range, while other sources produce perturbations over the whole frequency range. Thus some of the orbit motion spectrum integrals of Table 1 must be allocated to undulator perturbation limits. In other words, if 3 μm is the maximum allowable rms orbit motion in the x plane from all sources, then a smaller number, say, 1.0 μm, would have to be taken as the maximum allowable rms motion in the 0.01-1 Hz range for undulators.

NEW ALLEVIATING FACTORS

Restricting ID source perturbations to a small amount like 1 μm may seem impossible at first. However, there are many alleviating factors not considered until now and some complicating factors used for years that are no longer needed:

Previously it was assumed that ID gaps could be moving together. Actually, independently operated gaps rarely move together. This will remove a factor $\sqrt{N_{\mathrm{ID}}}$ due to the number of IDs.

If there are independent IDs whose gaps are scanned slowly for long periods, the perturbation frequency will be below the band (below 0.01 Hz), in which case orbit correction cancels the perturbation with very high (virtually "infinite") gain.

Two orbit correction systems are running full-time in different frequency bands and have particularly high gain (i.e., correction effectiveness) in the 0.01 - 1 Hz frequency range of interest. A high gain allows larger tolerances for ID perturbation. Figure 1 shows the gain of the orbit correction as presently configured.

ID gap feedforward on nearby storage ring dipole correctors can be used to reduce the effort from the feedback correctors by 90% in DC mode. However, we found that the EPICS network for communicating gap information is much slower than the dedicated reflective memory of the orbit feedback system. Thus a feedforward system for correcting the orbit perturbation would not be needed to improve stability.

The ID perturbation when the gap is moving is not really a sequence of steps but rather segments of ramp errors of

* Work supported by the U.S. Department of Energy, Office of Science, under Contract No. DE-AC02-06CH11357.

† lemery@aps.anl.gov
‡ sajaev@aps.anl.gov
§ xiaom@aps.anl.gov

Copyright © 2013 CC-BY-3.0 and by the respective authors

Table 1: Main Lattice Parameters and Beam Stability Requirements in rms and in Integrated Power Spectral Density in the 0.01 - 200 Hz Band

	Original specification	Achieved in APS Operation[1]	APS-U Require-ments [2]	Allocation for PM IDs[2]	Units
Goals or Performance in rms					
Δx	16	3.5	3	1.0	μm
$\Delta x'$	1.2		0.57	0.17	μrad
Δy	4.4	1.2	0.42	0.1	μm
$\Delta y'$	0.45		0.22	0.055	μrad
Goals in Integrated Power Spectral Density					
Δx			9.0	1.0	μm^2
$\Delta x'$			0.32	0.03	μrad^2
Δy			0.18	0.01	μm^2
$\Delta y'$			0.048	0.003	μrad^2

[1] 0.01 - 100 Hz band.
[2] All permanent magnet IDs, including APPLE, planar and revolver undulators.

various rates. An orbit correction will eventually compensate a step error, but will not be able to correct a perturbation that ramps in time. The resulting error, say, $e(t)$ is equal to the open-loop error orbit rate of change $r(t)$ times the DC correction time constant τ, i.e., $e(t) = r(t)\tau$. The time constant for DC orbit correction at APS is 0.25 seconds. (We might be able to reduce the time constant in the future.) If the ramp doesn't last too long, say, 10 seconds, then the AC-coupled fast orbit feedback (otherwise known as real-time feedback – RTFB) can further reduce the error because of the higher frequency components in the ramp perturbation.

Thus we conclude that the values of the field integrals as a function of gap are not the relevant quantity, rather the derivative is. This can loosen the requirements quite a lot.

The PSD integral from 0.01 to 200 Hz (and other ranges) of the BPM readbacks is continuously calculated by the APS control system with processing that exponentially averages the result with a 1-minute time constant, thus smoothing out spikes. The average over the BPMs at the ID sources will be compared to alarm limits and will be our criterion for stability during operations.

RAMP ERROR WITH FEEDBACK

The orbit perturbation produced by the first- and second-field integral errors of an ID is given by:

$$u(s) = \frac{e}{cp}\frac{\sqrt{\beta_s\beta_o}}{2\sin(\pi\nu)}\sqrt{I_1^2+\frac{I_2^2}{\beta_s^2}} \times \cos\left(|\phi(s)-\phi_s|-\pi\nu\right), \quad (1)$$

$$u_{\max} \approx \frac{e}{cp}\frac{\sqrt{\beta_s\beta_o}}{2\sin(\pi\nu)}\sqrt{I_1^2+\frac{I_2^2}{\beta_s^2}}, \quad (2)$$

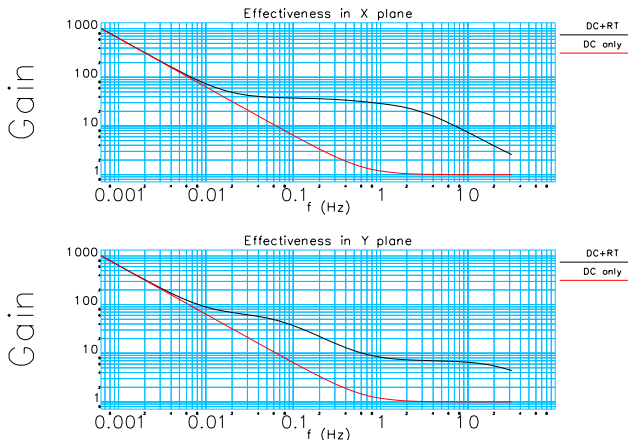


Figure 1: Correction effectiveness with slow correction only ("DC only") and with fast orbit feedback included ("DC+RT")

where u is either x or y; β_s and β_o are the beta functions at the source and the observation location respectively; $I_{1,2}$ are the normalized first- and second-field integrals (i.e., angle and position perturbation, respectively); ν is the betatron tune where we will assume values of $\nu_x = 0.18$ and $\nu_y = 0.22$; and $\phi(s)$ and ϕ_s are the phase advances at longitudinal coordinate s and at the source. The first- and second-field integrals have values roughly independent from each other and different limits will be imposed on each.

Equation (1) obviously indicates that the orbit error induced by a single perturbation is global around the ring, while Equation (2) gives the maximum expected orbit error at some other light source point around the ring. These equations remain valid with integrals and orbit varying slowly with time, of course.

Copyright © 2013 CC-BY-3.0 and by the respective authors

Table 2: Requirements for First- and Second-Field Integral Rate of Change.

Field Integral	No orbit correction[1]	Orbit correction of ramp error, 5-second duration	Orbit correction of ramp error, indefinite duration
Rate of $\int B_y dz$	1.2 G·cm	21 G·cm/s	5.0 G·cm/s
Rate of $\int B_x dz$	1.0 G·cm	16 G·cm/s	4.0 G·cm/s
Rate of $\int dz \int B_y dz'$	2500 G·cm^2	43,000 G·cm^2/s	10,000 G·cm^2/s
Rate of $\int dz \int B_x dz'$	300 G·cm^2	4900 G·cm^2/s	1200 G·cm^2/s

[1] Values in this column are limits on actual field integrals, not their rate.

Most of what follows explains the reduction of the global orbit due to the global orbit correction system. However, even for perfect or infinite time response of orbit correction, there will be remnant local photon beam steering errors because we don't have correcting elements in the straight section. This spatial-domain limitation, though important, will be not be discussed here.

A simple frequency-domain model of the global orbit correction was created using Matlab (building upon scalar-orbit models written by [3, 4]). Since we are interested in the low-frequency part of the response, the effect of time delays and corrector response can be ignored. The results were shown in Figure 1. The gain is found to vary approximately as $1/f$, which is expected for a system under integral control, plus some additional help from the AC-coupled real-time feedback in the important range 0.1 Hz to 1 Hz. Figure 2 shows the time-domain scalar-model orbit response of a unit ramp perturbation (taking orbit and perturbation as unit-less quantities for simplicity). Without correction the orbit error would be equal to the perturbation. With integral correction only (slow orbit feedback),

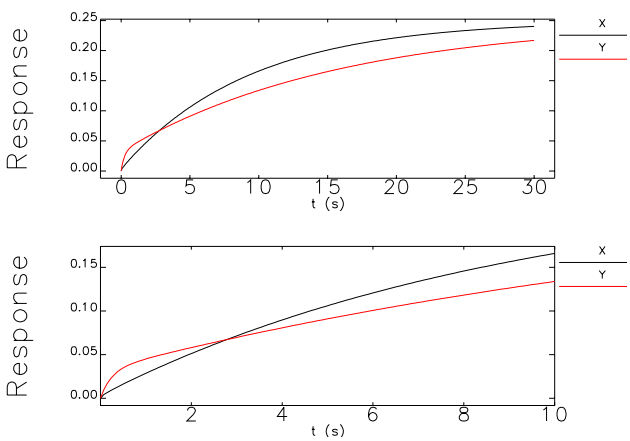


Figure 2: Response to unit-ramp orbit perturbation of our correction system. The average response within the first 5 seconds determines the ID perturbation specification.

the general error would be given by $e(t) = r(t)\tau$, where $r(t)$ = 1 s^{-1} (unit ramp) and τ = 0.25 s in our case. With the additional AC-coupled correction (fast orbit feedback), there is a short-term correction within the first 5 to 20 seconds. Taking the average orbit response over the first 5-second interval, we see that the net orbit response is 0.06 times the ramp rate in both planes. This small factor is reflected in the frequency domain plot of Figure 1, where the average effectiveness in the frequency range 0.1 to 1 Hz is about 20.

Because of the complex frequency dependence of the combined DC-AC system correction effectiveness, the actual orbit "ramp" error from IDs would have to be modeled on a case-by-case basis with orbit correction simulation for acceptance (using the present version of orbit correction).

ID INTEGRAL REQUIREMENTS

Finally we arrive at two sets of ID requirements: one for an arbitrarily long ramp and another (looser) set of stronger allowed perturbations assuming a 5-second ramp. The 5-second ramp-error duration was selected because it matches the worst-case behavior of most planar IDs perturbation.

Table 2 shows the specifications on the first- and second-field integral rates-of-change for these two ramp conditions assuming that each of these integrals will contribute to one half of the ID perturbation allocation of Table 1.

The requirement for the position stability is more severe than that of the angle coordinate, thus only the requirement based on position stability is given in the table.

According to this global orbit error analysis, an ID is allowed to have a somewhat large "peak" in the absolute value of field integrals as long as the peak is not come upon too quickly. One way to make a particularly difficult ID compliant to the rate limit is to make the gap move slowly in the gap-value range where the field integral changes quickly.

REFERENCES

[1] Y.-C. Chae and G. Decker, Proc. PAC 1995, RAR24, 3409 (1995).

[2] G. Decker, APS_1427507, APS (2012).

[3] C. Schwartz, Private Communication (2001).

[4] T. Berenc, Private Communication (2010).

Copyright © 2013 CC-BY-3.0 and by the respective authors

OPTICS DESIGN AND BEAM DYNAMICS OPTIMIZATION OF A FIVE-BEND ACHROMAT LATTICE FOR THE ADVANCED PHOTON SOURCE UPGRADE*

Yipeng Sun† and Michael Borland, ANL, Argonne, IL 60439, USA

Abstract

For the proposed future Advanced Photon Source (APS) upgrade, a multi-bend achromat design with very low emittance has been studied. Such a ring promises to enhance the photon brightness and transverse coherence by two orders of magnitude. In this paper, one possible lattice design is presented, which is composed of five-bend achromat arc cells. The linear optics design is done for an emittance of 150 pm at a beam energy of 6 GeV. The nonlinear optics are optimized using the Multi-objective Genetic Algorithm (MOGA) technique for good injection efficiency and beam lifetime. Beam dynamics performance is also preliminarily evaluated.

OVERVIEW

Storage rings based on alternate strong focusing have been widely used for many years in the design of colliders and synchrotron radiation light sources. Several focusing configurations have been invented and some of them applied in real ring construction and operation, including the separated-function FODO cell, combined function FD-cell, double-bend achromat (DBA), triple-bend achromat (TBA), and theoretical minimum emittance lattice (TME) [1].

In simplified form, the natural emittance in a storage ring scales as [2]

$$\epsilon_0 \sim \frac{F \cdot E^2}{(N_d N_s)^3 \cdot J_x}, \qquad (1)$$

where ϵ_0 is the equilibrium emittance in a storage ring, F is a dimensionless factor depending on the arc cell focusing, E is the electron energy, N_s is the number of sectors, N_d is the number of dipoles per sector, and J_x is the horizontal damping partition number.

To improve the photon brightness and coherence in a storage-ring-based light source, a low-emittance electron beam (matched to the photon beam) is needed. In general, the requirement to achieve very low emittance means employment of many weaker dipoles (smaller dispersion) and stronger quadrupoles (focusing). Stronger (or better) focusing approaches the ideal TME condition, while more dipole magnets direct us toward a multi-bend achromat (MBA) lattice where $M \geq 4$.

Such a lattice was first studied and proposed in the 1990s [3]. Similar ideas were also discussed for a future APS upgrade with MBA lattices [4] [5] [6], providing a lower natural emittance below 200 pm. The MAX-IV storage ring is the first MBA lattice being built and will be commissioned in 2015 [7]. It employs 20 seven-bend achromat (7BA) cells in a 528-m circumference, which provides an emittance of 330 pm at a beam energy of 3 GeV. ESRF is also proposing an upgrade using a hybrid multi-bend achromat lattice where larger dispersion is adopted to decrease sextupole strength [8].

Recently the APS has begun to explore replacing the current DBA lattice with a new MBA lattice as part of its ongoing upgrade project. A MAX-IV-like 7BA lattice [9], and an ESRF-like hybrid-7BA are being studied [5]. In this paper, another MBA design for the APS upgrade is presented, namely, a five-bend achromat lattice that provides an emittance of 150 pm at 6 GeV.

LINEAR OPTICS DESIGN

It is proposed to enhance the photon brightness and coherence by two orders of magnitude in the new APS MBA lattice. To achieve this goal, and to reuse as much existing hardware as possible, there are several optics design constraints:

- A natural emittance below 150 pm
- Match the existing ID beamline locations
- Maintain the bending-magnet beamlines
- 40 identical cells, each 27.6 m long
- Straight section length longer than 5 m
- Electron beam energy of 6 GeV
- Reuse the existing rf and injector system

Another important design constraint is from the available magnet technology. It is foreseen to use normal-conducting magnets with a bore radius around 12 mm. The drift length between magnets is limited to a minimum of 10 cm. The assumed maximum dipole, quadrupole, and sextupole strength are listed below.

- Combined dipole: dipole field $< 1\ T$; quadrupole gradient $< 50\ T/m$
- Quadrupole gradient $< 100\ T/m$
- Sextupole gradient $< 10000\ T/m^2$

Based on the above contraints, the linear optics matching is performed using ELEGANT [10]. The minimum magnet length is set to be 15 cm, with the magnet strength as low as possible. The linear optics in one sector is shown in Figure 1, where the starting and ending points are the insertion device (ID) center. One observes that the use of a triplet on either side of the ID straight has allowed tuning the beta

* Work supported by the U.S. Department of Energy, Office of Science, under Contract No. DE-AC02-06CH11357.

† yisun@aps.anl.gov

Copyright © 2013 CC-BY-3.0 and by the respective authors

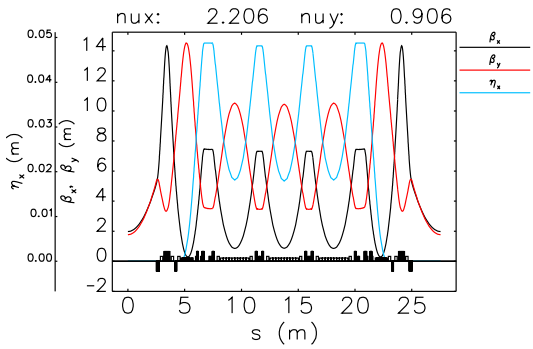


Figure 1: Twiss parameters in a sector with a length of 27.6 m. Natural emittance is 150 pm at a beam energy of 6 GeV. Black curve denotes horizontal beta function; red curve, vertical beta function; blue curve, horizontal dispersion function.

functions (β_x = 2 m, β_y = 1.9 m) at the ID to near the ideal value of L_u/π from the photon beam. In the central three TME-like cells, there are long dipoles combined with a quadrupole gradient. There are two quadrupoles in each dispersion-matching cell at the two ends. The maximum dipole field is 0.6 T, and the maximum quadrupole gradient is 65 T/m. The betatron phase advance is matched to be (2.206, 0.906), which generates a quasi-third-order achromat [11] in a storage ring consisting of 40 such identical 5BA cells.

There is limited space available for dedicated orbit/optics correction magnets and beam instrumentation. That means the correction magnets may need to be integrated into the main magnets. Alternatively, the main magnets could be made stronger and shorter, which would provide more free space. At a beam energy of 6 GeV, the main parameters of the storage ring are listed in Table 1.

Table 1: Parameters of the 5BA Storage Ring

Parameter	unit	value
Circumference	m	1104
Phase advance x/y per cell	2π	2.206/0.906
Tune x/y/s	2π	88.2/36.1/0.06
Natural chromaticity x/y		-166/-80
Rf voltage	MV	3.8
Rf frequency	MHz	352.8
Rf bucket height	%	3
Harmonic number		1296
Momentum compaction	10^{-5}	9
Natural emittance	$pm \cdot rad$	150
Damping time x/y/s	ms	12/20/14
Energy loss per turn	MeV	2.2
Energy spread	10^{-4}	9
RMS bunch length	mm	15

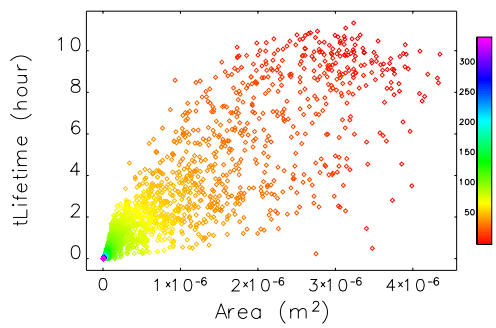


Figure 2: MOGA optimization plot. Horizontal axis is the dynamic acceptance area (β_x = 2 m, β_y = 1.9 m) and vertical axis is the Touschek lifetime.

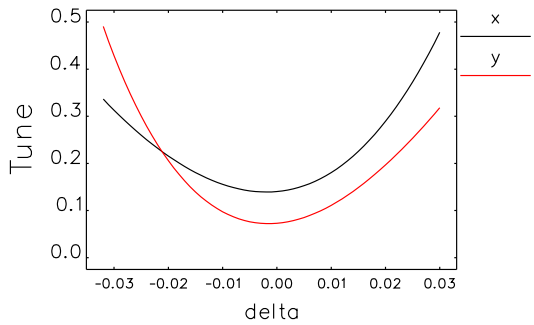


Figure 3: Horizontal (black curve) and vertical (red curve) betatron tune as a function of momentum offset $\Delta E/E$, dominated by second-order chromaticity.

NONLINEAR OPTICS OPTIMIZATION AND PERFORMANCE

In each 5BA cell, there are four families of focusing chromaticity sextupoles (SF) and another four families of defocusing chromaticity sextupoles (SD). The horizontal dispersion is zero in the straight section where there are six harmonic sextupoles. As with the linear optics, mirror symmetry is employed for the sextupole arrangement.

MOGA [12] is adopted to directly optimize both dynamic acceptance (DA) and Touschek ifetime from tracking simulations. The fractional tune is allowed to change in a range of (0.05, 0.45) while the linear optics is still matched. Six families of chromaticity sextupoles and three families of harmonic sextupoles are used as variables that may evolve "naturally" via the genetic algorithm. The two remaining chromaticity sextupoles (SF1 and SD1) are used to correct the first-order chromaticity to 1. A set of solutions with higher DA and lifetime are used as the parents for the next generation. The linear chromaticity penalty function also needs to be small. The MOGA optimization process is shown in Figure 2. It is observed that the DA area is increased from 2×10^{-7} mm^2 to 4×10^{-6} mm^2, and the Touschek lifetime is increased from 0.05 hours to

Copyright © 2013 CC-BY-3.0 and by the respective authors

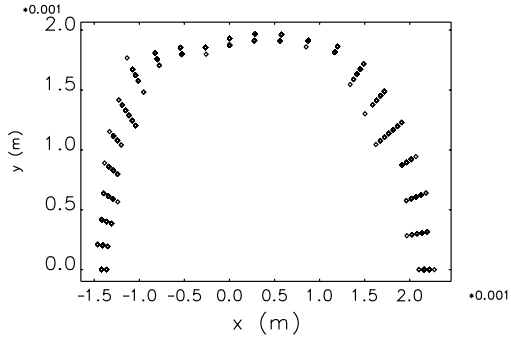


Figure 4: Dynamic acceptance with 50 ensembles of errors (random, systematic magnetic errors, and tilt errors on all the quadrupoles and sextupoles). Tracking is performed at the center of the ID where β_x = 2 m, β_y = 1.9 m.

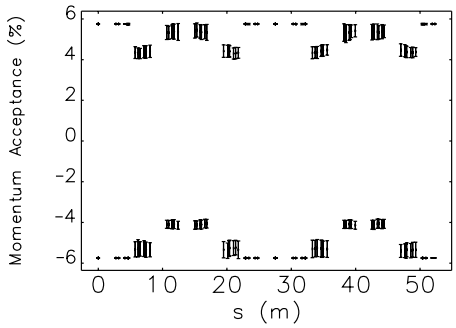


Figure 5: Local momentum acceptance with 50 ensembles of errors (random, systematic magnetic errors and tilt errors on quadrupoles and sextupoles). Tracking is performed at locations next to each magnet in two sectors (a total length of 55 m).

above 10 hours.

One of the best MOGA solutions was picked to be analyzed for its beam dynamics performance. The nominal dynamic acceptance area is 4.2×10^{-6} mm^2 and the Touschek lifetime is 10 hours. The sextupole gradient is less than 6000 T/m^2 with a sextupole length of 0.25 m. There is room to adopt longer sextupoles with lower strength. As mentioned above, the nonlinear optics aberrations are optimized using MOGA. The linear chromaticity is corrected to be 1, which counters the head-tail instability. Examining the solution found by MOGA, we find that the higher-order chromaticities are optimized such that the off-momentum tune spread is minimized. Given the fractional tune close to integer, the second order chromaticities are also optimized to be positive (less than 500), as shown in Figure 3. The global momentum acceptance is limited by the rf bucket, which is 3%.

Dynamic acceptance is the maximum stable transverse amplitude, which is determined by a single-particle numerical tracking simulation. It should ensure efficient acceptance of the injected beam with large emittance and energy spread. It may also impact on the circulating beam lifetime. As shown in Figure 4, the dynamic acceptance is 2 mm $\times$ 1.5 mm at the center of the ID where β_x = 2 m, β_y = 1.9 m. Fifty ensembles of magnetic errors and tilt errors are applied on the quadrupole and sextupole magnets. Note that errors are added to give optics beating of around 1%. No explicit misalignment errors are included, but the effect of such errors is nominally included by the choice of uncorrected optics beating. It is concluded that the DA is enough for on-axis swap-out injection. It is possible to increase the beta function in the injection area and reoptimize the DA for off-axis accumulation, which needs further investigation.

Scattering effects in the electron bunch change both transverse and longitudinal momentum of an electron. Local momentum acceptance is defined to be the maximum acceptable momentum change in a specified location. The mechanisms causing electrons to lose momentum may be physical aperture, DA, or rf bucket limitations. The LMA is determined by tracking and is shown in Figure 5. It is close to 4%, which ensures a good lifetime. (In this simulation we increased the rf voltage to reveal the limitation due solely to beam dynamics.) Collective effects are not studied yet, but expected to be on a smiliar level with the 7BA design [9].

CONCLUSION

A five-bend achromat lattice was developed for a possible future APS MBA upgrade. The linear and nonlinear optics are both optimized to improve the beam dynamic performance.

ACKNOWLEDGMENT

The authors would like to thank C. Wang, Z. Gu, V. Sajaev and L. Emery for helpful discussions.

REFERENCES

[1] L. Teng, Fermilab Report No. TM-1269 (1984).
[2] J. Murphy, Synchrotron Light Source Data Book, BNL 42333 (1989).
[3] D. Einfeld et al., NIM A 335 (1993) 402.
[4] L. Emery, M. Borland, Proc. PAC03, TOPA014, 256 (2003).
[5] M. Borland, private communication.
[6] M. Borland, NIM A 557 (2006) 230.
[7] S. C. Leemann et al., PRST-AB 12 (2009) 120701.
[8] L. Farvacque et al., Proc. IPAC13, MOPEA008, 79 (2013).
[9] M. Borland et al., MOPHO07, proceedings of NA-PAC13 (2013).
[10] M. Borland, Advanced Photon Source ANL/APS/LS-287 (2000).
[11] Y.-P. Sun and M. Borland, MOPHO13, proceedings of NA-PAC13 (2013).
[12] M. Borland et al., ANL/APS/LS-319 (2010).

Copyright © 2013 CC-BY-3.0 and by the respective authors

LINEAR SCALING ON CHOOSING A BUNCH COMPRESSION RATIO FOR AN FEL DRIVER*

Yipeng Sun†, ANL, Argonne, IL 60439, USA

Abstract

In this paper, a proper initial bunch length as a function of the main rf frequency and rf phase is estimated analytically by several approaches, assuming that no harmonic rf section is needed to linearize the energy modulation introduced during main rf acceleration. Next the upper limit of the bunch compression ratio in a single stage is evaluated analytically. The analytical relations derived on choosing a proper initial bunch length as a function of main rf frequency are confirmed by numerical simulation. These simple limits provide rough analytical estimations and may be beneficial for choosing bunch compression ratios in different stages of an FEL driver, especially in a first-stage bunch compression system where an harmonic rf linearization is usually applied.

OVERVIEW

A magnetic bunch compression system is normally adopted during the acceleration process of the electron beam, usually in several (two) stages. The basic idea is to first introduce an energy modulation (chirp) along the electron bunch in its longitudinal direction by an rf acceleration off-crest, then let the electron beam pass by a dispersive region where electrons in the head and tail of the bunch all move relatively towards the bunch center. Chicane- and wiggler-based bunch compressor designs were proposed and studied thoroughly in the 1990s, mainly for linear collider projects [1] [2] [3].

Due to the nonlinear nature of the rf sinusoidal wave and an initially long bunch length, higher-order energy chirps can not be neglected. Harmonic rf linearization of the longitudinal phase space of the electron bunch is normally employed to generate a more uniformly compressed bunch in a first-stage bunch compression. This paper discusses what is the limit on the bunch compression ratio in order to achieve a quasi-linear bunch compression without harmonic rf.

PROPER INITIAL BUNCH LENGTH WITHOUT HARMONIC RF

In this section, only the main rf acceleration section is considered, and a proper initial bunch length is derived as a function of rf frequency and rf phase, given that a quasi-linear compression is achieved with a reasonable bunch compression ratio adopted for each stage. There are two possible ways to quantify a quasi-linear compression. First, the contribution to final bunch length from nonlinearities (from rf acceleration and bunch compressors) could be evaluated and limited to a certain percentage. A second way is to compare the final bunch length calculated as the root mean square of the distribution with the one derived from a numerical fit of the final distribution (Gaussian fit if the initial distribution is Gaussian), and limit the difference between these two to a certain amount.

Energy Chirp Approach

First let us recall the energy modulation formula. For any one particle in a bunch, its relative energy offset after passing by an rf acceleration off-crest can be expressed as shown below:

$$\begin{aligned}\delta(z) &= \delta_i \frac{E_{i0}}{E_{f0}} + \frac{eV_0\cos(\phi + kz_i)}{E_{f0}} \\ &= a\cdot\delta_i + \frac{eV_0\cos(\phi+kz_i)}{E_{f0}}. \end{aligned} \quad (1)$$

where δ_i denotes the initial uncorrelated energy offset, E_{i0} is the central energy before rf acceleration, E_{f0} is the central energy after rf acceleration, e is the electron charge, V_0 is the rf voltage, ϕ is the rf phase, $k = \frac{2\pi}{\lambda}$ is the rf wave number, λ is the rf wavelength, z_i is the particle's longitudinal coordinate relative to the bunch center, and $a = E_{i0}/E_{f0}$ is the energy damping ratio.

The first- and second-order energy chirp from the main rf acceleration could be described by the rf wave number, rf voltage, and rf phase, solved from the same Taylor expansions discussed above, as shown below:

$$h_1 = -\frac{keV_0\sin\phi}{E_{f0}} \quad (2)$$

$$h_2 = -\frac{k^2eV_0\cos\phi}{2E_{f0}}. \quad (3)$$

Neglecting the energy chirp above the third order, the overall energy modulation from this main rf section can then be rewritten as

$$\delta(z) = a\cdot\delta_i + (h_1 + h_2\cdot z)z, \quad (4)$$

where $h_1 + h_2\cdot z$ denotes the effective first-order energy chirp.

One then observes that if z is small enough to make $h_1 + h_2\cdot z \approx h_1$, the overall energy modulation is almost linear; in that case harmonic rf linearization is no longer necessary. This condition could be interpreted as $|h_1| \gg |h_2\cdot\sigma_z|$ and further derived to be

$$\frac{c\cdot\tan\phi}{\pi\cdot f_{rf}\cdot\sigma_z} \gg 1. \quad (5)$$

* Work supported by the U.S. Department of Energy, Office of Science, under Contract No. DE-AC02-06CH11357. Work also supported by the U.S. Department of Energy under Contract DE-AC02-76SF00515.

† yisun@aps.anl.gov

Copyright © 2013 CC-BY-3.0 and by the respective authors

At this step, a proper initial bunch length can be expressed as a function of the main rf frequency and rf phase, as shown below. Here one assumes that a reasonable bunch compression ratio is adopted, with the detailed requirements discussed in the following section.

$$\sigma_{z,max} = D_0 \frac{2\tan\phi}{k_{rf}}, \tag{6}$$

where D_0 denotes an empirical constant whichthat is a small number much less than 1, which could be fitted from numerical simulation studies employing rf systems with different frequency (such as from L-band rf to X-band rf). As illustrated by the numerical simulation results below, in general D_0 should be less than 0.01 in order to maintain a relatively linear longitudinal phase space and a quasi-linear bunch compression without harmonic rf assistance. In general, the required value of D_0 depends on rf frequency, average rf phase adopted for introducing energy correlation, total compression ratio in all the stages, and the number of bunch compression stages. D_0 is inversely proportional to the rf phase and total compression ratio, while it is proportional to the number of bunch compression stages.

To generate a final hard X-ray FEL using normal photoinjector and undulator configurations, usually the electron bunch length needs to be compressed by 30-200 times of its initial value. If more stages of bunch compression are adopted, one only needs a smaller bunch compression ratio in each stage. This in turn requires only a small rf phase and small longitudinal dispersion (momentum compaction) of the bunch compressor systems. In this case, a larger constant D_0 and a longer initial bunch length can be tolerated.

Final Bunch Length Approach

A proper initial bunch length can also be evaluated by examing the expression of a final bunch length after bunch compression. Under a condition of linear optimal compression $1 + h_1 R_{56} = 0$, a similar required relationship is derived, $|h_1| \gg |h_2 \sigma_z|$. Assuming the electron bunch preserves a Gaussian distribution after passing by the dispersive region, the RMS bunch length can then be calculated as the integral shown below:

$$\sigma_z{}^2 = \int\int z_f{}^2(z,\delta) \cdot f(z,\delta) dz d\delta. \tag{7}$$

Then the expression $z_f(z,\delta)$ is derived with dispersion terms of the bunch compressor up to third order. After passing by the dispersive region, the longitudinal coordinate (relative to the bunch center) of any particle can be expressed as shown below:

$$z_f(\delta) = z_i + R_{56}\delta + T_{566}\delta^2 + U_{5666}\delta^3 + \ldots. \tag{8}$$

Take the correlated relative energy offset $\delta(z)$ in terms of energy chirp up to second order, keep the terms up to second order bunch compressor dispersion, and neglect the initial uncorrelated energy offset δ_i in higher-order terms above δ^2. The square of $z_f(\delta)$ is then calculated to be a polynomial of z.

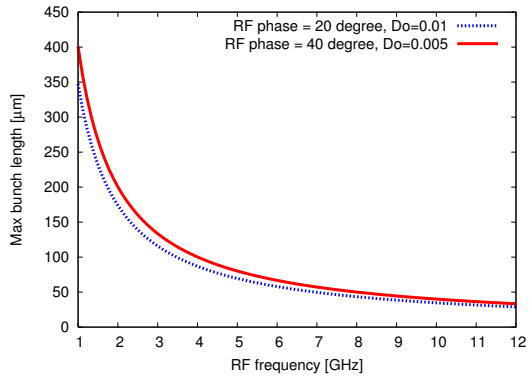


Figure 1: Proper initial bunch length as a funcion of rf frequency, for two given rf phases of 20 and 40 degrees. No harmonic rf linearization is included. A constant of $D_0 = 0.01$ is assumed for the 20-degree case, while $D_0 = 0.005$ is assumed for the 40-degree case.

One can then find the expression of the final bunch length by inserting $z_f^2(z,\delta_i)$ into the final bunch length formula andcalculate the integral. Here one needs to note that the integral of all the odd functions is zero, such as $\int\int z \cdot f(z,\delta) dz d\delta = 0$ and $\int\int z^3 \cdot f(z,\delta) dz d\delta = 0$. The expression of final bunch length only has entries from the integral of all the even functions. Under a condition of linear optimal compression, $1 + h_1 R_{56} = 0$, one finds that the final bunch length equals

$$\begin{aligned} \sigma_{z,f}^2 &= a^2 R_{56}^2 {\delta_i}^2 \\ &+ [2R_{56} a \delta_i (h_2 R_{56} + h_1^2 T_{566} + h_2^2 T_{566} \sigma_z^2) \\ &+ (h_1^2 \cdot T_{566} + h_2 \cdot R_{56})^2 \cdot \sigma_z^2] \cdot \sigma_z^2. \end{aligned} \tag{9}$$

Again, assuming a normal four-dipole chicane is employed as the bunch compressor, there is a fixed ratio between its first-order and second-order dispersion terms R_{56} and T_{566}, as $T_{566} = -1.5 R_{56}$. From the expression of final bunch length, one observes that the first term $a^2 R_{56}^2 {\delta_i}^2$ is from the initial uncorrelated energy spread, and the third term $(h_1^2 \cdot T_{566} + h_2 \cdot R_{56})^2 \cdot \sigma_z^2$ implies that the second-order chirp h_2 always adds on a first-order effect given as $T_{566} = -1.5 R_{56}$. However, a larger rf phase (close to on-crest point) can minimize the contribution from the third term. It is the second term that could be derived to give a similar final conclusion as discussed in the last section, with a required criteria of $|h_2 R_{56} + h_1^2 \cdot T_{566}| \gg |h_2^2 T_{566} \cdot \sigma_z^2|$. To repeat, the required relationship associated with the maximum tolerable bunch length is $|h_1| \gg |h_2 \sigma_z|$.

One could plot the proper initial bunch length as a function of rf frequency with different rf phase, as shown in Figure 1. One observes that for a lower rf frequency, the proper initial bunch length is longer, which is as expected. Another point is that if a higher rf phase can be employed, then the tolerable bunch length can be longer. In the next section, the analytical results derived above are checked

Copyright © 2013 CC-BY-3.0 and by the respective authors

and confirmed by numerical simulations with multi-stage bunch acceleration and compression based on rf systems with different frequencies.

Proper Compression Ratio in One Stage

In this subsection, a proper bunch compression ratio in one stage is discussed and an upper limit is drawn. Limited to first order, a compression ratio is approximated as shown below:

$$C = \frac{1}{1 + h_1 R_{56}}. \quad (10)$$

From the final bunch length expression one also observes that to keep an effectively linear bunch compression, there should be a limit applied on the bunch compression ratio. That means a bunch compression ratio can not be too large in one stage, otherwise the bunch compression is no longer linear.

Consider a first-order optimal bunch compression case. One has $1+h_1 R_{56} = 0$ and then could conclude that in this case, the final bunch distribution is only dependent on the nonlinear terms, which obviously breaks the linear compression requirement. So in general, there should be another criterion for a linear bunch compression that can be derived and shown in the following formula, up to second order. One needs to note that in the coefficient of term z^4, the relatively small uncorrelated initial energy offset δ_i and first-order associated term $4h_1 h_2 T_{566}(1 + h_1 R_{56})$ are neglected:

$$(1 + h_1 R_{56})^2 \gg (h_1^2 \cdot T_{566} + h_2 \cdot R_{56})^2 \cdot \sigma_z^2. \quad (11)$$

The above requirement in turn gives an upper limit on the bunch compression ratio in one stage. As there is a large acceleration in beam energy between subsequent stages, the nonlinear terms in the bunch energy chirp is also damped during acceleration. That damping effect helps to maintain a linear energy correlation. Also, as the bunch length becomes shorter from one stage to the next, the new contribution on the nonlinear energy chirp from the following linacs is smaller. Under this kind of configuration with more than two stages of bunch compression, a quasi-linear bunch profile should be easily achieved at the linac end. The requirement on bunch compression ratio in one stage (especially the first stage) is then approximated as shown below, which is a function of dispersion terms, energy chirp terms, and RMS bunch length:

$$C \ll \frac{1}{\sigma_z |h_1^2 \cdot T_{566} + h_2 \cdot R_{56}|}. \quad (12)$$

Combining all the above considerations, a bunch compression ratio between 5 and 10 may be adopted in one stage. The last point is that in general one should choose a weak chicane bunch compressor with small dispersion terms R_{56} and T_{566}, in order to minimize the contribution from higher-order terms.

Numerical simulation results [4] [5] are presented here, for two FEL driver designs based on different rf frequencies; these are the L-band rf (1.3 GHz) and the X-band rf (12 GHz) [6]. No harmonic rf correction is included here. The initial bunch length of $300\mu m$ and $40\mu m$ are adopted plus the rf frequency and phase. One could observe Figure 1 and find that $300\mu m$ and $40\mu m$ are the limited bunch lengths corresponding to the rf frequency of 1.3 GHz and 12 GHz, respectively. From the simulation results as shown below, one could conclude that the bunch compression process is quasi-linear, and a quasi-Gaussian bunch density profile is preserved. No spike in density profile is generated. These numerical simulation results confirm the validity of the above analytical derivations. It is noted that if one extends these two-stage bunch compression systems into three stages or more, the final bunch current profile could be more uniform, due to the reasons discussed above. In detail, the bunch compression ratio can be smaller in each single stage, and the dispersion terms R_{56} and T_{566} are also smaller in the bunch compressors. The relative energy-dependent-damping effect of the nonlinear energy chirp is also stronger given that more bunch compression stages are adopted.

CONCLUSION AND DISCUSSION

In this paper, analytical formulae are derived to estimate an initial proper bunch length as a function of rf frequency and rf phase in a linac-based FEL driver. These derivations may be benificial for an FEL driver design that has a mainly low bunch charge operation mode and that could achieve an initially short bunch length from the upstream photoinjector. It is also noted here that these limits only provide rough analytical estimations on the required bunch length and compression ratio, where assumptions have been made and no collective effects are included. A detailed bunch compression system design can start with these simple formulae and then be optimized by 3-D simulations with all effects included.

ACKNOWLEDGMENT

The author would like to thank C. Adolphsen, Y. Ding, P. Emma, Z. Huang, T. Raubenheimer, and J. Wu for helpful discussions. Most of this work was done at SLAC national laboratory. The paper was written at ANL national laboratory.

REFERENCES

[1] T. Raubenheimer, P. Emma and S. Kheifets, Proc. of PAC1993, p. 635 (1993); http://www.JACoW.org

[2] P. Emma, SLAC-PUB-1001, also in DESY TESLA-95-17 (1995).

[3] P. Emma, DESY TESLA-98-31 (1998).

[4] H. Grote and F.C. Iselin, MAD8 manual, CERN/SL/90-13 (AP), 1990.

[5] M. Borland, Advanced Photon Source LS-287, September 2000.

[6] Y.-P. Sun et al., Phys. Rev. ST Accel. Beams 15 (2012) 030703.

Copyright © 2013 CC-BY-3.0 and by the respective authors

SIMULATION OF AN X-BAND HARD X-RAY FEL WITH LCLS INJECTOR*

Yipeng Sun†, ANL, Argonne, IL 60439, USA
Tor Raubenheimer, SLAC, Menlo Park, California 94025, USA
Paul Emma, LBNL, Berkeley, California 94720, USA

Abstract

In this paper, the accelerator design and start-to-end 3D macro particle simulation (using ELEGANT and GENESIS) of an X-band rf-driven hard x-ray FEL with LCLS injector is briefly discussed. A preliminary design and LiTrack 1D simulation studies were presented earlier [1]. In numerical simulations this X-band rf-driven hard x-ray FEL achieves/exceeds LCLS-like performance in a much shorter overall length of 350 m, compared with 1200 m in the LCLS. One key feature of this design is that it may achieve a higher final beam current of 5 kA plus a uniform energy profile, mainly due to the employment of stronger longitudinal wakefields in the last X-band rf linac [2].

OVERVIEW AND ACCELERATOR DESIGN

LCLS is the world's first hard x-ray FEL in routine operation, providing soft and hard x-rays to its users with good spatial coherence at wavelengths from 2.2 nm to 0.12 nm by varying the bunch energy from 3.5 GeV to 15 GeV [3]. Design and beam dynamic studies are performed for several X-band rf-driven hard x-ray FEL drivers [4]. A low-charge hard x-ray FEL design [5] employs the entire X-band photoinjector and rf linac, which are optimized for a very low bunch charge of 10 pC and an average SASE FEL power of over 10 GW in a pulse length of 5 fs (start-to-end simulation in a short undulator length of 20 m). Thanks to the small 3D emittance associated with the low bunch charge (short initial bunch length from photoinjector, etc.), a linear bunch compression is achieved in two stages of bunch compressors without the assistance of harmonic rf linearization.

A second hard x-ray FEL design also features the entire X-band photoinjector and rf linac, but is dedicated for a normal bunch charge of 250 pC [6]. The longitudinal phase space linearization is done in its first-stage bunch compression with a specially designed bunch compressor composed of dipole, quadrupole, and sextupole magnets. From the start-to-end simulation using computer codes ASTRA [7], ELEGANT [8], and GENESIS [9], it is shown that this FEL achieves an average SASE FEL power of over 30 GW in a pulse length of 50 fs.

Both of these two hard X-ray FEL designs described above achieve a shorter SASE FEL saturation length due to a shorter undulator period and a weaker undulator field. It is also noted that the low-charge hard x-ray FEL design [5] achieves a better final beam quality than the LCLS case.

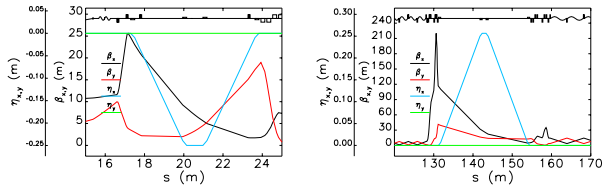


Figure 2: Beta functions and dispersion functions in the bunch compressors. Left: bunch compressor one, which is exactly the same as LCLS BC1; right: bunch compressor two, which is similar to LCLS BC2.

Analytical and numerical simulation studies show that the tolerance (charge and timing jitter, transverse misalignment) is acceptable for both of the above two hard X-ray FEL designs [5], [6].

A sketch of this compact (300 m) hard x-ray FEL driver using X-band accelerators plus an LCLS injector is shown in Figure 1. As previously mentioned, it employs an LCLS injector, which means that to the end of BC1 it is exactly the same as the LCLS. The only difference is that the S-band rf in Linac2 and Linac3 is replaced by an X-band rf. The BC2 design is similar to LCLS, at a beam energy of 4.3 GeV. For a bunch charge of 250 pC, the initial RMS bunch length is 690 μm from the S-band photoinjector. It is compressed to a final RMS length of either 6 μm (3-kA peak current) or 4 μm (5-kA peak current).

OPTICS DESIGN

The optics design of the linac, the bunch compressors, and the matching sections are done in MAD8 [10] and then converted to ELEGANT [8]. The TWISS parameters of bunch compressors one (BC1) and two (BC2), shown in Figure 2, are similar to the LCLS BC1 and BC2 (transverse phase-space matching to minimize CSR induced transverse emittance growth). The start-to-end TWISS parameters of the overall accelerator are shown in Figure 3. An average beta function of 10 meters and 20 meters are employed in Linac2X and Linac3X, respectively, to minimize both dispersive and wakefield-induced transverse emittance dilutions.

* Work at Argonne is supported by the U.S. Department of Energy, Office of Science, under Contract No. DE-AC02-06CH11357. Work also supported by the U.S. Department of Energy under Contract DE-AC02-76SF00515.

† yisun@aps.anl.gov

Copyright © 2013 CC-BY-3.0 and by the respective authors

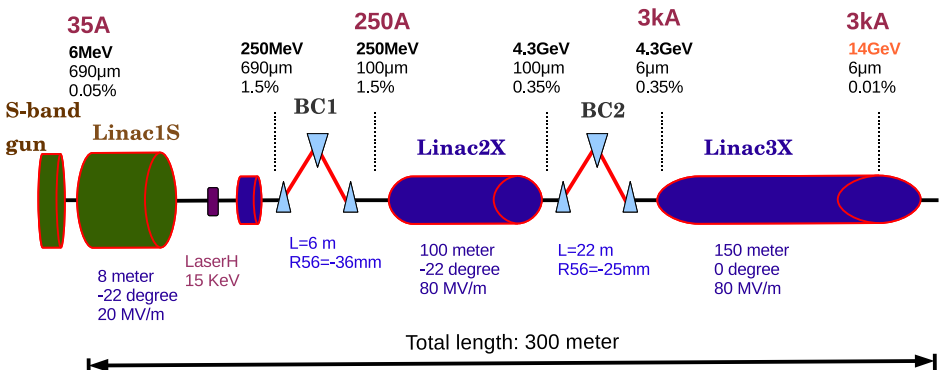


Figure 1: Sketch of a compact (300 m) hard x-ray FEL driver using X-band accelerators plus LCLS injector (up to the end of BC1). An average 'real estate' acceleration gradient of 60 MV/m is assumed in the X-band accelerator structures. The linac for the hard x-ray FEL achieves a final electron bunch energy of 14 GeV (same as the LCLS case) with a peak current between 3 kA and 5 kA (by tuning rf phase and then the bunch compression ratio). A final pulse duration length of 40-60 fs is achieved with a bunch charge of 250 pC. The sliced energy spread is between $0.01\% - 0.02\%$, and the sliced normalized transverse emittance is below 0.6 μm.

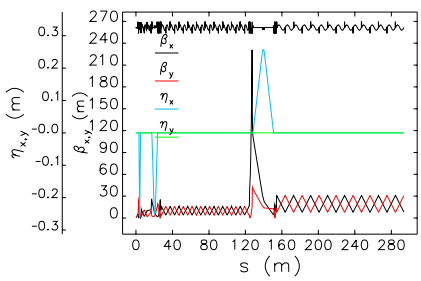


Figure 3: Beta functions and dispersion functions of the overall accelerator, from Linac1S (in Fig. 1) to the end of Linac3X (in Fig. 1) with a final beam energy of 14 GeV.

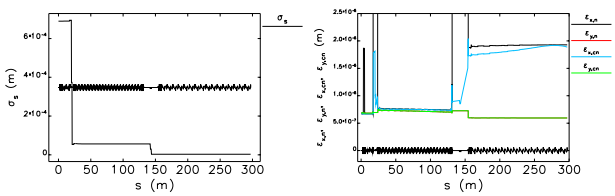


Figure 4: Left: RMS bunch length evolution along the linac, from ELEGANT simulation; right: projected and linear dispersion subtracted emittance evolution along the linac, from ELEGANT simulation.

ELEGANT SIMULATION

The beam dynamics simulation in the photoinjector is performed in ASTRA [7], and then a dumped beam is taken as the initial beam in the ELEGANT simulation. First-, second-, and third-order optics effects are included in the ELEGANT simulation, as well as all the collective effects, such as space-charge effect, incoherent and coherent synchrotron radiation, and transverse and longitudinal wakefields.

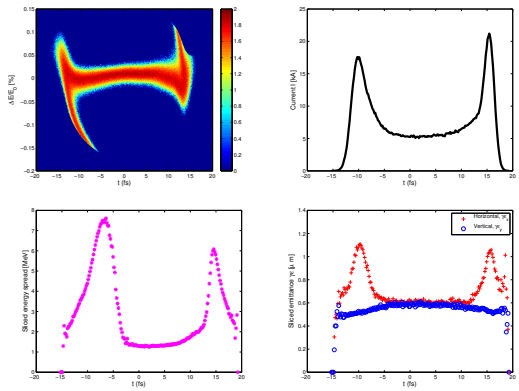


Figure 5: Electron beam properties at the end of Linac3X of this X-band-driven FEL driver, from ELEGANT simulation. Left top: longitudinal phase space; left bottom: longitudinally sliced energy spread; right top: current profile; right bottom: longitudinally sliced emittance.

The RMS bunch length and transverse emittance evolution along the accelerator are shown in Figure 4. Bunch compression ratios of 7 and 15 are achieved in a first- and second-stage bunch compressor. The final RMS bunch length is around 6-7 μm with a peak current over 3 kA. In the vertical plane the emittance is almost preserved. The horizontal emittance growth is mainly contributed from the coherent synchrotron radiation effects in the bunch compressors. Bunch compression ratios of 14 and 10 (for 5-kA final beam current case) could be achieved in a first- and second-stage bunch compression, respectively. The final beam current can be pushed to above 5 kA. The higher peak current at two ends (double horn) is due to compression with larger energy correlation (chirp) from longitudinal wakefields in Linac2X. There is a similar effect in the LCLS case.

Copyright © 2013 CC-BY-3.0 and by the respective authors

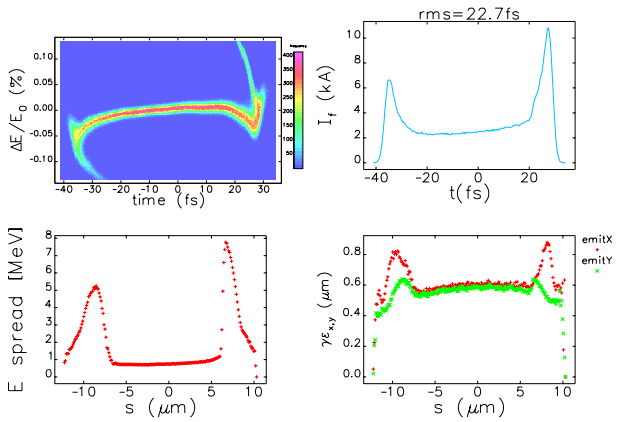


Figure 6: Electron beam properties at the end of LCLS Linac3, from ELEGANT simulation. Left top: longitudinal phase space; left bottom: longitudinally sliced energy spread; right top: current profile; right bottom: longitudinally sliced emittance.

Electron beam properties at the end of Linac3X of this X-band driven FEL driver are shown in Figure 5 from ELEGANT simulation, including longitudinal phase space, longitudinally sliced energy spread, current profile and longitudinally sliced emittance. A normalized transverse emittance of 0.6 μm is preserved at the core part of the electron bunch, with a pulse duration length of 40 fs. A peak current of 5 kA and a longitudinally sliced relative energy spread less than 2×10^{-4} is achieved. The residual correlated energy offset established in Linac1 and Linac2X is removed in Linac3X with the help of a strong X-band rf longitudinal wakefield, and a flat final energy profile is achieved at a final beam energy of 14 GeV.

A similar plot is shown in Figure 6 for the LCLS case. It is observed that the final beam current is over 5 kA in this X-band-driven FEL (3 kA for LCLS), and the sliced transverse emittance is similar for LCLS. A normalized transverse emittance of 0.5-0.6 μm is preserved at the core part of the electron bunch, with a pulse duration length of 70 fs. A peak current of 3 kA and a longitudinally sliced relative energy spread around 1×10^{-4} is achieved. The residual correlated energy offset established in Linac1 and Linac2 is removed in Linac3 with the help of an S-band rf longitudinal wakefield, and a flat final energy profile is achieved at a final beam energy of 14 GeV.

GENESIS SIMULATION

The electron bunch distribution generated from ELEGANT simulation is then fed into an undulator system, and the associated FEL performance is simulated and evaluated within the code GENESIS [9]. The same undulator setup is adopted for both this X-band-driven FEL and the LCLS, which is described below. An ideal undulator is designed to have a short period of $\lambda_w = 1.5$ cm, and the undulator strength K is chosen to tune the resonant FEL wavelength of $\lambda_r = 0.15$ nm, given the centroid energy of the electron bunch chosen at 14 GeV. No nonlinear magnetic field is included for the undulator model. No undulator tapering is adopted.

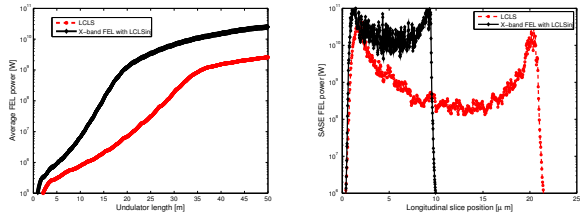


Figure 7: Left: FEL power evolution along the undulator; right: FEL power temporal profile at 50 m into the undulator. Red: LCLS case; black: the X-band-driven FEL.

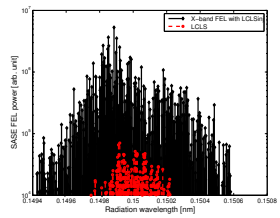


Figure 8: FEL power spectrum at 50 m into the undulator. Red: LCLS case; black: the X-band-driven FEL driver.

A comparison of the simulated FEL performance is shown in Figure 7 and Figure 8. As expected, this X-band-driven FEL achieves a shorter FEL gain length, a higher saturation power, and a higher FEL power at the same undulator length (benefiting from a higher peak current of 5 kA) as the LCLS case.

ACKNOWLEDGMENT

The author would like to thank C. Adolphsen, J. Wu, M. Woodley, A. Chao, Z. Huang, Y. Ding, and C. Limborg-Deprey for helpful discussions. The idea for this design is initially from C. Adolphsen et al. [1] and T. Raubenheimer. T. Raubenheimer proposed the push for higher peak current by employing stronger X-band wakefields [2]. Most of the work was done at SLAC. The paper was written at ANL.

REFERENCES

[1] C. Adolphsen et al., SLAC-PUB-14276 (2011).

[2] T. Raubenheimer, private communication (2011).

[3] P. Emma et al., SLAC-R-593, SLAC (2002); P. Emma et al., Nature Photonics 4 (2010) 641.

[4] Yipeng Sun et al., SLAC-PUB-14570 (2011); Proc. of IPAC2011, THPC103 , p. 3128 (2011).

[5] Yipeng Sun et al., Phys. Rev. ST Accel. Beams 15 (2012) 030703.

[6] Yipeng Sun et al., SLAC-PUB-14511 (2012).

[7] K. Floettmann, ASTRA user manual.

[8] M. Borland, Advanced Photon Source ANL/APS/LS-287 (2000).

[9] S. Reiche, Nucl. Instrum. Methods A 429 (1999) 243.

[10] H. Grote, F.C. Iselin, CERN/SL/90-13 (AP) (1990).

Copyright © 2013 CC-BY-3.0 and by the respective authors

ACHIEVING A QUASI-THIRD-ORDER ACHROMAT IN AN APS UPGRADE LATTICE*

Yipeng Sun† and Michael Borland, ANL, Argonne, IL 60439, USA

Abstract

The next-generation of storage rings will require stronger quadrupole focusing to achieve very low emittance. Stronger sextupoles (usually at smaller dispersion locations) are then necessary to correct the natural chromaticity and suppress the head-tail instability. The geometric and chromatic optics aberrations introduced by these sextupoles have a large impact on the beam dynamics performance. In this paper, it is discussed how to achieve a quasi-third-order achromat in a possible Advanced Photon Source (APS) multi-bend achromat (MBA) lattice. Repetitive identical MBA arc cells with specified phase advance and mirror symmetry are employed. The beam dynamics performance of such an achromat design is compared with a normal scheme.

OVERVIEW

The development of optical achromats started in the 1700s when achromatic doublets and triplets were invented to bring light of different frequencies to the same focal point. First-order achromats have been applied in particle accelerators for a long time. In the 1970s, K. Brown developed a systematic matrix-based approach to designing second-order achromats [1]. It adopts at least four identical cells with dipoles, quadrupoles, and sextupoles and can eliminate all geometric and chromatic aberrations up to second order. Two strong points being proposed are the integer phase advance in the entire beamline and the $-I$ phase separation between non-interleaved sextupoles to cancel even higher-order geometric aberrations. After that, similar third-order achromat design approaches were developed analytically and numerically [2] [3], where the concept of identical cells and integer phase advance is used again. Following these studies, W. Wan developed a general method with Lie algebra to design achromats to arbitrary order, taking advantage of mirror symmetry and using multipole magnets for each specified order (for example, octupoles for a third-order achromat) [4].

The latest PEPX design utilizes eight identical seven-bend achromat (7BA) cells in each arc section, where the total phase advance is an integer [5]. A third-order geometric achromat is achieved with the assistance of harmonic sextupoles [5]. In this paper, first a design similar to the APS storage ringe is presented. It employs more families of chromaticity sextupoles and may eliminate all geometric and chromatic aberrations up to third order. Then there is a discussion on how to achieve a quasi-third-order achromat in the APS upgrade lattices where 40 identical MBA cells have to be used and no dedicated straight sections are allowed.

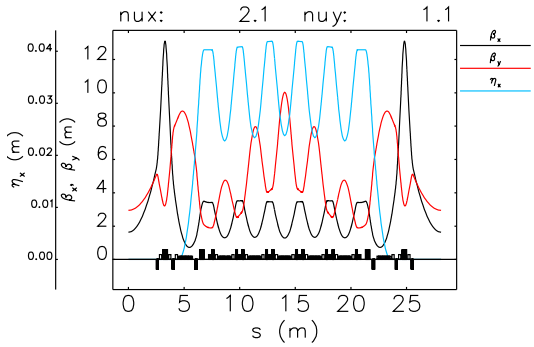


Figure 1: Twiss parameters in a 7BA arc cell with a length of 27.2 m. Natural emittance is 150 pm at a beam energy of 6 GeV. The black curve denotes horizontal beta function; red curve, vertical beta function; blue curve, horizontal dispersion function.

THIRD-ORDER ACHROMAT DESIGN

The current APS storage ring has a circumference of 1104 meters and is divided into 40 identical sectors. An APS-size ring is designed based on the third-order-achromat concept. Note that it may not fit in the current APS tunnel due to geometry, although the circumference is close to 1104 m. The ring consists of four arc sections plus short straight sections that are each 4 meters long. Each arc section has ten identical 7BA cells. The natural emittance is 150 pm at an electron beam energy of 6 GeV.

The linear and nonlinear optics optimization are performed with ELEGANT [6]. The Twiss parameters in a 7BA arc cell are shown in Figure 1. It is observed that in the central part there are five TME-like cells. Each cell consists of one combined function dipole (with defocusing quadrupole gradient), two focusing quadrupoles, and three sextupoles. The horizontal beta function and dispersion achieve a minimum in the center of the dipole magnet. The dispersion is matched to zero using two dedicated quadrupole magnets and an end dipole. A triplet is adopted outside of the end dipole to bring the beta functions down to β_x = 1.8 m and β_y = 3 m at the center of the insertion device (ID). The maximum dipole field is 0.45 Tesla and the maximum quadrupole gradient is 66 T/m.

The betatron phase advance of each 7BA cell is (2.1, 1.1) in units of 2π. The phase advance in each arc section is then (21, 11), i.e., multiples of 2π in both planes. In the 4-meter-

* Work supported by the U.S. Department of Energy, Office of Science, under Contract No. DE-AC02-06CH11357.

† yisun@aps.anl.gov

Copyright © 2013 CC-BY-3.0 and by the respective authors

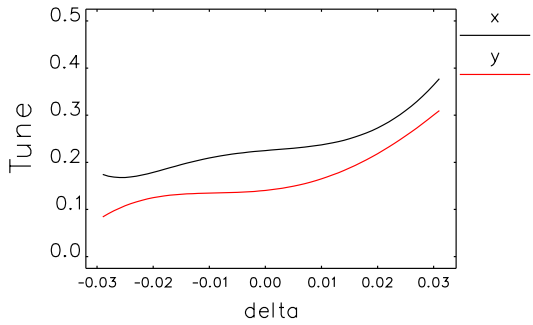


Figure 2: Horizontal (black curve) and vertical (red curve) betatron tune as a function of momentum offset $\Delta E/E$, dominated by third-order chromaticity.

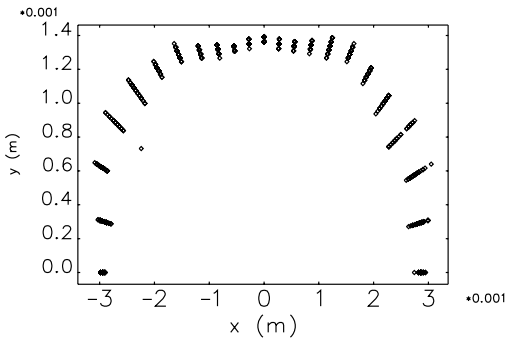


Figure 3: Dynamic acceptance with 50 ensembles of random, systematic, and tilt errors on quadrupoles and sextupoles. Tracking is performed at the center of the short straight section where β_x = 4 m, β_y = 1.2 m.

long straight section, which is between two arc sections, two triplets are placed with mirror symmetry. The linear optics is matched and the fractional tune of the storage ring is tunable in a range of (0.1, 0.4).

It is concluded that two families of sextupoles and five families of octupoles are enough to construct a third-order achromat [1] [2] [3]. In general, there are two independent linear chromaticity terms in the second-order matrix, and there are five independent terms in the third-order matrix (two second-order chromaticity terms, plus three transverse amplitude detuning terms). It is not realistic to use an octupoles plus sextupoles scheme due to limited space and maximum magnet strengths. Here only sextupoles are adopted to form a third-order achromat. Eight families of chromaticity sextupoles are placed in the dispersive region, while four families of harmonic sextupoles are placed between the end dipole and the ID.

Similar to the PEPX design [5], all third-order ($h10200$, $h10020$...) and most fourth-order ($h20200$, $h40000$...) betatron resonance driving terms are naturally cancelled between the ten identical cells [5]. These 12 families of sextupoles are tunable such that all the chromatic and geometric aberrations may be zero up to third order. In other words, the linear and second-order chromaticities ($d\nu/dp$ and $d\nu/dp^2$) can be tuned to zero, and the betatron resonance driving terms (up to fourth order) plus amplitude detuning terms ($d\nu_x/dJ_x$, $d\nu_x/dJ_y$ and $d\nu_y/dJ_y$) can be eliminated, too.

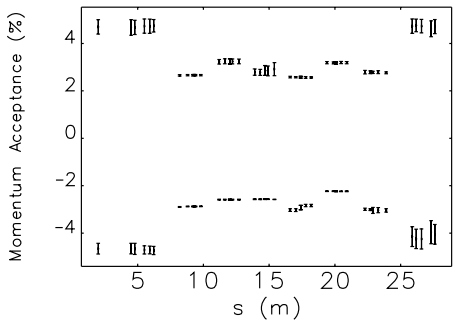


Figure 4: Local momentum acceptance with 50 ensembles of errors (random, systematic magnetic errors, and tilt errors on quadrupoles and sextupoles). Tracking is performed at locations next to each magnet in one 7BA arc cell (28 m).

As shown in Figure 2, the off-momentum tune variation is relatively small for a momentum offset up to 3%. The linear chromaticities are tuned to be 1 and the second-order chromaticities are close to zero. One observes that the off-momentum tunes are dominated by third-order chromaticities. We evaluated the lattice with 50 error ensembles, with 1% optics beating plus 1% coupling from strength and tilt errors in the quadrupoles and sextupoles. The dynamic acceptance (DA) was calculated by tracking for 400 turns, giving the results shown in Figure 3. We see that the DA is 3 mm (x) by 1.3 mm (y) at the straight section center where β_x = 4 m, β_y = 1.2 m. The shape of the DA curve is uniform and symmetric. The local momentum acceptance (LMA) was also evaluated at the exit of each magnet by tracking simulations. As observed in Figure 4, it is larger than 2%, which ensures a Touschek lifetime above four hours.

QUASI-THIRD-ORDER ACHROMAT AND BEAM DYNAMICS PERFORMANCE

"Quasi achromat" means that one wants to minimize/zero terms that are most relevant to the beam dynamics performance. For example, a chromatic achromat is essential in transporting a beam with large energy spread. As mentioned above, the lattice design described in the previous section may not fit the APS ring geometry. Alternatively, the following options are proposed and evaluated to achieve a quasi (or pure) third-order achromat in an APS MBA lattice. It is assumed to have 40 identical MBA cells.

- True third-order achromat with octupoles, excluded due to space constraints

Copyright © 2013 CC-BY-3.0 and by the respective authors

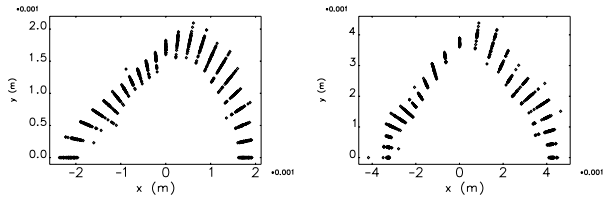


Figure 5: Comparison of dynamic acceptance shows that the quasi-third-order achromat scheme (right figure) has better performance.

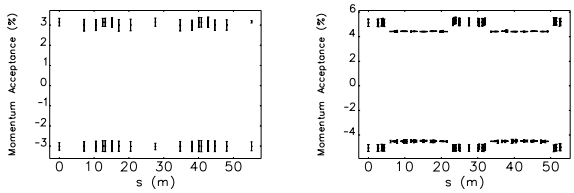


Figure 6: Comparison of local momentum acceptance shows that the quasi-third-order achromat scheme (right figure) has better performance.

- Add three additional quads at the two ends of every ten cells to change fractional tune, giving a superperiodicity of 4
- 40 identical cells, but each cell has phase advance like (2.104,1.103)

It is interesting to note that the third-order achromat condition is very sensitive to the phase advance. There will be large deviations of the resonance driving terms and detuning terms if the phase advance changes by 1×10^{-5} in each 7BA cell. Based on these considerations, option 3 is a good choice to achieve a quasi-third-order achromat in an APS MBA lattice. The 7BA cell phase advance is tuned to be something like (2.104,1.103), so that in ten repetitive cells the total phase advance is close to a multiple of 2π. The fractional tune is also naturally far away from integer resonance. Note that this scheme is also good for maintaining a large superperiodicity, which helps to suppress lower-order resonances.

A plain 7BA lattice was studied and optimized as one option for a future APS MBA upgrade [7]. It has a natural emittance of 150 pm at 6 GeV. The following two schemes are compared for their beam dynamics performance:

- Normal scheme with arbitrary phase advance in each 7BA cell
- Quasi-third-order achromat scheme, making a quasi-third-order achromat in ten 7BA cells

The lattice is almost the same for these two schemes. The arc sextupoles and harmonic sextupoles arrangements are exactly the same. The major difference is the phase advance. Both schemes are optimized for nonlinear beam dynamics performance, using a Multi-objective Genetic Algorithm [8]. As expected, the quasi-third-order achromat scheme has much smaller geometric and chromatic aberrations than the normal scheme. With the same error settings and tracking setup, the dynamic acceptance and local momentum acceptance are compared between these two schemes, as shown in Figure 5 and Figure 6, respectively. At a location with similar beta functions (roughly $\beta_x = \beta_y$ = 2 meters), the DA is 3.5×3.5 mm^2 for the achromat scheme, which is roughly a factor of two larger than the normal scheme. The LMA is also improved from 3% to 4%. As observed in Figure 7, there are fewer resonance lines showing up in the frequency map of the quasi- achromat scheme.

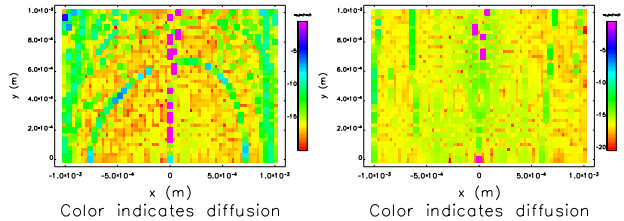


Figure 7: Comparison of frequency map analysis shows that the quasi-third-order achromat scheme (right figure) has better performance.

CONCLUSION

A true third-order achromat without octupoles was studied for an APS-size storage ring that has 150-pm emittance at 6 GeV. Quasi-third-order achromat schemes were also studied and implemented in APS MBA lattices. The effectiveness of the quasi-achromat scheme was confirmed for a plain 7BA lattice, as well as for a plain 5BA lattice [9] and a hybrid 7BA lattice.

ACKNOWLEDGMENT

The authors would like to thank C. Wang, Z. Gu, V. Sajaev and L. Emery for helpful discussions.

REFERENCES

[1] K. Brown, IEEE Trans. Nucl. Sci. NS-26(3), (1979) 3490.

[2] A. J. Dragt, Nucl. Instrum. Methods A 258 (1987) 339.

[3] F. Neri, Michigan State University Cyclotron Laboratory, Technical Report No. MSUCL-767 (1991).

[4] W. Wan and M. Berz, Phys. Rev. E 54 (1996) 2870.

[5] Y. Cai, Phys. Rev. ST Accel. Beams 15 (2012) 054002.

[6] M. Borland, Advanced Photon Source ANL/APS/LS-287 (2000).

[7] M. Borland, private communication.

[8] M. Borland et al., Advanced Photon Source ANL/APS/LS-319 (2010).

[9] Y.-P. Sun and M. Borland, MOPHO10, proceedings of NA-PAC13 (2013).

Copyright © 2013 CC-BY-3.0 and by the respective authors

ANALYTICAL EVALUATION OF CORRELATED TIMING JITTER CANCELLATION IN A STAGED BUNCH COMPRESSION SYSTEM*

Yipeng Sun†, ANL, Argonne, IL 60439, USA

Abstract

In this paper, the wakefield cancellation scheme on the timing jitter is revisited. The correlated timing jitter effects between the photoinjector laser and the linac rf phase are evaluated analytically. It is possible to minimize its impact on the final bunch length (peak current) variation by employing a longer linac with a lower acceleration gradient between bunch compressors one and two.

OVERVIEW

A staged magnetic bunch compression system is widely adopted in the acceleration process of the electron beam. It first introduces an energy modulation along the electron bunch in its longitudinal direction, then lets the electron beam pass by a dispersive region where electrons in the head and tail of the bunch all move relatively towards bunch center. Chicane- and wiggler-based bunch compressor designs were proposed and studied thoroughly in the 1990s, mainly for linear collider projects [1], [2], [3].

The stability of the final electron beam current depends on the timing and rf phase jitter, bunch compressor parameters, and electron beam charge variations. Gun laser to linac rf timing jitter (referred to as timing jitter)–the main timing error to be discussed in this paper–is considered to be correlated for all the linac sections as the sum of the uncorrelated (or random) rf phase jitter (different from rf source-to-source) tends to be small.

The bunch length variation due to jitter effects at the ends of the staged bunch compressors were studied in (and before) the LCLS initial design stage, and a longitudinal wakefield cancellation scheme was proposed with at least two stages of bunch compressions [4], [5], [6], [7], [8]. This scheme was also applied at the LCLS FEL [5], [7], [8]. A similar scheme is also proposed to reduce the energy chirp by employing the wake of coherent synchrotron radiation [9].

In this paper, this topic is revisited, while the associated formulae are rederived and extended analytically. The analytical result is verified by numerical simulations. It is possible to minimize the correlated timing jitter's impact on the final bunch length (peak current) variation by employing a longer linac with a lower acceleration gradient, between bunch compressors one and two.

* Work at Argonne is supported by the U.S. Department of Energy, Office of Science, under Contract No. DE-AC02-06CH11357. Work also supported by the U.S. Department of Energy under Contract DE-AC02-76SF00515.

† yisun@aps.anl.gov

ANALYTICAL DERIVATION

Neglecting the small initial un-correlated energy spread and considering only linear terms, the RMS bunch length after bunch compressor one can be expressed as

$$\sigma_{z1} = (1 + h_1 R_{56(1)}) \cdot \sigma_{z0}, \tag{1}$$

where σ_{z1} denotes the RMS bunch length after bunch compressor one, h_1 is the chirp of bunch compressor one, $R_{56(1)}$ is the first-order longitudinal dispersion in bunch compressor one, and σ_{z0} is the initial bunch length; and

$$h_1 = -\frac{k_1 e V_0 \sin\phi}{E_{f0}} \approx -k_1 \tan\phi \approx -k_1\phi_1, \tag{2}$$

where $k_1 = \frac{2\pi_1}{\lambda}$ denotes the rf wave number in the first rf section, E_{f0} is the central energy after rf acceleration, e is the electron charge, V_0 is the rf voltage, ϕ_1 is the rf phase, $k = \frac{2\pi}{\lambda}$ is the rf wave number, and λ is the rf wave length.

Given a timing jitter $\Delta\phi_1$, the change in the final bunch length is

$$\Delta\sigma_{z1} = -k_1 \Delta\phi_1 R_{56(1)} \cdot \sigma_{z0}. \tag{3}$$

Neglecting the residual damped energy chirp from the first rf linac $h_1 \cdot C_1 \cdot E_1/E_2$ ($C_1 = 1/(1 + h_1 R_{56(1)})$ denotes the compression ratio in BC1. Also the longitudinal wakefield effects in Linac2 only consider an energy chirp established in Linac2, which is h_2. The final RMS bunch length after the second bunch compressor can be calculated as

$$\sigma_{z2} = (1 + h_2 R_{56(2)}) \cdot \sigma_{z1}, \tag{4}$$

$$h_2 \approx -k_2\phi_2, \tag{5}$$

where σ_{z2} denotes the RMS bunch length after bunch compressor two, h_2 is the chirp of bunch compressor two, $R_{56(2)}$ is the first-order longitudinal dispersion in bunch compressor two, and $k_2 = \frac{2\pi_2}{\lambda}$ is the rf wave number in the second rf section.

After inserting the expression σ_{z1} into Eq. (4), one finds

$$\sigma_{z2} = (1 + h_2 R_{56(2)}) \cdot (1 + h_1 R_{56(1)}) \cdot \sigma_{z0}. \tag{6}$$

Given a linac rf timing jitter of $\Delta\phi_1$ and $\Delta\phi_2$ in the first and second rf linacs, the final bunch length is

$$\sigma_{z2} = \left[1 - k_2(\phi_2 + \Delta\phi_2) R_{56(2)}\right] \cdot \left[1 - k_1(\phi_1 + \Delta\phi_1) R_{56(1)}\right] \cdot \sigma_{z0}. \tag{7}$$

Copyright © 2013 CC-BY-3.0 and by the respective authors

The change of bunch length after the second bunch compressor is

$$\begin{aligned}\Delta\sigma_{z2} &= [-k_2\Delta\phi_2 R_{56(2)}(1-k_1\phi_1 R_{56(1)}) \\ &\quad -k_1\Delta\phi_1 R_{56(1)}(1-k_2\phi_2 R_{56(2)}) \\ &\quad +k_1k_2\Delta\phi_1\Delta\phi_2 R_{56(1)}R_{56(2)}]\cdot\sigma_{z0}. \quad (8)\end{aligned}$$

Inserting the bunch compression ratio in the first and second stage of bunch compressors, $C_1 = 1/(1+h_1R_{56(1)})$ and $C_2 = 1/(1+h_2R_{56(2)})$, into the above formulae, one finds

$$\begin{aligned}\Delta\sigma_{z2} &= [-k_2\Delta\phi_2 R_{56(2)}/C_1 \\ &\quad -k_1\Delta\phi_1 R_{56(1)}/C_2 \\ &\quad +k_1k_2\Delta\phi_1\Delta\phi_2 R_{56(1)}R_{56(2)}]\cdot\sigma_{z0}. \quad (9)\end{aligned}$$

Assuming the first and second rf linac have the same rf frequency $k_1 = k_2 = k$ (which also means that the same time jitter introduces the same change in the rf phase, $\Delta\phi_1 = \Delta\phi_2 = \Delta\phi$), one finds that the above formula can be simplified to

$$\begin{aligned}\Delta\sigma_{z2} &= k\Delta\phi[-R_{56(2)}/C_1 - R_{56(1)}/C_2 \\ &\quad +k\Delta\phi R_{56(1)}R_{56(2)}]\cdot\sigma_{z0}. \quad (10)\end{aligned}$$

From the above formula, one observes that in order to minimize the impact from timing jitter on the final bunch length, one needs to employ a linac with lower frequency rf (smaller k) and smaller longitudinal dispersion R_{56} in the bunch compressors. In order to keep similar compression ratios C_1 and C_2, a larger rf phase should be employed, given a required smaller longitudinal dispersion R_{56} in the bunch compressors. Further, assuming the same timing jitter for both the first and second rf linacs, the impact from both compression stages on the final bunch length always adds up.

Another effect that could be used to partially compensate the timing jitter is the longitudinal wakefield in the second rf linac [4], [5], [6], [7], [8]. The basic idea is that if a timing jitter in the first rf linac introduces a stronger compression in bunch compressor one, which in turn results in a shorter bunch length in the second rf linac, the energy chirp established by the longitudinal wakefield in the second rf linac is larger. For an under-compression scheme with normal four-dipole chicane compressor, the rising slope of the rf wave is employed (electron bunch is ahead of rf crest), which means that the bunch head has a lower energy than its tail. As the longitudinal wakefield always makes the bunch tail lose energy with respect to its head, the energy chirp from the wakefield has a sign opposite the rf chirp in the second rf linac. The timing jitter in the second rf linac is assumed to be the same as the one in the first rf linac, so this relative change in rf phase also introduces a stronger compression in bunch compressor two. However, the wakefield chirp fights the energy chirp established by the second rf linac and makes the bunch compression ratio smaller in this second stage, which partially compensates the timing jitter effects.

With the longitudinal wakefield effects in both the first and second rf linac included, the final bunch length is rewritten as

$$\begin{aligned}\sigma_{z2} &= \left[1+(h_2+h_{2w})R_{56(2)}\right] \\ &\quad \cdot\left[1+(h_1+h_{1w})R_{56(1)}\right]\cdot\sigma_{z0}, \quad (11)\end{aligned}$$

where h_{1w} denotes the linear energy chirp induced by longitudinal wakefield in the first rf linac, and h_{2w} is the linear wakefield energy chirp established in the second rf linac.

Given an electron beam energy of 250 MeV at bunch compressor one, a short first rf linac is employed, which means that the wakefield-induced chirp h_{1w} is relatively small and could be negligible. As discussed above, the wakefield chirp h_{2w} has a sign opposite the rf chirp h_2, which should be taken into account when the FEL bunch compression system is designed. Basically, it is the change in wakefield-generated energy chirp that could compensate a timing jitter between laser (electron bunch generation) and linac rf. Based on this point, a second rf linac with longer length should have a stronger relative change in wakefield-induced chirp when the electron bunch length is affected in a first-stage bunch compressor by timing jitter effect. A final electron bunch length at the end of bunch compressor two is then expressed as shown below, with timing jitter and wakefield effects considered up to first order. The rf phase ϕ_1 and ϕ_2 denote the ones that already have wakefield-induced energy chirp subtracted:

$$\begin{aligned}\sigma_{z2} &= [1-k_2(\phi_2+\Delta\phi_2 \\ &\quad -D(\sigma_{z1},k_2)\cdot L_{linac2})R_{56(2)}] \\ &\quad \cdot\left[1-k_1(\phi_1+\Delta\phi_1)R_{56(1)}\right]\cdot\sigma_{z0}, \quad (12)\end{aligned}$$

where $D(\sigma_{z1},k_2)$ denotes the unit-length change of wakefield-induced energy chirp in linac2, which is a function of rf structure (frequency) and electron bunch length in Linac2; and L_{linac2} is the length of Linac2.

In order to keep the same beam energy at BC2, the acceleration gradient in the second rf linac needs to be decreased. Another point is that, as the the second rf linac length is increased, the nominal wake-induced energy chirp is larger, which means that one has to adopt a larger rf phase in the second rf linac to cancel the wake effects and provide the necessary energy chirp. As discussed above, a larger rf phase also makes the timing jitter effect relatively smaller.

NUMERICAL SIMULATION

ELEGANT [10] simulations of a low-charge X-band hard x-ray FEL [11] are performed with timing jitter set on all linac rf phases up to 50 fs, which is successfully achieved in LCLS operation [12]. This timing jitter of 50 fs changes

Copyright © 2013 CC-BY-3.0 and by the respective authors

the Linac1 rf phase and in turn changes the electron bunch length at the end of bunch compressor one. The final relative RMS bunch length variation is around 20 % with the 35-meter-long Linac2, given a timing jitter of 50 fs between laser and linac rf.

One then can decrease the acceleration gradient in the second rf linac and increase the second rf linac length (employing more rf cavities), keep the same beam energy at bunch compressor two, and employ a stronger longitudinal wakefield in the second rf linac to cancel the timing jitter effect. However, a longer total accelerator length and a higher total cost are accompanied with increasing the second rf linac length and employing more rf cavities. A tradeoff needs to be made between the factors mentioned above and the tolerated timing jitter. Analytical and numerical studies show that decreasing the average acceleration gradient from 80 MV/m to 65 MV/m in the second rf linac could drop the final peak current variation to 12% [11]. The timing-jitter-induced peak current variation could be fully compensated if an average acceleration gradient of 50 MV/m is adopted in the second rf linac [11].

A second example is an X-band rf-driven hard x-ray FEL design with LCLS injector [13]. Similarly, the length of the second rf linac is tuned to compensate (or even overcompensate) the timing jitter impacts. As shown in Figure 1, the LCLS injector plus X-band linac case (blue curve) is much more sensitive to timing jitter than the normal LCLS case (red curve). This is due to the higher frequency of X-band rf. For these nominal cases, an acceleration gradient of 80 MV/m is adopted for X-band rf, while it is 20 MV/m for S-band rf in the LCLS. However, if one doubles the length of the second rf linac and adopts an acceleration gradient of 40 MV/m in the second X-band rf linac, the black curve shows that one could possibly cancel the timing jitter effect. In this specific example, the timing jitter effect on the final bunch length is over-compensated by the wakefields in the second X-band rf linac. One should also note that the rf phase in the second X-band rf linac is increased from 22 degrees to 33 degrees.

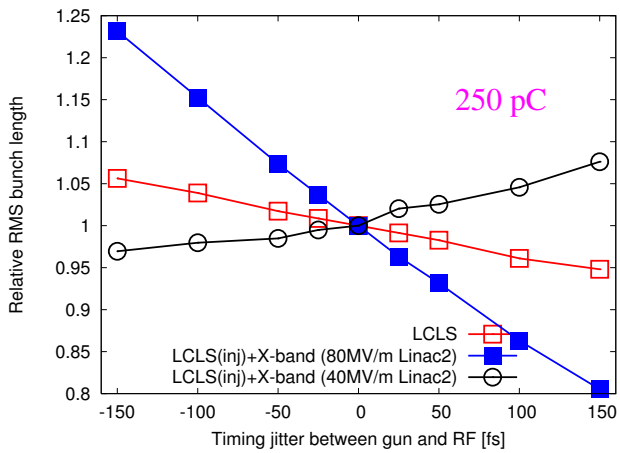


Figure 1: Relative bunch length after the final stage of bunch compression, as a function of timing jitter, for a bunch charge of 250 pC.

CONCLUSION

The longitudinal wakefield cancellation scheme is revisited in this paper. Analytical derivations are presented for bunch length and its variation in a staged bunch compression system. Under first-order approximation, the length of the second rf linac can be calculated analytically, which compensates the timing-jitter-induced bunch length variation. Simulation results of two X-band-rf-driven FEL drivers are presented where these cancellation schemes are applied.

ACKNOWLEDGMENT

The authors would like to thank P. Emma, Y. Ding, W. Wan, T. Raubenheimer, Z. Huang, and C. Adolphsen for helpful discussions. Most of this work was done at SLAC. The paper was written at ANL.

REFERENCES

[1] T. Raubenheimer, P. Emma and S. Kheifets, Proc. of PAC93, p. 633 (1993).

[2] P. Emma, SLAC-PUB-1001, DESY TESLA-95-17 (1995).

[3] P. Emma, DESY TESLA-98-31 (1998).

[4] T. Raubenheimer, Nucl. Instrum. Meth. in Phys. Res. A 358 (1995) 40.

[5] LCLS Design Study Report, SLAC-R-521 (1998).

[6] K. Bane, T. Raubenheimer and J. Seeman, Proc. of PAC93, p. 596 (1993).

[7] P. Emma, private communication.

[8] T. Raubenheimer, private communication.

[9] R. Bosch, Phys. Rev. ST Accel. Beams 13 (2010) 110702.

[10] M. Borland, Advanced Photon Source ANL/APS/LS-287, September 2000.

[11] Y.-P. Sun et al., Phys. Rev. ST Accel. Beams 15 (2012) 030703.

[12] P. Emma et al., Nature Photonics 4 (2010) 641.

[13] Y.-P. Sun et al., MOPHO12, Proceedings of NA-PAC13 (2013).

Copyright © 2013 CC-BY-3.0 and by the respective authors

X-BAND FEL DRIVER LINAC DESIGN WITH OPTICS LINEARIZATION*

Yipeng Sun†, ANL, Argonne, IL 60439, USA
Tor Raubenheimer, Juhao Wu, SLAC, Menlo Park, California 94025, USA
Paul Emma, LBNL, Berkeley, California 94720, USA

Abstract

In this paper, a compact hard x-ray FEL design is proposed with a single bunch charge of 250 pC, which is based on all X-band rf acceleration and two-stage bunch compression. It eliminates the need for a harmonic rf linearization section by employing optics linearization in its first-stage bunch compression. Emittance growth in the horizontal plane due to coherent synchrotron radiation (CSR) is investigated and minimized, to be on a similar level with the LCLS. An electron bunch distribution at the linac end is taken as the input for an FEL simulation in GENESIS, with a beam energy of 7 GeV. At an FEL radiation wavelength of 0.15 nm, a saturation length of roughly 40 meters can be achieved by employing an undulator with a period of 1.5 cm. Without tapering, an FEL radiation power above 10 GW is achieved with a photon pulse length of 50 fs, which is LCLS-like performance. The overall length of the accelerator plus undulator is around 250 meters, which is much shorter than the LCLS length of 1230 meters.

OVERVIEW AND ACCELERATOR DESIGN

In this paper, a very compact FEL driver is proposed with an accelerator length less than 200 m. An alternative way to do a linearized bunch compression in a first stage is proposed. The key point is to eliminate the harmonic rf section, and to apply an optics linearization instead, with a specially designed bunch compressor that includes quadrupole and sextupole magnets. Similar schemes have been proposed and studied preliminarily before, either in an analytical manner [1] [2] [3], by numerical simulations [1] [3] [4] [5], or in experimental measurements [3]. The second-order longitudinal dispersion T_{566} of this bunch compressor is precisely controlled and used to compensate the second-order curvature from the main rf acceleration. Third-order longitudinal dispersion U_{5666} can also be tuned to cancel the third-order rf curvature; however, in most cases this is not necessary as its impact is relatively small. Compared with a four-dipole chicane, this bunch compressor has the opposite sign of the linear longitudinal dispersion R_{56}. The main rf system in the first linac then has to work on the falling slope of the sinusoidal wave, which is the only way to shorten the bunch length; otherwise the bunch length is lengthened. In order to do a normal under-compression in the second stage, and still use longitudinal wakefields to remove the residual chirp in the last linac, one needs to do an over-compression in the first-stage bunch compressor. Over-compression may cause larger transverse emittance growth due to phase smear in the over-compression process, associated with energy change from coherent synchrotron radiation (CSR) in a dispersive region. The optics design of this bunch compressor needs to be investigated and optimized carefully to minimize these impacts.

The accelerator of this FEL driver is sketched in Figure 1. Compared with a similar hard x-ray FEL design based on S-band rf acceleration, this all X-band-based FEL has several potential advantages. One advantage is its compact size at the same final beam energy, due to the higher acceleration gradient provided by X-band rf cavities. In general the accelerator length is only one-fourth or one-third of the S-band-based accelerator. Besides, a shorter wavelength of X-band rf also makes the establishment of energy modulation easier, which then makes it possible to run on an rf phase closer to the crest and so save rf power. Another possible advantage is that it may be easier to manipulate the longitudinal phase space, especially in the second and last linac (for a two-stage bunch compression), mainly due to a much stronger longitudinal wake field of X-band rf. One may also benefit from a smaller CSR-induced emittance growth in bunch compressor two, as a larger energy correlation can be generated in Linac2 and then removed in Linac3, so the strength of the bunch compressor dipoles can be decreased.

NUMERICAL SIMULATION

In this section start-to-end ELEGANT [6] 6-D numerical simulation results are presented. The simulation starts at a beam energy of 50 MeV, where X-band photoinjector simulations show that an RMS bunch length of 160 μm could be achieved along with a normalized transverse emittance of 0.5 μm.rad at a bunch charge of 250 pC, by tuning the drive laser system, bunching system, and subsequent acceleration section [7]. Space-charge effect and velocity bunching are two dominant effects in this section from the production of the electron bunch and its acceleration to a beam energy of 50 MeV. The details on the simulation results of this part are not discussed here.

An electron bunch that consists of one million macro particles is then generated internally in ELEGANT, employing an RMS bunch length of 160 μm and a normalized transverse emittance of 0.5 μm.rad. The beam energy is 50 MeV and the single-bunch charge is 250 pC. The un-

* Work at Argonne is supported by the U.S. Department of Energy, Office of Science, under Contract No. DE-AC02-06CH11357. Work also supported by the U.S. Department of Energy under Contract DE-AC02-76SF00515.

† yisun@aps.anl.gov

Copyright © 2013 CC-BY-3.0 and by the respective authors

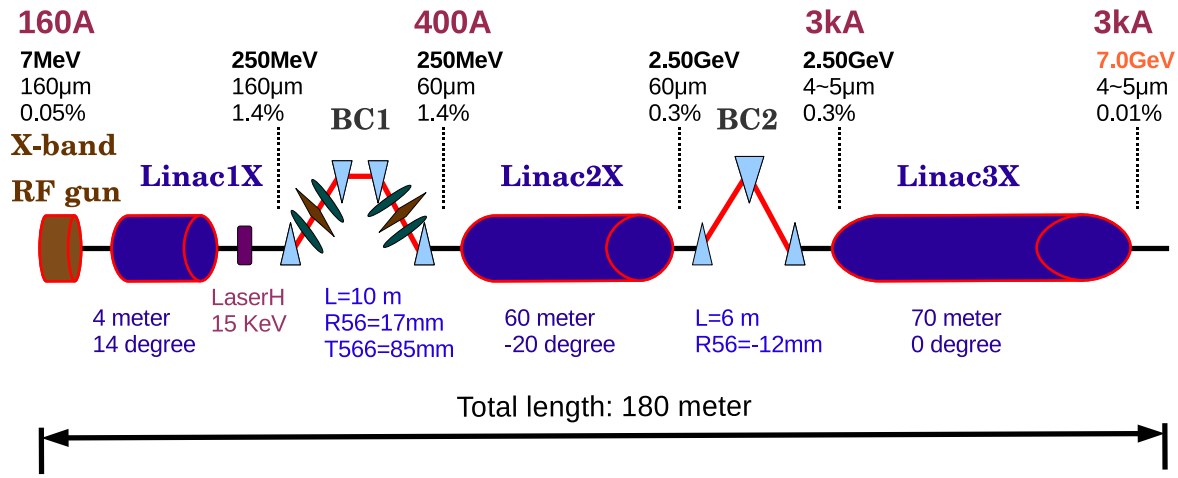


Figure 1: Sketch of an all X-band-based hard x-ray FEL accelerator design.

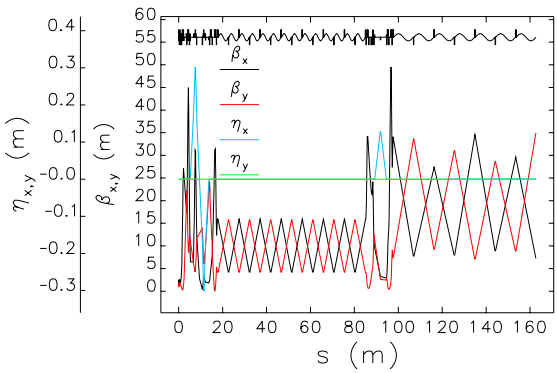


Figure 2: Start-to-end TWISS parameters, a beam energy from 50 MeV to 7 GeV. Black curve denotes horizontal beta function; red curve, vertical beta function; blue curve, horizontal dispersion function; and green curve, horizontal angular dispersion function.

correlated RMS energy spread is 12.5 keV. The distribution in both longitudinal and transverse planes is assumed to be a perfect Gaussian distribution. This electron bunch is transported through a first linac section (Linac1), bunch compressor one, a second linac section (Linac2), bunch compressor two, and a third linac section (Linac3). The start-to-end first order optics is illustrated in Figure 2, from entrance of Linac1 to the end of Linac3. The optics design is performed and optimized in an accelerator design code MAD8 [8] first, then translated into ELEGANT [6] format.

The CSR-induced transverse emittance growth is on a similar level between this X-band-driven FEL and the LCLS. In detail, while the vertical emittance is always preserved at 0.5 μm.rad during the acceleration and bunch compression, the horizontal emittance is increased to 0.55 μm.rad in the core part and 0.8-0.9 μm.rad in the bunch head and tail.

After the two-stage bunch compression, a peak current over 3 kA is achieved in a pulse length of roughly 50 fs. The vertical normalized emittance is preserved at 0.5 μm.rad, and the horizontal normalized emittance is increased by 20% on average. The residual correlated energy spread is removed in Linac3, mainly by the strong X-band rf longitudinal wakefield. The Linac3 runs on-crest with a total length of 70 meters. A final flat energy profile is achieved as shown in Figure 3, as well as the current profile, longitudinally sliced transverse emittance, and energy spread. This final electron beam is injected into the design undulator for a hard x-ray FEL with a radiation wavelength as short as 0.15 nm. The detailed FEL simulation and performance is presented below.

FEL SIMULATION

FEL performance is preliminarily studied, with the GENESIS simulation results presented in this section. In the following parts, we show a concrete example of FEL lasing at 0.15-nm wavelength, which is the same as achieved at LCLS. The undulator is designed to have a shorter period $\lambda_w = 1.5$ cm than the LCLS value of 3 cm, as the beam energy of 7 GeV is lower than the LCLS beam energy of 14 GeV. The undulator strength K is chosen so that the resonant FEL wavelength is $\lambda_r = 0.15$ nm according to Eq. 64 for $\theta = 0$ and $E = 7$ GeV. The electron bunch distribution generated from the ELEGANT simulation is then fed into an undulator system, and the associated FEL performance is simulated and evaluated within the code GENESIS [9]. The electron bunch transverse profile is matched into the undulator beamline where the average beta function is roughly 20 meters. No undulator tapering is adopted here to further

Copyright © 2013 CC-BY-3.0 and by the respective authors

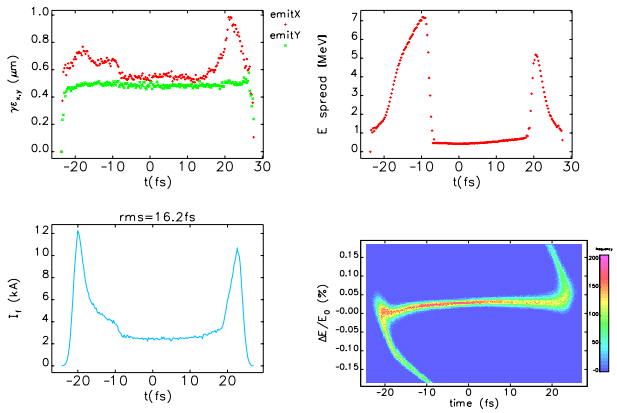


Figure 3: Beam properties at the end of Linac3, which is also the entrance of the undulator. Left top: longitudinally sliced emittance; left bottom: current profile along longitudinal direction; right top: longitudinally sliced energy spread; right bottom: longitudinal phase space.

increase the FEL saturation power.

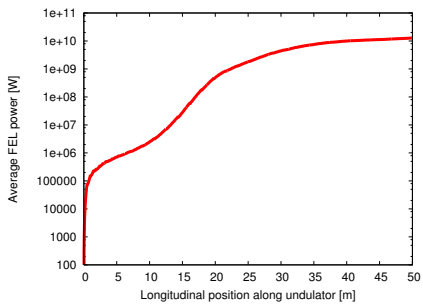


Figure 4: FEL power evolution along the undulator.

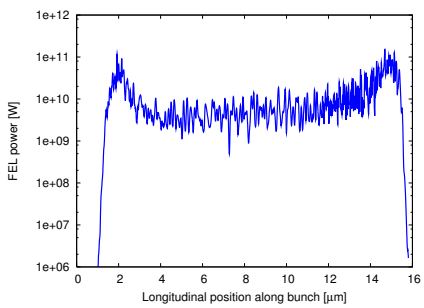


Figure 5: FEL power temporal profile at 40-m undulator.

Given a high peak current of 3 kA, plus a small sliced transverse emittance and energy spread, within a 40-m-long undulator the FEL radiation power can saturate at an average power of $P_{sat} \sim 10$ GW as shown in Figure 4. In comparison, LCLS achieves roughly 6 GW in 60 meters without tapering. An overall undulator length of 50 m is chosen to guarantee saturation. The temporal and spectrum profile of the FEL at 40 m of undulator is shown in Figure 5 and Figure 6, respectively.

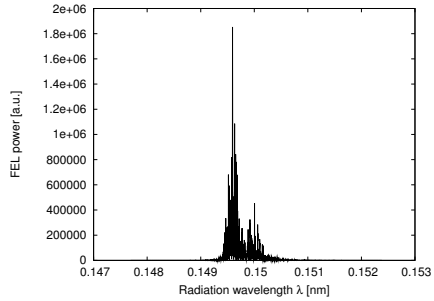


Figure 6: FEL power spectrum at 40-m undulator.

CONCLUSION

Start-to-end optics design and 6-D macro particle simulations are presented for an electron beam energy from 50 MeV to 7 GeV. The electron bunch is successfully compressed to a peak current above 3 kA, while its brightness is well preserved in both the transverse and longitudinal planes. The CSR-induced transverse emittance growth is at a similar level in both this X-band-driven FEL and the LCLS. This all X-band rf-based hard x-ray FEL could achieve LCLS-like performance in a shorter overall length of 250 meters.

ACKNOWLEDGMENT

The authors would like to thank M. Woodley, A. Chao, Z. Huang, C. Adolphsen, Y. Ding, and C. Limborg-Deprey for helpful discussions, and C. Adolphsen for the proofreading. Most of the work was done at SLAC. The paper was written at ANL.

REFERENCES

[1] P. Emma, "Bunch Compressor Options for the New TESLA Parameters," DESY TESLA-98-31 (1998).

[2] W. Decking, G. Hoffstatter and T. Limberg, "Bunch Compressor for the TESLA Linear Collider," Report TESLA-2000-40 (2000).

[3] R. England et al., Phys. Rev. ST Accel. Beams 8 (2005) 012801.

[4] S. Thorin et al., "Bunch Compression by Linearising Achromats for the MAX IV Injector," Proc. of FEL2010, WEPB34, p. 471 (2010).

[5] J. Thompson, "Bunch Compression for a Short-Pulse Mode in Cornell's ERL," Cornell internal report, ERL09-01 (2009).

[6] M. Borland, "elegant: A Flexible SDDS-Compliant Code for Accelerator Simulation," Advanced Photon Source ANL/APS/LS-287, (September 2000).

[7] C. Limborg-Deprey et al., "An X-Band gun test area at SLAC," Proceedings of PAC 2011, MOP015, p. 133 (2011).

[8] H. Grote, F.C. Iselin, "The MAD Program (Methodical Accelerator Design) Version 8.15," CERN/SL/90-13 (AP) (1990).

[9] S. Reiche, Nucl. Instrum. Methods A 429 (1999) 243.

Copyright © 2013 CC-BY-3.0 and by the respective authors

NSLS II COMMISSIONING TOOLS*

G.M. Wang#, T. Shaftan, B. Bacha, A. Blednykh, E. Blum, W.X. Cheng, J. Choi, M. Davidsaver, J. De Long, L. Dalesio, R. Fliller, M. Fulkerson, G. George, W. Guo, K. Ha, H. Hseuh, Y. Hu, W. Louie, M. Maggipinto, J. Mead, D. Padrazo, G. Shen, K. Shroff, O. Singh, K. Vetter; Y. Tian, H. Xu, L. Yang, X. Yang, F. Willeke. Photon Sciences, BNL, Upton, NY, 11973, U.S.A

V. Smalyuk, S. Karnaev, S. Sinyatkin, S. Gurov, A. Erokhin, E. Simonov, A. Derbenev, P. Cheblakov, R. Kadyrov BINP, SB, RUS

Abstract

NSLS-II is a state-of-the-art third-generation light source under construction at BNL. As many facilities worldwide, NSLS II uses the EPICS control system to monitor and control all accelerator hardware. CSS is used for simple tasks such as monitoring, display, setting of PVs and browsing the historical data. For more complex accelerator physics applications, a collection of scripts are mainly written in Python. The controls group developed the services, such as channel finder, machine snapshot, data archiving, twiss server, unit conversion etc. This paper will present the tools that we have been using for commissioning.

INTRODUCTION

The NSLS-II [1] is a state of the art 3 GeV synchrotron light source under construction at Brookhaven National Laboratory. It consists of a 200 MeV linac, a booster ring accelerating beam from 200 MeV to 3 GeV, a 3 GeV Storage ring and transport lines in between them.

As many other facilities [2,3], NSLS II chose the Experimental Physics and Industrial Control System (EPICS) as its control system to monitor and control the accelerator hardware. It interfaces to the accelerator instruments and devices (such as Power supply, digitizer, and motor) with IOC (Input Output Controllers). Channel Access is used as the interface to the machine process variables (PVs).

The typical control applications include two types, simple monitor/control device and complex accelerator physics application for studies and machine optimization (measurements, data analyses and applying correction). Mainly, we use cothread to access the process variables (PVs) in Python script for complex accelerator physics applications and the CSS (BOY) [4] panel for simple tasks such as monitoring, displaying and setting of the machine Process Variables (PVs). Besides, MATLAB is also available for programming and EDM panels are used for Linac control system from the linac vendor Research Instruments, GmbH. All source codes including panel configurations are controlled and managed by mercurial version in the control system.

To keep the beam commissioning time efficient, various tools were developed for data displaying, collecting and processing. Besides machine status and physics applications, we also developed the daily used operation tools, such as save/compare/restore tool, data archive, alarm and warning monitor, elog, eticket, channel finder service and applications.

Prior the beam commissioning, we have two stages test with above tools, subsystem integration testing (IT: the hardware system level function verification) and machine extended integration test (EIT: mimic the beam commissioning and tune the machine). These verifications require time and look boring and redundant, but it is necessary as it may take weeks of commissioning time to fix different technical problem.

MACHINE STATUS APPLICATION

All of the monitor and control panels are created with software tools in Control System Studio (CSS), which is an Eclipse-based collection of tools to monitor and operate large scale control systems. The interface allows the operators to edit the desired ramp/soak profiles and provides the option to use predefined recipes.

The NSLS-II operation panels [5] include the user panels and the expert panels. They display the device status and parameters (setpoint and readback) and show the device performance. A user panel shows only information that user is required, such as the magnet current setpoint and readback. The expert panel shows all the information that expert can fully control the device or diagnose the device, such as power supply operation mode and magnet temperature.

HIGH LEVEL APPLICATION

Besides the devices status and control, we also develop high level applications to realize the accelerator physics application tools. It is to translate the raw/processed data from PV to the "physics" parameters, such as from the beam size reading from flags for beam emittance or beam energy measurement. The code was programmed with Python. Although we programmed the high level applications with Python, some of their GUIs (depending on operation needs) are implemented in the CSS, as part of operator panels, so that the operators have consistent live information and interface environment. The user can set parameters and monitor the progress in GUI as regular device PV set and monitor. This feature is realized through soft IOCs.

* This manuscript has been authored by Brookhaven Science Associates, LLC under Contract No. DE-AC02-98CH10886 with the U.S. Department of Energy.

gwang@bnl.gov

Copyright © 2013 CC-BY-3.0 and by the respective authors

A screenshot of beam energy and energy spread measurement with flag VF2 is shown in Figure 1. It is in continuous mode, which means whenever the beam image updates, the beam energy and energy spread is updated correspondingly. It shows the beam image, horizontal beam profile, beam energy, beam energy spread, and the charge ratio in every 0.5% energy deviation.

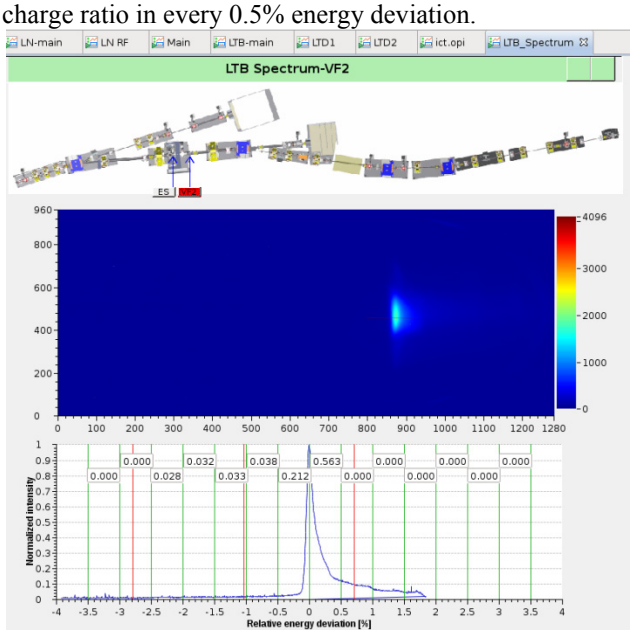


Figure 1: Screenshot of beam energy and energy spread measurement with flag VF2 in LTB transport line.

COMMISSIONING TOOLS

MASAR

The MASAR (MAchine Snapshot, Archiving, and Retrieve) [6] is an important tool used during the commissioning, which is developed by the NSLS-II Controls group for machine save/compare/restore function. MASAR is an EPICS V4 service, and it is a server-client based tool-set. The server and client are implemented in C++ and Python. The server takes machine snapshots, archives data in a relational database, and retrieves data from the database. The client provides a GUI that retrieves snapshot data, compares the data with the live machine, compare multiple snapshots, and restores the machine with given snapshot data.

The user creates a list of channels, which can be any record data type, such as scalar values, arrays or strings, that are important for the system in a configuration file and, then, MASAR saves the current configuration. To take a snapshot, the client specifies the name of the snapshot configuration and a name for this snapshot event. When the server receives a command to take a machine snapshot, the server retrieves the list of channel names in the configuration from the database. It then gets the current value of all the channels from IOC, and saves the data as a snapshot event into the database.

Channel Finder Service and Applications

The High level applications tend to prefer a hierarchical view of the control system where they can group channels by type (such as BPM, horizontal corrector) or location. These applications require retrieving a large set of channels' value or alarm state. Channel finder applications have simplified user interaction by requiring the user to providing only the channels' criteria that they are interested in, such as element type BPM or element Name ICT1, instead of the complete set of channels name.

User provides a list of channel names (PVs) with given properties and tags and channel finder service (CFS) [7] stores these information for different applications. The Properties are keyword-value pair data, where the keywords are predefined, such as element name with value P1, element type with value BPM, s Position with value P1 0.5 et. al, whereas the tags are plain strings, such as aphla.sys.LTB, aphla.sys.SR. The channel finder applications use CFS plugin, to query the service for a group of channels based on the set of criteria, which is based on one or any combination of channel name, properties and tags. The channel finder applications client are supported by CSS (such as channel viewer to show a group of PVs with their name, properties and tags, Channel line plot viewer to plot a group of PVs live data, waterfall plot to show time plot of all queried channels) or python (APHLA: accelerator physics high level application).

Channel Archiver

An EPICS Channel Archiver is installed to record the values of many interesting PVs over time (such as ICT charge, power supply readback, vacuum pressure, which are predefined by PVs' owner). This data is then available for online queries, for plotting with the CSS Data browser, and may be exported in several formats (such as spreadsheet, Matlab, h5) for analysis.

Figure 2 shows the historical view of the charge reading after linac from one ICT and two Faraday Cups with data browser.

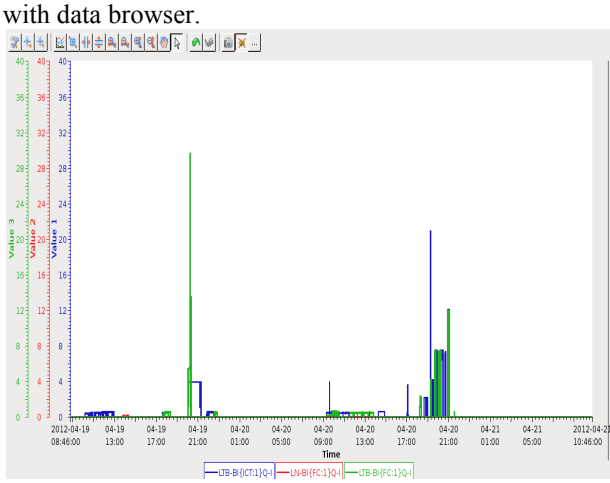


Figure 2: History view of charge reading.

Copyright © 2013 CC-BY-3.0 and by the respective authors

SUB-SYSTEM INTEGRATION TEST

The purpose of the sub-system integration test [8] is to verify the device function along with utilities, timing system and control system in control room environment. Meanwhile, we do the diagnostics system calibration and develop more functions to improve the control system features for users. The subsystem testing include all diagnostics (such as ICT, FCT, FC, Flags, BPMs) devices, power supplies and RF system. We developed the test procedure, which includes the system interface block diagram, the system physics parameters and ranges, the control parameters and procedures on mechanical/controls testing, calibration and check points. During the process, we use external "known" signal to simulate the real beam in various situations, such as 1 Hz/2 Hz/ stacking mode with low/high bunch charge at single bunch mode/long pulse mode.

Most of the technical issues are solved during the integration test. But this test cannot fix some possible problems, such as magnet polarity error, which could only be revealed by beam.

For example, during the BPM system integration testing [9], a number of hardware issues has been found out and fixed (such as cable loose connection on a patch panel). Some BPMs four buttons' signal shows different behaviour and noisy frequency up to a few kHz were observed. This is solved by modifying the oscillator and installing a microwave absorber. The BPM position noise level is now improved down to 1μm. During the BR flags test, a parasitic background was observed on the screen images, which will also affect the beam image. To fix this problem, A set of the absorbers has been produced by BINP and installed into the flag tubes. During the ICT test, the beam signal source is 'replaced' by a pulse generator. We found LTB-ICT2 connection issues and four ICTs exhibit the readback difference, which is larger than 5% due to calibration. After repeating the calibration, the four ICTs readback difference came down to be less than 1% and the charge readback noise reduced below 10 pC.

EXTENDED INTEGRATION TEST

Prior to the Booster (BR) beam commissioning, we carried out the beam commissioning with simulated beam signals, called extended integrated testing (EIT) to prepare for the booster ring commissioning by operating the whole system as during the actual beam commissioning. The beam signals are simulated and generated by a computer program, ELEGANT. Then they are transported by the same data channel as the real beam signal would travel.

We developed shift schedule, daily shift plans and shift summaries, closely corresponding to the actual beam commissioning. The EIT activities consist of 4 hour shifts per day with shift team from BNL and BINP. The short and long term shift plans are based on real beam commissioning steps. The whole test lasts 10 weeks.

During this process, we tested and optimized all the operation screens, the high level applications and upgraded the operation tools. With readbacks from the power supply and RF systems, commissioning activities such as injection, first turn steering, achieving circulating beam, RF capture, closed orbit, acceleration ramp optimization and extraction can be set up and optimized. This proved itself to be an efficient way of debugging the controls- and the correction systems, as the applications bug can be quickly revealed with the known 'beam' signal. Many small issues and bugs, which would have us slowed down during the commissioning, have already been discovered and fixed during the test. For example, the large dipole BD1 IGBT fail caused the PS broken, which takes power supply group ~1 month to find and fix the problems. The feedforward function in quads is implemented as the error is larger than specification. The MASAR function is upgraded to accommodate the waveform channels. The ramp manager application is upgraded so that RF control with sequence and limitation is included and RF voltage waveform setting can be easily correlated with PS setpoint.

Moreover, the testing is carried out from the control room in a way which is almost identical to the commissioning with real beam. The operations procedures, the shift routines, the use of the logbook and much more were practiced and improved during EIT. For example, the online shift summary service was developed for easy search.

ACKNOWLEDGEMENTS

All of this work would not have been possible without constant support of all the NSLS II teams and the close collaboration with the BINP team.

REFERENCES

[1] F.J. Willeke, Status of the NSLS-II Project, TUOBS3, PAC2011.
[2] Emery, L., Commissioning Software Tools at the Advanced Photon Source, p 2238 - 2240, PAC1995.
[3] R. Bartolini et al., High level software for DIAMOND commissioning and operation, THPCH112, EPAC2006.
[4] http://cs-studio.sourceforge.net/
[5] G.M. Wang et al., Preparation for NSLS II linac to booster transport line commissioning, MOPPR094, IPAC12.
[6] G.B Shen et. al, "NSLS II Middlelayer Services", MOPPC155, ICALEPCS 13.
[7] K. Shroff, et al, Multi Channel Applications for Control System Studio(CSS), MOPMN015, ICALEPCS2011.
[8] G.M. Wang et al., NSLS II injector integration test, THPEA063, IPAC2013.
[9] V. Smaluk et al., Status of beam diagnostics for NSLS II Booster, MOPC02, IBIC2013.

Copyright © 2013 CC-BY-3.0 and by the respective authors

A TUNABLE ENERGY CHIRP CORRECTION*

S. Antipov#, C. Jing, P. Schoessow, and A. Kanareykin,
Euclid Techlabs LLC, Solon, OH-44139
W. Gai, A. Zholents,
Argonne National Laboratory, Argonne, IL-60439
M. Fedurin, C. Swinson,
Brookhaven National Accelerator Laboratory, Upton, NY-11973
S. Baturin
St.Petersburg Electrotechnical University LETI, St.Petersburg Russia

Abstract

Short (subpicosecond) pulses are central to many of the next generation light source initiatives that are based on linear accelerators. Beam compression is performed by means of a chicane utilizing a correlated linear energy chirp. A small energy chirp is kept as the beam goes through the remaining accelerating stage to compensate for wakefield effects. It is necessary to compensate the residual energy spread before the beam enters the undulator stage. We present here a concept for a passive wakefield device - chirp corrector or dechirper, to perform this compensation. We have recently demonstrated a passive energy chirp correction by self-wakefield at the Brookhaven ATF facility. In this paper we present a progress report on development of these tunable chirp correction devices.

INTRODUCTION

Free Electron Laser (FEL) operation requires a high current beam. To reach high current, typically kA – level, the electron beam is compressed. Compression is performed by a chicane, a set of four dipole magnets arranged in a + - - + pattern. For the beam to be compressed by a chicane it has to have an energy chirp, a linear correlation between the energy and longitudinal coordinate. This correlation can be obtained by running beam off-crest in the accelerating section. A natural parameter to characterize the chirp is derived from the slope: the energy difference over the longitudinal coordinate difference in MeV/mm or equivalent. For compression in chicane a positive chirp required, i.e. the head of the beam has lower energy than the tail. In this case the lower energy particles (the head) have a longer path than the high energy particles in the tail. Hence the beam is compressed as the tail catches up with the head. After the compression the beam typically has a residual chirp on the order of 40 MeV/mm [1]. Prior to injection in the undulator this chirp has to be removed as it compromises the FEL lasing. In principle, this can be done by running the bunch off-crest in the accelerating section. Alternatively a passive wakefield device can be used by utilizing the self-acting wakefield induced by the electron bunch on itself [2]. In the original proposal such a device was called a "wakefield silencer". Similar proposals were also put forward in [3-5]. A new name "dechirper" or "chirp corrector" was used in [5] and adopted here as a generic name for the passive wake-inducing device whose sole purpose is to remove (or create) the energy chirp. Since the impact of the dechirper linearly scales with the length of the device and the charge of the electron bunch, it is convenient to characterize the dechirper strength in units of MeV/mm/m/nC. The experimental demonstration of the idea of the dechirper was first reported in [4] where a set of dielectric lined cylindrical waveguides with different apertures were used to produce wakefields with variable strengths. Although the use of different apertures in a cylindrical geometry gives a reasonable flexibility in adjusting the dechirper strength, a continuously tunable dechirper is nevertheless preferred. This device has been tested recently and in this paper we present some recent experimental results obtained using a tunable dechirper.

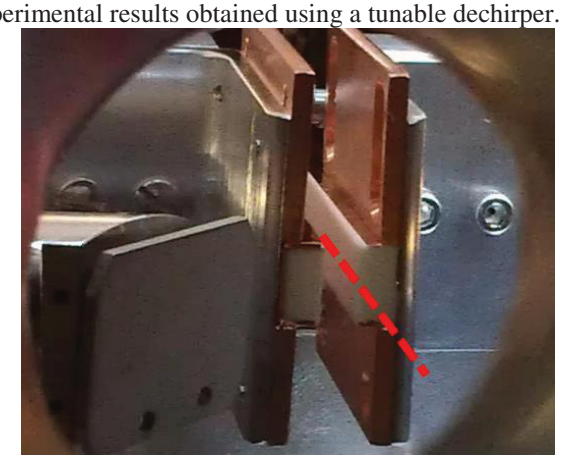


Figure 1: Tunable dechirper: two 10 cm long metallized alumina (ε=9.8) bars, 12 mm wide and 6.35 mm thick with 1 – 6 mm variable gap.

While propagating through the dechirper each electron emits Cherenkov radiation. For a particular structure this field can be simulated and in some cases calculated theoretically [6]. Integrating over the current distribution one can get the total wakefield inside the electron bunch. For dechirper operation we are interested in the self-wakefield, the fields inside the bunch. For a linear chirp correction the self-wakefield has to be quasi-linear. This can be obtained in a number of ways, using a single mode structure or a multimode structure. Naturally, a wake

*Work supported by the Department of Energy SBIR program under Contract #DE-SC0006299.
#s.antipov@euclidtechlabs.com

Copyright © 2013 CC-BY-3.0 and by the respective authors

generated by a beam can be represented by a set of modes excited in a structure. The dielectric-loaded waveguide can be made to support only one primary mode (with others having a weak coupling to the beam). This is typically done by using a thin layer of dielectric. If the wavelength of this mode is much larger than the length of the beam, then the self-wake is quasi-linear. This is obvious for a flattop beam as we convolve the constant current with the cosine wake to obtain a sine self-wake which is further approximated for short beams by a linear function of axial position. Similarly, a multimode structure would work in the case when most of the excited modes have wavelengths longer than the beam. We prefer working with a multimode structure as it is much simpler to handle in the experiment.

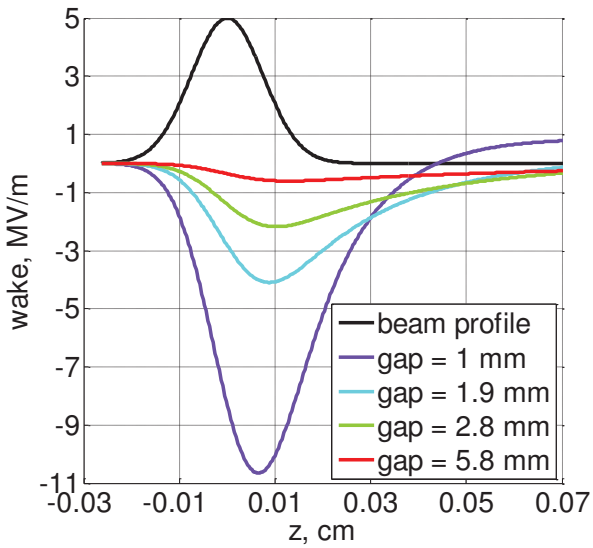


Figure 2: Principle of tunable dechirper: short range wakefields calculated for a Gaussian beam for four values of the dechirper gaps indicated on the plot. There is a linear part of the short range wake with amplitude changing as we change the dechirper gap.

The wake amplitude ~ $\eta \cdot q/a^2$, where η is the waveguide form factor, q is the charge and a is the characteristic size of the aperture. Hence tuning the transverse size of the aperture allows a corresponding adjustment of the strength of the chirp corrector (Fig. 2).

A chirp corrector also can be made using a corrugated structure [5]. Such structures typically operate as a single mode dechirpers. A multimode operation can be achieved by using deep corrugations, however, theoretical analysis in this case becomes complicated.

Defining the linear fit to the wakefield as illustrated in Fig. 3, we obtain for the dechirper strengths for a gaussian beam S_D = 45, 87, and 215 MeV/mm/m/nC using dechirper gaps = 2.8, 1.9 and 1 mm. It is important to point out that dechirper strength does depend on the beam distribution as illustrated in Figure 3. The self-wakefield slope differs slightly for gaussian and flattop beams.

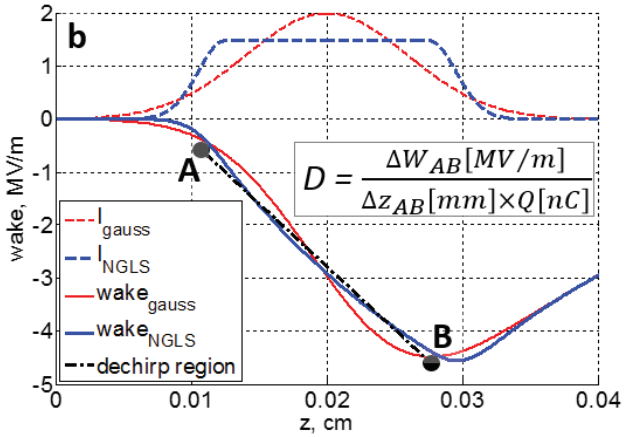


Figure 3: Illustration of the definition of the dechirper strength using the linear fit of the wakefield between points A and B (the case with a 1.9 mm dechirper gap is shown here). The red curve shows the profile of the electron charge distribution, NGLS-type 150 μm flattop beam (not to scale).

EXPERIMENTAL RESULTS

The experimental testing of a tunable dechirper was performed at the Accelerator Test Facility in the Brookhaven National Laboratory. We by accelerating electron bunch off-crest in the linac and obtaining an energy of 60 MeV and a positive 0.33 MeV/mm energy chirp. We had a longitudinal shaping setup for the beam that was part of another experiment and produced a quasi-triangular beam, 500 μm long with 54 pC charge. This was accomplished by a mask located at a point with a large energy dispersion between the two opposite sign dipole magnets [7]. The electron bunch length was measured with the interferometer using coherent transition radiation (CTR) from a foil located downstream of the second magnet.

The electron beam energy chirp was then manipulated by passing the electron bunch through a dechirper shown in Figure 1. After that, the electron bunch was sent into the spectrometer.

We measured the energy spread using a magnetic spectrometer. It was observed that the energy spread decreased as we closed the chirp corrector gap from 5.8 mm to 1 mm. Fig. 4 shows our experimental data: the beam is detected by a phosphor screen and imaged by a camera. On this image the horizontal dimension represents the particle energy, and the vertical dimension represents the vertical beam size. Due to the initial energy chirp one can see the correlation of the chirp value and the longitudinal projection of the beam on the spectrometer. Because the beam was quasi-triangular longitudinally and had an energy chirp, a linear correlation between the longitudinal coordinate and energy, the image on the spectrometer repeats the longitudinal beam profile, and we observe a triangular spot on the screen.

Copyright © 2013 CC-BY-3.0 and by the respective authors

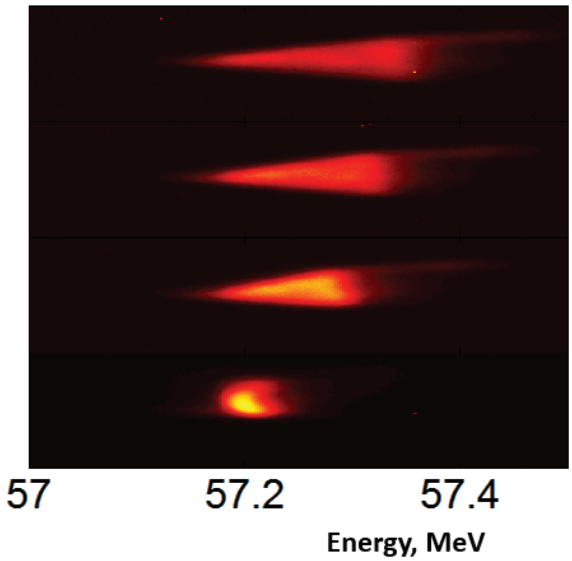


Figure 4: Experimental measurement: calibrated energy spectra of the beam passing through a chirp corrector with various gap sizes: 5.8, 2.8, 1.9 and 1 mm. The energy spread of the beam can be seen to decrease as the optimum gap size (1 mm) is approached.

When the dechirper gap was closed down to 1 mm we no longer observed any correlation and the energy spread was at a minimum. The energy chirp was calculated to be 0.33 MeV/mm (165 keV over a ~500 micron long triangular beam). This 0.33 MeV/mm was compensated in the 10 cm long dechirper. Since the total beam charge was 54 pC, the value of the dechirper strength in this case is 61±6 MeV/mm/m/nC.

In summary, our work has demonstrated a tunable dechirper, a passive wakefield device for reduction of the correlated energy spread. With this device, the 0.33 MeV/mm correlated energy spread of a 60 MeV, 54 pC electron bunch at the BNL Accelerator Test Facility (ATF) was completely removed by adjusting the gap between metallized alumina bars [8] (forming a planar dielectric structure) from 5.8 mm down to 1 mm.

REFERENCES

[1] J. M. Byrd, et al, in Proceedings of International Particle Accelerator Conference, 2012, pp. 2271–2272.
[2] M. Rosing, J. Simpson, Passive Momentum Spread Reduction, the Wakefield Silencer, ANL Report WF–144, April 1990.
[3] P. Craievich, PHYSICAL REVIEW SPECIAL TOPICS - ACCELERATORS AND BEAMS 13, 034401 (2010).
[4] S. Antipov, C. Jing, M. Fedurin, W. Gai, A. Kanareykin et al., Physical Review Letters 108 144801, (2012).
[5] K.L.F. Bane, G. Stupakov. Nucl.Instr. Meth. Phys.Res. A, 690, p.106, 2012.
[6] S. S. Baturin, I. L. Sheinman, A. M. Altmark and A. D. Kanareykin. Phys. Rev. ST-Accelerator Beams v. 16, 051302 (2013).
[7] P. Muggli, V. Yakimenko, M. Babzien, E. Kallos, and K. P. Kusche, Phys. Rev. Lett. 101, 054801 (2008).
[8] S. Antipov et al, arxiv: 1308.5646.

Copyright © 2013 CC-BY-3.0 and by the respective authors

DEMONSTRATION OF A COMPACT HIGH AVERAGE POWER THz LIGHT SOURCE AT THE IDAHO ACCELERATOR CENTER

Yujong Kim[†,‡,ǂ*], A. Andrews[†,‡], C. Eckman[†,‡], P. Buaphad[†,‡]
K. Folkman[†], C. O'Neill[†], B. Berls[†], J. Ralph[†], M. Smith[†], and A. V. Smirnov[⋕]
[†]Idaho Acccelerator Center, Idaho State University, Pocatello, ID 83201, USA
[‡]Department of Physics, Idaho State University, Pocatello, ID 83209, USA
[ǂ]Thomas Jefferson National Accelerator Facility, Newport News, VA 23606, USA
[⋕]RadiaBeam Technologies LLC, Santa Monica, CA 90404, USA

Abstract

The Idaho Accelerator Center (IAC) has been operating nine low energy accelerators for THz and X-ray light sources, nuclear physics, and medical isotope productions. In November 2012, the IAC and RadiaBeam collaborated to upgrade an IAC 44 MeV L-band RF linac with a chicane bunch compressor and a THz radiator with numerous periodic gratings for the resonant Cherenkov radiation. By using the THz radiator and the re-optimized L-band linac with a new operational energy of 5 MeV, we could demonstrate a THz resonant Cherenkov radiation with a high average power of about 17 W in an RF macropulse without using any sub-ps laser or undulator. In this paper, we describe our upgrades and accelerator optimization experiences to perform the proof-of-principle experiments at the IAC.

INTRODUCTION

As various user applications such as diagnosis of early stage cancers, 3D imaging of teeth, security and weapon scanning, and quality control of commercial products have been developing, recently, THz users strongly request coherent THz light source which can supply a high average power ($\geq$ 1 mW). Jefferson Lab and several other laboratories have demonstrated accelerator-based high average power THz light sources by using the Continuous Wave (CW) or Energy Recovery Linac (ERL) technology. However, we need a big budget to construct such an ERL based THz light source facility. To realize a compact and cheap high average THz light source facility, we have developed a resonant Cherenkov radiation based THz radiator [1–3], and performed its proof-of-principle experiments at the Idaho Accelerator Center (IAC) by upgrading an IAC 44 MeV L-band RF linac [4–6]. The parameters of the 44 MeV linac and the THz radiator are summarized in Table 1, and the layout of the upgraded IAC 44 MeV L-band linac is shown in Fig. 1. The upgraded linac has a 85 kV DC gun instead of an RF photoinjector and a THz radiator instead of a undulator as shown in Fig. 1. To perform the proof-of-principle experiments of narrow-bandwidth resonant Cherenkov radiation with a specially designed THz radiator, RF phases and gradients of the 44 MeV linac structures were re-optimized to have a new operational beam energy of 5 MeV and to have the shortest bunch length of about 500 fs (rms). It is well confirmed that the multi-bunch beam loading effects or the long-range longitudinal wakefields can be used to generate coherent narrow-bandwidth resonant Cherenkov radiation [1, 2, 7, 8]. In our experiments, we used a 85 kV DC gun to generate a long bunch train with 2600 short single bunches in a 2 μs long RF macropulse. By sending the 2600 short bunches with a single bunch charge of about 30 pC into the THz radiator, we could get strong multi-bunch beam loading effects to generate a high average power THz radiation at 0.316 THz. In this paper, we describe upgrades of the IAC L-band linac, the THz radiator, and linac optimization experiences to generate a high average power THz radiation at 0.316 THz with the compact THz radiator.

Table 1: Parameters of Linac and THz Radiator

Parameter	Value	Unit
Maximum beam energy	44	MeV
Minimum beam energy	5	MeV
RF frequency	1300	MHz
Repetition rate of RF macropulse	30	Hz
Length of RF macropulse	2	μs
Bunches in a macropulse	2600	·
Single bunch charge	30	pC
R_{56} of bunch compressor	13.7	mm
Minimum rms bunch length	500	fs
Resonance frequency of radiator	0.316	THz
Grating period	234	μm
Grating groove depth	80.86	μm
Grating structure length	30.4	mm
Grating structure width	6.3	mm
Grating structure gap	1.256	mm
Phase advance per period	88	deg
Quality factor	2150	·
Gap-averaged shunt impedance	4.3	MΩ/m
Nomalized group velocity	0.8	·
Average THz power per macropulse	17	W
Bandwidth of THz radiation	10	%

UPGRADES FOR EXPERIMENTS

For the THz experiments, as shown in Fig. 1, we installed a THz radiator, which had been fabricated with the conventional CNC milling, a chicane bunch com-

* Mail: yjkim@isu.edu

Copyright © 2013 CC-BY-3.0 and by the respective authors

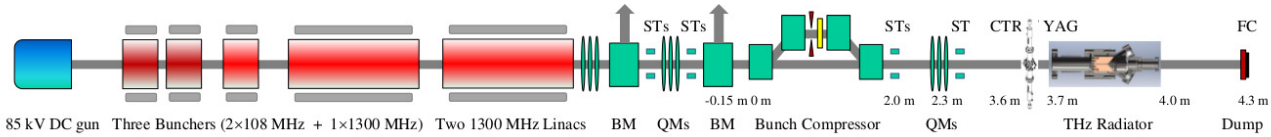


Figure 1: Layout of the IAC 44 MeV linac for the IAC-RadiaBeam THz project.

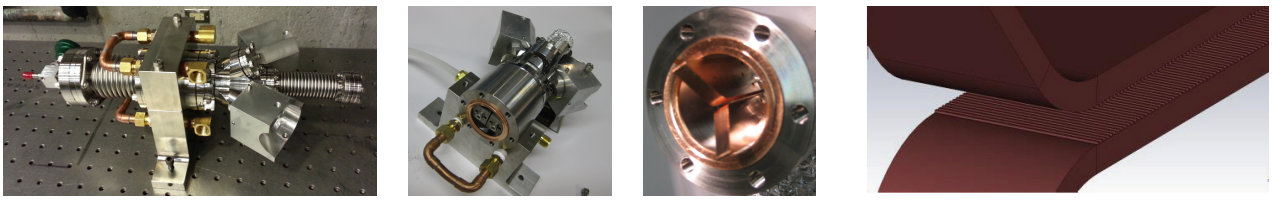


Figure 2: THz radiator: (first) entire THz radiator, (second) disassembled molybdenum collimator with a 1.2 mm wide gap, (third) copper side-open planar horn antenna with numorous gratings, (fourth) 3D images of the planar horn antenna.

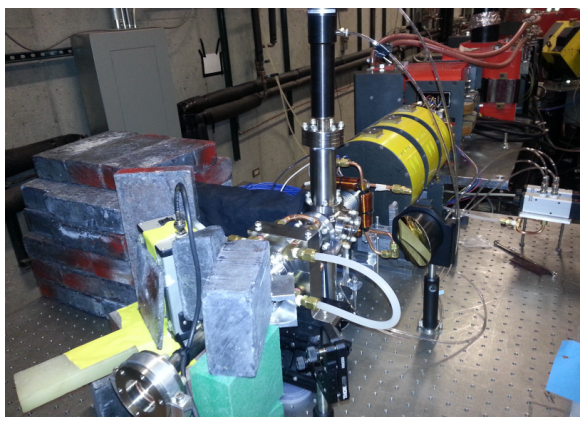


Figure 3: Upgraded beamline of the IAC 44 MeV linac for the IAC-RadiaBeam THz project.

pressor to compress electron bunch length, a quadrupole triplet (QMs) to change beam shape and to adjust focusing strength at the THz radiator, four horizontal and vertical steering magnets (STs) to adjust beam orbit along the beamline, a Coherent Transition Radiation (CTR) based interferometer to measure femtosecond long electron bunch length after the bunch compressor, an OTR screen to check the beam position and shape in front of the chicane bunch compressor, a YAG screen to check beam position and beam shape in front of the THz radiator, two Prosilica GigE CCD cameras to acquire beam shapes and positions at the OTR and YAG screens, a Faraday cup at the end of the beamline to measure electron beam charge going through the THz radiator [1, 5, 6]. In addition, as shown in Figs. 2 and 3, we had installed a homemade THz antenna in front of the left output-coupling Sapphire window of the THz radiator, and a GenTec QS-I-TEST SDX-1065 pyrodetector was installed in front of the right output-coupling Sapphire window of the THz radiator [1]. To acquire weak signals from the homemade antenna, we connected a Tektronix MSO72004 fast oscilloscope to the antenna with a 1.0 m long low loss copper coaxial cable. Since the cable length is only 1.0 m, we had to leave the oscilloscope in the linac tunnel with sufficient lead shielding. To control the oscilloscope from the linac control room, we used the remote desktop function of Windows XP. Since the cable is short and low loss one, it was very effective to find initial signals from the radiator [1]. The GenTec SDX-1065 pyrodetector was connected to a Tektronix TDS2014 slow oscilloscope with a 50 m long coaxial cable. Since the cable is long enough, the oscilloscope could be controlled at the control room directly.

To control newly installed magnets and Prosilica GigE CCD cameras remotely, we had installed EPICS accelerator control system. More details on the EPICS accelerator control system, the dipole magnets for the chicane and three quadrupoles for the triplet, and the Prosilica GigE CCD camera based beam imaging system can be found from references [4–6]. As shown in Fig. 1, the new 4.3 m long beamline for the THz experiments starts from the second 90 degree bending magnet (BM), which is located at right before the first 7 degree dipole magnet for the chicane bunch compressor. After installation of all components, the upgraded beamline is busy as shown in Fig 3. The 0.3 m long THz radiator consists of a molybdenum collimator set, cooling channels, two connecting flanges, and a pair of planar, side-open, copper gratings with symmetrical meander profile as shown in Fig. 2. Since the collimator has a 1.2 mm wide gap, good beam orbit steering is required to send electron beams through the THz radiator. Detailed design concepts of our THz radiator can be found from references [1, 2] and its parameters and performance are summarized in Table 1.

EXPERIMENTAL RESULTS

To detect THz signals from the THz radiator, first of all, we optimized the beam shape and orbit with steering magnets and the quadrupole triplet to get a weak transmission down to the Faraday cup. Then, we adjusted bunch length by optimizing RF phases of linac structures and chicane

Copyright © 2013 CC-BY-3.0 and by the respective authors

strength. After the bunch length optimization, we tried to improve beam transmission down to the Faraday cup with steering magnets and the quadrupole triplet. However, we could not get any THz signal from the GenTec SDX-1065 pyrodetector with 8 MeV electron beam, and the single bunch charge at the Faraday cup is much smaller than 1 pC. To overcome the high RF background noises, we installed a homemade THz antenna in front of the left output-coupling Sapphire window, and a Tektronix MSO72004 fast oscilloscope was connected to the antenna with a 1.0 m long low loss copper coaxial cable. Then, to improve the velocity bunching of the electron beam, we reduced beam energy from 8 MeV to 5 MeV. However, we could not get any signal from both the pyrodetector and the antenna either. In addition, the beam transmission to the Faraday cup was dramatically dropped at 5 MeV due to strong space charge forces at the THz radiator region when the beam was horizontally focused and longitudinally compressed at 5 MeV [1,6]. Therefore, we had to modify transverse beam shape from horizontally focused strip like one into uniformly distributed round one to reduce the beam spreading due to strong space charge forces in the THz radiator [1].

After the transverse beam shape modification, we could improve the beam transmission, and we could detect a weak cm-wavelength signal from the homemade THz antenna as shown in Fig. 4. The longer cm-wavelength radiation is generated by the wakefield induced at the 2 cm long horn antenna openings when the bunch length is longer than the grating period of 234 μm [1]. By adjusting RF phases for the velocity bunching, chicane strength for the magnetic compression, beam orbit, and beam uniformity against strong space charge forces, we could get good beam transmission down to the Faraday cup as well as the strong cm-wavelength signal from the homemade antenna as shown in Fig. 4. In that case, the single bunch charge at the Faraday cup was increased up to 30 pC. By compressing bunch length down to the grating period range, we could get a strong cm-wavelength signal from the homemade antenna and a strong THz signal from the pyrodetector as shown in Figs. 4 and 5. By analyzing signals from the pyrodetector, we found the fact that the average THz power of the RF macropulse with 2600 single bunches is about 17 W in the radiator [1]. We also got a similar power level by analyzing cm-wavelength signals from the homemade antenna. This is about two orders of magnitude higher average power than that was obtained with RF photoinjector based THz sources at low beam energies [8].

SUMMARY

Successfully, at 5 MeV, without any gun driving laser or undulator, we have demonstrated that a high average power THz radiation can be generated with a compact and cheap resonant Cherenkov radiation based THz radiator. The average THz power of an RF macropulse is about 17 W, which is is about two orders of magnitude higher average power than that was obtained with RF photoinjector based THz sources at low beam energies. We expect that

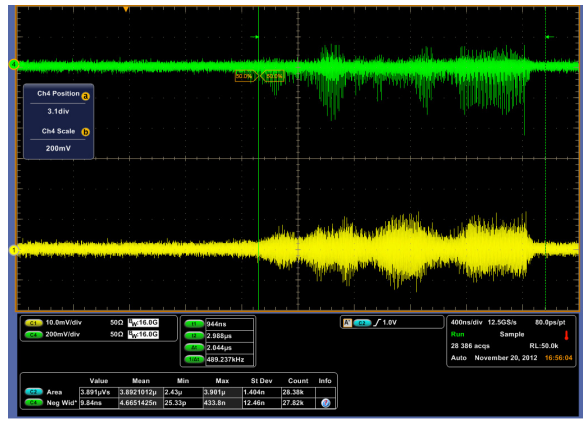


Figure 4: Tektronix MSO72004 oscilloscope signals at 5 MeV with a round beam shape: (top and green) signal from a Faraday cup, (bottom and yellow) signal from a THz antenna.

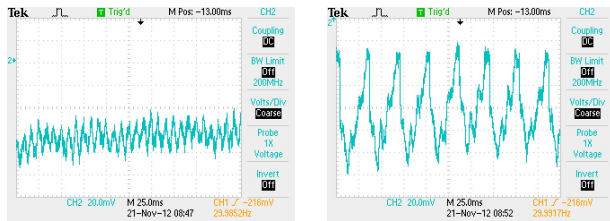


Figure 5: Tektronix TDS2014 oscilloscope signals from a GenTec pyrodetector at 5 MeV with a round beam shape: (left) when beam was off and (right) when the single bunch charge at the Faraday cup was about 30 pC, and the signal from THz antenna was strong as shown in Fig. 4.

the average power can be further increased by improving electron beam quality and by increasing RF macropulse length. By directly connecting the THz radiator to a multicell thermionic RF gun and an alpha magnet, we expect that the total length of the THz facility can be reduced down to several meters. By measuring average THz power from the THz radiator, hence the form factor of electron beam, we can also use the radiator to measure the femtosecond long bunch length of electron beams [1]. This work was supported by the U.S. Department of Energy (award No. DE-SC-FOA-0000760 and DE-FG02-07ER84877).

REFERENCES

[1] A. V. Smirnov *et al.*, in *Proc. IPAC2013*, Shanghai, China.

[2] A. V. Smirnov, Photonics Research Development, pp. 247-269, 2008.

[3] L.Sh. Grigoryan *et al.*, arXiv:1203.5429v1 [physics.acc-ph], 2012.

[4] A. Andrews *et al.*, in *Proc. IPAC2013*, Shanghai, China.

[5] P. Buaphad *et al.*, in *Proc. IPAC2013*, Shanghai, China.

[6] C. Eckman *et al.*, in *Proc. IPAC2013*, Shanghai, China.

[7] A.M. Cook *et al.*, Phys. Rev. Lett. **103**, 095003 (2009).

[8] G. Andonjan *et al.*, Appl. Phys. Lett. **98**, 202901 (2011).

Copyright © 2013 CC-BY-3.0 and by the respective authors

PSEUDO SINGLE BUNCH WITH ADJUSTABLE FREQUENCY*

C. Sun†, M. Hertlein, J. Kirz, M. A. Marcus, G. Portmann, D.S. Robin and C. Steier
Lawrence Berkeley National Laboratory (LBNL), Berkeley, CA 94720, USA

Abstract

We present the concept and results of pseudo-single bunch (PSB) operation - a new operational mode at the Advanced Light Source (ALS) - that can greatly expand the capabilities of synchrotron light sources to carry out dynamics and time-of-flight experiments. In PSB operation, a single electron bunch is displaced transversely from the other electron bunches using a short pulse, high repetition rate kicker magnet. Experiments that require light emitted only from a single bunch can stop the light emitted from the other bunches using a collimator. Other beamlines will only see a small reduction in flux due to the displaced bunch. As a result, PSB eliminates the need to schedule multi-bunch and timing experiments during different running periods. Furthermore, the time spacing of PSB pulses can be adjusted from milliseconds to microseconds with a novel "kick-and-cancel" scheme, which can significantly alleviate complications of using high power choppers and substantially reduce the rate of sample damage.

INTRODUCTION

A major limitation of synchrotron light sources is the ability to easily serve two classes of experiments simultaneously, namely, brightness or flux limited experiments and timing experiments. High brightness experiments require filling most of the rf buckets with electrons, thus maximizing the total current while minimizing the current per bunch. In such a multibunch filling pattern, the bunch spacing is typically only a few nanoseconds between electron bunches. On the other hand, timing experiments require longer times between x-ray pulses. For example, in the case of laser-pump x-ray-probe timing experiments, it is desirable to have only one x-ray pulse per laser pulse. Since such lasers operate between kHz and MHz rates, this implies a distance between pulses of ms to μs.

At the Advanced Light Source (ALS) facility, we have been exploring a new mode of operation that we call pseudo-single-bunch (PSB) operation, the goals of which are to allow multibunch and timing experiments to run simultaneously [1, 2, 3]. The idea behind PSB operation is to use a high-repetition (MHz)-rate, short-pulse (<100 ns) kicker [4] to vertically displace a single camshaft bunch relative to the bunch train. Experiments that require light emitted only from a single bunch can block the light emitted from the other bunches using a collimator with only light from the camshaft bunch reaching the experiment. The PSB timing could be at the orbital period (656 ns) or longer, depending upon how frequently the bunch is displaced.

Here we discuss the results of our studies on the PSB operational mode, especially the novel kick-and-cancel (KAC) scheme that can deliver a single pulse with adjustable frequency [3]. A similar idea was previously suggested [5], but to our knowledge this is the first time that it has been realized.

KICK-AND-CANCEL SCHEME

The idea of the KAC scheme is that by adjusting the ring tune and the PSB kick pattern, the camshaft bunch can first be displaced to a different orbit and then kicked back to its original one within a few turns. This KAC process can be repeated at will to create a PSB pulse with an adjustable repetition rate. Mathematically, the KAC scheme can be shown as follows. Assuming that a camshaft bunch is kicked at the i^{th} turn with a kick angle of θ_y, the orbit offset and angle at the n^{th} turn due to this kick are given by

$$\begin{aligned} y_n^i &= \theta_y \beta_y \sin[2\pi(n-i)\nu_y], \\ y_n'^i &= \theta_y \{\cos[2\pi(n-i)\nu_y] - \alpha_y \sin[2\pi(n-i)\nu_y]\}. \end{aligned} \quad (1)$$

To restore the orbit after the n^{th} turn, the superpositions of orbit offsets and angles from each kick need to be zero, i.e.,

$$\sum_{i=0}^{n} y_n^i = 0, \qquad \sum_{i=0}^{n} y_n'^i = 0. \quad (2)$$

Using the two equations above, we can solve the required vertical tune for given number of kicks and orbit turns. There are many possible solutions to Eq. (2). Just one example is presented here. In this example we wish to restore the orbit after two turns within two kicks. The orbit offsets and angles are created by these two kicks at the 2^{th} turn are

$$\begin{aligned} y_2^0 = \theta_y^0 \beta_y \sin 4\pi\nu_y, y_2'^0 &= \theta_y(\cos 4\pi\nu_y - \alpha_y \sin 4\pi\nu_y) \\ y_2^2 = 0, y_2'^2 &= \theta_y^0. \end{aligned} \quad (3)$$

Applying Eq. (2), we can solve the vertical tune $\nu_y = 0.25$.

To test this scheme at the ALS, the vertical tune of the storage ring needs to be adjusted to 9.25 from the nominal tune of 9.20. Figure 1 shows simulated beam orbits for this KAC scheme with the kick angle of 73 μrad. We can see that the beam orbit is displaced for two turns and then kicked back to the nominal one. For example, at the undulator beam line 6.0.1 as indicated in Fig. 1(c), the two orbits are displaced on both sides of the unkicked one, and

* Work supported by the Director Office of Science of the U.S. Department of Energy under Contract No. DE-AC02-05CH11231.
† ccsun@lbl.gov

Copyright © 2013 CC-BY-3.0 and by the respective authors

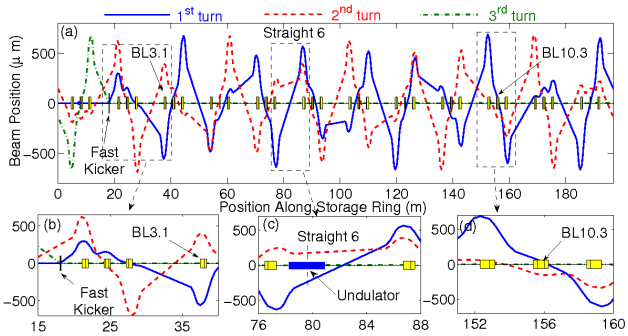


Figure 1: Orbits of the camshaft bunch for kick-and-cancel PSB operation mode at vertical tune 9.25 and kick angle θy=73 μrad: (a) Full 12 sectors; (b) close-up of sectors 2 and 3, where the kicker and beam line 3.1 are located. At the source point of beam line 3.1, the beam is displaced by -560 μm on the 1st turn and 395 μm on the 2nd turn; (c) close-up of straight 6. In the center of the insertion device the beam is displaced by -113 μm on the 1st turn and 188 μm on the 2nd turn; (d) close-up of beam line 10.3 source point. The beam is displaced by 10 μm on the 1st turn and -154 μm on the 2nd turn.

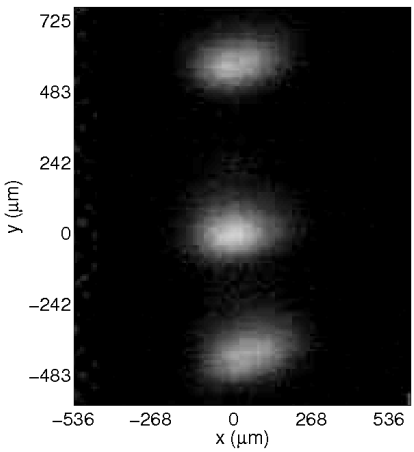


Figure 2: Beam image measurement at synchrotron diagnostic beam line 3.1. For this measurement, the storage ring was filled with a 5 mA single camshaft bunch, and the beam was kicked at the maximum kick-and-cancel frequency.

the maximum separation between them is about 250 μm at the center of the 6.0.1 insertion device.

It should be pointed out that the KAC may affect beam orbit stability through fluctuations of the kick amplitude, and affect the beam size by chromaticity and tune shift with amplitude. The reproducibility of the kick amplitude depends on the stability of the power supply. Measurements using an analog oscilloscope show that the relative fluctuations are approximately 2x10^{-3}, which gives rise to about 0.5 μm orbit motion (about 4% of the beam size). We have also carried out simulations using our accelerator modeling code to estimate the effects of chromaticity and tune shift with amplitude. The results show that beam size growth due to these effects is about 0.5 μm (rms) which is the same as the one caused by the fluctuations of the kick amplitude. These estimates indicate that for the ALS parameters beam orbit motion and beam size increase due to the KAC scheme should be acceptably small.

EXPERIMENTAL TESTS

We first tested this novel operation mode at our synchrotron diagnostic beam line 3.1. At this beam line, the x-ray pulse emitted from the bend magnet is first converted to visible light by a BGO crystal, and then imaged on a CCD camera. Figure 2 shows the measured beam image when the kicker is turned on. Clearly, there are three beam spots, the central one corresponding the un-kicked orbit and the other two the kicked orbits. The separation between the two kicked orbits is about 950 μm, which is consistent with the simulation. For this measurement, the storage ring was filled with a 5 mA single camshaft bunch, and the beam was kicked at the maximum kick-and-cancel frequency, i.e., there is no waiting period between each KAC process. Therefore, the three orbits have the same repetition rate of 500 kHz and the same current of 5/3 mA.

We tested this KAC operation mode at the bend magnet beam line 10.3.2. For this beam line, a side-deflecting toroid mirror forms a 1:1 image of the x-ray beam on a slit. The time-averaged x-ray intensity is measured using a YAG scintillator after the slit, the light from which is detected by a PIN diode. Figure 3 shows the x-ray signals by vertically scanning the slit when the kicker is turned on and off. For these measurements, the storage ring was filled with a 350 mA multibunch train and a 4 mA camshaft bunch. In the figure, the signal from the kicked camshaft is clearly seen on the shoulder of the main bunch background when the kicker is turned on. The signal to background ratio is about 10:1. Compared to the normal operation mode, the background from the main bunch train is suppressed by a factor of about 2500. The separation between the kicked camshaft signal and the main bunch peak is about 150 μm, which is consistent with the simulation.

We tested the KAC scheme at beam line 6.0.1 using a gated detector. The setup of the experiment is shown in Fig. 4(Top). For this test, the storage ring was filled with a 276 mA multibunch train and a 5 mA camshaft bunch. The x-ray pulse emitted from the undulator was measured using a gated avalanche photodiode at an end station of the beam line. Two measurements were carried out, one with a 50 μm slit centered on axis, and the other with the slit centered 190 μm off axis. For the on-axis measurement, the x-ray signals from the bunch train and unkicked camshaft bunches are clearly seen in Fig. 4(Middle); however, the pulses from the kicked camshaft bunch are missing for two turns since the camshaft bunch is displaced to different orbits during these two turns and the radiation from them is blocked by the slit. When the slit is moved off axis (up),

Copyright © 2013 CC-BY-3.0 and by the respective authors

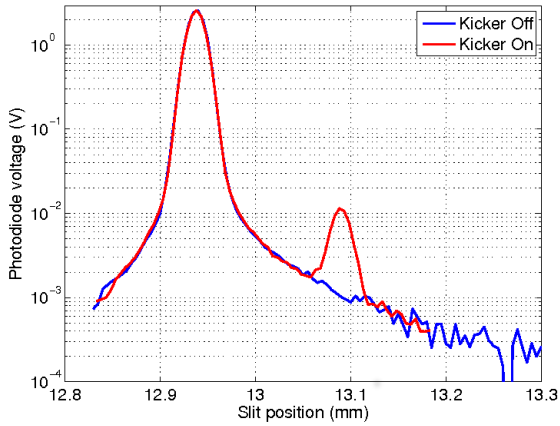


Figure 3: X-ray pulse measurements at a bend magnet beam line 10.3.2 with the kicker on and off. For these measurements, the storage ring was filled with a 350 mA multibunch train and a 4 mA camshaft bunch.

only the radiation from the displaced bunch at the second turn can pass through the slit. Therefore, we only see one pulse in Fig. 4(Bottom).

Finally, we tested this KAC scheme using an integrating (nongated) photodiode at beam line 6.0.1. For this test, the storage ring was filled with the same fill pattern as for the previous test, and the slit was moved off axis to a position where it would optimally transmit the light of the kicked bunch. At this slit position the background signal due to the unkicked bunches was suppressed by 3 orders of magnitude. This large suppression in the signal from the unkicked bunches directly translates to a substantial reduction in the sample damage rate.

CONCLUSIONS AND OUTLOOK

Our results show that with a relatively simple, inexpensive pulsed kicker magnet, it is possible to achieve both single-bunch and multibunch operations at the same time. With the proposed kick-and-cancel scheme, the pulse repetition rate of the PSB photon beam can be adjusted from Hz to MHz, which can significantly alleviate complications of using high-power choppers, substantially reduce the rate of sample damage, and greatly increase the variety and quality of experiments that can be done without using gated detectors.

Recently, ALS has successfully finished brightness upgrade [6]. The nominal working point of the storage ring lattice has been adjusted from the past (14.25, 9.20) to the current (16.25, 9.20). To make this KAC scheme available for beam users, we are planning to increase the vertical tune to 9.25. Horizontal tune scan has been carried out. The lattice with the tune of (16.18, 9.25) seems to be a very good candidate in terms of lifetime, injection efficiency and nonlinear beam dynamics. Further studies are undergoing to test this lattice and results look very promising. At this new working point, we could operate this KAC scheme during the normal operation, which would eventually allow to run

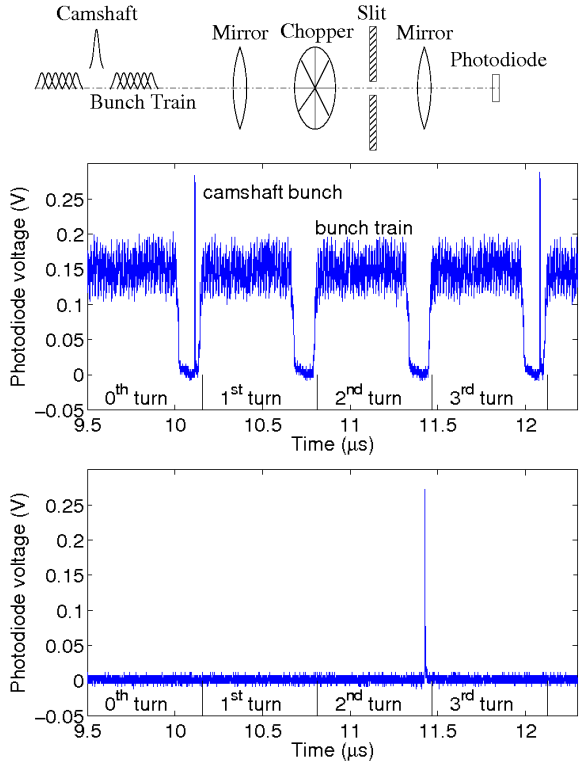


Figure 4: X-ray pulse measurements at an undulator beam line 6.0.1. (Top) Experiment setup; (Middle) On-axis measurement. The 50 μm slit is centered on axis. (Bottom) Off-axis measurement. The slit is off axis by 190 μm.

brightness and timing experiments simultaneously.

ACKNOWLEDGMENT

Authors would like to thank Tom Scarvie at LBNL for his help on the KAC lattice setup, and Slawomir Kwiatkowski, James Julian, David Plate, Ray Low and Ken Baptiste who constructed the PSB kicker and pulser. We also wish to thank the ALS management for their support and encouragement of these studies and LBNL's Engineering Division Director Kem Robinson for financial support for building the PSB kicker.

REFERENCES

[1] G. Portmann *et al.*, in *Proceedings of PAC07, Albuquerque, NM, USA, 2007* (IEEE, Albuquerque, NM), pp. 1182-1184.

[2] G. Portmann *et al.*, in *Proceedings of the Beam Instrumentation Workshop, Tahoe City, CA, 2008*, pp. 213-217.

[3] C. Sun, G. Portmann, M. Hertlein, J. Kirz, and D.S. Robin, Phys. Rev. Lett. 109, 264801 (2012).

[4] S. Kwiatkowski *et. al.*, in *Proceedings of EPAC06, Edinburgh, Scotland, 2006*, pp. 3547-3549.

[5] L. Blumberg, "VUV Wobbler", Brookhaven National Laboratory Memorandum, May 29, 1980.

[6] C. Steier *et al.*, in *Proceedings of PAC13, Pasadena, CA, USA, 2013*, TUOCB2.

Copyright © 2013 CC-BY-3.0 and by the respective authors

INITIAL LATTICE DESIGN STUDIES FOR A DIFFRACTION LIMITED UPGRADE OF THE ADVANCED LIGHT SOURCE

H. Tarawneh#, C. Steier, D. Robin, H. Nishimura, C. Sun, W. Wan
Lawrence Berkeley National Laboratory, 1 Cyclotron Rd., Berkeley, CA 94720 USA

Abstract

The Advanced Light Source (ALS) at Berkeley Lab has seen many upgrades over the years, keeping it one of the brightest sources for soft x-rays worldwide. Recent developments in magnet technology and lattice design appear to open the door for very large further increases in brightness [1], particularly by reducing the horizontal emittance, even within the space constraints of the existing tunnel. We are investigating the possibility of a new storage ring lattice that could approach the soft x-ray diffraction limit around 2 keV in both planes within the ALS footprint.

This note presents an overview of a candidate lattice for diffraction limited ALS and describes the optimization of the dynamical performance of the lattice. In addition on-axis injection scheme is foreseen for this ring and a candidate lattice for an accumulator ring, which will be built and housed either in the ALS storage ring tunnel or the booster tunnel, is also presented.

INTRODUCTION

A new compact lattice based on Multiple Bend Achromat [2] that is going to replace the existing ALS Triple Bend Achromat is being investigated. This design study of diffraction limited ALS (ALS-II) lattice has a goal of achieving a natural emittance of about 100 pm.rad and beam energy around 2 GeV.

This candidate lattice takes advantage of the fact that the ring admittance is defined by the small gap insertion devices and hence the use of small aperture magnets. This leads to the introduction of high magnetic strength where very low emittance with short circumference can be achieved.

The small emittance achieved by the candidate ALS-II lattice requires the usage of double RF system to lengthen the bunch and to operate with round beam to mitigate the effect of Intra Beam Scattering (IBS) and for lifetime considerations [3]. Bunch lengthening will also have large impact on mitigating the effect of beam interaction with the resistive metallic chamber and the chamber geometric discontinuities due small momentum compaction factor.

The ALS-II lattice strong focusing limits the dynamic aperture to few millimetres which requires an on-axis injection scheme based on swap-out [4]. A relatively small emittance ring, Accumulator ring, is proposed to inject into the ALS-II ring as the current ALS booster has a large emittance and will not deliver full charge in a single bunch needed by the swap-out injection scheme.

In the following sections, the choice of the ALS-II lattice and characterization of its dynamical properties and performance are discussed. The bunch lengthening with double RF system and the implications on emittance, lifetime will be discussed.

Also a candidate lattice for the accumulator ring and achieved dynamic performance will be presented.

(#) HITarawneh@lbl.gov

CANDIDATE ALS-II LATTICE

A study has been performed for a lattice that could approach the soft x-ray diffraction limit around 2 keV in both planes within the ALS footprint. This lattice, while not fully optimized, demonstrates the feasibility of the ALS-II concept. The new lattice is based on a Nine Bend Achromat replacing the existing ALS Triple Bend Achromat, see Figure 1. The lattice preserves the 12-fold symmetry and the circumference of the present ALS while ultimately achieving a natural emittance of about 100 pm.rad at 2 GeV beam energy. The proposed lattice follows the hybrid configuration of the ESRF upgrade design that takes advantage of a large number of combined function bending magnets to reduce the horizontal emittance [5]. The matched cell structure serves two goals, matching the dispersion to zero in the straight section since the lattice is optimized for high brightness production and to create a large horizontal dispersion bump and large beta function for efficient natural chromaticity correction. Figure 2 shows the layout of one arc of the candidate lattice.

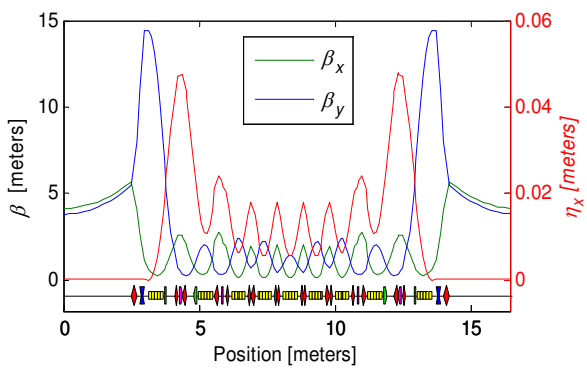


Figure 1: ALS-II candidate lattice Twiss functions.

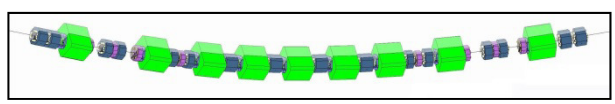


Figure 2: Layout of one arc of ALS-II lattice.

Multi-Objective Genetic Algorithm (MOGA) has been used to give an optimal solution based on the lattice elements [6]. The selected lattice provide identical optical functions in all straight sections with natural emittance of 100 pm.rad and horizontal and vertical beta functions of

Copyright © 2013 CC-BY-3.0 and by the respective authors

about 4 meters and zero dispersion. The choice is a compromise between matching the electron-photon phase spaces to maximize brightness at high photon energies and low natural chromaticities and hence adequate dynamic aperture needed for injection process. Table 1 summarizes the main parameters of the ALS-II lattice.

Table 1: Parameters of Candidate ALS-II Lattice

Parameter	Value
Beam energy [GeV]	2
Natural emittance [pm.rad]	100
Tune ν_x/ν_y	41.13/26.21
Natural $\xi_{x,y}$	-68/-64
Energy spread	8.13×10^{-4}
α_c	2.54×10^{-4}

NONLINEAR DYNAMICS

The proposed scheme for the chromaticity correction in the ALS-II lattice is based on compactness and flexibility. The small apertures in the sextupole magnets are used to introduce very strong sextupole fields. We avoided the introduction of these fields in the pole shape of the bending and quadrupole magnets where the flexibility of the lattice would have been compromised. The configuration of the matching cell which has relatively higher values of β_x, β_y and η_x functions is used to house four sextupole magnets families, two focusing and two defocusing ones, to correct the chromaticity.

The nonlinear effects driven by the strong sextupoles result in reduced dynamic aperture which hampers injection and reduces the Touschek lifetime. To overcome this, the ALS-II lattice will be operated at full coupling, i.e. with a round beam and an on-axis injection scheme. The dynamic aperture and momentum aperture of the candidate lattice is sufficient even when introducing errors ($> 200\sigma_{x,y}$) to allow high efficiency on-axis injection and provide decent beam lifetime (see Fig. 3). The off-momentum frequency map for the ALS-II lattice is shown in Fig. 4.

Mitigation of the impact of the IBS effect on the equilibrium emittance of the ALS-II lattice will be achieved by operating the lattice with full coupling where the vertical emittance is given entirely by betatron coupling and by bunch lengthening using a 3rd harmonic RF system. This leads to smaller electron density and hence less IBS growth rates in emittance. A factor of 4 lengthening, as shown in Fig. 5, gives an emittance growth of less than 20% using passive 3rd harmonic cavity at 500 MHz fundamental RF system and 500 mA beam current [7].

The momentum acceptance of the ALS-II lattice is dominated by dynamic aperture which will result in small Touschek lifetime. On the other hand, bunch lengthening is powerful mean to combat this effect where the particles loss due to Touschek scattering events is less with less dense bunches. Touschek lifetime for the ALS-II ring of 1.2 hour has been achieved with 100% coupling, i.e round beam and long bunches at 500 mA beam current [8].

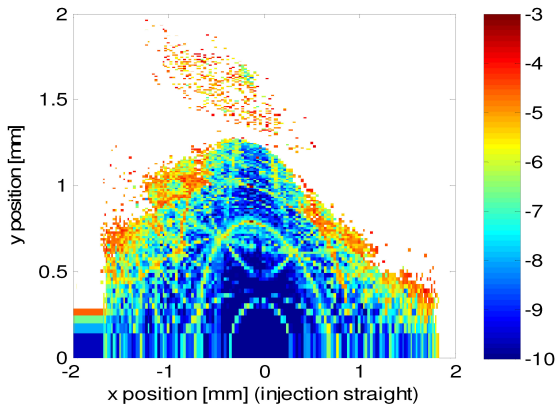


Figure 3: ALS-II lattice dynamic aperture with errors.

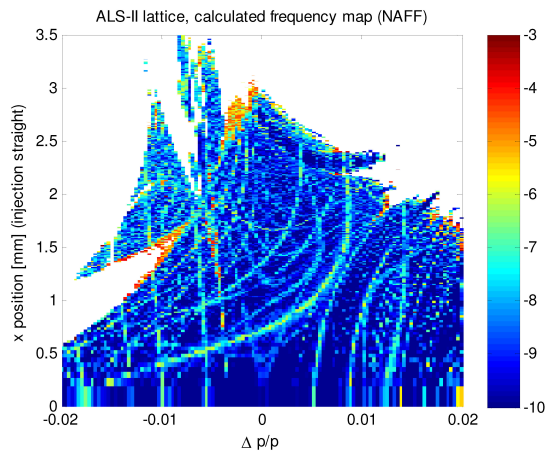


Figure 4: Dynamic momentum aperture of ALS-II candidate lattice.

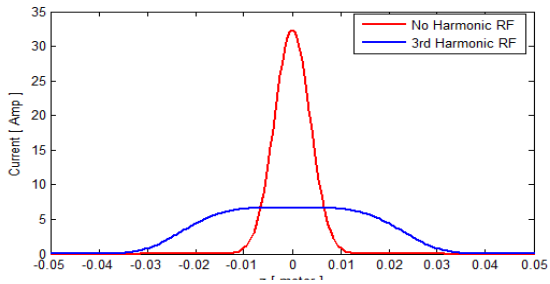


Figure 5: The bunch length of the standard and double RF system.

ON-AXIS INJECTION

The on-axis injection scheme is currently under study and it will be based on the swap-out scheme. A new accumulator ring will be built and housed either in the ALS storage ring tunnel or the booster tunnel. The

Copyright © 2013 CC-BY-3.0 and by the respective authors

accumulator ring will act as a damping ring where its lattice will allow for off-axis injection from the current ALS booster and the extracted low emittance beam is injected on-axis into the small dynamic aperture of the ALS-II ring. Figure 6 shows a candidate lattice for the accumulator ring that fits into the current booster tunnel with 78 m circumference and provides an emittance of 2 nm.rad at 2 GeV with sufficient dynamic aperture to allow for off-axis injection from the ALS booster, see Fig. 7. A partial swap-out injection into ALS-II ring is foreseen as a compromise between how fast the pulsed magnets systems for injection and extraction from the ALS-II ring and the accumulator ring vacuum and RF systems to accumulate the full current of the main ring in case of full swap-out option.

The partial swap-out option relaxes these requirements on the accumulator ring in terms of collective effects, RF power need and safety envelope of the current ALS shielding wall. Also partial swap-out helps to minimize the impact of injection transients. This is because only the fraction (say 10-20% of the full current) being swapped will have a larger emittance and thus a smaller brightness. Thus the brightness will decrease by the same factor and then recover in a few damping times (~20 ms). This small drop in brightness for a relatively short time compared with the time between swap-outs (~1 minute) makes swap-out virtually transparent to most of the users.

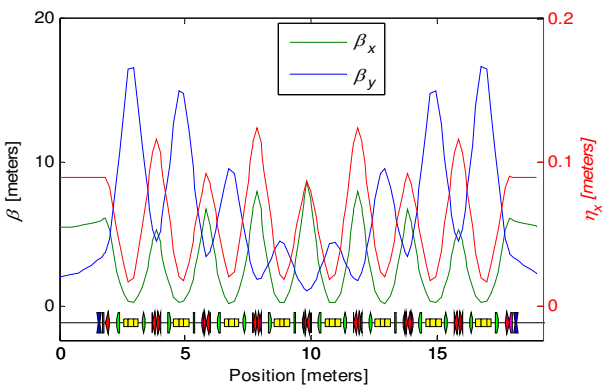


Figure 6: ALS Booster-size Accumulator ring lattice functions.

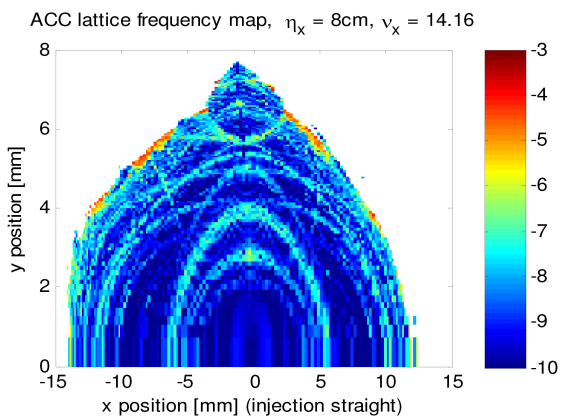


Figure 7: Accumulator ring dynamic aperture.

SUMMARY

The proposed baseline lattice for the ALS upgrade provides diffraction limited photon source up to 2 keV and fulfills the main constraints imposed by the fact that this upgrade is a replacement of the existing ALS storage ring. The lattice nonlinear effects are minimized by the proper configuration of the sextupole magnet families which results in a dynamic aperture sufficient for on-axis injection and lifetime with such strong focusing arrangement in one arc.

The use of double RF system to lengthen the bunches is powerful mean to mitigate IBS as a result strong focusing lattice and raise beam current threshold with decent Touschek lifetime.

Future work on achieving full coupling operation of the lattice and further optimization of the lattice momentum acceptance will be investigated. In addition studies of the injection process, fill pattern and accumulator ring choice need to be investigated to solidify the concept.

ACKNOWLEDGMENT

The Advanced Light Source is supported by the Director, Office of Science, Office of Basic Energy Sciences, of the U.S. Department of Energy under Contract No. DE-AC02-05CH11231.

REFERENCES

[1] M. Bai et al., Nucl. Instr. and Meth. A (2010), doi:10.1016/j.nima.2010.01.045
[2] D. Einfeld, J. Schaper, M. Plesko, Design of diffraction limited light source, Proceedings of IEEE Particle Accelerator Conference, PAC95.
[3] J. Bjorken, S. K. Mtingwa, Proceeding of Particle Accelerator 13, 115 (1983).
[4] M. Borland, AIP Conference Proceedings 1234, 2009.
[5] L. Farvacque, et.al. A Low-Emittance Lattice for the ESRF, Proceedings of IPAC2013, Shanghai, China. MOPEA008.
[6] C. Sun, et al., Phys. Rev. STAB 15, 054001 (2012).
[7] J. M. Byrd, M. Georgsson. Physical Review ST Accelerator and Beams, 4(3) 092001 Sept. 2002.
[8] A. Piwinski, DESY 98-179, Nov. 1998. ISSN 0418-9833.

Copyright © 2013 CC-BY-3.0 and by the respective authors

REMOVAL OF RESIDUAL CHIRP IN COMPRESSED BEAMS USING A PASSIVE WAKEFIELD TECHNIQUE

M. Harrison*, G. Andonian, T. Campese, A. Murokh, F. H. O'Shea, M. Ruelas,
RadiaBeam Technologies, Santa Monica, CA 90404, USA
P. Frigola, RadiaBeam Systems, Santa Monica, CA 90404, USA
M. Fedurin, Brookhaven National Laboratory, NY 11961, USA

Abstract

The removal of residual chirp in XFELs is of paramount importance for efficient lasing. Although current S-band XFELs remove the unwanted residual chirp using off-crest acceleration after the final bunch compressor, this technique is not possible for XFELs with soft X-ray lines as there are no further accelerating structures. The off-crest dechirping technique is also expensive for future superconducting XFELs. In response, RadiaBeam Systems presents its work, building upon the theoretical work of Bane and Stupakov [1], in RF-free residual chirp mitigation using only passive techniques. Beam-induced longitudinal wakefields are produced with opposing corrugated plates which allow for an entirely RF-free chirp removal. Theory, engineering, and experimental results are presented.

INTRODUCTION

Beam dechirping is crucial for current and future XFELs. Accelerating and compressing sections of beamlines leave beam bunches with a residual chirp that must be removed for lasing. In the SLAC LCLS, dechirping requires hundreds of meters of off-crest accelerating structures. This is costly both in terms of accelerating cavity efficiency and beamline space [2].

RadiaBeam Systems has designed and manufactured a compact, low-cost corrugated plate system with an adjustable gap for tunable beam dechirping. Its dechirping characteristics were measured at the Brookhaven National Laboratory (BNL) Accelerator Test Facility (ATF).

THEORY

The driving theory for designing the passive dechirper system has been presented in papers by Bane, Stupakov, and Emma [2] [3]. The longitudinal wakefield generated by a single electron passing between the corrugated plates is given by

$$w(z) = \left(\frac{\pi^2}{16}\right)\frac{Z_0 c}{\pi a^2} H(z) cos\left(\frac{2\pi z}{\lambda}\right), \qquad (1)$$

where $Z_0 = \sqrt{\mu_0/\epsilon_0}$ is the impedance of free space, $H(z)$ is the unit step function, c is the speed of light, z is the coordinate along the beam path, and λ is the wavelength of the dominant mode of the wakefield given by

$$\lambda = 2\pi\sqrt{\frac{a\delta g}{2p}}. \qquad (2)$$

The remaining variables describe the dimensions of the corrugated plates. a is the distance of the plates from the beamline (half the plate separation); δ is the depth of the corrugations; g is the gap between corrugations; p is the period of the corrugations. These dimensions are listed in Table 1 and pictured in Figure 2. For compliance with the derivation assumptions, $p, d \ll a$ and $\delta \gtrsim p$ [2]. The transverse dimension of the plates is taken to be infinite.

The $\pi^2/16$ factor comes from the differing geometry between parallel plates and the circular pipe that was used in Stupakov and Bane's original derivation [4]. The wakefield produced by the bunch is found by convolving the single particle wakefield (Equation 1) with the longitudinal beam bunch charge density profile. For rectangular longitudinal profiles, the wakefield is linear in the region of the beam bunch as shown in Figure 1. For plates that satisfy the constraints above, the dechirping strength, h, is given by the slope of the linear region and can be calculated by

$$h = \left(\frac{\pi^2}{16}\right)\frac{Z_0 c Q L}{\pi a^2 l}, \qquad (3)$$

where Q is the bunch charge, L is the length of the dechirper, and l is the bunch length.

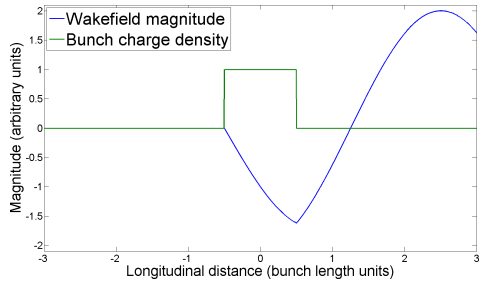


Figure 1: Bunch current profile and generated longitudinal wakefield.

CORRUGATED PLATE DIMENSIONS AND MANUFACTURE

The dimensions of the corrugated plates used in this experiment are listed in Table 1. The plates were fabricated

* harrison@radiabeam.com

Copyright © 2013 CC-BY-3.0 and by the respective authors

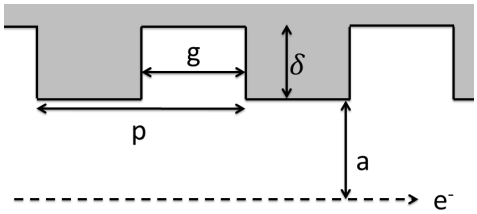


Figure 2: Diagram of corrugated plates.

Table 1: Corrugated Plate Dimensions

Dechirper dimensions			
Length	L	181	mm
Width		38.1	mm
Period	p	1.15	mm
Depth	δ	1.15	mm
Gap	g	0.77	mm
Plate separation	a	1–30	mm
Material		Aluminum	

from aluminum for its light weight and ease of machining. Note that the conductivity of the plates does not affect the function of the dechirper as long as the fundamental mode of the wakefield is dominant [5].

The plates were actuated by stepper motor-driven linear motion feedthroughs–one at each end of each plate. This allows for control of the plates' vertical position, separation, longitudinal angle, and alignment with the beam. Figure 3 shows the corrugated plates and the attachments to the linear actuators above. Figure 4 shows a close-up of the plates after alignment.

PROCEDURE

The plates were installed in a box chamber on Beamline 2 at the BNL ATF and were aligned to the beam using an alignment laser. The beam parameters for the experiment are given in Table 2.

The measured dechirping strength (h in Equation 3) of a configuration is defined as the change in energy spread divided by the bunch length. A beam with a known bunch length and energy spread was passed between the plates. As the plate separation was varied, the change in energy spread was measured by a downstream energy spectrometer. Photographs of the plates (e.g., Figure 4) taken with a calibrated camera are used to measure the separation.

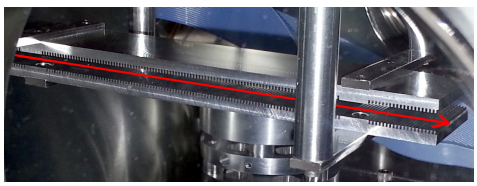


Figure 3: Full view of dechirper as installed. The red arrow indicates the electron beam path.

Table 2: BNL ATF Beam Properties

BNL ATF beam parameters			
Beam energy	E	57.6	MeV
Bunch charge	Q	340	pC
Initial chirp		400	keV/mm
Transverse beam size		100	microns
Pulse length (full width)	l	3.4	psec
Longitudinal profile		Rectangular	

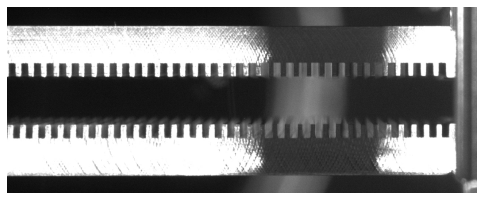


Figure 4: Side view of corrugated plates. Beam travels left to right. Note the corrugations are longitudinally misaligned by about a quarter of a period.

Bunch charge is measured by a downstream Faraday cup.

In a second round of measurements, the bunch charge was scanned at a fixed plate separation of 3.90 mm.

RESULTS

A selection of energy spectrum measurements at various plate separations can be seen in Figure 5. Figure 6 shows the dechirping strength of the corrugated plates as a function of plate separation. The blue line showing the dechirping strength was calculated by adding the wakefield-induced energy change (Equation 1 convolved with the bunch charge distribution and multiplied by the length of the dechirper) to the initial chirped beam. As the plate separation closes past a certain point, the theoretical dechirping strength peaks before reversing sign. This happens for two reasons. First, the beam gets over-dechirped and gains an increasing and oppositely-signed chirp. Second, the wavelength of the wakefield (Equation 1) shrinks to the extent that the wakefield is no longer linear. If the wakefield wavelength is sufficiently short, the bunch sees alternating positive and negative kicks along its length.

It can also be seen in Figure 6 that the measured dechirping power has the same behavior as the theoretical, but is weaker by about half. There are several possibilities for this that warrant further investigation:

- To what extent does the misalignment of the corrugations of the two plates reduce the strength of the dechirping wakefield? It was observed that the plates oscillated longitudinally by as much as half a corrugation period as they were actuated vertically (offset observable in Figure 4).

- Is the $\pi^2/16$ factor in Equations 1 and 3 sufficient to account for the different geometries (pipe vs. plates)?

Copyright © 2013 CC-BY-3.0 and by the respective authors

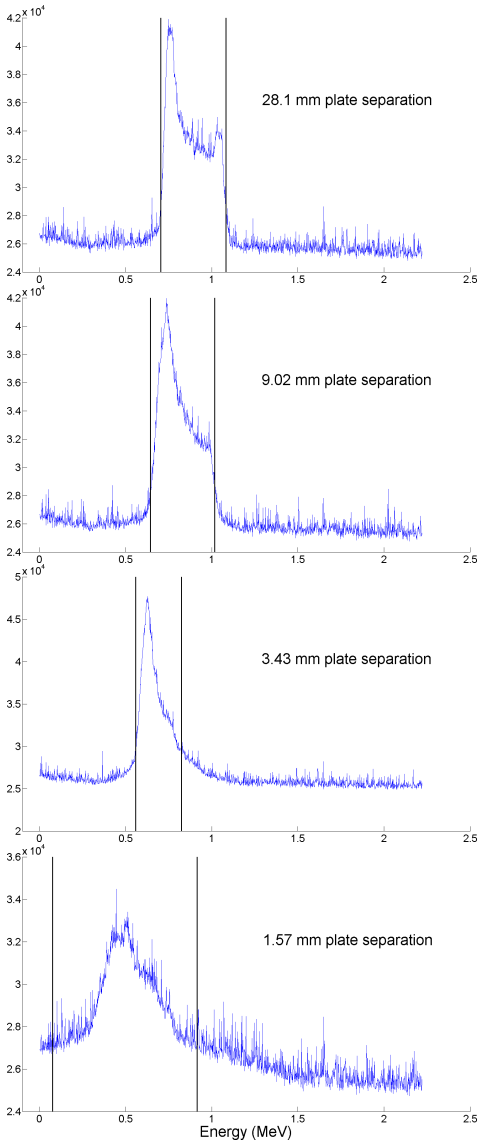


Figure 5: Energy spectrum plots at various plate separations. Note that closing the gap too much (smaller than ∼3.4 mm) results in a larger energy spread. The vertical lines designate the width where the intensity falls to 20% of the maximum height over the background.

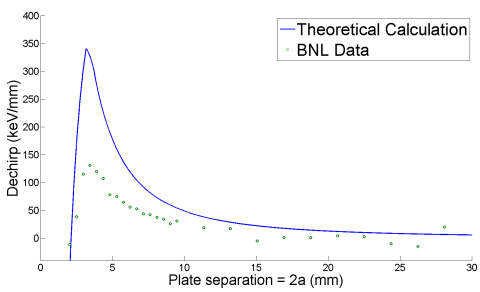


Figure 6: Dechirping Strength of parallel plates vs. Plate Separation, showing the measured dechirping strength at about half of theoretical predictions.

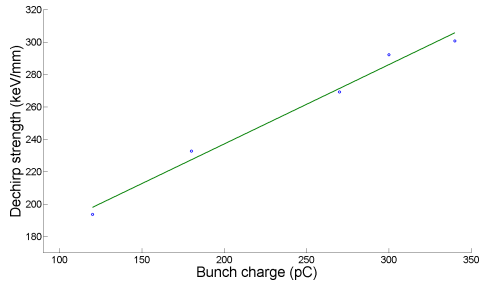


Figure 7: Dechirping Strength vs. bunch charge.

- How much of the measured energy spread is due to chirp, and how much is uncorrelated energy spread? The uncorrelated energy spread would result in an overestimation of the beam's initial chirp.

The result of the bunch charge variation experiment is shown in Figure 7. As expected, the relationship is linear.

FUTURE WORK

A second passive dechirping system is being planned that will involve a much longer corrugated plate section (>1 m) and an actuation system less prone to alignment errors. A longer dechirper is desirable because larger plate separations can be used, leading to longer wakefield wavelengths and a wider range of accepted bunch lengths. These are also more easily tuned by varying the plate separation for producing beams with near-zero chirp.

Furthermore, future experiments will make measurements with a deflecting cavity in addition to a dipole spectrometer to directly measure the beam's chirp. Transverse effects, especially any emittance blowup, will also be characterized.

ACKNOWLEDGMENTS

RadiaBeam Systems wishes to thank the staff at BNL ATF for their valuable assistance in this experiment. Special thanks to Karl Kusche and Christina Swinson for their personal involvement.

This is experiment is supported by an ongoing DOE Phase I Small Business Initiative for Research (SBIR) Grant, number DE–SC0009550.

REFERENCES

[1] K.L.F. Bane, G. Stupakov, Nucl. Inst. Meth. 690 (2012) 106–110.

[2] K. Bane, G. Stupakov, "Corrugated Pipe as a Beam Dechirper," SLAC-PUB-14925, April 2012.

[3] P. Emma, "Proposal for a Corrugated Beam Pipe Wakefield Experiment," NGLS Technical Note 24.

[4] K. Bane and A. Novokhatski, "The resonator impedance model of surface roughness applied to the LCLS parameters," LCLS-TN-99-1, SLAC, 1999.

[5] A. W. Chao, "Physics of collective beam instabilities in high energy accelerators" (John Wiley & Sons, New York, NY, 1993) 47–48.

Copyright © 2013 CC-BY-3.0 and by the respective authors

LASER-UNDULATOR FEL WITH NEARLY COPROPAGATING LASER PULSE*

R. A. Bosch#, J. E. Lawler, J. J. Bisognano, M. A. Green, K. D. Jacobs, R. Wehlitz, D. D. Yavuz,
University of Wisconsin-Madison, Madison, WI 53706, USA
R. C. York, Michigan State University, East Lansing, MI 48824, USA
T.-C. Chiang, T. J. Miller, University of Illinois, Urbana, IL 61801, USA

Abstract

A free-electron laser (FEL) may be obtained by interaction of an electron bunch and a nearly copropagating laser pulse, where the laser pulse is sheared to extend the interaction length. When the angle between the electron beam axis and the propagation direction of the laser pulse greatly exceeds the reciprocal of the relativistic factor, the output radiation is nearly on the axis, and the FEL may be approximated by an axially aligned magnetostatic undulator. For a feasible laser-undulator FEL, we calculate gain using a one-dimensional model, as well as a three-dimensional model that includes degradation from diffraction and electron velocity spread.

INTRODUCTION

An electromagnetic plane wave that collides head-on with an ultrarelativistic electron bunch may create an FEL [1] that amplifies xrays whose frequency is ~$4\gamma^2$ times that of the incident "pump" wave [2], where γ is the electron bunch's relativistic factor. To obtain softer xrays, one can propagate a pump wave in nearly the same direction as the electron beam. By using a sheared laser pulse [3, 4], the electromagnetic field affecting the bunch is similar to a plane wave over an extended interaction length [5–8].

For the case where the propagation directions of the electron beam and the pump wave differ by an angle >> $1/\gamma$, a one-dimensional (1D) FEL model predicts maximum gain for xrays whose propagation direction differs from that of the electron beam by an angle << $1/\gamma$, and nearly identical gain for xrays that propagate on the electron beam axis. For this practical case, a magnetostatic undulator that is aligned with the electron beam approximates the laser undulator.

For a circularly polarized laser-undulator FEL with output wavelength of 2.5 nm described in Ref. [8], we use this magnetostatic undulator to calculate gain using the 1D model as well as a three-dimensional (3D) model [9].

ONE-DIMENSIONAL MODEL

The 1D model describes a uniform density of cold electrons interacting with a plane electromagnetic pump wave. In this model, maximum gain occurs for the electromagnetic wave that is a 180º reflection of the pump wave, when viewed in the beam frame of reference where the average electron velocity is zero [10].

*Work supported by the University of Wisconsin-Madison
bosch@src.wisc.edu

In the laboratory frame, consider a uniform density of cold electrons drifting with average velocity $\beta^* c$, where c is the speed of light, interacting with a pump wave. Let the z-axis describe the direction of the average electron motion while interacting with the pump laser, which propagates at an angle of θ_{pump} w.r.t the z-axis. A head-on collision is described by $\theta_{pump} = 180º$.

For small laser intensity, the forced electron oscillations in the beam frame are nonrelativistic, and the average axial velocity of the electrons in the lab frame is given by $\beta^* \approx \beta = (1-1/\gamma^2)^{1/2}$. In this case, the Lorentz-invariant undulator parameter K is << 1, where [2, 5, 8]

$$K^2 = 2 r_e I \lambda_{pump}^2 / (\pi m c^3) , \quad (1a)$$

$$K^2 = r_e I \lambda_{pump}^2 / (\pi m c^3) . \quad (1b)$$

Equation (1a) describes a planar undulator created by a linearly polarized pump wave, while eq. (1b) describes a helical undulator created by circular polarization. Here, r_e is the classical radius of the electron, I is the pump laser intensity, λ_{pump} is the pump wavelength and m is the electron mass. For larger values of K, the forced electron oscillations are relativistic in the beam frame. In the lab frame, $(K/\gamma)c$ is the maximum transverse electron velocity driven by the pump wave.

In the laboratory frame, the angular 4-frequency (c times the 4-vector) of the pump wave is

$$\overline{\omega}_{pump} = (\omega_{pump}, \omega_{pump} \sin\theta_{pump}, 0, \omega_{pump} \cos\theta_{pump}) . \quad (2)$$

A Lorentz transform gives the angular 4-frequency in the beam frame, which is moving at the velocity $\beta^* c$ [11]

$$\overline{\omega}'_{pump} = (\gamma^* \omega_{pump}(1-\beta^* \cos\theta_{pump}), \omega_{pump} \sin\theta_{pump}, 0, \gamma^* \omega_{pump}(\cos\theta_{pump} - \beta^*)) , \quad (3)$$

where the axial relativistic factor is defined by $\gamma^* = (1-\beta^{*2})^{-1/2}$. In the beam frame, the pump wave has angular frequency

$$\omega'_{pump} = \gamma^* \omega_{pump}(1-\beta^* \cos\theta_{pump}) , \quad (4)$$

and direction of propagation obeying

$$\cos\theta'_{pump} = \frac{\cos\theta_{pump} - \beta^*}{1-\beta^* \cos\theta_{pump}} . \quad (5)$$

For many cycles of interaction, the maximum FEL gain occurs for the wave given in the beam frame by a 180º reflection of the pump wave [10]. This wave is given in the beam frame by the same frequency as the pump

Copyright © 2013 CC-BY-3.0 and by the respective authors

$$\omega'_{xray} = \omega'_{pump} = \gamma^* \omega_{pump}(1-\beta^* \cos\theta_{pump}), \quad (6)$$

and opposite direction of propagation as the pump

$$\cos\theta'_{xray} = -\cos\theta'_{pump} = -\frac{\cos\theta_{pump} - \beta^*}{1-\beta^* \cos\theta_{pump}}. \quad (7)$$

The 4-frequency of this wave, in the beam frame, is given by multiplying the spatial components of $\overline{\omega}'_{pump}$ by –1:

$$\overline{\omega}'_{xray} = (\gamma^* \omega_{pump}(1-\beta^* \cos\theta_{pump}), -\omega_{pump} \sin\theta_{pump}, 0, -\gamma^* \omega_{pump}(\cos\theta_{pump} - \beta^*)). \quad (8)$$

A Lorentz transformation gives the 4-frequency for maximum FEL gain in the laboratory frame

$$\overline{\omega}_{xray} = (\gamma^{*2} \omega_{pump}[1+\beta^{*2} - 2\beta^* \cos\theta_{pump}], -\omega_{pump} \sin\theta_{pump}, 0, \gamma^{*2} \omega_{pump}[2\beta^* - (1+\beta^{*2})\cos\theta_{pump}]). \quad (9)$$

In the laboratory frame, the wave with maximum FEL gain has angular frequency

$$\omega_{xray} = \gamma^{*2} \omega_{pump}(1+\beta^{*2} - 2\beta^* \cos\theta_{pump}), \quad (10)$$

and propagation angle w.r.t. the z-axis of θ_{xray}, where

$$\cos\theta_{xray} = \frac{2\beta^* - (1+\beta^{*2})\cos\theta_{pump}}{1+\beta^{*2} - 2\beta^* \cos\theta_{pump}}. \quad (11)$$

MODELING BY AN AXIALLY ALIGNED MAGNETOSTATIC UNDULATOR

Consider the practical case where the pump propagation direction differs sufficiently from that of the bunch so that $\theta_{pump} >> 1/\gamma$. In this case $\theta'_{pump} >> \pi/2$ and $\theta'_{xray} << \pi/2$, while the output angle obeys $\theta_{xray} << 1/\gamma$. Provided that the undulator strength K does not greatly exceed one, $K\theta_{xray} << 1/\gamma$ is obeyed, so that the FEL gain for a wave propagating in the z-direction nearly equals the maximum gain occurring in the direction θ_{xray} [12]. We approximate the FEL with a magnetostatic undulator aligned to the z-axis, whose xray wavelength and K equal those of the laser undulator. For magnetostatic undulator period λ_u and electron oscillation frequency $\omega_u = 2\pi\beta^* c/\lambda_u$, the xray wavelength and frequency obey [1]

$$\lambda_{xray} = \lambda_u/(2\gamma^{*2}) \quad , \quad \omega_{xray} = 2\gamma^{*2} \omega_u/\beta^* \quad , \quad (12)$$

Thus, the axially aligned magnetostatic undulator has period

$$\lambda_u = \frac{2}{1+\beta^{*2} - 2\beta^* \cos\theta_{pump}} \lambda_{pump} \approx \frac{\lambda_{pump}}{1-\beta^* \cos\theta_{pump}}, \quad (13)$$

and electron oscillation angular frequency

$$\omega_u = (\beta^*/2)(1+\beta^{*2} - 2\beta^* \cos\theta_{pump})\omega_{pump} \approx (1-\beta^* \cos\theta_{pump})\omega_{pump}. \quad (14)$$

For head-on laser interaction, $\omega_u \approx 2\omega_{pump}$ [2].

For a general value of K, the average axial electron velocity in the undulator is $\beta^* c$, where [1]

$$\beta^* = \sqrt{1-(1+K^2/2)/\gamma^2}, \quad (15a)$$

$$\beta^* = \sqrt{1-(1+K^2)/\gamma^2}. \quad (15b)$$

Equation (15a) describes a planar undulator, while eq. (15b) describes a helical undulator.

In the 1D model, the FEL gain is parameterized by the Pierce parameter ρ which obeys [1]

$$\rho^3 = (n_e e^2 K^2 [JJ]^2)/(32\omega_u^2 m\varepsilon_0 \gamma^3), \quad (16a)$$

$$\rho^3 = (n_e e^2 K^2)/(16\omega_u^2 m\varepsilon_0 \gamma^3), \quad (16b)$$

where eq. (16a) describes a planar undulator while eq. (16b) describes a helical undulator. Here, e is the electron charge, n_e is the electron density, and ε_0 is the permittivity of free space. The term $[JJ]$ is a Bessel function factor

$$[JJ] \equiv J_0(K^2/[4+2K^2]) - J_1(K^2/[4+2K^2]), \quad (17)$$

which is nearly equal to 1 for $K << 1$.

For low gain G << 1, the energy gain for a laser undulator with N cycles is [1]

$$G = 2(4\pi)^3 \rho^3 N^3 [(2-2\cos\phi - \phi\sin\phi)/\phi^3], \quad (18)$$

where $\phi \equiv 2\pi N - 2\pi N_{rad}$ is the phase slippage through the undulator, in which N_{rad} is the number of cycles of amplified radiation which overtake an average electron while passing through the undulator. For this low-gain case, an evaluation of the laser-undulator gain in the electron beam frame [10] confirms that it equals that of the axially aligned magnetostatic undulator. The largest gain occurs for a slippage of 2.61 radians [10]

$$G_{max} = 0.27(4\pi)^3 \rho^3 N^3. \quad (19)$$

In the high gain limit, the xray radiation power grows exponentially in a gain length [1, 2]

$$L_G = \lambda_u/(4\pi\sqrt{3}\rho). \quad (20)$$

In principle, a crab cavity can be used to tilt the bunch so that the gain medium provided by the electrons is aligned in the direction of maximum gain.

Without a crab cavity, the gain medium extends farthest in the axial direction, and the gain in the axial direction nearly equals the maximum in the direction θ_{xray} [12]. The self-amplified stimulated emission (SASE) is expected to propagate at a small angle equal to or smaller than that given by eq. (11), with gain nearly equal to that of the axially aligned magnetostatic undulator. For a seeded FEL, amplification of an axially propagating xray is nearly the same as in the axially aligned magnetostatic undulator.

THREE-DIMENSIONAL MODELING

In Ref. [8], a 300-period circularly polarized laser undulator with K = 0.4336, produced by a 750-nm pump

Copyright © 2013 CC-BY-3.0 and by the respective authors

laser propagating at an angle of θ_{pump} = 0.0572 radian w.r.t. a 168.65-MeV electron beam, produces output at λ_{xray} = 2.5 nm. Equation (11) predicts maximum gain for θ_{xray} = 0.19 mrad << 1/γ, in agreement with eqs. (5.42) and (5.43) of Ref. [6]. We approximate the laser undulator with an axially aligned helical magnetostatic undulator with period of 0.458 mm and length of 0.137 m.

In Ref. [9], M. Xie uses numerical fits to simulations to provide a 3D model for the degradation of high-gain FEL performance from diffraction and the electron axial velocity spread due to slice emittance and slice energy spread. Using 1D and 3D models, we evaluated gain for the ideal case where a cylindrically symmetric electron beam is focused in the center of a magnetostatic undulator where the horizontal and vertical beta functions equal one-half of the undulator length. The average beam size in the undulator is given by horizontal and vertical beta functions equal to 66% of the undulator length. Table 1 lists the parameters that were modeled.

Table 2 shows calculated FEL properties—the Pierce parameter, exponential gain length, gain saturation length, and saturation power—for the 1D and 3D models. Comparing the models shows that the gain length is increased 50% by diffraction and the bunch's axial velocity spread. According to the 3D model, the FEL gain is $e^{9.2}$ =10,000 within the 0.137-m interaction length. SASE saturation, which requires interaction over 19 gain lengths, is not achieved. Effects from nonuniformity of the laser undulator are not included in these models.

The FEL properties depend smoothly upon the beam parameters and *K*-value, indicating that a small deficiency in one parameter can be compensated by improving a different parameter. The 1D Pierce parameter of 0.00215 is comparable to the relative slice energy spread of 0.001, so that the 3D gain length increases substantially if the energy spread is increased, as shown in Fig. 1(a). Figure 1(b) shows that increasing the normalized emittance to 0.2 mm-mrad doubles the 3D gain length.

SUMMARY

For a 300-period laser-undulator FEL created by interaction of an electron bunch with a nearly copropagating laser pulse, the FEL gain and saturation have been calculated by approximating the laser undulator with an axially aligned magnetostatic undulator. Xrays with a wavelength of 2.5 nm are predicted to by amplified by $e^{9.2}$ = 10,000 within the 0.137-m interaction length.

Table 1: Electron Beam and Undulator Properties

Beam energy	168.65 MeV
Slice energy spread	168.65 keV
Slice emittance (normalized)	0.06 mm-mrad
Peak current	800 A
β-function ($\beta_x = \beta_y$)	0.09 m
Undulator *K* value	0.4336
Output xray wavelength	2.5 nm

Table 2: Calculated FEL Properties

Calculated parameter	**1D model**	**3D model**
Pierce parameter (ρ)	0.00215	0.00143
Gain length [mm]	9.78	14.8
Gain saturation length [m]	0.186	0.275
Saturation power [GW]	0.29	0.204

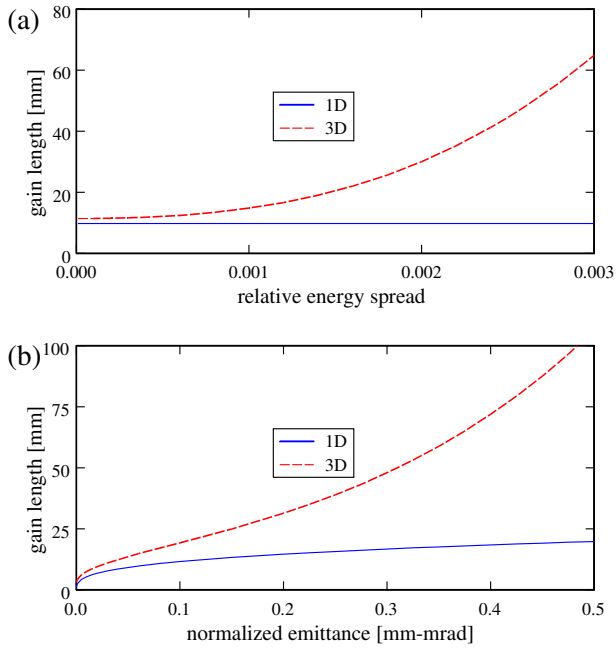


Figure 1: (a) Gain length vs. slice energy spread. (b) Gain length vs. normalized slice emittance.

REFERENCES

[1] R. Bonifacio, F. Casagrande, G. Cerchioni, L. de Salvo Souza, P. Pierini and N. Piovella, Riv. Nuovo Cimento 13, 1 (1990).
[2] G. Dattoli, V. Petrillo and J. V. Rau, Opt. Comm. 285, 5341 (2012).
[3] E. D. Treacy, IEEE J. Quantum Electron. QE-5, 454 (1969).
[4] J. Hebling, Opt. Quant. Electron. 28, 1759 (1996).
[5] A. D. Debus, M. Bussmann, M. Siebold, A. Jochmann, U. Schramm, T. E. Cowan and R. Sauerbrey, Appl. Phys. B 100, 61 (2010).
[6] A. Debus, Ph.D. thesis, Dresden University of Technology, Dresden, 2011.
[7] C. Chang, C. Tang and J. Wu, Phys. Rev. Lett. 110, 064802 (2013).
[8] J. E. Lawler et. al., J. Phys. D 46, 325501 (2013).
[9] M. Xie, in "Proceedings of the 1995 Particle Accelerator Conference, Dallas" (IEEE, Piscataway, NJ, 1996), p. 183.
[10] R. A. Bosch, in "Proceedings of the 2003 Particle Accelerator Conference, Portland, OR" (IEEE, Piscataway, NJ, 2003), p. 935.
[11] J. D. Jackson, Classical Electrodynamics (Wiley, New York, 1975), 2nd ed., p. 521.
[12] W. B. Colson, G. Dattoli and F. Ciocci, Phys. Rev. A 31, 828 (1985).

Copyright © 2013 CC-BY-3.0 and by the respective authors

STUDIES ON SHORT-BUNCH EXTRACTION AT CSNS RCS

Ye Zou, Jingyu Tang, Jinfang Chen
Institute of High Energy Physics, Chinese Academy of Sciences, Beijing 100049

Abstract

White neutron application requires short proton pulse length to obtain high time resolution for nuclear data measurements. Back-streaming neutron beam at the CSNS spallation target is to be exploited as a white neutron source. The available high RF voltage in the high intensity rapid cycling synchrotron (RCS) of the CSNS makes it possible to extract very short bunches by using the bunch rotation method. Special attentions have been paid to the bunch rotation during the slow acceleration, space charge effect and beam loading effect in the high-intensity RCS. Different extraction scenarios together with the changes in the injection have been studied. Together with the calculations, multi-particle simulations have been carried out to show the effectiveness of the method. With a sacrifice of about two-third beam power, the rms bunch length of the extracted beam can be reduced to about one eighth of the one in the nominal operation mode. Other scenarios also show the improvement in the bunch length.

INTRODUCTION

Back-streaming neutrons from the spallation target of CSNS (China Spallation Neutron Source) are very strong and harmful to the proton beam transport line if they are not well treated [1]. The studies found that the neutron beam has excellent properties of wide energy spectrum and time structure, and has been proposed to build a white neutron source for nuclear data measurement [2, 3]. The neutron pulse length is critical in defining the neutrons' energy by the time-of-flight method, and should be reduced as short as possible. The time structure of the back-streaming neutrons is jointly determined by the pulse length of the impinging proton beam and the thickness of the spallation target. Simulations show that the target thickness dominates the time resolution for the lower energy part of the wide-range energy neutrons, while the proton pulse length dominates the higher energy part. As the target length cannot be changed for this parasitic application, it would be interesting to shorten the proton pulse length by designing a special dedicated working mode for the CSNS accelerators. This paper presents the study about using the bunch rotation method in the RCS (Rapid Cycling Synchrotron of CSNS) to obtain very short proton beam bunches.

CSNS is a multi-disciplinary research facility under construction [4], which is to be built in two or three phases. In the first phase, the RCS is to accelerate beam from 80 MeV to 1.6 GeV in a repetition rate of 25 Hz, and the extracted beam power is 100 kW. Figure 1 and Table 1 show the layout and some parameters of the RCS.

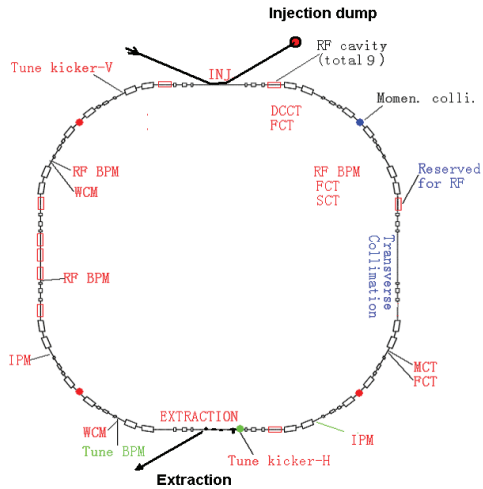


Figure 1: Layout of the CSNS RCS.

Table 1: Some Parameters of the CSNS RCS

Circumference (m)	227.92
Injection energy (GeV)	0.08
Extraction energy (GeV)	1.6
Maximum RF voltage (kV)	165
Betatron tunes (h/v)	4.82/4.80
RF harmonics	2
Transverse acceptance (πmm.mrad)	540
Collimation acceptance (πmm.mrad)	~350

SHORT-BUNCH EXTRACTION METHODS

There are two bunches per pulse in the extracted proton beam in the normal operation mode. The bunch length is determined by the RF voltage pattern and the longitudinal painting. The longitudinal painting is optimized to alleviate the space charge effects in such a high-intensity synchrotron. Compared with the simple method by designing a high RF voltage at the extraction, the bunch rotation method is more effective in shortening the bunch length for the extracted beam [5, 6]. The principle of the bunch rotation method is as follows: the RF voltage is adiabatically decreased from the normal extraction voltage to a low one, during which the bunch becomes gradually flat to follow the change of the RF bucket as long as the bucket still contain the beam with some margin. Then the RF voltage is quickly or non-

* zouye@ihep.ac.cn

Copyright © 2013 CC-BY-3.0 and by the respective authors

adiabatically increased to a high value. The mis-matched bunch will rotate in the enlarged RF bucket. After a quarter of synchrotron period, the bunch will reach the minimum length and then the single-turn extraction can be applied.

In small-amplitude or linear synchrotron motion approximation, the rms bunch length and height σ_τ and σ_δ in a matched RF bucket are expressed by

$$\sigma_\tau = \sqrt{\frac{A_{rms}}{\omega_0}}\left(\frac{2|\eta|}{\pi h e V \beta^2 E|\cos\varphi_s|}\right)^{\frac{1}{4}}, \quad (1)$$

$$\sigma_\delta = \sqrt{\frac{\omega_0 A_{rms}}{\pi\beta^2 E}}\left(\frac{heV|\cos\varphi_s|}{2\pi\beta^2 E|\eta|}\right)^{\frac{1}{4}}, \quad (2)$$

where $A_{\rm rms}$, ω_0, η, h and φ_s denote the invariant rms phase space area in eV-s, revolution frequency of the reference particles, phase-slip factor, harmonic number and synchronous phase, respectively. Suppose the RF voltage changes from the nominal setting V_i to V_1 adiabatically, and then to the maximum available value V_2 non-adiabatically. According to Eq. (1), the bunch extension ratio of the rms bunch length is equal to

$$r_{c\,max,V_i\to V_1} = \frac{\sigma_{\tau,i}}{\sigma_{\tau,m}} = \left(\frac{V_1}{V_i}\right)^{\frac{1}{4}} \quad (3)$$

where $\sigma_{\tau,i}$ and $\sigma_{\tau,m}$ denote the initial bunch length and the medium-stage bunch length, respectively.

After the non-adiabatic RF voltage change from V_1 to V_2, the bunch performs rigid quadrupole mode oscillations. After 1/4 of synchrotron period, the rms bunch length reaches the minimum, and can be expressed by

$$\sigma_{\tau,f} = \sqrt{\frac{A_{rms}}{\omega_0}}\left(\frac{2|\eta|}{\pi h\beta^2 E|\cos\varphi_s|}\right)^{\frac{1}{4}}\frac{(eV_1)^{1/4}}{(eV_2)^{1/2}}, \quad (4)$$

where $\sigma_{\tau,f}$ denotes the final bunch length. The compression ratio of the rms bunch length from V_1 to V_2 can be expressed by

$$r_{c\,max,V_1\to V_2} = \frac{\sigma_{\tau,m}}{\sigma_{\tau,f}} = \left(\frac{V_2}{V_1}\right)^{\frac{1}{2}}, \quad (5)$$

The total compression ratio of the rms bunch length from the initial voltage (V_i) to the low voltage (V_1) then to the final voltage (V_2) can be expressed as

$$R_{c\,max,V_i\to V_1\to V_2} = \frac{\sigma_{\tau,i}}{\sigma_{\tau,f}} = \left(\frac{V_1}{V_i}\right)^{\frac{1}{4}}\left(\frac{V_2}{V_1}\right)^{\frac{1}{2}}, \quad (6)$$

The bunch compression ratio depends only on the RF voltage ratio according to Eq. (6).

However, in practice, there are limitations to apply the bunch rotation method. In a high-intensity RCS, one has to consider the space charge effects during the bunch rotation process and the beam loading effect. The space charge effect may become strong when the bunch shortens during the bunch rotation. The initial beam emittance is also determined by the beam dynamics at the lower energy of the acceleration cycle, due to the space charge effects and the longitudinal microwave instability. The beam loading effect means that the circulating beam current detunes the RF cavities and becomes very important when the RF voltage is very low. To avoid the instability in the low-level RF control system, the ratio of the circulating beam current and the driving current from the RF amplifier should be controlled below a certain value, e.g. 6. This also limits the lowest RF voltage for V_1. The accumulated particles should be decreased to ease the above problems, and this leads to the reduction of the extracted beam power.

Different from its usual applications in compressor rings [7, 8] or slow cycling synchrotrons [9], in a high-intensity RCS, another important issue which should be considered seriously is the slow acceleration during the bunch rotation when the magnetic field is still ramping. The asymmetric RF bucket will deform the bunch shape and increase the final bunch length. The bunch rotation process should be started close to the maximum magnetic field, and this will delay the extraction moment slightly.

SIMULATION RESULTS

Multi-particle simulations with space charge with the ORBIT code [10] have been carried to show how effective the method in realistic cases is. Different injection scenarios and beam powers are studied in the simulations. The simulations are performed only in 1D longitudinal, while the transverse motion is kept in mind only by maintaining reasonable tune shifts with bunching factor because the transverse motion has no influence on the longitudinal one. In most cases, the chopping factor of 50% (defined as beam duty in the ring RF frequency) which is the one in the nominal working mode is used. With a reduced beam power or less accumulated particles, the RF voltage during the injection is reduced to obtain a small longitudinal emittance. In the nominal operation mode with full beam power, the RF voltage at injection is 29 kV. In a dedicated mode with 30% beam power, the RF voltage is decreased to 8.7 kV to keep the similar beam loading effect. Both chopping factors 50% and 30% are studied with the second giving smaller longitudinal emittance. The minimum and maximum RF voltage (V_1, V_2) before the bunch rotation are taken as 8.7 kV and 160 kV, respectively. During the last few turns of the bunch rotation which lasts about 0.2 ms or 200 turns, the Laslett tune shift reaches about -0.066, which is considered quite safe in a high-intensity RCS.

Figs. 2 and 3 show the longitudinal beam distributions just before the extraction in the nominal operation mode and in the dedicated operation mode, respectively. From the figures, one can see that a much shorter bunch length can be obtained in the dedicated operation mode. Fig. 4 shows the phase distribution of the extracted beam. For

Copyright © 2013 CC-BY-3.0 and by the respective authors

comparison, the rms bunch lengths for the extracted beam with different scenarios on injection and beam power reduction are shown in Table 2. With 30% chopping factor and 30% beam power together with the bunch rotation method, the rms bunch length of the extracted beam can be reduced to about one eighth of the one in the nominal operation mode. This can improve the time resolution of back-streaming neutrons almost by an order of magnitude at higher energy.

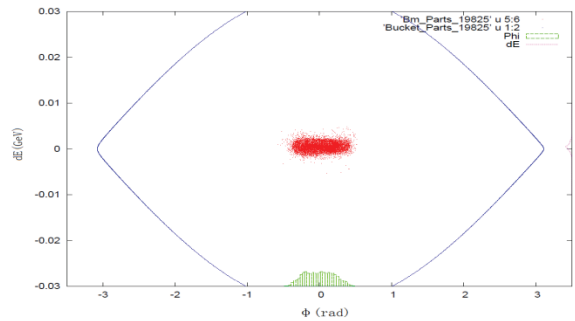


Figure 2: Longitudinal beam distribution just before the extraction in the nominal operation mode.

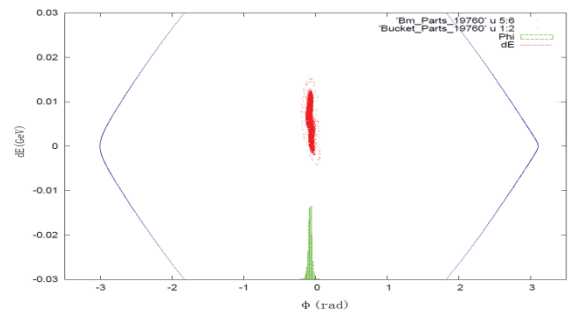


Figure 3: Longitudinal beam distribution just before the extraction in the dedicated operation mode with 30% chopping and 30% beam power.

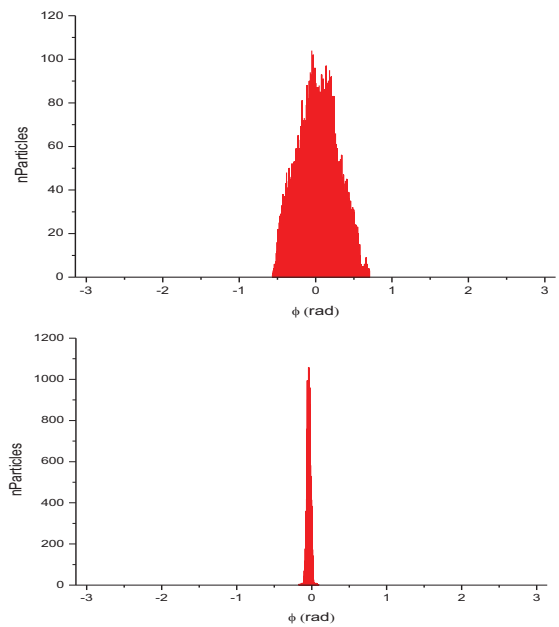


Figure 4: Phase distribution of the extracted beam. (Left: in the nominal operation mode; right: 30% beam chopping factor and 30% beam power).

Table 2: Rms Bunch Length with Different Chopping Factors and Beam Powers

Chopping factor (%)	Beam power remained (%)	rms length without rotation (ns)	rms length with rotation (ns)
50	100	13.0	7.5
50	50	11.0	3.5
50	30	9.3	3.3
30	30	7.2	1.7

CONCLUSIONS

The simulation studies show that the bunch rotation method by RF voltage manipulations is an effective one in short-bunch extraction in CSNS/RCS. In dedicated cases when the white neutron applications with high resolution are stressed, one can obtain a very short bunch length of about one eighth of the one in the nominal operation mode with a sacrifice of about two third beam power. Although the studies have been carried out with the CSNS parameters, the method should be applicable to other high-intensity proton synchrotrons with high available RF voltage.

ACKNOWLEDGMENTS

The authors would like to thank the CSNS colleagues for discussions. The study is supported by the CSNS project and National Natural Science Foundation of China (Projects 11235012 and 10875099).

REFERENCES

[1] H.T. Jing, J.Y. Tang, Z. YANG, Study on collimation and shielding of the back-streaming neutrons at the CSNS target, in publishing at Chinese Physics C.
[2] J.Y. Tang, S.N. Fu, H.T. Jing et al., Chinese Physics C, 2010, Vol. 34 (01): 121-125.
[3] H.T. Jing, J.Y. Tang, H.Q. Tang et al., Nucl. Instr. and Meth., A 621 (2010) 91-96.
[4] Jie Wei et al., Nucl. Instru. And Meth., A 600, (2009) 10-13.
[5] S.Y. Lee, Accelerator Physics, (World Scientific Publishing Co., Singapore, 1999).
[6] K. M. Fung et al., FERMILAB-Pub-00/198-E, 2000.
[7] R. Cappi, J. Gareyte, E. Métral, D. Möhl, Nucl. Instr. and Meth., A 472 (2001) 475-486.
[8] J. Pasternak, M. Aslaninejad, K. Long et al., Proc. of PAC09, Vancouver, (2009) p. 1433.
[9] P. Spiller, J. Ahrens, K. Blasche et al., Proc. of PAC2001, Chicago, (2001) p.3278.
[10] J.D. Galambos et al., ORBIT User Manual Version 1.10, July 1999.

Copyright © 2013 CC-BY-3.0 and by the respective authors

DESIGN CONSIDERATIONS FOR THE ESS ACCELERATOR-TO-TARGET REGION

Thomas J. Shea, Eric J. Pitcher, Ken Andersen, Phillip Bentley, Paul Henry,
Pascal Sabbagh, Alan Takibayev, ESS, Lund, Sweden
Heine Dølrath Thomsen, Søren Pape Møller, ISA, Aarhus, Denmark

Abstract

When the European Spallation Source (ESS) is completed in Lund, Sweden, a superconducting linac will deliver a 5 MW proton beam to a rotating tungsten target. Moderated neutrons from this target will be delivered to a suite of 22 neutron instruments. In the accelerator-to-target region, design choices must balance the demands of the accelerator, the target, and the neutron instruments. For example, the transport line upstream of the target station expands and shapes the small, low emittance linac beam into a large beam that is safe for the target components. It must do this with low loss in order to reduce activation of the beam line and minimize a potential source of background in the neutron instruments. To meet availability goals, beam-induced damage to critical components must be avoided by instrumenting beamline components, deploying a suite of beam instrumentation within the target monolith, and interfacing some of these devices to the machine protection system. This paper will describe recent design changes in this region, highlighting considerations that are applicable to most high power facilities and also those that are unique to a long-pulse source like the ESS.

GOALS

The accelerator-to-target region serves three primary stakeholders: Neutron Science, Target, and Accelerator. Because the long pulse concept couples these stakeholders, the design must balance the needs of all three.

Neutron Science

Neutron instrumentation at a long-pulse source requires a reproducible pulse, both in terms of the time structure and the brightness. Most long pulse instruments under development for ESS use a combination of choppers and the instrument's total flight path length to tailor the neutron pulse and the available wavelength band to the desired characteristics. For example, a truncated pulse will lead to a hole in the wavelength band at the sample position during the time-frame. Therefore, during neutron production, the facility should provide full length pulses with reproducible structure.

The long pulse places additional unique requirements on the neutron instrumentation in terms of dimensions and background. The optimal arrangement of the instrument geometry to exploit the long pulse requires measurement across a frame boundary. In other words, the instruments will perform measurements with slow-moving, meV-energy neutrons at the same time that the proton pulse hits the target for the next pulse. Any contamination from MeV particles emitted by the accelerator and target that can be picked up by the instrument appear as a time-dependent background superimposed on the weak meV signals of interest. This background manifests itself as a systematic error that is correlated with the measurement time (e.g. [5]), and is most efficiently mitigated at its source.

Target

To survive between reasonably long replacement intervals, target components that intercept the proton beam core impose restrictions on the beam's density. These components include the rotating tungsten target, and the proton beam window that separates this target's atmosphere from the accelerator's vacuum. In addition, surrounding components can only receive a limited volumetric power density, and this imposes a limit on beam outside of the core footprint.

Neutron moderator and reflector assemblies also reside within the target system. Because neutron intensity can depend on proton beam position and current, the time to moderate neutrons from the spallation spectrum down to desired energies will determine that timescale for allowable fluctuations in proton beam position and current.

Accelerator

To meet the target requirements above, the transport line leading to the target must expand the bright beam from the linac into an acceptable footprint. To meet the requirements for the neutron pulse, fluctuations in beam position and current must be repeatable and also limited in magnitude and/or characteristic timescale. The transport line should also allow hands-on maintenance by limiting beam loss to well under 1 W/m and by enabling isolation of the components from target back shine.

PROTON BEAM TRANSPORT

Table 1 summarizes the proton beam parameters at the output of the ESS linac. The accelerator-to-target line receives the beam with these parameters and transform it into a beam with the parameters at the proton beam window (PBW) and target (Tgt) listed in Table 2. It accomplishes this by scanning or rastering an expanded beamlet across the target surface.

Copyright © 2013 CC-BY-3.0 and by the respective authors

Table 1: Proton Beam Parameters at the End of the Linac

Parameter	Value
Nominal Power	5 MW
Energy	0.5 to 2 GeV
Pulse current	6.2 to 62.5 mA
Pulse Length	5 to 2860 μs
Repetition rate	14 Hz
Bunching frequency	352 MHz
RMS width in linac	2 mm

Table 2: Beam Parameters at the Target Station, Horizontal (H) and Vertical (V)

Parameter	Location	H	V
RMS size	CO	0.2 mm	0.4 mm
	PBW	10.0 mm	5.00 mm
	Tgt	12.6 mm	6.32 mm
Max. deflection	PBW	55.4 mm	12.7 mm
	Tgt	70.0 mm	16.0 mm
Avg. current density	PBW	88 μA/cm^2	
	Tgt	56 μA/cm^2	

Transport line optics are shown in Figure 1. The design proposal for the LANL MTS line [1] inspired this concept. The upstream matching quads, Q1–Q4, set the beamlet size on the target and provide a beam waist at the crossover (CO), where the beam deflections are minimized by design. Eight raster magnet dipoles (RMs) scan the beamlet, and they are centered on the action point (AP) with 4 acting in each plane. Downstream of the raster magnets, a quadrupole doublet, Q5+Q6, not only ensures the final beam size expansion, but imposes a transverse phase advance of π between the AP and the CO which becomes a pivot point for the deflections. In the presented optics, the peak integrated field per raster magnet is $\int B_y dL = 2.2\,\mathrm{mT.m}$ or $\int B_x dL = 3.8\,\mathrm{mT.m}$. To reduce modulation of the neutron intensity, the a rather high raster frequency of up to 40 kHz is specified.

As the location of the beamlet waist and also the pivot point for deflections, the CO becomes a suitable location for a small-aperture shield that absorbs most of the backstreaming neutrons. TraceWin [2] simulations including 3D space charge, demonstrate transport of 5×10^6 multiparticles through a $\lesssim 0.4$ mm RMS waist with no loss in the line or the aperture. This is an improvement over the previous design that was based upon nonlinear magnets [3]. Due to the limited magnification of the linac beamlet and the raster pattern's smearing of the beamlet, any transverse halo generated by the linac has a limited effect on the accumulated beam footprint at the target.

A suite of beam instrumentation supports tuning of the beam line [4]. During high power operations, a subset of this instrumentation also provides inputs to an interlock system that can suppress beam production upon detection of potentially damaging conditions.

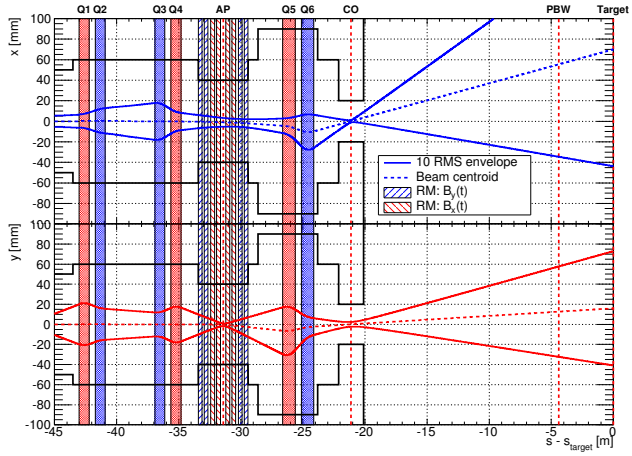


Figure 1: The final 45 m of the HEBT before the target surface. The optics are shown at maximum deflection.

TARGET

Rastering the beam the provides benefits described above, and with normal beam conditions, calculations show that the proton beam window, most delicate interceptive component, should provide the desired lifetime of about one year. However, off-normal situations must be considered and one of the most dramatic would be the simultaneous, undetected failure of all 8 raster magnet systems. In this case, a stationary beamlet with the parameters listed in Table 2 remains on the window. Beam instrumentation detects this condition and suppresses beam production before the arrival of the next pulse, but the window must survive the original errant pulse.

Finite element analysis has been used to analyse this situation. The calculations were performed using ANSYS and results were then post-processed using the RCC-MRx design standard, considering a dose up to 10 DPA. The calculation has been performed for a PBW made either from Al6061T6 or Ti6Al4V. The goal is indeed to fulfill RCC-MRx criteria from level A, meaning that the PBW can be used without inspection or replacement. The start values for this transient thermal analysis are those of a window subjected to nominal beam. A full unrastered pulse then induces a new temperature profile that is coupled one way to a transient structural analysis used for the RCC-MRx post-processing. The results summarized in Table 3 show that an aluminum window would require a replacement whereas a titanium window would not.

NEUTRONICS

As discussed above, the beam transport line employs a dynamic rastering system that scans a beamlet across the target surface. The impact on neutron beam characteristics has been assessed by incorporating time-dependent raster beams into a full MCNPX model of the target sta-

Copyright © 2013 CC-BY-3.0 and by the respective authors

Table 3: Usage Factors According to the RCC-MRx

	Al 6061T6		Ti6Al4V	
Criteria	**A**	**D**	**A**	**D**
$\overline{P_m}$	0.39	0.19	0.21	0.10
$\overline{P_L}$	0.26	0.12	0.14	0.07
$\overline{P_L + P_b}$	0.31	0.15	0.15	0.07
$\overline{P_m + Q_m}$	1.28	0.69	0.27	0.14
$\overline{P_L + P_b + Q + F}$	1.06	0.12	0.17	0.09
	unirr.	**irr.**	**unirr.**	**irr.**
J	4.8	4.8	9.4e-3	8.5e-2

tion monolith. Each moderator-reflector assembly in the ESS target station contains 3 moderators: a cold para-hydrogen moderator, an upstream thermal water moderator, and a downstream thermal water moderator. Time-dependent brightness was tallied for all 3 moderators. With a horizontal rastering frequency of about 40 kHz and a vertical rastering frequency of 29 kHz, fluctuations for cold neutrons (i.e. 2.5 Å) are very small - less than a few percent. Maximum fluctuations were observed out of the downstream thermal moderator, about 6% RMS at 0.8 Å.

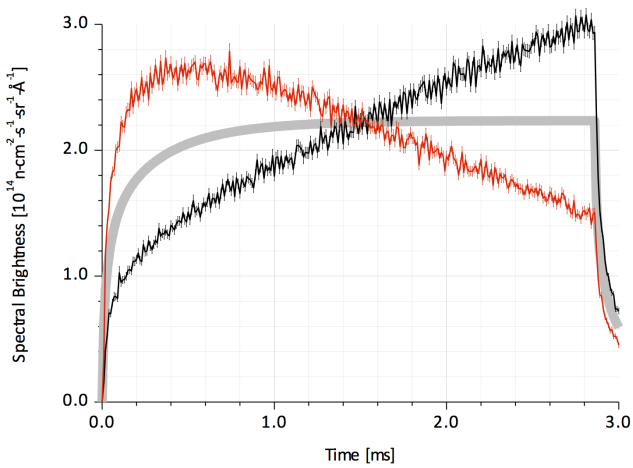


Figure 2: One example of an alternative scanning scenario. The beam is rastered vertically at 29 kHz and swept once horizontally during the 2.86 ms pulse. Thermal neutron pulses (0.8 Å) from upstream (red) and downstream (black) moderators are shown with the reference output from a square proton pulse shown in grey.

This effect on downstream thermal moderators can be exploited by using raster patterns like, for example, slow painting of the proton beam over the target in a horizontal direction while maintaining the rapid scanning in the vertical direction. In this case, high frequency deviations due to horizontal rastering are eliminated, while neutron pulse shapes exhibit rather interesting temporal features as depicted in Figure 2. Additionally, the study of the impact of beam rastering on updated conceptual designs of ESS moderators is underway.

NEUTRON INSTRUMENTS

The variations in the pulse structure as a result of the rastering of the proton beam onto the target offers several opportunities, particularly for thermal instruments, as the effect is most pronounced for short wavelength neutrons. By siting thermal instruments in the correct sector, the enhanced brightness of short wavelength neutrons at the end of the pulse can be harnessed by, for example, high-resolution diffraction instruments or a thermal chopper spectrometer. For example, through the use of a pulse-shaping chopper at 6-7m from the moderator surface, a wavelength band and wavelength uncertainty ($\Delta\lambda/\lambda$) is selected by a diffraction instrument. At the sample position, within the time-frame given by the 14 Hz repetition rate, the short wavelength neutrons (with a higher velocity) are selected from the end of the initial pulse, with enhanced intensity as shown in Figure 2. These neutrons give access to high Q at close to backscattering from the sample, which reveal the subtle structural details. As a general remark, boosting the neutron brightness for the short wavelengths will be very useful for all thermal instruments that employ pulse-shaping.

Delivery of the proton beam to the target with lower loss could also benefit neutron instruments. Reducing the potential for beam losses in this region by orders of magnitude could bring a proportional reduction in that contribution to the background. Other sources are now being investigated, with a focus on emission of particles from the accelerator berm that are transported as sky shine, and mechanisms of illumination of the instruments directly from the target, both external and internal to the neutron beamlines. Particular attention is being paid to the types of materials that can be used and the energies of the particles that illuminate them, and the physics processes that convert these transport mechanisms into measurable signals for detectors that are typically only sensitive up to 100s keV.

CONCLUSION

Particularly in a long pulse neutron source such as the ESS, the optimisation of the accelerator to target region can significantly enhance neutron source performance. Recent updates to the design, including the addition of raster scanning appear to provide performance benefits. This work is ongoing. In the near future, we plan to model updated moderator designs, and improve our understanding of neutron background with additional beam loss simulations.

REFERENCES

[1] B. Blind *et al.*, LINAC 2006, MOP055, p. 171 (2006).
[2] R. Duperrier *et al.*, ICCS'02, LNCS2331, p. 411 (2002).
[3] A.I.S. Holm *et al.*, IPAC'12, MOPPD049, p. 475 (2012).
[4] T. J. Shea *et al.*, IBIC 2013, TUPC02, Oxford (2013).
[5] B. Winn *et al.*, http://neutrons.ornl.gov/hyspec/_media/HYSPEC_Status_June_2012.pdf (2013).

Copyright © 2013 CC-BY-3.0 and by the respective authors

THERMAL DESIGN OF THE FETS CHOPPER BEAM DUMP

S. Mishra*, UROP student, Imperial College London
M. Aslaninejad, P. Savage§, P. A. Posocco, Imperial College London
J.K. Pozimski, Imperial College London and STFC/RAL
A.P. Letchford, STFC/RAL

Abstract

The Front End Test Stand Project (FETS) at RAL is being built to demonstrate fast beam chopping. This is required to create precisely defined gaps in the bunched H- beam which is essential in order to minimise beam losses in a synchrotron during injection. The gaps are created in the Medium Energy Beam Transport (MEBT) section of the FETS beam-line using a 'fast-slow' chopping scheme. This scheme uses two choppers, one fast and one slow, each kicks a portion of beam into its corresponding downstream beam dump. The challenge for the beam dump design is that it must occupy a limited longitudinal space to ensure that the beam transport is preserved and must absorb a beam power that is close to the sustainable stress limit of common engineering materials. This paper will describe the simulations made to study the cooling scheme required to absorb the power deposited in the dump plates for the fast and slow choppers.

INTRODUCTION

The FETS project requires two chopper beam dumps to withstand and safely dissipate power from the incident beam. The beam parameters, listed in Table 1, thus form the design criteria for these dumps [1].

Table 1: Parameters for the FETS Beam

Parameter	Value
Particle	H-
Beam Energy	3 MeV
Beam Current	60 mA
Pulse Length	20 ms
Duty Cycle	0.1
Maximum Power	180 kW
Average Power	18 kW

The beam is on for a 2 ms pulse in each 20 ms period. During this time, it is broken by choppers into a repeated cycle of ON/OFF states. The two choppers in the FETS project are denoted 'fast' and 'slow', based on their respective response times. During each ON stage of a chopper, it deflects beam particles to its corresponding downstream dump. The chopper timings have been designed in accordance with the ISIS synchrotron frequency of 1.5 MHz. The FETS beam has a frequency of 324 MHz, resulting in 216 periods of ON/OFF cycles, or beam bunches for each ISIS period [2]. Table 2 describes how these 216 beam bunches are broken by the fast and slow choppers.

*Supported by STFC
§ p.savage@imperial.ac.uk

Table 2: Sequenced Timing for the Fast / Slow Choppers

Number of bunches	Fast Chopper State	Slow Chopper State
4	ON	OFF
57	OFF	ON
4	ON	OFF
151	OFF	OFF

During an ON period of a chopper, its corresponding dump sees the full 180 kW of incident power. However, each chopper deflects only a certain proportion of the total 216 bunches, and the dump is required to dissipate power according to this proportion, as presented in Table 2. The sequence of states can be expressed in terms of the average power seen by the two dumps, shown in Table 3.

Table 3: Summary of Power Incident on Chopper Dumps

Number of bunches	Fast Chopper Dump	Slow Chopper Dump	Main FETS Dump
Percentage of total power dissipated	3.70%	26.39%	69.91%
Average power over 2 ms beam pulse	6.67 kW	47.50 kW	125.83 kW
Average power over 20 ms period	0.667 kW	4.750 kW	12.583 kW

PRELIMINARY DESIGN

This section describes the initial design decisions that have been taken for the chopper dumps. A rectangular plate-geometry was selected, with dimensions incorporating space constraints imposed by the FETS set-up. In this configuration, the deflected beam hits the plates at a shallow incident angle, with the power effectively distributed over a larger area, minimising the surface heat flux. Heat dissipates through the plate material, and is absorbed in water-cooled channels along the length of the plates.

The beam power must be safely dissipated by the plate and water cooling, and the material selection must be carried out accordingly. In order to select the material, existing beam dumps of similar specifications were first identified, and the materials used for these beam dumps were considered. Copper was then selected for the initial thermal analysis, with the possibility of using Nickel-coated copper in future simulations, should the radiation study deem this necessary. The subsequent analyses have all been carried out on a copper plate.

Copyright © 2013 CC-BY-3.0 and by the respective authors

THERMAL ANALYSIS

Thermal analysis has been performed using General Particle Tracer (GPT), MATLAB and ANSYS software to support the design for the chopper dump plates, and identify points for refinement of the preliminary design [3-5].

Particle Distribution

The beam is characterised by a Gaussian-like energy spread. In order to determine the power distribution on the chopper dump plates, GPT simulations were carried out to determine the distribution of particles hitting the plates. Each simulation was conducted using 95,200 macro-particles, with each particle carrying an equal proportion of the total beam power. For each dump plate, the output of the simulation was the co-ordinate location of the beam particles, in the plane of the plate. The particle distribution is shown in Figure 1.

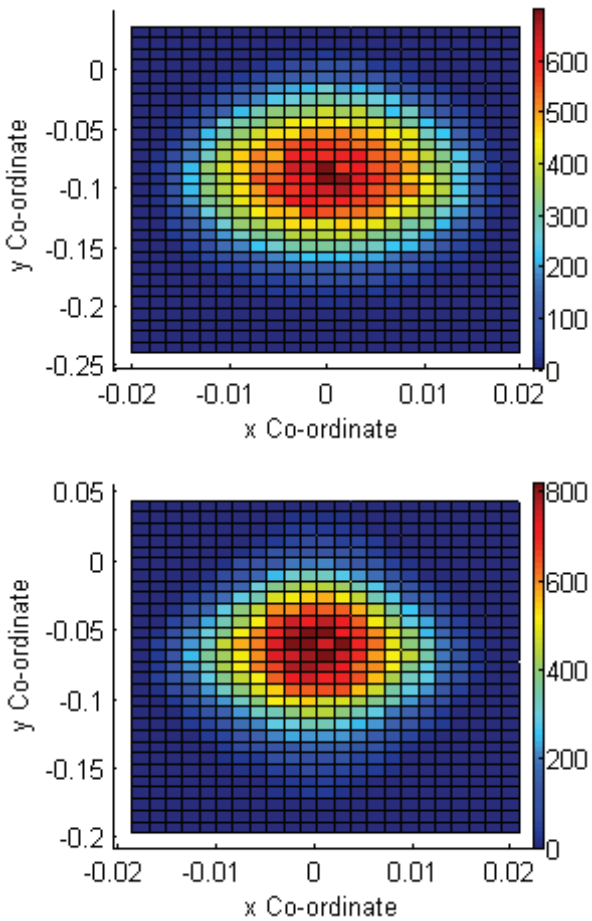


Figure 1: Particle distribution on the fast (top) and slow (bottom) chopper dump plates.

Finite Element Analysis Set Up

Finite element analysis (FEA) was conducted on the beam dump plate using the geometry described in the previous section. The boundary condition was a heat transfer from the beam on one surface, as obtained from the GPT simulations. For the transient and steady state analyses, the total power was distributed in proportion to the particle distribution described in Figure 1 for the fast and slow chopper dumps. The water-cooled channels were modelled using a convective heat transfer coefficient, with scope to extend to a full CFD analysis in future studies. The remaining plate surfaces were represented by a conservative zero heat flux model.

Steady State Analysis

The steady state temperature distribution for the two water-cooled plates under the influence of the time-averaged beam power of 0.666 kW and 4.75 kW to the fast and slow chopper dump plates respectively is presented in Figure 2.

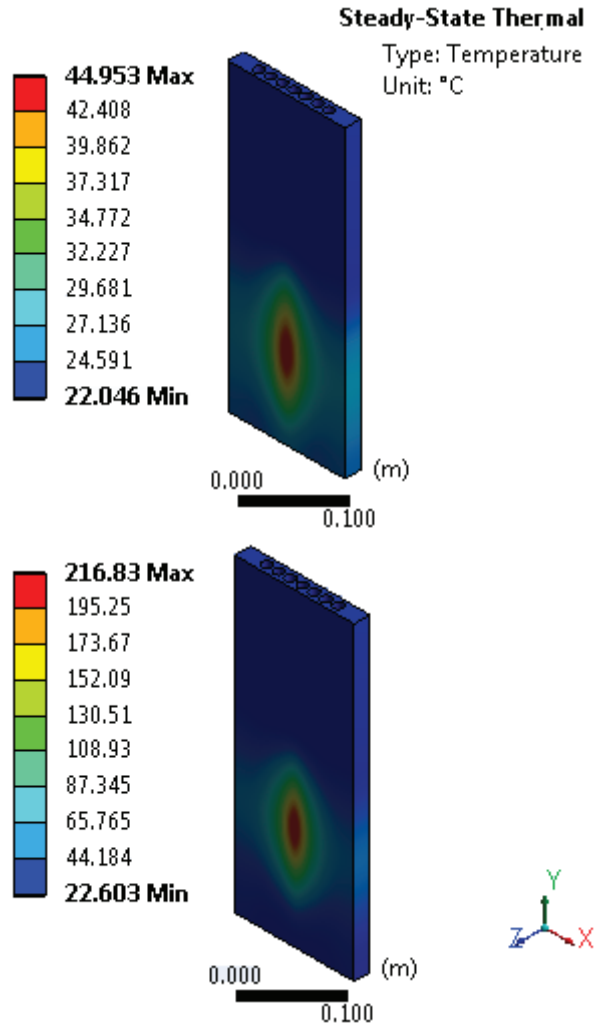


Figure 2: Steady state temperature distributions for the fast (top) and slow (bottom) chopper dump plates.

The maximum temperature obtained for the fast chopper dump, 45.0 °C is well below the creep temperature of copper, and the option of radiative cooling will be explored in future designs. The slow chopper dump has a maximum steady state temperature of 217 °C under active cooling by water. It is unlikely that radiative cooling alone will keep the maximum temperature below the creep temperature of copper.

Copyright © 2013 CC-BY-3.0 and by the respective authors

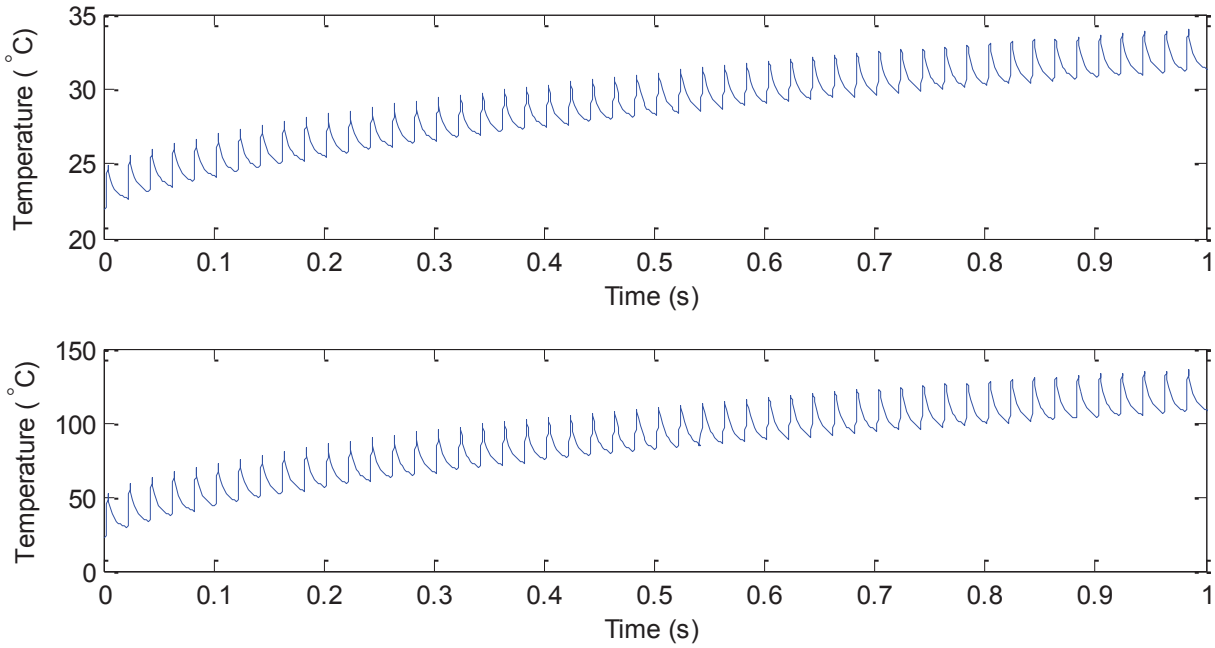


Figure 3: Graph of the maximum temperature as a function of time for the fast (top) and slow (bottom) chopper dump plates.

Transient Analysis

In the transient analysis, the beam power was applied for a period of 2 ms and then turned off for the next 18 ms, over consecutive cycles, in accordance with the data presented in Table 3. Time-averaged power over the 2 ms ON period of 6.67 kW and 47.5 kW were used for the fast and slow chopper dumps respectively, using the power distribution indicated in Figure 1.

Figure 3 illustrates the time history of maximum global temperatures of the two chopper dumps for the first 500 periods of these ON-OFF cycles. The difference in the vertical scale between the fast and slow chopper dumps should be noted; the slow chopper dump has a much larger ripple within each cycle. This represents the difference in heat flux applied to these dumps. Between subsequent cycles, it is seen that the temperature approaches the maximum steady state temperature for each dump, closely approximating an exponentially decaying trend. Within each cycle, the increase in temperature during the 2 ms period, followed by the decrease during the next 18 ms also follows similar kinetics.

CONCLUSION

The transient and steady state thermal effects of the incident beam on the two chopper dumps proposed for the FETS project have been investigated. The fast chopper dump has a maximum steady state temperature of 44.9 °C, and the slow chopper dump has a maximum steady state temperature of 217 °C. These results show that for the two chopper dumps, the material selected and geometry proposed are both thermally feasible.

The simulations done so far thus provide necessary groundwork for future analyses required in refining the design for the chopper dumps. Where approximations have been made to simplify the simulations, they have been conservative. There remains scope to incorporate a full computational fluid dynamics analysis to determine the variations in convective heat transfer coefficient along the water channels.

Additionally, it is necessary to translate the thermal analysis to determine the stress distribution, based on the plate mounting method. During the transient phase, temperatures vary by up to 30 °C in each pulse. This could lead to fatigue life problems if the stress levels are high. Subsequent work should also incorporate the effect of radiation on the material, to determine whether copper is feasible, or the copper bulk requires coating to enable the dumps to withstand the full beam power.

REFERENCES

[1] M.A. Clarke-Gayther, "The Development of a Fast Beam Chopper for Next Generation High Proton Drivers," IPAC'10, Kyoto, May 2010, p. 3320-3322 (2010) WEPD095.

[2] M.A. Clarke-Gayther, "A Two Stage Fast Beam Chopper for Next Generation High Proton Drivers," IPAC'11, San Sebastián, September 2011, p. 1786-1788 (2011) TUPS104.

[3] 'ANSYS® Academic Research, Release 14.0', www.ansys.com

[4] 'General Particle Tracer', www.pulsar.nl/GPT/

[5] 'MATLAB and Statistics Toolbox Release 2013a', The MathWorks, Inc., Natick, Massachusetts, United States

Copyright © 2013 CC-BY-3.0 and by the respective authors

PROPOSAL FOR SIMULTANEOUS ACCELERATION OF STABLE AND UNSTABLE IONS IN ATLAS†

A. Perry, ANL, Argonne, IL, 60439, USA; IIT, Chicago, IL, 60616, USA
B. Mustapha, P.N. Ostroumov, ANL, Argonne, IL, 60439, USA

Abstract

The Argonne Tandem Linac Accelerator System (ATLAS) is the only national user facility for low-energy stable heavy ion beams. With the recent commissioning of the Californium Rare Isotope Breeder Upgrade (CARIBU), ATLAS will also be used to accelerate radioactive beams. We here propose to convert ATLAS into a multi-user facility by simultaneously accelerating stable beams from the ECR ion source and radioactive beams from an Electron Beam Ion Source (EBIS) charge breeder under development for CARIBU. Radioactive beams produced from EBIS will contain several charge states of the same isotope, and could be injected into ATLAS in short (~10μs) pulses. We propose modifications of the existing ATLAS low energy beam transport line that will allow the simultaneous injection and acceleration of one or more charge states from EBIS and a stable ion beam from the ECR. Beam dynamics simulations using the code TRACK confirmed the feasibility of these modifications. The realization of this concept will increase the available beam time, the intensity of radioactive beams and improve the quality of the delivered beams as well.

INTRODUCTION

The Argonne Tandem Linac Accelerator System (ATLAS) is the only national user facility for low-energy stable heavy ion beams. On a yearly basis ATLAS provides beam time in excess of 5000 hours to domestic and international users.

Recently, the californium rare isotope breeder upgrade (CARIBU) had been successfully commissioned at ATLAS [1]. CARIBU will produce, at full capacity, beams of ~80-160 amu fission fragments from a 1 Curie ^{252}Cf source. After thermal stabilization and mass separation, the fragments will be charge bred in a charge breeder based on an electron beam ion source (EBIS) [2]. This type of charge breeders yield higher breeding efficiencies with fewer contaminations and shorter breeding times compared to electron cyclotron resonance (ECR) based charge breeders. After charge breeding in EBIS, the radioactive beams will be injected into ATLAS, used as a post accelerator.

When radioactive beams from CARIBU become available, the already high demand for ATLAS beam time is expected to further increase. It may therefore be necessary to upgrade ATLAS into a multi-user facility - capable of simultaneously accelerating multiple beams and delivering them to different experiments. The feasibility of the proposed upgrade project relies heavily on two features:

a. The accelerator structure of ATLAS, consisting of individually-phased superconducting cavities, is extremely versatile, as was best demonstrated in the simultaneous acceleration of 8 charge states of Uranium through the booster linac section [3]. This enables the acceleration of stable and radioactive beams with charge to mass ratios differing by as much as 5%. Amongst the beams available for injection into ATLAS are numerous examples that meet this criterion, as shown in Table 1 below.
b. The radioactive beam from CARIBU EBIS will be pulsed with a pulse repetition rate of ~30Hz and a pulse length of ~10μs for a duty cycle of 0.03%. During the remaining time it will be possible to feed the accelerator with the appropriate stable beam.

Table 1: Some Beams with Similar Charge-to-Mass Ratios which can be Accelerated Simultaneously in ATLAS

Nominal Charge/mass	Stable Beams from ECR2	Radioactive beams from EBIS
0.15	$^{20}Ne^{3+}$, $^{86}Kr^{13+}$ $^{238}U^{36+}$, $^{133}Cs^{20+}$	$^{86}As^{13+}$, $^{106}Nb^{16+}$ $^{93}Kr^{14+}$, $^{93}Rb^{14+}$
0.16	$^{208}Pb^{33+}$, $^{56}Fe^{9+}$	$^{100}Y^{16+}$, $^{87}Br^{14+}$
0.18	$^{128}Xe^{23+}$, $^{84}Kr^{15+}$	$^{111}Tc^{20+}$, $^{138}Te^{25+}$
0.20	$^{20}Ne^{4+}$, $^{90}Zr^{18+}$	$^{131}Sn^{26+}$, $^{124}Cd^{25+}$
0.23	$^{56}Fe^{13+}$	$^{105}Ru^{24+}$, $^{101}Mo^{23+}$ $^{91}Sr^{21+}$, $^{83}Se^{19+}$

In order to achieve multi-user capability, 3 main points were identified:

- Injection of beams from two sources into the ATLAS Low Energy Beam Transport (LEBT).
- Modification of the ATLAS LEBT, which contains a 180 degrees bend, to accommodate for the transport of two beams with slightly different charge-to-mass ratios while introducing minimal emittance growth.

† This work was supported by the U.S. Department of Energy, Office of Nuclear Physics, under Contract No. DE-AC02-06CH11357.

Copyright © 2013 CC-BY-3.0 and by the respective authors

- Extraction of the beams after acceleration in ATLAS and their delivery to the designated experimental areas.

The primary challenge presented would be addressing the above points in a cost effective way and within the constraints of the available infrastructure.

LEBT MODIFICATION

A general layout of the proposed ATLAS LEBT is depicted in Figure 1. The orientation of the EBIS charge breeder platform with respect to the ATLAS accelerator beam line dictates a total 180° bend of the radioactive beam. In order to accommodate the transport of multiple beams with different charge-to-mass ratios simultaneously, it is necessary to make the transport line achromat. This may be accomplished by using the Double Bend Achromat (DBA, also known as the Chasman Green lattice) [4]. In the DBA, each 90° bend is composed of two 45° bending magnets and an intermediate quadrupole lens. Using the mirror symmetry with respect to a plane through the middle of the quadrupole, it can be shown that the lattice is doubly achromatic in first order if the quadrupole strength k_0 satisfies the equation:

$$k_0 tan\left(\frac{k_0 Q}{2}\right) = \frac{(1-cos\theta)tan(u)+sin(\theta)}{\rho\left\{1-cos(\theta)+\frac{S_1}{\rho}\left[(1-cos(\theta))tan(u)+sin(\theta)\right]\right\}}$$

where Q is the quadrupole length and S_1 the distance from the bending magnet to the quadrupole. ρ, θ and u are the bending magnet's radius, bend angle and exit edge angle respectively.

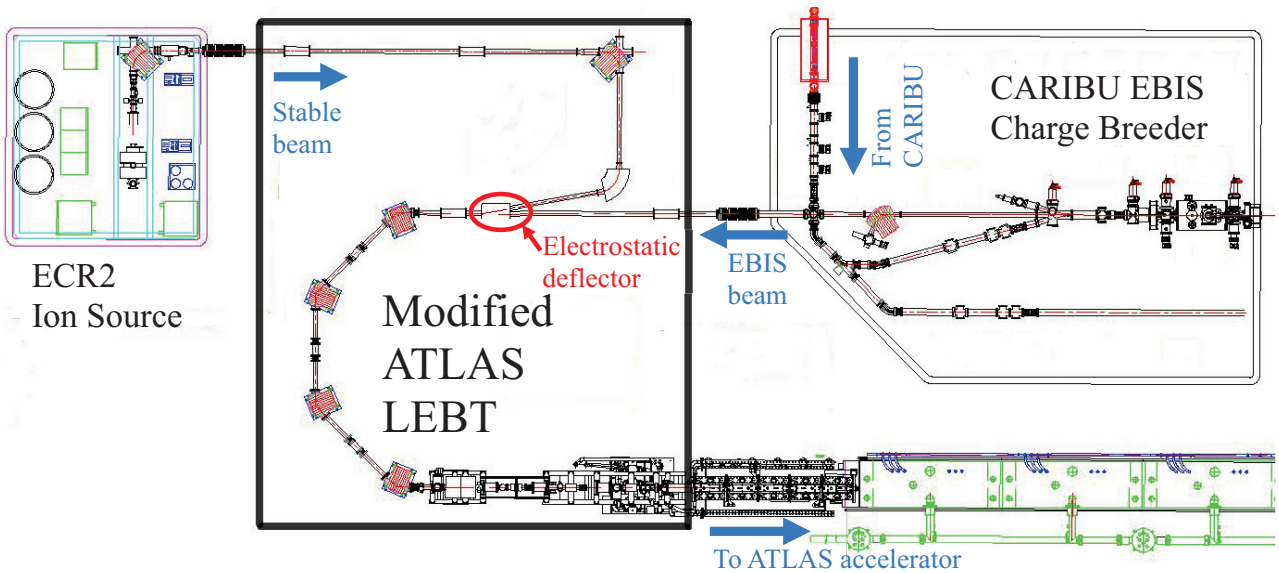


Figure 1: General layout of the proposed ATLAS low energy beam transport (LEBT) beam line. Arrows indicate the beam directions of the stable beam produced by ECR2, and the radioactive beam from EBIS.

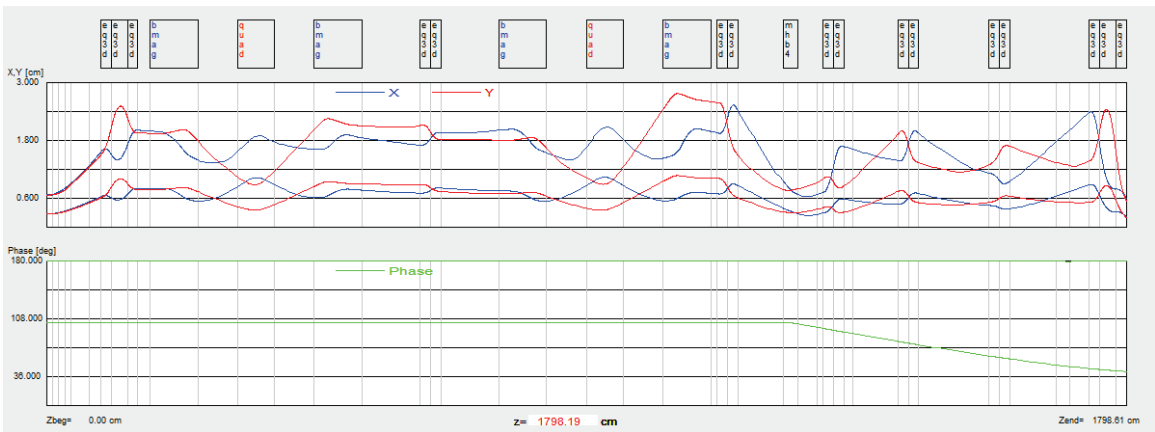


Figure 2: TRACK simulation results for the simultaneous transport of $^{132}Sn^{27+}$ from EBIS and $^{48}Ca^{10+}$ from ECR2. The RMS emittance growth in the 180° achromat bend is 1%.

Copyright © 2013 CC-BY-3.0 and by the respective authors

Furthermore, double focusing can be achieved by the appropriate choice of S_1 and u.

In addition to creating the achromat lattice, we also propose to replace all the magnetic focusing elements in the LEBT with electrostatic lenses. The latter are more compact and hence preferable to magnetic lenses in the low energy regime. The maximum of the dispersion function is obtained inside the intermediate quadrupole lens and is given by:

$$D_{max} = -\frac{1}{2k_0}\frac{sin(\theta)}{sin\left(\frac{k_0 Q}{2}\right)}$$

Hence these quadrupoles will have a 5 cm aperture radius which is larger than the standard used until now.

The code COSY Infinity [5] was used to evaluate the transfer matrix of the lattice and confirm its achromaticity in linear order, as well as the effects due to nonlinear terms. The beam dynamics code TRACK [6] was then used to simulate the simultaneous acceleration of $^{132}Sn^{27+}$ ions available from EBIS charge breeder and $^{48}Ca^{10+}$ ions available from ECR-2. The beams were first transported in the modified LEBT (Figure 2) and then injected into the ATLAS Radio Frequency Quadrupole (RFQ) accelerator and subsequent superconducting accelerator.

INJECTION AND EXTRACTION

The EBIS charge breeder will output approximately 30 batches of particles every second, each approximately 10μs long. In order to inject these batches and the batches produced from the ECR ion source into the same beam line, an electrostatic deflector (switch) will be used (as shown in Figure 1. The electrostatic deflector is to deflect the stable beam into the downstream beam line, but it will be synchronized to switch off with the arrival of the EBIS beam batches, so they continue downstream without deflection.

The design of the deflector will rely on the CARIBU EBIS electrostatic deflector and its 'diagonal cut' design. As shown in [2] this deflector design produces minimal emittance growth. However, due to the higher energy of the particles a higher deflecting voltage (evaluated at ~50kV) will be used for our purpose. If a total switching time (rise and fall) of 2ms is allowed then the requirements from the power supply are relatively relaxed, and a 94% duty cycle of the stable beam is still possible.

The Extraction of one of the beams and its subsequent delivery to the designated experimental hall is more complex due to the higher energy after acceleration and limited space available. The extraction will take place after acceleration in the Positive Ion Injector (PII) and the Booster, where the particles reach energies greater than 5.5MeV/u. A combination of a kicker magnet and a septum magnet will be used for the extraction.

SUMMARY

We propose a cost effective redesign of the ATLAS LEBT to accommodate the transport of multiple beams simultaneously. TRACK simulations show that with a modified LEBT, based on the Double Bend Achromat lattice, multiple beams with a charge-to-mass ratios differing by up to ~3% can be transported from two sources and accelerated in ATLAS. This will make ATLAS capable of multi-user operation, a capability which is important in light of the high demand for beam time, which is expected to further increase once radioactive beams from the EBIS CARIBU become available.

In addition to that, the radioactive beams from CARIBU EBIS will contain a range of charge states. If the LEBT is modified in accordance to our proposal, two of these charge states can be transported simultaneously and injected into different RF buckets in the RFQ. This will increase the intensity of the radioactive beams delivered to users.

Lastly, TRACK simulations indicate that transporting the CARIBU EBIS beam in the present LEBT may result in significant beam quality degradation. This is due to the high dispersion in the current layout and the energy spread of the beams produced by EBIS.

Further work on the injection, extraction and acceleration of multiple beams is still required.

REFERENCES

[1] G. Savard et al., "Radioactive beams from gas catchers: The CARIBU facility", Instruments and Methods in Physics Research B 266, 4086 (2008).

[2] C. Dickerson et al., "Simulation and design of an electron beam ion source charge breeder for the californium rare isotope breeder upgrade", Physical Review special topics - accelerators and beams 16, 024201 (2013).

[3] P. N. Ostroumov et al., "Simultaneous Acceleration of Multiply Charger Ions through a Superconducting Linac", Physical Review Letters 86, 2798 (2001).

[4] H. Wiedemann, "Particle Accelerator Physics I – Basic Principles and Linear Beam Dynamics", 2nd ed., Springer-Verlag Berlin Heidelberg New-York, 2004.

[5] http://www.bt.pa.msu.edu/index_cosy.htm

[6] The beam dynamics code Track [http://www.phy.anl.gov/atlas/TRACK]

Copyright © 2013 CC-BY-3.0 and by the respective authors

THE D-LINE PROJECT AT MICHIGAN STATE UNIVERSITY *

J.A. Rodriguez#, S. Chouhan, A. Lapierre, D. Leitner, G. Perdikakis, M. Portillo, S. Schwarz, M. Steiner, C. Sumithrarachchi, S.J. Williams, W. Wittmer, X. Wu, NSCL, East Lansing, MI, USA

Abstract

The Coupled Cyclotron Facility (CCF) at Michigan State University (MSU) has been used to produce rare isotope beams for more than a decade. Ions produced by an ECR source are accelerated using two superconducting cyclotrons in tandem with a stripper foil in between to boost their charge state. After the second cyclotron, a target and a fragment separator produce and select the rare isotope beam that is sent to the different experimental vaults. A gas stopper can be used to thermalize the beam before sending it to a low energy experimental area or to a charge breeder before the ReA re-accelerator. The D-line project includes a mass separator after the gas stopper and several beam transfer lines that connect it to the low energy experimental stations and to the charge breeder. In this paper, we will describe the project and give an update of its status including the results of the commissioning.

INTRODUCTION

One of the most important developments at the National Superconducting Cyclotron Laboratory (NSCL) during this past year has been the successful delivery of the first radioactive reaccelerated beam to users [1]. Together with the commissioning of the gas cell in the ion beam thermalization area [2], the charge breeder [3] and the reaccelerator [4], the completion of the D-line was one of the steps necessary to make this possible.

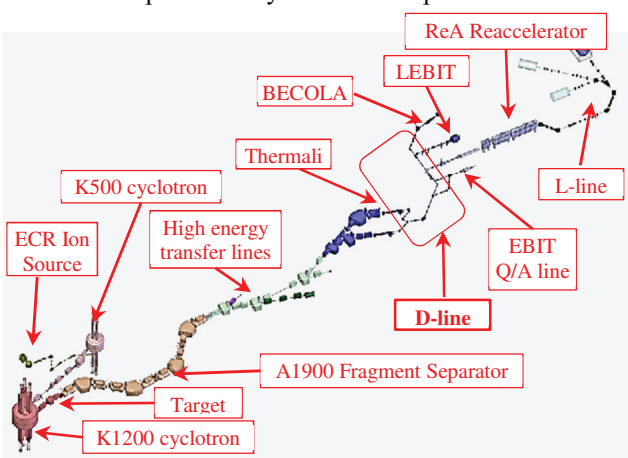


Figure 1: Layout of the CCF and ReA3 facilities (several high energy beam lines and experimental areas are not shown). The D-line connects the thermalization area with the low energy experimental hall and the charge breeder.

DESCRIPTION OF THE LINE

The main purpose of the D-line is to connect the beam thermalization area of the NSCL with the experimental devices in the low-energy experimental hall (LEBIT [5] and BECOLA [6]) or alternatively with the Q/A line before the charge breeder (EBIT) and the ReA3 reaccelerator. In addition, the line includes a mass separator that is used to select the Radioactive Isotope Beam (RIB) that is going to be studied and to clean the unwanted contaminants with a different momentum after extraction from the gas cell.

The line is designed to be able to transport efficiently beams with emittances of ~ 10 π·mm·mrad and energy lower than 60 keV. In its current configuration (Figure 3), the south line is used to transport stable beams from an off-line ion source. This beam has been used for commissioning of the D-line and downstream experimental devices. The north line is used to transport the RIBs previously thermalized in the gas cell.

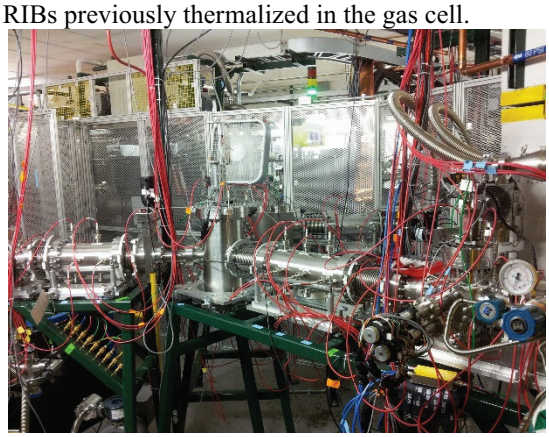


Figure 2: Merging point of the north and south lines. Starting from the left, the picture shows an electrostatic doublet, a bender and a triplet followed by the vacuum and diagnostic station before the mass separator.

With the exception of the dipole magnet used as a mass separator, all the other elements in the D-line are electrostatic. The beam is focused using electrostatic quads (10 cm long, 6 cm aperture, up to ±6 kV bias) normally grouped into doublets. In most cases, opposite electrodes are shorted inside the vacuum chamber and driven by a single power supply. However, some of them can be used as beam steerers since they can be biased independently. In addition, there are horizontal and vertical steering plates in all the diagnostic boxes. Spherical benders (up to ±10 kV bias) are used to deflect the beam 45 degrees at a time. Several of them have also been combined for deflection angles of 90 and 135 degrees. Some of them are mounted in movable drives in order to allow an inserted or retracted state to switch the desired beam and its destination.

A dipole magnet and two electrostatic doublets function

* This material is based upon work supported by the U.S. Department of Energy Office of Science under Cooperative Agreement DE-SC0000661, the State of Michigan and Michigan State University, and the National Science Foundation, under Cooperative Agreement PHY-1102511.
#rodriguez@frib.msu.edu

Copyright © 2013 CC-BY-3.0 and by the respective authors

as a mass separator with a resolving power M/ΔM higher than 100. Horizontal movable slits in the object and image planes can be used to collimate the incoming beam and to discard the unwanted masses.

The 61-degree magnet was designed using TOSCA to produce a 0.79 T field for a current of 217 A (with uniformity better than 10^{-3} in its ±5 cm central region). It has a bending radius of 68 cm, a 6 cm vertical aperture and a 22 cm pole width.

The lattice was designed using COSY INFINITY (Figure 4) to accept beam from both the north and south line and transport it to the object point of the separator, where both beams are matched to. The beam is then transported using point-to-point focus to one of the low-energy experimental stations or to the Q/A line for injection into the charge breeder. The optics of each segment of the line is independent of the destination of the beam and, only the matching triplet before the object point of the mass separator needs to be adjusted when the origin of the beam is changed.

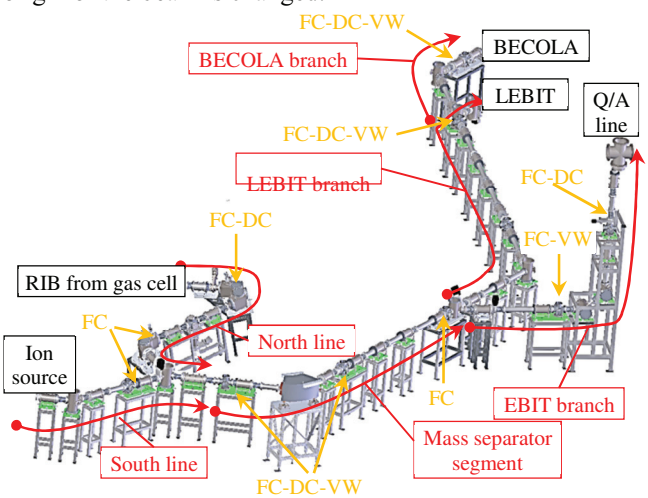


Figure 3: Layout of the D-line broken into different sections (in red), the beam origin/destination (in black) and a list of the diagnostics available at each location (in orange). FC stands for Faraday Cup, VW for MCP viewer and DC for decay counter.

There are ten diagnostic stations in the line and most of them are located at (or near) waists of the beam envelope (Figure 3). All the stations include Faraday cups and 5 mm diameter movable apertures (except for the ones in the object and image points of the separator which have movable horizontal slits). Six of the Faraday cups are equipped with silicon detectors to detect β-decays of the RIBs implanted in the Faraday cup current collector. Details of their design and associated DAQ can be found in [7]. In addition, there are five Multi Channel Plate (MCP) viewers and one more will be added in the future.

There are seven vacuum stations distributed throughout the beam lines. Each vacuum station includes a turbo pump with a gate valve, a cold-cathode gauge, two Pirani gauges and a venting valve. Each turbo pump is backed by a scroll pump (three of them directly, four of them through a common vacuum manifold). The beam line is split into six vacuum sections separated by gate valves to facilitate maintenance. The pressure in the lines typically reaches the 10^{-8} Torr range after two days of pumping.

The relative alignment of consecutive components in the line is better than 250 microns with the exception of some of the benders.

The high level controls have been built using Control System Studio (CSS). Using CSS to scale the energy of the line, to change the beam origin or destination or to complete mass scans is quick and convenient. However, at this time, different software is used to tune the lines and some additional work remains to integrate this capability in CSS.

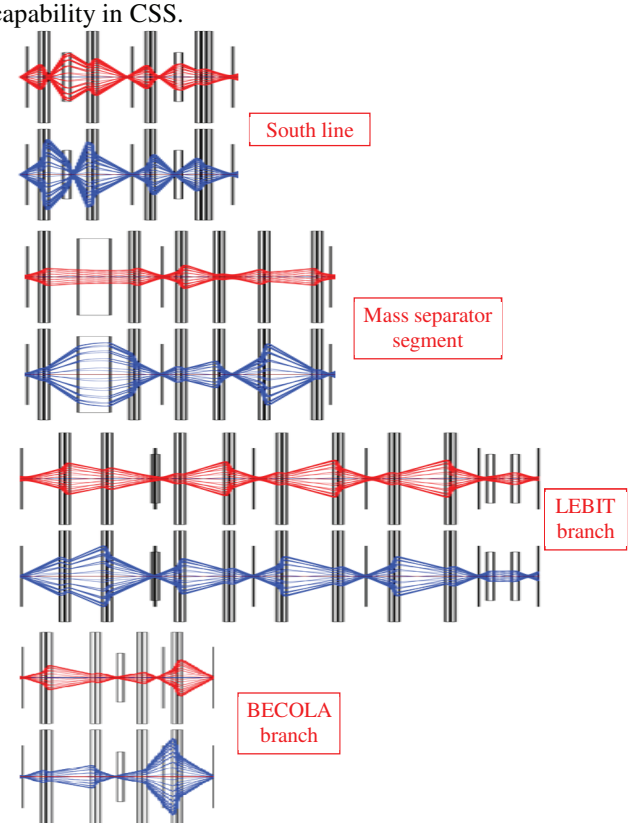


Figure 4: Ray calculations of beam transport in several segments of the line from South line to BECOLA (horizontal in blue, vertical in red)

COMMISSIONING OF THE LINE

Equipment Commissioning

The several hundred HV power supplies used in the line, their cables and connectors were tested during installation to confirm that none of them were damaged and that their polarity was correct. Several problems were identified and corrected during those tests.

The low-level controls and the interlock logic of the diagnostic drives were tested. The cables and electronics of the Faraday cups were checked using a calibrated current source and their electron suppressor biases were measured. Most of the decay counters and their data acquisition hardware and software were also tested using a Sr-90 radioactive source before installation. The low-

Copyright © 2013 CC-BY-3.0 and by the respective authors

level controls of the vacuum stations and the interlock logic of the gate valves were also checked.

Stable Beam Commissioning

Most of the segments of the D-line were commissioned using the off-line stable ion source upstream of the beam line. A ~2 mm misalignment in one of the doublets in the line was identified and tracked down to a faulty alignment monument. At the beginning of the commissioning with stable beam, 20-30 % of the beam was lost along the line and very strong non-linearities were observed in the MCP viewers. The problem was solved when the gas pressure in the ion extraction guide upstream of the D-line was increased. Originally, the beam was not cooled enough transversely and its emittance was larger than the acceptance of the line. Using the higher pressure now allows for only a few percent beam loss.

We have empirically found that the optimal settings of the last optical elements for injection into the experimental stations differ to a limited extent from those in the COSY model prediction. Also, slow beam jitter (with a period of several minutes) has been observed when the beam was injected into LEBIT. The sources of these problems have not been identified yet.

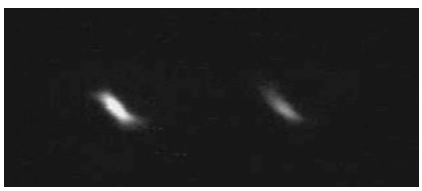


Figure 5: Image of two beams (corresponding to masses 76 and 77) as seen in the MCP viewer after the mass separator during one of the commissioning runs.

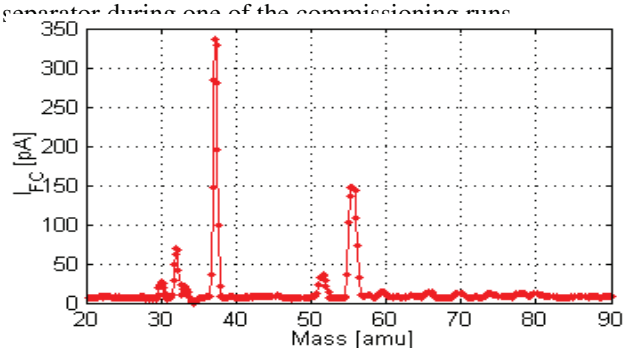


Figure 6: Mass scan during one of the Ga-76 commissioning runs. The different peaks correspond to different contaminant molecular beams produced in the gas cell as the high energy beam is slowed down and interacts with the residual gas. The two highest peaks correspond to mass 37 $[H_5O_2]^+$ and mass 55 $[H_7O_3]^+$.

Radioactive Beam Commissioning

Several commissioning runs with radioactive beams have been conducted during the last year. During these runs, the resolving power of the separator has been found sufficient (Figure 5) and the CSS-based mass scanning software developed for the separator has been tested (Figure 6).

In addition, the decay counters and their DAQ have been tested (Figure 7). The diagnostic team is working to improve their performance by reducing some of the EM

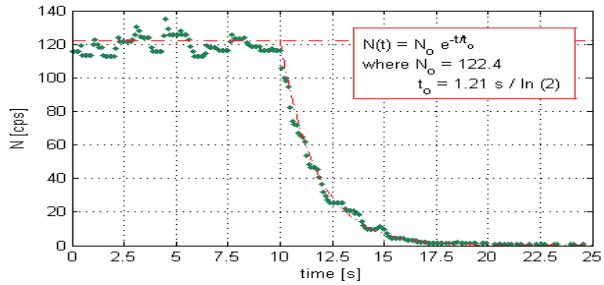


Figure 7: Decay curve for K-37 measured in the decay counter of the diagnostics station after the mass separator. The measured half-life is 1.21 s which is compatible with the expected value of 1.23 s.

CONCLUSION

The D-line project has been completed. All the segments of the line have been commissioned and the transport efficiency in all of them approaches 100 %. The line has been reliable at delivering hundreds of hours of stable and radioactive beams to both the low-energy experimental hall and to the charge breeder before the ReA3 reaccelerator.

ACKNOWLEDGMENT

Many people at the NSCL have worked together to complete this project. In particular, the authors would like to thank the machine shop, the controls, electrical engineering and mechanical design departments as well as the assembly, vacuum and alignment groups for their invaluable contribution to the project.

REFERENCES

[1] D. Leitner et al., "Status of the ReAccelerator Facility ReA for Rare Isotopes", NA-PAC'13 Proc.

[2] K. Cooper et al., "Status of the Beam Thermalization Area at the NSCL", APS-DNP fall 2013.

[3] A. Lapierre et al. "First Charge Breeding of a Rare-Isotope Beam with the Electron-Beam Ion Trap of the ReA Post-Accelerator at the NSCL", ICIS'13.

[4] W. Wittmer et al., "Results from the Linac Commissioning of the Rare Isotope Reaccelerator - ReA", NA-PAC'13 Proc.

[5] R. Ringle et al., "Penning trap mass spectrometry of rare isotopes produced via projectile fragmentation at the LEBIT facility" International Journal of Mass Spectrometry, 2013.

[6] K. Minamisono et al. "Commissioning of the collinear laser spectroscopy system in the BECOLA facility at NSCL", Nuclear Instrumentation and Methods in Physics Research A 709, 85 (2013).

[7] S.J. Williams et al., "Thermalized and Reaccelerated Beams at the National Superconducting Cyclotron Laboratory", IBIC'13.

Copyright © 2013 CC-BY-3.0 and by the respective authors

SYSTEMS ENGINEERING AND INTEGRATION ON THE FRIB PROJECT*

D. Stout#, T. Borden, N. Bultman, R. Frazee, M. Leitner, P. Nguyen, T. Russo, E. Tanke, C. Thronson, Facility for Rare Isotope Beams, Michigan State University, East Lansing MI, 48824 USA

Abstract

The Facility for Rare Isotope Beams (FRIB) will be a world-leading, DOE Office of Science national user facility for the study of nuclear structure, reactions, and astrophysics on the campus of Michigan State University (MSU).

Systems Engineering and Integration has been implemented at the outset to ensure that a requirements-driven design process is followed, and to ensure intra and inter-system compatibility. Top-level requirements have been allocated and subsequently elaborated between the Accelerator Systems, Experimental Systems, and Conventional Facilities. FRIB has developed a number of methods and tools to track requirements, establish interfaces, monitor design progress, and ensure overall system integration. These will be described in the paper.

FRIB PROJECT INTEGRATION

A superconducting, heavy-ion, driver linac will be used to provide stable beams of >200 MeV/u at beam powers up to 400 kW (~650 electrical micro-amps for uranium). The stable beams will be used to produce rare isotopes by in flight fragment separation. After fragment selection, the rare isotopes will be used at velocity (~0.5c), stopped, or reaccelerated. The MSU-led design and construction effort is supported by collaborations with many National Laboratories and other scientific institutions [1].

FRIB is integrated both vertically and horizontally. The vertical integration is achieved by the Systems Engineering methods discussed in the next section. Horizontal integration is achieved by the project organizational structure and by adherence to a consistent design process.

Project Engineers are identified within the three main FRIB Divisions, Accelerator, Conventional Facilities, and Experimental, and are responsible for integration within their Division.

The overall project design process is shown in Figure 1. At each significant project design phase, the key design products and expectations are defined with respect to the major design aspects: requirements, interfaces, drawings and specifications, manufacturing, and project management. At the beginning of each major design phase (i.e. preliminary or final design) deliverables for each sub-system are identified. These include specific analyses, tests, and prototypes that must be completed to demonstrate readiness for the next design phase, or for construction.

Defining the deliverables for each sub-system ensures coherence between the sub-systems, either by keeping their efforts on a similar schedule, or by clearly defining the interface points between sub-systems on different development schedules. This latter point is important since most projects usually cannot complete all design work simultaneously due to cost and design resource limitations. The other main advantage of clearly defining the deliverables and design expectations is that each sub-system manager then has a clear work plan for design. On FRIB these deliverables are used as part of the Earned Value Management System to measure and quantify design progress.

SYSTEMS ENGINEERING AND INTEGRATION OVERVIEW

Systems Engineering, as defined by the International Council on Systems Engineering [2], is an inter-disciplinary approach and means to enable the realization of successful systems. It focuses on defining customer needs and required functionality early in the development cycle, documenting requirements, then proceeding with design synthesis and system validation while considering the complete problem: Performance; Operations; Cost & Schedule; Training & Support; Test; Manufacturing and Disposal. Systems Engineering integrates all the disciplines and specialty groups into a team effort forming a structured development process that proceeds from concept to production to operation. Systems Engineering considers both the business and the technical needs of all customers with the goal of providing a quality product that meets the user needs.

Implementation of Systems Engineering can be tailored for a specific industry or laboratory. Many industries can amortize software, staffing, training, and set-up expenses over multiple platforms or projects. For one-off projects like FRIB, the same methods can be used, but off the shelf software and a leaner System Engineering staff are more appropriate.

Irrespective of the scale of the implementation, the "V" model is at the core of the Systems Engineering approach, and has been fully implemented for FRIB. This model breaks a system into sub-systems, equipment, and components, with specific requirements and interfaces at each level of decomposition. The right hand side of the "V" model is the subsequent aggregation of components, equipment, and sub-systems into a fully functioning system. This aggregation is accomplished by increasingly sophisticated levels of testing and integration. A requirements-based design is fundamental to the use of this model. By starting from a limited number of top-level system requirements, one can define the overall architecture and decompose the project into essential sub-

*This is based upon work supported by the U.S. Department of Energy Office of Science under Cooperative Agreement DE-SC0000661, by Michigan State University and by the State of Michigan.

#stout@frib.msu.edu

Copyright © 2013 CC-BY-3.0 and by the respective authors

System Design Process				
Project Phase:		Conceptual Design	Preliminary Design	Final Design
Design Aspect:	Requirements	Conceptual Design Report Parameter List	Parameter List System Req. Documents (SRDs)	Final Parameters and SRDs
	Interfaces	Interfaces defined	Interface Control Documents Interface Drawings	Final Interface Drawings
	Drawings	Process Flow Diagrams Block Diagrams CAD Model (for space reservation)	Piping and Instr. Diag (P&ID) Single Lines (electrical) General Arrangement/Assembly	Final Drawing Package
	Engineering & Specifications	Trade-off Studies and Analyses	Sub-system Specifications Engineering Analyses - Mech., Struct., Thermal - Dynamic, Electric., Circuit - Modeling, simulations	Final Component Specifications
	Manufacturing & Inspection	Manufacturing concept	Manufacturing Plan	Manufacturing Plan - Specs, procedures - Inspection/QA plan Assembly Installation Plan Factory Testing On-site Testing & Commissioning
	Project Management	Schedule Risk Assessment Cost Estimate Work Plan for Next Phase	Schedule (revised) Risk Assessment (revised) Cost Estimate (revised) Work Plan for Next Phase - Drawing Index - Specification Index	Schedule (revised) Risk Assessment (revised) Cost Estimate (revised) Work Plan for Next Phase

Figure 1: FRIB System Design Process Summary showing deliverables by phase and design aspect.

systems. Most sub-systems for FRIB are based on well-known accelerator technology.

REQUIREMENTS AND INTERFACE DEFINITION

Overall FRIB requirements were finalized during the conceptual design phase of the project. These requirements were captured in a draft Project Execution Plan, Project Requirements Document, and a Parameter list. The first two documents capture all requirements, and the Parameters list identifies the relevant sub-systems and some of their features. During preliminary design, these requirements were further divided into several "System Requirements Documents" for the accelerator, conventional facilities, experimental systems, personnel protection system, cryogenic plant and others. Because these are high level requirements, they were assigned to the specific sub-systems responsible for achieving them. The project captured these in a "Requirements Tracker", a spreadsheet capable of ensuring all requirements were assigned to a responsible system/sub-system. The tool also allows for selecting the requirements specific to a certain sub-system for verification at design reviews or during testing. Another important feature is that the tracker captures emerging safety requirements, assigns these requirements to a specific work element, and verifies their accomplishment. For example, radiation shielding and oxygen-deficiency hazard requirements are developed through calculations and analyses as the design progresses. The tracker facilitates capturing such evolving requirements.

Another essential area that requires definition and monitoring are interfaces, such as physical locations / connections, utility requirements, beam-handoff parameters, instrumentation and data interchanges, etc. FRIB developed an "Interface Tracker", an excerpt of which is shown in Figure 2, to identify interfaces and to retrieve the relevant information for a specific interface. Initial interface assignments, between magnets and power supplies for example, were identified. The appropriate interface documents were prepared, approved, and submitted to the FRIB document control center. The interface tracker visually identifies the interface and provides a hyperlink to the associated documents. It also quantifies the progress made in defining interfaces, so the project can ensure that interfaces are frozen before detailed design is started.

DESIGN VALIDATION

Initial design validation is the responsibility of the cognizant team. FRIB also conducts project-level reviews of all major sub-systems at the 30%, 60%, and 90%

Copyright © 2013 CC-BY-3.0 and by the respective authors

Avg.% 67			Cryogenic Systems	Target Area Utilities	Target Area Remote Handling	Target Area Non-Conv. Utilities	Frag. Sep. Beam Physics	Diagnostics	Preseparator Magnets	Preseparator Mechanical Systems	A1900 Reconfiguration	Power Supplies	Vacuum Systems
%avail.			T.3.02	T.4.02.01	T.4.02.02	T.4.02.03	T.4.03.01	T.4.03.02	T.4.03.03	T.4.03.04	T.4.03.05	T.4.03.06	T.4.03.07
71	Cryogenic Systems	T.3.02	O										
75	Target Area Utilities	T.4.02.01	O	O									
50	Target Area Remote Handling	T.4.02.02	O	O	O								
25	Target Area Non-Conv. Utilities	T.4.02.03	Y	Y	Y	O							
100	Frag. Sep. Beam Physics	T.4.03.01	O	O	O	O	O						
50	Diagnostics	T.4.03.02	O	O	Y	O	v	O					
78	Preseparator Magnets	T.4.03.03	v	O	v	Y	v	O	O				
43	Preseparator Mechanical Syst.	T.4.03.04	Y	O	Y	Y	O	Y	Y	O			
75	A1900 Reconfiguration	T.4.03.05	v	O	O	O	O	v	O	O	O		
100	Power Supplies	T.4.03.06	v	v	O	O	O	O	v	v	v	O	
100	Vacuum Systems	T.4.03.07	O	v	v	O	O	O	v	v	v	O	O

Figure 2: Excerpt from "FRIB Interface Tracker".

completion points. The 30% review corresponds to the completion of the Preliminary Design Phase in Figure 1, and the 60% and 90% reviews are conducted during the Final Design Phase.

Currently the project is conducting 60% and 90% reviews. The purpose of the 60% review is to ensure all requirements and interfaces are finalized, all engineering analyses have been completed and support final detailed design, and the design addresses quality, manufacturing, and environmental, safety and health requirements. The 90% review is conducted to confirm the design is complete and ready for procurement.

External expert reviewers are essential for effective reviews, and FRIB policy requires independent review of high level of care systems, such as personnel protection systems.

DESIGN MANAGEMENT

FRIB uses key performance indicators to summarize the engineering progress over time. Progress is based on completion of interfaces, completion of 60% and 90% reviews, and final drawing/specification completion. A excerpt of a Design Progress Dashboard is shown in Figure 3.

Experimental Systems Division

31-Aug-13		Interfaces (%) From Tracker	60% Design Review (%)	Drawing (BTP) or Specification (BTS) % Complete	90% Design Review (%)	Overall Design Progress (%)
Division Average:		68	41	17	10	45
Target Area Utilities	T.4.02.01	75	100	90		83
Target Area Remote Handling	T.4.02.02	50	0	10	10	41
Target Area Non-Conv. Utilities	T.4.02.03	25	100	10	10	52
Diagnostics	T.4.03.02	50	0	0	0	38
Magnets	T.4.03.03	78	50	30	0	54
Preseparator Mechanical Syst.	T.4.03.04	43	0	0	0	36
A1900 Reconfiguration	T.4.03.05	75	0	0	0	41
Power Supplies	T.4.03.06	100	100	50	0	68
Vacuum Systems	T.4.03.07	100	100	0	0	60
Low Level Controls	T.4.03.08	60	0	0	0	39
Machine Protection System	T.4.06.01	100	0	0	0	45
Personnel Protection Systems	T.4.06.02	88	100	10	0	61

Figure 3: "FRIB Design Dashboard" showing progress.

Progress is plotted monthly to make sure FRIB is on track for major milestones. A sample graph is shown in Figure 4.

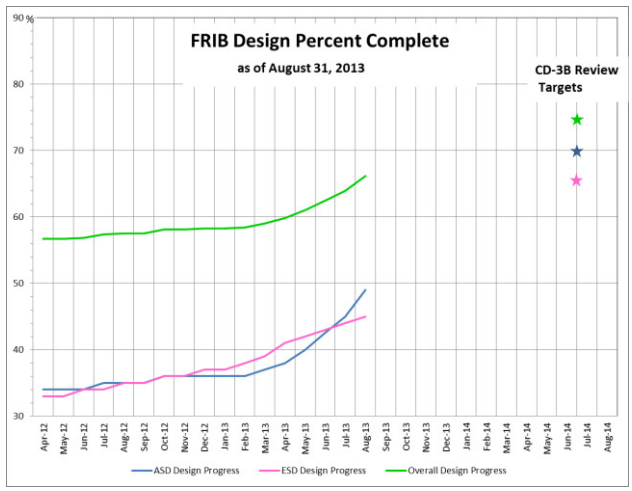


Figure 4: Sample Monthly Design Progress Report indicating progress and targets.

COMPONENT AND SUB-SYSTEM VALIDATION

The Project uses formal Acceptance Criteria checklists to identify the criteria that must be satisfied and to document the actual verification that the criteria is met. These lists are used for fabrication, testing, and will be used for installation and integrated testing. The Requirements Tracker previously mentioned supports criteria development, and it also captures the actual verification.

SUMMARY

FRIB has implemented an effective Systems Engineering and Integration Process:

- Tools are in place and used to manage requirements and interfaces; metrics provide managers current status of the design effort
- Review and validation processes will ensure designs meet requirements, including fabrication, installation and testing requirements.

REFERENCES

[1] J. Wie *et al*, "Progress towards the Facility for Rare Isotope Beams," These Proceedings.

[2] International Council on Systems Engineering, http://incose.org/

Copyright © 2013 CC-BY-3.0 and by the respective authors

STATUS AND OPPORTUNITIES AT PROJECT X: A MULTI-MW FACILITY FOR INTENSITY FRONTIER RESEARCH*

S. D. Holmes, M. Kaducak, R. Kephart, I.Kourbanis, V. Lebedev, S. Mishra, S. Nagaitsev, N. Solyak, R. Tschirhart, Fermilab, Batavia, IL 60510, USA

Abstract

Project X is a multi-megawatt proton facility being developed to support a world-leading program in Intensity Frontier physics at Fermilab. The facility will support programs in elementary particle and nuclear physics, with the potential for broader applications in materials and energy research. Project X is in the development stage with an R&D program focused on front end and superconducting rf acceleration technologies, and with design concepts for a staged implementation. This paper will review the status of the Project X conceptual development and the associated R&D programs.

PROJECT X MISSION AND GOALS

Project X is a high intensity proton facility that will support a world-leading U.S. program in Intensity Frontier physics over the next several decades. Project X is currently under development by Fermilab in collaboration with national and international partners. Project X will be unique in its ability to deliver, simultaneously, up to 6 MW of site-wide beam power to multiple experiments, at energies ranging from 235 MeV to 120 GeV, and with flexible and independently controlled beam time patterns. Project X will support a wide range of experiments utilizing neutrino, muon, kaon, nucleon, and atomic probes [1,2]. In addition, Project X will lay the foundation for the long-term development of a Neutrino Factory and/or Muon Collider.

PROJECT X REFERENCE DESIGN

A complete design concept, designated the Project X Reference Design [3], has been established supporting the above-described mission in an innovative and flexible manner. The Reference Design is based on a 3-GeV superconducting (SC) continuous wave (CW) linac, followed by an 8-GeV superconducting pulsed linac, and improvements to the Main Injector complex at Fermilab. The primary elements of the Reference Design are:

- An H^- front end based on a 162.5 MHz RFQ delivering 5 mA of beam current at 2.1 MeV into a medium energy beam transport (MEBT) line containing a wideband, bunch-by-bunch, chopper capable of accepting or rejecting bunches in arbitrary patterns and leaving 1 mA average (averaged over ~1 μsec) current for further acceleration;
- A 3-GeV SC linac operating in CW mode and capable of accelerating an average beam current of 1mA;
- A 3 to 8-GeV pulsed SC linac capable of accelerating a peak current of 1 mA with a duty factor of 4.3%;
- Rf splitters that can deliver beams at 1 and 3 GeV to at least three experimental areas;
- Experimental facilities to support experiments at 1 and 3 GeV;
- Modifications to the Main Injector (MI) and Recycler complex required to support 2-MW operations in the energy range of 60-to-120 GeV;
- All interconnecting beam lines.

STAGING STRATEGY

Fiscal considerations have motivated development of a staging plan for Project X, consistent with the following principles:

- The plan should provide compelling physics opportunities at each stage;
- Each stage should cost substantially less than $1B;
- Each stage should utilize existing infrastructure to the extent possible;
- The construction of each stage should minimize interruptions to the on-going research program;
- The full Reference Design capabilities should be achieved at end of the final stage.

The Reference Design has been developed consistent with these principles – the associated layout on the Fermilab site is shown in Fig. 1.

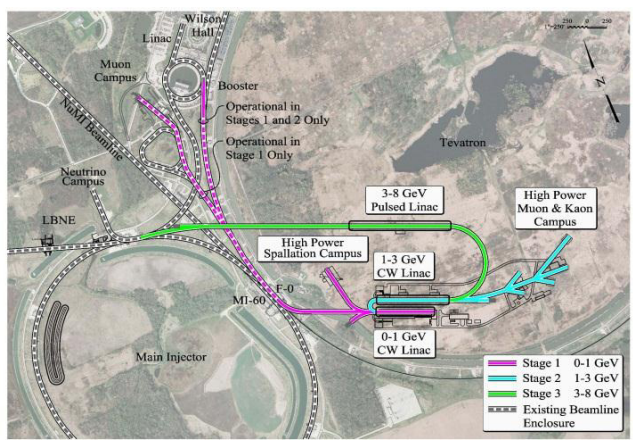


Figure 1: Project X Reference Design Stages.

Stage 1 is based on the 1-GeV CW linac. The 1-mA beam can be directed either to the existing 8-GeV Booster, the Muon Campus (currently under construction), or to a newly constructed High Power Spallation Campus. Stage 1 retires the existing 400-MeV linac and raises the Booster injection energy to 1 GeV,

* Work supported by the Fermi Research Alliance under U.S. Department of Energy contract number DE-AC02-07CH11359

Copyright © 2013 CC-BY-3.0 and by the respective authors

allowing a 50% increase in beam intensity. Stage 1 can simultaneously provide 1.2 MW to the long baseline neutrino target at 120 GeV, 80 kW to the Mu2e experiment [4], and 900 kW of beam power to the new Spallation Campus.

In Stage 2 the CW linac is extended to 3 GeV. The average beam current in the 1-GeV linac is increased to 2 mA with 1 mA available for the Booster and the Spallation Campus, and 1 mA passed into the 3-GeV linac for delivery to a newly constructed High Power Muon and Kaon Campus.

Stage 3 completes the Reference Design with the 8-GeV pulsed linac replacing the Booster as the injector into the Main Injector complex. The pulsed linac delivers a 1-mA peak beam current with a 4.3% duty factor (4.3 ms × 10 Hz). At Stage 3 the Main Injector can deliver 2.3 MW of beam power at any energy between 60-120 GeV. In addition, beam power is available for an 8 GeV program ranging from 0-170 kW, depending on the operating energy of the Main Injector.

The capabilities of Project X at each stage are given in Table 1.

Table 1: Project X Performance by Stage

	Stage 1	Stage 2	Stage 3
1 GeV Beam Power	0.9 MW	1 MW	1 MW
3 GeV Beam Power	---	3 MW	3 MW
8 GeV Beam Power	110 kW	110 kW	350 kW
120 GeV Beam Power	1.2 MW	1.2 MW	2.3 MW

R&D PROGRAM

The Reference Design provides the context for the Project X R&D program. The purpose of the R&D program is to mitigate technical and cost risks. The primary risks associated with Project X are identified as:

- Front End: The front end must provide an average beam current of 1-2 mA, with a peak current of 5-10 mA, with the beam assigned in a programmable manner into the linac rf buckets.
- H^- injection: All stages of Project X require injection via stripping over hundreds of turns. Space-charge mitigation requires foil painting. Other considerations include foil heating, and losses generated by partial stripping and/or or multiple scattering.
- High Intensity Main Injector and Recycler operations: Operations at intensities a factor of three beyond current experience require upgrades to the rf systems and control of a variety of beam instabilities.
- High Power Target Facilities: Target facilities for producing both secondary particle beams and spallation neutrons must accommodate >1 MW of incident beam power.
- Superconducting rf: A variety of cavities operating at different frequencies and with different geometric betas are required.

The R&D program as structured could support a Project X construction start in 2018.

Project X Injector Experiment (PXIE)

PXIE is an integrated front-end systems test, and is the centerpiece of the Project X R&D program [5]. PXIE will validate the concept for the Project X front end, thereby minimizing the primary technical risk element within the Reference Design. The PXIE layout is shown in Fig. 2.

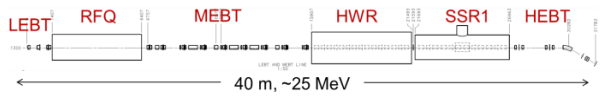


Figure 2: PXIE Layout.

PXIE will operate with the full Project X design parameters. These include delivering 5 mA average current from the RFQ, followed by 80% chopping within the MEBT for an average current delivered to the SC accelerating section of 1 mA. Two SC acceleration modules (HWR and SSR1) are expected to provide efficient acceleration with minimal emittance dilution to ~25 MeV. PXIE will utilize components constructed to Project X specifications wherever possible. This will provide an opportunity to re-utilize selected PXIE components within Project X.

PXIE is being undertaken by a collaboration of Fermilab with ANL, LBNL, ORNL/SNS, and four Indian institutions (BARC, IUAC, RRCAT, VECC).

Superconducting RF

The Project X linacs utilize modern SC radiofrequency (srf) technology as it has been developed over the last few decades. This technology is considered mature, and does not represent a significant technical risk within Project X; it is, however, a primary cost driver.

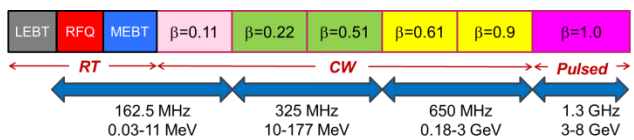


Figure 3: Project X Linac Technology Map.

Figure 3 displays the technology layout of the Project X linacs. A room temperature (RT) front end is followed immediately by superconducting accelerating modules extending from 2.1 MeV to 8 GeV. The linac operates in CW mode up to 3 GeV and in pulsed mode thereafter. Operation of a CW linac places a strong premium on achieving high Q_0 in order to reduce both operating costs and the capital investment in the cryogenic support systems [6]. A robust srf R&D program has been underway for several years at Fermilab in collaboration with national and international partners. This program

Copyright © 2013 CC-BY-3.0 and by the respective authors

originated as an initiative to develop 1300 MHz accelerating structures for the International Linear Collider [7] in the mid-2000s. The significant investment in ILC technologies made it natural to base the Project X design on sub-harmonics of 1300 MHz.

The status of srf development for Project X is summarized in Table 2. HWR and SSR signify half-wave and single-spoke resonators; LE650 and HE650 are both 5-cell elliptical cavities; while ILC is a 9-cell elliptical cavity (operating at lower gradient, but higher Q_0 than ILC) Substantial progress has been made on all cavity types. As an example Fig. 4 shows test results from six SSR1 cavities fabricated in industry, all of which meet the Project X performance specification and are planned to be used in PXIE and later in the Project X front end.

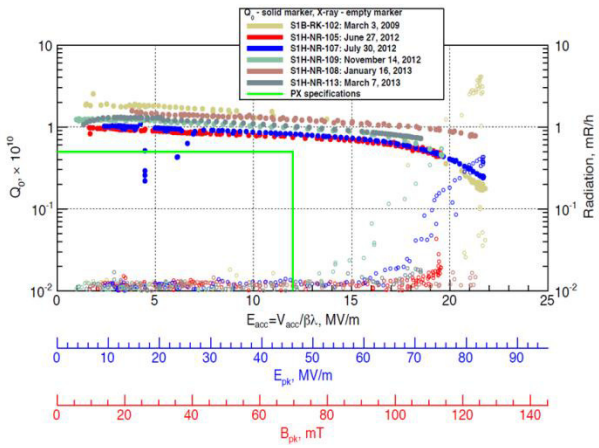


Figure 4: Dependence of Q_0 on accelerating gradient for SSR1 bare cavities at 2K. The green lines indicate the Project X specification.

SUMMARY

Project X is central to the strategy for future development of the Fermilab accelerator complex. A Reference Design has been developed that will support a world-leading program in neutrinos and other rare processes over the coming decades, and will provide a platform for future muon-based facilities. A staging strategy has been developed that provides compelling physics opportunities at each stage. An R&D program is underway with particular emphasis on front end and srf development. Project X could be ready to initiate construction in the second half of the current decade.

REFERENCES

[1] "Project X: Physics Opportunities", July 2013, arXiv:1306.5009.
[2] "Project X: Broader Impacts", July 2013, arXiv:1306.5024.
[3] "Project X: Accelerator Reference Design", June 2013, arXiv:1306.5022.
[4] "Mu2e Conceptual Design Report", November 2012, arXiv:1211.7019.
[5] S. Nagaitsev, "The Project-X Injector Experiment: A Novel High Performance Front-end for a Future High Power Proton Facility at Fermilab", contribution to NA-PAC'13.
[6] A. Grassellino, "Advances in SRF Materials Science aimed at High Q Cavities", contribution to NA-PAC'13.
[7] "ILC Technical Design Report", June 2013, http://www.linearcollider.org/ILC/Publications/Technical-Design-Report.

Table 2: Project X SRF Accelerating Cavity Requirements and Status

	Frequency (MHz)	Number Required	Gradient (MV/m)	Q_0@2K (10^{10})	Collab-orator	Status
HWR (β_{opt}=0.11)	162.5	8	8.2	0.5	ANL	Cavity and cryomodule design complete; prototype cavity on order
SSR1 (β_{opt}=0.22)	325	16	10	0.5	India	Ten cavities fabricated; 5/6 tested and meet spec; two cavities in fabrication at IUAC
SSR2 (β_{opt}=0.51)	325	35	11.2	1.2	India	Cavity electromagnetic and mechanical designs complete
LE650 (β_G=0.61)	650	30	16.5	1.5	India JLab	Cavity electromagnetic and mechanical designs complete
HE650 (β_G=0.9)	650	162	17	2.0	India	Cavity electromagnetic and mechanical designs complete; single cells meet spec; 5-cell protoypes received
ILC (β_G=1.0)	1300	224	17	2.0	DESY KEK	>40 cavities tested; two prototype cryomodules complete and tested to PX spec. (ILC program).

Copyright © 2013 CC-BY-3.0 and by the respective authors

STUDIES OF FAULT SCENARIOS IN SC CW PROJECT-X LINAC*

A. Saini†, J.-F. Ostiguy, N. Solyak, V. P. Yakovlev
Fermilab, Batavia, IL 60510 USA.

Abstract

The success of the Project-X accelerator facility crucially depends on reliable operation of the 1 GeV superconducting (SC) continuous wave (CW) linac at stage-I. Operation at high intensity in CW mode puts stringent tolerances on beamline elements. Any fault affecting nominal operation of an accelerating or transverse focusing element will result in beam mismatch in the downstream sections. This in turn leads to emittance growth, and ultimately triggers beam losses. A robust lattice design allowing local retuning can make the machine operable even in the event of a fault, limiting the need for long unscheduled downtime. This paper presents studies performed to understand the consequences of failure of various elements. The outcomes of local retuning for different fault scenarios at critical locations in the linac are discussed.

INTRODUCTION

Project-X is a proposed multi-megawatt (MW) accelerator facility to be built at Fermilab[1]. It is envisioned as a multiuser facility that would support a diversified experimental program at the intensity frontier. In the current economic environment, funding profile limitations led to development of a staging strategy. The facility would be built in three stages. The first stage involves construction of 1 mA (average current), 1 GeV SC CW linac. The second stage would double the average current through stage I. Half of the beam would then be further accelerated in a 1-3 GeV SC CW linac. The final and third stage involves construction of 3-8 GeV SC pulsed linac. A detailed description of staging approach is presented elsewhere[2]. A schematic of the CW linac baseline configuration is shown in Fig. 1. It comprises a room temperature front end and a SC linac. The front-end includes an ion source, a low energy beam transport (LEBT) section, an RFQ and a medium energy beam transport (MEBT) section. The DC ion source delivers a nominal current of 5 mA at 30 keV. The beam is transported through the LEBT and matched to the RFQ. The RFQ operates at room temperature at a frequency of 162.5 MHz and accelerates the beam up to 2.1 MeV. The beam then enters the MEBT where it gets chopped to acquire the time structure required to drive different simultaneous experiments. Following the MEBT is a SC CW linac segmented into five sections. The first section is based on 162.5 MHz Half Wave Resonators (HWR) and accelerate the beam to $\sim$ 9 MeV. The next two sections use two types of 325 MHz Single Spoke Resonators (SSR) i.e. SSR1 and SSR2, to reach a kinetic energy of 156 MeV. The two final sections dubbed low beta (LB) and high beta are based on 5-cell, 650 MHz elliptical shaped cavities respectively designed for β_G = 0.61 and β_G = 0.90 .

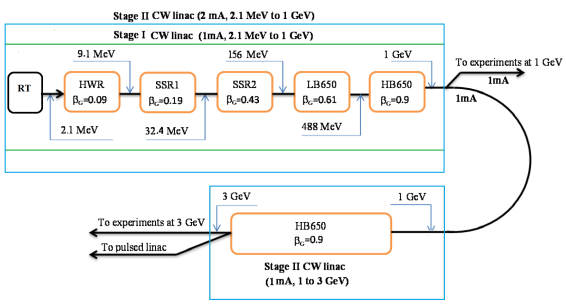


Figure 1: Acceleration scheme in Project-X CW linac.

GENERAL

Most of the complexity associated with a high intensity ion linac lays at low energy where dynamics is nonrelativistic and space charge effects are significant. The success of Project-X accelerator complex is therefore decisively dependent on reliable operation of the 1 GeV CW linac at stage-I. Failure of any element such as cavity, solenoid or quadrupole alters the focusing period of the beam, resulting in mismatch in the downstream sections. This, in turn, causes emittance growth and drives halo formation and beam losses. In some cases, the losses may be prevent safe operation. Unscheduled downtime is necessary to replace a faulty element and return to nominal operating conditions. Minimizing such unscheduled downtime is especially important in a multi-user facility where several experiments are running simultaneously. With that in mind, fault scenarios need to be accounted for in the optics design. The design should robust enough to allow localized compensation of the perturbation caused by an RF cavity or magnet failure. This paper presents studies performed to analyze various fault scenarios at critical locations in 1 GeV SC CW linac at stage-I of Project-X. Failure mitigation using localized compensation is demonstrated.

LOCAL COMPENSATION METHOD

The local compensation method involves re-tuning of elements in the vicinity of a failed element to restore a smooth beam envelope along the linac. Specifically, the RF phase and field amplitude of cavities are varied to recover the nominal beam energy and the longitudinal profile while

* Work supported by US DOE under contract DE- AC02-76CH03000.
† asaini@fnal.gov

Copyright © 2013 CC-BY-3.0 and by the respective authors

solenoids and quadrupoles are varied to restore the transverse dynamics. The constraints and assumptions applied during local compensation for Project-X SC CW linac are summarized below:

- Cavity accelerating fields: Fields are varied to recover nominal beam energy subject to the constraint that surface peak magnetic field in cavity should not exceed 70 mT.
- Cavity synchronous phases are varied in such a way that ratio of synchronous phase to longitudinal beam size is greater than 4. This assumption is made to achieve sufficient longitudinal acceptance.
- Field gradient in quadrupoles and axial magnetic field in solenoids are varied subject to the constraint that they cannot exceed design limits. These are 10 T/m and 6 T for quadrupoles and solenoids respectively.
- Minimum user disruption: The number of re-tuned elements is minimized in order to expedite the process of compensation.
- Local compensation cannot result in any losses (100% transmission).

FAULT SCENARIOS IN CW SC LINAC

Sensitivity of the linac performance to element failure is location dependent. Studies have been performed for different fault scenarios to understand their impact. The fault scenarios at the most critical locations are discussed in this section.

Failure of First SC Cavity in HWR Section

The HWR is the first SC section in the linac. It accelerates and focuses the beam coming out of the MEBT. One focusing period in the HWR section is composed of a solenoid and a HWR cavity. Failure of the first cavity in the HWR section is considered the most critical due to the large transverse and longitudinal beam size at this location. Since the beam is non-relativistic (2.1 MeV) failure of the first HWR cavity results in significant phase slippage that tends to grows in amplitude and ultimately causes beam losses in high energy section.

The local compensation method is applied to re-tune the beam optics. A bunching cavity and a triplet in the upstream MEBT, one solenoid in the same period of failed cavity and one solenoid and one HWR cavity in each of the three downstream HWR periods are used to recover a smooth beam profile. In addition, two HWR cavities (one in each of the two following periods) is used to recover the design energy at the end of the HWR section. Figure 2 and figure 3 show $1\sigma_{RMS}$ longitudinal beam size and normalized rms longitudinal emittance respectively. Abrupt changes in beam size and emittance characterize the beam losses which occur at the beginning of 650 MHz, LB section. It can be observed that there is no beam loss after

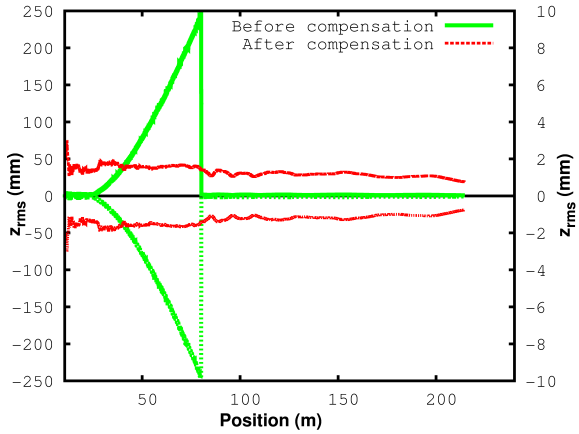


Figure 2: $1\sigma_{RMS}$ longitudinal beam size before (green) and after (red on secondary y-axis) local compensation of failure of first SC cavity in HWR section.

application of the local compensation method; the longitudinal emittance is also restored. Figure 4 shows the synchronous phase in the cavities and beam size for the re-tuned linac. Even with new setting of synchronous phases, the longitudinal acceptance is sufficient to accommodate a $6\sigma_{RMS}$ beam.

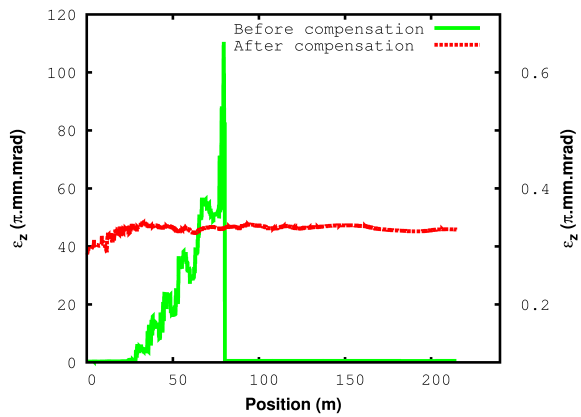


Figure 3: Normalized RMS longitudinal beam emittance before (green) and after (red on secondary y-axis) local compensation of failure of first SC cavity in HWR section.

Failure of First SC Quadrupole Doublet in LB Section

Solenoids are used to provide transverse focusing at low energy i.e. within the HWR, SSR1 and SSR2 sections. They are replaced with quadrupole doublets in the low beta (LB) and high beta (HB) sections. The nominal match between the SSR2 and LB section is very sensitive and involves outermost elements on both sides. Failure of the first SC quadrupole doublet is considered a critical event: it causes significant mismatch and envelope modulation in the downstream sections. Figure 5 shows $1\sigma_{RMS}$ transverse beam envelope before and after local compensation. It can be observed that failure of first SC quadrupole doublet in LB section results in significant distortion of trans-

Copyright © 2013 CC-BY-3.0 and by the respective authors

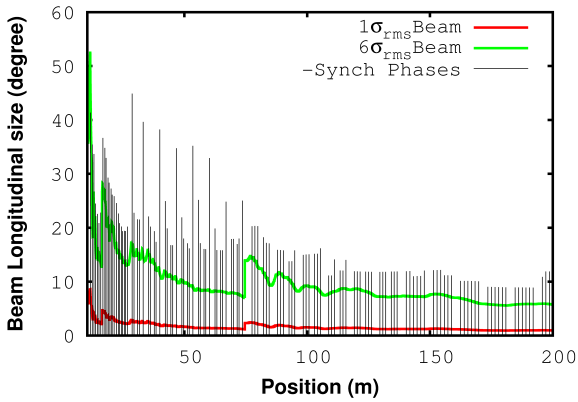


Figure 4: Longitudinal beam size in degree and synchronous phases after local compensation of failure of first SC cavity in HWR section.

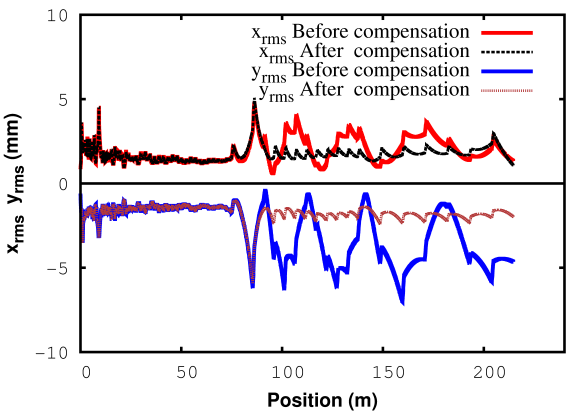


Figure 5: $1\sigma_{RMS}$ transverse beam envelopes before and after local compensation of failure of first SC quadrupole doublet in LB section.

verse beam profile, causing emittance growth in the downstream sections as shown in Figure 6. Again, application of the local compensation method results in a restored transverse beam profile and controlled emittance growth.

Failure of First Cavity in LB Section

Studies were performed to analyze the impact of a cavity failure at the frequency transition from 325 MHz to 650 MHz. It is found that failure of the first SC cavity in the LB section results in a 9 MeV beam energy reduction at 1 GeV linac output. However, no beam losses are observed. Fig. 7 shows that there are no abrupt changes in emittances. Emittance growth relative to baseline lattice [2] is less than 3% in longitudinal and horizontal plane and less than 7 % in vertical plane at the end of linac. We conclude that failure of cavity in the higher energy sections of the linac has minimal impact on performance.

CONCLUSION

Various fault scenarios were studied for the current Project-X baseline SC CW linac. Failures at critical locations, especially at low energy result in significant emittance growth and beam losses. Using local compensation, the optics design is flexible enough to allow recovery from failure of a RF single cavity or transverse focusing element. The output beam parameters and smooth beam profile in all planes are restored and 100% beam transmission is achieved.

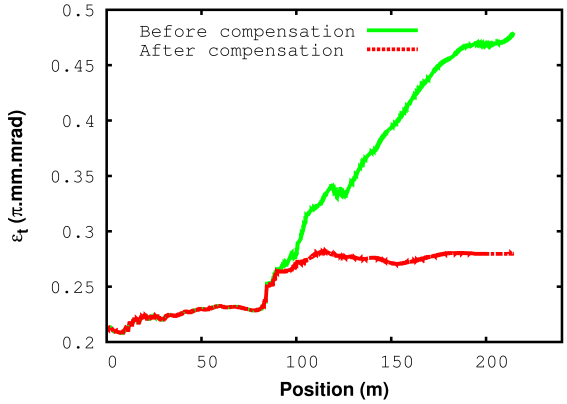


Figure 6: Normalized RMS transverse beam emittance before (green) and after (red) local compensation of failure of first quadrupole doublet in LB section.

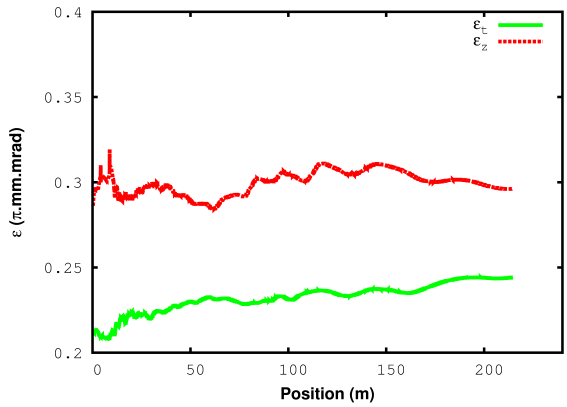


Figure 7: Normalized RMS longitudinal (red) and transverse (green) beam emittance in presence of failure of first SC cavity in LB section.

REFERENCES

[1] S. D. Holmes et al., Project-X Reference Design Report (June 2013), Project X-document 776-v7.

[2] N.Solyak et al., in Proceedings IPAC, Shanghai, May 2013, THPWO091, p. 3972 (2013).

Copyright © 2013 CC-BY-3.0 and by the respective authors

DESIGN ISSUES OF HIGH INTENSITY SC CW ION LINAC FOR PROJECT-X FACILITY*

A. Saini†, N. Solyak, V. P. Yakovlev, Fermilab, Batavia, IL 60510 U.S.A.

Abstract

Project-X is a high intensity proton facility which is primarily based on superconducting (SC) continuous wave (CW) linac. One of the most challenging tasks of Project-X facility is to have robust design of SC CW linac which can provide high quality beam to several experiments and subsequent pulsed linac simultaneously. Among the various technical problems associated with the SC CW linac, halo formation, beam mismatch, uncontrolled emittance growth and beam losses are the most crucial as they can limit overall performance and reliability. Scope of this paper is to address these issues for reference design of Project-X SC CW linac.

INTRODUCTION

The application horizon of particle accelerators has been widening significantly in recent decades. Where large accelerators have traditionally been the tools of the trade for high-energy nuclear and particle physics, applications in the last decade have grown to include large-scale accelerators like synchrotron light sources and spallation neutron sources. Applications like generation of rare isotopes, transmutation of nuclear reactor waste, sub-critical nuclear power, tritium production, radiation damage studies, studies of rare processes and generation of neutrino beams etc. are the next area of investigation for accelerator scientific community all over the world. Such applications require high beam power in the range of few mega-watts (MW). One such high intensity proton beam facility is proposed at Fermilab, named as Project-X [1]. The success of Project-X facility is primarily dependent on reliable operation of 1 GeV CW linac at first stage which is capable of delivering 2 MW beam power. A detailed description of baseline design of the CW linac is presented elsewhere [2].

Design of the high beam power accelerators are based on stringent beam losses limit. High beam losses can result in severe problem in terms of radio-activations. The cumulative experience of high intensity operation with existing facilities such as LANSCE [3] is utilized to set threshold limit of beam losses. In order to ensure hand-on-maintenance in safe environment, beam losses must be limited to 1 W/m for beam energy at 1 GeV. This paper addresses main characteristics and crucial beam dynamics design issues for the high intensity ion linac in framework of 1 GeV SC CW linac for the Project-X facility.

* Work supported by US DOE under contract DE- AC02-76CH03000.
† asaini@fnal.gov

EMITTANCE GROWTH

A low beam emittance ensures good output beam quality. Thus, minimal emittance growth along the linac is one of the primary objectives of optics design. The ion source determines initial transverse emittance of the beam which is transported to the RFQ through the low energy beam transport (LEBT) section. The magnets aberrations and non-linear space charge forces can result in a increase of transverse emittance in LEBT. It can be controlled, keeping beam size small and applying space charge neutralization. The longitudinal emittance is formed in the RFQ. A good beam matching at the upstream end of the RFQ minimizes transverse and longitudinal emittance growth along the RFQ. It is followed by the medium energy beam transport (MEBT) section which is comprised of bunching cavities and focusing magnets. Following is a SC CW linac. A robust design is capable to conserve emittance along the linac. It can be achieved using short regular focusing periods especially at low energy part of the linac. It results in smooth and linear changes in phase advance per meter (k). However, zero current phase advance in a focusing period should be kept below 90^0 to avoid envelope instability [4]. In order to avoid parametric resonance, focusing in linac is chosen such that $k_l \neq 2k_t$. Where k_l, k_t are wave numbers of the longitudinal and transverse oscillations respectively. Furthermore, non-linear space charge forces can result in excitation of coupling resonances which causes coupling between longitudinal and transverse motion. It results in abrupt emittance transfer between the planes. Figure 1 shows emittance coupling between longitudinal and transverse plane in first few sections of one of the variants of Project-X CW linac. It can be noticed that longitudinal emittance ϵ_l reduces at the expense of transverse emittance ϵ_t. In order to mitigate free energy transfer from one

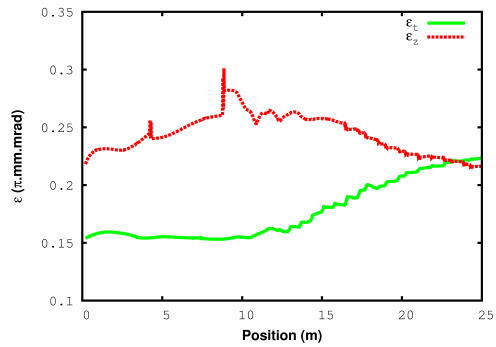


Figure 1: Emittance coupling between longitudinal and transverse plane.

Copyright © 2013 CC-BY-3.0 and by the respective authors

plane to another, equipartitoning is required. Condition of equipartitioning is:

$$\frac{T_t}{T_l} = \frac{k_t \epsilon_t}{k_l \epsilon_l} = 1 \qquad (1)$$

where T_t and T_l are temperatures in transverse and longitudinal plane respectively. In order to achieve efficient acceleration, focusing periods vary along the linac. Therefore, it is difficult to satisfy equipartition condition through out the linac. In this scenario, free energy transfer from one plane to another is suppressed by proper selection of working points (phase advance per period) in tune space where nonlinear space charge modes are stable. The Hofmann stability diagram [5] represents stability region in tune space that distinguishes stable modes from those which lead to coupling. Figure 2 shows working points of lattice that corresponds to Fig. 1. It can be noticed that some points are placed in stop-bands (region where space charge modes are unstable). It explains the reason of emittance exchange shown in Fig. 1.

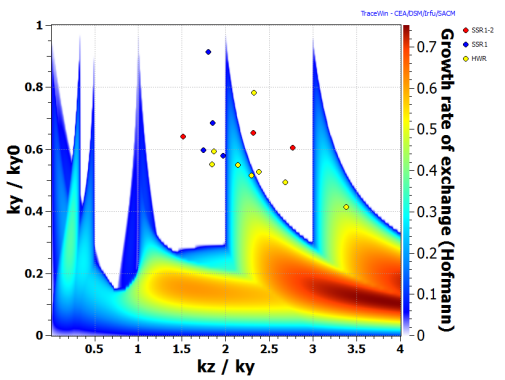


Figure 2: Hofmann stability chart: Distribution of working points in tune space.

The baseline design of Project-X CW linac involves no emittance exchange between the planes. Emittance growth [2] with respect to initial emittance is less than 4% in longitudinal plane, $\sim 10\%$ and 14% in horizontal and vertical planes respectively.

ACCEPTANCE

In high intensity linac, acceptance parameter is a vital mean to measure linac performance in term of beam losses. It is determined by largest beam size that can be transmitted through the linac without any particle losses. Thus, large beam acceptance corresponds to high tolerances against errors. A choice of physical aperture of beamline elements sets transverse acceptance of the machines. Preliminary beam-dynamics studies using numerical simulation codes helps to make optimal choice of aperture. Figure 3 shows transverse acceptance of 1 GeV SC CW linac for Project-X. An input distribution (shown in red) is generated with relatively very large emittance than nominal beam emittance in horizontal plane and relatively smaller in others. Distribution is tracked through the linac. Area occupied by initial coordinates of transmitted particles (shown in green) trace the acceptance of linac in this plane. It can be observed that transverse emittance is sufficient to accommodate 6σ beam (shown in blue).

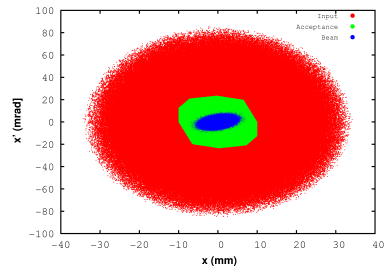


Figure 3: Transverse acceptance (green) of 1 GeV SC CW linac of Project-X with 6σ beam.

The complexity of ion linac is associated with the fact that beam velocity changes significantly during acceleration along the linac. Thus, to achieve efficient acceleration, different families of cavities are used along the linac. The Project-X SC CW linac is segmented into three section on the basis of operational frequencies of cavities (162.5 MHz, 325 MHz and 650 MHz). A careful matching is required between these sections otherwise it may introduce a discontinuity in average longitudinal force per period and limits longitudinal acceptance of the linac. In order to investigate most sensitive section in SC CW linac, longitudinal acceptance is analyzed at different locations in SC CW linac. It is found that longitudinal acceptance is primarily limited by the SSR2 section and no significant degradation is observed in subsequent sections. Figure 4 shows longitudinal acceptance after each section in linac. It is large enough to enclose 6σ beam (black). Thus no losses have been

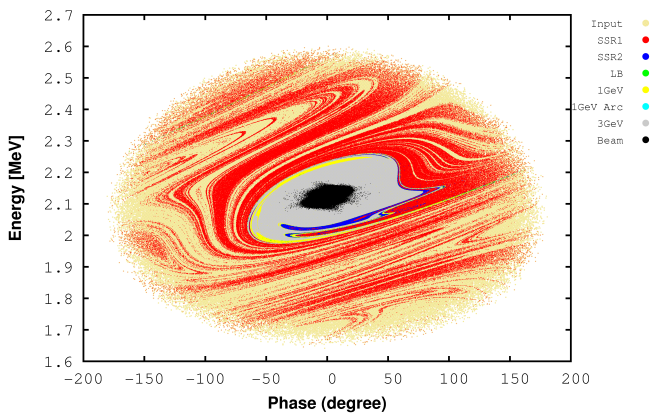


Figure 4: Longitudinal acceptance of SC CW linac of Project-X with 6σ beam (black).

observed for nominal operation of linac. Particles which fall out of longitudinal acceptance (grey region in Fig. 4) are no longer accelerated in linac, hence are not matched with downstream magnetic focusing elements which are designed for fully accelerated particles and consequently,

Copyright © 2013 CC-BY-3.0 and by the respective authors

they are lost due to transverse mismatch. Typically, the high intensity linac are designed to obtain large longitudinal acceptance in order to deal with longitudinal halo that usually results in beam losses at high energy part of linac.

HALO DEVELOPMENT

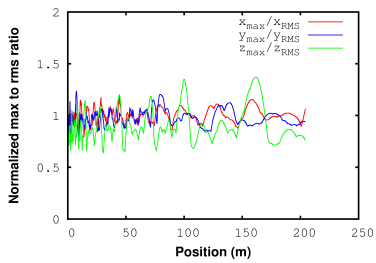


Figure 5: Normalized *maximum to RMS ratio* in all planes along 1 GeV SC linac.

The existence of beam halo is an important characteristics of the high intensity ion beam. Typically, beam halo is developed in low energy section and it is acquired large amplitude in high energy section that results in particle losses. It is most concerned aspect of the design of high intensity machine in the regime of stringent beam losses limit. There are several definition to quantify beam halo [6] but an important figure of merit that can be incorporated during lattice design is *max to RMS ratio*. It is ratio of maximum displacement to the RMS size of matched beam. Figure 5 shows *max to RMS ratio* normalized to initial value along the 1 GeV CW linac. Keeping this ratio close to one ensures that halo amplitude does not grow up along the linac. It is also useful to identify location of halo formation. It can be noticed from Fig. 5 that location around 100 m and 160 m is sensitive to longitudinal halo formation in linac.

Beam Mismatch

Beam mismatch is major source of halo development in linac. Studies are performed in order to analyze the impact of initial mismatch on halo formation for 1 GeV SC linac. Variation of 20% and 60% in initial Twiss Parameters in all planes are applied. All simulations are performed using a 6σ Gaussian distributed beam of 10^6 particles. Figure 6 shows longitudinal particle distribution at the end of linac for three cases no mismatch, 20% and 60% beam mismatch. Redistribution of particles can be observed in presence of mismatch which results in more particles in tail of distribution (radius >3). It is due to core oscillations that results in energy transfer from core movement to single particle orbit. It can also be noticed that redistribtion occurs faster in case of 60% mismatch (radius $\sim$ 2) than 20% (radius $\sim$3). It is a consequences of additional "free energy" introduced via mis-matched in the system. Similar

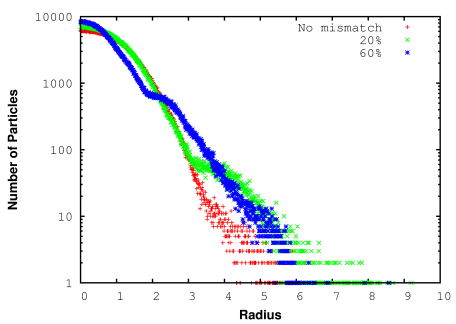


Figure 6: Longitudinal particle distribution at the end of 1 GeV linac (Radius = $|\sigma|$).

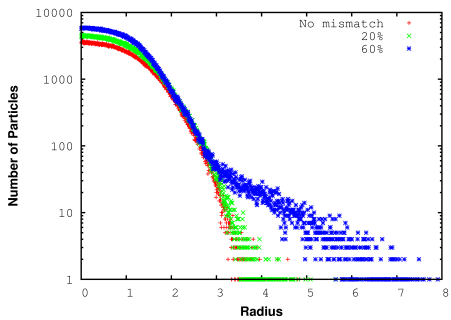


Figure 7: Transverse particle distribution at the end of 1 GeV linac (Radius = $|\sigma|$).

behavior is observed in horizontal plane. Figure 7 shows horizontal particle distribution at the end of linac. It can be noticed that only 60% mismatch results in significant halo development.

CONCLUSION

Controlled emittance growth and low beam losses are main objectives of the design of high intensity ion linac. Equipartition among the planes and avoiding stop-bands in the Hofmann stability diagram are possible way to avoid emittance exchange in presence of non-linear space charge forces. Large machine acceptance and suppression of mechanisms that lead to halo development are essential for reliable operation of the linac. Design of 1 GeV SC CW linac for Project-X is sufficiently robust to sustain stable operation even in presence of spread in design parameters. No beam losses are observed along the linac even in presence of 60 % initial mismatch of the beam.

REFERENCES

[1] S. D. Holmes et al., Project-X Reference Design Report (June 2013), Project X-document 776-v7.

[2] N.Solyak et al., in Proceedings IPAC, Shanghai, May 2013, THPWO091, p. 3972 (2013).

[3] http://lansce.lanl.gov/

[4] M. Reiser, "Theory and Design of Charge Particle Beams", Wiley (1994).

[5] I. Hofmann, in Proceedingd HB, Beijing, Sept. 2012, TUO3A01, p. 240 (2012).

[6] P. A. P. Nghiem et al., in Proceedingd HB, Beijing, Sept. 2012, THO03A04 p. 511 (2012).

Copyright © 2013 CC-BY-3.0 and by the respective authors

LAYOUT OF PROJECT-X FACILITY: A REFERENCE DESIGN*

A. Saini†, J.-P. Carneiro, D. Johnson, J.-F. Ostiguy, N. Solyak, V. P. Yakovlev
Fermilab, Batavia, IL 60510 USA.

Abstract

Project-X is a proposed high intensity proton facility to be built at Fermilab. It will be a multi-user facility which can support several experiments simultaneously. In the current scenario, the facility would be built in three stages. Each stage is associated with compelling scientific programs and is in synergy with existing Fermilab infrastructure. This paper presents the current reference design and discusses the main motivations and requirements driving the optics and physical layout.

INTRODUCTION

Project-X is a proposed high intensity proton facility to be built at Fermilab. Given the present economic environment, a staging strategy has been developed. The facility would be built in three stages. Each stage is associated with compelling scientific research programs and planned so that construction of each new stage has minimal influence on the operation of preceding ones. This approach has the benefit of limiting downtime during construction. A schematic of the Project-X facility is shown in Fig 1. A detailed description of the staging approach is presented elsewhere [1].

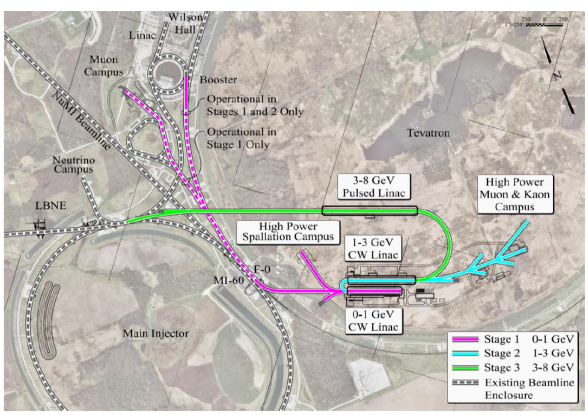


Figure 1: Layout of Project-X facility.

Success of the Project-X facility is critically dependent on the robustness of the superconducting (SC) continuous wave (CW) linear accelerator (Linac) design. While the reference design parameters [1] have been established, the optics is still evolving to incorporate technical constraints and to address issues that may potentially cause degradation of beam quality and particle losses. In this paper we describe recent changes in the beam optics.

* Work supported by US DOE under contract DE- AC02-76CH03000.
† asaini@fnal.gov

STAGE -I

The most challenging issues associated with Project-X facility would be addressed at Stage-1 which comprises a room temperature front-end followed by a 1 GeV SC CW linac delivering a 1 MW of beam power.

Ion Source, LEBT & RFQ

The front-end of Project-X consists of an ion source, a low energy beam transport (LEBT) section, an RFQ and a medium energy beam transport (MEBT) section. The ion source [2] operating in dc mode is capable of delivering a beam of H^- ion at 30 keV at maximum current of 10 mA. It is followed by the LEBT which includes three solenoids, a slow switching dipole magnet, a chopper assembly and diagnostic devices to characterize the beam. The chopper consists of a kicker and a beam absorber. It will primarily be used to produce variable low duty pulses during commissioning; it can also serve as pre-chopper to assist the MEBT high bandwidth chopping system. A detailed description of the LEBT layout and its component was presented elsewhere [1].

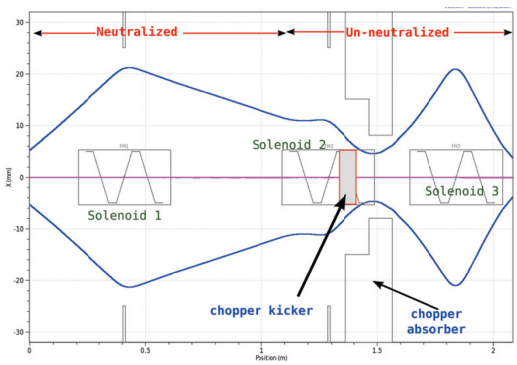


Figure 2: $3\sigma_{RMS}$ transverse beam envelope along LEBT (shown for fully neutralized operation).

A LEBT with solenoidal focusing usually requires neutralization to mitigate strong space charge defocusing. However, chopping of a neutralized beam can be problematic because the typical neutralization time is a few tens of micro-seconds, resulting in a time dependent optical perturbation. The Project-X LEBT design attempts to address this issue by incorporating two regions: (i) a fully neutralized region which extends from exit of the ion source to upstream edge of the second solenoid and (ii) an un-neutralized region from that point to the RFQ entrance port. Alternatively, the LEBT can also be operated in fully neutralized regime. Figure 2 shows a $3\sigma_{RMS}$ transverse beam envelope for fully neutralized operation. To

Copyright © 2013 CC-BY-3.0 and by the respective authors

minimize spherical aberrations through the solenoids, the beam transverse size is kept below half of the solenoids radial aperture [3]. Emittance growth in the LEBT occurs in the un-neutralized region and is driven by space charge. The LEBT is followed by an RFQ operating in CW mode at a resonant frequency of 162.5 MHz. It accelerates the beam to 2.1 MeV and provides longitudinal beam structure. Numerical simulations predict 99.8% beam transmission for nominal operation at 5 mA beam current. However, both transmission and output emittances strongly depend on beam matching at entrance of the RFQ. Figure 3 shows the evolution of the normalized RMS beam emittances through the LEBT and the RFQ for two modes of operation of the LEBT: (i) a partially neutralized LEBT (un-neutralized region after second solenoid) and (ii) a fully neutralized LEBT. It can be observed that beam emittances through the RFQ are significantly larger for partially neutralized LEBT operation. This is a consequence of non-linear space charge effects. Beam transmission through the RFQ is also reduced to 98.4 %.

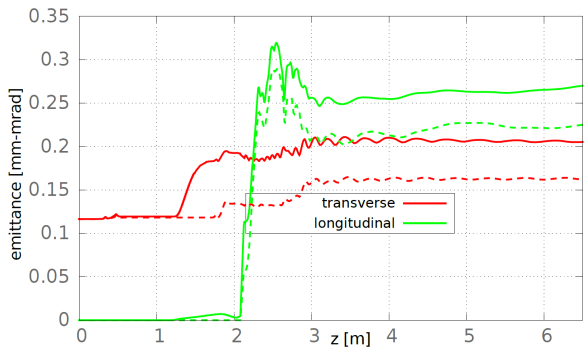


Figure 3: Normalized RMS beam emittances through LEBT and RFQ. Solid: LEBT with un-neutralized section. Dashed: fully neutralized LEBT.

MEBT & 1GeV SC CW Linac

The RFQ is followed by the MEBT and a 1 GeV SC CW linac. In order to improve the robustness of the design, the beam optics has been optimized. It can now accommodate, at the MEBT entrance, a longitudinal emittance larger than the reference design value [1]. The layout and beam optics are discussed elsewhere [4]. Changes in beamline elements are presented in [5]. A significant change is the introduction of a new β_G =0.92 cavity in the high energy 650 MHz section. This cavity has larger aperture (118 mm) which is beneficial in terms transverse acceptance in this section and avoids potential trapping of higher order modes. This cavity is therefor well suited to a future upgrade for higher current operation. The optics described in the reference design report was based on 5-cell, β_G =0.90, 650 MHz cavity (designed with aperture of 100 mm) in high energy section; the new cavity provides similar RF performance with minimal influence on beam optics.

1 GEV EXTRACTION LINE

Stage 1 of Project-X will provide 1 MW of beam power. This power will be distributed between a 1 GeV experimental area and the Booster/Muon campus using a special extraction scheme designed to allow both experimental facilities simultaneously. This is achieved by multiplexing the beam time structure. For stage 2, an additional MW of beam power will be delivered to the 1-3 GeV CW linac using the same extraction line. Figure 4 shows a conceptual layout of the extraction line which includes a vertical deflection unit (VDU) and a horizontally bending Lambertson magnet. The vertical deflection unit is composed of an RF deflecting cavity with trim dipoles positioned at the upstream and downstream ends.

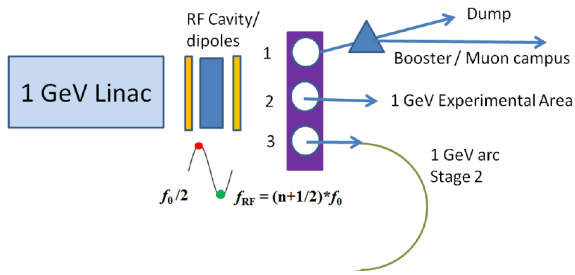


Figure 4: Conceptual design of 1 GeV extraction line.

RF Deflecting Cavity and Trim Dipole Magnets

The RF deflecting cavity at the end of 1 GeV linac splits the beam into two equal parts by imparting equal and opposite vertical kicks to successive bunches. The kick direction depends on the relation between the beam phase and the rf phase. Consequently, with f_0 representing the bunch frequency, the required rf frequency is

$$f_{RF} = (n + 1/2)f_0 \quad (1)$$

where n is an integer. The deflecting cavity at 1 GeV is designed to operate at 406.25 MHz (n and f_0 are equal to 2 and 162.5 MHz respectively). It is capable of providing maximum transverse voltage ($\Delta pc/e$) of 7 MV which corresponds to a deflecting angle θ of 4 mrad at 1 GeV. The trim dipoles on both sides of the cavity are identical and steer the beam in the vertical plane. Table 1 presents a summary of the cavity and dipole setting required to direct the beam to the different experimental facilities at stage I and stage II.

Lambertson Magnet

The VDU is followed by a 3-way Lambertson magnet. If there is no net deflection from the VDU, the beam goes through the field free region along the axis of Lambertson magnet and is delivered to the 1 GeV experimental area. However, when the beam experiences a net deflection from the VDU, it passes either through the upper or lower field region of the Lambertson and is steered horizontally. The direction of the horizontal steering is determined by the

Copyright © 2013 CC-BY-3.0 and by the respective authors

Table: 1 Operational scenarios for the VDU. 4th column (Dipole) is the total deflection from both dipoles.

Stage	Destination	deflecting cavity	Dipole	DSW
1	Muon Campus	+θ	+θ	
	1 GeV EA	-θ	+θ	
	Booster	off	+2θ	
	Dump	off	+2θ	on
2	1 GeV EA	+θ	-θ	
	Booster	off	+2θ	
	Dump	off	+2θ	on
	1 GeV arc	-θ	-θ	

sign of the net vertical deflection (+/-θ) from the VDU. Figure 5 shows beam separation scheme through Lambertson magnet.

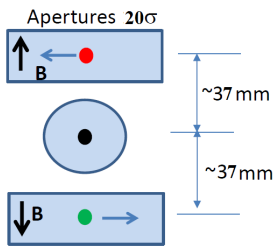


Figure 5: Schematic of 3-way Lambertson magnet. The beam is steered toward the left or the right depending on the sign of the vertical deflection imparted by the VDU.

Beam Optics through 1GeV Extraction Line

Figure 6 shows $1\sigma_{RMS}$ beam envelope through the 1 GeV extraction line. The RF deflecting cavity is set to provide a vertical deflection angle of 3 mrad while each dipole provides a 1.5 mrad vertical steering. A special quadrupole doublet with large aperture of 120 mm is placed just before the Lambertson magnet to cancel the vertical slope of the beam centroid so that it can enter the Lambertson magnet field region in the horizontal plane. The VDU to Lambertson distance is chosen to provide enough beam separation (15 - 20 σ_{RMS}) between deflected and undeflected beam. With the present settings, this separation is 20 σ_{RMS} (37 mm) (as mentioned in Fig 5). The Lambertson magnet is 1 m long; it provides an integral magnetic field of 0.2 T-m, corresponding to a ∼35 mrad deflection in the horizontal plane. The distance from the Lambertson to the first element of each beamline is optimized to provide enough horizontal separation. It can be observed from Fig 7 that introduction of the the extraction line does not contribute to emittance growth. The impact on the downstream optics is expected to be minimal. Minor retuning of the first section of the subsequent stage may be required to match the beam parameters at the entrance.

STAGE -II & STAGE -III

At stage II, 1 MW of beam power will be delivered to the 1-3 GeV SC CW linac through a 180^0 arc for further acceleration. Extraction line at the end of this stage will distribute 3 MW of beam power to different experimental facilities using a concept similar to the one discussed for

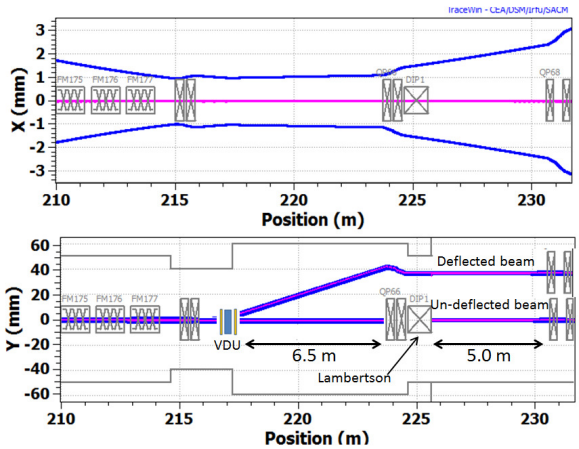


Figure 6: Beam RMS envelope in transverse plane through 1 GeV extraction line.

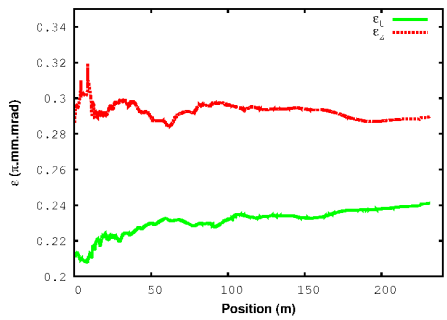


Figure 7: Longitudinal (green) and transverse (purple) beam emittance through stage 1.

the 1 GeV extraction line. In the final stage, 350 kW of beam power will be transported to a 3-8 GeV pulsed linac through another 180^0 arc. Details of the beam optics for the 1-3 GeV CW linac and the pulsed linac are discussed elsewhere [4].

SUMMARY

The beam optics is compatible with the Project-X staging strategy. Furthermore, it provides sufficient acceptance to accommodate, if necessary, larger emittances coming out of the RFQ.

REFERENCES

[1] S. D. Holmes et al., Project-X Reference Design Report (June 2013), Project X-document 776-v7.

[2] D. Li et al., "Progress of the Front-End System Development for Project-X at LBNL," IPAC'12, New Orleans, May 2012, THPPP092, p. 3951 (2012).

[3] L. Prost et al., Project-X document 1015-v2;http://projectx-docdb.fnal.gov/cgi-bin/ListAuthors

[4] N.Solyak et al., in Proceedings IPAC, Shanghai, May 2013, THPWO091, p. 3972 (2013).

[5] T. N. Khabiboulline et al., "Updates of Beam Optics and SRF cavities for Project X," IPAC'12, IPAC'13, Shanghai, May 2013, THPWO092, p. 3975 2013).

Copyright © 2013 CC-BY-3.0 and by the respective authors

STATUS OF THE LANSCE FRONT END UPGRADE*

R. W. Garnett#, Y. K. Batygin, I. N. Draganic, C. M. Fortgang, S. S. Kurennoy, R. C. McCrady, J. F. O'Hara, E. R. Olivas, R. J. Roybal, and L. J. Rybarcyk, LANL, Los Alamos, NM 87544, U.S.A., A. Schempp, IAP, Goethe University, Frankfurt am Main, Germany, J. Haeuser, Kress GmbH, Biebergemuend, Germany

Abstract

Initial acceleration of the beams in the LANSCE linear accelerator at Los Alamos National Laboratory is still presently accomplished through the use of two 750-keV Cockcroft-Walton (CW) based injectors. To reduce long-term operational risks and to realize future beam performance goals, plans are underway to replace the existing H^+ CW injector with a modern replacement, 4-rod Radio-Frequency Quadrupole (RFQ) based front end. Significant technical progress has been made since we last reported on this project. Status and progress of the design and fabrication of the RFQ, the RF system, beam transports, and integrated accelerator test stand will be discussed.

INTRODUCTION

The Los Alamos Neutron Science Center (LANSCE) currently supports a broad user base including the neutron scattering community, isotope production, basic science, and national security programs by providing multiple beams to several diverse experimental areas. The LANSCE linac accelerates negative hydrogen ions (H^-) and protons (H^+) simultaneously. An 800-MeV H^- beam is delivered at 20 Hz to the proton storage ring/moderated neutron production target for a suite of neutron-scattering instruments (Lujan Center), at 40 Hz to an un-moderated spallation target for nuclear physics cross-section measurements and microchip irradiations for industry (WNR), and on-demand at ~1 Hz for proton radiography (pRad), and at 20 Hz for ultra-cold neutron production (UCN). Protons are used for isotope production (IPF) at 100 MeV. High-power operation (10% total RF duty factor; 100 Hz x 625 μs; 16.5-mA peak proton beam current) has provided 800-kW average beam power at 800-MeV but was halted in 1998 after shut-down of the nuclear physics mission that supported high-power beam operations. Upgrades currently underway will restore full 120-Hz operations and allow high-power operation in support of planned new missions [1] that will require MW-level average beam powers.

Beams are delivered to the LANSCE experimental areas on a pulse-by-pulse basis, initially accelerated in two CW-based injectors, for H^+ and H^- beams, respectively. At present, LANSCE delivers up to three different H^- beams based on user requirements. The highest average-current H^- beam (100-125 μA) is first accumulated in the proton storage ring (PSR) and then extracted to the moderated neutron spallation target at the Lujan Center. This beam is chopped to provide an extraction gap in the PSR circulating bunch. By comparison, the WNR facility typically requires a single linac micropulse every few microseconds within the standard 625-μs macropulse. Producing the widely-spaced single micropulses requires the use of a chopper and low-frequency buncher in the H^- injector. These micropulses typically contain about 2.5 times more charge than the standard H^- linac microbunch. The other two H^- beam users, pRad and UCN, have beam requirements that require chopped and pre-bunched beams somewhat similar to the Lujan beam. The present dual-beam CW-based injector scheme for the LANSCE linac is shown in Fig. 1. The two beam species are merged into a common beam transport line and bunched before injection into the drift-tube linac (DTL) with a capture efficiency of approximately 80%.

Typical parameters for the 60-Hz (present maximum beam repetition rate) H^- beams are given in Table 1. Comparing chopping requirements against duty factor for these three beams, two categories emerge: low-duty factor beams with modest chopping requirements (Lujan, pRad) and a high-duty factor beam with demanding chopping requirements (WNR). H^+ beam parameters are also shown in Table 1. Future 120-Hz, H^+ beam requirements are shown in Table 2. An average H^+ beam power of 25 kW (250 μA) is required to be delivered to IPF at 100 MeV. An additional average beam power of 0.75 MW at 800 MeV is expected to be available for other applications beginning in 2017. Several options for enhanced future high-power beam operations can be found in Ref. 2.

Assessment of failure modes of our CW injectors revealed the potential for significant disruption of the beam operations at LANSCE [3] either due to catastrophic failure of major components and/or unavailability of spare parts.

Our strategy to reduce operational risks associated with the current CW-based injector systems involves the eventual replacement of these systems with modern radio-frequency quadrupole (RFQ) based injectors. Reliability is expected to improve due to reduced overall complexity of the systems and by modernization. RFQ accelerators are employed worldwide and have demonstrated stable and reliable operation.

To meet the above requirements while maintaining all existing beam delivery capabilities, including the high duty factor and demanding chopping requirements for the WNR beam, we are considering a 3-RFQ upgrade [3] to the present injector system that would be implemented in a staged approach with development of the H^+ RFQ having highest priority due to its impact on our near-term

* Work supported by the United States Department of Energy, National Nuclear Security Agency, under contract DE-AC52-06NA25396
# rgarnett@lanl.gov

Copyright © 2013 CC-BY-3.0 and by the respective authors

high-power performance goals. In this scheme (shown conceptually in Fig. 2), a single 201.25-MHz RFQ will provide bunched but un-chopped H^+ beam of up to 35 mA. A second 201.25-MHz RFQ will provide bunched and chopped H^- beam for Lujan, pRad and UCN. Finally, a third lower-frequency RFQ, at possibly 67 MHz, will produce the intense single H^- linac micropulses for WNR.

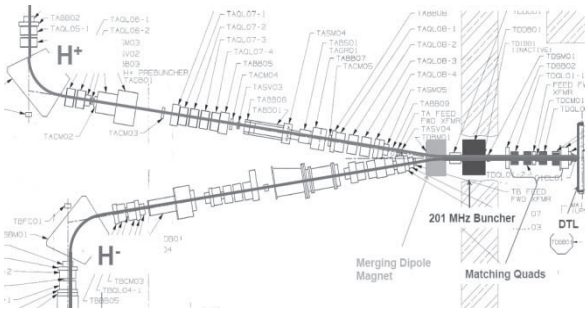


Figure 1: Present H^+/H^- CW injector layout.

Table 1: Typical 60-Hz LANSCE Beam Parameters

Beam/Area	Duty Factor	Chopping Specs
Lujan, H^-	20 Hz x 625 μs = 1.25%	290 ns burst every 358 ns
WNR, H^-	40 Hz x 625 μs = 2.5%	Single micropulse every 1.8 μs
pRad, H^-	1 Hz x 300 μs = 0.03%	20-30, 60 ns beam bursts, variable spacing
UCN, H^-	20 Hz x 625 μs = 1.25%	Variable
IPF, H^+	40 Hz x 625 μs = 2.5%	None

Table 2: Future 120-Hz LANSCE H^+ Beam Parameters

Beam/Area	Duty Factor	Ave. Current
IPF (100 MeV)	20 Hz x 770 μs = 1.54%	250 μA
Area A (800 MeV)	100 Hz x 770 μs = 7.7%	0.75-1.25 mA

We have developed an H^+ RFQ design and beam-transport layout compatible with the existing H^- CW injector that require no changes beyond the merging dipole upstream of the common H^+/H^- beam transport section (See Fig.1). This will allow for early implementation of the new H^+ system, independent of the longer-term plans to implement multiple RFQ injectors. Following completion of the RFQ, the RFQ will first be operated and commissioned on a separate test stand prior to integration at the front end of the LANSCE linac.

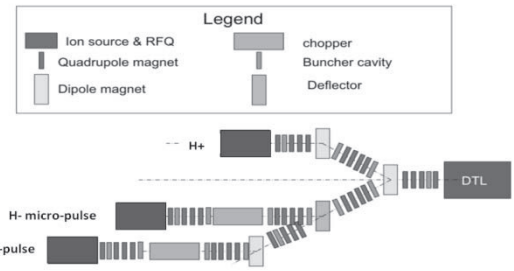


Figure 2: Conceptual layout of the 3-RFQ H^+/H^- injector system for LANSCE.

PROJECT STATUS

RFQ

The final physics design of the 4-rod RFQ has been completed and accepted. The physics design was completed and verified through a joint effort between the Institute of Applied Physics (IAP) at Goethe University, Frankfurt, Germany, and Los Alamos [4].

A final mechanical design review was held in April 2013. Fabrication of the RFQ is expected to take 9-12 months in Germany by our project partner Kress, GmbH, with delivery to Los Alamos before the end of 2014.

The RFQ is required to operate at a high duty factor of up to 15% and must meet strict beam performance requirements. Complementary simulations using the TRACE 2-D/3-D, PARMTEQM and PARMILA codes [5], Beampath [6], the CST Studio suite of codes [7] including Particle Studio, and the ANSYS [8] code were used to validate the design results.

To ensure mechanical and operational robustness of the RFQ, several technical evaluations were completed prior to acceptance of the design [9]. These included: addressing potential structure cooling issues, evaluation of tuning range, impact of stem spacing on frequency and field flatness, impact of vane cross-section and stem geometry on dipole fields, and investigation of end-region field effects on emittance growth and final output energy.

Ion Source and Low-Energy Beam Transport

The extraction geometry of our present H^+ duoplasmatron ion source, normally operated at a 35-kV extraction voltage, has been redesigned to produce a 35-mA beam with a transverse emittance of < 0.02 π-cm-mrad, normalized [10]. Modifications to an existing source and testing will be required to verify the new design.

Although previously a short electrostatic LEBT for beam matching from the ion source to the RFQ was considered, a new 2-solenoid magnetic LEBT has been designed and optimized to transport beams over a wide range of space-charge neutralization and transverse emittance, while allowing sufficient space for diagnostics and a beam deflector [10]. The design layout minimizes the beam size in the LEBT and potential emittance growth due to solenoid aberrations.

Copyright © 2013 CC-BY-3.0 and by the respective authors

RF System

After fabrication of the RFQ is complete, the alignment, tuning, and low-power testing will be done in Germany with Los Alamos participation. High-power testing will be done at Los Alamos and is expected to use the High Power Test Facility at LANSCE [11]. The RFQ will be tested at full peak power and the full 15% duty factor (120 Hz, 1250 μs RF pulse length) using the 201.25-MHz Thales TH781 Intermediate Power Amplifier and associated low-level RF controls capability of the test facility. The estimated full peak power required for the test is 90-100 kW, assuming a realistic surface conductivity and a 15%-20% additional power margin. Design of the final RFQ RF system has not yet started.

Medium-Energy Beam Transport

A new Medium-Energy Transport (MEBT) line to match the RFQ output beam into the DTL has been designed to replace the existing H^+ beam transport line shown in Fig. 1 [12]. The MEBT must be as compact as possible to preserve the beam emittances. To do so, we plan to use multiple compact 201.25-MHz quarter-wave bunchers [13] to minimize the beam phase spread and compact SNS-style MEBT quadrupoles for transverse beam focusing (See Fig. 3). Simulation studies have been completed using the TRACE-3D [5] and PARMILA [5] codes to validate the multi-particle beam dynamics and linac capture (estimated to be 81%).

RFQ Test Stand

Our original plan was to have all necessary preparations for the test stand completed at Los Alamos by the RFQ delivery date so that high-power testing and commissioning with beam could be completed, followed by demonstration over the course of a year of stable operations prior to implementation on the LANSCE linac. However, recent schedule and budget changes require a more phased approach to testing and commissioning of the RFQ.

As mentioned above, preparations are already underway to perform high-power testing of the RFQ. In parallel to fabrication of the RFQ, an intermediate-stage 35-keV ion-source test stand will be assembled, including the LEBT and sufficient diagnostics to confirm performance and reliability of the source, and to match and characterize the beam into the RFQ. Ion-source and high-voltage components have already been procured, with assembly of the test stand to begin soon.

Ongoing efforts to layout the full RFQ Test Stand that will include the ion source, 35-keV high-voltage system, LEBT, RFQ, RF system, MEBT, diagnostics, and controls will continue. These preparations include building support structures and beam transport-line components; procuring magnets, RF systems, and vacuum systems; as well as developing the appropriate diagnostics and controls required.

Particular emphases of the RFQ Test Stand will be long-term reliability and availability of the RFQ and associated systems, and the constraints imposed by dual-species operation of the LANSCE linac on the phase-space distributions of the beam from the RFQ injector. Good measurements of the beam properties, including matching to the DTL, are therefore required during the testing phase of the RFQ [14]. All components of the test stand are being designed to be compatible with implementation as a full replacement system on the LANSCE linac including support structures and all mechanical systems such as vacuum and cooling manifolds, etc.

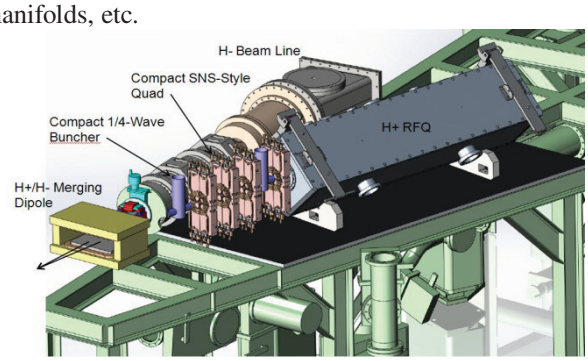


Figure 3: Shown is a preliminary engineering layout of the new H^+ RFQ injector, compact quads, and compact bunchers on the existing LANSCE beam transport line.

REFERENCES

[1] R. W. Garnett, "LANSCE as a High-Power Beam Applications Test Bed," AccApp'13, MOOFA05.
[2] R. Garnett, et al., "High-Power Options for LANSCE," PAC'11, THOCN4.
[3] R. W. Garnett, et al., "Progress towards an RFQ-based Front End for LANSCE," IPAC'11, WEPS068.
[4] L. Rybarcyk, et al., "Design Requirements and Expected Performance of the New LANSCE H^+ RFQ," MOPMA17, NA-PAC'13.
[5] See the Los Alamos Code Group web site at http://laacg.lanl.gov/.
[6] Yuri K. Batygin, "Particle-in-cell code BEAMPATH for beam dynamics simulations in linear accelerators and beamlines," Nucl. Instrum. Meth. A539 (2005).
[7] CST Studio Suite, CST GmbH, 2013, www.cst.com.
[8] ANSYS Engineering Simulation Software, www.ansys.com.
[9] S. Kurennoy, et al., "Design Analysis of the New LANL 4-Rod RFQ," MOPMA16, NA-PAC'13.
[10] C. Fortgang, et al., "Design of a Duoplasmatron Extraction Geometry and LEBT for the LANSCE H^+ RFQ Project," TUPSM18, NA-PAC'13.
[11] J. Lyles, et al., "New High Power Test Facility for VHF Power Amplifiers at LANSCE," PAC'11, TUP134.
[12] C. Fortgang, et al., "A Specialized MEBT Design for the LANSCE H^+ RFQ Project," TUPSM17, NA-PAC'13.
[13] L. Rybarcyk and S. Kurennoy, PAC'09, p. 4944.
[14] R. McCrady, et al., "Diagnostics for the LANSCE RFQ Front-End Test Stand," MOPSM05, NA-PAC'13.

Copyright © 2013 CC-BY-3.0 and by the respective authors

EXPERIMENTAL RESULTS FROM A "DIAGNOSTIC" PULSE FOR SINGLE-PARTICLE-LIKE BEAM POSITION MEASUREMENTS DURING ACCUMULATION/PRODUCTION MODE IN THE LOS ALAMOS PROTON STORAGE RING*

J. Kolski†, E. Bjorklund, M. Hall, M. Martinez, and F. Shelley, LANL, Los Alamos, NM, USA

Abstract

Beam position monitors (BPMs) are the diagnostic most used in setting up and documenting the Los Alamos Proton Storage Ring (PSR). One-turn injection can be approximated as single-particle injection with initial betatron position and angle (x_0 and x'_0). The turn-by-turn beam position data from single-turn injection allows measurement of the betatron tune, closed orbit (CO), and injection offset (x_0 and x'_0 at the injection point). In accumulation mode, many turns are injected into the ring, the transverse phase space is quickly filled, and there is no coherent betatron motion. The injection offset, which determines the accumulated beam size and is very sensitive to steering upstream of the ring, is not measurable during accumulation. We review our approach for measuring the injection offset during accumulation, focus discussion on recent experimental results, and compare measurements of the betatron tune, CO, and injection offset in single-turn injection mode and in a "diagnostic pulse" mode.

MOTIVATION

The PSR BPMs[1] are bi-directional, stripline-type with electrode length ∼37 cm (a quarter 201.25 MHz wavelength). The 201.25 MHz longitudinal beam structure, to which the PSR BPMs are sensitive, is imposed during acceleration and decoheres after ∼30 turns in the PSR due to momentum spread and synchrotron motion.

Single-turn injection mode is used to document the PSR. We measure 30 turns of beam position data before the longitudinal beam structure decoheres, which is sufficient to fit the betatron tunes, CO, and injection offset.

Normally, the PSR operates in production mode, where ∼1800 turns are accumulated. With the filled phase space, there is no coherent betatron motion in production mode, so the betatron tunes and injection offset can not be measured, but does yield the CO.

Aside from beam energy, the CO and betatron tunes are independent of machine operation upstream of the ring. The injection offset is very sensitive to steering upstream of the PSR, and we cannot measure this important operational parameter in production mode.

We develop an operation mode we call LBEG+ that enables us to document the PSR by measuring the betatron tunes, CO, and injection offset without affecting delivery of production beam[2]. The scheme is to inject a single turn (diagnostic pulse) on the same machine cycle as the production mode ∼50 μs after the accumulated beam is extracted, see Fig. 1. The 50 μs between production beam and the diagnostic pulse allows the linac RF to recover from the beam-off transient, the injection bump magnets to set to zero, and for residual field in the PSR buncher to dissipate. The diagnostic pulse coasts in the PSR and is lost.

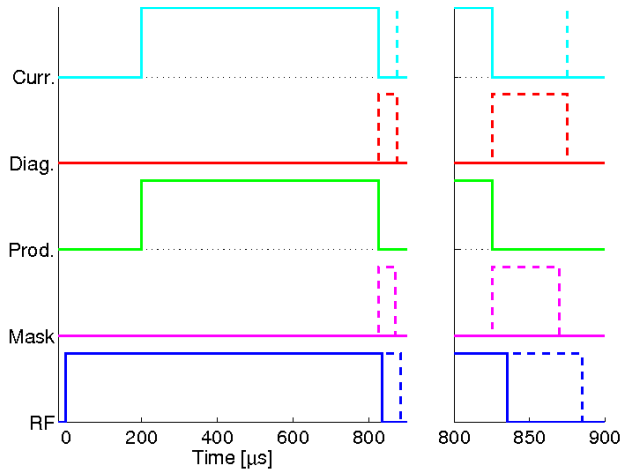


Figure 1: (Color) Timing scheme of one machine cycle for (from bottom to top) the linac RF gate (blue), RF system protect mask (magenta), production beam gate (green), diagnostic beam gate (red), and beam current in transport (cyan) for production (solid lines) and LBEG+ (dashed lines) modes. The right plot focuses on the end of the machine cycle.

LBEG+ AND SINGLE-SHOT MEASUREMENT COMPARISON

Operationally, the hope is for the LBEG+ scheme to replace the single-shot method for measurements of the CO, betatron tune, and injection offset during production. Thus, it is necessary for the CO, tune, and injection offset results measured via the LBEG+ scheme to be equal to the measurements taken in the single-shot scheme. We collected a set of BPM data in single-shot mode, and then collected another set of data in LBEG+ mode for comparison. In this section, we compare the LBEG+ and single-shot results for the CO, tune, and injection offset.

Thirty turns of betatron motion is digitized at each BPM.

* Work supported by in part by United States Department of Energy under contract DE-AC52-06NA25396. LA-UR 13-27450.

† Electronic address: jkolski@lanl.gov

Copyright © 2013 CC-BY-3.0 and by the respective authors

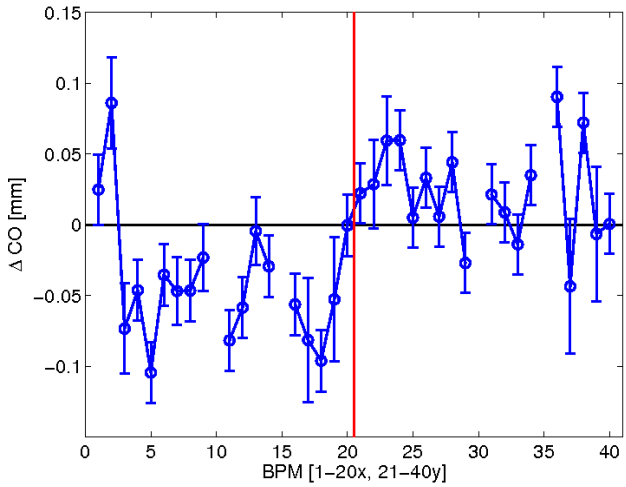


Figure 2: Difference in CO measurements using the single-shot and LBEG+ schemes with one rms uncertainty.

The beam position is fit with a cosine:

$$x_n = A\cos(2\pi\nu(n-1)+\phi) + O_{\text{ffset}} \qquad (1)$$

where A, ν, n, ϕ, and O_{ffest} are the amplitude of betatron motion, tune, turn index, phase, and CO respectively. We also compare the fitted amplitude and phase from single-shot and LBEG+ measurement schemes.

In the comparison plots, we use an ORM BPM indexing convention where BPMs are 1-20 horizontal, BPMs 21-40 are vertical such that BPM 1 and 21 are the horizontal and vertical planes of the first BPM.

Closed Orbit Measurement

The CO describes the accumulated beam centroid position average. For minimum beam loss, we center the CO at all BPMs. The CO measurement results between single-shot and LBEG+ measurement schemes are very similar, Fig. 2, within three rms uncertainties with maximum deviation of 0.1 mm, which is within acceptable tolerance. We conclude the CO measurements yield the same result in both schemes.

Tune Measurement

The tune measurement describes the frequency of betatron oscillation. The tune measurements are very close, Tab. 1, within one rms standard deviation. We conclude that the tune measurement is the same in both single-shot and LBEG+ schemes.

Table 1: Comparison of the Measured Tunes from Single-Shot and LEBG+ Schemes with One RMS Standard Deviation

	ν_x	ν_y
Single-Shot	$0.1898 \pm 4\times10^{-4}$	$0.1870 \pm 2\times10^{-4}$
LBEG+	$0.1900 \pm 4\times10^{-4}$	$0.1870 \pm 2\times10^{-4}$
Difference	2.48×10^{-4}	-5.7×10^{-5}

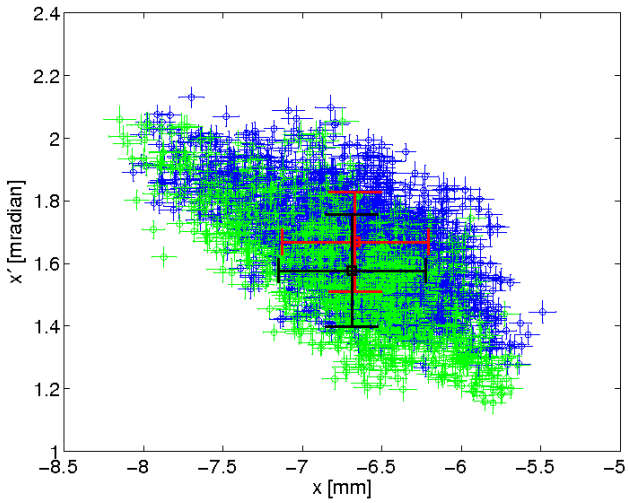


Figure 3: (Color) Horizontal injection offset measurement and the measurement distribution averages with one rms standard deviation from single-shot (blue, red) and LBEG+ (green, black) schemes.

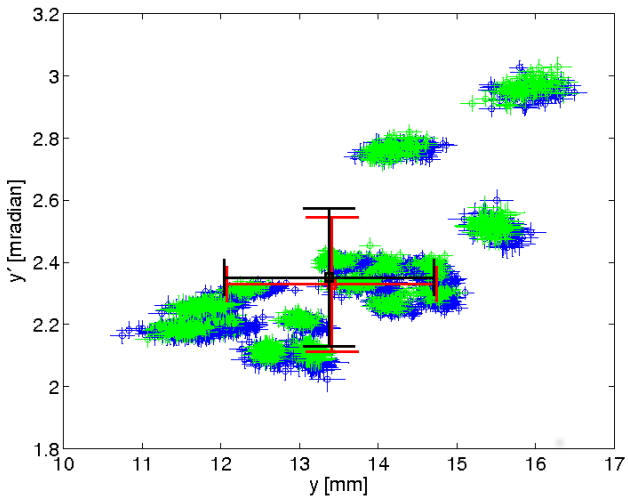


Figure 4: (Color) Vertical injection offset measurement and the measurement distribution averages with one rms standard deviation from single-shot (blue, red) and LBEG+ (green, black) schemes.

Injection Offset Measurement

The injection offset is fit to the turn-by-turn BPM data,

$$x_{i,n} = x_0\sqrt{\frac{\beta_i}{\beta_0}}(\sin\Theta + \alpha_0\cos\Theta) + x'_0\sqrt{\beta_i\beta_0}\sin\Theta - x_{CO_i}, \qquad (2)$$

where $\Theta = 2\pi\nu(n-1)+\mu_{0\to i}$, the indices i, 0, and n indicates values at the i^{th} BPM, the foil, or turn number re-

Copyright © 2013 CC-BY-3.0 and by the respective authors

Table 2: Comparison of the Measured Injection Offsets from Single-Shot and LEBG+ Schemes with One RMS Uncertainty on the Average

	x_0 [mm]	x_0' [mradian]
Single-Shot	$-6.669 \pm 1.1\times10^{-2}$	$1.669 \pm 4\times10^{-3}$
LBEG+	$-6.689 \pm 1.2\times10^{-2}$	$1.577 \pm 5\times10^{-3}$
Difference	2.0×10^{-2}	-9.2×10^{-2}
	y_0 [mm]	y_0' [mradian]
Single-Shot	$13.412 \pm 3.3\times10^{-2}$	$2.329 \pm 5\times10^{-3}$
LBEG+	$13.378 \pm 3.6\times10^{-2}$	$2.351 \pm 6\times10^{-3}$
Difference	-3.4×10^{-2}	2.2×10^{-2}

spectively, x and x' are the phase space position and angle, β, α, and μ are the beta function, its derivative, and the positive phase advance from the foil, and x_{CO} is the CO.

Figures 3 and 4 compare ∼100 measurements of the injection offset from each BPM. For typical operations, we set injection offset to $[x_0,\ x_0',\ y_0,\ y_0'] = [-3.8$ mm, 0.85 mradian, 16.5 mm, 2.8 mradian$]$. Table 2 compares the measurement distribution averages.

The measured injection offsets are quite different from our standard setup. This is an example of how the injection offset can change significantly with upstream tuning and why it is important to be able to measure the injection offset during production.

The islands in Fig. 4 are due to BPM measurement saturation for large beam positions. Each island is measurement from a different BPM, and each BPM has different degrees of measurement saturation depending on the type of BPM and the beam position. PSR BPM measurement saturation is the topic of a future paper.

We observe a statistically significant difference in the injection offset angles between the single-shot and LBEG+ measurements. The deviation is very small, $\sim 10^{-2}$ mradian and within tolerance. We conclude that the injection offset measurement from single-shot and LBEG+ schemes is the same.

Amplitude Measurement

The amplitude of betatron motion can be related to the beta function. Figure 5 compares the amplitude from single-shot and LBEG+ measurements. Note that the measurements agree within 3 rms uncertainties. We conclude the amplitude measurements from single-shot and LBEG+ schemes are the same.

Phase Measurement

The betatron phase can be related to the phase advance and is useful in model verification experiments. Figure 6 compares the phase measurements from single-shot and LBEG+ schemes. We observe a statistically significant and constant offset in the phase difference. The phase deviation is real and is due to the measured difference in injection offset angles discussed previously. Accounting for the very small change in injection offset, we conclude that the phase measurement from single-shot and LBEG+ schemes is the same.

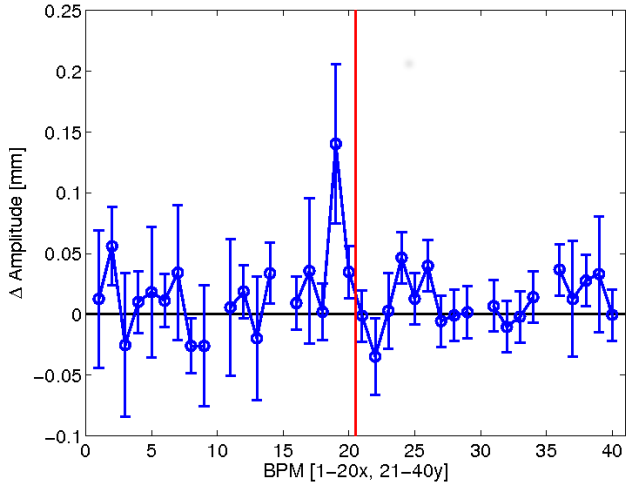


Figure 5: Difference in amplitude measurements using the single-shot and LBEG+ schemes with one rms uncertainty.

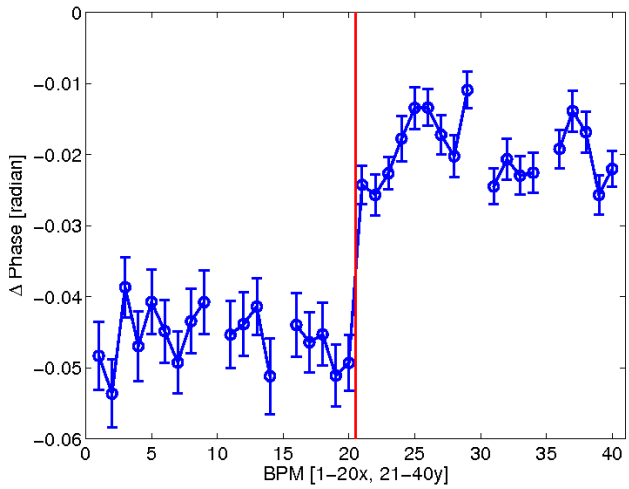


Figure 6: Difference in phase measurements using the single-shot and LBEG+ schemes with one rms uncertainty.

CONCLUSIONS

We demonstrate a proof of principle for the LBEG+ scheme to measure the CO, betatron tune, and injection offset during production. We compare measurements of the CO, tune, phase, amplitude, and injection offset from the single-shot and LBEG+ measurement schemes and show that both methods produce the same result.

REFERENCES

[1] J. Kolski, Ph.D. thesis, unpublished (Indiana University 2010).

[2] J. Kolski, et al. THPPP097, Proceedings of IPAC2012, New Orleans, Louisiana, USA.

Copyright © 2013 CC-BY-3.0 and by the respective authors

DESIGN ANALYSIS OF THE NEW LANL 4-ROD RFQ

S.S. Kurennoy, E.O. Olivas, and L.J. Rybarcyk, LANL, Los Alamos, NM 87545, USA

Abstract

An upgraded front end of the LANSCE linac will include a 4-rod RFQ replacing the aging Cockcroft-Walton injector, initially only for protons. We performed a detailed analysis of the proposed RFQ design using 3D modeling with the CST Studio Suite. The CAD-based RFQ model takes all design details into account. The electromagnetic analysis with MicroWave Studio (MWS) is followed by beam dynamics modeling with Particle Studio (PS) using the MWS-calculated fields. In addition, a thermal and stress analysis is performed with ANSYS, based on the power flux from MWS computations. Simulation results are used for design iterations aimed to satisfy special requirements imposed by an existing common transfer line for different beams injected into the 201.25-MHz drift-tube linac.

INTRODUCTION

LANL is moving forward with replacing the aging Cockcroft-Walton (C-W) injectors with an RFQ-based front end [1] for the LANSCE proton linac. A 4-rod type RFQ design was developed in collaboration between IAP (Frankfurt) and LANL. The LANL RFQ, operating at 201.25 MHz at the duty factor up to 15%, with 35-keV injection and 750-keV final energy, should satisfy special requirements due to its incorporation into the existing medium-energy beam transfer that works with multiple beams, see in [2]. The RFQ will be manufactured by Kress GmbH. We used the RFQ CAD files from Kress imported into CST Studio [3] to create a model of the LANL H^+ RFQ and evaluate its performance.

RFQ MODEL

The imported CAD model was simplified by removing details nonessential for EM analysis such as external supports, etc. The RFQ cavity walls were also removed, leaving only the resonator vacuum volume in the CST model. The resulting model is shown in Fig. 1. Here the RFQ vacuum vessel, in light-blue, is 175-cm long (wall-to-wall), 34-cm wide, and 30-cm high (along the stem direction, z). It also includes wide recesses on the thick end and front walls, of radius 8.5 cm and depth 1.5 cm, followed by 5-cm-long beam pipes of radius 2 cm. The RFQ vanes are supported by 24 stems that are spaced longitudinally with variable period, 75 mm in the center and 69.5 mm for three periods near each end. The tuners electrically short two adjacent stems and can be moved along them (in z direction) to adjust the mode frequency and voltage profile (flatness) along the structure length. The variable stem spacing simplifies tuning the voltage flatness along the structure. Our RFQ model uses the CAD model coordinates: x is along the RFQ axis, and the beam is moving in $-x$ direction (right to left in Fig. 1).

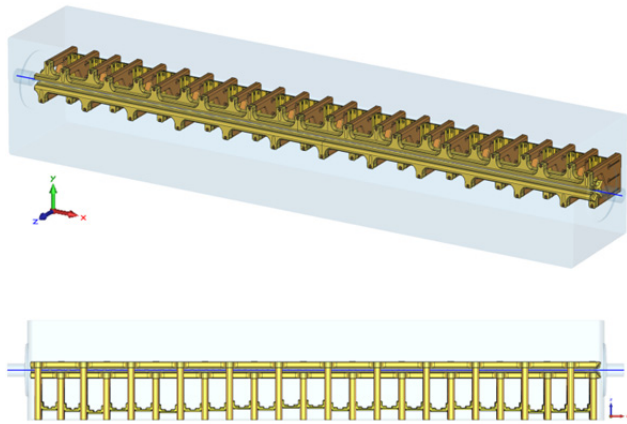


Figure 1: RFQ model (top) and its side view (bottom).

One can see in Fig. 1 (bottom) that the tuners are at different heights: they are adjusted to make the inter-vane voltage flat within ±1%. However, even with all tuners at the same height, the voltage is flat within ±5%, due to the variable stem spacing.

ELECTROMAGNETIC ANALYSIS

We studied the RFQ model using the CST MicroWave Studio (MWS). The mode frequencies and RF fields are calculated by the AKS eigensolver that provides more accurate surface approximations. The RF fields have some interesting features resembling those found in the FNAL 4-rod RFQ, see in [4, 5].

The first is the presence of a small transverse horizontal (parallel to the ground plane) electrical-field component, E_y, on the RFQ geometrical axis, sometimes referred to as a "dipole" component. This is due to the transverse electric fields being stronger between two upper vanes than between two lower ones, which results in the center of the transverse quadrupole field displaced down, to the ground plane, from the geometrical axis by 0.45 mm. The shift is small but not negligible when compared to the 4-mm vane aperture. This effect is known in 4-rod RFQs designed for higher frequencies [6]. The electric-field components on axis: longitudinal E_l, horizontal E_y, and vertical (along the stems) E_z are plotted in Fig. 2 versus the longitudinal coordinate $s = -x$. The fields are scaled to the nominal inter-vane voltage V_0=50 kV. In a similar plot along the axis shifted by -0.45 mm in z, the horizontal component E_y is close to zero, while the other two do not change much compared to Fig. 2.

Another important feature is the longitudinal electric field in the end gaps that separate the vane ends from the RFQ box walls (end-gap bumps). The red curve E_l in Fig. 2 shows the RFQ accelerating field – the oscillating part – produced by the vane modulation. The curve also has two peaks, near the entrance and exit.

Copyright © 2013 CC-BY-3.0 and by the respective authors

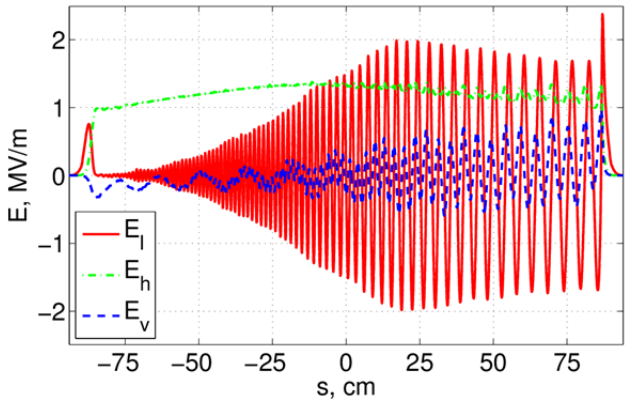


Figure 2: On-axis electric field in the RFQ model.

The RFQ cavity extends from s = -87.5 cm to s = 87.5 cm; the vanes start at s = -86.9 cm and end at 86.9 cm. It would make 6-mm gaps; however, the gaps are effectively wider by 1.5 cm due to the recesses cut out in the end walls and the beam pipes. This is why the entrance-gap peak of the longitudinal field is small. The large near-exit peak is due to a special end-vane design: one pair ends at a modulation maximum, another at minimum.

The end-gap longitudinal field exists because the quadrupole symmetry is broken near the RFQ ends; it would vanish in a perfectly symmetric structure. Moreover, in the end-gap areas there are transverse field components in addition to the usual quadrupole ones. Under some circumstances the end-gap fields, which are neither predicted nor taken into account by standard RFQ design codes, can change the exiting beam parameters such as energy and emittances [4, 5].

One important requirement for the RFQ operation is the inter-vane voltage flatness along the structure. The relative voltages, calculated at the midpoints of all 23 full periods, are presented in Fig. 3 for two cases: all tuners are at the same height, only the frequency is tuned to 201.25 MHz ("initial") and after some tuner adjustments in the MWS model ("tuned"). Even for the initial profile, the voltage was reasonably flat, within ±5% of the average value; this is due to the variable stem spacing.

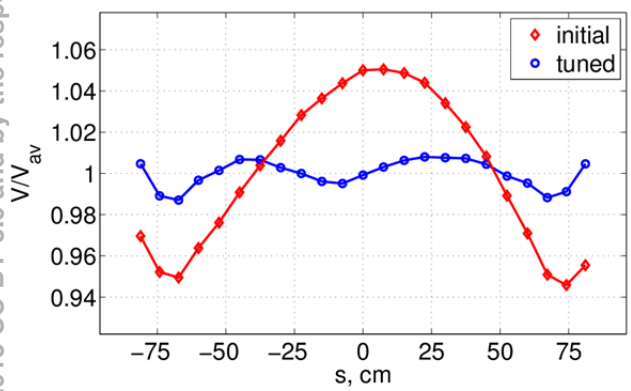


Figure 3: Voltage profile along the RFQ structure.

When all 23 tuners are moved together, by distance h up from the ground plane, the frequency sensitivity is df/dh = 0.75 MHz/mm. The frequency tuning range is comfortably sufficient in this design. In the shown tuned case, the displacements of individual tuner plates range from -9.5 mm to 8 mm.

The calculated maximal field at nominal voltage E_{max} = 23.5 MV/m ($1.6E_K$) is reached near the vane exit end. We use the fields calculated in the tuned case for our macro-particle simulations, and the related heat flux for thermal-stress analysis.

BEAM DYNAMICS RESULTS

The RF fields calculated by MWS are imported into the Particle Studio (PS) PIC solver. For macro-particle simulations, we used "matched" distributions generated with LAACG codes [7]. Matched CW proton beams of 10K macro-particles, one RF period long, were generated for a few different currents at the model boundary from Twiss-parameters that were back-traced from the match point at the RFQ vane entrance. The resulting distributions are converted to CST PS format and injected for 10 RF periods at 35 keV, (β_{in} = 0.0086), and accelerated to 750 keV, corresponding to β_{out} = 0.04. As an illustration, Fig. 4 shows macro-particles in the PS model with 12-mA current at t = 405 ns after the injection of 10x10K particles started. The total number of macro-particles at this moment is about 97.4K, most of them are densely packed in bunches. The particle energy is indicated by color; the energy scale is overlapped on the right. The particles propagate from right to left. More than 10 bunches are formed, due to the longitudinal space-charge push at the train ends; a few leading bunches in Fig. 4 are already accelerated and approaching the exit. Trailing low-energy particles are not captured in bunches.

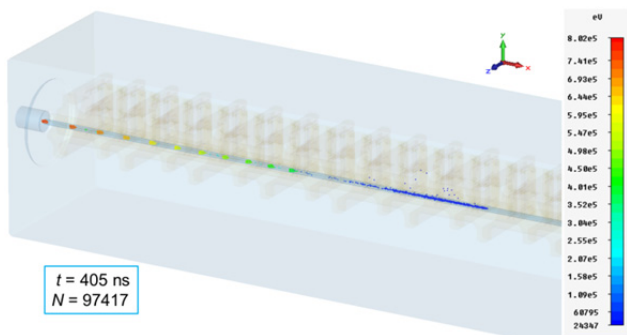


Figure 4: Particles in the RFQ model for 12 mA at 405 ns.

A convenient way to look at energy changes is with phase-space snapshots of the longitudinal phase space x-W (coordinate-energy). In Fig. 5, five such snapshots, from t = 405 ns to 409 ns with 1-ns step, are overlapped. Each snapshot is shown in a different color; together they cover a time interval equal to one RF period. One can see that the bunch energy increases until the end of the modulations (x = -869 mm), then remains constant in the

Copyright © 2013 CC-BY-3.0 and by the respective authors

exit beam pipe (x < -890 mm). Again, the beam propagates from positive to negative x in this model.

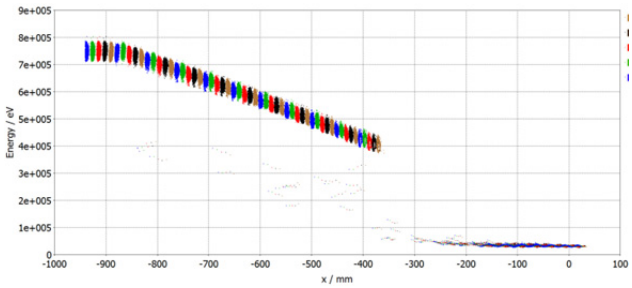


Figure 5: Longitudinal phase-space snapshots for 12 mA.

To exclude effects of space charge in the bunch-train head and tail, we analyzed only 4-6 central bunches from PS simulations with 10x10K beams injected. Some results – the average energy W of exiting bunches, their transverse normalized r.m.s. emittance ε_t, and current transmission – are summarized in Table 1. The initial distribution has a transverse normalized r.m.s. emittance 0.2 π mm·mrad in both transverse planes.

Table 1: PS Results for Different Beam Currents

I, mA	W, keV	ε_t, π mm·mrad	ε_l, keV·deg	transm.
0	756	0.40	20	0.99
12	756	0.55	13	0.97
35	753	0.62	15	0.89

The calculated growth of the transverse emittance, even in the matched low-current case, is large. On the other hand, the longitudinal emittances are smaller than expected. We consider the emittance results preliminary and will investigate this problem further.

THERMAL ANALYSIS

The total dissipated power in the RFQ model for ideal copper surfaces is 77 kW at 100% duty and is distributed as follows: 55% on stems, 28% on vanes, 17% on tuners, and less than 0.5% on the RFQ-vessel inner surface. Since the RFQ will operate at noticeable duty factors, up to 15%, the structure requires adequate cooling. It will be provided by water running at 2.5 m/s through cooling channels. Each stem has a separate inverse-V-shaped cooling channel. There are also cooling channels inside vanes, connected through a few stems to pipes under the ground plane. The heat flux calculated in post-processing MWS fields was used for thermal-stress analysis with ANSYS [8].

In the thermal analysis, a realistic contact copper-copper conductivity between vanes, stems, and tuners was taken into account. The calculated temperature distribution in a structure slice near the RFQ exit is shown in Fig. 6 for the duty of 18% (15% plus additional heating due to realistic surface conductivity). The maximal temperature of 335 K is at the near-end stem and the temperature range is less than 40° C even in this extreme case. Maximal deformations in the RFQ structure reach 80 μm but the relative vane displacements stay below 40 μm (< 0.002″).

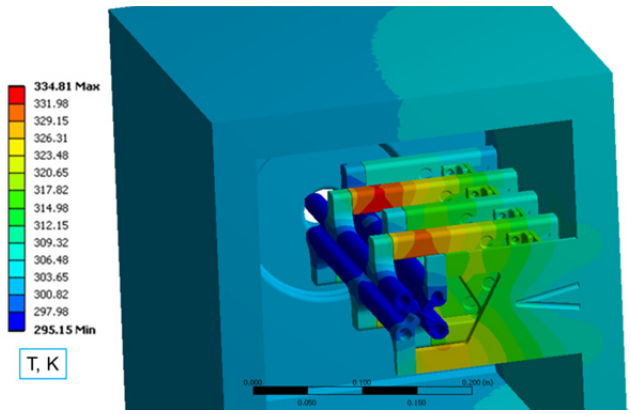


Figure 6: Temperature distribution at 18% duty.

SUMMARY

A detailed study of the new LANSCE 4-rod RFQ was performed with the CST Studio codes. The RFQ model is based on imported CAD files. The RF fields calculated with MicroWave Studio were used for beam dynamics modeling with Particle Studio and for thermal-stress analysis with ANSYS. Our modeling takes into account effects associated with 3-D field asymmetries such as end-gap fields, which are not predicted by standard RFQ design codes. We found that the RFQ output energy and transmission satisfy the design requirements and that the structure cooling is adequate. Reasons for the observed transverse emittance growth will be further investigated.

The authors would like to thank A. Schempp and J. Schmidt (IAP, Frankfurt), J. Haeuser (Kress GmbH), and Y. Batygin, R. Garnett, and J. O'Hara (LANL) for useful information and stimulating discussions.

REFERENCES

[1] R.W. Garnett et al, "Status of LANSCE RFQ front-end upgrade," MOPMA14 NA-PAC'13.
[2] L.J. Rybarcyk et al, "Design requirements and expected performance of the new LANSCE H^+ RFQ," MOPMA17 NA-PAC'13.
[3] CST Studio Suite, CST, 2013, www.cst.com
[4] S.S. Kurennoy et al, IPAC13, Shanghai, China, THPWO094, p. 3978 (2013); www.JACoW.org
[5] S.S. Kurennoy, reports LA-UR-12-26388 and LA-UR-13-21653, Los Alamos, 2012-2013.
[6] B. Koubek et al, PAC11, New York, p. 1888 (2011).
[7] Los Alamos Accelerator Code Group, laacg.lanl.gov
[8] ANSYS, ANSYS Inc., www.ansys.com

Copyright © 2013 CC-BY-3.0 and by the respective authors

DESIGN REQUIREMENTS AND EXPECTED PERFORMANCE OF THE NEW LANSCE H^+ RFQ*

L.J. Rybarcyk#, Y.K. Batygin, I.H. Draganic, C. M. Fortgang, R.W. Garnett, S.S. Kurennoy, R.C. McCrady, and T.P. Wangler, Los Alamos National Laboratory, Los Alamos, NM 87545, U.S.A
A. Schempp, IAP, Goethe University, Frankfurt am Main, Germany
J. Haeuser, Kress GmbH, Biebergemuend, Germany

Abstract

LANSCE provides H^- and H^+ beams to several user facilities for fundamental and applied research, including a 100-MeV, 250-μA proton beam to the Isotope Production facility (IPF). Each beam species is initially accelerated to 750 keV in separate Cockcroft-Walton (C-W) accelerators. Due to the age and possible failure modes of the C-W's and the potential impact of a C-W failure to the IPF program, we have begun the process of replacing the aging H^+ C-W with a modern Radio Frequency Quadrupole (RFQ) accelerator-based system. In addition, the complexity of combined species operations imposes further restrictions on the beam performance and configuration that must be incorporated into the design process. This paper will cover the physics design requirements of this new RFQ and the expected performance based upon the results of PARMTEQM simulations.

INTRODUCTION

The Los Alamos Neutron Science Center (LANSCE) facility has a diverse user program that is possible in part because of the dual species operation, i.e. acceleration of both H^+ and H^- beams. IPF is one of those facilities and receives 100-MeV beam generated by our H^+ injector. IPF is one of only a few installations that produce a key radioisotope for medical procedures used across the nation and so high beam availability and reliability is critical to meeting their programmatic milestones. The H^+ injector utilizes an ~40 year old 750-keV C-W accelerator. The C-W has possible failure modes that include a failure of the accelerator column, which has already been replaced once and required 4 months to complete, and the collapse of a support leg that could lead to a catastrophic failure of the C-W. Concern over the potential likelihood of these types of failures and the severe impact to the IPF program has provided the impetus to pursue an RFQ-based replacement for the H^+ injector.

The RFQ is being designed and verified as a joint effort between the Institute of Applied Physics (IAP), Goethe University, Frankfurt, Germany and Los Alamos. The IAP team used a combination of PARMTEQM [1] and proprietary algorithms to develop the physics design for the 4-rod RFQ, which the Los Alamos team verified using PARMTEQM. Our project partner Kress GmbH, with input from IAP, is responsible for the engineering design and fabrication of the RFQ.

*Work supported by US DOE under contract DE-AC52-06NA25396.
#lrybarcyk@lanl.gov

REQUIREMENTS

The new H^+ RFQ will need to provide sufficient beam current to meet present and anticipated future programmatic needs and do so within the context of dual species operation. This includes the capability to operate the RFQ for a range of input beam currents depending upon the requirements of the user programs and the available beam duty factor. The LANSCE dual injector beam line layout that maintains the existing H^- and common LEBTs requires the new RFQ to be located several meters upstream from the entrance to the next accelerating structure, i.e. the 100-MeV drift tube linac (DTL). This places additional constraints on the transverse and longitudinal emittances so that the beam can be transported and properly matched without significant losses. A list of the RFQ requirements and expected performance based upon PARMTEQM simulation results for the IAP-developed physics design are given in Table 1. The frequency and output energy were chosen to be consistent with our present linac base

Table 1: Comparison of the Final, 201.25-MHz 4-rod RFQ Design Parameters with the Design Specifications

Parameter	Specification	Final Design
Injection Energy	35 keV	35 keV
Final Energy	750 keV	750 keV
Transmission	≥ 90%	96%
Peak Current	35 mA	35 mA
Current Limit	≥ 70 mA	60 mA
Output Energy Spread (FWHM)	< 3.0%	2%
Length	< 2.5 m	1.75 m
Peak Electric Field (E_K)	1.7	1.6
Input Trans. Emittance rms (cm-mr, norm.)	0.020	0.020
Exit Trans. Emittance rms (cm-mr, norm.)	0.023	0.022
Exit Long. Emittance rms (deg-MeV @201.25 MHz)	< 0.08	0.071

Copyright © 2013 CC-BY-3.0 and by the respective authors

frequency and nominal injection energy to the DTL. The RFQ injection energy was chosen with the desire to keep it low, which helps reduce the overall length of the RFQ, and taking into consideration the successes of other RFQ projects with similar peak current, injection energy and frequency specifications [2][3]. The transmission specification was chosen to help ensure that the integrated performance of the new RFQ and DTL would have an overall beam capture up through the DTL at least as good as the present C-W based system. The current limit in the design of the RFQ was specified to be twice the maximum design current as a general rule-of-thumb. The output energy spread and longitudinal emittance were chosen to ensure successful transport and capture of the beam from the RFQ and was based upon results from PARMILA [4] beam dynamics simulation of the MEBT and DTL using PARMTEQM beam distributions [5]. The limit on the peak surface electric field was chosen to ensure reliable operation at design field strength. The input emittance represents the maximum that we expect to inject and was based upon the performance of our present duoplasmatron ion source, which we will use with the RFQ injector, and an estimate of the maximum emittance growth that might be sustained in the LEBT. However, based upon measurements of the existing H^+ beam, we expect the nominal input emittance to be somewhat smaller. The RFQ output emittance requirement was based upon expected performance for a carefully designed RFQ and the desired to keep the beam emittance in the MEBT at a level that will allow for easy transport and matching of the RFQ beam into the DTL [5].

EXPECTED PERFORMANCE

The IAP RFQ design was evaluated using the PARMTEQM design and simulation code. The simulations were done using the design parameters provided by IAP. The effects of the end regions that can be important in a 4-rod RFQ require the use of more sophisticated models that combine 3D EM fields with multiparticle tracking. This effort is in progress [6].

The results of the PARMTEQM simulations show the design meets our requirements in all but one aspect, the current limit, which is not significant as will be shown later. Figure 1 shows the beam dynamics along the RFQ and phase space distributions at the end of the RFQ for the design peak current and emittance input beam. The RFQ produces a good quality beam with high transmission. Figure 2 shows the results of the PARMTEQM simulation that indicate the design produces little transverse emittance growth along the RFQ. In initial studies performed by the Los Alamos team, we had found that an RFQ design employing equal transverse and longitudinal current limits, one common approach, produced significant transverse emittance growth. In a follow-on analysis we found that the emittance growth was due to parametric resonance conditions being met, but that could be avoided with properly chosen parameters [7]. This design effectively avoids the parametric resonance conditions and produces a beam with little, ~10%, emittance growth.

Because we plan on operating the RFQ for a range of input beam currents, likely values between 10 and 35 mA,

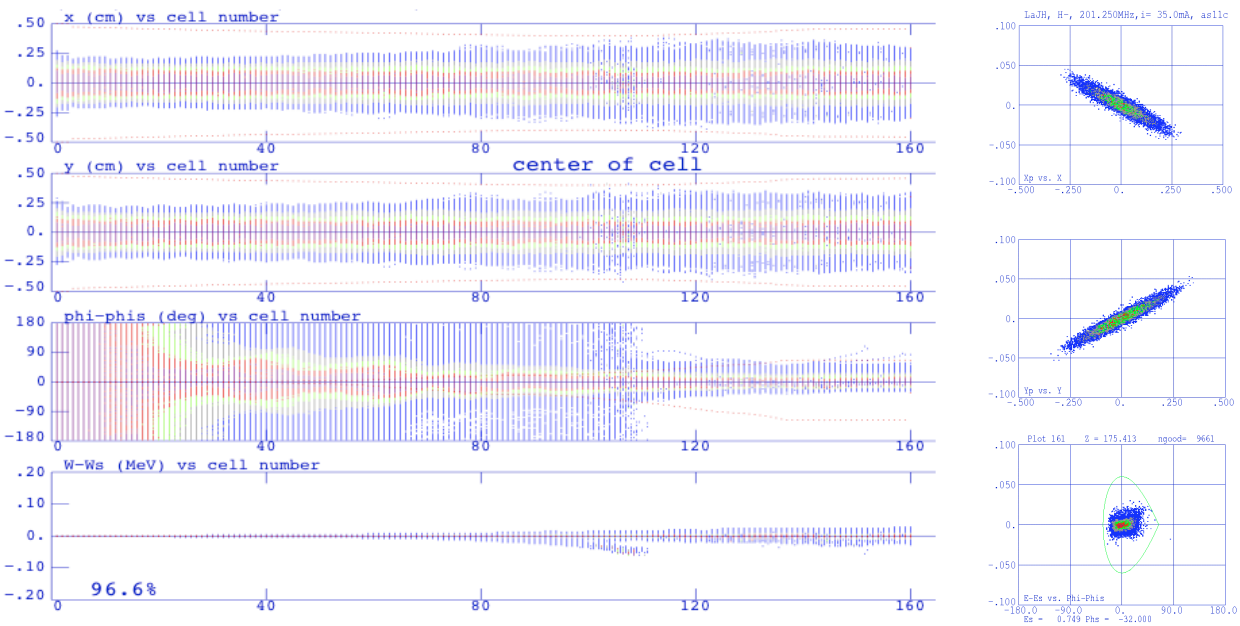


Figure 1: PARMTEQM beam dynamics results showing x, y beam size, phase and energy spread for the design input beam (left panel). RFQ output phase space distributions (right panel) x-x'(top), y-y' (middle) and phi-w (bottom).

Copyright © 2013 CC-BY-3.0 and by the respective authors

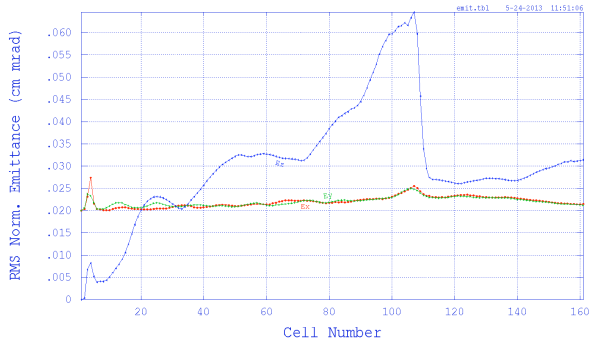


Figure 2: Transverse (red, green) and longitudinal (blue) rms, norm. beam emittances along the RFQ for the design input beam.

depending upon the average current required and the duty factor available for the user programs, we desire good performance over that range. Although the current limit characteristic for this design is somewhat lower than desired, it does not appear to affect the performance well beyond the design point and is therefore not an issue. As shown in Figures 3, 4 and 5, the simulated performance is quite good for input beam currents up to 60 mA, with the transmission falling off to about 80% at that point.

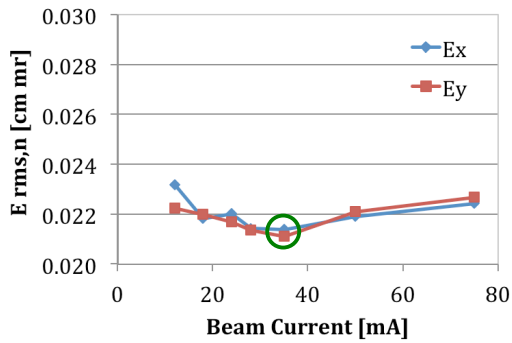


Figure 3: Transverse (red, blue) rms, norm. output beam emittance vs. input beam current. The green circle indicates the 35 mA design point.

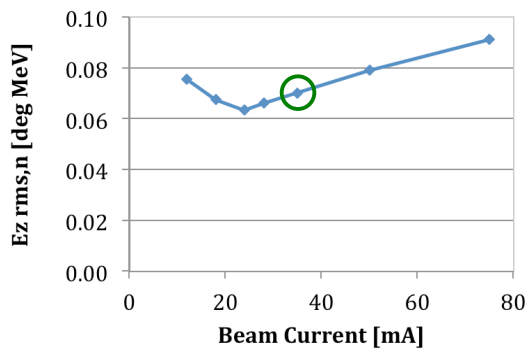


Figure 4: Longitudinal (blue) rms, norm. output beam emittance vs. input beam current. The green circle indicates the 35 mA design point.

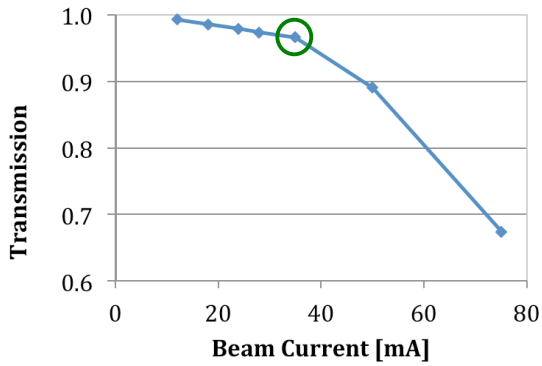


Figure 5: RFQ beam transmission vs. input beam current. The green circle indicates the 35 mA design point.

SUMMARY

The IAP approach has produced an RFQ design that has met the specified beam requirements as simulated with the PARMTEQM code. The performance is equally good for the range of beam currents over which we expect to operate.

REFERENCES

[1] K. Crandall et al., *RFQ Design Codes*, LANL publication, LA-UR-96-1836, revised Dec. 2005.

[2] A. P. Letchford et al., "Testing, Installation, Commissioning and First Operation of the ISIS RFQ Pre-Injector Upgrade," PAC2005, Knoxville, TN, May 2005, ROPC010, p. 695 (2005); http://www.JACoW.org

[3] V.E. Scarpine et al., "Instrumentation Developments and Beam Studies for the Fermilab Proton Improvement Plan Linac Upgrade and New RFQ Front-end," HB2012, Beijing, China, Sept. 2012, TUO1C06, p. 315, (2012); http://www.JACoW.org

[4] H. Takeda and J.H. Billen, *PARMILA*, LANL publication, LA-UR-98-4478, revised Mar. 2005.

[5] C. Fortgang, et al., "A Specialized MEBT Design for the LANSCE H^+ RFQ Project," this conference, TUPSM17.

[6] S. Kurennoy, et al., "Design Analysis of the New LANL 4-Rod RFQ," this conference, MOPMA16.

[7] Y. Batygin et al., "Beam Emittance Growth Effects in High-Intensity RFQ," IPAC2013, Shanghai, China, May 2013, TUPWA067, p. 1859 (2013); http://www.JACoW.org

Copyright © 2013 CC-BY-3.0 and by the respective authors

GPU ACCELERATED ONLINE MULTI-PARTICLE BEAM DYNAMICS SIMULATOR FOR THE LANSCE LINAC*

X. Pang†, L. Rybarcyk, S. A. Baily, Los Alamos National Laboratory, Los Alamos, NM, 87544, USA

Abstract

A GPU-accelerated online multi-particle beam dynamics simulator is being developed for use in the LANSCE linac operation. The goal is to provide new insights on the beam distribution inside the linac and to help understand the impact of set point adjustments on it. Details regarding the code structure design, GPU programming and performance, code validation and status will be presented.

INTRODUCTION

The Los Alamos Neutron Science Center (LANSCE) linac can provide H^+ and H^- beam up to 800 MeV. Due to a lack of direct beam measurements during high power operation, small adjustments to linac operating set points are made primarily on the basis of beam loss along the linac. To provide more insight on the beam distributions along the linac and to better understand the effects of machine parameter changes on the beam, we are creating a virtual beam diagnostic tool for use in the LANSCE control room [1]. This tool is a Graphics Processing Unit (GPU)-accelerated multi-particle simulator whose beam dynamics algorithms are based upon the ion linac design and simulation code PARMILA [2]. PARMILA is a z-code which uses the R matrices to transfer particles through accelerator elements. The simulator is designed using modern software design techniques and coded in C++ and Python. Using NVIDIAs CUDA technology [3], the algorithms are recast to fully harvest the computing power of a GPU. Once connected to the EPICS control system, the simulator can track the real time machine parameter changes, convert control set points to model quantities and quickly update the simulation.

CODE STRUCTURE

Since the simulator is developed for use in the control room, fast execution and ease of use are both important design criteria. To meet these criteria, a combination of a high-level scripting language, i.e. Python, and a low level compiled language, i.e. C++, were adopted. Figure 1 shows the hierarchy of code layers that allows the user to take advantage of the fast number-crunching kernels written in C++ and CUDA C without having to deal with the complex syntax and the lengthy compilation process that is associated with them. The outermost shell of the code structure that a user directly interfaces with is written in Python. Python is chosen as the high-level scripting language because of its shallow learning curve, pseudo code like syntax, lack of compilation phase, easy integration with the compiled languages and the rich numerical and visualization libraries. Figure 2 shows the major components of the core part of the code that is written in C++ and CUDA C. Following the CUDA convention [3], we refer to the CPU as the host and the GPU as the device in the rest of this paper. The components colored in blue (left) are the ones that reside on the host while those colored in yellow (right) reside on the device. The *BeamLine* component (middle) resides in pinned, or page-locked memory on the host and the information stored is shared between the host and device and denoted by the green block. Each major component is described in detail as follows:

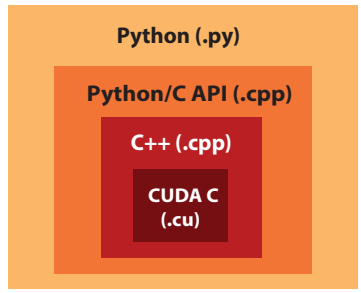


Figure 1: Code hierarchy. Lower level codes are wrapped by the higher level ones.

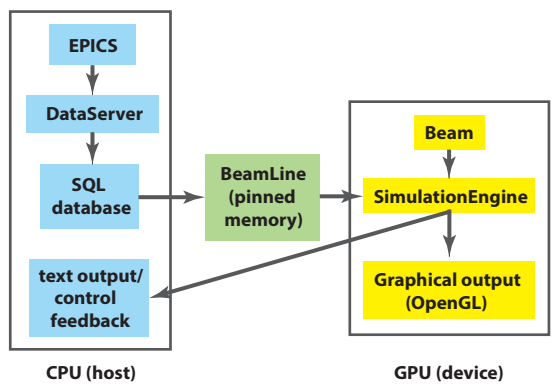


Figure 2: High level code structure and data flow indicated by the arrows.

The *DataServer* reads values from EPICS in multi-threaded fashion and stores the updated values to the SQL database.

The *SQL database* stores all the measured engineering values coming in from the *DataServer*, the conversion algorithms for every controllable accelerator element, and most importantly the converted physics quantities that are

* Work supported by U.S. DOE, NNSA under contract DE-AC52-06NA25396.

† xpang@lanl.gov

Copyright © 2013 CC-BY-3.0 and by the respective authors

eventually used in the beam dynamics simulations. A central database repository was chosen over flat files to guarantee data consistency and to provide historical tracking of data changes. Due to its light weight, self-contained and server-less features, *SQLite* was picked as the relational database management system (RDBMS) for the simulator.

The *BeamLine* component of the code is a data structure that stores the physics quantities of all the accelerator elements required in the simulation. It is updated in real-time once changes to the SQL database are detected so that the physics model used in the simulation is synchronized with the real world machine parameter settings. This data is stored in the pinned memory. In this way, modifications by either the host or the device can be reflected in the memory spaces of both sides, eliminating the need to first search for the element index for which the changes were made, then explicitly copying the new value from host to device.

The *Beam* class is used to store coordinate information for all the particles and some collective properties of the beam. Particle data are allocated on the global memory of the GPU in the format of structure-of-arrays (SoAs) to facilitate coalesced global memory access in the particle tracking simulation and beam property calculations. In order to reduce the expensive memory traffic between the host and the device, the *Beam* object is allocated on the GPU before the simulation starts and is kept on the GPU until the simulation ends. This class also provides methods to calculate different properties of the beam like centroid, size, emittance and beam loss etc. on the GPU.

The *SimulationEngine* component is the core of this simulator. All the physics algorithms for particle advancing and space charge effects are implemented in the *SimulationEngine*. These algorithms are stored in several CUDA kernel functions and are glued together by two overarching C++ classes, *SimulationEngine* and *SpaceCharge*. The *SimulationEngine* class orchestrates the whole simulation while the *SpaceCharge* class only manages the parameters and functions used in space charge calculations.

The *Output* of the code can be a graphical display, a text file or specific values sent back to the EPICS control system. A graphical display system is being developed using openGL so that simulation results sitting on the GPU can be conveniently displayed without copying back to the host when a graphical output enabled GPU is used.

GPU PERFORMANCE

The performance of the GPU accelerated simulator is compared with that of the optimized single CPU version of the code. The test system used for the comparison is a custom built workstation with Intel Xeon E5520 2.27GHz, 32 Gb of RAM, and a NVIDIA GTX 580 (Fermi architecture), running an x86_64 install of Scientific Linux 6.3 and CUDA 5.0.

The physics algorithm of the code consists of two major parts: particle advancing and space charge calculations. For particle advancing, the instruction level parallelism (ILP) was explored by assigning one thread to process four particles. This allows more computing resources to be used by a thread, more data to be reused and independent calculations within a thread to be processed in parallel, therefore more latency to be hidden. An overall faster execution can be achieved. In the space charge force calculation, particles are first binned onto a mesh and stored in a charge density table. Then an electric field table is calculated based on the charge density. Space charge kicks on the particles are applied by interpolating the electric field table based on individual particle's position on the mesh. Among these steps, the charge density table calculation accounts for the most computing time and is the bottleneck of the overall performance. To avoid the race condition when the density table is updated by multiple threads, the floating point atomic addition in the CUDA is used. This gives us about 12 times speedup in the charge density calculation compared to the CPU version.

Two LANSCE beam lines were used for the overall performance test: part of the H^+ low energy beam transport (LEBT) which consists of 8 quadrupoles, 4.32 meter long drift spaces (divided into 442 segments to apply space charge kicks), a RF cavity and a dipole and the drift tube linac (DTL), which includes 135 quadrupoles, 165 RF gaps and 1.68 meter long inter-tank drift spaces (divided into 171 segments). Typically using 32K particles in the simulation is sufficient to get an accurate estimate of many of the beam properties.

Without calculating the space charge effect, transporting 32K particles through an accelerator element using GPU can be 160 times faster than on a single CPU. Table 1 summarizes the total computing time including the space charge calculations and the speedup of simulations using different particle numbers. The overall performance is dominated by the space charge calculation which consumes between 70% to 90% of the computing time. One simulation through the transport structure on the GPU using 32K particles takes less than a second, whereas on a single CPU, it takes more than half a minute. In an accelerator control room where rapid response from any system is required, a reduction from half a minute to a fraction of a second makes this simulator a viable tool for pseudo-real-time computational turn-around in this demanding environment.

RESULTS

Before relying on the simulator to provide useful insight about the beam evolution in the linac under routine operating conditions, it must first be calibrated. Details about the calibration process is described in [4]. Figure 3 shows that after the calibration, we were able to get an excellent agreement between the results from the actual phase scan measurements made with the LANSCE H^+ beam and the results from the simulated phase scan following the adjustment of the relevant calibration factors. Figure 4 is a screen shot of the EPICS control channels and the simulator outputs for the simulation of H^- beams at LANSCE accelerated from 0.75 to 100 MeV through the DTL.

Copyright © 2013 CC-BY-3.0 and by the respective authors

Table 1: Computing Time and Speedup

Initial Particle Number	Beamline Structure	Overall Time [s]	Overall Speedup
16384	Transport	0.66	45.8
	DTL	0.37	26.7
32768	Transport	0.78	44.5
	DTL	0.47	34
65536	Transport	1.02	42.3
	DTL	0.71	39
131072	Transport	1.48	40.1
	DTL	1.15	45.2
262144	Transport	2.4	39.8
	DTL	2.07	48.6

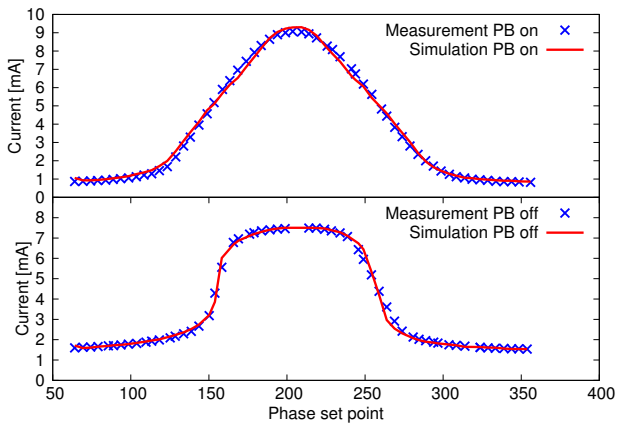


Figure 3: Phase scan measurements (blue x's) of the LANSCE DTL tank 1 with main buncher on and prebuncher on (top) and off (bottom). The simulated phase scan results following calibration factor adjustment are shown in red.

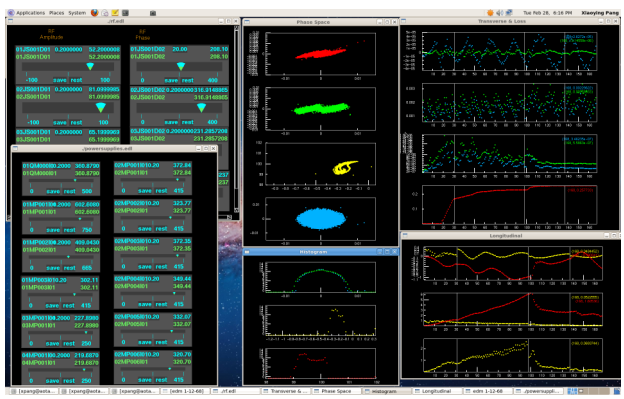


Figure 4: Screenshot of the EPICS control interfaces (left) and the simulator outputs (right).

Numerous beam properties such as phase space distributions and phase space projections at the end of the DTL as well as beam centroid, size, emittance, and fractional beam loss along the DTL are displayed. From this interface, changes that are made to relevant DTL operating parameters can be captured by the simulator and reflected in the simulation results in pseudo realtime. These 2D graphics displays were made using OpenGL, which maintains high throughput as additional communications through the CPU are minimized. This type of interface gives control room personnel additional information regarding beam performance and allows them to better understand the impact of any machine parameter changes to the overall accelerator performance.

STATUS AND FUTURE WORK

Currently, the simulator contains several standard transport elements and the DTL structure. The addition of the coupled-cavity linac (CCL) structure to the code is underway as well as improvements to the Python interface and data I/O. Following that, our near term plans include generation and calibration of the LANSCE CCL in the model and front-to-end simulations of the LANSCE linac from 0.75 to 800 MeV. More long range plans under consideration include simultaneously modeling multiple beam species, addition of other beam loss mechanism, e.g. H- stripping [5] and addition of a new space charge calculation routine based on a 3D Poisson solver.

CONCLUSION

By combining multi-particle tracking simulation algorithms with state-of-the-art GPU technology we have developed a powerful tool for use in the demanding accelerator control room environment. It has many applications not mentioned here [4][6][7]. Although more efforts are needed to further calibrate the existing model and to incorporate more accelerator structures, we believe this approach can greatly enhance operations and performance of existing and future accelerators.

REFERENCES

[1] X. Pang, L. Rybarcyk, S. A. Baily, IPAC, 2012.

[2] H. Takeda, J. H. Billen, Parmila, LA-UR-98-4478, 2005.

[3] NVIDIA Corporation, CUDA C Programming Guide, version 5.0, 2012.

[4] L. Rybarcyk, X. Pang, PAC 2013, 2013.

[5] L. Rybarcyk, C. Kelsey IV, R. McCrady, X. Pang, IPAC 12, 2012.

[6] A. Scheinker, X. Pang, and L. Rybarcyk, submitted for publication to Phys. Rev. ST-Accel. Beams.

[7] X. Pang, L. Rybarcyk, "Multi-objective Optimization for LANSCE Linac Operations", ICALEPCS 2013.

Copyright © 2013 CC-BY-3.0 and by the respective authors

PHASE STABILITY OF THE RF REFERENCE LINE FOR THE FRIB LINAC*

Q. Zhao#, J. Brandon, D. Morris, Y. Yamazaki, MSU, East Lansing, MI 48824, USA

Abstract

The phase stability of rf reference line is usually quite restricted in a high energy linac (very long linac, very high frequency). Due to the change of the ambience temperature in the linac tunnel, the electrical length of reference rf cables may change significantly, which results in unacceptable phase changes in cavities. So, sometimes the reference line is very expensive, for example, made of optical fiber housed in a lengthy thermostatic chamber. The frequencies of FRIB linac cavities are 80.5 and 322 MHz (not very high). We also take advantage of the double-folded linac geometry and feed the reference line in the center of the linac to effectively reduced the reference line by 6 times. Our studies show that the FRIB linac can tolerate up to 12ps phase stability of the rf reference line. Therefore, no is needed for the reference line.

INTRODUCTION

The Facility for Rare Isotope Beams (FRIB) [1], currently under establishment at the Michigan State University, will be a new national user facility for nuclear science. FRIB accelerator is a cw, high power, heavy-ion machine that will accelerate all stable isotopes to energies ≥ 200 MeV/u with a beam power of up to 400 kW. The driver linac consists of a front-end to generate ion beams and boost beam energy, a superconducting linac that is folded into three parallel segments and connected by a stripper station and two 180-degree bending sections, and a beam delivery system to transport output beam into the fragmentation target, as shown in Figure 1. The length of linac footprint is about 150m. Linac Segment 1 consists of 3 β=0.041 cryomodules and 11 β=0.085 cryomodules to increase the beam up to 20 MeV/u followed by a charge stripping system. All the cavities in Segment 1 are Quarter-wave Resonators (QWRs) with operating frequency of 80.5MHz. Half-wave Resonators (HWRs) with higher operating frequency of 322MHz are used for both Segment 2 and Segment 3. There are 12 β=0.29 cryomodules and 12 β=0.54 cryomodules in linac Segment 2 to accelerate beam energies ≥ 150 MeV/u. Additional 6 β=0.54 cryomodules in linac Segment 3 further push beam energies above 200 MeV/u, followed by a FODO quadruple lattice section that is reserved to place more cryomodules for future energy upgrade.

As a new generation national scientific user facility, the performance of FRIB has quite stringent requirements. Therefore, each system and its subassemblies become critical for the operation of such a complex machine. The rf field generated by cavities is one of the key factors that determine the beam performance of the linac. It is a challenging task to achieve good phase and amplitude regulation of the cavities in a large system. There are several types of errors or uncertainties related to the rf field of the cavities in linacs like the FRIB driver linac. For examples, (1) the random rf phase and amplitude fluctuation or jitter that changes very fast and dynamically and is regulated by low level rf controller, (2) misalignment of field axis with respect to the beam axis that is static and may be measureable thus be corrected or compensated, (3) deviation of amplitude settings with respect to the design that is static and determined mainly by calibration, (4) deviation of phase settings with respect to the design that is also static and usually more sensitive than that of field amplitude especially at low energy side, (5) phase change due to the variation of the electrical length of rf cable that is mainly due to thermal effect and thus a slow drift process. Therefore, each of them needs to be evaluated and controlled to meet requirements. In this paper, we discuss exclusively on the topic of the phase drift of the rf reference line for the FRIB linac.

CAVITY PHASE SETTINGS

There are total 330 cavities (including the rebuncher cryomodules between each segment) distributed in the three linac segments of the double-folded FRIB driver linac. All of the cavities (either QWRs or HWRs) have

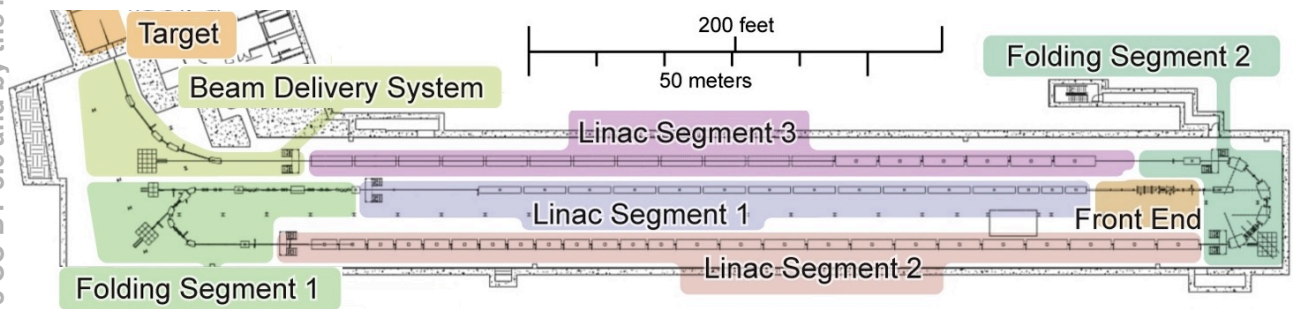


Figure 1: Layout of the FRIB driver linac.

* Work supported by the U.S. Department of Energy Office of Science under Cooperative Agreement DE-SC0000661
# zhao@frib.msu.edu

Copyright © 2013 CC-BY-3.0 and by the respective authors

two accelerating gaps excited in π-mode (that means the change of the electric field between the gaps is always opposite but at the same rate). Each cavity is powered individually, thus the amplitude and phase of each cavity can be independently adjusted. The field amplitude of cavity is usually set as high as allowed for reliable operation, while the phase of cavity that the beam experiences when transiting through the cavity (called synchronous phase) is determined by the beam dynamics design of the linac lattice. In a real machine, each cavity must be phase-scanned at least one time with beam by typically measuring the energy change (ΔE) as a function of the phase (φ), as illustrated in Fig. 2. The phase that corresponds the maximum energy is defined zero degree, and thus the synchronous phase φ_s (generally around -30º to tradeoff between the acceleration efficiency and the size of rf bucket) is set by retracting $|\varphi_s|$ degrees from the "zero". Once the synchronous phase is found, the low level rf controller will lock it. This procedure will be applied every cavity sequentially along the beam path. The synchronous phases of all cavities must be well-controlled over a long period of operation, so beam can always be accelerated along the linac synchronously in the stable region.

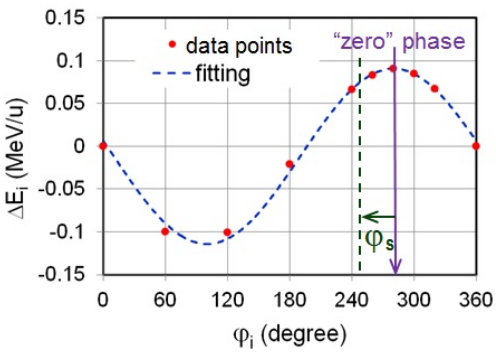


Figure 2: Phase scan of a β=0.041 QWR with uranium beam (q/A=33/238) at 0.5MeV/u to set the synchronous phase of the cavity.

RF REFERENCE LINE

The phase stability of rf reference line is usually quite restricted in a high energy linac where the linac is not only very long but also operates at high frequencies. High performance coaxial cables are widely used for rf reference line. It is well known that phase change in coaxial rf cables is sensitivity to the ambience temperature variations (due to the change of electrical length). So, sometimes the reference line is very expensive, for example, made of optical fiber housed in a lengthy thermostatic chamber. The global temperature at the FIRB linac tunnel will be controlled in the range of 72±6 ºF (22.2±3.3 ºC), which mainly implies some areas (e.g. near room temperature magnets) can have slightly higher temperature while other ones (e.g. near cryomodules) slightly lower. However, long-term temperature drift at a given location during normal operation will normally be much smaller than ±6 ºF.

A typical rf coaxial cable is a composite structure that consists of metal conductors separated by a polymer dielectric. The entire assembly is encapsulated with a polymer jacket. The phase length in degree of such a cable is given by

$$\varphi = \frac{360 f_0 \cdot l \cdot \sqrt{\varepsilon_r}}{c} \quad (1)$$

where c is the velocity of light in vacuum, f_o is the signal frequency, l is the mechanical length of the cable and ε_r is the dielectric constant of the insulating material between the center and the outer conductor of the coaxial cable. Therefore, for a given rf frequency (f_o), the phase change depends on the change of physical cable length (l) and/or the net dielectric constant of the propagation medium (ε_r). The metal conductor changes linearly with temperature, but the behavior of dielectric constant is usually very complicated when the temperature of cable changes.

The FRIB reference line will provide a stable signal of 10.0625 MHz which is compatible with rf system frequencies of 20.125, 40.25, 80.5, 120.75, 161, and 322 MHz. To minimize the temperature related phase change, the reference clock is fed from the center of the linac tunnel into six rf distribution lines through a 6-way splitter, as shown in Fig. 3. In this scheme, the reference line is effectively reduced by 6 times. The length of each linac segment is no more than 140m, so each rf reference line is about 70m long. In addition, low loss, phase stabilized cable (RFS 7/8" LCF78-50J) is selected for the rf reference lines. Foam polyethylene instead of polytetraflouoroethylene (teflon) is used as the insulating material in the cable to avoid the so-called teflon "knee" induced phase instability problem [2] (teflon itself undergoes a quick structural transition around 19 ºC, which results in a rapid change in the dielectric constant and thus an abrupt change in phase length).

To check the relation of phase change with temperature, a 136.8-meter-long coaxial cable (RFS 7/8" LCF78-50J)

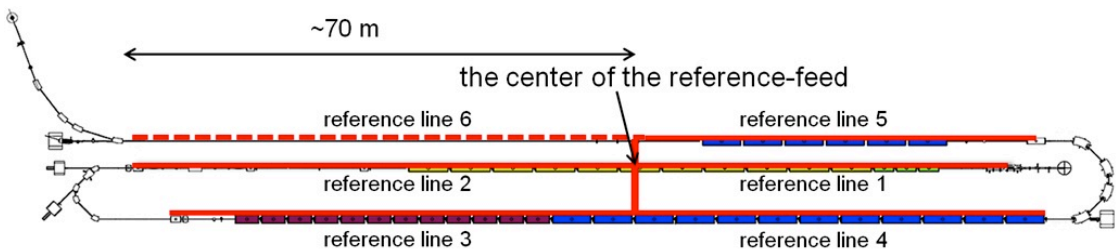


Figure 3: Schematic layout of the reference lines and the center of the reference-feed in the linac tunnel.

Copyright © 2013 CC-BY-3.0 and by the respective authors

from Radio Frequency System (RFS) company, same type as those to be used in FRIB linac, was tested at the FRIB lab with a 10.0625 MHz signal. The cable was rolled up and placed in a room where the temperature can be adjusted and controlled, as shown in Fig. 4. The oscillator, phase detectors and other devices were set up right outside the room, and can be seen through the window. Phase change of 0.105 degrees with respect to 10.0625 MHz was measured between the two different temperatures of 70.3 and 79.8 ºF, which is similar to the expected ambient temperature range within the FRIB linac environment.



Figure 4: Setup of the reference cable test at FRIB lab.

BEAM DYNAMICS STUDY

Beam dynamics study was performed to evaluate the FRIB linac performance with rf phase changes caused by the thermal effect of the rf reference lines. Based on the measured data, for a 100-meter-long cable and 1 degree Fahrenheit temperature increase, total phase change will be 0.06465 degrees at 80.5 MHz. Since the FRIB specs of the global temperature variation within the entire tunnel is 72±6 °F, cable temperature change of 12ºF is assumed in the study. Although this will unlikely happen, because the coherent change of the entire tunnel temperature should be much less than ±6 °F. So, the phase change of each cavity is calculated and shown in Figure 5, where the phase in degree corresponds the rf frequency of each cavity (80.5 MHz for QWRs, 322 MHz for HWRs).

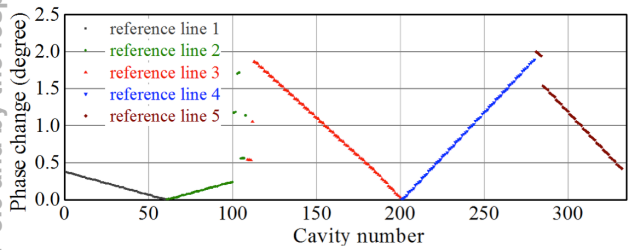


Figure 5: Phase change ("degree" corresponds to the cavity rf frequency) for each of the cavity along the linac.

Multi-charge-state uranium beam [3] carried from the frontend was tracked through the entire linac to the target. The results show the amount of phase change (shown in Fig. 5) is not sensitive to the beam performance. Sampled particle distributions on target are plot in Fig. 6 with the cases of phases changed and unchanged, which indicate the overall impact is insignificant. Although the maximum phase change is ~2 degrees for the HWRs in Segment 2 & 3, and ~0.5 degrees for the QWRs in Segment 1, the phase change between the neighbouring cavities is coherent and very small (unlike rf jitter), the particles still well follow the betatron oscillation in the longitudinal stable region. The amplitudes of the centroid oscillation in longitudinal phase space are negligible, as shown in Figure 7.

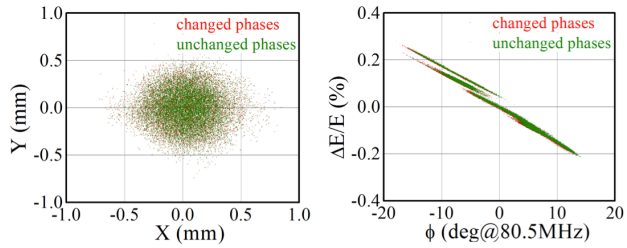


Figure 6: Sampled particle distributions on target with (in red) and without (in green) the phase changes. Both transverse (left) and longitudinal (right) are very similar for the two cases.

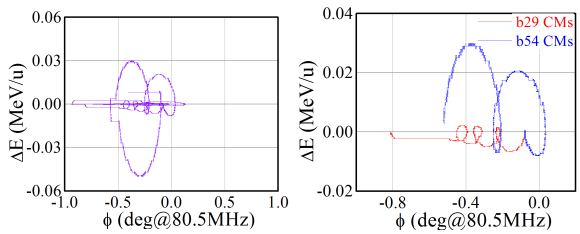


Figure 7: The centroid motion in longitudinal phase space with phase change included for the entire linac (left). Zoom of the Segment 2 only (right). The amplitudes of the oscillation are negligible.

SUMMARY

FRIB will feed the reference clock from the center of the linac tunnel into six rf distribution lines. The long-term thermal related phase change of each line shall be less than 12 ps. Beam dynamics studies using measured data confirm that the phase stability of the rf reference cable meet the requirement.

ACKNOWLEDGMENT

We thank P. Gibson, M. Holcome, M. Leitner, F. Marti, E. Pozdeyev, N. Usher, J. Wei, X. Wu, S. Zhao for their valuable discussions and assistance.

REFERENCES

[1] J. Wei, et al., "Progress Towards the Facility for Rare Isotope Beams", Proc. NA-PAC'13, FRYBA1.
[2] "Understanding phase versus temperature behaviour - the Teflon™ Knee", http://www.micro-coax.com
[3] Q. Zhao et al., "FRIB Accelerator Beam Dynamics Design and Challenges", Proc. of HB2012, WEO3B01.

Copyright © 2013 CC-BY-3.0 and by the respective authors

AN OPTIMIZATION STUDY OF THE TARGET SUBSYSTEM FOR THE NEW G-2 EXPERIMENT*

C. Yoshikawa#, C. Ankenbrandt, Muons, Inc., Batavia, IL 60510, USA
A. Leveling, N.V. Mokhov, J. Morgan, D. Neuffer, S. Striganov, Fermilab, Batavia, IL 60510, USA

Abstract

A precision measurement of the muon anomalous magnetic moment, $a_\mu = (g-2)/2$, was previously performed at BNL with a result of 2.2 - 2.7 standard deviations above the Standard Model (SM) theoretical calculations. The same experimental apparatus is being planned to run in the new Muon Campus at Fermilab, where the muon beam is expected to have less pion contamination and the extended dataset may provide a possible 7.5σ deviation from the SM, creating a sensitive and complementary benchmark for proposed SM extensions. We report here on a study performed on the target subsystem utilizing a new optimization technique that overcomes complexities of asymmetric particle production and depth of focus of a Li lens. This new technique is applied to an apparatus that is optimized for pions that have favourable phase space to create polarized daughter muons around the magic momentum of 3.094 GeV/c, which is needed by the downstream g 2 muon ring.

INTRODUCTION

The New g-2 Experiment at Fermilab [1] aims to measure the muon anomalous magnetic moment to a precision of ±0.14 ppm — a fourfold improvement over the 0.54 ppm precision obtained in the g-2 BNL E821 experiment [2]. The present discrepancy, Δa_μ(Expt. — SM) = (255±80)×10^{-11}, is already suggestive of possible new physics contributions to the muon anomaly. Assuming that the current theory error of 49×10^{-11} is reduced to 30×10^{-11} on the time scale of the completion of our experiment, a future Δa_μ comparison would have a combined uncertainty of ≈ 34 × 10^{-11}, resulting in a 7.5σ deviation from the Standard Model, which will be a sensitive and complementary benchmark for proposed extensions to the Standard Model. Most of the improvement will be due to increased statistics and thus it is essential to maximize production of useful pions that create polarized muons which are in the acceptance of the g-2 muon storage ring. Furthermore, cost considerations favour a design that reuses the existing pbar production subsystem that worked well during the Tevatron operation. Hence, the pion production subsystem will begin with the pbar production subsystem scaled from 8 GeV (kinetic energy) protons to 3.1 GeV/c pions.

A preliminary study [3] revealed complexities in optimizing the target where there is interplay between the asymmetric pion production, the need to have the pions created near the target edges to minimize reabsorption, and the depth of focus of the Li lens. An optimization procedure was proposed in that early study to overcome those complications and its application and result is the focus of the study reported here.

*Work supported by Fermi Research Alliance, LLC, under contract No. DE-AC02-07CH11359 with the U.S. Department of Energy
#cary.yoshikawa@muonsinc.com

THE LAYOUT

A graphical representation of the Fermilab pbar production target subsystem is shown in Figure 1 as implemented in Ref. [4] in the MARS15 code [5]. The proton beam with kinetic energy of 8 GeV impinges on the default target, which was previously used to create pbars. We considered two spot sizes for the proton. One is what we expect from a simple scaling from 120 GeV operation to 8 GeV. The other is the smallest we believe that can be achieved. Spot size information on both is provided in Table 1. The default pbar production target is a vertical cylinder (in-out of top view in Figure 1) composed primarily of inconel with a chord for the proton beam of ~7.5 cm. Pions produced in the target will be focused by the Li lens (yellow) that is 15 cm long, 1 cm in radius, and has a magnetic field gradient of 256.25 T/m, where the gradient has been scaled for 3.1 GeV/c pions to maintain proper focusing, while keeping the same focusing distance between centers of the target and Li lens of 25.16 cm. The focused pion beam is then collimated and bent through a pulsed magnet (PMAG) with a dipole field of 0.542219 T, also scaled for the 3.1 GeV/c pion beam, and bends the reference by 3 degrees to provide momentum selection.

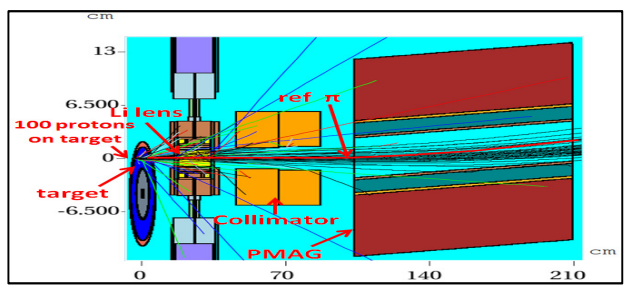


Figure 1: Zoomed in top view of pbar target subsystem.

Table 1: Proton Beam Spot Sizes

Proton spot size description	σ_x (mm)	σ_y (mm)	$\sigma_{x'}$ (mrad)	$\sigma_{y'}$ (mrad)
Default	0.55	1.1066	0.38	0.38
Small	0.15	0.15	0.6366	0.6366

A transition in our simulation between MARS that provides reliable particle generation and G4beamline [6] that is used for particle tracking, pion decay into muons, and effect of beam particles interacting with the beam line elements is shown in Figure 2. The MARS particle tracks that hit the virtual detector are converted and propagated in G4beamline through a set of four quads that refocuses

Copyright © 2013 CC-BY-3.0 and by the respective authors

the beam after the three degree bend from the PMAG. Figure 3 shows 100 such particle tracks traversing the four quads.

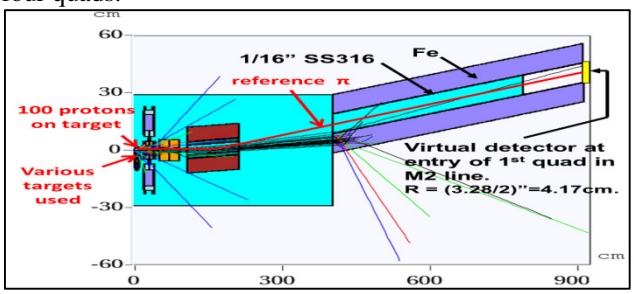


Figure 2: Top view of pbar target subsystem.

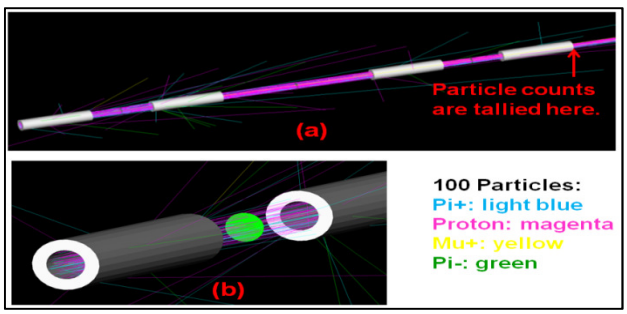


Figure 3: Particles after the conversion into G4beamline and propagated through the 4 quads. (a) Particle yields are tallied at end of the fourth quad with acceptance cuts appropriate for downstream elements. (b) Zoomed in view of particle trajectories between quads that are seen by a virtual detector (green).

The particle yields expected for the g-2 muon ring are estimated by particles simulated to the end of the fourth quad in the Fermilab M2 line as shown in Figure 3(a) and applying the acceptance of those downstream elements, which are:

- P(pi+) = 3.15588 GeV/c +/- 2% (1.02 x P_{magic} +/- 0.02 x P_{magic})
- 40π mm-mrad in each transverse dimension

THE OPTIMIZATION

The previous study [3] utilized thin inconel targets of varying widths, lengths (in direction of proton beam), and orientations (vertical and horizontal). In the current study, we assume pions emanating from the surface in the non-bend plane will give better yields downstream, so we considered only the horizontal orientation. Application of the horizontal slab target into a more realistic one that incorporates cooling would be via a rotating thin walled cylinder with the proton beam hitting either the top or bottom, as shown in Figure 4.

The earlier study also fixed the location of the target center to be at the focal point of the Li lens, while varying the target dimensions. Since pion production is greatest at the upstream end of the target, lengthening the target pushes the location of copious pion production ahead and out of the focal point of the Li lens. The solution to overcome the complexity between varying the target geometry and maintaining focus is to recognize that there will be much less useful pions produced at the downstream end of a long flat target. The procedure involves two stages, where the first optimizes for the location of the upstream edge of the target which is more critical, since that is where pion production is copious. It consists of the following steps as illustrated in Figure 5:

1. Placing the downstream end of a horizontal flat target far downstream as possible, near to the Li lens.
2. The upstream end of the target will be varied starting from the focal point and progressed upstream in each simulated configuration.

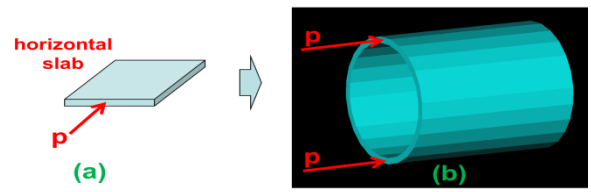


Figure 4: Association of simulated horizontal slab targets and a more practical rotating thin walled cylindrical target to accommodate cooling where protons impinge on either the top or bottom of the cylinder.

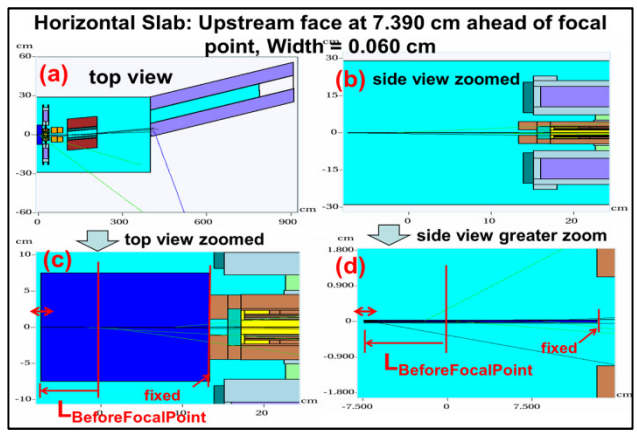


Figure 5: Illustration of optimization for location of upstream target edge. The downstream edge is fixed near the Li lens. The top view is shown in (a) which is similar to that shown in Fig. 2 for the default target. A zoomed in side view is shown in (b), while (d) is further zoomed to show the variation of upstream edge location relative to the Li lens focal point and (c) is similar for the top view.

The geometry of the targets studied, which included varying widths, are given in Table 2 and the anticipated small proton beam spot size described in Table 1 was used throughout the optimization. Results of this first stage of optimization are shown in Figure 6, where it is seen that there are two optimal configurations which provide similar yields:

- $L_{BeforeFocalPoint}$ = 56.12 mm & width = 0.60 mm
- $L_{BeforeFocalPoint}$ = 66.79 mm & width = 0.75 mm

Both configurations will be carried forward into the second stage of optimization.

Copyright © 2013 CC-BY-3.0 and by the respective authors

Table 2: Dimensions and Orientations of Targets Studied. Material of all targets is inconel.

Shape	$L_{BeforeFocalPoint}$ (mm)	Width (mm)
Horizontal Slab	0, 36.95, 73.9, 110.85 λ_{int} : 0, 0.25, 0.50, 0.75	0.60, 0.75, 1.00, 1.25
Default Pbar Target	chord ~75 mm	

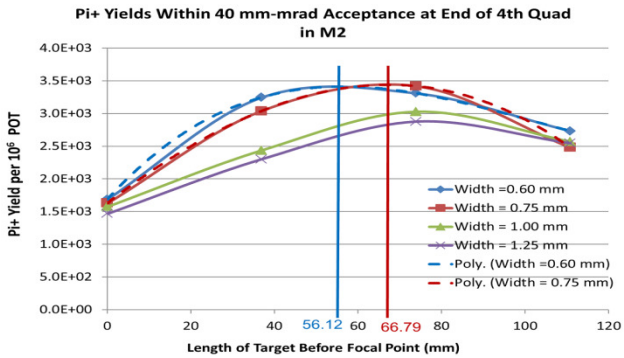


Figure 6: Yield of π^+s in first stage of optimization for location of upstream target edge.

The second stage of optimization consists of simply trimming the downstream end of the target; this automatically maximizes the yield taking into account the effects of:

- Widening birth of pions nearer the surface due to growth of transverse proton beam size as it traverses the target.
- Pions produced near the downstream edge.

The procedure for this second stage of optimization is to fix the location of the upstream edge of the target at locations determined from the first stage and vary the target length. Figure 7 illustrates this procedure for one of the optimal cases elucidated in the first stage.

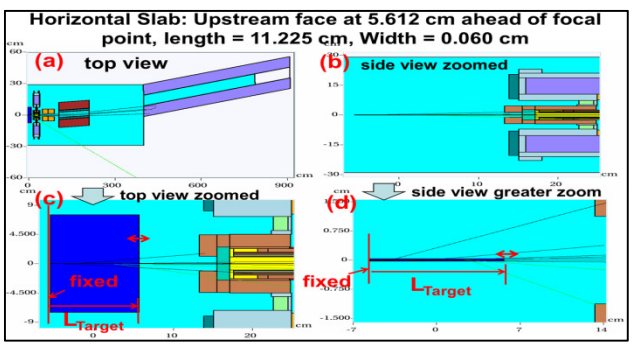


Figure 7: Illustration of optimization for location of downstream target edge. The upstream edge is fixed according to a result of first stage, while the downstream edge is varied. The top view is shown in (a) which is similar to that shown in Fig. 2 for the default target. A zoomed in side view is shown in (b), while (d) is further zoomed to show the variation of the downstream edge location and (c) is similar from the top view.

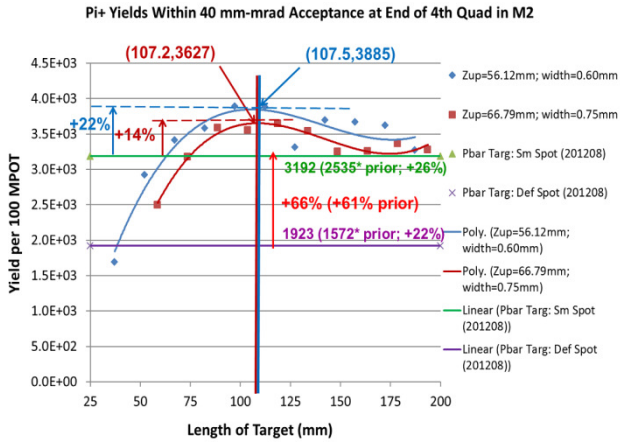


Figure 8: Yield of π+s in second stage of optimization for location of downstream target edge. Values designated "prior" refer to results obtained from MARS version 1510 used in the previous study [3], while the current results (also designated 201208) utilized MARS version 1512.

Results of the second stage of optimization as well as the effect of reducing the proton beam spot size on the default pbar target are shown in Figure 8. It is seen that the reduction of the proton beam spot size on the default pbar target increases the yield of useful pions by 66%! The optimized horizontal slab target using the same small proton beam spot size increases it further by 22%. While an increase of 22% is non-trivial, a cost-benefit and risk analysis resulted in the decision to keep the default pbar target design and reap the large benefit of the anticipated smaller proton beam size.

ACKNOWLEDGMENT

The support, encouragement, and contributions of Chris Polly, Mary Convery, and Dean Still of Fermilab are gratefully acknowledged.

SUMMARY

A study of the New g-2 Experiment target system at Fermilab was performed to optimize the yield of useful pions. An optimization procedure was invented that overcame the complexities of an asymmetric particle production and depth of focus of a Li lens. The best possible target modification yielded a 22% increase over that of the default pbar target and a cost-benefit decision was made by the New g-2 collaboration to resuse the existing pbar target design.

REFERENCES

[1] R. M. Carey et al., http://gm2.fnal.gov/public_docs/proposals/Proposal-APR5-Final.pdf
[2] G. W. Bennett et al., Phys. Rev. D 73 (2006) 072003.
[3] C. Yoshikawa et al., "Optimization of the Target Subsystem for the New g-2 Experiment," IPAC12 MOPPD044.
[4] N. Mokhov, g-2 collaboration meeting note (2009).
[5] MARS: N. Mokhov, http://www-ap.fnal.gov/MARS
[6] G4beamline: T. Roberts, http://g4beamline.muonsinc.com

Copyright © 2013 CC-BY-3.0 and by the respective authors

HIGH VOLTAGE STABILIZATION SYSTEM OF CARIBU/ECR FOR ATLAS

Yong Luo, Sergey Sharamentov, Richard Pardo, Rick Vondrasek, Guy Savard
ANL, Argonne, IL 60439, USA

Abstract

With the increased radioactive beam capabilities brought by new CARIBU (Californium Rare Isotope Breeder Upgrade) in ATLAS facility, highest charge breeder efficiency of ECR is desired. Experimental study shows that the best efficiency could be achieved when high voltages (up to 50 kV) of two platforms (CARIBU and ECR) are only different within less than 1V [1]. We have developed a system with some innovative ideas implemented to measure the required tiny voltage difference ratio (~0.002%) precisely and to protect the system too. High voltage (HV) filter is designed to protect it from severe HV sparks and multiple level of relays with high precision medium HV divider are used to protect it from possible power supply failure. Homemade HV divider is used for rough measurement and control. Measurement results are converted to optical signals and then used to control power supplies to achieve the desired platform voltages. The system has been partially tested and will be used in the future.

INTRODUCTION

When developing such a system with very high sensitivity and accuracy as mentioned above, at first we need to consider how to prevent damage from HV shock and power supply failure. We also need to think about how to measure the voltage difference precisely.

In ATLAS facility, both CARIBU and ECR1 are on a common HV platform of 350 kV. Then the 50 kV bias is applied to them on top of the 350 kV with separate power supplies. There are numerous instruments which are biased with different HV or high current power supplies on both platforms. Occasionally, HV sparks may occur. Those HV sparks are fatal to electronic measurement systems if they are not protected. Possible power supply failure is another threat we need to deal with. We cannot eliminate power supply failure, but we can protect the system with an appropriate design.

Using high voltage divider to measure the voltage difference is a simple and tempting idea. But careful study indicates that this approach has un-surmountable problem. Due to variation in resistor resistance caused by temperature and voltage bias variation, typical HV divider may only provide about 1% accuracy. Even for very expensive custom made high voltage divider with 0.1% tolerance, it still cannot provide the accuracy we need here. The high common mode noise also introduces more measurement error.

SOLUTION

Multiple levels of filter circuit are used to protect the system from HV, high current sparks in electrometer [2]. This kind of sixth-order low pass filter can achieve high-frequency attenuation exceeding 10^{+5}. So we adopted this approach for our HV spark protection.

Multiple levels of relay can be used to protect the system from power supply (PS) failure. Details will be explained in design and test section. Relays are turned off when PS fails. Homemade HV divider is used for coarse control and monitoring.

CARIBU side high voltage is used as floating GND for our measurement system. So when the tow platform HVs are very close, accurate measurement can be achieved without introducing big noise.

SIMULATION

Spice simulation is performed on a simplified low pass filter as shown in Fig. 1. In this simulation, a hypothetical high voltage spark source (I1, 20 kA, ~1ns rise time) shown in Fig. 1 is used.

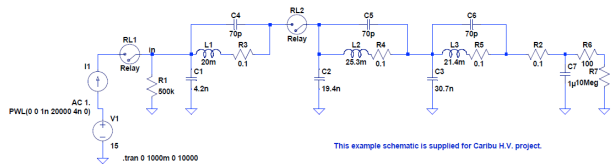


Figure 1: A simplified low pass filter with two relays.

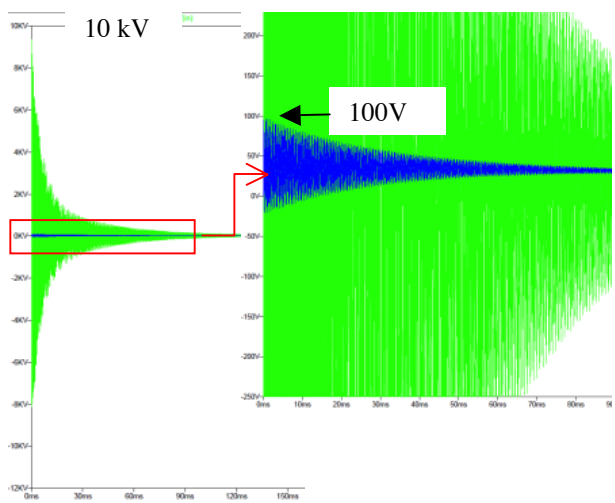


Figure 2: Simulation results of the filter shows the attenuation of HV shock

Copyright © 2013 CC-BY-3.0 and by the respective authors

The filter is similar as that which can be found in [2]. The simulation result is shown in Fig. 2. The plot at left shows the voltage waveform (green colour) at R1. It is about 10 kV peak. After filter, the peak voltage (peak of blue waveform) level drops to about 100V peak at C7/R6. The peak voltage attenuation is about 100 which is 40dB. The inset shows the zoomed view of area inside the red rectangle. Some components such as capacitors and resistors in the low pass filter are HV components.

DESIGN AND TEST

The system has been built by following the block diagram shown in Fig. 3. The voltage difference is measured by Delta V board and then converted to frequency. The frequency is then converted to optical signal and communicated to F-V converter. The signal is converted back to voltage before sampled by ADC. The computer checks the data and then goes back to control power supplies and control the system based on the data and control setting. A typical voltage to frequency converter used is shown in Fig. 4. It can be modified to use as frequency to voltage converter. The voltage after F-V converter can be used to control power supplies directly in case we need it.

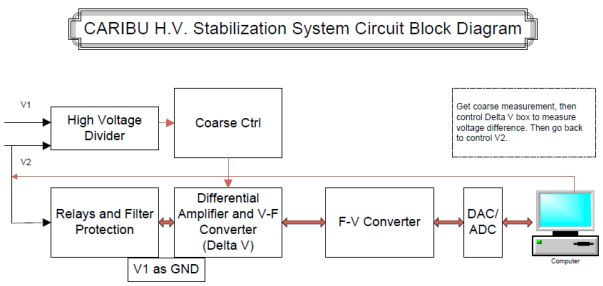


Figure 3: Block diagram of the HV stabilization system.

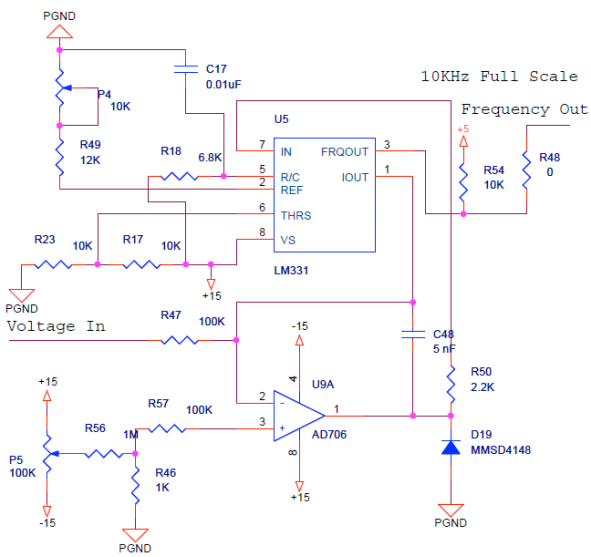


Figure 4: A typical voltage to frequency converter.

A FUG power supply with very high stability (10^{-5}/8h, ^{o}C) is used at CARIBU side platform voltage. This HV is used as the floating ground for the HV stabilization system. Power supply for Delta V board is referenced to CARIBU platform voltage.

A ultra precision medium high voltage divider (0.01% tolerance) with very low temperature coefficient is put on the Delta V board. It makes the accurate measurement feasible while also protecting this board from potential damage caused by medium high voltage up to 1500V after the low pass filter. A precision instrumentation amplifier AD8221 with high common-mode rejection ratio (CMRR) is used after the on-board divider. There is one relay on the Delta V board with release time ~1 ms. The 15 kV and 75 kV relay have release time ~2 ms and 15 ms respectively. Those two relays are RL2 and RL1 in Fig. 1. When there is a power supply failure, the one side voltage drop or increase due to the failure is estimated as 50V/ms, the relays in series are turned off by on-board monitoring circuitry to protect the system. Relays in series here are not for the purpose of protection from HV sparks. They are too slow for this but good for power supply failure protection.

A homemade HV divider provides ~1% accuracy and is used for coarse measurement and control in the system. Coarse control board is on 350 kV common HV platform and communicates with Delta V board through optical fiber cables.

The built system is show below in Fig. 5. The zoomed view of the low pass filter board and Delta V board is shown at right with the shield removed.

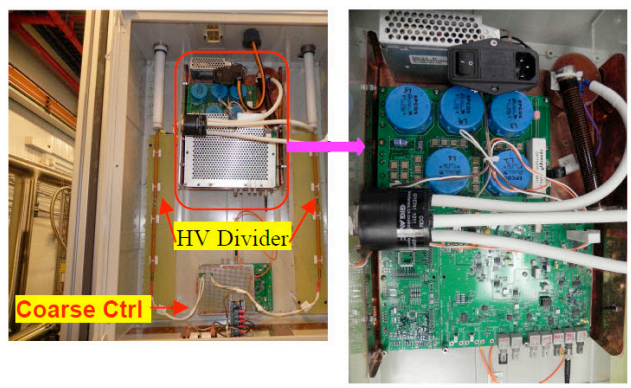


Figure 5: A simplified low pass filter with two relays.



Figure 6: F-V converter and control unit.

Copyright © 2013 CC-BY-3.0 and by the respective authors

Figure 6 shows the front and back panels of the F-V converter and control unit. This chassis can be placed on any platform close to ADC/DAC and it connects with Delta V board through optical fiber cables.

The whole system has been tested on bench and had some field tests too. Field test verified that it can stand at least 50 kV isolation which is one of the design goals. The voltage difference can be measured precisely to ~100 mV or less which exceeds another design goal of 1V. Final user interface software is in progress and the unit will be used in future in our facility.

ACKNOWLEDGMENT

This work was supported by the U.S. Department of Energy, Office of Nuclear Physics, under Contract No. DE-AC02-06-CH11357.

REFERENCES

[1] R.C. Vondrasek, R. Scott, J. Carr, and R.C. Pardo, "Status of the electron cyclotron resonance charge breeder for the ^{252}Cf fission source project at ATLAS", Review of Scientific Instruments 79, 02A901 (2008).

[2] K.S. Robinson, J.J. Coleman, "Spark protection circuit for measuring current in high-voltage circuit", Journal of Electrostatics, 63 (2005) 285-296.

Copyright © 2013 CC-BY-3.0 and by the respective authors

DESIGN AND SIMULATION OF THE ARGONNE INFLIGHT RADIOACTIVE ION SEPARATOR (AIRIS)*

B. Mustapha#, M. Alcorta, B.B. Back and P.N. Ostroumov
Physics Division, ANL, Argonne, IL 60439, USA

Abstract

A new inflight radioactive ion separator (AIRIS) is being designed for the ATLAS facility at Argonne. AIRIS will be used to separate and produce secondary radioactive beams from the interaction of ATLAS primary beams in a production target. AIRIS will be at least 10 times more efficient than the existing radioactive beam capability. We have made significant progress in the design and simulations of AIRIS including full 3D models of all the elements to consider their real dimensions and produce realistic 3D fields. The resolving power of the device has been studied for several reaction cases using realistic cross sections and kinematics. In addition to the magnetic separation of the device, an RF sweeper is being designed to take advantage of the time separation of the different beams and reject the primary beam tail and other potential contaminants in order to produce higher purity secondary beams. The latest AIRIS design and simulation results will be presented and discussed.

AIRIS AT ATLAS

The Argonne Tandem Linac Accelerator System is undergoing an efficiency and intensity upgrade [1]. Most of the stable beams will have their intensities increased by one to two orders of magnitude. To take advantage of this intensity upgrade and enhance the radioactive beam capabilities at ATLAS, a new inflight radioactive beam production and separation system is being proposed. The new system will consist of a production target placed at the end of ATLAS followed by an ion separator called AIRIS. Figure 1 shows the location of AIRIS downstream of ATLAS and upstream of any experimental area. The main constraint on the AIRIS design is to preserve stable beam operations by moving the target out and using AIRIS as a transport line. For this purpose, AIRIS should have the same beam axis as ATLAS and the existing beamline. A broadband design has been proposed and developed for AIRIS [2]. It consists of four dipoles and four multipoles (quadrupoles) as shown in Figure 1. The original design was developed and simulated using COSY [3]. In this work, we have performed detailed simulations and parameter feasibility studies using the code TRACK [4], which has led to the new design parameters listed in Table 1. The dimensions and spacing of the elements have changed but not the overall layout.

Table 1: AIRIS Design Parameters

Parameter	Value
Number of dipoles	4
Dipole bend angle, deg	22.5
Dipole radius, m	1
Dipole full gap, cm	10
Max. dipole field, T	1.75
Number of quadrupoles	4
Quadrupole length, cm	30
Quadrupole full aperture, cm	15
Max. quadrupole field, T	1.0
Shortest drift, cm	20
Total chicane length, m	7.1
Angular acceptance, mrad	50
Dispersion at mid-plane, mm/%	1.2

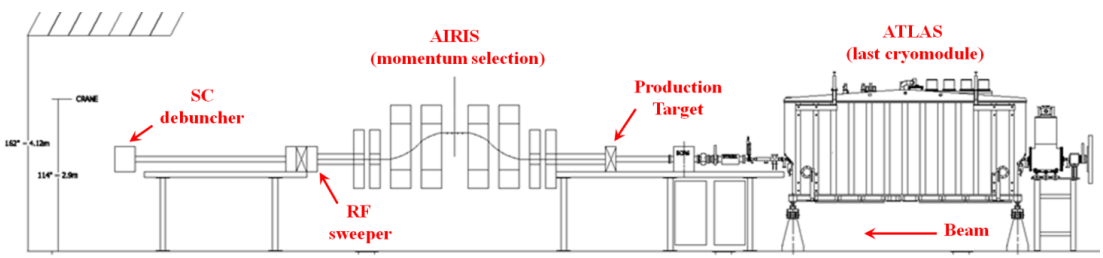


Figure 1: AIRIS, designed to be installed downstream of ATLAS and upstream of experimental areas for the production and separation of radioactive beams. An rf sweeper and a SC debuncher are included.

* This work was supported by the U.S. Department of Energy, Office of Nuclear Physics, under Contract DE-AC02-06CH11357.
# brahim@anl.gov

Copyright © 2013 CC-BY-3.0 and by the respective authors

TRACK FOR ION SEPARATOR DESIGN AND SIMULATION

The beam dynamics code TRACK has recently been modified for more accurate transfer matrix calculation of any element up to the second order in particle coordinates. These calculations were benchmarked against COSY's results with excellent agreement, as will be shown later. Combining the new features with the existing TRACK capabilities, we were able to study the AIRIS design in more detail, which allowed us to produce more realistic element parameters. TRACK can now be used for the design and simulation of any ion separator.

Benchmarking Against COSY

Figure 2 shows a comparison of transverse beam emittance along AIRIS calculated for a 14 MeV/u $^{14}O^{8+}$ beam using ray-tracing in TRACK and different order matrices in COSY. We clearly see that from 2nd to 5th order, COSY's results converge towards TRACK's results, which should be equivalent to infinite order.

Integration Steps in Bending Magnets

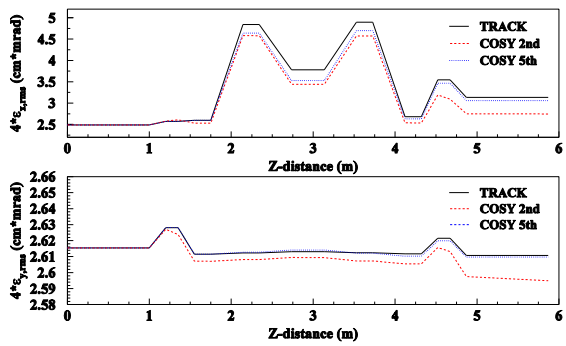


Figure 2: Transverse beam emittance along AIRIS calculated with TRACK and COSY at different orders.

Due to the curvature of a charged particle trajectory in a bending magnet, we expect a dependence of ray-tracing results in TRACK to the number of integration steps used for tracking. Figure 3 shows the dispersive horizontal beam centroid along AIRIS calculated in TRACK with increasing number of integration steps in the dipoles. We can see an improvement in the precision from 100 to 500 steps where it seems to saturate because we don't see a significant change when using 5000 steps.

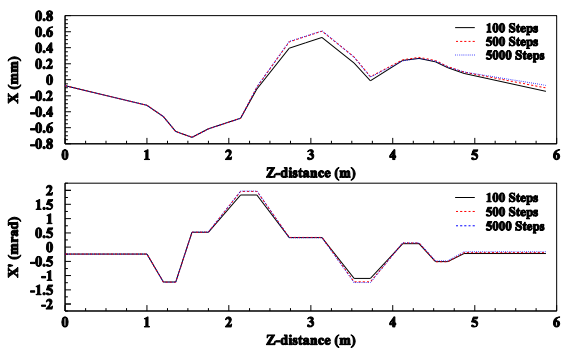


Figure 3: Horizontal (dispersive) beam centroid along AIRIS calculated in TRACK with different number of integration steps in the dipoles.

TRACK's 2nd Order Matrix for Correction

Using the 2nd order matrix calculation in TRACK and an internal optimization procedure, developed for high-order beam correction, we were able to optimize the sextupole component strength for a 2nd order correction. The results are shown in Figure 4.

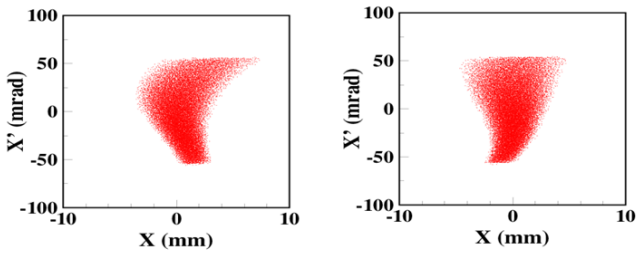


Figure 4: Horizontal beam phase space in AIRIS's mid-plane before and after 2nd order correction in TRACK.

Acceptance Calculation for Contaminants

TRACK already has an acceptance calculation procedure which could be easily applied to any potential contaminant to the radioactive beam selected in AIRIS. Figure 5 shows different regions of AIRIS acceptance in angle and energy, calculated with different mid-plane selection slit openings, for the $^{14}N^{7+}$ primary beam tail which is a potential contaminant to the $^{14}O^{8+}$ beam of interest. Such a calculation identifies the area of overlap with the primary beam and how to reject it.

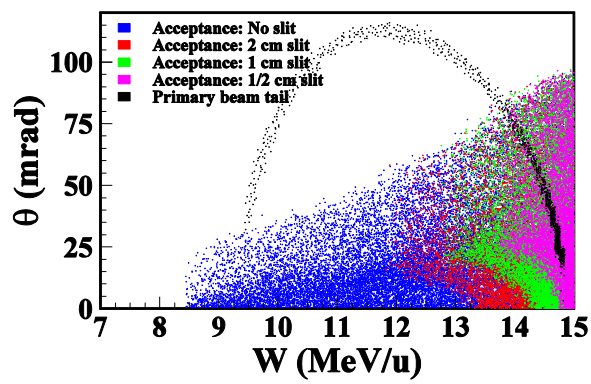


Figure 5: Regions of AIRIS acceptance (colors) calculated with TRACK for the $^{14}N^{7+}$ primary beam tail (black) with different mid-plane selection slit openings.

Copyright © 2013 CC-BY-3.0 and by the respective authors

Multi-Beam and Multi-Charge States

TRACK was the first beam dynamics code to support simultaneous tracking of multiple beams and, in particular, multi-charge state beams. It was used to prove and demonstrate the simultaneous acceleration of multiple charge states of a uranium beam in ATLAS [5]. Figure 6 shows one example of multi-beam simulation and one example of multi-charge state simulation applied to study the overlap of the different beams and select the beam of interest at the AIRIS mid-plane.

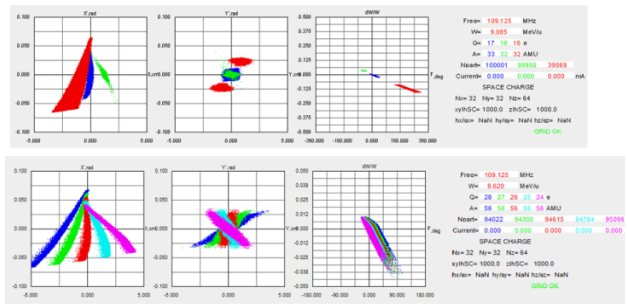


Figure 6: (top) Multi-beam phase space plots at AIRIS mid-plane for the $^{33}Cl^{17+}$ beam of interest and the $^{32}S^{16+}$ primary beam core and tail. (bottom) Multiple charge states of a ^{56}Ni beam at AIRIS mid-plane.

From Hard-Edge to 3D-Field Models

TRACK has internal models for most elements. These models range from simplified hard-edge to models with more realistic fringe fields. TRACK also supports external 3D fields calculated with other software. Although not always required, 3D field models could reveal more realistic non-linear effects. Figure 7 shows the $^{14}O^{8+}$ phase space in the AIRIS end plane simulated with hard-edge and 3D models for the dipoles and quadrupoles. We clearly see more beam distortions and tail formation in the 3D field case.

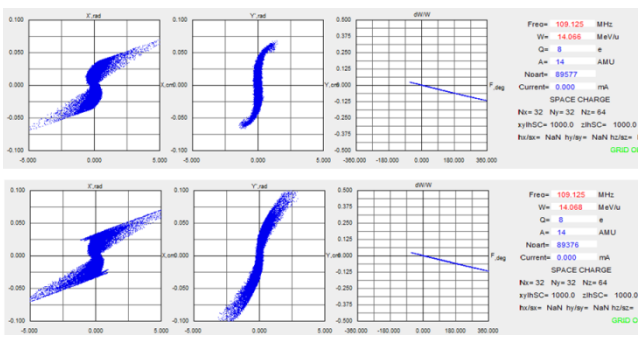


Figure 7: $^{14}O^{8+}$ phase space plots at the AIRIS end-plane calculated using hard-edge models (top) and 3D-field models (bottom) for the dipoles and quadrupoles.

3D MODELING OF AIRIS

In order to produce a more realistic model for AIRIS and check the feasibility of its elements, we have developed preliminary 3D designs for the dipoles and quadrupoles. For this purpose, EM-Studio of the CST package [6] was used and Figure 8 shows the full 3D model for AIRIS. The 3D modelling was essential to modify the AIRIS design parameters considering limitations on element dimensions, spacing and fields.

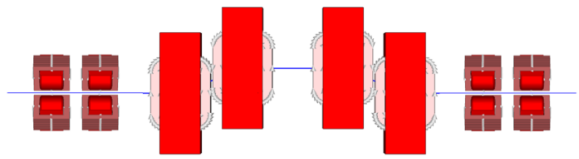


Figure 8: Full 3D model of AIRIS showing the dipoles and quadrupoles.

EXAMPLE OF AIRIS RESOLVING POWER

In order to study AIRIS's resolving power, we have simulated several radioactive beams. Realistic nuclear reaction models [7, 8] were used to generate the distributions for the secondary beam of interest, the scattered primary beam and the potential contaminants produced in the same reaction. Figure 9 shows an example of AIRIS performance in separating the secondary $^{56}Ni^{28+}$ beam of interest from the primary beam and other contaminants produced in the interaction of a 10 MeV/u ^{54}Fe beam on a carbon target.

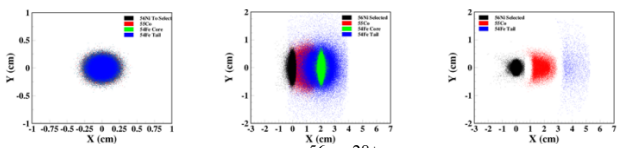


Figure 9: Separation of the $^{56}Ni^{28+}$ beam of interest from the primary beam and other contaminants. (left) All beams superposed at the target. (center) Clear separation of $^{56}Ni^{28+}$ (black) from the $^{54}Fe^{26+}$ primary beam core (green) at the AIRIS mid-plane. (right) Clear separation of $^{56}Ni^{28+}$ (black) from other contaminants, $^{55}Co^{27+}$ (red) and $^{54}Fe^{26+}$ primary beam tail (blue), at the AIRIS end-plane.

REFERENCES

[1] P.N. Ostroumov et al, "Upgrade of Argonne's CW SC Heavy Ion Accelerator", Proceedings of NA-PAC'13, WEOAB2, 2013.

[2] S. Manikonda et al., "Argonne In-flight Radioactive Ion Separator", Proceedings of HIAT-2012, June 18-21, 2012, Chicago, IL, USA

[3] COSY web page: http://cosy.pa.msu.edu

[4] TRACK web page: www.phy.anl.gov/atlas/TRACK

[5] P.N. Ostroumov et al, "Simultaneous Acceleration of Multiply Charged Ions through a Superconducting Linac", Phys. Rev. Lett. **86** (2001) p2798.

[6] CST web page: www.cst.com

[7] O.B. Tarasov and D. Bazin. "LISE++: Radioactive beam production with in-flight separators", NIM B **266** (2008) p. 4657.

[8] J.F. Ziegler, M.D. Ziegler, and J.P. Biersack, "SRIM- the stopping and range of ions in matter", NIM B **268** (2010) p. 1818.

Copyright © 2013 CC-BY-3.0 and by the respective authors

DIAGNOSTICS FOR THE LANSCE RFQ FRONT-END TEST STAND*

R. C. McCrady#, Y. K. Batygin, I. N. Draganic, C. M. Fortgang, R. W. Garnett, S. S. Kurennoy, J. F. O'Hara, E. R. Olivas, R. J. Roybal, L. J. Rybarcyk, Los Alamos National Laboratory, Los Alamos, NM 87544, USA.

Abstract

Plans are underway at the Los Alamos Neutron Science Center (LANSCE) to replace the existing H^+ Cockcroft-Walton injector with a modern 4-rod Radio-Frequency Quadrupole (RFQ) based front end. This will provide protons for injection into the downstream linac, where H^- ions are also accelerated. This dual-species operation of the linac imposes constraints on the injectors, resulting in particular requirements on the transverse and longitudinal emittances and phase-space distributions of the beam from the RFQ proton injector. Good measurements of these quantities are therefore required during the testing phase of the RFQ injector. In this paper we describe the measurements to be made and plans for the systems for carrying out the measurements.

INTRODUCTION

The existing injectors at LANSCE for protons and H^- ions are based on Cockcroft-Walton (CW) generators and have been in use since the initial construction circa 1970. These CW-based injectors provide unbunched beams of protons and H^- ions at 750 keV with very little uncertainties in the beam energies. Precise matching of the beam energies is required for good dual-beam operation of the subsequent portions of the linac consisting of drift-tube linac (DTL) and coupled-cavity linac (CCL) sections. Additionally, the high average currents of the beams require good transverse matching from the injectors into the DTL to prevent large beam spill that results in high radiation fields.

An effort is underway to replace the proton injector with an RFQ-based system [1]. The initial phases of commissioning this system will involve operation in a test stand to characterize the system and to ensure that it operates as desired prior to installation in the production environment.

The present 750 keV beam-transport lines from the CW injectors to the DTL are rather long, at about 16m. The two beam species are merged in a 9° dipole magnet about 2.3 meters upstream of the DTL and pass through an RF buncher and a 4-quadrupole matching lens in the common section after the merging magnet. The 18° separation between the two beamlines upstream of the merging magnet limits the transverse space available for equipment in the two beamlines. For this reason, the RFQ must be placed rather far upstream of the DTL, about 4 meters. This distance, combined with the large energy spread of the beam produced by the RFQ, necessitates the use of 2 additional RF bunching cavities in the new proton transport line (shown in Fig. 1) in order to maintain a bunch length that will fit easily into the acceptance of the DTL. For this reason it is imperative that we measure the longitudinal bunch shape of the beam; ideally a full longitudinal phase-space distribution would be measured.

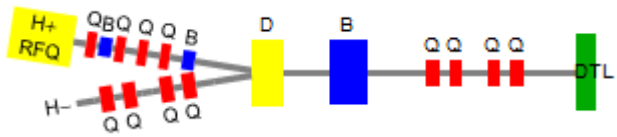


Figure 1: The proposed beam transport line from the proton (H^+) RFQ to the DTL. Also shown is a portion of the H^- transport line. Beamline elements are denoted by letters: Quadrupole magnets (Q), Dipole magnets (D) and Bunchers (B). Three of the bunchers are quarter-wave resonators, and one is a larger pillbox-style cavity.

The stringent requirements on the performance of the system drive the requirements for beam-measurement systems. In particular, we intend to measure beam current, transverse phase space, longitudinal bunch shape, and energy. The diagnostic systems for characterizing the beam produced by the new injector are described in the following sections.

TEST STAND

The RFQ-based proton injector will consist of a duoplasmatron proton source, a 35 kV accelerating column, a two-solenoid low-energy beam transport (LEBT), the RFQ, and a 750 keV medium-energy beam transport (MEBT) to the DTL.

We plan a phased approach to development of the RFQ test stand. The first phase will allow characterization of the LEBT that will transport the 35 keV beam from the source and extraction column to the entrance of the RFQ. The second phase will allow measurements of the beam delivered by the RFQ to assess its performance. The third phase will test the MEBT that will transport the beam from the RFQ to the DTL. Figure 2 shows the test stand phases and the associated beam measurements.

In the first phase, where the beam is not bunched, beam current and transverse emittance are of greatest importance. The beam energy is determined by the column voltage which can be measured precisely. The current and emittance provide input to models of the beam evolution in the LEBT. These models will be used in the process of transverse matching of the beam into the RFQ. We plan to have an emittance-measurement station near the middle of the LEBT; this apparatus will remain in place when the system transitions to the production

* Work supported by the United States Department of Energy, National Nuclear Security Agency, under contract DE-AC52-06NA25396
# mccrady@lanl.gov

Copyright © 2013 CC-BY-3.0 and by the respective authors

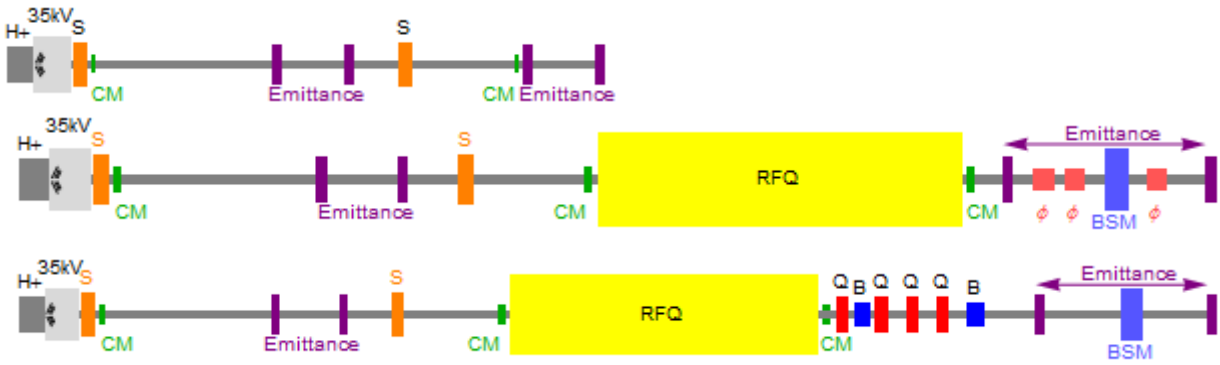


Figure 2: Phases 1 (top), 2 (middle), and 3 (bottom) of the RFQ test stand. Shown are the H^+ source, the 35kV accelerating column, two solenoid magnets (S), quadrupole magnets (Q), bunchers (B), beam-current monitors (CM), bunch-shape monitors (BSM), beam-phase monitors (ϕ), emittance-measurement stations, and the RFQ. Phase 1 allows testing the performance of the source and LEBT, including transverse matching into the RFQ. Phase 2 allows assessment of the RFQ performance, and Phase 3 allows characterization of the MEBT.

environment. An additional emittance station will be placed at the eventual location of the RFQ entrance. This will allow a direct measurement of the transverse phase space of the beam and provide a test of our models for predicting the match based upon measurements with the upstream emittance station.

The transverse evolution of the beam in the LEBT depends strongly upon space charge. The presence of multiple ion species (H^+, H_2^+, H_3^+) complicates modeling of the beam. We plan to remove most of the contaminating species near the middle of the LEBT in order to simplify the modeling of the beam within the RFQ. Beam-current monitors will be placed at a few locations along the LEBT, with one very close to the RFQ entrance.

TRANSVERSE PHASE SPACE

Presently at LANSCE we use several slit-and-collector emittance-measurement systems [2] in the 750 keV transport lines. These have proven to be very successful in tailoring the beams for injection into the DTL and for establishing other transverse conditions needed for proper beam bunching and collimation.

The slit-and-collector technique requires device actuators and many channels of analog signal conditioning and digitization; therefore they are costly. They also require scanning the slit across the beam, so a single measurement requires many beam pulses, making a single-pulse measurement impossible. However they also provide a complete phase-space measurement, allow an direct comparison to our existing LEBT performance, and the ability to distinguish the desired proton beam from other ions that are produced by the duoplasmatron proton ion source [3]. Additionally we have a great deal of experience with dealing with the subtleties of emittance measurement with this type of device, in particular the influence of secondary electrons produced by the beam interactions with the slits and collectors. While this type of scanner is relatively expensive to produce, several spares exist at LANSCE that can be exploited for the RFQ test stand.

Two other types of emittance measurement systems are under consideration: the Allison-type scanner [4] and the pepper-pot method [5]. These two methods have advantages and disadvantages in comparison to the slit-and-collector method, but the prospect of developing a new system and quickly gaining experience with it make it relatively unattractive from financial and logistical viewpoints.

BEAM CURRENT

Beam-current measurements are necessary for assessing the performance of the injector and provide space-charge information for the models of the beam evolution in the transport system. The LANSCE injectors typically produce 800μs-long beam pulses at 120Hz. The standard beam-current measurements are made using 100-turn toroidal current transformers with integrating electronics to provide an output signal that reproduces the beam-current time structure with a bandwidth of about 100 kHz. This system will meet most of our needs. Additional Pearson-type off-the-shelf current transformers may be used where higher bandwidth is needed for diagnosing problems.

BUNCH LENGTH

We have purchased a bunch-length measurement system [6] from INR and it is currently in fabrication. As mentioned above, the bunch length is a critical parameter for this injector due to the long distance from the RFQ to the DTL. While a full longitudinal phase-space measurement would be necessary to predict the evolution of the bunch, the projection of bunch length can validate models of the RFQ and beam-transport line.

The system will have a resolution of 1° of the 201.25 MHz RFQ frequency; this will fulfill the purpose mentioned above. This type of measurement requires partial interception of the beam by a tungsten wire, so it

Copyright © 2013 CC-BY-3.0 and by the respective authors

can be used with minimal impact during production operation.

BEAM ENERGY

Measurement of the beam energy is especially important for this system due to the use of two beam species in the linac. Directing both beams into the center of the linac acceptance provides a less problematic beam downstream in terms of uncontrolled beam spill.

A few options are available, but finding a technique to measure the RFQ output energy with high resolution is difficult. Options under consideration are: 1) magnetic spectrometer, 2) beam phase / time of flight, 3) solid-state detectors with scattered beam particles.

Detecting primary-beam protons scattered from a gaseous or solid target with solid-state detectors has been used previously in the commissioning of RFQs [7,8]. Resolution of a few keV is typical. While high-purity germanium detectors cooled to liquid-nitrogen temperature would be capable of <1keV resolution, this cooling is not possible without interposing some material in the path of the beam particles; this material would harm the resolution and provide a source of uncertainty in the absolute energy measurement.

A time-of-flight measurement using beam phase monitors [9] can provide energy resolution of a few hundred eV. Calibration of the system to provide an accurate absolute measure of kinetic energy is non-trivial, but can be accomplished.

Beam phase measurements can be made with a precision of <0.25°. To preserve this precision, mechanical alignment tolerances need to be about ±40μm. Uncertainties in cables lengths and in RF components could easily spoil the precision. We envision an in-situ absolute calibration using a metal conductor along the center of the beampipe.

The Fermilab PIP RFQ project, [9] used a system of three phase monitors to measure their RFQ output beam energy. Two of them were spaced at about 15 cm to provide a coarse measure of the beam velocity, and another was placed about 56 cm from the first to provide a fine measurement. Precision improves with greater spacing, but two complicating factors increase with the spacing: 1) Uncertainty in the number of RF cycles between the detectors; 2) De-bunching of the beam as it travels. We are evaluating these two factors to determine a set of phase-monitor spacings that will provide acceptable precision and accuracy for our measurements.

While beam-phase measurements can provide a precise measure of the average beam energy, it doesn't easily provide information on the energy distribution. We are evaluating the need for this type of measurement. A magnetic spectrometer is a good candidate to provide information on the energy distribution. To get good resolution in a magnetic spectrometer, two optical conditions are required: a small monochromatic spot size and high dispersion. Additionally, precise information about the path of the incoming beam is required. This can be accomplisheded with a pair of collimating slits. A fine map of the magnetic field is also needed to develop a map of the beam energy versus position at the exit of the magnet.

A magnet designed for use as a low-energy spectrometer is available at LANSCE; it has a bend angle of 120° and the pole faces are oriented to provide good focusing in the bend plane. Initial studies indicate that this magnet could provide sub-keV resolution, though space charge can compromise the resolution considerably.

A multi-wire electronic readout of the system would provide good dynamic range. Sub-millimeter wire spacing would be required in order to maintain resolution. The system used for the emittance scanners is a good candidate for the readout. Another possibility for readout is a phosphor/camera system.

SUMMARY

Several types of measurements are needed on the test stand for the new LANSCE proton RFQ in order to characterize the system performance, especially because of the dual-species operation of the downstream linac. We have identified systems for each measurement that can be implemented without extensive system development.

REFERENCES

[1] R. W. Garnett, et al., "Status of the LANSCE RFQ Front-End Upgrade," NAPAC'13, Pasadena, September 2013, MOPMA14.

[2] R. W. Goodwin, E. R. Gray, G. M. Lee, M. F. Shea, "Beam Diagnostics for the NAL 200-MeV Linac," Proc. 1970 Proton Linear Accel. Conf., Batavia, IL, 107 (1970).

[3] R. R. Stevens, et al., "Beam Measurements on the High-Intensity Proton Injector for LAMPF," Los Alamos National Laboratory internal report LA-4961-MS.

[4] P. W. Allison, J. D. Sherman, D. B. Holtkamp, "An Emittance Scanner for Intense Low-Energy Ion Beams," IEEE Trans. Nuc. Sci., Vol. NS-30, No. 4, 1983.

[5] M. Ripert, A. Buechel, A. Peters, J. Schreiner, T. Winkelmann, "A Low Energy Ion Beam Pepper Pot Emittance Device," BIW'10, Santa Fe, 2010, p. 297.

[6] A. V. Feschenko, "Methods and instrumentation for bunch shape measurements," PAC 2001, Chicago, p 517.

[7] J. P. Duke,D. J. S. Findlay, A. P. Letchford, J. Thomason, "Improved Results from the Gas Scattering Energy Spectrometer on the ISIS RFQ Test Stand," PAC 2003, Portland, May 2003, p. 2542.

[8] L. Weissman, et a;l., "First Experience at SARAF with Proton Beams Using the Rutherford Scattering Monitor," DIPAC 2009, Basel.

[9] V. Scarpine, "Beam Diagnostics for Low Energy Proton and H- Accelerators," BIW'12, Newport News, April 2012, http://www.jacow.org

Copyright © 2013 CC-BY-3.0 and by the respective authors

DESIGN AND COLD TEST OF A 17 GHz OVERMODED HYBRID PBG ACCELERATOR CAVITY*

JieXi Zhang†, Alan M. Cook, Brian J. Munroe, Michael A. Shapiro, Richard J. Temkin
MIT PSFC, Cambridge, MA 02139, USA

Abstract

An overmoded hybrid Photonic Band Gap (PBG) structure used as an accelerator cavity has been theoretically designed. The PBG structure consists of a triangular lattice of dielectric (sapphire) and metallic rods. The birefringence of the sapphire affects the PBG eigenmodes and must be taken into account. The PBG cavity formed by rods in between two copper plates will be operated in a TM_{02} mode at 17 GHz. Arrangement of the rods for higher-order-mode (HOM) damping demonstrates high frequency selectivity. Comparison with a disk-loaded waveguide (DLW) cavity gives a perspective of the dielectric PBG structure operated at an accelerating gradient of 100 MV/m. Cold test of a single hybrid PBG cell presents a high-Q resonance at 17 GHz. A standing-wave (SW) hybrid PBG structure will be tested in TM_{02} mode at 17 GHz.

INTRODUCTION

A periodic photonic structure, whose dispersion relation has photonic band gaps (PBG), can be applied to accelerators due to its good frequency selectivity [1]. A travelling-wave (TW) multi-cell metallic PBG structure has demonstrated successful acceleration of electrons with gradient of 35 MV/m [2]. More SW metallic PBG structures have been studied with high power breakdown tests at both SLAC and MIT [3, 4].

A theoretical study of a dielectric PBG structure was presented by Shapiro et al. [5]. A detailed design with isotropic sapphire rods using the commercially available code Ansys High Frequency Structure Simulator (HFSS) was reported in PAC11 [6]. The dielectric band gap allows a TM_{02}-mode operation without competing with the lower-frequency TM_{01} mode since the latter is not supported in the band gap. The TM_{02} mode helps in geometry design for a high frequency of 17 GHz and mitigates the central high field away from the innermost rods. Simulations showed an accelerating gradient of 100 MV/m with lower magnetic field than the metallic PBG structure, which may reduce the breakdown rate in high power testing. A sapphire rod structure was previously built and cold tested but not tested at high power [7].

In this paper, we analyze a sapphire PBG periodic unit cell with an anisotropic (birefringent) dielectric constant. 2D cross-section design in HFSS will give an optimal configuration of a hybrid PBG structure containing both dielectric rods and metallic rods. A single cell 3D structure has been theoretically designed and the cold test result will be presented.

ANISOTROPIC BAND GAP MAP

Sapphire is an optically anisotropic material with permittivity changing with the electromagnetic (EM) wave frequency [8]. At 17 GHz, with the orientation of the C-axis of the sapphire rods parallel to the particle beam axis in our design, the permittivity of the sapphire rod is $\epsilon_r = [9.398, 9.398, 11.587]$ by interpolation from [8].

Figure 1 shows the band gap map of a periodic sapphire lattice with the above anisotropic permittivity calculated in HFSS, as well as the comparison with an isotropic lattice of $\epsilon_r = 9.398$. The eigenmode frequency is normalized to $\omega b/2\pi c$ and the lattice is characterized by ratio $\frac{a}{b}$ with the rod radius a and the lattice spacing b. The lowest band gap can confine the TM_{02} mode while the TM_{01} mode is radiated out through the dielectric lattice.

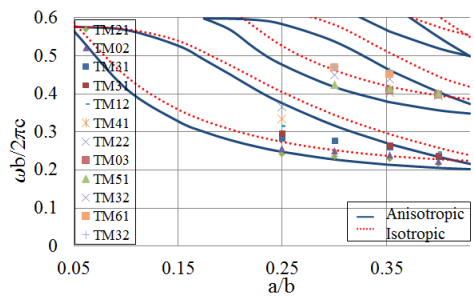


Figure 1: Band gap map of sapphire with isotropic and anisotropic permittivity.

In HFSS, to model a "2D structure", a very thin PBG layer is made with perfect E boundaries on top and bottom to limit the eigenmode solutions to TM modes. The calculated normalized frequencies of different modes in the 2D PBG structure are shown in Fig. 1; this helps to determine the design point $\frac{a}{b} \sim 0.35$, where the TM_{02} mode sits in the center of the band gap and few other modes are present in the same gap. The only HOM that is of concern is the TM_{31} mode. The final parameters of $a = 1.58$ mm and $b = 4.47$ mm have been chosen based on the 3D design shown later. Varying the arrangement of rods to achieve an improved Q of the TM_{02} mode and a reduced Q of the TM_{31} mode will be described in the following section.

CAVITY MODE IN 2D DESIGN

The birefringence of sapphire results in a discrepancy between the 2D and 3D simulations, but the study of the

* This work supported by Department of Energy High Energy Physics, Grant No. DE-SC0010075.
† zhangjx@mit.edu

Copyright © 2013 CC-BY-3.0 and by the respective authors

2D cross section of each mode with distinct rod patterns provides a basic idea of how to improve the Q of the TM_{02} mode and damp the HOMs. Figure 2 shows how the diffractive Q of the TM_{02} mode increases as we include additional rows of concentric sapphire rods. This shows that a large number of rods are needed in a pure dielectric cavity to get a Q of the TM_{02} mode that is comparable to the Q of the TM_{01} mode in a DLW ($Q > 1000$), leading to a large cavity geometry. To increase the diffractive Q of the TM_{02} mode, metallic rods are added to the outermost row.

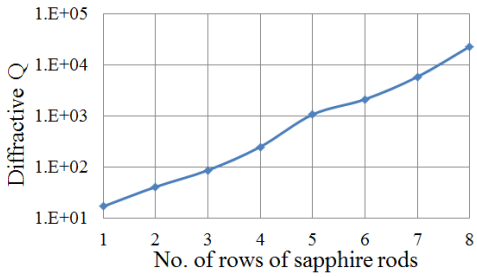


Figure 2: The diffractive Q vs. the number of concentric rows of sapphire rods.

Removing some rods makes the structure more azimuthally uniform and creates damping channels for the HOMs, which improves the Q of the TM_{02} mode and degrades the Q of the TM_{31} mode significantly. A 60° symmetric wedge of the optimal 2D structure is shown in Fig. 3, showing the E fields of the TM_{02} and TM_{31} modes. The calculated Q of the TM_{02} mode is ~ 6500 and the Q of the TM_{31} mode is ~ 30.

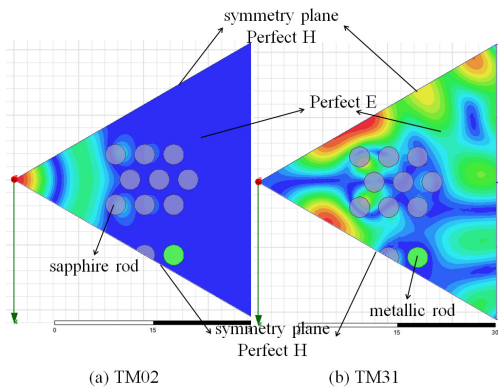


Figure 3: The 60° wedge cross section of E field of (a), the TM_{02} mode, and (b), the TM_{31} mode in the 2D model of the hybrid PBG structure.

SINGLE CELL 3D DESIGN

Based on the 2D design, a 3D HFSS model of a periodic single cell with three rows of sapphire rods and one row of metallic rods is shown in Fig. 4. Rods are inserted into two copper plates to form a cavity and irises are shaped to couple 17 GHz RF power. Design parameters are listed in Table 1.

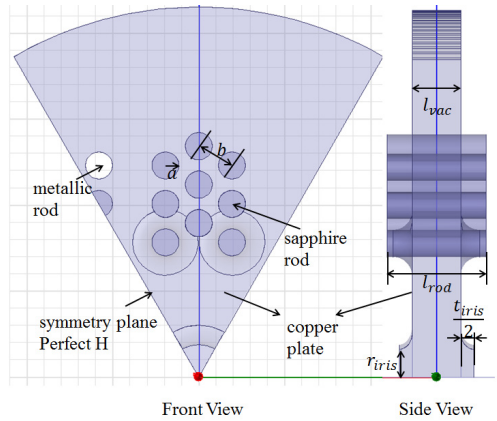


Figure 4: The 3D HFSS model of the periodic single cell hybrid PBG structure.

Table 1: Design Parameters of the Periodic Single Cell Structure

a **(mm)**	b **(mm)**	l_{rod} **(mm)**
1.58	4.47	11.68
r_{iris} **(mm)**	t_{iris} **(mm)**	l_{vac} **(mm)**
3.765	3.07	5.68

By using "Master" and "Slave" boundaries in HFSS, a phase shift of 180° is forced on the ends of irises to form a periodic boundary condition. The comparison of the EM field profile between the hybrid PBG cell (TM_{02} mode) and DLW cavity (TM_{01} mode) with the same irises is shown in Fig. 5, for an accelerating gradient [9] of 100 MV/m in each case.

The comparable field profile indicates a possibility to apply the hybrid PBG structure in high-gradient accelerators. The simulated result is listed in Table 2 as well as the experimental cold test measurement discussed next.

Table 2: Results of the Single Cell Structure

	f **(GHz)**	Q
Sim.	17.19	5800
Exp.	17.12	2700

SINGLE CELL COLD TEST

Cold test of a single cell of the hybrid PBG structure has been performed using a Vector Network Analyser (VNA) at MIT as shown in Fig. 6. Two antennas are held by three-axis translation stages to send and receive signals. Q is measured through the transmission parameter S_{21} [10].

Copyright © 2013 CC-BY-3.0 and by the respective authors

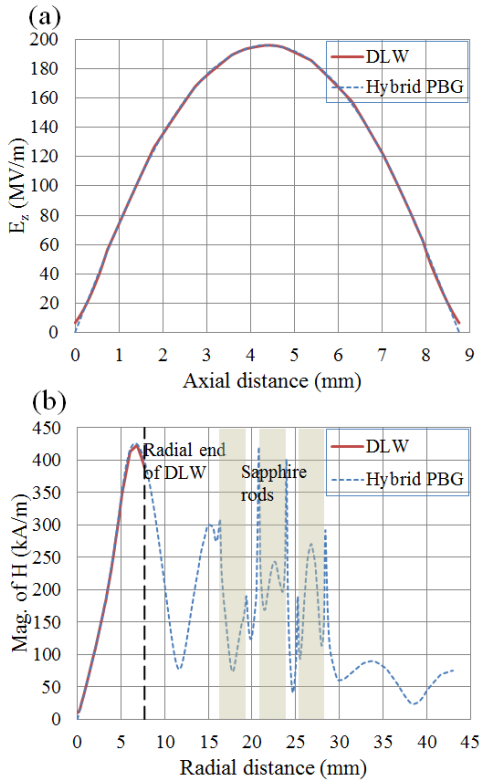


Figure 5: Comparison of the Hybrid PBG cell and the DLW cell of (a), E field axial profile and (b), H field radial profile.

The experimental result is shown in Fig. 7 with a single resonance at 17.12 GHz with $Q = 2700$, as listed in Table 2. No other modes are observed. The differences between theory and experiment in Table 2 may be due to approximations in the theory or fabrication errors. However, the presence of a single resonance close to the design frequency is very promising for future hot test experiments.

CONCLUSION

A hybrid PBG structure consisting of anisotropic dielectric rods and metallic rods has been optimized with 2D and 3D design in HFSS. With an accelerating gradient of 100 MV/m, the field profile of the single hybrid PBG cell is comparable to a DLW cell. A transmission measurement of a single cell of the hybrid PBG structure has been obtained in cold test, showing a single resonance at 17.12 GHz with a Q of 2700, providing a promising future for accelerator applications.

A SW 3-cell hybrid PBG structure is under design. By using the high power 17 GHz Haimson klystron at MIT, breakdown tests can be performed on the multi-cell structure.

REFERENCES

[1] S. Schultz, D.R. Smith and N. Kroll, "Photonic Band Gap Resonators for High Energy Accelerators", PAC'93 (1993).

[2] E.I. Smirnova et al., Phys. Rev. Lett. 95, 074812 (2005).

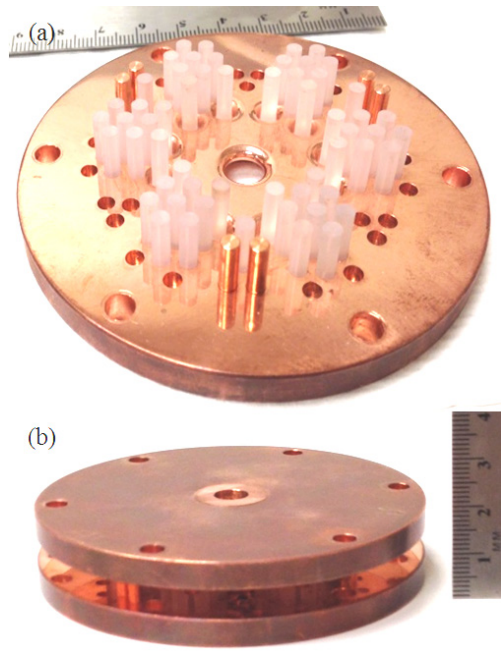


Figure 6: The cold test structure of the single hybrid PBG cell.

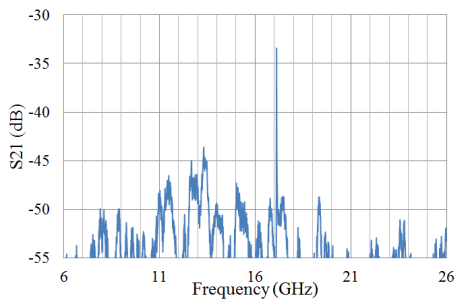


Figure 7: Transmission measurement of the single hybrid PBG cell.

[3] R.A. Marsh, *Experimental Study of Photonic Band Gap Accelerator Structures*, MIT-Thesis (2009).

[4] B.J. Munroe et al., Phys. Rev. ST Accel. Beams 16, 012005 (2013).

[5] M.A. Shapiro et al., Proc. Par. Accel. Conf. (PAC'03), IEEE Conf. Prof., pp.1255-1257 (2003).

[6] A.M. Cook et al., PAC'11 Proc. MOP041, p.175 (2011).

[7] M.R. Masullo et al., Microwave Opt. Techn. Lett. 48, p.2486 (2006).

[8] J. Krupka et al., Meas. Sci. Tech. 10, pp. 387-392 (1999).

[9] T.P. Wangler, *RF Linear Accelerators*, (Wiley-VCH, 2008), p. 41.

[10] E.L. Ginzton, *Microwave Measurements*, (McGraw-Hill, 1957), p. 405.

Copyright © 2013 CC-BY-3.0 and by the respective authors

RESULTS FROM THE LINAC COMMISSIONING OF THE RARE ISOTOPE REACCELERATOR - ReA*

Walter Wittmer†, Daniel Alt, Thomas Baumann, Carla Benatti, Shannon Wayne Krause, Alain Lapierre, Daniela Leitner, Ling-Ying Lin, Fernando Montes, Samuel Nash, Randall Rencsok, Jose Alberto Rodriguez, Michael Syphers, Eugene Tanke, Xiaoyu Wu (NSCL, East Lansing, Michigan)

Abstract

ReA [1] is a radioactive ion beams post accelerator currently being completed at the National Superconducting Cyclotron Laboratory at Michigan State University. ReA is designed to reaccelerate rare isotopes to energies of a few MeV/u following production by projectile fragmentation and thermalization in a gas cell. The facility consists of five main components: an electron beam ion trap (EBIT) charge breeder, an achromatic charge over mass separator, a radiofrequency quadrupole (RFQ) accelerator, a superconducting radio frequency linear accelerator (SRF LINAC) and a transport line into the experimental hall. The first sections up to the SRF LINAC of ReA have been commissioned in the last two years using an offline stable ion beam source and heavy ion beams from the EBIT charge breeder. The final section, transporting beam from the LINAC into the experimental hall, was completed and commissioned this summer. This paper presents the results of the SRF cryo module characterization and the progress of the machine optics model.

INTRODUCTION

The Facility for Rare Isotope Beams (FRIB)[2], a 400kW superconducting heavy-ion driver LINAC, will produce beams of exotic nuclear species with increased intensity of up to three orders of magnitude more than the CCF after fast fragmentation. ReA will reaccelerate these beams with improved characteristics for experiments. Initially the energy of the Rare Isotope Beams (RIBs) will be 3 MeV/u with future upgrades reaching 12 MeV/u. Currently ReA is coupled to the Coupled Cyclotron Facility (CCF) at the National Superconducting Cyclotron Lab (NSCL) at Michigan State University and provides beam of up to 2.4 MeV/u.

Stable beams are accelerated to energies of approx. 100 MeV/u by the CCF and fragmented on a solid target. The secondary beam, comprised of a melange of fragments, is separated achromatically in the A1900 fragment separator. The selected isotope is then thermalized in a He gas cell and extracted at energies up to 60 keV. Following mass selection at a dipole magnet the beam is injected into the Electron Beam Ion Trap (EBIT) where it is charge bred. The beam is then extracted at 12keV/u (RFQ injection energy) and transported through a Q/A achromatic charge-over-mass separator for charge selection and accelerated in the LINAC. The initial acceleration occurs in a four rod RFQ to an energy of 600 keV/u. The beam is then rebunched in a rebunching module with a single quarter wave cavity ($\beta = 0.041$) followed by an accelerating module containing six cavities of the same type. Next, the beam is delivered into the experimental hall. The final accelerating cryo module, comprised of 8 quarter wave cavities ($\beta = 0.085$), is currently in construction and will complete the initial ReA3 installation next year.

The commissioning of the current installation of the reaccelerator has been successfully completed following a commissioning experiment where a ^{37}K ($T_{\frac{1}{2}} = 1.23$s) beam was delivered to the ANASEN [3] detector.

SRF LINAC

The first rebunching module comprises a single quarter wave cavity ($\beta = 0.041$) and two superconducting 9 Tesla solenoids with integrated steering magnets. The second accelerating module houses 6 cavities and 3 solenoids of the same type. Both modules are shown in Figure 1.

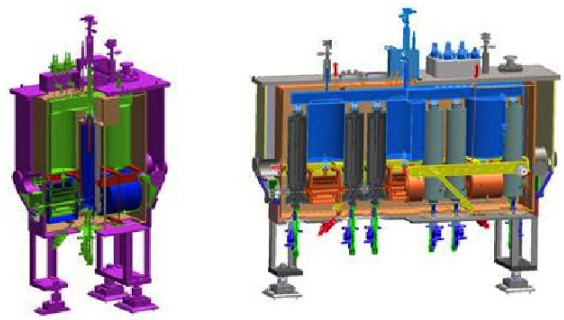


Figure 1: On the left the rebunching cryo module is shown with its cavity at the center between the solenoids. The right shows the first accelerating module with one cavity at each end and groups of two separated by the three solenoids.

Dipole Calibration and Energy Spread Measurement with CAESAR Detector

An experimental setup consisting of an Aluminum target inside the high-efficiency CsI(Na) scintillator array (CAESAR) [4] was used to obtain an energy calibration of a bend magnet, located after the second accelerating module, to measure the beam energy spread and to test the performance of the LINAC.

* Work supported by Michigan State University
† wittmer@nscl.msu.edu

Copyright © 2013 CC-BY-3.0 and by the respective authors

Preliminary analysis of the measurement data show good agreement of the derived energy spread and the predicted from the machine model as well as for the beam energy. A detailed analysis is ongoing an will soon be published.

Beam Based Cavity Amplitude Calibration

The initial calibration of the cavity amplitude was based on measurements performed in the SRF test dewar. It was soon noticed that the error of this calibration exceeded 10% and the calibration was repeated with beam based measurements. Two sets of measurements were performed. The first utilized a foil silicon detector where the beam is scattered through a gold foil to reduce the beam intensity and then the energy is measured with a silicon detector. The energy loss due to scattering has to be taken into account. The cavity phase is varied over 360 degrees and the beam energy is measured as shown in Figure 2. After calibrating

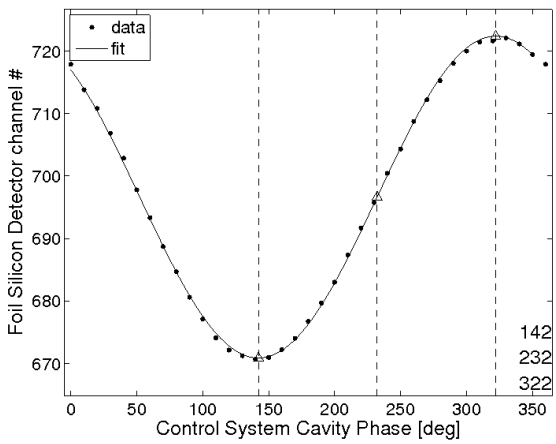


Figure 2: SRF cavity phase scan measured with a foil silicon detector. The dots represent the measured data, the line the fitted curve and the triangles with dashed lines, the location of maximum deceleration, zero crossing for the bunching slope and maximum acceleration.

the detector with an ^{241}Am source the energy difference between maximum deceleration and acceleration can be calculated. This allows calculating the accelerating field.

The second method uses two Beam Position Monitors (BPMs) [5] installed after the second cryo module and allows measuring the beam energy by means of time of flight measurements. A detailed description can be found in [6].

The established calibration factors have been verified with the bend magnet field, calibrated with the CESAR detector described above, and scattering measurements with the ANASEN detector. In both cases the differences were smaller than 2% which can be attributed to the uncertainty of the LINAC cavity phasing.

MACHINE MODEL

The DYNAC [7] code has been chosen for machine modeling based on its capability to simulate all devices in the ReA3 beam line except the EBIT. This includes the multi harmonic buncher, RFQ, superconducting quarter wave cavities, electrostatic and magnetic elements. This allows using a single code when performing beam optics calculations compared to 4 different sequencial codes.

SRF Quarter Wave Cavity Kick Measurements

An analytical model predicting the kick of a SRF quarter wave cavity (QWC) has recently been published [8]. A series of measurements were conducted with the goal to verify the model. If successful, it will allow to measure the cavity offset in the transverse position and minimize the overall kick the beam receives. Adding this effect to the machine model will improve its capability in the control room.

The asymmetric geometry of the QWC results in a vertical kick of the beam depending on the vertical displacement within the accelerating gap, the speed or energy of the particle upon entrance, as well as the cavity amplitude and phase. The location of the third cryo module is currently a drift space with a diagnostic station at each end capable of measuring the beam position. This allows measuring both position and angle of the beam exiting the second existing cryo module.

A first set of measurements was conducted using a molecular hydrogen beam H_2^+ at an RFQ energy of 600 keV/u. A parallel offset was induced to the beam trajectory through the last QWC of the LINAC, which was phased to the bunching zero crossing. The cavity amplitude was varied at each trajectory until the beam was lost in the drift space. A result of this measurement is shown in Figure 3.

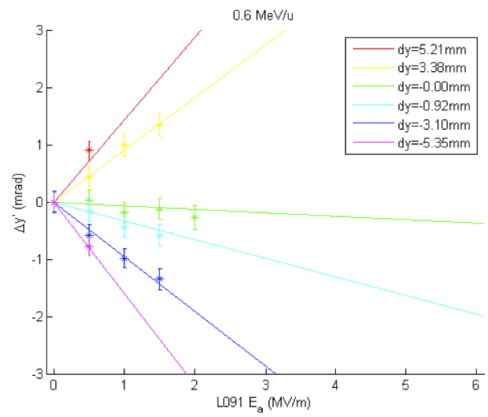


Figure 3: Vertical deflection angle vs. cavity voltage. Each line is the model prediction for different vertical displacement within the cavity from the beam's position. The diamonds including error bars represents the measured data.

All results agree with theoretical predictions. Based on this success a second series of measurements is planned for this fall, repeating this measurement at different beam energies and at different cavities.

Copyright © 2013 CC-BY-3.0 and by the respective authors

Results of the Application of the Model During Beam Line Commissioning

The model was completed beginning of 2013 and has been benchmarked in the accelerator over the past couple of months. The first practical application of the machine model occurred during the commissioning of the final beam line, connecting the ReA LINAC to the experimental end station. The beam line elements were set to their design values and the beam was transported to the end of this approx. 30-meter long line within three hours. During the following commissioning, the design optics in this area was preserved and the injected beam properties adjusted. Figure 4 shows the simulated (left) and measured (right) transverse beam profile on a scintillating viewer crystal in the

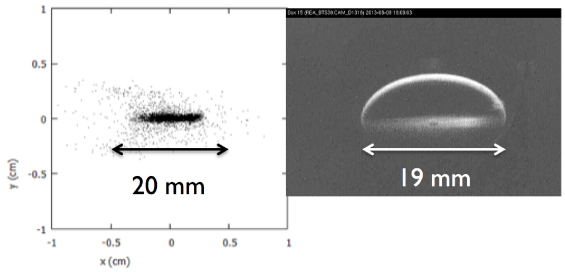


Figure 4: Transverse beam image in the location of a beam diagnostic station in the newly commissioned beam line. The left shows the simulated beam profile, the right the measured beam image.

diagnostic station. This particular location is at a high dispersion point, which explains the large horizontal beam.

To analyze the machine model a comparison of all settings was performed. Figure 5 shows as example the quadrupole magnet analysis. The first six magnets are located after the long drift and are part of the achromat that brings the beam line from the ReA deck onto the floor. The settings are optimized to cancel the dispersion. The following six quads are used to match the beam into the second achromat and final focus into the experimental end station. The settings of these element matches precisely the model. Only the final focus doublet needed to be adjusted. Overall the differences are small. The SRF cavity and RFQ settings are the same for model and machine. The solenoids in the SRF LINAC are deviating to a degree that is not fully understood. A possible source is a difference transverse emittance after the RFQ, as used in the simulation and in the machine. Work is ongoing to measure the emittance at this location. With the initial conditions of the beam entering the SRF LINAC section determined and the technique described in this paper, the benchmarking of the machine model will be completed.

The longitudinal emittance is fully understood. The model for the RFQ and SRF QWC is used to setup the beam. The transverse beam optics is well understood and a complete machine model will be available once the source for SC solenoid differences have been identified and incorporated in the model.

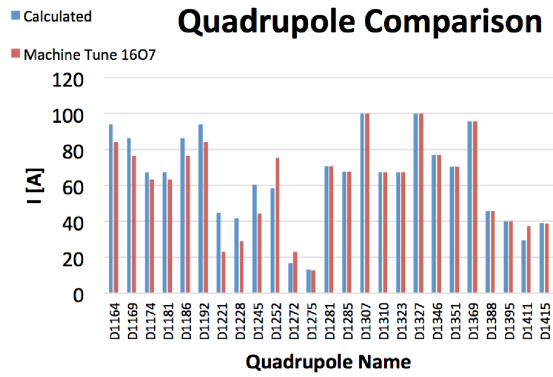


Figure 5: Comparison of quadrupole settings from machine model (blue) and as applied in machine (red).

CONCLUSIONS

The commissioning of the existing LINAC has been successfully completed and has shown a high level of reliability during the first beam delivery. The third cryo module is expected to be installed and commissioned by the end of summer next year. The experience and methods established during the initial commissioning will allow the integration of the final cryo module within a short period.

The machine model, implemented in a single code, has been established starting from the exit of the EBIT to the experiment's target point. The simulated longitudinal beam representation has been within 2% difference when compared to the measured beam. This has been verified by the measurements of the CAESAR and ANASEN detectors. The transverse description shows good agreement except in the cryo module area. Work is ongoing to determine the source of this difference.

REFERENCES

[1] D.Leitner, et al.,"Status of the ReAccelerator facility ReA for rare isotopes.", Proc. of 2013 NA-PAC'13, FRYBA2.

[2] J.Wei, et al., "Progress at MSU towards a Facility for Rare Isotope Beams.", Proc. of 2013 NA-PAC'13, FRYBA1.

[3] M. Matos, et al., "The Array for Nuclear Astrophysics Studies with Exotic Nuclei (ANASEN)." , In 14th International Symposium on Capture Gamma-Ray Spectroscopy and Related Topics, 2013.

[4] Weisshaar, D. et al.,"CAESAR - A high-efficiency CsI(Na) scintillator array for in-beam gamma-ray spectroscopy.", Nuclear Instrum. Methods Phys. Res. A 624, 615 (2010).

[5] J.Crisp, et al., "Beam position and phase measurements of microampere beams at the Michigan State University ReA3 facility.", Proc. of 2013 NA-PAC'13, THPAC20.

[6] B.Durickovic, et al., "RF cavity phase calibration using electromagnetic pickups.", Proc. of 2013 NA-PAC'13, THPHO14.

[7] E. Tanke, et al., "DYNAC: A multi-particle beam dynamics code for leptons and hadrons.", Gyeongju, TH429, p. 667 (2002)

[8] A.Facco and V.Zvyagintsev, Phys. Rev. ST-AB 14, 070101 (2011)

Copyright © 2013 CC-BY-3.0 and by the respective authors

BUNCHED BEAM ELECTRON COOLER FOR LOW-ENERGY RHIC OPERATION*

A.V. Fedotov[1#], S. Belomestnykh[1,2], I. Ben-Zvi[1,2], M. Blaskiewicz[1], D. Gassner[1], D. Kayran[1], V.N. Litvinenko[1,2], B. Martin[1], W. Meng[1], I. Pinayev[1], B. Sheehy[1], S. Tepikian[1], J. Tuozzolo[1], G. Wang[1]
[1)] Brookhaven National Laboratory, Upton, NY 11973, U.S.A.
[2)] Stony Brook University, Stony Brook, NY 11794, U.S.A.

Abstract

Electron cooling was proposed to increase the luminosity of the Relativistic Heavy Ion Collider (RHIC) operation for heavy ion beam energies below 10 GeV/nucleon. The electron cooling system should be able to deliver an electron beam of adequate quality in a wide range of electron beam energies (0.9-5 MeV). An attractive option is to use electron bunches produced with the superconducting RF (SRF) injector. Such a scheme of cooling with bunched electron beam is also a natural approach for high-energy electron cooling which requires RF acceleration. In this paper, we describe the requirements and design aspects of such an approach.

INTRODUCTION

Mapping the Quantum-Chromo-Dynamics (QCD) phase diagram is one of the fundamental goals in the heavy-ion collision experiments. The QCD critical point is a distinct feature of the phase diagram, the existence of which is predicted by various QCD models. The beam energy scan phase-I (BES-I) runs for physics, motivated by the search of the QCD critical point, were successfully conducted at RHIC in 2010-11. During BES-I physics runs data sets were collected for Au+Au (center of mass) energies of 7.7, 11.5, 19.6 and 39 GeV. Driven by physics and the BES-I results, the future physics program called BES-II is proposed for Au+Au energies below 20 GeV (γ=10.7). However, required event statistics is much higher than previously achieved and relies on significant luminosity improvement in RHIC at energies below γ=10.7. Electron cooling was proposed to increase luminosity of the RHIC collider for heavy ion beams at these low energies [1-2].

In a collider, the maximum achievable luminosity is typically limited by the beam-beam effects. For heavy ion beams significant luminosity degradation via the bunch length and the transverse emittance growth comes from the intra-beam scattering (IBS). For low-energy RHIC such IBS growth can be counteracted with electron cooling. If IBS were the only limitation, one could achieve a small hadron beam emittance and bunch length with the help of cooling, resulting in a dramatic luminosity increase. However, as a result of low energies, the direct space-charge force from the beam itself is expected to become the dominant limitation [3-4]. The main role of electron cooling for the lowest energy points is thus to counteract IBS: this prevents transverse emittance growth and intensity loss from the RF bucket due to the longitudinal IBS. As the energy is increased, the space-charge effect on the hadron beam becomes smaller which permits additional cooling of the transverse or longitudinal emittances of the hadron beams. This, in turn, allows us to reduce the β^*, providing larger luminosity gain. Recently, operation with long ion bunches and a new low-frequency RHIC RF system was suggested which should help to mitigate some observed limitations of beam lifetime at low energies offering a better path towards luminosity improvement [5-6].

This electron cooling technique requires electron beam to co-propagate with the same velocity as the ion beam in a localized portion of circular collider called the cooling section. An electron beam up to 5 MeV kinetic energy is needed to cover the full energy range of interest.

Such Low Energy RHIC electron Cooler (LEReC) based on the SRF linac is presently under design at BNL.

COOLING CONSIDERATIONS

The energies of electron beam needed for low-energy RHIC are sufficiently high (0.9-5 MeV), which allows us to consider cooling using bunched electron beam. One of the challenges for bunched beam cooling is providing beam transport of electron bunches without significant degradation of beam emittance and energy spread. A low-frequency 84.5 MHz RF gun can provide relatively long electron bunches. As a result, even for high bunch charges, space-charge effects remain under control. One can then deliver an electron beam of the necessary quality to the cooling section. In addition, the use of long ion bunches [5-6] allows us place several electrons bunches on a single ion bunch, which in turn relaxes requirements on charge in individual electron bunch and should allow us to achieve good beam quality needed for cooling.

Since non-magnetized cooling significantly simplifies electron beam transport and reduces the cost of the cooler, it was chosen as our baseline approach. Due to a relatively low beam current required for our cooler (Table 1), an approach with zero magnetic field on the cathode and thus no magnetic field in the cooling section is feasible. Short solenoids will be placed every 2 m to correct the angular spread accumulated due to the electron beam space-charge self field in the cooling section.

*Work supported by the US Department of Energy under contract No. DE-AC02-98CH10886.
#fedotov@bnl.gov

Copyright © 2013 CC-BY-3.0 and by the respective authors

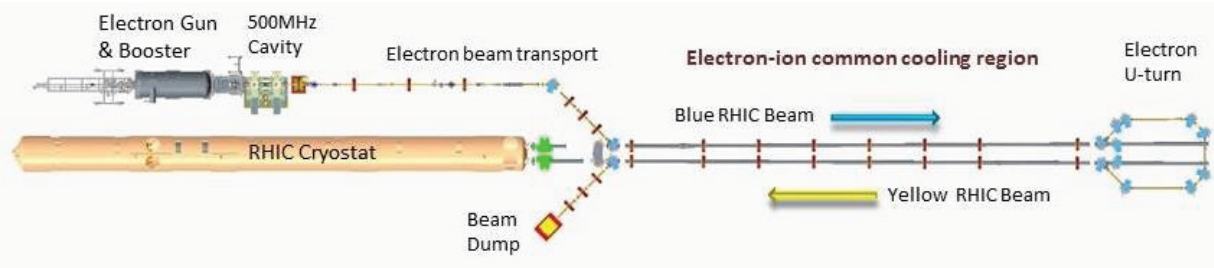


Figure 1: LEReC beam line layout. The cooling sections will be located in a RHIC warm region.

The use of undulators for recombination suppression in the cooling section is compatible with approach chosen. However, the use of undulators would require significant engineering additions to the cooling section while, in our case, the expected benefit for luminosity with recombination suppression seems rather modest. Thus, the recombination suppression with undulators is presently not included in the LEReC baseline.

ELECTRON ACCELERATOR

Beams for LEReC will be provided by a short SRF linac [7], which comprises a quarter wave resonator (QWR) photoemission electron gun, a QW SRF booster cavity and a normal conducting harmonic cavity to correct RF-induced energy spread. The two SRF structures will be housed in the same cryomodule with a superconducting solenoid in between the cavities. Preliminary optimization of the cavity shape is performed in collaboration with Argonne National Laboratory. Electron beam will be accelerated to the required energy and then transported from the SRF accelerator to the first cooling section in the Blue RHIC ring, cool ions in the first cooling section, turned around between Blue and Yellow RHIC rings (U-turn), cool ions in the Yellow ring and transported to the beam dump, as shown in Fig. 1.

Electron beam will be generated by illuminating a multi-alkali (CsK_2Sb or NaK_2Sb) photocathode with green (532 nm) light from a laser. The photocathode is inserted into a 84.5 MHz quarter-wave SRF cavity thus forming an SRF photoemission electron gun. The photocathode is located in a high electric field. Immediate acceleration of the electrons to a high energy reduces emittance degradation caused by a strong non-linear space-charge force. The low RF frequency of the gun reduces the effect of RF curvature on the beam.

The SRF gun will produce bunch trains (several bunches) with relatively long electron bunches, about 1 ns, at 84.5 MHz bunch repetition frequency. The bunch train repetition rate will be the same as the repetition rate of ion bunches in RHIC. The optical system will allow creating dedicated bunch patterns for different RHIC energies and ion bunch lengths with several bunches at 84.5 MHz frequency followed by a long gap corresponding to the frequency of ion bunches. For example, for very long ion bunches at lowest energies with new 4.5 MHz RHIC RF we can place up to 9 electrons bunches on a single ion bunch (see Fig. 2).

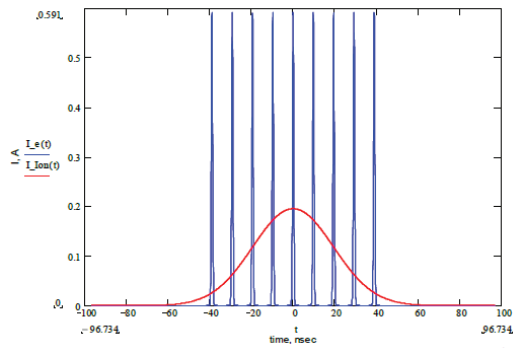


Figure 2: Nine electron bunches (blue) placed on a single ion bunch (red). Example for long ion bunches with proposed 4.5 MHz RHIC RF at $\gamma = 4$, time is in ns.

COOLER PARAMETERS

The requirement on the transverse angles of electron beam in the cooling section is given by the angular spread of the ion beam. For example, for the rms normalized emittance of 2.5 mm-mrad at γ=4.1, and 30 m beta function in the cooling section, the ion beam rms angular spread in the lab frame is 0.14 mrad. The ion beam will have rms longitudinal momentum spread in the range of σ_p=4-5×10^{-4}. This sets requirement on the rms momentum spread of electron beam of < 5×10^{-4}.

To keep the transverse angles of electron beam at an acceptable level (< 0.15 mrad) an integral of residual transverse magnetic field in the space used for cooling should be kept below 1 Gauss·cm (at γ=4). Shielding of residual magnetic field to such a level could be provided by several concentric cylindrical layers of high permeability alloy or by the correction coils.

Some cooling section space is taken up by very short (10 cm) weak (200 G) solenoids (to control angular spread due to the space charge), steering dipoles and beam position monitors to keep the electron and ion beam in close relative alignment. Diagnostics details for the LEReC project can be found in Ref. [8].

Since the electron beam does not have any magnetization, space used by the solenoids will be lost from the cooling process. Longitudinal field of 1 G produces rotational angles of 75 μrad at γ=4. Presently, design of these solenoids, placed every 2 m, is being optimized to maximize the space between them which satisfies requirement on B_z < 1 G. To allow for about 12 meters of effective cooling the full length of the cooling

Copyright © 2013 CC-BY-3.0 and by the respective authors

section, including solenoids, is presently 14 m. Basic parameters of electron beam are shown in Table 1 (see [9] for details). The charge per bunch needed depends on the energy at which cooling is applied and which RF system is being used in RHIC. For example, for γ=4 and 4.5 MHz RHIC RF the use of a bunch train allows us to split the total charge of 4 nC required for cooling, into 9 bunches with 0.44 nC per bunch. Although electron bunch occupies a small portion of the ion bunch, all ions could be cooled as a result of the synchrotron oscillations. To provide effective cooling of ions with different amplitudes a slow motion of the electron bunch through the ion bunch ("painting") is desired. With the present scenario of many electron bunches spread through the ion bunch such a painting maybe not necessary.

Table 1: Electron Beam Parameters

Electron Beam Energy	0.9-5 MeV
Charge per Bunch	0.4 –2 nC
Electron Beam Current	20-40 mA
RMS Norm Emittance	< 2.5 mm mrad
Transverse Angles	< 0.15 mrad
RMS Energy Spread	$< 5 \times 10^{-4}$
Bunch Length	750 ps

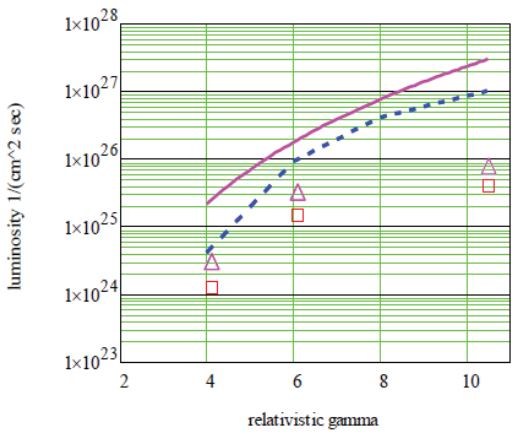


Figure 3: Luminosity in RHIC with and without the electron cooling upgrade. Red squares: measured average per store luminosity in BES-I; magenta triangles: measured maximum luminosity; blue dash line: luminosity with cooling (present RHIC RF); magenta top line: with cooling and long ion bunches (new RF system).

PERFORMANCE WITH COOLING

Projection of potential luminosity improvement as a function of energy is shown in Fig. 3. One can see that close to 10-fold improvement from cooling may be expected only at highest energies if one uses existing 28 MHz RHIC RF system (blue dash line in Fig. 3). At the lowest energies expected luminosity improvement could be rather modest (see [10] for details). A proposed low-frequency RHIC RF system (4.5 or 9 MHz) would allow for longer ion bunches and significant transverse cooling at low energies; the projected performance with this system is shown by the magenta curve in Fig 3. Performance in either scenario may be lower than indicated, due to remaining uncertainties in the beam lifetime improvement from cooling.

CHALLENGES

Successful operation of LEReC cooler requires stable and reliable CW operation of the SRF gun with electron beam current up to 40 mA. A long lifetime of the photocathode inside such a gun with a charge per bunch up to 2 nC is also required. Demonstration of some of the unique and challenging features is being planned with the existing 704 and 112 MHz SRF guns at BNL.

The achievement of very low transverse angular spread for the electron beam is challenging and is being addressed by a proper beam transport and engineering design [9]. The attainment of required low energy spread in the electron bunch relies on shielding of the longitudinal space-charge force with the vacuum chamber, use of long electron bunches and minimization of the length of beam transport. The repeatability of low energy electron transport is challenging due to remnant fields in the optics and hardware. Electron beam with small emittance and energy spread should be provided for several energies of interest. Quality of the beam should be preserved through the entire beam transport since the same beam will be used for cooling in both RHIC rings.

Besides many technical issues, this will be the first electron cooler to cool beams under collisions. This puts special requirements on the control of the ion beam profile under cooling. Careful optimizations between electron cooling and ion beam lifetime will determine how close one can actually get to the projected luminosity improvement.

ACKNOWLEDGMENTS

We would like to thank W. Fischer, C. Montag, T. Roser, A. Zaltsman and other members of the Collider-Accelerator Department for help and useful discussions.

REFERENCES

[1] A. Fedotov et al., Proc. of COOL'07 workshop (Bad Kreuznach, Germany), p. 243 (2007).
[2] A. Fedotov et al., Tech Note: C-A/AP/307 (2008).
[3] A. Fedotov et al., Proc. of HB2008 workshop (Nashville, TN), WGA10, p. 75 (2008).
[4] A. Fedotov et al., Proc. of PAC'11 (New York, NY), THP081, p. 2285 (2011).
[5] A. Fedotov and M. Blaskiewicz, BNL C-AD Tech Note: C-A/AP/449 (2012).
[6] V. Litvinenko, Tech Note: C-A/AP/476 (2012).
[7] S. Belomestnykh et al., Proc. of SRF'13 (Paris, France, September 2013), MOP17.
[8] D. Gassner et al., Proc. of IBIC'13 (Oxford, UK, September 2013), TUPF24.
[9] Low-Energy RHIC electron Cooling (LEReC) White Paper, C-AD BNL, September 2013.
[10] A. Fedotov, BNL Tech Note: C-A/AP/481 (2013).

Copyright © 2013 CC-BY-3.0 and by the respective authors

RHIC MACHINE STUDIES TOWARDS IMPROVING THE PERFORMANCE AT 2.5 GEV *

C. Montag, H. Huang, G. Marr, A. Marusic, G. Robert-Demolaize, T. Shrey, V. Schoefer, S. Tepikian, K. Zeno, BNL, Upton, NY 11973, USA

Abstract

To search for the critical point in the QCD phase diagram, Au-Au collisions at beam energies between 2.5 and 15 GeV/n are required. While RHIC has successfully operated at 3.85 and 5.75 GeV/n, the performance achieved at 2.5 GeV/n is not sufficient for a meaningful physics program. We report on dedicated beam experiments performed to understand and improve this situation.

INTRODUCTION

During the next 5 - 10 years, one of the major RHIC physics programs will be the search for the critical point in the QCD phase diagram, shown in Figure 1. This search requires a gold beam energy scan in the range between 2.5 and 15 GeV/nucleon, which extends well below the RHIC design energy range from 10 GeV/n at injection to 100 GeV/n at store.

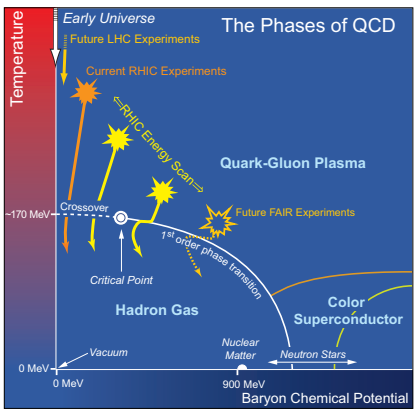


Figure 1: The QCD phase diagram, with the critical point expected in the center-of-mass energy range between $\sqrt{s_{\mathrm{NN}}} = 5$ and 30 GeV

Operating RHIC below its design energy range is very challenging for a number of reasons. First of all, beam emittances are large, resulting in a lower limit on the β-function at the interaction point, and therefore in low luminosity. Large space charge tune shifts are encountered even with moderate beam intensities. Last but not least, the multipole errors in the accelerator magnets are optimized at full energy, while they are an order of magnitude larger below the nominal injection energy.

* Work supported by Brookhaven Science Associates, LLC under Contract No. DE-AC02-98CH10886 with the U.S. Department of Energy.

Table 1: Beam Parameters Achieved at Three Different Energies During the Physics Runs of the First Phase of the Beam Energy Scan

	3.85 GeV	5.75 GeV	9.8 GeV
γ	4.1	6.1	10.7
σ_s [m]	1.5	1.5	1.5
ϵ_n [μm]	3	2.5	2.5
ϵ [μm]	0.73	0.41	0.23
I_{bunch} [10^9]	0.5	1.1	0.9
N_{bunches}	111	111	111
β^* [m]	6.0	6.0	2.5
ΔQ_{bb}	$1.2 \cdot 10^{-3}$	$1.7 \cdot 10^{-3}$	$1.4 \cdot 10^{-3}$
ΔQ_{sc}	0.035	0.047	0.012
τ_{beam} [sec]	1000	1500	3000

In the first phase of the beam energy scan in FY2010 and FY2011, RHIC operated at three different energies at and below its nominal injection energy [1, 2]. During these runs, beam lifetimes of roughly 15 minutes to one hour were achieved at gold bunch intensities of $0.5 \cdot 10^9$ to $1.1 \cdot 10^9$ ions per bunch; at the lower energies these intensities were limited by the space chage tune shift. Table 1 lists the beam parameters achieved during these runs.

In FY2012, RHIC operated for the first time successfully at a quarter of its nominal injection energy, namely at 2.5 GeV/nucleon [3]. During that test, beam lifetimes of approximately 4 minutes were achieved, see Figure 2. The bunch intensity was limited at $4 \cdot 10^7$ Au ions per bunch because of an injection efficiency of only 10 percent. Due to this short beam lifetime, only 27 bunches per ring were injected, since filling 110 bunches takes about two minutes per ring.

At these low bunch intensities, most of the RHIC beam instrumentation does not work properly, making it virtually impossible to understand and improve the machine performance. Most importantly, the transverse beam size and therefore the emittance were unknown because the ionization profile monitor (IPM) could not operate reliably.

EXPERIMENTS

In an effort to understand the single particle performance of the RHIC lattice at 2.5 GeV/nucleon Au beam energy, protons with the same rigidity of 19.3 Tm were injected and stored at an energy of 5.86 GeV, as listed in Table 2. Due to the different charge-to-mass ratio Z/A of protons compared to gold ions, the relativistic Lorentz factor γ is about

Copyright © 2013 CC-BY-3.0 and by the respective authors

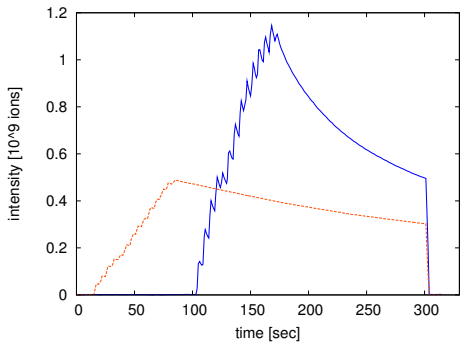


Figure 2: A typical Au-Au store at 2.5 GeV/n beam energy during a test run in 2012. While 27 bunches are being injected into the Blue ring, the intensity in the Yellow ring decreases by some 25 percent due to the short beam lifetime

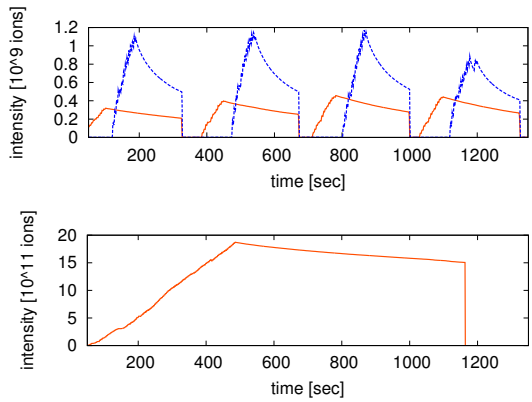


Figure 3: Comparison of the lifetime performance of typical Au-Au stores at 2.5 GeV/n in the Blue and Yellow ring (top) with a typical proton store at 5.86 GeV (bottom) in the Yellow ring

Table 2: Beam Parameters During the 5.86 GeV Proton Test Experiment

ramp	pp13-6GeV
$B\rho$	19.3 Tm
E	5.86 GeV
E_{kin}	4.92 GeV
γ	6.25
p	5.79 GeV/c
f_{rev}	77.187 kHz
h	363

a factor 2.5 higher than for gold ions at the same rigidity. Assuming identical normalized emittances ϵ_N for the two species, this results in smaller transverse beam sizes. Furthermore, the space charge tune shift

$$\Delta Q_{\mathrm{sc}} = -\frac{Z^2 r_p}{A}\frac{N}{4\pi\beta\gamma^2\epsilon_N}\frac{C}{\sqrt{2\pi}\sigma_s} \qquad (1)$$

for protons is also reduced by a factor $Z/(A\cdot\gamma^2) = 2.5^3$ as compared to gold ions with identical bunch charge $Z\cdot N$, normalized emittances ϵ_N, and bunch lengths σ_s.

After some tuning, intensities of $4\cdot 10^{10}$ protons per bunch were routinely injected and stored, with beam lifetimes of approximately one hour, as shown in Figure 3. Compared to the experience with gold ions in the same RHIC lattice, this was a huge improvement.

To characterize the single-particle performance of the lattice, we measured the dynamic aperture by two different methods. In the first attempt, we injected proton bunches with intentionally mis-steered orbits and measured the resulting beam emittances using the RHIC polarimeter target as a slow wire scanner. Mis-steering the injection orbit resulted in a drop of the injection efficiency and therefore the resulting stored beam intensity, Figure 4, thus indicating that an aperture limit was reached. During injection, losses were observed only in the RHIC abort kicker area, which is geometrically the tightest aperture at injection. Applying orbit bumps in an effort to reduce the losses in that location proved unsuccessful, which indicates that the beam orbit was well centered in the 2" × 3" aperture. However, regardless of the mis-steering efforts, the RMS beam sizes measured by the polarimeter target, at $\beta_x = \beta_y = 25\,\mathrm{m}$, remained constant at $\sigma_x = 2.4\,\mathrm{mm}$ and $\sigma_y = 2.0\,\mathrm{mm}$ which indicates that the beam already filled the available aperture even when it was injected without any intentional mis-steering, see Figure 6. At the abort kickers with $\beta_x = 41\,\mathrm{m}$, $\beta_y = 119\,\mathrm{m}$, this corresponds to RMS beam sizes of $\sigma_x = 3.1\,\mathrm{mm}$ and $\sigma_y = 4.4\,\mathrm{mm}$. These values are small compared to the abort kicker aperture, so it is safe to assume that the measured acceptance is limited by the dynamic aperture rather than the physical aperture.

This observation was confirmed by a second experiment in which the stored beam was transversely blown-up by the RHIC tunemeter. Again, this experiment resulted in RMS beam sizes of 2.4 mm horizontally and 2.0 mm vertically at the polarimeter. Furthermore, we observed a shrinking bunch length while the tunemeter was exciting the beam transversely, see Figure 5. We therefore conclude that the dynamic aperture is smallest for particles with large momentum deviation $\Delta p/p$.

The measured beam sizes of 2.4 mm horizontally and 2.0 mm vertically at the IPM with $\beta = 25\,\mathrm{m}$ correspond to RMS geometric emittances of $\epsilon_x = 0.23\,\mathrm{mm\,mrad}$ and $\epsilon_y = 0.16\,\mathrm{mm\,mrad}$. In contrast to this, Au beams with an RMS geometric emittance of $\epsilon = 0.73\,\mathrm{mm\,mrad}$ have been routinely stored at 3.85 GeV/nucleon. This indicates a dynamic aperture that is at least a factor 3 larger at the 50 percent higher rigidity of 29.7Tm at 3.85 GeV/nucleon compared to 19.3 Tm at 2.5 GeV/nucleon Au, or 5.86 GeV protons. The root cause of this large difference is not

Copyright © 2013 CC-BY-3.0 and by the respective authors

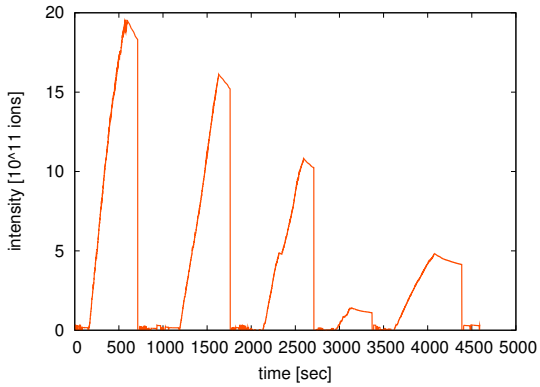


Figure 4: Total intensities of 110 bunches during the dynamic aperture measurement with mis-steered injection

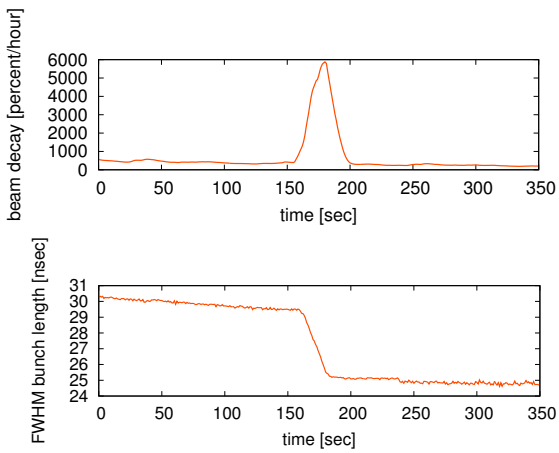


Figure 5: Hourly beam decay (top) and average bunch length during the dynamic aperture measurement using transverse emittance blow-up via the RHIC tunemeter

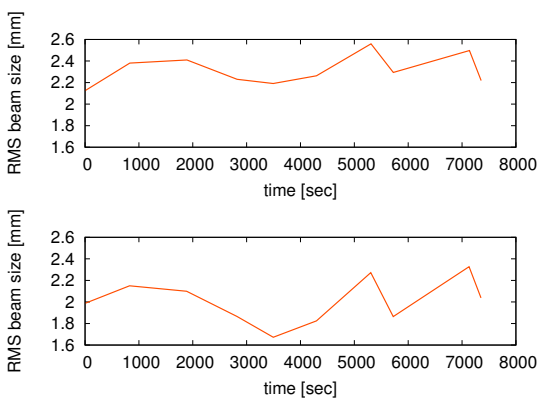


Figure 6: RMS beam sizes measured by using the RHIC polarimeter target as a wire scanner during the dynamic aperture studies

yet understood. Tracking studies are currently being performed in an affort to understand and improve the dynamic aperture at 2.5 GeV/nucleon Au.

SPACE CHARGE

Based on the measured emittance $\epsilon = 0.16\,\mathrm{mm\,mrad}$, corresponding to a normalized emittance of $\epsilon_n = 1\,\mathrm{mm\,mrad}$, an RMS bunch length of $\sigma_s = 3\,\mathrm{m}$, and a bunch intensity $N = 4 \cdot 10^{10}$ protons/bunch, the space charge tune shift achieved during our experiments with 5.86 GeV protons can be computed as

$$\Delta Q_{\mathrm{sc}} = -0.065, \tag{2}$$

which is consistent with the space charge tune shift limit of $\Delta Q_{\mathrm{sc}} \approx -0.05$ observed with Au beams at 3.85 and 5.75 GeV/nucleon.

Assuming the same geometric emittance of $\epsilon = 0.16\,\mathrm{mm\,mrad}$ for 2.5 GeV/nucleon gold, corresponding to a normalized emittance of $\epsilon_n = 0.4\,\mathrm{mm\,mrad}$, and a bunch length of $\sigma_s = 3\,\mathrm{m}$, this same space charge tune shift would be reached at a bunch intensity of $N_{\mathrm{Au}} = 8 \cdot 10^7$ gold ions per bunch, which is a factor 5 less than what was achieved at 3.85 GeV/nucleon. With 111 bunches per ring, this would result in a luminosity of $L = 2 \cdot 10^{22}\,\mathrm{cm^{-2}sec^{-1}}$.

CONCLUSION

Measuring the dynamic aperture of the 2.5 GeV/nucleon Au lattice by injecting and storing protons at the same rigity resulted in a dynamic aperture that is at least 3 times smaller than that for 3.85 GeV/nucleon Au. Improving this is the key to a higher beam intensity at the space charge limit, and therefore to higher luminosity. Tracking studies, including a frozen space charge model, are currently under way to understand and improve the dynamic aperture. However, multipole errors at these low energies are only known for a single dipole and a single quadrupole, which limits the predictive power of these simulations somewhat. As the next step, it is planned to inject gold beams with emittances taylored to the measured dynamic aperture to study the beam lifetime under these conditions.

ACKNOWLEDGMENTS

We would like to thank V. Litvinenko, K. Smith, T. Hayes, F. Severino, M. Costanzo, R. Schoenfeldt, K. Hartmann, J. Adessi, W. Dartiguenave, R. Michnoff, J. Jamilkowski, K. Mernick, M. Harvey, C. Liu, and C. Harper for stimulating discussions and their support in preparing and conducting the experiment.

REFERENCES

[1] C. Montag, T. Satogata, et al., C-A/AP/435.

[2] G. Marr et al., TUPZ038, Proc. IPAC 2011.

[3] C. Montag et al., TUPFI076, Proc. IPAC 2013.

Copyright © 2013 CC-BY-3.0 and by the respective authors

BURN-OFF DOMINATED URANIUM AND ASYMMETRIC COPPER-GOLD OPERATION IN RHIC*

Y. Luo, W. Fischer, M. Blaskiewicz, J.M. Brennan, N. Kling, K. Mernick, T. Roser,
Brookhaven National Laboratory, Upton, NY, USA

Abstract

In the 2012 RHIC heavy ion run, we collided uranium-uranium (U-U) ions at 96.4 GeV/nucleon and copper-gold (Cu-Au) ions at 100 GeV/nucleon for the first time in RHIC. The new Electron-Beam Ion Source (EBIS) was used for the first time to provide ions for the RHIC physics program. After adding the horizontal cooling, 3-D stochastic cooling became operational in RHIC for the first time, which greatly enhanced the luminosity. In this article, we first review the improvements and performances in the 2012 RHIC ion runs. Then we discuss the approaches to achieve the burn-off dominated uranium beam lifetime at physics stores. And we also discuss the low copper beam lifetime in the asymmetric copper-gold collision with different intra-beam scattering (IBS) and stochastic cooling rates and the operational solutions to maximize the integrated luminosity.

PERFORMANCES

Improvements

The first high energy U-U collisions in RHIC were enabled by the versatile new Electron-Beam Ion Source (EBIS) [1]. EBIS can produce beams of essentially any ion species, and can switch rapidly between two different species. It was used for the first time to provide ions for the RHIC physics program.

To counter the intra-beam scattering (IBS) caused emittance growth in the RHIC heavy ion runs, stochastic cooling was implemented in RHIC in the past few years [2]. The longitudinal system was implemented in the Yellow ring in 2007, and longitudinal cooling in the Blue ring and the vertical stochastic cooling in both rings in 2010. In 2012, by adding cooling in the horizontal plane, full 3-D stochastic cooling became operational for the first time in RHIC for both rings.

In the previous 2010 and 2011 Au-Au runs, we observed large beam loss after RF re-bucketing and at store with the vertical cooling on. These losses were from particles with large off-momentum deviation. For the 2012 ion run, we chose a lattice with integer tunes (28, 29), which are 3 units lower than what was used in the previous ion runs. With this lattice, simulation shows that the off-momentum dynamic aperture increases from 2 σ to 5 σ with the maximum relative off-momentum deviation $\Delta p/p_0 = 0.0018$ [3].

*This work was supported by Brookhaven Science Associates, LLC under Contract No. DE-AC02-98CH10886 with the U.S. Department of Energy.

The RHIC orbit feedback system became operational for the first time in the 2011 proton run. In the 2012 ion run, with numerous improvements in the control software and hardware, the orbit feedback became more robust. Together with tune/coupling feedback, the RHIC beam control feedback systems greatly reduces the beam time necessary for machine start-up and store tuning [4].

U-U Run

The 2012 RHIC U-U run began on April 19, 2012 and ended on May 15, 2012. The physics mode lasted for 22 days. Figure 1 shows the integrated luminosities for the two physics detectors PHENIX and STAR, together with their minimum and maximum projected luminosities. The minimum projected luminosity was based on the bunch intensity 0.6×10^9. However, the typical bunch intensity at the beginning of store was 0.3×10^9.

The luminosity in the U-U run was greatly enhanced with 3-D stochastic cooling. With 3-D cooling, the rms normalized transverse beam emittance was cooled down to 0.42 π mm mrad in 2 hours from 2.2 π mm mrad at the beginning of store. Figure 2 shows the luminosity with and without stochastic cooling. With 3-D cooling, the peak luminosity was 3 times the initial one, which was observed for the first time in a collider. The integrated luminosity per store is about 5 times that without any cooling. Despite the lower bunch intensity the integrated luminosity goals of both detectors were reached.

Figure 3 shows an example of the Zero Degree Calorimeter (ZDC) coincidence rates from the two detectors STAR and PHENIX, the actual beam loss rates, and the burn-off contributions to the beam loss in one store (fill number 16830). As mentioned above, this year we adopted a lattice which provides a large off-momentum dynamic aperture. The particle loss due to the momentum aperture limitation was essentially eliminated. Together with stochastic cooling, the beam loss was almost entirely due to burn-off [5], which is also the first time this was observed in a collider.

Cu-Au Run

The 2012 RHIC Cu-Au run began on May 15 and ended on June 25. Physics mode ran for 38 days. 3-D stochastic cooling was operational on May 23. Figure 4 shows the integrated luminosities for PHENIX and STAR. The achieved integrated luminosities for both detectors were above the maximum projection. We also reached

Copyright © 2013 CC-BY-3.0 and by the respective authors

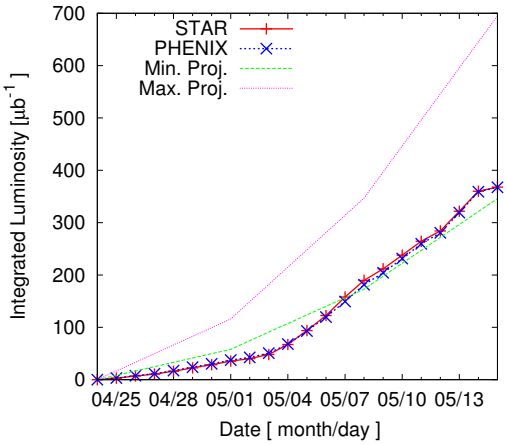


Figure 1: Integrated luminosities in 2012 RHIC U-U run. The minimum and maximum projections are shown.

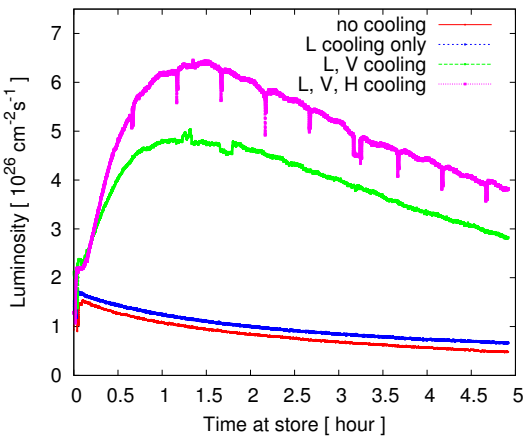


Figure 2: Luminosity without and with stochastic cooling in the 2012 RHIC U-U run. The rate drops every half hour were caused by the automatic store orbit corrections followed by interaction re-steering.

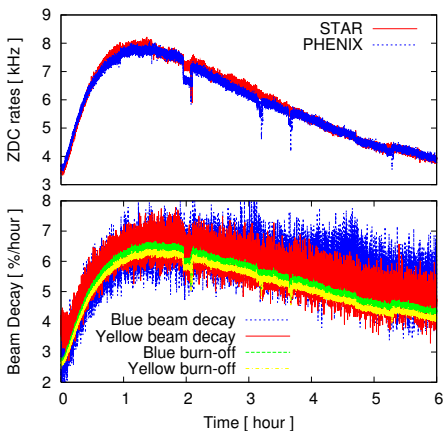


Figure 3: One example of the ZDC rates, beam decays, and burn-off contribution to the beam loss in 2012 RHIC U-U run. The burn-off is calculated based on the analytical cross section of 487.3 b [5].

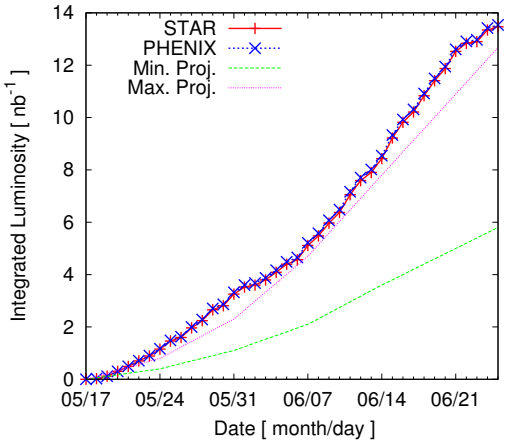


Figure 4: Integrated luminosities in 2012 RHIC Cu-Au run. The minimum and maximum projections are shown.

PHENIX's narrow vertex integrated luminosity goal. Narrow vertex luminosity only counts the collisions within ± 10 cm of the IP.

Figure 5 shows the averaged bunch intensities at the beginning of the store. To boost the bunch intensity in RHIC, double bunch merging in the Booster and AGS was tested and implemented. In principle, double bunch merging in the Booster and AGS could increase the bunch intensity in RHIC by a factor of 4. However, since double bunch merging increased the ion beams transverse and longitudinal emittances, careful tuning of the Booster, AGS, and the AGS-to-RHIC transfer line was always required. Continuous efforts were also made to improve the transmission efficiency from RHIC injection to store by fine tuning the working points, chromaticities, and transition loss. The Cu bunch intensity was doubled and the Au bunch intensity increased by 50% through out the course of the Cu-Au run. We achieved the most intense ion bunch in RHIC up to date.

In the Cu-Au run, Cu bunch intensity was more than 3 times the Au bunch intensity. The IBS emittance growth rate of the Cu beam is half of that of the Au ion beam, while the stochastic cooling rate of the Cu beam is one third of the Au ion beam. In the beginning of this run, we observed large Cu beam losses which were caused by the beam-beam interaction between the Cu and Au bunches with different transverse beam sizes. To maintain the Cu beam bunch intensity and to maximize the integrated luminosity, we intentionally reduced the Au beam's cooling rate in the first several hours of each store.

BURN-OFF DOMINATED BEAM LIFETIME IN U-U COLLISION

Beam Loss in Previous Runs

In the RHIC heavy ion runs, the IBS increases the longitudinal and transverse emittances. With a smooth ring

Copyright © 2013 CC-BY-3.0 and by the respective authors

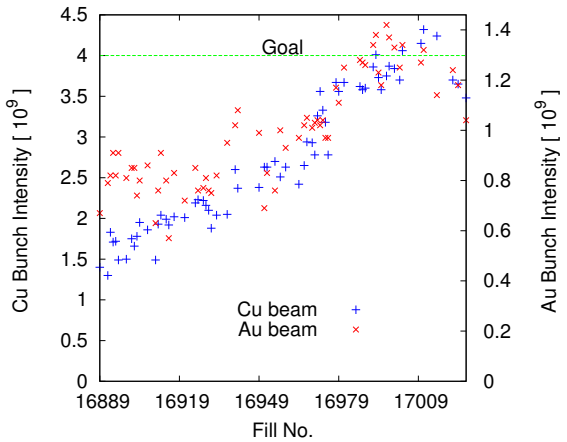


Figure 5: Averaged bunch intensities at the beginning of each individual store in the 2012 RHIC Cu-Au run.

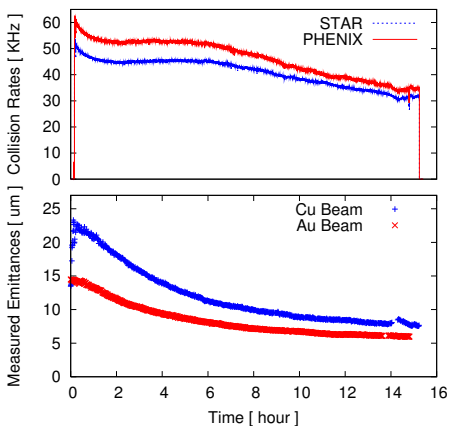


Figure 6: Experimental rates and beam transverse emittances in one physics store in 2012 RHIC Cu-Au run.

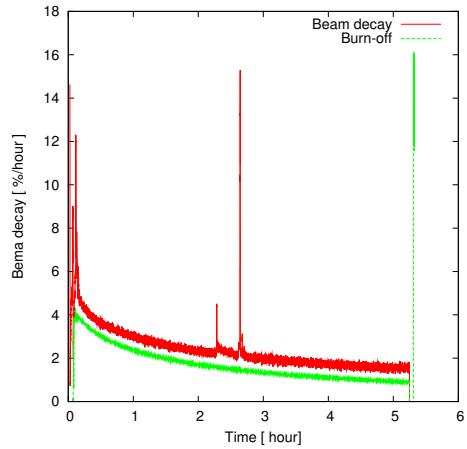


Figure 7: The Au beam decay in 2007 with only longitudinal cooling. RHIC Fill number is 9039.

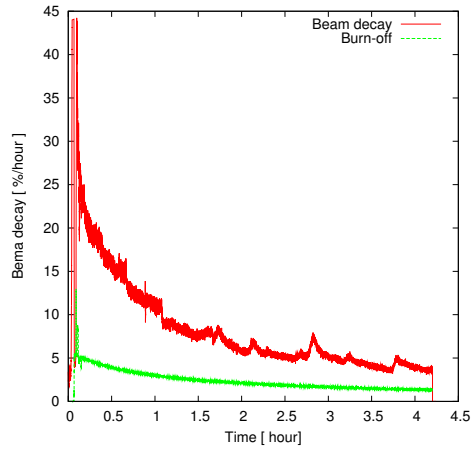


Figure 8: The Au beam decay in 2011 with only longitudinal cooling. RHIC Fill number is 15843.

approximation, the longitudinal and transverse IBS growth rates can be calculated as [6]

$$\tau_{||}^{-1} = \frac{1}{\sigma_p^2}\frac{d\sigma_p^2}{dt} \frac{r_i^2 c N_i \Lambda}{8\beta\gamma^3\epsilon_{n,rms,x}^{3/2} < \beta_x^{1/2} > \sqrt{\pi/2}\sigma_l\sigma_p^2}, \quad (1)$$

$$\tau_{\perp} = \frac{\sigma_p^2}{\epsilon_x} < \frac{H_X}{\beta_x} > \tau_{||}^{-1}. \quad (2)$$

According to Eqs. (1) and (2), it is possible to reduce $< \frac{H_X}{\beta_x} >$ to reduce the transverse emittance growth coupled from the longitudinal plane[7, 8]. Therefore, during the 2008-2011 RHIC ion runs, we used a lattice with FODO phase advances increased in the arcs and the integer tunes increased by 3 units. We named this lattices as "IBS-suppression" lattices and the previous lattices as "standard" lattices.

However, during the 2008-2011 RHIC heavy ion runs with the IBS-suppression lattice, we observed a large beam loss after RF re-bucketing and during store with transverse cooling [3]. RF re-bucketing aims to shorten the bunch length to increase luminosity but it increases the beam momentum spread. RF re-bucketing takes place in the beginning of the store without collision. The bunch's maximum momentum deviation is increased from 0.9×10^{-3} to 1.7×10^{-3} with RF re-bucketing.

Figures 7 and 8 show the beam decays in the Yellow ring in the fill 9039 in the 2007 Au-Au run and in the fill 15843 in the 2011 Au-Au run. In both fills, there was only longitudinal cooling. Along with the total beam decay, we also show the beam decay contributed by the beam burn-off due to luminosity. The burn-off is calculated from luminosity and the analytical value of total cross section of Au-Au collision. The IBS-suppression lattices caused much more non-luminosity particle loss than the standard lattices.

Off-Momentum DA

With longitudinal cooling, the beam loss in the longitudinal plane is eliminated. If there is any beam loss, it should happen in the transverse plane due to the limited transverse off-momentum dynamic aperture. From Figs. 7 and 8, the IBS-suppression lattices have smaller off-momentum dy-

Copyright © 2013 CC-BY-3.0 and by the respective authors

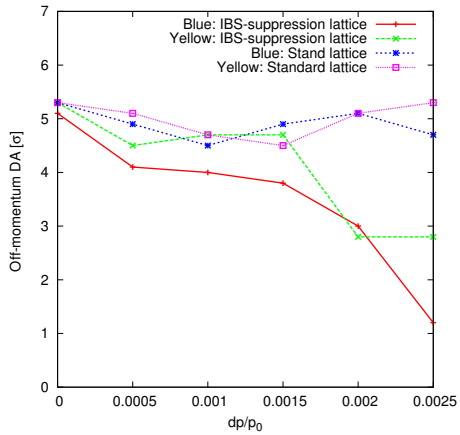


Figure 9: Off-momentum dynamic apertures with IBS-supression lattices and standard lattices for both rings.

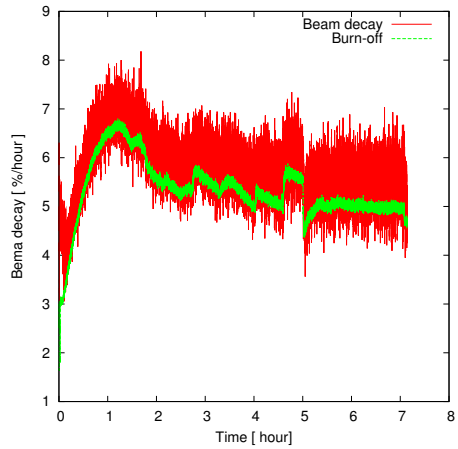


Figure 10: The Au beam decay in 2012 with transverse and longitudinal cooling. The beam loss was almost entirely from burn-off.

namic aperture than the standard lattices. In the 2011 Au-Au run with the longitudinal and vertical cooling, we observed about 50% of particle loss was non-luminous. According to Eq. (2), small transverse emittance increases the longitudinal IBS growth rate.

Figure 9 shows the calculated off-momentum aperture for both Blue and Yellow rings with IBS-suppression and standard lattices. For the IBS-suppression lattice, the off-momentum dynamic aperture begins to drop sharply to below 4σ when the relative momentum deviation is bigger than 0.0015. While for the standard lattice, the off-momentum DA is better than 4.7σ up to $dp/p_0 = 0.0025$. With RF re-bucketing, the RF bucket height is 1.9×10^{-3}.

Based on the beam loss observations in the previous runs and the calculated off-momentum apertures, we decided to adopt standard lattices for the 2012 U-U and Cu-Au runs. In the 2012 U-U run, 3-D stochastic cooling was fully operational in RHIC. The typical bunch intensity in RHIC is 0.3×10^9. Comparing to the previous Au-Au operation, the IBS growth rate is smaller and the stochastic cooling is more efficient.

Figure 10 shows the Au beam decay and the burn-off contribution in Fill 16830. With transverse cooling on, the initial luminosity is not the highest. Accordingly, the luminosity burn-off continues to increase until the peak luminosity is reached. The beam loss is almost entirely from the burn-off [5], which means that there is almost no loss due to limited transverse off-momentum dynamic aperture with the standard lattices.

BEAM-BEAM INTERACTION IN ASYMMETRIC CU-AU COLLISION

Different IBS and Cooling Rates

The IBS growth rate is proportional to $N_i Z^4/A^2$ while the stochastic cooling rate is proportional to $1/N_i$, where N_i is bunch intensity, Z and A are the ion charge state and atom number. In the 2012 Cu-Au run, the bunch intensities for the Cu and Au beam were about 4.0×10^9 and 1.3×10^9 respectively at the end of the run. Therefore, the IBS emittance growth rate of the Cu beam is half of that of the Au ion beam, while the stochastic cooling rate of the Cu beam is one third of the Au ion beam.

In the beginning of this run, with full cooling power for both beams, we observed that the Cu beam lifetime was significantly reduced when the two beams' emittances were quite different. The bigger difference between the emittances of the two beams was, the more Cu beam loss was observed. Later on we concluded that the bad Cu beam lifetime was caused by the beam-beam interaction between the Cu and Au beams with different transverse beam sizes [9]. As an example, Figure 11 shows the measured transverse emittances and the beam decays with 3-D cooling with full cooling power from the beginning of store.

Beam-Beam Interaction

For ion collisions, the beam-beam parameter, or the linear incoherent beam-beam tune shift, for the weak beam is

$$\xi_1 = -\frac{N_{i,2} r_p}{2\pi\epsilon_{n,rms,2}} \times \frac{Z_1 Z_2}{A_1}. \quad (3)$$

Here r_p is the classic proton radius. $\epsilon_{n,rms,2}$ is the rms normalized transverse emittance. The Z and A are the ion's charge state and atomic number. The subscript 1 is for the weak beam and the subscript 2 is for the strong beam.

In the previous RHIC Au runs, the beam-beam interaction was negligible since the beam-beam parameter was -0.003. In the 2012 Cu-Au run, when turning on 3-D cooling with full cooling power for the two beams from the beginning of store, the beam-beam parameter for the Cu beam reached -0.011 from initially -0.004.

Here we perform numerical simulation to calculate the beam-beam effect to the Cu beam's dynamic aperture. Figure 12 shows the Cu beam's dynamic aperture in the first 4.5 hours in the store. The measured bunch intensity and

Copyright © 2013 CC-BY-3.0 and by the respective authors

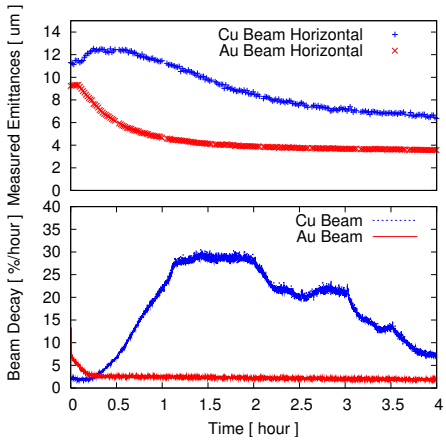


Figure 11: Bunch intensities and measured emittances in Cu-Au run. The fill number is 16911.

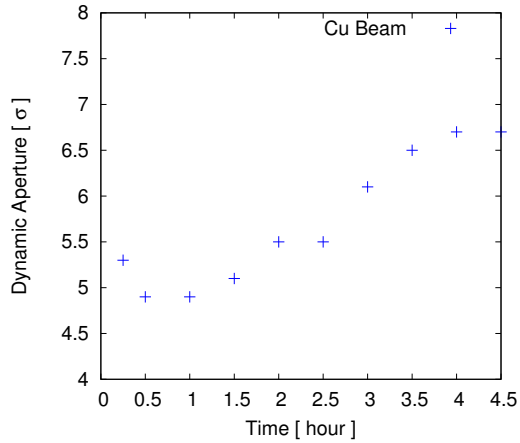


Figure 12: Calculated off-momentum dynamic aperture for fill 16911.

emittances in Fig. 11 were used. In this study, the initial relative momentum deviation is set to $dp/p_0 = 0.0015$. The dynamic aperture is given in units of Cu beam's rms transverse beam size. From Fig. 12, when the Au beam was fully cooled at 1 hour from the beginning of store, the Cu beam's dynamic aperture is lowest. With slow cooling of the Cu beam emittance, the Cu beam's dynamic aperture is slowly increased.

To avoid the large beam loss in the Cu beam and to maximize the integrated luminosity, we decided to turn off or reduce the Au beam's cooling gain in the beginning of the store until the Cu beam got cooled. Figure 13 shows the beam emittances and beam decays in the fill 16917 where we intentionally turned off the Au vertical cooling between 0.5 hour to 1.5 hour into the store. When the Cu and Au beam emittances were comparable to each other, then we turned on the yellow vertical cooling again. By doing so, we kept the Cu beam decay below 6%/ hour. Later on in the rest of 2012 Cu-Au run, we continued to balance the luminosity and the beam decay through the Au beam's stochastic cooling gains. The Cu beam decay was kept below 4%/hour in the whole stores. And the store length was set to 14 hours, which is the longest store length for the RHIC heavy ion runs.

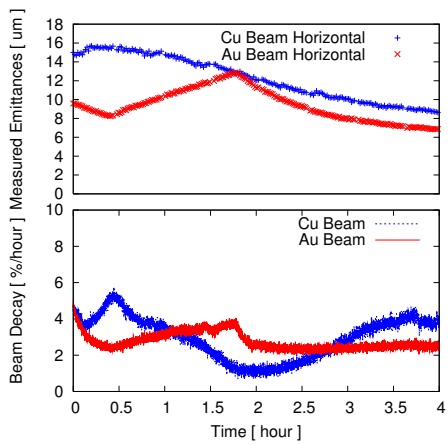


Figure 13: Bunch intensities and measured emittances with reduced Au cooling rate. The fill number is 16917.

CONCLUSIONS

The 2012 RHIC heavy ion run was a great success. It marked the first collisions of high energy U-U and Cu-Au ions in RHIC. With a versatile EBIS, powerful 3-D stochastic cooling, and double bunch merging in the injectors, high precision beam control systems, and many efforts of machine fine tuning, we reached both detectors' integrated luminosity goals. In the U-U run, with a new lattice which gives a higher off-momentum aperture and 3-D cooling, the particle loss is dominated by the burn-off. In the Cu-Au run, due to different IBS and cooling rates from both beams, we intentionally slowed down the Au beam cooling rate in the Yellow ring in the first several hours to match the two beams' transverse beam sizes and maximize the integrated luminosity.

REFERENCES

[1] J. Alessi, et al., WEP261, in Proceedings of 2011 PAC, New York City, USA (2010).

[2] M. Blaskiewicz, J. M. Brennan, and K. Mernick, Phys. Rev. Lett. 105, 094801 (2010).

[3] Y. Luo, et al., MOPPC022,in Proceedings of 2012 IPAC, New Orleans, USA (2012).

[4] M. Minty, et al., MOPO022, in Proceedings of 2011 IPAC, San Sebastian, Spain (2011).

[5] W. Fischer, et al, TUPFI078, in Proceedings of 2013 IPAC, Shanghai, China (2013). Submitted to Phys. Rev. C, 2013.

[6] A. Fedotov, BNL C-AD AP-Note 168, 2009.

[7] V. Litvinenko, etc., Proceedings of EPAC'08, Italy, 2008.

[8] A. Fedotov, et al., WGA28, ABDW-HB'08, Nashville, 2008.

[9] Y. Luo, et al., BNL C-AD AP-Note 463, 2012.

Copyright © 2013 CC-BY-3.0 and by the respective authors

THE PROJECT-X INJECTOR EXPERIMENT: A NOVEL HIGH PERFORMANCE FRONT-END FOR A FUTURE HIGH POWER PROTON FACILITY AT FERMILAB*

S. Nagaitsev#, S. Holmes, D. Johnson, M. Kaducak, R. Kephart, V. Lebedev, S. Mishra, A. Shemyakin, N. Solyak, R. Stanek, V. Yakovlev, Fermilab, Batavia, IL 60510, USA
P. Ostroumov, ANL, Argonne, IL 60439, USA
D. Li, LBNL, Berkeley, CA 94720, USA
P. Singh, M. Pande, S. Malhotra, Bhabha Atomic Research Centre, Mumbai-400085, India

Abstract

A multi-MW proton facility, Project X, has been proposed and is currently under development at Fermilab. We are carrying out a program of research and development aimed at integrated systems testing of critical components comprising the front end of Project X. This program, known as the Project X Injector Experiment (PXIE), is being undertaken as a key component of the larger Project X R&D program. The successful completion of this program will validate the concept for the Project X front end, thereby minimizing a primary technical risk element within Project X. PXIE is currently under construction at Fermilab and will be completed over the period FY12-17. PXIE will include an H^- ion source, a CW 2.1-MeV RFQ and two superconductive RF (SRF) cryomodules providing up to 25 MeV energy gain at an average beam current of 1 mA (upgradable to 2 mA). Successful systems testing will also demonstrate the viability of novel front end technologies that are expected find applications beyond Project X.

PXIE GOALS AND PLAN

A unique feature of Project X [1] is the capability of delivering a MW-range proton beam to several experiments quasi-simultaneously with a beam structure that can be adjusted to each experiment's needs. In the suggested scheme, this is achieved as follows:

(a) Prepare a "nearly CW" beam, in which many RF buckets may be empty but the beam current, averaged over several μs, is constant. The undesired bunches are removed in the Medium Energy Beam Transport (MEBT) by a chopping system. This quasi-CW beam has a repetitive time structure (RS).

(b) Accelerate the prepared beam. The optimum solution requires acceleration by SRF cavities after MEB at 2.1 MeV;

(c) Distribute the beam to experimental stations by an RF separator at 1 GeV and 3 GeV.

The RF separation of bunches successfully supports multiple experiments operation at CEBAF [2]. The acceleration with SRF at low energies has been used for a long time at ANL [3] (at much lower average currents) and recently is being commissioned at SARAF [4], but has not been demonstrated at parameters required for the Project X. The wideband chopper, needed to prepare bunch patterns, is a unique device currently beyond state of the art.

The PXIE program [5] will address both (a) and (b) with the specific goals of demonstrating effective bunch-by-bunch chopping of the CW beam delivered from the RFQ and efficient acceleration of the 1 mA RS beam with minimal emittance dilution through at least 15 MeV.

PXIE consists of an H- ion source (IS); a Low Energy Beam Transport (LEBT); a CW 2.1-MeV RFQ; a MEBT; two SRF cryomodules (CM) operating at 2K - a Half Wave Resonator (HWR) and a Single Spoke Resonator (SSR1); a High Energy Beam Transport (HEBT); and a beam dump (Fig.1).

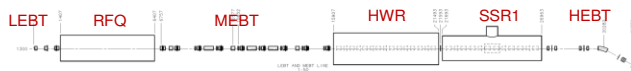


Figure 1: PXIE layout.

The concept of PXIE subsystems was described in [5]. The end-to-end simulations can be found in [6]. Main beam parameters are shown in Table 1.

Table 1: Nominal Beam Parameters at the Exit of Each Section

	IS/ LEBT	RFQ	MEBT	HWR	SSR1
Energy, MeV	0.03	2.1	2.1	11	25
Average current, mA	5	5	1	1	1
Time structure	DC	CW	RS	RS	RS
$\varepsilon_\perp$, μm					< 0.25
$\varepsilon_\parallel$, keV-ns					≤ 1

* $\varepsilon_\perp$ is the rms normalized transverse emittance, and $\varepsilon_\parallel$ is the rms longitudinal emittance.

The PXIE design and construction is being carried out by a collaboration between Fermilab, ANL, LBNL, SLAC, SNS, and Indian laboratories in a staged approach.

*Work supported by the U.S. Department of Energy under contract No. DE-AC02-07CH11359
#nsergei@fnal.gov

Copyright © 2013 CC-BY-3.0 and by the respective authors

The beam is planned to pass through the LEBT in FY14, through the RFQ in FY15, and full PXIE parameters are expected to be demonstrated by the end of 2018.

STATUS OF SUBSYSTEMS

The ion source has been procured from D-Pace Inc. [7], was characterized and used in the beam dynamics studies at LBNL, and presently is being assembled at Fermilab.

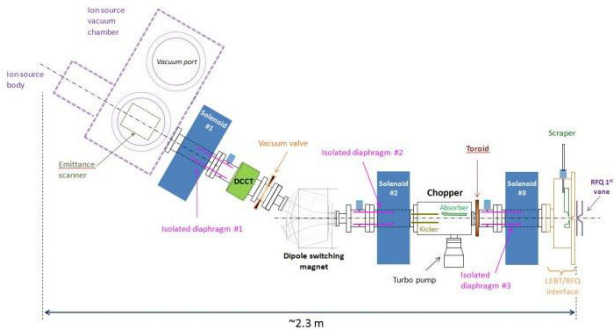


Figure 2: Conceptual design of the LEBT.

The LEBT has been conceptually designed (Fig. 2). The 2.2 m distance between the ion source and the RFQ entrance ensures a low hydrogen flux from the ion source into the RFQ. Because the design of the Project X front end includes two ion sources for redundancy, the final PXIE assembly will include a combining dipole magnet though only one ion source will be used. Focusing is provided by three solenoids. A chopping system will be used for several purposes: to generate a pulse mode during commissioning, in a normal operation, to shut down injection into the RFQ for machine protection, possibly, to interrupt the beam for the residual ion removal from the MEBT, and, if found necessary, to assist the MEBT chopper.

One of the concerns is a growth of effective emittance due to neutralization following chopper pulses. To address this, the LEBT will be assembled first in a simple, straight configuration, in which the beam can be neutralized either along the entire line or only upstream of the chopper. In the latter case, the large distance to the IS allows effective clearing of the residual ions by combination of a positive potential on a stopping electrode and a constant transverse electric field. The ion removal solves the issue with temporal changes of the beam envelope but increases the emittance growth due to space charge [6]. Experiments will show which mode is preferable. Presently, the LEBT elements are at various stages of designing, procurement, and assembly.

The 4-vane, 4.4 m 162.5 MHz RFQ (Fig. 3) has been designed and the fabrication has started in August, 2013 at LBNL. The detailed description of the RFQ design and status can be found in Ref. [8], and the design of the coupler is described in Ref. [9]. The complete assembly of the RFQ is planned to be delivered to Fermilab at the end of 2014.

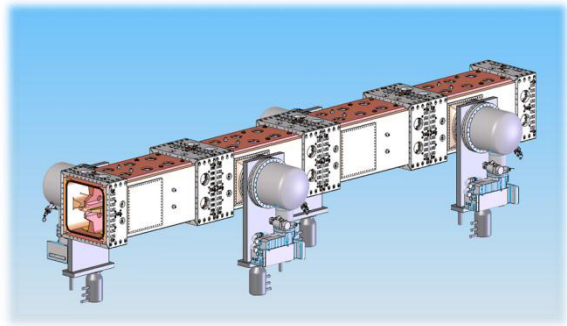


Figure 3: The RFQ conceptual design [9].

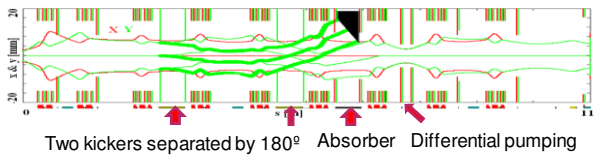


Figure 4: Scheme of MEBT optics and the beam envelope. The thin lines are the central trajectory and 3σ envelope (ε_{rms_n}=0.25 mm mrad) of the passing beam, and the thick lines are the Y envelope of the chopped-out beam. Red- quadrupoles, blue- bunching cavities.

The design of the ~10 m MEBT was presented in [10], and the beam trajectory is shown in Fig. 4. Its most challenging part is the chopping system that forms the required bunch pattern by deflecting the undesired bunches of the initially CW beam into an absorber. This deflection is made by two broadband, travelling-wave kickers separated by 180º of the betatron phase advance and operating synchronously. The electric length of each kicker is 0.5 m, the plate separation is 16 mm, and the plate voltage with respect to ground is ±250V. The plates have opposite polarity voltages for bunch passing and removal. Presently two versions of the kicker, distinguished by the characteristic impedance of the kicker structure (50 and 200 Ohm), are being developed.

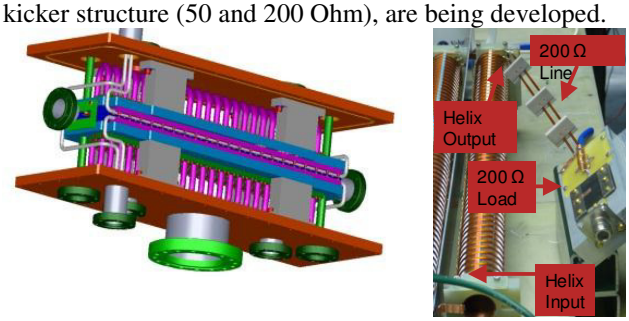


Figure 5: The MEBT kicker. A 3D model of the 50-Ohm kicker (left). Part of the vacuum box is removed for the presentation purpose. A model of the 200 Ohm kicker (right).

In the 50 Ohm version, the beam is deflected by the voltage applied to planar electrodes connected in vacuum by coaxial cables with the length providing the necessary delays (Fig. 5). The kicker prototype is being assembled.

Copyright © 2013 CC-BY-3.0 and by the respective authors

RF and thermal properties of an 8-plate model with electrodes and cable in the final version were successfully tested. The kicker will be powered by a commercially available RF-amplifier with a specially shaped driving signal [11].

The 200 Ohm kicker [12] consists of two helixes wound around grounded cylinders (Fig. 5). Presently it is at the stage of the pre-prototype fabrication.

The 200 Ohm kicker will be driven by broadband, DC coupled GaN switches in push-pull configuration being developed at Fermilab [12]. Operation of a single switch up to 500 V was demonstrated, and recently a fully functional 100V driver was successfully tested.

The kickers displace the undesired bunches by ~$6\sigma_y$ to the absorber surface. The absorber is specified to withstand 21 kW, twice the full nominal beam power, focused into a spot with $\sigma_{x,y}$ ~2mm. A preliminary conceptual design is complete, and ¼-size prototype has been successfully tested with an electron beam (Fig. 6). Preliminary results can be found in Ref. [13].

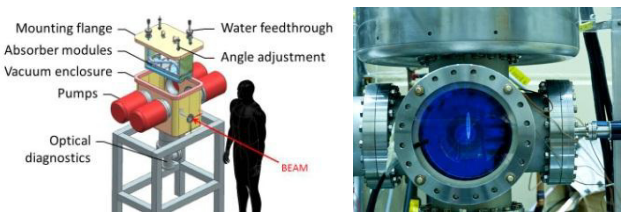


Figure 6: Absorber development: a conceptual design (left). Right – the OTR image of a 5.5-kW, 9-mm electron beam (bright ellipse) on the surface of the absorber prototype.

Transverse and longitudinal focusing in MEBT will be provided by 25 quadrupoles combined into doublets and triplets, and by three 162.5-MHz bunching cavities, correspondingly. The cavities are at the final stage of mechanical design at Fermilab. The quadrupoles and dipole correctors have been designed at BARC in India, and the prototypes are being tested.

The PXIE SRF cryomodules are being fabricated at ANL (HWR) and at Fermilab (SSR1). The HWR cryomodule [14] contains 8 162.5-MHz, nominally 1.7 MV, β = 0.11 cavities and 8 SC solenoids, with built-in dipole correctors and a BPM attached to each solenoid. Design of cavities and the cryomodule is complete (Fig. 7). Prototypes of the RF coupler and solenoid with dipole correctors have been build and successfully tested. Nb parts for all cavities have been fabricated, and two cavities will be tested in FY14.

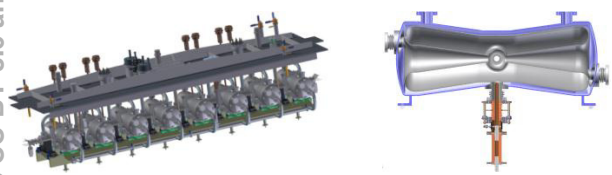


Figure 7: HWR CM design: a cavity-solenoid string attached to the top lid (left), a cavity with a coupler (right).

The SSR1 (Fig. 8) cryomodule consists of eight 325-MHz single-spoke resonators (β = 0.22) and 4 solenoids. Similar to the HWR CM, all solenoids will have corrector coils and BPMs. The conceptual design of the cryomodule is complete, and most of elements are at the stage of technical design.

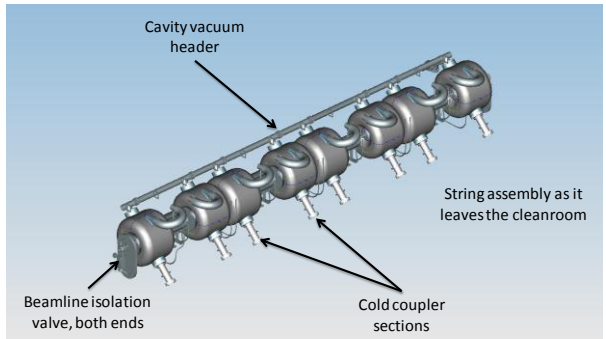


Figure 8: The SSR1 cavity and solenoid string assembly.

Details of the SSR1 cavity development is reported in [15]. The bare cavity and the He vessel are shown in Figure 9. The first SSR1 cavity prototype was manufactured by ZANON, the cavity was tested at Fermilab's Vertical Test Stand (VTS) and outfitted with a helium vessel. The second prototype was manufactured by ROARK, tested and showed acceptable performance. Subsequently, ten other SSR1 cavities were manufactured and delivered to Fermilab.



Figure 9: SSR1 cavity, bare (left) and dressed (right).

The SSR1 is followed by the HEBT that accommodates the beam diagnostics to measure the beam properties and the beam extinction for RF buckets emptied by the MEBT chopper. Its design is at the conceptual stage (Fig. 10) as well as is the PXIE beam dump at the end of the beam line.

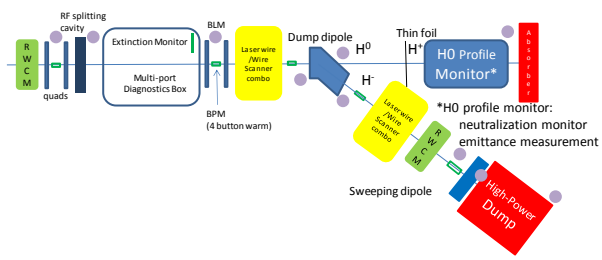


Figure 10: The HEBT scheme.

The PXIE will be located in the existing Cryomodule Test Facility (CMTF) building which will also include an enclosure for ILC and Project X cryomodules testing. A

Copyright © 2013 CC-BY-3.0 and by the respective authors

cryo-plant supporting operation of both installations, which will have 500 W cooling power at 2 K, is under construction. The upstream portion of the PXIE cave, long enough to accommodate the warm portion of PXIE, has been assembled with concrete shielding blocks. The infrastructure, controls, and diagnostics are at various stages of design and implementation.

REFERENCES

[1] Project X Reference Design Report, 2013, FERMILAB-TM-2557.
[2] C. Hovater et al., Proc. of LINAC'96, p. 79.
[3] J. Aron et al., Proc. of LINAC'79, p. 104.
[4] D. Berkovits, LINAC'12, MO1A01.
[5] S. Nagaitsev et al., Proc. of IPAC'12, THPPP058; also, "PXIE Design Handbook", Project X Document 1148, http://projectx-docdb.fnal.gov/
[6] J.-F.Ostiguy et al., Proc. of IPAC'13, TUPWA054.
[7] http://www.dehnel.com/
[8] D. Li et al., Proc. of IPAC'13, THPME047.
[9] S. Kazakov et al., Proc. of IPAC'13, WEPFI070.
[10] A. Shemyakin et al., Proc. of LINAC'12, MOPB095.
[11] V. Lebedev et al., Proc. of IPAC'12,WEPPD078.
[12] G. Saewert et al., Proc. NA-PAC13, THPBA17.
[13] A. Shemyakin et al., Proc. of IPAC'13, THPFI085 .
[14] Z.A. Conway et al., Proc. of IPAC'12, THPPP054.
[15] L. Ristori et al, Proc. of IPAC'13, WEPWO055.

Copyright © 2013 CC-BY-3.0 and by the respective authors

HIGH POWER (MW-CLASS) TARGETS FOR PARTICLE BEAMS

E.J. Pitcher, European Spallation Source ESS AB, Lund, Sweden
C. Densham, Rutherford Appleton Laboratory, Abingdon, UK

Abstract

Many applications that use accelerators are demanding ever-higher beam powers, which place greater demands on accelerator design and operation. Equally demanding is the design of targets that can operate safely and optimally at these power levels. High-power target design considerations include performance optimization, heat load, radiation damage and lifetime, safety, operability, reliability, and for pulsed beams, dynamic stresses from thermal cycling. The design and operation of these targets draws upon the experience gained in operating lower power targets.

HEAT LOAD

Heat load in high-power targets can be a major driver in target design. For traditional targets made of solid metal, heat load is normally limited by heat flux at the target-coolant interface. Deposited power density goes linearly with beam power and inversely proportional to beam spot area on target. One way to address higher beam power is by increasing the size of the beam spot on target.

As beam power on target increases, so does the engineering complexity of the target. Solutions that are viable at low power, such as cooling at the periphery, are no longer viable. Figure 1 shows a spent tungsten target from the Manuel Lujan Neutron Scattering Center at Los Alamos National Laboratory [1]. This target is a solid cylinder of tungsten, 10 cm in diameter by 7.5 cm long, encased in an Alloy 718 shell that served to contain the water which passed over the tungsten surface to carry away the 60 kW of heat deposited by the 800-MeV proton beam. Two features are clearly evident. First, the target is broken into four quadrants, most likely caused by unacceptably high thermal stresses in the target. Second, substantial corrosion of the tungsten has occurred, which is due to the creation of short-lived highly oxidizing radicals in the cooling water. These radicals have been shown to be highly corrosive to tungsten [2]. Radioactive spallation products within the tungsten enter the coolant stream as the tungsten corrodes, leaving the cooling components, such as filters, ion exchange columns, highly radioactive.

At the megawatt level and higher, innovative solutions to the problem of target cooling have been proposed, such as flowing liquid metal [3,4,5,6] and rotating solid targets [SNQ, SNS TS2, Bilbao, ESS]. A liquid metal target, such as that shown in Fig. 2, has the potential to handle very high power densities due to its high heat capacity. Two liquid metals that have been successfully demonstrated as spallation targets are mercury [4,5] and lead-bismuth eutectic [6]. Lithium is proposed as the target material for the International Fusion Materials Irradiation Facility, (IFMIF) with a baseline 10 MW, 40-MeV deuteron beam. This project is now completing its engineering development and demonstration phase, including development of the lithium target [7].

At the megawatt level, full-scale thermal testing of the target prior to putting it into service is difficult and normally cost prohibitive. This is compounded by the complexity of trying to simulate the power deposition profile of the accelerator beam. As a consequence, normally small-scale tests are conducted instead. These tests are normally designed to validate uncertainties that may exist in the data or models in the simulations used in the thermo-mechanical design of the target.

SAFETY

Targets for high-power accelerators become radioactive as a consequence of beam-induced nuclear reactions within the target. For >100-MeV beams, a good rule of thumb is that the radioactive inventory within an accelerator target is on par with a nuclear fission reactor with one order of magnitude less power, e.g., a 1-MW proton beam on a spallation target will have a radionuclide inventory, as measured in becquerels, on par with that of a 100-kW fission reactor. This inventory will generate decay heat, or afterheat, following beam shutdown that must be removed in a robust and reliable manner.

Because of the risk to workers and the public presented by this radioactive material, designers of high-power targets do well to adopt a “safety by design” philosophy, whereby safety is an omnipresent consideration in the design optimization process. A number of recently designed high-power targets [APT, SNS, MTS] draw from the safety philosophy developed for the nuclear

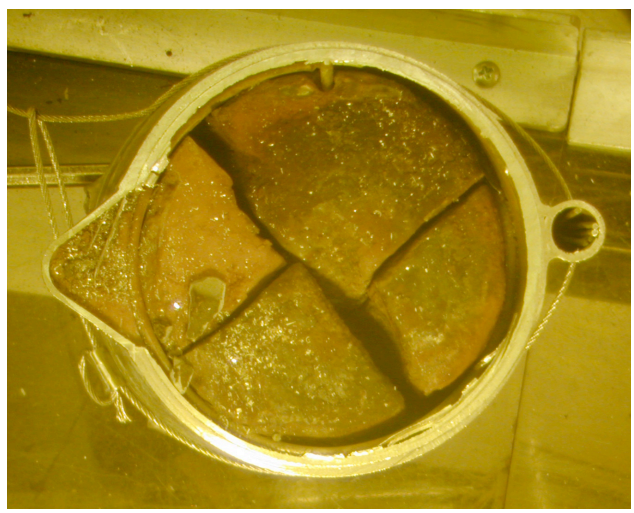


Figure 1: Broken and corroded Lujan Center tungsten target (from [1]).

Copyright © 2013 CC-BY-3.0 and by the respective authors

industry. First, hazards are identified, and initiating events that may produce these hazards are postulated. Those events with high frequency of occurrence and potentially high consequences are then selected as "design basis accidents." These postulated accidents undergo quantitative analyses to assess potential radiation doses to workers and the public. If needed to keep such doses within acceptable limits, mitigations are identified and incorporated into the design. These mitigations are credited safety controls that normally require a higher pedigree of design, procurement, installation, testing, and maintenance. Wherever possible, incorporation of passive safety features into the design is preferred over reliance on credited controls, as passively safe features are usually simpler to analyze (and therefore defend to regulators), more reliable, and lower cost.

PERFORMANCE

With respect to targets, beam power increases are normally addressed through the introduction of greater coolant volume fraction within the target, more structural material to accommodate larger thermal and mechanical stresses, larger gaps between components for ease of servicing, and similar features, which normally contribute to a degradation in target performance, for instance neutron production or neutrino production. A general rule of thumb is that an increase in beam power will not result in a proportional increase in performance, but rather will be proportional to (beam power)$^{0.8}$.

OPERATIONS

High-power targets operate in intense radiation environments. If the beam passes through water that is used to cool the target

As the radioactive inventory increases, the infra-structure required to operate accelerator targets becomes more substantial. Normally hot cells are located near the target operating position, and target maintenance or replacement requires a means to transfer the activated target from its operating position to the hot cell or other appropriate facility where the target can be prepared for disposal.

Transport of spent targets can require substantial infrastructure. This process normally requires shielded casks approved for the transport of radioactive material on public roads or railways. One example, shown in Fig. 2, is the cask used to transport the spent MEGAPIE target to less than 1 km, from the SINQ facility at the Paul Scherrer Institute to the Zwilag facility, where it was cut up for post-irradiation examination [MEAPIE PIE].

RADIATION DAMAGE AND LIFETIME

The structural material of high power targets is subjected to the most severe radiation damage of any application, more than fusion reactor first walls and fuel cladding in fast reactors (the fuel itself, a non-structural material, sees greater radiation damage). The damage is due both to displacements of atoms from their lattice sites and from the production of helium atoms that can cause embrittlement. Figure 4 shows the cross sections for proton-induced atomic displacements and helium production in iron. The displacement cross section is somewhat insensitive to the proton energy, while helium production increases steadily with increasing energy.

RELIABILITY

Target systems generally exhibit greater reliability and availability than high-power accelerators that drive them. This is due to the far fewer number of components in a target station as compared to a modern accelerator. However, the significant cost associated with some of the major systems of a target station usually preclude the ability to keep one or more spares in inventory. Further, many of the components must be handled and replaced remotely, which is labor- and time-intensive. The result is that, while target station component failures are usually rare, when they happen they have the potential to bring the facility down for weeks, or in the worse case, months.

CONCLUSIONS

Target designers are meeting the challenge of building targets that handle the ever-increasing beam power that today's modern accelerators are capable of delivering.



Figure 2: Transfer cask and custom trailer for the MEGAPIE target at the Paul Scherrer Institute.

REFERENCES

[1] M.J. Baumgartner, J.B. Donahue, R.D. Werbeck, "LANSCE Short-Pulse Spallation Target Change," Proceedings of the Fifth Topical Meeting on Accelerator Applications, San Diego, USA, June, 2003, p. 399.
[2] R.S. Lillard, D.L. Pile, D.P. Butt, J. Nucl. Mater. 278 (2000) 277.
[3] F. Groeschel et al., Nucl. Instrum. Meth. A 43 (2010) 345.
[4] J. Haines et al., Nucl. Eng. Design 23 (2007) 345.
[5] M. Futukawa et al., Nucl. Instrum. Meth. A 39 (2008) 345.
[6] F. Groeschel, C. Fazio, et al., J. Nucl. Mater. 335 (2004) 156.
[7] K. Kondo et al., Nucl. Fusion 51 (2011) 123008.

Copyright © 2013 CC-BY-3.0 and by the respective authors

BEAM INSTRUMENTATION FOR HIGH POWER HADRON BEAMS

A. Aleksandrov
Oak Ridge National Laboratory, Oak Ridge, TN 37830, USA

Abstract

This presentation will describe developments in the beam diagnostics which support the understanding and operation of high power hadron accelerators. These include the measurement of large dynamic range transverse and longitudinal beam profiles, beam loss detection, and non-interceptive diagnostics.

INTRODUCTION

Beam instrumentation is an important part of any accelerator. Modern machines are equipped with large numbers of diagnostics for measuring various beam parameters as illustrated by the Spallation Neutron Source diagnostics map in Fig. 1. Many of the diagnostics systems are common for different types of accelerators and accelerated particles but some can work in specific conditions only. In this paper we will discuss beam instrumentation systems used for megawatt-class hadron machines with relatively low energy of no more than a few GeV (essentially non-relativistic beams). There is a significant number of operating and emerging accelerators in this class, such as SNS, PSI, J-PARC, ESS, FRIB, Project-X and others. The major factors specific for these machines are related to their high average beam power:

- Small fraction of lost beam is of importance. Large dynamic range diagnostics are required to follow the dynamics of these small fractions.
- The damage threshold is reached quickly with high average beam power. Diagnostics systems for machine protection must have a fast response.
- The power density in the beam core can be very large. This can prevent the use of interceptive diagnostics.
- The average peak beam current is large. The space-charge effects can be significant and affect operation of some types of diagnostics.

Another important factor is the use of a superconducting RF linac for all or part of the acceleration. Although this is not a necessary requirement and some high power accelerators, like the PSI cyclotron, do not use it, the majority of new projects include high power superconducting linac in the design. This adds two more important factors:

- New damage mechanisms related to the superconducting cavities. Additional diagnostics may be required to protect the SRF linac [1].
- The SRF technology requires maintaining a very clean environment for the cavities and the surrounding vacuum chambers. This can impose severe restrictions on the design of the diagnostics in these areas up to complete a ban on using interceptive diagnostics, like in the case of the SNS SRF linac.

In the following sections we will discuss how the above factors affect the diagnostics requirements and the design choices.

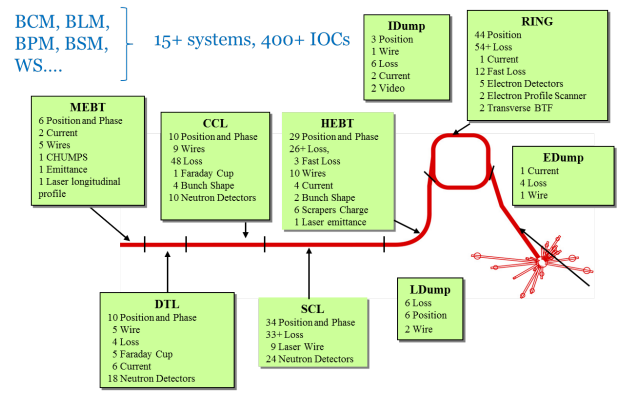


Figure 1: The Spallation Neutron Source diagnostics map.

MACHINE PROTECTION FROM LOST BEAM

Protecting the machine from damage by the lost beam is the most important application of the beam instrumentation. The main damaging factors are:

- Mechanical damage (melting, cracking, erosion). This mechanism is most important at lower energies (<10 MeV), where penetration depth for beam particles is relatively small. The damage threshold depends on many factors but typically it is of the order of magnitude of few hundred watts per meter, which represent a fraction of lost beam of few persent or higher. This level of fractional beam loss can be detected by a Differential Beam Current Monitor (DBCM) measuring beam current difference at two locations along the accelerator.
- Activation of the accelerator equipment. This mechanism is more important at higher energies and the commonly accepted threshold of 1 W/m is used for protons above 100 MeV, which corresponds to a very small fractional loss of $10^{-5} \div 10^{-7}$. As this threshold is significantly lower than the mechanical damage threshold, protection from the activation will automatically provide protection from the mechanical damage. Radiation Monitors (RM) are typically used for protection from small fractional beam loss at high energy [2].

The two above mechanisms are common for all types of the accelerators and a well-established protection strategy typically includes DBCMs at energy below 10 MeV, RMs

Copyright © 2013 CC-BY-3.0 and by the respective authors

at energy above 100 MeV and a combination of both in the transitional region. As was mentioned in the introduction, the use of SRF technology adds additional damage factors:

- Thermal load on the cryogenic system from the lost beam. The threshold is typically about 1W/m and it does not depend on the beam energy.
- Degradation of SRF cavity electrical strength due to repetitive instantaneous loss with the total energy deposition of about few hundreds of Joules.

At the beam energy above 100 MeV, the protection from the first factor is provided by the RMs as the threshold is the same as for protection from the activation. The situation becomes difficult in the region between 10 MeV and 100 Mev, where the 1 W/m thresholds is too low for detection by both DBCM and RM. As there is no high power SRF linac in operation at that low beam energy there is no established strategy for cryo-system protection.

The second factor was discovered during the SNS SRF linac operation. The baseline SNS Machine Protection System (MPS) did not provide protection from a sporadic loss of 100% of beam current within a 30-50 μs period of time because such events were considered to be safe if they happen so infrequently that the average lost power does not exceed 1 W/m. As the lost fraction is significant the RMs respond within a few microseconds but the signal propagation time within the MPS from the detector to the beam shut-off mechanism is typically of 15-30 μs so that overall response time is of 20-35 μs. A fast DBCM with a dedicated line to the beam shut off-device, as illustrated in Fig. 2, is being implemented for SRF linac protection at SNS [3]. The expected response time of 5-6 μs is mostly limited by the propagation time in the cables.

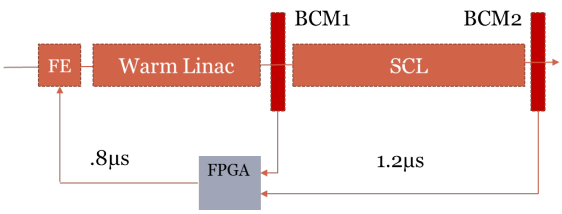


Figure 2: Diagram of the Fast DBCM protection system for the SNS Super Conducting Linac.

BEAM CURRENT AND POSITION MEASUREMENTS

Diagnostics for measuring the beam current and center of mass position are required for tuning of any accelerator independent of power. Typically, non-interceptive types of detectors are used: current transformers and electromagnetic pickups. With higher average beam power one can expect stronger signals from the detectors. An important caveat is that accelerator tuning is usually done at significantly lower beam power than in operation therefore the diagnostics should have a sufficient dynamic range or an adjustable gain to cover the required range of the signal strength. Also, depending on how the beam power reduction is implemented, an increased time response range maybe required. For example, the operational SNS beam parameters are 26 mA peak current, 1ms pulse width at 60 Hz repetition rate; the linac tuning is done with beam current reduced to 5 mA, pulse width shortened to 1 μs at 1 Hz. The reduced parameters are on the edge of the minimum design parameters for the beam position and phase monitors and do not provide the best signal-to-noise conditions but they had to be adopted to ensure the SRF linac safety.

TRANSVERSE BEAM CHARGE DISTRIBUTION MEASUREMENTS

Beam charge distribution measurements, usually in form of profiles or emittance, are the most challenging for high power beams. The biggest problem is that one has to have a "probe" inside the beam to sample the charge at different locations and the probe should be able to survive under a high beam power density. For high power beams specifically, as mentioned before, the dynamics of small fractions of the bunch are of interest, which requires measurement with large dynamic range. Typically, a dynamic range of 10^6 is desirable for understanding beam loss mechanism at the level of 1 W/m for 1 MW average beam power. In addition, if pulsed or chopped beam is accelerated, the diagnostics should have time resolution sufficient to resolve detail of the beam time structure. As we will show below, it is very difficult to combine all three requirements: non-intercepting, large dynamic range and good time resolution, in one diagnostic system.

Many different types of probes have been tried for high power beams. The results are summarized in Table 1 showing the best parameters demonstrated at high power hadron machines. The two numbers in parentheses show the expected parameters the existing systems are believed to be able to achieve with well understood modifications. We will discuss these options in more details in the next sections.

Table 1: Typical Parameters for Transverse Beam Charge Distribution Diagnostics

	Dynamic range	Time resolution	Non-intercepting
Solid material (wires, screens)	10^5 (10^6)	10 ps	No
Photons (laser beam)	10^2 (10^4)	10 ns	Yes
Charged particles (electrons, ions)	10	10 ns	Yes
Gas (residual, jet)	10^2	1 μs	Yes

Intercepting Diagnostics with Large Dynamic Range

The wire scanner is a typical example of a profile measuring system using solid material as a probe. As shown in Table 1, wire scanners can provide a very large

Copyright © 2013 CC-BY-3.0 and by the respective authors

dynamic range and a good time resolution. The simplest way of measuring the result of the beam interaction with the wire is to measure the charge collected on the wire. Figure 3 shows a typical transverse beam profile measured using the charge collection method at SNS. The system has a dynamic range of 10^5, which is currently limited by the digitizer resolution. It is believed the dynamic range can be improved further by upgrading the digital electronics. The advantage of the charge collection method is its simplicity and low cost. The disadvantage is the slow time response. It is not practical to achieve a good time resolution simultaneously with a large dynamic range for the charge collection method because the system bandwidth has to be limited in order to separate the DC coupled charge on the wire from the AC coupled signal induced by the electrostatic field of the beam.

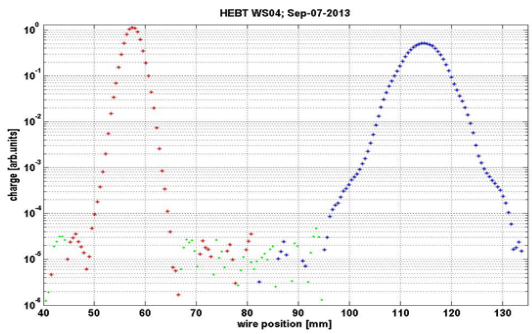


Figure 3: Typical transverse profiles measured with a wire scanner at SNS (red is vertical; blue is horizontal).

Measuring the number of beam particles scattered by the wire is another popular method of obtaining a signal from wire scanner. An example of an advanced wire scanner system of this type is described in [4] and a typical measured profile is shown in Fig. 4. The system allows profile measurements with very high temporal resolution of about 10 ps by detecting the arrival time of each scattered particle. The reported dynamic range is 10^5.

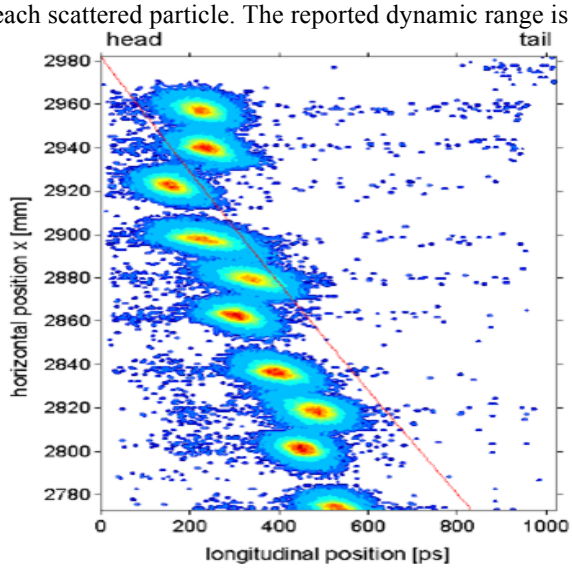


Figure 4: Typical transverse profiles with high temporal resolution measured at PSI (from [4]).

Important conditions for achieving large dynamic range in wire scanner measurements are good vacuum and small beam loss in the vicinity of the device. These conditions are difficult to satisfy at the low energy end of a linac or in the injector. A simple solution is to use a slit instead of the wire and measure charge collected in a Faraday Cup behind the slit. An example of slit system with large dynamic range and good temporal resolution is given in [5].

Non-Intercepting Diagnostics

The intercepting diagnostics discussed above are well developed, can provide large dynamic range and good temporal resolution, but they cannot be used if the beam power density is too high or clean environment requirements forbid any intercepting devices. Non-intercepting diagnostics are highly desirable in these situations. A very good general review of non-intercepting beam instrumentation is given in [6]. In this section we will give more focus to the techniques tested with high power hadron beams.

Laser Wire: A laser beam can provide an excellent probe for beam profile measurements if the interaction of the beam particles with the photons has a significant cross-section. In the case of H^- beam the cross-section for electron photo-detachment is large and peaks at the wavelengths of readily available commercial lasers as shown in Fig. 5. By crossing the beam with a narrow laser "wire" and detecting the products of the photo-detachment reaction (H^0 or electrons) the beam profile can be measured. An example of a large scale laser wire system with multiple measurement locations is described in [7]. It is possible to measure not just the profile but also the beam emittance using the laser wire as a slit as described in [8]. An example of an emittance measurement for a 1 GeV H^- beam at SNS is shown in Fig. 6. The profiles and emittance can be measured with high temporary resolution if a pulsed laser is used (about 10 ns for a typical Q-switched Nd-YAG laser). The dynamic range of about 10^2 of the SNS laser wire is limited by spurious reflections of the laser beam.

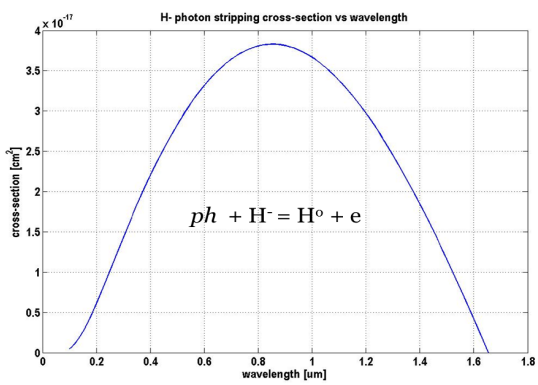


Figure 5: Electron photo-detachment cross-section vs. photon wavelength for H^-.

Copyright © 2013 CC-BY-3.0 and by the respective authors

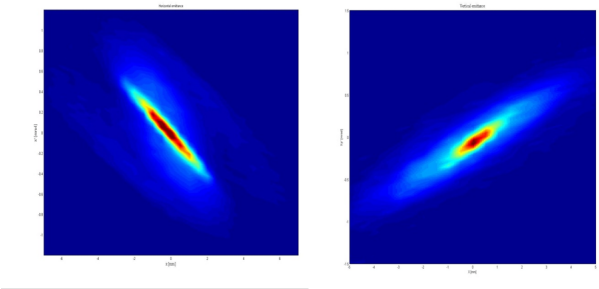


Figure 6: A typical emittance measurement using the SNS laser emittance monitor.

It is believed, based on the signal-to-noise measurements, that with proper engineering improvements the dynamic range could reach 10^4 or higher. In this case, the laser wire would be a rare case of the perfect diagnostic: non-intercepting, large dynamic range and with good temporal resolution. The biggest limitation of this diagnostic is its applicability for H^- beams only.

Ionization Profile Monitor (IPM): The Ionization Profile Monitor (IPM) is a popular non-intercepting diagnostic for beam profile measurement, widely used in proton and ion accelerators, especially in synchrotrons [6]. Its principle of operation is based on imaging of the ionization trace left by the beam in the residual gas by transferring the products of the ionization (ions or electrons) to a position sensitive charge collector. The dynamic range of an IPM is limited by the residual pressure gas and the ionization cross-section and typically does not exceed ~100. The time response can be of the order of few nanoseconds if electrons are collected. In order to mitigate distortion of the image by the space charge force of the beam a guiding electrical and/or magnetic field is used. In the case of high intensity beams the required field strength becomes the major factor determining the size, complexity and cost of the device. An example of an IPM designed for the SNS accumulator ring is shown in Fig. 7.

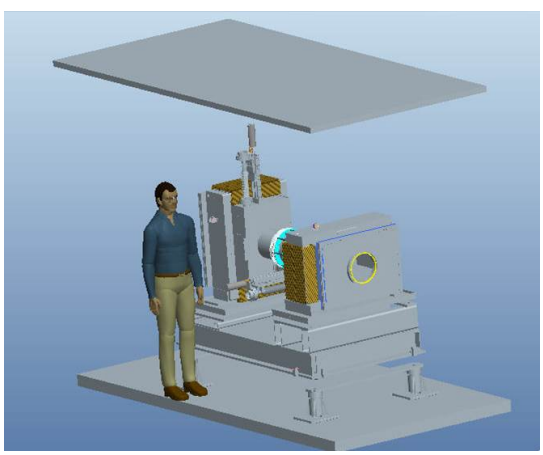


Figure 7: A model of an IPM design for the SNS accumulator ring.

Electron Beam Probe: The beam space charge force, detrimental for the IPM operation, can be used to an advantage in another type of transverse profile monitor: the electron beam probe [9]. The principle of operation is based on measuring the deflection of low energy electrons (or ions), typically in the 10 – 100 keV range, moving across the measured high intensity ion beam. The ion beam profile can be derived from the electrons deflection pattern under certain conditions. The dynamic ran is fundamentally limited by the principle of operation to a relatively low number of 10-15. The temporal resolution of few nanoseconds can be achieved with pulsed electron probe beam. An example of time resolved single turn profile measurement in the SNS accumulator ring is shown in Fig. 8.

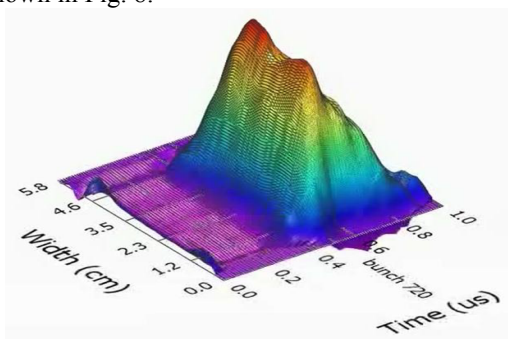


Figure 8: A typical result of a one turn transverse profile measurement with the electron beam probe monitor in the SNS accumulator ring.

Residual Gas Luminescence Monitor: Another type of a device not sensitive to the space charge forces of the high intensity beam is the residual gas luminescence monitor [6]. Its principle of operation is based on optical imaging of the residual gas luminescence induced by the measured beam. A relatively weak signal due to low cross section of the process, especially at high energy, requires long integration times and limits the dynamic range to no more than ~100.

LONGITUDINAL PROFILE MEASUREMENTS

Measuring the longitudinal bunch profile in high power non-relativistic beams is challenging for the same reason as transverse measurements discussed above: the necessity to put some kind of a probe inside the bunch. Naturally, the same types of probes used for the transverse measurements have been tried for the longitudinal diagnostics. The results are summarized in Table 2.

Table 2: Typical Parameters for Longitudinal Bunch Profile Diagnostics

	Dynamic range	Time resolution	Non-intercepting
Solid material (wires, screens)	10^4	1 ps	No
Photons (laser beam)	10^2	10 ps	Yes
Charged particles (electrons, ions)	?	?	Yes
Gas (residual, jet)	?	?	Yes

Copyright © 2013 CC-BY-3.0 and by the respective authors

Beam Shape Monitor (BSM)

Similar to the transverse measurements, the best results in terms of dynamic range and temporal resolution are achieved with an intercepting diagnostics using a metal wire as a probe. The BSM (aka Feschenko device) is a widely used device of this type [10]. Its principle of operation is based on measuring the profile of a low energy electron bunch created by the secondary emission from a wire positioned inside the measured ion beam. The electron bunch profile is measured using the RF deflection technique. A dynamic range of 10^4 with temporal resolution of a few picoseconds can be achieved as illustrated by Fig. 9. Further reduction of the temporal resolution is limited by space charge distortion of the low energy electron bunch. The dynamic range is limited by the ion beam scattering in the wire.

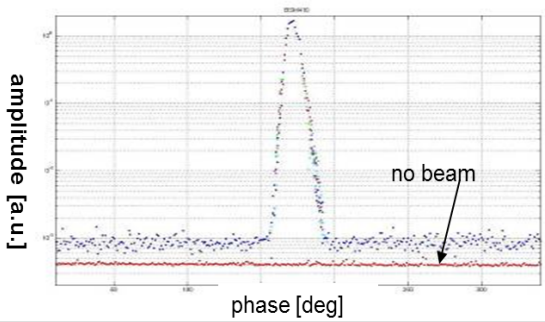


Figure 9: A typical measurement of the longitudinal bunch profile in SNS linac using BSM.

Laser Wire

The only operationally demonstrated non-intercepting type of longitudinal profile diagnostic with a good temporal resolution of few tens of picosecond and dynamic range of ~100 is based on the electron photo-detachment form H^-, similar to the laser wire described above [11]. A typical measurement of the longitudinal bunch profile in the SNS injector is shown in Fig. 10.

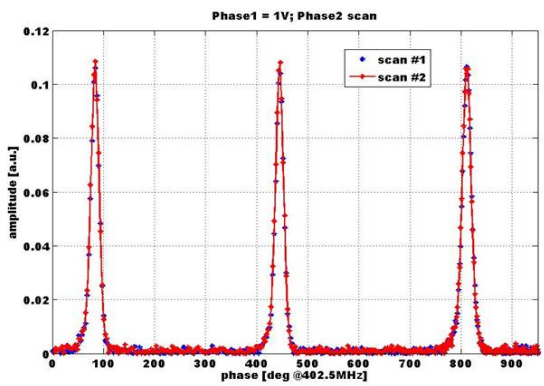


Figure 10: A typical measurement of the longitudinal bunch profile in the SNS injector using the laser wire

The dynamic range in this case is limited by a relatively poor vacuum at the device location. The temporal resolution is limited by the transverse ion beam size. The method is applicable for H^- beams only and this is its major limitation.

Non-intercepting BSM

There is an ongoing effort to develop a longitudinal diagnostic based on the IPM principle [12]. There are significant obstacles to overcome: complex electro-optical transport line, low signal and distortion from the ion beam space charge. A typical measurement with a low intensity heavy ion beam is shown in Fig. 11.

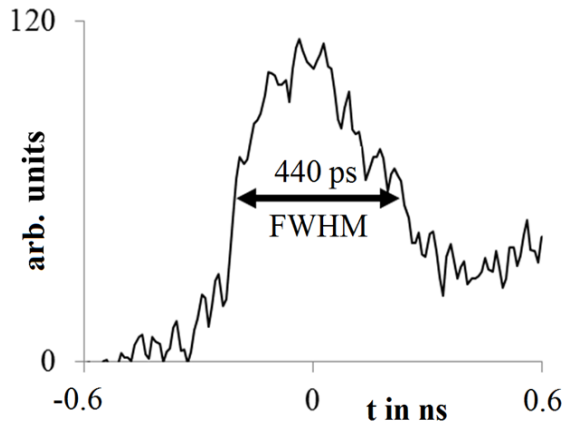


Figure 11: A typical measurement of the longitudinal bunch profile at GSI using the non-intercepting BSM (from [12]).

ACKNOWLEDGEMENT

ORNL/SNS is managed by UT-Battelle, LLC, for the U.S. Department of Energy under contract DE-AC05-00OR22725.

REFERENCES

[1] J. Galambos, Proc. of NA-PAC'13, FRYAA1.
[2] A. Zhukov, Proc. of NA-PAC'13, WEYA2.
[3] W. Blokland, *et al.*, Proc. of IBIC'13, THAL2.
[4] R. Dölling, Proc. of CYCLOTRONS'13, TU3PB01.
[5] A. Aleksandrov, *et al.*, Proc. of LINAC'12, p. 873.
[6] P. Forck, Proc. of IPAC'10, p. 1261.
[7] Y. Liu, *et al.*, PRSTAB **16**, 012801-1-10 (2013).
[8] Y. Liu, *et al.*, NIM A **675**, pp. 97-102, (2012).
[9] W. Blokland, *et al.*, Proc. of DIPAC'09, p. 155.
[10] A. Feschenko, *et al.*, Proc. of PAC2001, p. 517.
[11] C. Huang, *et al.*, APPLIED OPTICS / Vol. 52, No. 19, 2013 pp. 4462-4467.
[12] P. Forck, *et al.*, Proc. of IBIC'13, MOPF13.

Copyright © 2013 CC-BY-3.0 and by the respective authors

A FAST ROTATING WIRE SCANNER FOR USE IN HIGH CURRENT ACCELERATORS*

T. Moore, N.I. Agladze, I.V. Bazarov†, A. Bartnik, J. Dobbins, B. Dunham,
S. Full, Y. Li, X. Liu, J. Savino, K. Smolenski
CLASSE, Cornell University, Ithaca, New York 14853, USA

Abstract

We have developed a cost-effective, fast rotating wire scanner for use in accelerators where high beam currents would otherwise melt even carbon wires. This new design uses a simple planetary gear setup to rotate a carbon wire, fixed at one end, through the beam at speeds in excess of 20 m/s. We present results from bench tests, as well as transverse beam profile measurements taken at Cornells high-brightness ERL photoinjector, for a beam energy of 4 MeV and beam currents up to 35 mA.

INTRODUCTION

Recently, a new regime of beam parameters has become accessible with the advent of very intense photoinjectors, such as the Cornell ERL photoinjector, which feature very high average beam currents (up to 100 mA) and low transverse beam emittances (<1 mm-mrad rms normalized) [1, 2]. The beam energy out of the photoinjectors is near or below 10 MeV, with very large beam powers (on the order of MW) contained inside a small beam cross-section (diameter of 1 mm or less).

This parameter range poses special challenges for diagnostics at full beam current operation, particularly due to the beam's high charge density. First, the beam power density is high enough that any material intercepting the beam will melt on the order of 10's of microseconds or less. Second, the beam energy is low enough that synchrotron or diffraction radiation, which are often the method of choice for beam profile measurements at higher energies, are generally not available without introducing strong magnetic fields or placing apertures undesirably close to the beam for diffraction radiation.

One obvious candidate for a beam profile diagnostic capable of measuring MW type electron beams is a wire scanner that can sample the beam profile at a suitable transverse resolution (on the order of microns or even better) [3]. However, particle beams with small transverse dimensions and high intensities require a wire scanner with a very fast scanning speed, as these beams can melt even carbon wires - one of the best materials for withstanding extremely high temperature rises[4]. For example, a beam current of 100 mA and both an electron beam diameter and a wire diameter of $34\mu m$, like those found in the Cornell photoinjector, require a minimal scanning speed of 20 m/s. In this paper, we describe the design and show tests of a simplified wire scanner capable of reaching this speed and optimized for a large quantity reproduction, resulting in significant cost reduction.

WIRE SCANNER CONSTRUCTION

The principle of operation of the new wire scanner is illustrated in Fig. 1. It consists of a stationary gear G_1 and a smaller gear G_2 rotating around the gear G_1. The blade attached to the gear G_2 holds the carbon fiber cemented on its end. If the center of the small gear moves with the linear velocity v_g then the fiber scanning speed is

$$v_s = v_g\Big(\frac{R}{R_2} + 1\Big), \tag{1}$$

where R_2 is the radius of the gear G_2 and R is the distance from the center of the gear G_2 to the electron beam. Uncertainty of the beam position along the fiber results in the scanning speed variation

$$\frac{\delta v_s}{v_s} = \frac{\frac{\delta R}{R_2} + 1}{\frac{R}{R_2} + 1} \approx \frac{\delta R}{R}, \tag{2}$$

where it is assumed that $\delta R \ll R, R_2$. In the current prototype $R = 82.4$ mm, so for $\delta R = 5$ mm the relative scanning speed variation is $\delta v_s/v_s = 0.061$. This value sets the absolute precision of the transverse bunch profile measurement.

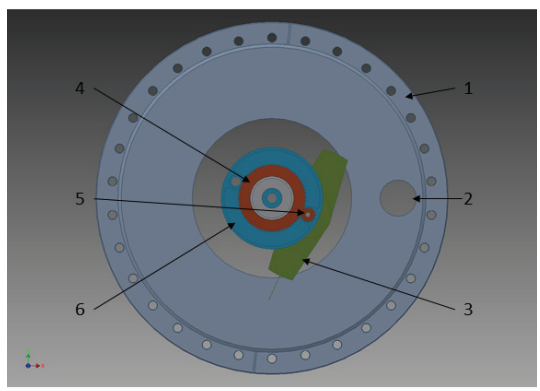


Figure 1: A 3D rendering of the gears setup. (1) - vacuum flange; (2) - beam pipe; (3) - blade with attached carbon wire; (4) - stationary gear G_1; (5) - rotating gear G_2; (6) - rotating gear box.

* This work was supported by the financial assistance from the National Science Foundation (Grant No. DMR-0807731).

† ib38@cornell.edu

Copyright © 2013 CC-BY-3.0 and by the respective authors

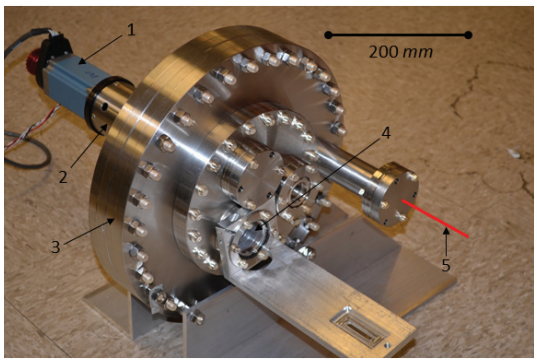


Figure 2: A photograph of the wire scanner. (1) - stepper motor; (2) - ferrofluidic rotary feadthrough; (3) - vacuum flanges; (4) - vacuum flange with viewports; (5) - beam direction.

A photograph of the wire scanner is shown in Fig. 2. The only custom made parts are the aluminum gear box and the fiber holding blade. These are installed between a pair of standard high vacuum flanges with a 337 mm outer diameter and an inner hole with a 152 mm diameter. Another set of two vacuum flanges of diameter 203.2 mm enclose the setup. One of the flanges is equipped with three optical view ports for monitoring the carbon fibers condition between scans. The rotation is provided by a ferrofluidic rotary feedthrough (Thermionics FRMRE-275-38CL) driven by a stepper motor. The maximum scanning speed is determined by the moment of inertia of the rotating parts (motor rotor, rotary feedthrough, gear box, and the blade), the friction in the gears and ball bearings, and the maximum torque rating of the rotary feedthrough. The gears and ball bearings were lubricated with Dicronite - a high vacuum compatible lubricant. Bench tests confirmed that mechanical friction is sufficiently small, and, with the existing moment of inertia of the system and torque limit of the feedthrough (1.06 Nm) scanning speeds can reach up to 30 m/s.

The starting position at the beginning of the scan is chosen so that the fiber is located slightly outside of the beam pipe. During the acceleration stage, the gear G_2 makes an almost complete revolution around the gear G_1 and the carbon fiber reaches its maximum velocity when it crosses the center of the beam pipe. Afterwards, the mechanism is decelerated and the fiber is stopped just outside the beam pipe, opposite its starting position. In order to avoid abrupt changes in the wire's acceleration, which lead to excessive vibrations, the velocity profile is programmed to follow a smooth sinusoidal curve for a nominal scanning speed of 20 m/s.

BENCH TESTS

In contrast to other wire scanners described in the literature [3, 5], the carbon fiber is attached to the rotating blade only by one end, so that a large amplitude vibration – up to 1 mm or more – can be easily excited. This should be compared to typical wire vibration amplitudes not exceeding $10\mu m$ in instruments with stretched wires fixed at both ends [6]. The oscillation speed will add to the wire scanning speed and, as a result can, affect the beam profile measurement. In the prototype instrument the oscillation frequency of the wire, $\omega = 75 \pm 2$ Hz, was determined experimentally by shining a laser onto the vibrating wire and tuning the laser pulse frequency until the image of the wire, obtained using a standard CCD camera, became stationary. Given the maximum amplitude of the oscillation $A_0 = 5mm$ (as determined by direct observation with the video camera), the wire scanning speed can be modulated by up to $\omega A_0 = 0.4m/s$.

In order to verify these estimates, a bench test designed to measure speed variations along the wire due to oscillations was performed. Specifically, a modulated laser was used to capture multiple images of the moving wire in a single CCD frame. The wire scanner was evacuated to a pressure of approximately 10^{-7} torr during these tests, and the laser beam was sent through the beam pipe using two flanges with optical windows. Figure 3 shows a frame obtained for a wire moving at 20 m/s using a laser pulse duration of 7 μs and a pulse frequency of 8 kHz. The laser pulse frequency of 8 kHz causes the wire oscillations to manifest as a slight broadening of the image. The laser light scattered by optical imperfections is removed by subtracting the frame without the wire.

The wire speed was calculated by measuring the distance between adjacent wire images in the scanning direction, and the results are shown in Fig. 4. Wire speed variations are observed both along the wire and in the scanning direction, pointing to the presence of the higher order vibrations. The average speeds determined at two wire scanning positions -2.0 mm and 0.4 mm are 20.2 $\pm$ 0.2 m/s and 20.0 $\pm$ 0.3 m/s respectively. The uncertainty is well within the estimate of 0.4 m/s based on the assumption that the amplitude of the fundamental wire vibration is less than 5 mm. The conclusion is that the wire scanning speed uncertainty is approximately (0.3 m/s)/(20 m/s) = 0.015, or 1.5%.

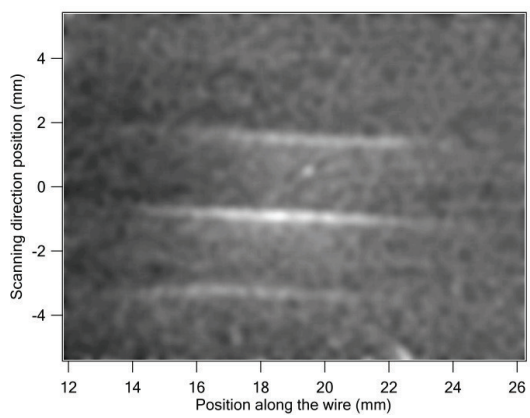


Figure 3: Three images of a wire captured on a single camera frame during a scan. The wire is moving at 20 m/s in the upward direction.

Copyright © 2013 CC-BY-3.0 and by the respective authors

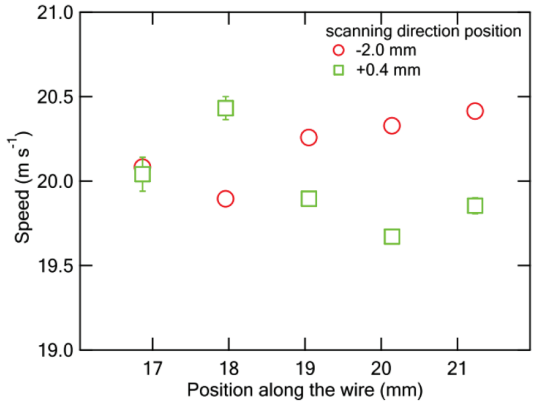


Figure 4: Wire speeds calculated at different locations along the adjacent wires shown in Fig. 3. The circles represent values calculated using the top and middle wires, while the squares use the middle and bottom wires. The error bars are smaller than the symbol size for some points.

BEAM TESTS

Beam tests of the new wire scanner were performed after installation in the chicane section of the Cornell ERL photoinjector [2]. X-rays produced when the wire crosses the electron beam were detected using a combination of a scintillator crystal and a silicon photomultiplier sensor (MicroSM-60035-X13 by SensL). The detector output was sampled at a rate 2 million samples per second with the aid of a digital acquisition device (Agilent U2500A USB DAQ). At a scanning speed of 20 m/s, this corresponds to a distance sampling interval of $10\mu m$, compared to the $34\pm1\mu m$ diameter of the carbon fiber used in these experiments. Data acquisition can be triggered either by the stepper motor controller (DMC-2183 by Galil Motion Control) at a preset wire position, or by the control software after a fixed time interval.

In order to test the dynamic range of the instrument, several sets of tests were performed for beam currents varying from $250\mu A$ to 35 mA, at a beam energy of 4 MeV and a bunch repetition rate of 1.3 GHz. The measured beam profiles were normalized by subtracting an offset and dividing the amplitude by the value of the current in mA. Results are shown in Fig. 5. The total area under the curve is preserved, confirming the good linearity of the detection system. As bunch charge is increased, a systematic broadening of the profile is observed that is the result of space charge repulsion.

At low beam currents the profiles can be obtained using a luminescent viewscreen. Figure 6 shows a comparison of the viewscreen and wire scanner profiles measured for the same beam current of $20\mu A$, which was obtained by decreasing bunch charge to 0.015 pC. A regular beam loss monitor photomultiplier was used for the wire scanner signal detection this time. Both curves are in very close agreement, confirming that both diagnostics are consistent for low bunch charge values.

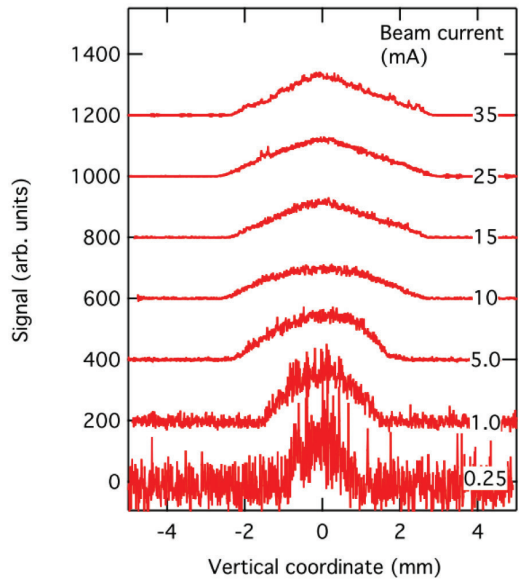


Figure 5: Wire scans at different beam currents, where the data is normalized to 1 mA current.

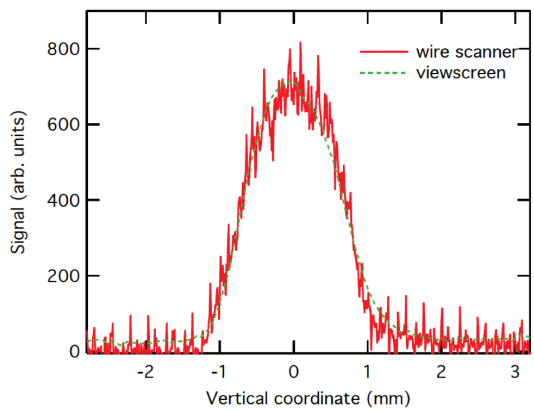


Figure 6: Comparison of the beam profile obtained with the wire scanner (solid line) and the luminescent viewscreen (broken line) for $20\mu A$ average beam current (0.015 pC bunch charge).

REFERENCES

[1] C. Gulliford, et al., arXiv:1304.2708v1

[2] B. Dunham, et al., App. Phys. Lett. 102 (3), 4 (2013).

[3] P. Tenenbaum and T. Shintake, Annu. Rev. Nucl. Part. Sci. 49, 125-162 (1999).

[4] M. Sapinski, CERN-AB-2008-030-BI, 2008.

[5] B. Dehning, et al., Proceedings of the Beam Instrumentation Workshop 2012, Newport News, VA, USA, TUPG029 021-023.

[6] N. Iida, et al., Proceedings of the APAC98, KEK, Japan.

Copyright © 2013 CC-BY-3.0 and by the respective authors

THE DOE-HEP ACCELERATOR R&D STEWARDSHIP PROGRAM*

Eric Colby, Michael S. Zisman#, U.S. Department of Energy, Washington, DC 20585, USA

Abstract

Since the Accelerators for America's Future (AfAF) Symposium in 2009, the U.S. Dept. of Energy's Office of High Energy Physics (DOE-HEP) has worked toward broadening its accelerator R&D activities beyond its support of only discovery science to include medicine, energy and environment, defense and security, and industry. Accelerators play a key role in many aspects of everyday life, and improving their capabilities will enhance U.S. economic competitiveness and the scientific research that drives it. In 2011, a community task force was initiated by DOE-HEP to develop more fully the information from the original AfAF Symposium. Subsequently, a DOE-HEP concept (coordinated with the other cognizant Office of Science program offices) was developed for accelerator R&D stewardship. Here, we describe the evolution of the stewardship task starting from its origins in the ongoing DOE-HEP accelerator R&D program, the mission of the new program, and initial steps being taken to implement it. Several initiatives are currently being considered to launch the program, and these will be indicated. Involvement of the accelerator community in developing ideas for future stewardship activities will be crucial to the ultimate success of the program.

ORIGIN AND MOTIVATION

Although DOE-HEP has historically taken a broad view of its accelerator R&D program, an effort to examine stewardship needs more formally began in 2009 with the sponsoring of the Accelerators for America's Future Symposium [1]. The report from this symposium, published in 2010 [2], identified the importance of accelerator technologies to broad sectors of the U.S. economy, including discovery science, medicine, defense and security, energy and environment, and industry. It also called out the needs for improved interagency, inter-program, and industry-agency coordination, and highlighted the value of expanded training and education of accelerator scientists and engineers.

In 2011, the Senate requested [3] DOE to prepare a 10-year strategic plan for "accelerator technology research and development to advance applications in energy and the environment, medicine, industry, national security, and discovery science." In preparation for developing such a strategic plan, Dr. Jim Siegrist, Associate Director of Science for High Energy Physics, in consultation with other Office of Science (SC) Associate Directors, asked Norbert Holtkamp from SLAC to convene a community task force to review and expand upon the findings of the earlier AfAF report. This group met during the period November 2011–February 2012 and provided information to:

- identify research opportunities with potential for broad national benefits
- summarize the status of key research and technology areas identified
- identify possible impediments to successful accelerator R&D stewardship activities for the broad user base envisioned

The task force report [4] was very helpful in preparing the DOE-HEP strategic plan, which was sent to Congress in October 2012.

DESCRIPTION OF STEWARDSHIP

Relationship with Current Program

The ongoing HEP accelerator R&D program develops the basic science and technologies needed to design, build, and operate state-of-the-art accelerators. Such accelerators are essential for making discoveries in HEP. Moreover, as is clear from the studies in Refs. [2] and [4], accelerators are likewise essential for serving the broader communities of medicine, defense and security, energy and environment, and industry as well as the discovery science community.

As indicated schematically in Fig. 1, there is already a strong connection between current R&D thrusts and stewardship program needs. The center portion of the figure lists the 8 program thrusts of the current HEP accelerator R&D program. The columns on the left indicate the science goals that motivate the program, namely, the desires for higher particle or photon beam quality, for higher beam intensity, and for higher beam energy (or, equivalently, more compact accelerators) and how they overlap with the program thrusts. The columns to the right indicate the overlap between the broader accelerator community needs and the ongoing R&D program thrust areas. The complete overlap with the needs of discovery science is by design, as this community has, to date, been the only consumer of the R&D work. It is interesting, however, that there is also substantial overlap with the needs of the other accelerator communities. We conclude from this that the existing skill set is already well matched to the needs of the broader accelerator community.

Accelerator Stewardship Mission

The mission of the accelerator R&D stewardship program is to support fundamental accelerator science and technology development of relevance to many fields, and to disseminate accelerator knowledge and training to the broad community of accelerator users and providers.

Carrying out this new mission—in addition to carrying out the current HEP programmatic accelerator R&D effort—will be accomplished through:

*Work supported by U.S. Dept. of Energy, Office of Science, Office of High Energy Physics
#michael.zisman@science.doe.gov

Copyright © 2013 CC-BY-3.0 and by the respective authors

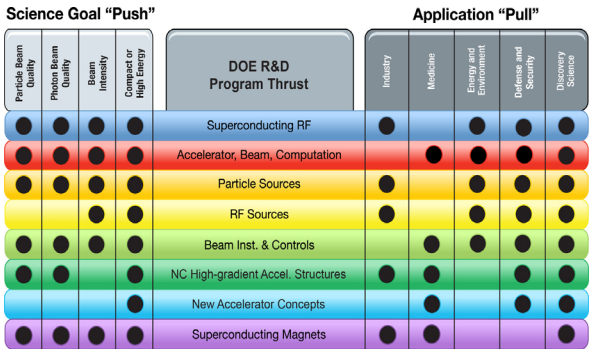


Figure 1: Connections between accelerator R&D thrust areas, science goals, and application needs (adapted from Ref. [4]).

- Facilitating access to national laboratory accelerator facilities and infrastructure for both industrial and other U.S. governmental agency users or developers of accelerators and related technology
- Working with accelerator user communities and industrial accelerator providers to develop innovative solutions to critical problems, to the benefit of both the broader user communities and the DOE discovery science community
- Serving as a catalyst to broaden and strengthen the community that relies on accelerators and accelerator technology

These elements are part of the accelerator R&D strategic plan.

STEWARDSHIP PROGRAM INITIATION

The steps envisioned to launch the stewardship program include:

1. Immediately augmenting existing programs to provide opportunities for industrial and federally funded users at DOE facilities by increasing support staff and funding for test facilities
2. In the mid-term (2–5 years), identifying a few topical areas with high impact for focused work; each area will have its own stakeholder board
3. In the longer term (5–10 years), select additional topical areas for focused work; new stakeholder boards will be created as topics are identified

In the steady state (depending, of course, on available resources), the HEP goal is to support at least three topical areas at any given time.

In preparation for item 1, an initial survey of available national laboratory infrastructure and capabilities was carried out in 2012. A follow-up meeting with the national laboratories to plan for stewardship activities at their test facilities is planned for early 2014.

Several potential topical areas have been identified for mid-term support (item 2). These include: improved particle beam delivery and control for cancer therapy facilities; laser development addressing the specific needs of the accelerator community, namely, high peak power, high average power, and high electrical efficiency; and energy and environmental applications of accelerators. One motivation for this last possibility is shown in Fig. 2, which gives the projected energy use of the SC accelerator laboratories compared with the anticipated mandated reductions. The SC accelerator complex energy usage is ~1000 GW-hr/yr, and is currently projected to increase about 50% by 2018. Without substantial improvements in efficiency, the challenge in meeting the mandated reductions is obvious.

For the longer term topics, we expect to solicit community input via workshops and discussions with other federal agencies.

Initial Topical Workshops

For the first two topics being considered under item 2 above, workshops were held to assess needs in these areas. The first, the Ion Beam Therapy Workshop, was organized jointly by DOE-HEP and the National Cancer Institute and took place in Bethesda, MD, from January 9–11, 2013. The second, the Laser Technology for Accelerators Workshop, was organized by LBNL and took place in Napa, CA from January 23–25, 2013. Both meetings were small and tightly focused, with attendance by invitation only. Representatives from the stakeholder agencies were also in attendance. Reports from the two workshops [5, 6] are available on the DOE-HEP website. A limited number of industrial observers were accommodated at each workshop, but did not participate in the preparation of the workshop reports.

Criteria for "Good" Accelerator R&D Stewardship Activities

In this section we provide some initial guidelines on choosing candidate activities for accelerator R&D stewardship. These should not be interpreted as hard and fast rules, but rather as an indication of the criteria that might be applied in the evaluation process.

1. The application must involve accelerators or accelerator-related technology having synergy with and benefitting the primary HEP mission.

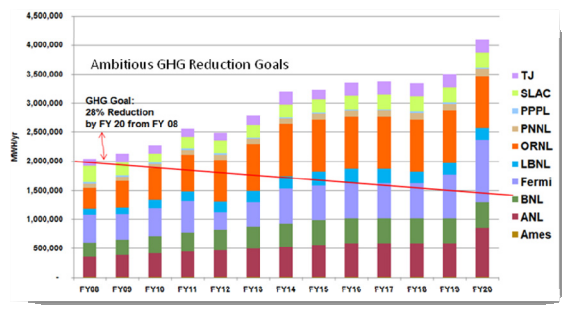


Figure 2: Projected energy usage of the SC accelerator complex through FY20 (bars). The red line indicates the decrease of 28% in green-house gasses (GHG) from FY08 to FY20 mandated by EO13514.

Copyright © 2013 CC-BY-3.0 and by the respective authors

2. There must be non-trivial intellectual involvement of the institution.
   Good: build an accelerator technology component (usually WFO*)
   Better: design an accelerator technology component (possibly WFO)
   Best: design, build, and test an accelerator technology component (stewardship)
3. The activity must be reasonably consistent with the mission of the institution and minimally impact its primary SC program(s).
   Good: activity maintains core skill or facility needed for the mission
   Better: activity expands core skill or facility needed for the mission
   Best: activity develops new core skill or facility needed for the mission
4. The institution must arguably be the best provider of the capability or service (and not compete with an existing business).
   Good: capability not unique, but institution is nearby to customer
   Better: capability is leading and institution is nearby to customer
   Best: capability is unique to provider
5. The customer benefitting from the stewardship activity must endorse the goals.
   Good: customer participates in task definition and writes letter of support
   Better: customer and institution partner; some cost sharing from customer (e.g., 1:10)
   Best: customer and institution partner; substantial cost sharing from customer (e.g., 1:1)

HOW YOU CAN ENGAGE

As we launch the accelerator R&D stewardship program, it is important that the accelerator community participate fully in its implementation. This can be done in a number of ways:

- Read the stewardship program description [7] and workshop reports found in Refs. [4–6].
- Respond to the Test Facilities Pilot Program call (national laboratories only) by identifying potential test facility customers and understanding their needs, and by responding to the meeting charge when it comes out.
- Prepare for topical area calls by starting to gather ideas and thinking about potential Collaborative Accelerator Research Teams (CARTs); be aware of related calls, e.g., the NIH P20 call for a National Center for Particle Beam Radiation Therapy Research [8] and the new DOE SBIR/STTR topical area for laser technology.
- Propose new, challenging topical areas; these should be "customer driven" and result in a potential solution that is broadly useful within a time frame of ≤ 10 years.

TAKE-HOME MESSAGES

Here we summarize the main points of the accelerator R&D stewardship program.

- Eligibility for the program will be broad; it is not a national-laboratory-only program.
- The "customer" must actively desire and participate in the activity; a pure technology push by potential providers is not sufficient.
- Activities should accrue some measureable intellectual benefit to HEP.
- Stewardship topical areas should address high-impact challenges on a roughly 5–10 year timescale; the intent is to solve problems and move on to other challenges.
- Handling intellectual property (IP) remains a challenge; existing WFO mechanisms provide a precedent, but IP will likely need to be handled case-by-case.

ACKNOWLEDGMENTS

We would like to thank Jim Deye (NCI) Cathy Bailey (NCI), and Christie Ashton (DOE) for help organizing the Ion Beam Therapy Workshop, and Wim Leemans and Martha Condon (both LBNL) for help organizing the Laser Technology Workshop. We are grateful to our DOE-HEP colleagues Jim Siegrist, Michael Procario, Glen Crawford, and L.K. Len for support and encouragement in launching the accelerator R&D stewardship effort.

REFERENCES

[1] http://www.acceleratorsamerica.org/workshops/agenda.html
[2] http://science.energy.gov/~/media/hep/pdf/accelerator-rd-stewardship/Report.pdf
[3] Senate Report 112-075, p. 93.
[4] http://science.energy.gov/~/media/hep/pdf/accelerator-rd-stewardship/Accelerator_Task_Force_Report.pdf
[5] http://science.energy.gov/~/media/hep/pdf/accelerator-rd-stewardship/Workshop_on_Ion_Beam_Therapy_Report_Final_R1.pdf
[6] http://science.energy.gov/~/media/hep/pdf/accelerator-rd-stewardship/Lasers_for_Accelerators_Report_Final.pdf
[7] http://science.energy.gov/hep/research/accelerator-rd-stewardship/
[8] http://grants.nih.gov/grants/guide/pa-files/PAR-13-096.html

* Work For Others activity.

Copyright © 2013 CC-BY-3.0 and by the respective authors

ADVANCES IN PHOTOCATHODE TECHNOLOGY AT CORNELL UNIVERSITY*

S. Karkare†, I. V. Bazarov, L. E. Boulet, M. Brown, L. Cultrera, B. Dunham, N. Erickson, G. Denham, A. Kim, B. Lillard, T. P. Moore, C. Nguyen, W. Schaff, K. W. Smolenski, H. Wang, CLASSE, Cornell University, Ithaca, New York, USA

Abstract

Beam brightness from modern day photoinjectors is limited by the photocathode. A multifaceted photocathode development program has been undertaken at Cornell University with a goal to develop the ultimate photocathode which has high quantum efficiency, low mean transverse energy, quick response time and a long lifetime. Positive affinity cathodes like CsK_2Sb and Na_2KSb have been grown using different kinds of alkali metal sources (alkali-azide and pure metal), characterized and tested in the Cornell ERL photoinjector. Novel layered structures of various III-V semiconductors like GaAs and AlGaAs grown using Molecular Beam Epitaxy (MBE) and activated to negative electron affinity using Cs and NF_3 are also being investigated. Surface and photoemission diagnostics like Auger spectroscopy, LEED, RHEED and the 2D-electron energy analyzers have been connected in vacuum to the photocathode growth and preparation chambers to fully characterize the surface and emission properties of the materials grown. A Monte Carlo based simulation has also been developed to predict photoemission from layered semiconductor structures and help design novel structures to optimize the photoemission properties.

INTRODUCTION

Photocathodes used in photoinjectors that power modern and future 4^{th} generation light sources like the ERL's and FEL's have extremely stringent requirements. Moreover, the maximum achievable beam brightness from photoinjectors is limited by the photocathode [1]. For example, the photocathode in the Cornell ERL injector is required to have a high ($> 3\%$) QE (quantum efficiency) at 520nm laser wavelength, short ($<$ 2ps) response time, minimum possible MTE (mean transverse energy) with typical values being 150meV and a long lifetime during high current ($\sim$100mA) operation. Metallic cathodes are rugged and have a fast response time, but have very low ($< 0.1\%$) QE. Semiconductor cathodes provide a high QE in the visible and UV range. For this reason semiconductor cathodes are the choice for several photoinjectors around the world. However, they have very stringent vacuum conditions for longevity [2].

Several of the key emission properties required from semiconductor cathodes are conflicting. For example, at longer wavelengths, negative electron affinity (NEA) semiconductor cathodes give a small MTE ($\sim$25meV) but have a long ($>$100ps) response time [3]. Furthermore, the detailed physics of photoemission and the origin of the key photoemission properties like QE, response time and MTE are not well understood for semiconductor cathodes. This is largely due to lack of conclusive and self-consistent experimental data hampered by the demanding vacuum requirements and experimental difficulties associated with measuring key photoemission properties of MTE and response time from these cathode materials.

EXPERIMENTAL FACILITIES

A campus-wide photocathode investigation program has been initiated at Cornell University in order to address the need for experimental data. Both positive electron affinity (PEA) alkali-antimonide and NEA semiconductor photocathodes are under investigation. The alkali-antimonide photocathode growth chamber and GaAs activation chambers are connected in vacuum to surface analysis chamber with auger spectroscopy, RHEED and LEED capabilities. Abilities to measure spectral response, surface QE scan, activate NEA semiconductor cathodes using Cs and NF_3 while measuring QE at different wavelengths simultaneously have also been incorporated. Advanced photocathode diagnostics such as the electron energy analyzer [4] to measure simultaneously, transverse and longitudinal electron energy distributions have also been developed and added to the setup. Figure 1 shows the picture of the multipurpose vacuum system devoted to photocathode research. The entire assembly is under ultra high vacuum with a pressure of less than 10^{-10} Torr throughout and less than 10^{-11} Torr in the GaAs preparation chamber and the surface analysis chamber. Samples can be transferred from one part of the assembly to another in vacuum via use of magnetically coupled transfer arms.

Multialkali photocathodes developed and characterized here can be transferred to the Cornell ERL injector for studying their performance in a DC photoemission gun under high voltage (350kV) and high beam currents ($>$ 70mA) [5] via a vacuum suitcase capable of maintaining a pressure of a few 10^{-10} Torr during the transfer. Another facility is a semiconductor MBE reactor used to grow and activate III-V semiconductor photocathode structures. New layered structures of GaAs/AlGaAs can be grown with graded doping levels in order to optimize photoemission characteristics. These structures, once grown in the MBE reactor can be capped with a thick As layer and be transported in air to either the multipurpose photocathode

*This work has been funded by NSF under grant number DMR-0807731, DOE under grant number DE-SC0003965

† ssk226@cornell.edu

Copyright © 2013 CC-BY-3.0 and by the respective authors

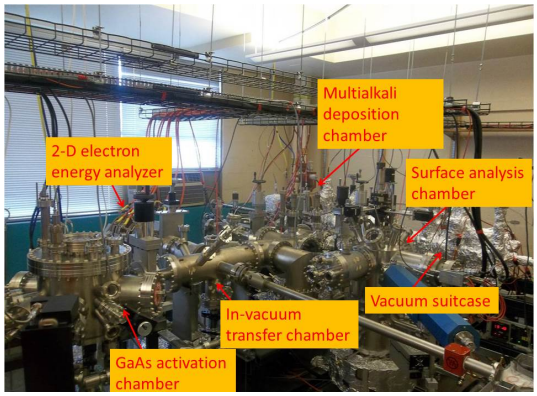


Figure 1: Photocathode growth and analysis chamber.

research chamber or to the DC photoemission gun, without contaminating the surface. The As layer can then be removed by heating the surface to about 350°C for one hour prior to the NEA activation.

ALKALI-ANTIMONIDE CATHODES

Characterization and High Current Operation

Various multialkali cathodes are routinely grown for use in the Cornell ERL injector using ALVATEC [6] alkali metal sources. Cs_3Sb, K_2CsSb and Na_2KSb have been successfully grown and characterized w.r.t their spectral response, MTE and response time in the photoinjector [7, 8, 9]. The results obtained have been summarized in Table 1. It can be seen that Na_2KSb gives a noticeably lower MTE than the Cs cathodes. Further Na_2KSb is also known to withstand higher temperatures making it more suitable for high current operation. Successful high current operation has been demonstrated by extracting 65mA of beam current from Na_2KSb cathode in the Cornell photoinjector for a period greater than 8hrs. The QE degradation during this operation had a 1/e lifetime constant of 66hrs [9].

Table 1: QE, MTE and Response Time Characterization of Multialkali Cathodes

Cathode	QE @ 532nm	MTE @ 532nm	Response time
Cs_3Sb	4-5%	160meV	$<$ 2ps
K_2CsSb	7-10%	160meV	$<$ 2ps
Na_2KSb	4-7%	120meV	$<$ 2ps

Investigating Alkali Metal Sources

Although multialkali cathodes have been successfully and reliably grown with the ALVATEC alkali metal sources, it has been found that the exact reproducibility of the growth process is difficult. The alkali metal flux changing over time and between individual dispensers is the main reason causing this lack of reproducibility. This makes it difficult to automate the cathode growth process. With this goal in mind various alkali metal sources are being investigated.

Along with ALVATEC sources, alkali antimonide cathode growth has been successfully demonstrated at Cornell using SAES dispensers [10], alkali azides and pure metal alkali sources. SAES dispensers are easy to handle and very reliable but have some drawbacks. They have to be heated to a temperature exceeding 600°C for alkali metal evaporation. Furthermore, the alkali metal flux from these sources is very small and hence they need to be placed very close to the substrate, increasing the substrate temperature due to radiative heating from the substrate and hindering cathode growth.

Alkali azides are stable compounds in air and decompose to release alkali metal vapor and nitrogen only when heated close to the melting point at about 300°C. This makes them easy to handle outside vacuum. They are cheap and the flux of alkali metal released is large. However, during the alkali metal evaporation the nitrogen released can cause the pressure to rise above 10^{-5} Torr. Very fine temperature control (to a fraction of a degree) of the furnaces is required to avoid excess pressure in the chamber. Such tight temperature control is one of the challenges to a successful use of these sources.

Pure metal alkali sources have been tested to some extent and have been found to be easy to operate for photocathode growth. But, pure alkali metals are strongly reactive and hazardous to handle in open air. A proper facility to insert these sources into the vacuum chamber through an inert gas atmosphere needs to be developed to avoid handling difficulty. Considering the stability and reliability of the sources, the pure metal alkali sources appear to be optimal. The above results are summarized in Table 2.

III-V SEMICONDUCTOR CATHODES

Monte-Carlo Simulation of Photoemission

A Monte-Carlo based simulation has been developed to explain the process of photoemission from GaAs [11]. This simulation is based on Spicer's 3-step photoemission model. Electrons are excited by photons from the valence band to the conduction band. The electrons are then transported within the GaAs bulk. During this transport they undergo scattering with phonons and holes and lose energy. The ones that reach the surface can get emitted into vacuum via tunneling through a surface potential barrier. This simulation successfully describes the spectral response and response time of GaAs cathodes without the use of any ad hoc parameters. Upon assumption of an elastic surface scattering that causes electrons to be emitted in a cosine angular distribution w.r.t. the surface normal, the Monte-Carlo code gives MTE values very close to the measured ones [12]. The exact value of NEA is extremely sensitive to the vacuum conditions and surface cleanliness. It can differ from activation to activation and hence is the only free parameter allowed in the simulations. The code has now been extended to layered structures with graded doping.

Copyright © 2013 CC-BY-3.0 and by the respective authors

Table 2: Comparison of Alkali Metal Sources

Source	Capacity	Stability	Thermal load on substrate	Effect on vacuum	Handling outside vacuum
SAES	Poor	Good	Significant	Negligible	Stable in air
ALVATEC	Good	Poor	Not measurable	Negligible	Stable when unused
Azides	Good	Poor	Not measurable	Rises to 10^{-5} Torr	Stable in air
Pure metal	Good	Good	Not measurable	Negligible	Needs inert gas environment

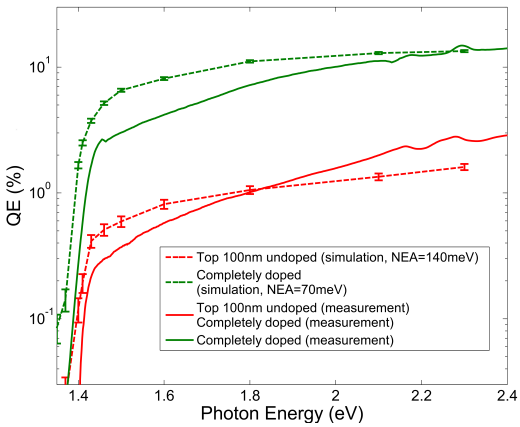


Figure 2: Measured and simulated spectral response of layered and non-layered GaAs cathode.

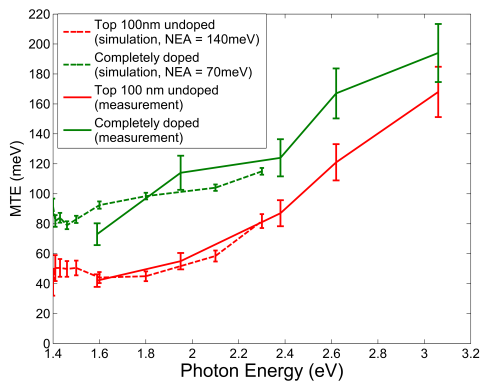


Figure 3: Measured and simulated MTE of layered and non-layered GaAs cathode.

Layered Structures

Novel layered structures of GaAs/AlGaAs with graded doping can be grown to optimize photoemission properties. So far layered structures have been grown to maximize QE [13]. The Monte-Carlo modeling predicted a simple structure consisting of 100nm undoped GaAs layer over a substrate doped to 5×10^{18}cm^{-3} using carbon would have a smaller MTE and a smaller QE as compared to completely p-doped GaAs. Such a structure was grown using MBE and activated to NEA. The MTE and spectral response were found to be in reasonable agreement with the values obtained from the Monte-Carlo simulation [14]. Figs. 2 and 3 show the comparison of the spectral response and MTE, respectively, of the layered and non-layered structures.

FUTURE WORK

We have concluded that pure metal sources are optimal for growing alkali-antimonide cathodes reproducibly. Developing an automated growth procedure using pure metal sources and growing advanced alkali-antimonide cathodes like the S-20 photocathode and characterizing it are among the next natural steps. The Monte-Carlo simulation has already allowed us to predict and realize new low emittance cathodes.This opens a way to systematic theory-driven investigations of more complicated layered structures optimizing certain photoemission properties. Simulations are continually being improved by including new relevant physics especially pertaining to the surface. Capability of activating and characterizing NEA cathodes within the MBE growth chamber is being implemented to skip the step of As capping and to ensure a clean and atomically flat surface.

REFERENCES

[1] I. V. Bazarov et al., Phys. Rev. Lett. 102, 104801 (2009).

[2] D. H. Dowell et al., Nucl. Instrum. Methods Phys. Res. A 622, 685 (2010).

[3] I. V. Bazarov et al., J. Appl. Phys. 103, 054901 (2008).

[4] D. A. Orlov et al,. Appl. Phys. Lett. 78, 2721 (2001).

[5] B. Dunham et al. Appl. Phys. Lett., 102, 034105 (2013).

[6] http://www.alvatec.com

[7] L. Cultrera et al. Appl. Phys. Lett., 99, 152110 (2011).

[8] I. Bazarov et al. Appl. Phys. Lett., 98, 224101 (2011).

[9] L. Cultrera et al. Appl. Phys Lett. (in press) (2013).

[10] http://www.saesgetters.com/products/alkali-metals-dispensers

[11] S. Karkare et al. J. Appl. Phys., 113, 104904 (2013).

[12] S. Karkare and I. V. Bazarov, Appl. Phys. Lett., 98, 094104 (2011).

[13] Y. Zhang et al. Appl. Phys. Lett., 99 101104 (2011).

[14] S. Karkare et al. In preparation.

Copyright © 2013 CC-BY-3.0 and by the respective authors

CONTINUED DEVELOPMENT AND TESTING OF CARBON NANOTUBE CATHODES AT RADIABEAM*

J.J. Hartzell#, L. Faillace, R. Agustsson, S. Boucher, A. Murokh, A. S. Smirnov, RadiaBeam Technologies, Santa Monica, CA 90404, USA
B. C. Regan, W. Hubbard, UCLA, Los Angeles, CA 90095, USA

Abstract

RadiaBeam is continuing to develop carbon nanotube (CNT) cathodes for DC-pulsed and radio frequency (RF) driven electron sources. CNT cathodes, if fully realized, are capable of producing very high current density with low thermal emittance, due to ambient operating temperature. Experimental results of CNT cathodes are presented, including the high-voltage tests, and life time studies. CNT cathodes potential applications in accelerator science and microwave industry are discussed, and near term plans to test the CNT cathodes in the RF environment are presented.

INTRODUCTION

Carbon nanotubes are allotropes of carbon with a cylindrical nanostructure and exceptional electrical and mechanical properties [1]. They are typically fibers with a diameter of 1 to 50 nm, coming in either single-wall or multi-wall strands and an aspect ratio of up to 1000. Due to this very high aspect ratio, they have extremely large field enhancement factors, allowing efficient emission of electrons [2] at fields of only a few MV/m. Stable currents of more than 1μA have been measured from a single CNT fiber [3]. CNTs can also be fabricated in large, dense arrays, making them ideal as a cathode material. Peak current densities as high as 50 A/cm^2 have been reported from a macroscopic cathode operating in pulsed mode [4].

The use of a cathode fabricated with CNT technology has a high potential to replace thermionic cathodes in vacuum electronic devices, such as TWTs. Due to their high field enhancement factor, it is possible to operate in a "cold" field emission regime with relatively high current densities and affordable voltages in a much wider temperature range, including at room temperature [5]. Moreover, CNT cathodes are able to provide high current beams from a very small total gun size.

CNT CATHODE PRODUCTION

After early initial testing, we have focused on producing CNT cathodes via electrophoretic deposition (EPD) (see Figure 1). This method has proven to be rapid and economical. We are able to produce and characterize approximately one cathode per week. This allows us to produce a large number of samples with varying properties (deposition density, annealing temperatures, etc) to find the best combination of performance and durability.

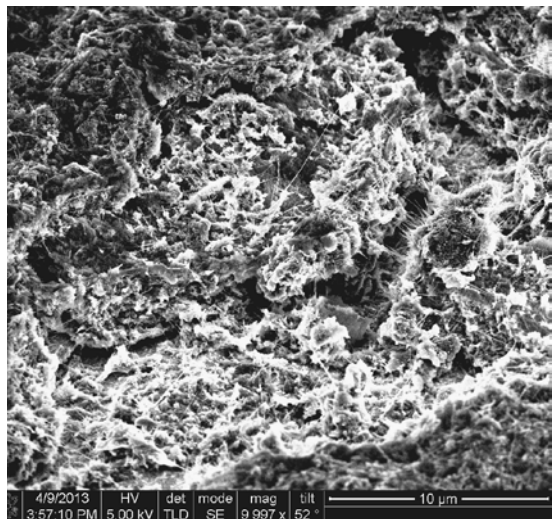


Figure 1: EPD deposition showing a very high density of CNTs.

As compared to earlier efforts, we have modified the substrate design to reduce the time required for machining and to accommodate the compact chemical vapor deposition (CVD) furnace that we helped our collaborators build. Our plan to eventually test the CNT cathodes inside the RF Gun at A0 (Fermilab) led to a design that has a reusable holder and removable cathode substrates. Figure 2 shows the new reusable holder with a variety of substrates ready for deposition.



Figure 2: Reusable cathode holder with molybdenum cathode substrate on the LEFT, based on Fermilab's A0 gun. Two undeposited cathodes (stainless steel and copper) on the RIGHT.

* This work is supported by DOE Grant DE-SC0004459
# Hartzell@radiabeam.com

Copyright © 2013 CC-BY-3.0 and by the respective authors

As we are near the point of having optimized our EPD process, we are beginning early production tests of the CVD process. A computer controlled quartz tube furnace and digital mass flow controllers comprise the basic CVD production system. Unlike EPD, CVD allows us to grow CNTs directly on the substrate, offering more control of the microscopic properties of the deposition. We begin with elemental nickel nanoparticles (20 nm diameter, MKnano), which we suspend in isopropanol and then spin-coat onto the desired substrate. Since single nanotubes tend to grow from each nanoparticle and tube diameter is proportional to catalyst size [6] we check nanoparticle density via SEM to ensure they are sufficiently dispersed. For initial CVD process optimization we used silicon wafers as growth substrates, exploring the gas flow and temperature parameter space and characterizing samples in a SEM to develop a suitable growth recipe. We then adapted this recipe for growth of CNT on Ni nanoparticles dispersed onto Cu substrates, as we eventually wish to grow nanotubes directly onto copper cathodes. After a few trial growths, adjusting to reduce the significant amount of carbon which deposits onto the copper as graphene, we were able to successfully grow carbon nanotubes directly onto copper surfaces (See Figure 3).

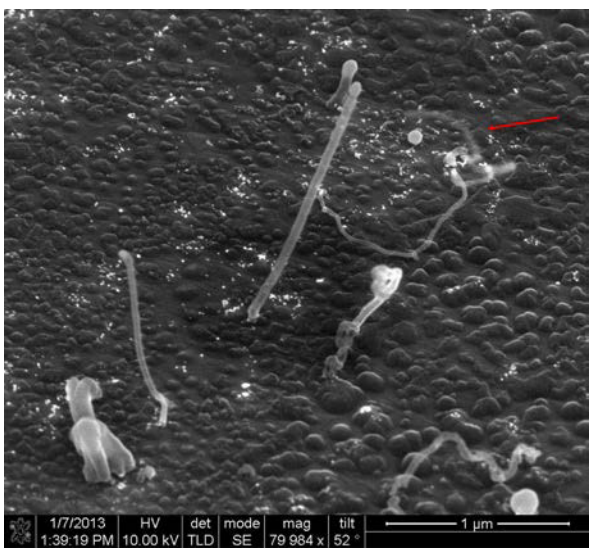


Figure 3: CNTs deposited onto a copper substrate via CVD. The red arrow points to a blurred CNT, indicating that it was only attached at one end, and was free to vibrate in the SEM.

CNT CATHODE TESTING

In order to be used in the gun (both DC and RF) for injection into an accelerator, the cathodes must have a sufficient current emitted at reasonable electric fields. Our initial goal is to make cathodes that are stable at ~20MV/m. We employ a pulsed mode test station for initial characterization. The test station has a variable gap of 0-25 ± 0.02 mm, can apply 0-2.5 kV, and a minimum pulse length of 5 µs.

For each cathode we study, we perform a series of individual runs, each at the same fixed electrode spacing. Each run consists of measuring the current while incrementally increase the voltage from 0 V until the cathode arcs. We then turn off the power supply to allow the system to stabilize and then repeat. Doing this allows us to progressively increase the maximum electric field the electrodes will support until we reach a stable operating point. From measuring the emitted current across the voltage range after each arc, we can clearly see that the emitted current is reduced as each arc damages a portion of the CNTs (see Figure 4). Once we reach a certain electric field, any loosely attached pieces of carbon are pulled off or a particularly long CNT is burnt off the cathode, initiating an arc. After the breakdown, the cathode can support a stronger field, albeit at a lower current, until the next breakdown. To confirm this idea, we used adhesive tape to mechanically remove all but the most strongly attached CNTs from the cathode the repeated the test. This substantially increased the voltage handling at the expense of reducing the emitted current.

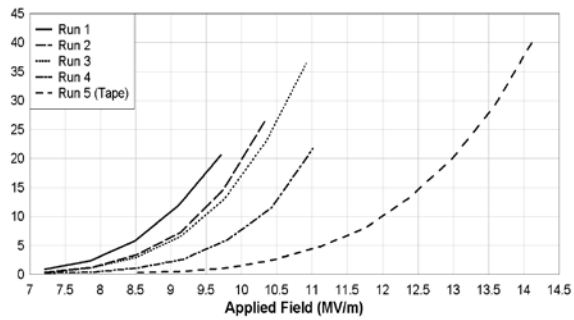


Figure 4: A series of runs on the same cathode, each ending in a breakdown. A final run after using tape to clean the cathode improves the voltage handling.

After using pulsed mode testing to evaluate a large number of cathodes, we select the best candidates and begin lifetime studies in a CW mode test station. This test station also has a variable gap of 0-25 mm, but the voltage range is extended up to 20 kV and continuous average current of 110 mA. A custom fabricated water cooled anode can dissipate the full energy the power supply can deliver.

Preliminary results show that after an initial burn-in period of approximately 4 hours, the cathode emission stabilizes at about 70% of the initial current (see Figure 5). Some degradation of emission is expected as the longest CNTs erode until all of the CNTs are approximately the same length and emitting the same average current.

Copyright © 2013 CC-BY-3.0 and by the respective authors

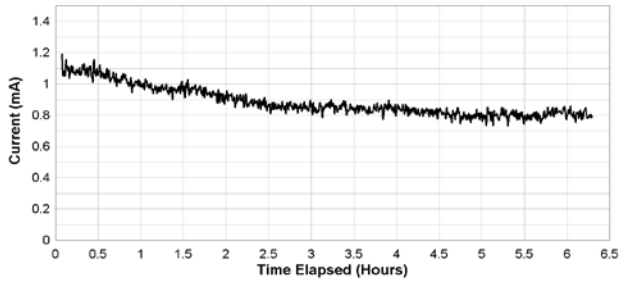


Figure 5: Lifetime study of small CNT cathode showing initial decay of current, stabilizing after approximately 4 hours.

PLAN FOR TESTS IN RF ENVIRONMENT

The initial high power tests inside an RF gun will be performed at the FNAL-A0 beamline at Fermilab. As discussed, our cathode design is compatible with their interchangeable cathode system. After verification in an RF environment, we will test our cathodes in a dual-frequency gun Radiabeam has designed and will fabricate (which will be given to Fermilab for general use after the experiments). The dual frequency gun uses the interference of a harmonic frequency with a primary accelerating frequency to effectively gate the emission of the CNT cathode to the proper phase of the acceleration RF. Since the CNT cathodes have a distinct threshold voltage, unlike thermionic cathodes, the bunch length can be made much shorter, eliminating the need for a bunching structure before injection into the accelerator.

We have started the RF design and engineering of a DESY/PITZ-like High-fidelity Gun. The preliminary 3D model is shown in Figure 6. The RF power is fed from the beam output pipe by means of a rectangular-coaxial transition. This will allow us to keep perfect field symmetry inside the Gun cells, eliminating any higher order mode field components that can deteriorate the beam quality. The cooling system, also shown in the picture, permits very high repetition rate operation.

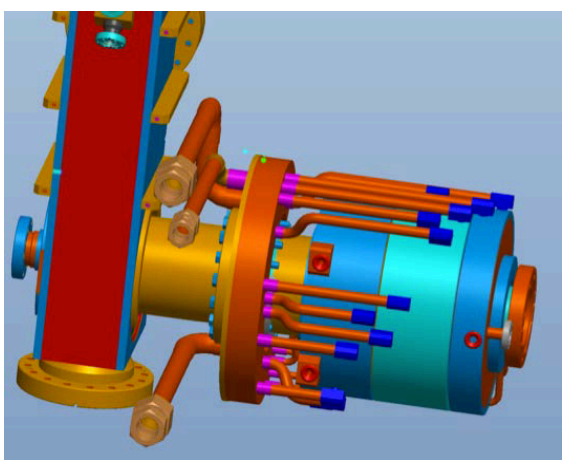


Figure 6: 3D CAD model of the high-fidelity RF Gun (Pitz-like).

This gun design will be adapted to use two frequencies (1.3 and 3.9 GHz) over the next several months. Fabrication is scheduled to begin in early 2014. The RF power test of the high-fidelity gun will be performed at Fermilab, with the CNT cathode, by the end of August 2014.

CONCLUSIONS

In summary, Radiabeam has made significant progress in bringing CNT cathodes to the point of experimental evaluation. Further testing must be done to fully characterize the emission and the lifetime, particularly for cathodes produced via CVD. The upgrades to the pulsed mode test system have greatly increased our throughput of samples, speeding up the optimization of our deposition processes. The CW mode test station was built and is evaluating samples under 100% duty cycle conditions to ascertain the effective lifetime of CNT cathodes.

REFERENCES

[1] M.S. Dresselhaus et al. Science of fullerenes and carbon nanotubes. New York: Academic Press, 1996.

[2] W. Zhu et al. Large current density from carbon nanotube field emitters. Applied Physics Letters (1999) vol. 75 pp. 873.

[3] J. Zhang et al. Efficient fabrication of carbon nanotube point electron sources by dielectrophoresis. Advanced Materials (2004) vol. 16 (14) pp. 1219-1222.

[4] D. Schiffler et al. A high-current, large-area, carbon nanotube cathode. IEEE Transactions on Plasma Science (2004) vol. 32 (5) pp. 2152-2154.

[5] J. Lewellen and J. Noonan. Field-emission cathode gating for rf electron guns. Phys. Rev. ST Accel. Beams (2005) vol. 8 (3) pp. 033502.

[6] M. Kumar and Y. Ando, "Chemical Vapor Deposition of Carbon Nanotubes: A Review on Growth Mechanism and Mass Production," Journal of Nanoscience and Nanotechnology 10, 3739–3758, 2010.

Copyright © 2013 CC-BY-3.0 and by the respective authors

NOVEL METHODS FOR EXPERIMENTAL CHARACTERIZATION OF 3D SUPERCONDUCTING LINAC BEAM DYNAMICS

A. Shishlo#, ORNL, Oak Ridge, TN 37831, USA

Abstract

This paper describes an approach to measure initial Twiss parameters in transverse and longitudinal directions at the entrance of a linac with independent short accelerating cavities. For the transverse plane the usual technique of transverse profiles is used, and for the longitudinal direction a recently developed non-intercepting method is applied. The new method is based on a beam position monitor amplitudes analysis. The applicability of the methods are discussed and demonstrated on an example of the Spallation Neutron Source superconducting linac.

INTRODUCTION

Beam loss in accelerators should be low enough to allow "hands on" maintenance. This goal is achieved by a good design of the machine and a precise tuning before the operation phase. According to its design, the superconducting linac (SCL) of the Spallation Neutron Source (SNS) accelerator should be a almost loss-free part of the machine due to large apertures and low residual gas pressure. During the commissioning, it was found that SCL had significant beam loss and could be activated above the "hands on" maintenance level when the beam power reaches a design value of 1.4 MW. Fortunately, this beam loss was reduced to an acceptable level by reducing the strength of the quadrupoles in the SCL without a clear understanding the loss mechanism. After that, the power of SNS accelerator was not limited by SCL beam loss. Recently, the SCL beam loss mechanism was identified as intra-beam stripping (IBSt) [1,2]. IBSt is a process of stripping one loosely-bound electron from one of two H^- ions colliding inside the bunch. The neutral hydrogen atom created in this collision will not see any focusing fields, and it will be lost on the beam pipe. The reaction rate of IBSt is proportional to the square of the particle bunch density, so the reducing of the SCL quadrupole strengths made the beam bigger transversely and reduced the density and beam loss. The process of a quadrupole focusing fields tuning is and was a purely empirical beam loss reduction based on readings of Beam Loss Monitors (BLM). All previous attempt to use a model based approach to the SCL loss reduction failed, and this paper is an attempt to explain why we did not succeeded before.

RATIONALE

IBSt beam loss is defined by the core of the bunch where the most particles are located. It allows us to describe this loss with a simple envelope model instead of complicated and slow particle-in-cell tracking codes. After certain assumptions (the Gaussian particles distribution in the bunch), the only parameters needed for the loss calculation are Twiss parameters of the bunch for all three directions along the linac [1]. To calculate these Twiss parameters we need the following components:

- A validated envelope tracking accelerator model.
- The measured initial Twiss parameters for all three dimensions.

The present work describes how to get these components for the SNS superconducting linac tuning. The problem of loss reduction based on this model and the initial Twiss parameters is a subject of future studies.

THE SNS SUPERCONDUCTING LINAC

The SNS superconducting linac consists of Medium and High Beta sections named in accordance with the two types of superconducting cavities designed for geometrical relativistic β= 0.61 and 0.81 beams. The first section has 11 cryomodules with 3 cavities in each module, and the High Beta section has 12 modules, 4 cavities per module. Each 805 MHz cavity has independent control of the field gradient and phase. According to the design, the cavity field gradients in each section should be all the same, but in reality they are not. Instead, the gradient of each cavity is set to be as high as possible for stable operation. The input energy of the SCL is 185.6 MeV; the output energy is about 930 MeV, and it is defined by existing cavity gradients; the design peak current is 38 mA and the design energy 1 GeV. The bunch frequency of 402.5 MHz is defined by a normal conducting part of the linac. The SCL has 32 stripline beam position monitors (BPMs) installed along the linac between cryomodules and in the cavity-free part of SCL. The BPMs measure the transverse positions of the beam, the arrival phases of the bunches, and the amplitudes of the Fourier harmonics of the bunch longitudinal distributions at the bunch frequency. The SCL is also equipped with 9 Laser Wire (LW) Stations to measure transverse profiles of the beam. Four LWs are installed at the beginning of each of the two sections (one LW after each of the first four superconducting cavities) and one LW at the end of SCL.

XAL ONLINE MODEL

All simulations and analysis performed for this work used the XAL Online Model (OM) [3]. The OM is an envelope tracking accelerator code similar to TRACE3D [4]. The OM tracks the envelope parameters through the SCL lattice using transport matrices for each quadrupole, each RF gap in the accelerating cavities, and each drift space. The space charge kicks are accumulated in the total

shishlo@ornl.gov

Copyright © 2013 CC-BY-3.0 and by the respective authors

transport matrix describing the transformation of the envelope from the beginning to an arbitrary point in SCL. The parameters of the lattice, such as the quadrupole field gradients, are taken from the control system. The field gradients and phases of the superconducting cavities are found after an analysis of the phase scans. The cavity phase scan is a process of collecting the BPM phases and amplitudes for a cavity phase changing from -180^0 to +180^0. All downstream cavities have the RF pulse blanked so they will not affect the beam, and the number of bunches in the pulse train is limited to about 200 to avoid beam loading of the cavities. Figure 1 shows the results of a phase scan of the first SCL cavity Cav01a. The phase difference between two BPMs are analysed as a time-of-flight measurement to get the amplitude of the cavity in the online model and the phase of its first accelerating gap. The phase set-point of each cavity was chosen to be 18^0 less than the position of the maximal acceleration (see Fig. 1). These settings are usual for the production tune of SCL.

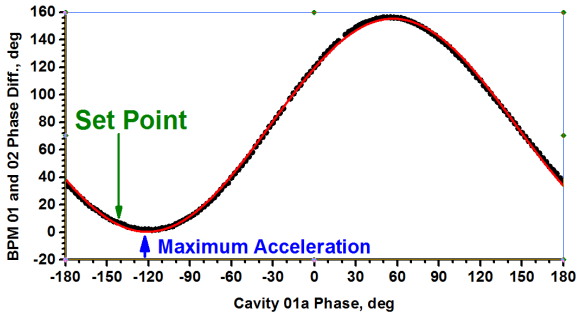


Figure 1: The BPM 01 and 02 phase difference during the phase scan of the first SCL cavity. Points are measurements, and the red line is an OM simulation.

After the online model lattice is initialized we can start the procedure of measuring the initial Twiss parameters for the transverse and longitudinal directions. In the presence of space charge forces these tasks are coupled, and they should be performed by iterations. We intend to do this in the future, but here we present analyses of the transverse and longitudinal data that were acquired about one year apart just to demonstrate the applicability of the methods. We will start with the algorithm and data analysis for horizontal and vertical directions.

TRANSVERSE PROFILES ANALYSIS

To get the initial Twiss for the horizontal and vertical directions from multiple profile measurements we will use the techniques described in [5]. Let's consider one direction. The transformation coordinates of the particle between the beginning of the lattice and the profile measurement device are defined by the transport matrix from the envelope model

$$\begin{pmatrix} x_1 \\ x_1' \end{pmatrix} = \begin{bmatrix} m_{11}^{(1)} & m_{12}^{(1)} \\ m_{21}^{(1)} & m_{22}^{(1)} \end{bmatrix} \cdot \begin{pmatrix} x_0 \\ x_0' \end{pmatrix}, \quad (1)$$

where x_0, x_0' and x_1, x_1' are coordinates of the particle at points 0 and 1, and $m^{(1)}$ is a transport matrix. By calculating the square of both sides of the first equation of the (1) system and averaging over the whole ensemble of particles in the bunch, we have the expression for the squared RMS beam size $\langle x_1^2 \rangle$

$$\langle x_1^2 \rangle = (m_{11}^{(1)})^2 \langle x_0^2 \rangle + 2 m_{11}^{(1)} m_{12}^{(1)} \langle x_0 x_0' \rangle + (m_{12}^{(1)})^2 \langle x_0'^2 \rangle,$$

where $\langle x_0^2 \rangle$, $\langle x_0\, x_0' \rangle$, and $\langle x_0'^2 \rangle$ are the correlations of the coordinates for the initial state. By using several profile monitors or modifying the optics of the lattice we can get as many different transport matrices $m^{(i)}, i = 1, \ldots, N$ and equations for the beam RMS sizes as we want. All this information can be represented by the following matrix equation

$$\begin{bmatrix} \langle x_1^2 \rangle \\ \cdots \\ \langle x_N^2 \rangle \end{bmatrix} = \begin{bmatrix} m_{11}^{(1)^2} & 2 m_{11}^{(1)} m_{11}^{(1)} & m_{12}^{(1)^2} \\ \cdots & \cdots & \cdots \\ m_{11}^{(N)^2} & 2 m_{11}^{(N)} m_{11}^{(N)} & m_{12}^{(N)^2} \end{bmatrix} \cdot \begin{bmatrix} \langle x_0^2 \rangle \\ \langle x_0 x_0' \rangle \\ \langle x_0'^2 \rangle \end{bmatrix}. \quad (2)$$

Assuming we have the measured RMS beam sizes s_1, s_2, … s_N we can find the initial correlations $\langle x_0^2 \rangle$, $\langle x_0\, x_0' \rangle$, and $\langle x_0'^2 \rangle$ by minimizing the sum

$$S = \sum_{i=1}^{N} \frac{\left(s_i^2 - \langle x_i^2 \rangle\right)^2}{\sigma_i^2}, \quad (3)$$

where σ_i denotes the rms error of the measured s_i^2. This error is obtained from the fit to the i-th profile which determines s_i.

The equation (3) is a typical linear Least Square Method problem, and the solution is

$$\begin{bmatrix} \langle x_0^2 \rangle \\ \langle x_0 x_0' \rangle \\ \langle x_0'^2 \rangle \end{bmatrix} = (M^T W M)^{-1} M^T W \begin{bmatrix} s_1^2 \\ \cdots \\ s_N^2 \end{bmatrix}, \quad (4)$$

where M is $N \times n$ matrix from equation (2) and W is a diagonal weight matrix

$$W_{ii} = 1/\sigma_i^2 . \quad (5)$$

A symmetric 3 x 3 covariance matrix

$$C = (M^T W M)^{-1} \quad (6)$$

defines the errors for the initial correlation values found from (4)

$$\sigma_{\langle x_0^2 \rangle} = \sqrt{C_{11}}, \quad \sigma_{\langle x_0 x_0' \rangle} = \sqrt{C_{22}}, \quad \sigma_{\langle x_0'^2 \rangle} = \sqrt{C_{33}} . \quad (7)$$

After the initial correlations are found, the Twiss parameters emittance, alpha, and beta are defined by equations

$$\varepsilon = \sqrt{\langle x_0^2 \rangle \langle x_0'^2 \rangle - (\langle x_0 x_0' \rangle)^2} , \quad (8)$$

$$\alpha = -\langle x_0 x_0' \rangle / \varepsilon , \quad (9)$$

$$\beta = \langle x_0^2 \rangle / \varepsilon . \quad (10)$$

The error of any scalar function of initial correlations $f(\vec{\tau})$

$$\vec{\tau} = [\langle x_0^2 \rangle, \langle x_0 x_0' \rangle, \langle x_0'^2 \rangle]^T \quad (11)$$

is given by

$$(\sigma(f))^2 = (\nabla_{\vec{\tau}} f)^T \cdot C \cdot (\nabla_{\vec{\tau}} f) . \quad (12)$$

Formulas (7) are special cases of this general formula. It also allows estimating the errors for the initial Twiss parameters (8-10).

All together formulas (4 – 12) describe the transverse profiles analysis including the error analysis.

Copyright © 2013 CC-BY-3.0 and by the respective authors

Space Charge Effects

In the presence of space charge the transport matrices in (2) will be dependent on the initial Twiss parameters for the longitudinal and transverse directions. As for the longitudinal Twiss parameters, there are several possible ways to find the initial values. First, we can blindly use the design parameters. Second, for the SCL we can use the methods described in this paper later. For the transverse parameters the transport matrices dependency makes the equation (2) a transcendental one, and there is no exact analytic solution for it.

To solve (2) in the presence of the strong space charge a two steps method was used. In the beginning, a general nonlinear fitting package was used to find the initial parameters that will minimize the S function (3). Then the transport matrices generated by the OM for these initial Twiss parameters were used in (4) and (7) to get a new set of these parameters and their error estimation. If these two sets were close enough assuming their errors, we concluded that the problem is solved. This method does not guarantee a uniqueness of the solution, because the fitting routine can find several local minima. This situation can be resolved by increasing the number of measurements with the lattice configurations providing the reduced errors (7). These additional measurements should be planned ahead by using the preliminary estimation for the initial Twiss. The rule of thumb from [5] is a 90^0/(N-1) betatron phase advance distance between each measurement. The exact effect of each additional measurement should be estimated by (7). Unfortunately, even these measures cannot guarantee a uniqueness of the solution and correctness of the error estimation.

Twiss Parameters Correlations

The diagonal elements of the covariance matrix C (6) include information about errors of $\langle x_0^2 \rangle$, $\langle x_0 x_0' \rangle$, and $\langle x_0'^2 \rangle$ parameters (7), and the non-diagonal elements of C describe their correlations. The graphical representation of these correlations on two dimensional plots like the (β, ε) plane could be very beneficial. As we will show later, sometimes it helps to explain the nature of very high errors of the Twiss parameters. The algorithm for plotting these correlations starts with the diagonalization of C

$$C = (M^T W M)^{-1} = V \cdot D \cdot V^T, \qquad (13)$$

where D is a diagonal matrix, and V is a transformation matrix for the $\langle x_0^2 \rangle$, $\langle x_0 x_0' \rangle$, and $\langle x_0'^2 \rangle$ parameters to a new set of variables $\vec{\theta}$

$$\vec{\theta} = V^T \cdot \vec{\tau}, \quad \vec{\tau} = [\langle x_0^2 \rangle, \langle x_0 x_0' \rangle, \langle x_0'^2 \rangle]^T . \qquad (14)$$

For $\vec{\theta}$ the covariance matrix D is diagonal. Therefore, the errors of $\vec{\theta}$ are defined by the diagonal elements of D (similar to (7)), and they are not correlated. The possible values of $\vec{\theta}$ are inside the rectangular region with the center defined by (14) and widths $\left[2 \cdot \sqrt{D_{11}},\ 2 \cdot \sqrt{D_{22}},\ 2 \cdot \sqrt{D_{33}}, \right]$. The surface points of this region can be easily projected onto any planes representing Twiss parameters correlations.

SCL LASER WIRE PROFILES ANALYSIS

To measure the transverse beam profiles in the SNS superconducting linac we use Laser Wire (LW) stations [6] instead of traditional wire scanners. LW stations perform nonintrusive measurements based on a photo-detachment process. The scans can be done even during 1 MW operation. The dynamic range of the LW measurement is lower than the traditional wire scanners, so in our analysis we used only beam sizes calculated as a Gaussian fit to the profiles. Figure 2 shows a typical laser wire profile with a fit, and the high level of noise does not allow us to calculate RMS of the profile directly. All measurements discussed in this section were performed in 2011 and 2012. Since then the SCL LW system was significantly improved [6].

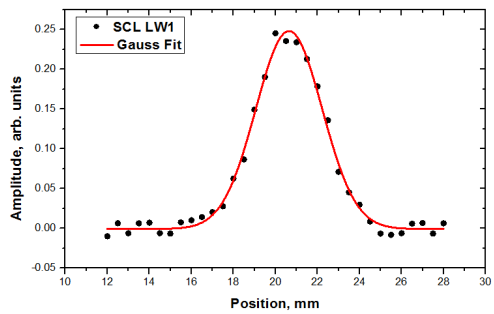


Figure 2: LW1 profile measurement and a Gaussian fit.

Earlier we reported that our attempts to improve SCL beam size beating failed because we could not find the initial Twiss parameters at the entrance [7]. After applying the analysis described in the previous section, it was found that the Twiss parameters errors were too big to make any meaningful conclusions. The detailed study of these errors showed the strong correlation between the emittance and Twiss beta parameter values.

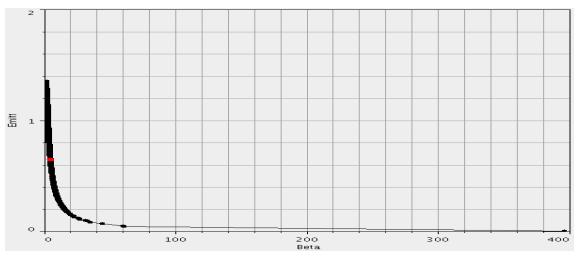


Figure 3: A correlation between the emittance and the beta Twiss parameter. The red dot is a central point found in the nonlinear fit.

As example, Fig. 3 shows this correlation with the region calculated with formulas (13) and (14) from the "Twiss Parameters Correlations" section of this paper. The possible range for the emittance is from almost 0 to 1.4 π*mm*mrad and the beta parameter is from 0 to 400 m. The beta range could be narrowed down if the emittance value is considered as a known parameter.

The initial transverse Twiss parameters measurement was improved after the error control (formulas (6) and (7) and multiple lattice configurations) was implemented. It

Copyright © 2013 CC-BY-3.0 and by the respective authors

was found that the quad gradients should be increased by 10% -15% to reduce the error to an acceptable level.

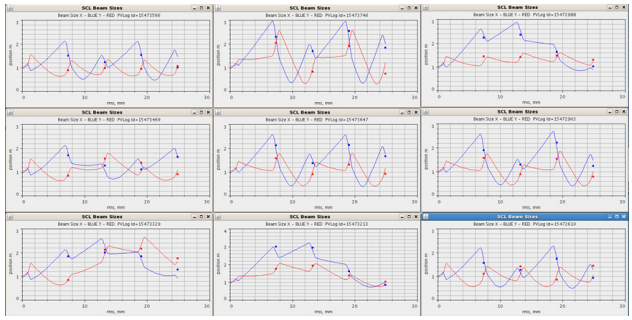


Figure 4: Transverse beam sizes at first 4 LW stations in SCL for 9 different quad settings. Blue and red colors are for horizontal and vertical directions respectively. Points are LW results, and curves are the model with the same initial Twiss.

Figure 4 shows the excellent agreement between LW measurements and the OM simulations for 9 lattice settings. These data were taken for all SCL cavities switched off and a low peak current to eliminate space charge effects. For the production peak currents 28-35 mA and the RF cavities switched on the agreement between the model and LW data was good for the first three LW stations. The measured transverse Twiss parameters at the entrance of SCL for the production tune for 37 mA peak current are shown in Table 1 (emittance normalized, rms). Unfortunately, we could not predict the transverse beam sizes downstream for the whole SCL linac. At that moment, we realized that we need more precise information about the longitudinal Twiss parameters and a verified model for the longitudinal dynamics calculations. The next section will describe our approach to this problem.

Table 1: Transverse Twiss Parameters

Direction	Alpha	Beta [m]	Emittance π*mm*mrad
Horizontal	-0.55±0.22	2.35±0.84	0.40±0.08
Vertical	0.66±0.14	7.7±1.8	0.38±0.05

LONGITUDINAL TWISS PARAMETERS

Recently at SNS, a new method of measuring of the rms longitudinal Twiss parameters of a beam in linear accelerators was developed [8]. The method is based on using sum signals from BPMs sensitive to the longitudinal charge distribution in the bunch. The applicability of the method was verified with direct longitudinal profile measurements by the Bunch Shape Monitor (BSM) at the end of Coupled Cavity Linac (CCL) which is a part of the linac preceding the SCL. The method is fast and simple, and can be used in linear accelerators where interceptive diagnostics are not desirable. The previously developed method based on transmission and beam loss measurements [7, 9] is less accurate and is much more time and effort consuming.

The new method is based on the same formulas (2-10), and the BPMs are used to measure the longitudinal rms sizes.

BPM and Longitudinal RMS Size of Bunch

At the SNS linac the sum signal of a BPM is proportional to the Fourier amplitude of the longitudinal bunch distribution at the frequency of the BPM system

$$u = J \cdot \zeta \cdot 1/I_0\left(\frac{\omega R}{\gamma\beta c}\right), \qquad (15)$$

where J is an amplitude of the beam current harmonic at the BPM frequency ω; ζ is a factor describing the transfer function of the BPM including the pickup geometry, amplifier gain etc.; R is the radius of the pickup aperture; c is the speed of light; β and γ are relativistic factors; and I_0 is the modified Bessel function. In the case of Gaussian longitudinal bunch shape

$$u = Q \cdot \zeta \cdot exp\{-(\omega s_z)^2/2\}/I_0\left(\frac{\omega R}{\gamma\beta c}\right), \qquad (16)$$

where Q is the total charge of the bunch and s_z is the RMS bunch time length. The calibration constant $(Q \cdot \zeta)$ can be measured as BPM amplitude at the production SCL tune when $\omega s_z \ll 1$. Inverting equation (16) with respect to s_z we get the bunch length from the BPM sum signal for formulas (2-10).

The main assumption that was used for the formula (16) is a Gaussian shape of the longitudinal density of the bunch. Figure 5 shows the longitudinal bunch distribution at the end of CCL which has an almost perfect Gaussian shape. For the production tune, during the acceleration of the bunch by SCL cavities, we keep the bunch short enough to avoid non-linear distortion from the cavities and beam loss. Therefore, we are confident that we keep the Gaussian shape of the bunch through the whole SCL.

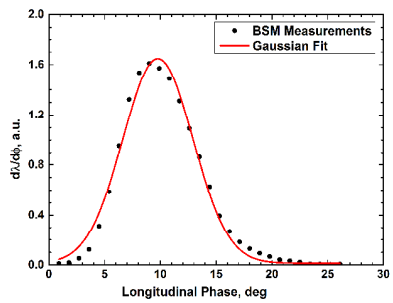


Figure 5: The longitudinal beam profile measured by the BSM in the CCL.

Longitudinal Twiss Parameters Analysis

In [8] it is shown that a simple measurement with a coasting beam is not accurate enough to get useful initial longitudinal Twiss parameters. The errors of these parameters are too big. As a solution, it was suggested to use a phase scan of the RF cavity placed between the initial point and the BPMs. In the case of the phase scan, the number of different longitudinal transport matrices $m^{(i)}$ in (2) increased to $N_\varphi \times N_{BPM}$ where N_φ and N_{BPM}

Copyright © 2013 CC-BY-3.0 and by the respective authors

are the number of the cavity phase points and the number of BPMs, respectively. For a phase scan step of 5^0 $N_\varphi \times N_{BPM} = 72 \times 15 = 1080$ measurements. It is also important that during the scan the cavity performs different focusing-defocusing transformations with the bunch in the longitudinal phase space. Fortunately, we already have the results of the phase scans of all SCL cavities that we used to initialize the SCL lattice of the OM model. A picture of the BPM amplitudes during the phase scan of the first SCL cavity is shown in Fig. 6.

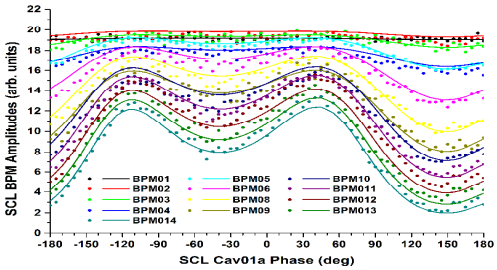


Figure 6: The BPM amplitudes during a Cav01a phase scan. Points are measurements, lines are from OM model.

The phase scan data were taken at the peak current of 30 mA which is different from the 37 mA during the transverse Twiss measurements, but we used the same transverse Twiss parameters anyway. This makes our analysis somewhat inconsistent, and in the future we plan to perform transverse and longitudinal analysis on the same set of data. After the analysis, we found longitudinal Twiss parameters at the entrance of the first SCL cavity are α = -0.78 ± 0.02 , β = 8.1 ± 0.2 [m/rad], ε = 0.60 ± 0.01 [π•mm•mrad] (XAL OM units).

Then we performed the same analysis for each SCL cavity in the Medium Beta section (unfortunately we scanned only this part). This gave us measured longitudinal Twiss parameters along the SCL. We also used the initial Twiss and the initialized OM lattice to simulate the same parameters. The Twiss parameters obtained two ways are shown in Fig. 7.

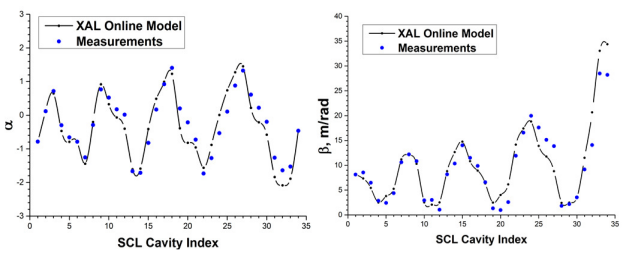


Figure 7: The longitudinal Twiss α and β parameters along SCL.

We have a relatively good agreement between the measured and simulated Twiss, but they do not agree inside error bars. The differences can be explained by the very strong longitudinal over-focusing of the bunch where the space charge effects are strong and the envelope model could be less accurate. Figure 7 demonstrates a poor matching in the longitudinal direction for the existing SCL tune.

CONCLUSIONS

The practical approach to the 3D beam characterization is suggested and tested on the example of the SNS superconducting linac. The new method of the longitudinal Twiss parameters measurement is developed and used. This is the first time the longitudinal parameters have been measured continuously along the linac. The role of the space charge effects should be studied further. The applicability of the XAL OM for the linac tuning is demonstrated.

ACKNOWLEDGMENT

The author is grateful to the members of SNS Beam Instrumentation team A. Aleksandrov, Y. Liu, and C. Long for the help in data acquisition and useful discussions.

ORNL/SNS is managed by UT-Battelle, LLC, for the U.S. Department of Energy under contract DE-AC05-00OR22725.

REFERENCES

[1] V. Lebedev et al., LINAC2010, Tsukuba, Japan, p. 929 (2010).

[2] A. Shishlo et al., Phys. Rev. Lett. 108, 114801 (2012).

[3] C. K. Allen, C. A. McChesney, C. P. Chu, J. D. Galambos, W.-D. Klotz, T. A. Pelaia, and A. Shislo, "A Novel Online Simulator for Applications Requiring a Model Reference," ICALEPCS 2003 Conference Proceedings, Kyongju, Korea, October 13-17, p. 315 (2003).

[4] K. R. Crandall and D. P. Rusthoi, Los Alamos National Laboratory Report No. LA-UR-97-886, 1997, http://laacg1.lanl.gov/laacg/services/traceman.pdf

[5] M. G. Minty, F. Zimmermann, "Measurements and Control of Charged Particle Beams," Springer-Verlag Berlin Heidelberg 2003, "Particle Acceleration and Detection" series. p. 104.

[6] Y. Liu et al., Phys. Rev. ST Accel. and Beams 16 (2013) 012801.

[7] Y. Zhang, "Experience and lessons with the SNS superconducting linac," Proceedings of IPAC'10, Kyoto, Japan, p. 26 (2010).

[8] A. Shishlo, A. Aleksandrov, Phys. ST Accel. and Beams 16 (2013) 062801.

[9] Y. Zhang et al., Phys. Rev. ST Accel. Beams 11 (2008) 104001.

Copyright © 2013 CC-BY-3.0 and by the respective authors

SPACE-CHARGE COMPENSATION FOR HIGH-INTENSITY LINEAR AND CIRCULAR ACCELERATORS AT FERMILAB*

M. Chung†, L. Prost, V. Shiltsev, Fermilab, Batavia, IL 60510, USA

Abstract

Space-charge effects have long been recognized as a fundamental intensity limitation in high-intensity linear and circular accelerators. As the mission of the US high energy physics program is pushing the Intensity Frontier, it is very timely to explore novel schemes of space-charge compensation that could significantly improve the performance of leading high-intensity proton accelerator facilities such as Project-X. In this work, we present two activities at Fermilab on space-charge compensation experiments based on residual gas ionization: 1) neutralized beam transport of continuous-wave (CW) H^- beam in Project-X Injector Experiment (PXIE); and 2) trapped electron plasmas for space-charge compensation in the newly proposed Integrable Optics Test Accelerator (IOTA) ring. Characteristics of the stability in the beam-plasma system, the dynamics of beam neutralization, and the transition between neutralized and un-neutralized beam transports are discussed for each experiment.

INTRODUCTION

The main idea of space-charge compensation considered in this work is based on the long-known fact that the negative effect of Coulomb repulsion can be mitigated if beams propagate through a plasma column of opposite charge. The plasma column can be formed by beam-induced residual gas ionization and/or by external plasma sources. This idea has been successfully applied to transport high-current low-energy proton and H^- beams into the RFQ in many linacs [1]. In circular machines, partial neutralization by ionization electrons was attempted with notable improvements in beam intensity, namely an order of magnitude higher than the space-charge limit [2].

BASIC DEFINITIONS

The time needed to generate enough electron-ion pairs for full space-charge compensation is called charge-neutralization time [1], $\tau_n = 1/n_g\sigma_i v_b$. The number density of the oppositely charged particles n_p (electrons for positive ion beams; positive ions for negative ion beams) grows linearly with time, and we have $n_p \approx n_b$ or $f_n \approx 1$ after the time duration of τ_n. Here, $f_n = n_p/n_b$ is the fractional charge neutralization. Note that the background gas density $n_g[\mathrm{m}^{-3}] = 3.54 \times 10^{22} \times p[\mathrm{Torr}] \gg n_b$ for nominal pressure range $p = 10^{-7} - 10^{-5}$ Torr. For the 30 keV H^- beam for the PXIE LEBT, $\sigma_i = 5 \times 10^{-20}\mathrm{m}^2$ and $\tau_n \approx 236$ μs for $p = 10^{-6}$ Torr. For a 2.5 MeV proton beam for the IOTA electron column, $\sigma_i = 1.5 \times 10^{-21}\mathrm{m}^2$ and $\tau_n \approx 862$ μs for $p = 10^{-6}$ Torr.

The electrostatic potential created by the uniform beam is $\phi(r=0) = V_s\left[1 + 2\ln\left(r_w/r_b\right)\right]$, where, $V_s = I_b(1 - f_n)/(4\pi\epsilon_0 v_b) > 0$ (< 0) for positive (negative) ion beams. Note that $\phi(r = r_b) = 2V_s \ln(r_w/r_b)$ and $\phi(r = r_w) = 0$. Here, r_b is the radius of the beam with constant density n_b and velocity v_b, and r_w is the radius of a perfectly conducting cylindrical wall.

PLASMA PROCESSES

We consider two cases: an H^- beam and a proton beam. Here, we listed only the dominant plasma processes for the space-charge compensation.

- H^- **beam:**

$$H^- + H_2 \rightarrow H(\mathrm{fast}) + H_2 + e \quad (1)$$

$$H^- + H_2 \rightarrow H^- + H_2^+(\mathrm{slow}) + e \quad (2)$$

$$e + H_2 \rightarrow H_2^+(\mathrm{slow}) + 2e \quad (3)$$

For the case with no solenoidal fields, ionization electrons are expelled by the beam space-charge immediately and the slow ions are oscillating inside the potential well of the beam. Initially, the ion density profile becomes highly peaked around beam center [3]. After a time duration of τ_n, a steady state is obtained. There is a critical value for the gas density, $n_{g,cr}$, in which $\tau_{i,exit} = \tau_n$, i.e., $n_{g,cr} \approx (1/\tau_{i,exit})/v_b\sigma_i$ [1]. Here, $\tau_{i,exit} = r_b/2v_i$ is the average time for an ion to exit the beam, and $v_i = \sqrt{T_i/m_i}$ is the ion thermal velocity. It is often assumed that T_i is on the order of 0.1 eV [1]. When $n_g = n_{g,cr}$, the potential difference between the beam center and edge, $V_s = 0$ and $f_n = 1$ at the steady state. For $n_g < n_{g,cr}$, $V_s < 0$ and $f_n < 1$. In this case, the beam is not fully neutralized and the system is essentially composed of two species ($n_e \ll n_i \sim n_b$). For $n_g > n_{g,cr}$, the beam becomes overcompensated, i.e., $V_s > 0$ and $f_n > 1$. In this case, $eV_s \sim T_e$ and $v_i \approx \sqrt{T_e/m_i}$.

For the nominal pressure range of PXIE, we always have $n_g < n_{g,cr}$, which is good for minimizing stripping loss, but not favorable for achieving full compensation. To achieve full compensation, use of Xe as a background gas is often considered, which decreases the critical density by a factor $\sim$ 45. Also, to reduce the loss of the H_2^+ ions through the longitudinal drift, positively biased electrodes may be used.

* Work supported by Fermilab Research Alliance, LLC under Contract No. DE-AC02-07CH11359 with the United States Department of Energy
† mchung@fnal.gov

Copyright © 2013 CC-BY-3.0 and by the respective authors

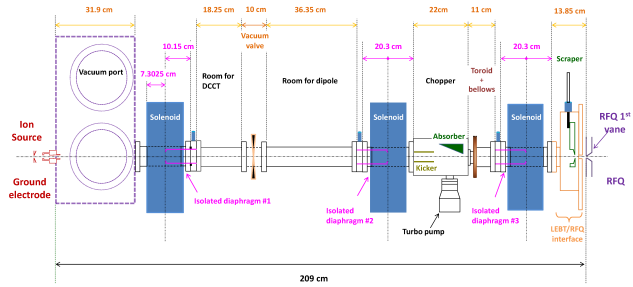


Figure 1: PXIE LEBT layout schematic.

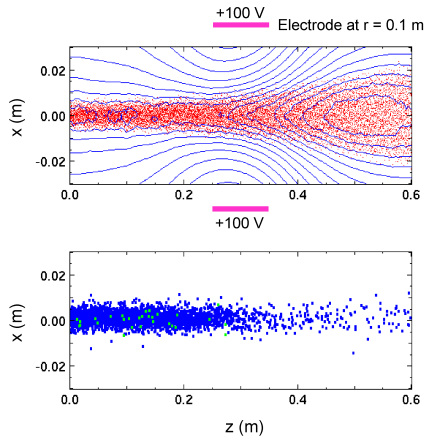


Figure 2: WARP 3D simulation of the transition from neutralized to un-neutralized transports in the PXIE LEBT. Electrode keeps positive ions (blue dots) from drifting into the un-neutralized region. For the un-neutralized region, we assume the vacuum is so good that there is little ionization processes. Note that most electrons (green dots) are expelled.

- **Proton beam:**

$$p + \mathrm{H_2} \rightarrow \mathrm{H(fast)} + \mathrm{H_2^+(slow)} \quad (4)$$

$$p + \mathrm{H_2} \rightarrow p + \mathrm{H_2^+(slow)} + e \quad (5)$$

$$e + \mathrm{H_2} \rightarrow \mathrm{H_2^+(slow)} + 2e \quad (6)$$

Positive ions are expelled by the beam space-charge, but at a much slower rate than the electrons. Therefore, space-charge compensation could exhibit a nonlinear phase in the beginning, particulary at high gas pressure. The ionization electrons have considerably higher thermal velocity than the ions, thus as V_s approaches to zero after a time duration τ_n, the electron loss increases and the space-charge compensation process slows down [3].

On the other hand, when we apply a uniform solenoidal field, the ionization electrons are confined close to the transverse position they are born from, and their density profile is similar to that of the proton beam. For non-relativistic electrons, the Larmor radius is $r_L = (3.37[\mu\mathrm{m}])\sqrt{T_\perp[\mathrm{eV}]}/(B_0[\mathrm{T}])$. In the 0.5 T normal-conducting solenoid considered in IOTA, we have $r_L < 0.1$ mm for perpendicular kinetic energy $T_\perp < 200$ eV.

PXIE LEBT: H$^-$ BEAM

PXIE will have a DC H$^-$ source (30 keV, up to 10 mA), a low energy beam transport (LEBT) system with three solenoid magnets (see Fig. 1), a CW RFQ, a medium energy beam transport (MEBT) system with wideband chopper, and two superconducting cryomoules (HWR and SSR1). The functions of the PXIE LEBT are 1) to transport and match the beam to the RFQ optical inputs; 2) to act as the first layer of the machine protection system; and 3) to provide pulsed (chopped) beam for commissioning of the beam line downstream [4].

Neutralization greatly reduces the beam space charge effects, most importantly, the emittance growth. As mentioned above, the PXIE LEBT should be operating in both pulsed and DC modes. In the pulsed mode, a chopper removes the neutralizing particles, and the beam becomes uncompensated and may behave quite differently than in the completely compensated case. For PXIE, the 5-mA beam space charge is relatively low, for instance, compared to the beam at SNS ($\sim$ 50 mA). Simulations showed that a scheme where the beam would be uncompensated in a part of the LEBT is possible, and such scheme was devised [4]. This scheme will minimize differences of the beam transport characteristics between the pulsed and DC operations, and allows for more space after the chopper for the absorber and diagnostics. Un-neutralized transport can be realized by properly biasing the electrodes and ensuring a good vacuum. However, the beam emittance will increase during the transition from neutralized to un-neutralized transports. In this regard, it is important to investigate whether the emittance growth is acceptable or not (e.g., by measuring the emittance using an Allison emittance scanner).

Up to the second solenoid, on the other hand, neutralization of the beam is maintained in a steady-state manner. Stability of this beam-plasma system can be affected by collective processes, such as dynamic decompensation, and electron and/or ion oscillations [5]. While beam neutralization experiments have been carried out elsewhere (see, for example, Refs. [1, 3, 5] and references therein) space-charge compensation in CW negative hydrogen beams is relatively less well understood. The PXIE LEBT configuration is quite unique as it allows to investigate both the transient and steady-state nature of the space-charge compensation of a negative hydrogen beam. Simulations using WARP 3D PIC code are in progress to address the unique characteristics of the PXIE LEBT (see Fig. 2) [6].

IOTA E-COLUMN: PROTON BEAM

A new storage ring (IOTA) is under construction at Fermilab to demonstrate the concept of nonlinear integrable lattices [7]. After initial experiments on the single-particle characteristics in the IOTA using electron beams, performance demonstrations in the space-charge dominated regime using proton beams will be followed [8]. One of

Copyright © 2013 CC-BY-3.0 and by the respective authors

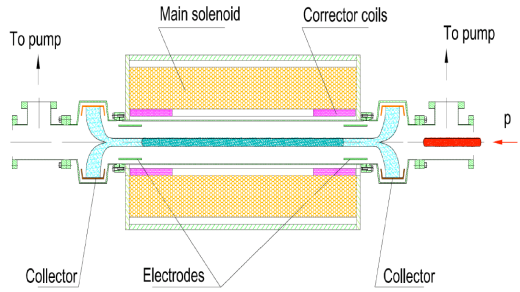


Figure 3: A conceptual layout of the electron-column apparatus for space-charge compensation in the IOTA ring.

the key R&D items is to investigate if space-charge compensation can be realized in the ring. The necessary conditions for effective space-charge compensation in the ring will be 1) the total defocusing effect by beam space charge over the ring is cancelled out by the focusing effect in the electron column; 2) the transverse profile of the electron density is the same as that of the proton beam; 3) the system of electrons and protons is dynamically stable [9, 10]. For the electron column concept considered here, electrons are generated internally through beam-induced residual gas ionization without special electron sources and optics. In the electron column concept, conditions 2 and 3 can be achieved if protons and electrons are immersed in a longitudinal magnetic field which is a) strong enough to freeze the electron density distribution; b) strong enough to suppress the e-p instability; c) weak enough to allow positive ions to escape transversely, in addition to longitudinal draining; and d) well matched to the ring optics to avoid beta-beat excitations.

The interaction between trapped electrons and circulating proton beams is subject to two-stream instability. It will degrade the quality of both the electron column and the main beam. It is well-known that the increase of the confining solenoidal field and Landau damping through momentum spread can suppress the instability. In addition, there are two unique instability suppression possibilities in the proposed experimental setup. One is self-stabilization of the e-p instability by the accumulation of secondary ions. It is observed [2] and also theoretically confirmed [11] that if there are not only electrons but also some residual ions in the cloud, the ions tend to short-out the electrostatic perturbations whose wavelengths are less than the transverse beam size r_b. The residual ion formation could be controlled by the proper choice of working pressure, solenoidal field, and electrode voltage (e.g., see a conceptual apparatus in Fig. 3). The other possibility is to increase Landau damping by a broad tune spread enabled by a special nonlinear lattice in the IOTA ring. This nonlinear lattice is designed to be integrable, and thus can create a large tune spread and zero resonance strength.

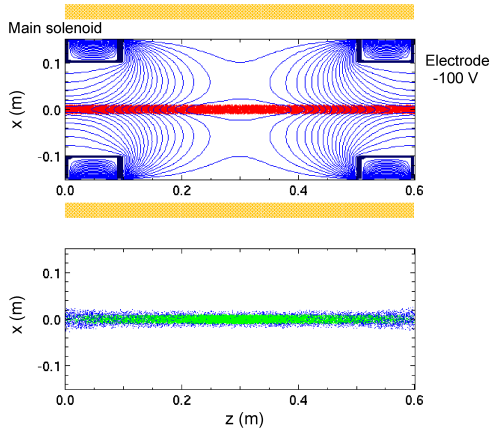


Figure 4: WARP 3D simulation of the plasma formation and trapping in the e-column. A uniform solenoid keeps both electrons (green dots) and ions (blue dots) in the beam path. Ions are slowly escaping longitudinally. To resolve cyclotron motion of the electron, the time step has been set to $\Delta t \leq 0.25 \times 2\pi/\omega_{ce}$.

Simulation of the plasma formation and trapping in the e-column is in progress using WARP 3D code (see Fig. 4). The simulation will eventually be coupled to a tracking code for the ring, to understand the effects of the nonlinear lattice and e-p instability.

CONCLUSION

Two experiments on space-charge compensation (one in a linac, and the other in a ring) are planned at Fermilab. Advanced simulation tools (e.g., WARP 3D PIC code [6]), and dedicated beam/plasma/gas diagnostics and controls could enable detailed understanding of the space-charge compensation processes, and eventually allow to achieve intense beams with improved stability and quality.

REFERENCES

[1] M. Reiser, *Theory and Design of Charged Particle Beams*, Wiley-VCH, Weiheim, 2008.

[2] G. I. Dimov et. al, Particle Accelerators 14, 155 (1984).

[3] A. BenIsmail et. al, Phys. Rev. ST. Accel. Beams 10, 070101 (2007).

[4] L. Prost et. al, Project X Document 1098-v3 (2012).

[5] I. A. Soloshenko, AIP Conf. Proc. 380, 345 (1995).

[6] Q. Ji et. al, Proceedings of HB2012, 546 (2012).

[7] V. Danilov et. al, Phys. Rev. ST Accel. Beams 13, 084002 (2010).

[8] ASTA proposal, see at http://asta.fnal.gov

[9] V. Shiltsev, Proc PAC'2007, p.1159 (2007).

[10] A. Burov et al, Fermilab TM-2125 (2000).

[11] R. A. Bosch, Phys. Rev. ST Accel. Beams 6, 074201 (2003).

Copyright © 2013 CC-BY-3.0 and by the respective authors

EXPERIMENTAL VERIFICATION OF SINGLE-BUNCH ACCUMULATION LIMIT DEPENDENCE ON IMPEDANCE AT THE APS *

V. Sajaev†, B. Borland, Y.-C. Chae, L. Emery, ANL, Argonne, IL 60439, USA

Abstract

One of the unique features of the Advanced Photon Source is operation with a small number of intense bunches — the standard operating mode has 24 16-nC bunches, while in a special operating mode one of the bunches has a charge of 60 nC. Such high single-bunch currents are achieved by a combination of high operational chromaticity and transverse bunch-by-bunch feedback. In the near future, more narrow-gap insertion device vacuum chambers will be installed, which will increase the impedance of the storage ring and make operation with high single-bunch current more problematic. Simulations exist that quantify the effects of increased impedance on the APS single-bunch accumulation limit; however, no direct experimental verification has yet been performed. In this paper, we will present a measurement of the single-bunch accumulation limit as a function of impedance. Different impedance values were achieved by changing the storage ring beta functions.

INTRODUCTION

The Advanced Photon Source (APS) is a 7-GeV third-generation synchrotron light source that has been in operation for almost 20 years. Presently, APS operates in three fill patterns: 24 equally spaced bunches — a pattern that is used for 60% of the time; 324 equally spaced bunches; and a special "hybrid" mode where one 60-nC bunch is separated from a train of weaker bunches by 1.5 μs. Total operating beam current is always 102 mA.

To achieve stable high-current single bunches, we operate at high chromaticities. Before introducing transverse bunch-by-bunch feedback, the operating chromaticity was +7 in both planes for the 24-bunch fill pattern and +11 for the "hybrid" pattern. The biggest downside of operating with high chromaticity is low lifetime. Even though APS operates in top-up mode, there is still a limit on how low the lifetime can be. The introduction of the feedback allowed us to lower chromaticity to +4 for the 24-bunches fill pattern and to +9 for the "hybrid" pattern.

The APS transverse impedance consists of three approximately equal parts [1]: the resistive-wall impedance of small-gap insertion device (ID) vacuum chambers, the geometrical impedance of the transitions from large- to small-gap chambers, and the geometrical impedance of the rest of the ring. Presently, there are 32 small-gap ID chambers installed. Of them, one has a 5-mm full gap, eight chambers have a 7.5-mm full gap, and the rest have an 8-mm gap. All ID chambers are 5 m long and are made of aluminum. At the time this work started, three ID locations were still unoccupied, meaning that three more small-gap vacuum chambers still needed to be installed. This would increase transverse impedance by about 6% and could affect our ability to provide users with 60 nC in a single bunch.

As we work on the APS Upgrade [2], a few things are clear: the lattice will be as strongly focusing as possible resulting in small dynamic aperture and short lifetime, the ID vacuum chambers will have as small gaps as possible resulting in higher impedance, and we still would need to provide high-charge bunches to the users performing timing experiments. In this situation, we need a good understanding of impedance effects in the APS and confidence in our simulation tools. We have developed an experimental program that would allow us to verify our simulation and predictive abilities.

SIMULATIONS

Simulation of the single-bunch accumulation limit is done by multi-particle tracking using `elegant` [3]. The impedance of the whole ring is represented as a single lumped element for each plane using the ZTRANSVERSE and ZLONGITUDINAL elements in `elegant`, which take calculated impedance as input. The ring itself is represented as a linear map of one sector (element ILMATRIX) with chromaticity. Special elements like cavities, radiation effects, etc. can be inserted between sectors. The simulated bunch consists of 200k particles, which is required for correct simulation of longitudinal effects. Wake potentials of all elements are computed using GdFidl [4] and a 1-mm-long bunch, in order to extend the resulting impedance bandwidth. Wake potentials are separated into dipole and quadrupolar components.

The simulated accumulation limit is strongly affected by the injection conditions, namely by the residual oscillations of the stored bunch. First, we used the most realistic approach and simulated both stored and injected bunches. But later we noticed that the losses that occur at the accumulation limit all come from the stored beam and are not affected by the injected bunch. After that, we simplified the simulation to a simple kick of the stored bunch. Ideally, there should be no vertical oscillations occurring after the injection, but due to small coupling inside the injection bump there is always some vertical motion of the

* Work supported by the U.S. Department of Energy, Office of Science, under Contract No. DE-AC02-06CH11357.

† sajaev@aps.anl.gov

Copyright © 2013 CC-BY-3.0 and by the respective authors

stored beam. This vertical motion is what affects the accumulation limit the most. The amplitude of the vertical motion is a free parameter that we used to reach an agreement with measurement. It was achieved at the amplitude of 0.3 mm. This amplitude of the vertical kick was then used for simulations that were intended to predict changes in the accumulation limit due to impedance variations. Figure 1 shows the result of the accumulation limit simulation as a function of vertical impedance, where the impedance is normalized to the present value. We can see that the accumulation limit changes very quickly in the vicinity of the present impedance value. Therefore, it is important to verify these results before any design decisions are made based on this plot.

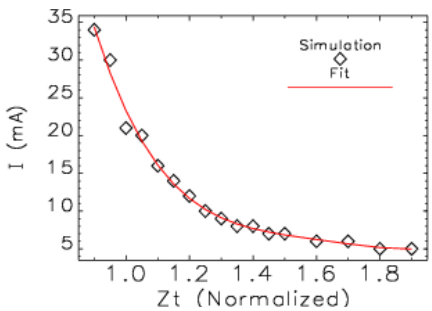


Figure 1: Single-bunch current limit as a function of vertical impedance. The impedance axis is normalized to the value for the current APS storage ring impedance.

To estimate the effect of different small-gap vacuum chambers on the accumulation limit, we have developed a simple spreadsheet that uses scaling laws taken from theory and simulations [5]: the effect of transitions is scaled as gap in the power of 2.4, and the resistive wall effect is scaled as gap in the third power, while the impedance effect is taken from a fit to the data in Figure 1. The spreadsheet was also used to calculate the expected results for the experiments described below.

EXPERIMENTAL RESULTS

The simplest way to vary the effective impedance in the storage ring is to change beta functions at impedance locations. Since about two-thirds of the vertical wake comes from the small-gap ID vacuum chambers, we need to change beta functions at ID locations. For operational convenience, we need to maintain the betatron tune close to its original value of 19.24; therefore, if beta function is increased at an ID location, it has to be decreased inside the sector. About one-third of the vertical wake is generated outside of the ID chambers; therefore, the reduction of vertical beta function outside of the ID chambers decreases the overall effect of beta function change on the effective impedance. Luckily, the simulations showed that the effect on the accumulation limit is still sufficiently large and should be visible in the experiment [6].

Lattice Development

We developed five lattices with vertical beta function in the ID ranging from 3.0 m to 5.0 m with 0.5-m steps. Figure 2 shows a set of five vertical beta functions for one sector (APS consists of 40 nearly identical sectors). The changes to the horizontal beta function were kept to a minimum. Also, when adjusting chromaticity, we excluded the sextupoles located inside the injection bump to keep injection conditions as close to the original as possible. All five lattices were implemented during machine studies. As always, the beta functions were measured and corrected to a high accuracy using the response matrix fit [7].

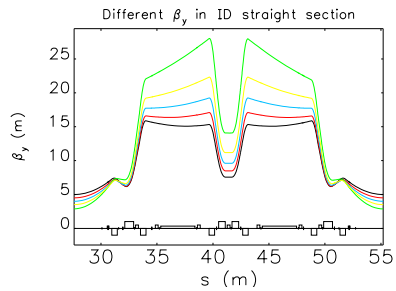


Figure 2: Vertical beta functions of one sector with ID value changing from 3 m to 5 m.

Accumulation Limit Measurement

The measurement of the accumulation limit is simple in essence: the injection is performed into a single bunch until no more charge can be injected or there is a drop-out of the stored bunch. In reality, however, it is hard to achieve a good reproducibility of this measurement because the accumulation limit is a complicated parameter depending on many variables. To ensure that all possible conditions are reproduced as closely as possible, for every lattice we followed the identical procedure:

- the lattice is corrected and coupling is minimized using the response matrix fit;
- the chromaticity is set to +11 in both planes, bunch-by-bunch feedback is tuned off;
- the orbit is well corrected;
- the injection conditions are reproduced — the injected beam trajectory is recovered, the stored beam closed bump in the horizontal plane is matched and spurious vertical oscillations of the stored beam after the kick are minimized;
- rf voltage is always maintained at 9 MV.

Figure 3 shows the results of the accumulation limit measurement for all five lattices as a function of the normalized effective vertical impedance. The accumulation limit is also normalized to the limit of the initial lattice. The vertical error bars show the accuracy of the accumulation limit

Copyright © 2013 CC-BY-3.0 and by the respective authors

measurement. The impedance error bars are calculated assuming 3% errors in the lattice beta functions. We can see a reasonable agreement between measurements and simulations.

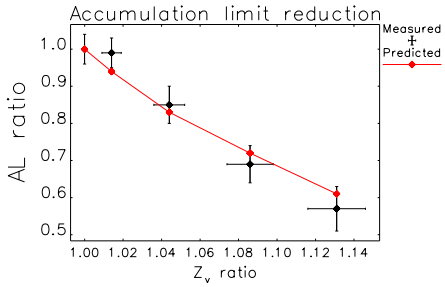


Figure 3: Comparison of measured and simulated accumulation limits as a function of vertical effective impedance.

To further validate our impedance model, two spare small-gap vacuum chambers were installed in two free sectors in May 2013. The expected increase of the vertical impedance due to this installation was 4% and the expected reduction of the accumulation limit was about 3 mA. The accumulation limit measurement procedure as described above was followed to measure the limit before and after the installation. A reduction by 2 mA was measured as shown in Figure 4, where the dependence of the accumulation limit on chromaticity is presented before and after the installation.

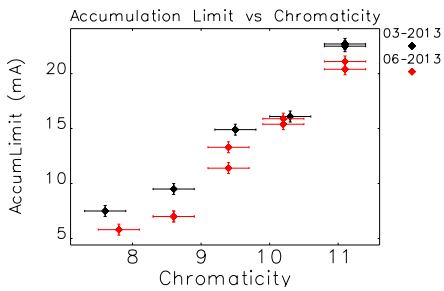


Figure 4: Accumulation limit as a function of chromaticity before and after the installation of two small-gap vacuum chambers.

Local Impedance Measurement

We also have measured the local impedance before and after installation of the two new chambers. The local impedance is obtained by analyzing response matrices measured at different values of the single-bunch current [8]. It is known that impedance acts on the beam as a defocusing element, so a response matrix fit can be used to measure this defocusing effect locally. In detail, the measurement and impedance determination is as follows: With a single bunch in the storage ring, the response matrix measurement is done for several beam currents. Then, the response matrix fit is performed for every measurement. The results of these fits is the set of beta function files — one for each beam current. The beta functions vary slightly from one file to another due to the defocusing effect of the impedance. The betatron phases from these files are combined for every location in the storage ring (for example, for all BPMs) to calculate the local betatron phase slope with current. The result of this processing is the betatron phase slope with current as a function of s along the storage ring. Then, a small number of artificial quadrupoles are used to reproduce the betatron phase slope dependence on s. The strengths of these quadrupoles will be proportional to the local impedance values. Here we need to emphasize that this approach works only for the vertical plane. In the horizontal plane at the APS the tune shift with current is very small due to smaller impedance and due to contributions from quadrupolar wakes that counteract the dipole wakes and make tune shift with current very small. Figure 5 shows the results of local impedance measurements before and after installation of new ID chambers. We can see a clear difference at the locations of the new chambers.

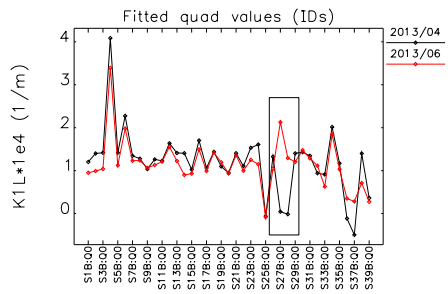


Figure 5: Local impedance distribution before and after installation of new vacuum chambers. A rectange shows where the chambers were installed.

CONCLUSIONS

We have developed a model that predicts how the single-bunch accumulation limit changes with storage ring impedance. We have varied the effective vertical impedance of the storage ring by changing beta functions at the small-gap vacuum chamber locations and measured the accumulation limit as a function of effective impedance. The measurements agreed reasonably well with the predictions. We have also verified the model by installing two new small-gap vacuum chambers and comparing the resulting accumulation limit reduction with predictions.

REFERENCES

[1] Y. Chae and Y. Wang, PAC 2007, FRPMN104, 4336 (2007).
[2] APS Upgrade Preliminary Design Report (2012).
[3] M. Borland, ANL/APS/LS-287 (2000).
[4] W. Bruns, LINAC 2002, TU444, 416 (2002).
[5] M. Borland, Private Communication (2012).
[6] M. Borland, Private Communication (2012).
[7] J. Safranek, NIM A 388 (1997).
[8] V. Sajaev, ICFA Beam Dynamics Newsletter 44 (2007).

Copyright © 2013 CC-BY-3.0 and by the respective authors

BEAM PHYSICS IN FUTURE ELECTRON HADRON COLLIDERS

A. Valloni*, O. Bruning, M. Klein, D. Schulte, F. Zimmermann, CERN, Geneva, Switzerland

Abstract

High-energy electron-hadron collisions could support a rich research programme in particle and nuclear physics. Several future projects are being proposed around the world, in particular eRHIC at BNL, MEIC at TJNAF in the US, and LHeC at CERN in Europe. This paper will highlight some of the accelerator physics issues, and describe related technical developments and challenges for these machines. In particular, optics design and beam dynamics studies are discussed, including longitudinal phase space manipulation, coherent synchrotron radiation, beam-beam kink instability, ion effects, as well as mitigation measures for beam break up and for space-charge induced emittance growth, all of which could limit the machine performance. Finally, first steps are presented towards an LHeC R&D facility, which should investigate relevant beam-physics processes.

INTRODUCTION

Particle colliders for high energy physics have been at the forefront of scientific discoveries for more than half a century. Leptons have been used to probe the partonic structure of the proton from the late 1960s, starting in fixed target deep inelastic scattering experiments, and continuing to the *e-p* collider HERA. With the first *e-p* collider HERA, remarkable results have been obtained on the parton structure of the proton, which are now crucial for the interpretation of the LHC data and include the discovery of a high density gluon and sea quark component in the proton. One can thus reflect on the valuable insight gained in revealing the structure of matter and evaluate priorities for future *e-p* or electron-ion (*e-A*) colliders [1]. Despite previous successes, many fundamental physics aspects have not yet been verified experimentally, and several future projects are under consideration in the USA and Europe and have good prospects of becoming operational and deliver results in the next 20 years. These projects intend to extend the knowledge achieved at HERA, and to provide new exploration tools by involving lepton collisions with heavy ions as well as with polarized protons and polarized light ions. These proposed colliders come in two varieties. One is an electron linear accelerator colliding with a proton or ion ring accelerator, the other, an *e*-ring accelerator colliding with a hadron ring. All of the future *e-A* colliders are based on the extension of already existing machines: LHeC at CERN [2], ENC at GSI [3], eRHIC at BNL [4] and MEIC at TJNAF [5]. Two colliders, ENC and MEIC are based on the ring-ring (RR) scenario, while the BNL and CERN teams selected the linac-ring (LR) option with energy recovery. The physics programs to a large degree are complimentary to each other and to the LHC physics [6]. In particular, with highest energies, the LHeC can be made a next Higgs factory. New ideas and technologies are applied in the accelerator designs and the intent of this paper is to present the key accelerator physics issues, referring to 3 possible future machines which are quite different in approach: eRHIC, MEIC and LHeC. This paper is organized as follows. The first part contains a brief overview on the parameter choices of the main future colliders worldwide. The focus here is on an understanding of the central characteristics of each machine and of the various common challenges. In the second part, among all the possible issues that these accelerators present, some selected subjects are described with related studies to analyze and compare the merits of different approaches. Special emphasis will be placed on the clear identification of the beam physics limits and accelerator technology limits highlighting aspects that need to be addressed by further research. The final section contains a summary of the future plans at CERN with special regard to the scientific and technical R&D activity for the development of an LHeC ERL test facility which will allow addressing relevant physics issues.

FUTURE ELECTRON-ION COLLIDERS

Since the very beginning, the focus of the *e-p* and *e-A* colliders studies has centered on achieving ultra-high luminosity and higher center-of-mass energy (CME). The eRHIC and ELIC machines consider their operation at the CME area of 20÷100 GeV, with luminosities ranging in 10^{32}÷10^{34} cm^{-2}s^{-1} values. Compared to the other machines, the LHeC provides the unique possibility of exploring *e-p* collisions in the TeV center of mass regime. The LHeC will collide the 7 TeV protons circulating in the LHC, therefore representing an interesting possibility for a further exploitation of the existing LHC infrastructure investment, with a high energy *e*-beam at a single collision point. As a result of the combination of SC accelerating structures and the energy recovery technique, a luminosity at least 2 orders of magnitude greater than the one achieved by HERA can be reached. The proposed machine layout consists of a 500 MeV polarized injector, two CW 10 GeV SC linacs and a recirculator system. Each beam recirculates up to 3 times through both linacs to boost the energy to 60 GeV. As the beam is focused and collided, it is bent by 180°, and then it is sent back through the first linac, at a decelerating phase. During deceleration the energy stored in the beam is converted to RF energy and the final beam, at its original injection energy, is directed to a beam dump. The baseline 60 GeV ERL option proposed can give an *e-p* luminosity of 10^{33} cm^{-2}s^{-1} (extensions to 10^{34} cm^{-2}s^{-1} and beyond are being considered), a beam current of 6.4 mA, with less than 100 MW total electrical power required.

* alessandra.valloni@cern.ch

Copyright © 2013 CC-BY-3.0 and by the respective authors

A similar approach of exploiting an existing beam facility and adding an accelerator for another species is taken in the collider projects eRHIC at BNL. The eRHIC design is based on one of the RHIC hadron rings which can accelerate polarized light ion beams to 100÷130 GeV/nucleon and polarized protons up to 325 GeV, and a new 5÷30 GeV multi-pass ERL to accelerate polarized electrons. It means that eRHIC will cover the CME range from 44.7 GeV to 197.5 GeV for polarized *e-p*, and from 31.6 GeV to 125 GeV for electron heavy-ion collisions. The machine will rely on SRF technology for production and acceleration of electrons, cooling of hadron beams and realizing crab crossing collision scheme. The injection system consists of a 10 MeV linac and 600 MeV single-pass ERL. Two 2.45 GeV SRF linacs in combination with six passes form the main ERL to generate 50 mA of polarized *e*-current. Multiple collision points are possible.

In the present baseline the central part of the proposed MEIC is a pair of figure-8 shaped storage rings, which accommodate the colliding electron and ion beams, respectively. The electron ring is made of normal conducting magnets and will store an *e*-beam of 3 to 11 GeV. The CEBAF SRF linac serves as a full-energy injector into the electron collider ring, requiring no further upgrade for energy, beam current, or polarization beyond the 12 GeV upgrade. The ion collider ring is made of high-field SC magnets and will store a beam with energy of 20 to 100 GeV for protons or up to 40 GeV per nucleon for light to heavy ions. The ion beams are generated and accelerated in a new ion injector complex. In addition, two large figure-8 high-energy collider rings will be added for a future energy upgrade for reaching up to 20 GeV electrons, 250 GeV protons or 100 GeV/u ions. The upgraded high-energy collider can use the same experimental halls and, possibly, the same detectors as MEIC, and the medium-energy ion collider ring would then serve as the final booster in the staged acceleration of ion beams.

CHALLENGES

Each of the future *e-A* colliders faces significant challenges and an intense accelerator R&D program is needed. A list of primary beam dynamics concerns is the following:

- *e*-beam energy losses and energy spread caused by the interaction with the beam environment (cavities, resistive walls, pipe roughness);
- incoherent and coherent synchrotron radiation (SR) related effects: energy losses, transverse and longitudinal emittance increase of the e-beam;
- effective energy loss and energy spread compensation schemes;
- *e*-beam filling patterns; ion accumulation;
- *e*-beam break-up (BBU), single beam and multi-pass;
- *e*-beam-ion and intra-beam scattering effects;
- *e*-beam polarization: depolarization effects;
- possible effects due to crab cavities;
- detailed beam dynamics with coherent electron cooling (CeC);
- beam-beam effects, including the *e*-beam disruption and the hadron beam kink instability.

Some of these topics will be discussed in the following sections.

Electron Beam Polarization

A key feature of *e-A* colliders is high polarization (over 80%) of the *e*-beam at all collision points. Many issues have to be carefully considered, such as a polarized source, self-polarization and depolarization, polarization time, and spin rotator. The MEIC electron ring is designed to store, manipulate and preserve a highly polarized *e*-beam. The MEIC polarized beam is provided by the CEBAF accelerator. Currently, the electron polarization from CEBAF at 6 GeV is above 85%. It is expected that a similarly high polarization will be achieved after completion of the 12 GeV upgrade. The equilibrium electron polarization is arranged to be vertical in the arcs of the figure-8 collider ring and anti-parallel to the arc dipole magnetic fields (see Fig. 1), in order to take advantage of the preservation of polarization by the Sokolov-Ternov (S-T) effect. Longitudinal

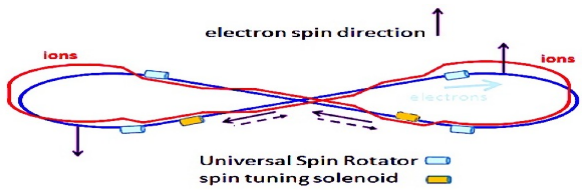


Figure 1: Diagram of polarization orientation at MEIC [5].

polarization is achieved at the collision points by utilizing 90° universal spin rotators (USR) each of which consists of a set of solenoids and dipoles placed at the end of an arc. To eliminate the transverse coupling introduced by the solenoids, each solenoid is split into two equal halves and 5 quadrupoles (in 3 families) are inserted between the halves. One or more spin tuning solenoids are needed to control the closed orbit spin tune and keep it away from resonances. Figure 2 illustrates how the USR works by showing a step-by-step rotation of an electron spin. The equilibrium

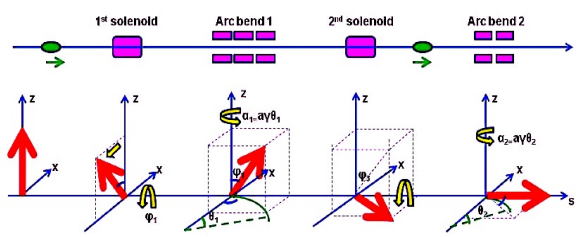


Figure 2: Schematic drawing of the USR at MEIC [5].

Copyright © 2013 CC-BY-3.0 and by the respective authors

beam polarization and its lifetime depend on competition between the S-T effect and radiative depolarization. The calculated equilibrium polarization and lifetime show significant depolarization even with perfect alignment. First calculations confirmed that the spin rotators and the sections between them are the main source of depolarization. The latter must be suppressed by spin matching which can be performed by manipulating the optics and layout of the lattice to achieve spin transparency between the two spin rotators. Regarding LHeC, Fig. 3 depicts the calculated spin vector spread, without any spin rotators, as a function of momentum spread for particles at 20, 40 and 60 GeV. While at eRHIC the loss of polarization is acceptable, for the high energy of LHeC the effective polarization can be reduced by 10% due to the spread of the spin vectors. For this reason to produce longitudinally oriented polarization at the LHeC collision point, a design with two spin rotators has been adopted. A low energy spin rotator first brings the polarization into the vertical direction and later a high energy spin rotator close to the IP realigns the spin vector in the longitudinal direction. The LHeC high energy spin

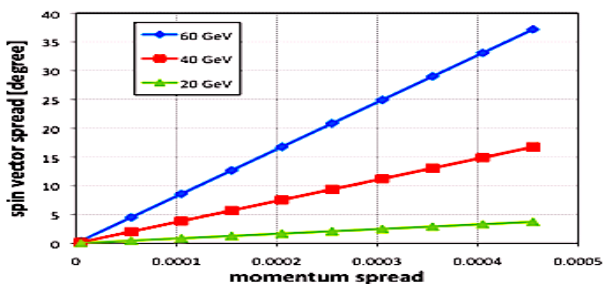


Figure 3: Angular spread of the spin vectors for off-momentum particles at 20, 40 and 60 GeV in the LHeC complex [7].

rotator consists of 4 helical dipoles with alternating helicity, similar to the RHIC proton spin rotator, placed in the straight section between the end of the second linac and the final focusing system. Besides saving space by being short, this approach also has the advantage of providing an independent full control of the direction of the polarization, as well as a nearly energy-independent spin rotation for the same magnetic field. The ∼MW SR power emitted by the 60 GeV *e*-beam passing through the spin rotator determines the minimum length of the system. In the present design, for a 60 GeV *e*-beam, the magnetic fields of the inner and outer pairs are 0.46 T and 0.37 T, respectively [2].

Optics Design and SR in Return Arcs

Control of SR effects on beam phase-space such as cumulative emittance and momentum growth due to quantum excitations is important for a high luminosity collider. In this section we briefly revisit the impact of SR from bending magnets for the intense beam at eRHIC and LHeC. The lattice design for both ERL based machines includes arcs placed above each other connected to the linacs by splitters and combiners. For LHeC a quasi isochronous arc optics design has been adopted, which simultaneously ensures a small value of emittance dilution and low momentum compaction, and therefore mitigates both transverse emittance growth and bunch length increase. The choice of large arc radius (1 km) is dictated by limiting energy loss due to SR at top energy (60 GeV) to less than 1%. Energy losses from resistive wall and coherent SR have both been shown to be negligible compared with the energy loss due to incoherent SR. The standard arc building block is 52 m long, and contains 4 quadrupoles and 2 (split into 10) dipoles. The values of the curly-H function and M_{56} are taylored as required by emittance dilution and isochronicity or beam size conditions, respectively, for arcs of different energies, transiting from a quasi-isochronous optics yielding a small beam size for the 2 lowest energy arcs, to a TME-optics for the 2 arcs at highest energy. The LHeC arc dipoles have a 25 mm gap and a maximum field of 0.264 T, at 60 GeV. The highest energy arc (before the final collision), gives a net normalized emittance increase of 4.5 μm. All the lower arcs together, with less emittance preserving optics, contribute a total of about 25% of the last arc, so that the total emittance dilution is 5.6 μm. At the interaction point, the SR induced RMS energy spread is only $2{\cdot}10^{-4}$, at the final arc, after deceleration, the energy spread reaches about 0.22%, while at the beam dump it grows to a full 4.5%. The *e*-beam looses about 2 GeV over all arc passes and the highest compensating RF voltage required is 750 MV for the energy loss at 60 GeV.

The lattice of the 6-passes for the eRHIC ERL arcs is based on low-emittance near-isochronous arc modules, supporting perfect isochronicity of complete paths. The standard building block is 35 m long, and contains 7 dipoles and 9 quadrupoles. The eRHIC arc dipoles have a gap of 5 mm and, at 30 GeV, a maximum field of 0.43 T. In view of the small gap and high beam current, resistive-wall wake fields and surface-roughness effects are under careful investigation. At 30 GeV peak lepton energy, with a dipole bending radius of 234 m, the total energy loss per electron due to SR is about 770 MeV over all arc passes; at 20 GeV it is only 150 MeV. A single double harmonic compensator at (almost) the highest energy delivering 389 MeV per passage compensates for the energy loss from SR and other, smaller effects like resistive wall and linac-cavity HOMs.

Multipass BBU and Beam-beam

In ERLs, the excitation of HOMs induced by the recirculating *e*-bunches can add up constructively and cause instabilities. Depending on the details of the machine optics, the deflection produced by a mode can translate into a transverse displacement at the cavity after recirculation. The recirculated beam induces, in turn, an HOM voltage which depends on the magnitude and direction of the beam displacement. Thus, the recirculated beam completes a feedback loop which can become unstable if the average beam current exceeds the threshold for stability. BBU is of particular concern in the design of high average current ERLs

Copyright © 2013 CC-BY-3.0 and by the respective authors

utilizing SRF technology. If not sufficiently damped by the HOM couplers, dipole modes with quality factors several orders of magnitude higher than in normal conducting cavities can exist, providing a threat for BBU to develop. The BBU threshold is increased by the natural chromaticity of the arcs if the latter is uncorrected [9]. A thorough suite of simulations to characterize the BBU instability have been conducted for the two ERL based machines LHeC and eRHIC. The LHeC BBU study is based on a new code that assumes point-like bunches and takes a number of dipole wakefield modes into account. A cavity-to-cavity frequency spread of the wakefield modes can also be modelled. In the simulation, one can offset a single bunch of a long train by one unit and determine the final position in phase space of all other bunches. Figure 4 shows the multi-bunch BBU adopting ILC-type (1.3 GHz) and SPL-type (720 MHz) cavities for a bunch with $3{\cdot}10^9$ electrons. The beam remains stable in both cases. Another key limit-

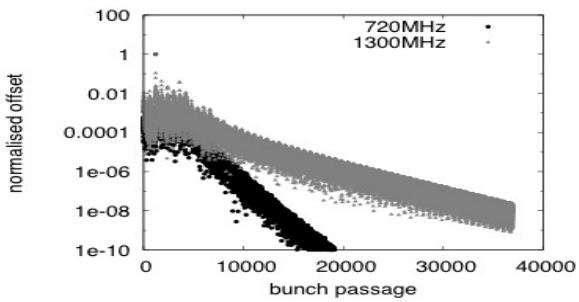


Figure 4: Multi-bunch BBU. Amplitudes along the full simulated train for the baseline lattice of LHeC [8].

ing factor to collider luminosity is beam-beam interactions. These can cause serious emittance growth of the colliding beams and fast reduction of luminosity. In particular the collision distorts the *e*-beam, which may be mitigated by proper matching of the exit beamline. The beam-beam effect can also amplify a perturbation and, thereby lower the BBU threshold. In Fig. 5 multi-bunch BBU including beam-beam effects is shown, again for two different cavity-types and for a bunch with 3×10^9 electrons. The beam remains stable in both cases but with a very small margin in the case of the ILC-type cavities.

Fast Beam-ion Instability

Collision of beam particles with the residual gas in the beam pipe leads to the production of positive ions that can be trapped in the beam. Their presence modifies the betatron function of the beam and can also lead to a BBU-like instability, since bunches with an offset will induce a coherent motion in the ions (and vice versa) [10]. This can in turn lead to a kick of the ions on the following bunches. The LHeC whole racetrack is ~9 km, 1/3 of the LHC circumference, so that ion clearing gaps can be incorporated in the bunch train whose arrival times for successive passes coincide in the linacs and which, in addition, always correspond to the same partner hadron bunches in the LHC (so

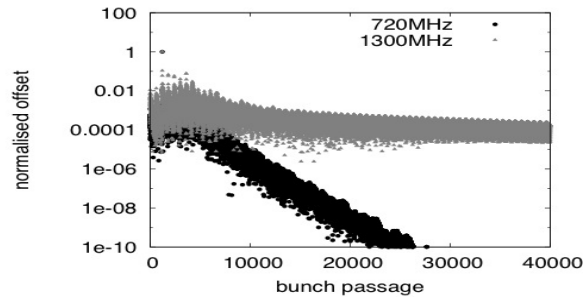


Figure 5: Multi-bunch BBU with beam-beam effect. Amplitudes along the full simulated train for the baseline lattice of LHeC [8].

that the LHC would comprise hadron bunches which collide on every turn and some others which never collide). In these clearing gaps the ions drift away from the beam orbit. A good vacuum quality is also needed to further slow down the build up of a significant ion density during the bunch train passages between successive clearing gaps. For the LHeC cold linacs, with a clearing gap of 10μs every 30μs, partial gas pressures of 10^{-11} hPa at 1.8 K are required at the position of the beam to render the residual fast beam-ion instability harmless, whereas a partial pressure below 10^{-9} hPa should be sufficient in the warm arcs. Similar tolerances apply to eRHIC.

Electron Cooling

Cooling of ion and hadron beams at collision energy is of critical importance for the performance of eRHIC and MEIC. An effective cooling process would allow to cool the beams beyond their natural emittances and also to either overcome or to significantly mitigate limitations caused by the hour-glass effect and intra-beam scattering. New concepts have been proposed recently to cool hadron beams. The most notable one among them is CeC. It is an *e*-beam based cooling system in which the accompanying *e*-beam provides feedback, similar to stochastic cooling, with an extremely high frequency bandwidth (THz range) by use of the FEL amplification mechanism in an undulator. This concept has been adopted for the eRHIC design. A sketch of the schematic layout is shown in Fig. 6. In the modula-

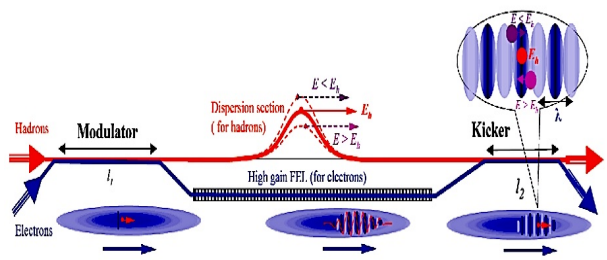


Figure 6: General schematic of CeC [11].

tor, each hadron induces density modulation in *e*-beam that is amplified in the high-gain FEL; in the kicker, the hadrons interact with the self-induced electric field of the *e*-beam

Copyright © 2013 CC-BY-3.0 and by the respective authors

and receive energy kicks toward their central energy. The process reduces the hadron energy spread, i.e. cools the hadron beam. A recent proposal is to use the microbunching instability instead of the FEL process as amplifier for the CeC scheme [12].

The MEIC baseline design does not invoke the CeC method, but it adopts a scheme of multi-stage cooling for supporting its high luminosities. Electron cooling is utilized not only for assisting ion beam formation but also during collisions. The latter is particularly important for preserving the collider luminosity and its lifetime by suppressing IBS induced heating. The scheme utilizes *e*-cooling at four different stages (at the pre-booster, injection and top energy, during collision) of the ion beam life cycle for achieving distinct goals in beam formation and maintenance. Figure 7 illustrates the *e*-cooler based on a magnetized photocathode gun, an ERL and a compact circulator ring. A high charge electron bunch from an injector is accelerated in an SRF linac up to 55 MeV and then sent to a circulator ring with an optically matched cooling channel for the ion bunch. The *e*-bunch circulates a large number of revolutions (up to 100) in the circulator cooler ring before its quality degrades significantly due to intra- and inter-beam scattering, and then returns to the same SRF linac for energy recovery. The *e*-cooling happens in both long straight sections as the circulator ring is placed in the vertex of the figure-8.

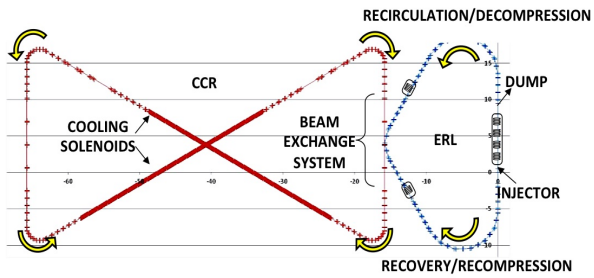


Figure 7: Schematic drawing of an ERL circulator cooling facility for MEIC [5].

FUTURE PLANS AT CERN

The development of a CW SC recirculating ERL for LHeC would prepare for many possible future projects. With some additional arcs, using 4 instead of 3 passes through the linacs, a machine like the LHeC ERL (without energy recovery) could also operate as Higgs factory $\gamma\gamma$ collider. The LHeC project will pursue the construction of a dedicated ERL test facility, the design of which will be prepared over the next two years. This test facilty could later be converted into the LHeC injector, including energy recovery. The purposes are first, confirming the feasibility of the LHeC ERL design by demonstrating stable intense *e*-beams with the intended parameters (current, bunch spacing, bunch length); secondly, testing novel components such as a (polarized) DC electron gun, SC RF cavities, cryomodule design and feedback diagnostics; finally, experimental studies of the lattice dependence of stability criteria. The realization of this facility will allow addressing several physics challenges such as maintaining high beam brightness through preservation of the 6D emittance, managing the phase space during acceleration and energy recovery, stable acceleration and deceleration of high current beams in CW mode operation. The design must also allow addressing other performance aspects such as longitudinal phase space manipulations, effects of coherent SR, longitudinal space charge and ions, halo and beam loss and microbunching instability.

SUMMARY

Electron-hadron colliders provide outstanding research potential. Several proposals aiming at very high luminosity, two-to-four orders of magnitude beyond the luminosity demonstrated by HERA, are under consideration in several laboratories all over the world. All these projects promote advanced research in accelerator physics and technologies. Additional R&D is needed. Further improvements to overcome the state-of-art include investigation of polarized electron guns, high-energy deuteron and proton polarization, integration of the detectors and colliders, high-energy *e*-cooling, high current and high brightness beam ERL operation, along with more detailed studies of multi-bunch BBU, beam-ion instability and beam-beam effects.

ACKNOWLEDGEMENTS

We wish to thank Vadim Ptitsyn and Yuhong Zhang for providing material for this paper. Helpful discussion and valuable input from all members of LHeC Study Group Collaboration are thankfully acknowledged. This work is supported by the European Commission within the oPAC project under Grant Agreement 289485.

REFERENCES

[1] ICFA Beam Dynamics Newsletter, 58, (2012).

[2] J. L. Abelleira Fernandez, *et al.*, [LHeC Study Group Collaboration], arXiv:1206.2913 [physics.acc-ph].

[3] A. Lehrach, *et al.* 2011, Journal of Physics: Conference Series, 295,1.

[4] V. Ptitsyn, *et al.*, at 42nd ICFA Advanced Beam Dynamics Workshop on High-Intensity.

[5] S. Abeyratne, *et al.*, arXiv:1209.0757 [physics.acc-ph].

[6] LHeC Collaboration, 'On the Relation of the LHC and the LHeC', arXiv:1211.5102, (2012).

[7] M. Bai, *et al.*, CERN-ATS-2011-110.

[8] D. Schulte, ICFA mini-workshop on "Beam-Beam Effects in Hadron Colliders", 2013.

[9] V. N. Litvinenko, PhysRevSTAB.15.074401.

[10] T. O. Raubenheimer, F. Zimmermann, PhysRevE.52.5487.

[11] V. N. Litvinenko, *et al.*, Proceedings of PAC '11, THOBN3.

[12] D. Ratner, PhysRevLett.111.084802.

Copyright © 2013 CC-BY-3.0 and by the respective authors

COLLIMATION WITH HOLLOW ELECTRON BEAMS: A PROPOSED DESIGN FOR THE LHC UPGRADE*

G. Stancari†, V. Previtali, A. Valishev, Fermilab, Batavia, IL 60510, USA
R. Bruce, S. Redaelli, A. Rossi, B. Salvachua Ferrando, CERN, Geneva, Switzerland
V. Moens, EPFL, Lausanne, Switzerland

Abstract

Collimation with hollow electron beams is a technique for halo removal in high-power hadron beams. The concept was tested experimentally at the Fermilab Tevatron collider using a hollow electron gun installed in one of the Tevatron electron lenses. Within the US LHC Accelerator Research Program and the European HiLumi LHC Design Study, we are investigating the applicability of this technique to the Large Hadron Collider and a conceptual design is being developed. We review some of the main topics related to this study: motivation; halo removal processes; development of hollow electron guns; effects on the proton beam core; and integration in the LHC machine.

INTRODUCTION

Hollow electron beam collimation is a new technique for beam collimation and halo scraping [1, 2, 3]. In a hollow electron beam collimator, a magnetically confined, pulsed, low-energy (a few keV) electron beam with a hollow current-density profile overlaps with the circulating beam over a short section of the ring. If the electron distribution is axially symmetric, the beam core is unperturbed, whereas the halo experiences smooth and tunable nonlinear transverse kicks. The electron beam is generated by a hollow cathode and transported by strong solenoidal fields. The size, position, intensity, and time structure of the electron beam can be controlled over a wide range of parameters.

The technique still relies on robust conventional collimators to absorb particles, but it has several features that can complement a classic multi-stage collimation system. In the case of high-power proton beams, for instance, scraping is smooth, controllable, and the issues of material damage and electromagnetic impedance of the collimator jaws are mitigated. In addition, a depletion zone is generated between the proton beam core and the collimator edges, making local energy deposition less sensitive to beam jitter, collimator movements, orbit and tune adjustments, or fast failures in the case of crab-cavity operation. In the case of ion collimation, it may be possible to reduce uncontrolled losses due to fragmentation. Hollow electron beam collimation is also being evaluated in comparison with other halo scraping techniques, such as tune modulation [4].

Hollow electron beam collimation is based on the technology of electron cooling and electron lenses. Electron lenses were developed for beam-beam compensation in colliders [5], enabling the first observation of long-range beam-beam compensation effects [6]. They were used for many years during regular Tevatron collider operations for cleaning uncaptured particles from the abort gap [7]. Thanks to the reliability of the hardware, one of the two Tevatron electron lenses could be used for experiments on head-on beam-beam compensation in 2009 [8], and for exploring hollow electron beam collimation in 2010–2011 [2, 3]. Electron lenses for beam-beam compensation were built for the Relativistic Heavy Ion Collider (RHIC) at Brookhaven National Laboratory and are currently being commissioned [9].

The Tevatron experiments on hollow electron beam collimation were conducted on antiprotons, mainly at the end of regular collider stores. In some cases, the electron beam was turned on for the whole duration of the fill. Because of the flexible pulsing pattern of the high-voltage modulator [10], the electron beam could be synchronized with a subset of bunches, providing a direct comparison with the unaffected beam.

The technique may provide a unique option to complement the LHC collimation system, but extending it from one machine to another is not trivial. To study these issues, a conceptual design of hollow electron beam collimation for the LHC upgrade is being developed within the US LHC Accelerator Research Program (LARP) and the European FP7 HiLumi LHC Design Study. If approved by the CERN management, this may then develop into a technical design in 2014, with the goal to build the devices in 2015–2017 and install them during the next long LHC shutdown, currently scheduled for 2018. In case of a resource-limited timeline, installation during the following long shutdown in 2022 is also an option.

HALO SCRAPING

For scraping the halo of a 7-TeV proton beam, we envision the inner radius of the electron beam to be placed between about 4σ and 6σ of the LHC proton rms beam size $\sigma = 0.32$ mm. This size is derived from the nominal normalized rms emittance $\varepsilon = 3.75\ \mu$m and the typical amplitude function at the candidate locations, $\beta = 200$ m. Scraping of elliptical proton beams is possible by displac-

* Fermilab is operated by Fermi Research Alliance, LLC under Contract No. DE-AC02-07CH11359 with the United States Department of Energy. This work was partially supported by the US DOE LHC Accelerator Research Program (LARP) and by the European FP7 HiLumi LHC Design Study, Grant Agreement 284404. Report number: FERMILAB-CONF-13-355-APC.

† Email: ⟨stancari@fnal.gov⟩.

Copyright © 2013 CC-BY-3.0 and by the respective authors

ing the electron beam, but for simplicity we focus on round beams.

For stability and for transport efficiency, the field in the guiding solenoids should be as large as possible. Based upon previous experience and technical feasibility, we consider configurations where the gun, main (superconducting), and collector solenoids have fields in the ranges $0.2\ \mathrm{T} \le B_g \le 0.4\ \mathrm{T}$, $2\ \mathrm{T} \le B_m \le 6\ \mathrm{T}$, and $0.2\ \mathrm{T} \le B_c \le 0.4\ \mathrm{T}$, respectively. This implies magnetic compression factors $k \equiv \sqrt{B_m/B_g}$ in the range $2.2 \le k \le 5.5$, which sets the required sizes of the cathode inner and outer radii. The 1-inch electron gun cathode built for this purpose, for instance, has inner radius $r_{ci} = 6.75$ mm and an outer radius $r_{co} = 12.7$ mm. After magnetic compression, these radii translate to $1.2\ \mathrm{mm} = 3.9\sigma \le r_{mi} \le 9.5\sigma = 3.0$ mm and $2.3\ \mathrm{mm} = 7.3\sigma \le r_{mo} \le 18\sigma = 5.7$ mm in the interaction region inside the main solenoid. The LHC primary collimators will be placed at around 6σ from the beam axis.

The scraping experiments at the Tevatron with 0.98 TeV antiprotons were done with peak electron beam currents up to 1.2 A, and halo removal times ranged between seconds and minutes, depending upon the radius and intensity of the electron beam.

The transverse kicks generated by the hollow electron beam are nonlinear and have a small random component due to noise in the electron beam current. These kicks interact with the lattice nonlinearities and with the sources of noise in the machine. Therefore, the kicks needed to obtain a given halo removal rate may not be directly proportional to the magnetic rigidity of the circulating beam — a linear machine with low noise may require larger electron beam intensities.

Tracking simulations in the Tevatron lattice with the Lifetrac code showed that relatively small electron currents can significantly enhance halo removal [11]. The removal rates are sensitive to the shape of the electron beam and to the distribution of the halo population. In the absence of experimental data, tracking codes can give rough but conservative estimates of the removal rates. Numerical simulations of the LHC lattice with the SixTrack code indicated that, in the absence of beam-beam interactions and of diffusion processes, removal of 7-TeV protons with a 1-A electron beam current would be slow [12]. Higher electron yields and different pulsing schemes were therefore pursued to extend the capabilities of the technique.

A 1-inch-diameter hollow electron gun based on a tungsten dispenser cathode was developed and characterized at the Fermilab electron-lens test stand [13, 14]. The perveance of this gun is 5.3 μperv. This implies a peak yield of over 5 A at 10 keV. This yield should be sufficient to have a detectable effect on 7-TeV protons.

One can also exploit the flexibility of the electron beam pulsing pattern. Most of the Tevatron scraping experiments were done with the same turn-by-turn excitation intensity on the bunches of interest, but, for beam-beam compensation purposes, the high-voltage modulator was designed to handle bunch-by-bunch adjustments, with 10%–90% rise times of 200 ns [10]. Fast abort-gap cleaning was achieved by turning on the electron beam every 7th turn, in resonance with the betatron oscillations of the uncaptured beam.

In the LHC, one could certainly change the electron beam current turn by turn, synchronizing the voltage change with the abort gap, for instance. (Bunch-by-bunch adjustments every 25 ns or 50 ns are probably unnecessary.) This flexibility opens up the possibility to operate the hollow electron lens in different pulsing modes: *continuous* — the same voltage is applied every turn; *resonant* — the voltage is changed turn by turn according to a sinusoidal function (possibly including a frequency sweep to cover the tune spread of the halo), or with the same amplitude, but skipping a given number of turns (as in the Tevatron abort-gap cleaning mode); *stochastic* — the voltage is turned on or off every turn according to a random function, or a random component is added to a constant voltage amplitude. These modes of operation were simulated with tracking codes [12]. Both the resonant and the stochastic mode give significant and tunable halo removal rates. While the first is sensitive to the details of the tune distribution (lattice nonlinearities, beam-beam parameter), the stochastic mode is much more robust.

Using collimator scans, it was possible to measure the effects of collisions and of the hollow electron lens on halo diffusion in the Tevatron as a function of betatron amplitude [15, 16]. Diffusivities in action space with and without collisions were also measured at the LHC [17]. Halo suppression is the main consequence of the drift and diffusion enhancement by the electron beam, but we intend to further investigate other important aspects, such as the increase in impact parameters and its effect on collimation efficiency.

UNDESIRED EFFECTS ON THE CORE

The core of the circulating beam is unaffected if the distribution of the electron charge is axially symmetric. One possible cause of asymmetry is the space-charge evolution of the electron beam. Other sources of asymmetry are the bends that are used to inject and extract the electron beam from the interaction region.

The electron beam was turned on for several hours during some Tevatron collider stores. With aligned beams and continuous operation, no deterioration of the core lifetimes or luminosities were observed. Only a limited number of experiments were done in resonant mode (by skipping turns).

The current-density profiles generated by the hollow electron guns were measured in the Fermilab electron-lens test stand as a function of beam current and axial magnetic field. Space-charge evolution of the electron beam profiles is mitigated by increasing the guiding magnetic fields. For main fields above 2 T and beam currents up to a few amperes, we estimate that transverse current-density profiles are practically frozen.

The calculation of the electric fields from the measured current density profiles and the generation of the kick maps

Copyright © 2013 CC-BY-3.0 and by the respective authors

caused by the bends is described in a separate paper [18]. These fields are being used as inputs for tracking simulations to estimate beam lifetimes and emittance growth rates. For the Tevatron lattice and working point, the only azimuthal asymmetry seen to cause extra losses in the core was the quadrupole component in a particular resonant mode (pulsing every 6th turn) [11].

FURTHER CONSIDERATIONS

The bunch structure in the LHC is very different from the one in the Tevatron. This translates into tighter requirements on the electromagnetic impedance of the electron-lens hardware. Another aspect being considered is the possible extension of this technique to different operational scenarios, such as scraping during the acceleration ramp, which do not present impediments in principle, but have never been tested experimentally.

Diagnostic instrumentation includes accurate beam position monitoring of the long electron pulses and measurement of the electron beam profiles with wires or with fluorescent screens, as done at RHIC. A sensitive local loss monitor is also required to verify relative beam alignment. A direct measurement of the halo population, although not strictly necessary, would greatly benefit this project.

The construction cost of each of 2 electron lenses (one per beam) for the LHC is estimated to be 2.5 M$ in materials and 3.0 M$ in labor. Construction of 2 devices would take about 3 years. Reuse of some of the Tevatron equipment, such as superconducting coils, is possible. Each electron lens occupies about 6 m of tunnel length. Installation time is dominated by cryogenic integration (similar to a stand-alone magnet) and requires at least 3 months for warm-up, connections, and cool-down. The Tevatron devices had static heat loads of 12 W for the helium vessel at 4 K and 25 W for the liquid nitrogen shield.

CONCLUSIONS

Experimental and numerical studies are being conducted to support the conceptual design of a hollow electron beam collimator for the LHC, a promising technique for controlled scraping of very intense beams. A hollow electron gun with geometrical features and peak current yields appropriate for the LHC was built. Several electron beam pulsing modes were studied in numerical simulations to extend the achievable halo removal rates. No effects on the beam core are expected in the continuous mode of operation. The effect of imperfections in the resonant and stochastic modes is being evaluated with tracking codes using kick maps generated from measured and calculated electron beam charge distributions. Options for instrumentation and diagnostics were considered. No major obstacles were identified in the integration of the devices in the LHC ring from the point of view of electromagnetic impedance, mechanical engineering, or cryogenics.

REFERENCES

[1] V. Shiltsev, in Proceedings of the 3rd CARE-HHH-APD Workshop (LHC-LUMI-06), Valencia, Spain, p. 92, CERN-2007-002 (2007); in Proceedings of the CARE-HHH-APD Workshop (BEAM07), Geneva, Switzerland, p. 46, CERN-2008-005 (2007).

[2] G. Stancari et al., Phys. Rev. Lett. **107**, 084802 (2011).

[3] G. Stancari, in Proceedings of the Meeting of the Division of Particles and Fields of the American Physical Society, Providence, RI, USA, August 2011, arXiv:1110.0144 [physics.acc-ph], FERMILAB-CONF-11-506-AD-APC.

[4] O. Brüning and F. Willeke, in Proceedings of the 4th European Particle Accelerator Conference (EPAC94), London, United Kingdom, June 1994, p. 991; Phys. Rev. Lett. **76**, 3719 (1996).

[5] V. Shiltsev et al., Phys. Rev. ST Accel. Beams **2**, 071001 (1999); Phys. Rev. ST Accel. Beams **11**, 103501 (2008); New J. Phys. **10**, 043042 (2008).

[6] V. Shiltsev et al., Phys. Rev. Lett. **99**, 244801 (2007).

[7] X. Zhang et al. Phys. Rev. ST Accel. Beams **11**, 051002 (2008).

[8] G. Stancari and A. Valishev, in Proceedings of the ICFA Workshop on Beam-Beam Effects in Hadron Colliders (BB2013), Geneva, Switzerland, March 2013, FERMILAB-CONF-13-046-APC.

[9] W. Fischer et al., in Proceedings of the 2013 International Particle Accelerator Conference (IPAC13), Shanghai, China, May 2013, p. 1526.

[10] H. Pfeffer and G. Saewert, J. Instrum. **6**, P11003 (2011).

[11] I. Morozov et al., in Proceedings of the 2012 International Particle Accelerator Conference (IPAC12), New Orleans, LA, USA, May 2012, p. 94, FERMILAB-CONF-12-126-APC.

[12] V. Previtali et al., in Proceedings of the 2013 International Particle Accelerator Conference (IPAC13), Shanghai, China, May 2013, p. 993, FERMILAB-CONF-13-154-APC; FERMILAB-TM-2560-APC (July 2013).

[13] S. Li and G. Stancari, FERMILAB-TM-2542-APC (August 2012).

[14] V. Moens, Masters Thesis, École Polytechnique Fédérale de Lausanne (EPFL), Switzerland, FERMILAB-MASTERS-2013-02 and CERN-THESIS-2013-126 (August 2013).

[15] G. Stancari et al., in Proceedings of the 52nd ICFA Advanced Beam Dynamics Workshop on High-Intensity and High-Brightness Hadron Beams (HB2012), Beijing, China, September 2012, FERMILAB-CONF-12-506-AD-APC.

[16] G. Stancari et al., in Proceedings of the ICFA Workshop on Beam-Beam Effects in Hadron Colliders (BB2013), Geneva, Switzerland, March 2013, FERMILAB-CONF-13-054-APC.

[17] G. Valentino et al., Phys. Rev. ST Accel. Beams **16**, 021003 (2013).

[18] G. Stancari et al., in these Proceedings, FERMILAB-CONF-13-356-APC.

Copyright © 2013 CC-BY-3.0 and by the respective authors

COMMISSIONING RHIC'S ELECTRON LENS *

X. Gu#, Z. Altinbas, M. Anerella, D. Bruno, M. Costanzo, W.C. Dawson, A.K. Drees, W. Fischer, B. M. Frak, D.M. Gassner, K. Hamdi, J. Hock, L.T. Hoff, A.K. Jain, J. Jamilkowski, R. Lambiase, Y. Luo, M. Mapes, A. Marone, C. Mi, R. Michnoff, T. Miller, M. Minty, C. Montag, S. Nemesure, W. Ng, D. Phillips, A.I. Pikin, S.R. Plate, P. J. Rosas, J. Sandberg, P. Sampson, L. Snydstrup, Y. Tan, R. Than, C.W. Theisen, P. Thieberger, J. Tuozzolo, P. Wanderer, and W. Zhang

Brookhaven National Laboratory, Upton, NY 11973

Abstract

In the 2013 RHIC polarized-proton run, it was found that the intensity of the RHIC bunch had reached a limit due to the head-on beam-beam interaction at intensity of $2x10^{11}$, as we expected from our simulations [1]. To overcome this limitation, we have planned to implement two electron lenses for beam-beam compensation. During and after the 2013 RHIC run, some e-lens systems were commissioned. The effect of the e-lens warm solenoids on the protons orbit was observed and corrected by orbit feedback. The blue electron-lens system was fully tested, except for the superconducting magnet; the electron beam was propagated from the gun to the collector, and most of the instrumentation for the blue e-lens was commissioned. The straightness of the superconducting solenoid #2 field was measured for the first time. The installation of the yellow e-lens system and two superconducting magnets are underway.

INTRODUCTION

Figure 1 schematically depicts the layout of the electron lens that was used during the 2013 run (A), and will be implemented for the upcoming 2014 run (B).

During the 2013 run, all e-lens warm magnets [2, 3] were ready and tested with proton beam; we placed the superconducting solenoid #1 on the yellow e-lens side and replaced the blue superconducting solenoid with a spare EBIS superconducting solenoid, which was operated at 3T. We tested the blue e-lens system with the electron beam.

For the 2014 run (Figure 1 B), the yellow e-lens system will also be available and the two e-lens systems will be ready for commissioning.

For commissioning the e-lens during the 2013 255 GeV polarized proton run, we first commissioned a new e-lens lattice [4]; then, we studied the effects of e-lens magnetic field on the proton beam with the e-lens warm solenoids. We found that when the currents from the warm solenoids were ramped up, there were some effects on the beam

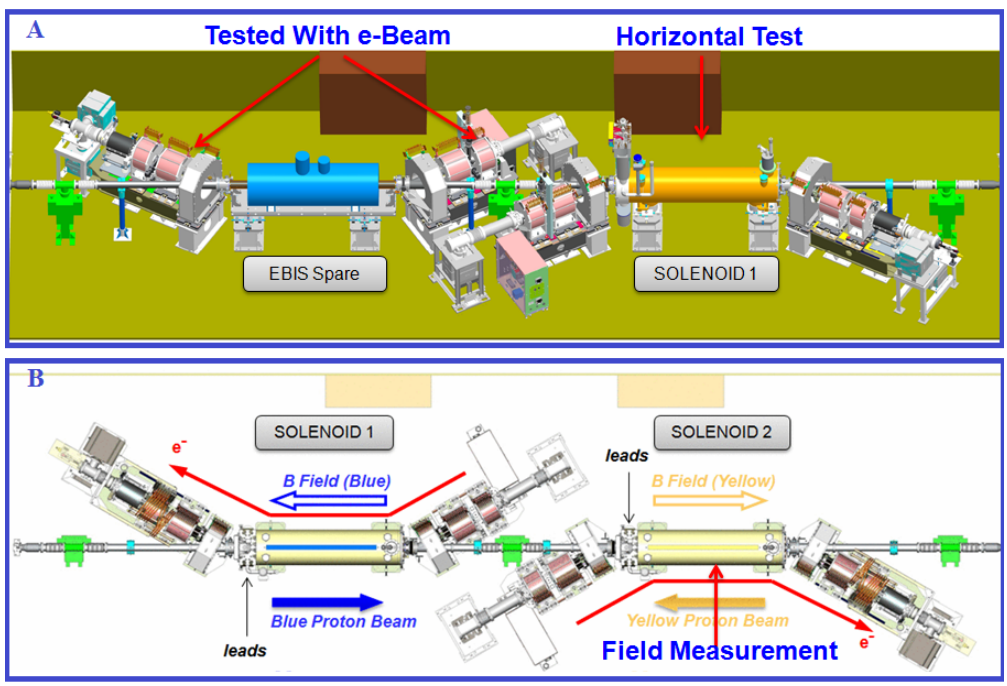


Figure 1: Schematic depictions of the layout of the electron lens during the 2013 run (upper) and the 2014 run (lower).

* Work supported by Brookhaven Science Associates, LLC under Contract No. DE-AC02-98CH10886 with the U.S. Department of Energy

#xgu@bnl.gov

Copyright © 2013 CC-BY-3.0 and by the respective authors

vertical orbit; we can correct this distortion by beam feedback. There were no apparent effects on beam loss, or on the beam intensity, emittance, or luminosity.

We also tested some instrumentation and applications for single-bunch beam-beam compensation during the 2013 polarized-proton run. Two BPMs were commissioned for the proton beam and electron beam.

For commissioning the blue e-lens, we propagated the electron beam through a system with a 3T EBIS spare superconducting-magnet. The properties of the cathode and the profile of the beam were measured with both a pinhole scanner and a YAG screen. The beam profile has Gaussian distribution. The modulator was commissioned with the 80 kHz and the DC beam for 14 and 9.5 hours respectively.

To further investigate the e-lens system reliability and make it more robust, several scenarios of system failure also were undertaken, such as Machine Protection System failure.

MAGNET EFFECTS DURING PROTON STORE

During the 2013 polarized proton run, we tested the e-lens warm solenoids with a proton beam. According to our simulation [5], the orbit of the proton beam is affected by the e-lens warm solenoids, especially in the vertical plane.

Figure 2 shows the distortion of the proton beam during the ramp-up of the e-lens warm solenoids with the orbit feedback on.

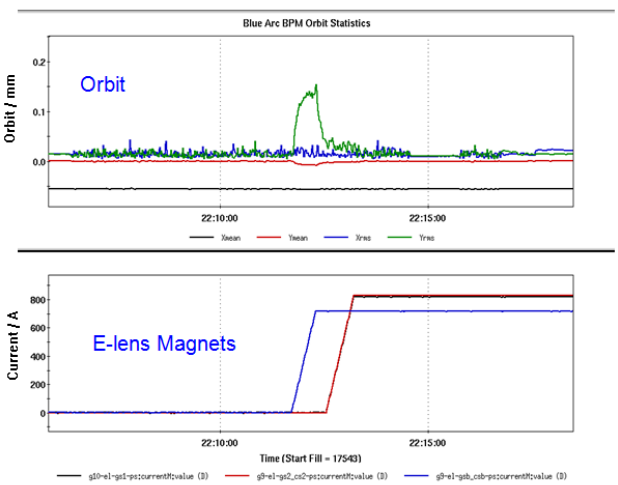


Figure 2: The vertical orbit rms with orbit feedback (top, in mm) and the warm magnet currents (bottom, in A).

The green (Yrms) trace in Figure 2, top, shows that the vertical beam rms position changes (~0.15mm) when the e-lens warm solenoid is ramped up even with the orbital feedback on, but recovered subsequently. A change in the orbit feedback parameters later reduced this effect. The effects on the horizontal plane were less.

Although e-lens warm magnets have some effects on the proton orbit, Figure 3, it is hard to discern any visible effects on RHIC luminosity.

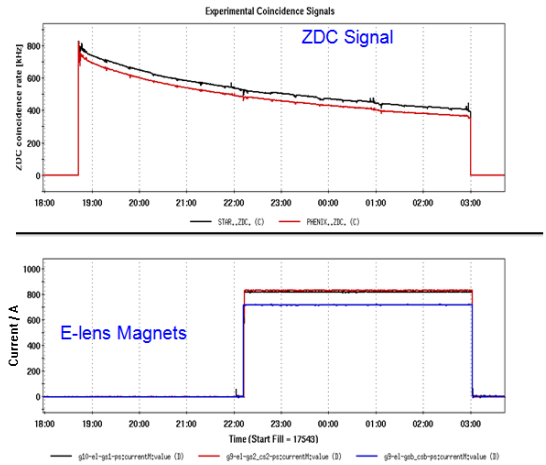


Figure 3: E-lens magnets current (bottom, in A) and luminosity (top).

ELECTRON BEAM COMMISSIONING

The blue e-lens system was fully commissioned with the help of the EBIS spare superconducting magnet, including the electron gun [6] and the collector. Figure 4 shows the perveance measurement of electron gun, which is 1.0×10^{-6} $AV^{-3/2}$.

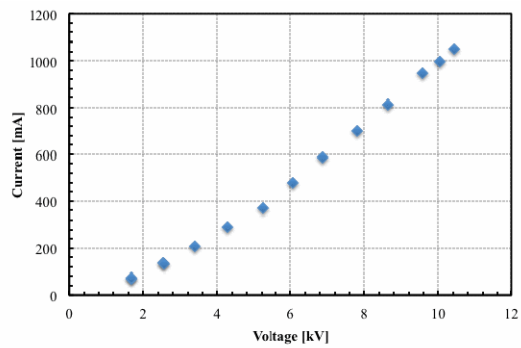


Figure 4: Perveance measurement of the electron gun.

We fully tested the electron beam running modes, and also demonstrated the system reliability. We ran the DC beam (1.256A) and the 80 kHz (parasitic) beam, respectively, for 9.5 hours and 14 hours; they were stopped intentionally for another test.

Figure 5 illustrates the 14 hour test of the 80 kHz electron beam. The bottom plot is the vacuum in the collector, which indicates that electron current was available in the collector; the upper plot, the anode voltage, denotes that the beam current was constant.

We also measured the electron beam profile with a YAG screen and a pinhole scanner [7]. Figure 6A shows the YAG profile for a 70 mA beam; Figure 6B shows the profile measured by the pinhole scanner for 1150 mA beam. The profile is Gaussian, with a small flat top, similar to the profile from the test bench [8, 9]. The total beam radius is 2.76 rms widths; the model yielded a value of 2.8.

Copyright © 2013 CC-BY-3.0 and by the respective authors

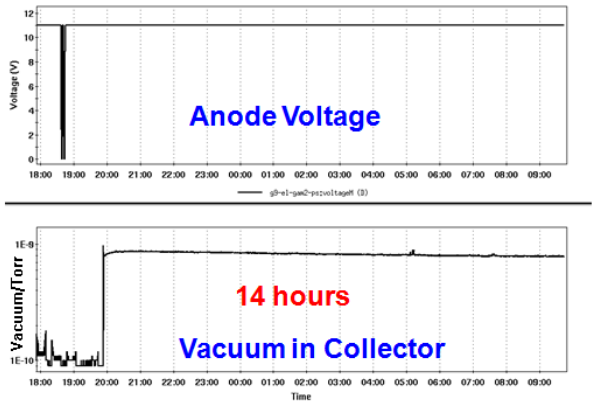


Figure 5: 80 kHz modulator test with more than a 1A beam.

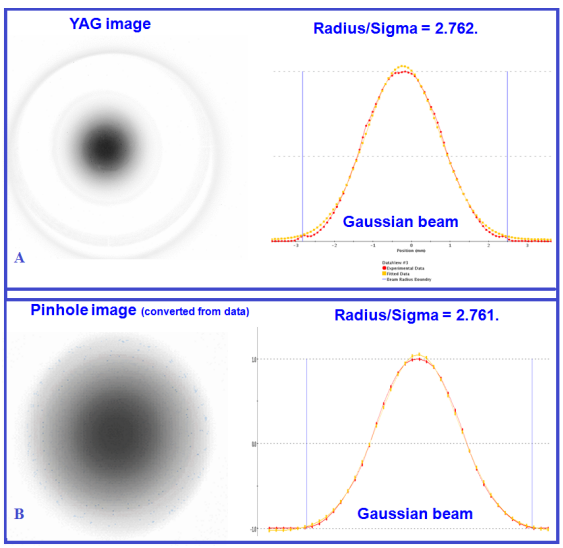


Figure 6: YAG screen (A) and pinhole (B) profile measurements of the electron beam.

E-LENS SUPERCONDUCTING MAGNETS

Two e-lens superconducting magnets were also tested. A horizontal test was done for both solenoid #1 and #2. With only 2 quenches, solenoid 1 reached 5 T. Solenoid #2 reached about 5.5 T. Both magnets have reached 6 T in a vertical test, and are expected to reach 6 T in the cryostat with further training quenches.

Figure 7 shows our measurements for the field straightness test at 2.83 T for solenoid #2, which was obtained at Brookhaven National Laboratory's Superconducting Magnet Department via magnetic needle [10]. The measurement was taken only with main coil and without fringe coil, anti-fringe coil, and correctors.

The green line in Figure7 is the field measurement and the red line is the measured deviation from a straight line. The blue line is the computed deviation after the application of five correctors.

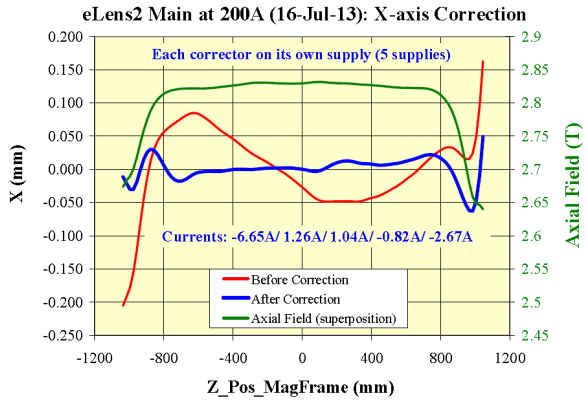


Figure 7: Measurement of the superconducting magnet field straightness in the horizontal plane.

As the blue line in Figure 7 shows, the straightness specification of ±50 μm is satisfied in X plane from about -900 mm to 900 mm without correctors. The uncorrected straightness deviation is even less in the Y (vertical) plane.

ACKNOWLEDGMENTS

The authors would like to acknowledge the help of the instrumentation group, vacuum group and controls group. The authors are also grateful to the valuable discussions with the FNAL TEL staff, in particular with V. Shiltsev, A. Valishev, and G. Stancari.

REFERENCES

[1] Y. Luo et al., "6-D weak-strong simulation of head-on beam-beam compensation in the Relativistic Heavy Ion Collider," Phys. Rev. ST Accel. Beams 15 (2012) 051004.

[2] W. Fischer et al., "Status of head-on beam-beam compensation in RHIC," Proc. of the ICFA Mini-Workshop on Beam-Beam Effects in Hadron Colliders (BB3013), CERN (2013).

[3] X. Gu et al., "Designing a Beam Transport System for RHIC's Electron Lens," PAC'11, New York, TUP208 (2011).

[4] V.H. Ranjbar et al., "RHIC Polarized Proton Operation for 2013," IPAC2013, Shanghai, China, p. 1544 (2013).

[5] X. Gu et al., "The Effects of The RHIC e-lenses Magnetic Structure Layout on The Proton Beam Trajectory," PAC'11, New York, USA TUP207.

[6] A. Pikin et al., PAC'11, New York, THP100, p. 2309 (2011).

[7] D. M. Gassner et al., "RHIC Electron Lens Test Bench Diagnostics," DIPAC'11, Hamburg, Germany, MOPD04.

[8] X. Gu et al., TUPHO01, NA-:PAC'13.

[9] T. Miller et al., "Electron-Lens Test Stand Instrumentation Progress," IBIC12, Tsukuba, Japan, THCB01 (2012).

[10] C. Crawford et al, Proc. Of PAC'99, New York, USA, pp. 3321-3323.

Copyright © 2013 CC-BY-3.0 and by the respective authors

HIGH PRESSURE GAS-FILLED RF CAVITIES FOR USE IN A MUON COOLING CHANNEL

B. Freemire*, P.M. Hanlet, Y. Torun, IIT, Chicago, IL 60616, USA
M. Chung, M.R. Jana, M. Leonova, A. Moretti, T. Schwarz, A.V. Tollestrup, K. Yonehara, FNAL, Batavia, IL 60510, USA
R.P. Johnson, Muons, Inc., Batavia, IL 60510, USA
M.G. Collura, Politecnico di Torino, Torino, Italy

Abstract

A high pressure hydrogen gas-filled RF (HPRF) cavity can operate in the multi-Tesla magnetic fields required for a muon accelerator cooling channel. A beam test was performed at the Fermilab MuCool Test Area by sending a 400 MeV proton beam through an 805 MHz cavity and quantifying the effects of the resulting plasma within the cavity. The resulting energy loss per electron-ion pair produced has been measured at 10^{-18} to 10^{-16} J every RF cycle. Doping the hydrogen gas with oxygen greatly decreases the lifetime of an electron, thereby improving the performance of the HPRF cavity. Electron lifetimes as short as 1 ns have been measured, and electron-ion recombination rates are on the order of 10^{-6} cm^3/s. The recombination rate of positive and negative ions in the cavity has been measured on the order of 10^{-8} cm^3/s. Extrapolation in both gas pressure and beam intensity are required to obtain Muon Collider parameters, however the results indicate HPRF cavities can be used in a muon accelerator cooling channel.

INTRODUCTION

A recent White Paper submitted to the 2013 U.S. Community Summer Study of the Division of Particles and Fields by the U.S. Muon Accelerator Program (MAP) outlines a staged Muon Accelerator facility based at Fermilab [1]. The report outlines two main programs; a Neutrino Factory (NF), and a Muon Collider (MC). For the case of a MC, a Higgs Factory and multi-TeV collider are described. Because muons are created with a large initial phase space, the colliders requires significant (roughly six orders of magnitude) cooling.

The only cooling method that can work within the muon's lifetime is ionization cooling, and a so-called Helical Cooling Channel (HCC) has been proposed to do so [2]. The HCC is composed of normal conducting RF cavities arranged in a helix within a solenoidal magnetic field (see Fig. 1 & 2). The RF cavities are filled with a high pressure gas to allow operation in multi-Tesla magnetic fields. A series of six HCC cells, approximately 230 m long, reduces the 6D emittance by a factor of 175,000 [3].

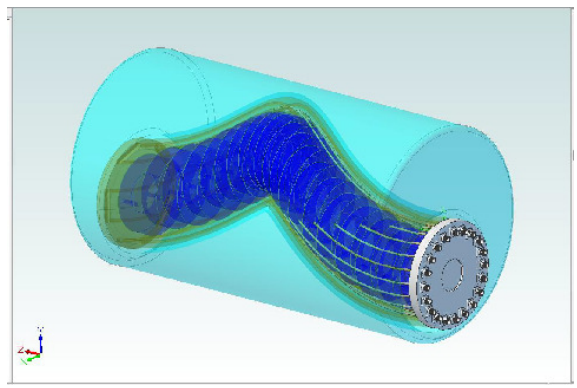


Figure 1: The 2D side view of one cell of the HCC, with components labeled. RF power is fed through the end. The solenoid coils are thermally isolated from the RF cavities [4].

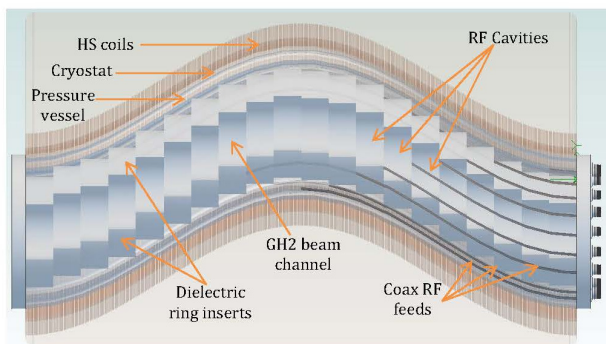


Figure 2: The 3D view of one cell of the HCC [4].

VALIDATION OF HIGH PRESSURE CAVITIES

A high pressure gas-filled RF (HPRF) cavity has been demonstrated to work in an external 3 T magnetic field without an ionizing beam [5, 6]. To validate its use in a HCC, a beam test using the 400 MeV Fermilab linac proton beam was performed at the MuCool Test Area (MTA). The cavity's performance using various beam intensities, gas pressures, dopant concentrations, and electric fields were studied with and without a 3 T magnetic field. Figure 3 shows a schematic of the experimental setup.

As the beam passes through the cavity, it ionizes the gas.

* freeben@iit.edu

Copyright © 2013 CC-BY-3.0 and by the respective authors

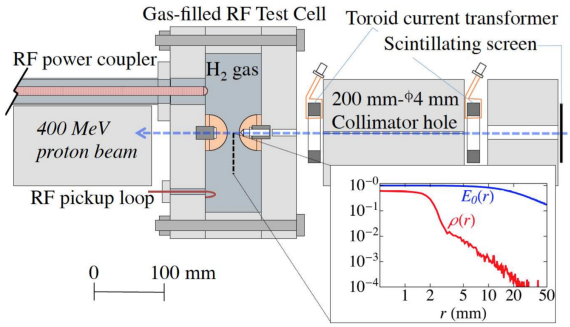


Figure 3: Schematic of the HPRF beam test setup. The beam enters from the right, passing through two collimators before impinging on the test cell. The inset plot shows the normalized electric field amplitude and simulated plasma density distribution as functions of radius.

The number of electron-ion pairs can be calculated:

$$N_{pairs} = \frac{\frac{dE}{dx}\,\rho\,L}{W_i} \tag{1}$$

where dE/dx is the stopping power, ρ is the gas density, L is the path length, and W_i is the average energy required to ionize a molecule.

Due to the high gas density, ionization electrons quickly come into equilibrium with the plasma, and drift with the cavity electric field. The electrons collide with gas molecules and transfer energy from the cavity to the plasma. The amount of energy transfered per charged particle can be evaluated by:

$$dw = q \int v\,E_0\,\sin(\omega\,t)\,dt \;=\; q \int \mu\,E_0^2\,\sin(\omega\,t)\,dt \tag{2}$$

where q is the charge of the particle, v is its drift velocity, E_0 is the amplitude of the electric field, and μ is the particle's mobility. The effect of the entire plasma is called plasma loading. To minimize the loading caused by electrons, an electronegative dopant gas can be used.

The results of the beam test are illustrated in Fig. 4 [7]. It can be seen that the addition of oxygen, present in dry air (DA), greatly decreases plasma loading. Additionally, there is very little difference between data taken with and without an external magnetic field.

The electric and magnetic fields inside the cavity as well as the ionization electrons' kinetic energy that would be present in a HCC were producible. However the maximum gas pressure was 100 atm while in a HCC it would be 180 atm. Additionally, the plasma density peaked at roughly 7×10^{11} cm^{-3} while in a real channel, due to the higher gas pressure and beam intensity, would be roughly 10^{16} cm^{-3}. Because of this, the results obtained in this beam test must be extrapolated to these higher densities.

The energy loss per particle, electron-ion and ion-ion recombination rates, and electron capture (by oxygen) time were measured as functions of electric field, gas pressure, and dopant concentration in order to extrapolate to the HCC parameters listed in Table 1.

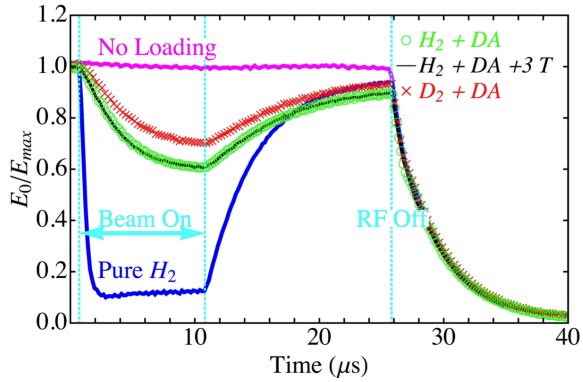


Figure 4: Typical RF envelopes recorded during the beam test. The beam is sent through the cavity once the flat top (E_{max}) has been reached. The magenta curve represents an RF pulse without beam.

Table 1: RF Parameters

Parameter	Unit	MTA Beam Test	HCC
RF frequency	MHz	801-808	325, 650
Gas pressure	atm	20-100	180
Oxygen conc.	%	2×10^{-4}-1	0.2
Peak E field	MV/m	5-50	20
External B field	T	0-3	4-14

Figure 5 shows the results of the electron attachment time, τ as a function of gas pressure. A fit to the data was used to extrapolate the time constant to 180 atm, which corresponds to 0.14 ns, indicated by the black lines on the plot.

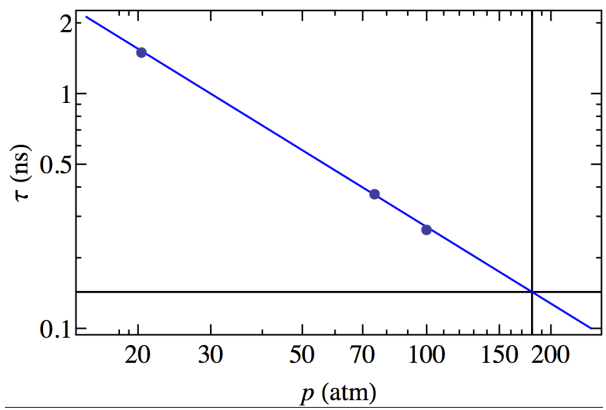


Figure 5: Electron attachment time as a function of gas pressure. The data (points) are taken from hydrogen gas doped with 1% DA (0.2% oxygen), and a fit was used to extrapolate the value of τ to 180 atm. The electron kinetic energy was kept constant at 0.4 eV.

PLASMA LOADING CALCULATION

A calculation of the plasma loading using muon accelerator beam and HCC RF parameters has been done. The beam parameters are given in Table 2. The beam bunches were assumed to be delta functions. The HPRF cavity's

Copyright © 2013 CC-BY-3.0 and by the respective authors

length was 10 cm and the stored energy was 19 J at 325 MHz and 4.7 J at 650 MHz.

The electron attachment time, electron-ion recombination rate, ion-ion recombination rate, and electron energy loss used in the calculation were based on extrapolations of measurements made at the MTA. The ion energy loss was based on classical values for the mobility.

Table 2: Beam Parameters

Parameter	Unit	Value
# of bunches	-	21
Bunch intensity	μ/bunch	10^{11}, 10^{12}
Bunch frequency	MHz	325
Injection phase	degrees	160

The results of the calculations are given in Table 3 & 4, for the two bunch intensities considered. Luminosity requirements dictate the bunch intensity before the final acceleration. To account for losses, the bunch intensity in the cooling channel will be between 10^{11} and 10^{12}.

Table 3: Plasma Loading Results for 10^{11} Muons per Bunch. The percent the accelerating voltage has dropped by the final bunch is given.

Parameter	Unit	325 MHz	650 MHz
Energy dissipated	J	0.292	0.317
% of total energy	-	1.5	6.7
% V_{accel} drop	-	0.8	3.4

Table 4: Plasma Loading Results for 10^{12} Muons per Bunch. The percent the accelerating voltage has dropped by the final bunch is given.

Parameter	Unit	325 MHz	650 MHz
Energy dissipated	J	1.84	1.98
% of total energy	-	9.7	42
% V_{accel} drops	-	5.0	24

It can be seen that, due to the larger stored energy, the 325 MHz cavity is only minimally loaded by the plasma, for either bunch intensity. The 650 MHz cavity experiences considerable plasma loading at the larger bunch intensity. This is due primarily to the buildup of ions over the course of the beam pulse. This is illustrated in Fig. 6. However, results obtained at the MTA indicate that the mobility of ions is smaller than the classical mobility, which was used here. This would have the effect of decreasing the loading due to ions.

CONCLUSIONS

The initial evidence suggests high pressure gas-filled cavities will work in a helical cooling channel for a muon accelerator. Extrapolation of parameters obtained at the MTA suggest that in the highest bunch intensity case, the accelerating gradient the final 10^{12} muon bunch would see would be degraded by 24%. The plasma dynamics inputs into this calculation were all taken to be conservative, and in reality the plasma loading should be less.

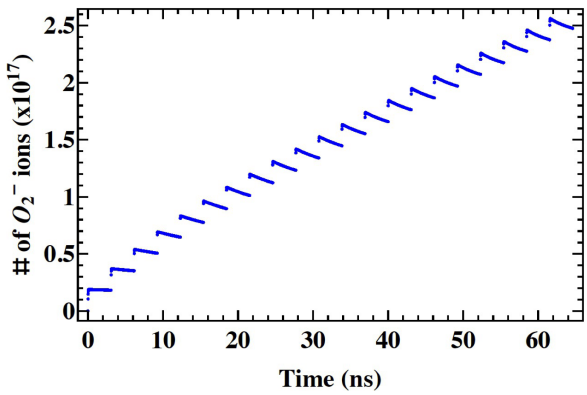


Figure 6: Number of O_2^- ions present in the cavity over the beam pulse.

The effects of higher gas and plasma density must be considered, and simulations [8] are underway to address this. Evidence suggests that higher densities have a positive effect on the cavity's performance.

Additionally, wakefields and beam loading have not yet been considered. These are not issues unique to gas-filled cavities, and may be a serious consideration for $10^{11}-10^{12}$ muons per bunch. The impact and mitigation are being investigated.

REFERENCES

[1] J-P. Delahaye et al., "Enabling Intensity and Energy Frontier Science with a Muon Accelerator Facility in the U.S.: A White Paper Submitted to the 2013 U.S. Community Summer Study of the Division of Particles and Fields of the American Physical Society," arXiv:1308.0494, August 2013.

[2] Y. Derbenev and R. P. Johnson, "Six-dimensional muon beam cooling using a homogeneous absorber: Concepts, beam dynamics, cooling decrements, and equilibrium emittances in a helical dipole channel," Phys. Rev. ST Accel. Beams, 8, 2005, 041002.

[3] R.P. Johnson et al., "Helical Muon Beam Cooling Channel Engineering Design," Proc. of NA-PAC'13, THPBA22.

[4] R.P. Johnson, private communication.

[5] K. Yonehara et al., "A Helical Cooling Channel System for Muon Colliders," IPAC 2010, Kyoto, May 2010, TU5PFP020, p. 870.

[6] P. Hanlet et al., "High Pressure RF Cavities in Magnetic Fields," EPAC 2006, Edinburgh, June 2006, TUPCH147, p. 1364-1366.

[7] M. Chung, et al., "Pressurized H_2 RF Cavities in Ionizing Beams and Magnetic Fields," accepted by Phys. Rev. Lett., October, 2013.

[8] R. Samulyak, et al., "Algorithms and Self-consistent Simulations of Beam-induced Plasma in Muon Cooling Devices," Proc. of NA-PAC'13, MOPBA06.

Copyright © 2013 CC-BY-3.0 and by the respective authors

TEST OF OPTICAL STOCHASTIC COOLING IN THE IOTA RING*

V. A. Lebedev# and Yu. Tokpanov, FNAL, Batavia, IL 60510, USA
M. S. Zolotorev, LBNL, Berkeley, CA 94720, USA

Abstract

A new 150 MeV electron storage ring is being built at Fermilab. The construction of a new machine pursues two goals a test of highly non-linear integrable optics and a test of optical stochastic cooling. This paper discusses details of OSC arrangements, choice of major parameters of the cooling scheme and incoming experimental tests of the optical amplifier prototype which uses highly doped Ti-sapphire crystal as amplification medium.

INTRODUCTION

The stochastic cooling has been successfully used in a number of machines for particle cooling and accumulation. Cooling rates of few hours required for luminosity control in hadron colliders cannot be achieved in microwave frequency range (~10^9-10^{10} Hz) usually used in stochastic cooling. Large longitudinal particle density, N/σ_s, used in such colliders requires an increase of cooling bandwidth by a few orders of magnitude. To achieve such increase one needs to make a transition to much higher frequencies. A practical scheme operating in the optical frequency range was suggested in Ref. [1]. The method is named the optical stochastic cooling (OSC). It is based on the same principles as the stochastic cooling but uses much higher frequencies. Thus it is expected to have a bandwidth of ~10^{14} Hz and can create a way to attain required damping rates. Fermilab plans to make an experimental test of the OSC in IOTA ring [2].

In the OSC a particle emits e.-m. radiation in the first (pickup) wiggler. Then, the radiation amplified in an optical amplifier (OA) makes a longitudinal kick to the same particle in the second (kicker) wiggler as shown in Fig. 1. A magnetic chicane is used to make space for the OA and to delay a particle so that to compensate for a delay of its radiation in the OA resulting in simultaneous arrival of the particle and its amplified radiation to the kicker wiggler. A particle passage through the chicane has a coordinate-dependent correction of particle longitudinal position which, consequently, results in a correction of relative particle momentum, $\delta p/p$, with amplitude ξ_0 so that:

$$\delta p / p = -\xi_0 \sin\left(k\,\Delta s\right) . \qquad (1)$$

Here $k = 2\pi/\lambda$ is the radiation wave-number,

$$\Delta s = M_{51}x + M_{52}\theta_x + M_{56}\left(\Delta p / p\right) , \qquad (2)$$

is the particle displacement on the way from pickup to kicker relative to the reference particle which experiences zero displacement and obtains zero kick, M_{5n} are the elements of 6x6 transfer matrix from pickup to kicker, x, θ_x and $\Delta p/p$ are the particle coordinate, angle and relative momentum deviation in the pickup.

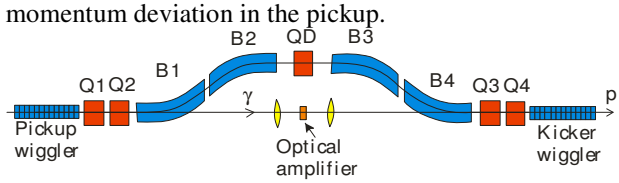


Figure 1: OSC schematic.

For small amplitude oscillations the horizontal and vertical cooling rates per turn are [3]:

$$\begin{bmatrix}\lambda_x\\ \lambda_s\end{bmatrix} = \frac{k\xi_0}{2}\begin{bmatrix}M_{56}-\tilde{M}_{56}\\ \tilde{M}_{56}\end{bmatrix} , \qquad (3)$$

where $\tilde{M}_{56} = M_{51}D_p + M_{52}D'_p + M_{56}$ is the partial slip-factor introduced so that for a particle without betatron oscillations and with momentum deviation $\Delta p/p$ the longitudinal displacement relative to the reference particle on the way from pickup to kicker is equal to $\tilde{M}_{56}\Delta p / p$, and D and D' are the dispersion and its derivative in the pickup. We assume that there is no x-y coupling in the chicane. Introduction of x-y coupling outside the cooling area allows a redistribution of the horizontal damping rate between two transverse planes. The sum of damping rates is: $\Sigma\lambda_n = k\xi_0 M_{56}/2$.

A non-linear dependence of kick on Δs in Eq. (1) results in a dependence of damping rates on amplitudes [3]:

$$\begin{aligned}\lambda_x(a_x,a_s) &= \left(2\,\mathrm{J}_0(a_s)\,\mathrm{J}_1(a_x)/a_x\right)\lambda_x \quad ,\\ \lambda_s(a_x,a_s) &= \left(2\,\mathrm{J}_0(a_x)\,\mathrm{J}_1(a_s)/a_s\right)\lambda_s \quad ,\end{aligned} \qquad (4)$$

where a_x and a_s are the amplitudes of longitudinal particle motion due to betatron and synchrotron oscillations expressed in the units of e.-m. wave phase:

$$\begin{aligned}a_x &= k\sqrt{\varepsilon_1\left(\beta_p M_{51}^{\,2} - 2\alpha_p M_{51}M_{52} + \left(1+\alpha_p^{\,2}\right)M_{52}^{\,2}\right)},\\ a_p &= k\left|\tilde{M}_{51}\right|\left(\Delta p / p\right) \quad ,\end{aligned} \qquad (5)$$

ε_1 is the Courant-Snyder invariant of a particle, and $(\Delta p/p)$ is the amplitude of particle synchrotron motion. As one can see from Eq. (4) each damping rate changes its sign if any of amplitudes exceeds the first root, μ_0, of the Bessel function $\mathrm{J}_0(x)$. That determines that at the cooling area boundary $a_x=\mu_0$ or $a_y=\mu_0$ where $\mu_0\approx2.405$. That yields the cooling area boundaries:

$$\begin{aligned}\varepsilon_{\max} &= \frac{\mu_0^{\,2}}{k^2\left(\beta_p M_{51}^{\,2} - 2\alpha_p M_{51}M_{52} + \left(1+\alpha_p^{\,2}\right)M_{52}^{\,2}\right)},\\ \left(\Delta p / p\right)_{\max} &= \mu_0 \Big/ \left(k\left|\tilde{M}_{51}\right|\right) \quad .\end{aligned} \qquad (6)$$

Although M_{56} and, consequently, the sum of damping rates depend only on focusing inside the chicane, $\tilde{M}_{56}$ and the ratio of damping rates depend on the dispersion at the chicane beginning, *i.e.* on the ring dispersion. Eq. (3) yields the ratio of damping rates,

*Work supported by Fermi Research Alliance, LLC, under Contract No. DE-AC02-07CH11359 with the United States Dep. of Energy
#val@fnal.gov

Copyright © 2013 CC-BY-3.0 and by the respective authors

$$\lambda_x / \lambda_s = M_{56} / \tilde{M}_{56} - 1 \ . \quad (7)$$

The relative cooling ranges are introduced as ratios of cooling area boundaries $(\Delta p/p)_{max}$ and ε_{max} to the rms values of momentum spread, σ_p, and horizontal emittance, ε, established by equilibrium between SR damping and heating. That yields:

$$n_{\sigma s} = (\Delta p / p)_{max} / \sigma_p \ , \quad n_{\sigma x} = \sqrt{\varepsilon_{max} / \varepsilon} \ . \quad (8)$$

As one can see the transverse cooling range does not depend on the dispersion but depends on the beta-function in the pickup wiggler.

BEAM OPTICS

The OSC system will take one of four straight sections with length of ~4 m. The cooling chicane consists of four dipoles with parallel edges (see Fig. 1) To obtain transverse cooling M_{56} and $\tilde{M}_{56}$ have to be different. It is achieved by placing a defocusing quad in the chicane center. Leaving only leading terms in the thin lens approximation one obtains:

$$M_{56} \approx 2\Delta s \ , \quad \tilde{M}_{56} \approx 2\Delta s - \Phi D^* h \ , \\ \lambda_x / \lambda_s \approx \Phi D^* h / \left(2\Delta s - \Phi D^* h\right) . \quad (9)$$

Here Δs and h are the path lengthening and the trajectory offset in the chicane, $\Phi=1/F$ is the defocusing strength of the quad, D^* is the dispersion in the chicane center, and we assume that $dD/ds=0$. The latter condition is required to minimize the equilibrium beam emittance. Similarly, using Eq. (8) one obtains estimates for the cooling ranges

$$n_{\sigma p} \approx \mu_0 / \left(\left(2\Delta s - \Phi D^* h\right) k \sigma_p\right) , \\ n_{\sigma x} \approx \mu_0 / \left(2kh\Phi\sqrt{\varepsilon\beta^*}\right) , \quad (10)$$

where $\beta^* \approx L^2 / \beta$ is the beta-function in the chicane center, and L is its half-length. As one can see from Eqs. (9) and (10) $\Phi D^* h$ determines the cooling dynamics. Using the bottom equation in (10) we obtain:

$$\Phi D^* h \approx \frac{\mu_0}{2kn_{\sigma x}} \sqrt{\frac{A^*}{\varepsilon}} \ , \quad (11)$$

where $A^*=D^{*2}/\beta^*$ is the dispersion invariant in the chicane center. As one can see the given wave-length, beam emittance and transverse cooling range uniquely determine $\Phi D^* h$ and, consequently, the cooling dynamics.

The choice of the wavelength of 800 nm was determined by choice of OA. Although the delay in the OA of 2 mm is quite small it still presents considerable challenges to the beam optics. Without redistribution of decrements it yields an acceptably low longitudinal cooling range, $n_{\sigma p}$ <1. Therefore a redistribution of decrements is required but its value is limited by reduction of the transverse cooling range. Decreasing the ring energy from 150 to 100 MeV reduces the equilibrium emittance and momentum spread and allows obtaining sufficiently large cooling ranges of >2 for both planes. Operation at the coupling resonance redistributes SR cooling rates between horizontal and vertical planes resulting approximately equal equilibrium transverse emittances and, consequently, twice smaller horizontal emittance. Tables 1 and 2 present the main parameters of the ring. The ring optics is symmetric relative to the chicane center. Figure 2 presents the dispersion and beta-functions for half of the ring. The optics was designed to minimize the equilibrium emittance. It requires a minimization of the dispersion invariant $A = \left(1+\alpha^2\right) D^2 / \beta + 2\alpha D D' + \beta D'^2$ in the dipoles. Its initial value of 11 m determined by requirements of OSC is quite large and, if not addressed, would result in an unacceptably large emittance. An adjustment of horizontal betatron phase advances between dipoles was crucial to obtain tolerable transverse emittances. Figure 3 presents the value of A along half of the ring.

Table 1: Main Parameters of IOTA storage ring for OSC

Circumference	40 m
Nominal beam energy	100 MeV
Bending field	4.8 kG
Tunes, Q_x/Q_y	6.36/2.36
Number of particles	$5 \cdot 10^8$
Transverse emittances, $\varepsilon=\varepsilon_x=\varepsilon_y$, rms	11.5 nm
Rms momentum spread, σ_p	$1.23 \cdot 10^{-4}$
SR damping times (ampl.), $\tau_s / (\tau_x = \tau_y)$	1.4 / 0.67 s

Table 2: Major parameters of cooling chicane

Delay in the chicane, Δs	2 mm
Horizontal beam offset, h	20.1 mm
M_{56}	3.95 mm
Dispersion in the chicane center, D^*	307 mm
Beta-function in the chicane center, β^*	8.59 mm
Cooling rates ratio, $(\lambda_x = \lambda_y)/\lambda_s$	1.18
Cooling ranges (before OSC), $n_{\sigma x}/n_{\sigma s}$	2.1 / 3.2
Dipole magnetic field	4.22 kG
Dipole length	10 cm
Strength of central quad, GdL	1.58 kG

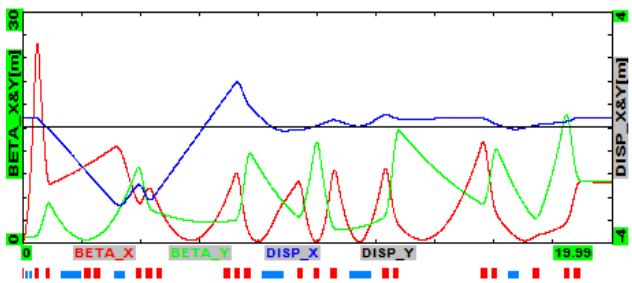


Figure 2: Optics functions for IOTA half ring starting from the OSC section.

OPTICAL AMPLIFIER

Choice of Ti:Sapphire OA has a few advantages. First, it has quite wide bandwidth (~20% FWHM). Second, it allows operation in the CW regime; and third, it can deliver significant amplification with only ~1 mm signal delay. For an OA prototype we bought a highly doped (0.5%wt Ti_2O_3) 2 mm thick Ti: Sapphire crystal from GT Crystal Systems. An estimated low power gain is ~100 (20 Db) with pumping power density of 1.8 MW/cm^2.

Copyright © 2013 CC-BY-3.0 and by the respective authors

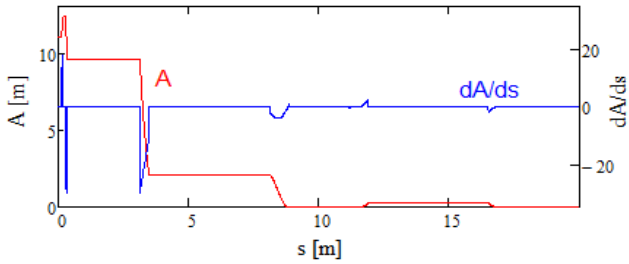


Figure 3: Dependence of the dispersion invariant, A, and its derivative for IOTA half-ring starting from the OSC section. dA/ds is non- zero at dipoles.

Optical system has two lenses (Fig. 1). The first lens focuses the beam radiation on the Ti:Sapphire crystal, and the second one focuses the amplified radiation into the kicker wiggler. The lenses have the same focal length and radius. The focal length was chosen to minimize the size of e.-m. radiation on the Ti:Sapphire crystal. A longer focal length decreases the spot size at the crystal entrance but increases the waist and effects of the field of depth. An optimal value of the focal length is 8 cm with lens radius of 3.5 mm. The lens radius was determined by a compromise between the damping rates growth with the radius and an increase of signal delay leading to a drastic deterioration of beam optics. The choice of lens parameters results in that the most radiation is within cylinder with 30 μm radius where amplification can happen. The radiation of pumping laser follows along beam radiation axis. Windows in vacuum chamber located along the axis allow the pumping light to get in and out together with the amplified radiation. The radiation of pumping laser comes through the same lenses. Additional matching lenses are installed outside the vacuum chamber. The pumping laser radiation is focused into 30 μm cylinder with close to rectangular power density distribution. It determines the laser power to be ~50 W. To reduce the effect of the depth of field a 50 cm gap between the cooling chicane and the wigglers is introduced.

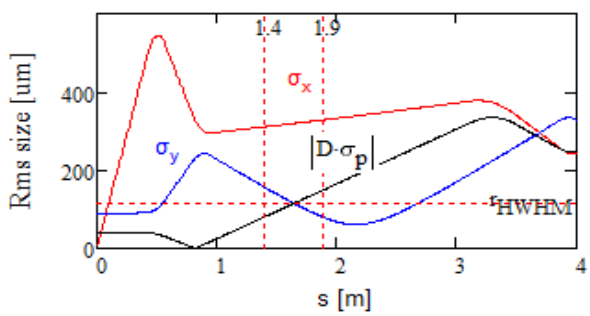


Figure 4: Rms beam sizes (horizontal – σ_x, vertical – σ_y, and due to momentum spread - $|D\sigma_p|$) in vicinity of cooling chicane starting from the center of OSC section. Vertical lines mark location of wiggler. The horizontal line shows diffraction limited spot size (HWHM) of amplified radiation in the kicker wiggler.

Cooling the OA to liquid nitrogen temperature is required. It increases the crystal thermal conductivity resulting in an acceptable temperature difference across the crystal (~8K) and thermal stresses. Cooling also reduces the dependence of refraction index on temperature and, thus, optics distortions related to the high pumping power.

Recently we assembled a prototype OA which will be operating in a pulsed regime to avoid problems with cooling required for CW regime. The goal of the measurements is to determine the dependence of phase and amplitude of amplified signal on frequency. It is achieved by inserting the OA into one leg of Michelson interferometer. The first measurements are expected soon.

COOLING RATES

Parameters of undulators and cooling rates are shown in Table 3. The undulator period was chosen so that the wavelength of the radiation at zero angle would be at the band boundary (750 nm). The cooling rates were computed using formulas developed in Ref. [4] where additional averaging over amplifier band was applied resulting in ~20% reduction of rates. It was assumed that only radiation within 2 mrad enters the OA. It sets the aperture of optical system to 2·3.5 mm and the upper boundary of the band to 850 nm. The effects of e.-m. wave dispersion in the OA amplifier were neglected. It was assumed that the dispersion in the amplifier is included into the gain, *i.e.* $G = 10$ implies an amplitude amplification of 10. Consequently, the dispersion makes the power gain to be somewhat larger than G^2. We also neglected incomplete overlap of light and particle beams in the kicker undulator at the beginning of cooling process when the beam size is determined by SR. Figure 4 shows the rms beam sizes in the cooling section for the uncooled beam. One can see that the beam sizes exceed the radiation spot size. It results in that the initial cooling rates are about factor of 5 lower. For the chosen number of particles in the bunch the system operates slightly below optimal gain at the beginning of cooling process. We would like to stress that even in the absence of amplification (passive system, $G = 1$) the OSC damping exceeds SR damping by more than an order of magnitude (see Tables 1 and 3).

Table 3: Main parameters of OSC

Undulator parameter, K	0.6
Undulator period	4.92 cm
Radiation wavelength at zero angle	750 nm
Number of periods, m	10
Total undulator length, L_w	0.50 m
Length from OA to undulator center	1.65 m
Amplifier gain (amplitude)	10
Telescope aperture, $2a$	7 mm
Lens focal length, F	80 mm
Damp. rates (x=y/s)	160/140 s^{-1}

REFERENCES

[1] M. S. Zolotorev and A. A Zholents, Phys. Rev. E, **50**, 4, p. 3087 (1994).
[2] S. Nagaitsev, *et. al.*, p.16, IPAC-2012, (2012).
[3] V. Lebedev, p. 644, HB-2010, (2010).
[4] V. Lebedev, p. 514, HB-2012, (2012).

Copyright © 2013 CC-BY-3.0 and by the respective authors

FREE-ELECTRON LASERS IN THE SOFT X-RAY REGIME*

J. N. Corlett#, LBNL, Berkeley, CA, USA

Abstract

X-ray science in imaging, structure determination, and spectroscopy, as well as diffraction/scattering, requires intense ultrafast pulses in the soft X-ray range, uniquely provided by free electron lasers (FELs). In addition to operational soft X-ray FEL facilities, there are FEL construction projects under way that include soft X-ray laser capabilities, and planned facilities with novel capabilities. This paper provides a review of the exciting field of existing and planned soft X-ray FELs with emphasis on new schemes and new technologies to achieve better performance.

SCIENCE NEEDS FOR SOFT X-RAY FELS

The scientific innovation expected from the construction and operation of X-ray FEL facilities lies in their ability to provide tools that offer extreme spatial, temporal, and energy resolution. Properties of FEL sources are expected to include the ability to reach to the ultrafast timescales of atomic motion (about 100 fs), spin motion (down to about 1 fs), and electronic motion (down to attoseconds), the spatial scale of the atomic bond (down to Angstroms), and energy resolution on the scale of the bond that holds electrons in correlated motion with near neighbors (~10 meV and greater). X-ray FEL sources offer unique capabilities to combine information on atomic length scales with data on full-scale functional systems under realistic operational conditions. In addition, these sources have an intensity and brightness needed to observe the subtlest of nature's secrets at these frontier space, time, and energy scales, and with elemental specificity.

Critical X-ray science in imaging, structure determination, and spectroscopy needs new capabilities in the soft X-ray range, accessing K- and L-edges of the earth-abundant elements, as well as diffraction/scattering in the few to several keV photon energy range. These scientific requirements give rise to the following desirable FEL performance features:

- X-ray time structure
  - Control of longitudinal phase space, with Fourier-transform-limited pulse structure extending from ~100 fs pulses with ~10 meV bandwidths to sub-femtosecond pulses with ~10 eV bandwidths
  - Control of longitudinal pulse shape, amplitude and phase
  - Synchronization and full integration with conventional pulsed laser sources
  - High repetition rate with regularly spaced pulses
- Full transverse coherence
  - Requirements set by real-space imaging, diffractive imaging, and photon-correlation spectroscopy
  - Optical systems to preserve and exploit transverse coherence
- High peak flux and brightness
  - Requirements set by non-linear effects in materials
- High average flux and brightness
  - Short-pulse sources with high repetition rates (100 kHz or greater) providing average flux and/or brightness substantially beyond existing sources
- Tunability, polarization control, and extended photon energies
  - Tunability throughout the transition-metal L-edges and polarization control and modulation
  - Two-color capability for non-linear spectroscopies and X-ray pump/X-ray probe
- High degree of amplitude and wavelength stability
- Multiple simultaneous users

SOFT X-RAY FEL OVERVIEW

High-gain single pass FELs at wavelengths in the EUV and shorter have been operating as photon science user facilities for almost a decade – the TESLA Test Facility (TTF) became the Free Electron Laser in Hamburg (FLASH) in 2003, and user operations began in 2005 with lasing at 25 nm [1]. FLASH now operates at wavelengths in the water-window (~4 nm) and longer. The LCLS at SLAC is the world's first hard X-ray FEL [2], and also operates in the soft X-ray regime with wavelength ~4.5 nm and shorter [3]. Both of these facilities currently operate in SASE mode in the soft X-ray range (although the LCLS also offers a hard X-ray self-seeded mode [4]). FERMI@elettra is a seeded FEL facility, offering improved temporal coherence, with tunable user beam currently offered down to 20 nm [5]. The SACLA facility currently operates the shortest wavelength FEL, in SASE mode [6].

Upgrades of these facilities are planned or are in progress and include development of soft X-ray capabilities, in capacity (adding FEL beamlines), and also in capability by extending the tuning range, seeding (either self-seeding or external laser-seeding) and offering tunable undulators and new operating regimes of pulse duration and time structure. The FERMI team is now commissioning a 2-stage harmonic cascade to reach into the water window [7]. Upgrade plans at SACLA include the re-location of the SCSS test facility as a soft X-ray FEL driver [8]. FLASH-II will add variable-gap undulators in a separate beamline driven by the existing linac, and seeding. LCLS-II is planned to provide self-seeded capability from 0.25–5 nm, using a new CW superconducting linac.

The European XFEL [9], SwissFEL [10], and Korean PAL-XFEL [11] facilities are under construction, and

*Work supported by the Director, Office of Science, of the U.S. Department of Energy under Contract No. DE-AC02-05CH11231
#jncorlett@lbl.gov

Copyright © 2013 CC-BY-3.0 and by the respective authors

plan for soft X-ray capability, in SASE or in self-seeded mode.

The FLASH and FLASH-II, European XFEL, and LCLS-II projects are based on superconducting RF technology, and offer very high repetition rate (up to ~100 kHz at each FEL) providing high average photon beam brightness and coherent power. Other facilities and projects use normal conducting accelerators and provide relatively low repetition rate (up to ~100 Hz). Use of normal conducting accelerators operated at high gradient is attractive in allowing for a small facility footprint.

Design studies elsewhere are developing concepts for soft X-ray FELs, including SXFEL (Shanghai), IRIDE (INFN-Frascati), and LUNEX5 (SOLEIL). Other soft X-ray FEL facility design studies have recently come to an end, including the NGLS at Berkeley Lab, and the NLS in the UK.

In addition to facilities, projects, and design studies, there are important R&D facilities contributing to understanding of FEL science and technology. Currently operating single-pass FEL R&D facilities are NLCTA (at SLAC), SPARC (at INFN Frascati), SDUV (Shanghai Institute of Applied Physics), and MAX-Lab (Lund, Sweden). Proposals for single-pass FEL R&D facilities include CLARA (STFC Daresbury).

OPERATING FACILITIES, AND THEIR UPGRADES AND EXPANSION PLANS

FLASH

The FLASH facility is a high-gain single pass SASE FEL driven by a pulsed superconducting L-band (1.3 GHz) linac based on TESLA technology, with maximum beam energy 1.25 GeV [12]. The time structure is a burst mode with up to 3 MHz bunch rate in an 800 μs macropulse, 10 Hz repetition rate, delivering up to 5000 pulses per second. Photon pulses in the wavelength range 4.2–44 nm, with 10–400 μJ per pulse, and duration in the range <50–250 fs, are produced in fixed-gap permanent-magnet undulators of period 27.3 mm. A Cs_2Te photocathode provides electron beam in a normal-conducting L-band RF gun, with charge per bunch 0.02–1 nC. Peak current at the FEL is typically 1–2 kA. Photon tuning is provided by adjusting the electron beam energy, and RF and beam-based feedback systems are used to enhance stability of beam energy, bunch compression, and timing. Development plans include production of shorter pulses, and enhanced temporal coherence through laser-seeding using XUV pulses from an HHG laser, as well as high gain harmonic generation (HGHG) using a UV seed [13].

FLASH-II

FLASH-II adds a second FEL beamline in a new undulator tunnel and a new experimental hall added to the facility at DESY. Driven by the same superconducting linac, both FLASH-I and FLASH-II are to be delivered electron beam in bursts at 10 Hz repetition rate by a beam kicker that will distribute bunches from within each macropulse [14]. Two photocathode lasers are used to generate sub-trains in a macropulse, allowing flexibility in intra-train repetition rate, number of pulses per train, longitudinal pulse shape, and pulse energy for both FELs. The bunch spacing for beam to FLASH-II is 1–25 μs. The undulators are 31.4 mm period, with variable gap, and allow tuning from 4–13.5 nm in SASE mode at beam energy of 1.2 GeV, and longer wavelengths at lower beam energy. Construction is under way, and commissioning with beam is expected to begin in early 2014. Seeded FEL operation is planned, using single-stage harmonic generation from a UV seed laser, and initially radiating in the range 20-40 nm.

LCLS

LCLS demonstrated the first hard X-ray laser operation in 2009, with an S-band (2856 MHz) photocathode gun and 14 GeV linac driving an FEL with 3 cm period fixed-gap permanent magnet undulators [2]. The facility provides photon wavelength from 4.5 nm to 1.2 Å, in pulses of ~3–500 fs, ~2–6 mJ per pulse, at a repetition rate of 120 Hz. Charge per pulse is typically ~250 pC to optimize brightness. Hard X-ray self-seeding at ~8.2 keV results in a factor ~50 reduction in bandwidth compared to SASE, and a brightness increase currently limited to a factor ~3. LCLS upgrade plans include development of capabilities for fs-scale pulses, hard and soft X-ray self-seeding, two-color generation, synchronized THz, multiple-bunch operation, and polarization control [3].

LCLS–II

LCLS-II is a major expansion of the FEL capabilities at SLAC, and plans are being developed to build a new 4 GeV superconducting L-band (1.3 GHz) linac based on ILC/XFEL technology developed for CW operation. The linac will drive two FELs, each an adjustable gap permanent magnet undulator design. Both FELs will be self-seeded, and one tunable over the range 1–5 nm (undulator period ~40 mm), the other 0.25–1.2 nm (undulator period ~26 mm). The latter will replace the existing LCLS undulator, and designed to be driven be either the new linac, or the existing S-band linac (for harder X-ray and higher per-pulse energy capability, at lower repetition rate). Bunch rate from the superconducting linac may be as high as 1 MHz, and each FEL will typically provide ~100 kHz X-ray pulses with uniform spacing, with energy per pulse up to ~2 mJ. A high-brightness, high repetition rate injector such as being developed at the APEX project may be used as an electron source [15]. The facility takes advantage of existing SLAC infrastructure in housing the injector, linac, RF power systems, beam transport, undulators, X-ray beamlines and endstations. This approach offers cost savings, and upgrade paths both in capacity by adding FELs, and capability by implementing new FEL designs. The construction project is estimated to complete in 2020.

Copyright © 2013 CC-BY-3.0 and by the respective authors

FERMI@elettra

The first seeded FEL user facility has been operational for users since 2012, and currently provides continuous tunability from the FEL-1 harmonic cascade over the range 20–65 nm (and longer wavelengths to 100 nm possible with specific machine setup). A UV seed laser is used to modulate the electron beam from a 1.2 GeV S-band (2998 MHz) GeV linac operating at 10 Hz, radiating at up to the 13th harmonic of the seed in 55 mm period variable-gap APPLE-II type undulators with polarization control. Peak current is ~500 A, as opposed to ~kA used in SASE FELs. Pulse energy of up to ~100 μJ can be delivered, and relative bandwidth as low as 0.05% (close to the Fourier transform limit), wavelength stability ~7x10^{-5}, and amplitude variations ~10% (measured in the EUV) [16, 17]. An upgrade to 50 Hz is under way, by implementing a new RF photocathode gun and klystron modulators.

FEL-2 is currently being commissioned, and uses a beam of energy ~1.5 GeV (by activating SLED cavities in the RF power systems) driving a two-stage harmonic cascade using a fresh-bunch approach. The two stages are each high gain harmonic generation FELs. The first stage is seeded by a UV pulse (~260 nm, the 3rd harmonic of a Ti:Sa laser system), and lases at the 4th-6th harmonic. The output of this first stage is used to seed the second stage modulator, using a chicane to delay the electron bunch such that the seed pulse overlaps and modulates an unperturbed ("fresh") part of the electron bunch. The final FEL output is obtained at up to ~65 harmonic of the initial UV seed. Tuning range is nominally 4–20 nm although coherent FEL emission with wavelength as short as 3 nm has been observed [18].

SACLA

SACLA opened to users in 2012 and is currently a hard X-ray facility, producing photon pulses in a range 5–15 keV, with 100-400 mJ per pulse in a duration of ~10–15 fs, at a repetition rate of 10 Hz (60 Hz maximum). The undulators are in-vacuum variable-gap, with period 18 mm. The machine uses an 8.5 GeV, C-band (5.7 GHz), linac, with a novel single-crystal CeB_6 thermionic cathode and combination of VHF, UHF, L-, S-, and C-band RF systems in the injector. Bunch charge is ~100–300 pC, and peak current >3 kA. SASE central wavelength stability is ~3x10^{-4}, and pulse energy variations ~10–20% [6,8].

Upgrades are being pursued to provide additional FEL beamlines (up to 5 and including one soft X-ray), a bunch-by-bunch beam distribution system, hard X-ray self-seeding, higher beam energy (to 9 GeV), and relocation of the SCSS (SPring-8 Compact SASE Source) test accelerator and increasing it's energy to 450 MeV (and potentially 1.4 GeV) to drive a EUV to soft X-ray FEL [8]. The soft X-ray FEL uses in-vacuum undulators with period 18 mm (same as hard X-ray undulators), and initial tuning range is ~15–60 nm, with 50–100 μJ per pulse. First operation of the soft X-ray FEL is planned for autumn 2015. The SCSS was built in 2005 to demonstrate the SACLA concept with a 250 MeV test accelerator, and successfully lased at 50 nm, with HHG seeding at 61.5 nm [19].

CONSTRUCTION PROJECTS

European XFEL

The European XFEL is under construction in Hamburg, Germany, and consists of a 17.5 GeV pulsed L-band (1.3 GHz) superconducting linac serving three initial SASE FELs, delivering photons from 0.05–4 nm in pulses of ~1–100 fs. The time structure is 2700 bunches per 600 μs macropulse, at a repetition rate of 10 Hz (average bunch rate 27 kHz, and a rate of 4.5 MHz within the macropulse). Kickers will provide flexible beam distribution with simultaneous operation of three experiments. Bunch charge is 0.02–1 nC, and average beam power over 500 kW. The injector is a normal-conducting L-band photo-cathode RF gun of the same type in operation at FLASH. The soft X-ray FEL is downstream from a hard X-ray FEL, using the same beam, and has 68 mm period permanent magnet undulators with adjustable gap; the tuning range is extended by adjusting the electron beam energy. Average soft X-ray power is greater than 100 W [20].

SwissFEL

Under construction in Villigen, Switzerland, SwissFEL is an X-ray laser facility with two FEL lines covering the wavelength range from 0.1-0.7 nm and 0.7-7 nm, respectively. An S-band injector delivers beam at 100 Hz to a normal-conducting C-band (5.72 GHz) linear accelerator. Two bunches of charge 10–200 pC are accelerated per RF pulse; one is extracted at 3 GeV for soft X-ray generation, while the other continues to be accelerated to 5.8 GeV for hard X-ray production. The soft X-ray FEL is self-seeded and uses 40 mm period APPLE-II type variable gap undulators with polarization control, and delivers per-pulse energy of ~100 μJ. Commissioning of the linear accelerator and the hard X-ray FEL will start in 2016; funding for the soft X-ray component requires additional approval and construction is planned to begin in 2018 [10].

PAL X-FEL

The PAL-XFEL is under construction, and designed to have three hard X-ray undulator lines at the end of a 10 GeV S-band (2856 MHz) linac, and a branch line at 3.15 GeV for two soft X-ray undulator lines. Initially, one hard X-ray and one soft X-ray FEL will be built. The injector uses an S-band photocathode gun which delivers two bunches of 20–200 pC charge at 60 Hz, bunch delivery to the soft X-ray beamline is to be controlled by a kicker system. A passive wakefield "dechirper" will be used to remove the correlated energy chirp following extraction from the linac [21]. The soft X-ray undulators are planned to be permanent-magnet adjustable-gap devices with 34 mm period, and APPLE-II type for the final few gain lengths to provide polarization control. Photon

Copyright © 2013 CC-BY-3.0 and by the respective authors

wavelength is in the range 1–4.5 nm (longer wavelengths using lower beam energy), with ~90 fs pulse duration. FEL experiments are planned to begin in late 2016 [11].

PROPOSALS AND DESIGN STUDIES

NGLS

The LBNL-led NGLS collaboration developed design concepts for a multi-beamline soft x-ray FEL array powered by a superconducting linear accelerator, operating with a high bunch repetition rate of ~1 MHz. The CW L-band (1.3 GHz) 2.4 GeV superconducting linear accelerator design is based on developments of TESLA and ILC technology, and is supplied by a high-brightness, high repetition rate VHF-frequency photocathode electron gun under development at the APEX facility [15]. 300 pC, 500 A peak current, ~300 fs electron bunches from the linac are distributed by RF deflecting cavities to the array of up to nine independently configurable FEL beamlines with nominal bunch rates of ~100 kHz in each FEL, with uniform pulse spacing, and some FELs capable of operating at the full linac bunch rate. Undulators are ~20 mm period, Nb_3Sn superconducting planar devices to provide optimal performance, and are being developed in an R&D program [22]. Individual FELs may be configured for different modes of operation, including self-seeded and external-laser-seeded, and each may produce high peak and average brightness x-rays with a flexible pulse format, including multiple approaches to deliver two-color X-rays with wide tuning range for each color, and with pulse durations in the range ~0.1–100 fs. RF and beam-based feedback systems, integrated with fiber-based timing and synchronization systems, would provide exceptional photon-beam stability and synchronization control in a high-rate, CW machine [23]. The effort is now stopped.

SXFEL

Baseline technical design studies for the Shanghai soft X-ray FEL (SXFEL) proposal have been completed. The initial configuration is planned to use a 10 Hz normal-conducting linac using S- and C-band technology and would deliver 840 MeV beam energy, driving a laser-seeded harmonic cascade to reach a wavelength of 8.8 nm. Upgrade to 1.2–1.3 GeV would provide photon wavelength down to 3 nm. The facility would be built at the Shanghai Synchrotron Radiation Facility, in collaboration with Tsinghua University [24].

LUNEX5

LUNEX5 is a multi-institution proposal coordinated by SOLEIL, for R&D and demonstration of advanced FEL concepts, including both RF linac and laser wakefield accelerators. Seeded FEL techniques, using in-vacuum cryogenically cooled PrFeB undulators with 15 mm period, would be developed with a 400 MeV superconducting linac, and a 0.4–1 GeV laser-plasma beam. HHG and EEHG seeding schemes would be explored to produce 4–40 nm FEL output in pulses of ~10 fs duration. A conceptual design report is completed, and the project is in an R&D stage [25].

IRIDE

The IRIDE concept under development and based at INFN Frascati [26] is a high brightness particle beams factory based on high duty cycle superconducting linacs. The design concept includes FEL oscillators and SASE and seeded FELs, operating over a very broad spectrum from IR to hard X-ray.

NLS

The NLS team in the U.K. developed a conceptual design for a 1 kHz coherent light source with FELs operating to wavelengths in the range ~1–25 nm, using a 2.25 GeV CW superconducting L-band (1.3 GHz) linac. The pulsed L-band photocathode gun would deliver 200 pC at 1 kHz, driving HHG-seeded FELs to provide temporal coherence and increased brightness. Three initial FELs were conceived, using harmonic cascade schemes and generating ~20 fs pulses. Upgrade paths to higher repetition rate (MHz), shorter X-ray pulses, higher energy photons (to 2 keV), and additional FELs and endstations were identified [27].

WiFEL

A concept for a Wisconsin FEL (WiFEL) has been developed based on a CW superconducting L-band (1.3 GHz) linac fed by a superconducting photocathode gun delivering bunches at MHz rate. A staged approach is suggested that includes incremental build-out of the accelerator and multiple seeded FELs, using harmonic cascades and covering a wavelength range down to ~1 nm, with ~10 fs pulses [28].

ACKNOWLEDGEMENTS

The author wishes to thank many people who have contributed to this review of projects, including Marie-Emanuelle Couprie, Paul Emma, Massimo Ferrario, Luca Giannessi, Winfried Decking, Heung-Sik Kang, Tor Raubenheimer, Sven Reiche, Robert Schoenlein, Siegfried Schreiber, Hitoshi Tanaka, and Zhentang Zhao.

REFERENCES

[1] V. Ayvazyan et al., "First operation of a free-electron laser generating GW power radiation at 32 nm wavelength", Eur. Phys. J. D **37**, 297–303 (2006)

[2] P. Emma, et al., "First lasing and operation of an angstrom-wavelength free-electron laser," Nature Photon. **4**, 641 (2010)

[3] T. Raubenheimer, "LCLS Operational Experience And LCLS-II Design", Proceedings of LINAC2012, Tel-Aviv, Israel, (2012)

[4] J. Amman et al, "Demonstration of self-seeding in a hard-X-ray free-electron laser" Nature Photonics **6**, 693–698 (2012)

Copyright © 2013 CC-BY-3.0 and by the respective authors

[5] E. Allaria et al., "Tunability experiments at the FERMI@Elettra free-electron laser", New Journal of Physics **14** (2012) 113009
[6] T. Ishikawa et al., "A compact X-ray free-electron laser emitting in the sub-ångström region", Nat. Photonics **6**, 540-544 (2012)
[7] L. Giannessi et al., "First Lasing of FERMI FEL-2", Proceedings of the 2013 FEL Conference, New York, USA (2013)
[8] T. Hara, K. Togawa, H. Tanaka, "Progress in SACLA Operation", Proceedings of FEL12, Nara, Japan (2012)
[9] M. Altarelli et al., "The European X-ray Free Electron Laser Technical Design Report", Hamburg, July 2007, DESY 2006-097.
[10] H.H. Braun, "SwissFEL, the X-ray Free Electron Laser at PSI", Proceedings of FEL12, Nara, Japan (2012)
[11] H.-S. Kang et al., "Current Status of PAL-XFEL Project", Proceedings of IPAC13, Shanghai, China (2013)
[12] K. Honkavaara et al., "Status of the FLASH Facility", Proceedings of the 2013 FEL Conference, New York, USA (2013).
[13] J. Boedewadt, C. Lechner, "Results and Perspectives of the FEL Seeding Activities at FLASH", Proceedings of the 2013 FEL Conference, New York, USA (2013)
[14] S. Schreiber et al., "Simultaneous Operation of FLASH1 and FLASH-2", Proceedings of the 2013 FEL Conference, New York, USA (2013).
[15] F. Sannibale, et al., "Advanced photoinjector experiment photogun commissioning results" PRST-AB **15**, 103501 (2012)
[16] E. Allaria et al., "Highly coherent and stable pulses from the FERMI seeded free-electron laser in the extreme ultraviolet", Nature Photonics **6**, 699–704 (2012)
[17] M. Svanderlik et al., "FERMI Seeded FEL Progress Report", Proceedings of IPAC13, Shanghai, China (2013)
[18] E. Allaria et al., "Double staged seeded FEL with fresh bunch injection technique at FERMI", Proceedings of the 2013 FEL Conference, New York, USA (2013)
[19] T. Tanaka et al., "SASE Saturation at the SCSS Test Accelerator Ranging from 50nm to 60nm", Proceedings of FEL08, Gyeongju, Korea (2008)
[20] W. Decking, "Status Of The European XFEL – Constructing the 17.5 GeV Superconducting Linear Accelerator", Proceedings of LINAC2012, Tel-Aviv, Israel, 2012.
[21] H.-S. Kang, "Control of Electron Beam Longitudinal Phase Space with a Novel Compact De-chirper", Proceedings of the 2013 FEL Conference, New York, USA (2013)
[22] E. Rochepault et al., "Error Analysis and Field Correction Methods in Superconducting Undulators", Proceedings of the 2013 International Conference on Magnet Technology, Boston, USA (2013)
[23] J. Corlett et al., "Design concepts for a next generation light source at LBNL", Proceedings of the 2013 FEL Conference, New York, USA (2013)
[24] Z. Zhao et al., "Shanghai Soft X-Ray Free Electron Laser Test Facility", Proceedings of IPAC'12, San Sebastian, Spain (2011)
[25] M.E. Couprie et al, "The LUNEX5 Project in France", Proc. SRI 2012, Journal of Physics: Conference Series **425** (2013) 072001
[26] http://www.lnf.infn.it/acceleratori/public/iride/IRIDE_White_Book.pdf
[27] "NLS Project Conceptual Design Report", Science and Technology Facilities Council, http://www.newlightsource.org/
[28] J. Bisognano et al., "Design Alternatives for a Free Electron Laser Facility," Proceedings of IPAC2012, New Orleans, Louisiana, USA (2012).

Copyright © 2013 CC-BY-3.0 and by the respective authors

MACHINE BASED OPTIMIZATION USING GENETIC ALGORITHMS IN A STORAGE RING *

K. Tian#, J. Safranek, Y. Yan, SLAC, Menlo Park, CA 94025

Abstract

In this paper, instead of applying GA in the conventional numerical calculations, we present a successful experimental demonstration of implementing GA in real machine based optimization. We conduct the optimization of the average vertical beam size of the SPEAR3 storage ring using GA. Beam loss rate is chosen as the sole objective function because it is inversely proportional to the vertical beam size and can be measured quickly in SPEAR3. The decision variables are the strengths of SPEAR3 skew quadrupoles, by varying which we can change both the betatron coupling and the vertical dispersion to search for the minimum beam size. The results in this paper can shed light on new applications of GAs in particle accelerator community, for example, optimizing the luminosity of the high energy collider in real time.

INTRODUCTION

GAs have been successfully applied in areas such as designing injector systems [1], diagnosing and designing accelerating cavities [2], and optimizing beam optics design in storage rings [3]. One core process of the GA is to evaluate objective functions from a given set of decision variables, i.e. knobs to be adjusted for optimum search. In spite of various approaches used in previous efforts, all of them evaluate the objective functions based on numerical simulations using particle tracking codes. In principle, when the optimization targets or their correlating parameters are measurable experimentally, it is possible to use the real machine as the function evaluator to directly measure the objective functions, rather than using a computer model. Compared to the simulation based optimization, the machine based optimization has the most accurate representation of the machine condition that includes all lattice errors. Moreover, when the physics quantities of interest can be measured quickly in experiment but cost long time to be calculated in simulations, the machine based optimization will excel in speed too. One example of such quantity is the luminosity of the high energy colliders. In SPEAR3, we have identified a similar parameter of interest that can be measured nearly instantaneously. In this paper, we report an innovative application of GA to minimize the average vertical beam size of the SPEAR3 storage ring in real time. To construct the GA, we use 13 skew quadrupoles in the storage ring as decision variables and the measured beam loss rates as the objective function. The results can serve as a proof of principle for using GA in machine based optimization.

*Work supported by U.S. Department of Energy Contract No. DE-AC02-76SF00515

#ktian@slac.stanford.edu

MINIMIZE THE VERTICAL BEAM SIZE

In a storage ring, circulating electrons are lost due to collisions with gas molecules and electron-electron scattering inside the bunch, where the latter is known as the Touschek effect [4]. As in most modern electron storage rings, the loss of stored beam current in SPEAR3 is mainly due to the Touschek scattering. Thus, one can derive the simple scaling law between beam loss rates *dI/dt* and vertical beam size as shown below:

$$\frac{\left|\frac{dI}{dt}\right|}{I^2} \propto \frac{1}{\bar{\sigma}_y}, \qquad (1)$$

where I is the stored current and $\bar{\sigma}_y$ is the average vertical beam size.

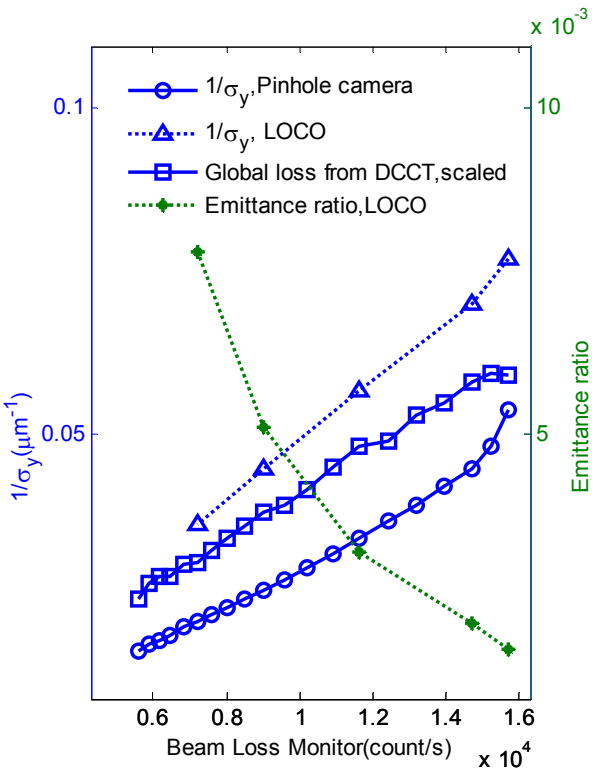


Figure 1: Experiment verification of Eq. (1).

In SPEAR3, Eq. (1) can be directly validated by experimentally measured data. During the experiment, 100 mA beam is filled in SPEAR3. We achieve 20 conditions in the ring by varying all skew quads in a fixed step size. For each condition, we measure the vertical beam size at 1Hz with an x-ray pinhole camera [5]. The beam loss rate is recorded instantaneously at 1Hz by a beam loss monitor (BLM) [6], installed next to the SPEAR3 beam horizontal scraper. The scraper is inserted close to the beam in order to capture nearly all of the beam loss at one point. The global beam loss is also

Copyright © 2013 CC-BY-3.0 and by the respective authors

acquired by recording the current decay during 2-minute period using a dc current transformer (DCCT). The current droop during the entire period of the experiment is less than 4%, thus, the stored current can be considered as a constant for the analysis in Eq. (1). Sampling 5 out of the 20 different cases, we measured the response matrix of the ring for each, and then fit the model to the measured data using LOCO. Emittance ratio and average vertical beam size then can be calculated from the fitted model. All results are shown in Figure 1, where the monotonic relationship of the measured beam loss monitor data, the vertical beam size, and the emittance prove the simple scaling law in Eq. (1).

ALGORITHM DESCRIPTION

In this section, we will detail the formation of a GA based technique in maximizing the beam loss rate of SPEAR3 in real time. The algorithm is based on NSGA – II [7].

Objective Functions and Decision Variables

The normalized beam loss rate measured by the BLM next to the scraper is the single objective function in our GA formation. The currents, which represent the strengths of the skew quadrupoles in SPEAR3, are the independent decision variables. After varying the currents of the 13 skew quadrupoles, the objective function is evaluated from the direct measurement of the BLM. Distinct from most other applications of GA, the accelerator serves as the function evaluator, instead of a numerical or analytical model. The SPEAR3 skew quadrupoles are powered by high precision MCOR power supplies featured with fast switching. The data acquisition from the BLM is also nearly instantaneous.

Genetic Operations

Except the first generation, all sequential generations are generated via the process of genetic operations. We use two of the most popular genetic operators: real-coded Simulated Binary Crossover (SBX) [8] and polynomial mutation [8]. In each genetic operation, one of the two operators is chosen randomly but conforms to a predefined ratio. During a crossover, two parents are picked to create two children, while one child is generated from one parent in the case of mutation. Once a child is created, its corresponding objective function is evaluated. Eventually, an offspring population is generated. Crossover and mutation are governed by the user-configurable nonnegative tuning parameters η_c and η_m respectively. A more detailed discussion of these two parameters can be found in the literature such as reference [8]. In short, these tuning parameters control the probability density function of the likeness between parents and children. For mutation, a smaller η_m represents less probability to have a similar child, which in turn provides a global search to the optimum regardless the parent solution. On the other hand, with a bigger η_m, it is very likely that the child only varies slightly from the parent and the operation is conducting a local search of optimum around the parent. The behavior of η_c is quite similar to η_m: the children tend to be close to one of the parents with large η_c or be randomly generated with small η_c.

The performance and speed of genetic algorithms highly depends on specific problems and can be adjusted with mutation and crossover tuning parameters. We have programmed the code to dynamically adjust these factors according to the diversity of the population in the new generation. It appears that the optimization progresses faster by promoting more global search with relatively small mutation tuning parameters in early generations. When the population starts to cluster toward the optimum region, it helps to save time by using large mutation tuning parameter or shrink the search space.

Replacement, Re-evaluation, and Stopping

To ensure an elitist approach, the current population is replaced by the best solutions chosen from both the offspring and the older generation. To maintain a fixed population size, the remaining solutions are discarded. As the objective functions are measured directly from the SPEAR3 machine, the results may change over time due to variation of machine condition. Therefore, we re-evaluate the surviving solutions from all previous generations every 10 generations. Limited by the machine time available for the experiment, we run the algorithm as long as possible, so normally we stop the program manually after a certain amount of time.

RESULTS

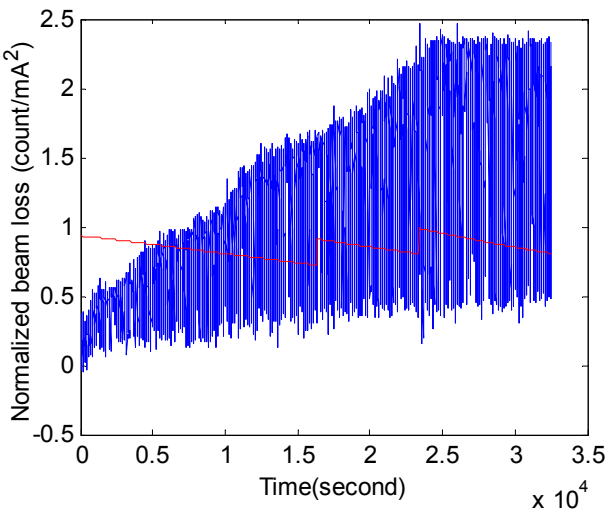


Figure 2: Normalized beam loss rates at the scraper during the experiment at 1Hz update rate.

We choose the population size of 120 in each generation for reasonably big sample size and relatively short time for generating the whole population during the experiment. As a result, it takes less than 3 minutes to generate one generation.

Figure 2 shows the results with 211 generations of GA optimization. To reduce the effect of stored beam current decay, we refilled SPEAR3 twice during this experiment

Copyright © 2013 CC-BY-3.0 and by the respective authors

as shown by the normalized stored beam current (scaled stored current shown as red curve). The optimization was paused during the refill and restarted by loading the dumped data after the fill. Overall, the algorithm behaved well. The normalized beam loss rates grow steadily for the first 150 generations, and then start to converge. In Figure 3, we compare the skew quadrupoles currents of the GA solution and the LOCO solution. The beam loss rates for the best solution found using GA are compared with the solution found using LOCO in Table 1. Average vertical beam size and emittance ratio of the ring with these two solutions are also calculated from the fitted model using LOCO.

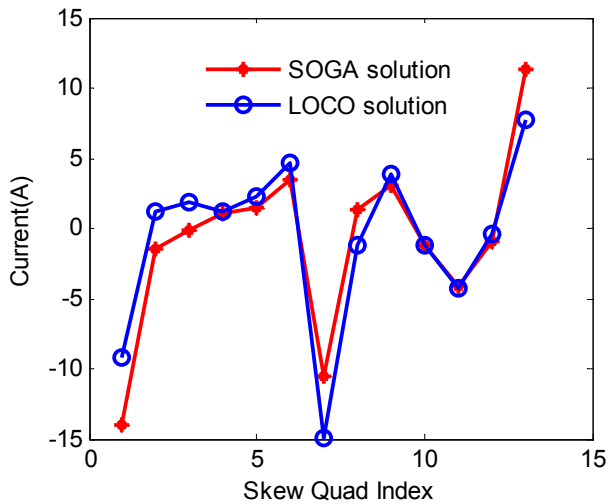


Figure 3: Comparison of the GA solutions and LOCO solution.

The normalized beam loss rate measured with the GA solution is increased by 17.9% from that with the LOCO solution. According to the scaling law in Eq. (1), this is translated to the reduction of vertical beam size by 15.18%. The calculated values using LOCO fitting show a 10.99% reduction of vertical beam size for the GA solution. The discrepancy comes from the accuracy of the fitting in LOCO, loss rates measurement, and the assumption of solely Touschek effect when deriving the scaling law in Eq. (1).

Table 1: Comparison of Solutions

	LOCO	GA
$\bar{\sigma}_y$ (μm)	7.9617	7.087
Emittance Ratio	0.0605%	0.0461%
Normalized Beam Loss rate	2.07	2.44

SUMMARY

Genetic algorithms are believed to be especially suitable for problems with high complexity where traditional gradient-based search methods normally fail to optimize. As the storage ring lattice is well designed, the coupling optimization of the ring tends to be a well behaved problem. This is evident from the final solution: out of 13 skew quadrupoles, only 3 are required to be set above 5A, while most of others are near zero. This fact weakens the advantage of using GA based optimization. Nevertheless, with machine based GA, we are able to find good solution regardless the time spent. Also, we have more confidence in its global validation. In addition, one should note that machine based GA may show advantage in speed over the traditional gradient based techniques when optimizing problems involved with more decision variables. As long as the corresponding hardware can be set roughly simultaneously, the time cost by machine based GA is independent of the number of decision variables. However, most traditional algorithms are scaled with the number of decision variables in high order. Thus, machine based GA can be more valuable for large machines.

The GA techniques we used are far from being refined. In future study, we will focus on improving speed and robustness. One possible approach is to create a hybrid algorithm that combines both GA and one of the traditional techniques for fast local search. When blending the two algorithms, it is challenging to maintain their original advantage, which requires thorough study.

ACKNOWLEDGMENT

We wish to acknowledge X. Huang and J. Corbett for valuable discussions and SPEAR3 operators for assisting in the experiment.

REFERENCES

[1] I.V. Bazarov and C. K. Sinclair, Phys. Rev. ST Accel. Beams 8, 034202 (2005).
[2] Y. Xiaowei and F. Mingwu, J. Appl. Sci. (Yingyong Kexue Xuebao) 17, 8 (1999).
[3] L. Yang, Y. Li, W. Guo, and Samuel Krinsky, Phys. Rev. ST Accel. Beams, 14 (2011), p. 054001.
[4] H. Wiedemann, Particle Accelerator Physics, Sringer-Verlag, 1993.
[5] J. Corbett, C. Limborg-Deprey, W. Mok, and A. Ringwall, in Proceedings of the 2005 Particle Accelerator Conference, Knoxville, Tennessee, USA, pp. 4057-4059.
[6] K. P. Wootton, M. J. Boland, and R. P. Rassool et. al., in Proceedings of the 2012 International Particle Accelerator Conference, New Orleans, Louisiana, USA, pp.771-773 .
[7] K. Deb, A.Pratap, S. Agarwal, and T. Meyarivan, IEEE Transactions on Evolutionary Computation, Vol.6, No. 2, April 2002; http://www.mathworks.com/matlabcentral/fileexchange/10429-nsga-ii-a-multi-objective-optimization-algorithm
[8] A. Holfler et. al, Phys. Rev. ST Accel. Beams 16, 010101 (2013).

Copyright © 2013 CC-BY-3.0 and by the respective authors

SUCCESSFUL COMPLETION OF THE ALS BRIGHTNESS UPGRADE*

C. Steier†, A. Madur, B. Bailey, K. Berg, A. Biocca, A. Black, P. Casey, D. Colomb, B. Gunion, N. Li, S. Marks, H. Nishimura, C. Pappas, K. Petermann, G. Portmann, S. Prestemon, A. Rawlins, D. Robin, S. Rossi, T. Scarvie, R. Schlueter, C. Sun, H. Tarwaneh, W. Wan, E. Williams, LBNL, Berkeley, CA 94720, USA;
L. Yin, Q. Zhou, J. Jin, J. Zhang, C. Chen, Y. Wen, J. Wu, SINAP, Shanghai, China

Abstract

The Advanced Light Source (ALS) at Berkeley Lab is one of the brightest sources for soft x-rays worldwide. A multiyear upgrade of the ALS is underway, which includes new and replacement x-ray beamlines, a replacement of many of the original insertion devices and many upgrades to the accelerator. The accelerator upgrade that affects the ALS performance most directly is the brightness upgrade, which reduced the horizontal emittance from 6.3 nm to 2.0 nm (2.5 nm effective), resulting in one of the lowest horizontal emittances of operating light sources. Magnets for this upgrade were installed in late 2012 and early 2013 followed by successful commissioning and user operation with 2.0 nm horizontal emittance.

INTRODUCTION

Over the years, the brightness of the ALS has been steadily improved, keeping the ALS the brightest third generation light source in the energy range below 1 keV (see Fig. 1). The upgrades included improvements in beam parameters (current and emittance), addition of new radiation producing devices (Superbends and advanced insertion devices) as well as stability improvements going hand-in-hand with the brightness improvements.

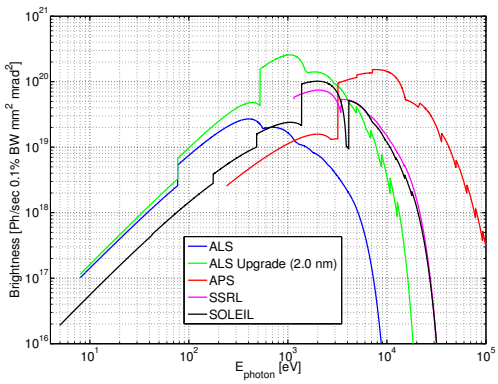


Figure 1: Comparison of the ALS brightness before and a after the low emittance upgrade with several other existing light sources.

The recent low emittance upgrade increased the brightness of the ALS by about a factor three in the bending magnet beamlines, and by about a factor two in the existing insertion device beamlines. The upgrade also opens the door to a potential further increase of the brightness by potentially implementing reduced horizontal beta functions in some straights.

BRIGHTNESS UPGRADE LATTICE

The ALS lattice has a triple bend achromat structure, with a fixed, large defocusing gradient in the bending magnets. Originally, there were only 2 families of sextupoles, with 4 sextupoles in each arc. An attractive set of possible upgrade lattices was found with higher straight section dispersion and an integer tune two units higher than the old lattice [1]. Those lattices have natural emittances of about 2 nm, compared to the more than 6 nm of the old lattice and horizontal beta functions of about 20 m in the straights.

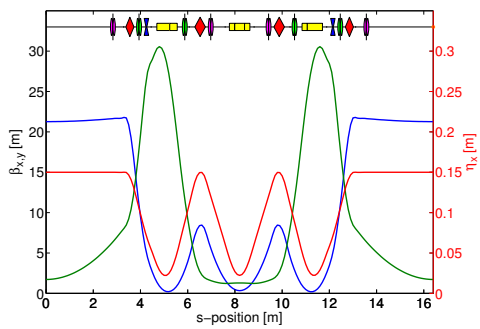


Figure 2: ALS upgrade lattice with 2.0 nm natural emittance at 1.9 GeV.

Later on, more systematic techniques [2, 3, 4] were used to find the global optimal lattices in terms of emittance or brightness. In those studies an additional family of low emittance lattices was found with very small horizontal beta function (order of 0.5 m) in the straights at much higher phase advance, which increase the brightness by better matching to the photon diffraction ellipse. Such low beta straights are still under investigation as an insertion for selected straights.

The high-beta lattices are within the range of the existing quadrupole magnets. However, the original sextupoles would not have been strong enough and the dynamic aperture would have been very poor. Both challenges were overcome with the addition of sextupoles in the straight sections.

* The Advanced Light Source is supported by the Director, Office of Science, Office of Basic Energy Sciences, of the U.S. Department of Energy under Contract No. DE-AC02-05CH11231.

† CSteier@lbl.gov

Copyright © 2013 CC-BY-3.0 and by the respective authors

MAGNET DESIGN AND PRODUCTION

The design [5] of the new sextupoles was performed in a collaboration by LBNL and SINAP and was finished in 2011. Because of space constraints, 3 different magnet designs are used. One of the families is optimized for small hysteresis and fast time response and has a closed yoke. It is used as the primary correctors in the fast orbit feedback. All new sextupoles also contain skew quadrupole coils (half of them have been initially connected to power supplies). This allows to improve the vertical beamsize stability in the ALS by providing aa local correction of the small skew quadrupole errors of the planar insertion devices. Some of the skew quadrupoles in three of the ALS arcs are also necessary to provide the vertical dispersion bump for the fs-slicing facility in the upgrade lattice.

Magnet production, carried out at SINAP, started with prototype magnets just after the design reviews in early 2011. The pole shapes were manufactured by wire edm on fully assembled magnet cores to achieve excellent field quality. Manufacturing was completed in summer 2012, on time to achieve the project installation milestones. During construction there was a detailed quality assurance program and all magnets were fully qualified by electrical, mechanical, and magnetic measurements. Precise fiducialization was carried out both mechanically and with the help of magnetic measurements. All magnets exceeded all important field quality requirements.

Installation

Thirteen of the new sextupoles were installed ahead of the main upgrade shutdown. This allowed to fully test their corrector functionality (time response, hysteresis) and to incorporate them into the slow and fast orbit feedback. The tests confirmed the excellent performance as corrector magnets and subsequently the remainder of the 48 magnets was installed during the 2013 spring shutdown (see Fig. 3). At the same time, all new power supplies and equipment protection systems were installed. Finally, the top-off interlock ranges were enlarged based on a complete new set of top-off safety calculations, and the interlocks were retested.



Figure 3: SHD magnet installed between the QF and QD quadrupoles.

Other Project Activities

In order to create sufficient space in all locations where new magnets were going to be installed, several modifications of vacuum chambers and stands were completed in 2012. Several candidate power supplies for the new magnets were tested and the control system interfaces for the selected power supplies were completed. Because of the new magnets and new strengths of existing interlocked magnets, parts of the safety analysis for top-off operation needed to be redone. The analysis was completed in time for the installation shutdown and no hardware changes were necessary. The new analysis allowed widening the interlock ranges on many of the top-off interlocked magnets allowing wide flexibility with the new lattices.

For the fs-slicing facility, the ALS has a complex lattice insertion that manipulates the local coupling and vertical dispersion to spatially separate the sliced beam. The new lattices required a completely new solution making use of the additional skew quadrupoles added to the new SHF magnets just adjacent to the insertion devices. The solution was found using genetic algorithms [6] and its lattice functions are shown in Fig. 4.

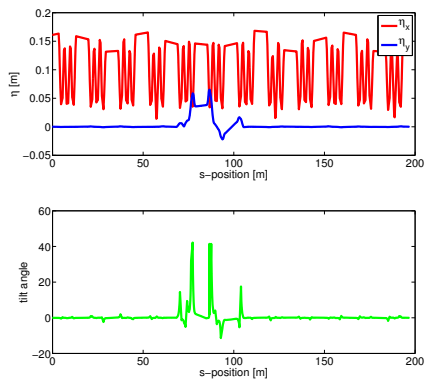


Figure 4: New fs-slicing optics that provides the spatial separation of the energy sliced beam in the new upgrade lattices.

Beyond the baseline of the project, which is aimed at delivering higher brightness, work is also going on to study low alpha modes of operation, which are enabled by the fact that the new sextupoles allow control of the second order momentum compaction factor.

COMMISSIONING

Simulations beforehand had predicted excellent dynamic and momentum aperture as well as lifetime for the optimized upgrade lattices [4, 7]. Fig. 5 shows an measurement of the momentum aperture of the upgrade lattice by recording the Touschek lifetime as a function of the RF acceptance. The measurement confirms that the upgrade lattice has a larger dynamic momentum aperture than the lattice used before the upgrade. In fact, during user operations the

Copyright © 2013 CC-BY-3.0 and by the respective authors

overall lifetime now is as high as before the upgrade, despite the large reduction in horizontal emittance which allowed to further reduce the vertical emittance as well (from almost 50 pm to below 30 pm).

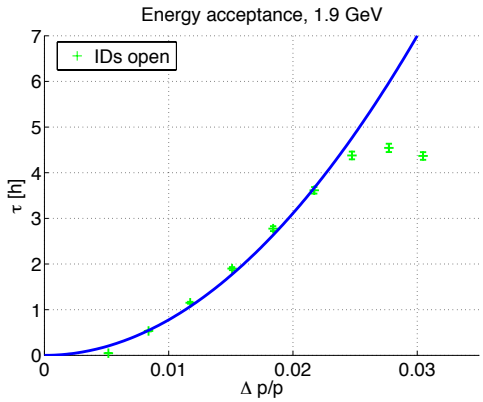


Figure 5: Lifetime versus RF amplitude scan confirming improved dynamic momentum aperture compared to the operation before the upgrade.

Migration to the new lattices was quick (few hours), after verifying all magnet polarities and magnet transfer functions in a beam based way in the old lattice. Further commissioning included optimizing the harmonic sextupole settings, updating the ID feed-forward (tune, beta beating, coupling) for the new lattice, implementing the new dispersion bump for fs-slicing facility and retesting the top-off interlocks with new ranges. The dispersion bump was refined after final lattice optimizations. The dynamic aperture and momentum aperture including the fs-slicing lattice insertion are similar to the bare lattice results and commissioning of the new solution went quickly. The new lattices also provide a larger, intrinsic horizontal separation of the sliced electron beam. We are currently in the process of evaluating how to make best use of this and expect that it will eventually allow a much better signal to noise ratio for the slicing facility.

Optimizing photon beamlines with new beam spots progressed quickly and user beamlines were able to resolve the brightness increase (see Fig. 6). The dynamic aperture and momentum aperture for the upgrade lattice were confirmed to be very close to the expected ones and the Touschek beam lifetime after the upgrade, despite the smaller horizontal and slightly smaller vertical emittance, as predicted is larger than before the upgrade, due to the larger dynamic momentum aperture.

SUMMARY

An upgrade project has been completed improving the brightness of the ALS by reducing the horizontal emittance from 6.3 to 2.0 nm. This resulted in a brightness increase by a factor of three for bend magnet beamlines and at least a factor of two for insertion device beamlines. The ALS now has one of the smallest horizontal emittance of all operating 3rd generation light sources. Initial user operations has been very successful. Most beamlines have been able to benefit significantly from the upgrade. No interruptions during the first 5 months of user operations have been related to the upgrade.

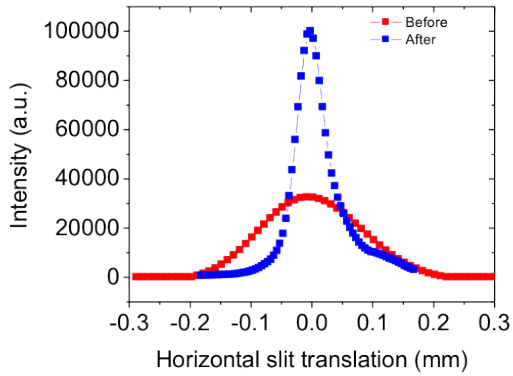


Figure 6: Comparison of the horizontal beam profile before and after the upgrade measured at one user beamline showing the factor of three improvement in brightness.

Building on the success of this upgrade, development work has now started towards a proposal for a more substantial upgrade of the ALS, that could provide diffraction limited performance for soft x-rays in the future. Such a ring, based on nine bend achromats appears feasible and could replace the current ring in the ALS tunnel [8].

ACKNOWLEDGEMENTS

The authors want to thank the ALS management, as well as the ALS user community for encouragement to keep developing the ALS further, as well as their support in securing funding for this upgrade project. We also would like to acknowledge our collaborators at SINAP, where the magnets were build. We are very grateful to D. Blough who helped us with Quality Assurance. We thank M. Kunz and N. Tamura at beamline 12.3.2 for the beam profile measurement.

REFERENCES

[1] H. Nishimura, et al., PAC 2007, Albuquerque, p. 1970.

[2] D. Robin, et al., Phys. Rev. STAB 024002 (2008).

[3] L. Yang et. al, Nucl. Instr. Meth. A 609 (2009) 50-57.

[4] C. Steier, et al., 10.1016/j.nima.2010.11.077.

[5] A. Madur, et al., IEEE Trans. Appl. Superc. 22

[6] C. Sun, et al., New fs-slicing optics, IPAC2012

[7] C. Sun, et al., Phys. Rev. STAB 15, 054001 (2012).

[8] H. Tarawneh, D. Robin, and C. Steier, Proc. of NA-PAC'13, MOPH023.

Copyright © 2013 CC-BY-3.0 and by the respective authors

STUDIES OF THE LOW ENERGY PROTON BEAM HALO EXPERIMENT

Hongping Jiang#,Shinian Fu, Jun Peng, Tao Huang, Fang Li, Peng Li, Huachang Liu, Cai Meng, Ming Meng, Zhencheng Mu, Huafu Ouyang, Peng Chen, Linyan Rong, Biao Sun, jianmin Tian, Biao Wang, Shengchang Wang, Wenqu Xin, Taoguang Xu, Lei Zeng, Fuxiang Zhao
Institute of High Energy Physic, Chinese Academy of Sciences, Beijing 100049, China

Abstract

We report measurements of transverse beam phase-space properties and transverse beam halo in mismatched proton beams in 28-quadrupole FODO transport channel following the 3.5-MeV IHEP RFQ. Beam profiles in both transverse planes are measured using beam-profile diagnostic. The gradients of the first four quadrupoles can be independently adjusted to match and mismatch the RFQ output beam into beam-transport channel. We also compare the measured beam profile with the 3-D nonlinear macro-particle code IMPACT simulations in the beam halo experiment. Quadrupole scans were used to determinate the transverse properties of the RFQ output beam. The Gaussian distribution was chosen as the initial particle distribution, which is well fit with the measured beam-core profile. We match the beam using the least-squares fitting procedure that adjusted the first four matching quadrupoles to produce equal rms beam size in the last six wire scanners. Simulations had been fairly successful in reproducing the core of the measured matched beam profiles, but there are some differences in the mismatched beam profiles.

INTRODUCTION

The interest in understanding the formation of a halo distribution around an intense proton beam has increased in recent years with the development of new applications requiring such beam, because the beam halo is a major source of beam loss and radioactivation in high-power and high-current proton linacs. Beam mismatch have been identified as the major source of the halo formation [1], space-charge forces in mismatched beam are the main source of beam halo in high current proton beams. Having well matched beam conditions is a fundamental requirement for the operation of proton linacs. And the macroparticle simulation method is widely used in modern accelerator design and beam dynamics studies [2].

In this paper, we present measurements of transverse beam phase-space properties and comparisons of simulation results using the code IMPACT [3] with experimental measurements of the beam profiles in a high-current matched and mismatched proton beam. The beam profiles were measured by the wire-scanners. The transport line was installed after the radio frequency quadrupole (RFQ) accelerator designated for ADS study at the Institute of High Energy Physics (IHEP).

Jianghp@ihep.ac.cn

THE BEAM-CORE MATCHING EXPERIMENT TRANSPORT LINE

The 28-quadrupole beam transport line is installed at the end of the IHEP RFQ, which accelerates the proton beam to 3.54MeV and operates at the frequency of 352MHz. The purpose of this transport line is the experimental study of the beam halo formation and the comparison of the experimental data with the simulations. The block diagram of this transport lattice is shown in Fig. 1. In this line, the first four quadrupoles are independently adjustable to match the beam or to produce mismatches; the last 24 quadrupoles form an FODO lattice.

The transverse beam profiles are measured using beam profile scanners, which consist of wire scanners for measurement of the dense beam core and halo scrapers for measurement of the outer halo regions [4]. In the beam halo experiment, we use the wire scanner to measure the beam profiles, and the wire scanner can provide intensity measurement over a dynamic range of about 10^3. The philosophy of the scanner placement is the following: the first group of two scanners is placed after quadrupole 5 and 6, they separately measure the beam vertical and horizontal profiles which are used to characterize the proton beam output from the RFQ. To observe beam profiles of matched or mismatched case, another two groups of scanners with 6 scanners for each group are placed after quadrupole 17 to 28, covering about two mismatch oscillations.

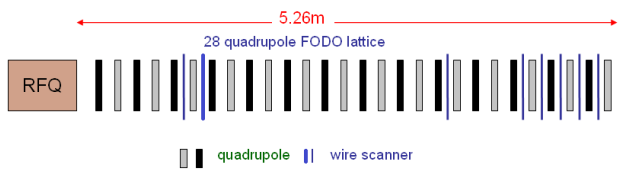


Figure 1: Block diagram of beam-core matching experiment transport line.

CHARACTERIZING THE PROTON BEAM OUTPUT FROM THE RFQ

In order to know the details of the beam, quadrupole scans and multi-wire scanner were used to characterize the transverse beam output from the IHEP RFQ [5]. In the scanning process, we kept the other three quadrupoles the same gradient 25.40T/m and obtained the Gaussian-like beam distributions with different rms radius compared with simulations shown in the Table 1 and Figure 2, the

Copyright © 2013 CC-BY-3.0 and by the respective authors

same with horizontal. Due to the lack of longitudinal measurements, the beam longitudinal Courant-Snyder parameters from the RFQ were predicted by the PARMTEQM [6] RFQ simulation code. Table 2 shows the results: the beam Courant-Snyder parameters and emittances. And the multi-wire scanner results will be show in the future, we can find the difference of parameters between the quadrupole-scan and the multi-wire scanners is about eight percent, which is acceptable in our experiments.

Table 1: The rms Vertical Radius Compared with Simulations under Different Focusing Strength

Q 1 (T/m)	Measurements	Simulation
-21.04	2.96±0.06 mm	2.94 mm
-23.57	2.46±0.05 mm	2.50 mm
-25.19	2.20±0.08 mm	2.27 mm
-26.90	2.10±0.06 mm	2.10 mm
-29.34	1.96±0.06 mm	1.98 mm

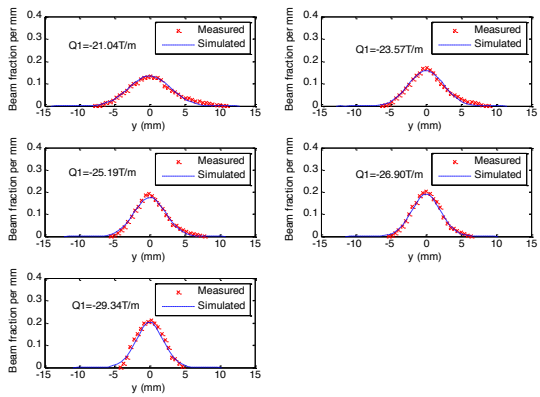


Figure 2: The beam measured vertical profiles compared with simulations under different focusing strength.

Table 2: Unnormalized Emittances and Initial Courant-Snyder Parameters from Quad Scan Analysis

	α	β (mm/mrad)	Emittance rms Unnormalized
Horizontal	3.443	0.42	3.66 mm-mrad
Vertical	-0.165	0.10	5.45 mm-mrad
Longitudinal	-1.564	3.16	0.32mm-mrad (normalized)

THE MATCHED BEAM

A least-squares-fitting procedure was used based on measurements of derivatives of rms sizes with respect to matching quadrupole gradients. Because the lack of vertical wire scanners at the end of transport line, beam was matched by adjusting the first four quadrupoles to produce equal rms sizes in horizontal position at the last 6 wire scanners. The measured results with different location equilibrium horizontal beam-core profiles were shown in Figure 3. As shown in the figure, the beam profiles with different locations have the similar distributions with an rms radius about 1.1mm.

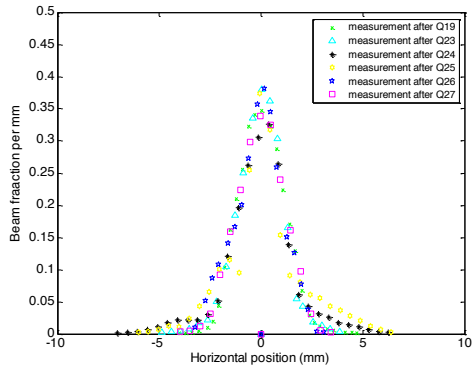


Figure 3: The equilibrium horizontal profiles measured at different locations.

Using the Gaussian distribution with a 24.7-mA beam current as the input distribution, we simulated the beam transported through the beam-core matching experiment. We have used 2×10^8 macroparticles per bunch with a computation grid of 64×64×128. The rms beam size and emittances at the centre of each drift space as a function of distance is given in Figure 4 compared with experimental data. From the figure we can see the rms radius predict an oscillation following the FODO periodic focusing channel and the wire scanner rms radius is perfectly fitting with the simulation, and the emittances are nearly constant. Besides the rms sizes, we also measured the projected density distribution, i.e., beam profiles in horizontal projections at seven locations along the transport channel. Figure 5 compares the simulations with the measured beam horizontal profiles. Simulations are fairly successful in reproducing the core of the measured matched-beam profiles (about 3 rms radius), but there are some discrepancies in the scope larger than 3-rms radius in some locations.

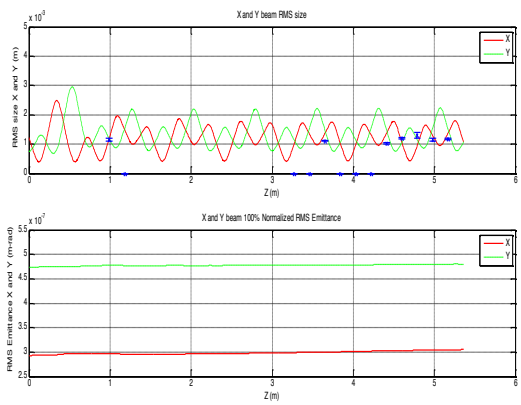


Figure 4: Results of beam rms radius and emittances as a function of distance for a matched beam.

Copyright © 2013 CC-BY-3.0 and by the respective authors

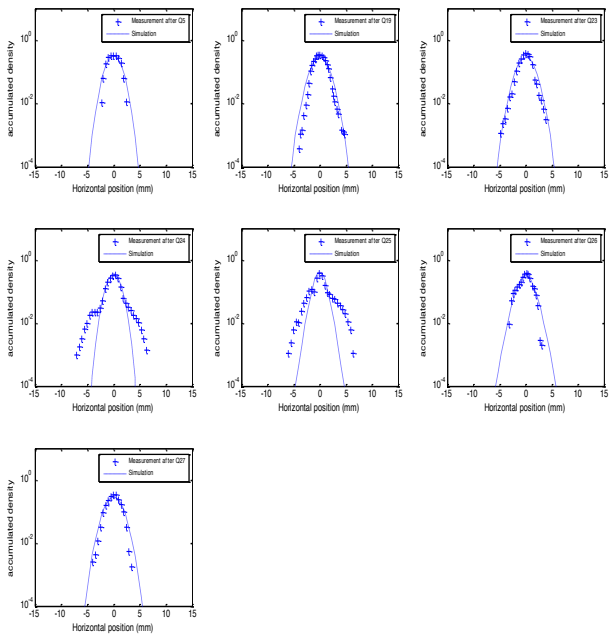


Figure 5: The horizontal profiles from measurements and simulations after Q5 Q19 Q23 Q24 Q25 Q26 Q27 for a 24.7 mA matched beam.

THE MISMATCHED BEAM

After we found the matched case, we adjusted the matching quadrupoles to obtain the mismatched beam. We measured the beam profiles and compared with simulations. The results were shown in Figure 6.

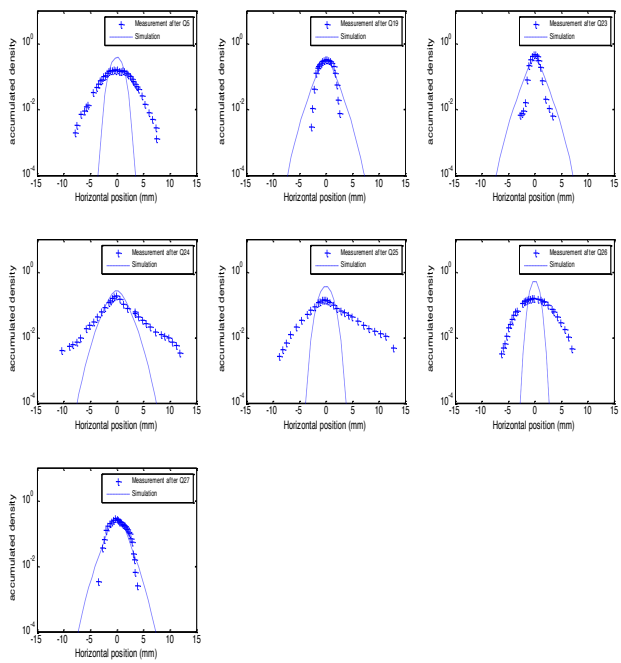


Figure 6: The horizontal profiles from measurements and simulations after Q5 Q19 Q23 Q24 Q25 Q26 Q27 for a 24.7 mA mismatched beam.

From the Figure 6 we can find only three locations beam profiles agree well with the simulations, the others have big differences. The simulation shows that the beam distribution is also a Gaussian distribution, but the measured beam profiles show the beam halo has formated. We need do further study to understand these questions.

CONCLUSIONS

We have used quadrupole scans and multi-wire scanner to determine the RFQ output beam Courant-Snyder parameters and emittances. In the simulation, we choose the Gaussian distribution with the obtained Courant-Snyder parameters as the initial beam-core distribution. We have compared the macroparticle simulations with the measurement data in a matched beam at 24.7mA. Simulations are fairly successful in reproducing the rms properties of the measured matched-beam, and the beam profiles in horizontal projections at the six locations shows that the beam is well matched, but for the mismatched case there are some discrepancies in the beam profiles in some locations. For explaining this phenomenon, we think there are more simulations with errors about the mismatched beam and beam offset to be analysed.

ACKNOWLEDGMENT

We thank Mr Ji Qiang for providing the IMPACT code and for help associated with its use.

REFERENCES

[1] Allen C K, Chan K C D, Colestock P L, et al. Beam-halo measurements in high-current proton beams [J]. Physical review letters, 2002, 89(21): 214802.

[2] J. Qiang, R. D. Ryne, B. Blind, J. H. Billen, T. Bhatia, R. W. Garnett, G. Neuschaefer, and H. Takeda, Nucl. Instrum.Methods Phys. Res., Sect. A 457, 1 (2001).

[3] J. Qiang, R. D. Ryne, S. Habib, and V.Decyk, J. Comput. Phys. 163, 434 (2000).

[4] Yu-Fang, Ruan, et al. "Design and simulation of a wire scanner for the CSNS linac." Chinese Physics C 34.10 (2010): 1655.

[5] Schulze M E, Allen C K, Colestock P L, et al. Characterization of the proton beam from the 6.7 MeV LEDA RFQ[C], PAC 2001, IEEE, 2001, 1: 591-593.

[6] K. R. Crandall et al.,"RFQ Design Codes", Los Alamos National Laboratory report LA-UR-96-1835 (revised February 12, 1997).

.

Copyright © 2013 CC-BY-3.0 and by the respective authors

LONGITUDINAL BEAM DYNAMICS AND LLRF REQUIREMENTS FOR THE PROJECT X PULSED LINAC*

A. Vivoli†, G. I. Cancelo, B. Chase, N. Solyak, P. Varghese, FNAL, Batavia, IL 60510, USA

Abstract

Project X is a high intensity proton facility being developed to support the intensity frontier physics program over the next two decades at Fermilab. The Reference Design [1] is based on a continuous wave (CW) superconducting (SC) 3 GeV linac providing up to 1 and 3 MW of beam power at 1 and 3 GeV respectively, while a superconducting pulsed linac provides acceleration of roughly 4.3% of the beam delivered from the CW linac to the 8 GeV injection energy of the existing Recycler/Main Injector complex. In this paper we present the results of simulations of longitudinal beam dynamics and Low Level RF (LLRF) control system in the pulsed linac, operated for long pulses in presence of errors and cavity detuning for different RF configurations and settings, and set the requirements for the LLRF necessary to fulfill the specifications of the design.

INTRODUCTION

The pulsed linac is the main part of the third stage of Project X and will accelerate pulses of 4.3 ms duration and 1 mA average current of the H^- beam coming from the 3 GeV linac (and downstream transport beamlines) up to 8 GeV at a repetition rate of 10 Hz. The constraints on the output beam parameters come from the acceptance of the downstream 8 GeV transport line and efficient injection in the Recycler/Main Injector ring. The lattice of the pulsed linac is studied with computer codes for accelerator optics and particle tracking simulating a single bunch. Once a configuration and set of parameters that provide acceptable output are found, multi-bunch simulations are performed to study the behavior of the system (accelerator and beam) during the length of the pulse and in multi-pulse mode. The focus of this study is on the RF system and longitudinal beam dynamics, neglecting beam optics and effects from elements of the beamline except for the accelerating cavities.

SINGLE BUNCH SIMULATIONS

Single bunch simulations are performed with the computer code TraceWin [2]. The current lattice of the pulsed linac and simulation results for the bunch envelopes are showed in Fig. 1. The linac is composed of 3 cryo strings of, respectively, 10, 9 and 9 ILC Type-IV cyomodules [3]. Each cryomodule contains 8 ILC 9-cell cavities and a SC quadrupole at the center.

Each cryo string is preceded and followed by a 2.5 m service box and between service boxes of adjacent cryo strings

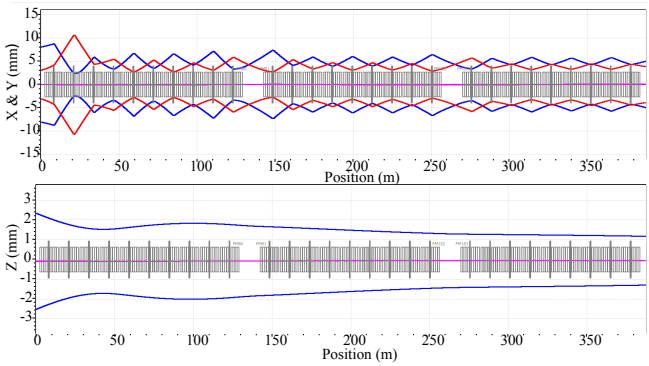


Figure 1: Beam envelopes (3 rms sigmas) in transverse (top) and longitudinal (bottom) coordinate spaces.

7.652 m room temperature areas are placed for beam collimation, diagnostics and maintenance operations. Table 1 shows relevant linac parameters and constraints to be fulfilled.

Table 1: Relevant Linac Parameters and Constraints

Beam Parameter	Initial value	Final value	Requirement
Kinetic Energy (MeV)	3000	8000	8000
Norm. hor. rms emit. (mm mrad)	0.516	0.516	≤ 0.6
Norm. vert. rms emit. (mm mrad)	0.281	0.311	≤ 0.6
Rms bunch length (ps)	2	1.3	≤ 100
Rms energy spread (MeV)	0.9	1.6	≤ 4

MULTI-BUNCH SIMULATIONS

Multi-bunch simulations are carried out employing a MATLAB based code written by the authors. The motivations for running multi-bunch simulations are various:

- To check that the configuration under study can fulfill consistently the specifications of the design during operation in presence of cavity detuning and errors in beam and RF components.
- To set the requirements for parameters of LLRF components to achieve an acceptable performance of the accelerator.

* Work supported by Fermi Research Alliance, LLC under Contract No. De-AC02-07CH11359 with the United States Department of Energy.
† vivoli@fnal.gov

Copyright © 2013 CC-BY-3.0 and by the respective authors

- To study the impact of gradient spread of the cavities fed by a singe RF station.
- To evaluate the reach capabilities of different configurations of the RF power system, like the number of cryomodules fed by each RF station.

The necessity to run the linac with different gradients for cavities fed by the same RF station comes from the fact that not all the cavities may be able to reach their design gradient. In this case, if the difference in voltage between the cavities is not too big, it is possible to adjust the ratios of the power couplers to set the loaded Q_L of each cavity such that they all have the same filling time. If the spectrum of the Q_Ls employed is in the range $7x10^6$–$1.2x10^7$ then operation is possible in presence of different detuning levels. The 2 configurations of the RF power system we want to study are with one power station feeding 8 cavities (1 cryomodule) or one station for 16 cavities (2 cryomodules).

Detuning Model

Most of the cavities in the pulsed linac are supposed to work at 25 MV voltage and around 5° phase. For these values for matched cavities (no reflection) the power needed to drive them is around 25 kW. To take into account power distribution losses, residual detuning after compensation and control overhead a value of 50 kW per cavity has been decided as a requirement for the linac power consumption. Lorentz Force Detuning (LFD) and microphonics cause voltage amplitude and phase of a cavity to change during the pulse and requires more power to drive the cavity at the design values. Methods to compensate them have been developed, resulting in a reduction of LFD at the level of 30 Hz or less for the cavity parameters given above, while microphonics level is around 3 Hz rms [4, 5]. In our simulations we assume LFD compensation is applied and we only use a model for the residual detuning. Analyses at Fermilab led to determine the lowest mechanical resonant frequencies of the cavities to be around 150, 250 and 390 Hz. In our model we assign to each cavity i mechanical frequencies $\omega_{1,i}, \omega_{2,i}, \omega_{3,i}$ around the above values, allowing a 5% of difference from cavity to cavity. Then we assign them three phases $\phi_{1,i}, \phi_{2,i}, \phi_{3,i}$ and 3 amplitudes $\alpha_{1,i}, \alpha_{2,i}, \alpha_{3,i}$ such that $\alpha_{1,i} + \alpha_{2,i} + \alpha_{3,i}$ equals the maximum measured LFD level. We also assign a value $\alpha_{0,i}$ for microphonics compatible with measures. We can write the detuning for each cavity as:

$$\begin{aligned}\Delta f_i = \alpha_{0,i} &+ \alpha_{1,i}\sin(\omega_{1,i}t + \phi_{1,i}) \\ &+ \alpha_{2,i}\sin(\omega_{2,i}t + \phi_{2,i}) \\ &+ \alpha_{3,i}\sin(\omega_{3,i}t + \phi_{3,i})\end{aligned} \quad (1)$$

In our simulations we used 2 types of detuning model: in the first one, uncorrelated, the phases and amplitudes of each cavity are independent. In the second type, correlated, the cavities inside a cryomodule share the same phases and amplitudes. For this second model the peak power delivered by the RF station must be bigger, since all the cavities reach the maximum detuning at the same time, requiring more power from the station at about the same instant. Results of measurements conducted, show some degree of correlation between the detuning of the cavities.

LLRF Control

In order to keep the voltage of the cavities at the design values, continuous correction of the power delivered by the RF station is necessary. Furthermore, different cavities require different corrections, but we can only control their common power source, thus the control can only be applied to the vector sum of the voltages of the cavities. This operation is executed automatically by the LLRF system. A schematic layout of the LLRF of the pulsed linac is showed in Fig. 2.

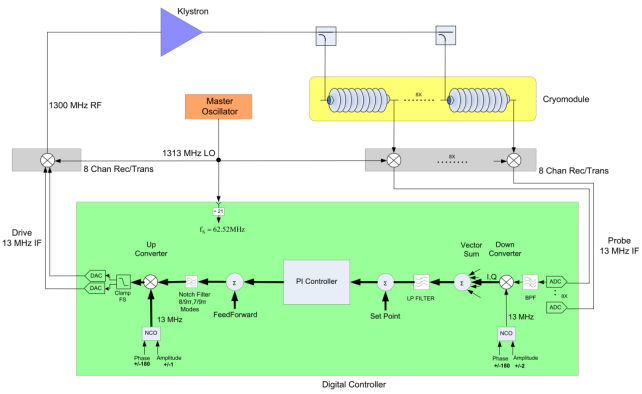


Figure 2: Schematic layout of the LLRF control of the pulsed linac.

More details of the system are available [6]. In our simulations it would be too time consuming to simulate the behavior of each element of the LLRF system, thus we simplify a little the scheme. Our simulated feedback works at a frequency of 1 MHz instead of 62.52 MHz. At each time step, the static and dynamic receiver errors are added to the voltages of the cavities (complex vector variables) and their vector sum is compared to the set point value. For the moment our system only has a proportional gain (no integral gain), so the difference just calculated is multiplied by the proportional gain and the result is summed to the feedforward value. We only simulate the fundamental mode of the cavity. The calculated power and phase are directly sent to the station (Klystron) with a delay of 1 time step (1 μs). The RF station delivers the power and phase requested with RF station errors added to them. Table 2 shows the LLRF parameters used in the simulations.

In addition to the above errors we also added beam intensity errors: 1 ps bunch time jitter (rms), 0.25 MeV bunch energy jitter (rms), 3% bunch-to-bunch intensity jitter (total) and 3% pulse-to-pulse intensity jitter (rms).

RESULTS

We considered two RF configurations with 8 or 16 cavities for RF station. In both cases we studied the dependence

Copyright © 2013 CC-BY-3.0 and by the respective authors

Table 2: LLRF Parameters Used in the Simulations

LLRF Parameter	Value
Cavity detuning level (peak)	30 Hz
Receiver amplitude rms error (static/dynamic)	0.667% / 0.009%
Receiver phase rms error (static/dynamic)	0.667° / 0.005°
Klystron gain	1
Proportional gain	250
Loop delay	1 μs
Klystron amplitude rms error (static)	0.2%
Klystron phase rms error (static)	1°

of the results on the cavity gradient spread. In particular we calculated the rms energy spread of the particles at the end of the linac and the peak power per cavity required during the simulation. As stated above the requirements are $\leq$ 4 MeV rms energy spread and $\leq$ 50 kW per cavity peak power. The other constraints resulted largely fulfilled by any scenario. First we compared the two models of detuning we used (correlated and uncorrelated) and found that in any case the correlated one required more power from the stations than the uncorrelated one (up to 50% more at 70 Hz detuning level) and resulted in larger energy spread (up to 50% at 45 Hz detuning level). Keeping all the other parameters at their nominal values, the difference in the results for a gradient spread varying from 0 to 10% resulted negligible for both the configurations. Since we first want to give conservative constraints we are giving results for simulations with correlated detuning, which are more pessimistic. The configuration with 8 cavities per station required 32 kW per cavity peak power at 0 detuning, resulting in final 1.86 MeV beam rms energy spread. The power needed grew up to 50 kW and more when exceeding 70 Hz of peak detuning. The energy spread grew up to 2 MeV at this detuning. At the nominal 30 Hz the power consumption was about 35 kW. For the 16 cavities configuration, the power consumption was few percent less than the other configuration, reaching the 50 kW limit at around 72 Hz. The energy spread is a more stringent constraint, since it grew from 1.87 MeV at 0 detuning up to around 3 MeV at 45 Hz and exceeding 5 MeV at 50 Hz. The power consumption dependence from the detuning is reported in Fig. 3.

A set of simulations where carried out to study the impact of the LLRF parameters (Table 2). We varied one parameter up to 10 times the nominal value, leaving the others constant, to evaluate the effect. For the moment we only applied this analysis to the receiver and generator errors. Varying the receiver amplitude error up to 0.09% produced a growth of 4% in the peak power, while the energy spread remained unchanged. Receiver phase error produced a 14%

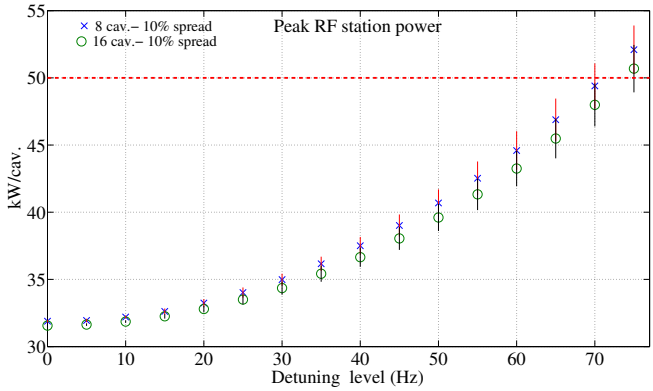


Figure 3: Peak power per cavity dependence on detuning for the 2 configurations studied.

increase in power and negligible in energy spread varying up to 0.5°. Generator amplitude error showed no impact up to 2% and its phase error produced 15% increase in energy spread and 2% peak power when increased to 10°.

CONCLUSION

In this paper we presented the ongoing study on Project X pulsed linac, showing some preliminary results of the multi-bunch simulations performed. Configurations with 8 and 16 cavities per station have been compared in presence of gradient spread and different level of detuning, showing similar performance with nominal parameters but more critical dependence of the 16 cavities configuration on the detuning level, concerning the final energy spread of the beam. Impact of some LLRF parameters have been preliminary studied showing particular importance of the phase errors. A more accurate and wider study of the parameters space is needed. Improvement of the code speed is desirable, giving the opportunity of more accurate simulations of the LLRF system.

REFERENCES

[1] Project X Reference Design Report, Project X-doc-776-v7.

[2] http://irfu.cea.fr/Sacm/logiciels/index3.php

[3] The International Linear Collider, Vol. 3, Part I: R&D in the Technical Design Phase.

[4] Y. Pischalnikov et al., "Lorentz Force Compensation for Long Pulses in SRF Cavities," IPAC2012, New Orleans, May 2012, THPPR012, p. 3990 (2012), http://www.JACoW.org

[5] W. Schappert, Y. Pischalnikov, "Recent Progress at Fermilab Controlling Lorentz Force Detuning and Microphonics in Superconducting Cavities," IPAC2013, Shanghai, May 2013, WEPWO058, p. 2438 (2013), http://www.JACoW.org

[6] P. Varghese et al., "A Vector Control and Data Acquisition System for the Multicavity LLRF System for Cryomodule1 at Fermilab," LINAC2010, Tsukuba, September 2010, MOP084, p. 250 (2010), http://www.JACoW.org

Copyright © 2013 CC-BY-3.0 and by the respective authors

MULTI-TURN INJECTION OF 50 MEV PROTONS INTO THE CERN PROTON SYNCHROTRON BOOSTER

V. Raginel, E. Benedetto, C. Carli, B. Mikulec, CERN, Geneva, Switzerland

Abstract

Since 1978, Linac2 produces beams of 50 MeV protons with a current around 160 mA, which are injected into the CERN Proton Synchrotron Booster (PSB) with conventional multi-turn injection using a horizontal septum. It is planned to replace Linac2 during a future long stop with a new H^- linac, Linac4, injecting at higher energy (160 MeV) and making use of the modern charge-exchange injection principle. Due to the age of Linac2 and to a delicate vacuum situation the risk of a serious Linac2 breakdown has to be considered. Therefore it is necessary to study if the PSB could produce beams useful for the LHC and other experiments injecting a Linac4 proton beam at 50 MeV with much lower average current compared to Linac2 and without the need for a long installation of the 160 MeV H^- injection hardware. Benchmarking of the PSB injection model with the existing injection system with Linac2 using the ORBIT code has been done for a LHC-type beam and then the injection model was used to estimate the brightness for LHC-type beams that could potentially be reached in one PSB ring with the injection of a Linac4 proton beam at 50 MeV.

INTRODUCTION

The Proton Synchrotron Booster located at CERN, Geneva, Switzerland, is currently boosting protons injected by Linac2 from 50 MeV to 1.4 GeV. It is the second accelerator of the LHC injector chain and consists of four superposed rings. Linac4 is a 160 MeV linac under construction aiming at boosting the performance of the CERN PSB with higher injection energy and replacing the present conventional multi-turn injection of 50 MeV protons with a septum by H^- charge exchange injection. General planning of the CERN complex foresees the connection Linac4 – PSB not before the end of the second LHC long run. In case of a serious breakdown of the presently used Linac2, which is ageing and showing weaknesses in terms of vacuum tightness, it is envisaged to inject 50 MeV proton beams with lower beam current and emittance from Linac4 as emergency scenario.

This work indicates the brightness that can be expected for a LHC beam (LHC-25ns) in the PSB after a multi-turn injection of 50 MeV protons from Linac4. The results are derived from simulations done with ORBIT. The reference parameters of the PSB injection with Linac2 are first used to test the model and then parameters of Linac4 are used as input of the simulation. An optimization of the injection process can be done to obtain an estimate of the highest reachable brightness for the LHC beam.

PSB MULTI-TURN INJECTION

During injection into the PSB, the beam is stacked in horizontal betatron phase-space using a closed orbit bump generated by four slow kickers to bring the stacked beam very close to the injection septum to minimize the transverse emittance of the resulting beam in the PSB. The incoming beam is deflected by the injection septum, which results in an injection with small position and angle errors. Subsequently the bump decreases and the beam moves to the reference closed orbit (see Fig. 1). The injection septum blade has a thickness of 1 mm and is 40 mm away from the closed central orbit.

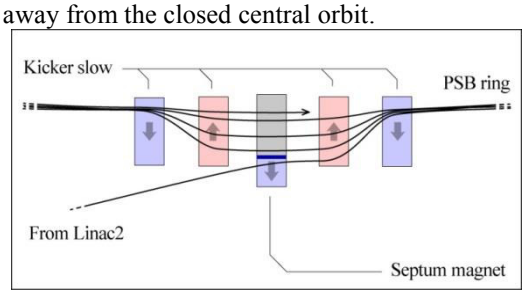


Figure 1: Multi-turn injection principle (after 4 turns).

During operation in order to produce all the required beam types, the following injection parameters can be optimized: the working point at injection, the injection timing and the horizontal and vertical positions and angles of the injected beam.

ORBIT CODE AND PSB MODEL

The ORBIT code (Objective Ring Beam Injection and Tracking) [1] was designed to track macro-particle coordinates through a set of accelerator elements and calculate space charge and other collective effects.

The model of the PSB lattice is composed of bending and quadrupole magnets imported with a special routine from MAD-8 [2] to ORBIT. The horizontal and vertical tune values are fixed in the MAD-8 model. The injection slow kickers are modelled in ORBIT with the ideal bump routine (linear decay of the bump). As ORBIT does not contain a septum module, a foil of thickness null as first element of the lattice and an aperture as last element of the lattice are used to simulate as realistically as possible the injection septum BI.SMH of the PSB [3]. The foil at the beginning of the lattice simulates the septum blade seen by the injected particles and the aperture at the end the septum blade seen by the circulating particles. The transverse space charge is modelled with the 2.5D FFT-PIC (Particle-In-Cell) modules without boundary condition(s). The FFT-PIC is a fast method to calculate transverse space charge, first by binning the

Copyright © 2013 CC-BY-3.0 and by the respective authors

macroparticles to a grid, then calculating the force distribution on the grid using a FFT method, and finally interpolating the force from the grid back to each macro-particle. Transverse space charge nodes are inserted after each transfer matrix included in the lattice file. The longitudinal space charge is modelled with one FFT node.

The 50 MeV proton beams from Linac2 and Linac4 are assumed to have a Gaussian distribution in transverse phase-space and a uniform distribution in longitudinal phase-space. At the injection point for Linac2 and Linac4, the horizontal beam size of the incoming beam is set to half of the PSB β_h [4], while the vertical beam size is matched to the PSB β_v and the waist positions $\beta'_h = \beta'_v$ are set to zero [5]. These parameters were optimized with simulations described in [4] and [5].

LINAC2 SIMULATIONS

The model has to be able to reproduce a LHC-25 beam with similar emittance and injection efficiency to that provided by the actual ring 3 of the PSB. The reference parameters of the PSB injection and of the Linac2 proton beam are listed in Table 1. The injection timing and the horizontal and vertical positions and angles of the injected beam are optimized to reach maximum intensity within the required emittance. The injection timing is defined by the delay between the moment when the injection kicker pulses at its maximum and the moment when the beam is injected.

Table 1: Reference Parameters of the Linac2 Beam and of the PSB Injection

Parameter	Symbol	Value
Linac2 normalized rms beam emittance	$\varepsilon^*_h = \varepsilon^*_v$	1.2 π mm mrad
Linac2 beam current		155 mA
Bump Collapse Time	TIKS	50 μs

In the real case for a LHC-25 beam, 2 turns are injected and the injection working point is Q_h=4.42 and Q_v=4.49. The normalized transverse rms emittances are $\varepsilon^*_h \approx 1.90$ π mm mrad and $\varepsilon^*_v \approx 1.75$ π mm mrad, respectively, and the injection efficiency is around 57% with an intensity of 1.85×10^{12} right after injection before small losses occur due to the capture process.

The simulations are carried out over 100 turns after the start of injection ending before the capture. The bump decay is completed after around 20 turns, with 100000 macroparticles injected per turn. The most optimized simulation shows an injection efficiency of 61%, with an intensity of 1.98×10^{12} protons and $\varepsilon^*_h \approx 1.88$ π mm mrad and $\varepsilon^*_v \approx 1.70$ π mm mrad. The simulations indicate an rms emittance blow-up of less than 4% during the first 10000 turns (~ 16 ms).

These results deduced from the PSB model match well the reality for the LHC-25 beam; however it has to be mentioned that there are still open questions for other beam types.

LINAC4 SIMULATIONS

The PSB model is then used to run simulations injecting a Linac4 50 MeV proton beam. The Linac4 50 MeV proton beam is expected to have a horizontal and vertical normalized rms emittance of 0.4 π mm mrad with a nominal current of 40 mA and a maximal average current of 50 mA. The current limit in Linac4 comes from the power available to compensate beam loading in the first tank of the DTL. The simulations are run for the nominal and for the maximal current and are optimized to produce a beam with the highest achievable intensity within the emittance of the LHC-25 beam currently produced by the PSB. The injection bump collapse time, the injection timing, the number of injected turns and the horizontal and vertical positions and angles of the injected beam are the parameters to tune. The injection working point is the same as for the Linac2 case. The simulations are carried out over 100 turns after injection with 50000 macroparticles injected per turn.

For both Linac4 currents, the simulations show optimum results with an injection of 9 turns and a bump collapse time of 90 μs (see Table 2). The injection efficiency is in the order of 45%, compared to 61% for Linac2.

Table 2: Optimum Results for the Simulation of a 50 MeV Proton Beam Injected from Linac4 into the PSB After 100 Turns

Injection Parameters and Resulting beam	L4 current 40 mA	L4 current 50 mA
Injection Timing [μs]	38.5	40
Initial horizontal offset [mm]	-43	-43
Initial vertical offset [mm]	1	1
Beam Intensity	1.68×10^{12}	2.19×10^{12}
Normalized rms emittance horizontal [π mm mrad]	1.87	1.81
Normalized rms emittance vertical [π mm mrad]	1.78	1.91

Simulations for the optimum cases indicate an emittance blow-up of around 2% for the 40 mA and of around 4% for the 50 mA cases during the first 10000 turns.

RESULTS

We introduce the brightness scaling as the ratio of the brightness obtained for the optimized case with Linac4 to the brightness obtained for the optimized case with Linac2.

Our simulations show that it is possible to reach 83% of today's LHC-25 beam brightness injecting a 40 mA Linac4 proton beam, while injecting a 50 mA Linac4 proton beam, 106% of today's LHC-25 beam brightness could be achieved. These results are slightly beyond expectation [6].

Copyright © 2013 CC-BY-3.0 and by the respective authors

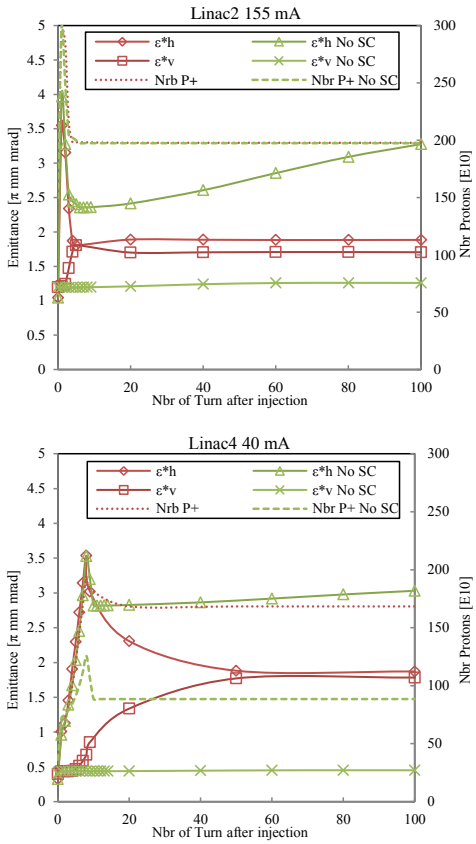


Figure 2: Horizontal and vertical normalized rms emittance (ε^*_h, ε^*_v) and number of protons as a function of number of turns after injection for optimized LHC-25 simulations with and without space charge with a Linac2 (top) and Linac4 40 mA beam(bottom).

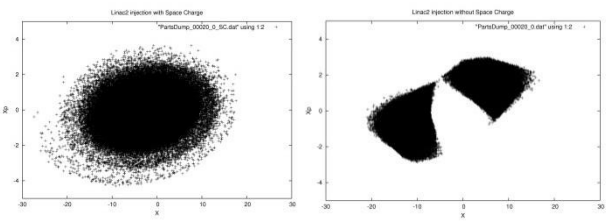


Figure 3: Horizontal phase-space profile of the resulting beam 20 turns after injection for 2 turns injected (Linac2) with space charge (left) and without space charge (right).

Figure 2 shows the results of the optimized simulations for Linac2 and Linac4 injection with and without space charge. In all the cases beam intensity and horizontal emittance increase during subsequent injection turn, i.e. 2 turns for Linac2 and 9 turns for Linac4. Once the injection is finished, beam intensity and horizontal emittance decrease due to horizontal losses at the septum blade. As the horizontal tune is 4.42, each beamlet interacts again with the blade ~2 turns after its injection inducing large horizontal losses. As the injection bump decays, the particles move away from the septum blade and the beam intensity stabilizes.

Space charge introduces a defocusing effect, which is dependent on the particle position inside the bunch and on the bunch distribution itself. It can be seen as an extra rotation in phase-space around the bunch centre and in the opposite direction than the betatron motion. If space charge is present, particles in the injected beamlets will have different tunes depending on their position inside the bunch. This mechanism explains for Linac2 and Linac4 cases with space charge the decrease of the horizontal emittance over few tens of turns after the end of injection, as the mixing of the beamlets and smoothing of the distribution is made possible by space charge. For the cases without space charge, the beamlets do not mix (see Fig. 3 right) and the horizontal emittance increases due to filamentation after injection until it reaches equilibrium (after a few 100 turns). For the Linac4 case the highest resulting beam intensity is reached for the space charge case. As explained before, with space charge the rotation of the particles with the strongest detuning close to the centre of the bunch will be slowed down and eventually they will not interact with the septum because, when they would be in the critical position, the painting bump would have already fallen enough to carry them away from the septum blade. The space charge mechanism is therefore helping in reducing the amount of losses with Linac4 and in producing beam with smaller horizontal emittance in case of Linac2.

CONCLUSION

The model of the PSB gives coherent results for the production of a LHC-25 beam with the present multi-turn injection of a Linac2 50 MeV proton beam. Comparing simulation results of the multi-turn injection with a Linac2 beam and with a Linac4 50 MeV proton beam with nominal average current, i.e. 40 mA, indicates that only 83% of today's brightness of the LHC-25 beams could be reached in the PSB. However assuming 50 mA for the average current of the Linac4 proton beam, i.e. its maximum deliverable current due to klystron power limitations, today's brightness for the LHC-25 type beams could be reached in the PSB. In conclusion Linac4 with a 50 MeV proton beam with 50 mA beam current could be used as backup solution in case of major failure of Linac2, at least to provide usable production beams for the LHC.

REFERENCES

[1] J.D. Galambos, J.A Holmes, D.K Olsen, A. Luccio, J. Beebee-Wang, "ORBIT User Manual", Version 1.10, July 1999.
[2] H. Grote, F. Christop Iselin, "The MAD program Version 8.19", CERN/SL/90-13(AP).
[3] CERN Technical Drawings SI.3.47.1020.0E.
[4] C. Bovet and al. Macroparticle computer simulation of the multiturn injection into the CERN PS Booster, Proc. Int. Particle Accelerator Conf. CERN 1972, p. 102.
[5] K. Schindl and P. van der Stok, "Present performance of PSB multiturn injection", CERN Internal report MPS/BR/Int/74-2, March 1974.
[6] A. Lombardi, "Linac4 Connection Options and Possibilities as a Backup for Linac2", IEFC Workshop 2011.

Copyright © 2013 CC-BY-3.0 and by the respective authors

nuSTORM: NEUTRINOS FROM STORED MUONS *

Alan D. Bross, Fermi National Accelerator Laboratory, Batavia, IL 60510, USA
for the nuSTORM Collaboration

Abstract

Neutrino beams produced from the decay of muons in a racetrack-like decay ring provide a powerful way to study short-baseline neutrino oscillation and neutrino interaction physics. In this paper, I describe the facility, nuSTORM, and show how the unique neutrino beam at the facility will enable experiments of unprecedented precision to be carried out. I will present sensitivity plots that indicated that this approach can provide 10 σ confirmation or rejection of the LSND/MinBooNE results and can be used to perform neutrino interaction measurements of unprecedented precision. The unique ν beam available at the nuSTORM facility has the potential to be transformational in our approach to ν interaction physics, offering a "ν light source" to physicists from a number of disciplines.

INTRODUCTION

The nuSTORM facility has been designed to deliver beams of $\overset{(-)}{\nu}_e$ and $\overset{(-)}{\nu}_\mu$ from the decay of a stored $\mu^{\pm}$ beam with a central momentum of 3.8 GeV/c and a momentum acceptance of 10% [1]. The facility is unique in that it will:

- Allow searches for sterile neutrinos of exquisite sensitivity to be carried out; and
- Serve future long- and short-baseline neutrino-oscillation programs by providing definitive measurements of $\overset{(-)}{\nu}_e N$ and $\overset{(-)}{\nu}_\mu N$ scattering cross sections with percent-level precision;
- Constitute the crucial first step in the development of muon accelerators as a powerful new technique for particle physics.

The nuSTORM facility represents the simplest implementation of the Neutrino Factory concept [2]. In our case, 120 GeV/c protons are used to produce pions off a conventional solid target. The pions are collected with a magnetic horn and quadrupole magnets and are then transported to, and injected into, a storage ring. The pions that decay in the first straight of the ring can yield muons that are captured in the ring. The circulating muons then subsequently decay into electrons and neutrinos. We are using a storage ring design that is optimized for 3.8 GeV/c muon central momentum. This momentum was selected to maximize the physics reach for both ν oscillation and the cross section physics. See Figure 1 for a schematic of the facility.

Muon decay yields a neutrino beam of precisely known flavor content and energy. In addition, if the circulating muon flux in the ring is measured accurately (with beam-current transformers, for example), then the neutrino beam flux is also accurately known. Near and far detectors are placed along the line of one of the straight sections of the racetrack decay ring. Purpose-specific near detectors can be located in the near hall and will measure neutrino-nucleon cross sections and can provide the first precision measurements of ν_e and $\bar{\nu}_e$ cross sections. A far detector at $\simeq$ 2000 m would study neutrino oscillation physics and would be capable of performing searches in both appearance and disappearance channels. The experiment will take advantage of the "golden channel" of oscillation appearance $\nu_e \rightarrow \nu_\mu$ (μ^+ stored in the ring), where the resulting final state has a muon of the wrong-sign from interactions of the $\bar{\nu}_\mu$ in the beam. This detector would need to be magnetized for the wrong-sign muon appearance channel, as is the case for the current baseline Neutrino Factory detector [3]. A number of possibilities for the far detector exist. However, a magnetized iron detector similar to that used in MINOS is seen to be the most straight forward and cost effective approach.

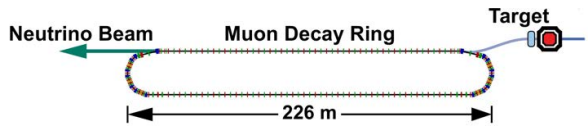


Figure 1: Schematic of the facility.

NUSTORM FACILITY OVERVIEW

The components of nuSTORM are anticipated to consist of six (6) functional areas consisting of the Primary Beamline, Target Station, Transport Line, Muon Decay Ring, Near and Far Detector Halls [4].

These areas will be located south of the existing Main Injector accelerator and west of Kautz Road on the Fermilab site. In general terms, a proton beam will be extracted from the Main Injector at the existing MI-40 absorber, directed east towards a new below grade target station, pion transport line and muon decay ring. The neutrino beam will be directed towards a Near Detector Hall located 20 m East of the muon decay ring and towards the Far Detector located approximately 1900 m away in the existing D0 Assembly Building (DAB). Figure 2 shows the nuSTORM facility components as they will be sited near the Fermilab Main Injector. The nuSTORM facility will follow, wherever possible (primary proton beam line, target, horn, etc.), NuMI [5] designs. Our plan is to extract one "booster batch" at

* Work supported by DOE under contract DE-AC02-07CH11359

Copyright © 2013 CC-BY-3.0 and by the respective authors

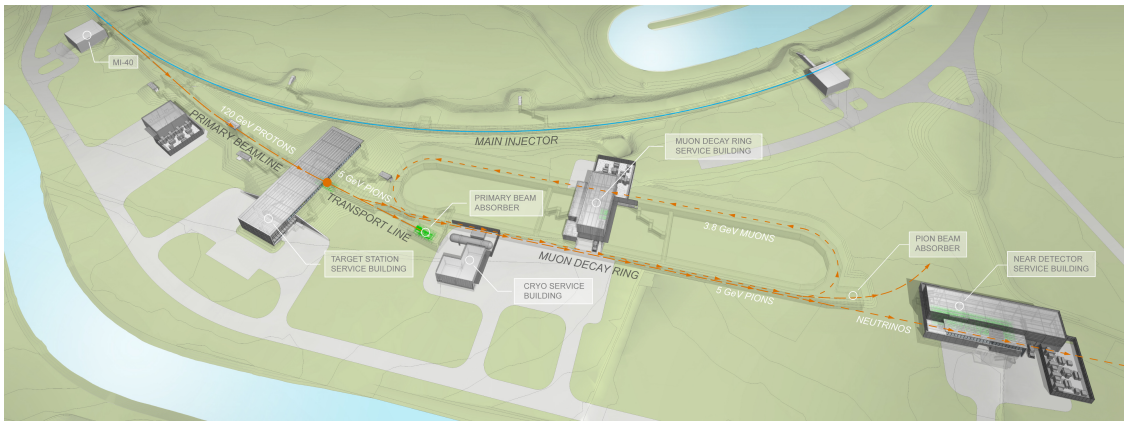


Figure 2: nuSTORM facility components.

120 GeV from the Main Injector ($\simeq 8 \times 10^{12}$ protons) and place this beam on a carbon target. Forward pions are focused by a horn into a capture and transport channel. Pions are then "stochastically" injected into the Decay Ring (see [6]). Pion decays within the first straight of the Decay Ring can yield a muon that is stored in the ring. Muon decay within the straight sections will produce ν beams of known flux and flavor via: $\mu^+ \rightarrow e^+ + \bar{\nu}_\mu + \nu_e$ or $\mu^- \rightarrow e^- + \nu_\mu + \bar{\nu}_e$. For the implementation which is described here, we chose a 3.8 GeV/c storage ring to obtain the desired spectrum of $\simeq 2$ GeV neutrinos. This means that we capture pions at a momentum of approximately 5 GeV/c.

FACILITY DETAILS

As mentioned above, the primary proton beam line and target station (and its components, i.e., target and horn) for nuSTORM follow the NuMI designs. From the downstream end of the horn, however, the nuSTORM beam system is longer similar to a conventional neutrino beam. From the downstream end of the horn, we continue the pion transport with several radiation-hard (MgO insulated) quadrupoles. Although conventional from a magnetic field point of view, the first two to four quads need special and careful treatment in their design in order to maximize their lifetime in this high-radiation environment. The pion beam is brought out of the Target Station and transported to the injection point of the Decay Ring, which we have called the "Beam Combination Section" or BCS. Figure 3 shows the pion transport line and the beginning of the Decay Ring FODO straight section. The Decay Ring straight-section FODO cells were designed to have betatron functions β_x, β_y (the Twiss parameters) optimized for beam acceptance and neutrino beam production (small divergence relative to the muon opening angle $(1/\gamma)$ from $\pi \rightarrow \mu$ decay. Large betatron functions increase the beam size leading to aperture losses, while smaller betatron functions increase the divergence of the muon beam. Balancing these criteria, we have chosen FODO cells with $\beta_{\max} \sim 30.2$ m, and $\beta_{\min} \sim 23.3$ m for the 3.8 GeV/c muons, which for the 5.0 GeV/c pions, implies ~ 38.5 m and ~ 31.6 m for the pion's $\beta_{\max}$ and $\beta_{\min}$, respectively.

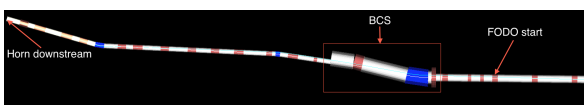


Figure 3: The G4beamline drawing from horn downstream to the FODO cells. Red: quadrupole, Blue: dipole, White: drift.

A large dispersion, D_x, is required at the injection point, in order to achieve π and μ beam separation. The BCS readily reaches this goal. A schematic drawing of the injection scenario is shown in Figure 4. The pure sector

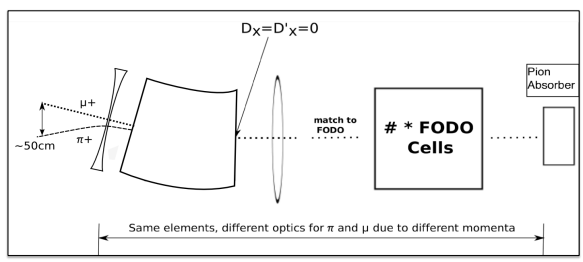


Figure 4: The schematic drawing of the injection scenario.

dipole for muons in the BCS has an exit angle for pions that is non-perpendicular to the edge, and the pure defocusing quadrupole in the BCS for muons is a combined-function dipole for the pions, with both entrance and exit angles non-perpendicular to the edges. The BCS will be followed by a short matching section to the decay FODO cells (see Figure 3). The performance of the injection scenario can be gauged by determining the number of muons at the end of the decay straight using a G4beamline simulation. In this simulation, we were able to obtain 0.012 muons per POT (see Figure 5). These muons have a wide momentum range (beyond that which the ring can accept, 3.8 GeV/c $\pm$ 10%) and thus will only be partly accepted by the ring. The green region in Figure 5 shows the 3.8$\pm$10% GeV/c acceptance of the ring, and the red region shows

Copyright © 2013 CC-BY-3.0 and by the respective authors

the high momentum muons which will be extracted by the mirror BCS at the end of the injection straight (see below). Within the acceptance of the decay ring, we obtain approximately 0.008 muons per POT.

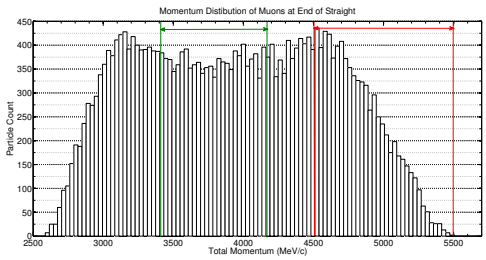


Figure 5: The muon momentum distribution at the end of decay straight.

Decay ring

We propose a compact racetrack ring design (480 m in circumference) based on large aperture, separate function magnets (dipoles and quadrupoles). The ring is configured with FODO cells combined with DBA (Double Bend Achromat) optics. The ring layout, including pion injection/extraction points, is illustrated in Figure 6 and the current ring design parameters are given in Table 1. With the 185 m length for the injection straight, $\sim 48\%$ of the pions decay before reaching the arc. Since the arcs are set for the central muon momentum of 3.8 GeV/c, the pions remaining at the end of the straight will not be transported by the arc, making it necessary to guide the remaining pion beam into an appropriate absorber. Another BCS, which is just a mirror reflection of the injection BCS, is placed at the end of the decay straight. It extracts the residual pions and muons which are in the 5±0.5 GeV/c momentum range. These extracted muons will enter the absorber along with pions in this same momentum band and can be used to produce an intense low-energy muon beam.



Figure 6: Racetrack ring layout. Pions are injected into the ring at the Beam Combination Section (BCS). Similarly, extraction of pions and muons at the end of the production straight is done using a mirror image of the BCS.

PERFORMANCE

With an exposure of 10^{21} 120 GeV protons on target, we obtain approximately 1.9 $\times 10^{18}$ useful μ decays. The appearance of ν_μ, via the channel $\nu_e \rightarrow \nu_\mu$, gives nuSTORM broad sensitivity to sterile neutrinos and directly tests the LSND/MiniBooNE anomaly [7]. A contour plot showing the sensitivity of the ν_μ appearance experiment to sterile neutrinos, utilizing a boosted-decision-tree (BDT) multivariate analysis, appears in Figure 7 for the exposure given above.

Table 1: Decay Ring Specifications

Parameter	Specification	Unit
Central momentum P_μ	3.8	GeV/c
Momentum acceptance	$\pm$ 10%	
Circumference	480	m
Straight length	185	m
Arc length	50	m
Arc cell	DBA	
Ring Tunes (ν_x, ν_y)	9.72, 7.87	
Number of dipoles	16	
Number of quadrupoles	128	
Number of sextupoles	12	

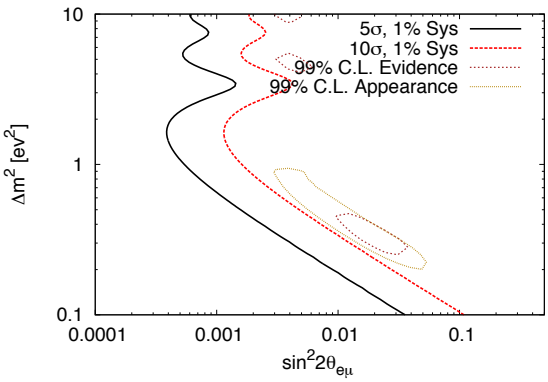


Figure 7: 5 and 10 σ contours for the BDT analysis. The 99% confidence level contours from a global fit to all experiments [8] are also shown.

REFERENCES

[1] D. Adey *et al.*,, nuSTORM Proposal, arXiv:1308.6822.

[2] S. Geer, "Neutrino beams from muon storage rings: Characteristics and physics potential", Phys.Rev., **D57**, 6989-6997, (1998).

[3] S. Choubey *et al.*,"Interim Design Report for the International Design Study for a Neutrino Factory", arXiv:1112.2853 (2011).

[4] T. Lackowski *et al.*, "nuSTORM Project Definition Report", arXiv:1309.1389.

[5] A. G. Abramov *et al.*,"Beam optics and target conceptual designs for the NuMI project," Nucl. Instrum. Meth. A **485**, 209 (2002).

[6] A. Liu *et al.*, "nuSTORM Pion Beamline Design Update," TUPBA18, these proceedings.

[7] K. N. Abazajian *et al.*,"Light Sterile Neutrinos: A White Paper," arXiv:1204.5379 [hep-ph].

[8] J. Kopp *et al.*, "Sterile Neutrino Oscillations: The Global Picture," JHEP **1305**, 050 (2013).

Copyright © 2013 CC-BY-3.0 and by the respective authors

KINETIC THEORY OF HALO FORMATION IN CHARGED PARTICLE BEAMS*

Wilson Simeoni Jr.† and Felipe B. Rizzato
IF-UFRGS, 91501-970, Porto Alegre, RS Brasil

Abstract

The proceeding proposes a derivation of the Vlasov-Poisson equation where the distribution function is splitted in a main part standing for the core and a fluctuating part standing for the halo, with which the kinetic theory of halo formations and core-halo dynamics are analysed.

INTRODUCTION

High-power hadron beams are more and more requested in multiple research fields like fusion material studies, neutrino physics, nuclear transmutation, accelerator-driven systems. Among the most recent projects, the IFMIF accelerators [1] break the record of high intensity, leading to a multi-MW beam power at relatively low energy. The concern for such accelerated beams is the predominance of the self-field energy upon the beam energy. In these conditions, the space charge effect is at its maximum, which triggers different non-linear mechanisms implying emittance growth, halo formation and sudden particle lost. The challenge is then to be able to control the total beam size, to maintain it well inside the beam pipe, and to avoid particle losses on its wall at the level of 10^{-6} in order to preserve hands-on maintenance. Careful studies of the dynamics of high intensity charged particles are thus mandatory to better understand and characterise the beam non-linear behaviour.

In the space-charge dominated regime, the space-charge effects result in emittance growth and halo formation, which contribute to beam losses. A change of focusing lattice or inadequate knowledge of proper injection conditions can cause a mismatch between the beam and the transport system. This mismatch may result in an oscillation of the beam envelope and generally excite a superposition of the envelope eigenmodes. These envelope modes possess additional free energy compared with the stationary distribution. Particles with appropriate oscillation frequencies can resonate with these envelope modes through the so called parametric $2:1$ resonance and attain large amplitude to form a halo [2]. These halo particles extract the energy from the envelope modes and convert free energy from mismatch into thermal energy, which causes beam emittance growth. The goal of this proceeding is proposes a derivation of the Vlasov-Poisson equation where the distribution function is splitted in a main part standing for the core and a fluctuating part standing for the halo, with which core-halo interactions will be analysed.

* Work supported by CNPq
† wilson.simeoni@ufrgs.br

CORE-HALO EQUATIONS

The beam is assumed to propagate with a constant axial velocity $v_z\hat{\mathbf{e}}_z$, so that the axial coordinate $s = z = v_z t$ play the role of time. The external focusing field is given by $\mathbf{B} = B_0\hat{\mathbf{e}}_z$ and is used to compensate the repulsive Coulomb force between the beam particles. It is convenient to work in the Larmor frame [3] which rotates with respect to the laboratory frame with angular velocity $\Omega_L = qB_0/2\gamma_b mc$, where c is the speed of light in vacuo, and q, m, and $\gamma_b = 1/\sqrt{1-\beta_b^2}$ are the charge, mass and relativistic factor of the beam particles respectively.

A collisionless charged particle beam is usually described in a self-consistent mean-field approximation by the Vlasov-Poisson system :

$$\frac{df_b}{dt} = \frac{\partial f_b}{\partial t} + \mathbf{v}\cdot\frac{\partial f_b}{\partial \mathbf{r}} + \mathbf{F}\cdot\frac{\partial f_b}{\partial \mathbf{v}} = 0, \quad (1a)$$

$$\mathbf{F} = -\kappa_z\mathbf{r} - \nabla\phi, \quad (1b)$$

$$\nabla^2\phi = -4\pi q n_b(\mathbf{r}, s). \quad (1c)$$

where N_b is the number of particles per unit axial length, $\mathbf{r}$ is the position vector in the tranverse plane, $\mathbf{v} = \frac{d\mathbf{r}}{ds}$ is the transverse velocity, $n_b(\mathbf{r}, s) = q_b\int d\mathbf{v}^2 f_b(\mathbf{r}, \mathbf{v}, s)$ is the transverse beam density, $\kappa_{z_0} = qB_0/2\gamma_b\beta_b mc^2$ is the focusing field, and $K = 2q^2B_0^2/\gamma_b^3 v_z^2 m^2 c^2$ is the perveance, which is a measure of the beam space charge. In Eq. (1), ϕ is a scalar potential that incorporates both self-electric and self-magnetic fields, $\mathbf{E}^s$ and $\mathbf{B}^s$. We shall take zero of the scalar potential to be at r_w, the position of the conducting channel wall. The distribution function is normalized so that $\int d\mathbf{v}^2 d\mathbf{r}^2 f_b = 1$. In the Larmor frame, the system corresponds to a two dimensional non-neutral plasma of pseudo particles of mass $m = 1$ and charge $q = \sqrt{K/N_b}$ interacting by a repulsive logarithmic potential $\phi(\mathbf{r}) = -q^2\ln(r/r_w)$ confined in a parabolic potential well of $U(\mathbf{r}) = \kappa_z r^2/2$.

The Vlasov equation (1) express the conservation of the distribution function in phase space. We assume that the initial condition in phase space consists of a patch of uniform distribution function ($f_0 = \eta_0$) surrounded by vacuum ($f_0 = 0$). After some evolution, the patch mixes with vacuum and the coarse-grained (i.e. locally averaged) distribution function $\bar{f}$ takes values between 0 and η_0. The fact that the coarse-grained distribution function cannot exceed the maximum value η_0 of the initial condition is responsible for an effective "exclusion principle "leading to degeneracy effects. This degeneracy, resulting from the incompressibility of the Vlasov equation in phase space , was first recognized by Lynden-Bell [4] is his study of equilibrium.

Suppose that the *coarse-grained* [5] distribution function is the distribution f_c for *core* of the beam and the fluctua-

Copyright © 2013 CC-BY-3.0 and by the respective authors

tions of the distribution function is the distribution f_h for the beam *halo* [6, 7].

We introduce the decomposition $f_b = \bar{f}_b + \tilde{f}_b$ $[f_b = f_{b_c} + f_{b_h}]$ where $\bar{f}_b$ $[f_{b_c}]$ is the *coarse-grained* distribution function and $\tilde{f}_b$ $[f_{b_h}]$ is the fluctuations. We assume that $\bar{f}_b$ $[f_{b_c}]$ results from the statistical average so that $\overline{\bar{f}_b} = \bar{f}_b$. Taking the local average of the Vlasov equation we obtain a convection-diffusion equation:

$$\frac{\partial f_{b_c}}{\partial t} + \mathbf{v}\cdot\frac{\partial f_{b_c}}{\partial \mathbf{r}} + \mathbf{F_c}\cdot\frac{\partial f_{b_c}}{\partial \mathbf{v}} = -\frac{\partial \mathbf{J}}{\partial \mathbf{v}}, \quad (2a)$$

$$\mathbf{J} = \overline{\mathbf{F_h} f_{b_h}}, \quad (2b)$$

for the *core* distribution function, with a diffusion current $\mathbf{J} = \overline{\mathbf{F_h} f_{b_h}}$ related to the correlations of the fine-grained fluctuations [8] (to describe the perturbations inside the *core* and to describe the retroaction of the *halo* on the *core* [7]). Note that the diffusion occurs only in velocity space. There is no diffusion in position space since the velocity $\mathbf{v}$ is a pure coordinate and therefore does not fluctuate. The problem in hand consists in determining the diffusion current $\mathbf{J}$. Since the diffusion current $\mathbf{J} = \overline{\mathbf{F_h} f_{b_h}}$ is related to the fine-grained fluctuations of the distribution function, any systematic calculation starting from the Vlasov equation must necessarily in corporate the evolution equation of f_{b_h}. This equation is simply obtained by substracting equation (1a) from (2a) :

$$\frac{\partial f_{b_h}}{\partial t} + \mathbf{v}\cdot\frac{\partial f_{b_h}}{\partial \mathbf{r}} + \mathbf{F_c}\cdot\frac{\partial f_{b_h}}{\partial \mathbf{v}} = -\mathbf{F_h}\cdot\frac{\partial f_{b_c}}{\partial \mathbf{v}} - \mathbf{F_h}\cdot\frac{\partial f_{b_h}}{\partial \mathbf{v}} + \frac{\partial \overline{\mathbf{F_h} f_{b_h}}}{\partial \mathbf{v}} \quad (3a)$$

The essence of the quasi-linear theory is to assume that the fluctuations are weak [9] and neglect the non-linear terms in (3) altogether. In that case (2a) and (3) reduce to the coupled system:

$$\frac{\partial f_{b_c}}{\partial t} + \mathbf{v}\cdot\frac{\partial f_{b_c}}{\partial \mathbf{r}} + \mathbf{F_c}\cdot\frac{\partial f_{b_c}}{\partial \mathbf{v}} = -\frac{\partial \overline{\mathbf{F_h} f_{b_h}}}{\partial \mathbf{v}}, \quad (4a)$$

$$\frac{\partial f_{b_h}}{\partial t} + \mathbf{v}\cdot\frac{\partial f_{b_h}}{\partial \mathbf{r}} + \mathbf{F_c}\cdot\frac{\partial f_{b_h}}{\partial \mathbf{v}} = -\mathbf{F_h}\cdot\frac{\partial f_{b_c}}{\partial \mathbf{v}} \quad (4b)$$

Physically, these equations describe the coupling between the *core* (*coarse-grained* distribution f_{b_c}) and the *halo* (the small-scale fluctuations f_{b_h}).

To resolve the equations (4a) and (4b) we assume during beam evolution, the system tends to maximize its rate of entropy production while satisfying all the constraints imposed by the dynamics.

Relaxation Process of the Beam Core and Halo Formation

The evolution of the system equations (4a) e (4b) is extremely complicated. Although the dynamics is collisionless, the fluctuations of the electromagnetic potential are able to redistribute energy between beam particles and provide an effective relaxation mechanism on a very short timescale (violent relaxation [4]).

The system develops an intricate filamentation in phase space (*phase mixing*). In physical space, this *mixing* process is associated with the heavily damped oscillations of beam away from mechanical equilibrium. In a strict sense, the distribution function $f_b = f_{b_c} + f_{b_h}$ does not reach an equilibrium distribution but develops smaller and smaller filaments. However if we introduce a coarse-graining procedure and locally average over the filaments, the coarse-grained distribution function $\bar{f}_b$ is expected to reach a stationary state on a short timescale. It is usually advocated that this metaequilibrium state is a particular stationary solution of the Vlasov equation [10]. A statistical theory appropriate for this process of violent relaxation has been developed by Lynden-Bell [4]. Unfortunately, the statistical prediction of Lynden-Bell is limited by the problem of incomplete relaxation [11]. Beams tend towards the equilibrium state during violent relaxation but cannot attain it: the fluctuations of the potential die away before the relaxation process is complete [12].

Equation (4b) is first solved formally with the help of Green functions [13]. This gives rise to an iterative process. This iterative process is truncated to quadratic order and the result is substituted back into (4a). The diffusion current $\mathbf{J}$ does not have yet a closed form as it involves the equal-time correlation function. To close the system, we assume that the fluctuations of the distribution function in two different macrocells are decorrelated. The resulting equation is now self-consistent [5].

Our working hypothesis is that during the stage of violent relaxation, the particles of beam extract their energy from the rapid fluctuations of the eletromagnetic field. By this process, some particles may acquire very high energies and escape from the beam forming the *halo*.

Process of the Core-Halo Interactions

With the halo formation, the relaxation of system from equilibrium becomes incomplete [14]. It starts a process of interaction *core-halo* where the terms on the right side of the equations (4a) and (4b) dominate the dynamic. The field energy generated by the core interact with the halo and the fluctuations tend to become weaker. The core reaches a stationary state [15].

Relaxation processes of Beam Halo via thermal bath

As the core is quasi-equilibrium state and the fluctuations are weakening, the core will serve as a thermal bath to the halo. This allows us to we find a quasi-equilibrium solution for the system core-halo in a relaxed state [16, 17, 18].

CONCLUSIONS

The maximum transportable current density of an ion beam with high space-charge intensity propagating in a periodic focusing lattice is a problem of practical importance.

Copyright © 2013 CC-BY-3.0 and by the respective authors

Accelerator applications such as Heavy Ion Fusion (*HIF*), High Energy Density Physics (*HEDP*), and transmutation of nuclear waste demand a large flux of particles on target. A limit to the maximum current density can result from a variety of factors: instability of low-order moments of the beam describing the centroid and envelope, instability of higher order collective modes internal to the beam, growth in statistical phase-space area (rms emittance growth) and excessive halo generation.

The most important examples of a nonstationary beam are a beam with an rms mismatch, a nonstationary distribution function (the distribution function is not a solution of the stationary Vlasov equation), and a misaligned beam. If the beam is initially nonstationary, it has a higher average energy per particle than the stationary beam. The energy difference represents the free energy that can be thermalized by nonlinear space charge forces, collisions, or instabilities. As a result of such a process, the emittance increases as the beam relaxes toward its final quasistationary state.

The deviation of beam distribution from the stationary state may be understood as the main cause of halo formation. Whenever a beam is not in its own stationary state, it naturally tries to approach closer to there, minimizing the nonlinear field energy. During this process, plasma oscillations are excited in the beam core, driving a portion of it into a halo. Inversely speaking, if a beam injected into a uniform channel is fine grainedly matched to it, there is no reason to expect the development of a halo unless the distribution itself is intrinsically unstable against perturbation. While several different factors have been considered as the possible sources of halo formation, it seems, after all, that the important point is how much a beam is deviated from the stationary state

In Linac the effective phase space volume occupied by a beam can grow rapidly if the beam intensity is sufficiently close to the space charge limit and if a source of instability is available. In principle there are three sources of instability: in a continuously focused beam it can be a nonmonotonic distribution function, like the K-V distribution; in two or three dimensional beams it can be an anisotropic distribution with different emittance and/or energy in two phase planes; in addition, periodic focusing can act as a source if an eigenoscillation is in resonance with the period of focusing.

In this proceeding a derivation of the Vlasov-Poisson equation where the distribution function is splitted in a main part standing for the core and a fluctuating part standing for the halo, with which the kinetic theory of halo formations and core-halo dynamics are analysed.

ACKNOWLEDGMENTS

The authors would like to thank the Conselho Nacional de Desenvolvimento Científico e Tecnológico (CNPq), Brazil.

REFERENCES

[1] A. Mosnier et al., Proc. of IPAC10, (2010). P.A.P. Nghiem et al., IFMIF-EVEDA Report : IFMIF-EVEDA-ASG-BD10-R006-A, (2010).

[2] R.L.Gluckstern, Phys.Rev.Lett.**73**, 1247 (1994). J. Qiang and D. Ryne, Phys.Rev. ST Accel. Beams **3**, 064201 (2000). R.L. Gluckstern et al., Phys.Rev. E **58**, 4977 (1998).

[3] R.C.Davidson and H.Qin, *Physics of Intense Charged Particle Beams in High Energy Accelerators* (World Scientific, Singapore, 2001).

[4] D. Lynden-Bell, *Statistical mechanics of violent relaxation in stellar systems*, Mon.Not.R.Astron.Soc. **136**, 101 (1967).

[5] G. Severne and M. Luwel, *Dynamical theory of collisionless relaxation*, Astrophysics and Space Science **72**, 293 (1980).

[6] C. L. Bohn and J. R. Delayen,*Fokker-Planck approach to the dynamics of mismatched charged-particle beams*, Phys. Rev. E **50**, 1516 1994.

[7] N. Piovella, A. Bourdier, P. Chaix and D. Iracane, *Perturbative Theory of the Core-Halo Interaction in a Continuous Focusing Channe*, EPAC94 Proceedings, 1186 (1994).

[8] P. Chavanis, *Hamiltonian and Brownian systems with long-range interactions: IV. General kinetic equations from the quasilinear theory*, Physica A, **387**, 1504 (2008).

[9] B. B. Kadomtsev and O. P. Pogutse, *Collisionless Relaxation in Systems with Coulomb Interactions*, Physical Review Letters, **25**, 1155 (1970).

[10] Y. Elskens, *From long-range interaction to collective behaviour and from Hamiltonian chaos to stochastic models*, Nuclear Instruments and Methods in Physics Research Section A, **561**, 129 (2006).

[11] P. Chavanis, *Quasi-stationary states and incomplete violent relaxation in systems with long-range interactions*, Physica A: Statistical Mechanics and its Applications, **365**, 102 (2006).

[12] Yan Levin, Renato Pakter and Tarcisio N. Teles, *Collisionless Relaxation in Non-Neutral Plasmas*, Physical Review Letters, **100**, 040604 (2008).

[13] P.H. Chavanis; *On the coarse-grained evolution of collisionless stellar systems*, Mon. Not. R. astr. Soc. **300**, 981 (1998). P.H. Chavanis; *Statistical mechanics of violent relaxation in stellar systems*, in: N. Antonic, C.J. van Duijn, W. Jager, A. Mikelic (Eds.), Multiscale Problems in Science and Technology, Springer, Berlin, 2002. astro-ph/0212205.

[14] R.A. Kishek, C.L. Bohn, I. Haber, P.G.O. Shea, M. Reiser and H.E. Kandrup, *Computational Investigation of Dissipation and Reversibility of Space-Charge Driven Processes in Beams*, Proceedings of the PAC01 (2001).

[15] Tarcisio N. Teles, Renato Pakter and Yan Levin, *Relaxation and emittance growth of a thermal charged-particle beam*, Applied Physics Letters, **95**, 173501 (2009).

[16] T.H. Dupree, *Theory of Phase Space Density Granulation in Plasma*, Physics of Fluids, **15**, 334 (1972).

[17] T.H. Dupree, *Theory of Phase-Space Density Holes*, Phys. Fluids, **25**, 277 (1982).

[18] T.H. Dupree, *Growth of phase-space density holes*, Phys. Fluids, **26**, 2460 (1983).

Copyright © 2013 CC-BY-3.0 and by the respective authors

BEAM DYNAMICS STUDIES OF A 30 MeV STANDING WAVE ELECTRON LINAC *

R. Dash#, HBNI, Mumbai 400094, India
J. Mondal, Archana Sharma, K.C. Mittal, BARC, Mumbai 400085, India

Abstract

For a high quality beam delivery to the users in application areas like material science and neutron spectroscopy, it is very important for the linac to keep the growth of transverse emittance and self field effects a minimum in order to limit the radioactivity and the cost of the linac itself and increase the transmission efficiency. This paper presents the results of electron beam tracking for a 30 MeV standing wave electron linac. This is a general purpose facility for neutron generation and will produce 10^{12}-10^{13} n/sec for measurement of neutron cross-section of (n, gamma), (n, xn) and (n, f) reactions. The effects of input beam size, divergence, field gradient and space charge effect on the beam quality have been studied with ASTRA beam dynamics code. This beam dynamics study explores the optimized beam parameters and beam quality for the linac operation.

INTRODUCTION

In this paper we have studied the beam dynamics of a 30 MeV, 6 kW bi-periodic coupled cavity standing wave electron linac under development at Electron Beam Centre (EBC) Kharghar, Navi Mumbai, India. In order to predict the quality of electron beam [1], [2], [3] the electron-tracking algorithm ASTRA [4] has been used. Although there are a few self-consistent space-charge codes that can be used to study the emittance evolution, we choose the ASTRA model in order to provide a fast parametric study.

The accelerating module (Fig. 1) contain a 85 keV thermionic electron gun, an injector section and two accelerating sections of 22 cell and 23 cell respectively operating in π/2 mode at a frequency of 2856 MHz. The injection section consists of three bunching cells and a power feed cell. The length of each accelerating cell is 52 mm, whereas the buncher cells are 45, 48 and 50 mm respectively. The bore radius is 5mm for all the buncher cells and accelerating cell. The effective shunt impedance for the buncher cells is ~ 80 MΩ/m, while for the accelerating cells, it is ~ 90 MΩ /m.

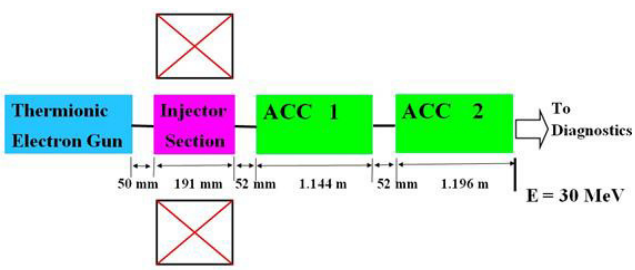


Figure 1: Schematic Layout of the 30 MeV Linac.

*Work supported by DAE, India
radhakanta.physics@gmail.com

MULTIPARTICLE SIMULATION WITH SPACE CHARGE

For the present work the longitudinal electric field components on the symmetry axis of the injector and accelerating sections have been computed using CST MWS [5]. The tracking code ASTRA does not need a geometrical description of the structures. For ASTRA code, the space-charge fields are calculated in the beam rest frame via Poisson's equation in free space and Lorentz's transformed back into the laboratory frame. ASTRA is based on Runge-Kutta integration of 4th order with fixed time step through the user defined external electric and magnetic fields, taking into account the space charge field of the particle cloud. A cylindrical grid, consisting of rings and slices, is set up over the bunch extension for the space charge calculations. The code automatically updates the mesh size as the simulation progresses. For all the simulations presented in the following, we have used 2.5 x 10^4 macro particles in uniform distribution. The initial energy of the particles injected in the guide is 85 keV. The particles are distributed quasi-randomly following the Hammersley sequence in such a way that statistical fluctuations are reduced and artificial correlations are avoided.

Effect of Space Charge on Beam Dynamics

Figure 2 gives the evolution of rms beam size for the nominal energy of 30 MeV. We have used a uniform distribution of particles having energy 85 ± 2 keV for the longitudinal direction with rms bunch length of 15.61 mm and bunch charge of 0.175 nC and Gaussian distribution in all transverse dimensions with rms beam sizes of 0.8 mm each. The results show that space charge gives rise to a transverse spread of the beam in the injection section and 1st cavity at low energies.

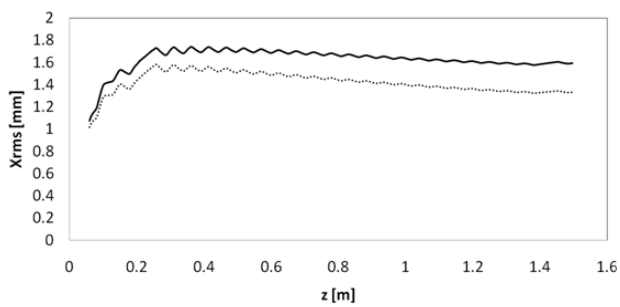


Figure 2: rms beam size without space charge (Dotted line) and with space charge (solid line).

Copyright © 2013 CC-BY-3.0 and by the respective authors

PARAMETRIC STUDY OF INPUT BEAM

Emittance of a beam is a suitable parameter to define the qualities of a beam in terms of size and divergence of the beam. Beam emittance is given approximately by the product of spot size and divergence, and is proportional to the volume of the bounding region that each bunch occupies in its region of six-dimensional phase space. The normalized RMS emittance is defined by [6]

$$\epsilon_{n,rms} = \beta\gamma\sqrt{\langle u^2\rangle\langle (u')^2\rangle - \langle uu'\rangle^2} \quad (1)$$

All the simulations data presented in this section have been noted at z = 2.64 m, that is at the end of the linac.

Evolution of Emittance with Space Charge

The general increasing nature of transverse emittance in Fig. 3 shows what we would expect: the beam has more of a tendency to diverge due to higher magnitude of self fields and leads to overall transmission loss. This curve changes significantly as we vary other parameters such as initial spot size, field strengths, cavity phases, etc.

For example, if we decrease the input rms beam size from 0.8 mm to 0.1 mm, the space charge effects becomes quite prominent and leads to growth of curve at a faster rate as shown in Fig. 3.

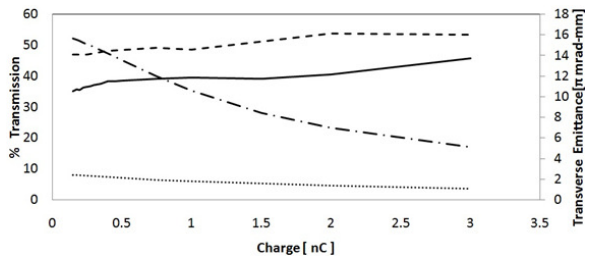


Figure 3: Effect of space charge on transverse emittance (solid line) and % transmission (Dash-dot-Dash) for rms beam size of 0.8mm .Transverse emittance (Dashed line) and % transmission (Dotted line) for rms beam size of 0.1 mm.

Evolution of Emittance with Beam Size

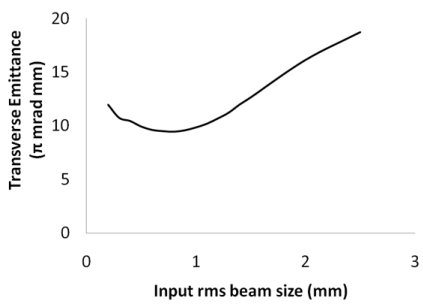


Figure 4: Evolution of transverse emittance with input beam size.

In rf cavities the radial component of the electric field grows quadratically with radius up to half of maximum radius of the rf cavity, whereas the longitudinal electric field increases linearly toward higher radii. As a result, the variation of the beam size (due to RF focussing) depends nonlinearly on the value of the beam size itself, therefore an increase of the emittance, proportional to the fourth power of the beam radius, is to be expected when a beam crosses a rf cavity .In order to numerically test this effect, we have tracked beams of charge 0.175 nC and of different transverse sizes through the rf cavity. Figure 4 describes the transverse emittance as a function of input rms beam size.

Evolution of Emittance with Divergence

In rf cavities the beam divergence strongly affects the beam behaviour. In order to study the emittance growth due to beam divergence we have taken an input beam of rms size 0.8 mm and varied the beam divergence as given in Table 1. We find that the transverse emittance shows a linear growth with increase in beam divergence, which leads to loss of electrons through the beam tube.

Table 1: Effect of Input Beam Divergence on Emittance

Input divergence	Transverse Emittance	Percentage transmission
2.1	7.71	55
6.2	8.53	54
9.4	9.67	53
12.5	10.65	52
15.6	11.48	50
18.7	12.52	47

Evolution of Emittance with Beam Aspect Ratio

We have studied the effect of the aspect ratio of the rms beam sizes in transverse direction and their effects on emittance growth. The summary of the results are given in Table 2. We observe that for any beam, the emittance growth in one transverse plane of the beam as compared to the other plane is within space-charge statistical error.

Table 2: Effect of Beam Aspect Ratio on Emittance

Beam Size x_{rms} (mm)	Beam Size y_{rms} (mm)	Emittance, ϵ_x (π mrad-mm)	Emittance, ϵ_y (π mrad-mm)
↑	1.5	11.25	12.67
0.82	2.0	9.24	17.83
↓	3.0	8.69	23.56
1.5	↑	13.65	10.33
2.0	0.82	18.18	8.91
3.0	↓	23.58	8.35

Copyright © 2013 CC-BY-3.0 and by the respective authors

Thus we treat each plane irrespective of the other plane, i.e. the two transverse planes behave independently of each other.

Effect of Variation of Field Gradient

We have studied the evolution of the beam subject to variation in field gradient. The results are given in Table 3 and from this we can estimate the changes in the output due to errors in the field gradient. An error of ± 4% in the field gradient changes the output energy gain ≈ ± 4% and error in gradient of ± 8% changes the output energy gain ≈ ± 8%.

Table 3: Effect of Field Gradient on Output Beam

Field Gradient (MV/m)	Output Energy (MeV)	Energy Spread (keV)	Transverse Emittance (π mrad-mm)
22	27.5	1230	11.78
23	28.8	908	11.21
24	30.0	720	10.65
25	31.2	648	10.03
26	32.4	678	9.58

Effect of Solenoid Focusing on Beam Quality

We have studied the quality of beam subjected to solenoid focusing. An air core solenoid of length 15 cm and 15000 ampere-turns is applied over the injection section as shown in the Fig. 1.The solenoid field reduce the beam diameter from ~ 8 mm to ~ 4.5 mm and improve the overall transmission ≈ 9%. Figure 5 describes the computed beam envelope over the entire length of the linac without solenoid and with solenoid.

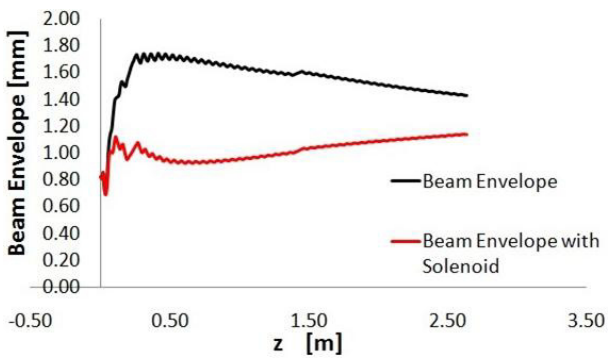


Figure 5: Computed beam envelope over the entire length of linac.

Transverse phase space of the electron beam at the end of the linac are shown in the Fig. 6 for without space charge effect and with space charge effect along with the focusing effect of the solenoid.

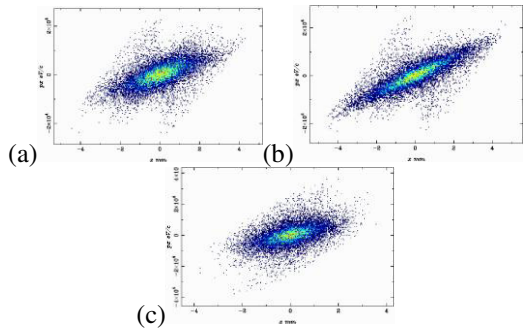


Figure 6: Transverse phase space of the electron beam at the end of the linac (a)without space charge, (b)with space charge, (c)with space charge and solenoid focusing.

CONCLUSION

We have investigated the effect of horizontal plane and vertical plane on beam dynamics and found that both the planes can be treated separately excluding space charge effect. A bunch charge of 0.175 nC is used to obtain a low emittance beam along the transverse and longitudinal direction with a reduced space charge effects. Also we have determined that a field gradient of 24 MV/m is to be maintained in order to have nominal energy gain of 30 MeV with minimum energy spread of 720 keV. We conclude from these beam dynamics studies that space charge effect plays a pivotal role in the injector section and 1st cavity of the 30 MeV linac. We have applied a solenoid of length 15 cm and 15000 ampere turns over the injector section to compensate the space charge effect. An energy spread of ~ 2.5% improves the quality of the output beam. With a beam size of ~ 4.5 mm in the bore of aperture diameter 10 mm, the beam loss on the cavity wall is minimized and the heavy irradiation of accelerator components is prevented.

ACKNOWLEDGMENT

Authors would like to acknowledge Dr. K. Floettmann (DESY, Germany) and Dr. M. Dohlus (DESY, Germany) for many valuable suggestions through private communications. R. Dash would like to thank Department of Atomic Energy, India for all kind of assistances and support under DAE Graduate Fellowship Scheme.

REFERENCES

[1] K. Floettmann, Phys. Rev. ST Accel. Beams 6 (2003) 034202.
[2] M. Reiser, Theory and Design of Charged Particle Beams, 2nd ed., Willey, New York (2008).
[3] T. P. Wangler, Los Alamos Report LA-8388, Los Alamos, 1980.
[4] http://www.desy.de/~mpyflo K. Floettmann, ASTRA, A Space charge Tracking Algorithm.
[5] http://www.cst.com CST Microwave Studio 2008.
[6] P. M. Lapostolle, IEEE Trans. Nucl. Sci. 18 (1971) 1101.

Copyright © 2013 CC-BY-3.0 and by the respective authors

PRE-SEPARATOR DESIGN OF THE IN-FLIGHT FRAGMENT SEPARATOR USING HIGH-POWER BEAM*

J.Y. Kim, C.C. Yun, D.G. Kim, E.H. Kim, M.J. Kim, M. Kim, J.W. Kim#,
Institute for Basic Science, Daejeon, Korea

Abstract

In-flight fragment separator of the rare isotope science project (RISP) is a main device to produce isotope beams for nuclear science research and applications. The separator is divided into pre and main stages. The pre-separator contains a thin target to produce the isotope beam and beam dump to remove unreacted primary beam. The maximum primary beam power is 400 kW. As a result, radiation level is very high in the target area and some of the magnets will utilize high-Tc superconductor coils operating at 20-50 K to efficiently remove the radiation heat deposited on the coil. A major function of the pre-separator is to remove the primary beam, which is complicated by different charge states produced when the primary beam passes through the target and wedge-shaped energy degrader. Some detailed calculations in beam optics and on the layout of the major separator components have been performed using GICOSY and LISE++ considering contaminant isotope beams due to nuclear reactions.

INTRODUCTION

In-flight fragment separator using the high power primary beam with large acceptance will allow researches for rare isotopes near the boundary of the nuclear chart. The next-generation in-flight separator is characterised by two major features: large acceptances of wanted isotope beam and two-stage scheme [1]. In-flight fragmentation and in-flight fission by using U beam are two major reactions to produce RI beam with an in-flight fragmentation method. It is expected new understanding on the nuclear physics can be obtained with this new device.

Currently, rare isotope science project (RISP) to construct a next-generation radio-active isotope (RI) beam facility is underway in Korea. Both Isotope separation on-line (ISOL) and the in-flight fragment separation methods will be utilized [2]. A super-conducting linear accelerator is the main driver that can accelerate a uranium beam to 200 MeV/u at a maximum beam power of 400 kW. The optical design of the in-flight separator has been performed by using GICOSY [3].

Figure 1 shows a schematic layout of the two-stage separator, in which superconducting magnets with large aperture are used to achieve large acceptance. The first stage serves to produce an RI beam of interest and to remove the unreacted primary and unwanted RI beams. The second stage aims to purify and to identify the isotope beam of interest. Major technical challenges are associated to the design and construction of the pre-separator, where the target and beam dump are located. The area including the target and beam dump is under the influence of high radiation.

In this paper, in-flight fragment separator of RISP is briefly introduced. Then optical properties and performance of the pre-separator are mainly discussed.

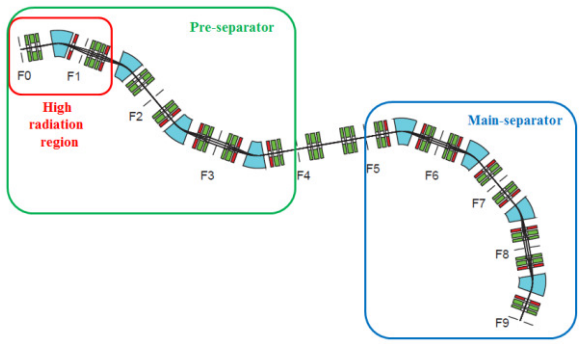


Figure 1: Schematic layout of the fragment separator.

DESIGN OF AN IN-FLIGHT SEPARATOR

The separator consists of pre and main separator, and a matching section in between is placed. The pre-separator from the production target to the F4 focus is composed of a four-bend achromatic spectrometer, consisting of four super-conducting dipole magnets with bending angle of 30 degree and seven superconducting quadrupole triplets.

As mentioned above, radiation level is very high in the target and beam dump area, so that radiation heating in superconducting coils is concerned. To remove the heat efficiently, one dipole and two quadrupole magnet triplets in the front end of the pre-separator will use high-Tc superconducting (HTS) coils. The rest of magnets in the pre-separator will use low-Tc superconducting (LTS) coils.

The main separator from the F5 focus to the F9 focus consists of eight superconducting quadrupole triplets and four dipole magnets. The F1, F3, F6 and F8 are momentum-dispersive focal planes, and the rest are achromatic planes. A wedge-shaped degrader can be used at each momentum dispersive focus to separate isotopes with the same q/A ratio by Z-dependent energy loss.

The goals of momentum acceptance and angular acceptance of the IF separator are ±5 % and ±50 mrad, respectively.

*Work supported by Rare Isotope Science Project
#jwkim@ibs.re.kr

Copyright © 2013 CC-BY-3.0 and by the respective authors

OPTICS OF THE PRE-SEPARATOR

The pre-separator contains four dipoles and seven quadrupole triplets, and its maximum magnetic rigidity is chosen to be 10 Tm considering the accelerator energy upgrade to 400 MeV/u for uranium beam in the future. The first-order optics of pre-separator is shown in Fig. 2. The production of RI beam using high power primary beam demands substantial radiation shielding compared to the facilities utilizing the maximum beam power of a few tens of kW. Radiation damage and shielding structure are main consideration in the design of pre-separator.

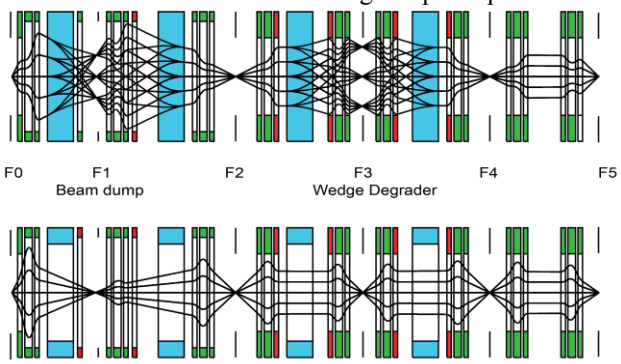


Figure 2: The first-order optics of pre-separator under consideration: The upper envelopes are in the horizontal plane, while the lower ones in the vertical plane.

To reduce radiation damage on magnetic components behind production target, the optics of pre-separator has a dispersive focus directly after the first dipole, where the dump is located. A merit of this solution is to limit an area of high level activation thereby minimizing the number of radiation resistant magnets.

For the space of the shielding walls, we leave long drift spaces of 2.6 m after second quadrupole triplets and 5.2 m between third and fourth triplets. A drift space of 1.95 m after the first dipole is to be occupied by the beam dump. Some parameters of the pre-separator are listed in table 1.

Table 1: Some Parameters of the Pre-Separator

Configuration	Four bends
Maximum magnetic rigidity	10 T/m
Momentum acceptance	±4.3%
Angular acceptance	±40 mrad (h)
	±50 mrad (v)
Momentum dispersion	+2.3 cm/% at F1
	-3.05 cm/% at F3

The large acceptance is needed to collect RI beam produced via ^{238}U fission. The angular and momentum spreads of RI beam produced by in-flight fission of uranium beam at 200 MeV/u can be over 100 mrad and 10%, respectively, when symmetric fission is assumed. The superconducting quadrupole triplets need to have large apertures and the dipole a large gap. The total length of pre-separator is currently about 57 m.

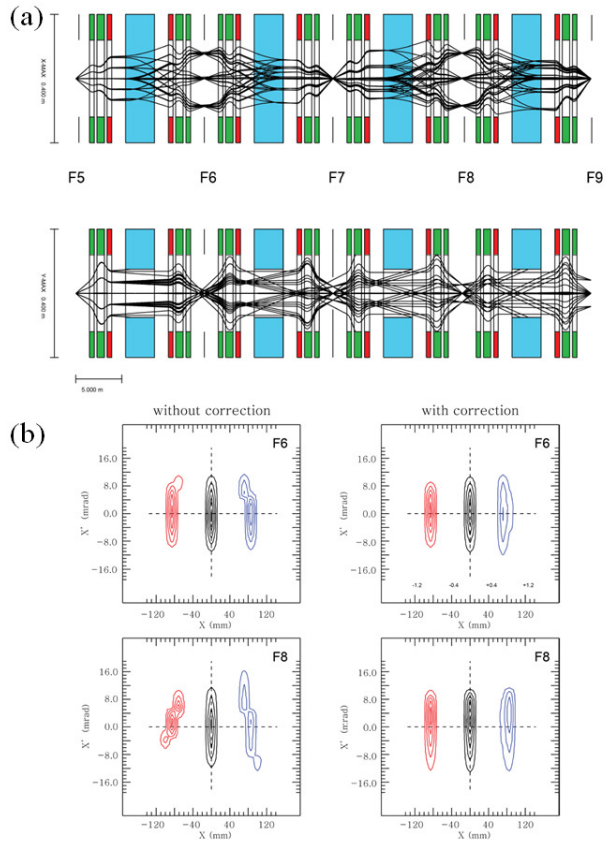


Figure 3: Correction of phase space distortion in the second order optics of pre-separator at F1 and F3.

Figure 3 is the result of 2nd order correction with hexapole magnet (red color). The beam phase spaces at F1 and F3 are compared before and after 2nd correction in Fig. 3 (b), which shows significant improvement.

PRE-SEPARATOR PERFORMANCE

Parameters of the pre-separator and the purity of ^{132}Sn at the exit of pre-separator were evaluated by simulations with the LISE++ code [4]. ^{132}Sn ion, which is double magic nucleus, is a main isotope beam of interest used for the separator design. A 200 MeV/u $^{238}U^{79+}$ primary beam was used with a graphite target of 303 mg/cm^2 thick to produce ^{132}Sn in the simulation. The momentum acceptance of ±3% was assumed using a wedge shaped degrader in F3 focus. The material of degrader is aluminium with central (on-rigidity) thickness of 1.57 mm corresponding to approximately 30% of ^{132}Sn beam range.

As can be seen in Fig. 4, the transmission of ^{132}Sn in 1st order simulation was calculated to be about 25.3%, when the selection slits in the pre-separator were completely open. Large losses of ^{132}Sn occur at the F1 focus, where the beam dump is located. Fission fragments are produced from the target with large spreads in both angle and

Copyright © 2013 CC-BY-3.0 and by the respective authors

momentum. Magnetic rigidities that are larger by 3% than the selected value are removed at the beam dumps, as shown in Fig. 5.

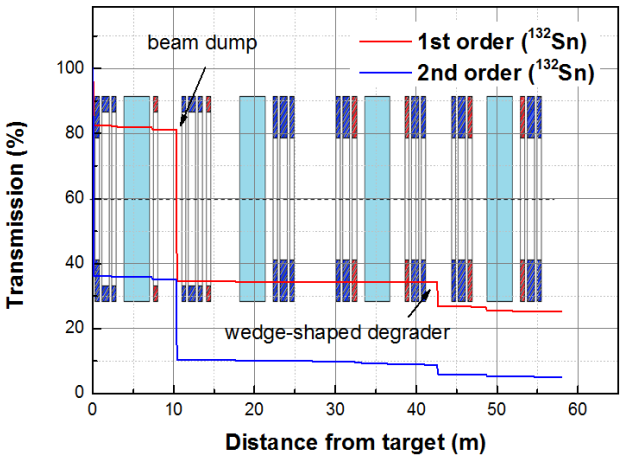


Figure 4: Comparison of transmission efficiency of ^{132}Sn produced via in-flight fission simulated in 1st and 2nd order optics on the pre-separator.

A less significant loss occurs due to multi charge states of ^{132}Sn ions generated by the electronic interactions in the wedge. The loss in transmission for ^{132}Sn derived from 2nd order aberrations is due to the increase in the size of the beam envelope compared to the first order beam envelope. The transmission of ^{132}Sn in 2nd order simulation is about 5.1%. Further optimization on high order aberration correction scheme is necessary to improve the 2nd order or higher order transmission efficiency.

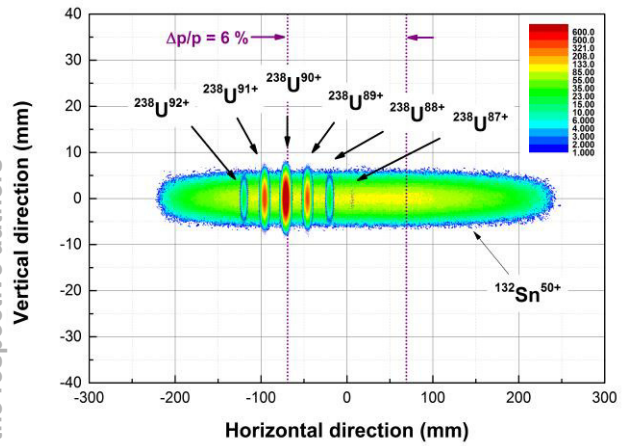


Figure 5: The primary beam and ^{132}Sn beam profiles at the F1 focus, where the beam dump are located.

Figure 6 is a part of the chart of nuclides indicating the yield rate of ^{132}Sn and un-wanted fragments at the end of the pre-separator. The production rate of ^{132}Sn is about 1.34×10^{7} pps with the purity of about 0.03%. The most intense contaminants are nuclei which are located closer to the valley of stability. The purity of ^{132}Sn can be improved by isotopic selection of the main separator.

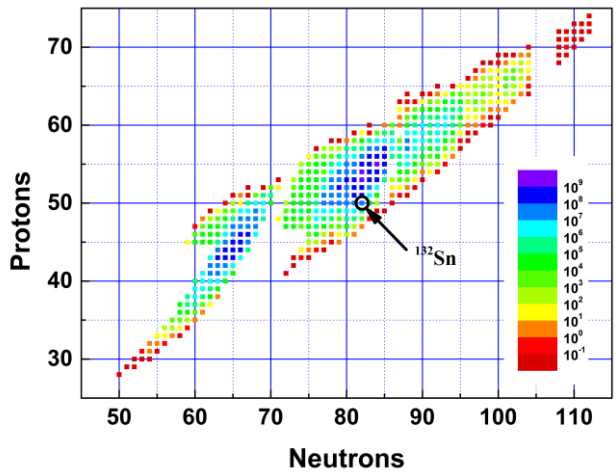


Figure 6: The rate of ^{132}Sn and un-wanted fragments transmitted to the end of pre-separator.

CONCLUSIONS

The design of in-flight separator using high-power primary beam has been carried out for the RISP in Korea. Main considerations on optical design of pre-separator are associated with shielding high-level radiation and removing the primary beam almost completely. The optimization process has been underway to deal with main considerations, and to improve the purity and the transmission of fragments. To evaluate the performance of current pre-separator, transmission efficiency and rate of ^{132}Sn were calculated by using LISE++ to be achieved 25.3 %, 1.34×10^{7} pps, respectively.

ACKNOWLEDGMENT

This research was supported by the Rare Isotope Science Project of the Ministry of Science, ICT and Future Planning (MSIP) and by the National Research Foundation (NRF) of Korea.

REFERENCES

[1] T. Kubo, Nucl. Instr. Meth. B 204 (2003) 97.
[2] J. W. Kim, "Status of the Rare Isotope Science Project in Korea" LINAC'12, Tel-Aviv, September 2012, TUPB028, p. 534(2012); http://www.JACoW.org
[3] M. Berz et al., Nucl. Instr. Meth. A 258 (1987) 402.
[4] O. Tarasov, D. Basin, Nucl. Instr. Meth. Phys. Res. B 266 (2008) 4657.

Copyright © 2013 CC-BY-3.0 and by the respective authors

HORIZONTAL DISPERSION STUDIES FOR THE CERN PROTON SYNCHROTRON BOOSTER RINGS

V. Raginel, B. Mikulec, S. Gilardoni, CERN, Geneva, Switzerland

Abstract

In order to confirm the value of horizontal dispersion of the CERN Proton Synchrotron Booster (PSB) given by the MADX model, the horizontal dispersion has been measured using pick-ups and wire scanners on its four rings. The dispersion value of the PSB rings is of interest for example as input for the emittance measurements critical for high-brightness beam production for the LHC, for future optics studies related to the planned upgrades of the PSB or for optics studies of the ejection lines. In this study, the dispersion measurement protocol and the analysis of the measurements are presented. The measurement results point out differences with respect to the MADX model and also differences between the four rings. It was then investigated using horizontal orbit measurement and MADX matching routines whether misalignments of quadrupole magnets could explain these differences.

INTRODUCTION

The knowledge of the dispersion of the Proton Synchrotron Booster (PSB) rings is of interest for cross check the optics of the ring currently in use, but also as input for the emittance measurements [1] or for the optics matching studies of the injection/ejection lines. While the dispersion in the PSB is estimated by a MADX model [2], measurements of dispersion are necessary to validate the simulated optics. The horizontal dispersion $D_x(s)$ can be defined by:

$$\Delta x(s) = D_x(s) \cdot \delta$$

where $\Delta x(s)$ is the horizontal beam centroid displacement at the location s and $\delta=\Delta p/p_0$ is the relative momentum offset with respect to the nominal momemtum p_0. The dispersion can be measured by changing the beam momentum via the RF system, observing the beam displacement at the location of the beam position monitors and the variation of the revolution frequency. The momentum deviation is evaluated via the momentum compaction factor and the measured frequency change. The measurements were done for all four rings of the PSB. The dispersion was obtained off-line using a fitting routine on the beam position monitors data and then compared to the MADX model.

DISPERSION MEASUREMENTS

The dispersion was measured using a LHC 50 ns beam (the luminosity production beam for the LHC 2012 run) for each ring using the programmable RF radial position function which converts a given change in the average orbit into energy offset. The radial position function was modified 760 ms after the start of the cycle, just before the extraction flat top of the magnetic cycle when the beam momentum is 2126 MeV/c. The horizontal beam displacement and the revolution frequency were acquired for various values of the radial position function averaging over three measurements. The horizontal beam displacement was observed by the sixteen pick-ups of each ring (BRi.UES1L3, BRi.UES2L3 ..., and BRi.UES16L3, with i=1, 2, 3, 4 indicating the fours PSB rings), one pick-up per section, and by one wire scanner in the section 2 of each ring (BRi.BWS.2L1). The pick-ups of the PSB rings are installed in-between the first focusing quadrupole (QF) and the defocussing quadrupole (QD) with the basic optics cell of the PSB being bending1-QF1-QD-QF2-bending2. The readout chain per section of the pick-ups is the same for each ring (multiplexing) [3].

A too large horizontal beam displacement can cause beam losses when the aperture limit is reached. The maximum variations of the radial position function with no beam losses were determined for both positive and negative displacement. The measurements were done between these maximum variations.

DISPERSION ANALYSIS AND RESULTS

Determination of the Dispersion in Each Ring

The measurements yield the displacement of the center of the beam and the corresponding revolution frequency. The relative momentum deviation was derived from the relative variation of the revolution frequency thanks to the following relation:

$$\Delta f / f_0 = -\eta \cdot \delta$$

where $\eta = \eta_0 + \eta_1 \delta + O(\delta^2)$ is the phase slip factor [4]. The frequency f_0 corresponds to the naturally centered orbit by introducing no offset in the radial loop function. A first assumption is to simplify the phase slip factor to the first order. The analysis was done using the relation

$$\Delta f / f_0 = -\eta_0 \cdot \delta$$

where $\eta_0 = \alpha_0 - 1/\gamma^2$ with α_0 being the first order momentum compaction factor, which is equal to 0.0609 in the PSB, and γ being the relativistic gamma of the proton beam. Δx vs. δ is then plotted for each pick-up and the wire scanner, examples of a plot of Δx vs. δ is shown in Figure 1 (black dashed line). The data fits show that the data is not linear, but rather parabolic.

Copyright © 2013 CC-BY-3.0 and by the respective authors

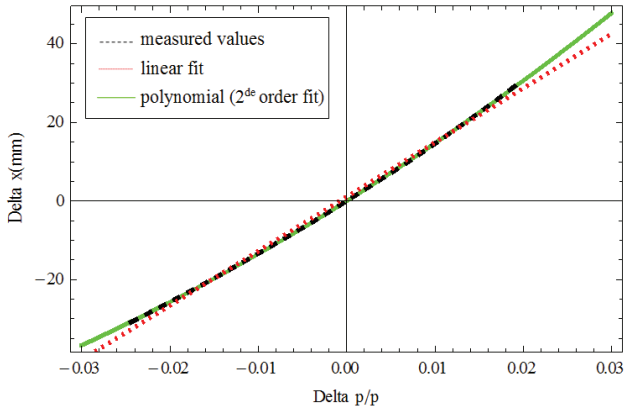


Figure 1: Plots of Δx vs. δ resulting from measurements done on the pick-up BR1.UES5L3 using the simplified relation $\Delta f/f_0 = -\eta_0 \cdot \delta$.

A second analysis was subsequently done using the relation

$$\Delta f / f_0 = -(\eta_0 + \eta_1 \cdot \delta) \cdot \delta$$

where $\eta_1 = \alpha_0 \cdot \alpha_1 + 3\beta^2 / 2\gamma^2 - \eta_0 / \gamma^2$ [5]

with α_0 being the first order momentum compaction factor and α_1 being the second order momentum compaction factor. The second order momentum compaction factor was determined for the PSB in the same way already used before in the PS [6]. The second order momentum compaction factor α_1 is related to the total momentum compaction factor α_p given by the MADX model of the PSB:

$$\alpha_p = \alpha_0 (1 + 2\alpha_1 \delta) + O(\delta^2) \text{ [4]}$$

The total momentum compaction factor α_p was simulated for nine momentum offsets Δp = ±40, ±30, ±20, ±10 and 0 MeV. α_1 was then derived from the slope of α_p vs. δ, and yields α_1 = 2.237. The resulting horizontal beam displacement as a function of the relative momentum spread becomes then a linear function. The relative position error of the pick-ups is considered to be within ±0.1 mm, except for the pick-ups 2L3 and 10L3 (±0.2 mm and ±0.3 mm, correspondingly) [7]. The calibration of the wire scanners indicates that the response of the wire scanners is linear in the range ±10 cm and that the relative horizontal position error is negligible. The data of the pick-ups BR2.UES6L3 and BR2.UES10L3 show some incoherency with the others pick-ups probably due to malfunctioning of the system and thus are excluded from the analysis. The slope of the linear fit gives the dispersion at each measurement point in the four rings. A comparison of the measured horizontal dispersion of all four rings and the horizontal dispersion D_x predicted by the PSB MADX model is shown in Figure 2. One can see in Figure 3 that the maximal relative differences of D_x predicted by the PSB MADX model and obtained by measurements on the 4 rings is ~10%. The dispersion values of MADX agree rather well with the measured values; however the dispersion of the MADX model shows an offset of ~0.05 m compared to the dispersion measured in the 4 rings, which is not well understood yet. The measurements show that dispersion is different from ring to ring, in the next section it is investigated whether misalignments of the defocusing quadrupoles explain these differences.

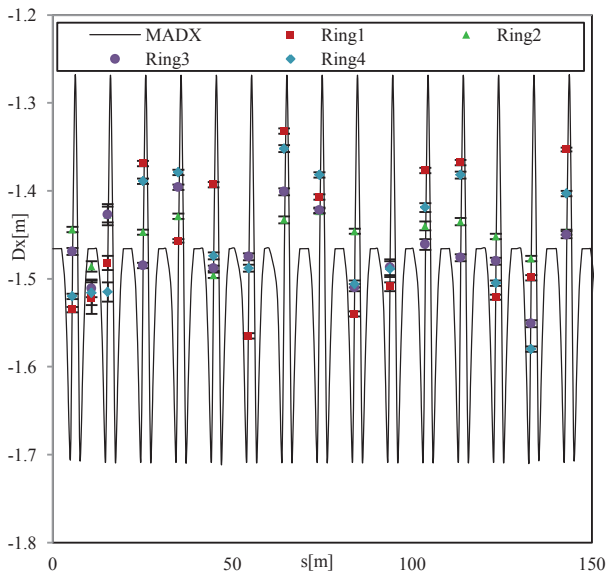


Figure 2: MADX simulation of the horizontal dispersion along the PSB ring (solid line) with the measurement points for the horizontal dispersion D_x for the 4 rings.

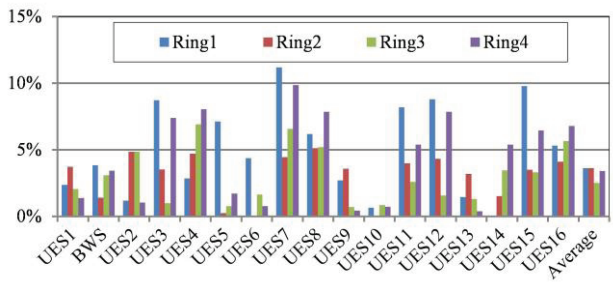


Figure 3: Relative differences of D_x given by the MADX model and obtained by measurements for the 4 rings. The pick-ups UES6 and UES10 of Ring2 are excluded from the analysis.

Analysis of the Differences Between the PSB Rings

It is investigated if the differences in dispersion between the four rings could be explained by the horizontal misalignments of the defocusing quadrupoles (QD). It has to be noted that a tilt of each QD affects differently the four superposed rings of the PSB because the alignment of the rings for the tilt is done by rotating the magnet stack around the centre of ring 3, which is at the same vertical level than the injection/extraction line. The method used was to estimate the horizontal misalignments of the QDs from closed orbit measurements for each of the four rings and then to

Copyright © 2013 CC-BY-3.0 and by the respective authors

compute the horizontal dispersion ring by ring inserting the estimated misalignments into the MADX model.

As the closed orbits in the PSB are dominated by misalignment effects [8], the horizontal misalignments of the defocusing quadrupoles can be estimated as follows. First the horizontal closed orbits were measured 760 ms after the start of the cycle for all the four rings averaging over three measurements, including the transversal misalignments of the pick-ups. Second in the MADX model, virtual horizontal kickers were inserted in the centre of each QD to represent the misalignments of the QDs. Their strength was then determined by reproducing the closed orbit via the MADX model. The kicks were then translated into misalignments using the relation $\Delta x_{QD} = \theta/(L \cdot k)$ with Δx_{QD} being the horizontal misalignment of the defocusing quadrupole, θ being the kick found by matching, L being the magnetic length of the quadrupole and k being the normalized gradient of the quadrupole. The estimation of the horizontal misalignment of the QDs was done independently ring by ring. Finally the estimated horizontal misalignments of the QDs were introduced into the original MADX model and the closed orbit and dispersion were computed. The dispersion function at the pick-ups is not strongly dependant on the number of misaligned QDs, when using two or more misaligned QDs.

From Figure 4, one can note that the offset between the measured dispersion and the one given by the MADX model is ~0.06 m. The misalignments of the QDs in the MADX model induce an oscillation of the dispersion around its average value. These oscillations agree rather well with the oscillations observed in the measured dispersion as shown in Figure 4 for rings 1, 3 and 4. For ring 2 it is difficult to conclude, as the dispersion measurement does not have a clear dispersion pattern due to the exclusion from the analysis of the pick-ups UES6 and UES10. It has to be noted that the absolute error of the pick-up orbit measurement is estimated to be ~1 mm [9], which leads to uncertainties on the estimated misalignments of the QDs and subsequently on the estimated dispersion with these misalignments.

However there are good indications that the misalignments of the QDs in the PSB explain the oscillations of the dispersion around its average value and thus explain partially the differences of the measured horizontal dispersion between the four rings.

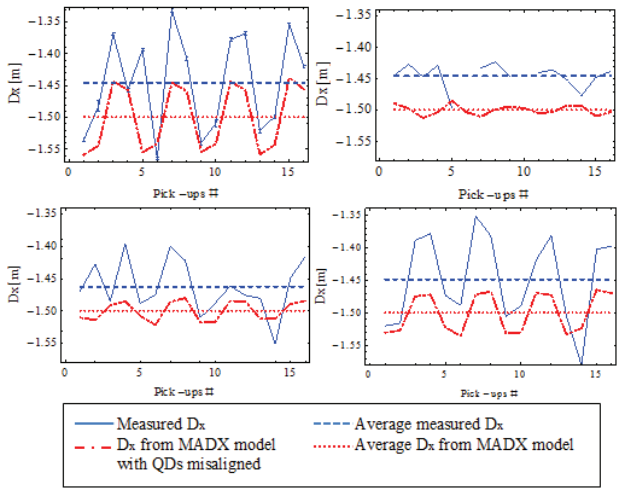


Figure 4: Comparison of the measured horizontal dispersion at the 16 pick-ups with the dispersions given by the PSB MADX model with misalignments of the QDs for ring 1 (top left), ring 2 (top right), ring 3 (bottom left) and ring 4 (bottom right).

CONCLUSION

The horizontal dispersion was measured using 16 ring pick-ups (1 per section) and a wire scanner (1 per ring) for the 4 rings of the PSB. The measured horizontal dispersion is consistent with the values of MADX within maximum 10% relative error and amounts to -1.45 m in average at the pick-ups. However slight differences between the four rings were observed. Using orbit measurements to estimate the misalignments of the QDs in each of the four rings it was shown that the difference in horizontal dispersion between the four rings could be partially explained by misalignments of the QDs. During the long shutdown 2013-2014 the PSB rings have been realigned; according to this study it can be expected to obtain a more uniform horizontal dispersion between the four rings after the 2014 restart.

REFERENCES

[1] P. Forck, Lecture Notes on Beam Instrumentation and Diagnostics, page 40, JUAS 2011.
[2] http://project-ps-optics.web.cern.ch/project-PS-optics/cps/Psb/2013
[3] D. Korchagin, M. Ludwig, L. Soby, BI Front end software functional specifications for the PSB Orbit measurement system [BPBNO], EDMS 691997, 2007.
[4] S.Y. Lee, Accelerator Physics, page 219, 1999.
[5] J.P. Shan, S.G. Peggs, S.A. Bogacz, Analytical evaluation of the second order momentum compaction factor and comparison with MAD results, Fermilab, 1993.
[6] S. Aumon, High Intensity Beam Issues in the CERN Proton Synchrotron, CERN-THESIS-2012-261.
[7] M. Chanel, B. Mikulec, G. Rumolo, R. Tomás, PS Booster Orbit Correction, CERN-AB-2008-034.
[8] C. Carli, Closed Orbit Estimates according to known misalignments in the PS Booster, PS/CA/Note 97-21.
[9] L. Soby, *private communications.*

Copyright © 2013 CC-BY-3.0 and by the respective authors

BEAM DYNAMICS AND WAKEFIELD SUPPRESION IN INTERLEAVED DAMPED AND DETUNED STRUCTURES FOR CLIC*

A. D'Elia[1,2,3], T. Higo[4], V.F. Khan[3], R.M. Jones[1,2], A. Latina[3], I. Nesmiyan[1,2] and G. Riddone[3]
[1]School of Physics and Astronomy, The University of Manchester, Manchester, U.K,
[2]The Cockcroft Institute of Accelerator Science and Technology, Daresbury, U.K,
[3]CERN, Geneva, Switzerland, [4]KEK, Tsukuba, Japan

Abstract

Acceleration of multiple bunches of charged particles in the main linacs of the Compact Linear Collider (CLIC) with high accelerating fields provides two major challenges: firstly, to ensure the surface electromagnetic fields do not cause electrical breakdown and subsequent surface damage, and secondly, to ensure the beam-excited wakefields are sufficiently suppressed to avoid appreciable emittance dilution. In the baseline design for CLIC, heavy wakefield suppression is used (Q ~ 10) [1] and this ensures the beam quality is well-preserved [2]. Here we discuss an alternative means to suppress the wakefield which relies on strong detuning of the cell dipole frequencies, together with moderate damping, effected by manifolds which are slot-coupled to each accelerating cell. This damped and detuned wakefield suppression scheme is based on the methodology developed for the Japanese Linear Collider/Next Linear Collider (JLC/NLC) [3]. Here we track the multi-bunch beam down the complete collider, under the influence of transverse wakefields and record the final emittance dilution at the end of the linac. We utilize the code PLACET [4] for all tracking simulations and include systematic and random fabrication errors; the latter are particularly beneficial in reducing the impact of the wakefield on the beam quality. Results of some initial alignment studies are also provided.

INTRODUCTION

The CLIC scheme entails two beams, one of which is the high-current drive beam (~ 100 A), and the other is a low-current accelerated beam. The drive beam is decelerated and provides an electromagnetic field which is coupled to the main accelerating linac. These main linacs are required to accelerate electron-positron beams to a final collision centre of mass energy of 3 TeV. Recent studies anticipate a staging to a reduced centre of mass energy of 375 GeV, as a prelude to the full collision energy. Here we focus on the 3 TeV design, which requires more than 71,000 accelerating structures. In this baseline design, each structure accelerates 312 bunches, each of which consists of ~ 4 x10^9 particles per bunch. The corresponding beam current of ~ 1 A removes energy from the accelerating electric field, and loads it down. The beam-loaded accelerating field is designed, on average, to be 100 MV/m. The electric field is a little more than a factor of two larger on the walls and the magnetic field is constrained to provide a pulse temperature rise on the copper walls of no more than 56 K [5]. A relatively compact accelerating structure is obtained by adopting an X-band accelerating frequency of 11.994 GHz. The iris radius of each accelerating cell largely determines the shunt impedance, which ideally should be maximized, but since shrinking it down also enhances the transverse dipole fields, a compromise must be achieved. In our design we focus on an average iris radius to free space wavelength: $\langle a \rangle/\lambda \sim 0.13$. The average iris radius determines the short-range wakefield, or the field experienced along the bunch itself. The transverse wakefield experienced by succeeding bunches in the multi-bunch train is influenced by several factors. In principle it can be suppressed by heavy damping, and this is indeed the method adopted in the baseline design for CLIC in which field is coupled out from each cell and immediately dissipated in attached ceramics. This ensures the wakefield on the first trailing bunch is constrained to less than 6.7 V/pC/mm/mm [5] and all subsequent bunches experience an even lower wakefield. Recent high power tests have indicated this structure is able to sustain the requisite surface electromagnetic fields at the design gradient [6].

However, here we discuss a method which entails changing the dipole frequency of each of the cells within a given structure and hence ensuring the eigenmodes, corresponding to these fields, add up in a deconstructive manner [3]. In our alternative design the iris is tapered down in an erf function manner, and this ensures the wakefield decays with a Gaussian envelope. However, the finite number of cells within each structure corresponds to a sampling of the field. This will ultimately lead to a point at which the eigenmodes add together coherently and hence will force the wakefield to rise above the constrained value. We provide four waveguide-like manifolds, slot-coupled to each cell in the structure, to ensure this recoherence in the wakefield is sufficiently suppressed. We have constrained our design to utilize the same number of cells as the baseline design, namely 24. This short structure is of course insufficient to provide adequate sampling, and hence we interleave the frequencies of several neighbouring structures in order to obtained the requisite wakefield suppression -12 and 16 fold interleaving is focused on in this article (corresponding to an equivalent structure of 288 and 384 cells, respectively).

This paper is organized such that the next section provides a description of the wakefield suppression used, followed by a section entailing tracking the beam throughout the complete linac under the influence of expected fabrication errors, and finally by a penultimate

* This research has received funding from European Commission under the FP7 Research Infrastructure grant no. 227579

Copyright © 2013 CC-BY-3.0 and by the respective authors

section concerned with an initial investigation of the implication of structure misalignment on emittance dilution. A final set of concluding remarks is also given.

DDS INTERLEAVED DESIGN

The accelerating structures investigated here are based on those optimised in [7], and a single one of these structures is referred to as CLIC_DDS_A. This optimisation was focussed on adhering to the semi-empirical design constraints specified for CLIC –and entails, *inter alia*, ensuring the surface electromagnetic fields are within given bounds [5], and the overall efficiency of the collider is maximised. The inter-bunch spacing was changed from the baseline value of 6 rf cycles to 8, in order to relax the required suppression on the first trailing bunch –which is governed by the frequency spread of the dipole modes. This allowed a bandwidth of 11.8 % (~ 2 GHz) with a span of 3.48σ to be assigned to the first dipole band. Higher order bands provide appreciably smaller transverse momentum kicks [8] to the beam and hence we focus on the first dipole band in this work.

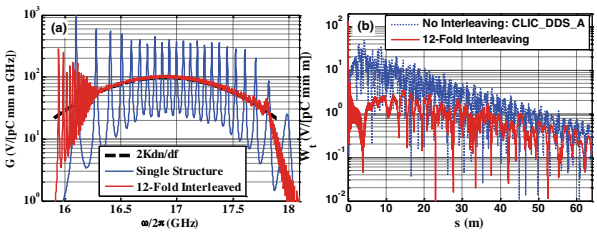


Figure 1: Spectral function (a) for a single structure (in blue) and a 12-fold interleaved series (in red), together with the Fourier transforms thereof, the corresponding wakefunctions W_t (b). Also shown is twice the kick factor weighted frequency density distribution (2Kdn/df).

Before discussing the wakefields, and beam dynamics of the multi-structure configurations relevant to CLIC, we note that a single structure, CLIC_DDS_A, has been fabricated and is being scheduled to be high power tested at CERN. All cells of this 24-cell structure have been precisely made by milling with a carbide tool on the outer area of each cell, followed by diamond-point turning in the beam-hole area and finally, chemically rinsed and diffusion bonded together. It remains to complete the process by attaching couplers and tuning stubs.

The transverse, long-range wakefield in these multi-cell structures is assessed using a spectral function method [9,10]. This method was developed to take into account the strong coupling of modes. The Fourier transform of the spectral function provides the wakefield experienced by the beam. A single structure consists of no more than 24 cells and hence will be woefully inadequate in suppressing the wakefield. However, provided the dipole modes are interleaved between successive structures, the wakefield will be well-suppressed. We have found 12-fold interleaving of modes to be sufficient (equivalent to a single structure consisting of 288 cells). The spectral function, and corresponding wakefunction, for a single structure and a 12-fold interleaved series of structures is shown in Fig 1. Also indicated is 2Kdn/df, the original uncoupled design. The short-range wakefield (the first 2 m or so), corresponding to the Fourier transform of the uncoupled design and coupled spectral functions, should be virtually identical and we have verified this during our calculations. It is interesting to note that the minimum spacing and indeed maximum spacing of the modes (corresponding to the spacing in the peaks in Fig. 1 (a) for example) provides an indication as to where the modes will recohere. The minimum and maximum separation of peaks in Fig. 1 (a) for a single structure is 61 MHz and 342 MHz, and for 12-fold interleaving of structure frequencies it is 5 MHz and 19 MHz. These separations correspond to recoherance positions of 5 m and 1 m for a single structure, and 60 m and 16 m for the interleaved structures. Inspection of the wakefields in Fig. 1 (b) confirms this behaviour. Clearly the interleaving enhances the overall sampling, and hence provides a better representation of the Gaussian distribution, and also pushes the recoherence position further down the bunch train.

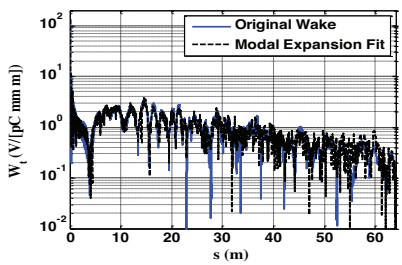


Figure 2: Envelope of fitted transverse wakefunction of (dashed and in black) together with that of the Fourier transform of the spectral function (solid blue) for a 12-fold interleaved structure.

The wakefield presented in Fig. 1 (b) is not that experienced by the beam, as the envelope, or worst case wakefield is illustrated. The tracking code we utilise, PLACET, requires the mode frequencies, Q's, and corresponding kick factors [4,11] as input parameters to assess the impact of these wakefields. We utilize the peaks in the spectral function and assign these to the modal frequencies, the remaining parameters are obtained by taking the usual modal expansion [12] and performing a non-linear least-square error fit. To provide some confidence in the fitting method, we compare the original Fourier transform of the spectral function to the fitted modal sum, and this is displayed in Fig. 2. We analyse the impact of these transverse long-range wakefields on the beam dynamics in the next section

BEAM DYNAMICS STUDIES

Here we assess the implications of these wakefields for two particular situations. In case I we investigate a 12-fold interleaved version of the original design, in which

Copyright © 2013 CC-BY-3.0 and by the respective authors

bunches were spaced from their neighbours by 8 rf cycles. In case II, we maintain the original distribution, but modify the bunch spacing to 6 rf cycles, and in this case we discover further interleaving, to the extent of 16-fold, is needed to contain the emittance dilution to acceptable limits. This of course has implications on the fabrication tolerances, as the minimum frequency spacing for the latter structure is 3.4 MHz**.** However, these tolerances are still compatible with those assigned to the accelerating mode –which is < 1 MHz. We performed beam tracking simulations down the complete linac, for a bunch train initially offset by σ_y (0.5 μm), and observed an emittance dilution in case I and II to be 4.4 % and 3.6 %, respectively.

However, these simulations neglected anticipated sources of experimental errors. To provide a more realistic assessment of the beam dynamics we conducted further simulations for both cases, in which systematic and random frequency errors were included. These beam dynamics simulations are time consuming, and in order to provide a rapid initial assessment of the effect of the wakefields on the beam dynamics, we also calculate S_{RMS} (the RMS of the sum wakefield [13]).

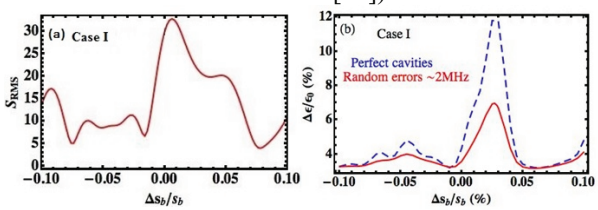


Figure 3: S_{RMS} (a) together with the vertical emittance dilution at the exit to the linac (b), as function of the fractional deviation in the bunch spacing from the nominal case for case I. A linac fabricated with no random errors, is simulated (shown dashed in blue), together with a linac incorporating random errors (the solid red curve).

The results of these beam dynamics simulations, alongside S_{RMS}, for both cases, are displayed in Figs 3 and 4. We note that the random errors adding in both cases had a Gaussian distribution and were restricted to 2 MHz RMS spread. Inspection of Fig. 3 reveals the maximum emittance dilution is 12 % for case I with no random errors. This is reduced to 7 % once random errors are added. Similarly, for case II, random errors bring the maximum emittance dilution down from 9 % to 6 %. We also note that S_{RMS} provides a qualitative guide as to the expected worst-case region for emittance dilution.

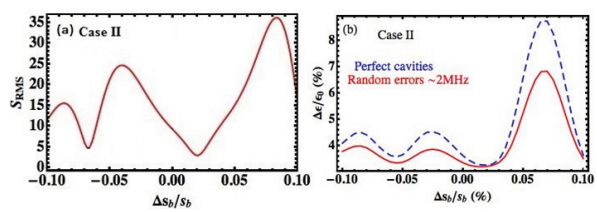


Figure 4: S_{RMS} (a) together with the vertical emittance dilution at the exit to the linac (b) for similar parameters as in Fig. 3, but for case II.

MISALIGNMENT STUDIES

The pre-alignment tolerance on the transverse positions of the components (accelerator structures, BPM, girders) of the CLIC linacs is 10 μm rms over distances of 200 m [14]. Beam-based alignment and emittance tuning bumps [15] are used to ensure the emittance dilution associated with this alignment is kept to acceptable limits.

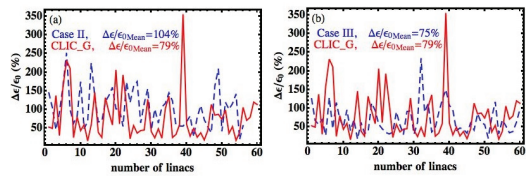


Figure 5: Emittance dilution for misaligned structures for CLIC_G (shown in red), together with case II (a) and III (b) -both shown dashed and in blue.

We investigated a case of which consisted of perfect linacs in which we added vertical random offsets of 10 μm rms to all the structures and this is compared to the baseline design, CLIC_G. We performed simulations for case II (Fig. 5 (a)), and also for case III (Fig. 5 (b)) which consists of 16-fold interleaving of mode frequencies and bunches spaced 8 rf cycles from their neighbours. However, the implications of not being able to accommodate 16 structures on a girder are not taken into account, as it is a considerable task to redesign the associated beam optics, and hence it remains a subject for a future publication.

FINAL REMARKS

A damped and detuned structure, with appropriately interleaved dipole mode frequencies, has been shown to be suitable for the CLIC main linacs. Two cases have been investigated, based on a bunch spacing of 6 and 8 rf cycles. The S_{RMS} parameter provides a qualitative indication as to the location of the worst-case emittance dilution. Preliminary studies on the dilution due to structure misalignments, based on case II and III indicate similar values to the baseline design.

REFERENCES

[1] A. Grudiev, *et. al*, PRST-AB, 10, 102001, 2009.
[2] D. Schulte, CLIC-Note-805, 2009.
[3] R.M. Jones, PRST-AB, 12, 104801, 2009.
[4] http://dschulte.home.cern.ch/dschulte/placet.html
[5] H. Braun *et al.,* CLIC-Note-764, 2008.
[6] T. Higo *et al.*, Proc. of IPAC13, 2013.
[7] V. F. Khan, *et al.*, NIM-A, 53639, 2011.
[8] D'Elia , *et al.*, Proc. of IPAC11, 2011.
[9] R.M. Jones, *et al*., New J. Phys. 11, 033013, 2009.
[10] R.M. Jones, *et al.,* PRST-AB, 9, 102001, 2006.
[11] I. Nesmiyan *et al.,* in press, NIM-A, 2013.
[12] R.M. Jones *et al.,* SLAC-PUB-10682, 2004.
[13] R.M.Jones*, et al.*, SLAC-PUB-8101, 1999.
[14] F.Becker, *et al.*, CLIC-Note-553, 2003.
[15] P. Eliasson *et al*., PRST-AB, 11, 011002, 2008.

Copyright © 2013 CC-BY-3.0 and by the respective authors

BEAM-BASED ALIGNMENT OF SEXTUPOLES AT THE APS *

A. Xiao †, V. Sajaev, ANL, Argonne, IL 60439, USA

Abstract

Sextupole magnet offsets play a large role in modern storage ring coupling control. Due to the non-linear field of sextupoles, their beam-based alignment becomes more difficult and often requires a sophisticated post-data process. A simple method had been developed at the APS that measures the vertical orbit variation (orbit change at BPMs with sextupole strength) versus beam trajectory through a sextupole in one plane while keeping the trajectory in the other plane fixed. This method converts the non-linear problem into a linear one, and experiment results show very good reproducibility and accuracy.

INTRODUCTION

Given the strong sextupoles used in modern storage rings, such as light sources with emittance for producing x-rays near the diffraction limits and/or colliders (B-Factory or damping ring) with very low vertical emittance, misaligned sextupoles tend to be the main sources of large coupling and optics perturbation. It affects the ability to model the machine, and correct orbit, tune and coupling, often resulting in a reduced dynamic aperture and beam lifetime.

For a sextupole installed next to a quadruple, the alignment is as simple as aligning its magnet center to the next quadrupole, and then performing a commonly used beam-based alignment (BBA) technique on the quadrupole. At the APS, however, the majority of sextupoles (four of seven per cell) are on "dipole" girders that do not have quadrupoles, thus we cannot rely on BBA of quadrupoles. Other means of measuring the sextupole magnet offsets need to be developed.

In a previous paper [1], we presented a matrix fitting method to fit all sextupole offset errors together with other machine errors, so that the fitted model agrees with the response matrix measurement. The advantage of this method is that one can quickly get results. The disadvantage is that results are obtained in an "indirect" way and could be mixed up with other effects.

Similar to the beam-based quadrupole offset measurement method, a "direct" beam-based sextupole offset measurement method has been developed since then. This method measures the vertical orbit variation (orbit change at BPM with variation of sextupole strength) versus beam trajectory through a sextupole in one plane while keeping the trajectory in the other plane fixed. The small change of data acquisition and manipulation converts the non-linear problem into a linear one, and experiment results show very good reproducibility and accuracy. Details of the method, simulation, and experiment results are discussed in this paper.

PRINCIPLE

The closed orbit displacement (COD) at position s, rising from a kick error θ at position s_0, is given by

$$u(s) = \frac{\sqrt{\beta_{u,s_0}\beta_{u,s}}}{2\sin\pi\nu_u}\theta\cos[\pi\nu_u - (\phi_{u,s} - \phi_{u,s_0})] = A\cdot\theta, \tag{1}$$

where $u(s)$ represents x or y; β and ϕ are the β-function and the betatron phase; and ν is the betatron tune. For a sextupole with misalignment of x and y, the kick angle is given by

$$\begin{aligned}\theta_x &= \frac{1}{2}\cdot K2L\cdot(x^2 - y^2),\\ \theta_y &= K2L\cdot x\cdot y,\end{aligned} \tag{2}$$

where $K2L = \frac{e}{cp}\partial^2 By/\partial x^2\cdot L$ is the integrated sextupole strength. The corresponding kick angle from a misaligned quadrupole is given by

$$\theta_x = K1L\cdot x \qquad \theta_y = K1L\cdot y. \tag{3}$$

Equations (2) and (3) have different character, one is linear and the other is non-linear. However, if we keep either x or y unchanged during the measurement, i.e., $\theta_y = (K2L\cdot x)\cdot y$ or $\theta_y = (K2L\cdot y)\cdot x$, Eq. (2) becomes as linear as Eq. (3). In other words, by fixing x while varying y and the sextupole strength, we are doing the vertical offset measurement of a quadrupole with strength $K1L = K2L\cdot x$. Similarly, by fixing y while varying x and the sextupole strength, we are doing the horizontal offset measurement of a quadrupole with strength $K1L = K2L\cdot y$. The only difference in this case is that we measure the vertical orbit variation instead of the horizontal orbit variation for a real quadrupole offset measurement.

SIMULATION STUDY

The principle of the method is simple and straightforward. However, other effects, such as coupling from misaligned sextupole etc., need to be considered, too. We studied different misalignment scenarios through simulations before testing with beam. The calibrated lattice model obtained from LOCO fit [2] (includes normal- and skew-quad errors) is used for simulation. One sextupole (S17B:S3) is misaligned intentionally in three different sets: $DX = 2$ mm, $DY = 1$ mm; $DX = 1$ mm, $DY = 1$ mm; and $DX = 0$ mm, $DY = 0$ mm. Sextupoles within the measurement bump are kept on or turned off.

* Work supported by the U.S. Department of Energy, Office of Science, under Contract No. DE-AC02-06CH11357.

† xiaoam@aps.anl.gov

Copyright © 2013 CC-BY-3.0 and by the respective authors

Similar to the BBA of quadrupoles, the simulation (and, later, measurement) is done in the following steps:

- Generate a local orbit bump at the BPM next to the sextupole, and scan the bump amplitude with $u_A = \pm 2$ mm in 1-mm steps (total $5 \times 5 = 25$ orbit sets).
- At each orbit bump, vary sextupole settings I between 0 and its maximum value in 4 steps. Record vertical orbit y at all BPMs.
- Calculate dy/dI (the slope of vertical orbit variation vs sextupole settings) at each BPM over the ring (Fig. 1).
- For the same x orbit, plot dy/dI over y; the crossing point is the sextupole's vertical offset (Fig. 2).
- For the same y orbit, plot dy/dI over x; the crossing point is the sextupole's horizontal offset (Fig. 3).

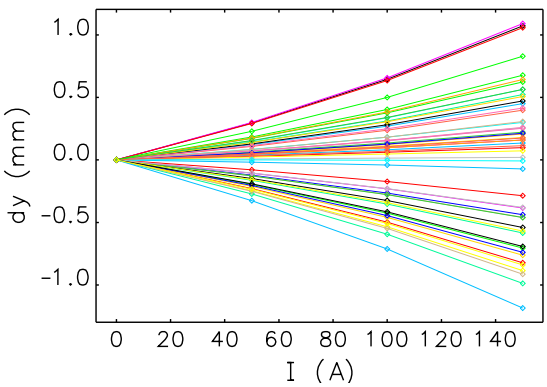


Figure 1: Vertical orbit variation dy vs. sextupole current change (symbols). Case for $DX = 2$ mm and $DY = 1$ mm. Data from the same BPM are connected; likewise for following figures.

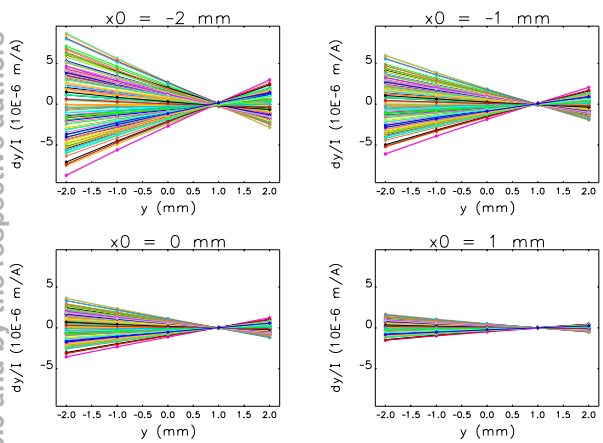


Figure 2: Calculated dy/dI vs. vertical beam orbit y (symbols). Results for different horizontal beam offsets (shown on top). Lines crossing at $y = 1.0$ mm indicate that the vertical sextupole offset is $y = 1$ mm.

Sextupole offset is determined where $dy/dI = 0$. The histogram distribution of $dy/dI = 0$ from all BPMs is shown in Figure 4. The average derived x and y offsets using this method are 1.83 mm and 0.98 mm, respectively. Compared with our initial assumption in simulation (2 mm in x and 1 mm in y), the agreement on vertical offset measurement is very good (better than 50 μ m), while the horizontal result seems to have a significant systematic error. Further simulations with different sextupole offsets or in cases when other sextupoles are turned off inside the bump all give similar results, i.e., good agreement on vertical offset prediction but large systematic errors for horizontal results.

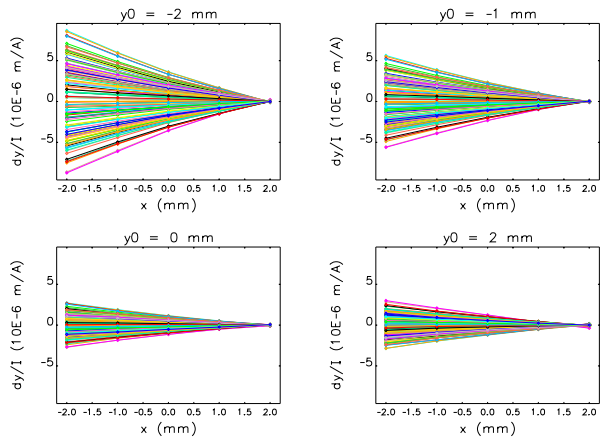
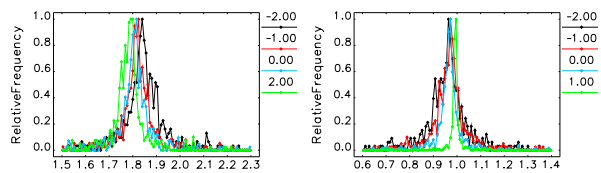


Figure 3: Calculated dy/dI vs. horizontal beam orbit x (dots). Results are grouped with the same vertical beam offsets (shown on top). Lines crossing at $x = 2.0$ indicate the horizontal sextupole offset is $x = 2$ mm.



(a) (b)

Figure 4: Histogram distribution of $dy/dI = 0$ vs. x (a) and vs y (b). Legend shows beam orbit in the other plane.

Further investigation of the method reveals that the linear dependence on x requires a fixed vertical orbit y inside the sextupole, while the strength change of the sextupole also causes y variation and leads to an additional vertical kick. This second-order effect has been ignored up to now. To include this effect we fit dy/I vs. $x(y)$ to the second order, and calculate the value to give $dy/I = 0$. Results including this second-order correction from the same data set are shown in Figure 5. The offset determined this way is closer to the input sextupole offset ($DX = 2$ mm).

The sensitivity of measurement depends on the product of beam offset "xy". As shown in Figure 5, a larger beam offset $y = -2$ mm gives more precise results. If either x or y are actually close to the sextupole offset (beam going through the sextupole center), the results become noisy, as

Copyright © 2013 CC-BY-3.0 and by the respective authors

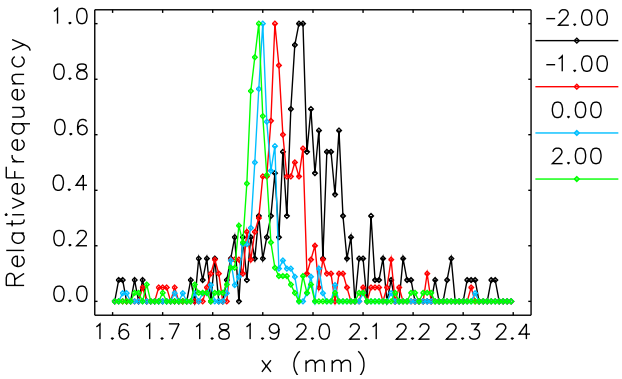
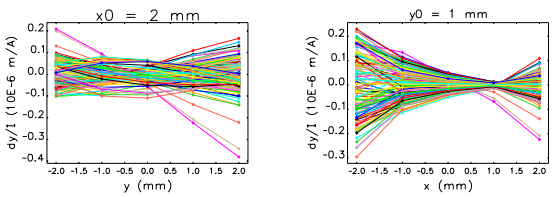


Figure 5: Histogram distribution of $dy/dI = 0$ vs x using second-order correction. Legend shows the beam orbit in y-plane.

can be seen in Figure 6. To have meaningful measurement results, two sextupole settings (to obtain dy/I) at each $3 \times 3 = 9$ orbit offset are needed.

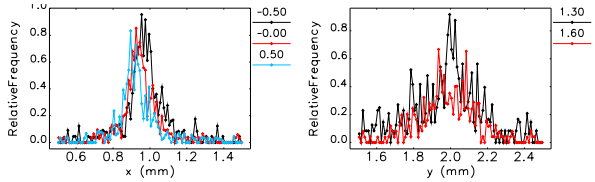


(a) (b)

Figure 6: Noisy results when beam is going through the sextupole center: $x0 = DX$ (a), and $y0 = DY$ (b).

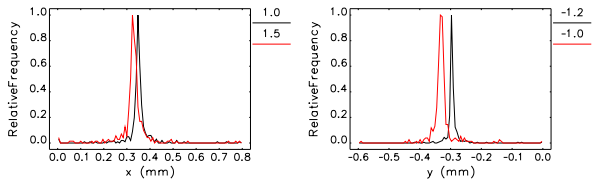
EXPERIMENT RESULTS

The method has been tested at the APS storage ring with beam. In preparing for the superconducting undulator (SCU) commissioning [3], we measured the sextupole offsets next to the 6BM (S6B:S2 and S6B:S3). Three x orbit offsets with $x = 1.0$, 1.3, and 1.6 mm and three y orbit offsets with $y = -0.5$, 0, and 0.5 mm were used in the measurement. Histogram distributions of $dy/dI = 0$ vs. beam orbit are shown in Figure 7. The predicted sextupole offsets are $DX = 0.95$ mm and $DY = 2$ mm. For DX measurement, all y orbits are moved away from the predicted sextupole center DY, so all measurement results are valid. We learned from simulation that the systematic error does exist and is reduced as y moves away from DY, as can be seen from both Figures 5 and 7. In this case, results from $y = -0.5$ mm should be taken as DX; the measurement error is believed to be within 50 μm. For DY measurement, the measurement made at $x = 1.0$ mm is too close to the sextupole center and gives noisy data similar to an example shown in Figure 6, and was discarded from the plot. Two other measurements predict the same DY results, agreeing with simulation. The accuracy of DY measurement is better than 50 μm. Similar results have been found with another sextupole (S18B:S3). Results are shown in Figure 8.



(a) (b)

Figure 7: S6B:S2 offset measurement results. Legend shows beam orbit in the other plane.



(a) (b)

Figure 8: S18B:S3 offset measurement results. Legend shows beam orbit in the other plane.

CONCLUSIONS

A direct beam-based sextupole offset measurement method has been developed at APS. This method converts the sextupole field from nonlinear to linear by keeping the beam orbit in the X plane unchanged while measuring the vertical beam orbit variation as a function of sextupole strength. The validity of the method had been tested through simulation and beam experiment. The second-order effect from orbit variation in the unmeasured plane was noticed and fixed through a second-order polynomial fit. The accuracy of this method is of the order of 50 μm.

The direct sextupole offset measurement takes more time compared with the "LOCO" fit method we originally reported in a previous paper [1]. Nevertheless, this is a suitable method if a direct measurement is required.

REFERENCES

[1] V. Sajaev, A. Xiao, "Simultaneous Measurement of All Sextupole Offsets Using The Response Matrix Fit," IPAC'10, Kyoto, (2010), THPE091, p. 4737, http://www.JACoW.org

[2] V. Sajaev, private communication.

[3] K. Harkay et al., "APS Superconducting Undulator Beam Commissioning Results," WEOAA3, Proceedings of NA-PAC 2013.

Copyright © 2013 CC-BY-3.0 and by the respective authors

ENERGY CALIBRATION IN THE AGS USING DEPOLARIZATION THROUGH VERTICAL INTRINSIC SPIN RESONANCES*

Y. Dutheil, L. Ahrens, H. Huang, F. Méot, V. Schoefer
BNL, Upton, Long Island, New York

Abstract

The AGS tune jump system consists of two fast pulsed quadrupoles used to accelerate the crossing of 82 horizontal intrinsic resonances. Timing of the tune jumps requires accurate tune and energy measurements. Although cross calibration using measurements of the beam revolution frequency shows good accuracy for most of the AGS energy range it is not adequately sensitive as the beam becomes highly relativistic. This drives a strong interest for a new independent energy measurement method.

Reduction in the vertical tune across vertical intrinsic spin resonances can induce significant depolarization of the beam. Therefore it was proposed to use the negative vertical tune shift created by this tune jump system to calibrate the energy measurement at few locations along the AGS acceleration cycle. The fast tune jump, of $\Delta Q \approx -0.02$ within $100\,\mu$s in the vertical plane, allows to accurately locate the spin resonant condition, independently from orbit or field conditions. Simulations using the AGS Zgoubi online model facilitate the interpretation of the experimental results. This paper introduces the experimental procedure and shows some of the latest results.

INTRODUCTION

The partial snakes configuration of the AGS creates horizontal intrinsic spin resonances by tilting the stable spin direction away from the vertical direction [1]. The resonant condition $Q_s \pm Q_x = n$ is satisfied twice per unit of $G\gamma$ during the ramp, inducing every time a small depolarization of the beam. The polarization losses are reduced by quickly changing the horizontal tune Q_x, increasing the crossing rate of the resonance [2].

The system is composed of two fast quadrupoles allowing a change in the horizontal tune of $\Delta Q_x = +0.04$ in $100\,\mu$s. One of the main challenge is the accurate timing required for each jump, such that the tune jump is centered around the resonance.

Tune Jump Timing

While the spin tune Q_s is a function of the energy, tune and energy measurements along the ramp allow precise timing of each jump. During the polarized protons operations these measurements are regularly used to generate new timings for the tune jumps. This is supposed to compensate for any drift in the location of the resonant condition, for instance due to a drift of the tune over time. During the AGS Polarized Proton Run 13, these measurements were regularly conducted to provide the highest polarization to the RHIC.

Table 1: Polarization Measurements During Run 13

Measurement date	Timings	Polarization
May 5th	from April 6th	$66.0 \pm 0.9\,\%$
May 5th	from April 29th	$59.7 \pm 1.1\,\%$
May 5th	from May 5th	$62.8 \pm 1.1\,\%$
June 6th	Uncalibrated	$64.4 \pm 3.9\,\%$
June 6th	Calibrated	$70.9 \pm 1.6\,\%$

In late April 2013, after a few weeks of running with the same tune jumps timings, new timings were generated but the polarization decreased. Table 1 shows that on May 5th the measured polarization was higher for the older timings. The two sets of timings more recently generated led to a consistently lower polarization.

To explain this deterioration the entire process from the computation of the jumps timing to the trigger of the pulsed power supply was verified, without finding any error. We decided to investigate on the measurements used to compute the jump timings : tune and energy measurements.

The tune measurement is based on the free oscillation of the beam, it is therefore an absolute measurement and is unlikely a source of significant error. The energy measurement is more complex and needs to be calibrated, making a possible suspect for our problems.

ENERGY MEASUREMENT IN THE AGS

The AGS uses a dedicated device called the *GgammaMeter* to measure the energy along the ramp. The energy is determined using the measured RF frequency f and average radius of the beam dR (Eq. 1) or the measured field $(B_{\text{inj}} + B_{\text{clock}}/C_{\text{scal}})$ and the average radius (Eq. 2) :

$$G\gamma = G\frac{1}{\sqrt{1-\frac{1}{c^2}\left(\frac{f}{h}\right)^2(2\pi)^2(R_0+dR)^2}} \quad (1)$$

$$G\gamma = G\sqrt{\left[\frac{(1+\gamma_{tr}^2 dR/R_0)\rho_0 c(B_{\text{inj}}+B_{\text{clock}}/C_{\text{scal}})}{M_0}\right]^2+1} \quad (2)$$

With γ_{tr} the transition energy, R_0 the radius and ρ_0 the radius of curvature of the AGS. The parameters in red (f, dR and B_{clock}) are measured quantities while the blue ones are machine parameters(R_0, γ_{tr}^2, ρ_0, B_{inj} and C_{scal}) that can be adjusted and the black are fixed physical constants.

The *GgammaMeter* is cross calibrated : at low energy the machine parameters in equations 2 and 1 are adjusted manually until the two methods report the same energy along

* Work supported by Brookhaven Science Associates, LLC under Contract No. DE-AC02-98CH10886 with the U.S. Department of Energy.

Copyright © 2013 CC-BY-3.0 and by the respective authors

the ramp. But at high energy the measurement based on the RF frequency (Eq. 1) is too sensitive, due to the highly relativistic beam.

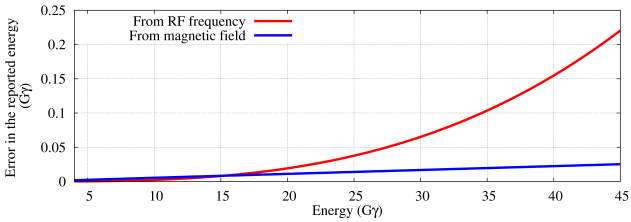


Figure 1: Error on the reported energy caused by an error of 1 mm in the measured average beam radius.

Figure 1 shows the derivative of equations 2 and 1 with respect to the measured average radius : $\partial G\gamma/\partial(dR)$. As the energy increases, we can see that the sensitivity of the energy measurement based on the revolution frequency becomes very large. While we consider that the measured average radius is known within a fraction of millimeter we also need an accuracy of around $0.01\,G\gamma$. It becomes apparent that the actual method of cross calibration is very hard at high energy.

This drives a strong interest to develop an independent method on energy measurement, possibly to calibrate the *GgammaMeter*.

Since the AGS accelerates polarized protons, methods based on the depolarization of the beam can be explored. A promising method using the current hardware of the AGS uses the tune jump system to accurately locate a strong vertical intrinsic resonance.

Tune Jump and Depolarization

While the tune jump system is used for its effect on the horizontal tune, it also induces a tune shift of $\Delta Q_y \sim -0.02$ in the vertical plane, within $100\,\mu$s. In addition, the partial snake configuration of the AGS modifies the spin tune, opening a forbidden band or "spin gap" in which the vertical tune is placed to avoid the vertical intrinsic resonances $Q_s \pm Q_y = n$. It is then possible to use a single tune jump to lower the vertical tune below the maximum value of the spin tune $Q_s^{\max}$, leading to a depolarization of the beam.

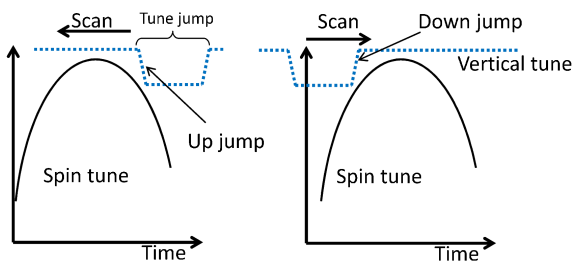


Figure 2: Illustration of the method used to locate the vertical intrinsic resonance.

Figure 2 shows the principle of the measurement. First the vertical tune is lowered to just above $Q_s^{\max}$, such that the tune jump is able to lower the vertical tune out of the spin gap. Then the timing of the tune jump is scanned across the spin resonance and the polarization at the end of the ramp is measured for each timing of the tune jump. If the spin tune crosses the vertical tune, a lower polarization is measured due to the depolarization across the resonance. The up-jump determines the location of the right side of the resonance and the down-jump allows to locate the left side.

The single crossing of the resonance, at the regular acceleration rate, has to strongly depolarize the beam in order for the difference in polarization to be clearly measured. Therefore the measurement is only carried at the two very strong vertical intrinsic resonances : $0+$ and $36+$.

While the method shown in figure 2 is very simple, several factors complicate the expected behavior :

- The vertical and spin tunes possess some spread due to energy spread of the beam and chromaticity of the machine, potentially blurring the transition between no depolarization and depolarization.
- The two resonances in each sides of $Q_s^{\max}$ can have different strengths, depending on the distance between them.

The experimental results are expected to be complex and no simple theoretical model can predict the observed polarization, the only solution to take everything into account would be to completely simulate the experiment. Thankfully the Zgoubi code[3] and the AGS Zgoubi online model[4] provide the perfect tools to simulate this experiment.

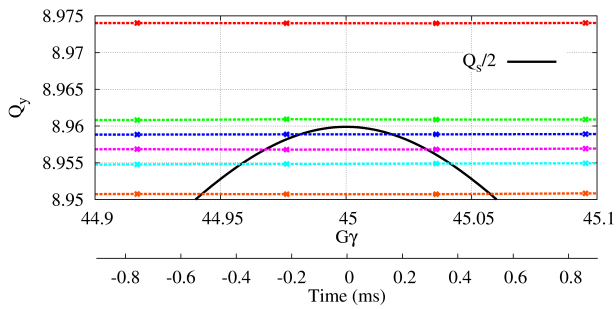


Figure 3: Vertical tune for the 5 different simulations and resonant condition for the second order snake resonance ($Q_s/2$) as a function of the energy or the time from $G\gamma = 45$.

Simulation at 36+

At $G\gamma = 45$, where the resonance $Q_y + 36 = Q_s$ is located, strong enough that the crossing of the second order snake resonance ($Q_s + 2Q_y = n$) induces a significant depolarization of the beam.

Multiparticle trackings using the Zgoubi code were done for a short simulation from $G\gamma = 44.5$ to $G\gamma = 45.5$. Realistic lattice conditions and acceleration rate were set up using the AGS Online model[4]. Each simulation consists

Copyright © 2013 CC-BY-3.0 and by the respective authors

in a tracking of 408 particles picked in a realistic 6-D Gaussian distribution for 3800 turns. The simulations total up around 20 000 CPU·hours[1].

Figure 3 shows the vertical tune without tune jump at $Q_y \sim 8.975$, lower than the operational tune across this resonance in order to cross the spin resonance when the jump quads are fired. Below, the different tunes on the jump were chosen across a wide range to determine the best configuration for the measurement.

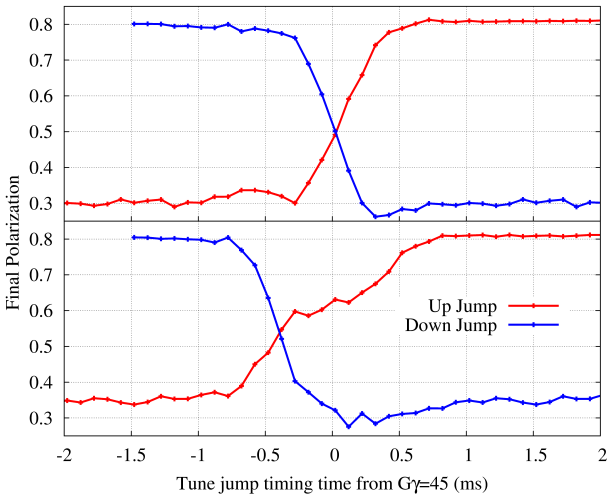


Figure 4: Final polarization for the up and down jump locations as a function of the time from $G\gamma = 45$ for the vertical tune on the jump just below the resonant condition (top plot) and for $Q_y = 8.951$ (bottom plot).

Figure 4 shows the experiment simulated for 2 different vertical tune on the jump. On the top plot the vertical tune on the jump is very close to the maximum value of the spin tune and the two vertical intrinsic resonances on either side of $G\gamma = 45$ are so close that they have the same effect on the beam and the figure is very symmetric, centered around $G\gamma = 45$. For a lower vertical tune the result is distorted due to the two resonances having different strengths when the distance separating them increases. These simulations show that the vertical tune on the jump should be positioned as close as possible from the maximum value of the spin tune.

Experiment at 36+

To correctly place the vertical tune we determined the maximum value reached by the spin tune across the resonance. By measuring the final polarization as a function of the vertical tune across $G\gamma = 45$ we determined that $Q_s^{\max}/2 = 0.956$. The vertical tune on the jump was placed at $Q_y = 8.954$ just below the resonant condition.

The polarization on the flat-top was measured as a function of the up and down jumps locations, by step of 200 μs. Figure 5 shows the measured data along with the simulation closest to the experimental conditions. The simulation results were numerically matched : vertically to account for the polarization lost outside the simulated range and horizontally shifted.

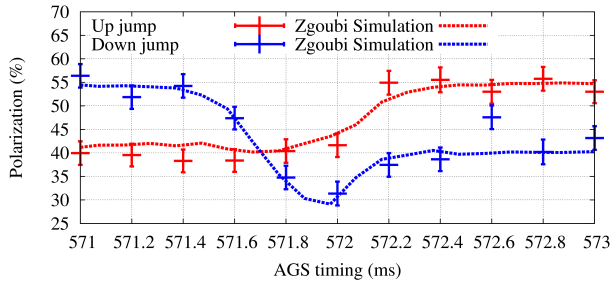


Figure 5: Final polarization for the up and down jump locations as a function of the time AGS time.

The matched horizontal shift of the simulation allows to determine that $G\gamma = 45$ is crossed at $T = 571.85$ ms. From the *GgammaMeter* data, we expected to see $G\gamma = 45$ at T = 572.7 ms. This difference is equivalent to $\sim 0.1\, G\gamma$.

RESULTS

The energy measurement at 36+ led to surprising results but the magnitude would suffice to explain an important loss of efficiency for the tune jumps. The same method was applied at $G\gamma = 9$ where a strong vertical intrinsic resonance is located, reporting a smaller disagreement with the energy measured by the *GgammaMeter* of $\Delta T = 0.1$ ms. Therefore it would appear that the energy reported by the *GgammaMeter* drifts along the ramp.

These results were used to recalibrate the the *GgammaMeter* and generate new tune jumps timings. Higher polarization was measured with the new timings on June 6th(Table 1), giving strong confidence into the energy measurement.

CONCLUSION

The energy measurement based on depolarization provided interesting results but the procedure is complex and the data taking is very long. But a faster method based on a continuous polarization measurement along the ramp is being developed and could be used for operation while the method described in this paper would be an important tool for experts to cross-check the results.

REFERENCES

[1] F. Lin *et al.*, "Exploration of horizontal intrinsic spin resonances with two partial Siberian snakes," Phys. Rev. ST Accel. Beams **10**, 044001 (2007).

[2] V. Schoefer *et al.*, "Increasing the AGS Beam Polarization with 80 Tune Jumps," Conf. Proc. C **1205201**, 1015 (2012).

[3] The ray-tracing code Zgoubi, F. Méot NIM-A 427 (1999) 353-356 ; http://sourceforge.net/projects/zgoubi/

[4] F. Méot *et al.*, "Modelling of the AGS Using Zgoubi - Status," Conf. Proc. C **1205201**, 181 (2012).

[1]This research used resources of the National Energy Research Scientific Computing Center, which is supported by the Office of Science of the U.S. Department of Energy under Contract No. DE-AC02-05CH11231.

Copyright © 2013 CC-BY-3.0 and by the respective authors

HALO CONTROL AND GENERATION IN RHIC *

C. Montag, K. A. Drees, BNL, Upton, NY 11973, USA

Abstract

In the next 5-10 years, RHIC will be colliding gold ions in the center-of-mass energy range of 5 to 20 GeV, which is below the regular injection energy. Though the machine has already successfully provided collisions at CM-energies of 7.7 and 11.5 GeV, a significantly higher luminosity than so far achieved is required for a meaningful physics program. While an electron cooler is presently being designed to provide the desired luminosity gain, this is a long-term project that is expected to be completed in 2018. As a short-term alternative the STAR collaboration has proposed installation of an internal halo target in the STAR detector beam pipe. To study the generation and control of the beam halo, we have performed dedicated beam experiments aimed at the bunch-by-bunch uniformity, and long as well as short-term stability of collimator loss rates.

INTRODUCTION

The Relativistic Heavy Ion Collider (RHIC) consists of two superconducting storage rings with a circumference of 3.8 km. In heavy ion collider mode, beams are injected at a rigidity of $B\rho = 81\,\mathrm{Tm}$ and accelerated to $B\rho = 833\,\mathrm{Tm}$ before they are brought into collision in the two detectors STAR and PHENIX. In the case of fully stripped gold ions, these beam rigidities correspond to an injection energy of 9.8 GeV/nucleon and a storage energy of 100 GeV/nucleon.

In recent years, nuclear physicists have become increasingly interested in searching for the critical point in the phase diagram of nuclear matter, which is expected to occur in the center-of-mass energy range between $\sqrt{s_{\mathrm{NN}}} = 5$ and 30 GeV, see Figure 1. To provide collisions in the desired energy range in collider mode, gold beams therefore have to be stored and collided at energies as low as a quarter of the nominal RHIC injection energy, which is extremely challenging due to large multipole errors in the superconducting magnets at these energies, as well as space charge and intrabeam scattering effects.

In 2010, RHIC has been successfully operated at center-of-mass energies of 7.7 and 11.5 GeV per nucleon pair [1]. However, to reach the desired integrated luminosities for the beam energy scan, RHIC would have to operate for a total of 70 weeks at these energies. Furthermore, performance at $\sqrt{s_{\mathrm{NN}}} = 5\,\mathrm{GeV}$ has not yet reached any level sufficient for meaningful physics operations, though beams have already been stored successfully at this energy [2], albeit at tiny intensities, and studies are underway to improve the performance [3].

* Work supported by Brookhaven Science Associates, LLC under Contract No. DE-AC02-98CH10886 with the U.S. Department of Energy.

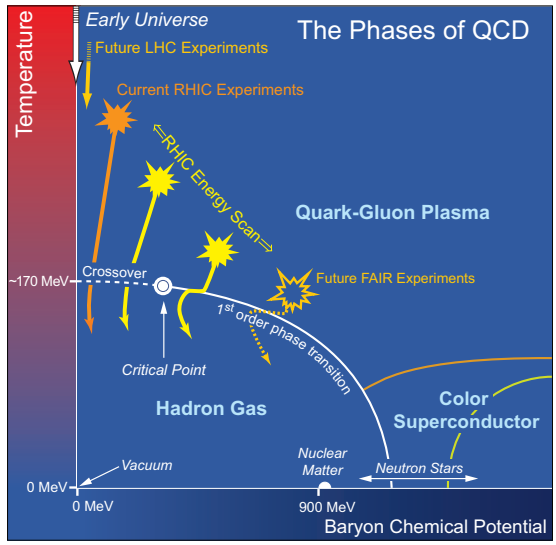


Figure 1: The QCD phase diagram, with the critical point expected in the center-of-mass energy range between $\sqrt{s_{\mathrm{NN}}} = 5$ and 30 GeV.

To improve the luminosity at low energies, an electron cooling system is currently being designed [4]. However, since this new device is scheduled to become operational in 2018, and because the lowest desired beam energy of 2.5 GeV per nucleon may turn out to be outside the useful reach of RHIC, the STAR collaboration has proposed the installation of a thin gold target in their detector area to study low energy gold-gold collisions in fix target mode rather than in collider mode [5].

The proposed internal target consists of a 30 mil (750 μm) thick gold foil that is installed in the RHIC beam pipe 2 m away from the STAR interaction point such that it intercepts the halo of the circulating Yellow beam upstream of the STAR detector, see Figure 2. To avoid potential damage to the target in case of an abort kicker pre-fire, which deflects the beam horizontally, the proposed target geometry is chosen such that it intercepts the beam halo only in the vertical plane. Furthermore, only the lower part of the beam pipe is equipped with the target foil, so in case the foil comes lose it does not drop into the beam path where it could block the aperture.

The aperture of the gold foil target needs to be chosen smaller than the 40 mm inner diameter detector beam pipe to make the target the local aperture limitation. On the

Copyright © 2013 CC-BY-3.0 and by the respective authors

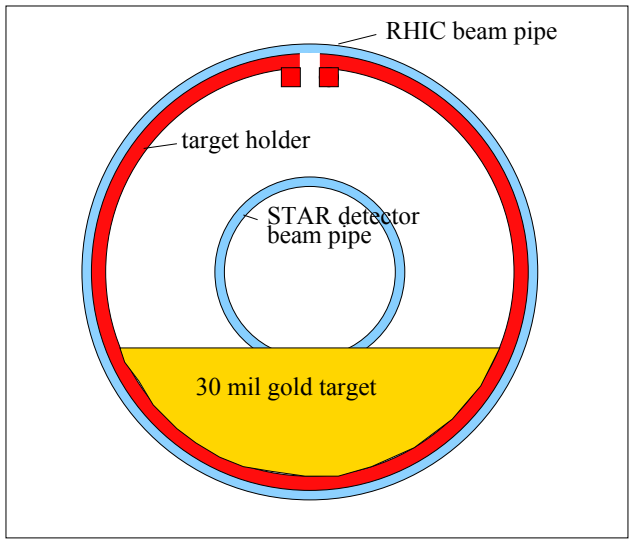


Figure 2: Schematic drawing of the proposed STAR internal target (Not to scale). The target will be installed at a distance of 2 m from the interaction point in the 3 inch inner diameter beam pipe. The aperture of the target is chosen slightly smaller than the 40 mm ID detector beam pipe.

other hand, the target must not interfere with regular collider operation. This can be accomplished by selecting a 16 mm half aperture for the target. This provides sufficient aperture at store as well as at injection, even when taking into account the $\pm 5\,\mathrm{mm}$ separation bumps around the interaction point. In dedicated target mode the target can deliberately be made the limiting aperture by increasing the separation bumps and blowing up the beam emittance.

Operating an internal halo target in a storage ring is challenging for various reasons, as the experience with the HERA-B target has shown [6, 7]. For instance, target interaction rates can vary greatly if the beam position is not stable enough due to mechanical vibrations of accelerator magnets, and/or the diffusion is not sufficient to replenish the transverse tails of the distribution. These large variations in the interaction rates tend to overwhelm the detectors with bursts of interactions, followed by periods without any rates at all, which makes data taking very difficult.

If transverse beam emittances vary greatly bunch-by-bunch, only the few bunches that have the largest emittances contribute to the interaction rates, resulting in similar detrimental effects as orbit jitter, albeit on a much faster time scale.

Finally, since the proposed STAR internal target is not moveable, interaction rate control has to be accomplished by manipulating the beam instead of adjusting the target position. While the target can be made the limiting aperture by applying a larger amplitude separation bump and increasing the emittance, sufficient diffusion has to be created to stabilize the interaction rates. Since the target will only be operated in a dedicated mode no special care has to be taken to preserve the emittance of the beam core for collider operation.

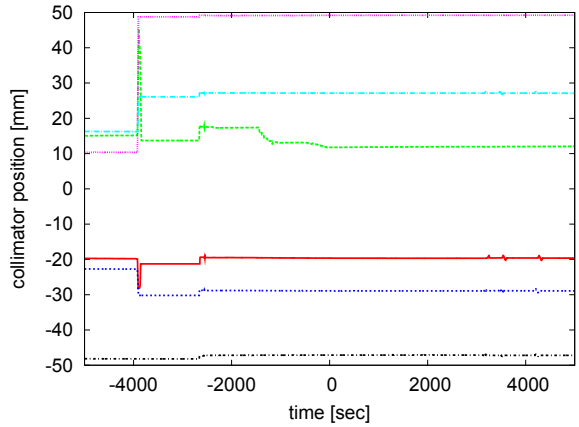


Figure 3: Recorded RHIC collimator positions during the beam experiment. The vertical collimator (green line) reached its final position at 11.5 mm. The horizontal axis is consistent with the one used in Figure 4.

To study the controlability and bunch-by-bunch uniformity of the target interaction rates as well as their stability at typical vibration frequencies up to hundreds of Hertz, beam experiments were performed during the FY 2013 polarized proton run.

EXPERIMENTS

Using the stored polarized proton beam at injection energy, a vertical collimator jaw was inserted into the beam halo until a loss rate of about 100 Hz per bunch was recorded by the local PIN diodes, which corresponds to a total rate of roughly 10 kHz from the 109 stored bunches. The resulting collimator position was measured by the BPMs and the collimator mechanics to be 11.5 mm from the beam center, as shown in Figure 3. With the tunes initially set to $(Q_x/Q_y) = (28.696/29.691)$, collimator loss rate control was attempted by moving the working point closer to the nonlinear resonances at $2/3$ and $7/10$, as shown in Figure 4.

In the first step, the horizontal tune was raised to $Q_x = 28.698$, which had little effect on the collimator loss rate, as can be expected since the collimator intercepts the halo vertically. Next, the vertical tune was raised towards $7/10$ as well, which also moves the working point closer to the coupling resonance. This resulted in the loss rates increasing from 100 to 200 Hz per bunch. However, when the tunes were kept constant at these new values the interaction rate dropped to its initial value within two to three minutes.

Finally, the vertical tune was slowly lowered towards the third order resonance at $2/3$, resulting in a rapid increase of the collimator loss rates as soon as it reached 28.683. Lowering it further to 28.678 raised the loss rates to 400 Hz per bunch. After about two minutes with stable tunes, the loss rate had dropped to 200 Hz per bunch, and remained

Copyright © 2013 CC-BY-3.0 and by the respective authors

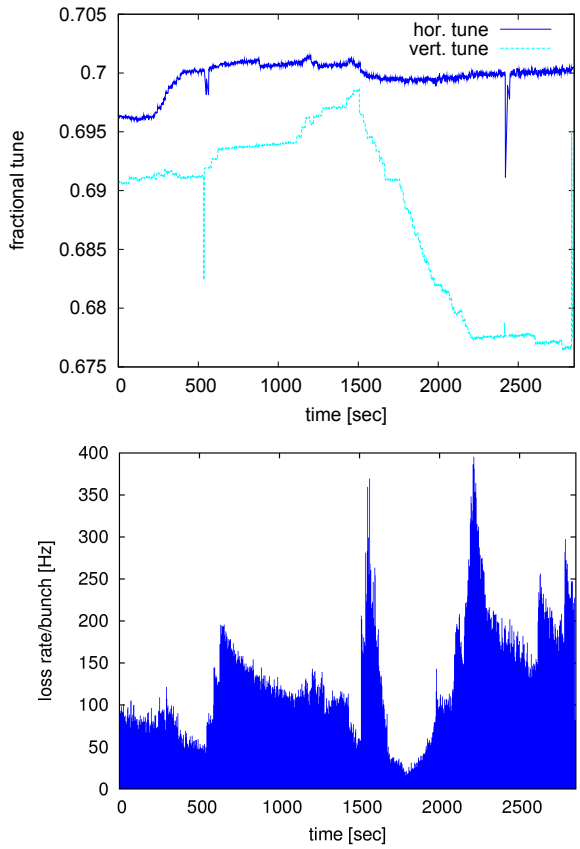


Figure 4: Loss rates during the tune scan. The horizontal scale is consistent with the one used in Figure 3, i.e. the tune scan starts after the collimators have reached their final position.

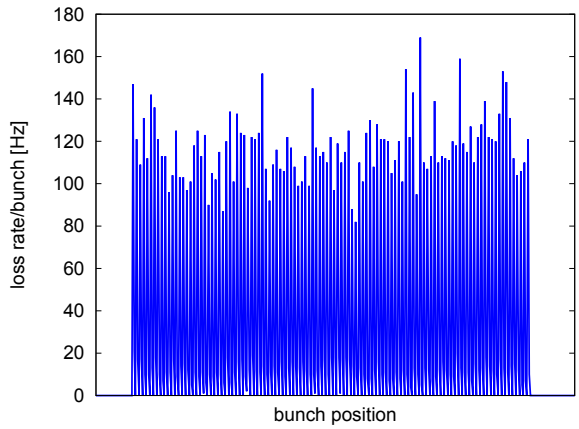


Figure 5: Bunch-by-bunch loss rates at a fixed point in time during the tune scan.

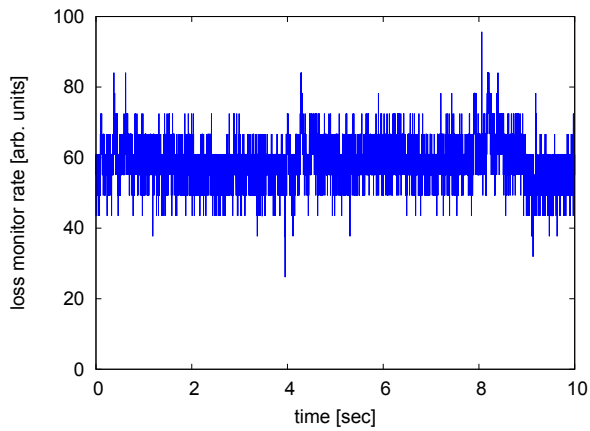


Figure 6: Loss monitor rates in the vicinity of the vertical collimator, sampled at 720 Hz.

reasonably constant there with a slow decrease from 200 to 120 Hz during the next five minutes.

Zooming in on the data during this stable period reveals the bunch-by-bunch structure of the collimator loss rates, Figure 5. As this plot shows, the bunch-by-bunch loss rate is very uniform along the entire train of 109 bunches.

Finally, the short-term stability of the target interaction rate can be studied using RHIC loss monitors in the collimator vicinity sampled at a high frequency of 720 Hz. As Figure 6 shows, the loss rates fluctuate very little over a time scale of 10 sec, indicating that high frequency rate variations due to effects like beam orbit jitter are practically non-existent.

SUMMARY

As these experiments have demonstrated, the interaction rate at the proposed internal target at STAR can be controlled by proper choice of a working point near a low-order resonance, in this case 2/3. While these experiments were carried out with a stored proton beam, the actual physics run will use gold ions. The higher IBS rates of such a gold beam compared to the proton beam used in this test are expected to improve the performance even further, making it possibly unnecessary to continuously move the tune towards a resonance to keep the interaction rate constant.

REFERENCES

[1] C. Montag, T. Satogata, et al., "Experience with low-energy gold-gold operations in RHIC during FY 2010," C-A/AP/435

[2] C. Montag et al., Proc. IPAC 2012, TUPFI076 (2012).

[3] C. Montag et al., TUOAA2, NA-PAC'13.

[4] A. Fedotov et al., TUOAA1, NA-PAC'13.

[5] STAR Beam Use Proposal 2013.

[6] C. Montag et al., Proc. PAC 2001, TPPH018, p. 1699 (2001).

[7] C. Montag, AIP Conf. Proc. 693 (2004) 144.

Copyright © 2013 CC-BY-3.0 and by the respective authors

A GRAPHIC INTERFACE FOR FULL CONTROL OF THE RHIC OPTICS*

G. Robert-Demolaize, M. Bai, Brookhaven National Laboratory, Upton, NY, USA
Xiaozhe Shen, Indiana University, Bloomington, IN, USA

Abstract

A high level application has been developed for the RHIC collider to provide a complete package for optics control. Optics can be measured using three different algorithms to process turn-by-turn (TBT) beam position monitor (BPM) data from either free (tune meter) or driven (AC dipole) betatron oscillations, and corrected via SVD on a response matrix built around specific sets of quadrupoles. The following reviews the details of those methods, and includes the first results of the operational commissioning of the application.

INTRODUCTION

One of the methods to measure the linear RHIC optics for any of its high energy heavy ions or polarized protons runs relies on AC dipoles (ACD's). In a particle accelerator, ACD's are designed to adiabatically drive coherent betatron beam oscillations with a frequency close to the beam tune. For RHIC, a GUI application called *loptics* was built to control the amplitude and frequency of the dipole field of a given ACD when measuring the optics of the corresponding beamline. Once the ACD is triggered, all BPM's around the considered ring record the beam oscillations over 1024 turns; linear optics are then derived using fitting algorithms on each BPM dataset [1]. With the recent successful developments of β_z-beating correction methods at RHIC in Run12 and Run13 [2], a major upgrade of *loptics* was to turn the application into a complete tool for measurement, correction as well as control of linear optic functions.

LINEAR OPTICS MEASUREMENTS

Fitting Driven and Free Oscillations

For coherent oscillations driven by an ACD at a tune $\nu_{\mathtt{AC}}$, the beam actually "sees" both $\nu_{\mathtt{AC}}$ and $1-\nu_{\mathtt{AC}}$ driving tunes according to the Nyquist sampling theorem. The transverse beam position $z_i^s(N)$ (for either plane) measured at the ith BPM and Nth turn at the longitudinal coordinate s in RHIC can then be derived as:

$$\begin{aligned} z_i^s(N) &= A_m \cos\left(2\pi\nu_{\mathtt{AC}}N + \psi_m(s)\right) \\ &- A_p \cos\left(2\pi\nu_{\mathtt{AC}}N - 2\pi\nu_{\mathtt{AC}} + 2\chi_{\mathtt{AC}} - \psi_m(s)\right), \end{aligned} \quad (1)$$

with $\psi_m(s) = -\pi\left(\nu_{\mathtt{AC}} - \nu_z\right) + \chi_{\mathtt{AC}} - \psi_z(s)$ and:

$$A_m = \frac{B_m L}{4\sin\left(\pi\left(\nu_{\mathtt{AC}} - \nu_z\right)\right) B\rho}\sqrt{\beta_z(s)\beta_z^0},$$

$$A_p = \frac{B_m L}{4\sin\left(\pi\left(\nu_{\mathtt{AC}} + \nu_z\right)\right) B\rho}\sqrt{\beta_z(s)\beta_z^0}.$$

where $B_m L$ is the integrated strength of the ACD field, $B\rho$ the magnetic rigidity, $\beta_z(s)$ and $\psi_z(s)$ the betatron function and phase advance at the ith BPM, β_z^0 the betatron function at the ACD, and $\chi_{\mathtt{AC}}$ the ACD initial phase. Eq. (1) can be written in both a compact form [3] (Eq. (2)) and a tune-phase dissociated form [4] (Eq. (3)):

$$z_i^s(N) = A_d\sqrt{\beta_d(s)}\cos\left(2\pi\nu_{\mathtt{AC}}N + \left[\psi_z(s) + \chi_{\mathtt{AC}}\right]\right), \quad (2)$$

$$z_i^s(N) = A_m\left[\cos(\psi_m(s))F_N - \sin(\psi_m(s))G_N\right]; \quad (3)$$

with $r = \sin\left(\pi\left(\nu_{\mathtt{AC}} + \nu_z\right)\right) / \sin\left(\pi\left(\nu_{\mathtt{AC}} - \nu_z\right)\right)$ one gets:

$$F_N = \cos\left(2\pi\nu_{\mathtt{AC}}N\right) - r\cos\left(2\pi\nu_{\mathtt{AC}}(N-1) + 2\chi_{\mathtt{AC}}\right),$$

$$G_N = \sin\left(2\pi\nu_{\mathtt{AC}}N\right) + r\sin\left(2\pi\nu_{\mathtt{AC}}(N-1) + 2\chi_{\mathtt{AC}}\right).$$

The compact form from Eq. (2) is then solved using the nonlinear Levenberg-Marquardt [5] fitting method on the three variables $A_{tot}(s) = A_d\sqrt{\beta_d(s)}$, $\nu_{\mathtt{AC}}$ and $\psi_{tot}(s) = \psi_z(s) + \chi_{\mathtt{AC}}$. The dissociated form in Eq. (3) can be solved with a linear fitting algorithm for the variables $A_m\cos(\psi_m(s))$ and $A_m\sin(\psi_m(s))$ once the driving tune $\nu_{\mathtt{AC}}$ is found using a fast Fourier transform (FFT) on the TBT data at the considered BPM. The ratio of amplitudes A_{tot} or A_m between two BPM's are then directly proportional to the ratio of the $\beta_z(s)$ functions at the BPM's locations. The phase advance $\psi_z(s)$ can only be calculated from $\psi_{tot}(s)$ or $\psi_m(s)$ with a precise knowledge of the initial ACD phase $\chi_{\mathtt{AC}}$; instead, *loptics* provides the phase difference $\Delta\psi_z(s)$ between two consecutive BPM's, which is independent of $\chi_{\mathtt{AC}}$.

The $\beta_z(s)$ and $\Delta\psi_z(s)$ derived from fitting Eq. (2) are actually the "driven" amplitude and phase of the beam oscillation. Results from the nonlinear fitting will therefore carry some artificial β_z-beating with an amplitude [6]:

$$\frac{\beta_d(s) - \beta_z(s)}{\beta_z(s)} \approx \frac{2\pi\left(\nu_{\mathtt{AC}} - \nu_z\right)}{\sin\left(2\pi\nu_z\right)}\cos\left(2\psi_z(s) - 2\pi\nu_z\right). \quad (4)$$

For typical ACD operations at RHIC, this amplitude is estimated at about 7% for $\nu_{\mathtt{AC}}$-ν_z=±0.01. For a linear machine, the artificial β_z-beat can be reduced experimentally to about 0.3% by driving the beam oscillations with $\nu_{\mathtt{AC}} > \nu_z$ in one measurement and $\nu_{\mathtt{AC}} < \nu_z$ in another, and averaging the fitted optics.

Free oscillations can be generated from beam injection oscillations or a coherent excitation by a single turn kicker magnet (e.g. for tune measurements), with $z_i^s(N)$ defined as:

* Work supported by Brookhaven Science Associates, LLC under Contract No. DE-AC02-98CH10886 with the U.S. Department of Energy.

Copyright © 2013 CC-BY-3.0 and by the respective authors

$$z_i^s(N) = A^s_{calc}\cos\left(2\pi\nu_{calc}N + A^s_3\right),$$
$$\text{with: } A^s_{calc} = A^s_1 \exp\left(-2.0\left(\frac{\pi N}{A^s_2}\right)^2\right). \quad (5)$$

The three variables $A^s_{1,2,3}$ are fitted similarly to driven oscillations using Levenberg-Marquardt. This allows the application to analyze any TBT oscillations dataset acquired during RHIC operations and derive the linear optics. Like in the nonlinear case, ν_{calc} is calculated for each BPM dataset via FFT and should be close to the machine tune ν_z. $\beta_z(s)$ and $\Delta\psi_z(s)$ are then determined from the fitted values A^s_1 and A^s_3 at each BPM.

Data Analysis in loptics

Figure 1 shows the graphical interface (GUI) of *loptics* with the ACD control options on the right hand side. Users can provide initial guesses for all parameters to be fitted in the bottom right side. The measured $\beta_z(s)$ and $\Delta\psi_z(s)$ are plotted against their respective design values as calculated by the RHIC online model. The corresponding β_z-beat and phase-beat plots are displayed in a separate tab and saved for further use with the optics correction algorithms. β^*_z and s^* at all IP's are also interpolated and displayed in a dedicated table. One of the upgrades to *loptics* is the calculation of horizontal and vertical phase advances between each IP, providing valuable information when commissioning the new RHIC lattices with e-lens compensation schemes [7].

More than one dataset can be analyzed at a time, with error bars calculated accordingly. Another recent upgrade to the application allows users to analyze datasets acquired with different $\nu_{\mathtt{AC}}$ in order to get rid of the artificial β_z-beat when using the linear fitting method. Each driving tune setpoint makes for an independent measurement, and all related datasets are grouped in the same data analysis process; all calculated average values and error bars are then recombined using the rules of propagation of uncertainty.

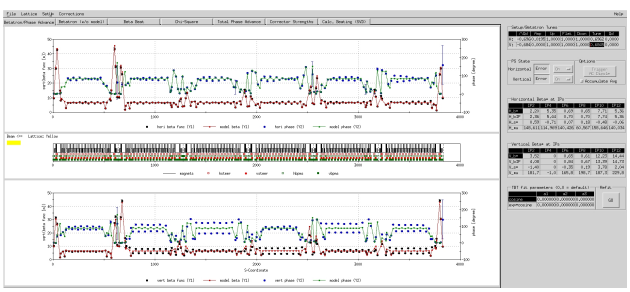


Figure 1: *loptics* graphic interface showing the results of data analysis of AC dipole driven Yellow polarized protons beam oscillations for 255 GeV optic functions (black dots) and phase advance (blue dots) measurements, compared to expected values from the RHIC online model (red and green traces respectively). Both horizontal (top) and vertical (bottom) planes were measured.

CORRECTION ALGORITHMS

In addition to new fitting methods, *loptics* now features a correction algorithms package for the RHIC linear optic functions. The first method is based on a singular value decomposition (SVD) of a response matrix R built around the machine settings as defined in the RHIC online model. Based on the wiring scheme of the RHIC insertions [8], one can find a group of n quadrupoles with individual power supplies to operate as a β_z knob for optics corrections. For all m BPM's in a given beamline, the online model can calculate $(\Delta\beta_z/\beta_z)_p, p = 1\ldots m$ at the pth BPM resulting from a small gradient error $\Delta k_j, j = 1\ldots n$ at the jth selected quadrupole. The matrix $R_{m,n}$ is then built as:

$$\begin{pmatrix}(\Delta\beta_z/\beta_z)_1\\ \vdots \\ (\Delta\beta_z/\beta_z)_m\end{pmatrix} = R_{m,n}\cdot\begin{pmatrix}\Delta k_1\\ \vdots\\ \Delta k_n\end{pmatrix}. \quad (6)$$

Following the data analysis and optics calculations previously described, *loptics* can solve Eq. (6) for $\Delta k^{err}_j, j = 1\ldots n$ by inverting $R_{m,n}$ with SVD:

$$\begin{pmatrix}\Delta k^{err}_1\\ \vdots\\ \Delta k^{err}_n\end{pmatrix} = -\left(R^{-1}_{m,n}\right)\cdot\begin{pmatrix}(\Delta\beta_z/\beta_z)_1\\ \vdots\\ (\Delta\beta_z/\beta_z)_m\end{pmatrix}_{meas} \quad (7)$$

The correction strengths derived from Eq. (7) can be tested in the online model before being applied to the machine, in full or in incremental steps. Figure 2 shows the calculated gradient errors and the corresponding predicted β_z-beat derived from a measurement of the RHIC Yellow lattice optic functions during a beam experiment with polarized protons at 255 GeV. One can notice that all quadrupole magnets selected for the optics corrections are located in all six RHIC interaction regions (IR's) to allow for the maximum number of power supplies to be used, therefore increasing the efficiency of the SVD package. Figure 3 presents the corrected β_z-beat from the optics shown in Figure 1 once 100% of the calculated correction strengths are applied to the Yellow lattice. There is a significant improvement especially in the vertical plane, where the peak-to-peak amplitude of the beating is reduced to about $\pm$ 20%. One should note that in *loptics* the size of $R_{m,n}$ takes into account the status bit of each BPM prior to SVD: any status other than "good" and the entire corresponding row in the response matrix is discarded. Another filter could be implemented that would discard BPM data (and matching $R_{m,n}$ row) if the measured β_z-beat appears to be too unrealistic (e.g. very large reported amplitude compared to other BPM's).

A segment-by-segment method (SBST) [2] is also currently being added to *loptics*. SBST can be used to determine significant gradient errors in individual IR magnets and would allow correcting optics locally, reducing the global β_z-beat to be corrected via SVD. Experiments with beam to test this two-pronged method are being discussed for the coming Run14 of RHIC.

Copyright © 2013 CC-BY-3.0 and by the respective authors

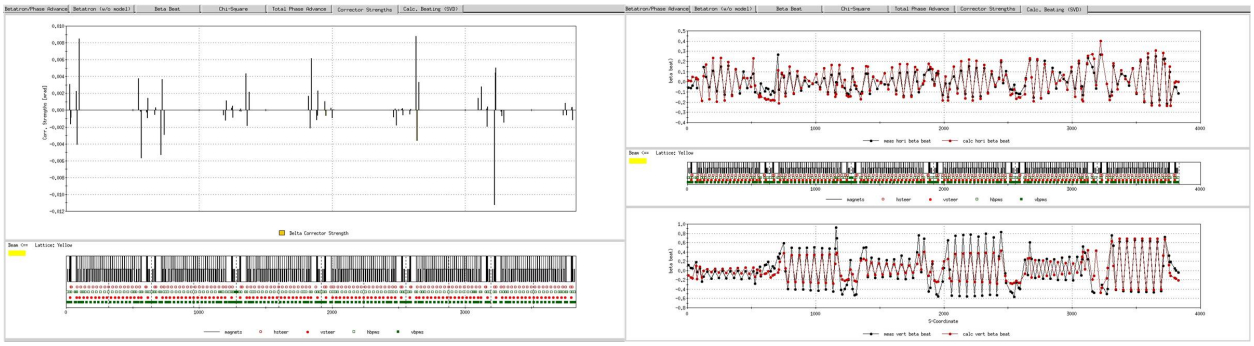


Figure 2: Strength of the gradient errors Δk_j^{err}, $j = 1 \ldots n$ (left) calculated using the global SVD correction scheme newly implemeted in *loptics* for the optics shown in Figure 1 and the selected quadrupole knob. The β_z-beat from these Δk_j^{err} as predicted by the RHIC online model (right, red trace) is compared to the measured one (right, black trace) to determine the quality of the determined solution.

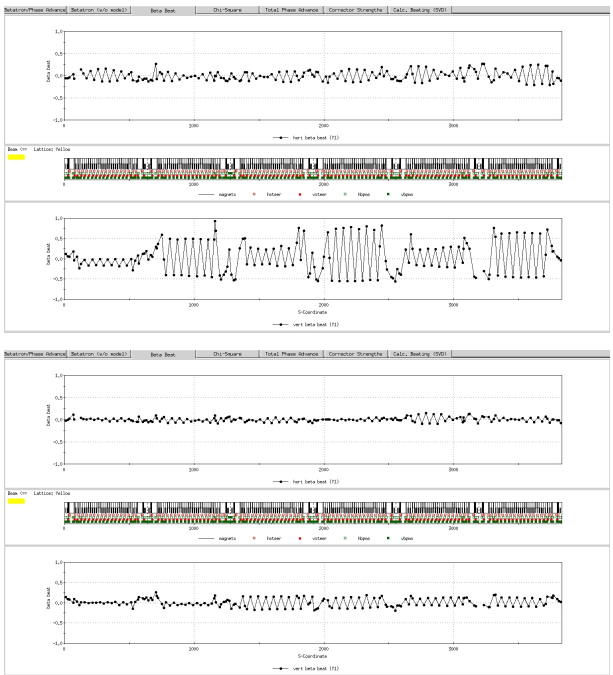


Figure 3: Measured (top) and corrected (bottom) Yellow 255 GeV polarized protons beam optics using the global SVD correction algorithm described in Figure 2.

CONCLUSION

loptics has been upgraded to allow for linear optics measurement using either free or driven turn-by-turn oscillations, with a graphic interface displaying all relevant parameters. Additionally, a correction algorithm based on SVD calculations on a response matrix built with the RHIC online model is now part of the application after being tested with beam as a standalone procedure. Its use in *loptics* allows predicting the accuracy of the correction before sending the knob values to the machine.

Further improvements include the combination of SBST and SVD correction methods, as well as adding an Independent Component Analysis (ICA) model for optics calculations [9]. ICA allows splitting the beam oscillations measured at each BPM into their betatron and synchrotron motions components, as well as filter out any background noise inherent to the electronics involved, leading to a more precise determination of β_z and $\Delta\psi_z(s)$ before corrections.

AKNOWLEDGEMENTS

The authors would like to thank Al Marusic and Simon White for their contribution in developing the new tools and their participation in the optics measurement experiments.

REFERENCES

[1] M. Bai *et. al.*, *Measuring Beta Function and Phase Advance in RHIC with an AC Dipole*, Proceedings of the 2003 Particle Accelerator Conference, p. 2204.

[2] M. Bai *et. al.*, *Optics Measurements and Corrections at RHIC*, Proceedings of the 2012 International Particle Accelerator Conference, p. 1299.

[3] R. Miyamoto *et. al.*, *Parametrization of the Driven Betatron Oscillation*, Phys. Rev. ST Accel. Beams 11, 084002.

[4] M. Bai *et. al.*, *Extracting Undistorted Twiss Parameters from Driven Oscillations*, RHIC Note C-A/AP/299, 2007.

[5] W. H. Press *et. al.*, *Numerical Recipes in C* (2nd ed.), *Ch 15.5 Modeling of Data / Nonlinear Models*, Cambridge University Press, 1992.

[6] R. Miyamoto *et. al.*, *Tevatron optics measurements using an AC dipole*, Proceedings of the 2007 Particle Accelerator Conference, p. 3465.

[7] W. Fischer *et. al.*, *Commissioning Progress of the RHIC Electron Lenses*, Proceedings of the 2013 International Particle Accelerator Conference, p. 1526.

[8] G. Robert-Demolaize *et. al.*, *Commissioning of a beta Knob for Dynamic IR Correction at RHIC*, Proceedings of the 2012 International Particle Accelerator Conference, p. 1314.

[9] X. Shen *et. al.*, *AC Dipole Based Optics Measurement and Correction at RHIC*, Proceedings of NA-PAC 2013.

Copyright © 2013 CC-BY-3.0 and by the respective authors

TRAJECTORIES OF LOW ENERGY ELECTRONS IN PARTICLE ACCELERATOR MAGNETIC STRUCTURES*

E.E. Cowan, Dept of Physics, Syracuse University, NY, USA
Kiran G. Sonnad†, CLASSE, Cornell University, NY, USA
Seth Veitzer, TechX Corp. Boulder, CO, USA

Abstract

It has been observed recently that low energy electrons, or electron clouds formed within quadrupoles can remain trapped for time periods beyond a beam revolution period at Cesr [1]. This paper provides some results obtained from analysis and numerical tracking of low energy electrons in quadrupoles under conditions similar to those when the above mentioned data was collected.

MOTION OF PARTICLES IN A NONUNIFORM MAGNETIC FIELD

Electron clouds generated in positively charged beams are known to negatively interfere with the beam. Most of the simulations done for various accelerators for estimating the cloud buildup have been for the duration of the passage of a single train of bunches. However if an electron remains trapped for long enough in a magnetic structure such as a quadrupole after the passage of a train, this trapped electron will encounter the next passage of a bunch train. The electron may then impinge upon the walls and potentially produce secondary electrons. Such a mechanism could lead to a progressive enhancement in cloud densities with repeated train passages and can have adverse consequences on the properties of the beam.

Trapping of electrons has been observed in the PSR [2]. In this experiment the proton beam was allowed to circulate and produce electrons and the beam was then deflected out of the storage ring, while the electron cloud was allowed to evolve. It was observed that electrons in quadrupoles persisted for a time period exceeding 50-100μs. More recently, experiments performed at Cesr observed electron trapping in quadrupoles in the presence of a beam [1]. The revolution period of the beam in Cesr is about 2.5 μs.

In this paper, we report results obtained from single particle tracking and compare them with theoretical expectations. The parameters of our computations were similar to those of the operating conditions when the data reported in Ref. [1] was taken. A similar study was performed earlier for the KEKB [3]. This study clearly showed that trapping of electron in quadrupoles can be important and requires a careful study.

Adiabatic Invariants

In dynamical systems exhibiting periodic motion, the quantity $\oint p \cdot dq$, which is the phase space area encompassed by the trajectory, also known as the Poincare invariant is a conserved quantity [4]. If a system undergoes a very gradual change, this quantity remains conserved so long as the relative value of this change over a full period of motion is very small, (see for example Ref. [4]). A classic example is a simple pendulum where the length of the string is gradually altered at a rate such that over the course of the oscillation period, $\delta l/l << 1$. Then the quantity E/ω remains constant and is the adiabatic invariant. The same principal of adiabatic invariance can be applied to a particle executing cyclotron motion in a magnetic field (see for example Ref. [5]). For a particle in this situation, the magnetic moment

$$\mu = IA = \frac{mv_\perp^2}{2B} \tag{1}$$

is conserved as long as $dB/B << 1$ over the cyclotron period T_c. This is equivalent to the following condition,

$$\frac{|\nabla B|}{B} r_c << 1, \tag{2}$$

where r_c is the cyclotron radius. On the other hand, energy which is given by

$$\mathcal{E} = \frac{1}{2} m(v_\perp^2 + v_\parallel^2) \tag{3}$$

being an absolute invariant always remains conserved. In the above equation, $v_\perp$ and $v_\parallel$ are velocities perpendicular and parallel with to the magnetic field, respectively.

Magnetic Mirroring

If energy and the magnetic moment are conserved, one can obtain a formula for magnetic mirroring. As B increases, $v_\perp$ increases and $v_\parallel$ decreases. If $v_\parallel$ decreases to zero, the trajectory turns around. This phenomenon is referred to magnetic mirroring. Since $v_\perp$ is rotating around the field line, one can associate this condition with a cone in velocity space. A particle would lie within the "loss" cone if

$$v_\parallel / v_\perp > 1 - (B_{bd}/B_{in})^{1/2}. \tag{4}$$

Here B_{in} is the magnetic field value at the initial point, and B_{bd} is the magnetic field on the same field line at the boundary of the vacuum chamber. A particle lying outside this cone in velocity space at the given point will remain trapped.

* Work supported by NSF (PHY-0734867, PHY-1002467, PHY-1068662), US DoE (DE-FC02-08ER41538)
† kgs52@cornell.edu

Copyright © 2013 CC-BY-3.0 and by the respective authors

Motion Transverse to Magnetic Field

Magnetic mirroring is a consequence of the effect of the particle motion along the magnetic field lines. Additionally, in the presence of a nonuniform field, the particle undergoes a "grad B" and a "curvature drift", which are perpendicular to the field lines. In the absence of any current sources, where $\nabla \times \mathbf{B} = \mathbf{0}$, the curvature of the field can be related to its gradient, and the expressions of the two drifts may be combined in the following form,

$$v_{curv} + v_{\nabla B} = \frac{m}{q} \frac{\mathbf{B} \times \nabla B}{|B|^3} (v_{\parallel}^2 + \frac{1}{2} v_{\perp}^2) \qquad (5)$$

The values of the magnetic field here correspond to points along the motion of the guiding center. While it is clear that a particle can never be trapped indefinitely because of this drift, what matters in our study is if the particle is trapped for the period of one beam revolution. Fringe field effects have been disregarded throughout this study, which would become important for electrons that are either formed in this region or drift into this region due to the effect described above. Nevertheless, we show that for electrons to undergo a prominent longitudinal drift, they have to acquire energies close to 1 KeV, which are typically high for electrons formed from multipacting.

RESULTS FROM TRACKING STUDIES IN QUADRUPOLE FIELDS

In order to test the validity of the loss cone and Eq. 4, five different initial positions were chosen. These points lay on a horizontal line parallel to the cross-section of the beam pipe and passing through the center of the cross-section. In order to determine the loss cone angle for these points, one needs to determine the field value at the given point as well as the "escape" point. The latter was determined with the help of a program we developed that traced the path along the field line. The point beyond which the particle was considered lost was located on this field line, very close to the boundary of the chamber. The chamber shape consists of two circular arcs (radius 0.075m) on the top and bottom, connected with flat side planes. It is about 0.090m from side to side and 0.050m between the apices of the arcs. The magnetic field is given by $B_x = ky$ and $B_y = kx$ with $k = 7.4T/m$, which is close to the value set during the operation of Cesr at 5.3 GeV.

Table 1: Cases Studied to Confirm Trapping

x(m)	B_{in} (T)	B_{bd}	θ_m (deg)	$\angle$ 1, $\angle$ 2
0.0005	0.0365	0.2261	66.2989	65, 67
0.015	0.1095	0.2386	47.3414	45, 48
0.025	0.1825	0.2626	33.507	32, 34
0.035	0.2555	0.2972	21.9773	20, 23
0.04	0.2920	0.3184	16.7044	15, 17

Table 1 shows all the initial positions from where electrons were tracked. The critical angle θ_m is equal to $90deg-$ (loss-cone-angle). Since the points lay on the horizontal axis, the magnetic field direction for all of them was vertical. Thus, if the particle launch angle with respect to the horizontal axis was less than θ_m one would expect it to be trapped. The tracking was performed using the plasma simulation program Vorpal [6]. The particles were launched at angles (with respect to the horizontal axis) just above and below the critical angle, indicated as $\angle 1$ and $\angle 2$ respectively. For each case, the energies used were 1eV, 10eV, 100eV and 1 KeV. In most cases, particles that started at $\angle 2$ remained confined while those with $\angle 1$ were lost. The only exceptions were when the particles were at $x = 0.05cm$ with energies 1Kev and 100eV, when particles at both the starting angles were lost. It was also confirmed that when particles were incrementally close to the center, they were lost within $2.5\mu s$ even at an energy of 1eV regardless of the initial direction of motion.

For a quadrupole magnetic field, one can easily verify that the condition of adiabatic invariance, given by Eq. (2) becomes weaker as one approaches the center. Depending on the particle energy, it becomes invalid at a certain point close enough to the origin. This explains the poor confinement for particles that cross points close enough to the center.

Overall, one could divide the trajectories into three classes, (1) Those that escape because their parallel and perpendicular velocities are distributed such that they lie within the loss cone. (2) Particles that remain trapped because they lie outside the loss cone, and the condition for adiabatic invariance remains satisfied. (3) Particles that cross points sufficiently close to the center that that the motion becomes non-adiabatic in the vicinity od the center. As these particles move away from the center due to inertia, they begin to move into an area of higher magnetic field, where the motion may become adiabatic. If they are within the loss cone, they escape. If they are outside the loss cone, they get reflected back toward the center. Depending upon the phase of the cyclotron motion they acquire near the center, they may stray away from the center in an entirely different direction. This process repeats itself until it enters the loss cone and impinges against the wall.

Figure 1 is an example of a particle that escapes because it is within the loss cone. Figure 2 is an example of particle that remained trapped for the period of $2.5\mu s$ because it was located outside the loss cone. Figure 3 was a particle very close to the center that exhibited non-adiabatic motion. The energy in all these cases was 1 KeV.

Figure 4 shows the three dimensional motion of a trapped particle at 1 KeV, clearly indicating the drift along the longitudinal direction. Figure 5 is a plot of the same z motion as a function of time. This plot compares the motion of the full trajectory, as computed by the tracking, the guiding center motion obtained from the tracking by numerically averaging over the cyclotron periods, and the motion as predicted by Eq. 5. We see that the analytic results agrees well with the numerically computed guiding center motion. The longitudinal distance covered by the

Copyright © 2013 CC-BY-3.0 and by the respective authors

particle in 2.5μs was found to be about 0.34m, while the length of the quadrupole is about 0.6m. Additionally, it is known from build up simulations that the fractional population of particles with energies of 1 KeV are not more than a few percent. Based on Eq. 5, one can state that the distance covered by the particles is roughly proportional to the energy (disregarding the details of the parallel vs perpendicular distribution of the velocities). Typical energies of the electrons is of the order of 100eV. One can thus argue that the longitudinal drift of trapped electrons does not contribute significantly to their escape before the arrival of a subsequent bunch train.

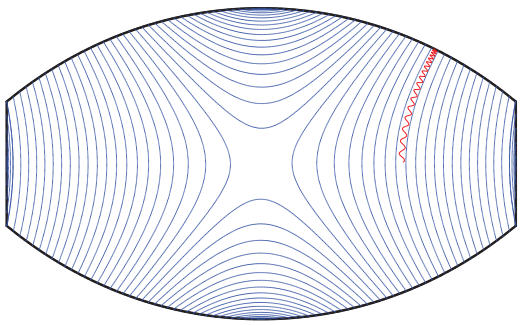


Figure 1: Escaped particle lying within the loss cone.

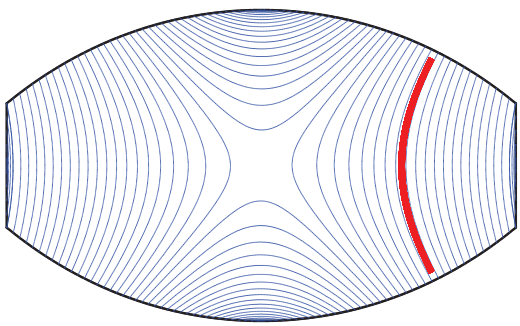


Figure 2: Trapped particle lying outside the loss cone.

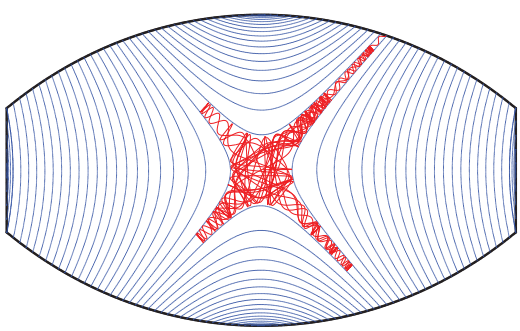


Figure 3: Particle executing non-adiabatic motion.

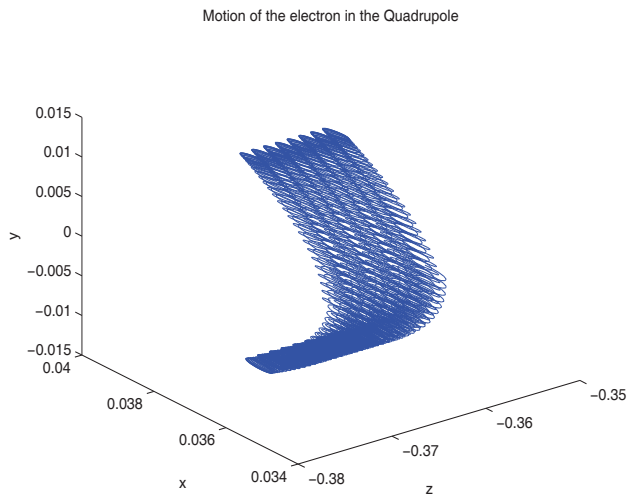


Figure 4: Three dimensional motion of a trapped particle showing longitudinal drift.

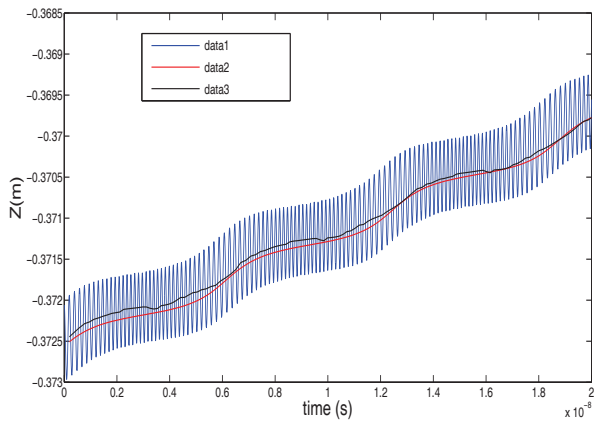


Figure 5: Validation of the combined grad-B and curvature drift, data1 is the full particle trajectory obtained from tracking, data2 the trajectory obtained from Eq. 5, data3 the tracked data averaged over the cyclotron motion.

REFERENCES

[1] J.A. Crittenden *et al*, "Observation of Electron Trapping in a Positron Storage Ring" Submitted to Phys Rev Lett, `http://arxiv.org/abs/1309.2625`

[2] R. Macek *et al.*, Phys. Rev. ST Accel. Beams 11, 010101 (2008).

[3] L.F. Wang, H. Fukuma, S. Kurokawa, and K. Oide, Phys. Rev. E 66, 036502, 2002.

[4] L.D. Landau, E.M. Lifshitz, Mechanics, Pergamon Press, Oxford (1976).

[5] Francis F. Chen, "Introduction to Plasma Physics and Controlled Fusion. Volume 1: Plasma Physics", Second Edition 1984.

[6] Chet Nieter and John R. Cary, Journal of Computational Physics, Volume 196, Issue 2, 20 May 2004, Pages 448–473.

Copyright © 2013 CC-BY-3.0 and by the respective authors

A LINEAR ENVELOPE MODEL FOR MULTI-CHARGE STATE LINAC*

Z. He#, FRIB, Michigan State University, USA; Tsinghua University, China
J. Wei, Y. Zhang, Z. Liu, FRIB, Michigan State University, USA
R. M. Talman, Cornell University, USA

Abstract

The traditional linear envelope tracking model is widely used in linac design and on-line tuning. However, for multi-charge state acceleration, where the transfer matrix acts differently on different charge-states, the linear envelope tracking model cannot be utilized. A direct way to handle multi-charge state acceleration is using multi-particle tracking, which is usually high in precision, but lacking in efficiency, therefore is not suitable for linac on-line beam tuning. In this paper, a new approach of adapting linear envelope tracking model to multi-charge state acceleration is proposed. The lattice of FRIB is used to test this technique in both linac segment and folding segment. The result is then benchmarked with a multi-particle tracking program IMPACT to ensure its precision with enhancement in efficiency.

INTRODUCTION

The traditional linear envelope tracking model is widely used. Instead of tracking every particle, the method is capable of keeping track of beam envelopes by knowing an initial theta matrix and the transfer matrix between the initial point and the objective point, which is shown below.

$$x_i^{(1)} = R_{ij} x_j^{(0)}$$

$$\sigma_{ij}^{(0)} = \frac{\sum_n \left(x_{ni}^{(0)} x_{nj}^{(0)} \right)}{N}$$

$$\sigma_{ij}^{(1)} = \frac{\sum_n \left(R_{ik} x_{nk}^{(0)} R_{jm} x_{nj}^{(0)} \right)}{N} = R_{ik} \sigma_{km}^{(0)} R_{jm}$$

Numbers of linac code are based on or contains this scheme, such as Trace 3D. The advantage of envelope tracking model is obvious: fast in calculation speed, simple and clear in physics, therefore, remains to be a preferable way in computational intensive applications like case-by-case based linac lattice global optimization, and time restricted applications like linac on-line beam tuning.

For traditional accelerators like electron or proton machines, only one charge state is presented and the traditional linear envelope tracking model can be directly adopted. However, Facility for Rare Isotope Beams (FRIB) is accelerating multiple charge states in order to enhance the beam current. For this kind of accelerators, the traditional linear envelope tracking model can no longer be adopted directly, extensions onto multi-charge states acceleration problems are needed.

*This work was supported by the U.S. National Science Foundation under Grant No. PHY-11-02511, and the U.S. Department of Energy Office of Science under Cooperative Agreement DE-SC0000661.

hez@frib.msu.edu

HOW TO DEAL WITH MULTI-CHARGE STATE ACCELERATION

There are three different schemes to handle multi-charge state acceleration problem. The most simple and straight forward one is multi-particle tracking. The advantage is we can expect minimum change of existing tracking code, attain high precision and detailed information. Particle tracking code like IMPACT, is utilizing this scheme. However, the shortcoming is high computational intensity and slow speed. And computer takes over all the calculation would result physics to be unclear.

The second way is to treat charge state deviation as momentum deviation for magnetic field. This method can give exact result on transverse coordinates and can reuse most part of existing code. But the problem the method can only handle all-magnetic field lattice. The imaginary extra momentum deviation can cause imaginary change in time-of-flight for non-relativistic cases. This method is sometimes quite useful when calculating multi-charge beam behaviour in a bending magnet.

THREE-STEP SCHEME

The third way is to treat different charge states separately using envelope tracking scheme. This method can be divided into three steps:

Step 1: Use an ideal particle with centre charge state to initiate the machine parameters, such as RF phases, bending magnet strength. Keep record of the particle and make it the reference of the whole beam.

Step 2: Choose the particle located at beam centre of each charge state as a reference particle and do single particle tracking according to the initialized lattice parameter. Keep record of each particle and make it the reference for each charge state beam.

Step 3: Do envelope tracking for each charge state beam. The transfer matrix should be adjusted according to its own charge state and reference orbit.

This method of handling multi-charge state is a combination of precision of particle tracking method and efficiency of envelope tracking. The calculation efficiency is quite high. Details can vary while the three step scheme concept is universal. For next part, the FRIB lattice would be analysed as an example using this method.

APPLICATION TO FRIB LATTICE

The FRIB project, built at the Michigan State University in corporation with the US Department of

Copyright © 2013 CC-BY-3.0 and by the respective authors

Energy (DOE), will deliver all stable ion beams with energy more than 200MeV/u and target beam power more than 400kW. In order to meet this goal, multi-charge state acceleration is needed, especially for heavy ions, to increase the beam current and beam power. For the Uranium case, the 33+, 34+ charge states are accelerated in linac segment 1, and after a charge stripped and charge selector, the 76+, 77+, 78+, 79+, 80+ charge states are selected and accelerated all the way to the target. Fig. 1 shows detailed layout of FRIB lattice.

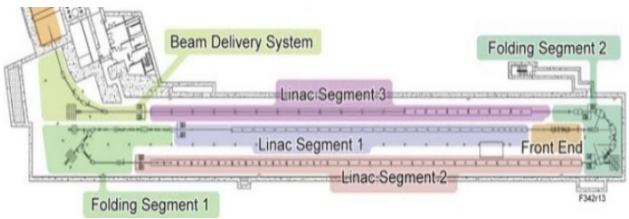


Figure 1: Layout of FRIB lattice.

Linac Segment

The linac segment is where heavy ions gain most part of its kinetic energy. For linac segment 1, superconducting quarter-wave resonators (QWRs), are used for accelerating ion beams while for linac segment 2, superconducting half-wave resonators (HWRs) are used. For both linac segment 1 and linac segment 2, superconducting solenoids are the main component used for focusing ion beams.

Linear Matrix Models: To track the energy and phase advance for synchronous particle in an RF cavity, the Drift-Kick-Drift thin lens model is utilized:

$$\begin{cases} W_f = W_i + qV_0T(k)\cos\varphi_i - qV_0S(k)\sin\varphi_i \\ \varphi_f = \varphi_i + \dfrac{qV_0}{2W_i}k[T'(k)\sin\varphi_i + S'(k)\cos\varphi_i] \end{cases}$$

T, T', S, S' are Transit Time factors. Two gap accelerating model is utilized to decrease the error caused by constant velocity assumption [1].

The longitudinal phase space transfer matrix comes from differentiation of the longitudinal Drift-Kick-Drift thin lens model and keeping the linear term of energy and phase deviation. The transverse phase space transfer matrix also comes from a Drift-Kick-Drift thin lens model. For each acceleration gap, the total transfer matrix can be decomposed into drift spaces between two focusing/ defocusing gaps and an acceleration.

A soft edge solenoid model is used in our model:

$$M_{soft\,sol} = M_{edge}M_{sol}M_{edge}$$

$$M_{edge} = \begin{bmatrix} 1 & 0 & 0 & 0 \\ -\Phi & 1 & 0 & 0 \\ 0 & 0 & 1 & 0 \\ 0 & 0 & -\Phi & 1 \end{bmatrix}$$

M_{sol} is the traditional hard edge solenoid transfer matrix M_{edge} describes the edge effect. $\Phi = -\frac{g^2a}{2}$, $= \frac{Bqc}{2\beta E_{tot}}$, and a is the solenoid radius [2].

These models have been verified by envelope tracking of single charge state after benchmark with a multi-particle tracking code IMPACT [3]. Then we can use the three step scheme to extend the model to handle multi-charge state acceleration.

Linac Segment 1: First step is to initialize the lattice parameters using a centre charge state. For linac segment 1 case where the two charge states are 33+ and 34+, either one can be used as reference charge state. Here we choose 33+ as the reference charge state and the lattice is initialized using an ideal 33+ particle. After initializing the lattice parameters, the centre particle for 33+ and 34+ charge states are tracked and results are recorded as reference orbit for each charge state. Then we can use envelope tracking scheme to track the envelope of 33+ and 34+ beam bunch separately. Transfer matrix can be influenced not only by charge states but also by reference orbit. Beam centre and RMS envelope evolution results can be seen in Fig. 2.

We can see from the figure that the 33+ charge state particle tends to have larger phase, because the 33+ charge state would always be dragged off and fall behind due to lack of acceleration efficiency compared to 34+. For transverse direction, the centre of beam for both charge states is coincident with the beam axis. Due to the different focusing strength for the different charge states, the focusing lattice cannot match both charge states at the same time, so we can see oscillation comes from mismatch for both charge states.

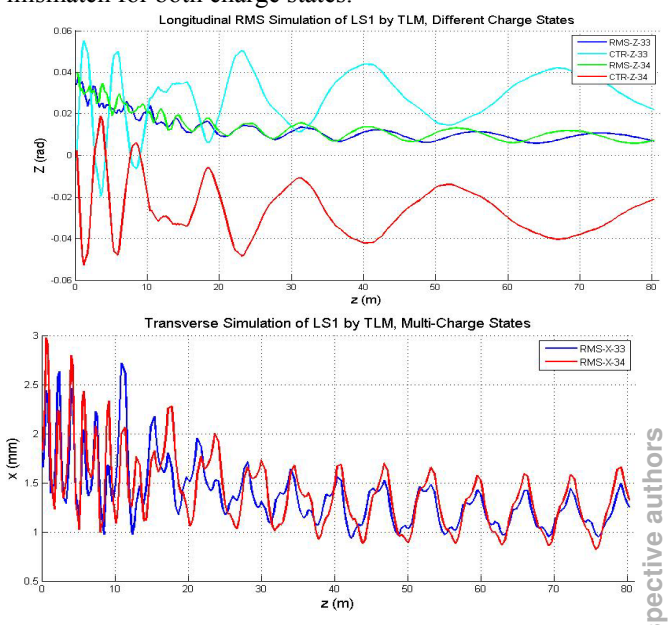


Figure 2: Upper: Linac segment 1 longitudinal phase centre deviation for the 33+ and 34+ two charge states and the phase spread RMS envelope in the centre of mass frame Lower: transverse beam RMS envelope for the 33+ and 34+ two charge states.

RMS Envelope Re-combine: For real experiment, we usually measure the whole bunch beam size. So, we need to calculate the total RMS beam size. In the centre of mass frame, $\bar{x}$ is centre of beam for each charge state, σ is the RMS size, N is particle number, foot note i represents different charge state, than the whole bunch RMS beam size equals:

Copyright © 2013 CC-BY-3.0 and by the respective authors

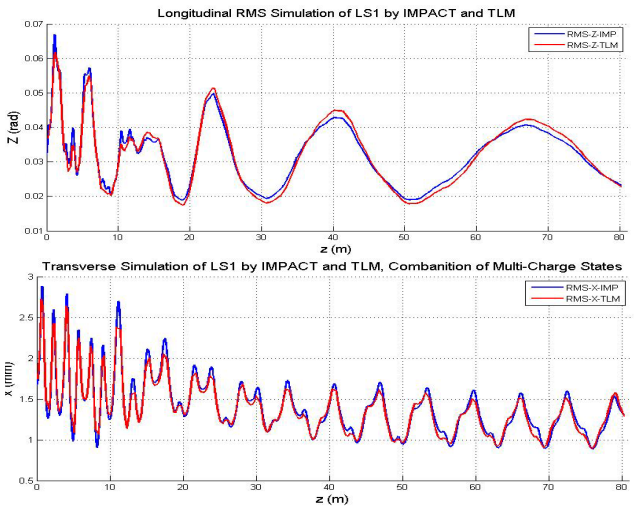


Figure 3: Re-combine of RMS envelope and benchmark with IMPACT. Upper figure, Re-combine of RMS envelope for the longitudinal direction, Lower figure, Re-combine of RMS envelope for the transverse direction.

$$\sigma = \sqrt{\frac{\sum_i N_i(\sigma_i^2 + \bar{x}_i^2)}{N}}$$

Using this scheme to recombine the beam size and benchmark with IMPACT, we can get the result shown as Fig. 3. We can see that the simple envelope model for handling multi-charge state benchmarks well with IMPACT simulation.

Folding Segment

There are two 180 degree benders linking three linac segments. For charge state far away from centre whose equivalent dispersion is quite high, higher order term may appear. In order to suppress the potential influence from higher order term, a new scheme has been proposed.

First, use a centre charge state to initialize lattice parameter, for uranium beam in bending segment 1 case where the charge states are 76+, 77+, 78+, 79+ 80+, the charge state 78+ is chosen to initialize the lattice. Then, for the centre particles of the remaining charge states, their own reference orbits are set up. Note that in order to suppress the possible higher order term coming from bending magnet, the exact transfer map is used to track the reference particles [4].

After setting up reference orbits, we can use envelope model to do envelope tracking. For this time, the traditional bending magnet transfer matrix for non-relativistic ion beams can be used.

By using the scheme, we can also obtain the beam centre and beam RMS size of each charge state in folding segment 1, the result is shown as Fig. 4. After recombination and benchmark with IMPACT, we arrive in the final result benchmark with IMPACT shown as Fig. 5. The thin lens model agrees well IMPACT result.

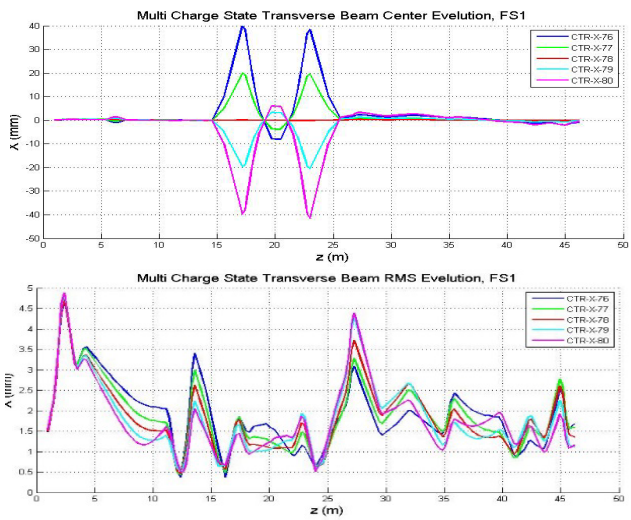


Figure 4: Transverse beam centre (upper) and beam RMS envelope (lower) evolution of five different charge states in folding segment 1.

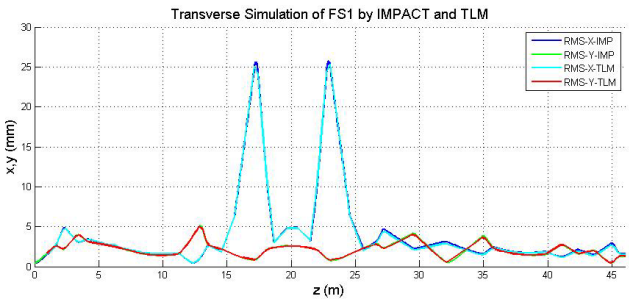


Figure 5: Re-combine of transverse RMS envelope of five different charge states in folding segment 1 and benchmark with IMPACT.

CONCLUSION

The multi-charge state envelope tracking model has proved to be precise and efficient. The result agrees well with multi-particle tracking. Very minor modification of currently available model is needed. The computational efficiency also turns out to be high. A beginning to end of FRIB lattice parallel computation of multi-particle tracking by IMPACT would take several minutes, while multi-charge state envelope tracking method would take only several seconds. The increment in efficiency makes the model promising in further development of on-line applications like fast beam tuning and lattice optimization for multi-charge state acceleration machine as FRIB.

REFERENCES

[1] Z. He et al. "An Analytical Cavity Model for Fast Linac-Beam Tuning", Proc. of LINAC'12, (2012).
[2] M. Aslaninejad, "Solenoid Fringe Field effects for the neutrino factory Linac", Proc. of IPAC'10, (2010).
[3] Ji Qiang, Rober D. Ryne, IMPACT code, LBNL; http://amac.lbl.gov/~jiqiang/IMPACT
[4] Etienne Forest, *Beam Dynamics, a new attitude and framework*, (Harwood Academic Pub. 1998).

Copyright © 2013 CC-BY-3.0 and by the respective authors

CALCULATION OF THE KICK MAPS GENERATED BY A HOLLOW ELECTRON LENS FOR STUDIES OF HIGH-ENERGY HADRON BEAM COLLIMATION*

G. Stancari†, M. Chung, A. Valishev, Fermilab, Batavia, IL 60510, USA
V. Moens, EPFL, Lausanne, Switzerland, H. J. Lee, Pusan National University, Korea

Abstract

Collimation with hollow electron beams is a technique for halo removal in high-power hadron beams. It was experimentally studied at the Fermilab Tevatron collider using electron lenses and it is being considered as an option to complement the collimation system for the LHC upgrades. In the ideal case, the magnetically confined electron beam has a hollow, axially symmetric current-density distribution, whose fields affect the beam halo, leaving the core of the circulating beam unperturbed. We address the effects of imperfections in the current density based upon profiles measured in the Fermilab electron lens test stand. We also study the effect of the bends used to inject and to extract the electron beam from the overlap region. The calculated field distributions will serve as inputs for tracking simulations, which are needed to estimate the effects of the electron lens imperfections on beam core dynamics, such as nonlinearities and emittance growth.

INTRODUCTION

Hollow electron beam collimation is a new technique for collimation and halo scraping of intense hadron beams in storage rings and colliders [1]. In a hollow electron beam collimator, a magnetically confined, pulsed, low-energy electron beam with a hollow current-density profile overlaps with the circulating beam over a short section of the ring. Figure 1 shows the layout of one of the Tevatron electron lenses. The beam is formed in the electron gun inside a conventional solenoid and guided by strong axial magnetic fields. Inside the superconducting main solenoid, the circulating beam interacts with the electromagnetic fields generated by the charge distribution of electrons. The electron beam is then extracted and deposited in the collector. The halo of the circulating beam can be smoothly scraped. The core is unaffected if the distribution of the electron charge is axially symmetric. One cause of asymmetry is the space-charge evolution of the electron beam as it propagates through the electron lens. Another source of asymmetry are the bends that are usually used to inject and extract the electron beam from the interaction region. Although small, these asymmetries may have detectable effects on core lifetimes and emittances because of their nonlinear nature, especially when the current of the electron pulse is changed turn by turn to enhance the halo removal effect by resonant excitation of selected particles.

In this paper, we discuss the effects of these asymmetries from experimental data and from calculations. In particular, the asymmetries in the charge distribution are translated into transverse kick maps for the circulating beam. These kick maps are provided as inputs for numerical tracking simulations of the Fermilab Tevatron collider and of the Large Hadron Collider at CERN with the Lifetrac or SixTrack codes. This work is in support of a conceptual design for a proposed hollow electron beam collimator for the LHC upgrade [2]. The same techniques can be applied to different current-density profiles (Gaussian, flat, etc.) to study perturbations in nonlinear integrable optics with electron lenses for the IOTA ring at the Fermilab ASTA facility [3].

AZIMUTHAL ASYMMETRIES

Two-dimensional azimuthal asymmetries of the electron current density in the overlap region inside the main solenoid (neglecting the injection and extraction regions) may be caused by the space-charge evolution of the hollow electron beam as it propagates through the electron lens (diocotron instability), or by imperfections in the electron gun geometry, magnetic field lines, etc.

Electron guns are characterized at the Fermilab electron-lens test stand. Current-density profiles are measured as a function of beam current and axial magnetic field. Space-charge evolution of the electron beam profiles is mitigated by increasing the guiding magnetic fields. The measured profiles are used to calculate the corresponding transverse electric fields inside the beam pipe using the Poisson

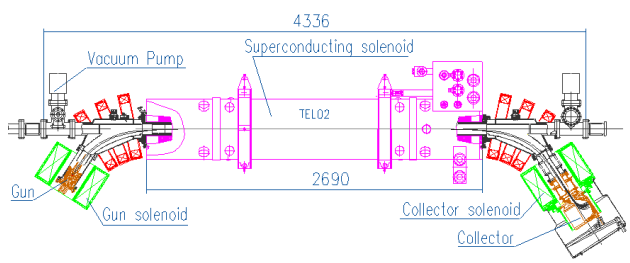


Figure 1: Layout of a Tevatron electron lens. (Dimensions in millimeters.)

* Fermilab is operated by Fermi Research Alliance, LLC under Contract No. DE-AC02-07CH11359 with the United States Department of Energy. This work was partially supported by the US LHC Accelerator Research Program (LARP) and by the European FP7 HiLumi LHC Design Study, Grant Agreement 284404. Report number: FERMILAB-CONF-13-356-APC.

† Email: ⟨stancari@fnal.gov⟩

Copyright © 2013 CC-BY-3.0 and by the respective authors

solvers of the Warp plasma particle-in-cell code [4]. A few examples of these calculations can be found in Ref. [5]. Inside the hole of the electron beam, where no charge is present, the potential satisfies Laplace's equation and the effect of the asymmetries can be characterized as a superposition of multipoles. Elsewhere, a more general parameterization is necessary. This approach was used to compare calculated and measured halo removal rates in the Tevatron [6]. For the Tevatron lattice and tune working point, the only azimuthal asymmetry seen to cause extra losses in the core was the quadrupole component in a particular resonant mode (pulsing the electron beam every 6th turn). Calculations for the LHC are under way and will be presented in the conceptual design report.

EFFECT OF BENDS

In an electron lens, toroidal bends are used for injecting and extracting the electron beam (Figure 1). To study whether the curved charge distribution of electrons has a significant effect on the dynamics of the circulating beam, we rely on the Tevatron experiments and on calculated kick maps.

Most of the Tevatron experiments on hollow electron beam collimation were done in continuous mode: the electron current was kept constant turn by turn. Under these conditions, no deteriorations of core lifetimes or luminosities were observed. For the LHC, to extend the range of achievable halo removal rates, resonant operation is also being considered: in this mode, the voltage in the electron gun is changed turn by turn according to a sinusoidal function, in resonance with betatron oscillations, or with the same amplitude, skipping a given number of turns [7]. Resonant operation was used for abort-gap cleaning in the Tevatron [8], but no systematic experimental studies were done on the effects of time-varying pulse amplitudes on the beam core. For this reason, numerical tracking studies are planned, and here we describe the calculation of the kick maps to be used as inputs.

The parameters of the proton beam are used to calculate beam sizes in the interaction region. We assume a round proton beam with a typical rms beam size $\sigma_p = 0.317$ mm. The hollow electron beam is represented by a cylindrical bent pipe with a curvature radius $R = 0.7$ m, inner radius $r_i = 1.27$ mm $= 4\sigma_p$, and outer radius $r_o = 2.39$ mm $= 7.5\sigma_p$. The ratio between the outer and the inner radius is chosen to reproduce the dimensions of the cathode in the existing 1-inch hollow electron gun [5, 9]: (12.7 mm)/(6.75 mm). The bent tube of electrons spans a bend angle of $\theta = 30$ deg. A total of $N_e = 1048576 = 2^{20}$ electron macroparticles is used to reproduce the static charge density distribution of a 1-A, 5-keV electron beam. The z-axis is chosen along the direction of the circulating proton beam. The x-axis points horizontally outward. The upward direction is represented by the y-axis. The origin of the coordinate system coincides with the point where the axis of the bent electron beam intersects the axis of the circulating beam (Figure 2).

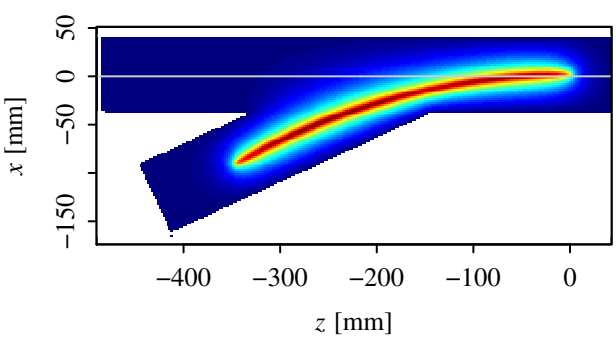


Figure 2: Conductor geometry and calculated electrostatic potential on the plane of the bent electron distribution. Dark red corresponds to −1.2 kV, dark blue represents 0 V. The horizontal gray line is the axis of the proton beam.

A multigrid Poisson solver within the Warp particle-in-cell code is used to calculate the electrostatic fields. The boundary conditions are defined by a long cylindrical main beam pipe and by a cylindrical injection beam pipe stub, joining the main pipe at an angle (Figure 2). This arrangement is a simplified version of the injection scheme in the Tevatron electron lenses (Figure 1). Both pipes have an inner radius $r_{\text{pipe}} = 40$ mm.

Space is subdivided into 2 discrete grids, a coarse one (2-mm spacing) covering the whole space, and a fine one (0.1 mm) around the central trajectory of protons. The transverse coverage of the fine mesh, $-10\sigma_p \le x, y \le 10\sigma_p$, is designed to obtain kick maps for both the core and the halo of the proton beam.

Figure 2 shows the electrostatic potential $V(x,y,z)$ on the xz-plane of the bend. The electrostatic fields E_x and E_y are integrated over straight paths to calculate the transverse momentum kicks $\Delta p_{x,y}$ experienced by the circulating proton beam:

$$k_{x,y}(x,y) \equiv \int_{z_1}^{z_2} E_{x,y}(x,y,z)\,dz, \qquad (1)$$

$$\Delta p_{x,y} = \int_{t_1}^{t_2} F_{x,y}\,dt = \frac{q}{v_z}\int_{z_1}^{z_2} E_{x,y}\,dz = \frac{q}{v_z}k_{x,y}, \qquad (2)$$

where q, v, and p are the charge, velocity, and momentum of the circulating beam, F is the electrostatic force, t is time, and the integrated fields k_x and k_y are later loosely referred to as 'kicks.' Only transverse kicks are considered, as the longitudinal kicks of two symmetric bends cancel out. The transverse kicks due to two bends, on the other hand, have the same sign and will add up. The typical angles of the proton trajectories are of the order of $\sigma_p' = 1.6\ \mu$rad, so the resulting position variations over the length of the bend can be neglected. For 7-TeV protons, an integrated field of 10 kV generates an angular deviation of 1.4 nrad. The kick maps on the fine mesh are represented as contour plots in Figure 3. Protons on axis experience a negative horizontal integrated field of −9.1 kV, whereas

Copyright © 2013 CC-BY-3.0 and by the respective authors

the vertical kick vanishes. The vertical kick on the plane of the bend is zero.

For tracking simulations, one can interpolate the given kick maps in 2 dimensions for each particle. Alternatively, to speed up calculations, one can use an analytical formulation of the functions $k_x(x,y)$ and $k_y(x,y)$. We use a parameterization in terms of the outer product of 1-dimensional Chebyshev polynomials in x and y up to a given order N. Because of the symmetry of the charge distribution, the horizontal kicks are even functions of y and only contain even powers of the vertical coordinate, whereas the vertical kicks are odd functions of y. At order $N = 7$, for instance, the standard deviation of the residuals of this interpolating model is about 150 V.

To study the sensitivity of the results to the geometry of the system, cases with different beam pipe radii and injection angles are simulated. The chosen beam pipe radii were 35 mm, 40 mm (reference case), and 45 mm. The chosen bend angles were 25 deg, 30 deg (reference case), and 35 deg. The changes in geometry considered in this study amount to a change in the kicks of less than 300 V.

Further details on the calculation of these kick maps can be found in Ref. [10].

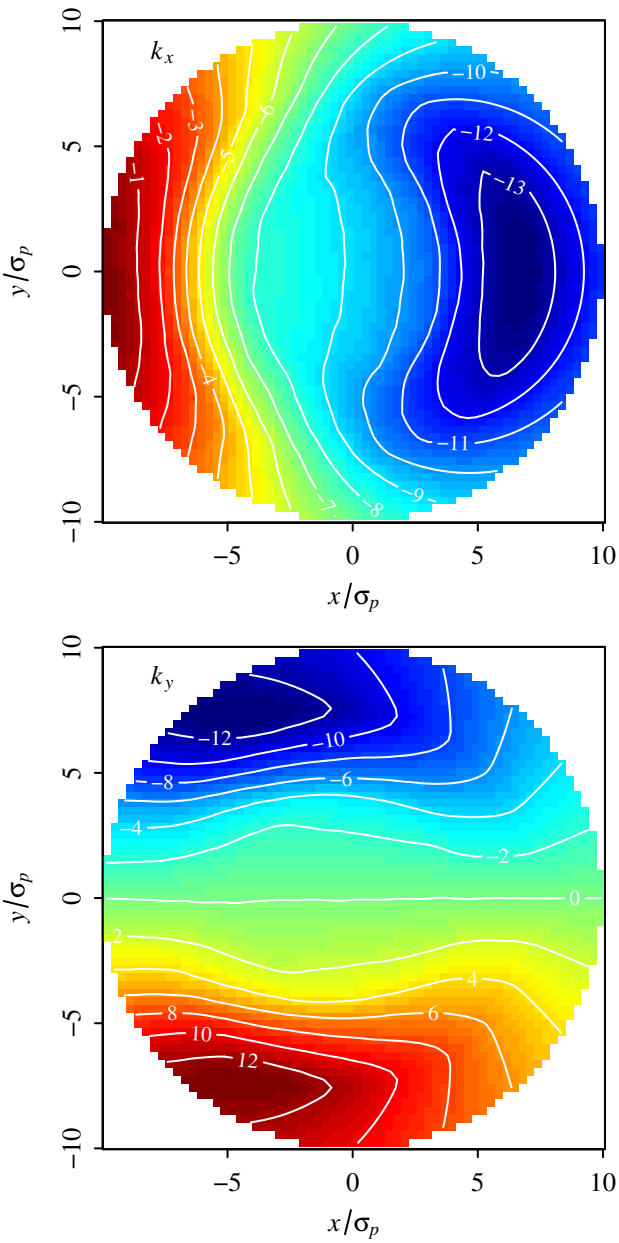


Figure 3: Contour plots of the integrated fields k_x (top) and k_y (bottom) as a function of scaled transverse coordinate. The contour lines are labeled with the value of the integrated field in kilovolts.

CONCLUSIONS

We studied some of the effects of electron-lens asymmetries on the circulating beam for hollow electron beam scraping. Two-dimensional current-density distributions are measured in the Fermilab electron-lens test stand and are used to calculate the transverse electric field distributions for tracking simulations. The electrostatic fields generated by the injection and extraction bends in an electron lens were also estimated. A bent, 1-A, 5-keV electron beam creates nonlinear transverse integrated electric fields of the order of 10 kV. Kick maps are provided on a fine grid for 2-dimensional interpolation and as coefficients of truncated power series of orthogonal polynomials for evaluation with analytical formulas in numerical tracking codes.

REFERENCES

[1] G. Stancari et al., Phys. Rev. Lett. **107**, 084802 (2011).

[2] G. Stancari et al., in these Proceedings, FERMILAB-CONF-13-355-APC.

[3] S. Nagaitsev et al., in Proceedings of the 2012 International Particle Accelerator Conference (IPAC12), New Orleans, LA, USA, May 2012, p. 16, FERMILAB-CONF-12-247-AD; A. Valishev et al., ibid., p. 1371, FERMILAB-CONF-12-209-AD-APC.

[4] J.-L. Vay, D. P. Grote, R. H. Cohen, and A. Friedman, Comput. Sci. Disc. **5**, 014019 (2012).

[5] V. Moens, Masters Thesis, École Polytechnique Fédérale de Lausanne (EPFL), Switzerland, FERMILAB-MASTERS-2013-02 and CERN-THESIS-2013-126 (August 2013).

[6] I. Morozov et al., in Proceedings of the 2012 International Particle Accelerator Conference (IPAC12), New Orleans, LA, USA, May 2012, p. 94, FERMILAB-CONF-12-126-APC.

[7] V. Previtali et al., in Proceedings of the 2013 International Particle Accelerator Conference (IPAC13), Shanghai, China, May 2013, p. 993, FERMILAB-CONF-13-154-APC; FERMILAB-TM-2560-APC (July 2013).

[8] X. Zhang et al., Phys. Rev. ST Accel. Beams **11**, 051002 (2008).

[9] S. Li and G. Stancari, FERMILAB-TM-2542-APC (August 2012).

[10] G. Stancari, FERMILAB-FN-0972-APC (September 2013).

Copyright © 2013 CC-BY-3.0 and by the respective authors

LIMITATIONS OF INCREASING THE INTENSITY OF A RELATIVISTIC ELECTRON BEAM*

J.E. Coleman#, D.C. Moir, C.A. Ekdahl, B.T. McCuistian, J.B. Johnson, G.A. Sullivan, and M.T. Crawford, LANL, Los Alamos, NM 87545, USA

Abstract

A 7 cm cathode has been deployed for use on a 3.8 MV, 80 ns (FWHM) Blumlein, to increase the extracted beam current from the nominal 1.7 kA to 2.9 kA. The intense relativistic electron bunch is accelerated and transported through a nested solenoid and ferrite induction core lattice consisting of 64 elements, exiting the accelerator with a nominal energy of 19.8 MeV. The principal objective of these experiments is to quantify the space charge limitations on the beam quality, in addition to its coupling with the corkscrew and the beam breakup (BBU) instabilities. Time resolved centroid measurements indicate a reduction in BBU >5x with simply a 20% increase in the average B-field used to transport the beam though the accelerator. A qualitative comparison of experimental and calculated results are presented, which include axial BBU amplitude with different accelerator lattice tunes.

INTRODUCTION

Relativistic electron beams used to study fundamental nuclear physics or provide intense sources of photons are challenged with instabilities to overcome when increasing the intensity of the beam. One of particular interest is the beam breakup (BBU) instability which manifests itself as a transverse magnet coupling to destroy the beam quality. BBU was first observed in the 1960s [1] and reported in detail by Stanford Linear Accelerator Center scientists in 1968 [2]. Shortly after its discovery, BBU was studied for the first time in detail on the Advanced Test Accelerator, a linear induction accelerator [3].

The first axis of the Dual-Axis Radiography for Hydrodynamic Testing (DARHT) facility is exploring the limitations of increasing the intensity of the electron beam for future radiographic capabilities. DARHT Axis-1 is unique for these studies because it is relatively simple to change the cathode emission size to increase or reduce the total current and therefore change the space charge of the beam while holding everything else constant. In order to effectively increase the intensity of the beam, the BBU instability must be quantitatively understood and effectively reduced. Beam Position Monitors (BPMs) provided time resolved centroid and BBU measurements.

EXPERIMENTAL SETUP

The experimental configuration used to study the BBU instability was the DARHT Axis-1 linear induction accelerator (Fig. 1). The accelerator is composed of a 4 MV Blumlein injector [4] and 32 Blumleins [5] used to drive at total of 64 induction cells (2 cells per Blumlein). The linear induction accelerator is broken up into 8 cell blocks consisting of 8 ferrite induction cores in each cell block for a total of 64 induction cells and 65 anode-cathode gaps. Each induction cell has the ability to impart 250 keV of energy into the beam for a total of 16 MeV in addition to the 3.8 MeV acquired in the diode.

Beam Position Monitors

The transported beam current and centroid is monitored by BPMs at the end of each cell block and internal to each cell block, so there is a BPM every 4 cells with axial spacing between 185-224 cm. The BPMs consist of 8 B-dots, or inductive monitors, oriented azimuthally every 45°. There are 4 position B-dots, 1 top and bottom for ±y measurements and 1 left and right for ±x measurements.

The ±x and ±y B-dots in each BPM were used to measure the BBU amplitude throughout the accelerator. This was done by measuring the unintegrated Δx and Δy which was sampled up to 8 GHz. A fast Fourier transform was applied to the signal over ± 50 ns in addition to the

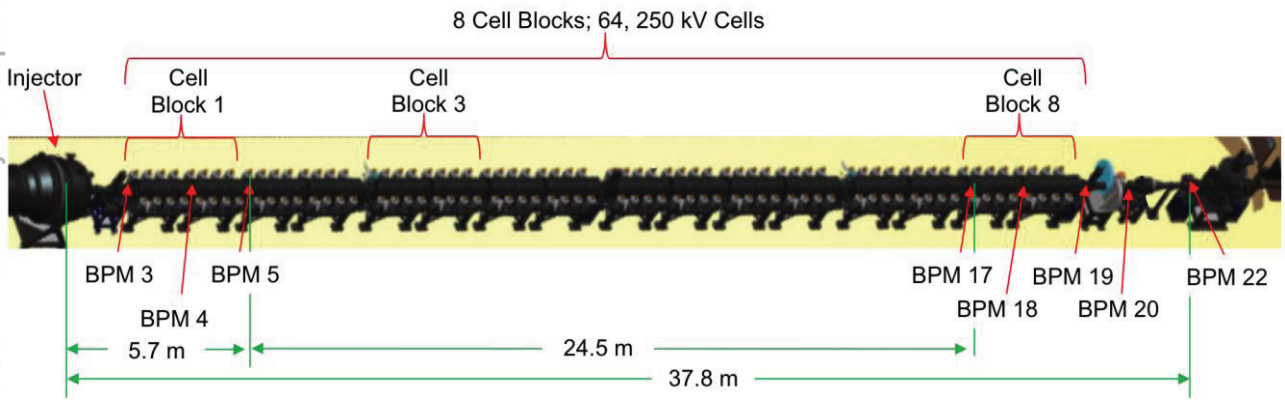


Figure 1: Model of the DARHT Axis-1 accelerator, consisting of the 4 MV injector, 64 induction cells and BPM located after every 4 cells.

* This work was supported by the National Nuclear Security Administration of the U.S. Department of Energy under contract DE-AC52-06NA25396.
#jecoleman@lanl.gov

Copyright © 2013 CC-BY-3.0 and by the respective authors

pulse length of the beam. The frequency spectrum was then integrated from 600-900 MHz to determine the BBU intensity

BEAM BREAKUP INSTABILITY

The BBU growth along the accelerator is characterized by the equation [6]:

$$\frac{\xi}{\xi_o} = \left(\frac{\gamma_o}{\gamma}\right)^{1/2} \exp\Gamma_m, \qquad (1)$$

where ξ is the measured BBU amplitude and ξ_o is the measured at the entrance of the accelerator. The amplitude decreases with acceleration to ½ power and increases exponentially with the growth factor, Γ_m

$$\Gamma_m = \frac{1}{c} I_b N_g Z_\perp \left\langle \frac{1}{B} \right\rangle, \qquad (2)$$

where c is the speed of light, I_b is the beam current, N_g is the number of gaps, $Z\perp$ is the transverse impedance, and $<1/B>$ is the average of the inverse magnetic field strength.

TRANSPORT AND BBU MEASUREMENTS

We began tuning the 2.9 kA beam envelope using the nominal tune for the 1.7 kA beam and the initial conditions measured from a sweep of the first transport magnet (Fig. 2). These measurements were also compared with calculations made with the TRAK code [7] and provided the initial conditions at z = 167 cm of a = 35 mm and a' = -17.5 mrad. Initially it was assumed because of the high space charge (K = 6 x 10^{-4}) of the beam coming out of the gun we could not converge the beam envelope too steeply because it would overfocus in the low or field-free regions between cell blocks. This first attempt is shown in Fig. 2 for Tune 4 where a gradual increase of the magnetic field from 360 G at the beginning of the first cell block to > 800 G at the end of the second cell block we were able to gradually converge the beam envelope down to ~13 mm. Evidence of the space-charge force quickly increasing the 2.9 kA beam radius between the cells is shown at z = 650 cm in Fig. 2(a). Initially only three magnets were changed in cells 8,9, and 10 to tune the envelope of the 2.9 kA beam from the nominal 1.7 kA tune, this is evident for the <B> calculated in Fig. 2(b) where there is only a slight difference after cells 5-8 (z = 572 cm) and cells 9-12 (z = 796 cm).

After initially attempting Tune 4 and examining Eqs. 1&2 it was expected that the BBU should increase by exp(2.9/1.7) ~ 5.5. However, after quickly investigating the signals on the downstream BPMs it was apparent that there was a substantial amount of BBU, which manifests itself as RF superimposed on the beam envelope. The top row of Fig. 3 shows the BBU on the raw signal of the 2.9 kA beam is ~20x higher than the 1.7 kA beam. After performing a fast Fourier transform over the 200 ns window of interest the frequency spectrum indicates nearly a ~40x increase in BBU. Both data sets indicate the BBU spectrum ranges from 700-850 MHz. Each of the cases shown here are a single shot representation of the average BBU amplitude for 5 shots.

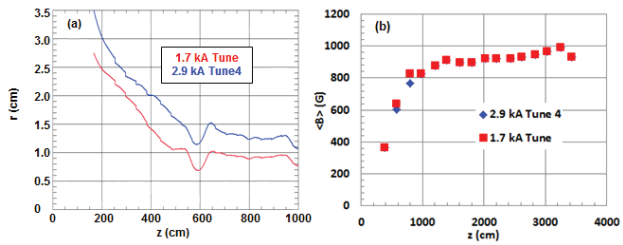


Figure 2: (a) Envelope comparison between the nominal 1.7 kA beam (red) and the first attempt at transporting the 2.9 kA beam (blue) in the first two cell blocks and; (b) <B> for 4 cells in each cell block for both tunes.

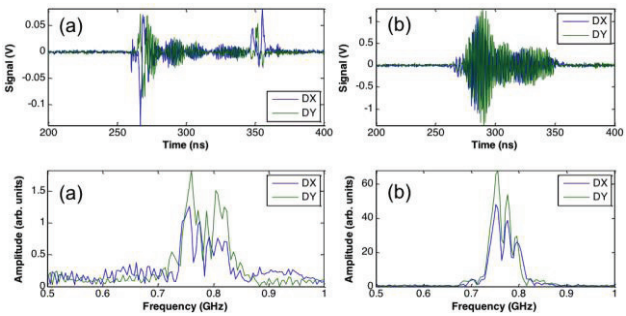


Figure 3: Top row: unintegrated Δx and Δy signals measured at BPM 20 (z = 36.1 m). Bottom row: fast Fourier transform of the signal above to indicate the amplitude and frequency of the BBU on the beam for: (a) the 1.7 kA beam; and (b) Tune 4 for the 2.9 kA beam.

A more detailed analysis made it apparent that the average BBU growth for the 2.9 kA tune was >10x higher than measured with the 1.7 kA beam (Fig. 4(a)). BBU is negligible for the nominal 1.7 kA tune until BPM07 (z = 980 cm) and the average measured value for 5 shots is $<\xi>$ = 0.044 ± 0.032. The BBU amplitude for Tune 4 matches the 1.7 kA tune at BPM07 (CB 2) and then increases ~11x the amplitude of the 1.7 kA beam at BPM09, through the 3rd cell block. The error bars in Fig. 4(a) indicate the shot to shot variation of the BBU amplitude which ranges from 10-60% depending on the amplitude and location. Over the length of the accelerator BBU increases 500x for the 1.7 kA beam and >10^3x for Tune 4, leading to factor of ~28x higher BBU for the 2.9 kA beam at BPM 20 (z = 3.6 m) (Fig. 4(b)). Direct comparison of the BBU measurements for the 1.7 kA beam with the 2.9 kA beam clearly shows $\xi_{2.9}/\xi_{1.7}$ >> exp(2.9/1.7) ~ 5.5. Applying a least squares fit to both data sets in Fig. 4(b) we are able to back out the slope of the exponential BBU growth and determine a

Copyright © 2013 CC-BY-3.0 and by the respective authors

measurement of the transverse impedance of the accelerator cells. The slopes are slightly different; the 1.7 kA data set yields 887 Ω/m and the 2.9 kA data set yields 1121 Ω/m. Each are within the measured and calculated cavity values of 400-1200 Ω/m over frequency ranges of 300-900 MHz.

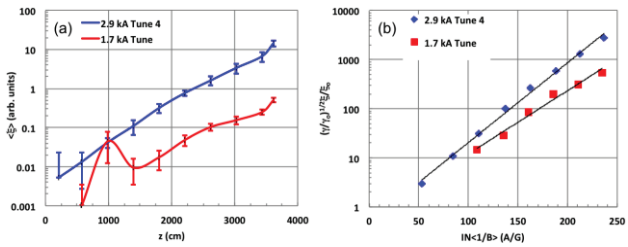


Figure 4: (a) Increase of the average BBU amplitude <ξ> over 5 shots due to the increased beam current from 1.7 (red) to 2.9 kA (blue); and (b) comparison of BBU growth along the accelerator. Each tune indicates a constant transverse impedance.

With this substantial growth in the BBU amplitude it was necessary to develop a tune with increased <B> along the length of the accelerator. The <B> in 4 cells of each cell block for each of the successive tunes and their corresponding envelopes are shown in Fig. 5. Each tune iteration brought the beam envelope down more steeply by increasing the <B> at the end of the accelerator, where the BBU amplitude was most apparent. Eventually we had to work our way upstream and begin tuning from the 1st cell block, in Tune 6, because of the lack of suppression.

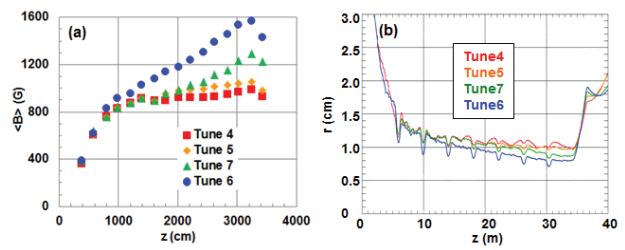


Figure 5: (a) <B> for 4 cells in each cell block used reduce BBU; and (b) the reduced 2.9 kA beam envelope for Tunes 4-7.

BBU at the upstream end of the accelerator is negligible for Tunes 5-7; it did not begin to become apparent until BPM 07 (z = 980 cm) as shown in Fig. 6(a). A reduction in <ξ> of ~5x is evident at BPMs 17-20 (z > 30 m) in Fig. 6(a) over tunes iterations from 4-6. The BBU growth along the accelerator for each successive tune is shown in Fig. 6(b). The initial BBU amplitude, ξ_o, is different for each tune contributing to the staggering of each curve. In addition the final product of growth factor, IN<1/B>, decreases for each successive tune as expected, from 237 A/G for Tune 4 to 194 A/G for Tune 6; an increase in <B> of 20%. Tune 7, which has a slightly reduced <B> compared to Tune 6, is shifted down on the BBU growth curve because its initial amplitude at BPM 7, 0.0275 >> <ξ> at BPM 7 for Tune 6. Each tune has nearly the same slope on the BBU growth curve (Fig. 6(b)) indicating the consistency in the transverse impedance of the induction cells in the accelerator lattice. The average transverse impedance for these four tunes is 1086 ± 26 Ω/m.

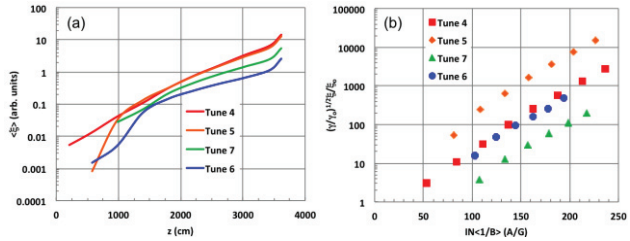


Figure 6: (a) Reduction in the average BBU amplitude, <ξ>, over 5 shots at each z-location due to the increased <B> with each successive tune; and (b) comparison of BBU growth along the accelerator for each successive tune. Each tune indicates a constant transverse impedance.

CONCLUSION

An increase in the intensity of the DARHT Axis-1 beam by 70%, with nearly the same transport lattice, lead to a ~28x increase in the final BBU amplitude. After several tune iterations, we successfully reduced the BBU amplitude 5x by simply increasing the <B> in the accelerator 20%. A more detailed explanation of these results and a further reduction in the BBU amplitude will be published elsewhere.

ACKNOWLEDGEMENT

I would like to take the opportunity to thank the DARHT Axis-1 operators and technicians James Carothers, Sam Snider, Melissa Reed, Jules Carson, Tim McCurdy, Rudy Valdez, and Edward Jacquez for their continued support.

REFERENCES

[1] M. G. Kelliher and R. Beadle, Nature 187 (1960) 1099.
[2] W.K.H. Panofsky and M. Bander, Rev. Sci. Instrum. 39 (1968) 206.
[3] G.J. Caporaso, "The control of beam dynamics in high energy induction linacs," in Proc. 1986 Linear Accel. Conf. p.17 (1986).
[4] J Fockler et al., "A 4 MV ± 1% Flat-top Electron Diode Driver," Eighth IEEE International Pulsed Power Conf., San Diego, CA, June 1991, p. 177 (1991).
[5] N.C. Jaitly et al., "Design and testing of a multi-output 300 kV prototype induction cell pulsed power supply for DARHT," Pulsed Power Conference, 1995, p. 1412 (1995).
[6] V. K. Neil, L. S. Hall, and R. K. Cooper, Particle Accel. 9 (1979) 213.
[7] S. Humphries Jr., AIP Conf. Proc. 297 (1993) 597.

Copyright © 2013 CC-BY-3.0 and by the respective authors

SYNCHROTRON RADIATION NEAR FIELD IN 3D*

C.-K. Huang#, B. E. Carlsten, and T. J. T. Kwan, Los Alamos National Laboratory,
Los Alamos, NM 87545, USA

Abstract

The Coherent Synchrotron Radiation (CSR) effect plays an important role in particle accelerators where high current electron beams are required, e.g., in X-ray Free Electron Laser. These electron beams are typically compressed to kA current in magnetic bends therefore they are subject to CSR effect. The widely used 1D CSR model relies on particle's radiation field along the circular trajectory near its present position, i.e., Green's function in 1D. We augment our previous 2D numerical CSR model by extending the synchrotron radiation near field calculation in the vertical direction. Our 3D calculation includes the dependence of the field on the relativistic beam energy through the scaled spatial variables and can be used to construct an efficient 3D CSR model due to the self-similarity of the field pattern in these variables.

INTRODUCTION

Coherent synchrotron radiation occurs in accelerators when high current beam bunches move along a circular beam path. It is a collective effect due to the coherence of the synchrotron radiation emitted by individual charge particle in the beam. As the radiation field on a particle is enhanced by the number of nearby particles if they emit coherently, the beam can undergo emittance growth or microbunching instabilities from interacting with its own coherent radiation. CSR is a major adverse effect on the performance of the FEL and has been investigated extensively in 1D and 2D [1-8]. As accurate understanding of the CSR effect requires modeling that accounts for the realistic beam shape and parameters, a 3D model will be essential and valuable. Although various CSR models have been developed so far, the most efficient and widely used models are based on a convolution approach using the time-independent longitudinal synchrotron radiation near-field, i.e., the "Green's function", of a single particle. We note that this near-field Green's function is relative to the present position of the radiating particle and in fact consists of both the near field and far field contributions from the particle at various retarded positions. Extending such CSR model into 3D requires an accurate description of the said Green's function in 3D, which is described in detail in the next two sections.

APPROXIMATE GREEN'S FUNCTION FOR RADIATION FIELD IN 2D

In this section we first review the 2D CSR model developed in Ref. [9]. This will serves as the premise of the 3D model discussed in the next section.

A diagram of the geometry is shown in Fig. 1. It is assumed that an electron is moving along a prescribed circular trajectory of radius R at constant angular velocity in the bending plane perpendicular to the magnetic field. The present and retarded positions of the particle are denoted as P and P', the corresponding velocities denoted as $\vec{\beta}$ and $\vec{\beta}'$, respectively. The field point A is represented by its coordinates (x, α) in this 2D geometry where x is the radial displacement of A relative to P and α is the angular difference between these two points.

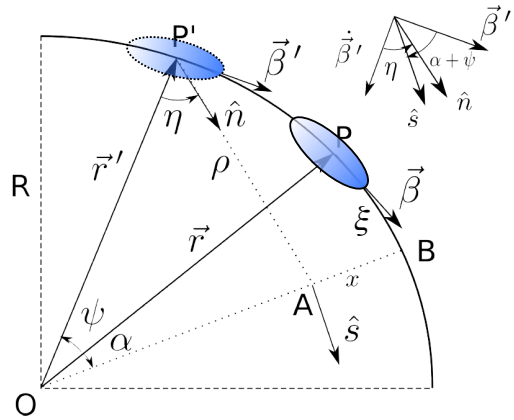


Figure 1: Geometry of the 2D model for calculating the longitudinal electric field from the synchrotron radiation of a particle in uniform circular motion. P and P' are the present and retarded positions of the particle, respectively.

The geometric relations that relate the present and retarded position of the particle are,

$$1+(1+x)^2-2(1+x)\cos(\alpha+\psi)=\psi^2/\beta^2 \qquad (1)$$

$$1+\psi^2/\beta^2-2(\psi/\beta)\cos\eta=(1+x)^2 \qquad (2)$$

where x has been normalized to R.

Using the Padé approximation

$$\cos(\zeta)\approx(1-5\zeta^2/12)/(1+\zeta^2/12)$$

and $|x|<<1$, $|\alpha|<<1$, $\psi^2<<12$, the transcendental equation Eq. (1) can be approximated as,

$$x^2+\alpha^2+2\alpha\psi+(x-\gamma^{-2}\beta^{-2})\psi^2-\psi^4/12\beta^2=0 \qquad (3)$$

After adopting the scaled variables $\tilde{x}=x\gamma^2$, $\tilde{\alpha}=\alpha\gamma^3$ and $\tilde{\psi}=\psi\gamma$, dropping the second term α^2 on the left hand side of Eq. (3) which is only important at the opposition

*Work supported by the LDRD program at LANL.
#huangck@lanl.gov

Copyright © 2013 CC-BY-3.0 and by the respective authors

direction of the forward radiation cone and β^2, this equation can be written in general form,

$$\tilde{x}^2 + 2\tilde{\alpha}\tilde{\psi} + (\tilde{x}-1)\tilde{\psi}^2 - \tilde{\psi}^4/12 = 0 \qquad (4)$$

Similarly, the longitudinal electric field from the particle's synchrotron radiation $E_s = -\partial(\phi - \beta A_s)/\partial\xi$, can be written into these scaled variables.

Since

$$(\phi - \beta A_s) = \frac{e\beta[1-\beta^2\cos(\alpha+\psi)]}{R\psi(1-\beta\sin\eta)} \qquad (5)$$

one can obtain,

$$(\phi - \beta A_s) \approx \frac{e\gamma(1+\beta\sin\eta)}{R\tilde{\psi}[1+(\tilde{\psi}/2-\tilde{x}/\tilde{\psi})^2]} \qquad (6)$$

It can be shown that $(1+\beta\sin\eta)$ weakly depends on γ in most regions at the $(\tilde{x},\ \tilde{\alpha})$ plane except for the vicinity of the negative $\tilde{\alpha}$ axis where radiation is negligible. Therefore,

$$E_s \approx \gamma^4 F(\tilde{x},\ \tilde{\alpha},\ \tilde{\psi})\ . \qquad (7)$$

Here $F(\tilde{x},\ \tilde{\alpha},\ \tilde{\psi})$ is the functional form of the longitudinal electric field that only depends on $\tilde{x}$, $\tilde{\alpha}$ and $\tilde{\psi}$. We can then introduce the normalization of the electric field $\tilde{E}_s = E_s/(e\gamma^4/R^2)$ which reveals its amplitude scaling with the particle's energy.

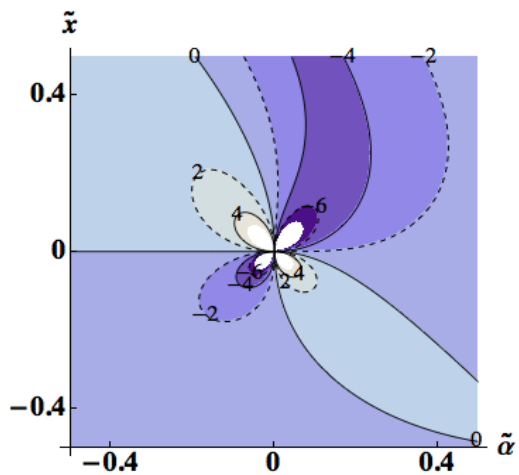


Figure 2: The general near field pattern of the longitudinal synchrotron radiation electric field in 2D for a particle in uniform circular motion.

Since $\tilde{\psi}$ implicitly depends on $\tilde{x}$, $\tilde{\alpha}$ from Eq. (4), Eq. (7) indicate that the longitudinal synchrotron radiation near field can be obtained, to a good approximation, from the invariant (with respect to γ) function $F(\tilde{x},\ \tilde{\alpha},\ \tilde{\psi}(\tilde{x},\ \tilde{\alpha}))$ with the proper scaling of the spatial variables and amplitude with the particle's energy.

Figure 2 shows the longitudinal electric field $\tilde{E}_s = E_s/(e\gamma^4/R^2)$ as a function of $\tilde{x}$, $\tilde{\alpha}$. The field's amplitude is large along the four diagonal directions, forming a cloverleaf like pattern. While the fields quickly decreases along the other three diagonal directions, it extends to far greater distance in the top-right corner as shown in Fig. 2.

APPROXIMATE GREEN'S FUNCTION FOR RADIATION FIELD IN 3D

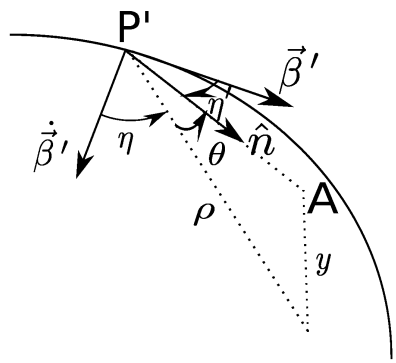


Figure 3: Schematic for the calculation in 3D.

We are now ready to extend the above result to 3D. In 3D, the position of field point A is denoted by its coordinates in the bending plane (x, α) and its vertical displacement y from this plane. Figure 3 shows the position of A and the angles it forms with respect to P'.

It is straightforward to show that in 3D Eq. (1) and (2) become,

$$1 + (1+x)^2 - 2(1+x)\cos(\alpha+\psi) = \psi^2/\beta^2 - y^2, \qquad (8)$$

$$1 + (\psi^2/\beta^2 - y^2) - 2\sqrt{\psi^2/\beta^2 - y^2}\cos\eta = (1+x)^2, \qquad (9)$$

where y is also normalized to R.

Since x^2 and y^2 appear together in Eq. (8) and (9), one can treat x and y similarly and define scaled variable $\tilde{y} = y\gamma^2$. With this scaled variable, Eq. (4) becomes,

$$\tilde{x}^2 + \tilde{y}^2 + 2\tilde{\alpha}\tilde{\psi} + (\tilde{x}-1)\tilde{\psi}^2 - \tilde{\psi}^4/12 = 0\,. \qquad (10)$$

In 3D, the unit vector $\hat{n}$ is not necessarily in the bending plane, thus $\hat{n}\cdot\vec{\beta}' = \beta\cos\eta' = \beta\sin\eta\cos\theta$. Hence,

$$(\phi - \beta A_s) = \frac{e\beta[1-\beta^2\cos(\alpha+\psi)]}{R\psi(1-\beta\sin\eta\cos\theta)}\ . \qquad (11)$$

Next we consider the $[1-\beta^2\cos(\alpha+\psi)]$ term and the $(1-\beta\sin\eta\cos\theta)^{-1}$ term in Eq. (11) separately. It is easy to show,

Copyright © 2013 CC-BY-3.0 and by the respective authors

$$1-\beta^2\cos(\alpha+\psi)=\gamma^{-2}\left[1-\frac{(\tilde{x}^2+\tilde{y}^2)\beta^2\gamma^{-2}-\tilde{\psi}^2}{2(1+\tilde{x}\gamma^{-2})}\right]\approx\gamma^{-2}, \quad (12)$$

and

$$(1-\beta\sin\eta\cos\theta)^{-1}=(1+\beta\sin\eta\cos\theta)(1-\beta^2\sin^2\eta\cos^2\theta)^{-1} \quad (13)$$

The first term on the right hand side of Eq. (13) varies slowly with particle energy and is bounded, $0\le(1+\beta\sin\eta\cos\theta)\le 2$. The second term can be further simplified using the following relation,

$$\gamma\beta\cos\eta\cos\theta=\gamma\psi/2-\gamma\beta^2(2x+x^2+y^2)/2\psi\approx\tilde{\psi}/2-\tilde{x}/\tilde{\psi} \quad (14)$$

leading to,

$$1-\beta^2\sin^2\eta\cos^2\theta\approx\gamma^{-2}\left[1+\tilde{y}^2/\tilde{\psi}^2+(\tilde{\psi}/2-\tilde{x}/\tilde{\psi})^2\right]. \quad (15)$$

With the above simplification, Eq. (11) reduces to a form akin to Eq. (6),

$$(\phi-\beta A_s)\approx\frac{e\gamma(1+\beta\sin\eta\cos\theta)}{R\tilde{\psi}[1+\tilde{y}^2/\tilde{\psi}^2+(\tilde{\psi}/2-\tilde{x}/\tilde{\psi})^2]}. \quad (16)$$

Therefore, in 3D, the functional form of Eq. (7) becomes

$$E_s\approx\gamma^4 G(\tilde{x},\ \tilde{y},\ \tilde{\alpha},\ \tilde{\psi}). \quad (17)$$

From the Liénard-Wiechert formula, the longitudinal radiation field is given by,

$$E_s=\frac{e}{c\rho}\cdot\frac{(\hat{n}\cdot\dot{\vec{\beta}}')(\hat{n}\cdot\hat{s}-\vec{\beta}'\cdot\hat{s})-(\hat{s}\cdot\dot{\vec{\beta}}')(1-\hat{n}\cdot\vec{\beta}')}{(1-\hat{n}\cdot\vec{\beta}')^3}. \quad (18)$$

After the retarded angle $\tilde{\psi}$ is solved from Eq. (10), one can use the following identities,

$$\hat{n}\cdot\vec{\beta}'=\beta\sin\eta\cos\theta,\ \hat{n}\cdot\dot{\vec{\beta}}'=(\beta^2 c\cos\eta\cos\theta)/R,\ \hat{n}\cdot\hat{s}=\sin(\alpha+\psi+\eta)\cos\theta \quad (19)$$

Eq. (18) becomes,

$$\tilde{E}_s=\frac{\beta^3}{\gamma^4\psi(1-\beta\sin\eta\cos\theta)^3}\cdot[(\sin\eta-\beta\cos\theta)\cdot\cos(\alpha+\psi+\eta)-\sin^2\theta\sin(\alpha+\psi+\eta)\cos\eta] \quad (20)$$

Figure 4 shows $\tilde{E}_s$ as a function of $\tilde{y}$ and $\tilde{\alpha}$ for $\tilde{x}=0$. It should be noted that the radiation field is strongest in the forward direction within a ~ 45 degree cone in the scaled variables $\tilde{y}$ and $\tilde{\alpha}$, which is consistent with the well-known $1/\gamma$ radiation cone in the un-scaled spatial variables. This also implies that for a beam that is sufficiently large in the vertical y direction, both the 1D and 2D models in the $(\tilde{x},\tilde{\alpha})$ plane will overestimate the longitudinal CSR force.

Similar to our previous 2D CSR model [9], the calculation presented here can be done once and applied to a range of beam parameters. The key to such flexibility is the recognition of the self-similarity of the radiation field in three spatial dimensions through the scaled variables. This follows the pioneering work in one spatial dimension by several other authors [5,6]. However, due to the complex radiation field pattern in 3D, it is rather difficult to derive an analytic formula for such field in the identified scaled variables. Numerical calculation for the 3D radiation field of a single particle is generally necessary and possible, as demonstrated in this paper, whose result can then be used to construct a 3D CSR model through the convolution with the beam shape.

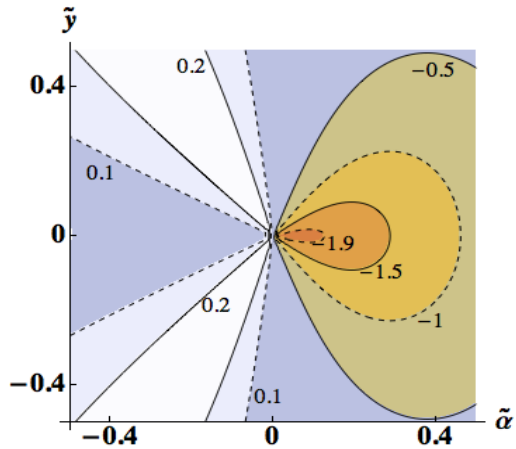


Figure 4: Longitudinal radiation field pattern for a highly relativistic in the vertical $(\tilde{y},\ \tilde{\alpha})$ plane at $\tilde{x}=0$.

ACKNOWLEDGMENT

We acknowledge useful discussion with Dr. N. Yampolsky and Dr. R. Ryne.

REFERENCES

[1] R. Li, Phys. Rev. ST-AB, 11, 024401 (2008).
[2] G. Bassi et al., Phys. Rev. ST-AB, 12, 080704 (2009).
[3] D. Gillingham et al., Phys. Rev. ST-AB, 10, 054402 (2007).
[4] A. Novokhatski, Phys. Rev. ST-AB, 14, 060707 (2011).
[5] J. Murphy et al., Part. Accel., 57, 9 (1997).
[6] E. Saldin et al., NIMA, 398, 373 (1997).
[7] C. Mayes et al., Phys. Rev. ST-AB 12, 024401 (2009).
[8] D. Sagan et al., Phys. Rev. ST-AB 12, 040703 (2009).
[9] C.-K. Huang et al., Phys. Rev. ST-AB, 16, 010701 (2013).

Copyright © 2013 CC-BY-3.0 and by the respective authors

EXPERIMENTAL VERIFICATION OF DIPOLE EDGE FOCUSING IN LINEAR MODEL BY OPERATING IN THE WEAK FOCUSING REGIME AT THE LOS ALAMOS PROTON STORAGE RING*

J. Kolski†, D. Barlow, R. Macek, and T. Spickermann, LANL, Los Alamos, NM, 87545, USA

Abstract

Linear optics models are important for the operation of circular accelerators because of their ability to predict the linear lattice functions, primarily betatron amplitude functions and betatron tunes. The accuracy of the liner model's prediction is dependent on how well the real machine's focusing lattice is known and represented. While quadrupoles may be mapped magnetically and their focusing properties well understood, the focusing effect due to dipole edge fields is less certain. For rings with rectangular dipoles like the Proton Storage Ring (PSR) at Los Alamos National Laboratory, the dipole edge focusing can be a significant contributor to the vertical focusing. Most accelerator modeling codes, like MAD and AT (Accelerator Toolbox), use the K. Brown formulation[1], but this approach can lead to errors ∼10% in the models betatron tune prediction[2]. Here we discuss particle tracking through simulated dipole fields, including edge effects, with TOSCA 3D to obtain the focal lengths of the edge focusing. We verify model and focal lengths by operating the PSR in the weak focusing regime (without vertically focusing quadrupoles) and show that the model predicts the betatron amplitude functions and tunes even in this unusual operating condition.

INTRODUCTION

The PSR is a 90 m circumference circular accelerator with broken ten-fold FODO cell symmetry, which occurs in the injection section (top of Fig. 1). While most cells have a 36° dipole magnet (SRBM), the injection section starts with a SRBM-type dipole that is shunted by 100 A (SRBM01) to allow room for RIBM09, which merges H- beam with the circulating H+ beam for charge-exchange injection. The dipole at the beginning of the next cell is replaced with two large gapped C-magnets (SRBM11 and SRBM12) accommodating a dump line. Relevant parameters for the five PSR dipoles types are listed in Tab. 1.

All PSR dipoles are rectangular, so including a good representation of the edge focusing is very important for the PSR linear model. There are three parameters in the edge focusing model: gap width, edge angle, and the fringe field integral (FINT) defined by

$$\kappa = \int_{-\infty}^{\infty} \frac{B_0 B_y(s) - B_y^2(s)}{g B_0^2} ds \qquad (1)$$

* Work supported by in part by United States Department of Energy under contract DE-AC52-06NA25396. LA-UR 13-27451.

† Electronic address: jkolski@lanl.gov

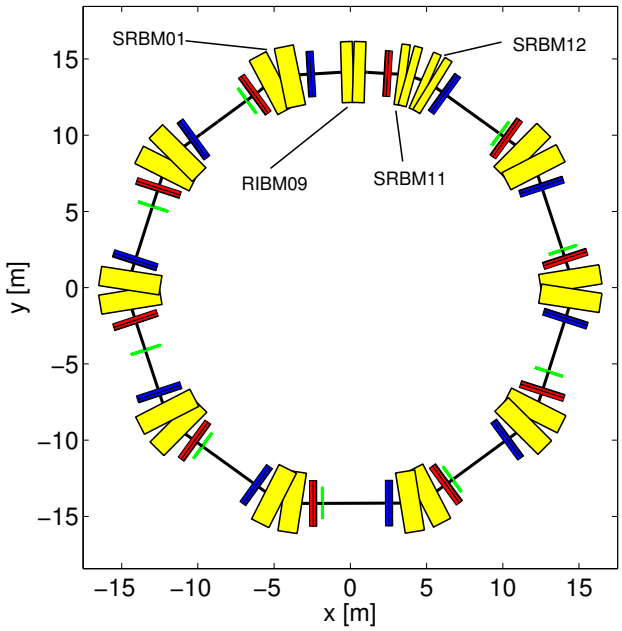


Figure 1: (Color) PSR model: dipoles (yellow) split into two model elements, focusing and defocusing quads (blue and red respectively), and vertical steering magnets (green).

Type	l [m]	θ°	$\theta/2$°	g [cm]
SRBM	2.550	36	18	10.478
RIBM09	1.553	6.8	3.4	12.852
SRBM01	2.542	32.8	11.9	10.478
SRBM11	1.095	16.2	8.1	18.059
SRBM12	1.080	16.2	8.1	12.852

Table 1: Five types of PSR rectangular dipoles.

and related to the edge focusing focal length by

$$\frac{1}{f} = \frac{1}{\rho} \tan\left(\frac{\theta}{2} - \psi\right), \qquad (2)$$

where

$$\psi = \frac{g\kappa}{\rho} \sec\left(\frac{\theta}{2}\right)\left(1 + \sin^2\frac{\theta}{2}\right). \qquad (3)$$

The initial (or baseline) PSR model uses gap width and edge angles from physical measurements and FINT based on applying Eq. (1) to results of a TOSCA 3D magnet field

Copyright © 2013 CC-BY-3.0 and by the respective authors

	Measured	Baseline	Improved
Horizontal	$3.2266 \pm 9 \times 10^{-4}$	3.2216	3.2251
Vertical	$2.2192 \pm 4 \times 10^{-4}$	2.2642	2.2154

Table 2: Betatron tunes from baseline and improved models and measurement.

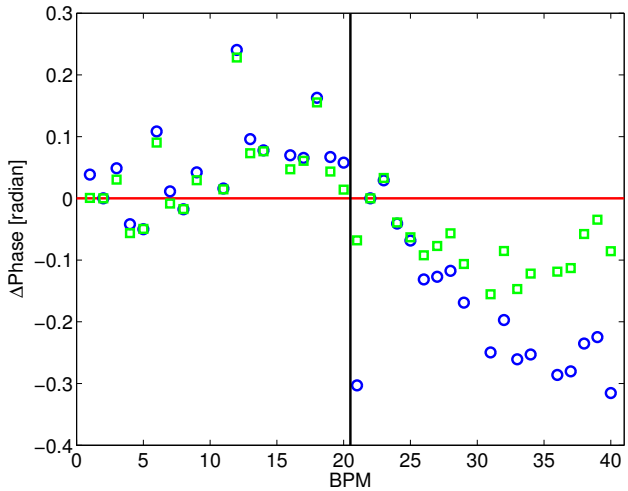


Figure 2: (Color) Difference between measured and baseline (blue) and improved (green) model phase advance from the first BPM after injection (2 and 22). ORM BPM indexing convention is used: horizontal BPMs (1-20), vertical BPMs (21-40) such that BPM 2 and 22 are the horizontal and vertical planes of first BPM after injection.

simulation to determine the dipole edge focusing. The resulting betatron tunes from the baseline model are compared with measurement in Tab. 2. We note that the vertical tune difference between baseline model and measurement is not good, 0.05. To understand the origin of the vertical tune difference between baseline model and measurement, we plot the difference between measured and baseline model phase advance in Fig. 2. Note the vertical phase demonstrates a systematically increasing phase difference between baseline model and measurement. We conclude that the baseline model systematically over focuses vertically. Since the baseline model horizontal tune result is good, we concentrate our model improvement efforts on the only model element that effects vertical and not horizontal focusing: the rectangular dipole edge focusing.

RAY TRACING THROUGH THE FRINGE FIELDS

Ultimately, the most important part in considering fringe fields from rectangular dipoles is obtaining the edge focusing focal length. To determine the edge focusing focal length, we traced on-momentum parallel rays through 3D magnetic field from TOSCA simulations of the PSR dipoles. The parallel rays were initially positioned on a 4×4 cm transverse grid with a ray every centimeter at

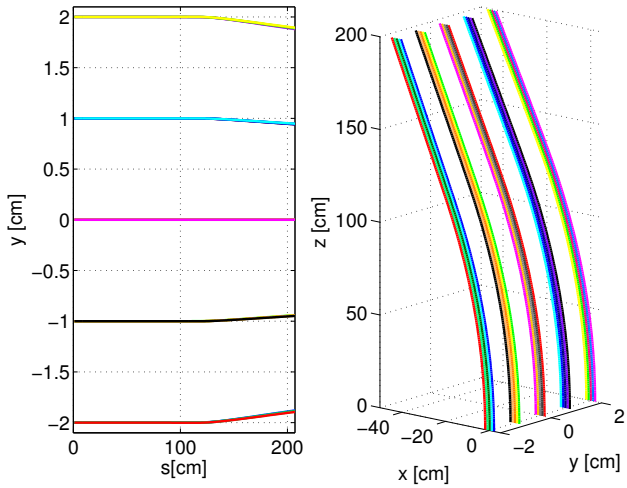


Figure 3: (Color) (Left) Rays' vertical position as a function of longitudinal coordinate, which encounter edge focusing $s \simeq 120$ cm. (Right) Ray position in the magnet-based coordinate system.

Magnet	Focal Length [m]		Fringe Field Integral	
	Baseline	Improved	Baseline	Improved
SRBM	13.208	13.733	.54150	.90291
SRBM01	13.208	13.733	.54150	1.2908
SRBM11	32.186	32.389	.44940	.46491
SRBM12	30.823	30.889	.51930	.52685
RIBM09	234.17	238.96	.35790	.47085

Table 3: The edge focusing focal length and FINT for each type of PSR horizontal bender from the baseline and improved models.

the longitudinal center of the dipole and traced through the downstream half of the PSR dipoles, Fig. 3. The fringe field focal length can be calculated from the ray tracing data for each of the PSR rectangular dipole types.

We can reverse engineer the K. Brown model of edge focusing, Eqs. (1) to (3), to produce the focal length calculated from the ray tracing data. We choose to modify the FINT parameter because the gap width and edge angle are physical parameters. In Tab. 3, we compare the edge focusing focal length and FINT from ray tracing, which we will call improved model, explained later, and the baseline model. Note the that the baseline model edge focusing focal lengths are systematically smaller than from ray tracing with the largest fractional difference in the SRBM and SRBM01 type dipoles. This is the cause of the vertical over focusing in the baseline model.

We construct an improved model using the FINT parameter determined by the ray tracing data and compare it with measurement in Tab. 2 and Fig. 2. Note the improved model has a much better prediction of the vertical tune and little systematic phase advance difference.

Copyright © 2013 CC-BY-3.0 and by the respective authors

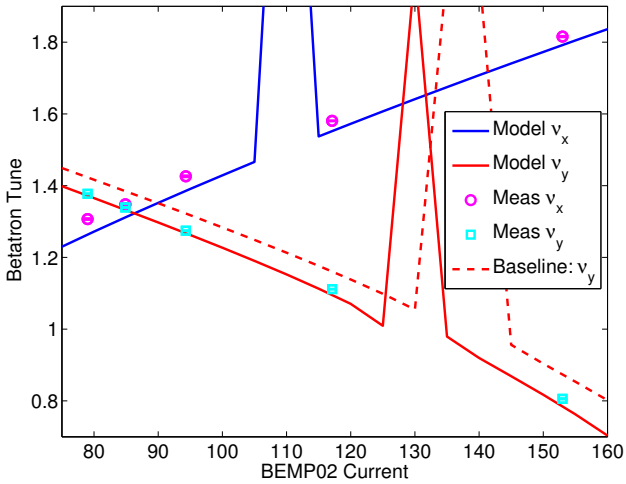


Figure 4: (Color) Model and measured tunes as a function of horizontal focusing quadrupole current: measured tunes (horizontal: magenta circles and vertical: cyan squares), model tunes (horizontal: blue line, and vertical baseline: dashed red line, vertical improved: solid red line).

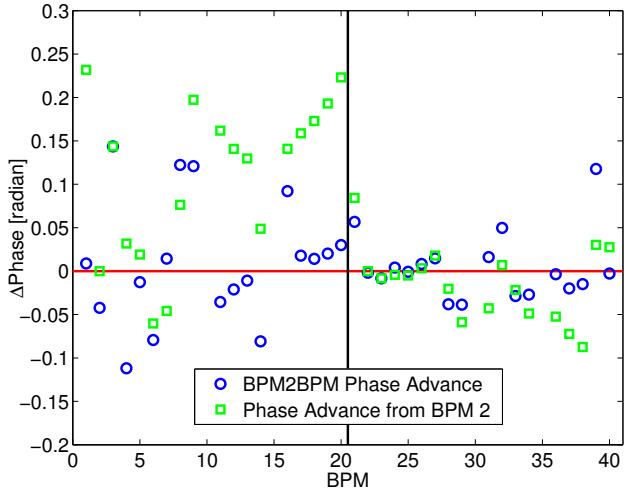


Figure 5: (Color) Difference in phase advance from the first BPM after injection (BPM 2 and 22, green) and the difference in BPM-to-BPM phase advance (blue) between measured and improved model at focusing quadrupole current 89.4 A. ORM BPM indexing convention is used as described in Fig. 2.

OPERATING THE PSR IN THE WEAK FOCUSING REGIME

The improved model uses an engineered FINT to produce the edge focusing focal lengths calculated from the ray tracing data. The edge focal focal length was not actually measured. Can we make a more direct, physical measurement? To isolate the edge focusing in a beam-based measurement, we operate the PSR with the vertically focusing quadrupoles at 0 A. To provide stable beam with this set up, the horizontally focusing quadrupole current (BEMP02) needs to be dramatically reduced so as to not overcome the edge focusing in the vertical. The improved model indicates that there are several regions of transverse stability, Fig. 4.

We measured the betatron tune at several stable points with reduced horizontally focusing quadrupole current and compared them with predictions from the improved model, Fig. 4. Note that even with the vertically focusing quadrupoles turned off, the improved model does a decent job at reproducing the measured vertical tunes, much better than the baseline model. Of course, we would like the model to yield closer results. Also note the greater discrepancy between the measured and model horizontal tune, as much as 0.03. This may be an indication that the current to gradient length conversions used in the model for the horizontally focusing quadrupoles do not work well due to a lack of magnet mapping data for such low currents and that we need to add the residual field effect in the vertically focusing quadrupoles.

Figure 5 compares the measured and model phase for horizontally focusing quadrupole current 89.4 A. Note in the vertical, both the phase advance from the first BPM after injection and the BPM-to-BPM phase advance deviation between the improved model and measurement is much smaller than in the horizontal.

We need to refine the improved model horizontal tune and phase predictions prior to fitting the edge focusing in the vertical. In continuing studies, we intend to fit the horizontally focusing quadrupole strengths to the measured horizontal tunes and then fit the FINT for each of the five PSR rectangular dipole types to match the measured vertical phase advance. Because the improved model performs well for normal operating conditions, we expect only a few percent adjustment to refine the improved model FINT.

CONCLUSIONS

We corrected the PSR linear model by engineering the FINT to yield the same focal length as found by tracing parallel rays through 3D magnetic fields resulting from TOSCA simulations. We compared linear lattice functions predicted by the improved model with measurement, in particular the betatron tune and phase advance. Although the improved model is better than the baseline model, we realize that we did not directly measure the FINT. To isolate the edge focusing in measurement, we operate the PSR without vertically focusing quadrupoles. We compare improved model predictions with measurements of the tune and find the model reproduces the measured vertical tunes well but not the horizontal. We need to correct the horizontal model before we can reliably fit the FINT.

REFERENCES

[1] K.L. Brown, SLAC-75 (1967).

[2] J. Kolski, Ph.D. thesis, unpublished (Indiana University 2010).

Copyright © 2013 CC-BY-3.0 and by the respective authors

COHERENT SPACE CHARGE TUNE SHIFT MEASUREMENTS IN THE LOS ALAMOS PROTON STORAGE RING*

J. Kolski†, R. Macek, and T. Spickermann, LANL, Los Alamos, NM, 87545, USA

Abstract

The coherent space charge tune shift describes the average frequency shift experienced by particles due to the effects of the beam's image charge and current and is proportional to the instantaneous beam current. For long beam pulses like the 290 ns long accumulated beam bunch in the Los Alamos Proton Storage Ring (PSR), we can observe the change in the coherent space charge tune shift longitudinally along the pulse. We measure an asymmetric betatron tune profile about the bunch center even though the beam current profile is symmetric about the peak intensity. In addition, we observe the coherent space charge tune shift to vary as a function of turn during a store. Quality measurements of the coherent space charge tune shift may provide a unique handle on interesting physics including wake field effects and electron cloud (EC) buildup. We digitize the vertical sum and difference signals from a beam position monitor, stack the digitized vector turn-by-turn, and fit the tune for each slice (0.5 ns digitization bin) along the pulse after a single-turn vertical kick. We compare the difference between the measured/fitted tune and the measured bare tune with the theoretical tune shift and infer a charge neutralization, which we relate to the EC density along the pulse and buildup in turn number.

INTRODUCTION

The coherent space charge tune shift (measured tune − bare tune) is due to image charge and current effects[1, 2],

$$\Delta\nu_y = -\frac{r_p N}{\pi\beta^2\gamma}\left[\frac{\bar{\beta}_y(\text{ring})}{2\gamma^2 B_f h^2}(1-\eta)+\frac{\pi^2\beta^2 C_2\bar{\beta}_y(\text{bend})}{24g^2}\right], \quad (1)$$

where r_p and N are the classical proton radius, number of protons, β and γ are the relativistic Lorentz factors, $\bar{\beta}_y$ is the average beta function either around the ring or in the dipoles, and B_f, h, η, C_2, and g are the bunching factor (average / peak or instantaneous current), beam pipe radius, beam neutralization, fraction of circumference occupied by dipoles, and the dipole half gap respectively. The first term in Eq. (1) describes the dependence of the coherent tune shift on the instantaneous current, while the second term relates the contribution from the average current. For the PSR, the second contributes ∼15% to the tune shift[1].

We construct a simple simulation of the coherent space charge tune shift using the model in Eq. (1) and a measured beam profile, Fig. 1. To match our measurements (described later), we divide the beam longitudinally into 0.5 ns slices. Initially the simulated beam centroid is offset transversely to produce coherent betatron oscillation, then the transverse beam centroid position is tracked for 420 turns. The FFT along turn for each slice's position yields the tune. The simulation results in a symmetric tune distribution along the bunch as expected because the beam

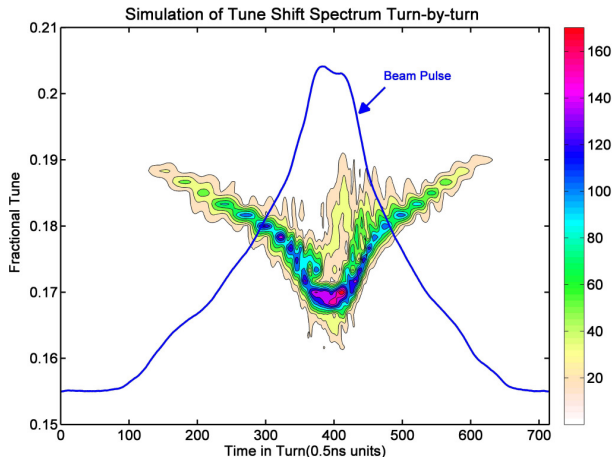


Figure 1: (Color) Simulation of tune distribution along the pulse using coherent space charge tune shift model Eq. (1) (contour) and measured longitudinal beam profile (blue line).

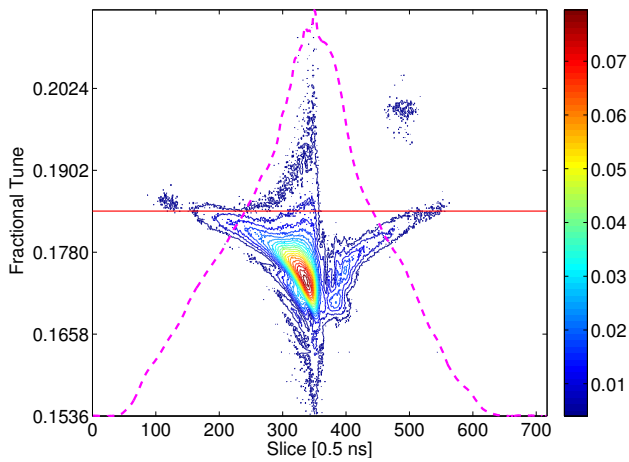


Figure 2: (Color) Measured tune distribution along the pulse (contour) and the last turn beam profile (dashed magenta line).

* Work supported by in part by United States Department of Energy under contract DE-AC52-06NA25396. LA-UR 13-27452.

† Electronic address: jkolski@lanl.gov

Copyright © 2013 CC-BY-3.0 and by the respective authors

profile is symmetric about the peak. Compare simulation with the measured coherent tune shift along the bunch, Fig. 2. Note that the measured tune distribution has much larger spread for slices on the leading edge than in simulation. This is because the tune for these slices is actually changing over the domain of the FFT.

From the model, we expect a symmetric tune distribution about the center of the bunch because the beam profile is symmetric about the bunch, but the measured tune distribution along the bunch is asymmetric about the bunch center. Note, the greatest discrepancy between model and measurement, particularly the magnitude of the tune FFT, occurs on the trailing edge. The difference could be due to many physical effects not included in the simple coherent space charge tune shift model of Eq. (1): EC multipactoring and neutralization, wake fields, etc. A recent study from Cornell[3] relates the coherent tune shift to beam neutralization due to the EC and changing tune shift along a train of bunches to EC build up. We will concentrate our efforts on determining the EC density.

The PSR is a harmonic one machine with only one beam bunch in the ring. For the purposes of EC buildup, the PSR beam can be thought of as a train of 100s - 1000s of bunches, so we may be able to relate changing coherent tune shift turn-by-turn to EC buildup. The PSR bunch is also a long 290 ns bunch, so we may be able to relate different coherent tune shifts along the bunch to EC density variations and gain insight into pinch dynamics and multipactoring of the EC.

MEASUREMENT AND ANALYSIS

To observe the coherent space charge tune shift, the beam must undergo coherent transverse motion, which we induce using a single-turn kick during a beam store after accumulation. The beam store is typically 200 - 400 μs. We digitize beam position and current signals at 2 GS/s (0.5 ns binning). Each digitization bin is a slice along the bunch. The digitized signal is stacked turn-by-turn such that all data for one slice is in the same row of the data matrix [# of slices, # of turns]. FFTs of data for each slice produced the contour in Fig. 2.

Hundreds of turns are required for precise frequency results from an FFT. The tune changes much faster, so we fit the position to a cosine to obtain the tune,

$$x_n = A\cos\left(2\pi\nu(n-1)+\phi\right)+O, \qquad (2)$$

where A, ν, n, ϕ, O are the amplitude, tune, turn index, phase, and offset respectively. To observe the tune change as a function of turn for each slice, we fit 30 turns. We step the domain of each successive fit by 10 turns to smooth the tune change as a function of turn. The tune fit is very good, typically yielding a fitting uncertainty $\sim 10^{-3}$.

We observe small but measurable changes in the tune as a function of turn number. Figure 3 shows the fitted tune as a function of fit number for slice 300. It is clear that we can measure a changing tune, but we are really interested in observing a change in beam neutralization.

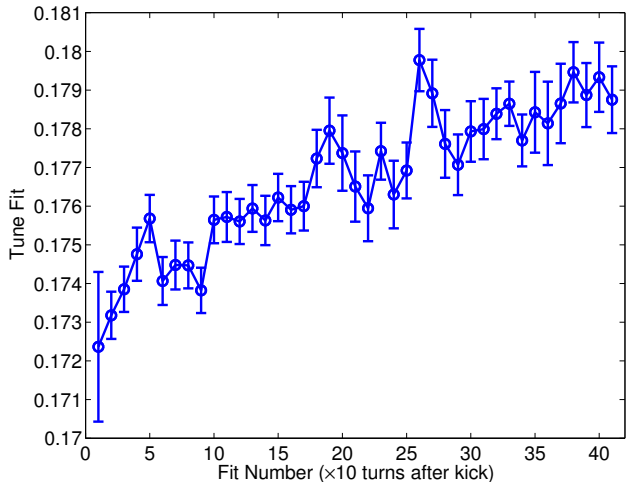


Figure 3: Fitted tune as a function of fit number (10 turn steps) after a single-turn kick for slice 300 (∼25 ns in front of the peak) with one rms fitting uncertainty.

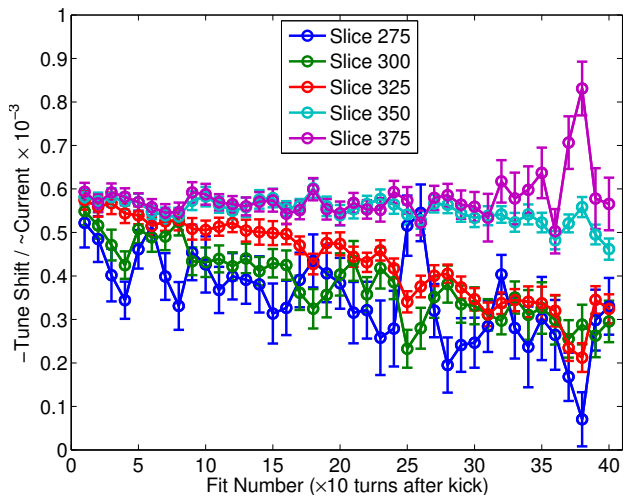


Figure 4: (Color) Normalized tune shift as a function of fit number for several slices along the bunch with one rms uncertainty. Slice 350 is the center of the bunch.

For the preliminary analysis and results reported in this paper, we note that the coherent space charge tune shift for a slice is proportional to the instantaneous current and simply normalize the measured tune shift for a slice to the average current during the fit for the slice to obtain a quantity proportional to the neutralization. If we observe the normalized tune shift measurably vary, we can conclude that the beam neutralization varies as well. We plot the normalized tune shift verses fit number for several slices in Fig. 4. The trend in the normalized tune shift is different for each time slice along the bunch. Note the normalized tune shift for slices 325 and 375, which are symmetric about the peak, has distinctly different slopes. We observe a steeper trend for slices located in front of the peak and observe lit-

Copyright © 2013 CC-BY-3.0 and by the respective authors

tle change in the slices on the trailing edge, which is similar to the measured tune distribution in Fig. 2.

Because the PSR bunch is a long 290 ns, in this measurement, we can also observe the measured normalized tune shift for each slice along the bunch as a function of fit number (turn number), Figs. 5 and 6.

Figure 5 plots the results for a bunched PSR production-like beam. Note the first fit after the single-turn kick yields a consistent normalized tune shift along the bunch. This is as expected if the neutralization along the bunch is constant. The structure along the bunch of the normalized tune shift is much more complicated 400 turns later. Note again the difference between leading and trailing edge. There are low frequency oscillations on the leading edge and high frequency oscillations on the trailing edge. This may be an indication of EC density variation along the long PSR bunch with EC pinch dynamics on the leading edge and multipactoring on the trailing edge.

Figure 6 plots the results for an accumulated bunched coasting beam with RF buncher off. Again, we observe for the first fit after the single-turn kick a constant normalized tune shift. Also notice the structure in the last fit, 800 turns after the single-turn kick. The spikes on the trailing edge start growing about 600 turns after the single-turn kick. Since the RF buncher is off, there is considerable beam in the gap between turns. This provides a very different beam potential that effects both EC pinch dynamics and multipactoring.

CONCLUSIONS

We measured the coherent space charge tune shift in the PSR. We digitized beam position and current signals at 2 GS/s, where each 0.5 ns digitization bin constitutes a slice longitudinally along the beam, stacked the beam signal turn-by-turn, and took an FFT along position for each slice to obtain the tune. We induced coherent transverse motion with a single-turn kick during a beam store after accumulation. We compared model and simulated tune distributions along the pulse and found the measured tune distribution was asymmetric about the peak even though the beam profile was symmetric.

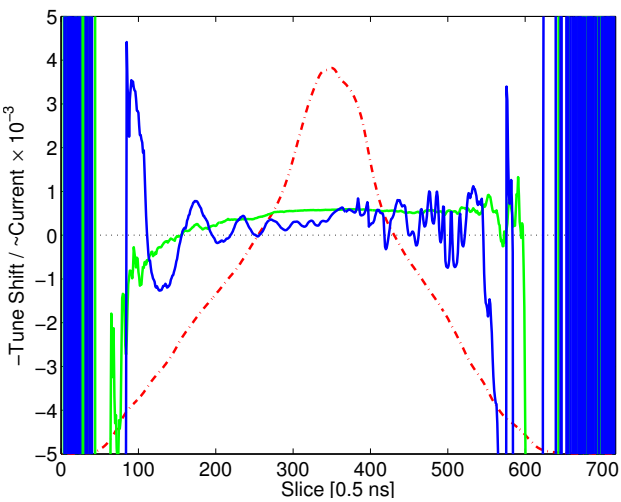


Figure 5: (Color) The measured normalized tune shift immediately after the single-turn kick (green) and 400 turns later (blue) as a function of slice along the bunch for bunched production-like beam with the RF buncher on and the last turn beam profile (red).

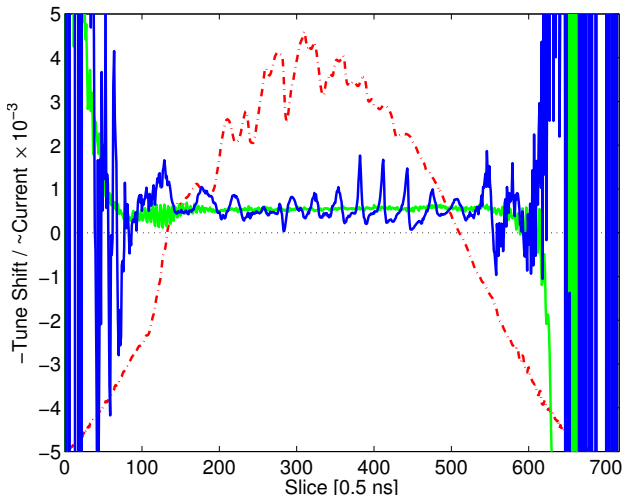


Figure 6: (Color) The measured normalized tune shift immediately after the single-turn kick (green) and 800 turns later (blue) as a function of slice along the bunch for bunched coasting beam with RF buncher off and the last turn beam profile (red).

We show the ability to measure small changes in the tune shift as a function of slices along the bunch and turns by fitting 30 turns of beam position to a cosine. When we take into account the instantaneous current, we observe a quantity proportional to beam neutralization that also varies with turn and slice along the bunch indicating EC density variations.

We have not positively identified the changing tune shift to be neutralization due to the EC. Further work to be done includes acquiring coherent space charge tune shift data at different beam intensities and bunch lengths and using Eq. (1) in the analysis to solve directly for the beam neutralization instead of simply normalizing the tune shift to the instantaneous beam current.

REFERENCES

[1] R. Macek, Log of the analysis of beam response to 1-turn kick Oct 9, 2006, 1/14/08, 1/15/08 draft (Unpublished).

[2] G. Giugnard, CERN 77-10 (1977).

[3] G. Dugan, M. Billing, et. al., Proceedings of IPAC2012, New Orleans, Louisiana, USA, WEYA02.

Copyright © 2013 CC-BY-3.0 and by the respective authors

PERFORMANCE COMPARISONS OF EMITTANCE-EXCHANGER BEAMLINES *

C.R. Prokop [1], P. Piot [1,2], B.E. Carlsten [3], M. Church[2]
[1] Department of Physics, Northern Illinois University DeKalb, IL 60115, USA
[2] Fermi National Accelerator Laboratory, Batavia, IL 60510, USA
[3] Los Alamos National Laboratory, Los Alamos, NM, 87544, USA

Abstract

Earlier experiments at Fermilab's A0 Photoinjector Laboratory demonstrated successful transverse-to-longitudinal emittance exchange (EEX) using a transverse-deflecting cavity (TDC) located between two identical doglegs. Such a design has the disadvantage of transversely displacing the beam. An alternative is an EEX beamline designed out of a variable R_{56} bunch compressor chicane. In this paper, we present designs and simulation comparisons for several emittance-exchanger beamlines, including the double-dogleg and chicane designs, as well as variations of the chicane design that allow for increasing its dispersion which proportionally decreases the field-strength requirements on the TDC. These comparisons are performed with PIC models of space charge and coherent synchrotron radiation.

INTRODUCTION

Transverse-to-longitudinal "emittance exchangers" (EEXs) allow for the exchange of a particle beam's transverse and longitudinal phase spaces. [1, 2] An early emittance exchanger design consisting of a transverse deflecting cavity (TDC) between two identical doglegs, each comprised of two opposite dipoles and a drift, was demonstrated at Fermilab's A0 Photoinjector Laboratory [3, 4]. A major disadvantage of such a configuration is its resulting offset of the beam's direction, which has significant impact on linac design as an elaborate dispersion correction scheme would be needed to operate the beamline in its non emittance-exchanging configuration.

A modification of the original design, based on a variable-R_{65} chicane, allows for the exiting beam to remain in-line with the incoming beam [5]. Furthermore, this design allows for almost-arbitrary adjustment of the dispersion at the TDC location, which reduces its power requirements. In this paper, we present three phase-space exchanger designs and performance comparisons between them.

We use two sets of beam parameters for these studies. The first is based on a study of partially compressed beams at ASTA [6], while the other is a smaller set of emittances used for comparisons with reduced second-order effects. Both are presented in Table 1.

* Work supported by LDRD project #20110067DR and by the U.S. DoE Contract No. DE-FG02-08ER41532 with NIU and No. DE-AC02-07CH11359 with Fermilab.

Table 1: Initial Beam Parameters

Parameter	symbol	Value (case 1)	Value (case 2)	Units
hor. emittance	$\varepsilon_{x,0}$	10.0	1.0	μm
vert. emittance	$\varepsilon_{y,0}$	10.0	1.0	μm
long. emittance	$\varepsilon_{z,0}$	39.1	10.0	μm
bunch length	$\sigma_{z,0}$	0.8	0.4	mm
LPS chirp	$\mathcal{C}_{z,0}$	0.0	0.0	m^{-1}

OVERVIEW OF PHASE SPACE EXCHANGER DESIGNS

In this Section we summarize the properties of the three beamlines considered through out this paper. Each of the designs must generally satisfy three different requirements [7]. For the dispersive section upstream of the TDC, M_-, we must control of the upstream dispersive section's x dispersion, η_-, and its derivative, $\eta_-\prime$. For TDC section, M_{TDC}, we must control the strength of the TDC as $\kappa = -\frac{1}{\eta_-}$, operated at zero-crossing. For the downstream section, M_+, the dispersive section's transfer matrix must be finely controlled such that the properties satisfy

$$\mathbf{D}_+ = \begin{pmatrix} R_{11,+} & R_{12,+} \\ R_{21,+} & R_{22,+} \end{pmatrix} \mathbf{D}_-, \text{and} \quad (1)$$

$$\kappa = -1/\eta_-. \quad (2)$$

where the $+$ and $-$ signs refer to values associated to respectively the downstream and upstream dispersive sections and $\widetilde{\mathbf{D}} \equiv (\eta, \eta' \equiv d\eta/ds)$ is the dispersion vector.

The most basic design is the Double Dogleg EEX (DDEEX), of a design similar to that implemented at A0. The dispersion η of each dogleg is 0.5 m, and the TDC is centered between the upstream and downstream doglegs. An accelerating-mode cavity is placed immediately downstream of the TDC to correct for the R_{65} term [8]. The dipoles are rectangular, and the exact lengths and distances are described in Fig. 1.

A similar design is a the Nominal-Dispersion EEX (NDEEX), in which the bend angles and geometry of each dogleg are the same, except the bend angles of one of them are reversed such that it forms a chicane rather than a pair of symmetric doglegs. Quadrupoles are placed inside the

Copyright © 2013 CC-BY-3.0 and by the respective authors

chicane between each of the existing elements, which allow for specific tailoring of the transfer matrix of the upstream and downstream doglegs. The quadrupole magnets are used to adjust the sign of the dispersion the upstream dogleg, while those of the downstream dogleg are used to meet the new requirements on the transfer matrix. For the simplest case, we choose the new dispersion of the upstream dogleg, M_-, to have the same magnitude as that of the DDEEX, i.e. $\eta_- = -0.5$. Diagrams of the DDEEX and NDEEX designs are presented in Fig. 1.

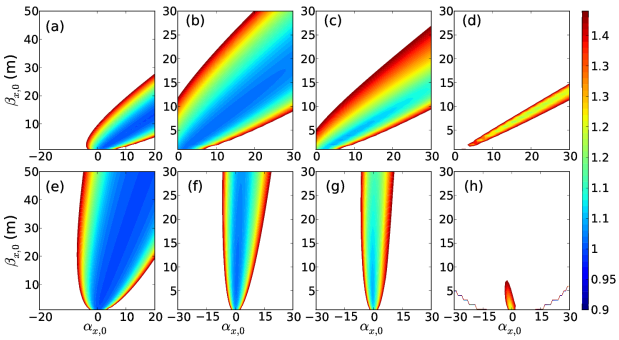


Figure 1: The DDEEX (top) and chicane-like (bottom) emittance-exchanger configurations. The TDC is centered between B2 and B3, and an accelerating mode cavity is placed immediately downstream.

The boosted-dispersion EEX (BDEEX) uses the same components and configuration of the NDEEX chicane. Rather than using the quadrupole magnets in M_- to change only the sign of its dispersion, we increase its magnitude as well, while correspondingly adjusting the downstream transfer matrix.. This has the crucial advantage of decreasing the requirement on the cavity kick-strength, as per Eq. 2. As the dispersion η_- increases, the requirements on η_+ become more difficult to satisfy while keeping the beam envelope well-constrained. We explore boosted values of $2\eta_-$ to $6\eta_-$.

Table 2: Beamline Parameters of the EEX Configurations in Fig. 1

Parameters	Value	Units
Dipole Length	0.30	m
Bend Angle	± 18	degrees
Beam Energy	50	MeV
$\lvert\eta_-\rvert$	[0.5, 1.0, 1.5,2.0,2.5,3.0]	m
$\lvert\eta'_-\rvert$	0.0	m
$\lvert\kappa\rvert$	[2.0,1.1,0.66,0.5,0.4,0.33]	m^{-1}

The exchanger beamlines were optimized in the simulation code ELEGANT [9], and then imported into IMPACT-Z [10], which allows for the implementation of SC effects with a three-dimensional PIC model, and with a one-dimensional model of CSR [11].

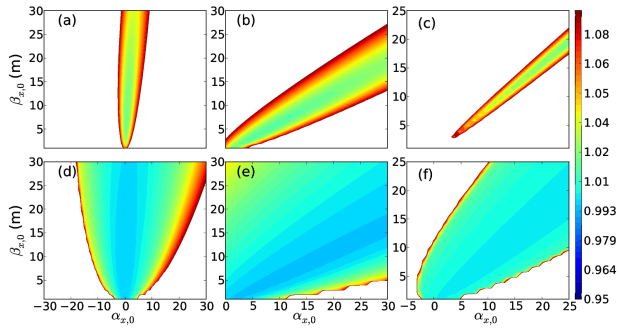


Figure 2: Contour plots comparison of three models (DDEEX (a,d), NDEEX (b,e), and BDEEX(c,f)) with IMPACT-Z for 0 nC for both $\mathcal{F}_{x\to z}$ (a-c) and $\mathcal{F}_{z\to x}$ (d-f), as functions of the C-S parameters at the EEX entrance, $\beta_{x,0}$ and $\alpha_{x,0}$.

BEAMLINE COMPARISONS

As a way to measure the relative performance of the various configurations, we performed scans of the initial Courant-Snyder (C-S) parameters, $\beta_{x,0}$ and $\alpha_{x,0}$ at the entrance of the EEX. This is required to account for varying optics between each of the configurations and the second-order effects of varying strengths that result from the differing optics.

We compare the core emittance exchanger designs for equivalent doglegs with dispersion of $|\eta_x| = 0.5$m, and the BDEEX design for $|\eta_x| = 1.0$m. Units for the color scales are μm when presenting the normalized emittances, mm for RMS bunch sizes, and unit-less when presenting the "exchange quality", $\mathcal{F}_{x\to z} \equiv \frac{\varepsilon_{z,f}}{\varepsilon_{x,0}}$ and $\mathcal{F}_{z\to x} \equiv \frac{\varepsilon_{x,f}}{\varepsilon_{z,0}}$, where perfect emittance exchange occurs at $\mathcal{F} = 1$. We also define the term "acceptance" with regards to the range over which the emittance exchange quality is near unity.

In Fig. 2, the DDEEX, NDEEX, and BDEEX are compared for the case of no collective effects. Boosting the dispersion causes a notable decrease in the acceptance of initial C-S parameters, as the quadrupole settings within the chicane cause the transverse beam sizes to be more erratic along the beamline.

When SC+CSR are introduced for a 1 nC bunch, as shown in Fig. 3, the acceptance is reduced for all three configurations. Comparisons of σ_z to the contour plots for the emittance exchange quality reveal a significant degradation to the emittance exchange quality that occurs when the beam size is at its minimum, i.e. when the final LPS is upright, a vital part of achieving optimal beam shaping. This indicates a significant barrier to achieving optimal shaping while also achieving optimal emittance exchange, and that there is some significant trade-off that must be determined when setting the EEX settings.

DISPERSION BOOSTING

Boosting the dispersion up to 6x of the nominal value (in this case, 3.0 m) introduces significant complications to

Copyright © 2013 CC-BY-3.0 and by the respective authors

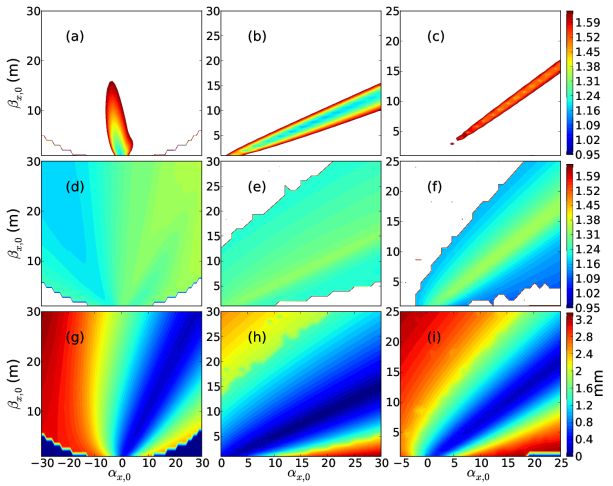


Figure 3: Contour plots comparison of three models (DDEEX, NDEEX, and BDEEX(2×) with IMPACT-Z for 0 nC for both $\mathcal{F}_{x\to z}$ and $\mathcal{F}_{z\to x}$, as functions of the C-S parameters at the EEX entrance, $\beta_{x,0}$ and $\alpha_{x,0}$.

beam control. As the x transfer matrix in the second dog-leg must be controlled to specifically satisfy the basic requirements for perfect emittance exchange, the y dynamics becomes difficult to control. For an example of optimized functions (via the same method of C-S scans presented earlier), see Fig. 4, using both ASTA and A0-style beam emittances.

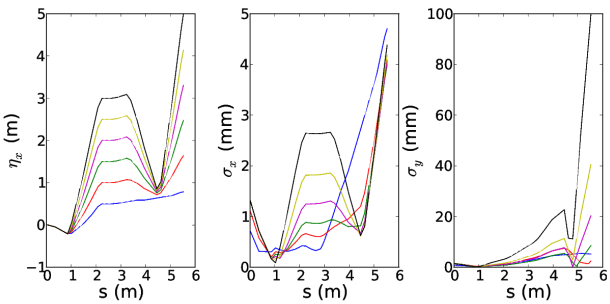


Figure 4: Horizontal dispersion η_x (left), σ_x (middle), and σ_y (right) along the NDEEX and BDEEX designs for $\eta_- =$ 0.5 m (blue), 1.0 m (red), 1.5 m (green), 2.0 m (magenta), 2.5 m (yellow) and 3.0 m (black).

The key difference between these simulations and those of the nominal-dispersion and double-boosted-dispersion is that σ_y is large and divergent, in addition to σ_x, which is large and divergent due to the kick from the TDC. Switching to smaller emittances reduces the beam size and the resultant emittance growth from second-order effects; see Table 3.

The key feature of dispersion boosting is the reduced requirements on the TDC, so while the quadrupole strengths are increased, the transverse beam size is less dominated by the TDC kick. The trade-offs that must be considered

Table 3: Quality of Emittance Exchange for Various Dispersions using the BDEEX Configuration, along with Which Emittances were Used

η_- (m)	Beam Type	$\mathcal{F}_{x\to z}$	$\mathcal{F}_{z\to x}$
0.5	1	1.00	1.00
0.5	2	1.00	1.00
1.0	1	1.04	1.02
1.0	2	1.01	1.00
1.5	1	1.08	1.01
1.5	2	1.01	1.000
2.0	1	2.407	1.05
2.0	2	1.22	1.000
2.5	1	10.42	1.12
2.5	2	3.43	1.01
3.0	1	79.98	1.75
3.0	2	25.35	1.04

are not simple, and depend greatly on both initial bunch length and transverse emittances. Dispersion-boosting up to 3x of the baseline dispersion is possible with ASTA-scale beam parameters, but greater dispersion is feasible for lower emittance regimes.

REFERENCES

[1] P. Emma, et. al, *PRST-AB* **9**, 100702 (2006).

[2] P.Piot, et. al, *PRST-AB*, **14** 022801 (2011).

[3] Y.-E. Sun, et. al, *PRL* **105**, 234801 (2010).

[4] J. Ruan, et. al, *PRL* **106**, 244801 (2011).

[5] D. Xiang, A. Chao, Phys. Rev. ST Accel. Beams **14**, 114001 (2011).

[6] C. R. Prokop, et. al, *NIM A*, **719**, p. 1728 (2013).

[7] R. Fliller, Fermilab Report, BeamDocs 2271-v2 (2007).

[8] A.A. Zholents, M.S. Zolotorev, ANL/APS/LS-327 (2011).

[9] M. Borland, APS LS-287, September 2000 (unpublished).

[10] Ji Qiang, et al., *Journal of Comp. Phys.* **163**, p. 434 (2000).

[11] E.L. Saldin, et. al, *NIM A*, **A 398** p. 373-394 (1997).

Copyright © 2013 CC-BY-3.0 and by the respective authors

ION BEAM CHARGE NEUTRALIZATION BY FERROELECTRIC DISCHARGE PLASMA *

A.D. Stepanov, E.P Gilson, L.R. Grisham, R.C. Davidson
Princeton Plasma Physics Laboratory, Princeton, New Jersey, 08543, USA

Abstract

Space-charge forces limit the possible transverse compression of high perveance ion beams that are used in ion-beam-driven high energy density physics applications; the minimum radius to which a beam can be focused is an increasing function of perveance. The limit can be overcome if a plasma is introduced in the beam path between the focusing element and the target in order to neutralize the space charge of the beam. This concept has been implemented on the Neutralized Drift Compression eXperiment (NDCX) at LBNL using Ferroelectric Plasma Sources (FEPS). In experiments at PPPL, a perveance-dominated ion beam was propagated through a FEPS and the transverse beam phase space was measured with a slit-slit emittance scanner to characterize the effect of charge-neutralizing plasma on beam divergence.

INTRODUCTION

To reduce the divergence of high-perveance ion beams due to space charge, electrons can be introduced into the beam volume. In most experimental applications, electrons are produced by ion impact ionization of background gas and from secondary electron emission (SEE) from surfaces impacted by the beam. Electrons become confined the electrostatic potential well of the ions, reducing the magnitude of the potential well, which decreases until equilibrium is established between electron production and loss rates. For charge neutralization by ionization of background neutrals, this process typically takes 50 μs.

For charge neutralization of pulsed ion beams with duration < 100 μs, a volume plasma can be introduced into the beam path to provide electrons. Ferroelectric Plasma Sources (FEPS) can produce volume plasmas with low electron temperatures, and have been used successfully on NDCX-I to neutralize the space charge of a converging high-perveance ion beam pulse. Herein, experiments on charge neutralization of a 32-42 keV Ar+ beam with a plasma produced in a ferroelectric discharge are presented.

FERROELECTRIC PLASMA SOURCES

Ferroelectric materials (FE), such as PZT and ($BaTiO_3$) are characterized by a high relative dielectric constant ($\epsilon_r > 1000$) and the presence of a spontaneous electric polarization. It was found that under the application of a fast-changing electric field, high electron current densities are be emitted from the FE surface [1, 2], and plasma can be produced. Plasma sources based on $BaTiO_3$ have been built for use on NDCX-I/II [3] for ion beam charge neutralization. The basic configuration of a ferroelectric plasma source (FEPS) is a slab of ferroelectric material placed between two flat electrodes, one of which is perforated. When a fast-rising voltage pulse (~ 5 kV) is applied between the electrodes, a plasma is formed at the side of the perforated electrode at points of juncture between metal, ceramic, and vacuum. In addition, gas desorption occurs during FEPS discharge, which most likely plays a role in plasma formation. The precise mechanism of operation of FEPS is still under investigation [4].

EXPERIMENTAL SETUP

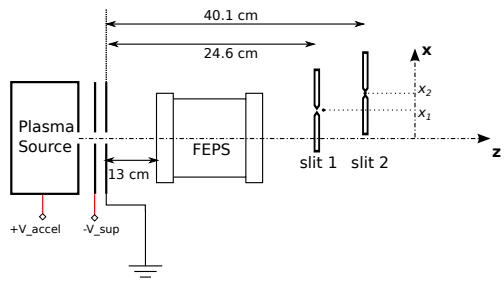


Figure 1: Diagram of the beamline used in the experiment. An Ar^+ beam, extracted from a plasma, propagates through a cylindrical FEPS. Downstream of the FEPS, the beam is intercepted by a two-slit emittance scanner which is used to measure the transverse current distribution of the beam.

The experiments were carried out on the Princeton Advanced Test Stand (PATS) at PPPL. Ar^+ ions are extracted from an RF-driven plasma and formed into a beam with a 3-electrode, accel-decel extraction system with gap length $d = 1.1$ cm and plasma aperture with radius $r_B = 1.5$ mm. The plasma is generated in a multicusp RF source with an internal antenna [5], driven by a pulsed RF power supply. Ion current density up to 28 mA/cm^2 can be extracted. Accelerating potential V_{accel} (30-60 kV) is supplied by an HV pulser [6].

The ion beam exits the accelerator through a grounded aperture at $z = 0$. At $z = 13$ cm, the beam enters a 10.1 cm long FEPS with an inner diameter of 7.62 cm. After the FEPS, the beam is intercepted by a slit-slit emittance scanner. The slits, located at $z_1 = 24.6$ cm and $z_2 = 40.1$ cm, are 2.5" long, 0.1 mm wide, and oriented horizontally. The second slit, referred to as the slit-cup, has a Faraday cup (FC) with SEE suppressor grid mounted directly behind it

* This work is supported by US DOE contract DE-AC02-09CH11466

Copyright © 2013 CC-BY-3.0 and by the respective authors

for measuring ion current. Both slits are mounted on linear motion feedthroughs and can be moved in the vertical direction. The feedthroughs are driven by stepper motors, which provide positioning accuracy better than 0.1 mil.

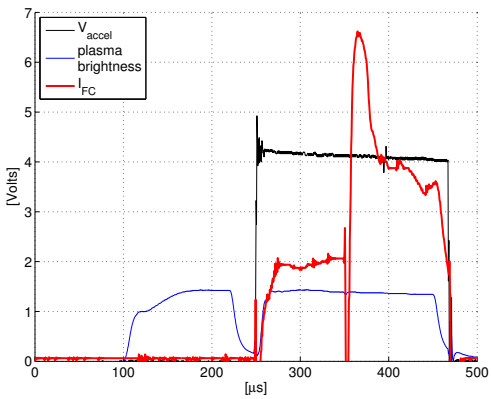


Figure 2: Waveforms of plasma density (blue trace), accelerating potential V_{accel} (black trace, 1 V = 10 kV), and FC current I_{FC} (red trace, 1 V = 1 μA) measured with the slit-cup positioned on beam axis. $V_{accel} = 42$ kV and $I_B = 0.7$ mA. FEPS was triggered at $t = 350$ μs. Plasma density is inferred from plasma light emission intensity.

The emittance scanner diagnostic provides $y-$integrated measurements of the transverse distribution $f(x, v_x, y, v_y)$. The first slit can be moved out of the way, so the beam is intercepted by the slit-cup only. Then, $y-$integrated transverse current density profiles $I_{FC}(x_2) = \int j(x_2, y)dy$ at $z = z_2 = 40.1$ cm can be obtained by recording I_{FC} for a range of slit-cup positions. If the beam is made to pass through both slits, then the current $I_{FC}(x_1, x_2)$ will be due to beam ions with $x = x_1$ and transverse angle $x' = (x_2 - x_1)/D$, where $D = z_2 - z_1 = 15.5$ cm is the $z-$ distance between the slits. In this way, the $y-$ integrated trace-space distribution $f(x, x')$ at $z = z_1 = 24.6$ cm can be measured.

In the experiment, ion beam pulses were generated every 2 seconds, with 200 μs-long RF and V_{accel} pulses applied concurrently. Afterglow plasma from an earlier RF pulse (from $t = -180$ μs to $t = -30$ μ s) was used as source of electrons to improve RF breakdown and plasma density rise-time. The FEPS was triggered 100 μs after the start of beam pulse. Typical waveforms of $I_{FC}(t)$, $V_{accel}(t)$ and plasma density are shown in Fig. 2.

EXPERIMENTAL RESULTS

In general, the beam divergence was greatly reduced when the FEPS was triggered, as can be seen in Fig. 2, showing $I_{FC}(t)$ for the slit-cup positioned on the beam axis. The increase in current after the FEPS is triggered at $t = 350$ μs, corresponds to the narrowing of the beam profile. $I_{FC}(t)$ reaches a maximum 15 μs after the FEPS discharge. Data from slit-cup profile scans and trace-space scans is used to investigate the timing and duration of charge neutralization and the minimum beam divergence that can be attained.

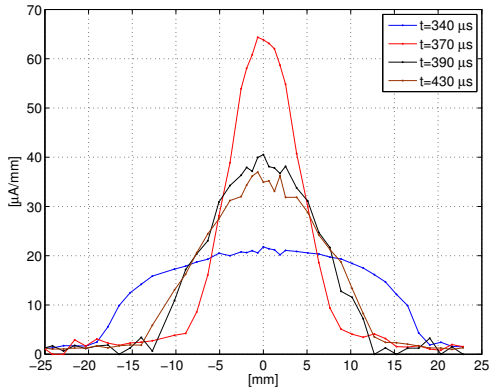


Figure 3: Transverse current density profiles $I_{FC}(x_2)$ taken with the slit cup at different times in the shot.

In the analysis, the effectiveness of neutralization is characterized by a decrease in beam divergence. For an ion beam extracted from a free plasma boundary, experimentally measured divergence is due several factors. The beam will expand due to space charge, characterized by generalized perveance $Q = (1/4\pi\epsilon_0)\sqrt{M/2e}I_B/V_{accel}^{3/2}$, and transverse emittance ϵ, due to finite temperature of plasma ions. These effects are included in the envelope equation for $r(z)$:

$$\frac{dr^2}{dz^2} = \frac{Q}{r} + \frac{\epsilon^2}{r^3} \quad (1)$$

Equation (1) can be solved numerically with initial conditions (r, r') at $z = 0$, which correspond to initial beam radius and divergence at the exit of the accelerator. In a plasma ion source, beam current and accelerating potential can be controlled independently, and the initial divergence of the beam depends on the perveance match. According to [7], the divergence angle $\omega = 0.29S(1 - 2.14Q/Q_0)$, where S is the aspect ration of the extraction gap and Q_0 is the optimal perveance. The optimal divergence that was obtained experimentally in [7] was 1.2°, as measured by $1/e$ Gaussian half-width.

In order to compare experimental results to the envelope model, transverse current density profiles $I(x)$ are measured with the slit-cup for beam energies of 32, 38, and 42 kV, and beam currents from 0.4 to 0.8 mA. Time evolution of total current $I_B(t)$ and HWHM profile width $x_{HWHM}(t)$, calculated from profiles of $I(x)$, is shown in Fig. 4. $I_B(t)$ remains the same before and after the FEPS is triggered, except for the dip in at 350 μs due to electrical noise from the FEPS HV pulse. The curve of $x_{HWHM}(t)$ shows that before neutralization, $x_{HWHM}(t)$ reaches steady state quickly. After the FEPS is triggered, $x_{HWHM}(t)$ decreases to a minimum at $t = 365$ μs, and then increases but remains smaller than before neutralization. Transverse current density profiles at different times are plotted in Fig. 3.

Copyright © 2013 CC-BY-3.0 and by the respective authors

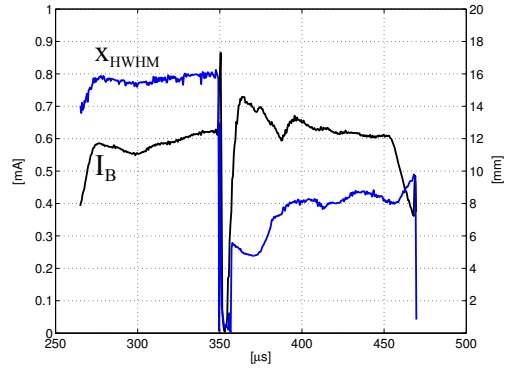


Figure 4: Time evolution of total beam current I_B (black trace) and x_{HWHM} (blue trace) computed from slit-cup profile data for $V_{accel} = 42$ kV, $I_B = 0.7$ mA

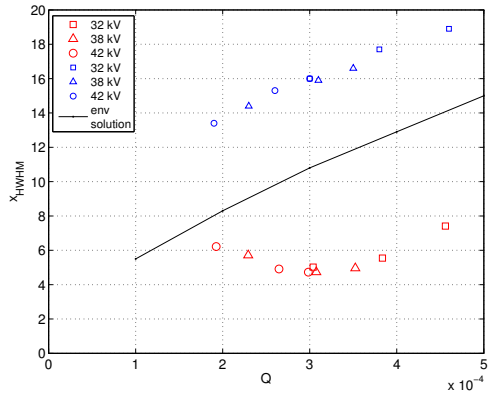


Figure 5: Profile widths characterized by x_{HWHM} versus generalized perveance Q for unneutralized (blue) and neutralized (red) cases at $z = 40.1$ cm. The solution to the envelope equation $r_B(Q)$ (black) is also plotted.

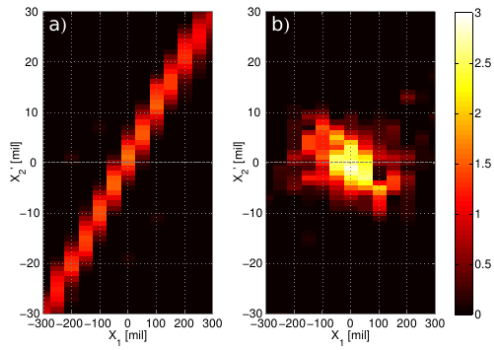


Figure 6: Trace-space data a) before neutralization ($t = 340$ μs) and b) after neutralization ($t = 365$ μs). The horizontal line $x_2' = 0$ corresponds to straight ion trajectories from the extraction aperture of the ion beam to the diagnostic.

Beam divergence, characterized by half-width, half-max of profiles $I(x)$ is plotted as a function of Q in Fig. 5 before neutralization ($t = 340$ μs, blue dots) and at optimal neutralization ($t = 365$ μs, red dots). Beam radius $r_B(Q)$ calculated from the envelope equation with $r(z = 0) = 0.15$ cm and $r'(z = 0) = 0$ is shown for comparison. For the unneutralized case, x_{HWHM} monotonically increases with Q, consistent with space charge expansion. For the neutralized case, x_{HWHM} vs Q has the shape of a perveance curve with a minimum at $Q \simeq 2.9 \times 10^{-4}$, suggesting that beam divergence is due to perveance match in the accelerating gap. At optimum perveance, the 1/e Gaussian half-width divergence angle is equal to 0.87°.

This angular divergence is close to optimal divergence of 1.2° obtained in [7] with a DC ion beam neutralized by ionization of neutral gas. This suggests that observed divergence is due to initial divergence at the exit of the accelerator, and that the beam propagated with $Q_{eff} \simeq 0$ from the source to the diagnostic. This means that that electrons from the FEPS plasma filled the volume of the whole beam and the beam propagated ballistically. This is evident from measurements of the trace-space distribution $f(x, x')$ with the two slit method.

In order to visualise the shape of the beam ellipse in $x - x'$ trace-space, a transformation $x' \rightarrow x_2'$ was applied:

$$x_2' = x_2 - \frac{D_2 + D_1}{D1} x_1 = x_2 - 1.61 x_1 \qquad (2)$$

Here, D_1 and D_2 are distances from the extractor to the first and second slits respectively. With this transformation, the horizontal line $x_2' = 0$ corresponds to the two slits being positioned on line-of-sight to the extractor. In Fig. 6, results of trace-space measurements are shown, comparing an unneutralized beam with the beam during optimal neutralization, which occurs 15 μs after the FEPS is triggered. The unneutralized beam has greater laminar divergence than lines-of-sight to the extractor, with the apparent source point located at $z = 3.6$ cm. This is consistent with space-charge expansion, when divergence angle r' increases with z. In the neutralized case, the beam trajectories are more convergent than lines-of-sight to the extractor, with the apparent source point located at $z < 0$. This indicates that the ion beam was completely charge-neutralized by FEPS plasma.

REFERENCES

[1] A. Dunaevsky et al, Journal of Applied Physics, 95:4621, 2004

[2] G. Rosenman et al, Appl. Phys. Rev., 88:6109, 2000

[3] E.P. Gilson, et al., Nuclear Instruments & Methods in Physics Research A (2013)

[4] V.T. Gurovich, et al, Journal of Applied Physics 106 (2009) 053301.

[5] G. Westenskow, et al. "Characterization of an RF-driven plasma ion source for Heavy Ion Fusion," PAC'03, pp.3300

[6] M.J. Wilson, D. Goerz, R. Speer, and R. Moal. "Heavy Ion Fusion (HIF) Impulse Injector Design, Construction, and Checkout". LLNL Report UCRL-ID-130764,1998.

[7] J.R. Coupland, et al, Review of Scientific Instruments, vol.44, no.9, pp.1258, 1973

Copyright © 2013 CC-BY-3.0 and by the respective authors

IDENTIFICATION OF INTRA-BUNCH DYNAMICS USING CERN SPS MACHINE MEASUREMENTS*

Ozhan Turgut†, John Cesaratto, John Dusatko, John D. Fox
Kristin Pollock, Claudio Rivetta, SLAC, Menlo Park 94025, USA

Abstract

Modern control techniques can be used to design feedback systems for stabilizing the intra-bunch dynamics in the presence of electron cloud (ECI) and transverse mode coupling (TMCI) instabilities. These techniques require reduced models of the bunch dynamics. We present a methodology to identify reduced order linear models representing single bunch dynamics using CERN SPS machine measurements. Vertical motion, in response to a wideband excitation signal, is sampled multiple times across the 5 ns bunch. The data and an observable canonical structure [1] are used to identify the dynamics, which is represented as a discrete time multi-input multi-output (MIMO) system. We focus on mode 0 (barycentric) and mode 1 (head-tail) data to identify a reduced order model. Results show that models clearly capture dominant dynamics and replicate machine measurements with corresponding central tune, damping value for each mode and correct separation between the modes.

INTRODUCTION

Electron cloud and machine impedance can cause intra-bunch instabilities [2]. Modern control techniques can be used to mitigate these problems but require reduced order models of intra-bunch dynamics to design optimal and robust controllers for wideband feedback systems [3]. We use system identification techniques to estimate parameters of linear models representing single bunch dynamics. We briefly explain the reduced order model and identification method. Experimental data was collected from a single bunch with 1×10^{11} protons at 26 GeV with low chromaticity configuration at CERN SPS. This paper includes results from mode 0 and mode 1 dynamics analysis but the methods are in principle applicable to N modes.

MODEL AND IDENTIFICATION

The physical system analyzed in this study is a nanosecond scale SPS bunch. The interaction with the bunch is done via control variables (momentum kick / driving signal) and measured variables (vertical displacement). The control variables and measured variables are discretized to represent the physical system in a MIMO form. The number of samples is arbitrary and depends on the sampling rate of the data acquisition system. These studies use 3.2 GS/s sampling rate allowing us to sample 16 different locations across 5 ns RF bucket [3]. The goal is to estimate the intra-bunch dynamics using these input and output signals.

Reduced Order Model

Any linear dynamical system can be represented in state space matrix form. A discrete time system sampled at every revolution period k with p inputs and q outputs is:

$$\begin{aligned} X_{k+1} &= AX_k + BU_k \\ Y_k &= CX_k \end{aligned} \tag{1}$$

where control variable (external excitation) $U \in R^p$, vertical displacement measurement $Y \in R^q$, system matrix $A \in R^{n\times n}$, input matrix $B \in R^{n\times p}$, and output matrix $C \in R^{q\times n}$. For a MIMO system, the model order determines the complexity.

Identification

Identification of a linear dynamical system is done by casting this problem into a linear least squares form. Assuming full observability, we can represent our state space in discrete time observable canonical form. This will enable us to estimate a minimum number of parameters [1]. However, even for linear systems there are two well known limitations for identification. These are the effect of noise and lack of persistent excitation.

Persistent Input

Input signal design and persistent excitation are critical aspects of system identification. Given a quasi-stationary input of u with a dimension nu and with a spectrum $\phi_u(\omega)$, $\phi_u(\omega) > 0$ should hold for at least n distinct frequencies for u to be a persistent excitation [4]. Random noise would be ideal to excite all the modes in the system but requires high excitation power and bandwidth. The hardware used in these measurements puts constraints on both power and bandwidth. The design of an input signal for identification under given constraints becomes an important question for the future studies.

Noise Sensitivity

Noise affects the performance of the identification, and in certain cases can make identification impossible. We can quantify the effect of the noise by adding noise on a known system until the identification can no longer clearly estimate the known dynamics. We drive a synthetic 2×2 coupled MIMO system using a frequency chirp signal with random noise added to the output signals. The effect of noise is tested by running the identification algorithm

* Work supported by U.S. Department of Energy under contract DE-AC02-76SF00515 and the US LHC Accelerator Research Program
† oturgut@stanford.edu

Copyright © 2013 CC-BY-3.0 and by the respective authors

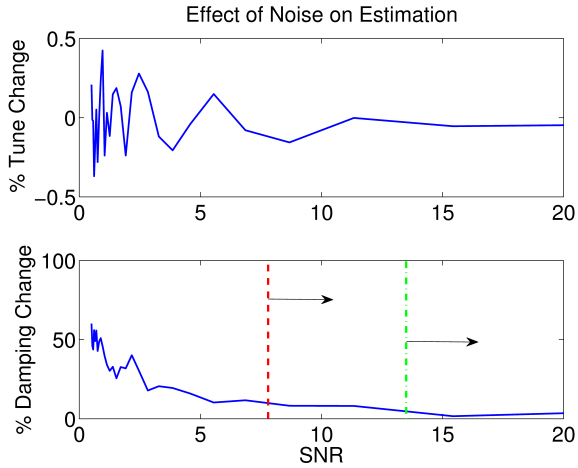


Figure 1: Deviation of estimated natural tune and damping of the 1^{st} mode from the true value for different SNR values. Red line shows min SNR to get errors less than 10%, green line is for errors less than 5%.

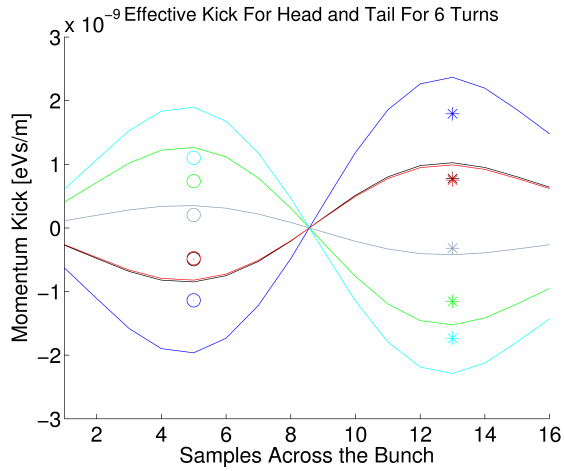


Figure 2: Amplitude modulated momentum signal used to kick particles in vertical plane. Each color represents the kick applied at a single turn. Average kicks, o : head, $*$: tail.

on input - output data as we increase the noise level. Parameters of the model and the corresponding modes of the identified model are estimated for different noise cases. We observe the effect of noise on the mode estimation by looking at the natural frequency and damping values of the first mode for different values of signal to noise ratio (SNR). Figure 1 shows the impact of noise on estimation of system parameters. For identification algorithm to perform well, we need to have SNR $>\sim 8$.

APPLICATION : SPS MEASUREMENTS

In this case the persistent excitation condition is satisfied because we are analyzing the dynamics of mode 0 and mode 1 excited by a chirp excitation, where the frequency changes over 15000 turns.

Our data processing uses a time varying bandpass filter to improve SNR to $\sim$ 20. A window of 500 turns is used to calculate corresponding center frequency of the filter, which follows the chirp excitation.

We focus on mode 0 (barycentric) and mode 1 (head-tail) dynamics. Dynamics, input-output relation of momentum kick and vertical displacement, can be defined by 2 coupled 2^{nd} order differential equations and represented as 2 $\times$ 2 MIMO system with $p = 2$, $q = 2$ and $n = 4$. As mentioned before the number of inputs and outputs depends on the sampling across the bunch. Measurement data should be arranged in such a way that we have 2 $\times$ 2 system. As an initial approach we separate the bunch into two parts. The samples lying in the first part (head) are represented by a macro particle. Its motion is calculated by taking the average motion of the all samples in the head. The same approach is used for the second part (tail) of the bunch. Similarly we calculate an effective kick for the head and the tail by using same technique. At each turn we calculate the effective kick that the head and tail experience by averaging the waveform between samples 1-8 and 9-16. Figure 2 shows 6 sequential traces (each represents a different turn) of the momentum waveform across the bunch and corresponding effective kicks for head and tail.

Results

In driven measurements we use both mode 0 and mode 1 excitations [3]. Excitations and corresponding bunch measurements are used to estimate the parameters of the model. In Fig. 3 the top left plot shows the vertical displacement of the centroid of the head with measurements in blue and the response of the model in red. The bottom left plot shows the same for the tail. Note that our reduced order model is linear time invariant. It cannot capture external perturbations or parameter variations in the bunch. Still the envelope of the amplitude of the centroid motions is captured in the time domain. The figures on the right show measurements and response of model in frequency domain. As an example of external perturbation, we see modulations in FFT data. One of mechanisms for these effects can be tune modulation. From both the time and frequency domains we observe that in this specific measurement, mode 0 is dominantly excited in the tail of the bunch. Although it is a frequency chirp sweeping both mode 0 and mode 1 frequencies, the excitation signal was generated and time aligned to dominantly excite mode 0. Figure 4 shows another data with strong excitation of mode 1. On the left, we see the RMS spectrogram of the driven measurement with clear mode 0 and mode 1 excitation around turns $\sim$ 4000 and $\sim$ 9000. On the right side, we show the RMS spectrogram of bunch's vertical motion predicted by reduced model. The model is able to capture dominant characteristics such as motions at mode 0 and mode 1 tune together with the effect of chirp and mode 0 residual motion.

Copyright © 2013 CC-BY-3.0 and by the respective authors

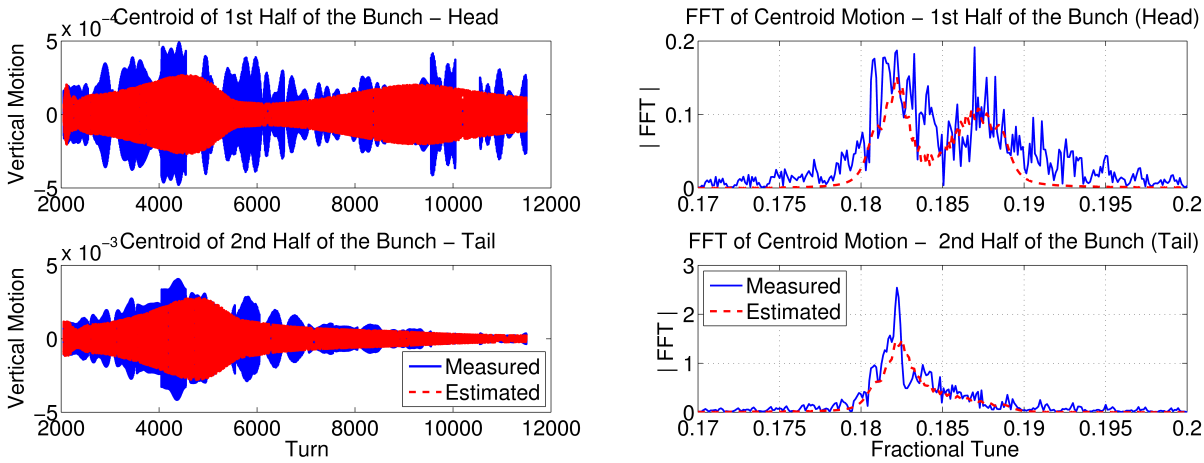


Figure 3: Comparison of the reduced order models response with machine measurements in time and frequency domain.

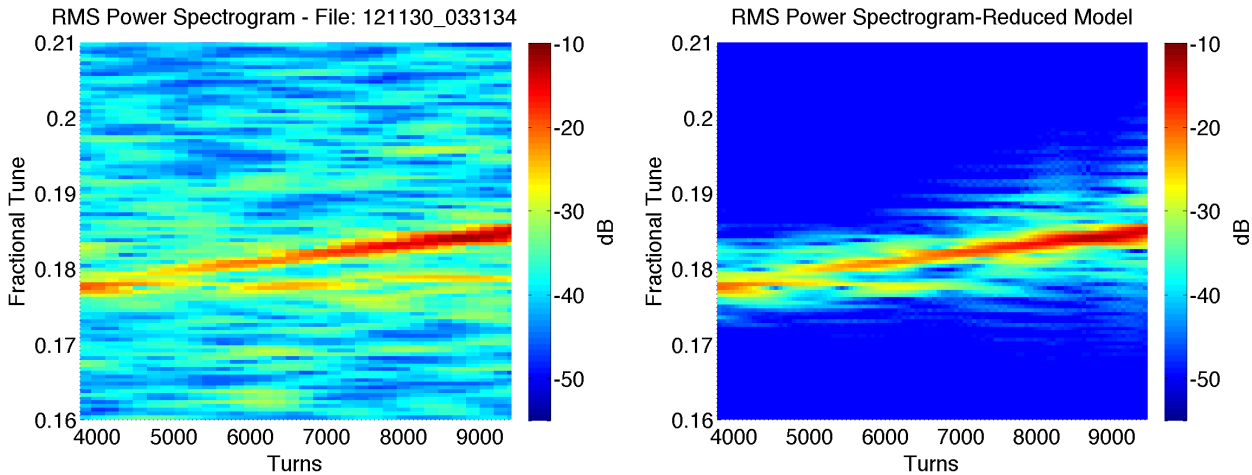


Figure 4: On the left we see the spectrogram of physical measurement showing both chirp excitation where we excite mode 0 and mode 1 around turns ~ 4000 and ~ 9000, respectively. On the right, we see the same excitation and analysis applied to the reduced order model.

CONCLUSION

Control of intra-bunch instabilities via a wideband feedback control system with optimal control algorithms requires a model of the intra-bunch dynamics. We show initial promising system identification results. We identify parameters of a reduced order model that captures mode 0 and mode 1 dynamics from CERN SPS machine measurements. The natural tunes, damping values and the separation of modes associated with the motion seen in measurements are estimated correctly using a linear model. Future work is aimed at estimating more internal modes as the wideband kicker is available late 2014. The techniques used are also applicable to explore optimal and robust control techniques using nonlinear simulation codes [5].

ACKNOWLEDGMENT

We thank H. Bartosik, A. Drago, G. Kotzian, U. Wehrle, CERN AB RF group, the CERN operations team and US-Japan Cooperative Program for their vital help.

REFERENCES

[1] NF. Al-Muthairi et al., "Identification of discrete-time MIMO system using observable canonical-form" , IEE Proceedings - Control Theory and Applications, 2002.

[2] G. Rumolo et al., "Experimental Study of the Electron Cloud Instability in the CERN-SPS" , EPAC 08, Genoa, Italy, pp TUPP065 June 2008.

[3] J. D. Fox et al., "A 4 GS/s Feedback Processing System for Control Of Intra-Bunch Instabilities", IBIC13, Oxford, UK 2013.

[4] M. A. Dahleh, "Lecture Notes - 6.435 System Identification", EECS, MIT, Spring-2005.

[5] M. Pivi et al., "Simulation Code Implementation to Include Models of a Novel Single-bunch Instability Feedback System and Intra-beam Scattering", IPAC 2012 conference, New Orleans, LA May 2012

Copyright © 2013 CC-BY-3.0 and by the respective authors

NONLINEAR BEAM DYNAMICS STUDIES OF HIGH-INTENSITY, HIGH-BRIGHTNESS PROTON DRIVERS *

Saeed Assadi#, Karie Melconian, Peter McIntyre, Texas A&M University, College Station, TX

Abstract

Space charge effects, beam losses, wake fields, and orbital control are significant collective effects that affect beam dynamics. The strong-focusing cyclotron incorporates helical orbits with a strong-focusing lattice and high-gradient cavities. It makes it possible to fully separate orbits and suppress interaction between bunches on neighboring orbits. We simulate nonlinear synchro-betratron coupling and explore methods to use the tools of strong-focusing to suppress beam blowup mechanisms.

INTRODUCTION

The Accelerator Resarch Lab at Texas A&M University is developing designs for a strong-focusing cyclotron (SFC) as a high-current (12 mA CW) proton driver for ADS fission [1], production of medical isotopes, and neutron damage studies [2]. The purpose of this paper is to explore how the unique features of the SFC can be used to control nonlinear dynamical effects that limit beam current in accelerators.

Particle motion in the SFC is described in terms of six phase space coordinates (x,x',y,y',ΔE,Δϕ]. The lattice of the Strong Focusing Cyclotron (SFC) requires inclusion of longitudinal or synchrotron motion as one cannot decouple longitudinal and transverse planes past mid-plane analysis. In this case synchrotron motion causes modulations of the parameters or forces and sidebands appear as a result in the tune space. The effects of synchrobetatron couplings and resonance-crossing should become dominant as intensity increases or bunch length elongates.

The SFC lattice combines periodic quad-focusing elements [FD] with common sector magnets and RF cavities, and in this respect it is similar to a combined-function synchrotron. The orbits however are spirals, and dynamics is strongly dependent on initial conditions, and in this respect it is similar to linacs. This results in synchrotron sidebands [1] in the betatron motion with chromaticity as developed by Orlov [2] and synchrobetatron resonances caused by chromaticity as analyzed in a review by Suzuki [3]. The SFC lattice is highly regulated by the arrangement of superconducting beam transport channels (BTCs) [4], Mobius-geometry RF cavities [5], and low-field superconducting sector dipoles [6] to produce matched beta function [β_x, β_y], dispersion [D] and D' to manage emittances. We simulate the SFC as a spiral transmission line, and we include forces from error fields, wake fields, cavity-coupling of bunches, and space charge.

Designs have been developed for a 6-sector 100 MeV SFC (TAMU100, shown in Figure 1) and for a 12-sector 800 MeV SFC (TAMU800) for which TAMU100 would serve as injector. A key element of the SFC is its use of the beam transport channels (BTC), installed along the equilibrium trajectory or each orbit in each sector as shown in Figure 1b. Each BTC contains an FD doublet of Panovsky quadrupoles (up to 6 T/m, used to local tune) and a window-frame dipole (up to .02 T, used to control isochronicity).

Simulation of beam dynamics in both SFCs starts by tracking a 4D map of a bunch propagating through the lattice elements and interacting with EM fields, similarly to the kick codes COSY-INFINITY, Elegant, MADx, and CERN Mathematica. We have started with that framework and added complexity to the simulation as the design progresses. The framework utilizes a combination of mathematical scripts based on COSY-INFINITY fed by Madtomma. Tracking is made using CSRtrack. Figure 2 shows the elements of one cell of an SFC lattice.

We impose a shell on the kick code that operates a simultaneous quadratic optimization, in which we can optimize up to 48 variables that define the isochronous orbits. The framework has evolved to include space charge, chromatic effects, and evolution of bunch-length.

Beam position monitors are provided in a gap at the end of each sector for each orbit. In the planning for commissioning of TAMU100, we plan to inject low-power beam into the first two turns of the lattice with RF off and capture it on a retractable beam dump. That will enable us to verify injection matching and BTC alignment before

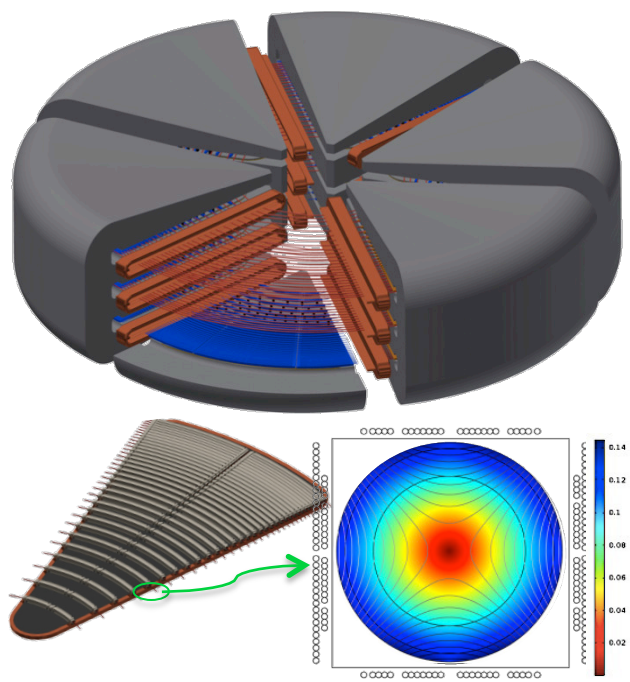


Figure 1. a) 3-stack of 100 MeV SFCs, with cutaway to show superconducting cavities, BTCs, and orbits; b) detail of a sector dipole flux plate and the arced BTCs.

*Work supported by grants from the State of Texas (ASE) and the George P. and Cynthia W. Mitchell Foundation.
assadi@tamu.edu

Copyright © 2013 CC-BY-3.0 and by the respective authors

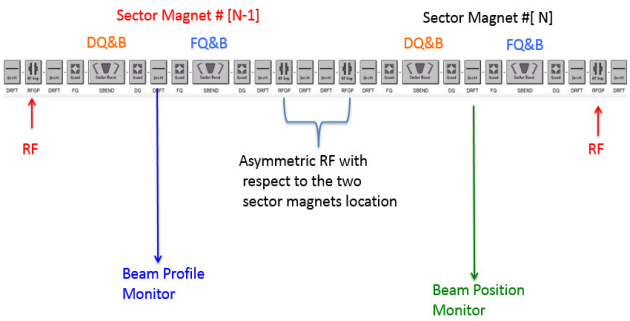


Figure 2. Lattice elements in the tracking simulation of one cell (sector dipoles) of the SFC lattice.

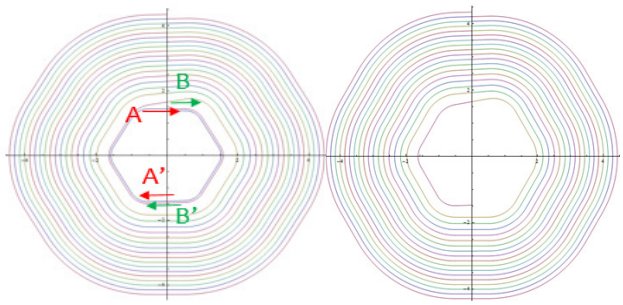


Figure 3, Reference orbits in the 6-sector TAMU100, before and after optimization of the injection orbit.

'threading the needle' of orbits with acceleration. The retractable beam dump can also be traversed to dump the beam after any desired orbit.

Figure 3 shows a first example of how the BTCs convey benefit in optimizing the SFC. Figure 3a shows a reference orbit for TAMU100 in which the orbit was launched from the extraction point and tracked back to injection, optimizing for isochronicity, maintaining stable phase advance in all cells, and holding constant betatron tunes from injection to extraction to a favorable operating point. Figure 3b shows a second optimization in which the optimization of the first two orbits was added to the optimizer criteria.

BEAM DYNAMICS STUDIES

We have studied beam dynamics using the tools described above. We established that the BTC quadrupoles can be grouped into 6 families (3x, 3y) and still provide excellent control with which to set tunes to any desired operating point and hold it there throughout acceleration.

We implemented a similarly grouped set of sextupoles at the exit from each sector to provide control of chromaticity, and a set of beam position monitors that will enable us to develop a correspondence between simulation and actual operation of the accelerator. With those tools, we proceeded to simulate the phase space dynamics of bunches, starting with low current and increasing to our design value.

Figure 4 shows Poincare plots for the 1σ-5σ contours of a bunch in a 3.5 mA 162 MHz SFC, tuned to hold $(\nu_x,\nu_y) = (3.196, 3.241)$. The first three plots show that the phase space has very regular motion throughout acceleration with no particles reaching the BTC apertures.

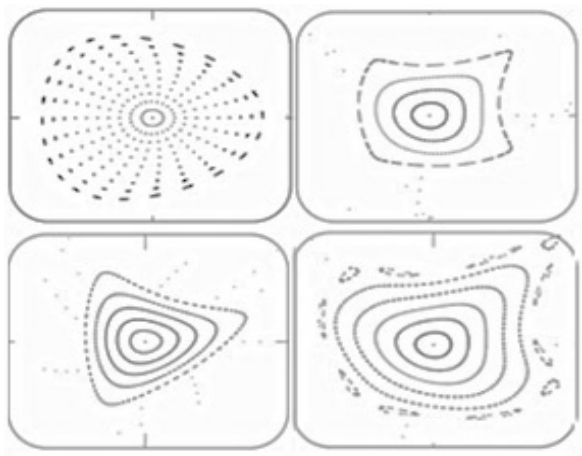


Figure 4. Poincare plots of a 3.5 mA 116 MHz bunch as it is accelerated in an optimized TAMU100 lattice.

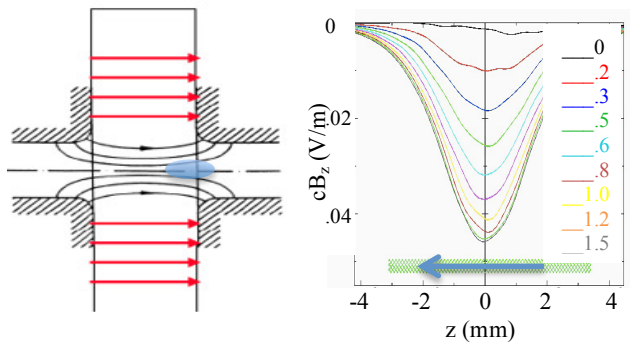


Figure 5. Effect of space charge on longitudinal bunch dynamics: a)bunch passing through cavity; b) longitudinal field inside bunch showing asymmetry from space charge.

For the last plot ν_x was moved near a 7th-order resonance. By the 9th orbit (40 MeV) beam breakup is evident on the 5σ plot. This result gives an example of the simulation at work, and it underscores the importance of controlling tune in a high-current cyclotron.

The nonlinearity and couplings are essentially due to two factors. First, off-momentum particles that go through cavity and then the edge of the sector magnet will go under a different chromatic affect. One aspect of this is shown in Figure 5b, where the space charge of the bunch produces asymmetric fields in the center of the bunch. Such chromatic effects result in synchrobetatron coupling.

We simulated the acceleration of the bunches in a 10 mA CW beam, for a favorable operating point and for tunes near 3rd- and 5th-order resonance. The favorable-tune case produced Poincare plots similar to those of Figure 4a-c; the cases near resonance are shown in Figure 6. When the tune is near a 3rd order resonance, clumping is evident by end of the 2nd orbit and the clumps can be seen driven apart. Similar clumping is evident when the tune is near a 5th order resonance, but clumps remain close. In both cases the beam was lost by 20 MeV. We conjecture that the clumps are driven apart in the 3rd order case by fringe fields of the sector dipoles and by cavity fields, both of which couple to 3rd order in the 6-sector lattice. For a favorable tune, clumping was not observed until near 100 MeV, and the beam profile remained intact.

Copyright © 2013 CC-BY-3.0 and by the respective authors

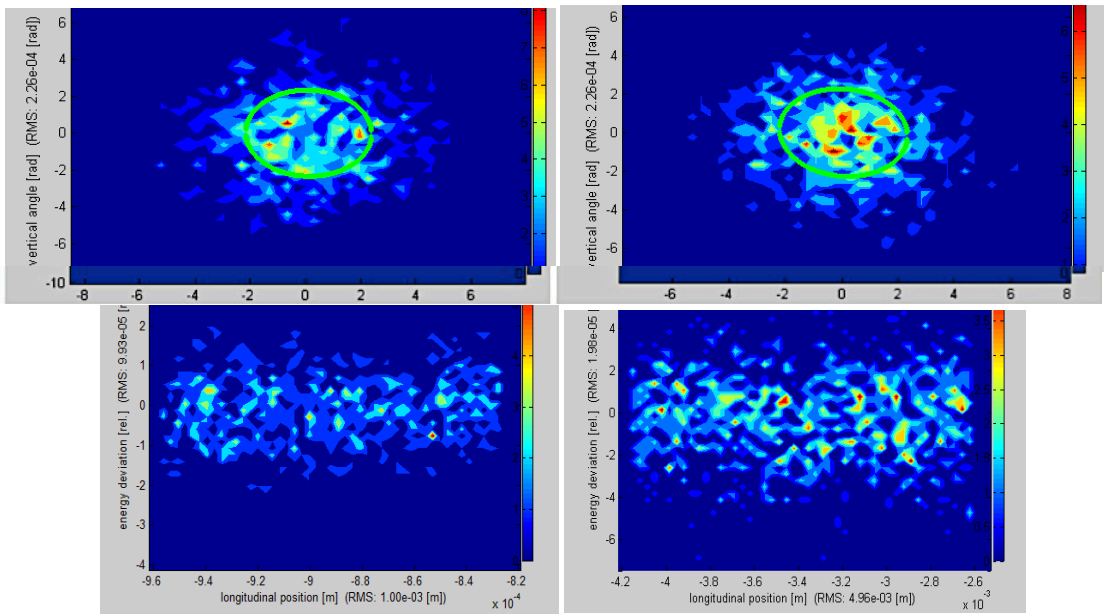


Figure 6. a) Beam breakup in transverse phase space after 2nd orbit when tune is near 3rd order and 5th-order resonances; b) beam breakup in longitudinal phase space when tune is near 5th order resonance.

Figure 7 shows similar dynamics for the longitudinal phase space of bunches in a 10 mA beam with favorable tune. ΔE grew from ±5° at injection to ±6° at extraction; Δϕ increased by 30%; the bunch was accelerated without loss from the 20 MV bucket.

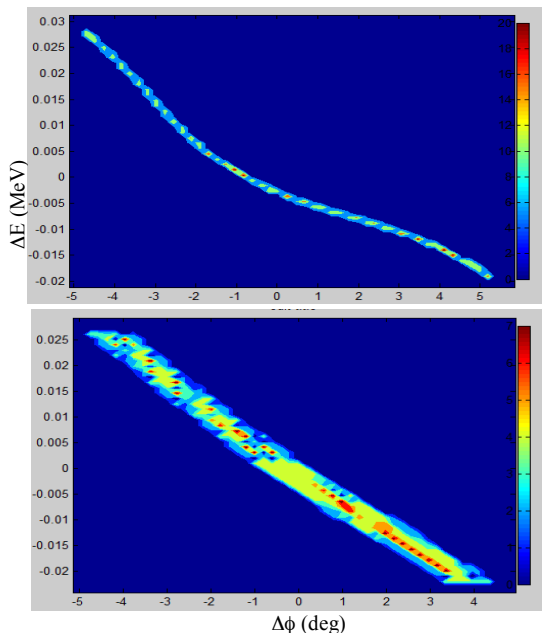


Figure 7. Longitudinal phase space of a bunch in a 10 mA beam: a) after first half-turn; b) 100 MeV.

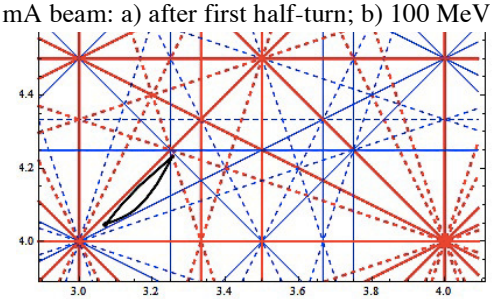


Figure 8. Tune distribution of points on the 5σ trajectory for a favorable tune.

Figure 8 shows a map of the tunes of individual particles on the 5σ contour of a bunch in 10 mA beam, accelerated using a favorable operating point. The tune can be positioned so no resonance crossing occurs, even at 5σ.

CONCLUSIONS

The above results are the beginning stages of a systematic investigation of non-linear dynamics in our strong-focusing cyclotron as it accelerates >10 mA of proton beam to 800 MeV for ADS fission and other applications.

REFERENCES

[1] C.L. Hammer, R.W. Pidd, and K.M. Terwilliger, "Betatron oscillations in the synchrotron," Rev. Sci. Instr. **26,** 555 (1955).

[2] I.F. Orlov, 'Excitation of betatron oscillations by synchrotron momentum oscillations in a strong focusing accelerator', Soviet Physics JETP **5**, 45 (1957).

[3] T. Suzuki, 'Synchro-betatron resonances', *Particle Accelerators*. **27**, 157 (1990).

[4] K. Melconian *et al.*, 'Design of a MgB_2 beam transport channel for a strong-focusing cyclotron," Int'l Conf. on Magnet Technology, Boston (2013).

[5] N. Pogue, P. McIntyre, and A. Sattarov, 'Superconducting RF cavity for high-current cyclotrons', Proc. IPAC, New Orleans (2012).

[6] A. Sattarov *et al.*, 'Flux-coupled stack of cyclotrons for a high-power ADS fission driver', *ibid*.

Copyright © 2013 CC-BY-3.0 and by the respective authors

INTERACTION REGION DESIGN AND DETECTOR INTEGRATION AT JLAB'S MEIC

F. Lin#, P. Brindza, Ya.S. Derbenev, V.S. Morozov, R. Ent, P. Nadel-Turonski, Y. Zhang,
Jefferson Lab, Newport News, VA, USA
C.E. Hyde, Old Dominion University, Norfolk, VA, USA
M. Sullivan, SLAC, Menlo Park, CA, USA

Abstract

The Electron Ion Collider (EIC) will be a next-generation facility for the study of the strong interaction (QCD). JLab's Medium-energy Electron Ion Collider (MEIC) is designed for high luminosities of up to 10^{34} $cm^{-2}s^{-1}$. This is achieved in part due to an aggressively small beta-star, which imposes stringent requirements on the collider rings' dynamical properties. Additionally, one of the unique features of MEIC is a full-acceptance detector with a dedicated, small-angle, high-resolution detection system, capable of covering a wide range of momenta (and charge-to-mass ratios) with respect to the original ion beam to enable access to new physics. The detector design relies on a number of features, such as a 50 mrad beam crossing angle, large-aperture ion and electron final focusing quads and spectrometer dipoles as well as a large machine-element-free detection space downstream of the final focusing quads. We present an interaction region (IR) design developed with close integration of the detection and beam dynamical aspects. The dynamical aspect of the design rests on a symmetry-based concept for compensation of non-linear effects. The optics and geometry have been optimized to accommodate the detection requirements and to ensure the interaction region's modularity for easiness of integration into the collider ring lattices. As a result, the design offers an excellent detector performance combined with the necessary non-linear dynamical properties.

INTRODUCTION

The MEIC accelerator complex at Jefferson Lab is designed to pursue a high luminosity to understand QCD in the nuclear physics programs [1]. As an interface between the beam acceleration/transport system and the detector, the interaction region (IR) is one of the most challenging parts of the MEIC design and largely determines the performance of the detectors and colliders. To achieve the required physics goals, the IR design should go through an optimization process between the physics requirements and accelerator performance. Besides, as part of the optics design of the complete accelerator complex, the IR design should also consider the modularity for its integration into the collider rings. This paper provides an overall consideration from the detection and accelerator performance points of view in the IR design and demonstrates a well-developed multi-function MEIC IR layout.

#fanglei@jlab.org

IR DESIGN REQUIREMENTS AND CONSTRAINTS

Detector Requirements

The primary full-acceptance detector has a sufficiently large magnet-free space near the interaction point (IP) for detection of particles down to about 0.5° in front of the final focus blocks. In addition, to allow detection of particles scattered between 0-0.5°, the hadrons and electrons need to pass through the large-aperture final focusing quadrupoles and are detected by the further downstream (up to 37 m) detector components. To maximize the detector's acceptance to the forwarding-scattered hadrons and electrons, both the ion and electron beams are focused downstream of the forward final focus so that small beam sizes at the focal points allow one to place the detectors closer to the beam centers. In combination with ~1 m dispersion at those points, this allows detection of particles with small momentum offset $\Delta p/p$. This optics was optimized to maximize its angular and momentum acceptance and detector resolution [2].

The considerations of detection performance in the IR design can be comprehensively described as follows,

1. large detector space (-4.4m / +7m) for a full-acceptance detector,
2. detection of forward scattered hadrons down to 0° achieved by
   - large aperture downstream ion final focusing quadrupoles,
   - strong spectrometer dipole,
   - large machine-element-free drift space after the spectrometer dipole,
   - secondary focus after the spectrometer dipole combined with large dispersion for better momentum resolution,
3. detection of low-Q^2 electrons and electron momentum analysis,
4. large 50 mrad crab crossing angle for faster beam separation to
   - reduce parasitic collisions due to high repetition rate,
   - increase space for magnets,
   - obtain better detector resolution,
5. IP locations
   - close to exit from ion arcs to reduce the residual gas scattering background,
   - far from exit from electron arcs to reduce synchrotron radiation background.

Copyright © 2013 CC-BY-3.0 and by the respective authors

Beam Dynamic Requirements

To achieve the required high luminosity, the colliding beams are strongly focused to a small spot at the IP, associated with a large transverse beam expansion before its focusing. This unavoidably induces a large chromatic betatron tune spread and chromatic beam smear at the collision point. The betatron tune spread is limited by the beam resonances and therefore restricts the ring's momentum aperture. The chromatic beam smear increases the beam spot size at the IP, resulting in a luminosity loss. A dedicated compensation approach to the chromatic effects has been reported and studied systematically by using a symmetric Chromaticity Compensation Block (CCB) [3,4,5,6,7]. The symmetries of particle's orbital motions and dispersion in the CCB allow simultaneous compensation of the 1st-order chromaticities and chromatic beam smear at the collision point without inducing significant 2nd-order aberrations and therefore preserving the ring's dynamic aperture.

In addition, the IR design was performed to consider a simultaneous optimization of chromatic compensation and detector requirements. Such an optimized optics is asymmetrically detector-optimized, with the upstream final focusing elements placed much closer to the IP than those on the downstream side, as shown in Figs. 1 and 2 for the MEIC ion and electron collider rings. This will be beneficial in reducing both the maximum betatron functions on the upstream side and the contribution to the chromaticity.

The layout of magnets in this detector-optimized optics is shown in Fig. 3, a complete 3D model of the detector region implemented using G4beamline/GEANT4 [7]. Special attention was paid to sizes and positions of the detector region elements to avoid interference with each other and with the detector functionality. For example, i) two permanent magnetic quadrupoles were used in the electron upstream final focusing block so that they are very close to the IP to maximize the detector acceptance by reducing the solid angle blocked by the final focusing quadrupoles; ii) the upstream ion final focusing block was designed using standard ring elements as much as possible and its layout was adjusted to minimize its interference with the forward electron detection; iii) the apertures and position of the downstream electron final focusing block were optimized to maximize the forward electron acceptance while ensuring proper fit of the electron and ion quads.

Geometric Constraints

The figure-8 MEIC collider rings are designed to have two collider rings' arcs vertically stacked in the same underground tunnel. Each arc bends the beam by 240° in the horizontal plane and two arcs in one ring are connected by straights with 60° crossing angle. With the 50 mrad crab crossing angle between the two collider rings at the IP, the geometry of the IR affects the overall ring geometry. The optics design decouples this dependence of the ring geometry from the IR design by imposing the following constraints to both electron and ion ring.

1. Electron ring
   - IR
     - zero net bend and zero transverse beam shift on each side of the IP,
   - Arcs
     - 240° bending angle including the spin rotators,

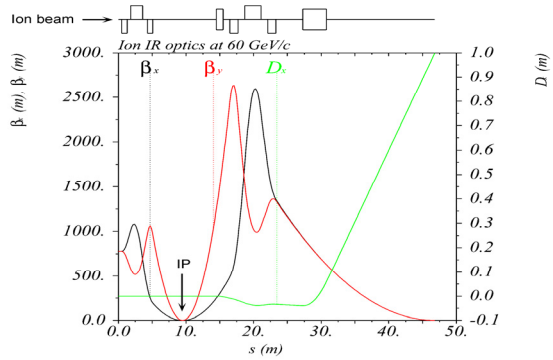


Figure 1: Detector region optics in the MEIC ion collider ring.

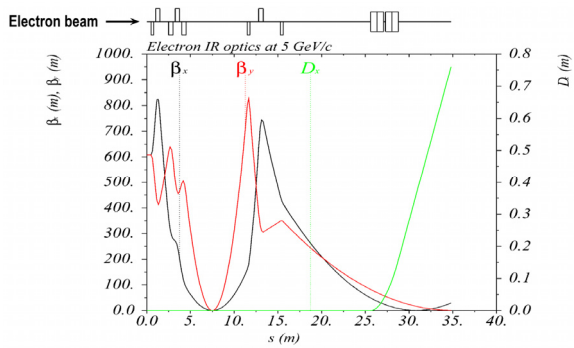


Figure 2: Detector region optics in the MEIC electron collider ring.

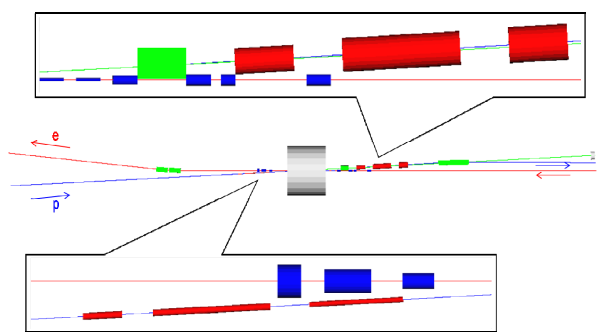


Figure 3: Layout of magnets in the detector region of MEIC collider rings.

2. Ion ring
   - IR
     - 50mrad net bend on each side of the IP to compensate the crossing angle (opposite bends on two sides of the IP),

Copyright © 2013 CC-BY-3.0 and by the respective authors

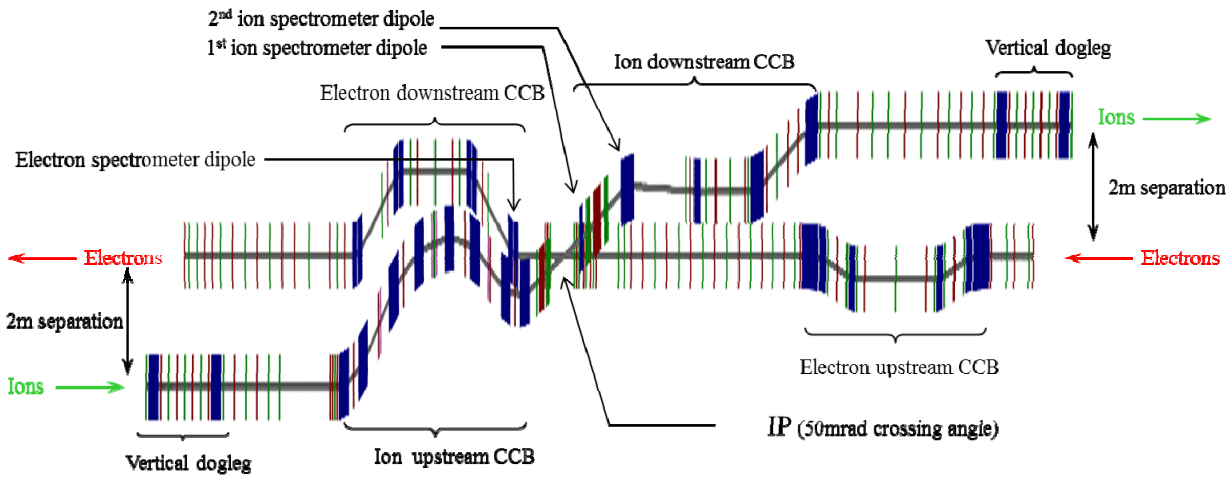


Figure 4: MEIC interaction region components and layout.

- ° 2m transverse beam shift on each side of the IP with respect to the electron ring,
- − Arcs
  - ° 240° arc bend,
  - ° 2m transverse separation from the electron ring at the arc ends.

These geometric constraints to the optics promise that the IR design is modular and any lattice changes in the IR will not interfere with the rest of the collider rings' configuration.

Combining all these considerations of detection, beam dynamics and geometry requirements, the interaction region components and its layout are shown in Fig. 4. Note that the two beam lines are parallel at the entrance and the exit of the interaction region with 2 m separation on each side. In order to compensate the chromatic aberrations at the IP and in the ring, each collider ring has two CCBs located upstream and downstream of the IP. The ion upstream and downstream CCBs produce a 50 mrad net bending angle for the crab crossing. The electron upstream CCB is moved away from the IP to avoid synchrotron radiation background in the detector.

CONCLUSIONS

An asymmetric detector-optimized IR optics design was developed for a full-acceptance detector simultaneously considering the detection requirements, chromatic compensation and rings' geometric constraints. The design provides the necessary properties of both the physics detection and beam dynamical aspects. In addition, such optics and geometry guarantee that the interaction region is modular and can be easily integrated into the collider ring lattices. We next plan to validate the design by tracking simulations.

ACKNOWLEDGEMENTS

This manuscript has been authored by Jefferson Science Associates, LLC under U.S. DOE Contract No. DE-AC05-06OR23177, DE-AC02-06CH11357 and DE-AC03-76SF00515. The U.S. Government retains a non-exclusive, paid-up, irrevocable, world-wide license to publish or reproduce this manuscript for U.S. Government purposes.

REFERENCES

[1] MEIC Design Report, edited by J. Bisognano and Y. Zhang (2012).
[2] V.S. Morozov, et al., Proc. IPAC'12, p. 2011, New Orleans, LA, USA (2012).
[3] Ya.S. Derbenev, presentation at LEMC'07, Batavia, IL, USA, (2007) [http://www.muonsinc.com/mcwfeb07/presentations/Derbenev 021307.doc]
[4] G. Wang, et al., Proc. PAC'09, p. 2649, Vancouver, Canada (2009).
[5] V.S. Morozov and Ya.S. Derbenev, Proc. IPAC'11, p.3723, San Sebastian, Spain (2011).
[6] F. Lin, et al., Proc. IPAC'12, p. 1389, New Orleans, LA, USA (2012).
[7] V.S. Morozov, et al., PRST-AB 16, 011004 (2013).

Copyright © 2013 CC-BY-3.0 and by the respective authors

MODELING SPACE CHARGE EFFECTS IN OPTICAL BUNCHERS*

L.V. Ho, P. Musumeci, J. P. Duris, R. K. Li, UCLA, Los Angeles, CA 90095, USA

Abstract

This paper introduces a 1-D, self-consistent simulation of Inverse Free Electron Laser (IFEL) based optical bunchers. Starting with a review of the conventional (monochromatic) IFEL bunching, we consider slow amplitude variation and multiple harmonics of the fundamental radiation wave. We model two new bunching schemes – the adiabatic and harmonic microbuncher and compare the bunching mechanisms between the optical bunchers as well as space charge effects to the modified IFEL interaction. Here, we present a model approximating the space charge fields and verification of the simulation with the well-known Free Electron Laser (FEL) simulator, Genesis 1.3.

INTRODUCTION

In recent years, the Inverse Free Electron Laser (IFEL) has gained popularity because of its accessibility as table-top accelerator with high energy gradient and most of all– because of its ability to microbunch beams on orders of the radiation scale [1]. Microbunched beams finds various applications throughout accelerator and beam physics including its use as a seed for high-gain harmonic generation (HGHG) FEL, preinjectors for advanced accelerators, and production of high quality, high current beams [2, 3].

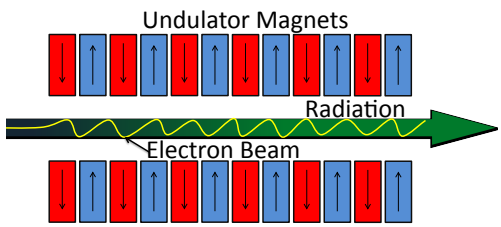


Figure 1: IFEL Interaction - Copropogating electron beam and laser within an undulator.

An IFEL consists of a laser and an electron beam copropogating within an undulator such that the electric field of the radiation is parallel to the wiggling of the electrons induced by the undulator (Figure 1). Efficient energy exchange between the beam and laser occurs when the resonant condition is satisfied – that is, when the electrons have energies such that the oscillation induced by the wiggler in its rest frame is in resonant with the electric field of the laser. This is satisfied when electrons has energy [1]:

$$\gamma_r^2 \simeq \frac{\lambda_\omega}{2\lambda}\left(1+\frac{K^2}{2}\right) \tag{1}$$

where γ_r is the resonant electron energy, λ_ω is the undulator wavelength, λ is the radiation wavelength, and $K = \frac{eB}{mck_\omega}$ is the normalized undulator parameter.

The IFEL was introduced by Palmer in 1972, who proposed the possibility of 10 GeV electron acceleration using the IFEL interaction [4]. In recent years, various experiments have shown the success of IFEL to achieve high-energy gradients with good beam quality [2], with experiments being done in national laboratories such as ATF and Livermore [5, 6]. In addition, the use of the IFEL microbunched beams have been demonstrated to increase radiation gain of over seven orders of magnitude in the HGHG FEL [3].

Here we present a 1-D IFEL simulation with the capability of including slow amplitude variation and multiple harmonics of the fundamental radiation wave. Thus, we can model the three different types of IFEL based optical bunchers: the conventional (monochromatic), harmonic, and the adiabatic microbuncher. With the newly proposed harmonic and adiabatic buncher, the ability to modulate the electron beam density is increased significantly, with bunching factors larger than 90 % [2, 7]. Space charge effects in ultra-relativistic electron beams may no longer be neglected, and considerations of its effects on the resulting beam becomes more important. We first present a review of the IFEL based optical bunchers. Then, we introduce a model approximating the space charge fields and verification of the bunching simulation with Genesis 1.3.

MICROBUNCHING THEORY

Monochromatic Microbuncher

The basic IFEL interaction of microbunching can be described in terms of phase space variables, γ and ψ, as alternative representations of the momentum and position of the electrons. The equations of motion are [1]:

$$\frac{d\gamma_i}{dz} = \frac{1}{2}kK_l\frac{KJJ}{\gamma_i}\sin\psi_i + \frac{e}{m_0c^2}E_i^{sc} \tag{2}$$

$$\frac{d\psi_i}{dz} \simeq k_\omega - k\frac{1+K^2/2}{2\gamma_i^2} \tag{3}$$

where the i denotes the i^{th} electron, $k_\omega = \frac{2\pi}{\lambda}$ is the undulator wavenumber, $k = \frac{2\pi}{\lambda}$ is the radiation wavenumber, $K_l = \frac{eE_0}{m_0c^2k}$ is the normalized radiation potential, and $JJ = J_0(G) - J_1(G)$ is the coupling factor due to the geometry of the undulator, where $G \approx \frac{K^2}{4+2K^2}$.

In the special case where there is no net energy exchange between the radiation and electrons, the resonant energy is constant, $d\gamma/dz = 0$, and modulation of the density of

* Work supported by DOE grant DE-FG02-92ER40693

Copyright © 2013 CC-BY-3.0 and by the respective authors

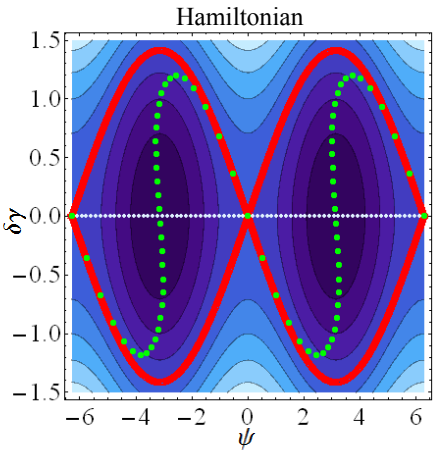


Figure 2: IFEL Hamiltonian for small oscillations and electron trajectories near resonant particle.

the electron beam occurs (microbunching). Figure 2 illustrates a contour of the Hamiltonian as well as the separatrix (bucket), denoted by the solid red line, and its reduction to a cosine-like potential for small oscillations about the resonant particle. In addition, Figure 2 shows the phase space evolution of electrons with energies close to the resonant energy (within the separatrix) reveal rotation within phase space, indicating the modulation of electron densities.

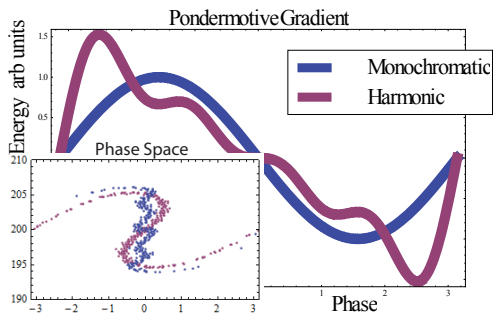


Figure 3: IFEL pondermotive gradients. The harmonic potential includes the first 4 harmonics of the fundamental radiation. The longtidunal phase space (lower left) illustrates the phase space of each gradient.

Harmonic Microbuncher

For the harmonic microbuncher, the novel change is the addition of multiple harmonics of the fundamental radiation to copropogate with the electron beam [8]. The pondermotive potential is no longer limited by the nonlinearities experiences by the monochromatic buncher, but becomes more like an ideal simple harmonic oscillator with the addition of more harmonics (Figure 3) [2]. In theory, a combination of infinite harmonics can produce a perfectly linear restoring force and thus perfect bunching and infinite current, limited only by space charge [2].

Adiabatic Buncher

The adiabatic buncher is another proposed microbuncher that eliminates the nonlinearities of the pondermotive potential [7]. An appreciable quality of the adiabatic microbuncher over the other two is its ability to preserve longitudinal beam emittance [7]. In this interaction, the radiation power is slowly increased along the undulator to fulfill the adiabatic condition – to change the amplitude of the pondermotive gradient on time scales much longer than the synchrotron period in order to preserve beam quality. In practice, the adiabatic condition is challenging to implement but can be approximated by utilizing the diffraction dominated regime of a gaussian wave and a very long undulator [7]. Figure 4 illustrates the validity of the approximation and the output longtidudinal phase space.

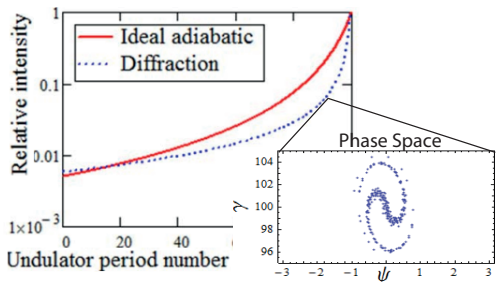


Figure 4: Fulfillment of the adiabatic condition and the approximation of the diffraction effects [7].

SIMULATION

Space Charge Approximation

The space charge fields are modeled by approximating each macroparticle as charged finite radial disks and summing the effects due all other macroparticles. In solving the coupled differential equations (2) and (3), we focus only on one bucket, with the assumption that all other buckets behave similarly. To evaluate the space charge effects, we must also account for the neighboring buckets and their contribution to the primary bucket.

Obtaining the electric field of one macroparticle on another and applying periodic boundary conditions, the electric field can be evaluated by:

$$E_0^{sc} = \epsilon \sum_{x}^{N} \sum_{b=-\infty}^{\infty} \operatorname{sgn}(\Delta_0 - b) \left(1 - \frac{1}{\sqrt{1 + \left(\frac{\Lambda}{\Delta_0 - b} \right)^2}} \right)$$

where $\epsilon = \frac{1}{2\epsilon_0} \frac{I_p \lambda}{Nc} \frac{1}{\pi \sigma_x^2}$, $\Delta_0 = \frac{\psi_x - \psi_0}{2\pi}$, $\Lambda = \frac{\sigma_x}{\lambda}$, I_p is the input peak current, N is the total number of macroparticles, b is the bucket, and σ_x is the transverse beam size.

When examining the sum over the buckets, we can see that contributions due to the buckets located to the left can be manipulated such that the buckets need only to be summed from $b = 0$ to $b = \infty$. In addition, because the

Copyright © 2013 CC-BY-3.0 and by the respective authors

sign function is defined to be 0 for $\mathrm{sgn}(0) = 0$, this avoids double counting of the particle in the bucket of interest. Then, the contribution of the electric field on the 0^{th} particle due to the x^{th} particle and its mirroring buckets can be written as:

$$E_0^{sc}(\psi_x) = \epsilon \,\mathrm{sgn}\,\Delta_0 \left(1 - \frac{1}{\sqrt{1+\left(\frac{\lambda}{\Delta_0}\right)^2}}\right) + \sum_{b=1}^{\infty} \frac{1}{\sqrt{1+\left(\frac{\lambda}{\Delta_0 - b}\right)^2}} - \frac{1}{\sqrt{1+\left(\frac{\lambda}{\Delta_0 + b}\right)^2}}$$

It is then possible to evaluate this sum for various phase positions, Δ_0, and use a n^{th} order fit function to replace this sum. This heavily simplifies the summation process by replacing an infinite sum to a simple polynomial function and reduces the space charge calculations to evaluating one sum that includes periodic boundary conditions.

Table 1: IFEL Monochromatic Bunching Parameters

Electron Beam	
Input Energy	100 MeV
Emittance	2 mm mrad
Peak Current	20000 Amps
Laser	
Power	50 TW
Wavelength	800 nm
Spot size $(1/e^2)$ at focus	3.56 mm
Rayleigh Range	50m
Undulator	
Undulator Length	0.96m
Undulator Period	.0639m
Undulator Parameter	.056

Verification of Simulation

The simulation, executed in Mathematica 8.0, was verified with the well-known FEL simulator, Genesis 1.3, developed by Sven Reiche [9]. This simulation is capable of modeling the conventional IFEL buncher, as well as the harmonic and adiabatic buncher.

In order to properly compare the models and the correctness of the space charge effects, we simulated in a particular case with parameters shown in Table 1. In this regime, the laser waist is much larger than the transverse size of the beam, reducing transverse effects and inducing a regime where 1-D simulations are justified. Additionally, in this regime, the gain length is much greater than the plasma length – that is $\frac{L_g}{L_p} >> 1$. This ensures that there is no radiation gain, which would otherwise counteract the space charge effects. Thus, we can clearly compare the effects of the pondermotive potential as well as space charge effects between the simulation and the Genesis 1.3 simulation without erroneous contributions existing in other particle simulators.

We found that the solutions of the equations of motion as well as the space charge calculations are consistent in the Mathematica simulation in comparison with Genesis 1.3. The bunching factors for space charge on and off are shown in Figure 5, showing the consistency between the models.

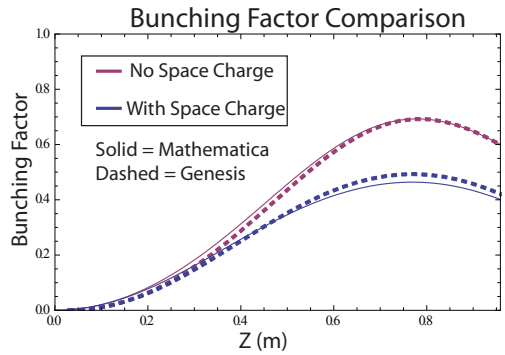


Figure 5: Comparison of Bunching Factor of monochromatic microbuncher between the simulations.

CONCLUSION

Verification with Genesis 1.3 and isolation the space charge effects validates the use of this simulation to adequately compare the different type of bunchers as well as the space charge effects.

Future plans include comparing the benefits and drawbacks of each – their experimental feasibility, bunching capabilities, and effects on the beam's final emittance, energy spread, peak current. Because space charge effects become much more dominant in the harmonic and adiabatic buncher, considerations of the extent of its affects on beam quality will also be analyzed.

REFERENCES

[1] P. Musumeci, "Acceleration Of Electrons By Inverse Free Electron Laser Interaction," UCLA, 2004.

[2] J. P. Duris *et al.*, Phys. Rev. STAB. **15**, 061301 (2012).

[3] S. Pottorf and X. J. Wang, "Harmonic Inverse Free Electron Laser Micro-Buncher," World Scientific, October 2000, ifel_gabp2kedited.

[4] R. B. Palmer, J. Appl. Phys. **43**, 3014 (1972).

[5] J. P. Duris *et al.*, WEPPP036, Proceedings of IPAC2012, New Orleans, Louisiana, USA.

[6] J. T. Moody *et al.*, in AIP Conf. Proc. 1507, pp. 482-487, Austin, Texas, USA.

[7] P. Musumeci, "SLAC National Accelerator Laboratory FACET & TEST BEAM FACILITIES PROPOSAL: Advanced IFEL bunching experiments at NLCTA," UCLA, June 2013.

[8] P. Musumeci *et al.*, Phys. Rev. Lett. **72**, 016501 (2005).

[9] S. Reiche, "Numerical Studies for a Single Pass High Gain Free-Electron Laser," Universitat Hamburg, 1999.

Copyright © 2013 CC-BY-3.0 and by the respective authors

STABILITY OF EMITTANCE VS. SPACE-CHARGE DOMINATED BEAMS IN AN ELECTRON RECIRCULATOR *

S. Bernal†, B. Beaudoin, M. Cornacchia, and D. Sutter
IREAP, University of Maryland, College Park, MD, USA

Abstract

We report on experiments and simulations of beam lifetime at the University of Maryland Electron Ring (UMER) for an emittance as well as a strongly space-charge dominated beam. We note the presence of expected (and strong) integer resonances for both beam currents and the absence, for moderate envelope mismatch, of some half-integer resonances for the high current beam only. The observations are related to particle-tracking simulations with the matrix code ELEGANT. The simulations employ a simple incoherent space charge model for a continuous beam, as well as lattice and magnet errors.

INTRODUCTION

The operation of all circular accelerators rely on careful selection of the betatron tunes for optimal beam quality and lifetime. In addition, when collective effects are an important factor, systematic study of current-dependent phenomena, e.g. envelope resonance conditions, is required. The basis for our investigation is the University of Maryland Electron Ring (UMER), a low-energy, high-current compact machine dedicated to beam physics research [1, 2]. We discuss the use of a simple computer model and show that the results are consistent with the main features of experimental beam lifetime charts, i.e. charts that display the surviving fraction of injected beam current at a given turn as a function of betatron bare tunes. Of particular interest is to compare the beam lifetimes of emittance-dominated and space-charge dominated beams.

When space charge is a factor, realistic 6D computer simulations of beam evolution over even a few turns is very computer intensive. Customarily, particle-in-cell codes are employed for tracking hundreds of thousands or even million of macroparticles. Other calculations with space charge such as transverse rms envelope matching are performed with matrix codes such as TRACE3D [3] which employ a linear space charge model and do not allow particle tracking. By contrast, the matrix code ELEGANT [4] can be adapted to do particle tracking in the presence of strong transverse space charge including non-linearities. The ELEGANT model of transverse space charge is only approximate but has yielded satisfactory results in envelope as well as dispersion calculations in UMER [5].

EXPERIMENTS

We have conducted experiments with two electron beams, 0.6 mA and 6.0 mA, both at 10 keV. The initial normalized rms emittances are 0.4 μm (0.6 mA) and 1.3 μm (6.0 mA); the bunch duration is 100 ns for both beams. In one set of experiments, all 70 DC magnetic ring quadrupoles are powered with currents varying from 1.65 to 2.10 A in 10 mA steps, while the injection (pulsed) quadrupoles (YQ and QR1) are kept fixed at the nominal operating currents. For each operating set of quad currents, the transmitted peak beam current is measured with a wall-current monitor located roughly half-way around the ring. In the second set of experiments, the value of one of the injection quads (QR1) is also varied so its focal length equals the corresponding one for the ring focusing quadrupoles. The other injection quadrupole (YQ) could not be varied because it plays a critical role for the injection angle into the closed orbit.

Figure 1a displays the results of beam lifetime at the 10th turn as a function of *estimated* bare tunes for the 0.6 mA beam (emittance dominated) when varying the strength of QR1. Deep red in the figures indicates 90-100% transmission while deep blue or purple near complete loss. The overall beam transmission for the 0.6 mA beam at the 10th turn is slightly improved by varying QR1 (the results with fixed QR1 are not shown), particularly far from the nominal operating point (I_F, I_D) = (1.826,1.826)A, indicated in Fig. 1a by "0". "$I_{F,D}$" refer to the currents of focussing and defocussing ring quadrupoles. Also worth noting is that good transmission for 0.6 mA occurs for $\nu_{0x} \gtrsim 6.5$, but it is greatly reduced for $\nu_{0x} \lesssim 6.5$.

Figures 1 b-c illustrate the beam lifetime results for the 6.0 mA beam (space-charge dominated at injection). The results of varying QR1 are more dramatic for the 6.0 mA beam. In this case, the beam losses near the nominal horizontal bare tune ν_{0x} = 7.5 are markedly reduced. Further, significant beam transmission occurs for highly asymmetric focusing, around (ν_{0x}, ν_{0y}) = (5.5, 8.5), unlike the case for 0.6 mA (Fig. 1a.) Finally, beam transmission for 6.0 mA displays an asymmetry around the line defined by $\nu_{0x} + \nu_{0y}$ = 13, corresponding to a sum resonance. Notice that beam transmission, overall, is noticeably better for the 6.0 mA beam than for the 0.6 mA, with e.g. no visible beam loss at ν_{0x} = 6.5 for the former.

The *estimated* bare tunes in Fig. 1 are determined through a transformation of the quadrupole current space, which is square [(1.65, 2.09) A×(1.65, 2.09) A in 10 mA steps], into the trapezoidal tune space using an effective quadrupole peak gradient per amp of g_0 = 3.95 G/cmA and standard matrix formulas (specifically, the inversion of eqs. 18-ab in Ref. [6].) The choice of g_0 corresponds to a calibration to the observed integer-resonance bands for the *low-current* beam (Fig. 1a). Another model of UMER in ELEGANT based on fitting g_0 to match results from response matrix measurements leads to a slightly different tune calibration [7]. We stress the fact that the plots in Fig. 1 are meant mostly as a guide to study beam lifetime

* Work supported by the U.S. Department of Energy.
† sabern@umd.edu

Copyright © 2013 CC-BY-3.0 and by the respective authors

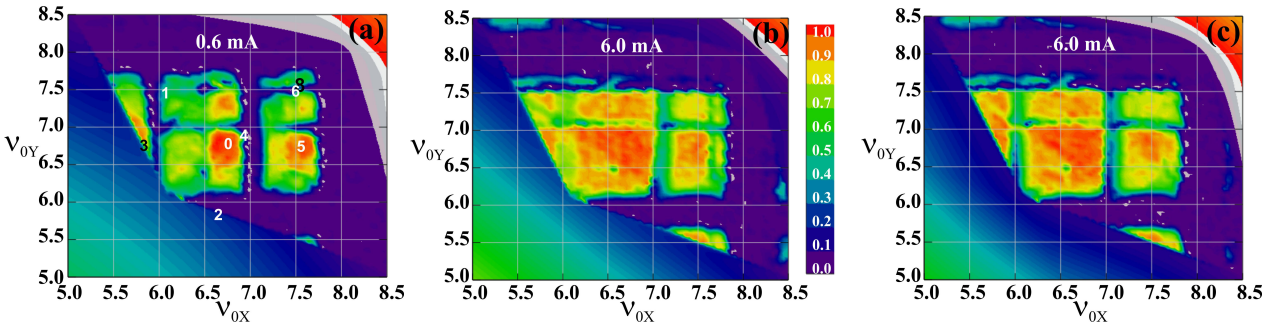


Figure 1: Beam lifetime charts at 10th turn as a function of estimated bare tunes (x: horizontal, y: vertical): (a) 0.6 mA beam (emittance dominated) with varying strength of injection quadrupole QR1 (see text ant Table 1); (b) 6.0 mA beam (space charge dominated) with fixed strength of QR1; and (c) 6.0 mA beam with varying strength of QR1. The green and red areas on opposite corners are artifacts of the graphics.

as a function of tunes, and that a more accurate calculation of tunes requires inclusion of all magnets. In fact, including the injection quadrupoles, and especially a realistic model of the main bending dipoles is important. The dipoles are used also as orbit correctors in UMER; the corrections compensate for the action of the vertical earth's field, the quadrupole radial displacement errors, and the machine imperfections.

Image forces also modify the tunes by values measured to be -0.003 and -0.03 for 0.6 and 6.0 mA beams, respectively, at the default operating point of 1.826 A [8]. The effect of image forces is seen by comparing Figs. 1a and 1b: e.g. the occurrence of the resonance at $\nu_{x0} = 7.0$ is shifted to an *apparently higher* value for the 6.0 mA beam relative to the 0.6 mA beam.

COMPUTER SIMULATIONS

The lattice model in ELEGANT employs hard-edge focusing and bending elements following the model described in [6], 3 injection elements (2 wide-aperture quadrupoles and one dipole), and a uniform 0.4 G earth's B-field pointing downward. A small quadrupole focusing term K1 = 3.45 m^{-2} is also included at every dipole; this arises from the presence of a sextupole component and the sagitta effect of particle orbits. Furthermore, *symplectic* quadrupoles and dipoles are employed.

We include magnet alignment and strength errors for the calculations: displacement errors of (rms) amplitude $(DX, DY) = (0.3, 0.1)$ mm; ring quadrupole strength error of amplitude $\Delta K1 = 1.0$ m^{-2}; and 2 mrad quadrupole and dipole tilt angle errors. The distribution of errors is Gaussian in all cases, with a cutoff of 2σ. Furthermore, we link the radial (DX) alignment errors of ring quadrupoles in groups of 4 as in the actual ring sections. We also implement a simple model of incoherent *transverse* space charge for a *continuous* beam [5], but image forces and momentum errors are *not* included. Also missing in the model are a number of vertical-steering corrector magnets.

The simulations are run over 10 turns with initial *beam* Courant-Snyder parameters that correspond to near rms-envelope matched conditions, and particle tracking is performed with 10K particles. We limit the simulations to 10 turns mainly because effects from debunching are not included. These effects, which manifest after about 20 turns for the 6.0 mA beam, render ineffective the measurement of the AC component of the beam current which is key for quantifying the beam lifetime as a function of tunes.

Out of the more than 2,000 operating tunes represented in Figs. 1, we focus our attention on a small number for tune measurements and for calculations in ELEGANT. The tunes are obtained by doing sinusoidal fits to 3 sets of difference orbits (for 6.0 mA); the resulting errors are 0.03 to 0.1. We calculate the small-amplitude tunes in ELEGANT by running a simple lattice model, with no magnet errors, over one turn. The Table below summarizes the results for 9 operating points; these are also indicated as numerals in Fig. 1a. The calculated and measured tunes agree in all cases but one to better than 0.08.

Table 1: Calculated (ELE.) and Measured (EXP.) Horizontal (x) and Vertical (y) Betatron *Linear* Tunes. Injection quad YQ is fixed at $K1 = -99.86$ m^{-2} (6.0 mA beam) for most points, while injection quad QR1 is varied (see text and Fig. 1a.)

	Ring Quad Currents I_F(A), I_D(A)	ν_{0x} ELE.	ν_{0y} ELE.	ν_{0x} EXP.	ν_{0y} EXP.
0	1.826, 1.826	6.744	6.850	6.677	6.850
1	1.750, 1.920	6.066	7.521	N/A	N/A
2	1.750, 1.650	6.641	5.908	N/A	N/A
3	1.650, 1.750	5.768	6.756	5.787	6.740
4	1.850, 1.850	6.852	6.950	6.727	6.902
5	1.960, 1.860	7.538	6.787	7.555	6.793
6	1.990[1], 1.990[1]	7.453	unst.	7.531	7.632
7	1.990[2], 1.990[2]	7.443	7.567	7.452	7.525
8	2.000[3], 2.000[3]	7.536	7.610	7.570	7.601

[1] Inj. quads: (YQ,QR1) = (−99.86,114.43) m^{-2}
[2] Inj. quads: (YQ,QR1) = (−114.43,114.43) m^{-2}
[3] Inj. quads: (YQ,QR1) = (−115.00,115.00) m^{-2}

At operating points like 0 and 5 in Table 1 and Fig. 1a, beam transmission at the 10th turn is essentially 100%. The magnet and lattice errors assumed (see above) lead in calculations to centroid oscillations of maximum amplitude of close to 6 mm and 10 mm in the horizontal and vertical planes, respectively, at point 0. At point 5, the calculated centroid oscillations are 4 mm and 10 mm, maximum amplitude. The magnitude of the oscillations in the vertical plane is about a factor of 2 larger than observed in beam-position-monitor data and also in results from simple calculations. Also regarding operating point 5, we note the

Copyright © 2013 CC-BY-3.0 and by the respective authors

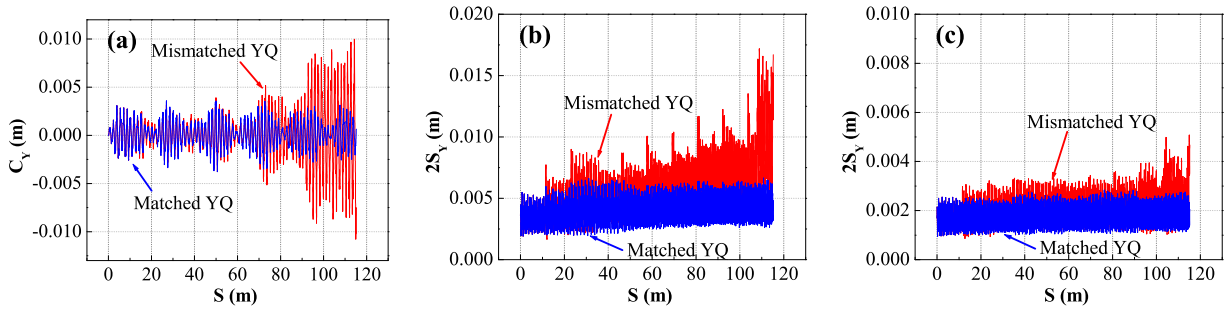


Figure 2: Results of calculations (*with* incoherent transverse space charge) in ELEGANT over 10 turns at (1.99, 1.99)A operating point in UMER: a) Vertical component of centroid motion for either 0.6 or 6.0 mA beams; b) 6.0 mA beam's vertical 2×rms semi-axis; and c) 0.6 mA beam's vertical 2×rms semi-axis. The strength of injection quadrupole YQ is increased by ∼15% to yield near-matched envelope conditions past $\nu_{0y} = 7.5$. The vacuum pipe radius is 0.025 m.

proximity to $\nu_{0x} = 7.5$, but the fact that beam transmission is unaffected at the 10th turn (Fig. 1c). Furthermore, envelope calculations with the "unmatched" original strength of the injection quad QR1, corresponding to Fig. 1b, show a steep increase in the 2×rms horizontal envelope of the 6.0 mA beam to almost 16 mm before the 10th turn, but only a modest increase for the 0.6 mA under the same conditions. Thus, retuning of QR1 in calculations makes a far more noticeable difference for high current than for low current, as in the experiment.

At four operating points (1, 2, 4, and 6 in Table 1), the beam circulates for 5 turns or less, insufficient to allow us to measure the tunes accurately at all these points. In ELEGANT, point 1 corresponds to tunes near (ν_{0x}, ν_{0y}) = (6.0, 7.5), while point 2 leads to tunes near (6.5, 6.0). The large centroid excursions seen in calculations for point 1 can explain the almost complete beam loss after only a few turns. Point 4 has (ν_{0x}, ν_{0y}) near (7.0, 7.0) and leads to the largest centroid oscillations and also to steep envelope growth after only 5 turns. Lastly, point 6 leads to an unstable vertical orbit and corresponding growing vertical centroid oscillations and envelope growth.

In Fig. 2a, we show the results of vertical centroid motion for two values of the strength of the injection quad YQ corresponding to "mismatched" and "matched" focal lengths, i.e. points 6 and 7 in Table 1. Also shown (Fig. 2b) are the vertical envelopes (2×rms semi-axis) for the 6.0 mA beam. These results are consistent with experiment: point 6 yields only 5 turns while point 7 recovers almost 80% beam transmission. A simple calculation using $\Delta\nu_0 = (4\pi)^{-1}\bar{\beta}(\Delta k_0)L$, where $\bar{\beta} = 0.22$ m, $\Delta k_0 = +15$ m^{-2}, $L = 7.45$ cm, shows that retuning YQ, as described above, leads to $\Delta\nu_{0y} = +0.020$, compared with $\Delta\nu_{0x} = -0.010$ from Table 1 (ELE.) However, no conclusive change in tunes can be measured because of the large errors, at least ± 0.05 near $\nu_{0y} = 7.5$.

Figure 2c shows the vertical 2×rms semi-axis of the 0.6 mA beam for "matched" and "mismatched" cases. The difference between the two cases is smaller than for the 6.0 mA beam. This example and results for a few additional operating points are in qualitative agreement with experiment, as little difference is seen in the beam lifetime chart for the 0.6 mA beam if the injection quad QR1 is adjusted to match the ring quads.

Naturally, without image forces in the model, the results for centroid motion do not change for the lower current beam, but those for the rms beam size yield about half the amplitude as for 6.0 mA because of the reduced incoherent space charge. At point 1, about half the peak beam current survives in the experiment at low current (Fig. 1a), unlike the case for 6.0 mA. Smaller envelope excursions, differences in orbit steering corrections and detuning from image forces may explain the different beam lifetimes.

To summarize, calculations of linear tunes with the code ELEGANT using a simple model are in good agreement with measurements in UMER. Further, calculated centroid and beam envelope evolution over 10 turns relate well to observed beam losses at points near integer and half-integer tunes. Other than reasonable assumptions for the magnitudes of magnet and lattice errors, the model has only one adjustable parameter, i.e. the transfer function of ring quadrupoles. The beam lifetime charts from experiments show that the emittance-dominated beam behaves more coherently than the space-charge dominated beam. Additional work for the near future includes more realistic modeling of lattice errors, improved tune measurements, and calculations and measurements of incoherent tunes.

We acknowledge helpful assistance from D. Brosius with typesetting the manuscript.

REFERENCES

[1] R. Kishek *et al*, Nucl. Instr. Methods in Phys. Res. A, in press (2013).
[2] Martin Reiser, *Theory and Design of Charged Particle Beams*, 2nd ed., (Wiley, V.C.H., 2008).
[3] Particle Beam Optics Laboratory Ver. 3.0.1.0, G.H. Gillespie Associates, Inc., 2010.
[4] M. Borland, Tech. Rep. Elegant: A Flexible SDDS-Compliant Code for Accelerator Simulations, Advanced Photon Source LS-287, Argonne Natl. Lab. (2000).
[5] S. Bernal, *et al*, Phys. Rev. ST. Accel. Beams, **14**, 104202 (2011).
[6] S. Bernal, *et al*, Phys. Rev. ST. Accel. Beams, **9**, 064202 (2006).
[7] M. Cornacchia, UMER Technical Note, June 10th, 2013 (unpublished).
[8] D. Sutter, *et al*, Proc. 2011 Part. Accel. Conf., New York, NY, p. 1668.

Copyright © 2013 CC-BY-3.0 and by the respective authors

EXPERIMENTAL DETECTION OF ENVELOPE RESONANCE IN A SPACE-CHARGE-DOMINATED ELECTRON RING*

W.D. Stem, T.W. Koeth, I. Haber, B. Beaudoin, IREAP, University of Maryand, College Park, MD 20742, USA

Abstract

Linear perturbation analysis of the RMS envelope equations predicts a frequency splitting of the transverse envelope modes with the onset of space charge. The resulting resonances are a potential source of beam degradation for circular particle accelerators and storage rings encountering space charge. Following WARP simulations that predict measurable consequences of these resonances, an experiment has been designed for their direct detection. This paper provides a detailed description and preliminary results of an experiment to study envelope resonances in the beam at the University of Maryland Electron Ring (UMER), a scalable high intensity electron storage ring.

INTRODUCTION

In a particle beam, the set of particles that make up the transverse extremes of the beam at any given time is called the envelope. Because each particle oscillates sinusoidally in and out of the bulk, the envelope make-up changes in time. Independently of these particle oscillations, the envelope itself oscillates as described by the K-V equations [1,2,3]. These oscillations can be two different types as shown in Figure 1. The first type is called the breathing or even mode, in which the envelope oscillates in an azimuthally symmetric sense. The second is called the quadrupole or odd mode, in which the oscillations of the envelope are 90 degrees out of phase.

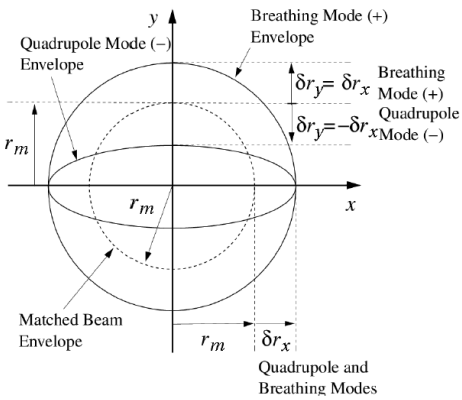


Figure 1: Transverse picture of the envelope modes [4].

At high energies, these envelope oscillations have the same frequency. This frequency occurs at a half-integer resonance, naturally determined from the geometry of the accelerator ring. At the onset of space charge a frequency splitting occurs and we can observe each of these oscillations independently. This frequency splitting is shown for UMER operating parameters in Figure 2.

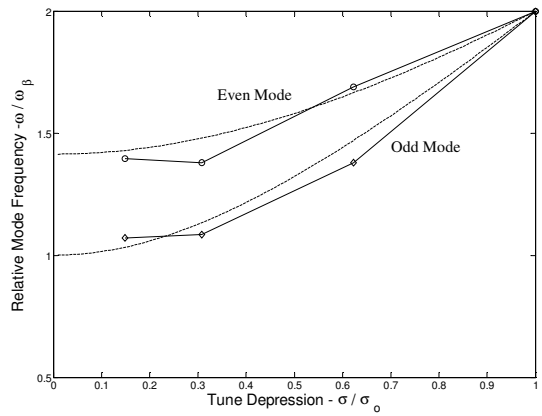


Figure 2: Relative envelope mode frequencies as a function of the tune depression for UMER operating parameters, plotted next to a calculation for the smooth approximation (dashed lines).

If we apply the appropriate perturbation to the envelope in phase with the mode we are trying to identify, the envelope will magnify in amplitude. This amplitude magnification results in the formation of a beam halo as shown in WARP simulation results [5]. After applying the perturbation, we can image the beam halo using a phosphor screen. Sweeping across frequencies, we can identify the resonant frequency of the oscillation as it will be proportional to the formation of beam halo. Applying the breathing mode perturbation may be possible with UMER's existing beam position monitors (BPMs), but the quadrupole mode requires the addition of an electrostatic quadrupole. This paper details the design, fabrication, and bench testing of the electrostatic quadrupole.

QUADRUPOLE DESIGN

In order to apply a quadrupole perturbation to the beam envelope, it is necessary to create a time-varying quadrupole field to match the oscillation frequency of the mode. To accomplish this, we create a resonant LC circuit using the quadrupole as a capacitor. The circuit design is shown in Figure 3.

*Work supported by US Dept. of Energy Offices of High Energy Physics and Fusion Energy Sciences, and by the Office of Naval Research and Joint Technology Office.

Copyright © 2013 CC-BY-3.0 and by the respective authors

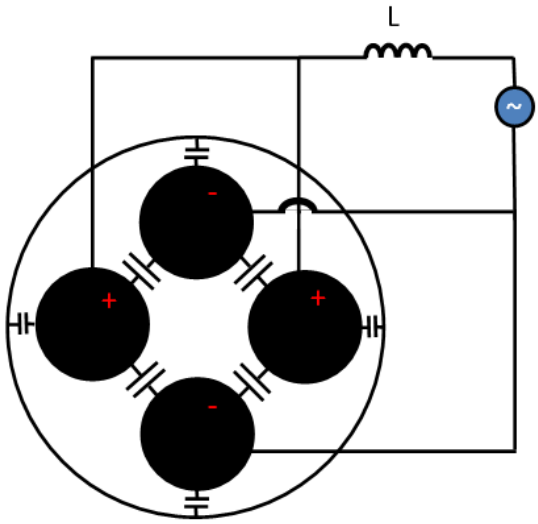


Figure 3: Circuit design for the electrostatic quadrupole. There is an undesired parasitic capacitance as the quadrupole interacts with the beam pipe wall.

Ideally, electrodes for a quadrupole field should have a hyperbolic cross section. However, fixing the ratio between the radius of the aperture and the radius of the electrode at 1:1.1468, a circular cross section approximates a hyperbolic cross section [6].

The quadrupole will replace an existing BPM in a BPM chamber. Due to the close proximity of the beam pipe wall, there exists a parasitic capacitance between the electrodes and the beam wall. To reduce this parasitic capacitance, the quadrupole's electrodes were designed to be half cylinders. The electric fields were simulated using a program developed by the Los Alamos Accelerator Code group called Poisson/Superfish [7]. The simulation is shown in Figure 4.

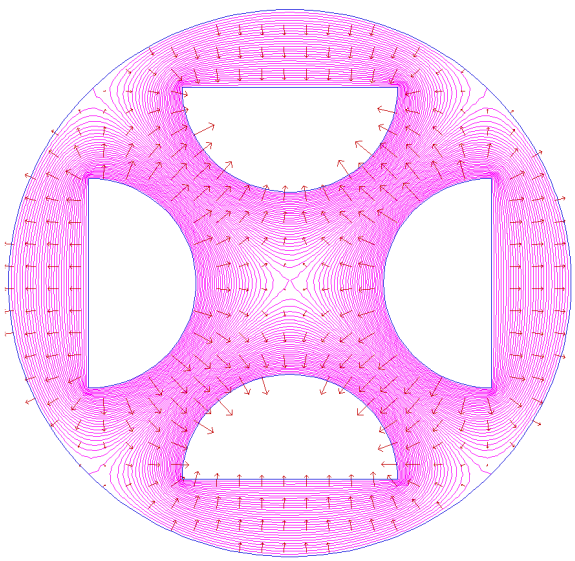


Figure 4: Poisson/Superfish electrostatic quadrupole simulation.

Since the opposing electrodes need to carry an identical, symmetrical voltage, the quadrupole was designed so that each group of opposing electrodes is in electrical contact through the base. Then the electrode pairs are attached by an insulating material. The CAD design for the quadrupole is shown in Figure 5.

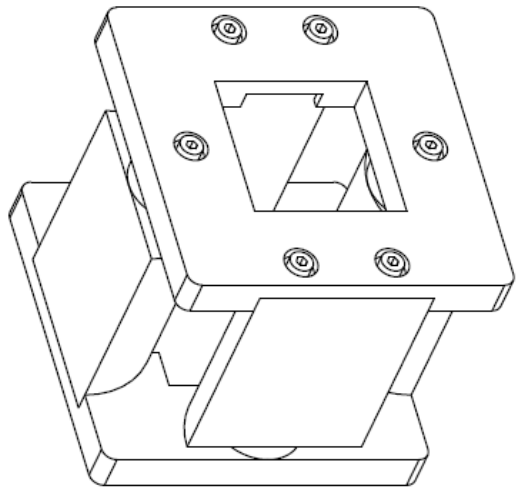


Figure 5: Pro/E diagram of machined quadrupole. Material is aluminum except for the insulating washers and insulating screws.

BENCH TESTS

Having machined the quadrupole to the CAD design in Figure 5, we proceeded to take measurements. By connecting a variable inductor to the bases of the quadrupole using the circuit design shown in Figure 3, a resonant circuit was formed. Using an MFJ-259B SWR Analyzer, the resonant frequency of the resonant circuit was measured. By finding the resonances for several values of inductance, we could plot the resonant frequency versus inductance and extract the capacitance according to the following equation:

$$C = \frac{1}{L(2\pi f_0)^2} \quad (1)$$

where f_0 is the resonant frequency of the circuit. This value was checked against a direct measurement of the capacitance using an SR715 LCR Meter. Initially, we used a stack of Mylar washers an inch in diameter for the insulating standoff. However, with a large area and a dielectric constant of 3.1, the capacitance between the electrodes and the base across the insulating gap was too great and it dominated the capacitance value between the electrodes. Instead, we opted for thinner, hollow plastic tubes to be used in place of the washers. Also, the base was unnecessarily large, so we fabricated new bases in the second bench model design shown in Figure 6.

Copyright © 2013 CC-BY-3.0 and by the respective authors

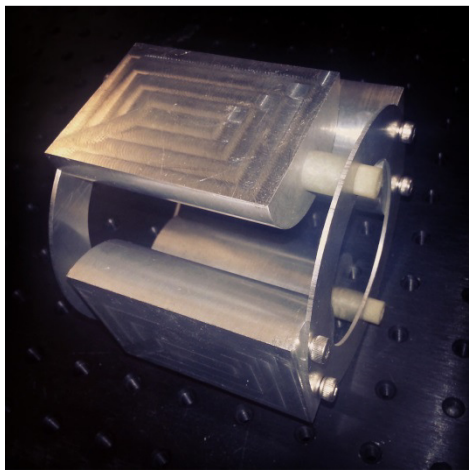


Figure 6: Finished bench model design using updated bases and insulating standoffs.

After completing a workable model of the quadrupole, we placed the quadrupole inside three sheets of wrapped sheet metal with a 6.9" inner diameter to simulate the parasitic capacitance from the beam pipe. Taking an S11 measurement with a network analyzer, the frequency spectrum for the resonant circuit was determined as shown in Figure 7. By perturbing the resonance in different ways, we have determined that the resonant peak for this circuit is just above 60 MHz. This of course can be varied by changing the value of the inductance in the LC circuit.

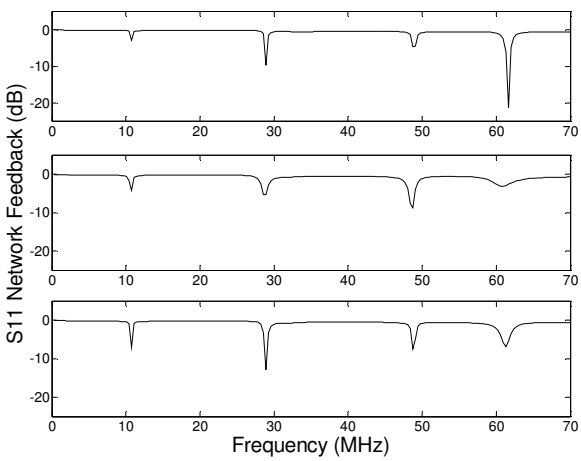


Figure 7: Frequency spectrum of the quadrupole from the network analyzer untouched (top) and touching each electrode (middle and bottom, respectively).

Using Matlab, the resonant peak was analyzed. The following formula was used to determine a Q of 444 for our resonant peak:

$$Q = \frac{f_0}{(f_{3dB} - f_{-3dB})} \qquad (2)$$

where f_{-3db} and f_{3db} represent the 3 dB bandwidth points. Using this analysis, we can verify that the parasitic capacitances from the beam pipe do not interfere with the capacitance of the quadrupole.

CONCLUSIONS

Envelope perturbations arising from resonant modes are present in space-charge-dominated particle accelerators and storage rings. It is important to understand these resonances when building and operating a high intensity accelerator to avoid emittance growth and beam loss. These modes can be observed experimentally using perturbative electric fields generated by an electrostatic quadrupole. After building a prototype and performing bench tests, we are certain that we can produce the fields necessary to induce envelope resonance in the beam. In the future, we plan to install a vacuum-ready electrostatic quadrupole into UMER and experimentally observe and manipulate high intensity envelope modes.

ACKNOWLEDGMENT

Thanks to John Pyle and Nolan Ballew of IREAP for their assistance in the fabrication of the electrostatic quadrupole. Also thanks to Timothy Ayo-Ajayi who assisted in the Pro/E CAD designs. Finally, we thank Alex Friedman, Dave Grote, and Jean-Luc-Vay for their support of the WARP code.

REFERENCES

[1] Kapchinsky, I.M. and Vladimirsky, V.V., *Proc. Int. Conference on High Energy Accelerators and Instrumentation*, CERN 1959, p. 274-288.

[2] Lapostolle, P.M., *IEEE Trans. Nucl. Sci.* **NS-18**, 1101 (1971).

[3] Sacherer, F.J., *IEEE Trans. Nucl. Sci.* **NS-18**, 1105 (1971).

[4] Lund, S.M. and Bukh, B. *Physical Review Special Topics: Accelerators and Beams*, 7 (2004), p. 024801-14.

[5] Stem, W.D. et al. *Envelope Perturbations in a Space-Charge-Dominated Electron Beam*. IPAC 2013 Proceedings, TUPME064, Shanghai, China.

[6] Hawkes, P.W. *Quadrupoles in Electron Lens Design*. Supplement 7. Academic Press. New York, 1970.

[7] Krawczyk, Frank. "Download Area for Poisson Superfish." *Los Alamos Accelerator Code Group*. 6 July 2012. 25 Sept. 2013.

Copyright © 2013 CC-BY-3.0 and by the respective authors

MEASUREMENT OF PLASMA WAVE SPEED FROM ELECTRON BEAM END EROSION*

D. F. Sutter and B.L. Beaudoin, Institute for Research in Electronics and Applied Physics, University of Maryland, College Park, MD 20742, USA

Abstract

The University of Maryland Electron Ring (UMER) normally injects a beam that is square in longitudinal profile (constant line density), filling one half the ring. When operating without longitudinal focusing, the beam head and tail erode at a constant plasma wave speed. Because the beam is very long (580 cm) compared to the beam pipe diameter (5 cm), the two eroding edges remain sharply defined until they meet. This paper describes how the plasma wave speed in the beam can be obtained experimentally by measuring only the initial pulse length, the time it takes for the eroding ends to meet and the kinetic energy. The plasma wave velocity can then be used to get an estimate of the average beam radius during the erosion time. Experimental results are compared to theoretical predictions.

INTRODUCTION

The University of Maryland Electron Ring (UMER) was built to explore the physics of non relativistic, space charge dominated beams that would be relevant for an ion accumulator ring of the type originally envisaged for application in heavy ion fusion. While the operating kinetic energy of 10 keV is very low, it is sufficient at the range of available operating currents, 0.6 to 100 mA, to serve as a good analog model for such accumulator rings. Moreover, because the relativistic gamma factor is only 1.02, there also exist a whole range of non neutral plasma phenomena that cannot be so easily observed in a highly relativistic beam. One of these is the ready generation and observation of plasma density waves. In UMER the beam can be operated with or with out longitudinal confinement [1]. When there is no longitudinal confinement, the initially almost square ends of the injected pulse begin to immediately disperse, or "erode" in a characteristic debunching pattern as shown in Figure 1. The electrons at the leading edge are pushed forward, gaining kinetic energy from the potential energy stored in the electrical potential of the beam charge, and electrons at the trailing edge are decelerated, in effect losing kinetic energy. The edges where the beam is actively eroding into the constant line charge density in the longitudinal beam center retain a sharp definition up to the point where the two edges come together in what is called the "breakpoint" in Figure 1. The rate at which each edge moves toward the center is the plasma wave velocity, c_s, and that is what is measured in this experiment.

* Work funded by the US Dept. of Energy Office of High Energy Physics and the US Dept. of Defense Office of Naval Research and Joint Technology Office.

accelphys@aol.com

PHYSICS OF THE EXPERIMENT

Boundary Conditions

The general operating parameters of UMER have been described elsewhere [2] as has the generation of density waves and solitons [3][4][5][6]. The specific properties that support the non neutral plasma experiments and modelling with cold fluid equations for space charge dominated beams are, the very long bunch length compared to the beam pipe diameter, the low beam velocity, the presence of strong space charge (for beam currents > 1 mA), and a beam density that is approximately constant over the radius. As a consequence, the radial component of the electric field, E_r, points outward and $E_z = 0$ in the region between the eroding edges. In the region between an eroding edge and the head or tail end point, E_z is proportional to the gradient in z of the line charge density, which is no longer constant. Of particular importance to the present technique, the 10 keV beam injected into UMER has an almost rectangular, constant initial line charge density profile with rise and fall times of a few nanoseconds, and a flat top of adjustable pulse length (~20 to 145 ns).

Computing the Wave velocity

The wave velocity, usually referred to as the "sound velocity" of the density wave because it is analogous to the ion acoustic velocity in neutral plasma, can be computed from [4],

$$c_s = \sqrt{\frac{e}{4\pi\varepsilon_0}\frac{1}{m_0 v_{bm}}\frac{g}{\gamma^5} I_{bm}} \quad , \text{ where } \quad g = 2\ln\frac{b}{a} \qquad (1)$$

for space charge dominated beams [3]. Noting that the classical radius of the electron r_e and the "characteristic current" I_0 are defined, respectively, by

$$r_e = \frac{e^2}{4\pi\varepsilon_0 m_0 c^2} \text{ and } I_0 = \frac{e\,c}{r_e},$$

Equation (1) can be rewritten in a more convenient form as

$$c_s = c\sqrt{\frac{1}{\beta\gamma^5}\frac{I_{bm}}{I_0} 2\ln\frac{b}{a}}, \qquad (2)$$

where c is the velocity of light, β and γ are the usual relativistic parameters, b is the beam pipe inner diameter and a is the beam radius. Given a set of beam radii corresponding to the relevant operating parameters,

Copyright © 2013 CC-BY-3.0 and by the respective authors

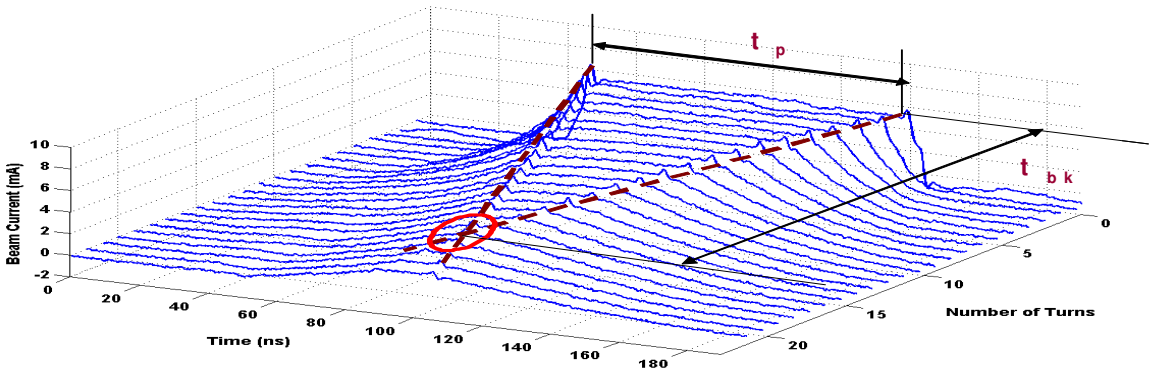


Figure 1: Mountain top plot of UMER 6 mA beam debunching past the "Break Point."

including the emittance at injection, and beam currents, equation (2) is used to compute the set of predicted values of c_s, shown in Table 1, column 3, corresponding to the initial beam radii shown in column 6. Solving equation (2) for the beam radius,

$$a = b\,e^{-A\frac{c_s^2}{I_{bm}}}, \text{ with } A = \frac{\beta\gamma^5 I_0}{2c^2} \qquad (3)$$

Equation (3) can then be used to compute a value of average beam radius based on the independent measurement of c_s described in the following section.

Sound Speed from Times

If the length of a beam pulse is t_p, and the velocity of the 10 keV beam is v_{bm}, the beam has a physical length l = $v_{bm}t_p$. But since the two edges are moving towards each other at the sound speed c_s, the edges will cover the same distance l in $2c_st_{bk}$, where t_{bk} is the break point time that it takes the two edges to come together. Since the distance is the same, $v_{bm}t_p = 2c_st_{bk}$ and

$$c_s = \frac{1}{2} v_{bm} \frac{t_p}{t_{bk}} \qquad (4)$$

So to measure the sound speed, it is only necessary to know three quantities: kinetic energy (to get v_{bm}) and the two times, the initial pulse length and the time to breakpoint. To compute the average beam radius for a measured c_s using equation (3), the corresponding beam current must also be measured.

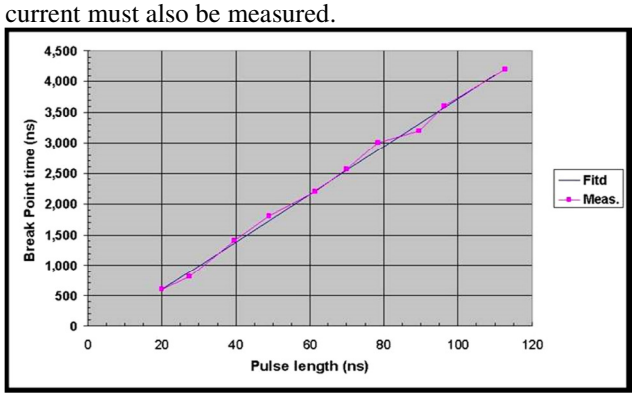


Figure 2: A plot of the measured values of t_{bk} vs t_p for a 6.0 mA beam.

MEASUREMENTS

In order to get a more accurate determination of the sound speed, t_{bk} was measured over a range of pulse lengths, and this was done for three different beam currents, I_{bm} = 0.6, 6.0 and 20.0 mA. The injected beam current is measured using a calibrated Bergoz integrating current monitor in the injection line and the values t_p and t_{bk} from a wall current monitor in the ring that displays the circulating beam current on a Tektronix DPO7254 oscilloscope. A plot of a typical data set is shown for the 6.0 mA beam in Figure 2. A linear fit is then made to the data which gives the slope and related errors as standard deviations. The fit also defines a linear relation

$$t_{bk} = mt_p + d\,,$$

where m is the slope and d the offset at $t_p = 0$, that can be used to predict t_{bk}. Using equation (4), the measured value of c_s in column 2 of Table 1 is computed from

$$c_s = \frac{1}{2}\frac{v_{bm}}{m}, \; where\; m = \left\langle \frac{t_{bk}}{t_p} \right\rangle_{fit}. \qquad (5)$$

Each of the measured values of c_s is an average over the time t_{bk}; so equation (5) gives a sort of "average of averages" of c_s over the t_{bk} versus t_p data sets.

All of the measurements were made with a beam kinetic energy of 10.000 keV giving a value of v_{bm} = 5.846 cm/ns, calculated from the special relativity relation for v_{bm} as a function of kinetic energy and electron rest energy. This was done to avoid a systematic error of ~ 1.4 % that would occur by using the nonrelativistic relation. The systematic error in equation (5) is calculated from,

$$\Delta c_s = \frac{1}{2m}\left(\Delta v_{bm} - \frac{v_{bm}}{m}\Delta m\right); \qquad (6)$$

Δm is the standard deviation of m obtained from the linear fitting routine. The results for three beam currents are shown in Table 1.

Copyright © 2013 CC-BY-3.0 and by the respective authors

Table 1: Results of measuring the sound speed in the core of the UMER beam for several beam currents. The predicted radii in column 6 are based on the computed emittance of the beam generated at the exit of the electron gun [7]. These emittances have been confirmed by independent measurements using tomographic techniques [8]. The predicted radii are used to compute the predicted c_s values in column 3.

Beam Current (mA)	Meas. c_s (cm/ns)	Pred. c_s (cm/ns)	Percent Difference	Est. Beam Radius(mm)	Pred. Beam Radius (mm)	Percent Diff.
0.58	0.0274 ± 0.0002	0.0276	0.7	1.78 ± 0.01	1.71	4.0
6.0	0.0750 ± 0.0015	0.0752	0.3	3.69 ± 0.04	3.64	1.4
20.5	0.1282 ± 0.0040	0.1223	3.5	4.87 ± 0.34	5.64	13.6

The average beam radii in column 5 of Table 1 are computed from equations (3). The contribution to the error in the exponential is dominated by the errors from values for c_s and $I_{bm;}$ so the much smaller error in A is ignored in the following expression for the error in measured beam radius,

$$\Delta a = \left\{ \frac{\Delta b}{b} - \left[2\frac{c_s}{I_{bm}}\Delta c_s - \left(\frac{c_s}{I_{bm}}\right)^2 \Delta I_{bm} \right] A \right\} a \quad (7)$$

We have used the following values in calculating the entries in table 1: b= 24.89 ± 0.089 mm, $\Delta \mathbf{I_{bm}}$ = ± 0.2 mA for all beam currents and v_{bm} = 5.846 ± .006 cm/ns based on our best estimate for momentum spread, Δp = ± 20 eV.

CONCLUSIONS

The derivation of equation (1) for c_s using the one dimensional fluid model in the cited references assumes that the electron beam is space charge dominated. The 0.6 mA beam, although it exhibits lots of serious space charge effects, is considered emittance dominated. So using the definition of equation (1) instead of the non space charge definition,

$$g = \left(\frac{1}{2} + 2\ln\frac{b}{a}\right),$$

was a question. The results in Table 1 confirm that the space charge dominated form of g works for 0.6 mA. Based on operating experience with UMER, there have been problems of beam blow up with the 0.6 mA beam, associated with injection line quadrupole settings, over the ~50 turns required to reach t_{bk}. We have found only a few sets of injection quad settings that reduce the blow up, and the presented results confirm the effectiveness of the settings used for the measurements. The lack of significant blow up for these quad values has been confirmed by kicking the 0.6 mA beam out, turn - by – turn, onto a phosphor screen for a direct, but laborious, measurement of beam radius.

Beam loss has a variety of causes, and all of these can change the assumed constant line charge density in the flattop region of the beam pulse. There are also a variety of potential causes of emittance blow up implying a corresponding radial size blow up. This experiment cannot distinguish among such causes, but the measured results for average c_s and a_{avg} for the 0.6 and 6.0 mA beams indicate that such effects are minimal over the corresponding times to t_{bk} (~50 turns for 0.6 mA and ~18 turns for 6.0 mA at t_p = 100 ns) and the machine operating parameters in place during the measurements. Beam and emittance blow up are known issues for the more strongly space charge dominated 20 mA beam. So the measured results are better than expected, but then the number of turns to t_{bk} is only ~10 or 11- not a very long sample of beam behaviour.

In summary, the work presented shows that the use of this simple c_s measurement technique is a quick and easy way to get an estimate of beam behaviour over the store time from injection to the breakpoint and is easier than the beam knockout and phosphor screen method that is our only other present alternative.

REFERENCES

[1] B. Beaudoin, I. Haber, R.A. Kishek, S. Bernal, T. Koeth, D. Sutter, P.G. O'Shea, and M. Reiser Physics of Plasmas **18**, 013104 (2011).
[2] R. Kishek, et al,"The University of Maryland Electron Ring Program," Proceedings, U.S. PAC 2013.
[3] K. Takayama and R. Briggs" Induction Accelerators," Springer, Berlin 2011.
[4] J.J. Deng et al, "Longitudinal Focusing of a Space-Charge Dominated Beams in the U of MD Electron Ring," U.S. PAC 1997.
[5] D.X. Wang et al, "Restoration of Rectangular Pulse Shape after Edge Erosion for a Space-Charge Dominated Electron Beam" PRL, 73, 1 (1994).
[6] Y. Mo, R.A. Kishek, D. Feldman, I. Haber, B. Beaudoin, P.G. O'Shea, and J.C.T. Thangaraj, Physical Review Letters **110**, 084802 (2012).
[7] Internal Note: UMER-09-0730-RAK.
[8] D. Stratakis, R.A. Kishek, S. Bernal, R.B. Fiorito, *et al.*, "Generalized Phase-Space Tomography for Intense Beams," Physics of Plasmas **17**, 056701 (2010).

Copyright © 2013 CC-BY-3.0 and by the respective authors

PRELIMINARY ACCELERATOR DESIGN OF A CIRCULAR HIGGS FACTORY IN CHINA

Q. Qin, J.Y. Tang, Y.W. An, S. Bai, J. Gao, H.P. Geng, Y.Y. Guo, D. Wang, S. Wang, Y.W. Wang, M. Xiao, G. Xu, S.Y. Xu, T. Yue, J.Y. Zhai, C. Zhang, Institute of High Energy Physics, Chinese Academy of Sciences, P.O. Box 918-9, Beijing 100049, P. R. China

Abstract

Since the Higgs boson was announced to find at LHC in CERN last July, many labs around the world have showed their interests on building electron positron colliders as Higgs factories to investigate the features of the Higgs boson. IHEP also proposed a circular Higgs factory last Sept. with a circumference of 50 – 70 km, and can be converted to a super proton-proton collider, which can be a discovery machine for new particles and physics. A preliminary design of circular electron positron collider as a Higgs factory is given here.

INTRODUCTION

On July 4, 2012, CERN announced that the Higgs boson was found at the Atlas and CMS experiments of LHC. The mass of the Higgs boson is about 125 GeV, which is only 20 GeV higher than the maximum beam energy LEP reached. After that moment, concept of Higgs factory were proposed, including circular e^+-e^- collider, linear collider, muon collider and γ-γ collider. Among these machines, the international linear collider has been studied by global efforts for more than 10 years, with the TDR [1] just released, but the accelerator technologies of circular machine seem more mature after being developed during the past decades. Muon and γ-γ colliders are also considered as the candidates of Higgs factory, but some of their technologies are still under development. Reviews of these machines can be found in [2].

As the development of future high energy accelerator , a circular e^+-e^- collider (CEPC) as the Higgs factory was proposed in IHEP, China, last Sept. with a circumference of 50–70 km. It can also be converted to a super p-p collider (SppC), with the beam energy of 50 TeV or more, as a discovery machine in the far future. Figure 1 shows a schematic graph of the whole machine (CEPC+SppC).

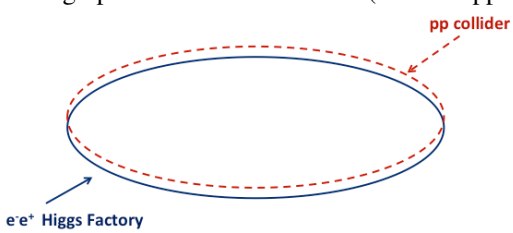


Figure 1: Schematic graph of the CEPC+SppC.

In this paper, we will first describe the determination of beam and machine parameters of the CEPC. Then, the linear lattice of the main ring will be given. The preliminary linear lattice design of the possible SppC converted from the CEPC by using the same tunnel is also presented. Some problems, covering both accelerator physics and technologies, are discussed at last.

PARAMETER DETERMINATION

In this section, main parameters for such a high energy collider will be given, after considering some important effects of beamstrahlung and the limit of synchrotron radiation power.

Beam Energy, Circumference, and Luminosity

As to a collider, beam energy and peak luminosity are the most important parameters.

Since the mass of Higgs particle is 125 GeV, the beam energy of CEPC can be set in the range of 120 – 125 GeV. In such a high energy region, beamstrahlung due to very strong synchrotron radiation (SR) when the two beams interact at IP, will be the main reason of the beam energy spread increase and thus the luminosity reduction. Under this concerning, we choose the lower limit of the Higgs particle, say 120 GeV, as the design energy of the storage ring of CEPC. Figure 2 shows the crossing-section of the Higgs at this energy region [3], from which we can see that though the lower beam energy was taken, the cross-section doesn't decrease too much.

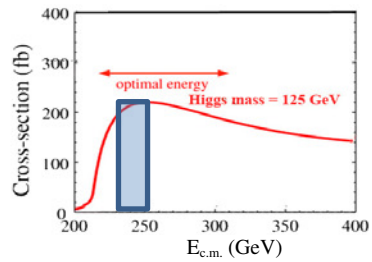


Figure 2: Cross-section at the Higgs energy region.

If we take cross-section of 200 fb and we need 20000 Higgs events per IP every year, we can easily get that the average luminosity will be $1\times10^{34}cm^{-2}s^{-1}$, which is then the design value for the CEPC.

The circumference of the CEPC storage ring can be determined by the future super p-p collider, converted from the CEPC. So the maximum proton beam energy, for example, E_{cm}=50–90 TeV, will be the energy of SppC, and thus we take 50–70 km as the circumference of the CEPC. Here we first use 50 km as the input parameter.

Considering the operation experience of LEP, we take the design value of vertical beam-beam parameter ξ_y as large as 0.1 for the CEPC, and 0.004 for the SppC. Besides these restrictions, another limit comes from the synchrotron radiation power of beam, which is taken as large as 50 MW. As to the 50 km circumference ring, if

Copyright © 2013 CC-BY-3.0 and by the respective authors

we take the filling factor of bending magnets around the ring as 0.78, we can get the bending radius of dipoles as ρ = 6.2 km. With these parameters, we can get the beam current from the following equation

$$P[kW] = 88.5\frac{E^4[GeV]}{\rho[m]}I[mA], \quad (1)$$

as $I = k_b I_b$ = 16.9mA. If we don't consider the hour glass effect, or beamstrahlung, the luminosity is expressed as

$$L[\mathrm{cm^{-2}s^{-1}}] = 2.17\times10^{34}(1+r)\xi_y\frac{E[\mathrm{GeV}]I[\mathrm{A}]}{\beta_y^*[\mathrm{cm}]}, \quad (2)$$

where r is the aspect factor, β_y^* the vertical beta function at IP, and I the beam current. With Eq. (2), we can get the luminosity can reach 4.42×10^{34}cm^{-2}s^{-1}if we take β_y^*=1mm.

Energy Spread, Emittance and Aspect Factor

Beamstrahlung plays an important role in such a high energy e$^+$-e$^-$ collider when two beams interact at the IP. Theories on how beamstrahlung affects beam parameters and the corresponding formulae can be found in [4]. Beam energy spread and lifetime are seriously influenced with the following equations

$$\delta_{BS} = \frac{2r_e^3N_e^2\gamma F}{3\sigma_x\sigma_y\sigma_z}, \quad R = \frac{\sigma_x}{\sigma_y}, F(R=1)=0.325, F(R>>1)\approx\frac{1.3}{R}, \quad (3)$$

and

$$\tau = \frac{20C\sqrt{6\pi}r_e\gamma}{\alpha^2\eta c\sigma_z}u^{3/2}e^u, \; u = \frac{\alpha\eta\sigma_x\sigma_z}{3r_e^2\gamma N_e}, \quad (4)$$

where C is the circumference, r_e the classical electron radius, N_e the number of particles per bunch, γ the relativistic energy factor, η the energy acceptance, and σ_x, σ_y and σ_z the 3-D bunch sizes. With some typical beam parameters, we can get the beam lifetime is about 10–20 min, which is much shorter than the existing or previous colliders. So the top-off injection should be adopted in the future CEPC.

Combining beam-beam parameter ξ_y with Eqs. (3) and (4), we can have the beam energy spread due to beamstrahlung as

$$\delta_{\mathrm{BS}} \equiv \frac{\langle\Delta E_{\mathrm{BS}}\rangle}{E\sigma r} = 0.864r_e^3\gamma\left(\frac{N_e}{\sigma_z(\sigma_x+\sigma_y)}\right)^2\beta_y \quad 0.864r_e^3\gamma\frac{r}{\sigma_z^2}\frac{2\pi\gamma}{e}\xi_yN_e \quad . \quad (5)$$

If we take ξ_y = 0.1, we will have $N_e = 5.26\times10^{19}\varepsilon_x$. From the above equations, one can find that small N_e can reduce the beam energy spread δ_{BS}, but one has to increase bunch number and decrease the horizontal emittance to keep the luminosity as high as possible. So, 50 bunches per beam can be adopted with the particle number of 3.52×10^{11} per bunch and the horizontal emittance of 6.69 nm.rad. Eq. (6) shows the luminosity concerning the beamstrahlung effect and limit of synchrotron radiation power.

$$L_{\mathrm{limit}} = 0.4565\times10^{34}\,\mathrm{cm^{-2}s^{-1}}\frac{\rho(\mathrm{km})P_{\mathrm{SR}}(100\mathrm{MW})\sqrt{\delta_{\mathrm{BS}}(0.1\%)}}{(E/100\mathrm{GeV})^{4.5}\sqrt{\varepsilon_y(\mathrm{nm})}}$$

$$= 0.4565 \quad 10^{34}\,\mathrm{cm^{-2}s^{-1}}\frac{\rho(\mathrm{km})P_{\mathrm{SR}}(100\mathrm{MW})}{(E/100\mathrm{GeV})^{4.5}}\times\frac{\sqrt{\delta_{\mathrm{BS}}(0.1\%)}}{\sqrt{r\varepsilon_x(\mathrm{nm})}} \quad . \quad (6)$$

Here, we can take the aspect factor, r, as small as 0.005, which was already realized in the existing particle factories, like KEKB, DAFNE and BEPCII.

Longitudinal and RF Parameters

Energy spread and acceptance due to synchrotron radiation are main parameters in longitudinal, together with bunch length and momentum compaction. Beam lifetime due to beamstrahlung as a function of V_{rf} at different RF frequency can be got and shown as Fig. 3.

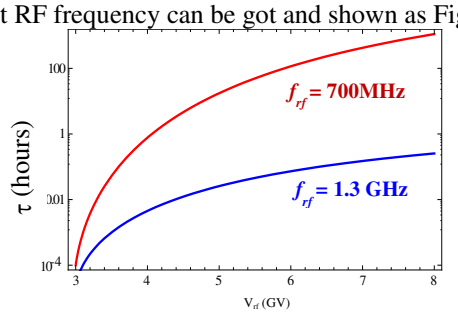


Figure 3: Beam lifetime as a function of RF voltage at different RF frequency.

If we take some typical values of σ_z<3mm, ν_s<0.3, δ_{BS} <σ_e/3, η<0.05 and τ>10 min, the correlation between α_p and V_{rf} can be got and shown as Fig. 4.

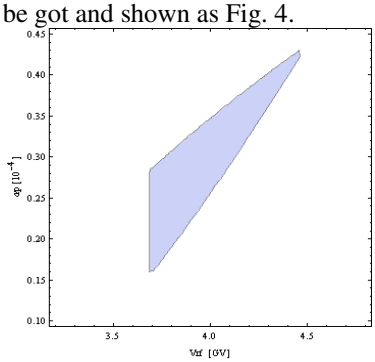


Figure 4: Momentum compaction vs. RF voltage (Grey: stable area).

If we choose the simplest FODO cell, as the basic unit of the arc, the momentum compaction can be got from

$$\alpha_p = \frac{\varphi^2}{4}\left(\frac{1}{sin^2\frac{\mu}{2}} - \frac{1}{12}\right), \quad (7)$$

and

$$\varepsilon_x = \frac{1-\frac{3}{4}sin^2\frac{\mu}{2}}{sin^3\frac{\mu}{2}cos\frac{\mu}{2}}C_q\gamma^2\frac{\varphi^2}{4}. \quad (8)$$

With ε_x = 6.69 nm.rad, we can choose $\alpha_p = 0.4\times10^{-4}$. Then from Fig. 4, we can get the total RF voltage V_{rf}= 4.2GV. The 5-cell RF cavity can be the candidate of the RF system, so we can take the acceleration field E_{acc}=10 MV/m with V_c=2 MV for each cavity. The total number of RF cavity will be 420.

Table 1 lists all the main parameters of the CEPC. The L_{limit} means the luminosity with the beamstrahlung effect. The luminosity with the beamstrahlung effect will be about half of the calculated luminosity. Here we take the hourglass coefficient as 0.6.

LINEAR LATTICE DESING OF CEPC

As we mentioned in previous section, the FODO cell is chosen as the basic unit of arcs. The phase advance of each cell is 60 degree for both horizontal and vertical

Copyright © 2013 CC-BY-3.0 and by the respective authors

planes. 16-folder symmetry is used for the whole ring and RF sections are distributed in each folder. A booster is assumed to be in the same tunnel as the main ring, with the energy range from 6 – 120 GeV. A 6-GeV linac is hoped to be the injector of the booster. For more IPs around the ring, pretzel scheme can be adopted. Figure 5 shows the Twiss functions for the standard cell in arcs.

Table 1: Main Parameters of the CEPS Storage Ring

Para.	Unit	Value	Para.	Unit	Value
Energy	GeV	120	Circum.	km	50
N_e	1E11	3.52	N_b/beam		50
Beam current	mA	16.9	SR power /beam	MW	50
Dipole field	T	0.065	Bending radius	km	6.2
$\varepsilon_{x,y}$	nm	6.69, 0.033	σ_x/σ_y	μm	36.6/0.2
β_{IP} (x/y)	mm	200/1	SR loss	GeV/ turn	2.96
$\xi_{x,y}$		0.1, 0.1	σ_z	mm	3
α_p	1E-4	0.4	IP No.		1
V_{rf}	GV	4.2	f_{rf}	GHz	0.7
ν_s		0.13	Harmonic		116747
δ_{SR}		0.0013	δ_{BS}		0.00014
η	%	2.7	τ_{BS}	hr	1.6
L_0/IP (10^{34})	/cm^2/s	2.65	L_{limit}/IP (10^{34})	/cm^2/s	1.26

To promote the luminosity at the same SR power, one has to increase the circumference of the ring. Another scheme with the circumference of 70 km is under design. Option for pretzel scheme is kept for more IPs, which can also have the luminosity enhanced, but not linearly with the number of IP. The final focusing system in the interaction region (IR) is still in its design, which will be one of the most difficult and critical parts of the machine.

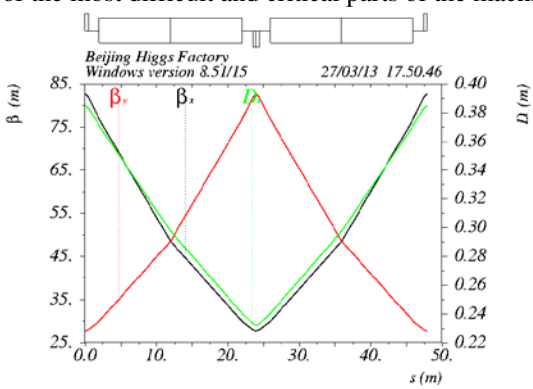


Figure 5: Twiss functions of a 60 degree cell.

The SppC, which will be constructed as a discovery machine using the tunnel of CEPC, can also have two scenarios with different circumferences, 50 km or 70 km. The maximum proton beam energy could reach 45 TeV, if the dipole field is about 20 Tesla using superconducting magnets. The energy limit mainly comes from the dipole field. The arc can also apply the standard cell with a phase advance of 60 or 90 degree.

With the empirical value of beam-beam parameter, say ξ_y = 0.004, beam current = 0.5mA, vertical beta function at the IP = 0.1m, we can get the luminosity of the SppC can be 2-3×10^{35}cm^{-2}s^{-1}. Table 2 gives the main parameters of SppC for 2 scenarios of 50 and 70 km circumference.

Table 2: Main Parameters of SppC for Two Schemes

Para.	SppC-1	SppC-2
Beam Energy (TeV)	20	45
Circumference (km)	50	70
No. of IPs	2	2
SR loss/turn (keV)	440	4090
N_p/bunch (10^{11})	1.3	0.98
Bunch No.	3000	6000
Beam current (mA)	0.5	0.405
SR power/ring(MW)	0.22	1.66
Dipole field (T)	12	19.24
Bending radius (km)	6.9	7.8
Momentum compaction (10^{-4})	3.5	2.5
β_{IP} x/y (m)	0.1/0.1	0.1/0.1
Norm. Trans. emit, x/y (μm.rad)	4	3
Geo. Lumi. reduction factor	0.8	0.9
L_0/IP (10^{35} cm^{-2}s^{-1})	2.15	2.85

DISCUSSION AND CONCLUSION

Although we have the preliminary design of the storage ring, but still a lot of problems remain. The accelerator physics related topics, such as dynamic aperture, low emittance ring design with pretzel orbits, beamstrahlung effect, design of the interaction ragion, beam background, beam polarization, collective effect and heat loading due to SR power, machine and detector interface (MDI), etc., are all very important to the machine design, and can influence the hardware system of the whole machine. Meanwhile, accelerator technology towards such a future machine needs to be developed too. The technique of very low field dipole and very high gradient quadrupole will be critical. Ultra-high field dipoles, such as 20 T, will be difficult for both superconducting and cryogenics system. How to realize the beam polarization at such a high beam energy, will be a challenge to both accelerator physics and technology.

In a word, the CEPC is very promising in physics, with some mature technologies. It could be converted to a p-p collider as a discovery machine. Some technologies need R&D, and accelerator physics studies need more efforts.

REFERENCE

[1] The International Linear Collider Technical Design Report, www.linearcollider.org/ILC/TDR, June 2013.
[2] A. Blondel et al., "Accelerators for a Higgs Factory: Linear vs. Circular", Report of ICFA Beam Dynamics Workshop, arXiv:1302.3318, Feb. 2013.
[3] S. Yamashita, Higgs at future linear collider, In Sitges 1999, Physics and experiments with future linear e+ e- colliders, vol. 1.
[4] V.I. Telnov, Restriction on the Energy and Luminosity of e$^+$e$^-$ Storage Rings due to Beamstrahlung, PRL 110, 114801 (2013).

Copyright © 2013 CC-BY-3.0 and by the respective authors

AC DIPOLE BASED OPTICS MEASUREMENT AND CORRECTION AT RHIC*

X. Shen†, S. Y. Lee, Indiana University of Bloomington, IN, 47405, USA
M. Bai, S. White, G. Robert-Domolaize, Y. Luo, A. Marusic, BNL, Upton, NY, 11973, USA
R. Tomás, CERN, CH1211 Geneva 23, Switzerland

Abstract

Independent component analysis (ICA) was applied to the AC dipole based optics measurement at RHIC to extract beta functions as well as phase advances at each BPM. Existence of excessive beta-beat was observed in both rings of RHIC at polarized proton store energy. A unique global optics correction scheme was then developed and tested successfully during the RHIC polarized proton run in 2013. The feasibility of using horizontal closed orbit bump at sextupole for arc beta-beat correction was also demonstrated.

INTRODUCTION

Accurate optics measurement and efficient optics correction schemes are highly demanded to provide more precise optics manipulation for further improvement of RHIC luminosity as well as its polarization performance.

ICA FOR AC DIPOLE BASED OPTICS MEASUREMENT

At RHIC, AC dipole has been routinely used to excite sustained coherent beam motion with large amplitude and preservation of beam emittance to facilitate acquisition of 1024 turn by turn beam position data at the beam position monitors (BPMs) [1]. Optical functions can then be extracted from the recorded BPM data by the technique of independent component analysis (ICA). ICA is more efficient than principle component analysis (PCA) because, in addition to correlations of data from all BPMs, it takes advantage of the time correlation between independent components to extract source signals with non-overlapping spectra [2]. From the spatial functions of source signals corresponding to AC dipole driven oscillation, one may extracted the modified betatron amplitude function β_d and phase advance ψ_d, which are related to the optical functions β_f and ψ_f of free betatron oscillation as [3]:

$$\beta_d = \frac{1+\lambda^2-2\lambda\cos[2(\psi_f-\pi\nu)]}{1-\lambda^2}\beta_f, \quad (1)$$

$$\tan(\psi_d-\pi\nu_d) = \frac{1+\lambda}{1-\lambda}\tan(\psi_f-\pi\nu_f), \quad (2)$$

where $\lambda = \sin[\pi(\nu_d-\nu_f)]/\sin[\pi(\nu_d+\nu_f)]$, ν_d is the driving tune of the AC dipole, and ν_f is the betatron tune of free oscillation. In Eq. (1) and (2), the reference point for phase advance is at the location of the AC dipole. In order to reconstruct the β_f and ψ_f, an accurate and efficient method was developed for routine operation. This method averages optical functions from two measurements in which ν_d is set on either side of ν_f with a distance of 0.01 to minimize the systematic errors from AC dipole driven oscillation. Details about the robustness of this averaging method against BPM errors can be found in Ref. [4].

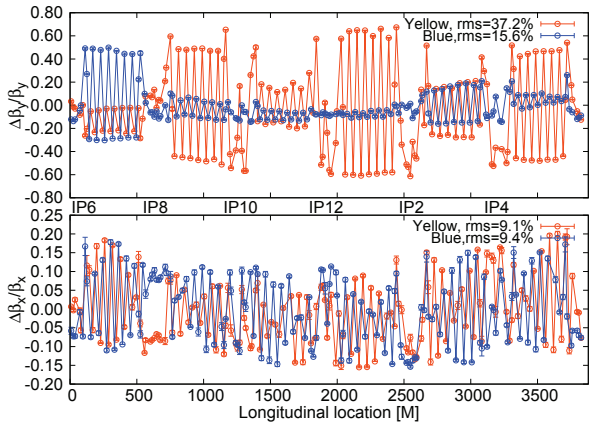


Figure 1: Measured beta-beat with error bars in the horizontal (bottom) and vertical (top) plane for both rings at RHIC. 15% peak beta-beat was observed in the horizontal plane for both rings. A 30% vertical peak beta-beat was found in the Blue ring and 60% in the Yellow ring

Figure 1 shows the beta-beat for the 255 GeV polarized proton beams in the Blue and Yellow rings during RHIC operation in 2013. In both rings, the horizontal peak beta-beat is approximately 15%. In the vertical plane, the peak beta-beat reaches 30% in the Blue ring and 60% in the Yellow ring. The excessively large beta-beat requires efficient correction to be explored.

BETA-BEAT RESPONSE MATRIX CORRECTION METHOD

The problem of beta-beat correction can be described by the following model:

$$\mathbf{WB} = \mathbf{WRK}, \quad (3)$$

where $\mathbf{B}^T = (\frac{\Delta\vec{\beta}_x}{\beta_x}, \frac{\Delta\vec{\beta}_y}{\beta_y}, \Delta\nu_x, \Delta\nu_y)$ is composed of the beta-beat vectors and tune variations, $\mathbf{K}^T = (\Delta K1L_1, \Delta K1L_2, \ldots, \Delta K1L_N)$ represents the change of integrated strength of N quadrupoles, and the superscript T means a transpose. $\mathbf{R}$ is the $M \times N$ beta-beat

* Work supported by grants from the US Department of Energy under contract DE-FG02-12ER41800 and the National Science Foundation NSF PHY-1205431.
† xiaoshen@indiana.edu

Copyright © 2013 CC-BY-3.0 and by the respective authors

response matrix. $\mathbf{W}$ is a diagonal matrix containing the weighting factors w_i $(i = 1, \ldots, M)$. To avoid beam loss and polarization loss, the tune variations receive high weights to be minimized. Beta-beat from noisy BPMs are assigned low weights. In reality, the number of independently powered quadrupoles is often very limited, i.e., $M \gg N$, such that Eq. (3) describes an overdetermined system in which the weighted measured beta-beat is minimized with the constraint of zero tune shifts. The required correction strength $\mathbf{K}_{\mathrm{cor}}$ is computed by using the generalized inverse $(\mathbf{WR})^{\dagger}$ of the weighted response matrix from singular value decomposition (SVD) as:

$$\mathbf{K}_{\mathrm{cor}} = -(\mathbf{WR})^{\dagger}\mathbf{WB}. \qquad (4)$$

Since the response matrix $\mathbf{R}$ is calculated from the ideal model, multiple iterations of correction based on Eq. (4) are necessary in the event of large beta-beat.

Based on the method discussed above, systematic computations were carried out to determine optimum correction for both rings of RHIC, in which a total of 72 triplet and trim quadrupoles in the interaction regions (IRs) with independent power supply are used as beta-beat correctors and two families of arc quadrupoles are included for tune compensation.

Figure 2 shows the relative correction strength for the Blue ring. All relative changes are below the maximum capability of power supplies. The large changes in trim quadrupoles are because the trim quadrupoles are initially set at a low field. Figure 3 shows the measured beta-beat with and without correction. The horizontal peak beta-beat was successfully reduced from 15% to 8%, while the vertical peak beta-beat was reduced from 40% to 14%. The experimental results were in good agreement with predictions.

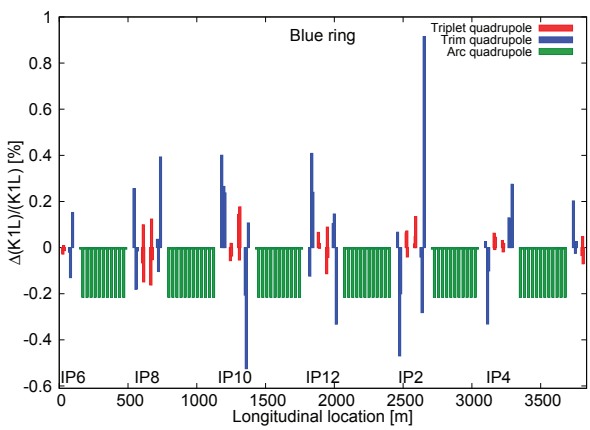


Figure 2: Relative changes of quadrupole integrated strength as a function of quadrupole locations in the Blue ring.

Due to the excessively large beta-beat in the vertical plane of the Yellow ring, two iterations of correction were implemented within the limited beam time. Figure 4 shows the computed relative corrections for the Yellow ring for the first and second iteration. Figures 5 and 6 show the

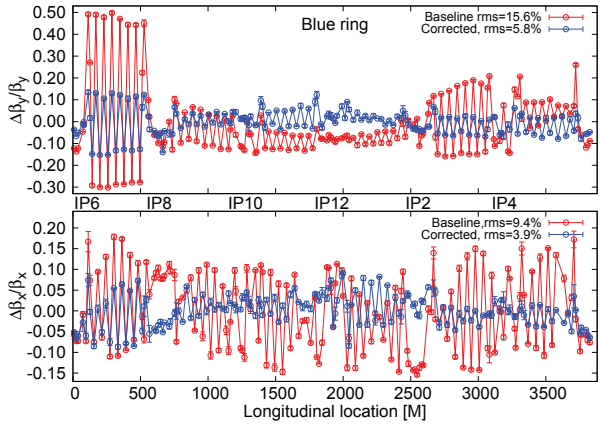


Figure 3: Baseline and corrected horizontal (bottom) and vertical (top) beta-beat with error bars for the Blue ring. Horizontal peak beta-beat was corrected from 15% to 8%, while vertical peak beta-beat from 40% to 14%.

measured horizontal and vertical beta-beat in the Yellow ring with and without corrections ,respectively. After the first iteration, the horizontal peak beta-beat was reduced to 12% which is consistent with the prediction, while the vertical peak beta-beat was reduced to 20% which still deviates quite much from the computation. Good agreement between experiment and prediction was found after the second iteration and peak beta-beat in both planes were reduced to 10%.

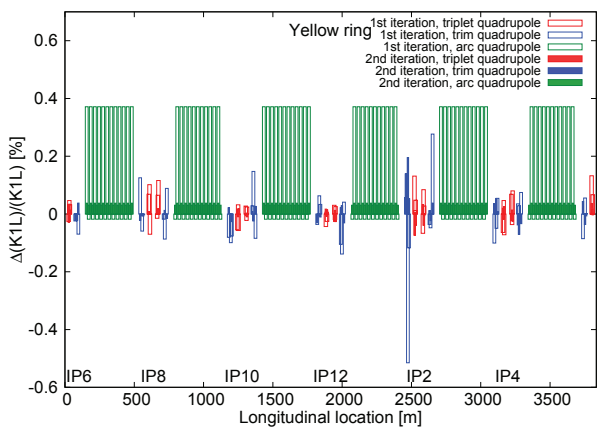


Figure 4: Relative changes of quadrupole integrated strength as a function of quadrupole locations in the Yellow ring for the first iteration (hollow bars) and second iteration (solid bars), respectively.

ARC BETA-BEAT CORRECTION USING CLOSED ORBIT BUMP AND SEXTUPOLE

In RHIC, there are no independently powered quadrupoles in the arcs such that gradient errors in these regions cannot be effectively corrected. However, feed-down normal quadrupole field from horizontal closed orbit bump at sextupole can be included as additional correctors to reduce beta-beat in these regions. This technique also provides capabilities of more precise optics

Copyright © 2013 CC-BY-3.0 and by the respective authors

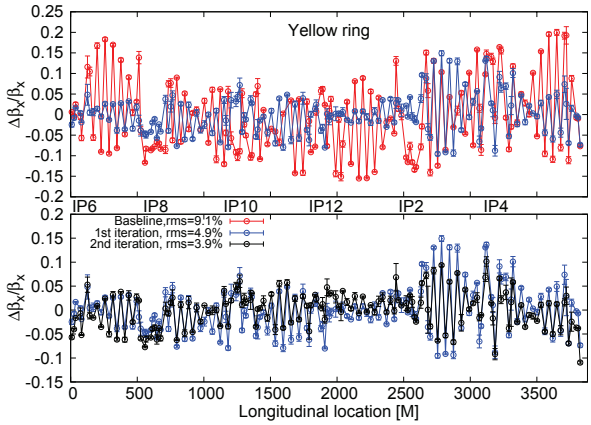


Figure 5: Baseline and corrected horizontal beta-beat with error bars for the Yellow ring. The peak beta-beat was reduced from 15% to 12% after the first iteration of correction, and further reduced to 10% after the second iteration.

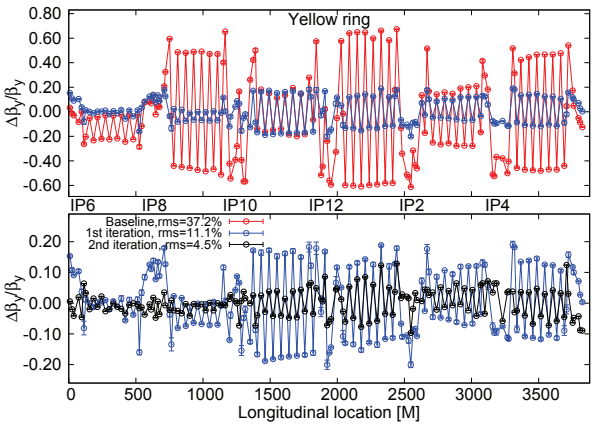


Figure 6: Baseline and corrected vertical beta-beat with error bars for the Yellow ring. The peak beta-beat was reduced from 60% to 20% after the first iteration of correction, and further reduced to 10% after the second iteration.

control to facilitate demanding optics manipulations. A proof-of-principle experiment of this technique was successfully carried out during the 2013 RHIC polarized proton operation.

Figure 7 shows the computed horizontal closed orbit required for arc beta-beat correction as well as the measured horizontal closed orbit. The computed and measured closed orbit are well matched in the arcs. The mismatches at around the interaction points (IPs) do not affect the correction performance because there are no sextupoles in these regions. The correction results are shown in Fig. 8. In the horizontal plane, beta-beat reduction was seen clearly in the arc between IP10 and IP12 as well as the arc between IP4 and IP6. In the vertical plane, significant beta-beat reduction was observed in the four arcs between IP10 and IP4. Overall, the peak beta-beat was reduced to 7%.

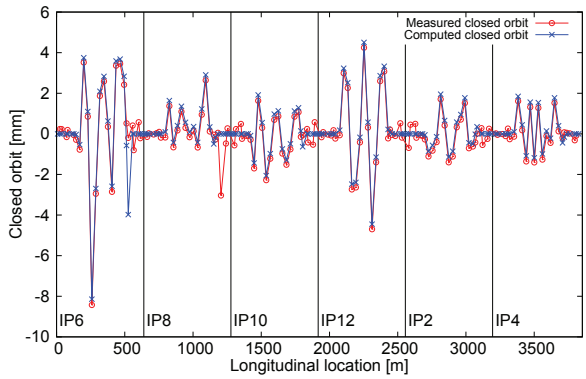


Figure 7: Measured and computed horizontal closed orbit for correction of arc beta-beat in the Yellow ring.

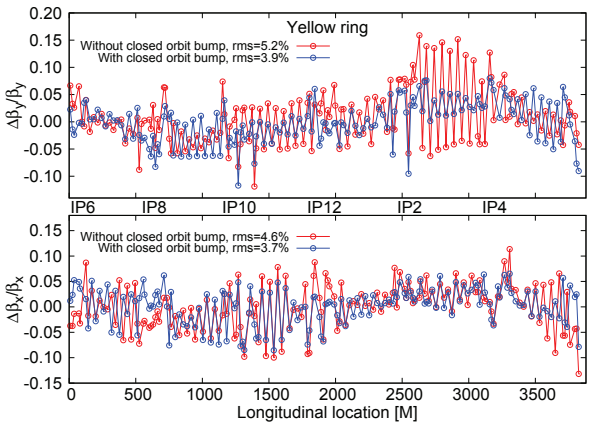


Figure 8: Horizontal (bottom) and vertical (top) residual beta-beat with and without the horizontal closed orbit bump displayed in Fig. 7 for the Yellow ring. Peak beta-beat was reduced to 7% for both planes with the closed orbit bump.

CONCLUSION

ICA was by the first time applied to RHIC to accurately extract optical functions from turn by turn BPM data of AC dipole driven betatron oscillation. With limited number of quadrupole correctors, a global correction scheme using beta-beat response matrix method was experimentally demonstrated to reduce the peak beta-beat to 10%. Peak beta-beat was further reduced to 7% during a proof-of-principle experiment of arc beta-beat correction using horizontal closed orbit bumps at sextupoles.

ACKNOWLEDGMENT

The authors would like to thank S. Tepikian for his help in providing RHIC design model, and the engineers in the beam instrumentation group as well as RHIC operators for their technical support.

REFERENCES

[1] M. Bai *et al.*, in Proc. of PAC 2003.

[2] X. Huang *et al.*, PRST-AB **8**, 064001 (2005).

[3] R. Mayimoto *et al.*, PRST-AB **11**, 084002 (2008).

[4] X. Shen *et al.*, submitted to PRST-AB.

Copyright © 2013 CC-BY-3.0 and by the respective authors

IMPLEMENTATION OF OPTICS CORRECTION ON THE RAMP IN RHIC*

C. Liu†, A. Marusic, M. Minty, BNL, Upton, NY 11973, USA

Abstract

In this report we describe and present experimental results from correction of the accelerator optics during acceleration and preparation for collisions at the Relativistic Heavy Ion Collider (RHIC) at BNL. Past experiences with beam optics correction at RHIC have concentrated on measurements and corrections at store beam energies. While well-corrected store beam optics is desirable for maximizing beam and polarization lifetime, well-corrected beam optics during the ramp is also desirable for example to reduce the strength of depolarizing resonances. With optics measurements on the ramp at every 2 or 4 seconds, corrections were computed for several fixed points on the ramp using a well-tested weighted Singular Value Decomposition algorithm. Successful implementation of correction on the second part of the ramp (rotator ramp), together with some observations on the first part of the ramp (the energy ramp) will be presented.

INTRODUCTION

Analysis of depolarizing resonances on the ramp and dynamic aperture study are part of the ramp optics design nowadays in RHIC [1]. Acceptable intrinsic resonance strength and dynamic aperture are ensured by design. With optics errors, both of these quantities are hard to predict. Most likely the machine performance in both aspects will degrade to some extent with optics errors. Therefore, it is desirable to correct the optics on the ramp for better polarization and intensity transmission efficiencies.

Besides continuous efforts for improving TbT (turn-by-turn) BPM data quality over the years [2], there are two developments in 2013 that make ramp optics correction feasible. One of the developments is the precision optics measurement based on ARTUS kicker [3] which is critical for ramp optics analysis. Firing the AC dipole for optics measurement is operational and robust at injection and store energies [4], however, it has not been demonstrated on the ramp during acceleration. Exciting the beam periodically with the ARTUS tune meter kicker has been done previously for the purpose of ramp chromaticity control, however, no successful effort has been applied to extract accurate linear optics information along the ramp. The other development is the successful demonstration of global optics corrections based on both the ARTUS kicker and the AC dipole [5, 6].

* The work was performed under Contract No. DE-AC02-98CH10886 with the U.S. Department of Energy.

† cliu1@bnl.gov

RAMP OPTICS MEASUREMENT

By firing the ARTUS kicker every 2 or 4 seconds on the ramp, TbT BPM data of free betatron oscillations can be recorded in both planes [2]. The timing of the excitations in the two transverse planes is shifted by 510 turns to reduce coupling effects. Special care was taken to avoid interference between TbT and average orbit data taking. The option of 1k, 2k and 4k turns TbT orbit is available. The option of 1k is chosen for the ramp optics measurement since usually the oscillation lasts less than 500 turns due to decoherence. Examples of TbT BPM data are shown Fig. 1.

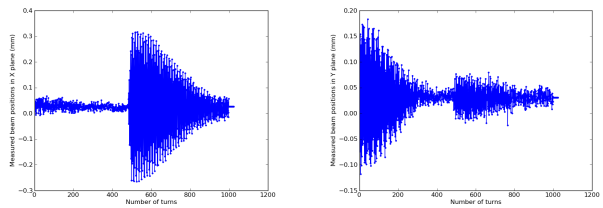


Figure 1: Turn by turn BPM positions in the horizontal (left) and the vertical (right) plane from ramp optics measurement, residual coupling (right) appears in the vertical plane where the horizontal oscillation starts.

As with usual optics analysis, beta functions and phase advances are determined for both planes from TbT BPM data. The analysis technique adopted by the author favors the data in the horizontal plane for better measurement resolution [3]. Therefore, the data in the vertical plane was shifted backwards by 500 turns (data after 500 turns being discarded) before windowed FFT being applied, which also reduces the impact of the residual coupling in the vertical plane after ∼500 turns.

The beta beats and phase errors at 289 s into the ramp are shown in Figs. 2 and 3. The whole ramp takes 320 s. Similar analyses were performed with data acquired every 4 seconds in the Blue ring and every 2 seconds for the Yellow ring. The overall trend of the optics errors is similar for both rings. As beam is being accelerated, the optics error decreases to its minmum in the middle of the ramp. Then the error goes up as beta stars are being squeezed.

RAMP OPTICS CORRECTION SCHEME

For the polarized proton program at RHIC in 2013, the ramp has two parts. The first one, during which the energy is ramped up and beta stars are squeezed, is called energy ramp. The second ramp, during which the rotator magnet ramps up, is called rotator ramp. There are 32 fixed points

Copyright © 2013 CC-BY-3.0 and by the respective authors

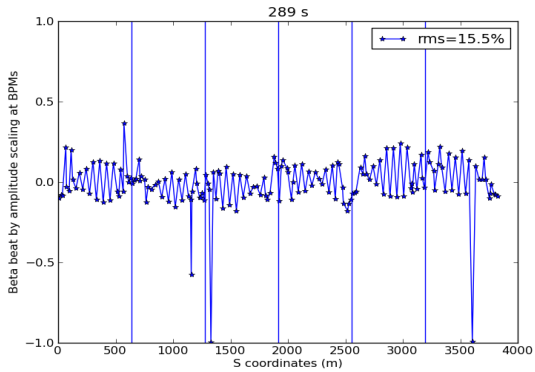


Figure 2: Beta beats at 289 s into ramp in the horizontal plane from ramp optics measurement.

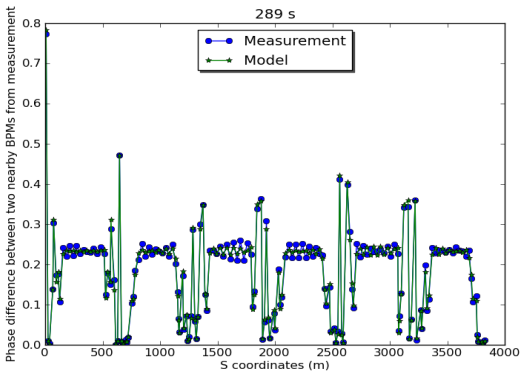


Figure 3: Phase errors at 289 s into ramp in the horizontal plane from ramp optics measurement.

(stepstones) for the energy ramp where magnet strengths are controllable for the energy ramp. The magnet strengths are interpolated between these stepstones. The rotator ramp has fewer stepstones since the optics is smoothier.

TbT orbits near stepstones are picked for optics analysis for the availability of optics models. Then corrections using the 72 trim quads are calculated based on the principle presented in [5]. Two scripts are designed for ramp optics correction. One of them goes through all the picked orbits for analyzing optics in both planes. The second one implements the corrections in RampEditor for all relevant stepstones. Due to the fact that the beam is not perfectly centered in quadrupoles, the closed orbit will vary with implementation of correction. Therefore, orbit feedback was turned on to keep the orbit stable. Besides that, tune feedback was used as well to avoid beam loss due to resonances. Chromaticity changes due to optics corrections were predicted by the online model (OptiCalc), which was then manually corrected before activation of corrections.

TEST ON ROTATOR RAMP

The concerns regarding ramp optics correction implementation are mostly related to the beam loss and beam emittance dilution. As a test, correction on a rotator ramp with fewer bunches (12 by 12) was attempted to study these effects. The test ramp was the same as a physics ramp except for the fewer bunches. The optics for the rotator ramp is considered as smooth regardless of the ramping of the rotators. Therefore, corrections calculated for the full energy were applied to all stepstones of the rotator ramp except the very first one. It means the correction strengths ramp up from the first to the second stepstone.

Beam loss of the test ramp and a physics ramp are shown in Fig. 4. The rising of beam loss around 1300 s in the Blue ring was due to other beam study. The oberservation is that the beam loss was slightly better for the test ramp during the rotator ramp and after beam collision. The IPM

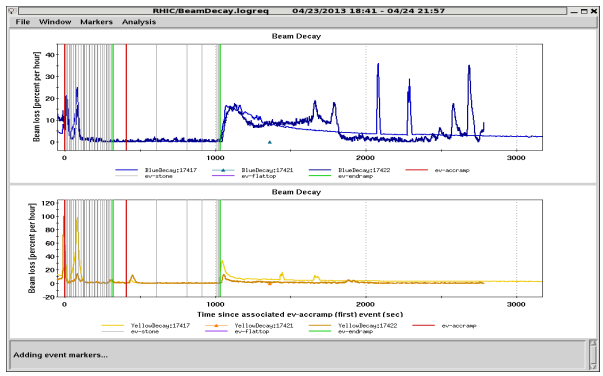


Figure 4: Comparison of beam loss between the test ramp and a physics ramp for both rings.

(Ionization Profile Monitor) reported emittance for the test ramp and a physics ramp are shown in Fig. 5. They are similar except for the large error bars due to fewer bunches. In addition, the calculated beam emittance inferred from beam collision signals are as good as in a good physics store.

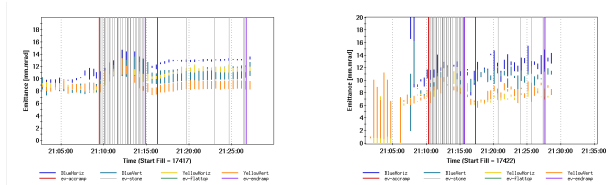


Figure 5: IPM measured emittance in a physics ramp (left) and the test ramp (right) for both rings.

The collision rate was expected to reach 1070 kHz at STAR by scaling beam intensities, which is ∼15% increase of luminosity.

The results of the test eliminate the concern of adverse effects of ramp optics corrections. Later on, the correction for the rotator ramp was implemented operationally for the physics program in the Yellow ring only due to other changes being made in the Blue ring. The rest of the program has been running with corrected optics without any complication.

Copyright © 2013 CC-BY-3.0 and by the respective authors

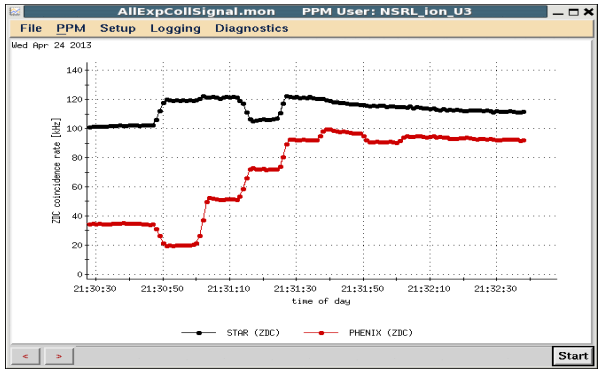


Figure 6: Beam collision signals in the test ramp for both experiments.

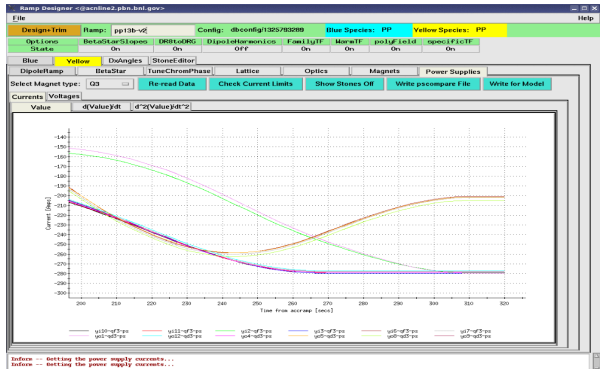


Figure 7: Current curves for selected magnets without ramp optics correction.

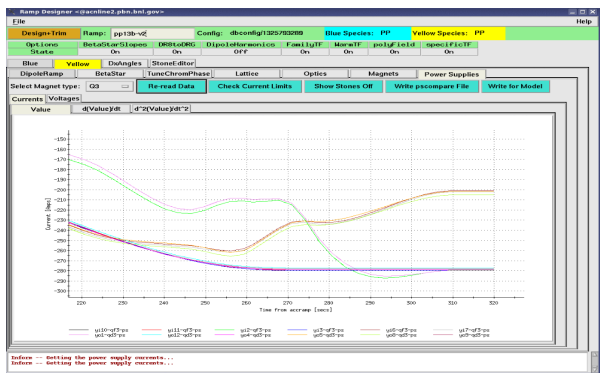


Figure 8: Current curves for selected magnets with ramp optics correction.

TEST ON ENERGY RAMP

Ramp optics correction for the energy ramp has been tested twice in 2013. We ran a 12 by 12 ramp for ramp optics measurement, ran a script to select the TBT orbit files near the stepstones and calculate optics corrections, ran script to send correction strengths to RampEditor and activated corrections. We were not able to ramp again for ramp optics measurement to verify the correction due to time limitations.

The problem encountered in the first attempt was that, each time a set of strengths were sent to a stepstone in RampEditor, the online model recalculated all relevant magnet strengths for the whole ramp which was too time-consuming. The solution was to send all correction strengths for a stepstone once, not separately. The other way around is to fix magnet strengths (anchoring) for the relevant stepstones so interpolation of magnet strengths will not occur after implementing correctons. The two ways are similar because changing strengths for a stepstone would anchor it as well. The problem encountered in the second attempt was that, anchoring stepstones changes the current curves for magnets dramatically, which caused magnets to exceed limits. The selected current curves before and after anchoring stepstones are shown in Figs. 7, 8. The ongoing effort is to change the RampManager code so that anchoring stepstones only fix the magnet strengths, but does not change the derivatives of the current curves.

SUMMARY

Precision analysis of the linear optics based on TbT BPM data by the ARTUS kicker opened out the possibility of ramp optics measurement at RHIC. Breakthrough of global optics correction added the critical piece for implementing ramp optics correction. Ramp optics correction for the rotator ramp has been implemented operationally at RHIC. Ramp optics correction for the energy ramp is in progress.

ACKNOWLEDGEMENTS

The author would like to thank the RHIC operation crew and the BPM team for their help during the beam studies. Special thanks to V. Ranjbar, M. Bai, M. Blaskiewicz, W. Fischer and T. Roser for their support of the work.

REFERENCES

[1] V. Ranjbar. Polarization transmission efficiency on ramp. Presented in RHIC retreat 2013, Brookhaven National Lab, Upton, NY, 2013.

[2] M. Minty et al. Measurement of beam optical functions during acceleration in RHIC. In *Proceedings of NA-PAC 2013*.

[3] C. Liu et al. Precision tune, phase and beta function measurement by frequency analysis in RHIC. In *Proceedings of the International Particle Accelerator Conference, 2013. IPAC 2013.*

[4] M. Bai et al. Measuring beta function and phase advance in RHIC with an AC dipole. In *Particle Accelerator Conference, 2003. Proceedings of the PAC 2003.*, volume 4, pages 2204–2206. IEEE, 2003.

[5] C. Liu et al. Global optics correction in RHIC based on turn-by-turn data from ARTUS tune meter. In *Proceedings of NA-PAC 2013*.

[6] X. Shen et al. AC dipole based optics measurement and correction at RHIC. In *Proceedings of NA-PAC 2013*.

Copyright © 2013 CC-BY-3.0 and by the respective authors

GLOBAL OPTICS CORRECTION IN RHIC BASED ON TURN-BY-TURN DATA FROM ARTUS TUNE METER*

C. Liu†, M. Blaskiewicz, K.A. Drees, A. Marusic, M. Minty, BNL, Upton, NY 11973, USA

Abstract

Deviation of the optical functions from the model may result in reduced dynamic aperture, luminosity and beam polarization all of which are of particular interest in the polarized proton program at RHIC. Peak to peak beta beats as large as +/- 80% have been observed. In Run-13, we demonstrated that the optical functions can be corrected globally by two different approaches, either beta beat or phase error correction. The optics measurement, correction algorithm and beta beat and phase error measurements before and after correction will be presented.

INTRODUCTION

RHIC (Relativistic Heavy Ion Collider) has been running with large beta beat over the years for both heavy ion and polarized proton programs. The impact on dynamic aperture and beam polarization from optics error are expected, however hard to quantify. The optics errors manifest themselves as beta beats (relative error of beta functions), or as phase advance errors, and as the integral, the tune errors. Usually, the luminosity decreases because of enlarged β^* from the presence of beta beat. Therefore, luminosity is expected to benefit from optics correction even though many other parameters contribute as well. Model optical functions are usually used in correction in accelerators, like orbit, tune and chromaticity corrections [1] since calibration of optical functions is non-trivial. The errors in optics obviously set a limitation on the best performance of the corrections. In addition, many critial diagnostics rely on model optics as well. For instance, IPM (Ionization Profile Monitor) uses model beta functions to calculate the beam emittance. The accuracy of all these diagnostics are expected to be improved with the measurement of optical functions and correction. The above facts justify the need of a robust fast turn-around optics measurement and correction scheme.

OPTICS MEASUREMENT

In RHIC, two types of TbT (turn-by-turn) BPM data can be acquired for optics measurement. One is the betatron oscillation driven by the AC dipole [2]; the other is the free betatron oscillation initiated by the ARTUS kicker [3] (tune meter). The oscillation caused by the AC dipole is adiabatical and renders high signal to noise ratio. The ARTUS kicker affects only one bunch, so it is more robust in practice. All measurments and corrections in this paper are based on TbT BPM data acquired using the ARTUS kicker.

* The work was performed under Contract No. DE-AC02-98CH10886 with the U.S. Department of Energy.

† cliu1@bnl.gov

TbT data analysis techniques, whether it is a time domain, frequency domain or any statistical method, should in principle deliver similar measurement resolutions provided they are employed to their best capacities. The author adopted a frequency domain method which produces ~0.2 deg phase measurement resolution [4] at RHIC.

In addition to measurements at BPM locations, beta functions at various critical devices can be interpolated based on the measured beta functions at nearby BPMs. First, one calculates the transfer matrices between the device and the upstream and downstream BPMs based on model optical functions. Then two equations can be established which relate the unknown beta and alpha at the device and the measured betas at the two BPMs.

$$\begin{cases} \beta_1 = R_{11}^2\beta_0 - 2R_{11}R_{12}\alpha_0 + R_{12}^2\frac{1+\alpha_0^2}{\beta_0} \\ \beta_2 = r_{11}^2\beta_0 - 2r_{11}r_{12}\alpha_0 + r_{12}^2\frac{1+\alpha_0^2}{\beta_0} \end{cases} \quad (1)$$

Here β_1, β_2 are the measured beta functions at BPM 1 and 2. R and r are the transfer matrices from the device to BPM 1 and 2 respectively. β_0 and α_0 are the unknown Twiss parameters at the device.

CORRECTION SCHEME

Global beta beat correction has been implemented on various accelerators successfully [5]. However, global phase error correction has been proposed but not demonstrated successfully [6]. The basics of the two corrections being applied in RHIC are similar. Suppose $(e_1, e_2, \ldots, e_m)'$ is the optics error (beta beat or phase error) being measured, M is the response of optics errors to quadrupole strength variationd in form of a matrix. The correction can be obtained by solving the following equations:

$$-\begin{pmatrix} e_1 \\ e_2 \\ \vdots \\ e_m \end{pmatrix} = \begin{pmatrix} M_{11} & M_{12} & \cdots & M_{1n} \\ M_{21} & M_{22} & \cdots & M_{2n} \\ \vdots & \vdots & \ddots & \vdots \\ M_{m1} & M_{m2} & \cdots & M_{mn} \end{pmatrix} * \begin{pmatrix} k_1 \\ k_2 \\ \vdots \\ k_n \end{pmatrix} \quad (2)$$

The optics error on the left side are from both planes, on which proper weights can be applied based on the scale of the errors. The correction knobs in RHIC are the 72 quadrupoles with trim power supplies which all reside in the interaction regions [7].

The response matrix for beta beat correction can be calculated either by an optics program (MAD-X) simulation or analytically based on the online model (OptiCalc) optical functions. The analytical formula are presented

Copyright © 2013 CC-BY-3.0 and by the respective authors

in Eq. 3. Betas in Eq. 3 are for the quadrupoles. The quadrupole integrated strength is assumed.

$$\begin{cases} M_{ij,x} = -\frac{\beta_{i,x}}{2\sin\pi\mu_x}\cos\left(2\pi\mu_x - 2|\phi_{i,x} - \phi_{j,x}|\right) \\ M_{ij,y} = \frac{\beta_{i,y}}{2\sin\pi\mu_y}\cos\left(2\pi\mu_y - 2|\phi_{i,y} - \phi_{j,y}|\right) \end{cases} \quad (3)$$

The results from both calculations were compared for RHIC at both the injection and store energies. Because of the fact that gamma-t quads are implemented in OptiCalc but not in the MAD-X model, the response matrices differ considerably from each other at injection energy. At full energy, the two results agree very well with each other since the contribution of gamma-t quads decreases with energy.

The response matrix for the phase error correction was only simulated with MAD-X. Therefore, the error in the phase response matrix is expected to be non-negligible due to the missing gamma-t quads at injection. At full energy, the impact of gamma-t quads on the phase response matrix should be minimal just like for the beta beat response matrix.

OPTICS CORRECTION

Due to time limitations and the known error in the model, a phase error correction was only attempted briefly at injection energy. With one iteration of corrections, the phase errors before and after correction at injection are shown in Figs. 1, 2, 3 and 4.

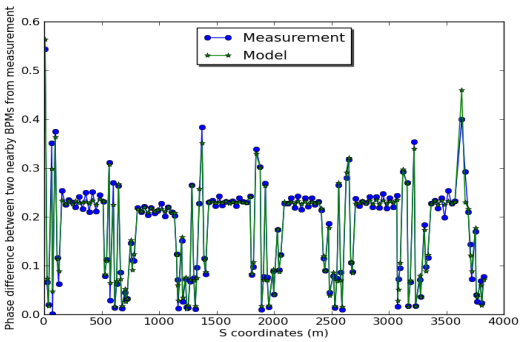


Figure 1: The measured and model phase advance in the horizontal plane before phase correction (in units of 2π).

The corresponding rms beta beat was reduced from 17.3% to 9.3% in the vertical plane, from 7.8% to 5.2% in the horizontal plane with the phase error correction.

Beta beat corrections were demonstrated in both rings at full energy. The beta beat before and after correction in the Blue ring are shown in Figs. 5 and 6. The applied integrated trim strengths for all 72 quads are shown in Fig. 7.

The phase measurement and correction has certain advantages over the beta beat correction. First, the phase measurement is model independent; secondly, the phase measurement is mostly immune to BPM calibration errors; and lastly, the phase correction will not introduce additional tune changes which have to be corrected. Phase error

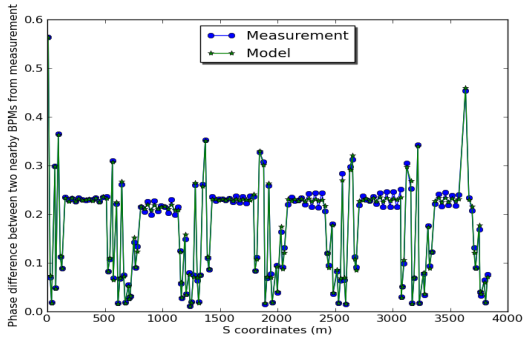


Figure 2: The measured and model phase advance in the horizontal plane after phase correction (in units of 2π).

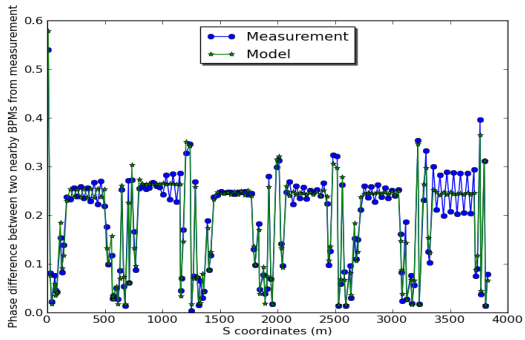


Figure 3: The measured and model phase advance in the vertical plane before phase correction (in units of 2π).

correction has been demonstrated successfully in RHIC at injection energy, however, not to its full capacity.

The beta functions at IPs (Interaction Points) are interpolated from the measurements before and after beta beat correction. The results are shown in Table 1 and 2. The numbers in parenthesis are the design values for the β^*.

SUMMARY

Both global optics correction schemes (beta beat and phase error correction) have been demonstrated successfully at RHIC based on ARTUS TbT BPM data. The beta

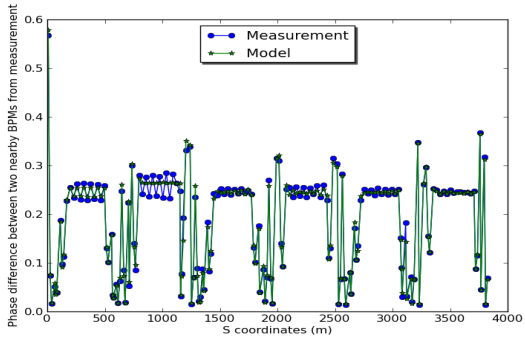


Figure 4: The measured and model phase advance in the vertical plane after phase correction (in units of 2π).

Copyright © 2013 CC-BY-3.0 and by the respective authors

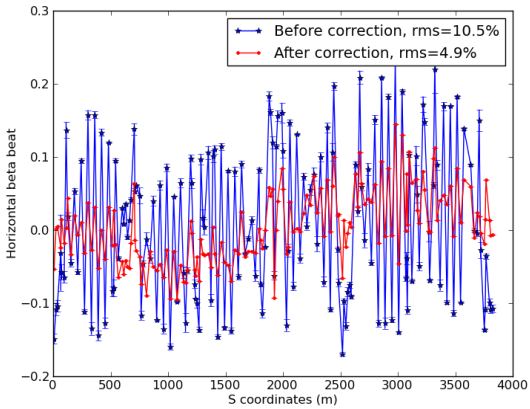


Figure 5: Beta beat in horizontal plane before (blue) and after correction (red).

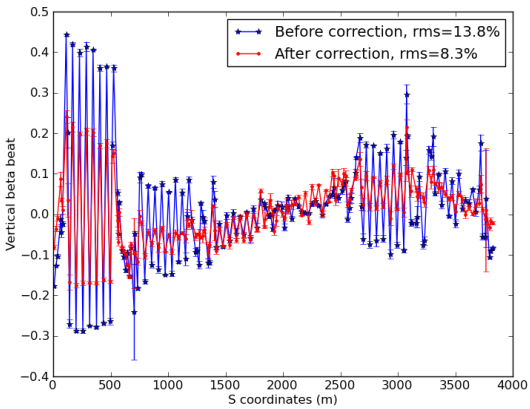


Figure 6: Beta beat in vertical plane before (blue) and after correction (red).

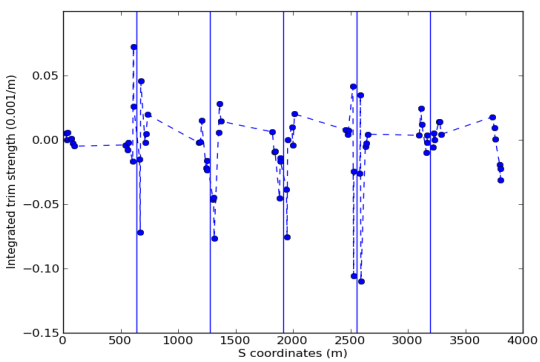


Figure 7: Applied integrated correction strength in the Blue ring at full energy.

Table 1: β^* at IPs in the Blue Ring Before and After Beta Beat Correction

	β_x **(IP6)**	β_x **(IP8)**	β_y **(IP6)**	β_y **(IP8)**
Before	0.74	0.63	0.82	0.73
After	0.66(0.64)	0.63(0.61)	0.69(0.63)	0.73(0.64)

Table 2: β^* at IPs in the Yellow Ring Before and After Beta Beat Correction

	β_x **(IP6)**	β_x **(IP8)**	β_y **(IP6)**	β_y **(IP8)**
Before	0.6	0.79	0.62	0.75
After	0.63(0.66)	0.66(0.6)	0.68(0.67)	0.70(0.68)

beat correction has since then been implemented operationally at store. The benefit on luminosity was observed [8]. The correction of β^* was verified by measurements after correction. Even though the phase response matrix has certain errors due to the missing gamma-t quads in the MAD-X model, phase error correction was demonstrated successfully at injection energy. Further studies are planned for the future. The result of a phase error correction is expected to be no worse than the beta beat correction.

ACKNOWLEDGEMENTS

The author would like to thank the RHIC operation crew and the BPM team for their assistance during the beam study. Special thanks to M. Bai and G. Robert-Demolaize for discussion, and to W. Fischer for his support and encouragement.

REFERENCES

[1] M. Minty et al. Simultaneous orbit, tune, coupling and chromaticity feedback at RHIC. *Proc. of PAC11, New York, NY*, 2011.

[2] M. Bai et al. Measuring beta function and phase advance in RHIC with an ac dipole. In *Proceedings of the PAC 2003.*, volume 4, pages 2204–2206. IEEE, 2003.

[3] A.K. Drees et al. Artus: The tune measurement system at RHIC. In *AIP Conference Proceedings*, volume 546, page 341, 2000.

[4] C. Liu et al. Precision tune, phase and beta function measurement by frequency analysis in RHIC. In *Proceedings of the IPAC 2013.*

[5] R. Tomás et al. Record low β beating in the LHC. *Physical Review Special Topics-Accelerators and Beams*, 15(9):091001, 2012.

[6] R. Calaga, R. Tomás, and F. Zimmermann. BPM calibration independent LHC optics correction. In *Particle Accelerator Conference, 2007. PAC. IEEE*, pages 3693–3695. IEEE, 2007.

[7] H. Hahn. RHIC design manual, revision of october 2000. pages 2000–2003, 2000.

[8] C. Liu et al. Implementation of optics correction on the ramp in RHIC. In *Proceedings of the NA-PAC 2013.*

Copyright © 2013 CC-BY-3.0 and by the respective authors

DYNAMIC APERTURE MAXIMIZATION WITH HEAD-ON BEAM-BEAM COMPENSATION IN RHIC*

Y. Luo, W. Fischer, S. White
Brookhaven National Laboratory, Upton, NY USA

Abstract

To reduce the large beam-beam tune spread and to compensate the beam-beam non-linear resonance driving terms, two electron lenses are being installed in the RHIC tunnel for head-on beam-beam compensation. In this article we discuss the approaches to maximize the proton dynamic aperture by adjusting the phase advances between beam-beam interaction points and the electron lenses. We present the beam-beam compensation lattice design, dynamic aperture calculation results, and comparisons between the lattices used in the previous RHIC proton operation.

INTRODUCTION

The working point in the polarized proton collision operation in the Relativistic Heavy Ion Collider (RHIC) is constrained between 2/3 and 7/10 to achieve a good beam lifetime with beam-beam interaction and to preserve the proton polarization on the energy acceleration and at the physics store. To further improve the luminosity, with an upgraded polarized proton source, the proton bunch intensity will be increased from currently 1.8×10^{11} up to 3.0×10^{11}. However, with such a high bunch intensity, there is not enough tune space between 2/3 and 7/10 to accommodate the large beam-beam tune spread.

To reduce the large beam-beam tune spread and compensate the large beam-beam resonance driving terms (RDTs), head-on beam-beam compensation with electron lenses (e-lenses) is adopted in RHIC [1]. Figure 1 shows the layout of RHIC head-on beam-beam compensation. The two proton beams collide at IP6 and IP8. Two e-lenses are being installed on either side of IP10, one for the Blue ring and one for the Yellow ring. To cancel the non-linear beam-beam RDTs from collision at IP8, we require the betatron phase advances between IP8 and the e-lens center to be $k\pi$, where k is an integer.

For the next 100 GeV polarized proton run, we will commission head-on beam-beam compensation for the first time in RHIC. To best utilize head-on beam-beam compensation and to maximize the proton dynamic aperture, we redesigned the proton lattices for both RHIC rings. On top of the above $k\pi$ phase advances between IP8 and the e-lenses, we also attempt to maximize the off-momentum dynamic aperture by adjusting the phase advances between the two collisional IP6 and IP8. In the following, we first discuss the phase requirements for head-on beam-beam compensation, then present the newly designed lattices and the calculated proton dynamic apertures compared with the previous RHIC proton operation lattices.

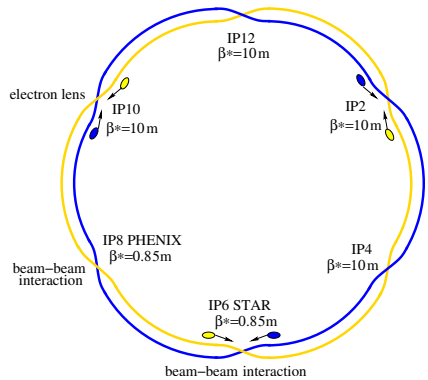


Figure 1: Layout of RHIC head-on beam-beam compensation. Proton beams collide at IP6 and IP8. E-lenses are located on both sides of IP10.

PHASE ADVANCE CONSIDERATIONS

For head-on beam-beam compensation in the proton operation in RHIC, simulation results show that full compensation gives a lower dynamic aperture than that with half beam-beam compensation. With half beam-beam comnpensation, if the phase advances between IP8 and the center of e-lenses is $k\pi$, k being an integer, the non-linear beam-beam RDTs from beam-beam interaction at IP8 will be exactly compensated by the e-lens at IP10 to the first order. For this purpose, we added two shunt power supplies to the main quadrupoles in the arc between IP8 and IP10.

In the previous proton runs, we observed that the particle loss at store took place in the transverse plane with beam-beam interaction. The proton loss rate was found to be proportional to the particle leakage rate from the proton bunch center to the tail. Since the particles in the bunch tail have bigger momentum errors, we concluded that the proton loss at store was caused by the low off-momentum dynamic aperture [2]. To improve it, we need to compensate the chromatic effects and compensate the higher order chromaticities.

In the early studies, we identified that the non-linear chromaticities for the RHIC proton lattices are mainly contributed by the triplet quadrupoles in the two interaction regions IR6 and IR8 where βs are much bigger than other non-collisional interaction regions [3]. From the

*This work was supported by Brookhaven Science Associates, LLC under Contract No. DE-AC02-98CH10886 with the U.S. Department of Energy.

Copyright © 2013 CC-BY-3.0 and by the respective authors

Table 1: Optics Parameters of E-lens and Standard Lattices.

Parameter	E-lens Lattices	Standard Lattice
Blue ring:		
Integer tunes	(27, 29)	(28, 29)
$\xi^{(2)}_{x,y}$	(167,-324)	(-1894, 213)
$\Delta\Phi_{x,y}\vert_{\rm IP6->IP8}$	(10.5π, 8.5π)	(10.9π, 8.5π)
$\Delta\Phi_{x,y}\vert_{\rm IP8->elens}$	(8π,11π)	(8.4π,10.1π)
Yellow ring:		
Tunes	(27,28)	(28, 29)
$\xi^{(2)}_{x,y}$	(-119,-60)	(-4160,-1045)
$\Delta\Phi_{x,y}\vert_{\rm IP6->IP8}$	(7.5π, 11.5π)	(8.3π, 11.0π)
$\Delta\Phi_{x,y}\vert_{\rm IP8->elens}$	(11π,9π)	(10.7π,8.8π)

perturbation theory, the second order contributions from quadrupoles are mostly determined by the first order off-momentum β-beat $d\beta/d\delta$, $\delta = dp/p_0$. Therefore, for the asymmetric optics at IP6 and IP8 in RHIC, we can minimize $d\beta/d\delta$ at the triplet quadrupoles by adjusting the phase advances between IP6 and IP8 to be $(p+1/2)\pi$, with p an integer [4].

OPTICS DESIGN

For the next RHIC proton run, the particle energy will be 100 GeV. According to the operational experiences in the previous RHIC 100 GeV proton runs, to obtain acceptable store beam lifetime, we choose $\beta^* = 0.85$ m, the same as in the 2012 100 GeV proton run. The luminosity gain will mainly come from the increased proton bunch intensity. With half beam-beam compensation with e-lenses, we expect that the maximum proton bunch intensity at store exceeds 2.5×10^{11}.

Table 1 shows the main optics parameters for the new lattice design for beam-beam compensation, together with the lattices used in the previous RHIC proton runs. For simplicity, we name the previous RHIC run lattices "standard lattices" and the newly designed lattices for beam-beam compensation "e-lens lattices". From Table 1, the e-lens lattices meet all above phase advance requirements: $k\pi$ between IP8 and e-lens and $(p+1/2)\pi$ between IP6 and IP8.

As an example, Figure 2 shows the fractional vertical tunes versus dp/p_0 for the e-lens lattices and the standard lattices. With the phase advances between IP6 and IP8 being $(p+1/2)\pi$, the second order chromacticities are largely reduced. Figure 3 shows the RDTs of $3Q_x$ along the ring. Large $3Q_x$ RDTs affect negatively the beam lifetime at injection and cause beam loss and emittance growth on the energy and rotator ramps. From Figure 3, for the e-lens lattices, the RDTs of $3Q_x$ in the Yellow ring are bigger than that from the Blue ring. To meet these phase advance requirements, the e-lens lattices reduce the arc FODO cell's phase advances from optimum 90° to 74° and generate extra β and dispersion beats between IP8 and IP10 with shunt qudrupole power supplies between them.

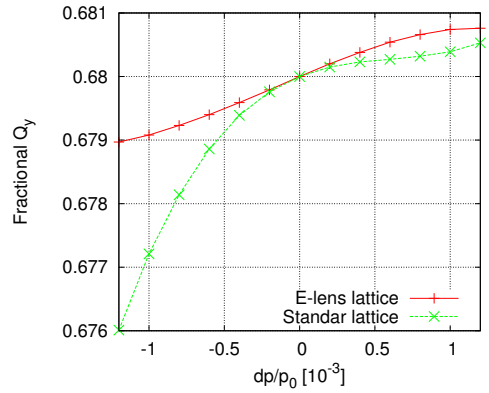


Figure 2: Yellow vertical tunes versus dp/p_0. Phase advances $(p+1/2)\pi$ between IP6 and IP8 reduce $\xi^{(2)}_{x,y}$. The Yellow vertical plane shows the largest nonlinear chromaticity in the standard lattice (Table 1).

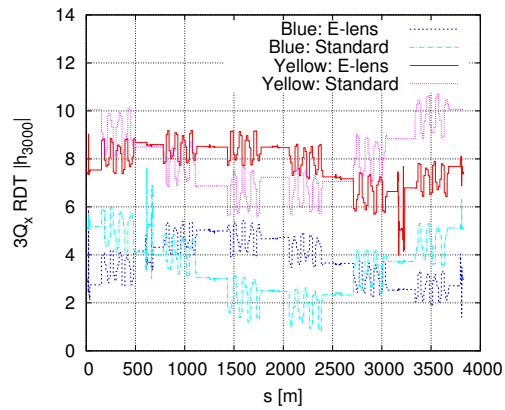


Figure 3: RDTs of the $3Q_x$ resonance for e-lens and standard lattices. $3Q_x$ RDTs are bigger in Yellow than Blue rings.

DYNAMIC APERTURE CALCULATIONS

Figure 4 shows the proton dynamic aperture without beam-beam interaction at store energy. The zero-amplitude tunes are scanned along the diagonal in the tune space. In this study, the vertical tune is always lower than the horizontal tune by 0.01. The Blue e-lens lattice gives a bigger dynamic aperture than the Yellow e-lens lattice when the tunes are close to 2/3. The Yellow standard lattice gives the lowest dynamic aperture in the scan, which is due to its large $3Q_x$ RDT and negative vertical second order chromaticity.

Figure 5 shows the dynamic aperture with beam-beam interaction at IP6 and IP8. The zero-amplitude tunes are (0.68,0.67). The dynamic aperture for the e-lens lattices are above 5 σ when the proton bunch intensity is below 2×10^{11}. The Yellow e-lens lattice gives a larger dynamic aperture than the standard Yellow lattice. The dynamic aperture begins to drop for all cases when the proton bunch intensity is above 2×10^{11}, which justifies head-

Copyright © 2013 CC-BY-3.0 and by the respective authors

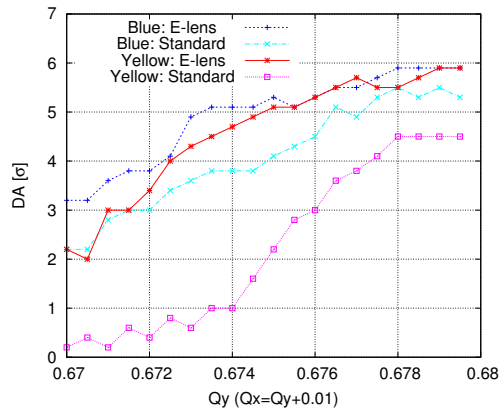


Figure 4: Dynamic aperture without beam-beam interaction at store. The initial $dp/p_0 = 12.5 \times 10^{-4}$.

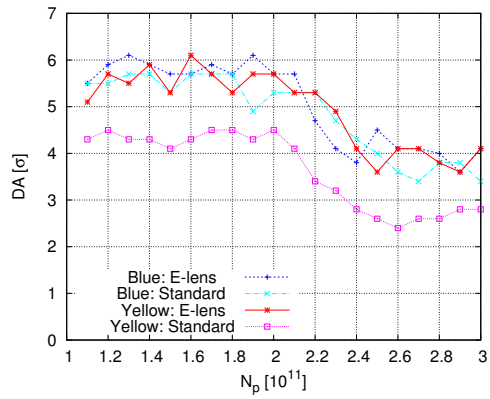


Figure 5: Dynamic aperture with beam-beam interaction at store. The zero-amplitude tunes are (0.68,0.67).

on beam-beam compensation for proton bunch intensities above 2×10^{11}.

Figure 6 shows the dynamic apertures with half head-on beam-beam compensation (HBBC). With HBBC the e-lens lattices give a bigger dynamic aperture than the standard lattices. For the Blue e-lens lattice the dynamic aperture is about 5 σ for all bunch intensities. While for the Yellow e-lens lattice, it is above 4.5σ for bunch intensities between 2.0-3.0$\times 10^{11}$.

The Yellow e-lens lattice gives a lower dynamic aperture than the Blue e-lens lattice when bunch intensities are below 2×10^{11}. One possible reason is the large Yellow $3Q_x$ RDT. Here we correct all the first order sextupole resonance driving terms with 12 sextupole families. The focusing or defocusing sextupoles in each arc are grouped into one family. With correction, the $3Q_x$ RDT is reduced by more than half and the second order chromaticties are still below 400. Figure 7 shows the dynamic apertures with the sextupole first order RDT correction. The dynamic aperture of HBBC with correction improves slightly but is still low when the proton bunch intensity is below 2.0$\times 10^{11}$.

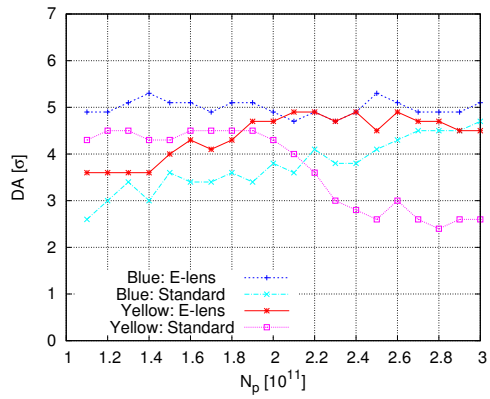


Figure 6: Dynamic aperture with half beam-beam compensation at store.

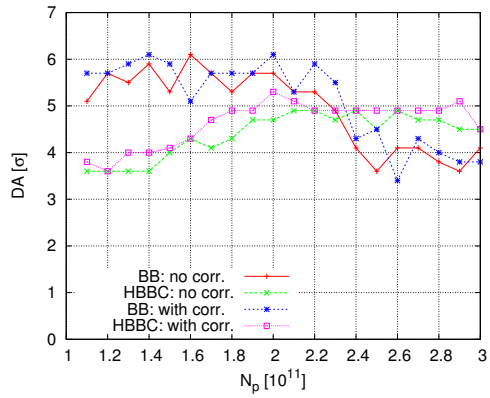


Figure 7: Dynamic aperture for the Yellow e-lens lattice with $3Q_x$ correction.

SUMMARY

We re-designed lattices for the head-on beam-beam compensation with e-lenses in RHIC. Phase advances between IP8 and the e-lenses are set to $k\pi$ to compensate non-linear beam-beam RDTs and the phase advances between IP6 and IP8 are set to $(p + 1/2)\pi$ to reduce the second order chromaticities. Dynamic aperture calculations show that the dynamic aperture is improved with e-lens lattices without and with beam-beam compensation, compared to the previous RHIC proton run lattices.

REFERENCES

[1] Y. Luo et al., Phys. Rev. ST Accel. Beams 15, 051004(2012).

[2] Y. Luo and Wolfram, ICFA mini-workshop on "Beam-Beam Effects in Hadron Colliders", CERN, 2013.

[3] Y. Luo, et al., THP059, PAC'2011.

[4] Y. Luo, et al., THP058, PAC'2011.

Copyright © 2013 CC-BY-3.0 and by the respective authors

MEASUREMENT OF BEAM OPTICS DURING ACCELERATION IN THE RELATIVISTIC HEAVY ION COLLIDER

M. Minty#, K.A. Drees, R. Hulsart, C. Liu, A. Marusic, R. Michnoff, P. Thieberger
Brookhaven National Laboratory, Upton, NY 11973, U.S.A.

Abstract

Measurements of the beam optics during acceleration have been performed at the Relativistic Heavy Ion Collider (RHIC). The results were used to obtain a measure of the maximum amplitude of the beta-beat envelope during acceleration which are of interest in the context of emittance and polarization preservation. The measured beta functions were then interpolated to locations of beam profile monitors for more accurate determination of the transverse beam emittances during the energy ramp. In this report we summarize recent improvements in the experimental methods, describe the measurement procedure and present experimental results.

INTRODUCTION

Optics measurements during acceleration are here based on excitation of the beam using pulsed kicker magnets (from the RHIC tune measurement system, ARTUS [1]) as opposed to driven excitations using AC dipoles [2], which are not well suited for measurements during the energy ramp. The response of the beam's change in centroid position was measured using beam position monitors (BPMs). Compared to measurements made previously [3] using the ARTUS kicker magnet [1], the measurement precision has been substantially improved by numerous enhancements made in the BPM and data delivery systems and by the application of continuously operating orbit and tune/coupling feedback [4] used to ensure reproducible and stable conditions during acceleration. For beam optics measurement during the energy ramp, a coherent beam oscillation was excited and single-bunch turn-by-turn (TBT) BPM measurements were acquired. These were carefully interleaved with average orbit measurements used by the orbit feedback. The TBT data were acquired at a selectable maximum rate possible (depending on whether acquisitions were desirable in both RHIC accelerators simultaneously) as limited by the data delivery times. The results were analyzed using slightly modified adaptations of existing frequency-based analyses [5-7] as described in Ref. [8].

In this report we summarize the improvements leading to reliable and robust measurements, describe the measurement procedure and present experimental results.

* The work was performed under Contract No. DE-AC02-98CH10886 with the U.S. Department of Energy.
#minty@bnl.gov

TURN-BY-TURN BEAM POSITION MEASUREMENTS

Past beam optics measurements in RHIC were sometimes compromised by poor BPM performance [9]. During the early years of RHIC operation, modifications (e.g. electronics relocation, gain relay modifications) were made and automated timing scans were developed which contributed to substantially improved performance [10, 11]. Then several issues specific to the turn-by-turn BPM system were resolved: timestamp errors were eliminated (2008), FireWire (IEEE serial bus interface) error checking and staggering using software loop delays were implemented (2009), a RAM data corruption source was located in the integrated front end of the signal processing electronics and corrected (2009), changes were made to interrupt priorities (2009), and Sederta-card memory corruption was identified and eliminated (2010).

DETERMINISTIC DATA DELIVERY

During the shutdown before the RHIC FY11 run, a digital test mode was developed to ensure reliable and robust delivery of TBT BPM data and executed over many months. For each of the ~650 BPMs in RHIC, a test pattern was set at a 0.25 Hz rate in the TBT data array of the local signal processing unit. The received patterns, as logged by the RHIC control system, were subtracted from the expected patterns to detect data handling errors. While the symptoms of data delivery errors were varied (values missing, values repeated, etc.), it was found that they were primarily due to stale data being read back (if overloaded, the Sederta card lost a portion of data and delivered data previously saved in the circular buffer). The errors were solved by further staggering of data transmitted over FireWire using now the RHIC beam sync link turn counter to more precisely stagger the delays to prevent data transmission time overlaps between BPMs. After these modifications, error-free data delivery using the digital test mode was demonstrated: >100,000 acquisitions were performed, where 1 acquisition corresponds to readout of 1024 turns from all BPMs, or about 70 billion readings, with no errors.

ACQUISITION METHODOLOGY

Measurements of the beam optics were made reproducible by ensuring reproducible beam orbits and betatron tunes using the now standard beam feedback systems during acceleration. While orbit and tune

Copyright © 2013 CC-BY-3.0 and by the respective authors

feedback operate independently, the BPM measurements used by orbit feedback and the turn-by-turn BPM measurements share the same networks for data delivery. The timing of the delivery of beam position measurements for these two systems was therefore carefully staggered to avoid data corruption.

A conceptual sketch showing the data acquisition methodology is shown in Fig. 1. Orbit feedback operated at its standard 1 Hz rate. We allowed 200 ms corresponding to an upper limit on the time to transmit all (4 planes from both accelerators) the average orbit BPM data well in excess of the 150 ms required based on previous measurements [12]. After delivery of the data for orbit feedback, the beam was excited in one plane followed a short time later by excitation in the other plane, where the spacing between applied excitations was set (~ 500 turns) to be longer than the decoherence time.

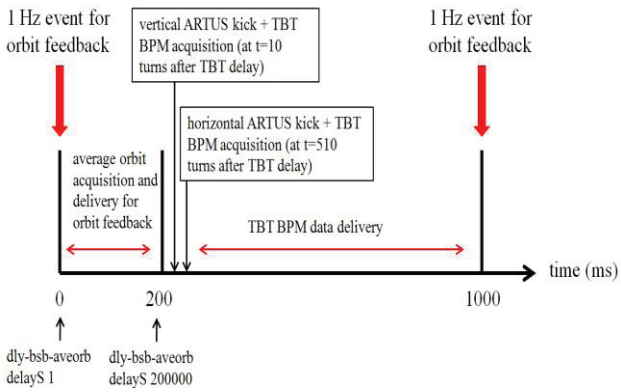


Figure 1: Conceptual sketch of carefully orchestrated timing to allow for turn-by-turn BPM acquisitions interleaved with BPM acquisitions required by orbit feedback during beam acceleration.

MEASUREMENT RESOLUTION

Following the above changes, the resolution of the turn-by-turn BPMs was first quantified using data acquired with continuous excitations provided by AC dipoles [13]. The resolution is here defined as the rms of the difference between the measurement and a sinusoidal fit to the measurement. In Fig. 2 is plotted in histogram format this rms for all BPMs for both transverse planes in both accelerators. Note that the resolution defined here represents an upper bound on the instrumental resolution; a correlation between poor resolution and large beta function (on either side of each interaction region) was determined by Fourier analysis to be due to residual oscillations of the beam (of about 10 Hz [11, 14], which for even higher precision analyses could be fit and removed from the data arrays).

APPLICATIONS

The Run-13 [15] ramp optics data were initially used [16] to determine the betatron tune spread along the energy ramp, which is important in the context of preservation of the proton beam polarization during acceleration. At that time a new beam optic designed for operation of new electron lenses [15,17] was being developed. An unexpected observation, namely reported shrinking beam emittances while establishing beams (i.e. "squeezing") for collision was observed in the yellow ring which provided motivation for interpolation of the beta function measurements [18] to the locations of the ionization profile monitors (IPMs, [19]) which measure the transverse beam sizes.

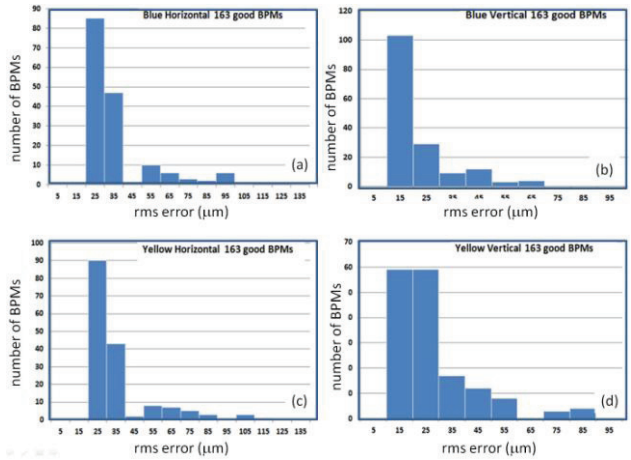


Figure 2: Resolution of turn-by-turn BPM measurements in histogram format for the blue/yellow ring horizontal plane (a)/(c) and vertical planes (b)/(d).

To investigate this further, ramp optics measurements were acquired. Shown in Fig. 3a/b are the model and measured beta functions at the IPMs in the two transverse planes. For reasons that are not yet understood the measured local beta function was observed to decrease while the model beta function, which is assumed for conversion of the beam size to emittance for online reporting, increased. The emittances (95%, normalized) derived using the model and measured beta functions are plotted in Figs. 3c/d. Using the measured beta functions, the emittances were constant - certainly not decreasing. These results are consistent with those acquired at the same time from the fluorescence monitor [20] which also indicated constant beam size while the model beta function increased.

Another example of beta function measurements at the RHIC IPMs is shown in Fig. 4 acquired with the lattice used for most of the FY13 run. The data shown here were acquired with a 1 Hz acquisition rate (ref. Fig. 1) in both accelerators. In all four planes the agreement between model and measured beta functions was observed to be best about midway during the acceleration cycle (which happens to be consistent with the tune errors seen by the tune feedback loops).

The evolution of the beta- and phase-beats during acceleration as measured by all BPMs was evaluated (and available in movie-style format). The amplitude of the envelope of the beta-beating in the accelerator arcs was consistent with those shown in Fig. 3.

Copyright © 2013 CC-BY-3.0 and by the respective authors

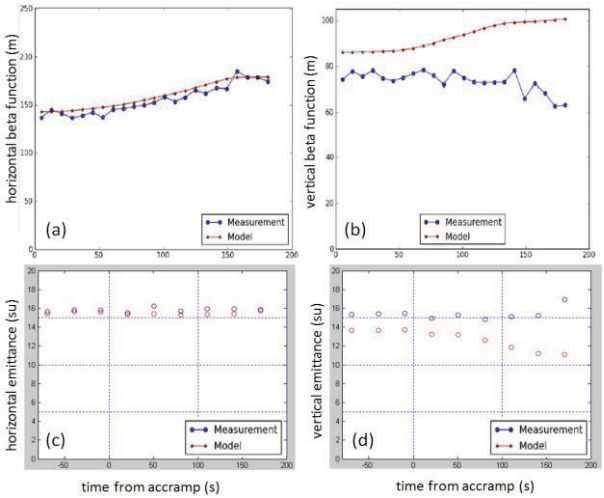


Figure 3: Model (red) and measured (blue) beta functions in the horizontal/vertical planes at 255 GeV during the final beta squeeze (a/b); IPM emittances (95%, normalized in mm-mrad) reported using the model (red) and measured (blue) beta functions in same planes (c/d).

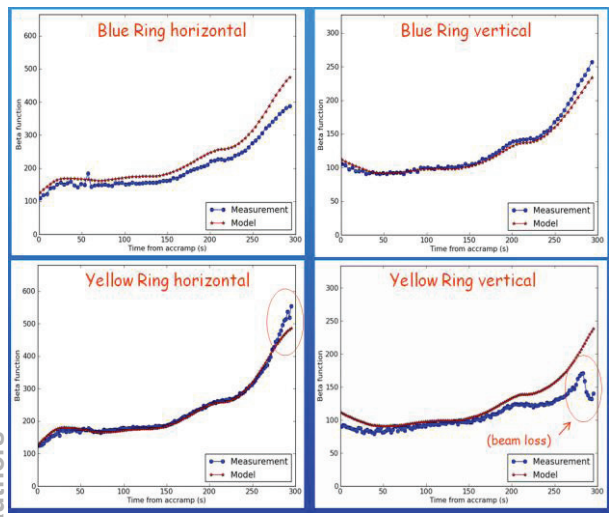


Figure 4: Model and measured beta functions at the 4 RHIC IPMs during acceleration of protons to 255 GeV.

SUMMARY

Numerous improvements in the BPM system have been completed over the years including most recently dedicated tests resulting in guaranteed error-free delivery of TBT data. The resulting resolution of the BPMs was measured and found to be excellent. This motivated further application of ARTUS-based beam optics measurements during beam acceleration in RHIC. With careful management of the transmission of BPM data used for orbit feedback and for TBT acquisitions, beta- and phase-beating were measured during the energy ramp and during the final beta squeeze in before collisions.

The results revealed that the presently used approach to optics correction based on fixed energy correction at injection and store with corrections propagated forward and backward, respectively, into the energy ramp [7,18] is appropriate. The measurements were also applied to better understand the beam emittances with measurement errors dominated by the uncertainty in the beta functions.

Efforts continue to utilize these ramp optics measurements for both validating corrections and for development of new methods for directly applying corrections during acceleration [21].

ACKNOWLEDGEMENTS

These beam optics studies – both measurement and analysis – result from many years of development and dedication of many individuals. Here thank M. Bai and C. Montag for use of the data obtained with the AC dipole for evaluation of the BPM resolution. We thank also the C-AD Operations and AP groups for their support.

REFERENCES

[1] K.A. Drees et al, "ARTUS: The Tune Measurement System at RHIC", BIW00, Cambridge, MA (2000).
[2] M. Bai et al, "RHIC AC Dipole Design and Construction", PAC01, Chicago, IL (2001).
[3] D. Trbojevic et al, "Improvements of the RHIC Ramp Efficiency", EPAC02, Paris, France (2002).
[4] M. Minty et al, "Simultaneous orbit, tune, coupling and chromaticity feedbacks at RHIC", PAC11, New York, NY (2011).
[5] G. Wang et al, "Linear Optics Measurement and Corrections Using AC Dipole in RHIC", IPAC10, Kyoto, Japan (2010).
[6] G. Vanbavinckhove et al, "Optics corrections at RHIC", IPAC2011, San Sebastian, Spain (2011).
[7] M. Bai et al, "Optics Measurement and Corrections at RHIC", IPAC2012, New Orleans, LA (2012).
[8] C. Liu et al, "Precision Tune, Phase and Beta Function Measurement by Frequency Analysis in RHIC", IPAC2013, Shanghai, China (2013).
[9] R. Calaga and R. Tomas, "Statistical analysis of RHIC beam position monitors performance", Phys. Rev. ST Accel. Beams **7**, 042801 (2004).
[10] T. Satogata et al, "RHIC BPM System Performance, Upgrades, and Tools", EPAC02, Paris, France (2002).
[11] T. Satogata et al, "RHIC BPM System Modifications and Performance", PAC05, Knoxville, TN (2005).
[12] M. Minty et al, "Global orbit Feedback in RHIC", IPAC10, Kyoto, Japan (2010).
[13] These TBT data are courtesy of M. Bai and C. Montag.
[14] C. Montag et al, Nucl. Instr. & Meth. A **564**, 26-31 (2006).
[15] V. Ranjbar et al, "RHIC Polarized Proton Operation for 2013", IPAC13, Shanghai, China (2013).
[16] M. Bai and X. Shen, private communication.
[17] X. Gu et al, "Commissioning RHIC's Electron Lens", NA-PAC' 13.
[18] C. Liu et al, Global Optics Correction in RHIC based on Turn-by-Turn Data from the ARTUS Tune Meter, NA-PAC' 13.
[19] R. Connolly et al, "Residual Gas Ionization Beam Profile Monitors in RHIC", BIW2010, Santa Fe, NM (2010).
[20] T. Tsang et al, Rev. of Sci. Instr. **79**, 105103 (2008).
[21] C. Liu et al, "Implementation of optics corrections on the ramp in RHIC", NA-PAC' 13.

Copyright © 2013 CC-BY-3.0 and by the respective authors

SIMULATION OF HIGH-POWER MERCURY JET TARGETS FOR NEUTRINO FACTORY AND MUON COLLIDER*

R. Samulyak†, Stony Brook University, Stony Brook, NY 11794, BNL, Upton, NY 11973, USA
H.C. Chen, Stony Brook University, Stony Brook, NY 11794, USA
H. Kirk, BNL, Upton, NY 11973, USA
K. McDonald, Princeton University, Princeton, NJ 08544, USA

Abstract

Hydrodynamic behavior of high power targets for future particle accelerators, in particular for the proposed neutrino factory and muon collider, has been investigated via numerical simulations. The target will contain a series of mercury jet pulses of about 1 cm in diameter, interacting with intense proton pulses in 15 – 20 T magnetic fields. Simulations used a smoothed particle hydrodynamics code designed to accurately resolve free surface 3D hydrodynamic flows. Simulation results have been compared with existing experimental data and previous simulations performed with the front tracking code FronTier. New target parameters have also been investigated.

INTRODUCTION

The key element of the target system being designed for the future muon collider and / or neutrino factory is a liquid mercury jet interacting with powerful proton pulses inside a 15 – 20 T magnetic solenoid. The stability of the mercury jet after the proton pulse disruption is a major concern for the target design. The proof-of-principles experiment for high-power mercury target system was conducted at CERN in 2007 [1].

The problem of the slow distortion of the mercury jet entering the solenoid has been evaluated numerically using the FronTier code [2, 3]. FronTier is a hydro- and magnetohydrodynamic code that resolves material interfaces using the method of front tracking. FronTier simulations of the mercury jet cavitation and disruption caused by interaction with proton pulses were presented in [4] and previous works referenced therein. Previous studies have demonstrated that modeling of cavitation and surface dynamics is critical for the simulation of the mercury jet interaction with proton pulses. Cavitation is intrinsically a multiscale phenomenon involving scales from micron-size at the cavitation onset to global scales in later phases of the evolution of bubbles. In FronTier, cavitation was modeled by creating numerically grid-dependent initial cavitation bubbles with tracked surfaces in rarefaction waves of critical strength. Such a cavitation model depends on a number of artificial parameters and makes it difficult to resolve small scales typical for clouds of cavitating bubbles. It is also non-conservative in nature as it removes the liquid and replaces the corresponding volume with gas bubbles. Difficulties with cavitation models prevented us from simulating long time dynamics of mercury jets in 3D.

To improve the modeling of small scales and simulation of long time dynamics of free surfaces flows, we have developed a parallel code based on the smoothed particle hydrodynamics (SPH) [5]. The code has been applied for the simulation of mercury jet targets in the parameter range typical for the muon collider, neutrino factory, and other experimental designs. The present paper only deals with hydrodynamic effects. The study of influence of MHD on the mercury jet cavitation and disruption using particle methods is in progress and will be reported in forthcoming work.

NUMERICAL METHODS

SPH [5] is a Lagrangian particle method in computational fluid dynamics in which deforming Lagrangian cells are replaced with particles. SPH eliminates the main mesh tangling difficulty of the original Lagrangian method while retaining many of its advantages. Due to its Lagrangian nature, SPH is strictly mass-preserving and capable of robustly handling interfaces of arbitrary complexity in the simulation of free surface and multiphase flows. It has known accuracy issues in the numerical approximation of differential operators but these are compensated by the SPH properties of nonlinear stability and conservation, enabling successful usage of SPH for a wide class of problems. We have also developed necessary physics models pertinent to the mercury target problem.

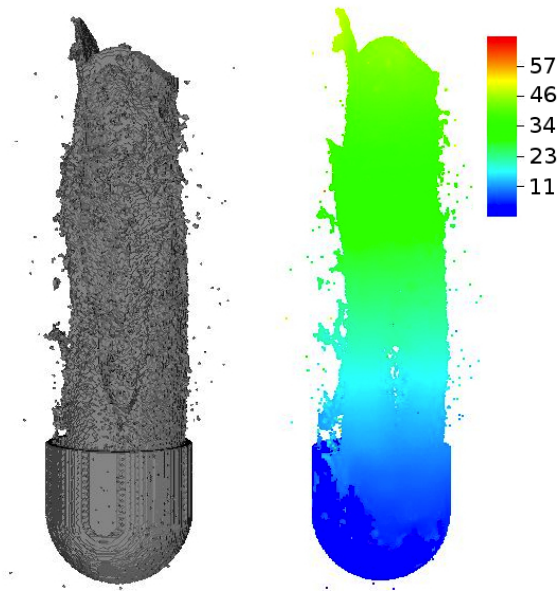
To model properties of mercury, we use the stiffened polytropic equation of state (EOS) [6]

$$P = (\gamma_l - 1)\rho(E + E_\infty) - \gamma_l P_\infty$$

with the adiabatic exponent $\gamma_l = 6.0$ and the stiffening constant $P_\infty = 47$ kbar . The stiffened polytropic EOS extends the range of pressure to negative values in order to account for the transient effect of tension in liquids. When the pressure falls below the cavitation threshold, the interaction between the corresponding particles is eliminated. This causes internal liquid breakups or cavitation. Using this method, cavities can appear on particle-scale length. The particle interactions are resumed if the pressure equilibrates and particles move close to each other causing the merger of fluid fragments.

* Work supported by DOE MAP
† roman.samulyak@stonybrook.edu

Copyright © 2013 CC-BY-3.0 and by the respective authors



(a) Mercury surface (b) z-velocity, m/s

Figure 1: Mercury thimble. Shape (left) and vertical velocity (right) of mercury splash column after 0.85 ms.

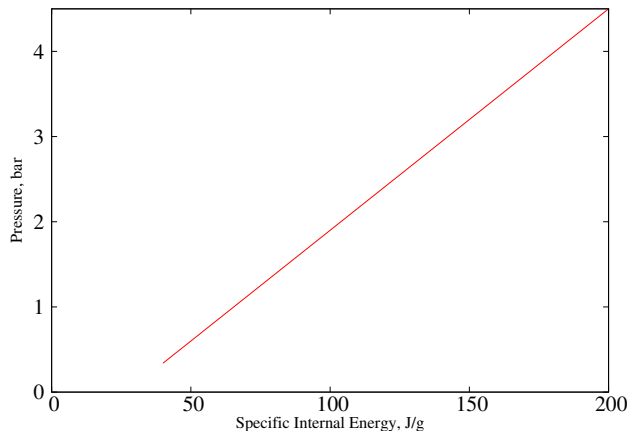


Figure 2: Isochoric increase of mercury pressure with increase of internal energy (cortesy Sandia National Lab).

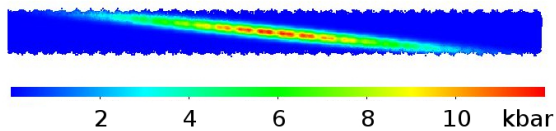


Figure 3: Initial pressure distribution in cross-section of the mercury jet due to neutrino factory beam energy deposition.

RESULTS AND DISCUSSION

Mercury Thimble Experiments

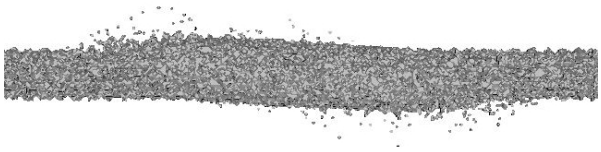
We have validated SPH simulations of the interaction of mercury with proton pulses using data of the mercury thimble experiments [7]. The volume of the thimble excavated in a stainless steel bar is 1.3 cm^3. It consists from bottom to top of a half sphere (r = 6 mm) and a vertical cylinder (r = h = 6 mm). The mercury has a free surface in up-direction, where it can expand to. The proton pulse has approximately Gaussian distribution and the intensity range of $0.6 - 17 \cdot 10^{12}$ protons at energy 24 GeV. We have performed numerical simulations of the thimble splash and observed that the splash velocity is sensitive to the value of the critical pressure used in the capitation model. Good agreement with experimental data was obtained for the critical pressure of 100 bar. This value was then used in all mercury jet simulations. Figure 1 depicts the shape of the mercury column in the thimble simulation.

Mercury Targets for Neutrino Factory and Muon Collider

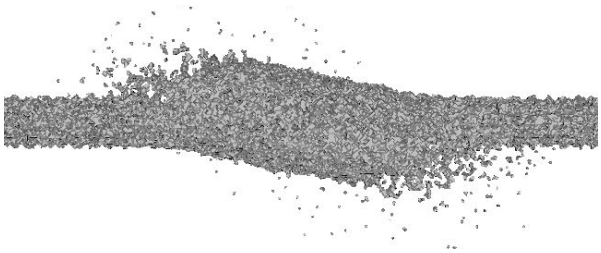
In this section, we report simulation results of the mercury jet interaction with proton pulses in the neutrino factory and muon collider power regimes. The 4 MW beam of 8 GeV protons will be delivered in 150 bunches per second for the neutrino factory and in 15 bunches per second for the muon collider. 20.8 teraproton bunches arrive at the neutrino factory target with the 6.67 ms interval that is large compared to hydrodynamic time scales of the mercury splash. In the case of the muon collider, 208 teraproton bunches arrive with the time interval of 66.7 ms. Therefore, it is sufficient to consider the interaction of the mercury jet with only one proton pulse. We use the corresponding energy deposition tables calculated at FNAL with the Monte Carlo code MARS. Assuming the isochoric regime of the energy deposition (the deposition time scale is mush smaller than the hydrodynamic time scale), the peak pressure is approximately 110 kbar in the muon collider target and 11 kbar in the target for the neutrino factory. Figure 2 shows the increase of pressure in mercury with the increase of internal energy. The proton pulse enters the jet under small angle and the energy deposition is not axially symmetric. The pressure profile in the jet is shown in Fig. 3.

After the energy deposition, strong pressure wave propagates to the jet surface and reflects from the mercury - vacuum interface as a rarefaction wave. Rarefaction waves focus in the center of the jet, break the liquid and create an extensive cavitation zone. After the jet is disintegrated by cavitation and surface instabilities, fragments of jet freely fly apart. The velocity of the neutrino factory target splash is in the range of 15 - 35 m/s, with some small droplets reaching velocities of the order of 40 - 50 m/s. These velocities are in the same range as ones observed in MERIT experiments. The exact comparison is not possible because of uncertainties in the energy deposition and spot sizes. In the muon collider case, main jet fragments disperse with the velocity of 90 - 110 m/s with some droplets reaching much higher velocities (see Fig. 4).

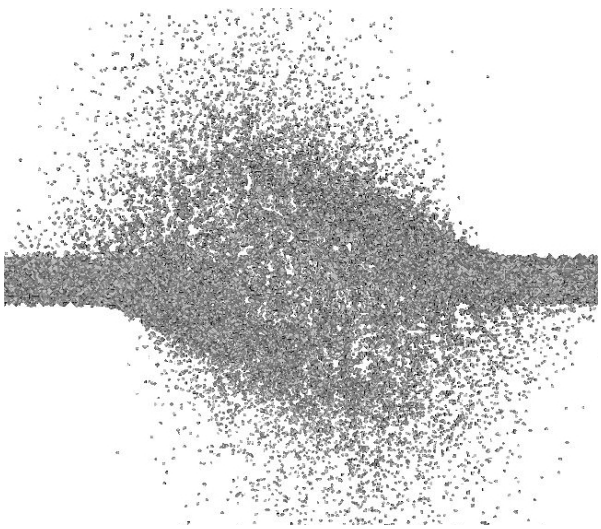
Copyright © 2013 CC-BY-3.0 and by the respective authors



(a) Neutrino factory, 0.35 ms



(b) Neutrino factory, 1.0 ms



(c) Muon collider, 0.35 ms

Figure 4: Mercury jet dispersal after deposition of 4 MW beam of 8 GeV protons. State of the neutrino factory target at 0.35 ms (a) and 1 ms (b), and the muon collider target at 0.35 ms (c).

Evaluation of Gallium Targets

The targetry group of the MAP collaboration is interested in evaluating the performance of lower-Z materials as targets for future accelerators / storage rings. We performed initial hydrodynamic simulations of the interaction of gallium jets with proton pulses. The density of gallium is $6.1\,g/cm^3$ and the sound speed is 2879 m/s. Detailed thermodynamic properties of gallium were not available at the time of simulations. Based on lower gallium density, we assumed that the pressure and internal energy density increase will be 50% of that in mercury for the same proton pulse. Using the muon collider proton beam parameters, the dispersal of the gallium jet was similar to that of the mercury jet (see Fig. 5). This observation is consistent with a simple extimate using the energy balance law. For the case of the neutrino factory proton beam, the jet expansion velocities were lower compared to the mercury jet and the gallium jet exhibited little distortion at 1 ms. This result could have been affected by inaccurate thermodynamic properties of gallium and the cavitation model. This issue will be addressed in the future work.



Figure 5: Gallium jet dispersal after proton beam energy deposition.

CONCLUSIONS AND FUTURE WORK

Hydrodynamic response of high power mercury targets interacting with proton pulses have been studies computationally using a smooth particle hydrodynamics (SPH) code. The mercury thimble experiments have been used for the validation of physics models, in particular cavitation, implemented in the SPH code. Simulated velocities of the mercury splash agree with experimental values. Furthermore, the sensitivity of the splash velocity to the value of the critical pressure has again demonstrated the importance of cavitation modeling for target simulations. With the critical pressure selected in the benchmark process, simulations of the neutrino factory and muon collider targets have been performed and mercury dispersal velocities have been calculated. Preliminary studies of gallium targets have also been performed. Future work will focus on MHD effects using the SPH code and its modifications.

REFERENCES

[1] K. McDonald *et al.*, Proc. PAC09 (Vancouver, Canada), TU4GRI03, 2009.

[2] R. Samulyak, J. Du, J. Glimm, Z. Xu, J. Comp. Phys., **226** (2007), 1532.

[3] T. Guo, R. Samulyak, S. Wang, Proc. Comp. Sci, **18** (2013), 511.

[4] R. Samulyak, W. Bo, X. Li, H. Kirk, K. McDonald, Condensed Matter Physics, 13 (2010), No 4, 43402: 1 - 12.

[5] J. J. Monaghan, Ann. Rev. Astron. Astrophys, 30 (1992), 543 574.

[6] R. Menikoff, B. Plohr, Rev. Mod. Phys., 1989, **61**, 75.

[7] A. Fabich, CERN-THESIS-2002-038, Vienna, November (2002).

Copyright © 2013 CC-BY-3.0 and by the respective authors

IMPACT OF THE INITIAL PROTON BUNCH LENGTH ON THE PERFORMANCE OF THE MUON FRONT END*

H.K. Sayed,† H.G. Kirk, J.S. Berg, Brookhaven National Laboratory, Upton, NY 11973, USA
K.T. McDonald, Joseph Henry Laboratories, Princeton University, NJ 08544, USA

Abstract

The dependence of the performance of the Front End of a Muon Collider/Neutrino Factory on the proton-beam bunch lengths of 0-20 ns is explored for beam kinetic energies of 3 and 8 GeV.

INTRODUCTION

Some of the requirements on the proton driver for a staged Neutrino Factory based on muons beams [1] are listed in Table 1. Efficient capture of muons in the Buncher of the Front End [2] of the Neutrino Factory favors very short proton bunch lengths. However, meeting the requirement of an intense proton bunch of length only 2 ns is challenging at 3-GeV beam energy because of space-charge effects [3]. We present here a study of the impact of a longer proton bunch on the performance of the Front End.

In the course of related studies [4], an advantage in capture efficiency was found in using a short "taper" to the profile of the capture-solenoid magnetic field, down from the 20 T peak at the target to 1.5-3.0 T at the beginning of the Decay Channel some 4-6 m downstream. Shorter tapers were found to deliver muon beams with smaller time spread at the Buncher for a given proton bunch length at the pion-production target, corresponding to increased capture efficiency of the Buncher. In this study we examined the performance of such short tapers, as well as long adiabatic ones, for proton bunches of 2-20 ns length.

The beam-dynamics simulations were performed using the ICOOL code [5], with input spectra of secondary particles produced at the proton-beam target as modeled by MARS15(2012) [6]. Figure 1 shows examples of pion beams at the end of the target, of length from 2-10 ns, before being tracked through the tapered capture-solenoid, Decay Channel, Buncher, Phase Rotator and Ionization Cooling sections.

CAPTURE EFFICIENCY VERSUS TARGET SOLENOID TAPER LENGTH

Pions (which later decay to muons) are generated at the target with a wide spread in transverse momentum, largely uncorrelated with their longitudinal momentum As they move through the high target solenoid field they develop a correlation between the longitudinal velocity and the initial transverse momentum. The higher the field integral $\int Bdl$ of the target solenoid leads to a larger time spread (*i.e.*, more muons sent out of the longitudinal acceptance of the buncher and rotator). Figure 2 shows the longitudinal phase space of muon beam at the end of the Decay Channel for a short taper of 4'm and a much longer adiabatic one of 40 m. The shorter solenoid taper delivers muon beam with smaller time spread at a fixed longitudinal momentum p_z to the Buncher. Consequently the short taper has an advantage over the more adiabatic long taper as it manages to pack more muons within the longitudinal acceptance of the buncher and phase rotation channels. Figure 3 shows the muon beam time spread at the end of decay channel (50 m from target) for various taper solenoid profiles.

Pions (later muons) produced off the target were tracked through the Front End starting from the end of the target, through the tapered solenoid, Decay Channel, Buncher,

Table 1: Proton-driver requirements for the final and initial stages of a Neutrino Factory.

Parameter	Final Stage	Initial Stage
Proton energy [GeV]	8	3
Beam power [MW]	4	1
Rep. frequency [Hz]	50	70
Bunch length [ns]	2 $\pm$1	2 $\pm$1

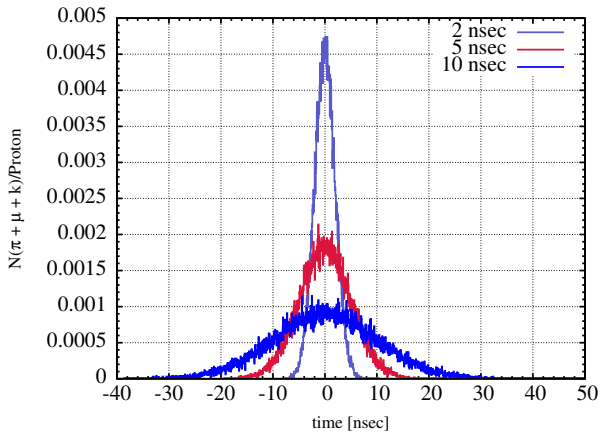
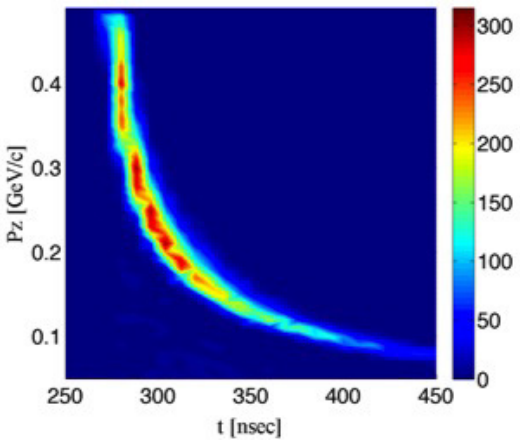


Figure 1: Pion beams with bunch lengths of 2-10 ns off the pion production target.

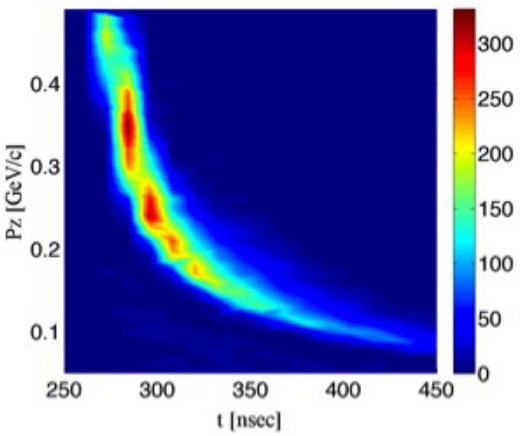
*Work supported by the US DOE Contract No. DE-AC02-98CHI10886.
† hsayed@bnl.gov

Copyright © 2013 CC-BY-3.0 and by the respective authors

Phase Rotator and Ionization Cooling channels. Fig. 4 shows the number of captured muons versus the solenoid taper length for various target solenoid configurations. The peak field of the target solenoid increases the transverse capture of the pions, as shown in Fig. 4. As the field tapers down to the constant field within the Buncher and Phase Rotator, the faster the taper the smaller the time spread and the better the performance. Increasing the taper-end field strength increases the acceptance of the Front End, as can be seen in Fig. 4).



(a) Short solenoid taper of 4 m.



(b) Long solenoid taper of 40 m.

Figure 2: Longitudinal phase space of pions and muons at the end of the Decay Channel, 50 m from the target.

As the initial pion bunch length gets longer the advantage of the short taper in preserving the time spread will not be the dominant effect on the performance of the Buncher and Rotator. To find the bunch-length limit over which the short solenoid taper holds its advantage, we tracked pions (muons) with bunch lengths varying from 1 to 30 ns through the Front End, Figure 5 shows the number of positive muons at the end of the Front End tracked through solenoid tapers of lengths 6, 20 and 40 m in case of

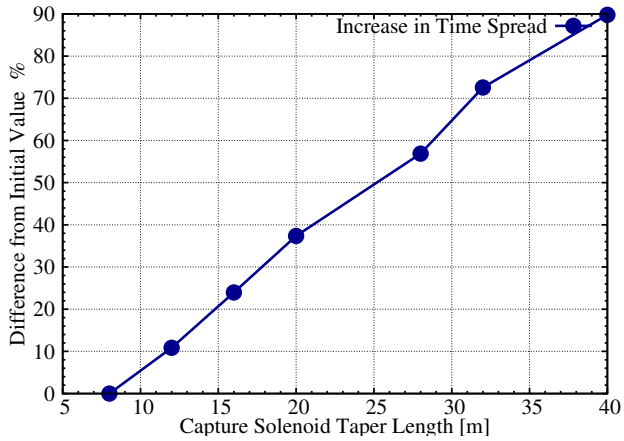


Figure 3: Relative increase in the time spread of the muon beam at the end of the Decay Channel as a function of the taper length. The distance from target to end of Decay Channel is constant.

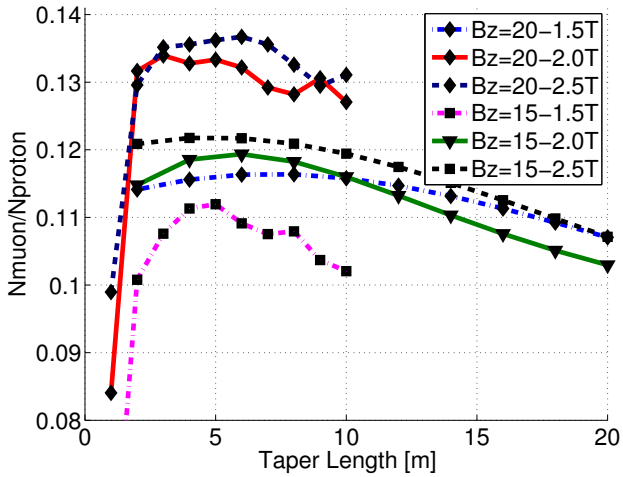


Figure 4: Muon yield after the transverse Ionization Cooling Channel, within the acceptance of the following accelerator chain, *vs.* the target solenoid taper length. Optimum yield is at taper length of 4-6 m.

an 8-GeV proton beam incident on a Hg-jet target, with solenoid-field profile tapering from 20 down to 2.5 T. The short taper looses its advantage gradually as bunch lengths increase from 1 to 20 ns. Bunches with length of 20 ns and longer will not benefit from the short-taper effect.

A similar study was carried for an initial Neutrino Factory with a 3-GeV proton beam on a graphite target and peak solenoid field of 15 T, with results shown in Fig. 6. The tracking study was done for a target solenoid taper length of 4 m and end field of 2.5 T. For this case the loss is $\approx 5\%$ per 1 ns increase in bunch length.

Copyright © 2013 CC-BY-3.0 and by the respective authors

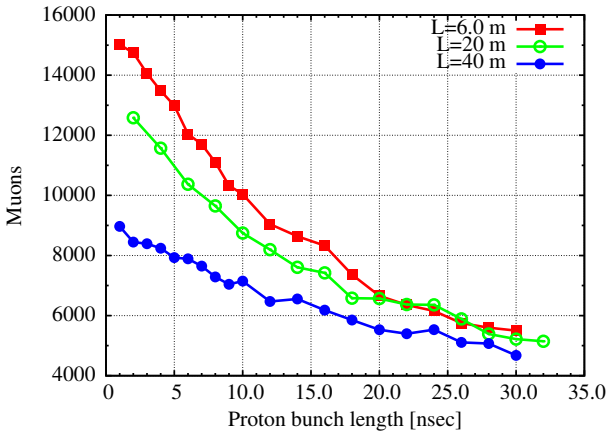


Figure 5: Number of positive muons within the accelerator chain acceptance *vs.* the initial proton bunch length for 8 GeV proton beam on a Hg-jet target. The tracking study was done for different target solenoid taper length of 6, 20, 40 m (red, green, blue). The short taper loses its advantage gradually as the bunches get longer.

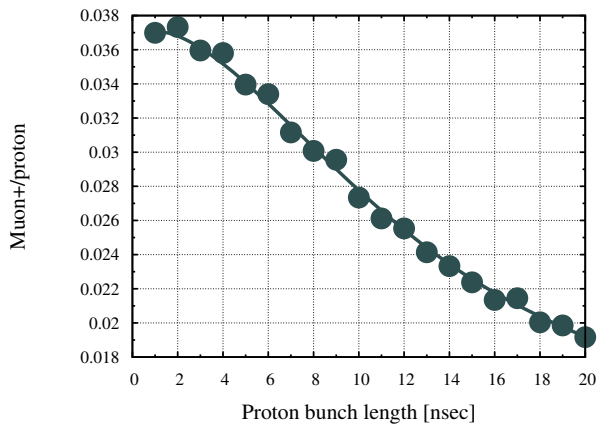


Figure 6: Number of positive muons within the accelerator-chain acceptance *vs.* the initial proton bunch length for 3-GeV proton beam on a graphite target. The tracking study was done for a target solenoid peak field of 15 T, taper length of 4 m, and end field of 2.5 T. For this case the loss is $\approx 5\%$ per 1 ns increase in bunch length.

PERFORMANCE OF THE DESIGN BUNCH LENGTH 2-8 NS

The performance of the Front End at various design bunch lengths of 2, 5, 8 ns *vs.* the target-solenoid taper length is shown in Fig. 7. For bunch lengths of interest for a Muon Collider and Neutrino Factory (2-8 ns), the short taper holds its advantage. The difference in performance of the front end between a 2 and 8 ns decreases gradually with the taper length.

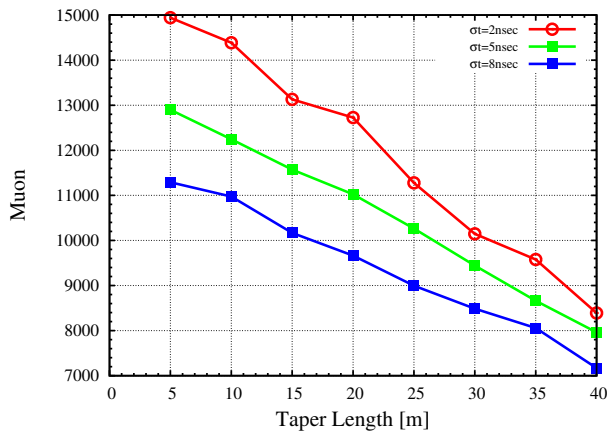


Figure 7: Number of positive muons within the accelerator-chain acceptance *vs.* the target solenoid taper length at three different bunch lengths of 2, 5, 8 ns.

ACKNOWLEDGMENT

The authors would like to thank X. Ding for useful discussions.

REFERENCES

[1] M.A. Palmer *et al.*, Muon Accelerators for the Next Generation of High Energy Physics Experiments, Proc. IPAC13, TUPFI057 (2013).

[2] C.T. Rogers *et al.*, Muon front end for the neutrino factory, Phys. Rev. ST Accel. Beams **16**, 040104 (2013).

[3] R. Palmer, Proton Bunching Options, Applications of High Intensity Proton Accelerators, BNL-90917-2010-CP, (2009).

[4] H.K. Sayed *et al.*, Optimization of the Capture Section of a Staged Neutrino Factory, THPHO11, NA-PAC'13.

[5] R.C. Fernow,Ionization Cooling Code, https://pubweb.bnl.gov/~fernow/icool/

[6] N.V. Mokhov, The MARS Code System User's Guide, Fermilab-FN-628 (1995); N.V. Mokhov and S.I. Striganov, MARS15 Overview, AIP Conf. Proc. **896**, 50 (2007), http://www-ap.fnal.gov/MARS/

Copyright © 2013 CC-BY-3.0 and by the respective authors

TOWARDS A GLOBAL OPTIMIZATION OF THE MUON ACCELERATOR FRONT END *

H.K. Sayed,† J.S. Berg, H.G. Kirk, R.B. Palmer, D. Stratakis, BNL, Upton, NY 11973, USA
K.T. McDonald, Princeton University, Princeton, NJ 08544, USA
D. Neuffer, Fermilab, Batavia, IL 60510, USA
J. Qiang, R.D. Ryne, LBNL, Berkeley, CA 94720, USA

Abstract

The baseline design for the Front End of a Neutrino Factory and Muon Collider consists of a five major components, namely the Target System, Decay Channel, Buncher, Phase Rotator, and the Ionization Cooling Channel. Although each of the mentioned systems has a complex design which is optimized for the best performance with its own set of local objectives, the integration of all of them into one overall system requires a global optimization to insure the effectiveness of the local objectives and overall performance. This global optimization represents a highly constrained multi-objective optimization problem. The objectives are the number of muons captured into stable bunches of specified transverse and longitudinal emittances, as constrained by the momentum-and dynamic-acceptance of the subsequent acceleration systems in addition to the overall cost. A multi-objective global evolutionary algorithm is employed to address such a challenge. In this study a statement of optimization strategy is discussed along with preliminary results of the optimization.

INTRODUCTION

The capture efficiency of muon Front End [1] of a Neutrino Factory and Muon Collider [2] determines the luminosity of both machines. In the Neutrino Factory scenario only a 4D transverse Cooling Channel is considered, while in the Muon Collider a charge separation follows the Front End before the 6D Ionization Cooling.

The muon beam is produced by bombarding a pion-production target with a 4-MW proton beam that is pulsed at 50 Hz. Produced pions travel through a constant-field solenoid Decay Channel where they decay into muons. Following the Decay Channel, muons go through bunching, phase rotation, cooling, and acceleration sections. Previous studies [3] have shown that using the global Front End performance as the figure of merit in the optimization of local systems improves the performance in a significant way. In this study we identify the parameters in each of the major subsystems of the Front End major that have an impact on the integrated performance, then we optimize the design accordingly.

* Work supported by the US DOE Contract No. DE-AC02-98CHI10886 and DE-AC05-00OR22725.

† hsayed@bnl.gov

TARGET AND MUON FRONT END

The Target System is designed to deliver intense muon beam of 10^{14} muons/sec from an incident beam of 10^{15} protons/s. In the baseline design a liquid-mercury jet target intercepts the 8-GeV proton beam inside a solenoid field that peaks at $B_i = 20$ T at the target and tapers down to $B_f = 1.5$ T over a distance of $L_{\rm taper} = 15$ m. The portion of the mercury jet disrupted by the proton beam is replaced before the arrival of the following proton pulse. This baseline configuration produces 0.8 muons/proton at the end of the Target System.

After the particles leave the tapered target solenoid they are transported in the Decay Channel, Buncher, and Phase Rotator in a constant solenoid field, nominally 1.5 T. At the end of the Decay Channel, $\approx$ 70 m from the target, most pions have decayed into muons and the beam is about 15 m long. The beam is then bunched over $\approx$ 33 m in a sequence of RF cavities with frequencies from 320 to 230 MHz that capture muons with kinetic energy ranging from 50-400 MeV. The bunching cavities RF voltage increases linearly along the channel from 3.4 to 9 MV/m.

In the 42-m-long phase-rotation section, lower-energy muons are accelerated and higher-energy ones are decelerated, until at the end of the Rotator the central momentum is 232 MeV/c, and the original 15-m-long bunch of muons of both signs has been formed into a 48-m-long train with 33 bunches of μ^+ interleaved with 33 bunches of μ^-. The muon beam is then matched into the alternating, 2.8-T solenoid field in the Cooling Channel.

OPTIMIZATION STRATEGY

In this section we identify the parameters in each subsystem that we consider in the global optimization. In the next section we will show the improvement on the performance after optimizing each of those parameters.

Capture Solenoid

The target-solenoid field is parameterized in three variables, the peak initial field at the target location, the taper length, and the end solenoid field. For this study the peak field was either 20 or 15 T The effect of solenoid field profile on the phase space density and distribution of the captured muons was studied by simulating the particles produced at the target and transported through the rest of the Front End. The target-solenoid field profile was shown to

Copyright © 2013 CC-BY-3.0 and by the respective authors

have a significant effect on the performance of the front end [4]. Here, we consider optimizing the capture efficiency as a function of the final asymptotic end field and the length of the taper as well.

Decay Channel, Buncher and Phase Rotator

Muons are confined in the Decay Channel, Buncher, and Phase Rotator by a series of constant-field focusing solenoid coils.

The muon/pion bunch lengthens as it drifts through the Decay Channel, developing a high-energy head and a low-energy tail which depends on the Channel length. We considered a multivariable optimization of the target-solenoid taper length, RF phase and the Decay Channel length at various taper end-field values. Figure 1 shows the process of optimizing the Decay Channel length with the figure of merit being the total number of muons within the acceptance cuts of the accelerator [5].

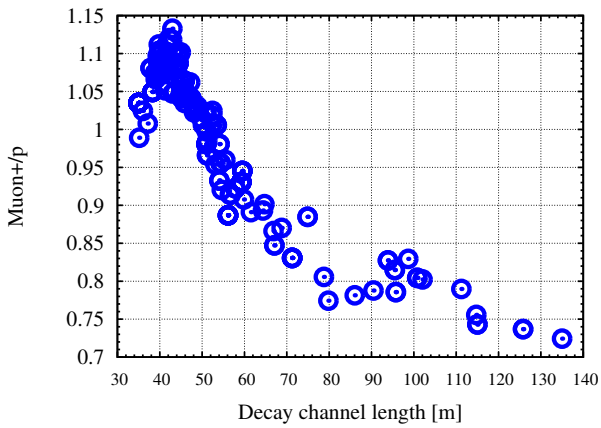


Figure 1: Optimizing the Decay Channel length using a differential evolution algorithm.

The effect of the solenoid field strength on the performance of the Front End was studied, including dynamic losses due to resonances ("stop bands") in the periodic field structure. The coil design was optimized to suppress those dynamic losses.

As the taper length of the target solenoid was optimized, the RF phases of the Buncher and Phase Rotator were also varied to find the optimal working point. Figure 2 illustrates an optimization of overall RF phase.

Broadband Match to Ionization Cooling Channel

While the muons are confined with a constant solenoid field starting from the Decay Channel to the end of the Rotator, the field in the Cooling Channel is generated by alternating solenoid coils of ± 2.8 T strength. The muon-beam phase-space ellipse would experience filamentation and emittance growth without matching between the region regions of constant and alternating solenoid fields. The muon beam out of the Phase Rotator has a large momentum spread, as shown in Fig. 3. A set of 9 solenoid coils

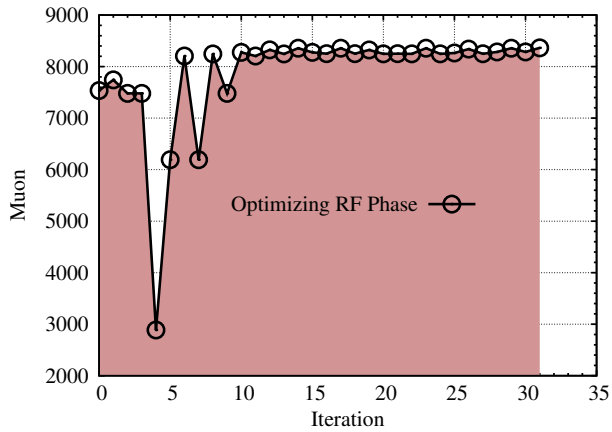


Figure 2: Optimization of the phase of the Buncher and Rotator RF cavities. Each iteration represent a trial value of the RF phase.

were considered to perform the match between the Rotator and the Cooling Channel. The objective of this optimization was constructed as a sum of the emittance magnification factor [6], eq. (1), at various momenta weighted by the number of muons within the vicinity of a central momentum,

$$EM = \frac{1}{2}\left[\frac{\beta_b}{\beta_s} + \frac{\beta_s}{\beta_b} + \left(\sqrt{\frac{\beta_b}{\beta_s}}\alpha_s - \sqrt{\frac{\beta_s}{\beta_b}}\alpha_b\right)^2\right], \quad (1)$$

where β_b and α_b are the beam ellipse parameters and β_s and α_s are the periodic solution for the Cooling Channel. Figure 4 shows the number of accepted muons along the Front End before and after the match.

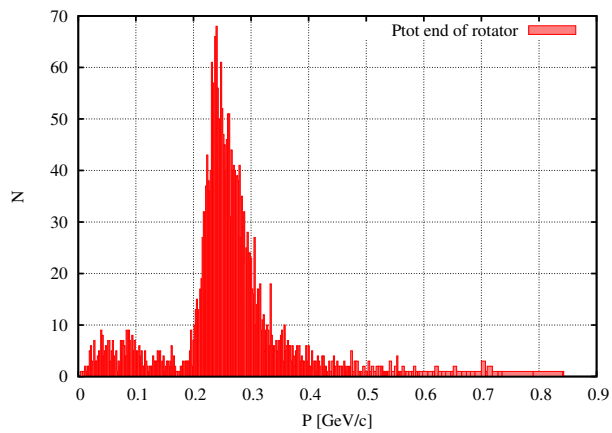


Figure 3: Muon beam momentum distribution at the end of the Phase Rotator.

HIGH PERFORMANCE COMPUTING OPTIMIZATION TECHNIQUES

A set of parallel, differential-evolutionary-optimization algorithms working on a CRAY based architecture [7] were

Copyright © 2013 CC-BY-3.0 and by the respective authors

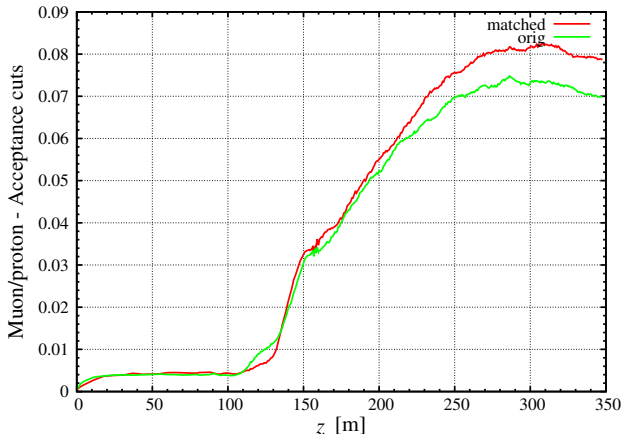


Figure 4: Performance of the Front End before and after optimizing the $B = 2.5$ T match to the ± 2.8 T alternating solenoid field in the Ionization Cooling Channel. The matching coils are located at $z \approx 150$ m from the target.

utilized and integrated with a parallel, Monte-Carlo-based, ionization-cooling-and-transport code ICOOL [8].

RESULTS

A first round of the global optimization of the Front End (which included parameters from the target solenoid taper, Buncher and Rotator RF phases, Decay Channel length and field strength, broadband matching to Cooling Channel) showed significant improvement of the performance of the Front End. Figure 5 shows the optimized performance of the Front End *vs.* the constant solenoid field, with an improvement of 15% above the unoptimized baseline field of 1.5 T, increases to 60% improvement at 3.5 T. An increase of the focusing field from 1.5 T to 2 T would improve the performance by 40% which represents a substantial increase in the performance of a mild rise in the cost.

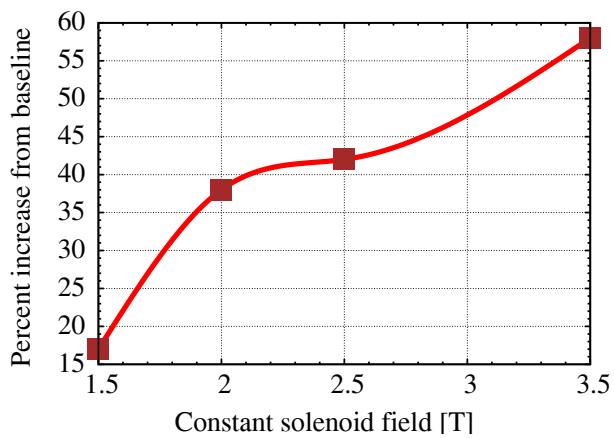


Figure 5: Optimized performance of the Front End *vs.* the constant solenoid field in the Decay Channel, Buncher, and Phase Rotator.

SUMMARY AND FUTURE WORK

A global optimization strategy for the muon Front End was presented. The first round of the multivariable optimization showed improvement by $15 - 60\%$ over the current baseline. Future work will include optimization of parameters of the Ionization Cooling Channel (focusing field, RF phase and RF gradient, absorber configuration).

ACKNOWLEDGMENT

Authors would like to thank C. Rogers for useful discussions and NERSC for the computing resources.

REFERENCES

[1] C.T. Rogers *et al.*, Muon front end for the neutrino factory, Phys. Rev. ST Accel. Beams **16**, 040104 (2013).

[2] M.A. Palmer *et al.*, Muon Accelerators for the Next Generation of High Energy Physics Experiments, Proc. IPAC13, TUPFI057.

[3] H.K. Sayed *et al.*, Progress On The Neutrino Factory Target System Design, Proc. Nufact12 (2012).

[4] H.K. Sayed *et al.*, Optimization of the Capture Section of a Staged Neutrino Factory, These Proceedings, THPHO11.

[5] J.S. Berg *et al.*, Muon front end for the neutrino factory, Phys. Rev. ST Accel. Beams **9**, 011001 (2006).

[6] C. Wang and K.-J. Kim, Beam parameterization and invariants in a periodic solenoidal channel, FERMILAB-MUCOOL-205 (2001).

[7] J. Qiang and R.D Ryne, Parallel Optimization of Beam-Beam Effects in High Energy Colliders, Proc. PAC2011, WEP152.

[8] R.C. Fernow, *Ionization Cooling Code*, https://pubweb.bnl.gov/~fernow/icool/

Copyright © 2013 CC-BY-3.0 and by the respective authors

DESIGN OF THE ILC RTML EXTRACTION LINES FOR THE RENOVATED TWO-STAGE BUNCH COMPRESSOR

S. Seletskiy#, NSLS, BNL, Upton, NY 11973, U.S.A.
N. Solyak, FNAL, Batavia, IL 60510, U.S.A.

Abstract

The renovated two-stage bunch compressor (BC) in the International Linear Collider (ILC) Damping Ring to the Main Linac (RTML) beamline requires new design for the extraction lines (ELs). The ELs located downstream of each stage of the BC will be used for both an emergency abort dumping of the beam and the tune-up continuous train-by-train extraction. They must accept both compressed and uncompressed beam with energy spread of 1.4% and 0.1% respectively. In this paper we report the design that allowed minimizing the length of such extraction lines while offsetting the beam dumps from the main line by 5 m distance required for acceptable radiation level in the service tunnel. Proposed extraction lines can accommodate beams with different energy spreads at the same time providing the beam size suitable for the aluminum ball dump window.

INTRODUCTION

It was decided [1-3] to incorporate a two stage bunch compressor [4] into the final design of the ILC [5]. The renovated two-stage BC compresses 6 mm long beam to 0.3 mm. The beam energy and energy spread after the first stage of the BC are 4.8 GeV and 1.4 % respectively. The beam energy after the second stage is 15 GeV and the beam energy spread, while it depends on the ILC operational mode, is 1.26 % at maximum.

The two extraction lines (ELBC1 and ELBC2) considered in this paper are located downstream of respective stages (BC1 and BC2) of the bunch compressor. The ELs can be used for either an emergency beam abort or for a train-by-train extraction. Since these ELs might receive both compressed and uncompressed beam, they must accept beams with both low and high energy spread.

Each extraction line is equipped with the 220 kW aluminum ball dump, which corresponds to the power of the continuously dumped beam with 5 GeV energy.

EXTRACTION LINES REQUIREMENTS

There are multiple requirements to the extraction lines:

- Due to the requirements of acceptable radiation levels in the service tunnel, horizontal offset of the dump from the main beamline must be at least 5 m center-to-center [6].
- The beam size on the dump window must be at least $\pi\sigma_x\sigma_y$=12 mm^2. Such beam size allows the use of an aluminum window on the dump.
- The beamline apertures have to be large enough to accommodate the beam. The RMS energy spread of the beam can be as large as 1.4% (for ELBC1). Additionally, a reasonable limit for the horizontal β-function is about 5 km. Since one might want to run beams with energy spread of 0.04% (for ELBC2 taking 15 GeV uncompressed beam) to the dump the beam size due to dispersion is no help in maintaining the required beam size on the dump window.
- The elements of the straight-ahead beamline and the extraction beamline must have enough transverse clearance.
- One has to arrange for both the train-by-train extraction and emergency abort of the beam, i.e., the emergency abort kicker has to ramp from zero to full strength in less than the minimum bunch spacing of 150 nsec.
- The magnets must be physically realizable. Here we limit ourselves to 1 T pole-tip fields for the quads, 1.5 T fields for the bends, and 0.05 T fields in septum magnets [6].
- The extraction line must be made as short as possible.

Requirements to the ELs in the final RTML are similar to the requirements specified in [6]. As a matter of fact the extraction system of new ELs is copied from 2008 solution.

EXTRACTION SYSTEM

The abort extraction of the beam is performed by four 2 m long fast kickers, which are powered to 35 G with a rise time of about 100 ns. Routine tune-up beam extraction is performed by a single 1 m long pulsed bend located between two central kickers. The bend is excited to 280 G to make its bending angle compatible with the cumulative angle provided by four fast kickers.

EXTRACTION LINES IN LINEAR APPROXIMATION

To satisfy aforementioned requirements, the linear lattices of ELBC1 and ELBC2 are designed in accordance with the concept considered in details in [6].

To decouple the dispersion and beam size issues we use Double Bend Achromats (DBA) as EL bending blocks. The extraction line is built of the cells, which have periodic solution for the Twiss parameters, and consist of DBA and focusing quads. Number of cells is determined by requirement to sufficient separation between the beam

#seletskiy@bnl.gov

Copyright © 2013 CC-BY-3.0 and by the respective authors

dump and the main line.

The linear solutions for the ELBC1 and ELBC2 are presented in Fig. 1 and 2 respectively.

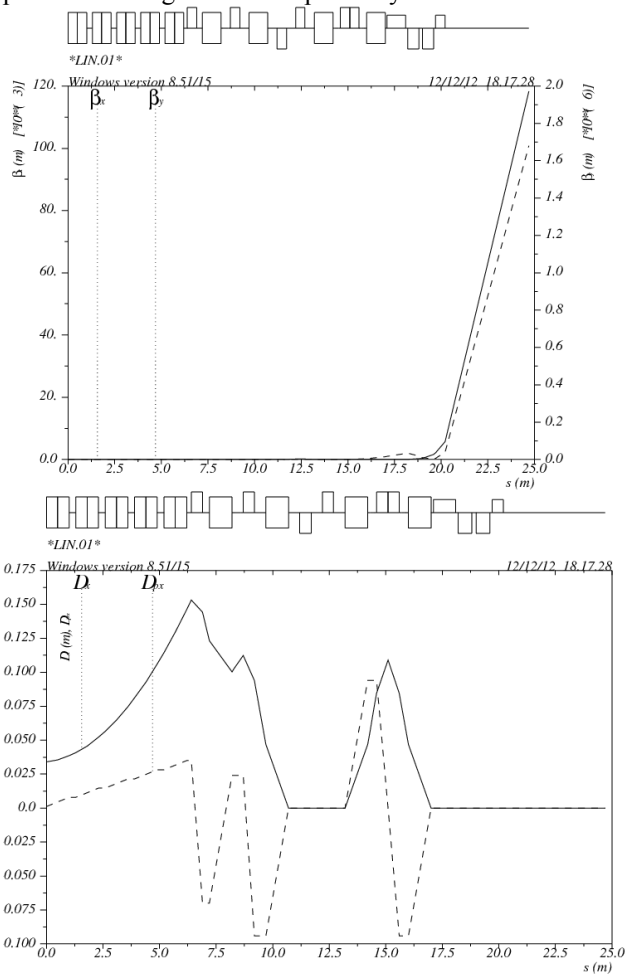


Figure 1: Twiss parameters and dispersion in ELBC1.

The extraction is initiated by a set of septum magnets (5 for ELBC1 and 6 for ELBC2) deflecting the beam from the main beamline by distance large enough to accommodate regular bends and quads. The septa are followed by a dispersion matching section consisting of two bends and two quads, which are tuned to zero the dispersion at the exit of the section.

The periodic cells (one for ELBC1 and two for ELBC2) following the dispersion matching section separate the dump from the main line by required distance. The quads at the end of the dump line are used to blow up the beam size on the dump window to the specified requirements. The resulting lengths of ELBC1 and ELBC2 are 24.7 m and 45.8 m respectively.

BEAM DUMP

The 220 kW aluminum ball dump [6] will be used for each of the lines. A nominal dump window diameter is 12.5 cm.

Calculations show that an aluminum window using a 1 mm thick hemispherical design is feasible for a suggested aluminum sphere dump. It has the promise of long term safe operation, with beam spot area on the dump window larger than 12 mm^2. There are no steady state heat transfer issues to reject the energy deposited by the beam to the cooling water.

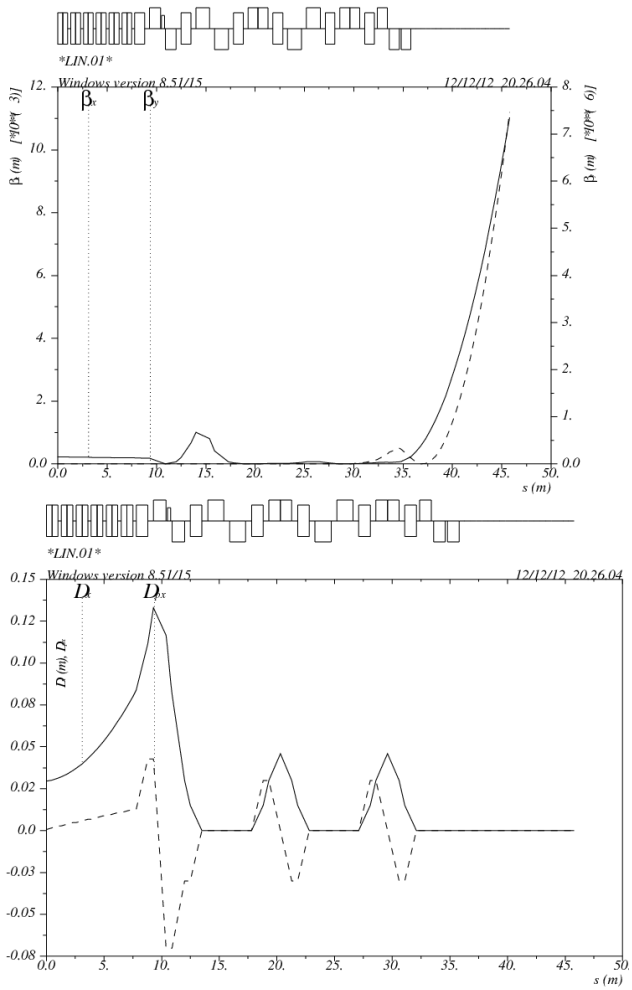


Figure 2: Twiss parameters and dispersion in ELBC2.

NONLINEAR EFFECTS

For a beam with a high energy spread there is a substantial blow-up of beam size at the end of the ELs. In Y direction the growth of the beam halo is due to chromatic aberrations, while in X direction it is because of both chromatic aberrations and nonlinear dispersion.

While the beam with small energy spread is contained within the envelope of reasonable size, the high energy spread beam explodes in horizontal size making the optical solution for the EL obtained in linear approximation unfeasible.

In the previous designs of the 2-stage BC extraction lines a number of solutions that mitigate the nonlinear halo were considered, including collimators, superconducting quads of large aperture and large diameter dump window. On the other hand, for the single stage BC there was found an extraction line solution [7] that uses relatively weak sextupoles for containing the nonlinear halo and doesn't require any additional beam collimation.

Copyright © 2013 CC-BY-3.0 and by the respective authors

Following the recipe adapted from single stage BC EL solution, we found that for ELBC1 the two sextupoles can contain the nonlinear hallo of the high energy spread beam. Such beam can be accommodated by the dump window of nominal 12.5 cm diameter, and there is no need in additional collimation. As Fig, 3 demonstrates, both high energy and low energy beam sizes are within the limits allowing for transporting through the EL and for utilization of nominal size dump window.

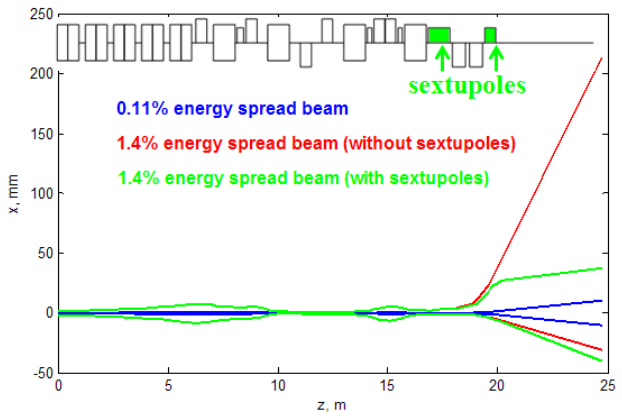


Figure 3: The horizontal beam size evolution through the extraction line for 1.4% (red – without sextupoles, green with sextupoles) and 0.11% (blue) energy spread beams.

In case of ELBC2 we found that the high energy spread beam can be contained with the help of only one sextupole strategically placed at the location of highest dispersion. Figure 4 shows that sizes of both low- and high-energy spread beams allow utilizing aluminum ball beam dump with a dump window of 12.5 cm diameter.

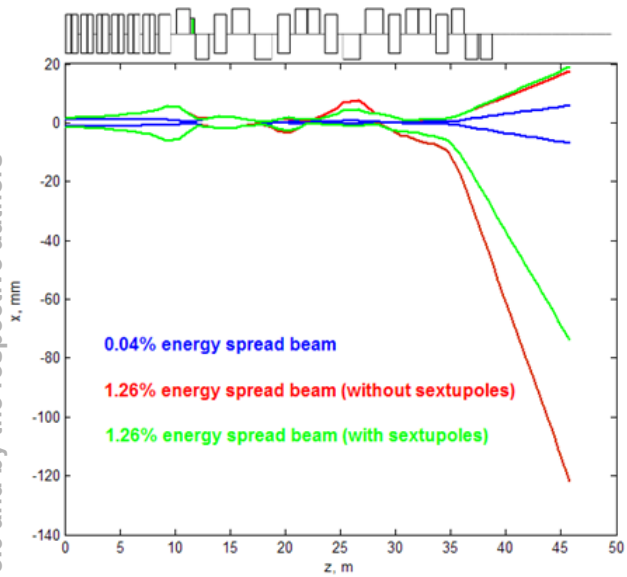


Figure 4: The horizontal beam size evolution through the extraction line for 1.26% (red – without sextupoles, green with sextupoles) and 0.04% (blue) energy spread beams.

CONCLUSION

We described the final design of the ILC RTML extraction lines located downstream of each stage of the renovated two-stage bunch compressor. The extraction lines are only 24.7 m and 45.8 m long. They are capable of accepting and transmitting 220 kW of beam power. The ELs can be used for both fast intra-train and continual extraction, and are capable of accepting both low- and high-energy spread beams.

REFERENCES

[1] S. Seletskiy, The Bunch Compressor options for the ILC RTML, ILC TBR Workshop, DESY, October 24-27, 2011.

[2] G. Dugan, Relative cost of one vs. two stage Compressors, ILC TBR Workshop, DESY, October 24-27, 2011.

[3] A. Latina, RTML beam dynamics (start-to-end), ILC TBR Workshop, DESY, October 24-27, 2011.

[4] S. Seletskiy, N. Solyak, Renovated 2-stage bunch compressor for the International Linear Collider, Proceedings of IPAC12, 2012.

[5] C. Adolphsen et al. (editors), The International Linear Collider Technical Design Report: Accelerator, 2013.

[6] S. Seletskiy, P. Tenenbaum, D. Walz, Design of the ILC RTML extraction lines, Proceedings of EPAC08, 2008.

[7] S. Seletskiy, N. Solyak, Final design of ILC RTML extraction line for single stage bunch compressor, Proceedings of IPAC11, 2011.

Copyright © 2013 CC-BY-3.0 and by the respective authors

NS-FFAG FOR ELECTRON-ION COLLIDER IN RHIC (ERHIC)*

D. Trbojevic, J. S. Berg, S. Brooks, O. Chubar, Y. Hao, V. N. Litvinenko, C. Liu, W. Meng, F. Meot, B. Parker, V. Ptitsyn, T. Roser, N. Tsoupas, and W. T. Weng, BNL, Upton, New York, USA

Abstract

A future electron ion collider "QCD test facility" is designed in the present Relativistic Heavy Ion Collider (eRHIC) tunnel. Electron acceleration and de-acceleration is preformed with energy recovery linac with multiple passes. We report on a combination of a multi-pass linac with the Non-Scaling Fixed Field Alternating Gradient (NS-FFAG) arcs. A single NS-FFAG arc allows electrons to pass, in the first stage of eRHIC, through the same structure with an energy range between 1.28 and 10 GeV. The NS-FFAG is placed in the existing RHIC tunnel. The 100 MeV injector bring the polarized electrons to the 0.9 GeV superconducting linac. After three passes through the linac 2.8 GeV electrons enter NS-FFAG arc and after 8 passes reach the energy of 10 GeV. After collisions the beam is brought back by the NS-FFAG, decelerated to the initial energy and directed to the dump.

INTRODUCTION

The eRHIC, future "QCD factory", will provide collisions between polarized electrons and: polarized protons in an energy range of 100-250 (325) GeV; light ions (d, Si, Cu); heavy ions 50-200 (130) GeV/u; and, polarized He^3 215 GeV/u. Electrons will circulate in the present RHIC tunnel as shown in Figure 1.

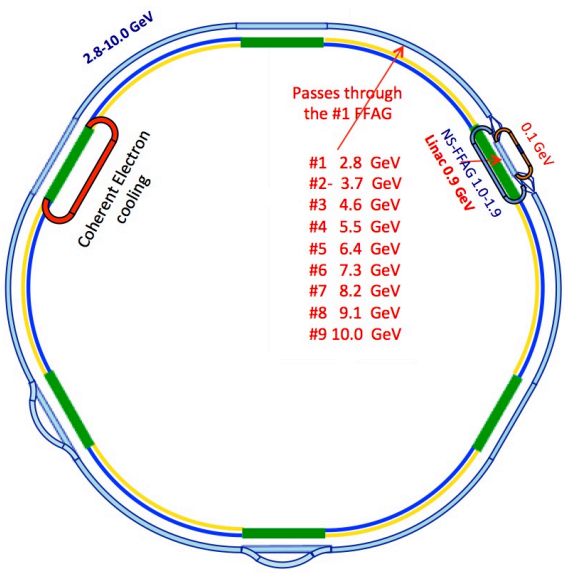


Figure1: Schematic layout of the electron NS-FFAG in the RHIC tunnel – blue and yellow superconducting ion rings are shown, as well as the position of the coherent electron cooling.

The Energy Recovery Linac (ERL) is proposed due to the beam-beam tune shift limitation in the ring-ring case for achieving higher luminosities and due to ability to recover the energy of ~1 GW with a dump energy equal to the injection energy. To reduce the cost and number of elements in the tunnel, a single NS-FFAG ring is proposed with an energy acceptance between 2.8-10 GeV for the first stage of eRHIC.

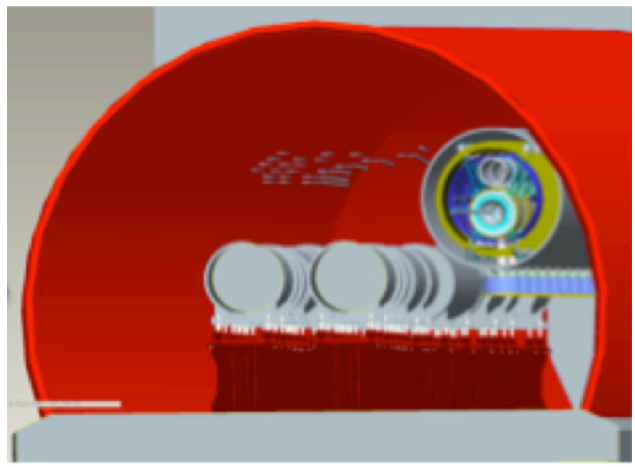


Figure 2: Two RHIC rings with electron linac on the right side above.

Non-Scaling FFAG

Revival of the Fixed Field Alternating Gradient (FFAG) accelerators previously developed in fifties [1,2,3] is very evident. They have very large momentum acceptance with beam accelerated under a constant magnetic field. The scaling FFAG have been mostly built in Japan: started with a the proof of principle (POP) proton accelerator at KEK, the 150 MeV proton accelerator (presently at the Kyushu University), 150 MeV accelerator at Osaka University, and many electron scaling FFAG's built for different applications. Although the scaling FFAG's have an advantage of the fixed magnetic field the synchrotrons are dominant accelerators in spite of magnetic field variation with energy. This is mostly due to significantly smaller aperture requirements. Large aperture magnets accommodate for the large orbit offsets. The aperture size is significantly reduced with the Non-Scaling FFAG's (NS-FFAG) [4]. The maximum of the orbit offsets are -18.6 mm$<\Delta x<0$ in the example presented. The NS-FFAG has fixed magnetic fields designed for the reference momentum. The maximum electron energy of 10 GeV, in the first stage of eRHIC, is selected for the reference energy with circular beam orbit. This is to reduce the synchrotron radiation, as the radius of the curvature is r=318 m.

NS-FFAG 2.8-10 GEV

The electron ring follows the shape of the RHIC tunnel and six arcs have 132 identical NS-FFAG cells. Each cell

* Work performed under Contract Number DE-AC02-98CH10886 with the auspices of the US Department of Energy

Copyright © 2013 CC-BY-3.0 and by the respective authors

is made of three combined function magnets: the central 1.25 m long is a defocusing magnet with a gradient of G_D=-17.9 T/m and dipole field of B_D=0.1T, while the two surrounding, 0.5m long, are focusing magnets with a gradient of G_F=23.7 T/m and dipole field of B_F=0.1 T. Properties of a NS-FFAG cell are shown in Figure 3.

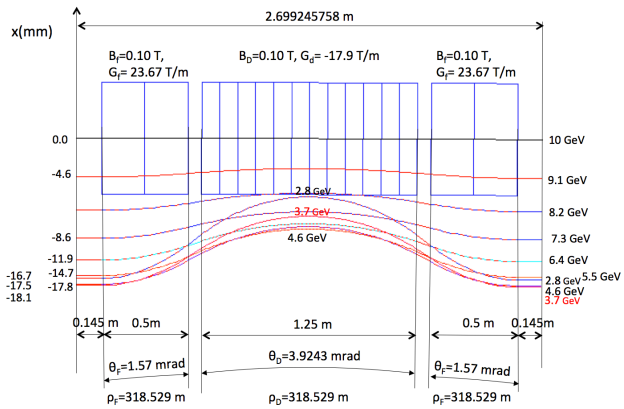


Figure 3: Basic NS-FFAG cell properties.

The tune dependence on energy is shown in Figure 4.

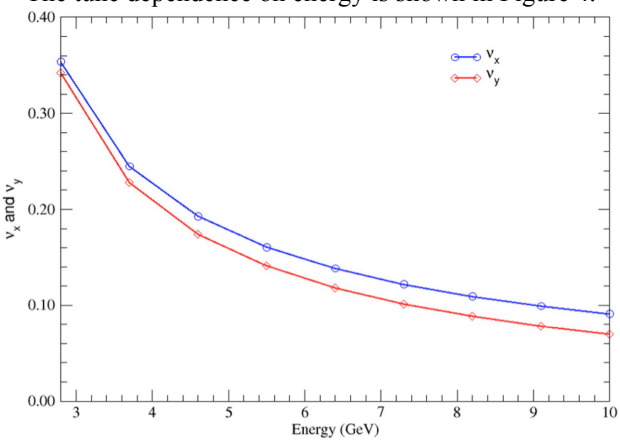


Figure 4: Betatron tunes dependence on energy.

The path length in NS-FFAG has a parabolic function with respect to the beam energy range with a minimum corresponding to the momentum compaction or transition energy equal to zero. A relation ship between bending angles Ratio=θ_F/θ_D of the two magnets defines the shape of the parabola as shown in Figure 5. The ratio of Ratio=θ_F/θ_D =0.4 was selected to allows for almost symmetric dependence in the time of flight with respect to the medium energy of E=6.4 GeV and the largest bending radius to reduce the synchrotron radiation.

A connection of the NS-FFAG to the linac is presented in Figure 6. The spreaders on one side of the linac and combiners on the other side allow at the same time adjustment of the time of flight for each energy so the bunches arrive at linac at the top of the linac RF wave or if they are decelerated to the bottom of it.

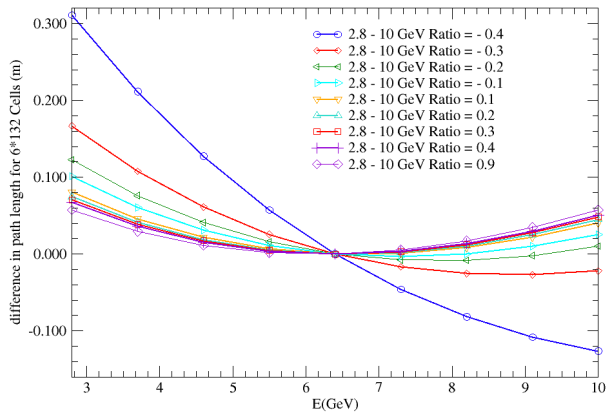


Figure 6: The six arcs time of flight dependence on the ratio between to angles of bending of the two magnets.

The maximum orbit offset dependence on the ratio between the two magnets is presented in Figure 7.

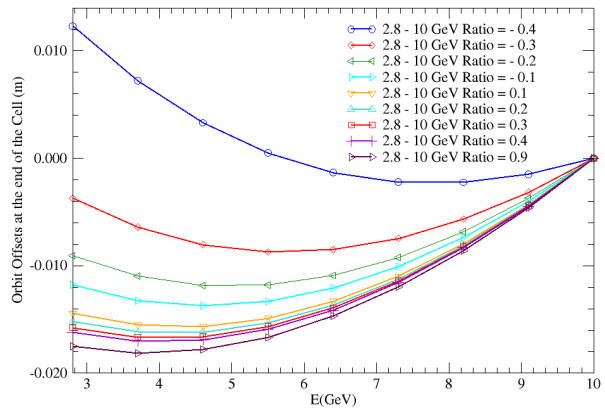


Figure 7: Maximum of the orbit offsets dependence on energy for different ratios of the bending angles θ_F/θ_D.

2.8-10 GeV Magnet Design

The defocusing combined function magnet made of combination between the permanent magnet SmCo is shown in Figure 8.

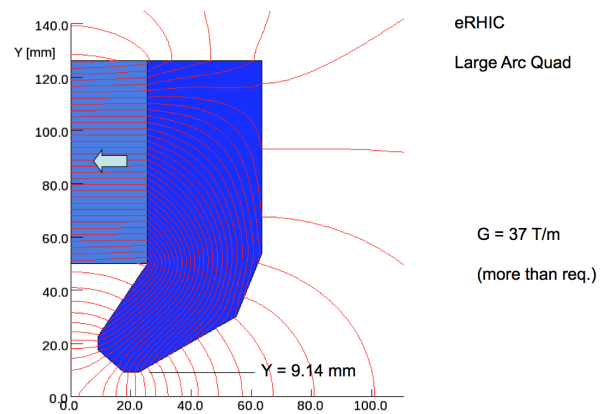


Figure 8: Defocusing combined function magnet.

Copyright © 2013 CC-BY-3.0 and by the respective authors

A magnet design for the focusing combined function magnet is shown in Figure 9.

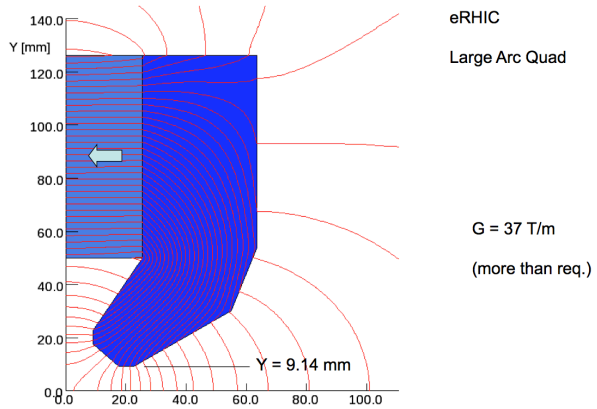


Figure 9: Focusing combined function magnet.

1-1.9 GEV NS-FFAG

The area around interaction region at 4 o'clock is selected for placement of the linac, injector and the NS-FFAG racetrack for two passes of electron beam with energy of 1 and 1.9 GeV. The 90 MeV injector receives electrons with energy of 10 MeV from the polarized electron source as schematically shown in Figure 10.

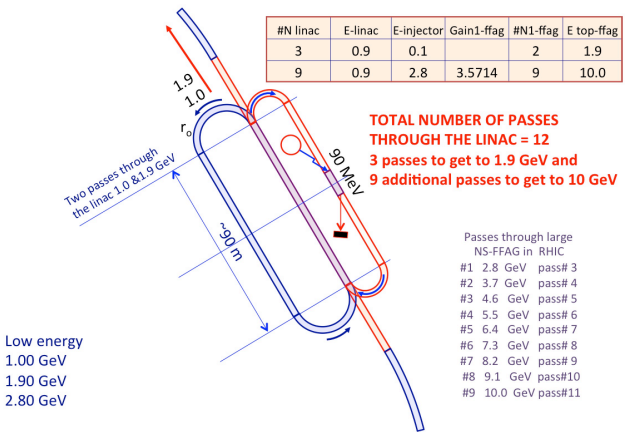


Figure 10: Schematic presentation of the linac with the injector, polarized electron source, and small NS-FFAG.

The new civil construction will be necessary for the small NS-FFAG ring as shown in Figure 11.

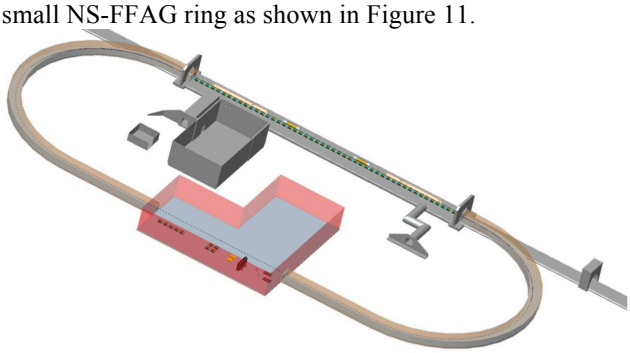


Figure 11: Linac and small NS-FFAG layout.

The basic NS-FFAG cell for the two passes with energies of 1 and 1.9 GeV is shown in Figure 12.

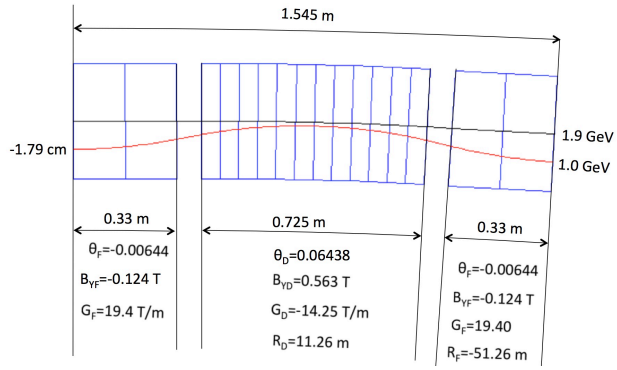


Figure 12: The NS-FFAG cell with two passes and 30 m radius of a curvature.

ORBIT CORRECTION

A random misalignment of the magnets, with a Gaussian distribution with maximum errors of 50, 100, and 150 μm, was implemented. Orbit for all energies were recorded and corrected with two correctors per cell.

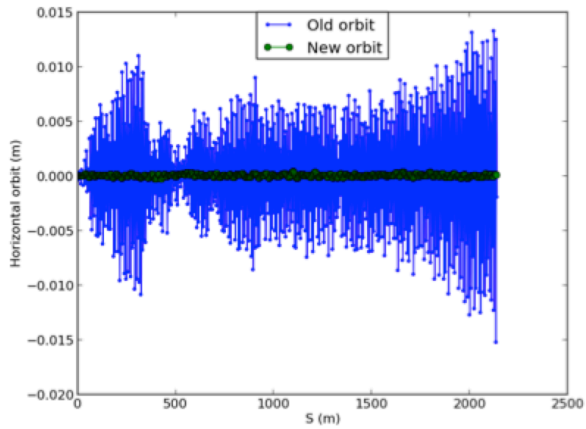


Figure 13: Correction of the orbit due to misalignment.

SUMMARY

A new approach of the NS-FFAG electron lattice design for the ERL eRHIC project is being studied. Two 2.8-10 GeV and 1-1.9 GeV NS-FFAG's lattices are designed and studied. Magnet design and beam dynamics studies are in progress.

REFERENCES

[1] T. Okawa, University of Tokyo, Japan, FFAG structure suggested at a Symposium on Nuclear Physics of the Phys. Society of Japan 1953.
[2] K.R. Symon, D.W. Kerst, L.W. Jones, L.J. Laslett, and K.M. Terwilliger, Phys. Rev. 103 (1956) 1837.
[3] A. Kolomensky et al., Zh. Eksp. Teor. Fiz. 33 (1957) 298.
[4] D. Trbojevic, E. D. Courant, and M. Blaskiewicz, Phys. Rev. ST Accel. Beams 8 (2005) 050101.

Copyright © 2013 CC-BY-3.0 and by the respective authors

DYNAMICAL BETA-SQUEEZE FROM 80 TO 40 CM AT RHIC*

Dejan Trbojevic, Jing Yichao, and Yun Luo, BNL, Upton, New York, USA

Abstract

Relativistic Heavy Ion Collider (RHIC) has been achieving record luminosities during the last decade. The latest stochastic cooling of the heavy ions, like uranium, achieved the largest luminosity at RHIC during the last heavy ion run. A betatron squeeze method, already used at LHC CERN, where a betatron wave is created through the arc up to the interaction region is applied at RHIC. When the heavy beam size is reduced due to stochastic cooling a dynamical beta squeeze is possible to apply in RHIC where the existing 75 cm value of beta-star could be reduced to 45 cm. This could be achieved by introducing the betatron wave in both planes throughout the arc before and after the interaction region. Higher values of dispersion and betatron functions in the arc, with a 90° degrees phase difference per FODO cell allow easier higher order chromatic corrections.

INTRODUCTION

The RHIC stunning discoveries in quark-gluon plasma in recent years went above any expectations that have captured worldwide attention. First and foremost was the unexpected "perfect"-liquid nature of the 4-trillion-degree quark-gluon plasma that permeated the early universe. RHIC is now closing in on the transition from this hot quark-gluon plasma into ordinary matter made of protons and neutrons—namely everything we see in today's world. This is a report on an attempt to improve on the RHIC existing large luminosity by dynamically squeezing the beam size as the stochastic cooling succeeds in reducing all three emittances. The stochastic cooling has already shown tremendous success during the previous RHIC runs. Under this assumption an additional step might be possible in an attempt to increase further the luminosity by additional beta squeeze at the interaction point (IP). This would be possible as the emittances are reduced and the triplet aperture would not present the aperture limitation anymore – as the beam is getting smaller at the IP the maximum of the betatron functions become larger at the focusing triplet quadrupoles. A complex of the RHIC accelerators used to make the latest achievements is shown in Figure 1.

RHIC 90° Lattice

Advantages of the 90° degrees per cell lattice have been well known [1]. The LHC chromatic and other non-linear compensations [2] were followed for the RHIC lattice chromatic corrections after encouraging results in the eRHIC lattice design.

* Work performed under Contract Number DE-AC02-98CH10886 with the auspices of the US Department of Energy



Figure 1: The RHIC accelerator complex shows the major components Linac, Booster, Alternating Gradient Synchrotron (AGS), and RHIC. The Electron Beam Ion Source EBIS is an additional important element.

Major advantage of the 90° lattice is not only reduction in the intra-beam scattering effect but easier linear and non-linear chromatic correction as there are 24 sextupole circuits available in RHIC. The sextupole correction has already shown very impressive results in dynamical aperture improvements during the eRHIC lattice study. The betatron functions of the 90° RHIC lattice with β^*=75 cm is shown in Figure 2.

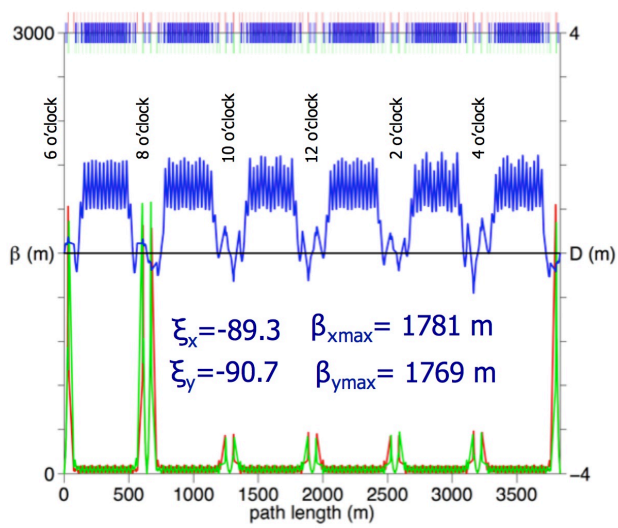


Figure 2: Betatron functions of the RHIC 90° degrees lattice with the β^*=80 cm. Two interaction regions at 6 and 8 o'clock have the same beam size.

Details of the lattice functions around one of interaction regions are shown in Figure 3. The maximum of the dispersion function is D_{max}=1.78 m. The lattice parameters

Copyright © 2013 CC-BY-3.0 and by the respective authors

in both cases with the β^*=75 cm and β^*=45 cm are shown in Table 1.

Table 1. Betatron Functions for β^*=75 and 45 cm

β^*(cm)	β_{xmax}(m)	β_{ymax}(m)	ζ_x	ζ_y	D_{xmax}	D_{xmin}
75	1781	1769	-89	-91	1.76	-0.6
40	2985	3317	-108	-119	2.52	-2.6

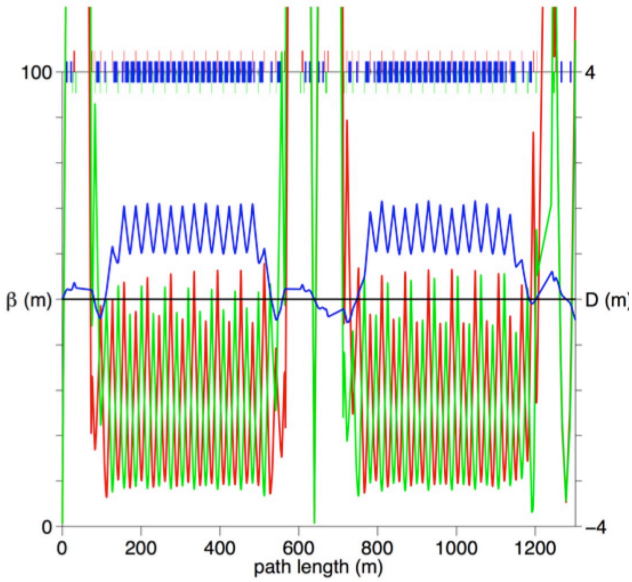


Figure 3: Details of the betatron functions around the IP for the β^*=75 cm.

The RHIC 24 sextupole circuits are shown in Figure 4.

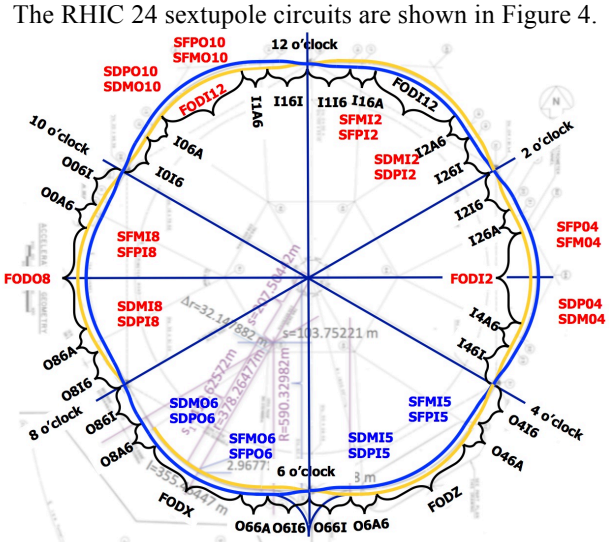


Figure 4: RHIC 24-sextupole circuits schematic.

Two pairs of quadrupoles are used around on each side of the interaction point IP-6 to induce the betatron wave through the IP6. At the end of the arc after the IP-6 there are two additional pairs in both horizontal and vertical plane used to cancel the wave, placed at correct betatron phase. A schematic presentation of the quadrupole pairs used in beta squeeze is shown in Figure 5. The quadrupoles in the pair are 90° degrees apart. The first quadrupole of the pair has a decrease in the gradient of ΔG=-7% while the second one has an increase of ΔG=+7%. The opposite is valid for the other plane at the beginning of the arc before the IP.

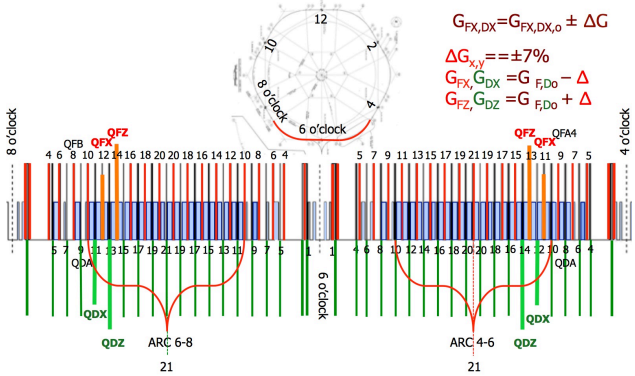


Figure 5: The quadrupole pairs to induce the beta wave are labeled QFX and QFZ, and QDX and QDZ at the beginning and end of the arcs.

The betatron functions in RHIC after introduction of the beta wave and beta squeeze is shown in Figure 6.

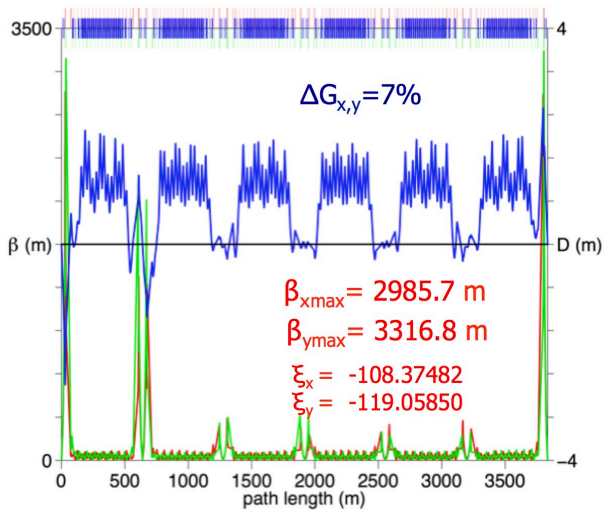


Figure 6: Betatron functions after the betatron wave is created through the IP 6.

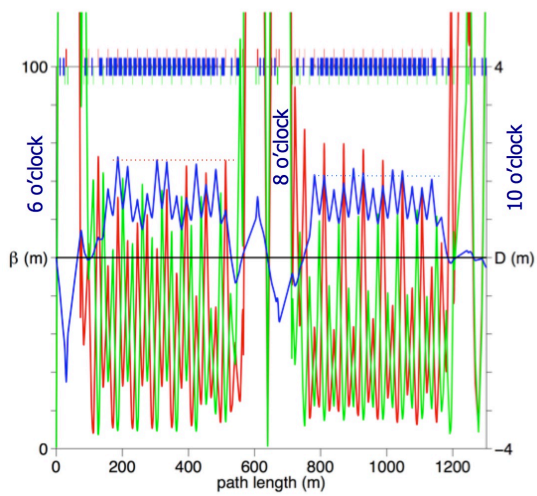


Figure 7: Details of the beta squeeze.

Copyright © 2013 CC-BY-3.0 and by the respective authors

Details of the beta squeeze from β^*=75 cm to β^*= 45 cm in two arcs around the IP-6 are shown in Figure 7.

SUMMARY

The stochastic cooling in RHIC has showed incredible success getting to the point that almost all beam loss comes from collisions with other beam. As the cooling reduces emittances in all three dimensions it would be possible to gain more in luminosity by dynamically squeezing the size at the collisions as the beam gets cooled, as the maximum of the betatron functions at the triplets are not a limitation any more. This is a study with the lattice design trying to double the luminosity. The LHC [2] method was followed. A betatron wave through the interaction point IP-6 succeeded in reducing the β^* from β^*= 75 cm to β^*= 45 cm with the beta wave creation through the two neighboring arcs. The larger betatron functions and dispersion in the arcs will allow easier chromatic correction as the correction is given by $\sim K_2 \beta D_x$. The dynamical aperture study in this case is in progress.

REFERENCES

[1] B. Autin, NIM, A 298 (1990) 85.
[2] S. Fartoukh, LHC Project Report 278, CERN.

Copyright © 2013 CC-BY-3.0 and by the respective authors

ERHIC INTRACTION REGION AND LATTICE DESIGN*

D. Trbojevic, E. C. Aschenauer, V. N. Litvinenko, Y. Luo, Jing Yichao, B. Parker, and V. Ptitsyn
BNL, Upton, New York, USA

Abstract

A proposal for the new high luminosity L=10^{34} $s^{-1}cm^{-2}$ polarized electron proton/3He and other un-polarized heavy ions eRHIC based on Electron Recovery Linac (ERL), assumes a location in the existing tunnel of the operating Relativistic Heavy Ion Collider (RHIC). Requests of the experiments for the interaction region are very challenging: allow detection of neutrons, allow deep virtual scattering for protons-electron collisions, detection of partons with lower momentum, etc. We present an interaction region (IR) design with a vey high focusing where at the collision point IP of 5 cm, and a 10-mrad collision angle between electrons and ions using the crab cavities. We are introducing a combined function magnet for the first element in the high focusing triplet configuration to provide neutron and the lower energy parton detection, and allow at 4.5 cm distance passage of electrons through free magnetic field region. The 200 T/m gradient quadrupoles provide very small beam size at the IP and allows a passage with a very small magnetic field for electrons.

ERHIC PHYSICS

The RHIC stunning discoveries in quark-gluon plasma in recent years went above any expectations that have captured worldwide attention. First and foremost was the unexpected "perfect"-liquid nature of the 4-trillion-degree quark-gluon plasma that permeated the early universe. RHIC is now closing in on the transition from this hot quark-gluon plasma into ordinary matter made of protons and neutrons—namely everything we see in today's world. Continuation of the RHIC success will be a new polarized electron-polarized proton/He^3 and electron-ion collider the QCD lab (the quantum chromodynamics describes the strong forces). It would be determining quark and gluon contribution to the proton spin, what is the polarization of gluons, and what is the flavor decomposition of the polarized sea, what is the spatial distribution of quarks and gluons in nuclei, and to explore the strong forces – understand in detail the transition to the non-linear regime of strong gluon fields and the physics of saturation, and have a probe to study deep inelastic scattering.

IR LATTICE FOR HIGH LUMINOSITY

A choice for ERL in the eRHIC is due possibilities of obtaining higher luminosity as the beam-beam effect represents a limitation the ring-ring option. From an injector the beam is accelerated by the superconducting linac using several passes and reaching energies up to 20-30 GeV to be able to reach luminosities of L=10^{34} $s^{-1}cm^{-1}$. We describe an ion lattice and Interaction Region (IR) design to allow small beam sizes with β^*= 10 and 5 cm. It is assumed that coherent electron cooling will reduce the ion beam emittances, allowing very short bunches in the longitudinal space. The strong focusing is possible by placing the first magnet of the triplet at 4.5 m distance from the IP. The IR design is being developed together with the detector physicist designers. The IR in RHIC is made to be symmetric as shown in Figure 1 and in more detail in Figure 2.

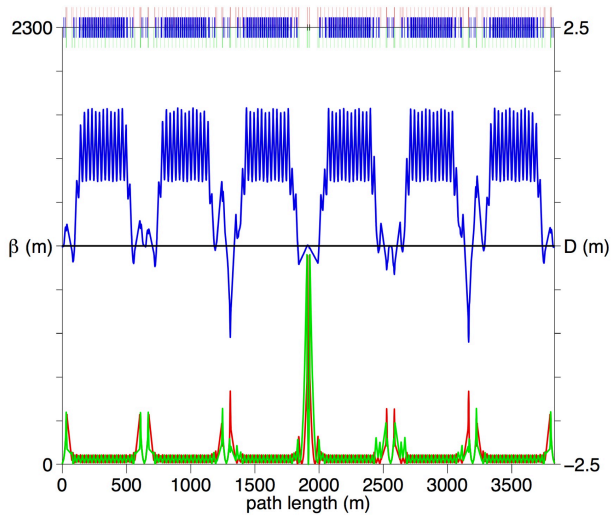


Figure 1: eRHIC lattice design with the β^*=10 cm at the single interaction region at 6 o'clock IP.

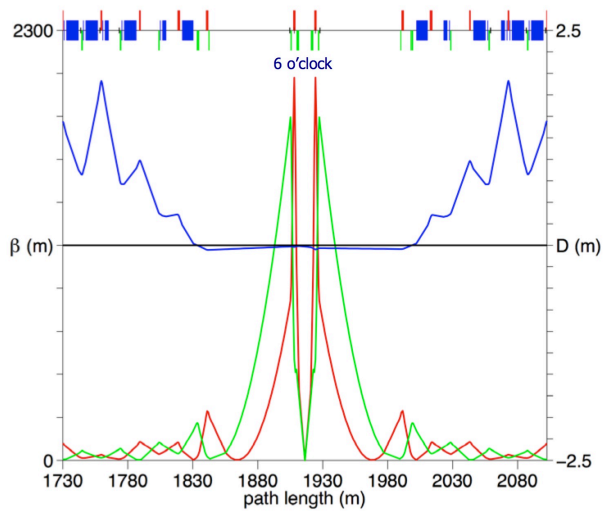


Figure 2: Details of betatron functions in the IR.

The maximum of the betatron function in the triplet magnets, the dispersion function, the chromaticities, and tunes for the β^*=10 cm are shown in Table 1. It is

* Work performed under Contract Number DE-AC02-98CH10886 with the auspices of the US Department of Energy

Copyright © 2013 CC-BY-3.0 and by the respective authors

important to note that the natural chromaticities of the ion eRHIC lattice are smaller than the RHIC chromaticities at RHIC the operating conditions.

Table 1. Betatron Functions for β^*=10, 5 cm

β^*(cm)	β_{xmax}(m)	β_{ymax}(m)	ζ_x	ζ_y	D_{xmax}	D_{xmin}
10	1100	1103	-89	-83	1.56	-1.1
5	2209	2210	-134	-113	1.94	-1.6

The layout of the interaction region in eRHIC is schematically presented in Figure 3.

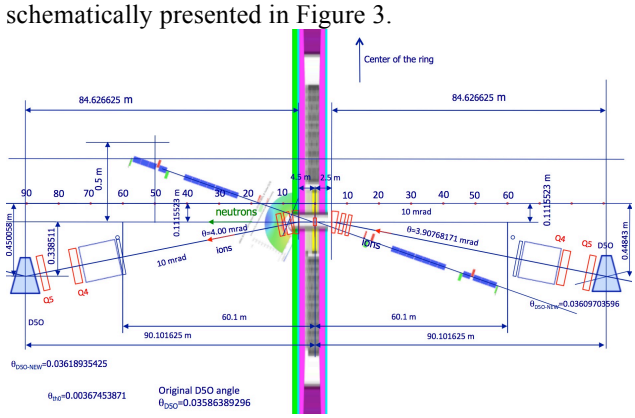


Figure 3: Layout of eRHIC interaction region.

Schematic presentation of the interaction region magnets downstream of the electron-ion or polarized proton or He^3 collisions is shown in Figure 4. The solid angle of neutron is obtained by use of a combined function magnet – (shown in orange color). The electron beam passes through the zero field region of the combined function magnet as shown in Figure 5.

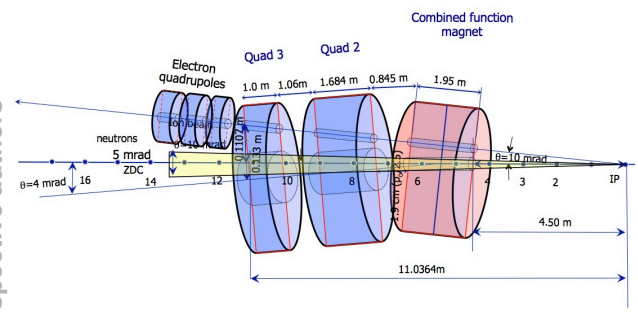


Figure 4: The triplets for both electron and ion lattice eRHIC IR layout with neutron solid angle (yellow).

A dipole coils are added to the solenoid of the detector to allow bending of electrons for an angle of 10 mrad. The combined function magnet is followed by the 200 T/m gradient quadrupoles. The combined function magnet bends the beam for 4.5 mrad allowing neutron detection downstream. The vertical axis in Figure 3 is centimeters while the horizontal axis is in meters. The detector is shown in looks distorted as due to different scale.

The RHIC lattice in the arcs is made of 90° phase difference per cell in the arcs. The LHC chromatic corrections were used in his design. The beam squeeze with a β^*=10 cm does not result in a very large natural chromaticities as shown in Table 1. The beam squeeze from 10 cm to 5 cm is realized by introduction of the betatron waves in both planes. The wave is created by changing the quadrupole gradients (ΔG= 7% with respect to the regular arc quadruple gradients) in two quadrupole pairs at the beginning of the arc before the IP.

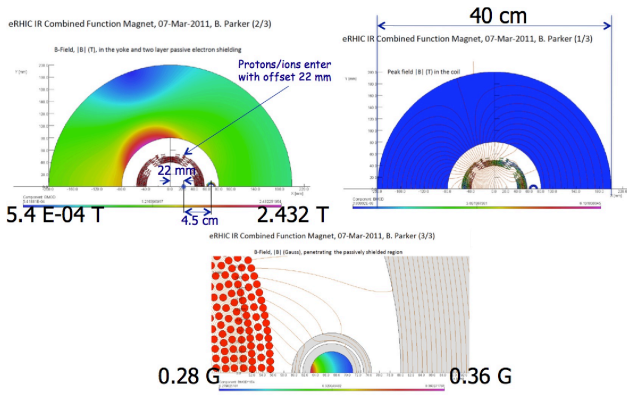


Figure 5: Combined function magnet with three different functions at the same time: bend the ions for 4.5 mrad, field free region for electron passage, and neutron detection downstream.

The layout of the sextupoles in the eRHIC ion lattice is shown in Figure 6.

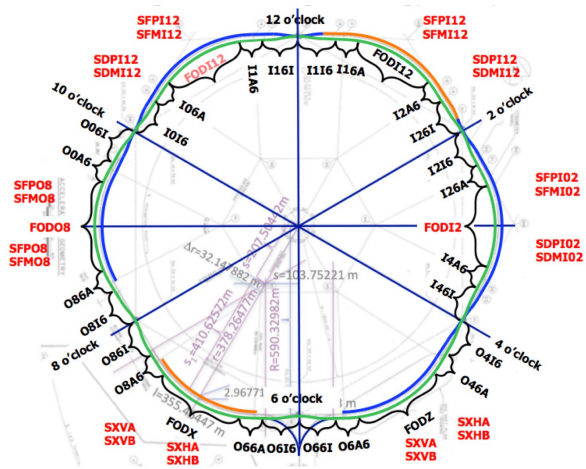


Figure 6: 24 families of sextupoles in the 90° degrees lattice are able to correct the first and higher orders of chromaticitiies in eRHIC lattice.

The betatron wave, as in the LHC design [1], not only achieves a reduction of the β^* from β^*=10 to β^*=5 cm, but also allow easier chromatic correction as the beta functions in the arcs before and after the IP are increased, as well as the dispersion function, reducing the strength of the sextupoles. The betatron functions after the beta squeeze to β^*=5 cm are shown in Figure 7 with detail of the sextupoles in the arcs in Figure 8.

Copyright © 2013 CC-BY-3.0 and by the respective authors

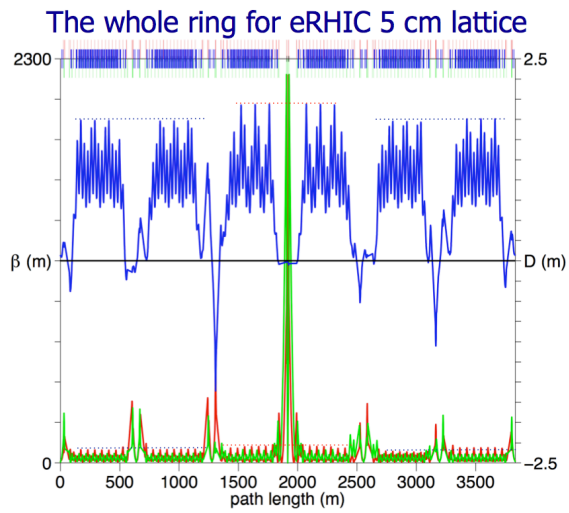


Figure 7. Betatron squeeze to β^*=5 cm.

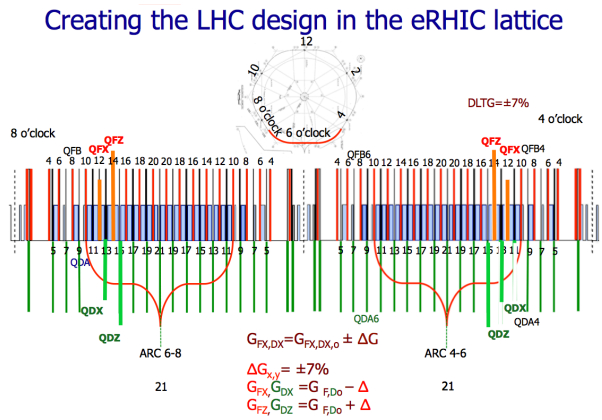


Figure 8. Sextupoles and pairs of quadrupoles used to create the wave in two arcs neighboring the IP.

The tune dependence on momentum after the sextupole corrections is shown in Figure 9.

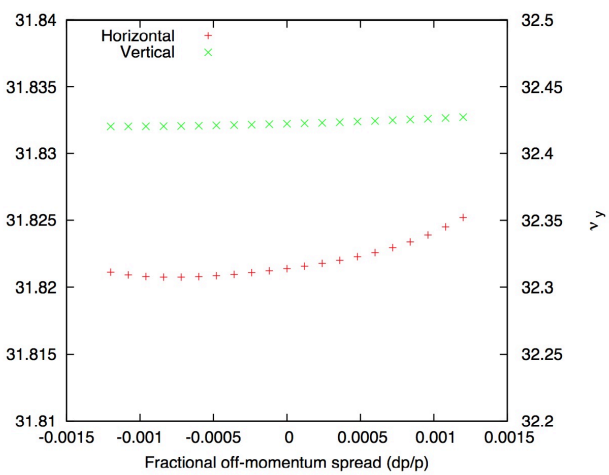


Figure 9: Tune dependence on momentum after sextupole correction

The dynamical aperture studied by applying only 8 families of sextupoles shown in Figure 10.

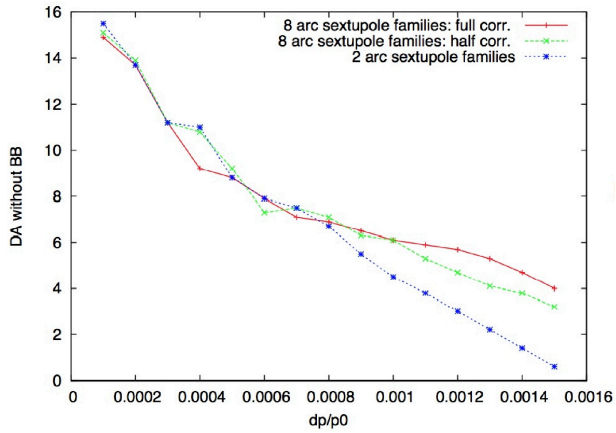


Figure 10: The dynamical aperture with 8 families of sextupoles.

The dynamical aperture after 24 families sextupole correction is shown in Figure 11.

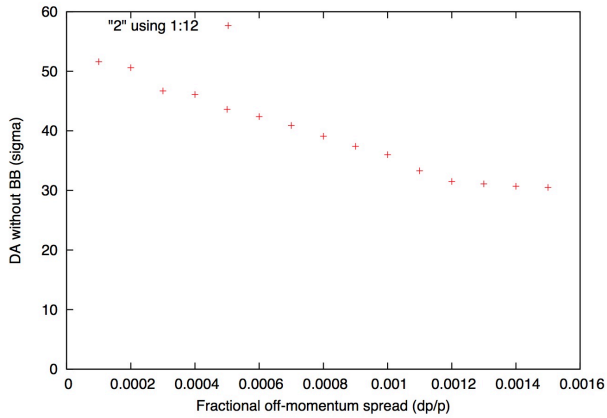


Figure 11: The dynamical aperture in the eRHIC lattice with β^*=10 cm after 24 family of sextupole correction.

SUMMARY

The eRHIC interaction region design with lattice design is presented. The LHC [1] beta squeeze was used as driving idea of the eRHIC lattice design. Initial results of the dynamical aperture are very favorable. A study of the dynamical aperture with the β^*=5 is in progress. Improvement in the interaction region design, with new superconducting triplet magnet design will follow.

REFERENCES

[1] S. Fartoukh, LHC Project Report 278, CERN.

Copyright © 2013 CC-BY-3.0 and by the respective authors

nuSTORM PION BEAMLINE DESIGN UPDATE*

A. Liu†, A. Bross, D. Neuffer, Fermilab, Batavia, IL, 60510, USA
S.Y. Lee, Department of Physics, Indiana University, Bloomington, IN, 47405, USA

Abstract

A facility producing neutrinos from muons that decay in a racetrack ring can provide extremely well understood neutrino beams for oscillation physics and the search for sterile neutrinos. The "neutrinos from STORed Muons"(nuSTORM) facility based on this idea has been introduced by Bross, Neuffer et al. The design of the nuSTORM facility and the particle tracking have been presented in the paper of Liu, et al. This paper demonstrates the recent optimization results of the pion beamline, with G4beamline simulations. The optimum choice of pion beam center momentum, a new algorithm on fitting bivariate Gaussian distribution to the pion phase space data at the downstream side of the horn, and the comparison of the beamline performance with the optics designed based on Graphite and Inconel targets are also described.

INTRODUCTION

The overview of the nuSTORM project can be found in the nuSTORM Fermilab proposal [1]. A possible nuSTORM facility design was described in the paper of Liu, et al. [2]. An overview of the facility is displayed in Figure 1. In order to obtain as many useful muons from pion decay as possible, the pion beamline is designed to capture and transport pions within a $P_0 \pm 10\%$ GeV/c momentum range, where P_0 is the design momentum of the pion beamline [3]. P_0 is chosen to maximize the muon flux within a $3.8 \pm 10\%$ GeV/c range. This paper finds P_0=5 GeV/c, as determined by G4Beamline[4] simulations. We also inspect the possibility of using an Inconel target where the pion productivity is checked and compared with the graphite target scenario we proposed in our previous papers.

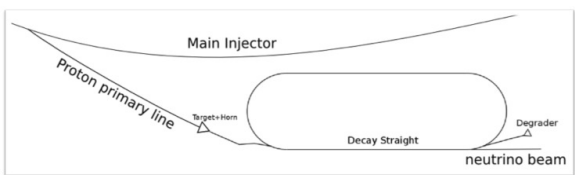


Figure 1: Overview of the nuSTORM facility. The Fermilab Main Injector places proton beam on a target, producing a large spectrum of secondary pions that are transported and injected into the decay ring. The pions then decay within the decay straight to muons , which are captured by the ring. Muons decay and produce neutrino beams with known flux and flavor in the decay straight.

* Work supported by DOE under contract DE-AC02-07CH11359
† aoliu@fnal.gov, also affiliated to Indiana University, supported in part by DE-FG02-12ER41800 and NSF Phys 1205431

Pions are produced by protons hitting the target, collected by a magnetic horn, transported and injected into the ring by a Beam Combination Section (BCS) and transmitted to the end of the decay straight until extracted. The beamline from the downstream end of the horn to the end of the racetrack ring decay straight is called the pion beamline of nuSTORM. A schematic drawing of the pion beamline in G4Beamline is shown in Figure 2.

PION PRODUCTION AND COLLECTION

nuSTORM is designed to use a 100 kW target station. A proton pulse with approximately 10^{13} protons at 120 GeV and pulse length of 1.6 μs will be extracted from the Fermilab Main Injector and bombarded onto a solid target. The target is partially inserted into a NuMI-like, 300 cm long magnetic horn to collect the pions produced from the target. The horn shape and length are designed to optimize the acceptance of pions within a momentum range of $P_0 \pm 10\%$. A schematic drawing of the horn with the target is shown in Figure 3

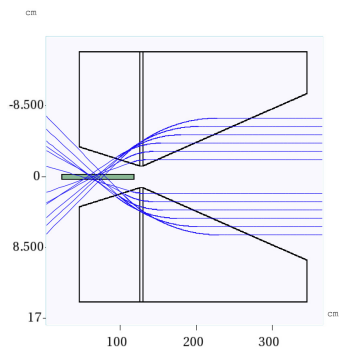


Figure 3: Schematic drawing of the nuSTORM horn and target (middle rod). Protons hit the target from the left.

Selecting The P_0 of The Pion Beam

The probability density of having a muon with momentum p_μ from the decay of a highly relativistic pion is $1/(2\gamma p'_\mu)$ for $0.573 P_0 \leq p_\mu \leq P_0$, where γ is the relativistic gamma of the pion, and $p'_\mu = 29.8$ MeV/c is the muon momentum in the rest frame of the pion. Assuming the pion beam has a uniform momentum distribution over the range $[0.9P_0, 1.1P_0]$, the probability of having a muon with momentum p_μ from this pion beam has a maximum constant value

$$f(p_\mu) = \int_{0.9P_0}^{1.1P_0} \frac{1}{0.2P_0} \frac{m'_\pi c}{2p_\pi p'_\mu} dp_\pi = \frac{2.35}{P_0} \left(\frac{\text{muons}}{\text{MeV/c}}\right)$$

Copyright © 2013 CC-BY-3.0 and by the respective authors

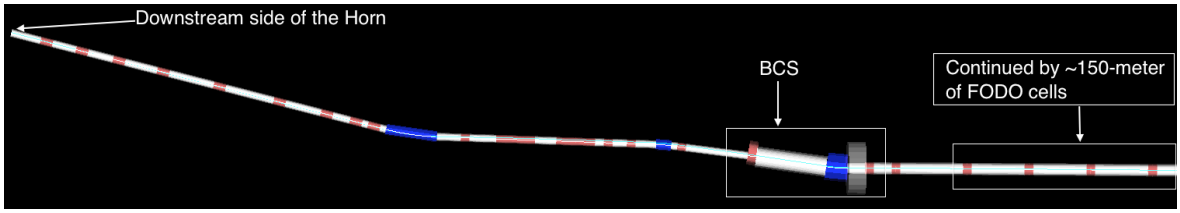


Figure 2: A schematic drawing of the pion beamline. The pions move from the downstream side of the horn (left) to the end of the decay ring straight section (right, not shown all).

for $0.63P_0 \leq p_\mu \leq 0.90P_0$. m'_π=139.6 MeV/c is the pion mass in the rest frame of the pion. This implies that the momentum distribution of the muons within the 3.8±10% GeV/c momentum acceptance of the ring is uniform as long as $P_0 \in$[4.644, 5.426] GeV/c. In addition, the value $2.35/P_0$ of the flat top of $f(p_\mu)$ is smaller when P_0 is larger. Having a lower P_0 will result in more muons within $3.8 \pm 10\%$ GeV/c, whereas having a higher P_0 will reduce the requirement on dispersion, D_x, created by the BCS and will reduce the emittance growth from pion decay. Figure 4 shows the trade-off by plotting the number of muons in the momentum acceptance with $\sigma_{x'}$ and $\sigma_{y'}$, which are the rms angle width of the muons. The smaller $\sigma_{x'}$ and $\sigma_{y'}$ are, the easier the muon beam can be captured. The criteria are well-balanced when P_0 is 5 GeV/c.

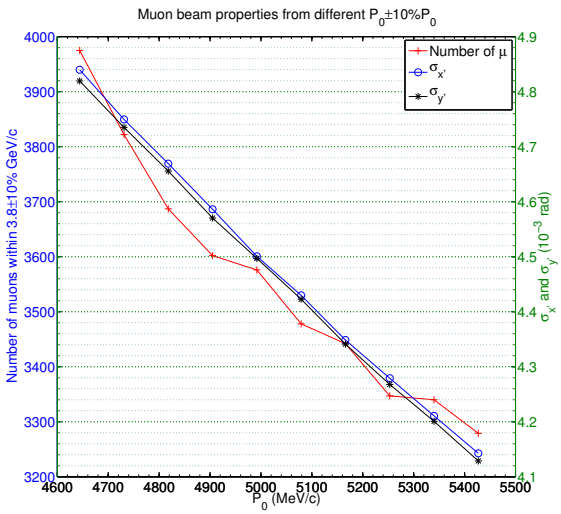


Figure 4: Number of muons within $3.8 \pm 10\%$ GeV/c from the decay of pion beams with different $P_0 \pm 10\% P_0$ (In red crosses, left vertical axis), $\sigma_{x'}$ and $\sigma_{y'}$ (In blue circles and black stars, right vertical axis) v.s P_0. The number of pions in each simulation bin is 10^4.

Target and Horn

We use a 95 cm graphite target (about two interaction lengths), with a radius of 3 mm as a baseline in our design. A 39 cm Inconel target (also two interaction lengths), with the same radius has also been considered and with it we obtain more pions within the above momentum range. The engineering prospects of the Inconel target are under study. The number of pions within 5±10% GeV/c we collect after the horn is 0.139 and 0.157 pions per POT for the graphite and Inconel targets, respectively.

Algorithm for Fitting a Gaussian Function to the Pion Distribution

In order to design the pion beamline optics, the TWISS parameters need to be matched at the downstream side of the horn. Because the pion distribution in the transverse phase space is dramatically distorted from an ideal Gaussian beam, we need to find an algorithm to fit a bivariate Gaussian distribution to the phase space data. One way to do so is by using a thorough scan on the TWISS parameters and including the maximum number of pions with the acceptance ellipse. However, this scan efficiency is greatly limited by its step size and the initial starting point of the parameters. We implemented the Gauss-Newton method of minimizing the sum of squared function $Q(\vec{\alpha}) = \sum_{i=1}^{n} r_i^2(\vec{\alpha})$ where $\vec{\alpha} = (\mu_t, \mu_{t'}, \sigma_t, \sigma_{t'}, \rho_{t,t'})$ represents a list of variables in the function r_i, which in our fitting purpose represents the residuals of $r_i(\vec{\alpha}) = \ln z(t,t')_i - \ln f((t,t')_i, \vec{\alpha})$. t and t' represent the transverse phase space coordinates in either x or y direction, $z(t,t')_i$ is the real bivariate probability density value at $(t,t')_i$ and $f((t,t')_i$ is the Gaussian function value at that point. The vector $\vec{\alpha}$ is optimized by iterating on m in the expression $\vec{\alpha}^{(m+1)} = \vec{\alpha}^{(m)} - (\vec{J}^\top \vec{J})^{-1} \vec{J}^\top \vec{r}(\vec{\alpha})$ until the difference of $\vec{\alpha}^{(m+1)}$ and $\vec{\alpha}^{(m)}$ has decreased to a critical value. Once the $\vec{\alpha}$ is found, we can use the covariance matrix to get the TWISS parameter values.

The direct Gauss-Newton method still has large inaccuracy because we include all the pions in the phase space in the fitting. However, some of those particles are far outside the 2×10^{-3}m·rad acceptance ellipse of the pion beamline. Thus we did another iteration on the Gauss-Newton method, where each time we discard a number of pions having the largest phase space emittance. The iteration is repeated until the rms phase space emittance of the beam has shrunk to 2×10^{-3}/6 m·rad, which is the conventional way of defining the relation between rms emittance and acceptance.

The comparison of the fitting results from the parameter scan method and the iterative Gauss-Newton method are shown in Figure 5, taking the pions produced by the

Copyright © 2013 CC-BY-3.0 and by the respective authors

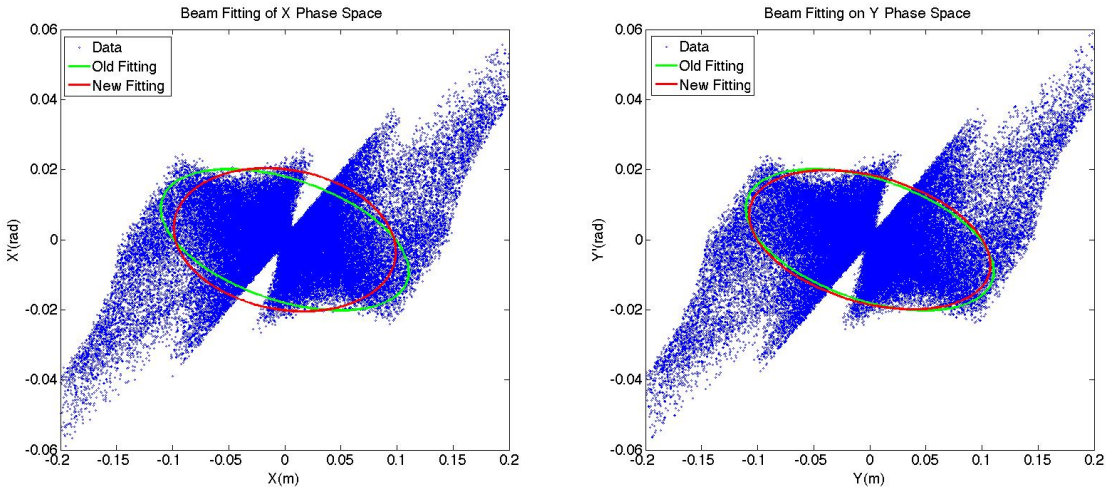


Figure 5: Comparison of acceptance ellipses in the horizontal phase space (left) and vertical phase space (right) using different fitting methods. The old scanning method and the new Gauss-Newton method are plotted in green and red, respectively.

graphite target as an example. The new acceptance ellipse contains approximately 1% more pions than the previous one does. The TWISS parameters from the direct Gauss-Newton method, parameter scan method, and the iterative Gauss-Newton method are shown in Table 1.

Table 1: TWISS Parameters from Different Fitting Methods

method	α_x(1)	β_x (m)	α_y (1)	β_y (m)
Direct Gauss-Newton	-0.21	5.28	-0.58	6.32
Parameter Scan	0.5	6.13	0.5	6.13
Iterative Gauss-Newton	0.17	4.91	0.38	5.8

Pion Beamline Performance

After the TWISS parameters are found at the downstream side of the horn, the optics of the pion beamline can then be matched to the racetrack ring decay straight, where the periodic TWISS parameters were set by optimizing a series of design criteria [5]. The performance comparison of pion beamlines designed based on the optics of pions from graphite and Inconel targets is shown in Table 2.

SUMMARY

The nuSTORM pion beamline design has been updated. The optimization of the beamline confirms an optimum center momentum of the pion beam at 5 GeV/c, and a new algorithm of particle distribution fitting has been tested. The yield of muons within 3.8±10% GeV/c within the first pass of the decay straight is about 0.008 for graphite target and 0.013 for Inconel target, per 120 GeV POT.

Table 2: Pion Beamline Performance Comparison

Target	π^+ at the downstream side of the horn (per POT)	π^+ at the end of the decay straight (per POT) (without decay)
Graphite	0.140	0.081
Inconel	0.157	0.114

Target	$\mu+$ in 3.8±10% GeV/c at the end of the decay straight (per POT) (with decay)
Graphite	0.008
Inconel	0.013

ACKNOWLEDGMENT

We thank the APC colleagues who provided comments and suggestions on the design of the nuSTORM facility.

REFERENCES

[1] P. Kyberd et al. "Neutrinos from STORed Muons: Proposal to the Fermilab Physics Advisory Committee" arXiv:1308.6288.

[2] A. Liu et al., "nuSTORM Facility Design And Simulation", proceedings of iPAC2013, p55 (2013).

[3] A. Liu et al., "Determining the pion reference momentum for nuSTORM injection design", Fermilab TechNote, Fermilab-TM-2563-APC (2013).

[4] G4beamline, T. Roberts, Muons, Inc.

[5] A. Liu et al., "Design and simulation of the nuSTORM pion beamline", submitted to PRST-AB (2013).

Copyright © 2013 CC-BY-3.0 and by the respective authors

A STAGED MUON-BASED FACILITY TO ENABLE INTENSITY AND ENERGY FRONTIER SCIENCE IN THE US*

Jean-Pierre Delahaye (SLAC, Menlo Park, California),
Charles Ankenbrandt, Stephen Brice, Alan David Bross, Dmitri Denisov, Estia Eichten, Ronald Lipton, David Neuffer, Mark Alan Palmer (Fermilab, Batavia, Illinois),
S.Alex Bogacz (JLAB, Newport News, Virginia),
Patrick Huber (Virginia Polytechnic Institute and State University, Blacksburg)
Daniel M. Kaplan, Pavel Snopok (Illinois Institute of Technology, Chicago, Illinois),
Harold G. Kirk, Robert B. Palmer (BNL, Upton, Long Island, New York),
Robert D. Ryne (LBNL, Berkeley, California),

Abstract

Muon-based facilities offer a unique potential to provide capabilities at both the Intensity Frontier with Neutrino Factories and the Energy Frontier with Muon Colliders ranging from the Higgs energy to the multi-TeV energy range. They rely on novel technology with challenging parameters, for which the feasibility is currently being assessed by the U.S. Muon Accelerator Program (MAP) [1]. A realistic scenario for a complementary series of staged facilities with increasing complexity and significant physics potential at each stage has been developed. It takes advantage of and leverages the capabilities already planned at Fermilab, especially Project X and LBNE. Each stage is defined in such a way as to provide an R&D platform to validate the technologies required for subsequent stages. The rationale and sequence of a realistic staging process are presented.

INTRODUCTION

The major discoveries made in 2012, namely the large flavour mixing angle θ_{13} measured at Daya Bay in China and the Higgs boson by the LHC at CERN dramatically modified the Particle Physics landscape. Although the Higgs discovery corresponds to a splendid confirmation of the Standard Model (SM) and no sign of new physics Beyond the Standard Model (BSM) has (yet) been detected at LHC up to at least 1 TeV, BSM physics is necessary to address basic questions which the Standard Model cannot address especially the dark matter, the matter-antimatter asymmetry and the neutrino mass. Therefore the quest for BSM physics constitutes a high priority for the future of High Energy Physics. It requires facilities at both high energy and high intensity frontiers. Neutrino oscillations are irrefutable evidence for BSM physics with the potential to probe up to an extremely high energy range. Neutrino Factories with an intense and well defined flux of neutrinos from muon decay provide an ideal tool for high precision flavour physics at the high intensity frontier. At the high energy frontier, a multi-TeV lepton collider will be necessary as a precision facility to complement the LHC, if and when confirmed, for Physics exploration beyond the Standard Model.

* Work supported by the U.S. Dept. of Energy under contracts DE-AC02-07CH11359 and DE-AC02-76SF00515.

THE BEAUTY AND CHALLENGES OF MUON-BASED FACILITIES

Muon-based facilities [2] offer the unique potential to provide the next generation of capabilities and world-leading experimental support spanning physics at both the Intensity and Energy Frontiers. Building on the foundation of Project X at FNAL, muon accelerators can provide that next step with a high-intensity and precise source of neutrinos to support a world-leading research program in neutrino physics. Furthermore, the infrastructure developed to support such an Intensity Frontier research program can also enable the return of the U.S. high energy physics program to the Energy Frontier. This capability would be provided in a subsequent stage of the facility that would support one or more Muon Colliders, which could operate at center-of-mass energies from the Higgs resonance at 126 GeV up to the multi-TeV scale.

An ensemble of facilities built in stages is made possible by the strong synergies between Neutrino Factories and Muon Colliders, both of which require a high power proton source and target for muon generation followed by similar front-end and ionization cooling channels. These muon facilities rely on a number of systems with conventional technologies whose required operating parameters exceed the present state of the art as well as novel technologies unique to muon colliders. An R&D program to evaluate the feasibility of these technologies is being actively pursued within the framework of the U.S. Muon Accelerator Program (MAP) [1] with impressive R&D results already achieved and a definitive answer expected by 2018 as to whether or not muon-based facilities built in stages can be realistically contemplated.

RATIONALE FOR A STAGED APPROACH

The feasibility of the technologies required for Neutrino Factories and/or Muon Colliders must be validated before a facility based upon these could be proposed. Such validation is usually made in dedicated test facilities which are rather expensive to build and to operate over several years. They are therefore difficult to justify and fund, given especially that they are usually useful only for technology development rather than for physics.

Copyright © 2013 CC-BY-3.0 and by the respective authors

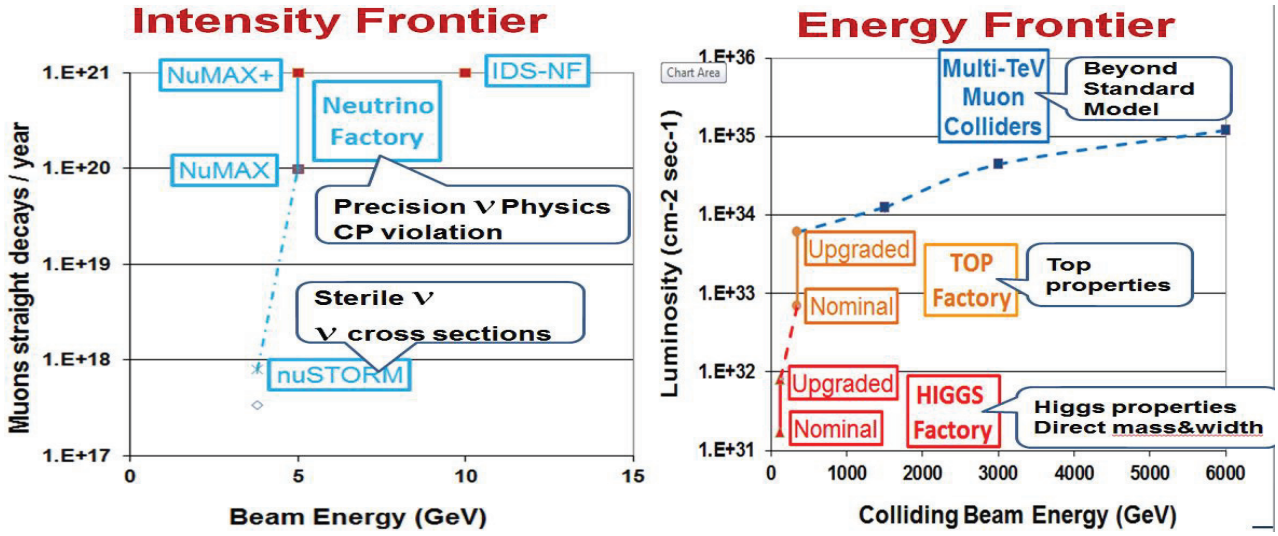


Figure 1: Performance and Physics of muon-based facilities over two frontiers and a wide energy range.

An alternative approach is proposed here. It consists of a series of facilities built in stages, where each stage offers:

- Unique physics capabilities such that the corresponding facility obtains support and is funded.
- In parallel with the physics program, integration of an R&D platform to develop, test with beam, validate and get operational experience with a new technology that is necessary for the following stages.
- Construction of each stage as an add-on to the previous stages, extensively reusing the equipment and systems already installed, such that the additional budget of each stage remains affordable.

Such a staging plan [3] thus provides clear decision points before embarking upon each subsequent stage. It is especially attractive at FNAL building on, and taking advantage of, existing or proposed facilities, specifically:

- Existing tunnels and other conventional facilities;
- Project X as the MW-class proton driver for muon generation;
- SURF as developed for the LBNE detector, which could then house the detector for a long-baseline Neutrino Factory.

It consists of a series of facilities with increasing complexity, each with performance characteristics providing unique physics reach (Fig.1):

- nuSTORM [4]: a short-baseline Neutrino Factory-like facility enabling a definitive search for sterile neutrinos, as well as neutrino cross-section measurements that will ultimately be required for precision measurements at any long-baseline experiment.
- NuMAX: an initial long-baseline 5GeV Neutrino Factory, optimized for a detector at SURF, affording a precise and well-characterized neutrino source that exceeds the capabilities of conventional superbeams.
- NuMAX+: a full-intensity Neutrino Factory, upgraded from NuMAX, with performances similar to IDS-NF [5] as ultimate source to enable precision CP-violation measurements in the neutrino sector
- Higgs Factory: a collider capable of providing between 3500 (startup) and 13,500 Higgs events per year (10^7 sec) with exquisite energy resolution enabling direct Higgs mass and width measurements.
- Multi-TeV Collider: if warranted by LHC results, a multi-TeV Muon Collider, with an ultimate energy reach up of to 10 TeV, likely offers the best performance and least cost and power consumption for any lepton collider operating in the multi-TeV regime.

Their main parameters are described in Table 1. A complex integrating all of the above facilities in a staged approach on the FNAL site is shown in Figure 2.

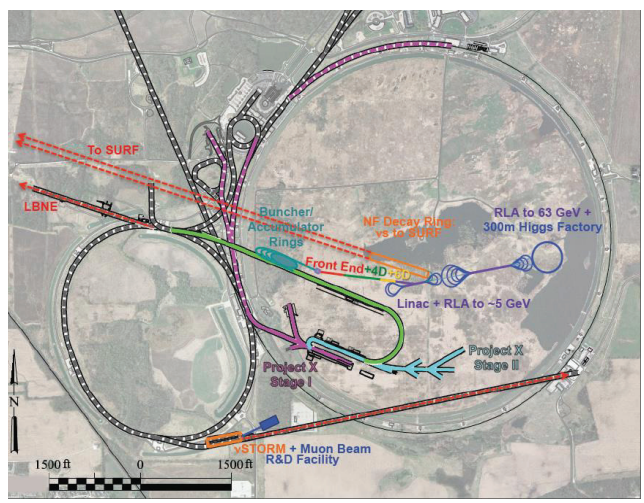


Figure 2: Footprint of Neutrino Factory and Higgs Factory Muon Collider facilities on the FNAL site.

Copyright © 2013 CC-BY-3.0 and by the respective authors

Table 1: Main parameters of the various Muon-based facilities in a phased approach

System	Parameters		Unit	nuSTORM	NuMAX	NuMAX+
Performance	Stored μ+ or μ-/year			8×10^{17}	2×10^{20}	1.2×10^{21}
	ν_e or ν_μ to detectors/yr			3×10^{17}	8×10^{19}	5×10^{20}
Detector	*Far Detector:*		Type	SuperBIND	MIND / Mag LAr	MIND / Mag LAr
	Distance from Ring		km	1.9	1300	1300
	Mass		kT	1.3	30 / 10	100 / 30
	Magnetic Field		T	2	0.5-2	0.5-2
	Near Detector:		Type	SuperBIND	Suite	Suite
	Distance from Ring		m	50	100	100
	Mass		kT	0.1	1	2.7
	Magnetic Field		T	Yes	Yes	Yes
Neutrino Ring	Ring Momentum (P_μ)		GeV/c	3.8	5	5
	Circumference (C)		m	480	600	600
	Straight section		m	184	235	235
	Arc Length		m	56	65	65
Acceleration	Initial Momentum		GeV/c	-	0.22	0.22
	Single-pass Linac		GeV/pass	-	0.95	0.95
			MHz	-	325	325
	4.5-pass RLA	RLA I	GeV/pass	-	0.85	0.85
			MHz	-	325	325
		RLA II	GeV/pass	-	-	-
			MHz	-	-	-
Cooling				No	No	4D
Proton Source	Proton Beam Power		MW	0.2	1	3
	Proton Beam Energy		GeV	120	3	3
	Protons/year		1×10^{21}	0.1	41	125
	Repetition		Hz	0.75	70	70

Muon Collider Parameters								
		Higgs Factory		Top Threshold Options		Multi-TeV Baselines		
Parameter	*Units*	*Startup Operation*	*Production Operation*	*High Resolution*	*High Luminosity*			*Accounts for Site Radiation Mitigation*
CoM Energy	TeV	0.126	0.126	0.35	0.35	1.5	3.0	6.0
Avg. Luminosity	$10^{34}cm^{-2}s^{-1}$	0.0017	0.008	0.07	0.6	1.25	4.4	12
Beam Energy Spread	%	0.003	0.004	0.01	0.1	0.1	0.1	0.1
Higgs* or Top* Production/10^7sec		3,500*	13,500*	7,000*	60,000*	37,500*	200,000*	820,000*
Circumference	km	0.3	0.3	0.7	0.7	2.5	4.5	6
No. of IPs		1	1	1	1	2	2	2
Repetition Rate	Hz	30	15	15	15	15	12	6
β*	cm	3.3	1.7	1.5	0.5	1 (0.5-2)	0.5 (0.3-3)	2.5
No. muons/bunch	10^{12}	2	4	4	3	2	2	2
No. bunches/beam		1	1	1	1	1	1	1
Norm. Trans. Emittance, ε_{TN}	π mm-rad	0.4	0.2	0.2	0.05	0.025	0.025	0.025
Norm. Long. Emittance, ε_{LN}	π mm-rad	1	1.5	1.5	10	70	70	70
Bunch Length, σ_s	cm	5.6	6.3	0.9	0.5	1	0.5	2
Proton Driver Power	MW	4#	4	4	4	4	4	1.6

TENTATIVE STAGED SCENARIO AND SCHEDULE

Three major items on the critical path have been clearly identified: i) MAP technology feasibility demonstration with results expected by 2018, ii) 6D cooling performance with beam validation by 2022 possibly using nuSTORM as an R&D platform in complement to the cooling principle and feasibility demonstration at MICE [6], iii) Proton beam power availability of 3 MW at 3 GeV from Project X (phase 2) by 2024 and 4MW at 8 GeV (phase 4) by 2032. A technically limited schedule could then be tentatively defined.

nuSTORM as the first stage could be launched as soon as funding is available since it does not require any technology development. A first beam could be provided by the end of the decade. It would serve as an R&D platform to test and validate the 6D cooling with a 10^8 muon beam. NuMAX which does not require any cooling could be launched by 2018 when the MAP technology feasibility will have been demonstrated. It would initially be driven by a proton beam power of 1MW at 3 GeV provided from 2024 by Project X phase 2 in parallel with its other users. This facility would then be upgraded to NuMAX+ by adding a limited amount of 4D cooling validated in NuMAX when used as an R&D platform with a beam of 10^{11} muons and by increasing the proton driver to the full power of 3 MW provided by Project X phase 2 at 3 GeV. The NuMAX+ injector & acceleration up to 5 GeV could then be used to drive a Muon Collider at the energy and luminosity as required by Physics at the time, possibly a Higgs factory, which could be launched by 2025. It would have to be upgraded by i) implementing a 6D cooling previously validated at full intensity using NuMAX+ as an R&D platform with a beam of 10^{12} muons, ii) upgrading the proton driver to 4 MW by the project X phase 4 at 8 GeV available from 2032, iii) extending the acceleration system up to 62.5GeV. A multi-TeV muon collider could then be launched if and when required by Physics for BSM studies by using the previously built injector system and adding the necessary final cooling, acceleration system and collider ring.

CONCLUSION

A staging approach for muon-based facilities has been developed with physics interest and technology validation at each phase taking advantage of the present and proposed facilities at Fermilab. Each stage is built as an addition to the previous stages, reusing as much as possible the systems already installed such that the additional budget of each stage remains affordable. Thanks to the great synergies between Neutrino Factory and Muon Collider technologies, these facilities are complementary and allow capabilities and world-leading experimental support spanning physics at both the Intensity and Energy Frontiers. Rather than building an expensive test facility without physics use, the approach uses each stage as an R&D platform at which to test and validate the technology required by the following stage. The critical issues of this novel and promising technology are thus all addressed in the most efficient and practical way within reasonable funding and scheduling constraints.

As deduced from the components on the critical path and a technically limited schedule, such a staging approach with integrated R&D would allow informed decisions by 2020 about Neutrino Factories at the Intensity Frontier and by 2025 about Muon Colliders at the Energy Frontier.

REFERENCES

[1] M.A.Palmer et al. MAP, http://map.fnal.gov/ and contribution to NA PAC'13
[2] ICFA Beam Dynamics Newsletter, No 55: http://icfa-usa.jlab.org/archive/newsletter/icfa_bd_nl_55.pdf
[3] MAP White Paper at CSS2013: arXiv:1308.0494.
[4] NuSTORM: arXiv: 1308.6228 (proposal) and arXiv: 1309.1389 (Project Definition Report).
[5] IDS-NF: https://www.ids-nf.org/wiki/FrontPage
[6] MICE: http://www.mice.iit.edu/

Copyright © 2013 CC-BY-3.0 and by the respective authors

BEAM-BEAM STUDIES FOR HL-LHC*

A. Valishev#, FNAL, Batavia, IL 60510, USA, D. Shatilov, BINP, Novosibirsk 630090, Russia
T. Pieloni, CERN, Geneva, Switzerland, D. Banfi, J. Barranco, EPFL, Lausanne

Abstract

The analysis of beam-beam effects for the High Luminosity LHC upgrade is in progress as a part of HiLumi LHC Design Study. We report on the current status of beam-beam simulations with the particular emphasis on single and multi-particle weak-strong tracking studies. We evaluate the LH-LHC performance scenarios, and outline the plan of further research.

MOTIVATION AND APPROACH

A major upgrade of the Large Hadron Collider aiming at a significant increase of its luminosity beyond the design value is planned for around 2020. The machine configuration, called High Luminosity LHC (HL-LHC) will incorporate a number of technological advances bringing the beam intensity, brightness and overall accelerator precision to an unprecedented level. The global HiLumi LHC Design Study is in progress with the goal of delivering an integrated design to facilitate the upgrade [1]. Quite naturally, the examination of beam dynamics aspects constitutes an essential part of the effort. In the HiLumi structure, Work Package 2 covers accelerator physics subjects and combines the following Tasks: Coordination and Communication; Optics and Layout; Intensity Limitations; Beam-Beam Effects; Beam Parameter and Luminosity Optimization. The Tasks work in close collaboration with each other to enable the development of a coherent view on the beam dynamics. The goal of Beam-Beam Task is to evaluate the possible performance limitations arising from beam-beam interactions, to define key parameters such as minimum required beam separation and maximum acceptable beam brightness values and to identify optimum beam configurations for the different operating scenarios.

The studies of beam-beam interactions at HL-LHC are grouped into two categories: the weak-strong (incoherent) and the strong-strong (coherent) effects. The proposed values of beam brightness at HL-LHC suggest that the weak-strong effects are more likely to result in performance limitation through the creation of resonances causing particle losses and emittance growth. As such, the incoherent effects are the focus of the present report. For the strong-strong effects see e.g. Ref. [2, 3].

*Fermi Research Alliance, LLC operates Fermilab under contract No. DE-AC02-07CH11359 with the U.S. Department of Energy. This work was partially supported by the US LHC Accelerator Research Program (LARP). The HiLumi LHC Design Study is included in the High Luminosity LHC project and is partly funded by the European Commission within the Framework Programme 7 Capacities Specific Programme, Grant Agreement 284404.

#valishev@fnal.gov

PERFORMANCE SCENARIOS

A detailed description of the baseline HL-LHC scenario can be found in Refs. [4, 5]. Here we present the parameters relevant to the simulations reported further.

The so-called 'stretched' baseline HL-LHC scenario presumes that at the beginning of a high-energy run (fill), the beams collide at IP1 and IP5 (Atlas and CMS experiments) at the full crossing angle of 590 μrad. Due to the large geometrical reduction, the total beam-beam tune shift is quite moderate and does not exceed 0.015 for the case of 3 head-on collisions. The transverse separation at long-range collision points is 12.5 beam sigma. As the beam intensity decays due to the luminosity burn-off, the bunches are gradually tilted with respect to the reference trajectory (crabbed) using RF crab cavities, which results in a head-on collision at the end of the fill. This achieves a constant (leveled) luminosity of 5×10^{34} cm^{-2}s^{-1}, thus allowing to maximize the luminosity integral. The beta-function at IP1/5 during leveling remains constant at 15 cm.

Table 1: 'Stretched' Baseline HL-LHC Parameters for 25ns Bunch Spacing

Parameter	Value
Protons/bunch	2.2×10^{11}
Number of bunches	2808
Crossing angle	590 μrad
β*	15 cm
Normalized emittance	2.5 μm
Energy spread	1.2×10^{-4}
Bunch length	7.5 cm
Beam-beam tune shift per IP	0.0033

In the baseline HL-LHC scenario the luminosity is leveled such that the number of events per crossing (pile-up) does not exceed the limit set by experiments. However, it was recently recognized that the longitudinal pile-up density (the number of events per unit length or unit time) also needs to be limited. This can be achieved through maximizing the length of luminous area by keeping the bunches always colliding fully head-on (crabbed). The luminosity leveling in this scheme is performed by the transverse offset or change of beta-function, i.e. β*=70 cm at the beginning of a fill, and then is gradually reduced to 15 cm.

Copyright © 2013 CC-BY-3.0 and by the respective authors

SIMULATION TOOLS

The weak-strong beam-beam simulations for HL-LHC were performed with two particle tracking codes: SixTrack [6] and Lifetrac [7]. Both codes have been extensively used for the development of such colliders as the Tevatron, DAFNE, and LHC, and have been well tested against available experimental data. Nevertheless, we performed additional benchmarking in order to ensure consistency of simulations. For example, Fig. 1 presents the Dynamic Aperture (DA) simulation for HL-LHC lattice with multipole errors in the absence of beam-beam interactions.

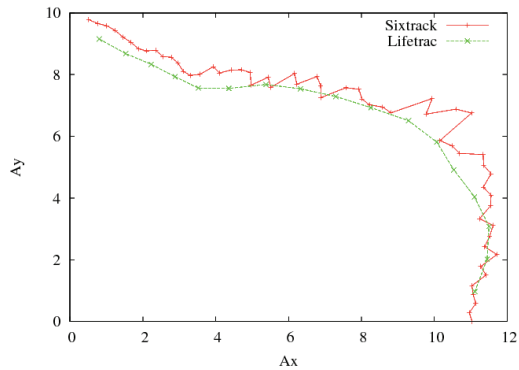


Figure 1: Dynamic aperture (Ax, Ay in units of beam σ) for HL-LHC lattice with multipole errors without beam-beam, simulated with two codes. Sixtrack data courtesy of M. Giovannozzi.

The two codes treat machine lattice with a symplectic thin-lens approach, and account for full set of machine features, including the focusing chromaticity and high-order multipole errors. The beam-beam kicks are realized through analytical formulae (the so-called Hirata formalism).

The standard figure of merit for the evaluation of performance is the dynamical aperture for particles with momentum deviation of 2.7×10^{-4}, based on 10^6 turns of tracking. However, a recent application of the Frequency Map Analysis [8] to beam-beam interactions [9,10] provides a useful insight into the dynamics of a system with much less intensive simulations. Throughout the report we provide comparisons of the two approaches.

BASELINE SCENARIO RESULTS

Figures 2, 3 present simulation results for the baseline scenario. The color on FMA plots depicts the tune variation along a particle's trajectory over 2^{12} turns (momentum deviation for these FMA simulations was zero). The logarithmic scale is provided in Fig. 2 on the right. One can see that the tune footprint is small and is not densely populated with resonances. The DA results based on 10^6 turns generally agree well with area in FMA plots where tune jitter is large, and resonances overlap (Chirikov criterion [11]).

Figure 4 shows the DA for various options of HL-LHC optics as a function of crossing angle (slhcv3.1b optics, 10^6 turns). The target minimum DA for a robust design is 6 σ, which determines the choice of crossing angle for the baseline scenario.

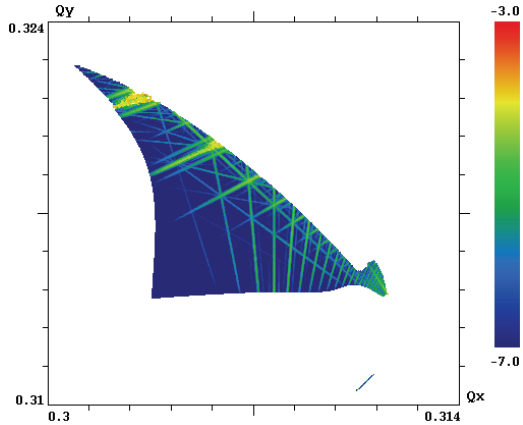


Figure 2: FMA plot in tune space (tune footprint) for HL-LHC baseline scenario.

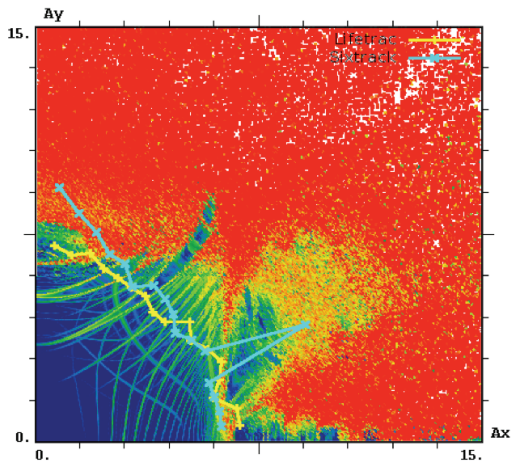


Figure 3: FMA plot in amplitude space for HL-LHC baseline scenario. Yellow line – Lifetrac dynamic aperture, cyan line – SixTrack dynamic aperture.

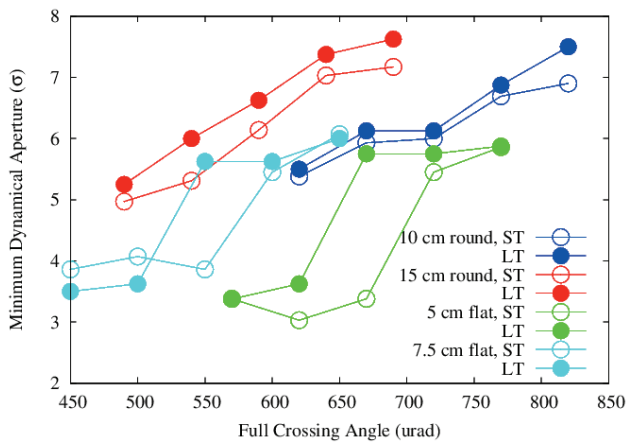


Figure 4: Minimum dynamical aperture for different types of HL-LHC optics as a function of crossing angle. ST – SixTrack (4D/5slices per IP), LT – Lifetrac data.

Copyright © 2013 CC-BY-3.0 and by the respective authors

BETA-FUNCTION LEVELING SCENARIO

The alternative leveling scenario is more demanding with respect to beam-beam interaction due to a relatively large beam-beam tune shift at the beginning of a fill (ξ=0.034). However, the results in Figs. 5, 6 suggest that at least for the case of machine without multipole imperfections, the first studies with Lifetrac show that DA is not reduced below 6 σ. The 7th order resonance does not cause significant diffusion of the core particles. The overlapping 10th and 13th order resonances cause some emittance growth, which reduced the luminosity lifetime to approximately 20 hours. However, it is likely the effect of these resonances could be mitigated by a careful choice of the betatron tune working point. We also explored the possibility to reduce the crossing angle towards the end of a fill, when the bunch intensity decays to Np=0.95×10^{11}, to 480 μrad (10 σ separation), and found that DA in this case remains over 6.5 σ.

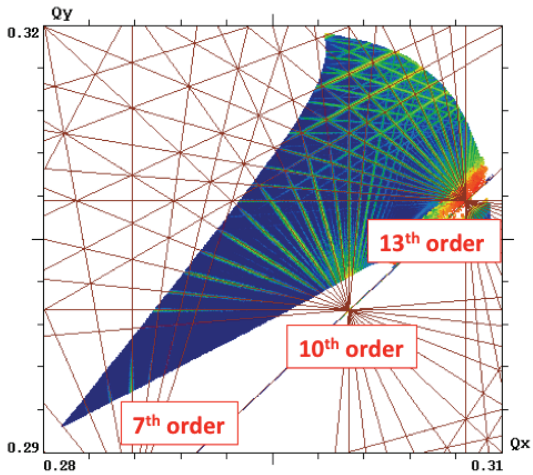


Figure 5: FMA plot in tune space for full head-on collision at IP1/5. β*=15 cm, crossing angle 590 μrad (12.5 σ separation).

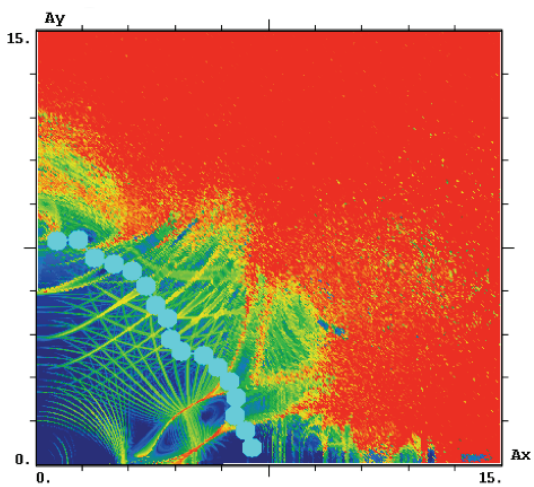


Figure 6: FMA plot in amplitude space for full head-on collision at IP1/5. Cyan points – 10^6 turns DA.

SUMMARY AND OUTLOOK

The weak-strong simulations of beam-beam effects in HL-LHC using two particle tracking codes demonstrate robustness of the baseline operational scenario. The dynamic aperture predicted by both codes is over the reference value of 6 σ for a machine with no multipole imperfections. Studies of an alternative luminosity leveling scenario making use of beta-function leveling and full head-on interactions, predict that despite the significantly larger beam-beam parameter in this scheme, the dynamical aperture is well within the specified limit. The alternative scheme may allow a decrease of the crossing angle and, consequently, the required crab-cavity voltage.

Future effort will be concentrated on the studies of sensitivity of the proposed schemes to machine imperfections. We also plan to investigate other options of achieving lower pile-up density, such as longitudinal beam density shaping.

ACKNOWLEDGMENTS

The authors would like to thank the experts of HiLumi Work Package 2, and Beam-Beam Task in particular, for numerous enlightening discussions. We are grateful for the support by SixTrack team. We are indebted to S. Fartoukh for his constant encouragement and attention to this work.

REFERENCES

[1] HiLumi LHC http://hilumilhc.web.cern.ch/HiLumiLHC/
[2] S. Paret and J. Qiang, "Coherent Instability Due to Beam-Beam Interaction in Hadron Colliders", TUPBA23, these proceedings.
[3] T. Pieloni et al., "Observations of Two-Beam Instabilities During the 2012 LHC Physics Run", TUPFI034, IPAC'13, Shanghai, China (2013)
[4] L. Rossi and O. Brüning, CERN-ATS-2012-236 (2012)
[5] O. Brüning and F. Zimmerman, "Parameter Space for the LHC High-Luminosity Upgrade", MOPPC005, IPAC'12, New Orleans, LA, USA (2012)
[6] R. De Maria et al., "Recent Developments and Future Plans for SixTrack", MOPWO02, IPAC'13, Shanghai, China (2013)
[7] D. Shatilov et al., "Lifetrac Code for the Weak-Strong Simulation of the Beam-Beam Effects in Tevatron", TPAT084, PAC'05, Knoxville, TN, USA (2005)
[8] J. Laskar, Icarus 88, 266 (1990)
[9] Y. Papaphilippou and F. Zimmermann, Phys. Rev. ST Accel. Beams **2**, 104001 (1999)
[10] D. Shatilov et al., Phys. Rev. ST Accel. Beams **14**, 014001 (2011)
[11] B.V.Chirikov, J. Nucl. Energy Part C: Plasma Phys. 1: 253 (1960)

Copyright © 2013 CC-BY-3.0 and by the respective authors

COHERENT INSTABILITY DUE TO BEAM-BEAM INTERACTION IN HADRON COLLIDERS*

S. Paret, J. Qiang, LNBL, Berkeley, CA, 94720, USA

Abstract

Beam-beam effects can excite coherent modes in circular colliding beams and can thereby cause coherent instabilities. Nevertheless the beams in LHC have been well behaved and no fundamental limitation to the beam-beam parameter has been found in head-on collisions. In this paper we consider beams with much higher intensities than ever collided in any hadron collider. By virtue of 3D strong-strong computer simulations, we investigate the coherent stability and emittance growth of proton beams in head-on collision. The impact of a crossing angle between the beams and of a transverse damper is examined.

INTRODUCTION

In lepton colliders, a changed scaling of the luminosity and the beam-beam parameter with intensity has been observed when the intensity exceeded a threshold [1]. The dynamics of colliding hadron beams differs qualitatively from that of electron beams because radiation damping is negligible for hadrons. Therefore hadron beams are assumed to be more prone to instabilities. In the LHC however, the intensity or beam-beam parameter have not been limited by beam-beam effects due to head-on collisions [2]. Beam-beam effects at the highest beam-beam parameter achieved in LHC are discussed in Ref. [3, 4]. In this paper we consider the coherent stability at intensities well beyond the performance of present colliders to identify possible inherent beam-beam limitations for future colliders.

Analytic models of the coherent stability apply only to simplified cases, like assuming linear self-fields and no crossing angle [5, 6]. These models predict unstable regions in the parameter space. Head-tail modes, on the other hand, have been found to be generally stable as long as impedances are neglected [7]. The computer simulations discussed here are not subject to the limitations of the analytic models. In the next section the setup of our simulations is outlined. A discussion of results and conclusions follow in the subsequent sections.

SETUP

The beam parameters chosen for our simulations loosely follow the LHC setup, except for the intensity. The intensity of the beams in our simulations was increased until strong coherent effects were observed. Table 1 lists the simulation parameters. Initially, the particle distribution was Gaussian. One pair of bunches collided once per turn. The corresponding beam-beam parameter without crossing angle is 0.067. According to the linear model developed in Ref. [6], these bunches will experience a quadrupolar instability.

Table 1: Simulation Parameters

Parameter	Value	Unit
N	21×10^{11}	-
ϵ	0.512	nm
β^*	0.5	m
σ_L	0.077	m
δ_p	1.11×10^{-4}	-
Q_x, Q_y, Q_z	0.31, 0.32, 0.00212	-
E	7	TeV
N_m	1,000,000	-
Slices	10	-

Table 2: The Four Cases Discussed in This Paper

Case	Crossing angle	Damper
A	0	off
B	0	on
C	0.15 mrad	off
D	0.15 mrad	on

The beam-beam kicks were computed self-consistently using a Green's function method [8]. The numerical noise in self-consistent simulations can drive emittance growth [9, 10]. However, in the cases considered here, the physical emittance growth is so large that the numerical contribution is negligible. In fact, using 4 times more macro particles in a simulation of case D changed the emittance growth by about 3 % only. Impedances and electron clouds have been neglected because they would obscure the pure beam-beam effects.

Collisions with and without crossing angle as well as with and without transverse damper are discussed. In the following section these 4 cases will be referred to by the letters specified in Tab. 2. The damper model is described in Ref. [10].

RESULTS

First we consider the case A. The offset and emittance are shown as a function of time in Fig. 1. The centroid motion is unstable and the emittance grows by several 10 %/s. From 12,000 to 50,000 turns, the horizontal oscillation is damped while the emittance growth is accelerated. A list of emittance growths after different time intervals for all cases is provided in Fig. 3. For either plane, the average growth of both beams is given.

* This work was partially supported by the U. S. LARP and NERSC of the U. S. Department of Energy under contract No. DE-AC02-05CH11231.

Copyright © 2013 CC-BY-3.0 and by the respective authors

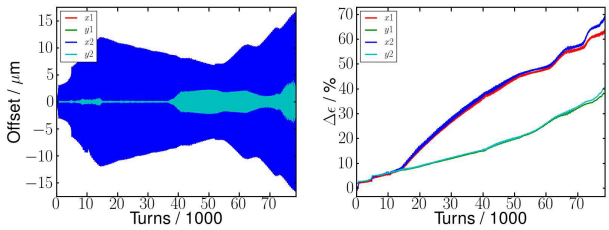


Figure 1: Case A, offset (left) and emittance growth (right) versus time.

Table 3: Emittance Growth (with respect to initial value) at Different Times for Cases A Through D. The simulation of case C did not arrive at 70,000 turns.

Turns	5000	25,000	70,000
A, hor.	8 %	26 %	61 %
A, ver.	7 %	13 %	35 %
B, hor.	33 %	35 %	41 %
B, ver.	13 %	16 %	21 %
C, hor.	7 %	43 %	-
C, ver.	6 %	22 %	-
D, hor.	78 %	116 %	134 %
D, ver.	43 %	70 %	81 %

The envelope spectrum of 2048 turns at the beginning of the simulation and after 30,000 turns is shown in Fig. 2. At the beginning there are peaks at 0.2 and 0.4, indicating a 5^{th} order envelope resonance. These peaks disappear, however, within 10,000 turns and several peaks close to 0 and 0.5 rise. Due to the large beam-beam parameter, the tune footprint is quite large and spreads over many resonance, as Fig. 3 illustrates.

Setting the damper gain to 0.02 (case B) stabilized the centroid, as Fig. 4 demonstrates. Larger gains yielded more emittance growth. The horizontal oscillation is quite large initially, with an amplitude of about 10 μm, and damped very slowly, though. The difference between the planes is attributed to the tunes since all other parameters are equal in both planes. There is a rapid emittance growth initially, which suddenly slows down, as shown in Fig. 4. The final growth rate is on the order of 1 %/s, presumably due to diffusion. Compared with case A, the emittance growth

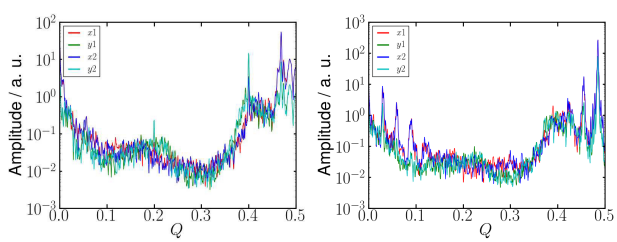


Figure 2: Case A, envelope spectrum after at the beginning and after 30,000 turns.

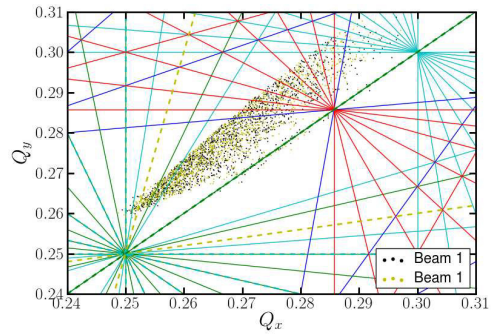


Figure 3: Case A, tune footprint. The visible resonance lines include 4^{th} order (cyan dashed), 6^{th} order (yellow dashed), 7^{th} order (red), 8^{th} order (green), 9^{th} order (blue) and 10^{th} order (cyan solid).

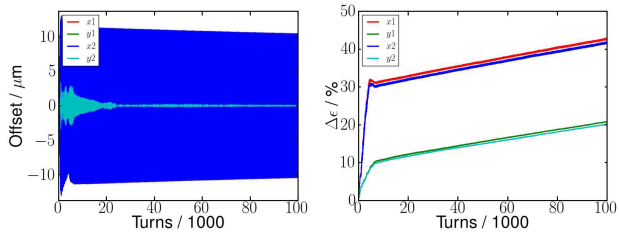


Figure 4: Case B, offset (left) and emittance growth (right) versus time.

is enhanced initially (s. Tab 3), but after a short time the damper proves beneficial.

The spectra of the offsets and envelopes during the fast growth period are shown in Fig. 5. There is a series of peaks in the spectra, indicating the excitation of the beams. After a few 1000 turns, when the beams stabilized, they mostly disappear. As a consequence of coupling, the spectra look all quite similar, despite the differences between the vertical and horizontal planes in the time domain.

Next we let the bunches collide with the nominal crossing angle, without damping (case C). The resulting centroid motion and emittance growth are displayed as a function of time in Fig. 6. The beams obviously suffer a dipolar instability. The emittance grows modestly at the beginning but accelerates as the instability evolves.

The spectrum of the centroid motion is shown in Fig. 7.

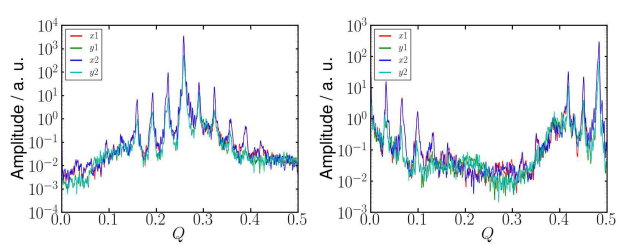


Figure 5: Case B, offset and envelope spectrum after 3000 turns.

Copyright © 2013 CC-BY-3.0 and by the respective authors

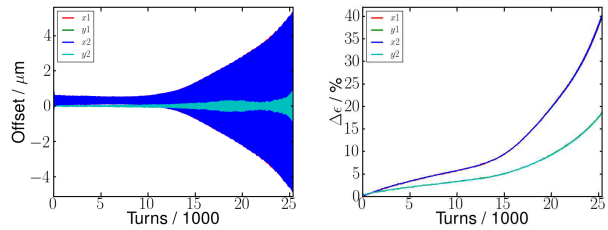


Figure 6: Case C, offset (left) and emittance growth (right) versus time.

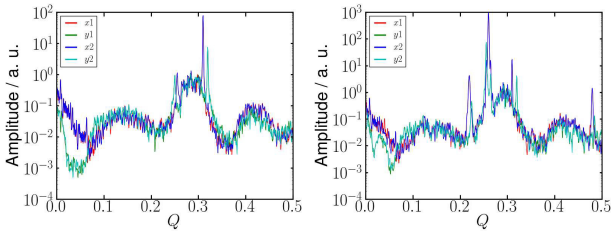


Figure 7: Case C, offset spectrum after 1000 turns and 20,000 turns. The π and σ beam-beam modes are clearly visible.

The spectra clearly reveal the σ (at Q_x and Q_y, respectively) and π (at lower frequency) BB modes. As the instability progresses, the π modes increase, which proves that they are driving the oscillation, but also new modes appear.

Finally the damper was turned on while the beams were colliding with crossing angle (case D). In this case the damper gain was set to 0.2. The corresponding offset and emittance are shown in Fig. 8. The damper stabilizes the centroids within 30.000 turns. By this time the emittance has already grown by 40 % to 50 %, respectively, in each plane. After the offset is under control, the emittance keeps growing at a decreasing rate. Similarly to the situation without crossing angle, the damper accelerates the initial emittance growth but mitigates it later on. The growth rate will possibly converge towards a constant determined by diffusion.

The spectra of the offset and envelope are shown in Fig. 9. Here we see one coherent mode at $q \approx 0.262$ in both planes. It appears that the π mode of both planes coupled to an oscillation with a single frequency while the damper completely suppresses the σ mode. The envelope spectrum features peaks at q, $1-2q$ and a broad band around $1-2$ times the working point.

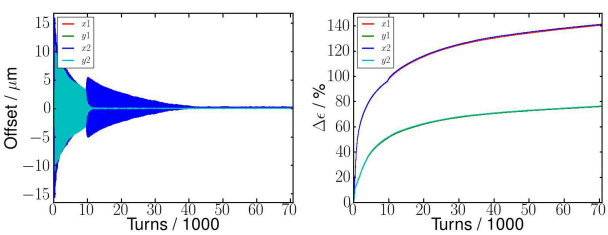


Figure 8: Case D, offset (left) and emittance growth (right) versus time.

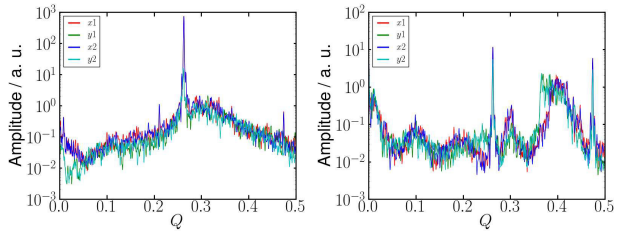


Figure 9: Case D, offset (left) and envelope (right) spectra after 20,000 turns.

CONCLUSIONS

At extremely high intensity beams colliding head on experience dipolar instabilities in our simulations. A transverse damper has proven able to suppress these instabilities, although the damping time can be very long. Employing the damper causes a short, drastic emittance growth, several 10 % within a few 10,000 turns, and cannot avert a subsequent continuous emittance growth with a rate of about 1 %/s. Although a crossing angle (without crab cavities) reduces the effective beam-beam parameter, the beams are stronger affected by beam-beam effects with a crossing angle. At a sufficiently large intensity, beam-beam effects severely challenge the control of the beams even in the absence of external perturbations.

ACKNOWLEDGMENT

The authors thank Simon White for helpful discussions.

REFERENCES

[1] J. T. Seeman, "Observations of the beam-beam interaction", Lecture Notes in Physics, Vol. 247, Springer, 1986.

[2] W. Herr et al., "Observations of beam-beam effects at high intensities in the LHC", IPAC2011, San Sebastian, Spain, WEODA01.

[3] K. Ohmi, "Beam-beam limit in a hadron collider", IPAC2012, New Orleans, USA, THYB01.

[4] S. Paret at al., "Tune studies with beam-beam effects in LHC", IPAC2013, Shanghai, China, TUPME060.

[5] K. Hirata, "Coherent betatron oscillation modes due to beam-beam interaction", NIM A269 (1988).

[6] M. Furman et al., "A symplectic model of coherent beam-beam quadrupole modes", Techn. report, SSC-174, 1988.

[7] E. A. Perevedentsev et al., "Simulation of the head-tail instability of colliding bunches", PRST-AB 4, 024403 (2001).

[8] J. Qiang et al., "Strong-strong beam-beam simulations using a Green function approach", PRST-AB 5, 104402 (2002).

[9] S. Paret et al., "Collisional effects in particle-in-cell beam-beam simulations", IPAC2013, Shanghai, China, TUPME059.

[10] S. Paret et al., "Simulation of colliding beams with feedback in LHC", IPAC2012, New Orleans, USA, TUPPC091.

Copyright © 2013 CC-BY-3.0 and by the respective authors

DESIGN AND HIGH ORDER OPTIMIZATION OF THE ATF2 LATTICES*

E. Marin†, G. White, M. Woodley, SLAC, Menlo Park, CA 94025, USA
K. Kubo, T. Okugi, T. Tauchi, J. Urakawa, KEK, Ibaraki, Japan
R. Tomás, CERN, Geneva, Switzerland

Abstract

The next generation of future linear colliders (LC) demands nano-meter beam sizes at the interaction point (IP) in order to reach the required luminosity. The final focus system (FFS) of a LC is meant to deliver such small beam sizes. The Accelerator Test Facility (ATF) aims to test the feasibility of the new local chromaticity correction scheme which the future LCs are based on. To this end the ATF2 nominal and ultra-low beta* lattices are design to vertically focus the beam at the IP to 37nm and 23nm, respectively if error-free lattices are considered. However simulations show that the measured field errors of the ATF2 magnets preclude to reach the mentioned spot sizes. This paper describes the optimization of high order aberrations of the ATF2 lattices in order to minimize the detrimental effect of the measured multipole components for both ATF2 lattices. Specifically three solutions are studied, the replacement of the last focusing quadrupole (QF1FF), insertion of octupole magnets and optics modification. By applying the mentioned cures the design vertical beam size at the IP is almost recovered for both ATF2 lattices.

INTRODUCTION

The International Linear Collider (ILC) [1] and the Compact Linear Collider (CLIC) [2] projects are designed to deliver a luminosity at the interaction point (IP) above $10^{34}\mathrm{cm}^{-2}\mathrm{s}^{-1}$ by colliding e^+e^- beams of vertical sizes in the nanometre scale. The final focus system (FFS) provides the required beam focusing by means of two strong quadrupole magnets, so called Final Doublet (FD), which are located at a distance L* upstream the collision point. The FD generates chromaticity due to the inherent energy spread of the particle beam which needs to be corrected in order to preserve the vertical IP beam size.

The ATF2 [3] beam line is the extension of the Accelerator Test Facility (ATF) meant to validate the feasibility of the final focus systems (FFS) based on the local chromaticity correction scheme, first proposed in [4]. To this end the ATF2 nominal and ultra-low lattices are designed to obtain a σ_y^* of 37 nm and 23 nm respectively. The nominal lattice is the scaled-down version of the FFS of ILC while the ATF2 ultra-low β^* lattice [5] features a β_y^* a factor 4 smaller than nominal, in order to increase the chromaticity to a value similar to that of the CLIC FFS. This challenging optics explores the feasibility of ultra-low β^* lattices.

Reducing the value of β_y^* imposes tight constraints on the magnetic field tolerances of the FFS magnets, particularly for those magnets located at high beta regions, e.g. FD. The lattice design that recovers the design vertical spot size σ_{y0}^* for both ATF2 lattices is described in the following.

LATTICE DESIGN

In order to overcome the destructive impact in terms $\sigma_{x,y}^*$ of the multipole components of the ATF2 magnets, described in [6], different solutions have been considered in [7]. These include replacing the FD, reducing the vertical emittance or increasing the β_x^*. Reducing the vertical emittance is not a cost effective solution. Increasing the value of the β_x^* by a factor 4 effectively reduces the impact of the multipole magnets for both ATF2 lattices, yet it is not the preferred solution since it deviates from the IP beam aspect ratio that the ATF2 nominal lattice was designed for to mirror that of the ILC FFS. In 2012 it was decided to insert 4 skew sextupole magnets [8] meant to compensate for the skew sextupole components of those quadrupole magnets that do not meet the required tolerances, see [9]. Further the focusing quadrupole magnet of the FD was replaced by a 4Q17 type recycled from the PEP-II ring, due to its better field quality. As a result of these beam line modifications the impact of the multipole components becomes negligible for the ATF2 nominal lattice. Although these modifications also minimise the impact of the multipole components for the ATF2 ultra-low β^* lattice, they are not sufficient. The σ_y^* obtained is still 30% larger than design value. The analysis of the high order aberrations of the IP beam size carried out in [10] by the MAPCLASS code [11] determines that a chromatic third order (octupole) component is the main contributor to the calculated $\Delta\sigma_y^*$. The insertion of a pair of octupole magnets is proposed in [10] as an effective solution for compensating this particular aberration.

Octupole Magnets

Two octupole magnets located at dispersion and dispersion-free regions of the ATF2 beam line, namely OCT1FF and OCT2FF respectively, counteract the effect of the chromatic octupole aberration on the vertical IP beam size. It is found that these octupole magnets can reduce the σ_y^* down to 24 nm. More details can be found in [10].

In terms of field quality, the tolerances have been evaluated for both decapole and dodecapole components, Table 1 summarises the tolerances for both octupole magnets. Tighter tolerances are found for the OCT1FF which is located at the dispersion region but all of them are easily achievable from the point of view of magnet design. CERN has taken the initiative to design and construct a pair

* Work supported by Department of Energy contract DE-AC02-76SF00515.
† emarinla@slac.stanford.edu

Copyright © 2013 CC-BY-3.0 and by the respective authors

Table 1: Relative Tolerance Evaluated at a Radius equal to 1 cm for the Octupole Magnets OCT1FF and OCT2FF. Each tolerance represents a vertical beam size growth at the IP of 2%.

Component	Decapole		Dodecapole	
	Normal	Skew	Normal	Skew
Units	$[10^{-1}]$	$[10^{-1}]$	$[10^{-1}]$	$[10^{-1}]$
OCT1FF	2	1	4	1
OCT2FF	7	4	6	12

of octupole magnets to be inserted in the ATF2 beam line, see [12] for more details.

TUNING PROCEDURE

The tuning procedure consists in bringing the accelerator to its design performance under realistic error imperfections. When errors are included into simulations, the IP beam sizes are well above their design values. The tuning procedure is applied to compensate for the IP beam size aberrations caused by the machine imperfections. The tuning determines the feasibility of a lattice. The procedure of tuning ATF2 consists of an initial alignment of the ATF2 magnets using the beam itself, so called BBA. This technique centres the beam at the magnetic center of the magnets within 100 μm [13]. The typical σ_y^* at this stage is of the order of a few μm respectively, see Fig. 1. The final IP spot tuning after the BBA is based on a set of orthogonal tuning knobs that target the residual beam size aberrations at the IP.

Tuning Errors Conditions

The error conditions considered in this simulation are transverse misalignments, rotations along the longitudinal axis and strength errors of the magnetic fields. 100 simulated machines are set up with different initial error conditions. Each error is assigned to the quadrupole, sextupole and octupole magnets following a random Gaussian distribution of width σ_{error}. Also the measured multipole content of the ATF2 magnets and a measurement error of the IP beam size monitor are included into the tuning study. Table 2 summarises the values of σ_{error} for each error.

Table 2: Errors σ_{error} Assumed for the Tuning Simulation Study.

Error	σ_{error}
Horizontal misalignment [μm]	100
Vertical misalignment [μm]	100
Tilt along s-coordinate [μm]	300
Strength [%]	0.1
IP measurement [%]	10

Tuning Knobs

The available 5 normal sextupole magnets of ATF2 are used to construct 8 linear knobs that target the waists α_x^*, α_y^* (longitudinal displacement of the focal point), energy dispersions η_x^*, η_y^* and $\eta_y'^*$ and couplings between x and y ($< x, y >$), p_x and y ($< p_x, y >$) and p_x and p_y (p_x, p_y) at the IP. Each knob uses different combinations of transverse displacements of the normal sextupole magnets. Since the orthogonality may not be fully guaranteed it is common practise to scan the whole set of knobs a few times. Figure 1 shows the evolution of the mean of the vertical IP spot size $< \sigma_y^* >$ (solid line) over 100 different seeds, after each scan of the linear knobs.

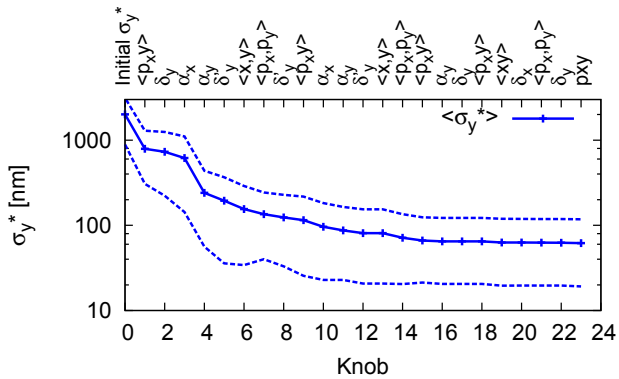


Figure 1: Evolution of $< \sigma_y^* >$ after scanning each of the linear knobs shown in the upper axis. The solid line refers to the mean value of σ_y^* of the 100 simulated machines and the upper and lower dashed curves represent the mean $\pm$ rms error, respectively.

The linear knobs bring σ_y^* from a few μm down to $\approx$ 100 nm in about ten knob scans, after that the tuning speed decreases notably and the beam size converges to above 60 nm after scanning the set of linear knobs 3 times. This $< \sigma_y^* >$ represents almost a factor 3 above the design value. In terms of the confidence level, only 33 % of the simulated machines reach a final $\sigma_y^* < 1.2\ \sigma_{y0}^*$ as shown by the red curve in Fig. 3.

At this stage, further study of the higher order aberrations of σ_y^* of the 100 different machines after scanning the linear knobs is conducted using the MAPCLASS code in combination with MADX [14]. MADX evaluates the map from the entrance of ATF2 to the IP to the desired order. MAPCLASS uses this map to transport a Gaussian distribution meant to represent the beam at ATF2. The study reveals that the 2$^{\text{nd}}$ order aberrations that contribute most to $\Delta\sigma_y^*$ using the so called *transport notation* are related to: $T_{y,p_x,y}$, T_{y,x,p_y}, $T_{y,\delta,\delta}$ and $T_{y,x,x}$ coefficients. In addition to these aberrations, it is also worth noting the contributions from the 3$^{\text{rd}}$ order which are more severe than those of the second order, the most notable being related to the coefficients: $U_{y,x,x,x}$, $U_{y,x,\delta,\delta}$, $U_{y,x,x,y}$, U_{y,x,x,p_x} and $U_{y,x,y,\delta}$, as shown in Fig. 2. The two line-points shown in Fig. 2 represent the average contribution to $\Delta\sigma_y^*$ over

Copyright © 2013 CC-BY-3.0 and by the respective authors

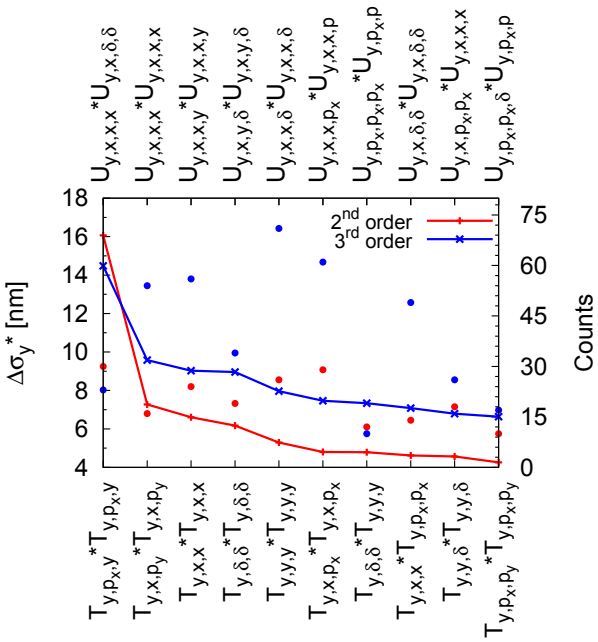


Figure 2: Most relevant high order aberrations that remain after applying the linear tuning knobs. Red curve refers to the 2nd order aberrations, namely $T_{i,j,k}$ (lower axis). Blue curve represents the 3rd order aberrations, namely $U_{i,j,k,l}$ (upper axis)

the simulated machines from the aberration labelled on the horizontal axes. The lower and upper axes show the 2nd (red) and 3rd (blue) order coefficients. The number of occurrences of each aberration is shown by the single points using the same color code, and should be read on the right axis.

Taking advantage of the 4 skew sextupole magnets installed along the ATF2 beam line, a set of 4 knobs are constructed in order to compensate for the above mentioned $T_{i,j,k}$ aberrations. The 2 octupole magnets are used to obtain 2 additional knobs for taking care of the $U_{y,x,x,x}$ and $U_{y,x,\delta,\delta}$ aberrations. These knobs are based on strength variations. The number of machines that reach a $\sigma_y^* < 1.2\ \sigma_{y0}^*$ increases from 33% to 54% after applying the linear and 2nd order knobs. When the octupole knobs are included into the tuning procedure, the percentage of tuned machines with $\sigma_y^* < 1.2\ \sigma_{y0}^*$ increases to 63% as shown in Fig. 3. Figure 3 compares the confidence level of the tuning strategies, namely linear knobs (red), linear plus 2nd order knobs (green) and linear plus 2nd order plus octupole knobs (blue). The confidence level represents the number machines that reach a $\sigma_y^* < 1.2\ \sigma_{y0}^*$.

SUMMARY

The present multipole content of the ATF2 magnets increases the vertical beam size at the IP by less than 5% when the ATF2 nominal lattice is considered in simulations. By contrast, the impact of these multipole errors

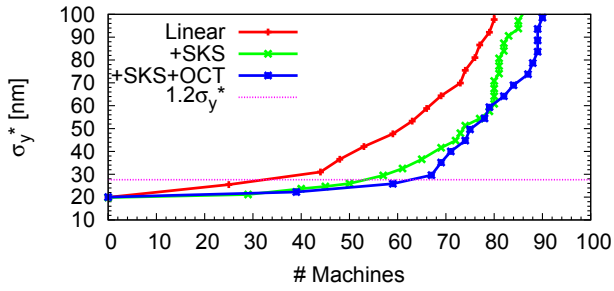


Figure 3: Confidence curves obtained for the 3 tuning strategies. The magenta line indicates the $1.2\ \sigma_{y0}^*$ value.

increases σ_y^* by 30% for the ATF2 ultra-low β^* design. Simulation shows that 2 octupole magnets can effectively reduce the impact on the beam size by less than 5%. The calculated tolerances of the magnetic field errors of these octupole magnets do not represent any difficulty from a magnet design point of view. An additional benefit is found when studying the tuning performance of the ultra-low β^* lattice under realistic error imperfections. Thanks to the knobs based on these octupole magnets, the percentage of machines that reach a final $\sigma_y^* < 1.2\ \sigma_{y0}^*$ increases from 54 % up to 63 %.

REFERENCES

[1] ILC Global Design Effort, "ILC Technical Design Report," http://www.linearcollider.org/ILC/Publications/Technical-Design-Report.

[2] "CLIC Conceptual Design Report," *CERN-2012-007*.

[3] H. Braun *et al*, "ATF2 Proposal. Vol. 1," *CLIC-Note-636*, (2005).

[4] P. Raimondi and A. Seryi, *Phys. Rev. Lett. 86*, (2001).

[5] P. Bambade *et al*, "ATF2 Ultra-Low IP Betas Proposal," *CLIC-Note-792*, (2009).

[6] R. Tomás *et al*, "ATF2 ultra-low IP betas proposal," *Proc. of PAC'09*, Vancouver, (2009).

[7] E. Marin *et al*, "Scenarios for the ATF2 Ultra-low betas proposal," Proc. of IPAC,10 (2010).

[8] T. Okugi *et al*, "Linear and 2nd order optics correction of ATF2 final focus beamline," to be submitted to *Phys. Rev. ST-AB*.

[9] E. Marin, "Design and higher order optimisation of FFS for linear colliders," *PhD Thesis*, (2012).

[10] E. Marin *et al*, submitted to *Phys. Rev. ST-AB*.

[11] R. Tomás, "MAPCLASS: a code to optimize high order aberrations," *CERN-AB AB-Note-2006-017 (ABP)*, (2006).

[12] M. Modena, "Progress with FFS magnets for CLIC, ILC and ATF2," Meeting: *CLIC and ILC BDS*, CERN (2013).

[13] M. Woodley, "EXT: Summary of activities, software development and tuning performance," *11th ATF2 Project Meeting*, 2011.

[14] "MAD-X Home page," `http://frs.home.cern.ch/frs/Xdoc/mad-X.html`

Copyright © 2013 CC-BY-3.0 and by the respective authors

COUPLING SPIN RESONANCES WITH SIBERIAN SNAKES*

Nermeen Khalil†, Stony Brook University, Stony Brook, NY 11794, U.S.A.
V. Ptitsyn, Brookhaven National Laboratory, Upton, NY 11973, U.S.A.

Abstract

The polarization of proton beam during the acceleration process in a particle accelerator is affected by the existence of spin resonances. Coupling spin resonances can be excited in the presence of the betatron coupling introduced by rolled quadrupoles and solenoids. A corresponding algorithm has been developed and added to the ASPIRRIN code to include the calculation of the first-order intrinsic resonance harmonics in the case of arbitrary strong betatron coupling and in the presence of Siberian Snakes and spin rotators.The analysis of the coupling resonance harmonics excited in RHIC collider is presented.

INTRODUCTION

Accelerating high energy polarized proton beams in a circular accelerator is complicated with the presence of depolarizing resonances. With the application of the various kind of spin rotating devices (like Snakes and spin rotators) the stable spin axis on the design closed orbit may deviate from the vertical, and an algorithm should be realized which would calculate the spin resonance harmonics with this complex configuration of the magnetic field on the design orbit. Main features of this algorithm for calculating the spin resonance strength were presented in [1]. In the work presented in this paper the algorithm has been extended to include the calculation of horizontal and vertical intrinsic spin resonance amplitudes for the case of strong betatron coupling, caused by rotated quadrupoles and solenoidal fields. We consider, as an example, the betatron coupling in RHIC accelerator which is originated mostly due to rolls of quadrupoles at the RHIC interaction regions and compensated using the local skew quadrupole correctors. In order to calculate the undesired coupling effects on the spin resonance strength an algorithm has been modified in ASPIRRIN [2] code to include the horizontal and vertical intrinsic spin resonance amplitude calculation for arbitrary rotated quadrupole in presence of the Siberian Snakes. In RHIC two Siberian Snakes are installed in each of the two RHIC rings [3].

ALGORITHM DESCRIPTION

In order to describe the spin motion which is initiated by the arbitrary rotated quadrupole , we would need to introduce the calculation of the spin perturbation in general. We consider the spin perturbation due to betatron oscillations as the linear form in the orbit variables $w_j = T_{iq}X_q$. The orbital coordinates and momenta of a particle will be defined as $X^T = (x, p_x, y, p_y)$, where x and y are the horizontal and vertical coordinates of a particle, and p_x and p_y are their conjugate momenta. The linear orbital motion can be defined as $X_q = F_{qr}A_r$ where F_{qr} is the matrix compiled from the complex eigenvectors of the orbital motion, and A_r is the vector of the betatron amplitudes.

Here we are considering the spin perturbation theory in the coordinate system $(\mathbf{l}, \mathbf{m}, \mathbf{n_0})$, where $\mathbf{n_0}$ is the stable spin solution on the design orbit. In this coordinate system a spin vector on the design orbit rotates with the constant spin precession tune ν around $\mathbf{n_0}$. The vector $\mathbf{k} = \mathbf{l}+\mathbf{im}$ is related with the spin eigenvector $\mathbf{k_0}$ by $\mathbf{k} = \mathbf{k_0}\cdot e^{i\nu\theta}$, where θ describes the accelerator azimuth. In Eq. 1 the first-order spin resonances are defined as the coefficients of Fourier decomposition of the spin perturbation term

$$\mathbf{w}\cdot\mathbf{k} = \sum_{r,p}\epsilon_{rp}e^{i(p+Q_r)\theta} = \sum_{r,p}A_r\tilde{v}_{rp}e^{i(p+Q_r)\theta} \qquad (1)$$

where p are integer numbers and Q_r present components of the orbital betatron tune vector $(Q_I, -Q_I, Q_{II}, -Q_{II})$. Q_I and Q_{II} are tunes of two betatron oscillation modes. In order to calculate $\tilde{v}_{rp}$ in the program the integral over one turn is taken doing element-by-element integration [1].

$$\tilde{v}_{rp} = \frac{1}{2\pi}\int_0^{2\pi} e^{i\delta_{rp}\theta}\sum_{j,q}T_{jq}\mathcal{F}_{qr}k_{0j}d\theta \qquad (2)$$

where $\delta_{rp} = \nu - (p + Q_r)$ describes detuning of the spin tune from a resonance tune.

In order to obtain $\tilde{v}_{rp}$ for rotated quadrupole we start with considering the following equations of motion of particle in arbitrary rotated quadrupole:

$$x'' = -g_c x - \kappa_c y \qquad y'' = g_c y - \kappa_c x \qquad (3)$$

where $g_c = g\cdot cos(2\phi)$ and $\kappa_c = g\cdot sin(2\phi)$ are defined by the quadrupole rotation angle ϕ and the quadrupole field gradient g.

From (3) we can get the expressions for the orbital motion eigenvectors which will be used later in the paper :

$$F_{3r} = -AF''_{3r} + BF''_{1r} \qquad F_{1r} = AF''_{1r} + BF''_{3r} \qquad (4)$$

Here:

$$A = -cos(2\phi)/g \qquad B = -sin(2\phi)/g \qquad (5)$$

The components of horizontal and vertical components of the spin perturbations in a quadrupole are given by:

$$w_x = (1+\nu_0)y'' \qquad w_y = -(1+\nu_0)x'' \qquad (6)$$

* Work supported by Brookhaven Science Associates, LLC under Contract No. DE-AC02-98CH10886 with the U.S. DOE
† nermeen.khalil@stonybrook.edu

Copyright © 2013 CC-BY-3.0 and by the respective authors

where $\nu_0 = G\gamma$, with magnetic moment anomaly G and relativistic factor γ. From (1) and (6) the contribution to a spin resonance harmonic produced by a betatron mode oscillating with the tune Q_r from a quadrupole can be formulated as the following:

$$\tilde{v}_{rp}^{quad} = (1+\nu_0)(k_{0x}I_3 - k_{0y}I_1) \quad (7)$$

where I_1 and I_2 are the integrals defined as

$$I_1 = \int_{\theta_1}^{\theta_2} F_{1r}^{''} e^{i\delta_{rp}\theta} d\theta \quad (8)$$

$$I_3 = \int_{\theta_1}^{\theta_2} F_{3r}^{''} e^{i\delta_{rp}\theta} d\theta \quad (9)$$

and θ_1 and θ_2 correspond to the entrance and the exit of the quadrupole.

To find the integrals (8) and(9) one can apply twice the integration by parts and the expressions (4) to get the set of linear equations for I_1 and I_3. Resolving the equations one gets the solution in the matrix form:

$$\begin{pmatrix} I_1 \\ I_3 \end{pmatrix} = M^{-1} \begin{pmatrix} C_1 \\ C_3 \end{pmatrix} \quad (10)$$

where M, C_1 and C_3 are expressed as

$$M = \begin{pmatrix} 1 + A\delta_{rp}^2 & B\delta_{rp}^2 \\ B\delta_{rp}^2 & 1 - A\delta_{rp}^2 \end{pmatrix} \quad (11)$$

$$C_3 = \left[(F_{3r}^{'} - i\delta_{rp}F_{3r}) e^{i\delta_{rp}\theta} \right]_{\theta_1}^{\theta_2} \quad (12)$$

$$C_1 = \left[(F_{1r}^{'} - i\delta_{rp}F_{1r}) e^{i\delta_{rp}\theta} \right]_{\theta_1}^{\theta_2} \quad (13)$$

Then the final formula which defines the contribution from an individual rotated quadrupole to the spin resonance harmonic is:

$$\tilde{v}_{rp}^{quad} = Y[k_{0x}(\delta_{rp}^2 \sin(2\phi)C_1 + (g - \delta_{rp}^2\cos(2\phi))C_3) - k_{0y}((g + \delta_{rp}^2\cos(2\phi))C_1 + \delta_{rp}^2 \sin(2\phi)C_3)] \quad (14)$$

where

$$Y = g(1+\nu_0)/(g^2 - \delta_{rp}^4) \quad (15)$$

Summing these contributions from all quadrupoles gives us the full spin resonance harmonic defined by r and p.

Using similar technique the spin resonance harmonics contribution from a solenoid was derived as:

$$\tilde{v}_{rp}^{sol} = \frac{(G-\nu_0)K_s}{\delta^2 - (GK_s)^2}(-i\delta_{rp}[e^{i\delta_{rp}\theta}((F_{2r} + \frac{1}{2}K_sF_{3r})k_{0x} + (F_{4r} - \frac{1}{2}K_sF_{1r})k_{0y})]_{\theta_1}^{\theta_2} + GK_s[e^{i\delta_{rp}\theta}((F_{2r} + \frac{1}{2}K_sF_{3r})k_{0y} - (F_{4r} - \frac{1}{2}K_sF_{1r})k_{0x})]_{\theta_1}^{\theta_2}) + \frac{(1+\nu_0)K_s}{2}\left[e^{i\delta_{rp}\theta}(F_{1r}k_{0x} + F_{3r}k_{0y})\right]_{\theta_1}^{\theta_2} \quad (16)$$

where K_s is the normalized field of the solenoid and the last term describes the contribution from the solenoid ends.

CALCULATIONS FOR THE BETATRON COUPLING AT RHIC

We would show some tests which have been done by ASPIRRIN after modifying it with the new algorithm. The main motivation for our calculation was to test the code ability of calculating the resonance strength amplitude in the general case for the betatron oscillation coupling. The calculations were done for the RHIC lattice with two Siberian Snakes, which had uncoupled tunes $Q_x = 27.685$, $Q_y = 29.673$ with betatron amplitudes of $10\mu m \cdot rad.$ in both planes.

The spin tune in RHIC with the Siberian Snakes is equal to 0.5. because of that in all plots in this section we show the result for resonance harmonics which are closest to 0.5 value (that is with the resonance tunes in $[0-1]$ range). Moreover, we add together the amplitudes of the two spin resonance harmonics, one below and other above 0.5, corresponding to the same betatron tune (Q_I or Q_{II}). That gives the resonance amplitude of the linear resonance harmonic, which is more natural when considering an accelerator with the Siberian Snake [1].

First we started by varying the field strength of different IR skew quadrupoles correctors, which are used to compensate for the coupling caused by the rolled quadrupoles, and observing how the spin resonance harmonics depend on the betatron coupling, which is characterized by minimum betatron tune split ΔQ_{min}. In figure 1 a typical behavior of the vertical and horizontal resonance harmonics are shown by varying the gradient strength of skew-quadrupole (SQ06C2B), the horizontal resonance amplitude would increase non linearly while the vertical amplitude would behave the opposite.

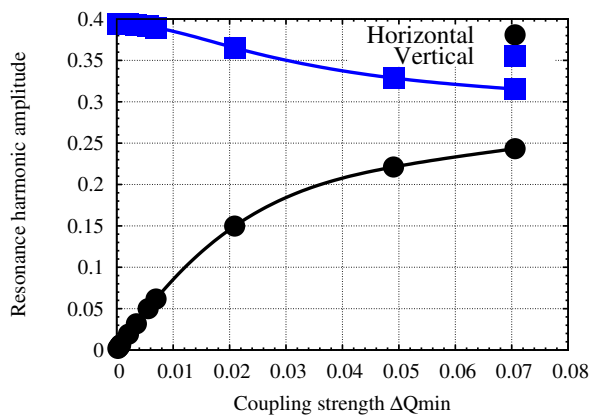


Figure 1: Dependence of the vertical and horizontal resonance harmonic amplitudes on the coupling strength when varying a skew quadrupole corrector. $G\gamma = 422.3$.

Figure 2 demonstrates another typical feature of the resonance harmonic dependence observed during the skew quadrupole variation studies. While the vertical and horizontal harmonics changes the sum of their squares remains approximately constant: $\tilde{v}_{hor}^2 + \tilde{v}_{ver}^2 \approx const.$ This in-

Copyright © 2013 CC-BY-3.0 and by the respective authors

dicates a rotational type transformation between the horizontal and vertical resonance harmonics when the betatron coupling is introduced.

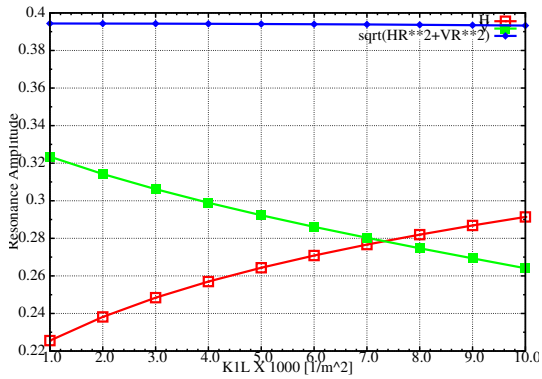


Figure 2: Conservation of the sum of squares of the horizontal and vertical resonance harmonic amplitudes when varying a skew quadrupole corrector(SQ08C2B). $G\gamma = 422.3$.

Next, we considered actual coupling errors present in RHIC, where strong sources of the the betatron coupling are due to the rolls of the IR quadrupoles. These quad rolls are well known from the beam-based and magnetic measurements. Thus, we applied the known rolls and well as local skew quadrupole corrector strengths used at RHIC operation [4]. Figure 3 shows the calculated values of the vertical resonance amplitudes versus $G\gamma$ in a region of strong resonances in RHIC. The figure shows some reduction of the values of vertical harmonics amplitude after applying the quad rolls and skew quad correction.

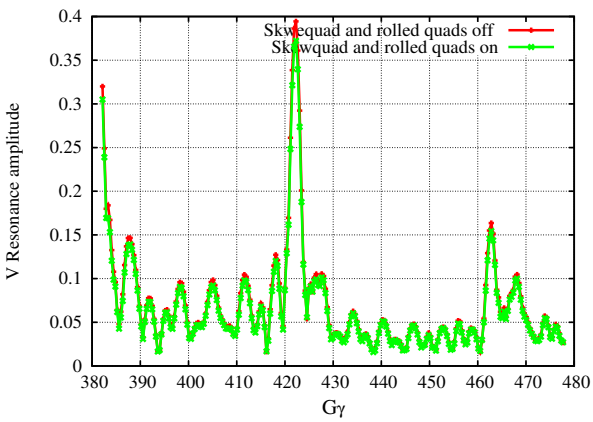


Figure 3: Calculated vertical spin resonance harmonics with and without the actual RHIC IR quadrupole rolls and local IR skew corrections.

Figure 4 shows the calculated values of the the horizontal resonance amplitude versus $G\gamma$ and it is observed that the horizontal resonance amplitudes are excited up to 0.15 when the actual quadrupole rolls and skew quad corrector strengths are used (in this case $\delta Q_{min} \approx 0.01$). After that we used optimized values for certain local skew quadrupole gradients, which reduced the δQ_{min} coupling parameter to 0.001. The horizontal resonance harmonics are clearly reduced in this case. The plot also shows that the horizontal resonance amplitudes are suppressed to zero when the skew quadrupoles are turned off and the quadrupole rolls are 0.

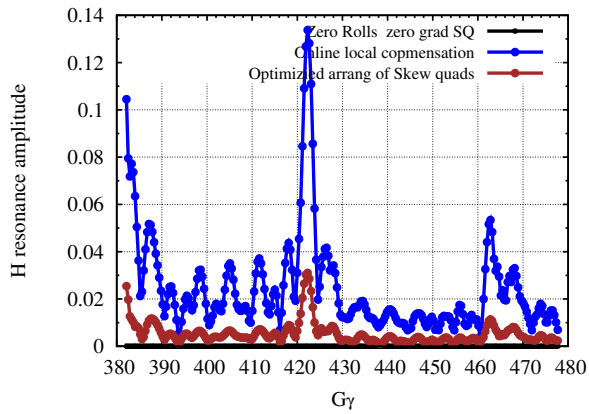


Figure 4: Calculated horizontal spin resonance harmonics with and without the actual RHIC IR quadrupole rolls and local IR skew corrections. The result for optimized corrections is also shown.

SUMMARY

The calculation of spin resonance harmonics with coupled transverse betatron motion was implemented in the ASPIRRIN code. We noticed a rotation-type transformation of the resonance strength of vertical and horizontal harmonics when introducing the betatron coupling. The local coupling correction for actual values of quad rolls and IR skew quad correctors at 6 Interaction regions in RHIC results in exciting the horizontal resonance strength up to 0.15 at $G\gamma$ of value of 422.3. Optimizing the skew quadrupoles arrangement for better compensation of the local coupling helps to reduce the horizontal spin resonance amplitudes even before applying the global coupling correction.

REFERENCES

[1] V. Ptitsyn and N. Khalil, "Calculation of spin resonance harmonics in an accelerator with Snakes' submitted to Proceed. of 20th Internat. Symposium on Spin Physics, Dubna, September 2012.

[2] V. Ptitsyn, S.R. Mane and Yu.M. Shatunov, Nucl. Instr. and Meth. A, V.608 2009 p.225;

[3] I. Alekseev, *et al.*, "Configuration Manual, Polarized Proton Collider at RHIC".

[4] Y. LUO, *et al.* , "REVISIT LOCAL COUPLING CORRECTION IN THE INTERACTION REGIONS OF RHIC", BNL Report C-A-AP-439 (2011)

Copyright © 2013 CC-BY-3.0 and by the respective authors

THE RHIC E-LENS TEST BENCH EXPERIMENTAL RESULTS *

X. Gu#, F.Z. Altinbas, J. Aronson, E. Beebe, W. Fischer, D.M. Gassner, K. Hamdi, J. Hock, L. Hoff, P. Kankiya, R. Lambiase, Y. Luo, M. Mapes, J. Mi, T. Miller, C. Montag, S. Nemesure, M. Okamura, R. H. Olsen, A.I. Pikin, D. Raparia, P. J. Rosas, J. Sandberg, Y. Tan, C. Theisen, P. Thieberger, J. Tuozzolo, and W. Zhang, BNL, Upton, NY 11973

Abstract

To commission some of the hardware and software for the RHIC electron lenses (e-lenses), we built a test bench based on BNL's EBIS test stand. Over several months, we tested the electron gun, the collector, the high-voltage gun-modulator, the instrumentation, the partial control system, and several software applications. A nominal DC-beam current of 0.85 A was demonstrated. And the electron beam transverse profiles were verified as being Gaussian with a small flat top. We also evaluated some e-lens power-supplies and the electronics for measuring current on our bench. The properties of the cathode and the profile of the beam were assessed. In this paper, we present some of our experimental findings.

INTRODUCTION

To improve the luminosity of the polarized protons in the Relativistic Heavy Ion Collider (RHIC), we are installing two electron lenses (e-lenses) in IR10 [1-4] to compensate for the head-on beam-beam effect. We designed an e-lens test bench to test some elements of the e-lens hardware, its controls, and some application software [5]. Figure 1 illustrates the layout of e-lens test bench; it encompasses an electron source, a beam-propagation system, an electron collector, and some instruments for beam diagnostics.

The electron source is an electron gun with a cathode designed to generate a beam with transverse Gaussian profile [3, 6]. After manufacturing it, we measured the actual shape of the cathode (its cross-sectional profile), then simulated the beam profile resulting from the cathode profile with the 2D program TRAK, and compared it to the obtained beam profile with the measured beam.

The system that propagates the beam encompasses a 4.6 T superconducting solenoid, a collector coil, gun dipoles, main dipoles, collector dipoles, and a drift tube.

When the electron beam arrives at the collector, we measured its current with the DCCT and the pulse CT [7]. The maximum temperature on the collector was determined by Resistance Temperature Detectors (RTDs) at the highest DC load. The eight RTDs on the cylindrical surface of the electron collector were arranged in two groups. Each group consisted of four RTDs in one longitudinal plane; the four thermocouples of one group were separated azimuthally by 90 degrees, while the two groups were separated longitudinally by 70 mm.

After several months of operation, we tested the electron gun, the collector, the high-voltage gun modulator and most of the instrumentation on the test bench. We also qualified parts of the control system and several software applications. The nominal pulse and the DC beam current of 0.85 A were demonstrated, and the electron beam transverse profiles were verified as being Gaussian. Some e-lens power supplies and the electronics for measuring the current were also assessed. The properties of the cathode and the profile of the beam were evaluated.

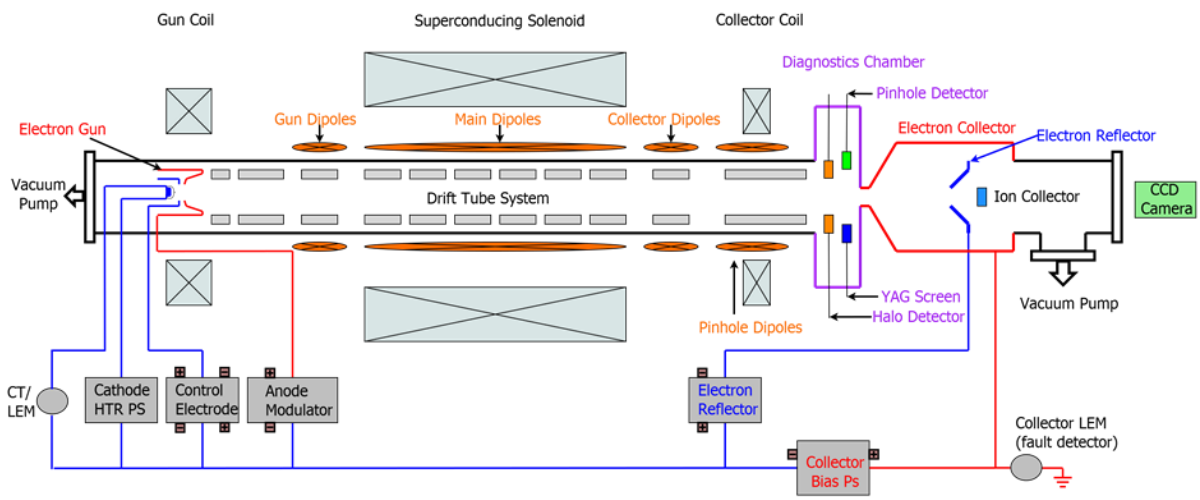


Figure 1: Layout of the electron lens test bench.

* Work supported by Brookhaven Science Associates, LLC under Contract No. DE-AC02-98CH10886 with the U.S. Department of Energy

#xgu@bnl.gov

Copyright © 2013 CC-BY-3.0 and by the respective authors

THE ELECTRON GUN AND BEAM

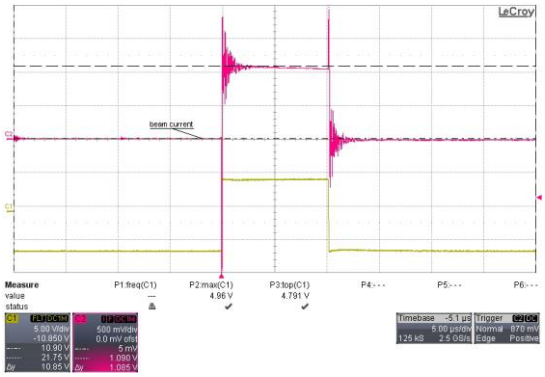


Figure 2: Example of the measurements of the 1085 mA current of the electron beam (yellow) and the anode voltage (red).

We demonstrated the capability of the electron gun on the test bench. Figure 2 shows an example of the measurements of the electron beam current (yellow) and the anode voltage (red). For the current, it is 500 mA/div; for the anode voltage, it is 5 kV/div; the pulse length is 5 μs/ div.

For the pulsed electron-beam, we used the gun-side pulse CT (Fig. 1) and obtained the anode voltage locally via the Tek P6015A probe. To obtain information on the beam loss, we evaluated the electron beam current on the collector side CT, and compared it with a similar measurement from the gun-side CT.

THE COLLECTOR

The temperature of the collector was recorded while the DC beam current was being increased to 1 A.

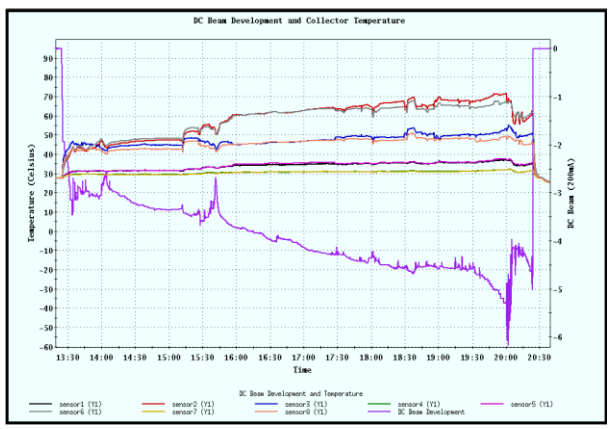


Figure 3: Collector temperature and DC beam.

Figure 3 shows the DC beam current (purple) and the RTDs temperature read-backs (other colors). The DC current is $I = 5.04 \times 200$ mA $= 1080$ mA, and the collector voltage is about 5 kV. The total beam power is 5.4 kW and the maximum temperature is about 70°C on the temperature sensor 2.

As it is apparent from Fig. 3, the eight temperature sensors yield four similar groups of readings, implying that the electron beam may be off-axis or not parallel to the collector axis. Similar readings were obtained from pairs of sensors located at the same angle along the beam, but at two different longitudinal positions.

THE MODULATOR

Figure 4 shows results from the modulator running at 80 kHz with a 10 kV anode voltage. The yellow waveform is the anode voltage, while the red waveform represents the electron beam current measured by the gun-side of the pulse current transformer. The two spikes on both sides of each pulse seemingly reflect the charging and discharging current between the modulator and the anode.

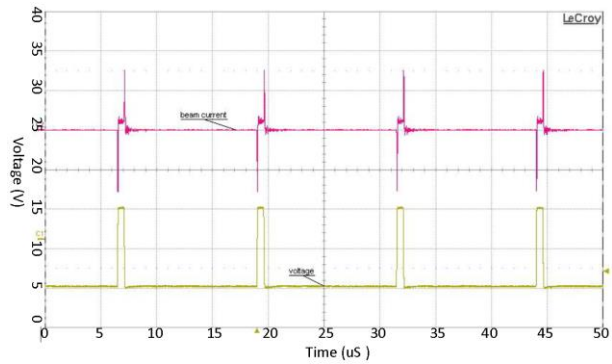


Figure 4: 80 kHz modulator test with beam-current pulse (red), and the anode-voltage pulse (yellow).

The BPMs will play a critical role in meeting the ambitious requirements for commissioning and operating the electron lenses. Two BPMs in the e-lens will measure the positions of both the proton and the electron beam. To assure beam alignment within 10% beam sigma precision for a 300-μm electron beam, we designed the modulator with a rise and fall time of only 50 ns.

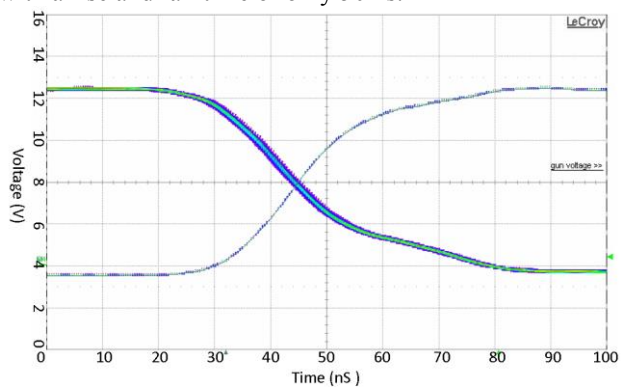


Figure 5: Rise and fall times of the electron beam measured via the anode voltage.

Although the beam current is a non-linear function of the voltage, the rise and fall times of the current signal are very close to the rise and fall times of the anode's voltage signal. Therefore, at first, we measured the electron beam rise and fall times via measuring those of the anode voltage.

Figure 5 plots the beam rise and fall time, measured with a waveform persistence setup; it reveals that the

Copyright © 2013 CC-BY-3.0 and by the respective authors

rising edge of the beam is more stable than the falling edge. The frequency is 80 kHz, and the anode voltage is 10 kV.

The rise and fall times for 98% of the amplitude are 60 ns and 70 ns, respectively. We located the Behlke switch of the anode modulator about 0.6 m away from the anode because of the test bench structural limitations. We will reduce the contribution of the capacitance and inductance of the connecting cable to the transitions of the modulator pulses in the e-lens by positioning the Behlke switch much closer, i.e., 10 cm, to the anode feed-through.

PINHOLE SCANNER AND YAG SCREEN

The pinhole scanner was fully tested, evaluated, and calibrated. By adding a bias voltage on the pinhole we found that the behaviour of the secondary electrons play an important role in the total signal at the integral pinhole scanner.

Figure 6 shows the beam profile, acquired by the pinhole scanner for a beam of 200 mA. The profile has a flat top at the center, and lesser intensity at the edges of the beam, as predicted by the 2D program TRAK with a measured cathode profile.

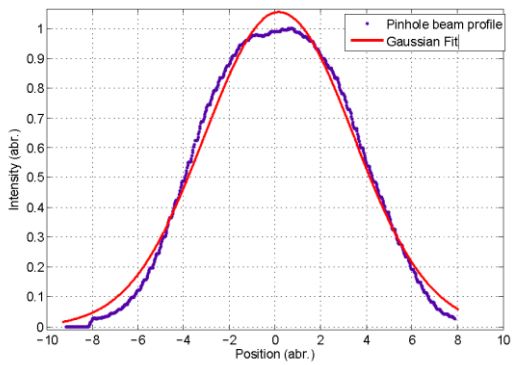


Figure 6: Beam profile obtained using pinhole scanner.

We also developed a YAG screen and camera system for measuring the beam profile. Our findings for a 144 mA electron beam are plotted in Fig. 7; the profile is similar to that depicting the pinhole results.

The YAG screen can obtain the beam profile within seconds. We acquired many beam profiles for different system configurations. However, caution is required here because the YAG screen is very fragile and can be damaged by unwanted beam current.

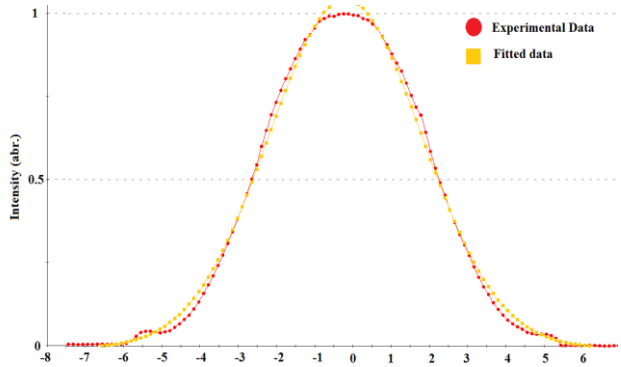


Figure 7: Beam profile from YAG screen, showing the correspondence between the experimental and fitted data.

SUMMARY

We tested and improved the electron gun, collector, some instrumentation, and some power supplies on the e-lens test bench. The software- and the machine-protection system were also prototyped. All of these tests resulted in a considerable savings in time for commissioning the 2013 e-lens, and later on.

ACKNOWLEDGMENTS

The authors would like to acknowledge the help of the instrumentation, vacuum and controls groups. The authors are also grateful for the valuable discussions with the FNAL TEL staff, in particular with V. Shiltsev, A. Valishev, and G. Stancari.

REFERENCES

[1] W. Fischer, et al., "Status of head-on beam-beam compensation in RHIC", proceedings of the ICFA Mini-Workshop on Beam-Beam Effects in Hadron Colliders (BB3013), CERN (2013).

[2] X. Gu, et al., “Designing a Beam Transport System for RHIC’s Electron Lens”, PAC’11, New York, USA TUP208.

[3] A. Pikin, et al., “Structure and Design of the Electron Lens for RHIC”, PAC’11, New York, USA THP100.

[4] X. Gu, et al., “The Effects of The RHIC e-lenses Magnetic Structure Layout on The Proton Beam Trajectory”, PAC’11, New York, USA TUP207.

[5] J.G. Alessi, et al., “Progress on Test EBIS and the Design of an EBIS-based RHIC Preinjector”, PAC’05, Knoxville, Tennessee, P363.

[6] Y. Luo, et al., “6-D weak-strong simulation of head-on beam-beam compensation in the Relativistic Heavy Ion Collider”. Phys. Rev. ST Accel. Beams 15, 051004 (2012).

[7] D. M. Gassner, et al., “RHIC Electron Lens Test Bench Diagnostics”. DIPAC’11, Hamburg, Germany, MOPD04.

Copyright © 2013 CC-BY-3.0 and by the respective authors

SINGLE PASS ELECTRON COOLING SIMULATIONS FOR MEIC*

G. I. Bell†, I. V. Pogorelov and B. T. Schwartz, Tech-X Corp, Boulder, CO, 80303, USA
Yuhong Zhang and He Zhang, Jefferson Lab, Newport News, VA, 23606, USA

Abstract

Cooling of medium energy protons is critical for the proposed Jefferson Lab Medium Energy Ion Collider (MEIC). We present simulations of electron cooling of protons up to 60 GeV. In the beam frame in which the proton and electrons are co-propagating, their motion is non-relativistic. We use a binary collision model which treats the cooling process as the sum of a large number of two-body collisions which are calculated exactly. This model can treat even very close collisions between an electron and ion with high accuracy. We also calculate dynamical friction using a δf PIC model. The parallel code VSim (formerly Vorpal) is used to perform the simulations. We compare the friction rates with that obtained by a 3D integral over electron velocities which is used by BETACOOL.

ELECTRON COOLING

In the simplest form of electron cooling [1], an electron beam is created with the same γ as a relativistic ion beam which we wish to cool. The two beams are then made to co-propagate over a section of a storage ring, the **cooling section**. In the **beam frame** traveling with the average velocity of the particles, their velocities are non-relativistic, and the particles interact by means of Coulomb collisions.

This paper explores the amount of dynamical friction which can be obtained in an (unmagnetized) cooling section of the Jefferson Lab Medium Energy Ion Collider. The particles to be cooled are protons with $\gamma = 65.4$. The cooling section is $s = 60$ m long. These simulations are done in 3D, where x and y are transverse coordinates and z is the direction of beam propagation.

The bunched electron beam is non-uniform, but suppose we consider a small region only a few Debye lengths wide in the center of the electron bunch. In this region, the electron density is nearly constant. We consider a distribution of electrons which is uniform in space and has a Maxwellian distribution in velocity

$$f_0(\vec{v}) = \frac{n_e}{(2\pi)^{3/2}\sigma_x\sigma_y\sigma_z}\exp\left[-\frac{v_x^2}{2\sigma_x^2}-\frac{v_y^2}{2\sigma_y^2}-\frac{v_z^2}{2\sigma_z^2}\right], \quad (1)$$

where n_e is the density in the center of the electron bunch. In the beam frame the RMS velocities $\vec{\sigma}$ are non-relativistic, specific values are given in Table 1. Note that

Table 1: Electron Beam Parameters Used in the Simulations, all Parameters are in the Beam Frame

parameter	symbol	value	unit
electrons per bunch		2.5	10^9 elec.
peak density	n_e	1.32	$10^{15}e/m^3$
plasma freq.	ω_p	3.26	10^8/sec
plasma per.		3.07	nanosec
interaction time	τ	3.06	nanosec
trans. RMS bunch size	r_x	303	μm
long. RMS bunch size	r_z	1.3	m
trans. RMS velocity	σ_x	2.35	10^5 m/sec
long. RMS velocity	σ_z	0.36	10^5 m/sec
trans. Debye length	λ_x	114	μm
long. Debye length	λ_z	17.5	μm

z is the direction of beam propagation, and because this is an accelerated beam it is not isotropic, and $\sigma_z < \sigma_x = \sigma_y$.

Consider now a single ion moving at velocity $\vec{v}_{ion}$, and let $\vec{v}_{\rm rel} = \vec{v}_{ion} - \vec{v}$ be the velocity of each electron relative to the ion. Assuming each collision is symmetric in time, the dynamical friction force on the ion can be calculated by the 3D integral over the electron velocity space [2]

$$\vec{F}_{\|} = -\frac{n_e Z^2 e^4}{4\pi\epsilon_0^2 m_e}\int_{-\infty}^{\infty}\Lambda\,\frac{\vec{v}_{\rm rel}}{|\vec{v}_{\rm rel}|^3}f_0(\vec{v})\,d^3\vec{v}. \quad (2)$$

Here Z is the ion charge number (for protons, $Z = 1$), $e < 0$ is the electron charge, and m_e is the electron mass. In the simplest case, the Coulomb logarithm

$$\Lambda = \log(\rho_{max}/\rho_\perp), \quad (3)$$

where ρ_{max} and $\rho_\perp$ are often called "the maximum and minimum impact parameters". This terminology is unfortunate, because equation (2) actually includes contributions from collisions with arbitrarily small impact parameters [2]. $\rho_\perp$ is the impact parameter for 90 degree scattering

$$\rho_\perp(\vec{v}_{\rm rel}) = \frac{Ze^2}{4\pi\epsilon_0 m_e|\vec{v}_{\rm rel}|^2}. \quad (4)$$

In the actual beam, collisions with arbitrarily small impact parameters can occur. In simulations, the problem is that very small impact collisions are rare, and there may not be enough of them to accumulate good statistics. Therefore, in simulations it is advantageous to introduce a cutoff

* This work is supported by the US DOE Office of Science, Office of Nuclear Physics, grant numbers DE-SC0009508 and DE-SC0000835; resources of NERSC were used under contract No. DE-AC02-05CH11231.
† gibell@txcorp.com

Copyright © 2013 CC-BY-3.0 and by the respective authors

ρ_c, and to ignore collisions with impact parameter less than ρ_c. A modified Coulomb logarithm for equation (2), which can take into account ρ_c as well as the finite interaction time is given by [2]

$$\Lambda = \frac{1}{2}\log\left[\left(\frac{\rho_{max}^2+\rho_\perp^2}{\rho_\perp^2+\rho_c^2}\right)\left(\frac{\rho_c^2+d^2}{\rho_{max}^2+d^2}\right)\right], \quad (5)$$

where $d = |\vec{v}_{\rm rel}|\tau/2$ and $\tau = s/(\gamma\beta c)$ is the interaction time in the beam frame. Note that the Coulomb logarithm (5) reduces to (3) in the case where $\rho_c = 0$ and $d \gg \rho_{max} \gg \rho_\perp$.

In general, the Coulomb logarithm Λ is different for each electron because of the dependence of $\rho_\perp$ and d on $\vec{v}_{\rm rel}$. We cannot hope to calculate the integral (2) analytically, but it is easily calculated numerically because the velocity distribution $f_0(\vec{v})$ decays exponentially.

If $\omega_p = (n_e e^2/(m_e\epsilon_0))^{1/2}$ is the plasma frequency, then the Debye lengths in x, y and z, respectively, are $\lambda_x = \sigma_x/\omega_p$, $\lambda_y = \sigma_y/\omega_p$ and $\lambda_z = \sigma_z/\omega_p$. For this accelerated beam the longitudinal Debye length is considerably less than the transverse Debye length.

Over one passage through the cooling section, suppose we need to accumulate more than N_c collisions of impact parameter less than ρ_c in order to get good statistics on these collisions. In [2] it is shown that for the isotropic case, N_c and ρ_c are related by the formula

$$\rho_c = \sqrt{\frac{N_c}{\langle|\vec{v}_{\rm rel}|\rangle\tau\pi n_e}}, \quad (6)$$

where $\langle|\vec{v}_{\rm rel}|\rangle$ is the average magnitude of the relative velocity over all electrons. This equation can be used in the numerical models to set the cutoff impact parameter ρ_c.

To estimate the dynamical friction in the actual beam, we numerically evaluate the friction (2) using the Coulomb logarithm (5) with $\rho_c = 0$ and $\rho_{max} = 3r_x$, where r_x is the transverse RMS bunch size. Figure 1 shows the friction force in eV/m obtained for protons moving at various velocities. If the electron velocity distribution were isotropic, Figure 1 would be radially symmetric in $|\vec{v}_{ion}|$. Instead it shows enhanced friction longitudinally, and the maximum friction force of 0.659 eV/m occurs for a proton moving purely longitudinally with $v_z = 0.90 \times 10^5$ m/s.

SIMULATION MODELS

Electron cooling is an extremely weak effect, and difficult to capture numerically. The Debye shielding cloud around one proton has a magnitude on the order of the proton charge, $|e|$. Therefore, the perturbation in the electron bunch due to the presence of a single proton is nine orders of magnitude smaller than the charge of the electron bunch, $(2.5 \times 10^9)e$.

The first model we consider is the **binary collision** model [2]. The Coulomb collisions are modeled as an n-body problem, although we ignore electron-electron interactions. The interaction between each ion and electron is calculated exactly as a 2-body problem, with the contributions summed over all particles. This produces an n-body solver which can accurately model any 2-body collision with a constant time step [2]. To accurately model 3-body and higher collisions the time step must be decreased during these interactions, however these collisions are rare and do not contribute appreciably to dynamical friction.

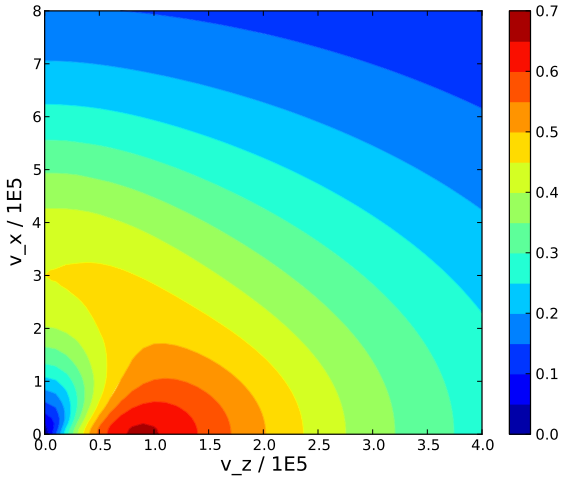


Figure 1: A contour plot of the friction force in eV/m as a function of the longitudinal and transverse ion velocity. This figure is only shown in one quadrant because it is symmetric in the other three.

In order to reduce the noise in these simulations, we add a positron over each electron with identical location and velocity. When an electron and positron interact with a proton, the diffusive velocity kicks cancel while the dynamical friction accumulates. Without this trick the dynamical friction would be dominated by particle noise.

Figures 2 and 3 show friction estimates from the binary collision model, the two figures are for purely longitudinal or transverse motion, the two axes of Figure 1. However, the theoretical curves are not the same as in Figure 1, because we have adjusted the theory to take into account the size of the numerical domain (L), and use a ρ_c corresponding to $N_c = 5$. The simulation domain is a cube $L = 800$ µm on a side, and in [2] it is shown that we should use $\rho_{max} = \min\{3r_x, 0.43L\}$ and $d = \min\{|\vec{v}_{\rm rel}|\tau/2, 0.43L\}$. These modifications of the Coulomb logarithm (5) reduce the friction by about 30% compared with the values in Figure 1. The theoretical friction values compare well with those predicted by the binary collision model. The error bars are derived by comparing friction rates for multiple ions. In the transverse case (figure 3) the errors can be large, probably because the electrons are hotter transversely ($\sigma_x > \sigma_z$).

The second model we consider is a **linear δf PIC model** [3–5]. We consider the shielding to be a perturbation from the equilibrium Vlasov-Poisson equation. The perturbation is modeled using weighted particles, where the particle weight represents the perturbation and all weights start at zero. The δf particles move in response to background

Copyright © 2013 CC-BY-3.0 and by the respective authors

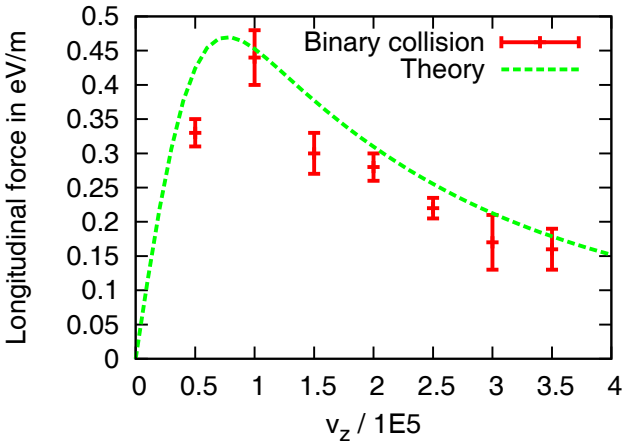


Figure 2: Theoretical longitudinal friction, eq. (2) versus that obtained from the binary collision model.

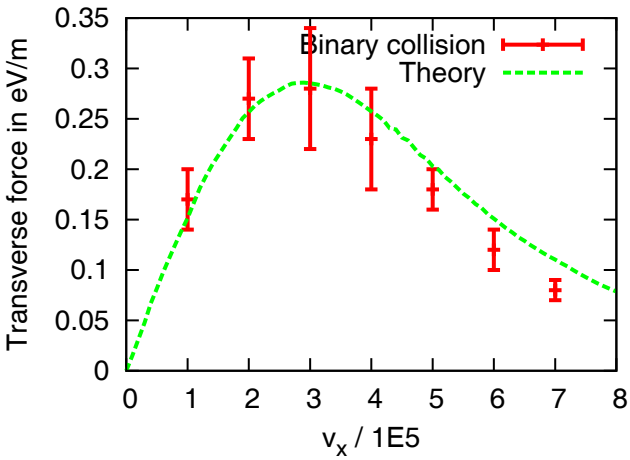


Figure 3: Theoretical transverse friction versus that obtained from the binary collision model.

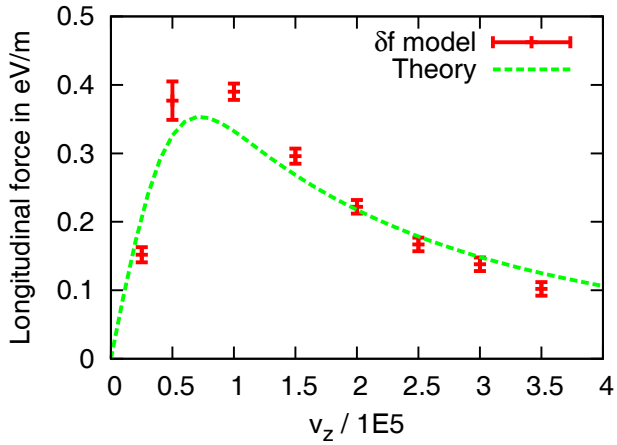


Figure 4: Theoretical longitudinal friction, eq. (2) versus that obtained from the δf model.

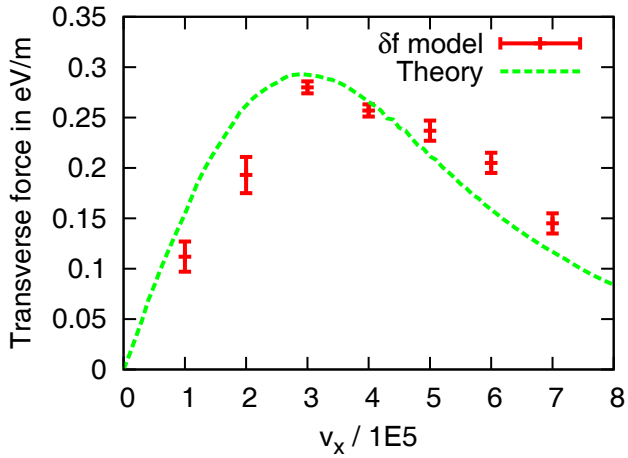


Figure 5: Theoretical transverse friction versus that obtained from the δf model.

fields, and their weights evolve to capture the shielding. The ions move in the electric field of the δf particles using the Boris push [6]. In all cases, the average force on each ion is calculated from the velocity change of the ion over the run. We note that a force of 0.5 eV/m results in a proton velocity change of 0.15 m/s over the cooling section, or about 1 part in 10^6 of the proton beam frame velocity.

Figures 4 and 5 show dynamical friction results for the δf model. The δf model uses a different domain size which is not cubical, therefore in the theoretical model we have inserted a different L. The error in the δf method is often very small, because different protons behave similarly. The δf method eliminates much of the particle noise present in the binary collision model.

SUMMARY

Theoretical estimates of dynamical friction (2) have been confirmed by two numerical simulations. The theoretical model includes effects from the finite interaction time τ, and also effects present in simulations such as finite domain size L and a lower cutoff in impact parameter, ρ_c. The numerical simulations agree well with the theoretical model when we insert appropriate values of these parameters.

REFERENCES

[1] G.I. Budker, Atomic Energy 22 (1967), p. 346.

[2] G.I. Bell et. al., J. Comput. Phys., 227, 87148735 (2008).

[3] N. Xiang, J.T. Cary, D.C. Barnes, Phys. Plasmas **13** 062111 (2006).

[4] G.I. Bell et. al., PAC 2011 Proceedings, MOP067.

[5] G.I. Bell et. al., "Modulator simulations for coherent electron cooling using a variable density electron beam", submitted to Phys. Rev. ST Accel. Beams, 2013

[6] J. Boris, in Proc. Fourth Conf. Num. Sim. Plasmas, eds. Boris and Shanny (NRL, 1970), p. 367.

Copyright © 2013 CC-BY-3.0 and by the respective authors

MEIC ELECTRON COOLING SIMULATION USING BETACOOL*

He Zhang†, Yuhong Zhang, Jefferson Lab, Newport News, VA 23606, USA

Abstract

Electron cooling of ion beams is one critical R&D issue in Jefferson Lab's medium energy electron-ion collider (MEIC). In the present MEIC design concept, a multi-phase cooling scheme is adopted. In the ion pre-booster, a DC electron cooler is responsible for assisting ion beam accumulation and initial cooling. In the ion collider ring, the ion beams with energies up to 100 GeV/u are cooled by a high current bunched electron beam driven by an energy-recovery SRF linac assisted by a circulator ring. It is essential to understand how efficient that electron cooling is, particularly in the high energy range, and how the cooling electron bunches in the circulator cooler ring are affected by the cooling process and other collective beam effects, in order to confirm the feasibility of the design. Here we present first results of the simulation studies of electron cooling processes of MEIC using BETACOOL code.

INTRODUCTION

The MEIC is designed to deliver a peak luminosity above 10^{34} $\mathrm{cm}^{-2}\mathrm{s}^{-1}$ and covers a CM energy range up to 65 GeV. It offers an electron energy up to 12 GeV, a proton energy up to 100 GeV, and corresponding energies per nucleon for heavy ions with the same magnetic rigidity [1]. The MEIC ion complex consists of ion sources, a linac, two boosters and a medium energy collider ring, as shown in Fig. 1. The conventional electron cooling is chosen to assist cumulation of ions from the linac and to reduce and preserve the emittance of the MEIC ion beam. We propose to have electron coolers installed both in the pre-booster and in the collider ring, and our multi-phase electron cooling scheme includes the following steps: (1) low energy (up to 2 MeV) DC cooling at the pre-booster, (2) bunched electron cooling at the ion injection energy (up to 20 GeV/u) of the collider ring, and (3) bunched cooling at the top ion energy (100 GeV/u) of the collider ring. An important feature of this scheme is continuous electron cooling of the ion beams during their collision with the electron beam.

While the electron cooling mechanism is well developed and successfully tested with low energy DC beam applications world wide, we are challenged by the high density and high energy of the MEIC ion beam [2, 3]. The present design concept calls for an ERL for the high energy cooler in the collider ring for meeting the request of a very high RF power and additionally a circulator ring for mitigating the electron gun life time challenge [1]. There are a number of critical R&Ds for this design concept, for example, (1) what is the cooling efficiency at the high energy range with a bunched electron beam; (2) how the cooling electron bunches in the circulator cooler ring are affected by the cooling process and other collective beam effects; and further (3) how the cooling efficiency is affected by the continually (slow) degradation of the cooling bunches during circulation of the cooling. In the report, we present our initial results for the simulation studies of the first issue listed above. For simplicity, the coupling to the electron beam dynamics in the circulator cooler ring is ignored. The latter is currently also under studied [4]. In other words, the cooling electron bunches in the simulations are assumed ideal, fresh from the electron source, for each cooling, instead of being a real beam circulating in the cooler ring. At a later time, these two studies will be combined as we expect.

Table 1: Key Parameters for Different Cooling Schemes

		Pre-Booster	Collider Ring
p^+ Energy	GeV	3	20/100
p^+ Bunch Length	cm	Coasting	Coasting/1
Cooler Type		DC	ERL circulator
Magnetization	T	1	0
Cooler Length	m	10	2×30
e^- Beam Current	A	3	1.5
e^- Bunch Length	cm		1.2
Cooling Scheme 1		✓	
Cooling Scheme 2			✓
Cooling Scheme 3		✓	✓

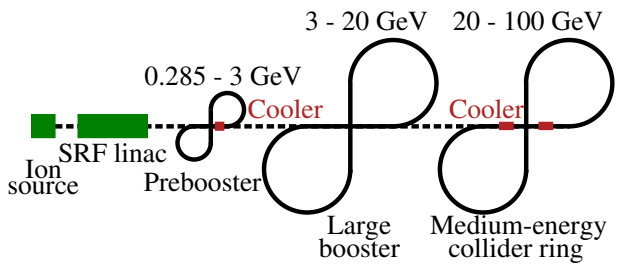


Figure 1: Components of MEIC ion complex

MODELS AND METHODS

Ideally a start-to-end simulation should be carried out for the entire process of MEIC ion beam formation and cooling, nevertheless, presently there is no such a code capa-

* Work supported by the U.S. Department of Energy, Office of Nuclear Physics, under Contract No. DE-AC05-06OR23177 and No. DE-AC02-06CH11357.

† hezhang@jlab.org

Copyright © 2013 CC-BY-3.0 and by the respective authors

ble of taking such a task. Therefore, we simulate various physics processes independently.

To explore the capability and limitations of both the low energy DC cooler and high energy ERL cooler, we have performed simulations for the following three hypothetical cooling schemes: (1) only the DC cooler in the pre-booster, (2) only the ERL circulator cooler in the collider ring, and (3) using both the DC cooler in the pre-booster and the ERL circulator cooler in the collider ring. It is expected that such simulations will shed the lights of the nominal MEIC cooling design scheme.

The highest kinetic energy of protons in the pre-booster is 3 GeV, the corresponding energy of the cooling electron energy is about 2 MeV. Space charge effect of the DC electron beam is included. In the collider ring, a Gaussian bunched electron beam of 1.5 A is used to cool a coasting (very long bunch) proton beam at the injection energy (20 GeV), and the same electron beam is used to cool a Gaussian bunched proton beam at the collision energy (60 GeV for the nominal design point). The beam and cooler parameters for the different cooling schemes are presented in Table 1.

We utilized the well developed BETACOOL code, which provides various formulas for the intra-beam scatterings (IBS) effect and cooling force calculation, along with various models for dynamic simulations [5]. As to the following results, Martini model [6] is used for IBS effect calculation, the model beam method is for DC cooling simulation and the RMS dynamic method with single particle model is for bunched electron beam cooling simulation [5].

SIMULATION RESULTS

Cooling in Pre-booster Only

In the pre-booster, the initial normalized emittance of the proton beam is assumed to be 3.15 $\pi \cdot \mathrm{mm} \cdot \mathrm{mrad}$ in both transverse directions, which is limited by the space charge tune shift. The momentum spread dp/p is assumed to be 0.001. The radius of the electron beam is 0.832 cm, which is three times of the rms radius of the proton beam. The current of the electron beam is 3A. Fig. 2(a) shows the evolvement of the normalized emittance and the momentum spread of the proton beam during the cooling process. After about 600 s, the transverse emittance of the proton beam reaches the equilibrium at about (0.6, 0.2) $\pi \cdot \mathrm{mm} \cdot \mathrm{mrad}$. Because we need to stack five injections in the collider ring, 600 s is too long. We would like to stop cooling after 200 s, when the emittance was reduced to (1.18, 0.99) $\pi \cdot \mathrm{mm} \cdot \mathrm{mrad}$. After the pre-booster, we inject the proton beam into the large booster, accelerate it to 20 GeV, and then inject it to the collider ring. The first long bunch needs to wait 800 s for the following four bunches before we accelerate them together to 60 GeV. During this 800 s, the horizontal emittance of the proton bunch will increase up to 1.45 $\pi \cdot \mathrm{mm} \cdot \mathrm{mrad}$ due to the IBS effect, which is shown in Fig. 2(b). After being accelerated to 60 GeV, without cooling the horizontal emittance keeps increasing due to IBS effect. As Fig. 2(c) shows, after two hours the horizontal emittance will be about 3.8 $\pi \cdot \mathrm{mm} \cdot \mathrm{mrad}$. For both energy stages, the vertical emittance remains almost unchanged because the vertical IBS effect is much smaller than the horizontal one.

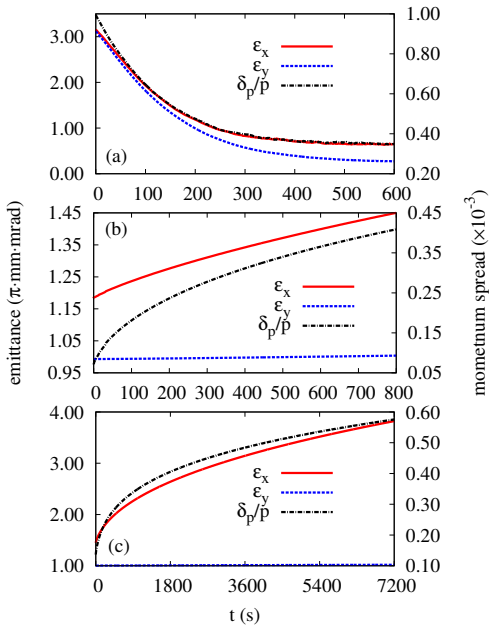


Figure 2: Cooling in the pre-booster (a) and IBS induced emittance and momentum spread expansion in the collider ring at 20 GeV (b) and 60 GeV (c).

Cooling in Collider Ring Only

Without cooling in the pre-booster, we assume the initial normalized emittance of the proton beam in the collider ring at 20 GeV to be 3.15 $\pi \cdot \mathrm{mm} \cdot \mathrm{mrad}$, limited by the space charge tune shift, and the momentum spread 3×10^{-3}. We will cool the coasting (very long bunch) proton beam at 20 GeV first, and then cool the bunched proton beam at 60 GeV. Cooling at 20 GeV turns out to be quite efficient as shown in Fig. 3(a). The emittance reaches the equilibrium within 250 s. When the proton beam is bunched at 60 GeV, its IBS effect is about two orders of magnitude higher in the horizontal direction than in the vertical direction, while the friction forces in both directions are roughly the same. Hence there is a tendency to over cool the beam in the vertical direction, which as a result of the over cooling makes the cooling in horizontal direction even more difficult. If the transverse motion of the proton beam is coupled, the emittance growth due to IBS effect will be redistributed in the two directions according to the coupling rate, which makes the cooling in the horizontal direction easier and also provides a way to control the transverse bunch sizes. Simulation results also support this hypothesis. If the emittance at 20 GeV is reduced to 0.30 $\pi \cdot \mathrm{mm} \cdot \mathrm{mrad}$, then at 60 GeV after the proton beam is bunched, the emittance can be further reduced to 0.17 $\pi \cdot \mathrm{mm} \cdot \mathrm{mrad}$ within 20 s with 100% coupling in trans-

Copyright © 2013 CC-BY-3.0 and by the respective authors

verse directions as shown in Fig. 3(b). Or the emittance can be reduced to (0.30,0.07) $\pi \cdot \mathrm{mm} \cdot \mathrm{mrad}$ with 40% transverse coupling as shown in Fig. 3(c), which provides a flat beam.

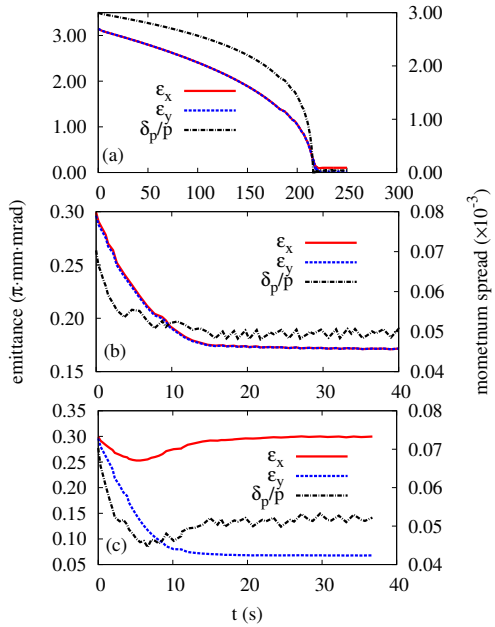


Figure 3: Cooling in the collider ring at 20 GeV (a) and at 60 GeV for 100% (b) and 40% (c) coupled p^+ beam.

Cooling in Pre-booster and Collider Ring

Now we consider both the DC cooling in the pre-booster and the ERL circulator Cooling in the collider ring. the DC cooling in the pre-booster is the same as shown in Fig. 2(a). Assuming the normalized emittance of the proton beam out of the pre-booster is (0.83,0.57) $\pi \cdot \mathrm{mm} \cdot \mathrm{mrad}$ and we start to cool from this emittance in the collider ring at 20 GeV, the evolvement of the emittance and momentum spread of the proton beam is shown in Fig. 4(a). Initially the longitudinal cooling is strong and the momentum spread reaches the lowest point within five seconds and then starts to increase again. When the emittance is reduced to about 0.3 $\pi \cdot \mathrm{mm} \cdot \mathrm{mrad}$, dp/p is in the order of 10^{-6} and it is increasing, according to Fig. 4(a), which means energy is transferring from the transverse directions to the longitudinal direction. If we stop cooling the coasting beam at this point, it is reasonable to assume dp/p will increase during the following accelerating and bunching process. In the following simulations for the cooling at 60 GeV, an initial dp/p of 3.7×10^{-4} is used. As Fig. 4(b) and Fig. 4(c) show, the emittance can be reduced to 0.23 $\pi \cdot \mathrm{mm} \cdot \mathrm{mrad}$ within 20 s when fully coupled in the transverse directions or (0.31,0.18) $\pi \cdot \mathrm{mm} \cdot \mathrm{mrad}$ within 30s when 50% coupled.

SUMMARY AND DISCUSSION

Preliminary simulation results suggest the design parameters of MEIC cooling system are achievable. We did simi-

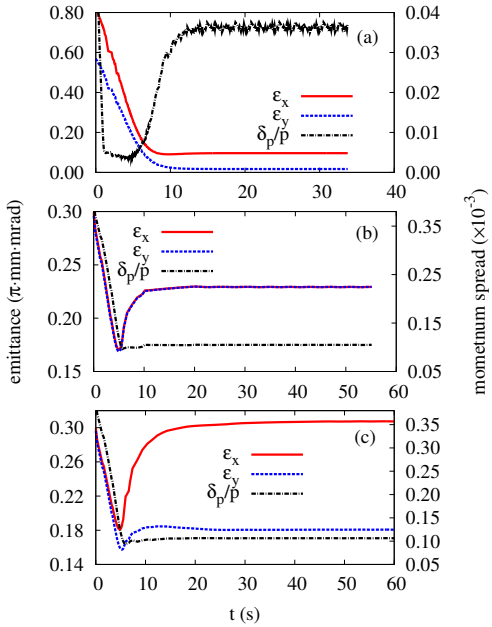


Figure 4: Cooling in the collider ring at 20 GeV (a) and at 60 GeV for 100% (b) and 50% (c) coupled p^+ beam.

lar simulations for heavy ions, the cooling of which turned out easier than that of protons. There are some points we want to note as follows. Transverse coupling is helpful for the cooling in the collider ring, but its dynamic effect needs to be studied. In the above simulations, we assume the ion beams always have Gaussian distributions. However, this is not necessarily true. We need to study how the ion beam distribution evolves in different cooling processes and how much it affects the results if the distribution deviates from Gaussian. Analytical formulas are used to calculate the friction force, and their accuracy under the MEIC parameters need to be checked and confirmed. We plan to use the electron bunches multiple times in cooling, so it is crucial to understand how the electron bunches are affected by the proton bunches, which is currently out of the ability of BETACOOL. New method, such as N-particle simulations, may need to be developed and applied.

ACKNOWLEDGMENT

The authors want to say thanks to Ya Derbenev and V. Morozov at JLab, A. Fedotov at BNL, L. Mao at IMP in China, and A. Smirnov at JINR in Russia for beneficial discussions.

REFERENCES

[1] MEIC Design Report, ed. by Y. Zhang, etc., 2012

[2] Ya. Derbenev, NIM A, vol. 532, p.307, 2012

[3] Ya. Derbenev and Y. Zhang, Proc. of COOL09,2009

[4] Private communication with E. Nissen

[5] I. Meshkov, et al., BETACOOL Physics Guide, 2007

[6] M. Martini, CERN PS/84-9 AA, 1984

Copyright © 2013 CC-BY-3.0 and by the respective authors

STATUS AND FUTURE PLAN OF THE DEVELOPMENT OF A COMPACT X-RAY SOURCE BASED ON ICS AT LASER UNDULATOR COMPACT X-RAY (LUCX)*

M. Fukuda#, S. Araki, A. Aryshev, Y. Honda, N. Terunuma, J. Urakawa, KEK, Ibaraki, Japan
K. Sakaue, M. Washio, RISE, Tokyo, Japan

Abstract

We have developed a compact X-ray source via inverse Compton scattering (ICS) between multi-bunch electron beam and a laser pulse stacked in an optical cavity at Laser Undulator Compact X-ray (LUCX) accelerator in KEK. Since the autumn of 2011, we have begun X-ray imaging test. In the beginning, it had taken two hours to get an X-ray image because of low intensity of X-ray with 10^4 photons/pulse. To get a clear X-ray image in a shorter period of times, we have upgraded the accelerator, which consists of a 3.6 cell photo-cathode rf-gun, a 12cell standing wave accelerating structure and a 4-mirror planar optical cavity. The target intensity of an electron beam is 500nC/pulse with 1000 bunches at 30 MeV. The one of laser pulse is also 6mJ/pulse. The expected number of X-ray is $1.7\text{x}10^7$ photons/pulse with 10% bandwidth. We have already started the multi-bunch beam generation and X-ray imaging test after upgrade. The accelerator produces 26.8 MeV beam with the total charge of 380nC in 300 bunches per pulse. The aging process is also continued to increase energy and intensity. We will report the results of the beam test and future plan of the development of a compact X-ray source at LUCX.

INTRODUCTION

X-rays have various fields of application, such as medial application, biological science, material science etc. Synchrotron radiation produced by GeV order storage ring is commonly used for high brightness X-ray source. However the device is generally huge and expensive. On the other hand, the X-ray source based on ICS is compact and inexpensive because this method can decrease this energy of an electron beam by more than an order of magnitude when producing X-rays with the same energy.

We have constructed the LUCX accelerator at KEK in order to develop the compact X-ray source based on ICS. Since the autumn of 2011, we have begun X-ray imaging test and succeeded to take the X-ray image of fish bone[1]. However, it took two hours to get the image due to low intensity of X-ray with 10^4 photons/pulse.

We have upgraded this accelerator in order to increase the intensity of X-rays in last year. The 3.6cell rf-gun, 12cell booster and 4mirror cavity have been designed and constructed for this upgrade. The X-ray generation and the X-ray imaging are already started after upgrade[2]. We will report the current status and future plan of the X-ray experiment in the accelerator.

*Work supported by the Quantum Beam Technology Program and Photon and Quantum Basic Research Coordinated Development Program of MEXT.
#mfukuda@post.kek.jp

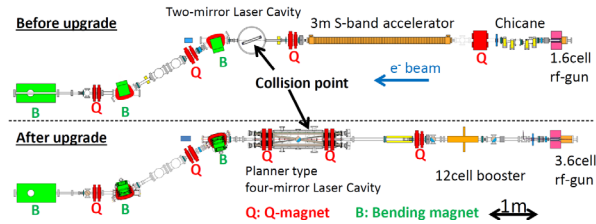


Figure 1: The beamline of the LUCX accelerator before/after upgrade.

LUCX ACCELERATOR

The upgraded beamline is shown in Fig. 1. A 3.6cell photo-cathode rf-gun generates an electron beam with the energy of 10MeV and then the beam is accelerated to 30MeV by a 12cell booster. After that, the beam is collided with a laser pulse in a 4-mirror planar optical cavity and then X-rays are generated by ICS. The X-rays are extracted into the atmosphere through a Be window with the thickness of 300μm. The electron beam is separated from the X-ray by a bending magnet and then is dumped to the beam dump.

3.6Cell Photo-Cathode Rf-Gun

An S-band 3.6cell rf-gun[3] has been installed instead of 1.6cell rf-gun to increase the beam energy. The cut view and the picture of the rf-gun is shown in Fig. 2. The cavity structure consists of smooth curves to increase the Q-value of the cavity and to reduce dark current from the surface. Cesium telluride (Cs_2Te) film is evaporated on the surface of the Mo cathode plug which is attached in the cavity by the load-lock system. An electron beam is emitted from the cathode by irradiating 266nm UV laser light. The beam is accelerated to 10MeV.

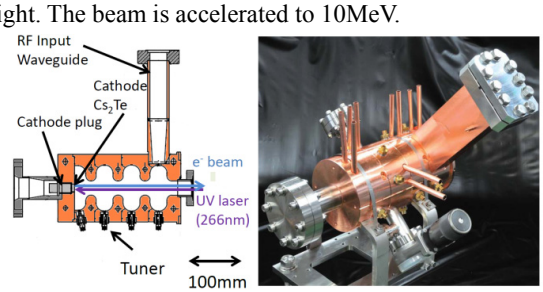


Figure 2: The cut view and the picture of 3.6cell rf-gun.

The cavity of the 3.6cell rf-gun has four resonance modes. Therefore the surface of the iris in the cavity has

Copyright © 2013 CC-BY-3.0 and by the respective authors

reduced 3mm rather than former in order to expand the mode separation. The separation between 2/3π mode and π mode is 2.8MHz. The size of rf input port is also enlarged to adjust the coupling β to close to 1. Table 1 shows the parameter of the rf-gun.

12Cell Booster

A 12cell booster[3], which is standing wave accelerating tube, has been installed instead of an S-band travelling wave accelerating tube in order to downsize the accelerator section. The length has been shortened from 5.7 to 2.5m. An electron beam is accelerated to from 10MeV to 30MeV here.

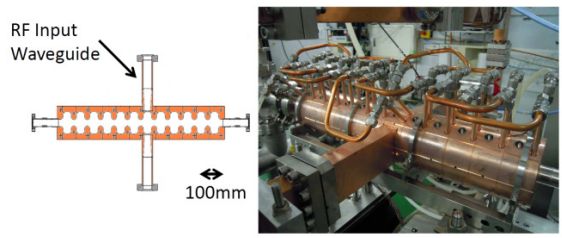


Figure 3: The cut view and the picture of the 12cell booster.

Figure 3 shows the cut view and the picture of the 12cell booster. The structure of the cavity is almost the same as that of the rf-gun. However, the accelerator has twelve resonant modes. Therefore the surface of the iris in the cavity has further reduced compared with that of the rf-gun to extend the mode separation. The separation between 10/11π mode and π mode is 1MHz. In addition, rf power is input through two input ports to obtain symmetrical electric field in a coupling cavity. The parameter of the 12cell booster is shown in Table 1.

Table 1: Parameters of the Rf-Gun and the Booster

	3.6cell rf-gun	12cell booster
Frequency(π-mode)	2856MHz	2856MHz
Q-value	15000	17800
Coupling β	0.99	1.1
R/Q	395Ω	420Ω
Mode separation	2.8MHz(π-2/3π)	1MHz(π-10/11π)

4-Mirror Planar Optical Cavity

A four-mirror planar optical cavity[2] is a four-mirror bow-tie ring resonator. The drawing is illustrated in Fig. 4. The cavity enhances the laser power and makes small laser size at the collision point. The spacing of laser pulses is equal to that of electron bunches. Therefore the laser pulses can collide with all bunches of multi-bunch electron beam.

To increase the luminosity of ICS by enhancing the stored power in the cavity and by bringing close to head-on collision, the 4mirror cavity is installed. The distance of the concave mirrors is made longer than former 2-mirror cavity to enhance the stored power and the laser size on the mirror is enlarged because the stored power is limited by the damage threshold of the mirrors. Moreover, the collision angle of an electron beam and a laser pulse is reduced to 7.5deg. The parameters are shown in Table 2.

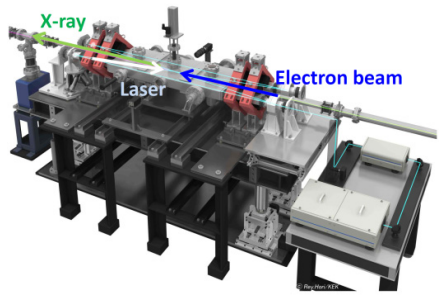


Figure 4: Drawing of the 4-mirror planar optical cavity.

Laser Master System

The length of 4-mirror cavity must be held in the accuracy less than angstrom to keep resonance. It is very difficult to also synchronize to the accelerator simultaneously with this. Therefore the master signal is generated from the signal of laser pulses injected to the cavity. That is to say the accelerator devices such as klystrons synchronize with the cavity and the rf frequency is determined by the length of the cavity. We call this method the laser master system, whose diagram is shown in Fig. 5. By using this method, the 4-mirror cavity should just maintain resonance and the stability has improved very much.

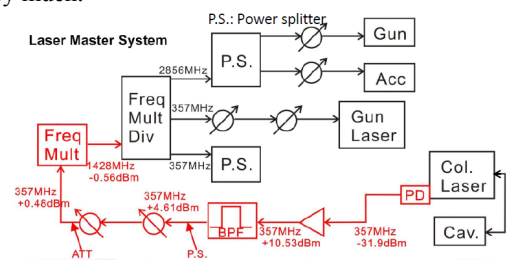


Figure 5: Diagram of the laser master system.

MULTI-BUNCH BEAM GENERATION

We have successfully generated the 300 bunches beam with 26.8 MeV and 380nC total charge now. The 3.6cell rf-gun produces 8.1MeV electron beam and the 12cell booster accelerates up to 26.8MeV.

The beam loading compensation is important issue when accelerating a multi-bunch beam. The loading effect is compensated by injecting the beam in the timing of the transition region when rf power is filled[4]. The compensation optimized by adjusting the timing between an electron beam and a rf pulse. In this upgrade, the accelerating tube is changed into the standing wave type cavity which has with the same Q-value as the rf-gun. This makes the compensation easy because these timings for the compensation become also almost same. Figure 6

Copyright © 2013 CC-BY-3.0 and by the respective authors

shows the measured energy of multi-bunch beam. The energy difference is within 1.2% (peak to peak). The energy spread(rms) of each bunch is also 0.1%.

Figure 7 shows the emittance when changing the solenoid field with the bunch charge of 1.25nC/bunch. The emittance at the solenoid current of 116A is about 5π mm mrad. The beam size at the collision point is also 80μm x 50μm.

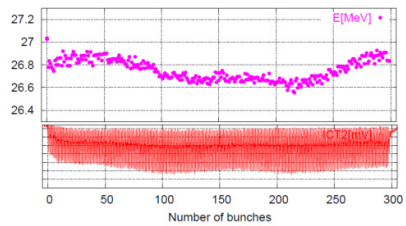


Figure 6: These graphs show the energy of multi-bunch beam and the current transformer waveform.

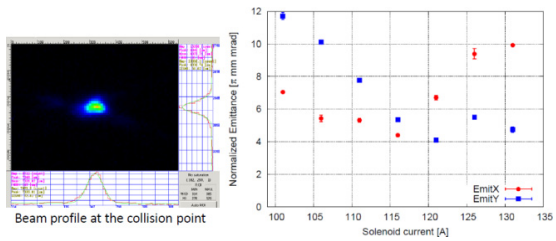


Figure 7: The left picture is the beam profile at the collision point. The right graph shows the result of emittance measurement.

X-RAY IMAGNING TEST

We already start to generate ICS X-rays and to take X-ray images after upgrade. A Micro-Channel Plate (MCP) and a Silicon-On-Insulator (SOI) pixel sensor[5] are used as X-ray detector. The MCP is utilized for measuring the intensity of X-rays. The SOI sensor can take the X-ray image with high spatial resolution because the SOI sensor has very small pixel size of 17μm. The sensor can also obtain the X-ray signal with high signal to noise ratio because the sensor can distinguish an X-ray and a high energy particle by measuring the deposit energy at each pixel or by checking whether the signal is detected along several pixel.

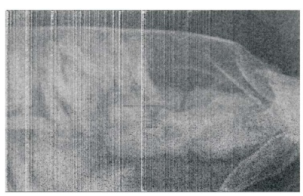


Figure 8: Captured image of chilli pepper by SOI sensor.

We have succeeded to obtain very clear image by the SOI sensor. Figure 8 shows the X-ray image of Chilli pepper[2]. The number of X-rays injected to SOI sensor is 5460 photons/pulse with the energy of 9keV. The number of total band is 5.1×10^5 photons/pulse. The total irradiated number of X-rays to the SOI sensor is 6.7×10^7 photons.

We are trying to increase the intensity of ICS X-ray by increasing the number of electron bunch and the intensity of a laser pulse after X-ray imaging test. Current number of X-rays in total band is 1.4×10^6 photons/train. It is about three times at the time of X-ray imaging test.

SUMMARY AND FUTURE PLAN

We have upgraded the LUCX accelerator and the laser cavity to increase the intensity of X-rays, which increased by about 10 times as compared with upgrade before. The clear image can also be obtained by the SOI pixel sensor.

Table 2 and 3 show the present and target parameters of an electron beam and a laser pulse respectively. The target intensity of X-rays is 1.7×10^7 photons/pulse 10%b.w. at the energy of 15keV in this upgrade. To achieve it, more number of electron bunch and higher energy electron beam is needed as the accelerator side. The target number of electron bunch is 1000bunches/pulse with 30MeV. Therefore we continue the rf processing of 3.6cell rf-gun and 12cell accelerating tube to expand the rf pulse width and to increase rf power. We will try X-ray phase imaging with Talbot-Lau interferometer if we could obtain the higher intensity of X-rays from now.

Table 2: Present and Target Parameters of Electron Beam

	Present	Target
Energy	26.8MeV	30MeV
Intensity	1.25nC/bunch	0.5nC/bunch
Number of bunch	300	1000
Beam size (rms)	33μm x 33μm	80μm x 50μm
Pulse length	15ps	---

Table 3: Present and Target Parameters of Laser

	Present	Target
Wave length	1064nm	---
Pulse energy	0.4mJ/pulse	6mJ/pulse
Beam size (rms)	89μm x 85μm	50μm x 25μm
Pulse length	7ps	---
Collsion angle	7.5deg	---

REFERENCES

[1] K. Sakaue et al., AIP Conf. Proc., 1466 272-277 (2012).
[2] K. Sakaue et al., "Development of Laser-Compton X-Ray Source Using Optical Storage Cavity," IPAC'13, Shanghai, May 2013, WEPWA017, p. 2165 (2013); http://www.JACoW.org
[3] T. Aoki et al., "Development of an S-band Multi-cell Accelerating Cavity for RF Gun and Booster Linac," IPAC'11, San Sebastian, September 2011, MOPC020, p. 110 (2011); http://www.JACoW.org
[4] S. Liu et al., Nucl. Instrum. Meth., A584, 1-8 (2008).
[5] Y. Arai et al., Nucl. Instrum. Meth., A636(2011)S31-S36.

Copyright © 2013 CC-BY-3.0 and by the respective authors

HIGH-CHROMATICITY OPTICS FOR THE MAX IV 3 GeV STORAGE RING

T. Olsson, S.C. Leemann, MAX IV Laboratory, Lund University, SE-22100 Lund, Sweden

Abstract

The ultralow emittance lattice of the MAX IV 3 GeV storage ring has a large negative natural chromaticity. This has to be corrected to positive values to prevent head-tail instabilities. On the other hand, high linear chromaticity can lead to a large tune footprint which limits Touschek lifetime. Therefore, the linear chromaticity is corrected to +1 in both planes with sextupoles while octupoles are used to further reduce the tune footprint. Studies indicate this design leads to threshold currents for resistive wall and transverse mode coupling instabilities beyond what is expected during regular user operation. However, since these are only preliminary studies based on approximations, the possibility of instability issues during commissioning needs to be considered. A short term solution is to operate the storage ring at a higher chromaticity. This paper describes the developed high-chromaticity optics for the MAX IV 3 GeV storage ring. It focuses on reduction of chromatic and amplitude-dependent tune shifts to maximize dynamic aperture and Touschek lifetime. A comparison between the performance of the new high-chromaticity optics and the design optics is also presented.

INTRODUCTION

The MAX IV facility is a 3rd generation state-of-the-art synchrotron light source currently under construction in Lund, Sweden [1]. The MAX IV 3 GeV storage ring has an ultralow emittance lattice with a large negative natural chromaticity in both planes [2]. To avoid head-tail instabilities, the linear chromaticity has to be corrected to positive values. On the other hand, a large linear chromaticity can lead to proximity to, or crossing of, potentially dangerous resonances, which can limit dynamic aperture and Touschek lifetime. To satisfy both constraints, the linear chromaticity in the design optics of the MAX IV 3 GeV storage ring has been corrected to +1 in both planes [2]. Initial instability studies indicate this design leads to threshold currents for resisitive wall instability and transverse mode coupling instability beyond what is expected during user operation [3]. However, since these are only preliminary studies based on initial estimates of the impedance budget the possibility of instability issues occurring during commissioning needs to be considered. The instability studies indicate that the threshold currents increase with chromaticity. A short term solution is therefore to operate the storage ring at a higher chromaticity. An alternate optics for the MAX IV 3 GeV storage ring with linear chromaticity +4 in both planes has therefore been developed [4]. This paper presents the performance of the newly developed high-chromaticity optics in comparison to the design optics. The challenges to achieve a high-chromaticity optics with sufficient performance are also described.

NONLINEAR OPTICS OPTIMIZATION

The MAX IV 3 GeV storage ring make use of strong sextupoles to correct the linear chromaticity, minimize chromatic tune shifts and tailor the chromatic tune footprint while minimizing first-order resonance driving terms. Octupoles are employed to minimize the amplitude-dependent tune shifts and further tailor the tune footprint. This approach is detailed in [5]. The same approach was used during the development of a high-chromaticity optics.

OPA [6] was used to correct the linear chromaticity to +4 in both planes using the two strongest chromatic sextupoles. All five sextupole families were then adjusted to optimize the chromatic tune footprint while constraining the linear chromaticities to +4.

The chromatic tune shifts for the high-chromaticity optics are displayed in Fig. 1. For both planes, the resulting chromatic tune shifts for the high-chromaticity optics are not unexpectedly larger than the corresponding tune shifts for the design optics across the entire range of interest.

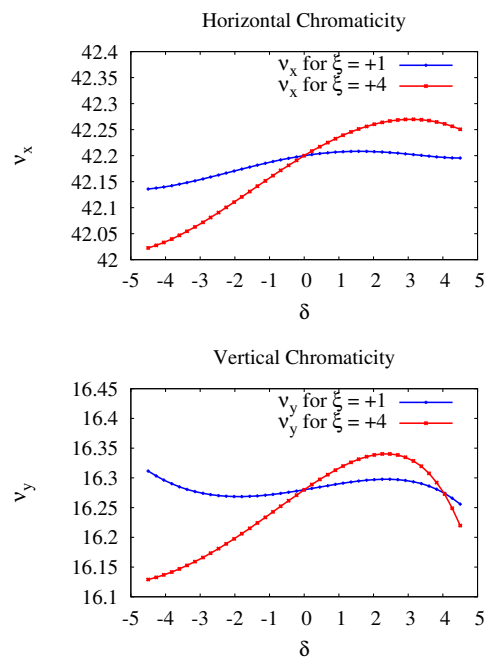


Figure 1: Chromatic tune shifts for the high-chromaticity optics calculated by TRACY-3 [7]. The chromatic tune shifts for the design optics are displayed for comparison.

Copyright © 2013 CC-BY-3.0 and by the respective authors

The chromatic tune footprint for the high-chromaticity optics is displayed in Fig. 2. The chromatic tune shifts were tailored with OPA to avoid the $\nu_x + 2\nu_y = 75$ resonance which is assumed to be potentially strongly driven. The resonances $\nu_x - \nu_y = 26$, $2\nu_x - \nu_y = 68$ and $3\nu_y = 49$ are all skew resonances. They were assumed to be weaker driven and less focus was put on avoiding them. The resulting chromatic tune footprint although not large, is not as compact as the chromatic tune footprint of the design optics detailed in [8].

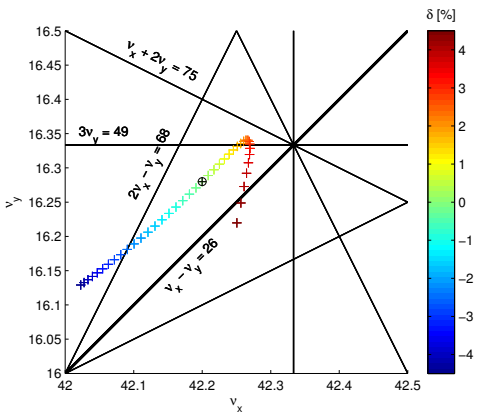


Figure 2: The chromatic tune footprint for the high-chromaticity optics calculated by OPA. Resonances up to third order are displayed.

The three families of octupoles were then used to tailor the amplitude-dependent tune shifts. The resulting amplitude-dependent tune shifts for the high-chromaticity optics are displayed in Fig. 3. It is evident that the amplitude-dependent tune shifts are larger for the high-chromaticity optics than for the design optics.

DYNAMIC APERTURE

The dynamic aperture for the high-chromaticity optics is displayed in Fig. 4. Comparison with the dynamic aperture for the design optics presented in [8] reveals that the dynamic aperture for the high-chromaticity optics is smaller. However, the required on-momentum dynamic aperture is achieved. The off-momentum dynamic aperture is smaller for $\delta = -4.5\%$ than for $\delta = +4.5\%$ which is a consequence of the chromatic tune shifts.

MOMENTUM ACCEPTANCE

The off-momentum diffusion map is displayed in Fig. 5. The momentum acceptance appears to be limited to within $\delta = -7\%$ and $\delta = +9\%$. Within the required momentum acceptance $\delta = \pm 4.5\%$ several areas with somewhat elevated diffusion and some bands and ring-shaped structures possibly indicating resonant behavior are visible. From frequency map analysis two resonances can be recognised, $4\nu_x = 169$ and $4\nu_y = 65$. These are both upright octupole resonances that are not expected to be driven strongly. For

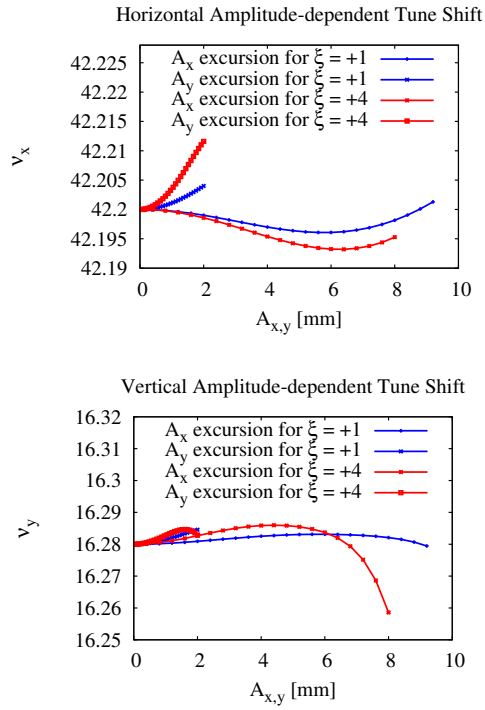


Figure 3: Amplitude-dependent tune shifts for the high-chromaticity optics calculated by TRACY-3. The amplitude-dependent tune shifts for the design optics are displayed for comparison.

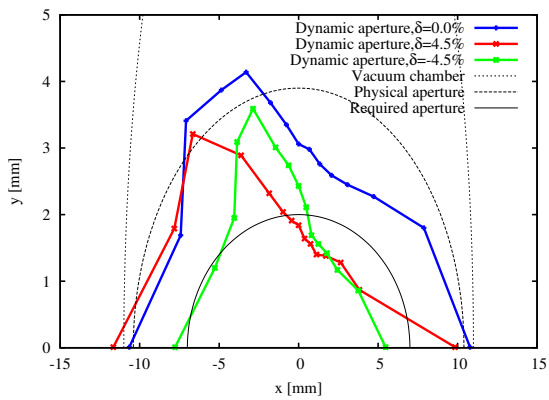


Figure 4: Dynamic aperture at the centre of the long straight sections for the high-chromaticity optics calculated by TRACY-3. The physical aperture originating from the vacuum chamber and the aperture required for injection and lifetime reasons are also shown.

$\delta < -5\%$ there appears to be an area with chaotic motion. Frequency map analysis indicates that this occurs close to the integer resonance.

TOUSCHEK LIFETIME

The Touschek lifetime of the high-chromaticity optics was determined by 6D tracking with TRACY-3 using actual

Copyright © 2013 CC-BY-3.0 and by the respective authors

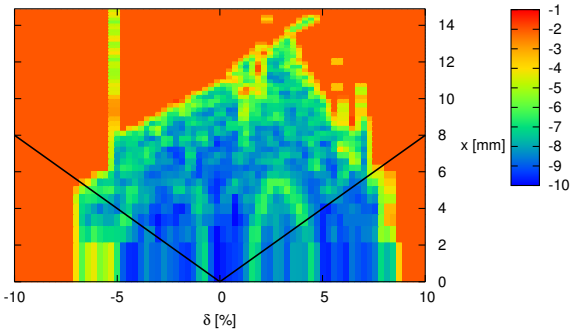


Figure 5: Diffusion map for off-momentum particles at the centre of the long straight sections for the high-chromaticity optics calculated by TRACY-3. Blue areas show low diffusion and red areas high diffusion. The vertical amplitude was set to +0.1 mm. The black line is an approximation of the maximum dispersive orbit.

vacuum chamber apertures. For the maximum stored beam current of 500 mA, vertical emittance 8 pm rad and maximum cavity voltage 1.8 MV, the Touschek lifetime was determined to be 8.98 hours. Neither the effects of IBS nor the Landau cavities present in the MAX IV 3 GeV lattice were included in this calculation. This is a reduction of roughly 5 hours compared to the corresponding Touschek lifetime of the design optics [8].

ERROR STUDIES

Initial error studies have been performed. These studies indicate that a lattice momentum acceptance of $\pm 4.5\%$ will not be achievable with the high-chromaticity optics, however an overall momentum acceptance of roughly $\pm 3.5\%$ is ensured. This will considerably reduce the Touschek lifetime. Initial estimates for the reduction of Touschek lifetime caused by magnet and alignment imperfections indicate that the Touschek lifetime could still be sufficient to allow the high-chromaticity optics to be used in the MAX IV 3 GeV storage ring as a short term solution should instability issues occur during commissioning. Further studies of the reduction of Touschek lifetime with errors need to be performed to fully validate this conclusion.

CHALLENGES FOR A HIGH-CHROMATICITY OPTICS

The correction of the linear chromaticity to +4 in both planes sets high demands on the nonlinear optics to achieve sufficiently large dynamic aperture to ensure an efficient injection process and sufficiently large Touschek lifetime. Since the linear chromaticity is set to +4 there is a need for strong sextupole magnets and skillful optimization of the chromatic tune footprint to accomplish small chromatic tune shifts which do not approach dangerous resonances. Because of the enlarged chromatic tune footprint caused by the increased linear chromaticity, the demand for small amplitude-dependent tune shifts is further increased.

The strong sextupole magnets and the need for small amplitude-dependent tune shifts call for strong octupole magnets. When the gradients of the octupole magnets are considerably enlarged they start to have a substantial effect on the chromatic tune shifts through higher order dispersion. Therefore, the chromatic tune shifts and the amplitude-dependent tune shifts have to be optimized with regard to each other. This results in a more complex design process. Several iterations and skillful design are required to achieve good performance. A possible alternative is to apply MOGA [9] to find a high-chromaticity optics with further improved performance.

CONCLUSIONS

A high-chromaticity optics with linear chromaticity +4 in both planes has been developed for the MAX IV 3 GeV storage ring. The high-chromaticity optics has a smaller dynamic aperture than the design optics, especially for off-momentum particles. The momentum acceptance of the high-chromaticity optics is therefore lower compared to the design optics. No major effect on the efficiency of the injection process is expected since the dynamic aperture requirements are fulfilled on-momentum. However, the reduction of momentum acceptance will result in a considerable reduction of Touschek lifetime. Initial estimates for the reduction of Touschek lifetime caused by errors indicate that the performance of the high-chromaticity optics should be sufficient to allow the optics to be applied in the MAX IV 3 GeV storage ring as a short term solution if instability issues occur during commissioning. Further studies are necessary to validate this conclusion. There also exist opportunities to revise the high-chromaticity optics and perhaps further improve its performance.

REFERENCES

[1] M. Eriksson et al., "The MAX IV Synchrotron Light Source", THPC058, IPAC 2011, San Sebastián, Spain.

[2] S.C. Leemann et al., Phys. Rev. ST Accel. Beams, **12**, 120701 (2009).

[3] P. F. Tavares et al., "Collective Effects in the MAX IV 3 GeV Ring", IPAC 2011, San Sebastián, Spain.

[4] T. Olsson, "High-chromaticity Optics for the MAX IV 3 GeV Storage Ring", Master's Thesis, Lund University (2013).

[5] S.C. Leemann et al., Phys. Rev. ST Accel. Beams, **14**, 030701 (2011).

[6] "OPA manual", available at `http://people.web.psi.ch/streun/opa/`

[7] "Tracy-2 User's Manual", unpublished.

[8] S.C. Leemann, MAX-lab Internal Note 20121107, available at `http://www.maxlab.lu.se/node/999`

[9] L. Yang et al., "Global optimization of an accelerator lattice using multiobjective genetic algorithms", Nucl. Inst. and Meth. in Phys. Res., **609**, pp. 50-57 (2009).

Copyright © 2013 CC-BY-3.0 and by the respective authors

CREATION OF HIGH-CHARGE BUNCH TRAINS FROM THE APS INJECTOR FOR SWAP-OUT INJECTION*

C.-Y. Yao, M. Borland, L. Emery, L. Donley, F. Lenkszus, B.-X. Yang
Advanced Photon Source, Argonne National Laboratory, Argonne, IL 60439, USA

Abstract

A multi-bend-achromat (MBA) low-emittance lattice is being explored for a future APS Upgrade [1]. Due to its small dynamic aperture, the traditional injection scheme must be replaced with a "swap-out" scheme [2]. Several options were considered for the creation of a high-charge bunch train from the injector, and we selected an option that builds the bunch train in the existing particle accumulator ring (PAR). This option enables both single-bunch mode, which is necessary to support current APS operation, and bunch-train mode. This report provides a description of the injection process, simulation results, and specifications of injector timing, kicker, and rf subsystems.

INTRODUCTION

The APS injector consists of a 450-MeV electron linac, a particle accumulator ring (PAR), and a synchrotron booster. The PAR has a 9.77-MHz cw fundamental system (RF1) and a 117.3-MHz pulsed 12th-harmonic system (RF12). In the first 250 ms, beam is accumulated into the RF1 bucket and damped to a bunch length of ~0.86 ns. RF12 is turned on at 250 ms of the PAR cycle and compresses the bunch length to 0.3 ns. Bunch cleaning is performed at 350 ms, and beam is further damped and extracted at 483 ms. Currently the injector runs at a 2-Hz rate and provides a single bunch with a beam charge of up to 4 nC. For an APS MBA low-emittance lattice, the injection scheme would be replaced with a single-bunch or bunch train swap-out scheme. Several bunch fill patterns are being considered: a single-bunch high-charge mode with up to 4 mA per bunch, and a multiple bunch mode that consists of multiple bunch trains, each with up to 5 bunches per train.

HIGH-CHARGE SINGLE-BUNCH AND BUNCH TRAIN GENERATION

The APS MBA upgrade now under exploration envisions two types of fill patterns: a 48-singlet fill pattern with a single-bunch charge of up to 15 nC, and a multi-bunch-train fill pattern with up to 432 bunches.

For 48-singlet mode the injector would need to deliver up to a 20-nC single-bunch with an emittance of 30 nm-rad in the x and y planes. The rf gun, without major upgrade, can deliver about 1 nC per pulse with 30-Hz repetition rate. To reach 20 nC we would need to extend the PAR accumulation cycle from the current value of 0.5 second to 1 second or longer. Figure 1 shows a possible 1-second PAR accumulation cycle. During the first 633.33 ms, 20 linac pulses are accumulated, while the next 100 ms is used to damp the beam to about 0.8 ns in length. The 12th-harmonic rf is turned on around 733.33 ms, following which the beam is captured into the 12th-harmonic bucket and compressed to a bunch length of 0.3 ns. Bunch cleaning is then turned on for 20 ms. After a final damping of 100 ms, beam is extracted to the PAR-to-booster (PTB) beam transport line. The current rf system, with modest upgrades, can support this operating cycle.

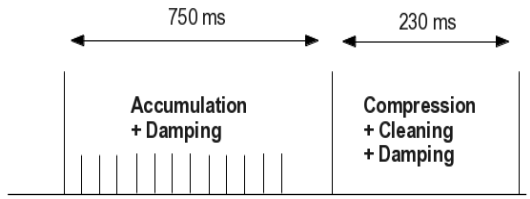


Figure 1: Accumulation of high-charge single-bunch beam in the PAR.

For the multiple bunch-train fill pattern, we consider 2 to 5 consecutive bunches per bunch train with a total of up to 432 bunches and flexible spacing between the trains. To build such bunch trains the PAR rf system must be replaced with a cw 352 MHz system. The bunches can be either accumulated one at a time with a linac micro-bunch length of less than 1.5 ns, or simultaneously with a long linac micro-bunch of up to 15 ns. In both cases a fast gun chopper with a rise time of ~1 ns is needed to accurately control the length of the linac micro-bunches. Bunch cleaning can be performed after accumulation to remove unwanted satellite bunches. Figure 2 shows one possible bunch-train fill pattern with 4 bunches per train.



Figure 2: A multiple bunch train fill pattern.

TIMING SYSTEM UPGRADE

The APS timing system would need to be upgraded to accommodate the new fill patterns and timing precision requirements. The "swap out" mode of operation and ns-level rise/fall time of the kickers requires much-reduced jitter time, estimated to be 50 ps or lower. The jitter time of the existing APS timing system, measured in the range of 200 to 500 ps, is apparently inadequate. A new timing infrastructure would need to be developed to achieve the required timing precision.

*Work supported by the U.S. Department of Energy, Office of Science, under Contract No. DE-ACO2-O6CH11357.
#cyao@aps.anl.gov

Copyright © 2013 CC-BY-3.0 and by the respective authors

STORAGE RING KICKER UPGRADE

The swap out injection scheme [3] requires extracting an old bunch or an old train of bunches and replacing it with a new one. The spacing between the singlet bunches or bunch trains can be as short as two or three buckets, i.e., 5 to 8 ns. The rise time and fall times must be shorter than this spacing. Since traditional ferrite-based kickers would not provide such fast response, we are exploring the use of multiple striplines driven with very fast pulse generators, e.g., similar those made by FID GmbH [4]. For on-axis injection we would need a 3-mrad total kick angle. A set of seven striplines could be used for injection with a total length of 2.8 m. Another set would be used for extraction. Development work on the stripline kicker is underway. Table 1 lists the main parameters for the stripline kickers.

Table 1: Main Parameters of the Stripline Kickers

Impedance (Ω)	Drive voltage (kV)	Kick angle (mrad)	Total kick (mrad)	Total length (m)
50	±20	0.4	3.0	2.8

RF POWER AND DETUNING REQUIREMENTS FOR HIGH SINGLE-BUNCH CHARGE

At 20-nC single-bunch charge the PAR average current is 200 mA and we expect to see much stronger beam loading effects. Upgrades of rf amplifiers and tuning loops would be needed to compensate for the high beam loading. The booster rf system (RF5) would also need to handle a beam current of 17 mA. An estimated 450 kW of rf power is required at extraction, 50 kW more than the current value, and much higher detuning is required at injection. Table 2 lists the required rf power and detuning angle for the upgraded rf systems. Based on these estimates, the current cavities, the RF1 amplifier, and the RF5 klystron can support the required power. The amplifier for the PAR RF12 system would need to be upgraded, and the detuning range for the PAR cavities must be measured and re-evaluated. The booster cavity uses mechanical tuners that can only react to slow changes. The large detuning range between the injection and extraction of the booster beam may require a fast tuner. We are considering installing ferrite tuners through a coupler installed in one of the ports of the cavity. If that is not practical then direct rf feedback must be considered to stabilize the beam.

Table 2: Rf Power and Detuning Requirements

System	Gap Volt V(kV)	Shunt imp. Rs (MΩ)	Power P (kW)	Detuning ψ (deg)
RF12	30	0.22	4.2	40
RF1	40	0.37	4.8	40
RF5@inj	620	221	1.8	80
RF5@inj	9000	221	460	20

Figure 3 and 4 shows the estimated power and detuning for the PAR RF12 system.

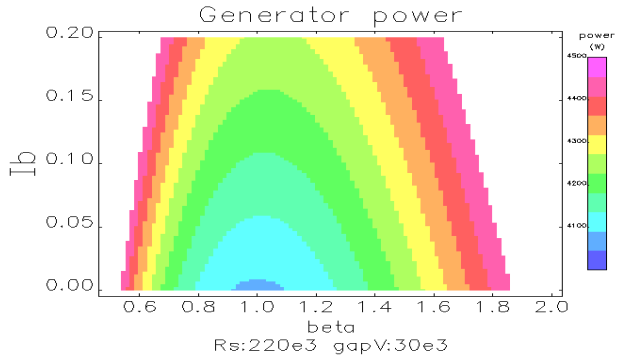


Figure 3: Power requirement as a function of beam current and coupling coefficient for RF12.

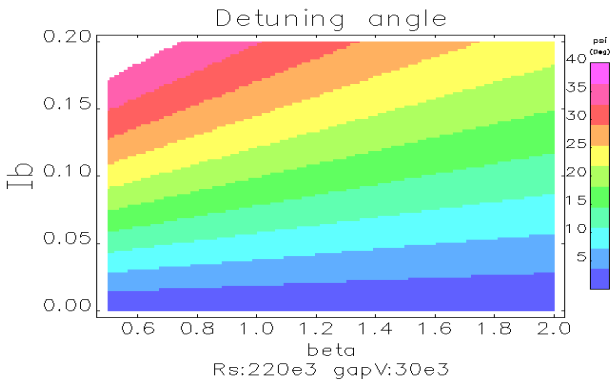


Figure 4: Detuning requirement as a function of beam current and coupling coefficient of the RF12 cavity.

BEAM INSTABILITIES

Resistive-wall, coupled-bunch, and ion instabilities are stronger with higher single-bunch charge. Chromaticity correction is perhaps the most effective compensation method. For the PAR, the sextupole magnets and corrector magnets are combined. A current limit of 4 A limits the chromaticity to 1 or 2 in both planes, even though the sextupole power supply can provide more than 10 A. We will perform magnetic measurements and evaluate the feasibility of increasing the sextupole current limit to 10 A, which will bring the chromaticity to 6 to 7. The booster sextupole magnets, especially the defocusing sextupoles (SD), are currently close to their power supply limit. We would need to upgrade these supplies to increase the sextupole field by a factor of 1.2 to 1.5. Pole-tip shimming is also being considered. Simulations show that adding 3-mm shims to the poles increases the sextupole field by 30%. Combining these two methods should give a 50% increase in booster sextupole strengths for a target chromaticity of ~7 in both planes.

Transverse feedback systems would need to be installed for both the PAR and booster in case dynamic aperture becomes a limiting factor with increased chromaticity.

BOOSTER BEAM EMITTANCE

The beam emittance of the booster 92-nm lattice, measured at the current energy of 7 GeV, is 72 nm-rad.

Copyright © 2013 CC-BY-3.0 and by the respective authors

The reduction in emittance is due to momentum offset caused by rf frequency change. At 6-GeV extraction energy of the APS MBA lattice, the booster emittance would be reduced to 53 nm-rad, much higher than the sub-100 pm MBA lattice emittance. Since the MBA lattice uses on-axis injection and also has nearly equal β-functions for both x- and y-planes, we can further reduce the effective booster emittance by full coupling. A study shows that full coupling can be realized by moving the booster tunes together along the ramp cycle. Figure 5 shows a tune measurement result. We measured a reduction of x-emittance by a factor of two. Hence, we anticipate that we can achieve a booster emittance of 30 nm in both planes.

BOOSTER RAMP SUPPLY UPGRADE

The booster ramp supplies employ 12-phase-SCR-based voltage regulation hardware. Current regulation is achieved with workstation-based ramp correction programs. The system runs well for normal operations. However the supplies, especially the dipole supply, are sensitive to AC line harmonic distortion and line voltage changes. To insure the stability and reliability of injector operation we may need to replace the power supply with switching-type power supplies with current regulation.

In addition, the corrector ramp control hardware would be upgraded to achieve a ramp update time of 1 to 2 seconds, which would enable us to run orbit correction with sufficient speed.

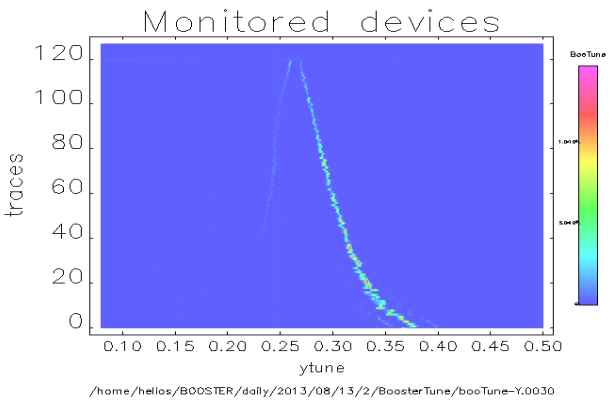


Figure 5: Tune plot of a fully coupled booster beam. The bright trace is the horizontal tune and the dim trace on the left is the vertical tune. Each trace represents 1.8 ms in time.

LINAC SYSTEM UPGRADE

The APS linac consists of dual thermionic rf guns and a photocathode gun, two non-SLEDed klystrons (L1 and L3), and three SLEDed klystrons (L3, L4, and L5) delivering a maximum beam energy of 450 MeV. During normal operations the linac delivers a 375-MeV beam. High single-bunch charge injection may require running the linac with more pulses per cycle and a beam energy of 450 MeV. This may impact linac reliability, so we may add a waveguide switching network so a spare klystron (L6) can be a hot spare for the L4 or L5 klystrons. A kicker that serves as a bunch length chopper, which has a rise/fall time of 50 ns, would be upgraded with a new power supply giving few-ns rise and fall times, in order to accurately control the linac micro-bunch length.

BEAM DIAGNOSTICS UPGRADE

The PAR beam position monitors (BPMs) have a strong beam intensity dependence and can only be used for slow orbit correction in a limited beam current range. New BPM electronics would be needed to increase the dynamic range of the BPMs. The new system would also provide turn-by-turn history capability for beam physics studies, e.g., analysis of instabilities and potential cures.

The booster BPM system was designed to read the average orbit at one time slot during a ramp. It can only be used to tune up beam orbit. A new booster BPM system would use the same BSP-100 module [5] used in the APS storage ring. The new system would provide averaged orbits for up to five time slots along the acceleration cycle, allowing orbit to operate continuously. The orbit correction program could be configured to treat each of the combinations of BPMs and time slots as an independent variable. Turn-by-turn histories would also be available for such tasks as injection trajectory correction, beam stability analysis, etc.

CONCLUSIONS

An MBA extreme low-emittance lattice is being explored for a future APS upgrade. A “swap out” scheme with a high-charge singlet fill pattern and a multiple-train hybrid fill pattern are under consideration. We considered the options and necessary upgrades in order to prepare the injection beam with the existing APS injector complex.

ACKNOWLEDGMENTS

The authors acknowledges the comments and suggestions by N. Sereno, Y. Chae, Lee Teng, T. Smith, A. Xiao, M. White, and D. Horan.

REFERENCES

[1] M. Borland et al., MOPHO07, these proceedings.
[2] L. Emery et al., PAC 2003, TOPA014, p. 256 (2003).
[3] A. Xiao et al., WEPSM13, NA-PAC 13.
[4] T. Naito, et al., IPAC’10, WEOBMH02, p. 2386 (2010).
[5] A. Pietryla et al., PAC’07, FRPMN116, p. 4390 (2007).

Copyright © 2013 CC-BY-3.0 and by the respective authors

OBSERVATION OF +1 BUCKET BUNCH IMPURITY GROWTH AT THE APS STORAGE RING*

C.-Y. Yao, B.-X. Yang, M. Borland, ANL, Argonne, IL 60439, USA

Abstract

The APS storage ring has three fill patterns: a 24-singlet, a 1+8x7 hybrid with a leading bunch of 16 mA, and a 324-singlet. Bunch purity of better than 1×10^{-6} is required for +3 and higher bucket numbers for the first two fill patterns during user operations. A PAR bunch cleaning system is used to clean the satellite bunches. During top-up user operation, beam charge in satellite bunches grows due to the long lifetime of the low charge satellites. Recent storage ring developments, including operating with the bunch-by-bunch feedback system, reduction of chromaticity, and lattice correction, have increased the dynamic and momentum aperture of the storage ring. We observed unusual beam charge growth in +1 buckets, which indicates leakage of electrons from the main bunches to the +1 satellite buckets. This report describes the observation and the dependence of leakage on chromaticity settings, and gives a brief analysis.

OBSERVATION OF ABNORMAL +1 BUNCH GROWTH

Figure 1 shows the normal growth of the +1 satellite bucket relative counts in the 24-singlet fill of the RHB (reduced horizontal β-function) lattice, recorded in the first run period of 2013. It has a typical growth rate of ~2×10^{-8} per hour. Figure 2 shows an abnormal growth of the +1 bucket counts with a growth rate of ~3×10^{-6}, about 150 times higher than normal value. Typical injector bunch impurity for the +1 satellite bucket is at the 8×10^{-7} level and can not explain this abnormal growth. A test was conducted with injected beam turned off and top-up injection systems continuously running. We observed significant growth of net counts in the +1 satellites while the -1 buckets showing no growth. A plot of the result is shown in Figure 3. This test confirmed that the +1 bucket counts come from leakage of main bunches.

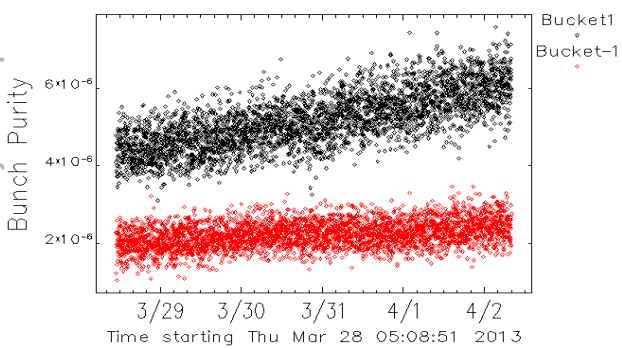


Figure 1: Normal accumulation of the +1 satellite bucket during user operations.

*Work supported by the U.S. Department of Energy, Office of Science, under Contract No. DE-ACO2-O6CH11357.
#cyao@aps.anl.gov

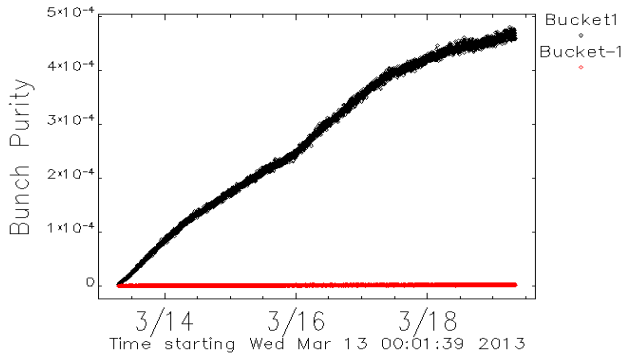


Figure 2: Abnormal growth of the +1 satellite bucket during top-up user operations with lower chromaticity.

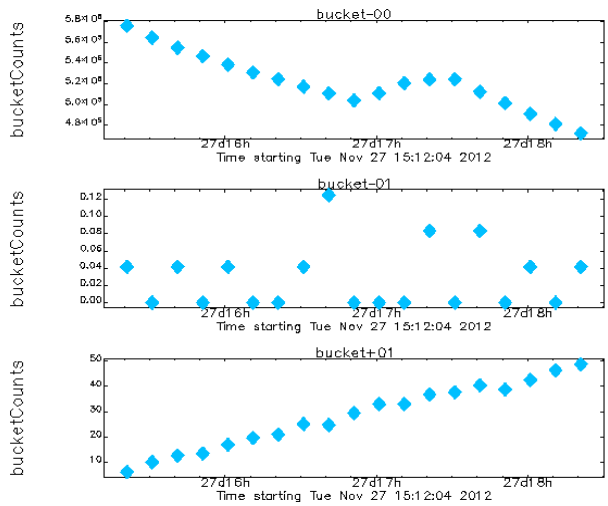


Figure 3: Average bucket count change during a test in which the injected beam is turned off while top-up injection systems were running. Top: main bucket. Middle: -1 bucket showing no growth. Bottom: +1 bucket showing steady growth.

LEAKAGE RATE FITTING

In order to find the relationship between the +1 bunch impurity and the change in storage ring chromaticity, we varied chromaticity in 0.5 steps and collected bunch purity data during Run-1 of 2013. We fit the resulting data with `sddsgenericfit` [1].

The +1 bucket relative counts can be expressed with the following differential equation:

$$dI = \frac{I_0}{T_0} C_{inj}\, dt - \frac{I}{T_b}\, dt + I_0\, R_{leak}\, dt \quad . \qquad (1)$$

The variables are defined as:
I_0 --- main bucket beam current

Copyright © 2013 CC-BY-3.0 and by the respective authors

I --- +1 satellite beam current
T_0 --- main bucket lifetime
R_{leak} --- defusing rate from main to +1 bucket
C_{inj} --- +1 bucket ratio of injected beam
T_b --- +1 bucket beam lifetime

The solution of this equation can be expressed as:

$$\frac{I(t)}{I_0}=\frac{I(0)}{I_0}e^{-\frac{t}{T_b}}+C_1[1-e^{-\frac{t}{T_b}}] \quad , \qquad (2)$$

where I(0) is the initial +1 satellite current, and C_1 is the expected final +1 bucket impurity defined as:

$$C_1=T_b\left(\frac{C_{inj}}{T_0}+R_{leak}\right) \quad . \qquad (3)$$

Injector +1 bunch impurity was estimated from bunch purity data taken immediately after a fill-from-zero. Average beam lifetime over the data collection time was used as T_0, mainly determined by the lifetime of the main bunches.

Table 1 lists fit results and other relevant parameters. The negative leakage rates in some cases are probably due to measurement error, which only indicates a very low or zero leakage rate. Figures 4 and 5 show plots of leakage rate and expected final +1 bunch purity versus chromaticity, respectively. The dependence of leakage rate on x-chromaticity is clear. The results also show that in order to avoid high +1 bucket counts we need to operate with a minimum x-chromaticity of ~4.0.

Table 1: Measured and Fit Parameters

Data date	x-chrom	+1 bucket asymptote impurity	+1 bucket lifetime (s)	Main bucket lifetime (s)	Leak rate (1/s)
03-13	3.122	$9.29e^{-04}$	$7.02e^{5}$	$4.04e^{4}$	$1.30e^{-9}$
03-20	3.625	$1.37e^{-04}$	$2.79e^{5}$	$3.90e^{4}$	$4.68e^{-10}$
03-27	5.638	$2.15e^{-06}$	$5.77e^{5}$	$3.49e^{4}$	$-2.0e^{-11}$
04-03	4.127	$1.82e^{-06}$	$5.47e^{5}$	$3.19e^{4}$	$-2.27e^{-11}$

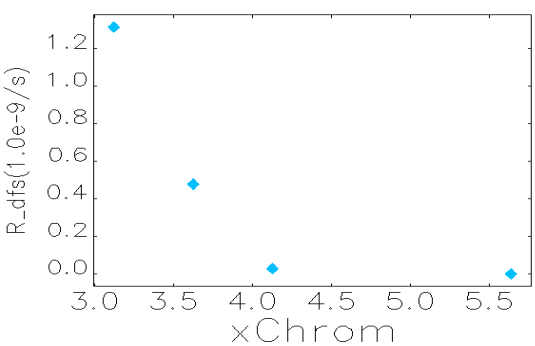


Figure 4: Fit leak rate versus x-chromaticity.

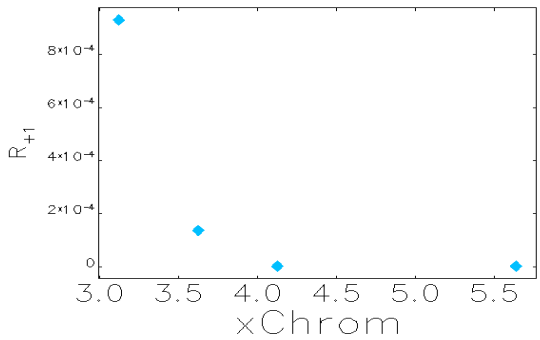


Figure 5: Expected final +1 impurity versus x-chromaticity.

ANALYSIS

The fact that +1 buckets gained electrons while -1 buckets did not implies occurrence of a longitudinal re-capture process.

Earlier studies of beam dynamic aperture and lifetime [2] found that decreasing chromaticity and subsequent reduction of non-linear tune shift extends the momentum acceptance of the APS storage ring beyond that of the normal-chromaticity lattice. We speculate that it is possible that "lost" electrons due to Touschek scattering or other processes stay longer around the longitudinal separatrix, as shown in Figure 6, and are recaptured in the following bucket due to another scattering event. However simulations we performed with `elegant` so far are unable to confirm this theory. One possible reason is that the required simulation time, on the order of 10^4 seconds scale, and total initial particle counts are too high for us to achieve in the limited time available. Further studies, such as varying gap voltage while observing change in the +1 bucket impurity and continued simulations with different parameters are planned.

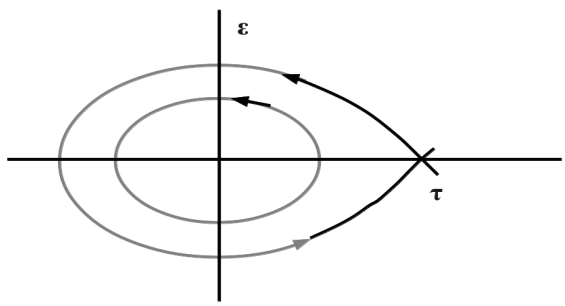


Figure 6: Longitudinal phase-space diagram of a storage ring bucket.

CONCLUSIONS

Recapture of electrons that are lost from the main bucket into the +1 satellite bucket has been observed during the most recent 24-singlet RHB lattice user run when x-chromaticity is +3.6 or lower. This is the first time we have observed this process in the APS storage ring. The leakage rate depends on the value of the x chromacity and

Copyright © 2013 CC-BY-3.0 and by the respective authors

is estimated to be around 10^{-9}/s. During a week-long top-up fill, the accumulated +1 bucket bunch impurity can be as high as a few times 10^{-4}. The recapture process stops completely when x-chromaticity is above 4.0. This observation may have implications for future APS storage ring lattice development.

ACKNOWLEDGEMENT

The authors acknowledge fruitful discussions with L. Emery, Y. Chae, K. Harkay, K. Schroeder and the assistance of APS operatons crew in collecting the data.

REFERENCES

[1] M. Borland et al., "User's Guide for SDDS Toolkit Version 2.8," http://www.aps.anl.gov/Accelerator_Systems_Division/Accelerator_Operations_Physics/manuals/SDDStoolkit/SDDStoolkit.html

[2] V. Sajaev and L. Emery, "Dynamic Aperture Study and Lifetime Improvement at the Advanced Photon Source," proc. of PAC'05, Knoxville, Tennessee, MPPE064, p. 3632 (2005); http://www.JACoW.org

Copyright © 2013 CC-BY-3.0 and by the respective authors

FUTURE NSLS-II INJECTOR UPGRADES*

T. Shaftan#, G. Wang, J. Rose, R. Fliller, R. Heese, F. Willeke, BNL, Upton, New York

Abstract

Last year we began commissioning of the NSLS-II injection system. In 2013 the NSLS-II injector, which consists of 200 MeV linac, 3 GeV booster, transport lines and storage ring injection straight section, will be entering operations. During injection system development we invested substantial efforts in preserving options for future injector upgrades and enhancements. In this paper we discuss our vision and plans of incremental evolution of the NSLS-II injector by implementing planned upgrades, such as the second gun, flexible bunch patterns, beam stacking in the booster, emittance compensation techniques in the transport lines, etc. These upgrades will expand the facility capabilities, improve the beam quality and increase operational reliability.

INTRODUCTION

The NSLS-II [1] is a state-of-the-art 3 GeV synchrotron light source under construction at Brookhaven National Laboratory. It will provide ultra-bright synchrotron radiation of 10^{21}·photons·s^{-1}·mm^{2}mrad^2·0.1%BW^{-1} at 2 keV and high photon flux of 10^{15}·photons·s^{-1}·0.1%BW^{-1}. The facility will support a minimum of 60 beamlines. Construction started in 2009 and commissioning is expected to be completed in 2014.

The NSLS-II injector [2] is now being commissioned to deliver beam performance sufficient for initial storage ring operations at low current. At a later stage the NSLS-II storage ring capabilities will continuously expand to include high intensity operations and top-off mode. This expansion will require the NSLS-II injector to reliably deliver electron beam at a high charge rate, with low losses and high stability in all six phase space coordinates. To meet the requirements of high-intensity ring operation we designed in a large scope of the injector upgrades. The upgrades, described in this paper, aimed to increase the NSLS-II facility capabilities, improve beam quality and reliability of the facility operations.

LINAC UPGRADES

Production of Short Pulses

The 200-MeV NSLS-II linac is a high-performance accelerator delivering up to 15 nC per shot with the emittance of 70 nm rad within trains of 20 ps (RMS) bunches. These excellent beam properties can find applications in generating bright flashes of radiation in THz-visible and hard X-ray wavelength range. Top-off time format (1 injection cycle per minute) permits using the injector linac for other purposes during at least 50 seconds every minute.

*This manuscript has been authored by Brookhaven Science Associates, LLC under Contract No. DE-AC02-98CH10886 with the U.S. Department of Energy.

#shaftan@bnl.gov

Some of these parameters (bunch length and beam emittance) can be greatly improved by addition of an RF gun that delivers an LCLS-like beam performance.

With an RF gun the NSLS-II injector linac will gain potential in generating short bursts of radiation via:

- Short pulses of THz/IR via CTR or in an undulator
- Coherent sources in IR – DUV range of wavelengths
- Short pulse X-rays via Compton Scattering

We designed the linac tunnel in such a way that there exist an ample space ahead of the linac for developing a user end station and upgrading the linac energy for building a short radiation pulse facility (Fig. 1).

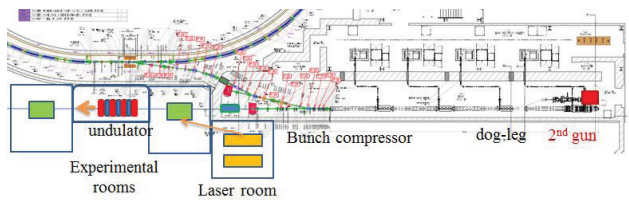


Figure 1: Potential layout of the short pulse facility.

Including the second gun [3] into the low-energy part of the linac will: a) increase reliability of the NSLS-II accelerator complex, b) enable more efficient operations in generating complex bunch patterns and, c) simplify switching between single-bunch and multi-bunch modes for the ring injection.

Generating Flexible Bunch Patterns

Specifications for the storage ring bunch pattern given by the NSLS-II users require sharp edges of the circulating bunch trains and uniform distribution of charge per bunch within a single train. This translates into challenging requirements on the gun pulser since its electronics defines the quality of the generated trains.

In order to enable generation of flat-top (relative bunch-to-bunch charge noise below 1%) trains with sharp edges (~2 ns) we proposed to include a short kicker (chopper) just upstream of the 100-keV gun (Fig. 2, [4]).

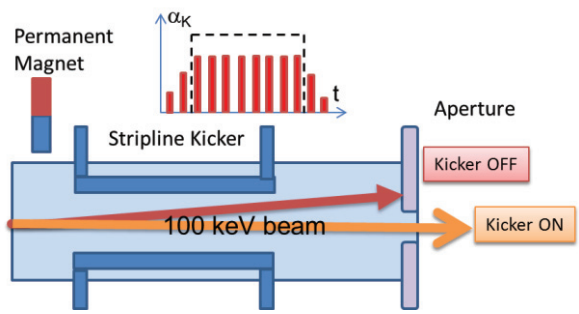


Figure 2: Schematics of the beam chopper.

This kicker will permit passing beam only inside the desired macropulse deflecting bunches outside to the

Copyright © 2013 CC-BY-3.0 and by the respective authors

chamber wall. The gun pulser performance is therefore simplified since the gun will be emitting long bunch trains with loose requirements on the train edges. The kicker will select the most uniform part of the bunch train and cleanly chop off the edges.

Another advantage of this compact device is in limiting the useless and harmful charge outside of the bunch train thus minimizing it from being accelerated and reducing beam loss at high energy.

During the design stage we allocated sufficient space for the chopper system in the linac front-end.

Beam Loading Compensation

The linac is designed to deliver charge 15 nC per shot with up to 150 bunches. The beam loading induces voltage in the sub-harmonic pre-buncher (SPB) and acceleration sections, which results in a large energy spread at the nominal beam current.

We designed an alternative way of beam loading compensation via using a BPM and a screen in the large dispersion region of the transport line upstream of the linac. BPM button signal is split into two paths: one follows to the regular BPM system and the other to the bunch-by-bunch system. The bunch-by-bunch energy slew along the train can be measured from the fast BPM system, while the bunch train energy spread is measured at the beam screen. We use the train average energy spread and bunch-by-bunch energy slew as the RF feed-forward signal to compensate the beam loading effect in the RF system. Then the bunch train beam quality will be optimized and the energy spread, induced by the beam loading, can be minimized.

Linac Digital RF Controller Upgrade

The linac will be upgraded to use the digital cavity controller developed for the NSLS-II booster and storage ring RF systems. Specialized firmware will provide double clocking of the output DAC to improve waveform ramp smoothness, add feed-forward capability to keep TW structure field constant in the presence of beam loading and fix a Master Oscillator reference ambiguity upon reset that we have with the original system.

BOOSTER UPGRADES

2-Hz Repetition Rate

While the NSLS-II booster will soon be commissioned at 1 Hz repetition rate, which is adequate for the initial phase of facility operations, we designed all of the injector subsystems to operate at the double frequency. Expanding the injector operations to 2 Hz will halve the demand of the injected charge per shot, increasing beam quality and reducing beam loss. It will also help to reduce the top-off injection cycle thus shortening perturbations on the stored beam orbit in the storage ring.

Beam Stacking

To further reduce requirements on the linac charge per shot we studied and then implemented beam stacking system in the booster [5]. The beam stacking is realized via closed bump with four booster injection kickers (Fig. 3) accommodating two consecutive bunch trains from the linac separated by 100 ms. Accumulated beam is accelerated and extracted from the booster as a single high-current train.

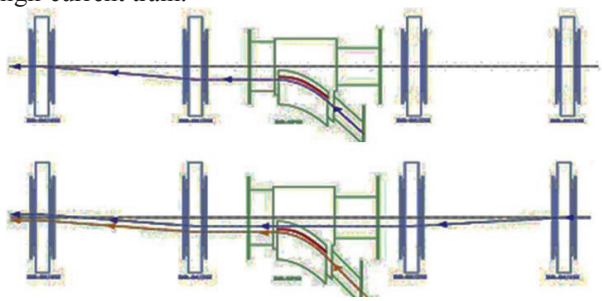


Figure 3: Concept of the beam stacking: upper and lower layouts show injection of the 1st and 2nd bunch trains.

Bunch Train Merging System

Another way of reducing linac output charge per bunch is in adding a high-frequency (i.e. 3 GHz) RF system and modifying the linac front-end to produce trains with 2ns/6=333ps bunch separation. After injection in the booster the 500 MHz RF system takes over and every six microbunches damp down into a single 500 MHz rf bucket. Decreasing charge per bunch should help increase capture efficiency in the linac front-end and reduce beam transverse emittance at 200 MeV for low-loss injection into the booster.

Bunch-by-Bunch Transverse Feedback System

High current circulating in the NSLS-II booster throughout the energy ramp may lead to development of instabilities, which will limit the injector output and create radiation losses in the injector complex. Sources of the potential instabilities include HOMs in the booster RF cavity, resistive wall, impedance of the vacuum chamber transitions and ion-related effects. In addition, bunch-by-bunch oscillations may lead to detrimental effects on the extracted beam quality. As such, the phase space area of the extracted beam may increase thereby increasing the beam emittance and creating losses in the storage ring.

Among the methods of battling the instabilities in the booster we assessed a concept of bunch-by-bunch feedback system, whose implementation for the booster may be similar to that in the storage ring. The diagnostics straight of the booster ring is long enough to accommodate a long stripline kicker fed by a broadband RF generator. The feedback will rely on measurements of bunch-by-bunch orbit deviations in the booster BPMs and adapt the waveform in accordance to the amplitudes of oscillations of consecutive bunches in the circulating train.

Emittance Correction System

Quality of the injector beam can be compromised by collective effects or through errors in the extraction line (i.e. ripples in the pulsed magnets). Consequently, bunches in the train may exit the booster with modulation

Copyright © 2013 CC-BY-3.0 and by the respective authors

in angle or position inflating the resulted projected beam emittance.

This parasitic bunch-by-bunch modulation can be corrected using a stripline installed at the exit of the booster, i.e. at the beginning of BSR transport line.

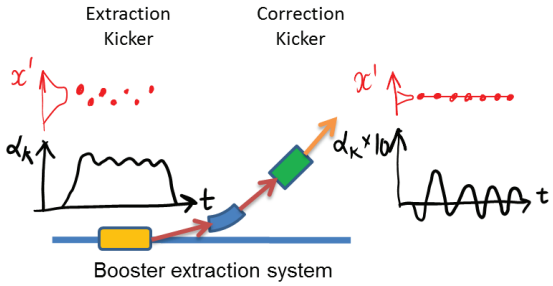


Figure 4: Concept of the horizontal emittance compensation.

The stripline will produce a modulated field waveform, so that bunches passing the stripline will receive negative angular kicks to minimize the angular spread along the extracted bunch train (Fig. 4, [6]).

STORAGE RING INJECTION SYSTEM UPGRADES

Slow Bump in the Injection Straight Section

Performance of the storage ring kickers will significantly contribute to the overall reliability of the NSLS-II accelerator complex. It is prudent therefore to reduce the maximum voltage on the kicker pulsers. We considered and analysed a solution of adding a 3 DC/Slow correctors [7] in the injection straight section, which will produce a closed bump helping the pulsed kickers. For sufficiently fast correctors the closed bump can be turn on during every injection cycle reducing the kicker maximum voltage by 30%. The storage ring injection straight section contains space sufficient for adding these three correctors.

Pulsed Sextupole

During the injection straight design we assessed injection via a pulsed multipole pioneered at SPring-8 [8]. In [9] and [10] we analysed the sextupole injection in details and concluded that integration of a strong pulsed sextupole into the storage ring injection straight will require substantial revisions of the BSR transport line optics. However we considered testing this alternative injection scheme at a later time.

Storage Ring and Booster Bunch Cleaning Systems

As demonstrated by experience of several synchrotron light sources the bunch cleaning systems are necessary to satisfy user requirements on quality of storage ring bunch pattern. Primarily for these experiments that deal with precise timing of their detectors it is required to maintain sharp edges of the storage ring bunch trains with the stray charge in the RF buckets between the trains below 0.01%.

There exist two sources of the stray electrons in the storage ring buckets: a) charge outside of the injected bunch trains and, b) electrons scattered out of full SR RF buckets via Touschek effect (multiple scattering). The latter is inherent property of a high-current storage ring and requires implementation of the SR bunch cleaning system. Estimates on the rates of accumulation of the Touschek-scattered electrons in the SR RF buckets are available in (Fig. 5, [11]).

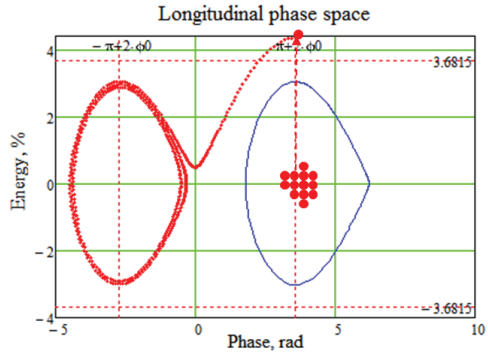


Figure 5: Accumulation of Touschek-scattered particles in an empty bucket.

Modern bunch cleaning system consists of a stripline driven by an RF generator, an aperture for constraining the vertical betatron amplitude of these electrons that are excited by the stripline, and a high-sensitivity bunch pattern monitor [12]. Motion of the unwanted bunches is driven by the stripline field until their vertical oscillation moves them outside the aperture. The bunch pattern monitor controls the purity of the circulating bunch train. We designed in provisions for integrating the required hardware for the bunch cleaners in both booster and storage ring.

REFERENCES

[1] F. Willeke, "Status of the NSLS-II Project," PAC2011, TUOBS3, p. 732 (2011).
[2] T. Shaftan et al., "Status of the NSLS-II Injector," IPAC2013, MOPEA080, p. 273 (2013).
[3] T. Shaftan, "Merging dog-leg for NSLS-II linac," NSLS-II Tech. note 104.
[4] G. Wang et al., PAC2011, THP133, p. 2372 (2011).
[5] R.P. Fliller et al., PRST-AB 14 (2011) 020101.
[6] T. Shaftan et al., IPAC10, TUPEC045, p. 1823 (2010).
[7] G. Wang et al., PAC2011, THP135, p. 2378 (2011).
[8] H. Takaki et al., EPAC08, WEPC091, p. 2204 (2008).
[9] R. Heese et al., PAC09, TU5RFP009, p. 1105 (2009).
[10] T. Shaftan et al., PAC09, TU5RFP012, p. 1114 (2009).
[11] T. Shaftan, "Estimate on migration rate of Touschek-scattered particles into the neighboring RF buckets," in TouchekMigrationRateN.xmcd, 3/11/2008.
[12] J. Weber et al., "FPGA-based "bunch cleaning" system at the advanced light source," NIM A 600 (2), 376 (2009).

Copyright © 2013 CC-BY-3.0 and by the respective authors

SUBPICOSECOND BUNCH TRAIN PRODUCTION FOR HIGH POWER TUNABLE THZ SOURCE

S. Antipov#, C. Jing, P. Schoessow, and A. Kanareykin,
Euclid Techlabs LLC, Solon, OH-44139
W. Gai, A. Zholents, Argonne National Laboratory, Argonne, IL-60439
M. Fedurin, M. Babzien, K. Kusche
Brookhaven National Accelerator Laboratory, Upton, NY-11973
V. Yakimenko,
SLAC National Accelerator Laboratory, Menlo Park, CA-94025

Abstract

An effective method of introducing an energy modulation in an electron bunch by passing it through a dielectric-lined waveguide was recently demonstrated [1]. In the follow up experiment we successfully converted this energy modulation into a density modulation by means of a chicane beamline. The density modulated beam was sent through a foil target, producing THz transition radiation which was characterized using interferometric techniques. By changing the initial energy chirp of the beam we tuned the center frequency of the generated THz radiation in the range 0.68 – 0.9 THz. A table top high power narrowband tunable THz source based on this technique is proposed.

INTRODUCTION

In recent years there has been a large interest in the production of sub-picosecond bunch trains consisting of series of equally spaced electron micro bunches [2-6]. These bunch trains can be used for production of high power THz radiation [4–6, and references therein] and to drive resonant wakefields in plasma and dielectric wakefield accelerators [2, 3].

Sub-picosecond bunch trains can be generated directly from a photocathode of an electron gun using a series of uniformly spaced laser pulses [6-8]. Alternatively, a transverse-to-longitudinal phase space exchange in combination with a multi-slit mask [9-12] can be used. Another approach is to use difference frequency generation by double energy modulation of electrons in an undulator via interaction with optical lasers having slightly different carrier frequencies [13, 14]. In this paper we present an approach using energy modulation by means of the self-excited wake fields in a dielectric-lined [1] or corrugated waveguide [15] with subsequent conversion into a sub-picosecond period density modulation.

A strong energy modulation in an electron bunch passing through a dielectric-lined waveguide was recently demonstrated in reference [1]. Here, we report the successful conversion of this energy modulation into a density modulation and production of a picosecond bunch train. This result provides a foundation for a compact, tunable source of intense THz radiation [RSI].

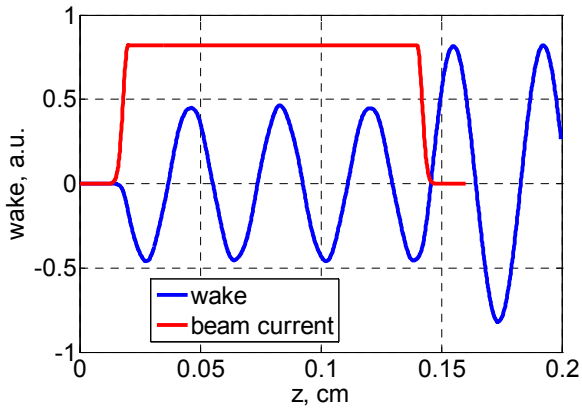


Figure 1: Periodic self-wakefield inside a long quasi-rectangular electron beam.

The principle of introducing an energy modulation in the beam is the following: when the bunch length is comparable or much longer than the wavelength of the fundamental mode of the wakefield, the wakefield inside the bunch will show an amplitude modulation, particularly for a triangular or rectangular shaped bunch (Fig. 1). If the beam has an energy chirp (linear correlation between energy and longitudinal coordinate) then the periodic self-wakefield (Fig. 1) produces an energy modulation (Fig. 2). This energy modulation can be converted into density modulation by means of chicane, a set of four dipoles arranged in a "+ - - +" fashion. Inside the chicane high energy particles travel a shorter distance than those at low energies, hence sections of the beam in which low energy particles are ahead of the high energy ones will be compressed (Fig. 2). If the beam has a positive chirp (head having a lower energy than the tail) initially, the whole beam is compresed as well. Hence the current is modulated at a higher frequency than the frequency of the wakefield mode that created the energy modulation in the first place!

Changing the energy chirp of the beam therefore allows us to tune the frequency of the current modulation. In the case of negative chirp the resulting modulation will be at a frequency lower than the energy-modulating frequency of the wakefield. This property allows us to tune the frequency over a wide range.

*Work supported by the Department of Energy SBIR program under Contract #DE-SC0006299.
#s.antipov@euclidtechlabs.com

Copyright © 2013 CC-BY-3.0 and by the respective authors

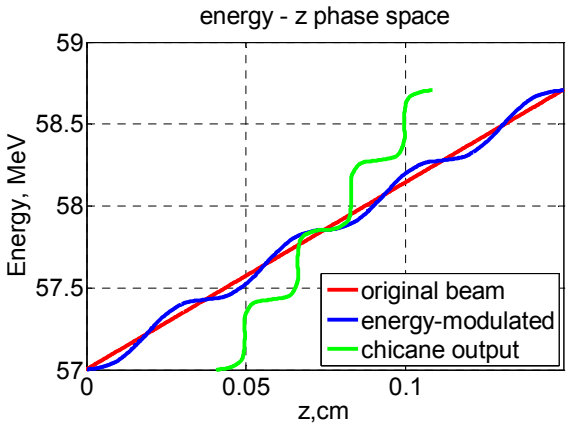


Figure 2: Illustration of the process of bunching and compression. Longitudinal phase space portraits for the incoming electron bunch (red), energy modulated bunch (blue) and density modulated bunch after the chicane (green).

If the original beam does not have an energy chirp (Fig. 3) then the current modulation after chicane is of the same frequency as the mode that created the energy modulation.

Chicanes are typically characterized by a so-called time-of-flight parameter, R_{56} (the transfer matrix element describing chicane's longitudinal dispersion). It relates the path length difference to the fractional energy offset [19] and has the units of cm.

$$\Delta\ell = R_{56}\left(\Delta E / E\right) \quad (1)$$

The time of flight parameter has to match the energy-longitudinal coordinate phase space to provide optimal compression. It is illustrated in Figure 3, where we plot the bunching factor b of an electron beam for various values of the chicane R_{56}.

$$b = \frac{1}{N}\sum_{i=1}^{N} e^{ikz} \quad (2)$$

While a time-of-flight parameter of 4.9 cm (Fig. 3) provides a density modulation of the beam, the corresponding bunching factor is on the order of 0.3. In contrast, R_{56} = 11 cm yields a maximum bunching factor of 0.5. These numbers, however, are rather large for practical realization. In the experiment we used a compact permanent magnet chicane with R_{56} = 1 cm. Even with a small time-of-flight parameter it is possible to have large bunching factors provided that initial beam is strongly modulated in energy prior entering the chicane [16].

EXPERIMENT

The experiment based on this concept was performed at the Accelerator Test Facility (ATF) at Brookhaven National Laboratory [16]. The electron bunches provided by the ATF beam line at 57 MeV had a rectangular peak current profile with a length of ~ 5 ps (1.5 mm) and amplitude of ~ 100 A. The current distribution is produced by passing the beam through two dispersive dipole magnets with a mask in between that cuts off the tails [10]. We can control the linear energy chirp along the electron bunch by changing the phase of the accelerating field in the linac. The head-to-tail energy variation was as large as 850 keV in the experiment, similar to the theoretical examples given previously. For a 1.5 mm long beam this would correspond to a chirp of 567 keV/mm.

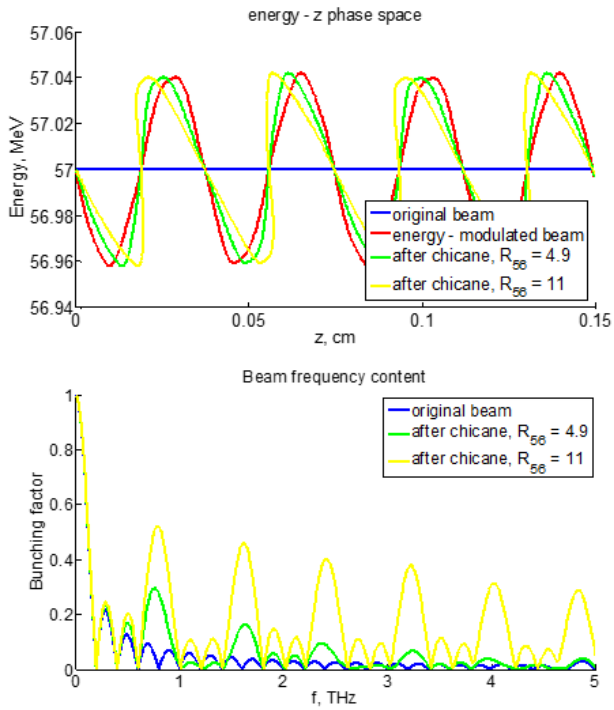


Figure 3: Bunching without compression. Top: Longitudinal phase space portraits for the incoming non-chirped electron bunch (blue), energy modulated bunch (red) and density modulated bunch after chicanes of different strengths (green and yellow). Bottom: frequency content of the beam. Initial beam (blue) and beam after chicanes of different strengths (green and yellow).

After acceleration, bunches were focused to a small transverse size (~ 100 μm rms) and transported through a 800 GHz, 2" long kapton (polyimide) tube, metallized on the outside and with a 300 micron inner radius and 28 micron wall thickness. The kapton has nearly constant permittivity ε in the range of frequencies between 0.5 THz and 1.5 THz. The chicane was made out of four identical permanent dipole magnets. Each magnet has 5 cm magnetic length and ~ 9.4 kG maximum magnetic field for a 5 mm magnetic gap. The distance between the first and the second magnet and the third and the fourth was 5 cm. This chicane had the matrix element value R_{56} =1 cm. We were able to move the chicane in and out of the beam line so that it was possible to measure the electron bunch properties both with and without the presence of the chicane. After the bunch passes through energy modulating structure and then through the chicane it becomes density modulated and this modulation can be measured by passing the bunch through a foil, producing coherent transition radiation (CTR).

Copyright © 2013 CC-BY-3.0 and by the respective authors

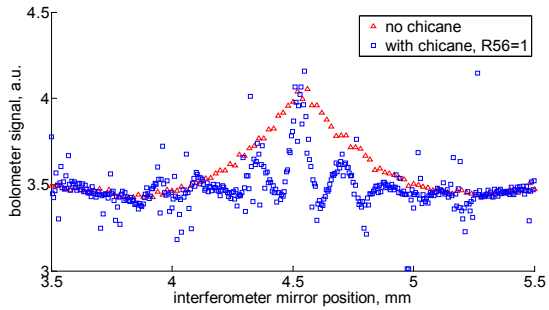


Figure 4: Measured THz CTR signal. Beam passing through chicane (blue rectangles) and chicane retracted (red triangles).

The time structure of the CTR signal is analyzed with a Michelson interferometer using a bolometer as the detector [9, 10]. The result of the interferometric measurement is the autocorrelation function (intensity as a function of the path length difference in the interferometer) of the CTR signal that has a periodicity related to the periodicity of electron bunch. The resulting bunching can be clearly observed through the periodicity of the autocorrelation function. Fig. 4 compares interferometric measurements of the original bunch (chicane retracted) and the density modulated bunch. The autocorrelation function is periodic for a signal produced by the density modulated beam, while the original long rectangular bunch does not produce periodicity over the distance spanned by interferometer mirror motion. We can also conclude that there are 4 beamlets in the density modulated beam (bunch train) because we have 7 pronounced peaks on the autocorrelation function plot. This determines that the bandwidth of the signal is about 25%. By changing the chirp of the beam we were able to tune the density modulation [16] over a range estimated at 0.68 to 0.9 THz.

Based on these encouraging results we have developed a concept for a beam based high peak power tunable THz source. All components are similar to those used in this experiment but adjusted to the specific needs of a dedicated THz radiation source. An electron bunch is produced in the gun and accelerated to a few MeV off-crest forming an energy chirp along the electron bunch. After that it passes through a dogleg (two dipole magnets of equal strength and opposite sign, Fig. 1) where a collimator is used to cut the bunch tails and to provide a uniform density distribution with a relatively sharp leading edge [10]. Next, similar to the experiment above this bunch traverses an energy modulating structure. The energy modulation acquired is converted into a density modulation in a chicane. The resulting bunch train is injected into the power extractor, which is essentially another wakefield producing structure, a dielectric loaded or corrugated metal waveguide equipped with a horn type antenna. Additional electron focusing optics may be needed to control the beam size as it loses energy in the extractor. For the 800 pC, 100 A, 57 MeV ATF beam we propose to use a 3 cm long quartz tube with ID = 0.3 mm and OD = 0.4 mm to produce a 0.7 THz, 170 ps long pulse with a peak power of 6 MW and 1 mJ energy per pulse.

REFERENCES

[1] S. Antipov, C. Jing, M. Fedurin, W. Gai, A. Kanareykin, K. Kusche, P. Schoessow, V. Yakimenko, and A. Zholents, Phys. Rev. Lett. 108, 144801 (2012)
[2] E. Kallos, T. Katsouleas, W.D. Kimura, K. Kusche, P. Muggli, I. Pavlishin, I. Pogorelsky, D. Stolyarov, V. Yakimenko, Phys. Rev. Lett. 100, 074802 (2008).
[3] G. Andonian, O. Williams, X. Wei, P. Niknejadi, E. Hemsing, J. B. Rosenzweig, P. Muggli, M. Babzien, M. Fedurin, K. Kusche, R. Malone, and V. Yakimenko Appl. Phys. Lett. 98, 202901 (2011).
[4] S. Antipov, C. Jing, P. Schoessow, A. Kanareykin, V. Yakimenko, A. Zholents, W. Gai, Rev. Sci. Instrum. 84, 022706 (2013).
[5] G. L. Carr, M. Martin, W. McKinney, K. Jordan, G. Neil, G. Williams, Nature 420, 153-156 (2002).
[6] J. Neumann, R. Fiorito, P. O'Shea, H. Loos, B. Sheehy, Y. Shen, and Z. Wu, J. Appl. Phys. 105, 053304 (2009).
[7] M. Boscolo, M. Ferrario, I. Boscolo, F. Castelli, S. Cialdi, Nucl. Instrum. Methods Phys. Res. A, 2007, 577: 409.
[8] J. Power, C. Jing, in 13th Advanced Accelerator Concepts Workshop 2008, AIP Conf. Proc. No. 1086, pp. 689–694.
[9] Y.-E Sun, P. Piot, A. Johnson, A. H. Lumpkin, T. J. Maxwell, J. Ruan, and R. Thurman-Keup, Phys. Rev. Lett. 105, 234801 (2010).
[10] P. Muggli, V. Yakimenko, M. Babzien, E. Kallos, and K. P. Kusche, Phys. Rev. Lett. 101, 054801 (2008).
[11] Y.C. Du, W.H. Huang, C.X. Tang, Chinese Phys. C 36 151, 2012.
[12] P. Piot, Y.-E Sun, T. J. Maxwell, J. Ruan, A. H. Lumpkin, M. M. Rihaoui, and R. Thurman-Keup, Appl. Phys. Lett. 98, 261501 (2011).
[13] D. Xiang and G. Stupakov, Phys. Rev. ST Accel. Beams 12, 080701 (2009).
[14] M. Dunning, C. Hast, E. Hemsing, K. Jobe, D. McCormick, J. Nelson, T. O. Raubenheimer, K. Soong, Z. Szalata, D. Walz, S. Weathersby, and D. Xiang, Phys. Rev. Lett. 109, 074801 (2012).
[15] K. Bane, G. Stupakov, Nucl. Instrum. Methods Phys. Res. A, 2012, 677: 67-73
[16] S. Antipov, M. Babzien, C. Jing, M. Fedurin, W. Gai, A. Kanareykin, K. Kusche, V. Yakimenko, and A. Zholents Phys. Rev. Lett. 111, 134802 (2013)

Copyright © 2013 CC-BY-3.0 and by the respective authors

ANALYSIS AND OPTIMIZATION OF COUPLER KICK IN APEX*

H. Qian#, S.Kwiatkowski, C.F. Papadopoulos, Z. Paret, F. Sannibale, J. Staples, R. Wells, LBNL, Berkeley, CA 94720, USA

Abstract

A high repetition rate (~MHz) and high brightness photoinjector, based on VHF band CW normal conducting (NC) RF gun, is being developed under Advanced Photoinjector EXperiment (APEX) at Lawrence Berkeley Lab. A NC 30 MeV L-band linac system will be added after the gun to demonstrate beam brightness with lower repetition rate (~10 Hz). In this paper, coupler kicks from APEX buncher and acceleration cavities are evaluated by 3D RF simulation, analytical model and beam tracking, and coupler cells are optimized to minimize emittance dilution due to coupler kicks.

INTRODUCTION

The Advanced Photo-injector Experiment (APEX) is for demonstration of MHz repetition rate high brightness electron beam (~300 pC, ~0.6 mm mrad) injection for the next generation high repetition rate X-ray free electron lasers [1]. APEX is staged in 3 phases. In phase 0, the VHF-band normal conducting RF gun was successfully conditioned to achieve CW operation at nominal beam energy (750 keV) with low vacuum pressure performance (10^{-11} – 10^{-9} Torr). In phase I, a 6D beam phase space characterization will be conducted at 750 keV in CW mode. In phase II, a NC 30 MeV linac will compress and accelerate the beam to reduce space charge effects, so that beam brightness will be more reliably characterized. The APEX beamline is shown in Fig. 1.

The designs of buncher cavity and booster cavity are based on the ALS harmonic cavity and the ANL-AWA acceleration cavity respectively [2, 3], as shown in Fig. 2, both of which are not optimized for low energy and low emittance photoinjectors in terms of coupler kick. The RF input coupler breaks cylindrical symmetry of acceleration field and induces RF multipoles, which may perturb beam alignment and emittance compensation. Such effects can be even worse for beam near the gun due to relatively lower beam energy and thus bigger beam sizes, and has been taken care of in previous low emittance photoinjectors [4-9].

In the following, the RF coupler kicks will be evaluated for the APEX buncher and acceleration cavities through both simulations and simplified analytical models, and geometry modifications are suggested and evaluated.

ANALYTICAL EVALUATION OF COUPLER KICK EFFECT

RF coupler induced emittance growth has been well investigated during the development of low emittance photoinjectors [4-9]. Here a simplified analytical model is used to summarize the coupler kick effects when beam travels through a coupler cell (Fig. 2). Inside the model, only RF force is considered and beam size inside the cell is assumed to be relatively constant. The longitudinal paraxial electric field is expressed as follows:

$$E_z(x,y,z,t) = E_z(x,y,z)e^{i(\omega_0 t+\varphi_0+\Delta(x,y,z))}. \quad (1)$$

where amplitude asymmetry is included in $E_z(x,y,z)$,and phase asymmetry is included in $\Delta(x,y,z)$. $\varphi_0 = 0$ is defined as maximum acceleration phase.

Considering first order phase asymmetry and amplitude asymmetries induced by dipole and quadrupole, RF phase and amplitude can be expressed as,

$$\Delta(x,y,z) = k_y y \, . \quad (2)$$

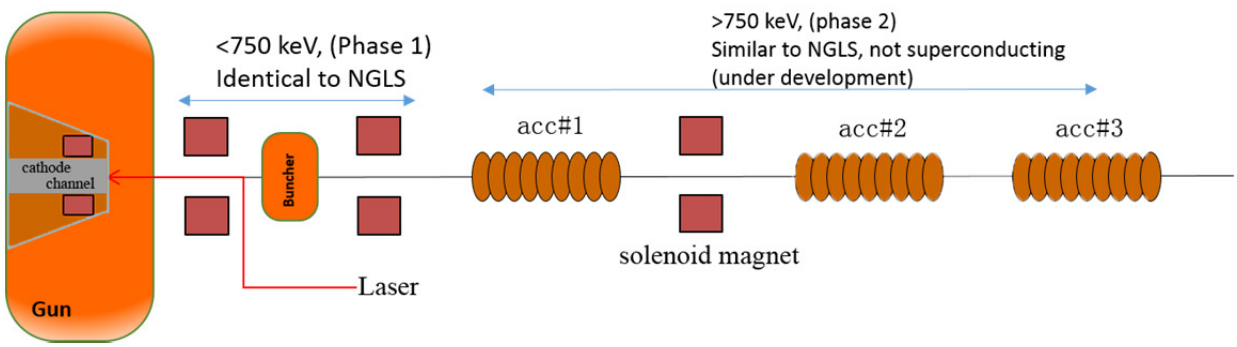


Figure 1: Schematic of the APEX injector beamline. Phase 1 is currently under operation. Phase 2 under development.

**This work was supported by the Director of the Office of Science of the US Department of Energy under Contract no. DEAC02-05CH11231
#hqian@lbl.gov

Copyright © 2013 CC-BY-3.0 and by the respective authors

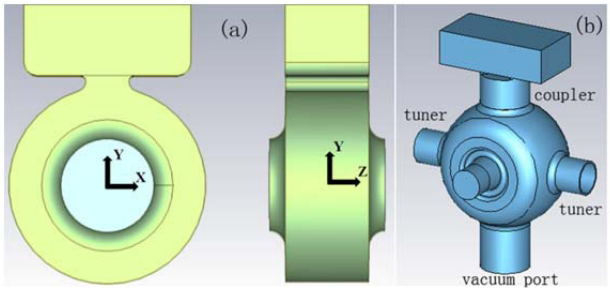


Figure 2: (a) Coupler cell of ANL-AWA cavity, (b) APEX buncher scaled from ALS harmonic cavity.

$$E_z(x,y,z) = E_0\cos(kz)(1-a_0(x^2+y^2) + a_1\,\mathrm{y} - a_2(x^2-y^2)) \quad (3)$$

where E_0 is the peak axial acceleration field, a_0, a_1 and a_2 are monopole, dipole and quadrupole coefficients, k_y is first order phase gradient.

RMS normalized projected emittance growth can be formulated as,

$$\Delta\varepsilon_{n,x}^{monopole} = \Delta\varepsilon_{n,y}^{monopole} = a_0\alpha\lambda\sigma_x^2\sigma_\varphi\cos\varphi_0\,. \quad (4)$$

$$\Delta\varepsilon_{n,y}^{dipole} = \frac{1}{2}a_1\alpha\lambda\sigma_y\sigma_\varphi\cos\varphi_0,\ \ \Delta\varepsilon_{n,x}^{dipole} = 0\,. \quad (5)$$

$$\Delta\varepsilon_{n,x}^{quadrupole} = \Delta\varepsilon_{n,y}^{quadrupole} = a_2\alpha\lambda\sigma_x^2\sigma_\varphi\cos\varphi_0\,. \quad (6)$$

$$\Delta\varepsilon_{n,y}^{phase} = \frac{1}{2}k_y\alpha\lambda\sigma_y\sigma_\varphi\sin\varphi_0\ \ \Delta\varepsilon_{n,x}^{phase} = 0\,. \quad (7)$$

where $\alpha = \dfrac{eE_0}{2mc^2k}$, λ is RF wavelength (twice coupler cell length), k is RF wave number, σ_x and σ_y are transverse RMS beam sizes, σ_φ is longitudinal RMS bunch length measured by RF phase. The total emittance growth is,

$$\Delta\varepsilon_{n,x} = \Delta\varepsilon_{n,x}^{monopole} + \Delta\varepsilon_{n,x}^{quadrupole}\,. \quad (8)$$

$$\Delta\varepsilon_{n,y} = \sqrt{\begin{matrix}(\Delta\varepsilon_{n,y}^{monopole} - \Delta\varepsilon_{n,y}^{quadrupole})^2 \\ +(\Delta\varepsilon_{n,y}^{dipole} - \Delta\varepsilon_{n,y}^{phase})^2\end{matrix}}\,. \quad (9)$$

RF SIMULATIONS

The preliminary APEX buncher cavity design (1.3 GHz) is scaled from ALS harmonic cavity (1.5 GHz), as shown in Fig. 2, and has a single waveguide coupler, a symmetric vacuum port and two RF tuner ports. The ANL-AWA cavity is a 1.3 GHz 7-cell standing wave cavity, and the RF power is fed into the cavity by a single waveguide coupler (Fig. 2). In order to feed the 7 cells, the coupling slot is big, which is expected to greatly distort the cylindrical field symmetry in coupler cell.

Coupler Kick Evaluation

CST Microwave studio is used to simulate 3D RF field map, and RF field in the middle plane of coupler cell is used to extract amplitude and phase asymmetry coefficients, as shown in Table 1. Eq. (5) to (7) are used to do a quick emittance growth evaluation based on Table 1 and one specific beamline optimization solution for 300 pC operation from ASTRA simulation [10, 11], as shown in Table 2.

Table 1: Amplitude and phase asymmetry coefficients

	Buncher	**AWA cavity**
a_1 (m^{-1})	0.007	0.9
a_2 (m^{-2})	8.7	1.4
k_y (mrad/m)	3.0	17

Table 2: Emittance growth (in mm mrad) evaluations for one APEX solution with 300 pC beam charge

	Buncher	**ACC #1**	**ACC #2**	**ACC #3**
$\Delta\varepsilon_{n,y}^{dipole}$	0.02	4.9	1.4	1.2
$\Delta\varepsilon_{n,x\ or\ y}^{quadruple}$	0.28	0.02	0.003	0.002
$\Delta\varepsilon_{n,y}^{phase}$	0.03	0.005	0.06	0.03

Table 2 shows coupler kick gives significant emittance growth in both buncher and acceleration cavities. Buncher cavity is dominated by quadrupole, and AWA cavity is dominated by dipole.

Coupler Cell Optimization

To minimize quadrupole in buncher cavity, tuner ports are made to be the same size as coupler port and vacuum port, and tuners are removed or retracted. To minimize dipole and phase asymmetry in AWA cavity, symmetric dual RF coupler is added (Fig. 3), and coupler size is tuned to restore the original power coupling factor. CST simulations show though dipole is minimized, quadruple is enhanced by an order of magnitude, so two dummy ports are added at 90 degree relative to coupler port to suppress quadrupole. Comparison between original and modified AWA coupler cell is displayed in Fig. 3.

After coupler cell optimization, with the same beamline settings as in Table 2, Eq. (5) to (7) predict coupler induced emittance growth are well below 0.05 mm mrad for both buncher and acceleration cavity.

Copyright © 2013 CC-BY-3.0 and by the respective authors

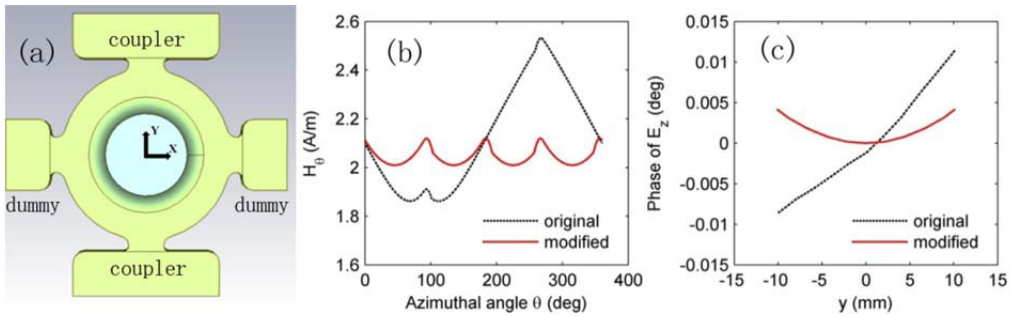


Figure 3: (a) 4-port optimization of AWA coupler cell, (b) azimuthal magnetic field amplitude at radius of 10 mm in central plane of coupler cell (z=0), (b) RF phase of E_z along line x=0 in plane z=0.

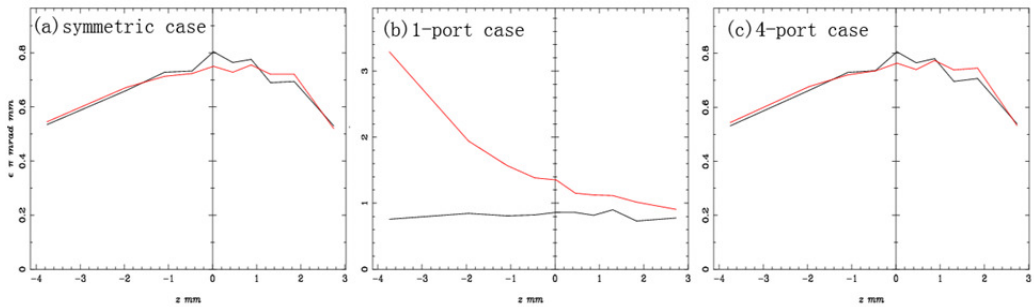


Figure 4: Slice emittance (x: blac, y: red) at ACC #3 exit (~14 MeV) for (a) symmetric map, (b) 1-port map, (c) 4-port map

BEAM TRACKING SIMULATIONS

To include both RF and other forces (space charge, solenoid focusing et al.), the 3D RF field maps from CST can be used in ASTRA simulations of the APEX beamline. In the following, three field maps of AWA cavity are used for one solution of the ongoing optimization process for the APEX beamline, as shown in Fig. 4. The "symmetric" case is based on input of the on-axis E_z field in ASTRA. In this case, ASTRA expands the fields E_r and B_φ around the axis up to 3rd order. This is by construction azimuthally symmetric and no emittance growth due to multipole field is possible. The "1-port" and "4-port" cases refer to 3D field maps based on the optimization described previously. Fig. 4 confirms the original AWA cavity (1-port) will cause huge emittance growth and the optimized AWA cavity (4-port) almost removes all coupler kicks.

CONCLUSION

Coupler kicks in the APEX injector are studied by RF simulation, analytical model and beam tracking, and huge emittance growth is found due to improper coupler cell designs of buncher and acceleration cavities. After symmetry optimization of coupler cell, coupler kicks are minimized and confirmed by ASTRA simulations.

REFERENCES

[1] F. Sannibale et al., Phys. Rev. ST Accel. Beams 15 (2012) 103501.

[2] R.A. Rimmer et al., "A Third-Harmonic RF Cavity for the Advanced Light Source," (1998), EPAC'98.

[3] J.G. Power et al., Upgrade of the Drive Linac for the AWA Facility Dielectric Two-Beam Accelerator, (2012) SLAC-PUB-15138.

[4] B. Dwersteg, Nuclear Instruments and Methods in Physics Research A 393 (1997) 93.

[5] D. Palmer, "The Next Generation Photoinjector" (PhD diss., Stanford University, 1998).

[6] Z. Li et al., Coupler Design for the LCLS Injector S-band Structures, (2005) SLAC-PUB-11728.

[7] M. Chae et al., Phys. Rev. ST Accel. Beams 14 (2011) 104203.

[8] B. Buckley and G.H. Hoffstaetter., Phys. Rev. ST Accel. Beams 10 (2007) 111002.

[9] C. Gulliford et al., Phys. Rev. ST Accel. Beams 14 (2011) 032002.

[10] C.F. Papadopoulos et al., "Injector Design Studies for NGLS," TUPS069, FEL'13.

[11] K. Flöttmann. ASTRA: A space charge tracking algorithm. user's manual available at http://www.desy.de/~mpyflo/Astra_dokumentation

Copyright © 2013 CC-BY-3.0 and by the respective authors

LLNL X-BAND TEST STATION STATUS*

R.A. Marsh†, F. Albert, G. Anderson, S.G. Anderson, E.T. Dayton,
S.E. Fisher, D.J. Gibson, S.S. Wu, F.V. Hartemann, C.P.J. Barty
Lawrence Livermore National Laboratory, Livermore, CA 94550, USA

Abstract

An X-band test station is being built at LLNL to support inverse Compton-scattering x-ray and gamma-ray source development. The major components for the X-band test station have been designed, fabricated, installed, and aligned. The XL-4 klystron has been delivered, dressed and installed in the ScandiNova modulator, and tested to full peak power. Final assembly and bakeout of RF transport, test station supports, and accelerator components is complete, and the current status of commissioning and first beam will be presented and discussed. Future upgrade paths and configuration for a variety of x-ray and gamma-ray applications will be discussed along with schedule for planned experiments.

INTRODUCTION

Extremely bright narrow bandwidth gamma-ray sources are expanding the application of accelerator technology and light sources in new directions. LLNL has a successful history utilizing gamma-rays generated by a linac-driven, laser-based Compton scattering gamma-ray source [1, 2, 3, 4]. Next generation advancements in linac-based x-ray and gamma-ray production require increasing the average flux of gamma-rays at a specific energy (that is, $N/eV/sec$ at the energy of interest). One way to accomplish this is to increase the effective repetition rate by operating the RF photoinjector in a multi-bunch mode, accelerating multiple electron bunches per RF pulse. This multi-bunch mode will have stringent requirements for the electron bunch properties including low emittance and energy spread, but across multiple bunches. An X-band test station is under construction at LLNL to develop multi-bunch electron beams and generate x-rays. This paper summarizes progress and describes the current status of the project.

The RF gun is described in detail in [5]. Test station parameters are summarized in Table 1. Beam dynamics are summarized in Fig. 1 for a 250 pC bunch generated in the Mark 1 X-band RF gun and accelerated by a single T53 traveling wave accelerating section. Beam steering will use X-Y windowpane dipole magnets, and two quadrupole triplets will focus the beam for transport and quad-scan emittance measurement. A dump dipole magnet will double as a spectrometer once it has been calibrated.

Table 1: Test Station Parameters

Charge	25–250 pC
Normalized Emittance	<1 mm mrad
Gun Energy	7 MeV
Cathode Field	200 MV/m
Coupling β	1.7
Section Gradient	~70 MV/m
Final Energy	30 MeV

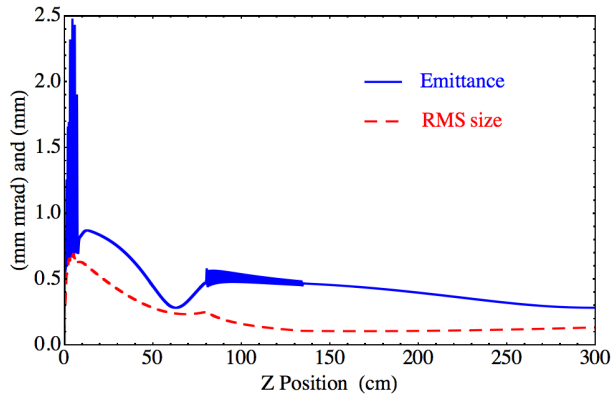


Figure 1: PARMELA beam dynamics simulation for a bunch charge of 250 pC.

TEST STATION

The test station layout is shown in Fig. 2. The high voltage modulator and X-band tube reside in a separate area with RF distribution fed through a hole in the wall to the linear accelerator. A manifold divides the power between the RF gun and the accelerating sections [6]. Testing of the klystron to full power is complete [7], and the RF load tree that was used for this testing is currently being disassembled to provide components for dressing the accelerating sections and provide components for the power division manifold. Support structures made from 80/20 mount to the laser tables and provide multi-dimensional adjustment for alignment of supported components to the beamline. The emittance compensation solenoid for the RF gun is mounted on precision ground rails so that it can be moved back to provide access to the gun. The gun support structure holds the RF gun, WR-90 pumpouts and pumps, as well as an RF gate valve on the beamline. The T53 accelerating structure is mounted on a SLAC designed strongback with end-to-end adjustment, which is then mounted on 80/20 supports that provide additional adjustment as well as support for RF distribution, loads, and vacuum pumps.

* This work performed under the auspices of the U.S. Department of Energy by Lawrence Livermore National Laboratory under Contract DE-AC52-07NA27344
† marsh19@llnl.gov

Copyright © 2013 CC-BY-3.0 and by the respective authors

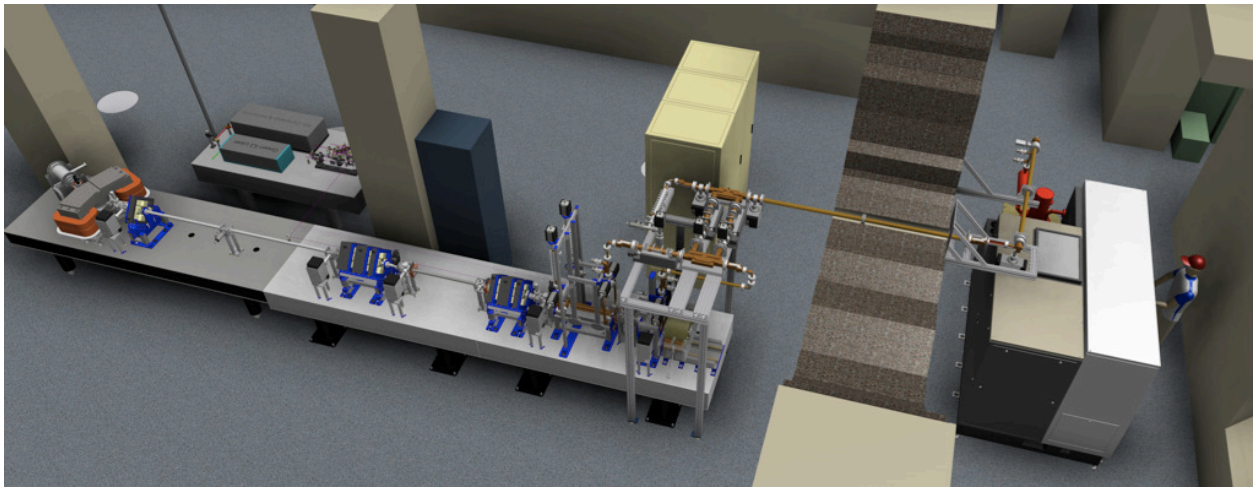


Figure 2: CAD rendering of the X-band test station. Test station position has been changed to optimize the RF distribution for minimal loss and permit for the expansion of the beamline for future experiments.

The quadrupole magnets are mounted together in triplets, with each stand having adjustability. The magnet alignment within their supports has been measured as reported in [8]. The steering magnets are mounted onto beamline vacuum flanges.

Alignment

The alignment specification on most components, driven by the desire to limit emittance growth, is ± 100 μm. As shown in [9], tolerances can become even tighter if emittance growth in low charge bunches is to be limited. An initial alignment procedure was developed for a 250 MeV X-band linac at LLNL [10], which has been adapted to the X-band test station. The general approach for alignment uses a precision CMM arm from Romer, with a quoted specification of ± 75 μm repeatability and volumetric accuracy over the full envelope reachable by the arm. The Romer arm and operating technician can be seen in Fig. 3. Physical contact with a probe tip allows encoders in the arm to map the exact position of each point input into the CMM software. The coordinate system of the arm is based on geometric features of individual components such as the cross-section of magnet pole pieces, or the outer radii of pillbox cell cups, combined with tooling ball fiducials that have been placed on magnets and accelerating structures. Initial measurement of the geometric features allows the external fiducials to be used in the future when features may be less accessible.

The emittance compensation solenoid is the heaviest component, and has the least adjustment (its height from the table is fixed). Magnet metrology measurements at SLAC confirmed that the magnetic and physical axes of the solenoid were aligned to within 25 μm. The solenoid was adjusted so that is was parallel with the laser table, and pointing along the table edge. Solenoid alignment set the coordinate system for subsequent components, with the beamline axis zero set by the mid plane of the Helmholtz pair outer pole faces: this will be the center for the RF gun so that there is no field on the cathode surface. Subsequent components are all aligned onto the beamline centerline, at an offset from the cathode driven by beam dynamics and mechanical design.



Figure 3: Photograph of X-band test station alignment. Romer CMM arm in use to precisely measure the 3D position of the T53 cells for proper alignment of the accelerating structure with respect to the beamline axis and cathode position.

The RF gun body was aligned on axis with the cathode cell backplane offset so that the internal cathode surface resides at the mid-plane of the solenoid. The RF gun beam-

Copyright © 2013 CC-BY-3.0 and by the respective authors

line gate valve was also used for alignment of the RF gun support structure given that it is the furthest component downstream of the gun. The T53 section was measured with respect to pillbox cells and fiducials on each WR-90 RF port. The beamline position of the T53 accelerator section has been fixed from beam dynamics modeling and was set with respect to the outer face of the accelerator coupling cell. The quadrupole triplet alignment in their 80/20 support has been confirmed with magnetic measurement [8] so that the physical pole positions were used to position them in space. Fiducials on the quadrupole triplets were also mapped so that they can be used in the future to align the magnets or other beamline components when beamline pipe is in place and the pole faces are not accessible to the arm probe. The critical test station components were realigned following final assembly of the RF distribution components to insure the accelerator section and gun retain their precise location. It was necessary to measure the accelerator structure and quadruple magnet fiducially because the bore of the magnets and surface of the section were no longer accessible.

Bakeout

The RF gun vacuum system is comprised of: an RF input window; a WR-90 pumpout; the Mark 1 RF gun; a custom weldment cross; an all-metal RF gate valve; a hot cathode vacuum gauge; two 10 L/s ion pumps; two 40 L/s ion pumps; and additional vacuum nipples, T's, blanks, and an all-metal angle valve to connect the major components. After final assembly and alignment of this unit, the entirety of the system excluding the pump magnet housings has been wrapped with heater tape and aluminum foil, and baked to 120°C for over a week. A base pressure of 2 10^{-9} Torr has been achieved.

Baking the completed vacuum system of the beamline and RF distribution will provide the best possible starting point for RF processing and commissioning. The T53 accelerator section, gun diagnostic pop-in and photocathode laser mirror box, as well as the full RF distribution up to the klystron output window form a single vacuum system. The complete system bake was planned using 13 independent heater tape and PID control channels. The system was baked to 100°C for over a week and base pressures of 1–4 10^{-9} Torr was achieved once the system cooled to room temperature.

Conditioning

RF processing of the T53 accelerator section is underway. The control system for critical accelerator diagnostics is in place and tied into the arc detection system that was used for RF commissioning of the XL-4 klystron [7]. The arc detection chassis is active on the klystron forward and reverse, the RF gun forward and reverse, and the accelerator section forward and reverse. In addition the same NI chassis that does the real time monitoring acts as a digitizer for the modulator voltage and current. In order to condition most safely, the accelerator section is being brought to full power first, so that the transport waveguide can be processed and the control system can be debugged.

CONCLUSION

The major components for the X-band test station have been designed, fabricated, installed, and aligned. The XL-4 klystron has been delivered, dressed and installed in the ScandiNova modulator, and tested to full peak power [7, 11]. Assembly of RF transport, test station supports, and accelerator components, final assembly and bakeout have been completed. RF conditioning of the vacuum RF transport, accelerator section, and RF gun is underway. Laser transport for the photocathode drive laser is complete, and the laser system will be brought into operation once the laser safety interlock system installation is complete.

Conditioning is focusing on processing the RF gun to full operating power, which corresponds to 200 MV/m peak electric field on the cathode surface. Single bunch commissioning of the Mark 1 design will provide confidence that this first structure operates as designed, and will serve as a solid starting point for subsequent changes, such as a removable photocathode, and the use of various cathode materials for enhanced quantum efficiency. Charge scaling experiments will follow, partly to confirm predictions, as well as to identify important causes of emittance growth, and their scaling with charge. Multi-bunch operation will conclude testing of the Mark 1 RF gun, and allow verification of code predictions, direct measurement of bunch-to-bunch effects, and initial implementation compensation mechanisms.

REFERENCES

[1] C.P.J. Barty, and F.V. Hartemann, *"T-REX: Thomson-Radiated Extreme X-rays Moving X-ray Science into the"Nuclear" Applications Space with Thomson Scattered Photons"*, **UCRL-TR-206825** (2004).

[2] F. Albert, *et al.*, Opt. Lett. **35**, 354 (2010).

[3] D.J. Gibson, *et al.*, Phys. Rev. STAB **13**, 070703 (2010).

[4] F. Albert, *et al.*, Phys. Rev. STAB **13**, 070704 (2010).

[5] R.A. Marsh, *et al.*, Phys. Rev. ST Accel. Beams, **15**, 102001 (2012).

[6] R.A. Marsh, *et al.*, *"50 MW X-Band RF System for a Photoinjector Test Station at LLNL"*, **TUP132**, *PAC 2011*.

[7] R.A. Marsh, *et al.*, *"LLNL X-band RF System"*, **WEPFI078**, *IPAC 2013*.

[8] R.A. Marsh, *et al.*, *"Precision Magnet Measurements for X-band Accelerator Quadrupole Triplets"*, **THPPD018**, *IPAC 2012*.

[9] R.A. Marsh, *et al.*, *"Modeling Multi-bunch X-band Photoinjector Challenges"*, **MOPPP042**, *IPAC 2012*.

[10] S.G. Anderson, *et al.*, Nucl. Instrum. Methods Phys. Res., Sect. A, **657** 1, pp. 140–149 (2011).

[11] R.A. Marsh, *et al.*, Nucl. Instrum. Methods Phys. Res., Sect. A, *in preparation* (2013).

Copyright © 2013 CC-BY-3.0 and by the respective authors

SHAPING ELECTRON BUNCHES FOR ULTRA-BRIGHT ELECTRON BEAM ACCELERATION IN DIELECTRIC LOADED WAVEGUIDES*

Evgenya I. Simakov#, Dmitry Yu. Shchegolkov, C. Huang, and T.J. Kwan,
Los Alamos National Laboratory, Los Alamos, NM 87545, U.S.A.

Abstract

We describe a possible design of an Emittance Exchanger (EEX) which may be employed to generate a pair of a double-triangular drive bunch and a trapezoidal witness bunch for a Dielectric Wakefield Accelerator (DWA). We consider the concept of a high-brightness DWA with the gradient of above 100 MV/m and less than 0.1% induced energy spread in the accelerated beam as a possible afterburner for the proposed Los Alamos Matter-Radiation Interactions in Extremes (MaRIE) signature facility. We present the results of simulations with Elegant which take into account non-linear effects of the EEX beamline. Possibilities for producing ideal beam shapes to demonstrate low induced energy spread in a DWA are discussed.

INTRODUCTION

The modern discovery science has an emerging need for a very hard X-ray source, with high-peak fluxes of coherent 42-keV photons (~ 0.3 angstrom wavelength). High energy photons will allow resolving grain boundaries in materials in extreme states such as experiencing shock waves and being able to penetrate μm-to-mm sized samples. High photon energies are also required to prevent samples from disintegrating from a single X-ray pulse, allowing multiple images of transient effects. High-resolution imaging of these effects will optimally require up to 10^{12} photons per X-ray pulse, well above the ability of current technology. Los Alamos National Laboratory (LANL) has identified this discovery science frontier as an important part of its future mission and has proposed the Matter-Radiation Interactions in Extremes (MaRIE) facility [1], which includes an X-ray free electron laser (XFEL) as described in [2].

The number and the energy of photons produced by the XFEL is strongly dependent on the energy of the electron beam produced by the linear accelerator with the more energetic beam delivering more high energy photons to the user. Although generally the baseline design needs to be conservative and rely on existing technology, any future upgrade would immediately call for looking into the advanced accelerator concepts capable of boosting the electron beam energy up by a few GeV in a very short distance without degrading the beam quality. Typical electron beam quality parameters for XFEL applications are electron bunch charges of 0.1 to 1 nC, normalized rms emittances of 0.1 to 1 μm, and rms energy spreads of < 0.1%. By decreasing the bunch energy spread and emittance, it is possible to increase the total X-ray flux by orders of magnitude [2]. Dielectric Wakefield Accelerator (DWA) [3,4] has a potential to satisfy the required constraints of the afterburner and produce acceleration gradients above 100 MV/m and less than 0.1% spread in the gained beam energy [5].

We have initiated a project at LANL to demonstrate the proof-of-principle operation of a DWA with shaped drive and witness bunches at high gradient, and with enhanced transformer ratio and reduced energy spread.

REDUCING WITNESS BUNCH ENERGY SPREADS IN DWAs

DWAs are formed by one or several dielectric layers surrounded by metal cladding (Figure 1). The dielectric constant and the inner and outer radii of the dielectric tubes (or single tube in the simplest case) are chosen so that the phase velocity of the fundamental monopole mode (TM_{01}) is approximately equal to the speed of light and the mode is effectively excited by the beam passing in the central vacuum channel. In a collinear DWA the field generated by a leading, high-charge drive bunch is used to accelerate a trailing, low-charge main bunch which contains a relatively small amount of charge. The wakefields excited by a leading bunch have the remarkable property that the axial electric field and the transverse electric field are transversely uniform and linear, respectively. If one can make the wakefield to be axially constant along the bunch it will result in no induced energy spread within the bunch, leading to an extraordinary condition of preserving the main beam brightness while providing high gradient acceleration. We have realized that it is possible that an accelerated beam in a DWA can achieve the needed small energy spread if the longitudinal witness bunch profile is properly customized [5].

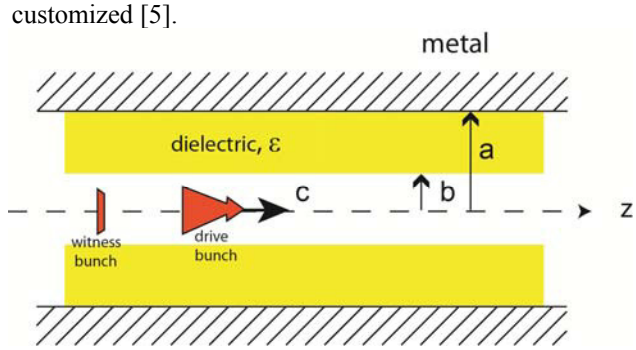


Figure 1: The schematic of a dielectric loaded waveguide with shaped electron beams traveling on axis.

Figure 2 shows the current profiles of the driving double triangular bunch and a trapezoidal witness bunch and their corresponding longitudinal wakefield generated

*Work is supported by the U.S. Department of Energy through the Laboratory Directed Research and Development (LDRD) program at Los Alamos National Laboratory.
#smirnova@lanl.gov

Copyright © 2013 CC-BY-3.0 and by the respective authors

in a single mode wakefield accelerator. The wakefield is computed using the Green function method for the DWA geometry with parameters summarized in Table 1. It can be seen from the figure that the wakefield excited by the witness bunch interferes with the wake excited by the drive bunch which results in a uniform gradient experienced by the witness bunch. As a result, the induced energy spread in the witness bunch is below 10^{-5}.

In addition, Figure 2 illustrates the high transformer ratio generated by the double triangular drive bunch. The enhanced transformer ratios which result from generating the wake with the shaped drive bunches are important for achieving high gradients in DWAs.

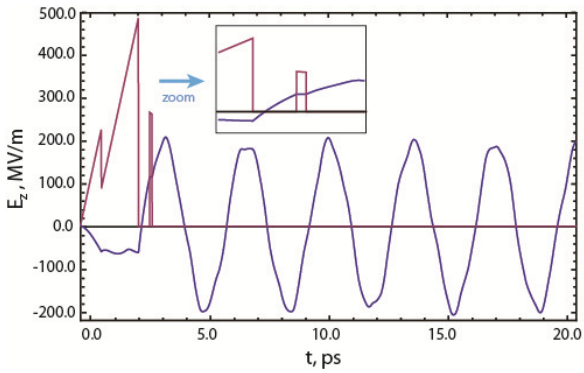


Figure 2: The current profiles of the drive and the witness bunches (red line) and the wakefield (blue line) excited by the pair of bunches in a proposed DWA configuration.

Table 1: Parameters of the 300 GHz Dielectric Wakefield Accelerator Configuration

Beam pipe ID, *2b*	1.14 mm
Dielectric tube ID, *2a*	1.24 mm
Waveguide cutoff	298 GHz
Charge of the drive bunch	5 nC
Length of the drive bunch	2.350 ps
Charge of the witness bunch	250 pC
Length of the witness bunch	100 fs
Time between the bunches	2.8017 ps
Transformer ratio	3.38
ΔG/G	$9*10^{-6}$

PRODUCING SHAPED BEAMS WITH EEX

In order to simultaneously generate the double triangular drive bunch and a trapezoidal witness bunch for a proof-of-principle demonstration, the recently proposed Emittance Exchanger (EEX) [6,7] can be employed. The schematic of a possible beamline is shown in Figure 3. The beamline starts with a mask which has two shaped slots. The slots have special shapes and are optimized to cut out the correct double triangular and trapezoidal beam profiles out of the Gaussian bunch (Figure 4). The mask is followed by an Emittance Exchanger which consists of two identical doglegs, a deflecting cavity in between them, and a number of corrective elements, such as a fundamental mode cavity, quadrupoles and possibly sextupoles. We conducted the extensive tuning of the EEX optics to convert the distribution of particles shaped in x direction into a distribution of particles similarly shaped in z direction.

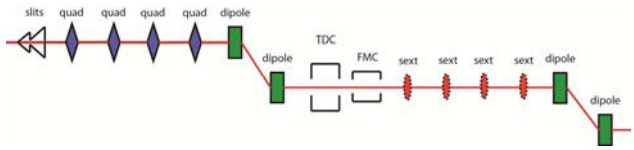


Figure 3: The schematic of a beamline for producing shaped electron bunches.

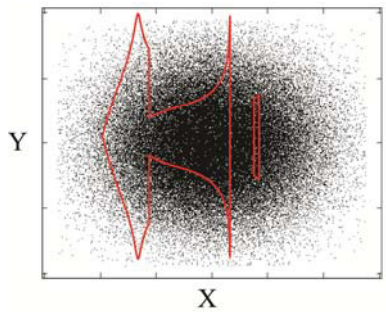


Figure 4: The shape of the mask plotted on top of the Gaussian bunch.

The beamline was modeled with Elegant [8], which is a matrix code. Without accounting for the space charge effect and coherent synchrotron radiation (CSR), the final 6-dimensional phase space coordinates of each particle in Elegant can be obtained from the initial phase space coordinates using different orders of transfer matrices of the beamline:

$$X_i^F = R_{ij}X_j + T_{ijk}X_jX_k + Q_{ijkl}X_jX_kX_l;\ \ i,j,k,l = 1,2,\dots 6.$$

In order to have the perfect transformation of the beam in the first (linear) order described by R-matrix, we want to have R_{5j}=0 except for R_{51}, which determines the stretch factor. The conditions R_{53}=R_{54}=0 are satisfied automatically in this configuration as the y-space remains uncoupled to both x and z spaces. In order to make R_{55}=R_{56}=0 the dispersion of the doglegs has to be matched to the deflecting cavity. Since the deflecting cavity of a finite length produces a time-correlated energy variation in the beam, it is necessary to include a fundamental mode cavity to compensate this effect.

Matrix elements R_{51} and R_{52} can be adjusted with the quadrupole magnets in front of the emittance exchanger. Using just two quadrupoles is sufficient to make R_{52}=0 and R_{51} equal to whatever required stretch factor. However, with only two quadrupoles we do not have any control over the width of the bunch (beta functions) along the beamline. The beta-functions may become quite large and the second order aberrations then become significant.

Copyright © 2013 CC-BY-3.0 and by the respective authors

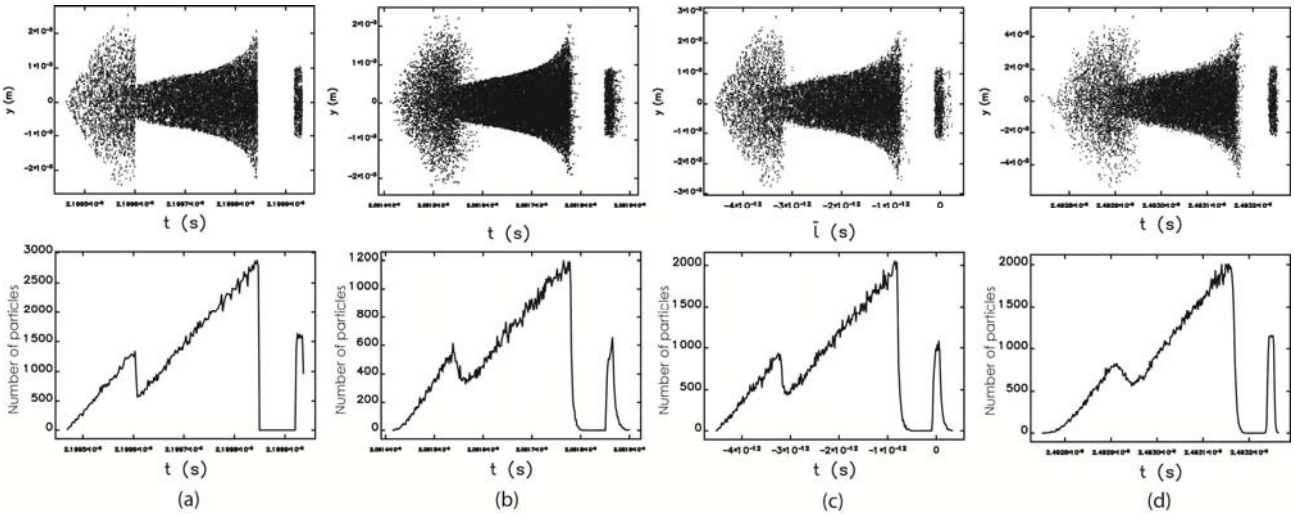


Figure 5: Distributions of the electrons (2D and integrated over y-axis) in the drive and witness bunches after the mask and the EEX as computed by Elegant: (a) in the first order of matrix elements, (b) in the third order of matrix elements, (c) in the first order with the second order matrix element T_{555} artificially included, and (d) in the third order with correcting sextupoles turned on.

With four quadrupole magnets before the EEX we have the control over R_{51}, R_{52}, beta functions and also over R_{61}, which we would like to keep small to avoid a longitudinal momentum chirp in the shaped bunch. Figure 5(a) shows the final distribution of particles and current in the shaped drive and witness bunches as computed with Elegant with only the first order of the transfer matrix.

The phase space exchange looks perfect in the first order simulations. However, when computations were performed to take into account the higher order matrices, aberrations were discovered (Figure 5(b)). We analysed the effects caused by different second and third order matrix elements and concluded that the observed changes in the shape of the witness bunch were mostly due to the effects of the second order matrix elements T_{555} and T_{551}. Figure 5(c) shows the distribution of electrons computed with the first order matrix and the T_{555} element artificially added. The aberrations due to the second order elements could be mitigated by placing a number of sextupole magnets in between the cavities and the second dogleg. Figure 5(d) shows the distribution of electrons with the sextupole corrections.

CONCLUSION

We have designed and optimized a beam shaping beamline to produce a double triangular drive and a trapezoidal witness bunches for a high transformer ratio low induced energy spread dielectric wakefield accelerator experiment. The beamline consisted of a mask followed by a tuned Emittance Exchanger. The EEX provides a unique tool for shaping beam currents in a small time scale. We realized that the EEX method is not perfect, as the higher order nonlinear effects in the beamline distort the desired pulse shape. Suppression of nonlinearities by inserting new elements into the beamline like quadrupoles, sextupoles or even octupoles can help reducing higher order nonlinearities, but will also increase complexity of the system that will eventually make tuning and aligning more difficult. The tighter focused beam may also become more prone to the space charge related effects. An experiment is planned in the near future to fully evaluate the nonlinearities and the space charge effects. We plan to conduct a beam shaping experiment with an EEX to evaluate the effects which are difficult to account for in simulations. This work may eventually evolve into a conceptual design of an afterburner for the proposed LANL future signature facility MaRIE. It also has the potential to advance the DWA technology to a level to make it suitable for a number of national security applications, including compact accelerators for warfighter support and active interrogation.

REFERENCES

[1] Matter-Radiation Interactions in Extremes (MaRIE) facility. http://marie.lanl.gov.

[2] B. E. Carlsten, K. A. Bishofberger, L. D. Duffy, C. E. Heath, Q. R. Marksteiner, D. C. Nguyen, R. D. Ryne, S. J. Russell, E. I. Simakov, and N. A. Yampolky, J. of Mod. Optics **58**(16), 1374 (2011).

[3] W. Gai, P. Schoessow, B. Coley, R. Konecy, J. Norem, J. Rosenzweig, and J. Simpson, Phys. Rev. Lett., **61**, 2756 (1988).

[4] M. Rosing and W. Gai, Phys. Rev. D, **45**, 1829 (1990).

[5] E.I. Simakov, B.E. Carlsten, D. Shchegolkov, AIP Conf. Proc. 1507, pp. 634-638 (2012).

[6] Y.-E. Sun, P. Piot, A. Johnson, A. H. Lumpkin, T. J. Maxwell, J. Ruan, and R. Thurman-Keup, Phys. Rev. Lett., 105, 234801 (2010).

[7] P. Emma, Z. Huang, K.-J. Kim, P. Piot, Phys. Rev. ST Accel. Beams **9**, 100702 (2006).

[8] M. Borland, Advanced Photon Source LS-287, September 2000.

Copyright © 2013 CC-BY-3.0 and by the respective authors

MONTE CARLO SIMULATIONS OF CHARGE TRANSPORT AND ELECTRON EMISSION FROM GaAs PHOTOCATHODES*

Yongjun Choi†, Dimitre A. Dimitrov, Chet Nieter, Tech-X Corp., Boulder, CO, USA
Siddharth Karkare, and Ivan Bazarov, CLASSE, Cornell University, Ithaca, New York, USA

Abstract

The need for a bright electron beam is increasing in the fields of x-ray science, electron diffraction and electron microscopy which are required for colliders. GaAs-based photocathodes have the potential to produce high-brightness, unpolarized and polarized, electron beams with performance that meets modern collider requirements. Even after decades of investigation, however, the exact mechanism of electron emission from GaAs is not well understood. Therefore, we investigate photoemission from a GaAs photocathode using detailed Monte Carlo electron transport simulations. Instead of a simple stepwise potential, we consider a triangular barrier including the effect of the image charge to take into account the effect of the applied field on the emission probability. The simulation results are compared with the experimental results for quantum efficiency and energy distributions of emitted electrons without the assumption of any ad hoc parameters.

INTRODUCTION

The successful operation of X-ray light sources, free electron laser (FEL), and linear accelerator facilities depends on providing reliable photocathodes [1] for generation of low emittance, high-brightness electron beams using conventional lasers.

An ideal photocathode must have a high quantum efficiency (QE), low mean transverse energy (MTE), a quick response time and a good operational lifetime. GaAs-based photocathodes have been experimentally tested and shown [2] to have the potential to produce high-brightness unpolarized and polarized, electron beams with performance (e.g., high QE and low emittance) that meets FEL and modern collider requirements. A better understanding of the physics of photoemission in GaAs will open new possibilities for creating very low emittance high efficiency photoemitters.

However, there are still a number of issues [3] to solve in order to develop an optimized photocathode design. It is of interest to better understand the quantum efficiency and energy distribution of generated beams as a function of temperature, laser frequency, cathode material, doping concentration, electron affinity, and surface properties (e.g., roughness, band bending, charge trapping).

* The authors wish to acknowledge the support of the U.S. Department of Energy (DOE) under SBIR grant DE-SC0006246 and Early Career DE-SC0003965.

† yjchoi@txcorp.com

Accurate simulation capabilities help to optimize the design of a semiconductor photocathode. Three dimensional, particle-in-cell (PIC) codes can accurately simulate the evolution of electron beams for these purposes.

The VSim simulation and modeling framework [4] includes a variety of physical models that make it useful for a broad range of research in plasma physics and computational electrodynamics. It can model a plasma as particles, a fluid, or a particle-fluid hybrid; it can treat electromagnetic fields either self-consistently or in the electrostatic limit; and it provides both explicit and implicit time updates.

In a previous work [5], we investigated effects of charge transport and surface properties on electron emission from GaAs with a specific surface potential. However, it did not include the image charge effect, zero applied field was assumed, and the space-charge field was not included in the models. Here, we have started to consider electron emission properties when the space-charge field is included and the applied field is non-zero. We have done simulations with a surface potential that is often used to investigate electron emission and includes the image charge effect. Finally, we have used a reduced model for the calculation of the electron emission probability that is fast to evaluate but potentially less accurate than the model in Ref. [5].

MODEL

The simulation is based on the three-step model initially proposed by Spicer [6]. The three valley model is used to describe the band structure of GaAs. Here, we briefly describe these models. More detailed explanation can be found in Ref. [5].

Three Step Model

The three-step model takes into account the dependence on photon energy and (implicitly) on temperature. Fig. 1 shows a schematic representation of the three-step model for *p*-doped GaAs photocathode. The creation of electron-hole pairs due to absorption of photons is treated in the first step. A photon with sufficient energy is absorbed by a valence band electron leading to its transition to the conduction band and the formation of a hole in the valence band. The difference between the photon energy and the energy gap of the semiconductor material is transferred into kinetic energy of the created free charge carriers. In the second step, created conduction band electrons undergo different scattering processes and propagate diffusively. Some of these electrons will reach the photocathode surface and be

Copyright © 2013 CC-BY-3.0 and by the respective authors

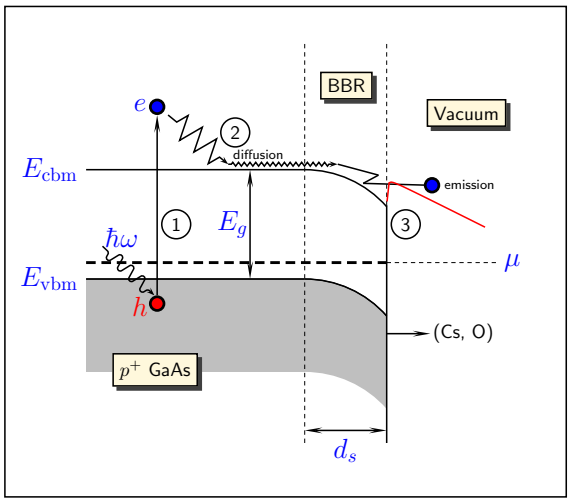


Figure 1: Schematic representation of the three-step model. First, a photon is absorbed causing the generation of an electron-hole pair. Next, the free electron undergoes phonon scattering and diffuses towards the GaAs cesiated electron affinity surface. In the final, third step, a conduction band electron undergoes emission (over barrier or tunneling) or reflection when impinging on the GaAs-vacuum interface.

emitted, during the third step as schematically shown in Figure 1.

Three Valley Model

In our simulation, we use the three valley model of GaAs, which assumes the top 3 valence bands (heave hole, light hole and the split-off) to be spherical and parabolic near the Γ point. The first conduction band is modelled as a combination of three valleys (Γ, L, and X valleys).

Electron-Hole Generation

As light propagates to a distance x in a photocathode (measured from its surface), its intensity decrease is given by the expression

$$I = I_o exp\left(-x/a\left(\hbar\omega\right)\right),$$

where $a\left(\hbar\omega\right)$ is the photon's energy-dependent absorption length. We assume that excitation of electrons from the valence band to the conduction band is the only dominant light absorption process. Doping dependent absorption length is calculated using the model developed by Lao *et al.* [7] The energy w.r.t. the conduction band minimum (CBM) of the electron excited into the Γ valley by a photon is calculated by equating the energy difference between the initial and final state of the electron to the energy of the photon [8].

Conduction Band Electron Transport

The charge transport of free carriers in the presence of applied electric field represents a drift-diffusion process. The simulation tracks electrons excited into the conduction band in both real space and k-space using semi-classical equation of motion. The main problem in modeling charge transport in GaAs is to determine the relevant scattering processes involved, how to calculate their rates as a function of electron energy, and how to determine final wave vectors in each type of scattering process. In this study, we considered impurity, phonon, and carrier-carrier scattering. For impurity scattering, we only consider scattering with charged impurities, because most impurities in GaAs are ionized at room temperatures. For phonon scattering, we consider acoustic, optical, and polar optical phonon scattering processes. Piezoelectric scattering is ignored. Here, we consider only electron-hole scattering (and neglect electron-electron and electron-plasmon processes) since it is the dominant carrier-carrier process for electrons in heavily *p*-doped GaAs. The density of free electrons is very small and plasma oscillations of the holes are heavily damped, therefore, electron-electron and electron-plasmon processes can be neglected.

Modeling Electron Emission

The simulation results we have reported here use the electron emission model developed by K. Jensen [9] with the image charge effect included in the surface potential. The potential energy of an electron in this surface potential is given by

$$V\left(x\right) = \chi - Fx - \frac{Q}{x}, \qquad (1)$$

where χ is the electron affinity (measured relative to the conduction band minimum at the surface), $Q = Q_0\left(K_s - 1\right)/\left(K_s + 1\right)$, $K_s \approx 13$ is the (static) dielectric constant for a GaAs cathode, and $Q_0 = q^2/\left(16\pi\varepsilon_0\right)$ with q the fundamental charge and ε_0 the permittivity of vacuum. The probability of emission is then given by Eq. (18) in Ref. [9] as a function of the electron's effective energy along the direction perpendicular to the emission surface. This approximate model for calculation of the emission probability, due to reducing the problem to one spatial dimension, requires us to extend our algorithm in VSim to explicitly preserve conservation of transverse momentum during emission. In the MATLAB code developed for the study by S. Karkare *et al.* [5], a transfer matrix (TM) approach was used to calculate the emission probability that explicitly takes into account conservation of transverse momentum. The TM method is currently being implemented in VSim and results with it will be presented elsewhere.

COMPARISON TO PHOTOEMISSION EXPERIMENTS

We use VSim with an electromagnetic pusher and include space charge effects. Band bending field and image charge effects are considered too. We also include the effect of an external applied field which was set to 1 MV/m. The values of GaAs parameters used in the simulations are given in Ref. [5]. The band bending region energy was 0.461 eV and its length was 8.4 nm calculated via the approach in Ref. [5]. Three-dimensional simulations are performed with

Copyright © 2013 CC-BY-3.0 and by the respective authors

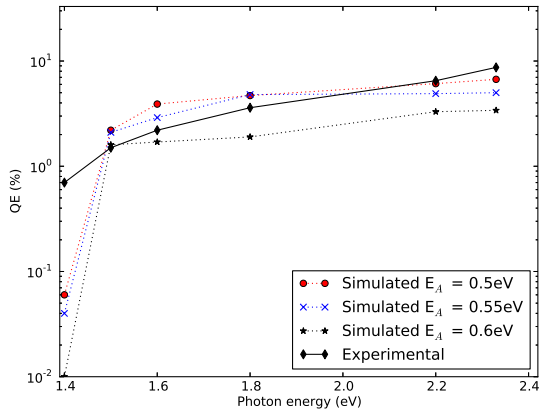


Figure 2: Comparison of measured and simulated spectral response. The electron affinity is an input parameter in the simulations. Results close to the experimental data are obtained for $\chi = 0.55$ eV.

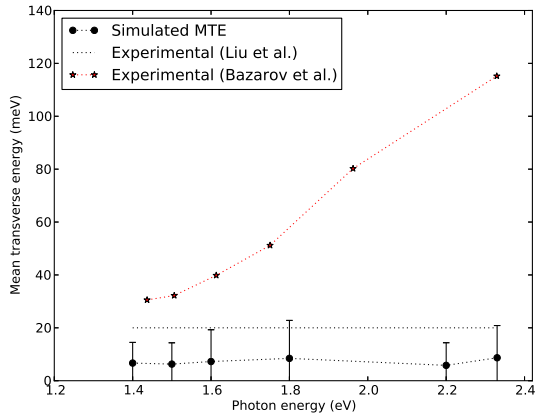


Figure 3: Comparison of measured (Liu *et al.* [10] and Bazarov *et al.* [11]) and simulated MTE using $\chi = 0.55$ eV in our simulations.

$30 \times 30 \times 30$ cells and 1000 electrons except for the lowest photon energy 1.4 eV in which case 10000 electrons were considered. We run simulations to 100 ps to collect data. The electron affinity is measured from the CBM at the GaAs surface (note that some authors consider χ relative to the CBM in bulk).

Spectral Response

Figure 2 shows the spectral response measurement along with the results obtained from the simulation for various values of electron affinity. The simulation results with electron affinity of 0.55 eV are overall closest to the experimental data. It is worth to mention that the simulation results are obtained entirely from the band structure and transport properties of GaAs and no ad-hoc parameters have been used. The only uncertain variable is the electron affinity which is deduced to be 0.55 eV (for the surface potential, Eq. (1), we considered) by comparing the simulated results to the experiment. In order to calculate the quantum efficiency, the reflectivity value of GaAs was taken from Ref. [5].

Mean Transverse Energy

We show MTE results from our simulations in Figure 3 together with data from two experimental measurements [10, 11]. The electron affinity was set to 0.55 eV in the simulations. Our results do not include scattering during emission process, and show very small MTE due to the narrow cone effect similar to the results from the MATLAB code [5]. The MTE deduced from the angular and energy distribution obtained by Liu *et al.* [10], using white light for excitation, is close to the simulation results. However, data from other experiments, including Bazarov *et al.* [11], give larger values outside of the narrow cone prediction. The reason for this discrepancy is still to be understood. Additional scattering during emission through the Cs layer was considered [5] leading to higher MTE values. However, emission dependence on surface roughness, orientation, surface cleanliness, and external electric field effects are still to be investigated in detail.

CONCLUSION

We presented simulation result on charge transport and electron emission from GaAs cathodes. Our model includes effects of applied field and image charge in the surface potential, space-charge fields and band bending. This model can achieve agreement with experimental data on QE with electron affinity the only free parameter varied. However, different surface potentials have been proposed and investigated in other studies [5] (and references therein). Further work is needed to determine the most relevant surface potential and related surface physics models (e.g. roughness and space-charge region in non-equilibrium) that could best describe observed experimental data.

REFERENCES

[1] D. H. Dowell *et al.*, *Nucl. Instr. Meth. Phys. Res.* A, 622:685-97 (2010).

[2] J. Clendenin *et al.*, *Technical Rev.*, SLAC-PUB-9581, Stanford Linear Accel. Center (2002).

[3] C. K. Sinclair, *Nucl. Instr. Meth. Phys. Res.* A., 557:69-74 (2006).

[4] C. Nieter, and J. R. Cary, *J. Comput. Phys.*, 196:448 (2004).

[5] S. Karkare *et al.*, *J. Appl. Phys.*, 113, 104904 (2013).

[6] W. E. Spicer, *Phys. Rev.*, 112:114-22 (1958).

[7] Y. F. Lao and A. G. U. Perera., *J. Appl. Phys.*, 109, 103528 (2011).

[8] M. A. Osman and D. K. Ferry, *Phys. Rev. B*, 36, 11 (1987).

[9] K. L. Jensen, *J. Vac. Sci. Technol.*, B 21, 1528 (2003).

[10] Z. Liu *et al.*, *J. Vac. Sci. Technol.* B 23, 2758 (2005).

[11] I. V. Bazarov *et al.*, *J. Appl. Phys.*, 103, 054901 (2008).

Copyright © 2013 CC-BY-3.0 and by the respective authors

HIGH CAPTURE LOW ENERGY SPREAD INVERSE FREE ELECTRON LASER ACCELERATOR

J. P. Duris, R. K. Li, P. Musumeci, E. Threlkeld
Department of Physics and Astronomy, UCLA, Los Angeles, CA 90095, USA

Abstract

We present the design and construction of a strongly period-, field-, and gap-tapered helical undulator for use in a high-gradient, high-efficiency helical IFEL experiment at Brookhaven ATF. The undulator design achieves efficient acceleration without prebunching by matching the ponderomotive and resonant energy gradients along the length of the interaction for the measured laser parameters. Simulations based on the measured undulator fields and experimental parameters suggest that as much as 43% of a 50 MeV beam will be accelerated to 94 MeV with 2.3% rms energy spread.

INTRODUCTION

Recent progress in inverse free electron laser acceleration (IFEL) has led to unprecedented acceleration gradients and energy gain for this class of accelerator. The STELLA experiment at ATF demonstrated efficient IFEL acceleration with gradients similar to conventional RF-accelerating cavities and captured up to 80% of the beam with the use of a prebunched beam [1]. The UCLA Neptune IFEL experiment first achieved accelerating gradients surpassing that of conventional rf-accelerators [2]. More recently, the UCLA-BNL helical IFEL collaboration at the Brookhaven Accelerator Test Facility (ATF) accelerated electrons from 52 MeV up to 106 MeV with a TW class CO_2 laser, averaging a 100 MeV/m accelerating gradient in the 54 cm long helical undulator [3]. The LLNL-UCLA IFEL effort currently underway at Lawrence Livermore National Lab aims to surpass these achievements by utilizing a multi-TW Ti:Sa laser [4] and has produced some significant initial results [5].

While IFEL accelerating gradients now outpace that of their rf counterparts, the higher gradients often come at the price of significant energy spread and low capture. One approach to improving capture is to match the longitudinal phase space of the beam to the longitudinal acceptance of the accelerator through microbunching as demonstrated by [1], and novel optical scale harmonic and adiabatic bunchers hold the promise of improved microbunching [6]. However, the efficiency of IFEL accelerators is often limited by spatiotemporal overlap of electron and laser beams as well as resonant energy and ponderomotive gradient mismatch. We aim to address these issues to allow monoenergetic acceleration with gradients larger than that of conventional accelerators without the use of prebunching.

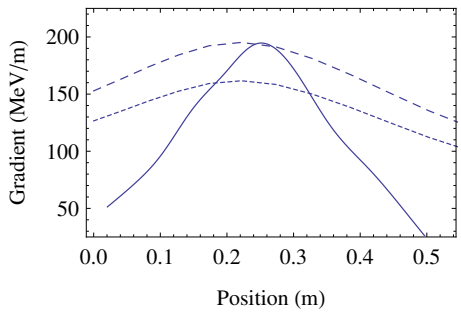


Figure 1: Resonant energy gradient set by the undulator tapering (solid) and ponderomotive gradients for the highest laser focal intensity of 23 TW/cm^2 (dashed) as well as for the median intensity of 18 TW/cm^2 (dotted).

GRADIENT MISMATCH

The UCLA-BNL helical IFEL collaboration at ATF was conceived to improve accelerating gradient through the use of the first strongly period- and field-tapered helical undulator. Whereas electrons propagating through a linear undulator undergo sinusoidal motion thereby reducing to zero twice per period their transverse velocity, the helical trajectories of the electrons propagating through the undulator provide continuous transverse velocity which in turn enables continuous energy transfer. This, coupled with a TW-class CO_2 laser, allowed for the acceleration of 52 MeV electrons up to 106 MeV [3].

The undulator was originally designed for use with a 9.6 cm Rayleigh range CO_2 laser. Unfortunately after construction, it was discovered that beam line space constraints and a restricting dipole aperture just upstream of the undulator necessitated a laser Rayleigh range of 30 cm. While the increased Rayleigh range had the positive benefit of easing transverse overlap tolerances by increasing the laser spot size, the on-axis intensity was reduced 3-fold, thereby significantly limiting the fraction captured and challenging the success of the experiment.

The problem can be better visualized by comparing the gradients set by the tapering of the undulator and that supplied by the ponderomotive interaction of the electrons in the combined undulator- and laser-fields. Figure 1 shows the resonant energy gradient set by the undulator and the ponderomotive gradient for various focal laser intensities (right plot). The resonant energy gradient usually exceeded the ponderomotive gradient, thereby significantly increasing the number of particles lost by reducing the ponderomotive bucket depth.

Copyright © 2013 CC-BY-3.0 and by the respective authors

HELICAL UNDULATOR

In order to improve the efficiency of the interaction, either the laser focusing must be changed to match the undulator design or the undulator tapering must be modified to match the laser. The former proved to be expensive as the dipole gap would have to be increased and impractical since due to the experimental hall layout, the focusing optics would have to be placed in the middle of a walkway, blocking access to vacuum equipment and interlock systems. The chosen solution was to redesign and rebuild the undulator to accommodate the more relaxed laser focusing.

The helical undulator is the superposition of two Halbach permanent magnet undulators rotated 90 degrees about their common axis and shifted in phase by a quarter wavelength [7]. Each of the four opposing pairs of NdFeB magnets per period determines the period and on-axis field of each undulator for a fixed gap of 15 mm. In order to relax the tapering, we tapered the gap of the undulator. This extra degree of freedom enabled us to change the undulator strength K while the period remained fixed.

Undulator Design

The undulator design follows closely the methods described in [8]. Equations 1 and 2 describe the approximate longitudinal dynamics of a particle undergoing helical IFEL interaction. Here, $K_l = \frac{eE_0\lambda}{m_0c^2 2\pi}$ and $K = \frac{eB\lambda_w}{m_0c2\pi}$ are the laser and undulator normalized vector potentials respectively.

$$\frac{d\gamma}{dz} = \frac{kK_lK}{\gamma}\sin\psi \tag{1}$$

$$\frac{d\psi}{dz} = k_w - k\frac{1+K^2}{2\gamma^2} \tag{2}$$

Equation 1 describes the ponderomotive gradient due to the combined interaction of undulator- and laser-fields as evident by the presence of K and K_l in the equation. For a stationary resonant phase, a resonant particle's energy is determined completely by setting the phase advance to zero in Equation 2, thereby yielding the energy of the resonant particle: $\gamma_r = \sqrt{\frac{\lambda_w}{2\lambda}(1+K^2)}$. This resonant energy depends only on the undulator field strength K and wavelength λ_w; therefore, the gradient in the resonant energy is determined completely by the undulator.

The undulator tapering is then determined by Equation 3 which is found by equating the ponderomotive gradient from Equation 1 with the gradient in the resonant energy set by the undulator tapering. When the undulator period and laser parameters are specified along with the initial condition that K at the entrance be such that the resonant energy is equal to the input beam's 50 MeV, the differential equation yields K which in turn determines the on-axis field strength along the undulator. The undulator builder equation can then be used to estimate the gap along the undulator needed to create the designed on-axis field. The measured laser and e-beam parameters used in the tapering

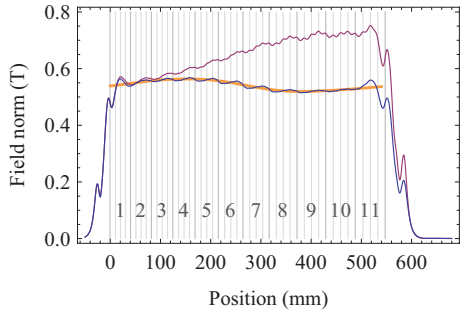


Figure 2: Design magnetic field amplitude along the undulator (orange) along with Radia simulation (blue) and the previous constant-gap undulator field (purple).

design are specified in Table 1. The design laser focal intensity dictates the threshold for full acceleration and was set to be 4 TW/cm^2 in order to be well within the capabilities of the laser in order to achieve full acceleration for most shots; furthermore, simulations show that this choice of design intensity maximizes capture for the more typical intensity of 18 TW/cm^2 observed previously. The resonant phase was chosen to be a constant $\pi/4$ as a compromise between bucket depth and ponderomotive gradient.

$$\frac{dK}{dz} = \frac{8\pi K K_l \sin\psi_r - \frac{d\lambda_w}{dz}\left(1+K^2\right)}{2\lambda_w K} \tag{3}$$

Table 1: Design Parameters

E-beam energy	50 MeV
Laser focal intensity	4 TW/cm^2
Laser wavelength	10.3 μm
Rayleigh range	30 cm
$1/e^2$ spot size	0.99 mm
M^2	1.07
Resonant phase	$\pi/4$
Laser waist	undulator midpoint

The 3D magnetostatic field solver Radia [9] was used to determine the placement of each magnet. Figure 2 shows the design field determined by the differential equation for K discussed above along with the field simulated by Radia with the design magnet gap configuration. The ripple in the Radia simulated field was introduced to minimize trajectory deflections for particles propagating on axis through the undulator. The trajectory is determined by the second integral of the field; however as the field increases towards the end of each period, the integral over one period is non-zero and the net effect is a kick to the particles. The ripple minimizes this deflection by canceling the second integral over each period.

Construction and Measurement

The undulator magnets are held in place by bolts which provide fine tuning of the gap over a range of a couple mm;

Copyright © 2013 CC-BY-3.0 and by the respective authors

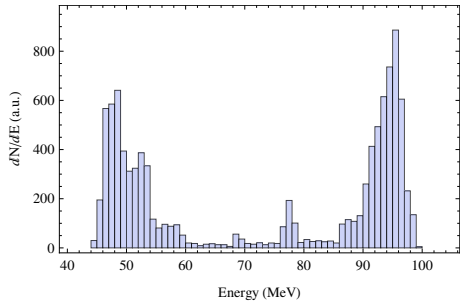


Figure 3: TREDI simulation utilizing the measured fields.

however since the half gap needed to be increased by about 2.5 mm towards the undulator's exit, aluminum shims were introduced to increase it by 3 mm. Measurements of the height of each magnet, width of the rails for each period, and the overall shim distance allowed for an estimate of the initial half gap with magnets retracted fully. The difference between design and measured half gap was calculated, and each magnet was driven into place. Since thread tolerances cause up to 200 μm play as each bolt was turned, a hall sensor was positioned on axis near each magnet before moving to detect movement as its corresponding bolt was turned.

After the initial magnet placement, the on-axis fields were measured and found to be systematically low by a couple percent. Magnets were then tuned slightly in pairs to increase the field to that of the Radia simulations. Finally, the fields were finely tuned to reduce the transverse kick and offset estimated by the first and second integrals of the field for a beam with energy 50 MeV. The final measured fields were found to agree to within 0.5% rms of the Radia simulations.

SIMULATIONS

Simulations were performed with the 3D IFEL code TREDI and are shown in Figure 3 for a 50 MeV input e-beam, laser focusing parameters listed in Table 1, and 18 TW/cm^2 laser focal intensity. TREDI solves the Lorentz force equations rather than averaging the motion of the electrons over an undulator period [10] and was previously bench-marked against IFEL experimental results in planar undulators [2]. The simulation includes time dependent effects, and the 1 ps long e-beam and 4.5 ps laser pulse are synchronized at the entrance to the undulator. The simulations show that for the expected experimental parameters, up to 43% of the beam is captured and transported to greater than 90 MeV. The accelerated beam has a mean energy of 94 MeV, energy spread of 2.3%, and is microbunched at 10.3 μm.

One of the benefits of the relaxed tapering is the relatively modest requirements on the laser performance. Figure 4 shows how the maximum particle energy varies as the input laser focal intensity is increased. While the laser focal intensity was previously seen to usually exceed 15 TW/m^2, the threshold for acceleration to 90 MeV for the measured undulator is just 5 TW/cm^2. This suggests that

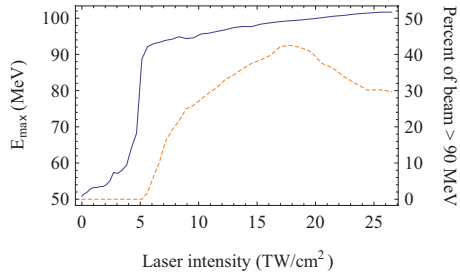


Figure 4: Maximum particle energy (solid) and fraction of beam with energy greater than 90 MeV (dashed) as a function of input laser focal intensity.

full energy acceleration should be obtained for most shots. Furthermore, a quarter of the beam is accelerated to greater than 90 MeV when the intensity is doubled to 10 TW/cm^2. These modest requirements on laser intensity for full acceleration open the door to studies of the accelerated beam.

CONCLUSIONS

While recent achievements in IFEL acceleration have focused on either high gradient or high efficiency acceleration, the UCLA-BNL helical IFEL collaboration aims to achieve both without the need for prebunching. The undulator tapering design achieves this by matching the resonant energy and ponderomotive accelerating gradients using the measured laser parameters through the novel strongly period-, field-, and gap-tapered helical undulator. The laser focal intensity threshold for full acceleration is well within the laser's observed limits leading to the possibility of studies of the accelerated beam. For moderate laser intensities, up to 43% of the e-beam should be transported to full energy, and production of a monoenergetic beam with few percent energy spread is expected.

This work was supported by DOE grant DE-FG02-92ER40693, Defense of Threat Reduction Agency award HDTRA1-10-1-0073 and University of California Office of the President award 09-LR-04-117055-MUSP.

REFERENCES

[1] W. Kimura et al., *Phys. Rev. Lett.*, 92:054801, 2004.

[2] P. Musumeci et al., *Phys. Rev. Lett.*, 94:154801, 2005.

[3] J. Duris et al. Submitted to *Phys. Rev. Lett.*

[4] J. Moody et al. in Proceedings of the 2012 International Particle Accelerator Conference, New Orleans, LA, 2012.

[5] J. Moody et al., MOPAC43, NA-PAC'13.

[6] L. Ho et al., TUPAC29, NA-PAC'13.

[7] J. Duris et al. in Proceedings of the 2012 International Particle Accelerator Conference, New Orleans, LA, 2012.

[8] J. Duris, P. Musumeci, R. Li. *Phys. Rev. ST Accel. Beams*, 15:061301, 2012.

[9] O. Chubar, P. Elleaume and J. Chavanne. *J. Synchrotron Rad.*, 5, 481- 484, 1998.

[10] L. Giannessi, P. Musumeci, M. Quattromini *Nucl. Instrum. Methods Phys. Res., Sect. A*, 436, 443, 1999.

Copyright © 2013 CC-BY-3.0 and by the respective authors

WISCONSIN SRF ELECTRON GUN COMMISSIONING*

J. Bisognano,# M. Bissen, R. Bosch, M. Efremov, D. Eisert, M. Fisher,+ M. Green, K. Jacobs,
R. Keil, K. Kleman, G. Rogers, M. Severson, D. D. Yavuz
University of Wisconsin-Madison, Stoughton, WI 53589, USA
R. Legg, R. Bachimanchi, C. Hovater, T. Plawski, T. Powers
Jefferson Laboratory, Newport News, VA 23606, USA

Abstract

The University of Wisconsin-Madison has completed installation of a superconducting electron gun. Its concept was optimized to be the source for a CW free electron laser facility with multiple megahertz repetition rate end stations. This VHF superconducting configuration holds the promise of the highest performance for CW injectors. Initial commissioning efforts show that the cavity can achieve gradients of 35 MV/m at the cathode position. With the cathode inserted CW operation has been achieved at 20 MV/m with good control of microphonics, negligible dark current, and $Q_0 > 3\times10^9$ at 4 K. Bunch charges of ~100 pC have been delivered, and first simple beam measurements made. These preliminary results are very encouraging for production of 100s pC bunches with millimeter-milliradian or smaller normalized emittances.

MOTIVATION

An FEL complex operating at high repetition rates and delivering intense, ultra-short, fully-coherent, variably-polarized beams to multiple experiments enables transformational research in diverse science disciplines. The Wisconsin SRF electron gun program is a response to the demand for a very bright electron source that can be used for these next generation light sources. SRF guns hold the promise to produce very bright, CW beams because of the correlation between high electric field on the cathode and brightness [1].

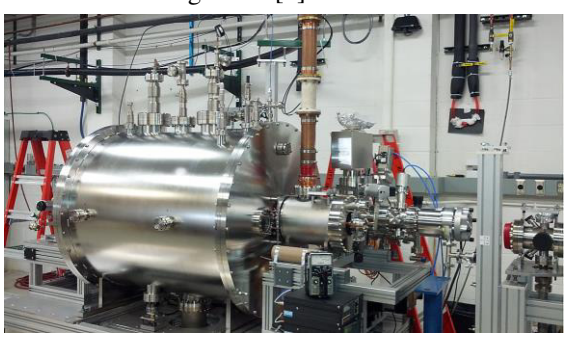


Figure 1: Electron gun installed in vault.

FACILITY OVERVIEW

The design uses a 199.6 MHz, quarter wave resonator geometry at a peak gradient up to 45 MV/m. Details of the superconducting cavity design, fabrication, and modeling have been presented in earlier publications [2]. The lower frequency design allows operation at 4 K and close to spatially constant electric field while the electron transits the accelerating gap. Thus, beam properties are expected to be superior to CW L-band guns, and relative to DC electron guns, should offer better performance with higher cathode fields. A copper photocathode was installed for initial testing with repetition rates limited to 1 kilohertz by the drive laser. Figure 1 shows the overall installation, and Table 1 contains key parameters for the gun.

Table 1: SRF Electron Gun Design Parameters

Max beam kinetic energy	4.0 MeV
Bunch charge	10–200 pC
Normalized trans. emittance	0.2–1 μm
Ultimate average beam current	1.0 mA
Peak current	50 A
Driving laser wavelength	266 nm

SUBSYSTEMS

RF System

The RF system utilizes a commercial, 30 kW, solid state transmitter driving coaxial waveguide through a circulator to the RF coupler. The low level RF controller (LLRF) [3] allows self-excited cavity operation and incorporates cavity fault and tuner control. It is based on the JLab upgrade design.

Magnets

The emittance compensation solenoid is of high temperature superconductor design. Nominal operating parameters are an integrated field of 3.1 T^2-mm at 38.45 A excitation at about 25-30 K (i.e., intermediate between LHe and LN_2 temperatures). An 18 bit AD7608 ADC is used to measure voltages at both ends and at the center of the solenoid for quench protection. The voltage difference between the two halves of the coil are compared and differences as small as 1 millivolt can be used to trigger a quench trip. There are two octupoles in the beamline. On each octupole the poles are independently powered with excitations mixed in software to produce normal and skew dipole and quadrupole correctors.

Cryostat

The cryostat consists of the helium vessel, internal tuner mechanism, cathode stalk, beam pipe, LN_2 cooled thermal radiation shield, magnetic shield, cryogenic plumbing and external vacuum vessel. The cavity is

*Work supported by DOE Award DE-SC0005264
#jbisognano@src.wisc.edu
+Current address: APS ANL

Copyright © 2013 CC-BY-3.0 and by the respective authors

immersed in 100 liters of batch fed LHe within the helium vessel. Minimizing static heat loss is critical since the LHe bath is not a closed loop system and the cryostat consumes LHe all the time that the cavity is held at 4.2 K. Calorimetric measurements using a heater in the helium vessel resulted in a static loss measurement of 6 W which agrees favorably with earlier calculated predictions of 7.5 W. Future plans include the addition of a LHe refrigerator, and the existing cryostat can be configured to run closed loop. The required modifications will most likely result in an increase in static thermal loss of approximately 2 W.

Photocathode Laser

The drive laser system consists of a Spectra Physics Tsunami titanium-sapphire oscillator seeding a Spitfire Pro Ultrafast Amplifier. It operates at 1 kHz and is synchronized to an external 80 MHz signal which is phase locked to the RF master oscillator. A Minioptic TPH tripler provides the frequency doubled and tripled beams at 400 nm and 266 nm respectively. The 800 nm light is used for laser diagnostics while the 266 nm light passes through an adjustable aperture optical transport system before being directed onto the photocathode.

The laser transport optical system consists of two nested Schiefspiegler telescopes with a 0.4 net magnification. A laser pulse length of 120 fs has been achieved.

Controls

The control system is based on EPICS utilizing several soft-IOCs running on a Scientific Linux server. Koyo DL205 PLCs are used to interface most of the beamline hardware. Additional soft-IOCs were written for cryogenic thermocouples, Faraday cup picoammeters, and motorized laser mirror mounts. Cameras are used to capture the YAG:Ce screen images. New capture software was written based on existing diagnostic cameras that implemented Gaussian fitting and automatic exposure control.

COMMISSIONING

Cooldown

Without a helium refrigerator, a two-step cool-down procedure has been utilized with vendor delivered LN_2 and LHe. The procedure takes two consecutive days. The first step, cooling down by LN_2, is performed on the first day followed by filling the cavity cryostat with liquid helium to complete the cool-down procedure on the second day. The first cool-down step also includes pre-cooling of the cavity cryostat by liquid nitrogen in a manual mode. Right before the liquid helium filling step (on the next day of the cool-down procedure) the cavity cryostat is purged by dry (boil-off) nitrogen until there is complete evaporation of the liquid nitrogen. Then, the gaseous nitrogen in the cryostat is purged by helium gas. Cooldown is about 29 hours to the most poorly cooled points. However, RF input can begin after about 10 hours.

Cathode Positioning

The cathode longitudinal position can be adjusted to ensure it is flush with the cavity surface. Although the cathode can be viewed axially through the cavity, the longitudinal positioning of the cathode face is complicated by the cryogenic contraction and flexure of the structure under vacuum load. Dead reckoning from warm measurements results in a ±2 mm error, which exceeds tolerances.

Our technique for positioning involves measurements of cavity resonant frequency versus cathode insertion. Comparable geometry runs were made in SuperFish [4]. The technique begins with frequency computations and measurements with the cathode withdrawn. From SuperFish one has the frequency shift expected with the cathode flush with the cavity's cathode snout; in this case it is nearly -3000 Hz. The cathode is then physically adjusted to achieve this frequency shift.

Microphonics

Generator Driven Resonator mode is an operating mode where the RF frequency is fixed and the cavity's mechanical tuner is used to keep the cavity frequency within a few hertz of the reference frequency. The field control chassis has the capability to send data on the phase difference between forward and transmitted power to a DAC output. The rms value of the frequency shift was 0.35 Hz and the peak-to-peak value was 2.7 Hz. The largest frequency component was a cavity frequency excursion of 0.14 Hz rms at a vibrational mode of 1.8 Hz The loaded Q of the cavity is 10^7. The microphonics are within the cavity bandwidth, and are well controlled by the LLRF system.

Plasma Processing and Q_0 Improvement

During the initial cold tests at Niowave, the cavity showed a low field Q_0 of 3×10^9 at 4 K. However, the cavity exhibited relatively severe field emission which limited operation to approximately 5 MV/m peak field at the cathode. To improve the anticipated initial performance, a novel surface preparation technique, plasma processing [5, 6], was used [7].

Figure 2 shows the Q_0 data plotted with the data from cold test at Niowave. Data show the cavity has a Q_0 of 3×10^9 at 4 K at a peak cathode gradient of 26 MV/m.

Performance Summary

Conditioning of the cavity and especially the cathode stalk has not been completed. The RF circulator failed at higher average powers and is currently under repair at the vendor, and further conditioning has been postponed. Following are performance limits achieved to date, but further improvements can be expected:

Highest CW gradient: 29 MV/m, cathode out
Highest CW gradient: 20 MV/m, cathode in
Highest pulsed gradient: 35 MV/m, cathode out
Highest pulsed gradient: 29 MV/m, cathode in
Dark current: < 1 pA at 20 MV/m CW

Copyright © 2013 CC-BY-3.0 and by the respective authors

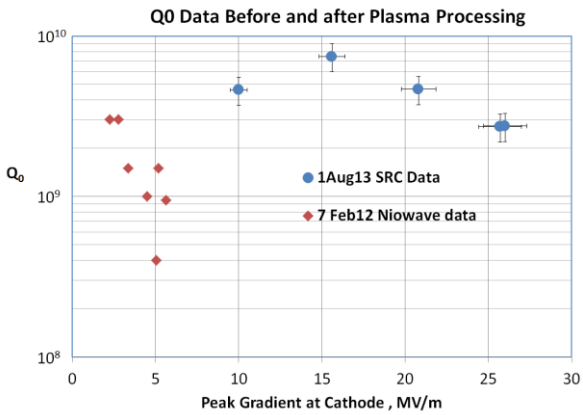


Figure 2: Calorimetric Q_0 data for cavity.

BEAM MEASUREMENTS

The gun and diagnostic beamline are shown in Figure 3. The transverse profile of the beam can be measured at three locations using 0.1 mm thick YAG:Ce screens. Two of the viewers, the first of which also contains a slit array, are located on the straight-ahead beamline, for use in

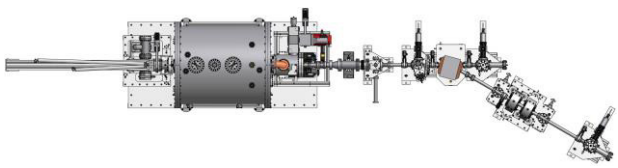


Figure 3: Layout of the gun and diagnostic beamline.

transverse emittance measurements. The third viewer is located on the 30° branch line, and is used to measure beam energy and energy spread. The beam is deflected down the branch line by an H-frame dipole. Both the straight-ahead line and the branch line are terminated with a Faraday cup/beam dump read by a picoammeter.

First beam measurements were made in mid-2013 although multipactor conditioning of the cathode stalk to higher gradients was still moving forward. To minimize cryogenic load during debugging of the diagnostics, first data were taken at 12 MV/m.

Initially there was 60 Hz motion of the beam that was traced to an AC solenoid on a vacuum valve. Additionally, it was found that the synchronization of the drive laser and the RF system was not stable. In particular, the 1 kHz repetition frequency from the drive laser is not well phase locked to the 200 MHz cavity fundamental, which results in an erratic bunch repetition rate and possible phase wandering. A laser upgrade is being provided by the vendor to correct this problem.

The electron energy was measured by centering the beam on the first beam viewer and the viewer on the 30° branch line. Based on the dipole calibration, the energy at 12 MV/m was 1.1 MeV. This is consistent what would be expected based on the accelerating gradient. The width of the beam spot on the 30° line viewer gave a projected energy spread of 2 % full width. The average bunch charge was measured to be roughly 100 pC.

Only one shift was devoted to transverse beam measurements before the RF circulator failure and only very limited data were acquired. We have initially used the quad-scan technique [8] for emittance measurement. To take space charge into account, ASTRA [9] simulations were compared to the measurements, and plausible emittances extracted. The estimated value for the normalized projected emittance is 1.5 mm-mrad. Given that laser/RF synchronization problem was present and that no systematic optimization was possible before the circulator failure, this result is surprisingly good and already near baseline goals. Since higher gradients can be obtained and optimization of phase tuning, cathode positioning, laser spot size, and emittance compensation has yet to be performed, considerable performance improvements can be expected.

FUTURE PLANS

A plan for a three year Phase II program is in place. We will work to fully characterize gun operation including exploration of tuning configurations (charge, peak current, RF phase, laser pulse length and spot size, emittance compensation, cavity gradient, etc.). The self-expanding blowout mode [10] and lower charge configurations for reduced emittance will be thoroughly investigated. A high repetition photocathode laser will be added together with a cathode preparation chamber for high quantum efficiency photocathode materials. Ultimately, exotic cathode materials for lowest emittance will be introduced. These improvements will allow operation at an average current of 1 mA at repetition rates up to 40 MHz.

SUMMARY

All together, the preliminary results are very encouraging for production of 100s pC bunches with millimeter-milliradian or smaller normalized emittances.

ACKNOWLEDGMENTS

We wish to thank Professor John Pfotenhauer and his cryogenics team for their help in the design of the cryostat and advice on cooldown procedures.

REFERENCES

[1] I.V. Bazarov, B.M. Dunham, C.K. Sinclair, Phys. Rev. Lett. 102 104801 (2009).
[2] R. Legg et al., IPAC2012, p. 661 (2012).
[3] C. Hovater et al., LINAC2010, p. 280 (2010).
[4] K. Halbach and R. F. Holsinger, Particle Accelerators 7 (1976) 213-222.
[5] Sang-ho Kim, LINAC2008, p. 11 (2008).
[6] J. Mammosser et al., IPAC2012, p. 3156 (2012).
[7] R. Legg et al., SRC Technical Note SRC-230, http://www.src.wisc.edu/users/SRC_230.pdf
[8] J. Rees and L. Rivkin, SLAC-PUB-3305 (1984).
[9] K. Flöttmann, ASTRA user manual.
[10] O. Leutein et al., Phys. Rev. Lett. 93 094802 (2004).

Copyright © 2013 CC-BY-3.0 and by the respective authors

EFFECT OF RF GRADIENT UPON THE PERFORMANCE OF THE WISCONSIN SRF ELECTRON GUN*

R. A. Bosch#, Synchrotron Radiation Center, University of Wisconsin-Madison,
3731 Schneider Dr., Stoughton, WI 53589, USA
R. A. Legg, Jefferson Lab, 12000 Jefferson Avenue, Newport News, VA 23606, USA

Abstract

The performance of the Wisconsin 200-MHz SRF electron gun is simulated for several values of the RF gradient. Bunches with charge of 200 pC are modeled for the case where emittance compensation is completed during post-acceleration to 85 MeV in a TESLA module. We first perform simulations in which the initial bunch radius is optimal for the design gradient of 41 MV/m. We then optimize the radius as a function of RF gradient to improve the performance for low gradients.

INTRODUCTION

A superconducting radiofrequency (SRF) electron gun has been designed and constructed to produce 200-pC bunches that are suitable for a high-repetition-rate (5 MHz) soft-xray free electron laser (FEL) [1–5]. Bunches are created by laser illumination of a photocathode and then accelerated to an energy of 4 MeV by a 200-MHz SRF cavity with peak electric field of 41 MV/m on the cathode. The electron gun utilizes a Cu photocathode, which can be replaced with a Cs_2Te photocathode whose higher quantum efficiency allows operation with lower laser power.

When a bunch is accelerated and compressed to achieve a peak current of ~1 kA for an FEL, current and energy modulations can cause microbunching that spoils the FEL process [1]. To minimize modulations in longitudinal phase space at the expense of slightly increased transverse emittance, "blowout" mode is employed, in which the initial bunch length is small compared to that of the accelerated bunch [6]. Simulations of blowout mode show that longitudinal and transverse modulations of the initial bunch distribution emitted from the photocathode are smoothed out by the self field space charge force [3].

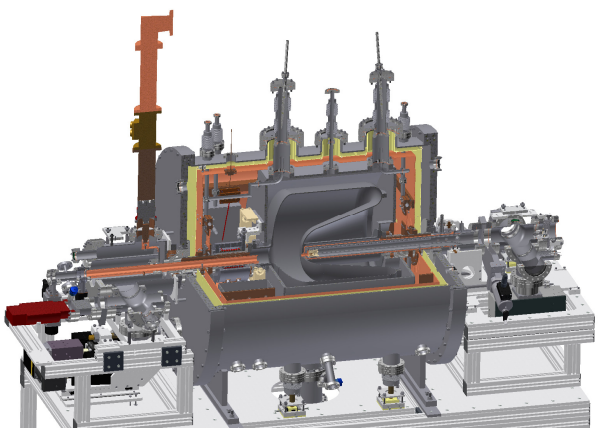


Figure 1: The photocathode, SRF cavity and high-temperature superconducting solenoid in the liquid-helium cryostat. Courtesy of G. C. Rogers.

We study the gun performance with simulations that include emittance compensation [7] from focusing the bunches in a high-temperature superconducting (HTS) solenoid [8] that is immediately downstream of the SRF cavity, and then accelerating them to 85 MeV in a cryomodule containing eight TESLA 1.3-GHz SRF cavities. The first TESLA cavity is used as a buncher, with the phase and gradient adjusted to control transverse focusing. The bunches become longitudinally frozen after travelling 3 m and reaching an energy of 6 MeV. For the design gradient of 41 MV/m, simulations indicate that bunches with normalized emittance of ~1 mm-mrad emerge from the cryomodule [5]. Figure 1 shows the photocathode, SRF cavity, and solenoid in the liquid-He-cooled cryostat.

In this article, we evaluate the production of 200-pC bunches when the peak electric field on the cathode of the 200-MHz cavity differs from the design gradient of 41 MV/m. The ASTRA [9] code is used to perform 100,000-particle simulations of a realistic bunch that initially has truncated Gaussian radial and longitudinal profiles, truncated at 0.8σ. (Note that for a Gaussian profile truncated at 0.8σ, σ is not the rms value.) For the Wisconsin electron gun, previous studies [5] have shown agreement between ASTRA simulations and simulations performed with the GPT code [10].

An initial longitudinal σ of 187.5 fs is studied; nearly identical results have been obtained with smaller values of the longitudinal σ, consistent with blowout mode. Since the electron velocity depends upon the RF gradient, we use the AUTOPHASE feature of the ASTRA code to set the RF phase when a bunch enters a TESLA cavity to equal the optimized phase for the design RF gradient of 41 MV/m.

A bunch is emitted from a Cu or Cs_2Te photocathode with initial transverse normalized slice emittances ε_x and ε_y that are related to the rms laser spot dimensions by $\varepsilon_{x,y}$ [mm-mrad] ≈ $\sigma_{x,y}$ [mm], and initial kinetic energy of ~0.5 eV [11, 12]. For a Gaussian radial profile truncated at $0.8\sigma_r$, the rms dimensions are given by $\sigma_{x,y} = 0.4\sigma_r$.

FIXED BUNCH RADIUS

We first considered the initial bunch radius that gives the lowest output emittance for the design gradient of 41 MV/m. For a truncated Gaussian radial profile truncated at $0.8\sigma_r$, this initial radius σ_r is 1.75 mm [5]. The rms

*Work supported by DOE Award DE-SC0005264
bosch@src.wisc.edu

Copyright © 2013 CC-BY-3.0 and by the respective authors

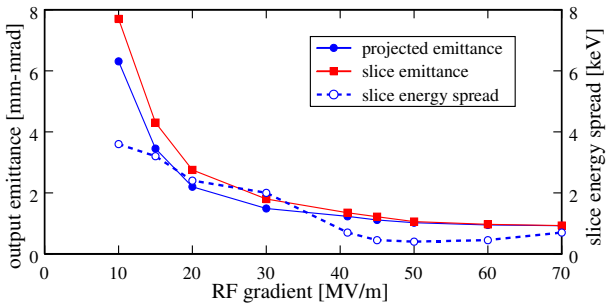


Figure 2: Bunch properties versus peak RF gradient, for a truncated Gaussian bunch distribution emitted from a Cu or Cs_2Te photocathode, with initial radial σ_r of 1.75 mm, initial longitudinal σ of 187.5 fs, and initial emittance of 0.7 mm-mrad. The focusing strength of the solenoid was optimized for each value of the RF gradient, in order to minimize the projected emittance. The normalized projected and slice emittances, and the slice energy spread, are evaluated at the exit of the TESLA module where the beam energy is 85 MeV.

bunch dimensions are $\sigma_{x,y}$ = 0.7 mm, so for a Cu or Cs_2Te photocathode, we assume that the initial normalized slice emittances are $\varepsilon_{x,y}$ = 0.7 mm-mrad. For the design gradient, the lowest projected emittance at the exit of the TESLA module is obtained when the longitudinal integral of the square of the solenoidal magnetic field, $\int B^2 dz$, equals 31.1 kG^2-cm. For this case, the normalized projected and slice emittances are 1.3 mm-mrad, the slice energy spread is 0.7 keV, and the peak current is 35 A.

For each value of the peak RF gradient that we studied, the solenoid field strength was optimized to obtain the lowest projected emittance at the exit of the TESLA module. Figure 2 shows the projected emittance of the bunch, and the slice emittance and slice energy spread in the longitudinal center of the bunch. To evaluate the slice properties, 200 slices—each containing 500 particles—were considered. Since the slice emittance is largest near the bunch center, it is possible for the projected emittance to be smaller than the slice emittance of the center slice. While the output emittances decrease with increasing RF gradient, the slice energy spread reaches a minimum value of 0.4 keV when the RF gradient is 50 MV/m.

OPTIMIZED BUNCH RADIUS

When the RF gradient is lower than the design value of 41 MV/m, the space-charge-induced emittance growth is increased for a given bunch radius. Consequently, the initial bunch radius that produces the smallest output emittance depends upon the RF gradient. We performed simulations in which the initial bunch radius and solenoid field strength were both optimized to obtain the smallest projected emittance for each value of the RF gradient, for a Cu or Cs_2Te photocathode with initial $\varepsilon_{x,y}$ [mm-mrad] = $\sigma_{x,y}$ [mm]. The results in Fig. 3(a) show that optimizing the initial bunch radius significantly improves the performance for RF gradients lower than the design value. The output emittances decrease with increasing RF

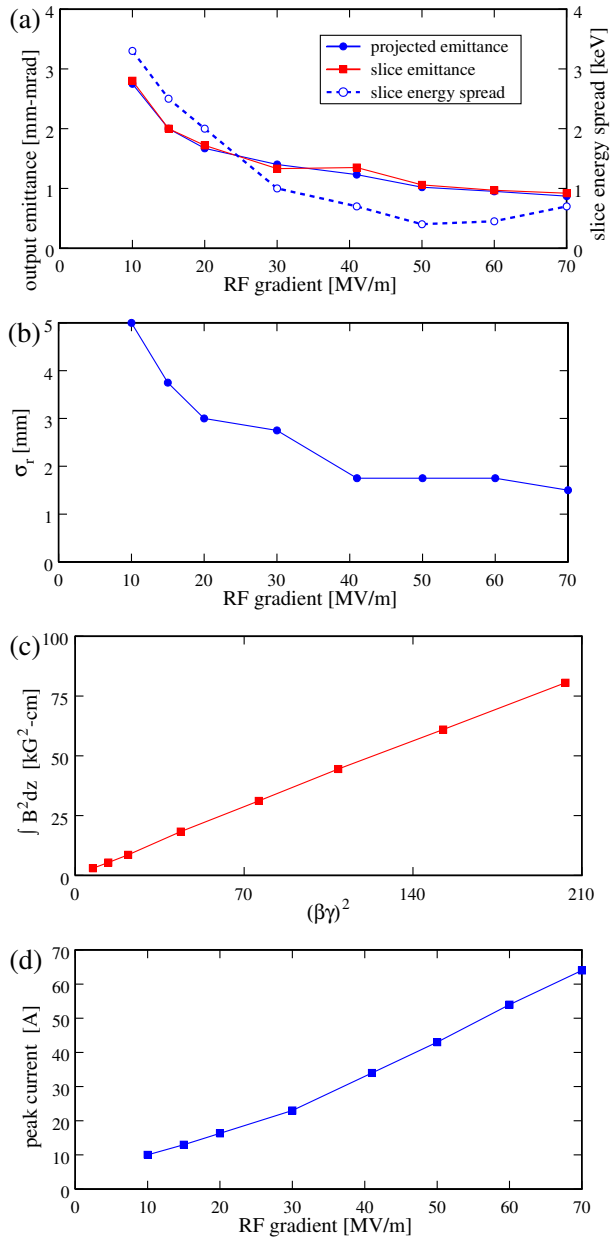


Figure 3: Bunch properties vs. peak RF gradient. The initial bunch radius and the solenoidal field are optimized for each value of the gradient to minimize the projected emittance for a Cu or Cs_2Te photocathode. (a) The normalized projected and slice emittances and slice energy spread at the exit of the TESLA module. (b) The optimal value of σ_r vs. RF gradient, for a Gaussian radial distribution truncated at $0.8\sigma_r$. (c) The integral of the square of the optimized solenoidal field, $\int B_z^2 dz$, vs. the bunch's $(\beta\gamma)^2$ in the solenoid. (d) Peak current at the exit of the TESLA module.

gradient, while the energy spread is minimized at 0.4 keV for a peak gradient of ~50 MV/m.

Figure 3(b) shows the optimal value of σ_r as a function of the RF gradient. For lower RF gradients, it is advantageous to have a larger initial radius, even though the initial emittance from the photocathode is increased.

Copyright © 2013 CC-BY-3.0 and by the respective authors

For the RF gradients studied, Fig. 3(c) shows that the longitudinal integral of the square of the solenoidal magnetic field, $\int B^2 dz$, is proportional to the bunch's $(\beta\gamma)^2$ in the solenoid, where β is the electron velocity divided by the speed of light, and γ is the relativistic factor. This indicates that the optimized focal length of the solenoid is independent of the RF gradient.

Neglecting space charge effects, the focal length of the solenoid, f, in the thin-lens approximation, obeys [13]

$$\frac{1}{f} = \left(\frac{e^2}{4m^2c^2} \right) \frac{\int B^2 dz}{(\beta\gamma)^2} , \quad (1)$$

where e is the electron charge, m is the electron mass, and c is the speed of light.

For the optimal solenoidal field strength, the calculated focal length is 0.29 m for all values of the RF gradient. The image of the cathode is located near to the entrance of the second RF cavity in the 8-cavity TESLA module, whose first RF cavity has phase and gradient adjusted for use as a buncher. The location of the cathode's image is consistent with the emittance compensation process, in which a beam waist is formed near to the entrance of the first RF cavity that is used for acceleration of the beam [1, 7].

Figure 3(d) shows the bunch's peak current at the exit of the TESLA module. The peak current increases with RF gradient because of decreasing longitudinal expansion due to space charge.

For simulations in which the initial bunch has a truncated Gaussian profile, a gradient of 15 MV/m is sufficient to produce a high-quality bunch with normalized transverse emittance of 2 mm-mrad, slice energy spread of 2.5 keV, and peak current of 13 A. For the design value of the gradient, 41 MV/m, a bunch is produced with normalized transverse emittance of 1.3 mm-mrad, slice energy spread of 0.7 keV, and peak current of 35 A. With a slightly larger gradient of 50 MV/m, the slice energy spread decreases to 0.4 keV, while the normalized emittance is 1 mm-mrad and the peak current is 43 A. For gradients exceeding 55 MV/m, the peak current exceeds 50 A.

SUMMARY

For the Wisconsin SRF electron gun, simulations have been performed to study the dependence of the output bunch properties upon the peak RF gradient on the cathode of the 200-MHz cavity. To model realistic bunches from laser illumination of a photocathode, we simulated bunches whose initial radial and longitudinal profiles are truncated Gaussian distributions, truncated at 0.8σ. To minimize the output emittance, we optimized the initial bunch radius and field strength of the emittance-compensation solenoid for each value of the RF gradient. For gradients of 10–70 MV/m, the output emittance decreases and the peak current increases with increasing gradient, while the slice energy spread is minimized at 0.4 keV for a gradient of 50 MV/m. For gradients exceeding 50 MV/m, the normalized output emittance is smaller than 1 mm-mrad, and for gradients exceeding 55 MV/m, the peak current exceeds 50 A.

For gradients exceeding 15 MV/m, the 200-pC bunches have normalized slice and projected emittances smaller than 2 mm-mrad, slice energy spreads smaller than 2.5 keV, and peak currents exceeding 13 A. These bunches are suitable for a soft xray FEL.

REFERENCES

[1] R. Legg, W. Graves, T. Grimm and P. Piot, in "Proceedings of the 11th European Particle Accelerator Conference, Genoa, Italy, 2008" (EPS-AG, Genoa, Italy, 2008), p. 469.

[2] R. Legg, in "Proceedings of the 24th Linear Accelerator Conference, Victoria, BC, Canada, 2008" (TRIUMF, Vancouver, BC, Canada, 2009), p. 658.

[3] R. Legg, M. Allen, M. Fisher, Z. Hjortland, K. Kleman, T. Grimm and M. Pruitt, in "Proceedings of the 45th ICFA Advanced Beam Dynamics Workshop on Energy Recovery Linacs, Ithaca, NY, 2009" (Cornell, Ithaca, NY, 2010), p. 45.

[4] R. Legg, J. J. Bisognano, M. Bissen, R. Bosch, D. Eisert, M. Fisher, M. Green, K. Jacobs, K. Kleman, J. Kulpin, G. Rogers, M. Severson and D. Yavuz, in "Proceedings of the 2012 International Particle Accelerator Conference, New Orleans" (JACoW, Geneva, 2012), p. 661.

[5] R. A. Bosch, K. J. Kleman and R. Legg, in "Proceedings of the 2012 International Particle Accelerator Conference, New Orleans" (JACoW, Geneva, 2012), p. 1572.

[6] O. J. Luiten, S. B. van der Geer, M. J. de Loos, F. G. Kiewiet and M. J. van der Wiel, Phys. Rev. Lett. 93, 094802 (2004).

[7] L. Serafini and J. B. Rosenzweig, Phys. Rev. E 55, 7565 (1997).

[8] R. Gupta, M. Anerella, I. Ben-Zvi, G. Ganetis, D. Kayran, G. McIntyre, J. Muratore, S. Plate, W. Sampson, M. Cole and D. Holmes, in "Proceedings of the 2011 Particle Accelerator Conference, New York" (PAC'11 OC / IEEE, NY, 2011), p. 1127.

[9] G. Pöplau, U. van Rienen and K. Flöttmann, in "Proceedings of the 10th European Particle Accelerator Conference, Edinburgh, 2006" (EPS-AG, Edinburgh, 2006), p. 2203.

[10] M. J. de Loos and S. B. van der Geer, in "Proceedings of the 5th European Particle Accelerator Conference, Sitges, Spain, 1996" (EPS-AG, Sitges, 1996), p. 1241.

[11] W. S. Graves, L. F. DiMauro, R. Heese, E. D. Johnson, J. Rose, J. Rudati, T. Shaftan and B. Sheey, in "Proceedings of the 2001 Particle Accelerator Conference, Chicago" (IEEE, Piscataway, NJ, 2001), p. 2227.

[12] V. Miltchev, "Investigations on the transverse phase space at a photo injector for minimized emittance," Ph.D. thesis, Humbolt University, Berlin, 2006.

[13] V. Kumar, Am. J. Phys. 77, 737 (2009).

Copyright © 2013 CC-BY-3.0 and by the respective authors

STUDY ON 2 CELL RF-DEFLECTOR CAVITY FOR ULTRA-SHORT ELECTRON BUNCH MEASUREMENT*

T. Takahashi†, Y. Nishimura, M. Nishiyama, K. Sakaue, M. Washio
Waseda University, Tokyo, Japan

T. Takatomi, J. Urakawa, KEK, Ibaraki, Japan

Abstract

We have been studying on an rf-deflector system to measure ultra-short electron beam bunch length at Waseda University. By using HFSS, we optimized the design of the 2 cell rf-deflector which is operating on π-mode, standing wave, dipole (TM_{110}-like) mode at 2856 MHz. We have finished manufacturing under the collaboration with High Energy Accelerator Research Organization (KEK) and installing the rf-deflector in the accelerator system of Waseda University. It is estimated that this rf-deflector has sufficient performance for measuring the ultra-short electron bunch. Now the experiment has just begun and confirmed electron beam is swept by this rf-deflector. Bunch length measurement will be soon carried out accurately. In this paper, the design of rf-deflector, the estimation for rf-deflector performance, the present progress and the future plan will be described.

INTRODUCTION

At Waseda University, a compact linear accelerator system based on photo-cathode rf electron gun is applied for the various researches and we have two kinds of rf electron guns as beam sources, 1.6 cell S-band Cs-Te photo-cathode rf gun (1.6 cell gun) for the pulse radiolysis [1] and the laser Compton scattering [2], Energy chirping cell attached rf gun (ECC gun) for the generation of coherent THz radiation [3]. It is necessary to measure time structure of electron beam on several picoseconds region on 1.6 cell gun and bunch length of several hundreds femtoseconds on ECC gun in the future. Therefore, we have been developing an rf-deflector system in order to achieve the bunch length measurement with high temporal resolution.

PRINCIPLE OF BUNCH LENGTH MEASUREMENT BY RF-DEFLECTOR

When rf electromagnetic wave is supplied into an rf-deflector, a proper resonant mode is excited. The resonant electromagnetic field in the beam line produces force on the beam. The magnitude of the force which influences on each part of the electron bunch is different in association with temporal change. When this force has vertical direction to the beam line, the beam after the passage of an rf-deflector is tilted as it drifts. This means the longitudinal distribution of the beam is converted to the transverse. The bunch length can be calculated by observing the transverse distribution. The outline of bunch length measurement by an rf-deflector is below (Fig.1).

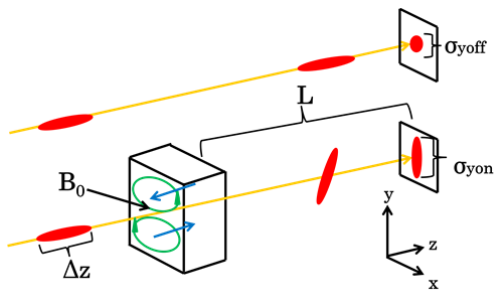


Figure 1: Outline of bunch length measurement.

In Waseda University, we have designed the rf-deflector which produces only Lorentz force to the beam by a magnetic field, using a TM110-like mode. By solving the equation of motion to electron, bunch length Δz is expressed by (assuming the Gaussian profile):

$$\Delta z = \frac{E\sqrt{{\sigma_{yon}}^2 - {\sigma_{yoff}}^2}}{2cB_0L\{\cos(\omega t_0 + \phi) - \cos\phi\}} \qquad (1)$$

where σ_{yon} and σ_{yoff} are the vertical beam size at the profile monitor when the rf-deflector is on and off, respectively, B_0 the peak magnetic field in the rf-deflector, L drift distance between the outlet of the rf-deflector and the profile monitor, φ the rf phase when the bunch enters the rf-deflector, ω the angular frequency of the rf-deflector, E the beam energy, t_0 the traveling time of the bunch in the rf-deflector, c the velocity of light. Then the number of 2 in the denominator represents the 2 cell structure of the rf-deflector. When σ_{yon} is measured, it is supposed that the time resolution becomes higher if the space covered by σ_{yoff} is smaller. So it is important to get large σ_{yon} and small σ_{yoff}. According to Eq. (1), the large magnitude of B_0 or L brings about the progress of time resolution, and ultra-short bunch length measurement could be possible. Because L has the limitation considering the size of the accelerator facility, we have designed the form of the rf-deflector with the larger

*Work supported by JSPS Grant-in-Aid for Scientific Research (A) 10001690 and the Quantum Beam Technology Program of MEXT.
†qwerty-ytrewq@toki.waseda.jp.

Copyright © 2013 CC-BY-3.0 and by the respective authors

magnitude of B_0 and adopted the rectangular-based 2 cell rf-deflector as a result.

DESIGN AND MANUFACTURING OF RF-DEFLECTOR

We have used HFSS simulating 3D full-wave electromagnetic fields for the design of the rf-deflector [4]. An rf-deflector is a kind of cavity, and proper resonant modes related to the form of a cavity are conducted by solving Maxwell equation. We have determined the cavity parameters to make TM110-like mode on 2856 MHz. The largest magnitude of B_0 has been obtained, adjusting the sizes of x and y directions.

We have improved the structure from 1 cell to 2 cell for the further progress of temporal resolution. The π-mode operation of 2 cell cavity provides larger tilt for electron bunch. The structure of the 2 cell rf-deflector is shown in Fig. 2. The magnetic field in 2 cell rf-deflector (Fig. 3) and the coupling with the waveguide have been optimized on HFSS.

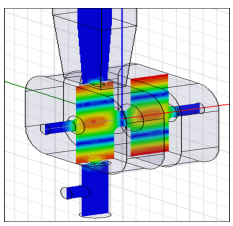


Figure 2: Structure of 2 cell rf-deflector (HFSS).

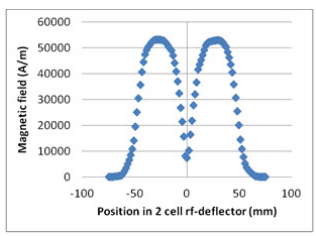


Figure 3: Magnetic field in 2 cell rf-deflector with 750 kW supply (HFSS).

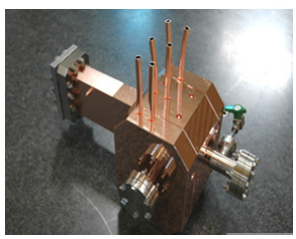


Figure 4: Structure of 2 cell rf-deflector.

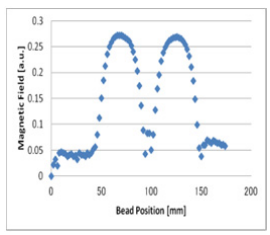


Figure 5: Magnetic field in 2 cell rf-deflector.

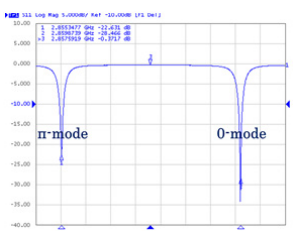


Figure 6: Reflecting method result.

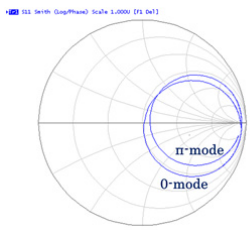


Figure 7: Smith chart.

On the basis of this design by HFSS we have manufactured the 2 cell rf-deflector under the collaboration with High Energy Accelerator Research Organization (KEK). The cavity was processed the fabrication-coordination of rf frequency iteration 4 times. After achieving the desired frequency, the each part was brazed. The finished 2 cell rf-deflector is shown in Fig. 4. Some tuners and water pipes are attached to each cell.

For the purpose of the installation in the accelerator system at Wasede University, we have tuned the rf-deflector by the tuners and temperature of the rf-deflector. The results after the tuning are shown in Fig. 5, Fig. 6, and Fig. 7. Figure 5 shows that the magnetic field strength in each cell is almost the same by the beads method. Figures 6 and 7 show the results of measurement by reflecting method and the smith chart on network analyzer. These indicate the coupling with the waveguide is suitable. The comparison of the cavity parameters after tuning and the desired value is shown on Table 1. The desired value has been set under air condition. The fabrication and tuning of the rf-deflector have successfully processed, as shown in Table 1.

Table 1: Target Parameters of RF-deflector Design

Parameters	Result	Desired value
π mode	2855.348MHz	2855.372MHz
0 mode	2859.874MHz	2859.922MHz
Δf	4.526MHz	4.55MHz(HFSS)
Q value on π mode	16298	17282(HFSS)
Ratio of magnetic field	1:0.9875	1:1
Coupling constant β	0.839	1.000

SETUP AND EXPERIMENT

After establishing the rf-deflector, we have installed in the accelerator system. The outline of the setup is shown in Fig.8 and the accelerator system after installation shown in Fig. 9. We can measure the beam energy by the bending magnet and the charge by the FCT in the downstream of the rf-deflector. Because of our systematic condition, we have installed the rf-deflector falling sideways. This means the beam is tilted in x direction, so we think of the beam size in x direction as σ_{yon} and σ_{yoff}. The rf-power for the rf-deflector is variable in the range of 0~750kW through the attenuator.

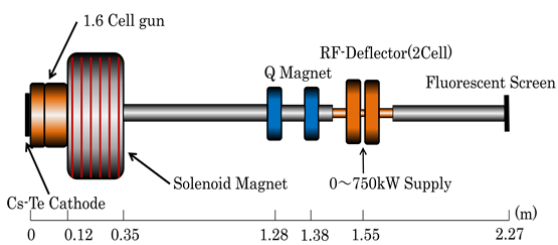


Figure 8: Setup of rf-deflector system.

Copyright © 2013 CC-BY-3.0 and by the respective authors

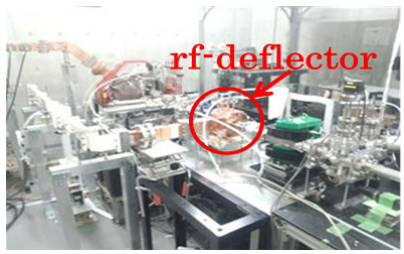
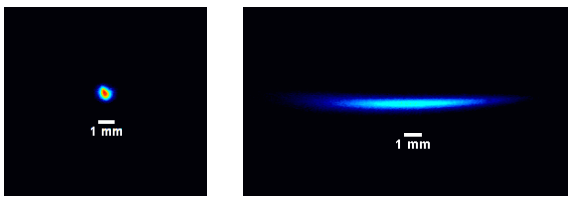


Figure 9: RF-deflector system.

Now the experiment has just begun. First of all, we had to confirm the rf-deflector is operating properly. We have observed the focused beam on the screen with the rf-deflector off to optimize the currents in the solenoid magnet and Q magnets. The deflected beam has been observed at the zero-crossing phase with the rf-deflector when 175kW rf-power was supplied. These profiles are shown in Fig. 10. The peak position of the beam doesn't move compared with Fig 10 (A) at the zero-crossing phase. The beam parameters were about 4.8MeV and 3pC. In Fig. 10, σ_{yoff} is about 220μm and σ_{yon} is about 3.26mm. This result indicates that the rf-deflector is operating properly.



(A) (B)

Figure 10: Observed beam profiles. (A): deflector is off, (B): deflected bunch at the zero-crossing phase.

Because B_0 is 320G with 175kW supply on HFSS simulation, the bunch length can be estimated to be 2.07ps from Eq. (1). The temporal resolution of the rf-deflector means the limitation of measurable bunch length and is derived as the bunch length in the case that σ_{yon} equals σ_{yoff}. Therefore, the temporal resolution is approximately 140fs from σ_{yoff}, σ_{yon}, and the bunch length.

The B_0 that we discussed above is not correct value. The actual B_0 in the rf-deflector is now under calibration, otherwise the accurate bunch length and temporal resolution can not be calculated. The B_0 calibration is accomplished by fitting the displacement about the peak of the beam, Δy, to the rf-deflector phase, φ_0. The displacement Δy is expressed by:

$$\Delta y = \frac{c^2 B_0 L}{E\omega}\{\sin(\omega t_0 + \phi_0) - \sin\phi_0\} \qquad (2)$$

These parameters are the same as described in Eq. (1). Since the actual B_0 is probably smaller than the value on HFSS due to the loss of the rf-power, the accurate bunch length and temporal resolution will come to be larger. However, the simulation result may not have much difference, thus we can estimate that this rf-deflector system has a capability of measuring ultra-short bunch. Concerning the short bunch beam, which has the several picoseconds length, the temporal structure of the electron bunch can be observed. The precise bunch length measurement will be soon carried out.

CONCLUSIONS AND PROSPECTS

In this paper, we introduced the rf-deflector system for the bunch length measurement with high temporal resolution and described the procedure for 2 cell rf-deflector. We have achieved 2 cell rf-deflector which will be able to measure several hundreds of femtoseconds bunch. Now we have finished installation in our accelerator system and confirmed the rf-deflector operating properly. The precise bunch length measurement and dynamics studies of rf-gun will be soon carried out.

RFERENCES

[1] K. Ogata, et al., Proc. of IPAC'11, THPS090,(2011)
[2] K. Sakaue, et al., Radiation. Phys. Chem. 77. 1136 –1141 (2008).
[3] Y. Koshiba, et al., "Development of an rf electron gun for ultra-short bunch generation", IPAC2012, TUPPD058,(2012).
[4] Y. Nishimura, et al., Proc. of IPAC 2013, WEPFI023 "STUDY ON TWO-CELL RF-DEFLECTOR CAVITY FOR ULTRA-SHORT ELECTRON BUNCH MEASUREMENT."

Copyright © 2013 CC-BY-3.0 and by the respective authors

10S FEMTOSECOND BUNCH LENGTH MEASUREMENT BASED ON COHERENT TRANSITION RADIATION*

Xianhai Lu†, Wenhui Huang, Chuanxiang Tang, Tsinghua University, Beijing 100084, P. R. China‡
K.G. Roberts, R.K. Li, P. Musumeci, H.S. To, UCLA, Los Angeles, CA 90095, USA

Abstract

In this paper, we discuss bunch length measurement based on coherent transition radiation for 10s femtosecond electron bunches with of several MeV energy and several pC charge. The ultrashort bunch length is obtained by velocity bunching using a compact dual slot resonantly coupled linac located after an RF photoinjector. Strong focusing with a solenoid is required to enhance the radiation generation. Filters are used to reconstruct coherent transition radiation spectrum. The transverse and longitudinal form factors are also studied with simulation.

INTRODUCTION

Bunch length measurement is a basic issue in beam diagnostic. Traditional methods for bunch length measurements includes using deflecting cavity[1], using radiation based spectrum methods[2] and electro-optic detection methods[3]. By using velocity bunching method, sub picosecond or 10s femtosecond bunch can be generated in several MeV energy and several pC charge regime, for applications such as ultrafast electron diffraction and Thomson scattering. To measure the bunch length at the maximum compression plain, coherent transition radiation (CTR) method is more appropriate than direct methods using deflecting cavity, since the latter measurements are extended in z and can only give an estimate for the average bunch length over the measurement distance. Another advantage of using CTR method for measuring ultrashort bunch is the energy of coherent transition radiation increases significantly as the bunch length decrease, which is favorable to detection.

In this paper, we discuss a bunch length measurement method based on coherent transition radiation, for 10s femtosecond electron bunch length obtained by velocity bunching using a linac. The method and setup are described in the following section. In the end, preliminary experimental results are also presented.

METHOD

For transition radiation generated by electron crossing metal boundary, the process can be viewed as collision process of electron with its image charge. The spectrum and angular distribution of energy generated in the collision can be obtained by calculating the Lienard-Wiechert potential as [4]:

$$\frac{\mathrm{d}E_s}{\mathrm{d}\omega\cdot\mathrm{d}\Omega}=\frac{e^2}{4\pi^2c^3}\left(\frac{\vec{v}\times\vec{n}}{1-\vec{n}\cdot\vec{v}/c}-\frac{\vec{v'}\times\vec{n}}{1-\vec{n}\cdot\vec{v'}/c}\right)^2, \quad (1)$$

where E_s is the radiation energy of single electron,ω is the angular frequency of radiation, Ω is the solid angle, e is the charge of electron, c is the speed of light in vacuum, $\vec{n}$ is the direction of radiation, $\vec{v}$ and $\vec{v'}$ are the velocities of electron and its image charge. It is noted that the angular distribution does not depend on frequency. For a 45 degree collision, the velocity $\vec{v}$ and $\vec{v'}$ are determined by the setup, then we can calculate the energy distribution by integrating over the solid angle collected by an off axis parabolic (OAP).

The total radiation energy of a bunch E_b is the sum of single electrons, taking consideration of phase effect into account. The expression can be written as:

$$\frac{\mathrm{d}E_b}{\mathrm{d}\omega\cdot\mathrm{d}\Omega}=|N\cdot f(\omega)|^2E_s(\omega) \quad (2)$$

$$=\frac{e^2|N\cdot f(\omega)|^2}{4\pi^2c^3}\left(\frac{\vec{v}\times\vec{n}}{1-\vec{n}\cdot\vec{v}/c}-\frac{\vec{v'}\times\vec{n}}{1-\vec{n}\cdot\vec{v'}/c}\right)^2, \quad (3)$$

where $f(\omega)$ is the coherent factor. When the longitudinal size of bunch is much longer than the transverse size and the radiation are concentrated in small angle around beam axis, transverse coherent effect can be neglect and the coherent factor can be written as:

$$f(\omega)=f_L(\omega)=\frac{1}{N}\sum_{j=1}^{N}e^{i\omega t_j}\cong\int_{-\infty}^{+\infty}\rho(t)e^{i\omega t}\mathrm{d}t, \quad (4)$$

where $\rho(t)$ is the normalized distribution function. For wavelength longer than bunch length, the field created by electrons are coherent and the total energy is proportional to the square of number of electrons. In the case of low energy bunch and comparable transverse bunch size and longitudinal size multiplied by γ ($\sigma_x \backsimeq \gamma\sigma_z$), the effect of transverse size of bunch should not be neglected. For a numerical example, the wavelength of CTR corresponding to 40 fs bunch ranges around 12 μm, assuming the transverse spot size is 100 μm, when viewed at the angle larger than 7 degree from the axis, the maximum phase difference of radiation emitting from different transverse position can be larger than one period. Then the coherent factor should be written as:

$$f(\omega)=f_L(\omega)f_T(\omega), \quad (5)$$

* U.S. DOE Grants No. DE-FG02-92ER40693, No. DEFG02-07ER46272
† sealuxh@gmail.com
‡ Key Laboratory of Particle & Radiation Imaging, Tsinghua University, Ministry of Education

Copyright © 2013 CC-BY-3.0 and by the respective authors

with the transverse coherent factor as:

$$f_T(\omega) \cong \int_{-\infty}^{+\infty} \tilde{\rho}(r) e^{i\omega(\vec{r}\cdot\vec{n}/c)} \mathrm{d}t, \qquad (6)$$

where $\vec{r}$ and $\tilde{\rho}(r)$ are the transverse position and transverse normalized distribution function respectively. To consider the exact coherent effect, we calculate both the longitudinal and transverse coherent factor at given wavelength and angle, for different spot size and different bunch length (assuming Gaussian profiles). Then we integrate the total energy over the solid angle (within 30 degrees from beam axis) and 10 % frequency (FWHM) using numerical method. The result of integration is displayed in Fig. 1.

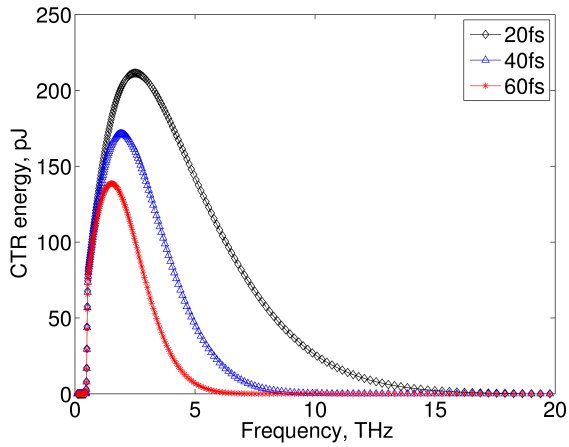


Figure 1: CTR spectrum for rms bunch length of 20 fs, 40 fs, 60fs of energy of 5 MeV, charge of 3 pC and rms spot size of 50 μm.

Figure 1 shows the CTR energy at 3∼5 THz is sensitive to the length of bunch, while the energy at low frequency (1 THz) is relatively insensitive. This characteristic implies we can use the ratio of high frequency CTR energy over low frequency one as a measurement of bunch length.

SETUP

Ultrashort Bunch Generation

The schematic of beam line is shown in Fig. 2. The first solenoid (soleA) right after RF gun is used to match the beam into a standing wave linac, which is operated at compressing phase. After the linac, the bunch drifts and compresses at the CTR target about 1.6 m downstream. The phase of linac determines the compressed point, which should be set coincident with the plain of CTR target. A second solenoid(soleB) is placed about 0.4 m upstream the CTR target to focus the beam to a minimal spot size on CTR target to enhance the transverse coherent effect. The CTR target is a 1/10 wavelength gold mirror of 1cm × 1cm, which can be treated as an infinity perfect boundary for electron of several MeV energy. The distance of CTR target from the cathode of RF gun is 3.78 m.

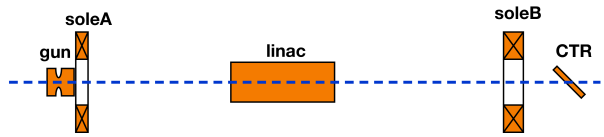


Figure 2: Schematic of beam line.

The energy and energy spread of the linac is calculated with GPT[5], shown in Fig.3. It shows the bunch is compressed to the minimal length at linac phase about 77 degree off crest. The minimal rms bunch length that can be achieved is as low as 21 fs. At the same time the second solenoid can be tuned to achieve spot size of rms 30 μm. It should be noted that there is a tradeoff between the smallest spot size and shortest bunch length, since it is easier to compress or focus in one dimension with a low charge density of the other dimension.

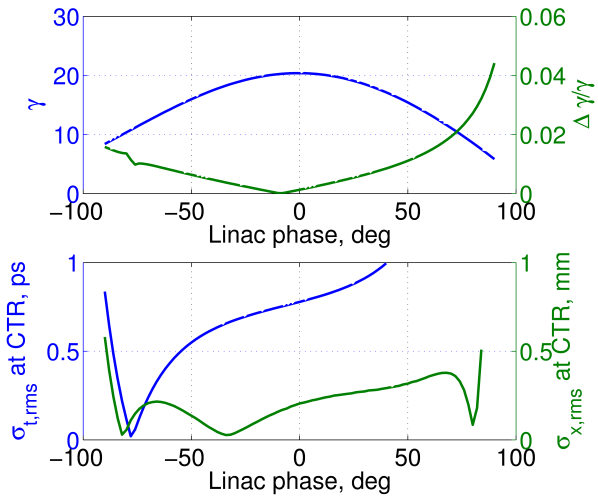


Figure 3: Energy, energy spread, spot size and bunch length with respect to linac phase.

CTR Collection and Spot Size Measurement

The whole setup of CTR collection is placed in a vacuum chamber. A moveable stage can insert the CTR target or a YAG screen onto the beamline. The thickness of YAG is 30 μm with spatial resolution smaller than 5 μm [6]. The measurement of spot size is important for deriving the bunch length. A 90 degree, 1 inch diameter OAP with parent focal length of 1 inch is well aligned and mounted near the CTR target. Two 1.5 inch diameter THz mirrors are used to guide the parallel radiation to a 3 inch diameter OAP with parent focal length of 6 inches. The focused radiation after second OAP passes through a 3 mm thick TPX window[7] on the wall of vacuum chamber and collected by a pyroelectric detector. Filters of different wavelength can be inserted before the detector.

Copyright © 2013 CC-BY-3.0 and by the respective authors

RESULT AND DISCUSSION

In the first round experiment, the energy of signal is sufficient to be detected with a pyroelectric detector with sensitivity of 0.3 mV/nJ. A solenoid scanning is performed and the total CTR energy is measured under 20 pC charge. The result is shown in Fig. 4.

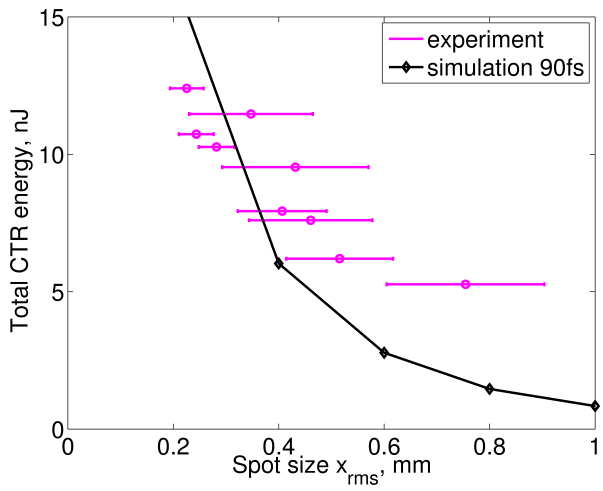


Figure 4: Total CTR energy detected with respect to rms spot size at CTR target under 20 pC charge.

Figure 4 show the total energy decreases as spot size increase, which is in consistent with the degraded transverse coherence of the bunch. However, since this total energy is not sensitive to bunch length, we can estimate a longitudinal bunch size larger than 10s fs order. With lower charge of 5 pC, linac phase scanning is also performed to study the effect of velocity compressing, shown in Fig. 5. Figure 5 shows the compressing point is important to generate CTR.

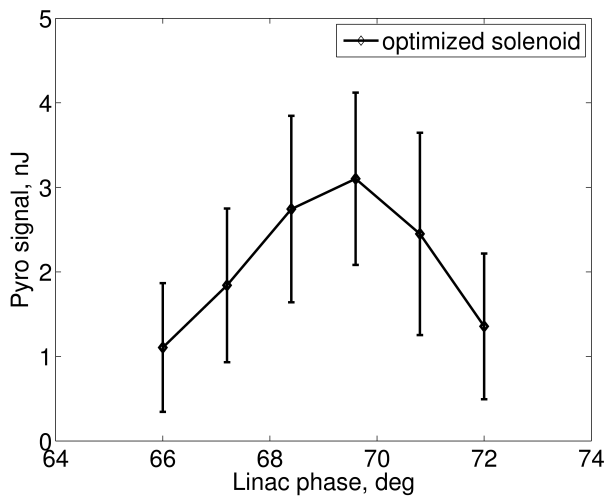


Figure 5: Total CTR energy detected with respect to phase of linac.

Large error bars in both Fig. 4 and Fig. 5 show instability of spot size and CTR energy. This is caused by the jitter of RF system, especially the jitter of gun phase, resulting in the mismatch of compressing point and CTR target. Another challenge is that the calibration of the transmission and detection efficiency for different wavelength. A second round experiment is planned to use more sensitive detectors for lower charge bunch, aiming at measuring the ratio of CTR energy at different frequency and deriving ultrashort bunch length.

CONCLUSION

In this paper, we discuss an CTR based bunch length measurement method for 10s fs bunch of several MeV energy and several pC charge. The CTR energy spectrum is precisely calculated using numerical integration method, considering transverse and longitudinal coherent effect. A relative CTR component ratio measurement is proposed to derive bunch length. Simulation is performed and predicts compressed bunch length of 20 fs (rms), with spot size of 30 μm (rms) at the CTR target. The preliminary experiment shows significant dependence of total CTR energy on spot size and linac phase.

ACKNOWLEDGMENT

The authors acknowledge the helpful discussions with Dr. Gerard Andonian, Phuc Hoang, Emma Curry and Peter Yu.

REFERENCES

[1] J. Shi et al., "Bunch Length Measurement With RF Deflecting Cavity At Tsinghua Thomson-scattering X-ray Source ", Proc. of PAC 2009, Vancouver, May 2009, TH5PFP094, p. 3429.

[2] G.L. Carr et al., "Coherent Radiation Measurements at the NSLS Source Development Lab", PAC01, Chicago, WPPH069, p. 2608.

[3] G. Berdon et al., "Single Shot Electron-beam Bunch Length Measurements", Proc. of DIPAC 2003, Mainz, May 2003, IT05, p. 24.

[4] A. Murokh et al., Nucl. Instr. and Meth. in Phys. Res. A 410 (1998) 452.

[5] http://www.pulsar.nl/gpt

[6] K.G. Roberts et al., "Measurement of Ultrasmall Transverse Spot Size", Proc. of NA-PAC 2013, TUOBB4.

[7] http://www.tydexoptics.com

Copyright © 2013 CC-BY-3.0 and by the respective authors

HIGH-CHARGE FEMTOSECOND ELECTRON GENERATIONS FOR ULTRAFAST, HIGH-BRIGHTNESS ELECTRON BEAM APPLICATIONS*

Jangho Park#, Hans Bluem, John Rathke, Tom Schultheiss, and Alan M. M. Todd
Advanced Energy Systems, Inc., Medford, New York 11763, USA

Abstract

Generation and preservation of ultrafast, high-brightness electron beams is one of the major challenges in accelerator research and development (R&D) for beam applications such as free electron lasers (FEL) and ultrafast electron diffraction (UED). Transverse and longitudinal space charge forces play a key role in emittance dilution and bunch lengthening respectively, for all high-brightness beams. We present a newly-designed, X-band, photocathode, radio frequency (RF), electron gun that utilizes radial bunch compression to deliver a compact ultrafast, high-brightness source. By compensating for the path length difference in an extremely-high-acceleration-gradient cavity with a curved cathode, we numerically demonstrate the potential for achieving more than an order of magnitude increase in beam brightness over existing electron guns. The thermo-mechanical analysis and conceptual design that demonstrate the viability and reliability of the concept are also presented.

INTRODUCTION

Ultrafast high-brightness electron beams are desired as injectors for light sources, including FELs, energy recovery linacs (ERL) and medical devices, amongst other applications. Brightness is the holy grail of most light sources and brighter, short-pulse electron injectors are to be prized where there are no downstream transport consequences of the short bunches. An example is micro bunching instabilities that can result from transport interactions with the energy modulations induced by the longitudinal space charge (LSC) forces in the bunches. These sources may also find direct application in advanced accelerators like the plasma wake-field accelerator (PWFA) and ultrafast electron diffraction (UED) [1]. Plasma accelerators promise orders-of magnitude increases in accelerating gradient to greater than 100 GeV/m and could lead to very compact and economical systems for those many accelerator applications that require high particle energies. Ultrafast diffraction techniques, which provide information about atomic-scale molecular structure, are critical to chemists and material scientist in their research and development activities.

In the generation of ultrafast, high-brightness electron beams, space-charge forces play a fundamental role in emittance dilution and bunch lengthening within the gun and subsequent emittance compensation drift. In order to generate and preserve the beam brightness, transverse and longitudinal space charge effects have to be precisely managed. Several different approaches have been reported and are being actively pursued within the worldwide accelerator community. These include various velocity bunching and magnetic compression techniques. However, each option suffers drawbacks that must be overcome in order to deliver a compact and economic ultrafast, high-brightness source.

In order to develop an improved ultrafast high-brightness electron source, we have proposed a scheme that compensates for path length differences by using a curved cathode [2]. This introduces radial compression that compensates for geometric bunch lengthening effects when coupled with extremely-high-acceleration-gradient to minimize the impact of space-charge forces. The AES-patented rear-fed coaxial cathode coupling eliminates contributions to transverse emittance from non-axisymmetric modes [3]. We show that combining these effects is feasible and does indeed deliver a more compact, economic, ultrafast high-brightness electron beam for the identified applications.

CAVITY AND COUPLING DESIGN

For a high-aspect-ratio (short bunch length) electron bunch, the asymptotic bunch length due to the space charge forces of a uniformly accelerated bunch is expressed by:

$$\Delta t_{sc}(\infty) = \frac{mc^2}{e}\frac{Q}{\pi R^2 \varepsilon_0 c E^2}. \qquad (1)$$

This ignores the drive laser duration and assumes prompt response from a copper cathode with a constant laser spot radius (R). Here, bunch lengthening due to space charge is inversely proportion to the square of the bunch radius (R) and the square of the accelerating field (E). The bunch lengthens due to the longer trajectories of the outer particles, compared to electrons emitted closer to the axis, and is proportional to the square of the beam radius.

Our previous upstream, coaxial, waveguide-fed gun cavity design had the drawback that the radial space for electron beam emission and drive laser insertion was relatively small [4]. We have now completed the RF analysis for a coaxial RF feed from the rear of the gun. Standard codes like the SLAC-developed S3P code [5] and SUPERFISH have been used to complete the RF design used in the reported beam dynamics analysis. Following Ref. [3], we focused on the geometry of the coaxial coupler and the iris between the cells, in order to maximize shunt impedance and thus minimize losses for a given cathode voltage. The coaxial coupler and the iris

* This work was supported by the U.S. Department of Energy, under Contract No. DE-SC0009556.
#jangho_park@mail.aesys.net

Copyright © 2013 CC-BY-3.0 and by the respective authors

changes required adjustment of the thermal stress analysis and the location of the cooling channels. The RF design in the cathode area also affects the beam dynamics design. To allow for flexibility in cathode materials, the cathode has been designed as a detachable and adjustable structure. A completely axisymmetric gun delivers improved emittance and permits optimal placement of the emittance compensating solenoid.

The physics design of an X-band RF gun cavity with a curved cathode and a coaxial RF coupling scheme, embedded in an emittance compensating magnetic field has been optimized. Various curved and flat cathode geometric models have been studied using the SUPERFISH. We varied the radius of curvature to optimize the beam dynamics output. The resultant SUPERFISH output field files were translated into input files for the [6] beam dynamics code. Figure 1 shows a cavity cross-section with field lines from SUPERFISH. The radius of the coaxial coupler has been chosen to prevent the transmission of the lowest high-order TE01 mode through the coaxial waveguide.

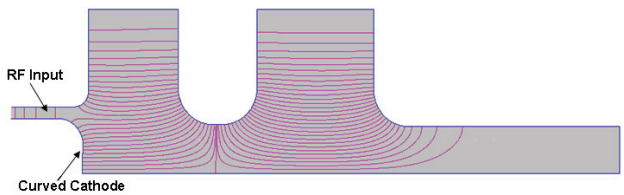


Figure 1: SUPERFISH model of the 1.6 cell, X-band, π-mode, RF gun cavity with rear-fed coaxial coupling.

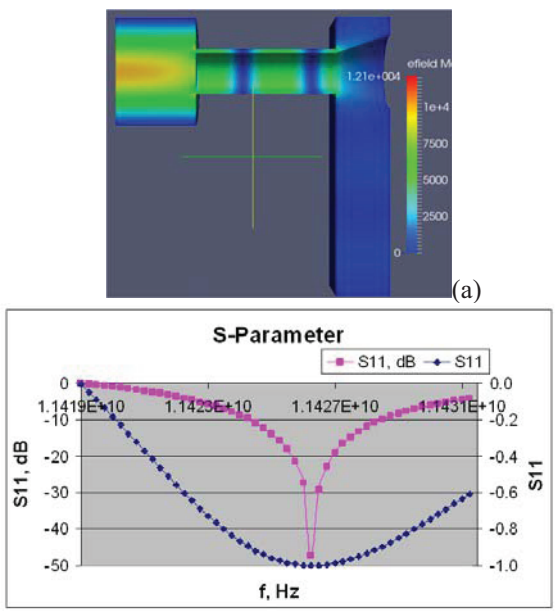


Figure 2: (a) Coupling structure electric fields in the rectangular to coaxial waveguide transition, and (b) the normalized S11 parameter for the coupling structure.

The waveguide to coaxial cavity coupling transition has been designed using by SLAC developed S3P code [5]. Figure 2(a) shows that WR-90 rectangular to coaxial waveguide transition. The coaxial waveguide and the cavity resonate as TEM and TM modes, respectively. Figure 2(b) shows the normalized S-parameter - the transmission/reflection coefficient for the coupling structure. The cavity resonant frequency is 11.426 GHz for the geometry shown.

BEAM DYNAMICS CACULATION

The beam dynamics analysis addressed several aspects of the gun design. Firstly, we anticipated that the higher accelerating field in the X-band cavity would reduce the longitudinal and transverse emittance growth produced by space charge forces, thereby delivering our goal of an ultrafast, high-brightness, electron bunch. Secondly, by utilizing a curved cathode, we expected that the focusing field near the cathode surface would lead to improved integrated transverse beam focusing and improved beam brightness. Finally, we predicted that the curved cathode would compensate for the bunch lengthening induced by path length variation across the cathode, due to the combined effect of the focusing elements and the RF in the cavity.

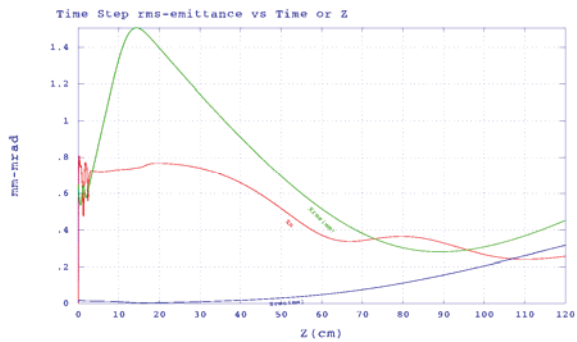


Figure 3: Evolution of the bunch length (blue), beam size (green) and emittance (red) along the beam axis.

Various simulations were performed using TStep [6], an evolved version of PARMELA, to investigate the effect of the bunch charge on the bunch length and beam brightness. Figure 3 shows the evolution of the bunch length, beam size and emittance along the beam axis. At the interaction point 45 cm from the cathode, we deliver a 2.5 MeV, 20 pC bunch with a transverse rms emittance of 0.81 π mm-mrad. The 82 fsec FWHM bunch has a transverse rms beam spot of 0.71 mm with an energy spread of 0.6 %. These results are very similar to those achieved with the upstream-fed coaxial RF design [4].

THERMAL DESIGN

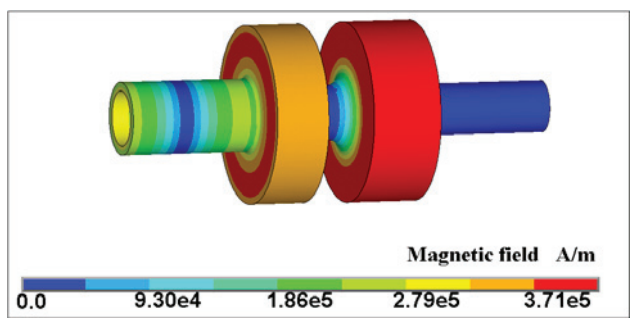


Figure 4: Magnetic field values during an RF pulse.

Copyright © 2013 CC-BY-3.0 and by the respective authors

SUPERFISH normalizes electric fields to a maximum of 1 MV/m. Our design maximum electric field is 250 MV/m in the gun. The wall losses thus scale from the indicated 467 watts to 4.23 MW, thus requiring pulsed RF power. Figure 4 shows the RF surface magnetic fields. The proposed RF pulse duration is 200 nsec and the repetition rate is 200 Hz, resulting in a duty factor of 4.0 x 10^{-5}. This low duty factor enables the adoption of a simplified cooling scheme for the design.

The magnetic fields in the waveguide and coaxial feed were determined from the geometry and the operating point power. The magnetic fields along with wall and the resistance were used to determine the local power loss on the walls, where the power loss is iterated to reflect the temperature dependent resistance of the walls. Figure 5 shows the resistive wall power densities.

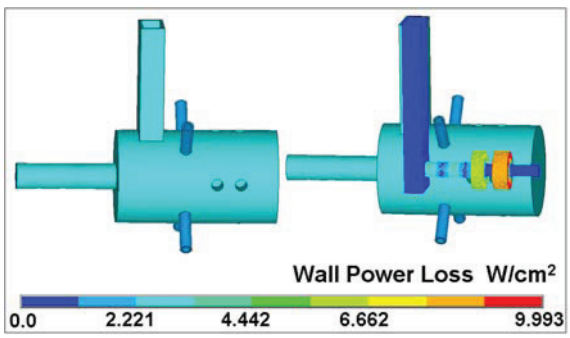


Figure 5: Average power loss on the cavity walls with a duty factor of 4.0 x 10^{-5}.

A cooling water flow rate of 2.3 gpm through the eight cooling channels is used to keep the temperatures within the acceptable range. Figure 6 shows the temperature distribution within the gun and on the cooling channel surfaces. The iris between the two cells is not cooled directly, but is cooled with thermal conduction through the copper walls. The temperature rise between the inlet cooling water and the maximum copper surface temperature is only 6.3ºC.

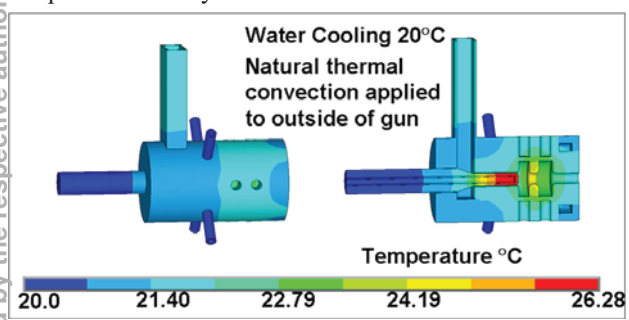


Figure 6: Temperature distribution in the gun body. The supplied water cooling temperature is 20ºC. Natural thermal convection is applied outside of the gun.

The displacements derived from the temperature variation were then applied to the RF model. The RF model was then rerun to determine a frequency comparison with the original geometry. This showed a shift of -644. kHz. This can easily be compensated by developing the geometry to be at the design frequency for an elevated design temperature. The inlet cooling temperature would then need to be about 3.4ºC below this design temperature to operate at the design frequency.

The waveguide and vacuum barrel were cooled by natural convection and conduction to the gun body. The rectangular waveguide was made of copper and the vacuum barrel and flanges were modelled as stainless steel. The ambient temperature was assumed to be 20ºC and the resulting temperature rising was only 1.2ºC. Thermal conduction in the waveguide was high enough and the field penetration of the perforations small enough, that the temperature rise was not significant. The thermo-structural and RF frequency shift analysis demonstrates that the design of this electron gun running at 4.0 x 10^{-5} duty factor is robust. The temperature rise of the gun body is small, less than 5ºC, the displacements are small, less than 0.8 x 10^{-4} inches, the Von Mises stresses are low, less than 1100 psi, and the frequency shift is manageable. Hence the design and thermal management of this gun have adequate head room for robust operation.

SUMMARY

AES has recently completed the design of an ultrafast, high-brightness, electron source for FEL, ERL and advanced accelerator injectors. The gun is particularly suited to UED analysis. The beam dynamics analysis of such an X-band, ultrafast, RF gun with a curved copper cathode has been demonstrated to deliver an order of magnitude increase in beam brightness over existing S-band electron guns. Thermo-structural analysis and mechanical design shows the achievement of robust operation at a duty factor of 4.0 x 10^{-5}. Proposals have been submitted to perform the experimental validation of the device at the BNL Accelerator Test Facility (ATF).

ACKNOWLEDGMENT

The authors would like to thank Dr. Ng of SLAC for permitting the use of and providing assistance with the ACE3P code.

REFERENCES

[1] X. J. Wang, D. Xiang, T. K. Kim and H. Ihee, J. Korean Phys. Soc. **48,** 390 (2006).
[2] M. J. de Loos et al., Phys. Rev. ST Accel. Beams **9**, 084201 (2006).
[3] H. Bluem et al., http://accelconf.web.cern.ch/accelconf/p07/PAPERS/THPMS070.PDF
[4] J. Park et. al., http://accelconf.web.cern.ch/AccelConf/IPAC2012/papers/tuppd080.pdf
[5] C.-K. Ng, et al., "State of the Art in EM Field Computation," Proc. EPAC06, Edinburg, Scotland.
[6] http://tstep.lmytechnology.com/

Copyright © 2013 CC-BY-3.0 and by the respective authors

STUDIES OF FIELD AND PHOTO-EMISSION IN A NEW SHORT-PULSE, HIGH-CHARGE Cs_2Te RF PHOTOCATHODE GUN

E. E. Wisniewski
Illinois Institute of Technology, Chicago, IL, USA and ANL/HEP, Argonne, IL, USA
M. Conde, W. Gai, C. Jing, W. Liu, and J. G. Power
ANL/HEP, Argonne, IL, USA
Z. Yusof and L. K. Spentzouris
Illinois Institute of Technology, Chicago, IL, USA

Abstract

A new high-charge RF gun is now operating at the Argonne Wakefield Accelerator (AWA) facility at Argonne National Laboratory (ANL). The 1.5 cell 1.3 GHz gun uses a Cesium telluride photocathode driven with a 248 nm laser to provide short-pulse, high charge electron beams for the new 75 MeV drive beamline. The high-gradient RF gun (peak field on the cathode $>$ 80MV/m) is a key piece of the facility upgrade. The large Cs_2Te photocathode (diameter $>$ 30 mm) is fabricated in-house. The photo-injector generates high-charge, short pulse, single bunches (Q $>$ 100 nC) or bunch-trains (Q$>$1000 nC) for wakefield experiments, typically involving dielectric-loaded accelerating structures. Field-emitted dark current from the Cs_2Te cathode was measured during RF conditioning. Fowler-Nordheim plots of the data are presented and compared to similar measurements made using a copper cathode in the initial phase of conditioning. Results of quantum efficiency (QE) studies are presented with the cathode operating in both single and bunch-train modes.

EMISSION STUDY PLAN AND GOALS

The 1.5 cell, 1.3 GHz, AWA drive-gun is now operating, using high Quantum Efficiency (QE) Cs_2Te photocathodes fabricated in-house [1]. The photocathode requirements are QE greater than 1% with a lifetime of weeks to months while experiencing a very high gradient (80 MV/m) peak RF field on the cathode. The primary function of the gun is to provide high-charge, short-pulse electron beams to drive wakefield structures [2]. As part of the turn-on process, we are conducting field emission and photoemission studies in the gun.

Photocathode Field Emission Study

We measured and characterized field emission from two different photocathodes used during the two phases of RF conditioning. Copper was used for the initial gun conditioning, followed by Cs_2Te thin film on Molybdenum for planned high-charge operation. We hope to use the data to better understand the relative impact of different factors influencing the level of field emission and its possible mitigation.

Photoemission Study

We characterized photoemission from the Cs_2Te photocathode under various conditions. Using 2-10 ps, 248 nm wavelength laser pulses, we are studying photoemission at high gradient to optimize the performance of the photocathode and the gun. At the time of the writing of this paper, QE measurements of the photocathode in the gun have been made over a period of about 6 weeks.

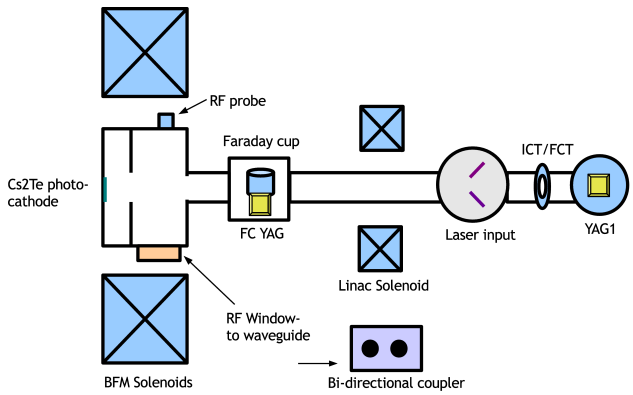


Figure 1: The L-band 1.5 cell photocathode gun with the relative positions of diagnostics to be used (cartoon - not to scale). The RF power input is measured near the RF window using a bi-directional coupler. The dark current is measured with a Faraday cup 58 cm from the cathode. The beam charge is measured using an Integrating Current Transformer (ICT). YAG(Ce) scintillating screens to image the beam and the dark current are available at two locations. In addition, an in-vacuum mirror at the Faraday cup location may be used to observe the photocathode and help to identify emission sites (not to scale).

EXPERIMENTAL SETUP

The beamline with the relative positions of diagnostics used for the experiments is depicted in a schematic shown in Fig. 1. RF power measurements were made using a dual-directional coupler connected in series in the waveguide just before the gun. The dark current was measured using a Faraday cup. The beam charge was measured using a Bergoz combination in-flange Integrating Current Transformer (ICT) and Fast Current Transformer (FCT).

Copyright © 2013 CC-BY-3.0 and by the respective authors

YAG(Ce) scintillator screens were used to image the beam at two locations.

RF CONDITIONING AND FIELD EMISSION

RF conditioning of the gun was begun in 2011 but was interrupted by AWA upgrade expansion construction. To protect the both the gun and the cesium telluride cathode from effects of RF damage, the first round of conditioning took about 160 hours to reach 88 MV/m. The RF pulse length was 8 microseconds and repetition rates varied from 1 to 10 Hz. Next, the first Cs_2Te photocathode was installed and conditioned to 25 MV/m. Both photocathodes were used to produce electron beams, but progress was halted due to upgrade activities. Drive gun operation and the studies discussed herein resumed in summer 2013 and are on-going.

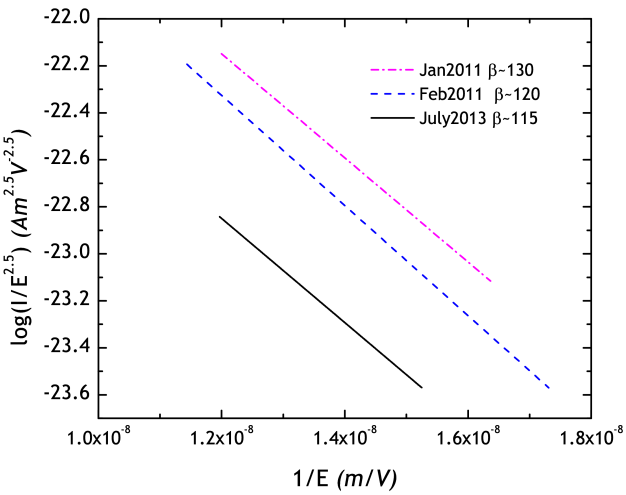


Figure 2: Initial RF conditioning was done with a copper photocathode. Linear fits of Fowler-Nordheim plots for the Cu cathode at several points in the conditioning process. The field enhancement factor (β) calculated from the slope of each fit indicate field enhancement in the gun with the Cu cathode is stable at about 120 after conditioning to 88 MV/m.

During conditioning, dark current data was taken with a Faraday cup located 58 cm from photocathode. The gun fields were measured using a diode at the bi-directional coupler in the waveguide near the RF window. Data from the copper cathode indicates a reasonable level of dark current and a field enhancement factor β=120.

Field emission from the cesium telluride photocathode was also measured with the Faraday cup during conditioning. Field emission from p-type semi-conductors has been shown to behave quite differently from metals and may result in non-linear Fowler-Nordheim plots [4]. As seen in Fig. 3 ,the preliminary results are suggestive of a field dependent, much lower β.

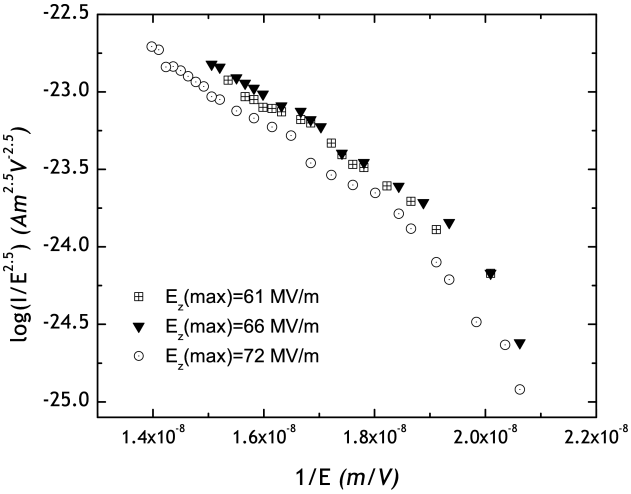


Figure 3: RF conditioning with Cs_2Te, a p-type semi-conductor thin-film photocathode. Three Fowler-Nordheim plots from data taken as conditioning proceeded appear non-linear, suggestive of β with a possible field dependence.

ONGOING PHOTOEMISSION STUDIES: PRELIMINARY RESULTS

Conditioning of the Cesium telluride cathode proceeded with some caution due to the vacuum requirement (low $10^{-}10$ torr). Arcing occurred fairly frequently as the field level was raised. The photocathode shows some small spots (about 0.5 mm in diameter), possibly indicating damage to the thin film from arcing during RF conditioning.

Once the photocathode was conditioned to about 30 MV/m, we began photoemission studies. Photoemission measurements were made using the experimental setup sketched in Figs. 1 and depend on laser power measurements concurrent with beam charge measurements in order to distinguish shot-to-shot variations in the laser or the QE. The diagnostics for the QE phase scan single bunch and bunch-train measurements [5] include the Bergoz in-flange ICT (to measure total charge) with FCT (to resolve individual bunches) described previously as well as a PD10-C OPHIR photodiode sensor with laser energy meter to measure laser power per pulse. We have been collecting data for QE lifetime studies on all the photocathodes we make for several years, but the data presented in this paper is from the first one operated for an extended period of time in the gun at high field. For a comparison, see Fig. 5

We performed QE-RF field dependence measurements by two methods: 1) by varying the peak RF power into the gun and 2) by varying the laser input phase with constant RF power. Plots of average QE values phase scans with 150 pC charge at several different RF field levels are plotted in Fig. 4. The QE remains relatively flat, showing little or no evidence of field enhancement. The laser photon energy at 5 eV is well above the photoemission threshold.

Copyright © 2013 CC-BY-3.0 and by the respective authors

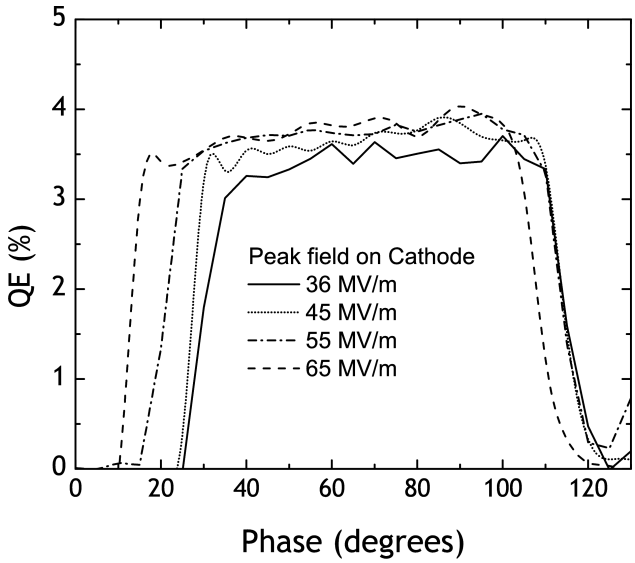


Figure 4: Averaged data from 4 phase scans at 36, 45, 55, and 65 MV/m. The scans are relatively flat showing little or no evidence of field enhancement.

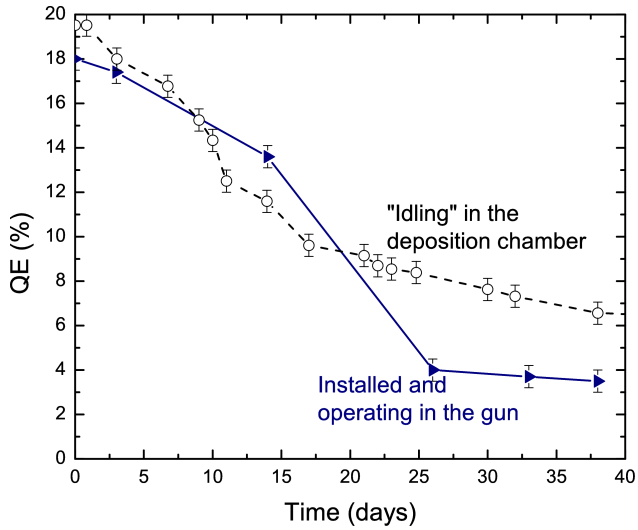


Figure 5: The QE for two photocathodes is plotted vs. time. The photocathode installed in the gun shows a promising QE lifetime, still near 4% in the gun after operating more than a month. Plotted for comparison is the QE lifetime of a photocathode "idling" in the deposition chamber.

Additional Studies and Analysis

The emission studies discussed here are broad in scope and continuing. For these reasons, only some of the highlights and preliminary results are presented. Additional work or data still to be analyzed includes: high charge phase scans, rastering the cathode with the laser to probe the spatial uniformity of QE, mapping the QE variations across the cathode and tracing them back to the deposition process or RF conditioning damage. Such a QE map may be of assistance in understanding variations in QE vs. laser spot size. Also planned are 1000 nC long bunch train QE measurements: generate from 4 to 32 bunches per train with 770 ps separation (1 RF period). The data will be analyzed for possible QE bunch-train position dependence.

SUMMARY

The first Cs_2Te photocathode is operating successfully at AWA in the new drive gun. In an effort to understand the performance limitations of the new gun and photocathode, photocathode emission studies will be conducted during conditioning and initial operation. RF conditioning of the Cesium telluride cathode has proceeded to 72 MV/m while maintaining QE at required levels. QE Phase scans using on-line laser energy and charge measurements indicate that the QE remains high after 1 month. Bunch train measurements have been performed, but the results are still being analyzed. The photocathode still in the gun shows a promising QE lifetime, plateauing near 4% in the gun after more than a month in the gun and over 6.6×10^{-10} RF pulses. Results from these studies will be analyzed and used to optimize the photocathode drive gun operation.

ACKNOWLEDGMENTS

The submitted manuscript has been created by UChicago Argonne, LLC, Operator of Argonne National Laboratory ("Argonne"). Argonne, a U.S.Department of Energy Office of Science laboratory, is operated under Contract No. DE-AC02-06CH11357. The U.S.Government retains for itself, and others acting on its behalf, a paid-up nonexclusive, irrevocable worldwide license in said article to reproduce, prepare derivative works, distribute copies to the public, and perform publicly and display publicly, by or on behalf of the Government.

REFERENCES

[1] Z.M. Yusof, M.E. Conde, W. Gai, E.E. Wisniewski, and L.K. Spentzouris, Proc. of IPAC12, TUPPD071, p.1569 (2012).

[2] M. Conde et al., Proc. of PAC2011, MOP008, p. 115 (2011).

[3] J. Wang and G. Loew, Field emission and rf breakdown in high-gradient room- temperature linac structures, Technical Report SLAC-PUB-7684, SLAC, 1997.

[4] R. Stratton, Theory of Field Emission from Semiconductors, Phys. Rev., 125, 1962.

[5] J. Power et al., Proc. of IPAC12 (2012).

Copyright © 2013 CC-BY-3.0 and by the respective authors

THE CATHODE PREPARATION CHAMBER FOR THE DC HIGH CURRENT HIGH POLARIZATION GUN*

O. Rahman†, I. Ben-Zvi, D. Gassner, A. Pikin, T. Rao, E. Riehn, B. Sheehy, J. Skartika, E. Wang, Q. Wu, BNL, Upton, NY 11973, USA.

Abstract

A compact cathode preparation chamber for the high current high polarization gun for the proposed eRHIC project has been designed and assembled at Brookhaven National Laboratory. This preparation chamber will be used to activate GaAs photocathodes to be used in the Gatling gun. The chamber is capable of achieving XHV on a consistent basis. Bulk GaAs samples were activated in this chamber with standard QE for the respective wavelength. In this paper, we discuss the design of this vacuum system, the heat cleaning and the activation procedure for the GaAs sample which will eventually be followed for the Gatling gun.

INTRODUCTION

The High Current High Polarization Electron Gun is one of the most important research projects for the proposed eRHIC project [1]. The average current is required to be 50 mA and the polarization requirement is more than 80%.For weekly exchange of cathodes, given that two guns are used, one cathode has to provide 50 mA of average current for 85 hours, which yields to 15300 C of charge. The maximum reported charge extracted is 1000 C, which is a order of magnitude lower than the requirement [2]. To solve this problem, 50 mA of current can be distributed over 20 photocathodes such that each cathode has to provide 2.5 mA of current for 85 hours, yielding 765 C of charge. This solution of combining 20 bunches to one common beam axis solves the problem of charge limitation without sacrificing the high average current requirement. The high polarization can be obtained using Superlattice GaAs which is able to provide polarization greater than 80% in a consistent basis [3]. For the R&D and "proof of principle" experiment, bulk GaAs will be used.

DESIGN OF THE CATHODE PREPARATION CHAMBER

The cathode preparation chamber is a compact design including 3 crosses, two of them are 6-way crosses and the other one is a standard 4 way cross. These three crosses are stacked on top of each other with the 4-way cross at the bottom. The cathode holder is moved up and down using a magnetic manipulator. One NEG pump and one turbo pump is attached to the bottom 4-way cross. The middle cross contains the tungsten filament, another NEG pump, one Ion pump and a view port. The top-most cross includes the Cs source, a pick up anode, a variable leak valve for Oxygen, an Extractor gauge to measure low pressure and a window through which laser shine the sample. A cross sectional view of the assembly is shown in Fig. 1 and the front view of the actual system is shown in Fig. 2. The vacuum and heat cleaning components are described in detail in the following sections.

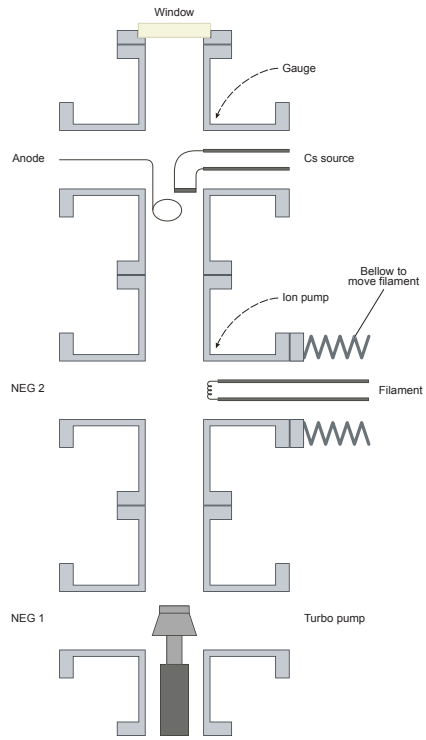


Figure 1: Cross sectional view of the cathode preparation chamber.

VACUUM COMPONENTS AND BAKE OUT PROCEDURE

The bake out procedure is extensive since activating GaAs requires XHV i.e low 10^{-11} Torr scale vacuum. The chamber at 200°C for approximately a week. Heater tapes are used to wrap the chamber and K-type thermocouples are used in 8 different locations of the chamber to make

* Work supported by Brookhaven Science Associates,LLC under contract no. DE-AC02-98CH10886 with the U.S. Department of Energy

† orahman@bnl.gov

Copyright © 2013 CC-BY-3.0 and by the respective authors

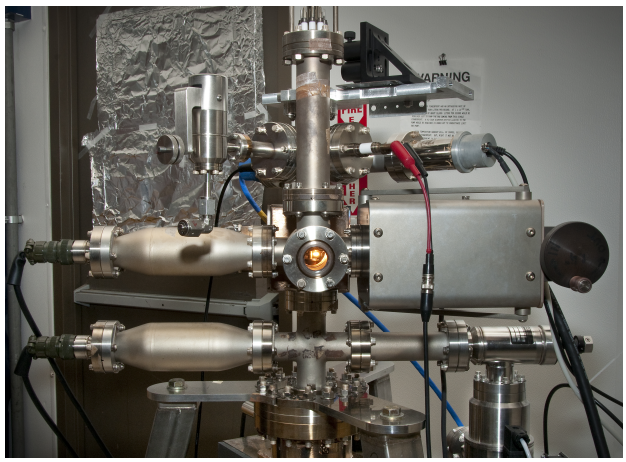


Figure 2: Front view of the cathode preparation chamber.

Table 1: Vacuum Pumps used in the Prep. Chamber

Pump	Pumping speed	location in the chamber
Ion pump	50 l/s	Middle cross
NEG 1	80 l/s	Bottom cross
NEG 2	80 l/s	Middle cross

sure that the temperature is uniform over the entire chamber.Different pumps that are installed in this system is described in Table 1.The NEG pumps are Capacitorr D400 units from SAES getters and the Ion pump is a standard Gamma Vacuum one.

Temperature data is saved to a computer using an Omega USB data acquisition module. The temperature of the chamber is increased gradually from room temperature to 200°C in 50°C increments over the course of two days.

One AxTRAN ISX2 gauge, a hot cathode extractor type gauge, is used to monitor pressure data. The NEG pumps are activated twice during the bakeout cycle, once the temperature of the system is 100°C and then right before the cooling of the system begins. Every other component of the system is also degassed during the heating cycle when the system is at 200°C including the filament, the Cs source, the cathode holder and the gauge.

A typical Pressure Vs Time graph is show in Fig. 3. While cooling down, the system is also brought down gradually from 200°C to 80°C to room temperature. While the system is at 80°C, the RGA is degassed.

HEAT CLEANING AND ACTIVATION

Before GaAs is activated, the surface of the sample needs to be cleaned either by conventional heat cleaning or atomic Hydrogen cleaning. We use a commercially available Tungsten filament from a 250W light bulb to heat up the sample by radiation to a desired temperature. The heat cleaning setup is shown in Fig. 4. The filament

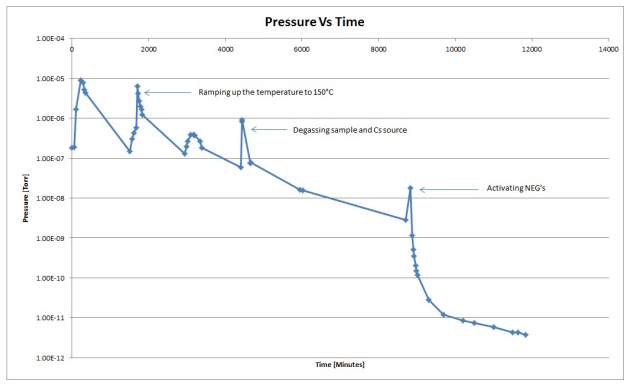


Figure 3: Pressure of the chamber during a bake-out procedure.

is inserted into the chamber using a feedthrough which is connected to a bellow that is compressible and the position of the filament can be adjusted.

It should be noted that the vertical position of the cathode

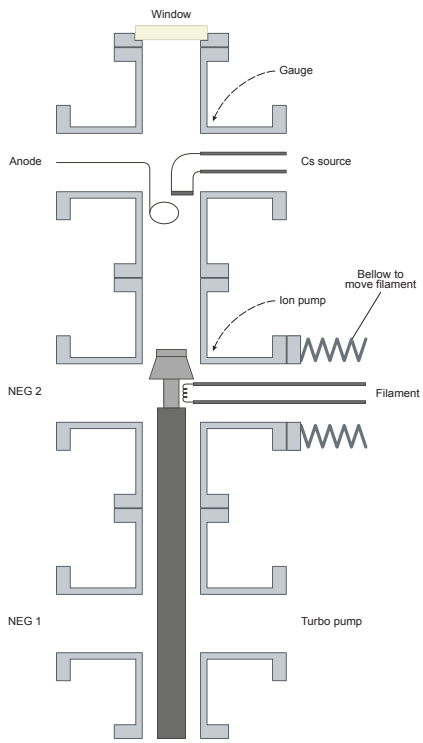


Figure 4: Schematic diagram of the heat cleaning procedure.

and the position of the filament has to be exact in order to have the right temperature on the surface of the sample. Meticulous calibration tests were performed to measure the surface temperature of the GaAs as a function of the driving current through the filament with a fixed vertical height and fixed filament position. For our heat cleaning procedure, we use the calibration curve to obtain

Copyright © 2013 CC-BY-3.0 and by the respective authors

a temperature of 580°C on the surface of the GaAs.

After the heat cleaning is done for 45 minutes, it takes approximately 2 hours for the sample to come back down to room temperature (also obtained from the calibration experiment). For activation, we use a standard evaporation Cs source from SAES getters. The laser is a 650 nm diode CW laser. A sample activation curve is shown in Fig. 5.

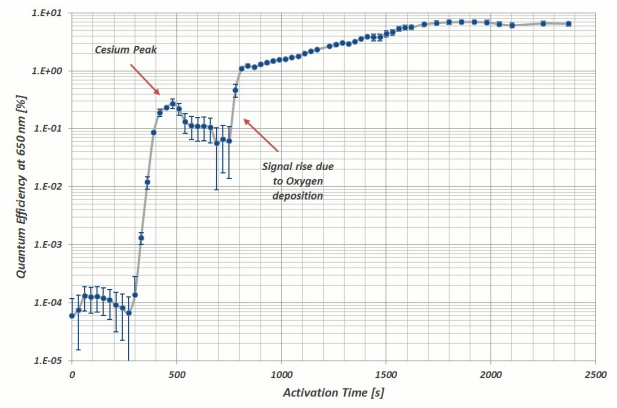


Figure 5: Typical activation curve.

Typically the first real signal is measured after 350 seconds and the Cs peak is seen after 500 seconds. This activation process is a co-deposition process where the Cs and Oxygen are applied to the surface simultaneously after the signal has reached the Cs peak. Multiple activations were performed using this technique and the QE ranges between 6% to 8% for 650 nm light.

CONCLUSION AND FUTURE PLAN

A compact prototype preparation chamber to activate GaAs photocathodes is assembled and tested. The chamber has shown to be XHV achievable and bulk GaAs samples were activated in the chamber with standard QE for 650 nm light. This chamber is scheduled to be installed on the storage chamber and a two cathode test is scheuled to be performed early next year. Eventually, this chamber prototype will be used to activate Superlattice GaAs photocathodes for the full operation of the High Current High Polarization Gun.

REFERENCES

[1] X. Chang et al., "A multiple cathode gun design for the eRHIC polarized electron source," Proc. of PAC2011, WEP263, p. 1969 (2011).

[2] J. Grames et al., "Charge and fluence lifetime measurements of a dc high voltage GaAs photogun at high average current," Physical Review Special Topics-Accelerators and Beams 14.4 (2011) 043501.

[3] T. Maruyama et al., "Systematic study of polarized electron emission from strained GaAs GaAsP superlattice photocathodes," Applied Physics Letters 85 (2004) 2640.

Copyright © 2013 CC-BY-3.0 and by the respective authors

PARMELA SIMULATION FOR BNL 704MHZ SRF GUN IN LOW EMITTANCE OPERATION

E. Wang, J, Kewisch, I. Ben-zvi, BNL, Upton, NY 11973

Abstract

The BNL 704MHz 0.5 cell SRF gun is designed for an ERL prototype with high bunch charge and high average current, but may ultimately be used to generate a high brightness electron beam for a high power far infrared free electron laser (FEL) without energy recovery. In simulations with the space charge tracking code PARMELA we obtained a transverse normalized beam emittance of 0.22 mm-mrad for a bunch charge of 300 pC. The schematic layout of 704 MHz gun and its preliminary beam dynamics are presented in this paper. The emittance of electron beam was optimized for 300 pC bunch charge, 20 ps bunch length and 20 MeV operations.

INTRODUCTION

A high repetition rate FELs requires an electron beam with an extremely good emittance and operating in CW mode. The transverse normalized emittance of the electron bunch is matched to a FEL beam if

$$\gamma\varepsilon_{x,y} < \frac{1}{4\pi}\gamma\lambda_r$$

where γ is the electron energy and λr is the FEL wavelength. The reduction the transverse emittance from the RF gun and the optimization beam optics are the goals of this paper. To realize the high repetition rate and high average power FEL, the gun has to work in CW mode.

SRF gun combines the high gradients of normal conducting RF gun with the CW mode operation of superconducting RF technology. It is demonstrated to be capable of generating a low emittance beam in CW mode operation. The 704MHz superconducting gun for BNL ERL prototype is commissioned now[1]. As an ERL injector, this gun must accelerate electrons to 2-2.5MeV with bunch charge up to 5nC dependent on the operational parameters. In pervious simulations it was shown that this gun is capable of providing the beams with 1.4μm rms normalized emittance with a bunch charge of 1.4nC.

In our PARMELA simulation we reduced the bunch charge to 300 pC and obtained a normalized transverse emittance of 0.22 mm-mrad after acceleration to energy of 20MeV. The optimization code RTX was used in this work as a wrapper around the PARMELA program. The 2D electric field map of the gun and cavities was obtained with Superfish and passed into PARMELA. The average axial electric field in the gun is assuming 9.4MV/m.

BEAM OPTICS ARRANGEMENT

The layout of the accelerator is shown on Figure 1. The beam energy at half cell SRF gun exit is 2MeV. Then it will be boosted to 20MeV by a 5 cell cavity. Two solenoids are used to maintain the beam size and space charge compensation. A 3rd harmonic cavity is used to reduce the energy spread. A uniform spatial and temporal distributions laser shape was assumed to drive the beam from cathode. The 704MHz cavity shape is shown on Figure 2. The initial beam and accelerator parameters are listed as Table 1.

Multiple parameters including laser spot size, emission phase, beam length, solenoids' field, 3rd harmonic cavity parameters must be optimized.

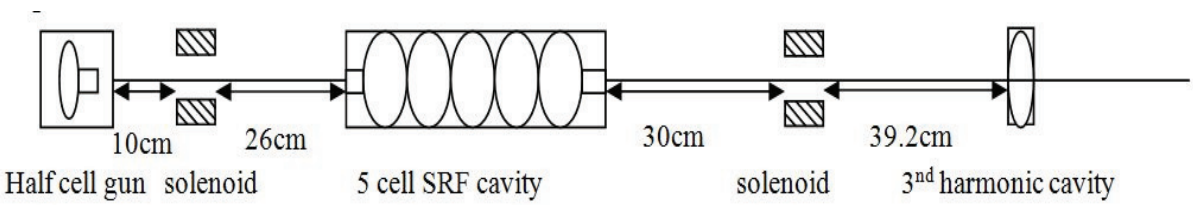


Figure 1: The layout of beam optics. The optimized distance is labelled.

*Work supported by Brookhaven Science associates, LLC under Contracts No.DE-AC02-98CH10886 with the U.S.DOE
#wange@bnl.gov

Copyright © 2013 CC-BY-3.0 and by the respective authors

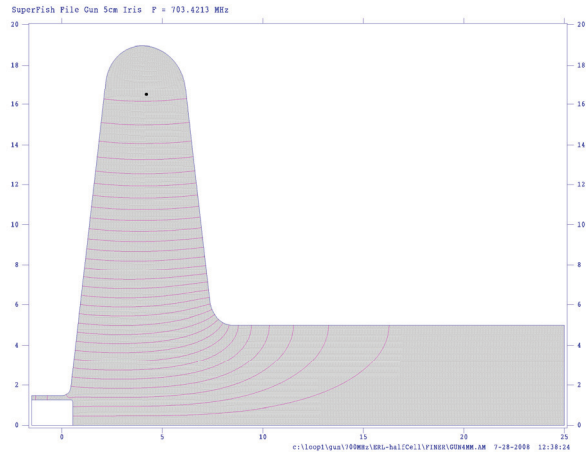


Figure 2: The fundamental mode in the 704Hz SRF gun. The cathode position can be adjusted.

The input parameters assumed for the PAMELA simulations are summarized in Table 1.

Table 1: The Optimized Parameter for Low Emittance Operation

Parameter	Value at 40MV/m
Bunch charge at cathode	300pC
Longitudinal charge distribution at cathode	Uniform
Transverse charge distribution at cathode	Uniform
Bunch length at cathode	20ps rms
Thermal emittance, $\varepsilon_{n,th}$	0.23μm
Gun gradient E_0	9.4MV/m
Injection phase	15.3 degrees
Boost gradient E_0	25MV/m

BEAM OPTICS OPTIMIZATION PROCEDURE

RTX code[2] is a beam optics optimization code which uses the Condor optimizer[3] and PARMELA for the calculation of the beam dynamics. The optimization is performed in several steps in order to limit the number of variables and reduce the optimization time:

- Define the gun geometry and calculate the EM fields using Superfish. The recess of the cathode was adjusted in 6 steps and the following optimization steps were executed for each position of the cathode.
- Single electron tracking to optimize the phase of RF gun and linac. The goal is to reach the maximum energy at the exit of the 5 cell cavity and the minimum energy at the exit of the 3rd harmonic cavity.
- With 5000 particles optimize the spot size on the cathode. The goal is to reach the minimum the normalized emittance at the gun exit.
- With 5000 particles find the strength of the solenoid strength and the distance between the solenoid and the 5 cell cavity, minimizing the normalized emittance at the end of the linac.
- With 5000 particles find the strength of the second solenoid, optimizing the emittance at the exit of 3rd harmonic cavity. The improvement in this step is small.
- Optimized the beam energy spread by varying the phase, gradient of 3rd harmonic cavity and the phase of the accelerating cavity.
- With 10000 particles perform a global optimization of spot size, emission phase, cavity phase, solenoids field and components distance.
- Confirm the final result with 100000 particles.

EMITTANCE OPTIMIZATION

The electron beam energy increases as the function of position is shown in Figure 3. The optimized beam injection phase is 15.3 degrees on the cathode.

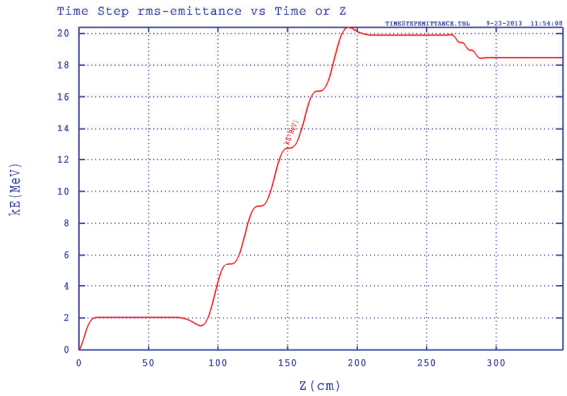


Figure 3: The electron energy as the function of longitudinal position.

The beam emittance from an RF gun is determined by the thermal emittance, the RF emittance and the space charge emittance. It can be written by

$$\varepsilon_n = \sqrt{\varepsilon_{\text{thermal}}^2 + \varepsilon_{\text{rf}}^2 + \varepsilon_{\text{sc}}^2}$$

where the thermal emittance refers to initial beam emittance at cathode emission surface, the RF emittance refers to time dependent focusing of the beam by RF field in the gun cavity and the space charge emittance refers to the repulsive force attributable to space charge cause the emittance to increase. To obtain optimized emittance result in a short time, 5000 particles were used in entire beam line simulation.

A larger laser beam size increases the thermal emittance while a smaller spot size increases the space charge emittance. Therefore varying the beam spot radius can be used to minimize the value of normalized emittance at the exit of gun. The optimized initial beam size is 0.67mm diameter. Here, we assume the beam has a beer can shape, i.e. a uniform transverse and longitudinal distribution.

In the gun the electrons in a bunch will experience different RF kicks depending on the longitudinal position along inside the. This will cause the projected emittance to increase[4]. The minimum RF emittance occurs when the bunch experiences the maximum field amplitude. To minimize the RF emittance, the initial emission phase and laser spot size are varied together.

Copyright © 2013 CC-BY-3.0 and by the respective authors

By recessing the cathode we obtain focusing of the beam by creating a radial electric field near the cathode. In a normal conducting gun this is accomplish using magnetic coils outside the copper cavity. This is not possible in a SRF gun. We found the best position of the cathode to be 5.4 mm behind the cavity wall at a peak RF field at the cathode of 40MV/m. Figure 4 shows the transverse normalized emittance as function of distance from cathode with the optimized parameter.

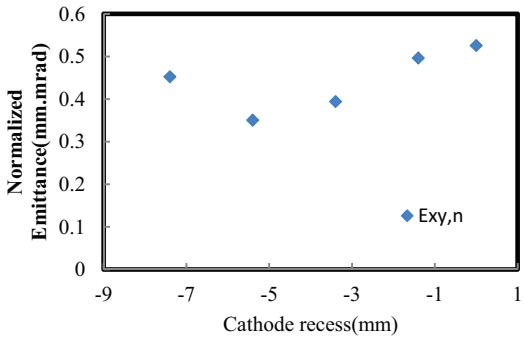


Figure 4: Transverse normalized emittance dependent on cathode insertion position.

The middle section of the bunch usually experiences higher defocusing from space charge forces then the head or tail of the bunch. This results in a bunch rotation in a phase space which is different for beam ends and middle section and increases the projected emittance. A focusing lens in combination with a drift is capable of compensating the overall emittance growth[5]. We place two solenoids to maintain the beam size and compensate emittance increase due to the linear space charge. The first solenoid is placed 10 cm from the gun exit to allow for the space needed for the cryostat. The RF focusing of the booster must match to the beam invariant envelope to damp the emittance oscillations. This matching requires the beam waist is at entrance to the booster linac. The optimized value of B_z is 891G. The optimized position of the booster entrance to the cathode was found to be 46.7 cm,

The beam energy is then boosted to 20 MeV by the 5 cell SRF cavity. A second solenoid is used to optimize the emittance at the end of beam line. A minimum emittance was found when the solenoid field is 197G and the location of the second solenoid entrance is 185.2 cm from the cathode.

As the electrons are accelerated in the 5 cell cavity the particles in the head and tail of the bunch gain less energy than the particles in the centre. This effect can be compensated by deceleration in a 3rd harmonic cavity with a frequency of 2111.1MHz. This cavity is placed downstream of booster cavity. By varying the phase of the 5 cell cavity together with the phase and voltage of the 3rd harmonic cavity we can eliminate the linear and quadratic components of the energy distribution.

At cavity exit, the beam energy spread is 960eV which corresponds to $5 \cdot 10^{-5}$ of full beam energy.

After the separate optimization of the parameters the laser spot size, the strength of both solenoids and the drift length are optimized together. Since the optimization starts close to the final values convergence is quickly reached. Finally, the complete beam line is calculated with 1 million particles to obtain final transverse emittance evolution in the beam line. (shown on Figure 5). A normalized transverse emittance of 0.22 mm-mrad was obtained.

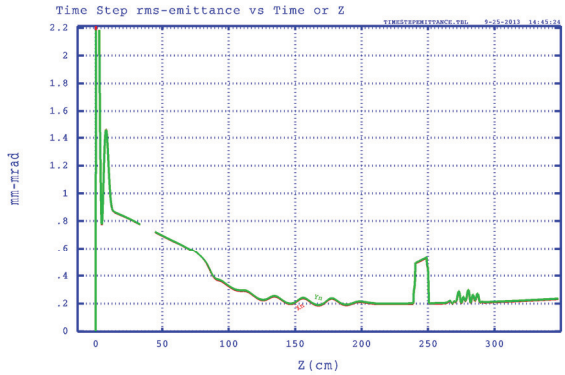


Figure 5: Transverse normalized emittance as function of longitudinal position.

CONCLUSION

We used PARMELA and RTX code to find the best beam optics arrangement for 300pC bunch charge operation of BNL 704MHz gun. 0.22 mm-mrad normalized transverse emittance was obtained. The beam energy spread is minimized to $5 \cdot 10^{-5}$.

REFERENCES

[1] W. Xu, "Commissioning SRF Gun for the R&D ERL at BNL," *ERL 2013*, 2013. http://ssrc.inp.nsk.su/conf/ERL2013/Presentations/WG105_talk.pdf

[2] Developed by J. Kewisch.

[3] F. Vanden Berghen and H. Bersini, "CONDOR, a new parallel, constrained extension of Powell's UOBYQA algorithm: Experimental results and comparison with the DFO algorithm" Journal of Computational and Applied Mathematics, vol. 181, no. 1, pp. 157–175, Sep. 2005.

[4] K.-J. Kim, "Rf and space-charge effects in laser-driven rf electron guns," NIMA vol. 275, no. 2, pp. 201–218, Feb. 1989.

[5] L. Serafini and J. B. Rosenzweig, "Envelope analysis of intense relativistic quasilaminar beams in rf photoinjectors: A theory of emittance compensation" Physical Review E, vol. 55, no. 6, pp. 7565–7590, Jun. 1997.

Copyright © 2013 CC-BY-3.0 and by the respective authors

BEAM DYNAMICS OF FUNNELING MULTIPLE BUNCHES ELECTRONS

E. Wang, I. Ben-zvi, D.M. Gassner, W. Meng, T. Rao, E. Riehn, J. Skaritka
Brookhaven National Laboratory, Upton, NY 11973, USA
O. Rahman, Stonybrook, NY 11974,USA

Abstract

The future electron ion collider (eRHIC) at Brookhaven National Laboratory requires a polarized electron source with high average current, short bunch length, and small emittance. The-state-of-the-art single polarized electron photocathode is far from delivering the required 50mA current due to ion back-bombardment limiting the cathode's lifetime and surface charge limit. In our design of the funnelling gun, currently under construction, the electron bunches generated from 20 photocathodes in a 220 kV DC gun are funnelled into a single common beam-axis. This article details design of the optics of our high-average-current polarized electron gun, and presents our simulation of the beam's dynamics and the design of the combiner. We also report herein our progress in constructing the funnelling gun.

INTRODUCTION

A key technological demand in constructing a future heavy-ion collider lies in assuring a high average-current, high-bunch-charge polarized electron source. To meet the requirements for luminosity and electron energy for an electron- and heavy-ion-collider, we are developing a polarized electron source with an average current of 50mA, and a 2.3A peak current. The quantum efficiency (QE) lifetime due to ion back-bombardment limits the level of the achievable average current, and bunch charge with a single GaAs photocathode in a DC gun. One approach to extending charge lifetime is to funnel the electron bunches generated from several photocathodes to a single common axis. In our design, each photocathode generates an average current of 2.5 mA. We placed twenty GaAs photocathodes along the rim of a 32 cm-diameter cathode electrode at a potential of -220 kV. A series of fixed magnetic field dipoles first bend the off-axis electron bunches that then are merged into the main axis by a rotating magnetic field. Figure 1 is the schematic layout of the funnelling gun for transporting current from the cathodes to the depressed collector that acts as a beam dump. Each cathode produces an electron bunch with a 700 kHz of repetition rate. The timing of the radiating laser to the cathode is such that each cathode emits with delay of 70ns after the previous one. After funnelling, the bunches' repetition frequency is 14 MHz; the total average current reaches 50 mA.

*Work supported by Brookhaven Science associates, LLC under Contracts No.DE-AC02-98CH10886 with the U.S.DOE
#wange@bnl.gov

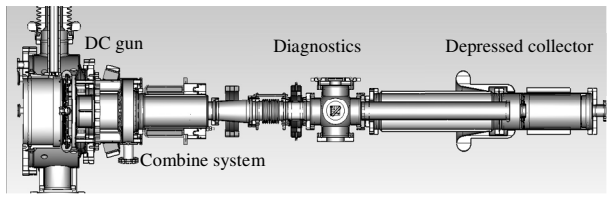


Figure 1: Schematic layout of funnelling gun.

GUN SETUP

The detailed design oft the gun was described earlier [1].We used a Pierce-like DC gun to accelerate the electrons. A focusing field near the cathode balances the effect of the strong space-charge from the bunch. The optimized angle between the cathode and the cathode's electrode is 157°; the gap voltage is 220V across 2.8mm. The maximum field on the cathode is 5.3MV/m. Solenoids placed after the anodes compensate for the defocusing of the space charge in the gun's DC gap. We designed compensated dogleg trajectories in the beam's funnelling system encompassing 20 fixed bending fields, one for each cathode, generated by 20 dipole-magnets, along with a single rotating bending-field generated by the magnetic combiner. Several components of the beam diagnostics are sited downstream, and finally, the beam will absorbed by a depressed collector. Two solenoids downstream of the combiner maintain the beam size.

SIMULATION OF THE COMBINER FIELD

We are using 20 dipole coils and 40 quadrupole ones with a sine AC current to generate rotational dipole- and quadrupole fields [2]. The OPERA AC steady-state solutions confirmed the degree of rotation of the fields, and also that the multicathode emitted beams are in phase. The effect on the beam of the rotating time-dependent field can be ignored. In simulating the gun , we used the static-field maps generated by Opera-3D/TOSCA for simulating the 3D beam in CST Particle Studio. We also generated a rotation dipole- and quadrupole-field from CST EM studio time-domain solver. The 20-sine excition signal is sent to the dipoles; each of them has an 18-degree phase shift. We obtained the animation of the rotating field in the time frame. We used the same setup for generating the rotational quadrupole field. Figure 2 shows the field distribution simulated by CST. The simulated rotated field was used in a PIC solver to assess the the funneling of the multiple bunches . However, the simulation consumed too much time and power due to the RAM limitation in the personal computer and its I/O speed.

Copyright © 2013 CC-BY-3.0 and by the respective authors

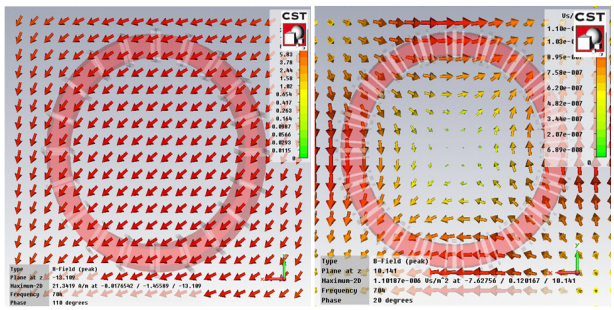


Figure 2: Dipole-field (left) and Quadrupole-field (right) of combiner simulated by CST.

BEAM DYNAMICS

The main problems in beam dynamics are the high bunch-charge, the three-dimensional geometry of the beam's path, and the non-axial symmetricity of the field at the DC gap and at the combiner's entrance about the beam's axis. Therefore, we studied the beam dynamics of the gun and the design of the beam line's optics using "Particle Studio", the 3D beam-tracking code and Particle In Cell (PIC) code developed by Computer Simulation Technology (CST). The following were the three goals of designing the beam line's optics for this gun : i) Prevent the beam from approaching the beam pipe; ii) minimize the beam's emittance at the place of diagnostic cross position, and, iii) focus the beam into the depressed collector. We started by simulating a single beam. The 3D CST Particle studio's tracking solver was used to obtain the beam's transverse parameters. Table I summarizes the optimized input parameters for the simulations.

Table I: Input parameters after optimization

Parameter	Value
Bunch charge	3.5nC
Longitudinal distribution	Gaussian distribution(σ=1.5ns)
Transverse distribution	Uniform
Bunch length at cathode	1.5ns
Bunch radius at cathode	4mm
Thermal emittance, ε_{th}	0.5 μm/mm(rms)
DC gap voltage	220kV
Combiner	Center field=24.5G; Physical length=20cm
First solenoid	Maximum field=560G; Physical length=5.4cm
Second solenoid	Maximum field=184G; Physical length=10.5cm
Third solenoid	Maximum field=366G; Physical length=6.3cm

The current density from the cathode is 4.6A/cm^2, i.e. lower than the limit of GaAs surface charge. Figure 3 shows that the beams' envelope and its transverse normalized RMS emittance as a function of distance with and without the combiner's quadrupole field.

The space-charge force at a 3.5nC bunch with 220keV energy dominates the growth of emittance. The combiner that generates a rotating dipole and a rotating quadrupole magnetic field is synchronized to the beam. Without the quadrupole, the beam lacks focusing in the direction of bending, but experiences excess focusing in the direction of the field. Changing the quadrupole current will equalize the focusing effect in two transverse directions; we obtained a diameter of 15 mm in the round beam's profile at the diagnostic cross when we apply a 7.5A current on the quadrupole coils wherein the divergence angle is x'/y'=23.6mrad/25.1mrad. The transverse normalized RMS emittance is $\varepsilon_{n,x}$/ $\varepsilon_{n,y}$=17.0mm mrad/14.9mm mrad when a quadrupole current is applied.

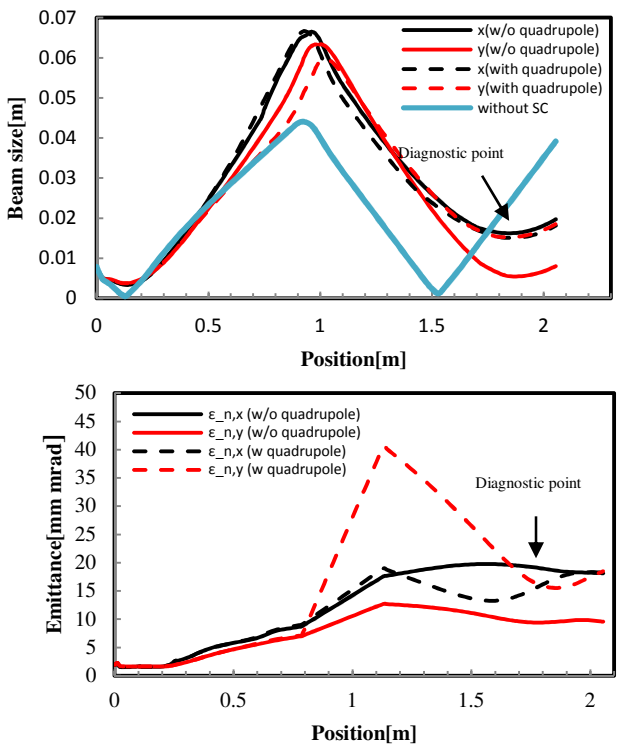


Figure 3 (top): The beam size as a function of distance with and without combiner quadrupole field. The blue curve shows the beam's size without space charge. (bottom) The normalized transverse RMS emittance as a function of distance with and without the combiner's quadrupole field.

Figure 4 illustrates the trajectory of the entire beam line based on the parameters given in Table 1. The beam expands downstream of the diagnostic cross. Therefore, we installed a third solenoid to focus the beam into the depressed collector. The diameter of the beam's waist at the entrance to the collector is 15mm, half that at the collector's entrance aperture. The beam's longitudinal character was simulated using the CST Particle Studio PIC code. The full-beam energy spread at the beam diagnostic cross is 22keV. The energy spread of 97% of the bunch particles is 8keV, viz., an acceptably small energy compared to its energy after the booster.

Copyright © 2013 CC-BY-3.0 and by the respective authors

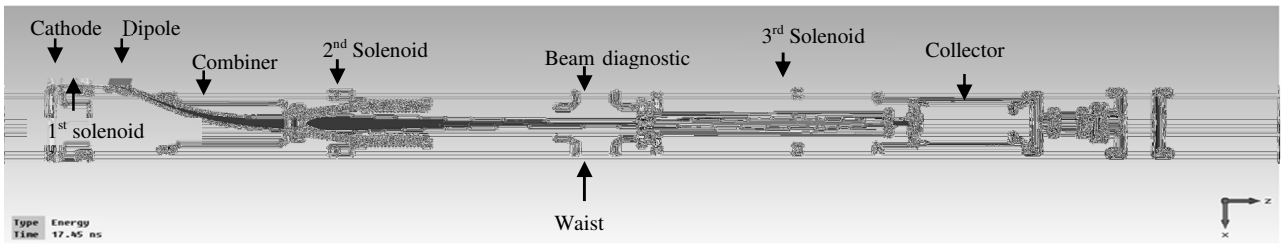


Figure 4: Tracking the entire beam-line. The black curve is the simulated bundle of beam trajectories using the CST particle-tracking solver.

ESTIMATION OF TOLERANCE

A single power-supply will drive the combiner coils' controlling stability to < 25 ppm. The machine's tolerance will be controlled to < 25μm. Based on current's vibration and assembly tolerance on the combiner, we estimate there is 1% non-uniformity transverse distribution on it. The multiple beam size will increase 9.8% and the normalized emittance will increase by 11.3% due to the field tolerance. To get the beam into the entrance aperture of the depressed collector, the tolerance of the timing of the combiner signal allows ±2 degree shift that corresponds to ±8ns.

BEAM-LOSS

Anywhere that a very small fraction of the electron beam strikes the gun's wall, oxidizing gas is desorbed, and the cathode can sustain damage. Several mechanisms contribute to beam loss, such as the formation of a halo round the beam, and the emission of electrons by scattering light or a dark current. We evaluated, in realistic geometry, the loss due to the beam halo by tracking test particles near the beam's edge while modelling the core beam as a slug of charge. The test particles have a different betatron oscillation period from that of the core beam due to defocusing by space charge; this mismatch contributes to the formation of the halo.

We first estimated the position from the cathode at which the beam halo was generated. e. Space-charge changes the force outside the beam, actually reducing the wavelength of betatron oscillation from its value without space charge. We expect the particles at the beam's edge to attain a maximum separation from the beam at one-quarter of that wavelength (λ+/4). The following calculation was based on reference [3].The generalized perveance of a single beam-let is 0.0002526 in combiner. For a constant beam radius, we must apply external focusing with the strength k_o^2, where k_o is the betatron wavenumber with no space charge.

$$K_0^2 = \frac{K}{a^2} + \frac{\varepsilon}{a^4}$$

Here, a is the 2*rms beam radius, and ε is the 4*rms non-normalized emittance. K is generalized perveance. We quantify the space-charge force by defining the intensity parameter χ.

$$\chi \equiv \frac{K}{K_0^2 a^2}$$

Using this notation, the reduction in betatron wavelength outside the beam is given by the factor sqrt(1+χ), so the surface particles separate position for the maximum excursion is

$$\frac{\lambda_+}{4} = \frac{2\pi}{4k_0\sqrt{1+\chi}}$$

Based on the beam parameters in Table 1, the calculation results in a distance of 62 cm where the halo beam is generated. It is further downstream of combiner exit.

We also studied the beam's halo by a particle-core model using the PIC code. Two annular-DC electron sources were placed at the cathode and the exit of the first solenoid. The cathode material was set as vacuum to avoid distorting the field. Fifty points uniformly distributed on the imaginary source generated the test particles. We set the average current at 1nA, allowing us to ignore the space-charge force from the test particles. These particles have the same energy and same divergence as the core beam at the site of the imaginary source. Once the beam reaches the annular source, the test particles surrounding the core beam feel its space charge. Tracking their position can identify the mechanism of halo formation and assess beam loss. The bunch approaches the beam pipe at two positions due to lack of focusing upstream of the combiner. One position is at the entrance to the combiner, and another is at the combiner's exit. Our simulation shows that the closest distance between the test particles and aperture at the first position is 11.2mm, and 19.2mm at the second position. Particles at surface of the bunch evidently cannot strike to the beam pipe and desorbs gases. Other mechanisms of beam loss remain to be determined experimentally.

ACKNOWLEDGMENT

The author thanks to Prof. R.A. Kishek for invaluable discussion on beam loss.

REFERENCES

[1] E. Wang, I. Ben-zvi, D. M. Gassner, in *PSTP 2013* (Proceedings of science, Charlottesville, 2013).

[2] I. Ben-Zvi, X. Chang, V. Litvinenko, Physical Review Special Topics - Accelerators and Beams **14**, 092001 (2011).

[3] S. Bernal, B. Quinn, M. Reiser,Physical Review Special Topics - Accelerators and Beams **5**, 064202 (2002).

Copyright © 2013 CC-BY-3.0 and by the respective authors

A TWO FREQUENCY GUN FOR HIGH CURRENT THERMIONIC CATHODE ELECTRON INJECTOR SYSTEMS

J. Edelen, S. Biedron, J. Harris, S.V. Milton, Colorado State University, Fort Collins, Colorado
J. Lewellen LANL, Los Alamos, NM

Abstract

This paper discusses work done at Colorado State University (CSU) on designing a radio frequency, thermionic cathode electron gun for high-current injection systems for free electron lasers. Some background and a brief overview of other facilities using this type of injector is provided followed by the basic theory of back-bombardment and why it is a problem for such high-current injectors. We then discuss the theory of how a second frequency in the gun could mitigate this back-bombardment effect. Scaling from a previous design to the relevant CSU frequencies and using beam simulations we show results comparable with previous work done in this field [1]. We found that for a 100-pC bunch charge operating at 10MV/m gradient the harmonic field produced a 63% reduction in the back-bombardment power.

INTRODUCTION

Production of 1) high-brightness, 2) low-emittance, and 3) high-average current beams is necessary for high average power free-electron lasers (FELs) and with regards to the first two the use of photocathode RF guns dominate. However, achieving high-average currents in the photocathode mode is complicated by the need of robust, high-quantum efficiency cathodes and complex laser systems. A simple thermionic cathode RF gun system can achieve quite high average currents and, properly designed, can achieve the high-brightness required for many FEL applications in the IR and longer wavelengths [2,3,4,5]; furthermore, the cathodes tend to be robust and long-lived (months to years).

While the use of thermionic cathodes can drastically increase the cathode lifetime, use of such cathodes presents two major complications. The first and foremost is how to prevent the potentially destructive electron back-bombardment, while of secondary concern is how to operate the accelerator in a pulsed mode, which is useful for characterizing the machine.

This paper does not address pulsed-power operation; however, previous work has analysed the possibility of both laser-gated thermionic emission or cathode grids to gate the emission [6]. Instead here we focus on a method to mitigate the electron back-bombardment heating effect.

BACK-BOMBARDMENT IN THERMIONIC RF GUNS

A thermionic cathode when held at a chosen elevated temperature will continuously emit electrons at a rate dependent on the cathode temperature. If the field on the cathode is positive there will be no emission because the field attracts the electrons back to the cathode. When the field is negative the emission from the cathode will be continuous. Some electrons, which are emitted late in the RF cycle, will not gain enough energy to exit the gun and will be accelerated back towards the cathode. These back-bombarded electrons transfer their energy to the cathode surface in the form of heat and subsequently can raise the cathode temperature. This effect is referred to as back-bombardment and is a negative feedback mechanism: higher temperatures produce more electrons, which in turn increase the back-bombardment. If left unchecked, cathode damage may occur.

Using a simple Newtonian model, we computed the trajectories of a single electron subjected to a time varying RF field. Figure 1 shows, as a function of injection phase, the resulting final position of these particles. A time domain overlay of the RF fields is also shown.

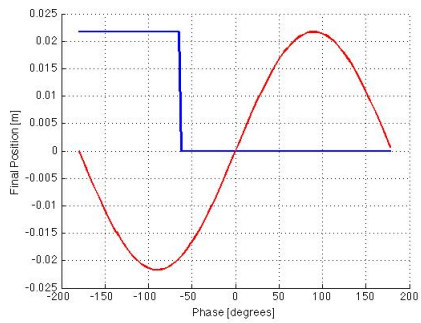


Figure 1: The resultant back-bombardment phase profile for a gap of 2cm and a RF frequency of 1.3GHz. Using a simple Newtonian model.

As stated previously, when the field is positive there is no emission so even though these particles have a final position of zero, they also never gain any energy. However for this model, there is a range of phases from roughly -63 to 0 degrees, where emission occurs but the particles ultimately are accelerated backwards by the rapidly changing field and strike the cathode. This corresponds to about 1/3rd of the region where emission is favourable and back-bombardment occurs.

THEORY OF BACK-BOMBARDMENT MITIGATION

In order to mitigate the back-bombardment effect we must consider what ideal waveform will completely eliminate this effect. A waveform that emits over some time, then holds zero long enough for the particles to

Copyright © 2013 CC-BY-3.0 and by the respective authors

leave the cavity before turning negative, should eliminate back-bombardment. This waveform and its resulting back-bombardment profile, similar to that of figure 1, are presented in figure 2.

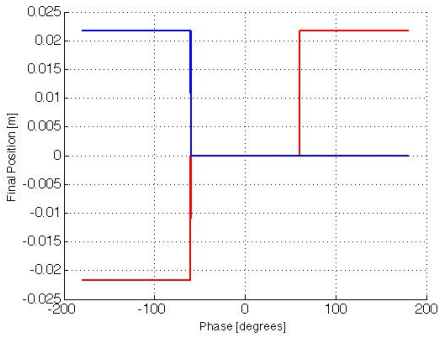


Figure 2: Ideal waveform (red) for complete back-bombardment mitigation with an overlay of its emission phase profile (blue).

This ideal waveform has practical limitations, so we must consider an approximation. We can express this periodic waveform through the use of a Fourier series. To eliminate possible adverse effects due to spurious overshoot caused by an incomplete set of harmonics we consider the first order approximation seen in equation 1.

$$E_z(t) = E_0 \sin(\omega t - \pi) + \frac{E_0}{2}\sin(2\omega t) \qquad (1)$$

The result of the back-bombardment phase profile, similar to those seen in figures 1 and 2, is presented in figure 3 with the overlay of our approximated ideal RF waveform.

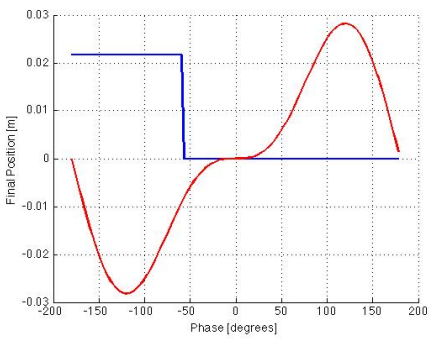


Figure 3: Phase profile for the two-frequency case using a simple Newtonian model (blue) with the temporal field envelope overlay (red).

Figure 4 compares the result of figure 1 and figure 3. This shows that we should see a decrease in the back-bombardment by the introduction of the first harmonic mode in the RF gun. This however was not optimized in relative field amplitude strength and relative phase or for other effects such as space charge. We need to consider a more general parameter space and do a proper scan over this space. Equation 2 represents a more general field profile where the harmonic phase and field ratio are given as variables.

$$E_z(t) = E_0(\sin(\omega t) + H\sin(2\omega t + \phi)) \qquad (2)$$

To better understand how the back-bombardment may vary, we performed a scan of these parameters on a 1D model for the back-bombardment.

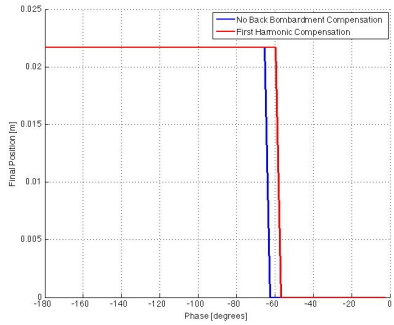


Figure 4: Comparison of the output phase profiles for the two-frequency case and the single frequency case.

Figure 5 shows the back-bombardment power in watts as a function of the harmonic field ratio and relative RF phase for the waveform defined by equation 2. The back-bombarded particle's energy is computed when it strikes the cathode, which is used to compute the energy deposited per RF cycle and consequently the back-bombardment power.

Our expected local minimum near 0.5 HFR and 180-degree phase offset is present, however the true local minimum occurs at 0.75 HFR and a 240-degree phase shift. This theoretical model predicts approximately a 40% reduction in the back-bombardment.

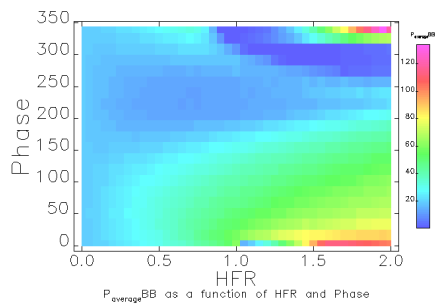


Figure 5: Theoretical result for the back-bombardment power as a function of the harmonic field ratio and the relative phase of the two RF powers.

There is also a minimum band in the upper right corner of the parameter space, since this does not appear in our simulations we believe this to be an artefact of the nonrelativistic approximation.

BEAM SIMULATIONS

The beam transport simulations were conducted using SPIFFE [7], a 2.5-D electromagnetic solver that includes space charge effects.

Copyright © 2013 CC-BY-3.0 and by the respective authors

Without Space Charge

To compare our theoretical model with the more complete and realistic relativistic simulation we begin by running the same parameter scan as before with space charge calculations turned off. The gradient of the cavity was 10MV/m. What we see is a general trend that corresponds with the basic non-relativistic approximation, though with some specific variances due to these approximations.

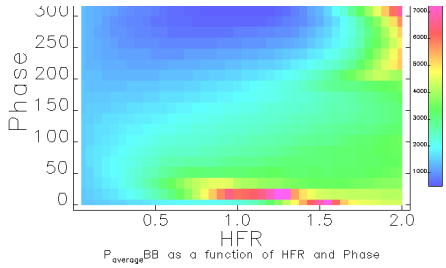


Figure 6: Back-bombardment simulation power as a function of harmonic field and the relative RF phase. The minimum is at 310 degrees and 1.1 HFR

With Space Charge

Having satisfied ourselves that the theoretical and non-space-charge simulations generally agree we turn on the space charge and execute a parameter scan over the same space as before. In this case we are assuming a modest amount of charge (100pC) emitted uniformly during a cycle. We see that the global minimum is roughly in the same location as in the non space charge region. This is indicative that in this modest charge case the space charge is not significantly affecting the ability of the harmonic mode to reduce the back-bombardment.

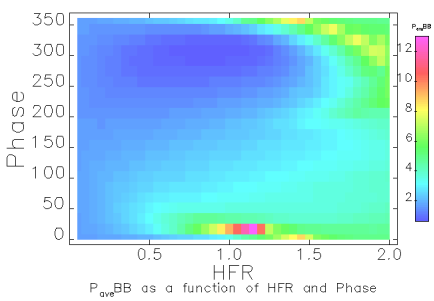


Figure 7: Back-bombardment as a function of the harmonic field ratio and the relative RF phase.

The back-bombardment power reaches a minimum at a relative phase of 310 degrees and a harmonic field ratio of 0.85. With no harmonic compensation the average back-bombardment power is 1.6kW. After introducing compensation the average back-bombardment power is reduced to 617W, about 37% of the baseline.

It should also be noted that while the harmonic field can mitigate the back-bombardment, improper tuning could increase it, which would greatly compound the cathode heating effects.

CONCLUSIONS

We have shown that the technique of using a harmonic field to reduce back-bombardment in thermionic guns can reduce the average back-bombardment power by about 63%.

AKNOWLEDGEMENTS

We wish to thank the office of Naval Research for funding this work.

REFERENCES

[1] S. Biedron, J.W. Lewellen, J. Noonan, “High Energy Laser” Joint Technology Office Presentation, December 2005.

[2] S.V. Milton, et al. “RESULTS FROM THE ADVANCED PHOTON SOURCE SASE FEL PROJECT,” EPAC 2000.

[3] N.D. Arnold et al. / Nuclear Instruments and Methods in Physics Research A 475 (2001) 28–37.

[4] Sandra G. Biedron, John W. Lewellen, Stephen V. Milton, N. Sami Gopalsami, John Schneider, Laura Skubal, Yuelin Li, Mathew Virgo, Gian Piero Gallerano, Andrea Doria, Emilio Giovenale, Giovanni Messina, Ivan Panov Spassovsky, “Compact, High Power Electron Beam Based Terahertz Sources,” Proceedings of the IEEE, Vol. 95, August 2007.

[5] H.P. Bluem, D. Dowell, A.M.M. Todd and L.M. Young “High Brightness Thermionic Electron Gun Performance” 2011 Proceedings of ERL2011 Tsukuba, Japan.

[6] Y.-E Sun, J. W. Lewellen, ANL, Argonne, IL 60439, USA, D. W. Feldman, IREAP, University of Maryland, College Park, MD 20742, USA, “PHOTOTHERMAL CATHODE MEASUREMENTS AT THE ADVANCED PHOTON SOURCE,” Proceedings of LINAC 2006, Knoxville, Tennessee USA.

[7] M. Borland “SPIFFE (SPace charge and Integration of Forces For Electrons) “ Argonne National Lab.

Copyright © 2013 CC-BY-3.0 and by the respective authors

THE CONCEPTUAL DESIGN OF PXIE VACUUM SYSTEM

A. Chen*, V. Lebedev, A. Shemyakin
Fermilab#, Batavia, IL 60510, USA

Abstract

The Project X Injector Experiment (PXIE) [1] will be a prototype of the Project X front end to validate the design concept and decrease technical risks. It consists of a 30 kV, 5mA DC H^- ion source (IS); Low Energy Beam Transport (LEBT); 2.1 MeV CW RFQ; Medium Energy Beam Transport (MEBT) that forms a desired bunch structure by removing ~80% of bunches; two SC cryomodules (CMs) accelerating the 1 mA beam to ~25 MeV; and High Energy Beam Transport with a dump (HEBT). Its vacuum system design will also establish the design guidance for the entire vacuum system of Project X, especially the requirement of low particulate vacuum that is sufficient in practise and at the same time is cost efficient to ensure the performance of CMs.

GAS LOADS AND LIMITATIONS

The PXIE vacuum system consists of four regions that can be separated by vacuum gate valves for commissioning or repairs: IS-LEBT-RFQ, MEBT, Cryomodules, and HEBT-DUMP. Different regions have different gas load sources and different limitations.

The main gas load in IS-LEBT-RFQ region is the gas flow from the IS, ~500 mTorr·l/s. Also, commissioning and machine tuning will be done in a pulse mode, when a chopper in the LEBT produces pulses of variable duration from 1 μs to 16 ms at 60 Hz repetition frequency. In this mode, almost all beam generated by the IS is absorbed in the chopper, and protons recombining inside the chopper's absorber into hydrogen, create an additional load ~1 mTorr·l/s. Vacuum limitations in this region are two-fold. First, the beam loss resulting from H^- stripping should be small, <5%. Second, the pressure in the RFQ and, consequently, gas flow from LEBT should be low to avoid discharges. From practical experience of other labs, pressure < 10^{-6} Torr should suffice.

The gas load in the MEBT region is a combination of outgassing of vacuum surfaces and gaskets; a hydrogen flux from the MEBT absorber irradiated by ~4 mA of the chopped-out beam; and a load from the MEBT scraping system. In the MEBT, vacuum restrictions are related to proximity to SRF. In addition to a gas and microparticles incoming to CMs, which is discussed in the next section, a flow of neutral hydrogen atoms created by stripping of H^- ions should be limited. Such atoms fly along the direction of the parent ions and can reach 2K surfaces of the cryomodules. To make irradiation of CMs by these atoms negligible (≤0.1 W of additional heat load), the vacuum integral over the MEBT length is limited to 1×10^{-6} Torr·m. Also, an aperture restriction after the MEBT absorber introduces differential pumping that dramatically improves pressure near the CM. Finally, scarpers installed at the end of MEBT additionally restrict the solid angle of penetration into the CMs.

Operating vacuum in the CMs is determined by the cryo-pumping and doesn't affect the beam directly. Vacuum limitations in the HEBT are determined mainly by the gas flow into SRF, and the main source of the gas is the beam dump.

Note that one of the vacuum-related effects considered in the course of PXIE design is a possibility of blistering. If hydrogen diffusion in a surface exposed to bombardment by the main beam or its tails is low, protons, implanted by an H^- ion impact, recombine in the bulk into hydrogen which is accumulated in dislocations until the built-up pressure breaks the overlaying material. Corresponding jump of local pressure can result in a beam loss. The issue is expected to be addressed by a system of collimation in LEBT and MEBT and preferential use of molybdenum for surfaces that are likely to be exposed to the beam irradiation.

THE SYSTEM DESIGN

A concept of beam line vacuum system derived from the limitations described above can be divided into three levels of vacuum environment (Figure 1):

1. Ultra High Vacuum and Low Particulate
2. High Vacuum areas (HV)
3. Transition areas

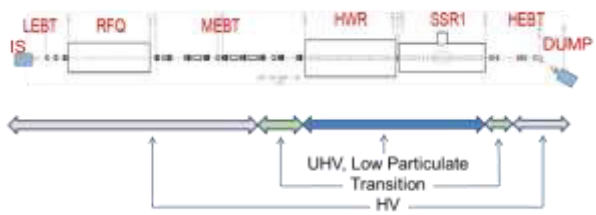


Figure 1: PXIE System Layout with classification of vacuum levels. HWR and SSR1 indicate location of two cryomodules.

UHV and Low Particulate Areas

These areas include two cryomodules, HWR and SSR1. With the cryomodules operating at 2K, cryo-pumping decreases the residual gas pressure below 10^{-10} Torr, mainly driven by the operation temperature. The challenge for this region is to achieve low enough pressure (10^{-7} Torr) at the room temperature before cooling down. Bypass vacuum pipe is designed to alleviate the conductance restriction due to the small aperture and large length of the cavity strings. To guarantee a low particulate environment for SRF operation, all necessary measures as proper handling,

Operated by Fermi Research Alliance, LLC, under Contract No. DE-AC02-07CH11359 with the United States Department of Energy
*alexchen@fnal.gov

Copyright © 2013 CC-BY-3.0 and by the respective authors

clean rooms, gas flow control during pumping and venting etc. are applied. Cold cathode (CC) gauges are used to minimize the heat load from gauging.

HV Areas

The areas from the H- ion source up to the beam absorber at MEBT and downstream of the transition area in HEBT, where the residual gas pressure is 10^{-7} Torr or above, are classified as HV. Turbo pumps are chosen for locations with the highest gas load: the ion source, LEBT chopper, RFQ, MEBT absorber, and the beam dump. Otherwise, pumping is provided by ion pumps.

The DC ion source is continuously supplied with hydrogen gas. Inside the plasma chamber, the hydrogen pressure of $3 \cdot 10^{-2}$ Torr is to be maintained while the pressure downstream is 10^{-6} Torr in order to avoid large beam loss due to H^- stripping. The pressure gradient is achieved by a differential pumping scheme with two 1000 l/s turbo pumps.

Pressure ~10^{-6} Torr in LEBT is achieved by installing a 300 l/s turbo pump at the chopper, where the large gas load is expected when the chopper intercepts major fraction of the beam, and by a 100 l/s ion pump in the middle of the beam line.

In the RFQ, ~10^{-7} Torr vacuum required for reliable operation is provided by two 1000 l/s turbo pumps. Additional two vacuum ports can be used to increase the total pumping capacity if found necessary.

The HV portion of the MEBT is from the RFQ to downstream of the absorber. The absorber, the largest source of the gas load in the MEBT, is pumped by two 1000 l/s turbo pumps, while two upstream ion pumps compensate outgassing of vacuum surfaces. The beam optics downstream of the absorber is adjusted to decrease the beam size and allow placing a 10 mm ID, 200 mm length tube for differential pumping.

The HEBT line consists of magnets and beam instrumentations at room temperature. Its portion starting ~2m downstream of the SSR1 cryomodule is designated as HV. Pumping here is done with several ion pumps. Because a large amount of hydrogen is produced in the beam dump, 2000 l/s turbo pumping is applied. A differential pumping scheme is applied in the first 2m region in order to achieve UHV in the vicinity of SSR1.

Transition Areas

The optimum design of areas providing transitions between UHV and HV will be one of the study goals for the PXIE experiments. These areas, the downstream portion of MEBT and upstream portion of HEBT, are used to minimize the risk of degrading SRF cryomodules due to migration of gas and microparticles from HV components. The gas flow to the cryomodules causes a gas deposition on cryogenic surfaces. While there are no exhaustive experiments or a cohesive theory on the subject, there are indications in the literature that such accumulation at the surface of cryogenic cavities degrades their performance. On the other hand, the closest analogue, a HWR in the Argonne National lab, successfully operates at the pressure of 5×10^{-8} Torr immediately upstream of the cryomodule, though with the residual gas composed primarily by water [2]. To be on a safe side, the pressure in the transition areas is specified to be $\leq 1 \times 10^{-9}$ Torr (H_2). In addition, the optics was designed so that the CM element closest to the room-temperature elements is a solenoid, so that the cryo surfaces inside it could effectively shield the SRF cavities.

A low particulate vacuum practices are applied to ~2m of immediate vicinity of the cryomodules. The roughing/venting ports are arranged in the way minimizing the particle migration towards CM, and the flow rate of roughing/venting is regulated to reduce the risk of particle migration. Note that specific of the PXIE

Table 1: Summary of System Parameters [3][4][5]

Pressure (torr)	10^{-2}-10^{-6}	10^{-7}	10^{-7}	10^{-7}	10^{-7} - 10^{-10}	10^{-10}	10^{-10}	10^{-10} - 10^{-7}	10^{-6}
Leak Check Sensitivity (mbar.l/s)	2×10^{-9}	2×10^{-9}	2×10^{-10}	2×10^{-9}	2×10^{-10}	2×10^{-10}	2×10^{-10}	2×10^{-10}	2×10^{-9}
Pumping	Turbo, Ion Pump				Ion Pump	Cryo Pumping		Ion Pump	Turbo, Ion Pump
Vacuum Seals of Joints	metal gaskets or elastomers; CF or KF				CF only; metal gasket only				
Part Cleaning	UHV procedures								
Gauging	Ion gauge					cc gauge		Ion Gauge	
Low Particulate practice	no	no	no	no	Yes	Yes	Yes	Yes	no
controllers	equipped with RS485 to communicate with control system ACNET via PLC								

Copyright © 2013 CC-BY-3.0 and by the respective authors

is a CW beam, which space charge may assist in transport of microparticles between different location during operation. We believe that such effect would manifest itself as degradation of properties of SRF cavities closest to the warm elements, and, if found, may require lengthening of the transition areas in the design of the Project X.

The transition areas also include fast acting valves on both ends of the cryomodules to prevent catastrophic failures in a case of vacuum accidents in the room temperature parts.

Vacuum requirements for various locations of the PXIE vacuum chamber are summarized in Table 1, and calculated pressure profiles are shown in Figures 2-4.

Other Vacuum Systems

Besides the beam vacuum, there are two other vacuum systems in cryomodules.

The RF couplers in the HWR cryomodule have two ceramic windows which separate coupler vacuum from the beam vacuum and atmosphere. The power coupler vacuum systems are at $\leq 10^{-6}$ Torr. These small volumes of vacuum are maintained by ion pumps (one per coupler). This vacuum system has to be monitored in real time because the ceramic window isolate it from cryomodule beam vacuum is under high RF power and is very delicate. Classified as HV region.

Insulating Vacuum in HWR and SSR1 is required for cryo-isolation. The pressure shall be 10^{-5} Torr prior to cooldown. These systems will be pumped with turbo and roughing pumps. Pressure shall be maintained 10^{-6} Torr or better at cold. CC gauges shall be used. The pumps once used in this system shall not be used for UHV system because of contamination.

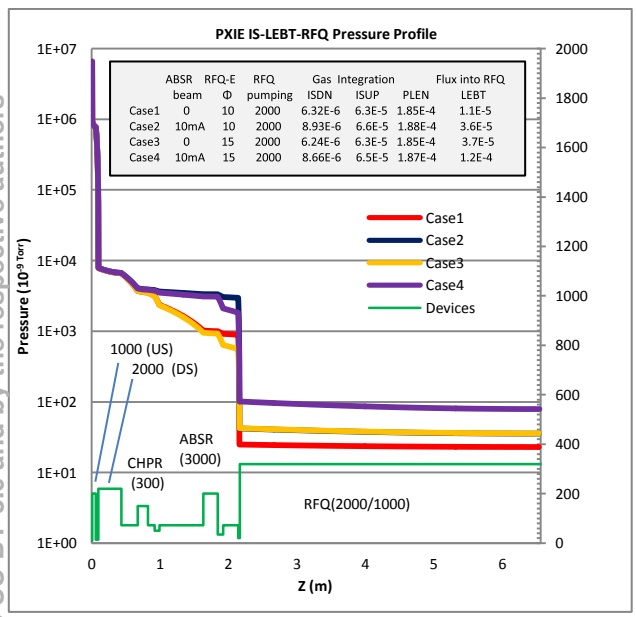


Figure 2: The pressure profile in IS-LEBT-RFQ. The number in parentheses is pumping speed in l/s. The IS has 1000 l/s turbo in its upstream chamber and 2000 l/s in down stream chamber. The flow rate of hydrogen is 0.5 torr·l/s. the gas integration is in Torr·m. the equivalent aperture of devices is in mm. there is no gas flow at the downstream end of RFQ.

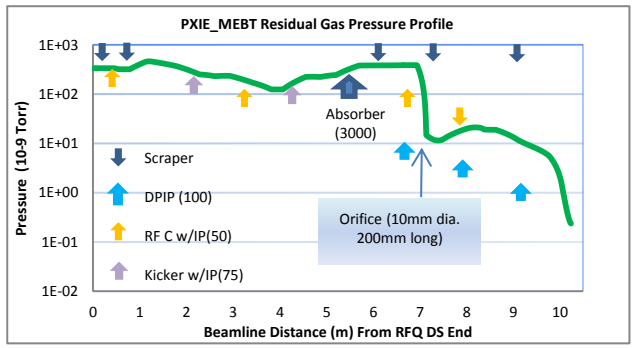


Figure 3: The pressure profile in MEBT. There is no gas flow at the both ends. The number in parentheses is pumping speed in l/s.

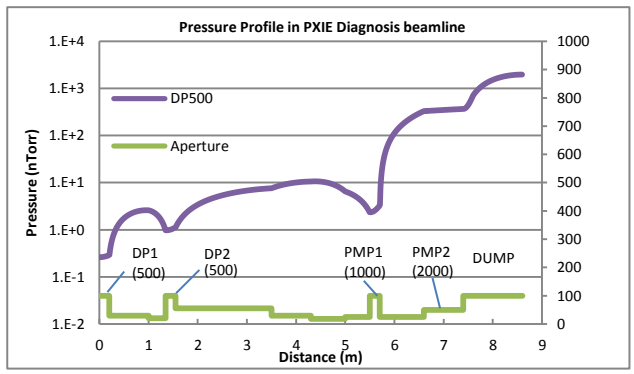


Figure 4: The pressure profile in HEBT-DUMP. The number in parentheses is pumping speed in l/s. there is no gas flow at the ends.

REFERENCES

[1] S. Nagaitsev et al, TUYAA1, NA-PAC'13.
[2] P. Ostroumov, G. Zinkann, private communication, 2012.
[3] A. Chen, L. Nobrega "PXIE Vacuum Considerations", Project X-doc-972-v1.
[4] V. Lebedev, "Beam related vacuum requirement", Project X-doc-971-v1.
[5] S. Nagaitsev et al , PXIE Design Handbook.

Copyright © 2013 CC-BY-3.0 and by the respective authors

DEVELOPMENT OF A COMPACT PHOTO-INJECTOR WITH RF-FOCUSING LENS FOR SHORT PULSE ELECTRON SOURCE APPLICATION

[1]Alenxander Grabenhofer, [2]Douglas W. Eaton, and [1, 3]Young-Min Shin
[1]Department of Physics, Northern Illinois University, Dekalb, IL, 60115, USA
[2]ScandiNova Systems AB, Uppsala, Sweden
[3]Fermi National Accelerator Laboratory (FNAL), Batavia, IL 60510, USA

Abstract

For development of compact ultrafast electron source system, we are currently designing a short-pulse RF-gun with RF focusing structure by means of a series of comprehensive modeling analysis processes. EM design of a 2.5 cell resonant cavity with input coupler, acceleration dynamics of photo-emitted electron bunch, EM design of RF-lens with input coupler, and phase-space analysis of focused electron bunch are systematically examined with multi-physics simulators. All the features of the 2.856 GHz cavity geometry were precisely engineered for acceleration energies ranging from 100 keV to 500 keV (safety limited) to be powered by our 5 MW S-band klystron. The klystron (Thales TH2163) and modulator system (ScandiNova K1 turnkey system) were successfully installed and tested. Performance tests of the klystron system show peak output power > 5 MW, as per operation specifications. At the quasi-relativistic energies, the electron source is capable of generating 100fC – 1 pC electron bunch with pulse duration close to 30 fs – 1 ps and transverse size of a few hundred microns. PIC simulations have shown that the electron bunch undergoes fast RF acceleration, rapidly reaching the desired energies, which can be controlled by tuning RF injection phase and input driving power. It has been shown that it is possible to also focus/compress the bunch longitudinally using a RF-lens, which would allow us to control the temporal resolution of the system as well. While our primary analysis has been performed on a 2.5 cell design, we are also looking into half-cell (single cavity) design that is expected to provide the same range of beam energy with a simple configuration.

INTRODUCTION

The ultrafast electron diffraction (UED) source is one of the most powerful time-resolved spectroscopic/ microscopic tools capable of visualizing the sub-atomic world in a femto-second time frame. A successfully developed UED system will enable us to observe various ultrafast phenomena in chemical and biological substances of solid, gas and liquid phases. The instrument will be a useful tool for a wide range of scientific experiments in chemistry, biology, physics, radiolysis, and engineering on which accurate spatiotemporal analysis methodology is highly demanded. Ultrafast technology with sub-atomic resolution within the femto-second range, while still immature, far exceeds the current technical capacity of commercially available electron microscopes. This technology is not achievable from any single unit or commercial product, as integral parts and their systematic integration are still under development. For spectroscopic application, the main advantage of electron diffraction is that the electrons scatter off all atoms and atom-atom pairs in the molecular sample. Thus, unlike spectroscopy wherein the probe is turned to specific transitions, the electron probe is sensitive to all species in its path and can hence uncover structures that spectroscopy may be blind to. This type of spectroscopic imaging technique can offer spatiotemporal information of transitional dynamics and chemical reaction in liquid and solid states that are of main interest in NIU, as described in the next section, and the proposed UED system is expected to secure sufficient spatial and temporal resolution with good spatial coherence for those kinds of studies. The UED technique employs time-delayed ultrafast pulses – a laser pulse to initiate the reaction and an electron pulse to probe the ensuing structural change in the molecular sample. The resulting electron diffraction patterns are then recorded on a CCD camera. These processes can only produce femto-second electron diffraction when all the elements are properly orchestrated in harmony, which requires a sophisticated design process. In particular, as a key element of a UED system, a short pulse electron source must be capable of producing highly mono-energetic electron bunches of a few hundred keV to a few MeV to create dynamic scattering images with femto-second/sub-angstrom spatiotemporal resolution. Currently, we have a 5.5 MW S-band klystron driver for a photo-injector that has been designed with a 2.5 cell RF-gun to produce 100 ~ 500 keV electron bunches.

BACKGROUND AND OBJECTIVES

Most of UED systems have employed the photocathode-based DC gun with an energy in the range of 30 ~ 100keV（Max. DC field = 10 ~ 12 MV/m）and 400 ~ 600 fs at 10^3~10^4 e-/pulse. However, with the DC guns, bunch length and energy spread are increased during beam transport. The bunch length of a 30 keV e-beam is, for instance, increased from fs to a few ps and the energy spread ($\Delta E/E$) becomes ~ 3×10^{-3} to a distance of 40 cm. It is thus difficult to obtain a < 100 fs electron bunch with $\Delta E/E < 10^{-3}$ using DC guns. Also, to reduce the space charge effect in low energy DC gun system, the distance between sample and cathode should be minimized (4 ~ 5 cm) and/or the number of electrons in bunch should be decreased to 10^3 e-/bunch with 400 fs. It is difficult to observe the ultrafast dynamics with single-

Copyright © 2013 CC-BY-3.0 and by the respective authors

shot measurement and the studies of low-energy UED are limited to the reversible processes. Recently, photocathode RF-guns with higher accelerating gradients and electron density are therefore widely investigated for femto-second UED system application, which is also considered in our approach. We plan to pursue mechanical design and manufacturing of a RF-gun and high vacuum chambers, including a cooling system. The machined parts will be inspected by the Engineering Department and our HP8510C VNA will be available for spectrum analysis of the manufactured RF cavity.

SYSTEM CONFIGURATION

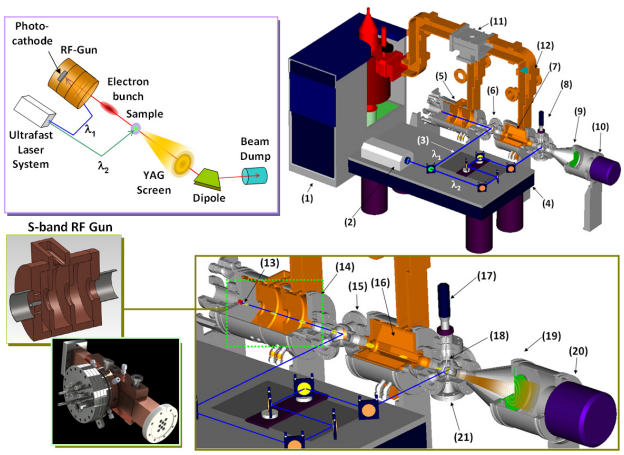


Figure 1: (a) Conceptual sketch of ultrafast electron diffraction system (b) engineering drawing of the designed NIU UED system. The RF power source (S-band klystron system) is already under installation with several other RF components (insets: designed 2.5 cell cavity and S-band photoinjector, courtesy of Radiabeam). See text for details.

Figure 1 is an engineering sketch of the proposed instrument that mainly consists of ultrafast laser system, a RF-gun, beam focusing devices, a 6-way cross sample chamber with a micrometer aligner, Yttrium aluminium garnet (YAG) screen with femto-second optoelectronic CCD camera, and electron beam dump with a bending section, if necessary. The electron bunch is photo-emitted by illuminating a photocathode with an ultra-short laser (that could eventually be spatiotemporally shaped). This pump-probe configuration, where the pump is a μJ laser pulse and the probe is the electron beam, could have enormous advantages in studying the dynamics of system in transient states with sub 100-fs (and eventually attosecond) time resolution. The short pulse electron source in the proposed UED unit mainly includes a femto-second laser system, a RF-gun, and a buncher for pulsed operation with femto-second electron packets. The system will employ a regeneratively mode-locked laser that produces ultra-short pulses of up to 10 ~ 100 nJ at 800 nm with variable pulse width (100 fs to 10 ps) and repetition rate (~ 80 MHz). The output pulses pass through two successive nonlinear crystals to be frequency tripled (267 nm). The harmonic is separated from the residual infrared radiation (IR) beam by dichroic mirrors, and the frequency-tripled pulses are introduced to the photocathode of the RF-gun for generating the electron pulse. The residual IR fundamental beam remains available to heat or excite samples and clock the time through a computer-controlled optical delay line for time-resolved applications. In order to pursue electron diffraction spectroscopy with sufficiently high signal-to-noise ratio, electron bunches need to contain > 10^6 electrons per a pulse. A photocathode with a quantum efficiency of 10^{-6} will require 10^{12} UV photons per a pulse to provide the 10^6 electrons/pulse. 10% efficiency in the two harmonic generation steps from the near IR to the UV implies 10^{14} IR photons/pulse. For the ~ 1eV IR photon energy, one then arrives at an IR laser pulse energy of ~ 10 μJ. A 10 μJ laser pulse energy is difficult to obtain from a fs laser oscillator directly as 0.1 – 1 μJ is about the limit with long cavity and/or cavity dumping techniques. A high QE (> ~ 10^{-4}) photocathode may thus be needed in order to create > 10^6 electrons/pulse with the laser energy. The first approach under our consideration is to use a Magnesium (Mg) photocathode (work function: 3.66 eV) at 267nm that has demonstrated relative high QE (10^{-3}) under modest vacuum condition [1].

SIMULATION MODELING ANALYSIS

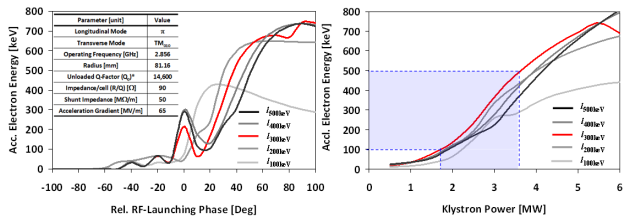


Figure 2: Optimally designed RF-gun parameters (table) and RF-launching phase and klystron power versus electron energy graphs obtained from tracking/PIC simulations with various cell-to-cell distances for beam-wave synchronization (1 pC bunch charge and 100 fs pulse).

As shown in Fig. 2, the acceleration performance of the design RF gun was examined with CST PIC solver. CST PIC code is the 3D particle-in-cell simulator based on finite-difference-time-domain (FDTD) algorithm that includes space charge effects of an electron bunch, represented by a collection of macro-particles, using real-time field profiles and ambient energy losses. The macro-particles are deposited on a grid and Poisson's equation is solved in the rest frame of the electron bunch and the electrostatic fields are Lorentz-transformed to compute the total force experienced by each macro-particle in laboratory frame. For the particle simulation, the electric and magnetic fields of 2.856 GHz, π, TM_{010}-mode, provided by CST Eigenmode solver, are imported into the cavity in particle-tracking and PIC simulation models. The initial laser distribution was taken to be an ultra-short

Copyright © 2013 CC-BY-3.0 and by the respective authors

laser pulse and a perfect three dimensional ellipsoidal distribution. At quasi-relativistic energies the electron source is capable of generating 100fC ~ 1 pC electron bunch with pulse

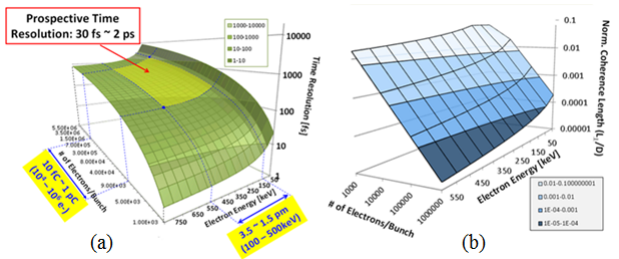


Figure 3: (a) spatiotemporal resolution and (b) coherence length versus # of electrons and electron energy.

duration close to 30 fs ~ 1 ps and transverse size of few hundred microns. At lower energies similar performances can be achieved with lower (100 fC) bunch charge. The space charge effect appears more dominant at the lower energies in that transverse and longitudinal emittances are diluted in the phase-space. A preliminary design is examined with the RF-gun by particle-tracking and PIC simulations. The electron bunch emitted from the cathode is slightly blown up for Columbic space charge force and then rapidly decreases toward the gun exit, but once entering in the focusing field region, it is rapidly squeezed in the axial directions. The simulations show that the bunch has improved momentum linearization in phase-space with spatial compression.

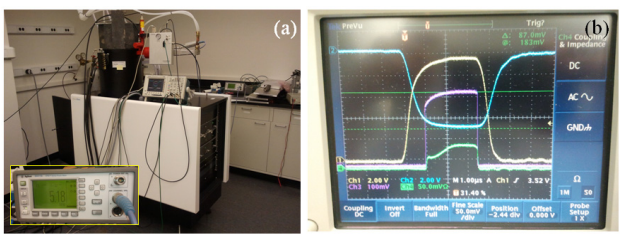


Figure 4: (a) Assembled S-band klystron (Thales TH2163) and modulator system (inset: output power measured by a power-meter) (b) waveforms of pulsed power measured by an oscilloscope.

A crucial component in the case of pump-probe experiment will be the precise measurement of the delay time between the laser pump and electron probe beams. Time stamping with 10 fs resolution will be achieved using an electro-optical modulator [2,3]. If the device does not offer fast enough response to distinct temporal evolution of diffracting patterns, it may be combined with streak camera to improve time resolution, which may also require a deflecting device. The time-resolution of the best optoelectronic streak cameras is around 100 femto-seconds. Measurement of pulses shorter than this duration requires other techniques such as optical autocorrelation and frequency-resolved optical gating (FROG) [4,5]. Figure 3 shows prospective specification of our designed UED system that is assessed by analytic calculations [6]. One can see in Fig. 3 that the 100 ~ 500 keV, corresponding to 1.5 ~ 3.5 pm spatial resolution, leads to 30 fs ~ 2 ps time resolution with ~ 10^4 ~ 10^6 electrons (~ 10 fC ~ 1 pC).

RF-TEST OF KLYSTRON SYSTEM

As a part of plan of a short pulse electron beam source construction, we installed and commissioned the S-band klystron (Thales TH2163) and modulator system (ScandiNova K1 turnkey system), as shown in Fig. 4. The high power RF-test ended up successfully demonstrating a ~ 5.2 MW peak power with 4 μs pulse width. The optical table and some waveguide components were added to the system, which will be used as a high power driver for the RF-gun once an accelerating mode cavity is added.

CONCLUSION

We have been developing a short pulse electron source for ultra-fast electron diffraction (UED) application at Northern Illinois University (NIU). The construction of the compact ultrafast electron source and associated detection equipment will be a great opportunity for the unique resource and technology in beam and laser physics, electrical engineering and other associated accelerator technologies, and support users from biology, chemistry, condensed matter physics, and medicine, among other fields.

REFERENCES

[1] X. J. Wang et al., Nucl. Instrum. Methods A 356 (1995) 159; X. J. Wang et al., to be published in Nucl. Instrum. Methods A, BNL – 65002 (1997).

[2] F. Loehl, K. Hacker, H. Schlarb, "A sub-50 fs bunch arrival time monitor for FLASH," in Proceedings of the 8th Workshop on Diagnostics and Instrumentation for Particle Accelerator (DIPAC07), 262-264; available at http://www.elettra.trieste.it/dipac07/

[3] T. Maxwell, P. Piot, "Proposal for a Non-Interceptive Spatio-Temporal Correlation Monitor," to appear in proceedings of the 2009 Particle Accelerator Conference. Preprint available at http://lss.fnal.gov/archive/test-preprint/fermilabconf-09-260-apc.shtml

[4] Rick Trebino (2002), *Frequency-Resolved Optical Gating: The Measurement of Ultrashort Laser Pulses*, Springer. ISBN 1-4020-7066-7. Read more: http://www.answers.com/topic/frequency-resolved-optical-gating#ixzz2LCyPzeRB

[5] R. Trebino, K. W. DeLong, D. N. Fittinghoff, J. N. Sweetser, M. A. Krumbügel, and D. J. Kane, "Measuring Ultrashort Laser Pulses in the Time-Frequency Domain Using Frequency-Resolved Optical Gating," Review of Scientific Instruments 68, 3277-3295 (1997). Read more: http://www.answers.com/topic/frequency-resolved-optical-gating#ixzz2LCyYYFlX

[6] Marcos Dantus, Scott B. Kim, J. Charles Williamson, and Ahmed H. Zewail, "Ultrafast Electron Diffraction. 5. Experimental Time Resolution and Applications," *J. Phys. Chem. 199498,* 2782-2796.

Copyright © 2013 CC-BY-3.0 and by the respective authors

HIGH POWER TEST OF A 3.9 GHZ 5-CELL DEFLECTING-MODE CAVITY IN A CRYOGENIC OPERATION

Young-Min Shin[1, 2], and Michael Church[2]
[1]Department of Physics, Northern Illinois University, Dekalb, IL, 60115, USA
[2]Fermi National Accelerator Laboratory (FNAL), Batavia, IL 60510, USA

Abstract

A 3.9 GHz deflecting mode (π, TM_{110}) cavity has been long used for six-dimensional phase-space beam manipulation tests [1-5] at the A0 Photo-Injector Lab (16 MeV) in Fermilab and their extended applications with vacuum cryomodules are currently planned at the Advanced Superconducting Test Accelerator (ASTA) user facility (> 50 MeV). Despite the successful test results, the cavity, however, demonstrated limited RF performance during liquid nitrogen (LN_2) ambient operation that was inferior to theoretical prediction. We have been performing full analysis of the designed cavity by analytic calculation and comprehensive system simulation analysis to solve complex thermodynamics and mechanical stresses. The re-assembled cryomodule is currently under the test with a 50 kW klystron at the Fermilab A0 beamline, which will benchmark the modeling analysis. The test result will be used to design vacuum cryomodules for the 3.9 GHz deflecting mode cavity that will be employed at the ASTA facility for beam diagnostics and phase-space control.

INTRODUCTION

Over the past decade, a multi-cell deflecting (TM_{110}) mode cavity has been employed for phase-space manipulation tests of high brightness beams [1-6] at the Fermilab A0 photoinjector (A0PI), and extended applications are currently scheduled at the ASTA user facility (> 50 MeV). Despite the past successful experimental results, the cavity demonstrated a limited RF performance during liquid nitrogen (LN_2) operation, which did not reach the theoretically predicted gradient. The designed cavity has been fully examined with theoretical calculations, based on the Panofsky-Wenzel theorem, using an integrated modeling tool with a comprehensive system analysis capacity to solve complex thermodynamics and the mechanical stress of the multi-cell. This paper discusses the cryogenic RF performance of the 5-cell deflecting mode cavity with numerical modeling analysis. It also presents up-to-date test simulation results of an integrated thermo-stress analysis modeling tool on the deflecting cavity vacuum-cryomodule and low power RF-test results of warm (room-temp, 297 K) and cold (LN_2-temp, 80K) cavities.

SYSTEM DESCRIPTION

At the Fermilab A0PI, the deflecting mode cavity has been used for various beam optics experiments. The cavity was designed with 5 cells to maximize kick strength and powered with a 50 kW (peak), S-band (3.9 GHz) klystron. The RF power was coupled into the cavity through the high power TEM-mode coaxial coupler that was built in the liquid nitrogen (LN_2) vessel. The coupler design includes a temperature gradient from cryogenic temperature (80K) of a LN_2-ambient cavity to room temperature of an input waveguide. As the emittance exchange only requires modest fields and short pulse lengths, the TM_{110} mode cavity was constructed out of oxygen-free, high conductivity (OFHC) copper [7]. A higher Q_0 was required than what was achievable at room temperature with the OFHC copper. We see that Q_0 is proportional to the square root of the copper's bulk conductivity. A Q_0 2.4 times greater was achieved by simply incorporating a LN_2 cryogenic jacket into the design.

The system is designed with the LN_2 vessel because the conductivity of normal conducting copper is increased 6 times from $5.8 \times 10^7\ \Omega^{-1}m^{-1}$ at room temperature to $3.5 \times 10^8\ \Omega^{-1}m^{-1}$ at 80 K, which doubles the cavity Q. The cryo-vessel was designed with three frequency tuning screws, attached to the chamber-outside body at one end and the flange, brazed with the beam pipe at the other end, across the flexible bellows. The tuners push the flange against the body and the mechanical pressure is transferred to the cavity through the beam pipe so the structural distortion by the tuner induces frequency change. As this simple design did not include vacuum insulation, the LN_2-temperature (~ 80 K) was maintained by shielding the outer body with foam insulation. The coaxial input coupler was designed with the critical matching condition, $\beta = Q_0/Q_e \sim 1$, for maximum RF power coupling into the cavity. The original design includes many practical considerations in various technical aspects. However, a high-Q cavity sensitively responds to dimensional deviations and external perturbations, which could significantly limit the deflecting performance in a cryostat. In particular, structural variation of the input coupler can significantly influence RF coupling characteristics producing an unevenly distributed field profile. It is thus highly probable that the limited deflecting performance of the 5 cell can be attributed to an off-resonance RF coupling presumably owing to design error, fabrication error, and/or cryo-cooling contraction. In order to completely identify the operational constraints, we thus investigated the cavity design and estimated its performance with a theoretical assessment incorporated with numerical data of RF simulation modeling analysis.

We conclude that the off-resonance coupling leads to a reduction in the kick strength because it more likely perturbs the field distribution, decreasing cell-to-cell field uniformity, rather than directly weakening the field

Copyright © 2013 CC-BY-3.0 and by the respective authors

strength. The accelerating potential vs. radial position and the deflecting force versus the field deviation. Note that the increasing rate of the deflecting field amplitude along the radial distance is noticeably reduced with loss of field uniformity, which is reflected in the deflecting force: kick strength drops down to 2.9 from 3.95 with 40 % non-uniformity (35.6 % reduction). Eventually, one can see that poorly coupled RF power, accompanying perturbation of the field distribution, possibly causes a 30 ~ 40 % deficiency of the deflecting strength.

SIMULATION MODELING

The frequency shift ($TM_{110,\pi}$ mode) due to the effective temperature declination from room temperature (300 K) to LN_2 (80 K) is explained by the uniform change of the cavity volume. The frequency is increased from 3.8725 GHz at 300 K to 3.8870 GHz at 80 K, which corresponds to 68 kHz/K. The simulation analysis estimates that cryo-cooling causes roughly a 24 MHz frequency deviation to the design cavity that would need to be considered in the process of determining cavity dimensions. This approximate analytic assessment is effective for quantifying an average deviation with the assumption that the entire cavity uniformly contracts with a decrease in temperature. However, it does not accurately predict local displacements due to RF-loading impacts over the structure, in particular on the system with fixed points. Moreover, it is limited in accurately implementing localized effects of critical heat sources such as RF loading and beam loading in the cryomodule analysis. Therefore, we extensively investigated RF-thermal characteristics of this 5-cell cryomodule with full 3D thermal and mechanical simulation modeling analysis. More details are discussed in the next section.

Figure 1 depicts the recently designed vacuum-cryomodule containing the 3.9 GHz 5-cell deflecting mode cavity that could be installed at the Fermilab ASTA user's facility. It is designed with the vacuum insulator, instead of the foam insulator. Volumetric contraction and thermal fluctuation resulting from LN_2 cooling is no longer a critical factor since the vacuum insulator tank is an excellent heat reservoir for the LN_2 vessel, which linearly cools the ambient temperature down to 77 – 80 K and maintains it consistently. Instead, it is more critical to consider RF loading and beam loading for CW or high duty operation of high intensity or high power machines. The frequency tuner is similar to the original design except that it is mounted on the vacuum tank with an additional flexible bellows. In this design, the amount of liquid nitrogen is controlled by the N_2 inlet and vent/relief and its level is monitored by the LN_2 level probe. The temperature of the LN_2 vessel remains constant by means of the vacuum insulation tank. However, even in the thermally insulated vacuum system energy of long pulse duration deposits a considerable amount of power on the cavity surfaces that can increase the ambient temperature so highly as to exceed the temperature threshold of bubble formation in the N_2 fluid.

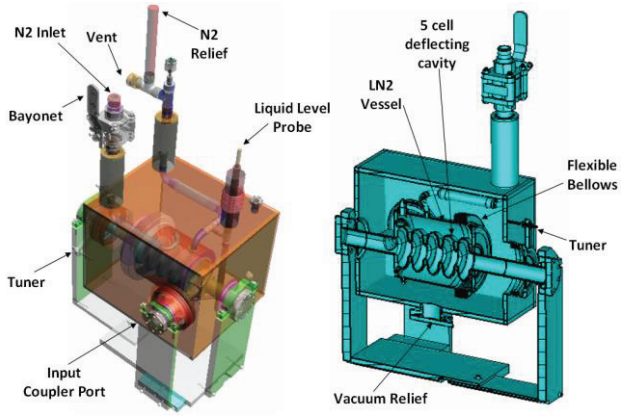


Figure 1: Designed vacuum-cryostat with a 5 cell deflecting mode cavity (a) x-ray image and (b) cross-sectional view

If a deposited power density on the cavity surface exceeds 1 W/cm^2 on average, it is highly probable that the ambient temperature exceeds the LN_2 boiling point (~ 77 – 80 K) so as to rapidly increase gap pressure and create N_2 bubbles that may change the ambient pressure around the cavity in the LN_2 vessel. The excessive fluctuation of vessel pressure could substantially impact cavity performance via frequency change, structural distortion, and even quench on the cavity. Therefore, we simply calculated average power densities deposited on the cavity surface with respect to pulse width and pulse repetition rate (PRR). For the calculation, it is assumed that the cavity receives 70 kW from the klystron and the surface area of the 5 cell is 97.96 cm^2 outside and 89.36 cm^2 inside, respectively. A pulse condition is with less than 1 W/cm^2 RF deposition on the outside and inside cavity surface. Although the calculation is based on the assumption that total RF power is deposited on the cavity surface, it appears that the RF pulse condition (1 ms/5 Hz) of 3.9 GHz deflecting mode cavity planned for the ASTA test facility surely exceeds 1 W/cm^2, which is about 4 W/cm^2 inside and 3.5 W/cm^2 outside. We examined the RF-loading characteristics with a full 3D simulation modeling analysis using an integrated multi-physics computational platform.

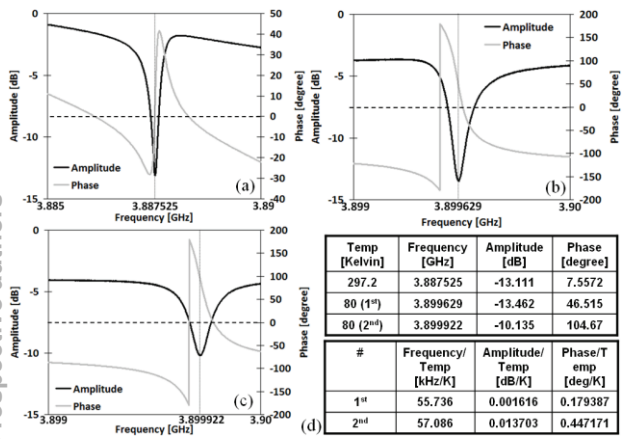
Simulations show S_{11} spectra of the original and deformed 5 cell structures, obtained from frequency domain solvers before and after RF-loading of 1 ms pulse to the cavity. The displacement of thermal energy deposition causes 7.32 MHz frequency shift, accompanied with 2.82 dB amplitude change and 59 degree phase deviation, on the $TM_{110,\pi}$ mode, which is beyond the FWHM (full-width-half-maximum) bandwidth of the input signal. The designed system has a thermal sensitivity of 1.32 MHz/K, corresponding to 0.51 dB/K and 10.7 degree/K.

HIGH POWER RF-TEST

The 5 cell cavity in the cryo-vessel, after completely shielded by thermal insulation foams, was tested at room-

Copyright © 2013 CC-BY-3.0 and by the respective authors

(297 K) and LN_2-temperature (80 K). The cold cavity parameters were measured twice after 0 day and 20 days long cooling operations to observe temporal variation of thermal stability. Figure 2 shows S_{11} spectra (amplitude and phase) of the warm and cold cavities and thermal variations of a TM_{110}-mode. It appears that the resonant frequency is up-shifted with ~ 12.1 MHz by the thermal transition from T = 297.2 K to T = 80 K, corresponding to 55.74 kHz/K, under the condition that cavity frequency varies linearly with temperature. The resonant frequency further rose to 3.899922 GHz after 20 days cooling, corresponding to converged thermal frequency variation of ~ 57 kHz/K, which is close to the simulation result, 64 kHz/K. The return loss remains steady at the initial cooling, while it is gradually increased to ~ - 10 dB, corresponding to 0.0137 dB/K. Even the reduction of coupling level will leave the system fairly operational as 90 % of driving power is still coupled in the system. The instantaneous phase deviation is ~ 0.18 degree/K, but it is also gradually increased up to 0.447 degree/K after 20 days cryo-operation. Therefore, the measurement implies that in the early stage of LN_2-operating mode the system can operate with temporal change of < 5 K in terms of amplitude/phase deviation. However, as the vessel loses cooling efficiency with increasing time, acceptable temperature range for the system drops down to < 2 K, which might exceed ambient thermal fluctuation beyond controllable range of the foam-insulated system. For a better thermal management, a cryo-vessel should thus be designed with a vacuum-insulation, which is currently planned with the ASTA 5-cell deflecting mode cavities.



Temp [Kelvin]	Frequency [GHz]	Amplitude [dB]	Phase [degree]
297.2	3.887525	-13.111	7.5572
80 (1st)	3.899629	-13.462	46.515
80 (2nd)	3.899922	-10.135	104.67

#	Frequency/ Temp [kHz/K]	Amplitude/ Temp [dB/K]	Phase/T emp [deg/K]
1st	55.736	0.001616	0.179387
2nd	57.086	0.013703	0.447171

Figure 2: Experimental S_{11}-spectal data of the 5 cell test cavity measured at (a) room temperature (T = 297.2 K), and LN_2-cooled temperature (T = 80 K) (b) 0-day and (c) 20 days after cooling started.

BEAM TEST

A deflecting force of the LN_2-cooled transverse deflecting cavity (TDC) is tested with a beam of p ~ 3.5 MeV/c and bunch length (σ_z) ~ 5 ps. We scanned RF launching phases to extrapolate transverse kick strength, $k = eV_\perp/E\rho$. Figure 3 is the phase-scanned beam position and envelope graphs. The drift distance of the beam monitor measuring a peak-to-peak deflection ~ 17 mm is ~ 1.22 m from the TDC, which corresponds to the deflection voltage of ~ 24.4 kV. The kick strength, k, from the data is calculated to be ~ 0.41 m^{-1}. We will continuously test the cavity to characterize a R_{65} term.

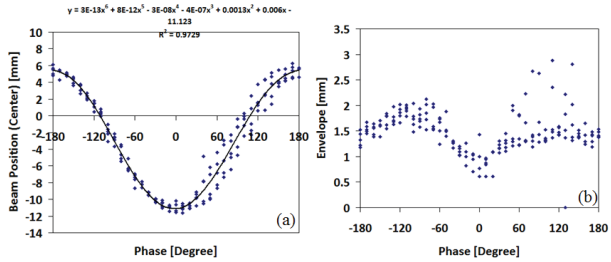


Figure 3: Beam Test result (p ~ 3.5 MeV/c): phase scans of (a) beam center position and (b) envelope.

CONCLUSION

A normal conducting multi-cell deflecting mode cavity has been used for various beam control applications in an LN_2-vessel at the Fermilab A0PI and currently it is planned to accommodate vacuum-cryomodules of either normal conducting or superconducting deflecting mode cavities in the ASTA beam line for higher energy beam tests. Despite successful test results of the previous experiments on 6D phase-space manipulation, the 5-cell cavity demonstrated limited performance. The preliminary high power RF-test and beam test were done and currently systematic optimization of the sensitivity modeling analysis on the deflecting mode vacuum-cryomodule is under consideration in comparison with experimental data.

ACKNOWLEDGMENT

We would like to acknowledge Philippe R. G. Piot for the support of the experiment. We also thank James Santucci, Jerry M. Makara, and Christopher Prokop for the technical support of the system setup for the experiment.

REFERENCES

[1] K. Bishofberger et al., Proc. of LINAC 2002, TU404 (2002).
[2] Y.-E Sun et al., Phys. Rev. ST-AB 7 (2004) 123501.
[3] P. Piot et al., Phys. Rev. ST-AB 9 (2006) 031001.
[4] J. Ruan et al., Phys. Rev. Lett. 106 (2011) 244801.
[5] Y.-E Sun et al., Phys. Rev. Lett. 105 (2010) 234801.
[6] T. W. Koeth, "An Observation of a Transverse to Longitudinal Emittance Exchange at the Fermilab A0 Photoinjector," PhD Thesis, 2009.
[7] T. W. Koeth, Proc of PAC2007 Albuquerque, NM, THPAS079, p. 3663 (2007).

Copyright © 2013 CC-BY-3.0 and by the respective authors

RF GUN WATER TEMPERATURE CONTROL SYSTEM AT ASTA *

P. Stabile#, M. Ball, J. Czajkowski, J. Firebaugh, P. Kasley, P.S. Prieto, T. Zuchnik,
Fermilab, Batavia, IL, 60510, USA

Abstract

A linear electron accelerator is in the late stage of construction at the Advanced Superconducting Test Accelerator (ASTA) facility at Fermilab. The purpose of this accelerator is to operate, study and develop the superconducting cavities and associated systems to be used in future superconducting accelerators. ASTA incorporates an L-band radiofrequency (RF) gun with a coaxial RF input operation at 1.3GHz, based on 1+1/2 cell DESY-type gun, followed by two superconducting cavities. A temperature control system regulates the RF power transmission between 5MW Klystron and the RF Gun. Its role is to maintain the resonant frequency by exploiting the 16.5ppm/ºC thermal expansion of the copper. Temperature is regulated by mixing chilled low conductivity water (LCW) with circulating water between the cavity and gun skid located outside the radiation cave. A fine pneumatic actuated valve controls the chilled water flow and in turn is controlled by a feedforward/feedback regulation algorithm. This paper will describe the water temperature control system used to stabilize the tuning frequency of the RF Gun.

INTRODUCTION

Fermilab is constructing ASTA at the existing New Muon Lab (NML) building. ASTA is part of Fermilab new state-of-the-art superconducting radio frequency (SRF) test facility complex. ASTA facility [1] consists of a shielding cave which houses the accelerator, as well as areas for support equipment and systems required for operation. The accelerator consists of three distinct sections: the injector, SRF accelerator, and the test beam lines including space for a small storage ring. The injector is a 1.3GHz photocathode electron RF gun which generates electron bunches repeated at 3MHz within a macro pulse of nominal duration of 1ms [2, 3].

The RF power to the gun is supplied by a 5MW, 1.3GHz klystron. The temperature control loop stabilizes the temperature of the RF Gun when RF power is applied and also during no RF power cycles.

The temperature control loop regulates the water temperature to ±0.18 ºC which, at a centre frequency of 1.3GHz, keeps the frequency shift of the Gun, within 5KHz (23KHz/ ºC). A 5KHz shift corresponds to a reflected power less than –22dB.

SYSTEM DESCRIPTION

The task of the cooling system is to mix the outgoing warm water with the supply LCW water regulating the desired temperature of the circulating water. Figure 1 shows the piping schematic of the RF gun cooling system. The cooling skid is located outside the radiation shielding and water is pumped through approximately 80 feet of piping. A PLC is integrated into the cooling skid to read back the temperature and flow measured by the different sensors and to control the flow rate of the LCW. The temperature of the LCW supply is stabilized to 90±1ºF (~32.22 ±0.5ºC) by an external control system running on an independent PLC. The amount of the incoming supply LCW is controlled by a fine pneumatic valve that allows a flow rate between 0 and 15GPM. The position of the valve is controlled by a dedicated PID loop build into the valve controller.

A heater is used to mix the LCW cold water and the warm water from the RF Gun and can supply between 0 and 12KW of power. The mixed water flows to the gun at a fixed rate of 15 GPM through nine cooling channels, seven with 10mm ID and two with 6mm ID tubing connections, cooling down the cavity. The return water from the gun is split between the heater and a return connection to the main chiller system.

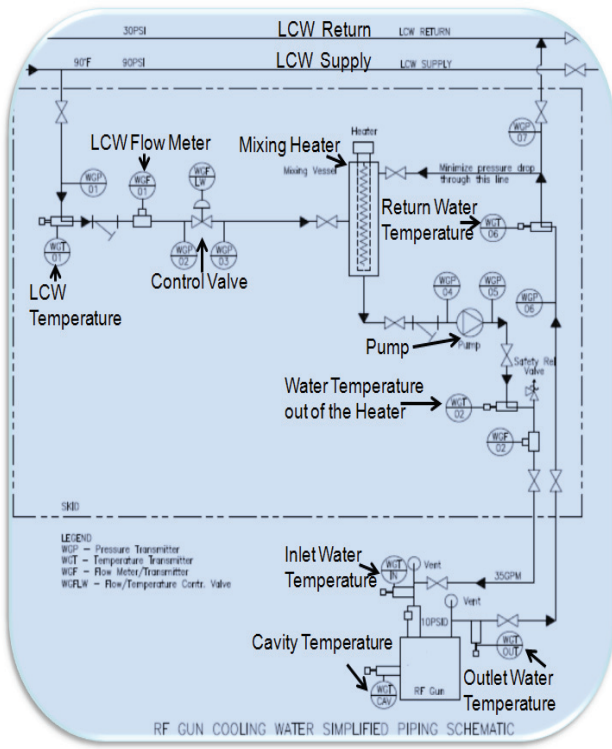


Figure 1: RF gun cooling system overview.

* This work was supported by the U.S. Department of Energy under contract No. DE-AC02-07CH11359

#stabile@fnal.gov

Copyright © 2013 CC-BY-3.0 and by the respective authors

SYSTEM MODELING

An appropriate model of the system was first made. The RF Gun cooling can be divided into a combination of two subsystems:

- Heater
- RF Gun

Heater

The heater has a fixed volume tank completely filled with almost 1.5 gallons of water. The LCW (m_1) is mixed with the return water from the gun (m_3). The output water (m_2) from the heater flows at constant rate to the gun and removes the necessary amount heat from the cavity.

The water temperature from the heater to the Gun has to be stable; avoiding fluctuations in temperature reduces power reflections from the gun.

The heater can be modeled as a mixing tank with two inputs and one output. The differential equations describing it are:

$$M_\sigma \frac{dT_{02}}{dt} c_p + m_3 T_{02} c_p = m_1 T_{01} c_p + m_2 T_{06} c_p + HPWR\,, \quad (1)$$

$$\frac{dV}{dt} = m_1 + m_2 - m_3\,, \quad (2)$$

where:

- M_σ = volume of water of the heater (US GALLONS)
- m_1 = LCW water flow rate (GPM)
- m_2 = Return flow rate from the gun (GPM)
- m_3 = Output flow rate from the heater (GPM)
- HPWR = Heater power (KW)
- c_p = Specific heat capacity of the water at constant pressure(J/g* ºC)
- T_{02} = water temperature at the output of the heater (ºC)
- T_{06} = return water temperature from the gun (ºC)
- T_{02} = supply water temperature (ºC)
- V = heater water volume (US GALLONS).

The total water flow in the Gun is constant and the time constant of the system is:

$$\tau = M_\sigma / m_3\,, \quad (3)$$

which is equal to 5.96 sec. The steady state point can be calculated using:

$$T_{02} = T_{01}\frac{m_1}{m_3} + T_{06}\frac{m_2}{m_3} + \frac{HPWR}{c_p m_3} \quad (4)$$

RF Gun

A cavity constructed of a single metal has as percent change in wavelength equals the percent change in linear dimension which is proportional to temperature. Frequency de-tuning of the cavity caused by expansion and deformation of the copper causes an increase of the reflected power and RF phase instability. If the frequency deviates from the drive frequency, the power reflected from the cavity will cause standing waves within the waveguide.

The thermal expansion of the copper is about 17.68ppm/ºC (1ppm/ºC more from the one expected) resulting in a 23KHz frequency shift per degree Celsius.

As a first approximation the cavity can be considered as a tank with water flowing through it that maintains a constant volume [4]. Assuming that the inlet water instantaneously and completely mixes into the volume, the thermal mass C will be at the outlet temperature T_{OUT}. The change in outlet temperature will be equal to the net power flowing into the volume divided by its thermal capacitance.

The following differential equation describes the system:

$$\frac{dTout}{dt} = \frac{P_{r\,f}}{C} + \frac{F}{AC}(Tin - Tout)\,. \quad (5)$$

The time constant is:

$$\tau = F / AC\,, \quad (6)$$

which depends on the set flow rate of the chilled water. The steady state point can be calculated:

$$Tout = \frac{A P_{r\,f}}{F} + Tin\,, \quad (7)$$

where:

- P_{rf} = Average RF power injected to the gun (KW)
- F = Flow rate of the chilled water (GPM)
- C = Heat capacity of the water(KJ/ ºC)
- A = Heat factor (ºC*GPM/KW)

IMPLEMENTATION

A combined feedforward/feedback control system has been implemented to improve performance over a simple feedback control (Figure 2).

When a step in the RF power or in the temperature set-point occurs, the feedforward algorithm calculates and sets the new LCW flow rate as a function of temperature variation of the cavity per unit of flow (ºC/GPM) and per unit of power (ºC/KW). The algorithm uses the initial conditions of the system (T_{CAV}, T_{SET}, T_{LCW}, T_{IN}, RF_{Power}) and the final steady state point calculates the new flow set-point. The controller take into consideration the effects of pure time delay due to pipe lengths and also the changes taking place in the return water flow temperature.

Copyright © 2013 CC-BY-3.0 and by the respective authors

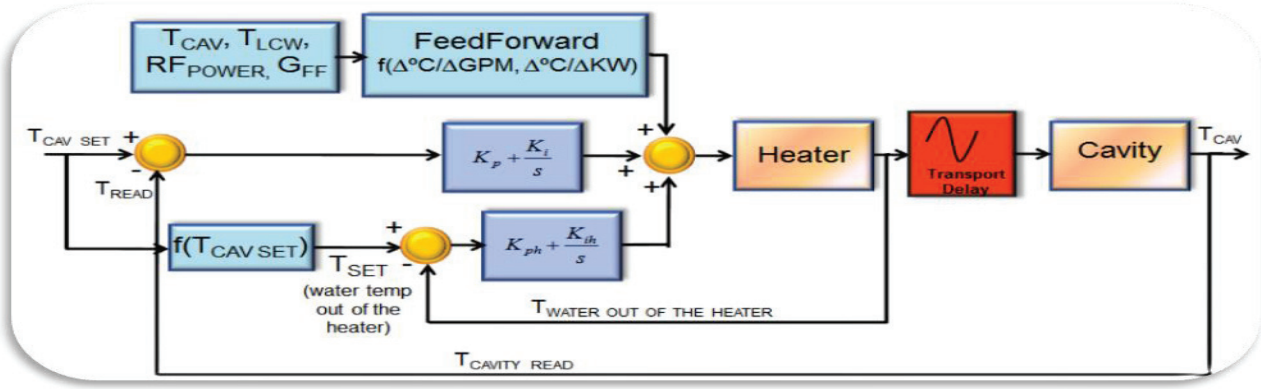


Figure 2: Feedforward/feedback block diagram.

The chilled water takes almost 40 sec. to reach the cavity enclosure, then an additional 20 sec. is required to reach the cavity.

The feedforward is an open loop response, therefore the controller needs to observe the effect of the feedforward loop on the gun temperature before closing the loop with the feedback loop. Once the steady state has been reached within ±0.24 ºC, the feedback suppresses the steady state error.

The cavity feedback was implemented as a proportional and an integral controller with a closed loop bandwidth of ω_{CL}=Kp(Tin- Tout)/AC ~0.005Hz. This makes the feedforward critical for improving the bandwidth of the controller. A conservative design has 45º phase margin.

The Ki/Kp gain ratios in the cavity feedback loop were chosen in order to minimize the overshoot of the system and meet the target phase margin. The water travel time is a "pure delay" that adds 100º to the total phase shift and can be overcame by the feedforward.

An inner feedback control loop has been added to the controller to stabilize the water temperature coming from the heater and it is still in the first stages of development.

This inner feedback loop doesn't have the pipe transport delay therefore its bandwidth is higher than the cavity loop.

RESULTS

The RF Gun is in final stages of conditioning and first electron beam has been produced.

Figure 3 shows the temperature control obtained with a constant power applied to the RF Gun. The temperature set-point is 42.1ºC and the peak RF Power is 1.7MW with a pulse rate of 1Hz and a pulse width of 800µsec. The orange trace is the cavity temperature. The data collected shows that the cavity temperature can be stabilized in a range of 42.1 ±0.18 ºC.

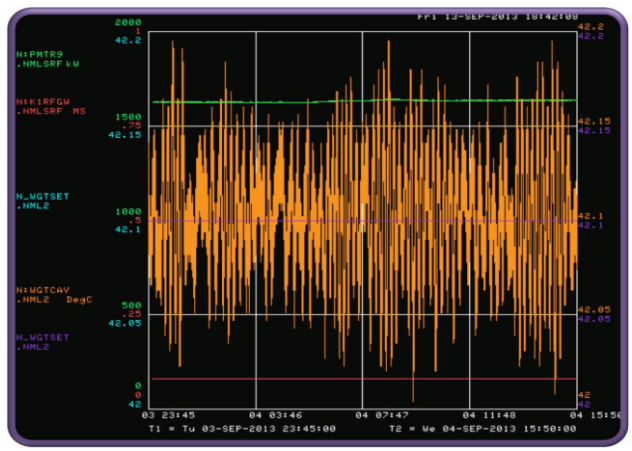


Figure 3: Cavity Temperature control with no RF power.

ACKNOWLEDGMENT

Authors would like to acknowledge all the ASTA project team for their support to this work.

REFERENCES

[1] J. Leibfritz et al., "Status and plans for a superconducting RF accelerator test facility at Fermilab," IPAC2012, New Orleans, Louisiana, MOOAC02, p. 58 (2012); http://www.JACoW.org

[2] M Church and S. Nagaitsev, "Plans for a 750MeV Electron Beam Test Facility at Fermilab," PAC'07, Albuquerque, New Mexico, THPMN098, p. 2939 (2007); http://www.JACoW.org

[3] M. Church et al., "Plans for a 750 MeV Electron Beam Test Facility at Fermilab," PAC'07, Albuquerque, New Mexico, THPMN099, p. 2942, (2007).

[4] J. Crisp and J. Satti, "Fermilab Linac Upgrade Side Coupled Cavity Temperature Control System"; http://beamdocs.fnal.gov/AD/DocDB/0035/003506/001/LinacUpgradeTempCntlSys-Crisp.pdf

Copyright © 2013 CC-BY-3.0 and by the respective authors

EPICS ACCELERATOR CONTROL SYSTEMS FOR LAMBDA EMS AND TCR MAGNET POWER SUPPLIES

Anthony Andrews[1,2*], Y. Kim[1,2,3], C. Eckman[1,2]
P. Buaphad[1,2], C. O'Neill[2], B. Berls[2], K. Folkman[2], and J. Ralph[2]
[1]Department of Physics, Idaho State University, Pocatello, ID 83209, USA
[2]Idaho Accelerator Center, Idaho State University, Pocatello, ID 83201, USA
[3]Thomas Jefferson National Accelerator Facility, Newport News, VA 23606, USA

Abstract

The Idaho Accelerator Center (IAC) of Idaho State University has been operating a 44 MeV L-band linac for high average power THz generation, various nuclear physic related applications, medical isotope generation, and Laser Compton Scattering (LCS) based X-ray generation [1]. As of August 2012, the IAC has been upgrading the 44 MeV linac with a new computer based EPICS accelerator control system to replace the old analog control system. So far, this upgrade includes control of two GigE CCD cameras, and several magnet power supplies with embedded IEEE controllers [2]. However, the 44 MeV linac also has some magnet power supplies which are controlled with external RSTL controllers. This paper describes the development of the EPICS accelerator control system to control Lambda EMS and TCR magnet power supplies with these external RSTL controllers.

INTRODUCTION

To improve the reproducibility and stability of the 44 MeV linac, the previous analog control system was upgraded to a computer based control system. The control system chosen for this upgrade was the Experimental Physics and Industrial Control System (EPICS). As of August 2012, this upgrade included a control system for 2 Prosilica GigE CCD cameras, 32 TDK-Lambda ZUP power supplies, and 15 Lambda EMS power supplies with embedded controllers [2]. However, the 44 MeV linac also contains 3 Lambda EMS power supplies and one Lambda TCR power supply with external RSTL controllers. Figure 1 shows half of the control system for the magnet power supplies including Lambda EMS power supplies with embedded controllers, Lambda EMS with the external RSTL controllers, and a solitary Lambda TCR power supply with an external RSTL controller [3,4][1]. This paper describes how the control of these magnet power supplies with external RSTL controllers was accomplished. The full description of the EPICS accelerator control system for the 44 MeV linac will be published at another conference [5]. As shown in Fig. 1, the EMS power supplies and TCR power supplies were connected to their own dedicated MOXA terminal server with RS485-RS232 conversion interfaces [6]. Then, the terminal server was connected to the EPICS server via an isolated network using an Ethernet cable and a 3Com network switching hub. After that, a means to communicate with the power supplies was developed by using two EPICS modules (ASYN and StreamDevice) supplied with the synApps package [2]. Then, device support applications were manually programmed for the power supplies, and the current was controlled by manipulating process variables (PVs) using MEDM Operator Interface (OPI) panels.

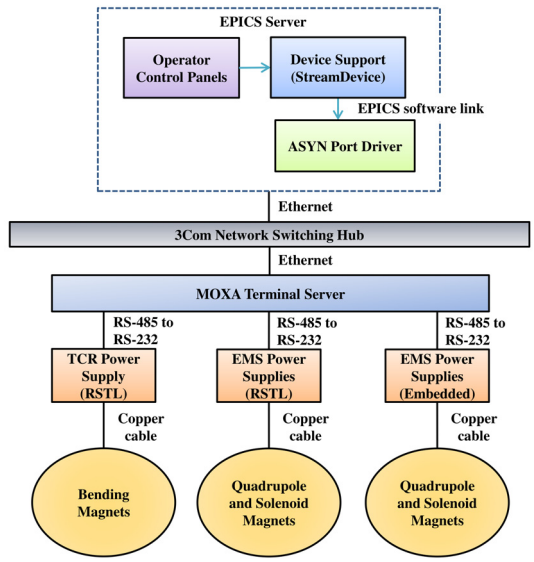


Figure 1: Experimental setup of EPICS server and hardware for the IAC 44 MeV linac.

HARDWARE CONFIGURATION

Before creating the PVs, the RSTL controllers had to be configured to work with the Lambda EMS and Lambda TCR power supplies. For the Lambda EMS power supplies, it was just a matter of following the connection diagram for the RSTL to TB1 connector in the manual [7]. However, the interface from the RSTL to the Lambda TCR power supply took some additional configuration for the RSTL. Since the RSTL was rated for a 40 V power supply and the Lambda TCR was a 160 V power supply, the first configuration detail was to add a couple resistors to the RSTL board. This was done to create a voltage divider and reduce the high voltage from the Lambda TCR to a level

* Mail: andranth@isu.edu
[1]For more information about the internally controlled EMS power supplies see reference [2,5]

Copyright © 2013 CC-BY-3.0 and by the respective authors

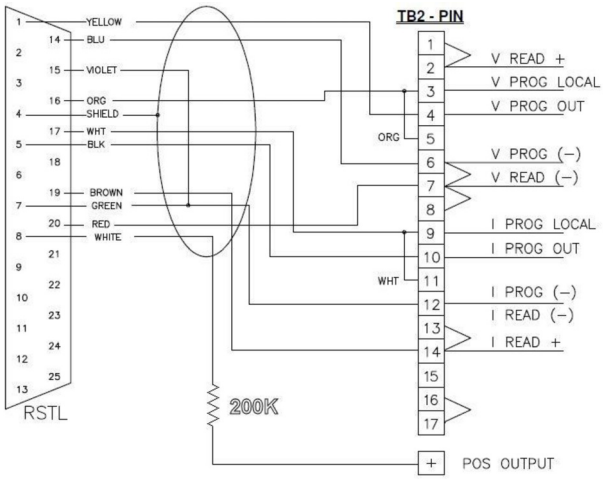


Figure 2: Connection diagram for cable going from RSTL to TB2 connector on Lambda TCR power supply [8].

that would not damage the analog to digital converter chip in the RSTL. After this, a 25 pin cable, which came with the RSTL, had to be connected from the RSTL to the TB2 connector as shown in Fig. 2 [8]. There was a 200 kΩ resistor added in series from the positive output busbar on the Lambda TCR to pin 8 on the RSTL 25 pin connector. This was done to reduce the voltage load on the 25 pin connector to within it's specifications. To complete the hardware configuration, the Lambda TCR power supply had to be calibrated to ensure that the current readback would follow the EPICS programmed current value as close as possible [7].

DEVICE SUPPORT APPLICATIONS

After the hardware configuration and calibration, the next step was to turn off the "echo" setting of the external RSTL controller. Then make a device support application containing the files to create PVs. The device communication was accomplished by installing the synApps software package including ASYN and StreamDevice [2].

Application Creation for Power Supplies

The creation of PVs for both types of power supplies was almost the same because they both use external RSTL controllers. To create the application, the following commands were used [2]:

- makeSupport.pl -t streamSCPI TCR_
- makeSupport.pl -t streamSCPI EMS_
- makeBaseApp.pl -t ioc EMS_and_TCR
- makeBaseApp.pl -t ioc -i EMS_and_TCR

The first two commands create support directories for the Lambda EMS and Lambda TCR power supplies. These support directories contain the files to create PVs. The third command creates a configure and an application directory. The fourth command creates an iocBoot directory, which contains the *st.cmd* file [2]. The "EMS_and_TCR" are arbitrary names for the application directory and the directory under iocBoot containing the *st.cmd* file.

Protocol Files

The module StreamDevice uses protocol files to translate commands that follow the SCPI (Standard Commands for Programmable Instruments) standard into a format that EPICS records can use [2]. For example, the SCPI command to measure the current (MC) from the RSTL manual looks like this [7]:

- getC{out "MC"; in "%6f"; in "";}

In this case, getC is a protocol, which sends the command MC "out" to the device and gets a response "in" from the device. The RSTL sends back two "in" responses, the first is a number with six floating digits, and the second is just a blank line that follows a command sent to and from the RSTL. The blank line serves as a form of confirmation that the RSTL received a command from the user. The other key component for making a PV is a record in a database file. [2]

Database File

The database files are where the records are located. The PVs are made by putting the protocol name (i.e. getC) into the input or output fields in the record [2]. Here is an example of a record to read the current:

```
record( ai, "$(P):90A_BENDS:curr_r") {
  field( DESC, "Readback Current")
  field( DTYP, "stream")
  field( INP, "@TCR.proto getC $(PORT19) $(A)")
  field( PREC, "3")
  field( EGU, "Amps")
  field( HOPR, "65")
  field( LOPR, "0")}
```

In this case, the only difference between the Lambda EMS and the Lambda TCR is the definition of the High Operational Range (HOPR) of the current. For the Lambda EMS this is 30 A and for the Lambda TCR it's 65 A. In the record above, a field of particular interest is the INP field. This field sends the command defined as the protocol "getC" located in the protocol file "TCR.proto" to the port and address of the device. The $(PORT19), $(A), and $(P) are all defined in the *st.cmd* file.

st.cmd File

This is an executable file that creates a channel between the RSTL and EPICS by using an IP address, a portName, and an address. This file also loads all of the records that are in the database files. An IP address is specified by entering the following line in the *st.cmd* file:

[2]For more protocol file information and more on SCPI commands, see reference [2].

Copyright © 2013 CC-BY-3.0 and by the respective authors

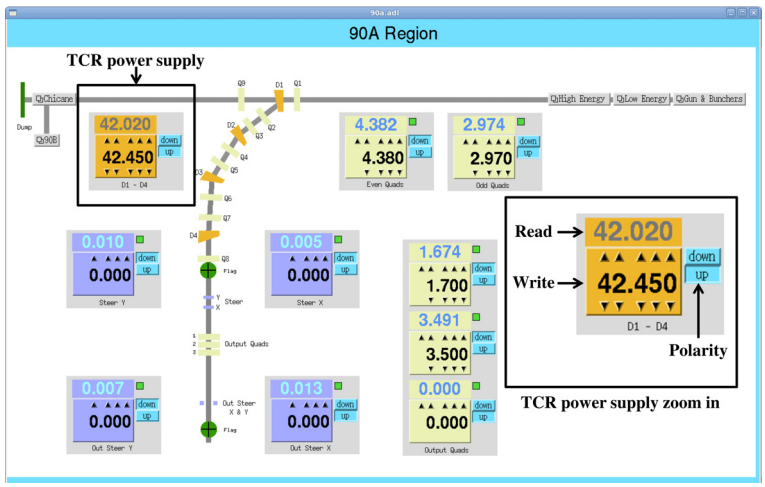


Figure 3: An MEDM OPI pannel to control and read the current of the magnet power supplies for the 44 MeV linac.

drvAsynIPPortConfigure("P19","134.50.x.y:4019",0,0,0)

Here P19 is a portName, which is an arbitrary identifier used to define $(PORT19) from records as an IP address (134.50.x.y) and a port (4019) on the MOXA terminal server [2]. In this case, P19 was used because this particular power supply was connected to the nineteenth port of the MOXA terminal server. The rest (0,0,0) specifies *priority, noAutoConnect,* and *noProcessEos* [2]. To specify a database in the *st.cmd* file, a line similar to the following was used:

dbLoadRecords("db/A.db","P=$(P),PORT19=P19,A=19")

Here the A.db is the database file that contains all of the needed records to control the power supply. The macro P is used as a linac identifier, in this case P is 44MeV. The PORT19 is the same as the portName. The address (A=19) for this set-up ran from 1 - 32, because there were 32 ports on each MOXA terminal server [2].

MEDM DISPLAY

Motif Editor and Display Manager (MEDM) is an EPICS extension which provides a way to create simple OPI's like the one shown in Fig. 3. This display contains a representation of the linac with the magnets being controlled. The circled box controls the TCR power supply, which controls all dipole magnets in this region of the linac. The operator changes the set (Write) current PV by clicking the black arrows or by typing a value manually. The actual readback value from the power supply is displayed in the box above write. Since all the power supplies are unipolar, the direction of the current has to be changed with external circuitry. The "Polarity" on the display gives the operator an indication of the direction of the current.[3]

[3]The other control widgets on this display are for embedded controlled power supplies, see reference [2].

CONCLUSION

The goal of this part of the 44 MeV control system upgrade was to control old Lambda EMS and TCR magnet power supplies with external RSTL controllers using EPICS. This was accomplished by using ASYN and StreamDevice to create a communication channel between EPICS and the power supplies, and then convert SCPI commands into PVs. Afterwards, MEDM OPIs were developed to control and monitor those PVs. The addition of the control system for these older magnet power supplies almost completes the EPICS upgrade for the 44 MeV linac, the rest of the control system with save/restore functionality will be described in the next conference paper [5].

ACKNOWLEDGMENTS

I would like to thank Jeff Bush, the technical group leader at TDK-Lambda Inc., for all of his help and advice in configuring the RSTL through email correspondence. I would also like to thank Dr. Kukhee Kim, Dr. Debbie Rogind, and Dr. Ernest Williams for teaching me a lot about developing EPICS device support applications through summer internships at SLAC national lab from 2011 to 2013.

REFERENCES

[1] http://www.iac.isu.edu

[2] A. Andrews et al., Proc. IPAC2013, THPEA061, Shanghai, China.

[3] http://www.us.tdk-lambda.com/hp/product_html/emspower.htm

[4] http://www.us.tdk-lambda.com/hp/product_html/tcrpower.htm

[5] A. Andrews et al., to be published at ICALEPCS 2013.

[6] http://www.moxa.com/product/nport_6650.htm

[7] http://www.us.tdk-lambda.com/hp/pdfs/Product_manuals/83468004.pdf

[8] A. Andrews, "Re: A problem with TDK Lambda ZUP power supply," message to Jeff Bush, 13 Mar. 2013, E-mail.

Copyright © 2013 CC-BY-3.0 and by the respective authors

PROGRESS REPORT OF H⁻ ION BEAM PRODUCTION AT THE LANL ION SOURCE TEST STAND*

I.N. Draganić#, Y.K. Batygin, C.M. Fortgang, R. W. Garnett, J. Gioia, S. S. Kurennoy, R. C. McCrady, J. F. O'Hara, G. Rouleau, L. Rybarcyk, LANL, Los Alamos, NM 87545, USA

Abstract

As part of the Los Alamos Neutron Science Center (LANSCE) the Ion Source Test Stand (ISTS) is a flexible, stand-alone facility used for H⁻ ion beam source development and studies of low energy beam transport. It consists of a surface converter ion source with a multi-cusp permanent-magnet plasma confinement structure, an 80-kV high-voltage electrostatic extraction column, a low-energy ion beam transport line, and beam phase-space diagnostics. After resolving several technical issues, the ISTS was successfully restarted during the summer of 2012. Since then we have performed several long duration experiments. A development program is ongoing with the goals of improving source performance (e.g. reliability, availability, increased current, etc.) and beam transport efficiency (beam neutralization at low energy, beam dynamics with/without noble gas injection, etc.). Several enhancements to performance are being investigated in order to achieve a forthcoming upgrade requirement of LANSCE operations in 2014: beam current of 16-18 mA, 120-Hz operation at a duty factor of 10% and a source lifetime of greater than 28 days. We present a short description of the ISTS apparatus, obtained results and forthcoming experiments.

H⁻ ION SOURCE TEST STAND

The ion source test stand (ISTS) (Figure 1) was developed to perform H⁻ beam research in support of operation of H⁻ source of LANSCE user facility [1, 2]. It is a replica of the 80 keV injector in the H⁻ dome of LANSCE which is used to accelerate beam to 750 keV using a Cockcroft-Walton high-voltage generator. The ion beam optics consists of a four electrode electrostatic accelerating column (Pierce electrode -80 kV, extraction electrode -67 kV, column electrode -27 kV and grounded electrode), two focusing solenoid magnets separated by a distance of 1.9 m, two emittance measurement stations (IDEM02 and IDEM03), an electrostatic beam deflector, and a 4° bending magnet to separate H⁻ beam from electrons (see Fig 1). Beam current is measured by a calibrated current monitor and Faraday cup. The beam line is equipped with a residual gas analyzer (RGA) to characterize outgassing processes and a noble gas injection subsystem (Ar, Xe, etc.).

The first long ISTS run (over four weeks) was successfully performed during August and September 2012. The H⁻ ion beam was extracted in the range of 10 to 14 mA using a pulsed source gate of 835μs with repetition rate of 120 Hz (or ion source duty factor of 0.102).

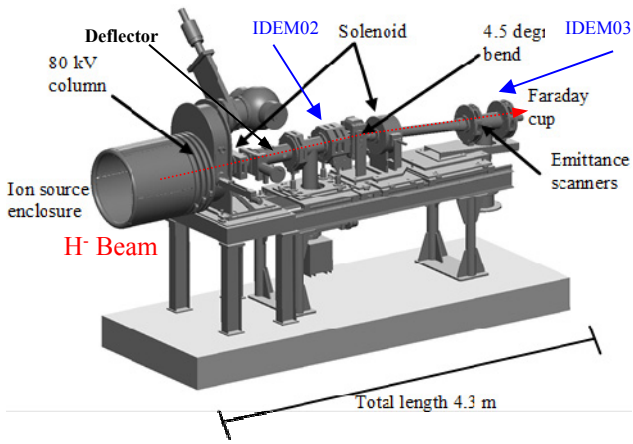


Figure 1: Schematic layout of the H⁻ ion source test stand.

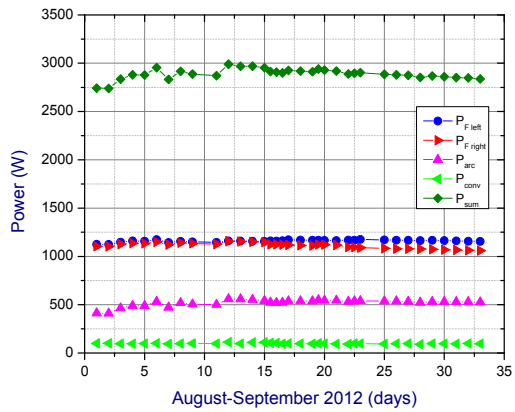


Figure 2: Source of power losses in the H⁻ ion source includes thermal dissipation of the two filaments, arc discharge and converter electrode loses at 120 Hz.

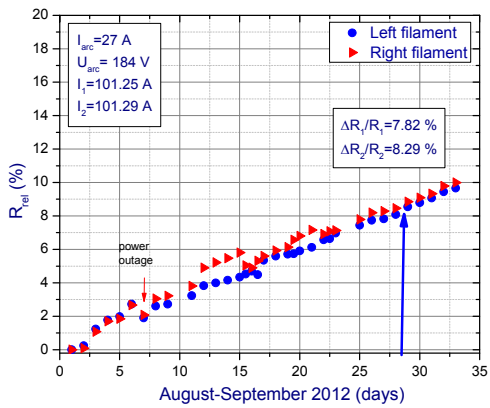


Figure 3: Recorded filament relative differential resistances (R1 - right filament and R2 - left filament).

*Work supported by the US Department of Energy under Contract Number DE-AC52-06NA25396.

#draganic@lanl.gov

Copyright © 2013 CC-BY-3.0 and by the respective authors

A set of standard operational parameters for the ISTS set were applied to achieve a nominal working regime for the ion source and beam transport at low energy of 80 KeV. The thermal power distribution is shown in Fig. 2. The total source power was less than 3 kW. The tungsten filament relative differential resistances were recorded during the entire run cycle as a diagnostic tool for the source lifetime. First preliminary data of the filament differential resistance of ~8.0% presented in Fig. 3 indicates that the a typical LANSCE H^- ion source will be able to last over 28 days at a high duty factor (0.102). In fact, the differential resistances of both filaments after 33 days did not exceed an empirical criterion for catastrophic failure of 12 % total increase in filaments resistance for this type of H^- surface converter ion source. Comprehensive tests of ion source reliability in "production like" operation conditions are underway. Detailed analysis of the source lifetime and filament differential resistance is described in Ref. [3]. The ISTS was used to produce a lower H^- ion beam at 35 keV in order to study H^- beam neutralization effects for the first time. Some recent results are described below.

SPACE-CHARGE NEUTRALIZATION STUDY

Beam emittance scans were performed using the IDEM02 and IDEM03 beam emittance stations. A typical emitance scan using the standard slit-and-collector emittance-measurement system is presented in Fig. 4. During beam measurements, the electrostatic deflector pulse was kept constant at a repetition rate of 4 Hz and pulse length of 625 μs, while emittance measurements were sampled within a 50 μs gate with variable delay of τ = 10 - 580 μs with respect to the beginning of the deflector pulse, reproducing different values of beam pulse at both stations. All measurements were performed at standard working vacuum pressure of $1.6 \cdot 10^{-6}$ Torr. The H^- beam intensity was 9.3 mA for beam energy of 80 keV. The purpose of this experiment was to determine the level of beam space charge neutralization as a fuction of tme in the beam pelse. Figures 5 and 6 show the variation of beam parameters versus beam pulse. The beam parameter values of are stabilized after 100 - 150 μs.

Determination of the level of compensated space charge was done through comparison of results of measurements and simulation. These results indicate that 100% neutralization is achieved after 120 μs for a beam energy of 80 keV, while the same level of neutralization is achieved after 200 μs with a beam energy of 35 keV achieves. The beam neutralization results are described in detail in Ref. [4].

HIGH CONVERTER VOLTAGE EXPERIMENTS

The extracted H^- beam current was tuned by adjusting converter voltage in the range from 220 to 500 V for a discharge current of 26 A. For each point a corresponding cesium oven temperature (200 to 240 C) was allowed to stabilize over several hours (3-4 hours per point) to get

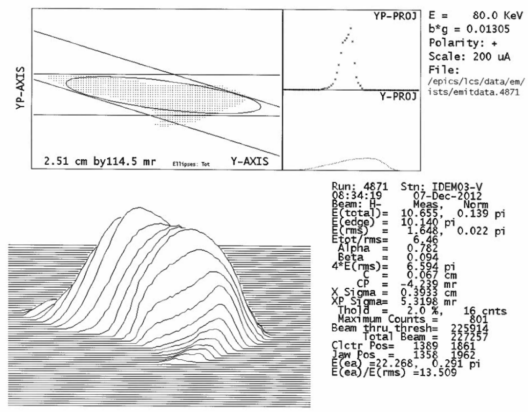


Figure 4: Characteristic transverse phase space data (H^- beam vertical emittance scan recorded using IDM03).

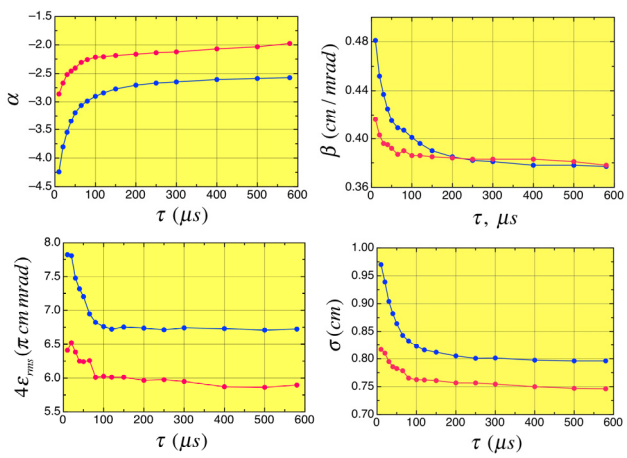


Figure 5: Parameters of 80 keV beam at IDEM02: (blue) horizontal, (red) vertical.

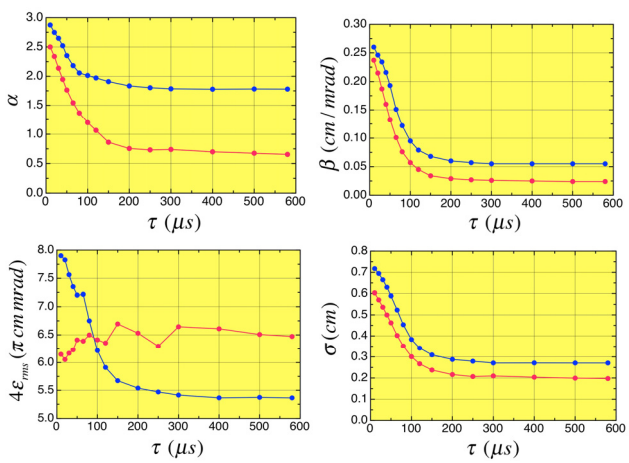


Figure 6: Parameters of 80 keV beam parameters at IDEM03: (blue) horizontal, (red) vertical.

the maximum output current. Optimal converter voltage increases with increasing cesium oven temperature (see Fig. 7A). Similar temperature dependence was measured and discussed in the previous ISTS work described in Ref.

Copyright © 2013 CC-BY-3.0 and by the respective authors

[5]. We have observed H- beam current increases up to 30 % with elevated converter voltage (Fig. 7B). The new results are in agreement with theoretical models, but different from results recorded before at the ISTS [5]. Previous beam intensity measurements were independent of high converter voltage and emittance measurements were not taken. In our set of measurements we were able to record emittance scans using both EM stations. Transverse emittance dependence on elevated converter voltage is shown in Fig 8A. Total emittance values are constant over the converter voltage range of 250 to 450 V, except for IDEM02 scans in vertical direction. 7 to 11 π-cm-mrad, 4-rms emittance increase in the vertical direction was measured on the second station. Beam brightness was constant for the whole range of high voltage (see Fig 8. B). We plan to repeat the same measurements with extracted beam over the beam current range of 16 -18 mA (production level for LANSCE) and converter voltages up to 600 V. We expect to see an increase of H- beam currents up to 21 - 23 mA. We hope that the new experiments will resolve disagreements between different experimental results and theoretical models for the formation of H- ions on the surface of negatively biased electrode (converter).

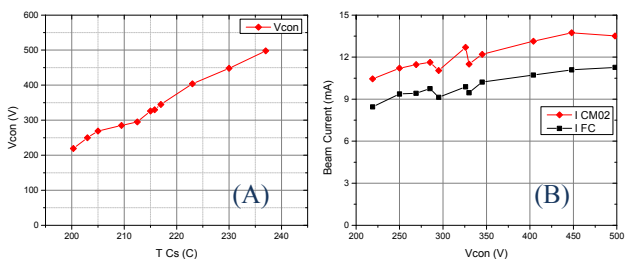


Figure 7: (A) The "peaked" converter voltage as a function of cesium oven temperature. (B) Beam currents measured using current monitor and Faraday cup as a function of converter voltage.

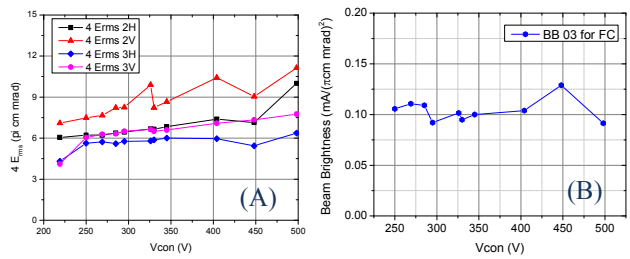


Figure 8: (A) Emittance measurements performed at IDEM02 and IDEM03 stations as a function of elevated converter voltage. (B) H- beam brightness as a function of converter voltage.

ISTS DEVELOPMENTS PLAN

The H- ion beam development plan for better performance consists of 28 different proposals. They are compatible with a previously described development plan for the ISTS [6]. The plan includes some of the following proposals:

- Improvement by elevating source body temperature by reduction the water flow in the source body/ side plates cooling loops or increasing input water temperature.
- Optimizing converter geometry and position.
- Modification of the converter electrode water cooling channels for more uniform current density production over the electrode surface.
- Addition of an inner hot liner (screen) for better control over Cs coverage of the converter and reduction in Cs dissipation.
- Installation of a third filament for higher discharge currents, plasma density and enhanced production of H- beam.
- Investigation of thicker filament diameters for increased electron emission area, higher discharge current and higher extraction of negative ion beams.
- AC versus DC voltage driven filament heating for prolongation of source lifetime and higher extracted beam currents.
- Continued space charge neutralization experiments: 80 keV/35 keV H- beam transport at different values of beam pulse length, different vacuum pressures, and different residual gases (by injection of heavy noble gases Ar, Kr, Xe into transport beam line).

These development efforts are expected to enhance performance of the LANSCE surface converter ion source in the long term. Upcoming, near-term ISTS experiments will focus on demonstrating reliable 120 HZ source operations for >28 days in support of 2014 LANSCE operation requirements.

ACKNOWLEDGEMENT

The authors are thankful to James Stelzer, Nathan Okamoto, and Jerry Paul for help in processing and preparation of the ion sources used for this study.

REFERENCES

[1] J. Sherman, et al. " Physical Insights and Test Stand Results for the LANSCE H- Surface Converter Source", AIP Conf. Proc. **763**, American Institute of Physics, Melville, NY, p. 254 (2005).

[2] R. Keller, et al. "H- Ion Source Development for the LANSCE Accelerator Systems", AIP Con. Proc. **1097**, American Institute of Physics, Melville, NY, p. 161 (2009).

[3] I. N. Draganic, et al. "Lifetime Study of Tungsten Filaments in an H- Surface Converter Ion Source", Proc. PAC 2013, Pasadena, USA, these proceedings.

[4] Y.K. Batygin, et al. "Space Charge Neutralization of Low Energy H- Beam" Proc. IPAC'13, Shanghai, China p 1865 (2013); http//www.JACoW.org

[5] O. Tarvainen, et al. "Experiments with LANSCE H- Ion Source at Elevated Converter Voltages and "Fast-Track Roadmap" to Improve Source Performances", LANL Report, LA-UR-09-07369 (2009).

[6] K. F. Johnson et al. "H- Ion Source Development for High Performances" LINAC'10, Tsukuba, Japan, p.1004 (2010); http//www.JACoW.org

Copyright © 2013 CC-BY-3.0 and by the respective authors

A SPECIALIZED MEBT DESIGN FOR THE LANSCE H+ RFQ UPGRADE PROJECT*

C. Fortgang#, Y. Batygin, R. Garnett, S. Kurennoy, L. Rybarcyk, LANL, Los Alamos, NM USA

Abstract

The LANSCE accelerator operates with both H^+ and H^- ions. Presently, each species has its own 750-keV Cockcroft-Walton (CW) and an initial transport line. The two transport lines merge into a common transport after which both species are injected into the 201.25-MHz DTL. The H^+ CW will be replaced with a 4-rod RFQ that is now in final design. Because of the complication of accommodating two beam species, the MEBT for the RFQ beam is much longer than usual. The length of the MEBT for the H+ beam, and a requirement to merge it with the existing common transport, present new and unique challenges for the MEBT design. In particular, multiple ¼-wave bunchers in addition to the existing final buncher upstream of the DTL are necessary to minimize phase spread of the RFQ output beam for DTL injection. Estimates of emittance growth, matching into the DTL over a range of H^+ beam currents, and simulations through the first two DTL tanks are presented.

INTRODUCTION

The LANSCE accelerator presently has 2 CWs for H^+ and H^- operation. The plan is to replace the H^+ CW with a 750-keV 4-rod RFQ being designed by IAP (Frankfurt) and Kress GmbH (with LANL input) and fabricated by Kress. The design of the RFQ transport line is complicated by the fact that it has to merge with the H^- transport line. The RFQ specifications that are relevant to the MEBT design are: RF frequency = 201.25 MHz, beam energy = 750 keV, RFQ maximum output emittance (rms, norm.) = 0.023 π cm-mrad, and maximum input current = 35 mA. The goals for the MEBT physics design are to minimize beam loss and emittance growth while maintaining the longitudinal bunching produced by the RFQ, under the constraint that the common transport for the 2 species not be modified. A discussion of the overall LANSCE RFQ project is given in [1].

PHYSICS DESIGN

Figure 1 shows the beam envelope and phase spread for the $5\varepsilon_{rms}$ beam from a TRACE-3D [2] simulation.

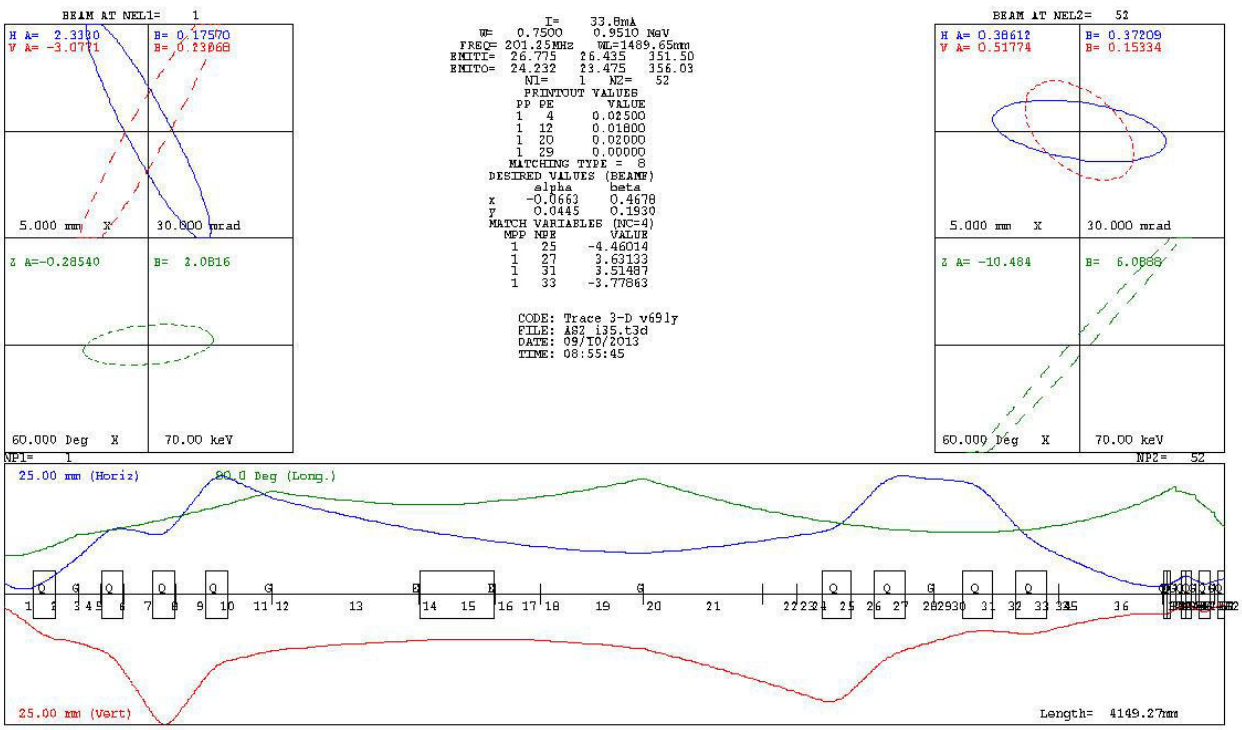


Figure 1: TRACE3D beam envelope for the $5\varepsilon_{rms}$ beam in the MEBT for ~34 mA.

*Work Supported by USDOE DE-AC52-06NA25396
cfortgang@lanl.gov

Copyright © 2013 CC-BY-3.0 and by the respective authors

The total length of the MEBT, 4.15 m, is much longer than would normally be desired. Figure 2 shows the present layout of the 2 transport lines and their merger before injection into the DTL.

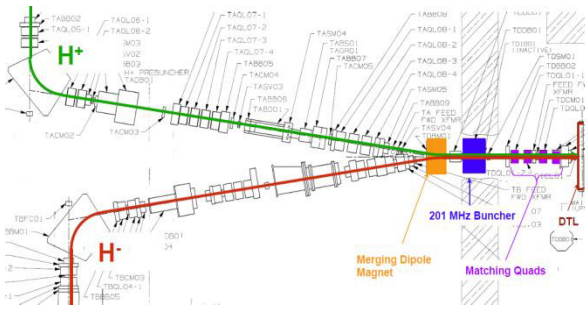


Figure 2: Present H^+/H^- CW injector layout.

The input beam for the TRACE simulation uses the output beam Twiss parameters from a PARMTEQM [3] RFQ simulation. The beam current is 33.8 mA at 750 keV. The rms normalized transverse emittance is 0.021 π cm-mrad and longitudinal rms emittance is 0.07 π MeV-deg. The RFQ beam is transported to the existing 9° bending magnet (element 15 in Fig. 1) using 4 quads and 2 quarter-wave bunching cavities [4]. We chose these cavities because they are compact. They require about 3 kW of RF peak power for 25 kV of cavity voltage. The 9° bending magnet is where the 2 species merge. Everything downstream of the bending magnet currently exists and will not be physically modified. Part of the design process is to have the beam small in the main buncher (MB) cavity (element 20) to manage the emittance growth due to non-linear RF fields. However, we found that if we insist on a waist in both transverse planes at the MB then there is too much beam loss due to scraping elsewhere in the MEBT. The asymmetric position of the waists allows us to have an acceptable beam size in the MB and at the same time minimizes the maximum beam size elsewhere. The first 4 quadrupole magnets are used to position the waists and the last 4 quadrupole magnets match the beam transversely into the DTL. Careful inspection of Fig. 1 shows that there is room for a 4th buncher in the middle of the last 4 quads but it has been decided not to use that space for a buncher because of our constraint to leave the existing common transport unmodified. The design as shown does not have a deflector for beam gating. In order to save on space we decided to put the deflector in the LEBT, upstream of the RFQ. The drift space just upstream of the bending magnet is not available for hardware because that is where the 2 merging beam lines come so close together that there is no available room transversely.

Longitudinal matching of the RFQ beam into the DTL is more challenging than the transverse match. The reasons are the long distant required to transport the beam and the limited allocation of beam line space for bunchers. Without space charge the longitudinal envelope equation for a drift can be integrated twice for the beam size. The result is,

$$\varphi(z) = z_o \left[(1+ z_o' \, z/z_o)^2 + (\varepsilon_z \; z / z_o^2)^2 \right]^{0.5} \; 360/(\beta\lambda) \quad (1)$$

where φ(z) is the beam size in degrees, z_o and z_o' are the initial longitudinal beam size and divergence, ε_z is 5 times the rms longitudinal emittance, β=v/c, and λ is the RF wavelength. If we consider the drift following a buncher, then z_o is the longitudinal beam size at the buncher and $z_o' < 0$ is proportional to the buncher cavity voltage. If we differentiate (1) and solve for the position of the waist following a buncher we obtain,

$$z_{waist} = |z_o'| \, z_o / (z_o'^2 + \varepsilon_z^2/z_o^2) \quad (2)$$

Examination of (2) shows that for a given z_o and ε_z there is a maximum value for z_{waist} with z_o' being an independent parameter. This can also be seen in Figure 3 where (1) is plotted for 6 different buncher focusing strengths. The black line connects the waist positions (circles) for each case. For this example the farthest distance from the buncher where the beam is at a longitudinal focus is ~550 mm (magenta waist).

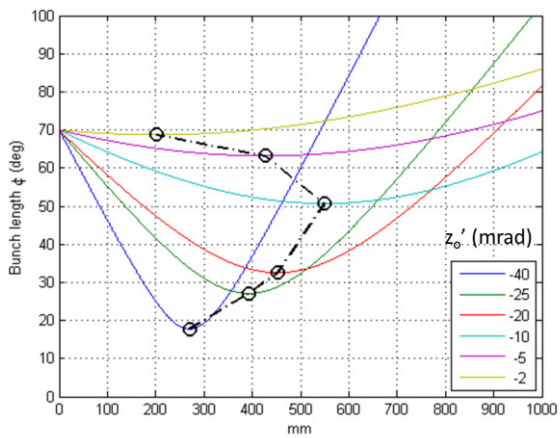


Figure 3: Bunch length downstream of a buncher cavity for 6 different focusing strengths. There is a limit to how far downstream the waist can be positioned.

The drift between the MB and the DTL entrance is larger than the farthest possible waist position downstream from the MB. Therefore, the beam cannot be focused to the proper size longitudinally at the DTL entrance using the MB and so the longitudinal match is less than ideal. However, our design gets the best possible match under the constraints and still results in a better capture by the DTL than is achieved presently with the DC beam produced by the CW.

Fig. 1 represents a point design for one particular current and emittance. We have checked that for lower currents and higher emittances we can still transversely match the beam into the DTL. However, a complication exists for dual species matching due to the common transport downstream of the 9° bending magnet where a

Copyright © 2013 CC-BY-3.0 and by the respective authors

compromise must be found to match both beams using the final 4 quads. Ideally, one can set the quads nearest the DTL for matching the H^+ beam and then use H^- quads (upstream of the merge point) to match the H^- beam into the DTL.

PARTICLE SIMULATION RESULTS

After doing a preliminary design with TRACE 3D we check and optimize the design with the multi-particle beam dynamics code PARMILA [5]. The PARMILA simulations start at the entrance to the MEBT and end after the 2nd DTL tank where the beam energy is 40 MeV. Table 1 shows the results of the particle simulations for 2 different RFQ input beam currents and an input emittance of $\varepsilon_{n,rms}$ = 0.02 π-cm-mrad.

Table 1: PARMILA simulation results for 2 different beam currents. The quantities in the last row are the transmission through the RFQ, MEBT, and DTL respectively.

RFQ I input	35 mA	24 mA
RFQ I output	33.8 mA	23.5 mA
εx, εy (π-cm-mrad)	0.021, 0.021	0.022, 0.022
εz (MeV-deg)	0.070	0.064
MEBT I output	33.0 mA	23 mA
εx, εy (π cm-mrad)	0 .036, 0.029	0.029, .028
εz (MeV-deg)	0.25	0.146
DTL Tanks2- I output	26.6 mA	21.05 mA
εx, εy (π-cm-mrad)	0.079, 0.041	0.059, 0.034
εz (MeV-deg)	0.345	0.295
Vgap Bunchers (kV)	20, 15, 22	22, 13, 24
Iout / Iin : RFQ,MEBT,DTL	.966, .976, .806	.979, .979, .915

The estimated beam loss, emittance growth, and transmission shown in Table 1 meets our requirements. In particular, the capture of 91.5% by the DTL for the 24-mA case is better than the ~80% capture presently achieved during routine LANSCE operation with lower beam current (~10.5 mA).

The PARMILA phase space plots at the exit of the MEBT for the case of 33.8 mA out of the RFQ (1st column of Table 1) are shown in Figure 4. Note the large longitudinal phase spread due to the long drifts without buncher cavities.

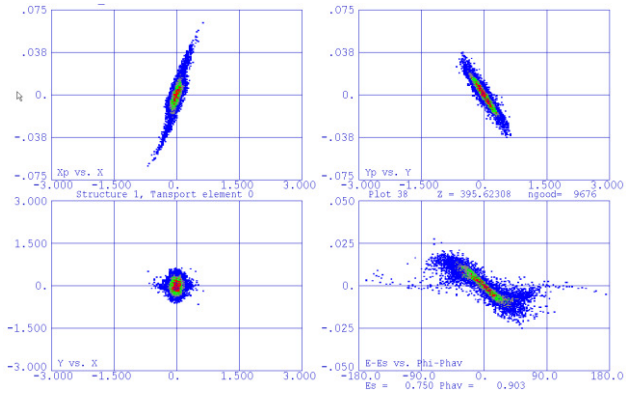


Figure 4: Beam phase space and x-y plots at the end of the MEBT for the case of 33.8 mA beam out of the RFQ.

SUMMARY

Design of a MEBT for the LANSCE H^+ RFQ project has been presented. Complications of the MEBT design because of the need to transport 2 species to the DTL has been discussed and addressed. A design using TRACE3D has been verified with particle simulations. The simulations predict good capture and transmission through the first 2 tanks of the DTL up to 40 MeV.

REFERENCES

[1] R. Garnett et al., "Status of the Lansce RFQ Front-End Upgrade," MOPMA14, NAPAC'13.

[2] K. Crandall and D. Rusthoi, "TRACE 3-D Documentation," Third Edition, LA-UR-97-886 (1997).

[3] K. Crandall et al., "RFQ Design Codes", LANL report LA-UR-96-1836, (revised 2005).

[4] L. Rybarcyk and S. Kurennoy, "Use of a Debuncher Cavity for Improving Multi-Beam Operations at LANSCE", PAC 09, Vancouver, May 2009, FR5REP072, p. 4944 (2009); http://www.JACoW.org

[5] H. Takeda and J. Billen, "PARMILA," Los Alamos National Laboratory report LA-UR-98-4478 (revised 2005).

Copyright © 2013 CC-BY-3.0 and by the respective authors

DESIGN OF A DUOPLASMATRON EXTRACTION GEOMETRY AND LEBT FOR THE LANSCE H^+ RFQ PROJECT *

C. Fortgang#, Y. Batygin, I. Draganic, R. Garnett, R. McCrady, L. Rybarcyk, LANL, Los Alamos, NM USA

Abstract

The 750-keV H^+ Cockcroft-Walton at LANSCE will be replaced with a 4-rod RFQ with injection energy of 35 keV. The existing duoplasmatron source extraction optics need to be modified to produce up to 35 mA of H^+ current with an emittance <0.02 pi-cm-mrad (rms,norm) for injection into the RFQ. In addition to source modifications we need a new LEBT for transport and matching into the RFQ. The LEBT uses 2 magnetic solenoids with enough drift space between them to accommodate diagnostics and a beam deflector. The LEBT is designed to work over a range of space-charge neutralized currents and emittances. The LEBT is optimized in the sense that it minimizes the beam size in both solenoids for a point design of a given neutralized current and emittance. Special attention has been given to estimating emittance growth due to solenoid aberrations. Examples of source-to-RFQ matching and emittance growth (due to both non-linear space charge and solenoid aberrations) are presented over a range of currents and emittances about the design point. A preliminary mechanical layout drawing will also be presented.

INTRODUCTION

The LANSCE accelerator presently has 2 CWs for H^+ and H^- operation. The plan is to replace the H^+ CW with a 750-keV 4-rod RFQ being designed by IAP (Frankfurt) and Kress GmbH (with LANL input) and fabricated by Kress. The input energy of the RFQ is 35 keV at a maximum beam current of 35 mA. The design emittance for the RFQ input beam is 0.02 π-cm-mrad, rms-normalized. Presently the LANSCE users of H^+ require about 18 mA of extracted beam. The current H^+ duoplasmatron source is very reliable and has been used for decades at LANSCE. We will use the existing duoplasmatron source with a newly designed extraction system and LEBT for beam injection into the RFQ. For the LEBT a magnetic focusing system was chosen. Careful attention has been paid to the solenoid design so that emittance growth due to non-linear focusing terms is made negligible.

SOURCE EXTRACTION DESIGN

Figure 1 shows the extraction geometry for the 35 keV source. The source design was done using the finite element code TRAK [1]. The relevant parameters are: Pierce, extractor, electron suppressor and ground electrode apertures equal 5 mm, 6 mm, 8 mm and 16 mm, respectively. The gap between the Pierce aperture and the extractor is 12 mm. The Pierce and electron suppressor electrodes are held at 35 kV and -2 kV. The extractor voltage is varied to minimize the emittance for each extracted beam current, mainly determined by the source plasma density and T_e (proportional to source arc current). In Fig. 1 the extractor gap voltage (ΔV) is 22.6 kV and the extracted current is 18 mA. The maximum electric field is 3.44 kV/cm. For 35 mA of extracted current the extractor gap voltage is 35 kV and the maximum electric field is 5.3 kV/cm which is still below our goal of Epeak < 7 kV/cm. A cutaway view of the source design is shown in Fig. 2.

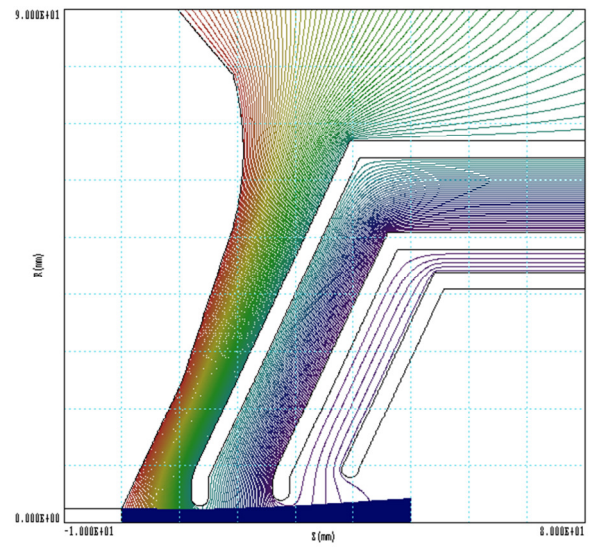


Figure 1: Electrode geometry and beam extraction for a 35 keV, 18 mA H^+ beam. Grid spacing is 10 mm/div.

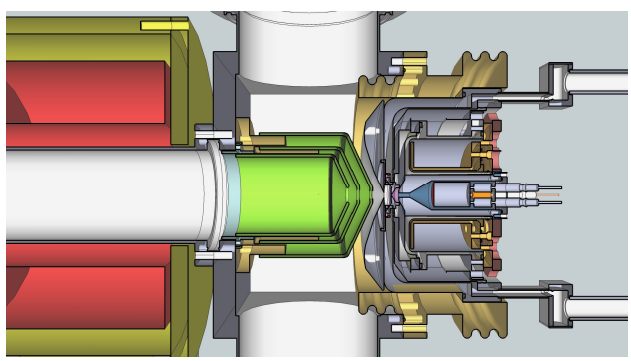
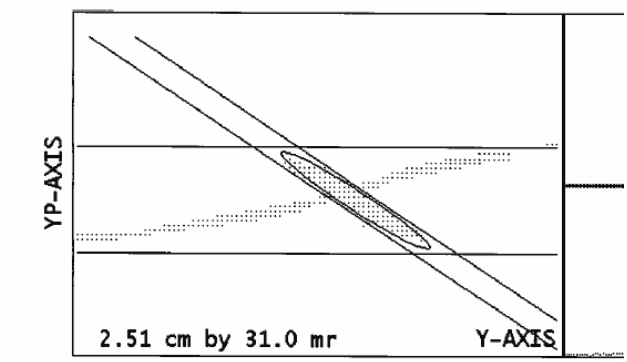


Figure 2: Duoplasmatron source is on the right. Extraction electrodes are in the center and the 1st LEBT solenoid is on the left. Pumps are above and below electrodes.

*Work Supported by USDOE DE-AC52-06NA25396
cfortgang@lanl.gov

Copyright © 2013 CC-BY-3.0 and by the respective authors

The TRAK code was used to adjust the electrode shapes to produce a uniform and laminar beam to minimize emittance growth due to nonlinear space charge fields and geometric optic aberrations in the first few centimeters downstream of the source aperture. Presently at LANSCE, with ≈15 mA of H^+ current at 750 keV the measured beam emittance is ≈ 0.004 π-cm-mrad, rms-normalized (Fig. 3). The second beam seen in the figure is H_2^+. The measured ratio $\varepsilon_{total}/\varepsilon_{rms}$ = 5.6 is indicative of a waterbag distribution ($\varepsilon_{total}/\varepsilon_{rms}$ = 6.0). For our LEBT design with 35 mA of extracted current we assume an emittance of 0.0075 π-cm-mrad.



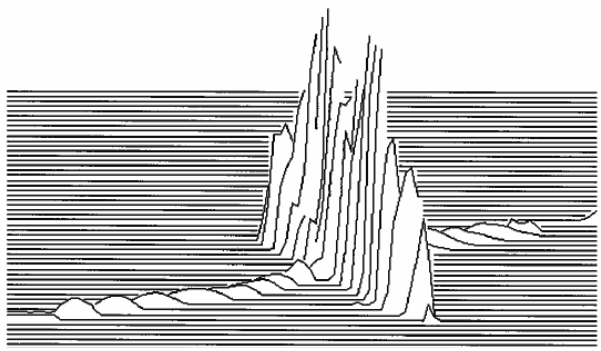


Figure 3: Measured H^+ transverse phase space at 750 keV for the LANSCE duoplasmatron source. H_2^+ beam is also observed.

LEBT DESIGN

A TRACE2D envelope simulation of the $4\varepsilon_{rms}$ beam is shown in Fig. 4.

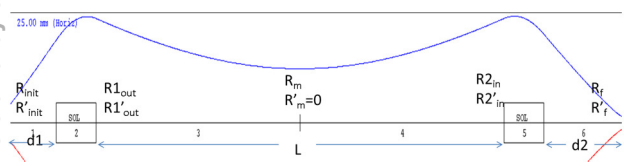


Figure 4: TRACE 2D envelope simulation with LEBT design variables defined. The source aperture is 50 mm upstream of the simulation starting point on the left.

A magnetic LEBT was selected instead of an electrostatic design so as to have a high degree of space charge neutralization via ionization of the background neutral gas. With less effective current, emittance growth due to the nonlinear space-charge force is reduced to a tolerable level. In addition, for the same focal length magnetostatic lenses have smaller aberrations than electrostatic lenses [2]. An electrostatic deflector (for beam gating), emittance diagnostic, steering magnet and valve (not shown) will be located in the drift between the 2 solenoids. Our design is an optimized point design [3] in the following sense: for a given drift distance L between solenoids, a beam waist at the center (R'_m=0), a given effective (partially neutralized) beam current, and a given beam emittance, there is one value for the beam size at the waist (R_m) that minimizes the beam size ($R1_{out}$ = $R2_{in}$) in both solenoids. This is desirable to minimize emittance growth due to nonlinear solenoid focusing. Once the beam size at the waist, R_m, is determined then $R1_{out}$, $R1'_{out}$, $R2_{in}$ and $R2'_{in}$ are determined. With that information the beam is matched backwards to the source with d1 and the strength of the 1st solenoid (B1) as matching variables. Similarly, the beam is matched to the RFQ input with d2 and B2 as matching variables. If the beam current or emittance are different from the optimized point design parameters, the beam can still be matched to the RFQ using different solenoid strengths but the symmetry of the design is broken. The beam size in the solenoids will grow if either the emittance or current is larger than the point design. Table 1 gives the LEBT parameters.

Table 1: LEBT Parameters

ε initial rms- normalized	0.0075 π cm-mrad
Source to d1	50 mm
d1	204 mm
L	1800 mm
d2	346 mm
Solenoids effective length	176 mm
R max in solenoids	24.5 mm
R waist between solenoids	11 mm
R final	1.38 mm
R' final	- 31.4 mrad
B1 max	2758 Gauss
B2 max	2536 Gauss

SOLENOID DESIGN

An important aspect of the LEBT design is to minimize emittance growth. If the beam size in the solenoids is not small compared to the solenoid aperture then there will be emittance growth due to non-linear effects. To second order the deflection of an ion after traversing a solenoid is,

$$\Delta r' = - e^2 / (4 (m \gamma v_z)^2) \quad x \int [Bz^2(0,z)\, r - \tfrac{1}{2}\, r^3\, Bz(0,z)\, \partial^2/\partial z^2 (Bz(0,z))]\, dz .$$

The first term in brackets is the usual linear focusing. The second term in brackets is non-linear. Smaller beams have less aberration because of the r^3 dependence.

Copyright © 2013 CC-BY-3.0 and by the respective authors

Longer solenoids that result in the same deflection as shorter solenoids will also have less aberration. This comes from the $\partial^2/\partial z^2$ (Bz(0,z)) factor which makes less of a contribution to the line integral if the magnetic field profile is flat and sharp (long solenoids) as opposed to peaked and rounded (short solenoids). The integrated second derivative term is <0 so the overall effect of the second term is >0 and thus larger radii particles are over focused. It is more practical to make a solenoid longer than it is to make the aperture larger. After iterating on solenoid designs and particle simulations, we settled on an iron yoke design with the following specifications: solenoid physical length = 250 mm, effective length = 176.3 mm, aperture = 54 mm, and coil current density ≈ 4.1 Amps/mm^2. A solenoid of these dimensions causes a small but acceptable amount of emittance growth.

PARTICLE SIMULATIONS

To simulate the effects of both solenoid aberrations and nonlinear space charge on emittance growth in the LEBT we use the particle tracking code BEAMPATH [4]. Figure 5 shows particle tracks through the LEBT for a waterbag distribution. This distribution was selected based on the emittance measurement results previously discussed. Based upon measurement and calculations we expect the level of space charge neutralization to be ~ 90%. Therefore, the effective beam current is 3.5 mA. Qualitatively the beam is mostly laminar though some ray crossing is observed.

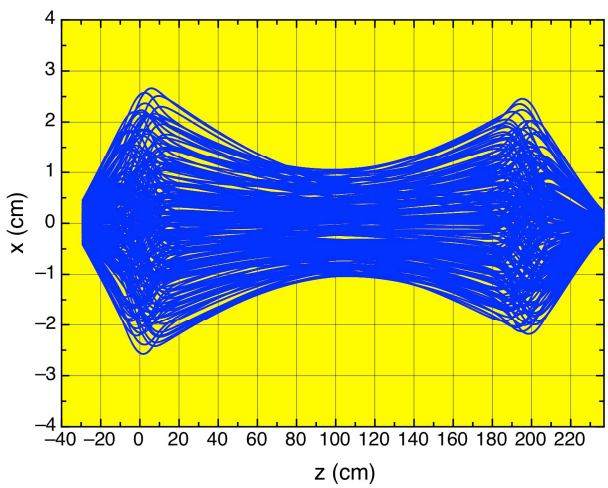


Figure 5: BEAMPATH simulation of matched beam in the LEBT. A waterbag distribution is assumed.

Figure 6 shows the emittance growth along the LEBT, again starting with a waterbag distribution and an effective current of 3.5 mA. The dashed line is the emittance growth with nonlinear space charge included but with the nonlinear solenoid focusing term turned off. The solid line includes the solenoid nonlinear focusing. The emittance growth due to solenoid aberrations is relatively small for the reasons given above. The simulated normalized rms emittance at the RFQ match point is comfortably below our requirement of 0.02 π cm-mrad.

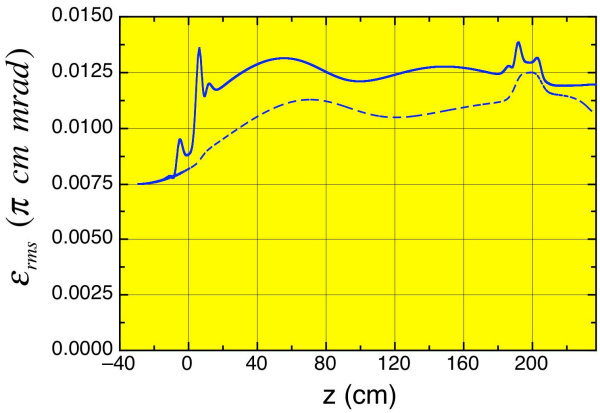


Figure 6: Emittance growth along the LEBT with (solid line) and without (dashed line) nonlinear solenoid focusing included.

SUMMARY

A new 35-keV extraction system for the H^+ duoplasmatron source and an optimized point design of a LEBT for matching into the H^+ RFQ has been presented. The physics design of the extraction system has been incorporated into a solid model. The LEBT design is optimized to minimize the beam size in the solenoids for the expected emittance, neutralized beam current, and desired drift space between the solenoids. Careful attention has been given to the solenoid design so that emittance growth due to nonlinear focusing is at an acceptable level. The physics design of the source extraction system and LEBT is complete and mechanical design will start this coming year.

REFERENCES

[1] TRAK, TRICOMP Series www.fieldp.com
[2] "Handbook of Charged Particle Optics", Edited by Jon Orloff, CRC Press LLC, p.191 (1997).
[3] Y.K.Batygin, "Design Issues of Low Energy Beam Transport", Proc. of IPAC2013, Shanghai, China, p.1853 (2013).
[4] Y.K.Batygin, "Particle-in-cell code BEAMPATH for beam dynamics simulations in linear accelerators and beamlines," Nucl. Instrum. Meth. A 539, p. 455 (2005).

Copyright © 2013 CC-BY-3.0 and by the respective authors

APPLICATION AND CALIBRATION ASPECTS OF A NEW HIGH-PERFORMANCE BEAM-DYNAMICS SIMULATOR FOR THE LANSCE LINAC *

L. J. Rybarcyk# and X. Pang, Los Alamos National Laboratory, Los Alamos, NM, 87545, USA

Abstract

The Los Alamos Neutron Science Center utilizes a linear accelerator (linac) consisting of two 750-keV injectors, a 100-MeV drift tube linac and an 800-MeV coupled cavity linac to provide both H^- and H^+ beams to several user facilities. We are presently developing a graphics processing unit (GPU)-based high-performance multiparticle beam-dynamics simulator to aid in tune-up and operation of the linac. Our primary goal is to create an on-line tool that will act as a virtual beam diagnostic and in pseudo real-time provide accelerator operators and physicists with insight into the evolution of the beam throughout the linac. This paper will discuss potential applications of this tool and aspects of the various calibrations that are a prerequisite to using the model.

INTRODUCTION

High power linacs, such as the Los Alamos Neutron Science Center (LANSCE) 800-MeV accelerator, use a combination of well defined physics-model based tune-up procedures and empirical optimization to establish low-loss operation under high-power beam conditions. Although the low beam power tune-up is typically performed with an array of beam diagnostics, the subsequent adjustments under high beam power conditions are performed with little or no direct beam information and focus mainly on reducing beam spill as measured with radiation monitors located along the linac and beam lines. A better situation would be one where tuning activities are guided by more detailed information about the beam properties along the linac. Although one possible option would be to install numerous beam diagnostic devices all along the accelerator, this is rather impractical due to cost considerations and the interceptive nature of many of the desired devices. Another possible option is to utilize a beam dynamics model along with a *realistic* beam distribution to predict the beam characteristics along the linac. The beam dynamics model would need to contain enough physics to predict with reasonable accuracy the properties of the beam along the linac, but also be fast enough to provide near real-time feedback, as an actual beam diagnostics device would. At LANSCE we are pursuing the latter approach as a means to provide additional information and insight into the evolution of the beam along the linac. Besides serving as a virtual beam diagnostic during tune-up and operation, this model can also serve other functions as will be discussed.

*Work supported by US DOE under contract DE-AC52-06NA25396.
#lrybarcyk@lanl.gov

THE SIMULATOR

The new high-performance, multi-particle, beam-dynamics simulator is based upon the widely used ion linac design and simulation code PARMILA [1], but rewritten in C++ and NVIDIA's CUDA C [2] to enable a modern code architecture that can utilize the power of the Graphics Processing Unit (GPU) technology for tremendous performance improvements [3]. PARMILA was chosen as it incorporates essential physics required to simulate a realistic beam distribution in various ion linac structures and beam line components, algorithms that have been tested and benchmarked and approximations that enable faster execution without sacrificing significant accuracy.

The physics model for the linac is based upon design and as-built information regarding the linac geometry and accelerating fields and is stored in an SQL database. When the simulator is used in an "on-line" mode, a *data server* reads in real-time the linac parameters from the EPICS control system and pipes the data into the SQL database, where they are converted into physics model quantities. Alternatively, in the "off-line" mode, the user may chose to modify the stored values of linac parameters, which are subsequently converted to physics model quantities. In either case, the simulator reads the database at the beginning of the simulation. This SQL database also contains the conversions and calibration constants that relate the data system set points to the corresponding physics model quantities. Specific procedures are performed to establish the correct value for each of the calibration constant required by the model.

APPLICATIONS

Although originally developed to serve as an online model for tune-up and operation of the linac, it has become clear that the high-performance, multi-particle, beam-dynamics simulator can also be used in other valuable ways. Many of the following activities could be performed with a standard off-line, "slow", beam dynamics code. However, the benefit for many of these applications is that the simulator response is rapid, i.e. pseudo real-time, and the connection to the accelerator control system conveys the sense of operating a real machine, not just a model, which facilitates these activities.

Virtual Beam Diagnostic

The main goal of the simulator development is to provide operations personnel with pseudo real-time information about the beam evolution along the linac to

Copyright © 2013 CC-BY-3.0 and by the respective authors

aid in the tune-up and subsequent empirical fine-tuning of machine parameters. In this case the simulator is configured to run in an online mode, continuously updating the model with the latest operational set points and then looping through the beam dynamics simulation before updating the graphical output of various quantities along the linac. An example of the simulator running H^- beam through the LANSCE drift tube linac (DTL) is shown in Figure 1. As various DTL parameters are adjusted via EPICS controls the simulator continually updates the display in pseudo real-time with beam information, such as profiles, emittances, losses and phase-space distributions.

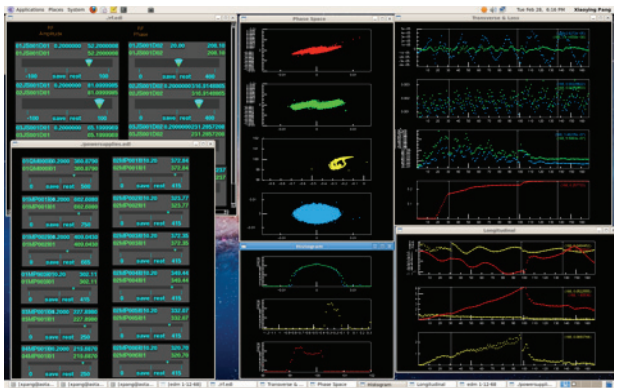


Figure 1: EPICS control sliders (left) and simulation output that includes profile, phase space, centroid, size, emittance and loss plots.

Training

In an off-line mode the simulator can be used to help train operators and physicists regarding the nuances of operating a high-power linac. Along this vein it can be used to develop better insight and understanding into the effect that various accelerator parameter changes have upon the beam along the linac.

Troubleshooting

Troubleshooting linac performance often occurs during the start-up phase when measurements do not meet expectation. The simulator can be invaluable here to help diagnosis and debug particular problems with the linac.

During the most recent start-up of the LANSCE linac, we observed characteristically different phase scans in the last tank of our DTL. About the same time we observed unexpected changes in the cavity field phase in the first DTL tank. Using the simulator we were able to reproduce similar phase scan results when a significant phase shift was introduced into the first tank. This led us to find and fix a problem with the signal path from the RF reference line to DTL tank 1 LLRF controls.

Test Bed

Another valuable use for the simulator is as a development and test facility for various feedback and control schemes. These are schemes that would normally require access to the linac control parameters via the EPICS control system. Recently, this was done using the simulator and was aimed at testing a model-independent optimization approach for establishing control set points in the linac. [4]

Optimization

Since the simulator is meant to provide detailed information about the beam along the linac, it can also be used to find a more optimal way to operate the accelerator. Over many years of high power beam operation at LANSCE, the operations staff has found lower beam loss solutions that require operating the machine away from design values. This can also be explored with the simulator. Evolutionary optimization approaches such as the multi-objective genetic algorithm (MOGA) and multi-objective particle swarm optimization (MOPSO) are being investigated as a way to help find stable, low beam-loss solutions that better define and quantify the beam conditions along the linac [5].

CALIBRATIONS

Before using the simulator to provide meaningful information about the beam evolution along the linac it must be calibrated. That is, the transformations associated with the control system set points to physics model parameters must be established. These calibrations include focusing magnet strengths, RF field phase and amplitude for the bunching and accelerating structures, and space-charge compensation in the low-energy beam transports. Some of the calibrations are done offline and some are beam-based.

The magnet calibrations relate power supply current to field. These are done offline and based upon fitting excitation curve data of field vs. current.

Depending upon the type of cavity, the RF bunchers and accelerating tanks utilize both offline and beam based approaches. The single-gap buncher cavities that are used in the 750-keV beam transports utilize an offline calibration. An EM-field calculation of the cavity was performed using SUPERFISH [6] to extract the theoretical E_oTL, Q_u and P_{cav}. In addition, measurements were made of the cavity Q along with each buncher cavity amplifiers output power vs. amplitude set point. These results were combined to produce the effective gap voltage vs. amplitude set point. The phase set point is calibrated with a beam-based measurement known as a phase scan and is described below.

The accelerating sections of the linac require beam-based measurements to establish the RF calibrations. For each section driven by one RF amplifier there is a separate phase offset and amplitude scale factor that must be determined to properly tie the control setting to the physics model. For the DTL these are calibrated using a standard phase scan method. The phase scan measures the beam current above an energy threshold as a function of the phase setting of the tank being scanned. The size and location of the current distribution is related to the

Copyright © 2013 CC-BY-3.0 and by the respective authors

amplitude and phase of the accelerating field in the tank. Figure 2 shows two measured phase scans of DTL tank 1 along with the fits produced by the simulator. The phase scans represent the cases with the first of two LEBT bunchers off and on, respectively. Tank 1 amplitude scale factor and the two buncher cavity phase offsets were extracted from the fits to these data.

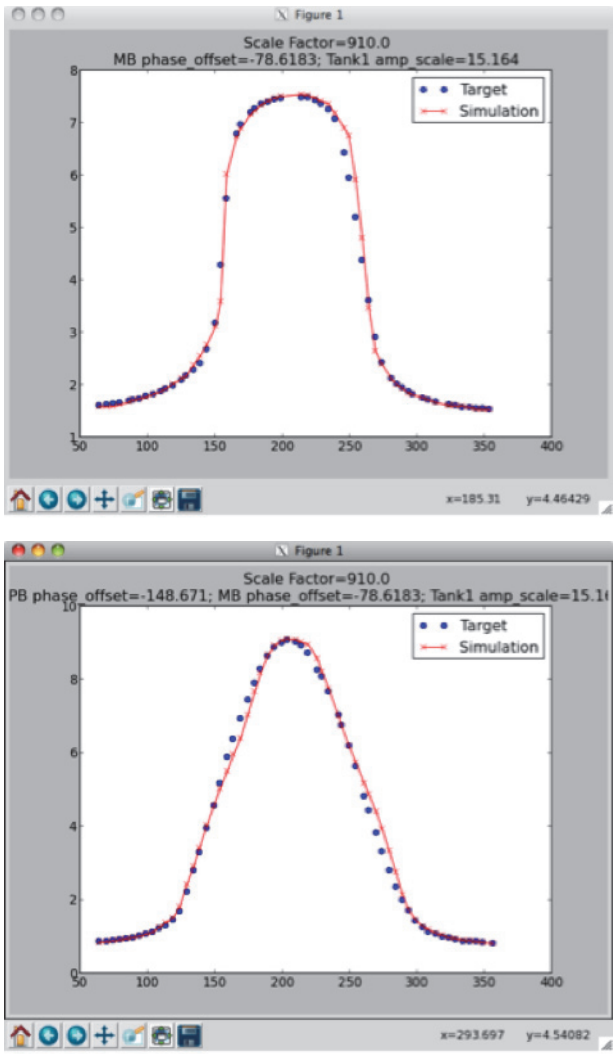


Figure 2: Measured (blue dots) and simulated (red line) phase scan data for Tank 1 of the DTL. Upper (lower) panel is for the case when the first of two LEBT buncher cavities is off (on).

The coupled cavity linac (CCL) is just now being incorporated into the simulator and therefore has not yet been include in LANSCE linac model. However, the calibration of the phase offset and amplitude scale factor for each CCL accelerating module will be performed by fitting measured phase scans similar to what has been done elsewhere [7].

An additional factor that we have chosen to include in the model is the space-charge compensation of the beam, which is the result of interactions with residual gas in the nominally evacuated beam line. Measurements in the low-energy beam transports (LEBT) where space-charge forces are significant showed different degrees of compensation present [8]. This space charge compensation factor is derived from a comparison of measured beam emittances and model predictions.

SUMMARY

A high-performance, multi-particle beam dynamics simulator is being developed for the LANSCE linac and will serve as a virtual beam diagnostic by providing staff with additional information about the beam along the linac during tune-up and operation of the facility. In addition it can also function as a tool for training linac operations personnel, troubleshooting issues associated with beam operations, as a test-bed for new control schemes and for optimization of the linac operation. The simulator requires the calibration of various constants that relate linac control system parameters to various physics model values. These are done using a combination of offline and beam-based procedures. The beam-based approach extracts calibration constants from fits to various tune-up measurements.

ACKNOWLEDGMENT

The authors want to thank Scott Bailey for his efforts in setting up the EPICS system on the GPU workstation that helped enable the development and testing of this simulator.

REFERENCES

[1] H. Takeda and J.H. Billen, *PARMILA*, LANL publication, LA-UR-98-4478, 2005.
[2] NVIDIA, *NVIDIA CUDA C Programming Guide, Version 4.0, 2011*.
[3] X. Pang, L. Rybarcyk and S. Bailey, "High-Performance Beam Simulator for the LANSCE Linac," IPAC2012, New Orleans, LA, May 2012, MOEPPB012, p. 103 (2012); http://www.JaCoW.org.
[4] A. Scheinker, X. Pang and L. Rybarcyk, "Model-Independent Particle Accelerator Tuning," LANL publication, LA-UR-13-26403, submitted for publication to Phys. Rev. ST-Accel. Beams.
[5] X. Pang and L. Rybarcyk, "Multi-objective Optimization for LANSCE Linac Operations," submitted to ICALEPCS 2013, THPPC087.
[6] J.H. Billen and L.M. Young, *POISSON SUPERFISH*, LANL publication, LA-UR-96-1834, 2004.
[7] T.L. Owen et al., "Phase Scan Signature Matching for Linac Tuning," Proceeding of the 1994 International Linac Conference, Tsukuba, Japan, 1994, p.893.
[8] Y.K. Batygin, C. Pillai and L.J. Rybarcyk, "Beam Performance in H- Injector of LANSCE," IPAC2011, San Sebastian, Spain, Sept. 2011, MOPS043, p. 697 (2011); http://www.JaCoW.org.

Copyright © 2013 CC-BY-3.0 and by the respective authors

INTEGRATION BETWEEN THE FRIB LINAC MECHANICAL CAD MODEL GEOMETRY AND THE ACCELERATOR PHYSICS LATTICE DATABASE*

M. Johnson#, N. Bultman, I. Grender, M. Leitner, G. Morgan, O. Yair, Q. Zhao
Facility for Rare Isotope Beams (FRIB), Michigan State University, E. Lansing, MI 48824, USA

Abstract

This paper will summarize the systems engineering techniques utilized to translate the FRIB accelerator physics lattice file to actual three-dimensional CAD geometry for linac components. An automated approach of using the accelerator physics lattice database used for optics and particle simulation has been implemented to generate data points used to position the technical 3-dimensional CAD geometry. This coordinated method ensures consistency between the technical and scientific design domains throughout the project design phases. The FRIB configuration management used to control lattice and CAD model revisions is also discussed. In addition, the paper discusses fiducialization plans and tolerance stack up analysis to meet positional requirements for FRIB cryomodules, diagnostics, and the beam delivery magnet systems.

DATA MANAGEMENT

The layout of the FRIB accelerator physics lattice file is composed of the basic element layouts of the driver linac. This layout is accomplished using spreadsheet file to define the undeveloped geometry of ion sources, focusing and steering magnets, accelerating cryomodules, radio frequency quadrupole (RFQ), The alignment placement requirements of the accelerator components are summarized in [1,2]. An automated script imports the lattice points into our mechanical CAD software generating local coordinates for the centers of each component, called a skeleton file. The three-dimensional design geometry is then located to each coordinate in the skeleton file making up the complete linac geometry. The Survey and Alignment Group will develop and maintain a proprietal data handling system composed of a relational database and a workable simplified wireframe graphics model [3]. This system will be integrated with the FRIB project database currently under development within the Controls and Computing Group. All components requiring alignment will have associated fiducials. The fiducials are placed on the wireframe component model and these in turn are placed at the correct location in the design lattice based upon the data gathered during the fiducialization process. The wireframe graphical model is a single graphical representation of every point that the Survey and Alignment Group is given as a design location. The relational database provides functionality for archiving and retrieving data from various epochs of the project's evolution in order to keep abreast of revisions and network re-observation campaigns. In addition to coordinate data and associated uncertainties the database will hold information regarding nomenclature, instrumentation, tooling, fiducialization, and ideal component design lattice positions.

General Layout

As shown in Figure 1, the driver accelerator consists of Electron Cyclotron Resonance (ECR) ion sources, a low energy beam transport containing a pre-buncher and electrostatic deflectors for machine protection, a Radiofrequency Quadrupole (RFQ) linac, linac segment 1 (with Quarter-wave Resonators (QWR) of β=0.041 and 0.085) accelerating the beam up to 20 MeV/u where the beam is stripped to higher charge states, linac segments 2 and 3 (with Half-wave Resonators (HWR) of β=0.29 and 0.53) accelerating the beam above 200 MeV/u, folding segments to confine the footprint and facilitate beam collimation, and a beam delivery system to transport to the target a tightly focused beam.

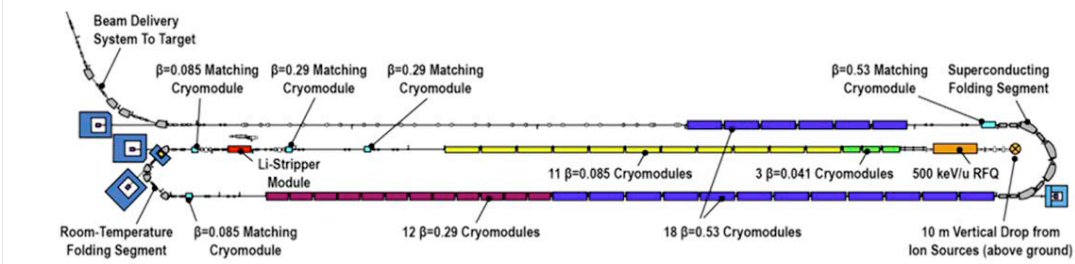


Figure 1: The FRIB accelerator layout at the tunnel level.

*This material is based upon work supported by the U.S. DOE Office of Science under Cooperative Agreement DE-SC0000661, the state of Michigan and Michigan State University
#mjohnson@frib.msu.edu

Copyright © 2013 CC-BY-3.0 and by the respective authors

ALIGNMENT NETWORK

At present the core processes are in the project-specific refinement phase. The FRIB global coordinate system (GCS) is the single cartesian site-wide reference system used by the Survey and Alignment Group to integrate the spatial information and placement requirements of the Accelerator Systems Division (ASD), the Experimental Facilities Division (ESD), the Conventional Facilities Division (CFD), and the civil construction effort. The network is an array of monuments permanently affixed in the floor and to walls to realize coordinate system. The Z-axis of the coordinate system is oriented to gravity at all locations, as the effect of earth curvature is to be regarded as insignificant with regard to project requirements. The floor monuments holes will be drilled and the monument bodies grouted in place when the concrete substrate is sufficiently cured, allowing the maximum time to elapse before the first network campaign begins. The monument body accepts a 1-1/2" spherically mounted retroreflector (SMR) the center of which is considered a geometric point and conceptually defines the monument location. The Spallation Neutron Source (SNS) floor monument design is to be adopted for FRIB. The SNS design requires no intermediate fixture for placing the SMR into the monument body. The wall monument design has yet to be chosen but several designs are under consideration with the main criteria being the method by which they are affixed and cost. Measurements are made to the SMR primarily by laser trackers and total station instruments. Digital level measurements are also made, but in that case the SMR is replaced by a solid sphere of the same dimension and measurements made to the sphere's uppermost point utilizing a bar-coded invar rod that are reduced to the sphere's center by its nominal radius.

Network observations are made to the monuments from a series of instrument stations. The series of instrument stations and observations through the front end, linac tunnel, target area and existing NSCL constitutes a network observation campaign. The objective of a network observation campaign will be the production of a triad of X, Y and Z coordinate values with the GCS.

The uncertainties associated with the monument locations represent an upper limit on the achievable global precision of alignment. The component-to-component tolerances are found in the FRIB Driver Linac Element Placement Requirements document and the Experimental Systems Alignment Requirements document.

The network path begins at the ECR ion source in the front end the beam transitions to the linac floor through a 13 m vertical drop. Monuments affixed to the walls through the vertical drop provide for the placement of instruments near the 6 m mark as well as above and below. In similar fashion, the nearby equipment hatch will also be utilized. Employing differential leveling techniques through narrow vertical passages is particularly difficult and special fixtures and aids will be needed. The linac is a folded design so there is no single corridor from which instruments may have lines of sight to all components within any particular cross section of the tunnel. Two corridors of linac floor allow for the necessary lines of sight. Along the length of the tunnel there will be monuments placed in 4 rows spaced 5 meters apart. Where available wall space will be utilized for monument placements. The rows will be spaced at 5 meter intervals along the beam path, resulting in an approximate total of 150 monuments.

COMPONENT ALIGNMENT SCHEMES

Vertical Drop Alignment

FRIB will write individual fiducialization procedure documents for each species of component in which unique or special considerations are addressed. The adjustment process should be fairly straighforward for many components, especially those spanning the linac floor. The vertical drop from the ECR to the linac floor offer significant challenges for the alignment process. The design makes use of two spaceframes, shown in figure 2, to which the individual components are affixed. In this region, the beamline components consists of 2 sets of 3 electrostatic quadrupoles residing in a common vacuum housing, vacuum pumps, profile monitor diagnostics. The individual components are mounted and aligned within the space frame in a horizontal orientation. Subsequently the individual component fiducial locations are verified and transferred to spaceframe fiducials. Alignment mounts are then placed in the drop and the spaceframe is installed and aligned. Using this method reduces alignment in the vertical drop to just two components.

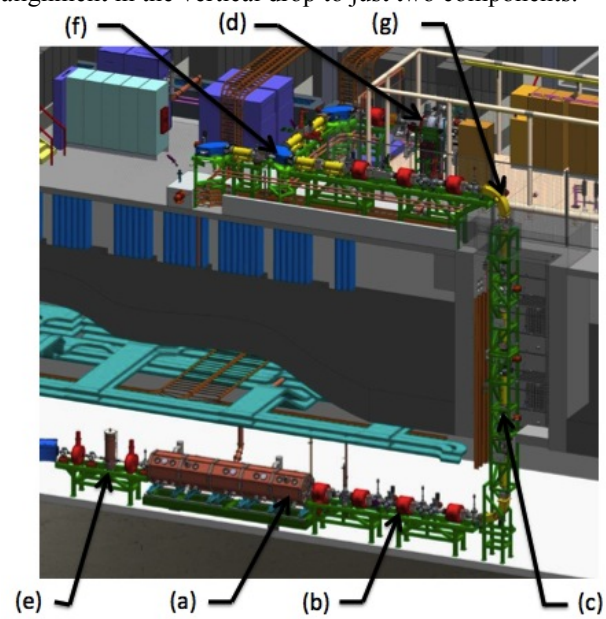


Figure 2: Vertical beamline transport section. (a) Radio Frequency Quadrupole, (b) RT solenoid, (c) vertical spaceframe, (d) SC ion source, (e) bunching resonator, (f and g) RT dipole magnet.

Copyright © 2013 CC-BY-3.0 and by the respective authors

Cryomodule Alignment

Resonator and solenoid alignment of the cryomodule is accomplished using a mechanical axis line established from the entrance and exit 3-3/8" gate valves. The gate valves are part of weldments that are assembled with dowel pins to the vacuum vessel bottom plate which doubles as a strong back with external fuducials visible for tunnel placement. The bottom plate also supports the superconducting resonators attached to cold rail structures via G-10 thermal insulating support posts.

During assembly the inside of the resonator's niobium beam tubes are fuducialized to temporary SMR nests on the helium vessel. Once assembled to the bottom plate the vessels locations are logged with respect to the bottom plate fuducials in order to transform the local fiducialization coordinates into design lattice coordinates to be used for alignment in the GCS. The bottom plate fuducials are then used to place the mechanical beam axis orientation into the design lattice.

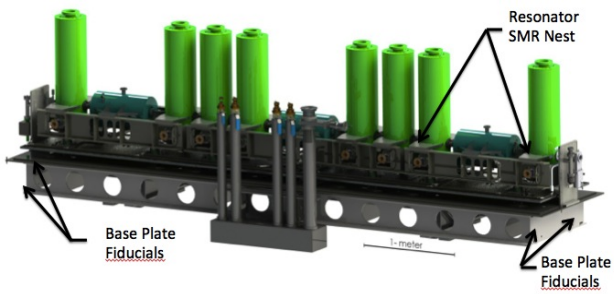


Figure 3: Cryomodule cold mass alignment setup.

Diagnostics Alignment

Beamline diagnostics located between cryomodules are integrated into the linac vacuum system boxes, shown in figure 4. These vacuum boxes and diagnostics assemblies consist of beam profile, beam current, beam position and the ability to house beam loss monitors.

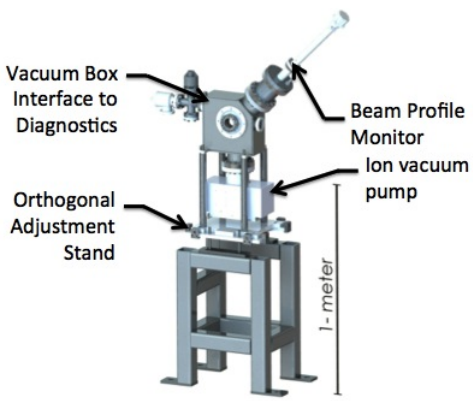


Figure 4: Integrated beam diagnostics, orthogonal adjustment and vacuum system.

Fidulization is performed during assembly and recorded into the alignment database. The diagnostic components are aligned via the vacuum box's external SMR nests. To do this efficiently the use of a coordinate measuring machine (CMM) arm may be used. The vacuum box is positioned to the tunnel network via the external SMR nests.

Magnet Alignment

The driver linac portion of the accelerator consist of room temperature (RT) X-Y correcting magnets, RT quadrupoles, super conducting (SC) dipole magnets, RT dipole magnets.

Magnetic field mapping is done with respect to 6.35 mm [.250"] holes in the pole tip steel, which are then fuducialed to SMR nests visible at tunnel installation. The SC dipole is shown in figure 5.

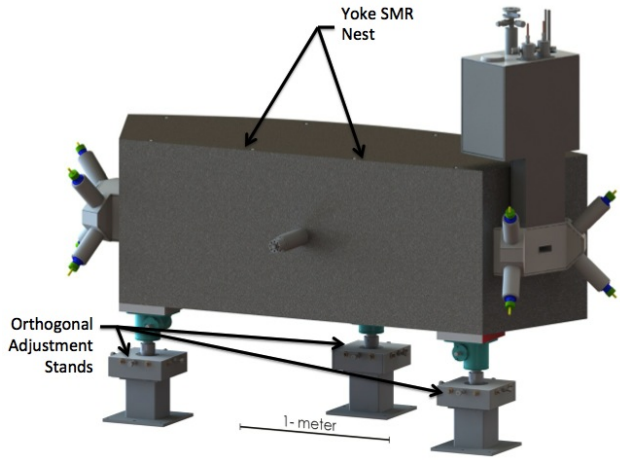


Figure 5: Folding segment 2 superconducting dipole magnet.

SYSTEMS ENGINEERING

The lattice file and corresponding 3D mechanical CAD geometry is stored in a read-only database after drafting checking and stakeholder approvals. The database is controlled using a commercial engineering software package [4]. Subsequent changes follow a formal engineering change order process that records the design history, requirements and subsequent specifications.

REFERENCES

[1] Y. Yamazaki, "FRIB Driver Linac Element Placement Requirements" FRIB T31201-PL-000032-R001.

[2] M. Hausmann "Experimental Systems Alignment Requirements", FRIB T40300-SP-000074-R001.

[3] I. Grender, "Preliminary FRIB Survey & Alignment Plan.", FRIB T31303-PL-000075-R001.

[4] Adept Synergis PDM (version 2013) [computer software]. Available from: http://www.synergissoftware.com/

Copyright © 2013 CC-BY-3.0 and by the respective authors

IMPROVING EFFICIENCY OF IONS PRODUCTION IN ION SOURCE WITH SADDLE ANTENNA*

V. Dudnikov#, R. Johnson, Muons, Inc., Batavia, IL 60510, USA, S. Murrey, T. Pinnisi, C. Piller, M. Santana, M. Stockli, R. Welton, ORNL, Oak Ridge, TN 37831, USA

Abstract

Extraction of positive and negative ions from a saddle antenna radio-frequency surface plasma source (SA RF SPS) is considered. Several versions of new plasma generators with different antennas and magnetic field configurations were tested in the small Test Stand. The efficiency of positive ion generation in plasma has been improved up to 80 times from 2.5 mA/cm^2 kW to ~0.2 A/cm^2 per 1 kW. For cesiation was used a heating of the cesium chromate cartridges. A small oven for cesium compounds and alloys decomposition by heating was developed and tested. After cesiation a current of negative ions to the collector was increased from ~1 mA to 10 mA with RF power ~ 1.5 kW in the plasma and longitudinal magnetic field B_l~250 Gauss. A specific efficiency of H$^-$ production was increased up to ~ 20 mA/ cm^2 kW from previous ~2.5 mA/ cm^2 kW.

INTRODUCTION

Development of the saddle antenna RF surface plasma source (SA RF SPS) was proposed for improve efficiency of H$^-$ ion production and improve SPS reliability and availability [1-4]. Now RF SPS for accelerators with emission aperture 7 mm have the efficiency of H$^-$ ion generation ~1 mA/kW and RF power ~ 50 kW is needed for 50 mA beam current production [5]. With this efficiency delivered current is enough for 1 MW proton beam production but the high RF power required for the sources can create problems for very long term operation at higher beam power. This efficiency is too low for CW operation with current ~10 mA necessary for Project X and for cyclotrons injection.

In tested version of SA RF SPS the specific efficiency of positive ion generation was increased to ~0.2 A/ cm^2 kW and a specific efficiency of H- production was increased up to ~ 20 mA/cm^2 kW from previous ~2.5 mA/ cm^2 kW.

The total efficiency of the surface plasma produced fraction of the H$^-$ beam is a product of the probability of secondary emission of H$^-$ caused by plasma bombardment of the collar surface around the emission aperture, the probability of extraction of emitted H$^-$, and the rate of bombarding plasma flux [6,7].

The coefficient of secondary emission of H- is determined by surface properties (proper cesiation) and the spectrum of the plasma particles bombarding the collar/emitter surface around the emission aperture. The cesiation was improved recently [5] and appears to be nearly optimal. The probability of extraction of H$^-$ emitted from the collar surface is dependent on the surface collar shape [4-7], which was optimized recently to improve H$^-$ emission. The problem of efficient plasma generation is being addressed by the development of new RF plasma generators with higher plasma generation efficiency and better concentration of useful plasma flux onto the internal surfaces of the collar around the emission aperture for lower RF power [1-4]. In this project, we use the saddle antenna, which has its RF magnetic field transverse to the source axis, combined with an axial DC magnetic field, to concentrate the plasma on the collar where the negative ions are formed by secondary emission [1-4,6,7].

SA SPS DESIGN

The schematic of a large RF SA SPS with the AlN ceramic discharge chamber, saddle antenna, and DC solenoid is shown in Fig. 1. The chamber has an ID=68 mm. The saddle antenna in this SPS with inductance L=3.5 μH is made from water cooled copper tube. RF assisted triggering plasma gun (TPG) is attached to discharge chamber from left. An extraction system is attached from right side.

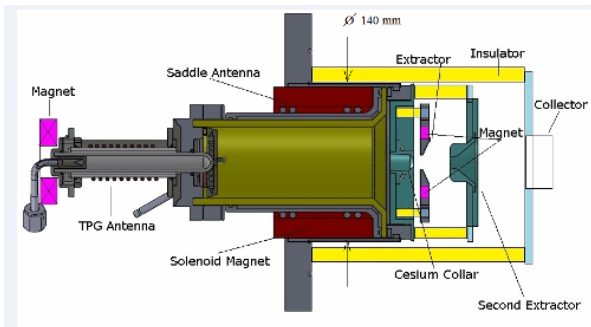


Figure 1: A schematic of the SA SPS with an extraction system and a collector.

Design of the extraction system is shown in Fig. 2. The strong transverse magnetic field (up to 1 kG) is created in the collar (4) by permanent magnets (7) inserted into water cooled extractor (6) attached to the plasma plate (1) through ceramic insulators (5). SA SPS was tested with emission and extractor's apertures of 6 mm diameters.
A Cesium vapor can be delivered to the emitter cone (2)

*Work supported by Contract DE-AC05-00OR22725 and by STTR grant DE-SC0002690.
#Vadim@muonsinc.com

Copyright © 2013 CC-BY-3.0 and by the respective authors

from Cs chromate cartridges (4) heated by plasma or from a resistive heated Cs oven (3).

Schematic of ion beam formation is shown in Fig. 3. Ions are extracted from the cone by extraction voltage Uex between the cone and the extractor and accelerated by voltage in the second gape. Co-extracted electrons are well collected to the extractor along magnetic field lines without drift in crossed ExB field.

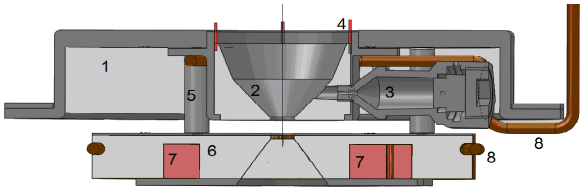


Figure 2: Extraction system of the RF SA SPS. 1- plasma electrode; 2-emitter/converter cone; 3-Cesium oven; 4-Cs cartridges; 5-ceramic insulators; 6- extraction electrode; 7- permanent magnet; 8-cooling tubes.

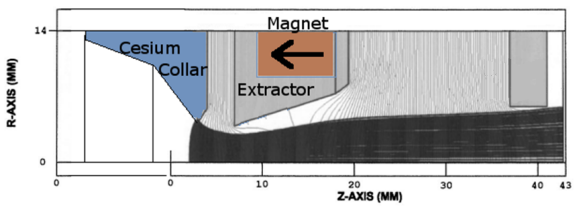


Figure 3: A schematic of ion beam formation (emission aperture is 6 mm diameter).

The strong transverse magnetic field B_t suppress electron collection by collector and the secondary emission is suppressed by magnet attached to the collector.

The RF discharge in the TPG was excited by RF (13.56 MHz) generator with power up to 0.6 kW. For the SA discharge excitation was used RF (13.56 MHz) generator with power up to 2.5 kW. The RF power loss in SA and matching network was ~1 kW and up to ~1.5 kW can be used for plasma generation.

The plasma electrode with Cs collar/cone was grounded. Extractor, accelerator electrode and collector were biased by high voltages Uex up to 15 kV and Uc up to 15 kV. Pulsed currents to these electrodes were registered by Pearson transformers with sensitivity 1 V/A.

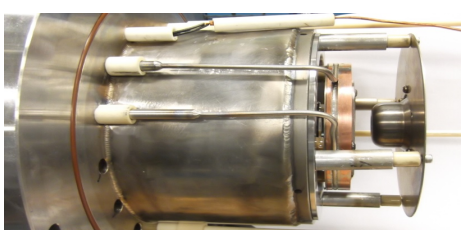


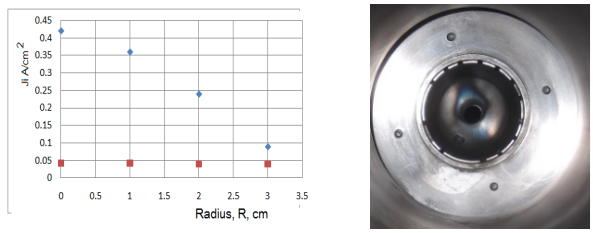
Figure 4: SA SPS with extractor and collector.

A photo of assembled SA SPS with extractor is shown in Fig. 4.

The magnetic field B_l up to 250 G is created by solenoid exited by current Im up to 70 A with voltage Um up to 8 V. A hydrogen gas flow was controlled by MKS mass flow controller.

EXPERIMENTAL RESULTS

Several versions of plasma generators with different antennas and magnetic field configurations were fabricated and tested in the test stand. A pulsed RF (13.56 MHz) discharges with duration 1-2 ms, up to 60Hz and power up to 1.5 kW in the plasma were tested. Produced positive ion emission current density distribution along the radius R is shown in Fig. 5.



a b

Figure 5: a) Ion emission current density Ji (A/cm^2) (plasma density) along the radius R (cm) at high magnetic field (blue) and at low magnetic field (brown) with RF power 1.5 kW in the plasma (observed by small collectors) without transverse magnetic field Bt. b) Trace of plasma flux on the collar converter wall with transverse magnetic field Bt~1 kG concentrated up to 8 mm of diameter.

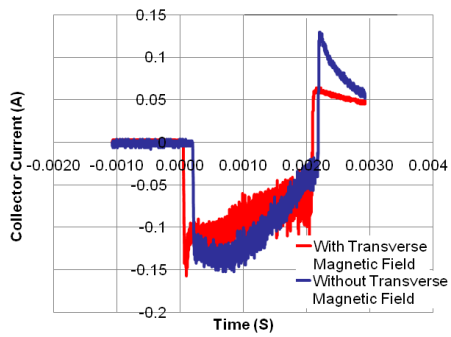


Figure 6: Traces of positive ion current to the collector with and without transverse magnetic field.

Up to 100 mA of positive ion was extracted with emission aperture 6 mm at RF power ~1.5 kW in plasma as shown in Fig. 6.

After cesiaion the negative ion current to the collector Ic was increased from 1 mA to 10 mA and electron current to the extractor Iex was reduced from 0.15 A to 0.1 A.

Examples of Ic and Iex signals are shown in Fig. 7.

Dependences of Ic on RF power in the plasma Prf is shown in Fig. 8 (upper scale). Dependences of Ic on the solenoid voltage Um is shown in Fig. 9. Dependences of Ic on the extraction voltage is shown in Fig. 10. The collector current I_c increases by a factor of 7 as the longitudinal magnetic field Bl increases from 0 to 250 G. and increases with the extraction voltage. The extraction

Copyright © 2013 CC-BY-3.0 and by the respective authors

electrode was biased up to Uex~15 kV and collector was biased up to Uc~15 kV. SA SPS can operate at the gas flow decreased down to Q=8.3 sccm (standard cm^3/minute), while the H^- current increased up to 10 mA at P_{rf}=1.5 kW (H^- generation efficiency was up to I_c/P_{rf} = 6 mA/kW with cesiation).

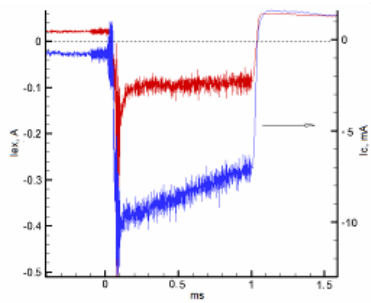


Figure 7: Signals from extractor Iex=0.1A (electron current, red) left scale and signal from collector Ic=10mA (negative ion current, blue) right scale. Signal slope connected with a low inductance of the Pearson transformer.

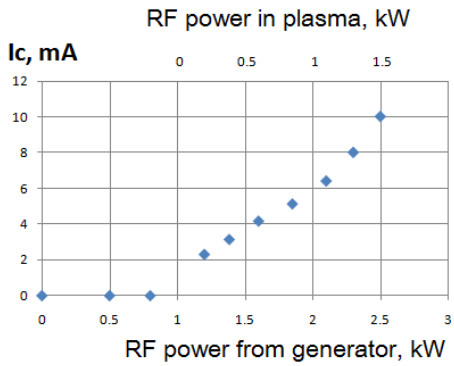


Figure 8: Dependence of Ic on RF power in the plasma Prf (upper scale) and from generator (bottom scale).

The longitudinal magnetic field from the solenoid at the emission aperture is below 50 G and does not change the suppression and deflection of co-extracted electrons by the transverse magnetic field Bt~1 kG.. However, the optimal cesiation was not reached because the extractor current Iex is high. Most efficient and stable cesiation was produced with a dark (carbon) film deposition on the emitter cone (2) in Fig.2.

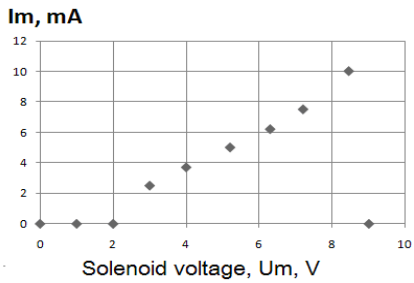


Figure 9: Dependence of Ic on the solenoid voltage Um.

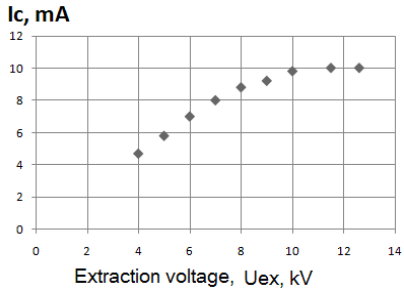


Figure 10: Dependence of the collector current Ic on the extraction voltage Uex. RF power in the plasma Prf=1.5 kW, the solenoid voltage Um=8.3 V. Gas flow Q=8.6 sccm.

Extraction current has a significant level of noise with frequencies fn~1-2 MHz. Ion beam shape is indicated by sputtering traces on the Molybdenum plate of the extractor electrode, on the accelerating electrode and on the collector as shown in Fig. 11.

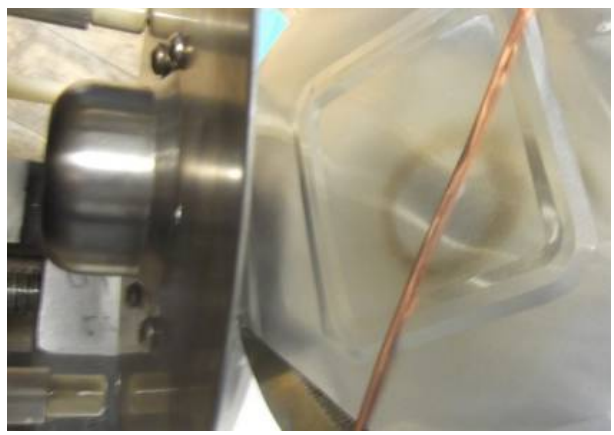


Figure 11: Accelerating electrode and a collector with a trace of sputtering by negative ion beams.

With demonstrated efficiency ~20 mA/cm2 kW it is enough ~10 kW of RF power for 60 mA of H- production, necessary for SNS operation with beam power 1.4 MW. RF SPS for CW operation with beam current ~10-15 mA can be developed with manageable RF power ~ 2 kW.

REFERENCES

[1] V. Dudnikov et al., THPS026, Proceedings of IPAC2011, San Sebastián, Spain, 2011. http://accelconf.web.cern.ch/AccelConf/IPAC2011/papers/thps026.pdf
[2] V. Dudnikov, et al, Rev. Sci. Instrum. 83, 02A712 (2012).
[3] V. Dudnikov, et al., AIP Conf. Proc. 1390, 411 (2011).
[4] V. Dudnikov, et al., AIP Conf. Proc. 1515, 456 (2013).
[5] R.F. Welton , et al., Rev. Sci. Instrum. 83, 02A725 (2012).
[6] V. Dudnikov, Rev. Sci. Instrum., 83, 02A708 (2012).
[7] Yu. I. Belchenko, G. I. Dimov, and V. G. Dudnikov, Nuclear Fusion,14(1),113-114 (1974).

Copyright © 2013 CC-BY-3.0 and by the respective authors

OPERATION OF A DIAMOND FIELD-EMISSION-ARRAY CATHODE IN A L-BAND RF GUN

P. Piot[1,2], B. Blomberg[1], C.A. Brau[3], B. K. Choi[4], W. Gabella[3], B. Ivanov[3],
J. D. Jarvis[5], M. Mendenhall[3], D. Mihalcea[1], H. Panuganti[1]
[1] Department of Physics and Northern Illinois Center for Accelerator &
Detector Development, Northern Illinois University DeKalb, IL 60115, USA
[2] Accelerator Physics Center, Fermi National Accelerator Laboratory, Batavia, IL 60510, USA
[3] Department of Physics and Astronomy, Vanderbilt University, Nashville, TN 37235, USA
[4] Department of Electrical Engineering and Computer Science, Vanderbilt University,
and Vanderbilt Institute of Nanoscale Science and Engineering, Vanderbilt University,
[5] Advanced Energy Systems Inc., Medford, NY 11763, USA.

Abstract

We report on the operation of a field-emission diamond cathode in a L-band RF-gun (1.3 GHz) at Fermilab's HBESL facility. The diamond cathode consists of an array of a million sub-micrometric pyramidal diamond tips.Beam currents in excess of 10 mA were observed and the cathode did not show appreciable signs of degradation after days of operation. Measured Fowler-Nordheim characteristics and transverse beam densities are also reported.

INTRODUCTION

Over the past years, field-emission (FE) electron sources have been the subject of intense researches due to several advantages they offer over photoemission and thermionic sources. The main advantages of FE sources stem from their ability to produce very low-emittance bunched beams, their capability to generate high-average current beams, and the absence of requirement for an auxiliary laser system. A single-tip FE emits electrons from a very small transverse area and can therefore produce beams with extremely small, quantum-degenerate, transverse emittances [1, 2]. When arranged as large arrays, field-emission-array (FEA) cathodes can provide substantial average currents [3] to the detriment of emittance which then scales linearly with the FEA macroscopic radius [4, 5].

Pulsed field-emission occurs when a FE cathode experiences a time-dependent field, e.g., when located in a resonant radiofrequency (RF) cavity and the root-mean-square (rms) duration of the bunch is $\sigma_t \simeq \omega^{-1}[\beta_e E_0/B(\phi)]^{-1/2}$ where $\omega \equiv 2\pi f$ where E_0 and f refer to the field amplitude and frequency. The latter pulse duration is obtained by taking the current density, $B(\phi)$ is a function of the workfunction ϕ associated to the cathode material and β_e is a field-enhancement factor [6, 7]. Nominally, the bunch rms duration is a significant fraction of the RF field period typically resulting in beams with large energy spread. This limitation can however be circumvented by exposing the FE cathode to superimposed electromagnetic fields [8].

In this paper we report on the first operation of a diamond FEA (DFEA) cathode in a conventional L-band RF gun nominally operated with a Cesium Telluride (Cs_2Te) photocathode. The DFEA is composed of ungated diamond pyramids which have proven to be rugged. Depending on the size and pitch of the pyramids, tests under DC voltages have showed field emission to begin at macroscopic fields $E_0 \simeq 5$ MV/m, and current density as high as 30 A.m^{-2} has been obtained [9].

EXPERIMENTAL SETUP

The geometry of the DFEA cathode used for the experiment reported below appears in Fig. 1(a,b). It consists of an array of $\sim 1000 \times 1000$ pyramidal diamond tips with their extremities separated by ~ 10 μm. The typical pyramid base is ~ 4 μm and the radius of curvature of the tip is on the order of 10 nm. Electrostatic simulations performed with the finite-difference element program POISSON [10], indicate that local fields in excess of ~ 0.9 GV/m are achieved at the tip when subjected to a macroscopic field $E_0 = 30$ MV/m (corresponding to $\beta_e \sim 30$).

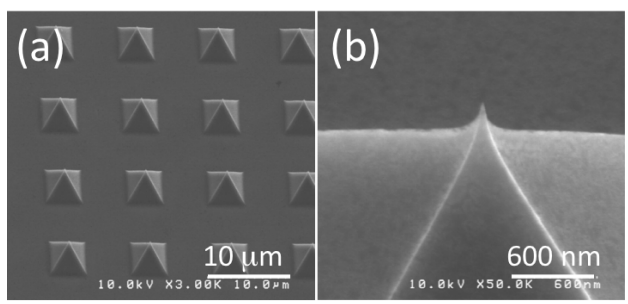


Figure 1: Electron-microscope photographs of the DFEA pattern (a) and close up of one pyramidal tip (b).

The cathode pattern was formed using a mold-transfer process whereby chemical vapor deposited (CVD) diamond is grown in sharpened silicon molds [11]. Using various techniques, DFEAs can be produced with single, double, or quadtip emitters. A variety of growth recipes

Copyright © 2013 CC-BY-3.0 and by the respective authors

are used to achieve a desired combination of sp^2 and sp^3 carbon, dopant concentration, and nitrogen content. The DFEA are brazed on a Molybdenum substrate.

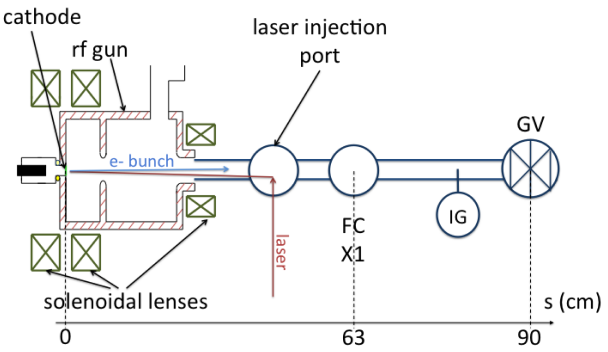


Figure 2: Experimental setup used to carry field-emission studies (a) . The legend is as follows: "FC": Faraday cup, "IG" ion gauge, "X1": scintillating screen for transverse beam density measurement.The insets are photograph of the DFEA cathode in its final position in the RF gun (b), and of the cathode holder with diamond coating on its font surface before insertion in the RF gun (c).

The DFEA cathode was located on the back plate of a 1.625-cell RF gun operating on the TM_{010} π mode at $f = 1.3$-GHz. The RF gun is powered by a $\leq$ 3-MW peak-power klystron pulsed at 1 Hz [12].

For the measurement presented below the RF macropulse width was set to 35 μs. The RF gun is surrounded by three solenoidal lenses that control the beam's transverse size. The charge and transverse distribution of the emitted electron beam can be measured with respectively a Faraday cup (FC) and scintillating screen (X1); see Fig. 2. Both diagnostics are located at $z = 0.63$ m from the cathode and are remotely insertable. The X1 screen is imaged on a charged-coupled-device (CCD) optical camera. A variable iris and neutral-density filters are used to attenuate the emitted optical radiation and mitigate saturation of the CCD. The optical resolution of the imaging system is $\sim$ 100 μm. A ion gauge (IG) located 0.5 m from the gun monitors the vacuum level in the section composed of the gun and diagnostics. Typical vacuum pressure levels in this beamline section are $\sim 1 \times 10^{-9}$ Torr. The forward RF power, P, injected in the RF gun cavity is measured using a calibrated RF diode detecting the low power from -30-dB directional coupler installed on the RF waveguide. The measured forward power can be used to infer the peak electric field at the cathode surface via $E_0[\mathrm{MV/m}] \simeq 2.234 \times 10^2 \sqrt{P[\mathrm{MW}]}$ where the RF-gun quality factor is taken to be $Q \simeq 2.3 \times 10^4$ and the cathode is assumed to be flushed with the RF-gun back plate.

The DFEA's substrate was brazed on a Molybdenum cathode holder compatible with the load-lock insertion mechanism used in the RF gun; see Fig. 3. The cathode holder was inserted in the RF gun and its position was adjusted to insure the gun resonant frequency remains at 1.3 GHz (as monitored with a spectrum analyzer). To insure electrical contact between the cathode holder and RF-gun-cavity walls, a Cu-Be spring is used. This spring is also found to be a source of spurious negligible field-emission current.

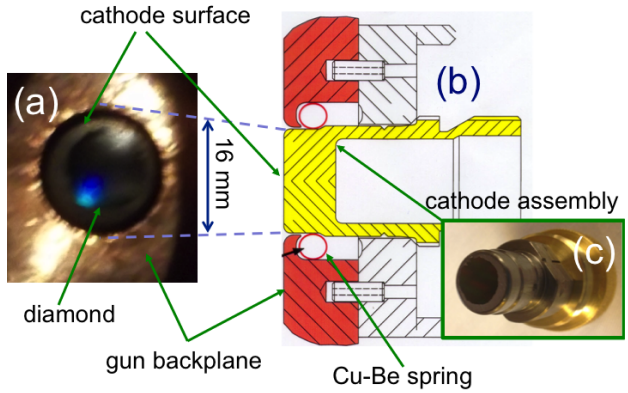


Figure 3: Photograph of the DFEA cathode (dark-blue area) inserted in the RF gun (copper back plate shown) (a). Cross-section sketch of the cathode insertion mechanism showing the RF gun back-plate (red) with cathode holder (yellow) (b). Photograph of the cathode holder (c).

MEASUREMENTS

A sample of F-N characteristics recorded over several days of operations appear in Fig. 4. The curves all have similar slopes at high fields [$\nu \equiv B(\phi)/\beta_e = 129.5 \pm 6.2$] for the cathode in its nominal position (with its emitting surface flushed with the RF gun backplate). A somewhat different slope is observed ($\nu' = 213.2 \pm 0.5$) when the cathode is retracted by a $\sim$ 2 mm. For these measurement the solenoids were turned off.

During the running period, the vacuum level was monitored and did not appreciably deteriorate ($\leq 1.2 \times 10^{-9}$ Torr). The current was also recorded for long period of time (typically up to one to two hours). An apparent current drift was observed by tracked back to klystron power drift over the time. Accounting for the E-field drift by computing an "instantaneous" F-N slope as $\mu \equiv E_0 \times \ln(I/E_0^2)$ indicates that the emission is stable with typical relative rms variation $\langle[(\delta\mu)/\mu]^2\rangle^{1/2} \simeq 0.37\%$. In practice correlated changes due to klystron-power drifts can easily be mitigated using a slow feedback loop.

The beam densities at X1 measured for a sample of operating conditions appear in Fig. 5. The beam sizes increase with field strength (due to larger emitting area) but can be

Copyright © 2013 CC-BY-3.0 and by the respective authors

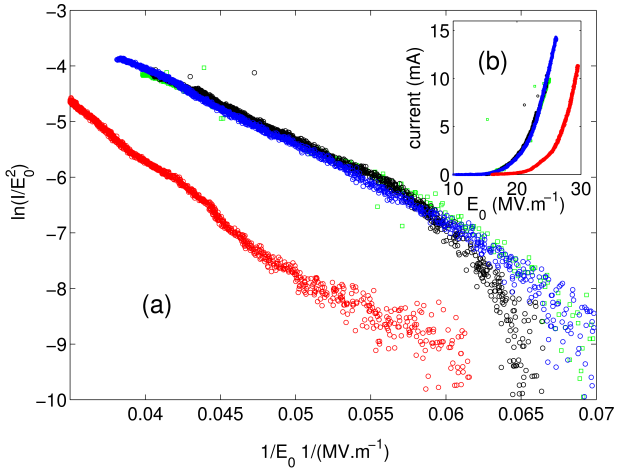


Figure 4: F-N plots (a) for the nominal (green, blue, black traces) and retracted (red) cathode position. For the nominal cases, the black and blue traces were respectively taken 10 and 59 days later than the black trace). The inset (b) displays the current evolution versus macroscopic field amplitude.

focused to a 1-mm (rms) spot size with the solenoids; see Fig. 5(d).

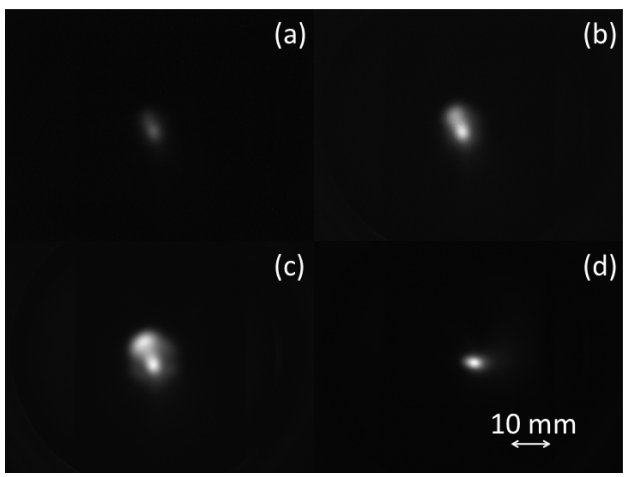


Figure 5: Transverse beam density measured at X1 for three cases of forward power $\hat{E}_0 \simeq 23.5$ (a), 25.5 (b) and 31 MV/m (c) with solenoids off and for a focused beam and $\hat{E}_0 = 31$ MV/m (d).

CONCLUSION

In summary we successfully demonstrated the operation of a DFEA cathode in a conventional L-band RF gun nominally design to operate using photocathodes. These results represent a significant step toward the realization of robust laser-free compact light sources for industrial, medical, and defense applications. Further tests will focus on characterizing the emittance of the beams generated from smaller-area FEA cathodes along with producing short bunch using gated DFEA cathodes currently under development [13].

We are indebted to M. Church, E. Harms , E. Lopez, J. Santucci, and V. Shiltsev for their support. This work is supported by the DARPA Axis contract AXIS N66001-11-1-4196 with Vanderbilt University, DOE Contracts No. DE-AC02-07CH11359 with the Fermi Research Alliance, LLC. and No. DE-FG02-08ER41532 with the Northern Illinois University.

REFERENCES

[1] K.L. Jensen, J. App. Phys 102 024911 (2007).

[2] J. D. Jarvis, H. L. Andrews, B. Ivanov, C. L. Stewar, N. de Jonge, E. C. Heeres, W.-P. Kang, Y.-M. Wong, J. L. Davidson, and C. A. Brau, J. Appl. Phys. **108**, 094322 (2010).

[3] K. B. K Teo, et al., Nature 437, p. 968 (2005).

[4] S. C. Leemann, A. Streun, A. F. Wrulich , Phys. Rev. ST Accel. Beams 10, 071302 (2007).

[5] J. D. Jarvis, B. K. Choi, A. B. Hmelo, B. Ivanov, C. A. Brau, J. Vac. Sci. Technol. B **30**, 042201 (2012)

[6] J. W. Wang and G. A. Loew, "Field Emission and RF breakdown in high-gradient room-temperature linac structure", report SLAC-PUB-7684 (unpublished, 1997).

[7] D.Y. Zhong, G.Y. Zhang, S. Liu, T. Sakurai, E.G. Wang, Appl. Phys. Lett. **80** 506 (2002).

[8] J. W. Lewellen and J. Noonan, Phys. Rev. ST Accel. Beams, **8**, 033502 (2005).

[9] J. D. Jarvis, H. L. Andrews, C. A. Brau, B. K. Choi, J. Davidson, W. P. Kang, Y. M. Wong, J. Vac. Sci. Technol. B **27**, 2264 (2009).

[10] J.H. Billen and L.M. Young, in Proceedings of the 1993 Particle Accelerator Conference, Washington, DC (IEEE, Piscataway, NJ, 1993), p. 790.

[11] W. P. Kang, J. L. Davidson, M. Howell, B. Bhuva, D. L. Kinser, D. V. Kerns, Q. Li, and J. F. Xu, J. Vac. Sci. Technol. B **14**, 2068 (1996).

[12] J.-P. Carneiro, et al., Phys. Rev. ST Accel. Beams **8**, 040101 (2005).

[13] J. D. Jarvis, H. L. Andrews, C. A. Brau, B. K. Choi, J. Davidson, W.-P. Kang, and Y.-M. Wong, in Proceedings of the 2009 free-electron-laser conference (FEL09), p. 376 (2009).

Copyright © 2013 CC-BY-3.0 and by the respective authors

MULTIPHOTON EMISSION FROM CESIUM TELLURIDE PHOTOCATHODES

H. Panuganti†, C. Prokop, Department of Physics, Northern Illinois University, DeKalb, IL, USA
P. Piot, Fermi National Accelerator Laboratory, Batavia, IL, USA

Abstract

The High-Brightness Electron Source Lab (HBESL) at Fermilab operates an L-band RF gun (1.3-GHz) that incorporates a Cesium Telluride (Cs_2Te) photocathode illuminated by an ultra-short (sub-100 fs) laser pulses. In this contribution we report recent studies on exploring the electron beam emission using 800 nm laser pulses (instead of the 266 nm nominal wavelength used for linear photoemission).

INTRODUCTION

Photocathodes are excellent sources for production of short electron bunches [1]. Production of short bunches is possible due to the advancements in the drive laser pulse times combined with availability of fast-response photocathodes. Photoemission allows generating higher charges compared to field- and thermionic emission, and also with small beam transverse emittance. One good parameter to characterize the performance of a photocathode is quantum efficiency (QE), which is defined as the number of electrons emitted for a unit photon. Cesium Telluride is considered to be an exceptionally high QE (up to 20 %) semiconductor photocathode [2]. The work function of Cs_2Te 4.6 eV corresponds to the laser wavelength of 266 nm falling in the ultraviolet (UV) region. Since most of the commercially available lasers include lasing media with high gain in the infrared (IR), frequency up-conversion to the UV is generally done for linear photoemission from metallic and some semiconductor cathodes. For titanium sapphire based laser systems (λ~800 nm), UV pulses for photoemission are obtained from frequency tripling of IR pulses using a two-stage process consisting of a second harmonic generation (SHG) stage followed by a sum frequency generation (SFG). In order to preserve the short pulse duration during the up-conversion process, both stages generally use thin BBO crystals which results in low IR-to-UV conversion efficiency typically < 10%. In this paper we present preliminary results toward attempting to generate electron bunches with commensurate charge directly using the amplifier IR pulse. We specifically report on the observation of two-photon emission from Cs_2Te.

PHOTOCATHODE THEORY

Spicer developed the first model in 1958 to explain photoemission in semiconductors, which is commonly referred to as the Three Step Model, which models the photoemission mechanism as a bulk effect [3]. In the first step, an electron absorbs a photon and gets excited from the valence band to the conduction band. In the second step, the excited electron transports to the surface. In the third step, the electron escapes to the vacuum level resulting in emission. The QE equation for a semi-infinite photocathode slab is given by [3]

$$QE = [1 - R]\frac{\frac{\alpha_{PE}}{\alpha}P_E}{1+\frac{1}{\alpha L}}$$

Where R is the reflectivity of the material; α is the intensity attenuation coefficient of the photocathode material; α_{PE} represents the coefficient of absorption for the vacuum level, or the number of electrons that are excited to the vacuum level that can possibly photoemit per unit laser intensity available; L is called the escape length which represents the strength of the electron scattering; P_E is the probability that an electron at the surface with sufficient energy to escape, escapes. Here all the parameters are functions of $h\upsilon$. Fowler-Dubridge model is derived for photoemission for metallic photocathodes based on similar approach. It is the first step (photo-absorption and excitation) that distinguishes between single-photon emission from multiphoton emission. Once the electrons get excited, the rest of the processes viz. electron transport to the surface and electron escape remain the same. In single photon emission the intensity dependence of QE goes away. But in multi-photon emission α_{PE} additionally depends on the intensity of the light (temporal) besides $h\upsilon$, as the non-linear "simultaneous" absorption of multiple photons (of lower energy) has to occur to excite an electron to the vacuum level. Hence shorter laser pulses are required for higher order photoemission.

EXPERIMENT

The experiment reported in this paper was carried at the high brightness electron source laboratory (HBESL). The HBESL facility consists of a 1.5 cell L-band 1.3 GHz RF gun powered by a 3 MW klystron. The photocathode drive laser consists of a broadband (200 nm) Octavius oscillator followed by a SpectraPhysics regenerative amplifier. The amplified IR pulse typically has 100 fs duration. The IR-to-UV SHG and SFG conversion processes incorporate respectively a 0.300 and 0.150 mm BBO crystals. The crystal thicknesses were optimized with SNLO and short UV pulse (130 fs), and were measured using a polarizing-gating UV FROG. The produced pulses were short enough to enable the production of uniformly charged ellipsoidal bunches using the blow-out regime [4]. A schematic of the experimental setup used for our experiment appears in Fig. 1. A 4 mJ amplified laser pulse is sent to the HBESL accelerator

† harsha.panuganti@gmail.com

Copyright © 2013 CC-BY-3.0 and by the respective authors

vault where it is converted to UV. The laser energy can also be measured prior to the injection into the accelerator beamline using an energy meter and a calibrated diode. A virtual cathode – a one-to-one optical image of the photocathode, located outside of the vacuum – enables the measurement of the laser transverse distribution on the photocathode. The laser hits the Cs_2Te photocathode under normal incidence angle. The charge emitted from the photocathode can be collected by a Faraday cup (FC) located immediately downstream of the gun; see Fig. 1. The FC was calibrated with an integrated current transformer (ICT) at high charge (nC) values and is used to measure the low charge values associated with the bunches produced via multiphoton emission.

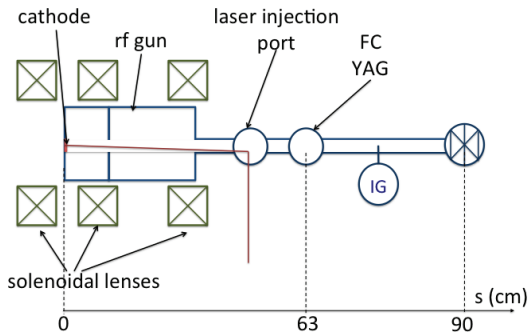


Figure 1: Overview of the HBESL electron source area. The IR pulse is injected through the laser injection port. The legend is *FC*: Faraday cup, *IG*: ion gauge, *YAG*: Yttrium Aluminum Garnet scintillating screen.

The produced bunch charge downstream of the RF gun strongly depends on the relative phase between the laser and the gun's RF field. Figure 2 shows the measured charge as a function of the launch phase referred with respect to the RF master oscillator. For this measurement the amplified IR laser pulse was directly sent to the cathode. The three traces correspond to three different laser transverse spot sizes of 3, 5 and 7 mm.

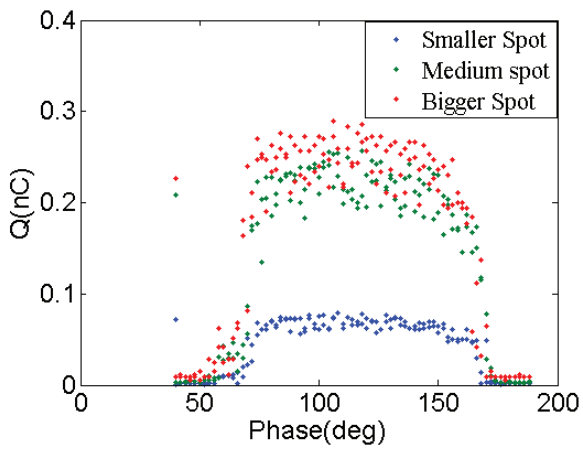


Figure 2: Charge dependence on laser phase relative to the gun (with an arbitrary phase offset). The blue, green, and red traces correspond respectively to laser spot diameter of 3, 5 and 7 mm on the photocathode.

The shape of the phase scan traces confirms that the charge emitted is from photoemission. Figure 3 shows the charge yield in the Faraday cup as a function of the laser energy for the same three different laser spot sizes.

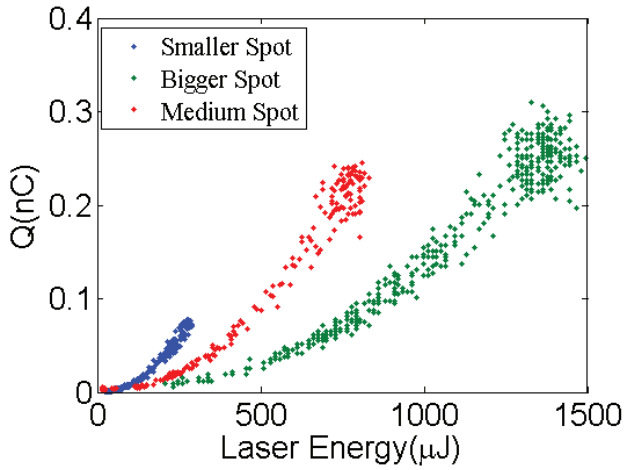


Figure 3: Charge variation as a function of laser energy for the three laser spot sizes considered in Fig. 2.

The stronger nonlinear dependence of the charge on the laser energy for the smaller spot size indicates that higher energy flux (J/m^2) produces higher charge in photoemission from the IR laser. Taking the laser's transverse density to follow a Gaussian distribution, smaller spot sizes obtained by clipping a larger spot impinges a higher laser flux for a given total laser energy and hence produces higher charge. The nonlinear signature of the charge–energy traces reported in Fig. 3 hint to a nonlinear photoemission process. To further quantify the dependence of the charge on the laser energy, we plot Fig. 3 on a log-log scale; see Fig. 4. The overall linear regression of the data confirms that the charge scales as $Q \propto I^2$ (where I is the laser intensity) suggesting that two-photon emission is the dominant process rather than the anticipated three-photon emission [5]. Some data points at lower charge/energy values with possible higher contribution from background noise (represented by '+') were omitted for linear curve fitting.

Photoemission is an independent process from charge acceleration, but the charge yield out of the RF gun which has a practical importance depends on the accelerating gradient in the gun due to the different electron beam dynamics. Figure 5 shows the log-log plots of charge vs. laser energy for different accelerating gradients (AD values) for the medium laser spot size. For a given logarithmic curve $logy = nlogx + C$, the coefficient A of $y = x^n$ can be calculated by using the relation $A = exp(C)$. In our case, $n = 2$ and A is the quadratic

Copyright © 2013 CC-BY-3.0 and by the respective authors

coefficient. The inset in Fig. 5 shows the variation in the quadratic coefficient with the accelerating gradient.

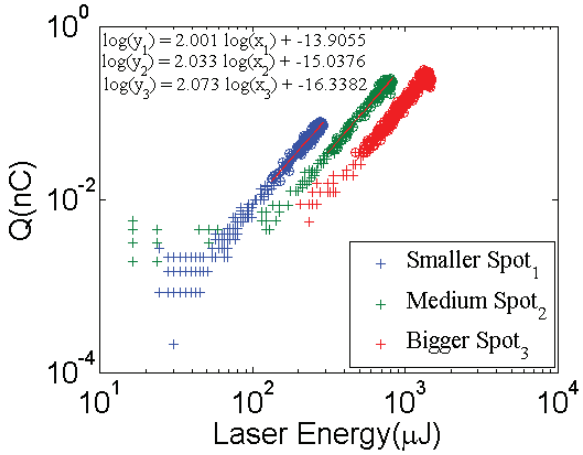


Figure 4: Logarithmic plots corresponding to the data presented in Fig. 3.

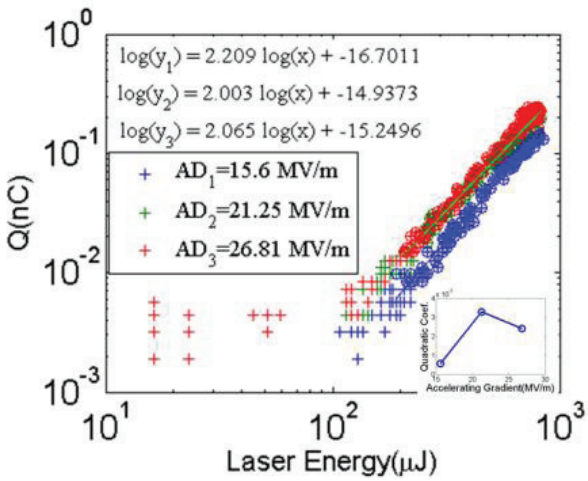


Figure 5: The effect of the accelerating gradient on the charge yield. Inset: The variation of the quadratic coefficient with the accelerating gradient.

Experimentally, we calculate the QE of a photocathode based on the correlation between the charge emitted Q by the given photocathode and the corresponding drive laser energy E as follows

$$QE \quad \frac{n(e)}{n(p)} \quad \frac{Q/e}{E/hc\lambda^{-1}} \quad \frac{Q}{E}\left(\frac{hc}{\lambda e}\right)$$

Where $n(e)$ is the number of electrons emitted, $n(p)$ is the number of photons impinged, λ is the wavelength of the drive laser, e is the electronic charge, λ is the wavelength of the laser, h is the Plank's constant, c is the velocity of light. Rewriting the above equation in more convenient units of charge and energy for the two wavelengths (of drive laser) of interest viz. 800 nm (IR) and 266 nm (UV) we get

$$QE_{UV} \quad 4.7\times10^{-6}\left(\frac{Q[pC]}{E[\mu J]}\right)$$

$$QE_{IR}(E) \quad 1.56\times10^{-6}\left(\frac{Q[pC]}{E[\mu J]}\right)$$

Figure 6 shows the charge vs. UV laser energy for the single photon emission from Cs_2Te.

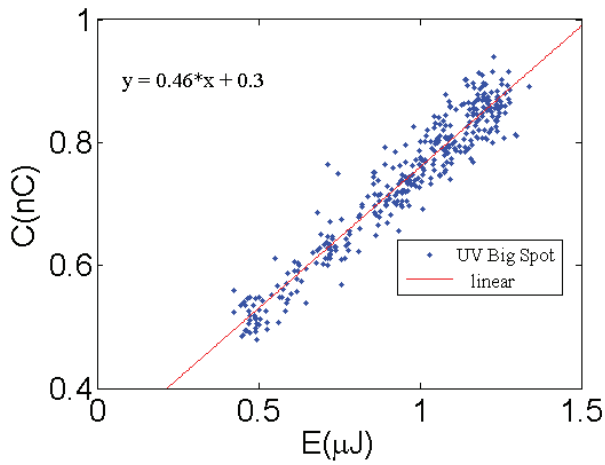


Figure 6: Charge vs. UV laser energy for Cs_2Te (single photon emission).

Typically, the QE is not defined for multiphoton emission as the ratio is not a constant like in the case of single photon emission. Or in other words increases with the laser energy, which possibly makes multiphoton emission preferable to obtain higher charge values at higher drive laser energy values, when compared to single photon emission. But we can define QE_{IR} as a function of E as in the previous equation and compare with that of UV.

REFERENCES

[1] K.L. Jensen, "Advances in Imaging and Electron Physics", Vol . 149, Elsevier Academic Press 2007).
[2] S. H. Kong, J. Kinross-Wright, D. C. Nguyen and R. L. Shieffield, J. Appl. Phys. **77**, 6031 (1995).
[3] W.E. Spicer; A. Herrera-Gomez, "Modern Theory and Applications of Photocathodes", SLAC-PUB-6306, August (1993).
[4] P. Piot et al., Phys. Rev. ST Accel & Beams **16**, 010102 (2013)
[5] P. Musumeci et al.,Phys. Rev. Lett. **104**, 084801 (2010).

Copyright © 2013 CC-BY-3.0 and by the respective authors

ANDROID APPLICATION FOR MONITORING THE STATUS OF THE ADVANCED PHOTON SOURCE

M. Borland*, Westmont, IL, USA

Abstract

Smartphones and tablets are nearly ubiquitous and have the ability to quickly access and display data from network sources. This suggests their suitability for remote monitoring of a facility such as the Advanced Photon Source (APS). While one possibility is to access data using a web browser running on the device, native applications offer attractive features, such as improved display and background execution. We report on development of an Android application for monitoring the status of the APS. In addition to displaying data, the application can issue alerts when beam is lost or restored. Home screen widgets of various sizes are also provided. We describe not only the features of the application, but also give details of the implementation. The application is free of advertising and is available free of charge on the Google Play store.

INTRODUCTION

Like many synchrotron radiation facilities, the Advanced Photon Source (APS) operates thousands of hours per year. During operating periods, it is expected to provide beam 24 hours a day, seven days a week. Getting information about status to accelerator staff, beamline staff, and beamline users is thus very important. The ubiquity of smartphones and tablets provides a way to do this.

These devices are internet-enabled, so it is of course possible to get information via a web browser. However, using a native Android application provides several advantages. One can provide high-level status on the notification bar, which is visible without unlocking the phone or opening the application. One can provide a home-screen widget that provides more information than will fit on the notification bar. The notification and widget can both be used to launch the full application. Another advantage of the native application over browser-based information delivery is that the native application can run in the background and provide audible alerts of significant events.

Inspired by these ideas, we developed an Android application that provides both high-level and detailed status data about the APS. The Android platform was chosen for its open-source nature and the low cost of entry for devices and development. Also, the Android home-screen widget feature provides a superior way to display very high level data without opening the application. Unlike other smartphone platforms, the Android Software Development Kit (SDK) is free and available for essentially all platforms, which allowed using Linux for development.

The application is called APSStatus and available free of charge on the Google Play store. The application is also free of advertising.

*michael.d.borland@gmail.com

FEATURES AND CAPABILITIES

The APSStatus package includes a main application and three home-screen widgets. The main application is organized into a series of pages or tabs, each of which displays information of a certain type. Presently there are tabs for overall status, status messages, 24-hour and 1-week history plots, superconducting undulator status, power supply summary status, power supply detailed status, vacuum system status, rf system status, personnel safety system status, and front-end equipment protection system status. Figure 1 shows the main status screen. This is typical of the status screens, in that it features a heading with a prominent date and time stamp, which allows the user to easily ascertain if the data is fresh. Data is updated at 1 minute intervals.

Since not all of the selections of data will be of interest to all users, the application menu's "Tab Settings" selection allows the user to determine which tabs will be displayed.

Most of the tabs supply snapshots of data without any history. One exception is the status messages display, which displays the history of recent status updates issued by control room staff. Two other exceptions are the 24-hour and 1-week history tabs, which provide plots of beam current, beam lifetime, rms beam motion, number of shutters open, horizontal emittance, and vertical emittance. Figure 3 shows an example of the 1-week history display. Touching a plot will bring up a zoomed-in version with pinch-to-zoom and scrolling features.

In addition to the main application, the user can add one or more of the three home-screen widgets to their home screen. These display small selections of data and require less than 300 bytes per update, i.e., less than 0.4 MB per day. Hence, these can be left running and provide the most essential information at a glance.

The largest of these widgets, which has some special features, is shown in Figure 4. It shows the beam current color-coded by status, the number of bunches, the beam lifetime, the number of operating beamlines, the horizontal and vertical emittance, and the injection efficiency on the last top-up shot. Unlike the other widgets, this widget also posts the beam current to the notification bar, where it can be seen from any home screen and even when the screen is locked. The beam current notification is color-coded to indicate whether it is within the expected range for the present machine mode or not.

Another special feature of this widget is that it can provide audible alerts when beam is lost or restored. The alerts are configured from the main application's menu. The user

Copyright © 2013 CC-BY-3.0 and by the respective authors

can elect to be alerted when beam is lost, when it is absent for an extended time, and when it is restored. The user can also set a quiet-time preference to avoid being disturbed while sleeping, for example.

SOFTWARE DESIGN

Those who are uninterested in software design may wish to skip this section, as it has little to do with how the application is used or what it can do. This section also assumes some familiarity with Android development.

We used the Eclipse Integrated Development Environment (IDE), which is advantageous in that it helps one quickly learn both the Java language and the specific methods provided by Android. The web contains many resources, such as Android tutorials and user forums (e.g., StackExchange).

The main application is organized into a series of Fragment objects, which are grouped together as a single application. Each Fragment displays a screen with data of a particular type, e.g., power supplies or vacuum. The interface is built using Peter Kuterna's SwipeyTabs class and SwipeyTabsSampleActivity, which is an extension of the FragmentActivity class. SwipeyTabs provides a convenient mechanism for switching between related activities by clicking on a tab at the top of the screen or swiping the screen left or right.

SwipeyTabs keeps three Fragments active at any time. These are the Fragment presently being viewed, plus the Fragments to the left and right. If the user swipes or tabs to the Fragment on the right, say, the new Fragment is generally displayed instantaneously because it is already active. Meanwhile, the next Fragment is triggered so it is more likely to be ready when the user swipes again. (If the user swipes too quickly, this may not be the case.)

The data that is displayed by APSStatus and its various widgets is provided by the APS web server from files written by a node that has read access to EPICS process variables and write access to the web server's file space. A common choice for sharing data on the web is XML (eXtensible Markup Language) files and APSStatus was originally written to use such files. However, XML has a well-deserved reputation for verbosity, resulting in a very poor ratio of data delivered to bandwidth used. Since excessive use of bandwidth is highly undesirable for mobile devices, we switched to gzipped SDDS (Self-Describing Data Sets) files. These have the additional advantage that they are easily created using the SDDS tools [1, 2] that are already part of the APS control system. There is also a convenient SDDS library for Java that reads from a URL directly [3].

Fragments are at present divided into three types: (1) those that read and display data from an SDDS file. (2) those that retrieve and display bitmap images. (3) those that retrieve and display text from the server. Most Fragments are of Type 1.

Each Type 1 Fragment has a corresponding SDDS file on the server that provides its data. This is done in part because Fragments do not share data, so there is no point in reading data from a common source. Also, reading from a common source would invariably mean using more bandwidth than needed. Hence, each Fragment is supplied with a minimalist data file containing only the relevant information. Each file contains a time-stamp, which is prominently displayed along with the other data. This ensures that the user will be able to tell if the data is stale for some reason. The update interval of the data is 1 minute. Updates for each active Fragment are handled by separate threads.

The displays for Type 1 Fragments require only stock Android widgets. In order to accommodate various screen sizes, the root widget is a ScrollView, which permits vertical scrolling. Inside the ScrollView are TextView widgets, often packed into TableLayout widgets.

The Type 2 Fragments display a series of small bitmaps that are provided directly by the server, i.e., they do not retain or plot the history data themselves. When a small bitmap is pressed by the user, a larger bitmap of the same data is retrieved and displayed. This reduces use of bandwidth and memory by not transmitting and storing large bitmaps that may be of no interest.

In addition to the main application, there are three home-screen widgets that provide various selections of very high-level information. The home-screen widgets are implemented using the AppWidgetProvider class and run independently of the main application. As with the main application, the home-screen widgets have a 1 minute update interval. Touching any of these widgets will open the main application.

Of the three home-screen widgets, one is larger and provides more information. It also provides an alarm service, which is configured from the main application, and places information in the notification bar. The alarm settings are communicated from the main application to this widget using the SharedPreferences facility.

On the server side, a cron job runs at 1 minute intervals to make the various SDDS data files. For each data file, there is generally a separate request file that is used in an invocation of `sddscasr` to create a snapshot. The snapshots are processed to, in particular, convert status and floating point data to a uniform format. This simplifies coding on the application side and also reduces the size of the data transmitted. Small data files just for the home-screen widgets help minimize use of bandwidth.

Other cron jobs run at intervals to create the bitmaps needed by the history displays. These jobs used pre-existing scripts that invoke the program `sddsplot`.

CONCLUSIONS

We have created an Android application that provides status information about the Advanced Photon Source, including history graphs and detailed status of major subsystems. The application includes home-screen widgets, notification bar posts, and optional audible alerts of beam loss or restoration. Bandwidth use is minimized in part through use of gzipped SDDS files. The application is available free of cost on the Google Play store, and is free of advertising.

Copyright © 2013 CC-BY-3.0 and by the respective authors

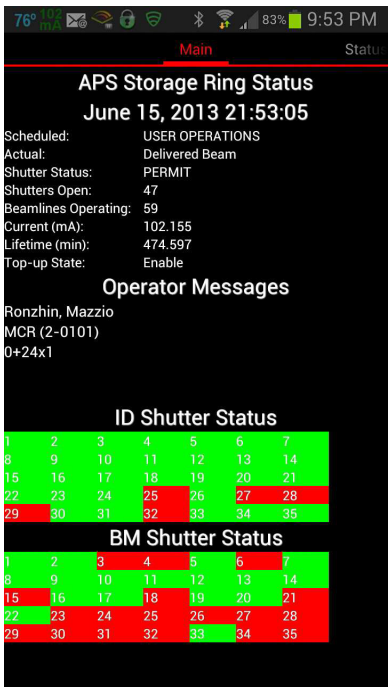


Figure 1: The main status tab of the APSStatus application.

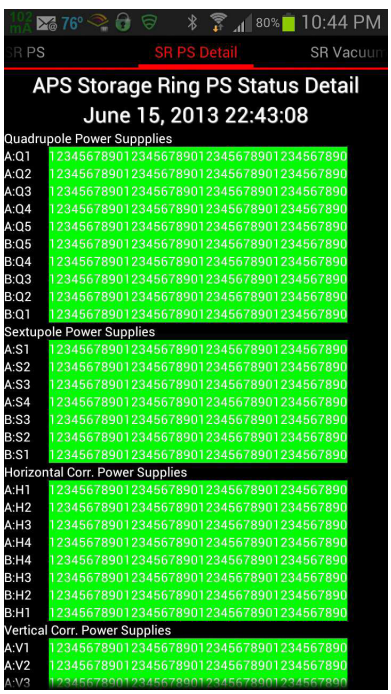


Figure 2: The power-supply detail tab of the APSStatus application.

REFERENCES

[1] H. Shang et al., PAC 2003, 3470 (2003).

[2] R. Soliday et al., PAC 2003, 3473 (2003).

[3] R. Soliday, ICALEPS 2001, 545 (2001).

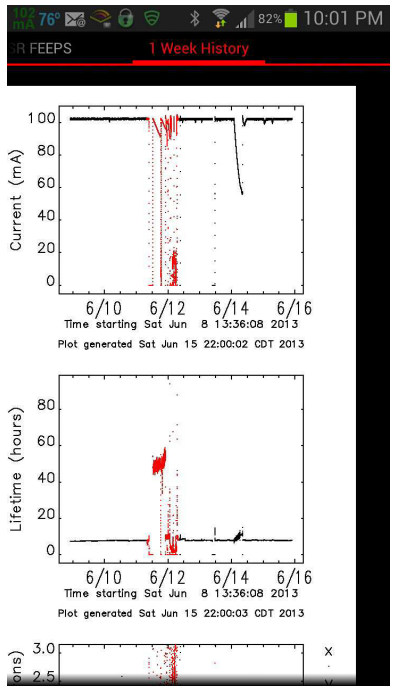


Figure 3: The one-week history tab of the APSStatus application. Scrolling vertically reveals additional plots, while pressing on a plot brings up a magnified view that can be zoomed and scrolled.

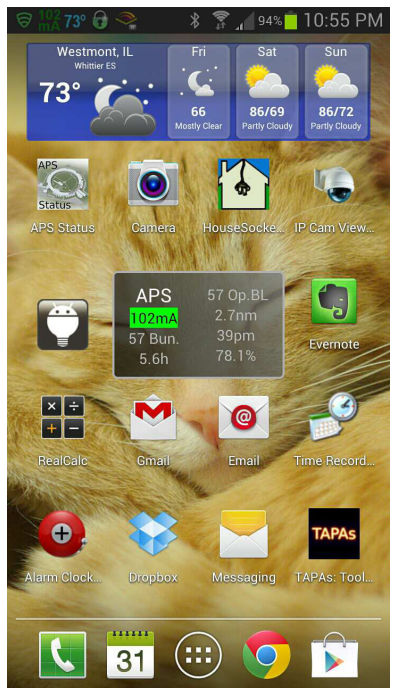


Figure 4: 2x1 APSstatus widget showing high-level APS information. Touching the widget brings up the full application. For clarity, we've removed most other widgets and apps from this screen. Note that the beam current also appears in the notification bar (top left).

Copyright © 2013 CC-BY-3.0 and by the respective authors

HIGH-POWER TESTS AND INITIAL ELECTRON BEAM MEASUREMENTS OF THE NEW HIGH-GRADIENT NORMAL CONDUCTING RF PHOTOINJECTOR SYSTEM FOR THE SINCROTRONE TRIESTE

L. Faillace#, R. Agustsson, P. Frigola, A. Verma, Radiabeam Technologies LLC, CA, USA
H. Badakov, A. Fukasawa, J. Rosenzweig, A. Yakub, Department of Physics and Astronomy, UCLA CA, USA
F. Cianciosi, P. Craievich, M. Trovo', Sincrotrone Trieste, Italy

Abstract

Radiabeam Technologies, in collaboration with UCLA, presents the development of a high gradient normal conducting radio frequency (NCRF) 1.6 cell photoinjector system, termed the Fermi Gun II, for the Sincrotrone Trieste (ST) facility. Designed to operate with a 120MV/m accelerating gradient, this single feed, fat lipped racetrack coupler design is modeled after the LCLS photoinjector with a novel demountable cathode which permits cost effective cathode exchange. Full overview of the project to date, installation, high-power RF conditioning and initial electron beam emittance measurements at Sincrotrone Trieste will be discussed along with basic design, engineering and manufacturing.

INTRODUCTION

Radiabeam is currently involved in the development of new technology aimed at high average power operation for a NCRF electron gun system, the FERMI II RF Gun, for the Sincrotrone Trieste facility operating at the frequency of 2.99801GHz with a repetition rate >50Hz.

The gun design was originally based on the UCLA-University of Roma-INFN-LNF [1] high repetition rate photoinjector for SPARX project, which borrowed the main features from the LCLS gun [2,3]. Nevertheless, the basic design was re-optimized by request of ST with two main changes: 1) an exchangeable cathode plate for easy exchange of different material samples; 2) single-feed for a cost-effective and more compact device.

RF GUN DESIGN

The RF design of the Gun has been performed by using the codes SuperFish [4] and HFSS [5]. Figure 1 shows half structure of the RF gun with surface electric field distribution calculated by HFSS. The RF power is fed through one waveguide only (top one); the symmetrical waveguide, acting as a dummy waveguide, forbids the propagation of the electromagnetic field that is below its cutoff value (i.e. the dummy waveguide has a width much smaller than the input one). The main purpose of the second waveguide is to cancel the field dipole component.

#faillace@radiabeam.com

Cell Design

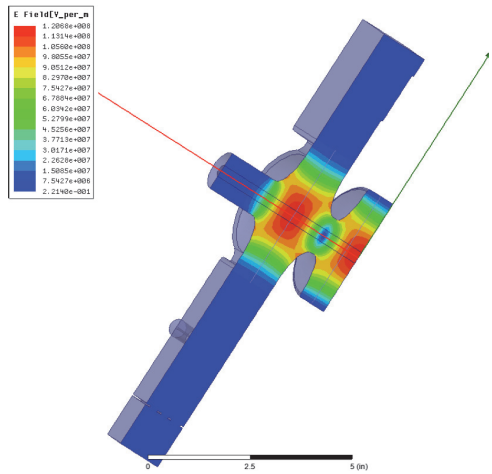


Figure 1: 3D model used for HFSS simulation. Surface electric field is shown.

The RF cavity shape, as proposed, has several innovative electromagnetic features, including Z-coupling and enhanced cell-to-cell coupling to produce higher mode separation, elliptical irises to reduce surface electric field, symmetric couplers for dipole mode minimization, racetrack geometry to minimize quadrupole field components. In contrast to the LCLS gun, which has these features, it is externally fed only by one side, avoiding the need of a power splitter and making the whole assembly much more compact, easier to handle and cost efficient.

In order to calculate the maximum surface electric field, we normalize the on-axis field to 120 MV/m at the cathode. The peak field on the iris is found to be 102 MV/m, below the breakdown safety threshold.

Per usual procedure, a first pass on the RF design was made with SUPERFISH and then HFSS was used to provide a complete picture of the RF performance, including mode frequencies, field balance, quality factor *Q,* shunt impedance and external coupling.

The design parameters achieved in simulation through this process are summarized below in Table 1.

Copyright © 2013 CC-BY-3.0 and by the respective authors

Table 1: Main RF Parameters

Parameter	Simulated value
π-mode frequency	2.998 GHz
0-π mode separation	14.2 MHz
Quality factor Q_0	13,750
External coupling β	1.8
Shunt Impedance R_{Shunt}	60.8 MΩ/m
Peak Surface *E* (120 MV/m @cathode)	102 MV/m
Input power *P*	<10 MW

Dipole and Quadrupole Component

The dipole and quadrupole components of the RF field have been evaluated using HFSS. The symmetry of the Z-coupling structure guarantees cancellation of the RF dipole component, apart from a negligible (in high-*Q* standing wave devices) transient from the single-side RF feed. The quadrupole field, on the other hand, is managed by adjusting the "race-track" spacing.

GUN FABRICATION, TUNING AND LOW-POWER MEASUREMENTS

The RF Gun was machined in-house and all the brazing cycles at SLAC, followed by final tuning. The Gun after the final brazing step is shown in Figure 2.

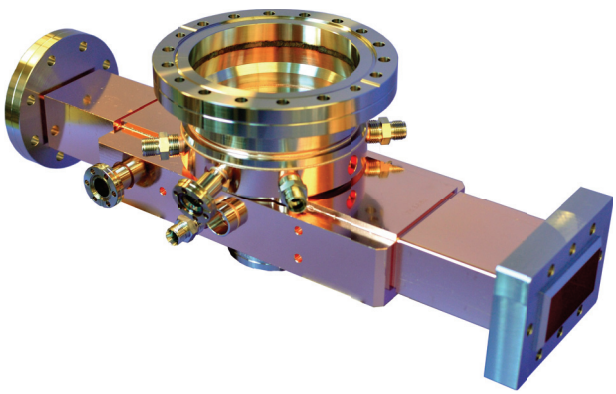


Figure 2: Picture of the Fermi II Gun after final brazing.

In order to check the simulated parameters, we performed low-power measurements by using a Vector Network Analyzer (VNA). The comparison is given in Table 2, showing good agreement.

Table 2: Comparison between Simulations and Measurements of the Main RF Parameters

	Measurement	HFSS
Frequency	2.99801 GHz (19 C, 40% humidity)	2.998GHz
Mode Separation	14.5 MHz	14.2 MHz
Q_0	13,350	13,750
Coupling beta	1.85	1.8

The reflection coefficient at the input RF waveguide is shown in Fig. 3. The tuning frequency was set to 2.99801, at 19°C and 40% humidity (assuming an operating temperature of 38°C).

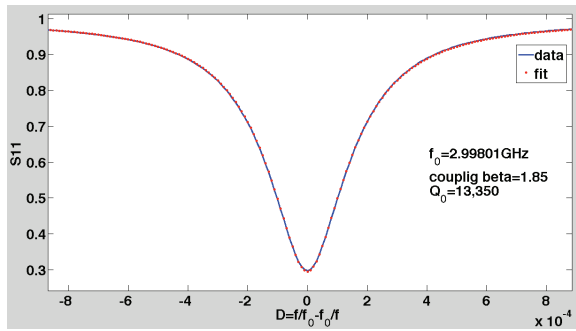


Figure 3: Reflection coefficient. Data (red dots) and fit (blue line).

The balance of the electric field profile was measured by means of the bead-drop procedure and using a 2mm dielectric spherical bead. The good agreement between data and fit is given in Fig. 4.

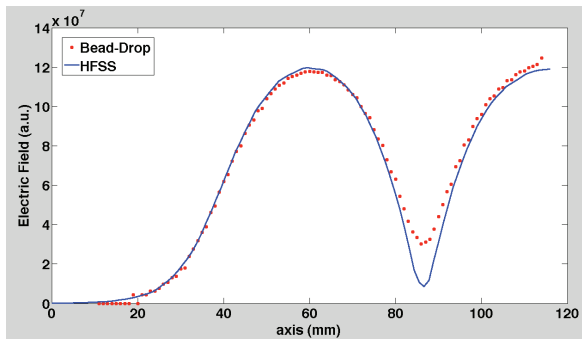


Figure 4: On-axis electric field profile. Data (red dots) and fit (blue line).

INSTALLATION AND HIGH-POWER RF CONDITIONING

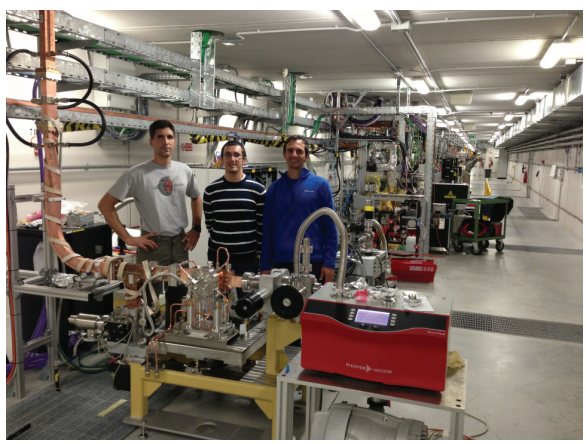


Figure 5: Installation of the Fermi II Gun inside the tunnel at Sincrotrone Trieste.

Copyright © 2013 CC-BY-3.0 and by the respective authors

The Fermi II Gun Installation started in Trieste on January 4th 2013 (Figure 5). The gun was brought under vacuum in a test area to check if any leaks were present as well as the frequency shift that resulted to be about 800 kHz, as expected.

A dedicated area for high-power gun testing is located behind the current RF gun station. The Fermi II gun was installed in this area to start high-power conditioning. The input power was raised up to 11MW and a repetition rate of 50Hz. The conditioning between 10Hz and 50Hz, given in the chart in Fig. 6, required a temperature variation of only -2°C. The vacuum base level was 2.4E-9 mbars.

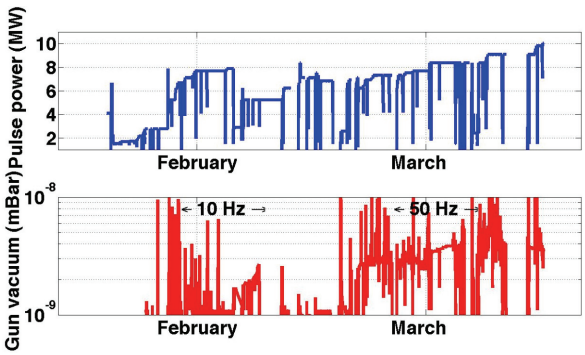


Figure 6: Monitoring of the high-power conditioning and vacuum levels.

The first electron beams were generated by using the laser profile shown in Figure 7.

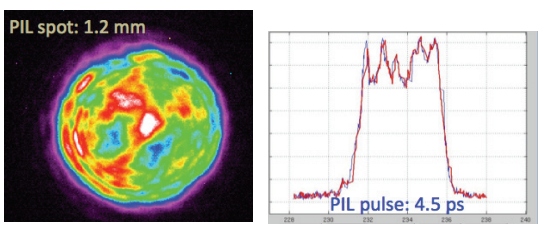


Figure 7: Left, laser spot transverse profile; right, pulse length profile.

The output energy was 5.1 MeV for 8MW of input RF power. Although the laser spot was not optimized yet, the quantum efficiency showed a good value of about QE=3.3E-5, see Figure 8.

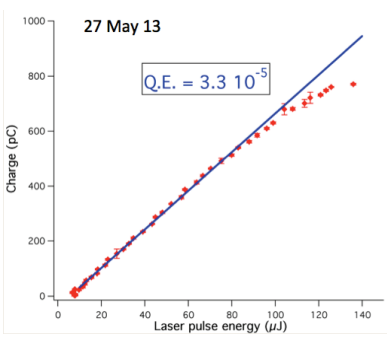


Figure 8: Charge yield as function of laser energy.

The first emittance measurement was performed with a 500 pC beam at 100 MeV, by using the quadrupole scan technique. In Figure 9, we show the result for the measured transverse normalized emittance on the vertical plane with a promising value of 0.67 microns.

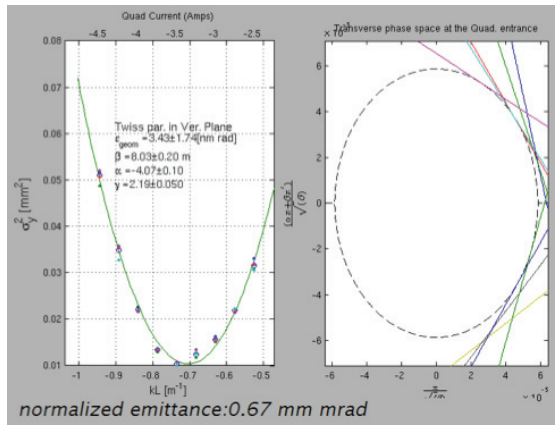


Figure 9: Initial emittance measurement of a 500pC beam.

CONCLUSIONS

We have presented the RF design, fabrication, high-power RF conditioning and initial beam measurements of the new Fermi II RF Gun. Innovative features to the class of RF Guns, such as elliptical irises and an exchangeable cathode system, improve the performance of this gun in terms of power handling and robustness. The removable cathode assembly showed good thermal performance even at 50Hz. The initial measurements of the beam normalized emittance are very promising.

ACKNOWLEDGMENT

I would like to thank Mauro Trovo' (ST) for providing material on the initial beam measurements.

REFERENCES

[1] L. Faillace *et al.*, " An Ultra-high repetition rate S-band RF Gun", FEL Conference 2008
[2] C.Limborg *et al.*, "RF Design of the LCLS Gun", LCLS Technical Note LCLS-TN-05-3 (Stanford, 2005).
[3] D.H. Dowell *et al.*, "The development of the Linac Coherent Light Source RF Gun", SLAC Menlo Park CA, published in the ICFA Beam Dynamics Newsletter No. 46.
[4] http://laacg1.lanl.gov/laacg/
[5] http://www.ansoft.com/products/hf/hfss

Copyright © 2013 CC-BY-3.0 and by the respective authors

INNOVATIVE LOW-ENERGY ULTRA-FAST ELECTRON DIFFRACTION (UED) SYSTEM*

E. Threlkeld, L. Faillace#, S. Boucher, RadiaBeam Technologies, Santa Monica, CA 90404, USA
P. Musumeci, University of California, Los Angeles, CA 90095, USA

Abstract

RadiaBeam, in collaboration with UCLA, is developing an innovative, inexpensive, low-energy ultra-fast electron diffraction (UED) system which allows us to reconstruct a single ultrafast event with a single pulse of electrons. Time resolved measurement of atomic motion is one of the frontiers of modern science, and advancements in this area will greatly improve our understanding of the basic processes in materials science, chemistry and biology. The high-frequency (GHz), high voltage, phase-locked RF field in the deflector allows temporal resolution as fine as sub-100 fs. In this paper, we show the complete design of the UED system based on this concept, including initial beam measurements.

INTRODUCTION

Time resolved measurement of atomic motion is one of the frontiers of modern science, and advancements in this area will greatly improve our understanding of the basic processes in materials science, chemistry and biology. One technique under active development in this area is ultrafast electron diffraction (UED), which has several distinct advantages over X-ray diffraction for certain applications. UED utilizes a less expensive source; the electrons are less damaging to the specimen (at comparable energies); the scattering length of electrons better matches the penetration depth of the probe laser; UED is more suitable for gas phase samples; and it allows direct measurement of atomic positions, since the electron scatter mostly from nuclei. UED has already been used to study solid-state phase transitions [1, 2], gas phase reactions [3, 4], strongly coupled systems [5, 6] and surface dynamics [7]. In light of these results, researchers are demanding ever-shorter electron bunches in order to improve the resolution of their UED measurements. However producing intense sub-ps pulses of electrons in the desired energy range (30 - 100 kV) is challenging, due to space-charged induced longitudinal spreading. To date, efforts in this area have concentrated on either minimizing the bunch charge, which reduces the signal-to-noise ratio (SNR), or on using higher-energy electron beams, which reduces the diffraction angle and increases the size and the cost of the system. RadiaBeam, in collaboration with UCLA, is developing an innovative, inexpensive, low to moderate energy UED system which allows to reconstruct a single ultrafast event with a single pulse of moderate energy electrons (100 keV). By implementing a fast Radio-Frequency (RF) deflecting cavity immediately after the sample, the diffracted electron beam can be "streaked," transforming the temporal evolution of the diffraction pattern into a transverse image (see Figure 1). The high-frequency (GHz), high voltage, phase-locked RF field in the deflector allows temporal resolution as fine as 100-fs and below, while the probe electron beam can remain comparatively long (10's of ps), and contain a large number of electrons (~10^8).

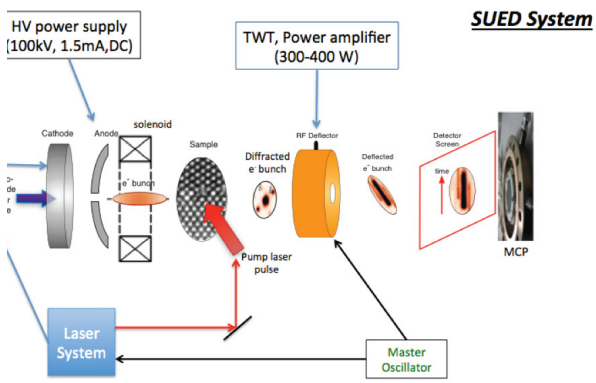


Figure 1: "streaked"- Ultra Electron Diffraction System.

ENGINEERING OF THE UED SYSTEM

The current setup of the UED system:

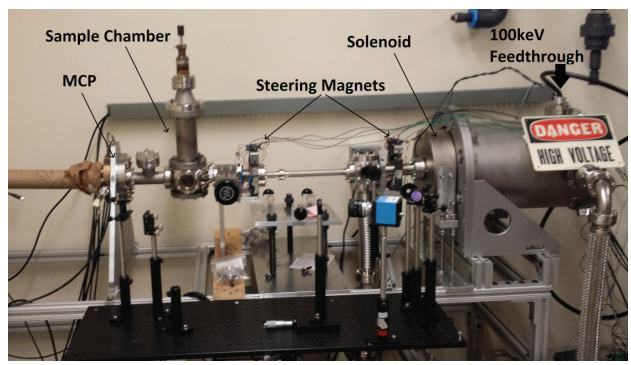


Figure 2: Current setup of the UED system.

The cathode location is set as z=0m. The solenoid is positioned at about z=6cm allowing a beam focusing point anywhere between the MCP (z=1m) and z=70cm. The sample is located at z=74cm and there is room for a second solenoid at z=40cm. Eventually the deflector can be put at z=50cm, just after the sample chamber to match previous resolution calculations.

PHOTOELECTRON GUN

The design of the 100 kV photocathode electron gun has been carried out by means of the 2D RF/Static simulation code SuperFish and the 2D gun design code

*Work supported by US DOE grant # DE-SC0006274
faillace@radiabeam.com

Copyright © 2013 CC-BY-3.0 and by the respective authors

EGUN2. As a starting point, we chose the 100 kV electron gun developed at Eindhoven University of Technology [8].

The main issue, when dealing with high DC field values, is represented by the transition between air and vacuum (vacuum feed-through) as well as the vacuum level inside the gun vessel. Both issues, addressed in the present section, can be the cause of overvoltage and high risk of breakdowns.

Special attention must be put on the feed-through design. A safe configuration would be to lay a high-insulating material around the inner conductor that will be electrically attached to the aluminum cathode holder. Also the interface geometry (such as an exponential cup filled with a dielectric) will be necessary.

The 2D profile used in simulations is given in Figure 3. The cathode is a flat disc with a 1 cm diameter. The holder, a hollow cylinder, allows for both back and front illumination and replaceability of the cathode piece itself. In the same figure, the axial electric field distribution is also shown. The field value at the cathode is about 9.8 MV/m. The maximum value is located at the round edge of the holder (11.8 MV/m). The above mentioned values of electric field are safe as far as breakdown is concerned, according to experimental results [9], showing that a high voltage of 250 kV is considered the safety threshold value inside a gap (cathode-anode) of about 1cm.

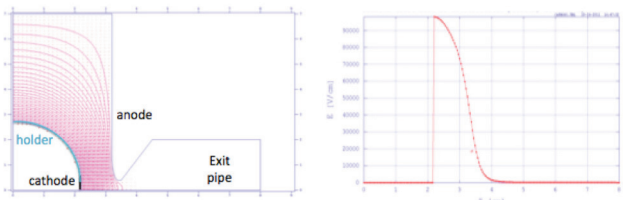


Figure 3: Left, 2D model from SuperFish (equipotential lines and field arrows are also shown); the cathode area is flat (1 cm dia.). Right, axial electric field (9.8 MV/m at the cathode).

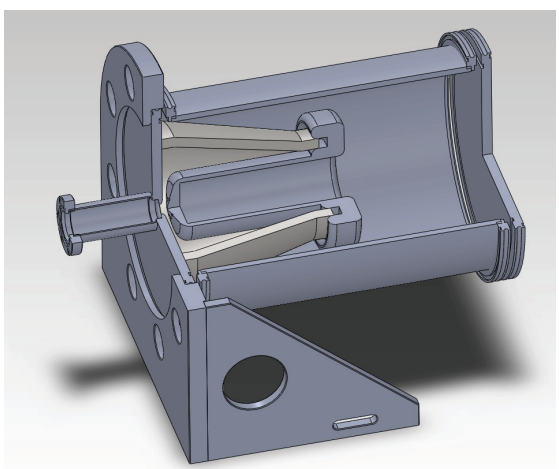


Figure 4: SolidWorks 3D model of the 100kV photo-gun.

A 3D mechanical model of the photo-gun, from SolidWorks, is shown in Figure 4. The replaceable cathode sample is made out of copper. The hollow cylindrical body that holds the cathode is made out of aluminum while the vacuum vessel, that the anode electrode is attached to, is stainless steel. In order to obtain very high vacuum level inside the gun (up to 10^{-14} mbar), a TMP pump will be used. The high-voltage feed-through and the TMP pump are attached to the vessel. The isolation between cathode and the anode is realized by using an insulating cone made out of Macor® (see: light grey conical piece in Figure 4).

PHOTOCATHODE DRIVE LASER

The laser used for this device is a Titanium-Sapphire 800nm 2GW (50fs pulse) source that goes through two BBO crystals (the first crystal is second harmonic generation while the second crystal is third harmonic generation) and gets converted to 266nm UV beam. This beam is sent to the photocathode using front illumination. A beam splitter is used to create a virtual cathode plane to enable measurement of the laser spot size with a CCD camera. A lens (f=50cm) is used to image onto the cathode an iris that can be used to adjust the spot size (see Figure 5).

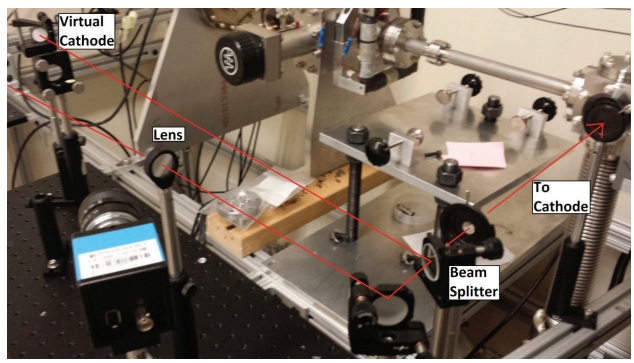


Figure 5: The optics just before the chamber including the imaging lens, beam splitter and virtual cathode.

BEAM CONTROL

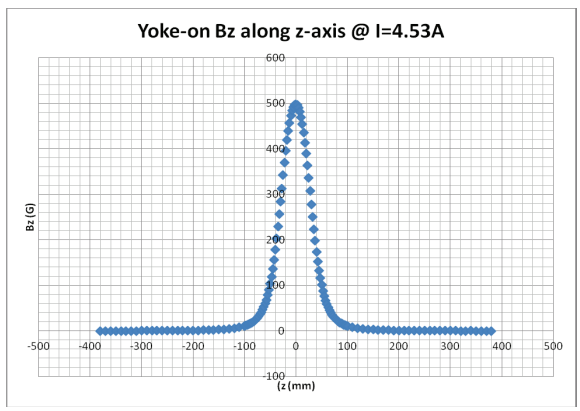


Figure 6: Plot of solenoid field at the center as a function of z.

Once the beam has been accelerated, it travels through the solenoid for focusing. See Figure 6 for the B vs Z of the solenoid. After, there are two 2-axis steering magnets for aiming and fine-tuning the position of the beam.

Copyright © 2013 CC-BY-3.0 and by the respective authors

DETECTOR SYSTEM

The micro channel plate (MCP) detector that will be used to image the beam is shown in Figure 7. The MCP basically works as an electron amplifier in which the incoming electrons generate secondary electrons. In this case, the incoming electrons enter channels in which they are accelerated by an electric field and generate the secondary electrons.

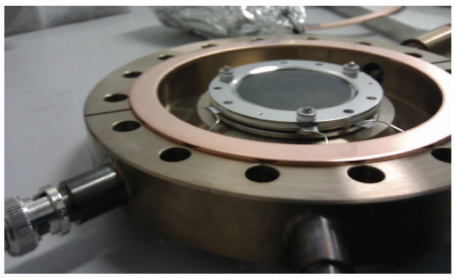


Figure 7: Multi Channel Plate Detector

The MCP is equipped with a phosphor screen that is imaged 1:1 onto the CCD camera, allowing a spatial resolution of 50 μm. The relation between the bunch duration and the length of the streak on the phosphor screen is obtained by integrating the Lorentz force that is acting on the electron bunch during its travel along the axis through the deflecting cavity. The MCP is located at the focusing point of the solenoid, in order to obtain a sharper diffraction pattern.

MEASUREMENTS

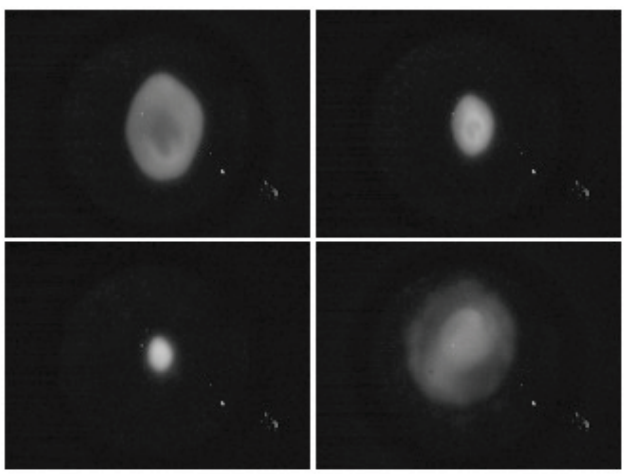


Figure 8: Beam images at different solenoid currents in order from top left to bottom right: 2.373A, 2.486A, 2.566A, 2.738A. The recurring white spots are dead pixels in the CCD camera.

In order to commission the system a solenoid scan was performed to compare the results with simulation and obtain first estimates on the beam parameters. We show in Fig. 8 a few representative images from the solenoid scan (Fig. 9). The minimum spot size at the MCP plane is obtained for a current of 2.566A. For these measurements the gun voltage was set at 40kV.

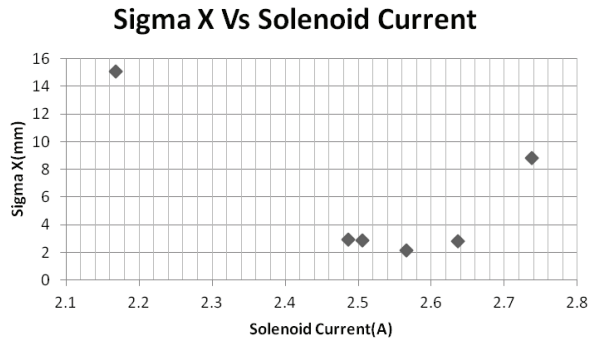


Figure 9: Measured Sigma X on the MCP as a function of solenoid current.

CONCLUSIONS

The UED technique has already been used to produce groundbreaking results in a number of areas of materials science and chemistry. It has been described as providing the capability to "make a movie" of events occurring on the atomic scale. Clearly, such a technology has the potential to enable new discoveries. The SUED system we are developing, with improved resolution and SNR, would enable even further breakthroughs in the understanding of ultrafast phenomena, stimulating new innovations in material science, chemistry and biology.

REFERENCES

[1] G. Mourou and S. Williamson, Picosecond electron diffraction, Applied Physics Letters 41 (1982) 44.

[2] B.J. Siwick et al., An atomic-level view of melting using femtosecond electron diffraction, Science 302 (5649), (2003) 1382.

[3] R.C. Dudek and P.M. Weber, Ultrafast diffraction imaging of the electrocyclic ring-opening reaction of 1, 3-cyclohexadiene, J. Phys. Chem. A 105(17), (2001) 4167.

[4] H. Ihee et al., Direct imaging of transient molecular structures with ultrafast diffraction, Science 291(5503), (2001) 458.

[5] N. Gedik, D. S. Yahg, G. Logvenov, I. Bozovic, and A. H. Zewail, Science 316 (2007) 425.

[6] F. Carbone, P. Baum, P. Rudolf and A. H. Zewail, Phys. Rev. Lett. 100 (2008) 035501.

[7] C.Y. Ruan et al., Ultrafast electron crystallography of interfacial water, Science 304(5667), (2004) 80.

[8] T. van Oudheusden, Electron source for sub-relativistic single-shot femtosecond diffraction. Ph.D. Thesis Dissertation (2010), Eindhoven University of Technology.

[9] L. L. Alston, High Voltage Technology, Oxford University Press, 1968.

Copyright © 2013 CC-BY-3.0 and by the respective authors

MODELING THE DEVELOPMENT AND MITIGATION OF CHARGE ACCUMULATION FOR PHOTO EMISSION ELECTRON GUNS*

C. Nieter†, D.A. Dimitrov, Y. Choi, Tech-X Corporation, Boulder, CO 80234, USA

Abstract

One potential problem with the operation of photo emission electron guns is the potential for charge to accumulate on the emission surface depending on how the biasing voltage is applied to the gun. If the voltage is applied away from the emission surface there is the potential for charge to accumulate on the emission surface since not all electrons will necessarily be emitted. This charge accumulation may affect the gun operation by reducing the accelerating field in the gun. We report on simulations that demonstrate this potential issue as well as simulations that test a potential solution where a secondary voltage is applied periodically to clear the accumulated charge.

INTRODUCTION

New design for photoinjectors has been proposed that will address the need for high current, high brightness beams for future particle accelerators [1, 2]. The design takes a primary electron beam from a conventional photocathode which is accelerated to a diamond window. The diamond window consists of a layer of diamond followed by a high-vacuum gap with an applied voltage across the window. The primary electrons scatter in the diamond generating cascade of secondary electrons. The electrons drift across the diamond where most of them are emitted into the vacuum gap and then into the accelerating cavity of the gun.

Since not all of the electrons are emitted from the diamond surface charge can build up at the diamond/vacuum interface. If enough charge builds up the field in the diamond can be shorted out preventing further electrons from drifting across the diamond. Experimental studies have shown for a primary electron beam whose pulse length is long enough there is a drop in the emission gain for the cathode [3]. It is believed that this drop off is due to electrons accumulating at the surface of the diamond reducing the electric field in the diamond.

We ran a series of simulations with the Vorpal multiphysics code [4] to study the process of charge accumulation in the diamond window from first principles. These simulations can be challenging due to the relative long time scales of the primary electron pulse length relative to the electron scattering rates in diamond. However, we were able to demonstrate the build up of charge at the surface and look at possible ways to clear the charge with a second voltage applied after the primary electron pulse has passed.

* Work supported by by DOE SBIR grant DE-SC0007577
† nieter@txcorp.com

SIMULATIONS

We use the parameters given for the diamond window from Ref. [3] as a starting point for our simulations. To be able to complete the simulations in a reasonable amount of time the physical size was scaled down by a factor of 100 giving us a diamond thickness of 3 microns and the thickness of the full window (diamond plus vacuum gap) of 5.5 microns. Similarly the beam radius was reduced by a similar amount to 4 microns. We reduce the applied voltage by the same factor of 100 to keep the same electric field magnitude giving us a voltage of 30 volts across the diamond window.

We performed 3D simulations of the diamond window. The simulation domain was 5.5 microns in the direction of beam propagation and 10 microns in the transverse direction. We used Vorpal's electrostatic solver to solve for the electric field generated by the various applied voltages as well as the fields generated by the electrons themselves. The electrons are represented using the particle-in-cell (PIC) method with the addition of recently developed scattering models for electron propagation in diamond [5].

Since the time scales needed to cover the pulse width from from Ref. [3] are very long compared to the time scale needed to resolve the highest scattering rate for diamond we increased the beam current so the charge will accumulate faster in the simulations. We also apply a fully reflecting boundary condition for the particles at the diamond/vacuum interface effectively setting the emission probably at the surface to be zero. We run the simulation for the twice the pulse width so we can study the accumulation of the charge while the pulse is on and the dissipation of the charge after the pulse has passed.

Charge Accumulation Simulations

In the first simulation we maintain the voltage across the diamond window while the beam pulse is on. Once the beam pulse has passed we shut off the voltage across the diamond window. Figure 1 shows a scatter plot of the macroparticle positions projected into a plane with one direction along the direction of beam propagation in the simulation shortly before the voltage is shut off. This plot shows the charge accumulating at the diamond/vacuum interface.

In Figure 2 the electric field perpendicular to the diamond surface at the diamond/vacuum interface is plotted versus time. The magnitude of the electric field drops as more charge is introduced to the diamond and begins to accumulate at the diamond/vacuum interface. Eventually the field drops to zero as enough charge has accumulated to short out the field. Once the pulse has passed and the voltage across the diamond window is shut off the electric

Copyright © 2013 CC-BY-3.0 and by the respective authors

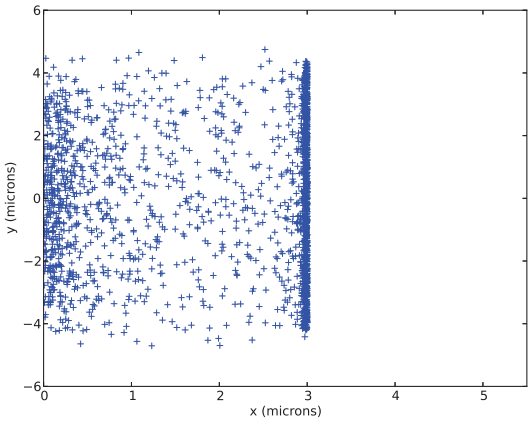


Figure 1: Macro-particles just before voltage across diamond window is shut off.

field changes sign as it is now the space charge of the electrons that dominates the electric field. The electrons that have now accumulated on the diamond surface are pushed back off by space charge forces. As the electrons leave the surface the magnitude of the electric field drops again but it begins to level off before reaching zero. This implies that a steady state may be reached or the rate of decrease could be slow enough that the charge accumulated may not be cleared before the next beam pulse hits the window negatively impacting the operation of the amplifier.

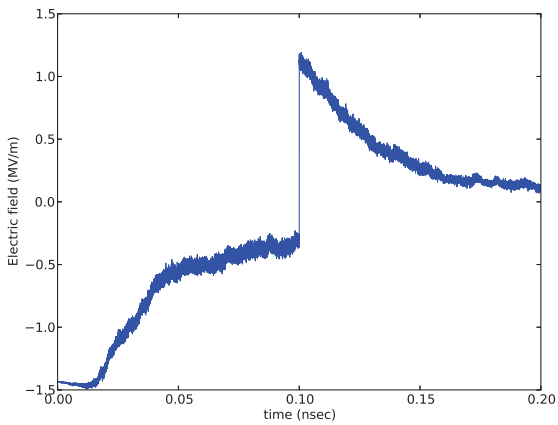


Figure 2: Electric field at diamond surface versus time.

Charge Clearing Simulations

A second simulation was run where after the beam pulsed as passed and the voltage across the diamond window is shut off a new voltage of the same magnitude is now applied parallel to the diamond surface. This produces an electric field parallel to the diamond surface that speeds up the clearing of the accumulated charge. This causes the charge transport to move parallel with the diamond surface and extract the electrons from the transverse sides of simulation. Figure 3 shows the number of macro-particles versus time for the original simulation (in green) and the new charge clearing simulation (in blue). The initial charge accumulation is the same for both simulations but the charge dissipates faster with the clearing voltage applied.

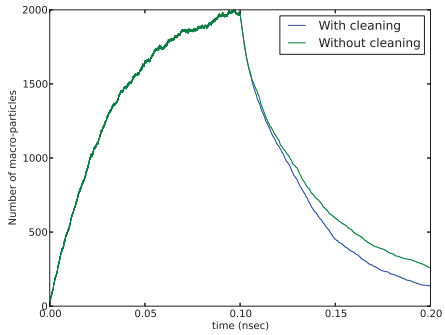


Figure 3: Number of macro-particles versus time for simulations with and without clearing voltage.

CONCLUSIONS

We have qualitatively shown that simulations can be used to study the process of charge accumulation in diamond amplifier designs proposed as part of new designs for photoinjectors. Both the build up and dissipation of the charge can be modeled and potential solutions to the charge accumulation can be studied.

Future plans include the addition of models for surface emission at the diamond/vacuum interface. This will better model both the process of charge accumulation and the process of charge dissipation after the voltage has been shut off since charges can now escape though the diamond/vacuum interface. Development work will be done to provide further flexibility in the particle boundaries so the clearing voltages can be applied directly to the diamond/vacuum interface.

Efforts will also be pursued to bring the simulation parameters closer to those found in a realistic device. These will include making use of HPC resources to allow for larger simulation sizes. Initial tests have shown that the diamond scattering may not require fully resolving the scattering rates since multiple scatter events can happen in a time step.

ACKNOWLEDGMENT

The authors are grateful to Drs. Ilan Ben-Zvi, Triveni Rao, Erdong Wang, and John Smedley for discussions to better understand their diamond emission experiments

REFERENCES

[1] I. Ben-Zvi, X. Chang, P. D. Johnson, J. Kewisch, and T. Rao, C-AD Accelerator Physics Report C-A/AP/149, Brookhaven National Lab (2004).

Copyright © 2013 CC-BY-3.0 and by the respective authors

[2] T. Rao, Ilan Ben-Zvi, A. Burrill, X. Chang, S. Hulbert, P. D. Johnson, and J. Kewisch. Diamond amplifier for photocathodes. In V. Yakimenko, editor, Advanced Accelerator Concepts: Eleventh Workshop. American Physical Society, (2004).

[3] Erdong Wang, Ilan Ben-Zvi, Triveni Rao, D. A. Dimitrov, Xiangyun Chang, Qiong Wu, and Tianmu Xin, Secondary-electron emission from hydrogen-terminated diamond: Experiments and model, Phys. Rev. ST AB 4 (2011) 111301.

[4] C. Nieter and J. R. Cary, VORPAL: a versatile plasma simulation code, J. Comput. Phys. 196 (2004) 448.

[5] D. A. Dimitrov, R. Busby, J. R. Cary, I. Ben-Zvi, T. Rao, J. Smedley, X. Chang, J. W. Keister, Q. Wu, and E. Muller, Multiscale three-dimensional simulations of charge gain and transport in diamond, J. Applied Phys. 108 (2010) 073712.

Copyright © 2013 CC-BY-3.0 and by the respective authors

APS SUPERCONDUCTING UNDULATOR BEAM COMMISSIONING RESULTS*

Katherine C. Harkay#, Laura Boon, Michael Borland, Louis Emery, Glenn Decker, Roger Dejus, Jeffrey Dooling, Charles Doose, Joseph Gagliano, Quentin Hasse, Yury Ivanyushenkov, Matthew Kasa, Jonathan Lang, Douglas Robinson, Vadim Sajaev, Nicholas Sereno, Karen Schroeder, Yuko Shiroyanagi, Denise Skiadopoulos, Martin Smith, Emil Trakhtenberg, Aimin Xiao, Alexander Zholents, Efim Gluskin, ANL, Argonne, IL 60439, USA

Abstract

The first test superconducting undulator (SCU0) was successfully installed and commissioned at the Advanced Photon Source (APS) and is delivering 80- to 100-keV photons for user science. All the requirements before operating the SCU0 in the storage ring were satisfied during a short but detailed beam commissioning. The cryogenic system performed very well in the presence of the beam. The total beam-induced heat load on the SCU0 agreed well with the predictions, and the SCU0 is protected from excessive heat loads through a combination of orbit control and SCU0 alignment. When powered, the field integral measured with the beam agreed well with the magnet measurements. An induced quench caused very little beam motion and did not cause loss of the beam. The device was found to quench during unintentional beam dumps, but quench recovery is transparent to storage ring operation. There were no beam chamber vacuum pressure issues and no negative effect observed on the beam. Finally, the SCU0 was operated well beyond its design requirements, and no significant issues were identified. The beam commissioning results are described in this paper.

INTRODUCTION

Superconducting technology was used to build a fully functioning short-period test undulator (SCU0) at APS [1, 2]. Superconducting undulators allow a higher peak magnetic field compared to conventional devices, which can greatly benefit the light source community [3]. The SCU0 was designed and developed at APS in collaboration with Budker Institute of Nuclear Physics (BINP), Fermi National Accelerator Laboratory (FNAL), and U. Wisconsin, Madison. The SCU0 has a period length of 16 mm, magnetic gap of 9.5 mm, magnetic length of 0.34 m, and operates with photon energy in the first harmonic of 20-25 keV. The design operating current is 500 A, giving a design field of 0.64 T. The SCU0 incorporates several unique features, including an out-of-vacuum design, a beam chamber that is thermally isolated from the magnet cores, and a cryocooler cooling system. The SCU0, with a 2-m-long cryostat, was installed in the APS storage ring in Dec. 2012 (see Fig. 1).

SCU0 commissioning was completed over approx. 110 hr during an extended machine start-up period, and the device was released for user operation on Jan. 29, 2013.

* Work supported by U. S. Department of Energy, Office of Science, under Contract No. DE-AC02-06CH11357.
#harkay@aps.anl.gov



Figure 1: SCU0 installed in the APS storage ring.

COMMISSIONING PLAN

Prior to installing the SCU0, a test chamber with virtually the same length, aperture, and transitions as the SCU0 was installed in the storage ring. Beam-induced heat loads on the test chamber and transitions were tested, and key design improvements were implemented for the SCU0; in particular, a standard-aperture bellows, rf liner, and gate valve replaced a 7.2-mm-aperture assembly on the chamber transition upstream of the SCU0.

A detailed beam commissioning plan was carried out, and all the requirements were satisfied: (a) unpowered SCU0 is transparent to normal user operation; i.e., does not measurably increase storage ring impedance, nor decrease injection efficiency or lifetime; (b) powered SCU0 only perturbs the beam within the specifications; and (c) SCU0 is sufficiently protected from beam-induced heat loads. There were several commissioning goals, including assessment of thermal and vacuum monitoring, alignment procedures, cryogenic performance, beam orbit stability, quench response, field correction, x-ray performance, and operation procedures.

SCU0 EFFECT ON THE BEAM

An unpowered SCU0 is transparent to the beam if its contribution to the storage ring impedance and/or local vacuum pressure neither decreases the beam lifetime or injection efficiency nor lowers the beam instability threshold. As expected from the successful test chamber results, the SCU0 chamber was also transparent: the single bunch limit of 16 mA was preserved, and 100 mA could be stored in all three user bunch patterns. The measured betatron tune shift with current, which is a measure of the transverse impedance, did not change within the expected experimental error. The beam lifetime and injection efficiency were both in the normal range after the standard startup procedures were carried out.

Copyright © 2013 CC-BY-3.0 and by the respective authors

Vacuum System

There were no beam chamber vacuum pressure issues and no negative effect observed on the beam. The beam chamber was cleaned using standard UHV techniques, but was necessarily exposed to air during the magnetic measurements. After the components were installed in the storage ring, the system was roughed down to the 2×10^{-7} Torr range on a cold cathode gauge (CCG) located in the downstream transition. A 24-hr, 130ºC bakeout was performed on the transitions upstream and downstream of the SCU0. The CCG pressure after the bakeout and before the SCU0 was activated was 3 nTorr. After cooldown and prior to injecting beam, the vacuum pressure was measured as 0.4 nTorr. The first 100-mA beam caused pressure transients in the 10-nTorr range, but after about four days of cold beam operation (10 Amp-hr), the pressure stabilized at ~3 nTorr. After 200 Amp-hr, the pressure was ~0.8 nTorr.

Mechanical Vibration

The cryocooler vibration was measured at three different locations: on the SCU0 support girder, on the SCU0 vacuum vessel near the beam level, and on the beam chamber about 0.4 m upstream of the SCU0. The cryocooler vibration power spectrum has a resonant frequency of 8.4 Hz. On the chamber, the integrated vibrational spectra power density (in the frequency range of 2-100 Hz) increased from 0.38 μm rms with the cryocoolers off to 0.68 μm rms with the cryocoolers on, less than a factor of two increase. The cryocooler vibration was not observed to adversely affect the beam motion.

Powered SCU0

The requirements on the SCU0 field-error tolerance are the same as that for the other planar IDs installed in APS [4]. The field-integral error tolerance was specified using simulations that include full-time orbit correction and real-time orbit feedback. Both an absolute limit as well as a rate-of-change requirement [5] were specified. Magnet measurements show that the SCU0 meets the specifications for all design parameters except the skew quadrupole component; the specification was 50 G and the measured value was 120 G at 500 A [6]. The skew component is due to the geometry of the coil winding opposite the pole face (a new coil winding scheme will be used for the next device.) The skew quadrupole error produced a 10% change in beam coupling over a 700-A range, but this effect was easily corrected by implementing feed-forward using the adjacent skew quadupoles. The first field integral was determined using the beam by measuring the corrector effort while scanning the SCU0 current. The agreement between the beam and magnet measurements is within 10%, as shown in Fig. 2.

Quenches may produce a field disturbance on a time scale that is too fast for the real-time orbit feedback to correct. If the perturbation is very large, the resulting beam trajectory displacement could exceed the beam position limit detector (BPLD) limits and cause a beam dump. The specification was given as a tolerance on the quantity $\sqrt{I_1^2 + (I_2^2/\beta_U^2)}$, where I_1 and I_2 are the first- and second-field integrals, respectively, and β_U is the average beta function at the undulator ends. The magnet measurements show that the SCU0 meets this specification during a heater-induced quench. Beam tests were performed with fast and slow orbit feedbacks in open loop to better observe the effect of a quench. An induced quench caused very little beam motion, ~60 μm, and did not cause loss of the beam. In Fig. 3, slow orbit recovery occurs over about 0.5 sec after the quench.

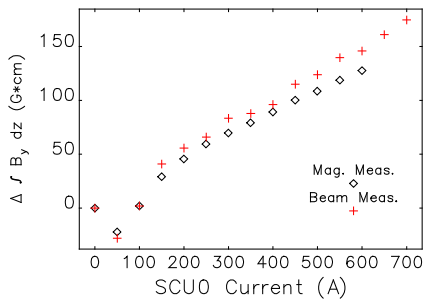


Figure 2: Field integral variation measured with beam.

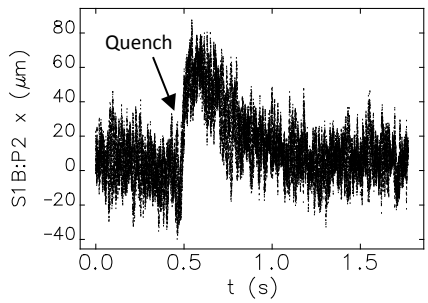


Figure 3: Effect of induced quench on the beam.

BEAM EFFECT ON THE SCU0

The total beam-induced heat load on the SCU0 agrees well with predictions (see Table 1), and the SCU0 is protected from excessive fault-induced heat loads through beam orbit control and SCU0 alignment. The cryogenic system performed very well in the presence of the beam, where magnet temperatures were maintained near 4 K while the beam chamber center temperatures were ≤13 K.

Beam-based Alignment

Precise alignment of the beam vacuum chamber with respect to both the electron beam orbit as well as synchrotron radiation generated in the upstream dipole magnet is extremely important. The beam vacuum chamber is instrumented with nine thermal sensors along its length [7]. Using the sensors and steering the beam, the chamber alignment was determined with 100-micron precision (see Fig. 4) [7]. This precision is more than 10 times better than what is achieved in a standard aperture scan. Other advantages of the thermal sensor beam-based alignment method include isolating the SCU0 alignment from other vacuum components in the orbit bump and providing good longitudinal spatial resolution.

Copyright © 2013 CC-BY-3.0 and by the respective authors

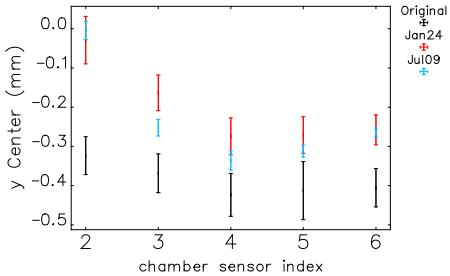


Figure 4: SCU0 chamber vertical alignment history (partial in-tunnel realignment shown in red).

Beam-induced Heat Load

Heat load predictions for standard 100-mA user operation were benchmarked using thermal sensors that measure temperatures at various locations in the SCU0 cryostat and along the electron beam chamber. Thermal analysis using the predicted electron beam heat loads, using three independent methods, agrees well with the observed measurements. Results are summarized in Table 1 for all three standard user bunch modes. For simplicity, the calculated values include only the dominant, image-current heating. In the chamber heater calibration, the predicted heat loads from Table 1 were converted to chamber temperatures by interpolating the heater data [8]. Using ANSYS, the heat load was modeled as a Gaussian image-current distribution. Agreement is excellent for both the central, Al part of the chamber as well as the SS warm-to-cold transitions [9]. Finally, the total 20-K heat load was measured using the bottom cryocooler 2nd-stage temperatures, fit to a model using vendor-supplied load map data [8]. There was no anomalous heat source; the agreement is remarkably within 1 K or 2 W.

Table 1: Predicted vs. Measured Center Chamber Temperatures and 20-K Heat Loads at 100 mA

No. of bunches	Chamb heater calib. (K)	ANSYS model (K)	Msrd. temp. (K)	Calc. heat load (W)	Msrd. heat load (W)
24	13.6	13.4	12.8	16.0	14.3
324	7.9	8.2	8.3	2.0	3.4
1+56	11.8	11.5	11.9	11.1	11.5

The device was found to quench due to beam losses during unintentional beam dumps. The SCU0 is powered off prior to intentional beam dumps. Over an 8-month operating period, only two quenches occurred with user-stored beam. These quenches did not cause any beam loss, and the cause is under investigation. Quench recovery is transparent to storage ring operation, and the impact of all quenches on SCU0 operation has been minimal due to rapid recovery.

PERFORMANCE

The SCU0 was operated at 650-700 A over 50% of the time, well beyond its 500-A design requirement. The SCU0 is routinely operated with 100-mA stored beam continuously near 650 A without a trip. The SCU0 was also operated at 150 mA, higher beam current than it was designed for, with no significant issues. Finally, no loss of He was observed over an 8-month operating period.

The x-ray source properties of the SCU0 were characterized by measuring the photon flux passing through a bent-Laue monochromator and comparing the SCU0 photon flux with that from an in-line 3.3-cm-period length permanent magnet hybrid undulator (U33). At 85 keV, the 0.34-m-long SCU0 produced ~45% higher photon flux than the 2.3-m-long U33. Figure 5 shows the simulated and measured photon flux at 85 keV for SCU0, and the measured photon flux for U33 (inset).

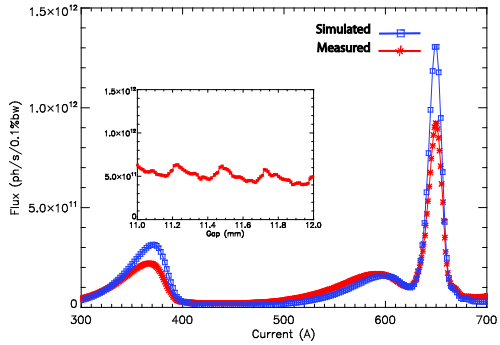


Figure 5: Photon flux comparisons at 85 keV. Main: Simulated and measured SCU0 photon flux. Inset: Measured photon flux of in-line U33.

SUMMARY

An almost decade-long R&D program on the development of superconducting undulators at the APS was successfully completed in 2012 with the installation into the APS storage ring of the first test undulator, SCU0. Beam commissioning was highly successful. The device has been in user operation since January 2013, delivering enhanced photon flux at energies above 50 keV.

ACKNOWLEDGMENT

We wish to thank the support of the APS management in long-term R&D and development of superconducting undulators. We also thank the APS team for their valuable contributions to the success of this project.

REFERENCES

[1] Y. Ivanyushenkov et al., IEEE Trans. on Appl. Superconductivity 21 (2011) 1717; Y. Ivanyushenkov et al., Proc. 2012 IPAC, MOPPP078, p. 744 (2012); journals.iucr.org/s/issues/2013/03/00/s130300aps.pdf
[2] Y. Ivanyushenkov, FRYBB1, NA-PAC'13.
[3] J. Bahrdt, Y. Ivanyushenkov, J. Phys. 425 (2013) 032001.
[4] Y.-C. Chae, G. Decker, Proc. of PAC1995, RAR24, p. 3409 (1996); http://www.JACoW.org
[5] APS Upgrade Preliminary Design Report (2012).
[6] C. Doose, M. Kasa, THPBA06, NA-PAC'13.
[7] K. Harkay et al., WEPSM07, NA-PAC'13.
[8] K. Harkay et al., WEPSM06, NA-PAC'13.
[9] Y. Shiroyanagi et al., THPAC07, NA-PAC'13.

Copyright © 2013 CC-BY-3.0 and by the respective authors

LOW EMITTANCE IN THE CORNELL ERL INJECTOR PROTOTYPE*

C. Gulliford, A. C. Bartnik, I. V. Bazarov, B. M. Dunham, for the Cornell ERL Team
CLASSE, Cornell University, Ithaca NY 14853 USA

Abstract

We present a detailed study of the six-dimensional phase space of the electron beam produced by the Cornell Energy Recovery Linac Photoinjector, a high-brightness, high repetition rate (1.3 GHz) DC photoemission source designed to drive a hard x-ray energy recovery linac (ERL). A complete simulation model of the injector has been constructed, verified by measurement, and optimized. Both the horizontal and vertical 2D transverse phase spaces, as well as the time-resolved (sliced) horizontal phase space, were simulated and directly measured at the end of the injector for 19 pC and 77 pC bunches at roughly 8 MeV. The resulting 90% normalized transverse emittances for 19 (77) pC/bunch were 0.23±0.02 (0.51±0.04) μm in the horizontal plane, and 0.14±0.01 (0.29±0.02) μm in the vertical plane, respectively. These emittances were measured with a corresponding bunch length of 2.1±0.1 (3.0±0.2) ps, respectively. In each case, the rms momentum spread was determined to be on the order of 10^{-3}. Excellent overall agreement between measurement and simulation has been demonstrated.

INTRODUCTION

Cornell University has recently designed, built, and commissioned a high repetition rate DC gun based photoinjector. One major goal for this project was the demonstration of low emittance at the end of the injector merger section. The results in this work demonstrate that it is possible to produce and transport beams from a DC source which have emittances at the point of injection approaching the diffraction limit for hard x-rays, and which have a bunch length and an energy spread within the parameter space required by the specifications of a full hard x-ray ERL. Table 1 shows these parameters for the Cornell Injector.

Table 1: List of Injector Design Specifications and Target Parameters

Parameter	Specification
Beam energy	5-15 MeV
Normalized emittance	$\epsilon_n \leq 0.3$ μm
RMS bunch length	$\sigma_t \leq 3$ ps
Bunch Charge	77 (19) pC
Average Current	100 (25) mA

One fundamental limit to achieving low emittance (high brightness) in a photoinjector occurs when the amount of charge extracted from the cathode nears the virtual cathode instability limit. A rough calculation shows that the lowest achievable emittance in this limit is proportional to the square root of the bunch charge q [1]:

$$\epsilon_n \propto \sqrt{q \cdot \frac{\mathrm{MTE}}{E_{\mathrm{cath}}}} \tag{1}$$

Here MTE and E_{cath} are the mean transverse energy of the cathode and the accelerating field at the cathode, respectively. Detailed simulations of well optimized DC gun photoinjectors support this square root dependence on the bunch charge and the cathode's MTE [2, 3]. In this paper, we show that the final measured emittance also scales in accordance with Eq. (1).

EXPERIMENTAL SET-UP

The injector features a high voltage DC gun operated at 350 kV, followed by emittance compensation solenoids and a buncher cavity. The beam is accelerated to 5-15 MeV using five superconducting srf cavities. The beamline section most relevant to this work is the B1 merger shown in detail in Fig. 1. The injector merger section is comprised of a conventional three-dipole achromat, a design chosen for its simplicity, and due to the limited space available for the injector experiment. The emittance measurement system (EMS) used for projected phase space measurements is the same two-slit system used in previous work [4]. For projected phase space measurements, the beamlet passed through the slits is collected using the Faraday cup at the end of the merger section. For time-resolved horizontal phase space measurements, the beamlet is passed through a horizontal deflecting cavity [5] in order to resolve the time axis of the beam on the viewscreen at the end of the merger [6]. The cathode used for this study was a GaAs wafer with a 4% quantum efficiency, and a MTE of 90 meV. The laser system used is a 50 MHz system, whose individual pulses have comparable pulse energy and duration to the our 1.3 GHz laser [7]. The final laser pulse train is chopped using a Pockells cell, and shaped using our temporal shaping system [8].

To arrive at the final optics used for these experiments, optimizations of a complete General Particle Tracer [9] model of the injector were carried out using a multi-objective genetic algorithm [2, 3]. For all optimizations, the gun voltage was fixed at 350 kV, and the beam energy was constrained to be $\leq$ 8 MeV to reduce neutron production from the tungsten slits in the EMS. The simulated temporal laser distribution was fixed to be roughly a flat-top

* Supported by NSF award DMR-0807731

Copyright © 2013 CC-BY-3.0 and by the respective authors

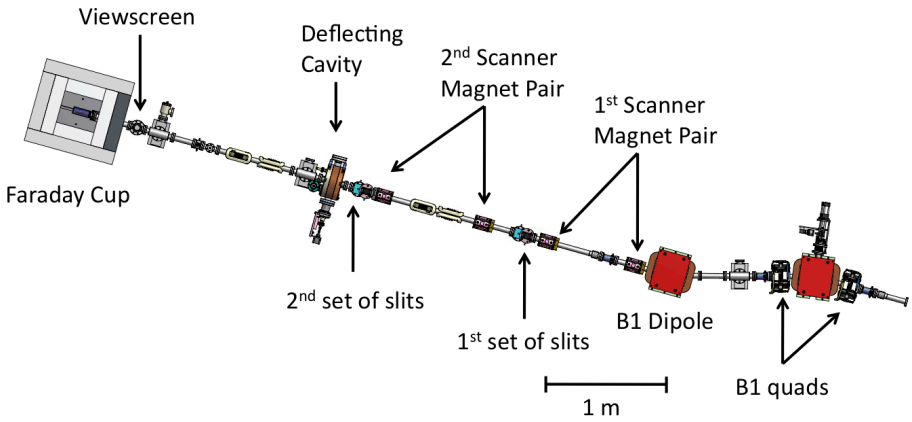


Figure 1: Top view of the B1 injector merger section showing the emittance measurement system.

with 8 ps rms length. Two settings, for 19 pC and 77 pC per bunch respectively, were derived from one optimization solution for 50 pC bunch charge, as this particular optics setting kept the beam sizes reasonably small through the entire injector. The final settings were loaded into the injector and the measured projected emittance was minimized by scanning both solenoid currents and adjusting the intensity cut off value in the measured transverse laser profile.

MEASUREMENTS

Data sets for 19 pC per bunch and 77 pC per bunch, corresponding to 25 mA and 100 mA average current when operating with the full 1.3 GHz repetition rate, were taken. Each data set consists of a measurement of the projected horizontal and vertical phase spaces, the time-resolved horizontal phase space, and the energy spread distribution. All data was taken at the end of the merger section except the energy spread data, which was measured near the entrance to the merger. From the projected phase spaces, the horizontal and vertical emittances as a function of beam fraction were computed. Similarly, from the time-resolved phase space data, the slice emittance was computed as a function of beam fraction, as well as the current profile along the bunch.

Tables 2 and 3 give the measured and simulated projected horizontal and vertical emittances for 19 (77) pC per bunch, respectively. The measured 19 (77) pC/bunch horizontal and vertical projected 100% emittances agreed with the GPT model to within 6 (5) % and 25 (8) %, respectively. Similarly, the measured horizontal and vertical 90% emittances agreed with GPT to within 21 (16) % and 27 (16) %, respectively. We point out that the measured horizontal and vertical 100%, 90%, and core emittances obey the expected scaling law $\epsilon_n \propto \sqrt{q}$. Also of note is the fact the horizontal core emittance for 77 pC meets the injector design specification for an ERL. In the vertical plane, both the 90% and core emittance meet this specification.

In order to satisfy the injector design requirements, it was important to verify that the emittance values were measured with an acceptable bunch length ($\sigma_t \leq 3$ ps). The rms bunch length was computed from the instantaneous current of each bunch measured with the time-resolved merger EMS. The rms bunch lengths for the 19 (77) pC per bunch settings were measured to be 2.1 ± 0.1 (3.0 ± 0.2) ps, respectively, while GPT gave bunch lengths of 2.2 (3.1) ps, respectively. The agreement between measurement and GPT was within 5% in both cases.

Table 4: Simulated and Measured RMS Energy Spread as a Function of Bunch Charge

Data Type	GPT Simulation	Measurement
19 pC/bunch, A4	0.16%	0.14 ± 0.01%
19 pC/bunch, B1	0.12%	N/A
77 pC/bunch, A4	0.27%	0.26 ± 0.01%
77 pC/bunch, B1	0.21%	N/A

The last quantity measured was the rms energy spread. To do so, the beam was sent through the A4 straight section, followed by a single dipole and viewscreen in the C2 section. Table 4 shows the simulated and measured rms energy spread in the straight section, as well as simulated values in the B1 merger. While the energy spread was not directly in the merger section, the agreement found between measurement and simulation for emittance and bunch length lead us to conclude that the values measured in the straight section at least provide an upper bound on the energy spread in the merger, following the same trend found in the simulation data.

CONCLUSION AND DISCUSSION

The projected and time-resolved phase spaces at the end of the Cornell ERL injector merger have been measured and simulated using the space charge code GPT for 19 pC and 77 pC bunch charges. In addition, the energy spread was measured in the straight section of the machine. Overall, we found excellent agreement between measurement and simulation. For both bunch charges, the agreement be-

Copyright © 2013 CC-BY-3.0 and by the respective authors

Table 2: Measured and Simulated Projected Horizontal Emittances

19 pC Measurement Type	$\epsilon_{n,x}(100\%)$	$\epsilon_{n,x}(90\%)$	$\epsilon_{n,x}(\text{core})$	f_{core}	$\epsilon_{n,x}(\text{core})/f_{\text{core}}$
Projected EMS	$0.33 \pm 0.02\ \mu$m	$0.23 \pm 0.02\ \mu$m	$0.14 \pm 0.01\ \mu$m	67%	$0.21 \pm 0.01\ \mu$m
Time-resolved EMS	$0.28 \pm 0.02\ \mu$m	$0.21 \pm 0.01\ \mu$m	$0.14 \pm 0.01\ \mu$m	72%	$0.19 \pm 0.01\ \mu$m
GPT Simulation	$0.31\ \mu$m	$0.19\ \mu$m	$0.07\pm\ \mu$m	59%	$0.12\ \mu$m
77 pC Measurement Type	$\epsilon_{n,x}(100\%)$	$\epsilon_{n,x}(90\%)$	$\epsilon_{n,x}(\text{core})$	f_{core}	$\epsilon_{n,x}(\text{core})/f_{\text{core}}$
Projected EMS	$0.69 \pm 0.05\ \mu$m	$0.51 \pm 0.04\ \mu$m	$0.28 \pm 0.2\ \mu$m	64%	$0.44 \pm 0.03\ \mu$m
Time-resolved EMS	$0.66 \pm 0.05\ \mu$m	$0.48 \pm 0.04\ \mu$m	$0.29 \pm 0.2\ \mu$m	67%	$0.43 \pm 0.03\ \mu$m
GPT Simulation	$0.72\ \mu$m	$0.44\ \mu$m	$0.17\ \mu$m	51%	$0.33\ \mu$m

Table 3: Measured and Simulated Projected Vertical Emittances

19 pC Measurement Type	$\epsilon_{n,y}(100\%)$	$\epsilon_{n,y}(90\%)$	$\epsilon_{n,y}(\text{core})$	f_{core}	$\epsilon_{n,y}(\text{core})/f_{\text{core}}$
Projected EMS	$0.20 \pm 0.01\ \mu$m	$0.14 \pm 0.01\ \mu$m	$0.09 \pm 0.01\ \mu$m	70%	$0.13 \pm 0.01\ \mu$m
GPT Simulation	$0.16\ \mu$m	$0.11\ \mu$m	$0.06\ \mu$m	64%	$0.09\ \mu$m
77 pC Measurement Type	$\epsilon_{n,y}(100\%)$	$\epsilon_{n,y}(90\%)$	$\epsilon_{n,y}(\text{core})$	f_{core}	$\epsilon_{n,y}(\text{core})/f_{\text{core}}$
Projected EMS	$0.40 \pm 0.03\ \mu$m	$0.29 \pm 0.02\ \mu$m	$0.19 \pm 0.01\ \mu$m	70%	$0.27 \pm 0.01\ \mu$m
GPT Simulation	$0.37\ \mu$m	$0.25\ \mu$m	$0.11\ \mu$m	59%	$0.19\ \mu$m

tween the measured projected 100 and 90% emittance values was within 30% of the simulated values in both transverse planes. We point out that for 77 pC/bunch, the measured 90% emittance in vertical plane, as well as the core emittance in both planes, meets the ERL design specification of $\epsilon_n \leq 0.3\ \mu$m. The projected emittance in both transverse planes demonstrates the correct scaling with bunch charge shown in Eq. (1). The measured rms bunch length for both bunch charges was at or below the 3 ps specification, and agreed with simulation to within 5%. Finally, an estimation of the energy spread of the beam in merger was found by measuring the energy spread in the straight section. Agreement between the measured and simulated rms energy spread was within 13% for both bunch charges. These results represent a significant advancement in high-brightness photoinjectors.

In looking to further reduce emittance, simulations indicate that lower emittances and shorter bunch lengths at the end of the merger are possible at higher beam energies (roughly 12 MeV) [10, 11]. Eq. (1) shows two more directions for further improvement. The emittance in this equation can be reduced by lowering photocathode MTE, or by increasing the accelerating field at the cathode. Currently, there is an active cathode research program at Cornell University dedicated to improving cathode performance [12]. In parallel, Cornell is developing an improved DC gun, in order to overcome the current voltage limitation. Lastly, improved laser shaping will aid in creating bunches with more linear space charge fields. According to Eq. (1), as well as more detailed calculations reported in [3, 11], these improvements are expected to reduce the emittance in the photoinjector by roughly a factor of 3, resulting in a beam brightness roughly 10 times higher than reported here.

REFERENCES

[1] I. V. Bazarov, B. M. Dunham, and C. K. Sinclair, Phys. Rev. Lett. **102**, 104801 (2009).

[2] I. V. Bazarov and C. K. Sinclair, Phys. Rev. ST Accel. Beams **8**, 034202 (2005).

[3] I. V. Bazarov, A. Kim, M. N. Lakshmanan, and J. M. Maxson, Phys. Rev. ST Accel. Beams **14**, 072001 (2011)

[4] I. V. Bazarov, B. M. Dunham, C. Gulliford, Y. Li, X. Liu, C. K. Sinclair, K. Soong, and F. Hannon, Phys. Rev. ST Accel. Beams **11**, 100703 (2008).

[5] S. Belomestnykh, I. Bazarov, V. Shemelin, J. Sikora, K. Smolenski, and V. Veshcherevich, Nuc. Inst. Methods A **614**, 179 (2010).

[6] H. Li, *Mutli-dimensional Characterization of the Laser and Electron Beams of the Cornell Energy Recovery Linac Photoinjector Prototype*, Ph.D. thesis, Cornell University (2012).

[7] Z. Zhao, B. M. Dunham, I. Bazarov, and F. W. Wise, Opt. Express **20**, 4850 (2012).

[8] I. V. Bazarov, D. G. Ouzounov, B. M. Dunham, S. A. Belomestnykh, Y. Li, X. Liu, R. E. Meller, J. Sikora, C. K. Sinclair, F. W. Wise, and T. Miyajima, Phys. Rev. ST Accel. Beams **11**, 040702 (2008).

[9] *http://www.pulsar.nl/gpt/*

[10] T. Miyajima and I. Bazarov, *Simulation Study of Cornell L0 Beamline*, ERL Internal Report 11-02 (Cornell University, 2011).

[11] Hoffstaetter, G. H., S. Gruner, & M. Tigner, *eds.*, Cornell ERL Project Definition Design Report (2011) `erl.chess.cornell.edu/PDDR`

[12] L. Cultrera, I. Bazarov, J. Conway, B. Dunham, Y. Hwang, Y. Li, X. Liu, T. Moore, R. Merluzzi, K. Smolenski, S. Karkare, J. Maxson, and W. Schaff, in Proceedings of IPAC2012, WEOAB02 (IPAC, New Orleans, Louisiana, USA, 2012).

Copyright © 2013 CC-BY-3.0 and by the respective authors

RECENT RESULTS FROM THE APEX PROJECT AT LBNL*

F. Sannibale, D. Filippetto, C. Cork, J. A. Doyle, G. Harris, T. Kramasz, S. Kwiatkoswski, R. E. Lellinger, V. Moroz, W. E. Norum, C. F. Papadopoulos, G. Portmann, H. Qian, J. Staples, R. Wells, K. Baptiste, J. Corlett, S. De Santis, L. Doolittle, G. Huang, R. Huang, M. Vinco, and M. Zolotorev, Lawrence Berkeley National Laboratory, Berkeley, CA 94720, USA

Abstract

The commissioning at the Lawrence Berkeley National Laboratory (LBNL) of a high-brightness high-repetition rate (MHz-class) photo-gun, based on a normal conducting 186 MHz (VHF-band) RF cavity operating in CW mode, is now completed. The gun has been designed to satisfy the requirements for operating high-repetition rate 4th generation light sources. Test of high quantum efficiency photocathodes with bunches of hundreds pC at MHz repetition rate are now underway. They include, Cs_2Te cathodes developed in collaboration with INFN-LASA and multialkali antimonides (CsK_2Sb), prepared by a collaborating group at LBNL. The present experimental results and the plan for future activities are presented.

INTRODUCTION

This paper describes the recent progress and experimental results obtained by the Advanced Photo-injector EXperiment (APEX) at the Lawrence Berkeley National Laboratory (LBNL).

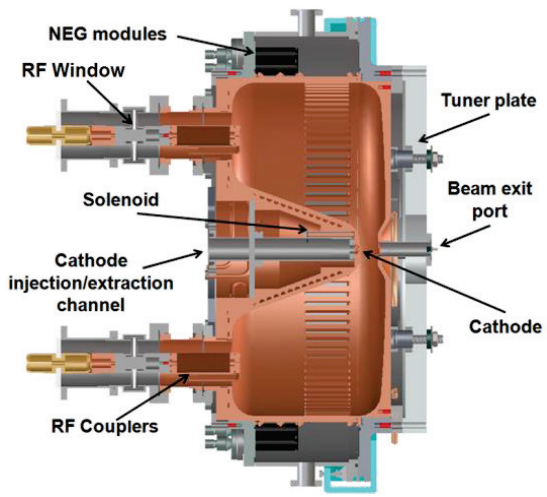


Figure 1: The VHF Gun cross sections.

The project main goal consists in the development and test of a new concept high-repetition rate high-brightness electron injector capable to operate in high-repetition rate free electron laser (FEL) and energy recovery linac (ERL) applications. The successful development of such an injector will critically impact the performance of future 4th generation light sources when high-repetition rates (> 10 kHz) are required, and of high repetition rate ultrafast electron diffraction (UED) and inverse Compton scattering (ICS) applications.

*Work supported by the Director of the Office of Science of the US Department of Energy under Contract no. DEAC02-05CH11231

The core of the system is represented by a normal-conducting (NC) continuous wave (CW) RF gun [1, 2] (see Fig. 1) where the electrons are generated by laser-induced photo-emission on high quantum efficiency (QE) photo-cathodes and accelerated by the cavity fields (~20 MV/m) to up to ~750 keV energy. The gun cavity has been designed to resonate at about 186 MHz (7^{th} subharmonic of 1.3 GHz) in the VHF frequency region. The low frequency choice makes the resonator size large enough to lower the power density on the structure walls at a level that conventional cooling techniques can be used when the cavity is run in CW mode.

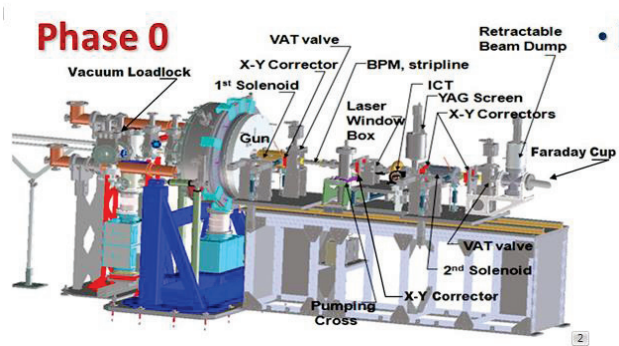


Figure 2: APEX Phase 0 CAD view.

A second advantage of the low frequency is the relatively long wavelength that allows for large apertures on the cavity walls with negligible distortion of the electromagnetic fields. Such apertures create the proper high-vacuum conductance path paving the way for the achievement of the very low pressures required by high-QE semiconductor cathodes (minimizing contamination and damage and hence ensuring longer QE lifetimes).

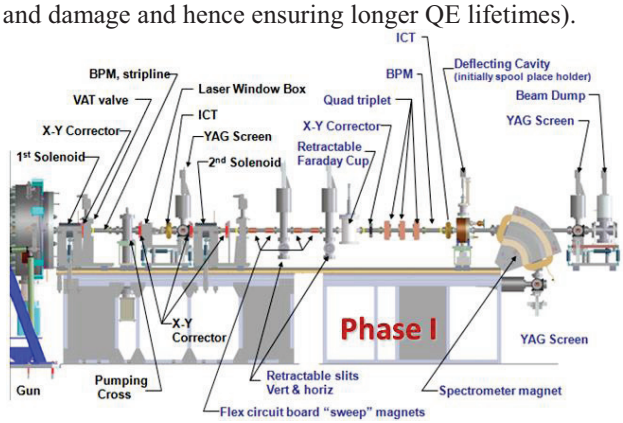


Figure 3: APEX Phase I CAD view.

Copyright © 2013 CC-BY-3.0 and by the respective authors

A last advantage of the VHF scheme is that it is based on mature and reliable RF and mechanical technology, a very important characteristic to achieve the reliability required to operate in a user facility.

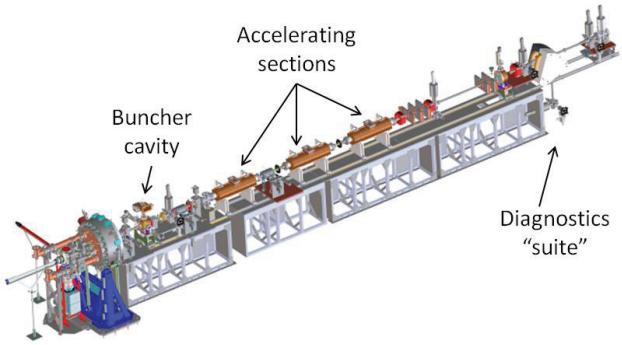


Figure 4: APEX Phase II CAD view.

The APEX project is organized in 3 main stages: Phases 0, I and II. Phase 0, shown in Fig. 2, is dedicated to the development and characterization performance of the gun, and to the testing and characterization of different types of cathodes. In Phase I, visible in Fig. 3, a complete suite of diagnostics [3] allows for the full 6D phase-space characterization of the electron beam at the gun energy. Beams of several hundreds of pC per bunch at MHz repetition rate will be characterized and compared with expected results from simulations. In Phase II, shown in Fig. 4, three pulsed NC 1.3 GHz accelerating sections [4] (a modified version of the AWA cavities at Argonne National Laboratory) and one 1.3 GHz buncher cavity are added to accelerate the beam up to about 30 MeV and compress it to the required lengths. Phase II configuration allows to reduce space charge forces at the level necessary to perform meaningful emittance measurements and be able to demonstrate the brightness performance of the gun. Due to cost and shielding limitations, Phase II operates in pulsed mode with 10 Hz repetition rate. Testing of different photocathodes will continue also during Phases I and II.

STATUS OF THE INSTALLATION

Phase 0 has been completely installed, and Figure 5 shows a picture of it inside the Beam Test Facility (BTF) at LBNL where the APEX project is located.

The vacuum loadlock system, which allows replacing cathodes without breaking the vacuum, is a clone of the system developed by INFN-LASA for PITZ and FLASH in Germany. The system is fully installed and successfully commissioned. The geometry of the extractable molybdenum cathode "plug", which supports the photo-emitting material, has been modified to allow for a smoother insertion in the gun and for minimizing the stress on the RF contact spring (see Fig. 6).

A vacuum leak in one of the two gun RF magnetic loop type couplers, revealed a design weakness in the part. The electrical contact between the coupler inner conductor and the loop cap, both copper parts, was ensured by the mechanical pressure created by two titanium screws. Due to the thermal stress generated when the cavity is switched on and off, the two copper parts gradually lost contact and all the current associated with the RF fields started to flow through the titanium screw creating overheating of the parts (see left part of Fig. 7).

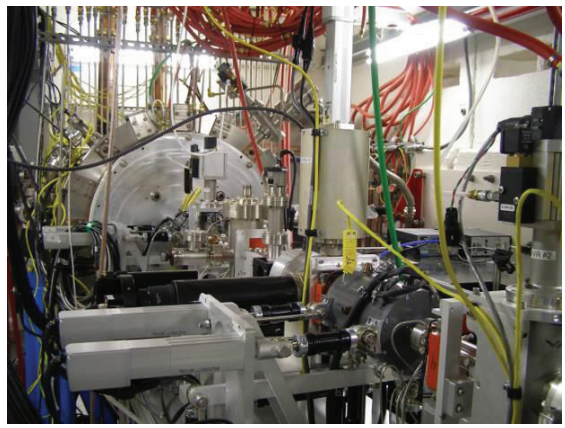


Figure 5: APEX Phase 0 installed in the BTF at LBNL.

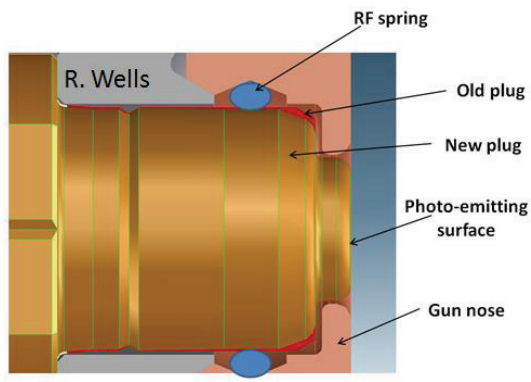


Figure 6: Comparison between the geometry of the previous (red) and new (gold color) cathode plugs.

The issue was serious enough that it was decided to completely redesign the couplers. The new design removed the screws, the copper parts were electron-beam welded together, and the copper cooling line cross section was enlarged for an increased flow of water.

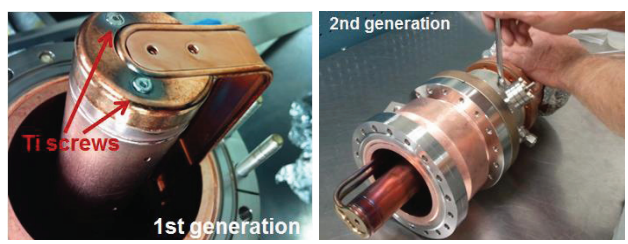


Figure 7: Left: 1st generation gun RF coupler. Right: the newly fabricated 2nd generation coupler being assembled.

The new design also addressed the presence of multipacting in the in vacuum coaxial line between the coupler loop and the RF window. The vacuum part of the coaxial was significantly shortened and all couplers components were coated with titanium nitride. In mid-

Copyright © 2013 CC-BY-3.0 and by the respective authors

February 2013, the two new couplers were installed and smoothly RF conditioned at full power in a few days. No evidence of multipacting was detected. Since then, the couplers have been reliably working at the nominal power.

The installation of the diagnostics suite components of Phase I is undergoing (in parallel with cathode tests) and systems as the double-slit emittance meter (based on a Cornell design), and the spectrometer are in advanced phase of installation (see Fig. 8). The 1.3 GHz deflecting cavity, a modified version of the Cornell design, required for "slice" transverse emittance and longitudinal phase space measurements is under fabrication at the LBNL mechanical shops.

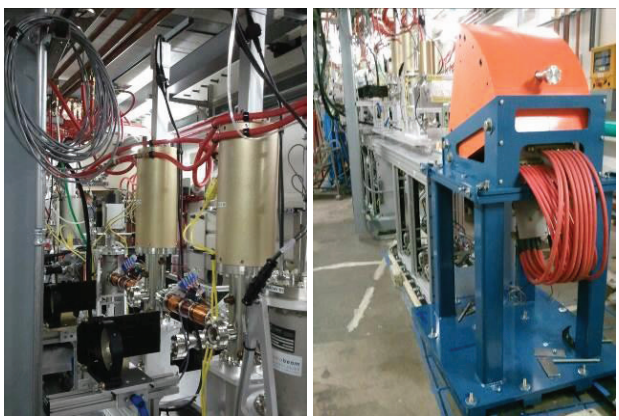


Figure 8: Phase I diagnostics systems in the BTF. Left: the 2-slit emittance meter. Right: the spectrometer dipole.

Phase II long delivery items, such as the klystron (Thales TV 2022F) and the related modulator (by DTI), have been ordered, and the complex RF distribution system, which distributes the 1.3 GHz RF power from the single klystron to the 3 accelerating sections, the buncher and the deflecting cavity, is fully designed (see Fig. 9), and parts are ready to be ordered.

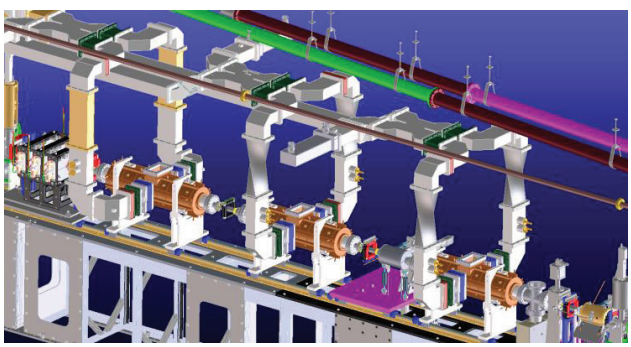


Figure 9: CAD view of part of the RF distribution system for APEX Phase II.

EXPERIMENTAL RESULTS

The VHF gun has been fully commissioned and demonstrated all major nominal parameters such as CW operation, accelerating field, beam energy, and vacuum performance. Detailed results of the gun commissioning have been reported elsewhere [5].

The photo-cathode drive laser, a ~1 W 1064 nm Yb-doped fiber-laser developed in collaboration with University of California Berkeley and Lawrence Livermore National Laboratory, is fully commissioned and in operation. The system, capable of MHz repetition rate operation with the required energies per pulse at the different wavelengths, includes 2nd and 4th harmonic generation, longitudinal and transverse pulse shaping, and pulse picking capabilities [6]. An additional commercial laser (Calmar) with higher power (~ 2 W in the infrared) is presently under installation.

The reliability of the VHF gun system, after almost 2 years of high power RF operation experience, revealed to be excellent. The large majority of the faults that rarely affect the system (once every few days) are due to cooling water supply fluctuations that trigger the interlock protection system.

The overall system performance stability is being tested. Figure 10 shows a relative RF power fluctuation in the VHF gun cavity of ~ 0.14% rms, indicating an accelerating field fluctuation of ~ 0.07%. Such result has been obtained by using a high-level MatLab feedback which reads the power in the cavity from the FPGA based LLRF system [7], and controls the RF power input to the RF amplifier for maintaining the power in cavity constant. The stability performance figure will be probably improved in the next future when the feedback will be implemented completely at the LLRF system level.

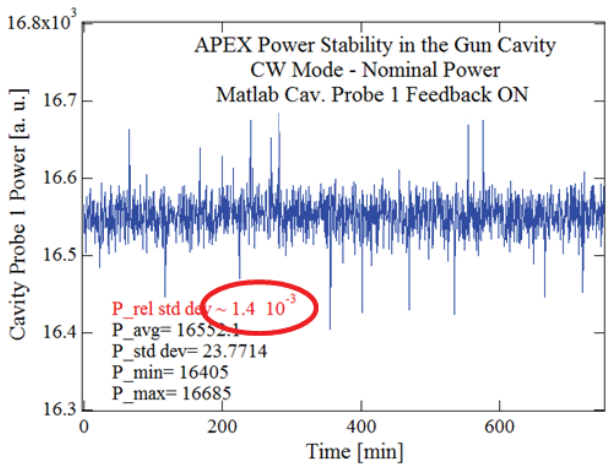


Figure 10: VHF Gun RF power fluctuation measurement.

The synchronization between the gun RF and the photocathode driving laser oscillator is performed by the LLRF system [7], and presently shows a measured time jitter of ~ 2 ps rms. Such a figure corresponds to a RF phase jitter (at the gun frequency) of ~ 0.15 degrees, and is dominated by the contribution of the non-ideally designed piezo/picomotor actuator controlling the position of one of mirrors in the laser oscillator cavity. Although the present jitter value is sufficiently small for the operation and tests to be performed at APEX, the near

Copyright © 2013 CC-BY-3.0 and by the respective authors

future upgrade to the new laser system (the Calmar laser mentioned above) should significantly decrease the jitter value.

The two main high-QE semiconductor photocathodes planned for testing include Cs_2Te produced by INFN/LASA (the same material used at the FLASH FEL in Germany), and the multi-alkali CsK_2Sb produced by a partner group at LBNL. Additional cathode materials are under consideration for future tests.

The completion of the vacuum loadlock system allowed to start the beam tests with the high-QE cathodes. After the activation of the 20 NEG modules in the gun (400 l/s pumping speed each, from SAES Getters), and several days of baking of the cavity [4], a vacuum pressure in the gun of ~ 1.0 10^{-11} Torr was obtained with no RF and of ~ 8.0 10^{-10} Torr when the RF is on at the nominal power. Partial pressures for "dangerous" molecules (H_2O, O, ...) are always 2 orders of magnitude smaller than the actual absolute pressure.

On March 18, 2013, the cathode tests initiated with one of the 3 available Cs_2Te cathodes prepared by LASA. Figure 11 shows the image of the very first beam from Cs_2Te on the YAG screen in the Phase 0 beamline (on March 18, 2013). The repetition rate was limited to 100 Hz to avoid damaging the screen, and because the fast equipment protection system (FEPS), required for high-current operation, was not commissioned yet. The charge monitors were not calibrated but the estimated charge per bunch was of several hundreds of pC.

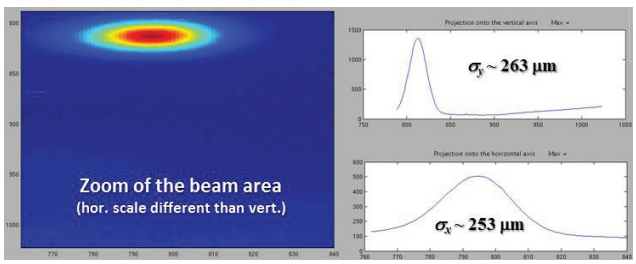


Figure 11: First high-charge beam from a Cs_2Te cathode.

In the subsequent days, following the successful commissioning of the FEPS and calibration of the current monitors, we started to operate at 1 MHz repetition rate. Figure 12 shows scope traces with 2 charge monitors (Bergoz ICTs) and a driving laser photodiode during one of these MHz runs.

At the end of April 2013, an almost continuous 1 MHz run of ~ 4 days integrated an extracted charge of ~ 40 C, roughly equivalent to the charge extracted from the same type of cathode during 3 months of FLASH operation. The top part of Fig. 13, shows the QE values measured during the run, and indicates a decrease of such a quantity from an initial ~ 10% to a final ~ 4%. Although preliminary, this is remarkably important result because it indicates a QE lifetime compatible with the operation of a MHz-class repetition rate x-ray FEL. Indeed, in a typical user facility scenario, the operation schedule includes a maintenance day for every week of user shifts. If the QE of the cathode stays higher than ~ 1% during such a period, then cathodes can be replaced (a ~20 minute operation) during the maintenance day with no impact on the user time.

The QE variations visible in the Figure are due to the fact that no laser pulse amplitude feedback was installed at the time, and the photon energy per pulse was drifting following the temperature variations associated with the alternating days and nights during the run, as visible in the bottom part of Fig. 13. The correlated charge-per-bunch variation is evident in the central part of the Figure.

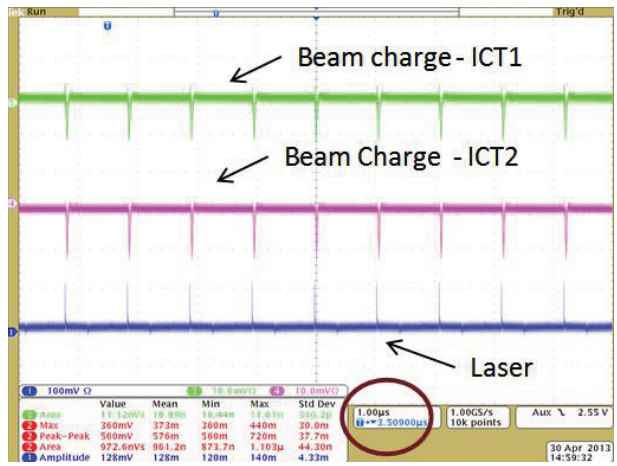


Figure 12: Scope traces from 2 charge monitors (ICTs) and a driving laser photodiode showing the 1 MHz time structure of the pulses.

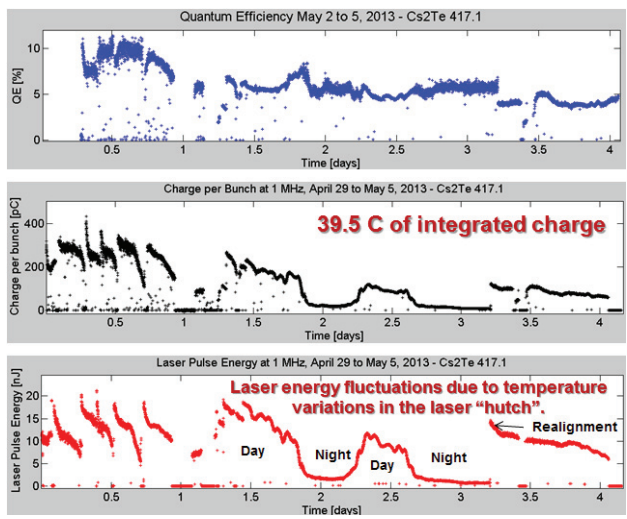


Figure 13: Results of a 4-day run with a Cs_2Te cathode at 1 MHz repetition rate. Top: QE values during the run. Center: charge per bunch, Bottom: laser energy per pulse

To stabilize the laser performance, we recently developed and installed two feedback systems to control the laser pulse energy and pointing. The systems use the image of the laser beam on the virtual cathode and the reading from a power meter to respectively control the horizontal and vertical angles of a mirror and a variable neutral density attenuator installed on a stage. The

Copyright © 2013 CC-BY-3.0 and by the respective authors

feedbacks have been successfully commissioned and the results of a 16 hour test are shown in Figure 14. With the laser stability now ensured by the new feedbacks, more systematic QE lifetime tests with the Cs_2Te will restart soon.

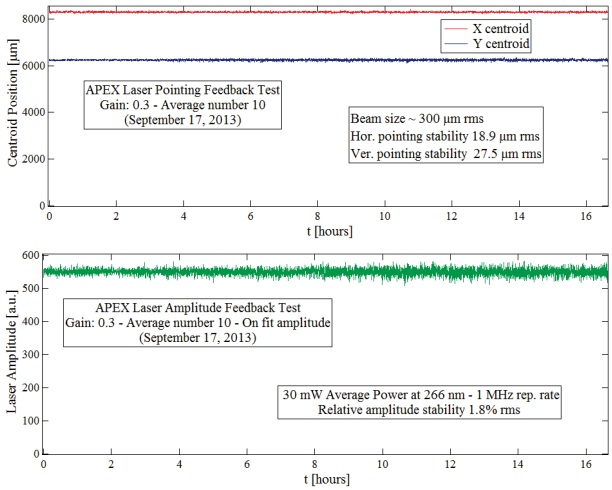


Figure 14: Test of the laser feedback systems. Top: pointing stability results. Bottom: energy per pulse results.

An initial preliminary thermal emittance measurement of the Cs_2Te cathode was performed by a solenoid scan at low charge per bunch (~900 fC) and at a beam energy of ~ 800 keV.

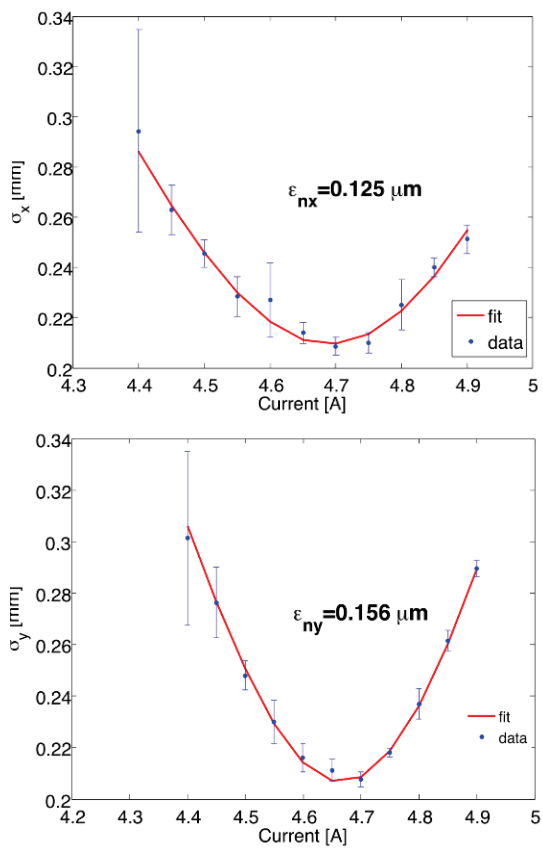


Figure 15: Cs_2Te cathode thermal emittance measurement by the solenoid scan technique. Top: horizontal plane result. Bottom: vertical plane result.

Figure 15 shows the results of the scan for both horizontal and vertical planes. For each of the solenoid current values, the average rms transverse size and standard deviation were calculated over ten individual beam images. The beam sizes at the virtual cathode during the measurements were of ~ 250 μm rms for the horizontal plane and of ~ 265 μm rms for the vertical one. The resulting normalized thermal emittance value for this preliminary measurement is:

$$\varepsilon_n/\sigma_R = 0.54 \pm 0.05 \text{ μm/mm}_{\text{rms}}$$

Such result is consistent with values measured by other groups. Additional more systematic measurements varying the laser transverse beam size at the cathode are scheduled for the near future.

FUTURE PLANS

After the completion of the tests with the presently installed Cs_2Te cathodes, CsK_2Sb multialkali cathodes will be inserted in the gun and characterized. One of such photocathodes, has been already successfully produced by our LBNL partner group and is ready for testing.

The installation (in the first half of 2014) of all the beam diagnostics systems included in APEX Phase I, will allow for the full 6D phase space characterization of beam at the gun energy, and for the comparison of the experimental results with the expected values predicted by the simulations.

Finally, in about 18 months from now (assuming the reception of the required funds), the completion of the installation of the Phase II components will allow for the final characterization of the brightness performance of the VHF gun.

ACKNOWLEDGMENTS

The authors want to express their appreciation for the support given to the project by the AFRD, ALS and Engineering Divisions of the Lawrence Berkeley National Laboratory.

REFERENCES

[1] J. Staples, F.Sannibale, and S. Virostek, VHF Band Injector, CBP Technical Note No. 366, LBNL October 2006.
[2] K. Baptiste et al., NIM A 599 (2009) 9 .
[3] D. Filippetto et al., Proceedings of IPAC2012, New Orleans, Louisiana, p. 963 (2012).
[4] H. Qiang et al., NA-PAC13, to be published.
[5] F. Sannibale et al., PRST-AB 15 (2012) 103501 .
[6] D. Filippetto et al., to appear in the Proceedings of 2013 Free Electron Laser Conference, New York, NY (2013).
[7] G. Huang et al., Proceedings of IPAC2012, New Orleans, Louisiana, p. 3488 (2012).

Copyright © 2013 CC-BY-3.0 and by the respective authors

EXPERIENCE WITH THE SNS LOSS MONITORING AND MACHINE PROTECTION

A. Zhukov, ORNL, Oak Ridge, TN, USA

Abstract

The Spallation Neutron Source (SNS) is a megawatt-class hadron accelerator. Beam loss monitoring is essential for machine protection, residual activation control and machine tuning. We discuss all parts of our beam loss monitoring system including its detectors, electronics, machine protection system (MPS) interface and its role in the accelerator tuning process. The system was designed more than 10 years ago, so we are now addressing obsolescence problems by designing a new FPGA based replacement. The plans for this next generation Beam Loss Monitor (BLM) system are presented.

INTRODUCTION

At SNS a 1ms long H^- beam (macro-pulse) consisting of ~1000 mini-pulses (700 nS pulse and 300 nS gap) is accelerated from 2.5 MeV to 1 GeV in a linac and then converted into H+ by a stripping foil for injection into a storage ring. The mini pulses are accumulated and the resulting, ~700 nS, accumulated beam pulse is extracted and then hits a mercury target. This process runs at 60 Hz and delivers up to 1.4 MW of power to the target. Average beam current is ~24 mA over 1 ms [1].

The SNS BLM system consists of 378 radiation detectors measuring secondary radiation due to beam loss. BLMs are used as MPS devices to shut down the current beam pulse if the integral loss is above threshold and to limit average loss to be under 1 W/m. The MPS system has to be software and timing independent to increase reliability.

Since the beam parameters are different in different parts of the machine, the nature of the losses are also very different.

DETECTORS

The BLM system is used as an MPS device as well as a beam tuning diagnostics. The same detectors are playing two roles and so have to combine reliability for MPS and flexibility for beam diagnostics. SNS uses ionization chambers (IC) as its main BLM device. This is due to their simple design and immunity to radiation damage. In addition to ICs we use several type of photomultiplier tube (PMT) based detectors. The neutron detectors (ND) are neutron sensitive detectors that are useful in low energy part of the linac (where ICs lack sensitivity). The ICs are not fast enough to provide macro-pulse structure to physicists so the PMTs can be used for such diagnostics purposes. Also all PMT devices can adjust their sensitivity significantly (factor of ~100-1000) by changing their HV bias.

Detector Distribution

BLMs are evenly distributed along the accelerator with a typical distance to the beam line of 0-90 cm. In addition to fixed detectors we found moveable detectors to be very useful for investigating unexpected activation patterns.

Table 1: BLM Distribution

Detector	DTL	CCL	SCL	HEBT	Ring	RTBT
IC	11	50	79	59	71	40
ND	12	8	23			
PMT	6	6	3			
DBLM		2	5			3

Figure 1 shows moveable BLMs placed in the transition area between warm and superconducting linacs.

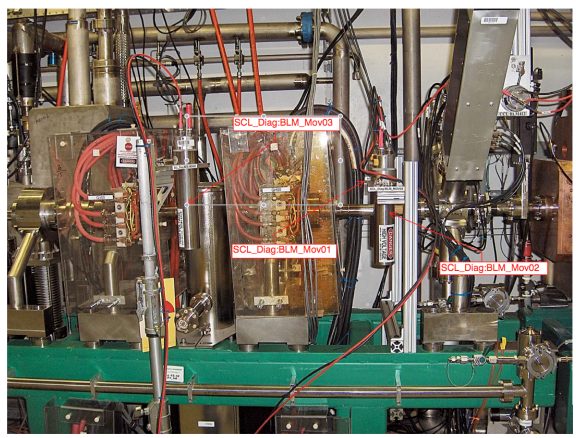


Figure 1: BLM placement for investigation of hot spot.

Detector Parameters

Most important detector parameters are shown in Table 2. Ionization chambers use daisy-chained HV lines since all of them have the same bias applied. All scintillator-based devices have dedicated HV power supply. In addition to signal and HV connections scintillator detectors have a test cable connected to an LED inside the detector. This connection allows testing and bias calibration for these detectors.

The slow response time of the neutron detector is caused by a polyethylene moderator that is needed to slow the neutrons down and increase cross section of neutron capture inside scintillator. Lead shielding around the scintillator helps to suppress sensitivity to x-rays (Fig. 2).

Copyright © 2013 CC-BY-3.0 and by the respective authors

Table 2: BLM Parameters [2]

Detector	IC	ND	PMT
Type	Ionization chamber	Neutron sensitive plastic scintillator + PMT	plastic scintillator + PMT
Detector medium	Gas Ar, 113 cm^3	Polyethylene moderator, ZnS(Ag) scint	EJ-208 scintillator
Typical HV Bias, V	-1000	-700	-700
Typical Sensitivity	70 nC/Rad	80 pC/n/cm2	2 mA/R/hr
Response time	~2 uS	~50 uS	~10 nS
Connectors	Sig (BNC), HV (SHV)	Sig (BNC), HV (SHV), Test (BNC)	Sig (BNC), HV (SHV), Test (BNC)

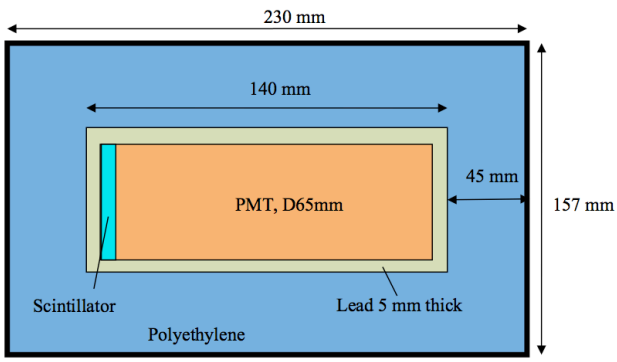


Figure 2: ND internals [2].

Detector Calibration

All ion chambers were calibrated with a gamma source. While that provided absolute calibration in terms of Rads per C of charge being measured, it was not very useful for estimating the fraction of beam being lost. For NDs we used a calibration with faraday cups imitating a full loss [3]. It agrees with simulation but doesn't emulate a real distributed loss.

In the SCL we were able to calibrate BLMs with a laser wire profile measurement device. The laser strips off an electron from the H^- and H^0 is subsequently lost. Knowing the number of H^0 created and measuring additional loss we concluded that SCL loss is around several 10^{-5} [4].

MACHINE PROTECTION AND CONTROLS

Front End Electronics

All detector types are effectively current sources and are interfaced to the same 8-channel analog front end (AFE) electronics that features transconductance amplifiers with jumper-settable gains (620, 6.2E3, 62E3 [Ohm]). The amplified signal is split between an MPS circuit (leaky integrator to integrate the total loss), a "view" circuit where the "fast" signal leaves the AFE and goes to a VME hosted ADC card where it is sampled at 100 kS/s (signal BW is 35 kHz) and the "slow" signal that is smoothed (BW 1 kHz) and also goes to a separate ADC channel [5]. Typical signals produced inside the AFE are shown on Fig. 3.

Hardware leaky integrators provides protection without relying on software or timing information. The system allows a shutdown of the macro-pulse within 15 uS of the integrated value exceeding a threshold. Software based integration over one second is used to limit average loss to stay below 1W/m and maintain residual activation of under 100 mRem/hr in the most parts of the tunnel.

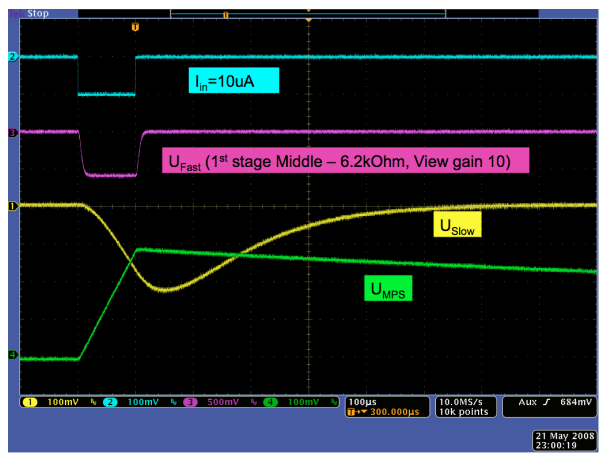


Figure 3: Signals in BLM AFE. Green shows MPS leaky integrator output.

The HV bias is shared by several (usually four) ICs that are daisy-chained in the accelerator tunnel. The HV is supplied by a VME HV module.

In addition to integrated loss, software monitors MPS detector health: gain settings, HV bias set points and read back, and HV bias current (that will detect cable problems in HV circuit).

Copyright © 2013 CC-BY-3.0 and by the respective authors

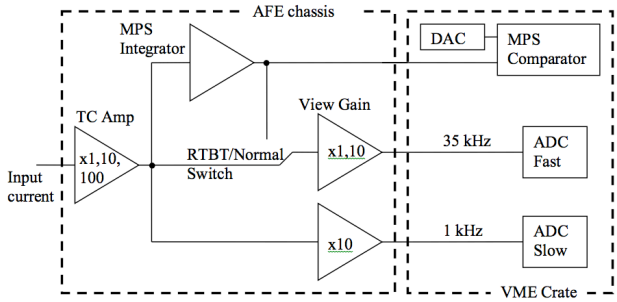


Figure 4: Analog front end [2].

Controls System [6]

The gain setting of the AFE is controlled and monitored by a VMIC VMIVME2510 64-bit digital IO module. The Machine Protection System (MPS) interface module compares AFE MPS loss to an MPS trip level and outputs the result to a separate MPS chassis. The MPS trip levels are set with the outputs of two Hytec8402 Industry Pack (IP) DAC cards (16 channels of 16-bit DAC each) residing on a GreenSpring VIPC616 IP Carrier board. There is a direct communication link from the Motorola MVME-5110 CPU board to the MPS Chassis through the PMC card attached to CPU board. Two ICS110B ADC cards read the AFE outputs of both the fast loss and slow loss signals. Each ICS110B card has 32 independent 24-bit Sigma-Delta ADCs. The ADC can sample up to 108 KHz (100 KHz is used). These data are then transferred and processed by the CPU board. The MVME-5110 features a 500MHz MPC7410 microprocessor, 512MB ECC SDRAM. The standard SNS timing configuration (V124S + V108S cards) provides a real-time data link of machine status as well as beam time synchronization and triggers. The VME crate used is an SNS-standard Weiner 21-slot crate.

The BLM IOC software is based on the Experimental Physics and Industrial Control System (EPICS) framework. Each programmable VME module in the crate has associated EPICS device driver software support which runs on the CPU board. For VME modules with common use at the SNS, beyond the BLM system (e.g. timing and MPS PMC), software is reused from the SNS standard software repository. Other BLM specific software drivers have been written for the remaining modules – the most significant and complex being that for the ICS110B ADC cards. The ICS110B driver is interrupt driven and relies on Direct Memory Access (DMA) for data transfer to the CPU card. It uses a specialized, hardware specific software driver. Alternating beam pulse data is captured by this ADC card into one of two internal "ping-pong" FIFO's. As one FIFO fills, the other, containing the prior pulse's data, is transferred via DMA to the CPU board and processed. For each 60 Hz beam pulse 400 samples (4 mS duration) are acquired for each fast and slow loss signal. Approximately 10 seconds of these data (600 pulses) are queued and internal to the system at any time. Various displays and display rates are available to visualize these data.

CAVITY X-RAYS

Beam loss is not the only source of radiation detected by BLMs. Significant x-ray background comes from RF cavities. To account for these x-rays, the SNS timing system generates a "blank" pulse every 10 seconds. During this blank pulse RF is switched on but there is no beam. The signal from the loss monitors is stored as a reference that is subtracted, in software, from the following normal pulses (with beam enabled). While this approach works, it cannot be used for fast protection because the leaky integrator cannot subtract the stored reference. This inherently compromises MPS because the loss limit set on the DAC has to include "losses" from x-rays.

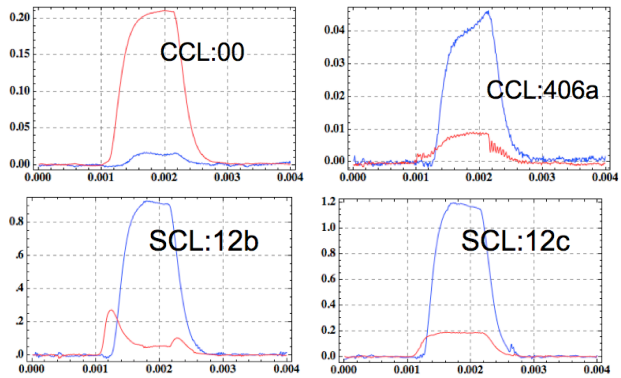


Figure 5: Loss waveforms showing Loss vs Time (s) in different locations. Red gives x-rays only signal (stored reference) and blue shows loss only signal (after subtraction of the reference).

As one can see in Fig. 5, the x-ray component is quite significant and can be even greater than the loss itself. A detector that is sensitive to neutrons and not sensitive to x-rays could be a possible solution. Unfortunately it is hard to create such a detector that would work in analog mode. We are currently experimenting with Dual BLM, which essentially consists of two scintillator-based detectors. One detector has increased sensitivity to neutrons and it measures neutrons and x-ray flux; the second detector measures x-rays only (its' neutron sensitivity is much lower than the first one). Thus by subtracting the "x-ray signal" from "neutron plus x-ray signal" we can get the signal from neutrons only.

NEXT GENERATION OF BLM SYSTEM

This BLM system was designed around 1999. The major problem now is part obsolescence. The AFE boards are using obsolete, discontinued parts and several VME boards are discontinued including the ADC board. Instead of designing replacement boards, we are developing a new system that will significantly differ from the current one.

We plan to use FPGA technology to add flexibility to the MPS setup. MPS functionality will be moved from software to FPGA. We will still have analog integration, but its output will be fed into the FPGA as well. Beam abort decision will be made inside the FPGA and software

Copyright © 2013 CC-BY-3.0 and by the respective authors

will be used for communication purposes only. Instead of having just two limits for single pulse loss and one second average loss we will have arbitrary integration windows that could be different for various regions of the accelerator following similar approach used in LHC [7]. For example, since the SCL requires a faster reaction time to high loss, the beam will be tripped if a single digitizer's sample exceeds a threshold level instead of the integral over several samples.

The multichannel AFE boards will be replaced with single channel modules (Fig. 6) of different types to accommodate different detectors.

Key features of a single channel AFE module:

- Analog subtraction using fader IC [8]
- PGA gain
- HV power supply
- Own MPS integrator
- DAC for threshold settings, HV control, subtraction control, test signal control
- Analog front end can have several options
  - Maximum configuration for Dual BLM (already designed and being under test)
  - Only MPS integrator and fixed gain amplifier for ion chamber with shared HV supply

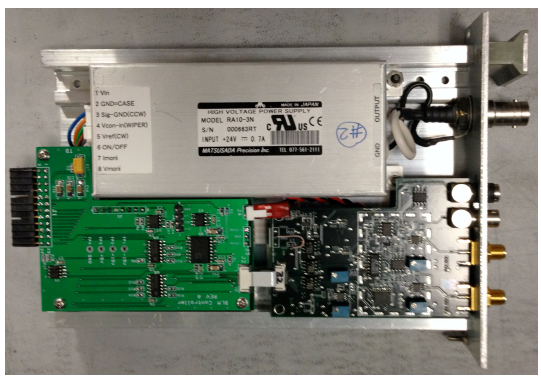


Figure 6: Single channel module with HV power supply and dual input for Dual BLM.

All modules will have amplified analog signals routed to the backplane and front panel for testing purposes. One chassis will host 8 (or 16) modules; analog signals in the same chassis will be digitized and processed in one FPGA (currently we consider cRIO system from National Instruments). This will add flexibility in defining trip conditions. We will be able to use the combination of losses from several detectors to determine if the beam is errant or not while having the MPS logic in hardware (FPGA). For example, the new system will be able to trip the beam if the weighted sum of losses exceeds a threshold; such testing can be performed on the fly on a point-by-point basis.

NON TYPICAL APPLICATIONS OF BLM

Fast BLMs for Beam Studies

We found it very useful to have fast BLMs (PMTs in Table 1). These devices are not connected to the MPS and are used for research only. They are fast enough to distinguish between mini-pulses of SNS beam. These detectors can be used as high time resolution devices for profile measurements. A PMT detects radiation caused by beam hitting a wire. Since it is not a beam line device it can be easily added anywhere in the tunnel. Another example where time resolution is essential is the injection area. Here PMTs can distinguish between loss from H^- hitting the foil and H^+ circulating in the ring.

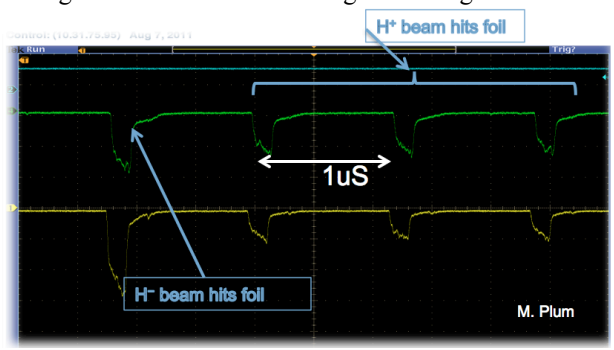


Figure 7: Fast BLM measurement revealing fine time structure of loss at injection area. One mini-pulse injected in the ring [9].

One of the main goals of the BLM system is controlling residual activation inside the accelerator tunnel. This is achieved by limiting one-second average loss. We also demonstrated that certain types of BLMs can be used to directly measure residual activation while beam is running. To achieve this we increase sensitivity of the scintillator-based detectors by ramping up their high voltage. Of course this causes saturation when beam is present (~ 1mS of 60 Hz period). But if we set the integration window to be well beyond the beam gate, the detectors are able to measure residual activation since there is no other radiation source when beam and RF are off. Figure 8 shows that one can see residual activation slowly decaying if beam is off for long time.

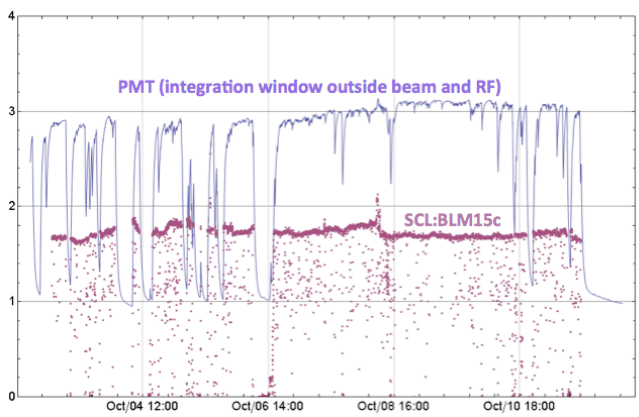


Figure 8: Residual activation in SCL measured by PMT vs. BLM (ion chamber) signal.

Installation of the new BLM system will make such residual activation measurement a standard procedure that will serve as additional guidance for tunnel surveys by radiation protection personnel.

Copyright © 2013 CC-BY-3.0 and by the respective authors

SUMMARY

The existing BLM system protects the SNS accelerator from beam related damage and controls residual activation by limiting average loss at specified 1 W/m level. The system covers all beam energies from 2.5 MeV to 1 GeV. The ionization chamber is the main detector used for MPS with dynamic range at least 10^5 and capable to measure down to 10^{-6} of fractional loss. It is capable to support beam power upgrades of at least doubling of beam power.

Low energy loss is hard to control with radiation detectors and other MPS devices are used in combination with the BLMs such as the differential BCM [10]. BLM systems are the main mechanism to trip errant beam; SCL downtime reduced by factor of six over last several years of operation by understanding causes of errant beam trips [1,10].

The system has proved to be quite reliable since SNS started operation in 2006. Total beam down time due to BLM malfunction is less than 12 hours; most of the downtime is related to software issues and VME power supplies failures.

Electronics obsolescence, including the ADC boards being discontinued, demands a system redesign. X-ray radiation from cavities presents an issue for hardware-implemented protection. Multi-channel AFE boards require beam shutdown for repair or troubleshooting. New FPGA-based [11] BLM system that will address the majority of these issues is currently under development.

ACKNOWLEDGMENT

ORNL/SNS is managed by UT-Battelle, LLC, for the U.S. Department of Energy under contract DE-AC05-00OR22725.

REFERENCES

[1] J. Galambos, "SNS Performance and the Next Generation of High Power Accelerators", FRYAA1, Proc. of NA-PAC'13.
[2] A. Zhukov et al., "SNS BLM System Evolution: Detectors, Electronics and Software", Proc. of PAC'09, Vancouver, BC, FR5REP038.
[3] A. Zhukov and S.Assadi, "Beam Loss Simulation of SNS LINAC", Proc. of PAC'07, Albuquerque, New Mexico, 25-29 Jun 2007, FRPMN060, p. 4138.
[4] A. Shishlo et al., Phys. Rev. Lett. **108**, 114801 (2012)
[5] R. Witkover and D. Gassner, "Preliminary Design of the Beam Loss Monitoring System for the SNS", Proc. of BIW'2010, Upton, NY, pp 345-352.
[6] R. Dickson, *private communication*.
[7] B. Dehning et al., "First Experience with the LHC Beam Loss Monitoring System", CERN-ATS-2009-025, Proc. of PAC'09, May 4-8 2009, Vancouver, Canada.
[8] J. Pogge and A. Zhukov "Results of Background Subtraction Techniques on the Spallation Neutron Source Beam Loss Monitors", Proc. of BIW'2010, Santa Fe, NM, TUPSM090.
[9] M. Plum, *private communication*.
[10] W. Blokland, C. Peters, "A New Differential and Errant Beam Current Monitor for the SNS Accelerator", Proc. of IBIC'2013, Oxford, UK, THAL2.
[11] W. Blokland, "The Use of LabVIEW FPGA in Accelerator Instrumentation", NIWeek'2010, https://decibel.ni.com/content/docs/DOC-15879

Copyright © 2013 CC-BY-3.0 and by the respective authors

ULTRA-SHORT ELECTRON BUNCH GENERATION BY A PHOTOCATHODE RF GUN*

M. Mizugaki#, Y. Koshiba, K. Sakaue, M. Washio, Waseda University, Tokyo, Japan
T. Takatomi, J. Urakawa, KEK, Ibaraki, Japan
R. Kuroda, AIST, Ibaraki, Japan

Abstract

We have been studying on the accelerator physics at Waseda University with BNL type 1.6cell RF gun. Such photocathode RF gun can generate low emittance and short bunch electron beam. Generating ultra-short electron bunch (shorter than 1ps) in a compact accelerator system would be meaningful because some applications need to be miniaturized, THz imaging, for example. However short the laser pulse is, the bunch length would be longer than 1ps due to the severe space charge effects. For the purpose of generating ultra-short electron bunch in compact system, we have newly designed Energy Chirping Cell attached RF gun (ECC RF gun). ECC is attached subsequently to the 1.6 cell. The role of ECC is to chirp the electron energy so that the electron bunch is compressed by velocity difference as it drifts. Simulation results show ECC RF gun can compress the electron bunch down to 200fs (rms) with 100pC electron charge. We have successfully measured the coherent THz light by synchrotron radiation and transition radiation. From these consequences, we infer that the bunch would be compressed into shorter than 500fs. In this paper, we report the results of the bunch length measuring experiments and future plans.

INTRODUCTION

At Waseda University, we have built a compact accelerator system (2m×3m), which consists of picosecond UV pulse laser and S-band Cs-Te photocathode RF electron gun . This RF gun is based on BNL type IV 1.6 cell cavity and capable accelerating high quality electron bunches up to the energy of 5MeV. In our system, the RF frequency is 2856MHz and Cs-Te is used for the cathode. Such photocathode RF guns can generate high-quality electron beam, that is to say low emittance, high brightness, and short pulse. At Waseda University, the beam has been used for applications such as pulse radiolysis experiment for radiation chemical reactions [1], soft X-ray generation via laser-Compton scattering [2] and a laser profiler [3]. Besides such beam applications, we have been developed an RF gun itself in cooperation with High Energy Accelerator Research Organization (KEK).

Ultra-short Electron Bunch

If ultra-short electron bunch (<1ps) is available from the RF gun, it leads some beam applications to be improved. At the least at Waseda, temporal resolution in pulse radiolysis system and luminosity in laser-Compton scattering will be improved. And in addition, ultra-short electron bunch is able to produce coherently enhanced THz radiation. At this time the intensity of THz radiation increases with the square of the bunch electron charge. Therefore in order to achieve high power THz radiation, it is necessary to keep a certain amount of the bunch charges besides bunch compression. The magnetic compression is widely used to compress energy chirped electron bunch. This method has made successful achievements [4], but leads the system to increase in size. The aim of our study is to generate ultra-short electron bunch by use of an RF gun alone.

BUNCH COMPRESSION

Generally in photocathode RF gun, the initial beam transverse/longitudinal profile can be controlled by the laser pulse. It seems that femtosecond laser would generate ultra-short bunch, but in simulation, we have confirmed that the bunch length gets longer than 1ps due to space charge effects. Therefore we have considered improving RF gun.

Energy Chirping Cell Attached RF Gun

Now we have newly designed an RF gun named Energy Chirping Cell attached RF gun (ECC RF gun) in order to achieve ultra-short bunch just with an RF gun itself [5][6].

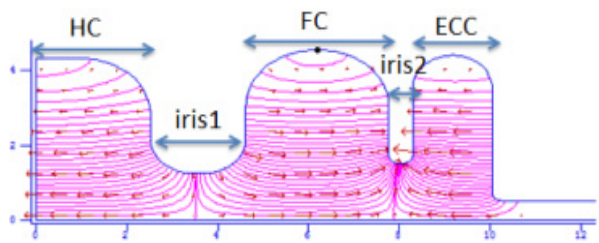


Figure 1: The cavity structure of the ECC RF gun.

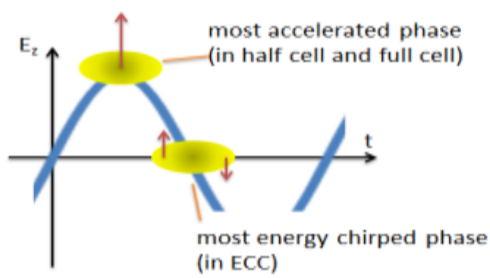


Figure 2: Off-crest acceleration in ECC.

*Work supported by JSPS Grant-in-Aid for Young Scientists (B) 23740203 and Scientific Research (A) 10001690
waterypersimmon7@fuji.waseda.jp

Copyright © 2013 CC-BY-3.0 and by the respective authors

As shown in Figure 1, the Energy Chirping Cell (ECC) is attached subsequently to the 1.6 cell: half cell and full cell. The ECC RF gun is designed to be operated in π mode, similar to the conventional RF gun. Figure 2 shows energy chirping is preceded at off-crest RF phase. In half cell and full cell, the bunch is accelerated around the crest, on the other hand the bunch energy is linearly modulated around zero-crossing phase in ECC.

Therefore in the ECC RF gun, the bunch is firstly accelerated up to around 4MeV in 1.6cell, after that the bunch energy is chirped linearly. The energy chirped bunch gets gradually compressed as it drifts. We have confirmed such velocity bunching by PARMELA and GPT, a beam tracking code. Shown in Figure 3, the bunch length in the longitudinal phase space gets most compressed down to around 200fs (rms) at the 3m from the cathode. At this time initial pulse width is 4.3ps (rms) and the bunch has enough charge (100pC). Moreover, initial RF phase significantly affects the ultra-short bunch generation. As shown in Figure 4, the bunch gets compressed only around 30 degree. And we show the simulation results in Table 5.

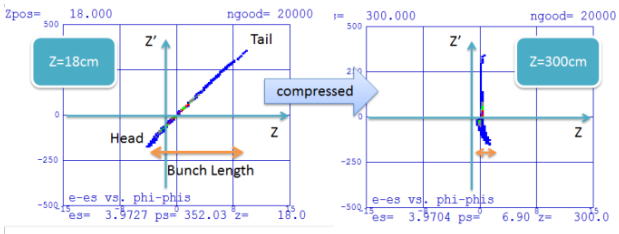


Figure 3:The longitudinal phase space distribution right after ECC (left), distance of 3m from cathode (right).

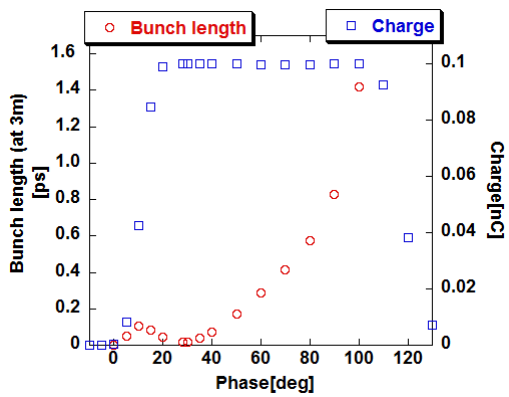


Figure 4: RF phase dependence of the bunch length.

Table 5: The Results of ECC RF Gun Simulation

Energy	3.98MeV
Charge	0.1nC
Minimum bunch length	158fs (rms)
The most compressed distance	3.07m
Normalized emittance	4.18πmm-mrad

By means of simulation, we have confirmed that the ECC RF gun generates ultra-short electron bunch, therefore we have started to manufacture the ECC RF gun. Figure 6 shows appearance of manufactured ECC RF gun.

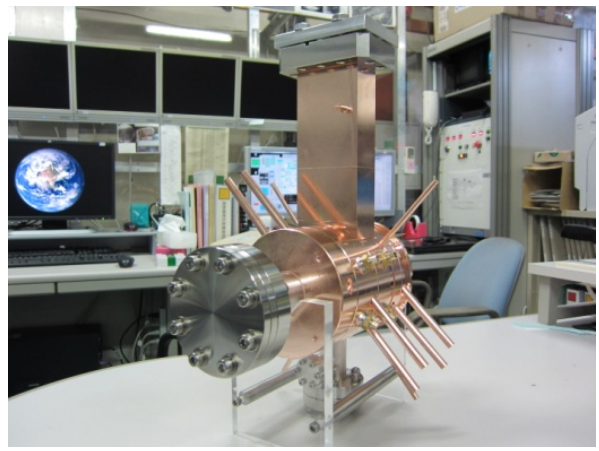


Figure 6: Manufactured ECC RF gun.

EXPERIMENTAL SETUP

We installed the ECC RF gun in our accelerator system. In order to measure a synchrotron radiation (SR), we built a beam line as illustrated in Figure 7. We put the bending magnet at the point of 3m from cathode, where the bunch got most compressed. And then SR passed through the z-cut quartz window, was measured by use of narrow band schottky barrier diodes (SBDs).

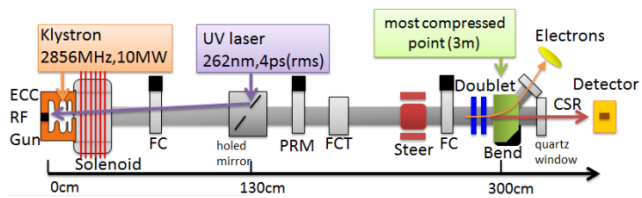


Figure 7: Experimental setup

Schottky Barrier Diode

In this spectroscopy experiment, we used several Schottky Barrier Diodes (SBDs), which have various narrow sensitive frequency ranges in THz region. The Table 8 shows the specs of these apparatuses.

Table 8: The Specifications of SBDs and BPF

Model	DXP-19	FAS-10SF-01	BPF
Manufacturer	Millitech	Wisewave	TYDEX
Sensitive range [THz]	0.04-0.06	0.075-0.11	0.18-0.22
Sensitivity [mV/mW]	1000	500	-
Name	0.05THz	0.1THz	0.2THz

Note that 0.2THz detector consists of 0.1THz SBD and 0.2THz BPF. 0.1THz SBD seems to have small sensitivity at 0.2THz.

Copyright © 2013 CC-BY-3.0 and by the respective authors

EXPERIMENTAL RESULTS AND DISCUSSION

Coherent Synchrotron Radiation Measurement

When the bunch length σ_z is regarded as short enough as the wave length of the radiation, the radiation gets enhanced coherently with square of bunch charge. Assuming the bunch form as Gaussian, the power of the synchrotron radiation is expressed as;

$$P_{\mathrm{all}}(\omega) = N(1+(N-1)e^{-(\omega\sigma_z)^2})P_0(\omega) \quad (1)$$

where N is the number of electrons and therefore when bunch charge is 100pC, N is 6×10^8. $P_0(\omega)$ is power of the radiation from one electron and $P_{all}(\omega)$ is power from the bunch. The spectrum of the SR and CSR is calculated by SPECTRA as shown in Figure 9. 3.7MeV electron bunch can generate THz radiation in our beam line. In our setup, the cut-off frequency is 0.6 THz. But considering the bunch is kicked by a fridge weak magnetic field the cut-off frequency becomes as lower as 0.3 THz. It is also obvious from Figure 9 and Equation (1) that shorter bunch can generate CSR at higher frequency. Therefore we can estimate the bunch length by measuring CSR frequency.

We have confirmed Coherent Synchrotron Radiation (CSR) by plotting THz intensity as a function of the bunch charge in Figure 10. It is evident from the plots that

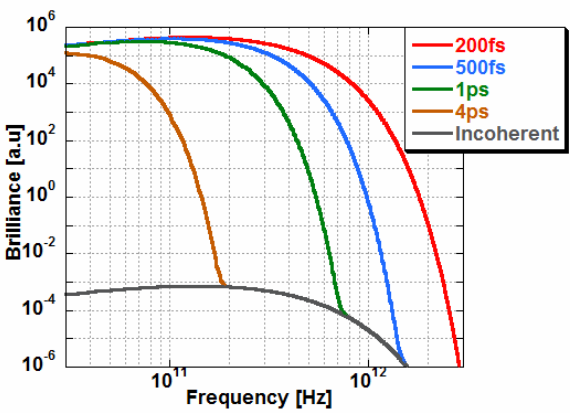


Figure 9: CSR spectrum calculated by SPECTRA (3.7MeV, 100pC).

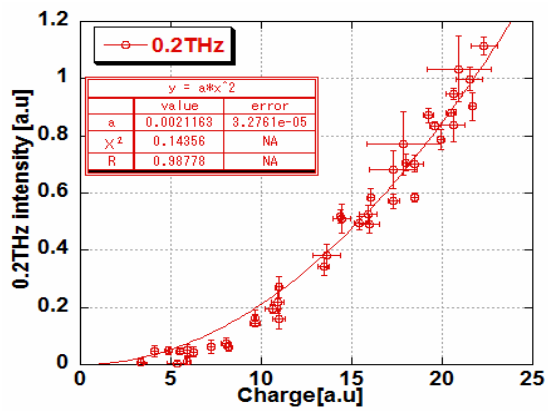


Figure 10: 0.2 THz coherent synchrotron radiation.

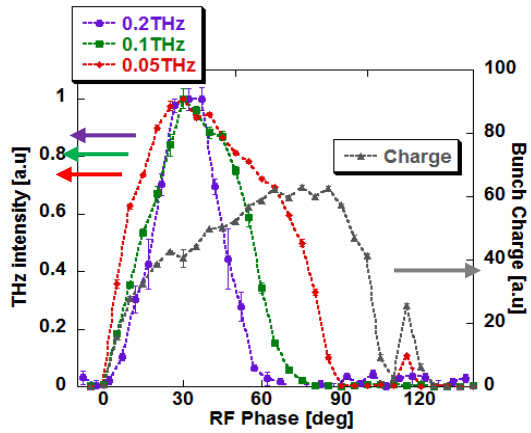


Figure 11: Phase dependence of several detectors.

we have obtained at least up to 0.2THz CSR.

We have successfully measured 3 various narrow THz regions, around 0.05THz, 0.1THz and 0.2THz. As shown in Figure 11, we compared the detectors. Each CSR has a peak at the 30 degree. Moreover, intensity plots become narrow as the frequency of the CSR becomes higher one. These are surely expected by the Figure 4.

From the CSR spectrum (Figure 9) and the successful results of 0.2 THz CSR detection (Figure 10), we can estimate the bunch length is shorter than 500fs. Moreover, having even 0.2 THz CSR the spread width intensity profile (Figure 11), this implies that the higher frequency CSR is produced at the optimum RF phase of 30 degree. We believe the bunch is exactly compressed down to the 200fs at the optimum phase.

SUMMARY AND FUTURE PLANS

In this paper, we described the ECC RF gun newly designed to generate ultra-short electron bunch. We have successfully measured the CSR, thus we estimated the bunch length was compressed down to 500fs (rms). As further bunch length measurement, we consider spectroscopy by use of an interferometer. In the near future, we intend to directly measure the bunch length by use of an RF deflector [7].

REFERENCES

[1] Y. Hosaka, et al., Radiat. Phys. Chem. 84.10-13, (2013)
[2] K. Sakaue, et al., Radiat. Phys. Chem. 77.1136-1141, (2008)
[3] Y. Yoshida, et al, Proc. of IPAC'12, THPPR049, (2012)
[4] M. Kumaki, et al, Proc. of IPAC'12, MOOBA03, (2012)
[5] K. Sakaue, et al., Proc. of IPAC'11, TUPC058, (2011)
[6] Y. Koshiba, et al., Proc. of IPAC'13, MOPFI024, (2012)
[7] Y. Nishimura, et al, Proc. of IPAC'13WEPF1023, (2013)

Copyright © 2013 CC-BY-3.0 and by the respective authors

REGULATOR / HARD SWITCH MODULATOR*

Ian Roth#, Neal Butler, Marcel Gaudreau, Michael Kempkes
Diversified Technologies, Inc., 35 Wiggins Avenue, Bedford, MA 01730

Abstract

Diversified Technologies Inc. (DTI) is developing a long-pulse modulator to meet the requirements of the Spallation Neutron Source (SNS) at Oak Ridge National Laboratory and the European Spallation Source (ESS), planned for Lund, Sweden. The modulator will deliver pulses at 100 kV at a pulse width of 3.5 ms, and a droop of less than 1%. The modulator will be delivered to Oak Ridge for conditioning klystron tubes before they are installed in the SNS accelerator.

INTRODUCTION

DTI is developing a long-pulse modulator as an alternative to the present Converter Modulator at SNS. The new Regulator / Hard Switch Modulator has two objectives: conditioning klystron tubes at SNS, and demonstrating the technology needed for future superconducting accelerators, such as ESS. The modulator specifications are given in Table 1. The key technical issue is meeting the 1% flatness specification without a large capacitor bank, using the minimum additional hardware. To meet these requirements, DTI's modulator has a small non-dissipative regulator that produces a tightly-controlled flattop and eliminates flicker on the input grid. The regulator is the major development for this new modulator design.

Table 1: Modulator Specifications (The frequency will be limited by the low-power supply used for klystron conditioning.)

Voltage (kV)	100
Current (A)	50
Pulse width (ms)	3.5
Frequency (Hz)	14
Voltage flatness (%)	<1
Ripple (% peak-peak)	<0.1

SYSTEM

Overview

The mechanical layout of the modulator is shown in Figure 1, and a highly-simplified schematic diagram is shown in Figure 2. The major elements of the system are the switch, regulator, capacitor, and transformer. This modulator is a 'hybrid' design, with a solid-state switch driving a pulse transformer. This design was chosen to accommodate the ESS preference to avoid DC high voltage and oil-immersed switching elements. The modulator could readily have been designed without a transformer; DTI has built many hard-switched solid-state modulators that reliably switch pulses over 100 kV, at much higher current and average power than required here.

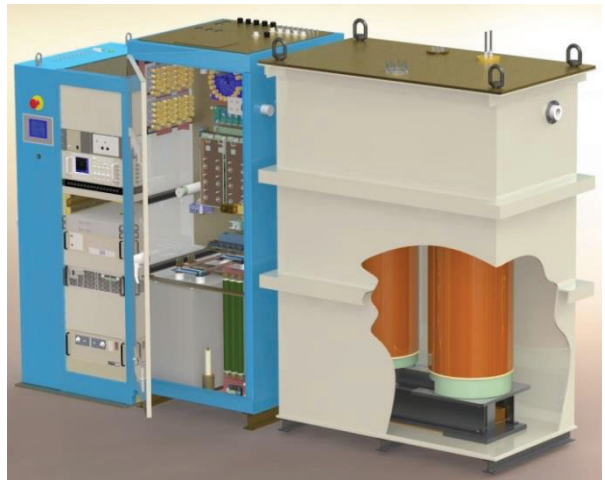


Figure 1: Mechanical layout of the system. The components are (from left to right) cabinet for PLC and AC power, rack-mount cabinet with power supplies and control boxes, power-conditioning cabinet (which contains the capacitor bank, switch, and regulator), and oil-filled transformer tank.

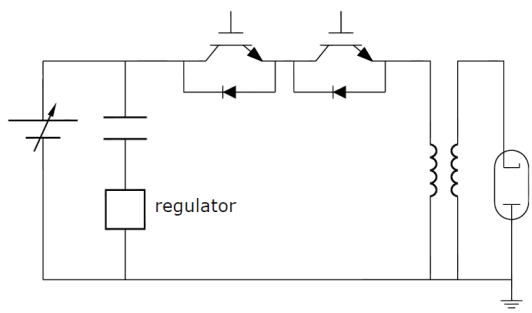


Figure 2: Highly-simplified schematic diagram. (The switch is made with seven IGBTs, not two.)

Switch

The switch is made with series-connected IGBTs, a well-established technology at DTI. The switch operates only once per pulse, in contrast to the 30 times needed by the SNS Converter Modulator. The lower switching frequency reduces the losses, and reduces the size of the switch.

The switch consists of seven modules in series; two of these are redundant. Since IGBTs fail short, if two modules short, the others will continue to support the voltage across the switch. The number of good IGBTs in the switch stack is monitored so that in the unlikely event

*Work supported by US DOE under an SBIR grant.
#roth@divtecs.com

Copyright © 2013 CC-BY-3.0 and by the respective authors

of a failure, repairs can be appropriately scheduled before a modulator failure occurs. The IGBTs are mounted on a cold plate to keep their temperature low, giving high reliability.

Regulator

The regulator is the key development for this program; it keeps the output voltage constant as the capacitor voltage droops. The regulator produces only the droop voltage (±7% of the output), rather than the full voltage produced by the converter modulator. This means that the regulator can be very small and efficient.

Representative voltage waveforms for this system are shown in Figure 3. The capacitor voltage droops during the pulse, then is recharged between pulses, returning to its original level. The regulator output is opposite to the variation in capacitor voltage. This produces both a flat output pulse and a constant power-supply voltage. As a result, the power supply can operate at constant current and constant power – and so does not produce flicker, regardless of the switching frequency. The regulator is non-dissipative, since it neither supplies nor sinks net power over a cycle.

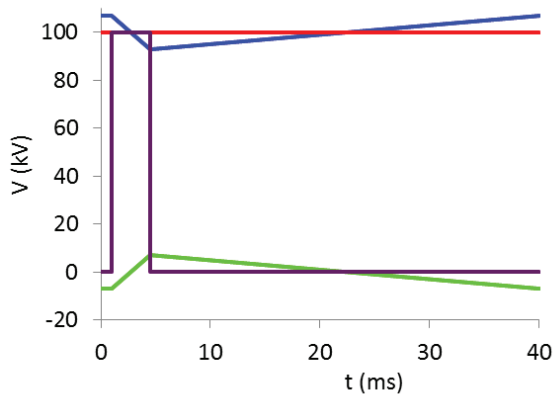


Figure 3: Voltage waveforms for the modulator system. Capacitor (blue), regulator (green), load (purple), main power supply (red).

The regulator is based on a full-bridge circuit rather than a half-bridge. A full bridge transfers all the energy in the filter inductor to the filter capacitor, unlike a half-bridge, which returns some of the energy to the bus capacitor. Because of this, a full-bridge can operate at a lower current (and correspondingly lower loss) than a half-bridge.

The bridge circuit has different phases of operation, depending on whether the modulator is pulsing or charging, and whether its output voltage is positive or negative. Operation during the first half of the pulse is shown in Figure 4. The A switch cycles on and off. When it is closed (top), current builds up in the inductor; when it is open (bottom), the current in the inductor discharges into the bus capacitor. The bridge circuit operates as a boost regulator, transferring energy from the filter capacitor (which is charged by the main capacitor) to the bus capacitor.

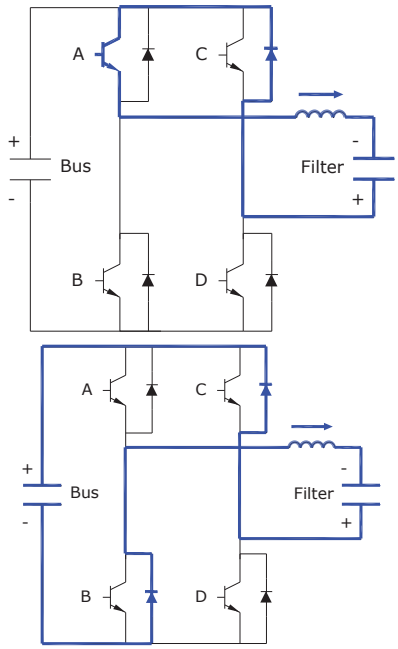


Figure 4: Regulator operation during the first half of the pulse, when the regulator output is negative. The blue traces show the current path. (Top) A switch is closed, and current builds up in the inductor. (Bottom) A switch is opened, and energy in the inductor discharges into the bus capacitor. Energy flows from the filter capacitor to the bus capacitor.

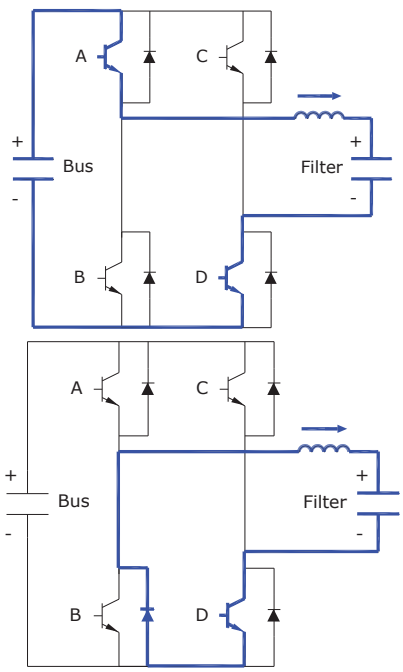


Figure 5: Regulator operation during the second half of the pulse, when the regulator output is positive. (Top) A and D switches are closed, and current builds up in the inductor. (Bottom) A switch is opened, and energy in the inductor discharges into the filter capacitor. Energy flows from the bus capacitor to the filter capacitor.

Copyright © 2013 CC-BY-3.0 and by the respective authors

Operation during the second half of the pulse is shown in Figure 5. In this case the D switch is closed. When the A switch is closed (top), current builds up in the inductor; when the A switch is open (bottom), the current in the inductor discharges into the filter capacitor. In this case the bridge circuit operates as a buck regulator, transferring energy from the bus capacitor to the filter capacitor (and then to the load).

Operation during charging is similar, but with the C and B switches operating, rather than the A and D switches.

The regulator is made with two bridges in parallel, connected to a common filter capacitor. The IGBTs in the bridges switch at 100 kHz during pulsing, and 5 kHz during charging. Their switching is staggered, making an effective switching frequency of 200 kHz during pulsing.

We have demonstrated regulator operation at its full output power. (While the switch voltage was low for this test, the regulator operation depends only on the regulator voltage and current.) The output voltage without the regulator is shown in Figure 6; the capacitor droop is exaggerated from the actual modulator design, and is obvious. Waveforms with the regulator operating are shown in Figure 7. The regulator produces up to ±400 V, and is clearly compensating for the droop. The initial dip in the voltage waveform is due to the initial voltage drop across the switch; this will be eliminated by feedback compensation in the regulator controls.

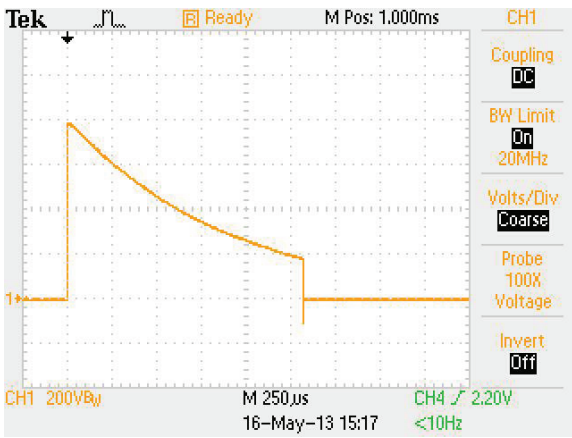


Figure 6: Pulse voltage without the regulator, 200 V/div, 250 µs/div.

Capacitor Bank

The capacitors are made with metallized film (also referred to as "self-healing"), allowing them to be roughly one-quarter of the volume and cost of capacitors made with film-foil technology. Metallized-film capacitors can tolerate arcs in the film, and so can operate at a relatively-high electric field. This is because when a metallized-film capacitor arcs, the metallization near the arc blows off, isolating the shorted section from the rest of the capacitor. The only impact is a small reduction in capacitance. In contrast, a film-foil capacitor cannot tolerate arcs, and must operate at a lower electric field. In general, the allowable current in metallized-film capacitors is lower than the current in a film-foil capacitor. However, the RMS current in the modulator (184 A) is low enough that is this not a concern.

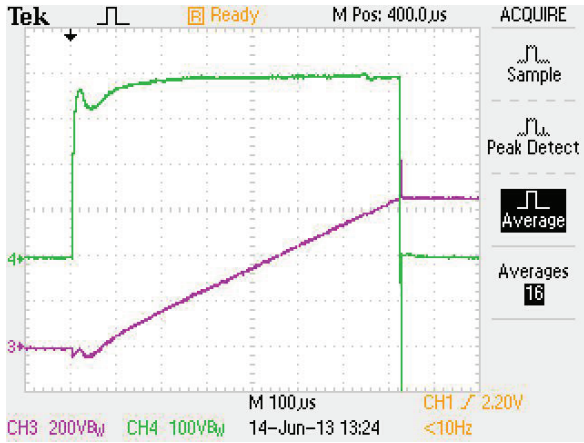


Figure 7: Pulse voltage (green) and regulator voltage (purple), 200 V/div, 250 µs/div.

The total bank capacitance is 4 mF; it stores 82 kJ at 6.4 kV. The bank is made of three 1333 µF capacitors in parallel, each 14" x 15" x 25" tall.

Transformer

The pulse transformer enables the DC power supply to operate at 6 kV, allowing the switch to be air-insulated. Since the pulse is 3.5 ms long, the transformer will be built like a power transformer, rather than the basket design typically used for microsecond pulses.

The long pulse width makes the transformer large, so the hybrid modulator is larger than a comparable hard-switch system. The leakage inductance of the transformer limits the pulse rise time. There is a design tradeoff between leakage inductance and size; reducing the leakage inductance increases the transformer size.

CONCLUSION

The droop control for long pulses provided by this regulator modulator makes it attractive for applications which would otherwise require prohibitively large and expensive capacitor banks, or more complex switching arrangements. The first system will be tested at DTI in early 2014, prior to its installation at SNS.

DTI's future efforts will include investigating directly-switched oil-cooled systems, and applying the regulator to correct pulse droop in long-pulse Marx modulators, rather than adding numerous corrector modules or complex Marx stages.

Copyright © 2013 CC-BY-3.0 and by the respective authors

INDUCTIVELY COUPLED PULSED ENERGY EXTRACTION SYSTEM FOR 2G WIRE-BASED MAGNETS *

R. Agustsson#, J. Hartzell, S. Storms, RadiaBeam Technologies, Santa Monica, CA 90404

Abstract

This project seeks to develop a novel method for quench protection of high-temperature superconducting (HTS) magnets based on coupling the magnet with a high-power resonant coil. The quench protection is realized by applying an electromagnetic pulse through the resonant coil and disrupting the superconducting state in the conductor. This creates a large (10s of meters) normal zone in less than 10 ms thus ensuring even distribution of the energy dissipation. The proposed protection system does not involve generation of high voltage on the coil leads and does not contribute to cryogenic losses. The system is easily scaled to a magnet of arbitrary size. Preliminary design and POC bench top test preparations are presented below.

INTRODUCTION

Recent progress in high-field performance of the second-generation (2G) HTS conductors [1, 2] has enabled design and development of ultra-high field magnets. This is possible because YBCO, the core material of 2G wire, holds the record for the upper critical field, Hc2. A combination of high Hc2 and high mechanical strength (700 MPa yield strength [3] for SuperPower Hastelloy-based wire) position the 2G wire as the only viable conductor for ultra-high field, > 20 Tesla, superconducting magnets.

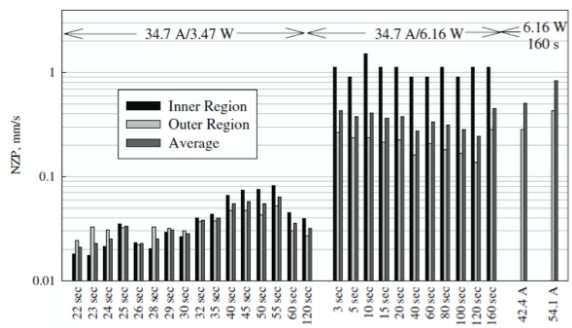


Figure 1: Typical NZP velocities measured in test 2G wire coils [4].

The key component of 2G wire is the epitaxial YBCO layer. This layer, which is only 1-1.5 micron thick, carries all the current of the superconductor. The major problem is its slow rate of Normal Zone Propagation (NZP). As shown in Figure 1, experimental measurement of NZP velocity in 2G wires yields values below 1 mm/s. Such a low propagation velocity results in concentrated energy dissipation and irreversible damage of the magnet during an unprotected quench. The problem is further exacerbated by the low thermal mass and poor thermal conductivity [5] of the YBCO layer. Thus carefully designed protection systems are required to protect 2G superconductors from catastrophic damage.

The established active and passive [6] quench protection systems for traditional low-temperature (LTS) magnets [7] are ill-suited for HTS magnets because their energy extraction is too slow. The measured NZP velocity means the stored energy has to be extracted or redistributed within a few seconds to prevent catastrophic damage. A traditional energy extraction system based on a dump resistor and a semiconducting switch would require several kilovolts on the coil to achieve fast extraction. Such a high voltage creates multiple problems for the interfacing electronics and the current source. Redistribution of the normal zone by resistive heaters is problematic since the thermal conductivity of insulating materials, used to separate the heater from the coil, drops at cryogenic temperatures due to the phonon freeze-out. This effect prevents efficient coupling of the heater elements to the superconductor.

TECHNICAL APPROACH

By inductively coupling a strong electromagnetic pulse via a resonant LC circuit, the normal zone propagation in the coil will be accelerated. The AC field induces currents in the superconducting layer with the current density exceeding that of the critical current density, J_c. This creates a large normal zone, uniformly distributing the dissipation through the magnet body. The method does not rely on thermal heating of the conductor, thus potentially enabling nearly instantaneous protection.

Quench Modeling

The 2G wire coil (in the following DC coil) was modeled as 120 mm OD, 80 mm ID double-pancacke stack. We used the following functional dependence to approximate the critical current field dependence: $I_c = I_0/(1+B/B_0)^a$, where I_0=300 A, critical current in self field, B_0=0.05 Tesla is the individual pinning field and a= 0.7 the pinning exponent. This is the typical I_c(H) behavior of SuperPower wire. The current density was calculated by dividing the current by the average area of the conductor, which was comprised of 50 micron Hastelloy substrate, 40 micron Copper stabilizer and 65

*Work supported by DOE Grant #DE-SC0009547

#agustsson@radiabeam.com

Copyright © 2013 CC-BY-3.0 and by the respective authors

micron Kapton insulation. The DC coil was excited at 80 % of Ic, generation the maximum DC field of 0.3 Tesla. The AC coil is modeled as a 6 turn flat coil wound from 4 mm copper wire. The AC coil is excited with a 200 A current, which is applied as a short burst during the quench protection phase.

The DC field profile was generated in the standard magnetostatic module of COMSOL 3.5, using axial symmetry. The AC field penetration process had two components: interaction of the AC field with inductive currents in the copper stabilizer and penetration of AC field into the superconducting layer. The inductive current interaction was modeled by the COMSOL "Azimuthal Induction Currents" module in 2D axial symmetry geometry. The penetration into the superconductor was simulated by a custom script using well-known Brandt equations [8].

Penetration of AC field into the coil winding is limited by the skin-effect in the copper stabilizer layer. Figure 2c shows that the optimum 50% penetration is achieved at frequencies below 200 Hz. In the design we choose 150 Hz as the operation frequency. This combines manageable size of reactive components with deep winding penetration.

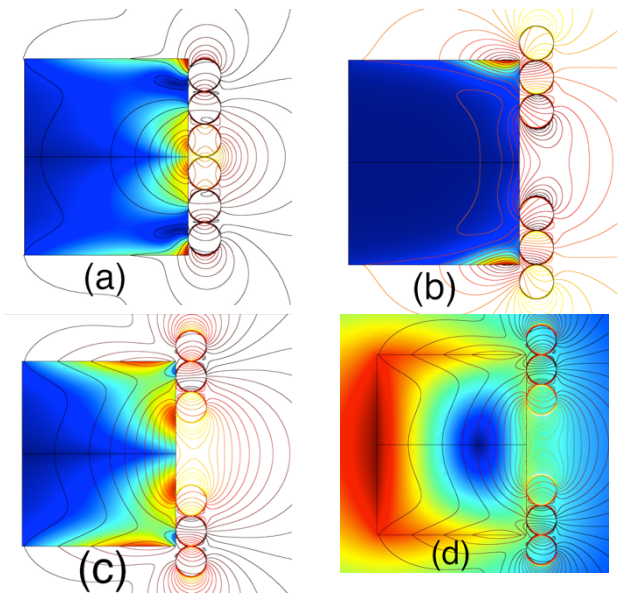


Figure 2: Resonant coil optimization showing field penetration color map and AC field contour map with initial geometry configuration (a), 1000Hz operation (b), final optimized geometry and frequency (c) and final DC magnetic field color map and AC field contour map (d).

Proof of Concept Design

The outputs from the optimal simulation results were slightly adjusted to account for simpler first pass implementation into the proof of concept (POC) system design and to use less HTS. Although slightly less penetration and NZP are expected due to this design change as seen in Figure 3, further Phase I efforts may approach the optimal design following initial system functional validation. The POC design parameters set the coil current at 100 A, resulting in a 0.1 T center, 0.22 T maximum field with a stored energy of 6.6J.

Double stack pancake coils with voltage taps for monitoring normal zone formation were envisioned. The stack would be sandwiched between G10 phenolic plates with slots cut in them for tap lead egress. The entire assembly will be immersed in a LN2 bath enclosed within a *Janis* cryochamber.

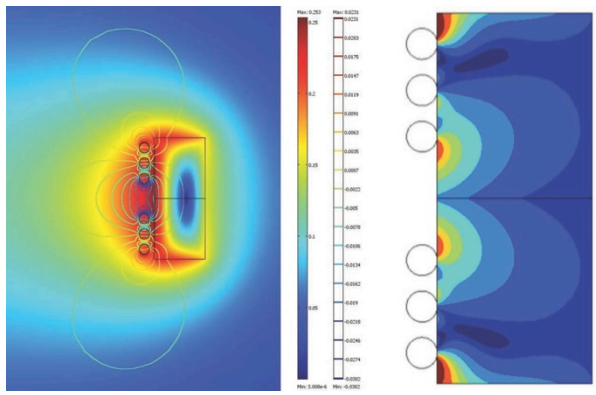


Figure 3: AC magnetic fields (left and shaded), DC magnetic fields (right contours) of the fabrication optimized simulations.

The main HTS coil is powered by a *TDK-Lamda* Genesys 3U 30V-333A power supply and the resonant coil is powered by a pair of *Kepco* BOP-10V-100A in parallel to provide the 200A resonant pulse. The main coil supply is protected with "low-side" switch (N-channel mosfet with the source tied to ground). The system only requires 150Hz pulsing and the *Kepco* BOP is capable of up to 800 Hz operation, permitting potential exploration of higher frequency spaces. This BOP replaced our original plan to build the resonant circuit, with the cost of the devices nearly equal to the projected parts and labor to build our own pulsed power supply.

For voltage tap monitoring, a *Measurement Computing* USB-2537 DAQ card was selected. This card can accommodate up to 64 single ended voltage channels that are needed for reasonable spatial resolution of the quench propagation. Moreover, this DAQ was also chosen for its 1 MS/s sampling speed and 16 bit resolution. Finally, the MC USB-2537 also offers a large common-mode voltage rejection of +/- 10 V, so that we can directly measure the voltage across all of the channels without signal isolation.

As the system utilizes 52 voltage taps on the super conducting coils, with an aggregate sampling speed of 1 MS/s, all 52 voltage taps can be sampled in just over 50 microseconds. Even with a factor of 2 allowance, 10 samples can be taken per tap every millisecond, thus defining the absolute temporal resolution limit of the system. Further, as the buffer size of the board is 1MS,

Copyright © 2013 CC-BY-3.0 and by the respective authors

all the data from a single event can be recorded without the necessity to clear the board buffer that would add further latency to the system.

FABRICATION AND INTEGRATION

A standard double stack pancake coil with HTS tape interconnects were manufactured at RadiaBeam Technologies. The turn to turn coil isolation was accomplished by co-winding the superconducting coil with kapton. To attach the voltage taps, a large copper block wrapped in heater tape was used as a warm backing plate while a precision temperature controllable soldering iron was used to heat the pre-tinned voltage taps until solder flow was observed. Pure Indium solder was used. The bare coil section was then carefully cleaned with isopropanol and lint free wipes prior to co-winding the kapton insulation tape. The pancake stack was dry wound on a custom-made mandrel, Figure 4 left, carefully designed to ensure the 10mm minimum bend radius of the HTS tape was not violated and ground wrapped with 0.006" DMD. The warm leads for the voltage taps were then soldered on and the assembled coil was sandwiched between a pair of G10 phenolic plates as seen in Figure 4 right. The warm leads are placed above the coil stack to ensure simpler assembly of the resonant coil around the perimeter of the assembly. The resonant coil was form wound in a flat pattern and bent to encompass the main HTS coil as shown in Figure 5, right.

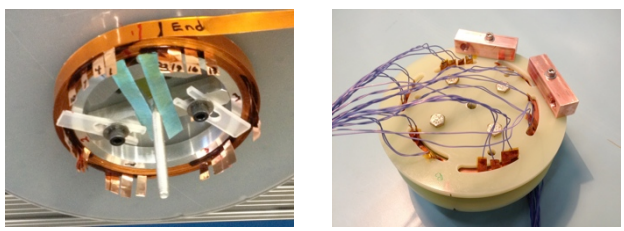


Figure 4: HTS coil on the winding fixture and shown with soldered voltage taps (left). Double pancake coil stack shown with tap leads soldered on and copper warm lead blocks.

EXPERIMENTAL PLANS

All the physical components have been completed and integrated into the cryostat as seen in Figure 5left. Final debugging of the controls and DAQ systems is currently ongoing with initial testing to start shortly. The experimental plans for testing this system will aim to search as broad a parameter space as possible. The main coil current, resonant coil current and frequency will be swept as we explore the system behavior. Further, various resonant coil geometries will be examined including the ideal optimized geometry as shown in Figure 2. Characterization of the NZP speed and optimizing the system to maximize the NZF will be the focus of these studies.

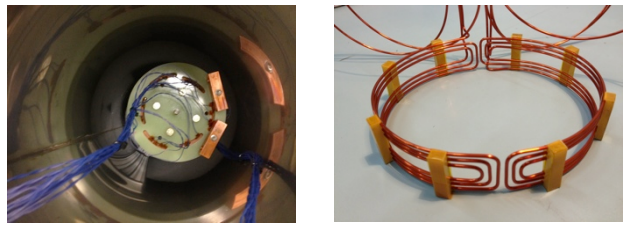


Figure 5: HTS coil placed cryochamber (left), resonant coils prior to forming around HTS coils (right).

CONCLUSIONS

The fundamental behavior of the induced quenching system has been examined through analytical studies and simulations demonstrating the potential viability of this system. Fabrication of the POC has been completed and the final debugging of the control system to be concluded in the very near future. The experimental work plan is in place with data to be acquired imminently.

REFERENCES

[1] Braccini et al. "Properties of recent IBAD–MOCVD coated conductors relevant to their high field, low temperature magnet use", Superconductor Science and Technology (2010) vol. 24 (3) pp. 035001

[2] Xu et al. "Angular dependence of Jc for YBCO coated conductors at low temperature and very high magnetic fields", Superconductor Science and Technology (2009) vol. 23 (1) pp. 014003

[3] van der Laan et al. "Anisotropic in-plane reversible strain effect in Y0. 5Gd0. 5Ba2Cu3O7− δ coated conductors", Superconductor Science and Technology (2011) vol. 24 (11) pp. 115010

[4] Sumption et al., Thermal diffusion and quench propagation in YBCO pancake coils wound with ZnO and Mylar insulations, Superconductor Science and Technology (2010) vol. 23 (7) pp. 075004

[5] Tomoyuki, N. and et al., "Thermal conductivity of YBCO coated conductors fabricated by IBAD–PLD method." Superconductor Science and Technology, 2010. 23(10): p. 105013.

[6] Schultz. "Protection of superconducting magnets", Applied Superconductivity, IEEE Transactions on (2002) vol. 12 (1) pp. 1390-1395

[7] Wilson, M.N., "Superconducting magnets", Monographs on cryogenics [2]1983, Oxford Oxfordshire

[8] E. Brandt, Type II Super Conductor Strip with Current in a Perpendicular Magnetic Field, Pys. Rev. B, Vol 48, #7, pp 893-905

Copyright © 2013 CC-BY-3.0 and by the respective authors

PHYSICS OF POLARIZED PROTONS IN ACCELERATORS*

M. Bai
Brookhaven National Laboratory, Upton, NY 11973, USA

Abstract

Polarized proton beams have been one of the essential elements in fundamental research such as unveiling the deep secret of proton spin structure. Polarized proton beams can also be the tool for direct measurement of the proton's electric dipole moment (EDM). However, due to the interaction between spin motion and electric and magnetic fields, it is very challenging to overcome various depolarizing mechanisms through acceleration, and necessary spin manipulations at a store energy to meet the physics program requirements. Several decades of efforts have been devoted to develop techniques to preserve polarization and spin manipulation, as well as further our understanding of spin dynamics. These efforts directly led to the successful spin program at the Brookhaven Relativistic Heavy Ion Collider (RHIC), the world's first high energy polarized proton collider. This tutorial presentation introduces basic physics which governs the spin dynamics in accelerators. A brief history of polarized protons development, as well as what have been achieved at RHIC are also reported.

INTRODUCTION OF SPIN DYNAMICS BASICS

Just like charge and mass, spin is also an intrinsic property of elementary particles. Spin vector $\vec{S}$ for a particle is then defined as

$$\vec{S} = \langle\psi|\vec{\sigma}|\psi\rangle, \tag{1}$$

where $\vec{\sigma}$ is the Paul matrices, and ψ is the particle spin state. Proton, a spin of $\frac{1}{2}$ particle, has two eigenstates, i.e. $\psi_+ = |\frac{1}{2}, +\frac{1}{2}\rangle$ (up state) and $\psi_- = |\frac{1}{2}, -\frac{1}{2}\rangle$ (down state). The intrinsic magnetic moment of a particle is then given by

$$\vec{\mu} = g\frac{e}{2m}\vec{S} \tag{2}$$

where e and m are the electric charge and rest mass of the particle. g-factor for a perfect point-like particle is $\frac{1}{2}$. For proton, the anomalous g-factor $G = \frac{g-2}{2}$ is 1.7928474.

For a beam of spin-$\frac{1}{2}$ particles, polarization P, on the other hand, is a classical concept defined as

$$P = \frac{N_+ - N_-}{N_+ + N_-} \tag{3}$$

where $N_\pm$ are the number of particles in the two spin states, respectively [1].

In a circular accelerator, the spin motion is governed by the Thomas-BMT equation [2]. In the frame of particles orbital revolution, it is given by

$$\frac{d\vec{S}}{dt} = \frac{e}{\gamma m}\vec{S}\times[G\gamma\vec{B}_\perp + (1+G)\vec{B}_\parallel + (G\gamma + \frac{\gamma}{\gamma+1})\frac{\vec{E}\times\vec{\beta}}{c}], \tag{4}$$

where $\vec{S}$ is the spin vector in the particle's rest frame, $\vec{B}_\perp$ and $\vec{B}_\parallel$ are the transverse and longitudinal components of the magnetic fields in the laboratory frame with respect to the particle's velocity $\vec{\beta}c$, $\vec{E}$ is the electric field particle encounters and γ is the relativistic Lorentz factor. Here, Eq. 4 shows that in a perfect planar circular accelerator, the spin vector precesses $G\gamma$ times in one orbital revolution. $Q_s = G\gamma$ is then defined as spin tune.

In general, the effect on spin motion from electric field in an accelerator is negligible. Equation 4 can then also be expressed as

$$\frac{d\vec{S}}{ds} = \vec{n}\times\vec{S} = [G\gamma\hat{y} + G\gamma\frac{B_x}{B\rho}\hat{x} + (1+G)\frac{B_s}{B\rho}\hat{s}]\times\vec{S}, \tag{5}$$

where $\hat{x}$, $\hat{y}$, $\hat{s}$ are the unit vector along the direction of radial, vertical and longitudinal, respectively. $ds = \rho d\theta$, where θ is the bending angle. The equation of motion for the spin state in Eq. 1 also known as spinor for a $\frac{1}{2}$ particle is

$$\frac{d\psi}{d\theta} = -\frac{i}{2}(\vec{\sigma}\cdot\vec{n})\psi = -\frac{i}{2}H\psi. \tag{6}$$

For a constant H, Eq. 6 can be rigorously solved as

$$\psi(\theta_2) = e^{-\frac{i}{2}H(\theta_2-\theta_1)}\psi(\theta_1) = M(\theta_2-\theta_1)\psi(\theta_1) \tag{7}$$

where $M(\theta_2-\theta_1)$ is a 2×2 spinor transfer matrix. For a main bending sector dipole, the spinor transfer matrix is just $M(\theta_2-\theta_1) = e^{-\frac{i}{2}G\gamma(\theta_2-\theta_1)\sigma_3}$. For a thin quadruple, the spinor transfer matrix is $M = e^{-\frac{i}{2}(1+G\gamma)kly\sigma_1}$, where kl is the normalized integrated strength of the quadrupole and y is the vertical displacement of the particle from the center of the quadrupole [1]. For any spin rotator which rotates spin vector by ϕ around an axis $\hat{n}_{rot}$ is $M = e^{-\frac{i}{2}\phi\hat{n}_{rot}\cdot\vec{\sigma}}$. In general, in a circular accelerator, the one turn spin transfer matrix for a particle on the closed orbit is

$$M = e^{-\frac{i}{2}Q_s 2\pi\vec{\sigma}\cdot\hat{n}_{co}}, \tag{8}$$

where Q_s is the spin tune, and $\hat{n}_{co}$ is the stable spin direction. Equation 8 shows that for the particle's spin vector always returns to the same direction if it is initially aligned with the stable spin direction $\hat{n}_{co}$. Otherwise, the spin vector just simply precesses around the stable spin direction $\hat{n}_{co}$ Q_s times per orbital revolution. For a particle in a perfect circular accelerator where it only sees vertically aligned guiding magnetic fields, the stable spin direction is vertical and spin tune is $Q_s = G\gamma$, linearly proportional

* The work was performed under the US Department of Energy Contract No. DE-AC02-98CH1-886, and with support of RIKEN(Japan)

Copyright © 2013 CC-BY-3.0 and by the respective authors

to the particle's energy. With the presence of any localized spin kick of ψ around an axis of n_e at location θ , the one turn transfer spinor transfer matrix of a particle on closed orbit then becomes

$$M(\theta+2\pi,\theta)=e^{-\frac{i}{2}G\gamma(2\pi-\theta)\sigma_3}e^{-\frac{i}{2}\phi\vec{\sigma}\cdot\hat{n}_e}e^{-\frac{i}{2}G\gamma\theta\sigma_3}, \quad (9)$$

and both spin tune and stable spin direction are changed [1].

In general, both spin tune and stable spin direction are function of particle's phase space coordinate, i.e.

$$\hat{n}_{co}(\vec{J}_z,\phi_z,\theta)=\hat{n}_{co}(\vec{J}_z,\phi_z+2\pi,\theta) \quad (10)$$

where $\vec{J}_z$ and , ϕ_z are particle's 6-D phase space coordinates. Spin tune is the number of spin precessions around $\hat{n}_{co}$ in one orbital revolution. Unless betatron tune is integer, spin tune and stable spin direction can no longer be computed by the simple one turn spin transfer matrix approach. Algorithms like SODOM, SLIM were developed to compute the stable spin direction for particles off closed orbit [3, 4]. For a single isolated resonance, an analytical solution of $\hat{n}_{co}$ was also found by Mane [5]. In the presence of overlapping resonances, the stable spin direction can be computed by numerical spin tracking using stroboscopic averaging developed by Heinemann and Hoffstaetter [6].

CHALLENGES IN ACCELERATING POLARIZED PROTONS TO HIGH ENERGY

Depolarizing Resonances

In a high energy planar accelerator, accelerating polarized protons operation is challenged by the presence of non-vertical magnetic fields due to magnetic field errors, quadrupole misalignments or vertical betatron oscillations, which kick the spin vector away from vertical direction. When the frequency of the perturbation on the spin motion coincides with the spin precession frequency, the kicks on the spin vector can be coherently added and result in polarization loss, i.e. a depolarizing spin resonance [1].

Depending on the source of the spin perturbing magnetic fields, there are two types of spin depolarizating resonances. The imperfection spin resonances at $G\gamma=k$ are due to dipole errors and quadrupole misalignments. Here k is an integer. The strength of this resonance is proportional to the size of the vertical closed orbit distortion. The intrinsic spin resonances at $G\gamma=kP\pm Q_y$, on the other hand, are driven by vertical betatron oscillation in the absence of coupling as well as other high order effects. Here, P is the super-periodicity of the machine and Q_y is the vertical betatron tune. The stronger the betatron oscillation, the stronger the intrinsic spin resonance. In general, for a resonance at $Q_s=K$, the resonance strength ϵ_K is defined as

$$\epsilon_K=\frac{1}{2\pi}\oint[(1+G\gamma)\frac{B_x}{B\rho}+(1+G)\frac{B_s}{B\rho}]e^{iK\theta}ds. \quad (11)$$

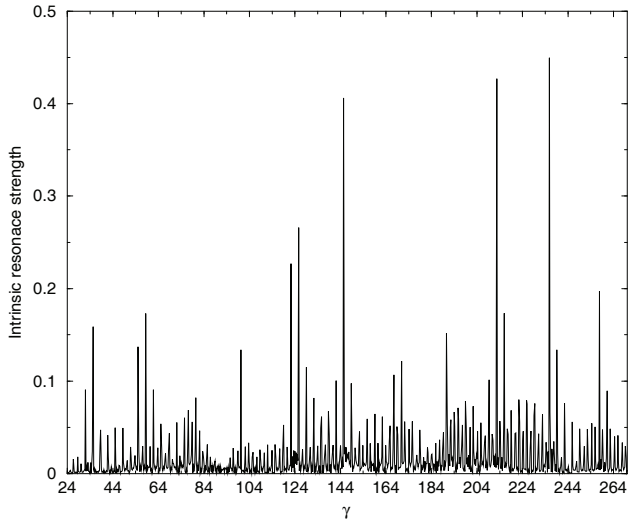


Figure 1: Strength of intrinsic spin resonances from injection energy to 250 GeV in RHIC. These are calculated from a RHIC lattice without any spin manipulation devices. The intrinsic spin resonance strength is calculated with a single particle at an emittance of 10π mm-mrad.

Evidently, for an imperfection resonance, its resonance strength is independent of particle's betatron oscillation amplitude. Intrinsic resonance strength, on the other hand, is different for particles at different betratron amplitude since they experience different magnetic field in a quadrupole. Fig. 1 shows the strength of intrinsic resonances as a function of energy in RHIC, calculated with Depol [7]. A total of 423 imperfection resonances lies between the RHIC injection energy and its designed store energy at 250 GeV, and the higher the beam energy, the stronger the imperfection resonance. The strong intrinsic spin resonances in RHIC are located at $81\pm(Q_y-12)$, $81+(Q_y-6)$, $2*81+(Q_y-12)$, $3*81-(Q_y-12)$ and $5*81\pm(Q_y-12)$. Clearly, no beam polarization can survive through all these depolarizing resonances.

The polarization change after crossing a resonance depends on the resonance strength as well as how fast the resonance is crossed. For a single isolated resonance, the ratio of the polarization after crossing the resonance P_f to the initial polarization P_i is given by the Froissart-Stora formula [8]

$$P_f=P_i(2e^{-\frac{\pi|\epsilon_k|^2}{2\alpha}}-1) \quad (12)$$

where $\alpha=\frac{dQ_s}{d\theta}$ is the resonance crossing rate and ϵ_k is the strength of the spin resonance. As indicated in Eq. 11, since intrinsic spin resonance strength is a function of the betatron oscillation amplitude, the average beam polarization of a Gaussian beam crossing an intrinsic resonance then becomes

$$P_f=P_i\frac{1-\frac{\pi|\epsilon_k|^2}{\alpha}}{1+\frac{\pi|\epsilon|^2}{\alpha}}, \quad (13)$$

Copyright © 2013 CC-BY-3.0 and by the respective authors

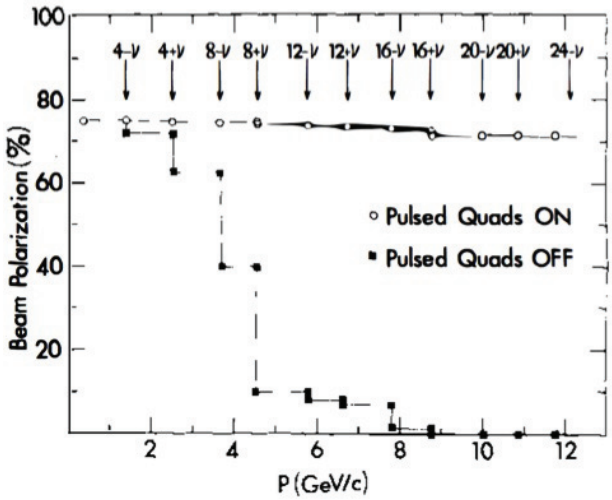


Figure 2: This plot shows the beam polarization as a function of the beam energy in the ZGS.

For a Gaussian beam, a polarization profile, i.e. polarization as function of betatron coordinates can be developed, of $P(x,x',y,y') = P_0 e^{\frac{x^2+x'^2}{2\sigma_{xp}^2}} e^{\frac{y^2+y'^2}{2\sigma_{yp}^2}}$ can be developed, The average beam polarization is $\langle P\rangle = P_0 \frac{1}{(1+R_x)(1+R_y)}$[9]. Here P_0 is the beam polarization of particle in the beam center, $\sigma_{x,p}$ and $\sigma_{y,p}$ are the rms size of horizontal and vertical polarization profile, respectively. $R_{x,y} = \sigma_{x,y}^2/\sigma_{x(y),p}^2$ where $\sigma_{x,y}$ is the rms beam size.

Overcome Imperfection Spin Resonance and Intrinsic Spin Resonance

Both imperfection resonances and intrinsic resonances can be overcome by correcting the closed orbit distortion at $G\gamma = K$ and fast jumping betatron tune at $G\gamma = kP \pm Q_y$ [1], respectively. Both techniques were first developed at the Argonne ZGS (Zero Gradient Synchrotron) [10, 11] in the early 70s. Fig. 2 shows the tune jump at each intrinsic resonance during acceleration. Both techniques were also applied to the AGS at BNL. With six fast tune jump quadrupoles and harmonic orbit corrections, polarized protons were accelerated to 22 GeV with 40% polarization in the AGS [12]. However, to achieve this, months of dedicated beam time were required [13].

For strong intrinsic spin resonances, one can use an RF dipole to excite a large amplitude coherent betatron oscillation to effectively enhances the intrinsic resonance strength and achieve full spin flip with regular resonance crossing rate. The advantage of this technique is to preserve the beam emittance by energizing the RF dipole adiabatically [14]. This technique was first successfully developed at the AGS [15] to obtain full spin flip at the four strong intrinsic resonances $G\gamma = 0 + Q_y$, $G\gamma = 12 + Q_y$ and $G\gamma = 36 \pm Q_y$. However, this technique is not applicable to weak intrinsic resonances due to the limit of physical aperture.

Partial Snake

For medium energy accelerators, the tedious and lengthy setup time of orbital harmonic correction for each imperfection resonance can be a serious impediment. Hence, an novel technique of using a partial snake, a magnetic which rotates spin vector around an axis in the horizontal plane by an angle of $\psi < 180^o$, to keep the spin tune away from all integers was proposed [16]. Equation 14 shows that spin tune, as a function of beam energy, becomes discontinuous at each integer. Hence, all imperfection resonances are avoided.

$$\cos(\pi \mathrm{Q_s}) = \cos(\mathrm{G}\gamma\pi)\cos(\frac{\psi}{2}). \qquad (14)$$

This technique was first developed at the BNL AGS [17]. A 5% solenoid snake, i.e. it rotates spin vector by 5% of 180^o, was installed in the AGS in the mid 1990s to overcome all the imperfection resonances [18].

In order to avoid the depolarization due to the weak resonances in the AGS, a dual partial snake scheme was developed in 2006. A 5.9% room temperature helical snake plus a super-conducting helical snake which can provide an maximum strength of 20% at the AGS extraction energy were installed located $\frac{1}{3}$ of the ring apart. With this configuration, spin tune then becomes [19]

$$\cos\pi \mathrm{Q_s} = \cos\mathrm{G}\gamma\pi\cos\frac{\psi_\mathrm{c}}{2}\cos\frac{\psi_\mathrm{w}}{2} - \cos\mathrm{G}\gamma\frac{\pi}{3}\sin\frac{\psi_1}{2}\sin\frac{\psi_2}{2}. \qquad (15)$$

Here, ψ_c and ψ_w are the amount of spin rotations of the strong super-conducting snake and the 5.9% snake, respectively. Equation 15 implies that not only the spin tune is forbidden in a gap around each integer but also that the width of the gap is modulated at an integer multiple of 3. The gap reaches its maximum width at each integer multiple of 3 where the two snakes are coherently added and otherwise reaches its minimum width when the two snakes are subtracted. Since the AGS has a super-periodicity of 12, all the strong intrinsic resonances are located at the integer multiple of 3 where the spin tune forbidden gap reaches its maximum. Hence, by placing the vertical betatron tune inside the spin tune forbidden gap, all imperfection and intrinsic spin resonances are avoided during the AGS acceleration [20].

Full Siberian Snake

To reach even higher energy polarized protons, it is operationally impossible to individually overcome each depolarizing resonance due to the amount of spin depolarizing resonances during the acceleration. Much stronger resonances also make it very difficult to preserve polarization with just partial snakes. Thanks to the invention of the Siberian snake by Derbenev and Kondratenko in 1976 [21], the polarized proton acceleration to high energies became practical. The Siberian snake is a special device which rotates the spin vector by 180° around an axis in the horizontal plane. Equation 9 shows in a ring with a single full snake, the spin tune becomes half integer, independent of

Copyright © 2013 CC-BY-3.0 and by the respective authors

beam energy and both imperfection resonances and intrinsic resonances are avoided [21]. This technique was first experimentally demonstrated in the cooler ring of Indiana University Cyclotron Facility in the 1980s[13].

For high energy accelerates like RHIC, intrinsic resonance can be so strong that more than one snakes are needed. In a ring with two full Siberian snakes located at 180^o apart from each other are used, the one turn spin transfer matrix is

$$M(\theta+2\pi,\theta)=e^{-\frac{i}{2}G\gamma(\pi-\theta)\sigma_3}(i\hat{n}_1\cdot\vec{\sigma})e^{-\frac{i}{2}\pi\sigma_3}(i\hat{n}_2\cdot\vec{\sigma})e^{-\frac{i}{2}\theta\sigma_3} \quad (16)$$

where $\hat{n}_1, 2$ are the axes of the two snakes, both are in the horizontal plane with an angle of $\Delta\phi$. It can easily show that the spin tune is $Q_s = \frac{1}{\pi}\Delta\phi$, where $\Delta\phi$ is the angle between the axes of the two snakes. With the axes of the two snakes perpendicular to each other, the spin precession tune is $\frac{1}{2}$. It is also easy to show that the stable spin direction stays vertical all around the ring. RHIC employs two full Siberian snakes in each of its two accelerators to preserve polarization through acceleration as well as collision at a store energy, and each RHIC snake consists of four helical dipoles [22].

The spin tune and stable spin direction mentioned above for one snake as well as dual snake setup are for a particle at zero betatron oscillation amplitude in a perfect ring. In reality, both spin tune and stable spin direction can become strongly dependent on the particle's phase space coordinates in the presence of strong spin depolarizing resonances, and can no longer be calculated through the simple one turn matrix approach as illustrated in Eq. 16. For a single isolated spin resonance case, an analytic solution was found by Mane [5]. Based on Mane's model, stable spin direction exhibits singularity at location of $mQ_y = Q_s + k$, and leads to significant depolarization. Here, m, k are integers, Q_y is the vertical betatron tune and Q_s is the spin precession tune. This is the so-called snake resonance, and was first observed during numerical simulation by Lee and Tepikian [23]. They are also experimentally observed at IUCF [24] as well as RHIC [25]. m is also called the order of the snake resonance. In an accelerator with only a single snake, an intrinsic spin resonance can drive both even order snake resonances (m is an even number) as well as odd order snake resonance (m is an odd number), and available betatron tune space for polarized beam operation can be rather limited.

With dual snake setup like RHIC, on the other hand, all the odd order snake resonances are eliminated and only the even order snake resonances exist in the absence of closed orbit distortion. This greatly opens up the available tune space for accelerating polarized beams. However, snake imperfections and imperfection resonances can bring back even order snake resonances, and result in significantly reduction of betatron tune space for preserving polarization. In addition, the imperfection of snake can deviate spin tune away from half integer, and causes each snake resonance to split [1]. Hence, optimizing snake configuration as well as minimizing closed orbit distortion are critical in avoiding snake resonances.

Careful choice and precise control of betatron tune to stay away from any snake resonances are critical to preserve polarization. For $Q_s = \frac{1}{2}$, one can see that snake resonance is forbidden at locations of $Q_y = \frac{n}{2m+1}$. For RHIC, $Q_y = 29.673$, at the vicinity of 3^{rd} order resonance, was chosen for accelerating polarized protons beyond 100 GeV, where three strong very strong intrinsic resonances are present.

In reality, the presence of snake imperfections and imperfections resonances brings back even order snake resonances. The imperfection of snake can deviate spin tune away from half integer, and causes each snake resonance to split [1]. Both can significantly shrink the available space for the betatron tune during the acceleration. Hence, optimizing snake configuration as well as minimizing closed orbit distortion are critical in minimizing polarization loss. In addition, it is also very critical to keep the spin tune as close to half integer as possible. In RHIC, spin tune shift can come from the error in the angle between the axes of the two snakes, and the horizontal orbital angle at the two snakes [26].

In the presence of very strong intrinsic resonance, i.e. $\epsilon_k > 0.5$, the snake resonances can be overwhelming and the tolerance on closed orbit and beam parameters can be at a level of impractical for operation. In this case, more snakes option should be explored. To accelerate He-3 in RHIC, because of the large anomalous g-factor, the intrinsic resonance for He-3 is about a factor of 2 stronger than the resonances for protons. Fig. 3 shows the snake resonance spectrum with current RHIC dual snake configuration. However, this can be greatly mitigated by adding two more pairs of snakes as shown in the bottom plot of Fig. 3. The 6-snake setup not only opens up available betatron tune spaces for acceleration, but also greatly relaxes the tolerance on other beam parameters [27]. As derivatived from the first order spin resonances like intrinsic resonance, the strength of snake resonance is tightly associated with strength of its driving resonance. Generally, the stronger the intrinsic resonance, the more harmful the snake resonance is. However, it is also worthwhile to point out the polarization crossing a snake resonance does not obey the Froissart-Stora formula. Currently, this is only studied through numerical spin tracking.

Polarization Lifetime

In high energy colliders like RHIC, at the store energy carefully chosen to be distant from major depolarizing resonances, both beams undergo beam-beam interaction, which leads to betatron tune shift as well as incoherent tune spread for each beam. For RHIC, the beam beam tune spread can be as large as 0.0075 per collision for polarized proton physics operation. This can populate particles in the beam sitting on a snake resonance, and polarization deterioration can happen during long hours of store as observed at RHIC [28].

Copyright © 2013 CC-BY-3.0 and by the respective authors

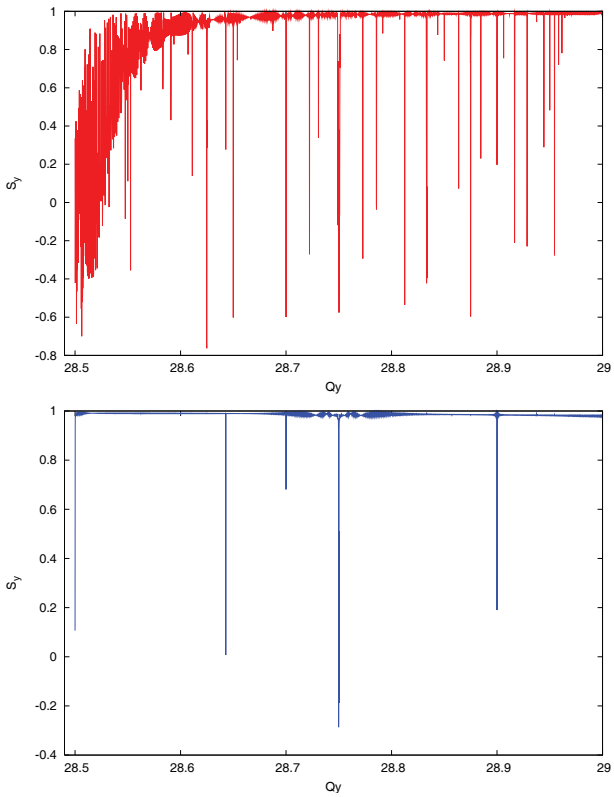


Figure 3: Top plot shows the snake resonance spectrum with RHIC dual snake setup, while bottom plot corresponds to 6-snake setup. Both plots show the vertical component of the spin vector as function of vertical betatron tune.

In addition to its impact on betatron motion, the beam-beam force also provides kick to spin motion. This effect was investigated by Batygin and others [29]. For a Gaussian distributed round relativistic beam, the electric field and magnetic field are $\vec{E} = \frac{qn}{2\pi\epsilon_0 r}[1 - (exp(-\frac{r^2}{2\sigma_2})]\hat{r}$ and $\vec{B} = \frac{1}{c}\vec{\beta} \times \vec{E}\hat{\phi}$, where qn is the charge line density of the beam, σ is the transverse beam rms size, $\hat{r}$ and $\hat{phi}$ are the unit vector along the radial and azimuthal direction of beam. The corresponding beam beam tune shift is $\xi = \frac{Nr_0\beta_*}{4\pi\gamma\sigma^2}$, where r_0 is the classic radius of the particle. Apply this to the Thomas-BMT equation, one can then estimate the maximum spin kick $2\pi\epsilon_{bb}$ from the beam-beam interaction as

$$\epsilon_{bb} = 2G\gamma\xi\sigma\frac{r}{\sigma}\frac{(1 - exp(-\frac{r^2}{2\sigma_2}))}{\frac{r^2}{2\sigma_2}}. \quad (17)$$

Fig. 4 shows the calculated maximum beam-beam spin kick as a function of distance from the center of beam for a beam of 15πmm-mrad emittance (95%, normalized) at RHIC store energy of $G\gamma = 487$. 0.7 m β-function at collision point and beam-beam tune shift $\xi = 0.01$ are assumed. In general, this is comparable to very weak lattice driven spin resonances. Thus, the beam-beam driven snake resonances are very weak for accelerators like RHIC that are equipped

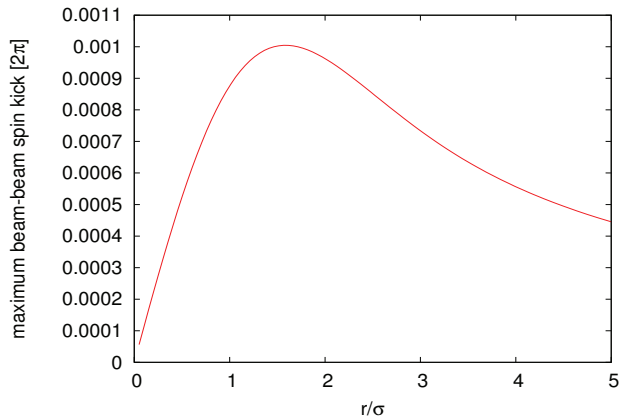


Figure 4: Maximum spin kick from beam-beam for a Gaussian round beam at RHIC store energy of $G\gamma = 487$. The β^* is 0.7m, and normalized 95% beam emittance is 15πmm-mrad for the calculation. The beam-beam parameter is chosen as 0.01 for this calculation.

with full snakes, and should be fully benign to beam polarization at store as long as the betatron tune stays away from the snake resonances. So far, detailed studies and analysis of the RHIC beam-beam impact on the polarization lifetime indicate that beam polarization deterioration at store is still due to the snake resonance at $5Q_y = Q_s + 3$ [28]. However, for accelerators with no snakes, beam-beam kick can drive additional spin resonances and result in polarization losses as observed at electro-positron collider LEP [30] and HERA, a polarized electron and proton collider [31]. Hence, it is critical for the choice of the working point, i.e. the tunes without collision to ensure long polarization lifetime.

CONCLUSION

Accelerating polarized protons to high energy is challenged by various depolarizing mechanisms driven by magnetic fields from manufacturing errors, misalignments, betatron oscillation and etc. Motivated by the need of having high energy polarized protons to study proton spin structure as well as other spin dependent physics, continuous efforts over the past couple of decades have been made in seeking ways to overcome spin depolarizing resonances and preserve polarization to high energy. Table 1 lists the achieved polarized proton performance at various facilities. The operating period for each facility is also listed. In Table 1, RHIC polarization is measured with an absolute polarimeter using H-jet [32]. It reflects the polarization averaged over a store, typically, 8 hours.

Physics of polarized protons in accelerators is a very rich topic, and this tutorial presentation can only cover the very basics of spin dynamics in a circular accelerator. The nonlinear aspects of spin dynamics, the effect of synchrotron radiation on polarization as well as challenges in robust numerical spin tracking are not covered in this presentation due to the complexity of each topic and limited space. In

Copyright © 2013 CC-BY-3.0 and by the respective authors

Table 1: Performance of Polarized Protons Facilities

facility	operating period	beam energy [GeV]	max polari--ration	beam intensity 10^{11}
ZGS	1969-1979	12	71%	0.9
AGS	1979-present	23	70%	2
IUCF	1982-1995	0.2	N/A	N/A
COSY	1985-present	3	N/A	N/A
RHIC	2000-present	255	57%	1.8

addition, this presentation also couldn't cover the topics of spin manipulation driven either by the physics program or by the needs of diagnostics like non-destructive spin tune measurement. The author can only hope this presentation serves as a brief introduction to attract those talented colleagues in the community to join the journey of this rich and interesting physics of polarized beams in accelerators.

ACKNOWLEDGMENT

The author would like to thank the NA-PAC organization committee for this opportunity. The author would like to thank Dr. T. Roser, Prof. S. Y. Lee, Dr. E. Courant, Prof. A. Chao, Prof. A. Krisch, and Dr. M. Syphers for introducing me to the field of high energy polarized proton beams. The author would also like to thank Dr. D. Barber, Prof. G. Hoffstatter, Dr. Ptitsyn, Dr. Derbenev, Dr. S. Mane and many others for introducing me to providing me with endless invaluable advises on spin dynamics. The author would also like to thank all her colleagues at BNL as well as her collaborators for their supports and fruitful discussions.

REFERENCES

[1] S. Y. Lee, *Spin Dynamics and Snakes in Synchrotrons*, World Scientific, Singapore, 1997.

[2] L. H. Thomas, Phil. Mag. 3, 1 (1927); V. Bargmann, L. Michel, V. L. Telegdi, Phys, Rev. Lett. 2, 435 (1959).

[3] K. Yokoya, Non-perturbative calculation of equilibrium polarization of stored electron beams, KEK Report 92-6, 1992

[4] A. Chao, Nucl. Instr. Meth. 29 (1981) 180

[5] S.R. Mane, Nucl. Instr. and Meth. A 485 (2002) 277.

[6] K. Heinemann, G. H. Hoffstatter, Tracking Algorithm for the Stable Spin Polarization Field in Storage Rings using Stroboscopic Averaging, PRE, Vol. 54, Number 4

[7] Courant E D and Ruth R 1980 BNL report BNL-51270

[8] M. Froissart and R. Stora, Nucl. Instrum. Methods Phys. Res. 7, 297 (1960).

[9] T. Roser, RHIC Polarized Collider and eRHIC, Proceedings of the 20th International Spin Physics Symposium, 2012

[10] D. L. Adams *et al.*, Phys. Lett. B276, 531 (1992).

[11] R. C. Fernow, A. D. Krisch, High Energy Physics with Polarized Proton Beams, Ann. Rev. Nucl, Part., Sci, 1981, 31:107-44, 1981

[12] F. Z. Khiari *et al.*, *Acceleration of polarized protons to 22GeV/c and the measurement of spin-spin effects in PP PP, Phys. Rev. D 39, 45-85*, (1989).

[13] A. Krisch, *ACCELERATING POLARIZED PROTONS WITH SIBERIAN SNAKES*, ACTA PHYSICA POLONICA B, No 5, Vol.20, 1998.

[14] M. Bai *et al.*, *Experimental test of coherent betatron resonance excitations*, Phys. Rev. E 56, 6002 (1997)

[15] M. Bai *et al.*, *Overcoming Intrinsic Spin Resonances with an rf Dipole*, Physical Review Letters 80, 4673(1998).

[16] T.Roser, *Partial Siberian Snake Test at the Brookhaven AGS*, in High Energy Spin Physics: 10th International Symposium, ed. T.Hasegawa, et al., Nagoya, Japan, 1992, (Univesal Academic Press, Inc.,1992), p.429.

[17] H.Huang, *et al.*, *Polarized Proton Beam in the AGS*, 13th International Symposium on High Energy Spin Physics, Protvino, (September,1998). 13th International Symposium on High Energy Spin Physics, Protvino, (September,1998).

[18] H. Huang, *et al.*, *Preservation of Proton Polarization by a Partial Siberian Snake*, Physical Review Letters 73, 2982(1994).

[19] T. Roser, *et al.*, *Acceleration of polarized beams using multiple strong partial siberian snakes*, proceedings of Spin2004, Trieste, Italy, 2004.

[20] H. Huang, *et al.*, *Polarized Proton Acceleration in the AGS with Two Helical Partial Snakes*, proceedings of Spin2006, Kyoto, Japan, 2006.

[21] Ya. S. Derbenev, A. M. Kondratenko, Sov. Phys. Dokl. 20, 562 (1976).

[22] I. Alexseev *et al.*, *Design Manual - Polarized Proton Collider at RHIC*, 1997.

[23] S. Y. Lee, S. Tepikian, Phys. Rev. Lett. 56 (1986) 1635

[24] V. A. Anferov etc, Siberian Snake Experiments at the IUCF Cooler Ring, Proceedings of PAC99, New York, 1999

[25] M. Bai, *et al.*, *Observation of Snake Resonances at RHIC*, Proceedings of the 19th International Spin Physics Symposium, 2010

[26] M. Bai, V. Ptitsyn, T. Roser, *Impact on Spin Tune From Horizontal Orbital Angle Between Snakes and Orbital Angle Between Spin Rotators*, C-A/AP/#334, 2008

[27] M. Bai, *et al.*, *Explore the Possibility of Accelerating He-3 at RHIC*, Proceedings of IPAC2012, New Orleans, 2012

[28] M. Bai, *et al.*, *Status and Plans for the Polarized Proton Collider at RHIC*, Proceedings of IPAC2013, Shanghai, 2013

[29] Y. K. Batygin, Spin depolarization due to beam-beam collisions, Phys. Rev. E, vol. 58, Num. 1, 1998

[30] R. Assmann et al, Experiments on Beam-Beam Depolarization at LEP, Proceedings of Particle Accelerator Conference, 1995

[31] D. Barber et al, Beam-Beam Depolarization at HERA, Proceedings of Particle Accelerator Conference, 1995

[32] H. Okada *et al.*, Phys. Lett. B 638 (2006)

Copyright © 2013 CC-BY-3.0 and by the respective authors

STATUS OF THE FRIB FRONT END*

E. Pozdeyev#, N. Bultman, G. Machicoane, G. Morgan, X. Rao, and Q. Zhao
FRIB, East Lansing, MI 48824, USA

Abstract

The FRIB Front End will provide beams of stable ions with a mass up to uranium at a beam energy of 500 keV/u and intensity required to achieve a power of 400 kW on the fragmentation target. In this paper, we describe progress with the design and construction of the Front End and its systems.

DESIGN AND PERFORMANCE REQUIREMENTS

FRIB will be a premier multiuser nuclear physics facility providing stable ion beams accelerated to energies above 200 MeV/u and with a beam power on the target up to 400 kW [1]. These project requirements are translated into stringent requirements on the front end design and performance. The FRIB front end will provide stable ion beams up to uranium with an energy of 500 keV/u. The required intensity of uranium beam is 13.5 pμA and the charge state is 33+. This intensity is at the edge of performance demonstrated by modern ECR ion sources. To decrease technical risks and reduce operational stress on the sources, the front end is designed to transport two charge states simultaneously for all ions heavier than xenon with a charge state of 25 and higher. To control losses in the linac and meet experimental requirements the front end includes a collimation system to limit the transverse beam phase space. The longitudinal phase space is controlled by means of limiting the longitudinal acceptance of the RFQ. In addition, the front end will provide required variability of the bunch intensity by up to nine orders of magnitude to meet experimental needs. Beyond controlling the bunch intensity, it is also required to control the beam pulse length and the pulse repetition rate to simplify linac tuning and safely ramp up the beam power on the target.

High availability, maintainability, reliability, and tunability are required for the front end to operate FRIB as a national scientific user facility. These requirements, as well as project budget and schedule limitations require using proven, reliable technical solution as much as possible. However, those solutions frequently have to be taken to new levels with evolutionary changes and upgrades to demonstrate world-breaking performance required by the project.

Finally, to meet possible future programmatic demands the front end has to be upgradable and includes required provisions for future enhancements.

FRONT END LAYOUT

The FRIB front end includes two ECR sources, one of which is a room temperature 14 GHz source based on the ARTEMIS source developed at NSCL, and the other is a superconducting 28 GHz source based on VENUS design [2]. The beam extracted from the sources is transported through LEBT to the tunnel, where it is accelerated by an RFQ and injected into the SRF driver linac. The sources are placed on high voltage platforms that can be biased up to 100 kV to match the RFQ injection energy for all beams. Table 1 shows principle parameters of the Front End. The Front End layout is shown in Figure 1.

Table 1: Front End Principle Parameters

LEBT (before RFQ)	
Energy (keV/u)	12
Nominal beam current (eμA, typ.)	400
Emittance (πμm, 99.5%, norm.)	0.9
MEBT (after RFQ)	
Energy (keV/u)	500
Nominal current (eμA, typ.)	330
Emittance (πμm, 99.5%, norm.)	1.1
Long. Emittance (πkeV/u·ns, 99.5%)	1.5
Bunch repetition rate (MHz)	40.25, 80.5
Beam pulse length (μs)	0.6 – CW

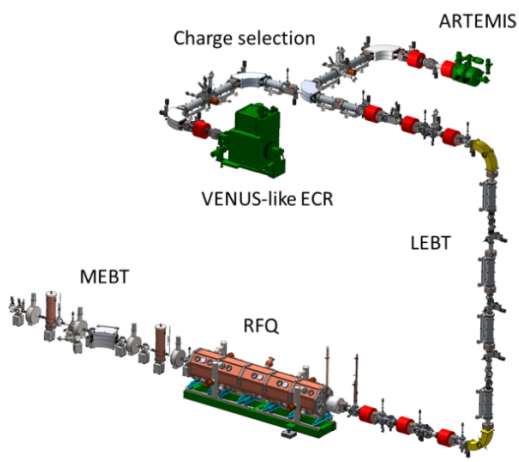


Figure 1: FRIB Front End layout.

FRONT END SYSTEMS

Ion Sources

The ARTEMIS ECR source, built at MSU and based on the AECR-U ECR developed at LBNL, operates at

*Work supported by the U.S. Department of Energy Office of Science under Cooperative Agreement DE-SC0000661 and grant #DE-FGO2-08ER41553
#pozdeyev@frib.msu.edu

Copyright © 2013 CC-BY-3.0 and by the respective authors

14.5 GHz with room temperature coils. The source will be used for commissioning FRIB and during some first years of operations for production of light and medium mass ions. Minimal re-configuration of the source is required to make the source compatible with operation on a high voltage platform and to boost its performance. The source currently produces 70 μA of Ar and Kr beams and will be able to generate up to 100 μA after upgrade.

The superconducting high-performance source will be based on the design of VENUS ECR ion source operating at a maximum frequency of 28 GHz. A world intensity record of 450 μA of U^{33+} was demonstrated by VENUS at LBNL in 2011. Figure 2 shows the M/Q scan with the source world-breaking record performance. The measured emittance for this charge state showed that 95% of the beam was within the FRIB acceptance.

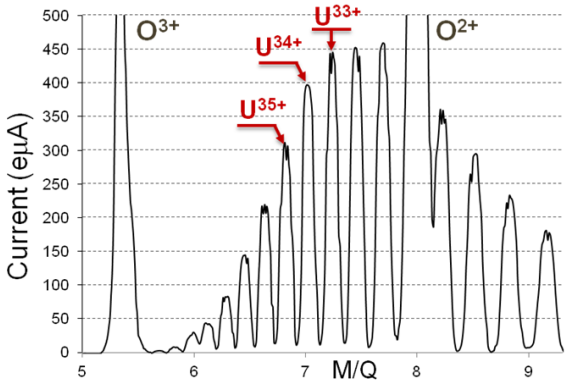


Figure 2: VENUS M/Q intensity scan for a uranium beam, demonstrating world record intensity of charge states 33+ and 34+.

The original VENUS cold mass design employs azimuthal bladders inflatable with liquid Indalloy to provide pre-stress. Once the metal is solid, the magnet could be disassembled only if the whole cold mass is warmed up above the metal's melting temperature, which has never been demonstrated. This design feature of the source was identified as a technical risk. To address the risk, a novel clamping scheme is pursued for the FRIB source. The scheme employs radial keys and water bladders to define the pre-stress state. This approach was developed by SUPERCON/LBNL for LARP high field magnets and allows for disassembling the magnet, changing components, and a fine control of the pre-stress state. A Collaboration between FRIB and LBNL was established to develop a design of the cold mass with radial keys.

In addition to the cold mass modifications, the cryostat will be modified comparatively to the original VENUS to include two GM-JT cryo-coolers to boost the cooling capacity from 6 W to 10 W to account for a higher dynamic heat load generated by the plasma Bremsstrahlung electrons and two Al-330 cryocoolers to cool the heat shield of the cryostat.

RFQ

The FRIB RFQ utilizes a 4-vane structure to accelerate single and two-charge state beams from 12 to 500 keV/u with estimated transmission efficiency above 80%. Table 2 shows main RFQ parameters.

Table 2: RFQ Principle Parameters

Frequency (MHz)	80.5
Injection/Output energy (keV/u)	12/500
Design charge-to-mass ratio	1/7-1/3
Accelerating voltage ramp (U, kV)	60 – 112
Surface electric field (Kilpatrick)	1.6
Quality factor	16500
Operational RF power (kW, O-U)	15-100
Dipole modes (closest, MHz)	78.3 / 83.2
Length (m)	5.04

The RFQ beam physics design is optimized to minimize the longitudinal emittance of the accelerated beam as described in [3][4]. To increase the RFQ output energy a linear accelerating voltage ramp is implemented. The linear voltage ramp is accomplished through proper sizing of the vane undercuts. Dipole mode suppression rods attached to the structure endplates are utilized to move dipole mode frequencies away from the accelerating mode frequency. The quadrupole and dipole mode local perturbations are fine-tuned during construction using 27 fixed mechanical slug tuners distributed along the length of the machine. A full 3D model of the RFQ, including undercuts, stabling rods, and the slug tuners, was implemented in the CST Microwave Studio (MWS) [5] to accurately select required parameters and simulate fields and surface losses.

Mechanical construction of the RFQ will be performed as a brazed structure with dual-circuit cooling water resonance control. Mechanical fabrication is performed in 5 longitudinal sections to optimize machining and handling. All components are made of high-conductivity copper and actively water cooled. The power is fed using a single magnetic-field loop-coupler drive. More information on the RFQ design can be found in [6].

Beam Transport and Other Systems

In 2007, VENUS demonstrated intensity required for FRIB for a 238U beam with the two charges states, 33+ and 34+, combined. Based on this result, the FRIB front end was designed achromatic, able to accelerate two charge states from an ion source to double intensity. Although recent tests demonstrated that significantly better performance from VENUS can be achieved, a decision was made to leave the front end design unchanged. To facilitate transport of two-charge state beams through the LEBT electrostatic quadrupoles and two 90° deflectors are used in the vertical transport line.

Copyright © 2013 CC-BY-3.0 and by the respective authors

The electrostatic quadrupoles were designed by Kurt Stiebing, manufactured by Roentdek Handles GMBH, and delivered to FRIB in August of 2013. The quadrupole assemblies were made of precision-stamped formed metal to reduce cost and weight of the assemblies. The measured manufacturing errors of the quadrupole assemblies are typically less than 200 μm that satisfies FRIB requirements. Figure 3 shows a photograph of a triplet assembly.

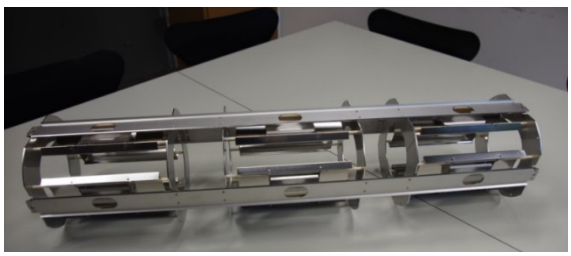


Figure 3: Electrostatic LEBT quadrupole triplet assembly. The length of the assembly is 91 cm.

Upstream of the RFQ, LEBT includes a multiharmonic buncher and a velocity equalizer, both are room-temperature low-power quarter wave resonator cavities. The former is used to bunch the DC beam and the latter is required to eliminate the energy spread of two charge state beams before injecting beams into the RFQ.

To reduce losses in the superconducting linac, the beam is collimated by several apertures in the LEBT. The front end includes a chopper to vary the duty cycle. The buncher will control the pulse length from several hundreds of ns to CW and the pulse frequency from 0 to 30 kHz. Several mesh screens installed in LEBT allow for reducing the beam intensity by up to nine orders of magnitude while keeping the nominal bunch frequency unchanged. Two 90° electrostatic deflectors in the vertical transport line are incorporated into the machine protection system. The voltage on the deflector electrodes is controlled by fast switches that receive the inhibit signal from the MPS with shut-off time below 1 μs.

Downstream of the RFQ, MEBT includes two room-temperature QWR bunchers, four SC solenoids, an energy analyzing dipole, and diagnostics. MEBT matches the beam to the SC linac and removes un-accelerated beam from the RFQ.

SUMMARY OF PROGRESS

The design of front end systems and early procurement of high priority items are ongoing. The low energy multi-harmonic buncher and electrostatic quads were manufactured and delivered. The commissioning source ARTMEIS is undergoing minor modifications to make it compatible with operations on a high voltage platform. The physics design and the preliminary engineering design of the RFQ have been completed. A design-build contract for the final design and manufacturing of the RFQ was awarded to industry. The final engineering design of the RFQ is in progress. Delivery of the RFQ and its high power test are expected in the summer of 2015. The design of the MEBT quarter wave resonators is in its final stage. Their procurement is expected to begin by the end of 2013. The design of the cold mass of the high performance source is being developed in collaboration with LBNL. It is important to emphasize that the high performance source is not required to start commissioning of the front end and will be brought online approximately a year after the start of commissioning but before the end of the project.

The front end design was integrated with civil facilities to allow for starting civil construction. Also, the front end was integrated with other accelerator and experimental systems. The design was value engineered. One example is the increase of the RFQ energy from the originally planned 300 keV/u to 500 keV/u by implementing voltage ramping that allowed eliminating one cryomodule. Commissioning of the front end with the room temperature source is expected to start in the fall of 2017.

ACKNOWLEDGMENT

The authors would like to thank A. Facco, L. Young, J. Stovall, S. Prestemon, S. Caspi, H. Felice, R. Hafalia, E. Rochepault, P. Ostroumov, R. Vondrasek, R. Pardo, A. Aleksandrov, D. Wang, X. Guan, and Q. Xing of Tsinghua University for their input to this work.

REFERENCES

[1] J. Wei et al., "Progress towards the facility for rare isotope beams", Proc. of NA-PAC 2013, FRYBA01.
[2] D. Leitner et al, Rev. Sci. Instru. 79 (2008) 02C710.
[3] P. Ostroumov, et al, Phys. Rev. ST Accel. Beams 5, 060101 (2002).
[4] Q. Zhao, et al, LINAC 2004, Lübeck, Germany, p. 599.
[5] CST Microwave Studio, v.12, CST GmbH (Darmstadt, Germany), 2012. www.cst-world.com
[6] N. Bultman et al, IPAC 2013, Shanghai, China, p. 2866, WEPFI075.

Copyright © 2013 CC-BY-3.0 and by the respective authors

UPGRADE OF ARGONNE'S CW SC HEAVY ION ACCELERATOR*

P.N. Ostroumov#, A. Barcikowski, Z. Conway, S. Gerbick, M. Kedzie, M.P. Kelly, S. Kim, S. Kutsaev, R. Murphy, B. Mustapha, R. Pardo, D. Paskvan, T. Reid, S. Sharamentov, G. Zinkann
ANL, Argonne, IL 60439, U.S.A.

Abstract

The ATLAS National User Facility at Argonne National Laboratory is the world's first CW superconducting ion linac. The accelerator is being continuously upgraded to extend its scientific reach. To increase the efficiency and intensity of both stable and radioactive beams [1], we have developed, built and installed a new normal conducting CW RFQ capable of providing a 295 keV/u for any ion from proton to uranium. The RFQ has been fully integrated into ATLAS and in routine operation since January 2013.

A new cryomodule containing 7 high-performance 72.75 MHz SC QWRs and 4 SC solenoids was completed this year and has been commissioned off-line. New design and fabrication techniques for these QWRs resulted in record voltages up to 4-5 MV per cavity and low residual resistances of 2-3 nΩ at 2K were demonstrated in individual cold tests of several QWRs. The primary purpose of the new cryomodule is to replace 3 old cryomodules and to increase the intensities of accelerated stable ion beams up to several hundred electrical micro amps. Beam commissioning is expected by the end of the year after significant modification of the accelerator tunnel for increased shielding and installation of a redesigned beam transport system.

CW RFQ

Last summer we commissioned a CW RFQ designed and built for the ATLAS Facility [2, 3]. Several innovative ideas were implemented in this CW RFQ. By selecting a multi-segment split-coaxial structure we have achieved moderate transverse dimensions for a 60.625 MHz resonator. For the design of the RFQ resonator and vane tip modulations we have developed a full 3D approach which includes MW-Studio and TRACK simulations of the entire structure [4]. A novel trapezoidal vane tip modulation is used in the acceleration section of the RFQ which resulted in increased shunt impedance. To form an axially symmetric beam exiting the RFQ, a very short output radial matcher, only $0.75\beta\lambda$ long, was developed. Figure 1 shows an internal view of the RFQ's last two segments. The openings in the vane and trapezoidal modulation of vane tips are clearly seen.

An advanced fabrication technology was applied for the construction of the RFQ which included precise machining and two-step high temperature brazing. Thanks to the high accuracy of the overall fabrication, the assembly of the 5-segment RFQ was straightforward and no additional alignment was required. The resonance frequency control system based on water temperature regulation showed excellent performance. The RF measurements show very good RF properties for the resonator, with a measured intrinsic Q equal to 94% of the simulated value for OFE copper. The multi-segment split-coaxial structure creates strong coupling between the quadrants and individual RFQ segments which reduces the effect of local frequency deviations on electromagnetic field distortions. Therefore, no bead-pull measurements were required to tune the accelerating field.

An O^{5+} ion beam extracted from an Electron Cyclotron Resonance (ECR) ion source was used for the RFQ commissioning. In off-line beam testing, we found excellent agreement of the measured beam parameters with the results of beam dynamics simulations [3]. The great success of this advanced design and fabrication technology is reflected in the measured beam parameters after the RFQ which are nearly identical to the simulated data.

After the successful off-line commissioning of the ATLAS CW RFQ accelerator with oxygen and helium beams, the device was moved, installed and integrated into the ATLAS system during the October-November 2012 period. Fig. 2 displays the current view of the ATLAS front end. The RFQ is directly attached to the first SC cryomodule. For the RFQ beam matching we have incorporated a MEBT which includes 3 SC solenoids and a SC cavity as a buncher [1]. Since January 2013, the RFQ is in routine operation. The beam parameters have been measured after the Positive Ion Injector (PII) of ATLAS which includes three SC cryomodules. The beam energy and time spectra have been measured using silicon barrier detectors (Fig. 3). The results of these measurements are consistent with the TRACK simulations. The efficiency of ATLAS beams on

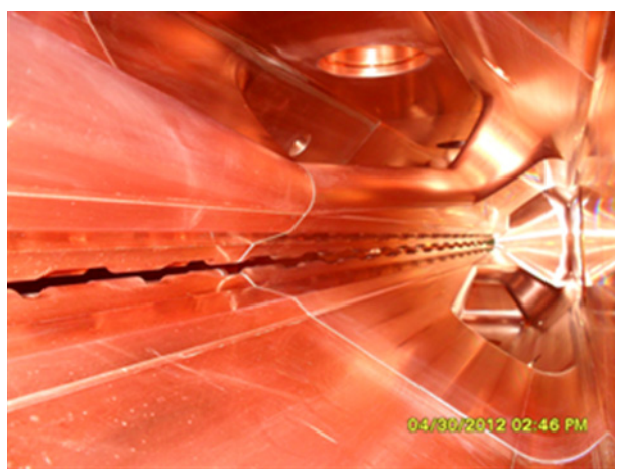


Figure 1: Internal view of the RFQ's high energy end.

* This work was supported by the U.S. Department of Energy, Office of High Energy Physics and Nuclear Physics, under Contract DE-AC02-06CH11357
#ostroumov@anl.gov

Copyright © 2013 CC-BY-3.0 and by the respective authors

target has doubled as compared to the pre-RFQ operation.

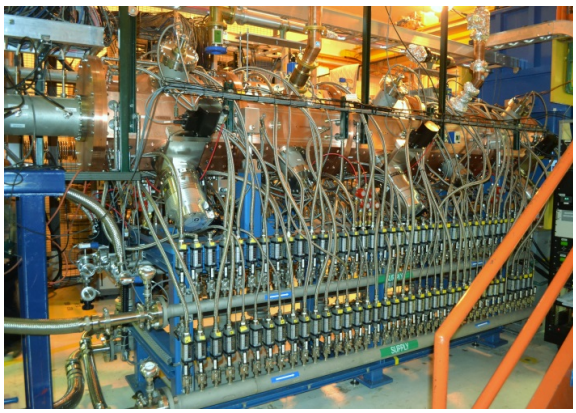


Figure 2: ATLAS front end with the RFQ in position.

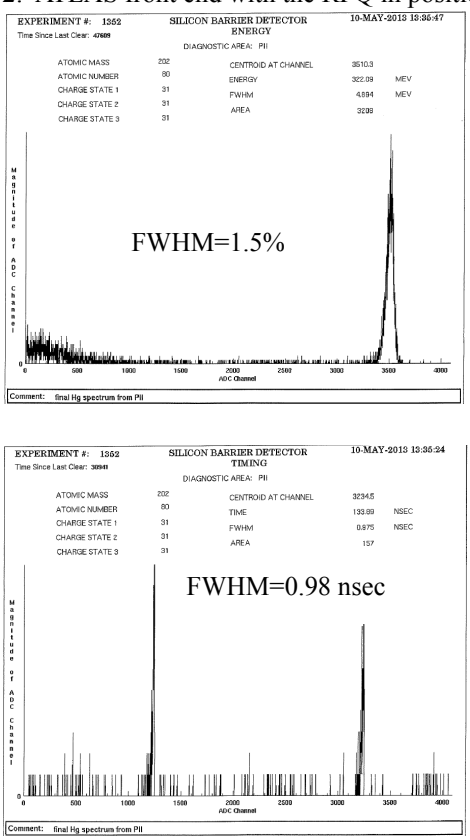


Figure 3: Mercury beam energy (top) and time spectra measured after the PII by elastic scattering at 7.5°.

QWR CRYOMODULE

While split-ring resonators are successfully operated at ATLAS with low-intensity ion beams, they exhibit a fundamental limit in the acceleration of high-intensity beams due to RF steering. Therefore we are replacing 16 ATLAS split-ring resonators with 7 QWRs. Four years ago we put into operation a new cryomodule containing seven 109 MHz β_{OPT}=0.15 QWRs to provide an additional 15 MV voltage to ATLAS. Now, we have developed and built a new cryomodule consisting of seven β_G=0.077 QWRs at 72.75 MHz SC cavities and four 9-Tesla SC solenoids. The new high-performance cryomodule will replace three existing ATLAS cryomodules of split-ring cavities to increase the intensities of accelerated ion beams.

Compared to the previous generation of quarter-wave resonators, several innovations were implemented into the cavity design, fabrication and RF surface treatment. The cavity geometry is highly optimized to reduce both electric and magnetic peak fields: both outer and inner conductors are conical as shown in Fig. 4a. During the fabrication of the niobium components, a wire EDM technique instead of machining was used to maintain clean surfaces prior to electron-beam welding. Electropolishing of the cavities was performed for a completed cavity with the integral helium vessel installed. Each cavity is equipped with a newly-developed double-window 4-kW adjustable RF coupler with a nitrogen cooled cold window [5]. To minimize microphonics due to pendulum vibration of the central conductor, the central drift tube in each QWR has been electrically centred by tuning to the highest resonant frequency [6]. An additional reduction in microphonics is achieved by installing mechanical dampers inside the central conductor [7].

The new QWRs will create accelerating gradients a factor of three higher, on average, than the existing split-ring cavities, and are designed to provide an accelerating voltage of 2.5 MV per cavity which results in a 17.5 MV total voltage gain in this cryomodule. Four 72.75 MHz QWRs were cold tested prior to installation in the cryomodule and all of them provided more than 4 MV without quenching achieving E_{PEAK}>70 MV/m and B_{PEAK}>105 mT [7,8].

CRYOMODULE COMMISSIONING

After the completion of the assembly in a clean room (Fig. 4b), the cavity-solenoid string was pumped out, sealed and moved outside the clean room. The following assembly work included the attachment of the cavity string to the box cryostat lid, installation of slow tuners, installation of nitrogen and helium distribution systems, alignment of cavities and solenoids, and plumbing of nitrogen and helium cooling systems. The appropriate choice of alignment mechanisms resulted in an accuracy of solenoid end positioning within ±250 μm [9]. After a thorough leak check of the nitrogen and helium systems, the cavity assembly was loaded into the box cryostat (Fig. 4c).

Due to the much higher beam intensity in the upgraded ATLAS, the linac radiation shielding is being significantly enhanced by the installation of 1-meter thick concrete walls. Meanwhile, the cryomodule has been cooled down and RF tested off-line. The following major tasks have been accomplished during the off-line commissioning:

- Each cavity was cooled down quickly in the temperature range from 150K to 50K as shown in Fig. 5.

Copyright © 2013 CC-BY-3.0 and by the respective authors

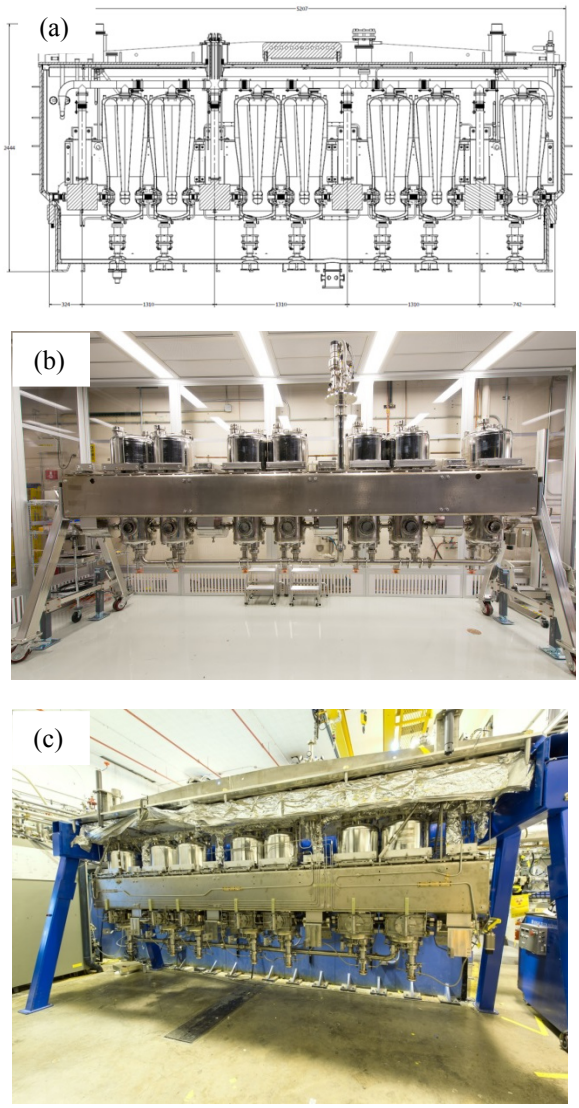


Figure 4: ATLAS intensity upgrade cryomodule. Side cross-sectional view (a), after completion of assembly in clean room (b) and after completion of full assembly prepared to load into the cryostat vacuum vessel (c).

- Due to the variable RF couplers, the multipactor conditioning took less than a couple of hours per cavity.
- RF testing demonstrated that each cavity is capable of providing an accelerating voltage greater than 3 MV.
- Microphonics were measured to be below 5 Hz at the 5σ-level in all cavities. Each cavity is equipped with a 4-kW RF amplifier and variable coupler which provide up to a 30 Hz bandwidth for RF control.
- The pneumatic slow tuner range varies from cavity to cavity and was from 17 kHz to 26 kHz at 70 psi. If necessary, the tuning range can be increased by applying up to 90 psi pressure to the helium gas used to drive the tuners.
- The cavities and solenoids are equipped with crosshair alignment targets. The latter were used for optical measurements of the cavity and solenoid positions in the cold cryomodule. At 4 K the solenoid alignment error was measured to be 80 μm rms.
- The static 4 K heat load of the entire assembly was measured to be 11 Watts which is an extremely low number for such a complex cryomodule.

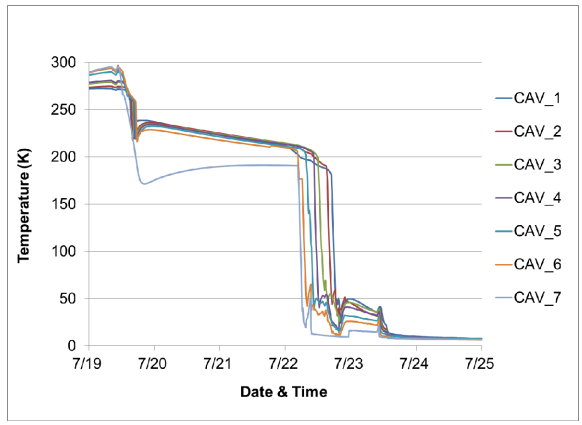


Figure 5: SC cavity temperatures vs time during the second cool down.

SUMMARY

A new CW RFQ with a suite of novel features has been developed, built and commissioned at ANL. The RFQ has doubled the ATLAS beam transport efficiency and demonstrated excellent performance since its integration into the accelerator in January 2013.

A new cryomodule with low-beta SC QWRs capable of providing 21 MV of accelerating voltage has been commissioned off-line and is being prepared for installation into the beamline. Beam commissioning through the new cryomodule is planned in December 2013.

REFERENCES

[1] P.N. Ostroumov, et al, PAC-11, March 28- April 1, New York, p. 2110.
[2] P. N. Ostroumov, et al., Phys. Rev. ST Accel. Beams 15, 110101 (2012).
[3] A. Perry, et al., "Beam Characterization of a New Continuous Wave RFQ Accelerator", accepted for publication in NIM A, August 2013.
[4] B. Mustapha, A.A. Kolomiets and P. N. Ostroumov, "A Full 3D Approach to the Design and Simulation of a Radio-Frequency Quadrupole", submitted for publication in PRST-AB.
[5] M. Kelly, et al, LINAC'10, Tsukuba, Japan, p. 884.
[6] Z. Conway et al., SRF'11, Chicago, USA, p. 943.
[7] M. Kelly, et al, Paper THIOC01 at SRF'13, Paris, France, September 23-27, 2013.
[8] Z. Conway, et al, Paper FRIOB01 at SRF'13, Paris, France, September 23-27, 2013.
[9] S. Kim, et al.,"4-Kelvin Alignment of the ATLAS Intensity Upgrade Cavities and Solenoids" In proc. of CEC/ICMC'13, Anchorage, Alaska, USA June 17-21, 2013.

Copyright © 2013 CC-BY-3.0 and by the respective authors

ION IMPLANTATION FOR SEMICONDUCTOR DEVICES: THE LARGEST USE OF INDUSTRIAL ACCELERATORS

S.B. Felch, Susan Felch Consulting, Los Altos Hills, CA 94022, USA
M.I. Current, Current Scientific, San Jose, CA 95124, USA
M.C. Taylor, Taylor Consulting, Lake Oswego, OR 97034, USA

Abstract

Ion acceleration of dopants and other ions is a critical and nearly universally employed tool for the fabrication of transistors in semiconductor devices and the various forms of electronic, photovoltaic and photonic materials. This paper reviews the major types of accelerators, ion sources, and scanning methods used in contemporary practice for ion implantation for electronic applications.

INTRODUCTION

The use of accelerated ions to dope and modify semiconductor materials, generally called ion implantation, is a core technology for the fabrication of integrated circuits (IC), which form the backbone of the global communications and advanced computation capabilities that have transformed modern life over the last half-century. The use of ion implanters in the IC industry, starting in the 1970s for precision doping of channel structures at doping densities of ~10^{-4} monolayers to set the threshold conditions for transistor switching, enabled the practical fabrication of complementary metal-oxide-semiconductor (CMOS) transistors that are now the dominant form of IC devices. Development of accelerator technologies capable of delivering highly stable and collimated ion beam currents, ranging from a few μA to 100 mA, and incident ion energies, ranging from 100 eV to ~10 MeV, have provided a broad and capable technology for fabrication of ICs for logic, memory, and analog operations, as well as an increasingly varied array of optical sensors and imaging devices. Ion implantation is now used for the overwhelming majority of applications for doping of semiconductor materials and in an increasing array of applications for creation and modification of electronic and photonic materials.

The yearly revenues from the sale of industrial ion implantation and materials modification tools are a US$1.5B market (in "normal" economic environments). In addition, there are substantial markets for suppliers of dopant species materials (~US$140M/year) and a diverse array of suppliers of spare and upgrade parts and services. Additional parts of the ion implantation commercial infrastructure include the suppliers of system components, magnets, power supplies, and vacuum pumps, and a varied array of metrology tools focused on process characterization and control applications.

The average number of commercial ion implantation systems sold per year, predominantly for fabrication of Si-based IC devices, has increased from ~250 to ~400 per year since 1980, as seen in Fig. 1. The year-to-year sales show large fluctuations due to the highly cyclic nature of IC fab construction trends, especially when driven by additional factors, such as shifts in dominant wafer sizes, introduction of new implanter machine types and IC devices, expansion into new global regions, and variations driven by general economic cycles. The combination of these technology and market factors has resulted in a rather steady "5-year" cycle in units sold per year over the last 3 decades.

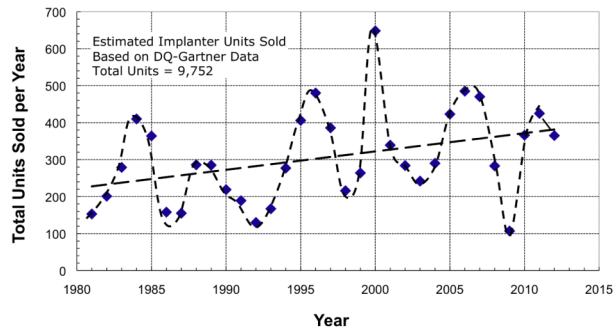


Figure 1: Estimates of the number of commercial ion implanters sold per year, mainly for IC fabrication. The data shown here are an underestimate, particularly for the earlier years.

SEMICONDUCTOR APPLICATIONS OF ION IMPLANTATION

The planar CMOS transistor, illustrated in Fig. 2, has been the workhorse device structure for IC devices for logic and memory applications since the mid-1980s.

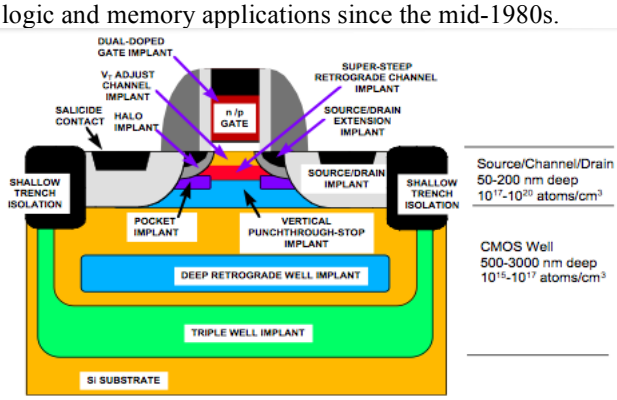


Figure 2: Sketch of major doped regions for a planar CMOS transistor.

For doping of near-surface (<100 nm) layers on Si with the common dopants B, As, and P, the beam energy

Copyright © 2013 CC-BY-3.0 and by the respective authors

requirement for atomic species is a fraction of a keV to a few tens of keV. Increasingly, the ion species of choice for low energy (sub-keV) implants is some form of molecular ion containing up to 18 dopant atoms (for $B_{18}H_{22}$), allowing for beamline operation at proportionally higher energies and significantly higher total beam flux for higher production throughputs. For deeper profiles to form CMOS wells for transistors and optical imagers, ion energies range up to several MeV.

The initial applications for ion implantation were for low dose (10^{11} to 10^{12} ions/cm^2) doping of CMOS channels to set the transistor switching, or "threshold", conditions. These implants required relatively modest beam currents, with 100 to 500 μA being common for "medium-current" implanters. By 1980, higher current sources and beamlines were developed for "high-current" machines, to produce beams of 1 to 30 mA of dopant ions. These machines were capable of efficient implants with doses of ~5x10^{15} ions/cm^2 used for CMOS source/drain junctions, as well as emitter, buried layer, and collector implants for bipolar devices.

By the late 1980s, implantation machines capable of ion energies of ~1-2 MeV were being used for doping deep "retrograde" wells in CMOS devices, to suppress latch-up instabilities between neighboring well structures and to reduce radiation-generated "soft failures" in Dynamic Random-Access Memory (DRAM) arrays. With the evolution of complex doping schemes to suppress lateral punch-through between source and drain junctions in short channel (<100 nm) transistors, ion implanters were developed with capabilities for mid-10^{14} ions/cm^2 doping at beam incidence angles up to 45°, to provide additional well doping in a "halo" surrounding shallow source-drain extension (SDE) junctions.

The CMOS transistors of the current decade are three-dimensional structures, called FinFETs or tri-gate transistors. The majority of implants for these devices continue to be the same, with over 40 implant steps per device for doping and materials modification applications. However, some of these implants, such as the source/drain extensions, need to be "conformal" in order to uniformly dope the sidewalls and top surface of the fins.

ACCELERATOR DESIGNS

Given the broad range of energies and doses in use for CMOS transistor doping and other materials processing, a variety of accelerators with quite different designs and beam scanning methods are used for each of the specific application segments shown in Fig. 3. The typical classifications for these general machine types are:

- Medium current — ion beam currents between 10 μA and ~2 mA
- High current — ion beam currents up to ~30 mA; ~100 mA for SIMOX (Separation by Implantation of Oxygen) beams
- High energy — ion energies above 200 keV and up to 10 MeV
- Very high dose — efficient implant of doses greater than 10^{16} ions/cm^2.

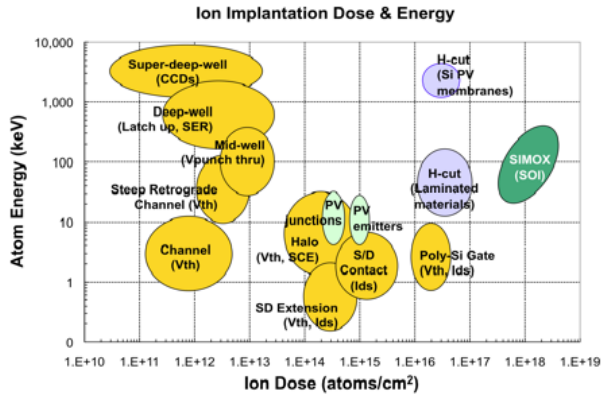


Figure 3: Dose and atom energy regions for CMOS transistor doping (gold), high dose hydrogen implants for Si layer splitting (lavender), and direct implantation of oxygen to form Silicon-on-Insulator (SOI) wafers (green).

Accelerator systems for ion implantation are provided commercially by a number of vendors, with the business being dominated by a few long-standing companies: Applied Materials/Varian Semiconductor Equipment (Gloucester, MA), the market leader; Nissin Ion Equipment (Kyoto, Japan), with a strong Asian market position; Advanced Ion Beam Technology (Hsinchu, Taiwan), a new high-current vendor; Axcelis Technologies (Danvers, MA), leading the high-energy market; and SEN Corporation (Shikoku, Japan), former Axcelis partner also with a strong Asian market presence. Other smaller vendors include Ion Beam Services (Rousset, France), a new Plasma Immersion Ion Implantation (PIII) and SiC implanter company; Ulvac Technologies (Japan), long-time vendor for research and development (R&D) tools; High Voltage Engineering (Netherlands) and National Electrostatics Corporation (Madison, WI), both supplying specialty R&D tools; and several radio frequency (RF) linac vendors known to be supplying R&D units for MeV proton beams for Si wafer cleaving for photovoltaic (PV) applications.

Beam current requirements for each machine type have increased as the wafer sizes and implanted areas increased from the early days of 75 mm diameter wafers to the present standard of 300 mm, with the contemplated increase to 450 mm after 2015. In addition, the increased requirements for dose accuracy (1% or better) and control of ion incidence angle (<0.5° for critical implants) place tight constraints on ion beam stability, scan uniformity, and beam collimation in the area near the wafer surface.

Beamline System Types

Each of the wide variety of ion implantation beamline designs contains certain general groups of functional components (see Fig. 4). The first major segment of an ion beamline includes a device known as an ion source to

Copyright © 2013 CC-BY-3.0 and by the respective authors

generate the ion species. The source is closely coupled to biased electrodes for extraction of the ions into the beamline and most often to some means of selecting a particular ion species for transport into the main accelerator section. The ion source usually is an arc-discharge plasma type, fed by a vapor of the atoms to be ionized, accelerated, and implanted. The "mass" selection is often accomplished by passage of the extracted ion beam through a magnetic field region with an exit path restricted by blocking apertures, or "slits", that allow only ions with a specific value of the product of mass and velocity/charge to continue down the beamline.

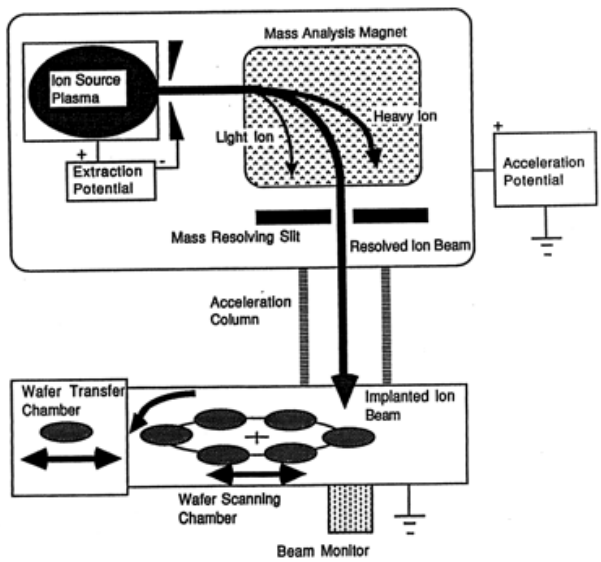


Figure 4: Major ion implantation beamline components.

If, as is often the case, the desired ion energy is different than the potential used to extract ions from the plasma source, the "selected" ion beam is accelerated (or decelerated) by additional sets of electrodes or RF fields. If the target surface is larger than the ion beam diameter and a uniform distribution of implanted dose is desired over the target surface, then some combination of beam scanning and wafer motion is used.

Finally, the implanted surface is coupled with some method for collecting the accumulated charge of the implanted ions, so that the delivered dose can be measured in a continuous fashion and the implant process can be stopped at the desired dose level. Sometimes the wafer is encased within a Faraday cup assembly, with appropriate methods of exclusion of extraneous charges from electrons and other ions within the beam plasma and charge losses due to secondary electrons and sputtered ions.

The design of an ion implantation beamline often needs additional components to satisfy the target requirements. These include components to make the scanned beam parallel at the surface of the target wafer and sources of electrons and ions to be injected into the ion beam plasma in the region close to the final target surface. These electrons and ions are needed to improve the space-charge balance in the ion beam, thus stabilizing the beam collimation and controlling the local potentials and current flows on the target surface.

The Varian VIISta 900XP [1], shown in Fig. 5, is an example of a medium-current beamline implanter with many of the components shown in Fig. 4. This beamline is capable of overall acceleration of single-charged ions to 300 kV (and P^{+3} ions to 900 keV) and contains a number of additional components, including a small deflection magnet and slit assembly placed directly after the source/extraction region and an electrode array for either accelerating or decelerating the selected ion beam prior to emerging from the main mass-selection (analyzer) magnet. The main function of the source filter magnet and slit is to prevent the P_2^+ and P_3^+ multimer ions (which can lead to energy and dose errors in P^{+2} and P^{+3} beams) from entering the main selection magnet and slit assembly and traveling to the target wafer.

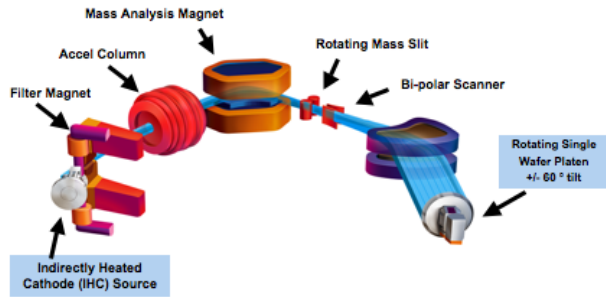


Figure 5: Beamline components of a Varian VIISta 900XP medium-current ion implanter.

Accel-Decel Beamlines

High-current beamlines, which are designed to maximize the ion flux delivered to the target wafer surface and often operate at low energies (1 keV or less), are usually shorter and contain fewer beamline components than medium-current designs. The short beamline path (often <2 m from source to wafer) and open geometries in the magnet analysis section result in improved ion transmission in "drift" mode with the only acceleration stage at the source extraction. To further increase the available ion flux for low energy (<1 keV) implants, an electrostatic deceleration lens is added just after the mass resolving slits. With the decel lens powered up, boron ion beams at energies as low as 0.2 keV can be delivered to the wafer surface with beam currents comparable to drift mode currents at 10x higher energies.

A limitation of this "accel-decel" mode of beam transport is that if dopant atom neutrals are formed by collisions with background gas molecules in the region following the mass analysis magnet and before the decel lens, neutral dopant atoms would be implanted at the extraction voltage energy along with the decelerated ions. This type of "energy contamination" is minimized by the operation of a turbopump in the region around the mass resolving slits (to reduce the ion neutralization rate from

Copyright © 2013 CC-BY-3.0 and by the respective authors

collisions with background gases) and by restricting the difference between the drift and decelerated ion energies.

Modulation of the ion energy along the beamline path is also a useful strategy to maximize beam transmission and facilitate beam shaping and focus. In the example of the AMAT/VSE VIISta Trident HC high-current implanter beamline shown in Fig. 6, a ribbon-shaped beam is formed by the extraction electrodes and focused at a mass resolving slit ("ion selection aperture") located downstream from the 90° mass analysis magnet [2]. The beam is then directed and shaped by another downstream magnet, prior to being implanted into a wafer scanned up and down in the ribbon beam. The ion beam can be decelerated at two stages along the way: directly after the mass resolving slits and after the final beam-shaping magnet.

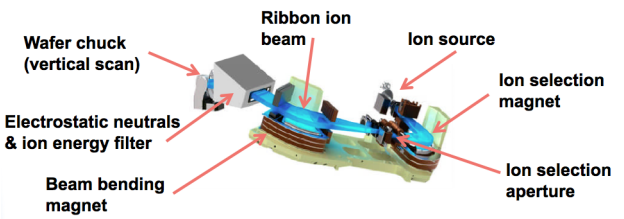


Figure 6: Example of advanced beamline architecture (AMAT/VSE VIISta Trident HC), which includes an inclined beamline, a neutrals and final ion energy filter just before the wafer, and a horizontally uniform ribbon beam for implanting a vertically scanned 300mm wafer that can be cryogenically cooled.

In a sophisticated combination of beam optics and system design, the AIBT high-current implanter, shown in Fig. 7, uses a number of electrodes to decelerate and deflect low-energy ions in a vertical ribbon beam along a "chicane" path (similar to turns in motorcycle racing tracks), before they emerge in front of the wafer scanning position [3]. Neutral dopant atoms that enter the decel stage continue undeflected into a beam trap. When higher energy ions are desired, the ribbon beam is switched back to a straight beam bath, thus bypassing the chicane decel electrode assembly.

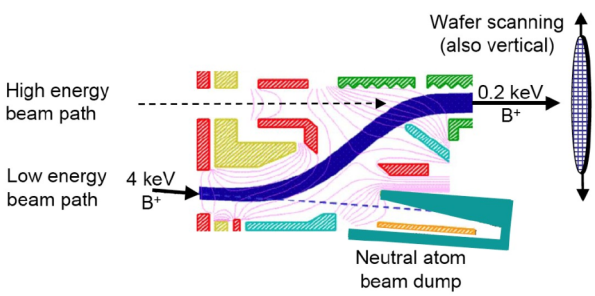


Figure 7: Schematic top view of the "chicane" beam path for deceleration of a vertical ribbon beam in the AIBT iPulsar high current implanter with a beam dump for neutral atom contaminants.

MeV Beamlines

When high-energy ions (>200 keV to several MeV) are needed, variations on either tandem or linear accelerators, developed in the 1930s for nuclear physics research, are used. In the tandem approach, multiple changes in the ion charge state along the beam path are induced to obtain a multiplication of the acceleration by a DC high-voltage potential, as seen in Fig. 8. First, positive ions are extracted from a plasma source and passed though a metallic vapor stream in order to form a beam of negative ions via collisional electron pickup. After undergoing mass selection in a magnet and slit assembly, the desired negative ions are accelerated toward a positive potential region, usually encased within a pressurized SF_6 atmosphere to allow for isolation of high potentials (up to several MV) in a compact chamber. At the center of this tandem beamline, the fast negative ions pass through a high level of Ar gas atoms, resulting in collisional charge exchange that transforms the negative ion beam to positive charged ions with various charge states. As the positive ions leave this shielded charge exchange region, they are accelerated away from the high positive potential in the center of the tandem. Single-charged positive ions leave the tandem beamline with a kinetic energy equal to twice the center positive potential. Double-charged positive ions have a final energy of three times the center potential. Useful, although low level, dopant beam currents with charge states up to +4 (with energy equal to 5 times the center potential) can be obtained for some ions with commercial tandem implanters. A magnetic selector segment placed at the exit of the tandem accelerator section allows only the ions with a desired charge state (and energy) to be passed to the target wafer.

In the Varian 3000XP tandem high-energy implanter shown in Fig. 8, positive ions are filtered by a magnetic field after the high-voltage acceleration stage to reject unwanted ions with undesirable energies and charge states [4]. The selected ions are then scanned along a horizontal beam path and directed through a magnetic beam-shaping element to produce a series of parallel beam paths at the wafer, which is moved up and down to produce vertical wafer scanning similar to the design shown in Fig. 5.

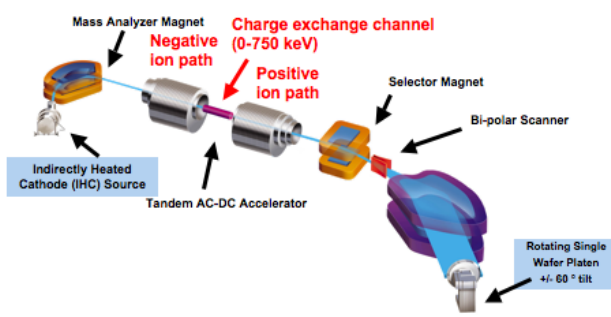


Figure 8: Schematic of the high-energy tandem accelerator beamline for the Varian 3000XP implanter with an operational range from 5 keV to 3 MeV.

Copyright © 2013 CC-BY-3.0 and by the respective authors

Commercial tandem accelerators are in operation with 2 MV potentials providing 8 MeV B^{+3} ions for doping profiles extending ~10 μm into Si. At these boron ion energies, control of gamma and neutron radiation calls for careful shielding and selection of beamline component materials, active radiation monitors, and limits to operating beam currents.

Phase-synchronized linear accelerators have also been used for high-energy ion implanters for over 20 years. In the Axcelis Purion XE high-energy implanter shown in Fig. 9, twelve RF cavities resonating at 13.57 MHz with maximum potentials up to 80 kV each combine to provide a beamline with mA-level beam currents for single-charged dopant ions at energies of ~1.5 MeV [5]. Double-charged P^{+2} ions can be accelerated to 2.9 MeV with 0.7 particle-mA beam currents for deep n-well applications. The positive ion beam from a plasma ion source enters the linac section after passing through a 70° mass-selection magnet (on the left in Fig. 9). After the beam is bunched and accelerated through the linac assembly, it is filtered with a 58.5° magnet (on the right in Fig. 9), that is tuned to select ions with the desired energy for transmission to the beam and wafer scanning stages.

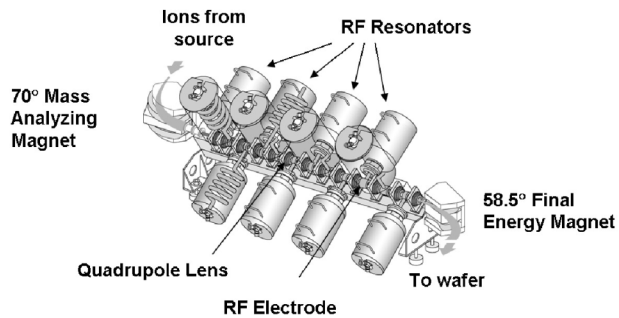


Figure 9: RF linac section of the Axcelis Purion XE high-energy implanter with an operation range from 5 keV to 1.5 MeV for B^+ (1.2 MeV for P^+ and 2.9 MeV for P^{+2}).

Plasma Immersion Ion Implanters

The systems used for very high dose (>10^{16} ions/cm^2) and low-energy (a few keV and less) implantation employ a radically simplified design. In PIII tools, the usual beamline components are eliminated, leaving only a means for generating a plasma containing dopant ions and a wafer mounted on a platen that can be biased. The ions in the plasma formed near the wafer are accelerated into the wafer surface by short (a few μs) negative potential pulses applied to the wafer platen at energies up to the maximum desired value.

PIII systems are remarkably compact in comparison to beamline accelerators, resembling the look of CVD and plasma etch systems. An example is shown in Fig. 10. The applications for these types of implanters include:

- High dose (~5x10^{16} B/cm^2) boron implants at energies of a few keV to counter-dope n^+ poly-Si to form p^+-doped gate electrodes in DRAM devices
- High dose doping of three-dimensional CMOS device structures, such as source-drain regions of finFETs
- High dose implantation of non-dopant ions for local enhancement or reduction of plasma etch rates and other materials modification applications.

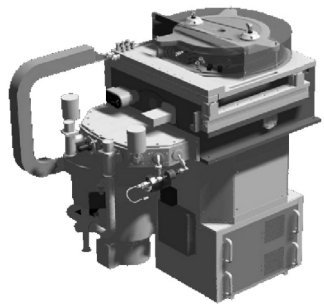


Figure 10: The Varian VIISta PLAD is an RF plasma doping tool, where a pulsed bias voltage is applied to the target wafer to implant ions from the plasma. The wafer bias voltages range from 0.1 to 10 kV [6].

SUMMARY

Ion implantation technology has been built on >40 years of experience, and accelerators are a key component of these tools. Even though commercial systems provide ion energies that span a range of 10^4 and implant doses that span a range of 10^8, the basic hardware designs are similar [7]. Implanter systems have evolved historically over time and will continue to evolve, as new device applications and CMOS device scaling brings more demanding requirements.

REFERENCES

[1] A. Renau, in Proc. 16th Int. Conf. on Ion Implantation Technology (IIT 06), AIP Conf. Proc. Vol. 866 (American Institute of Physics, Melville, 2006), p. 345.
[2] C. Campbell et al., in Proc. 19th Int. Conf. on Ion Implantation Technology (IIT 12), AIP Conf. Proc. Vol. 1496 (American Institute of Physics, Melville, 2012), p. 296.
[3] N. White et al., in Proc. 16th Int. Conf. on Ion Implantation Technology (IIT 06), AIP Conf. Proc. Vol. 866 (American Institute of Physics, Melville, 2006), p. 335.
[4] http://www.vsea.com/products.nsf/docs/viista3000xp
[5] Private communication, L. Rubin, Axcelis Technologies.
[6] E. Winder et al., in Proc. 16th Int. Conf. on Ion Implantation Technology (IIT 06), AIP Conf. Proc. Vol. 866 (American Institute of Physics, Melville, 2006), p. 511.
[7] M.I. Current, "Ion Implantation for Fabrication of Semiconductor Devices and Materials," in *Industrial Accelerators and Their Applications*, eds. R.W. Hamm, M.E. Hamm, World Scientific (2012), 9-56.

Copyright © 2013 CC-BY-3.0 and by the respective authors

ELECTRON BEAM IRRADIATION APPLICATIONS

Sunil Sabharwal#
Radioisotope Products and radiation Technology Section
International Atomic Energy Agency
Vienna, Austria

Abstract

The irradiation of materials with electron beams or X rays is used extensively to enhance or modify their physical, chemical or biological properties. These electron beam "irradiators" cover a very wide range of accelerators technology, beam current and energies to produce a wide variety of products, mostly with polymers. They also are used for curing ink, coatings, and adhesives as well as for the sterilization of medical products, disinfection and preservation of food. The emerging applications include treatment of waste waters and flue gases, and degradation of plastics for use in coatings and inks. The status of applications and the role of IAEA in enhancing these will be presented.

INTRODUCTION

High energy ionizing radiation has the unique ability to produce reactive species like free radicals in a variety of materials that can be used to modify physico-chemical properties of materials for a variety of industrial applications. Over the last 50 years, the subject of radiation chemistry and accelerator physics have developed simultaneously and from industrial applications point of view, the progress in one area has generally led to the advancement in the other area. While the basic radiation chemistry studies using the pulse radiolysis studies using nano-scale pulse electron beam accelerators led to understanding the basic fundamental aspects of radiation chemistry, the commercial applications based on radiation crosslinking of polymers or inactivation of pathogenic bacteria emerged as the driving force for developing high energy high current accelerators to ensure that the fruits of radiation chemical research are utilized for industrial applications. Radiation technologies based on electron beam accelerators today are used for applications such as crosslinking of wire& cables, producing heat-shrink materials, surface curing of materials, sterilization of medical products and for food irradiation [1]. Currently, world-wide, there are over 1400 industrial electron accelerators in operation that are being widely used for applications such as polymer processing, surface curing, sterilization of medical products and food irradiation [2]. A conservative market survey indicates that these high current EB units are providing an estimated over US $85 billion value added unique high-value products for mankind in an environmentally friendly manner [3]. Pollution of air, water and land resources due to industrial and human activities constitutes a major threat to sustainable development. While burning of fossil fuels lead to formation of sulphur oxides (SO_2 and SO_3), nitrogen oxides (NO_x), water resources are being polluted with industrial and human waste. The industrial effluents carry chemical contaminations like heavy metals, organic pollutants, petro-chemicals, pesticides and dyes while discharge of sewage and sludge giving rise to microbiological and chemical contamination of the water bodies. In the last few years, extensive work has been carried out for utilizing radiation technology for environmental remediation. Pilot or plant scale electron beam facilities have been set up to demonstrate the application of this technology for treatment of such pollutants in an effective and efficient manner [4,5]. This paper presents the present status of the established as well as emerging applications and the challenges that the accelerator technologists need to address for further implementation of this technology in these emerging areas.

TYPICAL CHARACRISTICS OF ELECTRON ACCELERATORS FOR INDUSTRIAL APPLICATIONS

For industrial radiation processing, the two main characteristics of an electron beam accelerator are energy and current. While energy of the accelerator determines the thickness of the product that can be uniformly processed, the current determines the productivity or the throughput of the process that can be achieved. A wide range of electron beams with energies varying from 0.15 to 10 MeV are used in radiation processing for varying applications (Table 1). The electron beam accelerators used in the industry typically have beam power (the product of electron energy and current) ranging from 5 to about 100 kW, although more powerful accelerators (400 kW and higher) have also been set up in recent years to demonstrate certain applications or for commercial irradiation. Low-energy accelerators having energies from 0.15 to 0.5 MeV, are generally constructed as self-shielded systems in the production. They are used mainly for the treatment of surfaces and the irradiation of coatings and thin materials, such as polymeric films. Medium-energy accelerators produce electrons with energies of 0.5 – 5 MeV at powers of up to 300 – 350 kW. High-energy accelerators, which for processing purposes generate electron beams with energies of 5 – 10 MeV, are linear accelerators giving pulsed beams of up to 50 kW. Such accelerators are used for radiation sterilization of medical products and, to a lesser extent, for the radiation treatment of foodstuffs. The applications of electron accelerators are summarized in Table 1.

#S.Sabharwal@iaea.org

Copyright © 2013 CC-BY-3.0 and by the respective authors

Table 1: EB Penetration for End Application

Application	Electron Energy	Typical Penetration (mm) for unit density product
Surface Curing	80–300 keV	0.4
Shrink Film	300–800 keV	2
Wire & Cable	0.4–3 MeV	5
Sterilization	3–10 MeV	38

FUNDAMENTAL PRINCIPLES FOR DEVELOPING ELECTRON BEAM TECHNOLOGY APPLICATIONS

Generation of radiation energy through electron beams is an expensive form of energy. It can therefore find applications under following conditions:

(i) Substantial benefits or change occur with a small input of energy. Polymerization reactions which are generally chain-reactions constitute one such class of reaction where radiation technologies can be used to initiate the chain reaction for a variety of industrial applications.

(ii) The small change produced results in a large change in the properties of the substrate. For example: in case of polymeric materials, the free radicals produced on polymer backbones can result in either joining of polymeric chains(crosslinking) or chain breakage (scission) resulting in dramatic change in the properties of the polymeric material. Similarly, the small change induced in the DNA structure may stop the reproduction of the microbial cell.

(iii) Situations where the value addition to the product is so high that cost of irradiation is not relevant

(iv) Where radiation is the only method of choice for the treatment process.

Based on these considerations, polymerization (surface curing), polymer modification, sterilization of medical products and food irradiation are the major established applications of electron beam technology.

ESTABLISHED APPLICATIONS OF ELECTRON ACCELERATORS

Polymer Modification

These applications are based on the ability of some polymeric materials, such as polyethylene to undergo crosslinking reaction between adjacent polymer chains, resembling vulcanization, resulting in improved thermal and mechanical properties as well as introduction of "memory effect" in polymeric materials after controlled irradiation. The electron beam crosslinking of the insulation jacketing on wire and cable is one of the most well established industrial uses of EB processing. Crosslink formation results in a three dimensional network structure in the polymeric material that prevents insulation from dripping off an overheated wire in case of a short circuit, or when exposed to elevated temperatures as in the case of an automotive engine or in case of a fire accident. The polymers that are typically used for such applications include polymers that cross-link on irradiation such as polyethylene, EVA or EPDM depending upon the end use application. Absorbed doses of the order of 100-150 kGy or higher are required to cross-link polyethylene wire and cable insulation. Crosslinking imparts two main properties to wire jacketing. if the wire become heated due to an electrical short circuit, the crosslinked jacketing will not melt off of the wire and thus will maintain its insulation. This is very important for under-the-hood wires used in automobiles. Second, when exposed to flames, the jacketing will not burn away nor drip and prevent or delay propagation of a fire.

Polymer cross-linking also forms the basis of radiation processing in the manufacture of heat-shrinkable plastic films and tubes. This application is based on the principle of "memory effect" in the crosslinked polymeric material. The crosslinked polymer deformed under stress at elevated temperatures, when reheated above its melting temperature remembers the shape before deformation and regains the shape before deformation. In a typical application, such materials are used to produce connectors for joining the wires or tubing. The crosslinked plastic behaves as a weak rubber that can be stretched or expanded by controlled mechanical or pneumatic differentials inside and outside the tubing. The stretched tubing is then quickly cooled to temperature below its melt transition temperature to allow the crystalline domains in the polymer to form again and hold the plastic in the stretched or expanded state. This tubing is then used to cover wire connections to be joined. When the tubing is heated during application, it contracts and conforms to the connector or object inside it. This simple application has resulted in forming a variety of high technology products such as heat recoverable closures for telecommunication splices, wraps for welded pipe joints and heat shrinkable food packaging film.

Radiation curing for printing inks especially with wide web presses for high volume production and for printed items requiring high quality graphics and colour highlights constitutes one of the most important applications of low energy electron beam accelerators and over 500 accelerators are used in the industry. Electrons from the accelerator generate free radicals in polymerisable monomers leading to simultaneous polymerization and crosslinking of the monomer onto the substrate. Since electron beam processing takes place at near ambient temperatures, drying of inks can be implemented even on heat sensitive plastic substrates. Absence of extractable initiators in EB curable inks and over print system allow development of over-print materials that are compliant with US Food & Drug Administration regulations for direct food contact and could replace film laminates used atop printed materials

Copyright © 2013 CC-BY-3.0 and by the respective authors

to prevent leaching of extractable for compliance with direct food contact regulations [6].

Sterilization of Medical Products and Food Irradiation

The use of electron beams for sterilization of medical products constituted one of the first commercial applications of radiation technology in 1950s. Since then, high energy 10 MeV accelerators have been used for many decades for sterilizing packaged medical devices. Mid energy accelerators at 3.0–5.0 MeV have also been used for medical device sterilization especially for products having a low bulk density so that the penetration of electrons is sufficient. The packages can be also be irradiated from two sides, thereby increasing the beam penetration to 2.4 times.. In recent years, X radiation produced from high energy high power electron beam accelerators (7 MeV, 700 kW). Even with a low conversion efficiency (typically 10%) for conversion to X rays, the facility allows production of 70 kW of X ray power that allows economic benefits for treatment of medical products by gamma radiation.

Food irradiation was one of the very first proposed uses of Roentgen's discovery of X rays and the subject has been investigated in details world over. The efficacy, minimal effect on nutritive value and general safety of irradiating food has been demonstrated over and over again. The World Health Organization (WHO) has long been on record as supportive of this method for processing food [7,8]. The industrial high energy electron beams (10 MeV) have been successfully used in irradiating food and foodstuffs to eliminate pathogens [9]. With increasing acceptance of food irradiation in many parts of the world, it is apparent that the use of electron beam accelerators for treatment of food is expected to increase in coming years.

EMERGING APPLICATIONS OF ELECTRON BEAM ACCELERATORS

The realization that the environmental problems associated with the development of human activities do not remain confined to local region, but also may affect people living far from contaminated sites has resulted in developing economically and technically feasible technologies for controlling solids, gaseous and liquid effluent streams. Radiation technology with electron beam accelerators with its unique ability to produce highly reactive species in an efficient manner has the capability to alleviate some of these problems and may play an important part in offering sustainable solutions. The unique features of this technology, being a room temperature and additive free process, makes radiation technology an environment-friendly process as compared to conventional thermo-chemical processes. Considerable efforts have been made in demonstrating use of radiation technology for environmental remediation. This includes application of radiation technology for simultaneous removal of sulphur oxides (SO_X) and oxides of nitrogen (NO_X) from flue gases. The electron beam technology for flue gas treatment has demonstrated very good removal efficiencies for the pollutants SO_X and NO_X. The by-product yield is of good quality with less moisture and is good for commercial fertilizer [4, 10].

Radiation processing of wastewater is non-chemical and uses short-lived reactive particles that can interact with a wide range of pollutants. Such reactive radicals are strong agents, oxidizing or reducing, that can transform the pollutants into liquid wastes. A pilot plant with an electron accelerator for treating textile dyeing wastewater was constructed in the Daegu Dyeing Complex (DYETEC) [11], and later an industrial plant for treatment of 10,000 m^3/day has been constructed and in successful operation [12]. A study on sludge hygienization using radiation is ongoing, and the experience of the research has shown that the process is simple, effective and easy to integrate with an existing sewage treatment plant, and that the radiation-hygienized sludge can be utilized as a fertilizer in agriculture [13].

CONCLUSION

The use of ionizing radiation has led to development of advanced polymeric materials for a wide range of applications in various industries. These include industries such as insulated wire and cable production, heat-shrink materials, surface curing, sterilization of medical products and food preservation. The commercial success of the technology is evident from the number of such machines operating and value added products that have emerged using this technology. The demonstration of electron beam based processes for treatment of flue gases and treatment of waste waters on an industrial scale is expected to offer unique solutions for environmental remediation in coming years. The development of reliable very high power electron beam machines will be crucial to extend the use of electron accelerators in these emerging applications.

REFERENCES

[1] R. J. Woods and A. K. Pikaev, Applied Radiation Chemistry: Radiation Processing (Wiley-Interscience, New York, 1994).
[2] S. Machi, Radiat. Phys. Chem. 22 (1983) 91.
[3] S.Machi, "Electron Accelerators for Industrial Applications in Japan," paper presented at IAEA Consultants Meeting, Vienna, July 21-25, 2008.
[4] A. G. Chmielewski, J. Licki and A. Pawelec, Radiat. Phys. Chem. 46 (1995) 1067.
[5] IAEA-TECDOC-1598, Vienna, Austria, 2008.
[6] S. Chatterjee, M. Laksin, D. Biro, J. D. Turgis, Radiation Curable Aqueous Compositions For Low Extractable Film Packaging, US Patent 6,803,112 (12 Oct. 2004).
[7] World Health Organization (WHO). Report of a Joint FOA/IAEA/Who Expert Committee: Wholesomeness of irradiated food. WHO Technical Report Series 659, Geneva, Switzerland (1981).

Copyright © 2013 CC-BY-3.0 and by the respective authors

[8] World Health Organization (WHO). Food Irradiation. In Point of Fact. 40 Geneva, Switzerland (1987).
[9] T. SADAT, "Electron beams processing in food industry technology and costs," Radiat. Phys. Chem. 25 (1985) 81.
[10] N. W. Frank, Radiat. Phys. Chem. 45 (1995) 989.
[11] B. Han, J. Ko, J. Kim, Y. Kim, W. Chung, I. E. Makarov, A. V. Ponomarev and A. K. Pikaev, Radiat. Phys. Chem. 64 (2002) 53.
[12] B. Han, J. Kim, Y. Kim, I. E. Makarov and A. V. Ponomarev, Water Sci. Technol. 52 (2005) 317.
[13] IAEA-TECDOC-1473, Vienna, Austria, 2005.

Copyright © 2013 CC-BY-3.0 and by the respective authors

OVERVIEW AND LESSONS LEARNED OF THE JEFFERSON LAB CRYOMODULE PRODUCTION FOR THE CEBAF 12GEV UPGRADE*

J. Hogan, A. Burrill, M. Drury, L. Harwood, C. Hovater, C. Reece and M. Wiseman
Thomas Jefferson National Accelerator Facility, Newport News, VA 23606, USA

Abstract

The Continuous Electron Beam Accelerator Facility (CEBAF) at Jefferson Lab is nearing completion of an energy upgrade from 6 to 12 GeV. An integral part of the upgrade is the addition of ten new cryomodules, each consisting of eight seven-cell superconducting radio-frequency (SRF) cavities. An average performance of 100+MV of acceleration per cryomodule is needed to achieve the 12 GeV beam energy goal. The production methodology was for industry to provide and deliver the major components to Jefferson Lab, where they were tested and assembled into cryomodules. The production process begins with an inspection upon receiving of all major components followed by individual performance qualification testing. The SRF cavities received their final chemical processing and cleaning at Jefferson Lab. The qualified components along with all associated hardware and instrumentation are assembled, tested, installed into CEBAF and run through an integrated system checkout in preparation for beam operations. The production process is complete and one of the first completed cryomodules has successfully produced 108 MV of acceleration with a linac beam current of 465 μA.

INTRODUCTION

The ten C100 cryomodules accounted for approximately one-quarter of the accelerator budget and 10% of the total budget for the 12 GeV upgrade project. The scope of the cryomodule production run consisted of the design, procurement, assembly, acceptance testing and a final integrated performance checkout with all associated CEBAF operating systems. The first superconducting radio frequency (SRF) niobium cavities were delivered in 2010. These SRF cavities were individually qualified in vertical dewars [1] at Jefferson Lab. In 2011, (ahead of the baseline schedule) the first two production 12GeV-C100 cryomodules were installed and commissioned in the CEBAF machine. These first two cryomodules accelerated and delivered beam for six months of physics experiments. In May 2012, one of the 12GeV-C100 cryomodules was successfully operated at a total energy of 108MV (with a linac current of 465uA) while delivering three-pass beam to the experimental halls [2]. This beam loaded performance demonstrated the design and production process of the C100 cryomodules would meet the 12 GeV requirements.

*Work supported by Jefferson Science Associates, LLC under U.S. DOE Contract No. DE-AC05-06OR23177. The U.S. Government retains a non-exclusive, paid-up, irrevocable, world-wide license to publish or reproduce this manuscript for U.S. Government purposes.

DESIGN

The original CEBAF cryomodule design consists of 8-five-cell cavities and produces a nominal voltage of 20 MV per cryomodule. 40 cryomodules (20/linac) were installed in the original CEBAF and produced enough voltage to run the machine at 4GeV. Over time the performance of these cryomodules was improved and optimized to increase CEBAF operation to 6GeV. The C100 cryomodule design consists of 8-seven-cell cavities and produces 100 MV per cryomodule (500 MV/linac). By adding the ten new C100 cryomodules and an additional 1/2-pass (tenth arc) to the existing accelerator, the maximum operating energy of CEBAF will be doubled from 6GeV to 12GeV.

Parameters

The C100 cryomodule design was developed over several years and is based on a set of early developmental cryomodules designed, built and operated in the Jefferson Lab CEBAF and FEL accelerators. The C100 cryomodule design parameters (see Table 1) were developed in concert with the other associated 12GeV accelerator system upgrades [3]; including the 4.6kW (at 2K) Central Helium Liquefier (CHL) [4], High power (13kW) radio-frequency klystrons (HPRF) and a new digital low-level radio-frequency (LLRF) control system [2].

Table 1: C100 Design Specifications

Parameter	Design Specification	Units
Slot length (includes warm section)	9.8	Meters (m)
Voltage/Cryomodule	108	MeV
2K heat load	<300	Watts
50K heat load	<300	Watts
HOM Damping (transverse)	$<2.4\times10^{10}$	Ohms/meter
HOM Damping (longitudinal)	$<6.5\times10^{11}$	Ohms
Cavity Gradient	19.2	MeV/m
Qo (@19.2 MV/m)	7.2E9	N/A

To meet the 12 GeV performance criteria, each of the ten cryomodules will need to provide 98 MeV of energy. In order to provide performance margin, the cryomodule is designed to produce 108 MeV. This additional performance capability provides the option to run some cryomodules higher in voltage in the event that more energy is needed to make up for lesser performing cryomodules. Similarly, the SRF niobium cavities were

Copyright © 2013 CC-BY-3.0 and by the respective authors

individually qualified at 19.2MV/m even though they only need to provide 17.5MV/m to meet the baseline performance. Subsequently, all of the cryomodule power related components (power couplers, cooling circuits, RF-windows, etc.) were also designed and specified to operate 10% above the baseline performance requirements.

Focused Areas of Design & Performance

The damping of higher order modes (HOM) in SRF cavities is a critical design parameter for recirculating accelerators. To mitigate against the possibility of having beam break-up (BBU) in the CEBAF accelerator an extensive effort was put into the measuring and characterizing the HOM spectrum of each cavity before it was built into a cryomodule [5]. Custom end-groups, that mimicked the boundary conditions the cavities would experience when assembled into a cryomodule, were designed and attached to each cavity during vertical testing (see Figure 1). These purpose built test end-groups allowed the HOM spectrum of each cavity to be characterized (and qualified) prior to being released for assembly into a cryomodule.

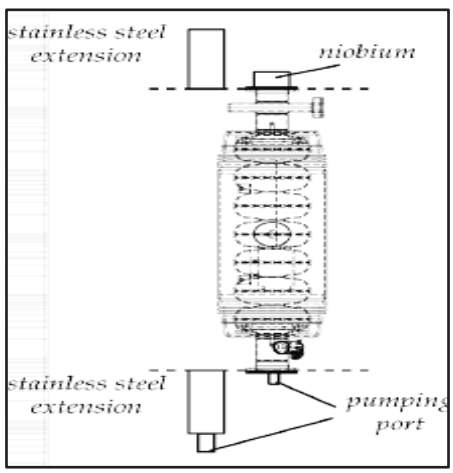


Figure 1: Custom SS end-groups assembled onto cavity during vertical testing.

The microphonic response of the SRF cavities to their environment is another design area that needed very careful attention. Excessive microphonic vibration creates dynamic detuning in the cavity and requires additional RF-power to keep the cavity on frequency with the power and control systems. In preparation for the 12 GeV project, a horizontal test bed (HTB) was assembled with two C100 cavities, helium vessels and tuners to investigate the microphonic response of the design. Results from this test demonstrated the design met the requirements.

Subsequently, the microphonic response was measured on the first production C100 cryomodule during final acceptance testing. Results from this acceptance test showed a higher than anticipated microphonic response. Upon further investigation, it was discovered the boundary conditions of the HTB did not fully represent the 'real' conditions of the C100 cryomodule. In response to these results, the tuner design was modified to reduce the microphonic response of the cavity/tuner system [6]. This cavity/tuner interface redesign was implemented on the final seven (of ten) cryomodules (see Figure 2).

At the point of implementation, production on the first three cryomodules had progressed beyond the point where the cavity/tuner interface could be retrofitted with the redesigned parts. Piezo elements will be used on these first three production units to minimize the additional detuning burden on the LLRF system.

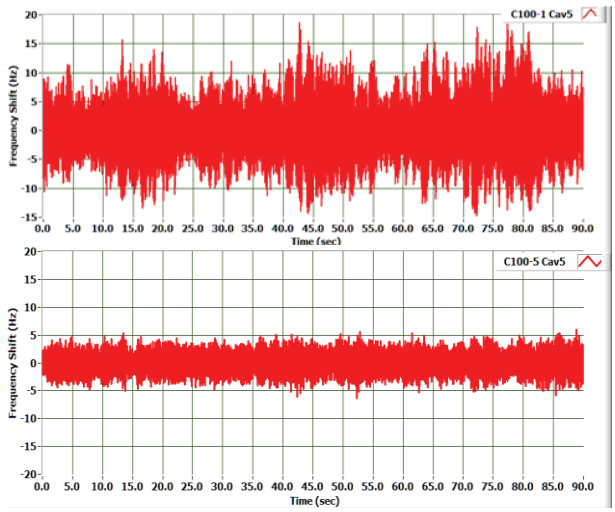


Figure 2: Microphonic detuning - Original design (top), redesigned (bottom) cavity/tuner system.

PRODUCTION

Cryomodule production began with the receiving inspections of the individual components that had been procured from industry. All components have established acceptance criteria that must be satisfied before components are released for use in cryomodule production. These receiving inspection criteria vary from simple visual inspections to multiple qualification processes including mandatory hold points for independent quality assurance.

The cavity qualification process was the first step in cryomodule production. Each C100 cavity was individually qualified after helium vessel welding in the Jefferson Lab SRF vertical test area (VTA). Each cavity was put through a standardized set of tests to verify the project performance parameters were met [7]. Each cavity must produce on average, 17.5 MV/m to meet the baseline performance goal of the 12 GeV project. To provide operational contingency, each cavity was qualified to 19.2 MV/m with a Qo of 7.2E9.

An administrative limit of 27 MV/m was periodically implemented on cavity qualification testing in order to reduce the risk of potentially degrading cavity performance and the need to re-test cavities (see Figure 3). Only one cavity (out of 86) failed to meet the gradient qualification goal of 19.2 MV/m. Two additional cavities were disqualified for use in production due to failure to meet the HOM damping and field flatness specifications.

Copyright © 2013 CC-BY-3.0 and by the respective authors

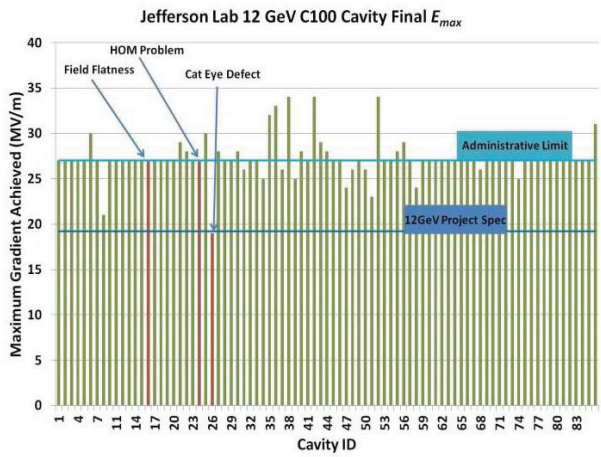


Figure 3: C100 cavity qualification in the VTA.

Once eight cavities were qualified for use in cryomodule production, they were assembled into a hermetically sealed cavity-string in a class 100 cleanroom (see Figure 4). The cavity string assembly was then moved to the cryomodule assembly area where the cold mass structure was constructed. Cold mass assembly includes the cold magnetic shielding (CRYOPERM), 2K helium piping, cold tuner section, instrumentation and multi-layer insulation (MLI).



Figure 4: Cavity string assembly in Class 100 cleanroom.

The cold mass assembly was then transferred to the space frame support structure with an integrated 50K thermal shield and MLI. The cavity string was then concentrically aligned to within 0.5mm. The final assembly consists of installing the vacuum vessel, cryogenic end cans, warm tuner sections and the waveguide fundamental power coupler assemblies. Once the cryomodule assembly was complete, a final QC check was performed to verify the mechanical, electrical and vacuum systems were functioning properly in preparation of final acceptance testing.

PERFORMANCE

Acceptance Testing

Each C100 cryomodule went through a final acceptance testing process in the Test Lab Cryomodule Testing Facility (CMTF) prior to being installed in the CEBAF machine. Acceptance testing is an operational checkout of the cavity performance and all of the cryomodule subsystems. Once all the cryogenic connections and control read-backs have been checked out, the C100 cryomodules were able to be slowly (10-20K/hr) cooled down from 300K to 4K without any degradation in performance due to Q-disease. This slow cooldown reduces the risk of creating a vacuum leak and allows for a lower temperature gradient within the cryomodule, thereby reducing the mechanical stresses associated with cooldown. Once the cryomodule was cooled to 4K, it was then pumped down to 2K for high power acceptance testing. Along with verifying all associated power and control signals were functioning properly, all the cryomodule operational parameters were measured for compliance with the design specifications.

High power RF was applied to each cavity to determine its maximum gradient (restricted only by an administrative limit of 25MV/m) while measuring the corresponding heat load (Qo). In addition, all the other operational systems such as tuners, HOM damping, cryogenic valves and instrumentation were qualified. One limitation is that high power can only be run into one cavity at a time. Therefore, the full cryomodule voltage must be estimated when based on acceptance testing results. With over twenty years of experience, these estimates have proven to be reliable for predicting operation in the tunnel.

Following final acceptance testing, the cryomodules were moved from the CMTF to the CEBAF tunnel for installation and commissioning. The installation process involves connecting the cryomodule to the cryogenic, RF-power, beamline vacuum and operational safety systems. Once all connections were complete and control signal read-backs have been verified, the cryomodule was again slow cooled to 4K, pumped down to 2K and refilled in preparation for the final integrated operational checkout and commissioning process [8].

As was done during acceptance testing, all the operational subsystems were checked out for proper function and the critical accelerating parameters were measured. To date 9 (of 10) of the C100 cryomodules have completed the commissioning process (see Table 2). The in-tunnel performances of all these cryomodules have exceeded the baseline required for 12 GeV operations. Two cryomodules did not achieved the design goal of 108 MV/m, however there is still more than adequate margin in the ensemble performance to meet the program goals.

Copyright © 2013 CC-BY-3.0 and by the respective authors

Table 2: C100 Commissioning Results

Cryomodule No.	Commission in CEBAF (MeV)	Operation with Beam (MeV)
C100-01	104.3	94.5
C100-02	109.6	108
C100-03	118.4	Jan 2014
C100-04	105.8	Jan 2014
C100-05	109.9	Jan 2014
C100-06	108.2	Jan 2014
C100-07	108.4	Jan 2014
C100-08	Oct 2013	Jan 2014
C100-09	113.7	Jan 2014
C100-10	109.8	Jan 2014

Gradient with Beam Loading

As stated above, the first two C100 production cryomodules were installed into the CEBAF machine in the fall of 2011. They were run with beam for the full six month physics run. This runtime was very beneficial with regard to gaining real operational experience running the C100 cryomodules while delivering physics quality beam to the experimental halls [2]. During beam studies time, the gradients on the C100 cryomodules were pushed up in order to test the performance of the entire 'vertical slice' (cryomodule, cryogenics, rf-power, digital LLRF controls, etc.) of the accelerating zone.

During one of these beam studies opportunities, C100-02 was operated at a maximum voltage of 108 MV while delivering multi-pass beam to the experimental halls. Having successfully demonstrated this capability early in the 12 GeV project was very encouraging for the future operations of the CEBAF machine.

Cost

From a cost standpoint, cryomodule production is >99% complete. For the purpose of this paper, the final 12 GeV cryomodule costs are broken down into three categories; procurements, expenses and labor (see Figure 5). These costs include all activities from the initial procurement process through assembly, acceptance testing, installation and commissioning.

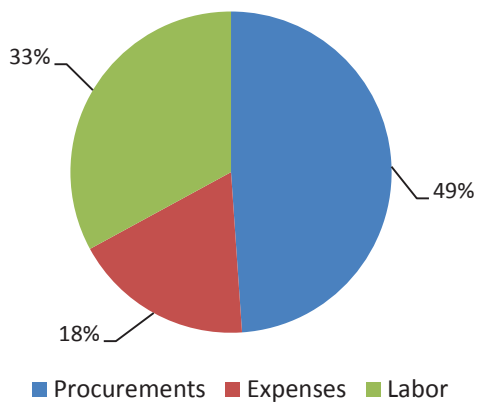


Figure 5: Cryomodule cost breakdown.

The procurement costs are the expenditures associated with the vendor subcontracts for the major cryomodule components such as the SRF-cavities, thermal & magnetic shields, tuners, helium vessels, space-frames, vacuum vessels and cryogenic end cans. The expenses category includes all "other" production costs such as consumables, minor procurements and travel to vendor sites. The labor costs include the labor associated with all cryomodule production activities from individual component QA receiving activities through assembly, installation and commissioning activities.

In order to better understand the level of effort that goes into cryomodule production activities, the labor costs are further broken down (see Figure 6). The labor breakdown shows that quality assurance accounts for approximately one-third of the total labor costs. These QA processes include the labor needed to create the procedures, perform the individual component receiving inspections, document the results and maintain the project database system.

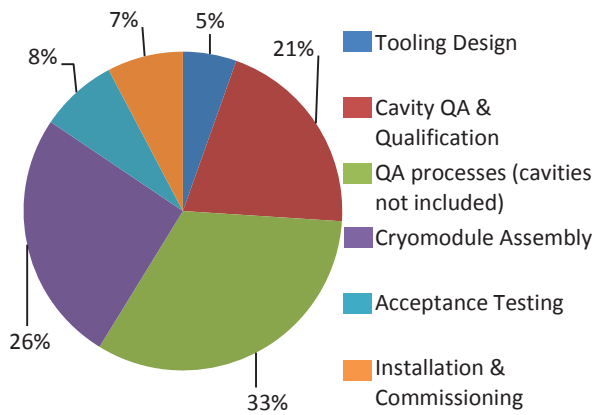


Figure 6: Cryomodule labor breakdown.

Cavity QA and qualification activities account for about one-fifth of the total labor costs. Each of the eighty-six cavities went through a thorough receiving inspection that includes both a dimensional check on a coordinate measurement machine (CMM) and an RF-check to verify that the cavity frequency and field flatness were within specification. Once accepted, the cavities were then run through final processing in preparation for qualification in the VTA. Vertical testing is a time consuming and expensive process, minimizing these testing cycles reduces both project cost and schedule. For this reason, a focused effort was dedicated to process control for cavity qualification. This aforethought and planning effort resulted in minimal retests for qualification (see Figure 7). 65% of all the C100 cavities were qualified on the first test cycle.

Copyright © 2013 CC-BY-3.0 and by the respective authors

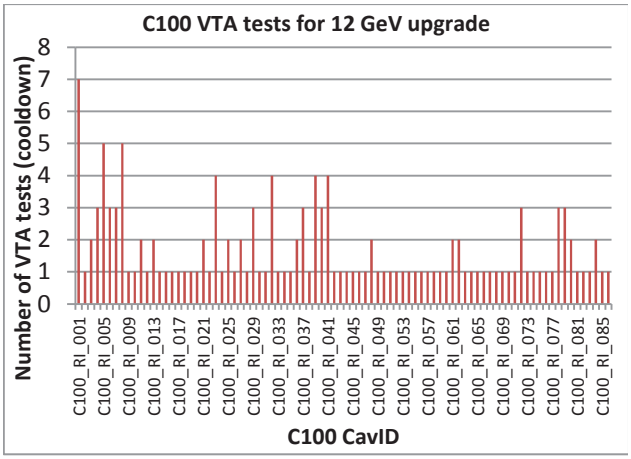


Figure 7: Cavity qualification test cycles in VTA.

Cryomodule assembly accounts for about one-quarter of the total labor costs. As stated above, the cryomodule assembly activities begin with the transfer of the cavity string from the cleanroom and run through final instrumentation checkout and leak check of the insulating vacuum (see Figure 8). There is a significant amount of skilled touch labor involved in these processes. The importance of the skilled staff to the success of this project cannot be understated; for this reason these resources need to be optimized. As with cavity qualification, a focused planning effort was dedicated to optimizing assembly activities and procedures to be efficient without compromising quality.



Figure 8: Cryomodule production group w/ C100-07&-08.

CONCLUSION

At the time this paper was written (Sep 2013), the 12 GeV-C100 cryomodule production run is virtually complete. All ten C100 cryomodules have been assembled, tested and installed in the CEBAF tunnel. Nine have completed their final integrated checkout and commissioning. The last cryomodule is scheduled to complete commissioning in October 2013.

CEBAF operations are scheduled to begin hot-checkout in November 2013. During this process all ten C100 cryomodules will be calibrated with the electron beam in preparation for 12 GeV physics. The lessons learned from the CEBAF 12 GeV Upgrade cryomodule production run include the importance of planning, prototyping, monitoring of performance throughout production and the clear definition of all acceptance criteria.

REFERENCES

[1] Andrew Burrill et al., "Production and Testing Experience with the SRF Cavities for the CEBAF 12 GeV Upgrade," IPAC2011, San Sebastian, Spain, MOOCA01 (2011); http://www.JACoW.org

[2] Curt Hovater et al., "Commissioning and Operation of the CEBAF 100 MeV Cryomodules," IPAC 2012, New Orleans, LA, WEPPC093 (2012); http://www.JACoW.org

[3] Leigh Harwood, "The JLab 12 GeV energy Upgrade of CEBAF", NA-PAC13, Pasadena, CA, MOZAA1.

[4] V. Ganni et al, "Commissioning of Helium Refrigeration System at JLab for 12 GeV Upgrade," CEC-ICMC 2013, Anchorage, AK.

[5] Frank Marhauser et al., "HOM Damping Sensitivity in SRF cavities," International Workshop on HOM Damping in SRF Cavities, Cornell University, Ithaca, NY, 11-13 October 2010.

[6] K. Davis et al, "Vibration Response Testing of the CEBAF 12 GeV Upgrade Cryomodules," LINAC 2012, Tel Aviv, Israel, MOPB031 (2012); http://www.JACoW.org

[7] Andrew Burrill et al., "SRF Cavity Performance Overview for the 12 GeV Upgrade," IPAC 2012, New Orleans, LA., WEPPC089 (2012); http://www.JACoW.org

[8] Michael Drury et al., "CEBAF Upgrade: Cryomodule Performance and Lessons Learned," SRF 2013, Paris, France, THIOB01.

Copyright © 2013 CC-BY-3.0 and by the respective authors

SRF CAVITIES BEYOND NIOBIUM: CHALLENGES AND POTENTIAL*

S. Posen† and M. Liepe
Cornell Laboratory for Accelerator-Based Sciences and Education, Ithaca, NY, USA

Abstract

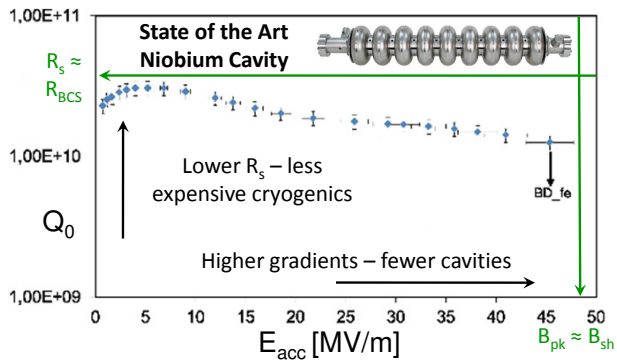
With niobium cavities now approaching the fundamental limits of the material, SRF researchers have begun a significant R&D effort to develop alternative materials to continue to keep up with the demands of new accelerator facilities. In this paper, the benefits of new materials are explored, as well as the critiria for selecting superconductors to use for SRF applications. The materials Nb_3Sn and MgB_2 are discussed in detail, including an exciting new result from a Nb_3Sn cavity that shows the great potential of alternative SRF materials. NbN and multilayers are also briefly discussed. The current status and the outlook for the future of alternative materials are reviewed.

WHY LOOK BEYOND NIOBIUM?

To accelerate beams of charged particles, superconducting radio-frequency (SRF) cavities are the technology of choice for many facilities. They can reach large accelerating gradients E_{acc} on the order of tens of MV/m, and though they require cryogenics for cooling below the superconducting transition temperature T_c of the material they are made from, they achieve high wall-power-to-beam-power efficiency due to their small surface resistances R_s. Modern SRF facilities use cavities made of niobium, either formed from bulk sheets, or sputtered in films onto copper. Early niobium cavities could operate at only small gradients of a few MV/m, but through years of research, preparation techniques were developed to avoid non-fundamental limitations, such as multipacting and field emission [1]. State-of-the-art production methods regularly produce cavities that operate very close to the fundamental limits of niobium: they have surface resistances R_s very close to the ideal BCS value at operating temperatures, and they sustain electromangetic fields very close to the material's superheating field B_{sh}, the field at which vortices penetrate the superconductor—creating unmanageable levels of heating in RF fields—for an ideal surface [2]. In Fig. 1, the qualification curve of a high-performing TESLA 9-cell niobium cavity (the proposed cavity design for ILC) is plotted. The curve tracks two figures of merit: E_{acc} and Q_0, which is inversely proportional to R_s. It shows that this cavity performs very close to the fundamental limits of the material.

To continue to keep up with continually increasing demands of future accelerator driven sciences, SRF researchers have begun a significant effort to develop alternative materials, chosen to have higher fundamental limits than niobium. The optimal material may depend on the type of facility. For low-duty-cycle high energy linacs, an alternative material would be chosen that can sustain very large surface magnetic fields, as this is what fundamentally limits E_{acc}, and therefore sets the minimum number of cavities requied to reach a given energy. On the other hand, for modern CW SRF linac designs, cryogenics is the cost driver, not the number of cavities. For niobium, low R_s operation requires the cavity to be cooled to ~2 K, where cryogenic efficiency often pushes the cost-optimum arrangement to using only modest gradients, because losses go quadratically with E_{acc}. At ~2 K, cavities made from an alternative material with lower R_s than niobium would have smaller losses at a given E_{acc}, so they would allow the cryogenic plant to be smaller and require less grid power, or they could operate at higher gradients, and therefore require fewer cavities. Furthermore, the temperature dependent part of R_s scales with $e^{-T_c/T}$, so if the alternative material had a large T_c, low R_s operation could be possible at 4.2 K, greatly simplifying the cryogenic plant by allowing it to operate at atmospheric pressure. Low R_s operation at even higher temperatures would open up the possibility of using helium gas for cooling.

Figure 1: Q_0 vs E_{acc} for a High Performing ILC 9-cell Niobium Cavity [3]. The maximum E_{acc} and the Q_0 over the entire range are very close to the fundamental limits of the material.



Long term R&D will be needed to reach the full potential of these alternative materials, but already new results (which will be shown later) on a Nb_3Sn cavity fabricated by Cornell show performances now superior to niobium for some applications requiring modest fields only.

* Work supported by DOE award number DE-SC0002329.
† sep93@cornell.edu

Copyright © 2013 CC-BY-3.0 and by the respective authors

WHAT PROPERTIES TO LOOK FOR IN ALTERNATIVE MATERIALS?

To determine which superconductors are viable candidates for producing high-performing SRF cavities, one should look for certain properties. To achieve large E_{acc}, a large superheating field B_{sh} is desirable, as this is the relevant critical field for RF applications. This is different from B_{irr}—the irreversibility field at which at which vortices that have penetrated into the sample become depinned—which is relevant for magnet applications. In SRF cavities, the objective is to exclude flux, not to pin it inside the superconductor; pinned normal conducting vortex cores dissipate strongly in RF fields. It is energetically favorable for vortices to be inside the superconductor above the first critical field B_{c1}, and only an energy barrier prevents flux penetration above this field. For an ideal surface, the barrier disappears at B_{sh}, making it the ultimate limit for SRF applications, but surface defects with size on the order of the coherence length ξ—roughly, the spacial amplitude of the superconducting wavefunction—can reduce the barrier to vortex penetration, such that fields close to B_{sh} cannot be realized without vortex entry. It is therefore important to have a large enough ξ to not be affected by small defects that would be present even on a well prepared surface, e.g. grain boundaries. It has been an open question how large of ξ is large enough—niobium cavities have reached fields quite close to B_{sh} and its ξ is ∼20 nm—but recent results (presented in a later section) on a Nb_3Sn cavity have shown that operation well into the metastable regime where only the energy barrier prevents vortex penetration is possible for ξ∼3 nm.

For small R_s, one must first consider the temperature-dependent surface resistance from BCS theory, R_{BCS}. As discussed previously, $R_{BCS} \propto e^{-T_c/T}$, so it is important for materials to have high T_c. Materials that have small R_{BCS} also tend to have small normal resistivity ρ_n [4]. However, there is also a temperature independent part of R_s, the "residual resistance" R_{res}: $R_s(T) = R_{BCS}(T) + R_{res}$. The factors contributing to R_{res} are not well understood, but previous SRF experience has made it clear that weak links between grains contribute to large R_{res} [1].

To be useful for cavity operation, alternative materials must also possess the following qualities: 1) it must be possible to fabricate it in a way that it conforms to a complex geometry over large area; 2) it must have decent thermal conductivity (and be able to be deposited on a substrate with decent thermal conductivity) for cooling to avoid thermal runaway; 3) it must have minimal surface roughness to avoid field enhancement; 4) it must be able to be made clean (for example, it cannot release potentially field emitting dust, and there must be a method to clean surface contaminants without affecting quality).

Some of the most promising alternative SRF materials and relevant properties are shown in Table 1, along with those of niobium. Experimental references for these properties were chosen to try to display realistic properties for polycrystalline films. However, material parameters vary depending on how the superconductor is fabricated, and some improvement in SRF qualities can be expected with R&D.

Table 1: Material Properties of Niobium and Three Promising Alternative SRF Materials. The penetration depth λ is calculated using Eqn 3.131 in [5]. The coherence length ξ is calculated using the equations in [6]. For Nb a RRR of 10 was assumed. For MgB_2, λ and ξ are not calculated, as the experimental values are given in the reference. B_{sh} for Nb is found from [7] and for others calculated from [2]. For B_{sh} calculations, $B_c = \phi_0/(2\sqrt{2}\pi\xi\lambda)$ is used, where ϕ_0 is the flux quantum [5]. Nb data from [8], Nb_3Sn data from [9], NbN data from [10], and MgB_2 data from [11] and [12]. Note that the two gap nature of MgB_2 may require more careful analysis than is performed here.

Material	$\lambda(0)$ [nm]	$\xi(0)$ [nm]	B_{sh} [mT]	T_c [K]	ρ_n [μΩcm]
Nb	50	22	210	9.2	2
Nb_3Sn	111	4.2	410	18	8
MgB_2	185	4.9	210	40	0.1
NbN	375	2.9	160	16	144

Potential and Challenges

Nb_3Sn is a material with tremendous potential for SRF applications. It has extremely small R_s, as a result of its small ρ_n and large T_c∼18 K (twice as high as niobium), as well as its small R_{res}, shown in cavity measurements [13]. It also is an excellent candidate for achieving large E_{acc}, with very large predicted B_{sh}∼400 mT (again twice as high as niobium), and a decent ξ∼3-4 nm. Furthermore, it can be coated onto niobium substrates, allowing existing niobium cavities to be upgraded. It is also non-reactive with water, and it adheres strongly to niobium when coated onto it, so that Nb_3Sn cavities can be cleaned using the high-pressure-water-rinsing methods developed for niobium.

Nb_3Sn is brittle, and it has low thermal conductivity, so it has to be used in film form. Therefore it faces challenges associated with using SRF films. These are detailed in a later section.

Preparation Methods

The Nb_3Sn fabrication method that has produced the most encouraging SRF results is vapor diffusion. The technique was developed at Siemens AG [14] and University of Wuppertal [15], and it is now being employed by researchers at Cornell University [16] and Jefferson Lab [17]. A niobium cavity is placed in an ultra-high-vacuum furnace with a small amount of tin. The temperatures of both are

Copyright © 2013 CC-BY-3.0 and by the respective authors

raised to around 1000°C, so that the tin has a high enough vapor pressure to reach the cavity, and once it reaches the surface, the temperature is high enough to encourage diffusion and alloying.

Researchers at several institutions have recently attempted to fabricate Nb_3Sn using other methods: liquid tin dipping and multilayer sputtering at INFN [18]; cathodic arc deposition at Alameda Applied Sciences Corp. [19]; and pulsed laser deposition at KEK [20] (note that AASC and KEK fabricated MgB_2 via the same methods). However, so far these studies have not produced encouraging RF results.

Development Status

Jefferson Lab has fabricated Nb_3Sn samples with excellent T_c. They have also performed low-field R_s measurements in a 7.4 GHz host cavity. A dedicated furnace has been delivered, and is currently being commissioned to coat full single-cell cavities. The apparatus is shown in Fig. 2.

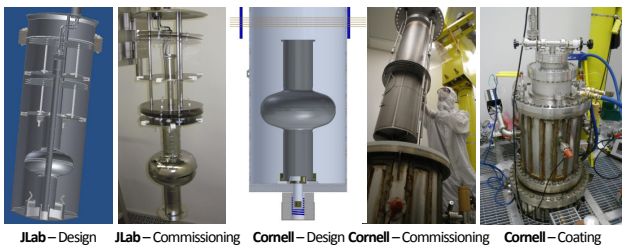


Figure 2: Apparatuses for coating cavities with Nb_3Sn at Jefferson Lab (left) and Cornell University (right).

The Nb_3Sn program at Cornell University (see coating apparatus in Fig. 2) has been ongoing for several years, and recently produced its second 1.3 GHz cavity, shown in Fig. 3, which showed exceptional performance in RF test [16]. As shown in Fig. 4, it achieved fields ∼12 MV/m at 4.2 K with a Q_0 of 10^{10}, 20 times higher than niobium. It is the first alternative material accelerator cavity to achieve significantly smaller R_s than niobium at useful gradients and temperatures. Previous Nb_3Sn cavities suffered from a strong increase in R_s with field, leading to speculation that the coherence length was too small, causing the barrier to vortex penetration to fail at surface imperfections. However, this new cavity proves that even with a ξ of only $\sim$ 3 nm, the energy barrier prevents observable vortex dissipation, the first clear indication that such a small ξ will not cause a fundamental limitation for cavities made from alternative materials.

MAGNESIUM DIBORIDE

Potential and Challenges

MgB_2 was discovered relatively recently, so it is not as well developed as Nb_3Sn, but it also has exciting potential. With a T_c of approximately 40 K, and a small ρ_n, it can have a very small R_{BCS} even well above liquid helium temperatures. Its superheating field is not clear at this early stage of development, but it could range from ∼200-600 mT, depending on the material properties. More development of SRF-quality MgB_2 films is needed to make a better estimate. It also has a decent ξ∼5 nm.

There are some challenges to developing MgB_2 as an SRF material. In fabrication, it is necessary to obtain a very small oxygen background in the coating chamber, as the magnesium is highly reactive with it. The coatings also react with water, which makes cleaning difficult. It might be necessary to coat an additional dielectric "capping" layer to allow a MgB_2 cavity to be cleaned. Additionally, because it is a two-gap material, its R_s is predicted to increase with field, but there might be methods to reduce this effect [21]. MgB_2, like Nb_3Sn is being developed in film form, so it will have the same film challenges detailed in a later section.

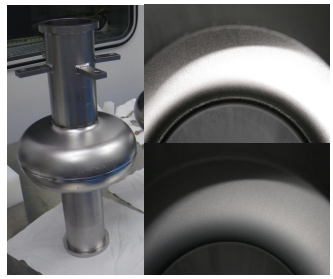


Figure 3: Cavity coated with Nb_3Sn at Cornell (left); view looking down into cavity before (top right) and after coating (bottom right). Notice the dark, matte gray appearance of the Nb_3Sn coating.

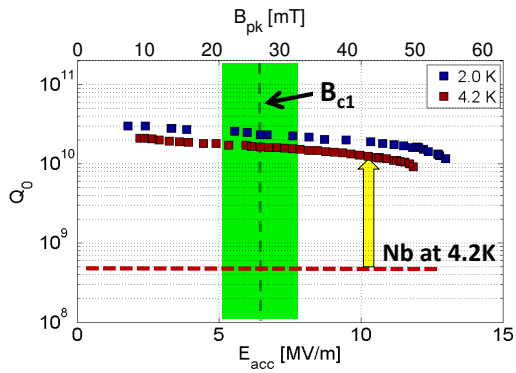


Figure 4: Q_0 vs E_{acc} for Cornell's Nb_3Sn cavity. At 10 MV/m, the Q_0 is a factor of 20 times higher than Nb at 4.2K. The maximum surface magnetic field is approximately 2 times higher than B_{c1}=27±5 mT, which was calculated using Ginzburg Landau theory from measured material parameters.

Copyright © 2013 CC-BY-3.0 and by the respective authors

Preparation Methods

Excellent preliminary results have been obtained using hybrid physical chemical vapor deposition at Temple University [22] and using reactive co-sputtering at Superconducting Technologies Inc. (STI) [23].

Development Status

Coating of accelerator cavities with MgB_2 is being developed by X. Xi at Temple University [22]. Studies of samples produced at Temple have repeatably shown films with T_c very close to the ideal literature value, and ρ_n of only 0.1 μΩcm [12]. Encouraging RF results have been obtained by researchers at Los Alamos and MIT Lincoln labs on MgB_2 stripline and dielectric resonators fabricated by STI, as shown in Fig. 5. Measurements still need to be done at smaller frequencies to determine if R_{res} can be small enough for SRF cavities, and if this can be maintained up to useful fields.

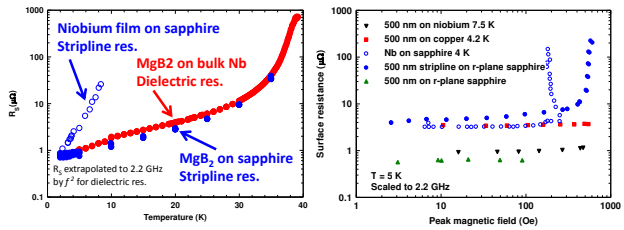


Figure 5: RF measurements of MgB_2 stripline and dielectric resonators show excellent R_s at high temperatures and high frequencies. Experimental data from D. Oates [23]. Note that scaling of the data from high frequencies may significantly underestimate the residual resistance at 2.2 GHz.

NIOBIUM NITRIDE

With a high T_c∼15-17 K, the δ phase of NbN has the potential to have R_{BCS} significantly smaller than niobium. For the relatively dirty films that are generally produced, it has a predicted B_{sh} of only around 150-200 mT, with a decent ξ∼3 nm. However, one additional argument in favor of pursuing NbN is that it might be possible to coat large niobium cavities in existing UHV furnaces—one of the methods of producing NbN involves bringing niobium to high temperatures in the presence of nitrogen gas, then quickly cooling it [24].

NbN has a very complex phase diagram, which makes it very challenging to achieve the superconducting δ phase. This is achievable with sputtering, but with heat treatment in a nitrogen atmosphere, no reliable procedure has been developed that could be applied to cavities. Recently an R_s reduction was observed in niobium cavities that were treated with nitrogen gas in a UHV furnace at Fermilab, and it was initially speculated that the cause was the growth of superconducting NbN. However, T_c and XRD measurements of samples revealed that another mechanism must have been responsible [25]. Another challenge is R_{res}—tests of sputtered NbN have shown a relatively high value. Additional investigations are needed to determine if this can be avoided.

MULTILAYERS

In 2006, A. Gurevich proposed that bulk films of alternative materials would be inferior to "SIS multilayer" films, which consist of alternating layers of thin superconductor (S) and insulator (I) on top of bulk superconductor, as shown in Fig. 6 [26]. It was suggested that the enhancement of the critical fields in thin films would help small-ξ materials to avoid vortex penetration from small surface defects. Several labs over the world have made excellent progress in the difficult process of fabricating SIS films, including CEA [27], Argonne [28], JLab [29], William and Mary [30], and Grenoble IPT [31]. However, recent theoretical work has shown that compared to bulk films, SIS multilayers can offer only a small enhancement of the superheating field, and only for a small parameter range [32].

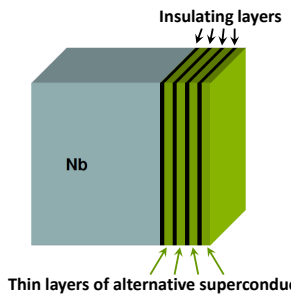


Figure 6: SIS multilayer structure proposed to protect alternative materials from vortex penetration. New theoretical work suggests that multilayers will not be superior to bulk films. Image adapted from [26].

FILM CHALLENGES

The alternative materials being researched are primarily used in film form over metal substrates. There are unique challenges associated with SRF films that are not encountered in cavities made form bulk material. The cooldown of a film cavity must be done slowly and uniformly to avoid temperature gradients over the surface. Gradients can cause thermocurrents due to the interface of the two materials, which in turn can create and trap flux that causes excess R_{res}. This also means that after a quench, the cavity must be warmed above T_c and cooled slowly again to regain a small R_s. Films cavities have fewer options available in case of a contaminated surface after coating—because the film is usually only a few μm thick, only light chemistry is available to clean the surface. Large cavities also present a significant challenge with films, since applying a film to a completed structure requires a very large coating apparatus. Coating pieces before welding is not possible in most cases because this would destroy the quality of the film at the weld.

Copyright © 2013 CC-BY-3.0 and by the respective authors

OTHER MATERIALS

Other potentially promising materials not presented here but for which there has been some recent activity include V_3Si, Mo_3Re [33], and Nb_3GaAl [34]. In addition, though they have very complex structures, the oxypnictides are an exciting possibility. More research is needed into these materials to understand if they might be useful for SRF applications.

CONCLUSIONS

Alternative SRF materials offer lower R_s, higher T_c, and higher B_{sh} than niobium. Cavities made from these materials would be much more cryogenicically efficient (likely a factor of 10-100), and they are predicted to reach higher gradients (up to a factor of $\sim$2), meaning that fewer cavities would be required to reach a given beam energy. Many labs worldwide are contributing to the effort, and while it is expected to be a long term R&D project, there has been significant progress recently. A Nb_3Sn cavity produced at Cornell achieved a breakthrough performance: at 4.2 K and $\sim$12 MV/m, it had a Q_0 of 10^{10}, 20 times higher than Nb, making it the first alternative material accelerator cavity to far outperform niobium at useful gradients and temperatures. MgB_2 is also showing great promise in small-scale RF tests, and the first MgB_2 accelerator cavities are planned to be produced soon.

ACKNOWLEDGEMENTS

The authors would like to express sincere thanks to the following contributors: Grigory Eremeev, JLab; Anne-Marie Valente-Feliciano, JLab; Enzo Palmieri, INFN; Xiaoxing Xi, Temple U.; Tsuyoshi Tajima, Los Alamos; Shinji Mitsunobu, KEK; Claire Antoine, CEA; Rosa Lukaszew, William and Mary; Daniel Oates, MIT Lincoln Labs; Mahadevan Krishnan, Alameda Applied Sciences Corp.; Franois Weiss, Institut Polytechnique de Grenoble. The authors would also like to thank authors of previous very helpful alternative SRF materials summaries, such as [35], [36], [37], [38], [21], and [39].

REFERENCES

[1] H. Padamsee, J. Knobloch, and T. Hays, *RF Superconductivity for Accelerators*, Wiley & Sons, New York, ISBN 0-471-15432-6, 1998.

[2] M. Transtrum, G. Catelani, and J. Sethna, Phys. Rev. B 83, 094505 (2011).

[3] A. Yamamoto, MOIOA02 (Presented at the SRF Conference, Chicago, USA, 2011).

[4] Vaglio, Particle Accelerators 61, 391 (1998).

[5] M. Tinkham, *Introduction to Superconductivity* (New York: Dover, 1996).

[6] T. Orlando, et al., Phys. Rev. B 19, 4545 (1979).

[7] A. J. Dolgert, S. J. Di Bartolo, and A. T. Dorsey, Phys. Rev. B 53, 5650 (1996); Phys. Rev. B 56, 2883 (1997).

[8] B. Maxfield and W. McLean, Phys. Rev. 139, A1515 (1965).

[9] M. Hein, *High-Temperature Superconductor Thin Films at Microwave Frequencies* (Berlin: Springer, 1999).

[10] D. Oates, et al., Phys. Rev. B 43, 7655 (1991).

[11] Y. Wang, T. Plackowski, and A. Junod, Physica C 355, 179 (2001).

[12] X.X. Xi, et al., Physica C, 456, 22-37, (2007).

[13] D. Proch, TESLA Report, TESLA 2000-15 (2000).

[14] B. Hillenbrand et al., IEEE Trans. Mag. 13, 481 (1997).

[15] G. Müller et al. EPAC 1996. p. 2085.

[16] S. Posen and M. Liepe, TUP087 (Presented at the SRF Conference, Paris, France, 2013).

[17] G. Eremeev et al., TUP071 (Presented at the SRF Conference, Paris, France, 2013).

[18] S. Deambrosis, Ph.D. Thesis, University of Padua (2008).

[19] M. Krishnan, C. James and B. Bures, (Presented at the TF-SRF Workshop, Newport News, USA, 2012).

[20] S. Mitsunobu, (Presented at the TFSRF Workshop, Padua, Italy, 2010).

[21] X. X. Xi, Supercond. Sci. Technol. 22, 043001 (2009).

[22] T. Tan, et al., TUP089, (Presented at the SRF Conference, Paris, France, 2013).

[23] T. Tajima, WEIOB01, (Presented at the SRF Conference, Paris, France, 2013).

[24] G. Gemme et al., J. App. Phys. 77 (1995).

[25] Y. Trenikhina, A. Grassellino, and A. S. Romanenko, TUP065, (Presented at the SRF Conference, Paris, France, 2013).

[26] A. Gurevich, App. Phys. Lett. 88, 012511 (2006).

[27] C. Antoine, J.-C. Villegier, and G. Martinet, APL 102, 102603 (2013).

[28] T. Proslier et al., WEIOC03, (Presented at the SRF Conference, Paris, France, 2013).

[29] A.-M. Valente Feliciano et al., TUP088, (Presented at the SRF Conference, Paris, France, 2013).

[30] W. M. Roach et al., IEEE Trans. App. SC., VOL. 23, NO. 3, JUNE 2013.

[31] F. Weiss et al., TUP081, (Presented at the SRF Conference, Paris, France, 2013).

[32] S. Posen et al., WEIOC04 (Presented at the SRF Conference, Paris, France, 2013).

[33] S. Deambrosis et al., Physica C 441 (2006) 108-113.

[34] A. Romero, Ph.D. Thesis, University of Padua (2011).

[35] A.-M. Valente Feliciano, (Presented at the SRF Conference, Beijing, China, 2007).

[36] G. Eremeev, TUOBAU08, (Presented at the SRF Conference, Berlin, Germany, 2009).

[37] A. Gurevich, (Presented at the TFSRF Workshop, Newport News, USA, 2008).

[38] T. Tajima et al., IEEE Trans. on Appl. Supercond., Vol. 17, No. 2 (2007).

[39] P. Kneisel, JLAB-TN-12-016 (2012).

Copyright © 2013 CC-BY-3.0 and by the respective authors

DESIGN OF THE SUPERCONDUCTING MAGNET SYSTEM FOR THE SUPERKEKB INTERACTION REGION

N. Ohuchi#, Y. Arimoto, N. Higashi, H. Koiso, A. Morita, Y. Ohnishi, K. Oide, H. Sugimoto, M. Tawada, K. Tsuchiya, H. Yamaoka, Z. Zong, KEK, Tsukuba, Japan
M. Anerella, J. Escallier, A. Jain, A. Marone, B. Parker, P. Wanderer, BNL, Upton, NY, U.S.A.

Abstract

SuperKEKB is the upgraded accelerator of KEKB aiming at an extremely high luminosity. The machine is designed on the basis of nano-beam scheme. The beam final focusing system is the most important element for achieving the luminosity of this accelerator. The system consists of 8 quadrupoles, 4 solenoids and 43 correctors.

INTRODUCTION

The target luminosity of SuperKEKB [1] is 40 times higher luminosity of 8×10^{35} cm^{-2} s^{-1} than that of KEKB. The 7 GeV electrons in the high-energy ring (HER) and the 4 GeV positrons in the low-energy ring (LER) collide at a single interaction point, IP, with a finite crossing angle of 83 mrad.

The accelerator is designed on the basis of the nano-beam scheme [2], and the final beam focusing system has been designed with superconducting quadrupole doublets for each beam. Since the positions of quadrupole magnets must be aligned very precisely within several nano meters, the alignment of quadrupoles is performed by the correctors [3]. In addition, from the requirement of beam optics, 43 corrector coils are installed in the system. The system has four compensation solenoids to reduce the effect of the detector solenoid field on the beams. All magnets and correctors are assembled into two cryostats.

In the paper, the design of the system is described.

SUPERCONDUCTING MAGNET SYSTEM

Magnet Layout in the IR

Figure 1 shows the layout of the superconducting magnets near the interaction point, IP [4]. The system consists of 8 main quadrupole magnets, 4 compensation solenoids, 35 corrector coils and 8 coils to cancel the leakage magnetic fields of QC1LP/RP. The main quadrupole magnets (QC1s and QC2s) are designed to form a quadrupole doublet for each beam. Table 1 shows the main parameters of the quadrupole magnets at the colliding energy of 11 GeV. The QC1LP/RP magnets are located at the closest position, +/- 935mm, to IP. They are quadrupole magnets without magnetic yokes in order to make the solenoid field profile for minimizing vertical beam emittance. The other quadrupole magnets have magnetic yokes.

Since the QC1LP/RP magnets are non-yoked magnets, the leakage field from the magnets to the e- beam line contains all field components as shown in Fig. 2. In order to cancel these components, the B_3, B_4, B_5 and B_6 cancel coils [3] are wound using the helium inner vessel as the coil bobbin. A small twist of the windings which produce the normal cancel components also generates the needed skew cancel components. The B_1 and B_2 field components are included in the optics design.

The compensation solenoids, ESL, ESR1, ESR2 and ESR3, are designed to cancel the Belle-II solenoid field integrally along the beam lines [5]. In the ESL and ESR1 solenoids, two or three quadrupoles are assembled, respectively, as shown in Fig. 1. In the right cryostat, the additional solenoids, ERS2 and ESR3, are also installed.

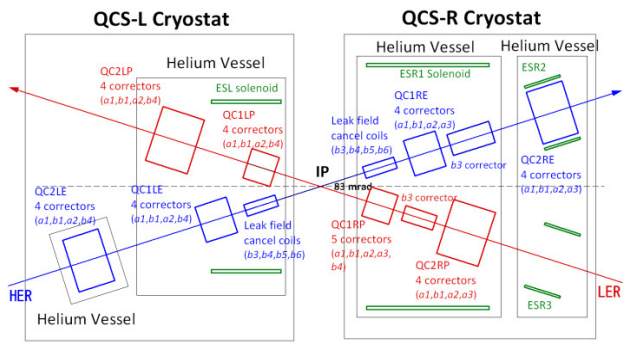


Figure 1: Layout of S.C. magnets near the IP of SuperKEKB.

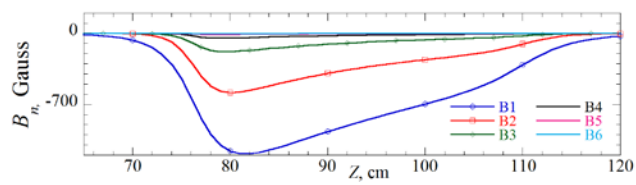


Figure 2: Leakage field profiles along the e- beam line.

Table 1: Main Quadrupole Parameters

Magnet	*GL*, T (T/m×m)	Type	*Z*, mm	*θ*, mrad
QC2RE	13.04 (31.12×0.419)	Yoke	2925	0
QC2RP	11.54 (28.15×0.410)	Yoke	1925	-2.114
QC1RE	25.39 (68.07×0.373)	Yoke	1410	0
QC1RP	22.96 (68.74×0.334)	no Yoke	935	7.204
QC1LP	22.96 (68.74×0.334)	no Yoke	-935	-13.65
QC1LE	26.94 (72.23×0.373)	Yoke	-1410	0
QC2LP	11.48 (28.00×0.410)	Yoke	-1925	-3.725
QC2LE	15.27 (28.44×0.537)	Yoke	-2700	0

GL is the integral field gradient (field gradient at center × effective magnetic length).

#norihito.ohuchi@kek.jp

Copyright © 2013 CC-BY-3.0 and by the respective authors

Alignment of Quadrupole Magnets

In Table 1, the quadrupole centers from IP and the mid-plane angles to the horizontal plane are listed. The quadrupole magnets for LER are assembled with these angles in the cryostats. Since the solenoid field and the leakage field of QC1P magnets change the e- beam orbits, the beam orbits will be controlled by dipole correctors. In order to optimize the corrector system, the magnet axes of QC1s and QC2s are shifted as shown in Table 2. In the table, ΔY is the shift amount in vertical direction from the horizontal plane including IP and the negative sign means downward. The plus ΔX means the horizontal shift toward the outer direction of the accelerator ring.

Table 2: Shift Amount of Magnet Axis

Magnet	ΔY	Magnet	ΔX
QC1RP	-1.0 mm	QC1RE	-0.7 mm
QC2RP	-1.0 mm	QC2RE	-0.7 mm
QC1LP	-1.5 mm	QC1LE	+0.7 mm
QC2LP	-1.5 mm	QC2LE	+0.7 mm

QUADRUPOLE MAGNETS

The four cross sections of the quadrupole magnets are shown in Fig. 3. The magnet designs are different in order to accommodate the change of the beam pipe diameters in the cryostats. Table 3 shows the design parameters of the magnets. The numerical values are for colliding energy of 12 GeV. The magnets consist of two layer coils, and the cables are same specification except for the keystone angle. The QC1P magnets are designed without iron yokes because in the location of these magnets the solenoid fields by ESL and ESR1 integrally cancel the Belle-II solenoid field. The QC1E and QC2P magnets have Permendur yokes to avoid magnetic saturation in yokes due to local imperfection in cancelling Belle-II field by ESL and ESR1. For the QC2E magnets, the yoke material is iron because the separation between two beams is more than 200 mm.

Table 3: Design Parameters of QC1 and QC2 Magnets

	QC1 P	QC1 E	QC2 P	QC2 LE/RE
Magnetic yoke	No	Perm.	Perm.	Iron
Coil I.R., mm	25.0	33.0	53.8	59.3
Coil O.R., mm	30.49	38.49	59.29	64.79
Collar/Yoke O.R., mm	35.5	70	93	115
Turns in a pole	25	34	54	58
Field grad.at I_d, G, T/m	76.4	91.6	32.0	36.4/39.3
Design curr., I_d, A	1800	2000	1000	1250/1350
Magnetic length, mm	333.6	373.1	409.9	537/419
$I_d/I_{c,\%}$	72	73	47	50/49

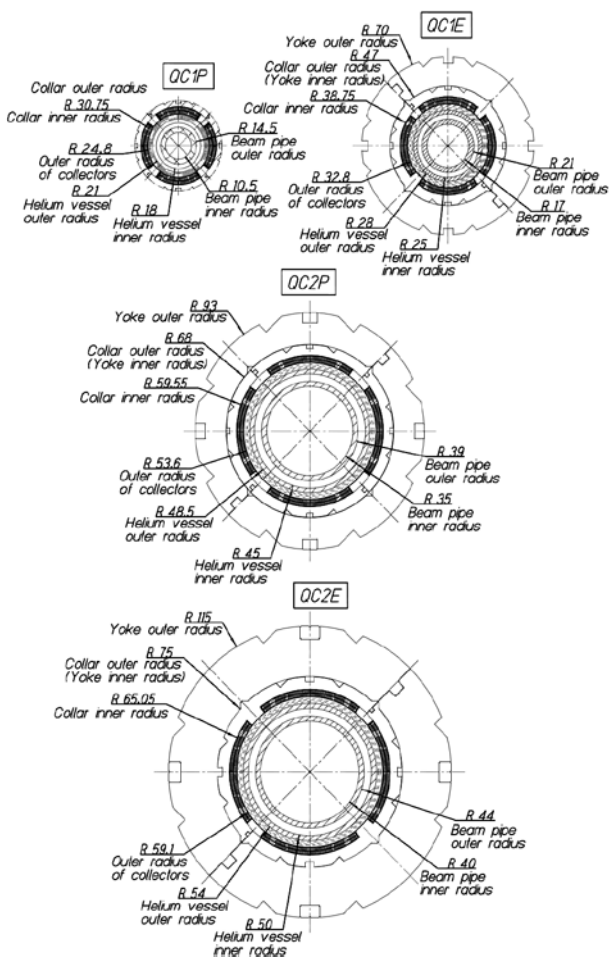


Figure 3: Quadrupole magnet cross sections.

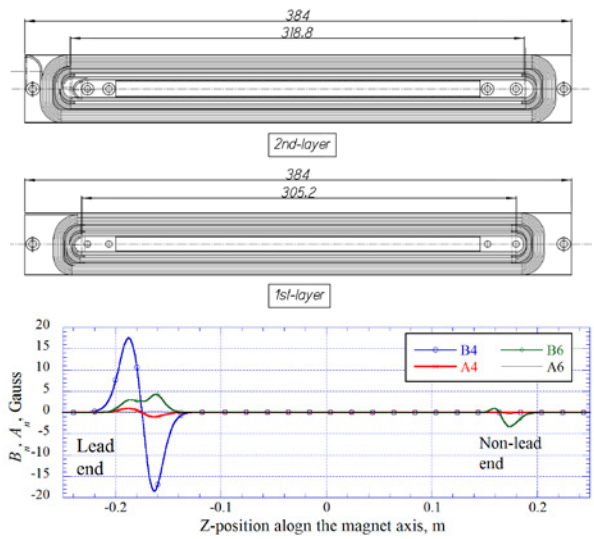


Figure 4: Coils of QC1P magnet and error field profiles.

In Fig. 4, the coils of QC1LP and the profiles of A_4, B_4, A_6 and B_6 components are shown. The coil ends are designed to reduce the absolute peaks of the error fields to less than 20 Gauss and the integral error fields to less than

Copyright © 2013 CC-BY-3.0 and by the respective authors

1 unit. From the asymmetry configuration of the lead end, the B_4 component has the peaks of +/- 18 Gauss. The Touschek life time are calculated with these field profiles. As the result, the lead ends of the magnets are positioned at the IP side in the cryostat because the smaller size beam at the IP side is less sensitive to the higher order error fields. The other quadrupole magnets are placed in the same way.

SUPERCONDUCTING CORRECTORS

The corrector specifications are summarized in Table 4. In Table 4, R_r is the reference radius, and A_n and B_n are the skew and normal correctors, respectively. The A_1 and B_1 correctors are designed to be able to shift the magnet axis in the range of 0.5 mm to 1.0 mm. The A_2 corrector can rotate the mid-plane angle of the quadrupoles from 12 mrad to 15 mrad. The sextupole A_3 and B_3 correctors cancel the error fields of the quadrupole magnets induced by magnet assembly errors. The required integral sextupole field strengths are equivalent to 1×10^{-3} of the quadrupole fields. R_r values of B_3 coils for LER and HER are 15 mm and 30 mm, respectively. Installation of sextupole correctors was decided from the results of QC1P/1E proto-type magnets [6]. The B_4 correctors increase the dynamic transverse aperture.

Table 4: Integral Field Strengths of Correctors

Magnet	R_r	A_1	B_1	A_2	A_3	B_3	B_4
	mm	T•m	T•m	T	T/m	T/m	T/m^2
QC1RP	10	0.016	0.016	0.64	7.6	17.2	60
QC2RP	30	0.03	0.03	0.31	1.36		-
QC1RE	15	0.027	0.046	0.75	7	27	-
QC2RE	35	0.015	0.015	0.37	1.5		-
QC1LP	10	0.016	0.016	0.64	-	-	60
QC2LP	30	0.03	0.03	0.31	-	-	60
QC1LE	15	0.027	0.046	0.75	-	-	60
QC2LE	35	0.015	0.015	0.37	-	-	60

COMPENSATION SOLENOIDS

Figure 5 shows the field profile of Belle-II solenoid and the combined field profile with ESL and ESRs. As shown in Fig. 5, Belle-II solenoid generates the solenoid field of 1.5 T, and the field is cancelled by the reverse solenoid fields in the areas of QC1LP and QC1RP. In order to produce the combined field profiles required by beam optics, ESL and ESR1 are divided into 12 and 15 small solenoids, and they produce the integral fields of 2.31 T•m and 3.69 T•m, respectively. These integral fields correspond to the integrated Belle-II solenoid fields from the IP. The maximum fields in ESL and ESR1 coils with the Belle-II fields are 3.4 T and 3.3 T, respectively.

Since QC1Es and QC2Ps have the Permendur yokes and the combined fields are designed to be less than 0.01 T, the residual solenoid fields are negligible on the beam lines. Between QC2RP and QC2RE, the Belle-II fringe field is in the range of 0.6 T because of no magnetic shields. The fringe field is cancelled by ESR2 or ESR3. The solenoid parameters are summarized in Table 5.

The design of the cryostat is difficult because the compensation solenoids have large repulsive electro-magnetic forces from the Belle-II field. The forces on ESL and ESR1 amount to 38 kN and 48 kN, respectively. The forces affect the magnet-cryostat alignment, and this is the next important problem to be solved.

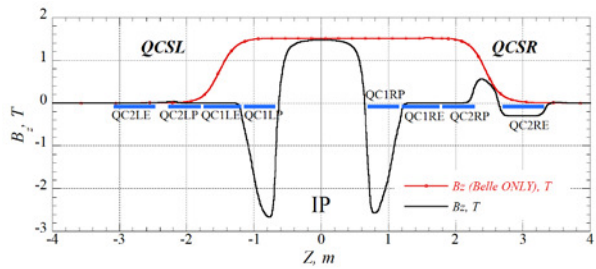


Figure 5: Solenoid field profiles along the beam lines.

Table 5: Design Parameters of Compensation Solenoids

	ESL	ESR1	ESR2/3
Integral field, T•m	2.31	3.69	0.17
Design current, A	348	462	210
Inductance, H	2.14	2.64	0.02
Maximum field, T	3.6	3.3	0.3
Magnet length, mm	905	1575	720
$I_d/I_{c,\%}$	68	72	<20

SUMMARY

The final focusing superconducting magnet system of SuperKEKB has been designed after many steps of iteration. The designed system consists of 8 quadrupole magnets, 4 compensation solenoids and 43 corrector coils. They are now in the construction stage, and the completion of the system is scheduled in 2015.

REFERENCES

[1] K. Akai et al., "Design Progress and Construction Status of SuperKEKB," IPAC2012, New Orleans, May 2012, TUPPR006, p. 1822 (2012); http://www.JACoW.org.
[2] P. Raimondi, 2nd SuperB Meeting, Frascati (2006).
[3] B. Parker et al., "Superconducting Corrector IR Magnet Production for SuperKEKB," THPBA07, NA-PAC'13.
[4] M. Tawada et al., "Design study of final focusing superconducting magnets for the SuperKEKB," IPAC2011, San Sebastian, September 2011, WEPO027, p. 2457 (2011); http://www.JACoW.org.
[5] H. Yamaoka et al., "Solenoid Field Calculation of the SuperKEKB Interaction Region," IPAC2012, New Orleans, May 2012, THPPD023, p. 3548 (2012); http://www.JACoW.org.
[6] N. Ohuchi et al., "Design and Construction of the Proto-type Quadrupole Magnets for the SuperKEKB Interaction Region," THPBA04, NA-PAC'13.

Copyright © 2013 CC-BY-3.0 and by the respective authors

RAPID CYCLING DIPOLE MAGNET*

H. Witte†, J.S. Berg, P. Kovach, M.D. Anerella, Brookhaven National Laboratory, Upton, NY, USA
M. L. Lopes, Fermilab, Batavia, IL, USA

Abstract

Accelerating muons to 750 GeV and higher is most efficiently accomplished using a hybrid synchrotron. Such a machine interleaves superconducting dipoles with bipolar dipoles ramping at an effective frequency of 400–1000 Hz and with maximum fields of around 1.8 T. Previous designs for the rapid cycling dipoles for this lattice have been based on grain oriented steel, which possesses good magnetic properties in the direction of the grains. Grain oriented steel however is highly anisotropic, which can potentially lead to field quality problems. In this paper we present an alternative design, which we expect to have lower losses, a higher peak field, and better field quality.

INTRODUCTION

A hybrid synchrotron is the most efficient known option for accelerating muons to their highest energies in a TeV-scale muon collider. A hybrid synchrotron bends particles by interleaving fixed field superconducting dipoles with bipolar rapid cycling dipoles. This permits rapid acceleration, to reduce muon decay, while making a significant number of RF cavity passes to achieve good efficiency. To maximize the RF efficiency, minimize decay, and maximize the energy range of a single ring, it is essential to have the highest field possible for both the superconducting and the rapid cycling dipoles.

A design accelerating muons from 375 to 750 GeV has been proposed [1] (shown schamatically in Fig. 1), which was a variation and refinement on earlier designs [2]. It has a circumference of 6300 m, with arc cells containing 2.7 m 8 T dipoles and 7.9 m rapid cycling dipoles. The field in the rapid cycling dipoles swings from -1.8 T to $+1.8$ T in 0.5 ms; there are about 2200 m of these dipoles in the ring. The beam will be accelerated 15 times per second.

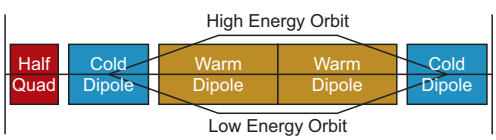


Figure 1: Structure of a quarter cell, showing the expected deviation of high and low energy closed orbits.

This report outlines a potential solution for the rapid cycling dipoles. We propose a solution operating at a frequency of 400 Hz (proposed in [2], gives more decays than [1]). The aperture required will be 60 mm horizontally (required for horizontal beam aperture) and 13 mm vertically (primarily to keep impedances reasonable). We also discuss a 25 mm vertical aperture, which might be required if a ceramic beam pipe is used.

MAGNET GEOMETRY

We consider the geometry shown in Fig. 2, which shows the 13 mm gap case. For a 25 mm gap the pole width increases to 132 mm because of field quality reasons. Each coil area is 87×30 mm^2 in cross-sectional area.

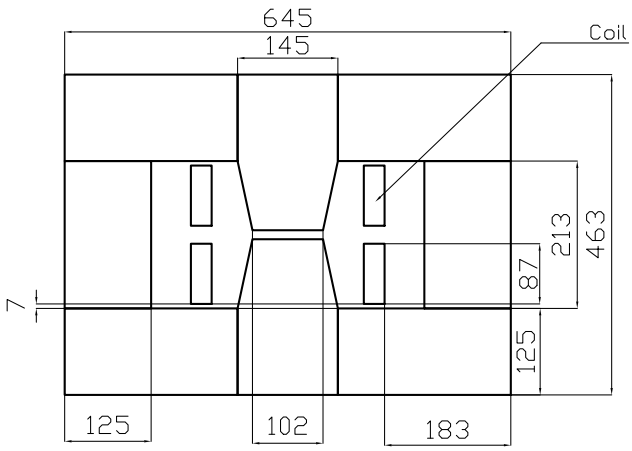


Figure 2: Geometry of the dipole magnet (in mm).

MATERIALS

Previous studies focused on grain-oriented 3% SiFe, which possesses good magnetic properties in the rolling direction [3]. A concern however is the high anisotropy of the material, which in studies has shown to affect the field quality.

For this study we focus on alternative isotropic materials, which promise lower losses while at the same time can achieve higher peak magnetic fields. The coil design employs two materials: 6.5 %SiFe and FeCo (49% Co, 1.9% V and 49% Fe). 6.5% SiFe, which has a relatively low magnetization saturation, is chosen for the very low losses. FeCo (with relatively large losses) has a very high magnetization saturation and is used for the poles of the magnet. For this design we consider Vacoflux 48 from Vac-

* Work supported by Brookhaven Science Associates, LLC under Contract No. DE-AC02-98CH10886 with the U.S. Department of Energy.
† hwitte@bnl.gov

Copyright © 2013 CC-BY-3.0 and by the respective authors

uumschmelze[1] and 10JNEX900 from JFE[2]. The material data for hysteresis, magnetization curves and loss calculations were obtained from the manufacturers [4, 5]. The laminates are assumed to be 100µm thick. For comparison reasons we also estimate performance and losses for a design using isotropic 3% SiFe with thicknesses of 178µ and 250µm [6, 7].

PERFORMANCE AND FIELD QUALITY

The magnet performance using the different materials was evaluated in a 2D non-linear static finite element simulation. For a field of 2T an average current density of 4 A/mm^2 is required (25 mm gap: 7.88 A/mm^2). Fig. 3 shows the expected field quality $\Delta B/B_0$ as a function of the peak magnetic field on the centre plane. The figure shows the obtained results for an all 3% SiFe yoke and FeCo/6.5 %SiFe (13 mm and 25 mm gap). As shown in the figure, the field quality using 3% SiFe starts to deteriorate for fields in excess of 1.5 T. Using FeCo in principle allows to achieve more than $1.9 - 2$ T assuming a required field quality of 1×10^{-3}.

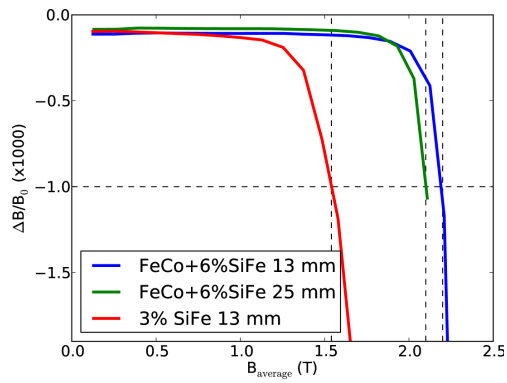


Figure 3: Field quality.

It was found that the field quality is unaffected by eddy currents in the yoke, hysteresis effects and mechanical tolerances other than the tolerance on the poles of the magnet.

POWER LOSSES

Resistive Losses in Coil

It was found that eddy current losses in the coils are a serious concern. To mitigate this the coils are placed in an area inside the yoke where field leakage is minimal. Instead of standard rectangular conductor (with a circular hole for water cooling) the coils are made of thin copper sheets, which are insulated against each other with 25µm thick Kapton tape. To determine the ideal thickness of the sheets a time-transient eddy current study was set-up. The simulation assumes that the coil area remains fixed, while the number of sheets is varied (and the thickness of each sheet is $d_{\mathrm{Sheet}} = w_{\mathrm{coil}}/N$, with N as the number of sheets).

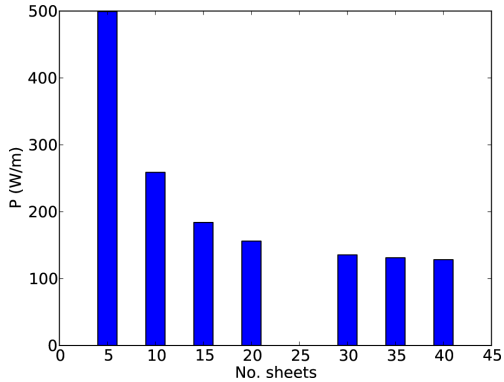


Figure 4: Power loss per m of magnet for different numbers of conducting sheets.

Fig. 4 shows the simulated power loss per pulse for a one meter long magnet. The figure shows that increasing the number of sheets up to 20 significantly reduces the power loss. A number of 30 sheets (each 1 mm thick) was chosen for the final design.

Core Losses

The core losses consist of eddy current losses, hysteresis losses and so-called anomalous losses. To estimate the core losses we rely on measured data from the manufacturers of the materials [4, 5]. Fig. 5 shows the results for an all 3% SiFe yoke with 178µ and 250µm thick laminates in comparison to a yoke made of 6.5% SiFe and FeCo. The losses are calculated assuming 2 km total dipole length in the ring.

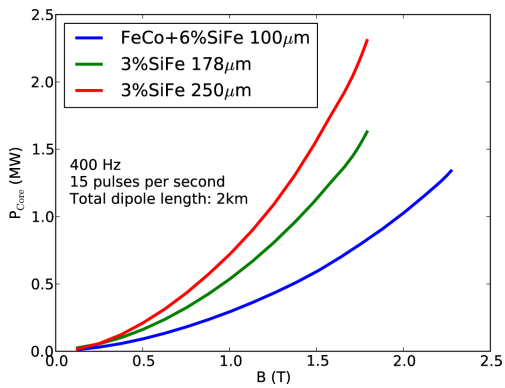


Figure 5: Core losses.

The figure shows that the here presented design is more efficient in comparison to a yoke made of 3% SiFe. For a peak field of 1.5 T the core losses are calculated to 0.5 MW for the entire ring in comparison to 1–1.5 MW for 3% SiFe. The core losses for 178µm thick 3% SiFe are expected to be lower than for 250µm thick laminates due to the better suppression of eddy currents.

[1] VACUUMSCHMELZE GmbH & Co. KG, Grüner Weg 37, D-63450 Hanau, Germany

[2] JFE Steel Corporation, Electrical Steel Section, Tokyo, Japan

Copyright © 2013 CC-BY-3.0 and by the respective authors

Total Power Loss

The total estimated power loss for the entire ring (core and coil losses, total dipole length 2 km) are shown in Fig. 6. The figure shows the losses assuming a 13 mm and 25 mm gap. The losses for the 178µm thick 3% SiFe laminates are shown as well. At 1.5 T the total losses using FeCo and 6.5 %SiFe are expected to be about 0.75 MW for the entire ring. At 2 T this increases to 1.5 MW. The power losses are lower by a factor of two or more in comparison to a design using 178µm thick 3% SiFe.

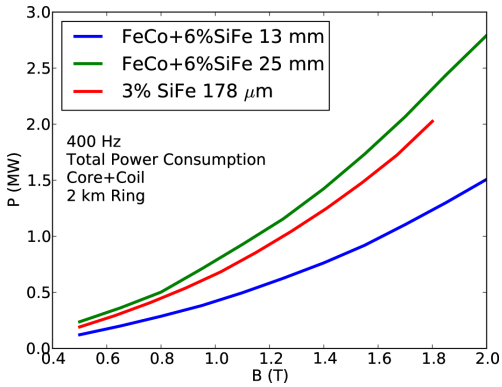


Figure 6: Total power loss for entire ring.

ENGINEERING CONSIDERATIONS

Mechanical Design

To contain the forces during operation the dipole magnet is housed in an external clamp. The peak forces during operation were evaluated using the Maxwell stress tensor and Biot-Savart-Law. It was found that the only significant force component acts on the poles, which is about 170 kN in vertical direction for a 1 m long magnet with a 13 mm gap (towards the centre of the magnet). The force acting on the coils is negligible.

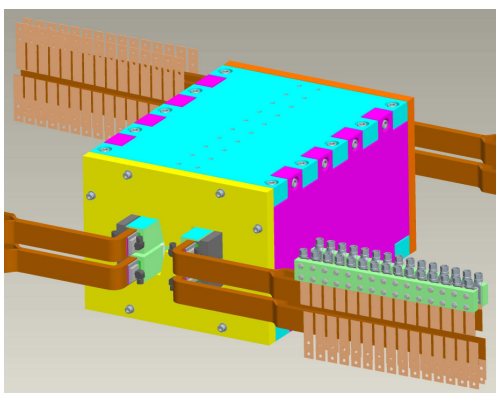


Figure 7: Rapid cycling dipole assembly.

The support structure of the magnet is designed to deal with the forces and to minimize the deflection to achieve the desired field quality. Fig. 7 shows the mechanical design of the dipole magnet.

Cooling

The average power dissipation in both the yoke as well as the coil is relatively low due to the repetition rate of 15 Hz. The coils can be conduction cooled on each side. A finite element simulation shows that the temperature gradient in the coil can be kept to 2 K or less provided 500 W (for a 1 m long dipole magnet) can be transferred to the coolant. The yoke can be conduction cooled via the external faces.

SUMMARY

A conceptual design of a dipole magnet is described in this paper which is suitable to be operated at 400 Hz with a repetition rate of 15 Hz. Using two different materials for the yoke (FeCo and 6.5 %SiFe), the losses can be minimized while at the same time achieving high magnetic fields. The presented design delivers a good field quality up to about 2T. For this field level the average power loss for an entire ring (2 km total dipole length) is about 1.5 MW.

It is planned to carry out activation studies of the yoke, which is a concern due to the cobalt content.

REFERENCES

[1] J. S. Berg and A. A. Garren. Hybrid Fast-Ramping Accelerator to 750 GeV/*c*: Refinement and Parameters over Full Energy Range. Technical Report BNL-98171-2012-IR, MAP-doc-4335, BNL, 2012.

[2] D. J. Summers, L. M. Cremaldi, R. Godang, B. R. Kipapa, H. E. Rice, and R. B. Palmer. Muon Acceleration to 750 GeV in the Tevatron Tunnel for a 1.5 TeV $\mu^+\mu^-$ Collider. In *Proceedings of PAC07, Albuquerque, New Mexico, USA*, page 3178. IEEE, 2007.

[3] D. Summers, L. Cremaldi, T. Hart, L. Perera, M. Reep, et al. Test of a 1.8 Tesla, 400 Hz Dipole for a Muon Synchrotron. *Conf.Proc.*, C1205201:3542–3544, 2012.

[4] C. Bach. Personal communication. VAC Sales USA LLC, 2935 Dolphin Drive, Suite 102, Elizabethtown, KY 42701, USA, 2012.

[5] H. Ninomiya. Personal communication. JFE Steel Corporation, Electrical Steel Section, Tokyo, Japan, 2012.

[6] AK Steel. DI-MAX HF-10, Cold Rolled Fully Processed Nonoriented Electrical Steel, Product Data Bulletin. Technical report, AK Steel Corporation, 9227 Centre Pointe Drive, West Chester, OH 45069, USA, 2013.

[7] Arnold Magnetic Technologies. Non Grain Oriented Electrical Steel Arnon 5. Online: `http://www.arnoldmagnetics.com/Non_Grain_Oriented_Electrical_Steel.aspx`, September 2013.

Copyright © 2013 CC-BY-3.0 and by the respective authors

THE ILLINOIS ACCELERATOR RESEARCH CENTER

R. Kephart#, J. Anderson, C. Cooper, S. Henderson, C. Schmidt
Fermi National Accelerator Laboratory, Batavia, IL 60510, USA

Abstract

Particle accelerators are an enabling technology not only utilized in their traditional role for fundamental research, but also in such diverse fields as medicine, industrial processes, environmental mitigation, and national security. In recognition of this large impact on the US economy, the Fermi National Accelerator Laboratory (FNAL) has partnered with the Illinois Department of Commerce and Economic Opportunity (DCEO) and the Department of Energy's Office of High Energy Physics (DOE/OHEP) to build the Illinois Accelerator Research Center (IARC). Located on the Fermilab campus, this 83,000 square foot facility will house office, technical, and educational space in a state-of-the-art facility for accelerator research, development, and education. With a strong focus on industrial application of accelerator technologies, IARC will attract high-tech companies to Illinois and help train Illinois citizens in advanced technologies.

INTRODUCTION

IARC was conceived and proposed by Fermilab and DOE to the State of Illinois in 2007. The need for a US facility like IARC was recognized at the Accelerators for America's Future symposium held in Washington DC in Oct 2009. The 2010 report from this symposium contains a wealth of information on the basic justification for investment in accelerator applications as well as the opportunities for new accelerator applications for a facility like IARC [1]. Following the lead of this symposium, the 2012 Senate Water and Energy Bill encouraged DOE to pursue the development of accelerator applications more aggressively [2,3]. It requested DOE/OHEP to provide a plan to address the opportunities made evident in the Accelerators for America's Future symposium. In 2011, OHEP convened an Accelerator R&D Task Force to offer advice on the creation of such a plan. An interim report from this committee was presented at the High Energy Physics Advisory Panel (HEPAP) meeting in March 2012 [4]. The final report to the House and Senate Appropriations Subcommittees was completed in September 2012. Through this request by Congress, OHEP is now the designated steward of accelerator science and technology within the DOE Office of Science complex, with a new thrust toward applied technology.

Key to the success of IARC will be a shared understanding at the national, state, and local levels that translational technology, namely developing ideas from the laboratory into commercial practice, only happens when the proper environment is cultivated. The proper environment promotes friendly, flexible collaboration with industry and universities and provides sufficient seed resources such that non-traditional and multi-disciplinary efforts can flourish.

In 2014 Fermilab plans to increase its partnerships with industry via Work for Others (WFO) and Cooperative Research and Development Agreements (CRADA's). When the physical plant is completed for occupancy in 2015, the IARC facility will attract industrial partners to develop technology for accelerator applications, encourage development of intellectual property by laboratory and university accelerator staff, and provide a National Center for Accelerator Education. The goal is a successful IARC program that exploits and leverages resources from DOE OHEP, Small Business Innovation Research (SBIR) programs, DCEO, and other public funding with substantial private investment from industry and the venture capital community. These funds will be used to translate ideas in accelerator technology into new high tech products and industries and to create an educational program to train the skilled workforce to build and operate the accelerators of the future.

A key concept for the IARC program is that it serves as a portal to allow industrial access, not just to the IARC physical plant, but also to the facilities and technical expertise of the entire laboratory. A successful program at IARC will lower barriers for Laboratory – Industry cooperation on accelerator technology and applications and enable an entire new class of projects to be undertaken as Government-Industry partnerships.

MISSION STATEMENT

The mission of IARC is to partner with Industry, University, and Laboratory collaborators to promote the development of accelerator technology and applications, leading to new products, capabilities, and businesses. The IARC education program will support and enable the creation of the high technology workforce required for its mission.

THE VISION

The vision for IARC is the creation of a friendly, flexible environment to facilitate collaboration with industry, universities, and other national labs and to help provide sufficient seed resources such that non-traditional and multi-disciplinary efforts can flourish. The IARC environment will allow access and leverage of Fermilab's unique facilities and staff to create an innovation hub for new Accelerator based technologies and industries.

When the IARC physical plant is complete in 2015, the laboratory envisions attracting industrial partners to develop technology for industrial accelerator applications; encouraging the development of advanced innovative accelerator science and technology as well as intellectual

Copyright © 2013 CC-BY-3.0 and by the respective authors

property by laboratory and university staff; and creating a National Center for Accelerator Education.

The key components of the IARC mission and vision are:

- Partnerships with industry, university, and laboratory collaborators to promote the development of accelerator technology, projects, and applications.
- Creation and support of entirely new U.S. based high tech industry sectors based on accelerator technology that enables new products and capabilities.
- Partnerships with universities to create a national educational center for accelerator science and technology.

IARC'S VALUE TO INDUSTRY

IARC will offer value to U.S. industrial companies and entrepreneurs by:

- Helping to overcome the technical barriers that currently impede development of ideas into new accelerator based applications and businesses.
- Serving as a portal organization to provide industry with better access to the extensive expertise in accelerator science and technology available from the Fermilab staff as well as the staff at nearby Argonne National Laboratory.
- Providing access to the specialized and unique accelerator infrastructure at Fermilab.
- Enabling and encouraging collaborations to propose and demonstrate the use of accelerator technology for new applications or markets.
- Serving as a Center for Accelerator Education allowing industrial staff to acquire needed technical skills to pursue businesses based on accelerator technology

CAPABILITIES AVAILABLE TO INDUSTRY THROUGH IARC

IARC will provide unique infrastructure for the development of new accelerator based products and businesses. However, key to its success is the powerful core capabilities available at the entire laboratory. The Accelerator Sector at Fermilab is made up of nearly 700 Scientists, Engineers, and Technical staff. Staff members have extensive experience spanning decades of design, construction, and operation of some of the most technically challenging accelerator components, accelerator systems, and facilities in the world. A brief summary of some specific areas of expertise and excellence that currently exist at the laboratory are listed in Table 1.

Table 1: Fermilab Core Capabilities Available to IARC Partners

Core capabilities	Areas of Expertise
Accelerator Science	Beam dynamics and theory Simulation and Modeling Phase-space manipulation Energy Deposition
Accelerator Operation	Operation and commissioning of large, complex accelerator systems
Accelerator Technology **(design, fabrication, test)**	Linear and circular particle accelerators Superconducting RF cavities Superconducting magnets Cryomodules Conventional, and pulsed magnets Magnet field mapping Beam Cooling systems Design of high power targets High and low-level RF systems Cryogenic Refrigeration systems
Accelerator Engineering	Accelerator design & fabrication Accelerator integration & commissioning Accelerator system cost estimates Design of accelerator RF systems Radio Frequency system modeling Low and High power electrical systems Water cooling systems Energy deposition and activation Cryogenic Engineering
Particle Detectors	Advanced Detector development Beam test of detectors Custom ASIC development
Controls Engineering	Control systems modeling and design Control & Interlock systems Data acquisition systems VHDL, PLD, PLC, DSP programming
Computing	Management, analysis of large data sets High speed parallel (GRID) computing High speed networks Data Storage and Cloud computing

The Fermilab accelerator sector staff and that of nearby Argonne National Laboratory represent the largest collection of Accelerator capability in North America. Similarly, the challenging experimental particle physics program at Fermilab has created world class capabilities in particle detector development and in advanced computing.

FACILITIES AVAILABLE TO INDUSTRY THROUGH IARC

IARC, located in the heart of the Industrial and Technical area of the Fermilab campus, will consist of 36,000 square feet of heavy assembly, technical, and office space in an existing Heavy Assembly Building (HAB) plus 47,000 square feet of new technical, office, and educational space in the State of Illinois funded addition. These two buildings make up the IARC complex.

The OTE building will provide office space for scientists, engineers, and administrative staff from Fermilab and IARC industrial, university, and laboratory partners. The OTE building provides meeting rooms, a

Copyright © 2013 CC-BY-3.0 and by the respective authors

lecture hall, and technical lab space. The layout of OTE and the nearby Heavy Assembly Building (HAB) is shown in Figure 1, which also indicates IARC's location in relation to the buildings that make up the Fermilab "Industrial Complex".

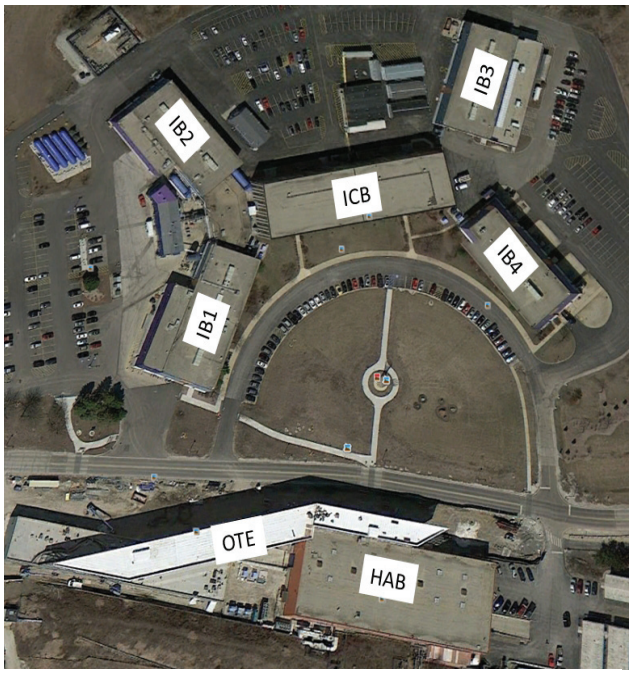


Figure 1: The IARC OTE & HAB Buildings shown in the Technical Division Complex.

The Industrial Complex houses the bulk of the Fermilab Technical Division (TD). TD staff located in the Industrial Complex includes experts in conventional and superconducting magnets, experts in warm and superconducting RF technology, and a powerful superconducting materials technology group. It is planned to move the Accelerator Physics Center (APC) to the OTE building with the goal of integrating FNAL staff with industrial and university partners encouraging exchange of information and true partnerships. APC has a long history of working with industrial partners on diverse topics. Members of the APC staff have strong Accelerator Physics, Beam simulation, and energy deposition capabilities.

The industrial complex includes extensive technical infrastructure for the development of accelerator components. Additional technical infrastructure at other locations on the Fermilab campus will also be available to IARC partners. Several test accelerators and beams will also be made available to IARC partners.

The IARC OTE Building can be seen in Figure 2. The IARC HAB, seen in Figure 3, was formerly used as the assembly building for the Collider Detector at Fermilab (CDF). CDF was a large 5000 ton experimental detector used at the Fermilab Tevatron collider. This building has a large assembly area equipped with 50 ton and 10 ton overhead crane coverage, and also has a deep pit that is ideal for testing or operating pilot scale accelerators or any similar equipment that will require radiation shielding. Extensive test and operation infrastructure already exists in this facility, including cryogenic refrigeration, low conductivity cooling water, and 1.5 MW of installed electrical power feeds. The HAB also has additional office space, meeting areas, and a technical shop with equipment for general machining.



Figure 2: Illinois Accelerator Research Center (Office Technical and Education addition) under construction at Fermilab.



Figure 3: Photo of the interior of the IARC Heavy Assembly Building.

A successful program at IARC will lower barriers for Laboratory – Industry cooperation on accelerator technology and applications and enable an entire new class of projects to be undertaken as Government-Industry partnerships. In this spirit we have compiled a list of the extensive technical infrastructure and test capabilities available at Fermilab via the IARC program. Table 2 lists fabrication and test capabilities at Fermilab, while Table 3 lists Fermilab test accelerator and beam test facilities.

Table 2: Fabrications and Test Capabilities at Fermilab

Facility	Capability	Specifications
Technical Division IB1	Superconducting RF cavity test facility.	3 vertical test Dewars 3.6 m in depth 0.86 m in diameter 1.4 K min temperature
	Conventional magnet test and mapping facility	3 horizontal test stands Pulsed power supply 750V, 25 kA, 2 HZ Complete magnet mapping capability
	Superconducting Magnet Test and Mapping facility.	Vertical Dewar 3.85 m deep 0.6 m diameter 1.8 K capability; Horizontal

Copyright © 2013 CC-BY-3.0 and by the respective authors

Facility	Capability	Specifications
		SC magnet test stands 2 or 4 K SC magnet Power supply (30 KA, 30 V); Interlocks and DAQ
	Cryogenic System	Helium refrigerator: 1,500 watts at 4.5K or 300 l/hour liquefaction
Technical Division IB2	Conventional magnet fabrications and repair.	25 ft long curing and de-bonding ovens 7 ft dia, 250 F, vacuum furnace; Lamination stacking and winding of large conventional magnet coils
Technical Division IB3	Superconducting magnet development and fabrication	SC cable machine; SC cable winding line 7 meter curing presses Nb3Sn reaction ovens Analytical equipment: Scanning electron microscope with Energy Dispersive Spectroscopy, Laser confocal and contact surface profilometry, FT-IR/TGA, Stress/Strain equipment, Residual resistivity ratio testing
Technical Division IB4	Quality Control Cavity Processing Lab	Large CMM machines State of the art cavity tumbling machine Electro-polish tool for SRF cavities; Class 10 clean room High purity, high pressure water rinse, Small and large 1000 C vacuum furnaces
Technical Division ICB	High Bay Assembly Area	Large high bay area with two 30 Ton overhead cranes and extensive Cryomodule assembly infrastructure
Technical Division MP9	Large Clean Rooms Clean SRF assembly Large Vacuum Oven	Large class 10- class 100 clean room; Fixtures for the clean string assembly of SRF cryomodules, Titanium welding infrastructure Large 1000 C high vacuum oven.
Technical Division MDB	Dressed Cavity Test Facility	Test of dressed SRF cavities at 2 K with pulsed or CW RF. 3 stands in 4 Shielded reconfigurable enclosures 1800 W @ 4K of cryogenic refrigerators Large vacuum pump provides 100 W at 2 K.
ANL-Fermilab Cavity Processing Facility	Surface processing and clean assembly of SRF cavities	Class 10 clean room for assembly; 2 EP/BCP tools for chemical surface processing of SRF cavities; 2 high pressure rinse systems; Ultra-clean water system; Trained Fermilab and ANL staff Facility located at Argonne Nat Lab.
Accelerator Division CMTF	CryoModule Test Facility	Test of SRF cryomodules at cryogenic operating temperatures and with RF Power. The facility is equipped with two large cryogenic refrigerators and can easily be adapted for other cryogenic testing activities.
Technical Division Solenoid Test Facility IB1 & CHL	Testing of large cryogenic magnets powered and at operating temperature	Proximate to the Tevatron Central Helium Liquefier. This facility and its large test Dewar is capable of testing very large magnets at 4 Kelvin.

Table 3: Fermilab Test Accelerator and Beam Test Facilities

Facility	Description
NML Pulsed SRF Facility	Currently this facility consists of a 40 MeV photo-injector and a facility to allow cold test of single 1300 Mhz cryomodule. Proposed as the basis of a world class Advanced Accelerator R&D (AARD) program. (see ASTA below)
Advanced Super-conducting Test Accelerator (ASTA)	ASTA is envisioned to contain 3 to 6 ILC/PX 1300 MHz cryomodules each containing eight cavities. Beam lines and test areas will support a user facility for a world class advanced accelerator research program. ASTA will provide intense electron beams from 50 to 800 MeV/c energies. A small storage ring IOTA with the capability of storing either electrons or protons is also planned to explore new techniques to store intense beams. See: http://apc.fnal.gov/programs2/ASTA_TEMP/index.shtml
Fermilab Test Beam Facility (FTBF) At MDB	A high energy beam facility devoted to Detector R&D. The facility consists of two versatile beamlines (MTest and MCenter) in which users can test equipment or detectors. Details can be found at http://www-ppd.fnal.gov/FTBF/.
MuCool Test Area (MTA)	Used for R&D on ionization cooling components for the Muon Accelerator Program (MAP). The facility includes an experimental hall with radiation shielding, a 600 W cryogenic plant , access to 400-MeV high-intensity H- beam from the Fermilab Linac, 201 & 805 MHz RF power, a large-bore solenoid magnet, liquid helium and nitrogen, vacuum and hydrogen safety systems, Details can be found at http://mice.iit.edu/mta/.

Copyright © 2013 CC-BY-3.0 and by the respective authors

Facility	Description
Project X Injector Experiment (PXIE)	PXIE is the integrated systems test for the Project X frontend. It is expected to accelerate a 1-mA CW beam up to 30 MeV with 1 mA average current. See: http://www-bdnew.fnal.gov/pxie/

SCHEDULE AND TIME LINE

The near term plans for IARC focus on construction of the IARC facilities and development of the business plan. This will be followed by launching the Accelerator Applications Program and then the Education Program.

The shell of the State funded OTE Building is finished and the building is scheduled to be complete in December of 2013. Building layouts that will optimize the different functions of IARC are being finalized so that outfitting of the OTE can begin in January of 2014. This will allow for beneficial occupancy of the OTE building in September of 2014.

Preparation of the HAB has 3 concurrent projects currently: Removal of old experimental equipment from the building, Life Safety Upgrades, and refurbishment. The main schedule driving element is decommissioning of the Tevatron CDF detector including heavy steel work and removal of over 2500 T of experimental equipment from the deep pit of HAB. Assuming adequate funding in FY14, it is envisioned that HAB Deconstruct and Decommission (D&D) will complete by the end of 2014. The HAB Life Safety Upgrades are scheduled to be complete in October of 2014.

Completion of OTE, HAB D&D, and HAB life safety projects will allow Industrial Partners to begin to utilize portions of the IARC facility in early 2015. The HAB Refurbishment project will modernize the 2nd and 3rd floors of HAB as the space is reconfigured into office, meeting, and technical spaces. A new HVAC system and controls, new insulated exterior, new windows and other modifications will allow the building to meet required energy and ADA standards.

In parallel with the construction of the IARC physical plant, the business plan and IARC program will be further developed by the IARC Staff, Fermilab Directorate, Fermilab DOE Site Office, and DOE Office of High Energy Physics leading to the launch of the formal IARC Accelerator Applications and Education programs.

THE PARTNERSHIP MANAGEMENT CHALLENGE

IARC is expected to drive significant changes in the way Fermilab interacts with industry. This Partnership Management Challenge has three major components:

- Forming new relationships
- Negotiating agreements
- Protecting Intellectual Property

Historically, Fermilab's communication program has focused on announcing scientific discoveries and promoting the Laboratory's technology transfer success stories to DOE, elected officials, industry, and the general public. As IARC develops, Fermilab will need a more comprehensive program to advertise licensing opportunities; coordinate events to attract new industrial partners; enlist the support and participation of industry groups and/or venture capital firms; and many other activities that require advanced marketing and sales techniques.

On a daily basis, IARC team members may be collaborating with other Fermilab scientists and engineers; industry or university partners; Department of Energy program managers or contracting officers; other research facilities, both U.S. and foreign; elected officials; or even the public. Each of these stakeholder groups has a different culture, a different language, and different expectations for partnering with the Lab. One of the top priorities for IARC and the Office of Partnerships and Technology Transfer (OPTT) is to establish simple and efficient processes for initiating, developing, negotiating, and administering a variety of partnership agreements that will meet the needs of these different stakeholder groups.

Ultimately, a key outcome of the IARC Program is to promote the commercialization of new technologies in support of U.S. competitiveness. In order to promote commercialization, these new technologies must be protected, which represents a major culture shift for Fermilab researchers. Intellectual property management is a very specialized field of knowledge covering the protection and licensing of intellectual property, such as copyrights, trademarks, patents, mask works, industrial design rights, tangible research products, and trade secrets. IARC Program management and OPTT are working together to develop an intellectual property management program that will provide the tools and training to help IARC team members work effectively in this new culture.

ACKNOWLEDGMENT

The authors would like to acknowledge Pier Oddone, for his personal support, Bob Hamm for his contributions to the business plan, Mike Weis, and Mark Bollinger, DOE Fermi Site Office for their strong support, and the Department of Energy, Office of High Energy Physics, and the Illinois Department of Commerce and Economic Opportunity without whose financial support the IARC would not exist.

REFERENCES

[1] Accelerators for America's Future, http://science.energy.gov/~/media/hep/pdf/accelerator-rd-stewardship/Report.pdf

[2] House Report 2354, http://thomas.loc.gov/cgi-bin/query/z?c112:H.R.2354:

[3] Senate Report 112-75 http://thomas.loc.gov/home/approp/app12.html

[4] Office of High Energy Physics Accelerator R&D Task Force Report, http://www.acceleratorsamerica.org/report/accelerator_task_force_report.pdf

Copyright © 2013 CC-BY-3.0 and by the respective authors

DIAGNOSTIC PROTON COMPUTED TOMOGRAPHY USING LASER-DRIVEN ION ACCELERATION

K. Woods#, S. Boucher, RadiaBeam Technologies LLC, Santa Monica, CA 90404, U.S.A.
B.M. Hegelich, University of Texas at Austin, Austin, TX 78712, U.S.A.
V. Bashkirov, R. Schulte, Loma Linda University Medical Center, Loma Linda, CA 92354, U.S.A.

Abstract

Although the growing utilization of computed tomography (CT)-based imaging has led to major advances in diagnostic capabilities, it has also resulted in higher cumulative radiation doses to patients. In order to fully exploit the benefits of high-resolution diagnostic CT scans while minimizing the risks of radiation-induced cancer, the realization of low-dose CT is crucial. Recent research has shown that the use of protons, rather than X-rays, for CT has the potential to greatly reduce the radiation dose delivered to the patient without reducing image quality. RadiaBeam Technologies, in collaboration with the Loma Linda University Medical Center and the University of Texas at Austin, is proposing the development of a proton CT scanner utilizing laser-driven ion acceleration (LDIA) techniques. The initial design of this system is presented.

NEED FOR LOW-DOSE CT

With over 62 million scans performed each year in the United States alone, computed tomography (CT) is a crucial tool for diagnostic radiology. Over the last 15 years, there has been a large increase in the utilization of diagnostic CT imaging procedures and therefore a subsequent increase in radiation exposure. As CT scans are responsible for nearly 50% of the radiation exposure from medical imaging in the U.S., the risks associated with its relatively high radiation dose, which can be two orders of magnitude greater than corresponding X-ray radiographs, become more and more of a concern [1]. Dose reduction is especially important for pediatric diagnosis, since children are both more sensitive to radiation and have more time for developing radiation-induced secondary cancers.

PROTON CT

Recent research has shown that the use of protons, rather than X-rays, for CT has the potential to reduce the radiation dose by an order of magnitude without reducing image quality [2], [3]. Ongoing studies of proton CT (pCT) at Loma Linda University Medical Center (LLUMC) are being performed to develop this technology for improving the accuracy of treatment planning in hadron therapy.

Principles of pCT

The first requirement for pCT is the production of a proton beam with high enough energy to fully penetrate the body part to be imaged. Protons with energies 200 - 250 MeV would be necessary for performing a typical head scan, while 330 MeV protons would be able to span most human torsos (60 cm range). Position-sensitive detectors are placed on either side of the subject to track the entry and exit points of each proton. The energy loss of individual protons is then measured with an energy detector/range counter, as shown in Figure 1.

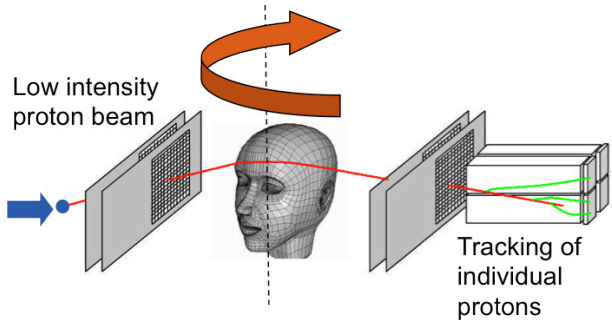


Figure 1: Conceptual design for a pCT scanner [Courtesy of R. Schulte, LLUMC].

Images can be created from the individual proton histories through the use of iterative reconstruction algorithms and path concepts such as the "most likely path" approach, as illustrated in Figure 2.

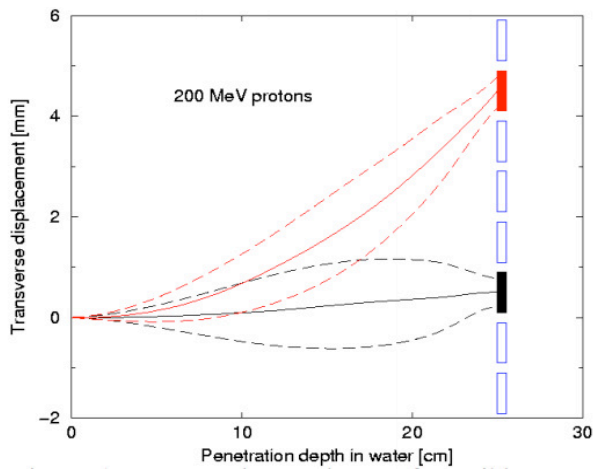


Figure 2: Monte Carlo simulation – solid lines: the most likely path of 200 MeV protons with exit displacements of 0 and 4 mm after traveling 25 cm in an object with water density; dashed lines: one sigma envelopes from Monte Carlo.

pCT Research at LLUMC

Over the last ten years, researchers at LLUMC have been developing pCT technology for improving the

Copyright © 2013 CC-BY-3.0 and by the respective authors

accuracy of treatment planning for hadron therapy. Currently, planning for proton therapy is done using X-ray CT, from which the relative stopping power of protons is reconstructed. However, there is a significant degree of error associated with this conversion that results in a range uncertainty between 3 and 5% for soft tissues [4]. This often causes conflict between the physician's desire to completely cover the tumor volume and the need to spare healthy surrounding tissue. When protons are used for treatment planning rather than X-rays, this conversion is bypassed and the stopping power can be reconstructed directly.

Between 2008 and 2010, LLUMC and their collaborators developed a Phase I scanner to prove the feasibility of pCT [5]. Rather than develop custom detectors for this prototype, they used the silicon strip detectors and data readout from the Fermi Space Telescope, which was a NASA GLAST Mission. They also used a multi-segmented crystal calorimeter for residual energy measurements, an FPGA-based data acquisition (DAQ) system, and a GPU-based reconstruction system. The scanner was then tested with different phantoms to demonstrate density resolution; the radiographs are shown in Figure 3.

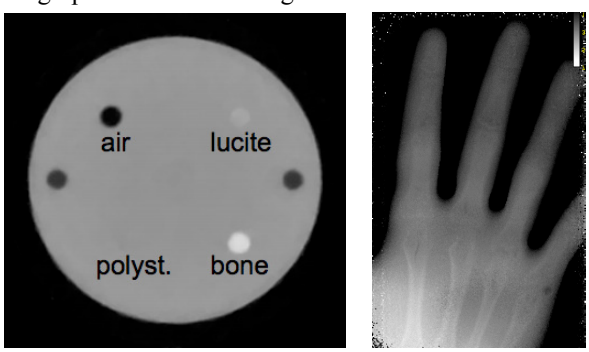


Figure 3: Left: Radiograph of a polystyrene head phantom with inserts of various densities (bone, polystyrene, Lucite, and air); right: radiograph of a hand phantom demonstrating high contrast between bone and soft tissue [Courtesy of R. Schulte, LLUMC].

In 2011, the group began the development of a Phase II pCT scanner featuring several major improvements. This scanner will have improved detectors with twice the active area (9 cm x 36 cm) and slim edges for reducing the dead space from overlapping silicon strips. It will also feature a simplified energy detector consisting of a 5-stage scintillator with a photomultiplier tube (PMT) readout scheme. The total scan time will be reduced to around five minutes through the development of a dedicated application-specific integrated readout (ASIC), and a GPU cluster will enable reconstruction in under ten minutes. This scanner is currently in the final stages of development.

DIAGNOSTIC PROTON CT

Although the research at LLUMC has clearly demonstrated the feasibility of pCT for improved treatment planning, the need for massive therapeutic proton accelerators and expensive proton gantries makes this development impractical for diagnostic applications. It can cost up to $150 million to build a proton therapy facility [6] (with an additional $21 million in yearly operational costs), compared to about $5 million for a conventional CT system.

In order for the diagnostic utilization of pCT to be possible, lighter, more compact accelerators that can be more easily rotated around the patient must be developed.

Advantages

The main advantage of diagnostic pCT is the major dose reduction from conventional X-ray CT. The estimated dose from a pCT scan is between 0.03 and 0.3 mGy, which is a potential reduction of about two orders of magnitude. This would justify the use of CT for a much broader range of diagnostic applications where the potential benefits were previously outweighed by the risks of excessive radiation exposure, such as pediatric diagnosis and patients with conditions requiring frequent imaging.

Another advantage of pCT over X-ray CT is its potential for quantitative imaging and its superior representation of electron density [4]. pCT has the potential to detect very small changes in density, which could make it useful for applications such as lung cancer screening. It could also provide better bone density measurements for patients with osteoporosis and improve detection of kidney or urinary stones, which are sometimes difficult to see on an X-ray image.

Collaboration

To meet this need, an international collaboration of scientists, doctors, and engineers has been established. The ultimate goal of this collaboration is the development of a compact diagnostic CT system for low-dose (sub-mSv) imaging. The institutions involved and their roles in the project are given in Table 1.

Table 1: Collaborating Institutions and Project Roles

Institution	Project role
RadiaBeam Technologies	Accelerator diagnostics and components
Loma Linda University, Dept. of Radiation Medicine	pCT expertise and medical input
University of Texas at Austin, Dept. of Physics	Acceleration scheme
Univ. of California, Santa Cruz, Institute of Particle Physics	Detector system
Baylor University, Dept. of Electrical and Computer Engineering	Computational scheme
Ludwig-Maximilians-Universität München, Dept. of Experimental Medical Physics	International collaborator
University of Haifa, Dept. of Mathematics	Reconstruction algorithms

Copyright © 2013 CC-BY-3.0 and by the respective authors

Approach

The crucial reduction in system size and cost for diagnostic pCT may be feasible with the implementation of innovative Laser-Driven Ion Acceleration (LDIA) technology. LDIA of highly energetic ion beams is a cutting-edge area in advanced accelerator research. Electrostatic fields in excess of 10^{12} V/m, produced via charge separation within a small area of several micrometers defined by the laser beam's focus, are theoretically capable of accelerating protons or heavier ions to energies suitable for imaging.

Dr. Manuel Hegelich, the main collaborator at UT Austin, is an expert in LDIA and will be leading the research efforts for the acceleration scheme. Dr. Hegelich was previously at Los Alamos National Laboratory, where his group demonstrated laser-driven protons with record-breaking energies of over 160 MeV [7]. Although this is still not quite high enough for imaging, this project will be utilizing a much more powerful laser. With the Texas Petawatt Laser at UT Austin, the most powerful laser in the world, energies of over 300 MeV should be achievable.

There are several requirements that must be met in order to develop a useful, accurate, and commercially relevant system. These specifications are outlined in Table 2.

Table 2: Requirements for a Diagnostic pCT System

Specifications	
Energy	330 MeV
Intensity	10^6 protons/second
Detection rate	1 MHz
Size	Single room
Scan time	~5 minutes
Cost	Comparable to X-ray CT (~$5 million)

POTENTIAL CHALLENGES

Although previous research strongly suggests the feasibility of the proposed system, there are several aspects of this project that may present challenges. The biggest challenge will be the development of a novel acceleration scheme to achieve the necessary beam specifications for imaging. Current LDIA techniques can produce a high-energy beam, but with very high intensity (~10^9 protons/pulse) and extremely low repetition rate. This is essentially the opposite of an ideal beam for pCT, which would be a rapid stream of individual protons to simplify detection and reconstruction. There are several acceleration techniques currently being explored to overcome this problem, but if the intensity cannot be sufficiently reduced, there is also the option of improving the spatial resolution of the detectors. In other words, it may be possible to compensate for the inability to temporally resolve each proton history by instead resolving them better spatially.

The system must also be sufficiently fast to acquire the scan quickly enough to ensure patient comfort and perform the image reconstruction in a relatively short amount of time. To achieve this level of speed, a DAQ and reconstruction system similar to LLUMC's Phase II scanner will have to be developed, with a dedicated ASIC and GPU cluster.

Although the development of diagnostic pCT will require many years of research, development, and testing, the success of such a system would have a major impact on diagnostic imaging and patient safety. While there are some challenges in the implementation of this technology, as previously mentioned, this strong collaboration of institutions should have the necessary expertise and experience to overcome such hurdles.

REFERENCES

[1] D. J. Brenner and E. J. Hall, "Computed Tomography — An Increasing Source of Radiation Exposure," *New England Journal of Medicine*, vol. 357, no. 22, pp. 2277–2284, 2007.

[2] R.H. Huesman, A.H. Rosenfeld, and F.T. Solmitz, "Comparison of Heavy Charged Particles and X-Rays for Axial Tomograpic Scanning," California Univ., Davis (USA). Dept. of Engineering, LBL--3040, Sep. 1975.

[3] A.M. Cormack and A.M. Koehler, "Quantitative proton tomography: preliminary experiments," *Phys. Med. Biol.*, vol. 21, no. 4, p. 560, 1976.

[4] V. A. Bashkirov, R. W. Schulte, S. N. Penfold, and A. B. Rosenfeld, "Proton computed tomography: Update on current status," in *IEEE Nuclear Science Symposium Conference Record, 2007. NSS '07*, 2007, vol. 6, pp. 4685–4688.

[5] H.F.-W. Sadrozinski, et al., Nuclear Instruments & Methods In Physics Research A (2012), http://dx.doi.org/ 10.1016/j.nima.2012.04.029.

[6] "Advancements in proton therapy cause for celebration | symmetry magazine."; http://www.symmetrymagazine.org/breaking/2011/10/21/advancements-in-proton-therapy-cause-for-celebration.

[7] D. Jung, "Ion acceleration from relativistic laser nano-target interaction," Ph.D. Dissertation, LMU München: Fakultät für Physik, Munich, Germany, 2012.

Copyright © 2013 CC-BY-3.0 and by the respective authors

OPTIMAL 3D QUADRUPOLE SHAPES*

R. Baartman, TRIUMF, 4004 Wesbrook Mall, Vancouver, BC, V6T 2A3, Canada

Abstract

The usual practice of constructing quadrupoles from truncated cylindrical hyperbolae is put into question. A new shape is proposed. This shape has an analytic potential function. The exact shape of the analytic quadrupole may be impractical, but in the short case where aspect ratio ≈ 1, pole shapes can be spherical. The optimal spherical radius is found to be 1.54 times the aperture radius. An example is also given demonstrating that in the long quad limit, the aberrations of order 5 and higher are much lower for the optimized shape.

A somewhat extended version of this paper has been published previously [1].

INTRODUCTION

The multipole elements commonly used to control charged particle beams correspond to solution terms of the Laplace equation $\nabla^2 V = 0$, namely, in polar coordinates (r, θ), $r^n \cos n\theta$ in the system where the potential on axis is zero. Thus $n = 2$ for a quadrupole, 3 for a sextupole, etc. This implicitly assumes the elements are infinitely extended in the axial (z) direction, and of course in real beamlines, they are not. For $n = 2$, the intended linear dependence of the fields upon transverse coordinate is thus broken by the finiteness of the quadrupole. This results in nonlinear force terms and aberrations.

It is not obvious how to axially terminate the poles of a quadrupole. Often, they are simply truncated. Does the shape in the longitudinal direction matter? And if so, what shape is optimal? For very long quadrupoles, it can be argued that hyperbolic equipotential surfaces given by $r^2 \cos 2\theta$ = constant are optimal. However, this is only true sufficiently far from the ends; for quadrupoles whose length is comparable to or shorter than the aperture, the 2-D hyperbolic shape is clearly not optimal. What then is the optimal shape of quadrupoles in the short limit? What is the optimal shape in the long limit? Answering these questions is the subject of this paper.

Hardness of the Fringe Field

In the limit where the fringe field extent is short compared with the focal length of the quadrupole, the lowest order aberration (cubic force) effect is independent of fringe field shape. This was shown in 1997 [2].

Let the strength function of the quadrupole be $k(z)$. Rigourously, this means $\partial_{xx} V = -\partial_{yy} V = k(z)$ along the axis $x = y = 0$, so that

$$V(x, y, z) \to \frac{k(z)}{2}(x^2 - y^2) \text{ as } (x, y) \to (0, 0), \quad (1)$$

In the "hard-edge" limit, k is a step function. But using a discontinuous step function instead of an analytic function to calculate the optics leads to dramatically incorrect results. It is thus regrettable that almost all the major higher order optics codes allow calculation of third order optics in the "no fringe field" case. This case is unphysical because it brings a particle from the field-free region outside the quadrupole instantaneously into the region where $k \neq 0$ without traversing intermediate fields. For example, for electrostatic quadrupoles, this violates conservation of energy as the potential energy is thereby incremented without changing the kinetic energy (in magnetic quadrupoles, angular momentum conservation is violated).

The beamline designer may have learned that the third order aberrations calculated without fringe fields are incorrect, but he/she is still left with the impression that the fringe field is at fault and customizing it in some way will improve the third order optics. Further, of quadrupoles with the same effective length, those with short fringe fields are erroneously thought to be superior even though this often means they have smaller aperture. In fact, such quadrupoles are inferior, as their fifth order aberrations are worse: it can be shown that in the hard-edge limit, fifth order aberrations are singular [3].

ANALYTIC QUAD

A technique for finding the potential in all space given only the strength function $k(z)$ is given by Derevjankin [4, this reference is in Russian, but referred to by Vasil'ev [5]]:

$$V(x, y, z) = -\Re\left\{\int_{z+iy}^{z+ix} dt \int_0^t k(\zeta) d\zeta\right\} \quad (2)$$

A particularly simple case that is realistic for short quads is

$$k(z) = \frac{K}{2}\,\mathrm{sech}^2 z. \quad (3)$$

We find:

$$V = \frac{K}{2}\,\Re\{-\log[\cos(x - iz)] + \log[\cos(y - iz)]\}. \quad (4)$$

See Fig. 1 where equipotential contours are plotted using as scaling potential $V_0 \equiv V(\frac{\pi}{4}, 0, 0) = \frac{K}{4}\log 2$. The transverse fields are locally nonlinear; at $z = 0$, $F_x \propto \tan x$, $F_y \propto \tan y$. Nevertheless, the integral of the transverse field is exactly linear:

$$\int_{-\infty}^{\infty} F_x dz = Kx, \quad (5)$$

and similarly, $\int F_y dz = -Ky$. The reason for this behaviour is that farther from axis, the transverse field is

*TRIUMF receives federal funding via a contribution agreement through the National Research Council of Canada.

Copyright © 2013 CC-BY-3.0 and by the respective authors

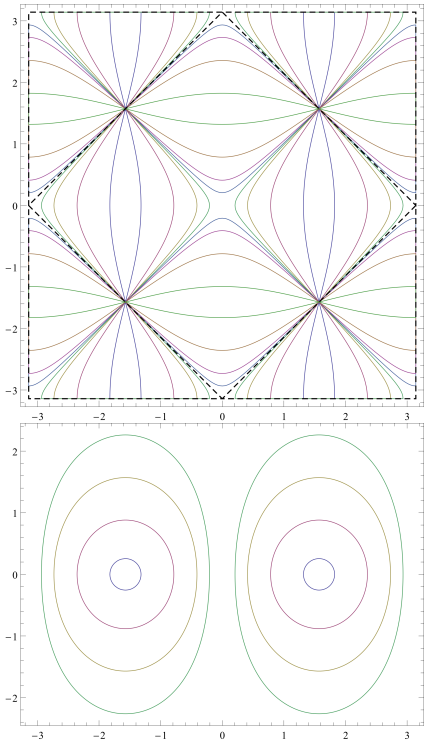


Figure 1: Equipotentials of Eq. 4. Upper: in $z = 0$ plane, contours $V = 4V_0$ (blue),$V = V_0$ (purple),$V = \frac{V_0}{4}$ (beige),$V = \frac{V_0}{16}$ (green), $V = -\frac{V_0}{16}$ (blue), $V = -\frac{V_0}{4}$ (purple), $V = -V_0$ (beige), $V = -4V_0$ (green). Lower: in $y = 0$ plane, contours $V = 4V_0$ (blue), $V = V_0$ (purple), $V = \frac{V_0}{4}$ (beige), $V = \frac{V_0}{16}$ (green).

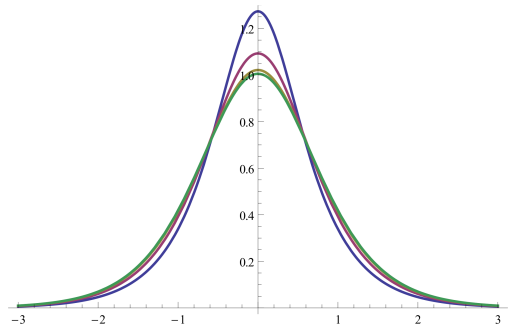


Figure 2: F_x/x vs. z for $x = \pi/4$ (blue), 0.5 (purple), 0.25 (brown), 0.125 (green).

stronger at $z = 0$, but weaker at the tails (it's 'peakier'). This is clarified in Fig. 2.

Integrated linearity from a locally nonlinear quad is not a surprise: from the symmetry and Laplace's equation, it can be shown that the following expansion holds:

$$V(x, y, z) = \frac{k}{2}(x^2 - y^2) - \frac{k''}{24}(x^4 - y^4) + \ldots \quad (6)$$

Taking derivatives to find the fields, and integrating for constant x, y, we see that Eq. 5 holds for any choice of $k(z)$.

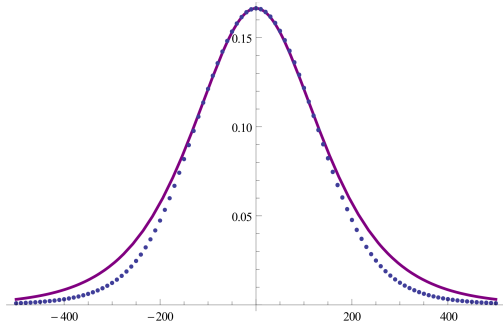


Figure 3: Magnetic field of the 12Q12 quadrupole (dots), measured at radius of 150 mm in the median plane vs. z in mm. The 12Q12 aperture radius is 155.6 mm, thus, $\sqrt{2}x = \sqrt{2}y = \frac{\pi}{4}\frac{150}{155.6}$. The continuous curve is the magnetic field at this same radius using Eq. 4, normalized to agree at $z = 0$.

EXAMPLE QUADRUPOLES

The potential V of the sech^2 quadrupole is periodic with period π in the x and y directions. At large z, the cancellation of this grid of alternating sign potentials ensures the rapid exponential falloff of the field. This is somewhat realistic. In the case of electrostatic quadrupoles, the ground planes dashed in Fig. 1 can be thought of as some approximation of the beam pipe. In magnetic quadrupoles the yoke takes the place of the ground surfaces. The yoke's proximity to the pole faces results in a characteristically quicker falloff as can be seen in Fig. 3, where the ideal sech^2 quadrupole is compared with a real quadrupole, namely, the TRIUMF 12Q12 (more on this quadrupole below).

Four choices of equipotential surfaces are shown in Fig. 4, oriented so that the quadrupole axis is vertical. Note the top left case is most like a long conventional quadrupole; the most significant difference being that the inside diameter varies along its length, as indicated by the $V = \pm\frac{V_0}{16}$ curves in the plot of Fig. 1. The lower right case in Fig. 4 would not give the correct fields without the 4 ground planes as the boundaries given by the 4 slender rods alone are insufficient. But the longer quadrupole (upper left in Fig. 4) case would work quite accurately without the ground planes.

As will be shown, this design has smaller aberrations than conventional designs, i.e. poles having constant xy cross section, truncated at each end. The only disadvantage is that the shape is rather more difficult to fabricate, having curvature on all directions.

Short Quadrupole Shapes

In the lower left of Fig. 4 (where the surfaces are strikingly similar in shape to four American regulation footballs) the potential of the shown surfaces is $\pm V_0$ and the curvature of the pole in the longitudinal direction is the same as in the transverse direction. This is an attractive feature because it allows as a good approximation for the pole to be symmetric along its axis, terminating in a spher-

Copyright © 2013 CC-BY-3.0 and by the respective authors

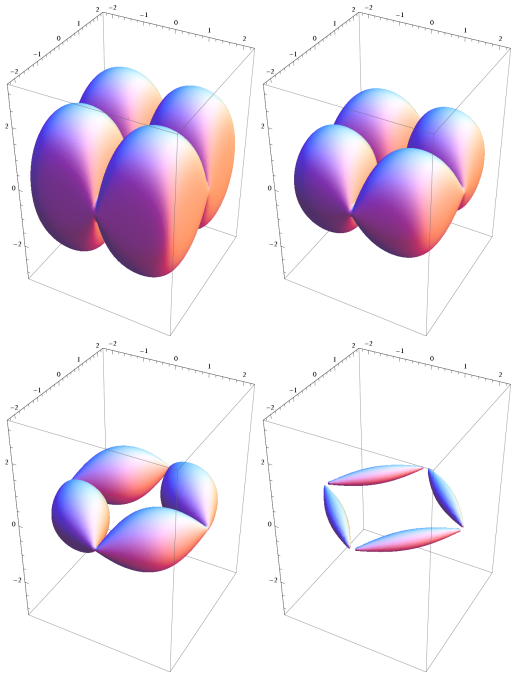


Figure 4: The coloured surfaces are 4 sets of equipotential surfaces of the potential (4). The quadrupole axis is vertical. In each case, the sides of the "box" containing the axes are also the 4 ground planes. All 4 give identical fields and the same sech^2 on-axis strength function if they are given the following potentials (left to right, top and then bottom), $\pm V_0/16, \pm V_0/4, \pm V_0, \pm 4V_0$ (adjacent surfaces have opposite sign).

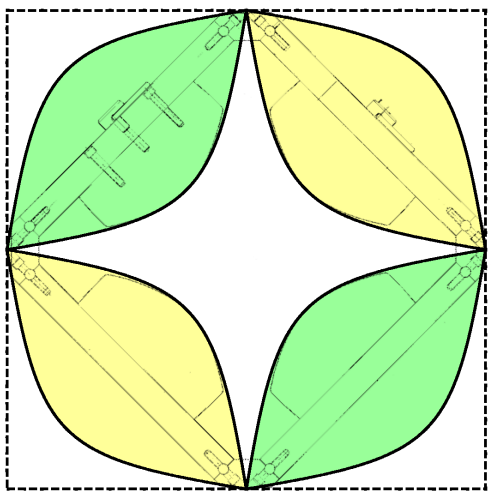


Figure 5: Cross section at $z = 0$ of the theoretical ideal sech^2 quadrupole (yellow and green) compared with drawing of the TRIUMF 12Q12 superposed. The yellow and green poles are circular in the orthogonal cross section, and hence shaped very much like the American football. The outer dashed square is at "ground" potential. Of the 12Q12 quadrupole, only the poles and the yoke are shown; coils are omitted. The black dot right of centre is the location of the Hall probe for measurements of Fig. 3.

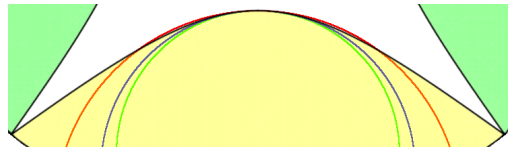


Figure 6: The "football" electrode with superposed, the circular arc of radius 1.15 times the aperture radius (green), $4/\pi$ (1.27) times the aperture radius (blue), and 1.54 times the aperture radius (red).

ical shape. What is the pole curvature that achieves this?

As the xy cross section is nearly hyperbolic, while the xz cross section is nearly a circle, it is clear that choosing a hyperboloid of revolution as shape is no better than choosing a spherical shape. The latter has the advantage that it is simpler to specify to the machinist.

As evident in the comparison in Fig. 5, the shape used for practicality, namely cylindrical poles terminating in a spherical pole-face, omits important parts of the "football" (the triangular regions either side of the poles in Fig. 5). This will have two effects: the quadrupole strength function $k(z)$ will not precisely follow a sech^2 law, and there will be some integrated 12-pole. The former is of little consequence, but the latter can cause aberration. However, just as with the case of the 2D quadrupole, we can alter the radius of curvature of the pole face to compensate the 12-pole. (20-pole and higher are not of course compensated in this technique but made slightly worse.)

In order to find the curvature radius that zeroes out the integrated 12-pole, Laplace's equation was solved for a 3D boundary model, using `OPERA`. I am indebted to Chris Philpott of Buckley Systems Ltd. (New Zealand) for performing the final optimization [6].

The result found is that the radius of curvature in units of the aperture radius is 1.54 ± 0.01:

$$\text{spherical pole-tip radius } = 1.54 \times (\text{aperture radius}). \quad (7)$$

The uncertainty arises from the grid coarseness and also from the variation due to surfaces "behind" the pole; surfaces which the engineer would be free to optimize for practicality. The potential on these surfaces also depends upon the insulator design in the case of electrostatic quadrupoles and the coil layout in the magnetic case.

This curvature is shown as the red curve in Fig. 6: one observes that it bulges past the "football" curve slightly on either side of centre. The blue curve is seen to properly match the "football" curve at the centre, and the green curvature, which is commonly used for such quadrupoles, is seen to not match the desired curvature at all. Reminder: the curvature of the ideal football shape in the direction orthogonal to the plane of the figure is essentially the blue curve.

The "12Q12" design

In the past, the short quadrupoles that have used rounded poles have used curvatures that are too sharp and as a result

Copyright © 2013 CC-BY-3.0 and by the respective authors

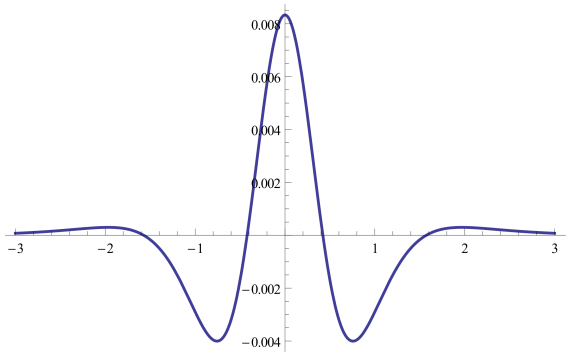


Figure 7: Fourth derivative of $k = \mathrm{sech}^2(z)$.

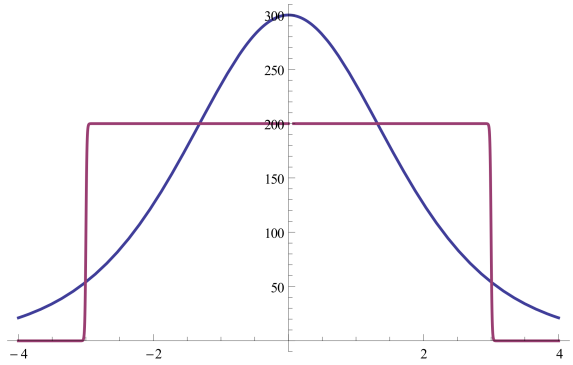


Figure 8: Gradient (in T/m) vs. z (in m) for the CERN LHC IP quadrupole (purple), compared with a sech^2 strength quadrupole of the same aperture (blue). Note that the latter quad would be impractical on two counts: its field extends outside the 6 m space allotted in the LHC, and it would need to be 1.5 times stronger at its peak. The comparison is only to illustrate that quads with optimally soft fringe fields have lower fifth and higher order aberrations.

the 12-pole does not integrate to zero. See Reeve et al. [7]. Of course, the point harmonic $A_6(z)$ is not zero, but $\propto k''''(z)$ even for the ideal pure quadrupole case. See Fig. 7 for $k = \mathrm{sech}^2(z)$. What is found in actuality is for example Fig. 11 of Reeve et al. (1976) [7]: the 12-pole looks like Fig. 7 on top of a nonzero background that is due to the incorrect pole curvature.

Recently, quadrupoles of the design "12Q12/1.5" were constructed by Scanditronix Magnet AB [8] for TRIUMF [9]. Their integrated multipole components were measured, also by Scanditronix, using a rotating coil. These magnets' radius of curvature near the pole centre is 1.14 times the aperture radius, which is too small by a factor 1.35, but this was partially offset by using a hyperboloid rather than a spherical shape. The 12-pole component was found to be roughly 20 times larger than the other multipoles: 0.0032 times the quadrupole field, at a radius of 94 mm, where the aperture radius is 155.6 mm.

Long Quadrupole Example

The aim of this example is to demonstrate that the conventional design quadrupole with a "tophat"-shaped strength function, has higher aberrations than the sech^2 quadrupole. Sech^2 quadrupoles need not be short. Refer to the $V = \pm\frac{V_0}{16}$ equipotentials in Fig. 1 to observe the shape of a long sech^2 quadrupole. The main difference in comparison with conventional quads is that the strength varies continuously along the quad. One method of obtaining this is to flare the aperture, varying it continuously from centre outward. Admittedly, this complicates the design and would increase the construction cost, especially for superconducting quads.

For illustration, we take as an extreme example the CERN LHC $\beta^\star$ quadrupoles. We take as round figures, a length of 6 m, aperture radius of 35 mm, gradient of 200 T/m, and use the Enge coefficients of the "LHCHGQ" [10]. We construct a model sech^2 quadrupole of the same integrated strength (1200 T), and same integrated squared strength of 240,000 T^2/m. This latter ensures that the third order aberrations are the same [2]. The Sech^2 strength function scaled to satisfy these two integrals is

$$k(z) = \left(300\,\frac{\mathrm{T}}{\mathrm{m}}\right)\,\mathrm{sech}^2\left(\frac{z}{2\,\mathrm{m}}\right) \tag{8}$$

Using COSY-∞ [11] and a proton energy of 7 TeV, we compared the aberrations to seventh order; these are shown in Table 1. (For the LHCHGQ, we had to modify slightly the COSY-∞ routine FFELE as the fringe field given in ref. [10] has an anomalously large extent). For the implementation of the sech^2 quadrupole in COSY-∞, see Ref. [1].

As expected, the third order aberrations are the same for the two types. The thin lens formula for the aberrations is [2]:

$$\begin{aligned}\Delta x' &= \frac{\int k^2 dz}{(B\rho)^2}\left(-\frac{1}{3}x^3 - xy^2\right) &(9)\\ &= -\frac{0.000147}{\mathrm{m}^3}x^3 - \frac{0.000440}{\mathrm{m}^3}xy^2\\ \Delta y' &= \frac{\int k^2 dz}{(B\rho)^2}\left(-x^2y - \frac{1}{3}y^3\right) &(10)\\ &= -\frac{0.000440}{\mathrm{m}^3}x^2y - \frac{0.000147}{\mathrm{m}^3}y^3\end{aligned}$$

These agree well with the values in Table 1, when the thick lens effect is taken into account. (This reduces the aberration effect in the focusing direction and exacerbates in the defocusing direction.)

But at higher than third order, the aberrations are not at all the same. The fifth order aberrations are about 200 times smaller for the sech^2 quadrupole, and the largest seventh order coefficients are roughly 100,000 times smaller for the sech^2 quadrupole. For ninth order, the ratio is 10^8.

It is doubtful that a superconducting quadrupole with Eq. 8 as strength function is at all feasible, and in any case would be too long to fit into the interaction region of the LHC. Further, there is nothing to suggest that the

Copyright © 2013 CC-BY-3.0 and by the respective authors

LHCHGQ quad	sech^2 quad	
$\Delta x'$ or $\Delta y'$	$\Delta x'$ or $\Delta y'$	mn
-0.4877909E-01	-0.4879330E-01	10
0.5406070E-01	0.5407527E-01	01
-0.1154336E-03	-0.1134717E-03	30
-0.3724576E-03	-0.4038506E-03	21
-0.4881636E-03	-0.4714397E-03	12
-0.1822114E-03	-0.1867242E-03	03
0.1017362E-02	-0.2979146E-05	50
-0.7305652E-02	-0.1326917E-04	41
0.4749991E-02	-0.2637724E-04	32
-0.7580379E-02	-0.3096770E-04	23
0.2348281E-02	-0.1566155E-04	14
-0.8101367E-03	-0.3084560E-05	05
-0.1109434	-0.1215269E-06	70
0.9689789	-0.6573820E-06	61
-0.7151169	-0.1949172E-05	52
1.312496	-0.2858019E-05	43
-0.2433022	-0.2866705E-05	34
0.5811675E-02	-0.2532962E-05	25
0.6676453	-0.8507323E-06	16
-0.1404954	-0.1333598E-06	07

Table 1: Aberration coefficients of the LHC "high gradient quadrupole", compared with quadrupole of sech^2 strength function. m and n are the exponents of x and y; for example, the fourth line is the coefficients for x^2y.

aberrations calculated for the LHCHGQ quads in any way limit the performance of the LHC. However, this comparative study puts to rest the notion that quadrupoles with smoothly varying strength function, being in a sense "all fringe field" [7], are optically inferior to more conventional quadrupoles with harder edges. In fact, quite the opposite is true.

The $k(z) \propto \text{sech}^2 z/D$ case is not special; any smoothly varying k would have similar low aberration properties. The advantage of the sech^2 case is that there is a handy, simple expression for the potential, and at least in the case of very short quads, this expression is a good approximation.

Thus our results can be understood as follows. In the traditional design, the poles terminate abruptly, and this results in aberrations that scale with the ratio of beam size to aperture, raised to a power appropriate for the order of the aberration. In the case of the design proposed here, the aberrations scale with the ratio of beam size to quadrupole length, raised to that same power.

CONCLUSIONS

We have derived an analytic potential for quadrupoles, both long and short. The strength function, instead of stepping up abruptly at the entrance and down at the exit, varies smoothly throughout the quadrupole. We have shown that this results in lower field aberrations.

REFERENCES

[1] R. Baartman, "Quadrupole shapes," *Phys Rev Special Topics Accelerators and Beams*, vol. 15, no. 7, p. 74002, 2012.

[2] R. Baartman, "Intrinsic third order aberrations in electrostatic and magnetic quadrupoles," in *Particle Accelerator Conference, 1997. Proceedings of the 1997*, vol. 2, pp. 1415–1417, IEEE, 1997.

[3] A. Dragt, April 1999. private communication.

[4] G. Derevjankin, "On the representation of the quadrupole lens potential," *Zh. Tkh. Fiz. (USSR)*, vol. 42, no. 6, pp. 1178–1181, 1972.

[5] G. Vasil'ev, "Spatial field of a quadrupole lens: An analytical approach," *Nuclear Instruments and Methods*, vol. 151, no. 1-2, pp. 65–68, 1978.

[6] C. Philpott, September 2012. private communication.

[7] P. Reeve, T. Gathright, and R. Fyvie, "Quadrupole magnet field measuring equipment at triumf," *Nuclear Instruments and Methods*, vol. 135, no. 3, pp. 459–472, 1976.

[8] tech. rep., Scanditronix Magnet, 2010. Newsletter.

[9] G. Morris, Sept 2011. private communication.

[10] M. Berz, B. Erdélyi, and K. Makino, "Fringe field effects in small rings of large acceptance," *Physical Review Special Topics-Accelerators and Beams*, vol. 3, no. 12, p. 124001, 2000.

[11] M. Berz, "Computational aspects of optics design and simulation: Cosy infinity," *Nuclear Instruments and Methods in Physics Research Section A: Accelerators, Spectrometers, Detectors and Associated Equipment*, vol. 298, no. 1-3, pp. 473–479, 1990.

Copyright © 2013 CC-BY-3.0 and by the respective authors

NEW METHOD FOR POINT-CHARGE WAKEFIELD CALCULATION*

Boris Podobedov#, Brookhaven National Laboratory, Upton, NY 11973, USA
Gennady Stupakov, SLAC National Accelerator Laboratory, Menlo Park, CA 94025, USA

Abstract

Extending our approach recently described in [1] we present a new method to accurately calculate point-charge geometric wakefields from wake potentials due to a much longer bunch, typically obtained with a time-domain EM field solver. By allowing a relatively long bunch in the EM solver, this method can significantly reduce the need for computer resources as well as drastically shorten the computing time. On top of that, the method provides valuable physics insights. Since the method, applied to longitudinal wakes, was described in [1], the goal of this paper is to extend it to transverse wakes.

METHOD DESCRIPTION

Knowledge of geometric wakefields is critically important for studies of accelerator beam dynamics. While analytical solutions are known for a number of simple geometries, detailed wakefield calculations for realistic vacuum chamber components are typically done utilizing time domain EM solvers. They compute the fields due to finite length bunches, forcing one to use extremely fine mesh (small fraction of the bunch length) to compute wakes at small distances. This is where the longitudinal wakes are usually dominated by singularities, so that a wake potential due a bunch of rms length σ scales as $W_{\parallel}^{\sigma}(z) \propto \sigma^{-q}$, $q>0$ [2,3]. Utilizing fine meshes has severe implications for computer memory requirements as well as calculation speed. Furthermore, EM solvers cannot calculate point-charge wakes, $W_{\parallel}^{\delta}(z)$ and $W_{\perp}^{\delta}(z)$, - functions that often provide significant physics insights and simplify beam dynamics analysis.

Recently we developed a method to calculate arbitrarily short bunch wakes, including point-charge, from the wake potentials due to a relatively long bunch, thus avoiding the fine mesh requirements in the EM solver. For longitudinal wakes the method is applied as follows [1].

1. Determine analytical singular wake model for a given geometry. For collimator and cavity type structures these are usually given by the optical and diffraction models respectively, see i.e. [2].
2. Determine the length parameter λ_g, which is the first $z\neq 0$ location where $W_{\parallel}^{\delta}(z=\lambda_g)$ has a discontinuity or a singularity of its higher derivative with respect to z. The recipe is given in [1] and it is illustrated below.
3. Pick $\sigma_0 \ll \lambda_g$ (but not too short to keep the computation time reasonable) and calculate the wake potential $W_{\parallel}^{\sigma_0}(z)$ with an EM solver.
4. Subtract the singular wake model from the result:
$$D_{\parallel}^{\sigma_0}(z) = W_{\parallel}^{\sigma_0}(z) - W_{\parallel,s}^{\sigma_0}(z). \quad (1)$$
5. Fit the remainder as follows:
$$D_{\parallel}^{\sigma_0}(z \le 3\sigma_0) = \frac{\alpha+\beta z}{2}\left(1+\mathrm{erf}\left(\frac{z}{\sqrt{2}\sigma_0}\right)\right) + \frac{\beta\sigma_0}{\sqrt{2\pi}}\exp\left(-\frac{z^2}{2\sigma_0^2}\right), \quad (2)$$
where α and β are fit parameters. Fit range used here, $|z/\sigma_0|\le 3$, works very well. However, this choice is rather flexible and may be influenced by practical trade-offs, i.e. fit quality vs. computation time. Maximum z, however, must obey λ_g-z_{max}>few σ_0.
6. For arbitrary short $\sigma \le \sigma_0$, the wake is given by:
$$W_{\parallel}^{\sigma}(z \le 3\sigma_0) = \frac{\alpha+\beta z}{2}\left(1+\mathrm{erf}\left(\frac{z}{\sqrt{2}\sigma}\right)\right) + \frac{\beta\sigma}{\sqrt{2\pi}}\exp\left(-\frac{z^2}{2\sigma^2}\right) + W_{\parallel,s}^{\sigma}(z), \quad (3)$$
$$W_{\parallel}^{\sigma}(z > 3\sigma_0) = W_{\parallel}^{\sigma_0}(z). \quad (4)$$
7. Similarly, for the point-charge:
$$W_{\parallel}^{\delta}(z \le 3\sigma_0) = (\alpha+\beta z)H(z) + W_{\parallel,s}^{\delta}(z), \quad (5)$$
$$W_{\parallel}^{\delta}(z > 3\sigma_0) = W_{\parallel}^{\sigma_0}(z), \quad (6)$$
where $H(z>0)=1$ is the step-function required by causality ($z<0$ is ahead of the bunch).

Summarizing the steps above, the method basically states that for $0<z<\lambda_g$ the point-charge wakefield (with subtracted singular part) is a smooth, slowly varying function. For $0<z\ll\lambda_g$ it is well approximated by a linear polynomial with coefficients easily found by fitting.

PARAMETER λ_g

λ_g can be determined by a straightforward geometric analysis combined with the causality principle [1]. Figure 1 illustrates how to find λ_g for a simple axially symmetric cavity. In the left pipe, a bunch moving with the speed of light c, carries only static EM fields. As the bunch enters the cavity, the fields get disturbed, exciting the radiation of EM waves. Some wave-fronts (i.e. red or orange)

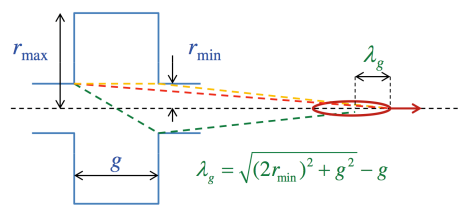


Figure 1: λ_g for a cavity with $r_{max}/r_{min}\ge 2$ and $g/r_{min}\ge 2^{-1/2}$.

*Work supported by DOE contracts DE-AC02-98CH10886 and DE-AC02-76SF00515.
#boris@bnl.gov

Copyright © 2013 CC-BY-3.0 and by the respective authors

eventually catch up with the bunch head, thus affecting $W_{\parallel}^{\delta}(z)$ for all values of z. Other wave-fronts (i.e. green) reflect and get delayed, so they can only affect $W_{\parallel}^{\delta}(z \geq d)$, where d is the delay times c.

Each type of reflections has two extreme values, d_e, of the delay, $d_e=d_{min}$ and $d_e=d_{max}$. For instance, all the rays that reflect once off the 2nd cross-sectional step at $r=r_{min}$, are delayed between $d_{min}=0$ (orange ray) and $d_{max}=(4r_{min}^2+g^2)^{1/2}-g$ (green). In general, parameters d_{min} and d_{max} define the z-range where a given reflection type affects $W_{\parallel}^{\delta}(z)$. Thus the points $z=d_e$ contain the discontinuities of the $W_{\parallel}^{\delta}(z)$ function or the singularities of its higher derivatives with respect to z.

The parameter λ_g can thus be found as the minimum of all the non-zero d_e values over all the possible reflection types. For the geometry of Fig. 1, the reflections off the 2nd cross-sectional step have the minimum positive d_e (for the green ray), compared to all the other reflection types, so λ_g is given by the formula shown in the figure.

For shallow cavities, outer-wall reflections result in yet smaller $d_e>0$, causing the replacement, $r_{min}\rightarrow r_{max}-r_{min}$, in the formula for λ_g. Finally, the smallest d_e for a short cavity is due to double reflections between the cavity side-walls, resulting in $\lambda_g=2g$. These three cases include all the possible formulas for λ_g for any r_{max}, r_{min} and g.

For complex geometries the number of different reflection types can be large, but since λ_g is defined by the minimum delay, identifying the relevant type is straightforward [1].

EXTENTION TO TRANSVERSE WAKES

The method above is directly applicable to transverse wakes except for a couple of simple changes. First, since these wakes are not singular, formally step 4 becomes obsolete. Nevertheless, if a short-bunch asymptotic wake model is known, subtracting it and then fitting the residual, $D_{\perp}^{\sigma_0}(z)$, may sometimes result in a better model of the point-charge wake. This will be illustrated later.

Second, the transverse counterpart of (5) should be generally written with an additional parameter κ,

$$W_{\perp}^{\delta}(z \leq 3\sigma_0) = \left(\kappa + \alpha z + \beta z^2\right) H(z), \qquad (7)$$

thus modifying (3) and (2) to, respectively, (8) and (9):

$$W_{\perp}^{\sigma}(z \leq 3\sigma_0) = \frac{\kappa+\alpha z+\beta(z^2+\sigma^2)}{2}\left(1+\mathrm{erf}\left(\frac{z}{\sqrt{2}\sigma}\right)\right) + \frac{(\alpha+z\beta)\sigma}{\sqrt{2\pi}}\exp\left(-\frac{z^2}{2\sigma^2}\right), \qquad (8)$$

$$D_{\perp}^{\sigma_0}(z \leq 3\sigma_0) = \frac{\kappa+\alpha z+\beta(z^2+\sigma_0^2)}{2}\left(1+\mathrm{erf}\left(\frac{z}{\sqrt{2}\sigma_0}\right)\right) + \frac{(\alpha+z\beta)\sigma_0}{\sqrt{2\pi}}\exp\left(-\frac{z^2}{2\sigma_0^2}\right). \qquad (9)$$

Note that here, the transverse wake parameters α and β are different from those in the (m=0) longitudinal wake above. Rather, they are related to the corresponding parameters of the m=1 longitudinal wake. Also, in most cases, $W_{\perp}^{\delta}(0)=0$ [3], so the parameter κ is often zero.

Finally, the transverse and the longitudinal wakes for a given structure must have the same parameter λ_g.

EXAMPLE FOR STEP-OUT GEOMETRY

We start by analyzing longitudinal wake potentials due to an axially symmetric step-out structure (Fig. 2, inset). Three wake potentials, computed with time domain EM solver ECHO [4] (used through the rest of this paper), are plotted in Fig. 2 (top).

As σ decreases, the wake potential inside the bunch attains larger negative values ($W_{\parallel}^{\sigma}(z)<0$ corresponds to the energy loss of the particle with longitudinal coordinate z). In the limit $\sigma\rightarrow 0$ this wake potential diverges as σ^{-1} and its singular part is given by the optical model, see i.e. [2],

$$W_{\parallel,s}^{\sigma}(z) = W_{\parallel,opt}^{\sigma}(z) = -\frac{Z_0 c}{(2\pi)^{1/2}\pi\sigma}\ln\frac{r_{max}}{r_{min}}e^{-\frac{z^2}{2\sigma^2}}, \qquad (10)$$

$$W_{\parallel,s}^{\delta}(z) = W_{\parallel,opt}^{\delta}(z) = -\frac{Z_0 c}{\pi}\ln\frac{r_{max}}{r_{min}}\delta(z), \qquad (11)$$

where Z_0 is the free space impedance.

The same ECHO wake potentials with (10) subtracted, are plotted at the bottom of Fig. 2 (dots). Clearly at $\sigma\rightarrow 0$ these curves approach a well-defined limit shown by the solid black line. This limit function has a discontinuity at z=0, and in the vicinity it can be well approximated by (cf. (5))

$$D_{\parallel}^{\delta}(z) = \left(\alpha+\beta z\right)H(z). \qquad (12)$$

Thus, if we determine the parameters α and β, we find the (short-range) point-charge wakefield, which can be written as (5) with the singular part replaced with (11).

For this particular geometry $\lambda_g = 2r_{min} = 2$ cm [1]. Following steps 3-5 above, we pick σ_0=2 mm<<λ_g, calculate $W_{\parallel}^{\sigma_0}(z)$ with ECHO and then determine the parameters α and β by fitting (2). All solid curves in Fig. 2 (bottom) are plotted using these values of α and β.

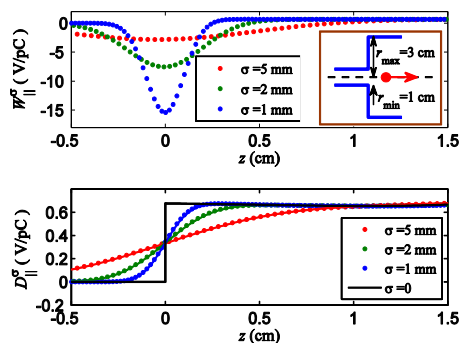


Figure 2: (inset) step-out geometry; (top) ECHO wake potentials; (bottom) same with singular parts subtracted (dots), and (solid) wakes reconstructed from $W_{\parallel,ECHO}^{2mm}$.

Copyright © 2013 CC-BY-3.0 and by the respective authors

Specifically, the green and blue curves plot (2) with the shown values of σ, while the black curve for the point-charge is the plot of (12). At z>6 mm, all three curves merge together as per (4) and (6). Finally, the red curve, with σ=5mm>σ_0, plots a (numerically performed) convolution of the Gaussian bunch shape with $D_{\|}^{\delta}(z)$ given by the black curve.

Figure 2 illustrates how to find the short-bunch wakes, including the point-charge, from EM solver results due to a relatively long bunch. While even for this simple case no analytical formula exists for $D_{\|}^{\delta}(z)$, the accuracy of this method can be tested further by performing ECHO calculations with shorter and shorter bunch, and observing the results converge to the black curve [1].

Similarly, point-charge wakefield reconstruction can be performed for transverse wakefields, which we will now illustrate for the same geometry of Fig. 2. As stated earlier, transverse wakes are non-singular, so step 4 could be skipped. Then the coefficients α, β and κ are found by fitting the σ_0=2 mm transverse ECHO wake with (9). Substituted in (7)-(8) they define the short-bunch wakes, including the point-charge one. At z>3σ_0 these wakes are given by the transverse analogs of (4) and (6).

Figure 3 shows the wake potentials found in this manner (solid) agreeing very well with the direct calculations by ECHO (dots). In addition, the point-charge wake (black line), agrees well, near z=0, with the optical model, [2],

$$W_{\perp,opt}^{\delta}(z) = -\frac{Z_0 c}{\pi}(r_{\min}^{-2} - r_{\max}^{-2})H(z). \qquad (13)$$

In fact, the fitted coefficient κ is within 2×10^{-4} of the value given by (13) (for z>0), which confirms the robustness of our fitting procedure.

Of course, the point-charge wake model found by our method gives a much better approximation away from the origin, where the transverse wake significantly deviates from the step-function behaviour of the optical model.

Alternatively, before the fitting, we could subtract the asymptotic wake due to (13), $W_{\perp,opt}^{2\text{mm}}(z)$. This fit, with κ set to 0, produces very close results to the fit above, i.e. the fitted parameters α are within 0.5% from each other. Therefore, in this example subtracting the asymptotic model is optional. Sometimes, however, asymptotic models are known only up to a numerical coefficient. In such cases fitting for the parameter κ is a must.

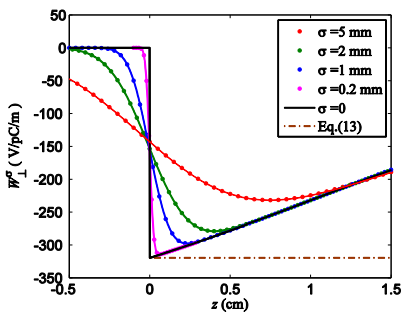


Figure 3: (dots) transverse ECHO wake potentials, and (solid) wakes reconstructed from $W_{\perp,ECHO}^{2\text{mm}}$.

EXAMPLE FOR CAVITY GEOMETRY

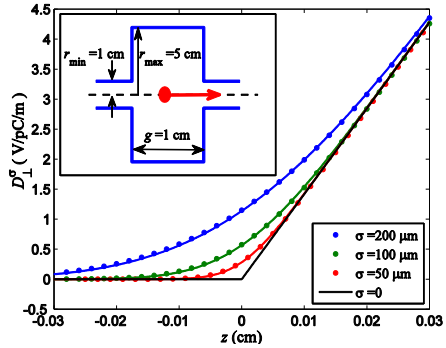


Figure 4: (inset) geometry; (dots) wakes calculated by ECHO and (solid) reconstructed from $W_{\perp,ECHO}^{1\text{mm}}$.

Here we apply the method to an axially symmetric cavity plotted in Fig. 4. Longitudinal wake reconstruction for this structure was described in [1]. For this geometry λ_g≈1.24 cm (see Fig. 1). To proceed with the transverse wake reconstruction, we take σ_0=1mm<<λ_g, and calculate $W_{\perp,ECHO}^{1\text{mm}}$. We then subtract the short-bunch wake asymptotic, $W_{\perp,d}^{1\text{mm}}$, given by the diffraction model, [2],

$$W_{\perp,d}^{\delta}(z) = 2k_d z^{1/2} \quad (z>0), \qquad (14)$$

$$W_{\perp,d}^{\sigma}(z) = k_d \sigma^{-1/2} \int f\left(z/\sigma\right) dz, \qquad (15)$$

where $f(s) = e^{-s^2/4}\sqrt{\frac{\pi}{8}|s|}(\mathrm{I}_{-1/4}(\frac{s^2}{4}) + \mathrm{sign}(s)\,\mathrm{I}_{1/4}(\frac{s^2}{4}))$,

$k_d = -Z_0 c \pi^{-2} r_{\min}^{-3}\sqrt{2g}$, and $\mathrm{I}_{\pm1/4}$ are the Bessel functions.

Unlike the previous example, here subtracting the short-bunch asymptotic substantially improves the final wake model. Indeed, according to (14), the short-bunch wakes are dominated by the $z^{1/2}$ term, which is fitted poorly by a polynomial function.

We proceed by fitting the residual, $D_{\perp,ECHO}^{\sigma_0}(z \le 3\sigma_0)$, to obtain the parameters α and β, and then reconstruct the point-charge wake, (7). With $W_{\perp,d}^{\delta}$ subtracted, it is plotted in Fig. 4 (solid black). Figure 4 also shows that the reconstructed short bunch wakes (solid color) agree perfectly with the direct ECHO calculations (dots).

In conclusion, we extended the point-charge wake reconstruction method of [1] to transverse wakes.

REFERENCES

[1] B. Podobedov, G. Stupakov, PRSTAB 16, 024401 (2013).
[2] K. Ng, K. Bane, in *Accelerator Physics and Engineering*, 3rd print, A. Chao, M. Tigner (Eds.), (World Scientific, 1999), p. 229; or in FERMILAB-FN-0901-APC (2010).
[3] A.W. Chao, *Physics of Collective Beam Instabilities in High Energy Accelerators*, (Wiley, NY, 1993).
[4] I. Zagorodnov, T. Weiland, PRSTAB 8, 042001 (2005).

Copyright © 2013 CC-BY-3.0 and by the respective authors

SPACE CHARGE MODELS FOR PARTICLE TRACKING ON LONG TIME SCALES*

J.A. Holmes, S. Cousineau, A. Shishlo, ORNL, Oak Ridge, TN, 37830, USA
R. Potts, University of Tennessee, Knoxville, TN 37996, USA

Abstract

In order to efficiently track charged particles over long times, most tracking codes use either analytic charge distributions or particle-in-cell (PIC) methods based on fast Fourier transforms (FFTs). While useful for theoretical studies, analytic distribution models do not allow accurate simulation of real machines. PIC calculations can utilize realistic space charge distributions, but these methods suffer from the presence of discretization errors. We examine the situation for particle tracking with space charge over long times, and consider possible ideas to improve the accuracy of such calculations.

INTRODUCTION

Space charge physics has been successfully incorporated into numerous computational particle-tracking studies of linacs, accumulator rings, and rapid cycling synchrotrons. These space charge models have allowed the successful simulation of phenomena that would have been impossible otherwise. Particle-tracking simulations for these machines all involve following particle distributions over short to moderate time scales. With the emergence of ever-higher beam intensities, it is now necessary to incorporate space charge effects into simulations of storage rings [1]. Calculations for storage rings require tracking beams for far longer times than those in linacs, accumulator rings, or rapid cycling synchrotrons. These long time scales place severe requirements on the speed and accuracy of the physics models and call for innovative methods of solution. For example, Lie Algebraic methods have been used with great success in single particle tracking to provide fast symplectic high order maps for storage rings. Although it is difficult to conceive of full turn maps for collective effects, such as space charge, advances will be necessary to incorporate this physics reliably into storage ring applications.

The problems of simulating space charge over long times arise partly from simplifications in the physics required to obtain a computational model and, more seriously, from the numerical properties of the model so obtained. From the physics perspective, a beam consists of many identical indistinguishable particles interacting quantum mechanically with each other and with their surroundings. In order to perform tracking studies, we make a series of approximations to arrive at a picture in which we treat the beam as a collection of distinguishable particles moving and interacting with each other and their surroundings primarily according to classical physics. Within this picture, space charge is the inter-particle Coulomb force, and its evaluation requires the solution of Poisson's equation.

Thus, even at the outset, space charge models represent a very simplified picture of reality. Their success in predicting and describing the physics of accelerators on short to intermediate time scales is some testimony to the validity of these approximations. However, for extension to long time scales, we must keep in mind that many other effects, such as lattice imperfections and nonlinearities, wake forces, neutral gas ionization and scattering, electron cloud interaction, intrabeam scattering, beam loss, and others may be important. These effects may be relatively unimportant at short or intermediate time scales, but critical at longer times. To study them in the presence of space charge, it is necessary understand and to mitigate the numerically induced noise and errors in the space charge models. The challenge of simulating space charge over long times lies in the representation of the beam distribution and the discretization of the problem.

CHOICE OF PHYSICAL MODEL

The first issue in space charge modeling is to determine what type of model contains physics sufficient to your needs. One criterion is the dimensionality of the model. 1D longitudinal models are used in longitudinal beam dynamics codes and also in conjunction with 2D transverse space charge calculations in 3D tracking codes. 2D transverse models, including bunch factor effects, are the most widely used for calculation in rings. If transverse properties vary longitudinally or transverse impedances are of interest, 2.5D models are necessary. These consist of a series of 2D model slices along the longitudinal direction that are connected by a common boundary condition. 2.5D models provide both the longitudinal and transverse space charge force components. All the above models are valid only for long bunches in which the bunch length greatly exceeds the beam pipe radius. Finally, there are full 3D space charge models. These are essential for short bunches, where the longitudinal and transverse dimensions are comparable, and are widely used in linac studies. Computational requirements rise steeply with the dimensionality of the model, so it is important to adopt the simplest model that contains the necessary physics.

* ORNL/SNS is managed by UT-Battelle, LLC, for the U.S. Department of Energy under contract DE-AC05-00OR22725

Copyright © 2013 CC-BY-3.0 and by the respective authors

REPRESENTATION AND DISCRETIZATION

Important issues that limit the applicability of space charge models are their representation of the beam distribution and the numerical discretization of the problem. Because the space charge forces depend on the charge distribution in the beam, the representation of the beam distribution in a simulation is very important. One simple class of space charge models, called envelope or particle core models, represents the space charge distribution as a uniform ellipsoidal core that propagates according to the envelope equation. The tracked particles feel the space charge force due to the propagating core. This force is linear inside the core. Envelope models are computationally fast and easy to apply. They have been used to study halo generation by mismatched beams and also the approach to the half integer resonance. One limitation of such models is that a constant emittance is specified in the envelope and thus constrains the evolution of the core. Accordingly, envelope models are simple, but far from realistic.

Conceptually, the opposite approach is to use the numerical distribution of tracked particles to provide the space charge forces. The implication in using this approach is that the tracked beam distribution realistically describes the actual beam distribution, which may require tracking many particles. Such methods, often called particle-in-cell (PIC) methods because of the techniques employed to evaluate the collective forces, are much more computationally intensive than envelope models and, as we shall see, they introduce discretization at more levels.

An intermediate class of methods for handling space charge involves the use of analytic or smoothed distributions for space charge evaluation, where the parameters of the smoothed distribution are fitted to those of a tracked beam consisting of particles. Such hybrid methods can, in principle, enjoy the speed and simplicity of envelope models while having parameters that evolve with the tracked beam distribution. A disadvantage could be that, depending on the details of chosen analytic representation or smoothing function, important features of the tracked distribution may be lost.

Any numerical space charge model will suffer from discretization error, but some methods are subject to more error than others. Time discretization is a feature of any space charge simulation, regardless of beam representation. While space charge forces act continuously in classical dynamics, simulations apply them as impulses, separated by single particle transport. If the time between impulses is too large, accuracy is lost. For example, nearby particles may become anomalously close in the single particle transport step. At the very least, it is necessary to include many space charge evaluations per betatron or synchrotron oscillation.

An additional level of discretization occurs when using the tracked particles directly to provide the charge/current distribution. Real accelerator bunches typically have 10^8 – 10^{14} particles, while accelerator simulations may use 10^4 – 10^9 macroparticles, with the lower end of this range being typical on workstations or small clusters. The impacts are an increased graininess of the force distribution and an increased potential for large binary collisions. Both of these effects introduce noise, or diffusion, into the particle evolution. The problem of the enhanced binary collisions is often handled by introducing into the inter-particle force Green's functions artificial smoothing parameters that reduce the force at close range.

A final source of discretization in many PIC methods relates to the use of spatial meshes. The straightforward direct evaluation of pairwise forces between N particles requires $O(N^2)$ computational work. Faster O(~N) methods have been developed. The most popular of these methods involve the distribution of the particle charges to a selected set of mesh points. This is followed by the solution of the resulting potential or forces at the mesh points, and then the interpolation of the forces back to the particle locations. Computational meshes are used in multigrid methods and also in algorithms using fast Fourier transforms (FFTs). Many of these are described in Refs. [2] and [3]. The approximations in distributing the charges to the mesh points and then interpolating the resulting forces from the mesh points back to the particles introduce additional noise into the space charge calculation that can be seen in the motion of individual particles. This is illustrated in Fig. 1, where the horizontal motion of three particles, initially at (x,y) = (3,0), (0,0), and (0,3) mm, selected from a cylindrical constant density beam of radius 7 mm in a uniform focusing channel, is plotted over 1000 betatron oscillations at the bear tune. The space charge tune reduction here is about one third. The space charge solution is carried out using a 2D FFT-based PIC solver. Without discretization noise, the amplitudes would remain constant. However, even with 400000 particles in a 2D problem, the effects of noise in diffusing the individual particle orbits are soon apparent.

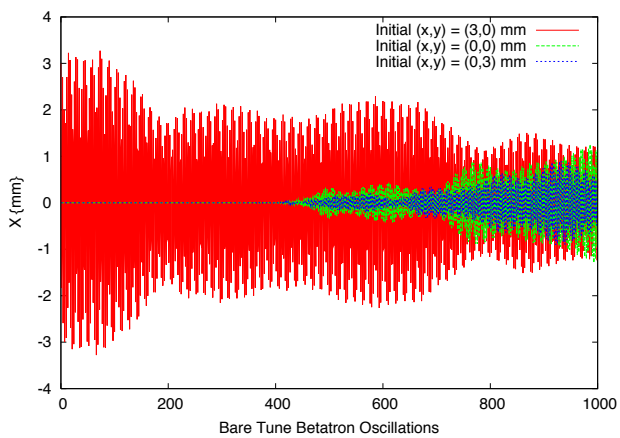


Figure 1. Horizontal motion of three particles in a uniform focusing channel with constant space charge, calculated using an FFT-based PIC algorithm. Without discretization noise, the amplitudes would remain constant.

Within the realm of fast grid-based methods, techniques have been devised to reduce the noise by using the grid for evaluating the forces of distant particles and calculating the forces due to nearby particles pairwise [2].

Copyright © 2013 CC-BY-3.0 and by the respective authors

Another fast method that uses pairwise force evaluations for nearby particles eliminates grid-based discretization errors completely. The fast multipole method [4] expands the individual particle potentials as multipoles at the centers of a collection of square gridded cells containing the particles. These expansions are then shifted and accumulated through a hierarchy of coarser "parent cells" and the resulting totals are converted to Taylor series expansions as they are shifted backwards through the hierarchy of "child cells". The result is a set of local Taylor series expansions for the potential and force within each starting cell. This method solves the N-body force evaluation to machine precision when enough terms are retained in the multipole and Taylor series expansions. Even so, the discretization effects of the time step and the numerical particle distribution remain.

OPTIONS FOR LONG TIME SCALES

Given the problems of properly representing the beam distribution and reducing the discretization noise, the question remains: What steps can be taken to extend space charge calculations reliably to long time scales? One possibility is the sledgehammer approach. It is possible to use smaller time steps, more particles, and finer meshes to reduce the level of noise due to discretization. This is feasible to some extent with the help of modern computer technology: clusters, GPUs, etc. Still, this approach is expensive and only delays the inevitable effects of the numerical noise. Another approach to reduce noise from discretization is to eliminate the discretization. At present, FFT-based methods are extremely popular for solving Poisson's equation. The fast multipole method can eliminate grid discretization errors associated with FFTs. However, the effects of the graininess of the particle distribution and discrete time steps are still present. Another approach with grid-based methods is to study different binning or smoothing algorithms for distributing space charge from the numerical particle distribution to the grid. Like low pass filters, such methods can alleviate noise due to gridding and the particle representation. One example is the template method of Vorobiev (presentation in Ref. [1]) in which the binned point charges on the grid are replaced by smoothed elements. Simplified or analytic distributions, based on statistically calculated parameters of the macroparticle distribution, are also worth exploring. For example, Figure 2 shows the evolution of the vertical beam size in three different tracking calculations through the SNS MEBT. Two of the calculations were carried out using grid-based 3D space charge models (PICNIC and SCHEFF) in the Parmila code, and the third utilized a uniform ellipsoid with parameters taken from tracking a distribution with 10% as many particles as in the 3D calculations. The RMS beam sizes from the three methods are virtually identical, although the ellipsoidal calculation required only 20% as much computer time as PICNIC and 40% as much as SCHEFF. Of course, these linac calculations are for short times, but similar hybrid models should be explored for calculations at long times.

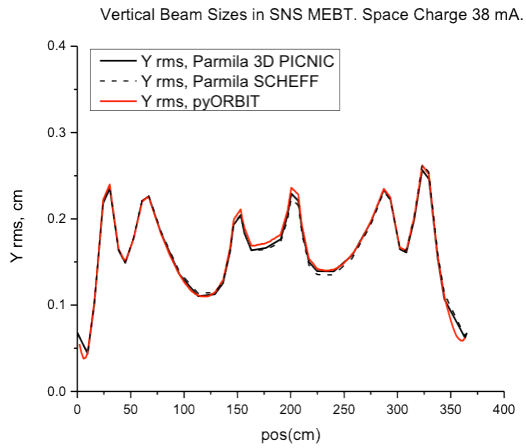


Figure 2. Vertical beam sizes from particle tracking calculations in the SNS MEBT. Space charge models include 3D PICNIC and SCHEFF PIC solvers and an ellipsoidal uniform density model with parameters set to those of a tracked distribution.

We are exploring all of these approaches in the ORBIT Code. At present, we have completed writing and are now testing a fast multipole method package. The intent is to compare the speed and numerical noise of this method with those of our existing FFT-based PIC solvers. In the future we plan to develop a number of fast hybrid models for long time scale calculations. All of these methods must be compared through careful benchmarking. As a final remark, we note that an excellent set of benchmark tests for space charge has been developed by Giuliano Franchetti, and can be found on-line [5]. These provide a thorough set of tests for space charge models, including some that involve long time scales.

REFERENCES

[1] Space Charge 2013, CERN, April 16-19, 2013, https://indico.cern.ch/conferenceDisplay.py?confId=221441

[2] R. W. Hockney and J. W. Eastwood, "Computer Simulation Using Particles", Institute of Physics Publishing, Bristol, 1988.

[3] J. Demmel, NSF-CBMS Short Course on Parallel Numerical Linear Algebra, especially Lectures 24-27, http://www.cs.berkeley.edu/~demmel/cs267-1995/

[4] L. Greengard and V. Rokhlin, "A Fast Algorithm for Particle Simulations", Journal of Computational Physics 73, (1987), 325.

[5] G. Franchetti, Code Benchmarking on Space Charge Induced Trapping, http://web-docs.gsi.de/~giuliano/

Copyright © 2013 CC-BY-3.0 and by the respective authors

TIME-RESOLVED TEMPERATURE MAPPING SYSTEM FOR THE APS DEFLECTING CAVITIES*

Y. Yang †‖, P. Dhakal#, J. Fuerst, J. Holzbauer, J. Kaluzny, J. Mammosser#,
A. Nassiri, H. Wang#, G. Wu, Argonne National Laboratory, Argonne, IL 60439, USA
#Thomas Jefferson National Accelerator Facility, Newport News, VA 23606, USA
‖Tsinghua University, Beijing 100084, China

Abstract

Time-resolved temperature mapping of a superconducting cavity can give valuable information on the limiting process of the cavity performance. A fast temperature mapping system has been developed at Argonne National Laboratory (ANL) for a superconducting deflecting cavity test. The time resolution of the temperature mapping could be up to 50 μs. Not only the spatial distribution of surface heating but also the thermodynamics can be recorded, which helps to understand the limitation mechanism. This new temperature mapping system has helped us to understand the rf performance limitations during the cavity vertical tests. Based on the findings from the temperature mapping, proper cavity treatment has been applied and the cavity performances have been improved.

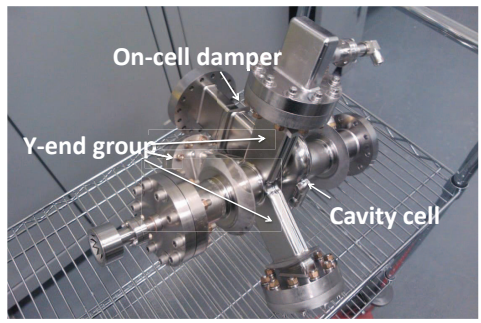


Figure 1: The APS superconducting deflecting cavity during assembling in a clean room. The cavity has a Y-end group on the beam pipe and a on-cell waveguide damper.

INTRODUCTION

The Advanced Photon Source (APS) at Argonne National Lab (ANL) has considered using the superconducting deflection technique to generate x-rays on the order of 2 ps or less [1]. A single-cell cavity design has been chosen as the baseline design and four superconducting deflecting cavities have been fabricated, as shown in Fig. 1. The cavity is a single squashed-cell cavity with an on-cell waveguide damper and a Y-end group on the beam pipe [2]. To provide sufficient deflecting modulation to the beam, a single-cavity deflecting voltage needs to reach 0.5 MV, which corresponds to a peak surface magnetic field of 106 mT. To accomplish this challenging goal, it is very important to understand the cavity performance limitations. Generally speaking, a number of processes, such as multipacting, field-emission, Q-slope, and thermal quench, might limit the superconducting cavity performance. All of these processes will eventually generate heat on the cavity wall. Temperature mapping is presently one of the most effective tools to gain insight into the cavity limitations.

Most conventional temperature mapping systems work for L-band accelerators [3][4]. Hundreds of sensors are required to cover the cavity surface. However, the sampling rate is limited to a few Hz, which is not fast enough to get a resolved signal. The APS deflecting cavity operates at 2815 MHz. The cavity size is much more compact compared to the L-band cavity, thus a fewer number of sensors are needed to cover the high magnetic field surface. A new time-resolved temperature mapping system has been developed for the APS deflecting cavity. It consists of 24 temperature sensors with a time resolution as high as 50 μs. A number of cavity tests made using this system have helped us understand cavity performance limitations. Compared to conventional temperature mapping, time-resolved temperature signals are much superior in classifying the limitations in terms of thermal dynamics. These findings from temperature mapping have led us to improve the cavity performance with the following treatment.

SENSOR MOUNTING AND DATA ACQUISITION

We used sensors made from Allen-Bradley carbon resistors. This resistor has a high thermal sensitivity of 10Ω/mK around 2 K. To thermally isolate the sensor from the helium bath, the resistor was enclosed in a G-10 container filled with epoxy. In order to make good thermal contact and provide electrical isolation to the cavity surface, the top surface of the resistor was ground away until the carbon was exposed and then a thin layer of a GE-varnish, toluene and alcohol mixture was applied.

The APS deflecting cavity operates at dipole mode, and the highest surface magnetic field region is the iris between the cavity cell and the Y-end group. The sensors were mounted around the cavity based on the surface magnetic field distribution, as shown in Fig. 2. Proper mounting techniques were developed. A cryogenic cable tie was applied as a band to mount the sensors around the iris. Two semi-circle bands made of cryogenic fiberglass weres used to attach the sensors on the cavity cell. Apiezon N grease

* Work supported by the U.S. Department of Energy, Office of Science, under Contract No. DE-AC02-06CH11357
† yaweiyang@aps.anl.gov

Copyright © 2013 CC-BY-3.0 and by the respective authors

is applied to all the sensor contacts to ensure good thermal contact with the cavity.

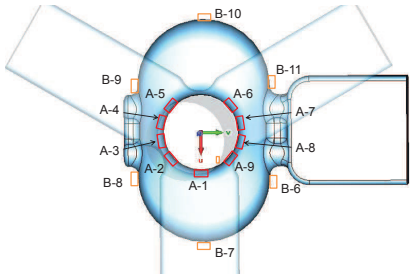


Figure 2: Sensor layout around the cell and the iris looking from the Y-end group side. The iris on the other side has similar sensors around the iris.

The data acquisition is based on a National Instrument data acquisition (DAQ) device. However, direct connection of the sensor to the DAQ will result in excessive current to the sensor. A proper circuit is designed to excite the sensors with a 15-μA current. As shown in Fig. 3 , the resistance values of the sensors are measured in terms of the voltage drop across the resistor. The cavity field level can be measured in terms of the output voltage of the cavity transmitted power crystal detector. All the data is processed and recorded by a LabVIEW program.

The software has three operation modes: calibration mode, continuous measurement mode, and pulse measurement mode. The calibration mode records how the resistance of different sensors changes with the helium gas pressure reading. Those correlations are used to calculate the temperature rise during the measurement. The calibration mode operates during the helium-bath cooling from 4 K to 2 K. The sampling rate is only 0.5 Hz, but the accuracy is better than 0.3 mK. During the cavity test, the software usually operates in continuous measurement mode. It quickly records the resistance values of different sensors. Then the temperature is calculated using the calibrated correlations. The sampling rate of continuous mode is 300 Hz with an accuracy of 2 mK, which is fast and accurate enough to obtain time-resolved heating. The pulse mode records the sensor reading with highest possible resolution up to 50 μs. However, the accuracy is limited to about 10 mK and the measurement only lasts for 2 seconds. This mode is designed to give the highest time-resolution.

CAVITY VERTICAL TEST WITH TIME-RESOLVED TEMPERATURE MAPPING

Eight cavity vertical tests have been performed with this temperature mapping system, and it has helped to identify the limitations of the cavity performances. With the help of this system, a number of defect mechanisms have been identified that have lead us to find appropriate treatment techniques to eliminate the obstacles and improve the cavity performance.

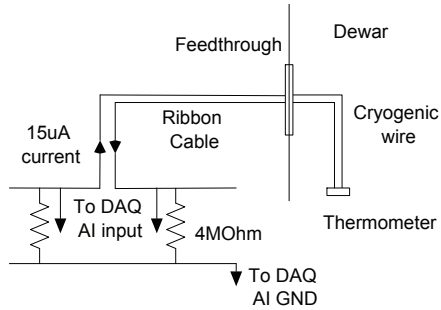


Figure 3: Schematic of the measurement circuit. A 15 μA current is used to excite the thermometer, and the voltage drop across the resistor is used to measure the resistance value.

Multipacting

The thermodynamics of multipacting (MP) on the cavity wall can be obtained using this system. It can be identified as an abrupt pulse heating when the field level reaches a barrier and then has a small and abrupt drop. An example is given in Fig. 4. Sensors A-3 and A-8 detected pulse heating signals during the vertical test when the cavity surface peak magnetic field first approached 85 mT.

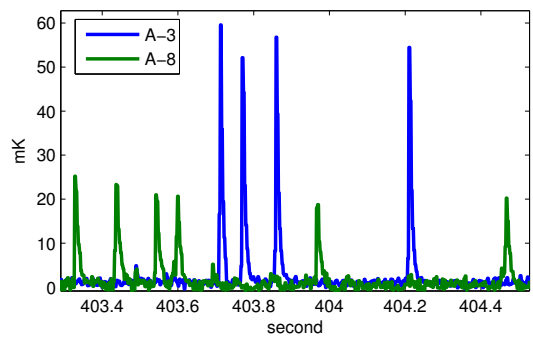


Figure 4: A soft MP barrier occurred at the A-3 and A-8 sensors when the maximum surface M-field approached 85 mT. Pulse heating can be detected when MP occurs

It can be seen that multipacting induced pulsed heatings at A-3 and A-8. They did not happen at the same time. On the other hand, both the A-3 and A-8 sensors were located at high magnetic field regions. The multipacting at either point is likely one-point multipacting.

All the multipacting found in the cavity tests turned out to be soft. The thermodynamic during multipacting processing was also obtained. The processing lasted from tens of seconds to several minutes. After that, the processing subsided and the Q gradually returned to normal. A continuous but not stable heating signal could be detected by time-resolved temperature mapping during the processing. Figure 5 shows an example of temperature signals during multipacting processing. The pulse heating signals became a continuous heating signal when the processing started. The processing happened at two points: the

Copyright © 2013 CC-BY-3.0 and by the respective authors

A-3 sensor location and the A-8 sensor location. An interesting phenomenon was that the processing at A-3 and A-8 took place alternately, which formed a rectangular-shaped temperature-rise signal. The processing gradually decayed as the temperature went down, and cavity Q gradually increased back to a normal level.

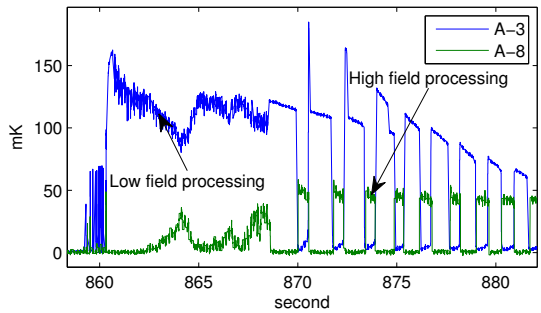


Figure 5: MP processing happened at A-3 and A-8 sensor when peak magnetic field approached 95 mT. The sudden "turn on" of the processing is shown with pulse heating changing into a continuous heating signal.

High-Field Q-Slope

High-field Q-slope was found in one of the cavities starting at 70 mT. The temperature mapping showed the Y-end group iris had a strong heating signal all around the iris [5]. The time-resolved signal showed the heating magnitude was constant at a given cavity field level. After the cavity showed a Q-slope at high field, the temperature rose exponentially in the power law ranging from 10 to 16. Those findings were consistent with the finding of Q-slope with convectional temperature mapping.

Quench Detection

Quench detection becomes more accurate with time-resolved temperature mapping. The thermodynamics of quench can be recorded. Figure 6 gives an example of quench. When quench happened, the A-3 sensor set at the location of the quench measured a pulse heating reading as soon as the cavity field dropped to zero. The pulse heating magnitude was very high (the highest reading was about 1.5K), which lasted about 50 ms. The sensors within 0,5 inch detected a small pulse reading of tens of mK. However, other hot spot temperatures would drop as the cavity quenched. The thermodynamics demonstrated by the time-resolved temperature mapping could help to determine the quench location with good accuracy.

CAVITY PERFORMANCE IMPROVEMENT

Of the four fabricated deflecting cavities, two of them have been explored in detail with this temperature mapping system. It has successfully located the defect spots or

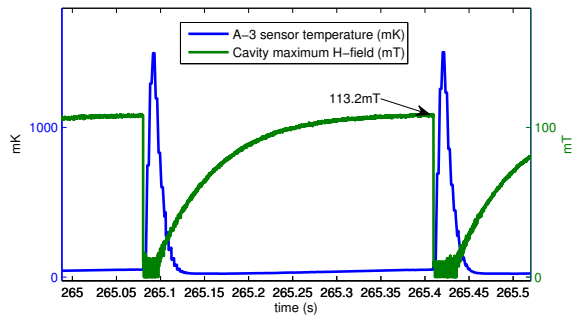


Figure 6: Quench pulse heating signal, the quench location temperature heating can go as high as 1.5K.

the heating area, and helped us to understand the performance limitations. Based on the findings from temperature mapping, the following treatments have helped to improve performance [6]. In one cavity, global heating was detected around the iris. A 40μm EP has helped to remove the Q-slope and improve the quench limit. In the other cavity, quench was detected at one spot on the cavity equator when the peak magnetic field approached 95 mT. A welding defect was found at the spot by optical inspection. The subsequent cosmetic E-beam welding smoothed the area and improved the gradient. Both of the cavities have reached design specifications.

SUMMARY

We described a time-resolved temperature mapping system to characterize the performance limitations of the APS deflecting cavity. Time-resolved temperature signals can be used to gain further insight into these limitations. Detailed studies were performed in two deflecting cavities. Based on our findings, proper treatment was applied and cavity performance reached design criteria in both cavities.

REFERENCES

[1] M. Borland, Physical Review Special Topics-Accelerators and Beams 8 (2005) 074001.

[2] A. Nassiri et al., "Status of the Short-Pulse X-Ray Project at the Advanced Photon Source," IPAC 2012, WEPPC038, p. 2292 (2012).

[3] A. Canabal et al., "Development of a temperature mapping system for 1.3-GHz 9-cell SRF cavities," PAC 2007, WEPMS031, p. 2406 (2007)

[4] G. Ciovati et al., "Temperature mapping system for single cell cavities," JLAB-TN-05-059, 2005.

[5] Y. Yang et al., "Electropolishing of the ANL deflecting cavity for the APS upgrade," SRF 2013, TUP055, to be published.

[6] J. Mammosser et at., "Fabrication and testing of defecting cavities for APS," SRF 2013, FRIOA03, to be published.

Copyright © 2013 CC-BY-3.0 and by the respective authors

MODE DAMPING MEASUREMENT FOR THE APS DEFLECTING CAVITY *

Y. Yang †‖, A. Nassiri, T. Smith, G. Waldschmidt, H. Wang#, G. Wu
Argonne National Laboratory, Argonne, IL 60439, USA,
‖Tsinghua University, Beijing 100084, China
#Thomas Jefferson National Accelerator Facility, Newport News, VA 23606, USA

Abstract

The Advanced Photon Source has considered using a deflecting-cavity-based scheme to produce short pulse x-rays. A deflecting cavity design has been completed. To verify the simulation result on this cavity, a copper prototype of the design has been fabricated for bench measurement. In this paper, we report our measurement results on this cavity. All the cavity modes below 5 GHz were identified by comparing the field distributions with calculations along different beam paths. After adding the damper, the measured Q_{ext}s of those modes were consistent with calculated values, which demonstrated that the cavity damping scheme was sufficient to reduce the wake impedances well below the safety thresholds.

INTRODUCTION

The Advanced Photon Source (APS) at Argonne National Lab (ANL) has considered using a superconducting deflecting-cavity-based scheme to generate x-rays on the order of 2 ps or less [1]. The unwanted cavity modes in cavities can drive coupled-bunch instabilities in high-current storage rings. Thus sufficient damping of those modes was very important. It is equally important to maximize the operating mode parameters and provide sufficient transverse kick to the beam. A cavity design has been proposed, as shown in Fig. 1. This cavity design is a single squashed-cell cavity with an on-cell waveguide damper and a Y-end group on the beam pipe [2]. The on-cell waveguide serves as lower-order mode (LOM) damper. One of the Y-end group waveguide damper works as a fundamental power coupler (FPC) and the other two dampers as higher-order mode (HOM) dampers. The cavity operates at 2815 MHz.

Extensive simulations have been performed, and we have demonstrated that the wake impedances are well below the stability thresholds [3]. In this paper, bench measurements were performed to verify numerical calculations. There were mainly two steps in the bench measurement. The first step was to identify the modes by measuring the field distributions using on-axis and off-axis bead-pulls. The second step was to characterize the damping performance by using actual high-power waveguide damper prototypes [4].

* Work supported by the U.S. Department of Energy, Office of Science, under Contract No. DE-AC02-06CH11357
† yaweiyang@aps.anl.gov

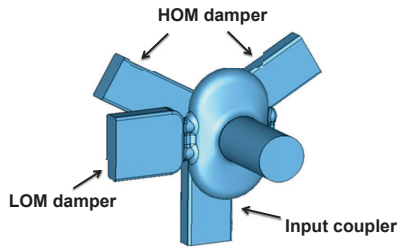


Figure 1: The APS deflecting cavity design.

COPPER PROTOTYPE CAVITY MEASUREMENT

Measurement Technique

The cavity modes were characterized by the Slater perturbation technique. With a small perturbing object, usually a dielectric bead or metal needle, passing through the cavity beam pipe, the longitudinal electrical field $E_z(r,\theta)$ along the beam path can be measured in terms of the frequency shift due to the perturbation. For a dielectric bead, the frequency perturbation can be related to the electric field strength as follows:

$$-\frac{\Delta\omega}{\omega} = g_1 e_{\parallel}^2 + g_2 e_{\perp}^2, \qquad (1)$$

where the coefficients g_1 and g_2 are geometric factors. They depend upon the bead size, material, and geometry. Eq. 1 shows that the electrical field in both longitudinal and transverse directions will contribute to the frequency change when the bead passes through the cavity. But for the R/Q measurement, only the longitudinal electrical field is of interest. In the APS deflecting cavity, there are many modes that have strong transverse electrical field compared to the longitudinal electrical field along the beam path. To get an accurate measurement of the R/Q, a slender bead with a length at least ten times larger than the diameter is required due to its insensitivity to the transverse electrical field with $g_1 \gg g_2$ [5]. However, our bead length needs to be relatively small to have adequate longitudinal resolution due to the compactness of the cavity. Given that, it is very difficult to have such a bead that can separate the transverse and longitudinal electrical fields. After exploring different beads and techniques, we selected a uniform dielectric bead with $g_1 \approx g_2$ to measure the electric field amplitude $E_{abs}(r,\theta)$ along different paths. Before the bead-pull mea-

Copyright © 2013 CC-BY-3.0 and by the respective authors

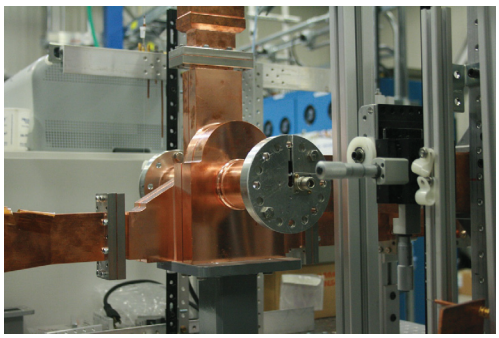


Figure 2: Copper prototype cavity in bead-pull measurement. The bead transverse location can be changed.

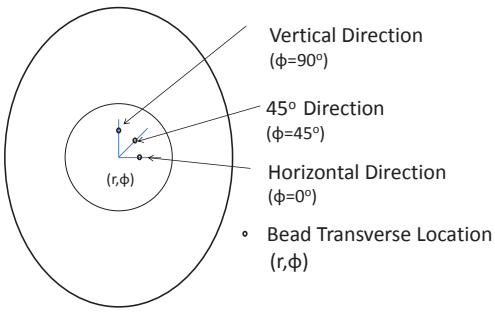


Figure 3: Bead pull measurement along different paths in horizontal, vertical, and 45^o directions.

surement on the copper prototype, we calibrated the beads with a pillbox cavity, in which the field distributions of different modes had been well understood. The geometric factors $g1$ and $g2$ were obtained by the monopole mode and dipole mode measurements.

Even though the azimuthal symmetry is broken in the APS deflecting cavity, the cavity modes can still be approximately classified as monopole mode, dipole mode, and quadrupole mode. It is hard to get the mode identity based on the field distribution E_{abs} on a single path. To fully characterize the mode azimuthal property (monopole, dipole, or higher) and identify the mode, bead-pull measurements were performed with different transverse offsets in different directions, as shown in Fig. 2 and Fig. 3. We focused on the horizontal , vertical, and 45^o angle displacement. The bead-pull measurements were performed using an Agilent E6362B network analyzer with a Labview program. With all waveguide ports and beam pipe ports shorted and sealed, the cavity mode was excited by a probe inserted through the beam pipe, and the signal was picked up through a probe on the waveguide damper or a probe inserted into the other side of the beam pipe. The frequency shift due to the bead perturbation was measured in terms of the phase shift, which was more sensitive than direct measurement. Different probes were developed for mode excitation. By changing the probes and varying the probe orientation, it was possible to enhance the profile of the mode we were measuring and reject the interfering mode.

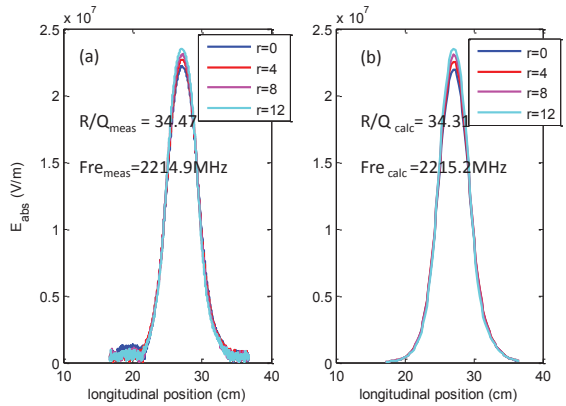


Figure 4: Measured (a) and calculated (b) field distribution of the TM010$_{like}$ mode along different paths with an increasing horizontal offset r. The measured R/Q value is very consistent with simulation.

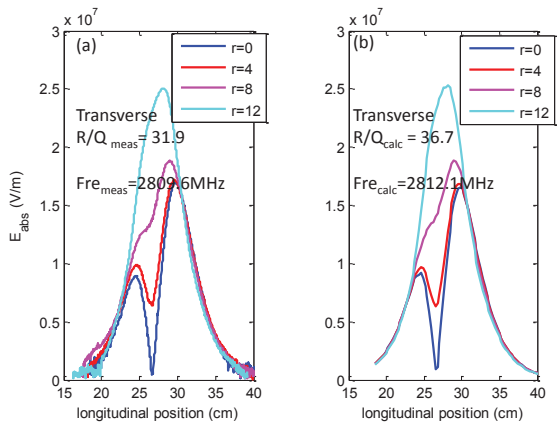


Figure 5: Measured (a) and calculated (b) field distribution of the TM110y$_{like}$ mode along different beam paths with an increasing vertical offset r.

Mode Characterization

Comparison of E_{abs} along different paths turned out to be a very effective way to identify all the cavity modes. Figure 4 compares calculated and measured field distributions of the monopole TM010$_{like}$ mode along different horizontal paths. This mode was the lowest mode of the cavity and it had very strong beam coupling. Due to the strong coupling with on-cell waveguide damper, the field amplitude had a gradient along the horizontal direction, which was confirmed by both calculation and bead-pull measurement. There was negligible transverse electrical field effect, and the R/Q measurement gave a very consistent result with the simulation. Figure 5 shows the field distributions of the operating dipole mode along different vertical paths. The measured field amplitude was the superposition of the longitudinal electrical field and the transverse electrical field; it was very hard to separate the longitudinal

Copyright © 2013 CC-BY-3.0 and by the respective authors

Table 1: Comparison of Mode Frequencies and Q_{ext}s with Prototype Dampers

Mode identity	Frequency *calc.* (MHz)	Q_{ext} *calc.*	Frequency *meas.* (MHz)	Q_{ext} *meas.*
$TM010_{like}$	2295.82	67.96	2294.2	76.4
$TM110y_{like}$	2812.12	1×10^6	2809.8	1.03×10^6
$TE111x_{like}$	2987.12	273	2985.23	256
$TE111y_{like}$	3027.2	515	3026.74	512
$TM110x_{like}$	3347.4	10.2	3326.74	24
$TM020_{like}$	3937.3	200.3	3935.4	152
$TM210_{like}$	4269.7	4270	4267.7	3890
$TE211a_{like}$	4505.7	1340	4520.4	1130
$TE211b_{like}$	4599.7	1376	4610.4	1425

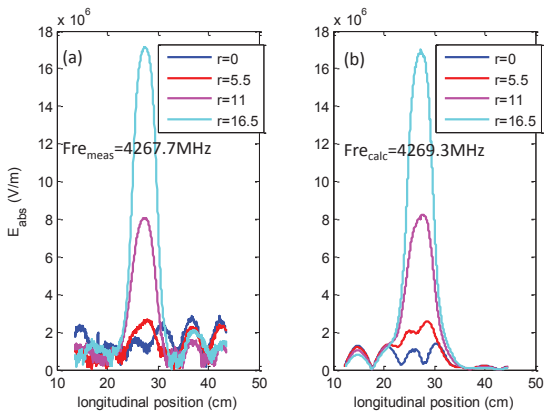


Figure 6: Measured (a) and calculated (b) field distribution of the $TM210_{like}$ mode along different beam paths with an increasing 45^o offset.

effect. Thus the measured transverse R/Q was less consistent with the simulation. Figure 6 shows the field distributions of the quadrupole $TM210_{like}$ mode along different 45^o paths. Around the cavity center, the field strength was very low but the field strength inside cavity increased significantly with a growing offset r in 45^o direction, as demonstrated in simulation and bead-pull measurement.

Mode Damping

After the cavity modes were identified by the bead-pull, all the waveguide couplers were connected with the proper loads. Q was measured by S_{21} transmission between the probes either inserted into the beam pipe or on the waveguide damper. After adding the damper, the loaded Qs of the cavity modes (except the operating mode) were much lower. Normally, we started the measurement with the same probes mounted in the same positions around the cavity as we did in the previous measurement when all the waveguides were shorted. The Q_{ext}s could be derived by the difference of the inverses of the measured Q_{load}s. If the mode Q_{ext} was very low, the probe location was adjusted to have stronger coupling. Table 1 compares the measured Qs with the calculation by ACE3P. It could be shown that the measured Q_{ext}s of the cavity mode were quite consistent with the simulation results.

One thing to note is that the measurement of the operation mode $TM110_y$ was different. The mode had a weak coupling with all the waveguides. To measure the coupling, a matched tophat was used on the waveguide coupler. The transmission S_{21} between the matched tophat and the tuned beam pipe probe was used to calculate the coupling through the waveguide.

SUMMARY

A copper prototype cavity has been fabricated and extensive measurements have been performed on the cavity. The bead-pull measurements were performed for all the modes below 5 GHz. The cavity modes were identified by comparing the measured field distributions with calculations along different paths. The field distribution of different modes were consistent with the calculated results. After adding the prototype damper, the measured Q_{ext}s were in agreement with the simulation results, which indicates that the fabricated cavity could meet the design criteria and the wake impedances were well below the stability thresholds for operating in the APS storage ring with 150-mA current.

ACKNOWLEDGMENT

The authors are particularly grateful to Tim Jonasson, William Yoder, and Charles Montiel for their help in cavity measurements.

REFERENCES

[1] M. Borland, Physical Review Special Topics-Accelerators and Beams 8 (2005) 074001.

[2] A. Nassiri et al., "Status of the Short-Pulse X-Ray Project at the Advanced Photon Source," IPAC 2012, WEPPC038, p. 2292 (2012).

[3] Haipeng Wang et al., "Crab cavity and cryomodule prototype development for the Advanced Photon Source," PAC11, WEOCS7, p. 1472 (2012).

[4] G. Waldschmidt et al., "High-Power waveguide dampers for the short-pulse X-ray project at the advanced photon source,"IPAC 2012, THPPC029, p. 3344 (2012).

[5] J. C. Amato and H. Herrmann, Review of Scientific Instruments 56(5) (1985) 696.

Copyright © 2013 CC-BY-3.0 and by the respective authors

ELECTRO-MAGNETIC OPTIMIZATION AND ANALYSIS OF A QUARTER WAVE RESONATOR *

Z. Zheng[#, 1, 2], A. Facco[1, 3], Z. He[1, 2], Z. Liu[1], J. Wei[1], Y. Xu[1], Y. Zhang[1]
[1]Facility for Rare Isotope Beams, Michigan State University, East Lansing, MI 48824 USA
[2]Tsinghua University of Beijing, Beijing, 100084 China
[3]INFN - Laboratori Nazionali di Legnaro, Padova, Italy

Abstract

A β=0.085 quarter wave resonator (QWR) with resonant frequency=80.5 MHz is used in the Facility of Rare Isotope Beam (FRIB). Its baseline structure is designed to achieve the FRIB specifications with optimum cost to performance ratio. Electro-magnetic optimization is introduced in this paper to modify its internal geometry to reach instead maximum accelerating gradient, while preserving the original flange to flange length. Reduced peak magnetic field and increased shunt impedance are well achieved in the optimization while keeping the same stored energy. The maximum accelerating voltage is raised accordingly. Multipacting and steering are also analyzed for the optimized cavity. This resonator could be used in the ReA linac at MSU and in all applications where the maximum accelerating voltage should be achieved in a limited space, or where the accelerator cost is mainly driven by the resonator gradient.

INTRODUCTION

The baseline structure of FRIB QWR cavity is designed to achieve its goal with optimum cost to performance ratio. By further optimizing the baseline cavity, we aimed at a cavity design (that we nicknamed "race car") which provides significantly more accelerating gradient (E_a) still being affordable in cost, like an economy car in the auto world. The optimization is achieved mainly by reducing the peak magnetic field B_p and increasing the cavity shunt impedance R_{sh}. Lower B_p can speed up the "car" to higher cavity gradient, and increased R_{sh} allows keeping power consumption low, like saving "gasoline" for the "car". With high gradient, low-β resonators like this "race car" design, compact accelerators which can reach several MeV per nucleon in a limited space can be built for different applications. In this paper, section 1 introduces the method and procedure of the electromagnetic optimization. Section 2 discusses multipacting and beam steering issues before and after the optimization.

ELECTRO-MAGNETIC OPTIMIZATION

The main goal of the optimization is reducing the peak magnetic field (B_p) and increasing shunt impedance (R_{sh}/Q) while keeping good values for the stored energy, the peak electric field (E_p) and the geometric factor ($R_s \times Q$). To achieve the "economy" concept, we should limit rising of the cavity cost as little as possible. Thus, we maintained the radius of cavity outer conductor and optimized the cavity inner part.

Performance of FRIB QWR

Before cavity optimization, simulation was performed to get the parameters of FRIB QWR with MWS [1]. Table 1 shows the simulation results (effective length=βλ).

Table 1: Cavity Parameters of FRIB QWR

Parameter	Value	Units
Frequency	80.50	MHz
E_p/E_a	5.9	Abs.
B_p/E_a	12.6	mT/(MV/m)
R_{sh}/Q	452	Ω
$R_s \times Q$	22.3	Ω

In superconducting low-β resonators, the highest reported surface peak fields before quench are approximately 80 MV/m and 150 mT in cw mode. So there is a tradeoff between E_p and B_p that should be taken into account when designing a cavity, and B_p/E_p~1.8 should be nearly an optimum. For the FRIB β=0.085 QWR, B_p/E_p=2.14 which means the cavity can be expected to quench at high accelerating gradient due to B_p. To raise the maximum achievable gradient to this cavity, the most effective method is reducing its B_p.

Procedures of Optimization

First step:

The peak magnetic field of FRIB QWR is located at the inner conductor near the short plate (Fig. 1). To reduce the B_p/E_p, we optimized the structure of inner conductor by scanning two geometric parameters (R_1 and L_1 in Fig.2).

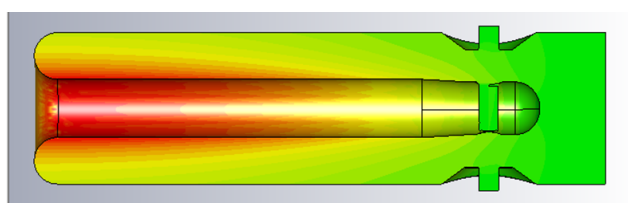


Figure 1: Magnetic field distribution of the FRIB QWR. Red means B_p. Cavity stored energy is normalized at 1J.

*Work supported by the U.S. Department of Energy Office of Science under Cooperative Agreement DE-SC0000661
#zhengw@frib.msu.edu

Copyright © 2013 CC-BY-3.0 and by the respective authors

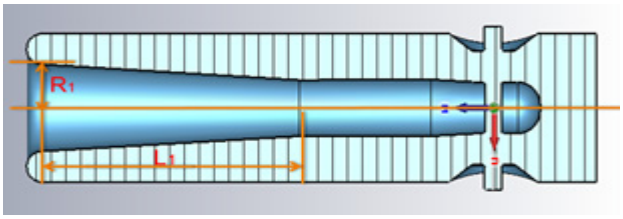


Figure 2: Diagram of the first step optimization.

The optimized parameters chosen are: R1=90 mm (the original value is 52 mm), L1=450 mm (As a reference: total length of the cavity is 1041 mm). After the first step, Bp/Ep is reduced significantly. But shunt impedance is lowered and cavity frequency is increased.

Second step:

We reduced the radius of inner conductor (R2 in Fig. 3) to increase shunt impedance and increased L2 to tune the resonant frequency back to 80.5 MHz. Optimization from scanning four parameters (R1, R2, L1 and L2) and the optimized parameters are chosen: R1=80 mm, R2=30 mm (the original value is 52 mm), L1=793 mm, L2=951 mm (the original value is 821 mm; cavity length extends 130 mm).

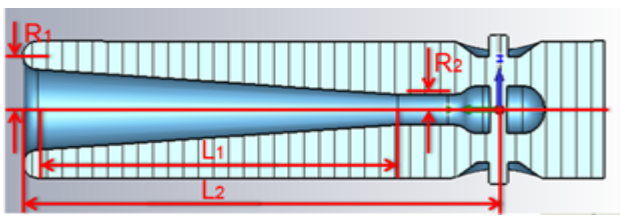


Figure 3: Diagram of the second step optimization.

Third step:

We tried to reduce the peak electric field to further improve cavity performance. E_p was located in the region of the inner conductor (IC) drift tube (nicknamed "donut"), so we optimized its shape. We tried three kinds of donuts during the optimization (see Fig. 4). Because the simulation results reconfirmed that even with tapered IC the original donut has minimum E_p, we kept it.

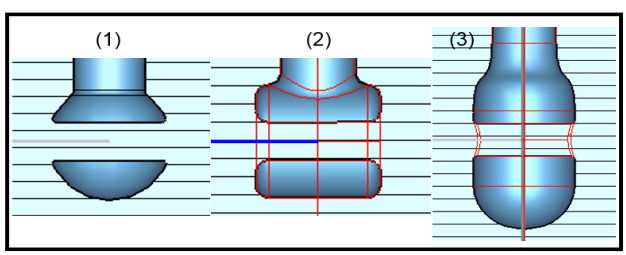


Figure 4: Three kinds of donuts in the third step optimization. (1) sphere donut, (2) cylindrical donut, (3) the original donut.

A final re-optimization was done by tuning all parameters together.

After these optimization steps, the cavity parameters resulted significantly modified regarding the maximum gradient capabilities, with rather limited rise of cost. We called this cavity design "race car" and its parameters are shown in Table 2 (effective length=βλ).

Table 2: Cavity Parameters of "race car"

Parameter	Value	Units
Frequency	80.48	MHz
E_p/E_a	5.8	Abs.
B_p/E_a	8.6	mT/(MV/m)
R_{sh}/Q	548	Ω
$R_s \times Q$	20.6	Ω

Comparing Table 2 with Table 1, the improvements from the FRIB QWR to the "race car" are as following: 1) peak magnetic field was reduced significantly; 2) shunt impedance was increased. We can see that B_p/E_p~1.5, significantly below 1.8. However, since staying at 1.8 would not reduce E_p anyhow, we decided to minimize B_p as much as allowed by our outer conductor diameter.

Thus, if we assume cavity will not quench below E_p=80 MV/m, the "race car" should provide a maximum accelerating gradient of 13.8MV/m if the effective length is defined as L_{eff}≡βλ=0.317 m, and 16.3 MV/m if L_{eff}≡D=0.27 m, where D is the real outer conductor diameter. If we assume – according to the ReA cavities test results – that operation at B_p=100 mT could be safely achieved, an acceleration of 3.7 MV in a cavity which is only 27 cm long might be feasible, if E_p=67 MV/m can be maintained as foreseen for elliptical cavities. This voltage until now for this range of beta was planned in operation only with cavities of considerably larger size.

MULTIPACTING AND BEAM STEERING

The "race car" design exceeds the expected FRIB cavity operation gradient, but some issues, such as multipacting and beam steering, needed to be studied carefully.

Multipacting Analysis

In the FRIB QWR, there are two types of multipacting: one is located at short plate [2], the other one is between inner and outer conductor (IC and OC). Both of them in clean cavities can be suppressed in a short time by RF conditioning during RF tests. For the "race car" cavity, the tapered IC may enhance multipacting near the short plate.

In Fig. 5, simulation of the FRIB QWR's multipacting was verified by the cavity vertical tests [3]. Thus, we can use simulations to predict multipacting of the "race car".

Copyright © 2013 CC-BY-3.0 and by the respective authors

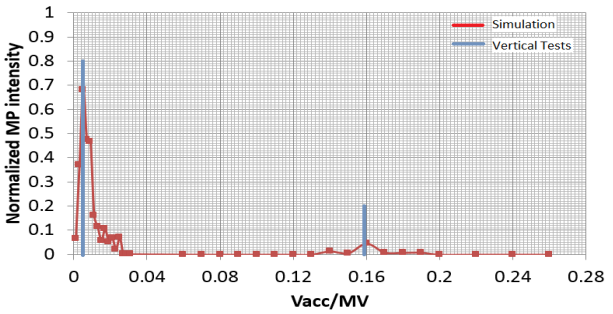


Figure 5: Multipacting barrier in simulation and vertical tests. In simulation, normalized MP intensity is proportion to the total number of secondary electrons in 10 RF cycles. In vertical tests, it is proportion to the frequency of multipacting (the number of multipacting processing tests over the total number of tests). The multipacting at lower accelerating gradient occurs between IC and OC while the higher one is on the short plate.

We simulated multipacting for both the FRIB QWR and the "race car", and compared them in Fig. 6. As a result, taper did enhance multipacting on the short plate. The multipacting barrier on short plate of the "race car" is shifted to a higher gradient and becomes wider. But the overall multipacting intensity doesn't increase much (maximum value increases from 0.7 to 1 in Fig. 6). Thus, the "race car" design might need more time than the FRIB one for RF conditioning to suppress multipacting.

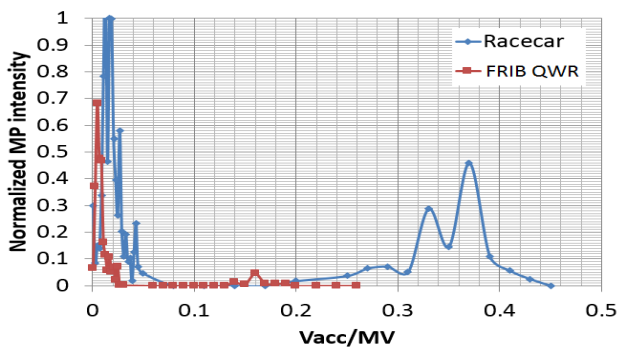


Figure 6: Multipacting comparison between FRIB QWR and "race car" by simulations. Normalized MP intensity is proportion to total number of secondary electrons in 10 RF cycles.

Beam Steering Analysis

In the FRIB QWR, beam steering can be corrected by offsetting the cavity down 1.5 mm [4]. Since in the "race car" radius of the inner conductor curvature is reduced from 52 mm to 30 mm above the beam axis, the vertical electric field distribution (E_y) is changed (see Fig. 7) and so the beam steering. Comparing with the FRIB QWR, the steering becomes weaker for $\beta<0.085$ but larger for $\beta>0.085$ (see Fig. 8). The disadvantage is that the previous correction method with the "race car" is not as good as with the FRIB cavity, although looking acceptable. Beam port shaping for better correction can be considered if necessary.

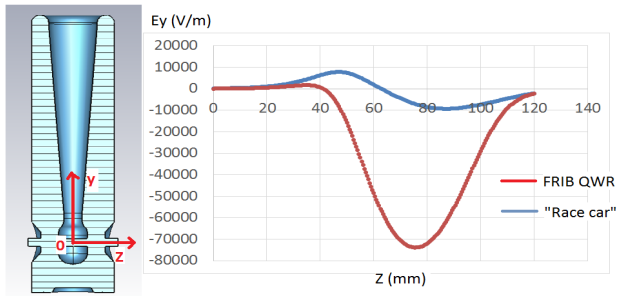


Figure 7: Ey comparison between the FRIB QWR and the "race car" cavity.

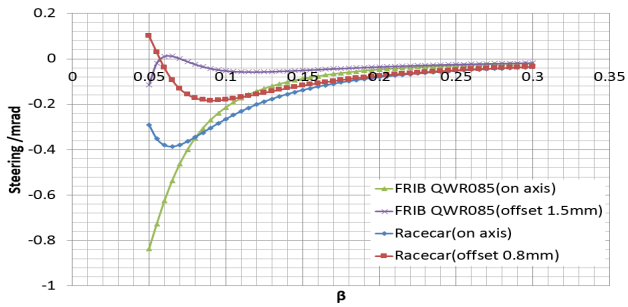


Figure 8: Steering and the correction comparison between the FRIB QWR and the "race car". By offsetting cavity down 1.5 mm we will have a minimum steering for the FRIB QWR, while for the "race car", the required correction will be 0.8 mm.

CONCLUSION

By simultaneously reducing peak magnetic field and increasing shunt impedance, the FRIB β=0.085 QWR geometry was optimized for maximum acceleration gradient without increasing the cavity longitudinal dimensions but only the vertical length by about 130mm. The cost increase for this new geometry appears to be rather affordable. This resonator type might benefit the ReA linac at MSU and other applications where maximum acceleration must be achieved in a limited space. Both multipacting and beam steering issues have been thoroughly studied with simulations. The construction of a prototype is planned for next year.

REFERENCES

[1] http://www.cst.com/
[2] Z. Zheng, "Multipacting suppression modeling for Half Wave Resonator and RF coupler", proceeding of Linac2012, Tel-Aviv, Israel.
[3] J. Popielarski, "Multipacting in FRIB prototype cavities", internal report.
[4] A. Facco, "Beam steering correction in FRIB quarter-wave resonators", proceedings of IPAC2012, New Orleans, Louisiana, USA.

Copyright © 2013 CC-BY-3.0 and by the respective authors

HYDROGEN DEGASSING STUDY DURING THE HEAT TREATMENT OF 1.3-GHZ SRF CAVITIES

M.J. Joung[1#], H.J. Kim[1], A. Rowe[2], M. Wong[2]
[1]IBS, Daejeon, South Korea
[2]Fermi National Accelerator Laboratory, Batavia, USA

Abstract

Superconducting radio frequency (SRF) cavities undergo a number of processes as part of its manufacturing procedure in order to optimize their performance. Among these processes is a high temperature hydrogen degas heat treatment used to prevent 'Q' decrease. The heat treatment occurs in the processing sequence after either chemically or mechanically polishing the cavity. This paper summarizes the hydrogen measurements during the heat treatment of a sample of chemically and mechanically polished single-cell and nine-cell 1.3-GHz cavities. The hydrogen measurements are analyzed according the polishing method, the polishing history, the amount of time that the cavity was baked at 800°C, and the temperature ramp rate.

INTRODUCTION

The performance of superconducting radio frequency cavities is most important fact for a high gradient accelerator. However it is limited by field emission and thermal magnetic breakdown.[1] Most of the SRF cavities receive surface treatment to improve the performance of the cavity. A high temperature heat treatment degases the hydrogen gas that comes from the polishing process. High temperature heat treatment provides some stress-relief in the material in addition to degassing hydrogen gas [2] Hydrogen degassing studies were carried out at Jefferson Laboratory and Institut fuer Kernphysik using defference cavity. [3-4] The goal of the analysis in this paper was to evaluate whether a dependency exists between the cavity surface processing techniques, the kind of cavity and the hydrogen evolution during the heat treatment. The different polishing techniques and sequence are described. The methodology of determining the amount of degassed hydrogen is explained. Finally, the conclusion shows a comparison of the hydrogen amount.

DESCRIPTION OF CAVITIES & PROCESSING HISTORY

Nineteen single cell cavities and three nine-cell cavities, all 1.3-GHz cavities, were analyzed. All had a variety of processing steps. The cavities were polished using either EP (Electropolishing) or CBP (Centrifugal Barrel Polishing, or tumbling) to a mirror finish. [5]

The EP process polishes the surface using electrical current in acid solution at 30°C. It is a type of chemical polishing. The CBP (or tumbling) process polishes the surface using material (media) for many hours between 30°C and 50°C. It is a type of mechanical polishing.

The 800°C heat treatment takes place after the cavities were polished. During the heat treatment the temperature ramp rate was either 3°C per minute or 10°C per minute and the soak time at 800°C was either 2 hours or 3 hours. Table 1 shows the various sequences that different cavities experienced. It is noted that the amount of material removed during polishing did not correlate with the amount of degassed hydrogen.

Table 1: Polishing and Bake Sequences for the Cavities

Cavity No.	Process
1, 2, 3, 4, 9, 11, 13, 14, 15, 16, 17, 18, 20, 23, 25, 26	EP / bake
10, 12	CBP / bake
7, 19	EP / CBP / EP / bake
6	EP / CBP / bake
22, 24	CBP / EP / bake
5	CBP / bake / EP / bake

MEASURING AND CALCULATING THE H_2 AMOUNT

The vacuum furnace has a SRS 100 residual gas analyzer that measures the partial pressures of gasses during a bake. The RGA sits outside the furnace's hot zone and on the opposite end of the chamber's cryopumps. Figure 1 shows the hydrogen partial pressure curves for an electropolished cavity, a tumbled cavity and the baseline from an empty chamber for a temperature soak of 3 hours and a ramp rate of 3°C per minute. Of interest is the pressure data within the temperature range of 300°C to 300°C, as is shown in Figure 1.

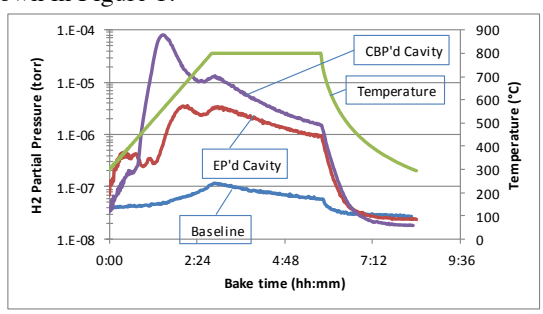


Figure 1: Typical H_2 partial pressures of an electropolished cavity, a tumbled cavity, and an empty chamber within 300°C to 300°C.

Copyright © 2013 CC-BY-3.0 and by the respective authors

A baseline hydrogen pressure curve was established by baking an empty furnace chamber. The empty chamber sat at room temperature at a vacuum pressure on the order of 1E-8 torr for eighteen days before the bake cycle started.

To calculate the total amount of degassed hydrogen from a cavity during a bake, the cavity's hydrogen pressure curve was integrated. The baseline hydrogen curve is also integrated, and the difference between the two values is the shaded area shown in Figure 2. This value is then multiplied by the effective pumping speed (~500 L/s) within the furnace to provide the total degassed hydrogen in units of torr-L.

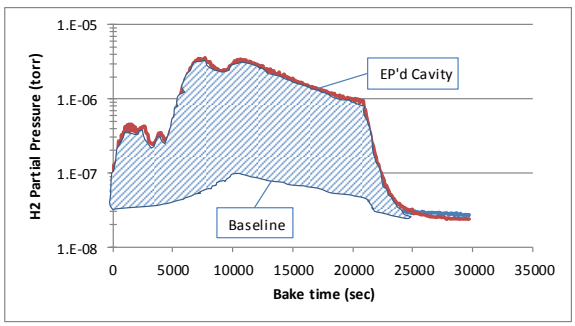


Figure 2: Area between the cavity and baseline H_2 pressure curves.

HYDROGEN ANALYSIS

Between Tumbled Cavity and EP Cavity

This section shows that tumbled cavity has a larger amount of hydrogen than the electropolished cavity. The tumbled cavities showed a hydrogen peak at temperatures between 500°C and 600°C. The hydrogen peak was typically an order of magnitude higher than the hydrogen level during the 800°C soak. Figure 2 compares the hydrogen amount for tumbled and electropolished cavities that had a three hour soak and a temperature ramp rate of 3°C per minute (cavities numbered 1 through 12). Cavities numbered 6, 7, 10, 11 and 12 were tumbled cavities. The rest of the cavities were electropolished.

Figure 3 shows the large of amount of hydrogen in the tumbled cavities compared with the electropolished cavities. It is likely that an electropolished cavity emits a small amount of hydrogen compared to the tumbled cavity. The H^+ ions that are produced tend to go into the cathode rather than the niobium surface. Also, the oxide surface layer which is produced during EP process prevents H^+ ions from penetrating easily into the niobium material. On the other hands, during the CBP process, the niobium oxide layer disappears and the H^+ ions can penetrate into the niobium material. Once the CBP process is complete, the oxide layer is reformed. During the heat treatment process, the oxide layer is removed and any hydrogen loaded into the niobium is released.

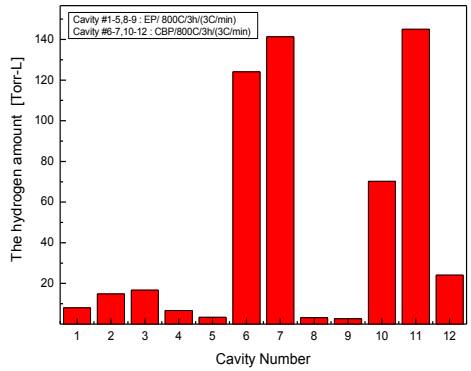


Figure 3: Comparing degassed H_2 in electropolished vs. tumbled cavities.

Between the Single-Cell Cavity and Nine-Cell Cavity

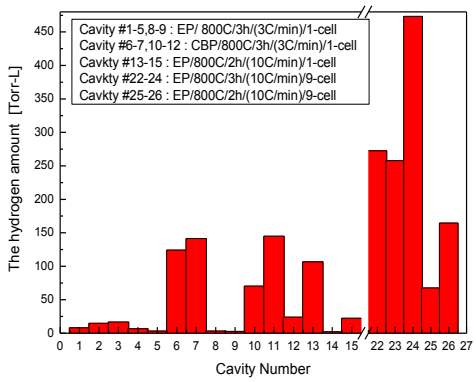


Figure 4: Comparing degassed H_2 in single-cell vs. nine-cell cavities.

Figure 4 shows the amount of hydrogen when comparing the single cell and nine cell cavities. Cavities 16-20 are single-cell cavities, and the cavities 22-24 are nine-cell cavities. Cavities 19, 22 and 24 are tumbled cavities. The nine-cell cavities show the degassed hydrogen amount more than nine times of the hydrogen amount from single-cell cavities, as expected.

By Polishing History

Each cavity received different kinds of polishing and polishing time, listed in Table 1. Two observations were found by comparing the polishing histories of the cavities. One observation confirms again that the amount of degassed hydrogen comes from the electropolished cavity is significantly less than the amount of hydrogen from the cavity that received CBP. The second observation is that the hydrogen amount from CBP cavity is larger no matter how many EP processes it received. So it turned out that EP process cannot remove hydrogen gas that comes from the CBP process. But when there is a baking process between CBP process and EP process, the baking process removes the hydrogen gas from the cavity that is left from the CBP process.

Copyright © 2013 CC-BY-3.0 and by the respective authors

CONCLUSIONS

This paper describes how the hydrogen data was collected and how the amount of hydrogen was calculated. The degassed hydrogen amount from electropolished and tumbled cavity was analyzed. It was confirmed that tumbled cavities degas a large of hydrogen gas compared with electropolished cavities and the basic principle was explained in the section of hydrogen analysis. It was found that the EP process cannot remove hydrogen gas that comes from the CBP process. Once the cavity received CBP process before baking, regardless of whether or when the cavity was EP'd the cavities degases a large of hydrogen amount. In comparing the single cell and nine-cell cavities, it was expected that the degassed hydrogen amount would be more, correlating with surface area. The amount of hydrogen from nine-cell cavities was much than expected. More studies will be done to understand the reason. The increasing rate of hydrogen amount to determine the real pump capacity and calculating the RGA accuracy has to be studied further in order to optimize the heat treatment process.

ACKNOWLEDGMENTS

This work was supported by the Rare Isotope Science Project which is funded by the Ministry of Science, ICT and Future Planning (MSIP) and the National Research Foundation (NRF) of the Republic of Korea under Contract 2011-0032011. My special thanks go to my colleagues at Fermilab: Charlie Cooper and the Cavity Processing R&D Group and Damon Bice and the Cavity Processing Group

REFERENCES

[1] P.Kneisel et al., "Performance of a CEBAF Production cavity after High-Temperature Heat Treatment", Proceedings of PAC 1993, pp. 927-9.

[2] G. Ciovati et al., "High-Temperature Heat Treatment Study on a Large-Grain Niobium Cavity", Proceedings of SRF 2011, TUPO051.

[3] B. Visentin et al., "Cavity Baking: A Cure for the High Accelerator Field Q_0 Drop", Proceedings of the 1999 Workshop on RF Superconductivity, TUP015.

[4] R. Eichhorn et al., "Results from an 850C Heat Treatment and Operational Findings from the 3 GHz Cavities at the S-DALINAC", Proceedings of SRF 2007, TUP19.

[5] Cooper et al., "Cavity Processing Research Laboratory at Fermilab: SRF Cavity Processing R&D", Proceedings of SRF 2011, Conf Proc. C11-07-25.4 (2011) 424-430.

Copyright © 2013 CC-BY-3.0 and by the respective authors

MEASUREMENT OF A SUPERCONDUCTING SOLENOID WITH APPLICATIONS TO LOW-BETA SRF CRYOMODULES*

S.H. Kim#, M.P. Kelly, Z.A. Conway, P.N. Ostroumov, ANL, Argonne, IL 60439, USA
E.E. Burkhardt, Cryomagnetics, Inc., Oak Ridge, TN 37830, USA

Abstract

Proton and heavy-ion linacs with superconducting cavities require compact lattices to suppress emittance growth in the low-velocity region. For beam focusing superconducting solenoids are superior in this regard to normal conducting quadrupoles. A superconducting solenoid with integral x-y steering coils has been fabricated for the Project-X Injector Experiment (PXIE) half-wave resonator cryomodule. It is capable of generating 6 T solenoidal fields and dipole steering fields of 30 T·mm field integrals in both of transverse directions. We experimentally investigated issues for practical use of this solenoid in cryomodules including: 1) the superposition of dipole steering fields on solenoidal fields, 2) the magnetic axis of the solenoid with respect to the mechanical references in cryogenic temperatures, and 3) the residual magnetic field generated by the solenoid on the superconducting RF cavity surfaces even after degaussing; a 72 MHz quarter wave resonator was used for this experiment. In this paper, we present details of experimental setup and results.

INTRODUCTION

Proton and ion linacs require a compact focusing lattice in the low-velocity region to minimize the required real-estate and to minimize emittance growth and corresponding beam loss [1]. Superconducting solenoids are superior in this regard to normal conducting quadrupoles. To reduce the real-estate requirements further dipole steering coils are integrated with solenoids [2]. This superconducting solenoid with dipole steering coils is to be installed in a cryomodule with superconducting RF cavities so the following questions regarding beam and cavity performance need to be verified: 1) Are the dipole fields linearly superposed with the solenoid fields? 2) Is the solenoid aligned to the beam in the cryomodule? 3) Are the residual magnetic fields generated by the solenoids small enough not to degrade the cavity Q-factor?

We studied these issues with a superconducting solenoid prototype fabricated for the Project-X Injector Experiment (PXIE) Half-Wave Resonator (HWR) cryomodule [3]. This solenoid generates 6 T solenoidal fields and each pair of the dipole steering coils integrated with the solenoid produces up to 30 T·mm integrated deflecting fields. In this paper, we will briefly introduce the solenoid used in these experiments and present the dipole field measurements with and without the solenoidal field to discuss field superposition. Then, we will present magnetic axis measurements relative to the mechanical axis and discuss accuracy of this measurement method. Another alignment issue, the alignment of the solenoid to the beam axis in the cryomodule, is not discussed in this paper [4]. Next, measurements of the residual magnetic fields generated by the solenoid on the surface of a 72 MHz superconducting Quarter-Wave Resonator (QWR) will be presented with a discussion of the degaussing employed to reduce the residual magnetic fields on the cavity surface. Finally, a summary of these experimental results will conclude this paper.

* Work supported by the U.S. Department of Energy, Office of High Energy Physics and Nuclear Physics, under Contract DE-AC02-76CH03000 and DE-AC02-06CH11357.
# shkim121@anl.gov

FIELD PROFILES AND SUPERPOSITION

The solenoid contains two bucking coils at either end. The bucking coils are wired in series with the main solenoid to produce an opposing field polarity relative to the solenoidal field. There are no iron return yokes or magnetic shields surrounding the solenoid. The bucking coils minimize the axial fringe fields and stray fields on the cavity surfaces. The measured axial field profile is shown in Fig. 1. The measured solenoid field in the high field region is in good agreement with the design values; this ensures that the focal length will be the same as the designed value. The fringe fields are slightly higher than the design but are still small enough for the residual magnetic fields around the cavity wall to be successfully reduced by degaussing as will be discussed later in this paper.

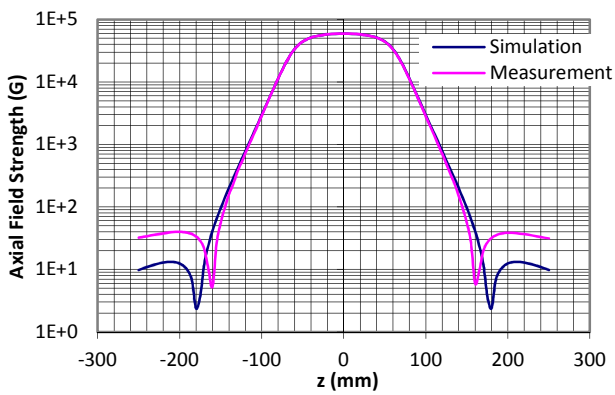


Figure 1: Axial field profiles on the axis. z is the longitudinal position which is 0 in the middle of the solenoid. Note that the magnetic field drops at z = ±160 mm in the measured data and at z = ±180 mm in the simulated response correspond to a polarity change in the axial field.

Copyright © 2013 CC-BY-3.0 and by the respective authors

Each dipole steering coil is composed of two racetrack shaped coils located outside of the solenoid coil; one is oriented vertically and the other is oriented horizontally. The dipole fields are measured on the z-axis of the solenoid bore with and without the solenoid field on. When the solenoid is energized to 6 T, the dipole field is 5~7% higher than when the solenoid is off, Fig. 2. With no current the solenoid coil, which is composed of multi-filamentary NbTi strands twisted within a copper matrix, is supposed to partly shield the dipole fields. However, the operating solenoid field of 6 T is high enough relative to the lower critical field of NbTi such that the dipole fields will be stable in actual operation. In the measurements presented here, the solenoid was turned on and off at each data point shown in Fig. 2. Notice that the measured field is axially symmetric with respect to the middle of the solenoid so the dipole coil is mechanically stable against Lorentz forces produced by the solenoid.

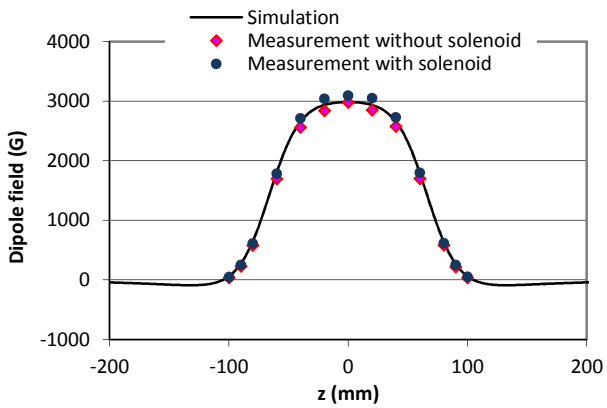


Figure 2: Dipole field profiles of simulation and measurement with and without solenoid fields.

MAGNETIC AXIS OF SOLENOID

The magnetic axis, here defined as the center of the solenoidal equipotential lines, is derived from an angular scan of the radial magnetic field using a hall probe. We measured the radial component of the magnetic field at two longitudinal positions, z = ±64 mm. These locations satisfy the following conditions; 1) the radial field is linear and 2) the radial field strength is large enough relative to the axial field component which reduces measurement errors arising from the misalignment of the probe. Because of the linearity this field sinusoidally oscillates with the azimuthal angle if the magnetic center has an offset from the mechanical center of the solenoid bore which is the center of probe rotation. The relationship between the magnetic field parameters and geometries is given by:

$$\Delta B/B_0 = d/R, \qquad (1)$$

where ΔB is the field amplitude, B_0 is the field offset of the measured magnetic fields, d is the offset of the magnetic center from the mechanical center, and R is the radius of the angular scan.

The measurement results are shown in Fig. 3, the measured offsets are 0.32 mm at z = -64 mm and 0.27 mm at z = +64 mm where R = 16 mm. The phase of each cosine curve corresponds to the angular offset of the magnetic center relative to the x-axis of the solenoid; so the magnetic center is located 145 degrees (z = -64 mm) and 115 degree (z = 64 mm) from the x-axis of the solenoid. Uncertainty in the longitudinal position of the measurements is the source of the field-offset difference between two curves in Fig. 3.

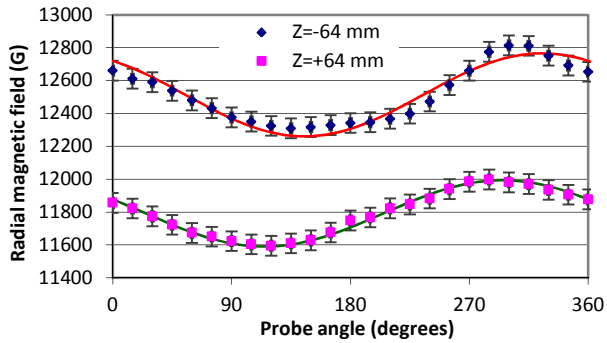


Figure 3: Angular scan of radial magnetic field to find the magnetic axis with respect to the mechanical axis (probe angle is 0 on the x-axis of the solenoid) measured at two different longitudinal positions.

Errors in these measurements are given by these factors: 1) uncertainty of the probe position in the radial and longitudinal directions, 2) misalignment of the hall probe, 3) contribution of the second or higher order of d/R because eq. (1) is derived with the first order approximation of d/R, 4) instrument errors of the probes and the gauss-meter, and 5) wobbling of the rotating rod on which the probes are attached during the angular scan. The factors from the first to the fourth totally give a fractional error of 5% in the result of d, which is negligible because typical transverse alignment tolerance of this solenoid is 0.25 mm. However, the last factor, which originates from the gap between the rotating rod and the rotation guide as shown in Fig. 4, gives uncertainty in the offset by the same amount of the gap distance which is ±70 μm after correction by thermal contraction. Multiple scans per angle would reduce this error statistically. It is measured once per angle in this study.

RESIDUAL MAGNETIC FIELDS

The solenoid test with the QWR is done to observe any residual magnetic field which is possibly generated by materials around the cavity, such as the helium jacket and the solenoid housing, magnetized after solenoid operation. To minimize the residual magnetic field, we degaussed the solenoid with a temporally sinusoidal current profile whose envelope is exponentially decayed with a decay time of 5 times the sinusoidal oscillation period and it finished when the field amplitude of the last degaussing cycle was 7 G in the middle of the solenoid.

Copyright © 2013 CC-BY-3.0 and by the respective authors

We installed the solenoid with the cavity in a cryostat as shown in Fig. 5 and measured magnetic fields during and after solenoid degaussing at two representative locations: one on the axis where the solenoid field is a maximum and the other on the cavity wall, which is the higher position in Fig. 5, where the RF magnetic field is a maximum when we use the PXIE HWR.

On the cavity wall, the magnetic field measured during the degaussing behaved like a hysteresis curve which is supposed to be dominated by the NbTi in the solenoid coil [5] and it came to the center of the hysteresis curve after degaussing was finished; therefore, there is no residual magnetic field after degaussing at that position except for leakage of the earth's magnetic fields, which cannot be degaussed by the solenoid, no matter what was magnetized during solenoid operation. On the other hand, the probe installed on the axis is too coarse to measure the residual magnetic field by accuracy of tens of mG because it is for measuring high level fields; note that the maximum field is 75 G on the axis whereas it is 55 mG on the cavity wall. The residual field on the axis was measured again after warming up scanning the low field probe and it was found that there were ~100 mG residual fields around the solenoid and the source of these fields was inside the solenoid housing; other than that, there are no significant residual field more than 10 mG except for leakage of earth's magnetic fields. For accurate measurements, we set the solenoid alone inside a good magnetic shield. The measurement results are shown in Fig. 6. Even though there still remain the residual magnetic fields inside the solenoid, the degaussing worked successfully so that the residual field at the position of the cavity surface is 2~3 mG.

SUMMARY

With the PXIE solenoid, we experimentally verified that 1) the dipole field of the steering coil is well superposed to the solenoid field and this coil is mechanically stable on solenoid operation, 2) the magnetic axis can be found with accuracy of less than 100 μm by scanning hall probes, 3) residual fields generated by the solenoid can be reduced to a few mG at the cavity surface by degaussing the solenoid.

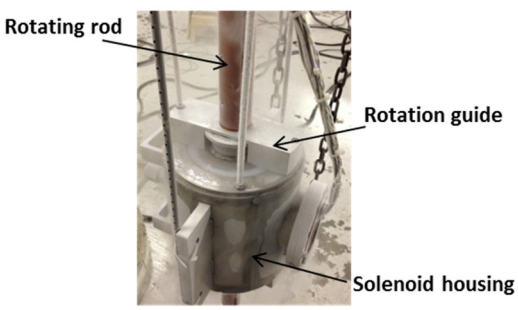


Figure 4: Setup for angular scan of the radial magnetic field. Hall probes are attached on the rotating rod which is composed of bakelite while the rotation guide is composed of aluminium and the solenoid housing is composed of stainless steel.

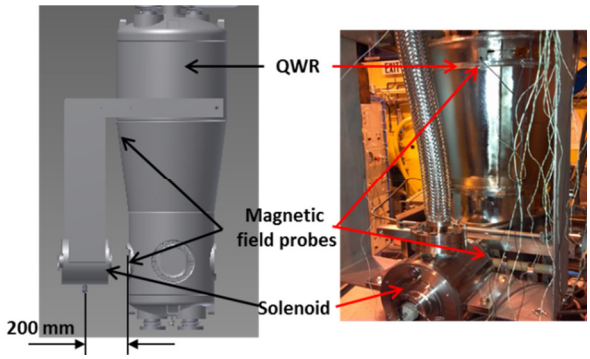


Figure 5: Magnetic field measurement setup in the cryostat. The QWR is hung on the cryostat lid. Each probe measures the magnetic field normal direction to the cavity wall; higher position on the cavity wall: low field probe (Bardington Fluxgate Magnetometer, Mag-01), lower position on the axis: high field probe (Lakeshore Hall Probe, HMCT-3160).

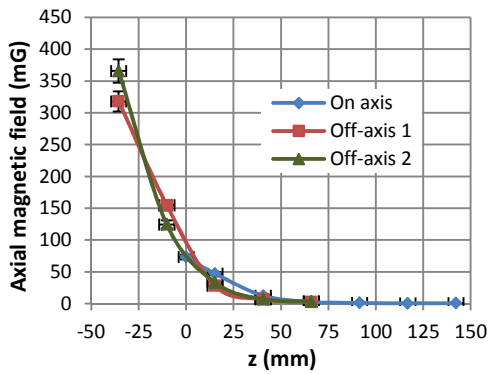


Figure 6: Axial scans of the residual magnetic field generated by magnetized materials in the solenoid. It is measured with the solenoid alone. The solenoid flange is placed at z=0 and the cavity flange will be placed at z=75 mm. The radial position of the "off-axis" scan is r=56 mm where the measured residual magnetic field is maximum.

ACKNOWLEDGMENT

The authors appreciate S.M. Gerbick, T.C. Reid, R.C. Murphy and M.J. Kedzie for their help to solenoid tests.

REFERENCES

[1] P.N. Ostroumov et al., Phys. Rev. ST Accel. Beams **7** (2004) 090101.

[2] P.N. Ostroumov et al., "A New Generation of Superconducting Solenoids for Heavy-Ion Linac Application," LINAC'02, Gyeongju, August 2002, TU413, p. 334 (2002); http://www.JACoW.org

[3] Z.A. Conway et al., "A New Half-Wave Resonator Cryomodule Design for Project-X," IPAC'12, New Orleans, May 2012, THPPP054, p. 3865 (2012); http://www.JACoW.org

[4] S.H. Kim et al., "4-Kelvin Alignment of the ATLAS Intensity Upgrade Cavities and Solenoids," CEC-ICMC 2013, Anchorage, June 2013, 4EOrB2-06.

[5] Y.B. Kim et al., Phys. Rev. **129** (1963) 528.

Copyright © 2013 CC-BY-3.0 and by the respective authors

MECHANICAL DESIGN OF THE 704 MHz 5-CELL SRF CAVITY COLD MASS FOR CeC PoP EXPERIMENT*

J. C. Brutus#,1, S. Belomestnykh1,2, I. Ben-Zvi1,2, T. Grimm3, Y. Huang1, R. Jecks3, V. Litvinenko1,2, I. Pinayev1, J. Skaritka1, L. Snydstrup1, R. Than1, J. Tuozzolo1, Wencan Xu1, J. Yancey3
1) Brookhaven National Laboratory, Upton, NY 11973-5000, U.S.A.
2) Stony Brook University, Stony Brook, NY 11794, U.S.A.
3) Niowave Inc., Lansing, MI 48906, U.S.A

Abstract

A 5-cell SRF cavity operating at 704 MHz will be used for Coherent Electron Cooling Proof of Principle (CeC PoP) system under development for the Relativistic Heavy Ion Collider (RHIC) at Brookhaven National Laboratory. The CeC PoP experiment will demonstrate the new technique of cooling proton and ion beams that may increase the beam luminosity in certain cases, by as much as tenfold. The 704 MHz cavity will accelerate 2 MeV electrons from a 112 MHz SRF gun up 22 MeV. Novel mechanical designs, including a super fluid heat exchanger, helium vessel, vacuum vessel, tuner mechanism, and fundamental power coupler (FPC) are presented. Structural and modal analysis, using ANSYS [1] were performed to confirm the cavity chamber and helium vessel structural stability and to calculate the tuning sensitivity of the cavity. This paper provides an overview of the design, the project status and schedule of the 704 MHz 5-cell SRF for CeC PoP experiment.

INTRODUCTION

The BNL3 5-cell 704 MHz SRF linac that is being designed and fabricated in collaboration between BNL and Niowave, will be used as the main 20 MeV accelerator for CeC PoP experiment under construction at IP2 of RHIC at BNL [2]. Phase II of this experiment is to be completed by the end of shutdown 2014 and will include the 704 MHz SRF linac. At the same time, with this project, BNL is pursuing R&D towards the electron-ion collider (eRHIC). This paper provides an overview of the design and structural analysis of the 704 MHz SRF linac. Two 5-cell Niobium cavities have been fabricated. The first one, BNL3-1 was manufactured by AES and the second one, BNL3-2 by Niowave.

704 MHZ DESIGN

Design Features

The 704 MHz 5-cell cavity cryostat consists of an internal phase separator, control valves, 5-cell cavity, two magnetic shields and a helium gas cooled thermal shield, a superfluid heat exchanger and an electrical heater. The helium supply and return lines are bayonet connections for quick assembly [3]. The layout of the 704 MHz SRF 5-cell SRF linac is shown in Figure 1.

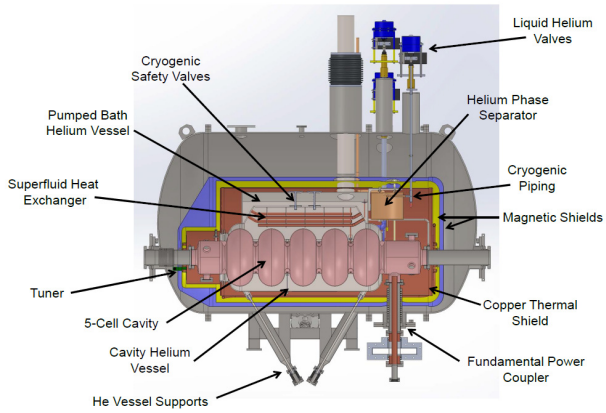


Figure 1: Layout of the 704 MHz SRF cryomodule.

The bottom of the helium vessel is a cylinder that incorporates the 5-cell cavity with the upper section modified to include the superfluid heat exchanger. Due to space constraint at IP2, the helium vessel was designed with the minimum real estate possible in order to keep the cryostat within the available space. The stiffeners shown in Figure 2 were added to the side of the helium vessel in order to reduce the deformation which translates to the cavity by deforming it through the supports attached to the helium vessel.

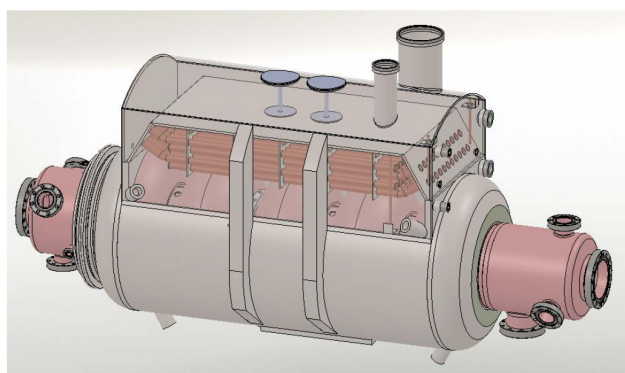


Figure 2: Layout of the 704 MHz cavity in a helium vessel.

Cavity Support

The support for the 5-cell cavity was designed in order to increase the natural frequency of the cavity in the helium vessel. The cavity is supported by three 1/8" Grade 5 titanium rods, symmetrically distributed around the beam axis. The support is located after the second

* Work is supported by Brookhaven Science Associates, LLC under contract No. DE-AC02-98CH10886 with the U.S. DOE.
#jcbrutus@bnl.gov

Copyright © 2013 CC-BY-3.0 and by the respective authors

cell, closer to the tuning bellows as shown in Figure 1. The support was designed to have no effect on the mechanical tuning of the cavity.

Mechanical Tuning System

The BNL3 cavity mechanical frequency tuning system was adopted from a design that has been successfully implemented by Dresden in Germany for their superconducting RF Photo-Injector [4]. The main reasons to use this design is for the mechanical advantage of the lever arms, the large tuning range, high resolution, hysteresis-free and linear operation. The design was modified to integrate a piezoelectric actuator for fast tuning and to accommodate larger cavity dimensions.

Fundamental Power Coupler

The fundamental power coupler is used to deliver up to 20 kW CW RF power to the SRF cavity. A cylindrical ceramic window is used to transmit the RF power from a reduced-height WR1150 waveguide to a coaxial line and to seal the cavity vacuum. The outer conductor of the coaxial line will be cooled by 5 K helium gas, and the RF window and inner conductor will be cooled by water. The final model of the fundamental power coupler is shown in Figure 3. The window material is 96% alumina with a dielectric constant of 9.4. The simulated S parameters are shown in Figure 4.

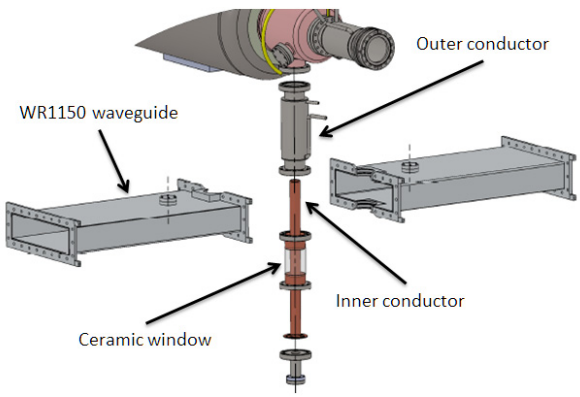


Figure 3: Fundamental power coupler model.

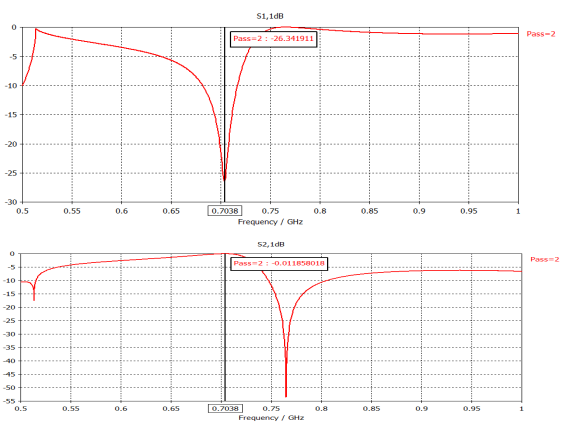


Figure 4: S-parameters for the FPC.

ANALYSIS

5-Cell Cavity

As mentioned earlier, structural and modal analyses, using ANSYS were performed to confirm the cavity chamber and He vessel structural stability and to calculate the tuning sensitivity of the cavity. When helium pressure is applied on the cavity, its deformed shape will change the resonance frequency. The sensitivity of the cavity is 10 Hz/mbar bases on the analysis. The location of the stiffeners between the cavities of the 5-cells had to be validated at maximum pressure condition (23 psia relief valve set pressure).

The second part of the analysis was to find the maximum allowable deformation of the cavity before yielding. One end was fixed in all degrees of freedom while allowing the other end to only move in the y direction. A 384 lbs force deformed the cavity by 0.442 mm with a maximum stress of 7507.4 psi. The yield strength of Niobium is 7500 psi. This corresponds to a tuning sensitivity of 171.6 kHz/mm. The relaxed and deformed shapes of the cavity are shown in Figure 5.

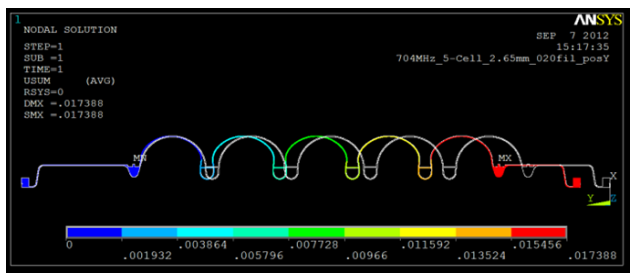


Figure 5: Relaxed and deformed shapes of the cavity.

Tuning Bellows

The tuning bellows was designed using titanium Ti-6Al-4V Grade 5 because of its high tensile yield strength of 120000 psi. The analysis was done at the maximum pressure condition (23 psia relief valve set pressure) applied on the inside of the bellows. The applied pressure resulted in a total deformation of .0065" and a maximum stress of 19927 psi in the convolutions of the bellows. Based on the results from the analysis, the helium vessel is determined to be safe under operating condition (14.7 psi) and the maximum condition (23 psi).

Modal Analysis

The goal was to design the struts to support the helium vessel and 5-cell cavity inside the vacuum cryostat, in order to keep the natural frequency above or close to 90 Hz. In the analysis, the three struts were at a 60° angle from the horizontal, symmetrically placed around the helium vessel about the axis of the beam on each side of the centre plane. Instead of using a solid rod for the struts, they are made of hollow ½" OD 0.022" WT Tube Ti Grade 2 in order to reduce the heat leak into the helium vessel and stiffening the structure. Based on the results from the analysis, the first mode reached 88.3 Hz. Although it is below 90 Hz, it is determined to be

Copyright © 2013 CC-BY-3.0 and by the respective authors

sufficient. Table 1 shows the results from ANSYS simulations.

Table 1: Mode Frequencies from ANSYS Modal Analysis

Mode	Frequency [Hz]
1	88.3
2	113.8
3	150.7

Helium Vessel

The deformation of the side of the helium vessel affects the 5-cell cavity by applying a force on it through the cavity support and deforming it. Under the maximum pressure condition (23 psi relief valve set pressure) the location of the stiffeners on the side of the helium vessel, shown in Figure 3, was optimized using ANSYS. The shape and size of the stiffeners was limited to the space available inside the heat shields. The maximum deformation of the helium vessel is 0.015", which deforms the 5-cell cavity by 0.007" in the radial direction. The maximum stress in all the components affected, are within the allowable limits. The deformed shapes of the helium vessel and 5-cell cavity are shown in Figure 6 and Figure 7.

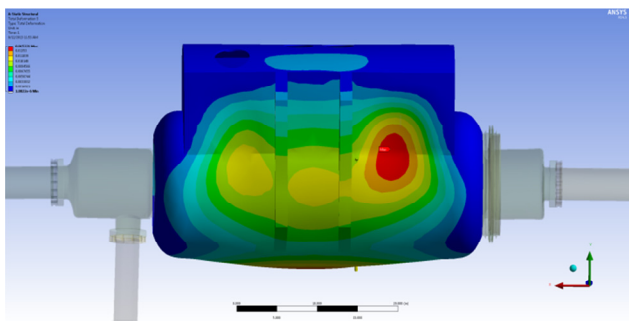


Figure 6: Deformed shape of the helium vessel.

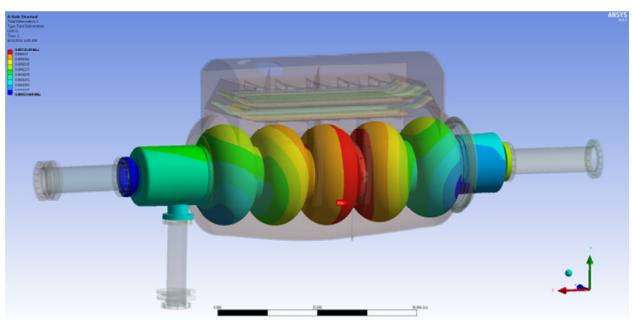


Figure 7: Deformed shape of the 5-cell cavity.

FABRICATION

Bulk buffer chemical polishing (BCP) of BNL3-1 (120 μm) was completed at AES and the cavity was baked at BNL at 600°C for 24 hrs. After baking, the cavity was sent back to AES for light BCP and HPR. BNL3-1 cavity is shown in Figure 8.

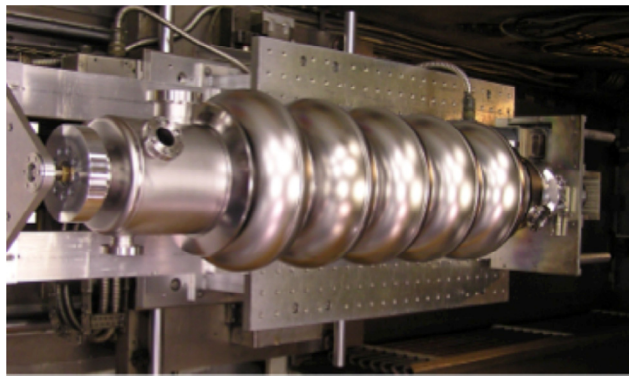


Figure 8: BNL3-1 cavity.

The second cavity, BNL3-2, and a cryomodule for CeC PoP are on order from Niowave. The fabrication and processing (bulk BCP, 600ºC vacuum bake, light BCP and HPR) of the cavity was completed recently at Niowave and BNL. The test in our vertical test facility for both cavities is scheduled for later this year. The better performed one of the two cavities will be integrated in the cryomodule.

CONCLUSION

The superfluid heat-exchanger, the tuner system and the cryogenic components make the mechanical design a challenging task. A preliminary design review of the cryomodule was completed in September at Niowave. We are working closely with Niowave to finalize the design and integration of the tuner system in the cryostat. The fabrication of the helium vessel and several components attached to the helium vessel is schedule to begin within the next couple weeks. The 704 MHz SRF linac is scheduled to be installed during RHIC summer shutdown 2014.

REFERENCES

[1] ANSYS Multiphysics Finite Element Code, ANSYS, Inc. Canonsburg, PA 15317.
[2] V. N. Litvinenko, et al., "Proof-of-Principle Experiment for FEL-Based Coherent Electron Cooling," PAC'2011, p. 2065.
[3] Y. Huang, et al., "Cryogenic Systems for Coherent Electron Cooling to be installed at RHIC," CEC/ICMC, 2013, 2EPoE5-01.
[4] J. Teichert, et al., "Cryomodule and tuning system of the superconduction RF Photo-Injector," Proc. of FEL 2006, BESSY, Germany, 2006, p. 575.

Copyright © 2013 CC-BY-3.0 and by the respective authors

MECHANICAL DESIGN OF 112 MHz SRF GUN FPC FOR CeC PoP EXPERIMENT*

J. C. Brutus#,1, S. Belomestnykh1,2, Y. Huang1,V. Litvinenko1,2, G. Mahler1, I. Pinayev1, J. Skaritka1, L. Snydstrup1, R. Than1, J. Tuozzolo1, Q. Wu1, T. Xin2
1) Brookhaven National Laboratory, Upton, NY 11973-5000, U.S.A.
2) Stony Brook University, Stony Brook, NY 11794, U.S.A.

Abstract

A Quarter-Wave Resonator (QWR) type SRF gun operating at 112 MHz will be used for Coherent Electron Cooling Proof of Principle (CeC PoP) system under development for the Relativistic Heavy Ion Collider (RHIC) at Brookhaven National Laboratory (BNL). The CeC PoP experiment will demonstrate the new technique of cooling proton and ion beams that may increase the beam luminosity in certain cases, by as much as tenfold. The 112 MHz cavity is designed to generate a 2 MeV, high charge (several nC), low repetition rate (78 kHz) electron beam using a new fundamental power coupler (FPC) design approach. Structural and thermal analysis, using ANSYS were performed to confirm the FPC structural stability and to calculate the deflection due to heat load from RF power generation. This paper provides an overview of the design, structural and thermal analysis, test results, and FPC tuning drive system for the 112 MHz gun.

INTRODUCTION

A 112 MHz superconducting quarter-wave resonator will be used as the injector for CeC PoP experiment under construction at IP2 of RHIC at BNL [1]. Phase I of this experiment is to be completed by the end of RHIC shutdown 2013 and will include the 112 MHz superconducting QWR and the fundamental power coupler that will be discussed in details in this paper. The paper provides an overview of the design, structural and thermal analysis, test results, and FPC tuning drive system for the 112 MHz gun.

112 MHZ FPC DESIGN AND FABRICATION

Design

The FPC is a coaxial structure, which provides tunable RF coupling and presents small interference to the electron beam output [2]. The FPC design couples the RF power into the cavity from the exit beam pipe of the cavity and allows the electron beam to travel through the hollow inner conductor of the FPC. An external linear motion system will be used to adjust the penetration of the coupling tube in order to fine tune the frequency of the cavity as well as to adjust the coupling strength [2]. The FPC was design to meet all the parameters listed in Table 1.

Table 1: Parameters of the Fundamental Power Coupler for 112 MHz QWR SRF gun

RF frequency	112 MHz
Frequency tuning range with FPC	3 kHz
FPC travel range	40 mm
Q_{ext} of FPC, min.	1.25×10^7
Max. RF power loss on the FPC inner conductor	898.6 W
Max. RF power loss on the FPC outer conductor	554.6 W
Available RF power	2 kW

The complete and detailed layout of the 112 MHz QWR and the FPC are shown in Figure 1 and Figure 2.

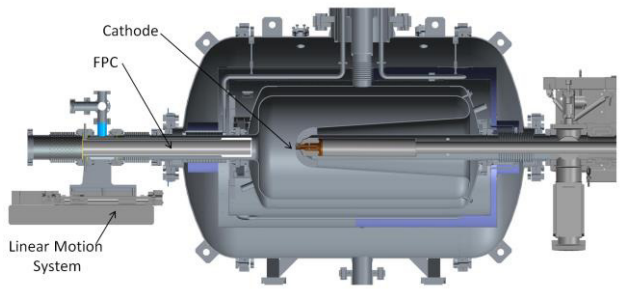


Figure 1: Layout of 112 MHz FPC in the QWR.

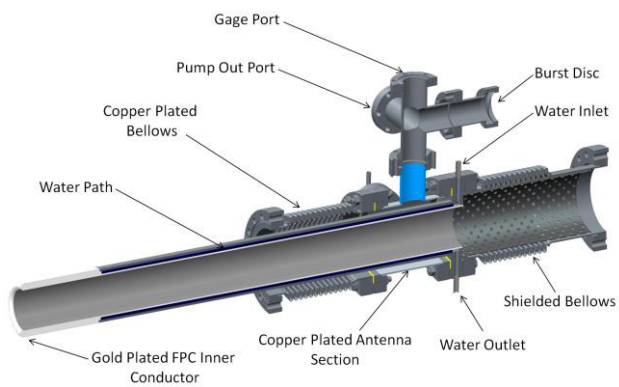


Figure 2: Detailed Layout of 112 MHz FPC.

In order to power the FPC, a BeCu connector was designed. The connector threads into the inner conductor of the FPC and slides inside an air cooled 7/16 UHF UHV cryogenic feedthrough designed by BNL. The FPC will be powered on both sides as shown in Figure 3.

* Work is supported by Brookhaven Science Associates, LLC under contract No. DE-AC02-98CH10886 with the U.S. DOE.
#jcbrutus@bnl.gov

Copyright © 2013 CC-BY-3.0 and by the respective authors

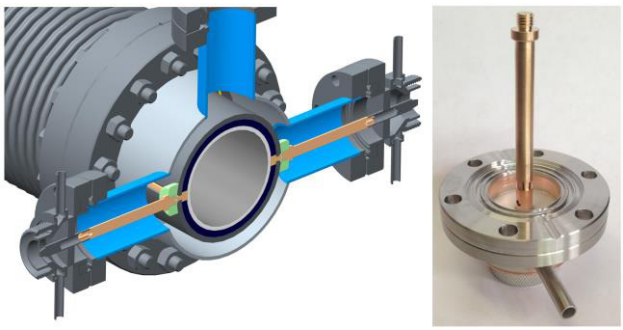


Figure 3: View of the vacuum feedthrough for connection of the coaxial cable to the FPC.

Analysis

One issue with the FPC design was to provide adequate cooling for removing heat due to RF power losses on the surfaces of the inner and outer conductor when the gun is operating. The outer conductor includes the copper plated bellows. Structural and thermal analyses, using ANSYS, were performed to confirm the FPC structural stability and to calculate the deflection and maximum temperature due to heat load from RF power generation. The distribution of RF power dissipated on the FPC inner and outer conductors is shown in Table 2.

Table 2: Distribution of RF power loses on the FPC

RF Power Loses	Value
On inner conductor hollow section	894.3 W
On inner conductor solid section	4.3 W
On bellows of outer conductor	554.6 W
On flange	21.9 W

In order to find out if cooling was needed for the bellows on the outer conductor of the FPC, ANSYS was used to determine the maximum temperature on the overall system. Several heat fluxes were applied on the inner surfaces corresponding to the values in Table 1 and a natural convection by air. A heat transfer coefficient of 15 W/m^{2}K was applied on the outer surfaces. A maximum temperature of 460 K was observed at the depth of the convolution. The result from ANSYS for the natural convection cooling of the outer conduction of the FPC is shown in Figure 4.

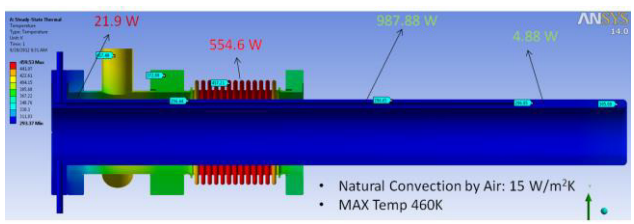


Figure 4: Temperature profile on the overall FPC.

The inner conductor of the FPC will be cooled using a temperature controlled water source. As shown in Figure 1, the inner conductor has a solid and hollow section. The solid section is designed to stiffen the structure and space out the channels from the 4K region of the QWR. The hollow section consists of two water channels, one on the upper half and the other one on the lower half. Both channels are connected towards the solid end of the FPC. The water flows through the upper half first and exits through the lower half of the FPC with a calculated temperature difference of approximately 1 K between inlet and outlet. The cooling system parameters are shown in Table 3.

Table 3: Cooling System Parameters FPC

Parameters	Value
Water volume flow rate, Q	4 GPM
Pressure drop	< 2 PSI
Local heat transfer coefficient, h	3217.4 W/m^{2}K
Inlet-Outlet temperature difference	0.88 K

The ANSYS results shown below in Figures 5, 6, and 7 indicate that the FPC will reach a maximum temperature of 305 K and a maximum deflection of 0.001" [3].

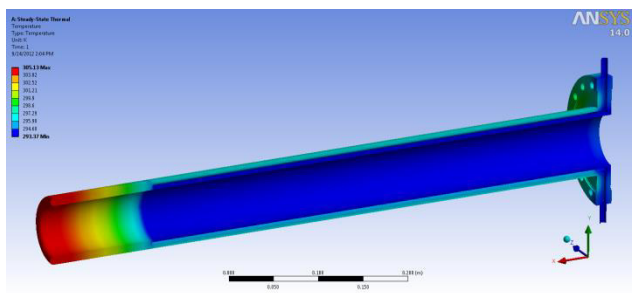


Figure 5: Temperature profile on the FPC inner conductor.

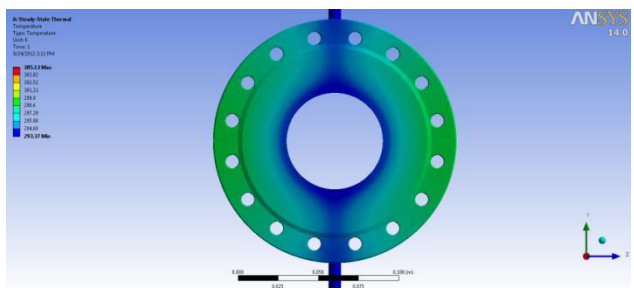


Figure 6: Temperature profile on the FPC water inlet/outlet flange.

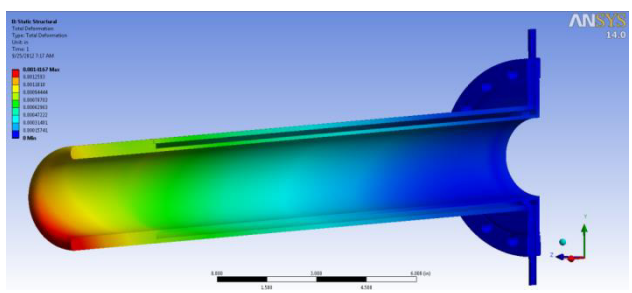


Figure 7: Deflection of FPC under thermal and structural load.

Copyright © 2013 CC-BY-3.0 and by the respective authors

Fabrication

The FPC was designed by BNL and fabricated in collaboration with Stony Brook University. The copper plated and the shielded bellows of the outer conductor of the FPC shown in Figure 2 were designed to provide a 1 inch travel with a low spring constant of 84 lbs/in in order to reduce the moments on the linear motion system. The plated bellows shown in Figure 8 have a minimum of 25 µm thick layer of copper on the inside of the convolutions.

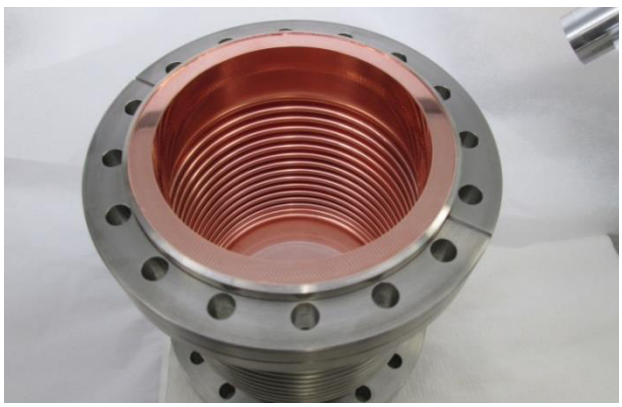


Figure 8: 112 MHz FPC copper plated bellows.

The inner conductor of the FPC was fabricated using 304 stainless steel because of its mechanical properties and for manufacturing purposes. The final assembly was copper plated with a 25 µm thick layer for the RF path, then plated with a 1 µm thick layer of gold to maintain a mirrored surface finish and bring the emissivity to as low as 0.02. This is done in order to reduce heat radiation to the 4 K environment of the 112 MHz superconducting QWR gun and prevent the cooling water from freezing in case of a failure.



Figure 9: 112 MHz FPC gold plated inner conductor.

112 MHZ FPC MOTION SYSTEM

The linear stage motion system for the FPC was designed and fabricated in collaboration between BNL and Ibex Engineering. The design uses a granite base in order to reduce deflection and vibration. The linear stage was successfully tested and met all the requirements listed in Table 4.

Table 4: Parameters of 112 MHz FPC linear stage

Parameters	Value
Travel range	40 mm
Response frequency	10 Hz
Position resolution	500 nm
Positioning accuracy	± 5 µm
Repeatability (no backlash- and hysteresis-free)	< ±500 nm
Straightness over travel range	± 5 mm
Flatness over travel range	± 5 mm
Speed	> 1 mm/s
Acceleration	> 60 mm/s^2
Position readback resolution	< 1 µm
Moment M1 transverse to the direction of travel	250 lbs.in
Moment M2 in the direction of travel	1000 lbs.in

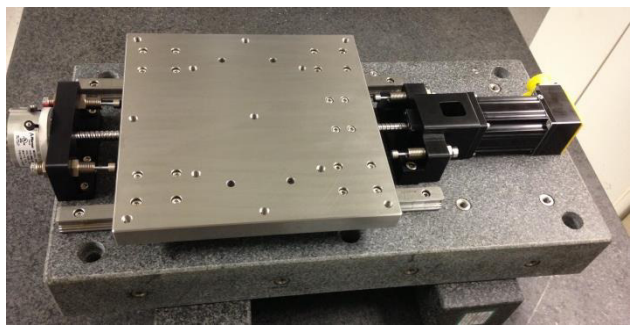


Figure 10: 112 MHz FPC linear motion system.

CONCLUSION

We successfully designed and manufactured all the components of the FPC. Most of the components have been tested individually to ensure that they meet all the requirements. The 112 MHz superconducting QWR gun is scheduled to be tested with the FPC and the cathode stalk during RHIC Run14. A safety interlock system is being designed to blow the cooling water in the FPC to prevent catastrophic failure, with the water freezing, in case of RF power loss.

REFERENCES

[1] V. N. Litvinenko, et al., "Proof-of-Principle Experiment for FEL-Based Coherent Electron Cooling," PAC'2011, p. 2065.

[2] T. Xin, et al., "Design of the Fundamental Power Coupler and Photocathode Inserts for the 112 MHz Superconducting Electron Gun," SRF2011, MOPO014.

[3] ANSYS Multiphysics Finite Element Code, ANSYS, Inc. Canonsburg, PA 15317.

Copyright © 2013 CC-BY-3.0 and by the respective authors

A TEMPERATURE-MAPPING SYSTEM FOR MULTI-CELL SRF ACCELERATING CAVITIES*

M. Ge, G. Hoffstaetter, F. Furuta, E. Smith, M. Liepe, S. Posen, H. Padamsee, D. Hartill, X. Mi,
Cornell University, Ithaca, NY 14850, USA.

Abstract

A Temperature mapping (T-map) system for Superconducting Radio Frequency (SRF) cavities consists of a thermometer array positioned precisely on an exterior cavity wall, capable of detecting small increases in temperature; therefore it is a powerful tool for research on the quality factor (Q_0) of SRF cavities. A new multi-cell T-mapping system has been developed at Cornell University. The system has nearly two thousand thermometers to cover 7-cell SRF cavities for Cornell's ERL project. A 1mK resolution of the temperature increase ΔT is achieved. A 9-cell cavity of TESLA geometry was tested with the T-map system.

INTRODUCTION

The quality factor (Q_0) of Superconducting Radio Frequency (SRF) cavities is a critical topic in the SRF field. High-Q cavities are able to save cryogenic capacities of accelerators. The definition of Q_0 is given by equation (1), where w is the angular frequency of the cavity, U is its stored energy, P_{loss} is the power loss on the cavity surface. The Q_0-value ranks the cavity's efficiency. If we define a geometry factor (G) as function (2), the Q_0 may be written as the ratio of the geometry factor and the surface resistance (R_s).

$$Q_0 = \frac{\omega U}{P_{loss}} = \frac{G}{R_s} \tag{1}$$

$$G = \frac{\omega\mu_0 \int_V \left|\vec{H}\right|^2 dV}{\int_A \left|\vec{H}\right|^2 dA} \tag{2}$$

The geometry factor is a constant determined by cavity geometry shapes, thus the Q_0 is dictated by cavity surface-resistance.

The T-map system, a thermometer array uniformly attached on a cavity exterior surface, is a powerful tool for surface resistance research. It is able to detect tiny heating on cavity wall during feeding RF power into cavity. Hence by the heating map of whole cavity, it is possible to calculate power loss and surface resistance, furthermore to calculate the Q_0-value of the cavity. The Q_0 of a multi-cell SRF cavity measured from RF is derived from the total value of all cells. The relationship between total Q_0 of a 9-cell cavity and Q_0-value of each cell at pi-mode is given by equation (3)

$$\frac{1}{Q_0^{tot}} = \frac{1}{n}\sum_{n=1}^{9} \frac{1}{Q_n^{cell}} \tag{3}$$

*This work has been supported by NSF award PHY-0969959 and DOE award DOE/SC00008431

Here Q_0^{tot} is total Q_0 of a 9-cell cavity, and Q_n^{tot} is Q_0 of cell n. The total Q_0 is unable to reflect which cell has low-Q and degrades the whole cavity. However, T-map can diagnose the Q_0-value of each cell by summing each cell's power loss. Hence T-map gives more information about cavity performance than RF measurement alone.

T-mapping history can be traced back to the 1980s. Cornell University was a pioneer in developing a 1-cell T-map system for 1.5GHz SRF cavity research [1, 2, and 3]. Now Jefferson Lab and Fermilab also have 1-cell or 2-cell T-map systems. These systems are used for fundamental SRF research via single-cell cavities. Therefore the development of a multi-cell T-mapping system is necessary and ultra-important. DESY and Los Alamos have multi-cell T-mapping systems for ILC 9-cell cavities [4, 5]. Those systems are mainly used to detect quench location.

TEMPERATURE-MAPPING SYSTEM DESCRIPTION

This multi-cell T-mapping system has been developed for the Cornell ERL project which requires the Q_0-value of 7-cell cavities to achieve 2×10^{10} at accelerating gradient 16MV/m [6]. For a 1.3GHz SRF cavity, the heating from RF causes on average about a 10mK temperature rise on the exterior wall at 25MV/m in a 2K helium bath [7]. Thus the resolution of this T-map is required to be approximately 1mK.

Thermometers and Boards

The Cornell multi-cell T-map has nearly two thousand thermometers. The temperature sensor is a 100Ω carbon Allen-Bradley resistor (5% 1/8 W). Carbon is a semiconductor, its resistance increases exponentially when temperature drops. Figure 1 (a) shows the schematic of sensor and its picture. APIEZON grease was applied on the varnished side of the thermometers prior to inserting the boards in cages. The sensor is able to detect the temperature rise of the cavity wall with 25% efficiency [3]. Two sets of 3-cell boards and one set of 1-cell boards were used for 7-cell SRF cavity. A 3-cell board has two channels addressed to the sensors for 3-cells. The sensor boards are spaced azimuthally every 15° around the cavity; totally it has 24 boards around the azimuth. Each cell is covered by an 11×24 thermometer array. Figure 1 (b) shows a 3-cell and a 1-cell board. The quantity of thermometers for the whole 7-cell cavity is 1848. Cornell constructed a new test insert for hanging the multi-cell cavity with full T-map. In Figure 1 (c) the left image shows the Cornell multi-cell T-map attached on middle 7-cells of a 1.3GHz 9-cell cavity; the right image is a picture showing several boards removed to expose the cavity. The

Copyright © 2013 CC-BY-3.0 and by the respective authors

insert has a feedthrough on the top-plate for extracting T-mapping cables out of the Dewar. A coupler motor and Ion pump were built on the insert as well, which allows us to adjust the coupler position as well as to keep the cavity under high-vacuum during the RF test. Three well-calibrated Cernox thermometers were attached on the insert for T-map calibration.

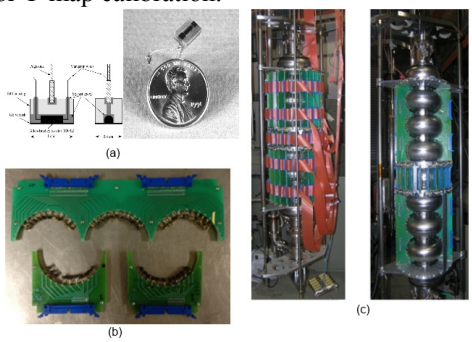


Figure 1: (a) Thermometer schematic, (b) T-map boards, (c) T-map insert.

CRYOGENIC TEST

We tested a 1.3GHz 9-cell cavity which is TESLA shape with the T-mapping system. The cavity was vertically electro-polished about 5μm, followed by high pressure water rinsing and clean assembly in a class 10 clean room. No 120°C baking was applied on the cavity.

Calibration and Sensitivity

A well-calibrated Lakeshore Cernox thermometer is utilized as a temperature reference for the helium bath during cooling down from 4.2K to 1.6K. Figure 2 (a) is a sensor's calibration curve.

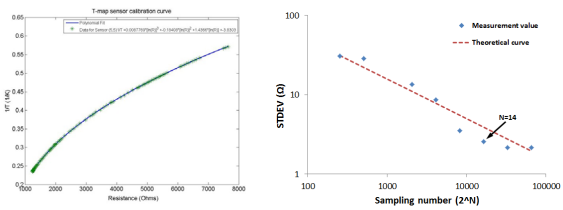


Figure 2 (a): 1/T vs. resistance curve during cooling down, (b) standard deviation vs. sampling number.

A polynomial function was adopted to fit the curve, shown in equation (4).

$$\frac{1}{T} = a_n x^3 + b_n x^2 + c_n x + d_n \qquad (4)$$
$$x = ln(R)$$

Here T is the bath temperature, R is the resistance of the carbon resistor, a_n, b_n, c_n, and d_n are fitting parameters for sensor n. By using fitting curves, it is possible to calculate $\frac{dR}{dT}$ which represents the sensitivity of each T-mapping sensor. An Allen-Bradley resistor value is about 12kΩ at 1.6K, $\frac{dR}{dT}$ is approximately 30Ω/mK; and $\frac{dR}{dT}$ is about 10Ω/mK at 2K.

Noise comes from the environment and the electronic system. Increasing measurement sampling number is an effective way to reduce noise from the electronic system. The PIXI controller can sample the sensor voltages at a 500 KHz rate, and average readings for 2^N samples. Figure 2 (b) shows the standard deviation of resistance decreasing with increasing sampling number. The dash line in the plot is a theoretical curve which is the standard deviation versus $\sqrt{1/2^N}$. The standard deviation is reduced to about 2Ω, when N is set to 14, corresponding to a sampling number of about 16000. We don't choose a higher N value because higher N will significantly extend scan time. The noise from the electronic system is about 200μK in a 2K helium bath; and 67μK in 1.6K helium. The total scan time is about 100s.

Thermal conductivity of grease as well as press-force of sensor against cavity-wall affects T-map noise level as well. Figure 3 is a lateral view of the subtraction between two T-map scans without applying RF field in 2K Helium bath. The total noise of the T-map system is about 1mK which achieved our initial goal.

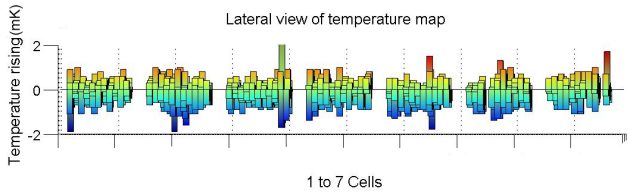
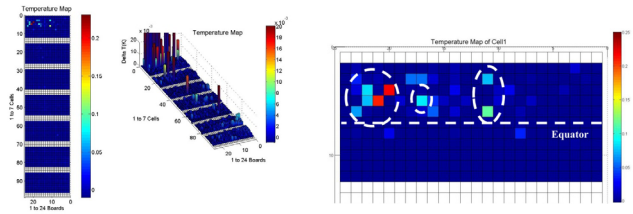


Figure 3: 3-sigma noise level of T-map system. The one sigma noise is only about 0.2mK.

Testing Results of T-map

The 9-cell cavity A9 was tested in a 2K helium bath and quenched at 21MV/m in pi-mode. The T-mapping boards covered the middle 7 cells of the cavity. Temperature-map data was taken at an accelerating gradient very close to quench. Figure 4 (a) depicts the temperature-rise (ΔT) map.



(a) (b)

Figure 4: (a) Map of temperature increase for 7-cells of an ILC cavity, (b) Detail T-map view of the dominantly heated Cell 1.

Most heating-spots were found on the top cell which is the top second cell of the 9-cell cavity. The highest ΔT is about 0.2K.

Figure 5 is the summary of ΔT versus H^2 curves; the axis on the right is the Q_0 of the cavity. Equation (5) depicts the ΔT and H^2 relationship of the sensor n. Here R_{sn} is the surface resistance close to the sensor n, $\vec{H}_n$ is the surface magnetic field at the sensor n, as the T-map sensors only cover the high magnetic-field region of each cell, thus $\vec{H}_n \approx H_{peak}$.

$$\Delta T_n = \frac{1}{2C} R_{s\,n} \vec{H}_n^{\,2} \qquad (5)$$

Copyright © 2013 CC-BY-3.0 and by the respective authors

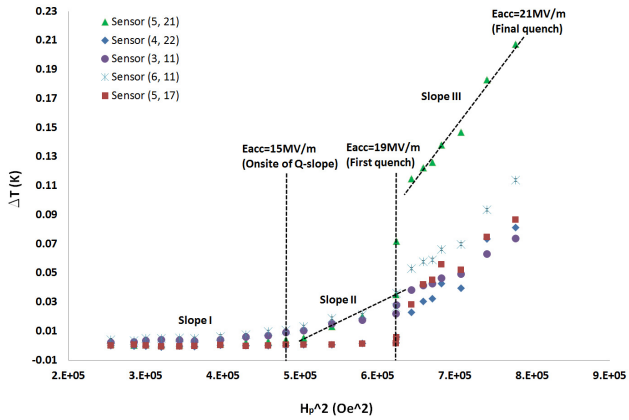


Figure 5: ΔT vs. H^2 curve.

The slopes of ΔT versus H^2 curves indicate R_s at the sensors from equation (5). Three slopes were observed. The slope I started from an acceleration gradient from 0 to 15MV/m. The surface resistance was consisted by BCS resistance and residual resistance. The slope II started at an accelerating gradient (E_{acc}) 15MV/m where the onset of Q-slope is. The surface resistance was increased due to the Q-slope. The heating increased dramatically around 19MV/m at the Multipacting barrier of the TESLA-shape cavity. The Multipacting triggered the first quench and processing of the cavity. After the Multipacting had been processed out, the heating increased with H^2 by the slope III until hard quench (21MV/m). The slope III indicates the surface resistance was increased further by flux trapping after the first quench.

Converting ΔT to Power Loss and Quality Factor

By summing the temperature rising of individual cells, we obtain power loss and quality factor of cavity and each cavity cell, shown in Figure 6 (a) and (b).

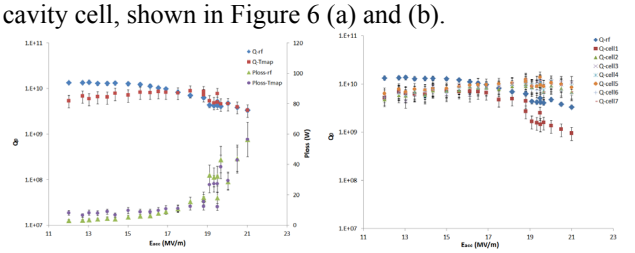


Figure 6 (a): Q_0, P_{loss} comparison between calculated from T-map and measured from RF. (b) The quality factor of individual cells compared to total Q_0.

The measurement curves match the calculated curve when the accelerating gradient is higher than 15MV/m where the heating started. Below 15MV/m, the heating from the cavity is too small to be detected accurately. The results from T-map indicate the measured cell 1 generated the most power loss on the surface, and degraded the total Q_0 starting from 15MV/m. The equation (3) suggests that the total Q_0 of the cavity is limited by the Q-value of the worst cell. The cavity test results also indicate that the Q-slope is possible to be a localized effect.

Surface Resistance Map

A surface resistance map is calculated from the ΔT of each thermometer, which is given by equation (6).

$$R_{s\,n} = \frac{2C\Delta T_n}{H_{peak}^{\ 2}} \qquad (6)$$

Figure 7 shows a surface resistance map when the cavity was at 21MV/m, close to quench.

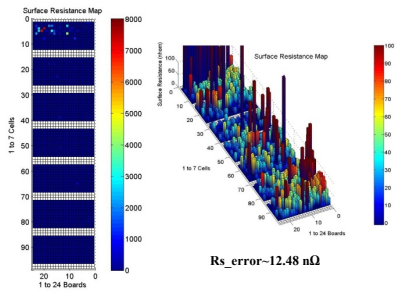


Figure 7: Map of the surface resistance R_s.

The maximum R_s value is close to 8000nΩ, and the average value of all R_s map is 74.26nΩ which agrees with the value (80.84nΩ) calculated from equation (1) by using the geometry factor and Q_0. The error of the surface resistance is about 16.8% calculated from the measurement error of ΔT, accelerating gradient (E_{acc}) and Q-value by uncertainty propagation formulas.

REFERENCES

[1] H. Padamsee, et al., "Field Emission Studies in Superconducting Cavities," PAC'89, Washington D.C., p. 1824 (1989).

[2] P. Kneisel, G. Mueller and C.Reece, "Investigation of the Surface Resistivity of Superconducting Niobium Using Thermometry in Superfluid Helium," 1986 Applied Superconductivity Conf., Baltimore, MD.

[3] J. Knobloch, Ph. D. thesis, CLNS THESIS 97-3(1997). http://www.lns.cornell.edu/public/CESR/SRF/dissertations/knobloch/knobloch.html

[4] Q.S. Shu *et al.*, "An Advanced Rotating T-R Mapping & It's Diagnoses of TESLA 9-Cell Superconducting Cavity," PAC'95, Dallas, TX, p. 1639 (1995).

[5] A. Canabal *et al.*, "Development of a Temperature Mapping system for 1.3-GHz 9-Cell SRF Cavities," PAC'07, Albuquerque, NM, p. 2406 (2007).

[6] M. Liepe *et al.*, "Progress on Superconducting RF Work for the Cornell ERL," IPAC 2012, WEPPC073, (2012).

[7] Y. Xie, "Relationship between Defects Pre-Heating and Defects Size," SRF2009, TUPPO049, p. 334, (2009).

Copyright © 2013 CC-BY-3.0 and by the respective authors

INVESTIGATION OF THE SURFACE RESISTIVITY OF SRF CAVITIES VIA THE HEAT AND SRIMP PROGRAM AS WELL AS THE MULTI-CELL T-MAP SYSTEM*

M. Ge#, F. Furuta, D. Gonnella, G.H. Hoffstaetter, M, Liepe, H. Padamsee,
Cornell University, Ithaca, NY, 14853, USA

Abstract

The thermal feedback model with the linear BCS resistance which were believed not strong enough to explain medium-field Q-slope (MFQS) is still valid. The HEAT and SRIMP program (H&S program) which adopted the SRIMP code for BCS resistance calculation allows inputting full material parameters, hence is able to simulate different cavity cases e.g. baked, unbaked, BCP'd, EP'd, and so on. The results agree with the measurement data from the low-field up to the hot-spots onset field. With the T-map data, it's a clear view that the localized hot-spots occur above MFQS region and caused high-field Q-slope.

INTRODUCTION

The surface resistance of superconductor under RF field is a critical topic, because it determines the Q-value of SRF cavity in accelerating fields. The thermal feedback model with the linear BCS resistance was developed for Medium-Field Q-Slope (MFQS) study [1]. However, the thermal feedback model was believed not strong enough to account for the observed MFQS [1, 2, and 3]. In this work, we explain the thermal feedback model with linear BCS model is still valid for MFQS and the localized hot-spots cause the Q-slope in high fields.

HEAT AND SRIMP PROGRAM

The surface resistance of superconductor under RF field includes two parts, one is BCS resistance (R_{BCS}) and the other is residual resistance (R_0), shown in equation (1). And equation (2) is the simplified R_{BCS} forms.

$$R_s = R_{BCS} + R_0 \quad (1)$$

$$R_{BCS} = A\left(\frac{1}{T}\right) f^2 \exp\left(-\frac{\Delta}{kT}\right) \quad (2)$$

Here, the factor A is a constant which determined by material property such as mean free path (l) *etc.*, Δ is the energy gap, f is the frequency.

The traditional HEAT program [4] uses Pippard approximation [5]:

$$R_{BCS}(T) = (2.78\times10^{-5}\Omega)\frac{\nu^2}{t}\left(\frac{148t}{\nu}\right)\exp\left[-\frac{1.81g(t)}{t}\right] \quad (3)$$

$$t = \frac{T}{T_c}, \quad \nu = \frac{f}{2.86GHz}, \quad g(t) = \left[\cos\left(\frac{\pi t^2}{2}\right)\right]^{1/2} \quad (4)$$

where f is the frequency of the RF field, T is the temperature. However in equation (3) and (4), it doesn't consider the Nb property. Comparison between baked and un-baked cases, the mean free path l is reduced by baking. Hence the factor A in equation (2) is changed and decreases the BCS resistance after baking. But equation (3) and (4) are unable to reflect the changes.

The improved HEAT program, HEAT and SRIMP code (H&S code), uses SRIMP [6, 7] to replace the equation (3) and (4). The SRIMP was written by Jurgen Halbritter for the BCS surface resistance calculation. The method of calculation incorporates the full BCS theory. Five material parameters are required to describe the superconductor:

- The superconducting transition temperature T_c;
- The energy gap (entered as Δ/kT);
- The London penetration depth, λ at T=0;
- The coherence length, ξ at T=0;
- The electron mean free path, l, at 4.2K.

MULTI-CELL T-MAP SYSTEM

The T-map system is known as a powerful tool for surface resistance research. It's able to detect tiny heating on exterior wall on cavities. Cornell University developed a multi-cell T-map system [8].

SURFACE RESISTANCE ANALYSIS

The EP'd and BCP'd Cavity Cases

Figure 1 is the comparison Q vs. E curves between H&S program calculation and RF measurement from 1.7 to 2K. The plot shows the calculation agrees with the measurement results well. The cavity is TELSA single-cell cavity NR1-3. The cavity was EP'd and 120°C baked. During the test, the cavity was FE and quench free.

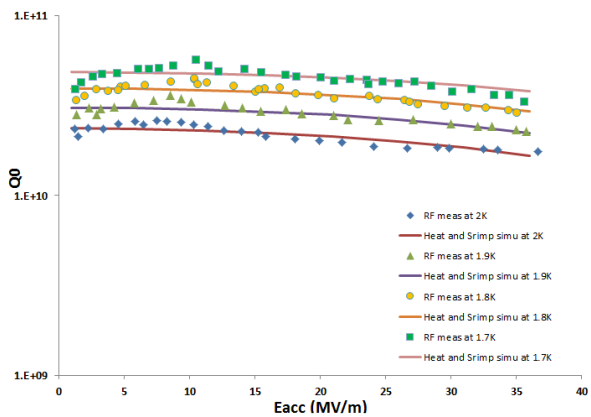


Figure 1: Comparison of H&S calculation and RF measurement at different temperatures for EP'd cavity.

*Work supported by NSF award PHY-0969959 and DOE award DOE/SC00008431
#mg574@cornell.edu

Copyright © 2013 CC-BY-3.0 and by the respective authors

The Q_0 versus Temperature data measured at low accelerating field was fitted by the SRIMP to obtain the material parameters described in previous section. In the fitting, we use surface RRR value to represent electron mean free path [9].

Here we selected the residual resistance, energy gap, and surface RRR as fitting parameters. The cavity was 120°C baked; therefore the surface RRR was reduced to 4.4. Converted the surface RRR to electron mean free path, the value is about 119 Angstrom. The detail of the conversion is discussed in the reference [9].The BCS resistance is minimum when mean free path is around 120 Angstrom [1].

Figure 2 shows the comparison of the BCP'd cavity case. The cavity is the 7-cell cavity ERL 7-4 for Cornell ERL project. The cavity was BCP'd more than 100μm; then the cavity was furnace treated under 650°C vacuum; after light-BCP, the cavity was 120°C baked in furnace followed by HR rinsed; and then the cavity was HPR'd and assembled in class 10 cleanroom.

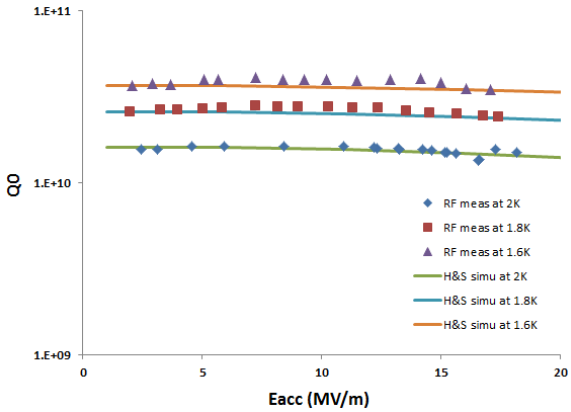


Figure 2: Comparison of H&S calculation and RF measurement at different temperatures for BCP'd cavity.

The SRIMP code fitting from the Q_0 versus temperature data indicates that the R_0 is about 5.6 $n\Omega$; the energy gap is 1.825; and the surface RRR is about 4.56. Using these parameters as the input of H&S program, the result agrees with the RF measurement very well at different temperatures.

The Baked and Unbaked Cavity Cases

In EP'd and BCP'd cavity cases, it suggests that 120°C baking plays an important role in reducing the BCS resistance to minimum. The H&S program is able to reflect the baking effect. In the Figure 3, there is the comparison between the cavity NR1-2 baked and un-baked cases. The NR1-2 cavity was EP'd about 30μm, and was tests before and after 120°C baking. Table 1 shows the material parameters comparison fitted by SRIMP. The surface RRR was reduced from 38 to 6.9, and energy gap was increased from 1.86 to 1.956. The changing of the parameters reduced BCS resistance from 13.78$n\Omega$ to 6.02$n\Omega$ at the accelerating gradient equalling 2MV/m; however the residual resistance was increased from 4.5 $n\Omega$ to 10.16 $n\Omega$; the total surface resistance was reduced from 18.27 $n\Omega$ to 16.18 $n\Omega$ at 2MV/m, which is shown in Table 2.

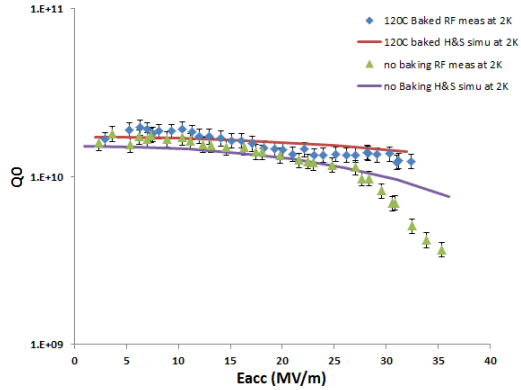


Figure 3: Comparison of H&S calculation and RF measurement between the baked and the un-baked cavity.

Table 1: Material Parameters Comparison of NR1-2

Parameters	Baked	Un-baked
T_c (K)	9.2	9.2
Energy gap	1.959	1.86
λ(A)	360	360
ξ(A)	640	640
Surface RRR	6.9	38
Residual resistance (R_0) ($n\Omega$)	10.16	4.5

Table 2: Surface Resistance Comparison of NR1-2

Parameters	Baked	Un-baked
BCS resistance at 2MV/m ($n\Omega$)	6.02	13.78
Residual resistance ($n\Omega$)	10.16	4.5
Surface resistance at 2MV/m ($n\Omega$)	16.18	18.27
Q_0 at 2MV/m	1.72×10^{10}	1.52×10^{10}

In the un-baked cavity case, the H&S program's calculation agrees with the measurement data up to 25MV/m above which the obvious discrepancy occurs. The cause of the discrepancy is the localized hot-spots based on the T-map data which will be shown in next section.

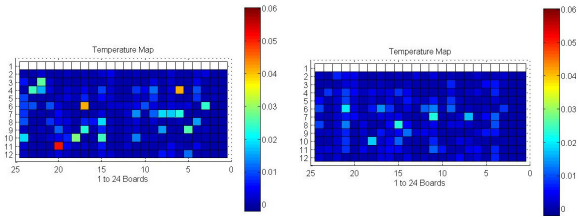
The Localized Hot-spots and High-field Q-slope

From the cavity NR1-2 measurement data (the un-baked case), we found that all the hot-spots present above the 25MV/m where the onset of the Q-slope is.

Figure 4 (a) is the temperature map of the cavity NR1-2 at 32MV/m, and (b) is the temperature map after the

Copyright © 2013 CC-BY-3.0 and by the respective authors

baking. By the contrast, we clearly see the hot-spots were suppressed by the baking, and the Q-value was recovered. Before the baking, the cavity was no quench; and the performance limited by RF power source. After the baking, the cavity limited by the hard quench at 32MV/m.



(a) Before the baking, (b) After the baking

Figure 4: Temperature map comparison of NR1-2 before and after the baking at 32MV/m.

The sensor in 11th row and 20th column shows the highest temperature increase in the Figure 4 (a), and the value is closed to 0.11K. The Figure 5 shows the heating versus accelerating gradient (E_{acc}) of the sensors (11, 20), (4, 6), (6, 17), (3, 22). The comparison curve from the sensor (3, 3) was selected because the sensor located in non-heating region.

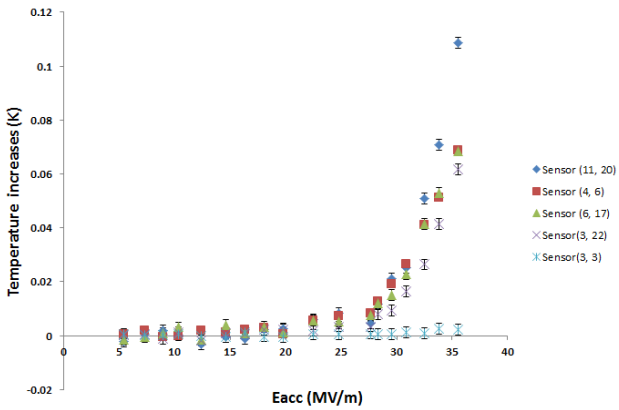


Figure 5: The temperature increases vs. accelerating gradient.

The H&S program is able to calculate the surface resistance of the hot-spots based on the T-map data. The program treats the residual resistance within one sensor coverage area as uniformed; in other words, the program utilizes the average residual resistance value within one sensor. To obtain the power loss on one hot-spot, the program gradually increases residual resistance thus increase the heating on exterior wall. The calculation ceases when the heating on exterior wall matches the T-map data. The power loss in none hot-spots region is mainly caused by BCS heating. Summing the power loss on each sensor region, the cavity Q_0 is obtained. The Figure 6 depicts the calculated Q_0 of NR1-2 compared with the RF measurement data. The scattering of the calculated result depends on the quality of the T-map data, e.g. the quantity of the broken sensors which misses the hot-spots detection.

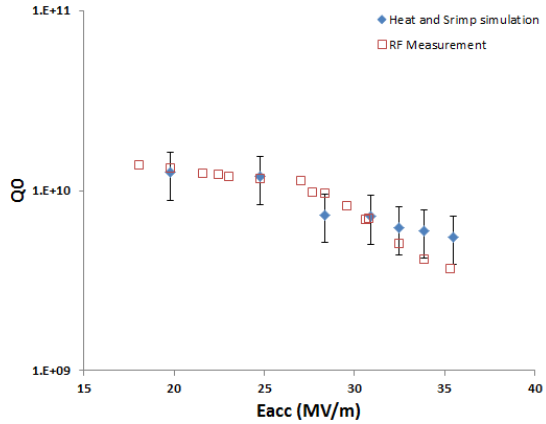


Figure 6: The Power loss on the Hot-spots comparison between H&S program and RF measurement.

CONCLUSION

The thermal feedback model with linear BCS resistance is valid for the medium-field Q-slope analysis. The H&S program's calculation indicates that the residual resistance is field-independent below the hot-spots onset field (25MV/m for NR1-2), and the residual resistance became field-dependent after the onset.

The distribution of the residual resistance isn't homogeneous. The high residual resistance region formed the hot-spots which degraded the Q-value in high-field.

The H&S program's calculations match up the measurement data perfectly. In this paper we checked the BCP and EP case as well as baked and un-baked case. It can be used to estimate the best performance of SRF cavities.

REFERENCES

[1] H. Padamsee, *RF Superconductivity, Vol. II Science, Technology, and Applications*, WILE-VCH, 2009.

[2] A. Gurevich, "Multiscale Mechanisms of SRF Breakdown", Proceedings of the 12th Workshop on RF superconductivity, Ithaca, (2005), p. 156.

[3] A. Gurevich, "Multiscale Mechanisms of SRF Breakdown", Physica C 441, 38 (2006).

[4] J. Vines, Y. Xie, H. Padamsee, "Systematic Trends for the Medium Field Q-Slope", Proceedings of SRF 2007, 2007, TUP27, p.178 Beijing, China.

[5] H. Padamsee. Calculations for breakdown induced by "large defects" in superconducting niobium cavities. CERN/EF/RF82-5, 1982.

[6] J. Halbritter, Zeitschrift für Physik 238 (1970) 466.

[7] J. Halbritter, "Fortran Program for the Computation of the Surface Impedance of Superconductors", Internal Notes KFZ Karlsruhe 3/70-6. June 1970.

[8] M. Ge, a temperature-mapping system for multi-cell SRF accelerating cavities.

[9] B. Bonin, Materials for superconducting cavities. (cds.cern.ch/record/399568/files/p191.pdf)

Copyright © 2013 CC-BY-3.0 and by the respective authors

CORNELL'S MAIN LINAC CRYO-MODULE PROTOTYPE

Ralf Eichhorn#, Yun He, Georg H. Hoffstaetter, Matthias Liepe, Tim O'Connel, Peter Quigley, Daniel Sabol, James Sears, Eric Smith, Vadim Veshcherevich
Cornell Laboratory for Accelerator-based Science and Education (CLASSE), Cornell University, Ithaca, NY 14853, USA

Abstract

In preparation for building an energy-recovery linac (ERL) based synchrotron-light facility at Cornell University which can provide greatly improved X-ray beams due to the high electron-beam quality that is available from a linac, a phase 1 R&D program was launched, addressing critical challenges in the design. One of them being a full linac cryo-module, housing 6 superconducting cavities operated at 1.8 K in continuous wave mode, 7 HOM absorbers and 1 magnet/ BPM section. The final design will be presented and a report on the fabrication status that started in late 2012 will be given.

INTRODUCTION

An NSF funded R&D program for the 5-GeV superconducting energy-recovery linac (ERL) [1] at Cornell University includes the design, build and thoroughly test all aspects of a complete cryomodule.

The almost 10 m long module (see Fig. 1) houses 6 superconducting cavities, operated in CW mode at 1.8 K. These 7-cells, 1.3 GHz cavities with an envisaged Q of $2*10^{10}$ will provide an energy gain of 16 MV/m. Each cavity is fed by a 5 kW power coupler. The Higher Order Modes (HOMs) absorbers are placed next to each cavity to obtain an efficient damping for the high beam current and short bunch operation. The series linac module will have a quadrupole/ steerer section which is omitted in the prototype as it technically does not present a challenge.

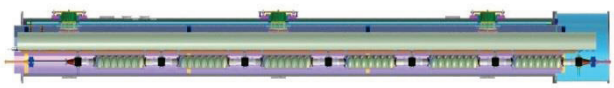


Figure 1: Cryomodule prototype.

COLD MASS SUPPORT SYSTEM

The beam-line string is suspended under the Helium Gas Return Pipe (HGRP) which acts as the beam-line backbone and is supported by three support posts to the vacuum vessel (see Fig. 2). The support system provides precision alignment and thermal insulation of the beamline string.

The HGRP is made of a Grade 2 Titanium pipe, with an outer diameter of 280 mm. With a 1 ton weight force of the beamline string, the maximum vertical displacement of the HGRP is estimated to be 0.1 mm and the natural frequency would be 88 Hz, indicating that a 3-posts support system is well suited to ensure an acceptable vertical displacement and vibration characteristics.

#r.eichhorn@cornell.edu

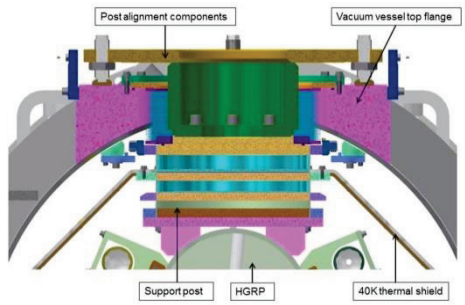


Figure 2: Cold mass support system.

The post has a same design as those used in the TTF cryomodule, which is an assembly of a low thermal conduction composite material pipe (G10 fiberglass pipe) and four stages of shrink-fit metal discs and rings. The two stainless steel disc/ring sets are connected respectively to the room temperature and to the 2 K cold mass environments. The two aluminum disc/ring sets provide thermal intercepts at 40 K and 5 K, with the 40 K set also providing structural support to the 40 K thermal shield. The heat load through conduction of each post (see Fig. 3) is estimated to be 8.58W to 40K, 0.54W to 5K and 0.05 W to 1.8K, respectively.

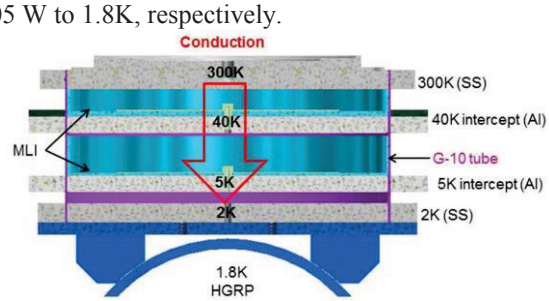


Figure 3: Support post.

The vacuum vessel is 965.2 mm in diameter, with a vessel cylinder made of carbon steel (A516 GR70) and stainless steel flanges that use O-ring seals. For the prototype the interior of the carbon steel portion will be painted with a low vapor pressure vacuum compatible epoxy, while the exterior will be painted with a marine paint product.

CYOGENIC PIPING SYSTEM

The cavities will be cooled by liquid helium sub-cooled to 1.8 K. Due to the fact that the half linac will be 350 m long, a big aperture (280 mm diameter) for the HGRP was chosen to provide the low flow impedance needed without excessive pressure drop. Connected to the HGRP at a single point in each module is a 100 mm diameter 2-phase helium manifold, show in Fig. 4. The purpose of this large 2-phase tube is to allow adequate surface area

Copyright © 2013 CC-BY-3.0 and by the respective authors

for evaporation and a sufficiently large cross-section for gas flow through it to the HGRP to avoid generation of waves on the liquid surface which could result in pressure fluctuations affecting frequency tuning of the cavities [2].

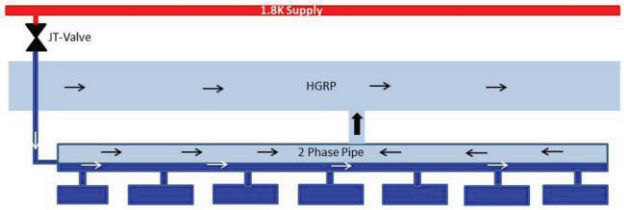


Figure 4: 1.8K flowchart.

A 5 K-6.5 K loop is used to cool the intercept all transitions to warmer temperatures in order to assure a minimal heat transfer to the 1.8 K system. A 40-80 K loop provides cooling for the coupler intercepts, cools the thermal radiation shield of the module and removes the heat generated in the Higher Order Mode (HOM) absorbers.

As show in Fig. 5, six lines of 50mm diameter run through the entire half-linac. In each module, local manifolds of smaller diameters deliver the cryogens via four valves (1.8 K, pre-cool, 4.5 K, and 40 K) which manage the flow division amongst the modules. The location and stiffness of piping supports were considered in the design to make sure the resonant frequencies are higher than 60 Hz (see Fig. 6 for details).

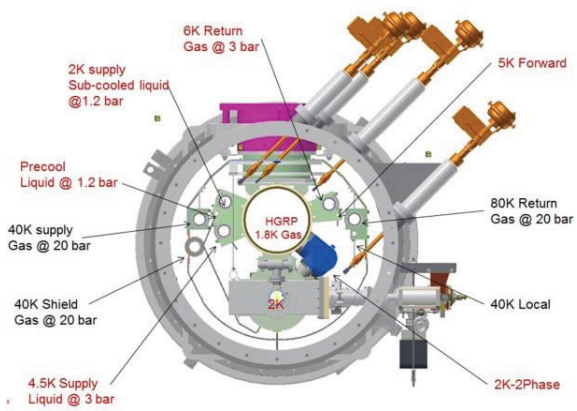


Figure 5: Piping system inside the cryomodule.

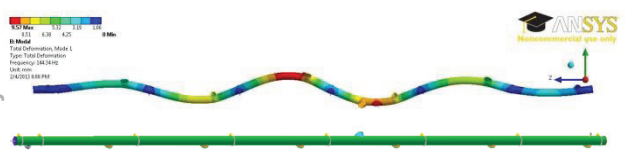


Figure 6: Natural frequency of the 1st mode of 2-phase pipe and the model showing the supports.

THERMAL SHIELD AND COOL DOWN

The radiation and convection heat loads are reduced by operating the shield at 40K and wrapping it with 30 layer multilayer insulation (MLI) blankets, in a vacuum environment. The magnetic shield, which is made of 0.5 mm Mu-metal sheets, will be mounted to the exterior of the 40K thermal shield to screen the Earth's field and any other stray magnetic field from the cavities.

The thermal shield is made from aluminum AL 1100-H14 sheets, with the upper section being thicker to support the weight. The sheets as shown in Fig. 7 are connected with fasteners as a rigid assembly with a good thermal contact. Reinforcement rings are attached to increase the mechanical stability.

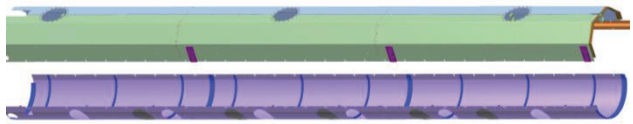


Figure 7: Upper and lower sections of the thermal shield.

To avoid excessive stress due to asymmetric cooling during the cool-down process, some slots (Fig. 8) are machined at the upper-lower section to unload the force.

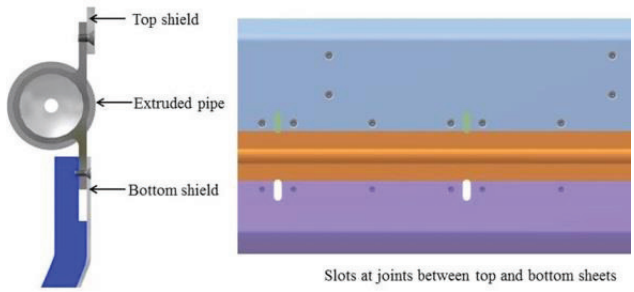


Figure 8: Joints between top and bottom sheets.

The thermal shield will be cooled by the 40 K delivery line which is connected to one side. As a result, the cool-down process will be asymmetric requiring a more detailed analysis.

Static heat loads includes conduction through the support post and radiation from room temperature vacuum vessel. With 30 MLI blankets covered on the shield, the radiation heat fluxes from room temperature are assumed to be 1.25 W/m^2. In the extruded pipe for the 40 K helium gas delivery, a convective heat transfer coefficient of 0.11 W/cm^2-K was estimated. The simulated results indicated that with a slow cooling rate of 4 K/hour, the temperature gradient reaches a maximum of 15 K on the entire shield, occurring 20 hours after the start of the cool down. Results are given in Fig. 9). Once

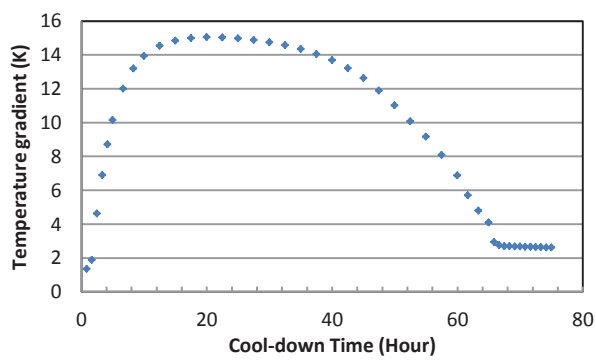
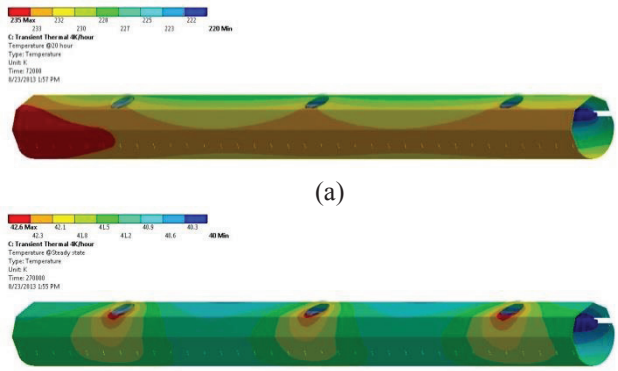


Figure 9: Temperature gradient on 40 K shield as a function of time during cool-down.

Copyright © 2013 CC-BY-3.0 and by the respective authors

fully cooled down, the steady state maximum temperature gradient will be only 2.6 K. At the worst scenario when the temperature gradient over the shield reaches the maximum, the thermal shield will be bent with a maximum relative deformation of 4.6 mm (Fig. 10), and the maximum stress will be about 60 MPa occurring at the corner of the slots.



(a)

(b)

Figure 10: Temperature distribution on the shield (a) at 20 hours after cool-down started and (b) at steady state.

ALIGNMENT AND ASSEMBLING

The HGRP defines the reference for the precision alignment of the beam-line string. Relative vertical alignment is ensured by precision machining on the interfacing surfaces of the supports, with a single machine tool setup at the final stage after all welding is done and a vibration stress relief is performed. The transverse and longitudinal alignment is obtained by the alignment pins on the support plates. The alignment key or a flexible cavity support allows the beam-line components to slide longitudinally relative to the HGRP during thermal cycling.

To accommodate the HGRP thermal contraction at cold relative to the vacuum vessel, the two side posts are slidable over the top flanges while the central post is locked in position. Details of the design are shown in Fig. 11. The central position of the side posts are pre-shifted at room temperature and will be concentric to the vacuum vessel flange at cold.

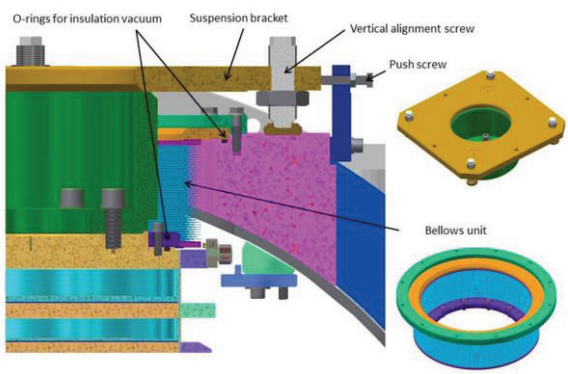


Figure 11: Post alignment components.

The prototype design foresees that it could be a spare module in the series linac that the final welding or connection for the cryogenic pipes will be made in-situ. In addition, the design also allows easy dismounting the whole assembly for replacing some components. The assembly sequence is that the beam-line string will be assembled in the clean room, and then attached to the HGRP. Once the cold mass is assembled, it will be rolled into the vacuum vessel on its rail system (see Fig 12).

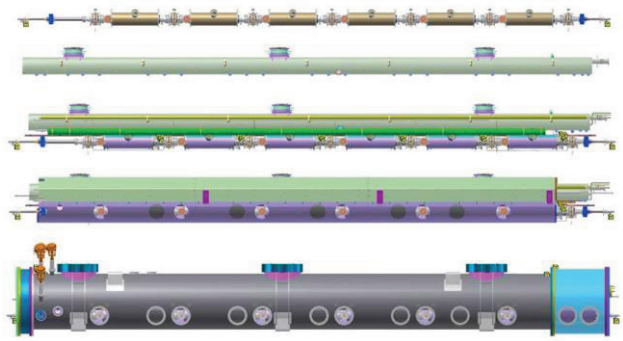


Figure 12: Prototype assembly sequence.

STATUS AND OUTLOOK

The major components of the cryomodule prototype are under fabrication. We anticipate starting the assembly process in November 2013, and have it completed and ready for test by the end of 2014.

ACKNOWLEDGMENTS

This design and construction work involves many people at CLASSE, which the authors gratefully acknowledge. Furthermore, we would like to thank Tom Peterson, Serge Claudet and John Weisend II for their help and their review during the design phase. This work has been supported by NSF awards PHY-0969959 and DMR-0807731 and DOE award DOE/SC00008431.

REFERENCES

[1] G. H. Hoffstaetter, S. Gruner, M. Tigner et al., *Cornell ERL Project Definition Design Report* (June 2013); http://erl.chess.cornell.edu/PDDR

[2] Eric Smith et al., Proc. of IPAC 12, MOPPP026, p. 619 (2012).

Copyright © 2013 CC-BY-3.0 and by the respective authors

THEORETICAL DESCRIPTION OF SIS MULTILAYER FILMS FOR SRF CAVITIES*

Sam Posen[1†], Gianluigi Catelani[2], Matthias U. Liepe[1], James P. Sethna[3], and Mark K. Transtrum[4]
[1]Cornell Laboratory for Accelerator-Based Sciences and Education, Ithaca, NY, USA
[2]Forschungszentrum Jülich Peter Grünberg Institut (PGI-2), Jülich, Germany
[3]LASSP, Physics Department, Clark Hall, Cornell University, Ithaca, NY, USA
[4] Department of Bioinformatics and Computational Biology,
University of Texas M. D. Anderson Cancer Center, Houston, Texas, USA

Abstract

The SIS structure—a thin superconducting film on a bulk superconductor separated by a thin insulating film—was propsed as a method to protect alternative SRF materials from flux penetration by enhancing the first critical field B_{c1}. In this work, we calculate the gibbs free energy of a vortex in a superconductor, and we show that an isolated thin film can enhance B_{c1}, but when it is placed in a SIS structure, due to the gradient in field across the film, we show that in fact B_{c1} = 0. We argue that the SIS structure is not beneficial for SRF cavities, but it may be useful in DC and low frequency applications. However, due to recent experiments showing low-surface-resistance performance above B_{c1} in cavities made of superconductors with small coherence lengths, we argue that enhancement of B_{c1} is not necessary, and that bulk films of alternative materials show great promise.

INTRODUCTION

SRF researchers have begun a significant effort to develop alternative materials to niobium, superconductors that could offer higher accelerating gradients E_{acc} and/or lower surface resistances R_s at a given temperature. There are several promising candidates, but most of them suffer from two potential liabilities. First, they have relatively small first critical fields B_{c1}, the magnetic field at which it becomes energetically favorable for a vortex to be inside the superconductor. Second, they have relatively small coherence lengths ξ. Vortex penetration is prevented at fields significantly above B_{c1} by an energy barrier, but surface defects on the order of ξ can reduce this barrier. These materials have ξ on the order of a few nm, compared to tens of nm for niobium, making even very small defects a potential vulnerability. As a result, there has been significant concern in the SRF community over whether vortex dissipation will occur if these materials are exposed to fields that bring them into the metastable state between B_{c1} and B_{sh}, the superheating field at which the energy barrier is reduced to zero for an ideal surface.

A. Gurevich proposed [1] a method to avoid the potentially vulnerable metastable state altogether. Pointing to the enhancement of parallel B_{c1} in films with thickness d smaller than the penetration depth λ, he suggested coating a niobium cavity with alternating layers of insulator (I) and thin film superconductor (S). With such a SIS structure, he proposed it might be possible to take advantage of the high B_{sh} and low R_s of the alternative superconductors used in the thin films without the disadvantage of their small B_{c1}. SRF researchers have been putting significant effort into developing SIS multilayers, and they are producing excellent work [2, 3, 4, 5, 6, 7, 8].

CALCULATING BC1

Tinkham [9] defines B_{c1} as the field at which "the Gibbs free energy [has] the same value whether the first vortex is in or out of the sample." For a SIS, the sample under consideration should be the full structure [10]. Stejic et al. [11] calculate the Gibbs free energy of a vortex in a thin film superconductor immersed in a parallel external field. They show that B_{c1} of the film is enhanced relative to the bulk value, according to

$$B_{c1} = \frac{2\phi_0}{\pi d^2}\left(\ln\frac{d}{\xi} + \gamma\right) \quad (1)$$

where ϕ_0 is the flux quantum, $\gamma = -0.07$ and $d << \lambda$. However, if a SIS structure is used to screen Nb SRF cavities, the geometry is quite different than that of an isolated film. How does Stejic's expression for B_{c1} change when the film is screening a bulk superconductor? In this case, it will have a B-field gradient across it, which will affect the free energy. We can use the same formalism as Stejic to calculate the Gibbs free energy for this case, and use it to find B_{c1} and B_{sh}[12].

Consider a single layer SIS structure, as shown in Fig. 1. A strongly type II superconducting film of thickness d, penetration depth λ_f, and coherence length ξ_f is separated from a bulk superconductor with with penetration depth λ_b by an insulating film of thickness δ. The superconducting film is screening the bulk from a parallel magnetic field with amplitude B_0. The screened field inside the bulk region has amplitude B_i. In our geometry, the x-axis is perpendicular to the film, pointing into it, with origin at the interface with the exterior. The z-axis is aligned with the magnetic field.

* Work supported by DOE award number DE-SC0002329 and in part by the EU under REA grant agreement CIG-618258.
† sep93@cornell.edu

Copyright © 2013 CC-BY-3.0 and by the respective authors

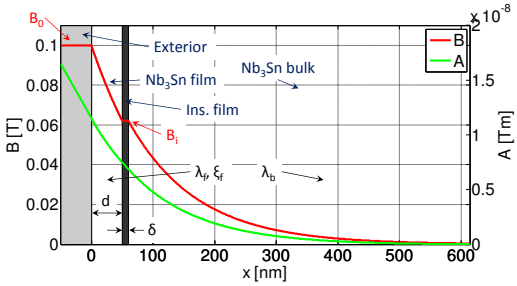


Figure 1: Geometry of the structure under consideration. The amplitudes of the magnetic field and the vector potential are plotted as a function of distance into the structure.

Stejic shows that the Gibbs free energy of a vortex in a superconductor can be determined from the value of two magnetic fields evaluated at the vortex location r_0: the Meissner-screened external field B_M and the field generated by the vortex in the film B_V.

$$\mathcal{G} = \frac{\phi_0}{\mu_0}\left(B_V(r_0)/2 + B_M(r_0)\right) \tag{2}$$

B_M can be found by minimizing the free energy in the structure when no vortex is present. This procedure gives:

$$B_M = \frac{B_0 + B_i}{2}\frac{\cosh\frac{x}{\lambda_f}}{\cosh\frac{d}{2\lambda_f}} - \frac{B_0 - B_i}{2}\frac{\sinh\frac{x}{\lambda_f}}{\sinh\frac{d}{2\lambda_f}} \tag{3}$$

where B_i is given by

$$B_i = B_0\left[\frac{\delta+\lambda_b}{\lambda_f}\sinh\frac{d}{\lambda_f} + \cosh\frac{d}{\lambda_f}\right]^{-1} \tag{4}$$

Stejic gives a relatively simple expression for B_V for the case when $d << \lambda$, but this would restrict us to very thin films. To study the full range of thicknesses, we turn to the more general expression from Shmidt [13] (this expression assumes $r_0 = (x_0, 0)$), which agrees with Stejic's expression for very small films:

$$B_V = \frac{2\phi_0}{\lambda^2 d}\sum_{n=1}^{\infty}\int_{-\infty}^{\infty}\frac{dk}{2\pi}e^{iky}\frac{\sin(\pi n x/d)\sin(\pi n x_0/d)}{k^2 + (\pi n x_0/d)^2 + 1/\lambda^2} \tag{5}$$

We can check our procedure by choosing $d >> \lambda$, such that the film behaves as a bulk supercondcutor. This calculation is shown in the top plot of Fig. 2. $B = B_{c1}$ when the free energy outside the superconductor is equal to that when a vortex is deep in the bulk. $B = B_{sh}$ when the barrier to flux penetration is reduced to zero (this plot is very similar to the one from Bean and Livingston's 1963 paper [14]).

We can study a single thin film (not in a SIS structure) by setting $B_i = 0$ in Eq. 3. This calculation is shown in the center plot of Fig. 2 (the free energy outside the film is

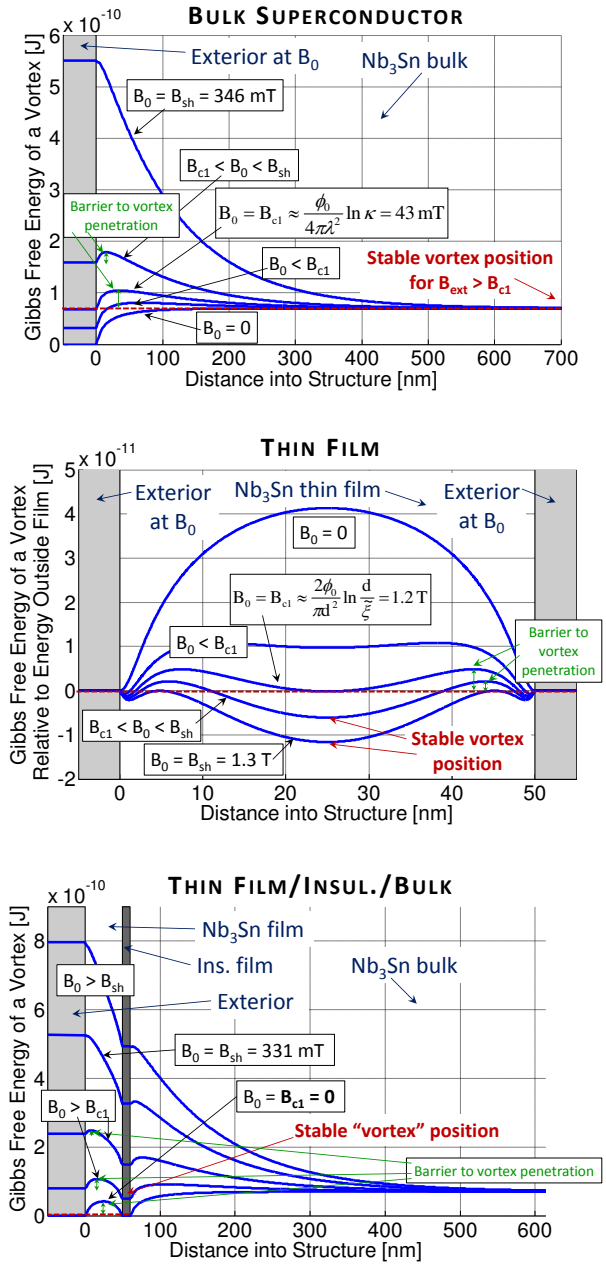


Figure 2: Gibbs free energy at various fields for a single vortex in (top) bulk Nb_3Sn, (center) a 50 nm Nb_3Sn thin film, and (bottom) a SIS structure with a 50 nm Nb_3Sn film on a Nb_3Sn bulk. B_{c1} is the smallest field at which there is a position inside the structure where the free energy for a vortex is smaller than the value outside. B_{sh} is the field at which the energy barrier to vortex penetration disappears. The top and center plots show the B_{c1} enhancement for a thin film compared to a bulk. The bottom plot shows that for a SIS structure $B_{c1} = 0$. The expression for the thin film B_{c1} is not valid for the SIS structure because it assumes that the first stable vortex position will be at the center of the film. However, for the SIS structure, the first stable vortex position occurs on the side of the film adjacent to the insulating layer.

Copyright © 2013 CC-BY-3.0 and by the respective authors

subracted from each of the plots for clarity). In this case, there is no bulk, so the first location at which the free energy drops below the external value at high fields is in the center of the film. This would be the stable position for a single vortex above B_{c1}. Both B_{c1} and B_{sh} are much higher for the film than the bulk.

Finally, we plot the free energy of vortex in a single SIS structure in the bottom plot of Fig. 2. In contrast to the previous case, only one side of the thin film is exposed to the external magnetic field. The field at the other side is smaller due to screening by film. Since $B_V = 0$ at the edges of the film, Eq. 2 shows that the free energy in the insulating layer is lower than the free energy outside. The film provides screening at any finite B_0 below the second critical field, so for $B_0 > 0$, the energetically favorable configuration is for flux to be trapped in the insulating layer. As we explain below, this implies that in practice for the SIS structure, B_{c1} is zero.

Why is Eq. 1 describing the enhancement of B_{c1} in a lone thin film not applicable for the SIS structure? This expression assumes that the first stable vortex position will occur in the center of the film. It predicts when the free energy at the center of the film will dip below the value of the free energy in the exterior. However, for the SIS structure, the free energy at the insulator side of the film will dip below the exterior value at fields much smaller than this.

DISCUSSION AND CONCLUSIONS

In this paper, we have shown that contrary to suggestions that SIS structures enhance B_{c1}, in fact they reduce it to zero. In [15], it is also shown that the B_{sh} of an SIS structure is only marginally larger than the bulk value and only for a small parameter space, and that using a multilayer only decreases B_{sh} of the film. In addition, [15] shows that SIS structures exhibit unmanageable levels of heating above B_{sh} at high frequencies. Therefore, it seems that SIS structures are not beneficial for SRF applications. However, they may be useful in DC and low frequency applications, where it should be possible to set up a gradient in the phase of the order parameter in the thin films, allowing them to screen very large fields.

Based on the results of this study, the authors of this paper recommend that SRF researchers developing alternative materials concentrate their efforts on bulk films. Bulk films are quite simple to fabricate compared to SIS films, but they offer a similar ideal SRF performance. And although we have shown that it is not possible to augment B_{c1} with SIS structures, there is still great promise for alternative materials. Because of recent experiments showing that low-surface-resistance operation above B_{c1} is possible with cavities made from short coherence lengths superconductors [16] [17], we now know that the potential of bulk films has not yet been realized.

REFERENCES

[1] A. Gurevich, App. Phys. Lett. 88, 012511 (2006).

[2] C. Antoine, Phys. Rev. ST-AB 13, 12 (2010).

[3] T. Tajima et al., AIP Conf. Proc. 1435, 297 (2012).

[4] D. Beringer et al., IEEE Trans. App. Superc. 23, 3 (2013).

[5] A.-M. Valente-Feliciano et al., Proc. of SRF2011, THPO074, (2011).

[6] X. Xi, Supercond. Sci. Technol. 22 (2009) 043001.

[7] T. Proslier et al., WEIOC03, SRF2013.

[8] D. Oates et al., (Presented at the Thin Films SRF Workshop, Newport News, USA, 2012).

[9] M. Tinkham, *Introduction to Superconductivity* (New York: Dover, 1996).

[10] This definition is chosen because if vortices move from the external region across the superconductor to become trapped flux in the insulating region, a very large amount of heating will occur. In other words, above B_{c1} as we have defined it, the film is in a metastable state, and only an energy barrier prevents strongly dissipative flux penetration.

[11] G. Stejic et al., Phys. Rev. B 49 (1994) 1274.

[12] These calculations use the London model, valid only for strongly type II materials. It neglects non-linearity, and likely overestimates B_{sh}.

[13] V. Shmidt and G. Mkrtchyan, Soviet Physics Uspekhi 17, (1974) 170.

[14] C. Bean and J. Livingston, Phys. Rev. Lett. 12 (1964).

[15] S. Posen and M. Liepe, WEIOC04, SRF2013.

[16] S. Posen and M. Liepe, TUP087, SRF2013.

[17] D. Gonnella and M. Liepe, TUP027, SRF2013.

Copyright © 2013 CC-BY-3.0 and by the respective authors

ACHIEVING HIGH ACCURACY IN CORNELL'S ERL CAVITY PRODUCTION

R. Eichhorn#, B. Bullock, B. Clasby, J. Kaufman, J. Sears, V. Shemelin,
Cornell Laboratory for Accelerator-Based Sciences and Education, Cornell University,
Ithaca, NY 14853-5001, USA
B. Kilpatrick, Kutztown University of Pennsylvania
T. Kuerzeder, TU Darmstadt, Institut fuer Kernphysik, D-64291 Darmstadt, Germany

Abstract

The phase 1 R&D program launched in preparation to building a 5 GeV Energy Recovery Linac (ERL) at Cornell, a full main linac cryomodule is currently built, housing six 7-cell cavities. In order to control the beam break-up limit, the shape of the cavity was highly optimized and stringent tolerances on the cavity production were targeted. We will report on the details of the cavity production, the accuracy of the cups forming the individual cells, the trimming procedure for the dumbbells, the cavity tuning and final accuracy of the cavity concerning field flatness, resonant frequency and overall length within this small series production.

INTRODUCTION

Six Cornell ERL 7-cell cavities will be connected in each cryomodule in the full LINAC. Between each cavity there are bellows and HOM absorbers. Therefore a tight tolerance of +/- 0.5mm must be applied to the length of each cavity (see Table 1). Unfortunately, due to space restrictions in Cornell's electron-beam welder, the beam tubes must be welded to the cavity before the final equator weld, which does not allow the cavity to be trimmed to its final length. Therefore, the cavity length must be controlled through other means.

Table 1: Length and Frequency Tolerances

Length (mm)	1160	+/- 1
Frequency (MHz)	1298.985	+/- 0.100

The first series production of three unstiffened ERL cavities at Cornell was completed some time ago. Each of the cavities did not meet the length or frequency tolerance. The results of the production can be seen in (Table 2). Each cavity was long, as well as low in frequency. Adjusting the frequency through the use of tuning served only to lengthen the cavities even further. In an effort to avoid a situation such as this in the second production series of three stiffened cavities, the previous production steps were analysed and a new strategy was formed.

#r.eichhorn@cornell.edu

Table 2: Length and Frequency of Production Cavities

Pre-Tuning

	Length (mm)	Frequency (MHz)
ERL7-002	1161	1298.46
ERL7-003	1161.5	1298.459
ERL7-004	1160.7	1298.498

Post-Tuning

	Length (mm)	Frequency (MHz)
ERL7-002	1165.9	1297.462
ERL7-003	1163.9	1297.504
ERL7-004	1162.1	1297.541

RF AND MECHANICAL TOLERANCES AND GRADIENTS

The half-cell contour was designed using FEM to calculate the correct resonant frequency at 1.8 K under vacuum. The room temperature frequency at STP is then extrapolated from this calculation.

The half-cell contour, when combined with the end-groups, drives the overall cavity length. However, several manufacturing and processing steps can have an effect on either length, frequency, or both. For example, etching the cavity will drive the frequency of the cavity down, but has no consequence on the overall length. However, field flatness tuning can be used to adjust the frequency of the cavity while simultaneously changing the overall length of the cavity.

It is important to know how each process will affect both the frequency and length of a cavity. To do so, each process' "gradient" must be known. For example, the tuning gradient is 430 kHz/mm. This means tuning the cavity will change its frequency by 430 kHz for every on millimetre. Other gradients are shown in Table 3.

The trimming gradient is, perhaps, the most salient variable during production. This gradient was calculated

Table 3: Various Manufacturing Gradients

Dumbbell Trimming	5	kHz/µm
Etching	10	kHz/µm
Tuning	430	kHz/mm

Copyright © 2013 CC-BY-3.0 and by the respective authors

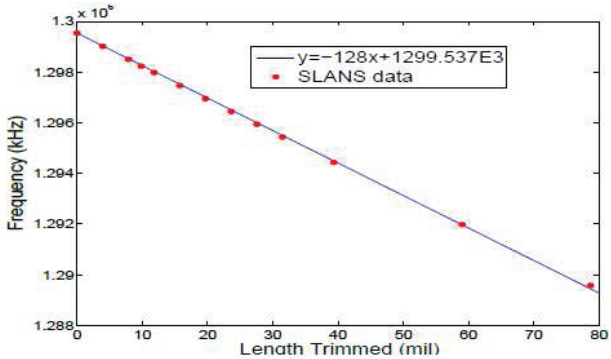


Figure 1: Calculated trimming gradient using the SLANS Code.

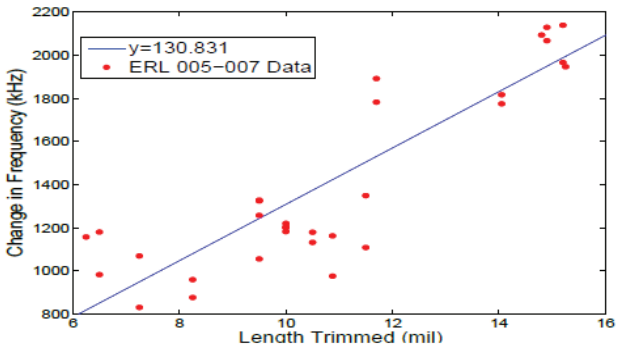


Figure 2: Measured trimming gradient using the newly designed dumbbell apparatus.

using SLANS and was found to be very linear (Fig. 1). Experimental trims of various dumbbells at various lengths confirmed this value (Fig. 2). The experimental trimming gradient is approximately 5.2 kHz/μm. This is within 1.5% of the theoretical value, giving good agreement between theory and experiment. The good agreement is partially due to the improved design for the RF measurement of the dumbbells which now ensures that the dumbbell does not deform under the load (see below).

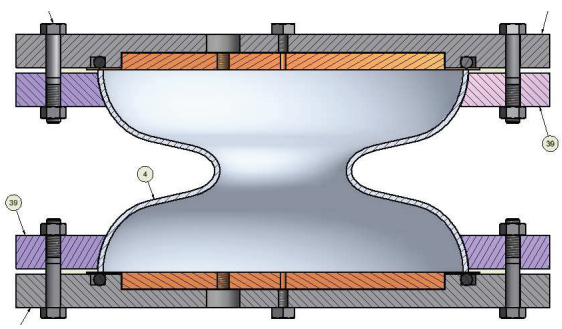


Figure 3: Improved dumbbell apparatus.

ROOT CAUSE OF FREQUENCY AND LENGTH DISCREPANCY

Before attempting to develop a protocol for frequency and length control during production, an effort to find the root cause of the discrepancy between the target cavity frequency and the manufactured cavity frequency was made. After many tests, it was determined that the fixture used to measure the resonant frequency of dumbbells reported an incorrect result. The original fixture, based on the JLab design [1,2], ensures adequate RF contact by pressing the dumbbell between two copper plates using a power screw. The middle of the dumbbell is unsupported. This can lead to a deformation of the dumbbell and subsequent shift in resonant frequency. To combat this problem, a new fixture was designed and constructed.

The revamped RF measurement fixture design was based off of the DESY design used for tesla cavities [3]. Figure 3 shows the new apparatus as built. Two aluminium plates are placed on the ends of the dumbbell. Inside these plates are copper RF contact plates. Aluminium plates are placed on the outer contour of the half-cells of each dumbbell. These plates are bolted to the equator plates for a good RF contact.

The middle plates in this fixture serve to brace the half-cells of the dumbbell so that adequate force may be applied to obtain a sufficient quality factor for measurement, while avoiding deformation of the half-cells.

LENGTH AND FREQUENCY CONTROL DURING THE SECOND SERIES PRODUCTION

During the second series of stiffened cavity production, the following quality control steps were applied:

- Coordinate measurement (CMM) of all half-cells in both untrimmed and trimmed states.
- CMM of untrimmed welded dumbbells.
- Frequency measurement of all dumbbells in the untrimmed state.
- CMM and RF measurement of all dumbbells after trimming.

Steps 1 & 2 were performed to verify all half-cell contours were within acceptable limits. Steps 3 & 4 were used to derive the cavities length and frequency.

To insure the cavity being produced would fall within both the frequency and length tolerances, the following algorithm was used:

$$\Delta L = d_{Trim} + d_{Tune} \ ,$$

$$\Delta F = d_{Trim} \times \Delta_{Trim} + d_{Tune} \times \Delta_{Tune} \ ,$$

where, d_{Trim} and d_{Tune} are the change in length due to trimming the dumbbells and tune the cavity, respectively. Δ_{Trim} and Δ_{Tune} are the trimming gradient and tuning gradient, respectively. Using these two equations, it is possible to find a solution that will yield the correct cavity length after frequency and length after trimming and tuning.

Copyright © 2013 CC-BY-3.0 and by the respective authors

Table 4: Dumbbell Length and Frequency (untrimmed, upper table and trimmed, lower table)

Dumbbell	A	B	Frequency (MHz) A	Frequency (MHz) B	fpi (mean) (MHz)	Length (mm)
CC	79	83	1296.815	1296.782	1296.800	115.443
CC	86	98	1296.686	1296.864	1296.777	115.900
CC	78	81	1296.661	1296.706	1296.685	115.938
CC	97	101	1296.763	1296.852	1296.809	115.900
CC	104	108	1296.647	1296.924	1296.788	115.653
CC	111	113	1296.818	1296.738	1296.780	115.741

Dumbbell	A	B	Frequency (MHz) A	Frequency (MHz) B	fpi (mean) (MHz)	Length (mm)
CC	79	83	1298.635	1298.635	1298.635	115.443
CC	86	98	1298.635	1298.635	1298.635	115.900
CC	78	81	1298.635	1298.635	1298.635	115.938
CC	97	101	1298.635	1298.635	1298.635	115.900
CC	104	108	1298.635	1298.635	1298.635	115.653
CC	111	113	1298.635	1298.635	1298.635	115.741

SECOND SERIES PRODUCTION OF STIFFENED CAVITIES

Six dumbbells were selected for a prototype fabrication in the second series of cavity production (ERL7-005). These dumbbells are listed, along with their pre- and post-trimmed lengths in Table 4. (Note: weld shrinkage has been accounted for in the overall length calculation.) At the target frequency of 1298.985 MHz, each these dumbbells would be shorter than the target dumbbells length, adding up to a cavity that was too short, but at the right frequency. Figure 4 shows the variance in both frequency and length of the six selected dumbbells before and after trimming. The pre-trim dumbbells have some variance in both length and frequency, but this is to be expected, as no frequency control protocols have been applied yet. The post-trim dumbbells, however, are very close in frequency relative to one another, while varying in length by approximately 0.5 mm.

The dumbbells' target frequency was changed to 1298.635 MHz in an effort to correct the lack of length at the correct frequency. By leaving an extra 0.7 mm per half-cell on each dumbbell after trimming, the resonant frequency of the cavity would be too low by 350 kHz, but the length would only be -+1.1 mm. It is assumed that, tuning the cavity by 350 kHz to the correct pi-mode frequency would lengthen the cavity by approximately 0.8mm, bring the finished cavity to the tolerable length, and correct frequency. (Note: The target length has been changed from 1160 mm to 1159 mm for this production series.)

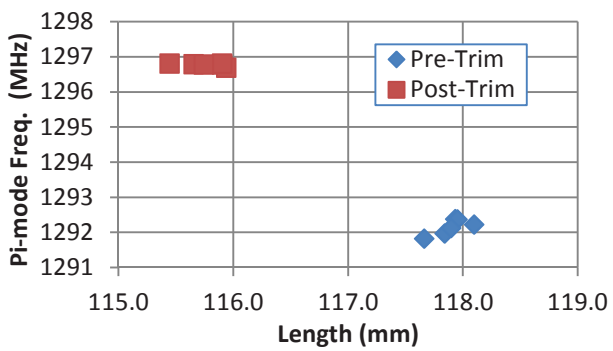


Figure 4: Variance of dumbbell frequency before and after trimming.

CONCLUSION

Cavity ERL7-005 has just recently come off of the production line. ERL7-005's length is 1157.1mm and its' pi-mode frequency is 1298.259 MHz with 79% field flatness. This results differs from the predicted above. ERL7-005 is approximately 1.1mm too short in length (1157.1mm overall) and 400 kHz (1298.259 MHz) too low in frequency. The cause of this is still under investigation.

REFERENCES

[1] F. Marhauser, JLab SRF Cavity fabrication errors, consequences and lessons learned. JLab-TN-10-021, August 2010

[2] V. Shemelin, "Frequency Control in the Cornell-ERL Main-LINAC Cavity Production", Proc. of the 2013 Int. Conf. on Part. Acc., Shanghai, China (2013).

[3] G. Kreps, et. al. "Half-Cell and Dumb-Bell Frequency Testing for the Correction of the TESLA Cavity Length", Proc. of the 1999 Workshop on SRF, Santa Fee, USA (1999).

Copyright © 2013 CC-BY-3.0 and by the respective authors

STUDIES OF THE SUPERCONDUCTING TRAVELLING WAVE CAVITY FOR HIGH GRADIENT LINAC*

Pavel Avrakhov#, Roman Kostin, Alexei Kanareykin (Euclid TechLabs, LLC, Solon, Ohio), Nikolay Solyak, Vyacheslav P. Yakovlev (Fermilab, Batavia)

Abstract

Use of a travelling wave (TW) accelerating structure with a small phase advance per cell instead of standing wave may provide a significant increase of accelerating gradient in a superconducting linear accelerator. The TW section achieves an accelerating gradient 1.2-1.4 larger than TESLA-shaped standing wave cavities for the same surface electric and magnetic fields [1]. Recent tests of an L-band single-cell cavity with a waveguide feedback [2] demonstrated an accelerating gradient comparable to the gradient in a single-cell ILC-type cavity from the same manufacturer. This article presents the next stage of the 3-cell TW resonance ring development which will be tested in the travelling wave regime. The main simulation results of the microphonics and Lorentz Force Detuning (LFD) are also considered.

INTRODUCTION

The primary advantage of a superconducting travelling wave accelerating (STWA) structure is an increased accelerating gradient up to a factor 1.24 for the same surface magnetic and electric field ratios E_{peak}/E_{acc} and B_{peak}/E_{acc} as for re-entrant [3] standing wave (SW) ILC [4] cavity. However, the TW regime for a high gradient linac requires too high level of RF power flux in the accelerating structure. Typical pulse power for L-band TW linac is a few hundred MW which is 10^3 times more than feeding power for superconducting SW cavities. Concept of the traveling wave resonator with a superconducting TW structure allows to keep pulse power on a reasonable low level

Figure 1 presents the first developed and tested 1.3 GHz prototype of a travelling wave SC resonator which consists of a single-cell cavity and a waveguide (WG) feedback [2]. The 1-cell model has the same shape as a regular full-sized cavity, which helped to understand the problems with mechanical manufacturing, assembly, and welding of this geometry as well as the surface processing issues.

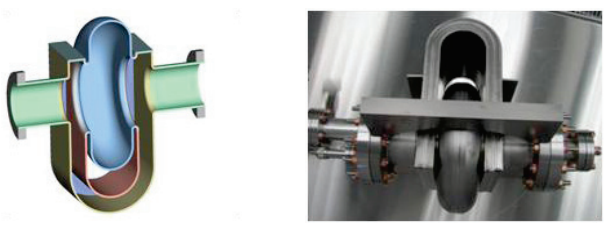


Figure 1: The single-cell model of a travelling wave cavity with waveguide loop.

*Work supported by US Department of Energy
p.avrakhov@euclidtechlabs.com

Two single cell resonators were manufactured at Advanced Energy System, Inc. (AES) and processed in Argonne and Fermi National Labs. Despite the fact that the STWR processing was without electropolishing, high gradient tests showed that the surface electric and magnetic fields reached the same values as 31 MV/m of TESLA-shaped cavity with no field emission. There were problems with the waveguide processing such as high pressure rinsing. But these problems did not lead to quenching in the waveguide because the surface electric and magnetic field amplitudes in the feedback loop were 2-3 times less than in the accelerating cavity. It should be noted the 1-cell STWR model could be tested only in SW regime.

The next step in SC TW cavity studies will be developing and manufacturing a multicell cavity and testing it in the travelling wave regime.

A NEW 3-CELL SC TW RESONATOR DESIGN STUDIES

According to plan, a new 3-cell TW cavity design (schematically depicted in Figure 2) was developed [5] and now is prepared for fabrication. In spite of the fact that the 3-cell structure has only one regular cell (in the middle of the cavity), it retains the same field distribution as for the full-sized 1 meter, 15-cell pattern.

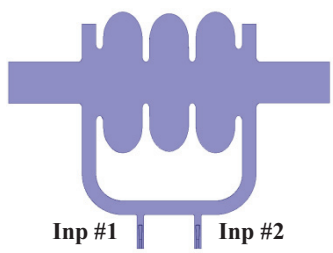


Figure 2: Traveling wave resonator with 3-cell TWaccelerating structure and two coaxial couplers.

As a standard for SC accelerating structure research it is testing on vertical test stand (VTS). Low level RF source of about 200-300 W at VTS requires the use of superconducting cavities with a high loaded quality factor Q_{load} of about 10^8. Well known problems for the SC high Q_{load} resonators are microphonics and Lorentz force detuning at the high gradient testing. But the TW structure detuning has specific feature when compared with the SW cavity - the degradation of the travelling wave regime. Unfortunately, TW operation cannot be restored only by frequency tuning as in the superconducting SW structure. Figure 3 illustrates

Copyright © 2013 CC-BY-3.0 and by the respective authors

forward and backward waves in the 3-cell superconducting travelling wave resonator (STWR) with 2.8 mm niobium walls deformed by external pressure. It is evident that a ±0.1 mbar pressure jump completely ruins the travelling wave regime in the non-reinforced STWR.

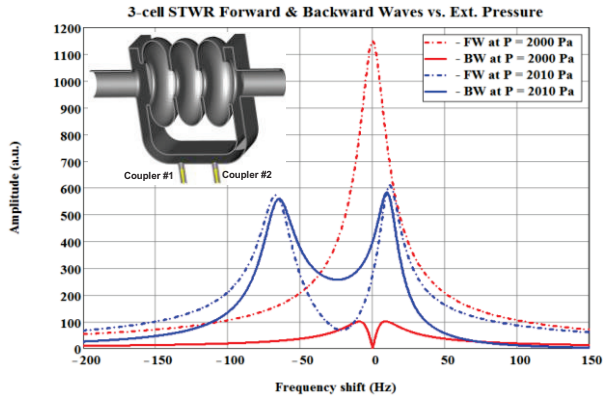


Figure 3: Microphonics detuning of the perfectly matched 3-cell superconducting travelling wave resonator with 2.8 mm niobium walls (pressure jump 10 Pa from 20 mbar to 20.1 mbar).

There are many ways to reinforce a low profile 160mm × 20mm rectangular WG, the most pressure-sensitive part of the STWR, but those involve other technical requirements for SC TW ring like the thermal conductivity of the WG wall and the capability for precise tuning. It imposes restrictions on the wall thickness and the WG loop shape. For instance, a WG loop with walls, more than 4 mm thick, could be overheated in CW regime. The most appropriate design, in our view, it is a waveguide with stiffening ribs on wide, or on both wide and narrow sides. Niobium ribs are a well-known way to reinforce large superconducting cavities such as 325 MHz SSR1, or low frequency 650 MHz 5-cell cavity for Project-X [6].

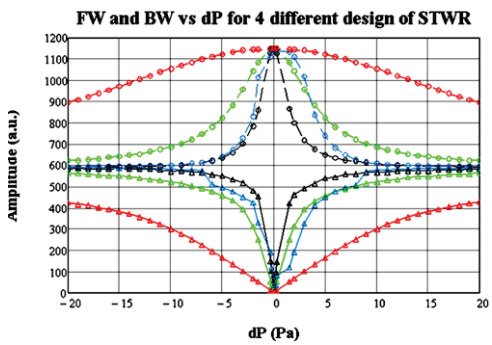


Figure 4: Amplitudes of forward (dash) and backward (solid) waves vs external pressure for 4 different designs of the 3-cell STWR: black curves - the non-reinforced model (all walls 2.8mm); blue curves – the model with cavity ribs only (thickness 4mm); green curves – the model with waveguide ribs only (4mm×10mm and 20mm between ribs); red curves - the most stiffened model with the cavity and waveguide ribs.

Figure 4 presents our efforts to reinforce the 3-cell STWR model to reduce the influence of microphonics. Stiffening ribs on the WG loop and on the cavity part dramatically improves the TW regime. Measured through the critical parameter $d\varphi/dP$, where $d\varphi$ is the phase shift caused by a pressure deviation dP, the last design has as a 57 and 12.6 times reduction (compared with the base design) of the microphonics sensitivity for waveguide loop and cavity part respectively.

It should be noted that the presented above results were obtained for fixed amplitudes and phases of the input signals: $P_{inp1} = P_{inp2}$, and a 90° phase difference between inputs. However, these parameters are fully controllable, and can considerably expand the acceptable external pressure variation. Figure 5 shows an example with suppression of microphonics detuning in the most stiffened STWR model only by adjustments of the inputs amplitude and phase. In this case the backward wave at a new operation frequency was completely suppressed, but the forward wave amplitude was kept almost the same (~94%). A 12% increase in power is required to obtain the nominal value of the forward wave amplitude.

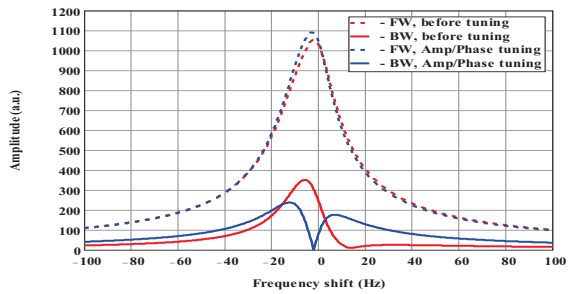


Figure 5: Forward and backward waves (FW & BW) under a 10 Pa external pressure variation in the TW resonator with stiffening ribs on the WG and the cavity parts: red curves – no tuning P_{inp1}/P_{inp2} = 1/1, $\Delta\varphi_{between_inp1\&inp2}$ = 90°; blue curves – after tuning P_{inp1}/P_{inp2} = 1.52/0.48, $\Delta\varphi_{between\ inp1\&inp2}$ = 96.3°

High gradient tests of the 1-cell STWR model have shown strong Lorentz forces in SW mode. Figure 6 demonstrates a comparison between the experimental results and the ANSYS simulation of the LFD in the real 1-cell cavity TW1AES002 (see Figure 1). 3-cell model simulations give similar cavity detuning behaviour.

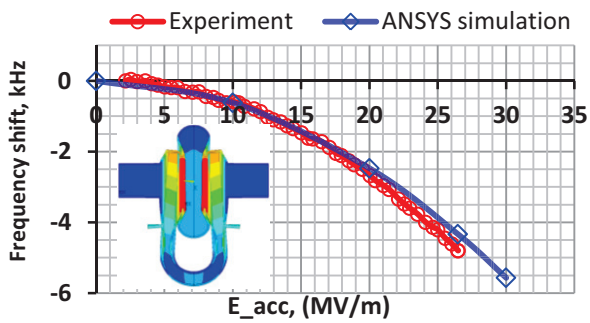


Figure 6: Lorentz force detuning data for 1-cell STWR cavity TW1AES002: experiment and simulation.

Copyright © 2013 CC-BY-3.0 and by the respective authors

The next series of graphs in Figure 7 illustrate simulations of a fine tuning procedure under strong LFD (E_{acc} = 31 MV/m, ring circulating power 631 MW) for the stiffened 3-cell STWR design. The frequency shift for this 3-cell model was -774 Hz and the TW regime was completely destroyed by LFD (Fig. 7-b).

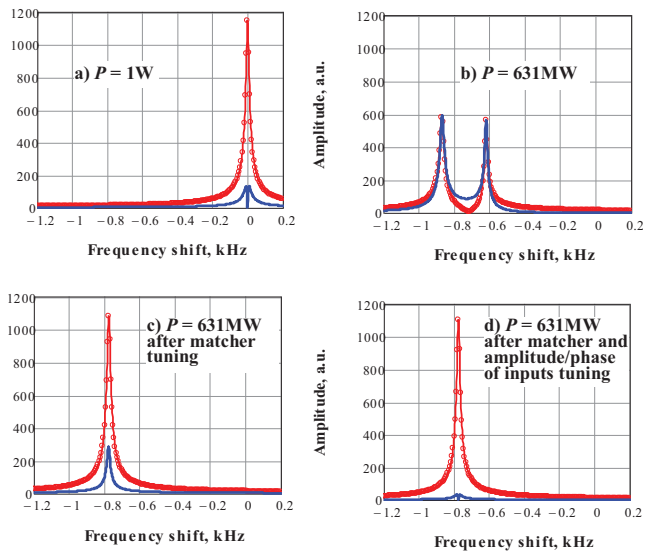


Figure 7: Tuning of the stiffened 3-cell STWR model after strong LFD: a) perfectly matched STWR before LFD; b) strong LFD under circulating power 631 MW; c) tuning by waveguide matcher deformation (+0.61 μm); d) the next stage of tuning is two inputs signal adjusting ($P_{inp1}/P_{inp2} \approx 1.245/0.755$, $\Delta\varphi_{between_inp1\&inp2} = 115°$, TW mode frequency shift is Δf_{TW} = -774.4 Hz)

This example of a strong LFD (about thirty STWR bandwidth) shows two needed stages of tuning – walls shape deformation by a special device named "matcher" (see in Figure 8) and more precise tuning by the redistribution of feeding power in the RF inputs. The first stage is stronger and might adjust both the TW mode and the STWR frequency. The input amplitude and phase control cannot change the cavity frequency and has a narrower acceptable range for detuned parameters. But according to our simulations (see Fig. 5) the fine tuning of RF inputs signals could be enough to withstand microphonics detuning in the stiffened STWR.

NEW 3-CELL DESIGN OF THE SUPERCONDUCTING TW CAVITY

The present design of the 3-cell STWR based on the obtained simulation results matched with the Fermilab VTS parameters. As SW superconducting accelerating structures the TW cavity has stiffening rings on accelerating cells and, in addition, stiffening ribs on the WG loop (see Figure 8). A new element for a VTS tested prototype will be waveguide matcher which will be used to maintain TW mode in the STWR. This will be achieved through one lever construction with two stepper motors and a movable pushing element. The first stepper motor (not seen in Fig. 8) is for WG shape deformations, which push or pull the pushing element. The second stepper motor is for moving the pushing element along the feedback waveguide in a specially designed cage. These stepper motors can provide up to a 10 nm displacement because of their gear ratios of up to 10^5 and their 1 mm shaft thread. Necessary matcher requirements obtained through the 3-cell model simulation are range and minimal step for shape deformation ±90μm / 20nm, and the longitudinal position ±4mm / 0.5μm, respectively.

There are five sleeves with conflate flanges for mounting pick-up antennas: three on the WG bend for calibration and TW directivity measurements, and two on the WG loop bottom side for power feeding.

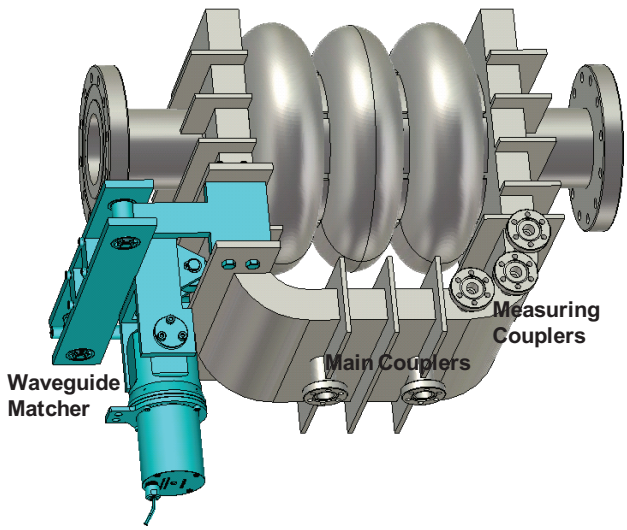


Figure 8: The 3-cell STWR assembly.

CONCLUSION

The results obtained in the STWR model simulation gave an understanding of the way to build a new 3-cell TW cavity design. Power limitation, strong microphonics, and Lorentz force detuning lead to reinforced niobium cavity, and a new tuning device in the new 3-cell design. Methods to create and support the travelling wave regime in this structure were discussed.

REFERENCES

[1] http://tesla.desy.de/new_pages/TDR_CD/start.html
[2] G. Wu et al, THPD048, Proceedings of IPAC'10, Kyoto, Japan.
[3] V.D. Shemelin, PAC 2005, p. 37481.
[4] International Linear Collider Reference Design Report, February 2007.
[5] P. Avrakhov et al, Proceedings of PAC'11, TUP066, p. 940, 2011.
[6] Project X: Accelerator Reference Design, Fermilab-TM-2557, June 2013

Copyright © 2013 CC-BY-3.0 and by the respective authors

STUDY ON PARTICULATE RETENTION ON POLISHED NIOBIUM SURFACES AFTER BCP ETCHING*

I. Malloch#, C. Compton, L. Popielarski, Facility for Rare Isotope Beams (FRIB), Michigan State University, East Lansing, MI 48824, USA

Abstract

Niobium surface defects and inclusions can be introduced during the manufacturing processes used in the production of SRF cavities. Bulk removal methods (sanding, polishing, etc...) are frequently utilized to remove or smooth away these defects on the surface of the niobium metal. It is hypothesized that these mechanical removal methods are capable of trapping performance-degrading particulates, which are then exposed during subsequent chemical processing, potentially contaminating the cavity prior to RF testing. This paper summarizes results of a series of surface roughness and etching experiments performed to determine the relationship between the extent of polishing and trapped particulate, and to determine a method for mitigating this particulate contamination through BCP etching. The relationship between these experiments and RF cavity performance will be explored as well.

INTRODUCTION

The construction of the Facility for Rare Isotope Beams (FRIB) driver linac will require more than 350 niobium superconducting radio frequency (SRF) cavities. Four types of cavities will be used in the linac: 80.5 MHz β = 0.041 and β = 0.085 quarter-wave resonators, and 322 MHz β = 0.29 and β = 0.53 half wave resonators. Each of these cavities must be fabricated with utmost precision to ensure proper functionality of the cavities during RF testing and during the operation of the completed accelerator. Of the many critical aspects of these RF cavities, the surface finish of the niobium exposed to RF fields is paramount to the proper functionality of these cavities during testing. Unfortunately, despite the best of intentions and the most well-defined procedures and quality assurance protocols, issues can arise that compromise these niobium surfaces. Weld spatter deposited on the niobium during electron-beam welding of cavity components, foreign debris and inclusions imbedded in the niobium during sheet rolling or part stamping, and gouges or scratches occurring due to mishandling or machining errors can all impact the quality of the cavity surface [1]. Fortunately, these defects can frequently be fixed by means of mechanical abrasion. While these repairs are necessary, unfortunately, the use of abrasive media to repair the niobium surface can cause lasting degradation of the surface finish, and, as a result, potential degradation of cavity performance due to particulate contamination on the cavity surface. This study seeks to examine the lasting impact of these repairs, and to determine a method for mitigating the consequences by means of processing and analyzing a series of niobium samples.

EXPERIMENTAL

Two lots of niobium samples were used in this experiment. Each lot consisted of a series of small grain, high-RRR (>250), 3 mm thick sheet stock samples, shear-cut to approximately 2.5 cm square. Each sample was stamped with a serial number, photographed, degreased with acetone, ultrasonic cleaned, and precision measured for thickness (±0.0025 mm) with an NDT Systems Model TG900 ultrasonic thickness gauge.

As is typically performed with RF cavities, following cleaning, the samples were chemically etched with a standard solution of buffered chemical polish (BCP). The BCP mixture used at FRIB is a 1:1:2 mixture of concentrated hydrofluoric (49% w/w), nitric (70% w/w), and phosphoric (85% w/w) acids. The first lot of samples was divided into eight sub-lots. The sub-lots were each submerged in BCP and etched for between 60 and 480 minutes, removing up to 300 microns of niobium from the surface of the samples. Upon completion of the etching, the samples were thoroughly rinsed with ultrapure water (UPW) and set to dry in an ISO 5 cleanroom. Once dry, the surface roughness (both R_a and R_z) at six different locations on each sample was measured with a Fowler 54-410-500 X-Pro Portable Surface Roughness Tester.

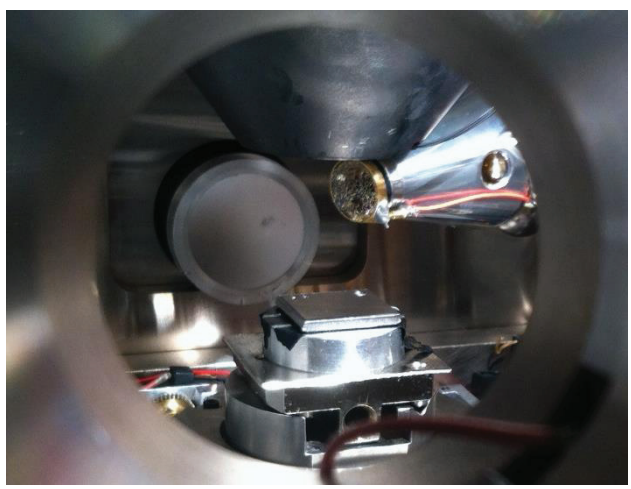


Figure 1: A niobium sample on the microscope stage as seen through the SEM's vacuum viewport.

To simulate a portion of an RF cavity repaired with an abrasive media, the second lot of samples was "polished"

* This material is based upon work supported by the U.S. Department of Energy Office of Science under Cooperative Agreement DE-SC0000661, The State of Michigan, and Michigan State University

malloch@frib.msu.edu

Copyright © 2013 CC-BY-3.0 and by the respective authors

for five seconds per sample with a pneumatic Dyno-File tool equipped with a medium-grit aluminium oxide conditioning belt. Ultrasonic thickness measurements showed that the abrasion did not remove an appreciable amount of material from the sample surface. Following the abrasion of the samples, they were divided into sub-lots, and ultrasonic cleaned once more. Once clean, the abraded samples were etched in the same manner as the as-received samples, then were rinsed and dried in the cleanroom and measured for surface roughness.

Once the surface roughness characterization of the samples had been performed, a representative set of samples were analyzed with a CamScan 44FE Field Emission Gun Scanning Electron Microscope to allow the topography and particulate retention of the samples to be observed in great detail (Fig. 1).

DISCUSSION

The development of the surface roughness for the as-received samples followed the same well-defined pattern that had been reported previously for chemically polished niobium surfaces [2, 3]. The surface roughness, R_z, prior to etching was very small, though it steadily increased for the first ~100 microns of etch removal. At this point, it began to plateau, and stayed relatively constant for the remainder of the etching procedure. The more surprising outcome was the evolution of the surface roughness for the abraded samples. Not surprisingly, the initial surface roughness of the abraded samples was significantly higher than was observed on the as-received samples (Fig. 2).

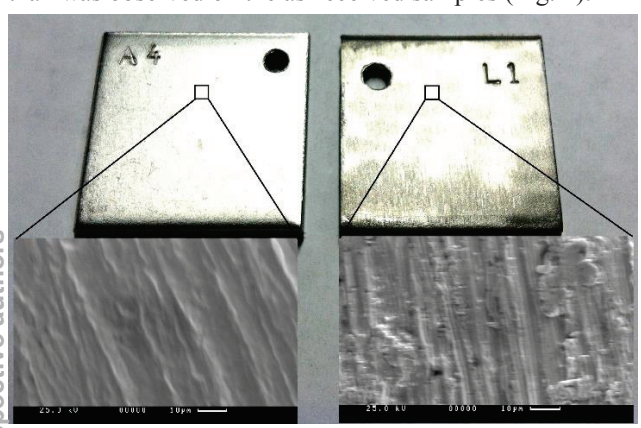


Figure 2: As-received niobium sample (left) compared to an abraded sample (right). Note the difference in surface roughness, both in the picture and in the SEM scans.

Once etching was commenced, the surface roughness fell sharply during the first 50 microns of removal, at which point the roughness began to climb, then plateau in a manner consistent with the as-received samples. The surprising finding was that the surface roughness of the abraded samples never converged with the as-received samples (Fig. 3). A similar pattern was observed with R_a measurements. The implication here is that under the conditions explored in this experiment, once a niobium surface has been abraded, the surface roughness will not return to a state consistent with a surface that has not been altered with an abrasive media. As can be seen in Figure 4, while the samples look very similar to one another with the naked eye, microscopy shows that they are not. Note the difference in the overall surface finish, and observe the valley that runs through the center of the image. These crevasses were seen in several locations on the abraded samples up until at least 100 microns of niobium had been removed from the surface. This has the potential to have serious consequences on RF cavity performance [4], since the increased surface area of a rougher material allows more room for particulates to become trapped on the surface, potentially resulting in field-emission and cavity quenching during operation.

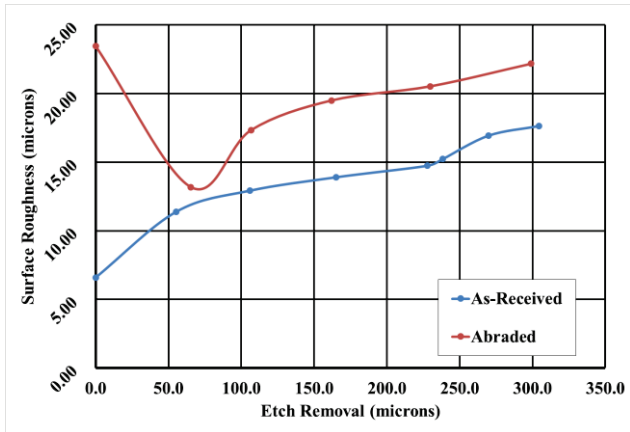


Figure 3: Plot of etch removal vs. surface roughness for the as-received and abraded niobium samples for different etch removal amounts.

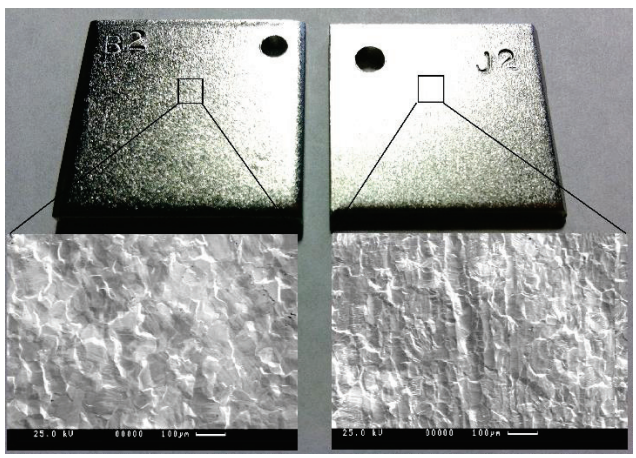


Figure 4: As-received niobium sample (left) compared to an abraded sample (right) following 70 microns of etching. Abraded sample has visibly worse surface finish under the microscope.

In addition to the concerns about the roughness of the niobium surface, there was also evidence to suggest that on top of the passive role that abrading can play in particulate retention, particulate was actively being ground into the surface of the niobium. These particulate were only exposed after significant amounts of etching had been performed (Fig. 5). While these particulate are not necessarily a *guarantee* of a bad cavity test, they are

Copyright © 2013 CC-BY-3.0 and by the respective authors

certainly not preferable, and can contribute to less than optimal cavity performance, especially at high-field.

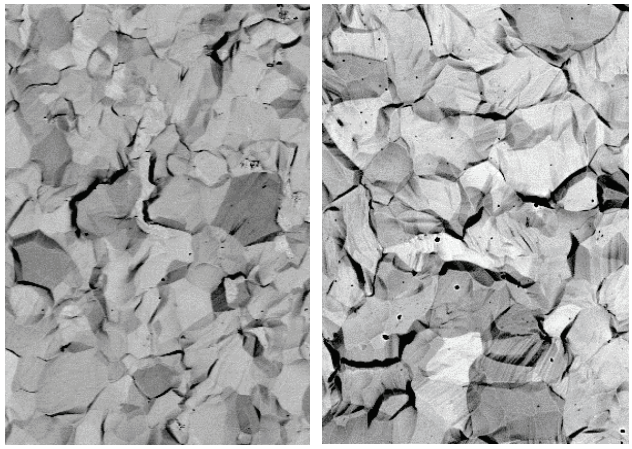


Figure 5: SEM scans of an as-received sample (left) and an abraded sample (right) after more than 100 microns of etching. Note the unusually high concentration of black particulate spots on the abraded sample.

SRF Cavity Repair: A Case Study

A β=0.085 quarter-wave resonator intended for use in the ReA3 coldmass was recently processed in the FRIB chemical etching and cleanroom facility. Once assembled and pumped down, the cavity demonstrated a large weld leak between the helium vessel and RF space along one of the cavity's flanges. At this point, the cavity was sent for repair at an electron-beam welding facility. During welding, suspected contamination in the weld area caused a significant amount of weld spatter to be deposited on the RF surfaces inside of the cavity.

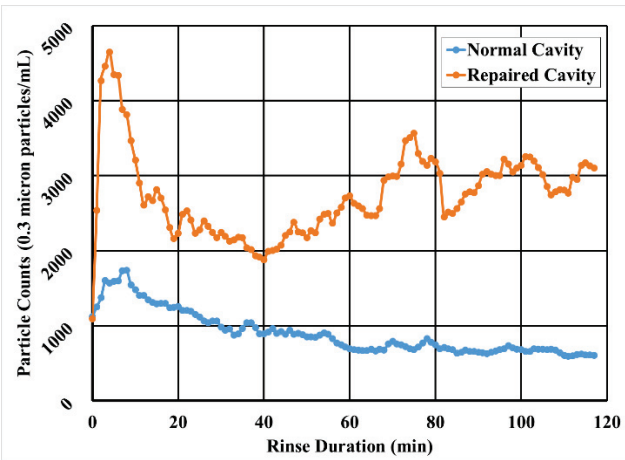


Figure 6: Liquid particle count comparison between a normal and repaired cavity during high-pressure rinsing.

The same abrasion method used in this experiment was used to remove the spatter and smooth out the resulting imperfections on the cavity surface prior to a chemical etch and high-pressure rinse (HPR) being performed. Liquid particle counts taken during the HPR were more than five times higher than were historically observed for a cavity of this type (Fig. 6). HPR was continued for an additional two hours, at which point the particle counts began to fall back to an acceptable range. Unfortunately, the subsequent cavity assembly and leak check revealed another leak requiring additional repair, so no comparison between cavity test results could be established. Despite the fact that no test results were gathered for this repaired cavity, data gathered over the course of many cavity processes indicates a correlation between low particle counts during HPR and superior cavity performance.

CONCLUSION

While the repair of surface defects on SRF cavities is often a necessity, careful consideration should be given to the methods and materials used. If abrasives must be used, as small of a surface area as possible should be affected. Care should also be taken to adjust processing procedures following these repairs to ensure the highest quality product possible. At a minimum, extended etching and high-pressure rinse cycles are recommended prior to assembly for RF testing. The necessity of repairs should be considered as well. Frequently, damage or inclusions on welded surfaces can cause defective welds; these must be repaired. However, if these issues are seen on other cavity surfaces, chemical polishing alone can often mitigate the damage without causing long-term impacts to the quality of the cavity surface. These less aggressive repair solutions should be pursued whenever possible.

ACKNOWLEDGMENTS

The authors would like to thank all the members of the NSCL & FRIB staff whose dedicated effort has made a significant contribution to this experiment. In particular, Ryan Brunk, Kyle Elliott, Doug Miller, Daniel Victory, Andrew Wisniowiecki, Ken Witgen, and Joseph Whaley. We would also like to extend our sincere gratitude to Di Kang for his assistance in gathering profilometry and microscopy data for this experiment.

REFERENCES

[1] C. Compton, et al., "Study Correlating Niobium Surface Roughness with Surface Particle Counts," in *Proceedings of the 15th International Conference on RF Superconductivity*, Chicago, IL, USA, 2011, TUPO016.

[2] K. Saito, "Techniques of SC Cavity Preparation for High Gradient," in *Proceedings of LINAC2002,* Gyeongju, Korea, 2002, pp. 534-538.

[3] K. Saito, et al., "Superiority of Electropolishing Over Chemical Polishing on High Gradients," in *Proceedings of the 1997 Workshop on RF Superconductivity,* Abano Terme (Padova), Italy, 1997, SRF97D02.

[4] G. Wu, et al., "Investigations of Surface Quality and SRF Cavity Performance" in *Proceedings of the 2010 Applied Superconductivity Conference,* Washington, D.C., 2010, 2LP1C-02.

Copyright © 2013 CC-BY-3.0 and by the respective authors

SRF CAVITY ETCHING DEVELOPMENTS FOR FRIB CAVITY PROCESSING*

K. Elliott#, I. Malloch, L. Popielarski, N. Putman, Facility for Rare Isotope Beams (FRIB), Michigan State University, East Lansing, MI 48824, USA

Abstract

Updates to the FRIB beta=0.53 half wave resonator (HWR) design have provided an opportunity to test new buffered chemical polish (BCP) flow control techniques. New processing fixtures have been fabricated and used to process the FRIB beta=0.53 HWR. This paper will present details of the fixture mechanical design iterations, the resulting BCP flow simulations, a qualitative evaluation of the agreement between simulations and measured results, and developments in process validation techniques.

INTRODUCTION

Buffered chemical polish (BCP) processing techniques continue to progress with the FRIB β=0.53 half wave resonator (HWR) cavity. With the updated cavity design we were able to use new fixturing concepts and take a variety of measurements to better understand the processing parameters. The new β=0.53 HWR cavity has an internal volume of 76 L, and an internal surface area of 1.4 m^2.

The objectives for the design of the new chemistry fixtures were to reduce fixture complexity, reduce fixture installation time, and increase the etch uniformity.

FIXTURE DESIGN

Twelve different configurations were analyzed to determine the best concept for achieving uniform etch removal. Seven of the configurations were a derivative of the directional quill injection system used on the previous β=0.53 HWR cavity [1]. The other five configurations consisted of a single directional quill. Ultimately the single directional quill was chosen. The analysis of the single directional quill, and the four injection quill design, can be seen in Figure 1.

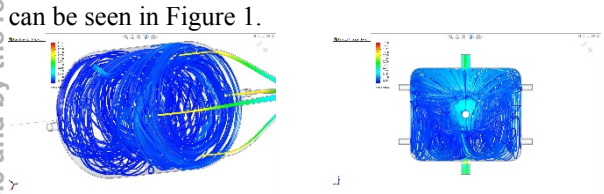


Figure 1: Left, analysis of four quill injection system. Right, analysis of single quill injection system.

* This material is based upon work supported by the U.S. Department of Energy Office of Science under Cooperative Agreement DE-SC0000661

#Elliott@FRIB.MSU.EDU

The single quill configuration shown in Figure 2 was chosen because it appeared to deliver equivalent mixing of the BCP compared to the four quill configuration, while reducing the complexity of the BCP delivery plumbing. The quality of the BCP mixing is determined qualitatively by choosing the fixture concept which produces the least velocity variation across the superconducting surface of the cavity.

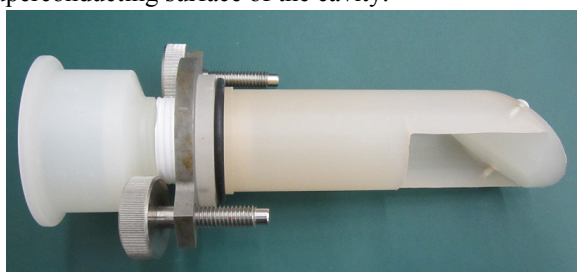


Figure 2: Single injection quill used for FRIB β=0.53 HWR cavity BCP processing.

One of the stated goals of this fixture iteration was to reduce installation time. This was done in two ways. First, the force needed to make the o-ring seal on each flange was carefully examined and revised. Second, we attempted to eliminate the need for tools during the fixture installation.

Past chemistry flanges were designed with a hole pattern to match the mating flange on the cavity. For example, one of the 2.75" ConFlat flanges of the prototype β=0.53 HWR cavity had six ¼" clearance holes (See Figure 3). Once the fasteners are were tightened there was nearly 12,000 lbs of force on the flange, though it is not known what portion of that force was transmitted to the o-ring.

O-ring Analysis

The Parker Hannifin o-ring handbook [2] indicates that only 20-30% compression is necessary to make a static o-ring seal. Given the o-ring hardness, thickness, and desired percent compression, the Parker Hannifin o-ring handbook indicates that 10-20 lbs of force per linear inch of o-ring is required to make a reliable seal. This means that only 300 lbs of force is needed for this seal.

A stainless steel backing plate was added to each flange to ensure that the tension from the fasteners was evenly distributed to the o-ring and, the number of fasteners was reduce from six to two. Because a well lubricated 1/4" fastener requires only 7.5 in*lbs of torque to produce 150 lbs of tension (half of the required 300 lbs), thumb screws

Copyright © 2013 CC-BY-3.0 and by the respective authors

were used in place of hex head cap screws. This eliminated the need for hand tools, and reduced the total BCP processing flange installation time from ~30 minutes to ~5 minutes.

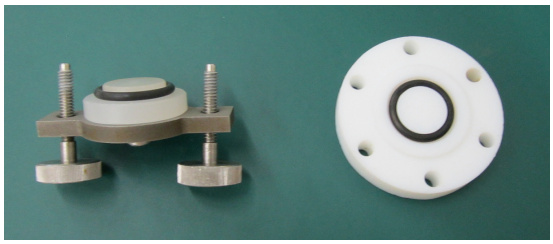


Figure 3: Left, new BCP blank flange design. Right, old BCP blank flange design.

EVALUATION OF SIMULATION

Ultrasonic thickness measurements (USTM) were taken on the new HWR cavity before and after each bulk etch step. The bulk etch removal for this cavity was taken in steps of 45 µm, 55 µm, and 30 µm respectively. The ultrasonic thickness measurements show strong correlation between the predicted flow path and the resulting etch patterns. Notice the high etch region which begins below the cavity beam port and broadens as the BCP impinges on the cavity surface. The black triangles in Figure 4 highlight this behavior. The new fixtures provided a more uniform etch in most locations on the cavity. One exception to this uniformity is the area near the radio frequency (RF) antenna ports indicated by the arrow in figure 4. The weld bead around this port allowed a gas bubble to form, reducing the local etch rate.



Figure 4: Left, Predicted flow pattern. Right, resulting etch removal measured by USTM.

PROCESS VALIDATION

Three different techniques were used to measure the amount of etching done to the cavity's RF surface. Those techniques were, ultrasonic thickness measurements, mass change analysis, and heat production analysis.

Ultrasonic Thickness Measurements

This method requires the user to take ultrasonic thickness measurements at numerous locations on the outside of the cavity before etching, and then repeat those measurements after etching. The thickness of material removed can then be calculated at each measurement location. This method is useful for determining locations of high etch removal, but it is also time consuming. If the removal has been calculated for the majority of the cavity's surface area all data points can be averaged to yield an accurate overall etch removal.

Mass Change Analysis

Unlike USTM's, this method does not provide information about removal rates in specific locations on the cavity. It is a useful way to quickly determine the overall etch removal. This method requires a mass measurement be taken before and after etching. Equation 1 below is used to calculate the average material removal from the cavity.

$$Removal = \frac{m_i - m_f}{\rho_{Nb} \times S.A.} \quad (1)$$

Where m is mass, ρ_{Nb} is the density of niobium, and S.A. is the surface area of the cavity.

Application of this method can be challenging because it requires a very accurate measurement of mass to yield accurate etch removal measurements.

Heat Production Analysis

Because the reaction between BCP and Niobium is very exothermic [3] a measurement of heat produced during the etching process can be used to determine the amount of niobium removed from the cavity's internal surface. The change in temperature of the flowing BCP is used to determine the amount of heat produced during the cavity etch. Equation 2 (below) is used to calculate the amount of heat which is put into the BCP.

$$Q(t) = \dot{V}(t) \times \rho_{BCP} \times c_{p,BCP} \times \Delta T(t) \quad (2)$$

Where $\dot{V}$ is the volumetric flow rate of the BCP, ρ_{BCP} is the density of the BCP, $c_{p,BCP}$ is the heat capacity of the BCP, and $\Delta T(t)$ is the temperature as a function of time. Now that the heat production known equation 3 (below) can be used to determine the amount of niobium removed from the cavity surface.

$$Removal = \frac{\int_{t_0}^{t_f} Q(t)dt}{M(Nb) \times \rho_{Nb} \times h_{RXN} \times S.A.} \quad (3)$$

Where M(Nb) is the molar mass of niobium, and h_{RXN} is the heat of the reaction.

One advantage of this method is that it can be applied during the etching process to determine when the cavity has received the desired amount of etching, and the resulting measurement is not affected by localized etch patterns.

Measurement Method Comparison

As mentioned earlier, this cavity was etched in three steps of 45, 55, and 30 micrometers respectively. Each measurement technique was used at every stage of the

Copyright © 2013 CC-BY-3.0 and by the respective authors

etching process. The result of each measurement technique are summarized in Figure 5 below.

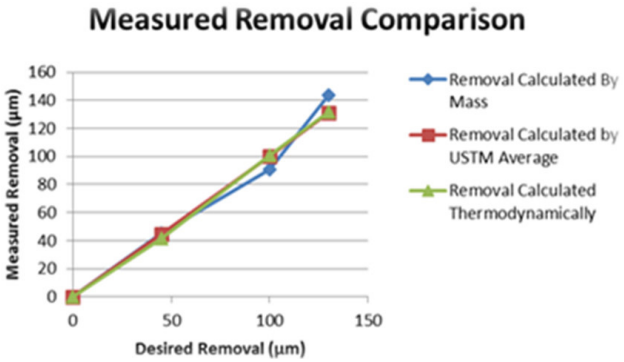


Figure 5: Comparison of measurement techniques for each stage of β=0.53 cavity bulk etch.

USTM is the most accurate technique at this time. The results of heat production analysis are in close agreement with the USTM method, as seen in Fig. 5. Measurements taken for the mass change analysis were done with a scale which had a resolution of .2 lbs., this can lead to measurement error of 7.5 µm.

CONCLUSION

Fluid flow simulations have proven to be effective in qualitatively predicting localized etch rates. Understanding predicted flow patterns will lead to accurate modeling of etch removal across the cavity's internal surface. After the removal patterns are understood the use of USTM's is no longer necessary. Instead mass change analysis or heat production analysis can be used to quickly and accurately verify etch removal.

ACKNOWLEDGMENTS

The authors would like to thank all the members of the NSCL & FRIB staff whose dedicated effort has made a significant contribution to the progress. In particular, Jim Loepke, Ken Witgen, for their work in flange design and fabrication, as well as, Dan Victory for patient and diligent data gathering.

REFERENCES

[1] L. Popielarski et al., "Buffered Chemical Polishing Development for the Beta=0.53 Half-wave Resonator at Michigan State University" TUPO057, SRF2011.

[2] Parker Hannifin O-Ring Division, *Parker O-Ring Handbook ORD 5700,* ©2007, http://www.parker.com/literature/ORD%205700%20Parker_O-Ring_Handbook.pdf

[3] I. Malloch et al., "Niobium Reaction Kinetics: An Investigation into the Reactions Between Buffered Chemical Polish and Niobium and the Impact on SRF Cavity Etching" WEPPC066, IPAC2012.

Copyright © 2013 CC-BY-3.0 and by the respective authors

MAGNETIC SHIELD OPTIMIZATION FOR THE FRIB SUPERCONDUCTING QUARTER-WAVE RESONATOR CRYOMODULE*

Y. Xu#, A. Fox, M. Johnson, M. Leitner, S. Miller, K. Saito, FRIB, East Lansing, MI 48824, USA

Abstract

The Facility for Rare Isotope Beams (FRIB) required 49 cryomodules containing 330 superconducting low-beta resonators, which have to be shielded from the earth magnetic field. Comprehensive magnetic shielding simulations have been conducted for 80.5 MHz β=0.085 cryomodules exposed to earth fields of 0.5 Gauss in different coordinate directions. The magnetic shield has to attenuate the earth magnetic field by a minimum factor of 33 (to less than 15 milli Gauss) in order to limit flux trapping in the resonators during cool-down. In the reported optimization studies, permeability of the magnetic shielding material, shield thickness, and number of magnetic shield layers have been varied. Different design concepts including global and local magnetic shielding have been evaluated. In addition, the design concepts are compared based on the cost of material, fabrication and assembly, the design complexity and compatibility with the overall cryomodule design to obtain an optimum solution.

INTRODUCTION

There are 49 cryomodules that will be built in FRIB: three 80.5 MHz β=0.041 cryomodules, eleven 80.5 MHz β=0.085 cryomodules, two 80.5 MHz β=0.085 matching cryomodules, twelve 322 MHz β=0.29 cryomodules, two 322 MHz β=0.29 matching cryomodules, eighteen 322 MHz β=0.53 cryomodules, and one 322 MHz β=0.53 matching cryomodule.

All cryomodules have to be shielded to attenuate the earth magnetic field in order to limit flux trapping in the cavities during cool-down to less than 15 milli Gauss. Two main different design concepts, room temperature global and low temperature local magnetic shielding as shown in Figure 1, have been compared on 80.5 MHz β=0.085 cryomodule from the attenuation ability, cost of material, fabrication and assembly, to the design and assembly complexity. The global magnetic shield locates between the vacuum vessel and the thermal shield and encompasses the entirety of cold mass, while the local magnetic shield is assembled around the resonators. Two local magnetic shielding designs are compared. One is to shield each resonator with individual shield, the other is to group the nearby resonators as much as possible.

ANSYS Magnetostatic is implemented to study the effects of permeability of material, size of magnetic shield, and the contribution from steel vacuum vessel. The magnetic flux on resonators is obtained to validate the effectiveness of the magnetic shield designs. Finally, Quality Function Deployment (QFD) is applied to compare different design concepts.

*Work supported by US DOE Cooperative Agreement DE-SC0000661
#xut@frib.msu.edu

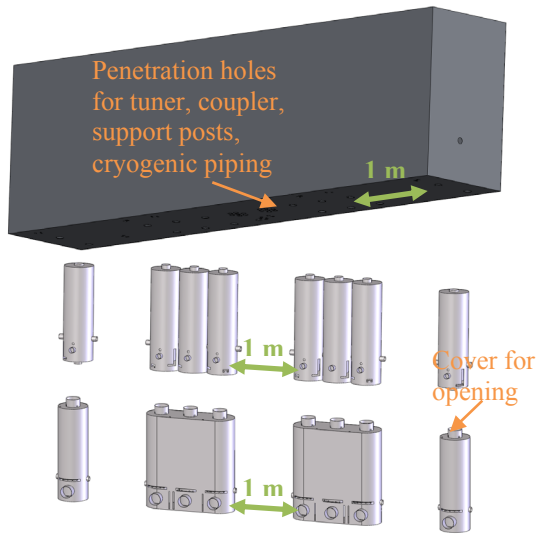


Figure 1: Global shield (top) and local single shield (middle) and local multi shield (bottom).

PERMEABILITY STUDY

The design of the magnetic shield starts with the proper material selection. Magnetic shielding materials should be chosen for their characteristic, usually in respect to permeability and saturation.

Manufacture Data

Amuneal Manufacturing Corporation compares the permeability of two products, Cryoperm 10 and Amumetal, as a function of ambient temperature shown in Figure 2 [1]. Amumetal has the maximum permeability at room temperature and is degraded at cryogenic temperature. Therefore, it is appropriate for the room temperature global magnetic shield. The permeability of Cryoperm 10 reaches its maximum at very low temperature (around 30 K) but is degraded at room temperature. Hence, it is proper for the low temperature local magnetic shield.

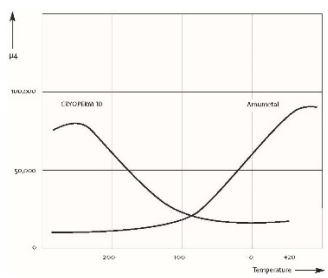


Figure 2: Permeability of Amumetal and Cryoperm 10 versus ambient temperature.

Recently, Amuneal developed a new shielding material Amuneal 4K (A4K) for cryogenic applications. A4K is

Copyright © 2013 CC-BY-3.0 and by the respective authors

claimed to have higher permeability than Cryoperm 10. Therefore, A4K will be employed in FRIB local magnetic shield design. However, Cryoperm 10 permeability will be utilized in the simulation for the sake of conservativeness.

Table 1 lists the permeability and saturation values of Amumetal and Cryoperm 10. Since a saturated shield is a poor attenuator, the selection of magnetic shield material must have adequate saturation characteristics.

Table 1: Permeability and Saturation

Material	Saturation (Gauss)	Permeability	
		μ Max	μ 40
Amumetal	8,000	400,000	60,000
Cryoperm 10	9,000	250,000	65,000

Measured and Simulation Data

It should be noted that the permeability provided above is the data obtained in the laboratory and has the optimum performance. However, the actual permeability of the shielding material depends on the heat treatment, fabrication and handling process of the material. Studies from CEA show that the actual performance of Cryoperm at low temperature is not as good as the one provided by manufacture. Therefore, simulations on FRIB Cryoperm magnetic shield are conducted at different permeability and compared with the measurement from other labs to determine a practical value of permeability. The comparison is made at the same shield thickness 1 mm.

Simulation of attenuation from FRIB local magnetic shield at different permeability with and without the vacuum vessel, 17500, 32500 and 65000, are displayed in Figure 3. It shows that the attenuation increases as the increase of the permeability. The measurement of CEA provides the attenuation from magnetic shield be 25 and that from both the magnetic shield and vacuum vessel be 100 [2]. In addition, the measurement of FNAL shows that the attenuation from both magnetic shield and vacuum vessel in their cryomodule is 120 [2].

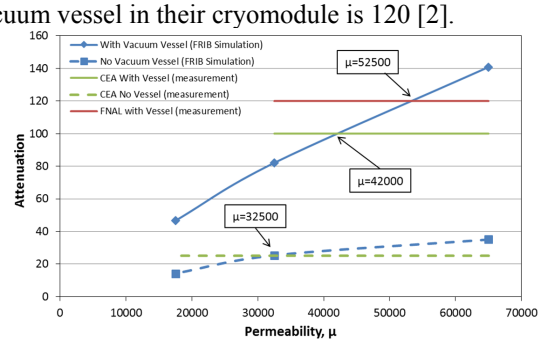


Figure 3: Permeability study.

The length of CEA test magnetic shield is 1.3 m, which is about the same as that of FRIB (1.25 m). Therefore, the performance of CEA and FRIB magnetic shields are similar. Although the permeability is not measured directly, it is reasonable to apply 32500 in the simulation to make direct comparison with the measurement of CEA. The length of FNAL 1.3 GHz cryomodule magnetic shield is 1 m, which is smaller than that of FRIB. Hence, higher attenuation is expected since the smaller the size the better the performance (also explained by Figure 4).

EFFECT OF MAGNETIC SHIELD LENGTH AND THICKNESS

Attenuation simulations on global magnetic shield with full, half, one third and quarter length are conducted and displayed in Figure 4. The shorter the magnetic shield length, the smaller the effective radius of the shield, hence the better its performance. Simulations on thickness 1.6 mm and 3.2 mm shields show that the attenuation increases 1.5 times as the shield thickness doubles. The theoretical study demonstrates that as the decrease of the effective radius of the shield, the attenuation ratio converges to 2 as the shield thickness doubles. For an infinitely large shield, the attenuation converges to 1 and is not affected by the shield thickness and material permeability. Therefore, the attenuation ratio is expected to be between 1 and 2 as the shield thickness doubles.

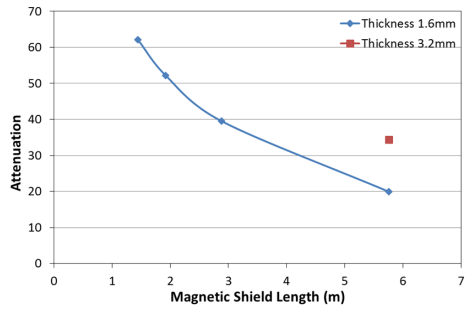


Figure 4: Effect of magnetic shield length and thickness.

STEEL VACUUM VESSEL

The contribution of steel vacuum vessel on the attenuation is displayed in Figure 3. Similar to the magnetic shield, the performance of vacuum vessel also depends on the material permeability, thickness and the vessel size. It can be observed from both the FRIB simulation and the CEA measurement that the contribution from the vacuum vessel is remarkable, especially with thick vessel wall (19 mm for FRIB).

GLOBAL MAGNETIC SHIELD

In the global magnetic shield design, no covers is implemented because of the relative small penetrations. The earth field is 0.5 Gauss in magnitude and varies in different directions for a thorough study. It is found out that the attenuation is the worst when earth field is -30° from the horizontal plane, which is the earth field direction at the FRIB location.

Global magnetic shield simulations are conducted on 1.6 mm, 3.2 mm and two layers of 1.6 mm shields with the contribution of vacuum vessel and the attenuation is 24, 34 and 34, respectively. Two layers of 1.6 mm shield is supposed to have better performance than one layer 3.2 mm shield. However, because of the space limit between the vacuum vessel and thermal shield in FRIB design, the spacing between two layers is very limited. Therefore, the enhancement on performance is not observed.

Copyright © 2013 CC-BY-3.0 and by the respective authors

Since the requirement for magnetic shield is the ability to attenuate the earth field by a minimum factor of 33, single layer of 1.6 mm shield is not appropriate for FRIB QWR cryomodule. The magnetic flux density profile on x-y plane with 3.2 mm magnetic shield is displayed in Figure **5**. Dark blue represents the ***B*** field below 15 milli Gauss. Therefore, 3.2 mm Amumetal global magnetic shield is able to meet the FRIB design requirement.

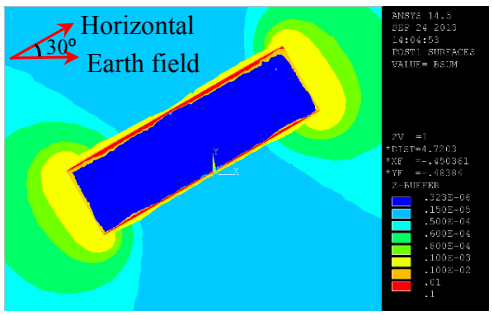


Figure 5: Magnetic flux density with global shield.

LOCAL MAGNETIC SHIELD

The same as the global magnetic shield simulation, the earth field is -30° from the horizontal plane and has magnitude of 0.5 Gauss in both local single shield and combined shield simulations. Tubular covers are necessary for the openings of power coupler, cryogenic supply, beam port and resonator supporting rail penetrations. The height of the cover is proportional to the diameter of the opening since magnetic fields can travel into an opening a distance equal to five times the diameter of the opening.

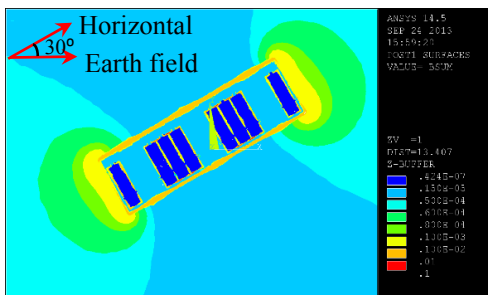


Figure 6: Magnetic flux density with local single shield.

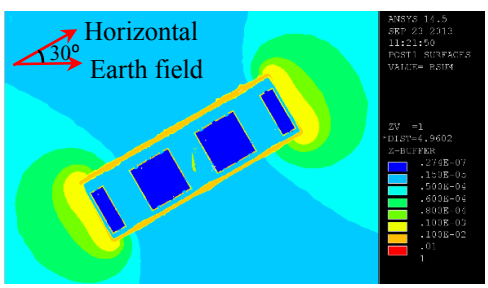


Figure 7: Magnetic flux density with local multi shield.

Simulations on local single shield and local combined shield indicate that the magnetic fields on resonator surfaces in both cases are less than 15 milli gauss (shown in dark blue in Figure 6 and Figure 7).

QFD

Quality function deployment (QFD) is a "method to transform user demands into design quality, to deploy the functions forming quality, and to deploy methods for achieving the design quality into subsystems and component parts, and ultimately to specific elements of the manufacturing process." [3] as described by Dr. Yoji Akao, who originally developed QFD in Japan in 1966.

The most important criteria is the inducted field less than 15 milli Gauss at resonator surface. It is shown in Figure 8 that all the designs meet the requirement but with different efforts. Global magnetic shield design requires more effort hence "bad relationship" is specified.

Other important factors include: design, assembly and fabrication complexity; compatibility with design of other systems such as bottom up design, cold mass, thermal shield, vacuum vessel, and cryogenic system; cost including material, fabrication and assembly cost. For example, the cost of 0.125" Amumetal global shield is the highest because of the highest material cost. In addition, the 2 layer 0.062" Amumetal global shield has the lowest compatibility with bottom up design, minimum spacing requirement and post-assembly accessibility to power coupler. In summary, the local A4K magnetic shield is the best design concept, especially with the multi-resonator configuration.

Max Relationship Value in Row		Relative Weight	Weight / Importance	Quality Characteristics (a.k.a. "Functional Requirements" or "Hows") / Demanded Quality (a.k.a. "Customer Requirements" or "Whats")	0.125" Mu-Metal global shield	Single Resonator A4K Shield	Multi-Resonator A4K Shield	2x .062" Mu-Metal shields	0.062" Mu-Metal global shield + A4K local shield
1	3	14.1	10.0	Inducted field is less than 15 mG at resonator surface	▲	O	O	▲	O
2	9	12.7	9.0	Minimal Complexity	Θ	O	O	▲	▲
2	9	11.3	8.0	Cost	▲	Θ	Θ	▲	O
3	9	11.3	8.0	Number of Parts	Θ	O	Θ	▲	O
4	9	12.7	9.0	Compatible with bottom up Design	Θ	Θ	Θ	O	Θ
5	9	12.7	9.0	Accommodates coldmass including FPC & tuner drive penetrations	O	Θ	Θ	O	O
6	9	12.7	9.0	Maintain 1" spacing to the Thermal Shield and 1" Spacing to Vacuum Vessel	O	Θ	Θ	▲	O
7	9	12.7	9.0	Allow for post-assembly access to FPC	O	Θ	Θ	▲	O
				Target or Limit Value					
				Difficulty (0=Easy to Accomplish, 10=Extremely Difficult)	2	3	3	8	5
				Max Relationship Value in Column	9	9	9	3	9
				Weight / Importance	469.0	671.8	739.4	150.7	350.7
				Relative Weight	19.7	28.2	31.0	6.3	14.7

Figure 8: QFD of magnetic shield design concepts (Θ: positive relationship; O: neutral; ▲: bad relationship).

REFERENCES

[1] http://amuneal.com/sites/default/files/AmunealDataSheet2.pdf

[2] FRIB Workshop on Magnetic Shielding for Cryomodules, March 6-7, 2013.

[3] Y. Akao, "Development History of Quality Function Deployment", *The Customer Driven Approach to Quality Planning and Deployment*, Minato, Tokyo 107 Japan: Asian Productivity Organization, pg. 339.

Copyright © 2013 CC-BY-3.0 and by the respective authors

TUNING PROCESS OF SSR1 CAVITY FOR PROJECT X AT FNAL*

P. Berrutti, M. Awida, T. Khabiboulline, D. Passarelli, L. Ristori, V. Yakovlev
Fermilab, Batavia, IL 60510, USA

Abstract

SSR1 is a family of single spoke resonators to be used in Project X at Fermi National Laboratory. These cavities operate in CW regime having nominal frequency of 325 MHz and optimal beta of 0.22. SSR1 cavities will accelerate H- ions after the Half Wave Resonator (HWR) section from 9 MeV to 32 MeV. In the near future this cavity will be used in Project X Injector Experiment (PXIE), which contains the ion source, the LEBT, the MEBT, the RFQ of Project X, and a cryogenic temperature section, having one HWR and one SSR1 cryomodule. SSR1 cavities have been built and tested at FNAL, the preparation of these resonators includes RF tuning which is the main focus of this paper. The frequency of the cavity is carefully chosen prior to the vertical test, and it is adjusted before welding the helium vessel to obtain 325 MHz nominal frequency for the dressed cavity in operating conditions. Several SSR1 cavities have been tuned at FNAL, the procedure, the hardware and the data are presented.

INTRODUCTION

SSR1 cavities have been built and tested at Fermilab [1] [2]. During cavity production it is necessary to set frequency goals throughout the entire process, to match the final target frequency of 325 MHz for a cold jacketed SSR1. After assembling and welding of the niobium, the cavity arrives at Fermilab and undergoes several quality control steps: visual inspection, CMM measurements, RF QC and leak check. The frequency is monitored throughout the entire cavity processing; when the cavity is received from the vendor several measurements are taken: fundamental frequency, high order modes frequencies, and field flatness. SSR1 cavity processing includes baking at high and low temperature and chemical polishing, bulk and light BCP. The leak check and the chemical processing are two main causes of frequency shifts. During the first vacuum check the cavity geometry is deformed by the atmospheric pressure, which shrinks the structure inducing permanent plastic deformations, even though very small. The average Δf for SSR1 due to the leak check is -80 kHz. The bulk BCP removes 150 µm in average from the cavity surface, while the light chemical processing results in 30 µm material removal. The Δf produced by the bulk BCP has been averaged over 10 cavities and it is 150 kHz, while the one due to light BCP is 30 kHz. Transition ring [3] and helium vessel welding makes the frequency change as well; the two processes have been recently started at FNAL. All these are causes of frequency deviations; in order to control and compensate for these shifts it is necessary to tune the cavities with a proper fixture.

*Work supported by D.O.E. Contract No. DE-AC02-07CH11359
#berrutti@fnal.gov

SSR1 BARE CAVITY TUNING

The first tuning step of SSR1 comes for the preparation to the vertical test, the frequency is adjusted to 324.6 MHz in order to reach approximately 325 MHz once the cavity is cooled down to 2 K in the test dewar. Usually the cavity received from the vendor has a resonant frequency of 325.6 (±0.2) MHz, after the leak check, first bake and bulk chemistry it is usually higher by 70 kHz. The total frequency shift to apply is approximately 1 MHz, taking into account the cavity sensitivity 540 kHz/mm (simulated) [4] and the spring constant 21 kN/mm, the tuning requires a robust fixture capable of delivering forces of several tens of kN. Figure 1 shows the tuning machine for SSR1 cavities, it consists in a box equipped with two rods which allow pushing or pulling on the cavity beam pipes. Two load cells measure the forces applied on each rod, four displacement gauges give reading of the deformations the cavity is subject to, and they are mounted between the beam pipes and the coupler ports. A set of antennae is mounted on the coupler ports to allow recording the frequency step by step with a network analyser.

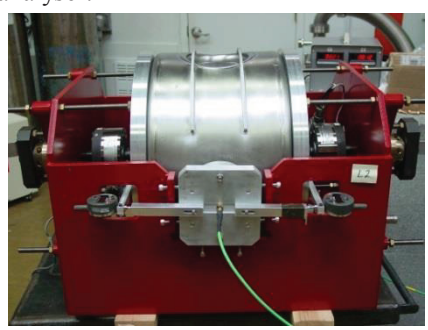


Figure 1: SSR1 tuning machine with a cavity in it.

To understand how the frequency changes when the tuning machine acts on the resonator, let us keep in mind Slater's rule:

$$\frac{\Delta f}{f_0} = \frac{1}{4W}\int_{V_i}^{V_f}(\varepsilon_0 E^2 - \mu_0 H^2)dV. \quad (1)$$

W is the stored energy in the cavity in initial conditions, V_i is the volume before tuning and V_f is the volume after deformations are applied. Since the rods are acting on the beam pipes the high electric field area is modified, consequently the change in frequency will have the same sign of the change in cavity volume: bigger volume means higher frequency.

Tuning Procedure

Before starting tuning the cavity, it has to be installed in the machine, which means have it fit centred in

Copyright © 2013 CC-BY-3.0 and by the respective authors

between the two rods to avoid any asymmetric deformation of the cavity structure. The tuning consists in applying a force on the cavity and then release it coming back to relaxed position. This is done in several steps, gradually, to avoid any abrupt change in the cavity geometry; RF measurements are taken for the stressed and relaxed conditions at each cycle. This process is repeated until the target frequency is achieved. Figure 2 shows the frequency of SSR1-112 during the tuning, one can see how for small forces applied the process is reversible and the frequency in the relaxed state is equal to the one before pushing or pulling. When the force overcomes the elastic limit of the material the cavity starts yielding, and as result the frequency for the relaxed cavity changes.

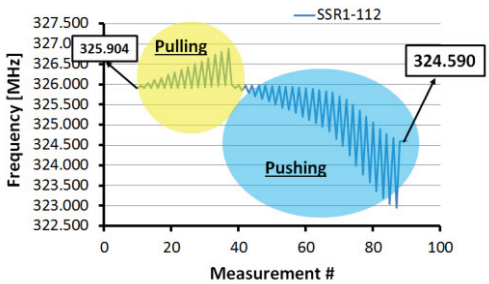


Figure 2: SSR1-112 frequency during tuning.

Frequency of the relaxed cavity is represented by the lower values for the pulling and higher values for the pushing. Despite the desired negative frequency shift, the first part of the tuning involves pulling which makes the frequency become higher. The reason why the tuning starts with pulling is to harden the material by stretching it; the frequency is not modified significantly usually a shift ranging from +80 to +100 kHz is sufficient. After the first pulling the real tuning by pushing starts, many cycle are usually required and the total force required can reach over 7000 lb_f.

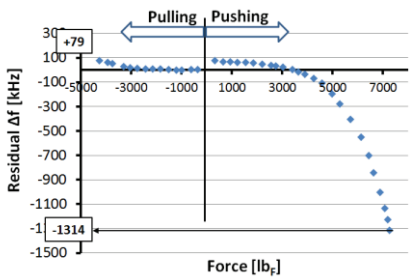


Figure 3: relaxed cavity frequency shift vs. force.

The figure above shows the Δf due to plastic deformation of the cavity, the pulling required almost 4300 lb_f while the pushing is over 7200 lb_f, the non-linearity of the last part of the plot is due to the yield of the material. When the value of frequency for the relaxed cavity is approaching the target, it is extremely important to increase the force by small steps since the material is yielding, and the frequency changes are much faster with the applied force. During the tuning it is possible to measure physical quantities related to cavity displacements, force applied and frequency shifts, in general it is interesting to look at frequency sensitivity as a function of the displacement and cavity spring constant. The frequency sensitivity $\frac{\Delta f}{l}$ measured in kHz/mm can be calculated from the plot of the frequency as a function of the average displacement, reported in figure 4. One can see two lines, one for the relaxed, one for the loaded cavity. The average of the parameter $\frac{\Delta f}{l}$ for all the cavities tuned is 460.7 kHz/mm, which is lower than the one predicted by simulations (540 kHz/mm). This mismatch is partly due to the residual asymmetry in the deformation induced by the rods; the error in evaluating the displacements is also not negligible, in addition the simulated sensitivity may differ from the real value.

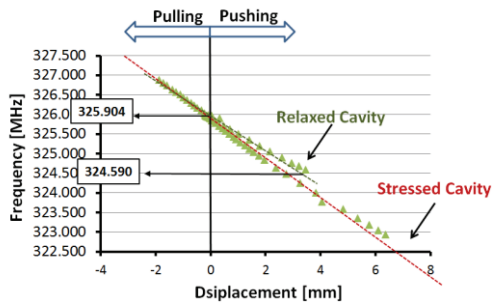


Figure 4: SSR1-112 frequency vs. average displacement.

Figure 5 shows the average displacement as a function of the force applied, from this plot it is possible to extract the spring constant value of the cavity evaluated as $\frac{\Delta F}{\Delta l}$, where ΔF is the difference in force applied; it is expressed in kN/mm, its average value is 22.2 kN/mm.

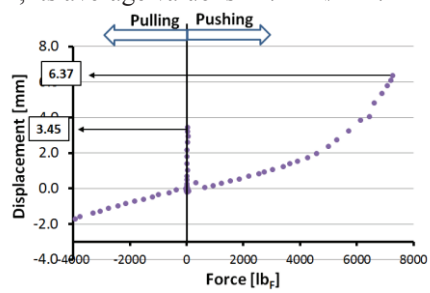


Figure 5: average displacement vs. force.

Tuning After Transition Ring Weld

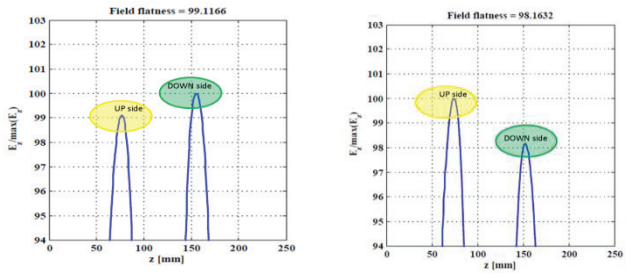
In the latest design of SSR1 helium vessel [4] a transition ring is used to attach the niobium cavity to the stainless steel vessel [3]. The ring is attached to the cavity by electron beam welding, see figure 6, this operation is done after the resonator qualifies from the VTS. Recently Fermilab received two SSR1 cavities which had the transition ring welded, SSR1-107 and SSR1-108. The expected frequency shift was initially thought to be very small, while it turned out to be around 500 kHz. The cause of this shift is the contraction of the beam pipe area on the transition ring side; the weld induces the material to shrink while it cools down, pushing the beam pipe in and consequently reducing the resonant frequency.

Copyright © 2013 CC-BY-3.0 and by the respective authors



Figure 6: SSR1 cavity with transition ring.

To prove this, bead pull measurements were taken on SSR1-108 before and after the weld, the normalized field amplitude plots are presented in figure 7, up side refers to the side of welding. Looking at figure 7(a) the maximum of the accelerating field is on the down side, opposite to the weld side, while for figure 7(b) the higher point appears on the transition ring side. Higher field means shorter gap, so this is an evidence of the shrinkage due to the weld.



(a) (b)

Figure 7: SSR1-108 field flatness before (a) and after (b) transition ring weld.

SSR1-107 has been tuned to compensate for the effects of the transition ring weld, following the procedure described in the previous paragraph but applying asymmetric forces to bring the gap length back to original value.

SSR1 DRESSED CAVITY

Fermilab recently received the first SSR1 cavity with helium vessel, in order to monitor the resonant frequency measurements have been taken during the entire welding process. Figure 8 shows the frequency history of SSR1-107 during the welding of the stainless steel helium vessel; the main steps are highlighted on the graph. The most critical procedure is the welding of the beam pipes to the vessel which brings up the resonator frequency significantly. The welds on the outer helium vessel shell do not induce significant shift, while the two ports (coupler and vacuum) may interfere with the helium vessel parts and put stress on the cavity: the lower peak in the yellow part of the graph is due to the ports pressing against the vessel parts, they have been machined during the welding procedure to solve this issue. The first cavity ended up having a total frequency shift of 264 kHz during the dressing process, the procedure and the design of the helium vessel parts will be revised in order to obtain lower shrinkage effect on the cavity geometry.

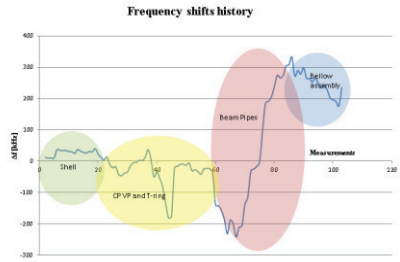


Figure 8: frequency shifts induced by helium vessel welding.

Once the resonator has been dressed it does not fit in the tuning machine anymore. A new fixture has been created to adjust the dressed SSR1 frequency: it consists in two stainless steel bars connected to the helium vessel on the tuner supports. Figure 9 shows the dummy tuner that will be used to adjust the frequency of the jacketed cavities; the device will allow tuning by pushing and pulling, unlike the real tuner device which will be able to compress the cavity only [4]. One rod is installed on each bar to allow tuning on the cavity wall, only on the side opposite to the transition ring, which has been connected to a bellow to allow movement.



Figure 9: SSR1-107 dummy tuner assembly.

CONCLUSIONS

Over ten SSR1 bare cavities have been tuned successfully at Fermilab, a new helium vessel design has been introduced and the first prototype has been built. The tuning procedure has been described and all the issues have been addressed. Currently tests and measurements are in progress on SSR1-107, to characterize all the features of the jacketed cavity; tuning will be done using the dummy tuner fixture, to assure that the target 325 MHz frequency is achieved.

REFERENCES

[1] V. Yakovlev et al., MOP015, Proceedings of SRF 2013, Paris, France.
[2] L. Ristori et al., FRIOB02, Proceedings of SRF 2013, Paris, France.
[3] L. Ristori et al., WEPPC058, Proceedings of IPAC2012, New Orleans, Louisiana, USA.
[4] L. Ristori et al., WEPPC057, Proceedings of IPAC2012, New Orleans, Louisiana, USA.

Copyright © 2013 CC-BY-3.0 and by the respective authors

SINGLE SPOKE RESONATOR INNER ELECTRODE OPTIMIZATION DRIVEN BY REDUCTION OF MULTIPOLES*

P. Berrutti#, T. Khabiboulline, L. Ristori, N. Solyak, V. Yakovlev,
Fermilab, Batavia, IL 60510, USA

Abstract

Accelerating cavities based on coaxial resonators, half wave and spoke resonators for example, do not have azimuthal symmetry. This lack of symmetry introduces a transverse field perturbation which affects negatively the beam dynamic, since the particles traveling through the structure are crossing two accelerating gaps separated by the inner electrode. The field asymmetry induces an asymmetric transverse momentum gain which, once expanded in multipoles, appears to be due to a quadrupole perturbation. Depending on the cavity geometry and particle velocity, the influence of electric and magnetic fields may vary quite significantly. One solution to obtain symmetric transverse fields in spoke resonators consists in modifying the inner electrode shape from a pole to amore elaborated structure resembling an X or a Y letter shape. The application of these changes symmetrizes both electric and magnetic fields and reduces the multipoles amplitudes to negligible values. This paper presents the study aimed at reducing the multi-pole amplitudes for SSR2 cavity for Project X; the presented procedure, in general, is valid for any spoke cavity.

INTRODUCTION

Coaxial resonators are widely used for low-beta applications At Fermilab one family of half wave resonators (HWR) and two families of single spoke resonators (SSR) will be used in Project X. The geometry of both HWR and SSR is obtained from a coaxial line approximately half of a wave length long. The accelerating gaps of these cavities are formed by the inner and outer conductors of the coaxial resonator. Particles are travel along an axis perpendicular to the inner electrode. Let us assume that the particles are traveling through the gaps along the z axis, the lack of azimuthal symmetry leads to a different transverse momentum gain on x and y axes, acting as a quadrupole on the beam [1]. This issue has already been examined at Fermilab [1], [2] and a solution has been implemented to overcome HWR field asymmetry [3]: the central part of the inner electrode was modified using a radially symmetric circular shape. Such modification allows to obtain regular transverse electric field reducing asymmetric effects on the beam envelope. When the same approach was used on SSR2, the second family of spoke resonators for Project X, results were quite unexpected: the field asymmetry was even higher than before. This was caused by the magnetic transverse fields, which are not negligible in SSR2 cavities.

TRANSVERSE FIELD ASYMMETRY

Half wave and spoke resonators accelerating mode is quasi-TEM mode, that has non-zero transverse components on paths slightly off the ideal electric axis of the cavity. Considering the z axis as the longitudinal direction, electric and magnetic fields will be present in x and y. In figure 1 transverse field components of SSR2 cavity are plotted along z, for an offset of ten millimetres on the x-y plane: along x axis E_x and H_y are present, while for an offset on y direction E_y and H_x.

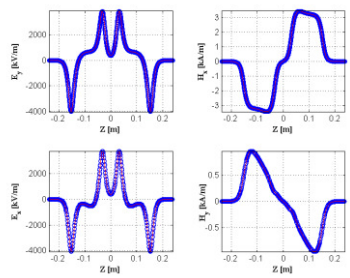


Figure 1: SSR2 electric and magnetic transverse fields.

A particle traveling with a radial offset r will experience a transverse kick due to the electric and magnetic fields:

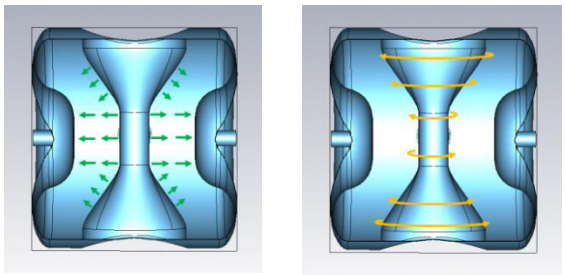
$$\Delta p_x(r,\alpha)c = \int_{z_i}^{z_f}\left(\frac{E_{x(r,\alpha)}}{\beta} - i\boldsymbol{Z}_0 H_y(r,\alpha)\right)e^{i\frac{kz}{\beta}}dz \quad (1)$$

$$\Delta p_y(r,\alpha)c = \int_{z_i}^{z_f}\left(\frac{E_{y(r,\alpha)}}{\beta} + i\boldsymbol{Z}_0 H_x(r,\alpha)\right)e^{i\frac{kz}{\beta}}dz. \quad (2)$$

Where $\boldsymbol{Z}_0$is the impedance of free space, $\beta = v/c$ and α is an angle, taken with respect to the x axis: α=0 corresponds to x axis and α=π/2 refers to y axis. The momentum gain can be calculated in the whole beta range for the accelerated particles, and its components can be evaluated separately to highlight the difference between electric and magnetic contribution. The electric field line are directed from the spoke to the outer walls, while the magnetic field lines spin around the inner post, hence the magnetic field component orthogonal to the electrode will be higher than the one parallel to it. Figure 2 shows SSR2 single spoke geometry, the green arrows on the left (a) represent a sketch of the electric field lines while the orange circles on the right (b) show the magnetic field spinning around the electrode.

*Work supported by D.O.E. Contract No. DE-AC02-07CH11359
#berrutti@fnal.gov

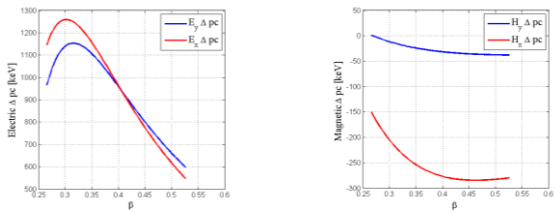
Copyright © 2013 CC-BY-3.0 and by the respective authors



(a) (b)

Figure 2: field line sketch of a spoke resonator (a) electric and (b) magnetic [1].

Assuming that the inner post lies along y, the magnetic field component orthogonal to the spoke will be H_x and the parallel one will be H_y; see plots in fig. 1 for comparison. All the transverse momentum gain components have been plotted in figure 3, the entire energy range of SSR2 cavity in Project X has been analysed (approximately from 40 MeV to 160 MeV). The left plot shows the electric field contribution; on the right the magnetic momentum gain is shown. Looking at fig. 3, it is immediately clear that the magnetic asymmetry is not negligible, especially for the higher beta region.



(a) (b)

Figure 3: (a) electric and (b) magnetic transverse momentum gain [1].

As a figure of merit for field asymmetry the following parameter Q can be used:

$$Q = \frac{\Delta p_x(r,0)c - \Delta p_y(r,\pi/2)c}{(\Delta p_x(r,0)c + \Delta p_y(r,\pi/2)c)/2}. \quad (3)$$

This parameter, evaluated on the full particle energy domain of SSR2, has been plotted in figure 4; its value is independent from the gradient or peak field because it is normalized over the sum of the two components: $\Delta p_x(r,0)c$ and $\Delta p_y(r,\pi/2)c$.

Calculating a multipole expansion of the transverse kick, it is possible to show that the asymmetry parameter is a measure of the quadrupole amplitude over the monopole.

ELECTRODE DESIGNS SHOWING NEGLIGIBLE FIELD ASYMMETRY

In order to bring symmetry to the cavity geometry it is necessary to re-design the inner electrode of the coaxial resonator. This modification consists in replicating half of the electrode with periodicity in the x-y plane, so the result will be an electrode resembling the shape of a letter Y or X. These two designs show very weak transverse field asymmetry for both electric and magnetic components. In the following subsections each design and its fields are described.

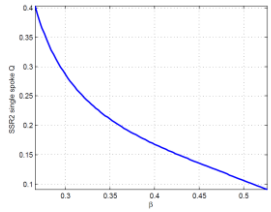
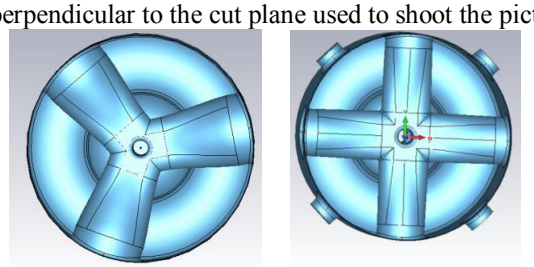


Figure 4: SSR2 single spoke asymmetry parameter vs. particle beta

Y-Shaped Spoke

The Y-shaped spoke, see fig. 5(a), consists of an inner electrode replicated and equally spaced at 120 degrees in the x-y plane. In figure 5(a) the x-y cross section of the Y-spoke design is shown, particles travel along z axis which is perpendicular to the cut plane used to shoot the picture.



(a) (b)

Figure 5: (a) Y-spoke design cross section, (b) X-spoke x-y section.

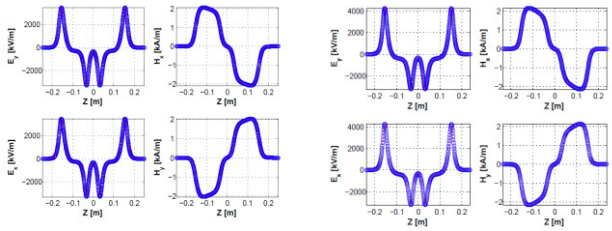
The transverse electric and magnetic fields benefit from the modified electrode. Transverse fields on a 10 mm offset are plotted in figure 6(a), electric on the left magnetic on the right. The x and y components of the two fields are in separate plots because an overlapping will not allow distinguishing one from the other, since they are almost identical. In figure 7 (a) the asymmetry parameter Q has been plotted versus the particle beta in the energy range of Project X, its maximum value is just ≈ 3% of the maximum Q for the single spoke. Figure 8 shows the magnetic (b) and the electric (a) transverse momentum gain on a 10 mm offset from the centre of the beam tube, the magnetic components (on the right) show some residual asymmetry.

X-Shaped Spoke

The X-spoke design has been made by intersecting two single spoke electrodes rotated by 90 degrees from each other; figure 5(b) shows the x-y cross section of the cavity geometry. Transverse field components and the transverse kicks are almost identical; this design does not have noticeable field asymmetry. Figure 9 shows the transverse momentum gain calculated for the full beta range, electric components are plotted on the left (a) and magnetic on the right (b). Since $\Delta p_x c$ and $\Delta p_y c$ electric and magnetic are identical in the plots, it is worth looking at the parameter

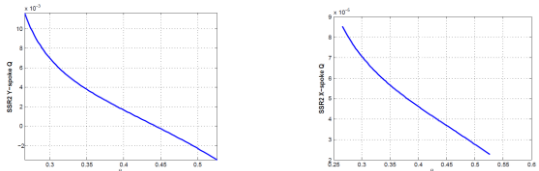
Copyright © 2013 CC-BY-3.0 and by the respective authors

Q versus particle beta: figure 7 (b) shows how small the residual asymmetry is. The parameter Q for this cavity dropped to the 10^{-5} range.



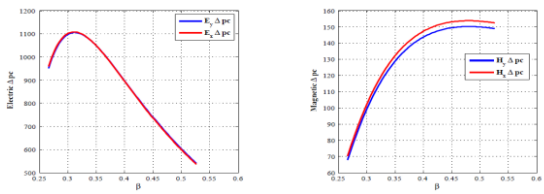
(a) (b)

Figure 6: SSR2 transverse field on 10 mm offset (a) Y-spoke, (b) X-spoke.



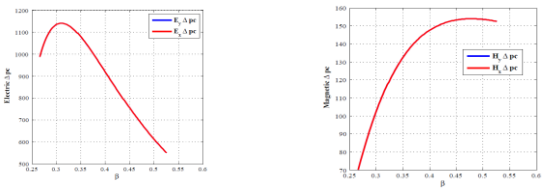
(a) (b)

Figure 7: Q parameter vs. beta (a) SSR2 Y-spoke, (b) SSR2 X-spoke.



(a) (b)

Figure 8: SSR2 Y-spoke transverse kicks vs. beta, (a) electric and (b) magnetic.

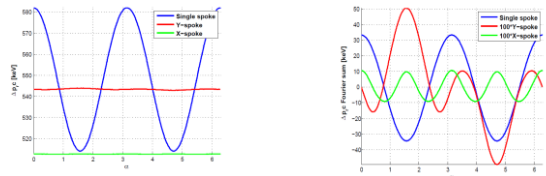


(a) (b)

Figure 9: X-spoke transverse kick components, (a) electric and (b) magnetic.

MULTIPOLE ANALYSYS

A more complete approach to the problem of transverse field asymmetry involves the expansion of $\Delta p_R c$ (the radial component of the transverse kick) in multipoles. One should to start by calculating the transverse kick at a given radial value, for all the angles on the x-y plane. Subsequently it is possible to decompose $\Delta p_R c(r, \alpha)$ in harmonics to evaluate the dipole, quadrupole, sextupole and octupole amplitudes. Figure 10(a) shows the angular dependence of $\Delta p_R c(r,\alpha)$ for all the three different designs of SSR2, calculated at r=10 mm for a synchronous particle (beta = 0.47) longitudinal energy gain of 4.5 MeV.



(a) (b)

Figure 10: (a) $\Delta p_R c$ as a function of the angle α, (b) Fourier sum of the radial kick, constant component excluded.

Figure 10(b) shows the Fourier series of $\Delta p_R c$, the plot does not include the constant radial component, included in 10(a) instead. In 10(b) the amplitudes of X and Y-spoke have been multiplied by a factor 100. Table 1 reports the values of the multipoles amplitudes, up to octupole; it confirms how beneficial the modification to the inner electrode is, quadrupole amplitude is highlighted.

Table 1: Multipoles Amplitudes Calculated at r=10 mm and 4.5 MeV Synchronous Particle Energy Gain

Amplitudes	Single spoke	Y-spoke	X-spoke
1st[keV]	5.812e-14	2.57E-01	6.31E-14
2nd[keV/mm]	3.391	1.76E-03	0.000717
3rd[keV/mm^2]	4.331e-16	2.43E-03	2.77E-16
4th[keV/mm^3]	4.747e-4	9.52E-07	9.67E-05
5th[keV/mm^4]	4.957e-18	3.58E-07	5.58E-18
6th[keV/mm^5]	2.338e-08	1.53E-07	2.89E-08
7th[keV/mm^6]	1.367e-19	4.31E-09	2.91E-20
8th[keV/mm^7]	2.719e-10	3.49E-10	6.35E-10

CONCLUSIONS

Alternative designs for a spoke resonator have been presented; the work has been driven by reduction of the field asymmetry which leads to a quadrupole perturbation on beam dynamic. Quadrupole amplitude has been reduced significantly and the X and Y-spoke designs have symmetric transverse fields (electric and magnetic). The approach to cavity design presented in this paper can be used for any spoke resonator which shows transverse field asymmetry.

REFERENCES

[1] P. Berrutti et al, "Multipole effects study for Project X front end cavities", WEPPC044, IPAC12 proceedings.

[2] J. Ostiguy, "Residual focusing asymmetry in superconducting spoke cavities", WEPS066, IPAC 2011 proceedings.

[3] P. Berrutti et al,"Effects of the RF Field Asymmetry in SC Cavities of the Project X", WEPPC047, IPAC12 proceedings.

Copyright © 2013 CC-BY-3.0 and by the respective authors

MULTIPACTING SIMULATIONS OF SSR2 CAVITY AT FNAL*

P. Berrutti#, T. Khabiboulline, L. Ristori, G. Romanov, A. Sukhanov, V. Yakovlev,
Fermilab, Batavia, IL 60510, USA

Abstract

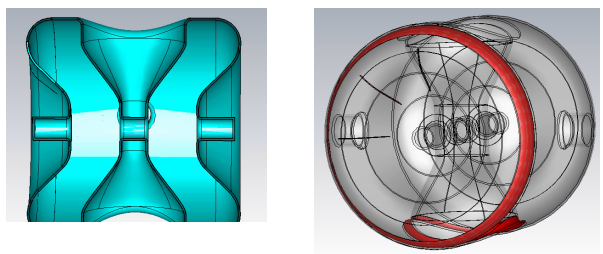
SSR2 is the second family of single spoke resonator under development at Fermi National Accelerator Laboratory (FNAL). These cavities will be placed in Project X front-end after SSR1 spoke resonators, which have already been built and tested and FNAL. Spoke cavities are affected by multipacting and the nature of their 3D geometry does not allow simulating the multipactor process using 2D tools. 3D tracking simulations, of electrons inside the cavity volume, have been carried out using CST Particle Studio. Different Secondary Emission Coefficients have been applied to the cavity walls in order to understand how strongly the multipacting depends on material properties. The power levels used in simulations cover the whole operating gradient range of SSR2 cavity. Results of these simulations are compared to the one given by SSR1 model, which demonstrated good agreement with experimental data. The purposes of this paper are to present the results gotten from the tracking solver, to give a prediction of what will be the multipacting scenario for SSR2 cavity and if there will be any dangerous zone for operation.

INTRODUCTION

Multipacting affects SRF cavities from high energy elliptical cavities to coaxial resonators for low-beta application. This work is focused on multipacting in low-beta structures; the main aim is to present the results of SSR2 cavity for Project X. SSR2 is a spoke resonator in development for Project X at Fermilab [1], it operates at 325 MHz and its optimal beta is 0.51. The design has been finalized recently it was necessary to understand at what level this resonator is affected by multipacting (MP), what the critical gradients are and where the MP develops in the cavity geometry. The software used for MP simulations is CST Particle Studio which provides a particle tracking solver that uses the field from the eigen-mode solver of Microwave Studio. The figure of merit chosen as a final result of tracking simulations is the growth rate, which gives information on how fast the number of particles increase with time. Simulation of MP in SSR2 cavity have been run for three different niobium secondary emission yields (SEY): in CST environment the highest emission for niobium is given by the wet treated material, a bake out model gives the intermediate one and the lowest yield is given by the discharge cleaned niobium. The growth rate has been calculated in a wide range of gradients and the MP locations have been identified for the major MP barriers. The experience of Fermilab with MP in low-beta structure started with SSR1, which is the lower optimal beta spoke resonator for Project X, operating at 325 MHz as well. Multipacting in SSR1 cavity has been simulated, using the same approach as for SSR2, and these results have been compared with experimental data from multipacting barriers found during the vertical test of SSR1 cavity [2], [3]. All this has been done in order to compare SSR1 and SSR2 multipacting simulations, and to understand how reliable and accurate the results of these simulations are.

SIMULATION SET UP

In order to simulate multipacting using CST particle studio it is necessary to create a shell all around the cavity volume to have an emitting material. The outer layer has been grown from the outside of the vacuum volume of the cavity, without interfering with the inner ideal surface. Figure 1(a) shows the geometry of SSR2 used for multipacting simulations in the x-y cut plane view. Once created the emitter shell the primary particle sources needed to be built. They were placed on the geometry taking advantage of the symmetry of the spoke resonator. Figure 1(b) shows the particle sources chosen for SSR2 MP simulations; red surfaces indicate sources of primary electrons. This set up has been used for SSR1 simulations as well; it has been previously described in [4] when the first multipacting simulations of SSR1 cavity were done.



(a) (b)

Figure 1: (a) outer shell built around SSR2 geometry x-y plane view, (b) particle sources are highlighted by red surfaces.

Primary particles were launched from the sources with an initial energy ranging from 2 to 6 eV, the angle was chosen randomly by the solver to get an isotropic electron emission. When simulating multipacting it is extremely important to have the mesh dense enough in the locations where the MP happens, the multipacting spatial scale is much smaller than the cavity dimensions. Multipacting occurs in regions where the electric field is not high, compared to the accelerating field, and the magnetic field bends the trajectories in a way that they satisfy the resonant condition. Electron trajectories could be very small compared to the cavity radius or length especially for complicated shapes like spoke resonators; thus a very fine mesh is required to get accurate EM field calculation

*Work supported by D.O.E. Contract No. DE-AC02-07CH11359
#berrutti@fnal.gov

Copyright © 2013 CC-BY-3.0 and by the respective authors

and reliable particle tracking in the multipacting regions. The emission model used is by Particle Studio is the Furman probabilistic model, which takes into account elastic backscattered, re-diffused and true electrons. The last ones are the responsible for electron growth since the backscattered and the re-diffused do not produce secondary particles. The available settings of secondary emission yield for niobium are three and all of them have been used in simulations, to understand how strongly the multipacting depends on the material property. Figure 2 compares the three SEY curves used, the plot is meant for a primary particle hitting the material perpendicularly to the surface.

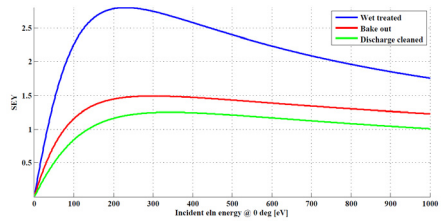
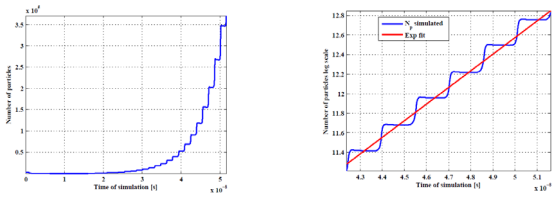


Figure 2: SEY of Nb as a function of the incident electron energy.

GROWTH RATE CALCULATION

A typical output from a multipacting simulation consists in a plot of the number of particles versus time of simulation. When multipacting occurs this curve can be approximated using an exponential function of time, the growth rate (GR) is the exponential coefficient that multiplies the time; after the MP is started the number of particles can be expressed by: $N(t) = N_0 e^{\alpha(t-t_0)}$. Where α is the growth rate, usually expressed in ns^{-1}, and N_0 is the number of particles at $t = t_0$, the time at which the MP process starts.



(a) (b)

Figure 3: (a) exponential particle growth vs. time, (b) last 3 RF periods of simulation time, particle number and its exponential fit.

Figure 3(a) shows the growth of particle with simulation time, usually the multipacting does not start immediately but it needs few RF periods to be engaged. Figure 3(b) shows the particle number and its approximation, y axis has been put in logarithmic scale; the figure shows the last 3 RF periods of simulation time, the one used to evaluate the growth rate value. From figure 3(b) it is clear that the resonant condition has been reached since the number of particles is increasing every half RF period, six steps appear over a simulation time of 3 RF cycles. The optimal number of RF periods to use for growth rate calculation has been chosen by looking at the GR values dependence on the RF cycles used for interpolation. Figure 4 shows the GR for number of RF periods going from 1 to 5, the optimal amount is considered to be around 3.

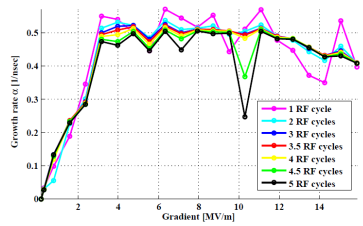


Figure 4: GR dependence on RF cycles used for the exponential fit.

The definition of gradient used in this paper is in agreement with the one used in Project X documents and it is based on a definition of effective length of the cavity expressed by $L_{eff} = \beta_{opt}\lambda$; the gradient is therefore $E_{acc} = \Delta W_{max}/L_{eff}$, where ΔW_{max} is the energy gain for a particle traveling at optimal beta through the cavity with zero synchronous phase.

SSR2 MP SIMULATIONS

SSR2 growth rate has been calculated for E_{acc} ranging from approximately 1 to 15 MV/m; the maximum energy gain for the cavity in Project X lattice is currently 5 MeV, which corresponds to $E_{acc} \simeq 10.6$ MV/m [5]. The growth rate summary plot is presented in figure 5, it includes all three different material used in simulations.

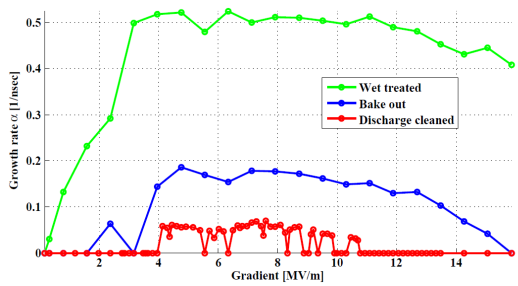
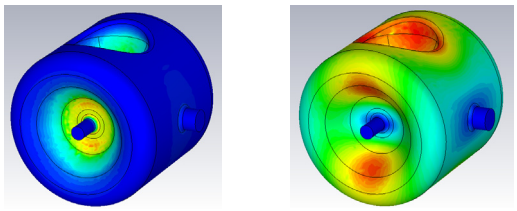


Figure 5: SSR2 GR vs. gradient summary.

The wet treated emission model has been allowing multipacting throughout the whole gradient range, so it did not give any information about particular barriers proper of the cavity geometry. Bake out SEY has helped in reducing the high number of secondary electrons generated, lowering the overall growth rate and some low gradient MP disappeared. The discharge cleaned material has allowed seeing different MP barriers in the medium-high gradient range, low and high power multipacting have not been observed. The number of points on the red curve has been increased to enhance its resolution and not to miss small barriers. Multipacting locations have been observed looking at the particle trajectory plots, in order to understand why and how the MP locations move from one spot to another it is fundamental to know the field distribution in the cavity. To increase the gradient means to increase the fields, electric and magnetic, the electrons move accordingly with field amplitude which can satisfy

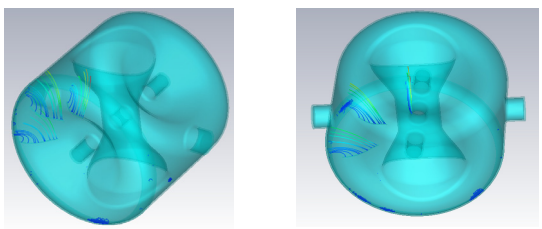
Copyright © 2013 CC-BY-3.0 and by the respective authors

the resonant condition. When the gradient is increasing linearly, MP moves to lower field areas to find the same field levels as for lower gradients. Figure 6 shows the field distribution is SSR2 (a) electric and (b) magnetic. Looking at fig. 7, which shows MP locations at different E_{acc} values, it seems that MP affects SSR2 cavity in the corners of the outer cavity wall. The MP spots move from the spoke vertical position, at low E_{acc}, to almost horizontal position on the corners, at higher gradients.



(a) (b)

Figure 6: SSR2 field distribution, (a) electric and (b) magnetic.



(a) $E_{acc} = 4.4$ MV/m (b) $E_{acc} = 6.6$ MV/m

(c) $E_{acc} = 8.7$ MV/m (d) $E_{acc} = 10.4$ MV/m

Figure 7: multipacting locations at different gradients.

SSR1 MP SIMULATIONS

Since several SSR1 resonators have been tested and multipacting barriers have been experimentally observed; the results of multipacting simulations of SSR1 have been compared with the data collected during the vertical tests of the cavities. Comparing the simulation results with the experimental data helps in understanding how accurate the simulations are, and how far from reality the model is. SSR1 simulations have been compared with experimental data and then with SSR2 MP, to see if the new cavity will have multipacting barriers whether softer or harder than the one observed during the tests of SSR1. The growth rate values of SSR1 and SSR2 are plotted in figure 8, the graph shows the data related to the lowest SEY model, since it is the only one the allows to see different MP barriers. SSR2 cavity shows harder multipacting barrier having higher growth rate values, the MP seems to occur for a wider power range as well. SSR1 has two main MP barriers according to simulations: the first ranges from 4 MV/m to 6 MV/m, the higher barrier starts at 6 MV/m and ends around 8 MV/m.

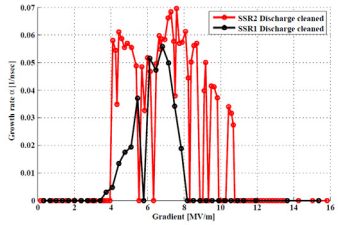


Figure 8: SSR1 and SSR2 GR comparison, discharge cleaned material.

The cold test data of all the SSR1 cavities is compared to the simulated growth rate in figure 9, which shows the time spent on each barrier for processing: around 4.5 and 6.5 MV/m all the cavities tested needed several hours for the MP to be processed, the black line in the plot represents the sum, on all cavities, of the time spent for processing. The simulations predict the two main barriers which all the tested cavities are showing during cold tests. The multipacting in SSR1 needs several hours to be processed and overcome; since SSR2 MP simulations showed an even worse scenario, the cavity may be subject to geometry changes to mitigate this phenomenon.

Figure 9: SSR1 MP processing time and growth rate.

CONCLUSIONS

MP has been simulated in SSR2 and SSR1 cavities for Project X, the results of SSR1 simulations have been compared with experimental data and the agreement seems good. SSR2 shows MP barriers harder and wider than SSR1, in the future SSR2 design may be slightly adjusted to mitigate the multipacting. Since the MP locations have been found the modification would involve slightly rearrangements of the outer wall corner.

REFERENCE

[1] M. Merio, P. Berrutti et al, WEPWO057, Proceedings of IPAC13.
[2] A. Sukhanov et al., MOP014, Proceedings of SRF 2013.
[3] T. Khabiboulline, Proceedings of IPAC12, WEPPC052.
[4] G. Romanov, MOP043, Proceedings of LINAC08.
[5] N. Solyak et al, THPWO092, Proceedings of IPAC13.

Copyright © 2013 CC-BY-3.0 and by the respective authors

New Helium Vessel and Lever Tuner for the 650 Mhz Cavities for Project X*

I. Gonin#, M. Awida, E. Borissov, M. Foley, C. Grimm, T. Khabiboulline, M. Merio, Y. Pischalnikov, L.Ristori, V. Yakovlev, FNAL, Batavia, IL 60510, USA

Abstract

The proposed design of the 3 GeV Project X Superconducting Linac employs two families of 650 MHz 5-cell elliptical cavities with different β. The β_G =0.61 will cover the 177-467 MeV range. To cover the range between 467-3000 MeV two versions of 650 MHz 5-cell elliptical cavities with β_G =0.9 and β_G =0.92 has been proposed. The low beam current for CW operation of the Project X requires cavities to operate at a high loaded Q and thus, narrow bandwidth. Therefore it requires the optimal mechanical design of cavities to minimize the sensitivity to microphonics.

INTRODUCTION

Fermilab is currently developing a multi-MW proton source, Project-X (PX) [1], which will provide intense muon, kaon, neutrino and nuclei beams for broad and diverse program at the intensity frontier of particle physics. Possible future upgrades of Project-X may require operating linac in a regime of a high beam current, when an average beam current is 5 mA or even 10 mA. The design of 5-cell elliptical 650 MHz β_G =0.9 is under development at Fermilab. An alternative design of elliptical cavity with a larger aperture (59 mm) and β_G=0.92 is suggested for HE 650 MHz section in order to comply with various upgrade scenarios of the Project X linac [2]. The design of a dressed cavity (both β_G =0.9 and β_G =0.92) has been mechanically optimized by minimizing df/dP, the sensitivity to microphonics detuning due to fluctuations in helium pressure. The results for β_G =0.9 version has been presented at IPAC 2013 [3]. In this paper we will present the results of COMSOL simulations of df/dP, mechanical resonances and cavity tunability of an alternative β_G =0.92 cavity. We will also present the mechanical design of tuners and ANSYS analysis of their properties. The tuner system will be identical for both versions of cavities design.

HELIUM VESSEL DESIGN

The helium vessel assembly is constructed from a single 5 mm thick sheet of grade 2 titanium that is rolled and seam welded into a tube with an inside diameter of 441 mm and a length of 930 mm. Two helium fill ports are featured to allow for an even cool-down of the cavity. The helium vessel assembly is shown in Figure 1. The weld joint designs on the helium vessel satisfy the ASME Boiler & Pressure Vessel Code Section VIII Division 2. It is important to note that the 5 mm wall thickness for the helium vessel specification was not because of the ASME code, but rather to help in reducing *df/dP* by using the helium vessel to help stiffen the cavity.

* Operated by Fermi Research Alliance, LLC, under Contract DE-AC02-07CH11359 with the U.S. DOE

gonin@fnal.gov

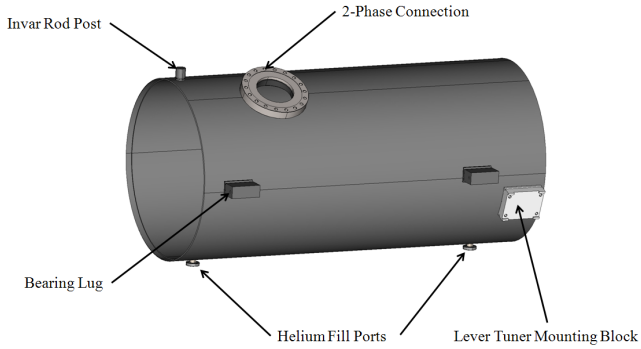


Figure 1: He vessel assembly.

The main coupler end and the field probe end of the helium vessel have slightly different joint designs due to the cavity installation sequence and variations in cavity lengths. The main coupler end of the vessel is considered a fixed position relative to the main coupler port of the cavity, and consistency between these key features for dressed cavities is maintained. Figure 2 shows the titanium-to-titanium TIG weld connection between the cavity and the helium vessel at the main coupler end. This joint design utilizes a backing ring and satisfies the ASME code.

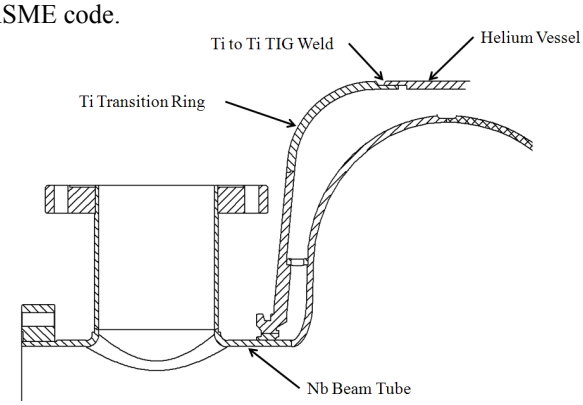


Figure 2: He vessel to cavity fixed joint design.

To allow for variations in the lengths of the manufactured cavities, the field probe end required a sliding joint design that would allow for cavity insertion from the field probe end to the main coupler end. As shown in Figure 3, cavities that vary by ±10 mm in length will not have any effect on the vessel design. This joint also satisfies the ASME code.

Copyright © 2013 CC-BY-3.0 and by the respective authors

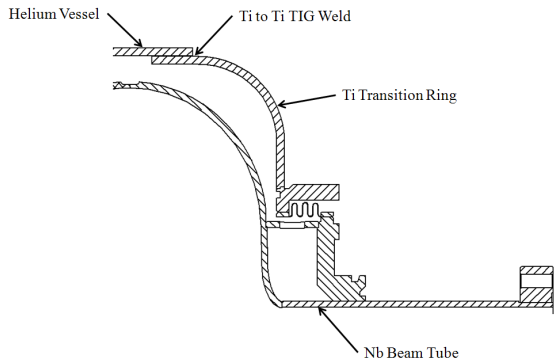


Figure 3: He vessel to cavity sliding joint design.

Dressed Cavity Pressure Boundary

Where practical, the overall cavity design must adhere to the ASME Boiler and Pressure Vessel Code. The pressure boundary will consist of the cavity walls, the connecting flanges, conical disks, and the helium vessel shell. This is outlined in Figure 4.

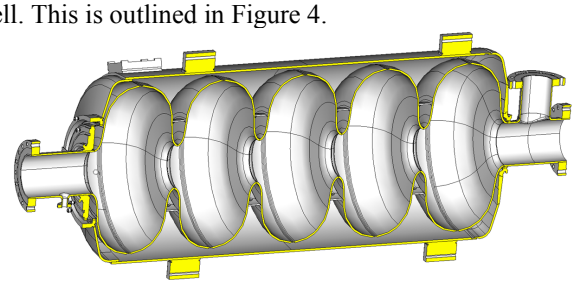


Figure 4: Pressure boundary of dressed cavity shown in yellow.

All electron-beam (EB) welds within the pressure boundary defined above are required to have a fully consumed joint: i.e. duel pass with full overlap or full penetration.

TUNER SYSTEM DESIGN

A compact fast/slow tuner for both versions of cavities has been developed for final tuning of the resonance frequency of the cavity after cooling down and to compensate frequency detuning due to the microphonics.

As shown in Figure 5, one end of the cavity is equipped with a lever tuner. The lever tuner was designed

- to tune cavity in the range of 200kHz.
- able to deliver up to 20kN forces on the cavity.
- fast tuning range up to 1kHz.

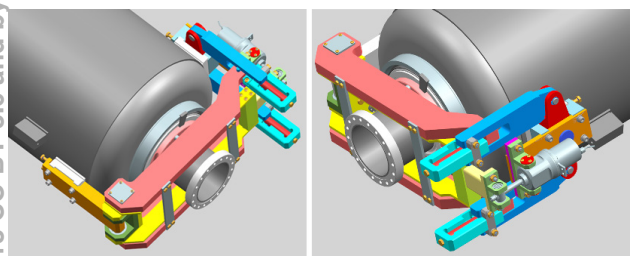


Figure 5: Lever tuner installed on dressed 5 cell cavity.

MECHANICAL ANALYSIS

The mechanical analysis of the β_G =0.92 650 MHz 5-cell elliptical cavity has been performed using the COMSOL and ANSYS FEA software. Figure 6 details a cross-section of the mechanical assembly including the niobium cavity shell and HV. Table 1 lists the material properties for 2K operating temperature used in the simulations. This assembly has different end groups – the left end group incorporates the slow and fast tuning systems and the right end group incorporates the main coupler.

The mechanical design of the cavity includes the following:

- Optimization of the df/dP, the sensitivity to microphonics detuning from fluctuations in helium pressure.
- Cavity tunability analysis.
- Incorporate the slow (stepper motor) and fast (piezo actuator) tuner designs. The slow tuner should be compact, reliable and provide the required tuning range, (about 200 kHz) keeping the cavity deformation below the yield limit.
- Simulations of cavity sensitivity to microphonics due to mechanical resonances and LFD.

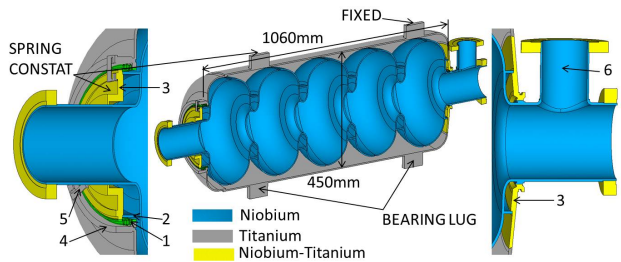


Figure 6: COMSOL model of mechanical assembly used in simulations. 1–bellows, 2–stiffening ring between end half-cell and conical flange, 3–conical flange, 4–bellows ring, 5–support brackets, 6–main coupler. Left – tuner end group. Right – main coupler end group.

Table 1: Mechanical Properties of Materials at 2K

	Young's modulus, GPa	Poisson's ratio	Density kg/m^3
Niobium	118	0.38	8700
Titanium	117	0.37	4540
Niobium-Titanium	68	0.33	5700

Optimization of df/dP

Initially the goal was to minimize df/dP as much as possible so we chose a middle stiffening ring radius of 134 mm (A) that resulted in df/dP < 5 Hz/mbar, however the cavity becomes quite stiff ~18 kN/mm at this ring radius. Room temperature RF tuning of the cavity was questionable. Afterwards, for an alternative β_G =0.92 cavity design we made a decision to sacrifice df/dP for the sake of making the cavity more tuneable and less stiff in order to avoid complicating the tuner design. A smaller

Copyright © 2013 CC-BY-3.0 and by the respective authors

diameter of bellows was proposed in order to help reduce df/dP of the dressed cavity.

COMSOL multiphysics 3D simulations of df/dP in the model presented in Fig. 6 has been done**.** The RF volume deformation induced by internal pressure determines the frequency shift. Boundary conditions used in calculations are:

- fixed displacement one of the bearing lug of Vessel.
- tuner stiffness is simulated by applying the spring constant K_{tuner}.

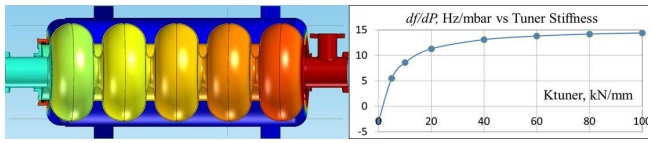


Figure 7: Total displacement for 1 bar internal pressure (K_{tuner} =20 kN/mm) and df/dP vs. stiffness of the tuner.

Fig. 7 shows the total displacements for an internal pressure of 1 bar with a 20 kN/mm tuner stiffness and dependence of df/dP vs. tuner stiffness. Modern cryogenic systems achieve rms pressure stabilities of ~0.2 mbar. It means, that even in case of infinite tuner stiffness, one can expect the maximum frequency deviation due to pressure fluctuation will be <4 Hz.

Mechanical Resonances

Mechanical resonances of cavities in a cryomodule can be excited by external vibrations. Fig. 8 represents the displacement plots of 10 lowest mechanical modes (7 of them are transverse T#1-T#7 and 3 longitudinal L#1-L#3). Boundary conditions used in the calculations are similar to the calculations described in the previous section. Fig. 8 shows the dependencies of the 3 lowest longitudinal modes vs. tuner stiffness.

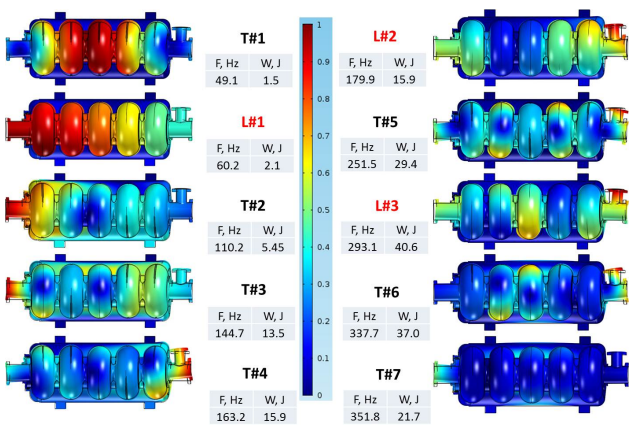


Figure 8: Frequencies, total energy, and COMSOL plots of normalized displacements of 10 lowest mechanical modes. Normalization is 1 mm maximum displacement.

ALLOWABLE WORKING PRESSURE

The dressed cavity has to be rated for a Maximum Allowable Working Pressure (MAWP) of 2 bar at Room Temperature (RT) and 4 bar at Cryogenic Temperature (CT). Preliminary structural analyses have been performed to verify that this requirement can be met. Different loading conditions have been studied; these are a combination of He pressure, dead weight, cooldown and tuner displacement. For each analysis, the Equivalent Stress is computed with finite element code and compared to the yield limit of the materials used (see Table 2). The results show that the MAWP required can be achieved under all the loading conditions.

Table 2: Yield Limit of the Materials Used for the Dressed Cavity

	Niobium	**Nb-45Ti**	**Titanium, grade 2**
RT (300 K)	38 MPa	475 MPa	275 MPa
CT (2 K)	317 MPa	544 MPa	834 MPa

Figure 9 shows the Von Mises Stress distribution for the cavity cooled down at 2 K and with a He pressure of 4 bar. The Equivalent Stress is below the yield of each material.

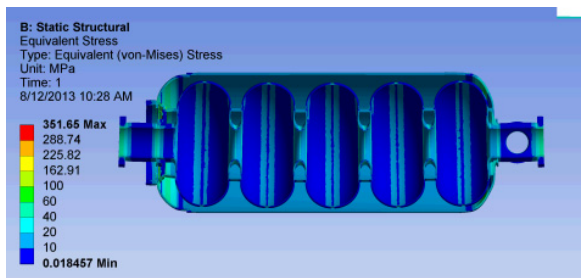


Figure 9: Equivalent Stress distribution at 2 K with 4 bar pressure applied.

Preliminary linear mechanical analyses have been done and show that the MAWP of 2 bar at RT and 4 bar at CT can be achieved. In the future, a set of linear, elastic plastic and local analyses will be performed to ensure that the dressed cavity complies with ASME Boiler and Pressure Vessel Code requirements.

REFERENCES

[1] http://projectx.fnal.gov/
[2] A. Lunin, A. Saini, A. Sukhanov, N. Solyak, V. Yakovlev, Alternative Cavity for the HE Part of the Project X Linac, IPAC 2012, New Orleans, Louisiana, USA, May 20–25, 2012.
[3] IPAC 2013, Shanghai China, WEPWO056.

Copyright © 2013 CC-BY-3.0 and by the respective authors

CM2, SECOND 1.3 GHZ CRYOMODULE FABRICATION AT FERMILAB*

T. Arkan#, M. Awida, P. Berrutti, E. Borissov, C. Ginsburg, C. Grimm, E. Harms, A. Hocker, T. Khabiboulline, Y. Orlov, T. Peterson, R. Pilipenko, Y. Pischalnikov, K. Premo, L. Ristori, W. Schappert, V. Yakovlev, FNAL, Batavia, IL 60510, USA

Abstract

CM2 is the second 1.3GHz Cryomodule assembled at the Cryomodule Assembly Facility (CAF) in Fermi National Accelerator Laboratory. The string has a corrector coil magnet, a beam position monitor and eight cavities. All cavities are qualified at >= 33 MV/m gradient at the Horizontal Test Facility (HTS) before assembly. The dressed cavities were outfitted with magnetic shielding, blade tuner. The cold mass was assembled based on the Tesla TTF Type III+ cryomodule design. CM2 is currently being installed into the test stand in NML where it will be cooled down and high power tested. CM2 will also be the first cryomodule to be tested with an electron beam at the NML facility. This paper describes the assembly steps, the quality assurance methods and the challenges experienced during assembly and qualification at CAF.

INTRODUCTION

Fermilab's second 1.3 GHz cryomodule (aka CM2 or RFCA002) was assembled between July 2011 and March 2012. During the installation of this module at NML test facility, a vacuum leak was discovered in the 2-phase helium circuit. The module was brought back to CAF in June 2012 and was partially disassembled to find the location of the leak and to repair it. The module was then reassembled and transported to NML in April 2013. The module is currently being installed on the test stand. The cool-down and high power radio frequency (RF) test of the module is planned to start in September 2013.

CAVITIES AND COLD MASS COMPONENTS

All eight cavities manufactured by industrial vendors were specifically selected to be likely to achieve the ILC design goal based on their performance in individual RF tests [1]. The cavities were first tested "bare" in a vertical liquid helium dewar using low-power continuous-wave RF. Cavities which met the ILC vertical test specification ($E_{acc} \geq 35$ MV/m, $Q_0 \geq 0.8 \times 10^{10}$) were then welded into individual helium jackets at CAF and outfitted with a high-power input coupler. The high power couplers were purchased from CPI. The couplers were cleaned and high power conditioned at SLAC. These "dressed" cavities were then tested in the HTS using high-power pulsed RF. Qualified cavities along with a corrector coil magnet outfitted with XFEL style helium jacket and a button style beam position monitor (BPM) were all assembled into a cavity string in the CAF cleanroom. INFN design blade tuners [2] were purchased from Incodema. The tuner motors and gears were purchased from Phytron and Harmonic Drive Inc. The magnetic shielding parts were designed by Fermilab and were purchased from Amuneal. The vacuum vessel, gas return helium pipe (GRHP) assembly and cold mass support posts were procured from Zanon in Italy.

*Work supported by the U.S. Department of Energy
#arkan@fnal.gov

CRYOMODULE ASSEMBLY

Cavity String Assembly

The assembly of the cavity string was done in the CAF cleanroom situated in the CAF-MP9 building. Eight qualified cavities, a magnet, a BPM and two gate valves were interconnected using bellows in the Class 10 cleanroom. The assembly of the cavity string is the most important step throughout the cryomodule assembly to ensure that the measured gradient of the qualified cavities is preserved. Particulate-free-flange-assembly techniques were developed and optimized throughout the years at various institutions working on SRF R&D. CAF cleanroom technicians have over 7 year experience in particulate free ultra-high vacuum applications. CM2 cavity string (See Figure 1) was assembled while following the assembly travelers and working with strict adherence to the CAF cleanroom working protocols.

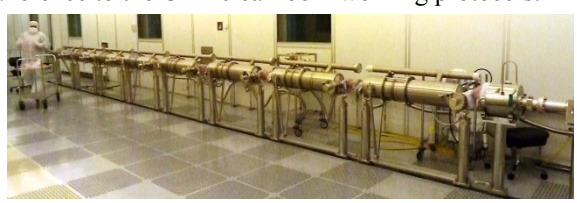


Figure 1: CM2 cavity string in the cleanroom.

Cold Mass and Final Assembly

After the string assembly was completed, the string was rolled out of the cleanroom into the cold mass assembly area at CAF-MP9 using the assembly rail. The 2-phase pipes of the cavities were interconnected using titanium (Ti) bellows welded using an automated orbital welding machine conforming to the ASME piping code. The cavities were then outfitted with magnetic shielding and blade tuner components. The cavity string was then lifted from the assembly fixtures and married to the GRHP assembly forming the cold mass assembly. The cold mass assembly was then transported to CAF-ICB building (See Figure 2). The X-Y axis alignment of the cavities to 250 microns was done using a laser tracker instrument. The cold mass was then transferred to the Big Bertha

Copyright © 2013 CC-BY-3.0 and by the respective authors

cantilever fixture for the welding of heat shields and multi-layer insulation (MLI) installation. (See Figure 3) The cold mass was then moved to the final assembly area in CAF-ICB where the warm end high power couplers and waveguides were assembled.



Figure 2: CM2 cold mass transport.

Throughout the cold mass assembly, several temperature sensors were installed on the critical components; RF measurements of the cavities were done several times and various vacuum leaks and pressure tests were conducted. After the final quality assurance checks, the fully assembled cryomodule was transported to the NML test area (see Figure 4).



Figure 3: CM2 cold mass on the Big Bertha fixture.



Figure 4: CM2 transport to NML.

CHALLENGES EXPERIENCED

Tuner Motor and Harmonic Drive Reliability

First tuner prototypes were designed and built at INFN and delivered to Fermilab. 50 blade tuners were later fabricated in U.S. industry. The Phytron brand tuner motor and the Harmonic Drive gearbox used for CM2 tuners were also used on most tuners worldwide. (See Figure 5)

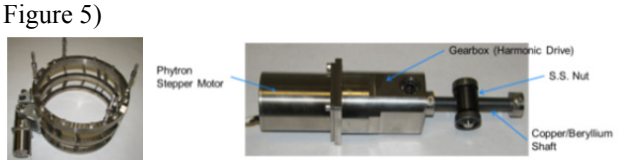


Figure 5: Blade tuner, motor, gearbox.

During the qualification and testing of the tuner components prior to the assembly of CM2 cavities, several mechanical problems were encountered:

1. Harmonic drive wave generator connection to the motor shaft: (See Figure 6)

- Phytron motor shaft has no provisions for a mechanical hard stop
- Dog-point set screws may lose grip on the shaft causing the wave generator to slip

Corrective Action – the motor shaft was cross-drilled and pointed set-screws were inserted with cryogenic grade Loctite.



Figure 6: Harmonic drive wave generator connection to the motor shaft.

2. Harmonic drive flex gear connection to copper/beryllium shaft: (See Figure 7)

- Screws may loosen causing gear to disengage from shaft causing gears to bind

Corrective Action – Internal lock washers were added under the screws and cryogenic grade Loctite was added.



Figure 7: Harmonic drive flex gear connection to copper/beryllium shaft.

Addressing CM2 coarse tuner reliability issues one tuner was tested at warm condition on the bench test. An automatic program ran actuator for 6 million steps to simulate real operating conditions. RF measurements were taken during the process to validate tuning progress. After test decision was made that "6millions steps at warm condition test" is too harsh to the shaft/nut coating. Instead all the eight CM2 motors installed on the cavities during cold mass assembly were subjected to 400-ksteps (~1% of the lifecycle).

In parallel with the warm testing, there was an opportunity to perform a cold full lifecycle test with a prototype cavity in HTS. The goal was to test the motor over a 10 day period to reach 30 million steps. The 30 million steps represents about 15-20 years of thermal cycling and cryomodule operation. This part of the test was completed successfully with the tuner/motor still functioning as predicted. Decisions were made to continue the cold test until a failure occurred or the system reached 60-million steps. At 31-million steps, the system suffered a failure. (See Figure 8) An autopsy was performed on the motor assembly and it was determined that the harmonic drive gear stripped and the wave generator got stuck in the spline gear.

Copyright © 2013 CC-BY-3.0 and by the respective authors

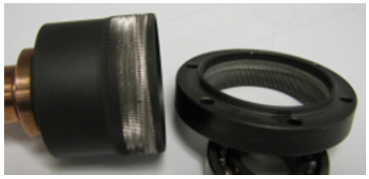


Figure 8: Harmonic drive gear failure.

Cavity HOM Antenna Shorts

During the electrical quality assurance checks of CM2 cryomodule, electrical shorts were found in three cavities at the high order mode (HOM) feedthrough connectors. An investigation of component dimensional tolerance stack up was undertaken to determine the cause. As it can be seen from Figure 9, the design distance between the antenna tip and the formteil is 0.5 mm. Taking into account that the antenna is assembled on the connector with a press-fit method in the cleanroom prior to the assembly of the feedthrough flange to the cavity, a tolerance stack up due to out of spec dimensions of individual components might cause an electrical short when the tip of the antenna touches the formteil.

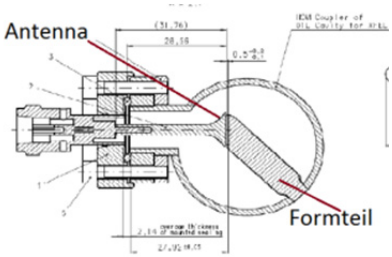


Figure 9: HOM Antenna assembly to the HOM coupler.

It was deemed that this problem will not be a critical issue for CM2 operations. However, all components in inventory were measured and the antenna tips were trimmed appropriately. It was also decided to conduct capacitance measurements on feedthrough flanges after these are assembled on the cavity in the cleanroom to ensure that there are no shorts.

Vacuum Leak on the 2-phase Circuit

During the vacuum leak checks of CM2 at NML testing facility, a vacuum leak was observed on the 2-phase helium circuit pipe. Initial leak checks at NML showed that the leak was in the vicinity of the Ti bellows between Cavity #8 and the magnet. (See Figure 10) The module was then transported back to CAF for partial disassembly and repair. The vacuum vessel, MLI and lower heat shields were disassembled in order to access the 2-phase pipe. After disassembly, it was observed that the magnet moved approximately 14 mm towards Cavity #8. Further investigation showed that the invar rod clamp designed to hold the spacing between the magnet and the cavity failed to restrain the magnet during vacuum pump down due to vacuum forces exerted on the clamp. After the magnet was moved back to its design distance, new clamps were designed and installed for the magnet and the cavities. We then started the leak check efforts and surprisingly no vacuum leaks were observed. Various leak checks, pressure tests in different configurations were done throughout a 3-month period to replicate the leak that was observed at NML.

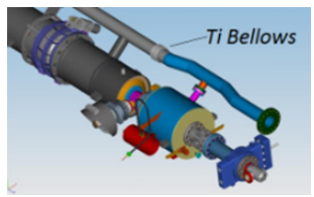


Figure 10: Ti bellows between magnet and cavity #8.

After several months of effort, a leak was observed. The leak appeared while checking the 2-phase helium circuit with the cold mass fully bagged and filled with helium. Further leak checks in the same morning without the bag showed a leak (mid 10^{-7} mbar x l/s) on the same Ti bellows that we observed a similar range leak at NML. Without changing the setup, the leak check inspector tried to confirm the leak in the afternoon. Surprisingly, the leak disappeared. We decided to replace the questionable Ti bellows with a new one. CM2 was then re-assembled. Further investigation was done on the removed Ti bellows to understand the strange leak behaviour. The bellows was sent out to an x-ray vendor but the analysis did not produce any useful results. Eventually, we were able to replicate the leak at Fermilab. First the bellows were cleaned and handled with UHV standards. The bellows were then pumped down and leak checked. The same range leak was observed on the seam weld of the bellows. If the technician touched the leak even with gloved fingers, the leak disappeared. Wiping with lint free cloths and using cleaning agents were not successful to open the leak. The bellows needed to be cleaned again with UHV standards in order to replicate the leak. It was deemed that the leak is so small that airborne dust particles, any residue from gloves might clog the leak and make it disappear. No further study was done on this bellows. Action items for future Ti bellows are to clean the bellows with UHV standards before incoming leak checks and always handle the UHV components with gloves and extreme care.

SUMMARY

The lessons learned during the fabrication of CM2 will be applied for future module assemblies at CAF.

ACKNOWLEDMENT

Special thanks to all the support (QC, RF, electrical, alignment & metrology, material handling) groups who helped CAF team during the CM2 fabrication.

REFERENCES

[1] C. Ginsburg, “Fermilab 1.3 GHz Superconducting RF Cavity and Cryomodule Program for Future Linacs”, LINAC’12, MOPB052.

[2] Y. Pischalnikov et al, “Test of a Coaxial Blade Tuner at HTS/FNAL”, PAC’11, TUP082.

Copyright © 2013 CC-BY-3.0 and by the respective authors

WAKEFIELD LOSS ANALYSIS OF THE ELLIPTICAL 3.9 GHZ THIRD HARMONIC CAVITY*

M. Awida#, P. Berrutti, A. Saini, T. Khabiboulline, and V. Yakovlev, Fermilab, Batavia, IL 60510, USA

Abstract

Third harmonic 3.9 GHz elliptical cavities are planned to be used in many particle accelerator projects such as XFEL, NGLS, and ASTA. In this paper, the wakefield losses due to bunches from 8 mm down to ultra short bunches of 10 μm are analysed. Both the loss and kick factors are numerically calculated for bunches of relatively long length (>1 mm) using CST wakefield solver. The data is then used to asymptotically extrapolate the values for ultra-short bunches by finding the wake functions. These calculations are essential to estimate the cryogenic losses in cryomodules and for beam dynamic analysis.

INTRODUCTION

Third harmonic cavities are commonly used in the particle accelerators of light sources to improve the bunch stability and compensate for the distortion that could happen between the sinusoidal accelerating field and the relatively long beam bunches [1-6].

Third harmonic 3.9 GHz cavities are currently under production for several projects. For instance, DESY's XFEL and FNAL's ASTA. Other future light sources (like NGLS) are also planning to use the third harmonic cavities.

In collaboration with DESY, Fermilab constructed a third harmonic cryomodule for the Free electron LASer in Hamburg (FLASH) facility [1-4]. Each cryomodule contains four superconducting radio frequency (SRF) cavities operating at 3.9 GHz. The third harmonic 9-cell cavities are designed to operate at 2 K in the TM_{010} π-mode at an accelerating gradient of 14 MV/m, summing up to a total energy gain of 20 MeV per cryomodule. These cavities operate in a decelerating phase of 179º relative to the beam phase, and are optimized for 9 mA of beam current.

In addition, another cryomodule will be fabricated for Fermilab Advanced Superconducting Test Accelerator (ASTA). ASTA plans to deliver 50 MeV beam for a broad range of beam-based experiments to push limits of particle-beam generation, acceleration and manipulation. ASTA plans to employ Superconducting 3.9 GHz cavities for bunch linearization.

Before accelerating beam with third harmonic cavities, it is imperative to estimate the cryogneic losses by analysing the wakefield losses. This paper reports on an extensive wakefield analysis, carried out on these third harmonic cavities, including the simulated loss and kick factors for sub cm beam bunches. Based on the simulated data and using an asymptotic approximation, we estimate the loss and kick factors for sub mm beam bunches.

WAKEFIELD SIMULATION FOR SUB CM BEAM BUNCHES

Figure 1 shows the geometry of the third harmonic 3.9 GHz 9-cells elliptical cavity. In different to the wakefield analysis in [5], we resorted to CST microwave studio to compute the wakefields inside a single cavity due to relatively long bunches, where the structure is excited by a longitudinal line current [7]. The line current is placed on the beam axis for the loss factor calculations, while the line is displaced off axis for the kick factor calculations. In both cases, the line current representing the beam is formed with a longitudinal, Gaussian shaped charge distribution.

Accuracy of the analysis was checked versus the mesh size. Typically, the ratio between the bunch sigma (standard deviation of the Gaussian distribution) to the mesh step size in the longitudinal direction *Sigma/h* is used to check the accuracy of the analysis with conventionally using *Sigma/h* of 20 as a satisfactory level of mesh refinement. In this analysis, we have used a *Sigma/h* of 30, as shown in Fig. 2. Mesh size of approximately 70 million elements (per quarter of cavity) was needed for the relatively short RMS bunch length of 2 mm, as shown in Fig. 2.

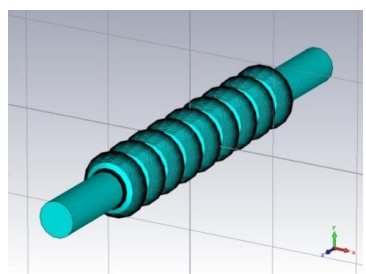


Figure 1: Geometry of the third harmonic 3.9 GHz cavity.

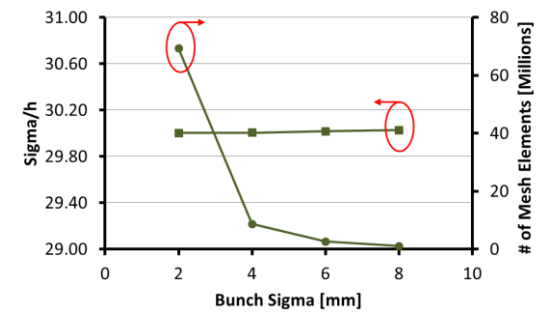


Figure 2: Sigma/h and number of mesh elements vs. bunch sigma.

*Operated by Fermi Research Alliance, LLC, under Contract DE-AC02-07CH11359 with the U.S. DOE

#mhassan@fnal.gov

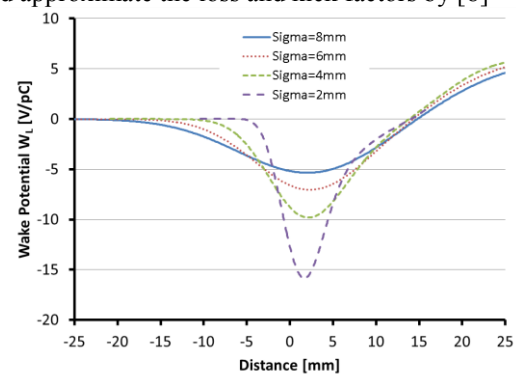
Copyright © 2013 CC-BY-3.0 and by the respective authors

Figure 3 shows the wake potential both in longitudinal and transverse directions for various RMS bunch lengths ranging from 8 mm to 2 mm. As expected, the peak absolute value of the wake potential increases as the RMS bunch length decreases. The longitudinal wake potential increases from 5 V/pC to 16 V/pC as the RMS bunch length decreases from 8 mm to 2 mm. On the other hand, the transverse wake potential increases from 0.4 V/pC/mm to 0.6 V/pC/mm as the RMS bunch length decreases from 8 mm to 2 mm. The peak of the longitudinal wake potential happens at approximately 2 mm distance for all bunch RMS lengths, while the peak transverse wake potential happens at approximately12 mm distance.

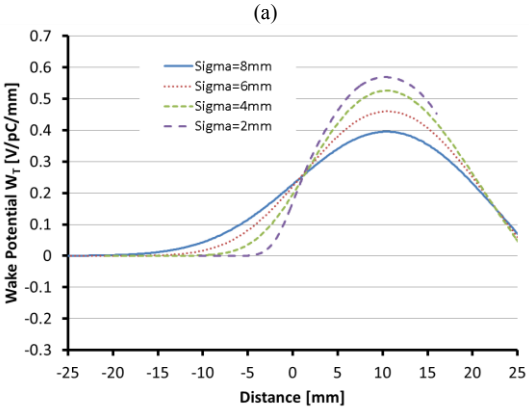
The loss and kick factors are shown in Fig. 4 (a) and (b), respectively. The loss factor varies from 3.5 V/pC to 10.5 V/pC as the RMS bunch length decreases from 8 mm to 2 mm, as shown in Fig. 4(a). On the other hand, the kick factor decreases from 0.22 V/pC/mm to 0.17 V/pC/mm over the same range.

ASYMPOTITIC APPROXIMATION FOR SUB MM BEAM BUNCHES

Computing the wakefield losses for ultra-short bunches is not possible using CST because of the mesh size limitation (for sub mm bunches, the mesh size would be in microns). In such case of ultra-short bunches, asymptotic approximation is typically used, where we could approximate the loss and kick factors by [8]

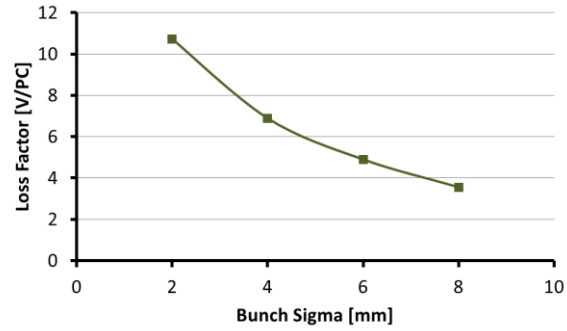


(a)

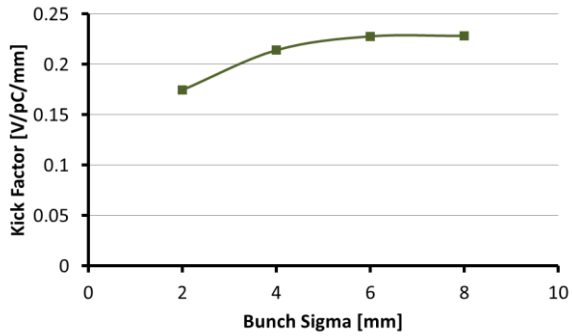


(b)

Figure 3: Wake potential for various bunch lengths. (a) Longitudinal. (b) Transverse.



(a)



(b)

Figure 4: Wakefield simulation results (a) Loss factor. (b) Kick factor.

$$L_{long} \cong \langle W^0_{long} \rangle = \frac{1}{Q}\int_{-\infty}^{\infty} W^0_{long}(s)q(s)ds$$

$$= \frac{1}{Q^2}\int_{-\infty}^{\infty}\int_{-\infty}^{s} w^0_{long}(s-s')q(s')q(s)ds'\,ds \quad (1)$$

$$L_{trans} \cong \langle W^1_{trans} \rangle = \frac{1}{Q}\int_{-\infty}^{\infty} W^1_{trans}(s)q(s)ds$$

$$= \frac{1}{Q^2}\int_{-\infty}^{\infty}\int_{-\infty}^{s} w^1_{trans}(s-s')q(s')q(s)ds'\,ds \quad (2)$$

where Q is the bunch charge, $q(s)$ is the longitudinal bunch distribution, W is the wake potential, and w is the wake function. However, the longitudinal and transverse wake functions at short distance s could be approximately related as [8]

$$w^1_{trans}(s) \cong \frac{2}{a^2}\int_0^s w^0_{long}(z)dz \quad (3)$$

where a is the iris radius

In the periodic structure the short range wake can be approximated as [8]

$$w_{long}(s) = A\frac{Z_0 c}{\pi^2 a}\exp\left(-\sqrt{s/s_0}\right) \quad (4)$$

$$w_{trans}(s) = \frac{2}{a^2}A\frac{Z_0 c}{\pi^2 a}2s_1\left(1-\left(1+\sqrt{s/s_1}\right)\exp\left(-\sqrt{s/s_0}\right)\right) \quad (5)$$

Upon substituting for the wake potential in the loss factor and kick factor equation and assuming Gaussian charge we could reach

$$L_{long} = \frac{A_1}{\sigma^2}\int_{-\infty}^{\infty}\int_{-\infty}^{s}\exp\left(-\sqrt{(s-s')/s_0}\right)\exp\left(-\frac{s'^2}{2\sigma^2}\right)\exp\left(-\frac{s^2}{2\sigma^2}\right)ds'\,ds \quad (6)$$

$$L_{trans} = \frac{4S_1}{a^2}\frac{A_1}{\sigma^2}\int_{-\infty}^{\infty}\int_{-\infty}^{s}\left(1-\left(1+\sqrt{(s-s')/s_1}\right)\exp\left(-\sqrt{(s-s')/s_0}\right)\right)\exp\left(-\frac{s'^2}{2\sigma^2}\right)\exp\left(-\frac{s^2}{2\sigma^2}\right)ds'\,ds \quad (7)$$

Copyright © 2013 CC-BY-3.0 and by the respective authors

Where A_1, S_0, S_1 are fit parameters.

Figure 5 shows the asymptotic approximation of the loss and kick factors based on the simulated data points calculated using CST microwave studio for relatively long bunches. In this perspective, the fit parameters for the loss factor are A_1=17 $V.mm^2/pC$ and S_0=0.5 mm, while the fit parameter for the kick factor is S_1=0.33 *mm* with an iris radius of a =15 mm.

Figure 5(a) demonstrates that the loss factor for a RMS bunch length of 50 µm is about 39.5 V/pC, increasing to 46 V/pC for a RMS bunch length of 10 µm. On the other hand, the kick factor decreases with decreasing the RMS bunch length as shown in Fig. 5(b), thus the kick factor is clearly not a concern for ultra-small bunches.

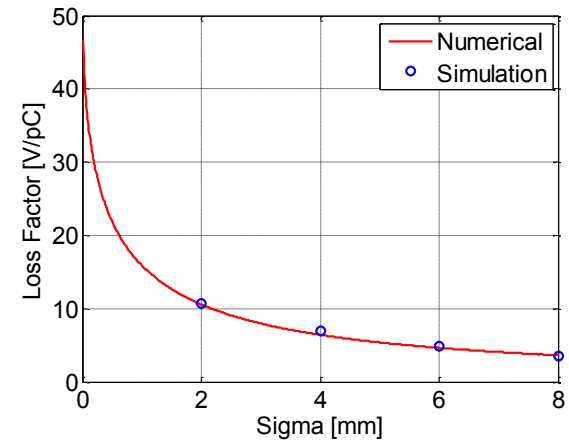


Figure 5: Asymptotic approximation (a) Loss factor. (b) Kick factor.

ESTIMATION OF CRYOGENIC LOSSES

Based on the aforementioned wakefield loss analysis, the cryogenic losses per cryomodule could be estimated as

$$L_{cyo} = nL_{long}QI$$

Where n is the number of cavities per cryomodule

For a particle beam of current 9 mA and charge 300 pC, the cryogenic losses of a four cavity cryomodule is listed in Table 1 for various bunch lengths.

Table 1: Cryogenic losses in W for a cryomodule of four cavities in case of beam current of 9 mA and beam charge of 300 pC.

Bunch RMS Length	Loss Factor [V/pC]	Cryogenic Losses [W]
8 mm	3.56	38.4
4 mm	6.89	74.4
2 mm	10.73	115.9
100 µm	35.1	379.1
50 µm	39.5	426.6
10 µm	46.5	502.2

CONCLUSION

Wakefield losses of the third harmonic 3.9 GHz elliptical cavity have been analysed. For relatively long bunches, the loss factor varies from 3.56 V/pC to 10.73 V/pC as the RMS bunch length decreases from 8 mm to 2 mm, while for ultra short bunches it reaches 46.5 V/pC for a RMS bunch length of 10 µm. The kick factor is not a concern for ultra-small bunches as it decreases with decreasing the RMS bunch length. The cryogenic losses for a cryomodule of four cavities would be 502.2 W for bunch RMS length of 10 µm, beam current of 9 mA and beam charge of 300 pC.

ACKNOWLEDGMENT

We acknowledge the feedback we received from Jim Steimel of Fermilab.

REFERENCES

[1] N. Solyak et al., “The progress in developing superconducting 3rd harmonic cavity,” EPAC 2006.
[2] E. Harms et al., “Status of 3.9-GHz superconducting RF cavity technology at Fermilab,” LINAC 2006.
[3] T. Khabiboulline et al., “New HOM coupler design for 3.9 GHz superconducting cavities at FNAL,” PAC 2007.
[4] E. Harms, et al., “Performance of 3.9 GHz superconducting cavities,” LINAC 2008.
[5] I. Zagorodnov, and T. Weiland, “Wake fields generated by the LOLA-IV structure and the 3rd harmonic section in TTF-II,” Dt. Elektronen-Synchrotron DESY, MHF-SL Group, 2004.
[6] R. Jones, et al., "Wakefields and beam dynamics simulations for the 3.9 GHz cavities of the ILC," LINAC 2006.
[7] CST microwave studio user’s manual.
[8] T. Weiland, and I. Zagorodnov, “The short-range transverse wake function for TESLA accelerating structure,” Dt. Elektronen-Synchrotron DESY, MHF-SL Group, 2003.

Copyright © 2013 CC-BY-3.0 and by the respective authors

RESULTS OF THE NEW HIGH POWER TESTS OF SUPERCONDUCTING PHOTONIC BAND GAP STRUCTURE CELLS*

Evgenya I. Simakov#, Sergey A. Arsenyev, W. Brian Haynes, Sergey S. Kurennoy, David Lizon, James F. O'Hara, Eric F. Olivas, Dmitry Yu. Shchegolkov, Natalya A. Suvorova, and Tsuyoshi Tajima, Los Alamos National Laboratory, Los Alamos, NM 87545, U.S.A.
Chase H. Boulware, Terry L. Grimm, Niowave, Inc., Lansing, MI, 48906, U.S.A.

Abstract

We report the results of the recent 2.1 GHz superconducting rf (SRF) photonic band gap (PBG) resonator experiment in Los Alamos. The new SRF PBG cell was designed with the particular emphasis on changing the shape of PBG rods to reduce the peak magnetic fields and at the same time to preserve its effectiveness for suppression of the higher order modes (HOMs). The new PBG cells have great potential for outcoupling long-range wakefields in SRF accelerator structures without affecting the fundamental accelerating mode. Two 2.1 GHz PBG cells with elliptical rods were fabricated and tested with high power in a liquid helium bath at the temperature of 4 K and 2 K. The cells performed in accordance with simulation and the maximum achieved accelerating gradient was 18.3 MV/m.

INTRODUCTION

Superconducting radio frequency (SRF) cavities are the natural choice for the future generation of high-duty-factor accelerators for the high power free-electron lasers (FELs) where the heat produced in the accelerating structure must be effectively extracted [1]. Operating the accelerator at high frequency and low bunch charge reduces the risks of brightness degradation in electron beam transport. However, high frequencies become a disadvantage with respect to excitation of higher order mode (HOM) wakefields in the linac which get excited more easily and interact with the accelerated beam causing instabilities, energy spread and ultimately the beam breakup.

Photonic Band Gap [2] (PBG) cavities have the unique potential to filter out much of the HOM power and reduce the wakefields. A PBG resonator is capable of supporting the accelerating mode and not supporting any higher order modes which propagate towards the peripheries of the cavity and get filtered out with waveguides.

The first ever demonstration of acceleration in a PBG resonator was conducted at Massachusetts Institute of Technology (MIT) in 2005 [3]. Since then, the importance of PBG structures for accelerators has been recognized by many research institutions worldwide. In the experiment reported in [3], the 6-cell open copper PBG structure was employed to construct a room-temperature travelling-wave accelerator at 17.137 GHz with inherit ability to filter out wakefields.

* Work is supported by the Department of Defense High Energy Laser Joint Technology Office through the Office of Naval Research.
#smirnova@lanl.gov

A project funded by the U.S. Department of Energy (DOE) Office of Science Early Career Research Program at Los Alamos National Laboratory has recently demonstrated fabrication and high power operation of single-cell SRF PBG resonators at 2.1 GHz [4]. Two resonators were fabricated in 2012 and demonstrated solid high gradient performance with the maximum achieved gradient of 15 MV/m limited by the magnetic quench.

We have initiated a project at LANL to push the high gradient limitations of the SRF PBG resonators and demonstrate the possibility of a resonator with significantly reduced peak surface magnetic field and still excellent performance with respect to filtering out higher order modes.

2.1 GHz SRF PBG RESONATORS WITH REDUCED SURFACE FIELDS

We have followed the idea of [5] and changed the shapes of the 6 inner rods of the PBG resonator from cylindrical to elliptical. This produced the desirable effect reducing the surface fields up to 40 per cent depending on the major radius of the elliptical rods [6]. The question however was if the new resonators with elliptical rods were as effective with respect to filtering out wakefields as resonators with round rods. To answer this question we used the time-domain solver of the CST Microwave Studio [7] and analyzed the confinement of HOMs and the fundamental mode in a PBG resonator with elliptical rods. We discovered that if the periodicity of the PBG structure is broken and the elliptical rods are moved slightly toward the center of the resonator, then the fundamental mode in this structure becomes better confined than in the structure with round rods. At the same time HOMs in this structure are confined worse and can be extracted more efficiently than in the structure with round rods [6].

The final dimensions and the accelerator characteristics of the structure with the shifted elliptical rods are summarized in Table 1. The cells were designed with 18 hollow cylindrical rods: 6 elliptical and 12 round. The maximum surface electric field in the PBG cell is reached on the blended edge of the beam pipe, as was in the case of the cavity with round cylindrical rods [4]. The maximum surface magnetic field is again reached on the rods of the PBG structure; however it is 40% lower than the maximum surface magnetic field in the cavity with round cylindrical rods operating at the same gradient.

Copyright © 2013 CC-BY-3.0 and by the respective authors

Table 1: Dimensions and Accelerator Characteristics of the 2.1 GHz SRF PBG Accelerator Cell with Elliptical Rods

Spacing between the rods, p	56.57 mm
OD of the round rods, d	17.04 mm = 0.3*p
Shift of elliptical rods, Δp	0.89 mm
Major OD of the elliptical rod, a	24.94 mm = 0.5*p
Minor OD of the elliptical rod, b	9.80 mm
ID of the equator, D0	300 mm
Length of the cell, L	71.43 mm (λ/2)
Beam pipe ID, Rb	1.25 inches = 31.75 mm
Radius of the beam pipe blend, rb	1 inch = 25.4 mm
Q_0 (4K)	$1.8*10^8$
Q_0 (2K)	$6.2*10^9$
R/Q	150.7 Ohm
E_{peak}/E_{acc}	2.37
B_{peak}/E_{acc}	5.66 mT/(MV/m)

Two resonators were fabricated by Niowave, Inc from a combination of stamped sheet metal niobium with the residual resistance ratio RRR>250 and machined ingot niobium components with RRR>220. After the electron beam welding, a buffered chemical polish etch was performed to prepare the RF surface for testing. The temperature of the acid was carefully monitored during the etching. The photograph of resonators right after fabrication is shown in Figure 1.



Figure 1: Photograph of the 2.1 GHz PBG cavities with elliptical rods ready to be tested.

HIGH GRADIENT TESTING OF THE 2.1 GHz SRF PBG RESONATORS

The resonators underwent high gradient testing at LANL in Summer of 2013. Each cavity delivered from Niowave was opened in a class 100 clean room and a pickup coupler flange and a movable bellow with a matched power input coupler were attached at the ends of the beam pipes. The cavity was then sealed and taken out of the clean room, set on the vertical cryostat insert, pumped down and leak checked. The testing procedure was the same as described in [4].

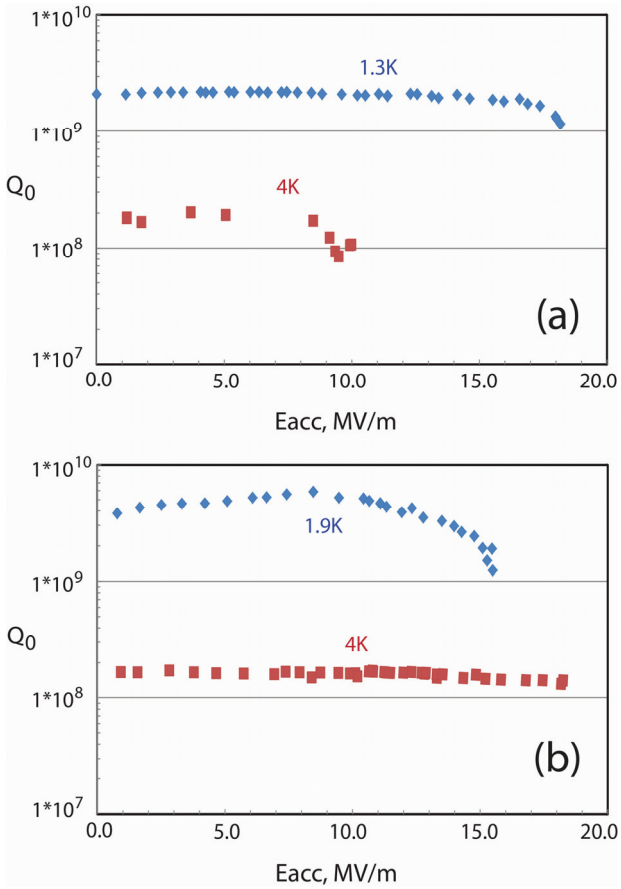


Figure 2: Unloaded Q (Q_0) as a function of accelerating gradient (E_{acc}) of the 2.1 GHz SRF PBG cavities with elliptical rods: (a) cavity #3 tested on 7/15/13, and (b) cavity #4 tested on 8/19/13.

Figure 2 shows the $Q_0 - E_{acc}$ curves at 4 K and 2 K for the two cavities with elliptical rods. Table 2 summarizes the test results. The cavities had somewhat longer beam pipes than the cavities with round rods, and Cavity #3 turned out to be undercoupled at 4 K even when the co-axial coupler was moved fully inwards. As a result, the 4 K measurements of this cavity were quite inaccurate. In addition, the magnetic field compensating coil was not turned on before the cool down, which explains the lower Q-values measured during the 2 K test. The cavity, however, performed excellent at 2 K and withstood a high 18.3 MV/m accelerating gradient. Cavity #4 was tested with a longer co-axial coupler probe. It performed excellent at 4 Kelvin and went up to 18.2 MV/m accelerating gradient and demonstrated high unloaded Qs. However, we observed a significant frequency shift in this cavity (300 kHz up vs. 30 kHz up in other three PBG cavities) when going from 4 Kelvin down to 2 Kelvin. Then during the testing at 2 K we observed a very strong

Copyright © 2013 CC-BY-3.0 and by the respective authors

Q-slope which was possibly due to field emission from a defect. The cavity quenched at 15.3 MV/m at 2 K.

Overall, the measurements totally confirmed the predicted improvement in the gradient performance of the cavities with elliptical rods as compared to the cavities with round rods.

Table 2: Measured Performance of Two 2.1 GHz SRF PBG Resonators with Elliptical Rods and Comparison to Theory

	Theory	Cavity #3	Cavity #4
Frequency	2.100 GHz	2.11524 GHz	2.11292 GHz
Q_0 (4K)	$1.8*10^8$	$1.6*10^8$	$1.6*10^8$
Q_0 (2K)	$6.2*10^9$	$2.2*10^9$	$3.9*10^9$
Maximum E_{acc} (4K)		10.0 MV/m	18.2 MV/m
Maximum E_{acc} (2K)		18.3 MV/m	15.3 MV/m
B_{peak} (4K)		57 mT	103 mT
B_{peak} (2K)		104 mT	87 mT

OBSERVATIONS OF THE FIRST SOUND GENERATED BY QUENCH

We have also attempted to put together a simplified quench diagnostics and installed 6 Buzzer Elements Piezo Benders 20 mm in diameter sensors, one next to each cooling hole of elliptical rods as shown in Figure 3. We observed ~10 kHz sound waves generated by quench at each road with the hope that the amplitude of the sound at each location could give us an indication of which of the six elliptical rods was experiencing quench.

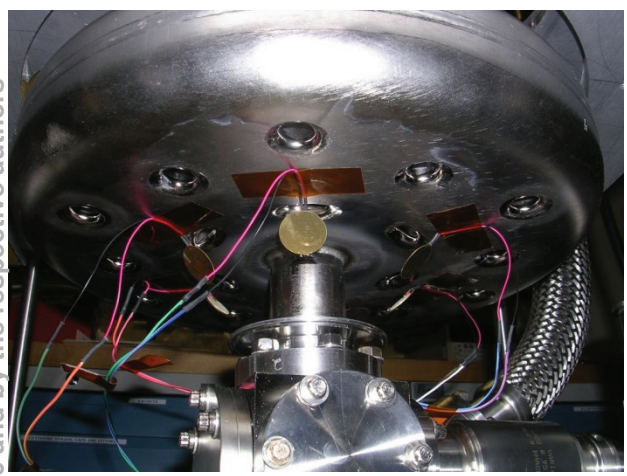


Figure 3: Piezoelectric sensors installed next to 6 hollow elliptical rods of the PBG structure.

The observed sound was similar in amplitude and timing at all six locations (Figure 4). This may suggest that quench occurred on the surface of the cavity outside of the rods, or that the sound mostly propagated through the metal body of the cavity instead of propagating through liquid helium. The detected sound traces looked very similar at both 4 K and 2 K.

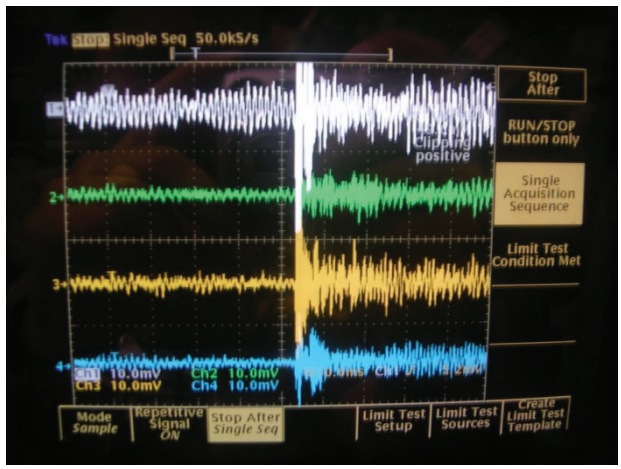


Figure 4: Sound traces from the piezoelectric sensors on an oscilloscope.

CONCLUSION

In summary, we have demonstrated the proof-of-principle fabrication and high gradient operation of superconducting photonic band gap cavities with elliptical rods. The cavities were tested at both 4K and 2K and performed quite well, demonstrating accelerating gradients as high as 18.3 MV/m. The two cavities with elliptical rods on average have performed 30 per cent better than the cavities with round rods tested earlier [4]. This is in perfect agreement with theoretical predictions. We believe that PBG technology will be successfully applied to design novel effective HOM couplers for high current SRF accelerators. As a result, it may significantly reduce the size the accelerators and allow increasing the brightness of the electron beam transport.

REFERENCES

[1] S. Belomestnykh, Reviews of Accelerator Science and Technology 5, p. 147 (2012).
[2] E. Yablonovitch. Phys. Rev. Lett., 258, p.2059 (1987).
[3] E.I. Smirnova, A.S. Kesar, I. Mastovsky, M.A. Shapiro, and R.J. Temkin, Phys. Rev. Lett. 95(7), p. 074801 (2005).
[4] E.I. Simakov, W.B. Haynes, M.A. Madrid, F.P. Romero, T. Tajima, W.M. Tuzel, C.H. Boulware, and T.L. Grimm, Phys. Rev. Lett., 109, p.164801 (2012).
[5] B.J. Munroe, A.M. Cook, M.A. Shapiro, R.J. Temkin, V.A. Dolgashev, L.L. Laurent, J.R. Lewandowski, A.D. Yeremian, S.G. Tantawi, and R.A. Marsh, Phys. Rev. ST-AB 16, p. 012005 (2013).
[6] Evgenya I. Simakov, W. Brian Haynes, Sergey S. Kurennoy, James F. O'Hara, Eric F. Olivas, Dmitry Yu. Shchegolkov, Proceedings of the IPAC 2012, p. WEPPP035 (2012).
[7] CST Microwave Studio, Computer Simulation Technology, www.cst.com

Copyright © 2013 CC-BY-3.0 and by the respective authors

UPDATE ON THE DESIGN OF A FIVE-CELL SUPERCONDUCTING RF MODULE WITH A PBG COUPLER CELL*

Sergey A. Arsenyev#, Massachusetts Institute of Technology, Cambridge, MA 02139, USA
Evgenya I. Simakov, Los Alamos National Laboratory, Los Alamos, NM 87545, USA

Abstract

We present a complete design of the 5-cell superconducting accelerating module incorporating a Photonic Band Gap (PBG) cell with couplers. The purpose of the PBG cell is to achieve better Higher Order Mode (HOM) damping which is vital for preserving the quality of high-current electron beams in novel linear accelerators used, for example, for free electron lasers. We first discuss the aspects of incorporating a PBG cell in a superconducting PBG module. The main goal is to ensure the equal probability of quench in each of the five cells, which can be achieved with significant geometry modifications. We then present the simulation data on HOM damping. Particularly, we calculate the external quality factors for the 10 most dangerous HOMs for this particular structure. HOM coupler configurations and modifications to the PBG geometry are discussed.

INTRODUCTION

Superconducting radio frequency (SRF) cavities are the natural choice for the future generation of high energy linacs, especially for high-duty-factor machines where the heat produced in the accelerating structure cannot be effectively extracted [1]. Going to higher frequencies in SRF cavities is desirable because of the lower cost and higher achievable luminosity of an electron beam. However, higher order mode (HOM) wakefields excited by a beam scale as frequency cubed and can easily destroy the beam in a high-frequency machine. If we want to go to the frequencies as high as 2.1 GHz, we have to find an effective way to suppress or outcouple HOMs.

PBG cavities are of interest to the particle accelerator community because they have reduced higher-order modes that can degrade beam quality [2, 3].

Waveguide couplers are commonly used as an HOM suppression mechanism (see, for example, [4]). Usually the couplers are attached to the beam pipe. In contrast with a room-temperature PBG cell, the superconducting cell is made closed in the transverse plane and utilizes waveguide couplers to extract the HOMs. Low field at the periphery of the PBG cell allows us to attach the waveguide couplers directly to the outside wall of the cell. This is beneficial to HOM damping because the HOMs are extracted at the point where their field is higher than at the beampipe. We also use less waveguides and increase real estate gradient.

*Work is supported by the U.S. Department of Energy (DOE) Office of Science Early Career Research Program
#arsenyev@mit.edu

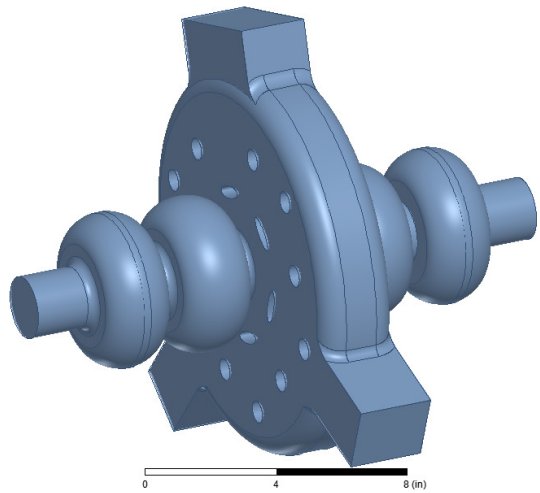


Figure 1: The 5-cell accelerating module with the central PBG cell.

Table 1: Dimensions and Accelerating Characteristics of the 5-cell Module

Frequency	2.1 GHz
Length of the module	14.05 in (35.69 cm)
Diameter of elliptical cells	4.95 in (12.57 cm)
Diameter of the PBG cell	12.32 in (31.3 cm)
Spacing of PBG rods	2.34 in (5.94 cm)
Radii of PBG rods	0.35 in (0.89 cm)
Beam pipe diameter	1.96 in (4.99 cm)
Angular position of the HOM couplers relative to the FM coupler	125°
r/Q	$1.44*10^3$ Ohm/m
E_{peak}/E_{acc}	2.65
B_{peak}/E_{acc}	4.48 mT/(MV/m)
Q_0 (4K)	$2.3*10^8$
Q_0 (2K)	$8.9*10^9$
Max theoretical gradient (for B_{peak}=200 mT)	45 MV/m

Copyright © 2013 CC-BY-3.0 and by the respective authors

FIVE CELL MODULE DESIGN

We incorporate a PBG cell into a module of five accelerator cells by using it instead of one of the conventional cells. As an example of a conventional accelerating module we take a high-current FEL accelerating module from [4]. The middle cell of the module [4] was replaced with a PBG cell (Fig. 1). A module with an incorporated PBG cell should be designed with lower accelerating gradient in the PBG cell than in other cells [5]. This is due to the fact that for the same accelerating gradient, the surface magnetic field in a PBG cell is higher than in a conventional cell because of the more sophisticated geometry [6]. If the module was designed to have a flat field profile, performance of the entire accelerator would be limited by a single PBG cell due to the higher probability of quench. To make the non-flat gradient profile, we introduce small differences in the eigenfrequencies of the cells. Like in a system of connected pendulums, this leads to different amplitudes of the fields in different cells [5].

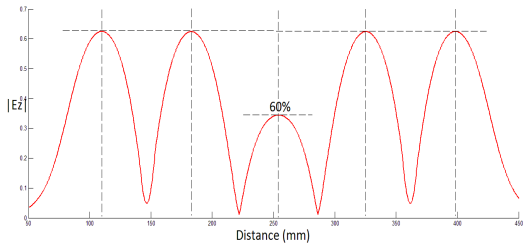


Figure 2: Electric field magnitude (accelerating gradient) along the central axis.

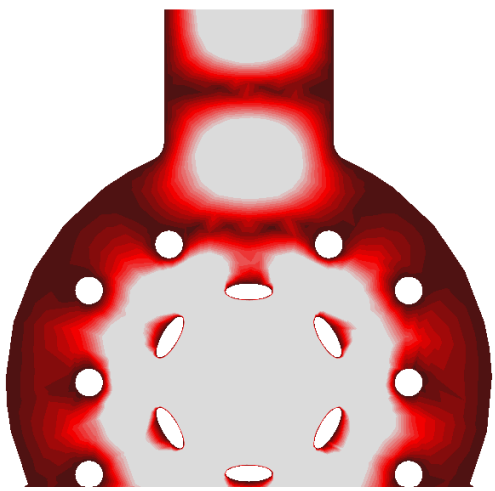


Figure 3: Magnitude of E-field in the fundamental mode coupled into the PBG structure thru the waveguide.

A conventional 2D PBG lattice has only rods with circular cross-section. The corresponding 5-cell module design was presented in [5]. However, it is beneficial to alter the shape of some rods to get better accelerating properties. In particular, the inner row of rods in the designed module is "squeezed" in radial direction and stretched in angular direction (Fig. 3) in order to produce lower ratio of the peak surface magnetic field to the accelerating gradient [7, 8]. Using elliptical rods allows us to push the gradient in the PBG cell higher, up to 60% of the gradient in the four conventional cells (Fig. 2). This is significantly better than we can do with a PBG cell which has only round rods (about 40%) [5]. Properties and dimensions of the accelerating module are listed in Table 1.

We are planning to use the Navy FEL beamline at LANL for the testing of the structure. The parameters of the experiment are listed in Table 2. The electron beam will be synchronous with the accelerating mode (beam on crest). Due to the negligible Ohmic losses almost all the power coupled to the module will go to the beam.

The fundamental mode coupler was designed to provide near critical coupling for the experiment with the electron beam (Fig. 3). Standard WR430 waveguide was used. One of the PBG rods was removed for coupling. The existing design can also be used for tests with the copper prototype and no beam – in that case Ohmic dissipation is approximately equal to the beam loading in the hot test and the coupling would still be close to critical. The beam tests will be conducted at much lower accelerating gradient (5 MV/m) than the cavity is capable to sustain. This ensures reliability of the structure.

Table 2: Parameters for the Planned Test

Charge per bunch	1 nC
Bunch repetition rate	100 MHz
Klystron power	200 kW
Average gradient	5.6 MV/m

HOM DAMPING

In order to understand what HOMs affect the beam the most, we performed a CST Particle Studio simulation with the beam displaced in either of the two transverse directions (X and Y). The computed wake impedance reflects the spectrum of the HOMs (Fig. 4). We used the areas underneath each peak as a criterion of whether or not the mode is dangerous. The area is related to a more commonly used quantity R/Q, which can be generalized for non-monopole modes. Each mode has two orthogonal polarizations, which are listed separately in Table 3. Generally we only have to look at the frequencies up to the beampipe cut-off, but one significant peak beyond the cut-off was examined as well (Table 3, modes 9 and 10). We then tried to minimize the quality factors for the most dangerous 10 HOMs. It was also verified that the frequencies of the monopole HOMs don't lie close enough to multiples of the beam frequency to allow the so-called "build-up" to happen.

There are dangerous HOMs with both the TE and the TM polarizations in the center cell. The HOM couplers should have cutoff below the frequencies of the modes with either polarization and therefore have customized dimensions (2.2in × 2.4in). The couplers and the PBG

Copyright © 2013 CC-BY-3.0 and by the respective authors

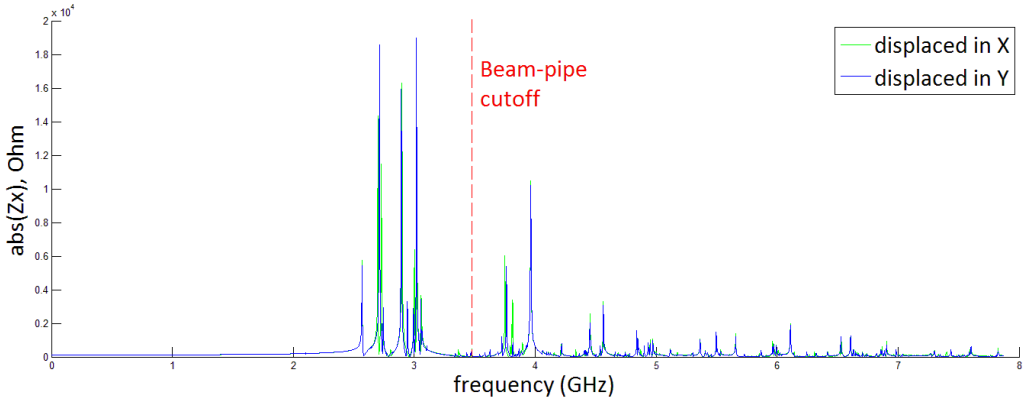


Figure 4: Transverse wake impedance profile for both X and Y beam displacements.

cell were optimized to provide sufficient dumping for all HOMs (Q less or about 1000). The final optimized Qs are listed in Table 3. The design also has advantage over the traditional solution of placing HOM couplers on the beam pipe because it utilizes only 3 couplers instead of 6.

Table 3: Quality Factors of the HOMs

Mode #	Peak area, Ohm/m*Hz	R/Q, Ohm	Frequency, GHz	Quality factor
1	27.1	32.4	2.556	1070
2	26.6	32.3	2.562	560
3	51.9	120.0	2.712	480
4	87.2	120.8	2.715	420
5	85.4	107.8	2.949	430
6	71.8	107.7	2.952	500
7	46.3	84.8	3.013	240
8	67.9	85.3	3.025	690
9*	73.9	79.0	3.943	200
10*	76.3	79.1	3.943	200

CONCLUSIONS

We designed a 5-cell SRF module with incorporated PBG cell and HOM couplers attached to the PBG cell. Using elliptical rods in the PBG structure enhanced the performance of the cavity (flatter gradient profile) relative to the round rods [5]. Fundamental mode coupler was designed to provide coupling close to critical for both hot-test and cold-test experiments. HOM couplers were designed to provide sufficient damping (Q less or about 1000) for the 10 most dangerous HOMs. We are planning to fabricate the copper prototype of the 5 cell structure first. It would let us measure quality factors of the HOMs and conduct a bead-pull test to determine the field profile. We then will fabricate the real superconducting module and mount it on the LANL Navy FEL beamline.

ACKNOWLEDGMENT

We would like to acknowledge people who helped this work: B. Munroe, E. Nanni, M. Shapiro, and R. Temkin. This work is supported by the U.S. Department of Energy (DOE) Office of Science Early Career Research Program.

REFERENCES

[1] Hasan Padamsee, Jens Knobloch and Tom Hays, "RF Superconductivity for Accelerators," Second Edition, Wiley-VCH (2011).
[2] John D. Joannopoulos, Steven G. Johnson, Joshua N. Winn, Robert D. Meade, "Photonic crystals. Molding the Flow of Light," Second Edition, Princeton University Press (2008).
[3] Evgenya I. Smirnova, "Novel Photonic Band Gap Structures for Accelerator Applications," PhD Thesis, Massachusetts Institute of Technology, June 2005.
[4] Haipeng Wang et al., Proc. of PAC2007, p. 2496 (2007).
[5] Sergey A. Arsenyev, Evgenya I. Simakov, AIP Conf. Proc. 1507, pp. 425-430 (2012).
[6] Roark A. Marsh, "Experimental Study of Photonic Band Gap Accelerator Structures," PhD Thesis, Massachusetts Institute of Technology, June 2009.
[7] Evgenya I. Simakov et al., Proc. of IPAC 2012, WEPPP035, (2012).
[8] Brian J. Munroe et al., Proc. of IPAC 2012, TUPRO71 (2012).

*above the beampipe cut-off

Copyright © 2013 CC-BY-3.0 and by the respective authors

INITIAL STUDIES OF MULTIPACTOR SUPPRESSION VIA TE AND TM MODES*

S. Rice[1] and J. Verboncoeur[2], Michigan State University, East Lansing, MI 48824, USA

Abstract

The formation of multipactor is strongly dependent upon the secondary electron yield (SEY) of a surface, and the emission velocities of the emitted electrons, in addition to the electric field. Since the secondary electron yield (SEY) of a material is dependent upon the kinetic energy and impact angle of the incident electron, we investigate use TE and TM coaxial cavity modes to modify the impacting electron velocities to reduce the average SEY and suppress multipactor, which builds upon our previous work examining TEM modes.

INTRODUCTION

Multipactor [1, 2] is a resonant phenomenon in which an electromagnetic field causes stray electrons to impact a surface, liberating secondary electrons, in such a way that the process can sustain itself. This phenomenon is of considerable practical interest in the design and operation of microwave windows, waveguides, and radio frequency resonant structures.

The formation of multipactor is strongly dependent upon the secondary electron yield (SEY) of a surface contributing to multipactor, since in order to initiate and sustain multipactor, the average number of emitted secondary electrons must be greater than or equal to unity. Multipactor is also dependent upon the system geometry and field excitation, which must be conducive to accelerating electrons into the boundaries at the proper RF phase to enable re-acceleration of the emitted secondary electrons.

When an electron impacts a boundary, the average secondary electron yield (SEY) is determined by the kinetic energy of the incident electron. Figure 1 shows a representative SEY curve. The specific SEY curve used in this present research was generated using Vaughan's model [3] with parameters chosen to match the impact energy location (E_{max}) and peak value (δ_{max}) of Furman's SEY model for copper [4], and is used for all the results presented in this study.

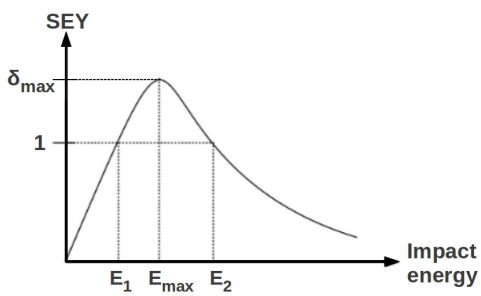


Figure 1: Typical SEY curve.

*Work supported by U.S. Air Force Office of Scientific Research (AFOSR) grant on the Basic Physics of Distributed Plasma Discharges.
[1]ricesco1@msu.com
[2]johnv@msu.edu

SIMULATION DESCRIPTION

Consider a coaxial cavity with conducting sidewalls, inner radius a, outer radius b, and longitudinal length L. The fundamental-mode TEM excitation at angular frequency ω can be parameterized by peak instantaneous voltage V_o and phase θ as $V_o \cdot \cos(\omega t+\theta) \cdot \sin(\pi z/L)$.

In our present research, we defined a=1 cm, b=5.65 cm, and L=1.86 m, and we used Vaughan's SEY model mentioned above. Unless otherwise noted, all secondary electron emission energies are set to zero to avoid the complication of the truly random (although typically low-energy) secondary emission energies. The selected geometrical values will allow a fundamental TEM mode to exist at 80.5 MHz, and the SEY model to yield maximum secondary electrons at $V_o \approx 1000$ V.

Electrons start from rest at the outer wall, and the net SEY is computed as the product of all the single-impact SEY values over 10 simulation steps, where each step is one fundamental mode period or boundary impact, whichever comes first. For each impact, a single simulated secondary electron is emitted and tracked. Only trajectories with at least two boundary impacts within ten fundamental-mode RF periods were considered to have net SEY > 0. The net SEY gives a proxy measure of the presence of the multipactor, since a net SEY < 1 would indicate that multipactor is not sustainable. Figure 2 shows the net SEY for the notional coaxial cavity for electrons starting at z values of 0.2L and 0.5L, where z=0 is defined to be the end of the cavity, and z=0.5L is halfway along the length of the cavity. The net SEY is displayed on a logarithmic scale, anything above 0 denotes a net increase in multipacting electrons. Note that to first order, the effect of changing z merely scales the multipactor voltage axis via the $\sin(\beta_z z)$ dependency.

MULTIPACTOR SUPPRESSION

Multipactor can only be sustained if the average SEY over the multipactor orbits is at least unity. This suggests a novel way to suppress multipactor, via the application of secondary excitation modes which result in the secondary electron impact energy being pushed away from the values where the SEY exceeds unity. Our previous work [5] explored multipactor suppression using an appropriately scaled and phase-referenced 3rd harmonic TEM mode, expressed mathematically as $-3V_o \cdot \cos(3\omega t+3\theta) \cdot \sin(3\pi z/L)$. The results are shown in Fig. 3, and it is apparent that the regions of sustainable multipactor have significantly decreased from the baseline case.

We now examine the use of TM and TE modes for the suppression of multipactor. This initial research examines the lowest order TM and TE modes, namely TM011 and TE011. The TM011 electric (E) and magnetic (H) field components are given by:

Copyright © 2013 CC-BY-3.0 and by the respective authors

$$E_\rho = \frac{j\beta_\rho\beta_z}{\omega\mu\epsilon}\left[A J'_0(\beta_\rho\rho) + B Y'_0(\beta_\rho\rho)\right]\sin(\beta_z z)$$
$$E_\phi = 0$$
$$E_z = \frac{-j\beta_\rho^2}{\omega\mu\epsilon}\left[A J_0(\beta_\rho\rho) + B Y_0(\beta_\rho\rho)\right]\cos(\beta_z z)$$
$$H_\rho = 0$$
$$H_\phi = \frac{-\beta_\rho}{\mu}\left[A J'_0(\beta_\rho\rho) + B Y'_0(\beta_\rho\rho)\right]\cos(\beta_z z)$$
$$H_z = 0$$

and the respective TE011 field components are given by:

$$E_\rho = 0$$
$$E_\phi = \frac{\beta_\rho}{\epsilon}\left[A J'_0(\beta_\rho\rho) + B Y'_0(\beta_\rho\rho)\right]\sin(\beta_z z)$$
$$E_z = 0$$
$$H_\rho = \frac{j\beta_\rho\beta_z}{\omega\mu\epsilon}\left[A J'_0(\beta_\rho\rho) + B Y'_0(\beta_\rho\rho)\right]\cos(\beta_z z)$$
$$H_\phi = 0$$
$$H_z = \frac{-j\beta_\rho^2}{\omega\mu\epsilon}\left[A J_0(\beta_\rho\rho) + B Y_0(\beta_\rho\rho)\right]\sin(\beta_z z)$$

where a cylindrical (ρ, φ, z) coordinate system is assumed, (βρ, βφ, βz) represent the respective wavenumber components, ω represents angular frequency, μ represents the magnetic permeability, ϵ represents the electric permittivity, J_0 and Y_0 respectively represent 0^{th}-order Bessel functions of the first and second kind, and primes denote derivatives. A and B are geometry-dependent constants which ensure that the tangential E-field goes to zero at the cavity boundaries. Since the electron speeds in our simulations are much less than the speed of light, the TM011 and TE011 magnetic field effect upon electron trajectory is negligible as compared to the electric field.

The plots in Fig. 4 show the net SEY for the same geometry and baseline excitation, but now with an additional mode of TM011 (top plots) or TE011 (bottom plots). The maximum field strength for each of these modes was set to 500 kV/m, which was somewhat arbitrarily chosen because this value is considered a strong but not unrealizable field strength. These modes were phase-referenced such that E_ρ started at zero phase at time=0 for the TM011 case, and E_φ started at zero phase at time=0 for the TE011 case. Additional phase shifts of 120º and 240º for the respective TM011 and TE011 fields were investigated. Although the specific multipactor-stable regions did exhibit some change, no qualitative difference was observed.

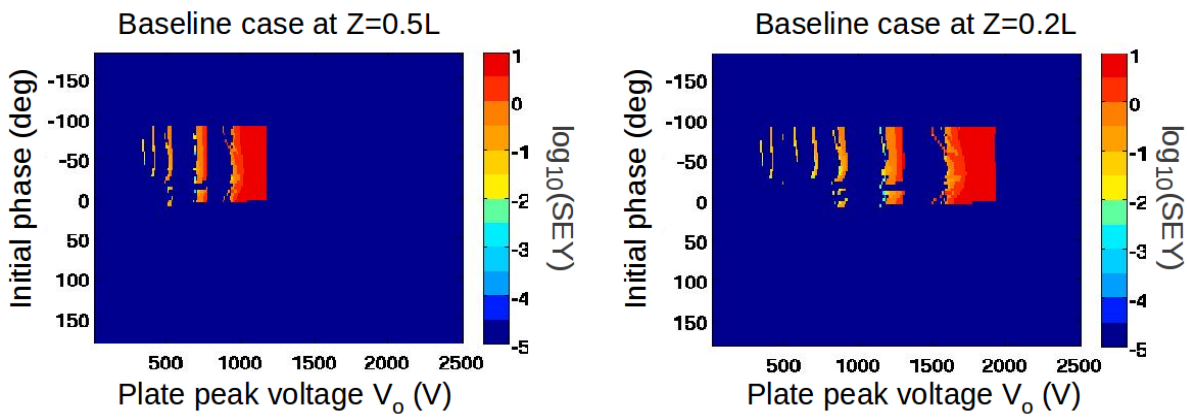


Figure 2: Simulated multipactor sustainability in a notional coaxial geometry, at two different z locations.

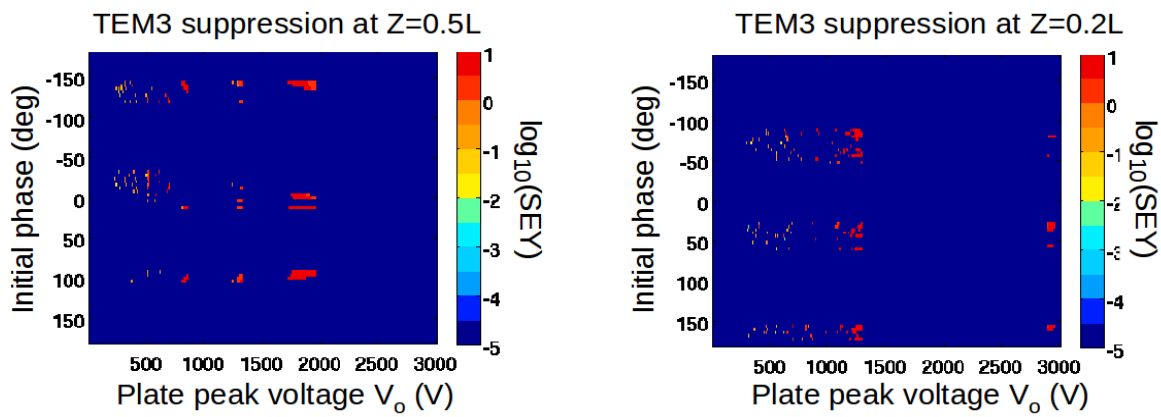


Figure 3: Multipactor sustainability in a notional coaxial geometry, at two different z locations, with a 3rd harmonic TEM suppression signal applied.

Copyright © 2013 CC-BY-3.0 and by the respective authors

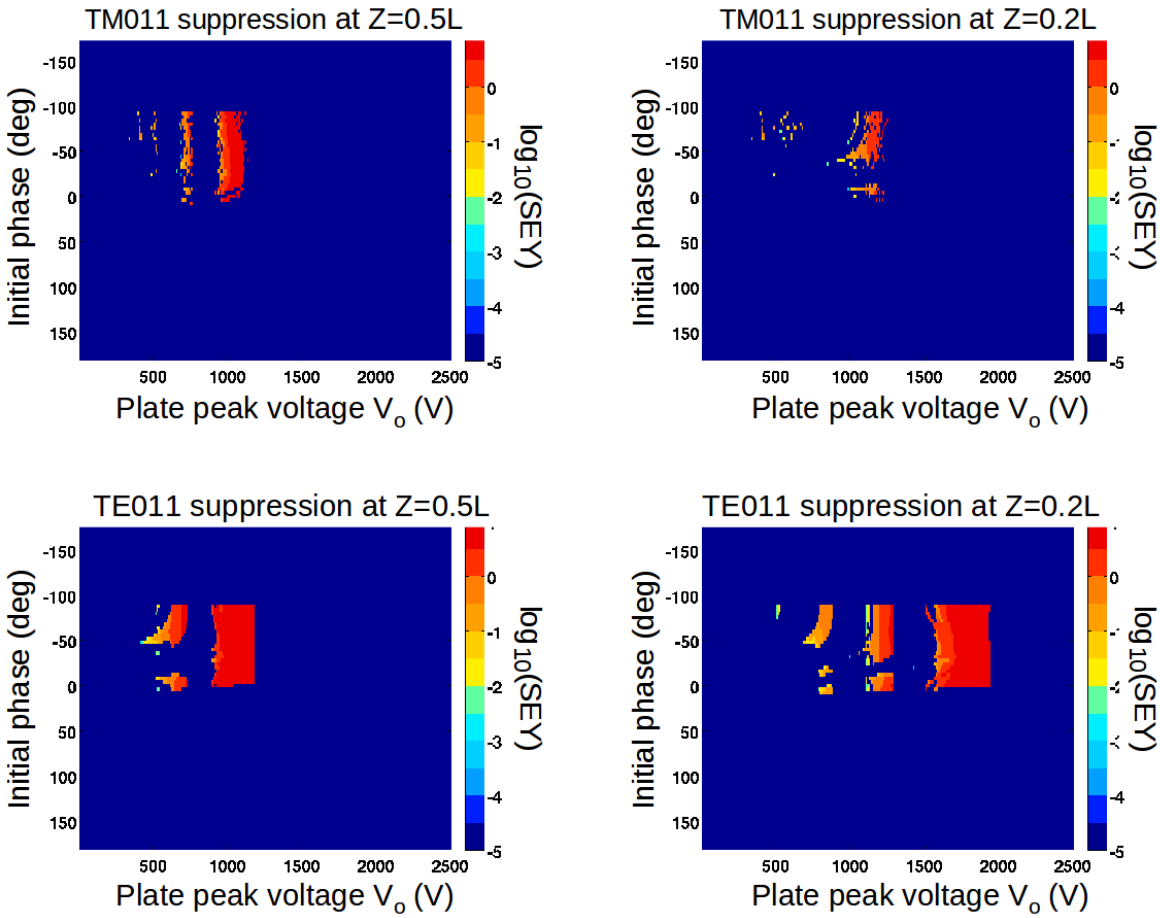


Figure 4: Multipactor sustainability with 500 kV/m TM011 (top) and TE011 (bottom) modes present, at z values of 0.5L (left) and 0.2L (right).

CONCLUSIONS AND FUTURE WORK

The TM011 and TE011 modes explored thus far do not suppress multipactor as much as the 3rd Harmonic TEM mode examined previously. [5] This is mainly attributable to the time scale of the different modes: the baseline TEM mode frequency is at 80.5 MHz, whereas the TE and TM modes considered here are at around 3.2 GHz, resulting in a small periodic perturbation to the overall trajectory of the particles. Additional work [6] presented in a poster at this conference also demonstrates the extreme sensitivity of multipactor simulation to the low-impact energy SEY and the secondary emission energies which are being neglected in the results presented above. Thus future work in this area will also take into account non-zero secondary emission energies.

REFERENCES

[1] Vaughan, “Multipactor”, IEEE Transactions on Electron Devices, Vol. 35, No. 7, July 1988, pp. 1172-1180

[2] Padamsee et. al, RF Superconductivity for Accelerators, Chapter 10: Multipacting, pp. 182-197

[3] Vaughan, “A New Formula for Secondary Emission Yield”, IEEE Transactions on Electron Devices, Vol. 36, (no. 9), pp. 1963-1967, (September 1989). See also the article revision by the same author published as “Secondary Emission Formulas”, IEEE Transactions on Electron Devices, Vol. 40, (no. 4), p. 830, April 1993

[4] Furman and Pivi, “Probabilistic model for the simulation of secondary electron emission”, Physical Review Special Topics – Accelerators and Beams, Vol. 5, (no. 124404), pp. 124404-1 through 124404-18, 2002

[5] Rice and Verboncoeur, "Multipactor Suppression in Resonant Cavities via Higher Order Modes", IEEE Conference on Pulsed Power & Plasma Science (PPPS 2013), San Francisco, CA., June 16-21, 2013

[6] Rice and Verboncoeur, "A Comparison of Multipactor Predictions Using Two Popular Secondary Electron Models", North American Particle Accelerator Conference 2013 (NA-PAC'13), Pasadena, CA., September 29 – October 4, 2013

Copyright © 2013 CC-BY-3.0 and by the respective authors

TESTS OF AN RF DIPOLE CRABBING CAVITY FOR AN ELECTRON-ION COLLIDER *

A. Castilla[1,2,3†], J. R. Delayen[1,2],
[1]Center for Accelerator Science, Old Dominion University, Norfolk, VA 23529, USA.
[2]Thomas Jefferson National Accelerator Facility, Newport News, VA 23606, USA.
[3]Universidad de Guanajuato (DCI-UG), Departamento de Fisica, Leon, Gto. 37150, Mex.

Abstract

On the scheme of developing a medium energy electron-ion collider (MEIC) at Jefferson Lab, we have designed a compact superconducting rf dipole cavity at 750 MHz to crab both electron and ion bunches and increase luminosities at the interaction points (IP) of the machine. Following the design optimization and characterization of the electromagnetic properties such as peak surface fields and shunt impedance, along with field nonuniformities, multipole components content, higher order modes (HOM) and multipacting, a prototype cavity was built by Niowave Inc. The 750 MHz prototype crab cavity has been tested at 4 K and is ready for re-testing at 4 K and 2 K at Jefferson Lab. In this paper we present the detailed results of the rf tests performed on the 750 MHz crab cavity prototype.

INTRODUCTION

The rf dipole geometry has been studied as a compact and efficient design for an electron-ion crabbing scheme for electron-ion colliders [1]. Among some of the most attractive properties of this design are the lower balanced surface fields with higher net deflection, higher shunt impedance, the advantage of having the operating deflecting/crabbing mode as the lowest mode, and the simple dependency of the rf properties on just a few geometrical parameters [2]. It is for all these reasons that the designed 750 MHz crab cavity prototype shown in Fig. 1 built by Niowave Inc. [3] has been tested and characterized at its facilities and the Center for Accelerator Science at Old Dominion University (CASODU) to corroborate that the fields' symmetry, operation performance, conditioning to multipacting and external Q factor are in agreement with the designed values.

ROOM TEMPERATURE TESTS

Bead-Pull

In a TE_{11} deflector/crabber such as the rf dipole, the transverse kick has contributions from both the electric and the magnetic components of the fundamental mode, thus the symmetry of the field profiles is a key point in the fabrication of the cavity to avoid introducing higher-order nonlinear field effects on the beams.

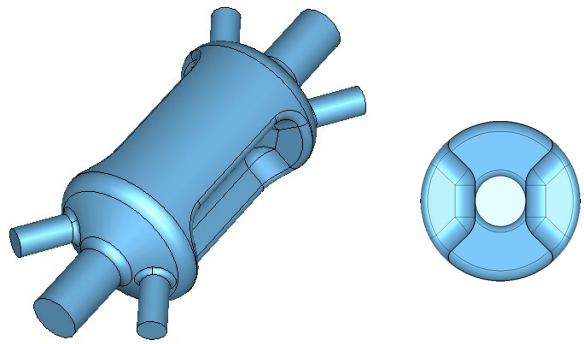


Figure 1: Rf dipole geometry and corresponding cross sections for the 750 MHz crab cavity design.

Table 1: Properties of the 750 MHz Crab Cavity

Parameter	750 MHz	Units
$\lambda/2$ of π mode	200.0	mm
Cavity length	341.2	mm
Cavity radius	93.7	mm
Aperture diameter d	60.0	mm
Deflecting voltage V_T^*	0.200	MV
Peak electric field E_P^*	4.45	MV/m
Peak magnetic field B_P^*	9.31	mT
B_P^*/E_P^*	2.09	mT/(MV/m)
Energy content U^*	0.068	J
Geometrical factor	131.4	Ω
$[R/Q]_T$	124.2	Ω
$R_T R_S$	1.65	$\times 10^4 \Omega^2$

At E_T^*= 1 MV/m

Once the electromagnetic design has been characterized using computer simulations, it is of utmost importance to characterize defects introduced during the fabrication and chemical treatment processes on the cavity, like assymmetries due to offsets on the load elements, perturbations induced by deformations on the volume, etc.

Different runs of bead-pull measurements were performed on the 750 MHz rf dipole crab cavity before and after e-welding using the automated bead-pull system set at CAS-ODU (see Fig. 2).

* Authored by Jefferson Science Associates, LLC under U.S. DOE Contract No. DE-AC05-06OR23177. The U.S. Government retains a nonexclusive, paid-up, irrevocable, world-wide license to publish or reproduce this manuscript for U.S. Government purposes. Part of this work was done in collaboration with and supported by Niowave Inc. under the DOE STTR Phase II program.

† acastill@jlab.org

Copyright © 2013 CC-BY-3.0 and by the respective authors

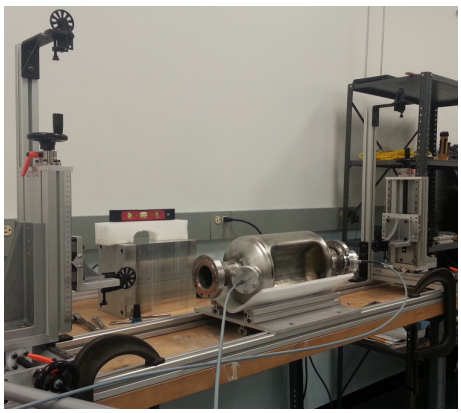


Figure 2: Bead-pull 750 MHz rf dipole set up at CAS-ODU.

The bead-pull results for both metallic and dielectric beads are presented in Figs. 3 and 4, compared with the calculations using the electric and magnetic fields for the crabbing mode found by simulations, showing a remarkable agreement at first order.

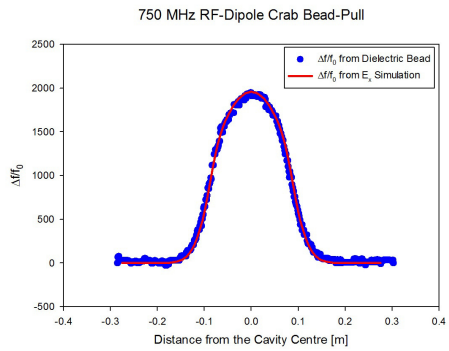


Figure 3: Frequency shift measured with a Teflon bead (blue) and calculated from the electric field by the simulations (red).

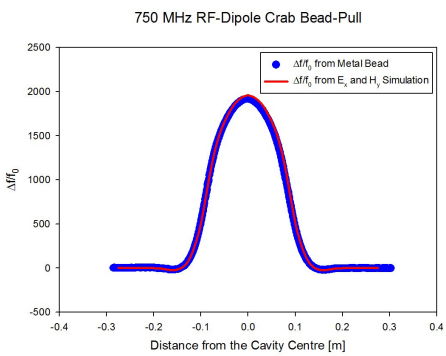


Figure 4: Frequency shift measured with a brass bead (blue) and calculated from the electric and magnetic field by the simulations (red).

Study of Losses at the Port Flanges

All the ports in the design are placed in the outer conductor regions with the lowest tangential surface magnetic fields, nevertheless these are not zero and there is still a fraction of them that can create currents on the nonsuperconducting flanges causing ohmic losses (see Fig. 5). The associated Q to these power dissipations can limit the final cavity Q_0 measured during operation or cryo-testing. For this reason a detailed numerical analysis was performed for the 750 MHz rf dipole crab cavity considering flanges both made of stainless steel and copper. The results are presented in Table 2.

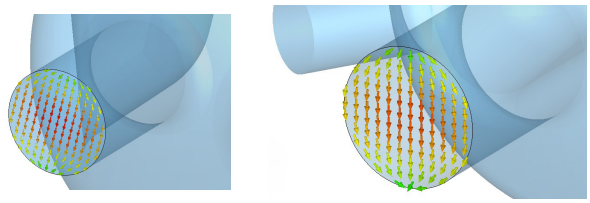


Figure 5: Visualization of the tangential magnetic field (H_y) obtained from CST Microwave Studio® simulations at the side-port flanges (left) and the beam-port flanges (right).

Table 2: Losses in the Port Flanges Due to Tangential Magnetic Field (H_y)

Copper			
Port	$\mathbf{P_{loss}}$ **[W]**	**Q**	**Total** $\mathbf{P_{loss}}$ **[W]**
2 Beam-ports	1.303×10^{-2}	3.61×10^{11}	
4 Side-ports	4.27×10^{-1}	1.102×10^{10}	
			$\mathbf{4.400 \times 10^{-1}}$
Stainless Steel			
2 Beam-ports	8.23×10^{-2}	5.713×10^{10}	
4 Side-ports	2.702	1.742×10^{9}	
			$\mathbf{27.844 \times 10^{-1}}$

Using for the flanges:

$$Q = \frac{\omega U}{P_{loss}}\,, \tag{1}$$

we have:

$$\begin{aligned} Q_{S.S.} &= 1.69 \times 10^{9}\,, \\ Q_{Cu} &= 1.07 \times 10^{10}\,. \end{aligned}$$

While for the cavity we have:

$$Q_0 = \frac{G}{R_s}\,. \tag{2}$$

And considering for 750 MHz: @4 K $R_s = 240\,n\Omega$ with $R_{BCS} = 20\,n\Omega$ and @2 K $R_s = 60\,n\Omega$, while from

Copyright © 2013 CC-BY-3.0 and by the respective authors

the simulations we obtained a $G = 131.4\,\Omega$. Then using Eqn. 2:

$$(Q_0)_{@4K} = 5.48 \times 10^8\,,$$
$$(Q_0)_{@2K} = 2.19 \times 10^9\,.$$

The results of this analysis showed us that the losses in stainless steel blanks and feed-throughs will not affect the measured Q_0 for the cavity on a test at 4 K, while in the case of 2 K we need to use Copper blank gaskets to minimize the losses at the flanges and reach the expected Q_0 values.

CRYOGENIC TESTS

For the performance test of the 750 MHz rf dipole crab cavity, the intrinsic quality factor (Q_0) achieved was measured as a function of the transverse voltage (V_T) at 4 K at the Niowave Inc. installations. During the testing a vertical dewar and a liquid He tank were used to cool the cavity down to 4.2 K while being driven by a 200 W amplifier (400-1000 MHz).

Among the important events during the testing to be noticed is that at low gradients a few multipacting barriers were present and conditioned without major problems and relatively quickly, this comes into agreement with the multipacting simulation results [4], even when no higher gradients were reached during this test. Due to that, the power dissipation on the cavity was enough to boil out the liquid He before we could move to higher gradients. No hard multipacting barriers or quenching occurred for the proof of principles cavity as can be appreciated in Fig. 6.

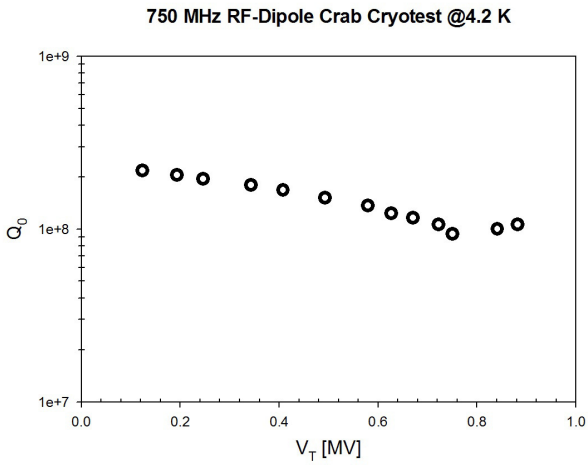


Figure 6: Q_0 curve obtained during the cryotesting of the cavity prototype up to ∼0.9 MV of transverse voltage.

Even when the curve describes a small slope it appears to be considerably flat around a value of $Q_0 \sim 1.5 \times 10^8$ (about a factor of 4 shorter with respect to the predicted value from the simulations). The region covered by the test corresponds to the region in which the multipacting barriers were expected to be present according to the analysis, having found no major problem to condition them without thermal breakdown or quenching. It can be observed around 0.8 MV of transverse voltage that the cavity presented a bigger multipacting conditioning, which was surpassed without further problem and the value of Q_0 reestablished.

All of the information compiled during the test supports that with the capability of keeping the temperatures, the cavity should reach the design specifications for the expected gradients without major problems. For this reason the cavity was shipped to ODU to be re-processed and retested at 4.2 K, and then at 2 K, when a leak on one of the brazings was detected and characterized. New parts have been purchased from Niowave Inc. and the cavity is scheduled to proceed with the corresponding cryotesting after repairing and re-processing at Jefferson Lab.

CONCLUSIONS

An rf crabber for both electron/ion bunches with designed values of $V_T = 1.6\,MV$, $E_p = 35.6\,\frac{MV}{m}$ and $B_p = 75.5\,mT$ per cavity was fabricated at Niowave Inc. After surface treatment [5] and high pressure rinsing, a thorough characterization of the rf properties and performance for the 750 MHz rf dipole prototype have been realized both at room temperature (low level rf) and at 4 K with satisfying results such as symmetry of the fields in agreement with the design simulations, capability of processing multipacting and absence of quenching at the reached gradients ($E_p = 20.0\,\frac{MV}{m}$, and $B_p = 41.9\,mT$) . Due to the success of this first test, a more detailed test at 4 K and 2 K to reach higher gradients was scheduled at the Jefferson Lab facilities, but having discovered a leak on one of the cavity brazings after shipping, the test has been rescheduled and the replacement of a new port by the cavity group at Jefferson Lab is currently undergoing.

AKNOWLEDGMENTS

We want to express our gratitude to the Niowave Inc. personnel, CAS-ODU members Subashini De Silva, Christopher Hopper and Kevin Mitchell as well as HyeKyoung Park and the cavity group at Jefferson Lab. This research used resources of the National Energy Research Scientific Center, which is supported by the Office of Science of the U.S. Department of Energy under contract No. DE-AC02-05CH11231.

REFERENCES

[1] A. Castilla et al., in Proc. of IPAC'12, New Orleans, Louisiana, p. 2447 (2012).

[2] S. U. De Silva and J. R. Delayen, Phys. Rev. ST Accel. Beams 16, 012004 (2013).

[3] D. Gorelov et al., in Proc. of IPAC'12, New Orleans, Louisiana, p. 2411 (2012).

[4] S.U. De Silva et al., in Proc. of IPAC'13, Shanghai, China, p. 2483 (2013).

[5] P. Kneisel, Nucl. Instrum. Methods 557, 1 (2006).

Copyright © 2013 CC-BY-3.0 and by the respective authors

MECHANICAL ANALYSIS OF THE 400 MHz RF-DIPOLE CRABBING CAVITY PROTOTYPE FOR LHC HIGH LUMINOSITY UPGRADE*

S. U. De Silva[1,2#], H. Park[2,1], J. R. Delayen[1,2], Z. Li[3]
[1]Center for Accelerator Science, Old Dominion University, Norfolk, VA 23529, USA
[2]Thomas Jefferson National Accelerator Facility, Newport News, VA 23606, USA
[3]SLAC National Accelerator Facility, Menlo Park, CA 94025, USA

Abstract

The proposed LHC high luminosity upgrade requires two crabbing systems in increasing the peak luminosity, operating both vertically and horizontally at two interaction points of IP_1 and IP_5. The required system has tight dimensional constraints and needs to achieve higher operational gradients. A proof-of-principle 400 MHz crabbing cavity design has been successfully tested and has proven to be an ideal candidate for the crabbing system. The cylindrical proof-of-principle rf-dipole design has been adapted in to a square shaped design to further meet the dimensional requirements. The new rf-dipole design has been optimized in meeting the requirements in rf-properties, higher order mode damping, and multipole components. A crabbing system in a cryomodule is expected to be tested on the SPS beam line prior to the test at LHC. The new prototype is required to achieve the mechanical and thermal specifications of the SPS test followed by the test at LHC. This paper discusses the detailed mechanical and thermal analysis in minimizing Lorentz force detuning and sensitivity to liquid He pressure fluctuations.

INTRODUCTION

The rf-dipole design is a favorable design for compact deflecting and crabbing applications especially at low operating frequencies [1]. The LHC high luminosity upgrade is one such current application that requires a crabbing cavity system with stringent dimensional constraints that will be operating at 400 MHz [2].

The rf-dipole cavity is one of proposed crabbing cavity designs. The design is proven to have improved rf-properties with low and balanced peak surface fields with high transverse deflection and high shunt impedance. The non-existence of lower order modes and widely separated higher order mode spectrum is an added advantage for this high current application of LHC.

An rf-dipole cavity with a cylindrical outer conductor has been designed and fabricated as a proof-of-principle cavity. The rf tests have been carried successfully [3]. The expected goal of 3.4 MV was exceeded and a transverse voltage of 7.0 MV was achieved. The major unknown in the rf-dipole geometry was the expected multipacting levels during operation. The conditions were simulated using the SLAC ACE3P code [4] and compared with rf results, show similar behavior. These multipacting levels were easily processed during the first cryogenic rf test and did not reoccur during the tests followed.

*Authored by Jefferson Science Associates, LLC under U.S. DOE Contract No. DE-AC05-06OR23177. The U.S. Government retains a non-exclusive, paid-up, irrevocable, world-wide license to publish or reproduce this manuscript for U.S. Government purposes.
#sdesilva@jlab.org

400 MHz CRABBING CAVITY PROTOTYPE

The transverse dimensions of the proof-of-principle cavity design exceed the dimensional specifications required by the LHC crabbing system. The cylindrical outer conductor restricts in reducing the cavity size as the operating frequency is directly related to the cavity frequency. The rf geometry is modified into a square shape outer conductor with similar loading elements, where the operating frequency is adjusted by rounding the edges of the cavity (Fig. 1) [5]. The rf properties of the prototype in comparison with the cylindrical cavity are shown in Table 1.

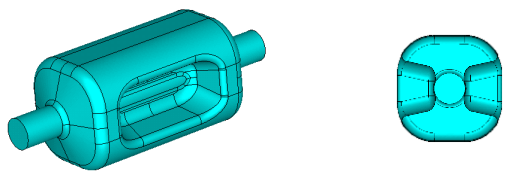


Figure 1: 400 MHz rf-dipole prototype with trapezoidal-shaped loading elements and the cross section.

Table 1: Properties of the Proof-of-principle and Prototype 400 MHz Rf-dipole Cavities

Parameter	Cylindrical shaped	Square shaped	Units
Cavity length	542.4	556.2	mm
Cavity diameter	339.9	281.0	mm
Aperture diameter (d)	84.0	84.0	mm
Bars length	350.3	293.0	mm
Bars inner height	80.0	117.5	mm
Angle	50.0	~12.0	deg
Deflecting voltage (V_T^*)	0.375	0.375	MV
Peak electric field (E_P^*)	4.02	3.65	MV/m
Peak magnetic field (B_P^*)	7.06	6.13	mT
B_P^* / E_P^*	1.76	1.68	
Energy content (U^*)	0.195	0.13	J
Geometrical factor	140.9	106.2	Ω
$[R/Q]_T$	287.0	429.2	Ω
$R_T R_S$	4.0×10^4	4.6×10^4	Ω^2

At $E_T^* = 1$ MV/m

The inner loading elements are curved to suppress the field non-uniformity across the beam aperture and to reduce the corresponding multipole components.

Copyright © 2013 CC-BY-3.0 and by the respective authors

The complete cavity with fundamental power coupler and HOM couplers are shown in Fig. 2. The HOM couplers have been designed to achieve the transverse and longitudinal damping thresholds [5].

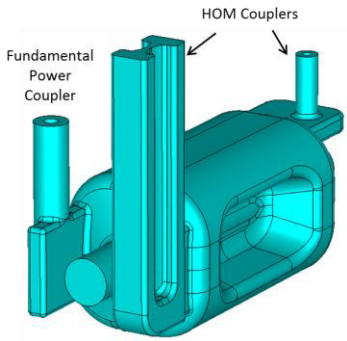


Figure 2: 400 MHz crabbing cavity proposed for LHC high luminosity upgrade.

The rf-dipole prototype design is finalized in terms of electromagnetic properties. The simulated multipacting conditions using the Tack3P in SLAC ACE3P suite [4] shows improved levels compared to the cylindrical proof-of-principle design [5].

MECHANICAL ANALYSIS

The 400 MHz crabbing cavity proposed for the LHC luminosity upgrade is expected to be tested at the SPS beam line prior to the tests at LHC. The SPS tests will include 1 or 2 cavities in a single cryomodule. Current work is focused in fabricating and testing of the first prototype, followed by the cryomodule assembly and testing at the SM18 test cryostat at CERN. The cavity will be beam tested at SPS beam line [2]. Prior to the cryostat assembly the cavity will be tested in a vertical test stand, preferably at the Jefferson Lab vertical test facility.

Stress Analysis

The rf cavity is expected to withstand different load conditions under different external pressures related to operational and safety conditions during vertical rf testing [6], cryomodule testing and beam line testing [7] as listed below:

- ❖ RF testing at the vertical test facility at Jefferson Lab
  - Testing condition – 1 atm external pressure at room temperature and during leak check
  - Operating condition – 1.1 atm external pressure and tuning force at 4 K. At 2 K the external pressure decreases to 0.03 atm
  - Safety condition – 1.4 atm external pressure at room temperature
- ❖ Cryomodule testing at the SM18 test cryostat at CERN
  - Maximum allowable pressure – 1.5 atm
  - Safety test pressure – 2.1 atm at room temperature
- ❖ Cryomodule testing in SPS at CERN
  - Maximum allowable pressure – 1.8 atm
  - Safety test pressure – 2.6 atm at room temperature

The rf dipole cavity fabricated with Nb sheets will experience stress levels under the different operating conditions. The estimated stress levels are required to be below the yield strength for Nb with material properties shown in Table 2.

Table 2: Material Properties of Nb at Room Temperature (RT) and Cryogenic Temperature of 4 K Used at CERN

Parameter	Value	Units
Density	8600	kg/m^3
Poisson's ratio	0.4	
Young's modulus at RT	1.0×10^{11}	Pa
Young's modulus at 4 K	1.23×10^{11}	Pa
Yield strength at RT	75	MPa
Max allowable stress at RT	70	MPa

The stresses analyzed using ANSYS [8] shows that the edges of the loading elements experience the highest stresses due to external pressure (Fig. 3), hence requires additional reinforcement to reduce the stresses below the yield strength.

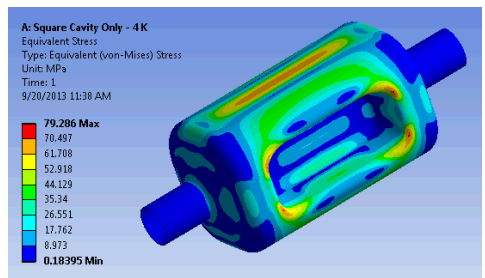


Figure 3: Stress distribution at 4 K and external pressure of 1 atm for a cavity with 3 mm uniform thickness.

Several options of cavity thicknesses with additional reinforcement were studied to achieve the design specifications for different operating conditions. Cavity with a uniform 3 mm thickness with stiffening plates added at the edges of the loading elements or a cavity with uniform thickness of 4 mm results similar stresses. The obtained stresses are below the yield strength for test conditions in a vertical test assembly, however does not meet the safety specifications for cryostat operation.

The cavity with uniform thickness of 4 mm is considered with additional 4 mm stiffening plates shown in Fig. 4, meets the operational and safety requirements for testing in a vertical test assembly as well as in a cryostat test.

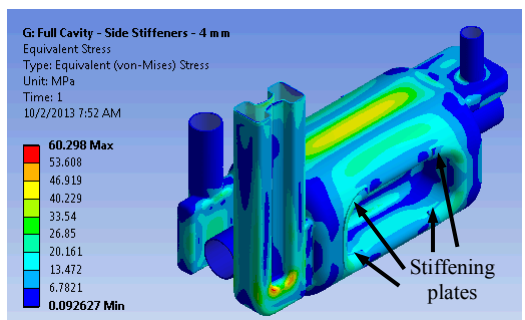


Figure 4: Stress distribution at 4 K and external pressure of 1.1 atm.

As shown in Fig. 5 at an external pressure of 2.1 atm the cavity body has a stress intensity below 70 MPa,

Copyright © 2013 CC-BY-3.0 and by the respective authors

which meets the specifications under cryostat operation. The higher stresses shown at the horizontal HOM coupler can be reduced with the fixed support by the addition of flange and helium tank mount.

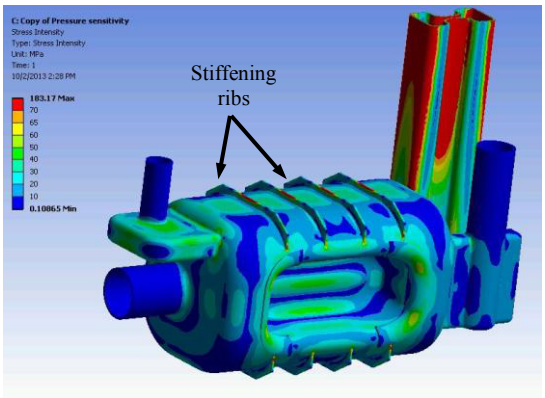


Figure 5: Stress intensity due to external pressure of 2.1 atm at room temperature.

Pressure Sensitivity

The flat surfaces at the top and bottom of the cavity experience the highest deformation due to external pressure. Table 3 shows the pressure sensitivity of the different cavity design options. The cavity with a 4 mm uniform thickness and stiffening ribs improved the sensitivity to pressure with a reduced ratio of -18.5 Hz/torr.

Table 3: Pressure Sensitivity for Different Cavity Designs

Cavity Design	***df/dP* [Hz/torr]**
Cavity with no coupler ports of 3 mm uniform thickness	-368.2
Cavity with coupler ports of:	
3 mm uniform thickness	-369.6
4 mm uniform thickness	-170.8
4 mm uniform thickness and stiffeners	-18.5

Lorentz Detuning

The Lorentz force detuning is an effect where the cavity is deformed by the radiation pressure. The magnetic field applies pressure and deforms the surface outward, while deformation due to electric field is inward as shown in Fig. 6. The curved loading elements around the beam aperture region reduce the deformation due to electric field while the outward deformation due to magnetic field counteracts the deformation due to external pressure to some extent.

The Lorentz coefficients (k_L) for different cavity designs:

- with 3 mm uniform thickness = -162.9 Hz/(MV/m)^2
- with 4 mm uniform thickness = -113.7 Hz/(MV/m)^2
- with 4 mm uniform thickness and stiffeners = -84.5 Hz/(MV/m)^2

The stiffeners were placed on the cavity to reduce the stresses for vertical testing, cryostat operation and safety conditions. The Lorentz coefficients can be improved with further reinforcement.

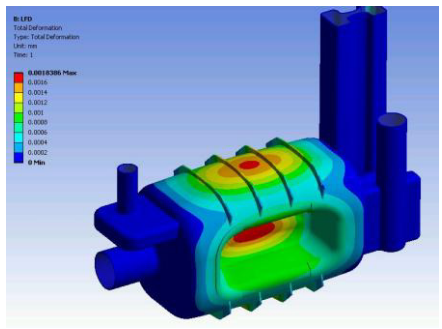


Figure 6: Deformation due to Lorentz force detuning.

CONCLUSION

The 400 MHz proof-of-principle cavity rf tests achieved a transverse voltage of 7.0 MV with high peak surface fields that gives the possibility of operating at a transverse voltage of 5.0 MV, which is above the expected goal of 3.4 MV. The preliminary mechanical analysis for the rf-dipole prototype cavity has been completed. Further analysis will be continued on reducing the pressure sensitivity and Lorentz detuning.

ACKNOWLEDGEMENTS

This work was partially supported by the U.S. DOE through the US LHC Accelerator Research Program (LARP), by the EU FP7 HiLumi LHC Grant Agreement 284404, and by the U.S. DOE HEP SBIR/STTR program through Niowave Inc., Lansing, MI.

We also would like to thank Gary G. Cheng for the support with ANSYS simulation.

REFERENCES

[1] S. U. De Silva and J. R. Delayen, Phys. Rev. ST Accel. Beams 16, 012004 (2013).

[2] P. Baudrenghien, et al., Functional Specifications of the LHC Prototype Crab Cavity System, Tech. Rep. CERN-ACC-NOTE-2013-003 (CERN, 2013).

[3] S. U. De Silva and J. R. Delayen, Phys. Rev. ST Accel. Beams 16, 082001 (2013).

[4] K. Ko, et al., in Proceedings of the 25th Linear Accelerator Conference, Tsukuba, Japan (2010), p. 1028.

[5] Z. Li, L. Ge, J. R. Delayen, and S. U. De Silva, in Proceedings of the 4th International Particle Accelerator Conference, Shanghai, China (2013), p. 2468.

[6] H. Park, J. R. Delayen and S. U. De Silva, in Proceedings of 15th Conference on RF Superconductivity, Chicago, Illinois (2011), p. 188.

[7] L. Alberty, "Prototype Cavity Stress Analysis", LHC Crab Cavity Engineering Meeting, FNAL, December, 2013.

[8] "ANSYS Academic Research, Release 13.0, Structural Mechanics Analysis, ANSYS, Inc.", (2010), http://www.ansys.com.

Copyright © 2013 CC-BY-3.0 and by the respective authors

COMPARISON OF ELECTROMAGNETIC, THERMAL AND MECHANICAL CALCULATIONS WITH RF TEST RESULTS IN RF-DIPOLE DEFLECTING/CRABBING CAVITIES*

H. Park[1,2#], S. U. De Silva[2,1], J. R. Delayen[2,1],
[1]Thomas Jefferson National Accelerator Facility, Newport News, VA 23606, USA.
[2]Center for Accelerator Science, Old Dominion University, Norfolk, VA 23529, USA.

Abstract

The current requirements of higher gradients and strict dimensional constraints in the emerging applications have required the designing of compact deflecting and crabbing rf structures. The superconducting rf-dipole cavity is one of the first novel compact designs with attractive properties such as higher gradients, higher shunt impedance and widely separated higher order modes. The recent tests performed on proof-of-principle designs of the rf-dipole geometry at 4.2 K and 2.0 K in the vertical test area at Jefferson Lab have proven the designs to achieve higher gradients with higher intrinsic quality factors and easily processed multipacting conditions. The cavity characteristics, such as pressure sensitivity and Lorentz force detuning, were studied using ANSYS before the fabrication. These characteristics were measured during the cavity test. The comparison between the simulation and the measurement provides insight how the simulation can be used for design and fabrication of future cavities.

INTRODUCTION

The Jefferson Lab 12 GeV [1] upgrade is in need of an rf separator system that separates the maximum energy beam in to the 3 experimental halls simultaneously. Figure 1 shows the 12 GeV beam line schematic with the rf separator systems required for the energy upgrade.

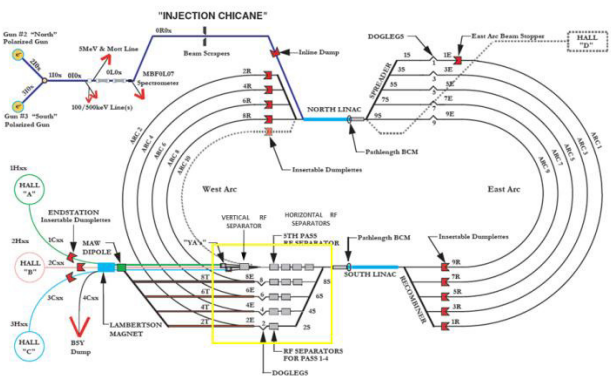


Figure 1: Jefferson Lab 12 GeV beam line.

The 6 GeV beam line has two separator systems for separating the beam horizontally and vertically. The horizontal separator system separates the beam that is recirculated into the linac from that sent to the experimental halls, where the vertical separator system separates the single beam into the 3 experimental halls. The existing rf separator system operates with a series of normal conducting rf separator cavities [2].

The 12 GeV energy upgrade requires a vertical rf separator system that operates at the increased beam energy. The superconducting rf-dipole cavity is one proposed options for the vertical separator system. Table 1 shows the optimized 499 MHz deflecting rf-dipole cavity [3]. The rf test results are shown in Figure 2.

Table 1: Properties of the 499 MHz Rf-dipole Deflecting Cavity

Parameter	Value	Units
Frequency	499.0	MHz
Cavity length	44	cm
Cavity diameter	25	cm
Aperture diameter (d)	40.0	mm
Deflecting voltage (V_T^*)	0.3	MV
Peak electric field (E_P^*)	2.86	MV/m
Peak magnetic field (B_P^*)	4.38	mT
Geometrical factor	105.9	Ω
$[R/Q]_T$	982.5	Ω
$R_T R_S$	1.0×10^5	Ω^2

At E_T^* = 1 MV/m

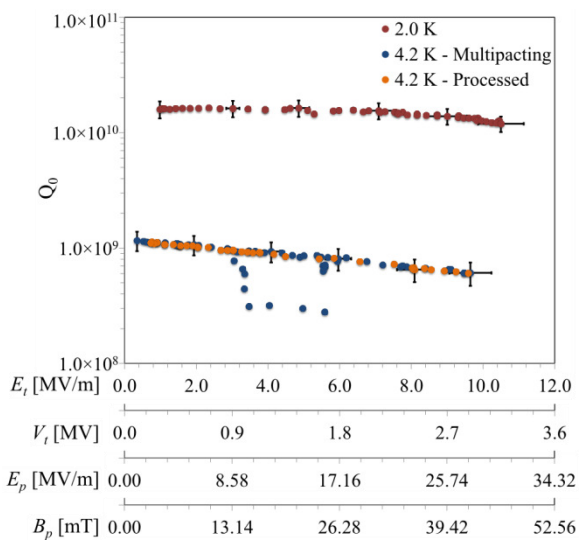


Figure 2: Q curve of the 499MHz rf dipole cavity.

*Authored by Jefferson Science Associates, LLC under U.S. DOE Contract No. DE-AC05-06OR23177. The U.S. Government retains a non-exclusive, paid-up, irrevocable, world-wide license to publish or reproduce this manuscript for U.S. Government purposes.

#hkpark@jlab.org

Copyright © 2013 CC-BY-3.0 and by the respective authors

FABRICATION

The rf-dipole cavity was fabricated in parts consisting of two end caps and the center body sub-assemblies. The driving factors of the fabrication process at JLAB were the available expertise and time line. Instead of traditional stamping, machining a part of cavity was chosen due to its forming complexity and high stress identified during the study. Machining gave the freedom to increase the thickness where needed. The stiffeners were considered but not used in order to see the unstiffened cavity characteristics and performance.

Figure 3 shows the fabrication sequence. Before the electron beam welding, all parts were trimmed and chemically etched.

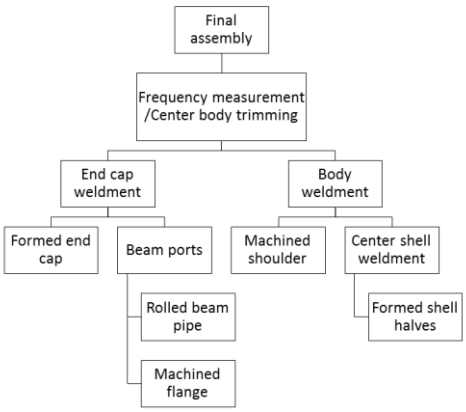


Figure 3: Fabrication sequence.

The end caps, center shell halves, and beam pipes were formed using the stamping dies. The center shell halves are open ended and they were conformed to the fixture during the longitudinal seam weld as shown in Figure 4. Figure 4 also shows the welded shell and the machined shoulder block.

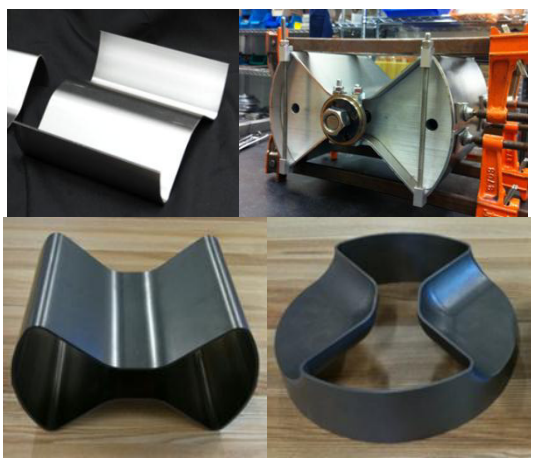


Figure 4: Formed shell halves and fixture assembly (top). Center shell weldment and shoulder block (bottom).

The sub-assemblies are then clamped tight and the frequency was measured (Figure 5). The frequency measurement and the center shell length trimming were repeated to achieve the target frequency.

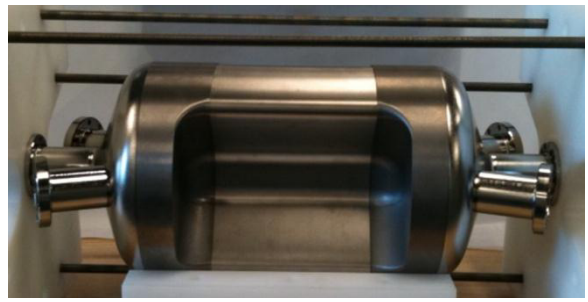


Figure 5: Clamped cavity for frequency measurement.

The next weld was to assemble the center shell body to the shoulder blocks. The center shell profile was slightly mismatched to the machined shoulder which would cause the stepped transition surface when it was welded. Therefore, the two profiles were constrained again with a collapsible fixture. This fixture was inserted between the center shell and the shoulder block as shown in Figure 6. Once it was tack welded in the electron beam welding machine, the fixture was taken out and inside and outside welds were performed.



Figure 6: Weld fixturing.

The final welds were the joints between the center body sub-assembly and end cap sub-assemblies. These joints required full penetration welds from outside.

COMPARISON

ANSYS was used for structural analyses under various conditions [4,5]. Additional analyses were conducted for predicting frequency change during the process, pressure sensitivity, Lorentz force detuning, and so on.

The target frequency of the cavity at room temperature before the final weld was calculated to be 497.8 MHz which would provide the operating frequency 499 MHz in the dewar.

Table 2 lists the cavity's frequency change along the process. The final trimming was done anticipating 498 MHz after final welding. However the welded cavity frequency was measured much lower. The investigation concluded that the deviations in the center shell weldment from the design profile the reason. During the trimming measurement (Figure 5) the center shell gap width was smaller due to the spring back. This resulted in higher capacitance and a higher frequency. Once the shell was conformed to the design profile during the weld the gap widened which lowered the frequency.

The total frequency shift from the welded cavity at room temperature to the cooled down evacuated cavity

Copyright © 2013 CC-BY-3.0 and by the respective authors

was calculated 0.97 MHz and the equivalent measurement was 1.01 MHz. The measurement and simulated frequency changes are in agreement.

Table 2: Frequency Changes of Cavity.

Process	Target/Simulation (MHz)	Measurement (MHz)
Before welding (clamped)	497.63	497.81
Welded cavity at room temperature	498.03	496.83
After bulk BCP	498.31	497.21
Evacuation and cool down to 4K*	499.00	497.84

* Simulation was separate but the measurements were made at the dewar simultaneously.

The rf tests on the 499 MHz rf-dipole cavity were performed at 2.0 K and 4.2 K. The results show high unloaded quality factor and low surface resistance [6].

The pressure sensitivity during the cool down process from 4.2 K to 2.0 K was measured to be -379.5 Hz/torr. As shown in Figure 7, the simulated results give a df/dP of -255.8 Hz/torr. The difference in the pressure sensitivity could be due to difference in material properties, and non-uniformity in the fabricated cavity. The higher sensitivity can be reduced by adding stiffeners at appropriate locations.

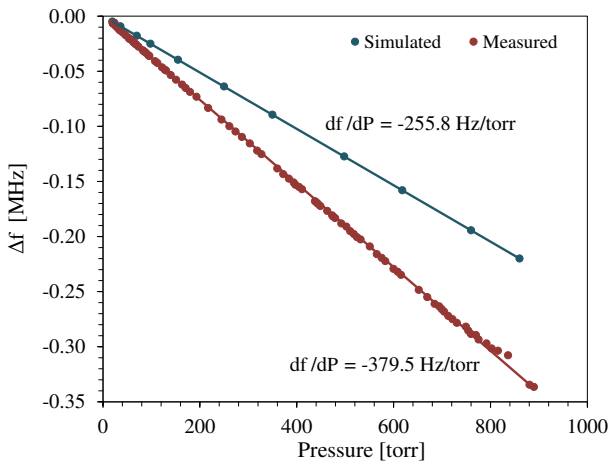


Figure 7: Pressure sensitivity of the 499 MHz rf-dipole cavity.

The Lorentz force detuning is an effect where the cavity is deformed by the radiation pressure. The magnetic field applies pressure and deforms the surface outward, while deformation due to electric field is inward. The change in cavity resonant frequency due to the deformation by Lorentz force was measured as shown in Figure 8. At 4.2 K and 2.0 K the Lorentz coefficients were calculated to be k_L = -57.7 and -53.7 Hz/(MV/m)^2, and the slight variation in the number is possibly due to ports calibration. The simulated coefficient is k_L = -52.4 Hz/(MV/m)^2 with a frequency shift of 5.2 kHz at a transverse voltage of 3.0 MV. This would also be reduced by adding stiffeners.

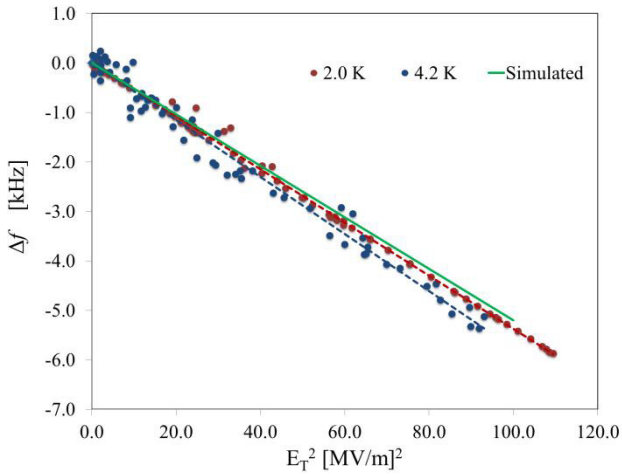


Figure 8: Lorentz force detuning at 4.2 K and 2.0 K rf tests.

CONCLUSION

The first rf test of the 499 MHz deflecting cavity was carried out and the test results were compared with the simulations. Differences between the simulation and the actual measurements are expected due to material and fabrication tolerances. The comparison of the 499 MHz rf dipole cavity case proves that these studies are useful to predict the behavior of the cavity and help to design to minimize the adverse effects of the cavity environment. In the case of the pressure sensitivity, further study is required to understand the deviation between simulation and measurement.

ACKNOWLEDGEMENTS

We thank Dave McCay and Casey Apeldoorn at Jefferson Lab Machine Shop for their tremendous help.

We also appreciate the support from Gary G. Cheng on the ANSYS simulation.

REFERENCES

[1] L. Merminga, et al., in Proceedings of the 21st Particle Accelerator Conference, Knoxville, Tennessee, Illinois (2005), p. 1482.

[2] C. W. Leemann and C. G. Yao, in Proceedings of the Linear Accelerator Conference, Albuquerque, New Mexico, (1990) p. 232.

[3] S. U. De Silva and J. R. Delayen, Phys. Rev. ST Accel. Beams 16, 012004 (2013).

[4] H. Park, S. U. De Silva and J. R. Delayen, in Proceedings of 3rd International Particle Accelerator Conference, New Orleans, Louisiana (2012), p. 2450.

[5] H. Park, J. R. Delayen and S. U. De Silva, in Proceedings of 15th Conference on RF Superconductivity, Chicago, Illinois (2012), p. 188.

[6] S. U. De Silva and J. R. Delayen, in Proceedings of 16th Conference on RF Superconductivity, Paris, France (2013).

Copyright © 2013 CC-BY-3.0 and by the respective authors

GEOMETRY EFFECTS ON MULTIPOLE COMPONENTS AND BEAM OPTICS IN HIGH-VELOCITY MULTI-SPOKE CAVITIES*

C. S. Hopper†, K. Deitrick, and J. R. Delayen
Center for Accelerator Science, Department of Physics,
Old Dominion University, Norfolk, VA, 23529, USA and
Thomas Jefferson National Accelerator Facility, Newport News, VA 23606, USA

Abstract

Velocity-of-light, multi-spoke cavities are being proposed to accelerate electrons in a compact light-source [1]. There are strict requirements on the beam quality which require that the linac have only small non-uniformities in the accelerating field. Beam dynamics simulations have uncovered varying levels of focusing and defocusing in the proposed cavities, which are dependent on the geometry of the spoke in the vicinity of the beam path. Here we present the results for the influence different spoke geometries have on the multipole components of the accelerating field and how these components, in turn, impact the simulated beam properties.

INTRODUCTION

To address the varying levels of focusing and defocusing that beam dynamics simulations have shown exist, we first evaluate the higher order multipole components contained in the accelerating field to better understand what contributions could lead to the observed behavior. The design of the cavities, and the linac, are then evaluated using results generated by ASTRA particle tracking simulation code.

MULTIPOLE COMPONENTS

The higher order multipole components are analyzed using the method given in [2, 3]. Various cavities have been considered for fabrication, and the field non-uniformity for each of these cavities is shown in Fig. 2. The difference in the models essentially comes down to the shape of the spoke aperture region. A standard racetrack is preferred because of the rf properties, but a rounded square, ring [4], and elliptical aperture have also been studied, and are shown in Fig. 1.

These geometries have varying degrees of symmetry. The ring and racetrack apertures, for similar cavities, have been studied and presented elsewhere [3]. Additional optimization of apertures (c) and (d) is necessary. However, it is likely that some compromise would have to be made, in terms of increased peak surface fields, to decrease the multipole components. Figures 3 and 4 show the $E_z^{(2)}$ and $E_z^{(4)}$ components as a function of position. All the cavities have the same mesh, and similar $E_z^{(2)}$ components, however there is a clear difference in the $E_z^{(4)}$ components.

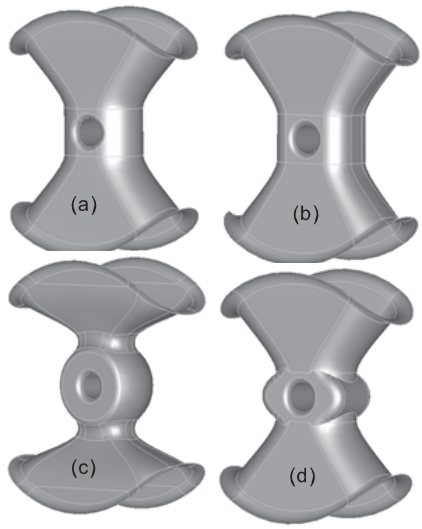


Figure 1: Various spoke aperture geometries studied. (a) racetrack, (b) rounded square, (c) ring, and (d) elliptical.

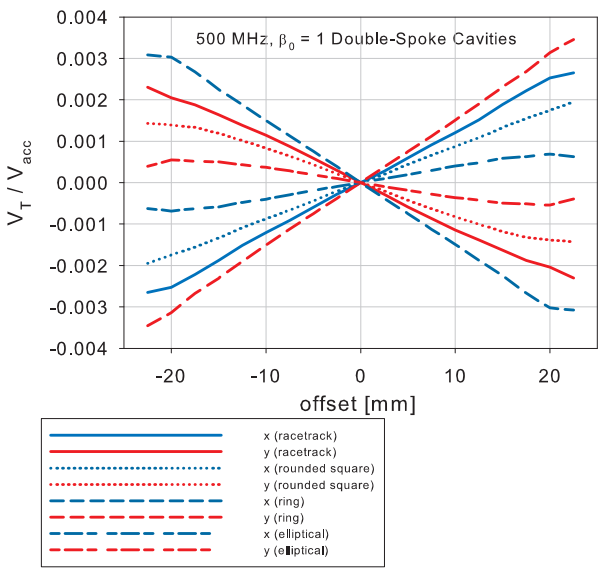


Figure 2: Dependence of transverse voltage (normalized to V_{acc}) on transverse offset for the aperture geometries presented in Fig. 1.

* Work supported by U.S. DOE Award No. DE-SC0004094
† chopp002@odu.edu

Copyright © 2013 CC-BY-3.0 and by the respective authors

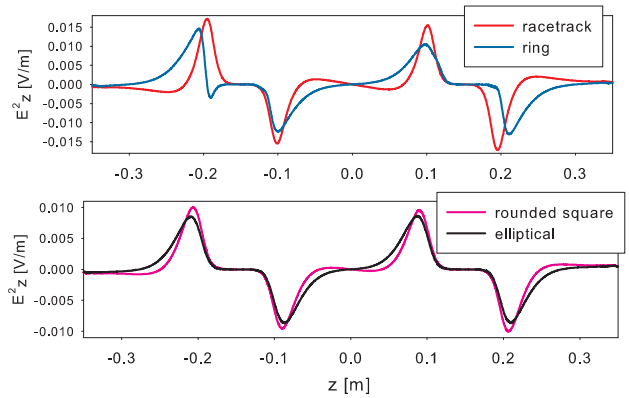


Figure 3: $E_z^{(2)}$ for various aperture geometries.

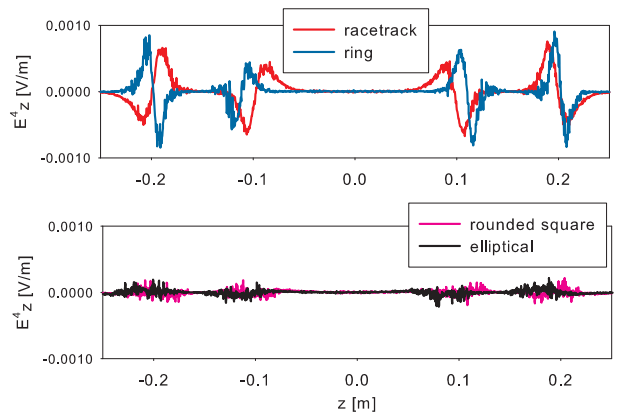


Figure 4: $E_z^{(4)}$ for various aperture geometries.

With the square and elliptical aperture, the octupole component is small enough to be obscured by noise.

While there are some similarities with the studies done by [4] and [5] on HWRs and single-spoke cavities, the geometry of the spokes presented here (other than the actual aperture region) is vastly different, which makes a direct comparison difficult.

BEAM DYNAMICS

The beam dynamics were simulated using the current cathode and gun specifications, detailed in [1]. After exiting the gun, the electron beam is defocusing in both transverse directions equally. The beam then gains 5.86 MeV in the initial double-spoke cavity. The optical parameters of the beam after a single cavity are presented in Tab. 2. As the spoke cavities are not symmetric with respect to the beam line, the transverse components are no longer equal, which is expected. However, the difference between the transverse components of either α or β differs between the four designs. With the least difference is the elliptical aperture, while the ring aperture has the most. Another noteworthy point is that after a single cavity, the β_x and β_y of the beam are diverging for the designs that are not the elliptical aperture.

Table 1: Multipole Components, 500 MHz, $\beta_0 = 1$

Aperture Geometry	$\mathbf{b}_2$ [mT]	$\mathbf{b}_4$ [mT/m^2]
Racetrack	0.37 + 0.006i	-3.9 + 720i
Rounded Square	0.25 - 0.001i	N/A
Ring	-0.45 - 0.07i	141 - 264i
Elliptical	-0.1 - 0.001i	N/A

At the exit of the cavity, a perfectly round beam would be such that $\beta_x = \beta_y$. After passing through a single cavity, the list of apertures in order of decreasing roundness is as follows: elliptical, rounded square, racetrack, and ring. This is also the order that would be obtained by listing apertures in order of increasing $|b_2|$. A comparison of the beam spots for the four designs with optimal configuration after one cavity is seen in Fig. 5.

The results become even more interesting when the electron beam passes through two cavities, shown in Tab. 3. The (-) entries correspond to an iris-to-iris distance of 0.619 m separating the two cavities, while (S) corresponds to a distance of 0.255 m. Entries with (R) correspond to the second cavity rotated 90° as in [1], so that the first spoke in the second cavity the beam traverses is orthogonal to the first spoke in the first cavity that the beam passes through. A few conclusions can be formed. Both the ring and elliptical apertures have β_x and β_y diverging, regardless of the separation or orientation of the second cavity. The racetrack and rounded square apertures diverge for either separation if the second cavity is unrotated, while the β_x and β_y converge for either separation if the second cavity is rotated.

More narrow observations can be made. For both distances, a rotated second cavity produces a rounder beam except for the (-) elliptical. Given that this technique works on the elliptical if there is a shorter separation distance, it may be that if a beam is round to the first order at the exit of an unrotated second cavity, rotating the second cavity decreases the roundness of the resulting beam. The beam behavior similar to a quadrupole is when the beam focuses in one direction while defocusing in the other, which corresponds to each transverse component of α having a different sign.

Since it has now become clear that the separation between the two cavities does have an impact that differs between designs, it is difficult to form any firm conclusions. It is possible to configure the racetrack and rounded square cavities to produce a converging beam for two cavities, while it is impossible to do so with the ring and elliptical designs, regardless of the distance between the two cavities. To develop further conclusions would require a systematic sweep over different separation distances and orientation of the second cavity for all four aperture designs. Though a worthwhile topic, it is beyond the scope of this paper.

As the quadrupole moment is significant in all four of the presented designs, it is difficult to discern the impact of

Copyright © 2013 CC-BY-3.0 and by the respective authors

Table 2: Beam Properties After a Single Cavity

Aperture Geometry	α_x	α_y	β_x [m]	β_y [m]
Racetrack	-19.58	-12.34	55.31	45.67
Rounded Square	-20.21	-16.34	55.51	49.46
Ring	-4.687	-26.27	44.38	56.87
Elliptical	-16.90	-18.47	53.42	51.28

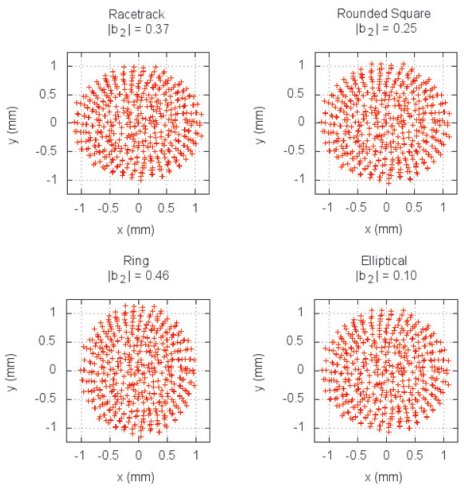


Figure 5: Beam spots of the different designs, with corresponding $|b_2|$ values, after a single cavitiy.

the octupole moment on the beam. Consequently, we are unable to form any conclusions about the relationship between $|b_4|$ and the behavior of the beam. A study of this aspect would require the quadrupole moment of the compared designs to be sufficiently constant. Additionally, it would also require a reliable method of accurately integrating $E_z^{(4)}$, which is difficult for the rounded square and elliptical apertures, as seen in Fig. 4.

To emphasize the connection between the beam behavior and $|b_2|$ for a given aperture design, this analysis begins with a single cavity. Once a second is added and it becomes clear that the separation between the two also has an impact, making it difficult to discern the consequences of separation and $|b_2|$ from the current set of results. Given a linac consisting of four cavities, separated as in [1], the optimum results are shown in Tab. 4. Optimal configurations for all designs except the elliptical are obtained by rotating the second and fourth cavity. For the elliptical, the optimum results are obtained by rotating only the third cavity.

CONCLUSION

The multipole components and beam optics have been studied for different spoke aperture geometries. A racetrack shaped aperture provides the most desirable rf properties, and with the proper orientation, an acceptable beam shape. The fabrication of this cavity is underway at Jefferson Lab.

Table 3: Beam Properties after Two Cavities, with the Second Cavity Rotated (R), Closer to the First Cavity (S), or Both (RS)

Aperture Geometry	α_x	α_y	β_x [m]	β_y [m]
Racetrack (-)	-15.6	0.234	106	65.1
Rounded Square (-)	-15.3	-5.13	107	81.6
Ring (-)	7.15	-27.5	45.2	128
Elliptical (-)	-8.98	-8.85	93.1	91.0
Racetrack (-R)	-4.40	-7.74	92.6	75.6
Rounded Sqare (-R)	-7.90	-11.4	97.1	90.4
Ring (-R)	-0.069	-8.45	49.2	118
Elliptical (-R)	-6.34	-11.6	87.3	97.2
Racetrack (S)	-13.8	-0.202	86.0	55.5
Rounded Square (S)	-13.6	-5.12	86.3	67.2
Ring (S)	6.95	-24.9	43.1	102
Elliptical (S)	6.13	-27.9	46.8	109
Racetrack (RS)	-4.98	-6.95	76.2	64.0
Rounded Square (RS)	-7.86	-10.3	79.0	74.2
Ring (RS)	0.148	-10.1	46.0	94.8
Elliptical (RS)	-1.22	-12.0	49.9	101

Table 4: Beam Properties After Four Cavities, Configured to Produce Roundest Beam

Aperture Geometry	α_x	α_y	β_x [m]	β_y [m]
Racetrack	5.555	2.035	94.68	78.64
Rounded Square	2.896	-0.1997	109.9	106.8
Ring	4.782	4.879	31.46	132.9
Elliptical	1.945	1.567	103.5	108.5

REFERENCES

[1] T. Satogata et al, "Compact Accelerator Design for a Compton Light Source," IPAC 2013, Shanghai, China, May 2013.

[2] J. Barranco Garcia et al, "Study of Multipolar RF Kicks from the Main Deflecting Mode in Compact Crab Cavities for LHC" IPAC 2012, New Orleans, LA, (2012), p. 1873.

[3] R. G. Olave, J. R. Delayen, and C. S. Hopper, "Multipole Expansion of the Fields in Superconducting High-Velocity Spoke Cavities," LINAC 2012, Tel Aviv, Israel, September 2012.

[4] B. Mustapha, P.N. Ostroumov and Z.A. Conway, "A Ring-Shaped Center Conductor Geometry for a Half-Wave Resonantor," IPAC 2012, New Orleans, LA, (2012), WEPPC037.

[5] P. Berrutti et al, "Effects of RF Field Asymmetry in SC Cavities of the Project X," IPAC 2012, New Orleans, LA, (2012), pp. 2318-2320.

Copyright © 2013 CC-BY-3.0 and by the respective authors

STUDY OF CAVITY IMPERFECTION IMPACT ON RF-PARAMETERS AND MULTIPOLE COMPONENTS IN A SUPERCONDUCTING RF-DIPOLE CAVITY*

R. G. Olave, J. R. Delayen†, S. U. De Silva, Old Dominion University, Norfolk, VA, USA
Z. Li, SLAC National Accelerator Laboratory, Menlo Park, CA, USA

Abstract

The ODU/SLAC superconducting rf-dipole cavity is under consideration for the crab-crossing system in the upcoming LHC luminosity upgrade. While the proposed cavity complies well within the rf-parameters and multipolar component restrictions for the LHC system, cavity imperfections arising from cavity fabrication, welding and frequency tuning may have a significant effect in these parameters. We report on an initial study of the impact of deviation from the ideal shape on the cavity's performance in terms of rf-parameters and multipolar components.

INTRODUCTION

Due to transverse geometry constraints at the nominal operating rf frequency of 400 MHz, novel compact cavities are under consideration for the upcoming LHC High Luminosity upgrade. The ODU/SLAC superconducting rf-dipole cavity is a suitable candidate as it satisfies the requirements for high gradients, high shunt impedance, low surface fields, no lower order modes, and well-defined and widely-spaced higher order modes [1]-[3]. The cavity geometry, while compact, is not azimuthally symmetric and therefore it becomes important to identify any higher order multipolar components at the operating frequency, since these can lead to beam instabilities in the LHC system. The ODU/SLAC rf-dipole cavity satisfies all specifications for the LHC crab cavity system in terms of rf parameters and in terms of multipole contributions up to the octupole term [4]; Table 1 presents a list of the relevant rf parameters for the cavity. As we prepare for fabrication of a prototype cavity, we are analyzing the impact of individual imperfections or departures from the ideal cavity geometry, that may arise from fabrication or welding errors, while additional distortions would result from the tuning process. In this paper, we present an initial analysis on how such geometry imperfections, particularly those due to welding of the poles, would result in the introduction of undesired higher order multipole components.

IMPERFECTIONS IN THE POLES VS FIELD UNIFORMITY

The design optimization of the cavity showed quite clearly that the geometry of the aperture region of the poles near the beam axis is of vital importance in minimizing the contribution of the sextupole component, which results in a more uniform deflecting voltage across the beam aperture region. For this reason, we start by looking into imperfections in the shape or welding of the poles. Using CST Microwave Studio® 2012 (CST MWS) we have altered the optimized design near the beamline to introduce individual defects in the alignment or geometry of one of the poles, according to the following list:

Table 1: RF Parameters of the 400 MHz Rf-dipole Cavity (at E_T = 1 MV/m and Reference Length $\beta_0\lambda$)

Parameter		Units
Frequency	400.28	MHz
$(R/Q)_T$	412.7	Ω
$(R/Q)_T * (QR_s)$	4.43x10^4	Ω^2
E_p/E_T	3.66	
B_p/E_T	6.14	mT (MV/m)

- (A) Yaw (rotation about y-axis) of one pole.
- (B) Pitch (rotation about x-axis) of one pole.
- (C) Roll (rotation about z-axis) of one pole.
- (D) Horizontal displacement of one pole.
- (E) Vertical displacement of one pole.
- (F) Blending radius at the outer corner of one pole.
- (G) Blending radius of the feather-like structure near the beamline of one pole.
- (H) Aperture radius in one pole.

Figure 1 shows transverse and longitudinal views of the cavity, where the optimized pole geometry can clearly be seen, as well as the places where deformations have been added according to the previous list.

The robustness of the cavity design is such that none of the individual imperfections introduced so far produces drastic changes in the rf-parameters. For items (A), (F) and (G), the transverse voltages (normalized to the transverse voltage at the ideal cavity's beamline) barely change as function of transverse offset from the ideal beamline, from those of the ideal cavity geometry. This can be seen for example in Fig. 2, which includes a plots for different yaw (rotation about the y-axis) angles, as well as a plot (red) of the transverse voltage as a function of transverse offset of the ideal cavity for reference. As can be seen, there is field uniformity in a large region within the cavity's aperture, even for large yaw angles in one of the poles.

* Work supported by U.S. DOE through the US LHC Accelerator Research Program (LARP)
† jdelayen@odu.edu

Copyright © 2013 CC-BY-3.0 and by the respective authors

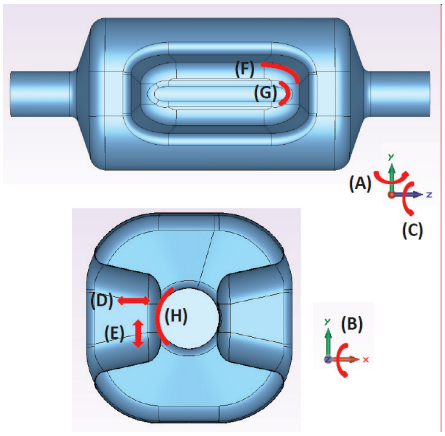


Figure 1: Longitudinal and transverse views of the optimized cavity, and individual imperfections that have been introduced in the geometry of the left pole.

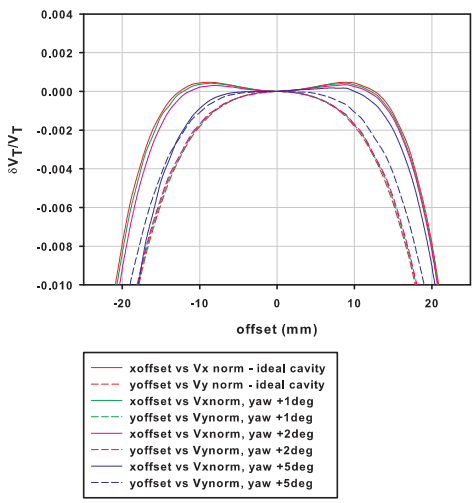


Figure 2: Effects of the yaw (rotation about the y-axis) of one pole on the normalized transverse voltages in the aperture region.

The introduction of a pitch angle results in changes similar to those of displacing a pole in the vertical direction, items (B) and (E). These result in an asymmetry in the horizontal (x-direction) voltage profile, accompanied by displacement of the electrical center of the cavity. This can clearly be seen in Fig. 3, which shows the effects of the pitch (rotation about the x-axis) of one of the poles on the normalized transverse voltage as a function of transverse offset.

The largest effects on the normalized transverse voltages seen so far are due to the roll (rotation about the z-axis) of one of the poles. These effects can be seen in Fig. 4 as a sharp asymmetry in the vertical (y-axis) voltage profile, as well as a displacement on the electrical center of the cavity.

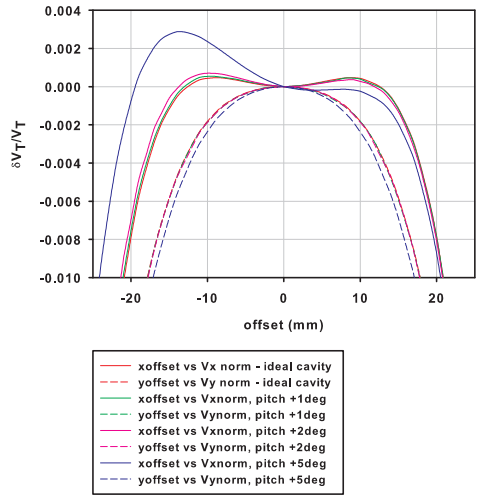


Figure 3: Effects of the pitch (rotation about the x-axis) of one pole on the normalized transverse voltages.

It is worthwhile to note that even for large imperfections, such as a roll angle of 5°, the change in the normalized transverse voltages is on the order of a few percent.

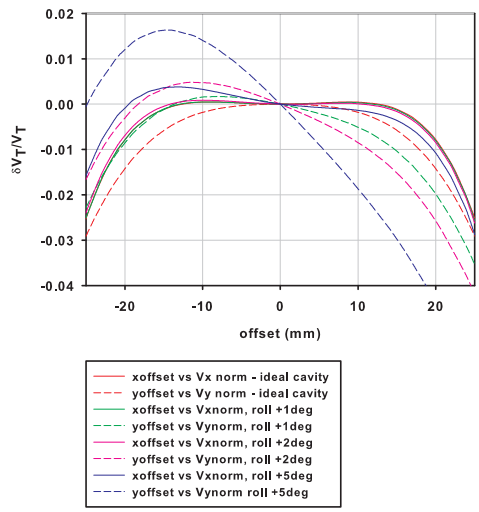


Figure 4: Effects of the roll (rotation about the z-axis) of one pole on the transverse voltages.

The effect of a horizontal displacement of one of the poles, item (D), is simply to shift the electrical center of the cavity. The effects of changing the aperture radius of one of the poles, item (H), is still under analysis.

IMPERFECTIONS OF THE POLES VS MULTIPOLE COMPONENTS

Following the procedure outlined in [5]-[8], from the interpolation of the electromagnetic fields on the surface of a virtual cylinder of radius R through the length of the cavity

Copyright © 2013 CC-BY-3.0 and by the respective authors

in a region free of charge, a general complete solution to the fields can be found. The accelerating electric field can then be expressed as:

$$E_z(r,\phi,z) = E_z e^{i\omega t} = \sum_{n=0}^{\infty} r^n \left(E_z^{(n)} cos(n\phi)\right) e^{i\omega t}, \quad (1)$$

where E_z is the electric field along the beamline direction z and ω is the rf frequency. If the field $E_z(R,\phi,z)$ is known, then the coefficients $E_z^{(n)}$ can be found via inverse Fourier integration of the surface fitted field.

Using the Panofsky-Wenzel theorem we may then calculate the transverse change in momentum (kick) of the particles as a series of multipolar RF kicks:

$$\Delta p_\perp = \left(\frac{e}{\omega}\right) \int_{-\infty}^{+\infty} (-i)\nabla_\perp E_z|_{t=z/v_z} dz \,. \quad (2)$$

Finally, we can express the transverse rf-kicks in the notation commonly used for the multipole magnetic kick strength for magnets. It is important to notice that in our case, the transverse rf-kicks are not static, but functions of time, and as such, they are complex numbers oscillating at the rf-frequency of interest (400 MHz).

$$B^{(n)}(z) = \frac{nj}{\omega} E_z^{(n)}(z), \quad b_n = \int_{-\infty}^{+\infty} B^{(n)}(z) dz \,. \quad (3)$$

Table 2 presents the multipolar components of the ideal cavity for reference. Because of the geometry of this cavity, all even b_n should be zero, so that gives us a reference for the degree of error in our calculations. Table 3 presents the multipole components for the cavities with the imperfections we have used as examples, namely for varying (A) yaw, (B) pitch, and (C) roll, normalized to V_T = 1 MV.

Table 2: RF Multipole Components, Normalized From Simulation Field Data to V_T = 1 MV, of the 400 MHz Rf-dipole Cavity

Multipole component		**Units**
V_T	1	MV
b_1	3.3	mT m
b_2	0.001	mT
b_3	37.4	mT/m
b_4	-1.8	mT/m^2
b_5	-1.94 x 10^5	mT/m^3

It can be seen that although higher order multipole components appear when the cavity is deformed, their contribution is not too significant (supported by the small percentage of variation in the transverse voltage profiles presented in the previous figures), and the cavity remains within the specifications required for the LHC crab cavity system.

Table 3: RF Multipole Components, Normalized From Simulation Field Data to $V_T = 1MV$, of the 400 MHz Rf-dipole Cavity. Units of mT m/m$^{(n-1)}$

Imperfection	b_1	b_2	b_3	b_4
yaw 1°	3.3	-0.003	36.1	41.1
yaw 2°	3.3	-0.0003	33.2	158.1
yaw 5°	3.3	-0.02	13.8	983.4
pitch 1°	3.3	-0.01	38.2	-18.1
pitch 2°	3.3	-0.05	40.4	-86.1
pitch 5°	3.3	-0.35	55.1	-561.4
roll 1°	3.3	-0.2	44.1	-171.0
roll 2°	3.3	-0.5	51.9	-374.6
roll 5°	3.3	-1.6	85.2	-1115.8

CONCLUSION

We are analyzing the impact of imperfections in the shape of the cavity on rf-parameters and multipole components. So far there are no deformations that would make the cavity non-compliant with the requirements for the LHC crab system. However, the analysis is not complete, and there can be significant shifts in the electrical center of the cavity. Our future plans include a comparison of these parameters for cavities normalized to the electrical center of the cavities, as opposed to normalization with respect to the ideal cavity.

REFERENCES

[1] S. U. De Silva and J. R. Delayen, "Design evolution and properties of superconducting parallel-bar rf-dipole deflecting and crabbing cavities," PRSTAB **16**, 012004 (2013).

[2] S. U. De Silva and J. R. Delayen, "Superconducting RF-Dipole Deflecting and Crabbing Cavities," SRF'13, Paris, France, September 2013, FRIOA04 (2013).

[3] Z. Li et al., "RF Modeling Using Parallel Codes ACE3P for the 400-MHz Parallel-Bar/Ridged-Waveguide Compact Crab Cavity for the LHC HiLumi Upgrade", IPAC'12 New Orleans, USA, May 2012, WEEPPB010 (2012).

[4] P. Baudrenghien, K. Brodzinski, R. Calaga, O. Capatina, E. Jensen, A. Macpherson, E. Montesinos, V. Parma, "Functional Specifications of the LHC Prototype Crab Cavity System", CERN-ACC-NOTE-2013-003 (2013).

[5] D. T. Abell, "Numerical computation of high-order transfer maps for rf cavities," PRSTAB **9**, 052001 (2006).

[6] J. Barranco Garcia et al., "Study of Multipolar RF Kicks from the main deflecting mode in compact crab cavities for LHC," IPAC'12, New Orleans, USA, May 2012, TUPPR027 (2012).

[7] R. G. Olave et al., "Multipole expansion of the fields in superconducting high-velocity spoke cavities" Proc. LINAC2012, Tel-Aviv Israel, MOPB072 (2012).

[8] S. U. De Silva and J. R. Delayen, "Multipole field effects for the superconducting parallel-bar/rf-dipole deflecting/crabbing cavities" Proc. LINAC2012, Tel-Aviv Israel, SUPB038 (2012).

Copyright © 2013 CC-BY-3.0 and by the respective authors

HIGHER ORDER MODES DAMPING AND MULTIPACTING ANALYSIS FOR THE SPX DEFLECTING CAVITY FOR THE APS UPGRADE*

Z. Li, L. Xiao, C. Ng, SLAC, Menlo Park, CA 94025, USA
A. Nassiri, G. Waldschmidt, G. Wu, ANL, Argonne, IL 60439, USA
H. Wang, R. Rimmer, Jefferson Lab, Newport News, VA 23606, USA

Abstract

A single-cell superconducting deflecting cavity operating at 2.815 GHz has been proposed and designed for the Short Pulse X-ray (SPX) project for the Advanced Photon Source (APS) upgrade. Each deflecting cavity is equipped with one fundamental power coupler (FPC), one lower order mode (LOM) coupler, and two higher order mode (HOM) couplers to achieve the stringent damping requirements for the unwanted modes. Using the electromagnetic simulation suite ACE3P, HOM damping was calculated for the cavity including the full engineering design waveguide configurations and rf windows. Trapped modes in the bellows located in the beampipes connecting the cavities in a two-cavity cryomodule were analyzed. Multipacting activities in the cavity and damping waveguides were simulated under the condition of field asymmetry due to a realistic cavity imperfection to assess possible problems during high power processing.

INTRODUCTION

The Advanced Photon Source (APS) can provide photon pulses of several tens to hundreds of picoseconds. There are growing requests from users to use shorter pulse X-rays (SPX) for the analysis of short time-scale physical processes. It has been proposed at APS [1,2] to utilize a pair of superconducting deflecting cavity modules to generate ~1ps X-ray pulses at one of the straight sections, without disrupting the regular X-ray pulse usage for other users. In the proposed scheme, the first set of cavities add a correlation between bunch longitudinal position and transverse momentum. X-Rays produced by this bunch will also have this correlation, and can be put through transverse slits to produce a much shorter X-Ray pulse. The second set of cavities are located a multiple of 180 degrees of phase advance to unchirp the beam, removing the effects of the first cavity set. A cryomodule of four such cavities on each side of the undulator will be needed to produce the required 2-MV deflecting voltage [3].

A two-cavity prototype cryomodule, Fig. 1, is currently under construction and to be tested before the full installation of the four-cavity cryomodules for the APS upgrade. Because of the added complicity of the multi-cavity system, understanding of potential trapped modes and multipacting issues in such a multi-cavity system is essential to validate the design concept. In addition to the planned test, detailed numerical analysis of the HOM damping and multipacting were carried out on the two-cavity prototype module. In this paper, we present the simulation results of HOM damping and multipacting analysis under realistic imperfection conditions.

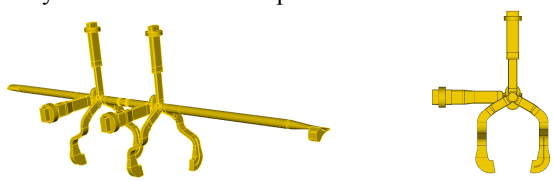


Figure 1: SPX two-cavity deflecting module, and the layout of the FPC and HOM/LOM damping couplers

TWO CAVITY PROTOTYPE MODULE

The layout of the two-cavity module, including the couplers, bellows, and extended beam pipes, is shown in Fig. 1. The cavity has a flattened oval shape and operates in the TM110 mode at 2.815 GHz, which has a strong magnetic field on the beam axis that produces transverse deflection. The RF power is fed from a fundamental power coupler (FPC) waveguide, the vertical waveguide in Fig. 1, which forms one of the legs of a ”Y”-end-group off-cell. The other two legs of the “Y”-end-group, the curved waveguide underneath the cavities, are for damping the higher-order modes. The cavity also supports a TM01 mode, which is at a lower frequency than the operating mode. An on-cell lower order mode (LOM) coupler, horizontal waveguide in Fig. 1, is directly attached to the cell at the cavity equator which offers a more compact geometry with enhanced LOM and HOM damping. Beampipe bellows are in between the two cavities for alignment flexibility.

We have used the parallel finite element EM code suite ACE3P [4] developed at SLAC to analyze the trapped mode damping and multipacting in the two-cavity cryomodule. Fig. 2 shows the finite element mesh around

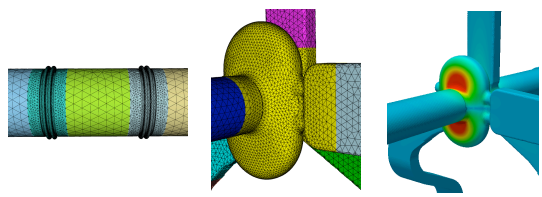


Figure 2: Finite-element mesh around the cavity and beam pipe bellows and the field profile of the operating mode.

*Work supported by the U.S. Department of Energy, Office of Science, Office of Basic Energy Sciences, under Contract No. DE-AC02-06CH11357

Copyright © 2013 CC-BY-3.0 and by the respective authors

the cavity and the bellows used by the ACE3P code. The electric field profile of the operating mode, which produces a vertical deflection, is also shown in Fig. 2.

TRAPPED MODES AND HOM DAMPING IN THE TWO-CAVITY MODULE

HOM Damping and Impedance

The HOMs up to 4.6 GHz were calculated using the Omega3P parallel eigensolver. The FPC, the LOM/HOM, and the beampipe ports are modelled with absorbing boundary conditions to evaluate the external Q_{ext}. Due to the geometry asymmetry, most of the HOMs are not centred at the geometric axis of the cavity. Because of this centre offset, a beam passing through the cavity centre will see multipole field components [5]. For example, a mode with a clear dipole mode pattern will have a finite monopole component when the centre is off the cavity axis. After the eigenmode calculations with Omega3P, the multipole components of each mode were calculated with respect to the beam centroid using a postprocessing tool. The impedances associate with the multipole field components of each mode were then calculated and are plotted in Fig. 3. The RF quantities plotted in Fig.3 are defined as the following, with "v" the voltage of the respective multipole component.

$$\left(\frac{R}{Q}\right)_T = \frac{|V_z(r_0)|^2}{\omega U (r_0\omega/c)^2} \qquad Z_T = \frac{\omega}{c}\left(\frac{R}{Q}\right)_T Q_{ext}$$

$$\left(\frac{R}{Q}\right)_L = \frac{|V_z(r_0)|^2}{\omega U} \qquad Z_L = \left(\frac{R}{Q}\right)_L Q_{ext}$$

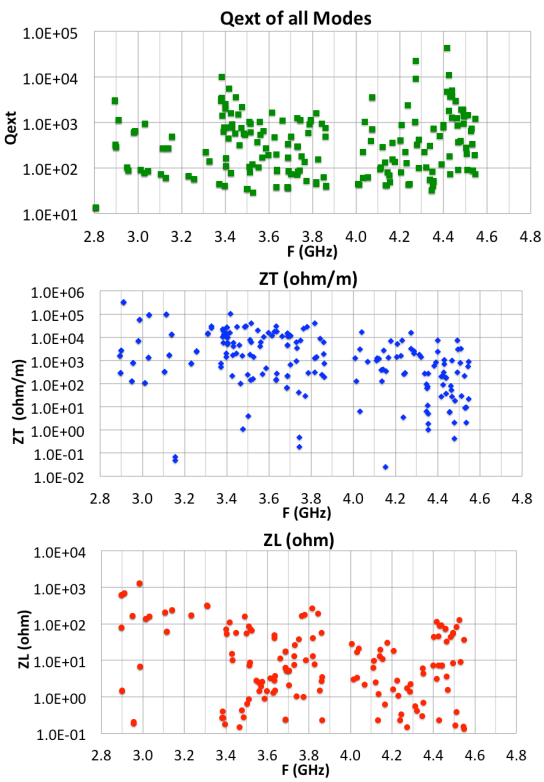


Figure 3: Q_{ext} and impedances of the HOMs in the two-cavity system.

Simulation results have shown that all the modes are well damped. There are no significant trapped modes found in the two-cavity system. Both transverse and longitudinal impedances met the requirements for beam stability [6].

HOMs in the Beam Pipe Bellows Region

There are a few modes above the beam pipe TM010 cutoff frequency of 4.41GHz that have longitudinal impedances of about 100 ohms. Two of these longitudinal modes are shown in Fig. 4. Both have relatively strong magnetic fields in the bellows region. These are the type of modes of concern in a multi-cavity module as they could produce RF heating to the bellows. Simulation results have showed that the two-cavity prototype module design can provide essential damping via the LOM and HOM couplers to these modes thus minimizes the beam coupling to the modes. As a result, the RF heating by these coupled modes does not seem to be of concern.

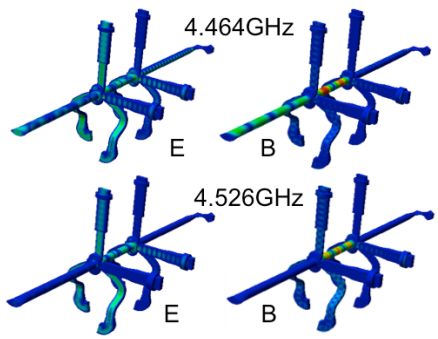


Figure 4: Monopole modes that have strong magnetic fields in the bellows region.

MULTIPACTING DUE TO FIELD ASYMMETRY

The rectangular LOM coupler has a TE10 mode cutoff frequency lower than the deflecting mode frequency. The rejection of the LOM coupler to the deflecting mode relies solely on the field symmetry. In an ideal case, the deflecting dipole mode can only couple to the TE20 mode of the LOM coupler which is cutoff at the operating dipole mode frequency. The asymmetric "Y"-end-group causes only a slight field asymmetry in the cavity which in turn induce negligible power leakage through the LOM coupler. However, the first horizontal test of a prototype cavity showed sharp heating at the LOM strongly correlated with a strong Q-switch and a significant power leakage through the LOM coupler [7]. This pointed to a field asymmetry caused by a shape imperfection and possible multipacting related to such a field that limited the cavity performance. Track3P multipacting simulation code was used to analyse multipacting resonances under a field asymmetry modeled with a simple "dent imperfection" on the cavity wall. The amount of "dent" induces an RF leakage that is comparable to the

Copyright © 2013 CC-BY-3.0 and by the respective authors

measurement. Fig. 5 shows the field leaking via the LOM coupler (horizontal) with the induced field asymmetry by a "dent". The multipacting map obtained for the "ideal" and "imperfect" cavities are shown in Fig. 6 for comparison.

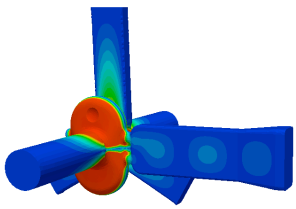


Figure 5: Power leakage through the LOM coupler in an imperfect geometry with a "dent", comparable to the leakage measured in the prototype cavity.

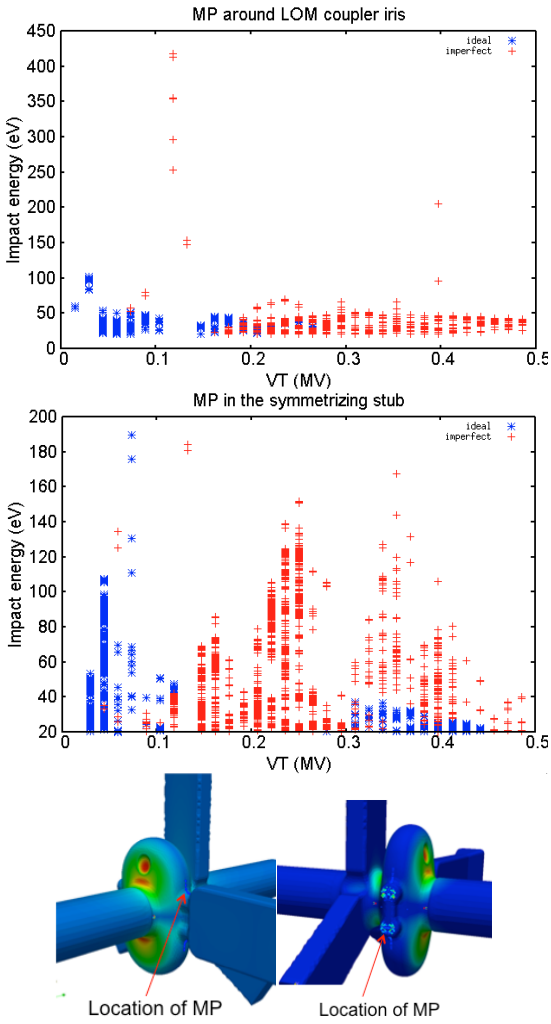


Figure 6: Effect of a field asymmetry on multipacting.

The multipacting band in the LOM coupling iris region is shifted to a higher field level in the case with the field asymmetry. The impact energies of the resonant trajectories in this band are mostly lower than 50 eV. The SEY for niobium at these energies are relatively low, and the multipacting bands in both "ideal" and "imperfect" cases are considered not strong barriers.

An enhanced multipacting band around 0.24 MV deflecting voltage was found in the symmetrizing dog-bone in the case with the field asymmetry. The energies of the resonant trajectories in this band are as high as 140 eV. The SEY of these trajectories is much higher than the ones around the LOM iris. Significant multipacting is possible in this region when a field asymmetry exists. This multipacting band was observed in the RF testing of the prototype cavity that has a imperfection asymmetry [6]. The multipacting band was eliminated in the RF test by tuning the LOM coupler to minimize the leakage and subsequently the field asymmetry, which agrees with the analogy of an ideal cavity.

SUMMARY

HOMs and trapped modes were calculated for the two-cavity prototype cryomodule using the parallel code Omega3P. No dangerous trapped modes were found in the two-cavity system. All modes were well damped. Both the transverse and logitudinal impedances are below the instability threshold. A few monopole modes above 4.41 GHz were found to have strong fields in the bellows region. These modes are well damped by the LOM/HOM couplers and are low in impedances. HOM heating of the bellows does not seem to be a significant issue. Multipacting in the cavity due to imperfection and asymmetry was analyzed using Track3P. An enhanced multipacting band in the symmetrizing stub was found when there is a finite RF power leakage through the LOM coupler due to a shape imperfection, which can be eliminated by tuning the LOM coupler. The simulation results are in good agreement with the RF test of a prototype cavity.

ACKNOWLEDGEMENT

The work used the resources of NERSC at LBNL which is supported by the Office of Science of the U.S. DOE under Contract No. DE-AC03-76SF00098.

REFERENCES

[1] A. Zholents, et al., NIM A 425 (1999) 385.
[2] G. Waldschmidt, et al., "Superconducting Cavity Design for Short-Pulse X-Rays at the Advanced Photon Source," Proc. PAC 2011, New York, USA.
[3] A. Nassiri et al., "Status of the Short-Pulse Project (SPX) at the Advanced Photon Source," Proc. IPAC 2012.
[4] K. Ko et al, "Advances in Parallel Electromagnetic Codes for Accelerator Science and Development," LINAC2010, Tsukuba, Japan.
[5] L. Xiao et al., "Higher Order Modes Damping Analysis for the SPX Deflecting Cavity Cryomodule," Proc. IPAC2012, New Orleans. USA.
[6] H. Wang et al., "Crab Cavity and Cryomodule Prototype Development for the Advanced Photon Source," Proc. PAC 2011, New York, USA.
[7] J. Mammosser et al., "Fabrication And Testing of Deflecting Cavities For APS," Proc. SRF 2013, Paris, France.

Copyright © 2013 CC-BY-3.0 and by the respective authors

WAKEFIELD COMPUTATIONS FOR A CORRUGATED PIPE AS A BEAM DECHIRPER FOR FEL APPLICATIONS*

C.-K. Ng, K.L.F. Bane, SLAC, Menlo Park, USA

Abstract

A beam "dechirper" based on a corrugated, metallic vacuum chamber has been proposed recently to cancel residual energy chirp in a beam before it enters the undulator in a linac-based X-ray FEL. Rather than the round geometry that was originally proposed, we consider a pipe composed of two parallel plates with corrugations. The advantage is that the strength of the wake effect can be tuned by adjusting the separation of the plates. The separation of the plates is on the order of millimeters, and the corrugations are fractions of a millimeter in size. The dechirper needs to be meters long in order to provide sufficient longitudinal wakefield to cancel the beam chirp. Considerable computation resources are required to determine accurately the wakefield for such a long structure with small corrugation gaps. Combining the moving window technique and parallel computing using multiple processors, the time domain module in the parallel finite-element electromagnetic suite ACE3P allows efficient determination of the wakefield through convergence studies. In this paper, we will calculate the longitudinal, dipole and quadrupole wakefields for the dechirper and compare the results with those of analytical and field matching approaches.

INTRODUCTION

In order to cancel the residual energy chirp in a beam before it enters the undulator in a linac-based FEL, a beam dechirper whose design consisting of periodic corrugations on the chamber walls has been proposed [1]. Such a dechirper is a passive device as it uses the longitudinal wakefield generated by the beam transit to compensate for the energy difference within the beam. The dechirper can be installed in machines such as LCLS-II where a superconducting linac will be used for beam acceleration and the wakefields generated in the superconducting cavities are not strong enough to dechirp the beam.

The original dechirper proposed for the light source NGLS was a round corrugated metallic pipe. The wakefields for the round geometry have been calculated using an analytical approach and formulas are available. Later, a flat rectangular geometry with corrugations on two parallel metallic plates was adopted and a dechirper was built and tested [2] at the injector test facility (ITF) for the PAL-XFEL in Korea [3]. The rectangular geometry has the advantage that the separation of the plates can be adjusted for different machine operation conditions. Formulas for the wakefields obtained by the analytical approach have been worked out recently for the rectangular case [4, 5]. Furthermore, numerical method using field matching in the frequency domain has been developed [4], which is believed to be more accurate than the analytical method.

The analytical approach is a good approximation when the depth and period of the corrugation are small compared with the separation of the plates. The corrugations in the dechirper being tested at PAL are small with respect to the chamber dimensions, but it is desirable to perform direct simulation by 3D electromagnetic code to verify the validity of the analytical approximation. This work focuses on numerical simulation using the finite-element electromagnetic code suite ACE3P [6] to calculate the wakefields of the dechirper and compare them with the analytical and field matching approaches. In addition to determining the longitudinal wakefield that is used to cancel the energy chirp of the beam, the dipole and quadrupole wakefields that kick and defocus the beam and hence increase its emittance will also be evaluated.

THE DECHIRPER MODEL

A sketch of the geometry of the dechirper is shown in Fig. 1. The corrugation is defined by the period p, the gap g, and the depth h. These corrugation parameters are fractions of a millimeter in size. The corrugations are located at the top and the bottom of the rectangular chamber with half height a and half width w. In order to provide sufficient longitudinal wakefield, the height of the dechirper needs to be small enough (on the order of millimeters), which is small compared with the chamber width, and the length of the dechirper needs to be long enough (on the order of meters). The dimension parameters of the dechirper tested at PAL are a = 3 mm, p = 0.5 mm, g = 0.3 mm, and h = 0.6 mm. In practice, a is adjustable from $2a$ = 5 mm to 28 mm. The validity of the analytical approximation is when p, $h << a$ and the corrugation depth h is much larger than its period p. It can be seen that the corrugation dimensions are about an order of magnitude smaller than the dechirper height. A direct 3D numerical simulation is required for cross check of the analytical calculation.

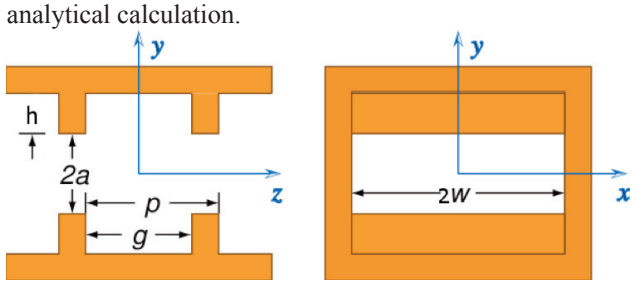


Figure 1: Sketch of the geometry of the dechirper.

* Work supported by the Department of Energy under Contract Number: DE-AC02-76SF00515.

Copyright © 2013 CC-BY-3.0 and by the respective authors

NUMERICAL APPROACH

The 3D numerical simulation is performed using the time domain module T3P of the code suite ACE3P. The wakefield computation in T3P is facilitated by the following simulation capabilities. First, T3P runs on computers at NERSC computing facility, which provides massively parallel computation to achieve fast computing speed. Second, a moving window technique for unstructured grids implemented in T3P confines short-range wakefield computation to the region of the mesh around the moving beam, thus substantially enhancing the computation efficiency. It should be pointed out that while it is straightforward to implement the moving window technique in the FDTD method with regular rectangular grids, its implementation in the finite-element method using unstructured grids is rather non-trivial [7, 8]. It requires careful mapping of field quantities when transferring the solution from the current window to the next one, especially under the computation environment where multiple computer processors are used.

Despite the above-mentioned computational advantages, simulating the full dechirper of meters long and with large chamber *w/a* aspect ratio is still challenging, if not infeasible. Fortunately, the wakefield will reach steady state after a certain catch-up distance, and the reflection from the sides of the chamber will be negligible when *w/a* is larger than a certain value. Therefore, a reduced model with much smaller length and width than the actual device can be used to obtain accurately the wakefield per unit length of the dechirper. Because of symmetry, only a quarter of the reduced model as shown in Fig. 2 is needed for T3P calculation.

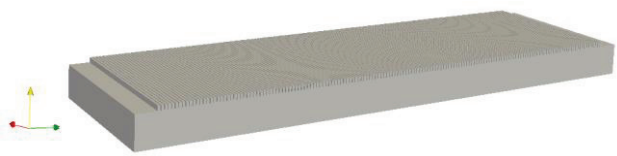


Figure 2: One quarter of the vacuum region of the dechirper model with corrugations situated on a half of the top plate used for T3P simulation. The full model is obtained by reflection with respect to the horizontal and vertical planes.

Figure 3 shows three snapshots of the beam transit in the dechirper with 160 corrugations. The computation at each time step in T3P is confined only in the colored region when the moving window technique is employed in following the transiting beam. Thus the computation domain is only a small fraction of the model, which drastically reduces the computation time.

Convergence studies have been performed by varying the number of corrugations and the width of the chamber, respectively. It was found that when the number of corrugations reaches 160, the longitudinal wakefield per unit length does not change. Fig. 4 shows the comparison of the longitudinal wakefields for a model with 144 and 160 periods. It can be seen that the two curves are almost the same. In a similar manner, when the chamber *w/a* aspect ratio is greater than about 2.5, the wakefield remains unchanged. In all the following numerical simulations, the dechirper model has 160 corrugations and *w/a* of the rectangular chamber is 3.

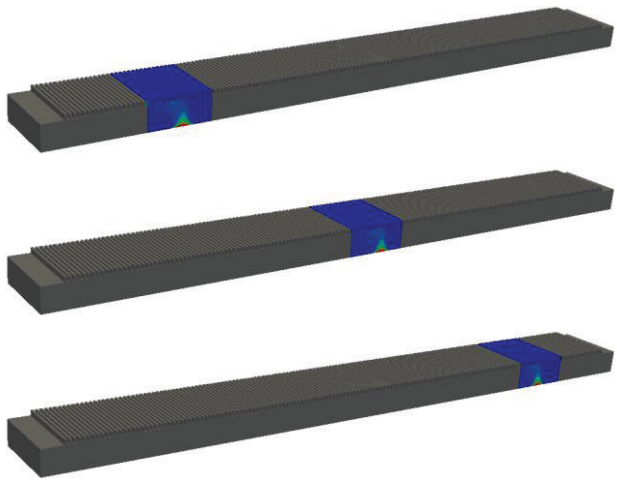


Figure 3: Snapshots of beam transit in the dechirper with 160 corrugation periods. The beam comes in from the left boundary at the origin (the lowest corner) and moves to the right. The colored region in each snapshot indicates the moving window at the corresponding time.

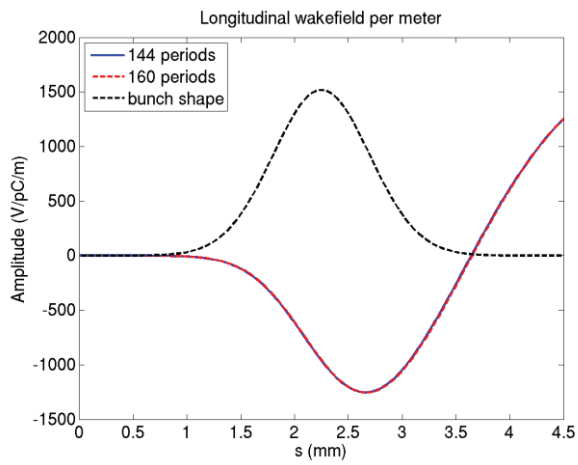


Figure 4: Longitudinal wakefield per unit length of the dechirper with 144 and 166 corrugations.

WAKEFIELDS OF DECHIRPER

The dimensions of the PAL dechirper have been listed in a previous section. To calculate the wakefields of the dechirper, a Gaussian bunch with σ = 0.45 mm is used, which corresponds to the rms beam size at the PAL test facility. Choosing appropriate boundary conditions at the symmetry planes in the quarter model shown in Fig. 2, one can determine the monopole and quadrupole wakefields with the beam transiting on the axis in a single T3P run, and the dipole wakefield with the beam transiting at an offset position in the vertical direction using different boundary conditions in another T3P run. The total transverse wakefield in the vertical direction is

Copyright © 2013 CC-BY-3.0 and by the respective authors

the sum of the dipole and quadrupole components and is given by

$$W_y = y_d W_{yd} + y_w W_{yq},$$

where W_{yd} and W_{yq} are the dipole and quadrupole wakefields, and y_d and y_w are the positions of the drive and witness particles, respectively. The wakefields are expressed in terms of per meter length so that the values for the actual dechirper can be readily obtained by multiplying with its length. In each of the monopole, dipole and quadrupole calculations, the T3P numerical results are compared with those evaluated by the analytical and field matching approaches.

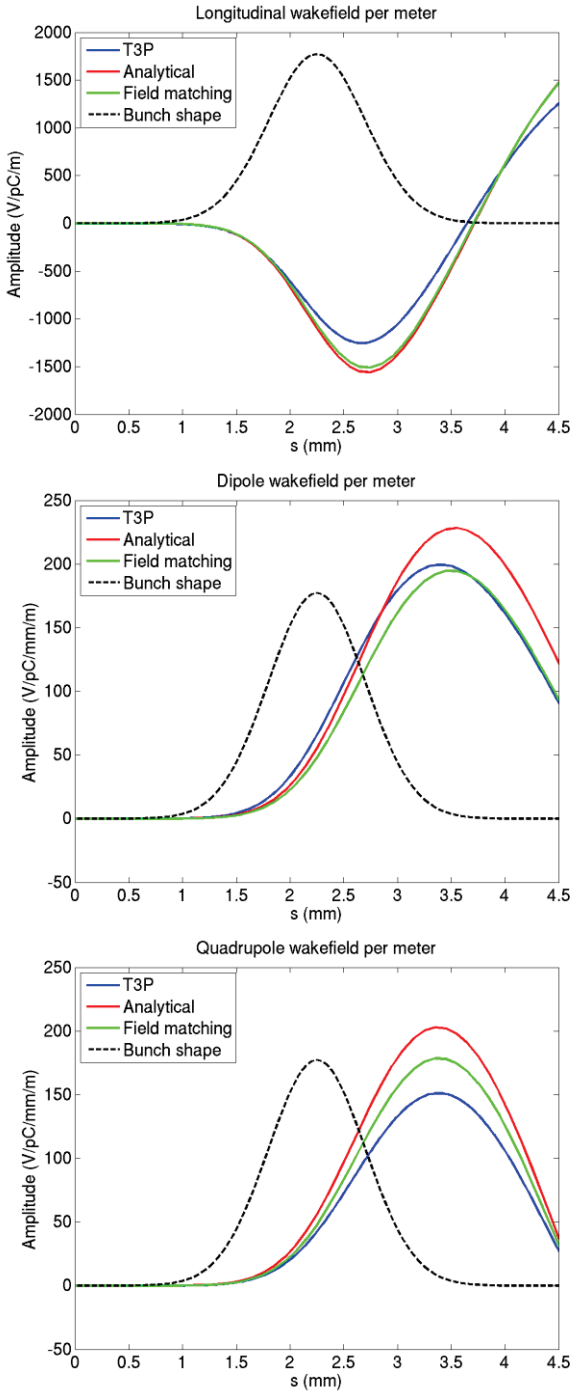


Figure 5: (Top) Longitudinal, (Middle) dipole, and (Bottom) quadrupole wakefield per meter length of the dechirper obtained by the analytical, field matching and numerical approaches.

Figure 5 shows the longitudinal, dipole and quadupole wakefields obtained by T3P numerical calculation, the analytical and field matching approaches. The loss factor obtained by numerical calculation is 821 V/pC/m, and the kick factors for the dipole and quadrupole components are 75 V/pC/mm/m and 52 V/pC/mm/m, respectively. In comparing the results of different approaches, Table 1 list the ratios of the loss or kick factors for any two of the approaches. In general, the analytical and field matching approaches agree with each other within 10%, while the numerical approach agrees either with the analytical approach or the field matching approach within 10-20%, depending on individual cases. This indicates that while analytical formulas render a fast means to determine the wakefields in a dechirper, in particular in exploring the parameter regime during the initial design phase, it is always desirable to further quantify the results with numerical methods for the final design.

Table 1: Comparison of the ratios of the loss factor or kick factors obtained by the analytical, field matching and numerical approaches.

Wake	FM/ Analytical	Numerical/ Analytical	Numerical/ FM
Monopole	0.97	0.84	0.87
Dipole	0.87	1.08	1.25
Quadrupole	0.86	0.73	0.85

ACKNOWLEDGMENTS

We would like to thank G. Stupakov for many useful discussions. This research used resources of the National Energy Research Scientific Computing Center, which is supported by the Office of Science of the U.S. Department of Energy under Contract No. DE-AC02-05CH11231.

REFERENCES

[1] K.L.F. Bane and G. Stupakov, Nucl. Instrum. Meth. A **690** (2012) 106.
[2] H.-S. Kang, "Control of Electron Beam Longitudinal Phase Space with a Novel Compact De-chirper," FEL 2013, August 26-30, Manhattan, NY.
[3] S.J. Park et al., "Construction of Injector Test Facility (ITF) for the PAL XFEL," Proc. IPAC 2013, Shanghai, China, WEPWA043, p. 2220 (2013).
[4] K.L.F. Bane and G. Stupakov, Phys. Rev. ST Accel. Beams **6** (2003) 024401.
[5] G. Stupakov, private communications.
[6] https://confluence.slac.stanford.edu/display/AdvComp/Materials+for+cw11
[7] L.-Q. Lee et al., J. Comput. Phys. **229** (2010) 9235.
[8] C.-K. Ng et al., "High Fidelity Calculation of Wakefields for Short Bunches," talk given at PAC 2011, March 28 – April 1, New York, USA.

Copyright © 2013 CC-BY-3.0 and by the respective authors

MECHANICAL DESIGN OF A NEW INJECTOR CRYOMODULE 2-CELL CAVITY AT CEBAF*

G. Cheng#, J. Henry, J. Mammosser, R. A. Rimmer, H. Wang, M. Wiseman, S. Yang, JLAB, Newport News, VA 23606, USA

Abstract

As a part of Jefferson Lab's 12 GeV upgrade, a new injector superconducting RF cryomodule is required. This unit consists of a 2-cell and 7-cell cavity, with the latter being refurbished from an existing cavity. The new 2-cell cavity requires electromagnetic design and optimization followed by mechanical design analyses. The electromagnetic design is reported elsewhere. This paper aims to present the procedures and conclusions of the analyses on cavity tuning sensitivity, pressure sensitivity, upset condition pressure induced stresses, and structural vibration frequencies. The purposes of such analyses include: 1) provide reference data for cavity tuner design; 2) examine the structural integrity of the cavity; and 3) evaluate the 2-cell cavity's resistance to microphonics. Design issues such as the location of stiffening rings, effect of tuner stiffness on cavity stress, choice of cavity wall thickness, etc. are investigated by conducting extensive finite element analyses. Progress in fabrication of the 2-cell cavity is also reported.

CEBAF NEW INJECTOR CRYOMODULE CAVITIES

Presently in the injector section of CEBAF there is a "Quarter Cryomodule", which has two 5-cell cavities. With the upgrade of operating energy from 6 GeV to 12 GeV, a few options for the booster cavity layout have been studied [1] and the 2-cell plus 7-cell cavities layout is deemed desirable. The demanded field amplitude for the 7-cell cavity is around 13 MV/m. An economic decision is made to refurbish a low loss JLAB Renascence cryomodule [2] 7-cell cavity, which is capable to provide 17-21 MV/m accelerating field amplitude, to be used in the new Injector Cryomodule. The 2-cell cavity is a new design based on the low loss cavity shape and is expected to provide approximately 4.6 MV/m accelerating field.

2-CELL CAVITY MECHANICAL DESIGN

The 2-cell cavity is made of high RRR fine grain niobium. Basic mechanical properties used in all design analyses are listed in Table 1. Note that the 2-cell cavity niobium material is the same as SNS cavity material and the cavity will be baked at 600 ^{o}C for 10 hours. Although niobium is not a "code material", the ASME Boiler & Pressure Vessel Code (BPVC) rules are referenced during the pressure induced stress analysis for the 2-cell cavity. The allowable stresses are determined per BPVC rules, i.e. the allowable stress is the lesser of 2/3 of yield strength or 1/3.5 of the tensile strength.

Among the major cavity mechanical design considerations, the choice of cavity wall thickness is mainly dictated by the upset condition pressure induced stress. The wall thickness also affects the cavity stiffness, tuning and pressure sensitivities, as well as vibration natural frequency. Similar theory applies to the option of using ring shape stiffeners. All mechanical design analyses are performed in ANSYS®. The tuning and pressure sensitivity calculations involve electromagnetic to structural coupled field analysis technique. Each design topics is addressed in a bit more details in the following sections.

Table 1: High RRR Niobium Mechanical Properties [3-5]

Properties	Room Temperature	Cryogenic Temperature
Young's Modulus, psi	1.49e7	1.79e7
Poisson's Ratio	0.38	0.38
Density, lb/in^3	0.31	0.31
Yield Strength, ksi	9.5	83.7
Tensile Strength, ksi	26.3	118.8
Allowable Stress, ksi	6.33	33.9

2-CELL CAVITY STRUCTURAL STRESS

Three loading conditions are examined for the stress state in the 2-cell cavity: 1) 2.2 atm pressure at room temperature (R.T.) simulating pressurization during the cryomodule cool down process, 2) 5 atm pressure at cryogenic temperature (C.T.) simulating pressurization caused by upset conditions [6], and 3) 5 atm pressure with 300 μm tuning displacement. The pressure chamber surrounding the niobium cavity is formed by the interior of a helium vessel and the cavity external surfaces. The helium vessel for this 2-cell cavity is made of stainless steel and has one bellows to mitigate the thermal stress developed during cool down and caused by the mismatch of expansion coefficients between niobium and stainless. The bellows also permits tuning of the cavity without holding up against an otherwise stiff helium vessel. Outside the helium vessel, a scissor-jack tuner is mounted. The helium vessel bellows and tuner are simulated as springs in the cavity stress analysis model. The bellows' longitudinal spring constant is relatively small. The tuner's warm and cold stiffnesses are analysed separately on a preliminary tuner design model.

*Authored by Jefferson Science Associates, LLC under U.S. DOE Contract No. DE-AC05-06OR23177. The U.S. Government retains a non-exclusive, paid-up, irrevocable, world-wide license to publish or reproduce this manuscript for U.S. Government purpose.
#cheng@jlab.org

Copyright © 2013 CC-BY-3.0 and by the respective authors

Two cavity wall thickness values are considered in the stress analyses: 3 mm and 4 mm. As to the stiffening rings, three design options, i.e. no rings, one ring between 2 cavity cells and 3 rings (2 added between the cells and helium vessels), are investigated. It is found that at least 3 rings are needed to reduce the pressure induced stress. The stiffening rings' radial locations are studied and it is found that large diameter rings would increase the cavity stiffness hence reduce the stresses, however, when the rings are too big, electron beam welding of these rings could affect the braze joint between niobium cavity and stainless steel helium vessel. In addition, if the cavity and helium vessel assembly is too stiff, tuning of the cavity will become difficult. The stiffening ring diameter is finally decided to be consistent with that for the 7-cell cavity. Table 2 shows the stress results for the 2-cell cavity with 3 stiffening rings and 3 mm or 4 mm wall thickness. Based on Table 2, the 4 mm cavity is selected. Note that the peak stresses typically occur at sharp corners where the stiffening rings are welded to the cavity. Such stresses are disregarded due to finite element model singularities that are incredible. The "body stress" is taken at "hotspots" that are away from the singularity points. Figure 1 shows the stress for the 4 mm thick cavity subjected to 2.2 atm pressure at R.T.

Table 2: Pressure Induced Stresses in Cavity with Different Wall Thicknesses

Cases	Tuner Stiffness (lbf/in)	Cavity stress (psi)	3 mm	Acceptable?	4 mm	Acceptable?
5 atms at C.T.	88,001	peak stress	22,036	-	18,656	-
		body stress	18,890	Yes	16,001	Yes
5 atms C.T. with 300 μm tuning	88,001	peak stress	24,756	-	23,104	-
		body stress	21,225	Yes	19,812	Yes
2.2 atms at R.T.	79,700	peak stress	9,177	-	7,850	-
		body stress	7,905	No!	6,172	Yes

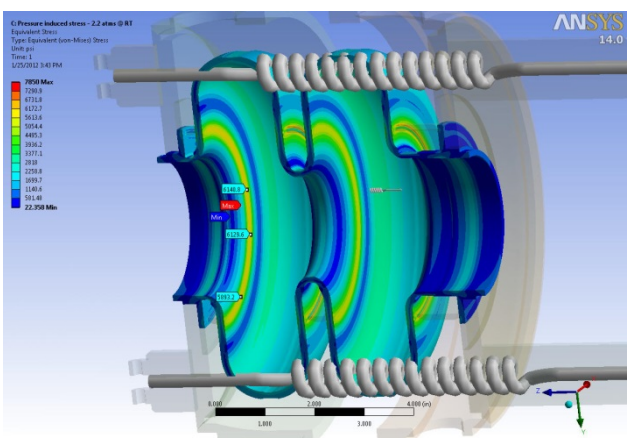


Figure 1: Stress in the 2-cell cavity (4 mm thick with 3 stiffening rings) subjected to 2.2 atm pressure at R.T.

2-CELL CAVITY TUNING AND PRESSURE SENSITIVITIES

The scissor-jack tuner exerts tuning force to the cavity through two pairs of tuner tabs that are mounted on the end plates of the helium vessel. The change of cavity electromagnetic frequency versus displacement between the pairs of tuner tabs is defined as the tuning sensitivity for the 2-cell cavity. Knowing the tuning sensitivity is important in tuner design as well as tuner operation.

Another important characteristic of the 2-cell cavity is its pressure sensitivity, that is, cavity electromagnetic frequency change with respect to helium vessel pressure fluctuation. Based on operational experiences, a ±0.1 torr pressure fluctuation is typical [7]. It is also learned from operational practices that such pressure fluctuation does not occur in a rapid manner. This means that the slow tuner can rectify the frequency shift in time. Ideally, one would want to control the pressure sensitivity to be a quite small number. This is affected by a number of factors, among which the size of the helium vessel bellows is crucial. The 2-cell cavity's helium vessel adopts a nominal 10″ diameter bellows design. This size of bellows is also used in Jefferson Lab's 12 GeV upgrade cryomodules (also called C100 cryomodules). It is expected that the pressure sensitivity of the 2-cell cavity to be at a similar level as C100 cryomodule cavities. Note that the stainless steel helium vessel and the 2-cell cavity (4 mm wall thickness and having 3 stiffening rings) itself are quite stiff, which helps in reducing the pressure sensitivity.

Coupled field analyses are carried out to solve for the tuning and pressure sensitivities. In principle, the model includes the vacuum volume that is enclosed by the niobium cavity. For tuning sensitivity analysis, the cavity and helium vessel are included in the model. For pressure sensitivity analysis, the tuner (simulated as a couple of equivalent springs) is also included. Frequency of the undeformed vacuum volume is calculated first. Then tuning displacement or pressure load is applied to the cavity and helium vessel. The niobium cavity deforms and the deformed shape of cavity is used to alter the vacuum volume. In the analysis model, the cavity and vacuum volumes share common interfaces so that nodal displacements at interfacial nodes can be conveniently transferred from the cavity to the vacuum. At last, the "deformed" vacuum is used to calculate a new frequency. The difference between the before and after structural deformation frequencies is then divided by the tuning distance or pressure applied to calculate the corresponding sensitivities.

For the 4 mm thick 2-cell cavity equipped with 3 stiffening rings, the tuning sensitivity is calculated to be 2.63 MHz/mm. Based on this, to achieve a coarse tuning range of 600 kHz, 228 μm tuning is needed. In the mechanical designs, this tuning distance is rounded up to 300 μm to be conservative. The cavity and helium vessel assembly's cold stiffness is estimated to be 8.93 N/μm.

Copyright © 2013 CC-BY-3.0 and by the respective authors



Figure 2: Fabricated 2-cell cavity major components.

The pressure sensitivity of the 2-cell cavity is calculated to be 382 Hz/torr. For the C100 7-cell cavity (3mm wall thickness, no stiffening rings), the measured pressure sensitivity is around 320 Hz/torr. So, the new 2-cell cavity's pressure sensitivity is comparable to that of the C100 7-cell cavity.

CAVITY VIBRATION FREQUENCY

To mitigate the detrimental effects brought by microphonics, "one should push the mechanical resonance frequencies as high as possible…" [8] In the 2-cell cavity design, 4 mm wall thickness and 3 stiffening rings are selected not only for resistance to the pressure loads, but also for high vibration frequencies. The 2-cell cavity is hosted by a helium vessel, which is supported by eight Nitronic rods in the transverse direction and two Nitronic rods in the axial (parallel to beam axis) direction. All rods are mounted to a spaceframe, which is bolted to a vacuum vessel that is anchored to the ground. Vibration analysis is very sensitive to the boundary conditions employed. However, it is impractical to build a mathematical model that reflects a real cryomodule's conditions precisely. In the 2-cell cavity vibration model, the vacuum vessel, spaceframe and Nitronic rods are assumed to be stationary, although in reality they pass environmental vibrations to the helium vessel and niobium cavity. The point is to examine the cavity's natural resistance to vibrational resonance. Therefore, the boundary conditions are that at the helium vessel end where 4 transverse rods and 2 axial rods exist, fixed support boundary condition is applied. At the other end where only 4 transverse rods exist, the helium vessel is fixed in transverse directions only. Basically, the cavity vibration model has a set of fixed-guided boundary conditions. The lowest vibration mode of the 2-cell cavity is found to be an axial mode, i.e. parallel to beam axis extension/compression oscillation, with a frequency of 218 Hz, which is much higher than the design criteria of 100 Hz. The 2-cell cavity is thus deemed as being robust in terms of its resistance to low frequency vibration resonances.

CAVITY FABRICATION

Fabrication of the 2-cell cavity has started. As shown in Fig. 2, major components such as the fundamental power coupler endgroup, end half cells, dumbbell, HOM endgroup, etc. are made. Special tools to help in dumbbell trimming and stiffening ring electron beam welding were designed and made. The amount of trimming on these components are determined per RF measurements. The 2-cell cavity is aimed to be finished in the Fall of 2013 and qualification tests will follow.

REFERENCES

[1] F. E. Hannon, A. Hofler and R. Kazimi, "Optimizing the CEBAF Injector for Beam Operation with a Higher Voltage Electron Gun," PAC'11, New York, March 2011, WEP288, pp. 2023-2025; http://www.JACoW.org

[2] C. Reece, "A 100 MV CW Cryomodule," JLAB-ACC-05-03. Invited Talk at 12th SRF Workshop, Cornell University, Ithaca, New York, USA.

[3] K. Wilson et al., "Mechanical Cavity Design for 100MV Upgrade Cryomodule," PAC'03, Portland, May 2003, RPAB064, p. 2866.

[4] G. Myneni and P. Kneisel, "High RRR Niobium Material Studies," JLAB-TN-02-01, Jefferson Lab, Newport News, VA.

[5] P. Kneisel and G. Myneni, "Preliminary Results of Tensile Test on Niobium at Room Temperature and 4.2K," JLAB-TN-88-097, Jefferson Lab, Newport News, VA.

[6] M. Wiseman et al., "Loss of Cavity Vacuum Experiment at CEBAF," Advances in Cryogenic Engineering, Vol. 39, Edited by P. Kittel, Plenum Press, New York, 1994, pp. 997-1003.

[7] Per communications with Jefferson Lab Cryogenic Group.

[8] H. Padamsee et al., RF Superconductivity for Accelerators, (John Wiley & Sons, Inc., 1998), p. 427.

Copyright © 2013 CC-BY-3.0 and by the respective authors

NOISE REDUCTION USING FILTERS ON TURN-BY-TURN LHC ORBITS TO OBTAIN MAGNETIC ERRORS WITH THE ACTION AND PHASE JUMP ANALYSIS METHOD

A.C. García B., J.F. Cardona, Universidad Nacional de Colombia*, Bogotá, Colombia

Abstract

The Action and Phase Jump analysis had been successfully used to obtain magnetic errors in RHIC. Analyses in LHC encountered significant noise. In this paper, a dual band-pass filter on LHC simulated orbits to reduce the noise is discussed. Gaussian and Uniform noise are studied independently. Results show that the best filter has a bandwidth of 0.0174 around the two transverse tunes. A low-pass band filter was also used to get the closed-orbit.

INTRODUCTION

The measurement of magnetic errors in an accelerator is an important task during the commissioning. One of the methods used to localize, to measure, and to correct magnetic errors is the Action and Phase Jump (APJ) Analysis. It is based on the theoretical principle of preservation of the Action and Phase variables in absence of a magnetic error. This method had been successfully tested in RHIC using closed-orbit data from experiments [1] and its theoretical development is fully presented in [2].

Preliminary analyses on turn-by-turn (TBT) orbits at the LHC show promising results [3, 4], but with a certain levels of noise than for the RHIC case, due to a bigger bandwidth of the LHC BPMs. Efforts to reduce the noise, like taking advantage of the thousands of turns provided by the LHC BPMs system (in contrast with the few orbits used in RHIC) have been done.

In this paper we discuss the use of pass-band digital filters to reduce noise in LHC TBT orbits; supplemented by an initial change of the PYTHON APJ code. A simulation of the beam trajectory, using MAD-X, is made for the thin LHC injection optics (V.6.5), where normal and skew linear quadrupole errors A_1 and B_1 were included, at the IR quadrupole MQXA.3L5 of beam 1.

Noise originated from the distribution of particles in the beam and noise originated from the misaligments of the BPMs are simulated using a Gaussian distribution and an Uniform distribution, respectively. The BPMs gain is also taking into account by using these distributions. This type of distributions had been used in noise studies for the closed-orbit measurement [5].

A BAND-PASS FILTER FOR THE LHC

The BPMs are the devices that provides measurements of the beam position in the transverse plane around the accelerator. For a fixed longitudinal position, the transverse position is sampled every turn leading to:

$$z(n) = \sqrt{2J_z\beta_{z,BPM}}\sin\left(\psi_{z,BPM} + 2\pi Q_z n - \delta_z\right) \quad (1)$$

where $z = \{x, y\}$ is the transverse plane coordinate, J_z is the Action, $\beta_{z,BPM}$ and $\psi_{z,BPM}$ are the beam β_z-function and phase advance at the BPM longitudinal position, δ_z is the Phase, and Q_z is the accelerator tune, at the transverse plane $z = \{x, y\}$. In this study, the data simulated with MAD-X on the acelerator LHC beam 1, is used to created new trajectories with simulated noise.In one case, the noise corresponds to a Gaussian distribution of $\sigma_{Gauss} = 0.1$ mm, which is added randomly to the each BPM data, and in the other case a Uniform distribution up to 0.3 mm is used. Then the resulting signal is filtered to evaluate wheter the filter help to reduce the uncertainty on the determination of magnetic errors using APJ method.

In this study, the filter was implemented using directly PYTHON functions, although trials were also made with own built transfer functions. From the available filters, the band-pass filter was chose, because it reduces the noise without damaging the magnetic error recovery. A second order filter is implemented, with Butterworth coefficients and the double run function [6].

Table 1: Frequencies Values for the Filter Bands. The overlapping is removed.

N.	$\omega_{pass}I$ [2π rad]	$\omega_{stop}I$ [2π rad]	$\Delta\omega$ [2π rad]	$\omega_{pass}II$ [2π rad]	$\omega_{stop}II$ [2π rad]
0	0.28025	0.28075	0.0005	0.30875	0.30925
1	0.28	0.281	0.001	0.3085	0.3095
...	...	...	...	...	...
25	0.01	0.49	0.48	0.01	0.49

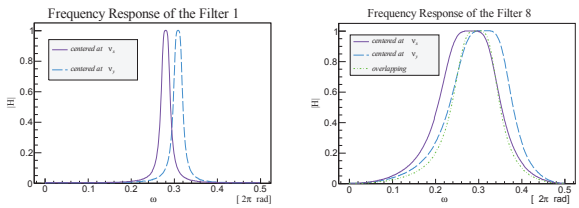


Figure 1: Dual Band-pass filter frequency response, if there is not overlapping (left) and with the corresponding overlapping band (right). Bands centered at 0.2805 and 0.309.

Also previous trials showed that the best results are obtained using a band-pass filter with two bands centered on the transverse tunes ν_x and ν_y (a 99% uncertainty is reached if only one tune band is used without noise). Table 1 presents the frequencies (ω) used to built the filter, where (N.) is the number of the case, the dots are the complementary values, such as an increment of 0.0005 in $\Delta\omega$ is

* Thanks to the DIB at Universidad Nacional de Colombia for the funding provided for computers and the support for this presentation.

Copyright © 2013 CC-BY-3.0 and by the respective authors

always made. The band centered at ν_x corresponds to the ω labeled with I, while the band for ν_y is labeled II. The bandwidth of the two bands are the same.

The filtered signal is the addition of the signals obtained with the two single band-pass filters, whose frequency response looks like Fig. 1.left, and in case of overlapping, the addition of the filtered signals is followed by the subtraction of a band-pass signal with the overlapping frequencies as the band, the frequency response looks like Fig. 1.right.

CHANGE IN THE APJ CODE

The phase obtained from the BPM measurements (eq.(14) in [2]) is implemented with the appropriate sign in the APJ computer code, in order to count on the four quadrants of a Cartesian coordinate. This and the fact that the trajectory function has a sinusoidal behavior allow to select 2 maximal and 2 minimal (i.e. negative maximal) orbits, for each transverse plane, and not only 1 as before.

The selection of the orbits is such as the final orbit has a maximum amplitude at the error position. As reported in [3] the selection is based on the phase of the trajectory. In this study the information from the two transverse planes is necessary, therefore 8 orbits are obtained, and the phase dispersion is 0.15 rad. Each orbit, called a formable orbit, is the average of the TBT orbits that have the maximum.

Also, an initial reformulation of the error position estimation is done in the PYTHON APJ code. The transverse error position is taken as:

$$z_{error} = \sqrt{2\bar{J}_0\beta_{z,error}}\sin\left(\psi_{z,error} - \bar{\delta}_0\right) \qquad (2)$$

where $\bar{J}_0$ and $\bar{\delta}_0$ are the average of the Action and Phase in a region before the error (generally the arc before the IR), respectively, and $\beta_{z,error}$ and $\psi_{z,error}$ are the beam β-function and phase advance, at the longitudinal position of the magnetic error, respectively.

To obtain the magnetic errors A_1 and B_1, the APJ uses the relations reported at [4] or [2]. Including different combinations of the orbits, new relations are obtained as reported in the *Appendix* of this paper. For more precise and exact results an implementation of a 2D independent fit is done. This allows to get A_1 and B_1 directly from:

$$\theta_x = -xB_1 + yA_1 \quad \text{and} \quad \theta_y = xA_1 + yB_1 \qquad (3)$$

where θ is the kick produced by the error, x and y are the estimate coordinates of the trajectory at the error. This is assuming that there is not other type of magnetic error.

RESULTS AND DISCUSSION

Figure 2 contains the beam y-trajectory in the frequency space for one BPM of the LHC. Four signals are plotted in the same axis, the FFT of: the simulated, with noise, and filtered, trajectories. This representation allows to observe how the amplitude of the noise signal is reduced in the filtered signals. The difference of the noise type used implies a higher amplitude of noise for the Gaussian case,

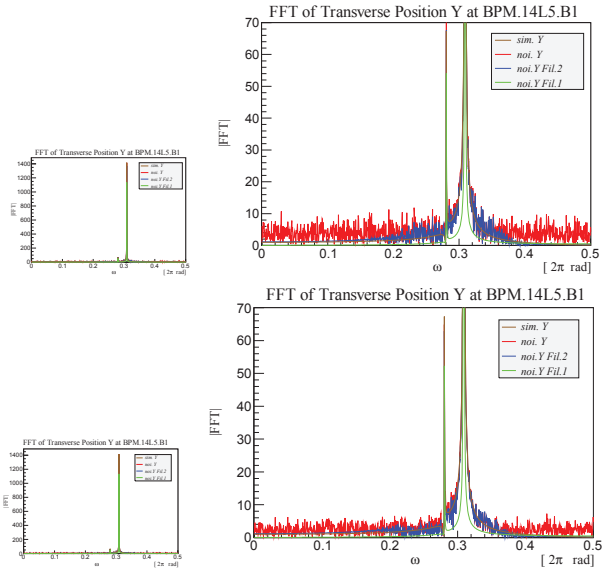


Figure 2: FFT of the Vertical Positions at BPM.14L5.B1 after 2000 turns, with Gaussian (top) and Uniform (bottom) noise. The left plots are the complete spectrumwhile the right plots is a close-up for the bottom of the spectra. All are a superimpose of a simulated (sim.) trajectory, a sim. with noise added (noi.), and a noise filtered signal for the cases N.1 (Fil. 1) and N.8 (Fil. 2) on Table 1.

observed as well in the plane x. This contrast the fact that the Gaussian distribution has a $\sigma_{Gauss} = 0.1$ mm while the Uniform distribution is up to 0.3 mm. [1].

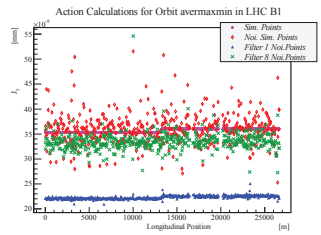


Figure 3: Action (J) along the LHC ring for one orbit type. Obtained from the simulation, without noise (Sim.), with Gaussian Noise (Noi. Sim.), and the filters N.1 and N.8 on Table 1. The magnetic errors are at 13271 m.

The Action (J) and Phase (δ) are modified with the presence of noise. Figure 3 contains J against s, without noise, for Gaussian noise and filtered, for y. The value of J is affected after the use of the filter Fil N.1, due to the difference of the trajectories amplitudes explained by the Frequency response of Fig. 1 (left). The Phase for the same orbit is in Fig. 4a. For both variables in x or y, the filter reduce the dispersion of their values. Something similar occurs with uniform noise, Fig. 5a shows δ against s, for the same type of orbit that is analyzed before, and the observations are the

[1] For both noise distributions, the BPMs resolution of 0.3 mm is the reference [7]. Because the beam distribution is Gaussian, we assumed that it is less probable to have particles of the bunche extremes affecting the BPM signal, therefore it is enough to have $\sigma_{Gauss} = 0.1$ mm.

Copyright © 2013 CC-BY-3.0 and by the respective authors

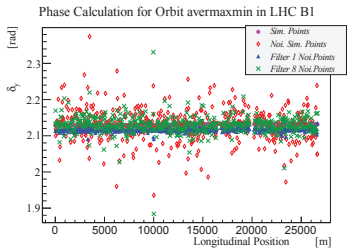


Figure 4a

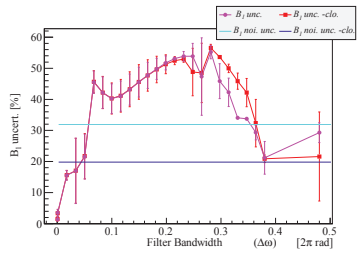


Figure 4b

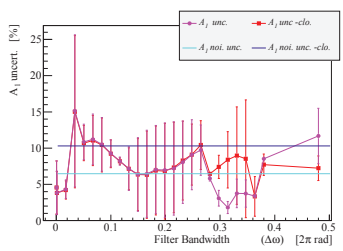


Figure 4c

Figure 4: Results for Gaussian Noise. Figure 4a contains the Phase (δ) along the LHC for the cases discussed in Fig. 3. The Uncertainty (uncert.) for B_1 and A_1 are showed in Fig. 4b and Fig. 4c, respectively, for the different bandwidths. The uncert. for the noised orbit is plotted as a horizontal line. A Low-pass filter to get the closed-orbit implies the -clo results.

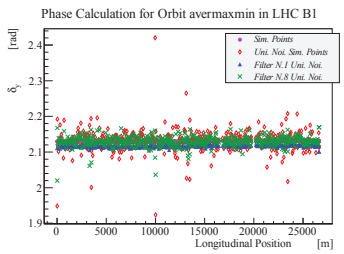


Figure 5a

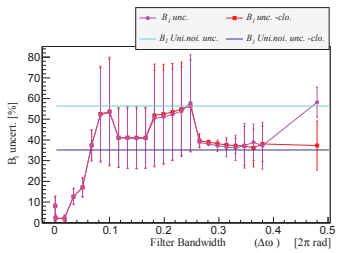


Figure 5b

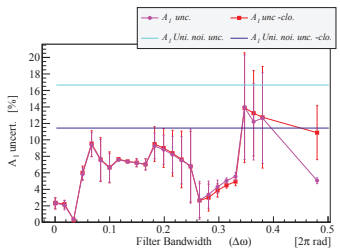


Figure 5c

Figure 5: Results for Uniform Noise in the same quantities as Fig. 4. Figure 5a contains δ while Fig. 5b and Fig. 5c contain the Uncertainty of B_1 and A_1. In the plots the precision and exactness is clearly lost for very small $\Delta\omega$.

same. Comparing the two distributions, the uniform noise implies a less dispersion.

To obtain A_1 and B_1, the selection of orbits implies that 8 points are available for the fit of Eq. 3. The magnetic errors uncertainty (taked as the Absolute Error of the measurements) of the two values obtained from the fit of Eq. 3., obtained from the fit with its dispersion (error bars), is plotted in figures Fig. 4b, Fig. 4c, Fig. 5b and Fig. 5c, against $\Delta\omega$.

Results using a low-pass band filter ($\omega_{cut} = 0.075$) for the closed-orbit calculation are reported with the line labeled as -clo. In the others, the closed-orbit is the average of the TBT trajectories. When there is noise at many frequencies, a discrepancy on the results is observed.

Also, the noise distribution affects the magnetic components in a different way. The horizontal lines, which are the uncertainty average on noised orbits (no filter used), have different values in Fig. 4b, Fig. 4c, Fig. 5b and Fig. 5c. The precision change according $\Delta\omega$ and the error.

The lesser uncertainty value for B_1 and A_1 with Gaussian and Uniform noise is obtained when $\Delta\omega = 0.0174$. This bandwidth has also a very high precision in the Uniform noise results. Diference on the noise reduction at the different bandwidths at the middle region could be corrected by setting an overlapping bandwith higher than the common ω values. In here, we are interested to take the lesser bandwidth that gives the lesser uncertainty.

CONCLUSION

A dual band-pass filter with a bandwidth of 0.0174 around the transverse tunes can be use to highly decrease Gaussian and Uniform noise in LHC orbits, when measure A_1 and B_1 at the same quadrupole using the APJ method as presented. Differences on how the closed-orbit is calculated are observed when there is noise at many frequencies.

APPENDIX

To obtain the magnetic errors, Equations (21) in [2] are used for every orbit. Other possibility is taking two orbits $(x^{(1)}, y^{(1)}, \theta_x^{(1)}, \theta_y^{(1)})$ and $(x^{(2)}, y^{(2)}, \theta_x^{(2)}, \theta_y^{(2)})$ to obtain one error, for example for B_1:

$$B_{1,x}=\frac{\theta_x^{(1)}y^{(2)} - \theta_x^{(2)}y^{(1)}}{x^{(2)}y^{(1)} - x^{(1)}y^{(2)}} \text{ and } B_{1,y}=\frac{\theta_y^{(1)}x^{(2)} - \theta_y^{(2)}x^{(1)}}{y^{(1)}x^{(2)} - y^{(2)}x^{(1)}} \quad (4)$$

The precision reached in this way is not as good as the presented results, but it could imply a faster and good measurement.

REFERENCES

[1] Javier Cardona, et. al, EPAC'04, Lucerne, TUPLT182, p.1553.

[2] Javier F. Cardona and Stephen G. Peggs, Phys. Rev. ST AB. 12 10988-4402, 2009 and Erratum 059901, 2010.

[3] J. Cardona, et. al, IPAC'11, San Sebas., WEPC004, p.2004.

[4] O.R. Blanco, et. al, PAC'11, New York, TUODN6, p.1.

[5] M. Aiba, et. al. EPAC'08, Genoa, 2008, WEPP025, p. 2572.

[6] SciPy Reference Guide (PYTHON). Functions *filtfilt*, *butter*. Pag 330-352. 2009.

[7] LHC Design Report: Vol 1 ch. 2, Geneva, CERN, 2009.

Copyright © 2013 CC-BY-3.0 and by the respective authors

POSSIBLE OBSERVATION OF TRANSVERSE LASER COOLED ULTIMATE COLD ION BEAM IN S-LSR*

Kouichi Jimbo#, IAE, Kyoto University, Uji-city, Kyoto, Japan
Hikaru Souda, Gunma University Heavy Ion Medical Center, Maebashi-city, Gunma, Japan
Yosuke Yuri, TARRI, Japan Atomic Energy Agency, Takasaki-city, Gunma, Japan
Hiromu Tongu, ICR, Kyoto University, Uji-city, Kyoto, Japan
Masao Nakao, Toshiyuki Shirai, and Akira Noda, NIRS, Chiba-city, Chiba, Japan

Abstract

Transverse laser cooling is pursued at an ion storage/cooler ring, S-LSR, Kyoto University. An RF bunched Mg^+ beam was cooled transversely through synchro-betatron resonance coupling by a co-propagating laser. We investigated peaks of synchrotron oscillation spectroscopically so that we can observe them stably. Oscillation signals from a parallel-plate pickup were observed by a spectrum analyzer. We also observed the coherent synchrotron modes. As the beam temperature decreases, the ion beam would be in space charge limited region. According to the computer simulation, in the case the beam turns to be space charge limited, the disappearance of peaks of synchrotron oscillation is expected. We would like to propose a capability of detecting space charge limited region by observing such a frozen synchrotron oscillation.

INTRODUCTION

In Small Laser-equipped Storage Ring (S-LSR) at ICR, Kyoto University, a frequency tuneable laser of ~280 nm is co-propagating with a 40keV Mg^+ beam, as shown in Fig.1. It was cooled in the transverse direction through resonant coupling method [1]. The Horizontal and longitudinal oscillations are coupled by an RF voltage applied at the position with a finite dispersion when a synchro-betatron resonance coupling condition (SBRC) is satisfied: a cooling force in the longitudinal direction is transferred to the transverse direction [2].

The ion beam was bunched by the RF wave of frequency 2.5192MHz. Since the revolution frequency was 25.192kHz, it corresponded to the harmonic number 100. Frequency spectra, which were obtained from preamp signals of a parallel-plate pickup in the ring, were observed by a spectrum analyzer [3]. We hope to use these frequency spectra for diagnostic purpose of ultra cold ion beams.

The RF frequency of 2.5192MHz will be printed as 2.5MHz for abbreviation, which corresponds to 0Hz in Figure 2, 3, and 5. In Figure 4, 0Hz represents 2×2.5MHz. At this stage of transverse laser cooling where the beam temperature was not yet ultra-cold to be in space charged limited region, there was no clear difference in frequency spectra whether the ion beam was laser cooled or not.

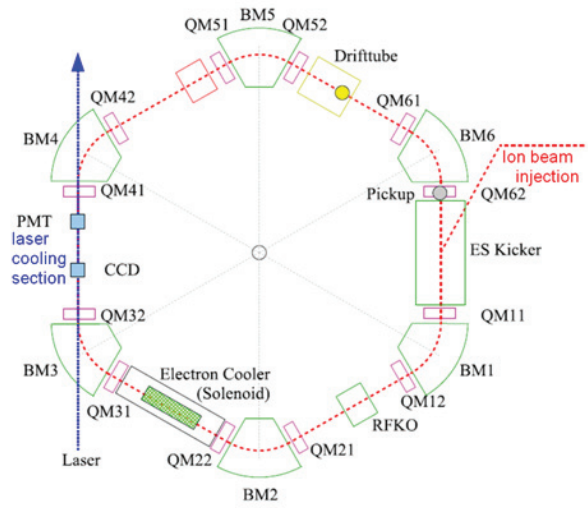


Figure 1: Layout of S-LSR.

Table 1 shows the main parameters of S-LSR.

Table 1: Main Parameter of S-LSR

Circumference	22.557 m
Average Radius	3.59 m
Length of straight section	1.86 m
Radius of curvature	1.05 m
Revolution frequency	25.192 kHz
Super periodicity	6
Ion species	$^{24}Mg^+$
Kinetic beam energy	40 keV
Transition wavelength	280 nm

EXPERIMENTAL RESULTS

The frequency spectra of around 2.5MHz, which is located at the centre, are shown in Fig. 2. To erase sidebands (2 peaks about ±1kHz, and about±2kHz from the centre), the RF frequency was varied ∓ 0.5kHz (Fig.2-a and 2-c) when SBRC was satisfied (Resonance tune ν_s=0.066、ν_h=2.066). However, we could not erase them. They were not noises. In fact the sidebands are small enough since the ordinate is the unit of dBm.

*Work supported by Advanced Compact Accelerator Development Project of MEXT, the Global COE program "The Next Generation of Physics, Spun from Universality and Emergence".
#jimbo@iae.kyoto-u.ac.jp

Copyright © 2013 CC-BY-3.0 and by the respective authors

In Fig. 3 and 4, sidebands of synchrotron frequencies were observed at both sides of each harmonic of the revolution frequency when SBRC was satisfied. These peaks were not observed under no beam. Therefore the ion beam caused them.

In Fig. 3, five peaks are recognizable. They correspond to frequencies of harmonic number h=98, 99, 100, 101, and 102 from the left. At h=98, 99, 101, and 102, synchrotron sidebands are accompanied in both sides of each harmonic. The 1st harmonic of RF frequency 2.5MHz is observed at the centre (h=100). An enlargement of the central peak is identical to Fig. 2-b.

In Fig.4, five peaks are also recognizable. They correspond to frequencies of harmonic number h=198, 199, 200, 201, and 202 from the left. At h=198, 199, 201, and 202, synchrotron sidebands are accompanied in both sides of each harmonic. The second harmonic of RF frequency (2 × 2.5MHz) is observed at the centre (h=200). The peak between 199 and 200 (about −1.6kHz from the centre 200) is a noise since it was observed under no beam.

The RF voltage was varied in Fig.5, which was recorded in higher resolution. Peaks indicated by blue arrows, of which synchrotron frequencies were shown, were moved among 5 peaks of +0kHz, about ±1kHz, and about±2kHz from the centre. Unexplainable low peaks were observed at ±1.7kHz in Fig5-a and ±1,5kHz in Fig5-b. They were not noises. Those low peaks were not observed under no beam.

Because of higher resolution, these peaks looks a little bit slender compared to those in Fig. 2. Synchrotron frequencies were evaluated according to the frequency formula of small amplitude synchrotron oscillation [4].

THE COHERENT SYNCHROTRON MODES

Fig. 2 manifests that sidebands are the coherent synchrotron modes (4 peaks about ±1kHz, and about± 2kHz from the centre), which occur when the RF frequency is a not exactly an integral multiple of the revolution frequency of each of circulating ions: this is the case when ions are circulating in bunches. A bunch is made of ions with different synchrotron amplitudes and phases. The coherent synchrotron modes of the bunch can be obtained by averaging synchrotron motions over the bunch distribution [5]. The coherent frequency spectra are located at harmonics of the RF frequency. Fig. 5, in which the RF voltage was varied, shows that the coherent synchrotron modes are independent of the RF voltage.

DISCUSSION

The computer simulation expects dumping of synchrotron oscillations when the ion beam is in space charge limited region [6]. When an ion beam is cooled to space charged limited region, it would be very difficult to detect it directly since the number of ions in the cold Mg^+ beam is very limited. In fact, the number of ions is estimated much less than ~10^4 [7]. A diagnostic method using scraping is already applied in a ultra-cold Mg^+ beam, which, however, was not sensitive enough to be usable in space charged limited region [8].

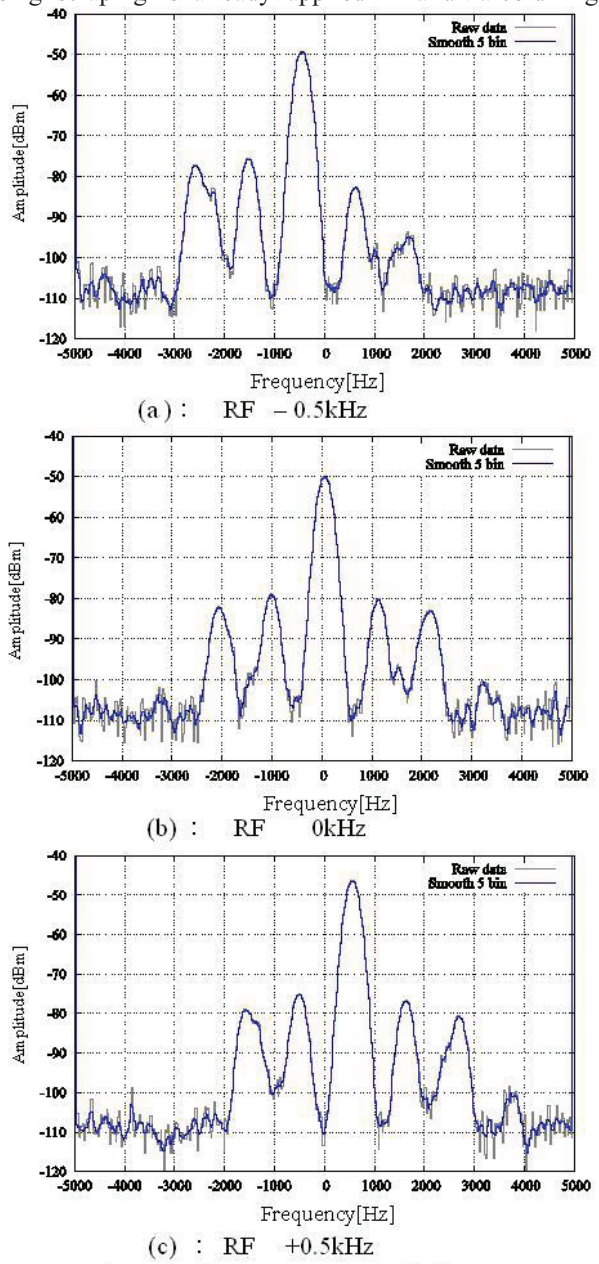


Figure 2 : Frequency spectra RF frequency was varied relative to RF frequency 2.5MHz (centre 0Hz).

We have observed synchrotron frequencies stably in frequency spectra. Observation of synchrotron frequencies would be helpful to confirm space charge limited ion beam since peaks of synchrotron oscillation would disappear in frequency spectra. Therefore we hope frequency spectra are usable as a diagnostic method of ultra cold ion beams.

It is also our great interest what will happen to the coherent synchrotron modes in space charged limited region, which we want to investigate with the use of the indirect transverse laser cooling when SBRC is satisfied in a near future.

Copyright © 2013 CC-BY-3.0 and by the respective authors

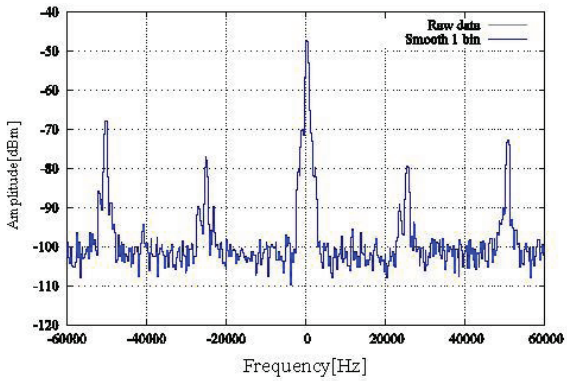


Figure 3: Frequency Spectrum from h=98 to 102. An enlargement of centre peaks (h=100) is physically the same as Figure 2-b.

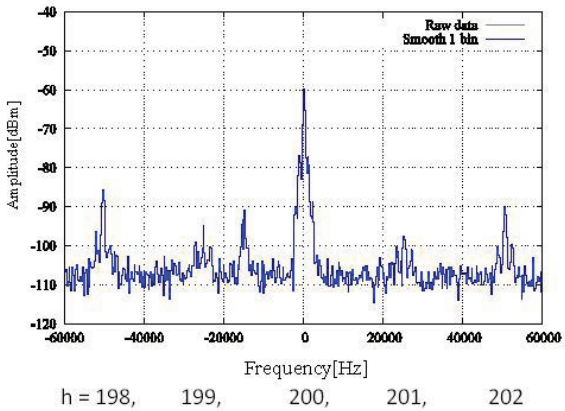
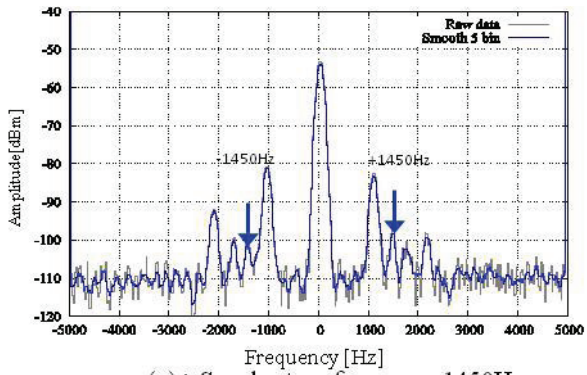


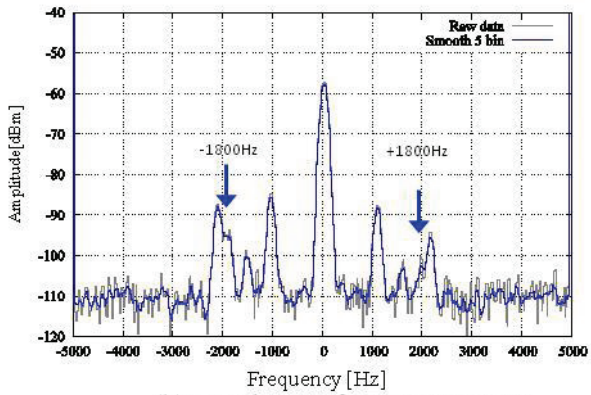
Figure 4: Frequency Spectrum from h=198 to 202. The peak between 199 and 200 is a noise since it was observed under no beam.

REFERENCE

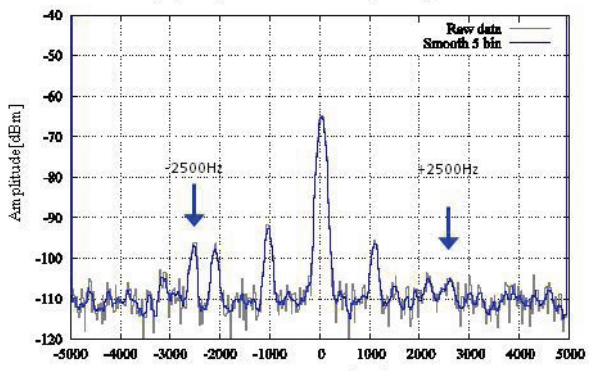
[1] M. Nakao et al., Physical Review Special Topics - Accelerator and Beams **15**, 110102 (2012).
[2] H. Okamoto et al., Phys. Rev. Lett. **72**, 3977 (1994).
[3] K. Jimbo et al., Proceedings of IPAC12, New Orleans, 2012, MOPPD011.
[4] S.Y.Lee, Accelator Physics (World Scientific, New Jersey 2012) 3rd ed. p234.
[5] ibid. p343.
[6] Y. Yuri et al., Proc. International Workshop on Beam Cooling and Related Topics COOL'13, Murren, Swizterland, 2013, THAMHA03.
[7] H. Souda et al., Jpn. J. Appl. Phys. **52** (2013).
[8] A. Noda et al., Proc. International Workshop on Beam Cooling and Related Topics COOL'13, Murren, Swizterland, 2013, THAMHA02.



(a) : Synchrotron frequency 1450Hz



(b) : Synchrotron frequency 1800Hz



(c) Synchrotron frequency 2500Hz

Figure 5: Frequency spectra when RF voltage was varied. RF frequency 2.5MHz is at the centre (0Hz). Synchrotron frequencies are indicated by blue arrows. Unexplainable low peaks were observed at ±1.7kHz in (a) and ±1,5kHz in (b). They were not noises. Those low peaks were not observed under no beam.

Copyright © 2013 CC-BY-3.0 and by the respective authors

LUMINOSITY ESTIMATION AND BEAM PHASE SPACE ANALYSIS AT VEPP-2000*

A. Romanov, I. Koop, E. Perevedentsev, D. Shwartz
BINP SB RAS and Novosibirsk State University

Abstract

Luminosity is the main output of colliders, so it is very important to measure it with speed and accuracy. VEPP-2000 has 16 beam profile monitors (BPM) which use CCD-cameras to register synchrotron light in the visible spectrum. Two luminosity estimation methods are presented, both based on beam size analysis. Although the luminosity measurements by particle detectors CMD-3 and SND are slow and have low statistical accuracy for low beam currents, their data can be used to test new faster methods. Additionally, an attempt of the phase space tomography is presented using the simulated BPM measurements of the particle distribution in a strongly non-gaussian beam.

INTRODUCTION

VEPP-2000 is used for hadron cross section measurements in the energy range of $0.4 \div 2$ GeV [1], hence it takes luminosity at several dozens of energies every season, thus emphasizing the tuning tools' importance. The collider has a two-fold symmetry lattice with 16 CCD cameras that take beam images using synchrotron light (Fig. 1). 8 CCDs are aimed at electrons and 8 at positrons.

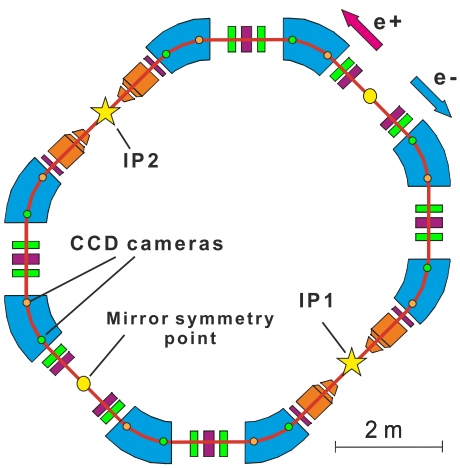


Figure 1: VEPP-2000 layout.

There are a number of theoretical and empirical considerations regarding lattice configuration depending on the energy [2], but the last step of the final tuning is almost always unique and done manually. To get the best luminosity output, the operator should tune parameters such as beta-functions at the IPs, closed orbit position, betatron tunes, chromaticity, betatron coupling and others. The crude effects such as "flip-flop" can be noticed by the naked eye, however fine tuning requires the fast and reliable luminosity estimation tools. Unfortunately, the speed and precision of the luminosity measurements from the detectors are not sufficient, especially at low energies.

Both presented methods of luminosity estimation assume that accurate optics model of the real accelerator ring is available. Assuming no focusing perturbations in the lattice other than those caused by the collision, and thus located at the IP, one can use known transport matrices to evaluate the beam sizes at the IP from the beam size measurements by CCDs.

FIRST LUMINOSITY ESTIMATION METHOD

Eight measurements are available for either transverse coordinates of the two beams, while there is only a pair of strongly indeterminate parameters - beam emittance ϵ and $\beta*$ - for each mode and each beam.

For the parameters fitting procedure, it is convenient to transport all the measured beam sizes to the point of mirror symmetry where Twiss $\alpha = 0$. The center of technical straight section is chosen since this point is not perturbed by the beam-beam focusing. The beta-function for $i-th$ profile monitor is transported as:

$$\beta_i = \beta_0 \cdot t_{11,i} + \beta_0^{-1} \cdot t_{12,i}, \quad (1)$$

where t_{kl} are the elements of known transport matrix. The fitting minimizes the difference between the model and measured beam sizes:

$$F = \sum_i \frac{\left(\sqrt{\epsilon\left(\beta_0 \cdot t_{11,i} + \beta_0^{-1} \cdot t_{12,i}\right)} - \sigma_i\right)^2}{\sigma_i^2 + o_i^2}. \quad (2)$$

Here, o_i is the size measurement error with a typical value of $3-5\mu m$, while the beam size σ_i is a pure betatron part of measured transverse size with excluded dispersion contribution

$$\sigma_\beta = \sigma - D \cdot \frac{\sigma_E}{E} \quad (3)$$

The fitted beta-function β_0 is transported to the IP together with the emittance that gives the size needed. The luminosity can be easily calculated as:

$$L = \frac{N_1 N_2 f_0}{2\pi\sqrt{\left(\sigma_{1x}^2 + \sigma_{2x}^2\right)\left(\sigma_{1y}^2 + \sigma_{2y}^2\right)}}. \quad (4)$$

The model is extremely simple, it uses several assumptions. 1) Well-known unperturbed optics between the IPs

* This work is supported by the Ministry of Education and Science of the Russian Federation.

Copyright © 2013 CC-BY-3.0 and by the respective authors

without betatron coupling. Strictly speaking it is not the case for VEPP-2000 but the rotation produced by the final focusing solenoids can be ignored. 2) Both arcs and IPs are identical. 3) All particle distributions remain Gaussian. This is not true in the case of very intensive beams close to the beam-beam limit. 4) Energy spread is not perturbed and formed by synchrotron radiation. Recently the bunch lengthening in the low energy range was observed, indicating the microwave instability for the beams that are intensive enough (Fig. 3). This phenomenon would modify the dispersion contribution to the beam sizes.

The comparison of this luminosity estimation technique is in good agreement with measurements from the detectors (Fig. 2).

SECOND LUMINOSITY ESTIMATION METHOD

General Outline

This method is also model dependent, but it is based on the second moments (SM) of the particles' distribution, some of which are obtained from the imaging BPMs. The idea is to transport the set of SM for both bunches over the ring and by adjusting initial values of the SM matrices and some other parameters fit the traced moments to the measured sizes. Given that the ring lattice is perfectly known, there are still interaction regions that have unknown effect on the distribution of particles in the bunches. To handle this problem the ideal ring lattice is appended with thin IP transformations.

Each IP is divided in two equal thin lenses to be able to find second moments in the center of the IP. The strength of the IP lens is calculated based on the size of the opposite bunch. First tests of this approach reveal discrepancies of the fitted and experimental second moments at large currents, when bunches became strongly non-Gaussian. The calculated luminosity also became unrealistic. To fix this effect, an additional set of fitting coefficients was introduced to adjust the counter beam focusing kick.

The final focus solenoids in the present VEPP-2000 lattice configuration cancel the rotation of the betatron oscillation planes after passage through the interaction straight. Since all the CCDs are located outside the IP's straight sections, the solenoids could be treated as axially symmetrical lenses without rotation. Due to the two-fold symmetry of the VEPP-2000 and by omitting the rotation from the solenoids, the SM in the center of each IP should be diagonal. Second moments of the electron and positron bunches in the first IP form the main part of the fitting parameters.

$$M_{IP1} = Diag[m_{1,00}, m_{1,11}, m_{1,22}, m_{1,33}, m_{1,44}, 0] \quad (5)$$

The longitudinal distribution has been set to zero because it has no effect on transverse beam size in VEPP-2000.

The total number of fitting parameters p_j is 18: 10 second moments and 8 from beam-beam force fitting parameters (2 IPs, 2 bunches, 2 dimensions). Experimental data from 16 working CCD cameras gives 32 points, which provides enough information to keep the task well overdetermined.

The target function is:

$$F = \sum_i \left(\frac{M_{exp,i} - M_{fit,i}}{M_{exp,i}} \right)^2 = \sum_i V_i^2. \quad (6)$$

The beam sizes vary strongly from CCD to CCD and this form gives equal weight to all data points.

Minimization Algorithm

To minimize F, the set of variations of parameters Δp_j must be found that leads to the cancellation of the V_i. Linearizing the $\Delta V_i(\Delta p_j)$ this goal can be written as:

$$\Delta V_i(\Delta p_j) \simeq \sum_j \frac{1}{k_j} \frac{\partial V_i}{\partial p_j} k_j \Delta p_j = -V_i, \quad (7)$$

here, k_j are normalization coefficients that can be used to adjust impacts of different model parameters. To find the desired set of parameters, the rectangular matrix $\frac{\partial V_i}{\partial p_j}$ should be inverted. The flexible way to find a pseudo-inverse matrix is provided by the singular value decomposition (SVD):

$$\Delta p_j = \sum_i \left(\frac{\partial V_i}{k_j \partial p_j} \right) \Big|_{SVD}^{-1} \frac{-V_i}{k_j}. \quad (8)$$

Implementation of the found corrections finishes the iteration that should be repeated several times, since the model depends nonlinearly on the parameters. After convergence of the fitting, luminosity is calculated with Eq. (4). The comparison of the second luminosity estimation method with others is shown in Fig. 2.

One of the differences between two algorithms is that latter has the energy spread in the beam as the fitting parameter. First runs supported the presence of microwave instability, first observed with phi-dissector – optical tool for bunch length measurements (see Fig. 3) [3, 4].

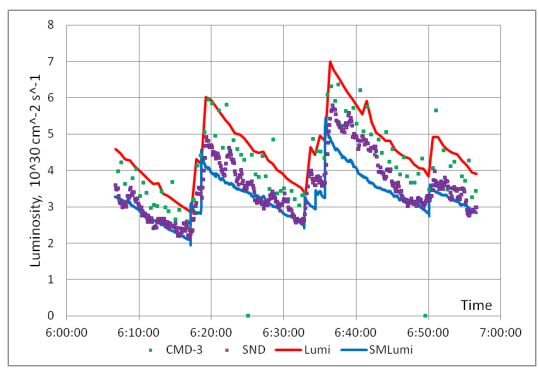


Figure 2: Comparison of the luminosity from different measurements: green dots – CMD-3, purple dots – SND, red and blue lines – estimation methods

Copyright © 2013 CC-BY-3.0 and by the respective authors

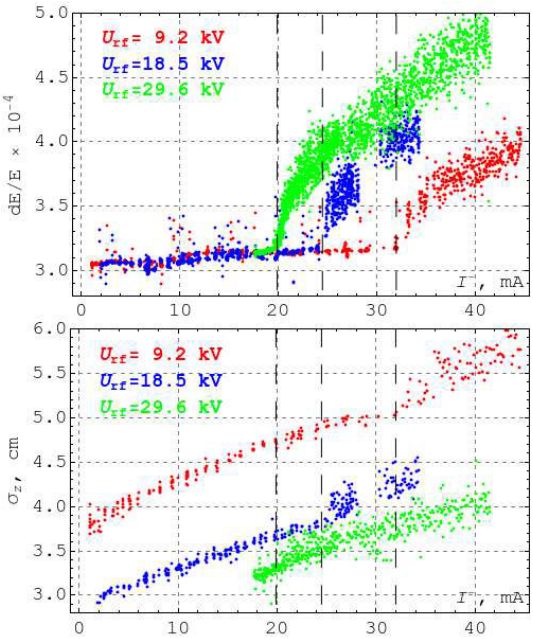


Figure 3: Correlation of the current dependence of the extracted energy spread and the measured bunch length.

PHASE SPACE TOMOGRAPHY

Relatively small number of CCDs – 8 for electrons and 8 for positrons – led to pessimistic estimations of classical approach to the beam phase space tomography methods which use several tens of projections [5]. Therefore, the feasibility study regarding this task was started after the shutdown of VEPP-2000.

The success in solving the inverse problems using the SVD inspired its use in the beam phase space tomography method. The fitting parameters p_j in this case describe the distribution of the particles in the phase space at some point. The experimental data $V_{exp,i}$ is composed of all projections' points from all the CCDs. For the known optics model, the transportation of the particles' distribution to the CCDs locations and calculation of the projections $V_{mod,i}$ is straightforward. To simplify the test problem, several assumptions were used: no transverse coupling; no energy spread; no lattice errors; no counter beam.

To describe the particles' distribution in the tested method the mesh in phase space is set so that values p_j describe the density in the mesh pointsand intermediate values are calculated by linear interpolation. One of the disadvantages of the method is that negative density is allowed. The main clue is to setup the mesh evenly with respect to the phase space. To do so, the point is selected where the Twiss parameter $\alpha = 0$. In this case, the phase trajectories represented in the normalized coordinates $(x/\sqrt{\beta}, x' \cdot \sqrt{\beta})$ form circles, and the mesh points' coordinates could be selected as (r_n, ϕ_m) plus $(0, 0)$ forming a polar mesh. The normalization coefficients k_j in Eq. (8) are proportional to the area related to the corresponding node.

Figure 4 demonstrates results of the fitting for three types of distributions with 5% noise level in the "experimental" projections. For the tests the real VEPP-2000 lattice in the horizontal plane was taken with 8 electrons' CCDs. The real lattice was taken for the tests. Except for some areas with very small negative densities, it is obvious that in general the reconstructed distributions are in good agreement with the original. Also, the integral of the negative density could be used to test the plausibility of found distributions.

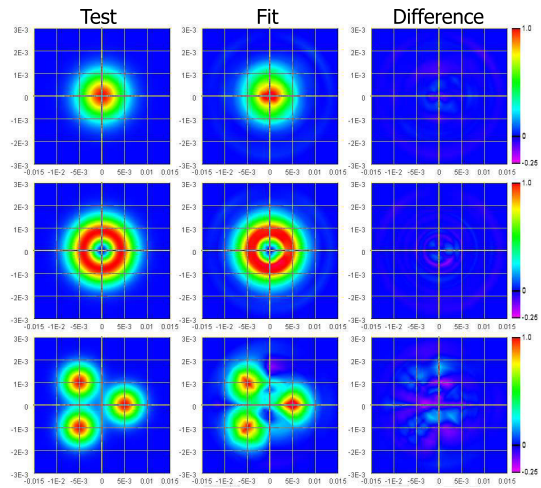


Figure 4: Test distribution, its fit and their difference for the Gaussian, ring-shaped and triple-Gauss distributions.

Further studies will include comparison of the tested method to the commonly used methods, such as inverse Radon transformation. Additionally, influences of various errors and mesh configurations should be thoroughly investigated.

The main practical goal of the beam phase space tomography at VEPP-2000 is to accurately estimate luminosity at high currents when the beam become strongly nongaussian and simpler methods may give unreliable results.

REFERENCES

[1] Yu. M. Shatunov et al., Project of a New Electron-Positron Collider VEPP-2000, in: Proc. 7th European Particle Accelerator Conf. (EPAC 2000), Vienna, Austria, p. 439 (2000).

[2] A. Romanov et al., Round Beam Lattice Correction using Response Matrix at VEPP-2000, Conf. Proc. IPAC 2010, THPE014 (2010).

[3] Yu.A.Rogovsky et al., "Status and perspectives of VEPP-2000", X International scientific workshop to the memory of Professor V.P. Sarantsev, 3 - 7 September 2013, Alushta, Ukraine (in Russian).

[4] E. Zinin, PhD Thesis, Budker Institute of Nuclear Physics, Novosibirsk, 1984 (in Russian).

[5] K.M. Hock et al., Beam tomography in transverse normalised phase space Nuclear Instruments and Methods in Physics Research A 642 (2011) 36.

Copyright © 2013 CC-BY-3.0 and by the respective authors

COMBINING MULTIPLE BPM MEASUREMENTS FOR PRECESSION AC DIPOLE BUMP CLOSURE*

P. Oddo, M. Bai, C. Dawson, J. Kewisch, Y. Makdisi, C. Pai, P. Pile, T. Roser
BNL, Upton, NY 11973, USA

Abstract

For the RHIC spin flipper to achieve a rotating field, it requires operating five AC dipoles as a pair of closed orbit bumps. One key requirement is to minimize the remnant AC dipole driven betatron oscillation outside of the spin flipper by 50 dB [1]. In the past, due to its inherent sensitivity, a single pickup with a direct-diode detector (3D) [2] and dynamic signal analyzer (DSA) were used to measure bump closure by measuring the remnant oscillations. This however proved to be inadequate, as the betatron phase advance between the AC dipoles is non-zero. A method of combining multiple BPMs into a sensitive measure of bump closure has been developed and was tested during RHIC polarized proton operation in 2013. This technique as well as the experimental results will be presented.

INTRODUCTION

A spin flipper for RHIC (Relativistic Heavy Ion Collider) has been developed for RHIC spin-physics experiments. It is needed to cancel systematic errors by reversing the spin direction of the two colliding beams multiple times during a store [3].

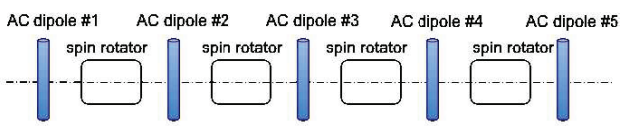


Figure 1: Spin flipper configuration.

The spin flipper system consists of four DC dipole magnets (spin rotators) and five AC dipole magnets (see fig. 1). The aim of this configuration is to produce a rotating field. Multiple AC dipoles are needed to localize the driven coherent betatron oscillation inside the spin flipper [1, 4]. While results from the 2012 run did suggest the presence of a rotating field, the polarization lifetime was degraded with the AC dipoles on. This suggested incomplete bump closure and/or incorrect phase between bumps [1] which lead to reinvestigating the method used to close the AC dipole bumps.

Operationally the AC dipoles form two bumps that minimize the effect of the AC dipoles outside of the spin flipper. The central AC dipole, #3 in figure 1, is common to both bumps. Both AC-dipole bumps operate at the same frequency, but are phase shifted from each other. The convention used when expressing closure in dB is to make the 0 dB reference the strongest AC dipole. In case of the dual bump, AC dipole #4 is used.

*Work supported by Brookhaven Science Associates, LLC under contract DE-AC02-98CH10886 with the U.S. Department of Energy and RIKEN, Japan.

BBQ 3D AFE & DSA

Up until the 2013 run the closure was only trimmed using the pickup and direct-diode detector (3D) analog front end (AFE) of the RHIC baseband tune meter (BBQ) processed via a DSA.

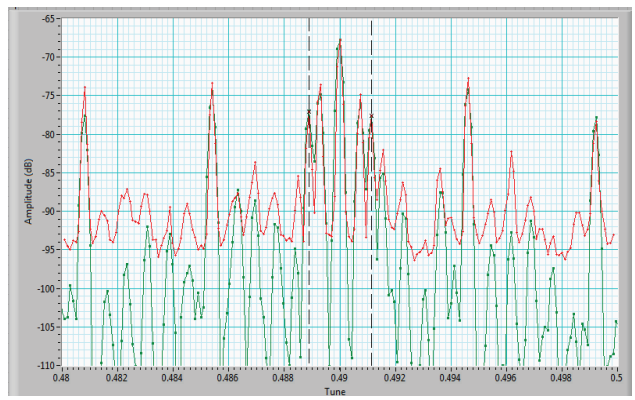


Figure 2: Closed bump DSA beam spectrum (green plot). The red plot is the fitted AC dipole magnet currents.

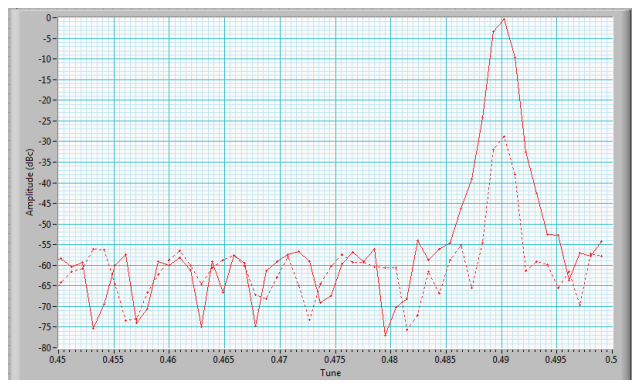


Figure 3: AC dipole #4 alone (solid) and closed bump (dotted) BPM beam spectrum of the most sensitive BPM.

The DSA spectrum in figure 2 (green plot) shows that the closure for the AC dipole bumps was 67 dB. However, the spectrum of the most sensitive BPM (fig. 3, dotted plot) shows a closure of only 28 dB. This nearly two order of magnitude difference clearly shows that it's not possible to determine closure using a single pickup (at a single frequency). The possibility of using a single pickup at multiple frequencies has not yet been fully explored.

COMBINING BPM MEASURMENTS

Even though discrete Fourier transform (DFT) spectrums, which typically are calculated using the fast Fourier transform (FFT) algorithm, are used here, these

Copyright © 2013 CC-BY-3.0 and by the respective authors

methods are not strictly DFT/FFT methods. As a matter of fact the BPM magnitude and phase used by software calculations used a sine/cosine fit, which can be thought of as the evaluation of the discrete time Fourier transform (DTFT) or z-transform at a single frequency.

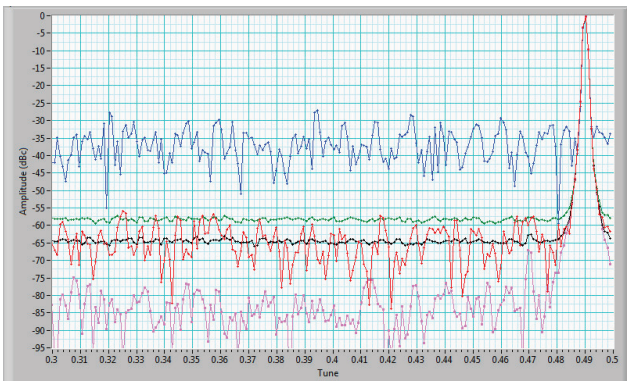


Figure 4: BPM spectrums of weakest (blue), strongest (red), average (green), weighted average (black) and vector average (purple) for AC dipole #4 at 90 A_{pk} (76 G·m) for PP at injection (23.8 GeV).

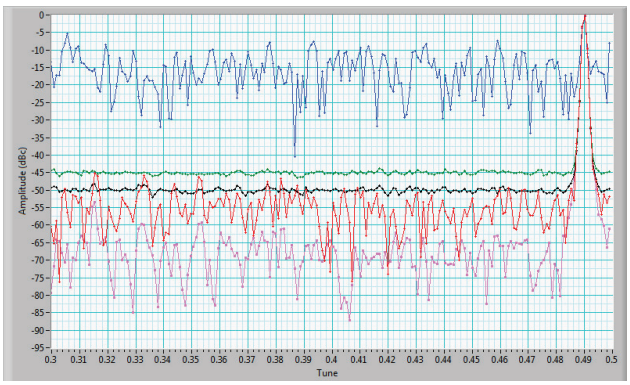


Figure 5: BPM spectrums of weakest (blue), strongest (red), average (green), weighted average (black) and vector average (purple) for AC dipole #4 at 117.9 A_{pk} (100 G·m) for PP at store (255 GeV).

Figures 4 and 5 show the weakest and strongest BPM spectrums and the spectrums for different methods of combining BPMs for polarized proton beam at injection and store respectively when excited by a single AC dipole (#4). In all cases the response is normalized to place the AC dipole peak at the driven frequency (0.49) at 0 dB. This is done as convenient way to visualize the signal to noise ratio. BPM data was taken with 1024 turn data records. For the 2013 run, 4096 turn records were available and these longer records would improve the signal to noise ratio by 6dB. Also note that the AC dipole excitation is 2 dB stronger for the data taken at store. The weakest BPM responses (blue traces) do change proportionally with the change in energy or magnetic rigidity (~20 dB). The strongest response (red traces) changes less (~12dB), which is just a direct result of the optics also being different. The weakest and strongest responses were also produced by different BPMs.

The average response (green trace) is just a simple magnitude average:

$$k_s \sum_{n=1}^{N} |Y_n| \tag{1}$$

Y_n is the frequency response for BPM n and k_s is a scale factor which normalizes the average to 1 (0 dB) when excited by a single AC. Since this is a magnitude response of all BPMs, all need to be zero for this to be zero and this would only happen for a closed bump. The noise floor for 1024 turn data at store was ~45 dB.

The weighted average (black trace) is a magnitude average weighted by each BPM's normalized signal to noise ratio squared:

$$\sum_{n=1}^{N} a_n |Y_n| \tag{2}$$

Software calculations for a_n use the mean magnitude of the DFT/FFT bins from 0.025 to 0.48 as the estimated noise value. The RMS error from a fit could also be used. The noise floor for 1024 turn data at store was ~50 dB.

The vector average (purple trace) scales frequency response of each BPM by the normalized signal to noise ratio squared, just as the weighted average, but also counter rotates the phase by measured phase:

$$\sum_{n=1}^{N} a_n \, e^{-i\phi_n} \, Y_n \tag{3}$$

Phase ϕ_n is the measured phase of BPM n when it was excited by a single AC dipole. The noise floor for 1024 turn data at store was ~70 dB. While this might look like a good candidate for determining bump closure, because this is a linear combination of BPMs, it is possible for it to be zero for combinations of only two AC dipoles and therefore not useful for definitely trimming bump closure (see eqn. 6 of next section).

Frequency Response of Multiple AC Dipoles

From previous treatments of transverse beam motion due to a single AC dipole [5] the basic equation of motion can be thought of as a discrete sampled time system, but the actual sampling is done by a particle or bunch.

Extending the model for an arbitrary number of AC dipoles in the time domain is:

$$\begin{pmatrix} y_0[n] \\ y_0'[n] \end{pmatrix} = \mathbf{M} \begin{pmatrix} y[n-1] \\ y'[n-1] \end{pmatrix} + \begin{pmatrix} e[n] \\ e'[n] \end{pmatrix} \tag{4}$$

$$\begin{pmatrix} e[n] \\ e'[n] \end{pmatrix} = g_{acd} \sum_{k=1}^{N} \mathbf{M}_{kN} \begin{pmatrix} 0 \\ i_1[n] \end{pmatrix} \tag{5}$$

Copyright © 2013 CC-BY-3.0 and by the respective authors

Functions $y_0[n]$ and $y'_0[n]$ are the beam position and slope at center of the last AC dipole, e[n] and e'[n] are the effective stimulus of all AC dipoles, matrix **M** is the transport matrix for a full turn, g_{acd} is a constant which converts magnet current into deflection (units A^{-1}) and matrix $\mathbf{M}_{kN}$ is the transport matrix from AC dipole k to the last AC dipole (N).

These equations illustrate that superposition can be used and that each AC dipole stimulus includes the path or optics to the reference point (center of last AC dipole).

Although not presented here, eqns. 4 and 5 can be transformed into the frequency domain. However, since this is a linear time invariant (LTI) system, certain assumptions can be made. The first is that the BPM position is a superposition of AC dipole currents:

$$Y_n(z) = \sum_{m=1}^{M} H_{nm}(z) I_m(z) \qquad (6)$$

$H_{nm}(z)$ is the transfer function from AC dipole m to BPM n, with M the number of AC dipoles.

Similarly, based on eqn. 5, BPM position is also a superposition of the error signals:

$$Y_n(z) = G_n(z)E(z) + G'_n(z)E'(z) \qquad (7)$$

$G_n(z)$ and $G_n'(z)$ are the transfer functions from AC dipole stimulus (or bump error) signal to BPM position n.

While both eqns. 6 & 7 were shown as continuous functions in z-transform form, actual calibrations are done at a fixed frequency ($z=e^{i2\pi Q_{acd}}$). The calibration process then just becomes a matter of multiplying complex constants. The transfer functions H_{nm} are also not calculated from a model, but a result of BPM position and AC dipole current measurements. For a single AC dipole on one at a time (superposition) eqn. 6 becomes:

$$H_{nm}(z) = \frac{Y_n(z)}{I_m(z)} \qquad (8)$$

Not shown, but it's also possible to derive these transfer functions from stepped AC dipole data.

Closing AC Dipole Bumps Using Calculated Correction Factors

Once the transfer functions have been determined, eqn. 6 can be used to solve for the precise currents needed to close a bump by setting $Y_n=0$ and solving for currents (or correction factors). Since the spin flipper contains two bumps, both need to be calculated separately using:

$$H_{n3} = 2k_2 H_{n2} - k_1 H_{n1} \qquad (9)$$

$$H_{n3} = 2k_4 H_{n4} - k_5 H_{n5} \qquad (10)$$

These equations assume a value for the shared AC dipole (#3) and calculate correction factors (k_1, k_2, k_4, and k_5) for the other four magnets assuming ideal settings.

Two methods have been used to calculate these correction factors. One involves a matrix operation using all BPMs at once for eqn. 9 and 10. The other method is a cutting method that involves iteratively calculating average correction factors for all combinations of BPM pairs and removing BPM pairs that produce correction factors that deviates more than four standard deviations from the average.

Measuring Bump Closure by Estimating AC Dipole Stimulus Components

A direct consequence of eqn. 7 is that the total AC dipole stimulus or bump error components (E, *E'*) can be calculated using pairs of BPMs using:

$$E = p_n Y_n + p_m Y_m \qquad (11)$$

$$E' = p'_n Y_n + p'_m Y_m \qquad (12)$$

The E and *E'* used are the ideal values calculated from the magnet current (based on eqn. 5). The scaling convention used is to make both E and *E'* equal 1 when excited by AC dipole #4 alone. Constants p_n, p_m, p'_n, and p'_m are then calculated using matrix operations while iterating over all BPM pairs (each of BPM n and m). These constants are summed and scaled to produce coefficients for each BPM so that producing the E and *E'* response only requires a single pass over the BPM data. The scaling used depends on which BPM pairs were used. When using all BPM pairs, the scaling should use the normalized signal to noise ratio squared to improve the resultant signal to noise ratio. When only using the final pairs used to calculate the bump correction factors, then the coefficients only need to be normalized by the number of pairs.

CONCLUSION

It is possible to combine multiple BPM measurements to close the AC dipole bumps. Using the calculated correction factors produced good results during the 2013 run. There are also numerous ways to verify closure, and this still includes the 3D pickup and DSA.

REFERENCES

[1] M. Bai et al, "RHIC Spin Flipper Commissioning Results," Proceedings of IPAC'12, 2012.
[2] M. Gasior et al, "The Principle and First Results of Betatron Tune Measurement by Direct Diode Detection," LHC-Project-Report 853, 2005.
[3] M. Bai et al, "RHIC Spin Flipper," Proc. 2007 IEEE U.S. Part. Accel. Conf., 2007.
[4] M. Bai et al, "Commissioning of RHIC Spin Flipper," Proceedings of IPAC'10, 2010.
[5] S. Peggs et al, "Nonlinear diagnostics using an AC dipole," RHIC/AP/159, 1998.

Copyright © 2013 CC-BY-3.0 and by the respective authors

STRIPLINE BEAM IMPEDANCE*

A. Blednykh#, W. Cheng, S. Krinsky
BNL, Photon Science, NY 19973-5000, USA

Abstract

We discuss the Lambertson and Shafer formalisms for the longitudinal and transverse beam impedances of a stripline. The required characteristic impedances and the geometric factors are determined by the solution of Laplace's equation in 2-dimensions, which we find using the 2-D POISSON code. Lambertson's equations are compared with numerical results obtained using the 3-D electromagnetic simulation code GdfidL. Good agreement is found at low frequencies. The results differ at high frequencies, since the analytic results do not take into account higher order modes.

INTRODUCTION

Striplines [1-4] are often used in accelerator systems to serve as either pick-ups or kickers. These devices are comprised of the conducting surfaces of the vacuum envelope and inner conducting electrodes as illustrated in Fig. 1. An important issue in the design of a stripline is the impedance that it presents to the particle beam traveling along the axis through the device.

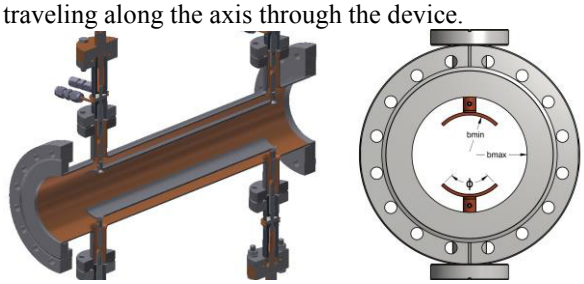


Figure 1: One half of the stripline kicker geometry. Two electrodes are located inside of the round pipe with $b_{min} = 24.1mm$ and $b_{max} = 38mm$ radii. The length of electrodes is 300mm. The electrode thickness is 2mm.

Lambertson [2,3] has presented a very interesting and comprehensive discussion of pick-ups and kickers. Following his formalism, one can express the longitudinal and transverse (vertical) beam impedances for a stripline in the form

$$Z_{||}(k) = g_{||}^2 Z_{ch,||}[sin^2(kL) + j\, sin(kL)cos(kL)] \quad (1)$$

$$Z_{\perp}(k) = \left(g_{\perp}^2 Z_{ch,\perp}/kb^2\right)[sin^2(kL) + jsin(kL)cos(kL)] \quad (2)$$

where k is the wave number, L is the longitudinal length of electrodes, b_{min} is the minimum distance between the beam axis and the electrodes, $g_{||}$ and $g_{\perp}$ are longitudinal and transverse geometric factors, and $Z_{ch,||}$ and $Z_{ch,\perp}$ are longitudinal and transverse characteristic impedances of the stripline. The geometric factors and the characteristic impedances are for the full structure containing all electrodes. We note that for a device comprised of two identical electrodes symmetrically placed as in Fig. 1, $Z_{ch,||} = Z_L/2$, where Z_L is the characteristic impedance of a single electrode.

At low frequency the longitudinal shunt impedance is related to the longitudinal beam impedance by [3]

$$R_{sh,||} = ReZ_{||}(k) \times 4, \quad (3)$$

and the transverse shunt impedance is related to the transverse beam impedance by

$$R_{sh,\perp} = ReZ_{\perp}(k) \times 4/k \quad (4)$$

To determine $Z_{ch,||}$ and $Z_{ch,\perp}$ for a given geometry, one needs to solve Laplace's equation in 2 dimensions. For this, we use the 2D POISSON electrostatic code [5]. The characteristic impedance is given by [6]

$$Z_{ch} = \frac{1}{cC}, \quad (5)$$

where c is the velocity of light and C is the capacitance of the stripline structure. For the longitudinal mode, both electrodes have voltage V_p, while for the transverse mode they have voltages of opposite polarity $\pm V_p$. In both cases, the capacitance is related to the stored energy W_e and voltage V_p via

$$C = \frac{2W_e}{V_p^2} \quad (6)$$

Given the magnitude of the voltage V_p, we calculate the stored energy using POISSON and in this manner determine the capacitance and thus the characteristic impedance for each mode.

First, as an illustration, we consider the ideal coaxial transmission line with geometric parameters $b_{min} = 24.1mm$ inner and $b_{max} = 38mm$ outer radius (Fig. 2a). The characteristic impedance determined from the stored energy computed by POISSON and using Eqs. (5 and 6) with specified positive voltage ($V_p = +1Volt$) on inner conductor is $Z_{ch}^{+} = 22.53\Omega$. This agrees with the well-known result, $Z_{ch}^{CXL} = \frac{Z_0}{2\pi} Log(b_{max}/b_{min})$ for the coaxial (CXL) transmission line.

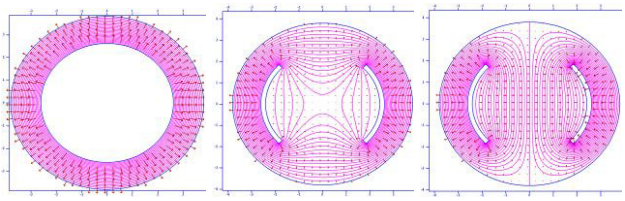
Next, we consider the longitudinal and transverse characteristic impedances for the round stripline geometry shown in Fig. 2b,c. The electrode radius b_{min} and outer radius b_{max} are fixed. The angle subtended by an electrode is varied from $\phi = 10^{\circ}$ to $\phi = 170^{\circ}$. The longitudinal and transverse characteristic impedances of the structure with the two electrodes as a function of the electrode angle are shown in Fig. 3. The longitudinal characteristic impedance tends to 23Ω for $\phi \to 180^{\circ}$, approaching the result for the coaxial transmission line, as it must.

As can be seen from Fig. 3, for electrode angle $\phi \to 180^{\circ}$, the transverse characteristic impedance $Z_{ch,\perp}$ is about a factor of two less than the longitudinal $Z_{ch,||}$. For electrode angle $\phi \to 90^{\circ}$, their difference becomes

*Work supported by DOE contract DE-AC02-98CH10886.
#blednykh@bnl.gov

Copyright © 2013 CC-BY-3.0 and by the respective authors

less but the fact that they are not equal means that a pair of electrodes matched to 25Ω transversally (50Ω single electrode) are mismatched longitudinally ($Z_{ch,||} = 18.2\Omega$) and vice versa.



a) b) c)

Figure 2: a) Coaxial transmission line with inner and outer radii of $b_{min} = 24.1mm$ and $b_{max} = 38mm$ respectively. b) Longitudinal excitation for $\phi = \pi/2$: two electrodes inside the round pipe at equal positive voltages V_p. c) Transverse excitation for $\phi = \pi/2$: two electrodes inside the round pipe at $\pm V_p$. Magenta lines are lines of constant scalar potential. Arrows are proportional to electric field strength.

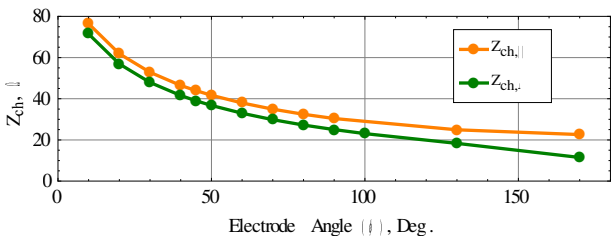


Figure 3: For the structure of Fig. 2b,c, we plot the longitudinal (orange) and transverse (green) characteristic impedances as a function of electrode angle ϕ calculated using the POISSON code.

The geometric factors for a pair of electrodes as a function of the electrode angle ϕ are shown in Fig. 4 (other geometric dimensions fixed). For $\phi \to \pi$, the longitudinal geometric factor $g_{||} \to 1$, while the transverse geometric factor, $g_{\perp} \to 4/\pi$.

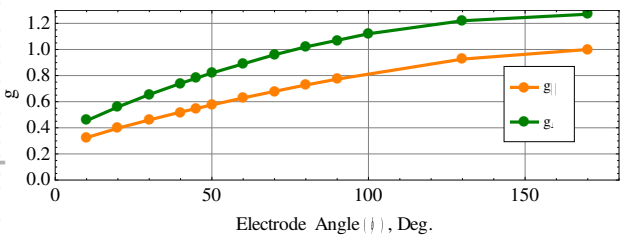


Figure 4: For the structure of Fig. 2b,c, we plot the longitudinal (orange) and transverse (green) geometric factors as a function of electrode angle ϕ calculated using the POISSON code.

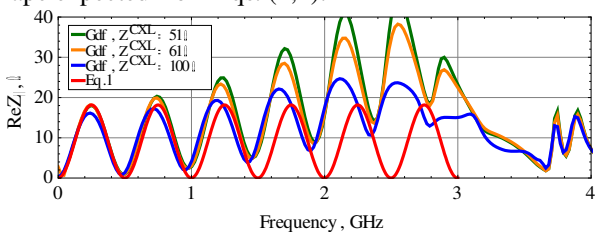
BEAM IMPEDANCES, $Z_{||}(k)$ AND $Z_{\perp}(k)$

The real and imaginary parts of the longitudinal beam impedance at low frequencies are shown in Eq. (1) [1].

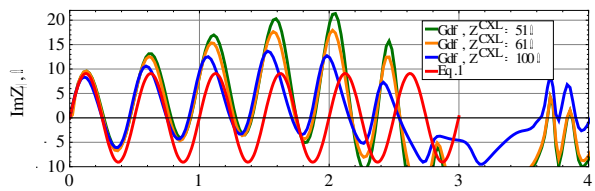
In Figs. 5a and 5b, we compare Eq. (1) with calculated data obtained using the 3D GdfidL electromagnetic simulation code [7] for the stripline geometry with 90° electrode angle, as shown in Fig. 1. The simulated longitudinal geometric factor and longitudinal characteristic impedance are $g_{||} = 0.774$ and $Z_{ch,||} = \frac{Z_L}{2} = 30.5\Omega$ (for two electrodes).

We varied the geometric dimensions of the coaxial feed-thru connectors to obtain three different longitudinal characteristic impedances of the external coaxial line, Z_{ch}^{CXL} =51Ω, 61Ω and 100Ω. This was done in order to check the deviation of the GdfidL calculated longitudinal beam impedance from Eq. (1), when electrodes are matched or mismatched to Z_{ch}^{CXL} of the feed-thru connectors.

First, we consider the characteristic impedance of feed-thru connectors $Z_{ch}^{CXL} = 51\Omega$. In this case, there is a good match to the transverse characteristic impedance ($Z_{ch,\perp}$) of each stripline electrode with 90° angle and a mismatch to the longitudinal characteristic impedance ($Z_L = 2Z_{ch,||} = 61\Omega$) of single electrode for the same angle. From Figs. 5a and 5b, we see that the longitudinal beam impedance (real and imaginary parts) agree well with Eq. (1) at low frequencies. The longitudinal impedance spectrum starts to deviate at high frequencies from the shape expected from Eqs. (1,2).



a)



b)

Figure 5: Real (a) and Imaginary (b) part of the longitudinal impedance for the stripline kicker with two 90° angle electrodes inside. The feed-thru connectors are matched to three different characteristic impedances $Z_{ch}^{CXL} = 51\Omega$ (green curve), $Z_{ch}^{CXL} = 61\Omega$ (orange curve) and $Z_{ch}^{CXL} = 100\Omega$ (blue curve). The longitudinal characteristic impedance of two 90° angle electrodes is $Z_{ch,||} = 30.5\Omega$. The red curves are the results of Eq. (1), with $Z_{ch,||} = 30.5\Omega$ and $g_{||} = 0.774$.

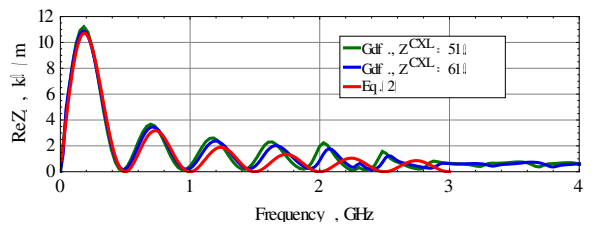
Next, we consider the characteristic impedance of feed-thru connectors to be $Z_{ch}^{CXL} = 61\Omega$. In this case the feed-thru connectors are matched to the longitudinal characteristic impedance of each individual electrode. The difference between the numerical results (orange curves in Figs. 5a and 5b) and the analytic results [Eqs. (1)] is reduced at high frequencies (below 3GHz) since matching is improved, but still there is significant

Copyright © 2013 CC-BY-3.0 and by the respective authors

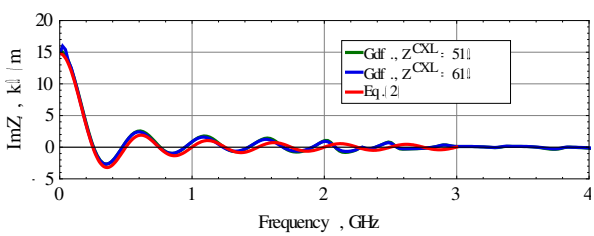
deviation. This can be explained due to gradual increase of the reflection coefficient (S_{11}-parameter) at higher frequencies. The coaxial feedthru connectors and electrode pair are perfectly matched at low frequencies. The reflection of the TEM-mode in the coaxial waveguide is around 10% for considered geometry at low frequencies and 50% at frequency ~2GHz (determined from a GdfidL calculation). Due to larger reflection of TEM-mode from output feed-thru connectors at high frequencies, electromagnetic fields radiate more into the vacuum chamber and the real part of the longitudinal coupling impedance $ReZ_{||}(k)$ deviates from quadratic sinusoidal wave. If the longitudinal characteristic impedance is over-matched ($Z_{ch}^{CXL} = 100\Omega$), then we observe frequency shift and reduction of $Z_{||}(k)$ at low frequencies.

The discussed equations provide a good approximate description of the beam impedance. We found excellent agreement between equation Eq. (1) and numerical calculations at low frequencies, when the electrodes and feed-thru connectors are matched or even slightly mismatched to each other

The real and imaginary parts of the transverse beam impedance are shown in Eq. (2). This equation is compared with GdfidL results for the stripline geometry as shown in Fig. 1. We analysed the effects of two electrodes with an angle of 90° each. The calculated transverse geometric factor and transverse characteristic impedance are $g_\perp = 1.1$ and $Z_{ch,\perp} = 25\Omega$ (for two electrodes). The transverse beam impedance is calculated for two different characteristic impedances of the feed-thru coaxial connectors, $Z_{ch}^{CXL} = 51\Omega$ and $Z_{ch}^{CXL} = 61\Omega$ (Fig. 6a and Fig. 6b).



a)



b)

Figure 6: Real (a) and Imaginary (b) part of the transverse impedance of the stripline kicker with two 90° angle electrodes inside. The feed-thru connector has two different characteristic impedances, $Z_{ch}^{CXL} = 51\Omega$ (green) and $Z_{ch}^{CXL} = 61\Omega$ (blue). The red curves are the result of Eq. (2).

As a result the electrodes are well matched in first case and slightly mismatched in the second. The real and imaginary parts of the transverse beam impedance agree well with Eq. (2) up to 2GHz. The imaginary part of the beam impedance at $\omega \to 0$ is $ImZ_\perp = 15k\Omega/m$. The small mismatch of electrodes with connectors has small effect on the transverse beam impedance.

TRANSVERSE SHUNT IMPEDANCE

The transverse shunt impedance has been calculated via Eq. (4). The real part of the transverse beam impedance of Eq. (2) with simulated transverse geometric factor and the transverse characteristic impedance has been implemented into Eq. (4) (green) and the result is shown at low frequency in Fig. 7. It agrees with $R_{sh,\perp}$ data obtained due to implementing the GdfidL data $ReZ_\perp(k)$ from Fig. 6a in to Eq. (4).

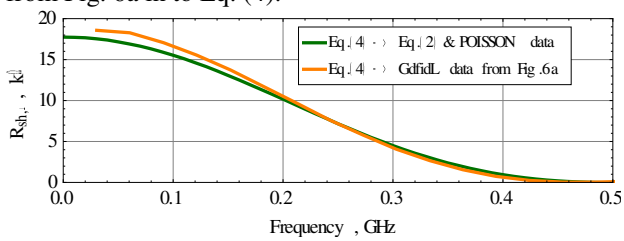


Figure 7: Transverse shunt impedance calculated via Eq. (4). Green curve is $R_{sh,\perp}$ due to Eq. (2) and numerically obtained vertical geometric factor and transverse characteristic impedance. Blue curve is the GdfidL data implemented in to Eq. (4).

SUMMARY

Analytical equations at low frequency for the beam impedances as well as the ratio between $Z(k)_{||,\perp}$ and $R_{sh,||,\perp}$ have been presented. Good agreement is found between the analytical results and 3D GdfidL simulations at low frequencies.

REFERENCES

[1] R. Shafer, IEEE Trans. Nucl. Sci. **NS-32**, 1933 (1985).
[2] G.R. Lambertson, "Dynamic Devices-Pickups and Kickers," in *Physics of Accelerators*, eds. M. Month and M. Dienes, AIP conf Proc**. 153,** 1414 (1987).
[3] D. A. Goldberg and G. R. Lambertson, "Dynamic Devices a Primer on Pickups and Kickers" LBL-31664, Nov. 1991.
[4] K.-Y. Ng, "Impedances of Stripline Beam-Position Monitors," Particle Accelerators, 1988, Vol. 23, pp. 93-102.
[5] J. H. Billen and L. M. Young, Poisson Superfish, LANL.
[6] R. E. Collin, *Field Theory of Guided Waves* (John Wiley & Sons, New York, 1991).
[7] W. Bruns, GdfidL, http://www.gdfidl.de.

Copyright © 2013 CC-BY-3.0 and by the respective authors

LONGITUDINAL WAKEFIELD FOR AN AXISYMMETRIC COLLIMATOR*

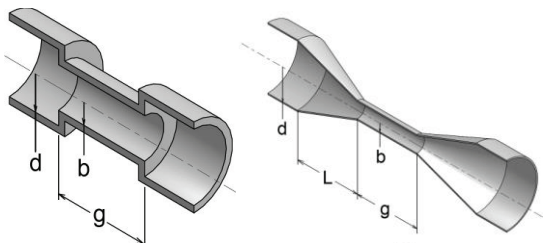
A. Blednykh# and S. Krinsky,
BNL, Photon Science, NY 11973-5000, USA

Abstract

We consider the longitudinal point-charge wakefield, *w(s),* for an axisymmetric collimator having inner radius *b*, outer radius *d*, inner length *g* and taper length *L*. The taper angle α is defined by $\tan\alpha = (d-b)/L$. Using the electromagnetic simulation code ECHO, we explore the dependence of the wakefield on a collimator's geometric parameters over a wide range of profiles: from small-angle tapers to step-function transitions.

INTRODUCTION

In this paper, using the 2-D electromagnetic simulation ECHO code [1,2], we carry out an investigation of the longitudinal short-range wakefield due to an axisymmetric collimator. More detail on this subject can be found in ref. [3].



a) b)

Figure 1: a) Step Collimator. b) Tapered Collimator.

We consider the highly relativistic limit in which a particle traveling at the speed of light *c*, passes through a step-function or tapered collimator illustrated in Figs. 1a,b. We denote: the smaller pipe radius by *b;* the larger radius by *d*; the length of the inner section of the collimator by *g;* and the length of the taper by *L*. The taper angle α is defined by $\tan\alpha = (d-b)/L$. The longitudinal wakefield produced by a point charge is denoted *w(s)*, where *s* is the distance of the test particle behind the driving particle.

Podobedov and Stupakov [4] have noted that the point-charge wakefield for a collimator can be written in the form,

$$w(s;b,d,g,L) = \frac{c\,Z_0}{\pi} log(d/b)\delta(s) + D(s;b,d,g,L), \quad (1)$$

where Z_0 is the impedance of free space. The delta function term corresponds to the result in the optical regime [5]. The causal function *D(s)*, vanishes for *s<0*, and is discontinuous at *s=0*. Since the impedance vanishes at zero frequency, it follows that

$$\int_0^\infty ds\, D(s) = -\frac{cZ_0}{\pi} log(d/b). \quad (2)$$

In this paper, in order to facilitate the illustration of the behavior of the wakefield over a wide range of parameters and for larger *s*, we prefer to introduce the normalized causal function $u(s)$, via

$$w(s;b,d,g,L) = \frac{c\,Z_0}{\pi} log(d/b)[\delta(s) - u(s;b,d,g,L)], \quad (3)$$

where

$$\int_0^\infty ds\, u(s) = 1. \quad (4)$$

Using this normalized function, the ratio of the loss factor k_{loss} to that in the optical regime [5,6] k_{loss}^{opt} is easily expressed. For a Gaussian bunch of rms width σ, this ratio is given by

$$k_{loss}(\sigma)/k_{loss}^{opt}(\sigma) = 1 - \int_0^\infty ds\, u(s) exp(-s^2/4\sigma^2), \quad (5)$$

where $k_{loss}^{opt}(\sigma) = \left(cZ_0/2\pi^{3/2}\sigma\right) log(d/b)$.

For a small-angle tapered collimator *(sat)*, it is shown in ref. [4] that,

$$D^{sat}(0) \cong -\frac{cZ_0}{\pi b\alpha}, \quad (6)$$

and for a step collimator *(st)*, it follows from the work of Okamoto, Jiang and Gluckstern [7] that

$$D^{st}(0) \cong -\frac{0.6\,cZ_0}{\pi b(\pi/2)}. \quad (7)$$

We now note that to within $\pm 10\%$ accuracy,

$$\frac{1}{\pi b} \cong \frac{log(d/b)}{d}, \quad (for\ 1.5 \leqslant d/b \leqslant 6). \quad (8)$$

In this paper, we shall restrict our attention to collimators with parameters within the range $1.5 \leqslant d/b \leqslant 6$. In this case, Eqs. (6,8) imply that for small-angle tapers,

$$u^{sat}(0) \cong \frac{\pi}{d\alpha}, \quad (9)$$

and Eqs. (7,8) show that for a step collimator,

$$u^{st}(0) \cong \frac{0.6\,\pi}{d(\pi/2)}. \quad (10)$$

The short-range wakefield depends predominantly on the two length scales $b\alpha$ and $d\alpha$. In illustrating its behavior, one can plot the wakefield versus the variable $s/b\alpha$ or $s/d\alpha$. In this paper, in order to illustrate more clearly the behavior of the wakefield at longer distances, we prefer to utilize the variable $s/d\alpha$.

For the short-range wakefield $(s/d\alpha \lesssim 0.3)$, our numerical calculations demonstrate that the dependence on g is very weak and they support the approximate validity of the scaling relation,

$$w(s;b,d,g,L) \cong \frac{c\,Z_0}{\pi} log\left(\frac{d}{b}\right)\left[\delta(s) - \frac{1}{d\alpha} f\left(\frac{s}{d\alpha}, \frac{b}{d}\right)\right]. \quad (11)$$

With the wakefield approximated by Eq. (11), it follows from Eq. (5) that the departure of the loss factor from the optical approximation for short bunches $(\sigma/d\alpha \lesssim 0.15)$ can be estimated by

$$k_{loss}(\sigma)/k_{loss}^{opt}(\sigma) \cong 1 - \sqrt{\pi} f\left(0, \frac{b}{d}\right)\frac{\sigma}{d\alpha}. \quad (12)$$

with $f\left(0, \frac{b}{d}\right)$ varying from ~3 for small-angle tapers to ~1.8 for step collimators. Eq. (12) is a more accurate expression for the loss factor than the similar relation given in Eq. (12.26) of ref. [8].

*Work supported by DOE contract DE-AC02-98CH10886.
#blednykh@bnl.gov

Copyright © 2013 CC-BY-3.0 and by the respective authors

DIMENSIONAL ANALYSIS

We motivate our discussion by using dimensional analysis and the longitudinal scaling relation introduced in ref. [9]. From dimensional analysis, we can write,

$$u(s;b,d,g,L)=\frac{1}{d}u_1\left(\frac{s}{d};\frac{b}{d},\frac{g}{d},\frac{L}{d}\right). \quad (13)$$

In the special case of a step collimator, for which L=0,

$$u^{st}(s;b,d,g)=\frac{1}{d}u_1^{st}\left(\frac{s}{d};\frac{b}{d},\frac{g}{d},0\right). \quad (14)$$

We have determined that when g is not too the wakefield depends very weakly on g, so we can simplify Eq. (14) to read,

$$u^{st}(s;b,d,g)\cong\frac{1}{d}u_2^{st}\left(\frac{s}{d};\frac{b}{d}\right). \quad (15)$$

The corresponding weak dependence of the impedance of a step collimator on g was found in the analysis of Ref. [7].

Our ECHO calculations have uncovered the surprising result that in the parameter range we are considering [see Eq. (8)], and for $s/d\gtrsim 0.5$, the dependence on b/d is very weak (see Fig. 2), so to a reasonable approximation,

$$u^{st}(s;b,d,g)\cong\frac{1}{d}u_3^{st}\left(\frac{s}{d}\right), \quad (16)$$

Clearly, in Eq. (13), we could have chosen to set the length scale with any of the lengths in the problem. Eq. (16) provides one motivation for our choice to single out the dependence on the larger radius d.

For a small-angle tapered collimator, it has been shown [9] that an important longitudinal scaling relation holds for the short-range wakefield,

$$w^{sat}(s;b,d,g,L)=\lambda\, w^{sat}\left(s\lambda;b,d,\frac{g}{\lambda},\frac{L}{\lambda}\right), \quad (17)$$

where λ is a dimensionless parameter. The scaling relation (17) holds trivially for the delta function term in Eq. (3). It therefore follows from Eqs. (13) and (17) that

$$u_1^{sat}\left(\frac{s}{d};\frac{b}{d},\frac{g}{d},\frac{L}{d}\right)=\lambda\, u_1^{sat}\left(\frac{s\lambda}{d};\frac{b}{d},\frac{g}{\lambda d},\frac{L}{\lambda d}\right). \quad (18)$$

We now choose $\lambda=L/(d-b)$, obtaining

$$u_1^{sat}\left(\frac{s}{d};\frac{b}{d},\frac{g}{d},\frac{L}{d}\right)=\frac{L}{d-b}\,u_1^{sat}\left(\frac{sL}{d(d-b)};\frac{b}{d},\frac{g(d-b)}{Ld},\frac{d-b}{d}\right) \quad (19)$$

and hence,

$$u^{sat}(s;b,d,g,L)=\frac{L}{d(d-b)}u_2^{sat}\left(\frac{sL}{d(d-b)};\frac{b}{d},\frac{g(d-b)}{Ld}\right). \quad (20)$$

Recall that the taper angle α is defined by $\tan\alpha=(d-b)/L$. We can rewrite Eq. (20) in the form

$$u^{sat}(s;b,d,g,L)=\frac{1}{d\tan\alpha}u_2^{sat}\left(\frac{s}{d\tan\alpha};\frac{b}{d},\frac{g\tan\alpha}{d}\right). \quad (21)$$

Based on the ECHO calculations, we have found that the dependence on g is weak for $s/d\alpha\lesssim 0.3$. Neglecting the dependence on g, and replacing $\tan\alpha$ by the angle α in the first argument of u_2^{sat}, we obtain the approximate scaling relation

$$u^{sat}(s;b,d,g,L)\cong\frac{1}{d\alpha}u_2^{sat}\left(\frac{s}{d\alpha};\frac{b}{d}\right). \quad (22)$$

Let us note that Eq. (22), which we have just introduced for the tapered collimator, has a form consistent with Eq. (15) found for the step collimator ($\alpha=\pi/2$). Therefore, we can hope that Eq. (15) will have an approximate validity for large collimator angles. Our numerical calculations show that replacing the tangent by the angle extends the range of usefulness of Eq. (15). In the context of the derivation of the scaling relation of Ref. [9], replacing $\tan\alpha$ by the angle α corresponds to moving out of the region of validity of the paraxial approximation, which is only applicable for a smooth, slowly-varying wall. Once the taper angle approaches $\pi/2$, the scaling is broken and the function f begins to depend also on the angle α itself. The special case of the wakefield of the step collimator ($\alpha=\pi/2$) turns out to exhibit very interesting behavior deserving individual attention.

APROXIMATE CALCULATION OF THE POINT-CHARGE WAKEFIELD

Using ECHO, we cannot directly calculate the point-charge wakefield. In Ref. [4], an approximate method for determining the point-charge wake has been introduced. Following this approach, we use ECHO to calculate the wakefield $W^{\sigma_0}(s)$ produced by a Gaussian bunch of rms width σ_0. We choose σ_0 small enough so that the wake is resistive. We then approximate Eq. (3) by

$$W^{\sigma_0}(s;b,d,g,L)=\frac{cZ_0}{\pi}log(d/b)\left[\frac{1}{\sqrt{2\pi}\sigma_0}exp\left(\frac{-s^2}{2\sigma_0^2}\right)-U^{\sigma_0}(s;b,d,g,L)\right]. \quad (23)$$

For $s\gg\sigma_0$, the point-charge wake is well-approximated by Eq. (23), hence

$$u(s;b,d,g,L)\cong U^{\sigma_0}(s;b,d,g,L)\qquad (s\gg\sigma_0). \quad (24)$$

In this manner, we approximate the scaling function introduced in Eq. (11) by

$$f\cong d\alpha\cdot U^{\sigma_0}(s;b,d,g,L)\qquad (s\gg\sigma_0). \quad (25)$$

STEP COLLIMATORS

In Fig. 2, we plot $f\cong d\alpha U^{\sigma_0}$ versus $s/d\alpha$ for step collimators with b=3mm and d=6mm (black), 12mm (green) and 18mm (orange), and with b=6mm and d=12mm (red). The rms length of the charge distribution $\sigma_0=50\mu m$ is chosen to be small enough to assure that the wake field is resistive. The close agreement of the wakefields for these different parameters is striking. These results clearly show that the dependence of the scaling function f on the ratio b/d is surprisingly weak, as noted in Eq. (16).

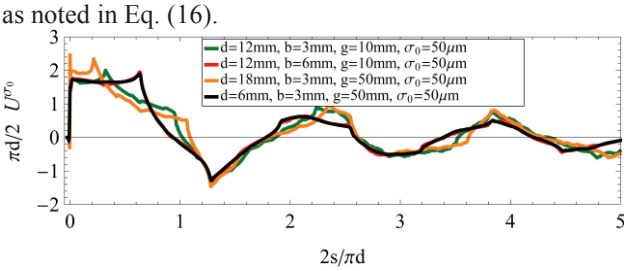


Figure 2: For step collimator, we plot $(\pi d/2)U^{\sigma_0}(s;b,d,g)$ versus $2s/\pi d$ for σ_0=50μm and: d=12mm, b=3mm, g=10mm (green); d=12mm, b=6mm, g=10mm (red); d=18mm, b=3mm,g=50mm (orange); d=6mm, b=3mm, g=50mm (black).

TAPERED COLLIMATOR

We note that for $s/d\alpha\lesssim 0.3$, f is quite independent of g. In Fig. 3, we plot the function $f\cong d\alpha U^{\sigma_0}$ versus $s/d\alpha$ for collimators with d=6mm and b=3mm. The cases with taper length $L\gtrsim 6.25mm$ (red, blue, orange) satisfy the

Copyright © 2013 CC-BY-3.0 and by the respective authors

longitudinal scaling (17) very accurately. The longitudinal scaling is seen to be broken when $L \lesssim 3.125mm$. The accuracy of the approximation of Eq. (11) for the cases of L=3.12mm (aqua) and L=1.56mm (green) has been significantly improved by the replacement of $\tan\alpha$ by the angle α as suggested following Eq. (21). Even in the case of the step collimator (black), Eq. (11) provides a rough approximation for small s. In Fig. 4, we plot the function $f \cong d\alpha U^{\sigma_0}$ versus $s/d\alpha$ for collimators with d=12mm and b=3mm. The cases with taper length $L \gtrsim 12.5mm$ (pink, black, orange) satisfy the longitudinal scaling (17) very accurately. The longitudinal scaling is seen to be broken for the cases of $L \lesssim 6.25mm$ (red, aqua, green). In Fig. 5, we plot the function $f \cong d\alpha U^{\sigma_0}$ versus $s/d\alpha$ for collimators with d=6mm, b=3mm, L=25mm (red); d=12mm, b=3mm, L=50mm (black); and d=18mm, b=3mm, L=50mm (green) for values of L sufficiently large to assure longitudinal scaling (17) is accurately satisfied. We see that for $s/d\alpha \lesssim 0.3$, there is approximate agreement between the curves corresponding to different values of b/d, illustrating the weak dependence on the ratio b/d in the approximate scaling relation (11).

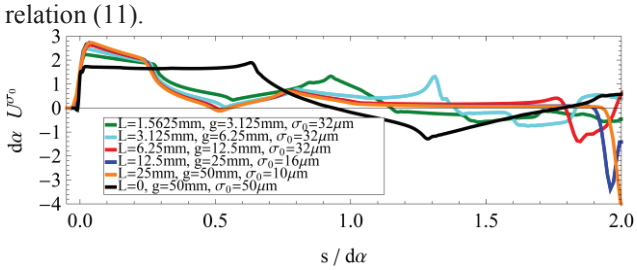


Figure 3: For tapered collimators, we plot $d\alpha U^{\sigma_0}$ versus $s/d\alpha$ for **d=6mm, b=3mm** and: g=3.12mm, L=1.56mm, σ_0=32μm (green); g=6.25mm, L=3.12mm, σ_0=32μm (aqua); g=12.5mm, L=6.25, σ_0=32μm (red); g=25mm, L=12.5mm, σ_0=16μm (blue); g=50mm, L=25mm, σ_0=8μm (orange). The black curve corresponds to a step collimator. We see that longitudinal scaling is only accurately satisfied for $L \gtrsim 6.25mm$.

SUMMARY

For a tapered collimator, we have shown that the short-range wakefield, for $s/d\alpha \lesssim 0.3$ and $\alpha \lesssim \pi/3$, is well-approximated by Eq. (11). Having factored out the $log(d/b)$ term, we have found that in the range $1.5 \leqslant \frac{d}{b} \leqslant 6$ of Eq. (8), the scaling function f depends only weakly on b/d. For small taper angle, $\alpha \lesssim \pi/4$, the ECHO calculations confirm that the longitudinal scaling [9] relation (17) is accurately satisfied. The approximation of Eq. (11) properly satisfies Eq. (17) for small taper angle. The longitudinal scaling is broken for angles large compared with $\pi/4$. We have found that using the taper angle α in Eq. (11), rather than its tangent, allows Eq. (11) to remain a good approximation for larger angles ($\alpha \sim \pi/3$), beyond the regime where Eq. (17) is satisfied. As the taper angle increases further, Eq. (11) becomes less accurate, and the function f begins to depend on the angle α itself.

The case of a step collimator ($\alpha = \pi/2$) is quite interesting. For the parameters that we have considered, its wakefield is well-approximated by,

$$w^{step}(s;b,d,g,L) \cong \frac{c\,Z_0}{\pi} log\left(\frac{d}{b}\right)\left[\delta(s) - \frac{1}{d}F^{step}\left(\frac{s}{d},\frac{b}{d}\right)\right], \quad (26)$$

where the dependence on b/d is very weak for s/d > 0.5 (see Fig. 2). The very weak dependence of F^{step} on b/d is quite remarkable, and we did not anticipate this simple behavior.

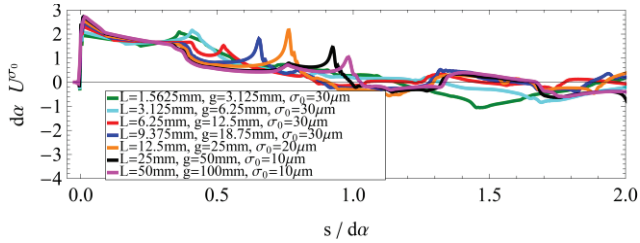


Figure 4: For tapered collimators, we plot $d\alpha U^{\sigma_0}$ versus $s/d\alpha$ for **d=12mm and b=3mm** and: g=3.12mm, L=1.56mm, σ_0=30μm (green); g=6.25mm, L=3.12mm, σ_0=30μm (aqua); g=12.5mm, L=6.25, σ_0=30μm (red); g=18.8mm, L=9.4mm, σ_0=30μm (blue); g=25mm, L=12.5mm, σ_0=20μm (orange); d=12mm, g=50mm, L=25mm, σ_0=10μm (black); g=100mm, L=50mm, σ_0=10μm (purple).

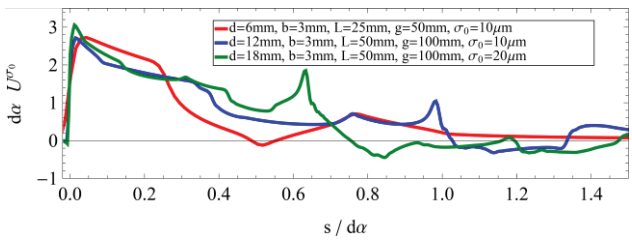


Figure 5: For small-angle tapered collimators satisfying longitudinal scaling, we plot $d\alpha U^{\sigma_0}$ versus $s/d\alpha$ for: d=6mm, b=3mm, L=25mm (red); d=12mm, b=3mm, L=50mm (black); and d=18mm, b=3mm, L=50mm (green).

REFERENCES

[1] I. Zagorodnov and T. Weiland, Phys. Rev. ST-AB 8, 042001 (2005).
[2] I. Zagorodnov, Phys. Rev. ST-AB 9, 102002 (2006).
[3] A. Blednykh and S. Krinsky, Phys. Rev. ST-AB 15, 054405 (2012).
[4] B. Podobedov and G. Stupakov, Phys. Rev. ST-AB 16, 024401 (2013).
[5] G. Stupakov, K.L.F. Bane and I Zagorodnov, Phys. Rev. ST-AB 10, 054401 (2007).
[6] S. Heifets and S. Kheifets, Rev. Mod. Phys. 63, 631 (1991).
[7] H. Okamoto, S. Jiang, R. Gluckstern, Phys. Rev. E, V50,#2 (1994).
[8] B. Zotter, S. Kheifets, Impedances and Wakes in High-Energy Particle Accelerators (World Scientific Publishing Co., 1997).
[9] G. Stupakov, K.L.F. Bane and I. Zagorodnov, Phys. Rev. ST-AB 14, 014402 (2011).

Copyright © 2013 CC-BY-3.0 and by the respective authors

WAKE FIELDS DUE TO WALL ROUGHNESS FOR REALISTIC SURFACES*

A.V. Fedotov#, I. Pinayev , BNL, Upton, NY 11973, USA
A. Novokhatski, SLAC National Accelerator Laboratory, Menlo Park, CA 94025, USA

Abstract

Wake fields due to the wall roughness of the vacuum chamber can catch up to the bunch causing energy spread and emittance growth. Several theoretical models were developed in the past which showed rather different importance of this effect. Some models suggest that the wall roughness effect can be minimized if the vacuum chamber surface is characterized by a large aspect ratio of the surface roughness (characteristic length to the height of the surface bumps). To explore these effects several surfaces were measured and direct numerical simulations were performed for such realistic surfaces. The studies were done both for the long bunches to provide estimates of this effect for parameters of the eRHIC project, as well as for very short bunches to explore parameter space of the wall roughness experiment proposed at BNL's ATF.

INTRODUCTION

This work was originally motivated by beam dynamics studies for the eRHIC project [1-3], which is a proposed upgrade of the Relativistic Heavy Ion Collider (RHIC). The present eRHIC design is based on the multi-pass electron beam transport in existing tunnel of RHIC. As a result of a high peak current and a very long beam transport, consideration of various collective beam dynamics effects becomes important [2, 3]. The contribution of the wall roughness to the coupling impedance (wake potential) can become significant, especially when the size of the vacuum chamber is small and length of the electron bunch is short.

Some models indicate that the wall roughness effects can be minimized if the vacuum chamber surface is characterized by a large aspect ratio of the surface roughness (characteristic length to the height of the surface bumps). We attempted to explore these effects for realistic surfaces by means of the direct numerical simulations. Several surfaces were measured, including extruded aluminium, for which such roughness aspect ratio is expected to be very large. The measured surface data was then used as an input parameter in electrodynamics code NOVO [4] to simulate the wake field.

Studies were done both for the long bunches (for the eRHIC parameters [2-3]) with the bunch length longer than a typical correlation length of the rough surface and for short bunches with bunch length much smaller than the correlation length of the surface roughness. In this paper, only results for the case of the short bunches are presented, as an illustrative example of our studies.

*Work supported by the US Department of Energy under contract No. DE-AC02-98CH10886 and DE-AC02-76SF00515.
#fedotov@bnl.gov

WALL ROUGHNESS

An effect of the wall roughness was first estimated based on the impedance of small protrusions of different configurations and orientations in Ref. [5]. Such an "inductive" model can lead to a very strict requirement on the surface polishing. The longitudinal wake potential in this model scales as h/b, where h is the height of the protrusion and b is the radius of the beam pipe.

Another model for the wall roughness was introduced in Refs. [6-7]. In this model the presence of roughness is equivalent to a pipe with a thin dielectric layer or periodic corrugation on the smooth wall surface. This model is typically referred to as the "dielectric" or "resonator" model. In the "resonator" model the coupling impedance also has a resistive part. A detailed comparison of the "resonator" and "inductive" models was given in [7]. The "resonator" model becomes invalid when the correlation length (or period of corrugation) is significantly larger than the height of the protrusion. This happens to be the case for realistic wall surfaces [8] and especially for the surfaces produced with extrusions.

The length of the protrusions along the surface (referred to as the "correlation length" l_c) was taken into account in the model developed in Refs. [8-9], which reduced the coupling impedance significantly for typical surfaces with the large correlation length, resulting in the scaling of the wake potential as $h \cdot h/(b \cdot l_c)$. A comparison of such model with the "inductive" model was given in Ref. [10].

In the eRHIC design, we relied on a significant reduction of the wall roughness effects due to the large aspect ratio of the wall roughness by choosing extruded aluminium vacuum chamber. Measurements of several surfaces were performed to allow systematic study of wake field dependences on the height and length of the roughness. In addition, rather than using measured surface data in approximate models for the estimates, we attempted to study wake fields directly, using numerical simulations with the code NOVO [4].

MEASURED SURFACES

In this paper, we limit our discussion to three measured surfaces: 1) "surface-1": sample of an extruded aluminium surface from the NSLS-II vacuum chamber; 2) "surface-2": rough aluminium surface without extrusions; 3) "surface-3": extruded aluminium surface from the superconducting undulator provided by ANL [11].

Copyright © 2013 CC-BY-3.0 and by the respective authors

NUMERICAL SIMULATIONS

Numerical calculation of wake fields due to real surface roughness is extremely demanding task. For this purpose, we used computer code NOVO which was specifically developed to handle calculation of wakes for very short bunches in very long accelerator structures. For solving Maxwell's equations in time domain, the NOVO code uses finite-difference method with improved characteristic of the dispersion curve in the region of minimum critical wavelength [4]. This code was used before to study effects of wall roughness for artificially created surfaces [6-7]. Here we performed simulations of wake fields with real measured surface data.

Although measured surface maps are three dimensional, the NOVO code is a 2-D code. For each numeric simulation, we took a single 1-D slice from the measured surface. Based on such a slice, the code generates azimuthally symmetric protrusions. The net effect of such 2-D simulation is that magnitude of the wake is somewhat over estimated compared to the real structure in 3-D [12]. Therefore, such 2-D simulations can be used for a conservative estimate.

The primary goal of our studies was to study wakes resulting from real surfaces produced with an extrusion technique, and thus very long correlation length. In addition, we studied dependences on the correlation length and height of the surface bumps; as well as different beam distribution from Gaussian to a more uniform bunch profiles. Due to a limited space in this paper, only few results for the case of bunches with a short edge are presented. Shown results are for the bunches with the flat centre region of 0.3 mm and bunch edges of 0.03 mm rms.

EXAMPLES AND RESULTS

Figure 1 shows 3-D measurement of extruded aluminium "surface-1".

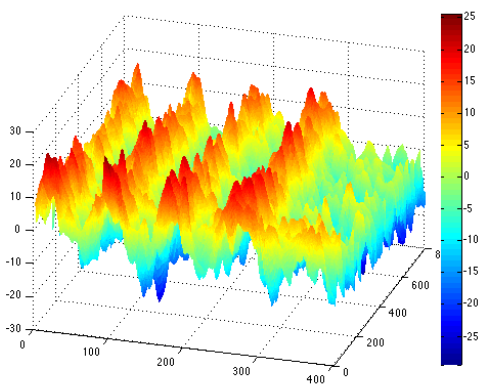


Figure 1: Measurement of "surface-1". Extrusions are along the mountain ridges (red). Vertical axis in μm; horizontal axes in pixels.

Due to a very large height of the roughness, resulting wake potential for "surface-1" is also large. Figure 2 shows a 1-D slice from the surface in Fig. 1 used in simulations. Figure 3 shows the bunch profile, the resulting wake potential and the loss factor.

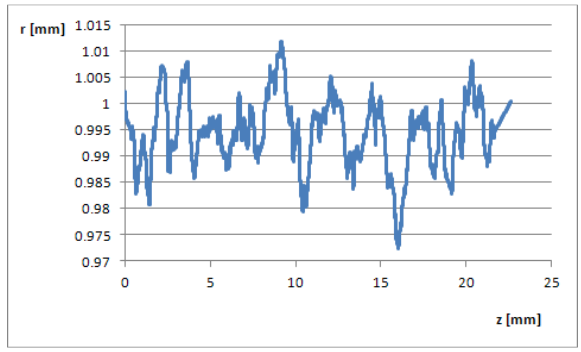


Figure 2: Slice from measured "surface-1" along one of the "mountain ridges" (along extrusion, beam direction z) added to the beam pipe radius of r=1 mm.

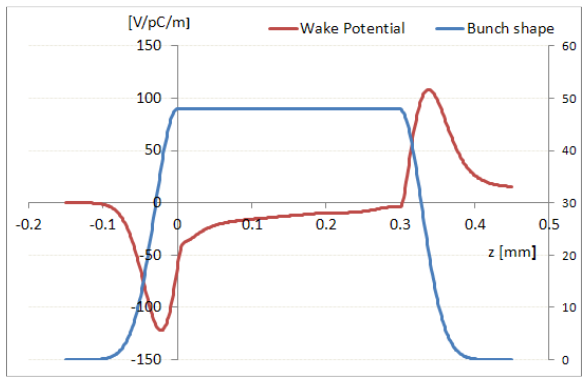


Figure 3: Blue: bunch profile; red: wake potential for "surface-1", radius r=1mm. Loss factor k=16 V/pC/m.

Simulations using "surface-1" data but with the characteristic length l_c artificially scaled by some factor showed that energy spread scales as $1/l_c$, as suggested in [8-9]. However, we did not observe expected h^2 dependence when the height h of the surface was also scaled by a factor. A possible scaling (more studies are needed) could be similar to $h \cdot g/(b \cdot l_c)$, where g is some additional surface parameter, describing the characteristic distance between the protrusions. For comparison, one obtains such $h \cdot g/(b \cdot l_c)$ dependence for a periodic structure with the depth h, gap size g and period l_c.

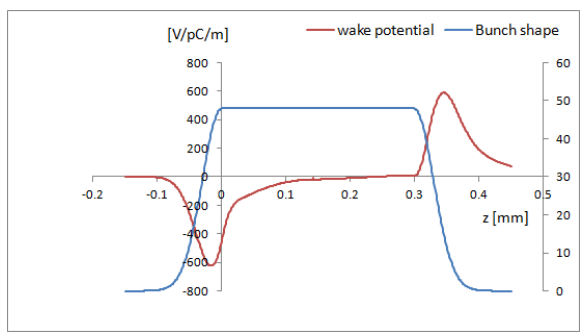


Figure 4: Blue: bunch profile; red: wake potential for "surface-1" with the correlation length 4 times smaller than in Figs. 2-3, r=1mm. Loss factor k=64 V/pC/m.

Copyright © 2013 CC-BY-3.0 and by the respective authors

As an example, Figure 4 shows resulting wake potential for the "surface-1" with the longitudinal structure of the surface in Fig. 1 compressed by a factor of four.

In further studies, a small-gap extruded aluminium vacuum chamber with a very smooth surface (Fig. 5), without applying possible polishing techniques, was provided by ANL [11]. The calculated wake potential and loss factor for such surface are shown in Fig. 6.

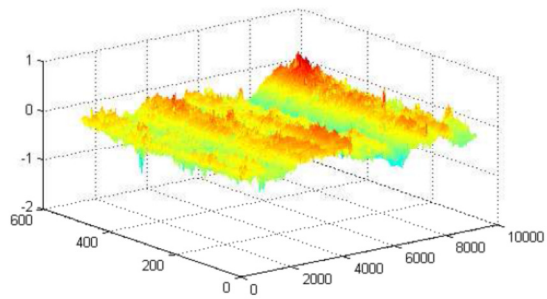


Figure 5: Measured surface for extruded aluminium "surface-3" provided by ANL. Vertical axis in μm; horizontal axes in pixels.

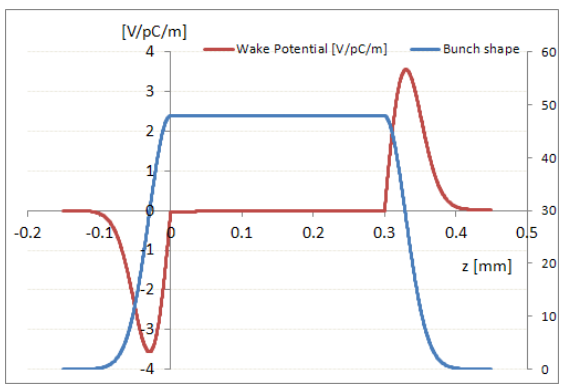


Figure 6: Blue: bunch profile; red: wake potential for "surface-3", r=1mm. Loss factor k=0.05 V/pC/m.

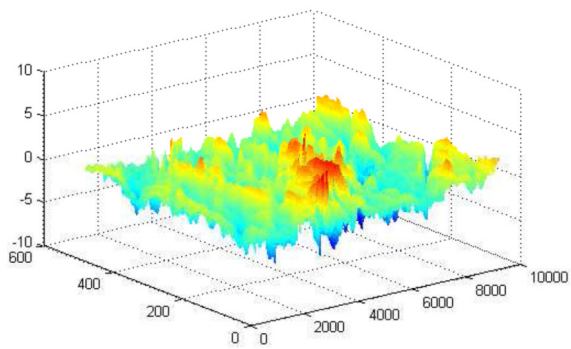


Figure 7: Measurement for aluminium surface without extrusions ("surface-2"). Vertical scale in μm.

We also studied wake potential for several aluminium surfaces without extrusions. Although these surfaces did not have large correlations lengths the height of the roughness bumps was not as large as for "surface-1". As a result, computed wake potential was of the same order as for "surface-1" with the extrusions, as shown in Figs. 7-8.

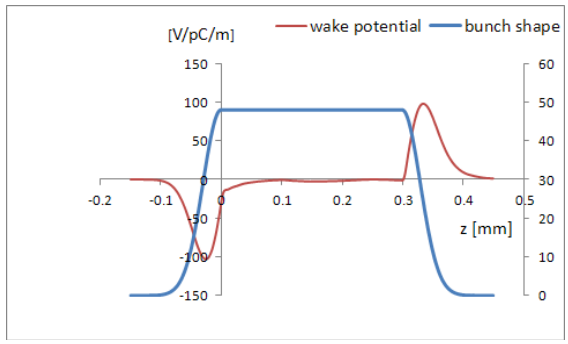


Figure 8: Blue: bunch profile; red: wake potential for "surface-2", r=1mm. Loss factor k=4 V/pC/m.

SUMMARY

In these studies we simulated wake potentials due to a wall roughness using real measured surface data. Some dependences on the correlation length and height of the surface bumps were examined. Several examples from our studies are reported in this paper.

Our simulations confirmed that the effect of the wall roughness can be strongly suppressed with the smooth extruded surfaces like the "surface-3". Simulation of wakes for the eRHIC parameters (not presented in this paper) showed that such a surface would be satisfactory for the eRHIC design.

ACKNOWLEDGMENT

We are indebted to Peter Takacs from the Instrumentation Division of BNL for surface measurements used in these studies. We would also like to thank I. Ben-Zvi, V. Litvinenko, E. Trakhtenberg and V. Yakimenko for help and useful discussions.

REFERENCES

[1] V. Ptitsyn et al., Proc. of IPAC'11 (San Sebastian, Spain, 2011), p. 3726, THPZ019.
[2] A. Fedotov and D. Kayran, Proc. of ERL2011 (Tsukuba, Japan, 2011), WG2014, p.64.
[3] A. Fedotov et al., Proc. of IPAC'12 (New Orleans, USA, 2012), WEPPR017, p. 2976.
[4] A. Novokhatski, "The computer code NOVO for the calculation of wake potentials of the very short ultra-relativistic bunches", SLAC-PUB-11556 (2005).
[5] K. Bane et al., Proc. of PAC97, p. 1738 (1997).
[6] A. Novokhatski and A. Mosnier, Proc. of PAC97, p. 1661; A. Novokhatski, M. Timm, T. Weiland, Proc. of ICAP'98, DESY Report TESLA 99-17.
[7] K. Bane and A. Novokhatski, SLAC-AP-117 (1999).
[8] G. Stupakov, Phys. Rev. ST AB 2, 060701 (1999).
[9] G. Stupakov, Phys. Rev. ST AB 1, 064401 (1998).
[10] K. Bane and G. Stupakov, SLAC-PUB 8023 (1998).
[11] Sample of extruded aluminium "surface-3" was provided by Emil Trakhtenberg from ANL.
[12] A. Novokhatski, M. Timm, T. Weiland, Proc. of PAC'99 (New York, NY, 1999), p. 2879.

Copyright © 2013 CC-BY-3.0 and by the respective authors

CHANGES IN ELECTRON CLOUD DENSITY WITH BEAM CONDITIONING AT CESRTA*

J.P. Sikora†, J.A. Crittenden, D.O. Duggins, Y. Li, X. Liu, CLASSE, Ithaca, New York 14853 USA

Abstract

We compare measurements of electron cloud (EC) buildup in uncoated and TiN-coated aluminum vacuum chambers as a function of integrated beam dose up to 1140 amp-hours. The EC density in newly installed bare aluminum chambers increases with beam dose, while the EC density in the TiN-coated chambers decreases with dose under the same beam conditions. Several techniques are used to monitor EC buildup. These include shielded pickups that measure the flux of cloud electrons onto the beam-pipe wall, and a TE wave resonance technique that measures the EC density within the volume of the beam-pipe. These measurements were made at the Cornell Electron Storage Ring, which has been reconfigured as a test accelerator CESRTA, providing positron and electron beams with energies ranging from 2 GeV to 5 GeV and a variety of bunch train configurations.

INTRODUCTION

New chambers were installed at three locations in the Cornell Electron Storage Ring Test Accelerator (CESRTA) in August 2012 as shown in Fig. 1. We have previously reported on the effects of beam conditioning measured immediately after chamber installation and then again after a significant beam dose of up to 1140 amp-hours [1]. Data with beam dose that is between these two extremes is presented here in order to estimate the dose required to obtain this conditioning. Table 1 shows the number of amp-hours for each beam. The chambers in L3 were let up to atmosphere as part of a separate project in January 2013, but the chambers at 15W and 15E have been under vacuum throughout this period. The table shows two values for the beam dose in April 2013 to reflect this.

Using the TE wave technique, data was collected in the TiN and bare aluminum chambers in L3 as well as the bare aluminum chamber at 15E. The raw data is in the form of phase modulation sideband amplitudes from which the peak electron cloud (EC) density can be calculated [2, 3]. The 10-bunch TE wave data taken in this study use 14 ns spaced bunches.

Shielded pickups (SPU) collect data from the TiN chamber at 15W and the bare aluminum chamber at 15E. This data is in the form of an oscilloscope trace as the SPU samples the flux of cloud electrons onto the vacuum surface [4]. For the purpose of plotting, the averaged scope trace is integrated to obtain the charge into the 50 Ω scope input for each turn (including the preamplifier voltage gain of 100). The data presented here is from two bunches of equal charge spaced by 14 ns. A turn at CESRTA is 2.5 μs and data is recorded with a 100 ns span, which is enough time to capture the non-zero signal from two bunches.

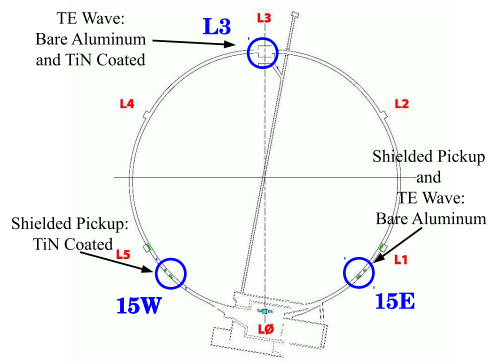


Figure 1: This sketch of the CESRTA storage ring shows the location of detectors used in this study: SPU in a chamber with TiN coating at 15W; SPU and TE wave measurements in the same aluminum chamber at 15E; TE wave measurements in the grooved TiN and bare aluminum chambers of L3.

Table 1: Beam Dose After Chamber Installation

Date (mm/dd/yy)	e- Amp-Hr	e+ Amp-Hr
08/22/12:	0.0068	0.028
08/23/12:	0.411	0.140
10/10/12:	167.9	166.2
11/19/12:	305.6	305.6
12/13/12:	306.0	308.0
(04/17/13):	(251.6)	(269.4)*
04/17/13:	558.8	579.7

*Since L3 at atmosphere during January 2013

CONDITIONING OF TITANIUM NITRIDE

There are two TiN-coated chambers in this study: the grooved chamber at L3 where there is TE wave data and the 15W chamber with SPU data. Figure 2 gives examples of the recorded 2-bunch SPU data at 8 mA/bunch. The signal from the first bunch peaks before 20 ns and is mostly composed of photo-electrons produced in the empty chamber. The larger second bunch signal at about 30 ns includes

*This work is supported by the US National Science Foundation PHY-0734867, PHY-1002467 and the US Department of Energy DE-FC02-08ER41538, DE-SC0006505.

† jps13@cornell.edu

Copyright © 2013 CC-BY-3.0 and by the respective authors

photo-electrons, but is dominated by the cloud electrons produced by the first bunch that are accelerated into the detector by the second bunch.

As a guide for interpretation of the SPU signals, simulations with ECLOUD [5] have shown that an increase in both the first and second bunch signal generally indicate an increase in the quantum efficiency for producing photoelectrons. Changes in the second bunch signal for the same first bunch signal generally indicate a change in the secondary emission coefficient. The data from April 2013 of Fig. 2 suggest a reduction in quantum efficiency with extensive conditioning, since there is a reduction in both the first and second bunch signals. The very early conditioning from August 22-23, 2012 (0.5 amp-hours) on the other hand appears to have an unchanged first bunch signal, while the second bunch signal is reduced by ten percent or so.

The integral of traces such as those shown in Fig. 2 become data points of Fig. 3 giving the SPU signal versus total beam current. The 2-bunch SPU data from the TiN chamber of Fig. 3 shows a noticable reduction in the SPU signal between the first beam in the storage ring on August 22nd and measurements taken the following day. Records also show that the vacuum improved under the same conditions from 100 nT to about 30 nT with a total beam dose of 0.551 amp-hours. The later measurements show small progressive reductions in the SPU signal with beam dose.

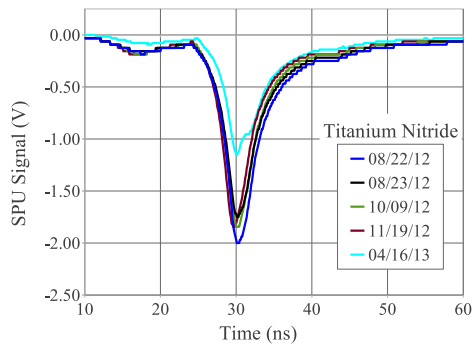


Figure 2: These plots are part of the 2-bunch SPU data that was taken in the TiN-coated chamber at 15W with 16 mA total positron current (8 mA/bunch = 1.28×10^{11} positrons/bunch).

The 10-bunch TE wave data from the L3 grooved TiN chamber in Fig. 4 is somewhat different. There is a step change in the EC density between the August 2012 data and all of the remaining measurements. The EC density measurement in October at 334 amp-hours is only slightly higher than the remaining measurements. This chamber was let up to atmosphere during maintenance in January 2013, so the April 2013 data in L3 corresponds to 521 amp-hours for that chamber. The TiN chamber at 15W (Fig. 3) had a total of 1140 amp-hours.

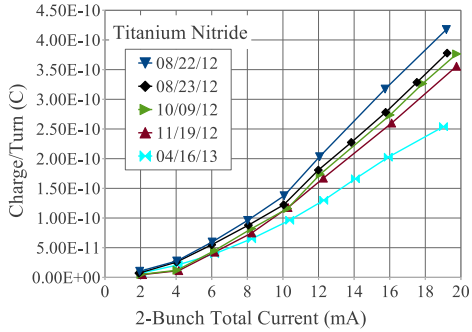


Figure 3: 2-bunch SPU data from the TiN-coated chamber at 15W (see Fig. 2) is integrated to obtain charge/turn. The data shows monotonic conditioning with beam dose. This includes the earliest conditioning with less than 0.5 amp-hours.

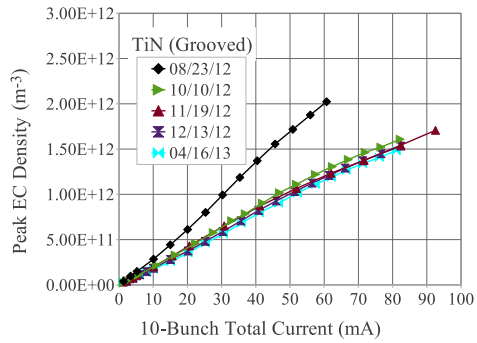


Figure 4: TE wave data with ten bunches from the grooved TiN-coated chamber at L3.

CONDITIONING OF BARE ALUMINUM

There are two bare aluminum chambers in this study: the grooved aluminum chamber in L3 with TE wave measurements and the 15E chamber where both TE wave and SPU measurements are made. Figure 5 shows some of the SPU data taken in the bare aluminum chamber at 15E. Following the interpretation used in the previous section on TiN SPU signals, Fig. 5 shows an overall increase in the signal from August 2012 to April 2013. There is an increase in both the first and second bunch signals, suggesting that this is due to an increase in quantum efficiency. The very early conditioning data (in the first 0.5 amp-hours) from August 22-23, 2012 shows a decrease in both the first and second bunch signals, suggesting a decrease in quantum efficiency. There were also substantial changes in the vacuum during the measurements on these two days, from 300 nT down to 30 nT at the peak currents. So it is possible that some of the electrons were produced by ionization.

Integrating the SPU signals, the charge/turn values are plotted versus total current in Fig. 6. As with the individual scope data plots, the trend of SPU signal versus current shows a decrease in signal amplitude with less than

Copyright © 2013 CC-BY-3.0 and by the respective authors

0.5 amp-hours, but after this, there an overall increase of EC density in the aluminum chamber with dose.

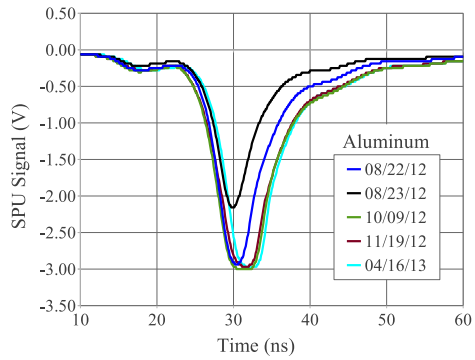


Figure 5: These plots are part of the 2-bunch SPU data in the aluminum chamber at 15E that was taken with 16 mA total positron current (8 mA/bunch = 1.28×10^{11}positrons/bunch). The preamplifier output is limited to 3 V resulting in some flattening of the highest amplitude signals.

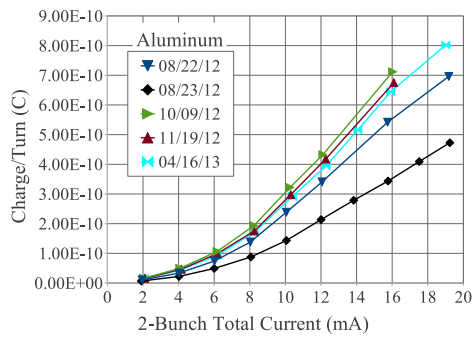


Figure 6: SPU two bunch data from the bare aluminum chamber at 15E shows an overall increase in signal with dose.

The 10-bunch TE wave data from the aluminum chamber at 15E is shown in Fig.7 and agrees with the SPU data in that the EC density becomes higher than its initial value after less than 170 amp-hours. No very early (less than 0.5 amp-hour) TE wave data is available in this data set. Data from the L3 grooved aluminum chamber in Fig. 8 shows a similar increase in EC density of about 40 percent after the earliest data.

CONCLUSIONS

Data taken using two very different techniques give similar information about the conditioning of bare aluminum and TiN-coated chambers. Bare aluminum shows a significant increase in EC density after modest conditioning and is mostly unchanged thereafter. There is some disagreement between the two techniques in data from TiN-coated chambers as to whether or not these chambers continue to

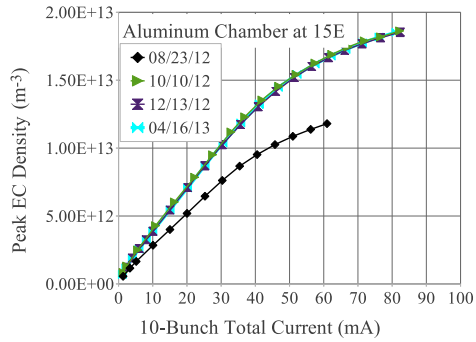


Figure 7: TE wave ten bunch data from the bare aluminum chamber at 15E shows a step increase of about 40 percent in EC density after the earliest measurement.

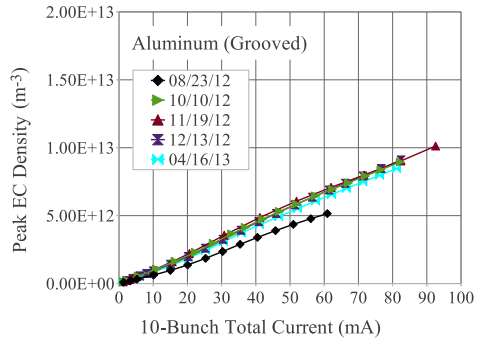


Figure 8: TE wave data from the grooved aluminum chamber in L3 also shows a step increase in EC denstity after the earliest measurement.

condition with beam dose. Interpretation is more difficult in this case because the TiN chambers have different photon dose and vacuum histories.

REFERENCES

[1] J.P. Sikora, *et al.*, "A Comparison of Electron Cloud Density Measurements at CESRTA", in Proc. of IPAC'13, Shanghai, China, May 2013, MOPWA071, (2013).

[2] J. P. Sikora *et al.*, "TE Wave Measurement and Modeling", in Proc. of ECLOUD'12, La Biodola, Isola d'Elba, Italy, June 5-8 2012, arXiv:1307.4315 [physics.acc-ph].

[3] J.P. Sikora, *et al.*, "Resonant TE Wave Measurement of Electron Cloud Density Using Multiple Sidebands", in Proc. of IBIC'13, Oxford, United Kingdom, September 2013, TUPF34, (2013).

[4] J. P. Sikora, *et al.*, "Time Resolved Measurement of Electron Clouds at CESRTA Using Shielded Pickups ," in Proc. of PAC'11, New York, NY, USA, August 2011, WEP195, p.1855, (2011).

[5] J.A. Crittenden and J. P. Sikora, "Electron Cloud Buildup Characterization Using Shielded Pickup Measurements and Custom Modeling Code at CESRTA", in Proc. of ECLOUD'12, La Biodola, Isola d'Elba, Italy, June 5-8 2012, arXiv:1307.4013 [physics.acc-ph].

Copyright © 2013 CC-BY-3.0 and by the respective authors

3D TOROIDAL FIELD MULTIPOLES FOR CURVED ACCELERATOR MAGNETS*

L. Brouwer †, S. Caspi, D. Robin, W. Wan, LBNL, Berkeley, CA 94720, USA

Abstract

Curved magnets producing continuously rotating field multipoles along the length of the bend can provide strong and continuous transverse focusing, making them of interest for accelerator systems such as compact ion beam gantries and synchrotron light sources. Evaluating the utility of such rotating multipole systems requires an accurate description of field behavior for beam physics calculations. This paper presents a helical scalar potential solution in 3D toroidal harmonics relevant to boundary conditions on the surface of a torus. The resulting fields are evaluated for a curved helical quadrupole channel to illustrate field rotation and the effect of magnet curvature.

INTRODUCTION

Previous analysis and use of accelerator magnets producing helical fields have focused on straight, cylindrical designs [1]-[5]. There is interest in studying the extension of this concept to curved magnets [6], requiring expressions for allowable fields rotating around the bend of torus. Previous work on field description and measurement of curved magnets is specific to cases of axial symmetry where the assumption of no field variation along the bend is made [7]-[9].

In these references Schinzer *et al.* present a method for finding scalar potential solutions in local polar coordinates using approximate R-separation of the scalar Laplace equation (expansion in the aspect ratio of the torus). In this paper a similar approach was taken to obtain expressions relevant to rotating fields on the bend of a torus, with the difference being the use of toroidal coordinates and full R-separation in 3D toroidal harmonics.

TOROIDAL COORDINATES

The right hand toroidal system of η, ξ, ϕ is formed by the rotation of bipolar coordinates η and ξ about the vertical axis (Fig. 1). Surfaces of constant η are tori, making toroidal coordinates a natural choice for problems with boundary conditions on the surface of a torus. Scale factors for this system are

$$h_\eta = h_\xi = \frac{a}{\cosh\eta - \cos\xi}$$
$$h_\phi = \frac{a\sinh\eta}{\cosh\eta - \cos\xi} \qquad (1)$$

where $(\pm a, 0)$ are foci of the bipolar system.

* Work supported by the U.S. Department of Energy under contract No. DE-AC02-05CH11231 and the National Science Foundation under grant No. DGE 1106400.

† lnbrouwer@lbl.gov

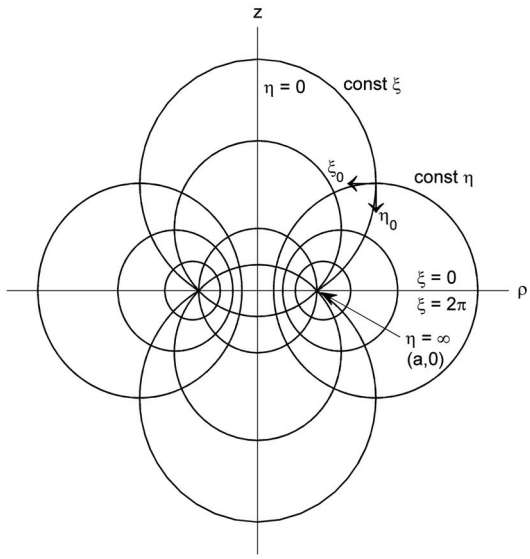


Figure 1: Bipolar coordinates $0 < \eta < \infty$ and $0 \le \xi \le 2\pi$ forming toroidal coordinates when rotated about the z-axis.

SCALAR LAPLACIAN

In a current free region the magnetic field can be expressed using only the gradient of a scalar potential $\vec{B} = -\nabla\psi$. The divergence of this field produces Laplace's equation for the scalar potential $\nabla\cdot\vec{B} = -\nabla^2\psi = 0$. In toroidal coordinates the scalar Laplace equation is

$$\nabla^2\psi = \frac{1}{h_\eta h_\xi h_\phi}\left[\frac{\partial}{\partial\eta}\left(\frac{h_\xi h_\phi}{h_\eta}\frac{\partial\psi}{\partial\eta}\right) + \frac{\partial}{\partial\xi}\left(\frac{h_\eta h_\phi}{h_\xi}\frac{\partial\psi}{\partial\xi}\right) + \frac{\partial}{\partial\phi}\left(\frac{h_\eta h_\xi}{h_\phi}\frac{\partial\psi}{\partial\phi}\right)\right] = 0. \qquad (2)$$

Substitution of the coordinate dependent scale factors (1) produces

$$\frac{k^2}{a^2}\left[\frac{\partial^2\psi}{\partial\eta^2} + \frac{\partial^2\psi}{\partial\xi^2} + \coth\eta\frac{\partial\psi}{\partial\eta} - k^{-1}\left(\sinh\eta\frac{\partial\psi}{\partial\eta} + \sin\xi\frac{\partial\psi}{\partial\xi}\right) + \frac{1}{\sinh^2\eta}\frac{\partial^2\psi}{\partial\phi^2}\right] = 0, \qquad (3)$$

where the simplification $k(\eta,\xi) = \cosh\eta - \cos\xi$ is made. The technique of R-separation is used, producing

$$\frac{k^{5/2}}{a^2}\left[\frac{\partial^2 u}{\partial\eta^2} + \frac{\partial^2 u}{\partial\xi^2} + \coth\eta\frac{\partial u}{\partial\eta} + \frac{1}{4}u + \frac{1}{\sinh^2\eta}\frac{\partial^2 u}{\partial\phi^2}\right] \qquad (4)$$

Copyright © 2013 CC-BY-3.0 and by the respective authors

which can be separated to obtain expressions for the substituted function $u = k^{-1/2}\psi$.

GENERAL HELICAL SOLUTION IN TOROIDAL HARMONICS

With u separable in each variable $u(\eta,\xi,\phi) = G(\eta)H(\xi)L(\phi)$, sinusoidal behavior in ξ and ϕ is assumed such that

$$L(\phi) = \sum_{m=0}^{\infty} \left[A_m \cos(m\phi) + B_m \sin(m\phi)\right] \quad (5)$$

$$H(\xi) = \sum_{n=0}^{\infty} \left[C_n \cos(n\xi) + D_n \sin(n\xi)\right]. \quad (6)$$

With these assumptions the separated "radial" equation for $G(\eta)$ can be obtained from (4) as

$$\frac{d^2G}{d\eta^2} + \coth\eta \frac{dG}{d\eta} + \left[\frac{1}{4} - n^2 - \frac{m^2}{\sinh^2\eta}\right] G = 0. \quad (7)$$

If a change of argument $Z = \cosh\eta$ is used, (7) can be reformulated into the associate Legendre differential equation

$$(1-Z^2)\frac{d^2G}{dZ^2} - 2Z\frac{dG}{dZ} + \left[\nu(\nu+1) - \frac{m^2}{1-Z^2}\right] G = 0 \quad (8)$$

with degree $\nu = n - \frac{1}{2}$ and order m. General solutions for $G(\eta)$ are the associate Legendre polynomials P_ν^m and Q_ν^m with argument $Z = \cosh\eta$.

$$G = \sum_{m=0}^{\infty}\sum_{n=0}^{\infty}\left[E_{n,m}P^m_{n-\frac{1}{2}}(\cosh\eta) + F_{n,m}Q^m_{n-\frac{1}{2}}(\cosh\eta)\right] \quad (9)$$

Combining the solutions of separable equations and the R-separation substitution, the general form of the helical potential is

$$\psi = k^{\frac{1}{2}}\sum_{m=0}^{\infty}\sum_{n=0}^{\infty}\left[E_{n,m}P^m_{n-\frac{1}{2}}(Z) + F_{n,m}Q^m_{n-\frac{1}{2}}(Z)\right]\times \left[C_n\cos(n\xi) + D_n\sin(n\xi)\right]\left[A_m\cos(m\phi) + B_m\sin(m\phi)\right] \quad (10)$$

which is in agreement with similar separable solutions of Laplace's equation in toroidal coordinates (see [10] for example).

BOUNDARY CONDITIONS ON A TORUS

A surface of constant $\eta = \eta_0$ forms a torus. If the minor and major radius of a torus are respectively R_c and R_0, the constants producing this surface are

$$\eta_0 = \cosh^{-1}\epsilon^{-1} \quad (11)$$

$$a = R_c\sinh\eta_0 = R_0(1-\epsilon^2)^{\frac{1}{2}}, \quad (12)$$

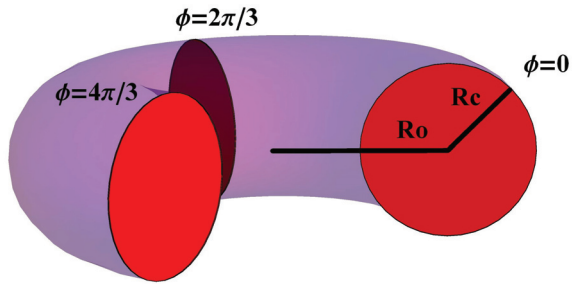


Figure 2: A partial torus of $\epsilon = 50/100$ is shown with bore cross sections at $\phi = 0$, $\frac{2\pi}{3}$, and $\frac{4\pi}{3}$ marked in red. The rotation of transverse fields through similar cross sections for a helical quadrupole channel is shown in Fig. 3.

where $\epsilon = R_c/R_0$ is the aspect ratio of the torus (Fig. 2). The potential inside and outside the torus' surface is given by

$$\psi^{in}(\eta_0 < \eta < \infty) = k^{\frac{1}{2}}A^{in}_{n,m}Q^m_{n-\frac{1}{2}}(\cosh\eta)\sin(n\xi - m\phi) \quad (13)$$

$$\psi^{out}(0 < \eta < \eta_0) = k^{\frac{1}{2}}A^{out}_{n,m}P^m_{n-\frac{1}{2}}(\cosh\eta)\sin(n\xi - m\phi), \quad (14)$$

where the Legendre polynomials are required to remain finite, and phase in ϕ and ξ is chosen such that $B_\xi(\eta,\xi,\phi = 0)$ is symmetric about the $\xi = 0$ axis.

Bore Fields

The fields inside the bore from $\vec{B} = -\nabla\psi^{in}$ (13) are,

$$B^{in}_\eta = -\frac{A^{in}}{a}k^{3/2}\left[\left(\frac{n-\frac{1}{2}}{\tanh\eta} + \frac{k^{-1}}{2}\sinh\eta\right)\times Q^m_{n-1/2}(\cosh\eta) - \frac{m+n-\frac{1}{2}}{\sinh\eta}Q^m_{n-3/2}(\cosh\eta)\right]\times \sin(n\xi - m\phi) \quad (15)$$

$$B^{in}_\xi = -\frac{A^{in}}{a}k^{3/2}Q^m_{n-1/2}(\cosh\eta)\left[n\cos(n\xi - m\phi) + \frac{k^{-1}}{4}\left[\cos((n-1)\xi - m\phi) - \cos((n+1)\xi - m\phi)\right]\right] \quad (16)$$

$$B^{in}_\phi = \frac{mA^{in}}{a\sinh\eta}k^{3/2}Q^m_{n-1/2}(\cosh\eta)\cos(n\xi - m\phi), \quad (17)$$

with use made of the properties of associate Legendre polynomials found in [11]. For the evaluation of the Legendre polynomials using the DTOR algorithms see [12].

Copyright © 2013 CC-BY-3.0 and by the respective authors

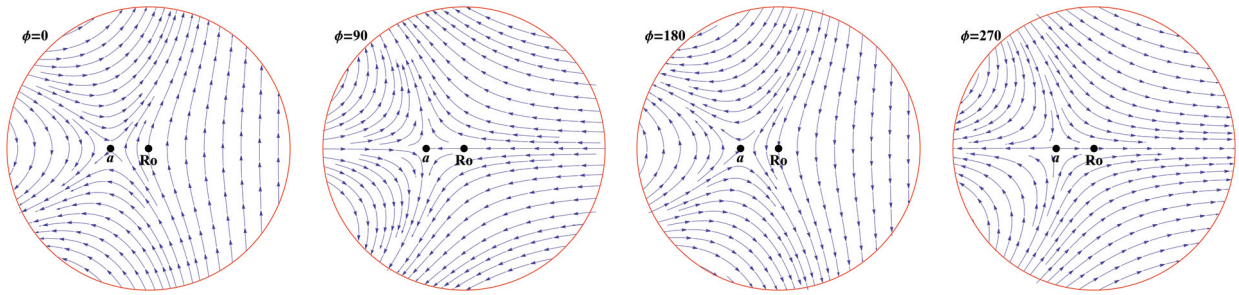
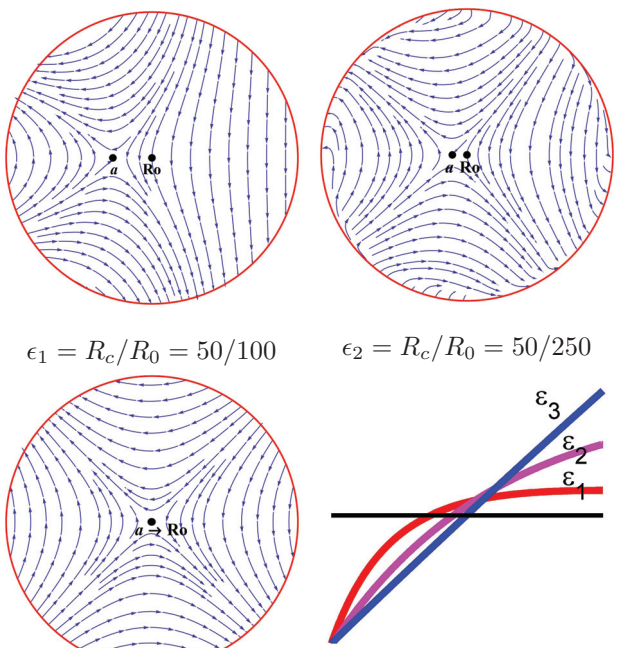


Figure 3: Transverse field rotation within a helical quadrupole channel ($n = 2$, $m = 1$) is shown for a torus of aspect ratio $\epsilon = 50/100$. The coordinate ϕ is the angle around the bend of the torus (see Fig. 2).

CURVED HELICAL "QUADRUPOLE" FOCUSING CHANNELS

The n=2 toroidal multipoles resemble quadrupole fields twisting along the length of the torus with m total rotations. This is illustrated in Fig. 3 for a curved quadrupole channel with one full period around the torus (m=1). The aspect ratio ϵ and field period length $2\pi R_0/m$ of the magnet determine the deviation of the helical toroidal field multipoles from traditional cylindrical multipoles. As the aspect ratio of the torus approaches zero and field period length approaches infinity, the fields approach those produced by a straight non-twisting quadrupole (see Fig. 4).



$\epsilon_1 = R_c/R_0 = 50/100$ $\epsilon_2 = R_c/R_0 = 50/250$

$\epsilon_3 = R_c/R_0 = 50/5000$ Normalized vertical field gradient along midplane

Figure 4: Axially symmetric quadrupole-like fields (n=2, m=0) are shown for a fixed bore radius R_c and increasing major radius R_0. As the aspect ratio of the torus $\epsilon = R_c/R_0$ tends to zero, the fields are seen approaching those of a straight cylindrical quadrupole.

CONCLUSION

A 3D scalar potential obtained through R-separation of Laplace's equation in toroidal coordinates was presented. This potential can be used to describe magnetic fields rotating helically along the length of a curved magnet in terms of toroidal harmonics. The deviation of these toroidal harmonics from straight cylindrical multipoles is influenced by the period of field rotation and the aspect ratio of the magnet (torus). This deviation tends to zero in the limit of no rotation and a aspect ratio of zero. A curved helical quadrupole channel was used to illustrate this behavior.

REFERENCES

[1] S. Caspi, *SC-MAG-464*, LBL-35928, 1994.

[2] T. Tominaka *et al.*, *Nucl. Instr. and Meth. A*, vol. 484, pp. 36-44, 2002.

[3] A. Morita and Y. Iwashita, *Phys. Rev. ST Accel. Beams*, vol. 6 , p. 014001, 2003.

[4] E. Willen *et al.*, *Proc. of the 2005 IPAC*, pp. 2935-2937, 2005.

[5] Y. Derbenev and R.P. Johnson, *Phys. Rev. ST Accel. Beams*, vol. 8 , p. 041002, 2005.

[6] W. Wan *et al.*, "A Preliminary Study on Possible Applications of Curved Helical Quadrupole Focusing Channel", *Proc. of the 2013 NAPAC*, submitted for publication. **

[7] P. Schnizer *et al.*, *COMPEL*, vol. 28, iss. 4, pp. 1044-1058, 2009.

[8] P. Schnizer *et al.*, *Nucl. Instr. Meth. A*, vol. 607, pp. 505-516, 2009.

[9] P. Schnizer *et al.*, *IEEE Trans. Appl. Supercond.*, vol. 22, no. 3, p. 4001505, 2012.

[10] P. Moon and D.E. Spencer, "Field Theory Handbook", ed. 2, pp. 112-115, Springer-Verlag, New York, 1971.

[11] M. Abramowitz and I. A. Stegun, "Handbook of Mathematical Functions", Dover, New York, 1972.

[12] J. Segura and A.Gil, *Computer Physics Communications*, vol. 124, pp. 104-122, 2000.

Copyright © 2013 CC-BY-3.0 and by the respective authors

RETRIEVAL OF EFFECTIVE PARAMETERS OF METAMATERIALS FOR ACCELERATOR AND VACUUM ELECTRON DEVICE APPLICATIONS *

Z. Y. Duan[1, 2, #], M. A. Shapiro[1], J. S. Hummelt[1], and R. J. Temkin[1]
[1]Plasma Science and Fusion Center, Massachusetts Institute of Technology, 167 Albany St., Cambridge, MA 02139, USA
[2]Institute of High Energy Electronics, School of Physical Electronics, University of Electronic Science and Technology of China, No.4, Section 2, North Jianshe Road, Chengdu 610054, China

Abstract

In this paper, we propose a new method to retrieve the effective material parameters, *i.e.*, the effective permittivity and permeability. We first obtain the effective permeability analytically and then retrieve the effective permittivity numerically from the structure's dispersion curve. This method is different from that one which is based on the scattering parameters for metamaterial slabs. The approach presented here offers an effective parameter retrieval for metamaterial-based accelerator and vacuum electron device applications.

INTRODUCTION

Metamaterials are artificial electromagnetic materials comprised of sub-wavelength elements. Metamaterials offer many new options for the design of components that use electromagnetic materials. A Double-Negative Metamaterial (DNM) has both negative permittivity and negative permeability and can be described by an effective medium theory [1, 2]. We investigate metamaterials at microwave, millimeter wave, and THz frequencies for application as accelerator structures, as interaction circuits of high-power microwave vacuum electron devices, and as beam diagnostics tools.

The present parameter retrieval method based on the scattering parameters (S_{11} and S_{21}) [3] is not suitable for the metamaterial-loaded waveguide case due to the waveguide dispersion and the anisotropy of the metamaterials as well as the complex mode. Up to now, the parameter retrieval method is only suitable for metamaterial slabs interacting with TEM mode in free space.

In this paper, we propose a metamaterial-loaded rectangular waveguide which is described by the effective medium theory and provide a method for the retrieval of the effective material parameters from the dispersion relation. The method presented here can offer a theoretical foundation for developing novel metamaterial-based accelerators and high-power vacuum electron devices [4]

*Work supported by DOE, High Energy Physics (Grant No. DE-SC0010075), AFOSR MURI Grant FA9550-12-1-0489 Administered by Univ. New Mexico and the Fundamental Research Funds for the Central Universities (Grant No. ZYGX2010X010).
#zhyduan@mit.edu

RETRIEVAL METHOD

A square waveguide operating below the cut-off frequency which is loaded by split-ring resonators (SRRs) was first proposed by Marques et al. [5] The empty waveguide can be considered as a negative permittivity medium only when the TE mode is excited, and the SRR array forms the effective negative permeability medium. As stated in [6], when metallic rods or stripes are loaded in the transverse direction of the waveguide operating below the cut-off frequency, the TM mode can be excited. Since TM modes are of interest in accelerator and vacuum electron device applications, we propose to use a rectangular waveguide loaded by complementary split-ring resonators (CSRRs) as shown in Fig. 1 (a). As opposed to SRRs on a dielectric in a waveguide where dielectrics can easily induce breakdown or damage [5], a CSRR-loaded waveguide is also completely composed of metallic elements and thus suitable for high-power applications.

The CSRR array can be characterized by an effective negative permittivity in the y direction. In addition, when the loss of the proposed waveguide is not considered, the corresponding empty rectangular waveguide operating below the cut-off frequency can be considered as a "magnetic" plasma and its relative permeability is given by [6]

$$\mathrm{Re}(\mu_{r,eff}) = 1 - \frac{\omega_c^2}{\omega^2}, \tag{1}$$

$$\omega_c = \frac{\pi}{\sqrt{\varepsilon_0 \mu_0}} \sqrt{\frac{1}{d^2} + \frac{1}{h^2}}. \tag{2}$$

Here ω_c is the cut-off frequency for the TM_{11} mode, ω is the angular frequency, and ε_0 and μ_0 are the vacuum permittivity and permeability, respectively, and d and h are the cross-section dimensions of the rectangular waveguide.

In Fig. 1 (b), two CSRR-loaded metallic plates are placed inside a rectangular waveguide and the beam is located between the two CSRR layers. In this waveguide, there is a TM-dominated hybrid mode. This mode is not pure TE or TM mode, but is a complex hybrid mode with field components both perpendicular and parallel to the electron beam direction. From the point of view of the effective medium theory, the "*macroscopic*" mode is

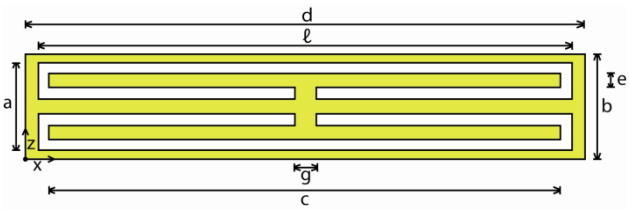
Copyright © 2013 CC-BY-3.0 and by the respective authors

approximately a "TEM" mode because the integrals of the longitudinal electric- and magnetic- fields in a period approximately vanish, respectively. Thus, from the simple physical model, once the dispersion is obtained, the phase velocity is determined. Therefore, for the approximate "macroscopic TEM" mode, the phase velocity can be easily written as

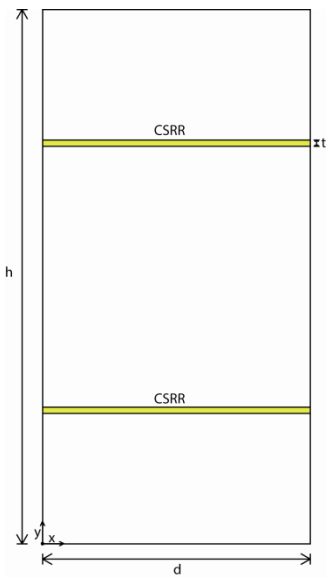
$$v_p = \frac{c_0}{\sqrt{\mathrm{Re}(\varepsilon_{r,eff})\,\mathrm{Re}(\mu_{r,eff})}}, \quad (3)$$

where c_0 is the light velocity in vacuum. Thus we can write the real part of the negative relative permeability as:

$$\mathrm{Re}(\varepsilon_{r,eff}) = \frac{c_0^2}{v_p^2\,\mathrm{Re}(\mu_{r,eff})}. \quad (4)$$



(a)



(b)

Figure 1: (a) a CSRR unit-cell, a=7.25 mm, b=8 mm, c= 39.18 mm, d=43.18 mm, e=0.75 mm, g=2.5 mm, l=41.38 mm; (b) the cross section of the proposed CSRRs-loaded rectangular waveguide, h=86.36 mm, t=1 mm.

Therefore, knowing the dispersion of the proposed waveguide and using the permeability given in Equation 1 we can completely determine the effective permittivity and permeability for the CSRR-loaded rectangular waveguide.

SIMULATIONS AND RESULTS

The two CSRR layers are symmetrically located in the waveguide along the z direction and the distance between the two CSRR layers is set to be 42 mm. The CSRRs are periodically placed along the axis of the structure with period 8 mm. Using the Eigen-mode solver of HFSS [7], we can get the dispersion curve for this structure which is shown in Fig. 2. Note that the material loss is not considered in the HFSS simulation. The cut-off frequency is ~3.89 GHz for the TM_{11}mode in the empty rectangular waveguide, as shown in Fig. 3. From the dispersion curve the phase velocity can easily be obtained by $v_p = \mathrm{Re}(\omega)/\beta$. For example, we can see that the double-negative frequency band is only from ~2.3 to 2.84 GHz for the l=41.18 mm case, where the directions of $\bar{v}_p$ and $\bar{v}_g = d\omega/d\beta$ (group velocity) are opposite. Here β is the phase constant.

Applying the parameter retrieval method presented here, the effective permeability can be found according to Equations (1) and (2), and it is shown in Fig. 3. Also, using Equations (3) and (4) and simulation results of the dispersion (from Fig. 2), we can retrieve the effective permittivity in the double-negative frequency band which is shown in Fig. 4. In the simulations d is kept as a constant and $c = l - 2$ is varied for three different values. Decreasing the resonator length l increases the resonant frequency of the CSRRs and thus the dispersion curve moves to the high frequencies (Fig. 2). The retrieved effective permittivity is dramatically changed (Fig. 4).

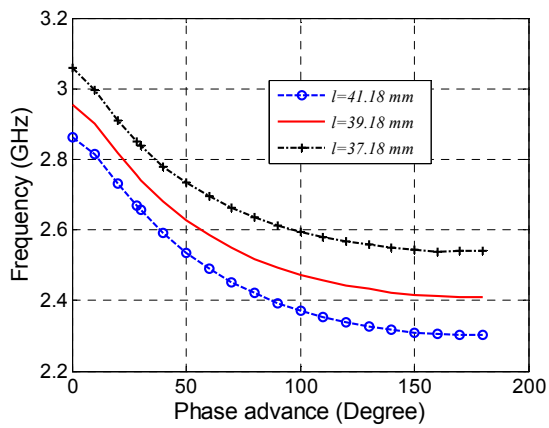


Figure 2: The dispersion curve for the proposed CSRR-loaded rectangular waveguide.

Here we are not interested in the frequencies beyond the double-negative frequency band, since this method is based on the effective medium concept and the dispersion characteristics. Note that this method is not rigorous, but it is approximately correct for the effective material parameters. Currently, we are developing another method based on the field analysis to retrieve the effective permittivity for the CSRRs which are filled in the waveguide.

Copyright © 2013 CC-BY-3.0 and by the respective authors

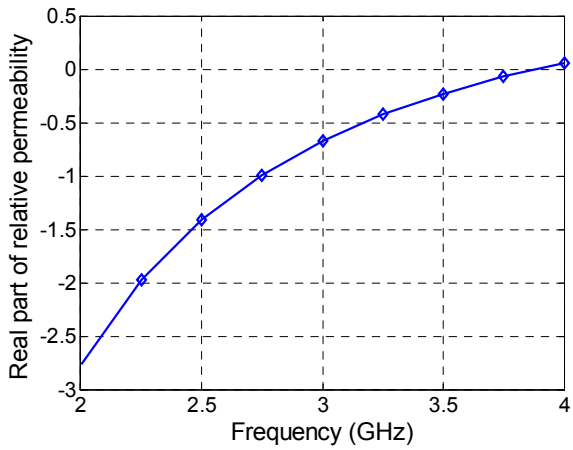


Figure 3: The real part of relative permeability vs. frequency.

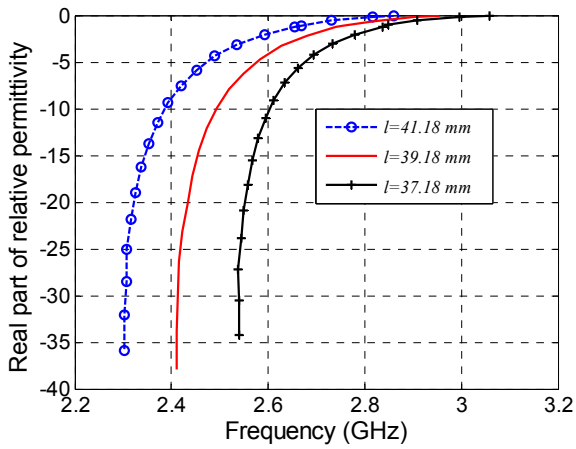


Figure 4: The real part of relative permittivity vs. frequency.

CONCLUSIONS

In this paper, we have proposed a CSRR-loaded waveguide. Using the effective medium theory and setting up a simple physical model, we have developed a method to retrieve the effective parameters for the CSRR-loaded waveguide. This method is based on the "magnetic plasma" concept and the structure's dispersion characteristics. It is different from the widely used scattering parameter method which is suitable for metamaterial slabs excited by TEM mode, but is not suitable for the metamaterial-loaded waveguide, where the waveguide affects the electromagnetic behaviour of the metamaterial.

REFERENCES

[1] R. Marques, F. Martin, and M. Sorolla, "Metamaterials with negative parameters: theory, design, and microwave applications," (John Wiley & Sons, New Jersey, 2008).

[2] Z. Y. Duan, B.-I. Wu, S. Xi, H. S. Chen, and M. Chen, Prog. Electromagn. Res., PIER, 90, 75 (2009).

[3] D. R. Smith, S. Schultz, P. Markos, and C. M. Soukoulis, Phys. Rev. B. 65, 195104 (2002).

[4] J. S. Hummelt, B. J. Munroe, M. A. Shapiro, and R. J. Temkin. "Simulations of wakefileds from an electron bunch in a metamaterial waveguide," NAPAC'13, Pasadena, September 29-October 4, 2013, (2013); Paper WEPBA14, www.JACoW.org

[5] R. Marqués, J. Martel, F. Mesa, and F. Medina, Phys. Rev. Lett. 89, 183901 (2002).

[6] J. Esteban, C. Camacho-Peñalosa, J. E. Page, T. M. Martín-Guerrero, and E. Márquez-Segura, IEEE Trans. Microwave Theory Tech. 53, 1506 (2005).

[7] ANSYS HFSS 14.0, www.ansys.com

Copyright © 2013 CC-BY-3.0 and by the respective authors

SIMULATION OF WAKEFIELDS FROM AN ELECTRON BUNCH IN A METAMATERIAL WAVEGUIDE*

J. S. Hummelt[1], B. J. Munroe[1], S. M. Lewis[1], M. A. Shapiro[1#], and R. J. Temkin[1]
[1]Plasma Science and Fusion Center, Massachusetts Institute of Technology,
Cambridge, MA 02139, USA

Abstract

A metamaterial waveguide is proposed for use in a linear accelerator. The waveguide walls are made of a metamaterial structure composed of complementary split-ring resonators (CSRRs). In such a metamaterial waveguide, a TM-like mode exists that can be excited by an electron bunch. A complementary split-ring resonator is formed by slots machined in a metallic plate. The fact that the metamaterial waveguide is both planar and composed of elements that are direct machined makes it both easy to build and easily scalable to higher frequency linear accelerators. The metamaterial waveguide is coupled to single mode rectangular waveguides. These waveguides can then be connected to a microwave network to couple power into or out of the waveguide. The metamaterial waveguide that is presented was designed using electromagnetic simulations in HFSS, and wakefield as well as PIC simulations of the structure were carried out using the CST Particle Studio code.

INTRODUCTION

Metamaterial (MTM) structures [1] are periodic structures that are both sub-wavelength and operate in a frequency range in which the structures are resonant. In contrast to the disk-loaded waveguides used as accelerator structures, spatial harmonics do not play a role in the accelerating properties of MTM structures. Basic studies of MTMs for use in or as accelerator structures, beam diagnostics, and interaction structures of higher power microwave sources are of interest due to the potential benefits of using frequency selective materials in microwave generation and the advances in MTM fabrication that may allow for high frequency design.

A complementary split-ring resonator (CSRR) with negative permittivity has been introduced [1]. A medium formed of an infinite array of parallel plates with CSRRs machined into them was proposed as an accelerator structure [2,3]. This system can be considered as an infinite array of electric dipoles, and the effective permittivity and permeability of this MTM were determined and simulations showed that this MTM has a negative refractive index.

The CSRR MTM has been modified to be used as an accelerator structure. Instead of using an infinite medium, a MTM waveguide is formed by placing the CSRRs in a waveguide that is below cutoff. In this paper we study the dispersion properties of the MTM waveguide and the electron beam interaction with its field.

*Work supported by AFOSR MURI Grant FA9550-12-1-0489 Administered by Univ. New Mexico and by DOE, High Energy Physics (Grant No. DE-SC0010075)
#shapiro@psfc.mit.edu

METAMATERIAL WAVEGUIDE

The MTM waveguide proposed (Fig. 1) is an assembly of four rectangular waveguides that have each had CSRRs machined into one of their faces as shown in Fig. 2. The waveguides are assembled such that the waveguide walls into which the CSRRs have been machined divide a 'cross' shaped pipe into four outer waveguide regions and one central waveguide region through which the electron beam passes. One period of the structure along the axial direction of the waveguide includes two split ring slots with openings facing each other, with total period p = 7 mm (Fig. 2). The MTM waveguide is designed in the S-band operating at 2.6 GHz. As the period is 7 mm, it is sub-wavelength at this frequency along the axial direction. The transverse dimension of the split rings is 41 mm. The slot width is g=2 mm and the CSRR thickness is 1.6 mm. In addition to the cross shaped structure shown in Fig. 1 we have investigated square, hexagonal, and triangular geometries as well.

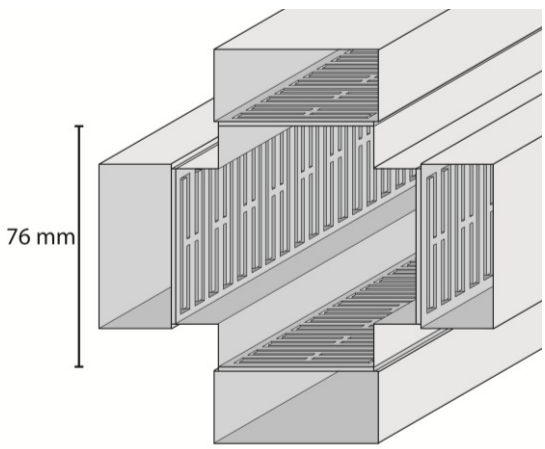


Figure 1: Metamaterial waveguide assembled from four WR187 waveguides (47.55 x 22.15 mm) with CSRRs machined into inner face of assembled structure.

Copyright © 2013 CC-BY-3.0 and by the respective authors

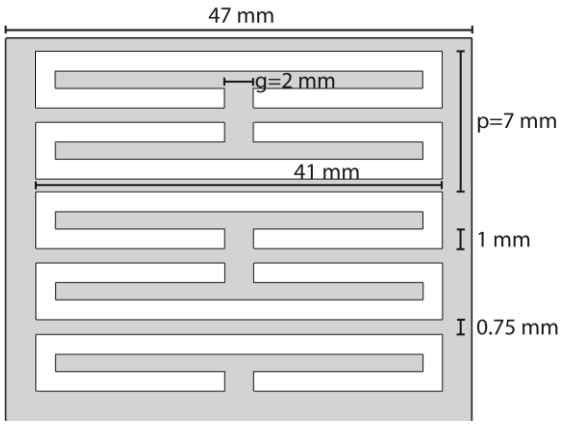


Figure 2: Metamaterial waveguide made from standard WR187 waveguide with CSRRs machined into one face of the guide.

Because of the electric response of the CSRRs, the MTM waveguide formed by the assembled waveguide structure has negative permittivity at 2.6 GHz. The structure's negative permeability is caused by the operation of the waveguide below its cutoff frequency for TM (HE) modes. The cutoff frequency of a waveguide with the same dimensions as the central region is near 5 GHz. The combination of negative permittivity and negative permeability provides a negative refractive index.

The HFSS simulation results showing the dispersion of the MTM waveguide are presented in Fig. 3. The frequency is shown as a function of phase advance per one period in degrees.

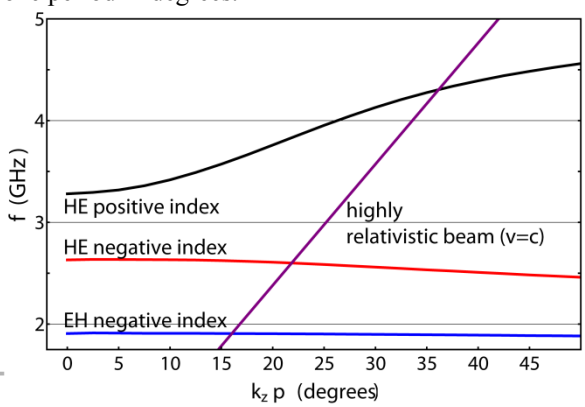


Figure 3: Dispersion curves of TM modes in the metamaterial waveguide. Two modes exist that couple to the electron beam, a negative refractive index mode at 2.5-2.6 GHz (red) and a positive index mode at 3.5-4.5 GHz (black). The relativistic electron beam dispersion line is also shown ($2\pi f = k_z c$, purple).

The negative group velocity, negative refractive TM-Hybrid mode is found at the frequency range of 2.5-2.6 GHz. In addition to this mode, the presence of the CSRRs also supports a lower group velocity mode at 1.9 GHz. The differences between these two modes have to do with the symmetry of fields between adjacent split rings. There is antisymmetry between split rings in the lowest order mode, which results in field cancellation and a very small axial field in the structure. Therefore, this mode is not expected to couple to the electron beam as well as the HE modes. At higher frequencies (3.5-4.5 GHz) a positive index mode is found. Shown in Fig. 3 is the dispersion line of a highly relativistic ($v \approx c$) electron beam. The beam excites the MTM modes at the frequencies where this beam line intersects the modal dispersion curves.

WAKEFIELD SIMULATION

The CST Particle Studio wakefield solver was employed to simulate the wakefield created from a single impulse bunch travelling through the structure. While the wakefield solver lacks the ability to characterize the full beam-wave interaction as a PIC code would, it is an efficient way to estimate the relative coupling of an electron beam to any particular mode in a structure when we examine the wake impedance as a function of frequency. The wake impedance as a function of frequency $Z_z(\omega)$ is found by taking the Fourier Transform of the wake potential $W_z(s)$, which is defined by the relation

$$Z_z(\omega) = -\frac{\int_{-\infty}^{\infty} W_z(s) e^{-i\omega s} ds}{\int_{-\infty}^{\infty} \lambda_z(s) e^{-i\omega s} ds}$$

where λ_z is the longitudinal charge distribution and s is the distance behind the impulse bunch. The wake potential created by the test bunch, shown in Fig. 4, is displayed in Fig. 5 as a function of s.

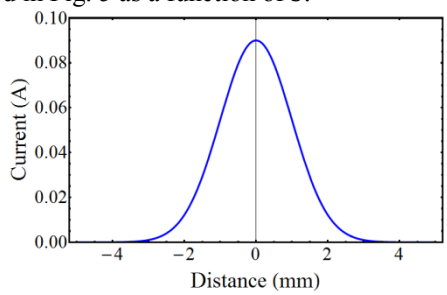


Figure 4: Test bunch current profile used in the wakefield simulations.

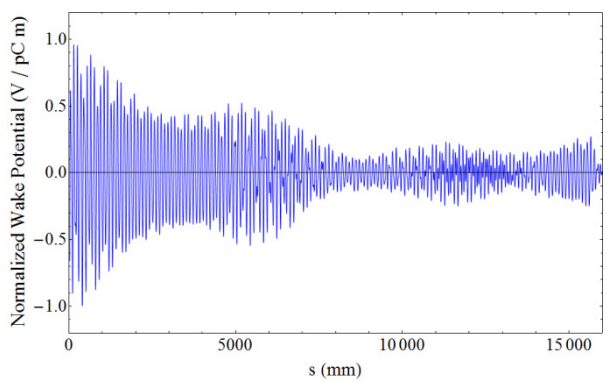


Figure 5: Longitudinal wake potential as a function of the distance behind the impulse bunch (s).

Copyright © 2013 CC-BY-3.0 and by the respective authors

For this simulation the bunch length used is much shorter than the wavelength of interest. Fig. 6 shows the longitudinal wake impedance as a function of frequency. The on-axis bunch excites the TM modes in the MTM waveguide and the longitudinal wake impedance indicates narrow band excitation at the frequencies of 2.6 GHz and 4.5 GHz. In addition to these two modes, there is slight excitation of the mode at 1.9 GHz because it does have a small, but nonzero axial field. The frequencies of each mode are in good agreement with the HFSS electromagnetic simulations.

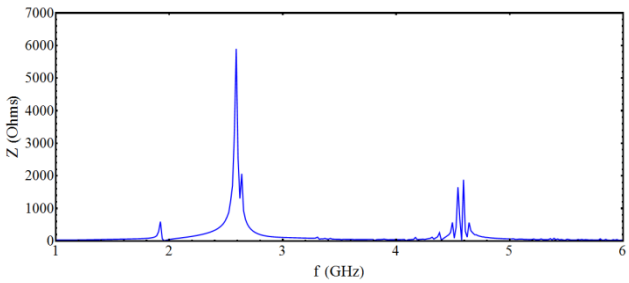


Figure 6: Longitudinal wake impedance shown as a function of frequency.

RADIATION OF A TRAIN OF BUNCHES

PIC simulations of a train of bunches in the 2.6 GHz MTM waveguide were performed using the CST Particle Studio code. This research is of interest for potential application at the beam line of the Haimson Research Corporation (HRC)/MIT 17 GHz linear accelerator, where the MTM waveguide simulated at 2.6 GHz is easily scalable to 17 GHz due to the frequency selectivity and planar geometry of the MTM. The HRC/MIT accelerator produces a train of sub-picosecond bunches with the repetition rate of 17.14 GHz. Radiation from this 17 GHz train of bunches has been used for bunch diagnostics, particularly bunch length measurement [4]. Radiation of the train of bunches in a photonic band gap structure was characterized in Ref [5].

These simulations were done for the S-band MTM waveguide and a train of bunches with a repetition rate of 2.6 GHz, an injected energy of 500 keV, and a time average current of 1 Amp. Fig. 7 shows the 1.1 m length of MTM waveguide with the electron bunches injected from the left.

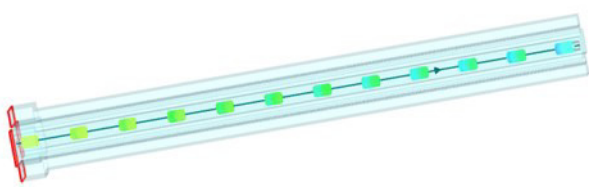


Figure 7: CST simulation of metamaterial waveguide structure with a train of bunches.

The radiation output is at the injection end of the structure because the radiation propagates backward, as predicted from the negative dispersion of the HFSS simulation. The energy distribution along the length of MTM waveguide in the train of bunches is shown in Fig. 8. Bunches give up their energy to radiation and the energy spread increases as the energy decreases.

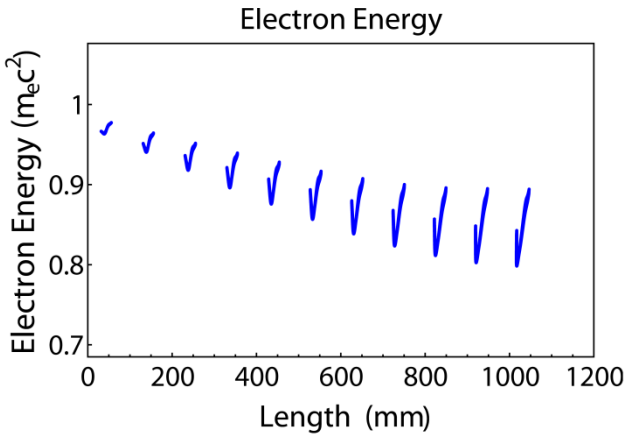


Figure 8: Electron energy distribution of the train of bunches as they travel through the structure. The bunches are injected at an energy of 500 keV (0.98 m_ec^2).

CONCLUSIONS

A metamaterial waveguide is proposed for use in an accelerator as a diagnostic or accelerating structure. The MTM waveguide is designed at the S-band but can be scaled to higher frequencies due to the simple and easily machined planar elements that give the waveguide its frequency response. A negative refractive index mode was identified for this MTM waveguide using the code HFSS, and this mode was also confirmed to both exist and couple strongly to the electron beam using the wakefield solver of CST Particle Studio. The excitation of the MTM waveguide by the electron beam was modelled and studied using the PIC solver of CST. A possible experiment using the HRC/MIT linac is presented.

REFERENCES

[1] R. Marques, F. Martin, and M. Sorolla. Metamaterials with Negative Parameters. Theory, Design, and Microwave Applications. John Wiley & Sons, 2008.

[2] M. A. Shapiro, J. R. Sirigiri, R. J. Temkin, and G. Shvets, Proc. of PAC09, Vancouver, BC, Canada, p. 2992.

[3] M. A. Shapiro, S. Trendafilov, Y. Urzhumov, A. Alu, R. J. Temkin, and G. Shvets, Phys. Rev. B 86, 085132 (2012).

[4] S. E. Korbly, A. S. Kesar, J. R. Sirigiri, and R. J. Temkin, Phys. Rev. Lett. 94, 054803 (2005).

[5] R. A. Marsh, M. A. Shapiro, R. J. Temkin, E. I. Smirnova, and J. F. DeFord, Nucl. Instr. & Meth. Phys. Res. A 618, pp. 16-21 (2010).

Copyright © 2013 CC-BY-3.0 and by the respective authors

RIBBON ELECTRON BEAM SOURCE FOR BUNCHED BEAM PROFILE MONITOR AND TOMOGRAPHY

V. Dudnikov, Muons, Inc., Batavia, IL 60510, USA
A. Aleksandrov, ORNL, Oak Ridge, TN 37831, USA

Abstract

Ribbon electron beam source with a strip cathode has been designed, fabricated and tested. Image of the ribbon electron beam with width up to 15 cm has been registered on the luminescent screen. This ribbon beam can be used for the large proton bunch profile monitoring in the Spallation Neutron Source (SNS) proton storage ring. Advanced beam diagnostics are essential for high performance accelerator beam production and for reliable accelerator operation. It is important to have non-invasive diagnostics which can be used continuously with intense beams of accelerated particles.

INTRODUCTION

Beam profile determination at high intensity ion accelerators requires the use of non-destructive methods. The basic physics and recent technical realizations of important non-intercepting profile diagnostics are summarized in Ref. [1]. Transverse electron beam scanners were realized recently for use in the SNS storage ring by Aleksandrov et al. [2, 3].

In the electron beam profile monitor (EBPM) developed at the SNS, a transverse beam profile is reconstructed from the deflection of electrons crossing the proton or ion beam after being influenced by the beam's space charge, as schematically shown in Fig. 1 [1]. A pencil electron probe is formed by an electron gun and scanned through the proton beam by the electric field of deflectors as in an oscilloscope tube. The position of the scanning electron probe after crossing the proton beam is visualized by a fluorescent screen and the image is captured by a camera for further processing. Assuming the electron beam has a much lower diameter than the proton or ion beam and the scan duration is much shorter than the ion bunch passage, the space charge field can be treated as constant. The beam profile can be reconstructed from the electron beam trace using the mathematical formalism given in Ref. [2].This method was considered for high energy synchrotrons and recently commissioned at the SNS [3]. A significant part of the scanner hardware is used for the extension of the scanning e-beam. Large quadrupole magnets also complicate the magnetic shielding of this version of scanner. For these reasons, electron beam profile monitors (EBPM) with electron beams formed by the deflection of pencil e-beams can be long, and fairly complex. Potentially more practical e-beam profile monitors that are more suitable for proton beam tomography can be developed using a strip cathode for formation of a ribbon beam as discussed below [4]. The analysis of the data for beam bunch transverse profiles for the system that we are proposing will be very similar to what has been developed for the EBPM as described below.

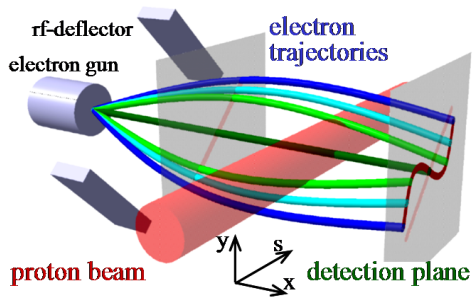


Figure 1: Schematic of an electron scanner for the vertical beam profile [1].

RIBBON ELECTRON BEAM PROFILE MONITOR (REBPM)

The ribbon electron probe beam profile monitor (REBPM) using a strip cathode is proposed as shown in Fig. 2. The electron ribbon (6) is generated by the strip cathode (1) with extractor (2). The transverse dimensions of the ribbon are defined by the collimator with two slits (3) and (5). The width or duration of the ribbon electron probe (6) is formed by the deflection of the ribbon electron beam across slit (5) by a pulsed voltage on the deflecting plates (4). Electrons of the ribbon electron probe after deflection by electric field of the proton bunch are visualized on the luminescent screen (7) and recorded by a fast CCD camera for further processing by the corresponding software discussed above.

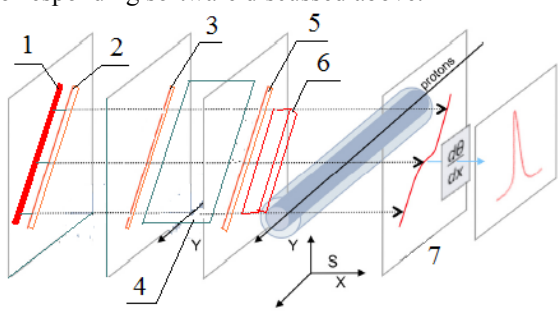


Figure 2: Electron probe beam profile monitor with a strip cathode.

The mechanical design of the system is shown in Fig. 3, the 3D models of the of the strip cathode electron gun with insulators and support insulators are shown in Figs. 4-6.

*Work supported by Contract DE-AC05-00OR22725 and by STTR grant DE-SC0007559.
#Vadim@muonsinc.com

Copyright © 2013 CC-BY-3.0 and by the respective authors

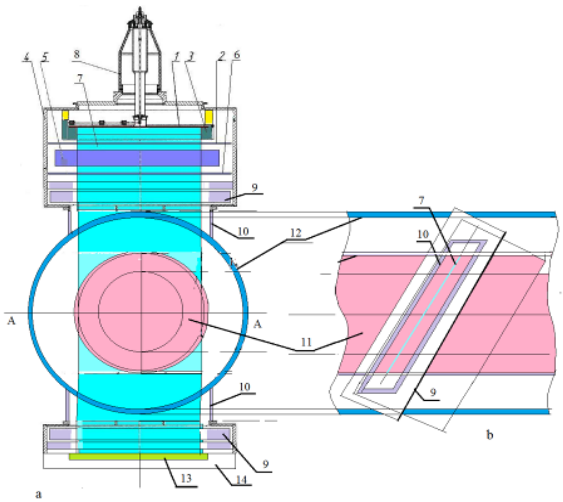


Figure 3: Mechanical design of the RBPM. a-cross-section in the plane of the ribbon electron beam; b- view of cross section in plane A-A. 1-strip cathode; 2-anode with slit; 3-extraction electrode with a slit; 4-vacuum vessel; 5-deflection plates; 6-beam forming electrode with collimating slit; 7-ribbon electron beam (up to 15 cm wide); 8-high voltage insulator; 9-slit valves for proton tube vacuum insulation (need slit ~50x180 mm^2); 10-electron beam vacuum chamber joined with proton vacuum tube 12; 11-proton bunch; 12-proton storage ring vacuum tube (OD=254 mm, ID=248 mm); 13-luminescent screen for electron beam observation; 14-vacuum window.

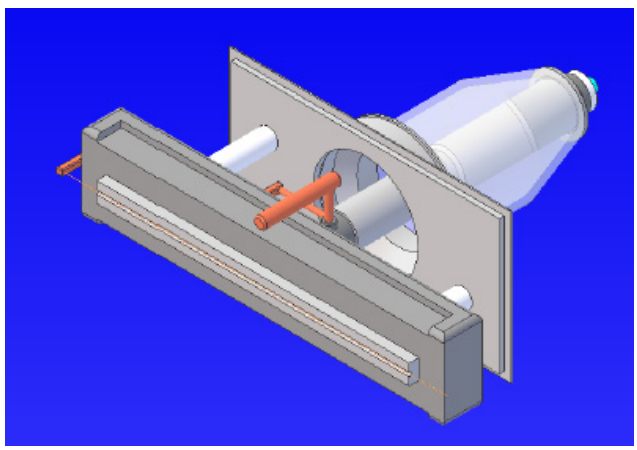


Figure 4: Design of Ribbon strip cathode electron gun.

Ribbon electron beam formation was optimized using the computer simulation code PBGUNS. The study below shows the optimization to reduce the electron beam divergence in the plane orthogonal to the ribbon. This is necessary to keep the image of the ribbon focused on the phosphor screen. The cross section of the electron gun for ribbon beam production is shown in Fig. 7. The scale of this drawing is 1 mm per division. The simulation grid step-size near the emitter can be up to 16 times smaller than the regular grid and the emission area can be simulated with high accuracy in an acceptable simulation time. The extracted electrons escape from the gun through a slit with width h=1 mm.

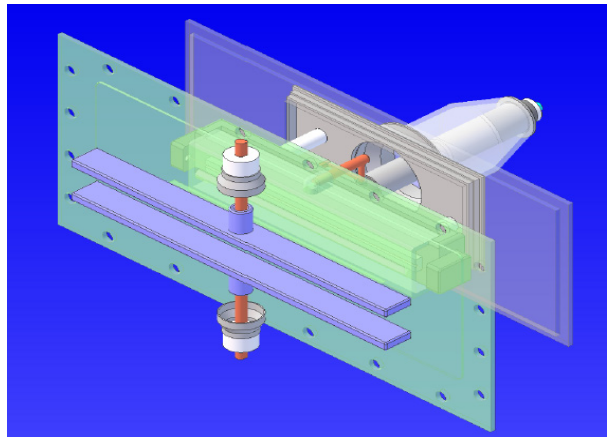


Figure 5: 3D design of RB electron gun with extraction electrode, accelerating anode, and deflection plates.

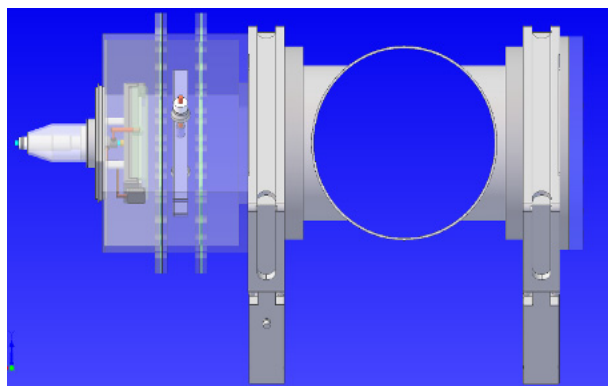


Figure 6: Adaptation of RB e-gun on the vacuum tube of the proton storage ring with vacuum valves.

The escaping electrons are accelerated by an anode (4) with voltage Ua= 100 kV located at coordinate Z_4=8 mm. Deflecting plates (5) with coordinates between Z4=9 mm and Z_5=13 mm are located between the anode (4) and electrode (6) with coordinate Z_6=14 mm. The ribbon electron beam can be deflected by the transverse electric field created between these plates and can be focused by electric fields near ends of these plates. This simulation was made with the potential of deflecting plates Ud=95 kV, which corresponds to the focusing voltage of a cylindrical (one dimensional) Einzel lens Uf=-5 kV.

The simulation was conducted with a space charge current limitation and with emission current limitation at the level of Je=100 mA/cm^2 ~ 1.5 mA per cm of the cathode filament (the simulation used a 1 m long filament). As can be seen from Fig. 7 the emitted flux of electrons is very divergent because of the cylindrical emission surface. The extraction electrode (first anode) intercepts a linear current density J1~0.23 mA/cm and J2~0.08 mA/cm is emitted from the gun. The central part of the beam has a regular divergence of α=40 mr/mm which must be compensated by additional focusing. This additional focusing was provided by the Einzel lens made by the fields between the deflection plates and the collimating slits.

Copyright © 2013 CC-BY-3.0 and by the respective authors

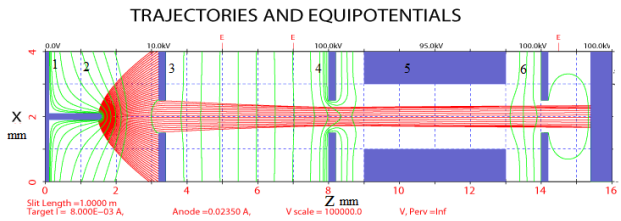


Figure 7: Edge view of the strip cathode electron gun showing the simulation of ribbon electron beam extraction, acceleration, and focusing by the deflector plates (extraction voltage Uex=10 kV, accelerating voltage Ua=100 kV, focusing voltage on the deflector system is Uf=-5 kV). Red lines are electron trajectories, green lines are equipotentials. The scale is 1 mm/division. The flat electrode (1) at Z_1=0 mm has zero potential, the same as the cylindrical emitter (2) with radius r=0.05 mm, located at coordinate Z_2=1.5 mm from the flat electrode. The electrons are extracted from the cylindrical emitter (2) by extraction electrode (3) located at coordinate Z_3=3.2 mm with potential Uex=+10 kV relative to the emitter.

A strip cathode with strong filament tension have been built and tested (see Fig. 8). The filament (1), (0.11 mm diameter thorium doped tungsten) has been attached to insulated holders (3) by spark welding with nickel foil interface and has been kept straight by a system of springs. The right holder is fixed on insulator 8. The left holder (3) can slide along a rod (4). Two direction plates with a glassy carbon inserts (5) can keep the left holder from rotating. The spring (6) can press the left holder to the left direction to keep the filament (1) straight. The filament (1) is positioned along the slit (2) of extractor (9). The anode (10) is used for further electron beam acceleration. The cathode is assembled on the base plate (7).

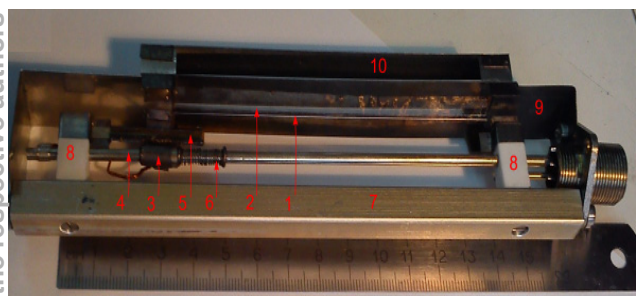


Figure 8: Design of a strip cathode gun with a tension by a spring. 1-filament thorium doped tungsten; 2-slit of extractor electrode; 3-cathode holder, sliding along support rod (4); 4- support rod; 5-plates for direction a cathode holder with a glassy carbon sliders; 6-spring 7-insulated base plate; 8- high voltage insulators;

The image of the ribbon beam from the e-beam gun prototype hitting the phosphor screen is shown in Fig. 9. The filament was heated by current Ih=1 A. The electron beam was extracted from the filament by pulsed extraction voltage Ue~ 1kV with the pulse duration T=1 μS and repetition up to f=10 Hz transmitted through an insulating transformer.

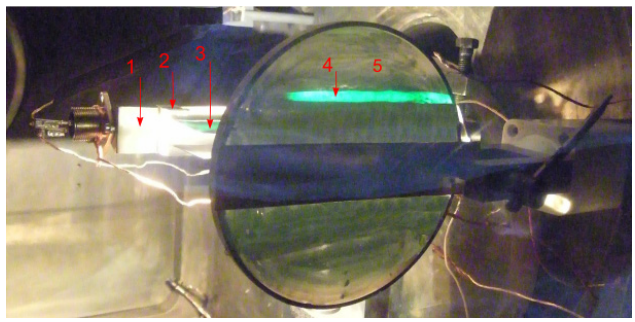


Figure 9: Ribbon electron beam on the luminescent screen deflected by deflection plates. 1-extractor electrode; 2-anode; 3-deflecting plates; 4-image of the ribbon electron beam on the screen; 5-luminescent screen. Diameter of luminescent screen is 110 mm, the shielding plate width is 25 mm.

The green line (4) on the screen (5) in Fig. 9 is an image of deflected ribbon electron beam. In this experiment, the beam line image was ~3 mm wide because the beam focusing by the deflecting plate electrostatic lens, as described in the section above on computer simulations, was not used. The beam trace visible on the screen can be seen and registered after one pulse.

With the electron beam energy increased to 100 keV, the luminescent screen trace can be seen with lower beam current. More-efficient luminescent screens with metallization will be used for the regular RBPM developed in Phase II. Increased accelerating voltage and fine focusing by the deflecting plates will produce a finely focused ribbon beam with thickness less than 1 mm, which is enough for good RBPM accuracy.

REFERENCES

[1] Peter Forck, "Minimal Invasive Beam Profile Monitors for High Intense Hadron Beams", IPAC 2010, Kyoto, Japan, 2010.

[2] A. Aleksandrov et al, "Feasibility Study of Using an Electron Beam for Profile Measurements in the SNS Accumulator Ring", PAC 2005, p. 2586-2588.

[3] W. Blokland, et al., "Electron Scanner for SNS Ring Profile Measurements", Proceedings of DIPAC09, TUOA03, Basel, Switzerland, 2009.

[4] V. Dudnikov and A. Aleksandrov, Rep. IPAC 2012, New Orleans, USA, 2012.

Copyright © 2013 CC-BY-3.0 and by the respective authors

POSSIBLE EXPERIMENTS ON WAVE FUNCTION LOCALIZATION DUE TO COMPTON SCATTERING

V. Danilov, A. Aleksandrov, J. Galambos, T. Gorlov, Y. Liu, A. Shishlo, ORNL, Oak Ridge, TN 37831, U.S.A.
S. Nagaitsev, Fermilab, Batavia, IL 60510, U.S.A.

Abstract

The reduction of a particle's wave function in the process of radiation or light scattering is a longstanding problem. Its solution will give a clue on processes that form, for example, wave functions of electrons constantly emitting synchrotron radiation quanta in storage rings. On a more global scale, it may shed light on wave function collapse due to the process of measurement. In this paper we consider various experimental options using Fermilab electron beams and a possible electron beam from the SNS linac and lasers to detect electron wave function change due to Compton scattering.

INTRODUCTION

The first dedicated experiments to measure the wave function of an electron in accelerator were started in Novosibirsk about two decades ago and described in [1, 2]. The experiments showed that the wave function of an electron in a storage ring is very localized, and its motion is similar to the motion of a classical particle with random kicks without any sign of phase space dilution due to the potential well (RF) nonlinearities.

The experiments were performed in the VEPP-3 storage ring with a single circulating electron [2] and the light from an undulator that was detected by photomultipliers. The standard Brown-Twiss intensity interferometer scheme used a splitter to send the photons to two photomultipliers. The basic idea to measure the longitudinal wave function size was to detect two photons by different photomultipliers during one passage of an electron through the undulator and the rms difference in time, multiplied by velocity of light, was supposed to give the wave function size. Unfortunately, the photomultipliers were slow – their response time (called the dispersion in [2]) was around 160 ps. The signal time difference from two photomultipliers was well within this number, therefore it was concluded that the wave function size is much shorter than the available resolution.

Here we pursue another approach. Using scattered instead of radiated quanta, and knowing the precise energy of electrons and photons, we can measure the resulting energy distribution (and, consequently, the electron wave function) after the scattered photon is measured by a detector and after we employ coincidence scheme, i.e. take only pairs of related electrons and Compton photons with very small angle with the beam velocity vector. This results in a very small transverse recoil and the electrons have mostly longitudinal momentum (or energy) change. This is possible if the resolution of detectors is high and the repetition rate of events is low. If the repetition rate is high, the electron beam energy spread in its left shoulder (see Figure 1) gives the energy spread of scattered electrons even without precise knowledge of the measured gamma quanta if the quanta don't introduce a large angular spread for electrons (we discuss this in the next sections).

An experiment outline is shown schematically in Figure 1. An electron beam with very small energy spread from a linac with energy in the range of hundreds of MeV collides with a laser beam producing rare Compton quanta. The backward scattered quanta are measured in a small scattering angle range (to have precise knowledge of their energy) by an X-ray detector and the electron that scattered the quanta is measured in an energy analyser that separates this electron from the rest of the beam by, e.g., magnetic field.

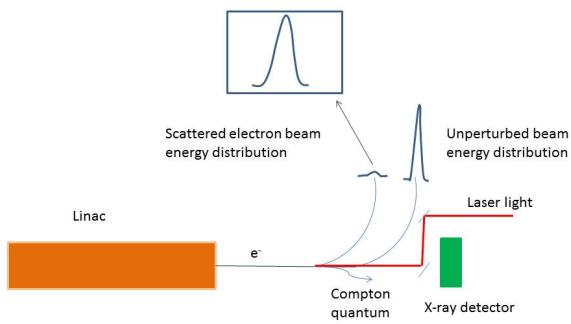


Figure 1: Experiment outline.

If the separation is larger than the width of the electron beam after the magnets, it is possible to measure the width of the energy distribution of the scattered electrons. This distribution, if different from the beam distribution, will give us the wave function width, or its localization, after the process of scattering and measurement of the photon. One has to notice that Figure 1 two-peak discontinuous distribution of electrons can be obtained if we cut out all electron-photon scatterings with large angles of Compton quanta with respect to beam axis pointing toward beam velocity. This procedure will eliminate the scattered-electron angular spread contribution to the left shoulder distribution and as a

Copyright © 2013 CC-BY-3.0 and by the respective authors

result will give more accurate details on the localization process.

In the next section we present calculations for the process probability and accuracy of the measurement. Last section presents simple estimations for the resulting wave package width – the technique is simple and related to the Heisenberg uncertainty principle.

ESTIMATIONS OF THE MAIN PROCESS PARAMETERS

Here we are interested in estimating for a given Compton quanta flux, the required laser and electron beam parameters, accuracies of the beams alignment, etc.

First of all, the electron beam should be as monochromatic as possible and the Compton quanta energy spread has to be minimal. The energy spread of the scattered electrons includes the energy spread of the incident electron beam and Compton quanta plus energy spread increase due to localization process. The smaller the first contribution is, the larger the accuracy of the energy spread increase measurement will be. In the limit of zero energy spread of the electron beam and Compton quanta energy, the energy spread of the scattered electrons (left screen in Figure 1) is a result of localization process and the Fourier image of the square root of the distribution gives us the localized electron wave function after the Compton quantum measurement (see the discussion of its physics in the last section).

Let's estimate separation of the beams – scattered (left trajectory in Figure 1) and unperturbed (right trajectory in Figure 1). Assuming a head-on collision, for backscattered quanta the energy ε_s is:

$$\varepsilon_s = 4\gamma^2\varepsilon, \quad (1)$$

where ε_s is the Compton quanta energy, and γ is the relativistic factor of the electron beam (here and below we assume that we are in Thompson regime, i.e. photon energy in the electron rest frame is much less than the electron rest energy). Assuming the electron energy E=405 MeV for SNS [3] and E=150 MeV for Fermilab IOTA injection line [4] we have roughly 8.8 MeV and 1.2 MeV backscattered quanta for these facilities, respectively, for readily available 355 nm light. More important is the relative energy change that is 2.2 % and 0.67 %, respectively. The typical relative electron beam energy spread is 0.01%. It shows both Fermilab and SNS electron beam energy separation could be made almost two orders of magnitude larger than the spread which gives us opportunity to make clean experiments on wave function localization.

The next step is to calculate the angle for quanta registration to reach the desired accuracy of scattered electron spread and the detection rates. The Compton cross section σ in electron rest frame in the Thompson regime is:

$$d\sigma = \frac{r_e^2}{2}(1+\cos^2\chi)d\Omega, \quad (2)$$

where r_e is the classical radius of the electron, and χ is the angle of the scattered photon with respect to the initial angle that is assumed to be exactly (or very close to) 180 degrees with the electron beam direction. We have to register backscattered photons very close to beam axis and, once a photon is registered, detect the scattered electron. In this way we minimize spread of scattered electron energies. If we want it to be small, the angle $\theta=\pi-\chi$ has to be small also. Recalculating the photon energy ε_s from the electron rest frame to laboratory frame yields:

$$\varepsilon_s = 2\gamma^2\varepsilon(1+\beta\cos\theta) \approx 4\gamma^2\varepsilon(1-\frac{\theta^2}{4}). \quad (3)$$

The spread of photon energies is about $\varepsilon_s\frac{\theta^2}{4}$, and has to be less than the electron beam energy spread δE which yields:

$$\theta \le 2\sqrt{\frac{\delta E}{E}\frac{E}{\varepsilon_s}}. \quad (4)$$

The rough estimate for both facilities (assuming $\frac{\delta E}{E} \approx 10^{-4}$) for 355 nm light is $\theta \le 0.2$ radians. Only photons within this angle have to be collected. We have to recall here that the Compton photon with a large angle gives a transverse kick (around 10^{-3} angle for our maximal angle of 0.2 rad in the beam's rest frame) and this reduces the accuracy of measurement because the electron separation due to dispersion and energy drop of scattered electrons will be smeared by the spread of the horizontal coordinates that appear due to Compton photon transverse momenta. We just have to reduce beta function at interaction region to mitigate this effect. In addition, the dispersion function after the magnets has to be as large as possible and the beta function at the electron position measurement has to be minimized – we leave these details for future work on more detailed design of the beam and laser optics.

At this point we have to estimate the needed electron flux and the detection rates for reasonable lasers. In the laboratory frame this photon angle becomes:

$$\theta_L \approx \frac{\theta}{2\gamma}, \quad (5)$$

that is around $0.3\text{x}10^{-3}$ for the Fermilab parameters. It means that the gamma detector, placed 10 meters from the beam, has to have an aperture diameter only 0.6 cm for the Fermilab case. SNS parameters have the similar values. For this small angle the cross section (2) becomes:

$$\sigma = \pi r_e^2\theta^2, \quad (6)$$

And the rate f of Compton quanta detection is:

$$f = \sigma f_{ph} N_e / S, \quad (7)$$

where f_{ph} is the number of photons per second, N_e is the number of electrons in the interaction volume, and S is the area of beams overlap.

Copyright © 2013 CC-BY-3.0 and by the respective authors

Estimation for the simplest SNS experiment can be done under following assumptions:

1) Electrons come from H^- stripping by a Q-switch laser with duration around 10 ns with repetition rate 30 Hz;
2) Only a small fraction (1%) of ions are stripped to prevent electron beam blow-up due to space charge force, therefore the total number of electrons per one laser shot is N_e=2x10^7;
3) The laser for interaction is also a 30 Hz Q-switch laser with the number of photons = 1.5x10^{18} per pulse assuming 25% efficiency conversion into 355 from 1064 nm light;
4) The area of overlap can be made around 1 mm^2;
5) We assume the electron beam spread can be reduced to 10^{-4} or below – either naturally or using some collimation.

The SNS events rate for 100% efficiency of gamma detector is $f \approx 0.9\,kHz$. This number is too high in order to use coincidence registration for electrons and gamma quanta. Probably, it is not necessary. But we can collimate the beam to reduce the energy spread and number of electrons will go down two orders of magnitude or so. That means the detection rate of around 9 Hz would be less than 30 Hz laser rate (0.3 Compton photons per shot), and we can use coincidence scheme to make clean measurements of electron energy distribution.

The Fermilab linac needs special low current injector producing monochromatic beam for such experiment. In the IOTA channel it is desirable to increase the dispersion as much as possible after the bend and reduce the betatron horizontal size. The counters for Gamma quants can be chosen different to see if the results of experiment depend on the boundary conditions for absorbed scattered photons.

Typical accuracies of the laser beam alignment have to be about 10^{-4}. The angular spread of the electron beam angles has to be about the same. All misalignments have to be less than acceptable angle of Compton quanta that is 0.3x10^{-3} for the typical beam parameters (see eq. [5]).

WAVE FUNCTION SIZE EXTRACTION

The expected result is that Compton energy spectrum for electrons doesn't change after the quantum measurement and we don't see any broadening of scattered electron distribution. The wave function localization is very weak then and can't be measured. If we see broadening of the left distribution in Figure 1, it will indicate that some localization took place.

Here we would like to speculate on how we calculate wave function size from a measured image on the screen (see Figure 1, left distribution). We assume that the dispersion function D can be made large enough so that the betatron size of the beam can be made much smaller than the energy spread-related size, that is $D\frac{\delta E}{E}$. In addition, we assume the electron spin doesn't influence its motion much, and ignore the rest mass of the electron. In this case its motion is similar to the light and the Fourier transform of the energy spectrum (taken as square root of the measured distribution) produces the wave function in time-space representation. There is always a question of wave function slow phase that can't be determined from the measurement of this type – we assume it is close to being a constant.

Simple arguments give us the following picture: if the wave function gets localized after the measurement to one photon wave length, the energy spread will be equal to the photon energy meaning the left image in Figure 1 will overlap the right one. If the localization is about 10 wave lengths, the energy spread is around 10% of the photon energy (the width of the right distribution is about 10% of the distance to the right one), etc.

The parameters, chosen in this paper, allow us to see the localization size if it is below 100 backscattered photon wave lengths. If the localization length is larger, meaning the increase of the energy spectrum width is not seen, one needs to decrease the electron beam and backscattered photons energy spread further.

SUMMARY

In this paper we have presented examples of possible experiments at SNS and Fermilab on electron wave function localization due to Compton quantum scattering and its measurement by a detector. It is shown that if the localization of the electron wave function is below 100 wave lengths of backscattered photons, it will be possible to measure it with moderate modifications of existing and future facilities at SNS and Fermilab.

ACKNOWLEDGMENTS

This work is supported by the U.S. Department of Energy under contracts No. DE-AC02-07CH11359 and No. DE-AC05-00OR22725.

REFERENCES

[1] N. Vinokurov, in Proceedings of Joint US-CERN-Japan-Russia accelerator school, World Scientific (1988) 108.
[2] T. Shaftan, PhD thesis, BINP, Novosibirsk (1997), in Russian.
[3] T. Gorlov, *et. al.*, "The Possibility of Generation of High-energy Electron Beam at the SNS facility", in Proceedings of IPAC 2013, Shanghai (2013), China.
[4] S. Nagaitsev, "IOTA - Integrable Optics Test Accelerator at Fermilab", in Proceedings of IPAC 2012, New Orleans (2012), USA.

Copyright © 2013 CC-BY-3.0 and by the respective authors

MEASUREMENT OF NON-LINEAR INSERT MAGNETS*

F. H. O'Shea†, R. Agustsson, A. Murokh, E. Spranza,
RadiaBeam Technologies, Santa Monica, CA 90404, USA
S. Nagaitsev, A Valishev, Fermilab, Batavia, IL 60510, USA

Abstract

Fermilab's Integrable Optics Test Accelerator (IOTA) is an electron storage ring designed for testing advanced accelerator physics concepts, including implementation of non-linear integrable beam optics and experiments on optical stochastic cooling. In this report we describe the contribution of RadiaBeam Technologies to the IOTA project which includes non-linear magnet engineering, prototype fabrication and measurement.

INTRODUCTION

IOTA is an electron ring designed as a proof-of-principle of non-linear integrable optics [1] at the ASTA facility [2]. Nonlinear optics are predicted to increase stability of the electron beam through Landau damping [3] and the natural tune spread of the electron beam will also increase dynamic aperture [1], leading to more intense beams in high-energy physics machines. The goal of the project is to study single particle dynamics in the non-linear regime using a 150 MeV electron beam in a ∼40 m circumference ring with 4 non-linear inserts that are each 2 m long [4]. While the beam dynamics of the non-linear optics system is being studied at Fermilab, the magnetic inserts are being designed and manufactured at RadiaBeam Technologies.

In this paper we discuss the magnetic design and tolerance requirements of the IOTA inserts and the measurement system being built to measure the first prototype of these unique magnets. The goals of the prototype magnet insert are to gain experience manufacturing a complex geometry, determine the cross-talk between adjacent magnet segments, and measure the field of a challenging insert that is tens of centimeters long with a sub-centimeter aperture.

DESIGN

The approach to this problem is the standard magnetostatic approach [5]: find the equipotential surfaces and choose one to fill with iron, correct the edge fields for the finite extent of the real magnets and then magnetize that iron via a current carrying coil on a "far off" yoke. The magnetostatic problem is defined in terms of the magnetic vector potential for a 2D object:

$$A_z(x,y,s) = \frac{B\rho\, c^2\, t}{\beta(s)} \sum_{n=1}^{\infty} \frac{2^{2n-1} n!(n-1)!}{(2n)!} \times \left(\frac{x^2+y^2}{\beta(s)\, c^2}\right)^n \cos\left[2n \arctan\left(\frac{y}{x}\right)\right]. \quad (1)$$

Where $B\rho$ is the magnetic rigidity of the particles, c is a scale factor with units $m^{1/2}$, t is a unitless strength parameter, x, y and s are the horizontal, vertical and longitudinal coordinates, respectively, and $\beta(s) = \beta^* + \frac{s^2}{\beta^*}$ is the beta-function in the non-linear insert with $\beta^* = 0.727$ m at the longitudinal center of the insert.

The vector potential (and as we will see, the scalar potential) is clearly continuous in the longitudinal coordinate but it would be very difficult to create a single 2 m long device that varies continuously to produce the desired scaling. Accordingly, the 2 m device is divided into 20 sections of constant parameters that are 6.5 cm long, between each section is a 3.5 cm long non-magnetic block (or air gap) used to separate the different segments. Because of the symmetry around the longitudinal center of the device, there are 10 different segments. The segments are labeled 1 through 10 with 1 being nearest the center of the 2 m device and 10

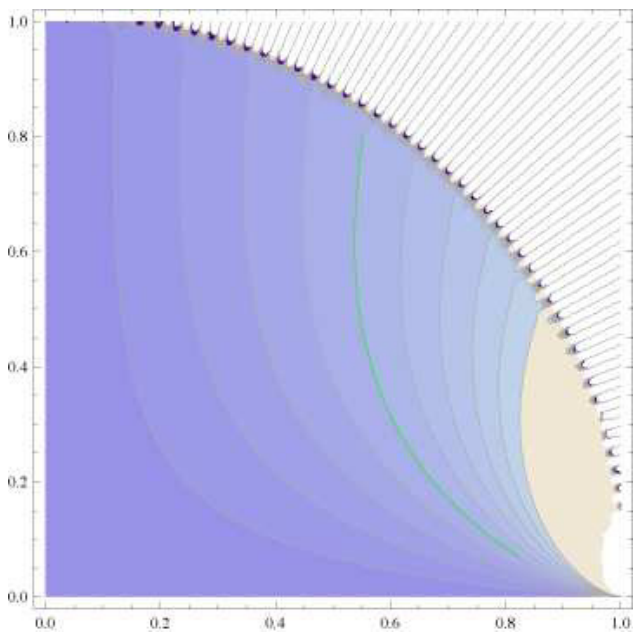


Figure 1: Contour plot of the equipotential lines of $\phi(x_N, y_N)$. The superimposed green line is the line taken for the face of the poles.

* Work supported by DOE under contract DE-SC0009531.
† oshea@radiabeam.com

Copyright © 2013 CC-BY-3.0 and by the respective authors

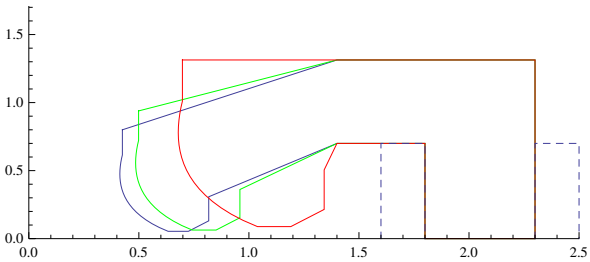


Figure 2: Real space outline of the 2D IOTA design for segments 1 (blue), 5 (green) and 10 (red), including a continuous return yoke. The dashed lines show the outline of the excitation coils. All dimensions are in centimeters.

being the outer most segment.

To lowest order, the problem is limited to a 2D plane, so the scalar potential is related to the vector potential via a $\pi/2$ rotation about the longitudinal axis [6]:

$$\phi(x_N, y_N) = t \sum_{n=1}^{\infty} \frac{2^{2n-1} n!(n-1)!}{(2n)!} \times \left(\frac{x_N^2 + y_N^2}{c^2} \right)^n \sin\left[2n \arctan\left(\frac{y_N}{x_N}\right)\right]. \quad (2)$$

Here, the scalar potential has been normalized such that $\Phi(x, y, s) \equiv \frac{B\rho c^2}{\beta(s)} \phi(x/\beta^{1/2}, y/\beta^{1/2})$ with $x_N \equiv x/\beta^{1/2}$ and $y_N \equiv y/\beta^{1/2}$. Because we know the scaled form of the potential and how the beta-function evolves through the non-linear magnet, we can solve for the pole face once and then scale it via the beta-function for all of the magnets. Further, because of the four-fold symmetry of the problem, we need only find the solution in one quadrant. The equipotential lines of the scalar potential in Eq. 2 are shown in Fig. 1. The green line in Fig. 1 shows the contour that will be used to define the pole faces. Because the solution is scaled by $\beta(s)$, this is the face for all of the magnets.

We note here that the potentials given by Eqs. 1 and 2 have singularities at ($x_N = \pm c$, $y_N = 0$), so whatever solution is found can never include normalized coordinates greater than c. Further, because the singularities are located on the $y = 0$ line, the vertical aperture is larger than the horizontal aperture.

In order to make the design easier to produce we have decided to make a single yoke design for all of the different pole tips. This way, the yokes can be produced en masse while the tighter tolerance pole tips are made for each of the segments separately. Fig. 2 shows a 2D outline of poles 1 (the smallest pole, it is the pole closest to the longitudinal symmetry point), 5 and 10 (the largest pole) of the IOTA insert design along with a continuous return yoke and a single excitation coil. The curved surface of each segment is given by the green line in Fig. 1.

Above the curved pole tip, a straight face is extended to 1.3 times the height of the highest point on the curved face. This straight corner improves the agreement between the simulation results and the desired field. The value was found via 2D optimization of the field using the code Poisson [7]. The height of the yoke is defined by the height of the pole face extension for the number 10 segment. On the lower side, the curved face is cut off by a flat section that is "chamfered" on the outside edge (to the right in Fig. 2) to prevent field concentration there. These underside changes are made in the scaled coordinate system, so they are different for each magnet.

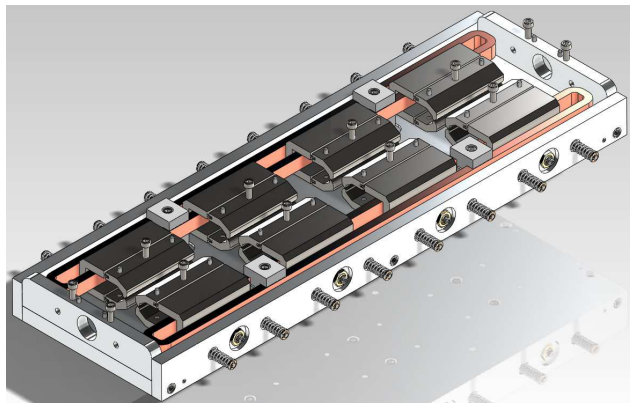


Figure 3: Isometric view of the IOTA insert prototype. A plate on top has been hidden to show detail below. The copper items are the excitation coils, the dark grey items are the steel poles and return yokes and light grey items are aluminum.

An isometric view of the prototype insert can be seen in Fig. 3. The prototype insert will contain 4 complete segments. Because the smallest aperture comes from the number 1 pole, the prototype insert will have the following segments (in order): 1, 1, 2, 3. This combination of segments allows us to measure the smallest aperture magnets and the coupling between segments. 3D simulation using the code Maxwell [8] has shown that the longitudinal symmetry point of a full length insert will be faithfully reproduced between the two number 1 poles in the prototype.

NONLINEAR MAGNET REQUIREMENTS



Figure 4: Close up image of the tongue and groove reluctance gap.

The magnets shown in Fig. 2 are closed yoke magnets. However, because the beta-function of the electron beam evolves along the length of the insert, each of the 10 segments requires a different excitation magnitude. To reduce the number of power supplies needed, we have decided to

Copyright © 2013 CC-BY-3.0 and by the respective authors

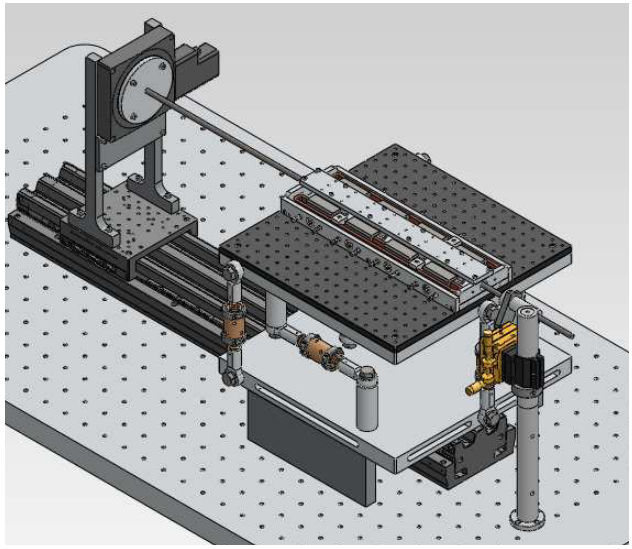


Figure 5: View of the IOTA insert measurement system.

use a single excitation coil for all of the yokes and to tune the field in each segment using a reluctance gap that can be set by moving the return yoke of each segment individually. If the reluctance gap were comprised of two flat faces, the required precision of the position of the yoke relative to a fixed pole tip is very tight, a few micrometers. To reduce the required tolerance we opted for a tongue and groove approach, this results in a required positional tolerance of $\sim$50 μm. A close up of the tongue and groove reluctance gap can be seen in Fig. 4.

The field quality requirements were defined using a frequency map analysis [4], the analysis indicates that a good field region of $|y| \approx c$ and $|x| \approx c/2$, with good being defined as difference from the ideal field by less than 1%, is required. Further, the magnetic center of the segments must be placed along the same line with an accuracy of 50 μm or less. To compare the magnetostatic simulations to the theoretical field, the simulated field is compared to the ideal field on the y-axis (B_x) and x-axis (B_y). Of the above defined magnets, the number 1 pole has the worst field quality: the difference is less than 0.5% at all points within ($x < 0.6c$,$y < 0.8c$). Therefore, simulations show that all magnets are potentially within the desired tolerance. Harmonic analysis of the fields produced by Poisson shows that the field faithfully reproduces the quadrupole and octopole moments with 0.1% of the desired values while the dodecapole moment is within 3% of the desired value (r_N = 0.5). The fields in the aperture are quite small at $B \leq$ 100 G, using t=0.45, c = 0.009 m$^{1/2}$ and $B\rho$ = 0.502 T-m, which are the design parameters for the prototype.

MEASUREMENT SYSTEM

To measure the magnetic field of the prototype insert requires that we design a measurement system with over 40 cm of travel in the longitudinal direction that can fit within circular gap of $\sim$10 mm diameter within the number 1 pole

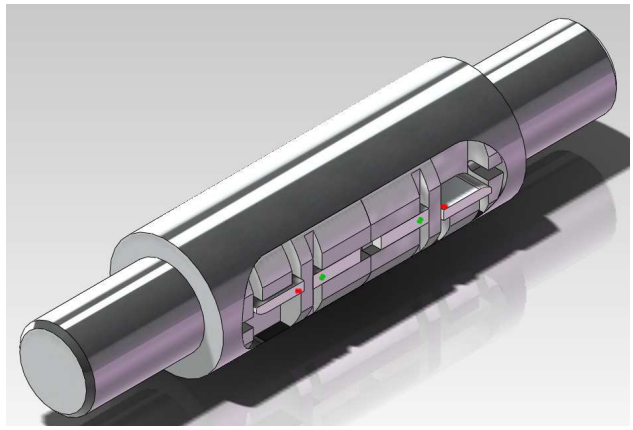


Figure 6: View of the hall probe holder showing the custom mechanics to allow probe motion in the radial direction. The red and green crosses are the locations of the hall probes.

(see Fig. 5). Additionally, the hall probe must be able to move within this 10 mm diameter gap. To accomplish this, we have designed a "rod and radius" system wherein a set of miniature hall probes [9] are mounted in a custom holder in a rod of the specified diameter (see Fig. 6). The rod is moved longitudinally via a linear motion stage and rotationally via a rotational stage. The radius is set manually with a set screw. This design will allow us to measure a large fraction of the desired aperture. We will use 4 hall probes that are separated longitudinally in the probe holder, such that two different radii within the IOTA insert aperture can be measured in a single, automated longitudinal scan (see Fig. 6). We intend to zero and measure each of the probes in a pair of common standards and to have an overlap region that can be measured by both sets of probes for direct comparison. At the time of publication, the IOTA insert is being manufactured and the measurement design is being completed.

REFERENCES

[1] V. Danilov and S. Nagaitsev, Phys. Rev. ST Accel. Beams 13, 084002 (2010).

[2] J. Leibfritz et al., IPAC'12, New Orleans, USA, May 2012, MOOAC02, p. 58, http://www.JACoW.org

[3] S. Nagaitsev, A. Valishev and V. Danilov, HB2010, Morschach, Switzerland, Sept. 2010, THO1D01, p. 676, http://epaper.kek.jp/HB2010/

[4] A. Valishev, et al., IPAC'12, New Orleans, USA, May 2012, TUPPC090, p. 1371, http://www.JACoW.org

[5] H. Wiedemann, *Particle Accelerator Physics, vol. I, 2nd Ed.*, (Berlin: Springer, 2003), 97.

[6] K. Halbach, Nucl. Instr. Meth. A 169, 1 (1980).

[7] K. Halbach and R. F. Holsinger, Particle Accel. 7, 213 (1976).

[8] http://www.ansys.com

[9] Arepoc s.r.o., http://www.arepok.sk

Copyright © 2013 CC-BY-3.0 and by the respective authors

PERFORMANCE OF PLANAR RADIATOR IN THE RADIABEAM-IAC EXPERIMENT*

A. V. Smirnov#, R. Agustsson, S. Boucher, J. J. Hartzell, S. Storms, RadiaBeam Technologies Inc., Santa Monica, CA 90404, USA and Y. Kim Idaho Accelerator Center and Idaho State University, Pocatello, ID 83209, USA

Abstract

Planar gratings structure for generation of mm-sub-mm wavelength long-range wakefields is analysed. The rugged, side-open, slow wave structure can sustain substantial beam loading including long multi-bunch trains up to CW operation. Electromagnetic performance of the structure is characterized numerically vs. experiment with emphasis to application to flat beams. It is shown that such an electrically wide, wavelength-gap structure can operate at significantly reduced tolerances whereas substantial flatness of the wakefield can be obtained at essentially non-flat eigenmode profile.

INTRODUCTION

In the experiment [1] conducted at Idaho Accelerator Center (IAC) a side-open gratings planar structure (see Fig. 1) was used to generate and partially extract mm-sub-mm wave radiation induced by wakefields. Since the structure is relatively new the radiator performance needs more detailed characterization as well as to substantiate the measurements made and to support other potential applications such as compact THz sources [2], energy dechirping [3] and collinear wakefield acceleration.

We analyse here the structure performance with GdfidL code [4] in eigen- and time domains. The side opening has been modelled as a large space enclosed by low conductivity walls (see Fig. 1) with negligible influence on the frequencies of the modes of our interest.

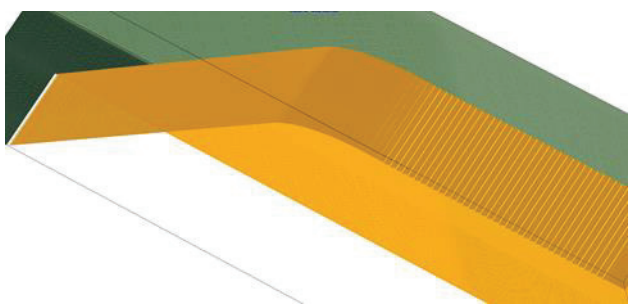


Figure 1: GdfidL model of one-quarter structure with horn antenna. Interaction gap: 1.26 mm, width: 6.3 mm, grating length L=30.4 mm (130 periods), period: 0.23 mm, and groove depth: 0.081 mm.

EIGENMODES

We analyse here eigenmodes that are in synchronism with the relativistic beam (v/c=0.996) using only one period of the regular part of the structure. Several modes with different horizontal variations can potentially interact with the beam in such an oversized structure. Field patterns for lowest modes are shown in Fig. 2. Side opening provides modal selection for the wakefield energy radiated forward [2,5] due to the side radiation losses via the factor $F = \left((1-\exp(-\alpha L))/\alpha L\right)^2$, where $\alpha = \pi f / Q v_{gr}$ is the modal attenuation. Simulation results for the first few eigenmodes are shown in Table 1.

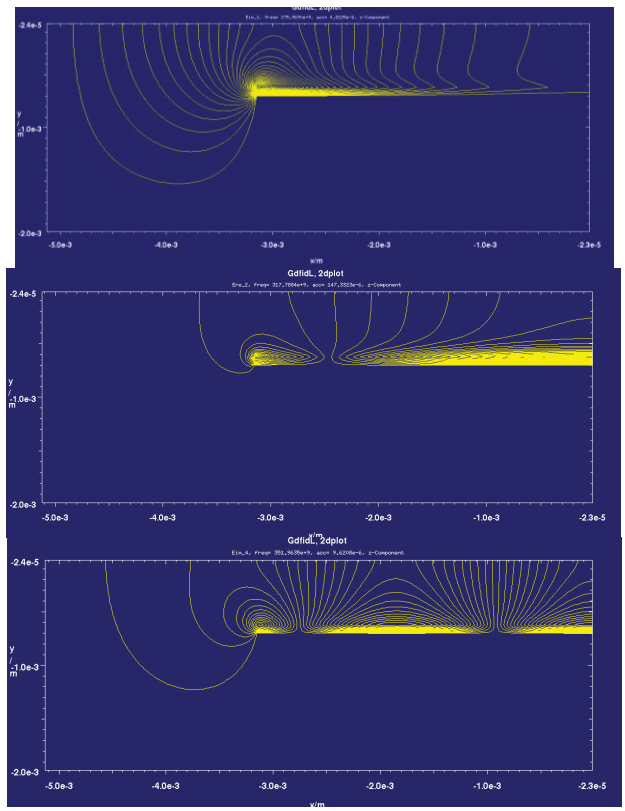


Figure 2: Contour plots in transverse XY plane for the Ez field for three lowest modes which are synchronous to 5MeV beam at 276, 312 and 352 GHz (one quarter model).

Table 1: F, group velocity, and r/Q [Ω/m] for different widths w [mm] of the beam filling the vertical gap.

f, GHz	F	r/Q, w=0	r/Q, w=2	r/Q, w=4.76	βgr
276	0.05	11	14.3	94	0.81
312	0.53	2450	2201	1343	0.844
352	0.27	1076	721	112	0.72
401	5e-4	459	180	23	0.79

*Work supported by US DoE Contract DE- SC-FOA-0000760
#asmirnov@radiabeam.com.

Copyright © 2013 CC-BY-3.0 and by the respective authors

One can see from Table 1 that with the absorbing periphery (having as low as 1 Sm/m surface conductivity) the factor F reduces fast as the modal order increases. This effect is similar to the spectrum rarefaction in open cavities and waveguides. One can see that mode #2 (at 312 GHz) strongly dominates in beam interaction due to radiation losses and higher r/Q at finite beam width.

TIME DOMAIN SIMULATIONS

Wakefield simulations have been performed here for filament and ribbon bunches having 30 pC charge at 500 and 700fs rms durations in various configurations: grating structure only, with horn attached, horn only (without the structure), and also in the structure with randomized geometrical parameters:

Wakefields induced by flat (ribbon) and filament bunches are illustrated in Fig. 3. Note the radiation patterns seen in Figs 3, 7 is significantly modified ("flattened") by the beam width.

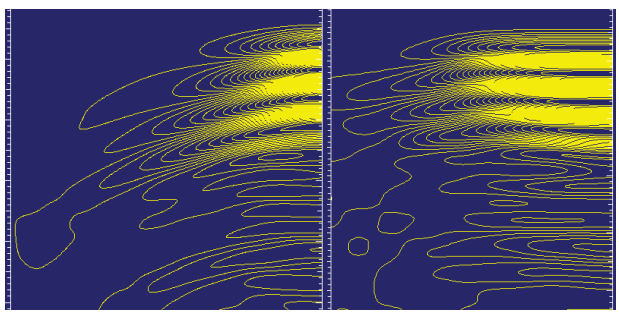


Figure 3. Ez field pattern in median XZ plane induced by a σz=150 μm bunch along 40 periods structure at t=31 ps for filament (left) and 4.8 mm wide (right) bunch filling the vertical gap.

Field spectra shown in Figs. 4, 5 confirm the dominant mode at ~300 GHz. Line splitting is caused by partial reflection of the power from the horn.

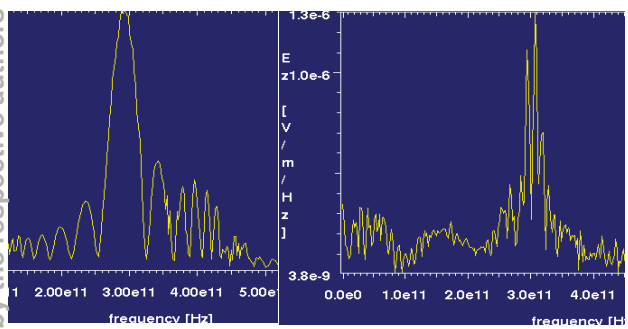


Figure 4: Ez field spectra on the output edge of the gratings (left) and on the horn opening (right) forσz=150 μm and w=2 mm bunch.

Longer bunch causes appearance of spectrum lime at lower frequencies (tens of GHz, see Fig. 5, right) and magnitude reduction at 300 GHz (compare to Fig. 4, right). We observed very similar behaviour experimentally [1], when we obtained signals from fast oscilloscope (~20 GHz bandwidth) whereas the pyrodetector signal was weak or not registered yet. That occurs when the chicane and RF phases were tuned incompletely.

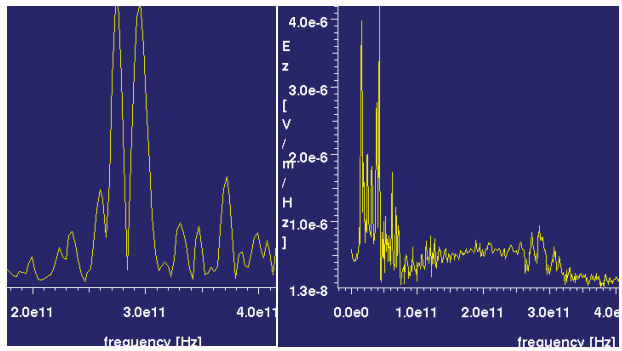


Figure 5: Ez field spectra on the output edge of the gratings (left) and on the horn opening (right) for a σz=210 μm, w=2 mm bunch.

Flux integral that determines radiated energy is plotted in Fig. 6 for full system and horn only. One can see that the radiated energy without gratings is negligible compared to that with gratings that occurs at ~ 310 GHz (see Fig. 4, right).

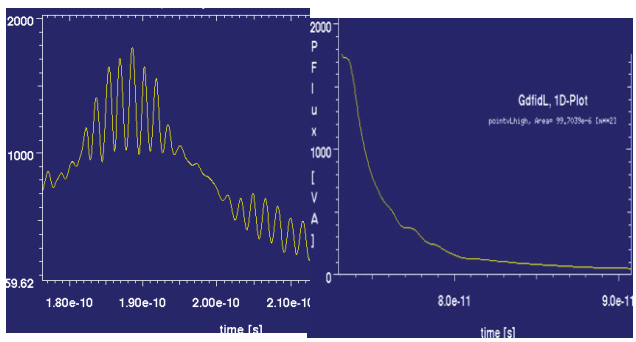


Figure 6: Total flux integral [W] (including quasi-static charge-induced fields) vs. time on the horn output with (left) and without the gratings (right) for a σz=150 μm, w=2 mm bunch.

From Fig. 6, left one can estimate the radiation micropulse time ~20 ps which corresponds well to the 18ps drain time determined as difference between slow wave structure filling time and time-of-flight. The tail of the plot corresponds to the bouncing caused by partial reflection.

One can also estimate from Fig. 6, left, ~40 nJ energy radiated by a 500 fs microbunch. For 1.3 GHz RF frequency and 2 μs pulse length it corresponds to ~100 μJ energy radiated per macropulse or ~3mW average power at 30 Hz rep rate. That corresponds well to pyrodetector measurements [1] and previous analytical estimations. From the analytical model and the simulations above we also estimate the rms bunch duration about 600-700 fs.

Wider bunches change field because of generation of higher and lower order modes (see Figs 7, 8).

From the field pattern induced by the bunch in the horn (Fig. 9) one can assume lobe direction angle about half of

Copyright © 2013 CC-BY-3.0 and by the respective authors

the opening angle. This is in agreement with preliminary far-field simulations.

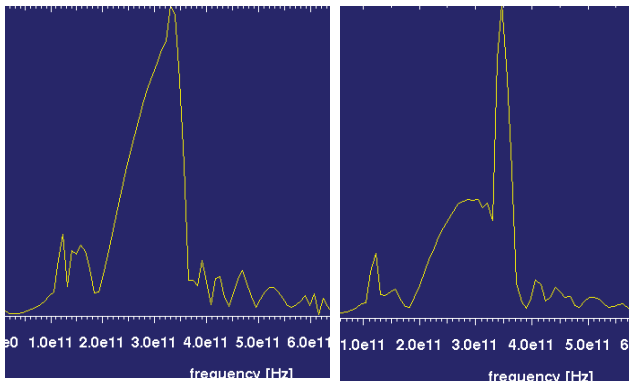


Figure 7: Ez field spectra induced in the 40-period gratings for 2 mm (left) and 4.76 mm (right) wide bunch at σz=150 μm.

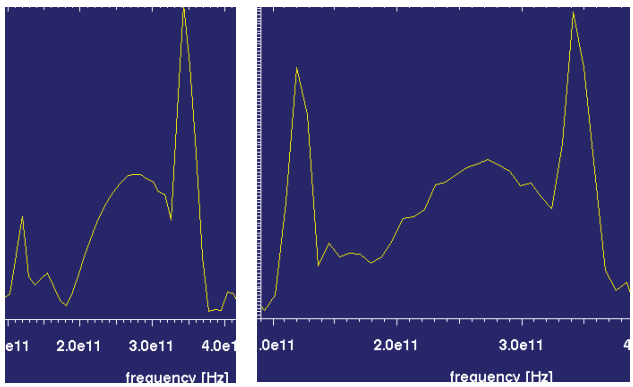


Figure 8: Ez field spectra induced in the 40-period gratings for 4.76mm (left) and 7 mm (right) wide bunch at σz=210 μm.

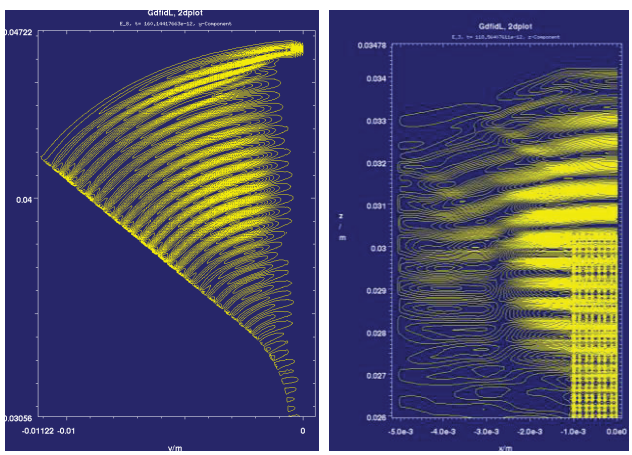


Figure 9: Ey in YZ (left, t=160ps) and Ez field plotted in XZ plane (right, t=118ps) forσz=150 μm bunch. The rectangular region on the right corresponds to the 2mm bunch width.

To model effect of CNC milling tolerances we introduced 0.5 mill randomization into the gratings parameters (period, groove depth, and thickness) in the full-length model (with the horn). The results for power and spectrum shown in Fig. 10 to be compared to Figs 4, 6.

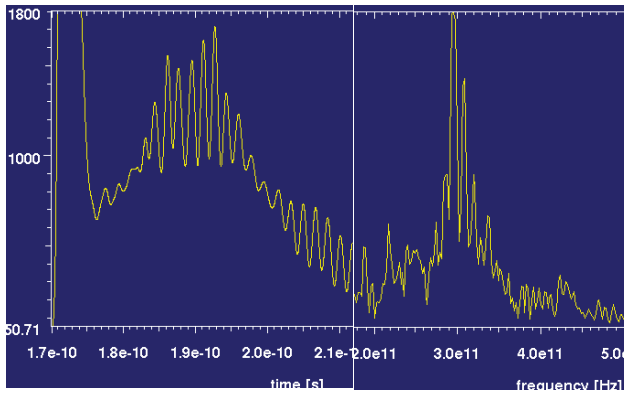


Figure 10: Full power [W] (left) and Ez field spectrum (right) for radiator with randomized gratings for 2 mm wide, σz=150 μm bunch.

CONCLUSION

Simulation confirmed ~mW power radiated from the insertion device at sub-THz frequency estimated earlier from measurements at negligible contribution of geometric wake induced by the antenna horn.

Flat beam considerably modifies wakefield pattern and can make it "flat" even if the eigenmode is not flat.

Wider beam (>5 mm) also results in appearance of ~120 GHz line and shift of the main peak to higher frequency (340 GHz at 7 mm width).

Radiation from longer bunches (≥650 fs) is dominated in the insertion device by lower frequencies (10-100 GHz) that was effectively used in the experiment for the pre-tuning of the beam compression system with fast oscilloscope.

At shorter bunches the radiation is strongly dominated by a single mode at ~310 GHz. That validates analytical simulations made previously to design the experiment [1].

Gratings randomization (~a mill) does not change much the coherent part of the wake making the high group velocity structure exceptionally attractive for applications.

ACKNOWLEDGMENTS

The authors are deeply grateful to Warner Bruns for the opportunity to use GdfidL code and help in simulations.

REFERENCES

[1] R. Agustsson, A. V. Smirnov et al., "Development of a Compact Insertion Device For Coherent Sub-Mm Generation", IPAC'13, WEPWA080, Shanghai, p. 2295 (2013).

[2] A. V. Smirnov. "Compact Schemes for Laser-Free THz-Sub-THz Source", THPSM19, these proceedings.

[3] K.L.F. Bane and G. Stupakov. SLAC Report No. SLAC-PUB-14925, 2012.

[4] W. Bruns, "The GdfidL Electromagnetic Field simulator," http://www.gdfidl.de/

[5] A.V. Smirnov, P. Musumeci. Nucl. Instrum. and Meth. in Phys. Res. A 721 (2013) 1.

Copyright © 2013 CC-BY-3.0 and by the respective authors

WAKEFIELD CALCULATIONS FOR SEPTUM MAGNET IN LCLS–II*

K.L.F. Bane, T. Raubenheimer, SLAC, Menlo Park, CA 94025, USA

INTRODUCTION

The LCLS-II would have delivered low emittance beams with an energy in the range 7–13.5 GeV to one of two undulators, one for generating soft x-rays (SXR) and the other for hard x-rays (HXR) [1]. To allow for flexibility in the distribution of the beams to the two undulators, a fast kicker and Lambertson-type septum magnet would be installed just upstream of the undulator region. The septum itself is 2 m long and the beam is meant to traverse it while passing within millimeters of metallic walls, which will induce resistive wall wakefields. The longitudinal wakes will take energy from the beam and add a longitudinally correlated energy variation—an energy chirp. The transverse wakefields can increase the beam's projected emittance.

In this report we perform calculations of the longitudinal and transverse wakefields of the septum, find their effects on the beam, and put the results in the context of the wakes of other objects in the downstream part of LCLS-II.

Figure 1 gives the layout of the LCLS-II beamlines upstream of the undulators, showing the location of the fast kicker and septum magnets. The septum magnet geometry we consider is shown in Fig. 2. The design orbit for the unkicked (free) beam is 1.6 mm above a curved SS surface; the (horizontally) kicked beam moves in the middle of a flat, rectangular chamber with a vertical aperture of 5 mm.

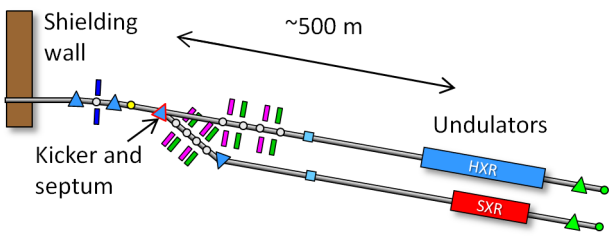


Figure 1: Layout of the LCLS-II beamlines in the vicinity and downstream of the fast kicker and septum magnet [2].

WAKES OF SHORT BUNCHES

Four bunch scenarios are considered for the operation of LCLS-II: short, relatively flat distributions with bunch charge $eN = 250$, 60, 12, 50 pC; peak current $\hat{I} = 3$, 3, 3, 4 kA; full width $t_{fw} = 70$, 15, 3, 10 fs. With the peak current (relatively) fixed and the bunches quite short, the wake strength of a bunch tends to vary $\sim t_{fw}$—since the wake is normalized to total charge eN. Thus it is the first scenario, the so-called "high charge" case with $eN = 250$ pC that will induce the largest wake effects by far, and

* Work supported by the U.S. Department of Energy under contract DE-AC02-76SF00515.

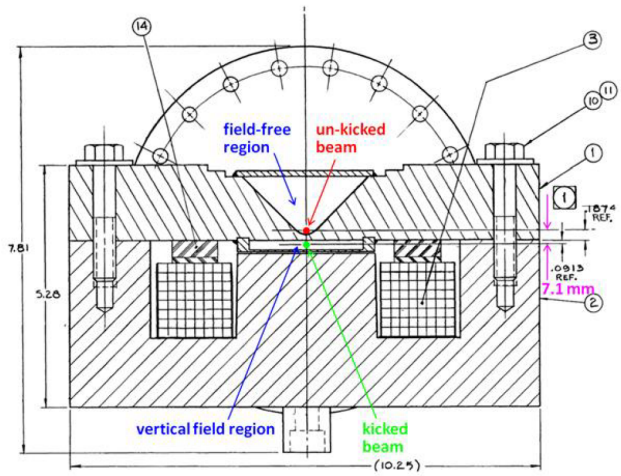


Figure 2: Cross-section the horizontally deflecting Lambertson septum magnet, "HLAM", considered in this report. The length of the chamber is 2.2 m. (Dimensions in the figure, unless otherwise specified, are in inches.)

in this report we limit our study to this case. The bunch distribution $I(s)$, to be used in calculations, is taken from the LCLS and is shown in Fig. 3 (the blue curve); note that the head is to the left, at positions $s < 0$. The distribution is double-horned, with an rms length $\sigma_z = 6.1$ μm; its core can be approximated by a uniform 3 kA (the red curve). Presumably, for the FEL we would like the entire beam core to reach saturation in the undulator together; thus the wake effects over the bunch core are most important.

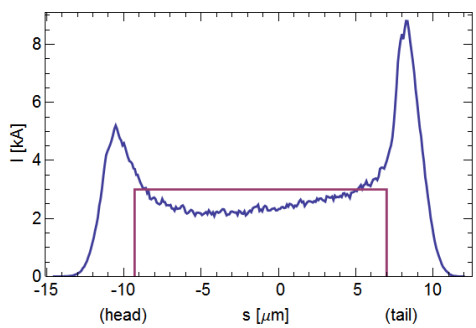


Figure 3: The bunch distribution used in the simulations, which represents the "high charge," 250 pC case (blue), and a uniform approximation of the core at 3 kA (red).

The energy variation induced in a bunch by the wake is

$$E_w(s) = -\frac{L}{c}\int_0^\infty W_z(s')I(s-s')\,ds' \,, \qquad (1)$$

Copyright © 2013 CC-BY-3.0 and by the respective authors

with L the structure length, c the speed of light, and $W_z(s)$ the longitudinal point charge wake ($W_z > 0$ means energy loss). The point charge wake of a periodic structure has a maximum value at $s = 0^+$. In a round structure that value is $W_z(0^+) = Z_0 c/(\pi a^2)$, with $Z_0 = 377\ \Omega$ and a the minimum radius of the boundary [3]. Similarly, for the dipole wake, for which $W_y(0) = 0$, the slope at origin is limited to $W_y'(0^+) = 2Z_0 c/(\pi a^4)$. For non-round structures the scaling will be the same but the constant factor will differ.

For bunches that are short compared to the zero-crossing distance of the wake, Eq. 1 can be approximated by $E_w(s) \approx -LW_z(0^+)Q(s)$, with $Q(s) = \int_{-\infty}^{s} I(s')\,ds'/c$. If, in addition, the core of the distribution is uniform, then over the core, $Q(s) \sim s$ and the wake-induced energy chirp will be approximately linear, with negative slope.

SEPTUM MAGNET

Free Beam

The resistive wall wakefields are weak forces for long bunches, *i.e.* when $\sigma_z \gg s_0 \equiv (2a^2/Z_0\sigma_c)^{1/3}$, where a is the offset of the beam from the wall, and σ_c is the conductivity of the wall metal. For the free, HXR beam, we find that $\sigma_z \ll s_0 = 21\ \mu$m ($a = 1.6$ mm, $\sigma_c = 1.4 \times 10^6\ \Omega^{-1}\mathrm{m}^{-1}$ for SS), and the effect is strong. In a round chamber, the longitudinal point charge wake (in the dc approximation) is given by [4]

$$W_z(\zeta) = \frac{4Z_0 c}{\pi a^2}\left(\frac{e^{-\zeta}}{3}\cos\sqrt{3}\zeta - \frac{\sqrt{2}}{\pi}\int_0^\infty \frac{x^2 e^{-x^2\zeta}}{x^6+8}dx\right) \quad (2)$$

with $\zeta = s/s_0$.

However, the chamber surrounding the free beam is only partially round, at the bottom (see Fig. 2). K. Yokoya has found the solution of the resistive wall wake for any boundary shape [5]. The solution is given in terms of an integral equation that he then solves numerically in a computer program. We use his program to find the wakes excited by the beam. In Fig. 4 we show in cross-section the lower part of the actual chamber shape (in red), the modified chamber that we use as boundary in our calculation (in blue), and the nominal position of the free beam (the olive dot).

The calculation results are given in Fig. 5. In frame (a) we present the point charge wake $W_z(s)$ for the model structure (blue), and the wake if the entire boundary were a circle of radius $a = 1.6$ mm (blue dashed, Eq. 2). Because of the vertical asymmetry in geometry, the energy loss varies linearly with vertical offset. However, for reasonable offsets ($\Delta y < 100\ \mu$m) Yokoya's program finds that the change in wake is small.

Using Eq. 1 we obtain the energy variation in the bunch, $-E_w(s)$[Figure 5(b)]. We see that the energy varies rather linearly over the bunch core, with a total $\Delta E_w = 1.3$ MeV; over the entire bunch the variation is $\Delta E_w = 2.6$ MeV. In the two frames we show also the wake and its effect if the surface were plated with Cu (the red curves). This reduces $\Delta E_w$to 0.4 (0.7) MeV over the core (the entire beam).

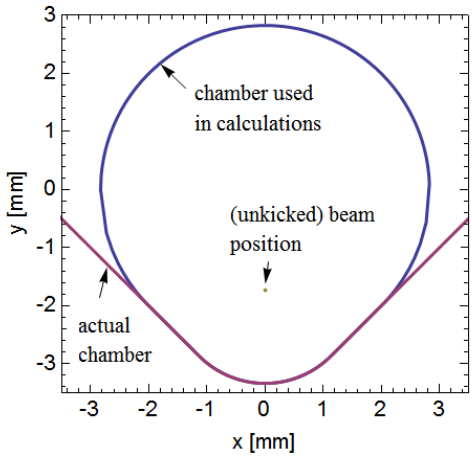


Figure 4: Position of unkicked beam, its relation to the chamber wall, and the model chamber used in calculations.

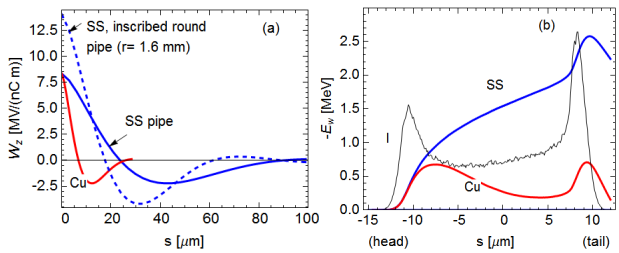


Figure 5: For the free beam: (a) Point charge wake in the SS structure (blue), if it were Cu plated (red); for an inscribed round pipe with SS, shown for comparison (dashes). (b) Total wake energy change for $eN = 250$ pC case. Bunch shape I is also shown (gray).

Transverse Wake

For our structure, with mirror symmetry in x and no symmetry in y, the transverse wake between two particles can be written as

$$\begin{aligned} W_y(s,y_1,y_2) &= W_{y0}(s) + y_1 W_{yd}(s) + y_2 W_{yq}(s) \\ W_x(s,x_1,x_2) &= x_1 W_{xd}(s) - x_2 W_{yq}(s) \end{aligned} \quad (3)$$

where x, y, indicate (small) offsets from the design orbit, and subscript 1 (2) refers to the leading (trailing) particle. Even on the design orbit, the vertical wake induced by the beam, $W_{y0}(s)$, will kick the beam downward and increase its projected emittance. The other wake functions $W_{xd}(s)$, $W_{yd}(s)$, $W_{yq}(s)$, are dipole and quad wake components. Yokoya's program finds all these components.

In Fig. 6(a) we plot the numerically obtained $-W_{y0}(s)$ (the blue curve). Convolving again like in Eq. 1 and dividing by the energy E, we obtain the kick angle $\Delta y'$. With normalized emittance $\epsilon_n = 0.4\ \mu$m, $E = 7$ GeV, $\beta_y = 30$ m, then $\sigma_{y'} = 1\ \mu$r. The normalized kick $\Delta y'/\sigma_{y'}$ is plotted in Fig. 6(b) (the blue curve); the average and rms values are 0.74, 0.54. The projected emittance growth on

Copyright © 2013 CC-BY-3.0 and by the respective authors

the design orbit is comparable to the slice emittance! Plating the septum wall with Cu can greatly reduce the effect (the red curves in Fig. 6). The relative average and rms kick values become 0.21, 0.11.

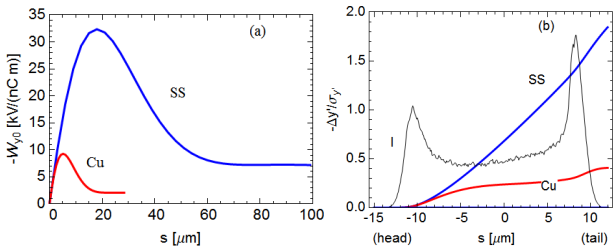


Figure 6: For the free beam: (a) Point charge vertical wake (on the design orbit) in the SS structure (blue) and if it were Cu plated (red). (b) Relative total vertical kick angle for $eN = 250$ pC case. Bunch shape I is also shown (gray).

The dipole wake functions W_{xd}, W_{yd}, were also computed. In an FEL the allowable pulse-to-pulse variation in orbit is similar to the beam size, which in the septum region is $\sigma_y = 30$ μm. Repeating the previous exercise with W_{yd} for a beam offset by σ_y, we find that the average and rms values of $\Delta y'/\sigma_{y'}$ are 0.01, 0.01, for SS, which are negligible (the results for W_{xd} are similar). As to the quad wake W_{yq}, it defocuses in y and is weak: the minimum effective focal length (near the tail of the bunch) is 6.5 km.

Kicked Beam

The SXR beam passes near the center of a rectangular chamber of width 76 mm and height 5 mm; its trajectory is bent horizontally. The bottom and sides are SS, the top is low carbon steel ($\sigma_c = 10^7\ \Omega^{-1}\mathrm{m}^{-1}$). For simplicity we will take as model parallel SS plates. The results will be slightly pessimistic for the longitudinal effect, and will miss the vertical kick on the symmetry plane (which we expect to be small).

The point charge wakefields between parallel, resistive plates have long been known [6, 7]. However, for convenience, we use Yokoya's program here again. In the flat case, the longitudinal wake at the origin, for plates separated by $2a$, is smaller than for the round case (with radius a) by the factor $\pi^2/16$. Performing the same calculations as for the free beam we find that the induced energy change E_w is similar to that given in Fig. 5(b) (the blue curve), though the amplitude is here about half as large. The energy variation over the bunch core (entire bunch) $\Delta E_w = 0.7$ (1.3) MeV.

The transverse wake for the parallel plate model follows Eq. 3, with $W_{y0} = 0$, $W_{xd}(s) = W_{yq}(s)$. In flat geometry $W_{yd}(s) \approx W_{yq}(s)$ over short distances. For a beam offset by σ_y, the maximum wake kick $\Delta y'/\sigma_{y'}$ (at the back of the bunch) is 0.02, with an average of 0.01, again a small effect. The quad wake defocuses vertically and is weak: the minimum focal length (at the back of the bunch) is 1 km.

The dispersion for the kicked beam can turn the wake induced energy spread into emittance growth as: $\delta\epsilon_x \approx \beta_x \eta_x'^2 \sigma_{\delta w}^2/(2\epsilon_x)$, with η_x' the derivative of the dispersion function and $\sigma_{\delta w}$ the relative rms energy spread due to the wake. Taking $\beta_x = 36$ m, $\eta_x' = 7 \times 10^{-3}$, $\sigma_{\delta w} = 0.7\ \mathrm{MeV}/(2\sqrt{3E}) = 3 \times 10^{-5}$, we obtain $\delta\epsilon_x = 0.03$, a negligible growth.

DISCUSSION

In Table 1 we show how the wake-induced energy variation ΔE_w in the septum compares with that in other vacuum chamber regions of LCLS-II downstream of the last bunch compressor, BC2: in the 580 m of Linac 3, the bypass line (1200 m), the linac-to-undulator transfer line (LTU) (300 m), and the undulator blank (in the HXR beam line) (170 m). Considering the septum is only 2.2 m long, its wake effect is relatively strong (assuming SS)—due to the extremely small chamber aperture. Note that for the septum as well as for the other regions in the table, the chirp is negative and mostly linear. In the LCLS-II the total wake-induced chirp serves an important function—to compensate the energy chirp left in the beam in BC2.

Finally, an important conclusion of this work is that, in order to avoid wake induced emittance growth, the septum surface in the vicinity of the free-beam orbit should be plated with a good conductor like Cu, even if the longitudinal wake adds a small nonlinearity to the energy chirp.

Table 1: Wake-induced Energy Variation ΔE_w in Different Regions of LCLS-II after BC2, for the High charge Case, $eN = 250$ pC [8]. Results are Given for the Core of the Beam, and the Entire Beam. The Septum Results Assume SS.

Region	Core	Total
Linac 3	19.8 MeV	36.0 MeV
Bypass	7.1	12.5
LTU	5.9	10.0
Septum, Free Beam	1.3	2.6
Undulator Blank	2.6	7.8
Total	36.7 MeV	68.9 MeV

ACKNOWLEDGEMENT

We thank K. Yokoya for supplying us with his Fortran program for calculating resistive wall wakes, and Y. Ding for providing the bunch shape used in the calculations.

REFERENCES

[1] LCLS-II Conceptual Design Report, SLAC-R-978, 2011.
[2] LCLS-II CD2 Lehman DOE Review, 21 August 2012, SLAC.
[3] See e.g. discussion in K. Bane and G. Stupakov, Phys. Rev. ST-AB 6 (2003) 024401.
[4] A. Chao, *Physics of collective beam instabilities in high energy accelerators*, (John Wiley & Sons, 1993) 47.
[5] K. Yokoya, Part. Accel. 41 (1993) 221, and KEK-PREPRINT-92-196.
[6] H. Henke and O. Napoly, Proc. EPAC90, p. 1046, 1990.
[7] K. Bane and G. Stupakov, Proc. PAC05, p. 3390, 2005.
[8] K. Bane, "Short-range, longitudinal wakefield effects in LCLS-II," talk at LCLS-II meeting, SLAC, June 2012.

Copyright © 2013 CC-BY-3.0 and by the respective authors

NEW TECHNIQUE TO MEASURE THE EMITTANCE OF BEAMS WITH SPACE CHARGE

K. Poorrezaei, R. B. Fiorito, and R. A. Kishek
Institute for Research in Electronics & Applied Physics,
University of Maryland, College Park, MD 20742, U.S.A.

Abstract

Characterization of the transverse phase space of electron beams with space charge is an important requirement for high brightness particle accelerators. We present a novel technique to measure the transverse rms emittance. The method uses the beam divergence, measured, e.g. with optical transition radiation interferometry, and the beam radius, obtained by imaging the beam, to determine the cross correlation term and thus all the terms in the equation for the rms emittance. The experimental data is obtained with a lens-drift-screen setup similar to what is used in a quadrupole scan. However, the analysis of the scan data is unique. It involves taking the cross-correlation term as a control variable in a procedure which matches the beam envelop radius and its derivative calculated from the envelope equation, with the measured radius and divergences at the screen. A linear space charge model is used in the envelope equations, hence the errors in the measurement relate to the nonuniformity of the beam transverse distribution. The technique is tested using simulated data.

INTRODUCTION

It is important to measure the transverse beam emittance in accelerators to quantify the beam quality and match the optics in an accelerator beam line. Most beams of interest are space-charge-dominated near the source and low energy transport section, where the beam dynamics are mostly determined by interparticle forces rather than the beam pressure represented by emittance. Space charge usually modifies and degrades the performance of emittance measurement methods such as quadrupole scan techniques [1]. Reference [2] presents a comprehensive analysis of space charge force effects on such measurements. Several amendments have been proposed in literature to enhance the accuracy of quadrupole scan method for high intensity beams [3].

From the symmetry of the expression for the rms emittance

$$\tilde{\epsilon}^2 = < x^2 >< x'^2 > - < x \cdot x' >^2$$

it is obviously possible to determine emittance with a quadrupole scan technique using measurements of either the beam radius or divergence . The usual implementation of the method is to perform a quadrupole scan of beam size only. However, it is possible to obtain simultaneous, high-quality measurements of beam size and divergence [4]. In this paper, we propose a method for measuring emittance, assuming a linear space charge model, from a small number of measurements of divergence and radius.

In order to use these observables to determine the rms emittance at arbitrary focus points we need a methodology which relates the measured observables, i.e. divergence and beam size to the cross-correlation ($< x \cdot x' >$) term. We will show how this can be done by taking the cross-correlation term as a control variable for matching beam envelopes to their actual envelopes with the constraint that the beam radii and divergences at the screen are same as the measured values.

MEASURING EMITTANCE FOR BEAM WITH SPACE CHARGE

Figure 1 shows a typical quadrupole scan setup. The focal length of the quadrupole (or solenoid) is scanned to achieve a minimum spot size on the screen located downstream at a distance L from the quadrupole.

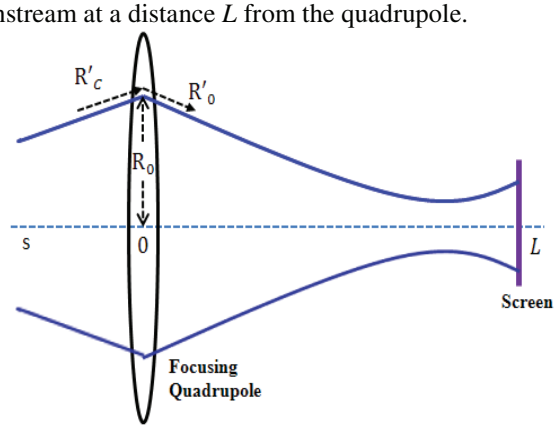


Figure 1: Diagram of a quadrupole scan setup to measure emittance. Beam enters the quadrupole with envelope R_0 and slope R'_C and leaves it with slope R'_0.

For a uniform round beam distribution where space charge is linear, the beam envelope evolution in a drift region is described by the following pair of coupled nonlinear ordinary differential equations (ODE):

$$R_j''(s) - \frac{K}{R_j(s)} - \frac{\epsilon_j^2}{R_j(s)^3} = 0 \quad (1)$$

where j ranges over transverse coordinates x and y, and dimensionless quantity

$$K = \frac{qI_b}{2\pi\epsilon_0 m(c\beta\gamma)^3} \quad (2)$$

is defined as the generalized perveance representing space charge defocusing forces. In Eq. (2), q is charge of the beam particles and I_b is the beam peak current.

Copyright © 2013 CC-BY-3.0 and by the respective authors

We present a method for deriving emittance from two samples of beam radius and divergence for a round beam. As R_x and R_y are equal in this case, we drop the index j and treat all parameters for x.

Multiplying Eq. (1) by R' and then integrating with respect to s leads to the following first order ODE:

$$R'(s) = \pm\left[{R_0}'^2 + \epsilon^2 \cdot \left(\frac{1}{{R_0}^2} - \frac{1}{R(s)^2}\right) + 2K \cdot \ln\left(\frac{R(s)}{R_0}\right)\right]^{1/2}, \quad (3)$$

where R_0 and ${R_0}'$, denote the radius and slope of the envelope at the lens. We need to have the beam envelope relation in terms of at-screen radius and slope quantities. This can be done simply by switching R_0 and ${R_0}'$ with beam quantities at the screen, $R(L)$ and $-R(L)'$, and applying a minus to the LHS of Eq. (3).

Such minuses are necessary as we are treating the envelope evolution along $-s$. Thus, envelope ODE in terms of envelope parameters at screen can be expressed as:

$$R'(s) = \mp\left[R(L)'^2 + \epsilon^2 \cdot \left(\frac{1}{R(L)^2} - \frac{1}{R(s)^2}\right) + 2K \cdot \ln\left(\frac{R(s)}{R(L)}\right)\right]^{1/2}. \quad (4)$$

This form of envelope ODE can easily be solved by numerical integration in packages like MATLAB.

As there is no closed form solution to this equation for large K, we cannot provide a closed form answer for emittance. The following procedure is devised to determine the emittance.

We start with a guess for cross-correlation term and try to infer focal setting applied to the lens by solving Eq. (4). Beam radius and divergence measurements at the screen are translated to $R(L)$ and $R(L)'$ and therefore inferred focal length is going to be a function of the guessed cross-correlation. We use the error between calculated focal length with actual focal length to correct our guess for cross-correlation and reiterate the procedure. Finally, after several steps, as the inferred focal length converge toward the actual one we come within a close vicinity of the actual cross-correlation.

Numerical Procedure

The detailed steps of the procedure are described here. As before we need two sets of beam radius and divergence measurements at two distinct focal lengths f_1 and f_2:

$$\begin{cases} f_1 \\ < x_1^2 > \\ < x'^2_1 > \end{cases}, \quad \begin{cases} f_2 \\ < x_2^2 > \\ < x'^2_2 > \end{cases}$$

Henceforth, we use subscript n, denoting the step number, alone or besides the measurement numbers 1 or 2 on all parameters that change over subsequent steps.

1. $XC1_1$, initial guess for the cross-correlation term at f_1, is chosen according to the discussion in next section.

2. $XC2_n$, the cross-correlation term at f_2, is calculated as:

$$XC2_n = \pm\sqrt{{XC1_n}^2 + < x_2^2 >< x'^2_2 > - < x_1^2 >< x'^2_1 >} \quad (5)$$

3. Next, ϵ_n (not to be confused with normalized emittance) and ${R'}_i(L)$ for two measurement sets ($i = 1,2$) are calculated as:

$$\begin{cases} \epsilon_n = 4[< x_1^2 >\cdot< x'^2_1 > - {XC1_n}^2]^{1/2} \\ {R'}_1(L)_n = 2\dfrac{XC1_n}{\sqrt{< x_1^2 >}} \\ {R'}_2(L)_n = 2\dfrac{XC2_n}{\sqrt{< x_2^2 >}} \end{cases} \quad (6)$$

Note that all three relations are in term of $XC1_n$.

4. ODE Eq. (4) can now be solved for finding at-lens envelope radius and slope conditions of measurements 1 and 2:

$$\begin{cases} R(0)_{1n} \ , & R'(0)_{1n} \\ R(0)_{2n} \ , & R'(0)_{2n} \end{cases}$$

5. For f_{1n} and f_{2n} estimates of focal lengths we have:

$$\begin{cases} f_{1n} = \dfrac{R(0)_{1n}}{{R'}_C - R'(0)_{1n}} \\ f_{2n} = \dfrac{R(0)_{2n}}{{R'}_C - R'(0)_{2n}} \end{cases} \quad (7)$$

Canceling the unknown ${R'}_C$ between these two equations and replacing f_{2n} with its final value f_2 leads to:

$$f_{1n} = \frac{f_2 \cdot R(0)_{1n}}{R(0)_{2n} + f_2 \cdot (R'(0)_{2n} - R'(0)_{1n})} \quad (8)$$

This equation is used to update f_{1n} at each step n. As before, the necessity for two pair of measurements arises from ${R'}_C$.

6. It can be easily checked that f_{1n} is a function of $XC1_n$. i.e. $f_{1n} = g(XC1_n)$. $XC1_n$ should be modified so that reiteration of the procedure from entry 2 makes f_{1n} closer to the target value f_1. In other words, $XC1_n$ is zero of this equation:

$$g(XC1_n) - f_1 = 0 \quad (9)$$

Copyright © 2013 CC-BY-3.0 and by the respective authors

Since derivative of the function g is not known, a modified form of Newton method [5] was used to find $XC1_n$ as zero of this equation.

After updating $XC1_n$ the procedure is repeated from entry 2 until f_{1n} converges with desired precision toward f_1. The process can also be stopped when the variation on emittance calculated at two consecutive steps is less than some $\delta\%$ of the calculated emittance, where δ is usually chosen between 1 and 10. Finally, beam effective emittance is the last ϵ_n calculated in entry 3.

SIMULATION RESULTS

In this section, we present results of tests of our proposed approach with simulated beams. We used the software WARP [6] to simulate the lens-drift experiment. Based on presumed beam parameters ϵ and K and an initial envelope radius at the lens, R_0, WARP generates a set of beam radius and divergence rms values $< x^2 >$ and $< x'^2 >$ at end of the drift section with length L where beam divergence and size are supposedly measured, e.g., using OTRI. The focal length of the lens, f, is calculated according to a hard edge model of the lens. The performance of the method for the several grades of the space charge was tested.

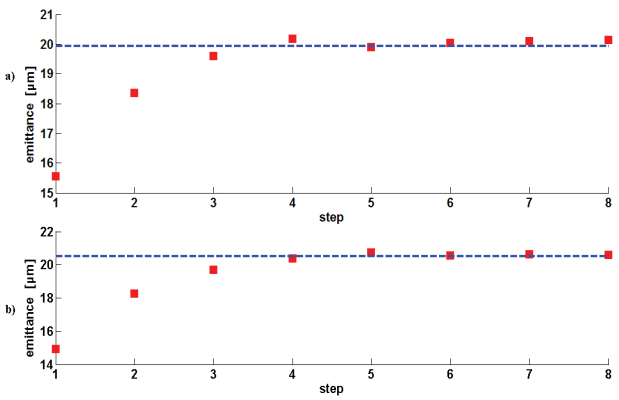


Figure 2: Plot showing convergence of emittance for (a) a medium space charge beam ($K = 2.83 \times 10^{-4}$), and (b) for a high space charge beam ($K = 7.06 \times 10^{-4}$).

Figures 2.a and 2.b show emittance convergence curves for space charge dominated beams with $K = 2.83 \times 10^{-4}$ and $K = 7.06 \times 10^{-4}$ respectively. The convergence is fast and errors in calculation of emittance are satisfactory.

To see effectiveness of the proposed procedure we tried to compare mentioned results with the emittance measured by conventional Courant Snyder (CS) parameter fitting and the minimum beam size method.

In figure 3 we compare the emittance obtained with different methods as a function of the parameter K. As expected the error in determining the emittance obtained using the CS quadratic fitting technique and the minimum beam size method, which are both accurate for emittance dominated beams, becomes increasingly large as space charge increases. In contrast, our two points fit method gives acceptable values for the emittance for all values of the K parameter shown.

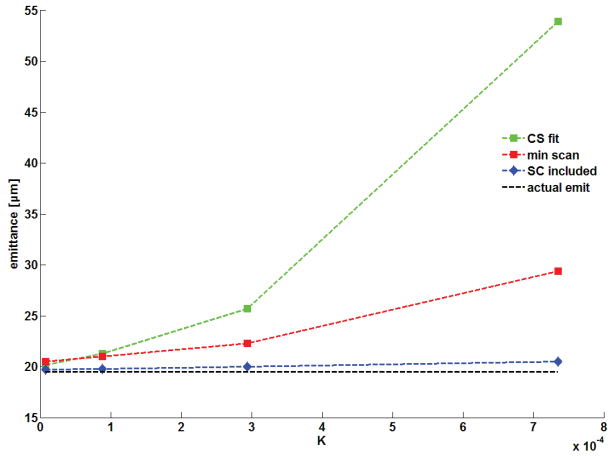


Figure 3: Comparison of the emittance measured using different methods as a function of beam perveance (K): dashed green curve: CS parameter fitting method, red curve: cross-correlation determination at minimum of quad beam size scan, blue curve: two value method including space charge, showing small deviation from the actual emittance.

ACKNOWLEDGMENT

We are grateful for inspiring discussions with J. G. Power, C. F. Papadapoulos, and I. Haber. We also thank J. L. Vay and D. P. Grote for their outstanding support of the WARP code. The work is supported by the U.S. Department of Energy, Office of High Energy Physics contract no. DEFG0207ER41489, the US Department of Defense, Office of Naval Research contract no. N000140711043 and the Joint Technology Office.

REFERENCES

[1] B. E. Carlsten., J. C. Goldstein, P. G. O'Shea, and E. J. Pitcher, "Measuring emittance of non-thermalized electron beams from photoinjectors," *Nuclear Instruments and Methods in Physics Research*, Section A 331 (1993) 791.

[2] S. G. Anderson, J. B. Rosenzweig, G. P. LeSage, and J. K. Crane, "Space-charge effects in high brightness electron beam emittance measurements," *Phys. Rev. ST Accel. Beams* 5 (2002) 014201.

[3] C. G. Limborg, S. M. Gierman, and J. G. Power, "A Modified Quad Scan Technique for Emittance Measurement of Space Charge Dominated Beams," *in Proceedings of the IEEE PAC 2003,* p. 2667 (2003).

[4] R. B. Fiorito and D. W. Rule, "Optical transition radiation beam emittance diagnostics," *AIP Conf. Proc. 319*, p. 21 (1994).

[5] G. J. Borse, *Numerical Methods with MATLAB* (PWS Publishing Company, 1997).

[6] A. Friedman, "Simulation of Intense Beams for Heavy Ion Fusion," *Nucl. Instrum.* Meth. *Phys. Res. A* 544 (2005) 160.

Copyright © 2013 CC-BY-3.0 and by the respective authors

HIGH POWER RF SYSTEM FOR e-linac FOR TRIUMF

A.K. Mitra, Z. Ang, I. Bylinskii, S. Calic, D. Dale, S.R. Koscielniak, R.E. Laxdal, F. Mammarella
TRIUMF, 4004 Wesbrook Mall, Vancouver, BC, Canada, V6T 2A3

Abstract

The TRIUMF e-linac high power system will be built in stages. For the first phase of installation to be completed by September 2014, the injector cryomodule (EINJ) will be fed by a 290 kW cw klystron at a reduced power level and the accelerating cryomodule (EACA) will be powered by an identical klystron. The first 290 kW 1.3 GHz klystron has been purchased from CPI, USA and the high power supply system has been bought from AMPEGON, Switzerland. The second klystron and second high voltage power supply are being procured from the same manufacturers. The 290 kW cw 1.3 GHz klystron is a factory tuned multi-cavity, high efficiency, high gain, broadband, water cooled tube. The klystron has been tested at the factory. The maximum usable linear range of the rf output power of the klystron is 270 kW and is governed by the incremental gain of 0.5 dB/dB. Thus, rf power required for EACA of 200 kW cw is adequately met by the klystron after taking into account the loss in the waveguide components. and waveguides. The high voltage power supply system (KPS) for the klystron, based on a voltage controlled power module technology, consists of 65 kV beam power supply, focus supply, filament power supply and vacuum ion pump power supply. The klystron will be tested to full power on a dummy load by October 2013. At the same time, the KPS will be tested fully with all controls, interlocks, protections and integration of the klystron and a 300 kW high power circulator.

INTRODUCTION

The TRIUMF e-linac consists of an electron gun, buncher cavity, injector cryomodule, and two main-linac cryomodules [1]. The injector module has one 9 cell cavity whereas each of the accelerating (main-linac) cryomodules contains two 9-cell cavities. The cavities operate at 1.3 GHz at 2 Kelvin. The nominal energy of the e-linac is 50 MeV kinetic with an average current of 10 mA. Each 9 cell cavity has two 60 kW high power couplers. Two 290 kW CW klystrons will be employed to feed injector cryomodule (EINJ) and the accelerating cryomodule (EACA). However, the klystron for the injector will be operated at reduced output power. The linac will be built in stages. In the first stage, to be completed by September 2014, a minimum beam energy of 25 MeV, 4 mA will be obtained using the 290 kW klystrons. In the second stage, to be implemented in 2017, a second accelerating cryomodule (EACB) will be added and a 120 kW rf generator will be procured which will feed the injector. The two 290 kW Klystrons will be restored to full power operation to feed the first and the second accelerator cryomodules, to achieve the final beam power goal of 500 kW.

BASIC SCHEME OF THE HPRF SYSTEM

The basic scheme of the high power rf system for the first accelerating cryomodules is shown in Figure 1. The injector has 1 9-cell cavity and will be powered by one 290 kW klystron at a reduced power level whereas the accelerating cryomodule EACA will be run by the second klystron operating at full power. A variable power divider has been employed to facilitate rf conditioning of the two 9-cell cavities in EACA cryomodule. Also, variable phase shifters are employed to achieve phase balance between two couplers in the same cavity and for phase balance between adjacent cryomodules. The major components of the high power rf system is outlined in the following sections.

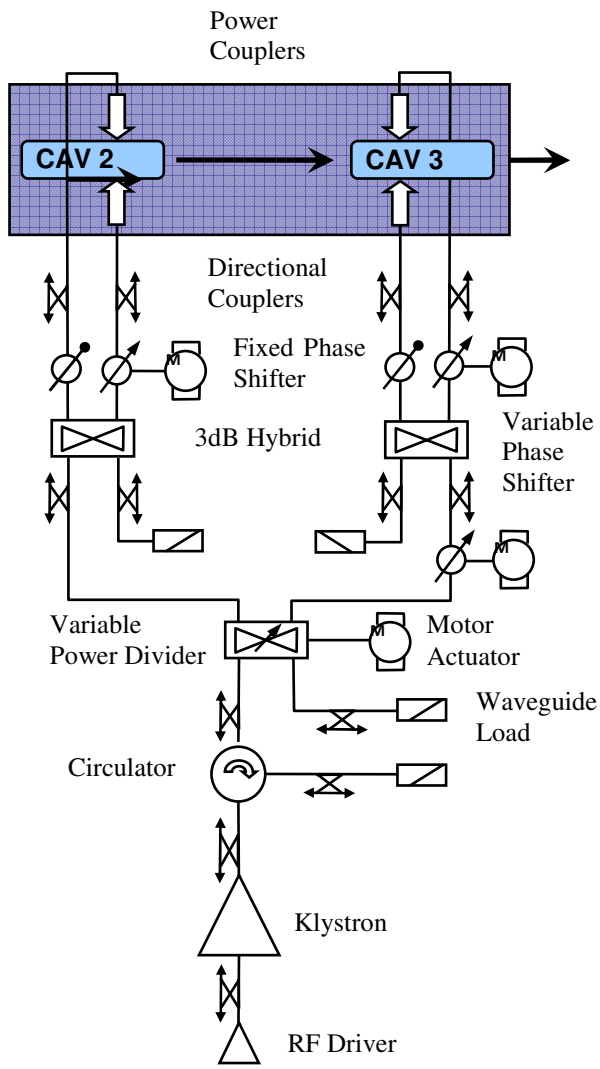


Figure 1: Basic schematic of HPRF system for the first accelerating cryomodule for e-linac

Copyright © 2013 CC-BY-3.0 and by the respective authors

CHOICE OF KLYSTRON

The choice of commercially available high power cw rf sources operating at 1.3 GHz is very limited. Using a 150 kW klystron (available power at the cavity is about 120 kW) for each cavity would have been the ideal choice for e-linac since it would have utilized fully the rf coupler power handling capacity (60 kW operational rating, 75 kW maximum) and provide simple and straight forward low level rf control. Such a system would be very expensive and also a 150 kW klystron is not commercially available. A 290 kW cw klystron, CPI type VKL7967A, shown in Figure 2, has been recently developed jointly with HZB, Berlin and TRIUMF and has been tested at the factory. This solution has been found to be suitable for the e-linac high power rf system and fits to the tight time schedule and available funding of the project. Figure 3 show the measured output power vs drive power for two different operating conditions. The basic parameters of the klystron are listed in Table 1. An oil tank houses the filament and the cathode of the klystron and a snubber is attached to the cathode circuit to limit the stored energy less than 15 joules. Some of the basic parameters for 290 kW and 150 kW operation are, beam voltage 60.5 kV/48.5 kV, beam current 8.1 A/6.8 A, rf drive power 8.0 w/11.0 w, rf efficiency 53%/48% respectively.



Figure 2: CPI type VKL7967A 1.3 GHz cw klystron

HIGH VOLTAGE POWER SUPPLY FOR THE KLYSTRON

A 65 kV, 10 A dc power supply (referred as KPS) has been developed by AMPEGON, Turgi, Switzerland for the CPI klystron. The power supply utilizes 12.5 kV AC 3 phase input and has a transformer with 48 secondary outputs. Each output is connected to a dc switching mode.

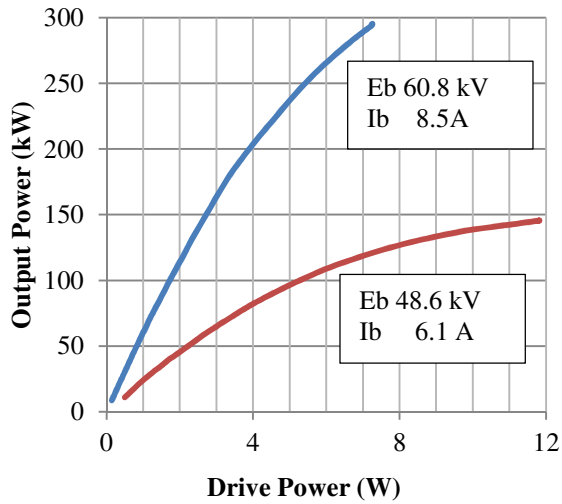


Figure 3: Output power vs drive power of the klystron module.

A novel low ripple enhanced PSM (power switching module) technology has been employed for the cathode power supply [2]. The dc voltage can be varied from 0 to 65 kV with a ripple <0.1% and a efficiency >96%. The KPS contains all required auxiliary power supplies to operate the klystron, rf driver amplifier, amplifier control and fast interlock system. For safety and maintenance of the KPS, a manual disconnect is interposed between the power supply and the Siemens switchgear which supplies all AC power requirement for e-linac. TRIUMF safety system will provide a +24 volt ENABLE control signal for the KPS and will initiate a trip by withdrawing this ENABLE control signal. The power supply has been tested at the factory for all functions, interlocks and local control. Short circuit was applied to a dc cable connected to the dc output of the KPS and the test showed that the output current increases from 0 to 40 amps in 10 µs while output voltage goes from 65 kV to 0 volts. The KPS is now installed at TRIUMF in its final location and is undergoing commissioning Figure 4 shows the photo of KPS being installed at TRIUMF.



Figure 4: AMPEGON KPS at final location at TRIUMF

Copyright © 2013 CC-BY-3.0 and by the respective authors

300 KW CW CIRCULATOR

A high power circulator is connected at the output of the klystron in order to protect it from high reflected power arriving at the klystron output window due to mismatch of the coupler-cavity impedance or arc in the waveguide components. The circulator, rated for 300 kW cw, is water cooled and has an arc protection system. A low-loss glass fiber cable transfers the light of an arc detected with a high sensitive photodiode to the optical input of the arc detector module. The circulator and two 300 kW dummy waveguide loads and system integration is provided by COMARK, USA.

VARIABLE POWER DIVIDER

A variable power divider was chosen to divide power for the two cavities of EACA and was procured from MEGA Industries. During normal operation of the accelerator, the power divider will be set to mid-value so that power from klystron is equally divided and is fed to the two EACA cavities. Since, the cavities are rf conditioned via a self excited mode dictated by low level rf system, the variable power divider will be set for maximum power transfer to the cavity to be conditioned. For rf conditioning the cavities, 2 to 4 kW cw and 5 to 15 kW pulse power may be required depending on the coupling of the power couplers to the cavity. Maximum attenuation of 37 dB of incident power can be achieved with a maximum insertion loss of 0.17 dB.

VARIABLE PHASE SHIFTER

Variable phase shifters are required to balance the phase of the RF input couplers on the same cavity. These variable phase shifters should have more than 120 degrees of phase shift to compensate for tolerances in the waveguide assembly. Also, phase shifter is required to compensate for phase shift between two adjacent 9-cell cavities in the same cryomodule. Multiple solutions were investigated using two stub phase shifter, three stub phase shifter and a hybrid based phase shifter. Simulations were conducted for each case. The two stub phase shifter is not capable of providing the required phase shift; however, the three stub phase shifter can provide the phase adjustment required but requires at least two motors (or three, if two are not ganged together) with independent controllers. The relationship between phase and position of the stubs is not straightforward, so calibration and intelligent control is needed. The hybrid coupler based phase shifter requires significantly more room but has an excellent phase shift characteristic with the movement of the short circuit. The simulation of such a phase shifter shows a phase change of 22.5 degrees occurs for 1 cm change in stub position The simulated insertion less and return loss are <0.1 dB and <-23 dB respectively for the complete range of phase shift.

Table 1: Parameters of CPI Klystron Type VKL 7967A

Operating Frequency Mid-band	1300 MHz
CW Output Power	290 kW
RF Power Gain at nominal beam voltage	42 dB
Usable CW Output Power[1]	270 kW
Usable DC to RF Efficiency[1]	52 %
VSWR Tolerance, maximum	1.2:1
-1 dB Bandwidth	2.0 MHz
-3 dB Bandwidth	6.0 MHz
Klystron Beam Voltage	62.5 to 65 kV
Klystron Beam Current, maximum	9.1A
Beam Perveance, minimum	0.55 μA/V$^{1.5}$
Collector Dissipation, maximum	600 kW
Body Dissipation (without Output)	1% P_{beam}
Tuning	Fixed tune
Beam Focusing	Electromagnet
Phase shift of Output Power to Beam Voltage shift at operating beam voltage	<0.05 degree/volt
Output Wave Guide	WR-650
Cooling	de-ionized water
RF Input, coaxial	Type“N”
Note 1: for incremental gain, IG >0.5dB/dB	

INSTALLATION AND TEST OF THE KLYSTRON

It is proposed to commission the KPS and test the klystron by October 2013. At first, the KPS will be tested for all interlock functions, safety switching on/off procedure with Siemens switch gear and manual disconnect and key sequence for lock out procedure. The front touch panel will be also tested to bring up the KPS in a controlled mode. After short circuit test of the dc output is done, the dc high voltage cables will be connected to the klystron. In the mean time, the klystron will have a snubber installed in the oil tank the focus, filament and vacuum ion power supplies connected and water cooling will installed. The circulator and the two dummy loads will be connected to begin the high power test of the system. EPICS control system interface will be commissioned. This will allow control of the KPS system as well as monitoring the temperature and flow of the water cooling system of the klystron, the circulator and the two loads and the dc parameters of the KPS-klystron system.

REFERENCES

[1] S. Koscielniak et al, “The ARIEL Superconducting Electron Linac”, LINAC12, Tel Aviv, Israel, Sept 9-14, 2012.

[2] M. Frei, M. Bader, et al, “Ampegon’s New Klystron Power Supply System for the Triumf E-Linac 1.3 GHz/270kW cw RF System”, IPAC13, Shanghai, China, 12-17 May 2013.

Copyright © 2013 CC-BY-3.0 and by the respective authors

THE LAYOUT OF 352 MHz 400 kW RF POWER AMPLIFIER

A. Smirnov, A. Krasnov, I. Rezanov, E. Ivanov, K. Nikolskiy, S. Polikhov, G. Sharkov
Siemens Research Center LLC, Moscow, Russia

Abstract

In this paper, we present the current status of the RF power amplifier under development for European Spallation Source (ESS, Sweden) normal conducting and superconducting accelerating sections based on solid-state architecture. A single 400 kW pulsed machine is represented with four standard 19" cabinets. Brief description and technical solutions regarding 8 kW (Class-AB, Si transistor based) RF modules, different power combiners and control system are shown.

INTRODUCTION

High power RF sources are important elements for most of linear accelerators that have found growing number of applications in science and medicine. Current power amplifier is being designed and developed to fulfil the requirements for superconducting cavities in ESS accelerator facility [1].

Main benefits of the generator under development are its smaller footprint, perspective of lower cost, better reliability and higher efficiency, achieved with class-AB operation, compared to conventional RF power sources like klystrons or other vacuum tubes generators. The solid-state microwave power amplifier modules based on Freescale LDMOS transistors arranged in parallel scheme with use of Wilkinson dividers/combiners are designed on PCB boards.

One machine is planned to be assembled inside set of four 19" cabinets. Each will contain 12 RF power amplifier modules with individual power combiner. All modules are connected to a power combiner with 50 Ohm coaxial cables. The set is terminated with a single common power combiner.

RF POWER MODULES

We have designed and manufactured compact RF power amplifier (RFPA) module prototype. The principal RFPA scheme is shown in Fig. 1. The driver stage is built using Freescale MRFE6VP100H transistor pair. The device is operated in Class-AB. Downstream the driver stage; there is a lumped element 1-to-8 Wilkinson-type splitter with final stage amplifiers at its outputs. All splitter ports have impedances of 50 Ohm.

Freescale MRFE6VP61K25H transistor pairs are being used for the final stage amplifying.

The second Wilkinson 8-to-1 power combiner is located downstream to the final stage amplifiers. The intermediate impedance of this combiner equals to 12.5 Ohms, which results in lower insertion loss. Additionally a lumped element mathing network is used to match the 12.5 Ohm intermediate impedance to output 50 Ohms. In Fig. 2, one of the fabricated RFPA modules is presented.

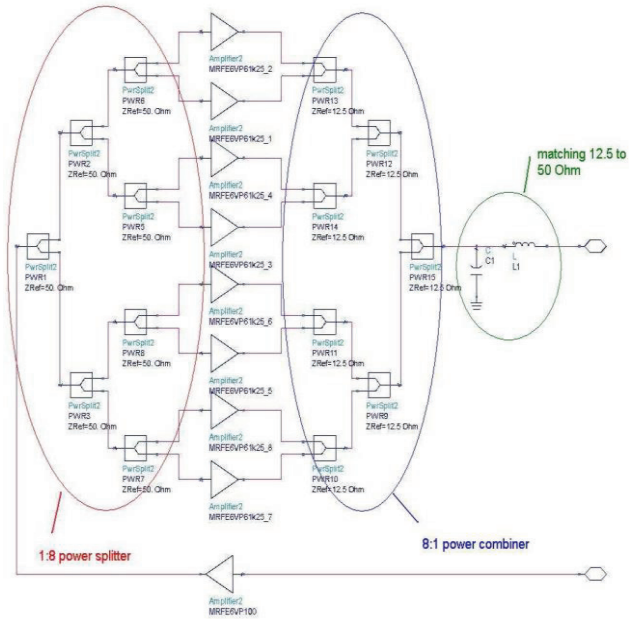


Figure 1: Single RFPA module principal scheme.

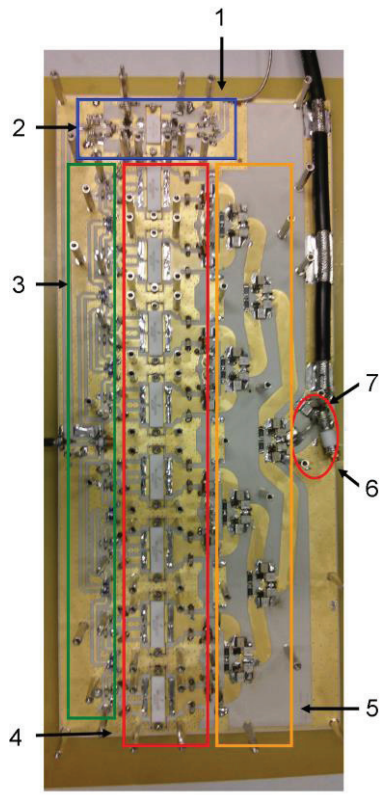


Figure 2: RFPA module: 1 – RF input; 2 – driver stage; 3 – input Wilkinson splitter; 4 – front-end amplifiers; 5 – output Wilkinson combiner; 6 – 12.5 to 50 Ohm matching circuit; 7 – RF output.

Copyright © 2013 CC-BY-3.0 and by the respective authors

Total efficiency dependence on the output RF power is shown in Fig. 3.

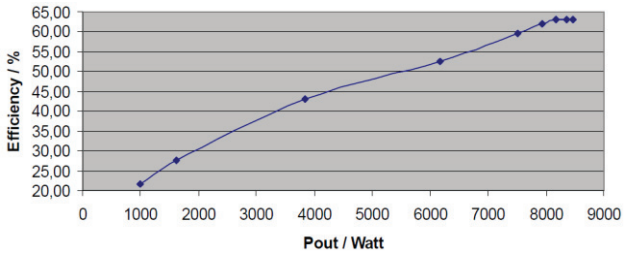


Figure 3: Efficiency vs. output RF power.

This prototype module is lying on a 5 mm thick copper plate that is air cooled, but in future it is planned to replace it with water based heat sink to guarantee heat sink temperature of less than 40°C.

RF performance features of a single RFPA are listed in Table 1.

Table 1: RFPA Specifications

Parameter	Value
Operation Frequency	352.21 MHz
Operation mode	max. 4 ms pulse, 5% duty cycle
Output RF power	8000 W
RF efficiency	~63%
Gain	50 dB
Input RF power	max. 10 W
Supply voltage	50 V
Input/Output impedance	50 Ohm
Dimensions	190×440×80 mm^3

POWER COMBINER

The current amplifier design implies an arrangement of 48 modules (giving required total RF power of 400 kW) in four 19" cabinets with 12 RFPAs and individual 12-to-1 power combiners in each of them. We have designed and fabricated compact power combiner based on rectangular-coaxial line with 12 7/16 input RF connectors and 3-1/8" EIA output flange like shown in Fig. 4. The 12 inputs are arranged in two rows with 6 in each.

The shapes of the copper inner conductor and coupling loops have been optimized to achieve best matching between inputs and 50 Ohm output, low surface fields and equal amplitude and phases of transmission coefficients between every input and output. The inner conductor plate is connected to the same outer case wall on which the inputs are located. This gives an opportunity to easily insert water cooling channels inside this plate as it is the hottest part of the combiner.

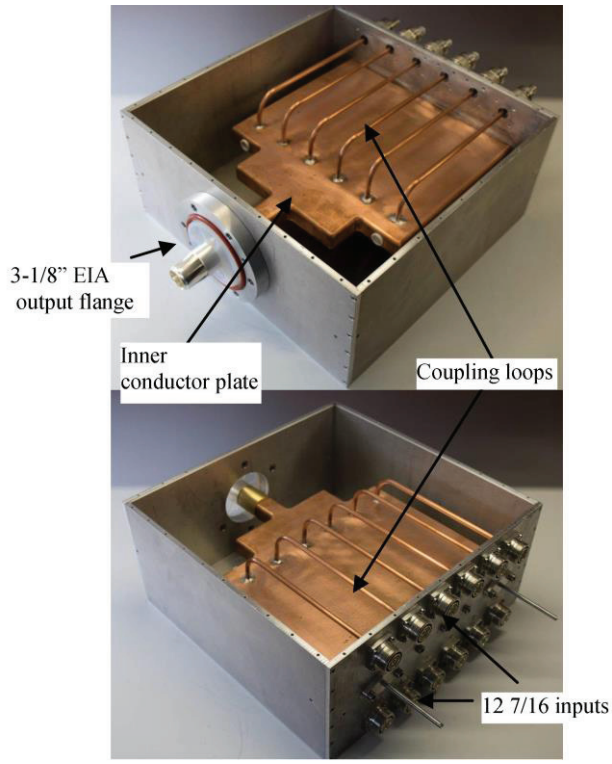


Figure 4: 12-to-1 power combiner prototype.

S11 measurement result referring to the common output port 1 is plotted in Fig. 5; other RF characteristics are listed in Table 2.

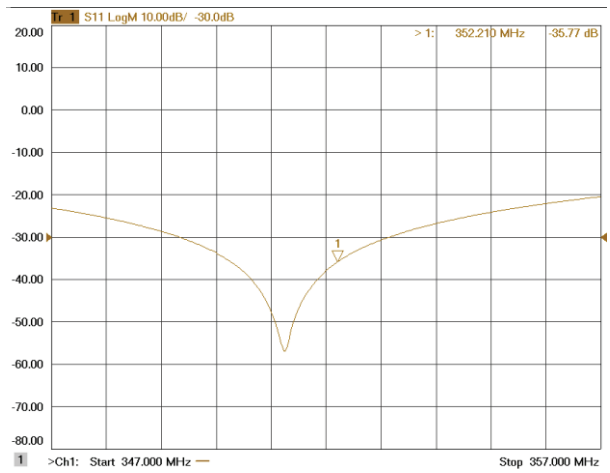


Figure 5: Measured return loss plot.

Table 2: Power Combiner Features

Parameter	Value
Operation frequency	352.21 MHz
Return loss	36 dB
Dissipated RF power ratio	0.5 %
Power splitting equality	~3 %
Dimensions	45×43×16 cm^3

Copyright © 2013 CC-BY-3.0 and by the respective authors

The device showed good performance and can be used in the amplifier. Currently the test bench for high power tests is under development. The next step will be to redesign this combiner so that inputs and output will be on the same side.

GENERATOR FORMFACTOR

All blocks including RFPA modules, power distribution, control, measurement and water-cooling systems will be assembled in four 19" cabinets ending up with a common 4-to-1 power combiner as shown in Fig. 6.

We assume that total height of the final generator assembly would not exceed 42 units (~190 cm) which is less than typical door height.



Figure 6: A row of 4 19" cabinets with common output power combiner.

An arrangement in each cabinet is in the following order from bottom to top: water-flow system, 12 19" racks with RFPAs, control system and 12-to-1 power combiner.

In each rack (see Fig. 7), there is a capacitor bank, supply power distribution system, 2 RFPA modules and water-cooling system with heat exchanger.

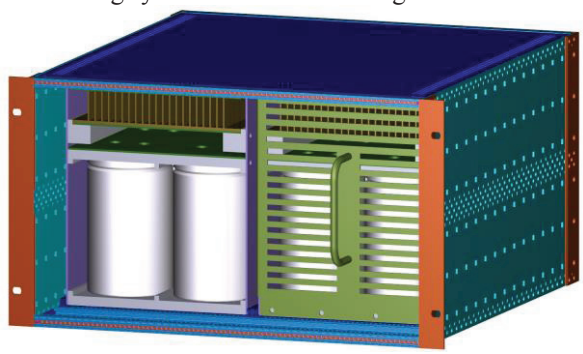


Figure 7: A single 19" rack with 2 RFPA modules arrangement scheme.

As for now the height of the racks is approx. 6 units (~27 cm) and is subject for further ompitimization.

The final 4-to-1 power combiner is assumed to have 4 3-1/8" EIA input flanges and a single 6-1/8" EIA output.

SUMMARY

The 352 MHz 400 kW pulsed machine is now in the design stage. In this paper, class-AB power amplifier modules based on Freescale 50V LDMOS transistors, box-shaped power combiner and the current system topology are described.

We are now working on the flexibility and scalability of the system so that it can be easily adapted to wide variety range of customers requirements on total output RF power, pulse length, duty cycles etc.

REFERENCES

[1] R.A. Yogi, A. Rydberg, et. al., Uppsala High-Power Test Stand For ESS Spoke Cavities, Proceedings of LINAC-12, Tel-Aviv, Israel, 2012.

Copyright © 2013 CC-BY-3.0 and by the respective authors

THE LAYOUT OF 72 MHz 16 kW RF POWER GENERATOR

A. Smirnov, A. Krasnov, I. Rezanov, E. Ivanov, K. Nikolskiy, S. Polikhov, G. Sharkov,
Siemens Research Center LLC, Moscow, Russia

Abstract

In this paper, we present the current design of the RF power generator for medical cyclotron Eclipse (Siemens Healthcare) based on solid-state architecture. The 16 kW machine operating at 72 MHz in continuous wave regime is being assembled into standard 19" cabinet. Brief description and technical solutions regarding 2 k W (Class-AB, Si transistor based) RF modules, power combiner and control system are shown.

INTRODUCTION

High power RF sources are important elements for most of accelerators that have found growing number of applications in physics and medicine. Current power amplifier will feed Eclipse cyclotron that is being used for PET isotopes production (^{18}F, ^{11}C, ^{13}N and ^{15}O) with H- ions at 11 MeV [1].

The main benefits of the generator under development are its smaller footprint, perspective of lower cost, better reliability and higher efficiency, achieved with class-AB operation, compared to conventional RF power sources like klystrons or other vacuum tubes generators. The solid-state microwave power amplifier modules based on Freescale LDMOS transistors arranged in parallel push-pull circuits, are designed on PCB boards.

All modules are connected to a power combiner with 50 Ohm coaxial cables.

RF POWER MODULES

We have designed and manufactured compact RF power amplifier (RFPA) modules with two pairs of Freescale™ MRF6V2010NR1 (driver stage) and MRFE6VP1K2H (main stage) transistors arranged in push-pull topology as shown on Fig. 1.

The frequency is adjustable between 72 and 73 MHz because cyclotron resonant frequency changes in this range during operation.

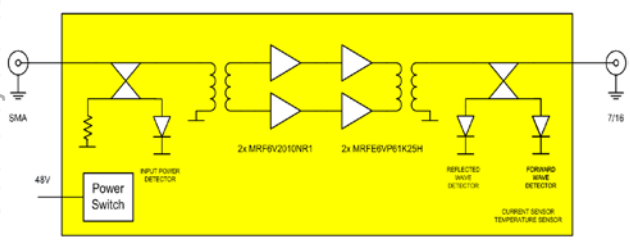


Figure 1: Parallel push-pull circuit.

The manufactured module prototype is presented on Fig. 2. Arlon AD255 with ε=2.55 is used a substrate material. The transistors are fed with 180^0 phaseshift, provided with an RF transformer. Achieved RF performance is shown in Table 1.

Table 1: RFPA Specifications

Parameter	Value
Bandwidth	72..73 MHz
Output RF power	max. 2100 W
RF efficiency	~75% (>80% planned)
Gain	52..55 dB
Input RF power	max. 30 mW
Supply voltage	48 V
Input/Output impedance	50 Ohm
Input/Output VSWR	max 1.3
Dimensions	16×25 cm^2

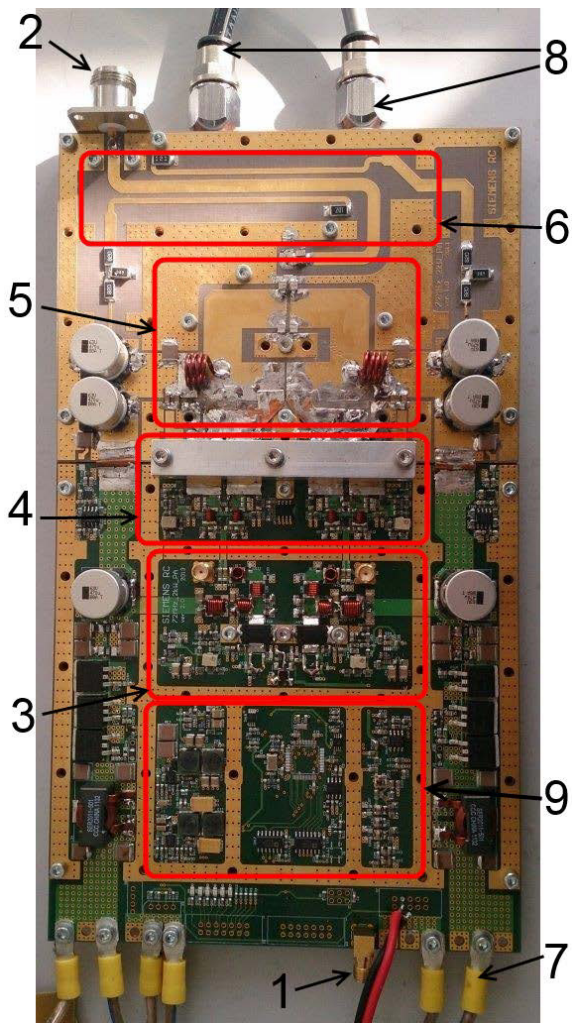


Figure 2: RFPA module: 1 – RF input; 2 – RF output; 3 – driver stage; 4 – main amp stage; 5 – output matching transformer; 6 – output directional coupler; 7 – DC supply; 8 – water cooling tubes; 9 – MCU unit.

Copyright © 2013 CC-BY-3.0 and by the respective authors

MCU (microcontroller unit) is a logic scheme that is able to collect the following measured parameters and and communicates with the external control system:

- Supply voltage and current;
- Input LLRF power level;
- Forward/reflected power at the RFPA output.

A set of nine of these RFPAs (giving total output RF power up to 18 kW) with individual off-shelf 3kW air-cooled AC-DC converters and EMI filters are packaged inside nine 19" racks of 2 units (~90 mm) height as shown on Fig. 3.

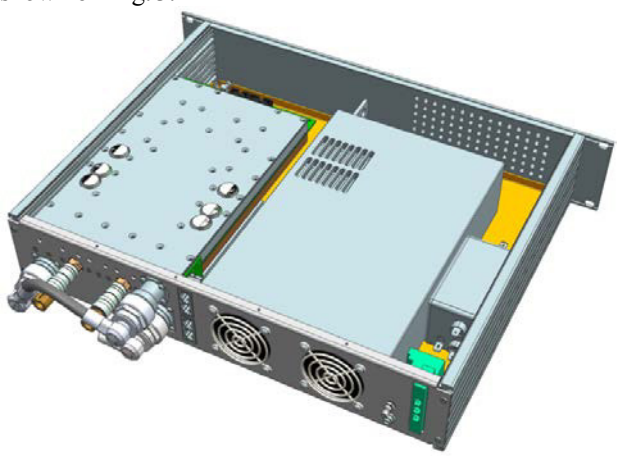


Figure 3: Single RFPA rack.

The RF efficiency dependence on output RF power is plotted on Fig. 4.

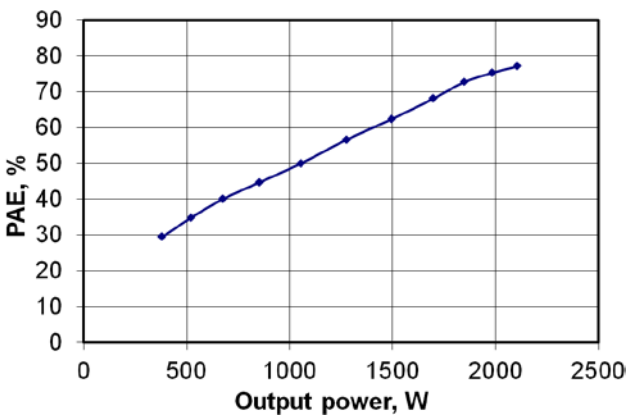


Figure 4: Measured RFPA efficiency vs. output RF power.

POWER COMBINER

Most of power combiners available on the market are based on coaxial geometry and are huge. In order to achieve the best compactness of the generator we have designed and manufactured the planar power combiner of 1 unit (~45 mm) height (see Fig. 5). It has nine 7-16 RF inputs and 1-5/8" EIA output coaxial flange.



Figure 5: 9-to-1 planar power combiner.

The inner conductor with the outer shielding aluminium case forms two sections of rectangular-coaxial serving as pre-combining and matching elements. The oval-shaped hole in the pre-combining part serves for input signals amplitude and phase balancing. The water-cooling tubes shapes have been optimized to introduce low perturbation of the EM fields.

Power combiner S-parameters measurement results referring to the common output port 1 are plotted on Fig. 6, other RF characteristics are listed in Table 2.

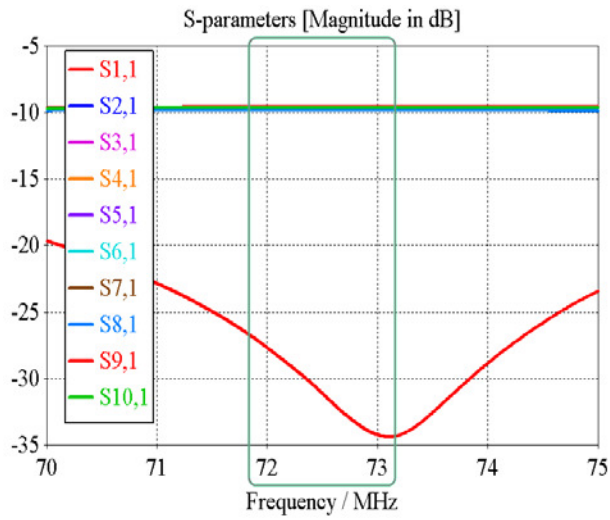


Figure 6: Measured S-parameters plot (operation frequency range is highlighted).

Table 2: Power Combiner Features

Parameter	Value
Bandwidth	72..73 MHz
Return loss	27..34 dB
Dissipated RF power ratio	0.1 %
Power splitting equality	<1 %
Dimensions	45×43×4.5 cm^3

Copyright © 2013 CC-BY-3.0 and by the respective authors

GENERATOR FORMFACTOR

All 12 blocks including power distribution, control, measurement and water-cooling systems will be assembled in 19" cabinet presented with components arrangement on Fig. 7.

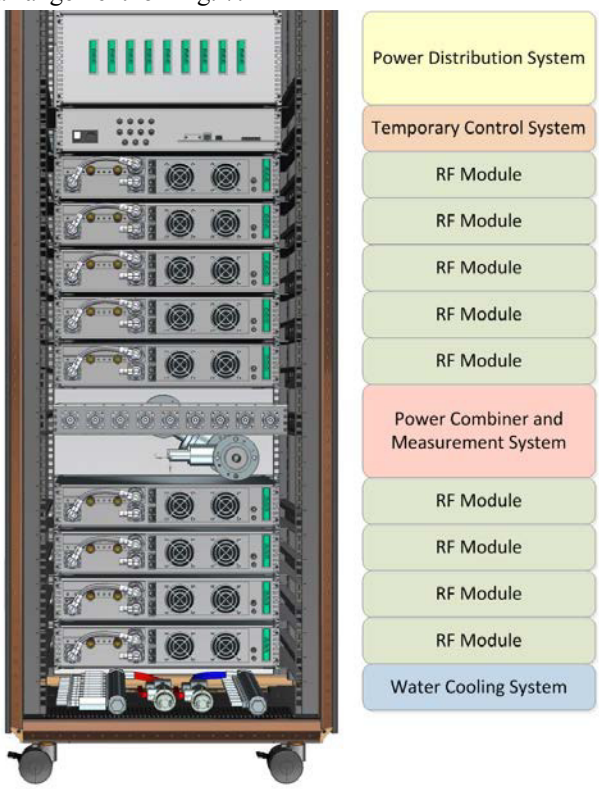


Figure 7: Generator assembly and arrangement scheme.

According to the current preliminary design the total height of the cabinet is 30 units (~1.4 m) and will be reduced down to 18 u nits (~80 cm) by arranging the components closer to each other – especially by putting all RFPAs into a single 4 units (~18 cm) high rack and uniting measurement system with the power combiner, as shown on Fig. 8.

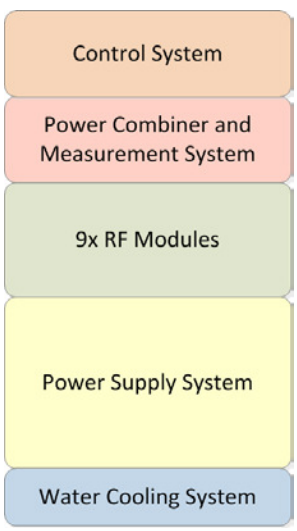


Figure 8: Goal scheme of the generator design.

The following is brief descriptions of the components.

Temporary Control System

The control system creates the reference signal, performs its splitting and amplifying. Each channel provides independent phase shift and adjustment of the transmission coefficients between master oscillator and the RFPA LLRF inputs. It is also possible to use an external reference signal.

Control system also examines the output RF signal and can adjust its phase and amplitude.

Power Distribution System

The generator can be used under 110V or 220V three-phase electrical network. The distribution system equally divides power between three phases by connecting three RFPA modules to each phase.

Cooling system located at the bottom of the cabinet provides the water flow through the RFPA modules and the power combiner.

SUMMARY

We have presented the current design of the 72 MHz 18kW (CW) power generator that is now being assembled and undergoing high power tests. The solid-state class-AB RF amplifiers show commendable efficiency of 75% at the operation output RF power level of 2 kW and will be improved to have over 80%.

As for now, the total height of the prototype device is 1.4 m and we are making efforts to shorten it down to 80 cm.

REFERENCE

[1] http://www.medical.siemens.com/siemens/en_GB/gg_nm_FBAs/files/dash/ds_09_eclipse.pdf

Copyright © 2013 CC-BY-3.0 and by the respective authors

OVERVIEW OF THE RHIC E-LENS SUPERCONDUCTING MAGNET POWER SUPPLY SYSTEM *

D. Bruno#, A.Di Lieto, G. Ganetis, R.F. Lambiase, W. Louie, C. Mi, T. Samms, J. Sandberg,
Brookhaven National Laboratory, Brookhaven Science Associates, Upton, NY, 11973, USA.

Abstract

A new superconducting solenoid magnet was installed in the yellow ring of RHIC before Run 13 as part of the e-lens project. The second solenoid superconducting magnet will be installed in RHIC after Run 13 is over. There are 6 power supplies required for the solenoid, fringe and anti-fringe coils for both magnets. Commercial off the shelf unipolar power supplies are used to power the solenoid, fringe and anti-fringe coils. There are 24 corrector power supplies required for both magnets. Custom built 50A bipolar power supplies are used to power the correctors. Quench protection and quench detection have also been installed in this power supply system. In addition, 4 new phase shift power supplies have been installed in RHIC which are needed for the new e-lens system. These phase shift power supplies have been installed across the yellow focusing and defocusing arcs as well as the blue focusing and defocusing arcs from sector 8 to sector 10. Power Supply technology, control system, connections, the quench detection/protection system, and status will be presented.

E-LENS POWER SUPPLIES

Power Supplies Description

There are thirty power supplies (p.s.'s) used in the e-lens p.s. system. Fifteen p.s.'s for each magnet. These are all current regulated power supplies with a DC Current Transformer (DCCT) current sensing element.

The two Solenoid p.s.'s are rated at 20Volts and 750Amps dc. The ac input to both Solenoid p.s.'s is 480Vac. The two Fringe and two Anti-Fringe p.s.'s are rated at 15Volts and 534Amps dc. The ac input to the Fringe and Anti-Fringe p.s.'s is 480Vac. The Solenoid and Helical p.s.'s are commercially available voltage regulated switchmode p.s.'s which are used within the BNL designed current regulator. The required p.s. current reproducibility is 0.01% of maximum current.

The twenty four bipolar trim p.s.'s are 20Volts and 50Amps dc. The ac input to the bipolar trim p.s.'s is 208VAc. These are the same bipolar p.s.'s that are used for the RHIC corrector magnets. The required p.s. current reproducibility for the trim p.s.'s is 0.1% of maximum current.

During normal operation these p.s.'s ramp up slowly to a dc level and stay there.

The Solenoid, Fringe and Anti-Fringe p.s.'s are all connected to their own quench protection assemblies (QPA's). These QPA's contain an energy extraction resistor across an IGBT switch as well as a diode across the output of the p.s. The IGBT and energy extraction resistor are connected to the positive output terminal of the p.s. and the magnet. The diode is connected across the dc terminals of the p.s. When a fault occurs in the p.s. or the QPA, or if the magnet quenches, the diode conducts across the p.s. and the IGBT opens so the energy extraction resistor is now in series with the load. The current from the load goes through the diode and through the energy extraction resistor. The supply also trips to the STANDBY-FAULT state. A DCCT was installed in the QPA for the regulation of the e-lens p.s. The trim p.s.'s don't have a separate QPA; they have a crowbar with an energy extraction resistor built into them.

There is a quench detector (qd) for the e-lens p.s. system which monitors the voltage across the magnets and the current of the magnets. The qd trips the p.s. to STANDBY-FAULT if a quench is detected. Whenever the p.s. trips to the STANDBY-FAULT state, the energy extraction resistor becomes part of the circuit.

e-Lens P.S. Magnet Loads

There are 17 superconducting magnets in one cryostat. The main Solenoid is connected to one p.s. The two Fringe magnets are connected in series to one p.s. The two Anti-Fringe magnets are connected in series to one p.s. The 12 trim magnets are connected to 12 individual p.s.'s. The Solenoid magnet has an inductance of 14H. Each Fringe magnet has an inductance of 515mH. Each Anti-Fringe magnet has an inductance of 38.4mH. The two long (vertical and horizontal) trim magnets are 5.34mH each. The 5 short vertical and 5 short horizontal trim magnets are 19.2mH each. The dc resistance of the corrector cables to the magnets is between 74mohms and 120mohms depending on the cable size used.

Quench Detection for e-Lens

The yellow solenoid magnet is made up of 11 double layers (coils). In order to protect the magnet during a quench the coil difference is taken between 5 coils and 6 coils. If this coil difference ever exceeds 125mV the qd will tell the QPA to open the series IGBT, then the energy extraction resistor is connected in series with the load. The p.s. contactor opens after the IGBT in the QPA opens. The blue solenoid magnet is made up of 10 double layers. The coil difference is taken between 6 coils and 4 coils because of the available voltage taps.

There are 2 Fringe coils in each magnet and 2 Anti-Fringe coils in each magnet. Each Fringe coil has dc terminals that come out of the magnet. The Two Fringe coils are connected in series outside of the magnet to one

* Work supported by Brookhaven Science Associates, LLC under Contract No. DE-AC02-98CH10886 with the U.S. Department of Energy
# bruno@bnl.gov

Copyright © 2013 CC-BY-3.0 and by the respective authors

p.s. The coil difference is taken between these two Fringe coils. The qd coil difference trip setting is 125mV. Each Anti-Fringe coil has dc terminals that come out of the magnet. The two Anti-Fringe coils are connected in series outside of the magnet to one p.s. The coil difference is taken between these two Anti-Fringe coils. The qd coil difference trip setting is 125mV.

The gas cooled leads for the Solenoid, Fringe and Anti-Fringe coils are set to trip at 250mV.

The super conducting leads for the Solenoid, Fringe and Anti-Fringe coils are set to trip at 25mV.

The corrector coils do not have qd on the coils, gas cooled leads or superconducting leads. The p.s.'s have an overvoltage interlock which fires a crowbar SCR and connects an energy extraction resistor in series with the magnet coil when the voltage crosses a threshold. The overvoltage trip has been adjusted to make sure that we stay below the Miits rating the corrector coils and superconducting leads when the corrector coil or superconducting leads quench.

Quench Protection for e-Lens

This is the Miits calculation for the solenoid magnet coil.

- The solenoid maximum voltage can see to is 600V across the magnet or +/-300V to ground.
- The maximum current for the magnet is 500A.
- The energy extraction resistor = 600V / 500A = 1.2ohms.
- The inductance of the magnet = 14H.
- The time constant τ = 11.67seconds.
- Miits rating of the solenoid = $I^2(\tau/2)*10^{-6}$=1.46Miits
- The Miits rating of the magnet must be at least 1.46Miits.

The original design of the solenoid magnet showed it could only absorb 0.5Miits. Diodes were added across each solenoid coil in order to raise the magnet's Miits rating from 0.5Miits to 1.5 Miits. These diodes are able to handle 1.5Miits.

The solenoid superconducting leads also had to have their Miits rating raised from 0.5Miits to 1.5 Miits. Stabilizing copper was added to the leads to increase the Miits rating.

The energy extraction resistor for the solenoid magnet was built to absorb 1.75MJ ($E=1/2LI^2$) with a temperature rise of 100C. A stainless steel resistor was used and it was assumed that all of the energy was dumped into the stainless steel. Using q = m x C x ΔT one can solve for m = mass of stainless steel resistor. C= specific heat of material, q=energy dumped into material and ΔT is the desired temperature rise. Once the mass is known the resistor can be constructed.

For the Fringe magnet, the maximum voltage to ground is +/-150V and the maximum current is 500A. For 2 coils in series the Miits rating needs to be at least 0.215 Miits. The Fringe coils are designed for 0.48Miits so no extra protection was required for the Fringe coils.

The energy extraction resistor for the Fringe magnet was built to absorb 128.75KJ ($E=1/2LI^2$) with a temperature rise of 100C. A stainless steel resistor was used.

For Anti-Fringe magnet, the maximum voltage to ground is +/-50V and the maximum current is 400A. For 2 coils in series the Miits rating needs to be at least 0.0215 Miits. The Fringe coils are designed for 0.48Miits so no extra protection was required for the Fringe coils.

The energy extraction resistor for the Anti-Fringe magnet was built to absorb 6.3KJ ($E=1/2LI^2$) with a temperature rise of 100C. A stainless steel resistor was used.

For the corrector the voltage threshold the SCR crowbar circuit is set to fire at 8V (and the current is limited to 45A) which tells us the magnet must absorb at 1847 Miits. The corrector coils, and superconducting leads, Miits rating is 2296 so we are well below the rating.

NEW PHASE SHIFT POWER SUPPLIES

Power Supply Configuration

Four new phase shift ps's (to shift the phase of the beam for e-lens) were installed in RHIC during RHIC runs 12 and 13.

Two new phase shift p.s.'s were installed in RHIC during Run 12. One was installed in the blue ring on the quad defocusing bus from sector 8 to sector 9 across the quad arc magnets. The other p.s. was installed in the yellow ring on the quad defocusing bus from sector 8 to sector 9 across the quad arc magnets.

In Run 13 two more phase shift ps's were installed in RHIC. One was installed in the blue ring on the quad focusing bus from sector 8 to sector 9 across the quad arc magnets. The other p.s. was installed in the yellow ring on the quad focusing bus from sector 8 to sector 9 across the quad arc magnets. All four phase shift p.s.'s were operational for run 13. Each p.s. is connected to 12 quad magnets in each arc. The total inductance each p.s. sees is about 18mH.

All four of the phase shift p.s.'s are located in one service building.

Power Supplies Description

The phase shift p.s.'s are commercially available voltage regulated switchmode p.s.'s which are used within the BNL designed current regulator. These p.s.'s are rated at 16Volts and 185Amps dc. The ac input to these p.s.'s is 208Volts ac and 12Amps rms.

The phase shift p.s.'s each have a QPA which operates in a similar way to the e-lens power supplies QPA's, however, a crowbar SCR was used to short out the p.s. instead of a diode.

Quench Detection Modification for Phase Shift P.S.'s

The qd's for the phase shift p.s.'s reside in two service buildings (1008B and 1010A) and one alcove (9B).

The voltage of the arc quad magnets was already being measured in the alcove 9B qd from the original design of RHIC. The calculation of the arc quad magnets voltage,

Copyright © 2013 CC-BY-3.0 and by the respective authors

using the di/dt method, is also done in the same qd. The voltage calculation had to modified to include the current contribution of the phase shift p.s.'s. This was achieved by sending the p.s. current readback signal from the p.s.'s in the service building (through the tunnel) to the alcove over fiber optics.

The qd voltage tap measurement of the gas cooled lead and super conducting lead was already being done in 2 service buildings (1008B and 1010A) from the original design of RHIC. These voltage taps had to be modified to include the contribution of the phase shift ps current. This was done by sending the p.s. current setpoint over the Real Time Data Link (RTDL) from the p.s. Waveform Generators (WFG's) located in 1010A to the qd's located in 1008B and 1010A.

CONTROL SYSTEM

e-lens and Phase Shift P.S. Control System

Both the e-lens and phase shift p.s.'s use the same 3u chassis control bucket. In this control bucket resides the setpoint card, the current regulator card, the buffer card, the DC overcurrent (DCOC) card, the digital isolation card and the control card. The setpoint card receives a 0-10V analog signal from a fiber optic interface card which resides in another bucket. This analog setpoint is sent over the 3u control chassis backplane to the BNL designed current regulator card. This current regulator card has a removable PC board for adjusting time constants to stabilize the p.s. current loop. The buffer card sends four analog signals back to the Multiplexed Analog to Digital Converter (MADC). These four signals are p.s. current setpoint, output current, output voltage and p.s. current error. The phase shift p.s.'s and the e-lens Fringe and Anti-Fringe p.s.'s use a 0-10V output DCCT head. The e-lens Solenoid p.s. uses a current output DCCT head. This current output is sent to a BNL designed DCCT card which converts the current to a voltage. The DCOC card receives the shunt input from the commercial p.s. shunt and uses this shunt on the DCOC card. The digital isolation card receives commands from a Node card which is external to the p.s. and sends p.s. statuses back to this Node card. The Node card communicates over a MODBUS Plus network to a MODICON Programmable Logic Controller (PLC).

OPERATIONAL EXPERIENCE & STATUS

Phase Shift P.S. Problems During Runs 12 & 13

During Run 12 some problems were encountered with the first two phase shift p.s.'s. We learned from these problems in order to improve the reliability of these p.s.'s for Run 13. The problems during Run 12 included:

- Running a copper BNC cable for the p.s. current readback to the qd through the tunnel. The current readback would move with beam. This was corrected by running a fiber through the tunnel.
- Workmanship problems with the wiring harness which caused a ground fault and other problems. Workmanship was improved to correct this problem and inspections were done.
- The p.s. isolation voltage rating was below the rating required for p.s.'s in the ring. This did not cause any problems but still was corrected. New p.s.'s were purchased with the correct voltage isolation rating.
- Open channels on the qd card picking up a signal from an adjacent channel, which had a p.s. current readback on it, would cause the qd to trip out. These open channels were shorted out.
- A hard reset was required for the yellow qd's to accept changes made for the yellow phase shift p.s.'s.

e-Lens P.S. Testing

The e-lens p.s.'s have not been used by operations for the RHIC runs yet but the yellow e-lens p.s's have been tested during RHIC run 13 and at the end of RHIC run 13.

The solenoid ps. was operated up to 392A maximum. The Fringe p.s. was operated up to 470A maximum and the Anti-Fringe p.s. was operated up to 330A.

One problem encountered with the e-lens p.s.'s was the placement of the DCCT head in the QPA. The DCCT head was placed too close to the energy extraction dc cable. When a quench would occur, and the energy extraction system would kick in, the DCCT head would see a spike on the current during the decay. The DCCT head was moved to correct this problem.

When the p.s.'s are off we have seen that the coil voltage taps pick up a signal when adjacent warm magnets are ramped. Injecting or dumping beam might also affect these coil taps. This has caused the qd to trip. This is currently being investigated.

The correctors were not been tested on the magnet as of yet but they have been tested on short circuits.

ACKNOWLEDGEMENTS

The authors would like to thank the technician's in the Collider Electrical p.s. group who worked very hard on these p.s.'s. They are Mitch DeLavergne, Joe Drozd, Don Gosline, Gregg Heppner, Brian Karpin, Rich Kurz, Tom Nolan, Fred Orsatti, Frank Scheifele, Jeff Wilke, and Ron Zapasek. This work was supported by Brookhaven Science Associates, LLC under Contract No. DE-AC02-98CH10886 with the U.S. Department of Energy.

REFERENCES

[1] The RHIC Configuration Manual.
[2] J. Muratore et al., "Test Results for the Electron Lens Superconducting Magnets at RHIC", MT23 Conference, Boston, July 2013.
[3] D. Bruno et al., "Overview of the AGS Cold Snake Power Supplies and the New RHIC Sextupole Power Supplies", PAC07, Albuquerque, MOPAS090, June 2007, p. 637 (2007); http://www.JACoW.org

Copyright © 2013 CC-BY-3.0 and by the respective authors

200 KW CW, 350 MHZ MULTIPLE BEAM INDUCTIVE OUTPUT TUBE

R. Lawrence Ives, Michael Read, David Marsden, George Collins, Rasul Karimov,
Calabazas Creek Research, Inc., San Mateo, CA 94404 USA
Takuji Kimura, Edward Eisen, Communications & Power Industries, LLC,
Palo Alto, CA 94304 USA

Abstract

Assembly is nearing completion of a 350 MHz, 200 kW CW, multiple beam, inductive output tube. The device incorporates seven electron beams interacting in a single, fundamental mode, output cavity. A single collector dissipates the spent beam power, and input and output power is transmitted in coaxial waveguide. Simulations predict 70 % efficiency with 23 dB gain. The tube is targeted for ion accelerators.

INTRODUCTION

Calabazas Creek Research, Inc. (CCR), in collaboration with Communications & Power Industries, LLC (CPI), is nearing completion of a 350 MHz, 200 kW CW, multiple beam, inductive output tube (MBIOT). This device is targeted for upgrade of the Advanced Photon Source (APS) at Argonne National Laboratory but will be applicable for a broad range of accelerator systems requiring RF power from 300 to 800 MHz. The MBIOT provides efficiencies higher than klystrons in a dramatically smaller device. The gain is limited to less than 24 dB; however, solid state drivers are commercially available providing several kilowatts of RF power. The principal challenge is designing an input cavity that will drive all electron guns at the same power and phase. This paper describes the design of the MBIOT and status of the assembly.

DESIGN

The MBIOT incorporates a single, coaxial input cavity to drive the seven electron guns. The tube uses electron guns produced by CPI for their single beam IOTs. The gun design is well established, and the performance has been verified through years of operation. Figure 1 shows the gun support plate and two of the guns.

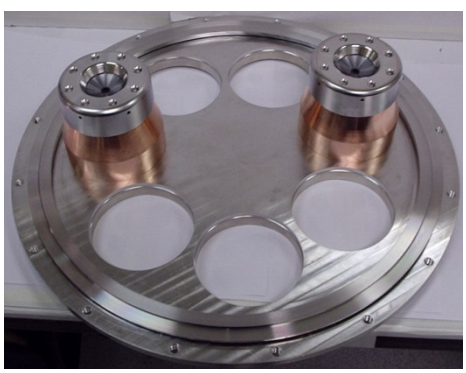


Figure 1: Gun support plate with two guns.

Figure 2 shows an HFSS simulation of the input cavity electric fields. The axis of the device is the Y-axis. Input power enters through a coax waveguide from the right. Heater power is provided by the leads emerging from the back of the gun and coupling to the top wall in the image.

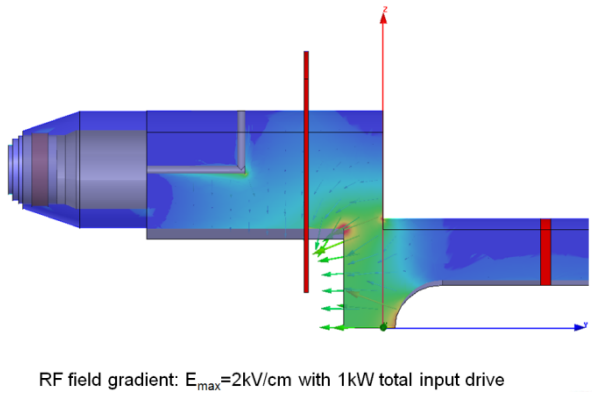


Figure 2: HFSS Simulation of MBIOT input cavity.

Figure 3 shows an HFSS simulation of the output cavity, with the beams entering from the left and the RF output power coupled to a coaxial waveguide on the axis. The external Q is determined by the penetration depth of the coax center conductor, which will be set during cold testing. The seven electron beams exit toward the right into a common collector that surrounds the output waveguide and window.

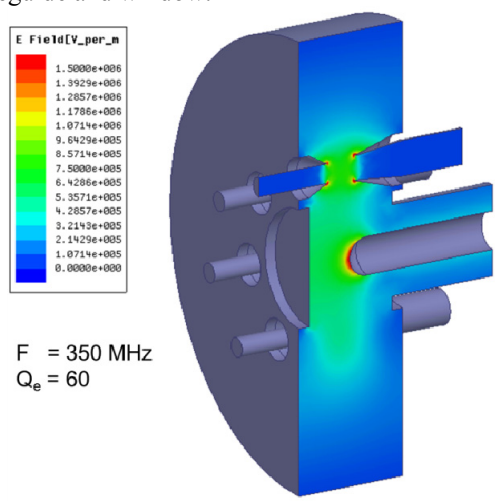


Figure 3: HFSS simulation of the output cavity.

Table 1 provides the performance specifications based on computer simulations. These satisfy the requirements for the APS upgrade and a number of anticipated accelerator systems.

Copyright © 2013 CC-BY-3.0 and by the respective authors

Table 1: MBIOT performance specifications.

Parameter	Value
Frequency	350 MHz
Bandwidth	4 MHz
Output Power	200 kW CW
Gain	23 dB
Operating Voltage	30 kV
Efficiency	70%
Total Current	9.5 A
Number of Beams	7
Average current per beam	1.4 A

FABRICATION

Fabrication is almost complete with only a few assembly steps remaining. The seven guns are complete, as are the input cavity assembly, HV ceramic assembly, collector, and output window. Figure 4 shows a photograph of the input cavity assembly. Tuners behind each electron gun should provide some adjustment of the fields to balance emission from the seven guns. Figure 5 shows a photograph of the collector and output window and waveguide assembly.



Figure 4: Input cavity assembly.

Several issues arose during assembly of the output cavity. Because of the presence of iron and numerous braze joints associated with the electron beams, brazing was a significant challenge. The differential expansion between copper and iron caused significant distortion of the large plates. Sufficient material was incorporated for subassembly machining; however, the distortion also impacted braze alloy flow. Consequently, numerous braze cycles were required before vacuum tight assemblies were achieved. These assemblies are now complete, and final assembly of the output cavity will begin when cold tests are completed. Figure 6 shows a solid model of the completed MBIOT.



Figure 5: Collector and output window and waveguide assembly.

SUMMARY

A multiple beam inductive output tube for accelerator applications is nearing completion. The device is designed to produce 200 KW CW at 350 MHz. The IOT incorporates seven electron beams driven by a single, coaxial input cavity and excites a fundamental mode output cavity. The tube is targeted for ion and proton accelerators and colliders.

ACKNOWLEDGEMENT

This program was funded by U.S. Department of Energy Grant No. DE-FG-3-07ER84876, the U.S. Naval Surface Weapons Laboratory, and Communications & Power Industries, LLC.

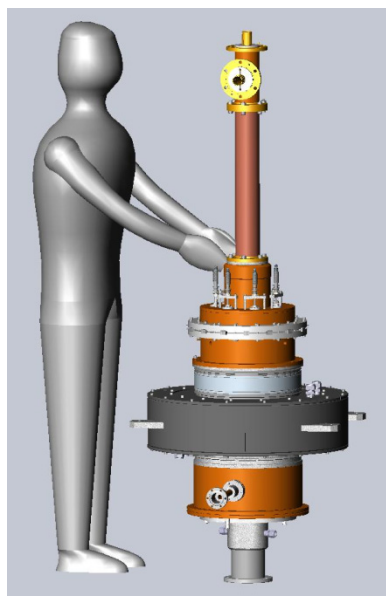


Figure 6: Solid model of completed MBIOT.

Copyright © 2013 CC-BY-3.0 and by the respective authors

DESIGN AND FABRICATION OF A 10 MW, L-BAND, ANNULAR BEAM KLYSTRON*

Michael Read, Patrick Ferguson, R. Lawrence Ives, Robert Jackson, David Marsden, and George Collins
Calabazas Creek Research, Inc., 690 Port Drive, San Mateo, CA 94404

Abstract

Design improvements and fabrication of a 10 MW, 1.3 GHz Annular Beam Klystron are described. The principal improvement is the electron gun. Utilization of a Controlled Porosity Reservoir (CPR) cathode allows the use of a zero-compression gun, resulting in improved beam quality and reductions in the gun and solenoid diameters.

INTRODUCTION

Efforts to achieve a high efficiency 1.3 GHz, RF source for the International Linear Collider (ILC) and similar accelerators are centered on multiple beam klystrons (MBK) and, more recently, on a sheet beam klystron (SBK). CCR is developing an annular beam klystron (ABK) to fulfill the stringent requirements imposed by the ILC. That is, the minimum efficiency should be 65% at an RF output power of 10 MW, and the cathode current density should be less than 5 A/cm^2. The pulse width must be 1.5 milliseconds at a pulse frequency of 15 Hz.

Like the MBK, the ABK perveance can be much higher than in a traditional klystron. In contrast to the MBK, the ABK uses a single beam with simple transverse magnetic (TM) mode resonators. Thus, the tube is similar a traditional klystron and much simpler than an MBK. The ABK length, efficiency and gain are similar to those of an MBK with the same power, perveance and frequency.

The CCR ABK electron beam current is 140 A at 120 kV with inner and outer beam radii of 3.2 cm and 3.6 cm, respectively. The drift tube radius is 4 cm. The tube includes six cavities, and the solenoidal magnetic field is 1.5 kG. A schematic of the ABK electron gun and simulated beam is shown in Figure 1.

As previously reported [1], CCR created a design that met all requirements and was not significantly affected by the diocotron instability. However, the 2 kG magnetic field required more power than desired. With an ideal beam, calculations of the efficiency showed no degradation with fields down to at least 1.5 kG. However, lowering the field increased the beam ripple, which in turn decreased the efficiency. This ripple was due to gun optics.

Design of a gun using compression to create an annular beam is intrinsically difficult, due largely to the fact that there is no radial force on the inside surface of the beam. The original design with a 2 kG field used a complex interaction of the cyclotron motion with the radial fields of the anode to minimize the ripple. Unfortunately, it was not possible to maintain the balance of forces at lower magnetic fields.

Generating an annular beam without compression, i.e. with a uniform axial magnetic field, is much more straightforward. But, for this case, the beam density of 16 A/cm^2 is too high for conventional cathodes. This difficulty is avoided using a CCR Controlled Porosity Reservoir (CPR) cathode. Current densities to 50 A/cm^2 have been demonstrated with this type of cathode. At the required density of 16 A/cm^2, the predicted lifetime is 100,000 hours. This is more than adequate for most applications, including the ILC.

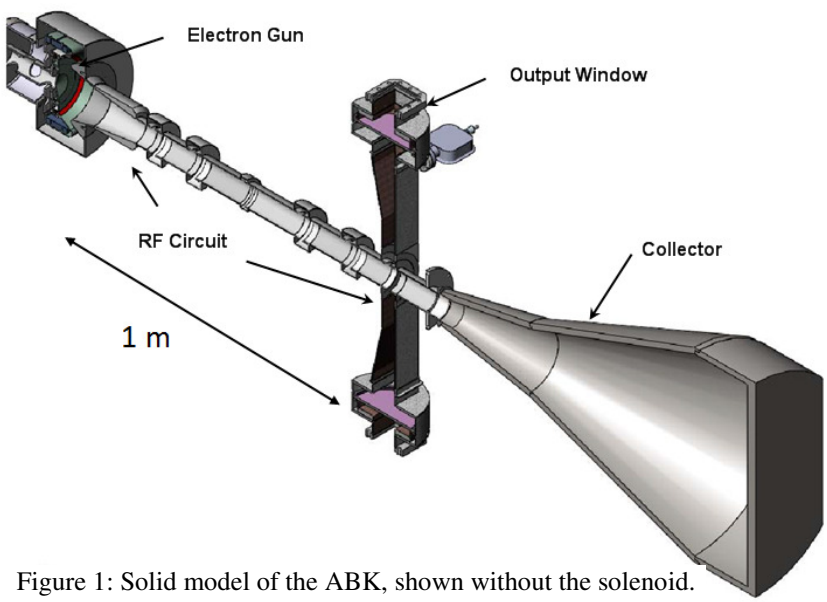


Figure 1: Solid model of the ABK, shown without the solenoid.

Copyright © 2013 CC-BY-3.0 and by the respective authors

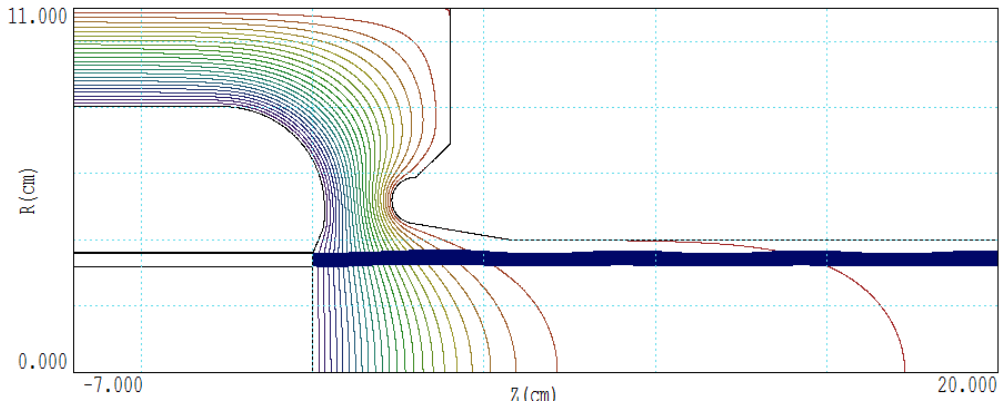


Figure 2: ABK gun with no compression of the beam.

ZERO COMPRESSION GUN

The new design for the gun is shown in Figure 2. There is still a modest ripple due to anode lensing, but, with a 1.5 kG magnetic field, the 4.7 mm peak-peak thickness is less than the original 5.1 mm with a 2 kG field. As with many guns with a high current density cathode, the electric field on the focus electrode was a concern. This, in fact, limited the shape of the focus electrode. In an ideal design, the focus electrode would extend further along an angle of roughly 67.5°, but this would have resulted in unacceptably high electric fields. As shown in Figure 3, the maximum field on the focus electrode is 63 kV/cm. This is under the engineering limit of 66 kV/cm for the design voltage and pulse width.

The average radius of the cathode is 3.4 cm, while the radius of the original cathode was 9 cm. The change in the cathode allowed reduction of the outer radius of the gun from 19 cm to 12 cm. This made it possible to decrease the radius of the solenoid, resulting in a 30% reduction in power required to produce the 1.5 kG field.

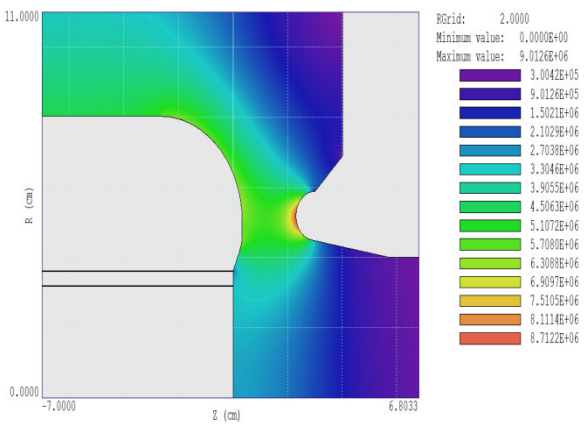


Figure 3: Electric field magnitude in the ABK gun.

FABRICATION

The ABK is being fabricated. Most of the tube uses conventional methods, but the cathode is unusual. Because of the nature of the CPR cathode material [2], the ABK cathode must be made in segments. The arrangement is shown in Figure 4. The cathode will be made in 6 modules,

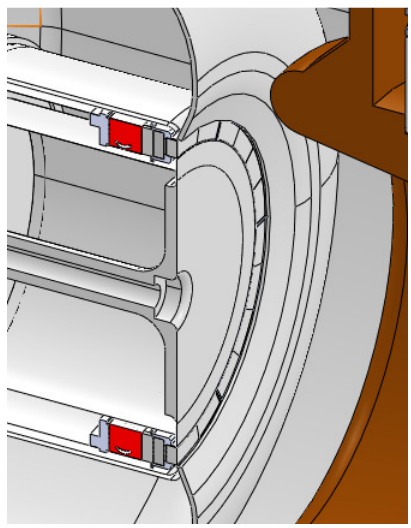


Figure 4: Cathode geometry.

each with 4 cathode segments. There was some concern that the asymmetries introduced by this fabrication method would degrade the beam optics. Simulations using the 3D trajectory code Beam Optics Analyzer (BOA) showed that this is not the case. In fact, even the removal of one of the segments has negligible impact on the beam trajectories. This is shown in Figures 5 and 6.

Copyright © 2013 CC-BY-3.0 and by the respective authors

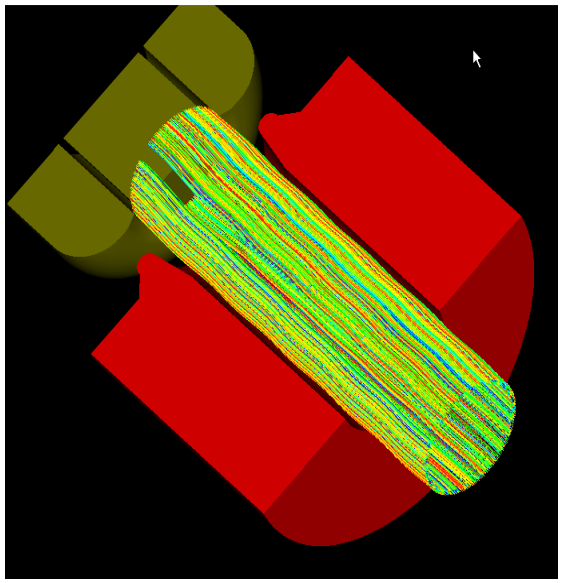


Figure 5: Trajectories generated by BOA, showing the effect of the deletion of a single segment of the cathode.

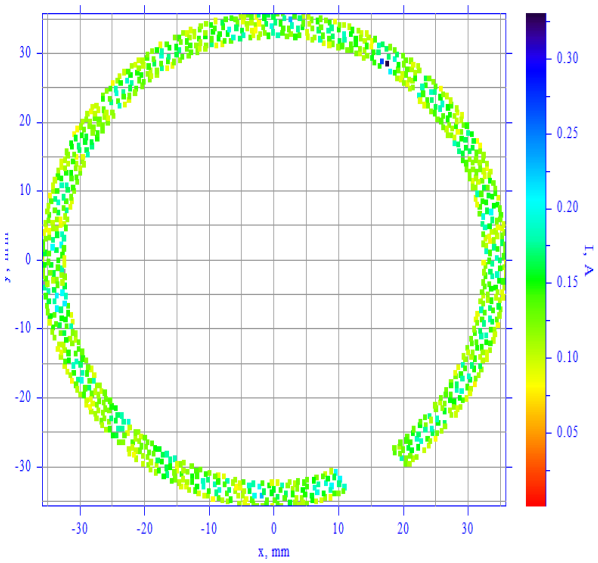


Figure 6: Cross section of the beam 70 cm downstream of the cathode. There is no visible distortion of the beam due to the missing cathode segment.

ACKNOWLEDGEMENT

*This research was performed under DOE SBIR contract DE-SC0006213.

REFERENCES

[1] Michael Read, et al., Optimized Design of a 10 MW, L-Band Annular Beam Klystron, IVEC 2012, p. 321 (2012).

[2] R. Lawrence Ives, Senior Member, IEEE, Louis R. Falce, George Miram, George Collins, "Controlled Porosity Cathodes for High Current Density Applications," IEEE Trans. Plasma Sci., Special Edition on High Power Microwave Sources, Vol. 38, No. 6, pp. 1345-1353, June 2010.

Copyright © 2013 CC-BY-3.0 and by the respective authors

X-BAND RF POWER GENERATION VIA AN L-BAND ACCELERATOR SYSTEM AND USES

N. Sipahi, T. Sipahi, S. G. Biedron, S. V. Milton, CSU, Fort Collins, Colorado, USA

Abstract

The development of compact, cost effective sources of high-energy electron beams is a major thrust of the Colorado State University Accelerator Laboratory team. In this paper we describe a way to generate usable X-Band RF power suitable for powering an X-Band accelerating structure to overall potentials significantly higher than what we are presently able to obtain from our L-Band photocathode RF gun system. The concept relies on the use of the L-band accelerator beam to generate the X-band power that is then delivered to a suitable X-band structure. Once powered this X-band structure can be used to accelerate an electron bunch to high beam energies.

GENERAL CONCEPT

The CSU Accelerator Facility will serve as a test bed for particle and laser beam research and development. Our major asset is an L-band rf gun system capable of delivering 6-MeV electron bunches [1], these parameters are given in Table 1. We would like to use this L-band linac as a drive source to generate X-band power for accelerating electron beam with an X-band rf structure without the need for an external X-band power source. This system could then be used to accelerate the beam to an even higher energy that possible with the L-band system alone.

Table 1: Parameters of CSU Accelerator Laboratory

Laser Frequency	81.25 MHz
L-Band RF Gun Frequency	1.3 GHz
L-Band RF Gun Energy	6 MeV
L-Band Macro pulse Length	10 μs
X-band Linac Frequency	11.7 GHz
Repetition Rate	10 Hz
RF gun Charge/Bunch	3.5 nC

From our earlier work, we found that although significant gradients could be achieved with an X-band structure powered via our L-band beam system the integrated potential in the X-band structure was fundamentally limited by the drive beam energy loss [2]. This led us to explore an alternative arrangement where power was generated in a TW structure and then transferred to a separate optimized structure used for acceleration of a secondary beam. This basic arrangement is shown in Figure 1.

Using such an arrangement, we would like to achieve the highest possible energies for our given beam parameters and proposed X-band drive system.

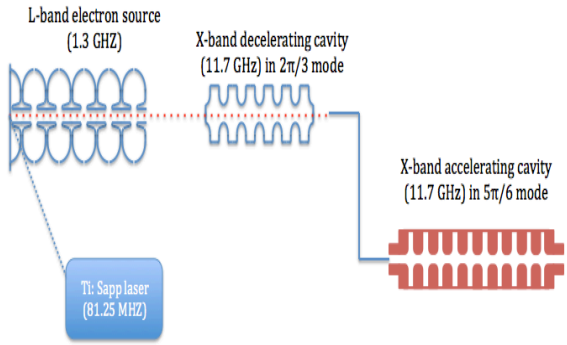


Figure 1: General layout of the two-beam X-band structure.

BEAM STUDIES FOR TWO DIFFERENT CAVITIES

Our study involves two different X-band accelerator structures, one to be used as a decelerating cavity that generates X-band power via the use of the beam from the L-band system, and the second one to be used as an accelerating cavity to achieve the highest practical potential for acceleration of the electron beam.

The one cell geometry for our X-band structures are defined in Figure 2 [3].

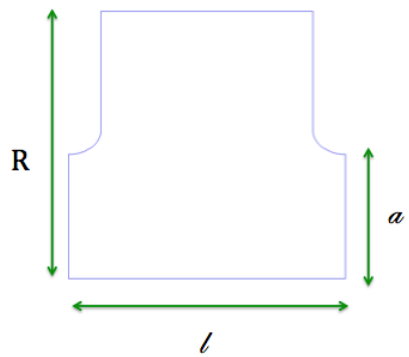


Figure 2: One cell structure of the X-band cavity.

The Beam – Cavity Interaction for the Decelerating Structure

In the decelerating cavity, the aim is to transfer energy from the L-Band RF system to the electron beam, consisting of bunches of charged particles, and then from the electron beam to the RF wave induced in the X-band decelerating structure, thus we design a structure that maximizes this interaction as in ref. 2.

The configuration is unconventional in that the X-band linac does not require a klystron system to achieve high accelerating fields. Rather it uses the power existing in the electron beam to resonantly power the fields in the structure.

Copyright © 2013 CC-BY-3.0 and by the respective authors

Once the X-band structure has been powered up to the full potential a properly phased electron bunch can then be injected and accelerated, and for a properly designed and configured system can raise the beam energy to nearly twice what would have been available from the L-band system alone.

In this decelerating linac geometry, the iris radius (a) is 0.00512466 m, cavity radius (R) is 0.0110955 and the cell length (l) is 0.0085411 m as in ref. 3. The general parameters of this $2\pi/3$ traveling wave (TW) structure are given in Table 2. The X-band power generated with these parameters is 1.4 MW.

Table 2: Beam – Cavity Interaction Parameters for X-band Decelerating Cavity Structure

L-Band Bunch Charge	3.5 nC
L-Band Final Beam Energy	6 MeV
X-band Max. Gradient	62.7 MV/m
X-Band Shunt Impedance	57 MΩ/m
X-Band Eff. Shunt Impedance	33.1 MΩ/m
X-Band Q	6656
Damping Factor (t/τ)	0.1
X-Band Cell length	0.0854 m
Number of X-Band cells	18
Total length of X-Band structure	15.3 cm
Available X-Band Potential	5 MV

The Accelerating Structure

In this design we wish to maximize the energy gain in an optimum length and get highest integrated potential at the end of one or more the cavities; therefore, we chose to design a new geometry, and change the phase advance from $2\pi/3$ to a higher mode, $5\pi/6$. This slows the group velocity and allows us to increase the length of structure and provide more opportunity to increase the integrated potential [4].

The resulting geometry of the accelerating structure becomes (a) is 0.002566233 m, the cell length (l) 0.010676375 m, and the cell radius (R) decreases in this case as in ref 3.The general parameters of this structure are given in Table 3.

Table 3: Beam – Cavity Parameters for X-band Accelerating Cavity Structure

Dec. Cavity Final Beam Energy	11 MeV
Phase Advance	$5\pi/6$
a/λ	0.1
Acc. Cavity Shunt Impedance	185.7 MΩ/m
Acc. Cavity Quality Factor	7474
Acc. Cavity Cell length	0.010676375 m
Group Velocity (v_g/c)	0.95%

This basic configuration, i.e. an L-band gun system beam powering a decelerating cavity used to generate X-band power and all the power fed into a single optimized accelerating cavity achieves an integrated potential significantly higher than our original direct attempt; however, we considered three different scenarios that allowed us to achieve a higher potential with our new proposed system. The two different configurations are shown in Figure 3.

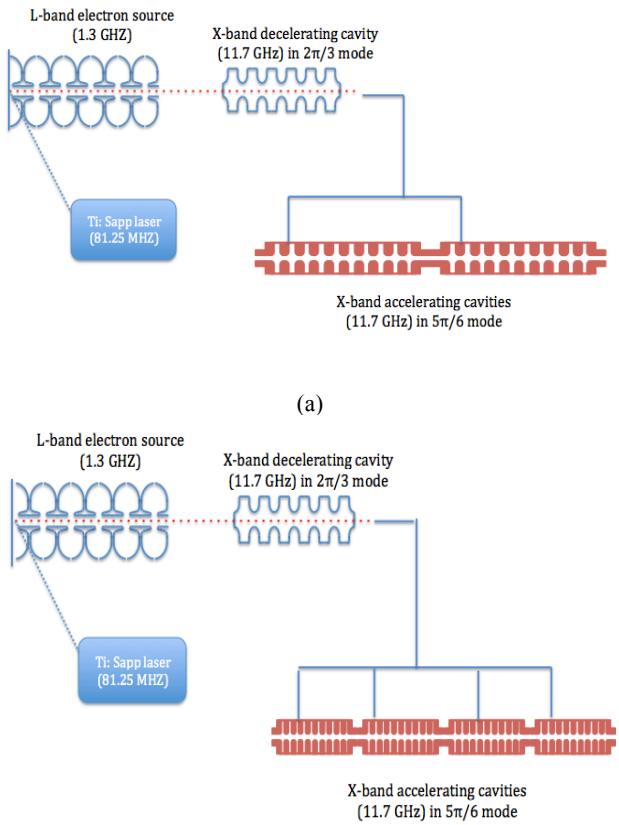


Figure 3: a) Two accelerating structure case b) Four accelerating structure case for the system under study.

In these configurations we divide the power into two or four different linacs to achieve a higher integrated potential than possible with a single structure; furthermore, if the input power and shunt impedance are fixed, the maximum energy gain over a structure of given length depends on maximizing the total attenuation parameter. In this case it becomes 1.26 [5]. Then, by using the quality factor and group velocity parameters from table 3, we can calculate the optimal accelerating cavity length. The beam loading parameters for the accelerating structures are given in Table 4.

Table 4: Available Potential and Maximum Energy Gain values for 0.72 m length accelerating cavity

Total Length of One Section	0.72 m
Number of X-Band cells	69.4

Copyright © 2013 CC-BY-3.0 and by the respective authors

Filling time for 1 Section	259 ns
Available Potential after 1 section	16.2 MV/m
Available Potential after 2 sections	22.9 MV/m
Available Potential after 4 sections	32.4 MV/m
Max. Energy gain after 1 section	12.6 MeV
Max. Energy gain after 2 sections	17.5 MeV
Max. Energy gain after 4 sections	24.8 MeV

As seen, by use of multiple accelerating structures, we can achieve a significantly higher integrated potential (Table 4) than in the single accelerating structure case.

DISCUSSION AND FUTURE STUDIES

We have shown that by proper design we can, by utilizing the beam from our L-band linac, resonantly excite an X-band decelerating structure to meaningful accelerating gradients. In our initial design example we achieved up to 5-MV additional accelerating gradient. Configured properly this implies that we can periodically achieve beam energies near double our original 6 MeV and potentially reach roughly 11 MeV in occasional single pulses without the need for an additional X-band power source after L-band structure. Additionally, after gaining 11 MeV, we can achieve higher potential by using accelerator structures that are designed and configured in a two-beam configuration. However, the amount of the potential that we can get depends on the higher mode of the cavities and the number of structures. Therefore, to optimize our case, we will continue to study the possible higher modes that can give higher integrated potential and check the limits of having more accelerating structures.

ACKNOWLEDGMENT

We wish to thank SLAC National Laboratory Facility for their support and funding and in particular the input from C. Adolphson. Also, we wish to thank the senior management of CSU for their support of the accelerator laboratory and accelerator education.

REFERENCES

[1] S. G. Biedron, T. Burleson, C. Carrico, A. Dong, J. Edelen, C. Hall, K. Horovitz, S.V. Milton, A. Morin, L. Rand, N. Sipahi, T. Sipahi, P. van der Slot, H. Yehudah, “ The CSU Accelerator And FEL Facility ”, FEL’12, Nara (2012).

[2] S. Biedron, S. Milton, N. Sipahi, T. Sipahi, C. Adolpsen, “Passively Driving X-Band Structures To Achieve Higher Beam Energies”, Proceedings of IPAC 2013, TUPEA075, p. 1304-1306 Shanghai (2013).

[3] T. Sipahi, N. Sipahi, S. Milton, S. Biedron, “Passively Driving X-Band Structures To Achieve Higher Beam Energies” NAPAC’13, Pasadena (2013) to be published.

[4] C. Christou, “X-band Linac Technology for a High Repetition Rate Light Source”, Nuclear Instruments and Methods in Physics Research A 657, p. 13-21 (2011).

[5] T. P. Wrangler, “RF Linear Accelerators” (Weinheim: Wiley,2008), p.68-76.

Copyright © 2013 CC-BY-3.0 and by the respective authors

COMPONENTS OF HEATING AND FUELING OF FUSION PLASMAS*

K. Schrock, M. Gaudreau, J. Kinross-Wright, Diversified Technologies, Inc.,
35 Wiggins Ave., Bedford, MA 01730, USA

Abstract

Diversified Technologies, Inc. (DTI) has bench-tested a table-top scale 'Buck Matrix' modulator with an efficiency of ~96% which uses a single set of IGBT switches for voltage regulation, arc protection, and pulse modulation.

INTRODUCTION

Next generation fusion facilities will require many megawatts of RF power from dozens of gyrotrons. Each gyrotron requires a power system that must deliver high-voltage power, modulate cathode voltage, and protect these expensive gyrotrons from arcing damage. It must be highly efficient to minimize both the power and cooling costs associated with operation and to ensure high facility availability.

Conventional DC power systems, built from WWII era components, have provided the typical approach to powering this class of high-power RF vacuum devices for the last 50 years. These systems, with their variacs, inductrols, spark gaps, ignitrons, and tetrodes, traditionally suffer from reliability and availability problems and are often only 50 – 70% efficient. Scaling conventional RF power electronics technology for next generation high power fusion facilities is not practical in either cost or reliability.

The technology for off-the-shelf, reliable solid-state modulators does exist, but currently requires two layers of solid-state switches – a voltage regulation step followed by a modulator / opening switch for arc protection. These two-step approaches are unnecessarily large and expensive, and an approved approach will be presented.

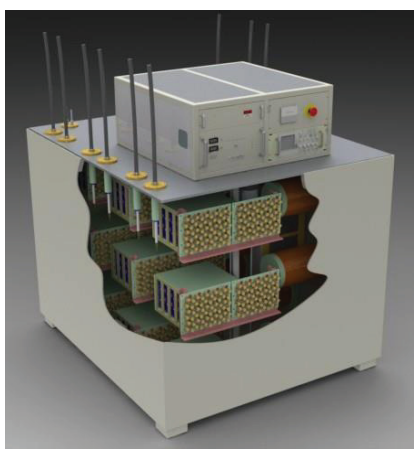


Figure 1: 75 kV, 45 A CW multi-phase buck-matrix regulator with low filter energy – serves dual purpose of regulating power and protecting a 1 - 1.5 MW gyrotron during arcs.

*Work supported by the Department of Energy

TECHNICAL APPROACH

Diversified Technologies, Inc. (DTI), under a DOE SBIR grant, has bench-tested a table-top scale 'Buck Matrix' modulator which uses a single set of IGBT switches for voltage regulation, arc protection, and pulse modulation.

DTI's Buck Matrix modulator (Figs. 1 and 2), with an efficiency of ~96%, cuts the size of the system in half, using a single layer of solid-state switches for both voltage regulation and arc protection/modulation. This cuts the total hardware costs by 30% or more, and eliminates the need for a separate opening switch or crowbar.

Although pulse step modulators also represent a one-step solution, their size and the complexity of their driving transformer make them more expensive than DTI's approach.

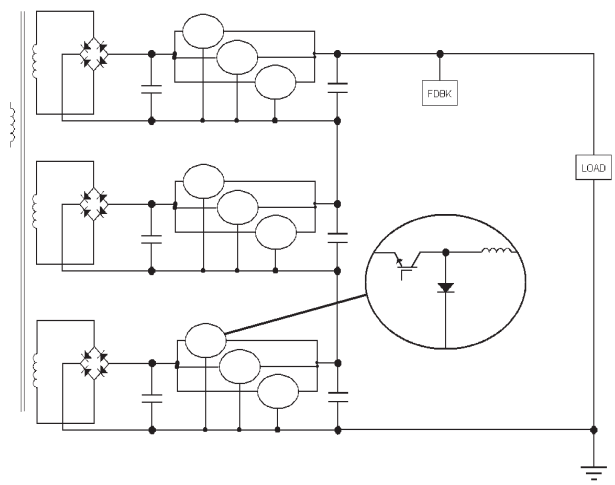


Figure 2: A series/parallel "Buck Matrix" topology combines superb ripple reduction and tube protection for minimum complexity and maximum efficiency. Transformer / Rectifier pairs are shown single-phase for simplicity.

OBJECTIVES

DTI focused on five primary objectives in developing the modulator. The first three focused on demonstrating the technical feasibility of the project: to assess any control system instabilities, to ensure the concept design would meet real gyrotron requirements, and to build and test a low voltage demonstration unit. The latter two tasks focused on the construction of a full-scale prototype. A high voltage electrical design for the full-scale system has been completed, as well as the ground work for the mechanical design, and the auxiliary systems have been

Copyright © 2013 CC-BY-3.0 and by the respective authors

defined, including the custom transformer-rectifier needed to power the Buck Matrix.

Design

Low stored energy is required in the Buck Matrix design to ensure that the tube is not damaged during arcs. This low stored energy is a major constraint of the design of the Buck Matrix; other key parameters are listed in Table 1.

Table 1: Key Specifications of the Prototype

Parameter	Full System	2x2 Demo	Units
Vin	95	2.5	kV
Vk	75	2.0	kV
Ik	45	2	A
Max Stored Energy	30	0.04	J
Max Voltage Ripple	1%	5%	

The principle behind the Buck Matrix converter is that very small output capacitors can be used, since the large out-of-phase ripple voltages will cancel each other out at the converter output. If we consider the case of a 2x2 Buck Matrix, the midpoint of the two sets of output stages sees significant ripple during the switching period.

Any ripple causes the current through each inductor to behave highly non-linearly. For example, a ground-side buck stage inductor will nominally see (Vi/2 - Vo/2) when its switch is turned on. If the ripple voltage at the midpoint swings 50% during a switch period, the voltage seen across the inductor would in reality vary from (Vi/2 - Vo/4) to (Vi/2 - 3Vo/4). The non-linear current waveform no longer has a predictable turn-off time, and the nominally stable operating point becomes marginally stable. Transient load or command changes have a nearly immediate effect on the output capacitor voltages, which can push the converter to a non-ideal operating point.

Simulation of the designed 2x2 Buck Matrix using fixed duty cycle control (open loop) showed a well-behaved circuit, with no output voltage overshoot and symmetric inductor waveforms.

A 3x3 system was later simulated (Figure 4). This system is harder to stabilize because of even smaller output capacitors and more component interactions in a 3x3 Buck Matrix. Simulations are not conclusive on whether fast peak-to-peak current regulation or slower voltage-mode feedback regulation result in a more stable system.

Experimentation

A low voltage 2x2 Buck Matrix was built to confirm the results of the simulation and analysis, and to demonstrate the feasibility of the Buck Matrix concept. Figure 3 shows the test setup.

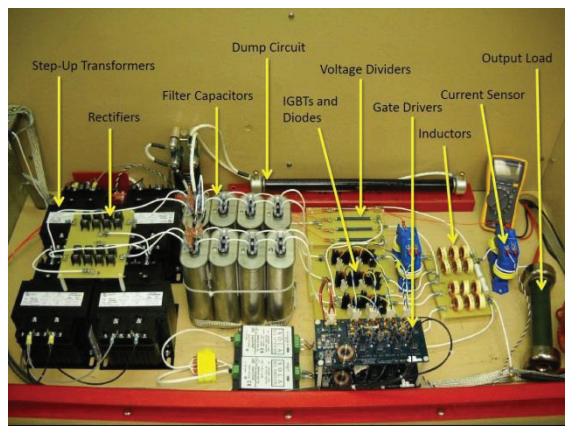


Figure 3: Components of the 2x2 experimental setup.

The 2x2 Buck Matrix performed as expected. Other than the inherent noise from the open hardware setup, the circuit waveforms nearly identically matched those from the simulations. The output ripples appropriately

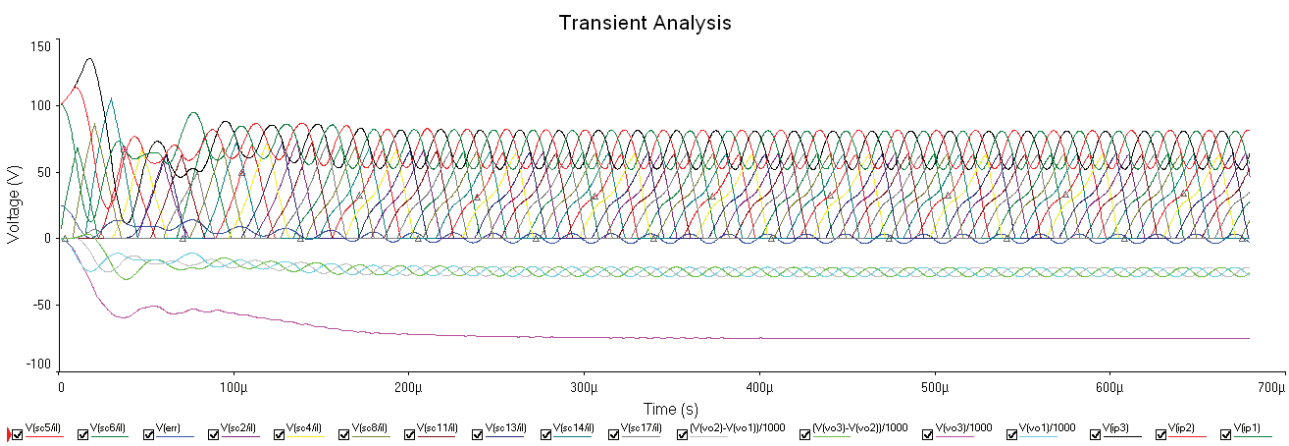


Figure 4: A 3x3 Buck Matrix under peak current mode control, with a fast PI voltage loop compensator. The response is fast, with symmetric inductor currents.

Copyright © 2013 CC-BY-3.0 and by the respective authors

cancelled each other due to phase interleaving. The measured output ripple was approximately 7%; theoretical ripple was 5%. This discrepancy is due to small timing and component value differences. With slightly different inductor and capacitor values, and with slightly different IGBT and diode transition times, the individual component contributions are not perfectly symmetric, thus perfect cancellation is not possible.

Switch Resilience

To verify if standard silicon IGBTs or SiC JFETs could be run at the planned power levels and frequency, two DTI 10 kV switchplates (Figure 5) were manufactured: one with the SiC JFETs, and one with the silicon IGBTs. A test setup was constructed to verify full voltage and full current switching and conduction losses of these different switch plates (Figure 6). The result of this testing allows us to predict with confidence what the expected junction temperature of the transistor will be in the real buck matrix system.



Figure 5: Three DTI 10 kV solid-state switchplates.

Transistor Selection

Silicon Carbide (SiC) transistors have recently become commercially available at reasonable prices. SiC boasts extremely fast commutation, essentially eliminating switching losses in power converters. 85 milliohm and 45 milliohm SiC JFETs [normally-on devices which need to be operated in a cascode circuit and controlled with a low voltage (40 V), extremely low on-resistance and low switching-loss MOSFET] were evaluated.

Two of the tests related to the device physics performed were to examine the JFETs' ability to reverse-conduct (similarly to the internal body diode of many IGBTs), and to determine if the intrinsic over-voltage avalanche characteristics would simplify operation of these devices in series for high voltage applications.

Reverse Conduction

The JFETs do reverse-conduct, but testing revealed that the devices will break if operated with significant current in the reverse direction—similar current levels as the forward conduction current is enough to damage the devices. If reverse conduction is required, blocking and antiparallel diodes should be added

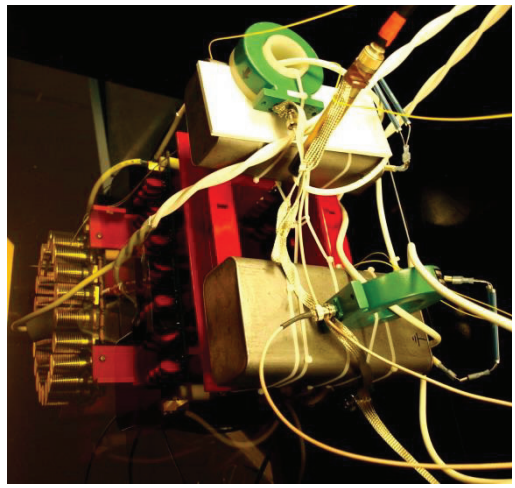


Figure 6: Switchplate test setup in dielectric oil. The assembly is vertically symmetric. A 20-stage switchplate with heatsinks is on the far left, at the bottom of the oil tank; above it is a high voltage diode assembly; on top are the two high voltage capacitors, and current sensors.

Avalanche

To test the avalanche characteristics, the JFETs were pulsed into an inductive load at very low pulsewidths (less than 1 microsecond) and low rep rate. When the JFET was turned off, the inductive voltage spike, which was a function of the input voltage and pulsewidth, would rise to above the device rating, and avalanche into the device. This worked as expected with very low avalanche energies, but damaged the device at higher avalanche energies.

Future Work

The huge reduction in ripple afforded by series/parallel multi-phasing allows the filters to become quite small, and it is precisely this reduction in stored energy in the filter – to below the threshold for arc damage – which enables the elimination of the second switch.

The results of this effort will eliminate half of this hardware, yielding approximately 30% savings, as well as improved system reliability and efficiency. The resulting design will be easily transferable to other voltage and current regimes, and is suitable for any CW or long pulse application – including future RF accelerators, light sources, and synchrotrons, and may also be applicable to other DOE programs, including the International Linear Collider (ILC). Other fusion power systems (e.g. ICRF, LHCD, neutral beam heating) may also make use of this technology with similar performance and cost advantages.

Copyright © 2013 CC-BY-3.0 and by the respective authors

AFFORDABLE, SHORT PULSE MARX MODULATOR*

R. Phillips, G. DelPriore, M. P.J. Gaudreau, R. Simpson
Diversified Technologies, Inc., 35 Wiggins Ave., Bedford, MA 01730, USA

J. Casey
Rockfield Research, Inc., 11010 Onslow Ct., Las Vegas, NV 89135, USA

Abstract

Under a U.S. Department of Energy grant, Diversified Technologies, Inc. (DTI) is developing a short pulse, solid-state Marx modulator (Fig. 1). The modulator is designed for high efficiency in the 100 kV to 500 kV range, for currents up to 250 A, pulse lengths of 0.2 to 5.0 μs, and risetimes <300 ns. Key objectives of the development effort are modularity and scalability, combined with low cost and ease of manufacture. For short-pulse modulators, this Marx topology provides a means to achieve fast risetimes and flattop control that are not available with hard switch or transformer-coupled topologies.

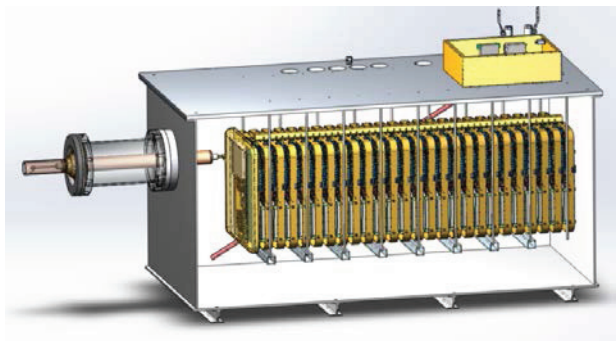


Figure 1 Planned 500 kV Marx modulator with an array of fifty of the plates shown in Figure 3.

INTRODUCTION

Under a DOE SBIR grant and based on research begun under the Next Generation Linear Collider (NLC) program, high energy, short-pulse modulators are being re-examined for the Compact Linear Collider (CLIC) and numerous X-Band accelerator designs. At the very high voltages required for these systems, however, all of the existing designs are based on pulse transformers, which significantly limit their performance and efficiency. There is not a fully optimized, transformerless modulator design capable of meeting the demanding requirements of very high voltage pulses at short pulsewidths.

BACKGROUND

A Marx generator is a system with energy storage capacitors which are charged in parallel at low voltage and discharged in series to provide high voltage output. This is a legacy idea, practiced for decades using resistor charging networks and spark-gaps for discharge. Constrained by the limits of closing switches, such systems required pulse forming networks and crowbars, with their attendant limitations

The Marx topology also enables features which are not common to hard switch modulators. Primary among these is the ability to control each module independently – and thus program the ultimate pulse voltage by choosing the number of modules triggered. The use of a bypass diode rated for full pulse current allows staggering of the modules' turn-on time, and ultimately enables full waveform synthesis in real-time.

TECHNICAL APPROACH

The Marx topology allows a new degree of freedom unavailable to other architectures – DTI can intentionally underdamp the series snubbing within the pulse circuit. This cannot be done conventionally – the reactive overshoot endangers the load. In a Marx, we can compensate for the overshoot by initially firing only a subset of the switches – thus "sling-shotting" the leading edge faster than otherwise possible. We can tune the number and timing of subsequent module firings to counter the reactive ringing, and hold a flattop pulse to the desired voltage and accuracy (Fig. 2).

Similarly, additional modules may be added to fire sequentially later in the pulse to compensate for capacitor droop. This is a critical enabling technology motivating Marx use for long-pulse accelerators (such as ILC), and yields valuable optimization even for very short-pulse systems. The reduction of capacitor size afforded by this flexibility further reduces parasitic capacitance, and thus reduces equipment size and cost while increasing power efficiency.

*Work supported by the Department of Energy

Copyright © 2013 CC-BY-3.0 and by the respective authors

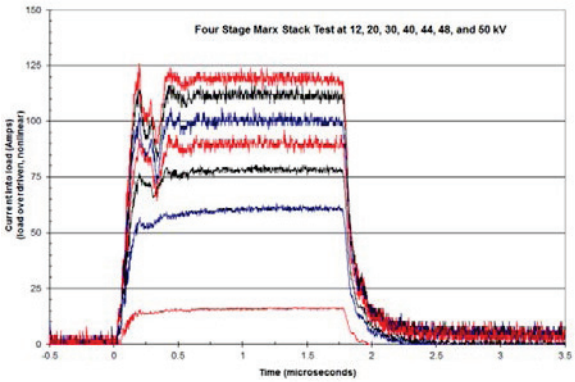


Figure 2 Test pulses of a four-stage Marx bank at 12, 20, 30, 40, 44, 48, and 50 kV. The notch at the beginning of the pulse is the intended result of induced overshoot, which decreases the rise time.

Architecture

The short-pulse modulator under development in this effort is a high peak-power pulse modulator of greater efficiency than presently available, in the 100 kV to 500 kV range, for currents of up to 250 A, pulse lengths of 0.2 to 5.0 us, and risetimes <300 ns (Table 1). A key objective of the development effort is a design which is modular and scalable, yet low cost, and easy to manufacture and maintain. Recently, DTI significantly reworked its original Marx bank architecture to achieve a low-cost, highly modular, and scalable design without compromising pulse performance.

Gate Drives

Table 1 Yale Marx Design Parameters

Pulse Voltage	500 kV
Pulse Current	250 A
Pulse Width	1.8 us
Repetition Rate	20 Hz
Module Voltage	12.5 kV
Module Capacitance	0.6 µF
# Modules for Base Pulse	40
Total # Modules in System	48 – 50
Expected Risetime	300 ns
Heater Voltage	24 VDC
Heater Current	21 A
Insulation	Oil

The relatively high per-module voltage (10-12.5 kV) precludes the use of single IGBTs within each module – thus series switch technology is an enabling feature for this system. For most high voltage modulators, all IGBTs pulse in unison, and a single ground based control system provides both motive power and timing control to all of the "floating" or "high-side" gate drives at the various successive stages. In this solid-state Marx modulator, the topology is such that each module can be independeltly controlled. With this flexibility, the externally supplied "command on" signal must be converted from a single command pulse into distinct ON-OFF commands, one for each module. The central ground-based control for the modulator performs this task, converting the input command into a sequence of ON-OFF commands to the modules to create the optimal pulse. An address – command structure between the controller and driver is used.

For this effort, we took the opportunity to redesign the gate drives with a different topology. Instead of the magnetically coupled gate pulses, we have chosen a more robust gate drive with independent magnetically coupled power and optically coupled gate triggers. This is a far more "brute force" approach, usually reserved for larger high voltage systems, but has the advantage that there is no asynchronous refresh, thus no opportunity for jitter.

Overall Topology

The physical layout of the Marx system has similarly undergone changes compared to our earlier work. In this effort, we revisited the ideal of a flat-pack design, where each module is a thin "pancake". Thus, the system-to-ground capacitance from each module is that of a thin segment of a coaxial capacitor. The large area of each "pancake" is exposed only to modules immediately above and below in the stack. Since the parasitic energy is proportional to V^2, rather than linear in V, we believe the new design will have better than a 10% parasitic capacitance reduction (hence faster risetime) than the prior approach, and far fewer mechanical components.

The co-location of devices inherent in the flat-pack design requires that all the shielding take place either within the multiple layers of the circuit board, or within shielding cans soldered onto the board. A peripheral corona shield minimizes voltage gradients between the Marx bank and the tank walls, as well as directing the parasitic charge into an appropriately stiff driven portion of the system circuitry.

Design Benefits

1) Reduced module costs

Through the use of PC board trace shielding and RF cans in sensitive areas of the circuit, we were able to co-locate controls directly on the board within reasonable proximity to pulsed current sections of the same board. By exposing the IGBTs directly to the oil, we can cool the devices effectively while eliminating machined parts and hardware, further reducing the module parts count, associated materials, and assembly costs. Since the flat-pack design significantly reduces voltage gradients from module to module within the Marx bank, the only significant need for corona and field reduction geometry is at the interface between the Marx bank stack and the walls of the tank. We anticipate more than a four-fold reduction in module mechanical costs, with the potential for additional reductions in manufacturing costs, compared to earlier designs.

Copyright © 2013 CC-BY-3.0 and by the respective authors

2) Simpler Interconnect

Each module in the redesigned Marx bank plugs directly into the two adjacent modules (Fig. 3; Fig. 5). We oriented the connectors and offset the board components and corona shields to allow any individual module to be added or removed from the stack, much like a book on a shelf, without any significant disassembly of support structures or disruption of the rest of the Marx bank. Since all module electrical connections and buswork are integral to the modules, only the fiber-optic control line (and optional fiber-optic monitor) needs to be externally connected. The first module in the stack plugs into a connector supplying charging HV, core bias current, auxiliary housekeeping power, and ground. A connector on the final module is connected to the Marx output coaxial cable, and includes a loopback for the common-mode choke bias current.

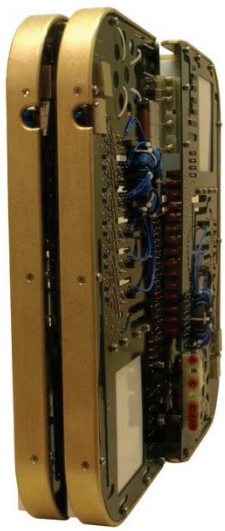


Figure 3 Stack of four connected modules viewed on edge. Fifty of these modules are shown connected in Fig. 1.

3) Scalability

The flat-pack Marx design is inherently modular and scalable, as additional plates may be added for a wide range of voltages. Whether at 100 or 500 kV, a Marx bank can use the same modules. The primary impact of additional plates is an increase in the charging current at the first plate, since it carries the current for all subsequent plates as well. Stray capacitance is also greatest at higher voltages, assuming constant spacing to the tank.

Prototype Testing

During testing of the prototype bank, we ran four modules with all modules simultaneously switched for a 1.5 µs pulse, with a 10 kV pre-charge into the system, resulting in a 40 kV output. The prototype modules performed flawlessly into high voltage, with none of the chatter or jitter that would otherwise be associated with gate drives impacted by noise coupling at high voltage. We then demonstrated the pulse-staggering capability of the Marx design by delaying the successive modules by 0, 0.5, 1.0, and 1.5 µs on a 2.3 µs pulse with a 7.5 kV pre-charge (Fig. 4). The distributed effect of the snubbing RL networks is clearly apparent here, with the fractional overshoot visible as each successive stage turns on into the high impedance load.

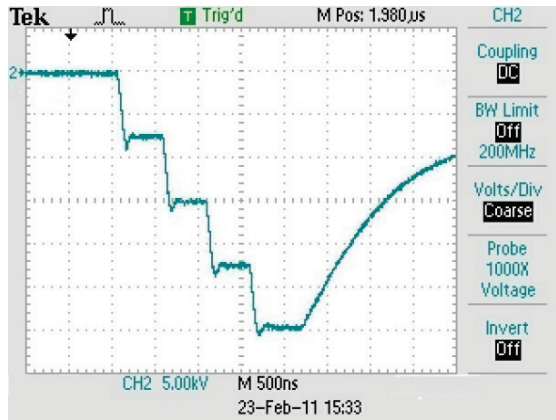


Figure 4 Four modules operated in staggered pulse mode, showing the individual control of each module.

Most recently, DTI has successfully tested a stack of 20 plates with a 12 kV pre-charge into a resistive load. The result was a 2 µs pulse output of approximately 240 kV and 200 amps. DTI will continue carefully constructing and testing modules to ensure the reliability and, above all else, safety of the equipment.

Plans/Conclusion

In Phase III, DTI will extend this design to future short-pulse, high voltage modulators for the next generation of planned accelerators, as well as transition this design to industrial / medical accelerators. We believe that the same combination of modular, low cost elements demonstrated in this Phase II effort will allow solid-state modulators to finally reach a price level that will supplant traditional (but low cost) thyratron / PFN designs currently used in these systems.

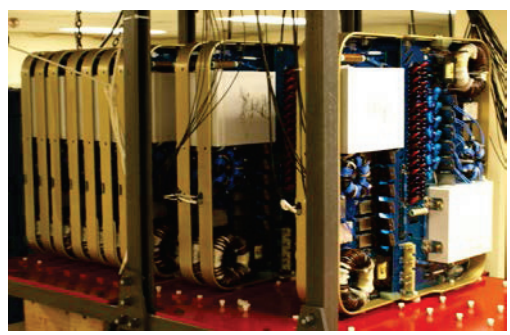


Figure 5 Stack of twenty-four connected modules.

Copyright © 2013 CC-BY-3.0 and by the respective authors

TEST OF AN L-BAND ENERGY-EFFICIENT SOLID STATE RF POWER SOURCE*

X. Chang, N. Barov, D.J. Newsham, and R. Wu, FAR-TECH, Inc., San Diego, CA 92121, USA

Abstract

We present the test results of a 1.497 GHz Solid State RF Power Source for the CEBAF linac at Thomas Jefferson National Accelerator Facility. The power amplifier was designed to operate at output power of 6.4 kW, with an overall efficiency greater than 55% at peak power, and is sufficiently compact to fit the existing rack space and cooling requirements at the installation site. Our solid state amplifier is designed for high efficiency, band width of more than ±5MHz at 1.497GHz, and long lifetime. The test results of the whole unit test will be shown.

INTRODUCTION

Thomas Jefferson National Accelerator Facility (TJNAF, JLab) is upgrading their RF system [1] for upgrading their electron beam energy. One of the options is to replace the klystron RF sources with the solid state amplifiers. Compared to a conventional klystron RF source, the solid state amplifier is easier to obtain high efficiency, long lifetime, and is safer due to low operating voltage, with a lower maintenance cost.

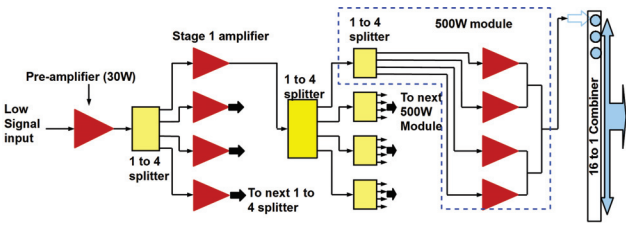


Figure 1: 8 kW Amplifier diagram. There are totally 16 of 500 W module.

Figure 1 is the diagram of an 8 kW solid state amplifier RF source. The low signal is amplified by a commercial 30 W amplifier (pre-amplifier) to drive the 4 transistors in the "stage 1" amplifier, which is contained in a single housing with 16 outputs. Each transistor in stage 1 has a peak output power of greater than 125 W. The output from each stage 1 transistor is split into 16 signals by two 1-to-4 splitters (one contained in the stage 1 amplifier housing and one contained in the 500 W module) and drive the 16 transistors in 4 of the 500 W modules. Isolators are placed between the two levels of splitting. Each transistor in the 500 W module has a circulator with load to prevent cross talking between transistor boards and to isolate the transistors from any reflected power. There are a total of 16 500 W modules and their outputs are combined in a 16-to-1 combiner.

*Work supported by DOE Office of Nuclear Physics, DOE-SBIR #DE-SC0002529

EXPERIMENTS

Transistor Board Development

Our chose RF3934 [2] as our amplifier transistors. It's a wideband transistor which an operate at 120W power. Previous testing to combine the output of 4 transistor boards with a commercial combiner [3] helped improve the performance of the transistor board prior to incorporating the transistors and in-house 4-to-1 combiner into a single module. Figure 2 shows the test set up for testing the 500 W module.

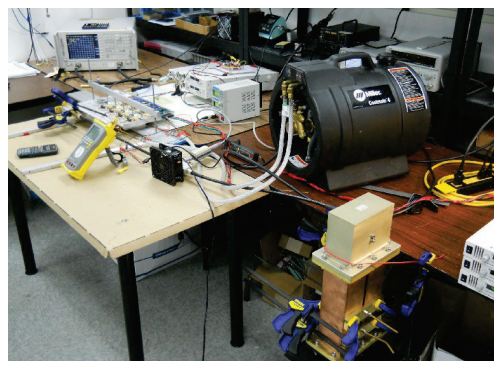


Figure 2: 500 W module test set-up. Output is connected through a 7/8" EIA connector.

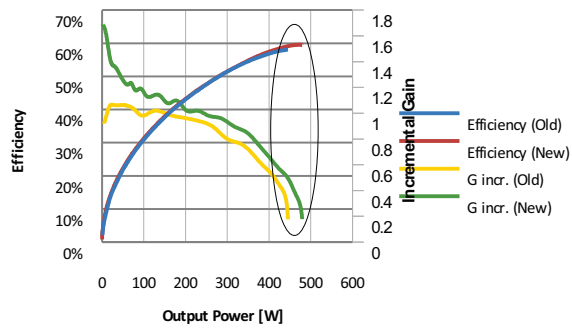


Figure 3: Peak power, efficiency, and incremental gain improvement by board modification.

The improvement of the 500 W module performance is shown in figure 3. With the improvement, the peak power increased from 445 W to 480 W, the peak drain efficiency increased from 58.2% to 59.5%, and incremental gain increased from 0.44 at 425 W to 0.57 at 425 W. The incremental gain here is defined as the change of output power in dB (P_{output}[dB]) divided by the change of input power in dB (P_{input}[dB]).

Copyright © 2013 CC-BY-3.0 and by the respective authors

16-to-1 High Power Combiner



Figure 4: High power 16-to-1 combiner cold test.

The final element of the power amplifier is a high power 16-to-1 combiner shown in Figure 4. It uses coaxial scheme for low insertion loss. The geometries of the inner and outer conductors are optimized to phase and power balance between input ports. HFSS [4] simulation indicates an insertion loss of 0.08 dB, input power imbalance of 0.01dB and phase imbalance of 1° .

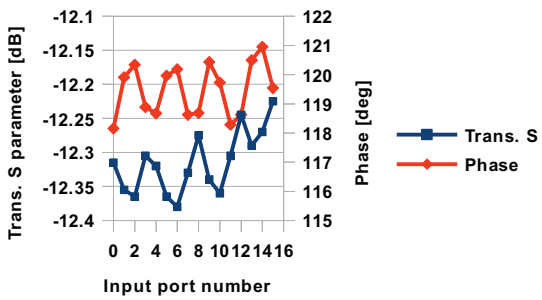


Figure 5: Transmission S-parameter and phase of each input port of the high power combiner.

Cold testing of the 16-to-1 combiner (figure 5) shows an insertion loss of 0.15 dB, an input power imbalance of ±0.03 dB rms, and a phase imbalance of ± 1° rms. The small deviation between the simulation and measurement come from machining and assembling errors.

Cooling System

Proper component cooling is critical to the amplifier performance. Better cooling can not only improve the transistor efficiency and peak power, but also increase the lifetime.

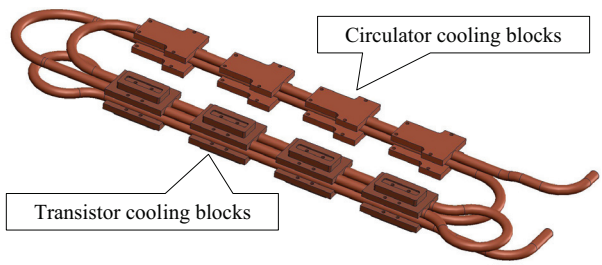


Figure 6: Cooling blocks for transistors and circulators.

Figure 6 shows the cooling scheme for the transistors and circulators (including 50 Ω circulator loads). Each pair of 500 W modules has a single cooling set for the 8 transistors and 8 circulators. The transistors are directly mounted onto the copper cooling blocks with thermal paste. The cooling blocks themselves are soldered onto thick wall (0.065" wall) 5/16" outer diameter copper tubing. The temperature difference between transistor case and cooling water at peak output power is 15 ºC. The temperature of the cooling water in the JLab facility is maintained at 35 ºC, so the peak transistor case temperature is 50 ºC, which provides a large safety margin over the rated transistor case temperature of 85 ºC. For each cooling set, the tubing is bent from a single piece eliminating the need for tubing joints making the system more robust and reliable.

Circulators and circulator loads made an indirect thermal contact to the circulator cooling blocks. The cooling blocks were mounted on outside surface of the 500 W cases. Circulators and their loads were mounted on inside surface of the 500 W case at the same locations of their corresponding cooling blocks. All interfaces were mediated with thermal paste. Each circulator generates about 6 W heating power at operating point. Circulator loads usually has no heating power and the peak power could be about 100 W in the worst case (output power full reflection). As the loads could operate at high temperature (150°C), the 100 W heating power could be easily handled.

Stage 1 Amplifier Test

The Stage 1 amplifier uses transistor boards the are similar to those used in the 500 W modules. The efficiency of these boards are less critical than those used in the 500 W modules because the total efficiency of the amplifier is less sensitive to the efficiency of the earlier stages. To achieve optimal performance, the stage 1 transistors must be more uniform and have higher incremental gain than those in the 500 W module. The boards used for stage 1 were selected and retuned to have well matched gain and incremental gain throughout the operating range.

Compact Design

The whole amplifier was designed sufficiently compact that it fit in the original klystron space. The amplifier is 22" high, 19" wide, and 20" (51 cm) deep, and fits in the original klystron rack.

Full Amplifier Test

The load for the full amplifier test uses a pair of 5 kW water-cooled loads. A high power 1-to-2 coaxial power splitter with an integrated directional coupler was designed and constructed in a 1-5/8" EIA coaxial geometry. The output from the full amplifier was split to into 2 outputs and connected to the loads. The reflection coefficient of the splitter with loads was measured to be better than -24 dB.

Water cooling for both the amplifier and the loads was provided by a circulating water system with a large radiator surface area, and can handle greater than 12 kW total power.

Copyright © 2013 CC-BY-3.0 and by the respective authors

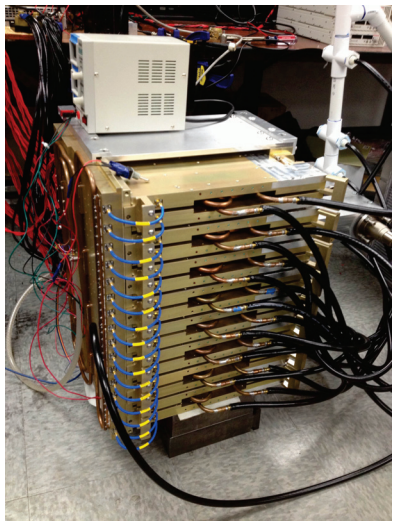


Figure 7: Full amplifier test set-up.

Figure 7 shows our whole unit amplifier and its test set up. The following lists the results near the operating point (6.4 kW) for the full amplifier test:

- Pre-amplifier input power: -7.1 dBm (0.2 mW)
- Pre-amplifier output power: 43.2 dBm (20.7 W)
- Output power: 68.1 dBm (6440 W)
- Pre-amplifier gain: 50.3 dB
- Total gain: 75.2 dB
- Power added efficiency: 54.4%
- Power supply wire loss: ~0.5% of total power
- Cooling water temperature: 37.1 ºC

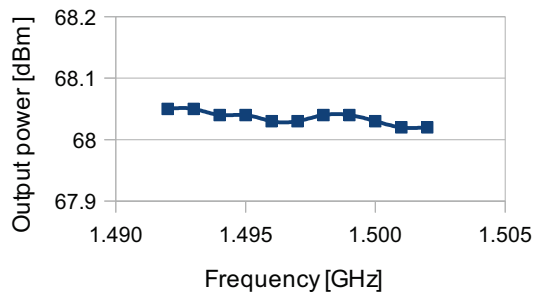


Figure 8: Frequency response of the full amplifier.

The frequency response of the amplifier was measured near the operating point. Figure 8 shows we see that the band width was larger than ± 5 MHz with this limit determined by the range of testing and not the amplifier itself.

CONCLUSION

The transistor boards were improved in peak power, efficiency, and incremental gain. Our high power 16-to-1 combiner has low insertion loss and small input imbalance and can easily handle the power output of the amplifier. The amplifier is compact with a robust and reliable cooling system. The peak power of the amplifier was 7 kW. The power added efficiency of 55% at 6.4 kW output and is expected to be better at higher output power. The band width is greater than 10 MHz.

ACKNOWLEDGEMENT

We would like to express our gratitude to colleagues at TJNAF from whom we received technical support. Special thanks to Dr. Rick Nelson for his helpful discussions.

REFERENCES

[1]. R. Nelson and A. Kimber, “RF Power Upgrade for CEBAF at Jefferson Laboratory,” PAC'11, New York, March 2011, THOCS4, p. 2127.

[2]. See the RFMD website: http://www.rfmd.com/CS/Documents/RF3934DS.pdf

[3]. X. Chang, N. Barov, D. Newsham, D. Wu, “Development of the Energy-Efficient Solid State RF Power Source for the Jefferson Laboratory CEBAF Linac”, proceedings of IPAC12, New Orleans, Louisiana, USA, May 20-25, 2012, THPPC073.

[4]. See the HFSS website: http://www.ansys.com/Products/Simulation+Technology/Electromagnetics/High-Performance+Electronic+Design/ANSYS+HFSS

Copyright © 2013 CC-BY-3.0 and by the respective authors

SYSTEM CONSIDERATIONS FOR 201.25 MHz RF SYSTEM FOR LANSCE*

John Lyles#, Walter Barkley, Jerry Davis, Angela Naranjo, Dan Rees, Gilbert Sandoval,
AOT Division, Los Alamos National Laboratory, Los Alamos, NM
D. Baca, R. Bratton, R. Summers, Compa Industries, Los Alamos, NM

Abstract

Acceleration of long pulses of proton current at high repetition rates (1 mS, 120 pps) at LANSCE have been impacted by reduced capability of the original 201.25 MHz RF system driving the 100 MeV DTL. The present operating point of the existing triode power amplifiers doesn't allow margin for tuning excursions with voltage standing wave effects or for tube manufacturing variations. This has led to the undesirable consequence of operating LANSCE at half of its original duty factor for the past seven years to maintain acceptable beam availability. A recent program has been initiated to restore the accelerator to its original high current operation. Investigated alternatives for high power RF included the development of physically large klystrons, solid-state and new power grid tube (tetrode) amplifiers. The power grid tube was favored as it reused much of the existing infrastructure including water-cooling systems, coaxial transmission lines, high voltage power supplies and capacitor banks. High duty factor tetrodes called Diacrodes®, are capable of supplying the DTL requirements with ample headroom. A LANL-designed power amplifier using the TH628L Diacrode® has produced 3 MW peak and 300 kW of mean power with > 14 dB of power gain and > 60% efficiency. It has been operating for over seven thousand hours generating RF power with a test load. Installation of the first new system begins in January of 2014.

RF SYSTEM SHORTCOMINGS

The LANSCE proton linac uses a DTL powered at 201.25 MHz, to accelerate both H^+ and H^- ions from 0.75 to 100 MeV in four Alvarez cavities, before injection into a coupled-cavity linac. The beam loading is 16.5 mA peak proton current at 120 pps. Nominal 8.7% beam duty factor (DF), with 1 pps of 1225 uS length. DTL cavity 2 has the highest energy gain of ~36 MeV, and requires the highest peak RF power of 3.6 MW, including excitation power. Significant average power (~430 KW) is required for each of three room temperature cavities to accelerate the long beam macro pulses. This is in contrast to the high-peak/low-average power regimes found at 200 MHz proton injector linacs at Fermilab, CERN, and BNL. Over the past 25 years, the manufacture of RF amplifier triodes with consistent lifetime has been challenging, when operating at the high average power needed at LANSCE. These tubes were originally commercialized in 1960, using unique processes such as pressed (non-brazed) seals. In the 1980s the company (RCA) quit the business, which was then bought by individuals. At this time there was concern about the longevity of the 7835 triode as a product.

Studies made in 1987-89 discussed alternatives to the triodes, including new tetrodes, klystrons, or IOTs. Through the last part of that century recurring problems were managed by having a larger supply of tested spare triodes. In 2006, the operating point of the power amplifiers had to be reduced in order to hold operating costs on budget (for all-too-frequent tube replacements) and prevent excess downtime. This led to the decision to operate LANSCE at half of its original duty factor to maintain acceptable beam availability.

A primary goal of the LANSCE Risk Mitigation (LRM) project has been to replace the original 201.25 MHz amplifiers with modern circuits having higher average power capability. Another goal has been to modernize the low level RF controls, to improve operational efficiency and reduce beam losses. In addition, end-of-life klystrons for the CCL are being replaced with forty-five new CPI VA862A1 klystrons.

ALTERNATIVES CONSIDERED

Solid State Amplifier

Broadcast transmitters have led development of solid state PAs. Units with up to 2 MW of modulated power have been installed at low frequencies up to a few MHz. In the VHF/UHF bands, however, power levels are predominantly in the tens of kW. In the past decade, development of CW PAs capable of 180kW was done at 352 MHz [1]. The Soleil group has pioneered using DMOS transistors in large combined circular arrays with 726 individual amplifier pallets for a booster synchrotron. Others have followed with similar designs. Transistors work best with continuous (CW) operation as wire bonds are weakened with pulsed currents, resulting in device derating [2]. The number of particular dies for a pulsed amplifier become similar to a CW rated amplifier, unlike with tubes where significantly higher peak power may be obtained from the same device. Technical problems are known to exist with LDMOS transistors, such as drift in quiescent current over time (aging and radiation-induced). MTBF for transistors are frequently quoted in tens to hundreds of years. In practical high power amplifiers such as at Soleil, the large number of passive and active devices required pushes down the MTBF to about 1 year, despite the inherent redundancies.

* Work supported by the United States Department of Energy, National Nuclear Security Agency, under contract DE-AC52-06NA25396
# jtml@lanl.gov

Copyright © 2013 CC-BY-3.0 and by the respective authors

In 2009, LANL evaluated a 1600-watt silicon carbide static induction transistor amplifier from Microsemi. It was biased above 100 volts. The device topology (common gate) limited power gain to 9 dB, requiring additional stages for preamplification. It was not pursued for various reasons.

Solid-state devices frequently have short manufacturing life cycles, being marketed for rapidly changing industries such as wireless communications. For this reason, there is a gamble to select the part that will stand out and survive in the market for a decade or more. Transistorized power amplifiers are very useful below 10 kilowatts at LANSCE - as high gain driver stages for tubes. There are no megawatt-level pulsed VHF amplifiers that would fit into the equipment hall, so this avenue was not pursued further.

Klystron or Inductive Output Tube

In the 1980s, LANL investigated high gain conventional klystrons with 40-50 dB gain. The closest commercial device was an ionospheric scatter radar amplifier at 224 MHz (EISCAT), 2.5 MW and 12% DF. Those devices were 5.5 m long and operated at 110 kV. Valvo and Varian both worked on tubes, but Varian preferred to offer multiple 1.5 MW Klystrodes (IOT) to LANL [3]. A multibeam IOT was also proposed using radial stripe beams but the development estimate was too costly and lengthy for LANL to consider at the time. Eimac had previously developed a 267 MHz 250 kW CW IOT for Chalk River Lab. It worked but was plagued with grid contamination from the cathode, which caused loss of control if not corrected. Thompson Tubes Electroniques proposed a 5.7 m long 200 MHz klystron at the time. Valvo eventually left the business. LANL also investigated building in-house, having large hydrogen-braze furnaces from the making of the first coupled-cavity linac. This was not pursued further when we shifted away from in-house klystron remanufacturing.

In 2004, CPI published a concept for a 250 kW coaxial IOT for 200 MHz [4]. Most recently, CPI has proposed a multibeam klystron for 200 MHz for 7 MW peak/52kW average power for Fermilab's DTL. Efficiency is estimated at about 50%. None of these developments has addressed the 3.6 MW peak, 430 kW average power required for the LANSCE DTL, however. In 2010 discussions with CPI led to the concept of a reduced gain (32 dB) high average power klystron with one-less fundamental cavity. In this way the tube length could be less than 4.7 meters. This klystron option was a viable contender for the replacement DTL RF amplifier.

Gridded Tube

The caveat for gridded tubes is that a matching cavity amplifier circuit must be developed around the chosen device. This requires that the tube manufacturer or an independent producer commercialize this complex unit into an amplifier system. An acceptable solution may also have the amplifier development done by the laboratories, although costs must be weighed against industrialization.

Several alternatives were proposed by Eimac in 1987-89 using tubes derived from the 8973, a conventional tetrode. None of these were deemed acceptable for high average or peak power without first testing at 200 MHz, requiring development funding for a circuit. In 1989 Thompson proposed a new tetrode that used the favorable double-ended RF circuit topology of the old triode but with much higher average power due to new grid materials, improved anode cooling, and brazed ceramic seals. This device was eventually developed and tested for resistive heating for fusion research as the TH628 Diacrode® [5]. This tube is a high DF (CW) device with over 3 times the anode dissipation rating of the original triode. The cathode is designed for long life typical of tetrodes, with 2.6 times the emitting area of the RCA triode. Emission current density of 0.95 Amps/cm^2 at the peak cathode current compares very favorably to 3 Amps/cm^2 in the triode for the same RF level. In 1998 LANL started development of a cavity amplifier for this device. The objective was to power combine two of the units for the highest power DTL cavity at 3.6 MW, and using a single amplifier for cavities 3 and 4 for 3 MW [6]. What began as a partial-time effort moved into a fully funded development by the author after the 2006 crisis happened. In 2009 a new test facility was assembled simultaneously with the building of a prototype PA for operation [7].

In 2010, Thales (former Thompson) made a change to the grid material for safety and environmental factors. As a consequence, the modified pyrolytic graphite had increased RF loss at 200 MHz. This lowered the screen grid (g2) RF power dissipation rating. While this didn't affect the intended fusion application below 80 MHz, it required the baseline design for LANSCE to use two amplifiers for all three of the largest DTL cavities. This increased the installed cost but provided ample headroom in the design, allowing the individual Diacrodes® to operate at 55% of their rating. Increased reliability and mean time to replacement for the tubes will result from this pairing of amplifiers.

As the prototype amplifier was being built, the total installed cost was estimated for both dual-Diacrode® and klystron options, based on the recent low gain klystron proposal from CPI. The complexity of the grid tube plant was weighed against the new cost and schedule of development for klystrons plus their new 1.2 MW 110 kV beam power supplies. With the in-house amplifier development about to reach its milestone to produce RF power, a decision was made to install with the Diacrodes® at LANSCE.

Construction of the final configuration of the amplifier was completed in 2010. The common-grid amplifier configuration uses a full wavelength double-ended circuit, and forced air/water cooling. Subsequent power testing

Copyright © 2013 CC-BY-3.0 and by the respective authors

resulted in minor improvements that were implemented in 2011 followed by testing up to 2.5 MW peak power at 12% duty factor. The amplifier has been tested at the 3 MW operating point to demonstrate design margins as well as cathode emission capabilities of the tube. Testing has continued for over 7000 hours with the amplifier using three different Diacrodes®, while also testing the remaining components for the plant. Mechanical and electrical design of the PA, supporting electronics and intermediate power amplifier (IPA) are discussed elsewhere [8][9][10]. The Diacrode® option reuses the same cooling water plant, the HV power supplies, capacitor banks and the 35.5 cm diameter coaxial transmission lines of the old RCA plant.

A tender for manufacturing the LANL-designed PA was issued in 2012 and the work was awarded to Continental Electronics Corporation. One PA has been delivered for testing in October with two more presently in manufacturing. Four more are scheduled to be purchased in the next two years. Two new TH628 Diacrodes® have been tested and accepted and 3 more are in manufacturing, with 3 more to be ordered in the future. Two IPAs have been ordered and delivered from Betatron Electronics, with 2 more expected in the coming years. The lab and the fabricator jointly designed these, based on the LANL prototype. This amplifier uses a Thales TH781 tetrode, and matching TH18781 cavity amplifier. One IPA will drive two combined TH628s at each RF station.

PASSIVE RF COMPONENTS

The 3 1/8 inch diameter coaxial transmission line from the 175 kW IPA is split by a λ/4 hybrid into two paths. One path has a passive phase shifter made like a trombone, with +/- 10 degrees of variability. The other path uses a fixed length delay to compensate for the phase shifter. The outputs from the two final PAs (FPA) are combined in a λ/4 branchline hybrid made from coaxial line. Normally this would shift any reflected power from the DTL into two components 90 degrees apart at the two Diacrodes®, causing difficulty in maintaining power balance with varying reflected power. A separate λ/4 phase delay is placed in the 9 3/16 inch diameter coaxial line on one FPA to make the two tubes operate into the same reflected phase. A similar delay is placed in the input line of the opposite amplifier to place the two amplifiers back in a quadrature relationship for the combiner. Figure 1 shows this configuration with the IPA removed for clarity.

CONCLUSION

The new gridded tube power amplifiers meet the technical requirements for the LANSCE DTL, and also provide a basis for new driver amplifiers for a future RFQ. They are being commercially produced, and installation of the first pair of amplifiers starts in January of 2014. Collaboration with CERN has been ongoing with the Diacrode® option considered for the SPS RF upgrade and for a 6D Muon ionization cooling facility through the TIARA R&D objectives [11].

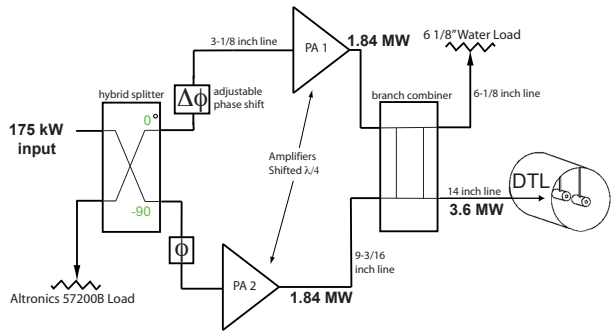


Figure 1: Diagram of combined power amplifiers.

REFERENCES

[1] D. Massamba, R. Lopes, P. Marchand, F. Ribeiro, "Developments of High power CW SSAs at Soleil", TIARA Workshop on RF Power Generation for Accelerators", Uppsala, Sweden, June 17-19, 2013.

[2] C. Martins, "Thermal Cycling of Power Semiconductors in Long Pulse Applications", TIARA Workshop on RF Power Generation for Accelerators, Uppsala, Sweden, June 17-19, 2013.

[3] Letter from M. Shrader, Eimac/Varian Associates, to R. Newell, LANL, Nov. 18, 1987.

[4] Kimura, T., Bohlen, H., et al, "Design of a 200 MHz, 250 kW Coaxial IOT", International Vacuum Electronics Conference, 2008, pp. 451-452.

[5] G. Clerc, J.P. Ichac, C. Robert, "A New Generation of Gridded Tubes for Higher Power and Frequencies", PAC'97, Vancouver, pp. 2899-2901.

[6] J. Lyles, C. Friedrichs, M. Lynch, "New High Power 200 MHz RF System for the LANSCE Drift Tube Linac", Linac98, pp. 228-230.

[7] J. Lyles, J. Davis, D. Rees, et al., "A High Power Test Facility for New 201.25 MHz Power Amplifiers and Components", IPAC'12, New Orleans, LA, pp. 3449-3451.

[8] Z. Chen, D. Baca, et al, "Mechanical Design and Fabrication of a New RF Power Amplifier for LANSCE", PAC'11, New York, NY, pp. 1085-1087.

[9] J. Lyles, Z.Chen, J. Davis, et al, "Design, Test and Implementation of New 201.25 MHz RF Power Amplifier for the LANSCE Linac", IPAC'12, New Orleans, LA, pp. 3446-3448.

[10] J. Lyles, S. Archuletta, J. Davis, et al., "Test Results for the 201.25 MHz Tetrode Power Amplifier at LANSCE", EPAC'04, Lucerne, Switzerland, pp. 1078-80.

[11] E. Montesinos, J. Lyles, TIARA Report WP7/Task 7.2, "Novel Pulsed RF Power Amplifier Design", http://www.eu-tiara.eu/database/index.php?wp=WP7

Copyright © 2013 CC-BY-3.0 and by the respective authors

MODELING OF MAGNETRON TRANSMITTER FOR THE PROJECT X CW 1 GeV LINAC*

Grigory Kazakevich#, Rolland Johnson,
Muons, Inc., Batavia, 60510 IL, USA

Vyacheslav P. Yakovlev, Brian E. Chase, Ralph J. Pasquinelli,
Fermilab, Batavia, 60510 IL, USA

Abstract

A 650 MHz 50 kW transmitter with a wide-band control in phase and power, based on injection-locked CW magnetrons has been proposed to drive individually Superconducting RF (SRF) cavities for the Project X CW 1 GeV H^- linac. Utilization of the magnetron RF sources for the intensity-frontier project will save a significant capital cost in comparison with traditional RF sources based on klystrons, Inductive Output Tubes (IOTs), solid-state amplifiers. The transmitter setup has been modelled experimentally using 2.45 GHz CW magnetrons with output power up to 1 kW operating in injection-locked mode in pulsed regime with long pulse duration. Measurements with the modelling setups indicated capability of the proposed transmitter to power the SRF cavities suppressing parasitic modulation of the accelerating field caused by mechanical oscillation (the microphonics), beam loading, dynamic tuning errors, and the low-frequency disturbances of the magnetron performance. Results of the experimental tests are analyzed and discussed in this paper.

INTRODUCTION

State of the art the intensity-frontier Project X H^- superconducting 1 GeV linac requires CW, 650 MHz RF sources to power SRF cavities. One of general requirements following from dynamic of non-relativistic or weakly relativistic beam is conservation of a small emittance during the process of acceleration. For this is necessary keeping the accelerating voltage phase and amplitude deviations to be less than 1 degree and 1% of nominal, respectively, [1].

To keep amplitude of accelerating voltage with the required accuracy in spite of microphonics, a dynamic control of the accelerating voltage is required, [2, 3].

The average RF power to feed each SRF cavity, providing an energy gain of ~17 MeV/m for average beam current of 2 mA at the microphonics magnitude, δf=20 Hz, one can determine by the following equation:

$$P_g = \frac{V^2}{4Q_E(r/Q)}\left[\left(1+\frac{I\cos\varphi(r/Q)Q_E}{V}\right)^2+\left(Q_E\frac{2\delta f}{f}\right)^2\right].$$

Here P_g is the RF source power, V is gradient of the accelerating field in the 1 m long SRF cavity for zero synchronous phase, (r/Q) is the cavity impedance, Q_E is the cavity external Q-factor, *f* is the cavity frequency, δ*f* is the microphonics magnitude, φ is the synchronous phase.

For ILC-type 650 MHz SRF cavity with (r/Q)≈ 638 and φ ≈-10 degrees the equation gives P_g≈ 38.5 kW at the necessary range of the power variation of ~ 5 kW. Considering reflections and insertion losses in the RF system one can evaluate the RF source nominal power of ≈ 50 kW necessary for each individual SRF cavity of the CW linac.

To compensate perturbations caused by beam loading, and dynamic tuning errors, a control of phase of the RF field is necessary in each individual SRF cavity.

Traditional RF sources based on klystrons, Inductive Output Tubes (IOTs), solid-state amplifiers are acceptable to provide the required power and the phase control, but the capital cost of the RF system is a significant part of the accelerator project. MW-scale CW klystrons powering groups of the cavities can reduce the costs, but this technique only allows a control of the vector sum of the accelerating voltage in the group. The vector sum control has not been tested in driving SRF cavities for non-relativistic or weakly relativistic particles; it may cause emittance growth because of non-optimized values of phase and amplitude of the field in individual SRF cavities.

The CW injection-locked magnetrons are efficient and less expensive than the aforementioned RF sources, [4].

Analysis of operation of magnetrons injection-locked by a phase-modulated signal, [5-7] demonstrates that the magnetron response on the locking signal is quite linear, has small phase error and quite fast, [8]. The features of the injection-locked magnetrons allow developing the RF source based on the CW magnetrons controlled in phase and power to suppress the perturbations of the magnetron phase performance inherent in magnetrons and moreover to satisfy requirements of the Project X H^- linac as well.

The experiments performed with CW 1 kW injection-locked magnetrons and evaluations presented in this paper indicate that the phase controlled transmitter based on the injection-locked magnetrons with a Low Level RF system including a closed wideband loop will allow eliminating all expected low-frequency perturbations of the accelerating field in SRF cavity including the perturbations caused by the phase performance of the injection-locked magnetron.

Results of the experimental tests are analyzed and discussed in this paper.

*Work is supported by the Fermilab and Muons, Inc. collaboration
#grigory@muonsinc.com; gkazakevitch@yahoo.com

Copyright © 2013 CC-BY-3.0 and by the respective authors

THE MAGNETRON TRANSMITTER FOR THE PROJECT X CW H⁻ LINAC

A concept of the 650 MHz, 50 kW magnetron transmitter (with phase and power to be controlled by a LLRF) for the Project X H⁻ CW linac is presented in Figure 1, [9].

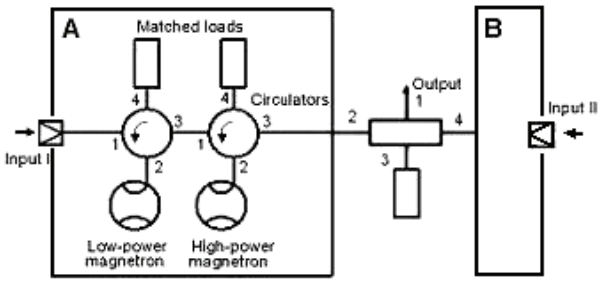


Figure 1: Block-diagram of the magnetron transmitter available for a fast control in phase and power.

The transmitter consists of two identical channels (A and B) of cascaded injection-locked magnetrons, combined in power by a 3-dB hybrid. The phase management is provided by controlled simultaneously and equally the phases at inputs of both 2-cascade magnetrons. The power management is provided at a control by phase difference at the inputs of the 2-cascade magnetrons. The 2-cascade injection-locked magnetron system allows reducing the required locking power.

EXPERIMENTAL FACILITY

The facility was developed for experimental tests of the CW transmitter active components using two CW, 1 kW microwave oven magnetrons. The magnetrons with free run frequencies differing by ≤ 5.7 MHz operated in injection-locked mode at the locking frequency of 2.469 GHz in pulsed regime, at pulse duration of 2.5-15 ms at low repetition rate. Each magnetron was installed in a separate module with necessary RF components, Figure 2. The modules were used to test performance of all active components of the proposed transmitter in various setups.

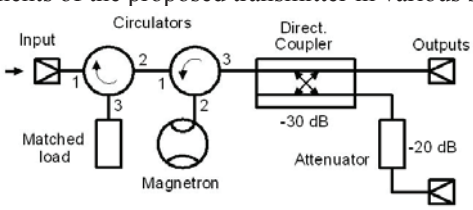


Figure 2: The magnetron experimental module for tests of the transmitter setup.

The experimental apparatus for the tests included a pulsed modulator to power the magnetrons, wide-band CW Travelling-Wave Tube (TWT) amplifiers driven by N5181A Agilent generator, to lock the magnetrons, and measuring equipment.

The modulator with partial discharge of storage capacitor provided simultaneous operation of the both magnetrons, having dissimilar Volt-Amps characteristics; the magnetron with lower anode voltage was fed by a compensated divider. The HV power supply ripple were negligibly low at the modulator output, however the modulator introduced a slope of the output voltage caused by discharge of the storage capacitor. The slope at pulse duration of 5 ms did not exceed 0.4% when 2 magnetrons operated simultaneously.

TESTS OF SINGLE AND 2-CASCADE INJECTION-LOCKED MAGNETRONS

Setup for tests of operation of injection-locked singles and 2-cascade magnetrons is shown in Figure 3, [8].

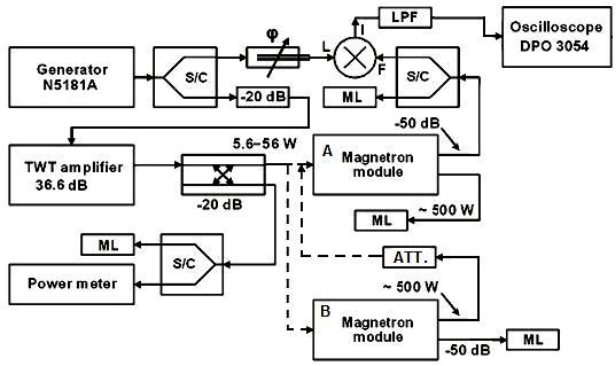


Figure 3: Setup to test operation of single and 2-cascade injection-locked magnetrons. S/C is a splitter/combiner, LPF is a low pass filter, ML is a matched load, and ATT is an attenuator. Powers of the magnetrons are depicted in this figure.

The single injection-locked magnetrons were tested in configuration using module A with the magnetron locked by the TWT amplifier and fed by the modulator, while the module B was disconnected from the amplifier and the modulator. The 2-cascade magnetron was tested in configuration, in which the magnetron module B was locked by the TWT amplifier while the module A magnetron was connected via attenuator to the module B output. In this case the magnetron in the module A was locked by the pulsed signal of magnetron B lowered in the attenuator. The modulator fed both the magnetrons.

Traces of the magnetron intrapulse phase variations are plotted in Figure 4.

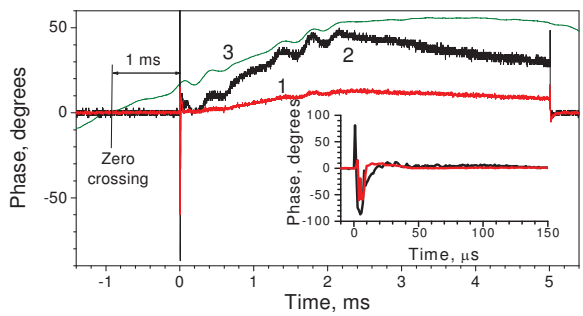


Figure 4: Phase performance of the single, trace 1, and 2-cascade, trace 2, injection-locked magnetrons. Trace 3 shows voltage of the AC line. Trace 1 was measured at the magnetron locking power of -15.6 dB; Trace 2 was measured at the locking power of the magnetron B of -15 dB and the attenuator value of 15 dB. Considering the attenuator value the locking power of the 2-cascade magnetron is -30 dB of the output power.

Copyright © 2013 CC-BY-3.0 and by the respective authors

Shift of the triggering of the modulator vs. zero crossing of the AC line voltage minimized the magnitude (peak-to-peak) of the magnetrons phase perturbations resulted from the magnetic field induced by the filament circuitry, [10].

POWER CONTROL OF INJECTION-LOCKED MAGNETRONS

The fast power control of the injection-locked magnetrons using power combining first was realized in the setup shown in Figure 5, [10].

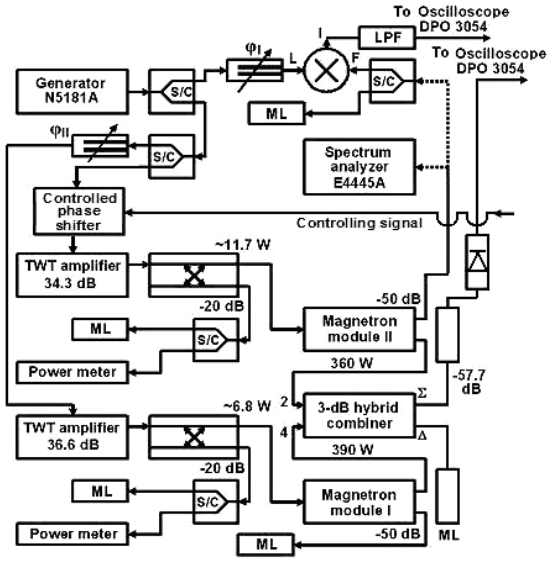


Figure 5: Setup with the injection-locked magnetrons for test of the power control by power combining.

The power control, Figures 1 and 5, is realized by a vector summation of output signals of the injection-locked magnetrons controlled by the phase difference.

Performance of the injection-locked magnetrons at fast power control was demonstrated controlling the analogue phase shifter JSPHS-2484 by a sequence of meander-like pulses with period of ≈30 μs, Figure 6.

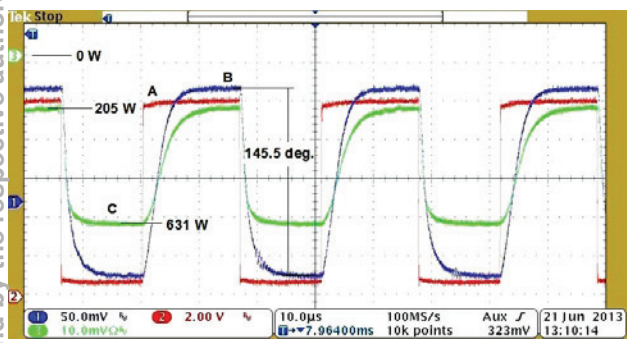


Figure 6: Trace A is shape of the voltage, controlling the phase shifter JSPHS-2484, trace B is the magnetron II phase response on the shifter fast control, trace C shows variation of the power measured by the calibrated detector at the port "Σ" of the 3 dB 180 degrees hybrid.

The high-frequency noise measured for single, 2-cascade injection-locked magnetrons and magnetrons with power combining does not exceed 0.4, 0.7 and 0.5 degrees (rms), respectively.

The bandwidth of the phase control was measured in setups, Figures 3, 5, by a phase modulation in generator N5181A at various modulating frequencies. Measured with Signal Analyzer MXA N9020A in the phase modulation domain the magnitude transfer characteristics of the magnetrons locked by the phase-modulated signal showed that the frequency cut-off at the locking power of ≥-13 dB for single and ≥-27 dB for 2-cascade magnetron setup is ≥1 MHz. It implies that the injection-locked magnetron RF source managed in phase and power by a LLRF controller with a closed feedback loop at the bandwidth of ≈100 kHz will be able to suppress all expected low-frequency perturbations in SRF cavities including the perturbations resulted from the magnetrons.

CONCLUSION

Setups of all active components of the proposed magnetron transmitter rapidly controllable in phase and power by the phase-modulated signal and intended for CW H^- linac of the Project X have been tested using 2.45 GHz 1 kW magnetrons operating in injection-locked mode. The experimental tests verified that the response of all active components of the transmitter based on the injection-locked magnetrons at the control is quite linear, provides small phase error and is quite fast to use a Low Level RF (LLRF) controlling system with a wideband closed loop. The ratio of locking power to output power of -27 dB for 2-cascade magnetron looks feasible at bandwidth of the magnetron phase control of ≥1 MHz. Measured high-frequency phase noise of the transmitter components <1 degree, rms, satisfies requirements of the Project X H^- superconducting linac. The magnetron transmitter with the LLRF controller will be able eliminating all expected low-frequency perturbations of the accelerating field in the SRF cavity including perturbations caused by mechanical oscillations, beam loading, dynamic detuning errors and perturbations resulted from performance of the injection-locked magnetrons, including phase pushing and perturbation caused by induced alternative magnetic field.

REFERENCES

[1] N. Solyak et al., WE101, LINAC10, Tsukuba, Japan
[2] H. Padamsee et al., *in* "RF Superconductivity for Accelerators", Wiley & Sons, Inc, 1998.
[3] J. R. Delayen, "Electronic damping of microphonics in superconducting cavities", PAC 01 Proceedings, Chicago, IL, USA, 2001.
[4] A.C. Dexter et al., PRST-AB,14, 032001, 2011.
[5] G. Kazakevitch et al., NIM A 528 (2004) 115–119.
[6] G.M. Kazakevich et al., PRST-AB, 12, 040701, 2009.
[7] G.M. Kazakevich et al., NIM A 647 (2011) 10-16.
[8] G. Kazakevich et al., WEPPC059, IPAC12. Proceedings, New Orleans, USA.
[9] G. Kazakevich and V. Yakovlev, Project X. document 896, http://projectx-docdb.fnal.gov
[10] G. Kazakevich et al., TUOAT12 report at 11-th International Topical Meeting AccApp 13, Bruges, Belgium, 2013.

Copyright © 2013 CC-BY-3.0 and by the respective authors

AN EFFICIENT RF SOURCE FOR JLAB*

M. Neubauer, A. Dudas, Muons, Inc. Batavia, IL 60510, USA
R. Rimmer, H. Wang, JLAB, Newport News, VA 23606, USA

Abstract

The original CEBAF accelerator at Thomas Jefferson National Accelerator Facility (JLAB) currently uses a system of 340 klystrons with relatively low efficiency, but an MTBF approaching 170,000 hours. Over the lifetime of the project 60% of the tubes have been replaced, giving an MTBF for a single tube of about five to six years. 45% of the klystrons were replaced over the thirteen years of full operation (1995-2007) with an average filament on time of 80% and high voltage on time of 75%, thus a utilization rate of 61% per year or ~4300 high voltage operating hours per year with an overall system efficiency of 35%. This represents 1.6M$ per year of electricity costs and over 20% of the total electricity usage of the high energy mission specific facilities (HEMSF).

We propose the development of a highly reliable high efficiency RF source for JLAB operating at ~80% efficiency yielding system operating costs of only about 0.7M$/year for the 6 GeV machine. A number of RF source designs are being evaluated including the concept of two injection locked magnetrons in a novel combining architecture for amplitude modulation. A cost analysis including efficiency and reliability will be performed to determine the optimum system architecture.

INTRODUCTION

The RF source for the CEBAF machine currently uses 5-8 kW klystrons operating at ~35% efficiency [1]. The annual electricity usage for the HEMSF for the 6 GeV machine is 130,000 MWhrs [2]. As shown in Table 1, the annual savings for the RF source alone would be about 1M$ per year, neglecting various cooling requirements for the power supply and microwave tube. The savings represent a reduction in the HEMSF usage from 130,000 MWhrs to about 113,000 MWhrs for the 6 GeV machine.

Table 1: Example calculations of the impact of a high efficiency RF source on the operating costs and electricity usage per year.

RF output power	5	5	kW
tube efficiency	35%	80%	
DC input power to each station	14.3	6.25	kW
number of stations	340	340	
DC Input power for HPRF sources	4857	2125	kW
Power supply conversion rate	95%	95%	
Total station input power for HPRF	5113	2237	kW
70% utilization rate	6132	6132	hrs/year
Yearly Electrical Useage	29784	13031	Mwh/year
Cost at 61$/Mwh	$1.82	$0.79	($M)
Savings		**$1.02**	**($M) per year**

The MTBF of individual tubes in the CEBAF system can be estimated to be 5-6 years or about 37,000 tube hours with a 75% utilization rate, while the MTBF of the system of 340 tubes is approximately 170,000 system hours (see Figure 1). Magnetrons have a similar MTBF. Varian (now CPII) reported lifetimes of 27,600 MTBF for a 65-80kW X-band coaxial magnetron [3]. In 2006, a study was made at the Naval Post Graduate School in Monterey, of the Total Ownership Cost (TOC) of the Aegis microwave power tubes. In the Aegis system, the MTBF of CFAs was improved from 6000 hours to 45,000 hours from 1983-2002 [4]. Cross-field amplifiers (CFA) are in the same class as magnetrons.

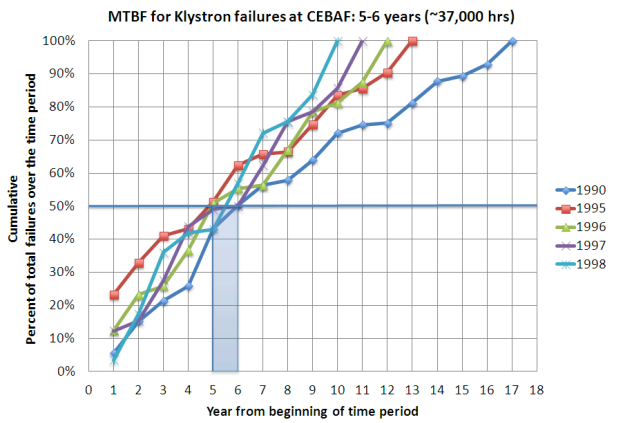


Figure 1: Data Collected from JLAB presentation, "Operating Experience and Reliability Update on the 5 kW CW klystrons at Jefferson Lab," [5].

Another primary use of magnetrons is in medical linear accelerators where they are operated at high peak powers with low utilization rates. The MTBF of the magnetrons in one linac system architecture was doubled from 20 months to 43 months over a four year period [6].

The point to be made is that, the system design and the interface between the tube(s) and power supplies dominates the MTBF of the RF source. It is reasonable to assume that the MTBF of a magnetron based system can be as good if not better, than the klystron MTBF when the system design is optimized at an early stage of development.

APPROACH

We have determined two basic designs which will be further analyzed. The first consists of a single RF source (klystron, magnetron, IOT, etc.), and the second would be a dual magnetron source in which the outputs of two injection locked magnetrons would be phased and combined to produce a required output power level and phase.

An initial power balance spreadsheet analysis has shown that a single magnetron would be more efficient that using either a klystron or IOT device. Thus our focus has narrowed to either a single or dual magnetron system.

*Work supported by DE-SC0009693

Copyright © 2013 CC-BY-3.0 and by the respective authors

Figures 2 & 3 show the system diagrams for each of those two options.

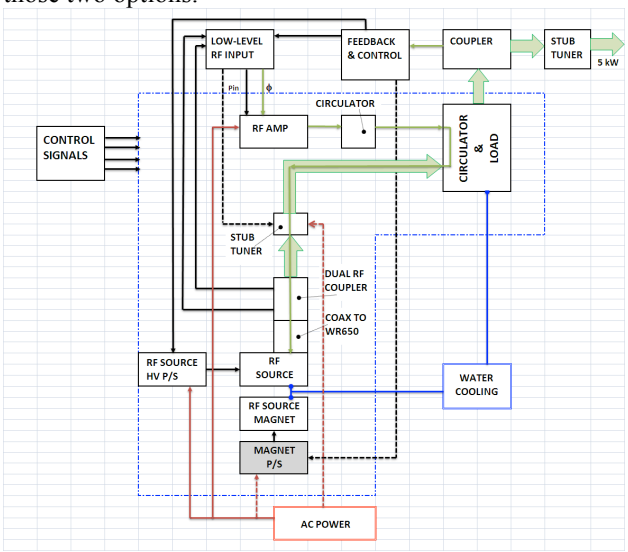


Figure 2: Single RF source system diagram.

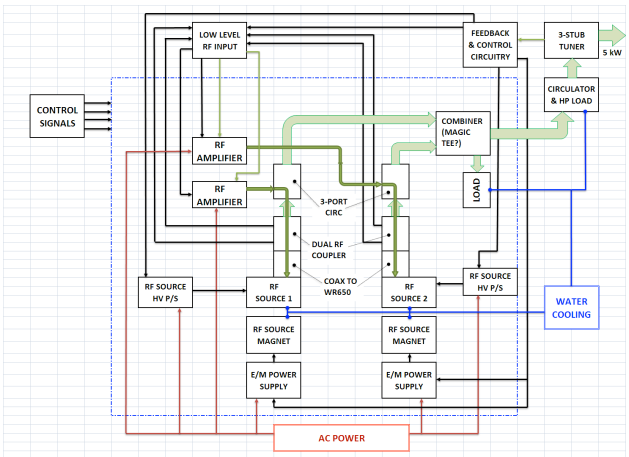


Figure 3: Dual Magnetron source system diagram.

Figure 2 is similar to the current CEBAF system using a single klystron. Figure 3 however shows an injection signal fed through a circulator into a combining network which may be as simple as a magic TEE. Both magnetrons are fed with this signal, injection locked, and deliver their output to combine in the fourth leg of the magic TEE. To adjust the output amplitude, the amplitude and phase of one magnetron is adjusted relative to the other (via the Feedback & Control system). The sum is sent to the output, and the difference is sent back through the circulator to a load. This is a straightforward system, just like the others, but the devil is in the details.

The first of those details is controlling the output phase of one magnetron relative to the other. In the work already done by JLAB, 0.8° phase stability was achieved, limited by noise from the digital power supply used.

Additional details being analyzed and optimized are:

1) What design elements or improvements are required to meet the AM requirements of the combined system?
2) What is the most cost effective combining system?
3) Will an electro magnet be used for the magnetron focusing to optimize efficiency?
4) Will the design of the 1497 MHz magnetron include a side coupling for improved locking?
5) Will phase shifters be required in addition to magnetron pushing by the beam voltage to achieve the required amplitude modulation?
6) What is the overall efficiency of the system under realistic operating conditions? How does it impact TOC?
7) Can a low gain cross-field amplifier (CFA) be used in addition to the phase locked magnetrons to meet the 12 GeV upgrade requirements?

System Efficiency and TOC

The system efficiency of various system architectures is being studied to determine the optimum design. The methodology is shown in Figure 4 (shown on the next page). Each element of the system architecture will be analyzed in terms of input power, efficiency, and heat loss. The TOC is a summation of acquisition cost and operating costs. The payback of the acquisition cost, in terms of cost savings from operating costs, is being determined.

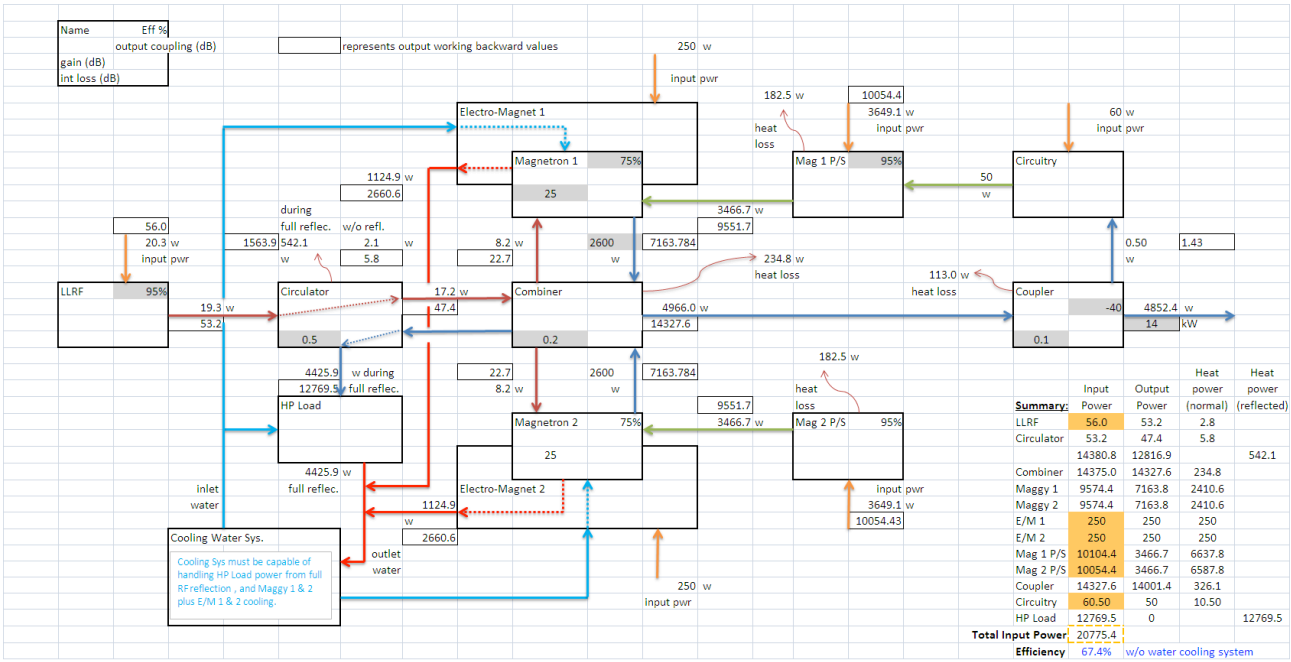
New components will need to be designed, such as the 1497 MHz magnetron, and the methodology to determine the design effort (cost) as well as the TOC without knowing exactly which elements will be involved will utilize a scoring method similar to that shown in Figure 5. In this method, various elements of the designs are "scored" for cost, ease of design, complexity, etc. (1 being easy / low cost, and 3 being difficult / high cost).

	Sum	Total Tube Cost	# of tubes	Eff	Tube Cost (each)	Gun	Interaction Region	Collector	Total System Cost	RF Driver	waveguide system	Feedback System	Power Supply
Klystron	19	15	1	0.4	6	1	3	2	4	1	1	1	1
IOT	14	8.57	1	0.7	6	2	2	2	5	2	1	1	1
2 Magnetrons													
master slave	19	8	2	0.5	2	1	1		11	3	3	3	2
peer to peer	19	8	2	0.5	2	1	1		11	3	3	3	2
2 CFAs	16	8	2	0.5	2	1	1		8	3	2	1	2
1 Magnetron													
Anode V Modulated	12	2.5	1	0.8	2	1	1		9	2	1	3	3
B-Field Modulated	11	2.5	1	0.8	2	1	1		8	2	1	3	2
Gridded	9.8	3.75	1	0.8	3	2	1		6	1	1	1	3

Figure 5: Example of a risk assessment used to determine the optimum architecture for the RF source in this project.

For example, since 340 units are anticipated in the full replacement of the klystrons, there will be learning curve applied to the unit cost of the RF source designed in this Phase I program. This will include a risk assessment and median pricing for the most probable cost of 680 magnetrons. The MTBF of the RF source will be applied to arrive at a total quantity of magnetrons needed, which may exceed 1000 magnetrons over ten years. Cost estimates from various suppliers will also be used where applicable. With this methodology in place, the most cost effective system architecture will be determined.

Copyright © 2013 CC-BY-3.0 and by the respective authors



Summary:	Input Power	Output Power	Heat power (normal)	Heat power (reflected)
LLRF	56.0	53.2	2.8	
Circulator	53.2	47.4	5.8	
	14380.8	12816.9		542.1
Combiner	14375.0	14327.6	234.8	
Maggy 1	9574.4	7163.8	2410.6	
Maggy 2	9574.4	7163.8	2410.6	
E/M 1	250	250	250	
E/M 2	250	250	250	
Mag 1 P/S	10104.4	3466.7	6637.8	
Mag 2 P/S	10054.4	3466.7	6587.8	
Coupler	14327.6	14001.4	326.1	
Circuitry	60.50	50	10.50	
HP Load	12769.5	0		12769.5
Total Input Power	20775.4			
Efficiency	67.4%	w/o water cooling system		

Figure 4: An example analysis for the system of Figure 3, showing elements of the analysis for total operating efficiency including the cooling system.

1497 MHz Magnetron

The RF source will be based upon a modest scaling of the common water-cooled industrial cooker magnetron: a 3 kW 2450 MHz magnetron [7]. The efficiency of this magnetron is about 70%. The efficiency of the similar 915 MHz water cooled magnetron is over 90%, so it is reasonable to assume a 1497 MHz magnetron can be designed to operate at ~ 80% efficiency. A paper design of a 1497 MHz magnetron is part of our program. Details of the anode structure can be designed in Comsol or CST. The details of the heater package, coupling, cooling, and other mechanical elements of the design will be made in sufficient detail so that bids for a total quantity of 1000 tubes can be obtained.

CONCLUSION

Initial work has shown that design of a more efficient CEBAF RF source system is reasonable, and should save JLAB 1M$+ in electricity costs per year. Technical performance and reliability equivalent to or better than the existing sources needs to be demonstrated. Total cost of ownership and time to recoup the initial investment will be calculated.

REFERENCES

[1] C Hovater et al., "RF System Development for theCEBAF Energy Upgrade," 2002.

[2] "Jefferson Lab 2012 Site Sustainability Plan" (January 2, 2012): 1–28; http://wwwold.jlab.org/fm/energymanagement/sustain_plan.pdf

[3] A C Johnson, W A Gerard, and R A Washburn, "Development of a 250 kW, X-Band, Accusweep Magnetron," (presented at the International Electron Devices Meeting 1991 [Technical Digest], IEEE, 1991), 601–604.

[4] Aruna U Apte and Eugene Dutkowski, "Total Ownership Cost Reduction Case Study: AEGIS Microwave Power Tubes" (May 31, 2006).

[5] R Nelson and S Holben, "Operating Experience and Reliability Improvements on the 5 Kw Cw Klystron at Jefferson Lab," vol. 3, (presented at the 1997 Particle Accelerator Conference, IEEE, 1997), 3165–3167.

[6] G T Konrad, "Application of Magnetrons with Medical Linear Accelerators," *Proc 1st Int Workshop on Crossed-Field Devices* (1995).

[7] Private conversation with Peter Campbell, retired marketing manager at CTL L-3.

Copyright © 2013 CC-BY-3.0 and by the respective authors

HIGH POWER CO-AXIAL COUPLER*

M. Neubauer, A. Dudas, Muons, Inc., Batavia, IL 60510, USA
R. Rimmer, J. Guo, S. Williams, JLAB, Newport News, VA 23606, USA

Abstract

A superconducting RF (SRF) power coupler capable of handling 500 kW CW RF power at 750 MHz is required for present and future storage rings and linacs. There are over 35 coupler designs for SRF cavities ranging in frequency from 325 to 1500 MHz. Coupler windows vary from cylinders to cones to disks and RF power couplers will always be limited by the ability of ceramic windows and their matching systems to withstand the stresses due to non-uniform heating from dielectric and wall losses, multipactor, and mechanical flexure.

We have fabricated and tested a novel robust co-axial SRF coupler (400 MHz, 6 kW CW) design that uses two windows manufactured with compression ring technology and no matching elements in the coax line. This technology allows the use of high thermally conductive materials for cryogenic windows because the braze joint will be in compression. We have also incorporated "explosion bonded" technology into this design to reduce needed parts and simplify fabrication. In this phase, a scaled down version of the 500kW CW double window assembly has been built and tested.

A compressed co-axial window was designed and fabricated using standard ceramics [1]. Low power tests confirmed the broadband match characteristics of a double window design.

Double-window, coaxial input couplers or coaxial pressure barriers have high power CW applications ranging from RF guns for injectors to high power magnetron sputtering systems. Single half-wavelength coaxial windows built with our compression technology will handle significantly more power than standard windows.

INTRODUCTION

Dual-Window Concept

When two coax windows are placed in a length of line, the distance between them can be adjusted to create a perfect match. That distance is approximately a quarter-wavelength. The thickness of the window and its dielectric constant determine the exact distance for the cancellation of reflections. For EIA 3-1/8 50Ω coax line, the ceramic window has the same dimensions as the coax (76.9 mm and 33.4 mm). In our Phase I construction of a compressed window we used a window thickness of 7.6 mm. Using those dimensions the optimum spacing for various frequencies can be determined by various simulation tools. For EIA 3-1/8 coaxial line, Figure 1 shows the window spacing as a function of frequency, which provides a near perfect match.

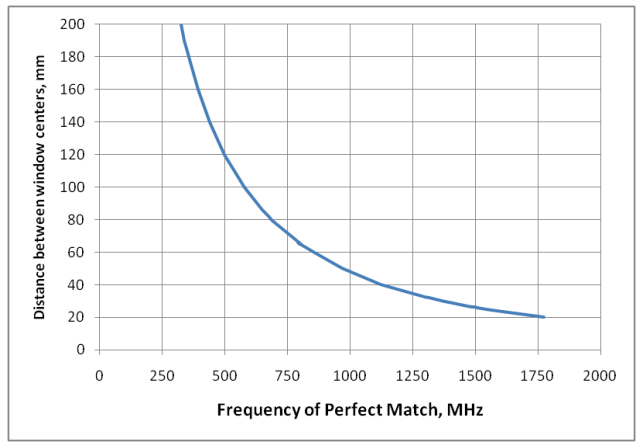


Figure 1: Two alumina windows 7.6 mm thick modeled in EIA 3-1/8 coax for the distance between them which creates a near perfect match.

As the thickness of the window becomes large compared to the wavelength of the match frequency, the actual distance to cancel reflections becomes smaller than the theoretical $\lambda_g/4$. The bandwidth of the match was calculated to be about 2-3% at a VSWR of 1.01:1.

Two windows of different materials can be matched in a similar manner by slightly changing the thickness of one window or the spacing between the two windows.

Explosion Bonding

Our coupler design was discussed previously [2], and illustrates the usefulness of fabricating the outer conductor, vacuum assembly, and window Compression Rings as one piece. A braze joint between the copper outer conductor and stainless vacuum tube, would be very difficult to make due to the large surface areas involved. Explosion Bonding (EB) a thin layer of copper onto the inner surface of a stainless steel tube then machining to size is a good and cost effective solution.

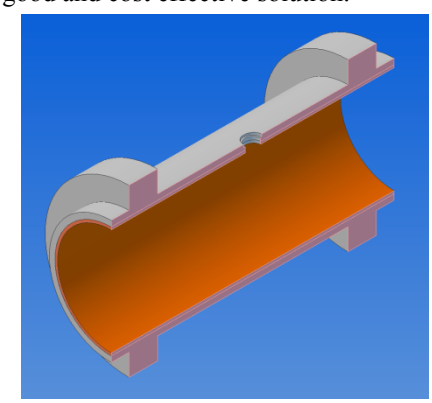


Figure 2: Explosion bonded copper outer conductor, compression rings, and vacuum tube assembly.

*Work supported by Dept. of Energy grant no. DE-SC0002769

Copyright © 2013 CC-BY-3.0 and by the respective authors

One challenge in getting a useable tube lies in the explosion "expanding" the tube in a non-uniform way (bulging), the strength of the explosion, the desired final machined dimensions, and thickness of the copper layer. This is a learning process and depends upon factors such as material, diameter, tube thickness, desired copper thickness, etc. It took two iterations before we determined acceptable initial (pre-explosion) dimensions, and the EB fabricator determined the proper amount of explosive.

Figure 3 is a graphic of the relevant dimensions for the third EB tube. The graphic clearly shows the bulging of the 1" thick stainless steel tube due to the explosive charge. With the earlier trials we, along with the supplier High Energy Metals, Inc., determined that the pre-bonding ID of the stainless steel tube needed to be ~3 inches, after bonding the ID of the Cu sleeve was as shown by the red squares, and the bond line between the Cu and the stainless steel is shown by the green triangles. Thus, the thickness of the Cu layer is approximately 0.300". The ID of the Cu was machined to 3.032" as shown by the dashed line, which leaves the Cu thickness as half the distance between the dashed line and the triangle at that axial location. The gray rectangles indicate the approximate location of the coax windows, and the Cu layer radial thickness is about 0.050" in those locations.

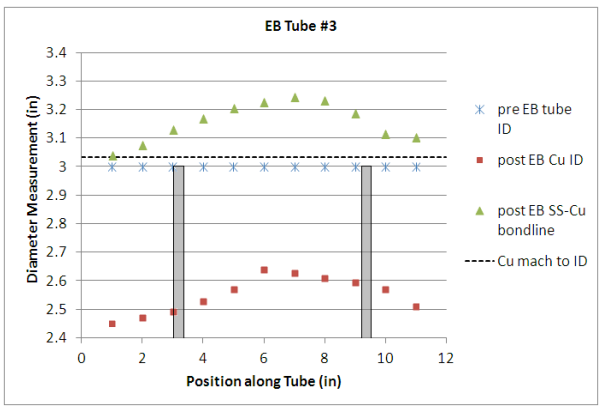


Figure 3: The relevant dimensions for the 3rd Explosion Bonded tube fabrication.

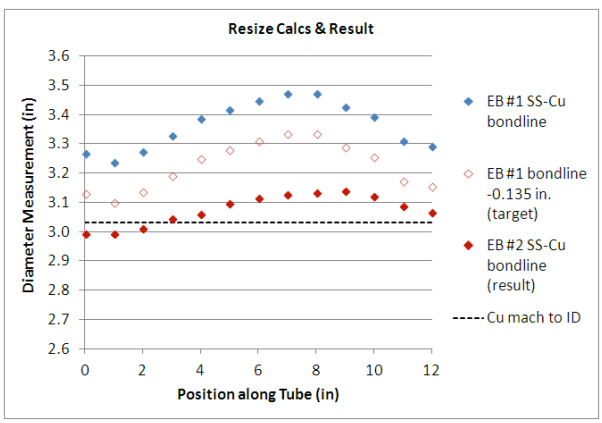


Figure 4: Determination of pre-EB tube ID.

As can be seen from Figure 3 and Figure 4, getting the exact thickness desired is still not exact. Figure 4 shows that there can be a bonding variation (for our size and geometry) of approximately 0.100 to 0.200 inches in diameter. This variation, along with the "bulging" issue requires careful planning and coordination with the EB supplier.

The earlier EB tubes were not wasted as portions of the explosion bonded tube were of suitable dimensions for braze tests to be made. Slices of the tube sufficiently long (~0.8") for two separate window braze tests were machined from the tube, and coaxial windows similar to those discussed in reference 1 were fabricated. In these windows the explosion bonded copper buffer layer surrounding the window ceramic was substantially thicker than in the windows discussed in reference 1, however, the window braze assembly was perfect (Figure 5) and the windows were vacuum tight, and survived a thermal cycle test down to cryogenic temperatures.

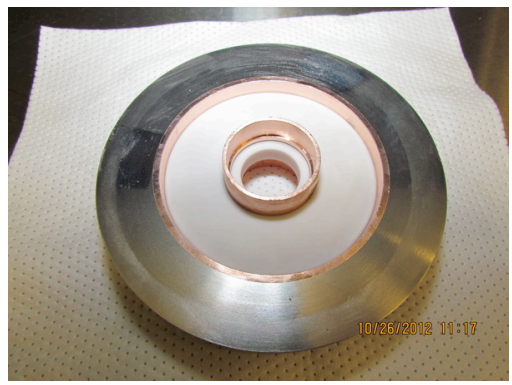


Figure 5: Coaxial window (~3" dia. ceramic) brazed into an Explosion Bonded copper / SS outer Compression Ring.

TECHNICAL APPROACH

Figure 6 shows the hot test assembly as a cut-away concept drawing. The brazed portion of the assembly will be made in two stages. First is the inner window assembly which consists of the inner conductor, the ceramic backing rings, and the two Alumina windows (Figure 7). The second braze bonds the inner conductor assembly to the explosion bonded (EB) assembly, such that the windows are aligned with the thick compression rings of the EB part. EIA adapter flanges and coax are connected for testing purposes.

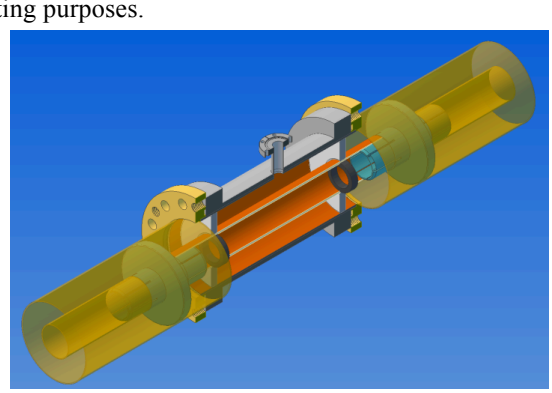


Figure 6: Dual-window Coupler hot test assembly drawing.

Copyright © 2013 CC-BY-3.0 and by the respective authors

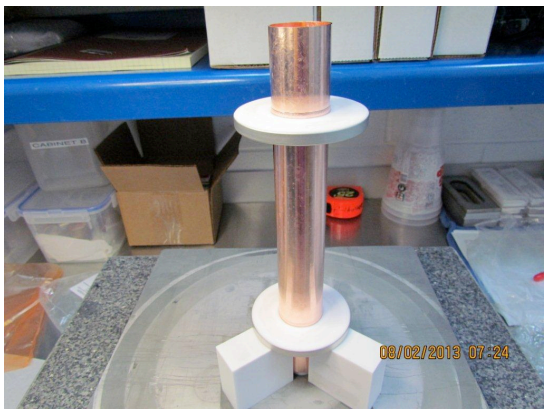
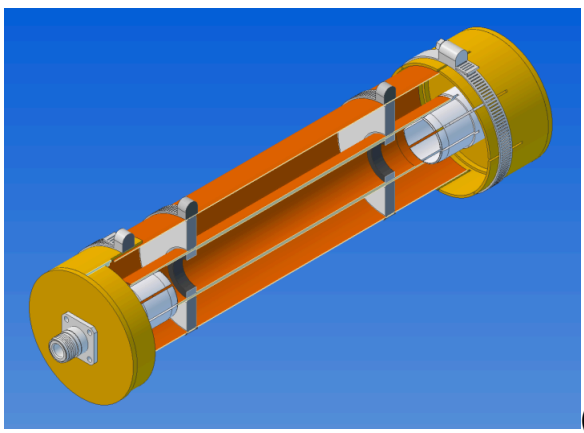


Figure 7: The dual coaxial window inner braze assembly.

Preliminary Testing / Measurements

Prior to the second braze, the inner conductor assembly was tested in a low power RF test (Figure 8). The RF test assembly could be easily made using a thin aluminum sheet rolled and hose-clamped around the metalized OD of the windows. The results are shown in Figure 9. Where the reflection has a -30 dB bandwidth of ~30 MHz, and the S21 transmission loss was measured at <0.01 dB.

Another single brazed window assembly was cycled to 4°K and back in JLab's vertical test dewar, then checked for leak tightness and dimensional changes.



(a)



(b)

Figure 8: Low Power RF test set-up for testing window / inner conductor braze assembly (a – 3D drawing, b – as fabricated).

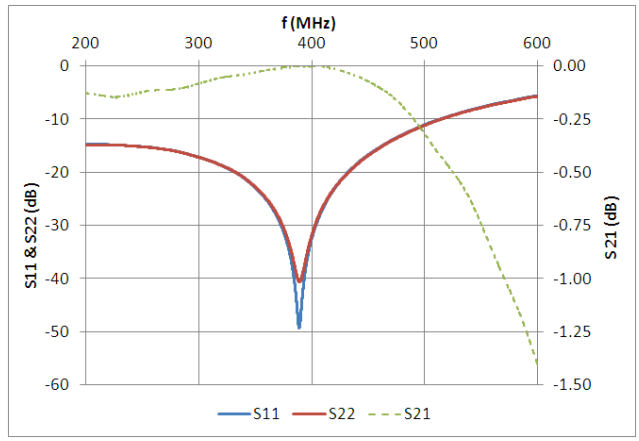


Figure 9: Plot of the S-parameters for the inner conductor low power RF test of Figure 8.

Final Assembly Braze

After measurements of the inner braze assembly, a final braze will be performed between the machined EB tube and the inner braze assembly. Figure 10 below shows the two parts before brazing.

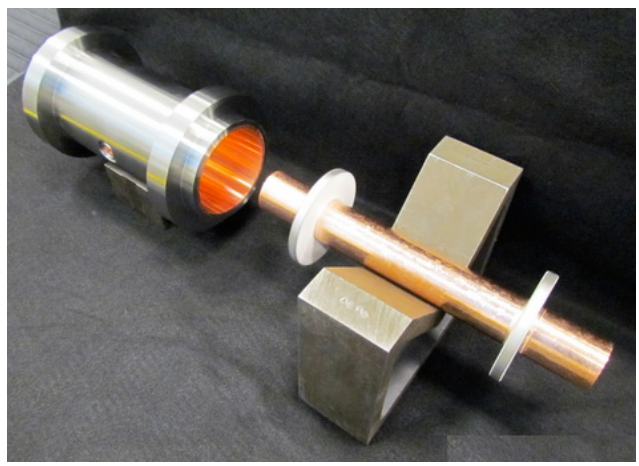


Figure 10: Shown are the inner braze assembly and the machined Explosion Bonded tube.

High Power RF Testing

The Coupler will be thermally cycle tested and vacuum checked to assure a leak tight assembly, then tested at high power using the set-up of Figure 6.

CONCLUSIONS

A dual coaxial window matched coupler has been designed and fabricated using compression ring technology for the windows and explosion bonding to combine the outer conductor to the vacuum wall.

REFERENCES

[1] Neubauer, M., et. al. "High Power Coax Window", PAC11.

[2] Neubauer, M., et. al. "High Power Co-Axial SRF Coupler", PAC12.

Copyright © 2013 CC-BY-3.0 and by the respective authors

S-BAND LOAD DESIGN FOR SLAC*

M. Neubauer, A. Dudas, Muons, Inc., Batavia, IL 60510, USA
A. Krasnykh, SLAC, Menlo Park, CA 94025, USA

Abstract

S-Band vacuum loads at the SLAC linac are encountering operational problems, now that they have to operate under the stringent requirements of 50 MW peak power, 6 kW average power, and extremely-tight phase stability for the linac. Failure mechanisms have been studied which suggest an RF surface breakdown of the 200 µm Kanthal layer in original RF loads.

Currently there are two approaches for RF load design. The first is based on employing highly resistive materials inside of WR284 waveguide [see SLAC-PUB-15229 or MOPB087 in LINAC12]. An alternative approach is based on using lossy dielectric. This is the approach discussed in this paper.

We have proposed a novel solution which incorporates mode conversion from TE10 in rectangular waveguide to TE01 in round waveguide. Lossy material will be placed in the round waveguide, and the selection of the TE01 mode minimizes the electric field normal to the surface of the lossy material. This lossy material in the TE01 round waveguide will be mechanically confined in compression (without brazing), in order to eliminate tensile stresses in the lossy material. The mode converter will be based upon an X-band mode converter invented at SLAC, and the TE01waveguide load design is based upon HOM load designs developed by Muons, Inc.

We are presently performing additional materials testing, in preparation for fabrication of a full power prototype load. A TE10 to TE01 SLAC converter design will be fabricate for both cold and hot testing.

Operational improvements to the SLAC LCLS linac may require the replacement of all SLAC linac vacuum RF loads. The new design can be scaled for use at other frequencies in a multitude of commercial RF applications.

INTRODUCTION

Recently at SLAC, the increasingly-stringent requirements for phase and amplitude stability of the linac beam have increased the sensitivity to the performance of the present load design. Ten of the current Kanthal loads were inspected, and all ten showed evidence of multipactor. Fifteen spare loads were tested and exhibited multipactor between 1 and 20 MW. An attempt to shift the multipactoring resonance using permanent magnets was not successful.

Dry loads are generally designed using high strength lossy ceramics due to the manufacturing processes used in the construction of such loads. The interface between the lossy ceramic and the support structure is brazed or soldered to make a thermally conductive path between the lossy ceramic, mechanical support, and the cooling circuit. The fact that brazing or soldering is used requires the lossy ceramic to survive large tensile stresses due to the mismatch in thermal expansion between the ceramic and the mechanical support. Efforts to either reduce these thermal stresses, or survive these stresses during thermal cycling, has led to creating strengthened ceramics such as $SiC_{whiskers}$ + Al_2O_3, or using thermally matched materials for the mechanical support such as W_{powder} + Cu in a sintered alloy. Both of these techniques have led to expensive structures due to low manufacturing yields. These low yields are typically due to large manufacturing variables, and narrow process limits, for successful fabrication of dry loads.

In our design, the dry load operates in the TE01 mode to significantly reduce the chance of multipactor, and incorporates mode converters designed by SLAC. The lossy ceramic components are cast into cylinders, from slurries composed of mixtures of SiC and porcelain, and processed to full densification and vitrification. These lossy cylinders are held in mechanical compression rather than being brazed. The microwave characteristics of the lossy ceramic cylinders have been measured, and further measurements will be made to determine the optimum mixture for various loading elements.

TECHNICAL APPROACH

TE01 Mode

The most reliable high peak power load will have no normal electric field components on the lossy material. This should simply eliminate the occurrence of multipactoring and arcing. Since the TE01 mode is a low loss mode, the uniformity of loss within the lossy dielectric is not as critical as it would be if compared to operation using other modes. This fact serves to relax the manufacturing process limits, as compared to those which are required in loads utilizing other modes and designs, such as the TE10 mode in rectangular waveguide utilizing lossy walls.

A SLAC designed TE10 - TE01 mode converter from WR284 rectangular waveguide to 6 inch round waveguide was used for the initial measurements (Figure 1). With two mode converters the insertion loss of lossy cylinders can be measured in the TE01 circular mode. The wrap-around mode converter is primarily scaled from the X-band version that was invented by Sami Tantawi of SLAC [1]. The VSWR of these mode converters back-to-back was 1.13 at 2856 MHz, likely due to out-of-round circular waveguide and non-matching edges at the mating flanges. Some slight tuning on the endplates could improve that number to less than 1.11 at 2856 MHz.

*Work supported by Dept. of Energy contract DE-SC0007559

Copyright © 2013 CC-BY-3.0 and by the respective authors



Figure 1: Two wrap-around mode converters for insertion loss measurements of lossy ceramic cylinders. S11 was measured to be less than -23.2 dB at the center frequency.

Novel Lossy Ceramic Cylinders

The lossy material chosen during the program was SiC_{powder} + porcelain. This lossy ceramic material is our new contribution to the design of high power microwave loads. It was chosen because of our system approach to the design and fabrication of a dry load. The fundamental concept that allows for its use is simply that high tensile strength lossy material is not a requirement of our design, as the ceramic material is held in compression.

The comparison of various mechanical properties of alumina and porcelain is shown in Table 1.

Table 1: Comparison of Porcelain and Alumina

	Porcelain	Alumina	
Flexural Strength	130(19)	380(55)	Mpa(ksi)
Tensile Strength	105(15)	170(25)	Mpa(ksi)
Compression	590(86)	2700(391)	Mpa(ksi)
Youngs Modulus	70	370	
Dielectric Strength	25	8.6	MV/m
Fracture Toughness	2	4.5	$MPa\text{-}m^{1/2}$
Thermal Conductivity	5	30	W/m-K

From these values it is clear that porcelain is mechanically inferior to alumina, which explains to a large degree why porcelain has not been used as a lossy ceramic the way that alumina and aluminum nitride have been. This again points to the very important and critical aspect of our systems design approach to this load. *The lossy ceramic is held in compression. It is not brazed and the assembly technique never allows for tensile stress to build up within the material.*

Tests

A number of lossy porcelain ceramics were fabricated with varying amounts of SiC_{powder} incorporated.



Figure 2: Photo of a 6" diameter lossy cylinder.

Their loss was measured using the back-to-back converters configuration of Figure 1 and a Network Analyzer. Using an Agilent 85070E the dielectric constant was measured for similarly made porcelain test disks which incorporated various amounts of SiC_{powder}.

The test disk results indicated that with percentages of SiC_{powder} less than 30% by dry volume, the uniformity of the material was difficult to control. With greater than 30%, the standard deviation was 5-6% of the real part of the dielectric constant, and the standard deviation of the loss tangent was less than 25%. The case where 52% by dry volume of the SiC_{powder} was used produced a lossy ceramic with an average dielectric constant of 7.44-0.37i, yielding a loss tangent of 0.05 as measured by the Agilent probe method.

It should be noted that the Agilent probe is not recommended for materials with loss tangents less than .05, and for materials with ε_r'>5 with loss tangents <0.5[2]. Unfortunately these measured values are exactly in that range, so it is best to assume the error around these values is fairly large. Fortunately, it does suggest the material concentrations that will be best suited for the lossy ceramic cylinders, in terms of tolerances in the manufacturing process, are in the range of 30-50% SiC.

The test assembly of Figure 1 was also modeled on Comsol (Figure 3) to compare measured results with simulated results. Once the model agrees well with the measured results, we will be able to model the loss effects of varying material parameters thus allowing a complete multi-section load model to be simulated with varying amounts of loss per section.

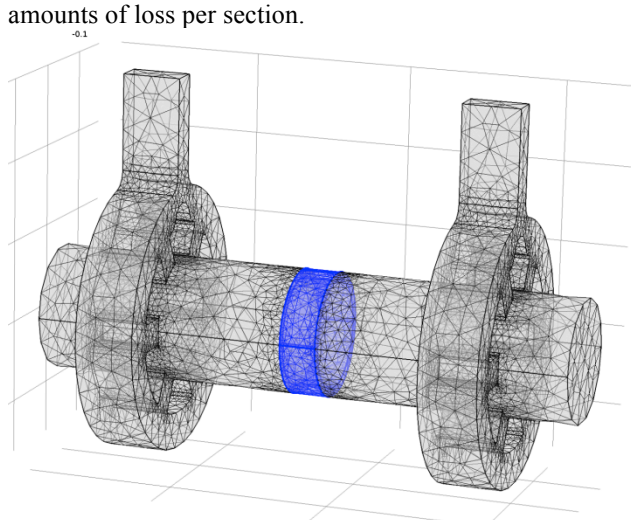


Figure 3: Comsol model of the back-to-back converters and a porcelain test cylinder.

The test cylinders were made by a slip casting process, ground on the outside diameter to 5.990 inches, and placed in the Figure 1 test fixture for S-parameter measurements. As expected, the results show a loss proportional to the percentage of SiC in the cylinder.

The measurements of each test cylinder are considered to be roughly the equivalent of what would comprise a single section of the load, the full load being approximately 10 such sections. Based upon our initial

Copyright © 2013 CC-BY-3.0 and by the respective authors

measurements, Table 2 shows the approximate %SiC needed for the cylinder of each load section, in order to distribute the losses evenly along the length of the load.

Table 2: Typical Loss Requirements for Each Section of the Load and %SiC

Section #	Input	1	2	3	4	5	6	7	8	9	10
Watts	6000	5400	4800	4200	3600	3000	2400	1200	600	300	150
db	67.8	67.3	66.8	66.2	65.6	64.8	63.8	60.8	57.8	54.8	51.8
db/section		0.46	0.51	0.58	0.67	0.79	0.97	3.01	3.01	3.01	3.01
Reflected											51.8
Return Loss	-32.0	35.7	36.2	36.7	37.3	38.0	38.8	39.7	42.7	45.7	48.8
Loss (db/in)*		0.18	0.20	0.23	0.27	0.32	0.39	1.20	1.20	1.20	1.20
% SiC		*25*	*26*	*28*	*29*	*31*	*32*	*43*	*43*	*43*	*43*
*assuming 2.5 inch long cylinders .25 inches thick											

RF Design

The final load design will consist of a number of "identical" (in appearance) sections, with each section designed to be self-matching. That is, for a cylinder length of λ/4 the reflection off the leading edge of the lossy ceramic cylinder is canceled by the reflection off the back edge of the cylinder.

For a cylinder with a dielectric constant of 8 and a loss tangent of 0.04, a 1.1:1 VSWR (26 dB return loss) is achieved over 50 MHz, and the sensitivity to length is ±0.1 inch for a VSWR of less than 1.1:1.

We are currently exploring a manufacturing process that we feel will improve the mixing of the slip and casting of the cylinders, in order to produce a high degree of uniformity throughout the volume of the cylinder.

Mechanical Design

As shown in Table 2, the load is currently planned to be made up of 10 sections with a loss per section of about 600 watts to balance the heat load along the load length. Each section of the load will be constructed to be self-matching as described above, and in a compression assembly similar to what is shown in Figure 4.

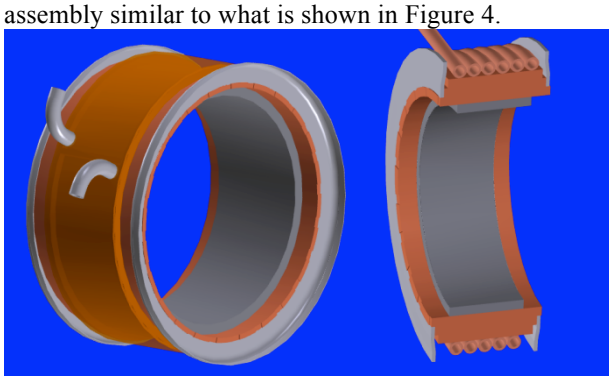


Figure 4: Cross section view of the lossy ceramic cylinder in the compression assembly and different cooling channel options for the prototype assembly.

The compression assembly is designed to be an interference fit at room and operating temperatures. Assembly is accomplished by flowing 100°C water through the cooling channel of the compression ring. The copper expands and easily slips over the lossy ceramic cylinder. This process has been successfully utilized by Muons, Inc. in a number of applications, from HOM load construction techniques to braze assemblies for coaxial RF windows.

The exact details of the construction of the compression ring will be worked out during Phase II.

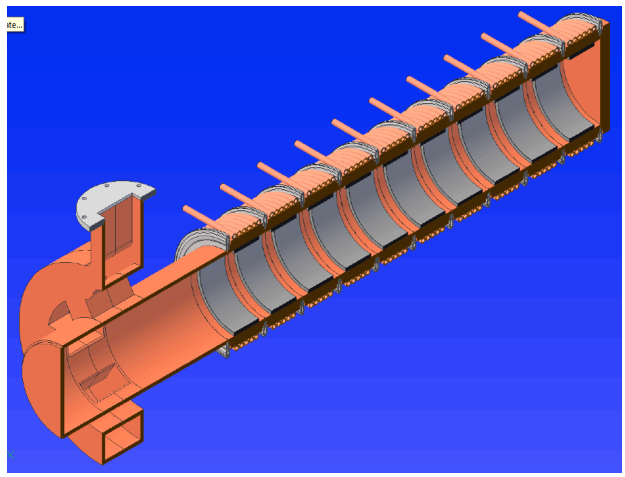


Figure 5: Final prototype configuration of the complete dry vacuum load.

Figure 6 shows ANSYS calculations of the cooling and anticipated operating temperature of the lossy ceramic. It shows that the conservative value of 600 watts of power dissipation raises the maximum temperature of the lossy ceramic by only 2 °C above the cooling water temperature. The reason for this low value is that the surface area of the 6" × 2.5" cylinder is quite large. Thus, we do not expect thermal issues to be significant in this load design.

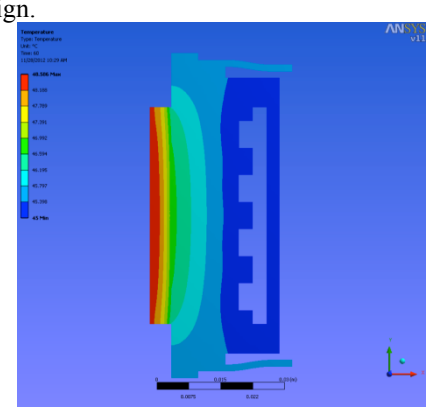


Figure 6: ANSYS results for a single section model.

ACKNOWLEDGEMENTS

Warren Teteak, Grand Island Ranch Machining.

REFERENCES

[1] S. Tantawi, "The Wrap-around Mode converter: A Compact TE10-TE01 Mode Transducer", to be published.

[2] Agilent 85070E Dielectric Probe Kit 200 MHz to 50 GHz. Technical Overview. Published in USA, June 14, 2012 5989-0222EN.

Copyright © 2013 CC-BY-3.0 and by the respective authors

HIGH-POWER LOW-VOLTAGE MULTI-BEAM KLYSTRONS FOR ILC AND PROJECT-X*

V. Teryaev[1], S.V. Shchelkunov[1,2], J.L. Hirshfield[1,2], N. Solyak[3], V. Yakovlev[3], S. Yu. Kazakov[3]
[1]Omega-P, Inc, New Haven, CT 06510, USA
[2]Yale University, New Haven, CT 06511, USA
[3]Fermilab, Batavia, IL 60510, USA

Abstract

Designs of two multi-beam klystrons with parameters suitable for ILC and for the 8-GeV pulsed stage of Project X (PX) have been developed. The chief distinction of these tubes from other MBKs is their low operating voltage, namely 60 kV for the ILC tube and 30 kV for the PX tube. Advantages of low voltage include no requirement for pulse transformers or oil-tanks for high-voltage components, and simpler modulators. A 6-beamlet quadrant of the ILC tube has been built and is soon to undergo tests; it is designed to produce 2.5 MW at 1.3 GHz in a 1.6 ms wide pulse at a 10 Hz pulse rate; a four-quadrant future version would produce 10 MW. The 6-beamlet PX tube is to produce 520kW, and would operate in one of two regimes, either at a repetition rate of 2 Hz delivering 30 ms pulses, or at 10 Hz delivering 8.5 ms-long pulses. The PX tube is currently undergoing engineering design, with construction scheduled for completion by the end of 2014.

INTRODUCTION

Multi-beam klystrons (MBKs) are the most advanced stage in the evolution of high-power klystron design. The distinct feature of MBKs is their relatively low-voltage beams (beam-lets) as compared to the single beam in traditional tubes. This provides numerous advantages: MBKs can use a simpler (and thus, a cheaper) modulator—or even a switched power supply; no pulse-transformer is required; and there is no need for a high-voltage oil tank to insulate the gun. An MBK can be made significantly shorter (e.g. by a factor at least 2) than a single-beam tube delivering the same power and pulse; in particular the collector length can be greatly reduced. The challenges associated with MBKs are typically to design the cavity chain where all parasitic modes are sufficiently detuned, which is accomplished by using a set of metal shunts inserted in some of the cavities to cause either inductive or capacitive detuning, particularly in the input and/or output cavities where the RF field interacts with all the beam-lets, or by using individual gain and penultimate cavities each serving a sub-group of beam-lets (beam-let cluster) and working at the fundamental mode. To easily match the beam between the gun, the cavities, and collector, the magnetic system is typically divided by iron pole-pieces into regions of independent control. An associated challenge is to have coil and pole-piece configurations where the transverse magnetic field on the axis of each beam-let is less than 0.5% of the longitudinal field, while keeping the magnetic system design relatively simple. In [1] and refs therein, detailed descriptions can be found of tools, methods, approaches and recipes to address the aforementioned challenges; in particular, contemporary state-of-the-art codes such as MAGIC [2], MERMAID [3], and DGUN [4] are invaluable in designing MBKs.

*Work supported by Office of High Energy Physics, U.S. Department of Energy;
sergey.shchelkunov@gmail.com

MBK FOR ILC

In [1], the tube's conceptual design was presented. Herein we mention briefly its parameters and main features. Figure 1 presents the layout; the design parameters are shown in Table 1.

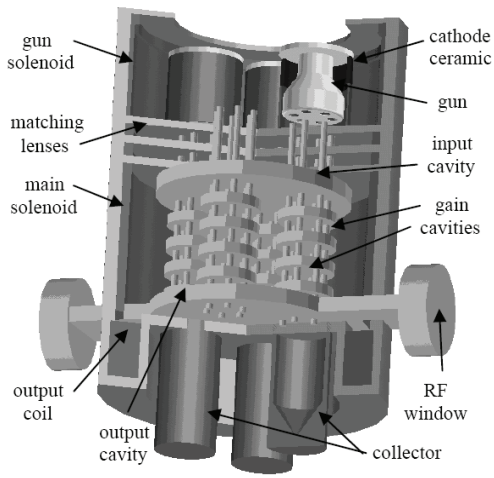


Figure 1: Layout of ILC MBK.

Table 1: Design Parameters of ILC–MBK

Operating frequency, MHz	1,300
Beam voltage, kV	60
Beam-let microperveance	0.85
Number of beam-lets	24
Beam-let current, Amps	12.5
Total current, Amps	300
Efficiency, %	65
Output RF power, MW	10
Average output power, kW	150
Pulse width, ms	1.6
Saturated gain, dB	50
Cathode loading, Amps/cm^2	2.7
Gun surface electric field, kV/cm	65
Total tube length, m	1

Copyright © 2013 CC-BY-3.0 and by the respective authors

Note that the electron gun is divided into 4 sectors, each delivering 6 beam-lets. The input and output cavity are common for all beam-lets. The gain cavities are clustered, each serving a group of 6 beam-lets.

At present, to validate the design of the entire tube, and to minimize technical risk, Omega-P is building a single quadrant of the tube that has only 6 beam-lets. The 6-beamlet quadrant is to produce 2.5 MW at a 10 Hz repetition rate; the rest of its parameters are as shown in Table 1.

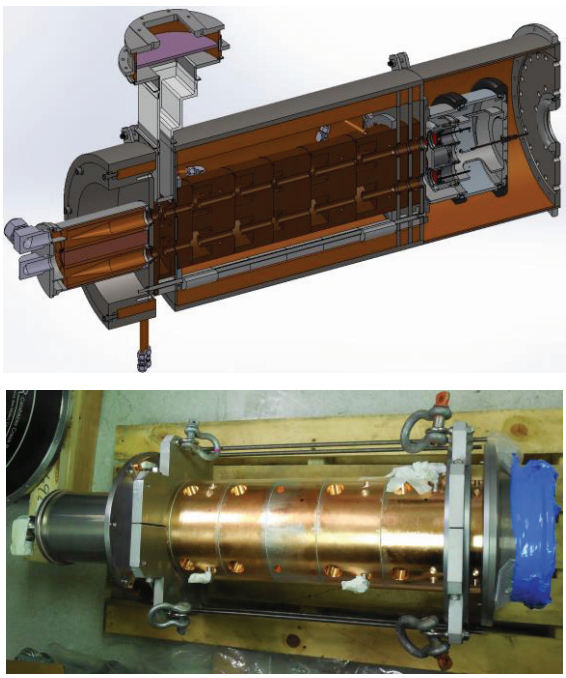


Figure 2: The 6-beamlet quadrant is to produce 2.5 MW at a 10 Hz repetition rate; the tube (at top) is shown inside the solenoid, and the cavity structure with the collector (at bottom) is photographed without the gun.

The 6-beamlet quadrant structure is being built for Omega-P by Calabasas Creek Research Inc. Presently the structure is undergoing final brazing. The magnetic system has been built by Stangenes Industries Inc. and is presently undergoing certification. The expectation is that the 6-beamlet quadrant will be ready for testing in the beginning of 2014.

MBK FOR PROJECT-X

The design parameters of this MBK are shown in Table 2. The tube is to operate at a gun voltage of only 30 kV.

Figure 3 shows a schematic of the tube. Its design incorporates many features found in the 6-beamlet quadrant of the ILC tube. The simulation work has been completed, and presently the engineering designs are nearly complete for the gun, collector, and the chain of gain, second-harmonic and penultimate cavities; the input and output cavities still require some simulation work to optimize the coupling (with a loop-like coupling element for the input cavity, and waveguide for the output cavity) while having the RF field distribution at the location of all 6-beam-lets as identical as possible. Fabrication of the magnetic system will begin soon.

Table 2: Design Parameters of PX–MBK

Operating frequency, MHz	1,300
Beam voltage, kV	30
Beam-let microperveance	0.85
Number of beam-lets	6
Beam-let current, Amps	4.4
Total current, Amps	26.4
Efficiency, %	65
Output RF power, kW	515
Average output power, kW	30/ 42.5
Pulse width, ms	30/ 8.5
Repetition rate, Hz	2 /10
Saturated gain, dB	46
Cathode loading, Amps/cm^2	2.1
Total tube length, m	0.85

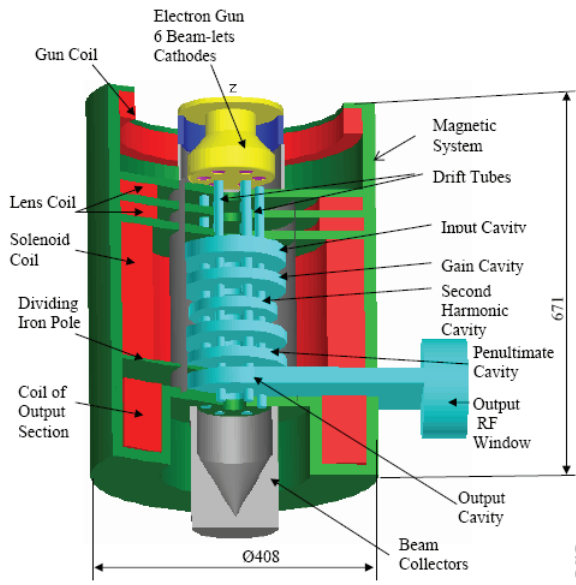


Figure 3: MBK for Project X.

As with the ILC MBK, the PX MBK has its magnetic system divided into several independent regions to allow good beam matching between the gun, cavities and the collector: an example is shown in Fig. 4. In addition, the solenoid around the cavity chain has a special periodic spacing which allows it to have very little transverse magnetic field (0.22 G max.) and only small ripples in longitudinal magnetic field (0.56 G peak-to-peak) at the locations of all 6 beam-lets.

The collector, shown in Fig. 5 is of a cellular design with cells uncoupled from one other; this feature helps to greatly reduce any space charge effects and parasitic mode oscillations.

The cavities operate in the fundamental TM_{010} mode; thus dealing with detuning of parasitic modes which would be required if operation were at higher-order modes is avoided.

Copyright © 2013 CC-BY-3.0 and by the respective authors

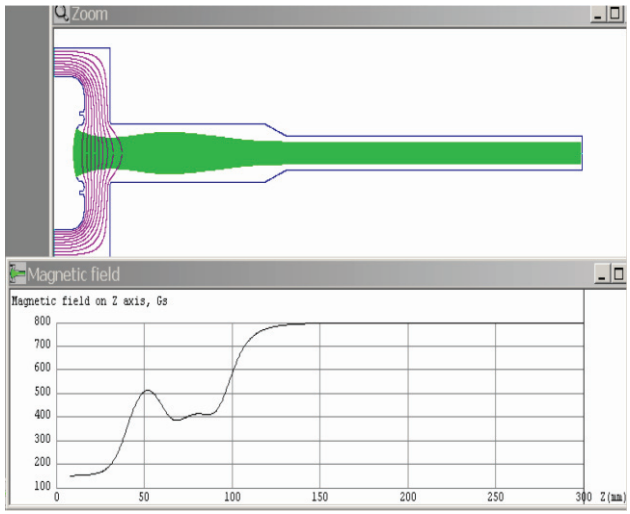


Figure 4: an example of electron beam matching in PX MBK. Horizontal divisions are 50 mm, and vertical divisions are 100 G.

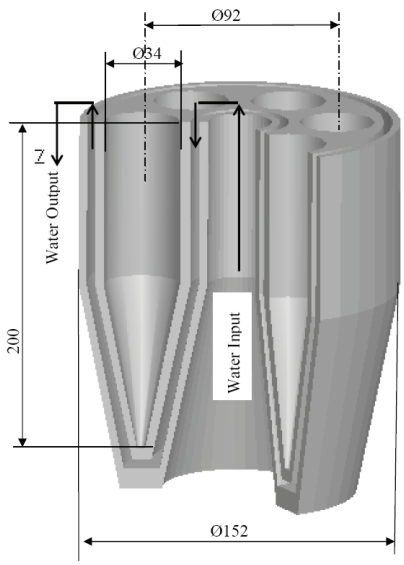


Figure 5: The collector with 6 cells for 6 beam-lets (see explanations in the text).

Figure 6 shows the typical distribution of electric field in a cavity. All cavities, except for the second harmonic cavity operate near 1300 MHz, while the second harmonic cavity operates near 2600 MHz; the latter is introduced to reduce the length of the interaction region and boost the tube efficiency.

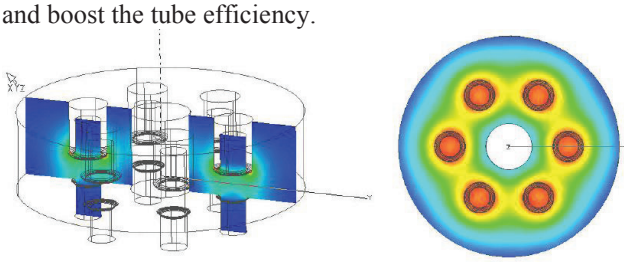
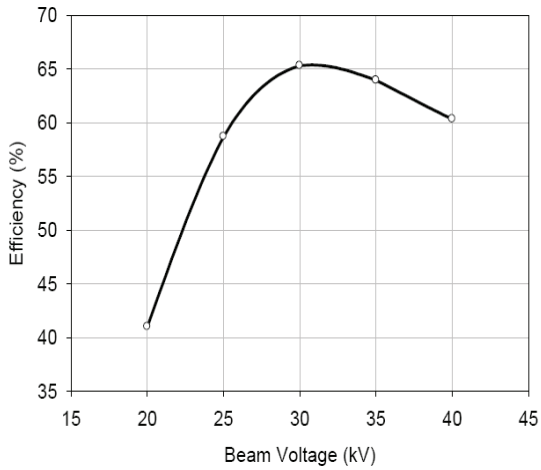
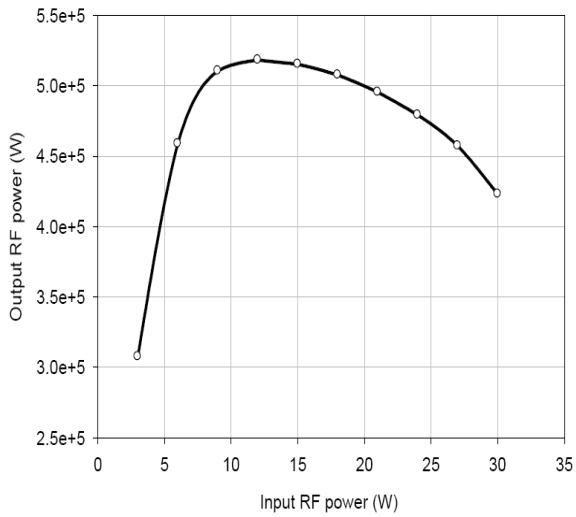


Figure 6: electric field in a cavity (see explanation in the text).

The computed efficiency and output power for the tube are shown in Fig. 7.



(a)



(b)

Figure 7: (a) efficiency vs. the beam voltage, and (b) the output power vs. the input one.

REFERENCES

[1] V. Teryaev et al., "Low Beam Voltage, 10MW, L-Band Cluster Klystron," Proc. of PAC09, Vancouver, BC, Canada, and refs. therein.

[2] MAGIC, User's Manual, see e.g., Mission Research Corp. MRC/WDC-R-409, 1997.

[3] MERMAID, User's Guide, see e.g., SIM Limited, 2005.

[4] "DGUN-code for simulation of intense axial-symmetric electron beams," p. 172, 6th Inter. Comp. Accel. Physics Conf, TU Darmstadt, Germany, 2000.

Copyright © 2013 CC-BY-3.0 and by the respective authors

OPTIMIZATION OF THE SLED PHASE MODULATION PARAMETERS OF THE FERMI LINAC*

C. Serpico, M. Dal Forno, A. Fabris, Elettra-Sincrotrone Trieste S.C.p.A., Trieste, ITALY

Abstract

FERMI is a single-pass, linac-based, FEL user-facility covering the wavelength range from 80 nm to 4 nm and is located next to the third generation synchrotron radiation facility Elettra in Trieste, Italy. The first FEL line in operation (FEL-1) has been opened to users at the end of 2012, while the second FEL line (FEL-2) covering the shorter wavelength down to 4 nm is in commissioning. The linac is composed of 16 S-band accelerating structures. Seven of them are Backward Traveling Wave (BTW) structures equipped with SLED system. Following the preliminary tests on one plant, in order to increase the operational accelerating gradient, phase modulation of the SLED drive power has been implemented on all BTW structures. The shape of the phase modulation is applied via the LLRF system firmware and can be modified if needed. This paper discusses the optimization of the phase modulation parameters.

INTRODUCTION

FERMI is a single-pass Free Electron Laser (FEL) driven by a normal conducting S-band linac composed of 16 accelerating structures. Seven of them are Backward Traveling Wave structures (BTW), coming from the old Elettra injector, with a filling time of 0.757μs. Each structure is fed by a $45MW$ peak power, 4.5μs pulse width Thales klystron. Taking advantage from the short accelerating structure filling time, the peak power to the structure is increased by shortening the pulse length: each power plant is equipped with PEN (Pulse Enhancement Network) system [1] that stores the energy at the beginning of the pulse and release it near the end of it.

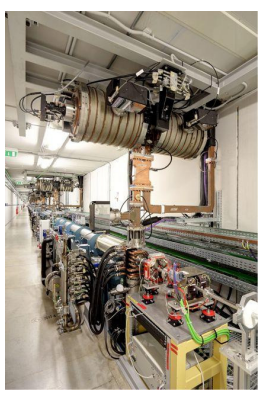


Figure 1: Pulse enhancement network system for a backward traveling wave structure.

* Work supported in part by the Italian Ministry of University and Research under grants FIRB-RBAP045JF2 and FIRB-RBAP06AWK3.

To achieve the Linac target energy of 1.5 GeV, each BTW structure needs to be operated at a gradient of 26 MV/m corresponding to an energy gain of about 155 MeV. Past operation of those structures, showed that breakdown problems inside the sections, associated with the very high peak-field built up during conventional SLED operation, prevented from reaching the desired gradient in a reliable way.

A phase modulation technique was implemented to lower the high peak field inhered with conventional SLED operation: while a preliminary linear phase modulation has allowed to demonstrate the utility of this technique in our application and has allowed to increase the energy gain in the structures, the possibility of an optimization of the phase modulation parameters has been studied to get the optimal trade-off between lowering the peak field, thus improving reliability, and still having an acceptable energy gain.

PRELIMINARY PHASE MODULATION

The phase modulation feature was integrated in the LLRF firmware of FERMI. The preliminary implementation of the phase modulation technique foresees just a linear modulation [2] where two parameters (i.e. the initial phase ϕ_0 and the phase modulation slope m) can be modified to change the shape of the modulation as depicted in Figure2.

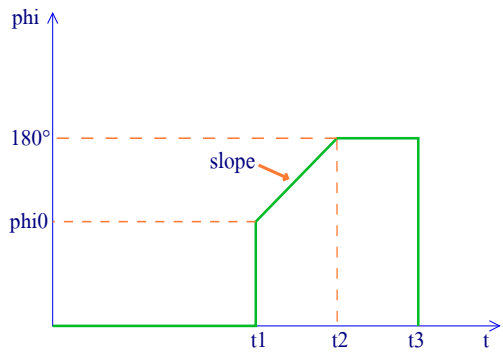


Figure 2: Linear phase modulation.

During a dedicated machine commissioning shift, different sets of parameters were tested: the optimal results (in terms of a trade-off between peak field and gradient loss) were achieved using an initial phase offset ϕ_0 of 95° and a slope m of 149 deg/μs.

A comparison between the pulse shape in case of conventional SLED operation and the one with the optimized linear phase modulation showed that for the same RF pulse

Copyright © 2013 CC-BY-3.0 and by the respective authors

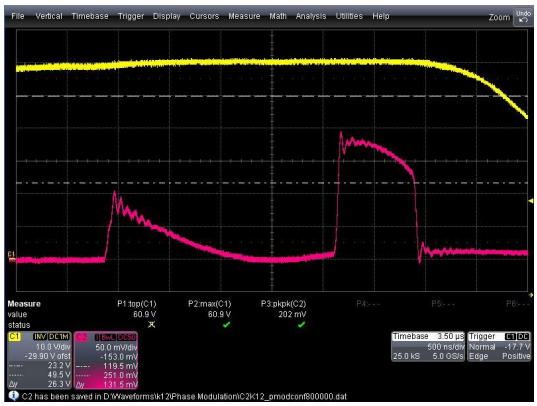


Figure 3: Input cavity field with phase modulation.

length (3000 ns), the peak field is reduced by almost 20%; correspondingly the energy gain loss is about 4%.

It must be noted that by simply using a linear phase modulation it was not possible to achieve a rectangular-like pulse shape. As depicted in Figure3 during the 770 ns pulse duration the normalized field amplitude varies from about 1.8 up to 1.4 (i.e. about 20% variation). Also, it can be pointed out that a huge phase slippage of about 46 degree between the begin and the end of the pulse occurs.

A way to get flatter pulse and smaller phase variations is to implement a continuous non-linear phase modulation.

NUMERICAL EVALUATION FOR A NON-LINEAR PHASE MODULATION

The phase modulation program for rectangular pulse shape has been numerically evaluated by solving the equations 1a and 1b for constant v_0 amplitude during pulse compression [3] [4]:

$$\begin{cases} \tau \dot{v}_c + v_c = -\alpha v_k & \text{(1a)} \\ v_0 = v_c + v_k & \text{(1b)} \end{cases}$$

where v_k and v_c are the generator and the pulse compressor equivalent complex voltages, β is the coupling coefficient between the SLED and the transmission line, $\alpha = 2\beta/(1+\beta)$ and τ is the filling time of the SLED cavities equal to $2Q_0/[(1+\beta)\omega_0]$. In the previous expression Q_0 is the unloaded quality factor of the SLED cavities and ω_0 is the angular frequency of the RF wave.

In our case, β is 10 and Q_0 is 190000. Accordingly, α is about 1.8 and the filling time τ is 1.832μs.

Equation 1a assumes that the resonant frequencies of the SLED cavities and of the RF wave are equal. In case there is a small difference between these two frequencies the equation 1a must be replaced by 2a where $\Delta\omega = \omega_0 - \omega_c$ and ω_c is the angular frequency of SLED cavities [4] [5]. This is necessary to minimize the phase variation during the flat-top of the pulse delivered to the structure.

$$\begin{cases} \tau \dot{v}_c + v_c\left(1 + j\tau\Delta\omega\right) = -\alpha v_k & \text{(2a)} \\ v_0 = v_c + v_k & \text{(2b)} \end{cases}$$

Replacing $v_c = v_0 - v_k$ in equation 2a as derived from equation 2b and discretizing the differential equation 2a we get:

$$\begin{aligned} v_{k_{i+1}} = v_{0_{i+1}} - v_{0_i}\left[1 - (1 + j\tau d\omega)\frac{dt}{\tau}\right] + \\ + v_{k_i}\left[1 - (1 - \alpha + j\tau d\omega)\frac{dt}{\tau}\right] \end{aligned} \quad (3)$$

Let's put:

$$\begin{aligned} w_i = v_{0_i}\left[1 - (1 + j\tau d\omega)\frac{dt}{\tau}\right] + \\ - v_{k_i}\left[1 - (1 - \alpha + j\tau d\omega)\frac{dt}{\tau}\right] \end{aligned} \quad (4)$$

where w_i groups all the term at time instant i. We can write:

$$v_{k_{i+1}} = v_{0_{i+1}} - w_i \quad (5)$$

The goal of a non-linear phase modulation is to get a rectangluar-like pulse shape to the structure during the pulse compression. The amplitude square of the voltage to the structure at time instant $i+1$ can be written into the form:

$$\begin{aligned} \left|v_{0_{i+1}}\right|^2 &= \left|v_{k_{i+1}} + w_i\right|^2 \\ &= \left|v_{k_{i+1}}\right|^2 + \left|w_i\right|^2 + 2Re\left\{v_{k_{i+1}}\bar{w}_i\right\} \end{aligned} \quad (6)$$

So, we have:

$$\begin{aligned} \left|v_{0_{i+1}}\right|^2 = \left|v_{k_{i+1}}\right|^2 + \left|w_i\right|^2 + \\ + 2\left|v_{k_{i+1}}\right|\left|w_i\right| cos\left(\angle v_{k_{i+1}} - \angle w_i\right) \end{aligned} \quad (7)$$

The phase modulation program must set the phase of the generator $\angle v_{k_{i+1}}$ such that the amplitude $v_{0_{i+1}}$ of the compressed pulse is kept as constant as possible.

If we call $v_{0_{PR}}$ the amplitude of the compressed pulse at the phase reversal time t_1, the phase of the generator at time instant $i+1$ for getting a constant amplitude pulse shape (i.e. equal to $v_{0_{PR}}$) could be then calculated with the following equation:

$$\angle v_{k_{i+1}} = arccos\left(\frac{\left|v_{0_{PR}}\right|^2 - \left|v_{k_{i+1}}\right|^2 - \left|w_i\right|^2}{2\left|v_{k_{i+1}}\right|\left|w_i\right|}\right) + \angle w_i \quad (8)$$

SIMULATION RESULTS

Running the simulation code it was possible to find a phase modulation program resulting in a flat amplitude pulse shape. Even if reaching a flat amplitude pulse for a given klystron power and pulse width is at expenses of the energy gain, lowering the peak fields could allow to increase the klystron output power without suffering of heavy breakdown phenomena in the structures' couplers and cells: in the end, this could finally result in a higher energy gain.

To reach a flat-top pulse it is necessary to change the phase by less than 180° at the phase reversal time and then

Copyright © 2013 CC-BY-3.0 and by the respective authors

increase it slowly to keep the pulse flat. As depicted in Figure4 as the phase reaches 180° it cannot further keep the pulse amplitude constant, so it decays exponentially. To get more power to the structure, the phase jump at the phase reversal time should be larger, but then the power cannot be kept constant until the end of the pulse.

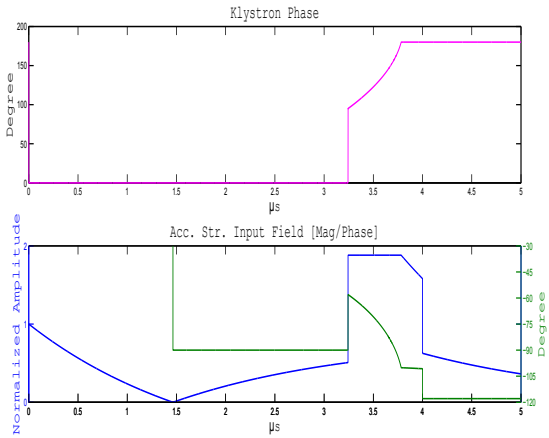


Figure 4: Non-linear phase modulation scheme.

So, for a 4μs pulse width, it was chosen an initial phase jump of 86 degrees: in this condition, the field amplitude at the phase reversal time is limited to about 1.75 (i.e. ≈ 3 in power). A non linear phase modulation than guarantees a constant amplitude field during the 770 ns pulse width. However, with this parameters the phase slippage along the RF pulse is about 50° as showed in Figure5.

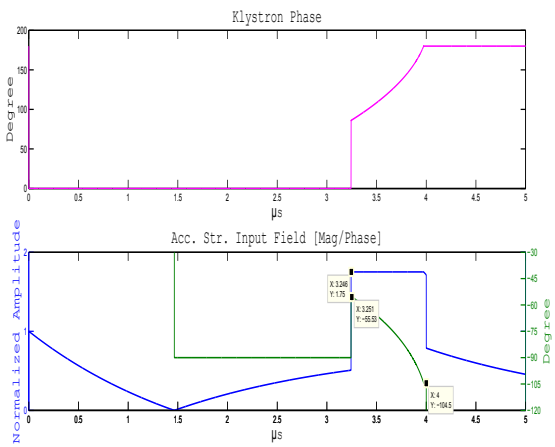


Figure 5: Pulse shape with non-linear phase modulation.

Nonetheless, the phase variation during the flat-top pulse can be minimized by slightly detuning the SLED cavities: this corresponds to choose a suitable $\Delta\omega$ in equation 2a. The frequency shift must be then compensated with a linear ramp of the phase in the first part of the klystron pulse. Figure6 shows the final pulse shape that could achievable with the new phase modulation program.

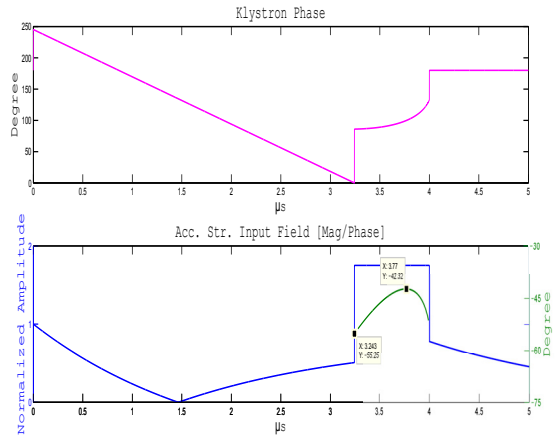


Figure 6: Pulse shape with non-linear phase modulation and SLED cavities detuning.

CONCLUSION

Based on our experience, we can say that our BTW accelerating structures can handle in a reliable way an input peak power of about 97 MW: using the actual linear phase modulation program, to stay below this limit, we operate the klystron at about 32 MW peak power with a 3.5μs pulse width resulting in a accelerating gradient of about 150 MeV.

The new phase modulation program, resulting in a flat amplitude pulse shape, lowers the peak field in the accelerating structure. This could allow to push the power of the klystron up to 36 MW and 4 μs pulse width while still keeping the peak power to the structure under the limit of 97 MW: in this operating conditions, the effective energy gain for each structure should reach about 165 MeV, assuring in this way a reliable margin for the operation of the FERMI Linac at the final target energy of 1.5 GeV.

REFERENCES

[1] G. D'Auria et alii, "The Impact of PSK Timing on Energy Stability of e-beam at FERMI@Elettra", EPAC'08, Genoa, Italy, MOPC008.

[2] C. Serpico et alii, "Phase-Modulation SLED Operation Mode at ELETTRA ", IPAC'11, San Sebastian, Spain, MOPC010.

[3] A. Fiebig, Ch. Schieblich, "A SLED Type Pulse Compressor with Rectangular Pulse Shape", EPAC'90, Nice, France.

[4] S.H. Shaker et alii, "Phase Modulator Programming to Get Flat Pulses with Desired Length and Power from the CTF3 Pulse Compressors", IPAC'10, Kyoto, Japan, TUPEA043.

[5] R. Bossart, P. Brawn, J. Mourier, I. Syratchev, L. Tanner, "High-power Microwave Pulse Compression of Klystrons by Phase-Modulation of High-Q Storage Cavities", CLIC-NOTE-592, June 2004.

Copyright © 2013 CC-BY-3.0 and by the respective authors

ENERGY AND REPETITION RATE UPGRADE OF THE S-BAND RF SYSTEM OF THE FERMI LINAC*

A. Fabris#, P. Delgiusto, F. Gelmetti, M. Milloch, A. Milocco, F. Pribaz, C. Serpico, N. Sodomaco, R. Umer, L. Veljak, Elettra - Sincrotrone Trieste, S.S. 14 – km. 163,5, in Area Science Park, 34149 Basovizza, Trieste, Italy

Abstract

FERMI is a single-pass linac-based FEL user facility covering the wavelength range from 80 nm to 4 nm and is located next to the third generation synchrotron radiation facility Elettra in Trieste, Italy. The first FEL line in operation (FEL-1) has been opened to users at the end of 2012, while the second FEL line (FEL-2) covering the shorter wavelength range down to 4 nm is in commissioning. In 2013 the linac energy will be increased following the full RF conditioning of the backward traveling wave accelerating structures and of the SLED cavities. The repetition rate has been also increased to 50 Hz following the installation of the new RF gun and the completion of the upgrade program of the klystron modulators. This paper discusses the strategies adopted for the energy and repetition rate upgrade of the S-band linac and provides a description of the status and of the first results.

INTRODUCTION

FERMI is a FEL facility based on a warm linac followed by a single pass FEL [1]. Two FEL lines are installed: FEL-1 and FEL-2. The accelerator mainly consists of an RF photocathode gun, an S-band linac, an X-band structure, a laser heater, two bunch compressors and the beam transport line to the undulators of the two FEL lines.

The S-band linac is presently composed of sixteen accelerating structures. The first nine structures are forward traveling wave (TW) ones. Two of them are 3 m long and are from the old Elettra injector, while the remaining seven are 4.5 m long and are LIL type coming from CERN. The last seven structures of the machine are 6.2 m long backward traveling wave (BTW) type and are equipped with SLED systems. Also these structures were used in the old Elettra linac injector. The machine layout reserves the space for two more accelerating structures that will be added in the future [2].

Fifteen S-band 45 MW, 4.5 μs. pulsed klystrons are installed, powering the structures, the gun and the three RF diagnostic deflectors. Typical powering scheme is two structures per klystron for the TW case and one structure per klystron for the BTW one. The system is in operation on a 24h/day basis and the total operating hours/year is higher than 6000.

The commissioning of the facility is rapidly advancing [3]. The first FEL line (FEL-1) has been opened to the external users, while the commissioning of the second one (FEL-2) is advancing. FEL-1 is typically operating at 1.2 GeV beam energy and 10 Hz repetition rate. FEL-2 requires the increase of the beam energy to reach the final specifications in term of shorter wavelength. At the same time the installation of the new gun, capable of operating at 50 Hz, and the upgrade of the modulators, completed at the beginning of 2013, will allow to push the repetition rate of the machine from the present 10 Hz value to the design one, once the conditioning of the structures is completed.

REPETITION RATE UPGRADE

All the modulators installed in the machine are pulse forming network (pfn) type (see Fig.1). The first six modulators installed in the machine were assembled using the hardware of the plants of the old Elettra injector to allow the start of the commissioning studies. For this reason they were limited to 10 Hz by the hardware. The pulse forming network, the pulse transformer and the klystron tank were replaced to allow higher dissipation due to the augmented duty factor. The pfn is now water-cooled and has a better pulse flatness, while the pulse transformer has a reduced core dissipation and pulse droop. The klystron tank is water-cooled and additional lead shielding was added to the tube. The high voltage power supply was also replaced with a new one that has a higher range of current and voltage and better stability.



Figure 1: One of the RF power plants.

In addition to the replacement of some of the major components, a revision of the modulators was carried on in order to optimize the operation at 50 Hz and the stability of the klystron anodic voltage. The resonant charging scheme has been replaced by direct charging of the pfn. This allows to avoid the use of big storage capacitors and inductors, which means a reduction in stored energy, in space and in the dielectric oil. Other

*Work supported in part by the Italian Ministry of University and Research under grants FIRB-RBAP045JF2 and FIRB-RBAP06AWK3
#alessandro.fabris@elettra.eu

Copyright © 2013 CC-BY-3.0 and by the respective authors

advantages of the solution adopted are the improvements in the end of charge voltage repeatability and the reduction of the parasitic capacitance and inductance in the high current path.

Minor upgrades were also performed in the remaining modulators, already designed and assembled for the 50 Hz case. The upgrade activities of all the modulators were organized in order not to affect the commissioning calendar and were completed in time in January 2013.

ENERGY UPGRADE

The energy of the electron beam should be increased to 1.5 GeV for FEL-2 to reach the shorter value of the design wavelength range. Table 1 reports the parameters of the energy gain and power from the klystrons for FEL-1 used until May 2013.

Table 1: Energy Gain (on crest) for FEL-1 (May 2013)

Section type	Energy gain	Klystron power
TW - 3m	~ 47 MeV	32 MW @ 2 μs
TW - 4.5 m	~ 55 MeV	32 MW @ 2 μs
BTW - 6.2 m	~ 120 MeV	22 MW @ 3 μs

Although the energy target should be achievable with the present set of structures, it must be remembered that the machine foresees the installation of two more structures, both in terms of space and available power from the not used output ports of the already installed klystrons. These two structures will contribute with additional 100 MeV to the electron beam energy budget.

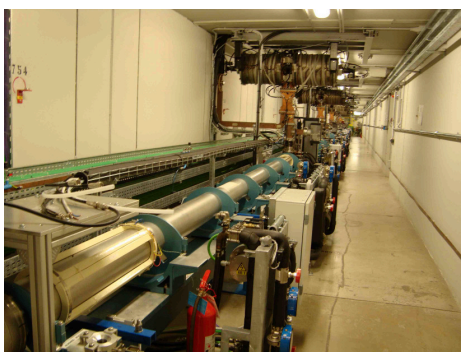


Figure 2: One of the SLED equipped BTW structures.

The increase of energy is obtained by raising the accelerating gradient in the BTW structures (Fig.2) so that their energy gain is in the 150 MeV/structure range. For these structures, equipped with SLED, there is RF power available still maintaining a reasonable safety margin, since operating peak power will be around 32 MW. However, it should be considered that in the past operation in the former injector of Elettra these structures suffered of heavy breakdown phenomena when pushed to high gradient. For this reason till the beginning, a phase modulation of the SLED phase reversal was introduced to lower the peak electric field. Following the preliminary test that showed the advantages of this technique [4], this procedure was routinely applied on all the plants.

For the TW structures, which are powered in pairs, the possible increase in energy is limited by the available power with the present set-up. Since the target energy could be reached only with the improved gain in the BTW structures and considering also that increasing the energy gain in the TW structures would require a re-optimization of the present working parameters at the first bunch compressor, it was decided to leave them untouched.

CONDTIONING RESULTS AND OPERATION

For the commissioning of the plants at 50 Hz and for the conditioning to 1.5 GeV, two periods were allocated so far in the present year: four weeks in May and one week in August. During the first period, both 50 Hz and RF conditioning was performed, while in the second only further 10 Hz RF conditioning was done.

At the end of the first period 1.5 GeV (on crest) at 50 Hz were reached. However, due to the fact that the breakdown rate was still too high, there was no possibility to extend the conditioning period and since the machine was required to operate at 10 Hz in the following runs, it was decided to set the maximum working energy of the machine at 1.46 GeV (on crest) at 10 Hz. In August further conditioning was performed at 10 Hz and the peak energy achieved was increased to 1.54 GeV. It must be noted that the result was only limited by the allocated time.

Table 2: Energy Budget after the Conditioning Periods

Section	50 Hz -May'13	10 Hz -Aug'13
TW – 3m	~ 47 MeV	~ 47 MeV
TW- 4.5 m	~ 55 MeV	~ 55 MeV
BTW -6.2 m	~139 MeV	~149 MeV
Linac energy (on crest)	1.46 GeV	1.54 GeV

The increase to 50 Hz of the power plants was achieved without any issue. In particular there was no change in the plant fault rate and in the frequency of the klystron arcs, which account for the major number of trips of the system. The TW structures, where only frequency rate upgrade was performed and no increase in gradient was required, reached the target value in few days.

The BTW structures operation at the gradient for 1.5 GeV at 50 Hz showed a still too high breakdown rate and therefore they need further conditioning to assess their ultimate performance. During the RF conditioning most of the vacuum spikes were detected by the ion pumps near to the structure input, which seems to suggest that breakdown events took place in the structure input coupler and cells. This is in-line with the observation

Copyright © 2013 CC-BY-3.0 and by the respective authors

performed on these structures in the past and with the simulation performed [5]. The main hardware issue was the failure of the ceramics of the reflected power port of the directional couplers between the SLED output and the accelerating structures input, which occurred three times.

Following the conditioning period, the structure are normally set to the maximum gradient reached that allows both sufficient reliability for the machine operation and consolidation of the results. The experience shows a nice decrease of the total number of vacuum trips with time (Fig. 3).

As for the next conditioning phases, since most of the time, for example when working for FEL-1, the beam energy required is lower than the maximum available, one or two sections are set off-line. On these structures, conditioning can continue without the need of dedicated time. The target is to establish the operation at 50 Hz in view of the experiments with internal users that are scheduled for Fall 2014.

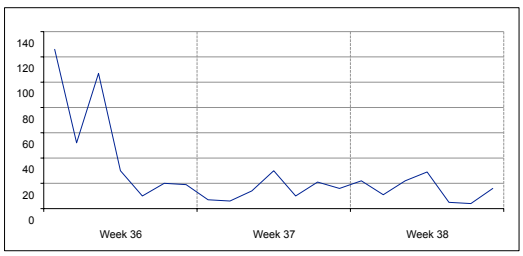


Figure 3: Trend of vacuum faults/week after conditioning.

OUTLOOK AND NEXT ACTIVITIES

The experience has shown that the performance of the directional couplers installed between SLED and structures input must be improved. Numerical simulations have been carried on to revise the design with the support of the components supplier. According to the simulations, the simple reduction of the coupling hole diameter, to reduce the coupling from the present 50 to 65 dB, should allow a reduction of the maximum electric field to an expected safe value. This should allow to operate in a safer condition without the need to revise the waveguide circuit layout. The amplitude of the RF samples from the coupler is still sufficient for the needs of monitoring and measurements with the LLRF. Other alternatives are also under investigation, but these should be seen in conjunction with the boundary conditions of the space available between SLED output and structure input. Other interlocks will be added on the reverse power from the structure, as the one that already protects the klystron, to preventively stop the operation of the plant.

On all the SLEDs a simple linear phase modulation has been applied up to now. A study on the optimization of the parameters of the phase modulation is in course with the target of obtaining a flatter pulse and a lower peak field in the accelerating structure while keeping the energy gain [6].

Although the target energy of FEL-2 should be achieved with the present layout of the machine, the energy budget will be further increased with the installation of the two remaining structures. The procedure for their acquisition is in course and it is expected to install them in 2015. This installation will provide additional 100 MeV.

Another possibility to increase the energy could be to install SLED cavities for the CERN type structures, as also suggested by the MAC committee. Although the filling time of these structures will not allow a maximum efficiency of the SLED process, from a preliminary calculation this could allow to obtain an additional margin of 100 MeV at a relatively moderate cost. Of course this possibility should also be verified with the operating range of other parts of the machine, such as the bunch compressors, and with eventual interferences with the present layout of the machine.

CONCLUSIONS

The S-band RF system of the FERMI linac is in routine operation, accumulating more 6000 operating hours per year. The upgrade of all the plants to 50 Hz has been completed.

The increase of the linac energy is in course, up to now 1.54 GeV at 10 Hz were reached on crest. Further conditioning is required to further slightly increase of some tens of MeV this value, as required for the lower wavelength range, taking into account the margin needed for the X-band and the need to operate some structures off-crest, and to extend these results at 50 Hz.

Further increase in the maximum energy could be reached with the installation of the two accelerating structures foreseen in the machine layout and with the possible upgrade with SLED of some of the TW structures.

REFERENCES

[1] C.J. Bocchetta et al., “Conceptual Design Report for the FERMI@Elettra Project”, ST/F_TN-07/12 (2007).

[2] A. Fabris et al., “Progress of the S-band RF System for the FERMI@Elettra Linac”, PAC’09, Vancouver, May 2009, WE5PFP022, p. 2039 (2009), http://www.JACoW.org

[3] M. Svandrlik et al., “FERMI Seeded FEL Progress Report”, IPAC’13, Shangai, May 2013, TUPEA010, p. 1182 (2013), http://www.JACoW.org

[4] C. Serpico et al., “Phase Modulation SLED Operation Mode at Elettra”, IPAC’11, San Sebastian, May 2011, MOPC010, p. 83 (2011), http://www.JACoW.org

[5] C. Serpico et al., “The Backward TW Structures for the FERMI@Elettra Linac, PAC’09, Vancouver, May 2009, WE5PFP023, p. 2044 (2009), http://www.JACoW.org

[6] C. Serpico et al., “Optimization of the SLED Phase Modulation Parameters of the FERMI Linac,” WEPMA01, NA-PAC'13.

Copyright © 2013 CC-BY-3.0 and by the respective authors

TUNER SYSTEM ASSEMBLY AND TESTS FOR THE 201-MHZ MICE CAVITY

L.Somaschini, INFN-Pisa, Pisa, Italy
A. Moretti, R. J. Pasquinelli, D. W. Peterson, Y. Torun, FNAL, Batavia, USA
P. M. Hanlet, IIT, Chicago, USA
A. J. DeMello, D. Li, S. Virostek, LBNL, Berkeley, USA

Abstract

The MICE cavities include a mechanical tuning system consisting of stainless steel flexure forks attached to the cavity body and driven by pneumatic actuators. The first of these systems was assembled and tested at Fermilab for use at the MuCool Test Area. The actuators were calibrated on a test hoop. The cavity body was measured and the fork contact pads machined to fit. Actuators are going to be mounted on the vacuum vessel housing the cavity. The transfer function of the tuning system and the quality factor of the cavity will be measured with the recently implemented frequency control software.

MICE CAVITY AND TUNER

Each acceleration module (RFCC) of the MICE experiment [1] is composed of four normal-conducting cavities made of copper with a nominal resonant frequency of 201.25 MHz (fig. 1) [2]. The four cavities will be mounted into a vacuum vessel in order to have the same pressure on both sides and avoid deformation of the cavity when pulling vacuum. The cavities will have to work in a high magnetic field that can reach 3T on some points of the cavities surface [3]: a tuning system able to work in such an environment had to be designed. Each cavity will be equipped with a pneumatic system of 6 tuners composed of an actuator and a fork. Each fork, made of stainless steel, will be inside the vacuum vessel and it will stretch and squeeze the cavity when operated by the respective actuator. The actuators will be located outside of the vacuum vessel and will share vacuum with the vessel by means of bellows. All 6 actuators will be connected in parallel and will be controlled by two electronic valves, one responsible for pushing the actuator shaft and the other one for pulling the shaft. The main aim of the tuner will be to compensate for thermal drift of the cavity and for structural differences between the 4 of them, keeping all the cavities at the same resonant frequency.

A test module with only one cavity has been built and is about to be tested in the MuCool Test Area (MTA) at FNAL [4].

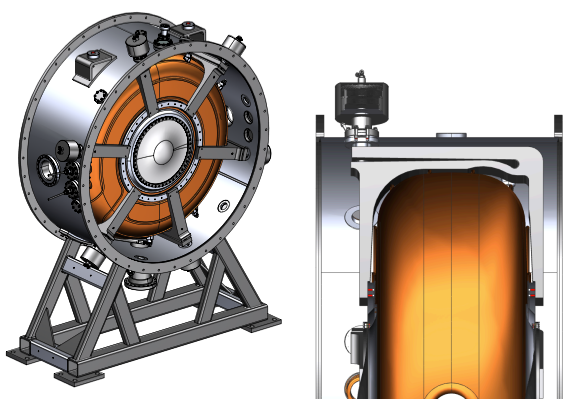


Figure 1: The MTA cavity module and the tuning system.

TEST STAND

Equipment

The six actuators, since working in parallel, had to be tested for possible gas leaks and for uniform response. To do that, a test stand was built at LBNL (fig. 2): a tuning fork was mounted on an aluminum hoop with a spring constant equal to 1/6 of the spring constant of the cavity. The test hoop was placed on an aluminum plate embedding a conflat flange necessary to screw the vacuum bellows of the actuators under test.

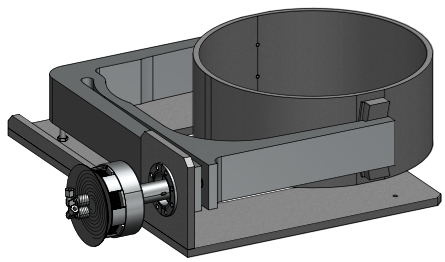


Figure 2: Tuning fork and actuator.

The actuators were controlled by two QPV proportional valves by ProportionAir. Those were connected to a computer running a LabView program. During the test, the pressure applied to each actuator was recorded from proportional valve readout and checked against an analog pressure gauge. The deflection on the test hoop diameter was measured with a dial gauge with a precision of 0.0005 inches, while a linear potentiometer was placed on the fork and aligned with the actuator shaft. The linear potentiometer used is by Novotechnik and it offers a 5 kΩ resistance over a mechanical range of 10 cm. It is powered with a stable 10V signal provided by a voltage regulator. The output voltage is directly proportional to the position of the shaft and consequently the voltage variation is proportional to the actuator shaft movement and to the variation in the fork gap (fig. 3). The voltage was read with a National Instrument ADC and recorded with a LabView code.

Copyright © 2013 CC-BY-3.0 and by the respective authors

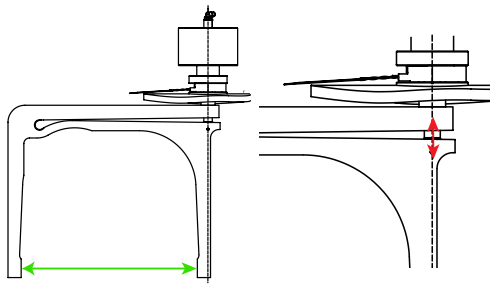


Figure 3: Deflection (left) and fork gap variation (right).

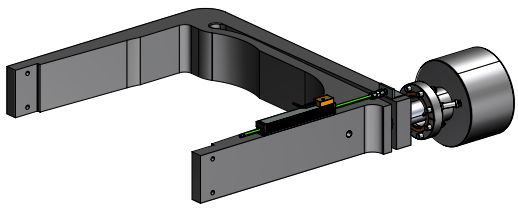


Figure 4: Linear potentiometer on the fork.

Test

In the following, +/- pressures refer to squeeze/stretch mode. For each actuator, the test started at 0 PSI and then the pressure was raised directly to 80 PSI. From this value it was lowered to -80 PSI in steps of 10 PSI and then raised again to 80 PSI with the same step size. The plot of hoop deflection as a function of pressure (fig. 5) shows a clear hysteresis cycle and also a small difference between the slope at positive and negative pressures. The same features appear also in the plot of fork gap variation as a function of pressure. However, when the deflection was plotted as a function of the fork gap variation, the hysteresis almost disappeared and the slopes at positive and negative pressures were much more similar. The tuning fork can be viewed as a mechanical system whose transfer function connects the actuator shaft position (input) and hoop deflection (output). Since its transfer function is linear, the nonlinearity is due to something external and cannot depend on friction between the hoop and the aluminum plate, as initially suspected. The small nonlinearity is likely caused by the actuators and in order to confirm this thesis, the mean of the two points at the same pressure in the hysteresis cycle was computed. The plots of deflection as a function of pressure and deflection as a function of fork gap variation showed a 13% difference between the squeeze and stretch slopes, as expected. On the other hand, the plot of deflection as a function of fork gap variation showed the same slopes (0.13% difference), confirming the actuators as the main source of nonlinearity (fig. 6).

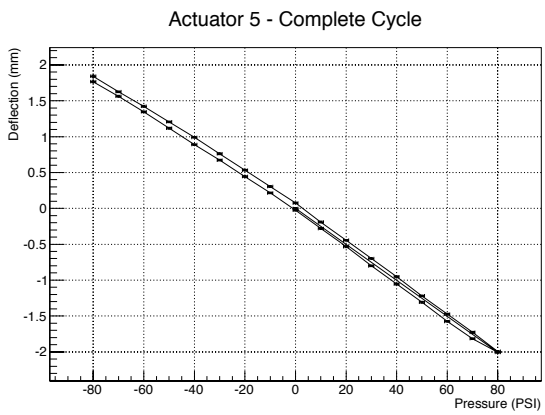


Figure 5: Plot of Deflection vs Pressure for actuator 5.

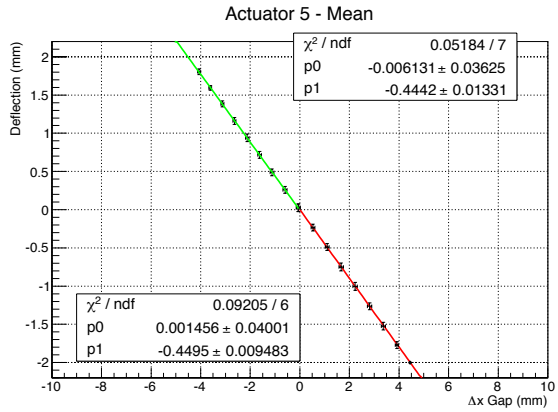


Figure 6: Slopes for stretch (green) and squeeze (red) mode.

Figure 7 shows the slopes for all 6 actuators. In the squeeze mode, all the actuators responded similarly and the results were compatible within the errors. In the stretch mode, the behavior was not as uniform as expected (tab. 1). The maximum slope difference between two actuators was 0.0011 mm/PSI which translates into a difference of 0.11mm or 12% at the maximum tuning pressure of 100 PSI. All 6 actuators will operate simultaneously and the resulting behavior will be the sum of the responses, so this small spread in slope will have no significant operational effect.

Table 1: Actuator Slopes

Actuator	Stretch (mm/PSI)	Squeeze (mm/PSI)
1	0.0224	0.0252
2	0.0225	0.0255
3	0.0233	0.0255
4	0.0227	0.0255
5	0.0222	0.0253
6	0.0229	0.0256

Copyright © 2013 CC-BY-3.0 and by the respective authors

ASSEMBLY

Upgrade

After the measurements on the test stand were completed, the equipment was moved to Lab 6 where a clean room is located. The cavity and the vacuum vessel were surveyed using a laser scanner. The fork contact pads were shaved to match the ring on the cavity that they will be bolted onto and to achieve precise alignment with

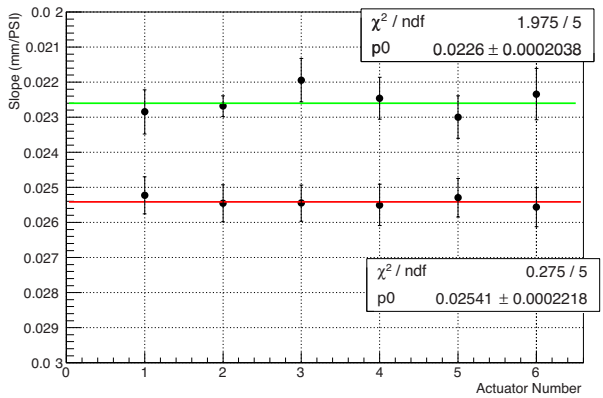


Figure 7: Actuators group behavior.

the vacuum vessel ports. Stainless steel shims will be used as needed between fork contact pads and the mounting rings for fine alignment.

The actuator control system was upgraded. The analog pressure gauges were replaced by electronic units by Omega with 4-20 mA current output. All plastic lines and fittings were replaced with copper tubing and brass fittings. Teflon tape used for thread sealing was replaced with radiation compatible Hercules real-tuff sealant. A valve panel was designed and assembled to allow for manual isolation of each of the 6 actuators and will be mounted directly on the vessel.

Since the cleanroom ceiling is low, the vacuum vessel was placed on a lower stand during assembly. However there isn't enough clearance at the bottom for mounting one of the actuators in this configuration. The test actuator was slightly modified to fit under the shorter stand. It has the same internal components and the same response but it has no vacuum bellows or housing.

A programmable logic controller (PLC) was added to the electronic chain. This is now responsible for the communication with the proportional valves and the electronic pressure gauges. Valve control and pressure readout are currently performed by the PLC at a rate of 1 Hz. The LabView control software is now interfaced with the PLC and not directly with the valves.

Preliminary RF measurements on the cavity were performed while it was positioned on a vertical stand and aluminum windows were installed. The measurements were completed with two B field couplers, a small loop and a bigger one as the input port to obtain critical coupling. The loaded Q measured in transmission mode was 19700 and the unloaded Q, measured in reflection mode, was 40300. The resonant frequency was 200.801 MHz with a drift of about 5 kHz depending on the room temperature.

Future Tests

For tuning tests on the cavity, both the cavity and the vacuum vessel will be moved into a clean room. The tuning forks will be installed on the cavity while it will be mounted horizontally on a fixture. Another custom fixture will be used to install the cavity in the vacuum vessel. The actuators will be screwed onto the forks and low level RF tests will begin in order to measure the transfer function of the tuning system. The vacuum vessel will have no side covers and there will be no vacuum inside or outside the cavity. Linear potentiometers will be mounted on the forks with C-clamps to measure the fork gap variation. Because of mechanical interference, it is not easy to measure cavity ring deflection and we will rely on the gap readout from the potentiometers. During the test, we will measure not only the applied pressure and the fork gap variation, but also the resonant frequency and the loaded and unloaded Q.

The RF measurements have been automated using LabView code and a network analyzer with GPIB interface.

Besides testing the tuning system with all the actuators working as expected, we will also simulate the failure of one or more actuators by isolating their air lines. This will provide knowledge of the limit of the tuning system in case of actuator failure.

SUMMARY AND PERSPECTIVES

The actuators have been tested intensively and their performances have been validated. A control system based on a LabView code and a PLC has been assembled and it's ready for the test with the cavity. The variation in fork gaps will be measured using linear potentiometers.

Changes in the resonant frequency of the cavity as a function of the applied pressure will be measured. The loaded and unloaded Q will be recorded by an automated program and a network analyzer.

REFERENCES

[1] Y.Torun and M. Zisman, "Status of the Muon Ionization Cooling Experiment", THPHO18, NA-PAC'13.

[2] D. Li et al., "The normal conducting RF cavity for the MICE experiment," EPAC'08, Genova.

[3] Tianhuan Luo et al., "Progress on the MICE 201 MHz cavity at LBNL", IPAC 2012, New Orleans.

[4] Y. Torun et al., "Assembly and Testing of the First 201-MHz MICE Cavity at Fermilab", WEPMA16, NA-PAC'13.

Copyright © 2013 CC-BY-3.0 and by the respective authors

RF DESIGN OPTIMIZATION OF A 176 MHZ CW RFQ*

B. Mustapha#, S.V. Kutsaev and P.N. Ostroumov
Physics Division, ANL, Argonne, IL 60439, USA

Abstract

We have recently designed a 176 MHz CW RFQ for the SARAF upgrade project. A full 3D model of the structure including vane modulation was developed. The design was heavily optimized using large scale electromagnetic simulations. Following the choice of the vane type and geometry, the shape and dimensions of the undercuts were optimized to produce a flat field along the structure. Simulations of the same structure with different lengths were performed to verify that the design length produced the best separation of the operating mode from neighboring modes. If built as designed, the RFQ should not need dipole rods for mode separation, but their effect were studied in the case of manufacturing errors. Finally, the tuners were designed and optimized to tune the main mode without affecting the field flatness. The design optimization was mainly performed using CST Micro-Wave Studio and the results were verified using both HFSS and ANSYS. The results of these studies will be presented and discussed.

INTRODUCTION

Soreq NRC, Israel's national laboratory, is exploring the possibilities of upgrading the existing SARAF linac [1]. One of the potential projects is an RFQ upgrade in collaboration with Argonne. In this paper, we present the rf design optimization for a 176 MHz cw RFQ. The proposed design is based on the successful ATLAS upgrade RFQ design [2].

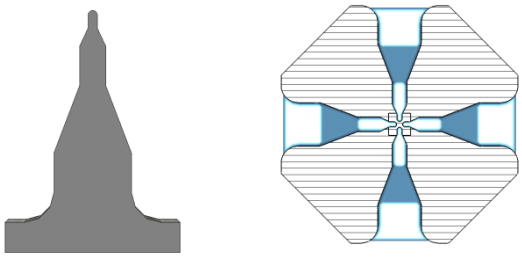


Figure 1: Vane profile (left) and RFQ cross section (right) with an inner diameter of ~ 36 cm.

RFQ STRUCTURE AND PARAMETERS

The selected structure for this RFQ is a 4-vane. The vane profile is based on the ATLAS upgrade RFQ except that this design is a full-vane, not a split-coaxial. At this frequency the transverse size of the RFQ is manageable. Both the vane profile and the RFQ cross section are shown in Figure 1. The structure is about 4 m long divided into 4 segments. The RFQ design parameters are summarized in Table 1. The output energy could be increased by applying trapezoidal modulation while keeping the same vane voltage and power.

Table 1: RFQ Design Parameters

Parameter	Value
q/A	½
Input energy, keV/u	20
Output energy, keV/u	1300
Frequency, MHz	176
Voltage, kV	75
Design current, mA	5
Power, kW	125
Average radius, mm	4.4
Max. modulation	2
Min. transverse phase advance, deg	33
Norm. trans. acceptance, π mm·mrad	2.2
Peak surface field, Kilpatrick units	1.6
Number of cells	250

RF MODELING AND OPTIMIZATION

The electromagnetic design and optimization were mainly performed using the CST Micro-Wave Studio (MWS) [3] and the final results were verified using HFSS and ANSYS. A full 3D model of the RFQ was developed in MWS. Detailed views of the geometry including the undercuts and the modulations are shown in figure 2. This model has pure sinusoidal modulations along the whole RFQ.

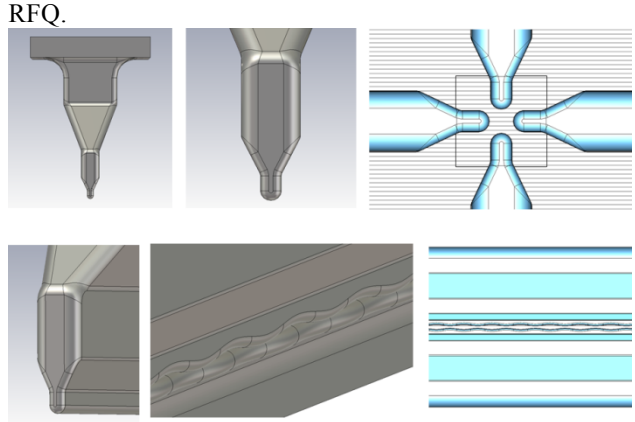


Figure 2: 3D modelling of the RFQ in MWS.

* This work was supported by the U.S. Department of Energy, Office of Nuclear Physics, under Contract DE-AC02-06CH11357 and ANL WFO No. 85Y4.
# brahim@anl.gov

Copyright © 2013 CC-BY-3.0 and by the respective authors

Optimization of Vane Undercuts

In full-vane RFQ structures, vane undercuts are often used to flatten the inter-vane field along the RFQ. These undercuts are applied at both ends of the RFQ and could in principle be of any geometry. We have studied two types of vane undercuts, the first is trapezoidal while the second is square as shown on Figure 3. By optimizing the

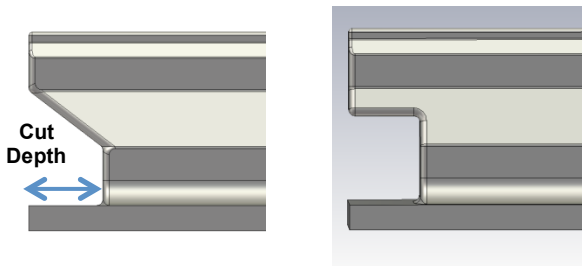


Figure 3: Trapezoidal (left) and square (right) vane undercuts.

cut depth, we were able to obtain a flat inter-vane voltage for both options as shown on Figure 4. However when checking the peak surface magnetic field on the cut planes we realized that it is about 10% lower for the trapezoidal cut shape which should lead to a lower power dissipation.

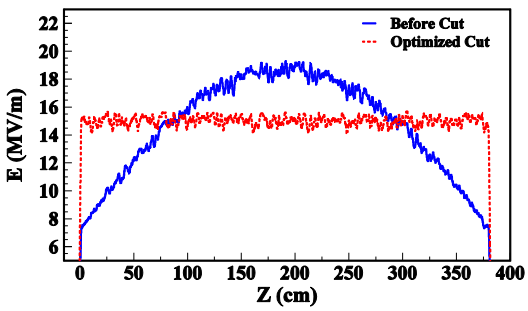


Figure 4: Inter-vane field along the RFQ before and after applying the appropriate vane undercuts.

Therefore we selected the trapezoidal undercut geometry for this RFQ. It is worth noting that these optimizations were done including vane modulations, which has led to non-symmetric entrance and exit undercut depths while before modulations the cuts were symmetric.

RFQ Modes as Function of Length

In order to study the RFQ mode separation as function of length, we have simulated several RFQs with the same cross section and undercuts but with different lengths. The results are shown on figure 5 for mode frequencies as function of length. The modes are identified as Q for quadrupole and D for dipole. The dipole modes marked by (2) are degenerates, their separation shows up for longer structures due only to memory limit in the simulations. The cut-off frequency for this structure is about 170 MHz. At a length of about 1.63 segments, the lowest quadrupole and dipole modes have the same frequency which corresponds to about 0.9×λ. This length is to be avoided because it would be hard to tune the structure for the operating quadrupole mode. The mode separation is best for a length of 4 segments where it is about 3 MHz wide and symmetric around the design frequency. At a length of about 5.5 segments the second dipole mode crosses the main quadrupole mode frequency which will also lead to tuning problems and superposition of quadrupole and dipole fields. The current RFQ design is 4 segments long and has the best mode separation.

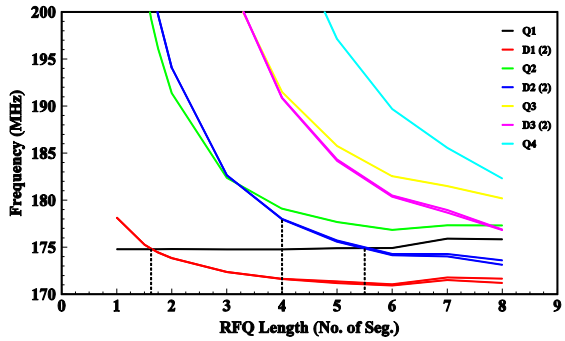


Figure 5: RFQ modes frequencies as function of length in segments (~ 1m).

DIPOLE RODS DESIGN AND OPTIMIZATION

Dipole rods are movable finger-shaped rods attached to the RFQ end plates which could be inserted into the RF volume as needed. Their main purpose is to produce additional separation of the main mode from the neighbouring dipole modes if needed. They are inserted into the quadrupole symmetry planes so they do not affect the quadrupole modes but they are capable of changing the frequency and fields of dipole modes. Based on the actual mode separation for the 4-segments RFQ, we should not need the dipole rods but in the event of manufacturing errors, they are may be useful for correction. The first study performed on the 4-segment RFQ showed low sensitivity of the mode separation to variations in the parameters of the dipole rods, namely the radius, location and penetration. Based on the previous section's results, their effect should be more significant for the 1.63 segment model where the main mode and the first dipole mode have the same frequency. The corresponding results are shown on Figure 6. We clearly see that the dipole mode frequency is more sensitive to the location of the rods with respect to the beam axis. The closer to the axis, the more effective they are. However, the main mode frequency and field are least affected by the rods when they are at mid distance between the beam axis and the cavity side walls, which is the location of maximal quadrupole symmetry. At this location the rods have to be inserted 15" into the RF volume to see a 0.5 MHz separation between the main mode and the dipole mode. The frequencies are not very sensitive to the rod diameter beyond 0.5" and when checking the field stability, a thicker rod disturbs the field more, so a 0.5" rod diameter is near optimal.

Copyright © 2013 CC-BY-3.0 and by the respective authors

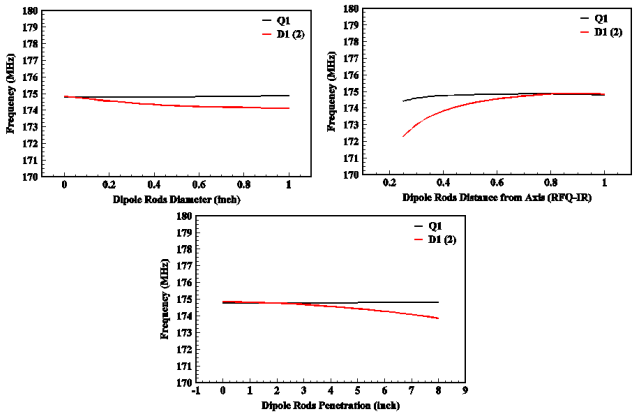


Figure 6: Effect of dipole rods geometric parameters on mode separation for a 1.63 segments RFQ.

TUNERS DESIGN AND STUDIES

A four-vane RFQ is usually built for a frequency just below the operating frequency to make sure it is tunable to that frequency. For the SARAF RFQ, the design target frequency is 175.4 MHz including all the geometry details. The simulation error is estimated not to exceed 0.2 MHz. So the tuners should have a range of at least 1 MHz. The RFQ will have two tuners per quadrant per segment making a total of 32 tuners as shown in Fig. 7. The tuner diameter is 2.5" and could go in up to 2" deep. Figure 8 shows a comparison of the inter-vane field between a case where the tuners are inserted to the same depth uniformly and a case of non-uniform tuning. The latter shows a slope in the inter-vane field which cannot be corrected. Based on these results we decided that the tuners ports should be separate from coupling and vacuum ports to allow for uniform tuning that preserves the field flatness. The simulated frequency sensitivity to the tuners is 37.5 kHz per tuner per inch, which is a 2.4 MHz tuning range if all tuners were inserted 2 inches deep into the cavity.

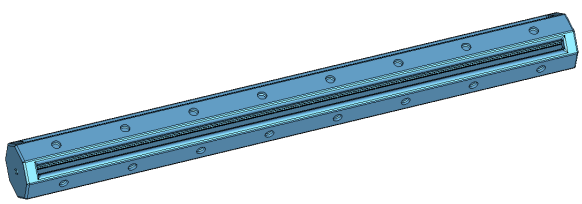


Figure 7: Full RFQ model showing the location of the tuners.

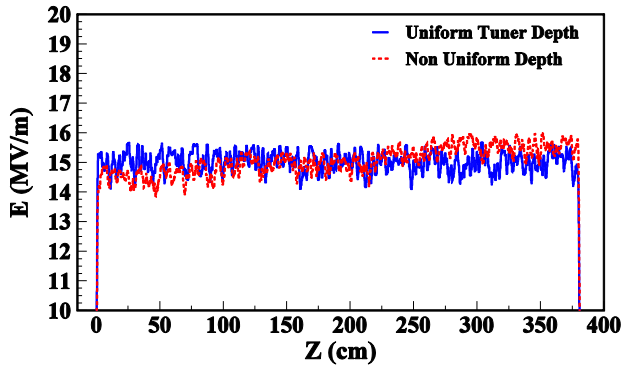


Figure 8: Uniform and non-uniform tuning effect on the inter-vane field along the RFQ.

SUMMARY

We have optimized the RF design for a 176 MHz CW RFQ. The RFQ is a 4-vane structure with optimized trapezoidal vane undercuts for a flat inter-vane field. It is a ~ 4 m long structure made of 4 segments with the best mode separation as function of length. This design should not need dipole rods but we have designed and optimized them to correct eventual manufacturing errors. The RFQ has 2 tuners per quadrant per segment, a total of 32 with a full tuning range of 2.4 MHz. The tuners ports will be separate from the coupling and vacuum ports to allow uniform tuning with minimal effect on field flatness. As successfully implemented in the ATLAS upgrade RFQ, we are planning to design trapezoidal vane modulation which would increase the output energy for the same RFQ length and power.

REFERENCES

[1] L. Weissman et al, "The status of the SARAF linac project", Proceedings of LINAC-2010, Tsukuba, Japan.

[2] P.N. Ostroumov et al, "Development and beam test of a continuous wave radio frequency quadrupole accelerator", Phys. Rev. ST-AB, 15 (2012) 110101.

[3] CST Simulation packages @ www.cst.com.

Copyright © 2013 CC-BY-3.0 and by the respective authors

MODELING VACUUM ARCS IN LINAC STRUCTURES*

J. Norem#, ANL, Argonne, IL 60439, USA
A Moretti, Fermilab, Batavia, IL 60510 USA
Z. Insepov, S. Nurkenov, Nano Synergy Inc, Downers Grove, IL 60516 USA

Abstract

We describe our vacuum arc model, which divides breakdown into four stages: trigger, plasma formation, plasma evolution and surface damage. We have modeled all four stages numerically and find that the properties of surface cracks and unipolar arcs can explain essentially all the experimental data we have seen. In addition to linac breakdown, the model should apply to arcs in a wide variety of applications, such as laser ablation, tokamak edge plasmas and micrometeorite impacts. We also outline differences with other work.

THE MODEL

This effort began as an attempt to understand gradient limits in 805 MHz cavities used for muon cooling. We have described the overall picture of the model and some of the details in a number of papers in the context of accelerator breakdown [1-7].

Recent work has shown that the development of the arc can be explained by two mechanisms: 1) mechanical failure of the solid surface due to Coulomb explosions caused by high surface fields at crack junctions (see ref [5]) and, 2) the development of unipolar arcs that can act as virtual cathodes and produce currents that short the driving potential [3]. Once an arc starts, the surface electric field and field emission increase, increasing ionization of neutrals, increasing in the plasma density [4]. The density increase then reduces the Debye length that increases the surface electric field, thus both the electric field and the density increase approximately exponentially with time. PIC simulations of the unipolar arc model for vacuum arcs relevant to rf cavity breakdown show that the density of plasma formed above the field emitting asperities can be as high as 10^{26} m^{-3} [6]. The temperature of such plasma is low, in the range of 1-10 eV. These high densities can make the Debye screening length, λ_D, become smaller than the mean inter-particle distance or the number of particles in the Debye sphere, to become less that unity. This implies the failure of the ideal plasma approximation, as well as most of the assumptions used in simple calculations. Processes in such a dense plasma can be affected by three body particle collisions so that the Particle In Cell (PIC) method which relies on a simple collisional model, with two body collisions, becomes inappropriate and different methods, such as Molecular Dynamics (MD) must be used

Arrays of cracks are seen in many SEM images of arc damage. We believe these cracks are the result of the cooling of the melted surface that takes place in two stages; first cooling from high temperatures to the solidification point of the metal, followed by cooling from the freezing temperature to room temperature, where the solid contracts by an amount $\Delta x/x = \alpha\,\Delta T \sim 2$ %, where ΔT is the temperature change, x represents the dimension of the damage and α is the coefficient of linear expansion. The model is diagrammed in Fig. 1.

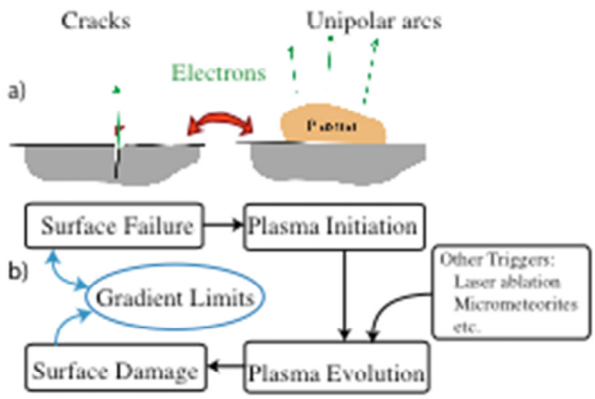


Figure 1: Breakdown proceeds through surface failure, plasma initiation, plasma evolution and surface damage. Part a) shows the physical picture, part b) shows active mechanisms.

The model provides a framework for prediction and experimental study of all aspects of the breakdown process in a variety of environments.

USING THE MODEL

In order to explore the reach of the model we consider the following issues:

Multipactor

We have reported surface damage in coupling cells where the scale of the structure was on the order of 10 nm, rather then the 1 μm commonly seen in 805 MHz Breakdown events. These are consistent with unipolar arcs caused by multipactor, and evidently are not associated with significant shorting currents. These occur at lower gradients and do not seem to be gradient limiting.

Magnetic Field Effects

The geometries of crack junctions can explain magnetic field effects. Data show similar breakdown thresholds with magnetic fields parallel and perpendicular to the surface, arguing for single surface breakdown. With B=0, melted areas are irregularly shaped, and cool so that

*Work supported by Office of High Energy Physics, USDOE
#norem@aps.gov

Copyright © 2013 CC-BY-3.0 and by the respective authors

primary cracks remove strain in one direction and secondary cracks form perpendicular to the primary cracks. Thus, crack junctions occur at right angles. From previous work, this geometry would produce a narrow range of enhancement factors. In a magnetic field, however, symmetric heating from shorting currents pinned to magnetic field lines results in radial strain and circumferential cracking. These cracks occur at variety of acute angles, producing higher enhancements, a wider range of enhancement factors and lower and wider range of breakdown fields [1].

Sheath Parameters

Numerical analysis of plasma sheath properties using MD has produced simple dependence on plasma densities, shown in Figure 2.

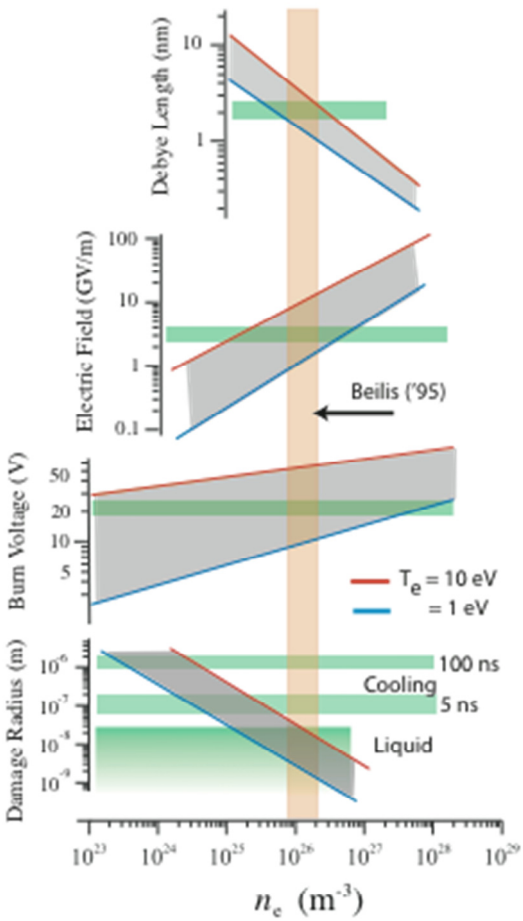


Figure 2: the dependence of experimental parameters on the density of the unipolar arc. More details are presented in Refs. [1] and [2].

If we assume that the plasma density rises until field emission currents short out the sheath, this process 1) sets a limit on the maximum plasma density, 2) determines the dimensions of the unipolar arc, and 3) seems to be compatible with unstable modes (oscillations) in plasma properties. The model can predict plasma dimensions, oscillation frequencies, thermal behavior, burn voltages, shorting currents, time evolution, frequency dependence and the nature of the surface damage produced. All these phenomena are consistent with experimental data [1-2].

Beam Deflection

The immediate results of a breakdown event in an accelerating cavity is a deflection of the beam by the shorting current and the loss of acceleration in the parts of the cavity that are no longer powered. This model assumes that shorting currents, flowing from unipolar arcs functioning as virtual cathodes, on consecutive irises will steer the beam by an angle $\theta = Bl/B\rho$, where θ is the bend angle, B is the magnetic field, l is the cell length and $B\rho$ is the rigidity of the beam. The magnetic field B can be calculated in a straightforward way from the shorting current, however it is unclear if the shorting current is operates on one or both phases of the rf, and how the time structure of the current depends on the electric field, so measurements are useful.

Surface Damage

During the liquid cooling phase, surface tension would smooth the surface, and the relation between the cooling time and the scale of surface irregularities seen in SEM images can be estimated from the dispersion relation,

$$\omega^2 = \sigma |k|^3 / \rho$$

where ω, σ and ρ are the frequency, surface tension constant and density of the liquid metal, and k is the wave number. This smoothing flattens the surface on the scale of microns and eliminates a class of possible field enhancement sites. In accelerator cavities, arcs last for on the order of 100 ns, which is not long enough to heat up the bulk copper, so thin heated surface volumes sit on essentially cold heat sinks and thermal contraction is approximately 2 % of the dimensions of the melted area. We calculate that the typical cooling time constants are in the range of a few hundred ns for accelerator cavities and the structures seen in SEM images of rf cavity damage have radial dimensions on the order of a few microns, see Fig 3. These cooling times are consistent with estimates in Ref [1]. The two stage cooling process seems to result in SEM surfaces that are somewhat smooth at the 1 micron level, but contain cracks with sharp edges at the 1 - 10 nm level that cover 2 % of any large solidified area of copper.

Frequency Scaling, Cooling and βs

Experimental data shows that 805 MHz rf cavities breakdown when the maximum local surface fields reach 10 GV/m, the same breakdown field assumed by Lord Kelvin to explain experimental results in 1904 [7]. We argue that there is minimal frequency scaling if the local field is the primary variable. Different geometries, power sources, frequencies and materials do, however, produce cavities with different maximum surface fields. This can be explained from differences in cooling and field enhancement factors, β. Assuming the plasma properties are similar, size and time history can produce quite different damage. Tiny hot spots cool rapidly and large surface areas will cool more slowly. Above the melting

Copyright © 2013 CC-BY-3.0 and by the respective authors

point surface tension will reduce surface fine structure, and below the melting point, some annealing may also produce significant smoothing,

We have produced estimates of cooling profiles dut to thermal diffusion for a variety of geometries using COMSOL [8], to show how the cooling depends on the nature of the arc parameters. We find three classes of heated surfaces that can be numerically evaluated: 1) tiny (~ micron) melted areas that cool very quickly, 2) large, more or less homogeneous areas with dimensions on the order of a few mm and, 3) intermediate sized regions (10 μm – mm), which are the dimensions seen in 805 MHz cavity damage.

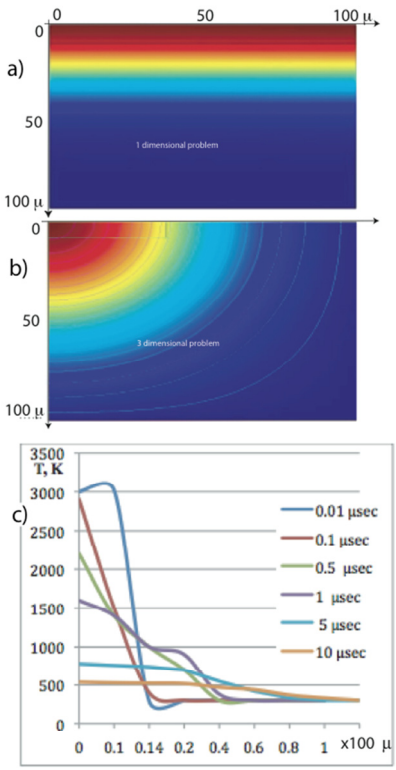


Figure 3: Extreme geometries modeled in COMSOL [8], a) planar, b)point, with c) the cooling profiles produced the case a).

COMPARISON WITH OTHER WORK

The field of vacuum breakdown is quite old, and ideas and methods have been around for a long time. We believe the model we are describing is conceptually simple and the range of applicability is large. We find, however, that this model and the conventional wisdom, do not always agree. We also question models that claim to predict frequency or magnetic field dependence without making any assumptions on the nature of the breakdown process or the damage it produces.

The conventional wisdom of breakdown is that structures producing field enhancements should look like polished fenceposts with hemispherical caps, their properties can be evaluated using a Fowler-Nordheim plot, breakdown is caused by high densities of Joule heating caused by field emission current densities, and these Joule heating events continue during the burn phase of the arc in the form of micro-explosions. While we do not specifically argue against these ideas, we find that more prosaic mechanisms alternatives seem to fit the existing data more easily. Fencepost geometries for field emitters are not seen in SEM images of arc damage, but surfaces are covered with submicron cracks. The efficiency of Joule heating depends very strongly on the geometry and the dimensions of suspected field emitters, and implies that Joule heating must be much less than heat loss to the copper bulk, making significant temperatures very hard to achieve in very small structures. Likewise, if the Debye length of the plasma sheath is on the order of a few nm, it seems hard to understand how localized current densities could produce micro-explosions phenomena due to Joule heating, and, if they could short the sheath, how these current densities could exist at all.

CONCLUSIONS

We have outlined the general principles and some details of our model of breakdown and gradient limits. We feel that this model provides a simpler and yet more general model of breakdown than other alternatives and we are continuing to develop details relevant to other applications. This model seems compatible with a wide variety of experimental data, but disagrees with some conventional wisdom.

ACKNOWLEDGEMENTS

We would like to thank DOE/OHEP, the MAP Program and the staff at Fermilab for support during this work.

REFERENCES

[1] Z. Insepov, J. Norem, J. Vac. Sci. Technol. A **31**, 011302 (2013).
[2] I. V. Morozov, G. E. Norman, Z. Insepov and J. Norem, Phys. Rev. STAB, **15** 053501 (2012).
[3] A. E. Robson and P. C. Thonemann, Proc. Phys. Soc., **73**, 508 (1959).
[4] J. Norem, V. Wu, A. Moretti, M. Popovic, Z. Qian, L. Ducas, Y. Torun, and N. Solomey, Phys. Rev. STAB **6**, 072001 (2003).
[5] Z. Insepov, J. Norem, S. Veitzer, S. Mahalingam, Proceedings of RF2011, June 1-3, Newport R. I. AIP Conference Proceedings 1406 AIP Millville, New York (2011), and arXiv:1108.086.
[6] Z. Insepov, J. Norem and A. Hassanein, Phys. Rev. STAB **7** 122001 (2004).
[7] Z. Insepov, J. Norem, Th. Proslier, A. Moretti D. Huang, S. Mahalingam, S. Veitzer; arXiv:1003.1736 (2010).
[8] COMSOL, http://www.comsol.com

Copyright © 2013 CC-BY-3.0 and by the respective authors

TUNING, CONDITIONING, AND DARK CURRENT MEASUREMENTS: 1300 MHZ NCRF CAVITIES AT THE ARGONNE WAKEFIELD ACCELERATOR (AWA) FACILITY*

J.G. Power#, M. E. Conde, S.D. Doran, W. Gai, and E. Wisniewski ANL, Argonne, IL 60439
C. Jing, Euclid Techlabs, 5900 Harper Rd, Solon, OH 44139

Abstract

In this paper, we present data on: (i) tuning and balancing; (ii) high-power rf conditioning; and (iii) dark current measurements; of normal conducting, standing wave, 7 cell, 1300 MHz accelerating cavities. The six cavities were tuned to 1300 MHz and were balanced to >96% in all cells. They are designed to operate with 10 MW of rf input power but are being rf conditioned beyond this operating point to insure low dark current during operation. During rf conditioning, dark current measurements are being recorded to provide a history of the cavity's surface field enhancement factor, *"β"*, throughout the rf conditioning period. Finally, as the final step we plan to record the breakdown rate at 10 MW to add to the breakdown literature for L-band cavities.

INTRODUCTION

Six normal-conducting, L-band rf cavities are currently undergoing commissioning as part of the linac upgrade to the AWA facility [1] to increase the drive beam energy from 15 MeV to 75 MeV. The cavity design (Fig. 1) is a seven-cell, standing-wave, 1300 MHz cavity made with OFE copper and was reported on earlier [2]. As of September 2013, all six cavities have been tuned and balanced but only one of the six cavities has been conditioned. In the first section of this paper we describe the tuning and balancing of all six cavities and in the second half of the paper we describe the rf conditioning of the first of the six cavities including measurements of dark current and the field enhancement factor, β, during the rf conditioning process. The remaining 5 rf accelerating cavities will be rf conditioned during the Fall of 2013.

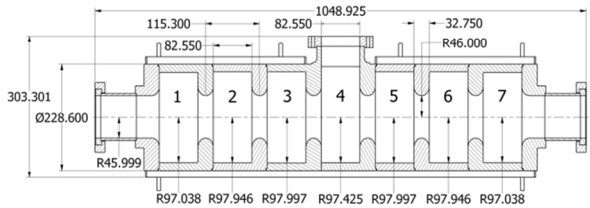


Figure 1: Cross section of the AWA rf cavity.

RF CAVITIES UPON ARRIVAL

Turnkey fabrication of the AWA cavities was enabled by a combination of high fidelity simulations using Omega3p [3], tight machining tolerances, push-pull tuning divots, and the adaptation of a well understood braze joint based on a SLAC design. Using this approach, the cavities were machined to final dimensions (i.e. without iterations), brazed together, and sent immediately to Argonne for tuning and balancing.

Table 1 lists the major figures of merit of the six cavities upon arrival from the vendor. The cavity Q0 was ~98% of ideal and the inter-cell coupling constant, k, was 99.5% of design. While neither of these is subject to adjustments during tuning they were within acceptable limits anyway. The cavities came back from the vendor with resonant frequency, f_0, that were between 290-568 kHz low and all cells had voltage field balance better than 87%. These values, for f_0 and balance, were very nearly acceptable without any tuning and balancing. Moreover, all cavities were within the estimated tuning range based on the combination of the push-pull divots and the temperature adjustment of the cooling water.

Table 1: Designed vs. Achieved Cavity Figures of Merit (upon arrival from vendor)

Parameter	Design	Cavity #1	Cavity #2	Cavity #3	Cavity #4	Cavity #5	Cavity #6
f0@38C	1300	-344 kHz	-290 kHz	-406 kHz	-568 kHz	-424 kHz	-360 kHz
T@1300	38^{0}C	38^{0}C	20.8^{0}C	23.6^{0}C	17.7^{0}C	9.6^{0}C	20.0^{0}C
Q0	25147	24911	24006	24798	24975	24768	24798
Beta	1.28	1.31	1.21	1.27	1.27	1.25	1.27
S11		-19.4dB	-20.2dB	-18.4	-18.5	-19.1	-18.5
Balance	100%	>93%	>90%	>95%	>93%	>87%	>99%
k	2.21%	2.2%	2.2%	2.2%	2.2%	2.2%	2.20%
S21-probe	-60dB				-61.95dB		-61.0dB

*The work is supported by the U.S. Department of Energy under Contract No. DE-AC02-06CH11357 with ANL.
#E-mail jp@anl.gov.

Copyright © 2013 CC-BY-3.0 and by the respective authors

TUNING AND BALANCING

Tuning Divots

Four push-pull tuners (Fig. 2) were used on each of the 7 cells of the rf cavities for a total of 28 divots. The advantage of push-pull tuners over push divots is that they allow for correction of machining errors in either direction. Tuning studs were brazed into holes on the side walls that had I.D. = 1.0" and a floor thickness = 1/8". Based on these dimensions, we estimated that the maximum tuning divot range was equal to half of the floor thickness or 62.5 thousandths. Estimating the volume this would displace, we used SUPERFISH to estimate that the maximum frequency range of the divots would be +/- 80 kHz per cell for a total tuning range of 560 kHz. However, not all of this tuning range can be applied to the frequency shift of the π-mode since the divots must also be used to correct the field imbalance.

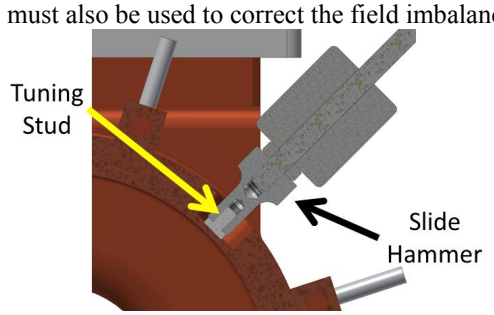


Figure 2: Cross section of a cell with tuning stud brazed in place and slide hammer screwed onto stud.

Beadpull

The beadpull measurement was simulated with SUPERFISH to optimize the size of the bead and the step size to use during the bead pull. The bead used was a metal (Al) needle of length = 0.2", O.D.=0.25", and I.D.=0.008" and was pulled through a horizontal mounted cavity by a 10 pound nylon fishing line with O.D. = 0.007. Beadpull results for all cavities upon arrival from the vendor are shown in Figure 3.

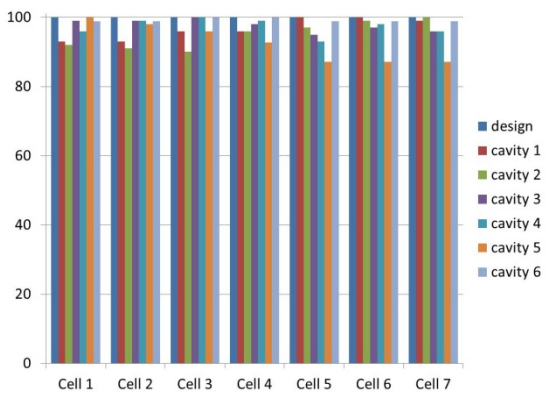


Figure 3: Initial beadpull results before tuning.

Tuning Algorithm

The standard tuning algorithm [4] uses a coupled circuit to model the ideal eigenmodes and eigenvectors while using perturbation theory to model the cavity errors. This algorithm was implemented with an in-house set of matlab codes. The general procedure was to input the frequency shifts due to imbalances from the beadpull measurements into the code to determine the frequency corrections (δf_c) and add that to the overall frequency offset of the π-mode(δf_π). The sum of these ($\delta f_c + \delta f_\pi$) is then applied to the cavity via the tuning divots.

Tuning and Balancing Results

Given that the cavity's frequency tunes were off by 290-568 kHz and that field balance was within 87% of design, then the range of the divots (~560 kHz) is slightly insufficient for a total correction. Several options were considered. We could add 4 more divots per cell but this has the risk of damaging the cavity. We could push divots beyond 62.5 thousandths. In the end, these two ideas were considered too risky and, instead, we decided to lower the operating temperature from 38°C to 20.7°C. Since the tunnel where the linac is installed is air conditioned and the dew point is below 13°C there is no downside to this.

The calculated frequency corrections for the field imbalances were within the range of the tuning divots (80 Hz per cell) in the vast majority of the cases. However, in 3 cases the correction for the largest cell was larger than 80 kHz (Table 2, bold) so the corrections were scaled down. The actual corrections that were applied to each cavity are shown in Table 2.

Table 2: Tuning Applied with the Divots

	Cav 1	Cav 2	Cav 3	Cav 4	Cav 5	Cav 6
Cell 1	0	-28.2	18.9	42.7	-12.4	1.8
Cell 2	0	-15.0	10.991	26.497	4.7	19.6
Cell 3	-10.9	-20.3	-41.6	2	-1.3	-23.2
Cell 4	-37.0	-50.6	-25.0	3.2	-14.5	-29.2
Cell 5	18.6	80.0	**81.2**	**85.656**	**80.9**	40.5
Cell 6	22.1	-22.9	-5.2	38.575	6.8	1.2
Cell 7	12	-11	8.5	25.2	8.8	-10.7

The final frequency of the π-mode was 1300 MHz at an operating temperature of 20.7 °C. The final field balance, obtained after adjusting the divots, (Fig. 4) had a mean value of 99% and was greater than 96% for all the cells in all the cavities.

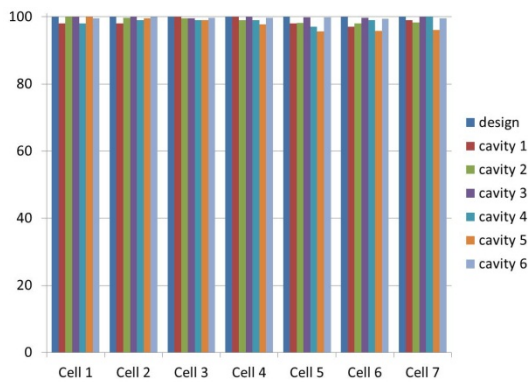


Figure 4: Final beadpull results after tuning.

Copyright © 2013 CC-BY-3.0 and by the respective authors

RF CONDITIONING

The AWA rf accelerating cavities were conservatively designed to operate a peak surface electric field of Ez=33.5 MV/m at an input power of P=10 MW. The cavities are being rf conditioned beyond this operating point to insure low dark current during operation. As of September 2013, only 1 cavity has been conditioned and we present the results here.

Dark Current

During rf conditioning, dark current measurements were recorded at the end of each phase of conditioning. The dark current was not directly measured but the x-rays generated by the dark current (verified to be linear with dark current) was measured instead (Fig. 5) with the light emitted from a phosphor screen and a PMT.

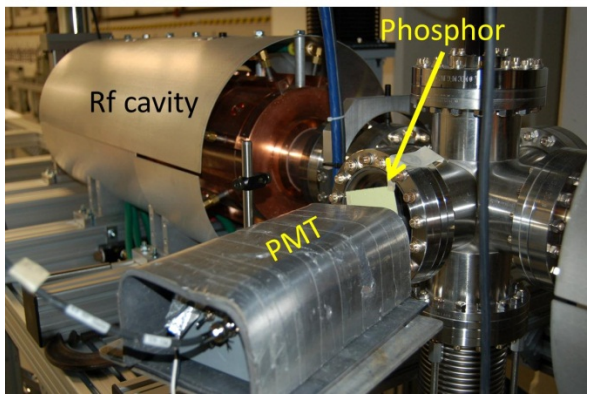


Figure 5: Setup used to measure x-rays from dark current.

Dark current was measured immediately after we had conditioning up to one of the fixed power levels (3, 6, 9, 12, 14 MW) for the first time. This insures that the cavity surface had never seen higher fields than the conditioned level. At that point, the power was lowered back to P=0 MW and the intensity of the phosphor light (proportional to the x-rays which is a proxy for dark current) was recorded as a function of input power (Fig. 6). The data clearly shows that the dark current emitted by the surface is less at the same field after the cavity has been conditioned beyond that point.

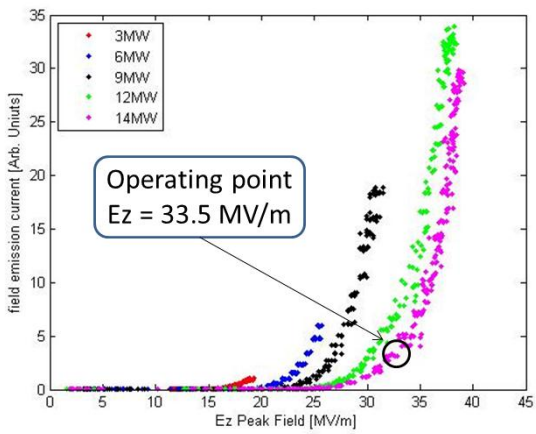


Figure 6: Conditioning History. (dark current vs. field)

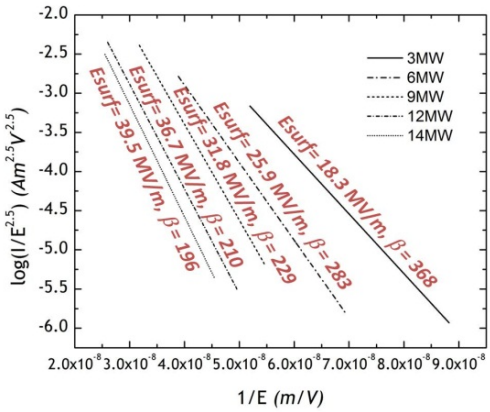


Figure 7: Conditioning History. (β enhancement factor)

The dark current data (Fig. 6) was used to make Fowler-Nordheim (FN) plots (Fig. 7) to get fits of the cavity's surface field enhancement factor, "β", throughout the rf conditioning period. Interestingly, this confirms the not so commonly known rule-of-thumb that the highest field to which the cavity has been conditioned to (E_{SURF}) multiplied by the field enhancement factor (β) is equal to a constant. We can convert the conditioning rf power levels tested to field using the cavity normalization E_{surf}=33.5 MV/m at P=10 MW. Using this, the fields are E_{SURF} = {18.3, 25.9, 31.8, 36.7, 39.5} MV/m. Fitting to the FN data gives β = {368, 283, 229, 210, 196}. Finally, we calculate the product βE_{SURF} = {6.7, 7.3, 7.3, 7.7, 7.7} GV/m and the rule βE_{SURF} = 5-10 GV/m is confirmed.

SUMMARY

Six normal conducting, standing wave, 7 cell, 1300 MHz accelerating cavities for the AWA linac upgrade have all been tuned and balanced. The first of the six cavities has been conditioned to 14 MW and dark current measurements were made. The remaining cavities will undergo rf conditioning soon and we plan to repeat dark current measurements for each cavity. Finally, we will record the breakdown rate at the operating power, P=10 MW, for each cavity.

REFERENCES

[1] M.E. Conde et al, "Argonne Wakefield Accelerator: A Facility for the Development of High Gradient Accel Structures and Wakefield Measurements," IPAC 2013.

[2] J.G. Power et al, "Upgrade of the Drive Linac for the AWA Facility Dielectric Two-Beam Accelerator," IPAC 2010.

[3] L. Lee et al., Omega3P, Tech. Rep., SLAC-PUB-13529, 2009.

[4] H. Padamsee et al., "Rf Superconductivity for Accelerators", John Wiley & Sons Inc., New York, (1998). {See Chapter 7}

Copyright © 2013 CC-BY-3.0 and by the respective authors

PPM KLYSTRONS FOR ACCELERATOR SYSTEMS

Patrick Ferguson, Michael Read, R. Lawrence Ives and David Marsden
Calabazas Creek Research, Inc., 690 Port Drive, San Mateo, CA 94404

Abstract

Calabazas Creek Research, Inc. (CCR) is engaged in the development of high power periodic permanent magnetic (PPM) focused klystrons for Accelerator Systems. There are at present 3 ongoing development programs. A 10 kW CW S-band klystron for the Advanced Photon Source at Argonne National Laboratory is nearing completion. An SBIR Phase II grant to develop an S-band 5.5 MW pulsed klystron for the Varian Medical Systems, Inc. CLINAC was funded in April, 2013. An SBIR Phase I grant to develop an S-band 75 MW pulsed klystron for the X-FEL linac at Los Alamos National Laboratory was received in February, 2013. The present development status of these 3 klystrons will be presented.

INTRODUCTION

The impetus to develop high power CW and pulsed PPM focused klystrons is to reduce the cost of producing a large number of klystrons as required by pending high energy linacs. The electron beams for the majority of klystrons for these linacs are focused using electromagnets. These electromagnets require a DC power supply and external fluid cooling. In addition, the electromagnet adds size and weight to the klystron. Employing a PPM structure in lieu of the electromagnet with DC power supply reduces the cost, size and weight substantially with no degradation in operation and life time.

CCR is nearing completion of the fabrication of the 10 kW CW S-band klystron. A 3D pictorial of this klystron is shown in Figure 1 below. The PPM structure consists of as standard geometry with a fixed period where the conventional ring magnets have been replaced by 4 pill box magnets in each half period. This geometry allows ready access to cavity tuners and cooling lines. The four long magnets around the RF output cavity are required to focus the spent electron beam as it loses energy. Initial simulations predicted an efficiency of 70%. However, after determining that the spent electron beam was intercepted just after the output cavity, the PPM structure was redesigned to include the large magnets with the efficiency decreasing to 55%. The electrical parameters for this PPM klystron are listed in Table 1.

Table 1. Electrical Parameters for the APS Klystron

Frequency	2.815 GHz
Beam Voltage	20 kV
Beam Current	1.0 A
Efficiency	55%
RF Output Power	11 MW
Saturated Gain	49 dB
Frequency	>5 MHz

The second PPM program is the development of a 5.5 MW pulsed S-band klystron similar to the solenoid focused klystron presently used in the Varian Medical Systems, Inc. CLINAC. The CLINAC is an X-ray source for treating cancer. The initial SBIR Phase I addressed the L-band RF sources for Project X at Fermi National Laboratory. It was redirected to the 5.5 MW S-band klystron due to the reduction in funding for Project X. The revised program is

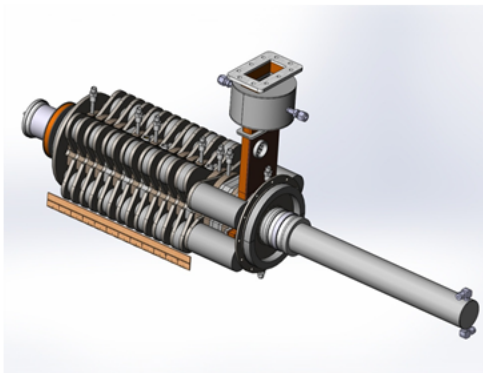


Figure 1: The 10 kW CW S-Band PPM Klystron.

Copyright © 2013 CC-BY-3.0 and by the respective authors

focused on reducing the size, weight and cost of the klystron and associated systems. The techniques established in this Phase II can be directly applied to all DOE klystron programs. The results are listed in Table 2.

Table 2. Electrical Parameters for the CLINAC PPM Klystron

Frequency	2.856 GHz
Beam Voltage	127 kV
Beam Current	90.5 A
Efficiency	48.8%
RF Output Power	5.61 MW
Saturated Gain	48 dB
-1 dB Bandwidth	>10 MHz

One goal is to include using as many existing subassemblies from the present solenoid focused klystron including the electron gun and output waveguide and vacuum window. The cathode will require a slight change in spherical radius with a small change in the focus electrode geometry.

The third PPM klystron development began in February, 2013. The initial specifications stated that a 50 MW klystron operating at 2.8175 GHz was required. At a meeting at LANL after receipt of the grant, the parameters were changed to the higher frequency of 2.856 GHz where there is more knowledge and hardware available and the RF output power was increased to 75 MW with an increase in pulse width from 3 microseconds to 12 microseconds. Further restrictions were imposed on the beam voltage not to exceed 450 kV and the beam current not to exceed 450 A. The resulting electrical parameters are listed in Table 3.

Table 3. Electrical Parameters for the LANL Klystron

Frequency	2.865 GHz
Beam Voltage	450 kV
Beam Current	379 A
Efficiency	48.2%
RF Output Power	82.2 MW
Saturated Gain	51 dB

SUMMARY

Several new klystrons are in development that use PPM focusing to reduce the size, weight and cost of RF systems. The novel approach to PPM focusing provides access to the RF circuit for cavity tuners, and water cooling and eliminates shunting to achieve axially symmetric magnetic fields. PPM focused klystrons can significantly reduce the cost of future accelerator and collider systems.

ACKNOWLEDGEMENT

These programs are funded by US Department of Energy grants DE-SC0004558, DE-SC0007591and DE-SC0009582.

REFERENCE

[1] Patrick Ferguson, et al., “Development of a 10 kW CW High Efficiency S-Band PPM Klystron” ICOPS, June, 2013, San Francisco.

Copyright © 2013 CC-BY-3.0 and by the respective authors

PASSIVELY DRIVEN X-BAND STRUCTURES

T. Sipahi, N. Sipahi, S. G. Biedron, S. V. Milton, CSU, Fort Collins, Colorado, USA

Abstract

Accelerating structures operated at X-band frequencies have been shown to regularly achieve gradients of around 100 MV/m or better. Obviously, use of such technology can lead to more compact particle accelerators. At the Colorado State University Accelerator Laboratory (CSUAL) we would like to adapt this technology to our L-band (1.3 GHz) accelerator system via a 2-beam configuration that capitalizes on the high gradients achievable in X-band accelerating structures in order to increase our overall beam energy in a manner that does not require investment in an expensive, custom, high-power X-band klystron system. Here we provide the design details of the X-band accelerator structures that will allow us to achieve our goal of reaching the maximum practical net potential across the X-band accelerating structure.

GENERAL CONCEPT

The CSUAL linac is an L-band system capable of generating 6-MeV electron bunches [1]. The parameters of L-band linac system are given in Table 1. For many reasons we would like to further increase the electron beam energy without additional significant investment. Our idea is to utilize the electron beam from our linac as a drive source for an otherwise unpowered (passive) X-band linac structure, thus allowing us to increase the beam energy by using the L-band power together with the inherent high shunt impedance of the X-band structure. In our previous study [2] we showed that by using a passive standing wave (SW) X-band cavity driven by our linac we had the potential to increase our 6-MeV electron bunch energy to 11 MeV in 15 cm, but there was a fundamental limit of that configuration. Here we utilize a two-beam configuration based on two traveling wave (TW) X-band structures, one used as an X-band power generator (the decelerator), and one as an accelerator. This configuration is shown in Figure 1. We exploit the TW structure's ability to provide continuous X-band power generated from the passing of the L-band system beam through it and then transfer this power to a second cavity that can be filled in a manner that does not limit as before the achievable integrated potential.

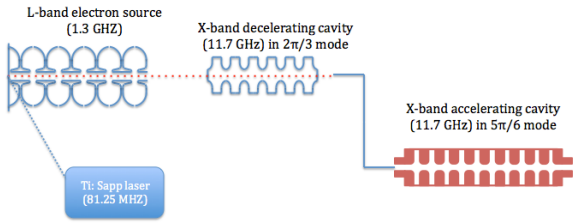


Figure 1: General layout of the two-beam X-band cavity structures [3].

Table 1: Parameters of CSU Accelerator Laboratory

Laser Frequency	81.25 MHz
L-Band RF Gun Frequency	1.3 GHz
L-Band RF Gun Energy	6 MeV
L-Band Macropulse Length	10 μs
X-band Linac Frequency	11.7 GHz
Repetition Rate	10 Hz
RF gun Charge/Bunch	3.5 nC

CAVITY CHOICE

General

We must design two separate cavities, one to be used as a decelerator and optimized to efficiently generate and allow extraction of X-band power without significant disruption to the passing beam, and the other optimized to efficiently accept X-band power and generate the highest practical integrated potential to be used for accelerating electron bunches.

We use a consistent description of cavity geometries as shown in Figure 2 where a is the iris radius, R is the cavity radius, h(=2r_1) is the disc thickness, l is the basic cell length, λ is the wavelength and r_1 is the radius of the iris poles.

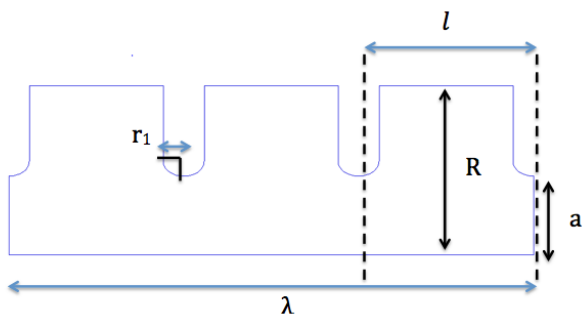


Figure 2: Schematic view of a generic X-band cavity.

In this example we show a configuration for a 2π/3 TW structure.

Copyright © 2013 CC-BY-3.0 and by the respective authors

Decelerating Cavity

Here we choose to use a $2\pi/3$ mode TW X-band structure with parameters given in Table 2 and as computed by the design code SUPERFISH [5].

As we plan on passing through the structure a fairly high current beam we must concern ourselves with HOM effects, thus the optimal tends to larger iris dimensions at the expense of shunt impedance [4]. Figure 3 shows the loss parameter k as a function of the iris radius.

$$k = \frac{\omega R_s}{4Q}$$

where ω is the angular frequency of the RF, Q is the unloaded quality factor of the structure and R_s is the cavity shunt impedance. Clearly a larger iris is desired. This is OK as we found in our earlier paper that even for moderate shunt impedance the structure is relatively short as we are limited by the maximum amount of energy we can remove from the drive beam. Based on our previous study the length of this cavity should be 15.3 cm in order to decelerate the beam from 6 MeV down to 1 MeV. Under such conditions the net X-band rf power that can be generated is 1.4 MW.

Figure 4 shows the power dissipated in the cavity walls as a function of the iris radius. As can be seen this is small compared to the available power generated even for larger values of a/λ and so is not a significant factor.

The resulting X-band power is then coupled out of the cavity and transferred to the accelerating structure.

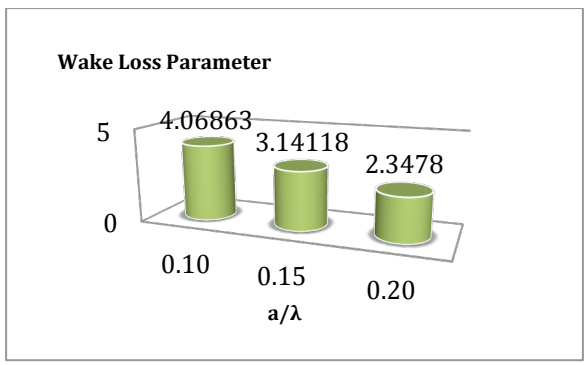


Figure 3: Wake loss parameter vs. a/λ.

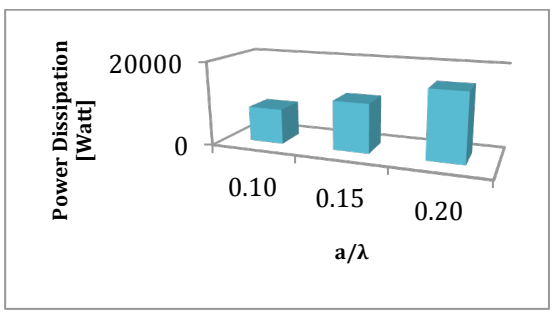
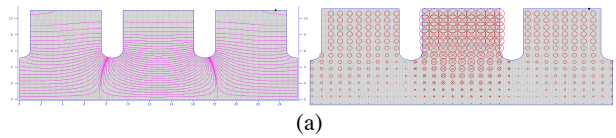


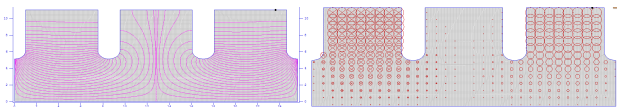
Figure 4: Power dissipation vs. a/λ.

As this structure is powered in a global fashion via the electron beam there is no need to complicate the design with a constant gradient design. Rather we choose a simple constant impedance device.

Figure 5 shows the cavity fields, both electric and magnetic, as computed by SUPERFISH for both Neumann and Dirichlet boundary conditions as specified at the end walls.



(a)



(b)

Figure 5: Electric and magnetic field patterns for $a/\lambda = 0.2$ in (a) Neumann boundary condition at end walls for $2\pi/3$mode (b) Dirichlet boundary condition at end walls for$2\pi/3$mode.

Table 2: Parameters for Decelerating Cavity

a/λ	0.2
Phase Advance per cell (ψ)	$2\pi/3$ radian
Iris radius (a)	0.00512466 m
Cavity Radius (R)	0.0110955 m
Disk Thickness (h= $2r_1$)	0.002 m
Quality factor	6456
Length	0.153 m
Frequency	11.7 GHz
Shunt impedance	79.15 MΩ
Power Dissipation	8360.779

Accelerating Cavity

The optimization for the accelerating cavities follows a different path. This cavity will see a single, relatively low charge pulse, so the aperture requirements are not as severe. Further we wish to maximize the overall integrated voltage seen by the beam during its passage. This clearly argues for high shunt impedance and as long a structure as reasonable.

Our L-band system is also capable of generating beam for over 10 μs, i.e. significantly longer than the fill time of typical X-band structures. We will therefore operate the L-band system with shorter pulses, but pulses long enough to completely fill the X-band structure. This then argues for a structure with a very slow group velocity as it will allow us to fill a longer cavity and capitalize on the long L-band rf pulses.

All structure parameters for the TW accelerator can be deduced from those of the SW structure. In particular, the group velocity can be computed by

$$\vartheta_g = \frac{d\omega}{dk_z} = \frac{2(2.405)c}{3\pi J_1^2(2.405)}\left(\frac{a}{R}\right)^2 \sin\psi e^{-\alpha h}$$

Copyright © 2013 CC-BY-3.0 and by the respective authors

where ψ is the phase advance per cavity traveling wave and α is the attenuation per unit length of the field for the TM_{010} mode through an iris of wall thickness h.

If we wish to decrease the group velocity and we have chosen a minimum a, we are left only with ψ as a variable. This then argues for a large TW mode number defined as n in $2\pi/n$. This is shown in Figure 6 where the relative velocity coming from the sine term is plotted vs. n. A value of n equal to 2 is the SW π-mode. This certainly would argue that the $2\pi/3$–mode is not the best choice and that a mode number of more like 15 or 16 would be better and might still be practical.

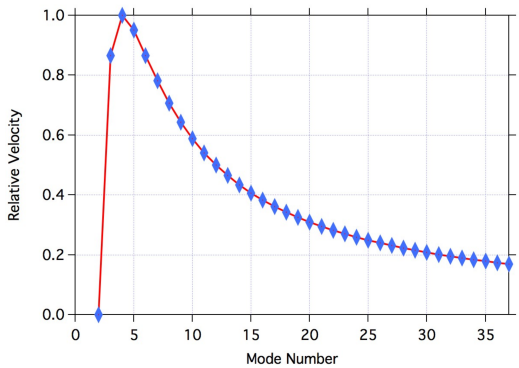


Figure 6: Relative velocity vs. mode number.

For that purpose moving the RF phase advance to $5\pi/6$ (for $a/\lambda = 0.1$) and using a longer cell length compared to that of the $2\pi/3$ (for $a/\lambda = 0.15$) mode in order to preserve synchronous acceleration of the electron bunch slows down the group velocity to 0.95% c and increases α_0 to 1.69 from its $2\pi/3$ value of 0.30 allowing more efficient deposition of the RF power in the accelerating structure [6,7]. Table 3 shows the parameters of this accelerator structure.

Table 3: Parameters for Accelerating Cavity

a/λ	0.15	0.1
Inner radius	0.00512466 m	0.00256233 m
Phase Advance	$2\pi/3$ radians	$5\pi/6$ radians
Cavity Radius	0.0110955 m	0.00999 m
Disk Thickness	0.002 m	0.002 m
Frequency [GHz]	11.7 GHz	11.7 GHz
Quality factor	6456	7474
Shunt impedance	79.15 MΩ	185.67 MΩ
Group Velocity	6.38 %	0.95 %

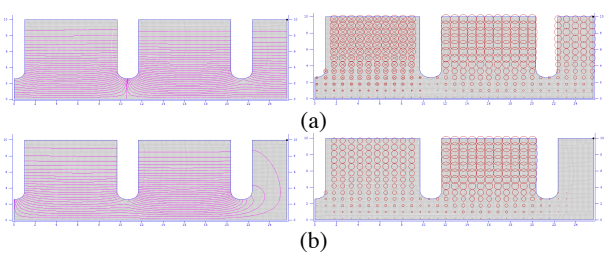


Figure 7: Electric and magnetic field patterns for $a/\lambda = 0.1$ in (a) Neumann boundary condition for $5\pi/6$ mode (b) Dirichlet boundary condition for $5\pi/6$ mode.

Figure 7 shows the cavity fields, both electric and magnetic, as computed by SUPERFISH for both Neumann and Dirichlet boundary conditions as specified at the end walls for the accelerating cavity.

DISCUSSION AND CONCLUSION

In this study we provide designs for two different TW X-band structures that would allow us to achieve higher energies in a compact way. To achieve higher potential one really needs to extract the X-band power from the X-band decelerating cavity and transfer it to a low group velocity traveling wave structure. Optimizing the group velocity by adjusting the inner radius of the constant-impedance structure and using a more relevant mode both improves the power efficiency and overall integrated potential.

ACKNOWLEDGMENT

We wish to thank the SLAC National Laboratory Facility for their support and funding and in particular the input from C. Adolphsen. Finally, we wish to thank the senior management of CSU for their support of the accelerator laboratory and accelerator education.

REFERENCES

[1] S. G. Biedron, T. Burleson, C. Carrico, A. Dong, J. Edelen, C. Hall, K. Horovitz, S.V. Milton, A. Morin, L. Rand, N. Sipahi, T. Sipahi, P. van der Slot, H. Yehudah, " The CSU Accelerator And FEL Facility ", FEL'12, Nara (2012).

[2] S. G. Biedron, S.V. Milton, N. Sipahi, T. Sipahi, C. Adolphsen, "Passively Driving X-band Structure to Achieving Higher Beam Energies", IPAC 2013, Shanghai, China, May 12-17, 2013.

[3] N. Sipahi, T. Sipahi, S. V. Milton, S. G. Biedron, "X-band RF power Generation via L-band Accelerator System and Uses" NAPAC 2013, Pasadena (2013) (to be published).

[4] J. W. Wang, RF Properties Structures of Periodic For Linear Accelerating Colliders*, SLAC-339, UC-28 (A), Stanford Linear Accelerator Center, Stanford University, Stanford, California, Ph. D. Dissertation (1989).

[5] J. Warren, et al., "POISSON/SUPERFISH Reference Manual," Los Alamos National Laboratory report LA-UR-87-126 (1987).

[6] C. Christou, "X-band Linac Technology for a High Repetition Rate Light Source", Nuclear Instruments and Methods in Physics Research A 657, p. 13-21 (2011).

[7] G. Burt, P.K. Ambattu, A.C. Dexter, T. Abram, V. Dolgashev, S. Tantawi, R.M. Jones, "X-Band Crab Cavities For The Clic Beam Delivery System", 44th ICFA Advanced Beam Dynamics Workshop: X-Band RF Structure and Beam Dynamics, Warrington, United Kingdom, December, 2008.

Copyright © 2013 CC-BY-3.0 and by the respective authors

PROGRESS TOWARD THE DEVELOPMENT OF A RAPIDLY TUNABLE RF CAVITY*

D.J. Newsham, X. Chang, and J.R. Thompson, FAR-TECH, Inc., San Diego, CA 92121, USA

Abstract

A major bottleneck in the development of compact, rapid-cycling particle accelerators is the ability to maintain phase coherence between the short orbit time of the particle bunch and the phase of the accelerating RF field. A ferroelectric loaded RF cavity can achieve the needed phase shift in a significantly shorter time than alternative technologies. The current status of the development of such a cavity including the cold test of a preliminary cartridge and the testing of the bias voltage subsystem will be presented.

INTRODUCTION

FAR-TECH, Inc. is developing a rapidly tunable RF cavity [1][2] that is specifically designed to provide the speed of frequency tuning required for use in modern rapid-cycling accelerator systems (rapid-cycling synchrotron or FFAG). Adjustment of the accelerating frequency between each cavity crossing of the particle bunch will maintain a synchronous phase between the bunch arrival time and the accelerating field on each pass.

The tuning is achieved by applying a bias voltage across a BST(M) [3] ferroelectric based load element placed within the cavity. The speed of frequency tuning is a combination of the fast response time of the BST(M) ($\lesssim$ 10 ns) and the response time of the bias system ($\sim$ 55 ns). Several cooled tuning elements with bias voltages ramped to 40 kV placed near the periphery of pill-box structure can provide a few percent frequency shift on the microsecond time scale.

CARTRIDGE TESTING

The heart of the tunable cavity is the ferroelectric biasing cartridge. This cartridge contains the ferroelectric sample and biasing copper electrodes. This cartridge can be inserted and removed without breaking the vacuum of the main cavity. This separation from the vacuum will also allow a coolant flow of a dielectric fluid to cool the cartridge. Further, using a ferroelectric tube, rather than a solid cylinder will allow both the inner and outer surface to be cooled. To test the performance of the cavity a simplified cartridge and cavity structure was designed, simulated, constructed, and tested. Although an actual cavity would have multiple cartridges place off axis, the test cavity purposefully placed the cartridge on axis to increase the RF field and reduce the power requirement and increase the tuning range for the test. The structure was designed in SolidWorks and simulated with HFSS with several values of the dielectric constant and loss tangent.

Cavity parts and cartridges were constructed as shown in Fig. 1. The cartridge pieces were soldered in two stages using the appropriate alloy for each contact. Soldering was performed in a solder reflow oven with PID temperature control. Frequency and cavity Q-factor were measured at several bias voltages using an Agilent 8720ES network analyzer and a high voltage supply. Because the ferroelectric cylinders are 1 cm long, the conversion from bias voltage to bias electric field is trivial. Full air breakdown occurred at approximately 18 kV bias.

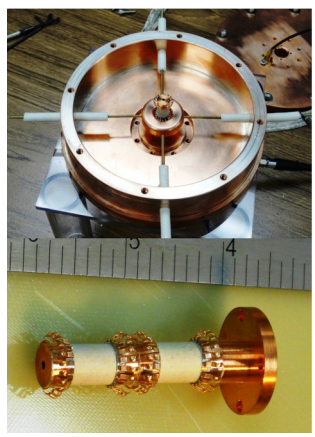


Figure 1: RF cavity used to characterize the biasing cartridge. Test cavity without top plate (*top*). Biasing cartridge (*bottom*).

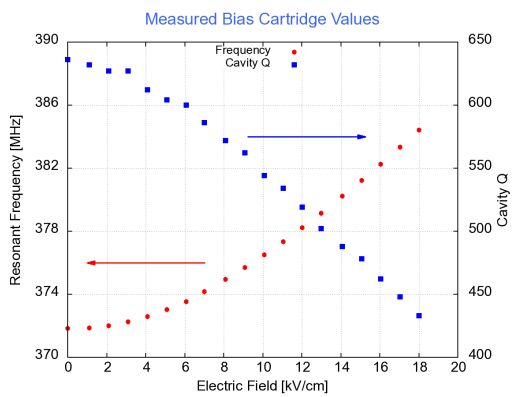


Figure 2: Measured resonant frequency and Q factor for the biasing cartridge in the test cell.

The measured frequency and Q-factor at different voltages are shown in Fig. 2. The HFSS simulation data relating dielectric constant and loss tangent to resonant frequency and Q-factor was inverted to convert the measure values to the values of interest. The result of this inversion are shown in Fig. 3 (dielectric constant) and Fig. 4 (loss tangent). Also included in these figures is

*Work supported by DOE Office of High Energy Physics, DOE-SBIR #DE-SC0006225

#newsham@far-tech.com

Copyright © 2013 CC-BY-3.0 and by the respective authors

estimated reduction in the loss tangent because the simulated wall losses are less than the real cavity that used bolted end plates resulting in a real wall Q that was 80% of the perfect copper wall Q value. This reduction in the wall Q results in a reduced loss tangent.

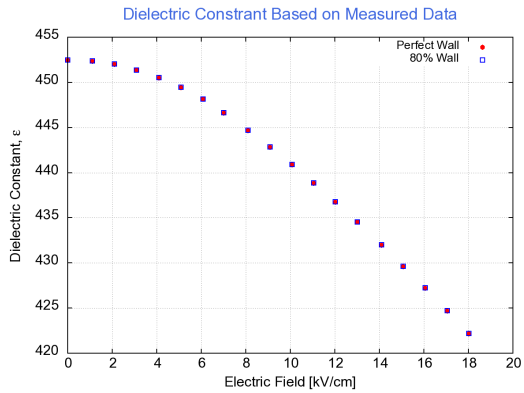


Figure 3: Calculated dielectric constant of the ferroelectric biasing cartridge. The 80% wall value represents a compensation for non-ideal wall losses.

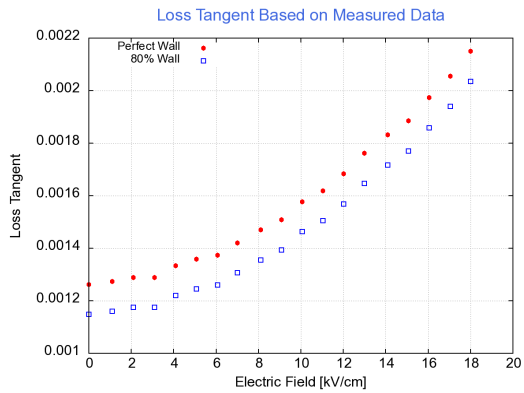


Figure 4: Calculated loss tangent of the ferroelectric biasing cartridge. The 80% wall value represents a compensation for non-ideal wall losses.

With a bias field of ~18 kV/cm there is a greater than 6% decrease in the dielectric constant. The lack of dependance of the dielectric constant on the wall losses indicate that load pulling of the cavity by the ferroelectric was not significant. As the bias voltage increases, the loss tangent becomes greater. When the portion of the total losses that is attributable to the walls is increased, there is the expected decrease in the loss tangent. Although all of the dielectric losses has been attributed to a bulk loss tangent, in reality there is a combination of effects related to the ferroelectric making it an effective loss tangent. In addition to the loss tangent, there is increased RF loss at the joint between the ferroelectric and the copper electrode including: RF electric field enhancement due to micro-irregularities on the ferroelectric surface upon which the metalization is placed; and residual surface charge. These "anomalous" losses can be reduced by specialized dielectric coatings before metalization.

BIAS VOLTAGE DRIVER

The high voltage biasing circuit is critical to the full testing and operation of the rapidly tunable RF cavity. The basic layout for a single stage of the Marx-like bias driver is shown in Fig. 5. For testing, the ferroelectric capacitance is replaced by a fixed load capacitor that is connected to the generator through an external inductor. Each stage consists of 2 storage capacitors and 2 MOSFET transistors for switching each capacitor (4 MOSFETs in total). Switching a storage capacitor in or out requires opening one transistor followed by closing the other transistor in the pair. In order to achieve minimum energy loss, there is a required minimum time (~150 ns) between the opening of one transistor and the closing of the other. When a storage capacitor is switched in, the voltage at the load will begin to oscillate (charge), switching in the second storage capacitor after a half-oscillation (determined by the inductor and load capacitor) will terminate the oscillation at the load (park). The voltage on the load will be nominally constant and twice the voltage on each of the storage capacitors. Reducing the voltage at the cartridge (discharge & park) is performed by sequentially switching out the storage capacitors. By this use of zero current switching, it is possible to recover some of the energy that has be stored in the load. In the process of charging & parking or discharging & parking, the time between the initial firing and the park firing is critical to minimize oscillation in the load.

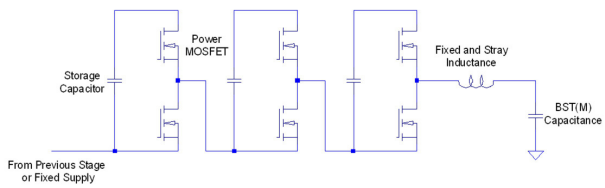


Figure 5: Simplified schematic 1-1/2 stages of the bias voltage generator.

A bias voltage driver board with 2 storage capacitors and a timing control control board capable of driving up to 4 bias voltage driver boards were designed and fabricated. Preliminary testing of a single bias voltage driver board with 1 kV on each of the 2 storage capacitors was started and is currently ongoing.

Voltage Driver Board

Two critical characteristics of the biasing circuit are the switching speed and energy efficiency. The switching speed determines the achievable ramp time, while the energy efficiency determines the bias circuit power requirements.

The choice of MOSFET was between Si based transistors which are faster with lower voltage standoff and SiC based transistors which are slower, have higher voltage standoff, and less mature in the development process. For the demonstration of the ferroelectric biasing cartridge concept, energy efficiency was more important than ramp speed and SiC transistors were chosen. Much

Copyright © 2013 CC-BY-3.0 and by the respective authors

like with Si, as the SiC technology matures, faster SiC devices should become available. Although the SiC transistors are "slower" the anticipated switching time will be faster than the 55 ns currently used. The higher voltage standoff available in SiC transistors allow the stage voltage to increase to 1000 V from the ~600 V initially planned. This reduces the number of stages needed to achieve 40 kV from 68 to 40. Two candidate Cree SiC MOSFET switches, CMF10120D (single die) and CMF20120D (a dual die). Currently, we have only begun testing the single dye transistor. Comparing the performance of these transistors will help determine if the drain to source on-state resistance, or the drain to source capacitance is more important in terms of energy loss, or if they are both minimal compared with the losses associated with the stray capacitance of the stage isolation.

Fig. 6 shows a voltage driver board. Power is delivered from an isolated +24 VDC power buss on the left, running up the edge of the board, which can be common to several. Component and 1 kV power is generated using isolated DC/DC converters from the power buss. Fiber optic coupling was used to provide ground and high voltage isolation between the timing control board and the voltage driver boards, as the voltages at the local ground references ("star points") can vary from ground by as much as the full output voltage. Each transistor is driven by a separate fiber to eliminate the need for digital circuitry on the voltage driver board which can have a high level of noise and because the on/off propagation delays of the transmitter/receiver are significantly different. The storage capacitors are charged with isolated 1 kV DC/DC converters. It is hoped that by using these supplies will have significantly less noise than rectified power from an isolated multi-tap transformer secondary, although there may be a significant loss of efficiency by using multiple DC/DC converters in series.

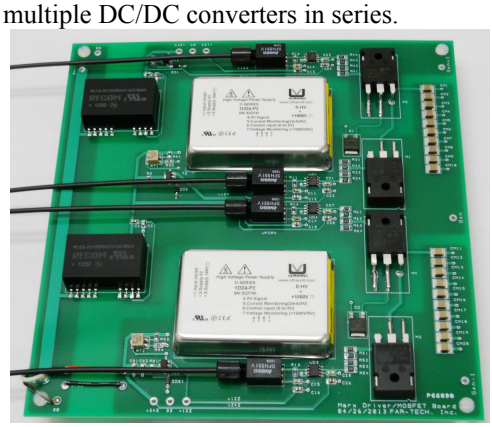


Figure 6: Populated voltage driver board without fiber receiver shields.

Timing Control Board

The timing control board which generates and sequences the appropriate MOSFET gate signals is shown in Fig. 7. As shown, it has only been sufficiently populated to test a single Marx board. The timing and sequencing is provided by an external pulse generator and on board sequencer, with associated individual switch timing delays. The timing delays, which in principle can be programmed in real-time, are hardwired through rocker switches for the prototype. The timing control board will remotely couple to the bias voltage driver board via fiber optics.

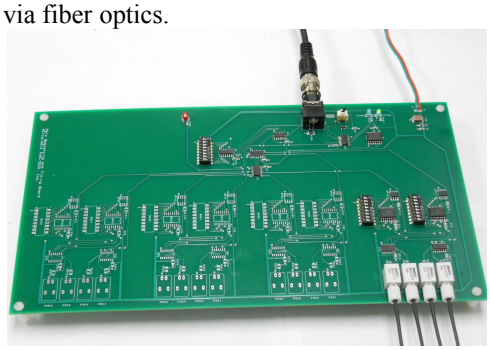


Figure 7: Timing control board with components for a single voltage driver board populated.

Preliminary Testing

The voltage voltage system was initially tested at 100 V per storage capacitor and increased incrementally to the full 1 kV per capacitor. The storage capacitance was reduced to 100 nF (designed for 1 μF) to provide better resolution of the energy loss. At each voltage the charging and discharging delay times were adjusted to achieve a minimum voltage ripple after parking. In general, this ripple could not be reduced below ~4%, possibly because of the voltage droop from switching losses and loss to stray capacitance. At storage capacitor voltages above ~400 V there was a problem of an open transistor suddenly closing and shorting the storage capacitor through the transistor pair. Ultimately, this problem was traced to the fiber receiver which was picking up transient noise and mimicking a "high" output. The problem was solved by adding shielding around the receiver that was electrically connected to the local "star" point. At 1 kV per storage capacitor, the energy loss in each storage capacitor, as measured by the reduction in voltage after the discharge/park was ~2mJ per storage capacitor. This loss is a factor of 3 higher than expected and is currently under investigation. The dual die MOSFET will also be tested; and will help identify the source of the losses.

REFERENCES

[1] D. Newsham et al., IPAC2012, New Orleans, May 2012, p. 3386.
[2] US Patent #8508319.
[3] A. Kanareykin, et. al., PAC2005, Knoxville, May 2009 p. 4305.

Copyright © 2013 CC-BY-3.0 and by the respective authors

INVESTIGATION OF BREAKDOWN INDUCED SURFACE DAMAGE ON 805 MHZ PILLBOX CAVITY INTERIOR SURFACES

M. R. Jana, M. Chung, M. Leonova, A. Moretti, A. Tollestrup and K. Yonehara,
Fermi National Accelerator Laboratory, Batavia, IL - 60510, USA
B. Freemire, and Y. Torun, IIT, Chicago, IL - 60616, USA
D. Bowring, LBNL, Berkeley, California - 94720, USA
G. Flanagan, Muons, Inc., Batavia, IL - 60134

Abstract

The MuCool Test Area (MTA) at Fermilab is a facility to develop the technology required for ionization cooling for a future Muon Collider and/or Neutrino Factory. As part of this research program, we have tested two 805 MHz vacuum RF cavities in a multi-Tesla magnetic field to study the effects of the static magnetic field on the cavity operation. This study gives useful information on field emitters in the cavity, dark current, surface conditioning, breakdown mechanisms and material properties of the cavity. All these factors determine the maximum accelerating gradient in the cavity. This paper discusses the image processing technique for quantitative estimation of spark damage spot distribution on cavity interior surfaces. The distribution is compared with the electric field distribution predicted by a computer code calculation. The local spark density is proportional to probability of surface breakdown and shows a power law dependence on the maximum electric field (E). This E dependence is consistent with the dark current calculated from the Fowler-Nordheim equation.

INTRODUCTION

High intensity, low emittance muon beams are essential requirements for a future Muon Collider and/or Neutrino Factory. Low emittance muon beams can be produced by ionization cooling. This consists of passing muon beams through low-Z absorber material (liquid H), to reduce all components of the momentum and replacing only longitudinal momentum with accelerating fields using RF cavities. At the same time, to keep the muon beam focused, both the absorbing material and RF cavities are placed inside a strong magnetic field provided by a superconducting solenoid. The ionization cooling process is most efficient if both the accelerating fields and magnetic fields are high. To study the interactions of a static magnetic field with operation at high accelerating fields, two 805 MHz RF cavities e.g. (i) LBNL-Pillbox (ii) All-Season have been tested in a multi-Tesla magnetic field at the Fermilab MuCool Test Area (MTA). During operation with high magnetic field B = 2 - 5 T, the cavity's accelerating field degrades significantly, dark current and X-rays are produced and interior surfaces suffer severe breakdown damage [1-3]. In this paper, we present the spatial distribution of the breakdown damage spots on the interior surface of the RF cavity using ImageJ [4] and Mathematica software [5]. The measured number of breakdown spots per unit area is compared with both the electric field distribution (calculated by computer code) and the dark current calculated from the Fowler-Nordheim equation. Finally a power law dependence on the maximum electric field is discussed.

805 MHZ CAVITIES

LBNL-Pill Box Cavity

A cross sectional view of the 805 MHz cylindrical pillbox cavity of inner diameter 312.4 mm is shown in Fig. 1. Two irises are covered by specially designed copper windows (separately shown). Each window has a radius of 97.9 mm. RF power at 805 MHz is fed in through a kidney shaped coupling slot on the cavity wall using WR975 rectangular waveguide [3] with 20 μs pulse duration and repetition rate of 15 Hz. The cavity is mounted inside a 44 cm bore diameter superconducting solenoid magnet which can generate magnetic fields up to 5 T. The peak electric field was 40 MV/m with RF power 4.2 MW at B=0 field and 16 MV/m with RF power 0.67 MW at B = 3 T.

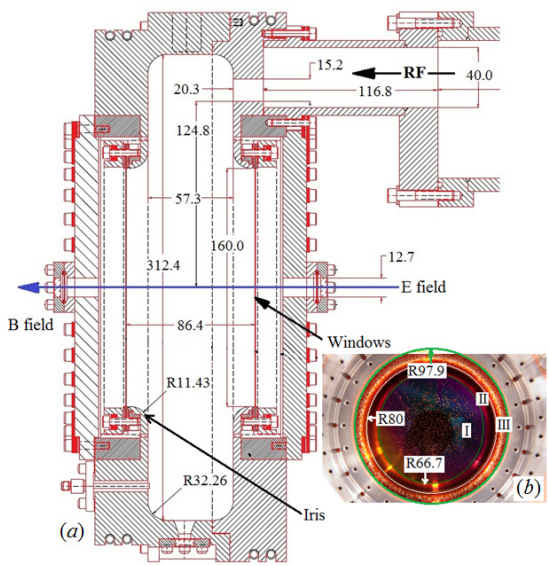


Figure 1: (*a*) Cross sectional view 805 MHz Pillbox RF cavity with copper window [3], (*b*) Copper window of radius 80 mm and iris of outer radius 97.95 mm.

Breakdown damaged spots on vacuum window is shown in Fig. 1(b) and the location of damaged spots are marked by crosshairs using ImageJ software shown in Fig. 2.

Copyright © 2013 CC-BY-3.0 and by the respective authors

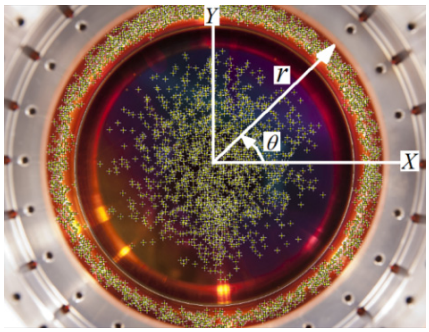


Figure 2: Photograph of copper window and iris with distribution of RF breakdown damage spots, marked with crosshairs using ImageJ software.

All Season Cavity

Another cavity tested at the MTA known as the All Seasons cavity, is shown in Fig.3 [6]. This cavity was designed for both vacuum (3×10^{-8} Torr) and 100 atm compressed hydrogen gas operation. It consists of a SS316 cylindrical body [Fig. 3(b)] of outer diameter 366.9 mm and two end plates. The top [Fig.3(c)] and bottom [Fig. 3(d)] both have a diameter of 290.7 mm.

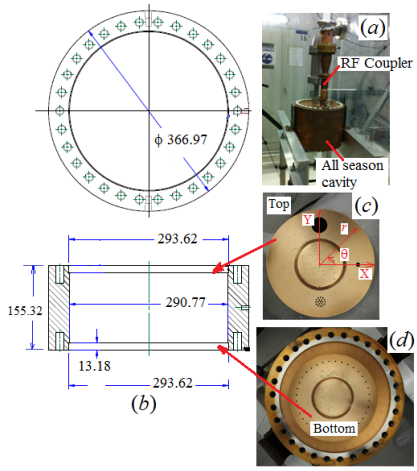


Figure 3: (a) All Seasons cavity (b) cross sectional view (c) top plate (d) bottom plate with cylindrical wall.

RF power was fed to the cavity through a coax coupler [Fig. 3(a)] with 20 μs pulse duration and 15 Hz repetition rate. The cavity was operated at peak electric field of 25 MV/m with RF power 1.2 MW, B=0 T and 22 MV/m with RF power 0.93 MW, B= 3T magnetic field [7].

ANALYSIS AND RESULTS

LBNL-Pillbox Cavity

For the sake of analysis, the surface of the pillbox cavity window was divided into 3 regions as shown in Fig. 1(b). Region I is a circular area of radius 66.7 mm, region II is a ring of inner radius 66.7 mm and outer radius 80 mm. Both region I and region II are part of flat circular window. Region III (iris) is also a ring of inner radius 80 mm and outer radius 97.9 mm. The center of the window is the origin of the coordinate system (X, Y or *r*,θ) shown in Fig.2 where Breakdown Damage (BD) spot locations are identified by crosshairs using the image processing software ImageJ. The BD spot distribution is calculated with the help of Mathematica software. Figure 4(*a*) shows the BD spot distribution in the X-Y plane. The upper half of the iris is close to the RF coupler and has more damage spots than the lower half. The BD spot distribution in r-θ plane is shown in Fig. 4(*b*).

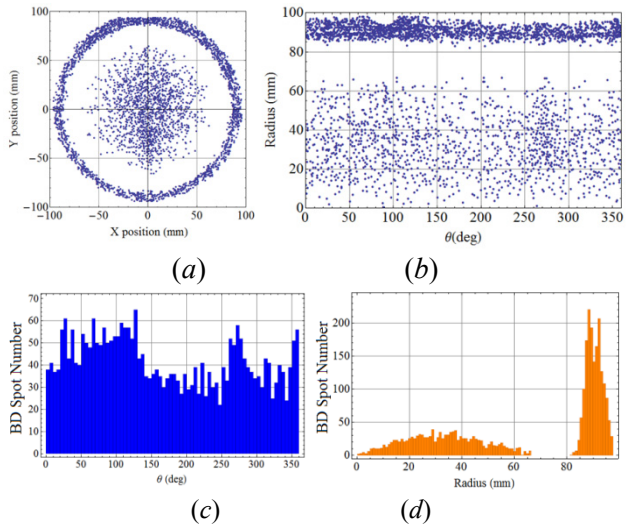


Figure 4: BD spot distribution in X-Y plane (*a*) and r-θ plane (*b*), BD spot no. vs θ plot (*c*) with bin size: 5° and BD spot no. vs *r* plot (*d*) with bin size 0.9 mm.

The number of BD spots at different values of θ and *r* are depicted in Fig. 4(*c*) and Fig. 4(*d*) respectively. The electric field distribution was calculated using computer code [8] and field emission dark current density was calculated from the Fowler-Nordheim equation where we have taken the work function (ϕ) for copper to be 4.65 eV and the field enhancement factor (β) to be 200. Figure 5 illustrates the results of the electric field, dark current density and number of BD spot density. Figure 6 shows the BD spot density vs electric field in the window area. The solid circles represent the data obtained from image processing and the line indicates an electric field (E^n) power fit. This shows the data fit well with $E^{6.28}$.

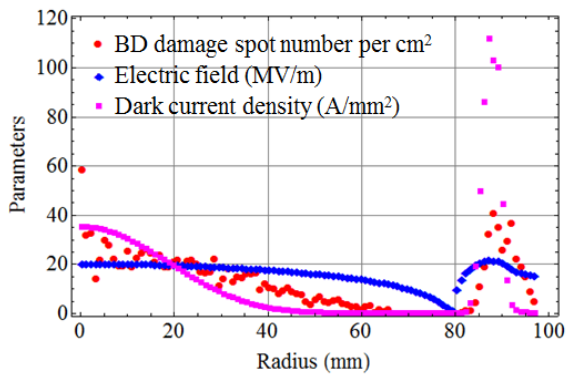


Figure 5: BD spot number per cm^2, RF electric field and dark current density vs radial distance plot.

Copyright © 2013 CC-BY-3.0 and by the respective authors

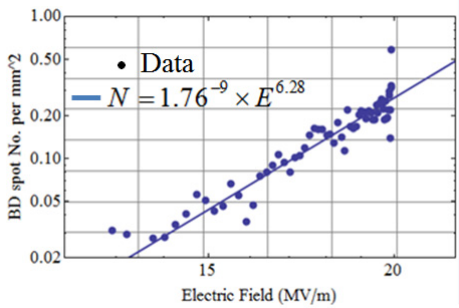


Figure 6: BD spot density vs electric field plot for flat window area.

All Seasons Cavity

Distributions of BD spot are shown in X-Y [Fig. 7(*a*)] and r-θ plane [Fig. 7(*b*)]. The number of BD spots at different values of θ and r are shown in Figs. 7(c) and 7(d) respectively. Fig. 8(a) illustrates the BD spot no. per mm^2 at different radii for the top plate at given θ values and Fig. 8(b) shows the same for the bottom plate. Fig. 9 depicts the computed electric field (with 10 times magnification) distribution and dark current density distribution. This is the same for both plates.

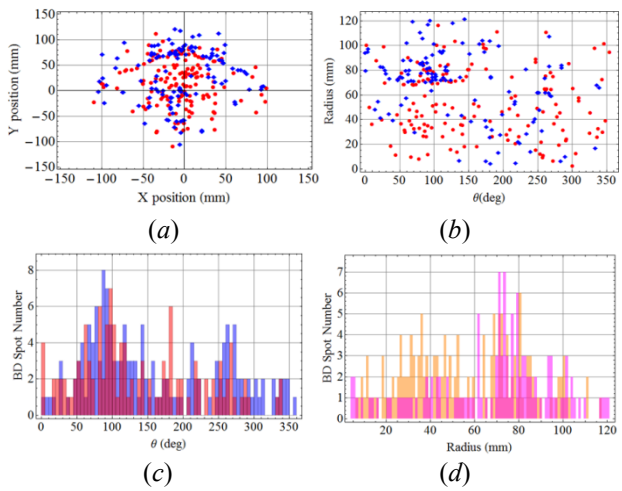


Figure 7: BD spot distribution in X-Y plane (*a*) and r-θ plane (*b*) (in both plots red/blue for top/bottom plate), BD spot no. vs θ plot (c) [blue/brown for top/bottom plate with bin size 5°], BD spot number vs *r* plot (d) [orange/magenta for top/bottom plate with bin size 1.2 mm].

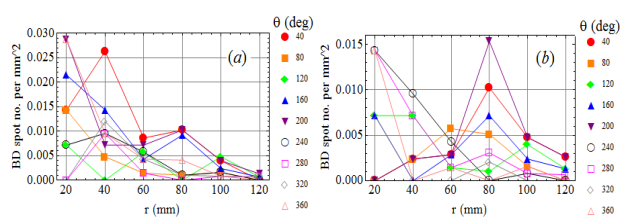


Figure 8: Plot of BD spot number per mm^2 at different radius for given θ (e.g. Red Circle for 40°, Orange Square for 80° and so on) (*a*) for top plate and (*b*) for bottom plate.

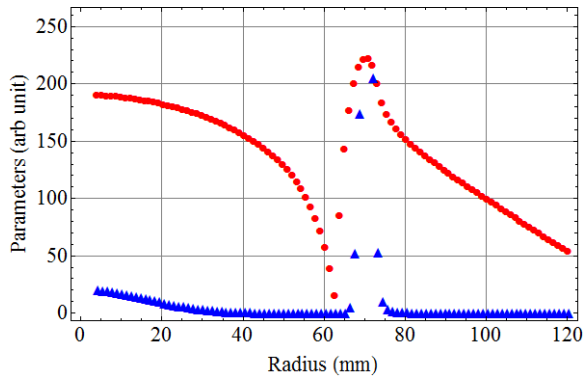


Figure 9: Electric field and dark current density distribution at different radii.

CONCLUSIONS

The BD spot distributions in both cavities are generally consistent with the electric field profiles but there are some differences. In the LBNL-Pillbox cavity, BD spots were distributed more densely over the iris region where the electric field and dark current are high. Note that the iris region includes accumulated damage from more runs than the window. In the flat window region the BD spot density data correlates with 6.28th power of the electric field. In the All Season cavity, fewer damage spots are observed because the surface inspection was carried out at an early stage of the run. In both plates most of the spots are within a radius of 100 mm. Note that in both cavities, data was taken both with and without magnetic field before the surface inspection. In future experiments, inspection will be done separately after runs with and without magnetic field to explore the role of magnetic field in the breakdown process.

REFERENCES

[1] J. Norem et al., Phys. Rev. ST Accel. Beams 6 (2003) 072001.
[2] A. Moretti et al., Phys. Rev. ST Accel. Beams 8 (2005) 072001.
[3] D. Li et al., "Design and fabrication of an 805 MHz Rf cavity with Be windows for a high RF power testing for Muon cooling experiment", Proceedings of PAC 2001, Chicago, USA, p. 918 (2001).
[4] W.S. Rasband, "ImageJ", U.S. National Institute of Health, Bethesda, Maryland, USA, http//rsb.info.nih.gov/ij (1997-2010).
[5] Wolfram Research, Inc. USA, www.wolfram.com
[6] G. Kazakevich et al., "Conditioning and future plans for a multi-purpose 805 MHz pillbox cavity for Muon acceleration", Proceedings of IPAC 2012, New Orleans, USA, THPPC032, p. 3353 (2012).
[7] Y. Torun et al., "Extended RF Testing of the 805 MHz Pillbox "All-Season" cavity for Muon Cooling", WEPMA17, NA-PAC'13.
[8] A. Moretti, Fermilab, USA (private communication).

Copyright © 2013 CC-BY-3.0 and by the respective authors

DESIGN AND HIGH POWER TESTING OF 52.809 MHZ RF CAVITIES FOR SLIP STACKING IN THE FERMILAB RECYCLER*

R. Madrak#, D. Wildman, FNAL, Batavia, IL 60510, USA

Abstract

For NOvA and future experiments requiring high intensity proton beams, Fermilab is in the process of upgrading the existing accelerator complex for increased proton production. One such improvement is to reduce the Main Injector cycle time, by performing slip stacking, previously done in the Main Injector, in the now repurposed Recycler Ring. Recycler slip stacking requires two new RF cavities operating at slightly different frequencies (df = 1260Hz). These are copper, coaxial, quarter wave cavities with R/Q =13 ohms. They operate at a peak gap voltage of 150 kV with 150 kW peak drive power (60% duty factor), and are resonant at 52.809 MHz with a 10 kHz tuning range. Two have been completed and installed. The design, high power test results, and status of the cavities are presented.

INTRODUCTION

To increase beam power, the Recycler Ring has been converted from an antiproton storage ring to a proton preinjector for proton injection/slip stacking. The increase in power, which is projected to be 80%, is due to a shorter Main Injector cycle time (decreased from 2s to 1.33s), since injection/stacking and acceleration can now be performed in parallel. [1]

Slip stacking is a process in which 6 batches of 8 GeV protons from the Fermilab Booster are 'stacked' on top of an additional 6 batches of beam. It has been performed and studied previously in the Main Injector [2], using an RF system which was designed primarily for the acceleration of beam. The process is as follows: Six Booster batches are injected into the Recycler Ring and captured by one RF system at 52.809 MHz, and then decelerated slightly by changing the frequency of the RF system by 1260 Hz. Then, six more batches are injected and captured by a second RF system operating at 52.809 MHz. Since the two sets of batches have slightly different energies, one set 'slips' azimuthally with respect to the other. When the two sets of batches are aligned, they are injected into the Main Injector, captured, and then accelerated to 120 GeV.

CAVITY DESIGN PARAMETERS

Slip stacking requires two cavities with f_0 = 52.809 MHz, a maximum V_{peak}= 150 kV and approximately 10 kHz of tuning range. The cavities must be tuneable by 1260 Hz for slip stacking itself, and must also have compensation for frequency drift due to heating and variation of cooling water temperature (~ 0.5 kHz/°F). The maximum duty factor will be 60% with a pulse length of 0.8 s.

In the interest of minimizing beam loading, the cavity dimensions were chosen to minimize R/Q while taking into account other practical constraints, such as being able to fit in the allowed area in the tunnel.

The cavity geometry is shown in Figure 1. This is a quarter wave coaxial resonator. The R/Q of 13 Ω is substantially smaller than that in the Main Injector cavities (103 Ω). This is due mainly to the large ratio of diameters of the outer and center conductors. Other key parameters are shown in Table 1.

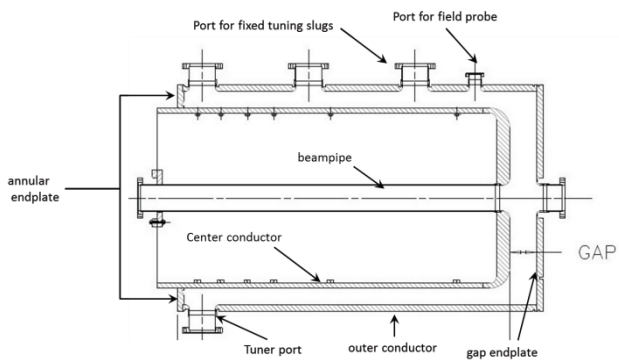


Figure 1: Cavity geometry and features.

Table 1: Cavity Design Parameters

f_0	52.809 MHz
Z_0	10.2 Ω
Vpeak (max)	150 kV
Maximum power	150 kW
Rshunt	75 kΩ
Q	5800
R/Q	13 Ω
Outer conductor ID	32 in
Inner conductor OD	27 in
nominal gap width*	2.9 in
Inner conductor length**	49.75 in
Step up ratio	6

*Based on pre-weld dimensions. Varied between cavities.
**Nominal length from cavity short to gap end

The initial design parameters and calculations were checked by constructing a model cavity from copper sheet metal [3]. Obviously this did not allow for vacuum or any high power tests, however, it was very useful for verifying and/or measuring key quantities at low power. These include factors such as resonant frequency

*Operated by Fermi Research Alliance, LLC under Contract No. DE-AC02-07CH11359 with the United States Department of Energy.
#madrak@fnal.gov

Copyright © 2013 CC-BY-3.0 and by the respective authors

dependence on various dimensions, higher order modes, and fast tuner development.

Input Coupler

The cavity input coupler is a loop type coupler which connects to a 9-3/16″ , 50 ohm transmission line through a copper and stainless steel bellows. The vacuum window is constructed from a conical 94% alumina ceramic brazed to copper rings. The rings are welded to additional copper sections to form the coupler outer and inner conductors. The coupler 2″ diameter inner conductor is welded to the cavity inner conductor 7.5″ from the shorted end, and the coupler outer conductor is welded to the cavity outer conductor. This results in a cavity accelerating gap to input coupler voltage step-up ratio of 6.

CAVITY CONSTRUCTION

The cavity center and outer conductors were forged at Scot Forge, Spring Grove, IL from OFHC copper ingots. Following the forging they were machined to final dimensions and ports were added. The circular and annular regions which form the ends of the cavity were also machined from solid blocks of OFHC copper.

The cavity center conductor, outer conductor, annual and circular end sections were electron beam welded at Sciaky Inc., Chicago, IL. Figure 2 shows the outer conductor being placed over the center conductor, after the annular end piece was welded to the center conductor. The cavity frequency was tuned after welding the center conductor to the annular ring by adjusting (by machining) the thickness of the endplate near the gap. This was necessary since the cavity frequency changed from pre- to post-weld, presumably because of changes in the effective dimensions due to the welding. The frequency dependence on gap width was measured to be 1.2±0.2 kHz/mil.



Figure 2: Positioning of outer conductor before electron beam welding.

In order to maintain a uniform temperature at high duty factor, there are 12 cooling lines each on the cavity center and outer conductors. Each set has a flow rate of 60 gal/min of 95 °F cooling water. The outer cooling lines and were brazed to the cavity. The lines on the ID of the center conductor were shrink-fit. At completion, each cavity weighs 4500 lbs. Some additional aspects of the cavity mechanical design are discussed in [4].

Cavity Ports

The cavity outer conductor has eight 3.87″ diameter (“larger”) and four 1.65″ diameter (“smaller”) ports. Furnace brazed copper to stainless steel transitions are used to connect either 6″ or 2-3/4″ Conflat® flanges (depending on the port size) to the copper cavity body. One exception is one of the larger ports used for a fast tuner, which uses a copper flange and not a Conflat.

Three of the larger ports located 35″ (on center) from the cavity shorted end were used for fixed tuning slugs. The slugs are OFHC copper cylinders with a diameter of 3.8″ and a 0.5″ radius on the cavity end. They are attached to water cooled Conflat blanks and protrude nominally 1″ into the cavity. Final machining of the length of the tuning slugs sets the cavity center frequency to 52.809 MHz.

The four smaller ports are all located near the cavity gap end: 44″ from the cavity short. Two of these contain disk shaped capacitively coupled field probes for measurement of cavity gap voltage. These were calibrated by simultaneously measuring the field probe power and the cavity gap voltage with an Agilent 85024A High Frequency Probe and network analyzer. The voltage ratio is nominally 10^5:1.

A third smaller port contains a 1″ diameter copper gap shorting slug which can be used in the case where there is a third inactive cavity installed in the ring. The slug is mounted on a linear vacuum feedthrough, which can be remotely moved into the cavity to contact the center conductor.

In one of the larger ports located 3″ from the cavity shorted end and opposite the input coupling loop, a fast tuner is loop-coupled to the cavity through a 2.5″ diameter coaxial ceramic window. The loop area is adjusted to give a nominal coupling impedance of 50 Ω. The tuner is a half-wavelength 50 ohm transmission line which is partially loaded with Al doped YIG and shorted at one end. The garnet section is immersed in a variable solenoidal magnetic field which provides for fast cavity tuning. The fast tuner, which has a range of 10 kHz, is described in more detail in a separate contribution to these proceedings [5].

RF POWER

The Fermilab Tevatron has been decommissioned and we were thus able to reuse the Tevatron RF Stations; this includes the power amplifiers, modulators, 9-3/16” transmission line, and impedance matching anode resonators. The Tevatron RF systems used essentially the

Copyright © 2013 CC-BY-3.0 and by the respective authors

same power amplifiers as does the Main Injector, and these are described in [6].

Power is provided by a cathode driven Eimac Y567B (4CW150000E) 150kW power tetrode. The tetrode is coupled with a monolithic ceramic blocking capacitor to a cylindrical aluminium quarter wave resonator which is used to match the power amplifier output impedance into a 9-3/16″, 50 ohm transmission line. This tap point is at one half the peak voltage. The transmission line includes a variable length phase shifter and a 3:1 coaxial transformer with 3λ/2 between the transformer voltage maximum and the cavity input. Taking into account the cavity input coupler step-up ratio of 6, the 3:1 transformer, and the half voltage tap point on the anode resonator, the total cavity step up ratio from the plate of the tetrode to the cavity gap is 9.

HIGHER ORDER MODES

Both the measured and calculated lowest frequency higher order modes of the cavity are shown in Table 2. Modes are classified as TEM or TE. The TEM modes are of more concern as they can be easily excited by the beam. All TM modes have frequencies of above ~2 GHz. The 3rd harmonic TEM mode is damped by a ½″ Heliax® quarter wave coaxial line with a capacitive pickup on the 9-3/16" transmission line (near a voltage maximum). For damping, a 5 W, 50 Ω load is connected to the heliax line near the 50 Ω tap point.

For the modes listed in Table 2, the frequencies of the TE modes are calculated analytically for a coaxial waveguide, assuming a line length of 50″, and using $\lambda=\lambda_g/(1+(\lambda_g/\lambda_c)^2)^{1/2}$, where λ_g and λ_c are the guide and cutoff wavelengths of the coaxial line [7]. The TEM modes were calculated using the LANL Superfish program [8].

Table 2: Higher Order Modes

Calculated f (MHz)	Measured f (MHz)	Type	order	Calculated f (MHz)	Measured f (MHz)	Type	order
52.809	52.809	TEM	λ/4	385.8	388	TE_{31}	$\lambda_g/4$
140.36	151.72	TE_{11}	$\lambda_g/4$	389.79	392.44	TE_{21}	$5\lambda_g/4$
	154.695				393.085		
154.748	157.780	TEM	3λ/4	421	428.15	TE_{31}	$3\lambda_g/4$
218.081	222.19	TE_{11}	$3\lambda_g/4$		428.870		
	226.13			429.882	437.130	TEM	9λ/4
245.228	247.17	TEM	5λ/4	432.281	432.42	TE_{11}	$7\lambda_g/4$
261.45	267.795	TE_{21}	$\lambda_g/4$	482.74	470.9	TE_{31}	$5\lambda_g/4$
	271.630				473.165		
310.186	308.890	TE_{21}	$3\lambda_g/4$	485.32	475.13	TE_{21}	$7\lambda_g/4$
	312				486.66		
318.485	318.63	TE_{11}	$5\lambda_g/4$	512.8	516.635	TE_{41}	$\lambda_g/4$
	323.81				518.15		
331.111	337.80	TEM	7λ/4				

CAVITY TESTING, INSTALLATION, AND COMMISSIONING

Prior to their installation in the tunnel, two cavities were tested to full power in a cavity test cave. The cavities were first subjected to low power (up to 500 W) CW RF for one week, to condition away multipacting between the outer and inner conductors. In this case the cavity was driven through the fast tuner port (with the tuner disconnected). A photo of the cavities installed in the Main Injector tunnel is shown in Figure 3.



Figure 3: Two complete cavities installed in the Recycler.

ACKNOWLEDGMENTS

We would like to acknowledge the huge efforts of the Accelerator Division Mechanical Support and RF Groups, and everyone involved in this project. We would also like to thank Marty Murphy for the photograph in Figure 3.

REFERENCES

[1] J. Cooper et al., "Technical Design Report for CD-2/3a," NOVA Document 2678-v8, October 2007, Ch8-3.

[2] K. Seiya et al., "Progress in Multi-Batch Slip Stacking in the Fermilab Main Injector and Future Plans," PAC'09, Vancouver, May 2009, TU6PFP061, p. 1424 (2009).

[3] H. Elnaiem, "Prototype NOvA RF Cavity for the Fermilab Recycler Ring," Aug 2009 (unpublished); https://indico.fnal.gov/getFile.py/access?contribId=10&resId=1&materialId=paper&confId=2665

[4] C. Ader and D. Wildman, "Design Methodology and Considerations for NOvA 53 MHz RF Cavities," IPAC'10, Kyoto, May 2010, THPEC044, p. 4158 (2010).

[5] R. Madrak and D. Wildman, "Perpendicularly Biased YIG Tuners for the Fermilab Recycler 52.809 MHz RF Cavities," WEPMA014, NA-PAC'13.

[6] J. Reid and H. Miller, "A 200 kW Power Amplifier and Solid State Driver for the Fermilab Main Injector," PAC'95, Dallas, May 1995, TAQ11, p. 1544 (1996).

[7] N. Marcuvitz, *Waveguide Handbook*, (London: The Institute of Engineering and Technology, (2009), p 72-80.

[8] http://laacg.lanl.gov/laacg/services/download_sf.phtml

Copyright © 2013 CC-BY-3.0 and by the respective authors

PERPENDICULARLY BIASED YIG TUNERS FOR THE FERMILAB RECYCLER 52.809 MHZ RF CAVITIES*

R. Madrak#, V. Kashikhin, A. Makarov, D. Wildman, FNAL, Batavia, IL 60510, USA

Abstract

For NOvA and future experiments requiring high intensity proton beams, Fermilab is in the process of upgrading the existing accelerator complex for increased proton production. One such improvement is to reduce the Main Injector cycle time, by performing slip stacking, previously done in the Main Injector, in the now repurposed Recycler Ring. Recycler slip stacking requires new tuneable RF cavities, discussed separately in these proceedings. These are quarter wave cavities resonant at 52.809 MHz with a 10 kHz tuning range. The 10 kHz range is achieved by use of a tuner which has an electrical length of approximately one half wavelength at 52.809 MHz. The tuner is constructed from 3⅛″ diameter rigid coaxial line, with 5 inches of its length containing perpendicularly biased, Al doped Yttrium Iron Garnet (YIG). The tuner design, measurements, and high power test results are presented.

INTRODUCTION

Two new quarter wave copper cavities have been constructed and installed in the Fermilab Recycler Ring for the purpose of slip stacking protons to increase beam power. These have been described in detail in [1]. They are to operate at 52.809 MHz with a tuning range of 10 kHz. Tuning by 1260 Hz is required for slip stacking itself, and additional tuning is needed to compensate for temperature changes. The cavity maximum peak gap voltage is 150 kV with a shunt impedance of 75 kΩ and Q ~ 6000. The cavities will be pulsed for a maximum of 0.8 s every 1.33 s (the Main Injector cycle time).

The cavities are tuned using perpendicularly biased garnet in a coaxial line. This has been done previously and is described in [2] and [3]. The original concept, though not for cavity tuning in particular, is described in [4].

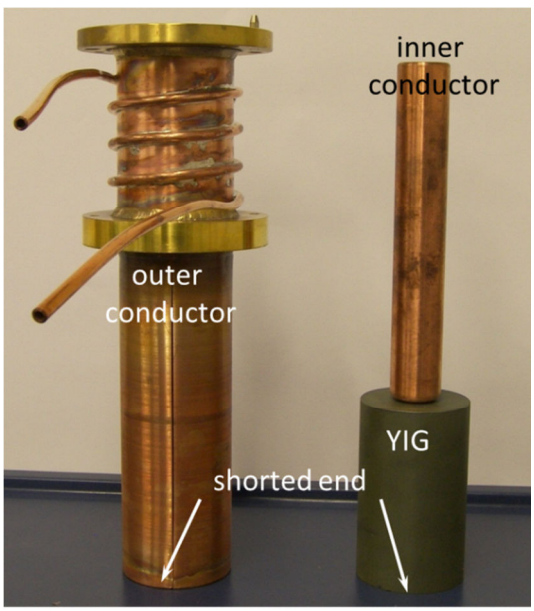


Figure 1: Tuner adjustable section with the inner conductor removed from the outer conductor.

DESIGN

In one of the ports located 3″ (on center) from the cavity shorted end, a fast tuner is loop-coupled to the cavity. The coupling is through a 2.5″ diameter coaxial ceramic window. The tuner loop area of 2.5 in^2 was adjusted to give a nominal coupling impedance of 50 Ω. The tuner is slightly less than a half-wavelength long and is made up of standard EIA 3⅛″ diameter, 50 Ω rigid copper transmission line, in addition to an "adjustable section" which is partially loaded with a 5″ long piece of Al doped Yttrium Iron Garnet (YIG). This section is immersed in a variable solenoidal magnetic field which provides a perpendicular bias for cavity tuning. A photo of the adjustable section, with the center conductor assembly removed from the outer conductor, is shown in Figure 1. The tuner line is shorted at the end opposite the cavity.

The garnet (TCI Ceramics type AL-400) has a saturation magnetization ($4\pi M_s$) of 400 gauss. Its OD and ID are 3.0″ and 0.65″ respectively. The center conductor used in the 15.75″ long adjustable section, which does not have the dimensions of standard 3⅛″ coax line, is shrink fit into the garnet. Over the 9″ length closest to the short, the outer conductor thickness has been reduced from the standard 3⅛″ coax line wall thickness to 0.020″. Both this 9″ section and the bottom copper shorting plate have a 0.0197″ wide slot machined through the copper to reduce eddy current effects.

For heat removal, the outer conductor is water cooled and the adjustable section is filled with a dielectric fluid (Diala AX).

The adjustable section had previously been designed for use as a fast phase shifter in vector modulators operating at 325 MHz [5].

The entire tuner, attached to the cavity and installed in the Recycler, is shown in Figure 2.

*Operated by Fermi Research Alliance, LLC under Contract No. DE-AC02-07CH11359 with the United States Department of Energy.
#madrak@fnal.gov

Copyright © 2013 CC-BY-3.0 and by the respective authors

Solenoid

The 112 turn solenoid (with TCI Ceramics G4 ferrite flux return) was designed to work at relatively high DC current (80A), but also at high frequency (~2 kHz) AC current. While the AC response is not absolutely required, the ability to tune at ~2 kHz will be an advantage. Obtaining the desired DC and AC response necessitated the use of Litz Cable of sufficient cross section (1/0 AWG) with 270 copper strands of 24 AWG wire insulated from each other. The total strand cross section reduces the losses in the DC regime, and the insulation between strands minimizes the eddy currents in the cable (for the AC regime). A cooling tube was wound on the outer surface of the solenoid as a bifilar coil in order to eliminate the effect of magnetic fields caused by eddy currents induced in it. A DC magnetic field simulation predicted the resulting minimum and maximum magnetic fields in the tuner garnet of 0.058 T and 0.081 T, for 8000 solenoid ampere-turns.

The solenoid current is supplied by a Copley Controls Model 266 amplifier which has a nominal bandwidth of

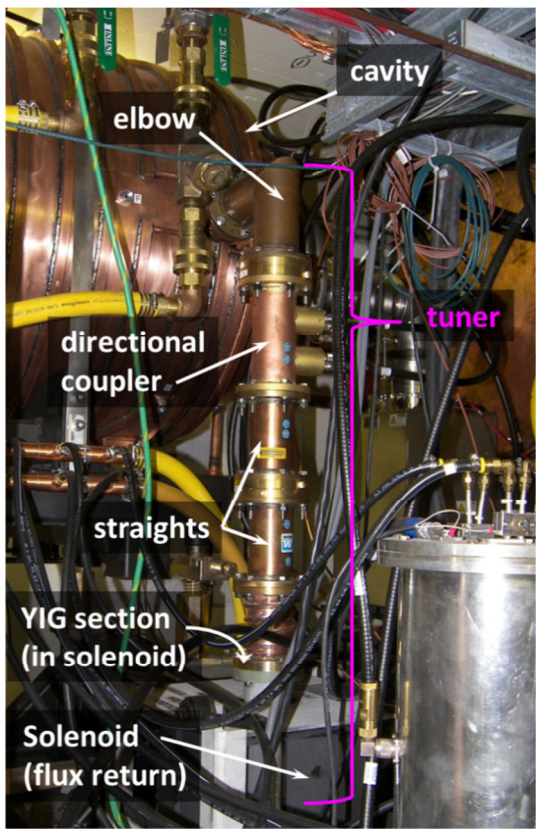


Figure 2: Tuner attached to the cavity, installed in the Recycler. The tuner is made up several 3⅛″ coax sections: an elbow, directional coupler, several straight sections, and finally the YIG loaded adjustable section (here obscured by the solenoid) which is shown in Figure 1.

5 kHz. The tuner response is currently limited by the solenoid inductance of 1.9 mH and the 60V max/80 A max DC supply for the Copley amplifier.

TUNER PERFORMANCE AND MEASUREMENTS

The tuner is characterized apart from the cavity by the measurements plotted in Figure 3. This shows network analyzer S_{11} amplitude and phase measurements as a function of DC solenoid bias. Large phase shifts

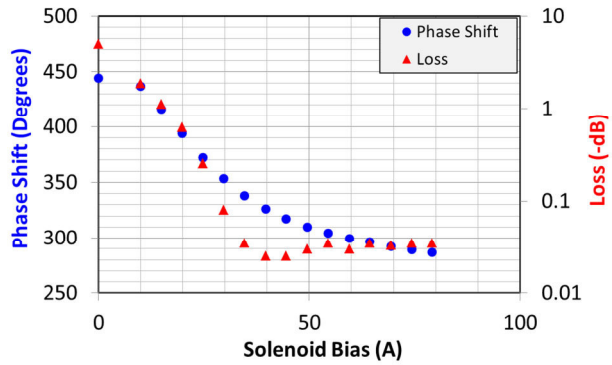


Figure 3: Two-way phase shift in tuner 15.75″ adjustable section at 52.809 MHz (left y-axis) and Loss (right y-axis) as a function of solenoid bias.

correspond to a large frequency change (tuning) in the cavity/tuner system. Operation must be above ~35A, below which the garnet becomes lossy.

The next set of measurements quantifies the operation of the cavity/tuner system as a whole. Figure 4 (wide range) and Figure 5 (operation range) show the frequency (left y-axis) and the Q of the cavity/tuner system (right y-axis) as a function of solenoid bias current. The bias at which we observe a large change in frequency and a minimum in Q corresponds to the case where the tuner is one half wavelength long.

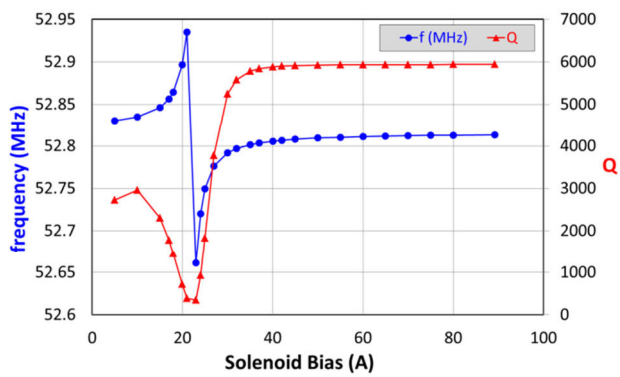


Figure 4: Frequency and Q of the cavity/tuner system as a function of solenoid bias current, for a wide range of tuner biases.

An additional restriction on tuner range is due to the peak voltage that can be sustained in the tuner without sparking. Figure 6 shows low level

Copyright © 2013 CC-BY-3.0 and by the respective authors

measurements of frequency and the corresponding tuner voltage. In this case, the cavity was powered with a relatively small signal. Cavity peak accelerating gap voltage and tuner peak voltage were measured simultaneously. The values were then scaled to cavity gap

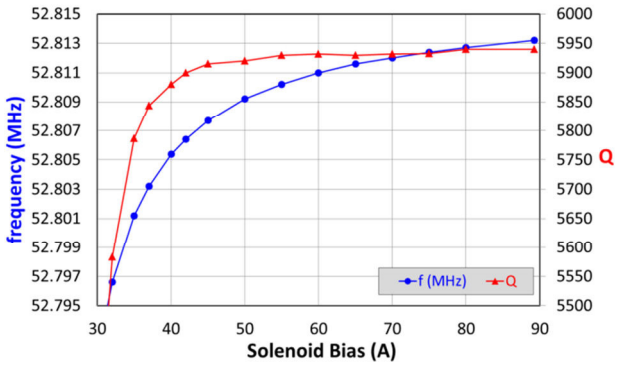


Figure 5: Frequency and Q of the cavity/tuner system as a function of solenoid bias current, for solenoid biases in the range that the tuner is operated (> 35 A).

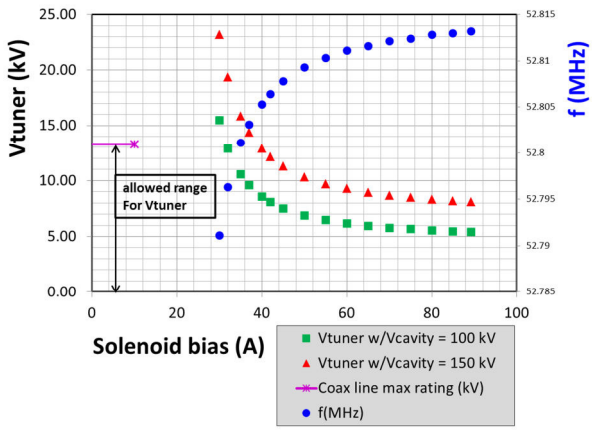


Figure 6: Tuner voltage and frequency of cavity/tuner system as a function of tuner bias. The maximum peak voltage for the tuner 3⅛″ line is also shown. (These measurements were taken from the cavity field probe and the directional coupler which is part of the tuner.)

voltages of 100 and 150 kV. Operating with a tuner voltage above the peak voltage limit for 3⅛″ coaxial line of 13.3 kV will cause arcing and must be avoided. Not only is arcing in the coax line undesirable, but this can also lead to high voltages near the garnet which could be destructive.

Measurements shown indicate I ≥ 32 A and I ≥ 40 A to respect the 13.3 kV limit, for cavity voltages of 100 kV and 150 kV. With no other adjustments, and taking into account the 35 A limit imposed due to losses in the garnet, the tuning ranges are 11.7 kHz and 7.5 kHz for cavity peak voltages of 100 kV and 150 kV.

TUNER SPARK PROTECTION

To avoid destruction of the garnet, several methods of protection are in place to shut off RF power to the cavity in the event of a tuner spark.

The tuner line contains a 60 dB directional coupler with both forward and reverse power taps. The first tuner protection system shuts off the RF drive if a change of more than 3dB/μs is detected in the reverse power.

In the second protection system, a phase detector monitors the phase difference between forward and reverse power. If the phase changes more quickly than that due to normal tuning, the RF drive is again shut off. This is accomplished using a capacitive differentiator and a comparator.

STATUS AND HIGH POWER TESTING

Before being installed in the Recycler, both cavities were high power tested in a shielded "cavity test cave". The cavity and tuner systems have been operated successfully at high power in the Recycler.

ACKNOWLEDGMENTS

We would like to acknowledge the huge efforts of the Accelerator Division Mechanical Support and RF Groups, and everyone involved in this project. In addition, we would like to thank all of those in Technical Division involved in the design and construction of the solenoids.

REFERENCES

[1] R. Madrak and D. Wildman, "Design and High Power Testing of 52.809 MHz RF Cavities for Slip Stacking in the Fermilab Recycler", WEPMA013, NA PAC 13.

[2] S. M. Hanna et.al, "YIG Tuners for RF Cavities", IEEE Transactions on Magnetics, Vol 28, No. 5, p. 3210, Sept 1992.

[3] R. L. Porier, "Perpendicular Biased Ferrite –Tuned Cavities", PAC'93, Washington, D. C., May 1993, p. 753, (1993).

[4] A. S. Boxer , S. Hershenov and E. F. Landry "A High-Power Coaxial Ferrite Phase Shifter", *IRE Trans. Microwave Theory and Techniques (Correspondence)*, vol. MTT-9, pp.577, 1961.

[5] R. Madrak and D. Wildman, "High Power 325 MHz Vector Modulators for the Fermilab High Intensity Neutrino Source (HINS)", LINAC'08, Victoria, B.C., Oct 2008, THP088.

Copyright © 2013 CC-BY-3.0 and by the respective authors

ASSEMBLY AND TESTING OF THE FIRST 201-MHz MICE CAVITY AT FERMILAB*

Y. Torun †, P. Hanlet, Illinois Institute of Technology, Chicago, IL 60616, USA
M. Leonova, A. Moretti, R. J. Pasquinelli, D. W. Peterson,
R. P. Schultz, J. T. Volk, Fermilab, Batavia, IL 60510, USA
L. Somaschini, INFN, Pisa, Italy
J. Gaynier, Kettering University, Flint, MI, 48504, USA
D. Bowring, A. J. DeMello, D. Li, S. P. Virostek, LBNL, Berkeley, CA 94720, USA
T. Luo, University of Mississippi, University, MS 38677, USA

Abstract

The International Muon Ionization Cooling Experiment (MICE) [1] includes two linear accelerator sections with four RF cavities each within a shared vacuum vessel. Ten cavity bodies have been fabricated for MICE including two spares and one was electropolished at LBNL. A special vacuum vessel was built to house this cavity and form the 201-MHz Single-Cavity Module (SCM). The module and its instrumentation are being assembled and tested at Fermilab for installation and operation in the MuCool Test Area.

MICE RF SYSTEM

MICE is a demonstration of ionization cooling using a full cooling cell surrounded by tracking and particle identification detectors to measure each muon before and after it traverses the cooling cell [2]. It is under construction at Rutherford Appleton Laboratory (RAL). Figure 1 shows the RFCC (RF cavity and coupling coil) module [3, 4] which includes a large-diameter coil around a linac section. Each pair of cavities will be driven by a 2-MW amplifier system for a gradient of 8 MV/m per cavity. Parts of the power distribution network and LLRF system are being procured, developed, built and tested by teams from LBNL, University of Mississippi, Illinois Institute of Technology and Fermilab in the US and Strathclyde University, Daresbury Laboratory, Imperial College and RAL in the UK.

SINGLE CAVITY MODULE

In order to develop the assembly procedure for the RFCC modules and test cavity operation early on at the Fermilab MuCool Test Area (MTA), a special vacuum vessel was designed at LBNL to house a single MICE cavity. The single-cavity vacuum vessel has mostly the same mechanical interfaces as the RFCC module. Figure 2 shows the single-cavity module assembly. Ten RF cavity bodies have been manufactured in industry using techniques developed at LBNL. Cavity half shells were spun from 6mm-thick Cu sheet e-beam welded at the equator. Four ports were pulled around the equator on each cavity for couplers, vacuum pumping and instrumentation. Copper cooling tubes were brazed onto the cavity bodies. Each cavity has a pair of 0.35mm-thick curved beryllium windows for a pillbox-like geometry. Power is brought in through a pair of coaxial loop couplers. The first set of couplers is under fabrication at LBNL. The tuning system comprises stainless steel flexure arms driven by pneumatic actuators [5]. Figure 3 shows the basic design. The actuator body includes two concentric shafts screwed onto threaded holes in the tuner arm. As the shafts are pulled together or pushed apart by pneumatic action, the forces are transmitted to the cavity stiffener rings to elastically deform the cavity body. The actuator cover is attached to a vacuum vessel port with vacuum bellows while the body is thermally isolated from the

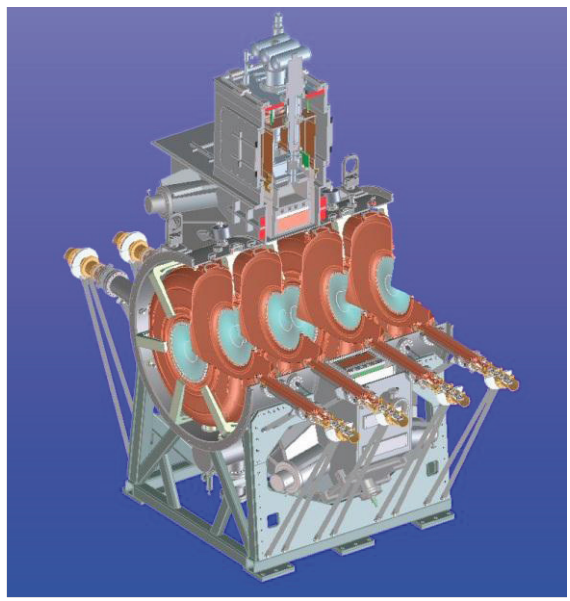


Figure 1: Partial cross section of a MICE RFCC module showing RF cavities, couplers and Be windows.

* This work was supported by the Office of Science, U.S. Department of Energy, through the Muon Accelerator Program.
† torun@iit.edu

Copyright © 2013 CC-BY-3.0 and by the respective authors

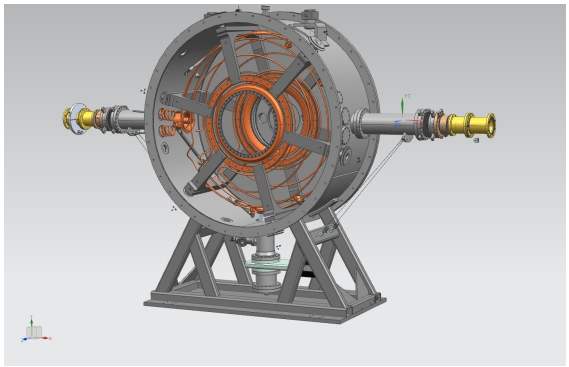


Figure 2: Single Cavity Module assembly view showing parts of the vacuum vessel body, couplers, tuning forks, actuators and cooling tubes. Stiffener and window clamp rings and cavity mounting struts are also visible while the cavity body and Be windows are suppressed for clarity.

vessel. One of the cavities was electropolished at LBNL [6] and sent to Fermilab for installation and testing in this vessel. A prototype tuner arm was mounted on an aluminum test hoop with one sixth the spring constant of the cavity body for initial tests at LBNL. The first set of six production tuner forks and actuators were built at Fermilab and LBNL respectively. The test setup was used at Fermilab to qualify the actuators.

ASSEMBLY STATUS AND PLANS

Clean Room

A class 100 (ISO 5) assembly environment is needed to minimize contamination of the vacuum vessel and cavity interior. The clean room chosen in Lab 6 at Fermilab had been unused for many years but after interior cleaning and curtain repair, it was down to class 10 (ISO 4). Air quality is monitored using a particle counter, all cavity ports are capped during mechanical work and full clean room garb is used by personnel during assembly. Cavity and vessel exterior surfaces were cleaned before and after being moved into the clean room. Flat aluminum cover plates were installed on the cavity in place of the Be windows to keep the interior clean during initial assembly work without risking damage to the thin windows. Covers for the vacuum vessel have to be removed to reduce the size during transport. Transparent plastic plates were used to keep the vessel interior clean during storage and transport.



Figure 3: Tuner model (left), actuator prototype (center) and test setup (right).

Mechanical Setup

The initial hardware configuration is shown in Fig. 4. Due to limited height in the clean room during assembly and in the hallway leading to the MTA experimental hall during transport, a shorter stand was built and the vacuum vessel moved onto this temporary stand. A portable gantry crane was cleaned and placed in the clean room to lift the cavity which weighed in at 227 kg and should be about 400 kg with the tuners installed. Initial measurement of cavity parameters was performed with the cavity mounted on a vertical measurement stand. A rotation fixture was built to hold the cavity locked in a horizontal orientation for tuning fork installation as well as rotate it to a vertical orientation for handling by the crane. The cavity will be mounted in the vacuum vessel using struts forming a six-axis (Stewart) platform. An attachment was designed for use with a portable lift to insert the cavity into the vacuum vessel and hold it while the struts are connected.

Tuner System

In order for the tuning system to work correctly, all the forks should be in a plane parallel to the cavity plane of symmetry and the actuator shafts aligned with vessel ports. Extra material was included on the contact pads in the drawings for the flexure tuning forks. The ports on the vacuum vessel, the stiffener rings on the cavity body (which the forks are attached to) and the forks were surveyed with a laser tracker. Tuner fork contact pads were machined to match the largest gap between stiffener ring surfaces on the cavity and shims were prepared to take up the gaps as needed. The forks have been installed as shown in Fig. 5. A simple alignment tool was designed consisting of a rod with an outside thread on one end so it could be screwed into the tuner fork and a flat surface with a hole at the other end to accept a laser tracker target. These were mounted on



Figure 4: Clean room interior with the cavity (back) mounted on the vertical measurement stand under the portable crane, the vacuum vessel (left) with transparent cover plates on the temporary stand and part of the rotation fixture (front).

Copyright © 2013 CC-BY-3.0 and by the respective authors

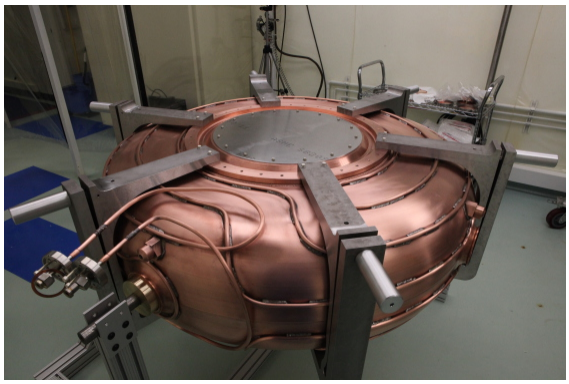


Figure 5: Cavity on rotation fixture with the tuner forks and alignment tools installed. Note the temporary aluminum cover instead of the Be window.

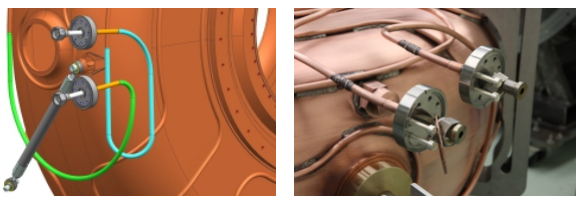


Figure 6: Cooling tube feed-throughs: model (left), installed on cavity (right).

the forks to be used for alignment of the forks on the cavity and alignment of the cavity within the vacuum vessel.

Water Connection

No water fittings are allowed inside vacuum volumes in MICE. The copper cooling water tube on the cavity body goes through a pair of stainless steel two-piece feed-through assemblies on the vacuum vessel (Fig. 6). A section of stainless steel tubing was vacuum brazed to a section of copper tubing. The stainless steel tube was then welded to the feed-through flange and a stainless steel fitting for the water connection on the air side. The copper tubing end was silfos brazed to the copper tube from the cavity body to complete the connection on the vacuum side. The feed-through assemblies were water pressure tested and vacuum leak checked before and after installation.

Diagnostics

The following instrumentation is in preparation for monitoring various aspects of cavity operation:

- On the cavity, couplers and vacuum vessel
  - Two pickup loops inside cavity to monitor the RF field
  - Vacuum gauges for the cavity, vessel and couplers
  - Thermocouples on cavity body
  - Infrared sensors pointed at the thin Be windows for temperature measurement
  - Fiber light guides viewing the cavity interior to detect sparking
  - Piezoelectric sensors on cavity body to detect and localize breakdown through acoustic signals
  - Electron pickups near the coupler ceramic vacuum windows to monitor coupler conditioning
  - Viewports near the vacuum windows to detect light in couplers due to breakdown
- In the experimental hall
  - Water pressure and flow. Note that there are five cooling tubes in the system: one for the cavity body and one for each of the coupler loops and RF windows
  - Gas pressure for tuner actuators
  - Radiation detectors
    - ionization chambers for overall dose rate
    - scintillator+PMT counters for X-ray rates
    - NaI crystal+PMT counter for X-ray spectra
  - Forward and reflected power waveforms from directional couplers near the cavity

Remaining Steps

The cavity will be installed in the vacuum vessel and the transfer function for the tuning system measured shortly. The vessel will be moved to the MTA hall after tuners and instrumentation are fully tested and assembly will be finished in the MTA clean room. The vessel will be initially placed in the fringe field of the MTA solenoid and moved next to the coupling coil prototype for testing in the full magnetic field configuration when that magnet is available. RF power station controls have been upgraded and commissioned with a test load and frequency tuning will be incorporated into the conditioning control software [7].

REFERENCES

[1] `http://mice.iit.edu`

[2] Y. Torun and M. Zisman, "Status of the Muon Ionization Cooling Experiment (MICE)", THPHO18, NA-PAC'13.

[3] D. Li *et al.*, "Progress of MICE RFCC Module," IPAC2012, New Orleans, THPPP093, p. 3954.

[4] K. Ronald *et al.*, "The RF System for the MICE Experiment," IPAC2013, Shanghai, WEPFI066, p. 2848.

[5] L. Somaschini *et al.*, "Tuner System Assembly and Tests for the 201-MHz MICE Cavity," WEPMA03, NA-PAC'13.

[6] T. Luo *et al.*, "Progress on the MICE 201 MHz RF Cavity at LBNL," IPAC2012, New Orleans, THPPC049, p. 3398.

[7] D. W. Peterson and Y. Torun, "Fermilab MuCool Test Area Cavity Conditioning Control Using LabVIEW," THPMA08, NA-PAC'13.

Copyright © 2013 CC-BY-3.0 and by the respective authors

PROGRESS ON THE FABRICATION OF A CW RADIO-FREQUENCY QUADRUPOLE (RFQ) FOR THE PROJECT X INJECTOR EXPERIMENT (PXIE)*

M. D. Hoff, A. J. DeMello, A. R. Lambert, D. Li, J. W. Staples, and S. P. Virostek
Lawrence Berkeley National Laboratory, Berkeley CA 94720, USA

Abstract

The Project X Injector Experiment (PXIE), a prototype front end of the Project X accelerator [1] proposed by Fermilab, is currently under construction. The complete PXIE beamline [2] is made up of an H^- ion source, a low-energy beam transport (LEBT), a 2.1 MeV, 162.5 MHz radio-frequency quadrupole (RFQ) accelerator, a medium-energy beam transport (MEBT) and a 30 MeV section of superconducting cryomodules. The 4.45 m long CW RFQ consists of four separate modules that are joined by means of specially designed bolted joints. Each module consists of four solid copper vanes that are brazed together to form a 4-quadrant accelerating cavity. The ~100 kW of total wall power heat is removed by means of gun drilled water cooling passages. Mode stabilization is provided by a series of brazed, water cooled pi-mode rods. Tuning is achieved using a total of 80 fixed slug tuners. Fabrication of the PXIE RFQ is now under way at LBNL. Details of the RFQ mechanical design and an update of the fabrication progress are presented in this paper.

MODULES

The 4.45 m long RFQ is assembled from four approximately equal length modules. The modules are sized based on the available copper C101 billet size, available milling machine capacity, general handling considerations and the desire to minimize joints. Each module is fabricated from four tee shaped pieces of copper that weigh approximately 940 kg each before machining (see Fig. 1).

MACHINING

The outer wall features are machined first. The outer wall is machined flat, followed by the pi-mode rod holes, slug tuner ports, sensing loop ports and the vacuum pump port are cut. Then the vane is flipped over and mounted to a 3 inch stainless steel plate for cavity machining. The stainless plate allows easy handling and mounting of the part in the milling machines. The precise cavity contours, pi-mode rod clearance holes and then the four mating braze surfaces are cut with a standard shaped end mill (see Fig. 2 and Fig. 3). The last step is the machining of the vane tip modulations, as described later in this paper.



Figure 1: Raw tee shaped copper for vane fabrication.

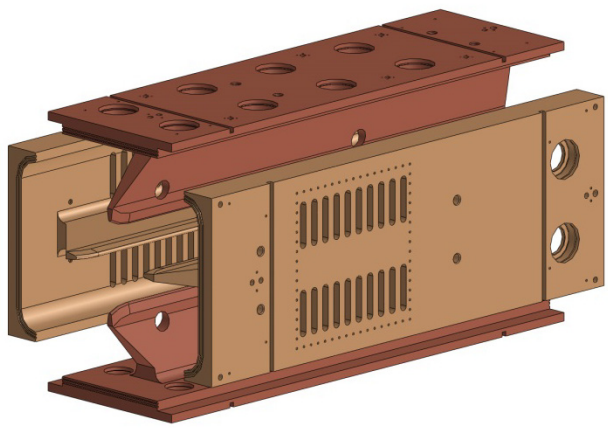


Figure 2: Exploded CAD model of four machined vane.

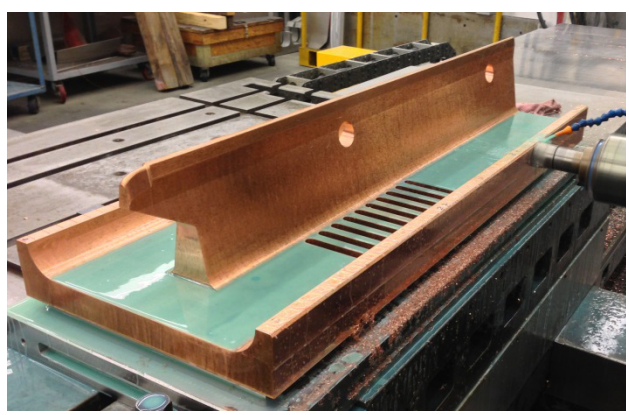


Figure 3: Module 1, horizontal vane being machined.

* This work is supported by the Office of Science, United States Department of Energy under DOE contract DE-AC02-05CH11231.

Copyright © 2013 CC-BY-3.0 and by the respective authors

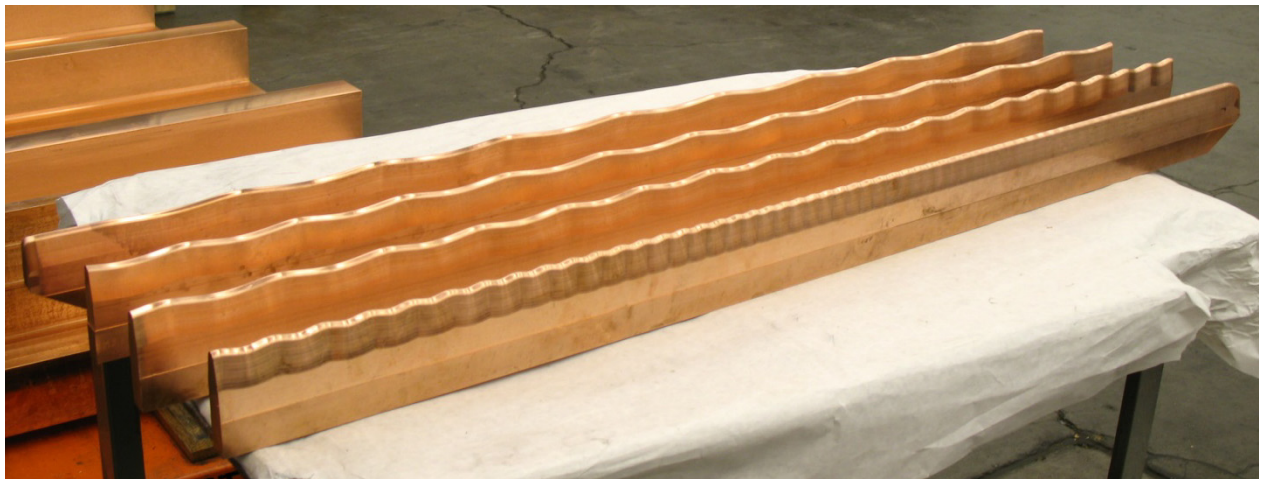


Figure 4: Modulation cut test piece.

PI-MODE RODS

RF mode stabilization between cavity quadrants is accomplished with 8 hollow copper rods per module, 32 total [3]. The rods are approximately 10 mm O.D. by 5 mm I.D. by 425 mm long (see Fig. 5). The rods are hollow to allow coolant to flow inside the rods during operation. The rods are brazed to the cavity walls at the same time the four vanes are brazed together. The rod passes through a clearance hole in the vane that divides the quadrants (see Fig. 6).



Figure 5: Pi-mode rod with two ferrules.

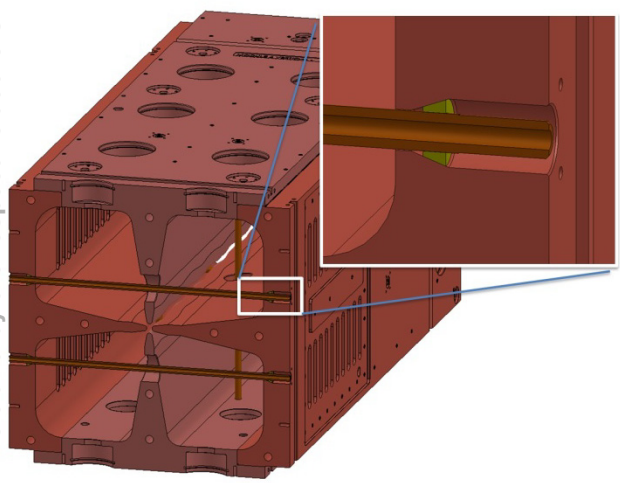


Figure 6: Pi-mode rod with ferrule detail.

VANE TIP MODULATIONS

Vane tip modulations are machined using a specially made carbide cutting tool. Using a profile cutting mill is much faster than a ball end mill (see Fig. 4 and Fig. 7).



Figure 7: Modulation profile cutting tool.

COOLING PASSAGES

Cooling of the RFQ body is accomplished by blind gun drilling ∅12 mm holes most of the long length of the vane. The long gun drilled hole is connected to the outside vane wall by cross-drilled holes at each end. The entry point for the gun drilled hole is then sealed with a tight fitting copper plug that is electron beam welded vacuum tight (see Fig. 8).

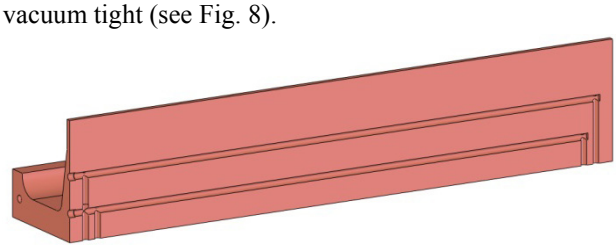


Figure 8: CAD model of gun drilled cooling passages.

BRAZING

When the majority of the machining is complete, the four vanes of a module are gently brought together using

Copyright © 2013 CC-BY-3.0 and by the respective authors

a kinematic, 6 strut fixture to check braze surface fits and measure RF cavity resonance. After the test fit, the vanes are separated, cleaned and CuSiL [4] braze alloy in the form of ∅1 mm wire is loaded into pre-machined grooves. The vanes are then brought back together and clamped into position. Pi-mode rods are then installed and clamped into position too. Brazing is done in a hydrogen furnace in the vertical position. The engineered clamps, using Inconel [5] Belleville washers, allow the copper to expand, yet maintain a firm clamping force during the heat up and cool down cycle (see Fig. 9).

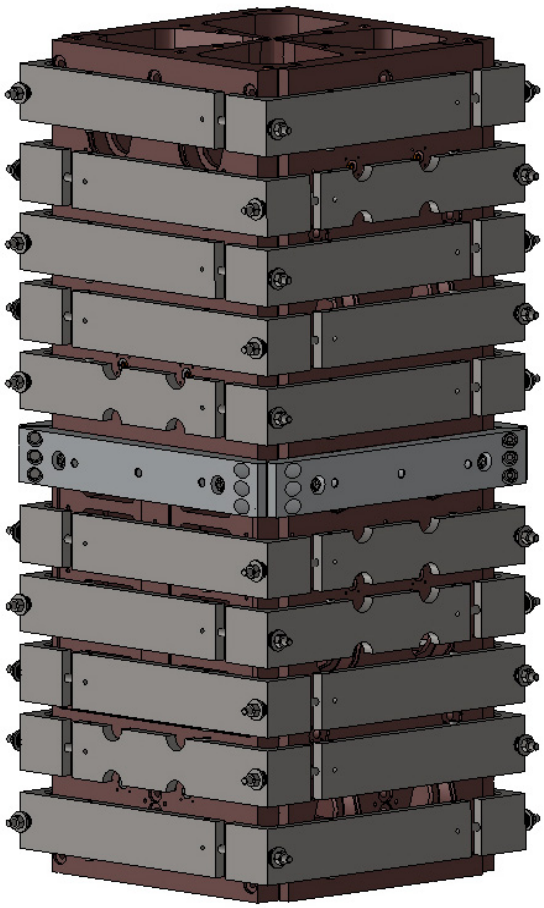


Figure 9: CAD model of vertical module braze with clamps.

POST BRAZE

After brazing the four vanes and 8 pi-mode rods together, the module is machined to its final length with O-ring and RF sealing geometry added to the ends.

Coarse tuning of the RFQ cavity is accomplished with 80 approximately equally spaced slug tuners. First temporary, length adjustable tuners are installed and RF resonance measurement are taken. The temporary tuners are adjusted in length until the desired RF resonance is achieved. The temporary tuners are removed, measured and replaced by non-adjustable, slug tuners. The slug tuners are sealed with an RF joint and O-ring. The slug tuners are held in place with a commercial snap ring.

JOINT PLATES

Modules are joined together using stainless steel plates that form a collar around the soft copper. The collar is tied to the module with a keyed groove and bolts. The collar contains pockets for bolts and nuts to clamp the modules together, squeezing the RF seal and O-rings in place (see Fig. 10).

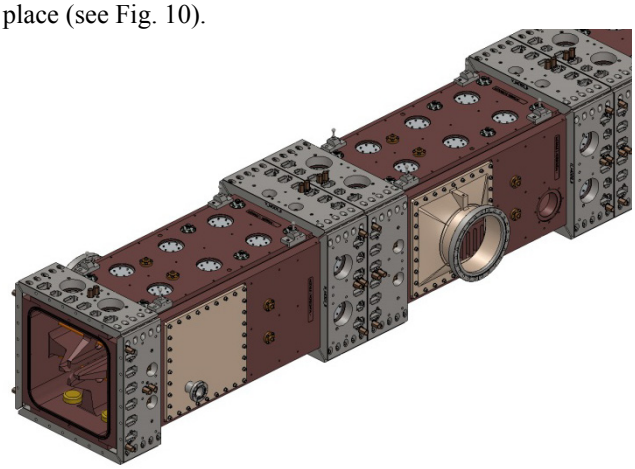


Figure 10: Joint Plates connecting modules.

SUMMARY

LBNL is currently constructing an RFQ for the Project X front end. The RFQ is being fabricated with solid copper vanes that are hydrogen furnace brazed together into four modules 4.45 m long total. Cooling will be accomplished with gun drill passages along the length of individual vanes. 32 Pi-mode rods linking adjacent cavities will provide RF stabilization. Brazed modules are mechanically connected using a special joint plate with bolts. Final tuning is accomplished with 80 static slug tuners. Fabrication is underway at LBNL with expected delivery of the RFQ to FNAL in 2014.

REFERENCES

[1] S. Nagaitsev, et al, "Project X – A New Multimegawatt Proton Source at Fermilab," PAC'11, New York, NY, USA, pp. 2566-2569.

[2] S. Nagaitsev, et al, "PXIE: Project X Injector Experiment," IPAC'12, New Orleans, May 2012, THPPP058, p. 3874 (2012).

[3] S. Virostek, et al., "Design and Analysis of the PXIE CW Radio-Frequency Quadrupole (RFQ)," IPAC'12, New Orleans, May 2012, THPPC034, p. 3359 (2012).

[4] CuSil is a brand name of Morgan Technical Ceramics-WESGO Metals, Hayward, California.

[5] Inconel is a brand name of Special Metals Corporation, New Hartford, New York.

Copyright © 2013 CC-BY-3.0 and by the respective authors

RF, THERMAL, AND STRUCTURAL FINITE ELEMENT ANALYSIS OF THE PROJECT X INJECTOR EXPERIMENT (PXIE)* CW RADIO-FREQUENCY QUADRUPOLE (RFQ)

A.R. Lambert#, M.D. Hoff, D. Li, J.W. Staples, and S.P. Virostek
Lawrence Berkeley National Laboratory, Berkeley, CA 94804

ABSTRACT

PXIE (Project X Injector Experiment) is a prototype front end system for the proposed Project X accelerator complex at Fermilab [1]. An integral component of the front end is a 162.5 MHz normal conducting CW (continuous wave) radio-frequency quadrupole (RFQ) accelerator that has been designed and is being fabricated by LBNL. The RFQ will accelerate H^- ions from 30 keV to 2.1 MeV [2]. The four-vane RFQ consists of four modules with a total length of 4.45 meters. Through application of finite element analysis (FEA), the electromagnetic fields and their resultant effect on the RFQ body temperature and the subsequent deformations due to thermal expansion have been simulated. The analysis methodology developed at LBNL allows for quick evaluation of RFQ temperature, stress, deformation and the resulting effect on frequency without requiring the construction of a prototype. The technique has been applied to the following: RFQ body, RFQ cutbacks, fixed slug tuners, and pi-mode rods. The analysis indicates that the total heat load on the RFQ will be approximately 80 kW, which is removed via water-cooled passages.

INTRODUCTION

The PXIE RFQ is a front end injector for the proposed Project X experiment at FNAL. As this RFQ will operate in continuous-wave (CW) mode, the engineering design and analysis is critical for managing the thermal performance. The aim of this paper is to introduce that analysis method used to determine the heat loads experienced by the RFQ, how these loads affect operating temperature, and how temperature increase affects frequency and the methods by which the cooling water can be used to mitigate the RF heating effects on frequency.

RFQ BODY SIMULATION

The body of the RFQ is simulated using a thin 3D slice of the RFQ cross section. Only one-quarter of the geometry is simulated due to symmetry. The first step of this step in the simulation is to create a vacuum geometry that corresponds to the solid RFQ body. Once created, ANSYS Multiphysics [4] performs RF analysis on the vacuum geometry. Once complete, the RF heat load is calculated and applied to the inner cavity walls of the RFQ body model. Convective water cooling is applied to the gun-drilled cooling channels, as shown in Fig. 1.

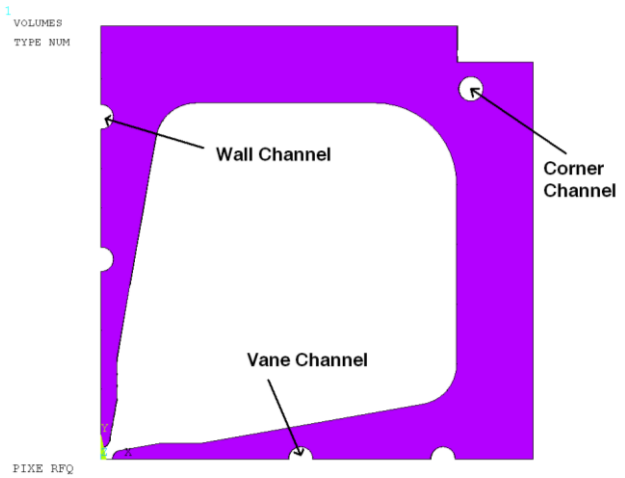


Figure 1: RFQ body cross section with gun-drilled cooling channels.

Assuming that the cooling water is at 30 °C, the resulting temperature profile at steady-state operation is shown in Fig. 2.

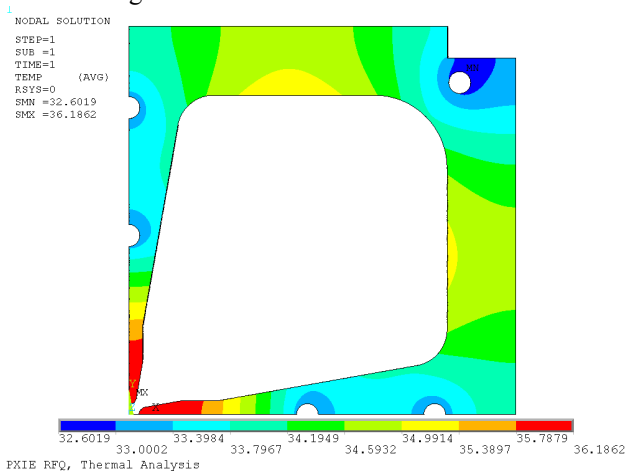


Figure 2: Temperature contours (°C) for steady-state RFQ operation.

The maximum temperature is 36.2 °C and is located at the vanetips. Minimum temperature is approximately 32.6 °C, and is found in the corner cooling passage. Overall, it is evident that with the current cooling scheme, the RFQ body temperature only rises 2.0 – 6.0 °C above nominal water temperature. This temperature rise causes expansion of the cavity walls away from the beam axis, and growth of the vanetips towards the beam axis. Both of these affect the resonant frequency of the cavity. The thermal results are piped into a structural analysis which determines the displacements due to thermal expansion, the results of which are shown in Fig. 3.

*Work supported by the Office of Science, U.S. Department of Energy under DOE contract number DE-AC02-05CH11231
#arlambert@lbl.gov

Copyright © 2013 CC-BY-3.0 and by the respective authors

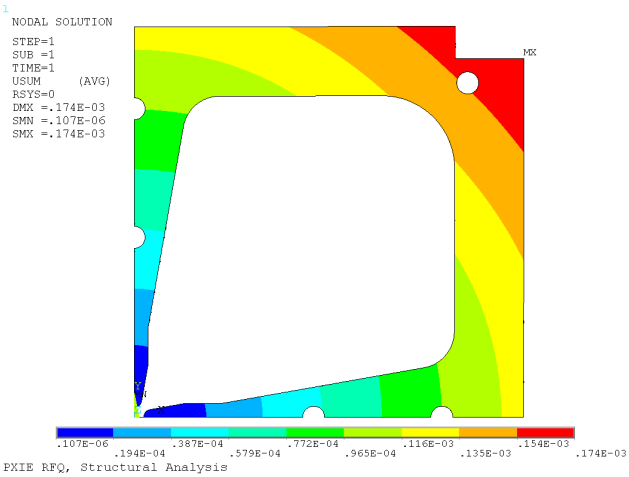


Figure 3: Thermal displacement (m) due to RF heating.

As surface nodes are shared between the vacuum and solid body meshes, the displacements are used to morph the vacuum mesh such that it reflects the deformed geometry. This new cavity geometry, which represents the steady-state operating condition, is used for a final RF analysis to determine the frequency shift due to RF heating and subsequent steady-state frequency. The uncorrected ideal, nominal and steady-state frequencies are shown in Table 1.

Table 1: RFQ Frequencies

Condition	Frequency (MHz)
Ideal	164.36
Nominal	164.28
Steady State	164.27

As Table 1 shows, the frequency drop from initial start up, i.e. nominal frequency, to the final steady state frequency is approximately 10 kHz. This drop is due to RF heating, with thermal equilibrium achieved roughly 10 minutes after RF power turn on. Varying the cooling water temperature in the vanes and walls provides some differential dynamic tuning capabilities that mitigate the frequency shift due to RF heating. The frequency sensitivity to cooling water temperature change is shown in Table 2.

Table 2: Frequency Shift Due to Cooling Water Temperature Change

PXIE Frequency Shift	Average Result
Overall (kHz/ °C)	-2.8
Vane (kHz/ °C)	-16.7
Wall (kHz/ °C)	13.9
Theoretical Shift (kHz/ °C)	-2.9

As the table shows, the theoretical shift closely matches the simulated overall shift, evidencing the accuracy of the FEA model.

RFQ BODY SIMULATION

The RFQ cutbacks are simulated in a similar fashion as the thin slice model. A sub-model of the cutbacks was created and RF analysis in ANSYS was carried out. The result is piped into a thermal simulation, the outcome of which is shown in Fig. 4.

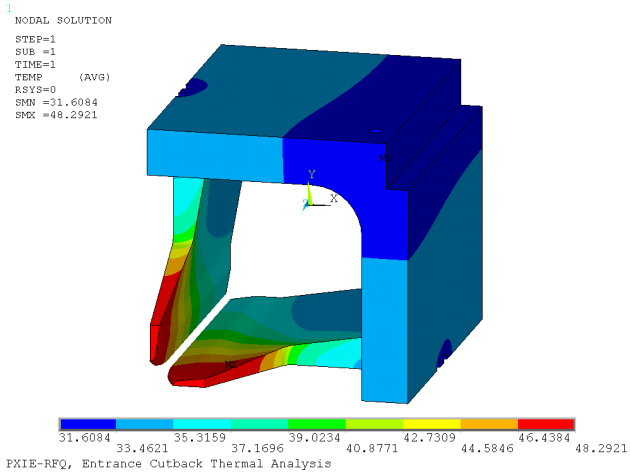


Figure 4: RFQ cutback temperatures (°C) at entrance.

As Fig. 4 shows, the maximum temperature occurs at the tips of the cutbacks, which is the location is the farthest from the cooling channels.

PI-MODE RODS

ANSYS Workbench is used to simulate the heating in the pi-mode rods, which are made from OFHC copper. The pi-rods are brazed into the RFQ structure and cooled via water that is pumped through their inner bore. Heat loads are approximated from ANSYS Multiphysics and CST Microwave Studio. The temperature results are shown in Fig. 5.

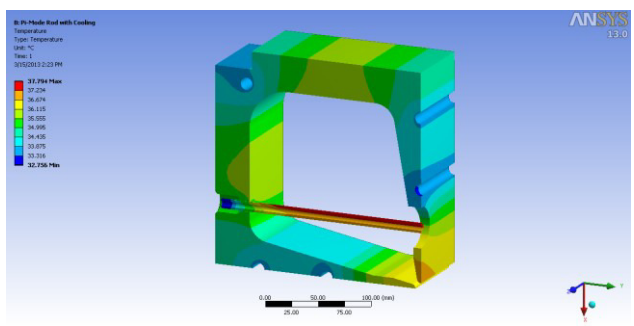


Figure 5: RFQ body and pi-mode rod temperatures (°C).

As Fig. 5 shows, assuming a nominal cooling water temperature of 30.0 °C, the resulting maximum rod temperature is 37.8 °C. As long as cooling water is flowing, the pi-rod temperature is effectively managed. However, in the event of a cooling water failure, failsafe systems will shut down RF power; this is to avoid

Copyright © 2013 CC-BY-3.0 and by the respective authors

excessive heating of the pi-rods, which could cause material yielding due to thermal expansion.

RFQ FIXED SLUG TUNERS

The slug tuners are made from OFHC copper and are installed in their respective ports using a snap ring. An RF spring mitigates any RF leakage at the mating surfaces, and an O-ring is used to seal the vacuum. The slug tuners do not have any active cooling, but instead rely on conductive heat transfer to the RFQ body.

The heat load on a given slug tuner is a function of its penetration depth into the RF cavity; nominal intrusion is 20.0 mm, while min and max intrusion is +/- 20.0 mm from nominal, which gives a tuning bandwidth of +/- 1.4 MHz. The worst-case heating situation corresponds to a slug tuner at maximum intrusion of 40.0 mm, located at the cutbacks. Evaluation of this situation yields a conservative estimate of the conductive cooling capability of the slug tuner to RFQ body interface. The heat flux into a slug tuner for the described condition is shown in Fig. 6.

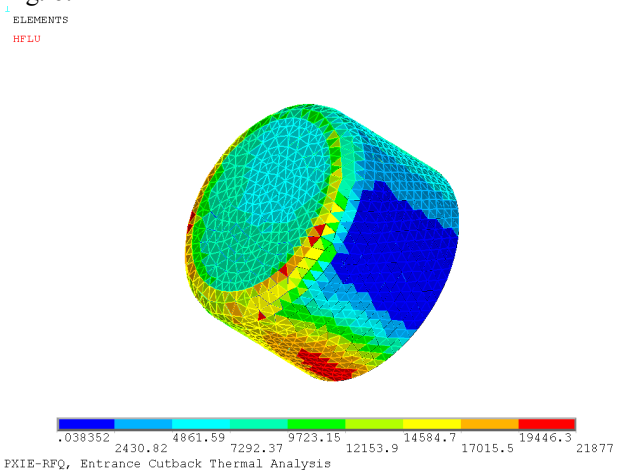


Figure 6: Slug tuner heat flux (W/m^2) at 40.0 mm intrusion.

The heat flux is integrated over the area of the slug tuner to provide the total heat flow into the tuner, which is ~80 W. This heat flow is then used in ANSYS workbench to simulate heat transfer from the slug tuner to the RFQ body. To mimic the effect of contact resistance, the effective area for conductive heat transfer is reduced to less than 10% of its actual area. The resulting temperature profiles are shown in Fig. 7.

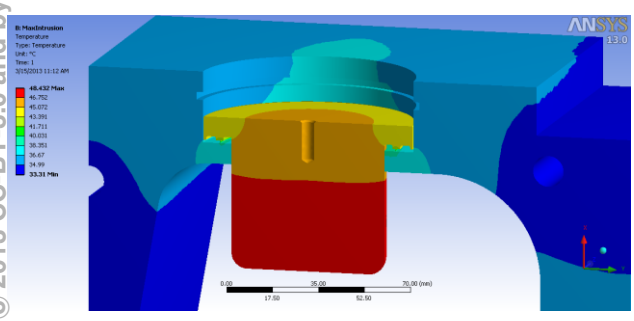


Figure 7: Slug tuner temperatures profiles (^{o}C)

The maximum tuner temperature is 48.4 ^{o}C, which is not problematic. It is unlikely that any of the slug tuners will experience this worst-case scenario; however, in the event that this situation does occur, the conductive heat transfer to the RFQ body is sufficient to cool the slug tuners.

TOTAL RFQ HEAT LOAD

From this analyses, it is possible to calculate the total RFQ heat load, and hence the required cooling that must be supplied to maintain stable operating temperatures. The total heat load of each module is tabulated in Table 3, with the overall total heat load summed at the bottom.

Table 3: Module Heat Loads Due to RF

Component	Heat Load (kW)
Module 1	19.2
Module 2	19.7
Module 3	19.7
Module 4	19.4
Total	**78.0**

As Table 3 shows, the total RFQ heat load is approximately 78.0 kW. This includes the heat of the RFQ body, cutbacks, pi-rods and slug tuners. Assuming a 30% contingency factor, the required cooling system should have a cooling capacity of ~100 kW.

CONCLUSION

This paper illustrates how the use of FEA provides successful prediction of RFQ operating parameters, as well as providing information that helps to size external systems without requiring a prototype module or rigorous experimental testing.

ACKNOWLEDGEMENTS

The author would like to acknowledge the efforts of the LBNL physics, engineering, and mechanical design teams, as well as the efforts of colleagues at Fermi National Accelerator Laboratory in Batavia, Il, and colleagues at the Institute of Modern Physics in Lanzhou, China.

REFERENCES

[1] S. Nagaitsev, et al, “Project X – A New Multimegawatt Proton Source at Fermilab,” PAC ’11, New York, NY, USA, pp. 2566-2569.
[2] S. Nagaitsev, et al, “PXIE: Project X Injector Experiment,” IPAC’12, New Orleans, May 2012, THPPP058, p. 3874 (2012) ; http://www.JACoW.org
[3] S. Virostek, et al., “Design and Analysis of the PXIE CW Radio-Frequency Quadrupole (RFQ),” IPAC’12, New Orleans, May 2012, THPPC034, p. 3359 (2012)
[4] ANSYS, Inc. (http://www.ansys.com).

Copyright © 2013 CC-BY-3.0 and by the respective authors

FINAL DESIGN OF A CW RADIO-FREQUENCY QUADRUPOLE (RFQ) FOR THE PROJECT X INJECTOR EXPERIMENT (PXIE)*

S. P. Virostek#, A. J. DeMello, M. D. Hoff, A. R. Lambert, D. Li, and J. W. Staples
Lawrence Berkeley National Laboratory, Berkeley, CA, USA

Abstract

The Project X Injector Experiment (PXIE) now under construction at Fermilab is a prototype front end of the proposed Project X accelerator [1]. PXIE will consist of an H^- ion source, a low-energy beam transport (LEBT), a radio-frequency quadrupole (RFQ) accelerator, a medium-energy beam transport (MEBT) and a section of superconducting cryomodules [2]. The PXIE system will accelerate the beam from 30 keV to 30 MeV. The four-vane, brazed, solid copper design is a 4.45 m long CW RF accelerator with a resonant frequency of 162.5 MHz. The RFQ will provide bunching and acceleration of a nominal 5 mA H^- beam to an energy of 2.1 MeV. The average power density on the RFQ cavity walls is <0.7 W/cm^2 such that the total wall power losses are ~80 kW. LBNL has completed the final design of the PXIE RFQ, and fabrication is now under way. The completed PXIE RFQ will be assembled at LBNL and tested with low-level RF prior to shipping to Fermilab. Several aspects of the final RFQ mechanical design along with associated fabrication techniques are presented in this paper.

INTRODUCTION

The PXIE RFQ will operate at a 162.5 MHz resonant frequency and will accelerate a 5 mA H^- beam to 2.1 MeV using a 60 kV vane-to-vane voltage. The 4.45 m long, four-vane CW structure will be comprised of four approximately 1.1 m long longitudinal modules. Only about 12% of the total RF input power goes to beam loading with the rest dissipated on the cavity walls to generate the necessary RF field. The modules will consist of four solid OFHC copper sections that are fully machined with the vane tips modulated prior to being brazed together. Due to the high power CW operation of the PXIE RFQ, a brazed copper structure design has been developed. Final frequency adjustment and local field perturbation correction is accomplished by means of 80 evenly spaced fixed slug tuners. Quadrupole mode stabilization is achieved through a set of 32 water-cooled pi-mode rods. The overall approach for the PXIE RFQ was to combine specific proven fabrication and assembly techniques with other high reliability, low cost features in order to develop a design that poses low risk and is easily manufactured using readily available machinery.

Images from a 3-D CAD model of the completed RFQ design are used in this paper to present detailed descriptions of various design characteristics. A realistic CAD rendering of the full four-module RFQ is shown in Fig. 1 (rendering by Don Mitchell of Fermilab).

*This work was supported by the Office of Science, U. S. Department of Energy, under Contract No. DE-AC02-05CH11231.
spvirostek@lbl.gov



Figure 1: CAD model of the assembled RFQ.

RFQ DESIGN DETAILS

Cavity Body

Each module consists of four vanes that are to be machined from a single piece of OFHC copper and will incorporate simple cooling channels produced using a readily available gun drilling technique. Modulations will be machined on the RFQ vane tips with a custom designed fly cutter used in a computer controlled horizontal mill. In order to provide high precision during both machining and assembly, the mating surfaces where the vanes join together also serve as fiducial surfaces. Two different vane geometries will be used in each module (horizontal and vertical) with the opposing vanes being identical. Features located on the outer surface of the vanes such as tuner ports, RF coupling ports, cooling taps, vacuum pumping ports, pi-mode rod penetrations, sensing loop ports and tapped holes for the stainless steel module joining plates will be machined prior to finish machining of the inner cavity surfaces and vane tips. All of the vacuum and RF sealing surfaces for the cavity penetrations are recessed into the outer surface of the RFQ copper body to prevent damage during handling.

The modules will be formed by brazing together the finished vanes along the axially running joints. In order to maintain the tight vane tip-to-vane tip tolerances and ensure that the required field flatness and cavity resonant frequency can be achieved using the slug tuners, a zero-thickness brazing process will be used. Wire braze alloy will be loaded into grooves that are recessed into the joint surfaces. A series of specially designed clamps will hold the vane joints tightly together during the hydrogen oven braze. The alloy spreads throughout the close fitting joint during the braze cycle by means of capillary action. This

Copyright © 2013 CC-BY-3.0 and by the respective authors

technique permits the RFQ modules to be assembled and the cavity frequency and fields measured prior to the braze cycle to allow for dimensional adjustments, if necessary. The braze alloy to be used is Cusil, a copper-silver eutectic that has very low viscosity when liquid. An exploded view showing the four vanes of a single RFQ module is provided in Fig. 2.

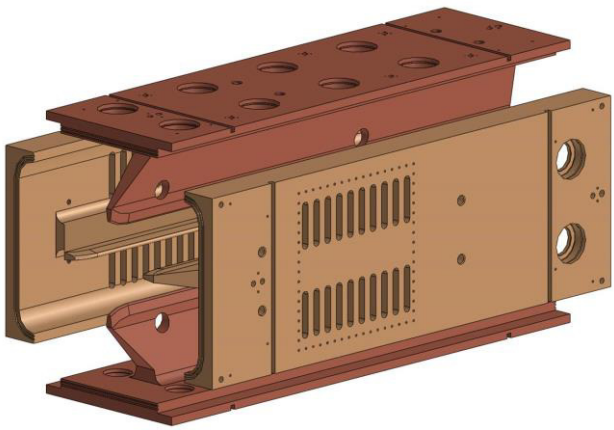


Figure 2: Exploded CAD view of a single module.

The final RFQ cavity is a four vane structure with four identically sized quadrants. A cross sectional view of the RFQ body showing the cavity geometry with cooling passages, tuners and pi-mode rods is shown in Fig. 3. Details of the RFQ features are discussed in the following sections.

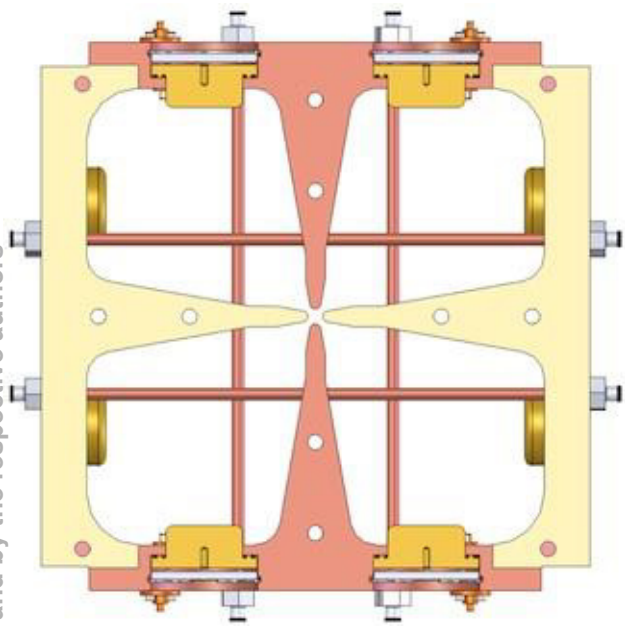


Figure 3: CAD model cross sectional view of the RFQ.

Cavity Cooling

The four cooling channels located in the RFQ vane tips will be supplied and temperature controlled separately from the eight cooling passages in the RFQ cavity walls. During operation, the combined effect of RF generated heat flux on the cavity walls and heat removal through the cooling passages will cause cavity distortion and a shift in the resonant frequency. By holding the wall cooling water constant and adjusting the vane tip water temperature, the structure frequency can be fine-tuned during operation. Due to the fact that the cavity frequency is very sensitive to the vane tip spacing, separate temperature control of the vane tip water provides approximately six times the frequency tuning range of a single cooling circuit.

The passages will be blind gun drilled into the vanes with e-beam plug welds at the end penetrations. Each of the 12 mm diameter passages will carry approximately 4 gallons per minute of cooling water. Vane cutbacks for proper termination of the RF cavity are located at the beginning of the first module and at the end of the fourth module. The cross drilled connection to the vane cooling passages will pass close to the root of the cutbacks to accommodate the higher local heat loads at the ends.

Cavity Tuning

Fixed slug tuners distributed along the length of the RFQ modules will provide cavity tuning. The final design uses 20 tuners per RFQ module (one per quadrant at five approximately evenly spaced locations). The tuners will be machined from solid slugs of OFHC copper.

The lengths of the tuners will be based on automated bead pull field measurements of the fully assembled RFQ modules. Each set of four tuners at a given axial location will be custom machined to the appropriate lengths. RF sealing of the tuners will be accomplished with a canted coil spring that will fit in a groove and be pressed against a recessed lip in the cavity wall. An O-ring outside the RF spring will provide vacuum sealing. A load plate using set screws will be held in place by a snap ring recessed in the RFQ wall and will provide the necessary sealing load on the tuner. The tuner components are shown in Fig. 4.



Figure 4: Fixed slug tuner components.

Copyright © 2013 CC-BY-3.0 and by the respective authors

Pi-mode Rods

In order to minimize the dipole mode and maximize the quadrupole mode, four pairs of pi-mode stabilizer rods per module will be used to provide RF mode stabilization. The rods pass through holes in the vanes and provide a direct connection between opposing cavity walls. The pi-mode rods will be brazed into the cavity walls at the same time that the four vanes are brazed together. The rods are 10 mm diameter hollow OFHC copper tubes that are water-cooled.

RF and Vacuum Seals

A 3 mm wide, 250 μm high raised surface will be machined into the module ends around the periphery of the cavity to provide a primary RF connection between modules. The primary sealing surface will be backed up by a canted coil spring to absorb any RF that leaks past the initial seal. An O-ring outside of the canted spring will provide the vacuum seal. The modules will be joined together using a 'flangeless' joint design in which connecting bolts and nuts are recessed into stainless steel joint plates. The joint plates are connected to the RFQ body by means of a series of bolts and are keyed to a lateral groove in the RFQ outer wall to provide resistance to the axial forces. Fig. 5 shows a CAD view of the module-to-module joint configuration

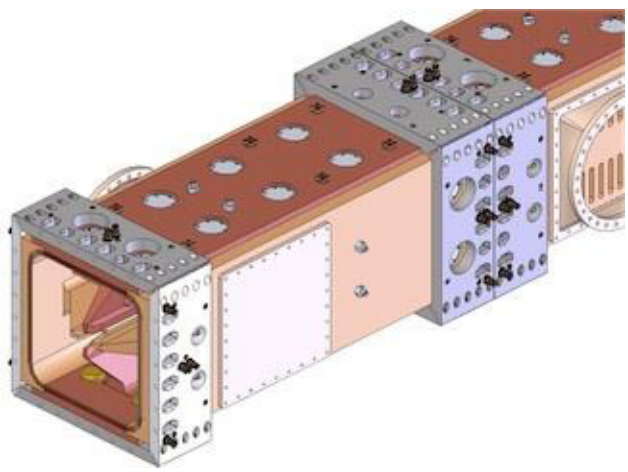


Figure 5: CAD showing a module-to-module joint.

Both RF and vacuum sealing are also required at the numerous penetrations into the RFQ cavities. The RF feed and sensing pick-up ports have sealing schemes that are similar to that previously described for the tuners. The vacuum ports will consist of slotted holes that penetrate the copper cavity walls and that were designed to maximize gas conductance while preventing RF leakage into the pumps. O-rings will provide the vacuum sealing for these ports.

RFQ Assembly

The RFQ modules are easily aligned during assembly as the ends are designed to be self-aligning through the use of dowel pins embedded in the walls at the ends. The bolted end connections are sufficiently strong and stiff such that the fully assembled RFQ can be supported as a single unit. This characteristic allows the RFQ body to be supported using a simple kinematic 6-strut system that cannot impart any direct bending stresses on the assembled RFQ. A CAD image of the full, four module RFQ is shown in Fig. 6.

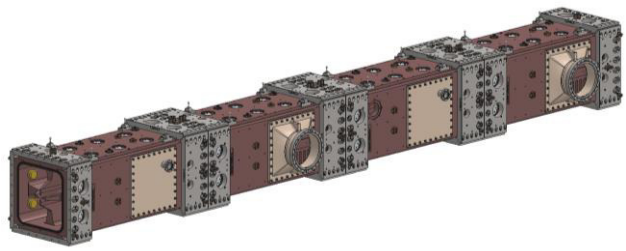


Figure 6: CAD model of the entire RFQ.

THERMAL PERFORMANCE

A series of RF, thermal and structural analyses were performed during the design of the PXIE RFQ. The details of these analyses, which were carried out using ANSYS [3], are provided in [4]. From the RF analysis, the average linear power density was determined to be 137 W/cm with a peak heat flux on the cavity wall of only 0.7 W/cm^2. The peak temperatures in the cavity copper were found to be only 4 to 5°C higher than the cooling water inlet temperature.

The RFQ cooling scheme will use differential water temperature control in the vane and wall passages. This technique provides active tuning of the RFQ by holding the wall water temperature constant and adjusting the vane water temperature up and down. The frequency of the RFQ can be shifted by -16.7 kHz for every 1°C rise in the vane tip cooling water temperature. For uniform water temperature control, the shift would only be -2.8 kHz/°C.

SUMMARY

LBNL has completed the final RFQ design for the Project X Injector Experiment at Fermilab. The overall design scheme was presented in this paper. Construction of the actual RFQ modules is now under way at LBNL and is expected to be completed by the end of 2014. Details of the fabrication progress can be found in [5].

REFERENCES

[1] Project-X ICD reference (http://projectx.fnal.gov/).
[2] D.Li, et al, "Design Study of the Front-end System for Project X," LINAC '10, Tsukuba, Japan.
[3] ANSYS, Inc. (http://www.ansys.com).
[4] A. Lambert, et al, "RF, Thermal, and Structural Finite Element Analysis of the Project X Injector Experiment (PXIE) CW Radio-frequency Quadrupole (RFQ)", NAPAC13.
[5] M. Hoff, et al, "Progress on the Fabrication of a CW Radio-frequency Quadrupole (RFQ) for the Project X Injector Experiment (PXIE)", these proceedings.

Copyright © 2013 CC-BY-3.0 and by the respective authors

INVESTIGATION ON DOUBLE DIPOLE FOUR-VANE RFQ STRUCTURE

Ki R. Shin[1], Yoon W. Kang, Aly E. Fathy[1], and Mark S. Champion
ORNL, Oak Ridge, TN 37831, [1]University of Tennessee, Knoxville, TN 37996, U. S. A.

Abstract

Four-vane RFQ is a general choice for the low energy injector of light ion accelerators. In this commonly used four-vane RFQ structure, each vane has undercuts at both ends to create open magnetic field paths that realize uniform electromagnetic fields along longitudinal direction. Meanwhile, there exists another undercut method called as double dipole (DD) that requires undercuts only on 2 vanes [1] that are interleaved with vanes with no undercut. The RFQ with DD cutback can provide a design option besides the traditional 4 vane cutback (4C) method. In this paper, we investigate and discuss some important DD RFQ features in detail: 1) Finite on-axis field at DD RFQ end section, 2) Dipole mode properties, and 3) Mode spectrum with respect to structure length. 3D simulation is utilized for this DD RFQ analysis.

INTRODUCTION

The radio frequency quadrupole (RFQ) has been widely used for focusing, bunching, and acceleration of ion particles [2]. The four-vane RFQ [3] with four vane cut-backs (4C) [2][4] is common design choice for light ion accelerator systems.

The four-vane RFQ is derived from the quadrupole ridge waveguide [3], and requires cut-backs on each vane ends. The cut-back is necessary to avoid perfect electric boundary condition on vane ends, which is essential to provide the required electric field uniformity in whole structure.

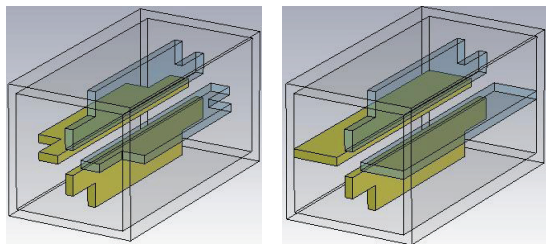
Researchers found that two other cut-back methods are possible to maintain the uniform quadrupole mode: double dipole (DD) and folded dipole (FD) [1][5]. These schemes were used in a $< 2.0\ \lambda$ length structure demonstration RFQ model at Chalk River. One drawback of the DD and FD structures is the generation of finite on-axis field at RFQ ends in quadrupole mode. However, these problems may be relieved by adjusting ion source energy level and RFQ radial matching section design [8].

The DD structure is of special interest in this paper because of its unique characteristics on dipole mode that leads to different mode spectrum results. This may provide an alternative design option in some cases where 4C RFQ mode separation is very small.

Therefore in this paper, we investigate some important features of DD RFQ. First, we discuss the on-axis voltage generation in DD RFQ. Next, some interesting dipole mode properties in DD RFQ are covered with qualitative description and discussion. Finally, a DD RFQ mode spectrum result with the Spallation Neutron Source (SNS) RFQ geometry is presented as an example case. The 3D simulation tool CST Microwave Studio [6] is utilized in this study.

ON-AXIS FIELD AT DD RFQ ENDS

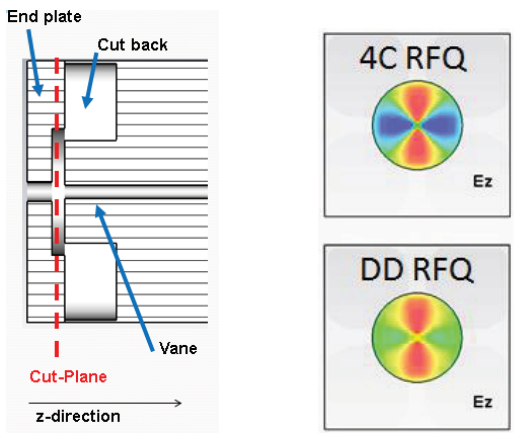
Fig. 1 shows a perspective view of 4C and DD RFQ cut-back geometries. In conventional 4C RFQ, all four vanes are not electrically touching the both end-plates. Meanwhile, only two opposing vanes make contacts to the end-plate in DD RFQ.



(a) (b)

Figure 1: RFQ cut-back - (a) 4C, (b) DD.

Because of this electrical contact of two vanes, DD RFQ generates a finite on-axis voltage. Fig. 2 describes how the on-axis voltage in z-direction is created. In 4C RFQ, the sum of Ez field on beam axis becomes zero. Each RFQ vane induces RF voltage of π phase difference from the adjacent vanes; hence cancellation of on-axis voltage occurs in 4C RFQ [7]. The short circuit condition of two vanes in DD RFQ, however, diminishes this cancellation and finite on-axis potential remains.



(a) (b)

Figure 2: RFQ end region - (a) geometry, (b) Ez field.

The existence of a finite on-axis voltage requires a different end-region design scheme as shown in Fig. 3. The conventional design for 4C RFQ in Fig. 3 (a) is not optimized to reduce the axial voltage. Previous work [1] suggested the design in Fig. 3 (b) which can decrease this axial voltage the most, however it may induce gas flow

Copyright © 2013 CC-BY-3.0 and by the respective authors

issue due to large bore. An intermediate design between these two is the conical one shown in Fig. 3 (c). This design has advantages of small bore with reduced axial voltage.

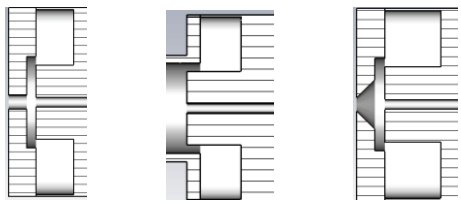


Figure 3: Plate geometry - (a) closed (b) open (c) conical.

The results of simulated axial voltage are summarized in Table 1. The SNS RFQ body geometry with 5λ length is utilized in this simulation study. The 550 kW peak power is assumed to have a similar operating condition in the SNS RFQ. The simulated axial voltage with conical end-plate geometry is 6.38 kV, about 9.8% of SNS RFQ 65kV input beam energy. This axial voltage can be further decreased by introducing a radial matching section (RMS) [8] in RFQ inlet. In this example with SNS RFQ RMS design, 4.77kV axial voltage, about 7.4% of the input beam energy, could be observed.

Table 1: On-Axis Voltage Results by Plate Geometry

	On-axis voltage	*Ratio / 65 kV*
Closed	9.87 kV	15.2 %
Open	3.75 kV	5.8 %
Conical	6.38 kV	9.8 %
Conical + RMS	4.77 kV	7.4 %

DIPOLE MODE CHARACTERISTICS

The DD RFQ provides a unique mode spectrum because of different cavity coupling and dipole mode boundary condition from 4C RFQ.

Figs.4 show how the quadrupole and dipole modes are generated in 4C RFQs. The RFQ magnetic field line path should be closed through circulation in cut-back areas [9]. When the magnetic field in two diagonal quadrants have the same polarity, it becomes the quadrupole mode. Otherwise, it becomes a dipole mode.

In azimuthal plane, the 4C RFQ fundamental quadrupole and dipole modes have π and π/2 phase difference per each quadrant, respectively. For a short RFQ, the magnetic coupling through end-region is stronger than the electric coupling via vane gaps. Hence, the fundamental quadrupole frequency with π phase difference becomes lower than the fundamental dipole frequency with π/2 phase difference [10]. For a long RFQ, however, the electric coupling dominates and the fundamental quadrupole frequency has higher value than the fundamental dipole frequency.

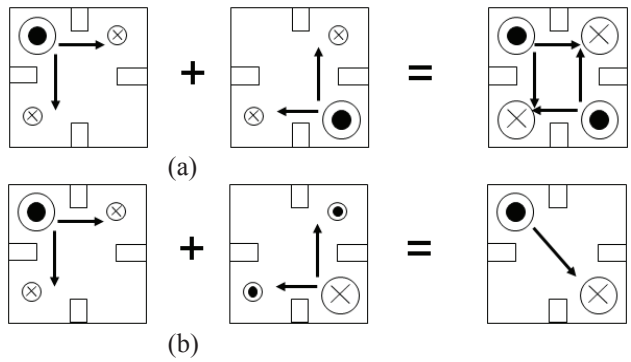


Figure 4: H field circulation at 4C RFQ end-region - (a) quadrupole, (b) dipole mode.

On the other hand, the DD RFQ modes are generated by electrically coupled two dipole cavities. Likewise 4C RFQ, the RF phase difference of each set determines the quadrupole and dipole modes. When two dipoles have 0 or π phase difference, it becomes the dipole or quadrupole mode. Since the two dipoles are connected only through electric coupling, the fundamental quadrupole frequency with π phase difference is always higher than the fundamental dipole frequency with open boundary in Fig. 5 (b). Therefore, the tuning method can be always kept same in DD RFQ independent to the structure length.

The vane pair short circuited to end-plates shown as red box in Fig. 5 causes the DD dipole modes not to degenerate as 4C RFQ dipoles. The DD modes are formed by combination of two dipoles, and the horizontal and vertical dipoles do not have same boundary condition because of the end-plate. H field in one dipole (Fig. 5 (b)) circulates through cut-back area that can be considered as an open boundary. Meanwhile, the other dipole in Fig. 5 (c) experiences the short circuit boundary. The magnetic field path is closed through the small bore openings in this short dipole.

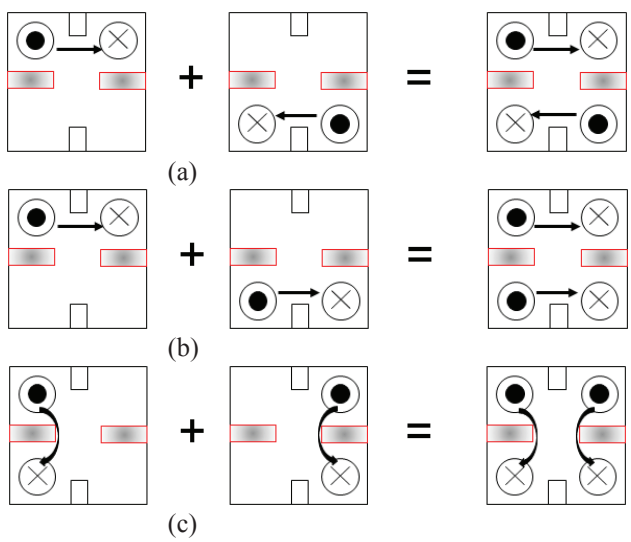


Figure 5: H field circulation at DD RFQ end-region- (a) quadrupole, (b) dipole (open), (c) dipole (short) mode.

Copyright © 2013 CC-BY-3.0 and by the respective authors

Although two dipole modes are not degenerate in DD RFQ, the entire mode spectrum is not complex. Since the open and short circuit boundary dipoles can be approximated as the waveguide and cavity modes, those can be related by cavity length l_v as (1) [11]. The frequency of short fundamental dipole $f_{TE(S)}$ is similar to the first harmonic frequency of the open fundamental dipole $f_{TE(O)}$ and so on. Their harmonic frequencies have similar relations as well.

$$f_{TE(S)} \cong \frac{c}{2\pi}\sqrt{\left(\frac{2\pi}{c}\cdot f_{TE(O)}\right)^2+\left(\frac{\pi}{l_v}\right)^2} \qquad (1)$$

MODE SPECTRUM BY RFQ LENGTH

Figs. 6-7 show the simulation results of 4C and DD RFQ mode spectrum with structure length. The SNS RFQ transverse geometry is used in this simulation. DD dipole frequencies are different from 4C ones, hence DD RFQ could be an alternate design option in some structure lengths. The open boundary dipole in DD RFQ (TE01n+1) has similar frequency with the short dipole (TE10n) by a harmonic order difference. The fundamental open dipole frequency TE010 is always lower than the fundamental quadrupole frequency TE110. With SNS geometry, DD RFQ has good mode separation around 3λ, 5λ, and < 1.5λ lengths.

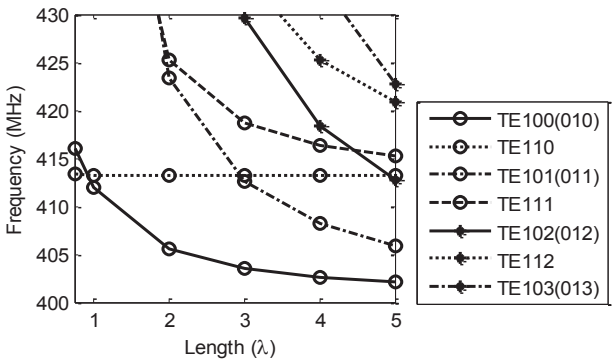


Figure 6: Mode spectrum results of 4C RFQ.

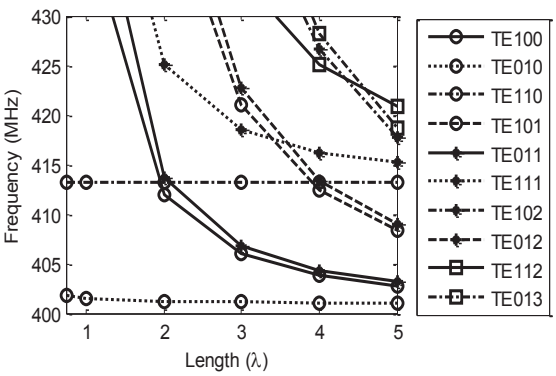


Figure 7: Mode spectrum results of DD RFQ.

CONCLUSIONS

Some results of investigation on the properties of DD RFQ are discussed. The on-axis field generation and end-region design examples are presented. An end gap axial voltage of 4.77 kV is expected with 550 kW peak power. Dipole mode properties of DD RFQ are compared with the 4C RFQ with qualitative discussion. Although dipole modes do not degenerate in DD RFQ, overall mode spectrum is still shows their harmonic relation. The simulation results of mode spectrum are in good agreement with expectation from qualitative approach. The DD RFQ can be an alternative design option in some RFQ lengths where it provides better mode separation than 4C RFQ.

ACKNOWLEDGMENT

This work was supported by SNS through UT-Battelle, LLC, under contract DE-AC05-00OR22725 for the U.S. DOE. The Authors thank the Basic Energy Sciences program of the U.S. DOE and the Research Accelerator Division of SNS for supporting this work.

REFERENCES

[1] R. Hutcheon et.al., "RFQ linac structure development at CRNL", IEEE Trans. on Nuc. Sci. Vol. NS-30, No. 4, Aug. 1983.
[2] I.M. Kapchinskiy and V.A. Tepliakov, Prib. Tekh. Eksp. 2, 19-22 (1970) & 4, 17-19 (1970).
[3] L. Young, "25 years of technical advances in RFQ accelerators," Proceedings of 2003 particle accelerator conference, Portland, OR.
[4] M. Browman et. al., "Studying the end regions of RFQs using the MAFIA codes", Proceedings of 1988 linear accelerator conference, Williamsburg, VA.
[5] R.M. Hutcheon et. al., "100% duty factor RFQ linac systems at CRNL," IEEE Transactions on Nuclear Science, Vol. NS-30, No. 4, August 1983.
[6] CST Microwave Studio, www.cst.com
[7] P. Balleyguier et. al., "Simulations vs. measurements on IPHI RFQ cold model," Proceedings of 2002 European Particle Accelerator Conference, France.
[8] K. Crandall et. al., "RF quadrupole beam dynamics design studies," Proc. 10th Linear Accelerator Conf. Montauk, NY, 1979.
[9] T. Wangler, "RF linear accelerators," 2nd edition, Weinheim, Germany: Wiley, 2008.
[10] P. Lapostolle, A. Septier, "Linear accelerators," North-Holland Publishing Company, Amsterdam, 1970.
[11] R. Collin, "Foundations for microwave engineering, "second edition, IEEE press series on electromagnetic wave theory, 1992.

Copyright © 2013 CC-BY-3.0 and by the respective authors

DESIGN AND MEASUREMENT OF DOUBLE GAP BUNCHER CAVITY PROPOSED FOR REDUCTION OF X-RAY RADIATION

Ki R. Shin[1], Yoon W. Kang, Aly E. Fathy[1], and Mark S. Champion
ORNL, Oak Ridge, TN 37831, [1]University of Tennessee, Knoxville, TN 37996, U. S. A.

Abstract

X-ray radiation from accelerating cavities can be serious problem not only in high energy section but also in certain low energy system including beam matching section with buncher cavity. In this paper we propose a double gap buncher cavity design for low energy part of H- ion accelerators which can reduce X-ray radiation. The cavity utilizes Transverse Magnetic (TM) mode at about 400MHz as the operating mode. A drift tube supported by a stem in the cavity can form two gaps that can divide the required gap voltage to a half per each gap. Lower peak field can be realized since this double gap cavity can avoid sharp geometry. 3D simulation is utilized to address the analysis of non-axisymmetric structure. An Aluminum scaled model is built and tested with low power measurement. The measured results are in good agreement with simulations.

INTRODUCTION

For safety, radiation shielding is an important part of a high energy accelerator design [1]. Concrete material surrounds accelerator system in a tunnel to shield any hazardous radiations. Often bunching cavities in low energy section of ion accelerator < 3MeV are placed outside the tunnel only with fundamental radiation shield. X-radiation with non-negligible level can occur, however, if cavities are not under good vacuum condition [2]. Therefore, more conservative design to prevent X-radiation can help to improve system operability.

Assuming a constant vacuum level, X-radiation intensity is related to the cavity gap voltage and discharge current [3][4]. Ref. [3][4] expects that the radiation intensity has quadratic to cubic relation with gap voltage. The radiation wavelength is inversely related to the gap voltage as well [4]. Consequently, lower gap voltage may decrease a radiation dose and hard X-ray generation.

The mechanism of discharge current is rather complex, but in general it is relevant to the field emission and explosive emission mechanism [5]. The electric field in cavity determines the discharge current, and lower electric field is expected. In other words, lower electric peak field with smooth gap geometry may help to minimize discharge current and radiation intensity.

With regarding these voltage and peak field requirements, a double gap buncher cavity design is proposed and its lab type measurement is presented in this paper. This design is aimed to fit the requirement of the cavity 4 with 30mm bore diameter in medium energy beam transport (MEBT) section in the Spallation Neutron Source (SNS) [6]. The cavity length and particle speed are about 13cm and 0.073 v/c, respectively.

X-RADIATION BY VACUUM DISCHARGE

At cavity gap, the X-ray radiation dose D_X is determined by the integration of the radiation intensity J_X over the particle commutation time t_c (1) [3][5].

$$D_X \cong \int_0^{t_c} J_X(t)dt \quad (1)$$

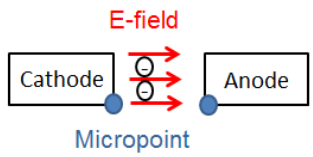
$$J_X \propto i(t)\cdot V^n(t) \quad (2)$$

The radiation intensity J_X is related to the discharge current i(t) at cavity gap and the gap voltage V(t) likewise (2) [3][5]. The variable n commonly has values in range of 1.8~3.0 [3-5]. As a result, V(t) becomes an important parameter to determine J_X. The maximum X-radiation frequency also rises as the gap potential energy increases. This may induce a generation of hard X-ray. Therefore, low cavity gap voltage is desired to decrease X-radiation.

In accelerating cavities with high electric field intensity, the discharge current is generally formed by Fowler-Nordheim field emission mechanism [5]. Fig. 1 describes the field emission process at cavity gap (between cathode and anode), and the current density definition.

In field emission mechanism, some cathode electrons are stripped by strong electric field and collide to the anode. The emission current is a function of electric field; hence smaller electric field is desirable to decrease X-radiation by discharge current.

Most RF cavities are designed to have enough design margins until to reach the field breakdown limit, however, some micropoints on cathode and anode surface (Fig. 1) may lower the barrier of discharging. These micropoints can generate plasma around cathode, and as a result the discharging process starts earlier than as expected. This mechanism is called as explosive electron emission [5]. The anode part can also suffer from extra heating, evaporation, and ionization.



$$j = A\cdot E^2\cdot e^{-\frac{B}{E}}$$

A and B are constants

Figure 1: Field emission at cavity gap and Fowler-Nordheim current density.

The sharp gap shape in low energy ion accelerator section can be more vulnerable to explosive electron

Copyright © 2013 CC-BY-3.0 and by the respective authors

emission mechanism; because the geometry would have more chance to contain micropoints than flat shape.

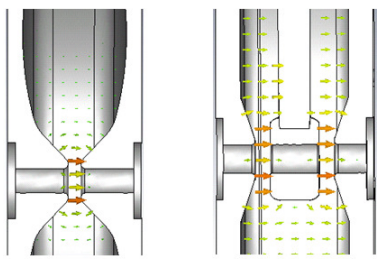
Regarding all considerations above, we propose a double gap cavity design which can help to relieve X-radiation problem. This design decreases gap voltage and peak electric field that is directly related to X-radiation. The voltage is reduced to a half by using double gap, and the peak electric field can be decreased with flat gap geometry.

DOUBLE-GAP TM MODE CAVITY

Buncher cavity operates with -90º phase from the RF electric field maximum, as a result the average particle speed does not change. For that reason, the multi gap cavity geometry can be symmetrical. The transverse magnetic (TM) electromagnetic mode can be more reliable from the multipacting issues than transverse electromagnetic (TEM) cavity design [7]. The benefit of higher R/Q in TEM cavity diminishes at higher frequency about 400MHz [8] because of very low Q. The TEM cavity efficiency further decreases for the requirement of SNS MEBT buncher cavity, which has a large bore diameter about 30mm. Therefore, TM mode is adopted as the operating mode.

The design of double gap cavity requires 3D RF analysis because of rotational asymmetry. The CST Microwave Studio [9] is utilized in the cavity design and parameter study.

Fig. 2 shows the electric field formation of the single and double gap cavities. About a half voltage of single gap cavity is formed in each gap of the double gap cavity. Each double gap cavity gap dimension is slightly bigger than the single gap cavity to decrease the electric peak field. Each gap field has the same RF phase in the double gap cavity and matched to the particle velocity.



(a) (b)

Figure 2: Electric field and cavity geometry around on axis- (a) single gap, (b) double gap.

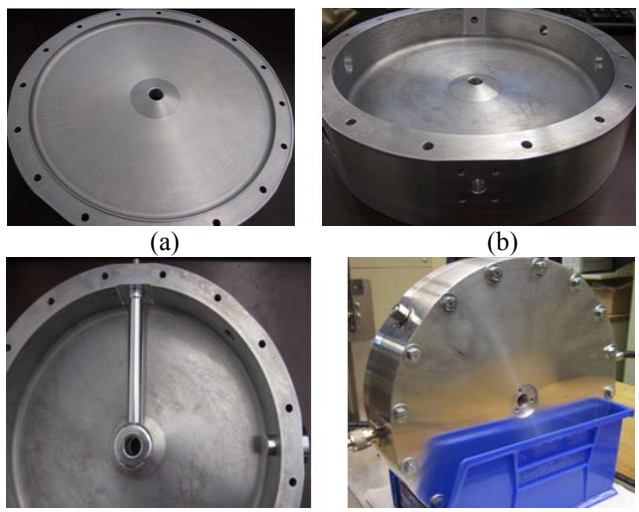
A summary of the cavity parameters are shown in Table 1. The double gap design obviously can decrease peak electric field by 55% and generate half voltage per each gap, which can help to decrease X-radiation intensity. Although this design gives slightly lower power efficiency and may become mechanically slightly bigger due to additional gap spacing. The power efficiency can be improved further by optimizing the cavity gap geometry.

Table 1: Parameter Comparison (3.0cm bore/ 28.2kW rms)

	Single Gap	Double Gap
Frequency (MHz)	401.9	400.1
Gap size (mm)	12.30	14.23 14.23
Q (unloaded, Copper)	21413	20903
r/Q	29.35	27.83
R_s/L (Mohm/m)	5.48	4.47
V_0 (kV)	119.08	57.28 57.28 (Total : 114.45)
T	0.447	0.452
E_0 (MV/m)	2.32	1.93
E_{pk} (MV/m)	29.9	13.26
H_{pk} (A/m)	6565	8644

½ SCALED MODEL FABRICATION

A scaled prototype model of half size is built with Solidworks [10] to verify the design. AL 6061 T6 material with 42% of copper conductivity is used as a cavity material. As shown in Fig. 3, the drift tube assembly is attached on the equator of the cavity main body. Next, the minor piece is mounted to the main piece to complete the assembly. This prototype model is designed for low power measurement; hence does not include the design of cooling channel.



(a) (b) (c) (d)

Figure 3. Fabricated ½ scale double gap cavity (a) minor piece, (b) major piece, (c) major piece with tube, (d) final assembly with 2 ports.

FREQUENCY AND Q MEASUREMENT

Table 2 shows the comparison of the simulated and measured TM010 mode frequency and Q value. S21 parameter is measured with a two port vector network analyser (VNA). The simulation and the measurement showed an excellent agreement in frequency. The 12%

Copyright © 2013 CC-BY-3.0 and by the respective authors

difference in Q measurement comes from extra power loss on the cavity seam plane and coupler ports.

Table 2: Simulation vs. Measurement – Frequency and Q

	Simulation	Measurement
Frequency	800.49	800.56
Q	9286	8179

R/Q MEASUREMENT

One of the cavity figures of merit, shunt impedance, is both RF loss and frequency dependent. Hence R/Q [11], which is independent of the loss and frequency is measured and compared.

Fig. 4 shows a beadpull system setup for R/Q measurement. A spherical metallic bead was used. We try the phase shift measurement to find R/Q since this method is rather simple and accurate [12].

The measured phase shift results in Fig. 5 are all integrated on the cavity beam axis to calculate R/Q. The reference phase outside of the cavity gap is set to zero, and two shifting curves are shown due to the double gap. The same method used in Ref. [13] is utilized to calculate R/Q.

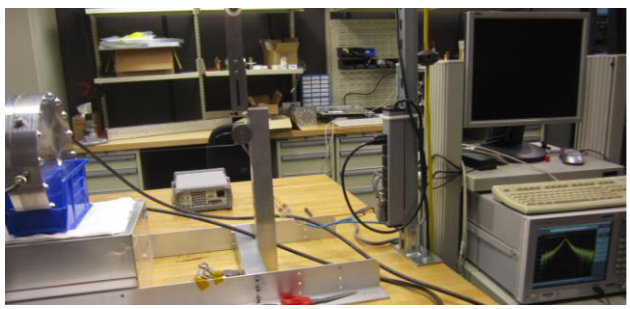


Figure 4: R/Q measurement system.

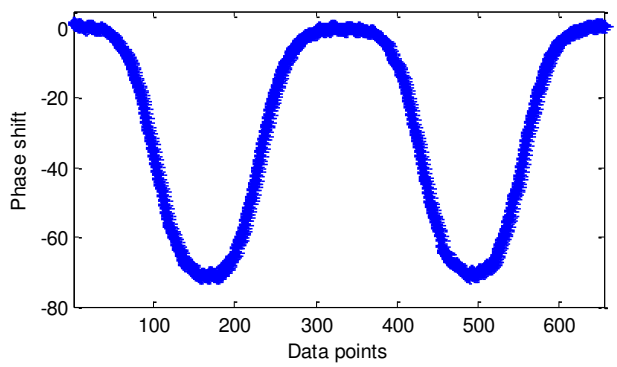


Figure 5: Measured phased shift by perturbation method.

The measured R/Q is in good agreement with the simulation with 94% accuracy as shown in Table 3. The estimated shunt impedance Rs is lower in accuracy with about 83%, because of 12% Q discrepancy already discussed in Table 2. R/Q value will be the same for 400MHz as well.

Table 3: Simulation vs. Measurement – R/Q

	Simulation	Measurement
R/Q	27.83	26.12
Rs (Mohm)	0.258	0.213

CONCLUSIONS

A buncher cavity design to reduce X-ray radiation for better operability is proposed for the low energy ion accelerator section with SNS MEBT cavity example. Gap voltage and peak electric field drastically decreases with this double gap design. Measurement results with scaled model are in good agreement with simulations.

ACKNOWLEDGMENT

This work was supported by SNS through UT-Battelle, LLC, under contract DE-AC05-00OR22725 for the U.S. DOE. The Authors thank the Basic Energy Sciences program of the U.S. DOE and the Research Accelerator Division of SNS for supporting this work.

REFERENCES

[1] J. Cossairt, “Radiation Physics for Personal and Environmental Protection”, FNAL Report TM-1834.
[2] A. Aleksandrov, “The SNS beam diagnotics experience and lessons learned”, Proceeding of the 2010 Beam Instrumentation Workshop.
[3] J. Haimson, “Some Aspects of Electron Beam Optics and X-Ray Production with the Linear Accelerator”, IRE Trans. On Nuc. Sci. Vol. 9, Issue 2, April 1962.
[4] A. Oppelt, “Imaging systems for medical diagnotics”, J. Wiley and Sons, 2006.
[5] G. Mesyats et. al., “Pulsed Electrical Discharge in Vacuum”, Springer-Verlag, 2012.
[6] J. Staples et al., “Design of the SNS MEBT”, XX International Linac Conference, California.
[7] A. Millich et al., “Comparison of Three Buncher Structure Designs for the 3MeV SPL Chopping Line”, CERN PS/RF/Note 2002-028.
[8] T. Enegren, “The SSC RFQ-DTL Matching Section Buncher Cavities”, 15th Particle Accelerator Conference, May. 1993.
[9] CST Microwave Studio, www.cst.com
[10] Solidworks, www.solidworks.com
[11] L. Maier et. al., “Field Strength Measurements in Resonant Cavities”, J. Appl. Phys. 23, 68, 1952.
[12] J. Slater, “Microwave Electronics”, Van Nostrand, 1950.
[13] P. Matthews et. al., “Electromagnetic Field Measurements on a Millimeter Wave Linear Accelerator”, IEEE Trans. on Micro. Theory and Tech. Aug. 1996.

Copyright © 2013 CC-BY-3.0 and by the respective authors

HARMONIC RATCHETING FOR FAST ACCELERATION*

N. Cook†, Stony Brook University, Stony Brook, NY 11790 USA
M. Brennan, S. Peggs, BNL, Upton, NY 11973, USA

Abstract

From medical synchrotrons to accelerator driven systems, there is a need for fast acceleration of protons and light ions. This can be a costly undertaking, requiring specially designed ferrite loaded cavities to be tuned across a wide range of frequencies. Ferromagnetic materials allow for the precise adjustment of cavity resonant frequency, but rapid tuning changes and operation outside material specific frequencies result in significant Q-loss. This leads to a considerable increase in power requirements. We introduce an acceleration scheme known as harmonic ratcheting which reduces the cavity frequency range when accelerating an ion beam in a synchrotron. This scheme addresses the needs of high repetition rate machines for applications in which low beam intensity is needed. We demonstrate with simulations the type of ramps achievable with ratcheting and consider its advantages.

INTRODUCTION

The potential for fast acceleration of low energy ion beams remains rich, with a host of applications proposed to take advantage of rapid cycling synchrotrons or FFAGs. Nonetheless, conventional acceleration of low β charged particles remains expensive and inefficient. The primary challenge of accelerating such particles lies in achieving robust and flexible tuning. Using speciality ferrites, tuning can be obtained at the cost of efficiency. Ferrite materials suffer dramatic loss effects when driven at high bias fields and high magnetic flux [1] [2]. These difficulties have stemmed the advancement of fast and efficient accelerators for low energy ion beams.

The integer harmonic number h relates the RF and revolution frequencies through the relationship $f_{RF} = h\, f_{ref}$. The relative RF frequency range can be significantly reduced below the revolution frequency range by decreasing h in steps as the ions accelerate and f_{rev} increases. This is the motivation and basic method of *harmonic ratcheting*.

HARMONIC RATCHETING

Suppose that two (or more) RF cavities take turns accelerating the beam – one turns on when the other turns off, at different RF frequencies – so that the RF frequency is always constrained to remain in the range

$$f_{min} \;\leq\; f_{RF} \;\leq\; f_{max} \tag{1}$$

where f_{min} and f_{max} are externally determined design parameters. It is possible to make the transition back or forth between harmonic numbers

$$\begin{aligned} h &= n \\ \text{and}\quad h &= n+\Delta \end{aligned} \tag{2}$$

where n and Δ are positive integers, if

$$\frac{f_{max}}{n+\Delta} \;>\; \frac{f_{min}}{n} \tag{3}$$

Equivalently, we have

$$\Delta \;<\; n\,r \tag{4}$$

where

$$r \;\equiv\; \frac{f_{max}}{f_{min}} - 1 \;>\; 0 \tag{5}$$

is the "ratcheting parameter". Equation 4 shows that Δ has a maximum permissible value, which must be greater than 1 if a harmonic transition is to be possible. A ratcheting transition is possible if the following conditions are met.

$$\begin{aligned} n &> 1 \quad &, r &> 1 \\ n &> \frac{1}{r} \quad &, r &< 1 \end{aligned} \tag{6}$$

Several harmonic ratchets can take place during one acceleration ramp. Figure 1 show an example with $r = 0.50$, where the revolution frequency increases from 0.61 MHz to 3.35 MHz, while the RF frequency is constrained to lie between 5.5 MHz and 8.25 MHz.

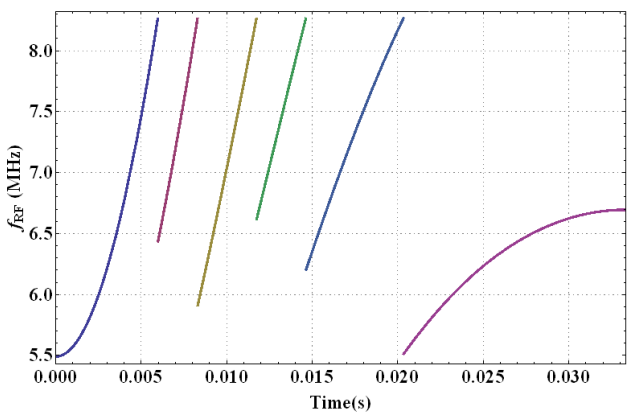


Figure 1: An example of harmonic ratcheting with $r = 0.50$. The plot shows one possible solution – with the harmonic number sequence $h = 9, 7, 5, 4, 3, 2$ – that maximizes RF frequency while minimizing ratcheting number.

* Work supported by Brookhaven Science Associates, LLC under Contract No. DE-AC02-98CH10886 with the U.S. Department of Energy.
† ncook@bnl.gov

Copyright © 2013 CC-BY-3.0 and by the respective authors

Designing a Ratcheting Ramp

The selection of the initial harmonic number in the ratcheting ramp is determined by considering the minimum required bucket length, t_{inj} to accept particles into a single bucket at injection. This length sets a maximum possible initial harmonic. Moreover, the energy acceptance at injection also scales inversely with ${h_{max}}^2$. These requirements can be summarized by

$$\begin{aligned} h_{max} &\leq \frac{1}{t_{inj} f_{rev}(0)} \\ \text{and } {h_{max}}^2 &\leq \frac{2QV_g\beta^2 E_s}{\pi|\eta_s|\Delta {E_0}^2} \end{aligned} \tag{7}$$

Here, Q is particle charge, E_s is synchronous energy, and η_s is the phase slip factor. As the initial harmonic increases, a corresponding increase in voltage is necessary to keep the acceptance the same. Ferrite tuning time poses an additional constraint on the ratcheting permutation. Tuning the inactive cavity from a high frequency down to a low frequency requires circumnavigating the hysteresis curve. This tuning time, τ_t, is on the order of a few ms, which sets a lower limit on the active time for any cavity between ratcheting transitions $\tau_{active} > \tau_t$.

Emittance Growth at Ratcheting Transition

During the harmonic transition, the voltage on the cavity operating near f_{max} at harmonic $h = n + \Delta$ is reduced while a second cavity operating at harmonic $h = n$ has its voltage raised from a feedback level to provide the desired gap voltage at the new harmonic. Assume that this change happens quickly and that both the synchronous phase and total accelerating voltage are smoothly varying when the ratcheting takes place.

The result of the harmonic ratcheting is a relaxation of the bucket potential. As a result, large amplitude particles stray further in phase from the design particle in order to feel the same restoring force, thereby increasing longitudinal emittance S. Similarly, the bucket area A will grow as h is reduced. Both quantities grow as

$$\frac{S_2}{S_1} \propto \frac{A_2}{A_1} \propto \left(\frac{n+\Delta}{n}\right)^{\frac{3}{2}} \tag{8}$$

The emittance growth due to the harmonic number transition matches with the bucket area growth during the ratcheting process. Thus, for small or slow changes in harmonic number, the ratcheting process is inherently stable, as illustrated in figure 4. This transition is calculated non-adiabatically. The transfer of voltage takes place over some time period τ_r. A particle will make $n_t = \beta c \tau_r / C$ turns in that time. If $\tau_r = 100\mu s$, a $\beta = 0.1$ particle makes 50 turns of a 60 m synchrotron.

FERRITE-LOADED CAVITIES

The resonant frequency of a ferrite-loaded cavity is $f = \frac{1}{2\pi} \frac{1}{\sqrt{LC}}$ where L, the inductance of the cavity, is adjustable between minimum and maximum values L_{min} and L_{max}. Consider a cavity with a total ferrite length of l, made of many rings with inner and outer radii r_a and r_b. The inductance is $L = \frac{l}{2\pi} \mu' \ln \frac{r_b}{r_a}$ where the *incremental* complex permeability of the ferrite is written $\mu = \mu' + j\mu''$. The component μ' and the inductance of the cavity are tuned by biasing the ferrite with a pseudo-constant azimuthal magnetic field driven by a tuning current. Ignoring the stray inductance, the required dynamic range of L and of μ' is

$$\frac{L_{min}}{L_{max}} = \frac{\mu'_{min}}{\mu'_{max}} = \frac{1}{(1+r)^2} \tag{9}$$

The voltage across the gap of a cavity is

$$V_{gap} = 2\pi f \, B_{max} \, l \, r_a \ln \frac{r_b}{r_a} \sim f \, l \tag{10}$$

where $B_{max} \approx 0.01$ T is the maximum RF magnetic field that is allowed at the inner radius of the ferrite rings. This shows that for a fixed maximum field B_{max}, the ferrite length l can be reduced if the RF frequency in the cavity is increased. Thus, harmonic ratcheting allows a given acceleration waveform to be achieved with shorter cavities.

The total length of ferrite required with a ratcheting parameter r, relative to a non-ratcheting scheme in which ions are accelerated over the full dynamic range is given approximately by

$$\frac{l_{ratchet}}{l_{non-ratchet}} = \frac{f_{min,non-ratchet}}{f_{min,ratchet}} \approx 2\,\frac{1+r}{D} \tag{11}$$

where $D = \frac{\beta_{max}}{\beta_{min}}$, and the factor of 2 recognizes that only half the cavities are active at any one time. For example, Figure 1 illustrates acceleration over a dynamic range of $D = 5.5$, using a ratcheting parameter of $r = 0.50$. In this case ratcheting makes it possible to decrease the total length of ferrite by a factor of 0.55. Conversely, the gap voltage can be nearly doubled for a fixed cavity length, almost doubling the potential repetition rate of a rapid cycling synchrotron.

EXAMPLE: A RAPID CYCLING MEDICAL SYNCHROTRON

Consider a rapid cycling synchrotron for acceleration of C^{6+} ions for radiation therapy applications. Assume a 15 Hz repetition rate and a circumference $C = \sim 65$ m. Ions must accelerated through a range 8 to 400 MeV/μ.

Once the initial harmonic is determined, the initial RF frequency is set at $f_{RF}(0) = h_0 \beta c / C$. Appropriate selection of a frequency ceiling limits the ferrite to operate within a more efficient permeability range. In this instance, we choose a ratcheting parameter of $r = 0.5$ via a final harmonic transition of $h = 3$ to $h = 2$. Figure 1 shows the RF frequency and figure 2 plots the active harmonic.

When the frequency ceiling is reached at the current harmonic, RF power is transferred to the second cavity system at a lower harmonic number. Each time the harmonic

Copyright © 2013 CC-BY-3.0 and by the respective authors

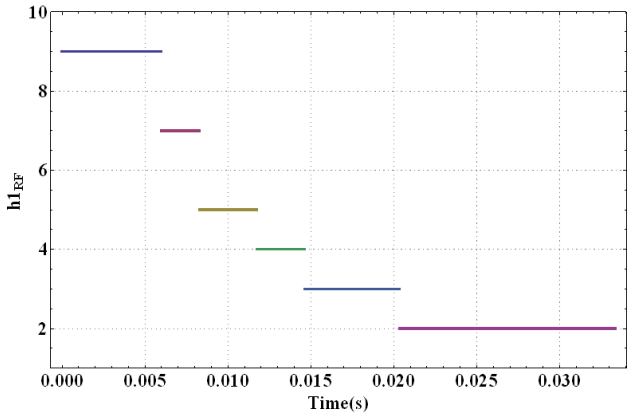


Figure 2: Active cavity harmonic for the ∼65 m Carbon synchrotron harmonic ratcheting ramp.

number is reduced, the RF frequency is reduced by a factor $\frac{h_n}{h_{n-1}}$ where h_n is the new harmonic, and h_{n-1} is the previous value. The maximum frequency swing during the ramp is determined by the maximum value of this ratio, or equivalently the ratcheting parameter r, according to

$$\frac{\Delta f}{f_0} = r \tag{12}$$

For example, if the largest transition in a particular ratcheting scheme is from $h = 3$ to $h = 2$, then the ratcheting parameter is $r = 0.5$, and that particular ramp is limited to a 50% frequency swing.

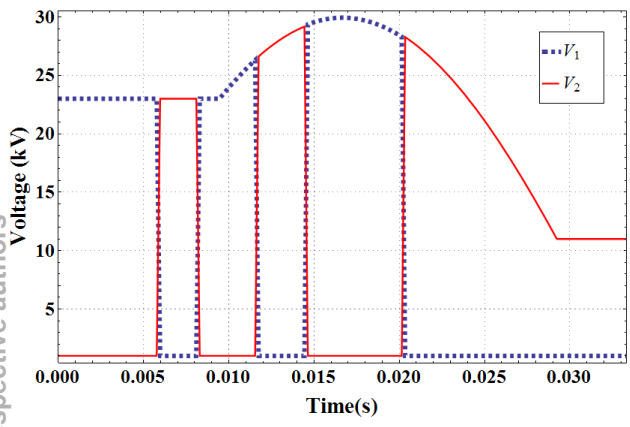


Figure 3: Output voltage for each cavity system. The voltage is calculated to meet the constraint $\phi_s \leq 33°$.

Figure 3 outlines the output voltage needed for each cavity system in our example ramp. The harmonic transition and transfer of power to the inactive cavity cannot be performed instantaneously; the voltage may be raised over $\sim 100\mu s$. Detailed feedforward and diagnostic systems are required in order to maintain the proper voltage. The emittance evolution for our example case is shown in 4.

Ratcheting may also reduce losses due to anomalous effects in ferrite. At sustained high fields, ferrites demonstrate a Q-loss effect (QLE) which can result in a reduction of 20% of maximum field. High bias fields can increase

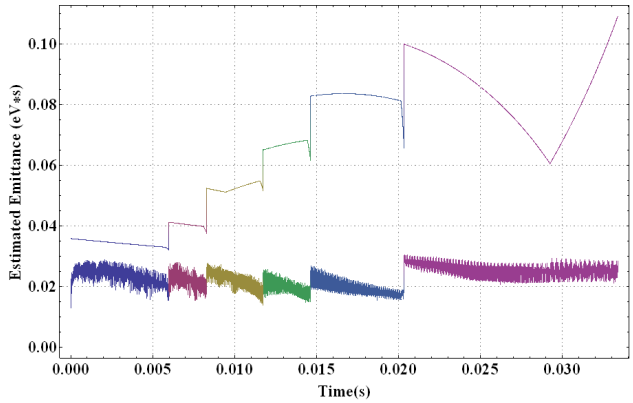


Figure 4: Estimated emittance and bucket area is shown for a simulated ramp with fixed synchronous phase.

this effect by reducing the threshold of Q-loss onset. However, at high bias rates the threshold for this effect is significantly raised [1]. A ratcheting scheme should mitigate QLE by reducing total biasing. Rapid bias field changes may also induce a dynamic loss effect in the ferrite. These losses can lower a cavity's Q value by up to 40%. Unlike the QLE, this effect appears to be more dependent on the temperature and duration of the biasing. By decreasing the time spent biasing at high fields, this effect can be reduced considerably [2].

CONCLUSION

A new scheme for accelerating low energy ions quickly and over a large frequency range is presented. By adjusting the harmonic number during acceleration in a manor specifically tailored to the desired acceleration cycle, a significant reduction in the frequency range is obtained, easing the ferrite's tuning requirement. Moreover, the frequency increase allows potentially several times larger gap voltages to be obtained for the same amount of ferrite, making higher machine repetition rates possible. Alternatively, cavity length could be reduced by an equivalent factor. This approach is particularly suited to low intensity ion beams which do not require filling a ring but necessitate fast acceleration across a range of energies.

ACKNOWLEDGMENT

We thank D. Trbojevic for many encouraging discussions on this topic.

REFERENCES

[1] K. Kaspar, H. G. König, and T. Winnefeld., "Studies on the maximum RF voltages in ferrite-tuned accelerating cavities," TUPKF013, Proceedings of EPAC 2004, 985-7.

[2] J.E. Griffin and G. Nicholls. IEEE Trans, Nucl. Sci. 26 (1979) 3965-7.

Copyright © 2013 CC-BY-3.0 and by the respective authors

MULTIPACTING STUDY FOR THE RF TEST OF THE MICE 201 MHz RF CAVITY AT FERMILAB MTA*

T. Luo†, D. Summers, University of Mississippi, University, Mississippi, USA
A. DeMello, D. Li, H. Pan, S. Virostek, M. Zisman, LBNL, Berkeley, California, USA

Abstract

In this paper, we present a study of multipacting effects for the high power RF test, to be done at Fermilab's Mucool Test Area, of the 201 MHz RF cavity for the Muon Ionization Cooling Experiment. We show how the fringe field of the Lab_G magnet affects the cavity performance due to multipacting and predict the possible multipacting bands in the high power RF test with different magnetic field strengths.

INTRODUCTION

One cavity for the international Muon Ionization Cooling Experiment (MICE) [1], after being manufactured and electro-polished at LBNL, has been shipped to the Fermilab Mucool Test Area (MTA) for the single cavity test. To study the cavity performance in a strong magnetic field, this cavity will be tested in the fringe field of the 5-T Lab_G magnet before the MICE Coupling Coil is ready for operation.

In this paper, we study multipacting (MP) effects for the single cavity with and without the Lab_G magnet fringe field. We show possible MP bands with different magnetic field strengths expected in the high power RF test. The Lab_G magnetic field is calculated by ANSYS, the cavity RF field by S3p [2] and the MP effect by Track3p [3].

MAGNETIC FIELD OF THE LAB_G MAGNET

The magnetic field of the Lab_G magnet has been mapped both experimentally and numerically [4, 5]. However, none of the previous mappings cover the full region where the 201 MHz cavity will be placed. Thus we used ANSYS to recalculate the magnetic field. The field along the central axis is compared with previous mapping and shows good agreement, as shown in Fig. 1. Due to the uniqueness of the solution of Poisson equation, the ANSYS result should also give the correct field everywhere in space, including the fringe field region where the cavity will be placed, which is about 1.0 m away from the Lab_G magnet (center-to-center) if the Single Cavity Vessel is located as closely as possible to the Lab_G magnet.

* Work supported by NSF MRI Award 0959000, and by Office of Science, U.S. Department of Energy under DOE contract number DE-AC02-05CH11231, US Muon Accelerator Program.

† tluo@lbl.gov

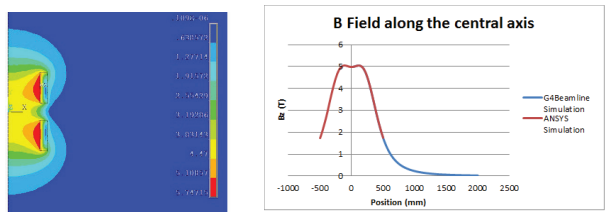


Figure 1: The ANSYS magnetic field calculation of the Lab_G magnet. The left figure is the contour plot of the field magnitude. The right figure is the comparison of magnetic fields from ANSYS with previous G4Beamline results [5] along the central axis.

RF FIELD IN THE 201 MHz CAVITY

The cavity model is built from its CAD drawing, including the curved beryllium windows, the coaxial waveguide and the loop coupler. To build an RF field with power propagating into the cavity and dissipating on the cavity walls, we use S3p with a "waveguide" boundary condition (BC) at the coaxial port and " impedance " BC on the cavity wall. The orientation of the coupler is adjusted to achieve critical coupling ($\beta \approx 1$), with coupling angle at about 17°. The E and B fields in the cavity are shown in Fig. 2.

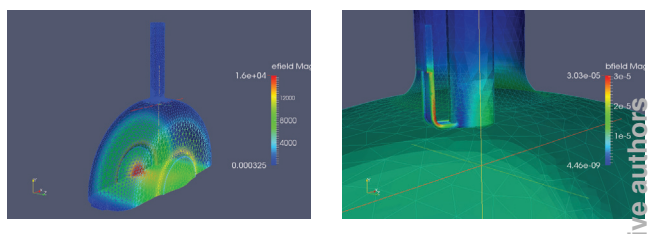


Figure 2: RF field of the cavity. The left figure shows the E field magnitude in the cavity. The right figure shows the maximum B field in the cavity on the coupler loop, where sufficient cooling should be supplied.

MULTIPACTING EFFECT ON 201 MHz CAVITY WITH LAB_G MAGNET

The MP effect is evaluated by the Enhancement Counter (EC) in the Track3P code. The electron is launched from its primary emission surface and tracked for 50 RF cycles, until its energy is too high or too low for MP, or until it hits the absorber surface. Every time it hits the second emission surface, the probability η to generate a secondary electron, which depends on impact energy and surface material, is

Copyright © 2013 CC-BY-3.0 and by the respective authors

recorded. After 50 RF cycles, the enhancement counter:

$$EC = \Pi_{i=1}^{N} \eta_1 \cdot \eta_2 \ldots \eta_N \,,$$

when $EC > 1$, it indicates a possible MP case. The larger the EC, the more likely the MP will happen. The SEY data of copper we used in this paper are for the Argon Glow Discharge (AGD) treated copper [6]. Since Be windows will be TiN coated, we treat these as an absorber surface.

According to its geometry, the cavity is divided into three parts: the coaxial waveguide, the coupler and the cavity body. We study the MP with different magnetic field strengths: $B_{max} = 0$ T, 1.25 T, 2.5 T, 3.75 T and 5 T on the central axis.

The required cavity field gradient for the neutrino factory is 16 MV/m, which corresponds to about 2.8 MW input power per port. Thus we will study the MP from 10 kW up to 3 MW.

MP In the Coaxial Waveguide

Without B field, the MP in the coaxial waveguide can be solved analytically for low-order modes and has been studied thoroughly. With the fringe field of the Lab_G magnet, the MP pattern changes significantly.

- The EC spectrum is shown in Fig. 3. Without B field, there is a narrow MP band at low power from 40 kW to 70 kW. Beyond that, there is no more MP. The Lab_G magnet fringe field induces a resonant pattern at higher power. As the B field increases, more resonant patterns show up at high power but the EC is small compared to the MP at low power.

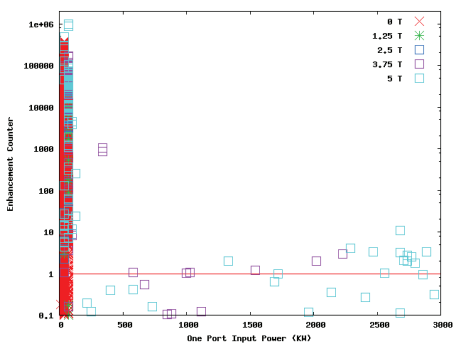


Figure 3: The EC spectrum in the coaxial waveguide.

- The MP impact location is shown in Fig. 4. With Lab_G B field, many resonant patters show up near the RF window with high EC. Most of them happen under 100 kW. Looking into the trajectories of these electrons, they are emitted near the RF window and build the resonance pattern bouncing between the inner and outer conductor of the waveguide. This may explain the copper deposition on the RF window observed in the previous test of the 201 MHz prototype cavity [7].

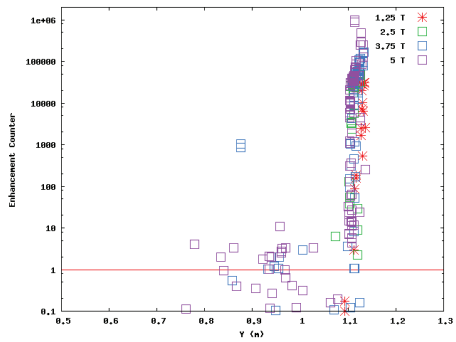


Figure 4: The MP impact location in the coaxial waveguide, where $Y = 1.1$ m is near the RF window.

MP In the Coupler Region

Due to the detailed geometry in the coupler region, the meshing at this area needs to be very dense to achieve an accurate RF field. The computation time would be too long if we carried out the MP calculation in the whole region. Therefore, we choose three typical locations in the upper, the middle and the bottom part of the couple and combine their results.

- The EC spectrum is shown in Fig. 5. Without external B field, MP happens only below 200 kW. As the Lab_G magnet increases its strength, the MP decreases in the low power region but shows up at higher power with smaller EC. No MP is observed above 750 kW.

- The MP impact location is shown in Fig. 6. Without external B field, the electrons emitted at the coupler region migrate up into the coaxial waveguide and build up a resonance there. When the external magnetic field is present, some electrons start to migrate into the cavity body and build up resonance along the curved torus. The stronger the external B field, the more resonance in the cavity.

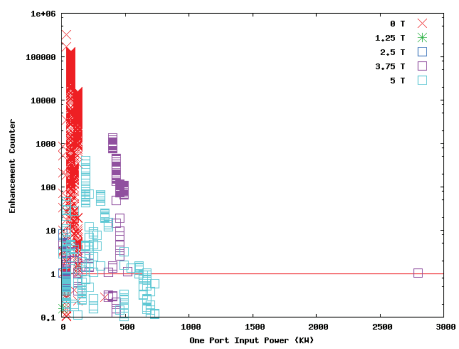


Figure 5: The EC spectrum in the coupler.

MP In the Cavity Body

When studying the MP in the cavity body, for simplicity, we study the cavity without the coaxial waveguide and

Copyright © 2013 CC-BY-3.0 and by the respective authors

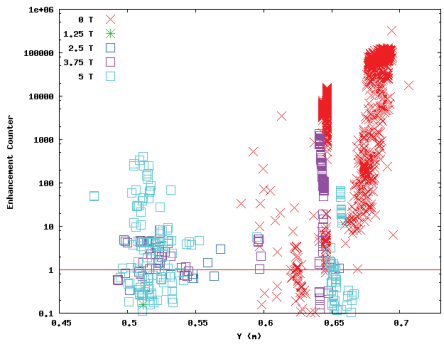


Figure 6: The MP impact location in the coupler. For reference, the extrusion transition between cavity and waveguide is from $Y = 0.601$ m to 0.627 m.

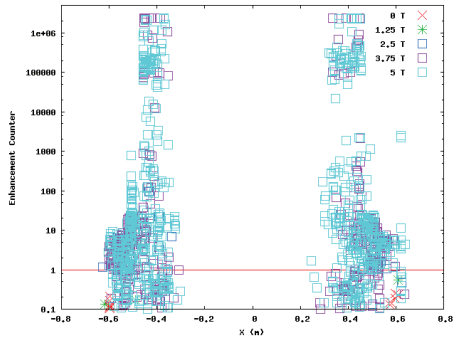


Figure 8: The MP impact location in the cavity body. For reference, the extrusion edge of the vacuum port and instrumentation port are at $X = -0.6$ m and 0.6 m, respectively.

coupler. Without the power input port, we use the E field gradient instead of the input power in the MP EC spectrum.

- The EC spectrum is shown in Fig. 7. When the external B field is zero or small, there is no MP in the cavity. As the B field increases, MP starts to show up in the cavity. The maximum MP happens at around 2 MV/m.

- The MP impact location is shown in Fig. 8. Above 50% of the full field of Lab_G magnet, stong MP starts to show up on the cavity copper side walls around $x \approx \pm 0.4$ m.

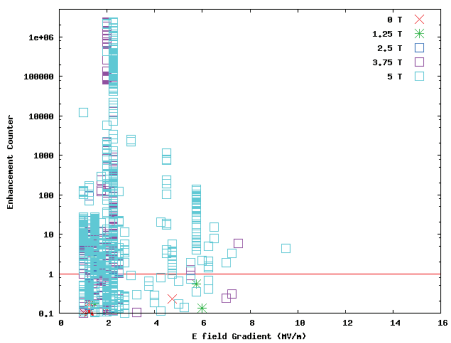


Figure 7: The EC spectrum in the cavity body.

CONCLUSION

In this paper we have studied the MP in the MICE 201 MHz cavity in the Lab_G magnet fringe field for the upcoming single cavity test at Fermilab MTA. Our study has shown that:

1. Without external magnetic field, in the coaxial waveguide, there is a narrow MP band at around 40-70 kW; in the coupler, some electrons migrate into the waveguide and build up MP there; no MP shows up in the cavity body.

2. The Lab_G magnet fringe field will change the MP, and its effects depend on the field strength. With the Lab_G field, simulation shows strong MP near the RF window in the waveguide, which might explain the copper deposition on the RF window seen in the previous test. In the coupler region, the B field guides the electrons into the cavity body and builds up MP along the curved torus. In the cavity body, when the Lab_G magnet operates above 50% of its full field, MP shows up on the copper side walls at low power.

We have applied several approximations in the simulations, such as ignoring other ferrite materials near the cavity, simplifying the loop coupler and RF window structure, using SEY data of AGD copper instead of electropolished copper, tuning the cavity to exact critical coupling, etc. All these factors will affect the MP results. Nonetheless this paper provides a qualitative, or semi-quantitative, description of the MP effect in the MICE 201 MHz cavity in the upcoming single cavity test.

ACKNOWLEDGMENT

The authors want to thank the SLAC ACD group for the support on ACE3P simulation tools, Rob Ryne of LBNL for the computation time on NERSC and Yagmur Torun of IIT/Fermilab for the field mapping data of LabG magnet.

REFERENCES

[1] M. Bogomilov et al., (MICE Coll.), JINST 7, P05009 (2012).

[2] K. Ko et al., "Advances in Electromagnetic Modeling through High Performance Computing", Physica C441,258 (2006).

[3] Lixin Ge et al., "Multipacting simulation for Muon Collider Cavity", Proceedings of PAC09, Vancouver, BC, Canada.

[4] Mike Green, "A Test Report for the MUCOOL RF Solenoid", LBNL-45148.

[5] http://mice.iit.edu/mta/magnet/magnet.html

[6] Bagline V., et al, Proceeding of PAC2001, Vol. 3. IEEE, 2001, pp. 2153.

[7] Alan Bross, "The Muon Accelerator Program "High" Gradient Normal Conducting RF R&D", US HG Workshop 2011.

Copyright © 2013 CC-BY-3.0 and by the respective authors

MULTI-HARMONIC ACCELERATING CAVITIES FOR RF BREAKDOWN STUDIES*

Y. Jiang#, J. L. Hirshfield, Yale University, New Haven, CT 06511, USA

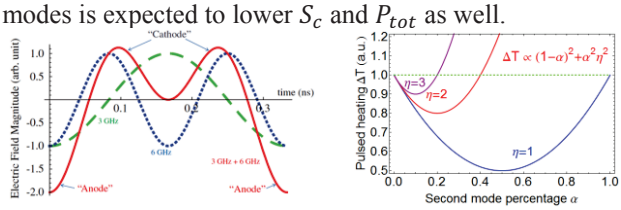
Abstract

Multi-harmonic accelerating cavities that are explicitly designed for RF breakdown experiments are described. The fundamental TM_{010} and its higher harmonic TM_{011} or TM_{012} modes of the cavities are to be excited coherently by an external RF source in the expectation of lowering surface pulsed heating and/or surface electric field, so as to reduce breakdown probability and possibly achieve an increase in acceleration gradient.

INTRODUCTION

In this paper, microwave cavities that support the superposition of the fundamental TM_{010} mode and at least one more mode whose eigen-frequency is a harmonic of the TM_{010} eigen-frequency are described. These bimodal cavities are explicitly intended to be vehicles that may deepen understanding of RF breakdown and pulsed heating, and as possible candidates for incorporation into multi-cavity high-gradient accelerator structures.

By selectively exciting synchronized multi-harmonic cavity modes driven externally in a precisely-controlled manner from a novel multi-frequency RF source available at Yale [1], unconventional spatiotemporal distributions of electromagnetic fields within a cavity can be realized, with the potential to lower field emission and/or pulsed heating at a given level of acceleration gradient; these effects are believed to be precursors to RF breakdown. In particular, two phenomena provide the main motivation for introduction of a 2nd mode at a harmonic frequency, namely: (a) the so-called anode-cathode effect [2]. In a longitudinally *asymmetric* cavity [2], phase-locked two-frequency operation, with the 2nd mode at a frequency double that of the fundamental, can allow the electric field pointing into one wall (cathode-like) to be significantly smaller than the field pointing out of that wall (anode-like), as shown in Fig. 1. A strong anode field will raise the work function barrier to suppress field and secondary emission; and (b) the suppression of pulsed heating, which is the focus of this paper. To model pulsed heating in a bimodal cavity, we characterize E-field superposition as $E_{total} = (1-\alpha)E_1 + \alpha E_2$, where $E_{1,2}$ is each electric field component with its associated acceleration gradient normalized to the same value, and α is the percentage of the 2nd mode such that E_{total} provides the same acceleration gradient. Similarly, the surface RF H-field is $H_{total} = (1-\alpha)H_1 + \alpha H_2$. Pulsed heating temperature rise ΔT can then be approximately scaled in terms of H_1 and H_2 as $\Delta T \propto (1-\alpha)^2 < H_1^2 > +\alpha^2\sqrt{f_2/f_1} < H_2^2 > =< H_1^2 > [(1-\alpha)^2 + \alpha^2\eta^2]$, where the frequency term $\sqrt{f_2/f_1}$ is related to the ratio of surface resistivities, $\eta = \sqrt{(f_2/f_1)^{1/2} < H_2^2 > / < H_1^2 >}$, and the cross term averages out over one period. Due to the quadratic dependence of ΔT upon α, it is possible to choose an optimal α such that $(1-\alpha)^2 + \alpha^2\eta^2 < 1$. In other words, to have lower temperature rise than for a single mode alone, while maintaining the same acceleration gradient; this is shown quantitatively in Fig. 1(b). The modified Poynting vector S_c [3], and total required RF power P_{tot}, also follow a quadratic dependence on the mode percentage α, so use of two modes is expected to lower S_c and P_{tot} as well.



(a) (b)

Figure 1: (a) Time dependence for a composite field (red line) excited at 3 GHz (green dashed) and 6 GHz (blue dotted), showing a factor-of-two anode-cathode field difference. (b) Dependence of the surface pulsed heating temperature rise ΔT on the 2nd mode percentage α. There is seen to be a range of α within which ΔT can be smaller than for a single mode (the green dashed horizontal line).

TM_{010} +TM_{011} CAVITY

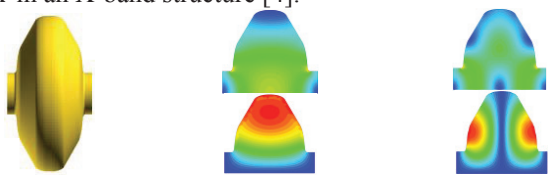
For a simple pillbox designed as a bimodal cavity with a typical iris size of $0.1\lambda - 0.2\lambda$ to support the TM_{010} mode and a 2nd harmonic TM_{011} mode, our analysis shows that $\eta > 3$. This implies that ΔT could not decrease by more than 10% for a simple pillbox cavity. Consequently, a new software package is being developed by us to optimize cavity geometry to support multi-harmonic modes with desired RF properties, such as high shunt impedance and low surface fields, and maximize reduction in temperature rise ΔT. This code integrates *Finite Element Method* and *Generic Algorithm*, so that it can find global optimization of RF parameters. Currently the code package is to include beam-cavity interactions that allow multipactor, wake field, and beam dynamics studies to be carried out in our unconventional structures, so as to provide a single software suite to expedite cavity design and optimization of RF properties and beam dynamics.

Optimization of design for a bimodal cavity supporting the TM_{010} mode and its 2nd harmonic TM_{011} mode can be realized using this code, as shown in Fig. 2. It is a full π-mode accelerating cavity, longitudinally symmetric with iris and beam pipe. Its fundamental frequency is at X-

*Work supported by U.S. DOE
#yong.jiang@aya.yale.edu

Copyright © 2013 CC-BY-3.0 and by the respective authors

band (12 GHz), to benchmark against the empirical criteria recently proposed within the worldwide High Gradient Collaboration: namely, a surface electric field $E_{sur}^{max} < 260\ MV/m$ and pulsed surface heating $\Delta T^{max} < 56\ K$ in an X-band structure [4].



(a) (b) (c)

Figure 2: Field patterns in an optimized bimodal cavity (a) for the TM_{010} mode (b), and its 2nd harmonic TM_{011} mode (c). Top patterns are *E*-field, bottom are *H*-field.

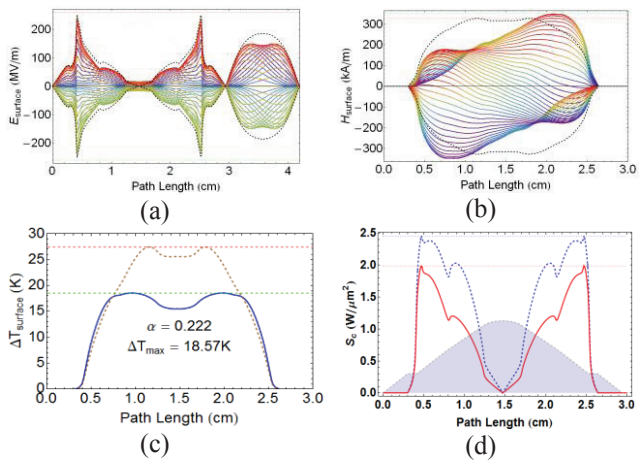
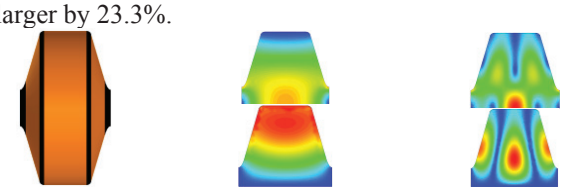


Figure 3: (a) Surface *E*-field and (b) surface *H*-field along the cavity periphery at different times for superposition of TM_{010} and TM_{011} modes, where the dotted line indicates fields of mode TM_{010} alone. *H*-field asymmetry is due to field distribution and chosen phase of the TM_{011} mode. (c) Optimized maximum pulsed heating temperature rise ΔT (blue line) is 18.57 K, compared to that of single mode 27.5 K (brown dotted line), both for a 200 ns pulse width; (d) maximum modified Poynting vector S_c (red line) is $1.95\ W/\mu m^2$ compared to a single mode value (blue dashed line) of $2.45\ W/\mu m^2$. The factor α for the 2nd mode in this example is 0.222. The gray area in (d) indicates the stretched cavity profile.

With this optimized cavity profile, the benefits of reducing surface pulsed heating, modified Poynting vector, and total RF power are demonstrated, as shown in Fig. 3 and Table 1. In Fig. 3, the pulsed heating temperature rise for our 2-mode superposition can be 32% smaller than that for the fundamental mode alone for the same cavity; and the maximum modified Poynting vector S_c can be lower by 20%, with a 22% 2nd harmonic component and a relative phase between the two modes of 90° (both modes are in sychromization should this bimodal cavity be operated in an accelerating structure). The peak surface *E*-field is the same as that of the fundamental mode due to this phase relationship, and no anode-cathode effect is present. Note, that even for a single TM_{010} mode, S_c is small due to the reduced *H*-field around the iris as a result of optimization. In Table 1, RF parameters of this bimodal cavity are listed in comparison with other cavity configurations. Although the instantaneous surface *H*-field is increased, the pulsed heating temperature rise is lowered since the exposure time to the peak *H*-field is shortened, and temperature rise is a time-averaged effect quadratically dependent on the mode percentage α in our 2-mode superposition. The total RF power is reduced, while maintaing the same acceleration gradient, so its effective shunt impedance is significantly increased.

TM_{010}+TM_{012} CAVITY

Because of different magnitudes and profiles of field distributions along the cavity walls for different modes in bimodal cavities, it is possible to have partial electric field cancellation on walls so that the maximum surface *E*-field can be smaller than that of single mode. We have analysed a π-mode accelerating cavity shown in Fig. 4 that supports the TM_{010} mode and its 3rd harmonic TM_{012} mode. When both modes reach the peak axial accelerating fields synchronously, the TM_{012} mode has its surface electric field opposite in direction to that of the fundamental TM_{010} mode on the side walls, and hence lowers the surface electric field significantly, as shown in Fig. 5. Preliminary analyses show that reductions in the maximum pulsed heating temperature rise of up to 21.5%, of the modified Poynting vector by 29.5%, peak surface *E*-field by 19.4%, total RF power by 18.9% are predicted for this bimodal cavity, than those for single mode operation at the same acceleration gradient for the same cavity. Also, its effect shunt impedance of 124.2 $M\Omega$/m is larger by 23.3%.



(a) (b) (c)

Figure 4: (a) Optimized bimodal cavity profile, with $a/\lambda = 0.1$. Field patterns for the TM_{010} mode (b), and its 3rd harmonic TM_{012} mode. Top patterns are *E*-field, bottom are *H*-field.

RF BREAKDOWN STUDY

It is of obvious interest to measure RF breakdown statistics for these bimodal cavity designs, comparing single mode and 2-mode superpostion, and to investigate surface fatigue on cavity surfaces after pulsed heating. An RF breakdown study is to be carried out based on availability in the Yale Beam Physics Lab of a unique 2-frequency phase synchronous RF source at S-band (2.856 GHz) and its higher harmonics, either at C-band (5.712 GHz) or X-band (8.856 GHz). The 2-frequency RF source will provide mutually phase-locked multi-MW ~1 μs pulses at both fundamental and higher harmonic

Copyright © 2013 CC-BY-3.0 and by the respective authors

Table 1: Comparison of RF parameters between an optimized bimodal TM_{010}+TM_{011} cavity and single mode cavities, where effective acceleration gradient is equalized at 100 MV/m, with red/green arrows showing up/down improvements. Pillbox A has the same maximum surface *H*-field as that of the fundamental mode in bimodal cavity; Pillbox B the same maximum surface *E*-field; and the nose-cone cavity is a single-mode cavity optimized to increase shunt impedance and lower surface pulse heating using the same code.

a/λ=0.12 π mode standing wave effective gradient $E_a = 100MV/m$	**TM_{010} + TM_{011} Bimodal Cavity**			**Pillbox A**	**Pillbox B**	**Nose-cone**
	1st harmonic alone	**2nd harmonic alone**	**78% 1st +22% 2nd**	**1st harmonic only**	**1st harmonic only**	**1st harmonic only**
frequency (GHz)	11.9942	23.9884		11.9942	11.9942	11.9942
effective shunt impedance (MΩ/m)	95.7	38.3	▲131.4	89.7	99.1	113.9
transit time factor	0.765	0.786		0.768	0.753	0.758
max E_{surf} (MV/m)	246.8	367.4	246.8	209.7	246.8	225.0
max H_{surf} (MA/m)	0.327	0.634	0.350	0.327	0.298	0.289
max S_c $(W/\mu m^2)$	2.45	10.3	▼1.95	3.75	3.02	4.20
max ΔT (K) @ 200ns pulse length	27.5	148.2	▼18.6	27.5	22.87	21.5
wall loss (MW)	1.306	3.263	▼0.95	1.392	1.262	1.097

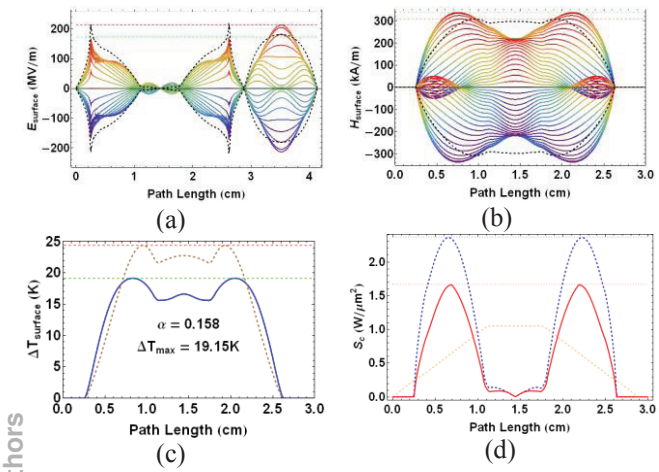


Figure. 5: (a) surface E-field and (b) surface H-field along the cavity periphery at different times for superposition of TM010 and TM012 modes, where the dotted line indicates fields of single mode TM010. (c) Optimized maximum pulsed heating temperature rise (blue line) is 19.15 K, compared to that of single mode 23.7 K (brown dotted line) with a 200 ns pulse width; (d) the maximum modified Poynting vector S_c (red line) is 1.67 $W/\mu m^2$ compared to a single mode value (blue dashed line) of 2.37 $W/\mu m^2$. α for the 2nd mode is 0.158.

frequencies with continuously-adjustable amplitudes and relative phase difference. The cavity geometry suitable for RF breakdown tests at Yale using S-band (2.856 GHz) as the fundamental frequency can be directly scaled from the optimized geometries shown above. RF breakdown tests in travelling wave or standing wave single cell structures [5] can be devised to benchmark with the existing RF breakdown data [3]. With better understanding of RF breakdown physics supported by experimental evidence and further development of computational tools, design concepts for accelerator structures comprising multi-harmonic cavities will be developed.

Bimodal cavities with the necessary tight dimensional tolerances require meticulous machining; but should be possible using recently described techniques that maintained dimensions to within 5 μm [6]. Further evidence for precision tuning of a not-dissimilar bimodal cavity has also been reported [1].

CONCLUSION

This paper describes use of multi-harmonic cavities powered by a dual frequency RF source to systematically study mechanisms which seem likely to influence the onset of RF breakdown. It is anticipated that deepened understanding of these mechanisms could lead to improved design of accelerator structures with higher shunt impedance, higher accelerator gradient, and lower breakdown probability than can be built at present.

ACKNOWLEDGMENT

The authors would like to thank Professor R.M. Jones from Manchester Univ. (UK) for valuable discussions.

REFERENCES

[1] Y. Jiang, et al, NIM A, v657, pp 71-77 (2011).
[2] S.V. Kuzikov et al, Phys. Rev. Lett. 104, 214801 (2010).
[3] A. Grudiev, et al, Phys. Rev. ST Accel. Beams, 12, 102001 (2009); and citations therein.
[4] A. Grudiev, et al, Proceedings of LINAC08, Victoria, Canada THP062, pp.923-935 (2008).
[5] V.A. Dolgashev, et al, SLAC-PUB-10667 (2004).
[6] S. Atieh, et al, IPAC2011, pp. 1768-1770 (2011).

Copyright © 2013 CC-BY-3.0 and by the respective authors

DESIGN STUDY OF KNOT-APPLE UNDULATOR FOR PES-BEAMLINE AT SSRF

Shigemi Sasaki#, Atsushi Miyamoto,
Hiroshima Synchrotron Radiation Center, Hiroshima University, Higashi-Hiroshima, Japan
Shan Qiao
Shanghai Institute of Microsystem and Information Technology, Chinese Academy of Sciences, People's Republic of China

Abstract

An intense on-axis radiation power from a linear undulator is a serious problem for a VUV/soft-X-ray beamline at medium or high energy light source facility. This problem may be solved by using a specially designed linear undulator such as the Figure-8, Pera, or Knot undulators. However, a permanent magnet undulator of such kind is not capable of changing polarization state. On the other hand, an APPLE undulator is able to generate variable polarization, but is not capable to reduce on-axis power density in linear modes. To solve these problems, we investigated various magnetic structures and found that the combination of Knot and APPLE undulator scheme works to generate low on-axis power density in every polarization mode.

INTRODUCTION

In order to generate the undulator radiation in VUV region at a medium energy storage ring facility, the undulator should have a very long period and a high K-value. In this case, especially for a linear undulator, unwanted high radiation power for higher harmonics concentrates on the radiation beam axis, and hence it give a heave heat load on optical components such as a mirror and a monochromator. To reduce the on-axis heat load, the Figure-8 undulator was proposed [1] and have been used in several synchrotron radiation facilities. Also, similar ides for the same purpose were proposed [2-4]. However, all those ideas except the Figure-8 were not realized may be due to the complicated structure and the advantages are not so significant compared with Figure-8. More importantly, all those exotic devices including the Figure-8 are not capable of varying polarization states. On the other hand, the APPLE-type undulators can generate various polarization states such as the right/left circular polarization, tilted linear polarization, and horizontal/vertical linear polarization. However, in the linear polarization modes, on-axis high power problem form higher harmonics is remaining as a serious problem.

In order to solve all problems described above, we propose a new scheme which is called a Knot-APPLE undulator to reduce on-axis radiation power in every polarization mode.

KNOT UNDULATOR

Figure 1 shows the magnetic structure of Knot undulator. This structure, similar to the Figure-8 undulator, the Halbach structure permanent magnet arrays locate above and below the beam axis, and magnet rows for generating horizontal magnetic field on the beam axis locate at both sides of central magnet rows. As shown in Figure 1, the dimension in the direction of beam axis of each magnet block in the horizontal row is the same with that in the vertical rows except the end structure.

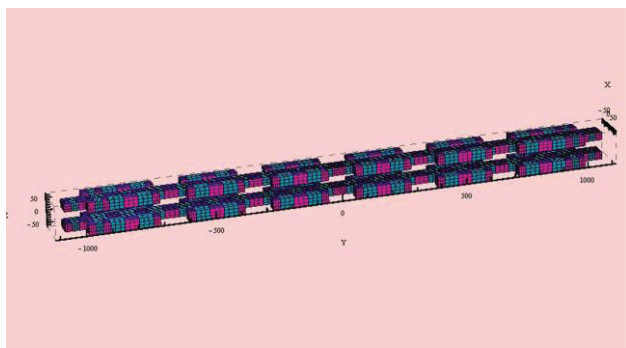


Figure 1: RADIA model of magnet structure for a Knot undulator.

As is seen in Figure 1, there is an empty space between segments in the horizontal structure in order to create the zero-field region. With this structure, the period length of horizontal field is one and a half of vertical field. Figure 2 shows the magnetic field distribution of Knot undulator having the structure of Figure 1.

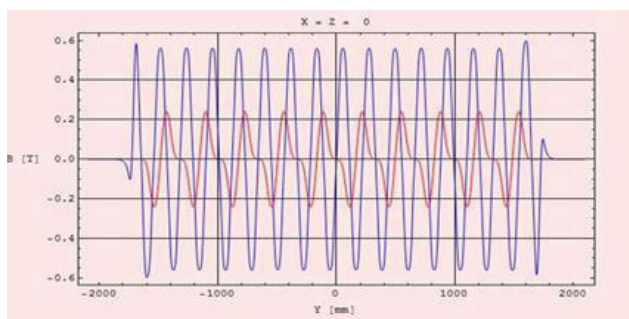


Figure 2: Field distribution of Knot undulator.

In Figure 2, blue line represents the vertical field and red line represents the horizontal field. The period lengths are 220 mm and 330 mm for vertical and horizontal, respectively. The magnet gap to generate the field in this figure is 40 mm.

Figure 3 shows the kick-angle map in an undulator having the field shown in Figure 2 for an electron beam with the energy of 3.5 GeV.

#sasakis@hiroshima-u.ac.jp

Copyright © 2013 CC-BY-3.0 and by the respective authors

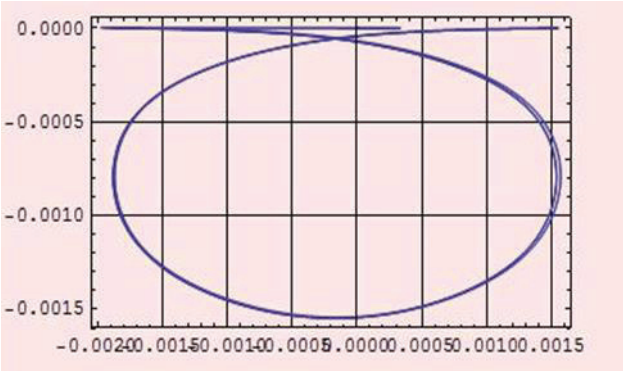


Figure 3: Kick map of Knot undulator.

The on-axis angular flux density spectrum is shown in Figure 4. At 6.2 eV peak position, the horizontal linear polarization with P_L > 99 % is achieved. For the calculation, parameters of the storage ring at Shanghai Synchrotron Radiation Facility (SSRF) are used which are E=3.5 GeV, I=200 mA, and ε_0=11.2 nmrad.

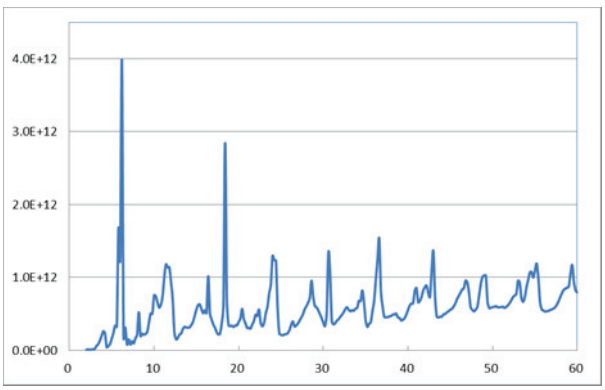


Figure 4: On-axis spatial flux density of the horizontal polarization mode.

KNOT-APPLE UNDULATOR

The Knot-APPLE undulator can be made by dividing central magnet rows into two parts in the same manner for creating the APPLE device. To create a magnet row in one quadrant, one has to combine the vertical row and horizontal row in a fixed position in the same magnet holder. Then, one has to introduce the same motion mechanism with that of APPLE undulator.

Vertical Polarization Mode

To reach to the vertical polarization mode, the magnet row phase has to be moved $\pm\pi$ ($\pm$110 mm) in anti-parallel direction. The antiparallel motion causes tilt of linear polarization which is different form the parallel motion that generates elliptical polarization.

Figure 5 shows the magnet row positions for the vertical polarization mode.

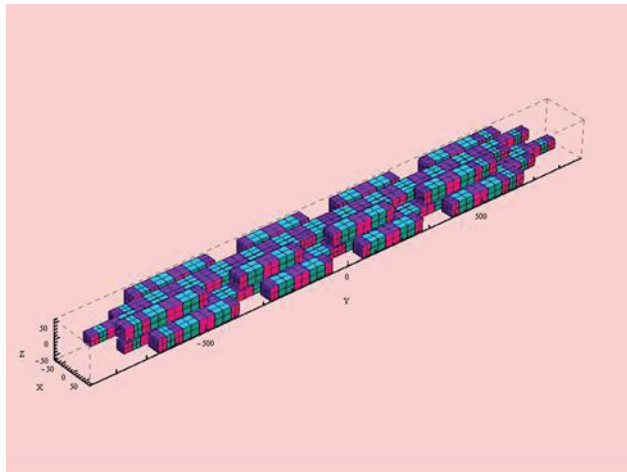


Figure 5: Magnet Structure of Knot-APPLE undulator in the vertical polarization mode.

Figure 6 shows the magnetic field distribution and Figure 7 shows the kick-angle map for vertical polarization mode. As it is obvious by comparing the field distribution for the horizontal polarization mode in Figure 2, the period length of vertical field component is one and a half larger than that of horizontal polarization.

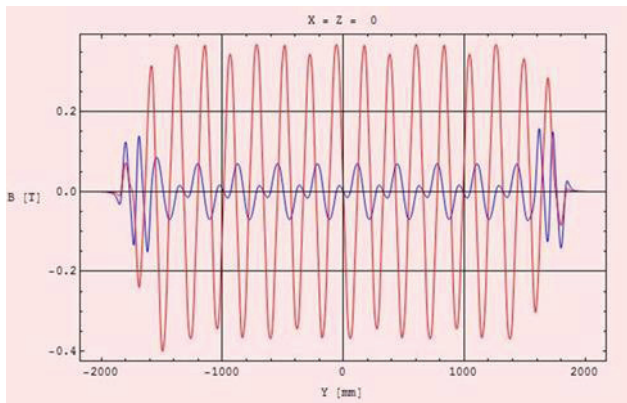


Figure 6: Field distribution of Knot-APPLE undulator in the vertical polarization mode.

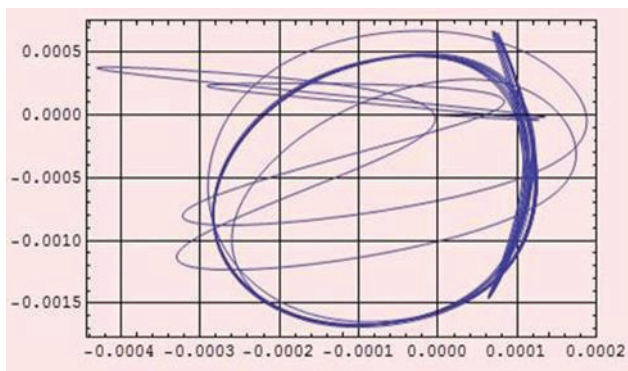


Figure 7: Kick map in the vertical polarization mode.

The on-axis flux density spectrum for the vertical polarization mode is shown in Figure 8. For the calculation, the ring parameters are assumed to be the same with those of horizontal polarization mode. The

Copyright © 2013 CC-BY-3.0 and by the respective authors

degree of vertical linear polarization in this mode is above 97 % at the fundamental (17.4 eV) peak position.

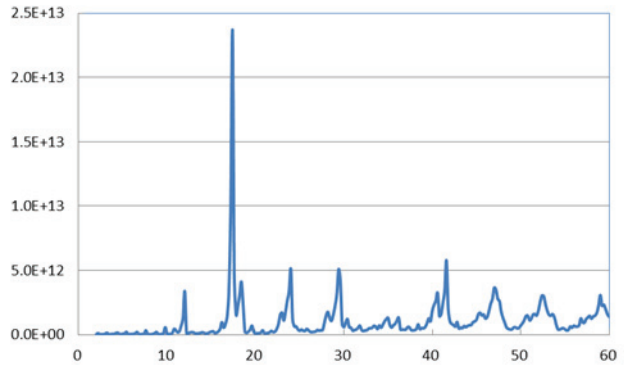


Figure 8: On-axis spatial flux density of the vertical polarization mode.

Elliptical Polarization Mode

To realize the elliptical polarization, different form the antiparallel motion for tilting linear polarization, the parallel motion is required. Figure 9 shows the magnet structure for the elliptical mode.

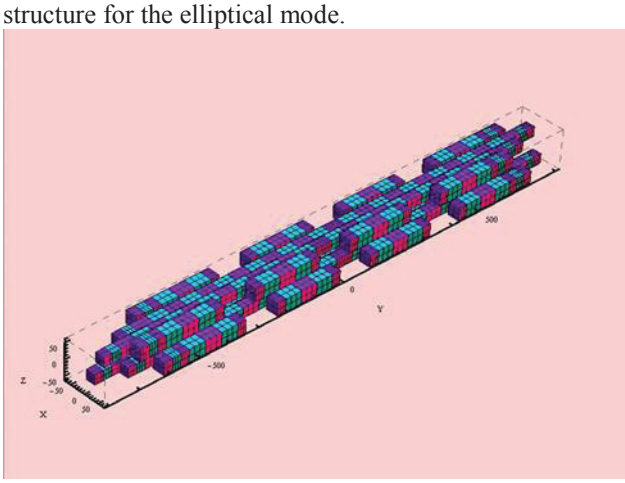


Figure 9: Magnet Structure of Knot-APPLE undulator in the elliptical polarization mode.

Figure 10 shows the magnetic field distribution for the elliptical polarization mode at the magnet row phase of 65 mm, and Figure 11 shows the kick-angle map of this mode.

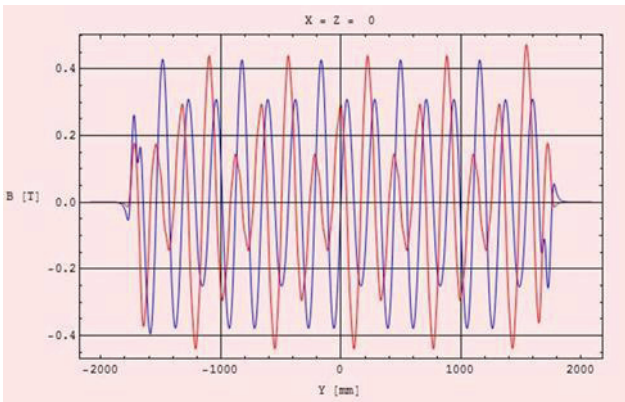


Figure 10: Field distribution of the elliptical mode at magnet row phase D = 65 mm.

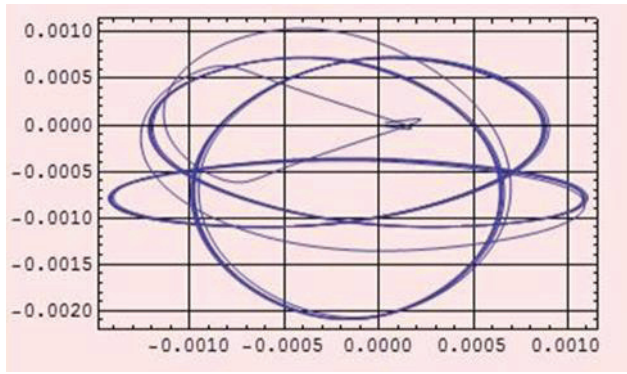


Figure 11: Kick map in the elliptical mode.

The on-axis flux density spectrum of elliptical polarization mode is shown in Figure 12. For the calculation, the ring parameters and the undulator gap were assumed to be the same with previous two cases. The degree of circular polarization in this mode is above 90 % at 9.8 eV peak position.

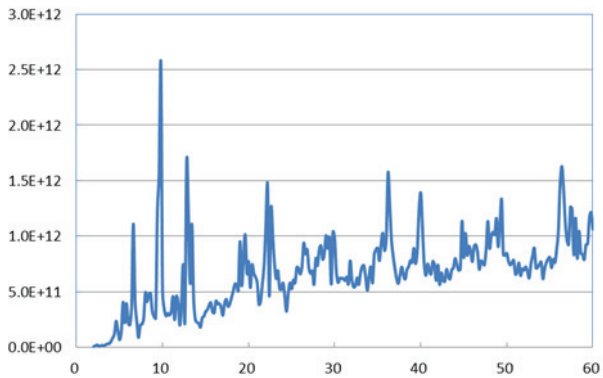


Figure 12: On-axis spatial flux density of elliptical polarization mode.

SUMMARY

In this paper, the Knot-APPLE undulator that is capable to vary polarization states with low on-axis power density at every polarization mode is proposed. This new device can be useful for synchrotron radiation users who use relatively low photon energies at medium/high energy ring facilities.

REFERENCES

[1] T. Tanaka and H. Kitamura, Nucl. Instrum. Meth. A 364 (1995) 368.
[2] S. Sasaki, *Undulators, wigglers and their applications*, pp. 237-243 (Ed. by H. Onuki and P. Elleaume, Taylor & Francis Inc, New York, 2003).
[3] S. Qiao et. Al., Rev. Sci. Instrum. 80 (2009) 085108.
[4] J. Yan and S. Qiao, Rev. Sci. Instrum. 81 (2010) 056101.

Copyright © 2013 CC-BY-3.0 and by the respective authors

CONCEPTS FOR SHORT PERIOD RF UNDULATORS

S.V. Kuzikov#, A.V. Savilov, A.A. Vikharev, IAP RAS, Nizhny Novgorod, Russia

Abstract

Two concepts for room-temperature RF undulators, fed by cm- or mm- wavelength radiation and aimed to produce ~1 nm wavelength radiation using relatively low energy electron beams, are considered. In accordance with the first considered concept each undulator segment introduces a high-Q cavity fed by its own multi-megawatt RF source. The 30 GHz pulsed gyroklystron or gyrotrons at 30 - 300 GHz, already elaborated and tested in IAP RAS, are appealing candidates. These sources can provide the effective undulator period of 0.5 - 0.05 cm, the undulator parameter up to 1, and the effective field length of 50 cm for each segment. The second concept implies using high-power short pulse propagating in a long helically corrugated waveguide where the -1st field harmonic is responsible for particle wiggling. High group velocity of this pulse allows providing long interaction of particles with RF fields.

RF UNDULATORS BASED ON HIGH-QUALITY CAVITIES

RF undulator in comparison with traditional undulator, consisting of DC magnets, introduces a strong appeal to use less energetic electron beam, in order to produce the same wavelength of Compton's scattered radiation [1-3]. For example, in order to achieve radiation of nanometer wavelength instead of 1-2 GeV beam in conventional undulator with several centimeters period, one can use several hundreds of MeV beam in RF undulator with period ~1 cm [4]. The inevitable payment for this evident advantage is a necessity to provide high power level of microwaves, in order to have acceptable undulator parameter to be competitive with conventional undulators. In Ka-band the necessary power of the wave (to be counter-propagating to electrons) in waveguide of ~1 cm size reaches GW level. That is why, the modern projects of RF undulators assume cavities of high Q-factors to be powered by existing RF sources (klystrons, gyroklystrons, magnikons) which itself are able to provide tens of megawatts. According to such a concept full RF undulator consists of many relatively short sections to be mutually phased ones. At centimeter wavelength range the bimodal TE_{01}-TE_{02} resonator looks promising [4], at millimeter or sub-millimeter range a multi-mirror Gaussian beam resonator is preferable.

High-Q cavities bring a threat of destroying phenomena like RF breakdown and pulsed heating [5-6]. In order to avoid these undesirable phenomena, a short-pulse RF radiation of GW power level is appealing. In particular, experiments carried out with particle accelerators show that nanosecond RF pulses of GW level can travel through electrodynamic structure without breakdown [7].

There are necessary RF sources of GW power level based on relativistic BWOs [8]. Such sources can deliver more than 1 GW power in X-band and about 1 GW in Ka-band in pulses of 0.1-20 ns duration with repetition rate as high as several kHz. It was proven in experiments that phases of separate sources might be mutually locked [9].

SHORT-PULSE, TRAVELING WAVE RF UNDULATOR BASED ON HELICAL CORRUGATED WAVEGUIDE

A short RF pulse of duration τ, propagating in a smooth waveguide with group velocity closed to light velocity c and directed toward an ultrarelativistic electron bunch, causes wiggling of particles at length $L_{eff}^{count} = c\tau/2$. If one takes 10 ns RF pulse, the interaction length does not exceed 2 m. Interaction distance can be much longer, if RF pulse is co-propagating with electrons. In this case the effective interaction length is:

$$L_{eff}^{co} = \frac{v_{gr}\tau}{1 - v_{gr}/c}, \qquad (1)$$

where v_{gr} – is a group velocity along electron beam.

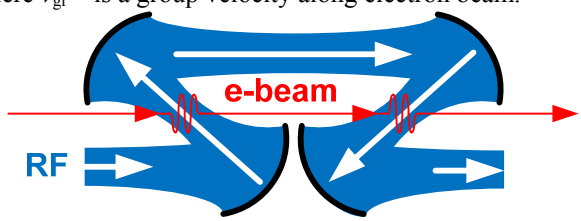


Figure 1: Mirror transfer line employing the "flying" RF undulator.

Of course, the co-propagating RF pulse in a smooth waveguide does not promise considerable Doppler's frequency up-shift. This problem is solved by using a so-called "flying" RF undulator, where a wavebeam spends a part of time moving toward electrons (Fig. 1).

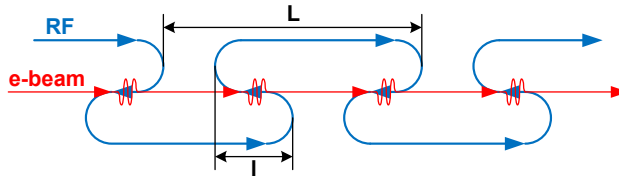


Figure 2: Equivalent scheme of "flying" RF undulator.

The simplified equivalent scheme of the "flying" undulator in Fig. 2 allows writing group velocity along beam in the mirror line:

$$v_{gr} = \frac{c}{1 + 2l/L}. \qquad (2)$$

#kuzikov@appl.sci-nnov.ru

Copyright © 2013 CC-BY-3.0 and by the respective authors

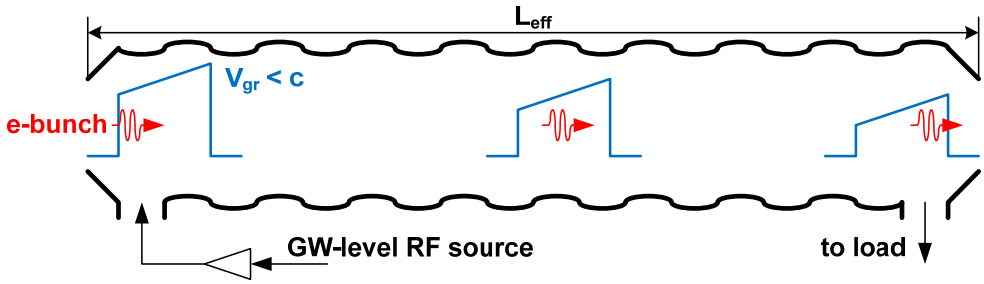


Figure 3: "Flying" RF undulator in form of helical corrugated waveguide section.

Any undulator can be described by dimensionless undulator parameter K, which is proportional to deflecting field amplitude. In an undulator with parameter K the optical radiation (in small signal approach) grows along electron path on z coordinate as $\sim \exp(K^{2/3} z)$ [4]. Let us introduce gain parameter as $\eta = K^{2/3} \cdot L_{eff}$, which can be used, in order to compare the "flying" RF undulator with the undulator, where RF pulse is counter-propagating. Ratio of gain parameters η_F (for the co-propagating 'flying' RF pulse) and η_0 (for the counter propagating RF pulse) is given using equations (1) and (2):

$$\frac{\eta_F}{\eta_0} = \frac{L}{l}. \qquad (3)$$

If the condition l=L is satisfied, then the "flying" RF undulator does not have advantages in comparison with smooth undulator with counter-propagating wave. Maximum of the ratio (4) is achievable, if l goes to zero. In this case the effective interaction length goes to infinity. However, there are big gaps where the interaction is absent at all. Such klystron-type configuration is more sensible to energy spread and beam emittance than configuration with simple counter-propagating wave [10].

In Fig. 3 the improved concept of the "flying" RF undulator, based on helical corrugated waveguide, is shown. Here bunch has continuous interaction with RF fields. In comparison with undulator based on counter-propagating wave in smooth waveguide (with parameter K_0), undulator parameter K in the corrugated waveguide is less, so let us take K=$K_0 \cdot \chi$. Nevertheless, the effective interaction is longer so that normalized gain parameter:

$$\frac{\eta_F}{\eta_0} = 2\chi^{2/3} \frac{v_{gr}/c}{1 - v_{gr}/c}, \qquad (4)$$

is more than unity, if group velocity is high enough:

$$\frac{v_{gr}}{c} > \frac{1}{1 + 2\chi^{2/3}}. \qquad (5)$$

In a corrugated waveguide of the fundamental period D there is an infinite number of the spatial harmonics those phase velocities could be either positive or negative relative to sign of electron velocity. Let us consider the "flying" RF undulator where co-propagating 0-th harmonic has the positive propagation constant h_0 and phase velocity, but -1-st harmonic has the negative propagation constant h_{-1} and negative phase velocity. The group velocity is less than c, positive and constant for all spatial harmonics. Particles oscillate in the transverse fields of the -1-st harmonic with equivalent undulator period:

$$\lambda_u = \frac{2\pi}{|h_{-1}| + k}, . \qquad (6)$$

where $h_{-1} = h_0 - 2\pi / D$, k=ω/c – is a vacuum wavenumber.

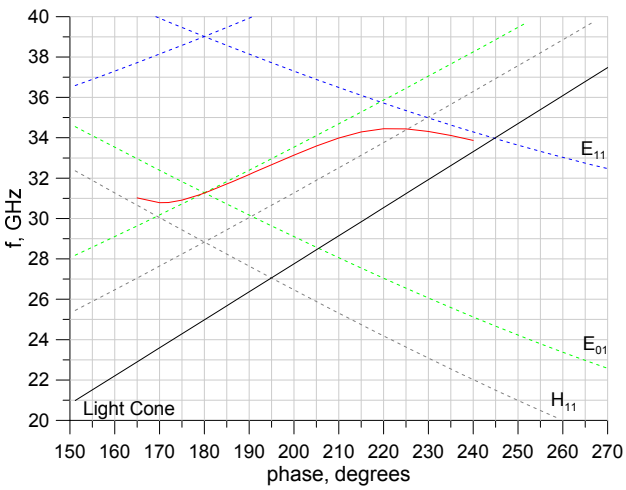


Figure 4: Dispersion characteristic of normal TM_{01}-TM_{11} wave in helical waveguide (red curve).

As it was proven in the paper [3], the co-propagating wave causes large-scale particle motion and dramatically spoils radiation spectra in RF undulator. In the proposed RF undulator the 0-th harmonic always exists and cannot be avoided. Nevertheless, in a helical corrugated waveguide the 0-th and -1-st harmonics can be represented by modes of different transverse structures.

Copyright © 2013 CC-BY-3.0 and by the respective authors

The 0-th harmonic should be chosen so that it does not possess transverse fields in the center where the thin electron beam travels. We suggest RF undulator based on TM_{01} (0^{th} harmonic) – TM_{11} (-1^{st} harmonic) in the one-thread helical waveguide. Dispersion curve of this operating normal wave, i.e. eigen frequency Vs phase h_0D in degrees, is shown in Fig. 4 for parameters: the average radius is R_0=6.1 mm, the period is D=6 mm, and the amplitude of corrugation is a=3 mm. The dashed curves correspond to partial modes in the smooth circular waveguide. The light cone is shown by black solid curve.

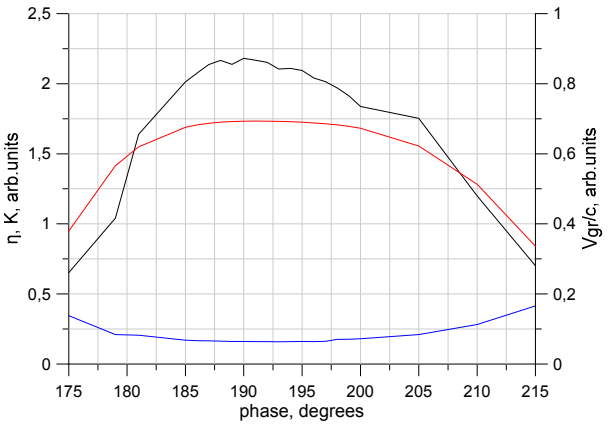


Figure 5: Normalized characteristics of TM_{01}-TM_{11} wave. The blue curve is undulator parameter. The red curve describes group velocity. The black curve is gain factor.

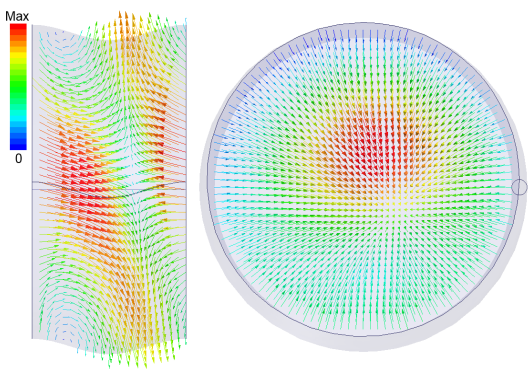


Figure 6: Instantaneous field structure of TM01-TM11 operating wave at phase 190 degrees.

In Fig. 5 K-parameter is plotted for the mentioned waveguide parameters and 1 GW RF power in dependence on the phase. In the same figure one can see group velocity and gain parameter also plotted in dependence on the phase. The highest value of parameter η (near 190 degrees in Fig. 5) corresponds to moderate fields, λ_u=5.4 mm, and group velocity about 0.7c. So we suggest to choose the point 190° as operating one. Such "flying" undulator is the equivalent of 10 m of usual undulator. Field structure of the operating TM_{01}-TM_{11} mode is shown in Fig. 6. Note that at the operating frequency partial TM_{11} mode is evanescent in the smooth circular waveguide.

The surface fields near phase 190° are 2.5 times higher than fields at axis so that Ohmic losses are not negligible. At phase=190° the power loss corresponds to factor $\alpha=6\cdot10^{-2}$ m^{-1} at room temperature. This loss is as high as about 60% of the incident RF power in 10 m helical waveguide. That is why, the pulse shape with the higher amplitude in front in comparison with the rear part of the pulse is desirable (Fig. 3). This pulse shape might provide constant acting fields for the electron bunch at whole undulator.

Schemes TE_{21}-TM_{11} and TM_{01}-TE_{11} are also possible.

CONCLUSION

The proposed concept, based on using GW level, 10-20 ns pulses in Ka-band, makes possible to use alone or a few number of RF sources in long enough "flying" undulator in order to create effective SASE XFEL.

REFERENCES

[1] T.Shintake et al. Development of microwave undulator. Japanese J. of Appl. Phys. 22, 844 (1983).
[2] V.L. Bratman et al. Stimulated scattering of waves in microwave generators with high-current relativisticelectron beams: simulation of two-stage free-electron lasers. Int. J. Electronics, Vol. 59, No. 3, pp. 247-289 (1985).
[3] S.G. Tantawi, CLIC Workshop 2013, High Gradient Session, CERN, January 31, 2013 (https://indico.cern.ch/contributionDisplay.py?contribId=41&sessionId=10&confId=204269)
[4] S.V. Kuzikov et al. Configurations for short period rf undulators, Phys. Rev. ST AB 16, Issue 7, 070701 (2013).
[5] V. Dolgashev et al. Geometric dependence of radio-frequency breakdown in normal conducting accelerating structures, Appl. Phys. Lett. 97, 171501 (2010).
[6] L. Laurent et al. Experimental study of rf pulsed heating, Physical Review Special Topics - AB 14, 041001 (2011).
[7] Thompson M.C. et al. Breakdown limits on Gigavolt-per-Meter Dielectric Wakefields, Phys. Rev. Lett. 2008. V. 100. p. 21.
[8] S.D. Korovin et al. Generation of Cherenkov superradiance pulses with a peak power exceeding the power of the driving short electron beam, Phys. Rev. E 74, 016501 (2006).
[9] V.V. Rostov et al. High Power Nanosecond Microwave Oscillators with Phase Synchronization. Strong Microwaves and Terahertz Waves: Source and Applications. Proceeding of 8th International Workshop, Russia. July 9–16, 2011. pp. 63–64.
[10] P. Elleaume et al. Design Considerations for a 1 Angstrom SASE Undulator, Nuclear Instruments and Methods in Physics Research. Section A, Vol. 455, No. 3, 2000, pp. 503-523.

Copyright © 2013 CC-BY-3.0 and by the respective authors

HELICAL SELF FOCUSING AND COOLING ACCELERATING STRUCTURE

S.V. Kuzikov#, S.V. Mishakin, A.A. Vikharev, IAP RAS, Nizhny Novgorod, Russia

Abstract

A new helical RF accelerating structure, which can provide emittance control of the electron beam, is proposed. This structure combines properties of a linear accelerator and a damping ring simultaneously. It makes acceleration of straight on-axis beam as well as beam cooling due to the synchrotron radiation of particles. These properties are provided by specific slow eigen mode which consists of two partial waves, TM_{01} and TM_{11} (near to cut off). The longitudinal field of the first wave is synchronous with electrons, the transverse fields of the second wave are far from synchronous condition and they cause electron wiggling like it occurs in RF undulator. As a result the emittance control might be employed at linear trajectory of the high-energy beam without decrease of the average gradient. Calculations show that surface electric field at level ~0,31 (relative to accelerating field) and shunt impedance ~20 MOhm/m at 30 GHz are achievable. Cooling rate at gradient 100 MV/m corresponds to the equivalent magnetic field ~0,75 T.

INTRODUCTION

High luminosity of colliding particles in meeting point is achievable for compact, well focused bunches. Such bunches are achievable using systems of particle's cooling. At energies up to several GeV dampling rings provides effective cooling [1]. In these rings particles move in spatially-periodic fields of DC magnets. There is cooling effect due to synchrotron radiation of particles [2]. In order to reach TeV level of energy, behind a cooling ring particles are directed in main linac. Unfortunately emittances of bunches propagating in high-gradient accelerator have tendency to increase, because long trains of particles inevitably excite wakefields which spoil beam quality.

At high energies (more than 10 GeV) rings cannot be used, because too high level of energy dissipation caused by radiation, and too big radius of a ring would be necessary. That is why, cooling undulator can be installed at the linear trajectory only. However, DC magnets around the accelerating structure would conflict with feeding, focusing, and diagnostic systems, and inevitably large period does not allow reaching small emittances, because the smallest achievable emittance is proportional to squared wiggler period [3]. Suggested in the paper [3] accelerator with alternating accelerating sections and wigglers would reduce effective gradient.

An accelerating RF structure, which also plays a role of RF undulator, does not reduce gradient. Such structure might be based on helical corrugated waveguide, where the operating normal mode consists of the 0^{th} spatial harmonic (with positive phase velocity), which is actually the accelerating mode, and the -1^{st} harmonic (with negative phase velocity) which is responsible for particle wiggling. The transverse non-synchronous field components can provide emittance control and beam focusing due to ponderomotive force which depends on transverse electric field gradient of the -1^{st} harmonic wave.

The enumerated properties allow to distinguish our new helical self focusing and cooling structure (HSFC) [4] among other helical structures investigated earlier [5, 6]. Nevertheless, there are important properties to be common for all helical structures. For example, like other helical structure a new structure has smooth shape of the constant circular cross-section (no expansions or narrowings) and big aperture (no small irises). A new technology of the mass production, based on a "corkscrew" in a copper mandrel, seems also possible which allows avoiding junctions inside sections.

TM01-TM11 HELICAL ACCELERATING STRUCTURE

Let us consider the accelerating structure based on helical waveguide described in cylindrical system of coordinates (r, z, φ) by equation:

$$r(z,\varphi) = R + a \cdot \sin\left(\frac{2\pi \cdot z}{L} + m\varphi\right). \qquad (1)$$

where R – is a waveguide radius, a and L – are amplitude and period of the corrugation. Period of the corrugation is close to $2\pi/h_{TM01}$, where h_{TM01} – is a propagation constant of the partial TM_{01} mode in smooth circular waveguide of the radius R. If index m equals 1, such helical structure couples partial waves TM_{01} and rotating on azimuth TM_{11}. The TM_{01} does not perturb transverse movement of on-axis electrons, the TM_{11} does not have longitudinal E_z component on axis.

Table 1: Parameters of TM_{01}-TM_{11} HSFC Structure

Radius, R	6.09 mm
Period, L	8 mm
Corrugation amplitude, a	1.25 mm
Azimuth index, m	1
Frequency, f	28.2 GHz
Phase advance, h_0L	4.727
Q-factor (copper)	10800
Norm. accelerating field, E_a / E_s^{max}	0.307
Shunt impedance, R_{sh}/L	18.9 MOhm/m

#kuzikov@apppl.sci-nnov.ru

Copyright © 2013 CC-BY-3.0 and by the respective authors

Parameters of helical structure TM_{01}-TM_{11} was optimized to reach maximum of the accelerating field relative to maximum of the arisen surface field E_a / E_s^{max}, maximum of shunt impedance R_{sh} was also necessary. Results of optimization for geometry at frequency 28GHz are shown in the Table 1. At acceleration gradient 100 MV/m the equivalent magnetic field is as high as 0.75 T. Dispersion relation for the optimized structure in a form of dependence of the eigen frequency f on phase advance h_0L (h_0 – is a Floquet propagation constant) is plotted in Figure 1. The line 1 in Fig. 1 is actually light cone which corresponds to the condition $h_0=k$. The operating mode (curve 2) has low group velocity (several per cents of light velocity). Of course, the operating point is the cross point of the curves 1 and 2.

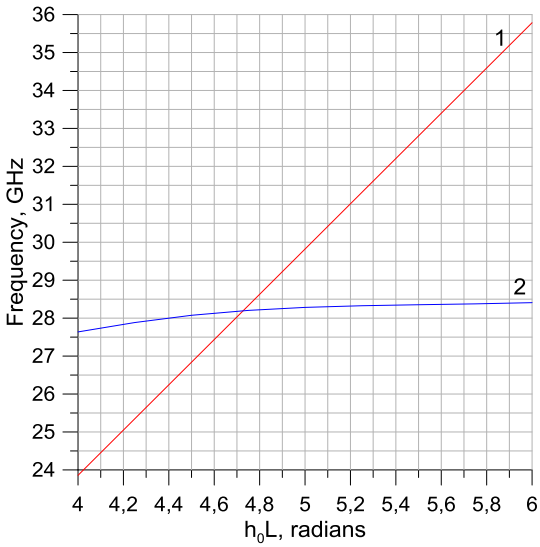


Figure 1: Dispersion characteristics: 1 – light cone line, 2 – dispersion curve of TM_{01}-TM_{11} wave in HSFC structure.

Field structure of the operating mode is shown in Fig. 2 (at middle plane) and in Fig. 3 (at two cross-sections). Accelerating field magnitude is uniform at beam line (Fig. 2).

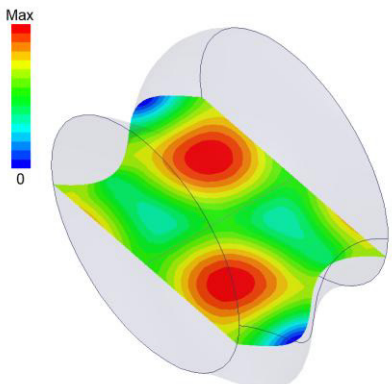


Figure 2: Module of electric field in middle plane.

Transverse field components are also uniform (Fig. 3), but phase velocities of longitudinal component and both transverse components have opposite signs (Fig. 4). Phase velocities of the transverse magnetic components are directed like phase velocities of transverse electric field components.

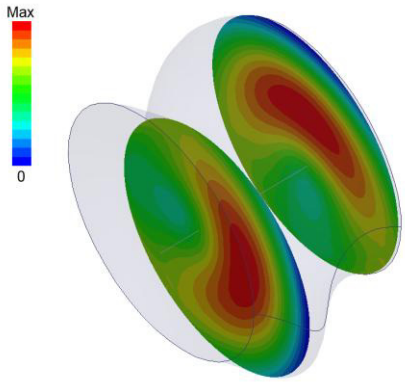


Figure 3: Module of electric field in two sequent cross-sections.

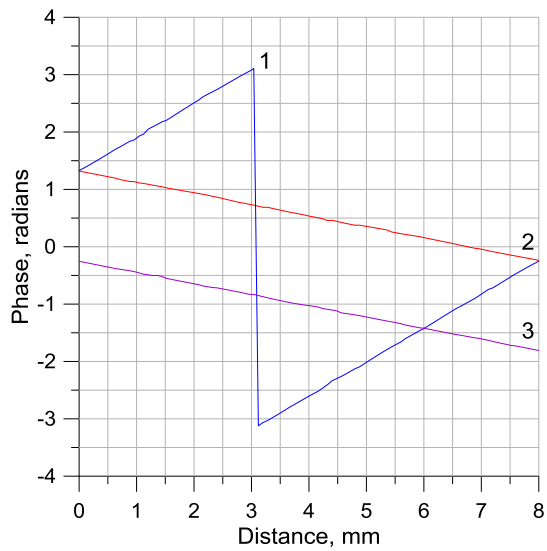


Figure 4: Phases of E_z (longitudinal) field component (curve 1) and phases of E_x (curve 2) and E_y (curve 3) field components.

The helpful feature of TM_{01}-TM_{11} HSFC structure is a flexible focusing of electrons. Physically the reason is that electric field of the -1st spatial harmonic has non-uniform distribution with minimum at axis of the structure. In such system moving electrons "sees" focusing ponderomotive (Miller) force:

$$F_\perp = -\frac{e^2}{4m(\omega + |h_{-1}| v_e)^2 \gamma^2} \nabla_\perp |E|^2 . \qquad (2)$$

where e and m – are charge and mass of an electron respectively, $v_e \approx c$ - is a velocity of electrons, γ - Lorentz's factor, $h_{-1} = h_0 - 2\pi / L$ - is a propagation constant of the -1st spatial harmonic.

Copyright © 2013 CC-BY-3.0 and by the respective authors

Near cut off condition the TM_{11} mode has field maxima determined by E_z components which are far from axis. That is why, there is the focusing force. In the rotating TM_{11} mode E_z component is distributed uniformly on azimuth, but the superposition of TM_{11} and TM_{01} produces field distribution with maxima rotating on azimuth and moving along z coordinate (Fig. 3). The average value of this force does not depend neither on azimuth nor distance.

In order to show focusing effect in TM_{01}-TM_{11} HSFC structure, we calculated by CST Microwave Studio 100 MV/m accelerating section consisted of ten periods. Initial energy of electrons at entrance of the structure was 10 GeV, bunch length was 1 ps, bunch diameter was taken as 3 mm, full charge was as high as 100 nc. In Fig. 5a one can see input transverse bunch population, in Fig. 5b output bunch population is shown. One can see that particles near the centre of the bunch are not perturbed by RF fields, but bunches at bunch periphery are shifted in direction to the origin. This shift is caused by the mentioned action of the ponderomotive force.

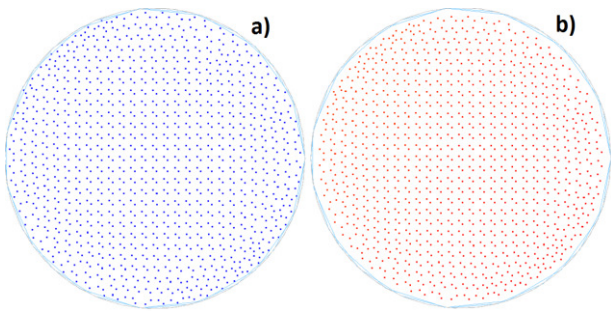


Figure 5: Bunch population at entrance of structure (a) and bunch population at output of structure (b).

Calculations of long HSFC structure, aimed to provide gradient as high as 100 MV/m, show that at distance 3 km energy spread is reduced by factor 40%, transverse emittance becomes less by factor 50%, full energy is less in comparison with classical structure without cooling by factor 17%.

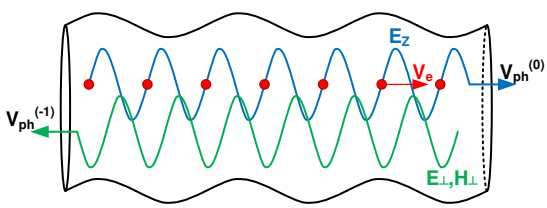


Figure 6: RF undulator excited by bunches itself.

Note that HSFC structure can be used as RF undulator only. In this case there are several appealing features. In particular, the same bunches (if its quality is high enough) could be used, in order to excite the operating mode, and in order to produce undulator radiation. The second reason to use HSFC structure as RF undulator could be important for sources of THz radiation where low-energy (MeV) electrons are used. These bunches experience an influence of Coulomb force, so longitudinal bunch size grows very fast on length. The longitudinal size could be controlled by E_z wave component in the helical structure, if one synchronizes bunches with RF field, like it is shown in the Fig. 6.

OTHER SCHEMES

Schemes, where only properties of RF undulator or only properties of acceleration occur, are also possible.

In particular, helical accelerating structures TM_{01}-TM_{21} or TM_{01}-TE_{21} of elliptic cross-sections do not have on-axis transverse fields. Nevertheless, properties of beam focusing in these structures still exist. The first mentioned structure has $E_a / E_s^{max} \approx 0.3$, but the shunt impedance is less than in the considered TM_{01}-TM_{11} structure.

In the structure $TE_{11} - TM_{01}$, where the 0^{th} harmonic is TE_{11}, and the -1^{st} harmonic is TM_{01}, the shunt impedance is high enough, but the parameter E_a / E_s^{max} is less than in the TM_{01}-TM_{11} structure.

CONCLUSION

Helical waveguides might be used as accelerating structures. These waveguides allows to accelerate electrons (or positrons), to control beam emittances and energy spread due to cooling, to provide self focusing due to transverse ponderomotive force or to combine all the mentioned effects simultaneously.

ACKNOWLEDGMENT

The authors would like to thank Prof. J.Hirshfield for his stimulating interest to this work and for helpful discussions with him.

REFERENCES

[1] G.K. O'Neill. Storage Ring Synchrotron: Device for High Energy Physics Research. Physical Review, No. 5, v.102, pp.1418–1419, 1956.

[2] J.M.J. Madey. Stimulated Emission of Radiation in Periodically Deflected Electron Beams. Journal of Applied Physics, Vol. 42, No. 1, pp. 1906-1913, 1971.

[3] H.H. Braun, M. Korostelev, F. Zimmermann. "Potential of Non-standard Emittance Damping Schemes for Linear Colliders". Proceedings of APAC 2004, Gyeongju, Korea, pp. 306-308, 2004.

[4] S.V. Kuzikov, A.A. Vikharev, J.L. Hirshfield. "Helical Accelerating Structure with Controllable Beam Emittance", 1st European Advanced Accelerator Concepts Workshop, Isola d'Elba, 2013. https://agenda.infn.it/conferenceOtherViews.py?confId=5564&view=standard

[5] Wilson, J. L., Fathy, A. E., Kang, Y. W., & Wang, C. "Applications of twisted hollow waveguides as accelerating structures". IEEE Transactions on Nuclear Science. Vol. 56, No. 3, pp. 1479-1486, 2009.

[6] Awida M. H. "Investigation of Beam-RF Interactions in Twisted Waveguide Accelerating Structures Using Beam Tracking Codes". Proceedings of PAC09, Vancouver, BC, Canada, 2009, WE2PBC03, pp. 1855-1857.

Copyright © 2013 CC-BY-3.0 and by the respective authors

PROGRESS ON PULSED MULTIPOLE INJECTION FOR THE MAX IV STORAGE RINGS

S.C. Leemann*, MAX IV Laboratory, Lund University, SE-22100 Lund, Sweden
L.O. Dallin, Canadian Light Source, Saskatoon, Saskatchewan, S7N 2V3, Canada

Abstract

Injection into the MAX IV storage rings will not make use of a conventional local injection bump with four dipole kickers. Instead, pulsed multipole injection will be applied. Previously, it was foreseen to use a pulsed sextupole magnet similar to what KEK had originally designed for the PF ring. But after seeing encouraging results with a prototype nonlinear kicker magnet developed for BESSY II, pulsed multipole injection for the MAX IV storage rings was revisited. A nonlinear kicker magnet similar to the BESSY-type can be realized for both MAX IV storage rings. Such a nonlinear kicker offers a broad zero-field region around the center which does not perturb the stored beam, while offering a high-field region around the location of the injected beam making it ideal for top-up injection. This paper summarizes the proposed kicker magnet design and shows beam dynamics results from multi-particle tracking studies. A comparison with the previous PSM design is also included.

INTRODUCTION

Early in the design process of the MAX IV storage rings it was considered that injection into the rings could be performed using a single dipole kicker installed downstream of the DC Lambertson septum. In the meantime, detailed studies have demonstrated feasibility [1] and fabrication of these dipole kickers is well underway. However, a single dipole kicker is not suitable for top-up injection because injection and capture cannot be made transparent to users. Therefore, injection with a pulsed sextupole magnet (PSM) was studied as a means to perform fully transparent top-up injection. This avoids having to balance the four dipole kickers and pulsers required to cleanly open and close a local injection bump over prolonged periods of time. Detailed analysis [2] revealed the great potential of PSM injection and a reference design for the magnet was initiated following the experience gained at KEK in the design of the PSM for the PF ring [3].

The MAX IV storage rings require roughly the same kick from the PSM as the PSM in the KEK PF. However, the position of the injected beam in the MAX IV PSM's is only a third of that in the PF and therefore the required sextupole gradient in the MAX IV PSM is considerably higher. On the other hand, the aperture requirements in the MAX IV storage rings are significantly lower, thus allowing a reduction of magnet aperture and an increase in field strength. An initial reference design for a 300 mm long solid iron magnet (cf. Fig. 1) supplied roughly 1.2 mrad kick (at 3 GeV) at −4.7 mm from the center. The bore is 32 mm leading to a pole-tip field roughly 0.5 T. A single coil per yoke called for 2125 A current. With a stored energy of 20.6 J, the required pulser voltage was 19.3 kV for single-turn injection into the MAX IV 3 GeV storage ring. For the MAX IV 1.5 GeV storage ring a similar magnet was designed which relies on 1527 A current at 400 mm length. Here, however, single-turn injection calls for 640 ns pulse length which increases the required pulser voltage to 92.9 kV. Although two-turn injection is possible and reduces the voltage requirement by 50%, it remains desirable to further reduce this voltage, i.e. lower the inductance of the PSM. However, since the magnet bore already lies within only several mm of the beam-stay-clear area, a significant reduction of the inductance could not be expected for this type of magnet.

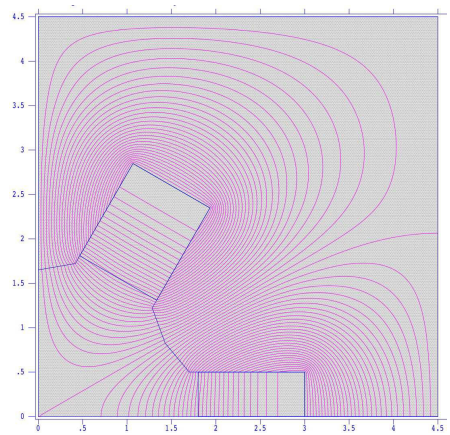


Figure 1: Pulsed sextupole magnet reference design for the MAX IV 3 GeV storage ring. One quarter of the magnet is shown. Scales are in cm. The magnet bore is 32 mm.

NONLINEAR INJECTION KICKER

Around the same time, first reports appeared of a novel nonlinear injection kicker (NLK) developed for BESSY II [4]. This kicker design expands on the original PSM idea to have a high field at the injected beam while keeping the field at the stored beam close to zero. It makes use of a stripline-like design with a geometry intended to create a high-field area strongly localized around the injected beam while suppressing the field at the stored beam through symmetry. Figure 2 shows an initial reference design for the MAX IV 3 GeV storage ring along with the

* simon.leemann@maxlab.lu.se

Copyright © 2013 CC-BY-3.0 and by the respective authors

generated field profile in the midplane compared to that of the PSM and a pure octupole.

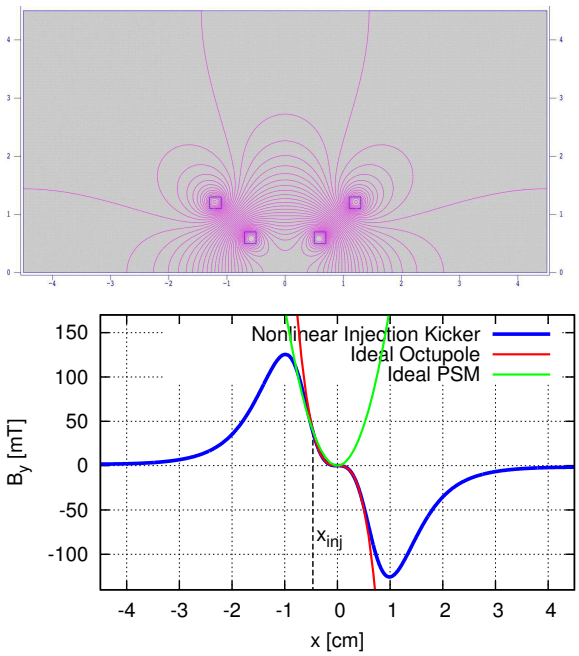


Figure 2: Upper half geometry (top) and resulting field profile in the midplane (bottom) of the reference design for a nonlinear injection kicker for the MAX IV storage rings calculated in POISSON. The design is adapted from the NLK developed for BESSY II.

Such a NLK has several distinct advantages over a PSM. Around the center the field is zero and flat. Between the center and the high-field area the profile is octupole-like (cf. Fig. 2, bottom). This leads to very small perturbations of the stored beam which is crucial given the very tight stability tolerances in MAX IV [2]. While imperfections in the PSM can lead to residual dipole kicks to the stored beam [5, 6], the field in the NLK always has a zero-crossing and therefore offers a field-free area for the stored beam. This area can be found with stored beam via orbit bumps thus enabling beam-based re-alignment of the magnet.

In principle, another advantage of the NLK is the flat area around the field maximum. Ideally the injected beam passes the NLK at this location thus enabling good capture efficiency even for injection of high-emittance bunches. In MAX IV, however, this NLK property cannot be exploited as there is an inherent trade-off between vertical position of the inner rods (in Fig. 2 they are 6 mm from the midplane) and the horizontal position of the field maximum (in Fig. 2 at 10 mm from the center). Since the injected beam in the MAX IV storage rings lies at roughly 5 mm from the stored beam, the inner rods would have to be brought so close to the midplane that the kicker would encroach into the vertical acceptance. On the other hand, as previous studies had demonstrated [2], with the low-emittance beam injected into the MAX IV storage rings[1], capture does not suffer from the gradient sampled in the PSM. Therefore, it was expected that the injected beam can sample the gradient of the NLK field, despite its steeper slope, without suffering significant smearing. This is confirmed by the comparison shown in Fig. 3: although NLK injection increases smearing compared to the PSM, the effective emittance of the injected bunch is still dominated by the large injection amplitudes. The gradient of the NLK at the injected beam does not lead to decreased capture efficiency.

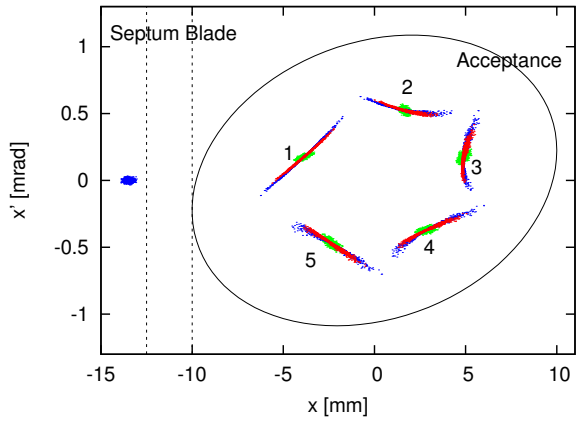


Figure 3: Tracking of the injected bunch with DIMAD during the first five turns in the MAX IV 3 GeV storage ring using single-turn injection. Injection with the NLK (blue) is compared to the PSM (red). For reference, a pure dipole kick (green) has been included. The latter is has no gradient, but it does not allow for transparent top-up injection.

The NLK can therefore be operated in the MAX IV storage rings with the injected beam on the slope. Although such application of the NLK does not exploit the elegant BESSY concept to full extent, it allows using the low-inductance NLK design for pulsed multipole injection (PMI) in MAX IV. The reference design for a NLK adapted to the MAX IV 3 GeV storage ring (cf. Fig. 2) calls for 2855 A and has a stored energy four times lower than the solid iron PSM. The pulser voltage[2] is estimated to be 5.7 kV. In the MAX IV 1.5 GeV storage ring the required current reduces to 1790 A and, with a required pulser voltage of 19.5 kV, single-turn injection becomes feasible. With the NLK two-turn injection is no longer feasible in the MAX IV 3 GeV storage ring as originally designed [2] because the kick of the NLK on the second turn has the wrong sign. However, with the relaxed voltage requirements, this is not considered a problem. For the MAX IV 1.5 GeV storage ring two-turn injection remains feasible as it relies on negligible amplitude of the injected bunch at the kicker during the second passage.

[1] A benefit of using the MAX IV 3 GeV linac as a full-energy injector into both MAX IV storage rings.

[2] This result relies on preliminary assumptions for the inductance of the circuit which is non-negligible compared to the low inductance of the magnet.

Copyright © 2013 CC-BY-3.0 and by the respective authors

DETAILED DESIGN PROGRESS

Because of the minimized perturbation of the stored beam as well as the low magnet inductance, it has been decided to use a BESSY-type NLK for injection into the MAX IV storage rings rather than the originally foreseen PSM. For this purpose MAX IV and SOLEIL have initiated a collaboration with the goal to design and build injection kickers for the SOLEIL storage ring as well as the two MAX IV storage rings based on further development of the BESSY-type NLK. The SOLEIL requirements for PMI are similar to those for MAX IV. While PMI in SOLEIL calls for a stronger kick than in MAX IV, the injected beam is farther away from the magnet center. Vertical beam-stay-clear requirements are comparable. In fact, it has been realized that the same magnet can be used for both MAX IV storage rings if the vertical beam-stay-clear aperture is set to 8 mm as a compromise between bringing the maximum kicker field closer to the injected beam and maintaining sufficient vertical acceptance in the MAX IV 1.5 GeV storage ring. Therefore, the only difference between the injection kickers in the two MAX IV storage rings will be the pulsers.

In comparison to the BESSY NLK, the SOLEIL Multipole Injection Kicker (MIK) design [7] foresees a pulser with a single transducer and all four loops connected in series. The parallel connections in the BESSY NLK were suspected of creating a field imbalance leading to residual kicks to the stored beam [8]. Furthermore, the SOLEIL MIK design does not include metallic walls and uses the ceramic chamber as a vacuum vessel allowing for better cooling and access. A large horizontal aperture (45 mm) prevents synchrotron radiation heating of the chamber without increasing the inductance of the magnet. The minimum ceramic thickness is presently being studied as it limits the vertical separation between the inner rods. Any increase of this separation has to be analyzed carefully as it leads to a significant growth of required current.

The ceramic chamber needs a conductive coating. Different coating thicknesses have been studied in terms of heating from ohmic losses, image currents, and Eddy currents. Furthermore the effect of the coating on the field and therefore on the stored beam have been investigated. Presently 5 μm Ti appears to be a suitable choice for the MAX IV 3 GeV storage ring. With such a coating a minor increase in current compensates for field attenuation, but a small quadrupole gradient at the stored beam remains. If any residual kick, $\phi_{\mathrm{res}}(\mathrm{at}\ 1\sigma_x)$, is to be limited in terms of divergence spread, $10\% \times \sigma_{x'}$, it can be shown that the maximum tolerable residual quadrupole gradient is independent of the stored beam emittance: $(\partial B_y/\partial x)_{\mathrm{res}} < 10\% \times B\rho/(\beta_x L)$. The SOLEIL MIK with 5$\mu$m Ti coating gives a residual gradient of 0.18 T/m, significantly below the 0.36 T/m [0.28 T/m] acceptable in the MAX IV 3 GeV [1.5 GeV] storage ring. This is corroborated by tracking studies where the effect of such a residual quadrupole gradient on the stored beam has been analyzed (cf. Fig. 4) and shown to be negligible. Another study has indicated that the end geometry of the rods and terminals leads to perturbations on an even lower level.

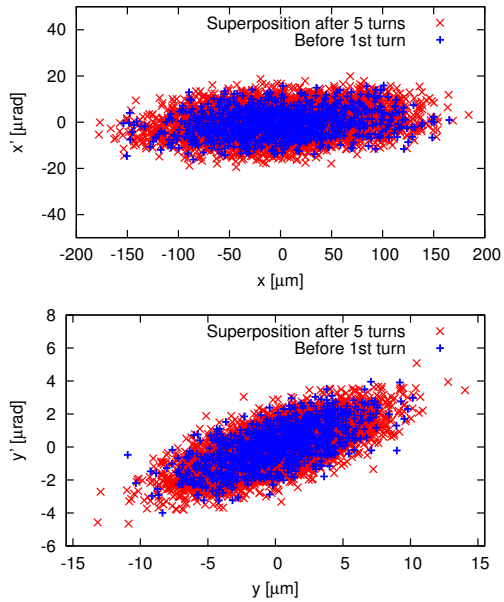


Figure 4: Tracking of the stored beam with DIMAD in the MAX IV 3 GeV storage ring through the SOLEIL MIK in single-turn injection mode. The residual gradient of the MIK leads to negligible perturbation of the stored beam.

ACKNOWLEDGMENTS

The authors would like to thank Peter Kuske and Olaf Dreßler from HZB as well as Pierre Lebasque and his team at SOLEIL for many interesting discussions on pulsed multipole kicker design.

REFERENCES

[1] S.C. Leemann, Nucl. Instr. and Meth. A **693** (2012) 117-129.

[2] S.C. Leemann, Phys. Rev. ST Accel. Beams, **15**, 050705 (2012).

[3] H. Takaki et al., Phys. Rev. ST Accel. Beams, **13**, 020705 (2010).

[4] T. Atkinson et al., "Development of a Non-linear Kicker System to Facilitate a New Injection Scheme for the BESSY II Storage Ring", THPO024, IPAC 2011, San Sebastián, Spain.

[5] H. Takaki et al., "Stored Beam Stability During Pulsed Sextupole Injection at the Photon Factory Storage Ring", TU6RFP045, PAC'09, Vancouver, BC, Canada.

[6] R. Takai et al., "Beam Profile Measurement During Top-up Injection with a Pulsed Sextupole Magnet", TUPD03, DIPAC2011, Hamburg, Germany.

[7] P. Lebasque, Preliminary Design Reports for the SOLEIL MIK, unpublished.

[8] O. Dreßler, P. Kuske, "Development and Commissioning of a Single Nonlinear Kicker Magnet System for the BESSY II Storage Ring Injection", USR Workshop, Huairou, Beijing, China, Oct. 30 – Nov. 1, 2012.

Copyright © 2013 CC-BY-3.0 and by the respective authors

BEAM-INDUCED HEAT LOAD PREDICTIONS AND MEASUREMENTS IN THE APS SUPERCONDUCTING UNDULATOR*

Katherine C. Harkay#, Laura Boon, Michael Borland, Yong-chul Chae, Roger Dejus, Jeffrey Dooling, Charles Doose, Louis Emery, Yury Ivanyushenkov, Mark Jaski, Matthew Kasa, Suk H. Kim, Robert L. Kustom, Vadim Sajaev, Yuko Shiroyanagi, Xiang Sun
ANL, Argonne, IL 60439, USA

Abstract

The first test superconducting undulator (SCU0) was successfully installed and commissioned at the Advanced Photon Source (APS) and is delivering 80- to 100-keV photons for user science. The cryosystem was designed to handle a beam-induced heat load of 40 W. Prior to operations, detailed predictions of this heat load were made, including that produced by resistive wall heating by the image current, geometric wakefields, synchrotron radiation, electron cloud, and beam losses. The dominant continuous wave (cw) source is the resistive wall heat load. The heat load predictions for standard 100-mA user operation were benchmarked using thermal sensors that measure temperatures along the SCU0 beam chamber. Analysis using the predicted heat loads from the electron beam agrees well with the observed measurements.

INTRODUCTION

A test superconducting undulator (SCU0) has been developed at APS [1] and was recently installed in the storage ring. A key design criterion was a vacuum and cooling system that keeps the NbTi coils cooled to 4 K in the presence of heating caused by the electron beam passing through the undulator beam chamber. The SCU0 beam chamber cooling system was designed for 40 W (at 20 K) of cooling capacity based on preliminary calculations of the beam-induced heat load [2]. In this paper, updated predicted heat loads are compared with measurements carried out during SCU0 commissioning [3].

Sources of beam-induced heat load on the SCU0 beam chamber include resistive-wall heating due to beam-induced image currents, synchrotron radiation generated in upstream dipole magnets, wakefield effects, direct beam interception and, potentially, electron cloud-induced multipacting effects. Under nominal operating conditions cw heat loads are present, while specific machine fault conditions may occur that give rise to individual transient heat loads.

Estimates of the various contributions to the heat load due to the beam are shown in Tables 1 and 2 for cw and transient sources, respectively, assuming 24-bunch operation. The central part of the chamber is nominally 20 K and is thermally isolated from the 4-K magnetic structure. The chamber transitions are in the 60- to 300-K cold-to-warm transition region. Where appropriate, the heat loads at 20 K and 60/300 K are given separately.

* Work supported by U. S. Department of Energy, Office of Science, under Contract No. DE-AC02-06CH11357.
#harkay@aps.anl.gov

Table 1: Estimated cw Beam-induced Heat Loads on the SCU0 Chamber, in 100-mA User Operations

Heat Source	Value at 20 K (60/300 K)
Resistive wall	4.7 W (11.3 W)
Wakefields	< 0.5 W (0.8 W)
Injection losses	2 W (non-top-up mode) 0.1 W (top-up mode)
Synchrotron radiation	0.2 W
Beam lifetime losses	<< 1 W
Electron cloud	< 2 W
Total heat load	10 W (12 W)

Table 2: Estimated Max. Transient Beam-induced Heat Loads on the SCU0 Chamber, in 100-mA User Operations

Heat Source	Value
Injected beam loss	13 W
Corrector failure	20 W
Synchrotron radiation with steering errors	25 W
Electron beam steering errors	20 W
Max. transient heat load	25 W

MEASUREMENTS

The beam-induced heating on the SCU0 beam chamber was measured using nine Cernox cryogenic thermal sensors mounted on the beam chamber, shown in Fig. 1 (Temp0-8). Sensors Temp2-6 are mounted on the outboard side of the aluminum section of the chamber, and Temp0,1,7,8 are mounted on the top side of the stainless steel (SS) cold-to-warm transition. The chamber heater is connected to a copper block mounted adjacent to sensor Temp5. A calibrated heat load was applied to the heater using a variable power supply. The chamber heater was used to calibrate the thermal sensors, allowing determination of the heat load from the temperature measurements. This calibration was used to both predict and benchmark the chamber temperatures for storage ring beam operation.

Chamber Heater Calibration

To simulate SCU0 operating conditions, the main coil current was set to 500 A, but there was no stored beam. An external supply current was used to vary the chamber heater power based on the known heater resistance. The chamber temperatures were recorded for P=0, 5, 10, 20, and 30 W, waiting 10-20 min per step. The equilibrium chamber temperatures were determined by fitting the measurements to an exponential function. The zero-power

Copyright © 2013 CC-BY-3.0 and by the respective authors

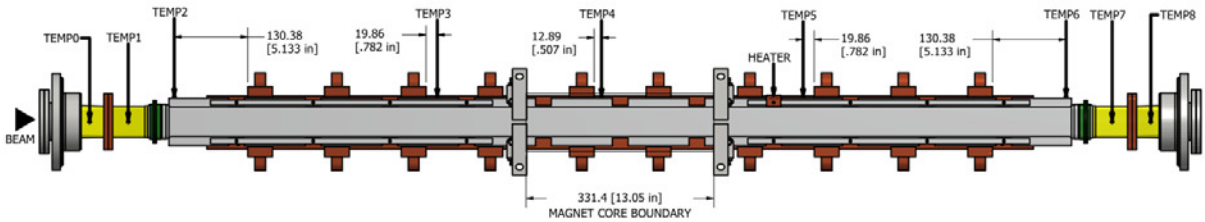


Figure 1: Thermal sensor (TEMP 0-8) locations are noted on a SCU0 beam chamber schematic, top view. The chamber heater is adjacent to TEMP5. Copper thermal links, shown in brown, connect the chamber to the cryocoolers via a common Cu bar. The Al section of the chamber is shown in grey and the stainless steel (SS) section in yellow.

temperature was averaged over 15 min prior to the start of the heater studies.

The temperature gains vs. chamber heater power for sensors 1-7 are shown in Fig. 2 as a function of their positions, s. Sensor 5 shows the largest temperature gain, as expected. The adjacent sensors 4 and 6 show a much smaller temperature gain; heat is extracted between these points by thermal links to the cryocoolers. Ideally, the heater on the Cu bar connecting all the thermal links could have been used, but the heat transfer is not known between the Cu bar and the chamber. The chamber heater calibration is also not exact, but was implemented knowing these limitations.

Because the chamber heater and sensor 5 are collocated between the same thermal links, sensor 5 is used to calibrate the temperature response to a known heat load. A polynomial fit for the temperature gain ΔT as a function of calibrated power P gives:

$$\Delta T = 1.974P - 0.0667P^2 + 0.00119P^3 \qquad (1)$$

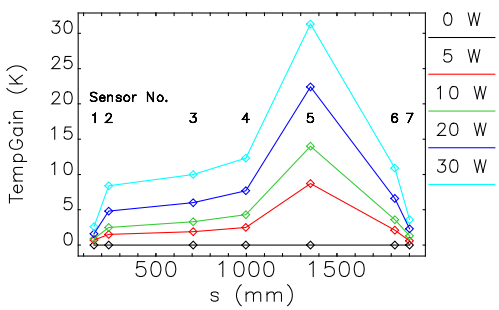


Figure 2: Chamber heater results for sensors 1-7, shown as a function of their positions, s.

Results

The chamber temperatures under stable cw conditions (no beam injection) were predicted using the dominant resistive-wall heat load only. In Table 1, the heat load at 20 K was obtained by multiplying the linear power density over the entire Al chamber length of 1.62 m. The power density varies with the number of bunches; for 24 bunches, it is 2.88 W/m [4,5]. However, the heater calibration should only be valid in the segments within the thermal links, a total length of 1.33 m. Therefore, this shorter length was used to estimate P, and the expected temperature gain was computed using Eq. (1). Also, the calibration was only applied to the central sensors 3-5, since these three sensors are located between thermal links. The baseline, no-beam temperature of the Al chamber central region is 7 K. The predicted power and expected final temperatures (7 K + ΔT) are given in Table 3 for the three standard bunch patterns at 100 mA (nominal user operations), and for 324 bunches at 150 mA (special operations). These predictions were available prior to SCU0 commissioning. The measured temperature (averaged at sensors 3-5) is also shown in the table, and the agreement with the expectations is very good. Finally, the power inferred from the measured temperatures was determined using Eq. (1) and is listed in the table.

Table 3: Comparison of Predicted and Measured SCU0 Chamber Heat Load and Temperatures at Sensors 3-5.

Beam current (mA)	No. bunches	Predicted power (W)	Expected T (K)	Msrd T (K)	Inferred power (W)
100	24	3.8	13.6	12.8	3.3
100	1+56	2.7	11.8	11.9	2.7
100	324	0.5	7.9	8.2	0.6
150	324	1.2	9.3	9.5	1.3

DISCUSSION

The SCU0 cryogenic system performed very well in the presence of the beam, with the magnet temperatures being maintained near 4 K while the beam chamber center temperature reached ~13 K. The 20-K cooling system for the beam chamber, with its 40-W capacity, provides a comfortable margin for normal user operation.

The predicted cw heat load, using only the resistive-wall heating, agrees remarkably well with the measurements using the chamber heater calibration. An independent thermal modeling using finite-element analysis also gives very good agreement with the measured temperatures over the entire length of the chamber [6]. The resistive-wall heating calculation for the Al section includes the anomalous skin effect, where the skin depth is small compared to the electron mean-free path. In this regime, only a fraction of the conduction electrons carry the current, which effectively decreases the wall conductivity [7]. The anomalous skin effect begins to show a difference for a resistivity ratio (RR) > 9 [5]; at 20 K, RR = 11 for 6063-T5 Al. The surface

Copyright © 2013 CC-BY-3.0 and by the respective authors

resistance also increases with surface roughness, and the effect can be computed using an empirical formula. For the SCU0 chamber, a surface roughness of 0.2 μm rms would increase the power loss by as much as 15% [4]. The SCU0 Al chamber was processed using an abrasive-flow polishing technique [8], and the measured surface roughness is on the order of 0.1 μm rms [9]; therefore, the surface roughness effect could be neglected.

All other contributions to the heat load are inferred to be small. The predicted synchrotron radiation heat load of 0.2 W in Table 1 [10-12] is small compared to the resistive-wall heat load for all bunch patterns except for the 324-bunch mode, where the predicted temperatures are underestimated. If the electron beam was mis-steered in the upstream dipole or corrector magnets and/or the chamber was not well-aligned, the synchrotron radiation heat load could be much higher, up to 25 W [13]. The results suggest that both the beam steering and the chamber alignment are within tolerance. The surface roughness of the SCU0 beam chamber has another effect: it can increase the synchrotron radiation absorption in the SCU0 chamber, which can increase the heat load. While this effect has not yet been analyzed, the results in Table 3 suggest that if it exists, the effect is very small.

Wakefields are predominantly in the chamber transitions outside the SCU0 cryostat, and the heat load was predicted to be dissipated primarily in the cooled Cu tapered transition upstream of the SCU0 [14]. The results in Table 3 are consistent with the absence of significant wakefield heating in the center of the chamber. Any potential heat load from beam lifetime losses is also inferred to be negligible, as predicted in Table 1.

So far, there is no evidence of anomalous heat loads on the SCU0 chamber. This is noteworthy, since measured beam-induced heat loads that are 2-10 times greater than what was expected have been reported for in-vacuum superconducting wigglers [15] and in-vacuum cryocooled permanent magnet undulators [16]. In the case of MAX [15], the discrepancy is assumed to depend on the fact that the Cu plating of the inner surfaces of the cold bore has a lower electrical conductivity than foreseen. The SCU0 is an out-of-vacuum device designed with a solid Al chamber wall for which resistive-wall heating is well understood. Calculations predict that high-current closely spaced bunches (such as in the case of 324 bunches) are more likely to drive an electron-cloud-induced multipacting resonance in the APS [2]. In SCU0 so far, there is no evidence of multipacting. Multipacting is believed to be responsible for an anomalous beam heat load and pressure rise at the ANKA in-vacuum superconducting undulator [17].

TRANSIENT HEAT LOADS

Transient heat load predictions in Table 2 assumed that the power is incident on the beam chamber. The maximum transient heat load of 25 W is within the SCU0 cooling capacity. The device was found to quench during unintentional beam dumps that have occurred during user operation due to fault conditions unrelated to SCU0. A beam loss in the magnet coils of ~1 nC (< 0.3% of the full store) could potentially cause a quench [18]. Procedures to mitigate these quenches are under investigation. With the exception of beam dumps, the device has quenched only twice in eight months of user operations, operating above its 500-A design current. The SCU0 magnet current is switched off prior to intentional beam dumps and during machine studies to avoid quenching.

SUMMARY

The cw beam-induced heat load predictions for the SCU0 beam chamber in standard APS user operation were compared with measurements using a simple chamber heater calibration. The expected chamber temperatures were used as a guide during SCU0 commissioning. The agreement between the expected and measured temperatures was very good, within 10%. The resistive-wall heat load is the dominant source, and all other contributions are inferred to be small, as predicted. There were no anomalous heat load sources detected. The SCU0 cryogenic system performed very well in the presence of the beam, as designed.

ACKNOWLEDGMENT

We thank the entire APS SCU0 team for their valuable contributions to the success of this project.

REFERENCES

[1] Y. Ivanyushenkov et al., IEEE Trans. on Applied Superconductivity, 21 (2011) 1717; Y. Ivanyushenkov et al., Proc. IPAC2012, MOPPP078, p. 744 (2012); journals.iucr.org/s/issues/2013/03/00/s130300aps.pdf
[2] M. Petra, R.L. Kustom, private communication (2004); R.L. Kustom, private communication (2010).
[3] K. Harkay et al., WEOAA3, NA-PAC'13.
[4] R.L. Kustom, private communication (2011, 2012).
[5] S.H. Kim, APS Light Source Note ANL/APS/LS-329 (2012).
[6] Y. Shiroyanagi et al., THPAC07, NA-PAC'13.
[7] B. Podobedov, PRST-AB 12 (2009) 044401.
[8] E. Trakhtenberg et al., Proc. PAC2011, p. 2093 (2011).
[9] L. Boon, K. Harkay, Proc. 2012 Electron Cloud Workshop (ECLOUD12), Isola d'Elba, Italy (2012).
[10] M. Jaski, private communication (2012).
[11] R. Dejus, private communication (2012).
[12] L. Boon et al., Proc. IPAC2011, THPC186, p. 3332 (2011).
[13] L. Boon et al., THPAC06, NA-PAC'13.
[14] L. Emery, X. Sun, private communication (2013).
[15] E. Wallen and G. LeBlanc, Cryogenics 44 (2004) 879.
[16] P. Elleaume, "Cryogenic Permanent Magnet Undulator Development at the ESRF," Three-Way Meeting, Argonne; http://www.aps.anl.gov/News/Conferences/2008/3WM08/3WM08Accelerator_R&D.htm
[17] S. Casalbuoni et al., PRST-AB 13 (2010) 073201.
[18] J. Dooling, private communication (2013).

Copyright © 2013 CC-BY-3.0 and by the respective authors

BEAM-BASED ALIGNMENT OF THE FIRST SUPERCONDUCTING UNDULATOR AT THE APS*

Katherine C. Harkay#, Laura Boon, Michael Borland, Louis Emery,
Robert L. Kustom, Vadim Sajaev, Yuko Shiroyanagi, Aimin Xiao
ANL, Argonne, IL 60439, USA

Abstract

The first test superconducting undulator (SCU0) was successfully installed and commissioned at the Advanced Photon Source (APS) and is delivering 80- to 100-keV photons for user science. The magnet cores are mounted on but thermally isolated from the beam vacuum chamber. Protecting the SCU0 from high beam-induced heat loads was an important requirement before operating the SCU0 in the storage ring. Precise alignment of the beam vacuum chamber with respect to both the electron beam orbit as well as the synchrotron radiation generated in the upstream dipole magnet was therefore extremely important. The beam vacuum chamber was instrumented with nine thermal sensors. Using the sensors, the chamber alignment was determined with 100-micron accuracy. This accuracy is 10 times higher than in a standard aperture scan. Other advantages of the thermal sensor-based alignment method include isolating the SCU0 alignment from other components in the orbit bump and providing good longitudinal spatial resolution. The chamber temperatures agreed well with the predicted heat load and dependence on steering. This novel beam-based alignment method and results will be presented.

INTRODUCTION

One of the many challenges of operating a small-gap superconducting undulator in a high-energy synchrotron light source is protection from excessive beam-induced heat loads [1]. For the test superconducting undulator (SCU0) recently installed in the APS [2], this is accomplished through several key features, including an out-of-vacuum design, thermal isolation of the beam chamber from the magnet coils, 40-W cooling capacity on the beam chamber, and a photon absorber to shield the SCU0 from synchrotron radiation from the upstream bending magnet (BM). Precise alignment of the magnet structure and beam vacuum chamber is also essential for proper heat-load protection, as is a well-controlled beam orbit while the device is in operation. Prior to installation in the APS, the SCU0 beam vacuum chamber and magnetic structure were transversely aligned to within ±150 μm relative to fiducials mounted on the vacuum vessel. Correction values were determined for a "cold fiducialization," based on measurements before and after cooldown on the test stand [3]. After installation and cooldown *in situ*, beam-based alignment was used to confirm that the SCU0 chamber position was reproduced and that it remained stable during operation. A standard aperture scan was performed first, followed by beam-based alignment using thermal sensors. The results are described below.

APERTURE SCAN

A standard aperture scan involves steering the electron beam vertically through the chamber until the edge of the beam scrapes the walls and the beam lifetime decays to a small value (typically < 10 min). The extreme values of the vertical beam position monitors (BPMs) are recorded to give a measure of the aperture. With a standard 5-m-long ID chamber, a combination of parallel- and angle-bumps can be used to determine the chamber alignment. However, the SCU0 was installed in sector 6 (ID6) downstream of a half-length ID chamber. Sector 6 thus has two small-aperture chambers and several transitions. Therefore, only parallel orbit bumps were implemented to confirm the overall chamber alignment.

The full vertical aperture of the SCU0 chamber is nominally 7.2 mm and the ID chamber is 7.5 mm. The aperture scan was performed using 2 mA in a single bunch, chosen low to protect the SCU0 but with sufficient BPM response. For comparison, the same measurement was repeated in ID21, a 5-m-long, 7.5-mm, full-height ID chamber known to be well aligned. A model four-corrector parallel bump was used to change the correctors, and a special global orbit configuration closes the bump, with the P1 BPM readings allowed to vary. P0 BPMs are located at the ends of the insertion device (ID) chamber, but they have inaccurate response at large orbit values (> 1 mm). P1 BPMs have a better response at large orbit values but there is a defocusing quadrupole between the P1s and the ID chamber ends. Because a model orbit bump produces a parallel orbit shift in the ID, it can be assumed that the orbit at P1 is nearly the same as P0. The aperture was determined from the P1 readings.

The results are given in Table 1. The ID6 results are very good in terms of symmetry, and the full range is comparable to ID21. The accuracy of this method in determining the chamber center is estimated to be about ±1 mm, given that the full range determined from the scan is ~3 mm smaller than the nominal chamber aperture.

Table 1: Aperture Scan Results for ID6/SCU0 and ID21

Sector	Steer up (mm)	Steer down (mm)	Full range (mm)
ID6	2.2	-2.2	4.4
ID21	2.2	-1.8	4.0

* Work supported by U. S. Department of Energy, Office of Science, under Contract No. DE-AC02-06CH11357.
#harkay@aps.anl.gov

Copyright © 2013 CC-BY-3.0 and by the respective authors

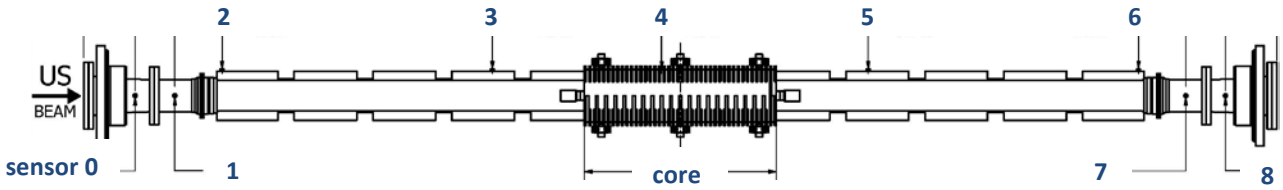


Figure 1: Thermal sensor locations, SCU0 beam chamber (top view). The chamber is stainless steel at sensors 0, 1, 7, and 8 and aluminium at sensors 2-6. The chamber is 2.06 m and the undulator core is 0.34 m in length.

ID STEERING

The SCU0 chamber is instrumented with nine thermal sensors mounted along its length; the locations are shown schematically in Fig. 1. The thermal sensors were used in a novel method of determining the chamber alignment, which is to steer the electron beam in the chamber and observe the temperature response of the thermal sensors. The beam steering was performed by changing the P1 set points and using a global orbit configuration to close the bump, keeping the P1 errors close to zero. The model orbit bump method (as used in the aperture scan) would be preferred since BPMs are not as accurate as correctors. However, the set point method was more straightforward given that it permitted a more complex orbit bump that did not also steer the beam in the BM (see next section). In this case, the image-current resistive-wall heat load dominates. The net resistive-wall heat load increases when the chamber is not centered in the chamber. Therefore, the sensor temperature variation can be used to determine the center of the chamber with respect to the user beam orbit. To maximize the effect, a relatively high image-current heat load is preferred (high bunch current). At the same time, to minimize the risk of accidentally steering high total bending-magnet radiation heat load into the chamber, low current, 25 mA, was used in 24 bunches. Figure 2 shows a typical measurement at sensor 3. The equilibrium temperatures for different vertical orbit offsets were fit to a parabolas to find the minima.

The effect of moving the beam vertically off the median plane was analyzed using the method of images in a planar geometry [4]. The surface current density variation was computed as a function of beam offset. The total power in both walls was then computed and normalized to the total power at zero beam offset. To compare with the data, the measured sensor temperature rise was converted to power using the chamber heater calibration [5]. The agreement is very good (see Fig. 3).

The SCU0 chamber vertical alignment as measured by the chamber thermal sensor minima is shown in Fig. 4. The accuracy is about ±100 μm. The original alignment (black) revealed an offset of 0.3-0.5 mm with respect to the user beam orbit. Partial in-tunnel realignment (red) reduced the offset to < 0.3 mm. Measurements after six months of operation (blue) show that the chamber position remains stable. In addition to the high accuracy, this method isolates the SCU0 alignment from other vacuum components and provides longitudinal spatial resolution limited only by the sensor spacing.

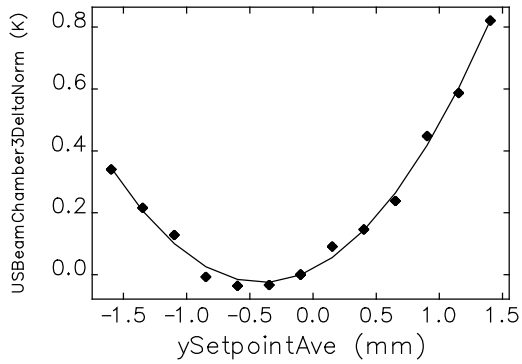


Figure 2: Temperature variation at sensor 3 with vertical beam steering in SCU0.

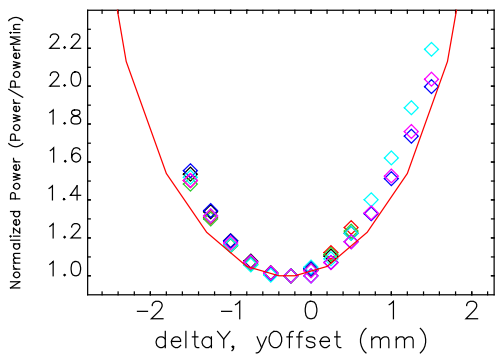


Figure 3: Normalized heat load using calibrated chamber temperatures (sensors 3-5) as a function of the vertical beam offset in the SCU0. The red line shows the theoretical normalized total power (offset by -0.3 mm).

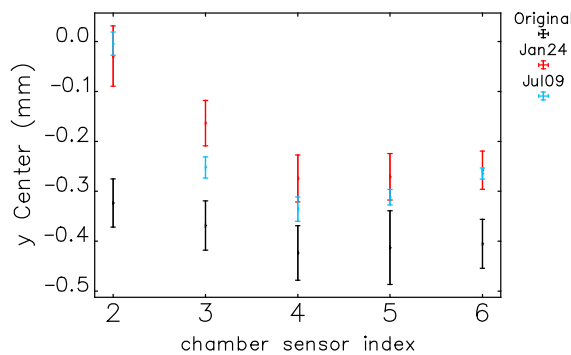


Figure 4: SCU0 chamber vertical alignment history.

Copyright © 2013 CC-BY-3.0 and by the respective authors

BM STEERING

The availability of thermal sensors on the SCU0 chamber allows a measurement that is rather unique. With perfect alignment and vertical beam steering exactly at the midplane in the main bending magnet (BM), the out-of-plane BM radiation power on the SCU0 chamber is only ~0.2 W. However, vertical ray tracing [6] and photon beam power calculations [7, 8] show that significant synchrotron radiation power (10s of W) can intercept the chamber when the beam is steered in the bending magnet, which steers the photon beam. Studies of BM steering serve two purposes: to measure the relative alignment between the BM and the SCU0, and to establish allowable limits on the photon beam steering.

In order to minimize the image-current heating of the SCU0 chamber by the beam, low bunch current was used (324 bunches). The global orbit configuration was set up to steer the BM exit source point while keeping the ID/SCU0 source point fixed. To limit the maximum BM power to below ~30 W, the beam current was limited to 20 mA. Figure 5 shows a typical measurement at sensor 6. The data show a vertical chamber displacement consistent with ID beam steering (see Fig. 2). The data also show that vertical beam offsets of less than ±1 mm at the BM exit give relatively small temperature increases. Larger steering can potentially steer x-rays in the BM radiation centroid into the SCU0 undulator core, which should be avoided.

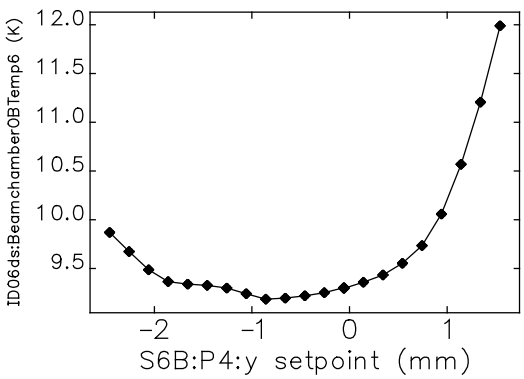


Figure 5: Temperature at sensor 6 with vertical beam steering in the BM.

SUMMARY

The beam was used to measure the alignment of the beam vacuum chamber of the test superconducting undulator (SCU0) at APS using two different methods. A conventional aperture scan confirmed that the overall alignment of ID6/SCU0 was consistent with a well-aligned ID chamber. Beam-based alignment was also carried out using thermal sensors mounted on the SCU0 chamber. The thermal sensor method allowed the vertical chamber alignment to be measured with 100-μm accuracy, which is 10 times higher than the aperture scan. After partial in-tunnel realignment, the SCU0 chamber was confirmed to be aligned to within 0.3 mm, and its position has remained stable over six months of operation. Steering the beam in the BM gives vertical chamber offsets that are consistent with steering in the SCU0, and confirms good relative alignment between the SCU0 chamber and the BM source. Standard beam orbit control and a beam position limiting detector interlock are implemented during SCU0 operation.

ACKNOWLEDGMENT

The authors wish to thank APS staff who contributed to the SCU0 project, especially in the following areas—alignment: J. Penicka, W. Jansma, S. Wesling; installation: J. Gagliano, J. Hoyt, R. Bechtold; wiring: S. Bettenhausen; and design: D. Skiadopoulos, E. Trakhtenberg.

REFERENCES

[1] Y. Ivanyushenkov et al., IEEE Trans. on Applied Superconductivity, 21 (2011) 1717; Y. Ivanyushenkov et al., Proc. IPAC2012, p. 744 (2012); journals.iucr.org/s/issues/2013/03/00/s130300aps.pdf
[2] K. Harkay et al., WEOAA3, NA-PAC'13.
[3] J.M. Penicka and W. Jansma, private communication (2012).
[4] R.L. Kustom, private communication (2012).
[5] K. Harkay et al., WEPSM06, NA-PAC'13.
[6] M. Jaski, private communication (2012).
[7] R. Dejus, private communication (2012).
[8] L. Boon et al., Proc. IPAC2011, THPC186, p. 3332 (2011); L. Boon et al., THPAC06, NA-PAC'13.

Copyright © 2013 CC-BY-3.0 and by the respective authors

FAST-SWITCHING VARIABLY POLARIZING UNDULATOR*

M. Jaski, R. Dejus, B. Deriy, E. Moog, I. Vasserman, J. Wang, A. Xiao, E. Gluskin
Advanced Photon Source, Argonne National Laboratory, Argonne, Illinois 60439, USA

Abstract

Development of a new fast-switching electromagnetic variably polarizing undulator (EMVPU) is underway at the Advanced Photon Source (APS). The EMVPU can produce x-rays with left- and right-handed circular polarizations and horizontal and vertical linear polarizations in the energy range 400-2000 eV. The undulator will be able to switch between left- and right-handed circular polarizations at 10 Hz, fast enough to allow for magnetic circular dichroism studies that rely on lock-in amplifier techniques. The handedness switch will be accomplished by switching only the vertical component of the field while the horizontal component stays constant. Details of the EMVPU and its initial experimental test models are presented.

INTRODUCTION

The new EMVPU will join other all-electromagnetic undulators that are presently in use at APS—the CPU (circularly polarizing undulator) [1], with Eγ ≥ 500 eV and 1-Hz switching, that has been in operation since 2001; and the recently installed IEX undulator, a quasi-periodic variably polarizing undulator (Eγ ≥ 250 eV) that was designed and built at the APS [2] and commissioned successfully in 2012 [3]. The EMVPU, like those devices, will provide linear polarization (horizontal and vertical) and circular polarization (right- and left-handed) capabilities, but adds the capability of switching the circular polarization handedness at 10 Hz (with an 80% duty cycle), faster than previously available at APS. Fast-switching undulators are also in operation at ESRF [4] and SOLEIL [5] using a combination of electromagnets and permanent magnets.

The requirement for rapid handedness switching of the circular polarization is driven by the users' need to use lock-in detection for their magnetic scattering experiments. They require ample time between handedness switches—time when the photons produced are of the desired energy and polarization and when measurements can be made with a stable photon beam. Not only must the current in the coil stabilize to its new value rapidly, but any eddy currents and associated stray fields induced by the switching must be minimized.

In order to achieve fast switching in the EMVPU, the vertical (By) field coils are single-turn coils machined from a solid piece of copper. This minimizes the coil inductance to allow for the fastest possible switching speed. One-turn coils also provide right/left symmetry near the pole tips, reducing undesirable magnetic multipoles. Transient fields during the switching must also be minimized. Laminated cores minimize eddy currents in the By poles. Eddy currents in the vacuum chamber can significantly slow the switching speed so a vacuum chamber material with low electrical conductivity must be used. Any residual e-beam steering or multipole transients will be compensated during switching using corrector magnets on each end of the device.

*Work supported by U.S. Department of Energy, Office of Science, under Contract No. DE-AC02-06CH11357.

PARAMETERS

Table 1 lists selected parameters for the EMVPU.

Table 1: Selected Parameters

Parameter	Value	Unit
Period	12.5	cm
Gap	8.5	mm
Maximum effective field for linear polarization (horizontal or vertical)	3491	Gauss
Maximum effective field for circular polarization	2469	Gauss
Switching speed between right- and left-handed circular polarization	10	Hz

ONE-PERIOD TEST MODEL

General Concept

Figure 1 shows the general layout of the Bx and By coils, poles, and core for the lower jaw of the one-period test model. The upper jaw has similar geometry. The By coils are single-turn coils machined from oxygen-free copper. The By core is made from 0.64-mm-thick M-22 silicon steel laminations with a C5 coating. The laminations are laser-cut and epoxied together. The epoxy-impregnated Bx coils have 46 turns of square copper solid wire [6]. The Bx poles are made of heat-treated vanadium permendur, chosen because it gives 5% higher field than low-carbon steel. The Bx core is low-carbon steel with slots for stainless steel cooling-water tubes. These cooling-water tubes cool the Bx core, which cools the Bx poles; both in turn cool the Bx coils.

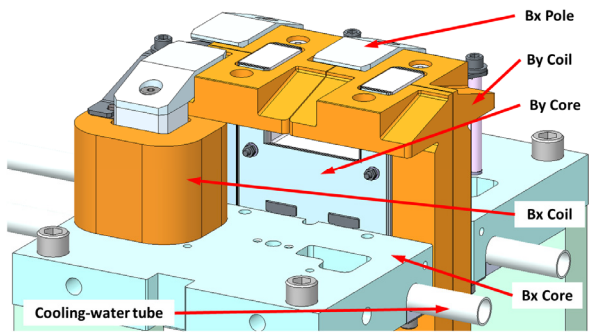


Figure 1: A 3-D CAD model of the one-period test model lower jaw (one Bx coil/pole assembly is hidden to show the By core).

Figure 2 shows a close-up of the one-period test model. The By coils are soldered to bus bars, after being tin plated to ease the soldering. The bus bars are water cooled

Copyright © 2013 CC-BY-3.0 and by the respective authors

with deionized cooling water and in turn cool the By coils.

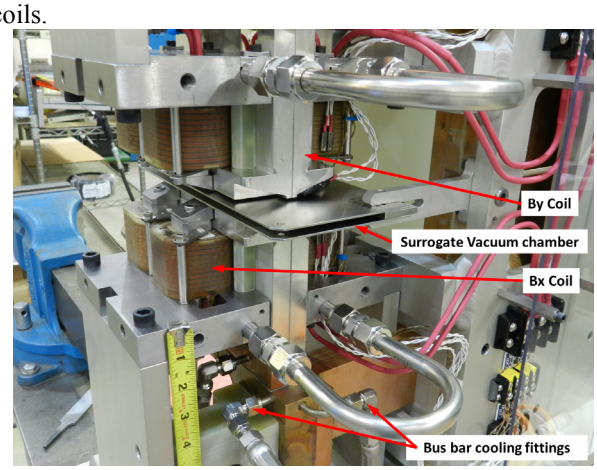


Figure 2: One-period test model.

Thorough testing of the switching speed of the one-period test model requires that the vacuum chamber be present so the eddy currents in the vacuum chamber can be properly taken into account. The final vacuum chamber will be made of stainless steel with a copper coating on the inside. For these tests, a surrogate vacuum chamber was used that would allow side insertion of a Hall probe for magnetic field measurement. The surrogate chamber, seen in Figure 2, is made from two pieces of 1.5-mm-thick 316 stainless separated by a 5-mm gap. The stainless steel pieces are plated with a 75-micron-thick copper strip on the inside.

Measured Field

The final power supply for the EMVPU is not yet available, so the original CPU power supply [7] was used for the testing. Switching rates as high as 10 Hz at 1400 amperes were achieved with the test model, as shown by the measured vertical peak field in Figure 3. The Hall probe was positioned inside the surrogate vacuum chamber. The rise time of the current was 16 ms; the rise time of the field was also 16 ms, showing that the limitation on rise time comes from this power supply rather than the device.

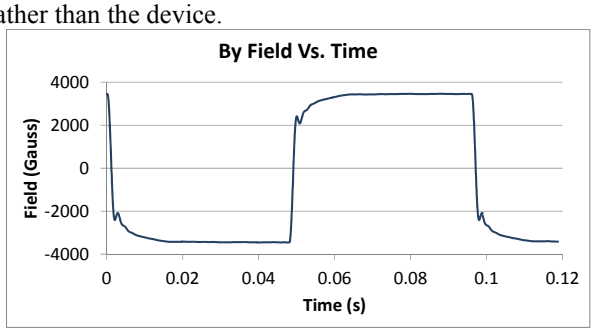


Figure 3: Time-dependence measurement of a one-period test model. The vertical field was ±3500 Gauss, switched at 10 Hz.

Solder Joint

The bus-bar solder joints are produced with a 50-micron-thick Sn60Pb40 (60/40) solder sheet, chosen because it has a melting temperature of 220°C as compared to over 500°C for silver solders. Because soldering needs to be done while the bus bars are assembled on the core, the lower temperature reduces the possibility of the core warping. All solder joints are assembled with a screw and spring washers. The spring washers take up the excess space produced as the solder melts. The joint screws are re-torqued after soldering to provide a full-contact solid joint. Figure 4 shows the solder joints of the By coils to the bus bars. The air gaps are filled with Nema Grade G-10 sheets after soldering.

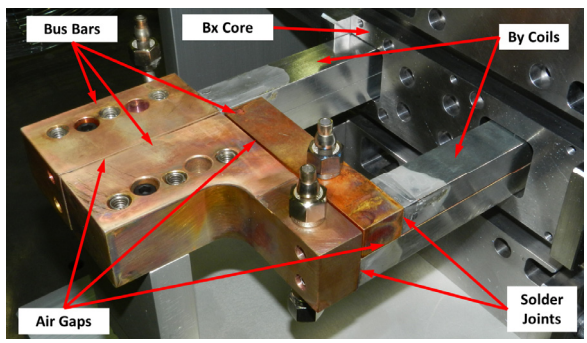


Figure 4: Solder joints of the By coils to the bus bars.

Simulated forces on the By coils and solder joints during switching are less than 1.8-kg force. A stress test was performed on the one-period test model to show how the coil supports and solder joints hold up. A nine-hour run with a current of 1400 amperes at 6 Hz was completed. There appeared to be no effect at all from the test.

FOUR-PERIOD TEST MODEL

A four-period test model is now under development at the APS. Figure 5 shows the model used for magnetic field analysis [8]. A new power supply is also under development at the APS. The new power supply will switch the current from -1400 to 1400 amperes within

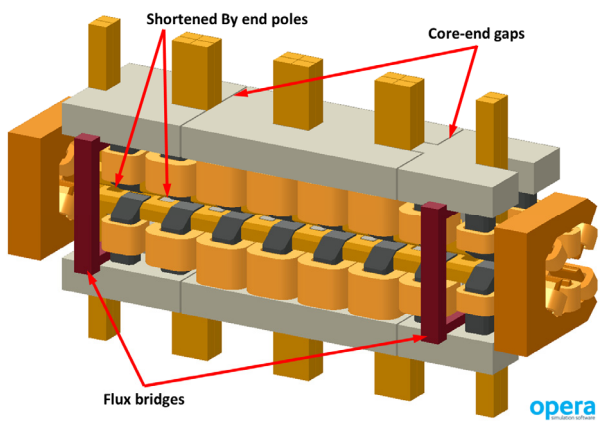


Figure 5: Magnetic field analysis model of the four-period test model.

Copyright © 2013 CC-BY-3.0 and by the respective authors

6 ms. This will allow the field to fully switch within 10 ms (determined from simulations), giving the user 40 ms to take data between each switching event (80% duty cycle).

The two By end poles on each end are shortened vertically to produce the ¼-¾ full-field configuration on each end that minimizes the first and second integrals (i.e., keeps the horizontal beam steering straight and on axis). Simulations guided the addition of flux bridges and 2-mm-wide gaps in the core near the ends to reduce the large horizontal missteering during switching of the By field. An initial missteering of up to 180 micro-radians was reduced to less than 75 micro-radians. Fast end corrector magnets will correct the remaining missteering.

The ¼-¾ full-field configuration is achieved for the Bx field at each end by reducing the number of turns on the end Bx coils and also by shortening the Bx pole tips horizontally. Any further correction will be done with the end corrector magnets.

Figure 6 shows a 3-D CAD model of the four-period test model without the support frames. Corrector magnets with six laminated poles and separate power supplies for each coil are included at the upstream and downstream ends of the device. Table 2 gives the maximum integrated multipoles that each corrector magnet can produce. The horizontal dipole also comes with a skew sextupole component (66 G/cm). This additional skew sextupole component is used to correct the integrated skew sextupole component through the whole device, as was done for the electromagnetic variably polarizing quasi-periodic (IEX) undulator [2, 3].

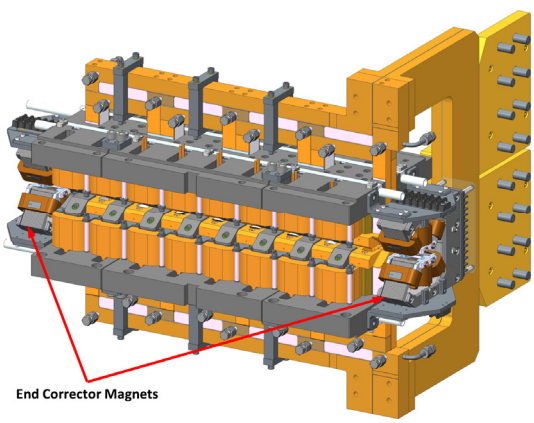


Figure 6: A 3-D CAD model of the four-period test model.

Table 2: Corrector Magnet Maximum Integrated Multipoles

Multipole	Value	Unit
Vertical dipole	958	G-cm
Normal quadrupole	469	G
Normal sextupole	569	G/cm
Horizontal dipole	653	G-cm
Skew quadrupole	69	G
Skew octupole	27	G/cm^2

VACUUM CHAMBER

APS typically uses aluminum insertion device vacuum chambers, but simulations show that the fastest possible switching through an aluminum vacuum chamber is 30 ms, due to the high electrical conductivity and resulting eddy currents in the Al. Figure 7 shows the simulated eddy currents in an aluminum vacuum chamber 130 microseconds after the start of switching.

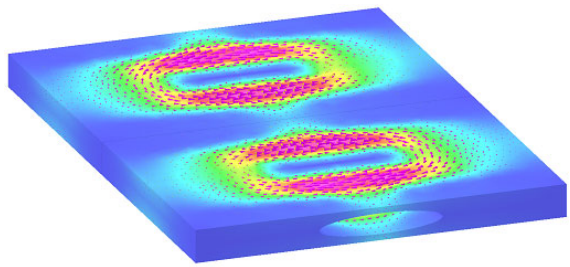


Figure 7: Simulated eddy currents in an aluminum vacuum chamber.

Stainless steel is much less electrically conductive than aluminum, reducing the switching time to 10 ms. The inside wall of the chamber must retain high conductivity, however, to minimize the resistive-wall impedance seen by the electron beam. Therefore, the inside wall will be coated with 75 microns of copper. Simulations show that a 75-micron Cu coating has a negligible effect on the switching speed. Further investigation into a stainless steel copper-coated insertion device vacuum chamber is ongoing at the APS.

REFERENCES

[1] E. Gluskin et al., AIP Conf. Proc. 521 (2000) 344.
[2] M. Jaski et al., "An Electromagnetic Variably Polarizing Quasi-periodic Undulator," WEPSM09, NA-PAC13.
[3] A. Xiao et al., "The Intermediate Energy X-Ray (IEX) Undulator Commissioning Results," WEPSM11, NA-PAC13.
[4] J. Chavanne, P. Elleaume, and P. Van Vaerenbergh, "A Novel Fast-Switching Linear/Helical Undulator," Proc. of EPAC 1998, TUOB02A, p. 317 (1998); http://www.JACoW.org
[5] F. Marteau et al., "Description of an Electromagnetic/Permanent Magnet Helical Undulator for Fast Polarization Switching," Proceedings of Magnet Technology MT-22, IEEE Trans. Appl. Superconductivity 22(3), (2012) 4102004.
[6] M. Jaski, "Design and Fabrication of Magnet Coils," Diamond Light Source Proceedings, Volume 1, Issue MEDSI-6, p. e7, November 2010.
[7] Yu. Evtushenko et al., "Precision Power Supply of Trapezoidal Current for the Undulator," Proc. of EPAC 2002, MOPLE104, p. 2469 (2002); http://www.JACoW.org
[8] Opera 3D finite element code (ELEKTRA), Cobham Technical Services, Oxfordshire, England.

Copyright © 2013 CC-BY-3.0 and by the respective authors

AN ELECTROMAGNETIC VARIABLY POLARIZING QUASI-PERIODIC UNDULATOR*

M. Jaski, M. Abliz, R. Dejus, B. Deriy, E. Moog, I. Vasserman, A. Xiao, E. Gluskin
Advanced Photon Source, Argonne National Laboratory, Argonne, IL 60439, USA

Abstract

An electromagnetic variably polarizing quasi-periodic undulator was installed in the Advanced Photon Source (APS) storage ring in April 2012 and has been successfully commissioned with stored beam. This device is identified as the Intermediate Energy X-ray (IEX) undulator. The IEX undulator takes its name from the IEX beamline where it is installed. The IEX undulator is able to produce a variety of polarizations: linear vertical, linear horizontal, and right- or left-handed elliptical or circular. Ten pairs of poles, distributed quasi-periodically along the undulator length, are powered separately, allowing the field strength of the quasi-periodic poles to be adjusted. This adjustability allows the user to seek a balance between the suppression of the higher harmonics and the loss of flux in the fundamental that best suits the measurement being made. The IEX undulator has a 12.5-cm period and can achieve photon energies as low as 250 eV in horizontal polarization and 440 eV in vertical polarization. A description of the IEX undulator will be presented.

INTRODUCTION

The IEX beamline team, consisting of APS staff members along with researchers from the Universities of Illinois at Chicago and at Urbana-Champaign, is commissioning a new dual beamline with one leg dedicated to angle-resolved photoemission spectroscopy (ARPES) measurements and the other dedicated to resonant soft x-ray scattering (RSXS) [1]. The undulator needs to provide photons ranging from 250 to 2500 eV, with horizontal and vertical linear, and left- and right-circular and elliptical polarizations. (Vertical linear polarization only goes as low as 440 eV.) The presence of high harmonics in the spectrum degrades the signal-to-noise ratio in both techniques, so a quasiperiodic undulator is sought for its ability to shift the high harmonics in energy so they are eliminated by the beamline optics.

Several possible variably polarizing undulator designs were considered, including an Apple II (all permanent magnet), an electromagnetic/permanent magnet, and an all-electromagnetic design similar to the circularly polarizing undulator (CPU) [2] presently installed at the APS. The all-electromagnetic design was chosen, largely because of its ability to vary the magnetic strength reduction in the quasiperiodic poles so trade-offs could be made between additional high-harmonic reductions at the expense of a loss in photon beam intensity. Magnetic field simulation and optimization [3] were done, and prototypes were built and tested before building the full-length device. The full-length device was successfully commissioned at the APS in 2012 [4].

*Work supported by U.S. Department of Energy, Office of Science, under Contract No. DE-AC02-06CH11357.

PARAMETERS

Table 1 lists selected parameters for the IEX undulator.

Table 1: IEX Undulator Selected Parameters

Title	Description	Value	Unit
General	Period	12.5	cm
	Gap	10.5	mm
	Periods per device (including end poles)	38	periods
Horizontal Linear Polarization	Minimum photon energy	240	eV
	Measured maximum vertical effective field	4614	Gauss
Vertical Linear Polarization	Minimum photon energy	440	eV
	Measured maximum horizontal effective field	3312	Gauss
Circular Polarization	Minimum photon energy	234	eV
	horizontal and vertical effective field	3312	Gauss

DESIGN AND ASSEMBLY

Figure 1 shows the IEX undulator at the magnetic measurement bench. The device is 958 mm wide × 2118 mm tall × 5044 mm long (37.7" × 83.4" × 198.6") and weighs 6350 kg (14,000 lbs). Casters attached to the base allow it to be manually rolled across a flat concrete floor by six people. The undulator is installed onto floor bases that are grouted to the floor. The undulator gap is fixed at 10.5 mm. The jaw assembly is mounted to high-precision linear roller bearings and can manually be moved



Figure 1: The IEX undulator at the magnet measurement bench.

Copyright © 2013 CC-BY-3.0 and by the respective authors

horizontally in and out of operating position, allowing for well-controlled alignment of the fixed gap around the vacuum chamber during installation. There are fine adjustments for longitudinal, vertical, and horizontal positions as well as roll, pitch, and yaw. The undulator is designed with a calculated mechanical fundamental natural frequency of 34 Hz.

Figure 2 shows the coil and pole arrangement for a single jaw. There are a total of 304 B_x (horizontal field) poles and 152 B_y (vertical field) poles. The coils are vacuum impregnated with epoxy [5].

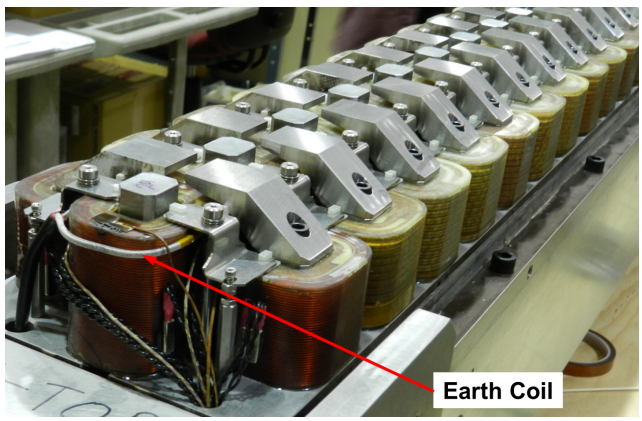


Figure 2: Top jaw coil and pole configuration. The centered vertical field poles alternate with pairs of horizontal poles along the undulator axis. The bottom jaw configuration mirrors this arrangement.

CORRECTOR COILS

End Coils

To minimize the first and second field integrals through the ends of the undulator, fewer turns are used in the endmost coils at both ends. The strength of the last pole is ¼ and the next-to-last pole is ¾ of full field. This leaves room around the end poles to add corrector windings. Six corrector coils are supplied on both the upstream and downstream ends of the undulator to provide a means for electron beam steering and multipole control. Figure 3 shows the configuration of the upstream corrector coils. The coils are labeled top (T), bottom (B), and quadrants Q1, Q2, Q3, and Q4. To minimize the imbalance between the 25% and 75% end poles that causes flux leakage into the full-field poles, a flux bridge is added on each end.

Each corrector coil has its own power supply. Figure 4 shows the coil field directions needed to obtain the various multipole moments. Table 2 lists the maximum achievable integrated multipole corrections, where the limit is imposed by the power supply and by the coil becoming hot. These corrections are more than was needed to meet specifications so the coil currents were limited to 20% of the maximum.

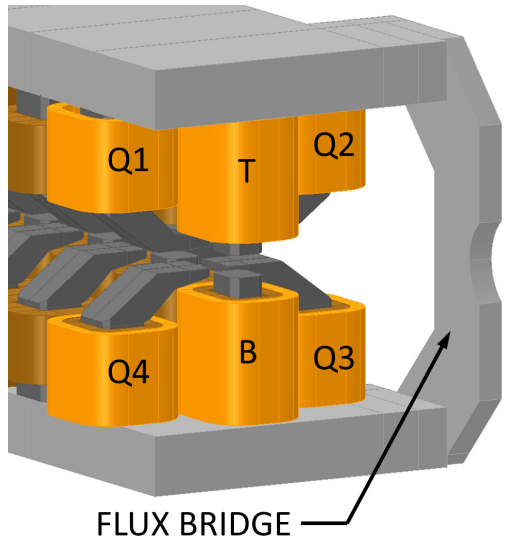


Figure 3: Configuration of the upstream corrector coils.

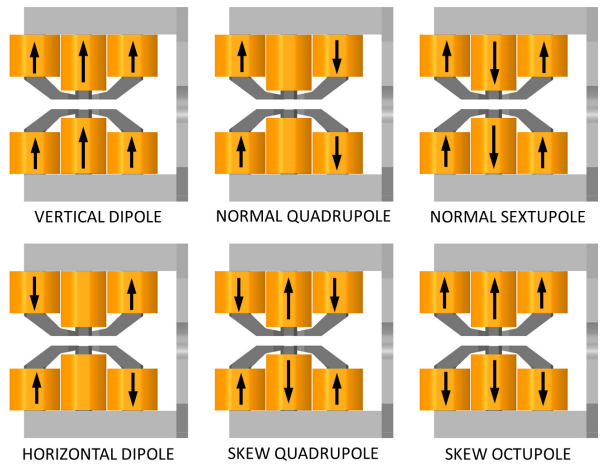


Figure 4: Coil field directions for the various multipole moments.

Table 2: IEX Undulator Maximum Achievable Integrated Multipole Corrections from the Corrector Coils

Multipole	Value	Unit
DS Horizontal Dipole	9021	G-cm
DS Vertical Dipole	13153	G-cm
DS Skew Quadrupole	4251	G
DS Normal Quadrupole	15158	G
DS Normal Sextupole	10236	G/cm
DS Skew Octupole	346	G/cm^2
US Horizontal Dipole	8043	G-cm
US Vertical Dipole	13054	G-cm
US Skew Quadrupole	4569	G
US Normal Quadrupole	15144	G
US Normal Sextupole	10140	G/cm
US Skew Octupole	375	G/cm^2

Copyright © 2013 CC-BY-3.0 and by the respective authors

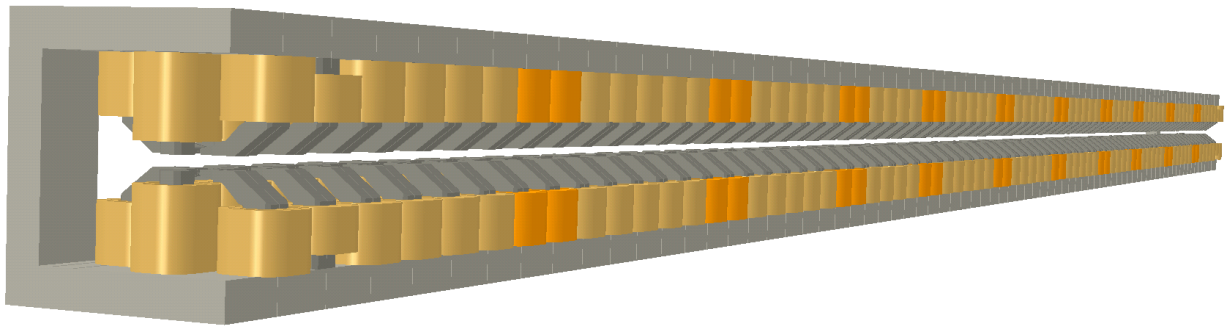


Figure 5: IEX undulator quasi-periodic pole positions.

Skew Sextupole Correction

An integrated skew sextupole component that was out of specification was discovered during magnetic simulations. No combination of end correctors provides a correction that is mainly skew sextupole, but the horizontal dipole corrector also produces a small skew sextupole component. The relative amounts of horizontal dipole and skew sextupole were adjusted by shortening the tips of the downstream horizontal dipole end poles, then increasing the current in those coils. A series of simulations was used to minimize the skew sextupole component.

Earth Coil

An earth coil is provided to compensate for the earth's magnetic field. The earth coil consists of a one-turn coil around the B_y poles on both the top and bottom jaws. The top jaw portion of the earth coil can be seen in Figure 2. The earth coil can supply an integrated B_y field up to 3900 G-cm. This is more than enough to correct the earth's field along with the approximately four-fold enhancement by the steel poles.

THERMAL

The coils are indirectly water cooled. Water lines directly cool the cores. The poles are bolted to the cores, and the coils are epoxied to the poles to ensure good thermal contact. At full power the device operates at 12,000 W; 9,500 W is removed by water cooling. The remaining 2,500 W is removed by air cooling. Blowers and a baffle draw air over the coils and exhaust the warm air (2,500 W) directly into the storage ring tunnel air handling exhaust. This immediately removes the heat from the tunnel so it will not interfere with storage ring tunnel temperature control. The heat loads given above were empirically obtained by building and testing a four-period test model.

QUASI-PERIODICITY

Quasi-periodicity suppresses the higher-order radiation harmonics [6]. The IEX undulator is supplied with quasi-periodic capabilities in both horizontal and vertical polarizations. For a 38-period undulator there are 76 pole sets (two pole sets per period). Coils are numbered 1 to 76. The quasi-periodic coils for the IEX undulator are 7, 8, 14, 15, 20, 21, 27, 28, 34, 35, 40, 41, 47, 48, 54, 55, 61, 62, 67, and 68. Figure 5 shows the configuration of the quasi-periodic coils. The B_x quasi-periodic coils are connected in series and have their own power supply. The remaining B_x coils are connected in series and have their own separate power supply. Similar connections are done for the B_y coils. The quasi-periodic coils can be operated at a reduced current (~85%) that will shift the higher spectral harmonics to a lower energy.

POWER SUPPLIES

Seventeen power supplies are required to operate the IEX undulator: B_x and B_y main power supplies, B_x and B_y quasi-periodic power supplies, twelve end-coil power supplies, and one Earth-coil power supply. Each power supply is bi-polar to allow for degaussing.

REFERENCES

[1] IEX Collaborative Development Team Final Design Report, available online at: http://www.aps.anl.gov/Sectors/Sector29/beamline/fdr/index.php
[2] E. Gluskin et al., AIP Conf. Proc. 521 (2000) 344.
[3] M. Jaski et al., "Magnetic Simulation of an Electromagnetic Variably Polarizing Undulator," PAC'11, New York, TUP244, p. 1289 (2011).
[4] A. Xiao et al., "The Intermediate Energy X-Ray (IEX) Undulator Commissioning Results," WEPSM11, NA-PAC'13.
[5] M. Jaski, "Design and Fabrication of Magnet Coils," Diamond Light Source Proceedings, Volume 1, Issue MEDSI-6, p. e7, November 2010.
[6] R. Dejus et al., "Spectral Performance of Circular Polarizing Quasi-Periodic Undulators for Soft X-Rays at the Advanced Photon Source," PAC'09, Vancouver, BC, Canada, MO6PFP076, p. 307 (2010).

Copyright © 2013 CC-BY-3.0 and by the respective authors

DESIGN OF A 17.2-MM-PERIOD PLANAR UNDULATOR FOR THE APS *

E.R. Moog#, M. Abliz, R.J. Dejus, J.H. Grimmer, and M. Jaski, ANL, Argonne, IL 60439, USA

Abstract

The design process for a short-period planar undulator is described. This is a conventional planar design based on Nd-Fe-B magnets and vanadium permendur poles. The period length was driven by the users' request for a high flux of photons at 23.7 keV, with minimal tuning range. A shorter period gives higher flux; 17.2 mm was the shortest value consistent with the gap limitations of the vacuum chamber and with reaching the desired photon energy. Details of the design, especially the various chamfers of edges of the magnet and pole, were examined more closely than has been the standard past practice in order to minimize the period length.

INTRODUCTION

The majority of the insertion devices at the Advanced Photon Source (APS) are of the planar permanent magnet hybrid type, and a variety of period lengths have been installed. This 17.2-mm-period undulator will have the shortest period; it is being designed to meet the specific needs of a group of users who want to maximize their photon flux at 23.7 keV without any need for a significant tuning range. The ideal choice for such a short-period undulator would be to use superconducting technology, but that technology is only now being commissioned at the APS [1]. It will be several years before a customized device can be designed and built for these users. They have opted not to wait.

Keeping the beam impedance from the insertion device vacuum chamber walls low results in a minimum gap for the undulator of 10.4 mm (with a new ID vacuum chamber that is in the design stage; the present typical minimum gap is 11.0 mm). This, combined with the 23.7 keV desired energy, means that the operating point of the undulator is not at the peak in the tuning curve but rather on a slope where a small change in undulator period can have a noticeable effect on the on-axis flux, as shown in Fig. 1 where there is a 15% flux increase between the 17.5 and 17.2-mm period lengths. Shortening the undulator period gives more flux, until the field strength needed to reach the desired energy no longer lies within the achievable gap range. The steepness of the tuning curve for this design project places a high premium on achieving the shortest period possible, and the need for a single specific photon energy means that the magnetic field cannot be lower than expected. To add to the challenge, the required undulator field increases as the undulator period decreases, while a decrease in period generally comes with a decrease in field.

*Work supported by U.S. Dept. of Energy, Office of Science, under Contract No. DE-AC02-06CH11357.
#emoog@aps.anl.gov

CHOICE OF MAGNET GRADE

The considerations that drive the choice of a magnet grade are the remanent field B_r and the coercivity H_{cJ} of that grade. Recent magnet grades used for APS undulators are Shin-Etsu's N39UH and N42SH. With $B_r \geq 12.7$ kG and $H_{cJ} \geq 21$ kOe, N42SH has been used when the highest field strength was needed. Otherwise, N39UH with $B_r \geq 12.2$ kG and $H_{cJ} \geq 25$ kOe has been chosen for its higher coercivity.

The higher coercivity is desirable for two reasons: 1) for a particular demagnetizing field in the magnet, the higher-coercivity magnet can survive higher temperatures without ill effects, and 2) the higher coercivity correlates with higher resistance to radiation-induced demagnetization. Magnets of either grade, when installed in an undulator whose magnetic design considerations include maintaining a moderate demagnetizing field, will survive a hot day with broken air conditioning. Radiation susceptibility is harder to quantify because of many unknowns, including the spectral sensitivity of the magnets and the spectral distribution of the radiation at the magnets' locations. At the APS, except for two extremely high-dose sectors, the undulators have not been affected by radiation enough to affect users' programs, though small effects have been seen. A common difference between the maximum demagnetizing field and the magnet's H_{cJ} has been ~4 kOe, so a goal is to keep the demagnetizing field at least that far below H_{cJ}. For this short a period, a higher H_{cJ} than N42SH is not necessary.

The magnet grade characteristics given here are from the manufacturer's data sheets and are for 20°C. The temperature of the APS storage ring tunnel, however, is 25°C. Since the on-axis field in the simulations must be met in the real device, the reduction in the manufacturer's B_r due to the higher temperature must be taken into

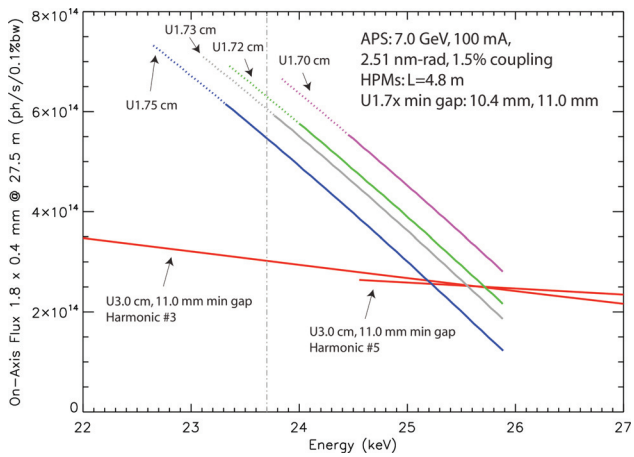


Figure 1: Tuning curves over a narrow photon energy range, for a few period lengths. The solid lines are for a minimum gap of 11 mm; the dotted extensions are for a reduction to 10.4-mm gap.

Copyright © 2013 CC-BY-3.0 and by the respective authors

account. Thus the B_r used in magnetic design calculations is 12.63 kG, after applying the -0.11%/K thermal coefficient correction.

DESIGN PROCESS

In order to finalize the period length, a series of quick calculations was carried out to determine approximately what field strength could be obtained from a variety of period lengths. Both 2-D and 3-D modules from the Vector Fields suite of magnetic design codes [2] were used. The only optimization was to ensure that the relative thicknesses of magnet and pole were close to optimal. From these results, a period length of 17.2 mm was chosen (see Fig. 1). The field requirement would be met with the new ID vacuum chamber; it might be met if a gap smaller than 11 mm could be achieved with the present chamber and if the delivered magnets are stronger than the minimum for the magnet grade.

2-D Design Work

Some initial magnetic design tasks can be carried out using the 2-dimensional codes. The calculations are slightly quicker and the optimization of the chamfering was found to be somewhat quieter than in 3-D. The results were later confirmed in 3-D.

The 2-D magnet model is shown in Fig. 2. The entire non-air part of the model is shown along with an inset showing an enlargement of the gap region. (The entire model includes more air on the non-gap side—enough so the boundary condition there doesn't matter.) Symmetry conditions allow just the quarter-period section shown, with only one jaw, to be calculated. Perpendicular field boundary conditions are applied along the beam axis (i.e., the undulator midplane) and the top boundary, which is the center of the magnet in the beam direction. The lower boundary (the center of the pole) has the magnetic field parallel to the boundary. The pole protrudes into the gap beyond the magnet, leaving a 0.5-mm magnet recess space available for shims to be placed during magnetic tuning of the completed undulator without affecting the minimum undulator gap. This space is needed despite its cost in on-axis field. A small air gap of 0.08 mm is allowed between the magnet and pole, reflecting the tolerance in the magnet and pole dimensions. The chamfers on the corners of the magnet and pole can also be seen.

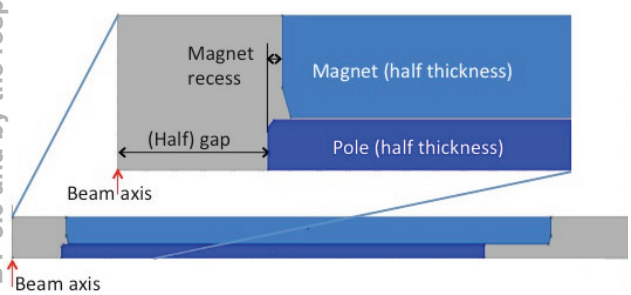


Figure 2: The two-dimensional magnetic model is shown at the bottom, with additional air space at the right omitted. The top section is an enlargement of the gap region, showing the chamfers and the thin air gap between magnet and pole.

The goal of the magnetic design is to maximize the on-axis field of the undulator while not allowing the demagnetizing field in the magnet (the H component parallel to the beam axis, since the magnetization direction of the magnet is parallel to the beam axis) to become too large compared to the magnet grade's H_{cJ}.

The field strength is very sensitive to the thickness (in the beam direction) of the magnet and pole, so it is optimized first. It is also rechecked last, once everything else has been set. Model calculations as a function of magnet thickness find an optimum peak field on axis at a magnet thickness of 5.67 mm. The peak field changes by 1 in 1000 at a thickness change of ±0.047 mm, leading to a tolerance on magnet thickness of ±0.05 mm. (The final recheck of the magnet thickness resulted in an adjustment to 5.63 mm. The pole thickness then becomes 2.81 mm.)

There isn't an optimum magnet height—a taller magnet will always give more field, albeit with diminishing returns, as long as the pole height is sensible. Therefore, the height chosen for the magnet, 52.5 mm, was the tallest that would fit without any redesign of the strongback or gap separation mechanism and without reducing the maximum achievable gap.

The pole height was adjusted to maximize on-axis field, giving a height of 45 mm. This is a broad maximum—it takes a 3-mm change to change the peak by 1 in 1000.

The remaining parameters to set using the 2-D model are the chamfers. There are four parameters to set: the y (vertical) and z (beam direction) dimensions on both the pole and magnet. An attempt to use the Optimizer module from Vector Fields [2] to set all four parameters at once was unsuccessful, but showed that the largest on-axis field was for the least pole material removed by the chamfering. Following the mechanical engineers' advice that the edges should be broken at least slightly, both pole chamfer dimensions are set to 0.15 mm.

Setting the magnet chamfers involves a trade-off between the on-axis field and the demagnetizing field inside the magnet. The surface plots in Fig. 3 show the behavior of both as a function of the magnet chamfer z dimension, Chzz, and the magnet chamfer y dimension, Chzy. (The z in the name is a reminder that this is a chamfer on the edge at the z end of the magnet. The chamfer at the x end will be considered below.) The top panel shows the effective field $B_{y\,eff}$ as a function of the chamfer dimensions. A ridge of higher field can be seen, with a sharper drop-off on the right side in the figure. The lower panel shows the worst value of the demagnetizing field in the magnet block, with the value closest to zero being desirable. It too shows a ridge, but one that runs perpendicular to that in the top panel. Originally the red point was chosen, where the two ridges cross. A slightly higher $B_{y\,eff}$ (by ~1 G) could be reached, but the decision was made to save a few kOe instead. Later, concerns were raised that the zz chamfer was too long to allow shims to be placed stably on the magnet faces, so Chzz was

Copyright © 2013 CC-BY-3.0 and by the respective authors

reduced to 0.5 mm. This change reduced the field by 0.9 G, a negligible amount, and made $H_{z\,max}$ worse by 660 Oe.

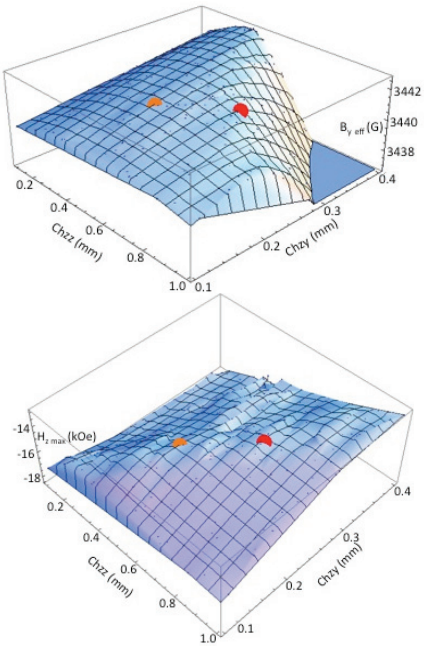


Figure 3: Surface plots showing the dependence of the effective field $B_{y\,eff}$ (top) and the strongest demagnetizing field in the magnet block $H_{z\,max}$ (bottom) on the chamfer dimensions in z, Chzz, and in y, Chzy. The red point, at (Chzz, Chzy) = (0.73, 0.26) mm was initially selected. Undulator tuning considerations prompted a change to the orange point at (Chzz, Chzy) = (0.5, 0.2) mm.

3-D Design Work

The aspects of the design that must be done using 3-D codes are those that involve the roll-off of the on-axis field in the lateral (x) direction, the widths of the magnet and pole in x, and the chamfers at the x end of the magnet and pole.

The 'good-field' region in the undulator is ±5 mm in x to allow for steering of the beam through the undulator and for beam displacements during injection. The roll-off is the peak-to-peak change of field over the range from -5 to +5 mm in the x direction, at the center of the pole in z. The limit on the field roll-off is set by requiring that the photon energies from electrons traveling within the 'good-field' region are the same as far as the user can tell, or specifically, to within 10% of the intrinsic width of the 3rd harmonic. (The roll-off is not used to limit the integrated multipole moments; those are separate requirements.) The full width at half maximum of the 3rd harmonic for a 4.8-m-long undulator is $\Delta E_\gamma/E_\gamma = 5.54*10^{-3}$, and for a 2.4-m-long undulator it is $7.10*10^{-3}$. These translate to $\Delta B/B$ = 0.0019 or 0.0024. For B ~3460 G, the roll-off limit becomes 6.6 to 8.3 G.

The width of the pole is limited by the need to fit around the vacuum chamber, with some allowance for clamping, so 44 mm is chosen, the same as many of the recent APS undulators. As with the magnet height, the on-axis field keeps growing the wider the magnet. The limit on the width then becomes what fits with the existing vacuum chamber. Sixty-seven mm is chosen; at that width any gain from a wider magnet is diminishing anyway. The chamfers at the x edge of the magnet are entirely determined by engineering requirements for the clamping scheme and fitting around the vacuum chamber.

The chamfer on the x edge of the pole remains to be set. The surface plots in Fig. 4 show the effects of the x and y dimensions of the chamfer (Chxx and Chxy, respectively) on the effective undulator field (top) and on the field roll-off (bottom). As the x chamfer dimension becomes larger, the pole is effectively narrowed and the on-axis field grows. As the pole narrows, there is initially no effect on the roll-off, but then the roll-off begins to grow rapidly. The red dot marks the selected pole x chamfer dimensions (Chxx, Chxy) of (7, 4) mm. There is noise on the right side of the roll-off plot, probably due to a meshing issue, but since its level is ~1 G it was not pursued.

The production of the 17.2-mm-period undulator is now underway.

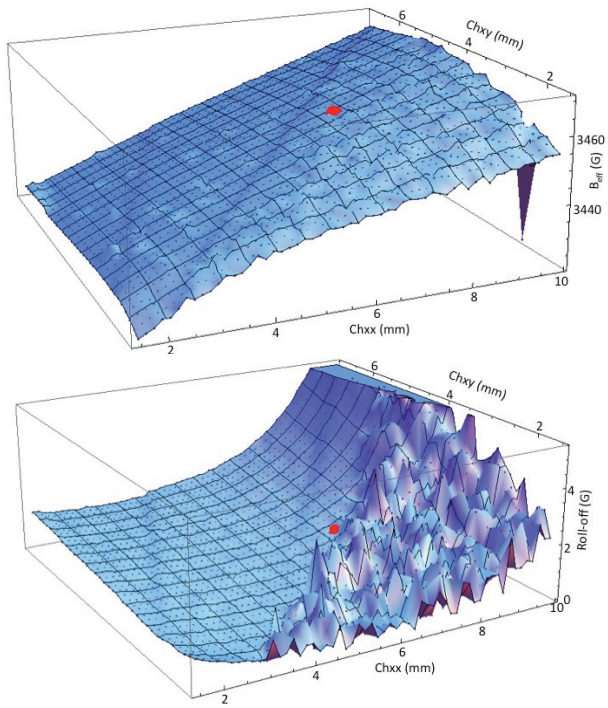


Figure 4: Surface plots showing the dependence of the effective field (top) and the field roll-off (bottom) on the chamfer dimensions in x, Chxx, and in y, Chxy. The red point, at (Chxx, Chxy) = (7, 4) mm is the selected value.

REFERENCES

[1] K. C. Harkay et al., "APS Superconducting Undulator Beam Commissioning Results," WEOAA3, NA-PAC'13.

[2] Opera Electromagnetics Finite Element Software Suite, Cobham Technical Services – Vector Fields Software.

Copyright © 2013 CC-BY-3.0 and by the respective authors

THE INTERMEDIATE-ENERGY X-RAY (IEX) UNDULATOR COMMISSIONING RESULTS *

A. Xiao, M. Abliz, B. Deriy, M. Jaski, M. Smith, I. Vasserman, J. Xu
Argonne National Laboratory, Argonne, IL 60439, USA

Abstract

Strong beam perturbation from the intermediate-energy x-ray (IEX) undulator operation has been expected from the beginning. This paper describes our efforts including the initial magnet design, field measurements and compensation, special considerations of power supplies and the control system, and the final commissioning results with beam. Perturbations are well within the specified limits, and the IEX was made ready for user operation in less than six months.

INTRODUCTION

A 4.8-m electromagnetic undulator was designed, built, and installed at the APS to provide the Intermediate-Energy X-ray (IEX) beamline with variably polarized radiation. Details on the device itself are presented separately [1]. The main parameters of this device are listed in Table 1. Simulation results show that strong nonlinear fields are present in this device. To eliminate beam perturbations, 13 correction coils are included, which correct stray fields, orbit, tune, coupling, and some high-order perturbations. Together with four main coils (By, By-Quasi, Bx, Bx-Quasi), there are 17 power supplies for this single device. Besides the complexity of the device itself, special requirements from user operations are:

Table 1: IEX Main Parameters

Title	Description	Value	Unit
General	Length	4.8	m
	Period length	12.5	cm
Horizontal Linear	Energy	0.25-3	keV
	K Value	5.271-0.694	
Vertical Linear	Energy	0.44-3	keV
	K Value	3.863-0.694	
Circular Mode	Energy	0.44-3	keV
	K Value	3.863-0.694	

- Generates four polarization modes. Horizontal- and vertical-linear modes [H/V], clockwise and counter-clockwise circular modes [CW/CCW].
- In each mode, the quasi-periodic property can be switched on and off [1].
- Precise photon energy reproducibility.
- Polarization refinement at the sample location.

* Work supported by the U.S. Department of Energy, Office of Science, under Contract No. DE-AC02-06CH11357.

To satisfy requirements on energy reproducibility, the device is required to operate on a hysteresis loop. A special magnet degaussing and conditioning procedure also needs to be followed. The device provides radiation to two beamline branches in which, due to different properties of optical elements, different IEX settings are required for different branches to reach $> 99\%$ polarization purity at the sample location.

All facts added up together made IEX commissioning a difficult task. Commissioning started on May 2012 and by November 2012 all operational modes had been successfully commissioned with beam. This paper describes details of the commissioning efforts leading to eventual success.

MAGNET DESIGN AND MEASUREMENT

The magnet design and measurement were done in close coordination with simulation work. Simulation results [2] showed this device would be the strongest nonlinear perturbation source among all IDs that have been installed in the APS storage ring. Special measures were taken during the magnet design phase, including 2×6 correction coils added to each side of the device for making further corrections.

After magnet assembly, the field was measured over the entire excitation curve for each operational mode. Unlike other ID measurements, which measure B_y only in the xz plane (y=0) — i.e., 2D measurement—both B_x and B_y fields were measured in a 3D volume. One assembly fault (a magnet block was inadvertently made from a prototype part) was found through fitting the measured field map to the design model, and corrected. After fixing the fault, the IEX was re-measured and a full set of simulation work was done using the measured field map. For these simulations [3], field data were fitted to the wiggler field expansions while measured field error was represented by a kickmap element; other machine errors were also included. Simulation results showed that the magnet quality met our expections. The simulated dynamic aperture (see Figure 1) was only slightly reduced due to the strong nonlinear field errors. This reduction was expected based on design simulations and can be mitigated using the local correction coils based on later beam test.

POWER SUPPLY

As described in the previous section, the IEX has 17 individual power supplies (PSs) to provide field excitation and local beam perturbation corrections, making it one of the single most complicated powered elements in the ring. To reduce beam perturbations, all PSs are synchronized, and

Copyright © 2013 CC-BY-3.0 and by the respective authors

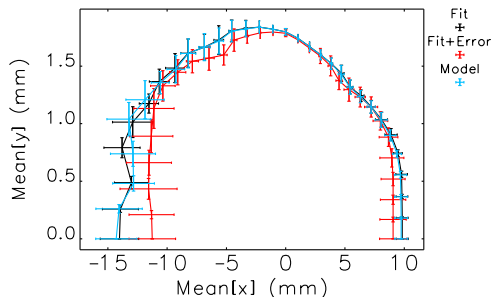
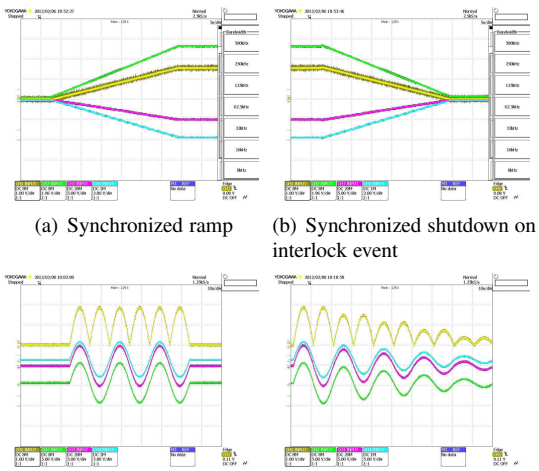


Figure 1: Dynamic aperture with machine errors. Black — field map from magnet measurement (fitted model); red — fitted model + measured field errors; blue — field map from IEX design.

a smooth linear ramp is made in between for each current change. This feature is built into the PSs local control system. Also, to simplify and standardize the required magnet conditioning and degaussing, these features are also built into the PSs local control system. Results are shown in Figure 2.



(a) Synchronized ramp (b) Synchronized shutdown on interlock event

(c) Conditioning curve (d) Degaussing curve

Figure 2: Waveform of PSs on different events.

CONTROLS

As described in the introduction, the IEX can be operated in many ways. The total operational states comprise 3 (modes, combined CW/CCW to C mode) × 2 (quasi) × 2 (direction) × 2 (beamline) = 24. Each state could generate different beam perturbations and thus needs a separate correction table. We have used a 24-page SDDS file to include all the correction tables, where each page corresponds to one operational state. In each table, there are columns containing photon energies, plus main [H/V] and Earth coil settings. These values are from magnet measurements. There are another 12 columns—6 for upstream (US) and 6 for downstream (DS)—including correctors for horizontal and vertical dipole, normal and skew quad, normal sextupole, and skew octupole. These corrector settings are beam-based and tuned to remove orbit, tune, and coupling variations from IEX operation and restore injection efficiency using higher-order correctors. The IEX local correctors are made from different combinations of the extra windings on the end poles [1]. The correction moments contained in the correction table need to be converted inside the control system before being sent to the PSs.

In summary, besides many general control tasks, the IEX control system needs to accomplish many special requirements. They are contained in the state program code, as illustrated in Figure 3, and include:

- Determine current and future IEX status.
- Choose the proper correction table.
- Convert correction moments to power supply settings and send to power supply.
- Choose the proper way to do mode switch.
- Perform magnet conditioning and degaussing.

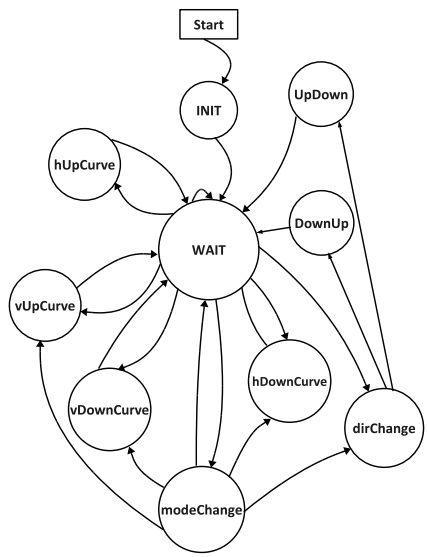


Figure 3: Diagram of IEX control state program.

COMMISSIONING WITH BEAM

The IEX was installed in the APS storage ring during the May 2012 shutdown. Thanks to thorough and careful work at every step (some of which is mentioned in the previous sections), in its first test with beam it was turned on and ramped to full strength step by step without beam loss. In this first beam test, there was no local correction—only regular APS orbit correction and feedback systems were employed. This clearly indicated that the device was working properly and that our assumptions and simulations had validity. Then we measured the tune shift and the dispersion perturbations with IEX on, and compared the results to our previous simulations, see Figure 4. We found very good agreement, which shows that the device is very close

Copyright © 2013 CC-BY-3.0 and by the respective authors

to the model and that various field errors were well controlled. After confirming that the device is well within our

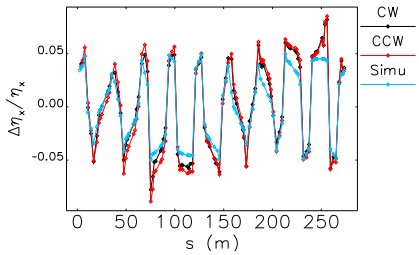
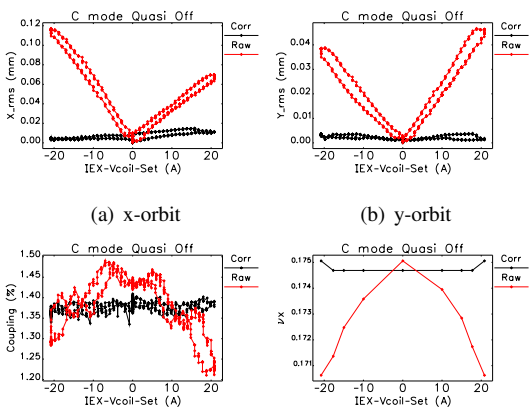


Figure 4: Dispersion error from IEX (quad ring): black/red - measurements made at CW and CCW mode; blue - simulation result.

expections and working properly, we started to debug our entire control program, simulate all possible user operation scenarios, and test the protection features with various simulated faults. At the same time, we started to build the local correction table (the 24-page SDDS file) for each operational state.

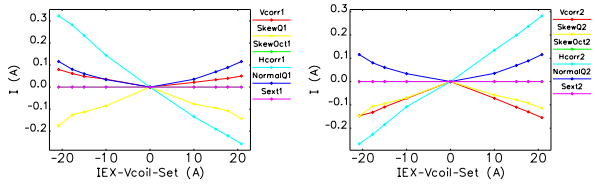
Techniques used for correction of similar APS devices [4, 5] have been adopted here with some adjustments. First, we measured beam response to the IEX local correction coils individually with IEX off. Then we measured beam perturbations while turning on the IEX. All corrector settings are then determined by multiplying beam perturbations with the inverse of the measured correction coil response. Normally, the tune and coupling variation is less sensitive to beam orbit going through the IEX magnet and had been corrected first, then the orbit perturbations are corrected. After several iterations (generally two is enough), most perturbations have been removed by the local correction coils. Some of the correction coil settings vs. the IEX main coil current and resulting orbit, tune, coupling variation with and without correction are shown in Figure 5 and 6. After about six months commissioning, the IEX was turned over for full user operation.



(a) x-orbit (b) y-orbit

(c) Coupling (d) Tune

Figure 5: Beam perturbations before (red) and after (black) local correction.



(a) Upstream correctors (b) Downstream correctors

Figure 6: IEX corrector settings (example of one page).

SUMMARY

IEX is the second circular polarized undulator to be installed in the APS. It has the strongest nonlinear field owing to its complex structure and high field. To eliminate its perturbation to the beam, we took great care in each step to ensure the device properties were within specifications and satisfied all user requirements. The device was able to run at full strength without losing beam immediately upon being turned on. Full correction table generation and debugging/troubleshooting of the control program took about six months (including a one-month shutdown in between). The device is now fully available for user operation with no restrictions.

ACKNOWLEDGMENTS

The successful IEX commissioning is the outcome of flawless work by many physicists, engineers, and technicians. We want to thank all of them sincerely for their great ideas and contributions. Methods developed from previous circular polarizing device commissioning, largely originated by L. Emery, also played a great role in the entire commissioning process. L. Emery's and V. Sajaev's rich experience on commissioning of new devices and their many suggestions helped us to avoid many mistakes.

REFERENCES

[1] M. Jaski et al., "An Electromagnetic Variably Polarizing Quasi-periodic Undulator," WEPSM09, NA-PAC'13.

[2] A. Xiao et al., "Beam Dynamics Study of the Intermediate Energy x-ray Wiggler for the Advanced Photon Source," Proc. of PAC'11, WEP064, p. 1594 (2011); http://www.JACoW.org

[3] A. Xiao, M. Borland, L. Emery, V. Sajaev, "Non-Linear Effects of Insertion Devices: Simulation And Experiment Results," WEPSM12, these proceedings.

[4] L. Emery et al., "Feedforward Correction of the Pulsed Circularly Polarizing Undulator at the Advanced Photon Source," Proc. of PAC'03, WPAG001, p. 2261 (2003); http://www.JACoW.org

[5] L. Emery, "Coupling Correction of A Circularly Polarizing Undulator at the Advanced Photon Source," Proc. of PAC'05, RPAE002, p. 805 (2005); http://www.JACoW.org

Copyright © 2013 CC-BY-3.0 and by the respective authors

NON-LINEAR EFFECTS OF INSERTION DEVICES: SIMULATION AND EXPERIMENT RESULTS *

A. Xiao, M. Borland, L. Emery, V. Sajaev
Argonne National Laboratory, Argonne, IL 60439, USA

Abstract

The Advanced Photon Source (APS) Upgrade includes adding more insertion devices (IDs) to the storage ring. Perturbations from IDs have been reviewed, with the most significant sources coming from IDs that generate circular polarized light. To address this, we measured non-linear effects from the existing circular polarized undulator (CPU) and intermediate-energy x-ray (IEX) undulator. Measurement results were compared with simulation results. Proposed correction schemes were tested experimentally.

INTRODUCTION

The ongoing APS Upgrade (APS-U) project includes installing IDs in unused straights and replacing some IDs with devices better-optimized for user requirements. ID perturbations to the beam can be qualitatively expressed by [1]

$$\Delta x'(x) \propto \frac{L_w}{E^2} K^2 \frac{d}{dx} F^2(x), \qquad (1)$$

where L_w is the length of the wiggler, E is the beam energy, K is the wiggler strength, and $F(x) = B_y(x)/B_y(0)$. Non-linear effects come from the roll-off in $F(x)$.

For planar IDs, only one on-axis field (typically B_y) needs to be non-zero. Thus a generally wider ID pole and flatter $F(x)$ is possible, which reduces non-linearities. For IDs that generate elliptical radiation, both B_x and B_y are necessarily non-zero on axis. The required magnet structure is much more complicated, with narrower poles and, as a consequence, larger variation of $F(x)$. Figure 1 illustrates this difference for some of the typical and planned APS IDs. ID parameters are listed in Table 1.

To better understand the beam dynamics effects of ID field non-linearity, several simulation methods have been implemented in `elegant` [2]. Some of the methods require an analytical wiggler field expansion, which can be obtained through fitting a 3D magnetic field map to a model. In this paper, we first describe these simulation tools, fitting methods, and methods to reduce artificial errors from fitting. Then, using IEX as an example, we show simulation results from a measured field map. Finally, we present some experimental results from CPU and IEX operations.

SIMULATION TOOLS AND FITTING METHOD

There are four elements in `elegant` that simulate IDs: CWIGGLER, GFWIGGLER, UKICKMAP, and FTABLE.

* Work supported by the U. S. Department of Energy, Office of Science, under Contract No. DE-AC02-06CH11357.

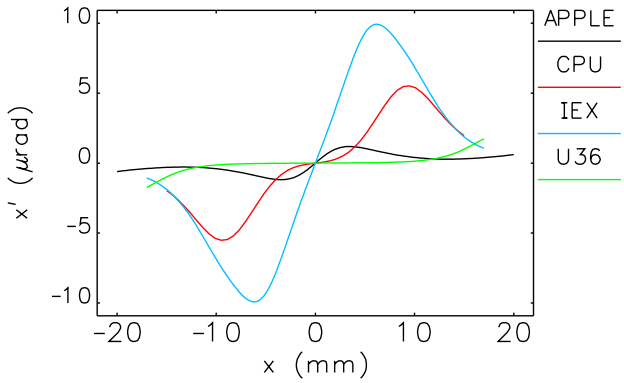


Figure 1: Comparison of simulated in-plane kick map ($y = 0$) for different types of IDs.

Table 1: Typical ID Parameters

ID Type	Length (m)	K_max+	By Pole Width (mm)
U33 *	2.4	2.75	51
U36 *	2.1	3.31	39.5
CPU*	1.8	2.77(H) 2.77(V) 2.5(C)	24
IEX*	4.75	5.27(H) 3.86(V) 3.86(C)	18.2
APPLE#	2.1	3.57(H) 2.7(V) 3.03(C)	35×35

+ H/V/C are different polarization mode for elliptical ID.
* Currently operated at APS.
# ID is under development, parameters are under consideration.

UKICKMAP uses kick maps [3] obtained from magnet design directly or from tracking results of the other three methods. All other methods use 3D field maps from ID design or field measurement. FTABLE uses the field map directly and is non-canonical, while CWIGGLER and GFWIGGLER require an analytical wiggler field expansion (from the 3D field map fitting) and are canonical. Our typical procedure for simulating nonlinear ID effects is: fit the 3D field map to a field expansion; using CWIGGLER or GFWIGGLER, track a bunch of particles through the element in a "grid" distribution on the $x - y$ plane with $x' = y' = 0$, and determine the kick map at the exit; use the kick map as input to UKICKMAP to perform various

Copyright © 2013 CC-BY-3.0 and by the respective authors

simulations. The key to the entire procedure is fitting a field map to the field expansion. The general field expansion of an elliptical undulator is written as [4]:

$$\begin{aligned} B_x^H &= B_0^H \sum_{m,n} A_{mn}^H \frac{k_{x,mn}^H}{k_{y,mn}^H} \sin(k_{x,mn}^H x) \\ &\quad \cdot \sinh(k_{y,mn}^H y) \cdot \cos(k_{zn} z), \\ B_y^H &= -B_0^H \sum_{m,n} A_{mn}^H \cos(k_{x,mn}^H x) \\ &\quad \cdot \cosh(k_{y,mn}^H y) \cdot \cos(k_{zn} z), \end{aligned} \tag{2}$$

with $(k_{y,mn}^H)^2 = (k_{x,mn}^H)^2 + (k_{zn})^2$ for the field generated from the two middle poles, and

$$\begin{aligned} B_x^V &= B_0^V \sum_{m,n} A_{mn}^V \cos(k_{x,mn}^V x) \\ &\quad \cdot \cosh(k_{y,mn}^V y) \cdot \cos(k_{zn} z + \tfrac{\pi}{2}), \\ B_y^V &= B_0^V \sum_{m,n} A_{mn}^V \frac{k_{y,mn}^V}{k_{x,mn}^V} \sin(k_{x,mn}^V x) \\ &\quad \cdot \sinh(k_{y,mn}^V y) \cdot \cos(k_{zn} z + \tfrac{\pi}{2}), \end{aligned} \tag{3}$$

with $(k_{y,mn}^V)^2 = (k_{x,mn}^V)^2 + (k_{zn})^2$ for the field generated from the four side poles. Here, $k_{zn} = 2\pi n/\lambda_u$, λ_u is the period, and B_0^H and B_0^V are the maximum on-axis horizontal and vertical fields, respectively. The total field is given by

$$\begin{aligned} B_y^C &= B_y^H + B_y^V \\ B_x^C &= B_x^H + B_x^V. \end{aligned} \tag{4}$$

ID field profiles greatly differ from a pure sinusoidal shape and have high harmonic components, making direct fitting very difficult. We thus developed a linear fit method. First, the field data are fit to longitudinal harmonics:

$$\begin{aligned} B_x^C &= \sum_n G_{H,n} \cdot \cos(k_{zn} z) + \sum_n G_{V,n} \cdot \cos(k_{zn} z), \\ B_y^C &= \sum_n F_{H,n} \cdot \cos(k_{zn} z) + \sum_n F_{V,n} \cdot \cos(k_{zn} z), \end{aligned} \tag{5}$$

where $\cos(k_{zn} z)$ are known values at each data point, and $F_{H/V,n}$ and $G_{H/V,n}$ are fit parameters. These F and G parameters are in turn decomposed into transverse harmonics following

$$\begin{aligned} F_{H,n} &= \sum_m \left[-B_0^H A_{mn}^H \cdot \cosh(k_{y,mn}^H y) \right] \cdot \cos(k_{x,mn}^H x) \\ &= \sum_m f_{H,n,m} \cdot \cos(k_{x,mn}^H x). \end{aligned} \tag{6}$$

Note that $k_{y,mn}^H$ and $k_{x,mn}^H$ are still related. Both $k_{x,mn}^H$ and A_{mn}^H are unknown parameters to be fitted. In order to turn this into a linear fit, we give an initial value to $k_{x,mn}^H$, then fit $f_{H,n,m}$. The proper $k_{x,mn}^H$ value is obtained by scanning $k_{x,mn}^H$ over a suitable range and choosing the value that gives the smallest residuals. The same technique is applied to the other F and G parameters.

Depending on the original field data errors and the available field map region, the fit results may be invalid. The F and G coefficients are interrelated via Maxwell's equations, so fitting one will give the other. Usually we fit F_H and G_V as they give the non-zero on-axis field. In the case of large (measured or modeled) field errors, this results in large field errors at the boundary of the available field map. Fitting F and G parameters together will eliminate such errors (see Figure 2). For best results, the field map region

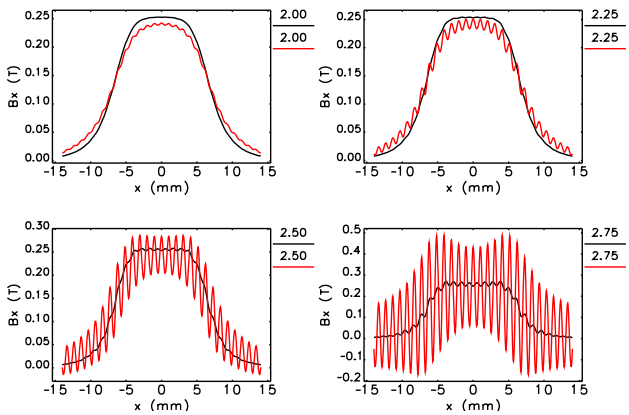


Figure 2: Fitted field profile at different y positions (legend value in mm). Red — fit F_H and G_V only; black — fit all F and G. Large fitting errors appears near the field map boundary.

should extend well beyond the expected dynamic aperture (DA). If an adequate field map region is unavailable, which we encountered in our EMVPU [5] simulation, we must use fewer small transverse harmonics (m) or manually set up boundary conditions that will help constrain the fitting results (see Figure 3).

SIMULATION RESULTS AND BEAM TEST

Figure 1 shows that IEX presents the strongest nonlinearity among all IDs that have been installed in the APS. Thus, detailed simulations were made with both designed and measured field maps. Due to large errors represented in the measured field data, the measured field map was fitted to its design model by adjusting its alignment (x, y, z), peak field (B_0), and roll-off parameter K_x slightly away from the value of the model simulation. Fitting results show that $K_{x,meas} \approx 0.96 K_{x,design}$. A slightly larger magnet field roll-off appears in the real device (see Figure 4). To include field errors, the IEX was sliced into several segments, each segment containing several periods. The error field was represented by a kick map at the end of each segment, calculated using the first field integral of the same

Copyright © 2013 CC-BY-3.0 and by the respective authors

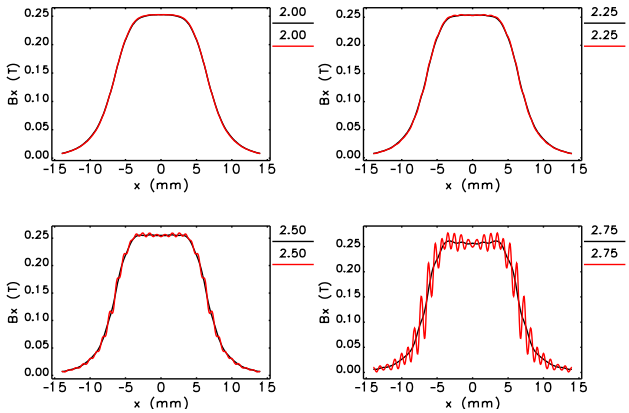


Figure 3: Fitted field profile at several y positions (legend value in mm). Black — harmonic m up to 30; red — harmonic m up to 50.

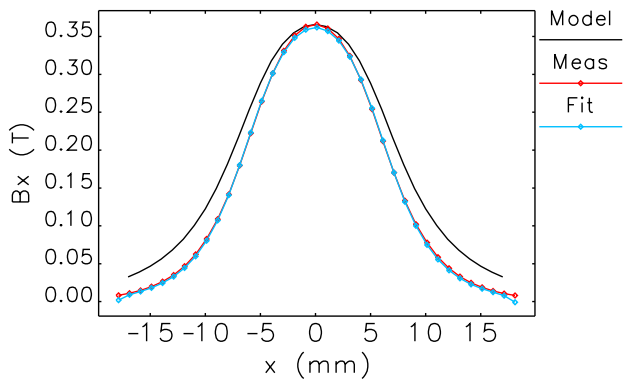


Figure 4: Peak Bx filed profile vs. x. Black — designed model; red — measured data; blue — fitted model.

segment. Simulated DA results for various conditions are shown in Figure 5. The simulation results predicted that the APS DA would be reduced slightly by IEX operation. This was confirmed by our beam-based measurements, as seen in Figure 6.

Another device with strong non-linearity is the Circularly Polarizing Undulator (CPU), for which we have a model field map, but no measured one. The non-linearity of the ideal CPU model is weaker than IEX, but the measured beam perturbations, such as orbit, tune, and coupling variations, indicate some larger field errors. The measured DA reduction from the CPU is also more severe than the IEX (see Figure 6). Unfortunately, we cannot simulate these field errors as we have no measured field map.

SUMMARY

Simulation of ID nonlinear effects can be accomplished in several ways. This paper explains how a field map can be fit to a field expansion used by `elegant` and what precautions are required for a valid result. Using the IEX device as an example, we illustrated how a measured field map was used to check the field quality and for DA simulation. Experimental results from both CPU and IEX operation show the importance of such simulation work.

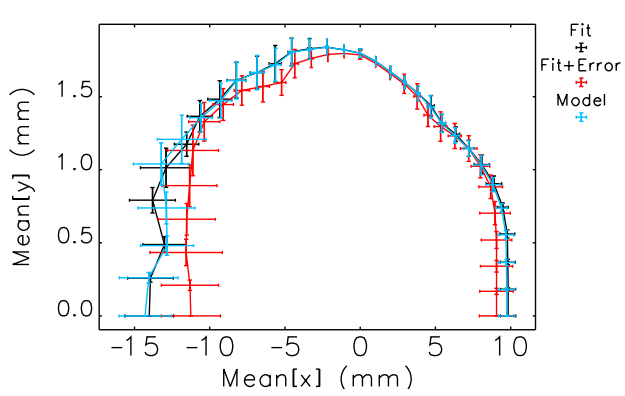
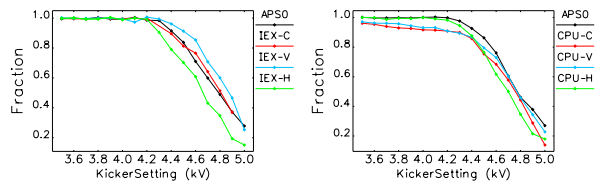


Figure 5: Dynamic aperture with machine errors. Black — field map from magnet measurement (fitted model); red — fitted model + measured field errors; blue — field map from IEX design.



(a) IEX—DA is decreased at large kick strength

(b) CPU—DA is decreased from small kick strength

Figure 6: A fraction of beam survived after a kicker pulse vs kicker strength (DA) for the APS baseline (APS0 — CPU and IEX are off), and CPU or IEX running at different polarization modes (H/V/C).

REFERENCES

[1] J. Safranek et al., "Nonlinear dynamics in a SPEAR wiggler," Phys. Rev. ST Accel. Beams, 5, (2002), 010701.

[2] M. Borland, ANL/APS/LS-287 (2000).

[3] P. Elleaume, "A New Approach to the Electron Beam Dynamics in Undulators and Wigglers," Proc. of EPAC'92, p. 661 (1992); http://www.JACoW.org

[4] A. Xiao et al., Proc. PAC11, WEP064, p. 1594 (2011); http://www.JACoW.org

[5] M. Jaski, private communication.

Copyright © 2013 CC-BY-3.0 and by the respective authors

ON-AXIS INJECTION SCHEME FOR ULTRA-LOW-EMITTANCE LIGHT SOURCES *

A. Xiao†, M. Borland, C. Yao, ANL, Argonne, IL 60439, USA

Abstract

Injection design for an ultra-low-emittance light source is mainly limited by two effects. Due to intrabeam scattering and beam instabilities, multiple bunches with tight bunch spacing are injected into the ring to reach high average beam current, which limits the choices of injection technology. Strong non-linear effects due to the significant focusing force applied and the resultant strong sextupoles make the dynamic aperture very small, so that only on-axis "swap-out" beam injection is workable. Using a seven-bend-achromat (7BA) lattice designed for the Advanced Photon Source (APS) storage ring as an example, this paper presents an on-axis injection scheme based on the fast stripline technique together with discussions of the different configuration choices.

INTRODUCTION

When pushing a storage-ring-based light source emittance close to very low emittance, two primary consequences emerge: insufficient dynamic aperture for accumulation-based injection, so that only on-axis "swap-out" injection is workable [1]; and the maximum single-bunch intensity is significantly reduced due to the intrabeam scattering (IBS) and beam instabilities, so a significant fraction of the ring may need to be filled with beam to reach the required average beam current. Both factors put strict restrictions on the choice of injection technology and optics design.

In the scheme envisioned here, a single "swap-out" beam injection only replaces a portion of the stored beam, see Figure 1. The target bunches must be extracted and injected without affecting the emittance and stability of the remaining stored beam. For this to be the case, the kicker field must be negligible at the next upstream or downstream bunches, which requires kicker rise- and fall-times less than the spacing between bunches—usually one to a few rf buckets depending on the specific design, e.g., 10 rf buckets @500 MHz implies 20 ns. Commonly used ferrite kicker magnets cannot meet such requirements, but the stripline kicker technology proposed for the ILC damping ring [2] seems promising and is adopted in this paper.

A series of 40-sector, 6-GeV seven-bend achromat (7BA) lattices [3] have been studied for the future APS Upgrade. The lattice used is shown in Figure 2. In this paper, we will present an injection and extraction design for the 7BA lattice, with discussion of the different injection schemes.

* Work supported by the U.S. Department of Energy, Office of Science, under Contract No. DE-AC02-06CH11357.

† xiaoam@aps.anl.gov

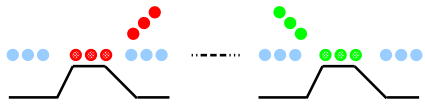


Figure 1: Sketch of on-axis "swap-out" injection (red: extraction bunches; green: injection bunches).

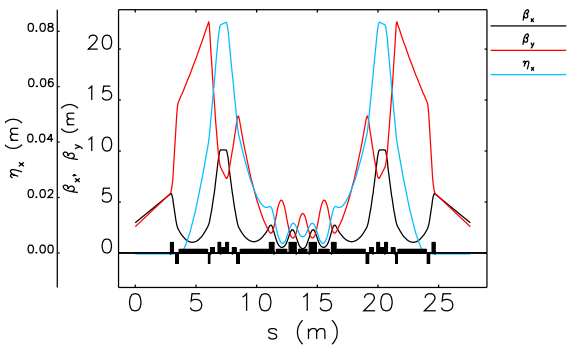


Figure 2: Single-cell optical functions of a 7BA lattice.

MAIN PARAMETERS

The kick angle from a stripline of length L with gap d between the electrodes is given by

$$\Delta\theta = 2g\frac{eV}{E}\frac{L}{d}, \tag{1}$$

where V is the voltage applied to the two electrodes, E is the beam energy, $g \leq 1$ is the geometry factor, and the factor 2 includes the force from both electric and magnetic fields. Using the stripline tested at ATF [4] (60 cm long, 10 mm gap, with $\pm$10 kV pulsers), the kick angle is 0.4 mrad.

The maximum achievable kick angle depends on two major factors: the available pulser strength V and the size of the stripline. Unlike the ILC damping ring, the required injection frequency is much lower, so a pulser with much higher output voltage [5] is available; V is then limited by the detailed design of the stripline (feed through). A smaller gap d increases $\Delta\theta$ for the same gap voltage V, while the maximum achievable V is also reduced due to reduction in the stripline size. As there is yet no detailed stripline design, we assume $V = 30$ kV at $d = 10$-mm gap compared with $V = 20$ kV at the same gap for the ILC damping ring. Larger L will make more efficient use of the limited space, but the maximum L is limited by the required rise/fall time. We choose $L = 0.6$ m, so that the rise/fall time is less than 5 ns. Altogether, the kick strength from a single stripline is 0.6 mrad. To accomplish the injection task, multiple striplines are needed.

Unlike other storage ring designs, an ultra-low-

Copyright © 2013 CC-BY-3.0 and by the respective authors

emittance light source like the 7BA discussed here usually has no more free drift space left inside the arc. The only space available is in the straight sections, which are mainly preserved for insertion devices. Assuming a single straight injection, the separation Δx between injected and stored beam center at the edge of the septum is given by

$$\Delta x \approx N\Delta\theta\frac{NL}{2} = \frac{\Delta\theta}{L}\frac{(NL)^2}{2}, \quad (2)$$

where N is the total number of striplines and $\frac{\Delta\theta}{L}$ is the normalized kick strength in mrad/m.

The minimum separation Δx_{min} is given by

$$\Delta x_{min} = x_{inj} + x_{err} + s_a + s_d, \quad (3)$$

where x_{inj} is the injected beam size, x_{err} is the allowed orbit error from all sources, s_a is the minimum septum aperture determined by other factors (for example, impedance), and s_d is the septum thickness.

Similar to the current APS design, two septums are used. We have set $s_a = 3$ mm and $s_d = 1$ mm for the thin septum in our simulation. The fully coupled injected beam emittance is assumed to be 30 nm. x_{inj} and x_{err} are related to the local beta function at the edge of the thin septum and will be discussed in later sections. All main parameters are listed in Table 1.

Table 1: Main Parameters for Injection

Title	Description	Value	Unit
General	Energy	6	GeV
	Stored Beam Emit.	81	pm
	Inj. Beam Emit.	30	nm
	Beta function at Inj.	≈3	m
	Orbit error (x_{err})	0.4	mm
Stripline	Length	0.6	m
	Gap	10	mm
	Gap Voltage	30	kV
Thin Septum	Length	0.25	m
	Thickness	1	mm
	Field Strength	0.7	T
	Inner Aperture	3	mm
Thick Septum	Length	1.5	m
	Thickness	2	mm
	Field Strength	1	T

BETA FUNCTION AT SEPTUM

A high-beta insertion is often used for the injection section design of a storage ring. Two pairs of kicks with phase advance close to π are located at either side of the septum, while the septum is located at the place of a high-beta function. The advantages of such a design are to minimize the kicker strength and reduce residual betatron oscillation of injected beam.

This kind of injection scheme is not applicable to the ultra-low-emittance light source (USR) for the following reasons:

- Phase advance. Since a light source tends to have a very crowded arc cell, there is insufficient space for multiple stripline kickers. Most likely, the stripline kickers will be placed in the same section as the septum.
- Optics perturbation. A specially designed high-beta injection section will break the lattice symmetry, which will typically reduce the dynamic aperture (DA) and momentum aperture (MA) significantly. Having sufficient DA/MA is already a big challenge for a USR lattice design.
- Impedance issues. Injection/extraction regions contribute a large portion to the entire ring's impedance budget. High-beta function makes the problem even more severe.
- Stripline aperture. High-beta function means larger beam size. Accommodation of the injection beam requires larger stripline gap, which reduces the stripline strength.

Due to the above reasons, a high-beta injection scheme was evaluated and abandoned. Those simulation results are not shown here. Note that if striplines and septum need to be put in the same section, then the beam separation is given by Eq. (2). From Eq. (3), a low-beta function at the thin septum, which minimizes x_{inj} and x_{err}, is preferable.

SINGLE STRAIGHT INJECTION AND EXTRACTION

If possible, putting injection and extraction to the same straight section is preferable. The minimum separation for beam extraction $x_{min,ext}$ is also given by Eq. (3) with replacing of x_{inj} to x_{sto} (beam size of stored beam). Using the parameters listed in Table 1, $x_{min,inj} = 5.3$ mm and $x_{min,ext} = 4.5$ mm. From Eq. (2), the minimum total stripline length for injection is 3.25 m, while the minimum total stripline length for extraction is 3 m. To accommodate the thin septum and including space between each element, $\sim$ 1 m of extra space is needed. Thus a minimum 7.5-m-long straight section is required to accommodate both on-axis injection/extraction in one straight section for a 6-GeV ring. Since the straight section length of our design is 5.8 m, injection and extraction require separate straight sections. In our design, sector 38 is used for beam extraction and sector 39 is used for beam injection.

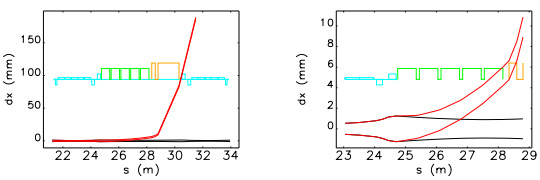
SEPARATED INJECTION AND EXTRACTION

As just discussed, injection and extraction need to be separated into two sectors. The difference between injection and extraction is that the required minimum separation at the thin septum is slightly different. For simulation

Copyright © 2013 CC-BY-3.0 and by the respective authors

convenience, we illustrate here the extraction line using parameters of beam injection as listed in Table 1.

To allow a 3-mm inner aperture for the thin septum, a minimum 5.3-mm beam separation must be provided by the stripline kickers. This number assumes 1-mm septum thickness, 3 sigma of injected beam size ($\sigma = 0.9$ mm at $\beta_x = 3$ m), and 0.4-mm orbit error from various sources. Using a normalized kick strength of 1 mrad/m, the total stripline length is 3.25 m from Eq. (2), requiring five 0.6-m-long striplines. Figure 3 shows the extraction line configuration (injected beam is from right to left), the envelope of injected beam (red line), and the envelope of the first turn of injected beam. This plot also shows why high-beta injection is not preferable, because in that scheme the stripline gap has to be increased to accommodate the entire injected beam envelope, which becomes much wider when using high-beta injection. Since now the minimum aperture limitation around the ring is the thin septum (3 mm), some stripline apertures (for example, 1 and 2) could be reduced to increase the normalized kick strength. The potential benefit from reducing stripline aperture is limited by the feedthrough, so this must be evaluated when we have a detailed stripline design. The separation at the first quadruople is 0.1 m and needs to be considered in the magnet design.



(a) Inj. layout (b) Zoom In

Figure 3: Injection configuration: black - first turn injected beam, red - injected beam, green - stripline, and yellow - septum.

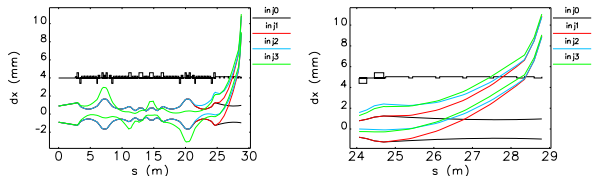
OTHER CHOICES

Besides putting all injection elements into the same straight section, other injection schemes have been studied. For example, we looked at putting striplines in the arc where sufficient drifts are present or using the straight section in the next sector. Results are shown in Figure 4.

The effectiveness of these choices strongly depends on the detailed optical design, i.e., the phase advance between the thin septum and an available space for installing an extra stripline. One could make this a special requirement to the optical design, or modify the existing optical design to make a special section to suit the required phase advance. Other issues make such choices unwelcome, including:

- Broken symmetry. It makes the already challenging nonlinear effects correction even more difficult.
- Less flexibility. A modification of the optical design will require a re-design of the injection line. It becomes more difficult due to the strong nonlinear effects.
- Large orbit oscillation inside arc, see Figure 4. This also causes nonlinear effects and may harm injection efficiency.

These effects can be seen from Figure 4. The additional stripline inside arc (inj2) doesn't increase beam separation at the septum due to the wrong phase advance. The additional stripline installed in other sectors (inj3) does increase beam separation at the septum at the expense of large orbit oscillation inside the arc, which means every change of the chromaticity configuration could result in rematching of the injection line. We have abandoned such options due to unclear benefits and these potential problems.



(a) Overview of different injection schemes (b) Zoom in of different injection schemes

Figure 4: Comparison of different injection schemes: inj0 - first turn injected beam, inj1 - all stripline in one straight, inj2 - one stripline in arc, inj3 - one stripline from the next sector. See how beam orbit varies inside the arc (a) and beam separation at the thin septum (b).

CONCLUSION

Using an APS 7BA lattice design as an example, several on-axis injection schemes have been studied. Results reveal the possible choice of injection technology, the main parameters determining the injection design (injection beam size, minimum septum aperture, etc.), and as a consequence, the requirements on the optics design (drift space, beta function, etc.). Our results show that on-axis injection into the 7BA lattice can be achieved. We attempted to make our discussions here as general as possible, so results can be used for other USR designs.

REFERENCES

[1] L. Emery and M. Borland, Proc. PAC 2003, TOPA014, 256 (2003).

[2] ILC Technical Design Report, Volumn 3 - Accelerator, Part I, http://www.linearcollider.org/ILC/Publications/Technical-Design-Report.

[3] M. Borland, Vadim Sajaev, Yipeng Sun, private communication; similar to M. Borland et al., MOPHO07, these proceedings.

[4] T. Naito et al., "Multibunch beam extraction using the stripline kicker at the KEK Accelerator Test Facility," PRST-AB 14 (2011), 051002.

[5] http://www.fidtechnology.com/

Copyright © 2013 CC-BY-3.0 and by the respective authors

ADVANCED X-RAY BEAM POSITION MONITOR SYSTEM DESIGN AT THE APS*

B.X. Yang†, G. Decker, J. Downey, Y. Jaski, T. Kruy, S. H. Lee, M. Ramanathan and F. Westferro
Advanced Photon Source, Argonne National Laboratory, Argonne, IL 60439, USA

Abstract

As part of the Advanced Photon Source (APS) Upgrade, new x-ray beamline front ends are planned that include extensive integrated x-ray diagnostic capability. The high-heat-load front-end (HHLFE) design includes a grazing-incidence insertion device x-ray beam position monitor (GRID-XBPM) utilizing Cu K-edge x-ray fluorescence from x-rays striking a pair of copper absorbers. At a 1.0˚ grazing incidence angle, the XBPM assembly is designed to withstand 17 kW power from two inline Undulator A devices at 150-mA stored beam. A second XBPM located outside of the accelerator enclosure monitors fluorescence from the beamline exit mask, which is a critical beamline-defining aperture. In addition, an intensity monitor is used to detect x-ray flux passing through a front-end mask inside the enclosure, while a second intensity monitor is located immediately downstream of the exit mask. Details of these designs and expected performance will be presented.

INTRODUCTION

The ongoing Advanced Photon Source Upgrade (APS-U) requires major improvements in x-ray beam stability. The stability goals are to be achieved on multiple beamlines with two inline Undulators A's delivering beam power up to 17 kW at 150-mA stored current. Since the modern storage ring orbit feedback systems have demonstrated submicron stabilities, the actual x-ray beam stability delivered to the user is determined by the accuracy of the beam position monitors. In the past several years, the APS has made a major effort in developing a hard x-ray BPM. The new device uses the 8-keV Cu K-edge x-ray fluorescence (XRF) from the front-end limiting apertures to infer the undulator beam's core position [1,2]. An experimental test with two inline undulators showed that the XBPM has nearly 70-fold improvement in rejection of bend magnet radiation background and a gap-independent calibration in one of the two dimensions [3]. Based on this successful demonstration, the GRID-XBPM was included as a standard device for the new HHLFEs being developed for the APS-U. In this paper, we report the engineering design of the new XBPM system, including a GRID-XBPM, the second XBPM at the end of the front end, and the two intensity monitors to assist for beam-based alignment of front end apertures. We will also report on the latest design development of a new XBPM based on Compton scattering.

*Work supported by the U.S. Department of Energy, Office of Science, under Contract No. DE-AC02-06CH11357.
†bxyang@aps.anl.gov

THE FIRST XBPM

Figure 1 shows the first XBPM. It is a GRID-XBPM consisting of two GlidCop absorbers, positioned on the left and right sides of the undulator beam axis. At 1.0˚ grazing incidence angle, they intercept up to 11.5 kW of undulator power during user operations and are able to withstand the full beam in case of mis-steering. The XBPM reads out vertical positions using x-ray pinhole camera optics, with a calibration independent of undulator gaps. It derives horizontal beam position from the difference/sum of the x-ray detector signals from the left and right absorbers. Hence the horizontal position calibration depends on the beam sizes, or undulator gaps. To meet the stringent stability requirements, the pinhole camera and detectors are mechanically isolated from the absorbers, and its height above the floor is monitored in real time by a mechanical motion sensor mounted on an Invar rod. External perturbations to the XBPM include: (1) the annual air pressure variation of 0.6% [4], which distorts the XBPM support plate; and (2) the thermal load of the x-ray beam on the XBPM assembly. Table 1 summarizes the ANSYS analyses for the impacts of these external perturbations. We can see that most distortions are within specifications. The thermal-distortion-induced vertical detector position change will be monitored and corrected in real time with the mechanical motion sensor or treated as gap-dependent XBPM offset.

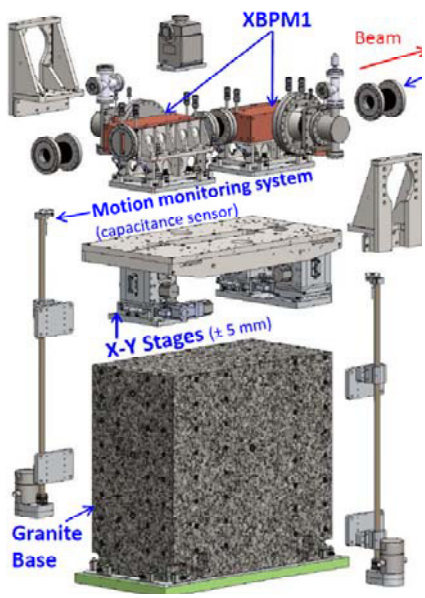


Figure 1: The GRID-XBPM for the APS-U high-heat-load front end.

Copyright © 2013 CC-BY-3.0 and by the respective authors

Table 1: Externally Induced XBPM Position Change

	Angular	Vertical
Barometric Pressure (0.6% rms)	±0.4 µrad	0.04 µm
Beam Load	±0.4 µrad	7 µm
Specifications	2 µrad	3 µm

THE SECOND XBPM

The exit mask of the HHLFE is a critical component of the beamline. It defines the exit aperture of the front end and protects the downstream bremsstrahlung shield from radiation damage. During normal beam operations, it intercepts up to 3.5 kW x-ray power. The fluorescence photons generated by the intercepted beam will be used by the second XBPM to infer the core beam position utilizing yet another set of pinhole camera optics. Figure 2 shows the arrangement of the XBPM2 components. Four silicon photodiodes are used to read out the horizontal and vertical positions of the x-ray footprint on the exit mask. This XBPM will not be linked to the orbit feedback system, but its information will be recorded and logged during user operations.

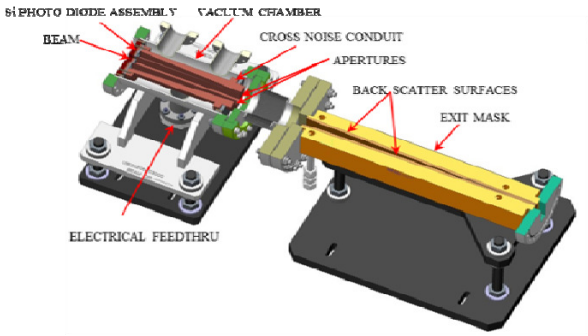


Figure 2: XBPM 2 design. A pair of apertures and four Si PIN diodes form a pinhole camera to read out the position of the x-ray footprint on the exit mask.

THE INTENSITY MONITORS

Two beam intensity monitors, IM1 and IM2, are planned for the new front ends. During normal operations, up to 100-W x-ray photons will be removed from the beam by the front-end beryllium windows, including 30-W x-rays by Rayleigh and Compton scatterings. These scattered photons can be detected using metallic photocathodes or silicon photodiodes, and the signal can be used to center the undulator beam on the exit mask by scanning the electron beam. The symmetry points of the scanning curve serve as the fiducial marks of the XBPM, allowing the operator to put the XBPM back to its standard state after each shutdown, or after the XBPM and its electronics are repaired or serviced. Figure 3 shows the design of the IM2: A large-area gold-coated photocathode is used to capture the scattered radiation from the Be window. The inset shows the estimate photocurrent as a function of undulator K-value, using known x-ray scattering cross sections [5]. For the operating range of Undulator A, the signal current remains in microampere range within a dynamic range of 1:7.

The first intensity monitor (IM1) uses the x-ray fluorescence from the photon shutter to measure the beam intensity passing through the upstream apertures inside the front end. By design, it will be used to fiducialize the GRID-XBPM during machine studies before user operations. Since it is a retrofit to existing photon shutters, the challenging part is to make the signal proportional to the total beam intensity but independent of the beam position on the grazing incidence shutter. Figure 4 shows the arrangement of IM1 components: a combination of an aperture edge and an EDM'd detector mask is used to minimize the signal's beam position dependence.

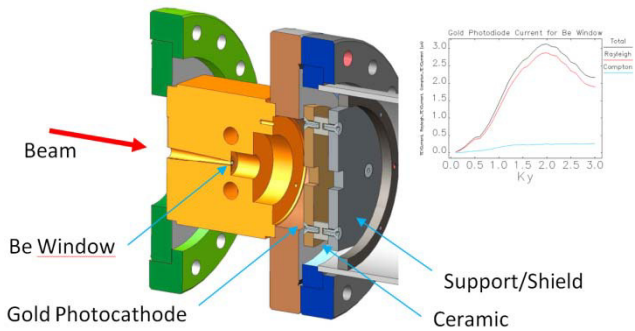


Figure 3: IM2 uses Rayleigh- and Compton-scattered x-rays from the Be window to monitor the x-ray beam intensity. Inset: A photodiode is used to detect x-rays.

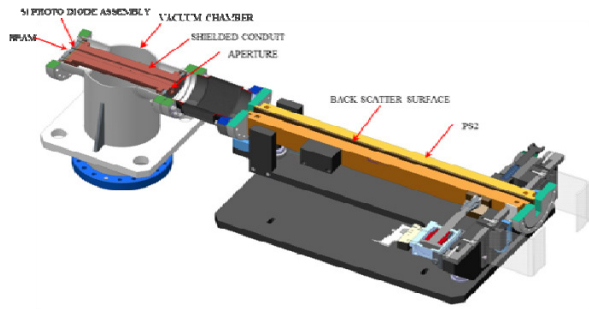


Figure 4: IM1 uses Cu K-edge XRF to measure the x-ray beam intensity when the photon shutter is closed.

SYSTEM DESIGN

Figure 5 shows the schematic of the new XBPM system inside the new orbit feedback system for the APS-U. With a reference from a common hydrostatic leveling system, real-time motion sensors will be used to monitor the positions of the RFBPM and the XBPM to compensate for the thermal expansion/distortion of the vacuum chamber supports. The RFBPM and GRID-XBPM will be used to monitor beam position and angle changes, and to provide information for orbit corrections.

For the x-ray beam exiting the front end, IM2 and XBPM2 will record its intensity and position information in real time and serve as independent validation of the x-ray beam stability achieved by the entire system.

Copyright © 2013 CC-BY-3.0 and by the respective authors

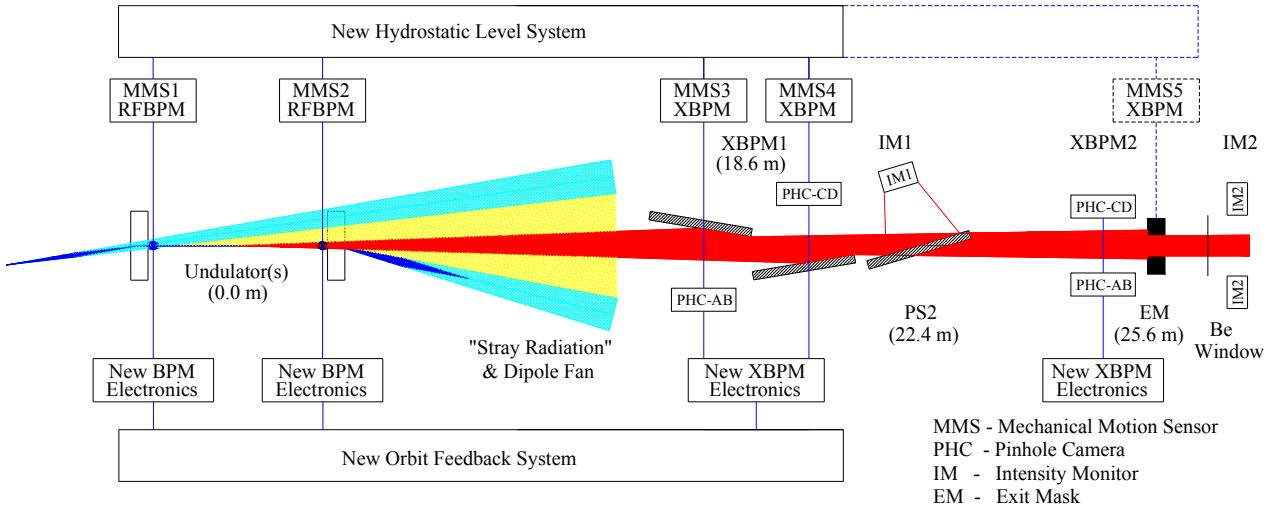


Figure 5: In the APS-U orbit feedback system, the XBPM system is responsible for measuring the x-ray beam angle and monitoring the x-ray beam intensity and position outside of the feedback loop.

SUMMARY AND DEVELOPMENTS

The engineering designs of the x-ray beam position monitor system for the APS high-heat-load front ends are complete. The components are being procured and manufactured. Installation of the first complete set is planned for early 2014.

The grazing-incidence design has demonstrated that a reliable XBPM can be built wherever a beam aperture can survive the beam, and the combination of beam apertures with position measurements simplifies operations of the beam-based alignment and improves its accuracy. However, the design also carries higher cost and requires longer beamline space.

For canted undulator front ends, where two undulator beams are separated by 1 mrad, with each carrying only 8.5-kW power, we are currently developing a different design based on Compton scattering from low-Z materials. Figure 6 shows a prototype: two grazing-incidence diamond blades are inserted from the top and bottom of the beam. At ~ 1.75 mm from the axis, they intercept ~ 500 W from each undulator. A set of pinhole optics and diamond detectors are mounted below and above the diamond blades to read out the horizontal beam position; the vertical beam position is derived from the difference/sum of the signals from the two blades. Initial ANSYS analysis shows that the diamond blades will survive a direct hit by the undulator beam during mis-steering if an appropriate heat spreader material, e.g., Mo-Cu, is used. A preliminary x-ray simulation shows that the signal current will be in the range of tens of μA for closed undulator gap (10.5 mm), and hundreds of nA for open gap (30 mm). This is welcome news for the data acquisition system since the dynamic range requirement is less stringent than that for the HHLFE GRID-XBPM with vertical absorbers. Optimization of the design is still in progress and experimental tests are planned for the near future.

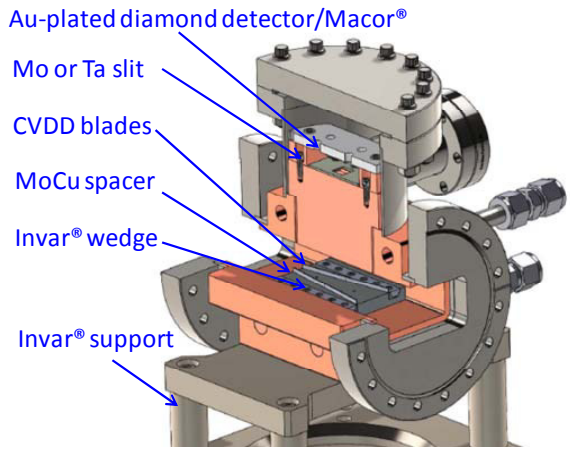


Figure 6: Compton-scattering XBPM conceptual design for the APS canted undulator front end.

REFERENCES

[1] B. X. Yang, G. Decker, S. H. Lee, and P. Den Hartog, Proc. of BIW0210, Santa Fe, NM, TUPSM043, p. 233, (2010); http://www.JACoW.org

[2] B.X. Yang, G. Decker, S. H. Lee, P. Den Hartog, and K. W. Schlax, "Progress in the development of a grazing-incidence insertion device x-ray beam position monitor," Proc. of PAC'11, New York, MOP189, p. 441 (2011); http://www.JACoW.org

[3] B.X.Yang, G. Decker, S. H. Lee, P. Den Hartog, T.-L. Kruy, J. Collins, M. Ramanathan, and N. G. Kujala, Proc. of BIW2012, Newport News, VA, WECP01, p. 235, (2012); http://www.JACoW.org

[4] Argonne National Laboratory atmospheric data, (ANLMET); http://www.atmos.anl.gov/ANLMET/

[5] A. Brunetti, M. Sanchez del Rio, B. Golosio, A. Simionovici and A. Somogyi, Spectrochimica Acta B 59 (2004) 1725.

Copyright © 2013 CC-BY-3.0 and by the respective authors

NON-INVASIVE BEAM DETECTION IN A HIGH-AVERAGE POWER ELECTRON ACCELERATOR

J. Williams, S. Biedron, J. Harris, J. Martinez, S. V. Milton, J. VanKeuren
Electrical and Computer Engineering, Colorado State University, Fort Collins, Colorado
S. V. Benson, P. Evtushenko, G. R. Neil, S. Zhang
Jefferson National Lab, Newport News, Virginia

Abstract

For a free-electron laser (FEL) to work effectively the electron beam quality must meet exceptional standards. In the case of an FEL operating at infrared wavelengths the critical phase space tends to be in the longitudinal direction. Achieving high enough longitudinal phase space density directly from the electron injector system in an FEL is difficult due to space charge effects, thus one needs to manipulate the longitudinal phase space once the beam energy reaches a sufficiently high value. However, this is fraught with problems. Longitudinal space charge and coherent synchrotron radiation can both disrupt the overall phase space, furthermore, the phase space disruption is exacerbated by the longitudinal phase space manipulation process required to achieve high peak current. To achieve and maintain good FEL performance one needs to investigate the longitudinal emittance and be able to measure it during operation preferably in a non-invasive manner. Using electro-optical (EO) methods, we plan to measure the bunch longitudinal profile of an energy (~120-MeV), high-power (~10kW or more average FEL output power) beam. Such a diagnostic could be critical in efforts to diagnose and help mitigate deleterious beam effects for high output power FELs.

INTRODUCTION

In order to operate an FEL of high quality, an electron beam with high-peak current, low transverse emittance and low energy spread is required. An operational understanding of electron bunch parameters through diagnostics is needed if one wishes to achieve the optimal desired beam qualities. There are a number of diagnostics of both invasive and non-invasive genres used to determine electron bunch parameters. Invasive diagnostics such as transition radiation (CTR) screens placed directly into the beam of electrons are great if one has a low power beam and does not care if operation is momentarily interrupted. Such diagnostics are not suitable for high power operation as they will be destroyed by the beam, or operational monitoring as they severly disrupt the beam properties upon impact with the diagnostic. As an FEL requires high longitudinal phase space density for optimal output, the required manipulations of the electron bunches can lend to undesirable additional effects which need to be monitored in-situ, and, if possible, avoided. One needs a non-invasive longitudinal phase space diagnostic to allow for the achievement and maintenance of the beam properties.

A method to sample the bunch's electric field without prohibitively disrupting the beam is to utilize a crystal with a birefringent property influenced by an electric field, known as the electro-optical (EO) method. This property is caused by the Pockel's effect and the crystal acts as a Pockel's Cell driven by the electric fields of the electron bunches. The different polarizations of light within a pulse traversing the crystal will have altered path lengths created by the birefringence. The altered pulse becomes elliptically polarized in a manner proportional to the influence of induced birefringence. Equation (1) (derived in Jamison, et al. [1]), gives the resultant Fourier transform of the electron beam's Coulomb field with a probing optical pulse, and the resultant inverse transform in Equation (2). The functions *R(t)* and *R(ω)* are the response of the crystal due its nonlinearity and phase matching.

$$E_{out}^{opt}(\omega) = E_{in}^{opt}(\omega) + i\omega E_{in}^{opt}(\omega) * [E^{Coul}(\omega)R(\omega)], \quad (1)$$

$$E_{out}^{opt}(t) = E_{in}^{opt}(t) + a[E^{Coul}(t) * R(t)]\frac{d}{dt}E_{in}^{opt}(t). \quad (2)$$

The Coulomb field becomes encoded in the optical pulse to later be processed in order to determine the longitudinal bunch profile.

For a relativistic electron, the radial Coulomb field is oriented perpendicular to propagation with an opening angle $\propto 1/\gamma^2$, where γ is the relativistic Lorentz factor. The strength of the field is a function of electron bunch distance, b, from the crystal as found in Eqn (3) below. This field is found to have an effect similar to radiation in the Terahertz region of the electromagnetic spectrum (~100-900μm wavelengths) [2]. Placing the desired (EO) crystal near the longitudinally propagating bunch charge encodes the electric field information in the crystal without directly altering the bunch. The induced birefringence is probed and encoded within an optical pulse incident normally on the crystal.

$$E_{y=b} = \frac{e}{4\pi\varepsilon_0}\frac{\gamma b}{(b^2+\gamma^2 z^2)^{3/2}} \quad (3)$$

The facilities where EO diagnostics have been implemented are in contrast to the CSU and JLab accelerators, typically feature beamline parameters with short bunches, low average power and high electron beam energies. As an example, one facility that has employed an EOS diagnostic is FERMI@Elettra [3], which features a bunch length of ~.54 ps FWHM, operational beam

Copyright © 2013 CC-BY-3.0 and by the respective authors

energy of 1.2 GeV, but at a much lower average power (10s of Watts). These differences in parameters, particularly the electron beam energy and average beam power, lead to modification of previous designs to suit our conditions.

METHODS

There are a variety of EO techniques utilized by different accelerator facilities, chosen based on their intrinsic strengths and weaknesses. It was shown at FELIX [4] that a scanning-delay method employed was capable of sub-picosecond measurements of longitudinal beam profile. In this diagnostic an initially linearly polarized 12-fs, 800-nm Ti:sapphire laser incident upon a ZnTe EO crystal placed near (6 mm from the bunch center) an electron pulse train is induced to elliptical polarization. The signal is further refined via use of a quarter wave plate and subsequent Wollaston prism to separate the polarization affected beam and the reference beam through a balance detector. Because the delay between the laser and the bunch train is scanned, this technique is subject to the natural laser pulse train jitter with respect to the beam and asmearing of the resultant profile limiting the resolution further due to averaging of the signal over many pules.

Another technique, known as spectral decoding, uses a chirped laser pulse to create a time-frequency relationship between the laser spectrum and the traversing electron bunch. This technique has been demonstrated at a number of facilities (FELIX, NSLS and FLASH [5-7]); however, there is a bunch length resolution limit, τ_{lim}, created by temporal distortion of the chirped pulse given by $\tau_{lim} = 2.6\sqrt{T_C T_0}$ [1], where T_C is the duration of the pulse generated by the electron beam and T_0 is that of the optical pulse length. A bunch length shorter than the resolution limit will distort the pulse signal due to Fourier transform artifacts [8]. An advantage of this method is that it is a single shot and so timing jitters and averaging of the signal do not affect resolution.

Similar to the previous method, another technique decodes the temporal profile of the electron bunch electrical field and is aptly known as temporal decoding. Using cross-correlation through second harmonic generation of the probe pulse that has been modified by the beam's electric field within the EO crystal, with a reference pulse (both split from a single pulse prior to probing of the crystal), a spatial mapping of the temporal intensity is created. This measurement is done in a single shot giving rise to individual bunch measurements. The FELIX facility has used this method to measure pulses with sub picosecond resolution [2,9]. A schematic of this method is given in Figure 1.

A fourth EO technique that differs in the manner of EO crystal probing is known as spatial encoding. Rather than probe the crystal with a laser pulse normal to the surface, a pulse broadened by a cylindrical telescope travels at an angle such that an encoding of the temporal profile of the Coulomb field is achieved across the transverse direction of the pulse. The spatial signal is now a measure of the temporal changes of the Coulomb field. As seen in Figure 2, the electron beam still propagates normal to the EO crystal. Because the probe is broadened, any anisotropy of the birefringence may lead to signal errors and quality measurements rely on ideal EO crystals. Employed at SLAC [10,11] and DESY, this single-shot measurement is shown to be capable of <300 fs FWHM bunch length measurements.

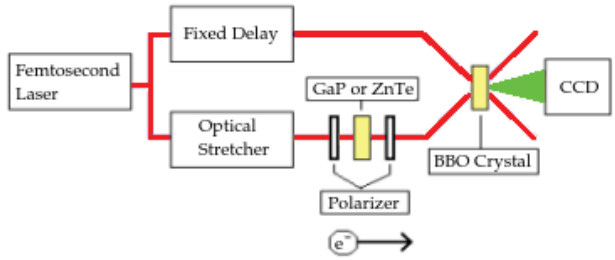


Figure 1: Electro-optical temporal decoding: A pulse is split such that a reference pulse travels through a fixed delay to be later combined the EO probe pulse in a non-linear crystal to create a pulse shape through Second Harmonic Generation (SHG).

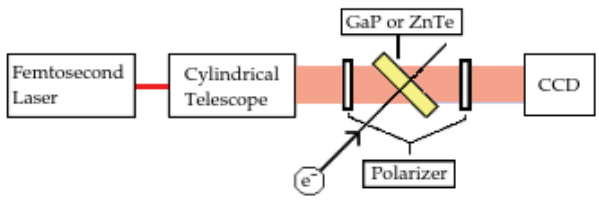


Figure 2: Diagram of electro-optical spatial encoding technique. Electron bunch still passes normal of the crystal, however, the probe pulse is incident obliquely. A cylindrical telescope is used to increase optical pulse transverse dimensions.

When designing the appropriate diagnostic to be implemented at CSU and Jefferson Lab, considerations of accuracy and effective measurement led us to choose the latter two introduced methods: EO temporal decoding and EO spatial encoding. Both of these are carried out in single-shot measurements allowing for single bunch signal probing. The spatial encoding method was found to be a relatively cheap option with a simple design. Where spatial encoding is limited in temporal resolution and noise susceptibility, temporal decoding compensates for these problems by providing excellent temporal resolution and low noise susceptibility due to the more complex cross-correlation design.

The beam energy for application at CSU, as well as the injection energy for the JLab accelerator, are both around 6 MeV. The beam energy for the second desired diagnostic location at Jefferson Lab is over 100 MeV and has a sub-picosecond bunch length. Based on Equation 3, there is a definite Coulomb field signal strength relation to distance from the beamline (b) which will have to be considered for our various applications. Clearly, placing an EO material further from the beamline is acceptable

Copyright © 2013 CC-BY-3.0 and by the respective authors

for higher energies and desirable to mitigate crystal damage, and therefore the crystal holder will be designed accordingly.

Prior to beam line implementation, a THz generation kit from Newport [12] will be used to simulate the desired diagnostic situation. The kit produces a THz wave through AC-biased plasma collapse, which is made to co-propagate with a reference pulse through a ZnTe crystal. Emulation of a real electron beam will be enhanced in the future to more accurately recreate the perpendicularly propagating Coulomb field of an electron bunch passing near the crystal.

ELECTRO-OPTICAL CRYSTAL DEPENDENCE

In order to determine the ideal EO crystal to be used for an actual diagnostic, considerations of crystal damage threshold, resonance and effective radiation birefringence will be made pertinent to our beam conditions. Figures 3 and 4 show the expected electric field intensity and resolution limits for energies around 6 MeV, which is our design beam energy. It is clear that the longitudinal resolution time will be limited to picoseconds measurements, and the low expected intensity may require us to place the crystal in close proximity to the passing bunch(<5mm), possibly subjecting the crystal to heavy radiation and beam halo damage.

DEVELOPMENT AND IMPLEMENTATION

Prior to implementation of an EO system within the CSU and JLab beamlines, several steps must be taken. Initially, we must study how our high average power beams will affect various EO crystals.

After deciding on the optimal crystal, the EO techniques must be developed on a setup that is a physical realization of the apparatus to be installed on the beamline. Currently the THz kit is being assembled. This kit will be bench tested to confirm functionality of the parts and then it will be modified for single shot capability so that a single bunch measurement can be made. Additional modifications will be made to accommodate radiation pulses similar to those generated by the CSU electron beam.

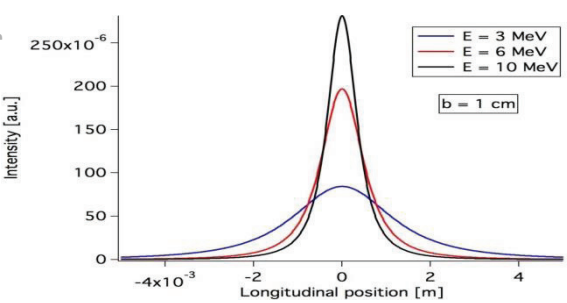


Figure 3: This figure shows the relative intensity of electron bunch electric field as a function of beam energy and position.

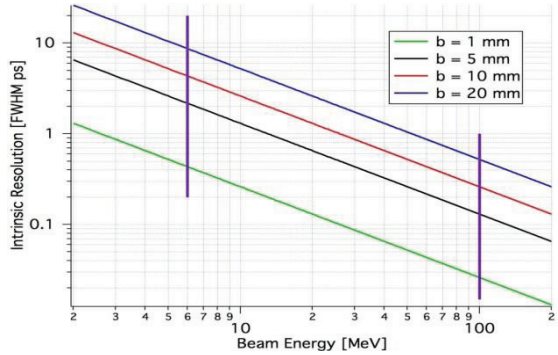


Figure 4: The time resolution of electron bunch EO signal is shown for various crystal distances and beam energies. The vertical bars mark the energies to be explored at CSU and JLab.

REFERENCES

[1] S.P. Jamison et al., "Femtosecond Resolution Bunch Profile Measurements," Proc. of EPAC'06, Edinburgh, Scotland, TUYPA01, p. 915 (2006); http://www.JACoW.org
[2] G. Berden et al., Phys. Rev. Lett. 93 (2004) 11.
[3] M. Veronese et al., "First Operation of the Electro Optical Sampling Diagnostics of the FERMI@ ELETTRA FEL," IBIC'12, Tsukuba, Japan, TUPA43, p. 449 (2012); http://www.JACoW.org
[4] X. Yan et al., Phys. Rev. Lett. 85 (2000) 16.
[5] I. Wilke et al., Phys. Rev. Lett 88 (2004) 12.
[6] H. Loos et al., "Electro-optic Longitudinal Electron Beam Diagnostic at SDL," Proc. of PAC'03, WPPB021, p. 2455 (2003); http://www.JACoW.org
[7] B. Steffen et al., "Spectral Decoding Electro Optic Bunch Length and Arrival Time Jitter Measurements at the DESY VUV-FEL," FEL'05, Palo Alto, CA, THPP039, p. 549 (2005); http://www.JACoW.org
[8] B. Steffen and S. Casalbuoni et al., "Electro Optic Bunch Length Measurements at the VUV-FEL at DESY," Proc. of PAC'05, Knoxville, TN, RPAT080, p. 3111 (2005); http://www.JACoW.org
[9] G. Berden et al., Phys. Rev. Lett. 99 (2007) 11.
[10] A. L. Cavalieri et al., Phys. Rev. Lett. 94 (2005) 11.
[11] H. Schlarb et al., "Comparative Study of Bunch Length and Arrival Time Measurements at FLASH," EPAC'06, Edinburgh, Scotland, TUPCH024, p.1049 (2006); http://www.JACoW.org
[12] Newport Corporation, "Application Note 44: Terahertz Spectrometer based on Generation of Ultrafast Terahertz Pulses in Air Plasma," (2011).

Copyright © 2013 CC-BY-3.0 and by the respective authors

INVESTIGATION OF UPSTREAM TRANSIENT WAKEFIELDS DUE TO COHERENT SYNCHROTRON RADIATION IN BUNCH COMPRESSION CHICANES

Chad Mitchell* and Ji Qiang, LBNL, Berkeley, CA 94720, USA

Abstract

The longitudinal wakefield due to coherent synchrotron radiation (CSR) in the bending magnets of bunch compression chicanes can significantly impact the beam quality in high-brightness FEL light-sources. In addition to single-bend CSR effects, transient radiation that is generated within a bend can follow the electron bunch downstream through one or more lattice elements before interacting with the bunch. An analytical 1-D model is used to estimate the size of these upstream wakefields in the absence of vacuum chamber shielding, and an FFT-based, integrated Green function method for computing these wakefields has been implemented in the code IMPACT to investigate their dynamical effects in the second bunch compressor of a Next Generation Light Source.

INTRODUCTION

The bend-induced collective interaction due to CSR in bunch compression chicanes can pose a significant challenge in the design of FEL light sources, producing transverse emittance growth and increased energy spread in the beam delivery system that can result in decreased quality of the resulting FEL radiation. A variety of 1-D wakefield models of CSR have been developed to study these effects [1]-[3], and the primary difference between these models lies in the approximations made regarding the history of the particles over the transit time of the radiation.

The model described in [2] includes transient radiation due to bend entry and exit by assuming that all particles that lie upstream of the nearest dipole at their retarded times lie within an infinitely long drift space. By contrast, the model described in [3] makes use of more detailed information about the upstream lattice. As a result, it also includes radiation that has been emitted within upstream bending elements. This paper investigates the size of these upstream transient effects for chicanes of practical interest.

ANALYTICAL AND NUMERICAL MODELS

For a bunch with a longitudinal density profile λ, the longitudinal CSR wakefield in units of energy loss per unit length takes the form:

$$W(z,s) = \int_{-\infty}^{z} \lambda(z') K_{CSR}(z+s, z'+s) dz', \qquad (1)$$

where K_{CSR} is determined from the Liénard-Wiechert electric field of a point charge and the layout of the lattice [3], z is the longitudinal bunch coordinate, and s is a parameter that specifies the location of the bunch centroid within the lattice. The function K_{CSR} varies on a scale $\sim R/\gamma^3$ that can be many orders of magnitude shorter than the bunch length. One method for evaluating the integral (1) numerically given the density $\lambda(z_j)$ at a collection of longitudinal locations $z_j = z_0 + jh$, $(j = 0, \ldots, n)$ is to represent the density by an interpolating polynomial and to evaluate the integral analytically over each subinterval [4, 5]. For the case of piecewise constant interpolation, the result can be written in the form:

$$W(z_k, s) = \sum_{j=0}^{k} \lambda(z_j) w_{igf}^{k,j}(s), \qquad (2)$$

where for terms with $0 < j < k$,

$$w_{igf}^{k,j}(s) = \qquad (3)$$
$$I_{CSR}\left(z_k + s, z_j - \frac{h}{2} + s\right) - I_{CSR}\left(z_k, z_j + \frac{h}{2} + s\right),$$

and

$$I_{CSR}(s, s') = -\int_{-\infty}^{s'} K_{CSR}(s, s'') ds''. \qquad (4)$$

An explicit expression for I_{CSR} in the case of small bending angles and high energy for an arbitrary lattice consisting of circular arcs (bends) and drifts can be found in [3].

Implementation in IMPACT

The IMPACT code is a parallel particle-in-cell code suite for modeling high intensity, high brightness beams in rf proton linacs, electron linacs and photoinjectors [6]. The model for upstream radiation in equations (2-4) was implemented in IMPACT-Z using an FFT-based, integrated Green function algorithm [4, 5]. This feature provides a fast capability for computing the free-space 1D wakefield due to CSR in an arbitrary lattice consisting of bends and drifts.

To use this feature, an additional input parameter is required for the specification of each dipole and drift element in the IMPACT-Z input file. This parameter specifies the number of upstream elements whose CSR contribution is to be included in the wakefield calculation within that element. In order to provide consistency with the model of [2], it is assumed that the farthest upstream element used in the CSR calculation is an infinitely long drift space.

Upstream Radiation Effects

Consider a 4-bend magnetic chicane whose bends will be denoted as Bend $1, \ldots, 4$, moving downstream from the chicane entry. In this section, we will examine the CSR

* ChadMitchell@lbl.gov

Copyright © 2013 CC-BY-3.0 and by the respective authors

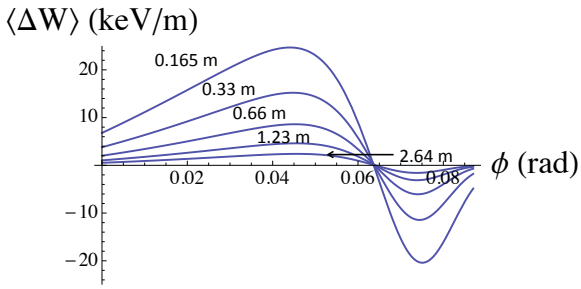


Figure 1: Approximate expression (8) for the difference in mean energy loss with and without the effect of upstream bends for a linearly compressing Gaussian bunch propagating through Bend 3 of the chicane of Table 1. The result is shown for various values of the central drift length.

wakefield when the bunch centroid lies within Bend 3. A portion of the particles within the bunch will lie within Bend 2 at their retarded times. Following a procedure similar to [7], one can use the results of [3] to show that in the limit $\gamma \to \infty$, the contribution of these particles to the total wakefield in Bend 3 takes the approximate form:

$$W_L(z,s) = \kappa F_L \lambda(z - \zeta_L), \tag{5}$$

where

$$\kappa = N r_c mc^2/R \tag{6}$$

and

$$F_L = \frac{4\psi(\phi+\psi+2L)}{\phi\{(\phi+\psi)^2+2L\psi\}}, \qquad \frac{\zeta_L}{R} = \frac{\phi^3}{24}\frac{\phi+4L}{\phi+L}. \tag{7}$$

Here ψ is the total bending angle of Bend 2, L is the ratio of the central drift length to the bending radius, and ϕ is the angle of the bunch centroid from the entry to Bend 3. By contrast, if we suppose that these particles at their retarded times lie within an infinitely long drift, then we recover Case A of [2]. In the limit $\gamma \to \infty$, it follows that (5) holds with $L \to \infty$ [7].

A convenient measure for the size of the upstream effects is the mean and rms value of the difference ΔW between the wakefields predicted from the two models. Making use of (5) in the case of a Gaussian bunch gives:

$$\langle \Delta W \rangle \approx \frac{\kappa}{\sqrt{4\pi}\sigma}\left[F_L e^{-\zeta_L^2/4\sigma^2} - F_\infty e^{-\zeta_\infty^2/4\sigma^2}\right]. \tag{8}$$

Consider a Gaussian bunch undergoing compression in a chicane described by the parameters of Table 1. Figure 1 shows the quantity (8) as a function of the entry angle ϕ into Bend 3 for various values of the central drift length L_c. In computing these curves, the compression of the bunch is modeled by taking $\sigma_z = \sigma_{z0}/[1 + (C-1)\phi/|\theta|]$ where $|\theta| = 87$ mrad and $C \approx 5$ is the compression factor at the chicane exit.

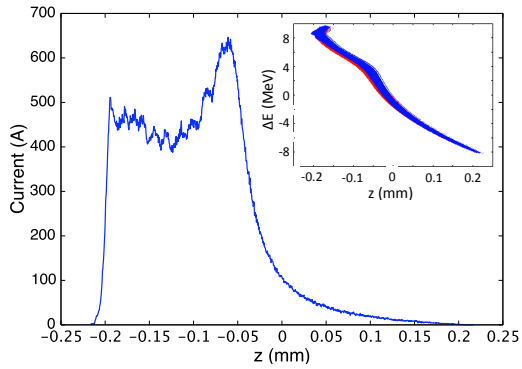


Figure 2: Current profile at the exit of BC2. The head of the bunch appears on the left ($z < 0$). (Inset) Longitudinal phase space at the exit of BC2 with (blue) and without (red) the effects of longitudinal CSR included.

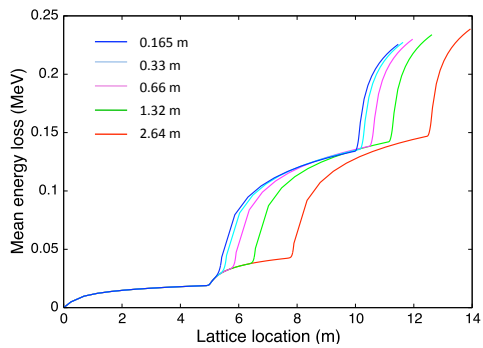


Figure 3: The cumulative loss in the mean energy of the bunch along the length of the chicane is shown for the values $L_c = 2.64$ m, 1.32 m, 0.66 m, 0.33 m, and 0.165 m.

APPLICATION TO A NEXT GENERATION LIGHT SOURCE

This algorithm was used to investigate CSR-induced dynamical effects in the second bunch compressor of a previously proposed Next Generation Light Source X-ray FEL being studied at Lawrence Berkeley National Laboratory [8]. Basic parameters for the chicane are provided in Table 1. Figure 2 shows the compressed current profile at the exit of BC2, together with the longitudinal phase space at the same location, both with and without the effect of the longitudinal CSR wakefield. The CSR interaction throughout the chicane induces a growth in the rms horizontal emittance of 23% relative to the initial value of 0.65 μm.

We study the effect of varying the length of the central drift L_c, leaving the compression factor of the chicane unaffected while controlling the strength of the upstream wakefield within Bend 3. Figure 3 illustrates the CSR-induced loss in the mean energy of the bunch along the length of the chicane for several values of the central drift length L_c. In order to illustrate the contribution of upstream radiation, Fig. 4 illustrates the difference between

Copyright © 2013 CC-BY-3.0 and by the respective authors

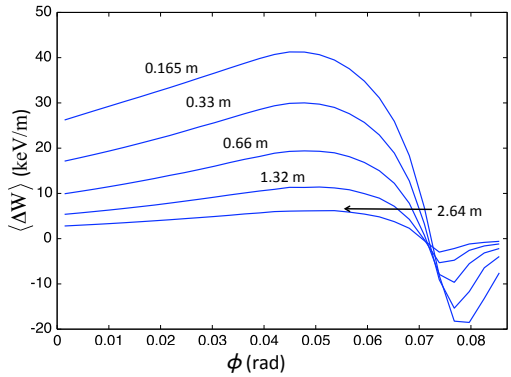


Figure 4: Difference between the longitudinal CSR wakefield in Bend 3 of BC2 as computed using the model of [2] (without upstream transient effects) and [3] (with upstream transient effects) during IMPACT-Z simulation. The average of this quantity over the length of the bunch is shown as a function of bend entry angle. Compare Fig. 1.

the mean CSR-induced energy loss as computed using the two wakefield models [2] and [3] along the length of Bend 3 for the same values of L_c. This difference attains a maximum at 40-50 mrad into the bend and changes sign 10-20 mrad upstream of the bend exit, similar to the curves shown in Fig. 1. The choice of model has a very weak ($\sim 10^{-3}$) relative effect on the final transverse emittance and the second beam moments for all values of L_c considered. The dominant effect of the upstream transient radiation is to introduce a displacement of the bunch centroid in both the horizontal coordinate and momentum, and these quantities are shown in Fig. 5 as a function of the central drift length.

Table 1: Parameters for NGLS BC2 (Factor of 5 Compression). The Initial Beam Distribution is Taken from IMPACT Simulation of the NGLS Design from the Cathode to the Chicane Entrance.

Chicane parameters	**symbol**	**value**
Bend magnet length (projected)	L_B	0.25 m
Drift length (B1→B2, B3→B4)	ΔL	4.5 m
Drift length (B2→B3)	L_c	2.64 m
Bend angle	$\|\theta\|$	87 mrad
Bend radius	$\|R\|$	2.88 m
Momentum compaction factor	R_{56}	-70.6 mm
Electron beam parameters	**symbol**	**value**
Nominal energy	E_0	717 MeV
Bunch charge	Q_0	300 pC
Uncorr. initial rms energy spread	$\sigma_{\delta 0}$	4.2×10^{-5}
Linear energy chirp	h	11.4 m^{-1}
Init. rms bunch length	σ_{z0}	373 μm
Init. rms norm. emittance	$\gamma\epsilon_x$	0.65 μm
Init. horizontal size	σ_{x0}	0.22 mm

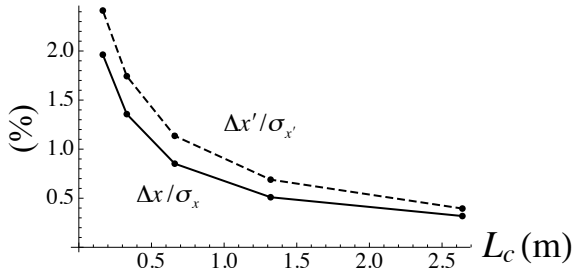


Figure 5: (Solid) Difference between the mean horizontal coordinate as computed using the models of [2] and [3] at the exit of BC2. (Dashed) Difference between the mean horizontal divergence in the two models.

DISCUSSION AND CONCLUSIONS

A one-dimensional free-space wakefield model of CSR including upstream radiation has been implemented in the code IMPACT-Z and used to investigate CSR wakefield effects in the second bunch compressor chicane of a Next Generation Light Source. The difference in mean energy loss due to the coupling with upstream radiation introduces a steering error of 1-3% in the transverse phase plane at the chicane exit. A previous study has investigated upstream radiation effects on the CSR-induced microbunching gain for this system [9], and future work will investigate the effects of vacuum chamber shielding.

ACKNOWLEDGEMENTS

This research was supported by the U.S. Department of Energy under Contract No. DE-AC02-05CH11231 and made use of computer resources at the National Energy Research Scientific Computing Center.

REFERENCES

[1] J. Murphy et al, Particle Accelerators, **57**, pp. 9-64 (1997).

[2] E. L. Saldin et al., Instrum. Meth. Phys. Res. A **398**, 373 (1997).

[3] D. Sagan, G. Hoffstaetter, C. Mayes, and U. Sae-Ueng, Phys. Rev. ST-Accel. Beams, **12**, 040703 (2009).

[4] R. D. Ryne, B. Carlsten, J. Qiang, and N. Yampolsky, http://arxiv.org/abs/1202.2409

[5] C. Mitchell, J. Qiang, and R. Ryne, Nucl. Instrum. Meth. Phys. Res. A **715**, 119 (2013).

[6] J. Qiang, R. D. Ryne, S. Habib, and V. Decyk, J. Comp. Phys. **163**, 434-451 (2000).

[7] G. Stupakov and P. Emma, Proceedings of EPAC 2002, Paris, France, 1479 (2002).

[8] J. Corlett et al, Proc. of ICAP 2012, New Orleans, LA (2012) 1762-1764.

[9] C. Mitchell and J. Qiang, Proc. of IPAC 2013, Shanghai, China, 1832 (2013).

Copyright © 2013 CC-BY-3.0 and by the respective authors

HIGH-GRADIENT METALLIC PHOTONIC BAND-GAP (PBG) STRUCTURE BREAKDOWN TESTING AT 17 GHz*

B.J. Munroe†, M.A. Shapiro, R.J. Temkin, MIT PSFC, Cambridge, MA 02139, USA

Abstract

Photonic Band-gap (PBG) structures continue to be a promising area of research for future accelerator structures. Previous experiments at X-Band have demonstrated that PBG structures can operate at high gradient and low breakdown probability, provided that pulsed heating is controlled. A metallic single-cell standing-wave structure has been constructed at MIT to investigate breakdown performance of PBG structures with very high surface temperature rise. The MIT standing-wave structure test stand has an available power of 4 MW for a maximum gradient of 130 MV/m; the actual realized gradient may be lower due to breakdown limitations. The MIT test stand will also utilize novel diagnostics, including fast camera imaging and optical spectroscopy of breakdowns.

INTRODUCTION

Photonic band-gap (PBG) structures, which use a lattice of metallic or dielectric rods to confine an accelerator mode while damping higher-order modes (HOMs), are a topic of ongoing experimental and theoretical work [1, 2, 3, 4]. Previous experimental work has demonstrated successful acceleration using a traveling-wave PBG structure [1] as well as suppression of wakefields [4, 5]. More recent work by MIT and SLAC National Accelerator Lab has shown that metallic PBG structures can operate at high gradient and low breakdown probability, achieving gradients of greater than 100 MV/m with a breakdown probability of less than 10^{-3} per pulse per meter of structure [6]. To expand on this X-band (11.4 GHz) testing a metallic PBG structure has been designed for testing at Ku-band (17.1 GHz). This metallic structure will be used to further investigate the role of pulsed heating on breakdown probability.

STRUCTURE DESIGN

The metallic PBG structure designed for high-gradient testing at MIT is designed as a scaled version of the round-rod PBG structure previously tested at SLAC and reported in [3]. The structure is axially powered via a scaled version of the SLAC $TM_{0,1}$ mode launcher. The PBG lattice has a filling factor, i.e. the ratio between the rod radius to the rod spacing, of $a/b = 0.18$, the same as the X-band structure. The high-field irises on either side of the PBG cell have an aperture of 0.216λ and a thickness of 0.176λ, again in agreement with the X-band structure. The main variation in structure design is that the Ku-band PBG cell has three rows of round rods, as opposed to the X-band structure's two, which is required by the Ku-band structure's open outer wall, as seen in Fig. 1. This open wall allows a direct line of sight to the high-field surface of the inner rods, allowing significantly greater diagnostic access to the structure during testing.

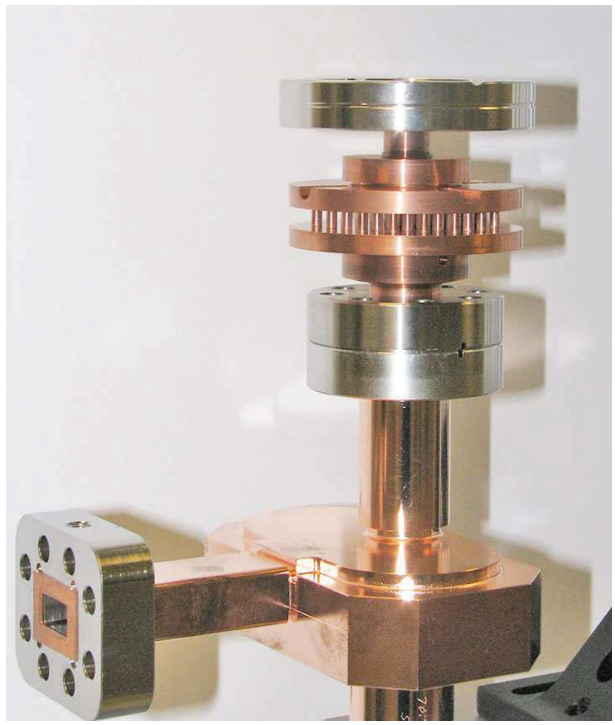


Figure 1: Metallic PBG structure and $TM_{0,1}$ mode launcher at MIT prior to structure brazing. Note the open outer wall of the PBG cell.

This structure will investigate the frequency scaling of breakdown behavior first observed in the testing of the PBG structure at X-band at SLAC, namely the effect of high surface magnetic fields on breakdown probability. To provide an accurate comparison the structure needs to be exposed, as limited by the breakdown probability, to gradients greater than 100 MV/m. The metallic PBG structure is expected to achieve 100 MV/m gradient at 2.4 MW of input rf power, as shown in Table 1. Note that the pulsed heating for this structure is higher than the X-band structure because of the increase in both the surface resistivity of copper and the power density with frequency. This power level is well below the approximately 4 MW of rf power available at the MIT test stand. The advanced optical diagnostics available at MIT combined with testing the structure at very high gradient should provide insight into how the structure fails and criteria for evaluating structure condition during testing.

* This work supported by Department of Energy High Energy Physics, Grant No. DE-SC0010075

† bmunroe@mit.edu

Copyright © 2013 CC-BY-3.0 and by the respective authors

Table 1: Performance of 17 GHz Round-rod PBG Structure at 100 MV/m

Power	2.4 MW
Peak Surface Electric Field	200 MV/m
Peak Surface Magnetic Field	900 kA/m
Pulsed Heating for 150 ns flat pulse	163 K

This structure has been fabricated using direct machining of the structure into cups which are then brazed together. The structure can be tuned after fabrication by perturbing the coupling cells using stainless steel tuning studs.

STRUCTURE COLD TEST

Prior to hot testing the PBG structures are cold tested using a vector network analyzer (VNA) to confirm that the quality factor, frequency, and coupling match the design values, shown in Table 2. This is necessary to ensure proper operation in hot test, and to properly model the fields in the structure, as described in [6]. By coupling through the input port of the mode launcher single port measurements of the coupling and quality factor can be made. Single port measurement of the field profile can also be measured using the dielectric perturbation technique described in [6]. The results of this field profile measurement can be seen in Fig.2. This PBG structure showed an asymmetric field profile, reduced coupling, and reduced quality factor, as seen in the cold test results. This structure was installed in the test stand, but sufficient coupling could not be obtained, so a new structure was fabricated.

Table 2: Design values of 17 GHz Round-rod PBG Structure

Frequency	17.140 GHz
Q factor	5600
S11	−46 dB

This new structure was fabricated in the same fashion as the first structure. Prior to brazing the performance of the structure was characterized using two coaxial probes situated on-axis in the structure. The transmission between these probes allowed a measurement of the quality factor of the modes independent of coupling through the mode launcher, which suffers when the structure is press-fit instead of brazed. The results of this measurement can be seen in Fig. 3. Note that this measurement shows a lower Q and a shift in frequency relative to the design point; both these values are expected to be closer to the design values after brazing. This structure will undergo both single-port and transmission Q measurements, as well as field profile measurements using a dielectric perturbation, after brazing to confirm that Q, frequency, and coupling are all within acceptable limits of the design values.

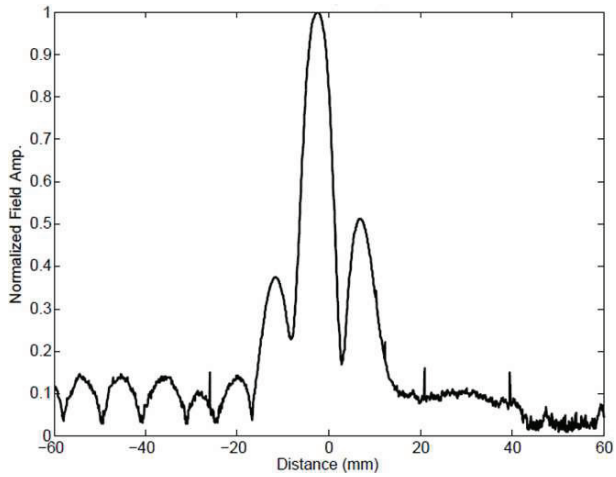


Figure 2: Measured field profile of first 17 GHz metallic PBG structure, obtained via use of a dielectric perturbation technique.

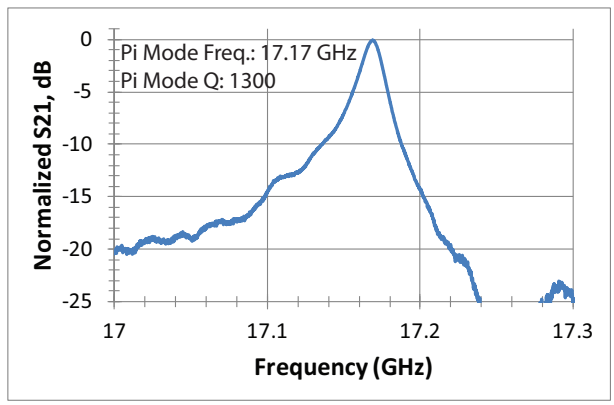


Figure 3: Transmission measurement of the second 17 GHz metallic PBG structure, prior to brazing. The Q of the mode of interest is found to be 1300 at a frequency of 17.169 GHz.

MIT 17 GHz TEST STAND

The standing wave test stand at MIT will be powered by the MIT/Haimson Research Corporation (HRC) relativistic beam klystron operating at 17.1 GHz. The klystron output that can be coupled to the test stand is limited to 12 MW to avoid breakdowns on the microwave window in the transmission line to the test stand. When coupled through a 4.2 dB hybrid (Fig. 4), which is inserted to protect the klystron from reflected power, the power available at the test stand is limited to 4 MW. Because the power density increases with frequency, this amount of available power is more than sufficient to conduct breakdown experiments similar to those at SLAC, as seen in Table 1.

The MIT standing wave test stand will utilize diagnostics. This is made possible through the use of an external vacuum chamber used to contain the device under test. This allows line of sight diagnostic access to the high-field regions of the PBG structure through view ports in the vac-

Copyright © 2013 CC-BY-3.0 and by the respective authors

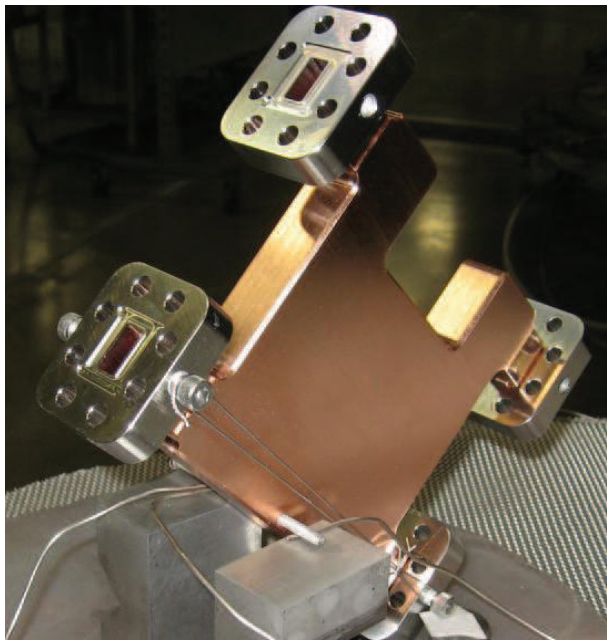


Figure 4: 4.2 dB hybrid from Haimson Research Corporation.

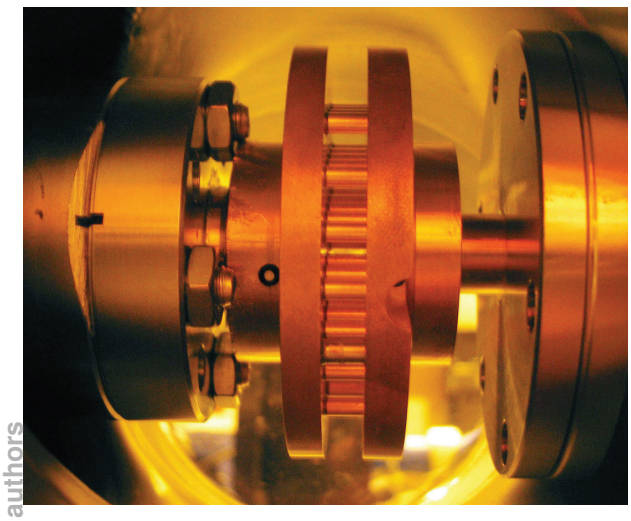


Figure 5: Metallic PBG structure installed in MIT test stand.

uum chamber. A nanosecond-gated ICCD camera will be used to observe and locate breakdown events, and a broadband optical spectrometer will be used to identify breakdown materials. Optical access to the structure can be seen in Fig. 5.

STRUCTURE HOT TEST

The operation of the MIT 17 GHz test stand was validated with the use of the first PBG structure described above. The microwave diagnostics functioned properly, confirming the cold test results that very little power was coupled into the design mode for that structure. Optical diagnostics were not used during this test, but their feasibility was verified as shown in Fig. 5. The second structure should allow proper testing of the high power test stand.

CONCLUSION

A metallic PBG structure has been designed and undergone preliminary tests at MIT. This structure will further investigate the relationship between pulsed heating and breakdown probability in high-gradient accelerator structures. The first iteration of the structure showed reduced coupling and quality factor, likely due to fabrication errors. This structure was used to validate both the cold and hot test procedures at MIT. The Q of the design mode was measured using both single port and transmission techniques, and a dielectric perturbation was used to determine the field profile of the design mode. The structure was briefly placed under hot test. The microwave diagnostics were confirmed to work properly, and optical access to the structure after installation was confirmed. A second iteration of the structure has been constructed and shows improved performance in cold tests of the structure prior to brazing. This structure will undergo further testing after brazing to confirm proper fabrication prior to being installed for hot testing.

REFERENCES

[1] E. I. Smirnova et al., Phys. Rev. Lett. 95, 074801 (2005).

[2] G. R. Werner et al., Phys. Rev. -STAB, Vol. 12, Article Number: 071301 (2009).

[3] R. A. Marsh et al., Phys. Rev. -STAB, Vol. 14, Article Number: 021301, (2011)

[4] C. Jing et al., Phys. Rev. -STAB, Vol. 12, Article Number: 121302 (2009).

[5] R. A. Marsh et al., Nucl. Inst. Meth. Phys. Rev. A, Vol. 618, pp. 16-21 (2010).

[6] B. J. Munroe et al., Phys. Rev. -STAB, Vol. 16, Article Number: 012005 (2009).

Copyright © 2013 CC-BY-3.0 and by the respective authors

FIRST CAVITY RESULTS FROM THE CORNELL SRF GROUP'S Nb_3Sn PROGRAM*

S. Posen† and M. Liepe
Cornell Laboratory for Accelerator-Based Sciences and Education, Ithaca, NY

Abstract

Breakthrough performance levels were achieved for a 1.3 GHz single cell cavity that was fabricated, coated with Nb_3Sn, and tested at Cornell. Unlike previous Nb_3Sn cavities, this cavity showed minimal R_s-increase up to medium fields. This disproves speculation that the R_s-increase in previous cavities was caused by vortex dissipation for $B > B_{c1}$, as surface fields far higher than the measured B_{c1} for this cavity were reached. At 2 K, quench occurred at ∼55 mT, apparently due to a defect, so additional treatment may increase the maximum gradient to even higher fields. At 4.2 K, at ∼12 MV/m, the cavity achieved Q_0∼1×10^{10}, approximately 20 times higher than niobium at this temperature. This makes it the first accelerator cavity made with an alternative superconductor to far outperform niobium at useable gradients.

INTRODUCTION

Superconducting Radio-Frequency (SRF) researchers have been highly effective at finding preparation methods that suppress performance-limiting effects in niobium particle accelerator cavities. Now cavities are regularly produced that operate very close to the fundamental limits of niobium: they have surface resistances R_s close to the ideal BCS value at operating temperatures, and they reach maximum surface magnetic fields close to the superheating field B_{sh}. To keep up with continually increasing demands of future SRF facilities, researchers have begun a significant effort to develop alternative materials to niobium, materials with smaller R_s and/or larger predicted B_{sh}.

Nb_3Sn is one of the most promising alternative SRF materials. Because it has a high critical temperature T_c of ∼18 K, compared to 9.2 K for niobium, its R_{BCS} at a given temperature is much smaller. This makes the material ideal for continuous wave (CW) linacs: benefits include a smaller and simpler cryogenic plant, the possibility of 4.2 K operation (no superfluid; atmospheric operation), and higher cost-optimum accelerating gradients in CW operation. Its predicted B_{sh} is nearly twice that of Nb, up to ∼400 mT depending on the material parameters used for the calculation. This makes the material ideal also for high energy linacs: it would allow Nb_3Sn cavities to operate at higher accelerating gradients than Nb cavities, and therefore fewer cavities would be required.

In the seventies, Siemens AG developed a method to fabricate Nb_3Sn coatings via vapor diffusion, which produced excellent RF results [1]. The University of Wuppertal applied this coating mechanism to particle accelerator cavities, achieving very small R_s at low fields, but their cavities showed a strong increase in surface resistance with increasing field (this effect is called Q-slope, for the shape of the graph of quality factor Q versus accelerating gradient E_{acc}). The Q_0 vs E_{acc} curve of one of the best cavities produced by University of Wuppertal and tested at JLab is shown in Fig. 1 [2].

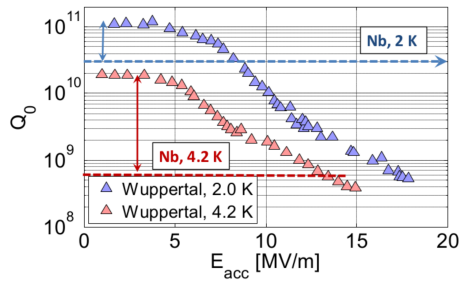


Figure 1: Q vs E curves at 2 K and 4.2 K for one of the best Nb_3Sn cavities produced by U. Wuppertal [2]. The approximate values for a Nb cavity are shown for comparison.

Various causes for the Q-slope were suggested, such as intergrain losses, imperfect stoichiometry [3], and dissipation due to vortex penetration beginning at the lower critical field B_{c1} [4]. As a result, it has been unclear whether or not this Q-slope behavior is fundamental to Nb_3Sn. In a recent historical review, Kneisel called finding the answer to this question and determining the origin of the Q-slope "the next important steps" for Nb_3Sn [5]. More importantly, if vortex penetration at B_{c1} were unavoidable, then bulk alternative SRF materials in general—which tend to have relatively small B_{c1} values—would be severely limited in the fields they could reach without strong dissipation. There is an energy barrier to vortex penetration, which for an ideal surface prevents strong vortex dissipation up to the superheating field B_{sh} [6], but small defects with size on the order of the coherence length ξ can decrease it. Other alternative materials also tend to have relatively small ξ, so the possiblity of vortex penetration above B_{c1} has been a serious concern.

Cornell University is now leading the program for new R&D efforts on Nb_3Sn SRF cavities. In 2009, Nb_3Sn development at Cornell began with the design, fabrication, and commissioning of a small coating chamber for samples. After establishing the capability to repeatably produce Nb_3Sn films of sufficiently high quality for cavity RF surfaces [7], Cornell researchers began work on a large coating chamber for single cell 1.3 GHz cavities, shown in

* Work supported by NSF Career award PHY-0841213, DOE award ER41628, and the Alfred P. Sloan Foundation.
† sep93@cornell.edu

Copyright © 2013 CC-BY-3.0 and by the respective authors

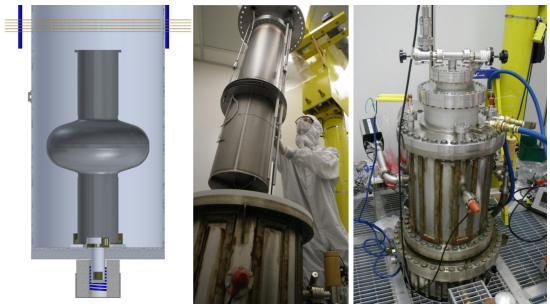


Figure 2: Cross-section of coating chamber (left), coating chamber being lowered into furnace (center), and UHV furnace with chamber inside (right).

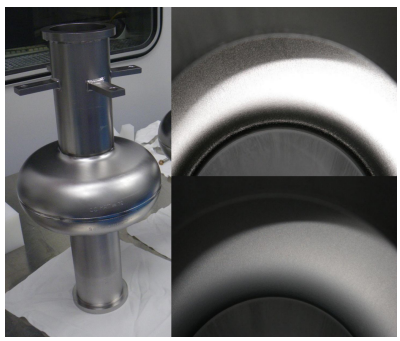


Figure 3: Coated cavity (left); view looking down into cavity before (top right) and after coating (bottom right).

Fig. 2. The first cavity coated showed unusually high R_s in RF testing, which was attributed to problems with the niobium cavity substrate. The performance of the second cavity coated will be presented here.

RF MEASUREMENTS

ERL1-4, a 1.3 GHz Cornell ERL-shaped (similar to TESLA shape) single cell cavity, was coated with Nb_3Sn via thermal vapor diffusion. Visually, the Nb_3Sn surface is a darker gray than niobium, and it is matte rather than shiny, as shown in Fig. 3. After the coating process it was treated with only a high pressure rinse (HPR) before mounting to a vertical test stand for cryogenic performance test. Before insertion to the dewar, the outside cavity surface was covered with an array of temperature sensors (temperature map) to obtain information about the loss distribution. The cavity was cooled at a very slow rate, $\gtrsim$ 6 min/K, as specified by Wuppertal researchers, to reduce trapped flux due to thermocurrents [2].

The Q vs E curve of ERL1-4 is shown in Fig. 4, along with that of the Wuppertal cavity from Fig. 1 for comparison. Overall, the performance is excellent. Unlike the cavities produced by Wuppertal, it does not show a strong reduction in Q_0 above 5 MV/m. At 4.2 K, at medium fields the Q_0 is up to approximately 10 times higher than that of the Wuppertal cavity, and approximately 20 times higher than a niobium cavity. At 2 K, the Q_0 is only slightly higher, indicating that residual resitance dominates over

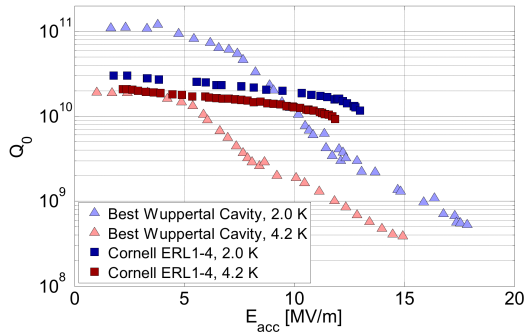


Figure 4: Q vs E curve from the new Cornell Nb_3Sn cavity, showing a small residual resistance at low fields and a large improvement in Q_0 at usable gradients over one of the best U. Wuppertal cavities. Uncertainty in Q and E is approximately 10%.

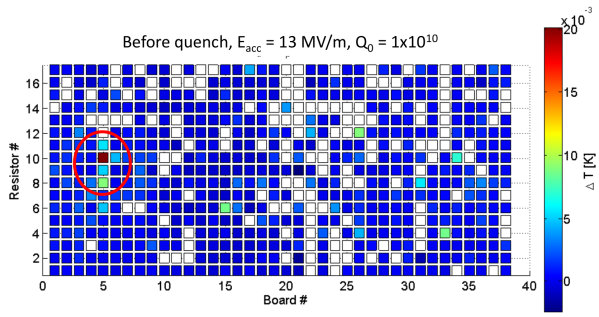


Figure 5: Temperature maps (which show the heating of the outer cavity surface relative to the helium bath) before quench, close to the quench field (top) and after the first quench (bottom). The region of strong localized heating is circled. Notice the difference in scale between the top and bottom.

BCS, with very low R_{res} value of $\sim$9 nΩ, similar to most Wuppertal cavities [2]. Above 9 MV/m, due to its relatively flat Q_0, ERL1-4 has a higher Q_0 than even this exceptional Wuppertal cavity at 2 K.

Quench occurred at approximately 55 mT at 2 K, which was preceeded by a sharp drop in Q_0 on the order of 10%, as well as pre-heating on the temperature map. The pre-heating was highly localized, as shown in Fig. 5. After quench, the same area showed further increased heating, consistent with this being the quench location. Our observations suggest that the limitation is a defect that becomes normal conducting when the Q_0 drop occurs, and triggers breakdown at higher fields. The dominance of this spot on the temperature map shows that this is a local problem—a defect—not a global problem with Nb_3Sn.

Q_0 was measured as a function of temperature, as shown in the left side of Fig. 6. There was no sign of Q_0 change near the T_c of niobium, 9.2 K, indicating excellent Nb_3Sn coverage of the surface. The high-temperature range is highlighted in the inset, from which a T_c of 18.0 ± 0.1 K is measured. Q_0 was converted to an estimated average surface resistance via $R_s = G/Q_0$, where G is the geometry

Copyright © 2013 CC-BY-3.0 and by the respective authors

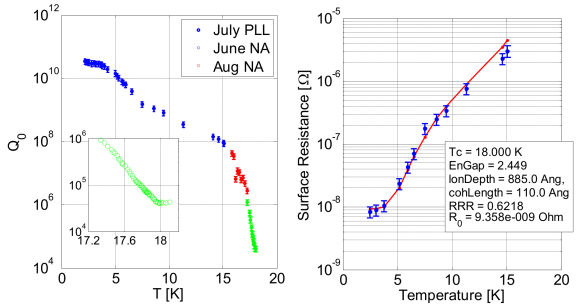


Figure 6: Q vs T measured with phase lock loop (PLL) or with network analyzer (NA) with weak coupling such that the $Q_0 \sim Q_L$ (left); R_s vs T and BCS fit (right).

Table 1: Measured and Calculated Nb_3Sn Film Properties

Property	Value
T_c [K]	18.0 ± 0.1
Δ/k_bT_c	2.4 ± 0.1
l [nm]	3.7 ± 0.5
$R_{\rm res}$ [nΩ]	9 ± 2
$\lambda_{\rm eff}(0)$ [nm]	150 ± 20
$\xi_{GL}(0)$ [nm]	3.2 ± 0.2
κ	47 ± 6
$B_c(0)$ [T]	0.47 ± 0.6
$B_{c1}(0)$ [T]	0.027 ± 0.005
$B_{sh}(0)$ [T]	0.39 ± 0.05

constant of the cavity. The resulting R_s vs T data was fit using a polymorphic BCS analysis [8]. The fit is shown in the right side of Fig. 6, and the fit parameters and derived values are summarized in Table 1. Δ/k_BT_c and B_c are in good agreement with literature values.

Table 1 lists the material parameters obtained from the $R_s(T)$ fit, together with additional parameters calculated from the fit parameters using Ginzburg-Landau theory (see [9] for derivation of each value). The so obtained B_{c1} value agrees well with a B_{c1} measurement performed with μ-SR by A. Grassellino et al [10] on a Nb_3Sn witness sample produced by Cornell. Figure 7 compares B_{c1} to the Q vs B data, showing that the cavity far exceeds B_{c1} without a significant increase in surface resistance. This is important, as it shows that vortex penetration does not occur at B_{c1} for bulk films of superconductors with small coherence length. The energy barrier keeps Meissner state metastable, even with the small ξ of Nb_3Sn. The Q-slope seen in the Wuppertal cavities therefore does not represent a fundamental problem for alternative SRF materials.

CONCLUSIONS

Exceptional SRF performance was observed in tests of a new Nb_3Sn cavity at Cornell. At 2 K, the surface magnetic field reached 55 ± 6 mT, far exceeding $B_{c1} = 27 \pm 5$ mT without any sign of vortex penetration. This disproves spectulation that the Q-slope observed in previous Nb_3Sn cavities was an inevitable result of exceeding B_{c1}. The gradient was quench limited at a defect, and there is no indication of any fundamental mechanism that would prevent future Nb_3Sn cavities from reaching even higher fields. Future research on preparation methods to achieve better Nb_3Sn surfaces can be expected to overcome non-fundamental limitations as they have in niobium, allowing fields close to $B_{sh} \sim 400$ mT to be reached. Even with the current performance achieved, Nb_3Sn now becomes a promising alternative material for certain future accelerators, as at usable accelerating fields $\sim$12 MV/m, we have shown that at 4.2 K Nb_3Sn cavities can achieve a Q_0 of 10^{10}, $\sim$20 times higher than niobium.

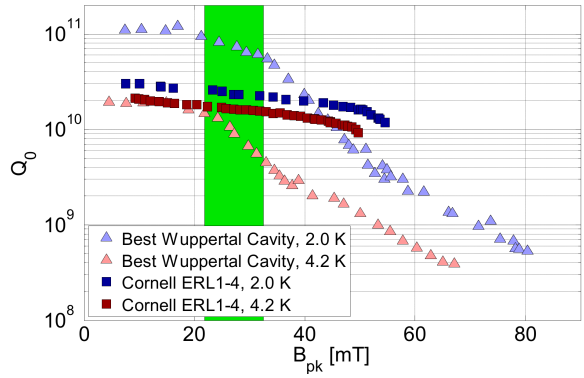


Figure 7: Q vs B curves of the Cornell and Wuppertal cavities. In green is the Cornell cavity's $B_{c1} = 27 \pm 5$ mT, which is exceeded without indication of vortex dissipation.

ACKNOWLEDGEMENTS

The authors would like to express sincere thanks to summer student assistant F. Wohlfarth; A. Grassellino et al. for sample B_{c1} measurement; N. Valles for polymorphic fit program; J. Halbritter, author of the SRIMP program; P. Kneisel for excellent summary of Nb_3Sn SRF history [5]; and H. Padamsee for helpful discussions.

REFERENCES

[1] B. Hillenbrand et al., IEEE Trans. Mag. 13, 481 (1997).
[2] G. Müller et al. EPAC 1996. p. 2085.
[3] H. Padamsee, J. Knobloch, and T. Hays, *RF Superconductivity for Accelerators*, Wiley & Sons, New York, 1998.
[4] A. Gurevich, App. Phys. Lett. 88, 012511 (2006).
[5] P. Kneisel, JLAB-TN-12-016 (2012).
[6] M. Transtrum, G. Catelani, and J. Sethna, Phys. Rev. B 83, 094505 (2011).
[7] S. Posen and M. Liepe, THPO066 (Presented at the SRF Conference, Chicago, USA, 2011).
[8] N. Valles, Ph.D. Thesis, Cornell University (in progress).
[9] S. Posen and M. Liepe, TUP087 (Presented at the SRF Conference, Paris, France, 2013).
[10] A. Grassellino et al., TUP029 (Presented at the SRF Conference, Paris, France, 2013).

Copyright © 2013 CC-BY-3.0 and by the respective authors

DEVELOPMENT OF Yb LASER FOR HIGH POWER ULTRA-SHORT PULSE*

Y. Matsumura†, K. Koyama, M. Uesaka,
The University of Tokyo, Bunkyo-ku, Tokyo, JAPAN
M. Yoshida, X. Zhou,
High Energy Accelerator Research Organization, Tsukuba, Ibaraki, Japan

Abstract

Ytterbium (Yb) lasers have good thermal and optical properties. The Yb lasers can be pumped by laser diodes. The oscillation wavelength is near the excitation wavelength. Yb can be highly doped in YAG crystal, so Yb-doped crystal has large gain even if the crystal is thin. These properties are advantages for high power operation. Additionally, because of broad emission spectrum of Yb, the passively mode-locked Yb lasers can easily generate femtosecond pulse at high repetition rate. The Yb lasers have been applied to many fields such as optical frequency comb and X-ray generation. Now, femtosecond pulse of much higher energy at high repetition rate is being required for dielectric laser accelerator (DLA) and lasertron. We have developed high power mode-locked Yb laser, and aim to generate 500 fs pulse of 500 W average power at 50 Hz. In this research, e acheived 20 W mode-locked Yb fiber laser amplification system at 1MHz. We report this achievement and the structure of our Yb laser system to achieve our final goal.

INTRODUCTION

Passively mode-locked lasers can easily generate femtosecond pulse at high repetition rate. The femtosecond pulses have been used in many scientific fields. In the accelerator field, femtosecond pulse of much higher energy at high repetition rate is required for new acceleration technologies such as DLA [1], lasertron [2] and laser wakefield plasma acceleration.

Yb lasers have many advantages for high power operation. Yb can be pumped directly by laser diodes (LD), which can convert electricity into light with as high efficiency as 60 percent. Since the difference between the oscillation wavelength and the excitation wavelength is as low as 90 nm, the quantum efficiency of Yb is very high. Furthermore, Yb can be doped in YAG crystal with high concentration, which enables thin disk lasers. The large surface to volume ratio of the thin disk enables efficient heat removal from the laser material and decreases the wavefront distortion due to the thermal lens effect.

Although the Ti:Sapphire lasers excel at less than 100 fs pulse generation, the Yb lasers have advantages over the Ti:Sapphire lasers when we need several hundreds fs pulse generation for high power operation.

* Work partly supported by KAKENHI, Grants-in-Aid for Scientific Research(C)24510120

† matsumura@nuclear.jp

In this research, we have developed a high power mode-locked Yb laser, and are aiming to generate 500 fs pulse with 500 W average power at 50 Hz for the new acceleration applications.

CPA SYSTEM OF YB LASER

To achieve the generation of 500 fs pulse of 500 W average power at 50 Hz, CPA was adopted. The schematic layout of the Yb laser is shown in Fig. 1. For amplification, Yb fiber and Yb:YAG lasers were used. The Yb fiber lasers have higher gain than the Yb solid lasers, and fibers can be cooled sufficiently by air. However, LDs for fiber lasers cost more than those for solid lasers, and power scaling cannot be applied for the fiber lasers. Additionally, the fiber lasers can't amplify high intensity pulse because of its damage threshold. For these reasons, the Yb fiber amplifiers were adopted at the first half part, while the Yb:YAG amplifiers were adopted at the second half part.

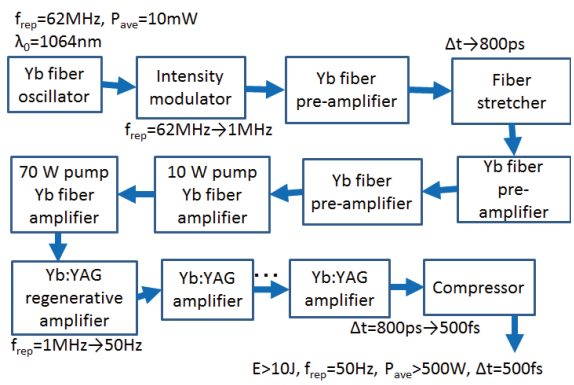


Figure 1: Schematic layout of Yb CPA system.

The ultra-short pulse at 62 MHz was emitted from a Yb fiber oscillator. After that, the pulse was picked up from the pulse train by an electro-optical (EO) module. The repetition rate was reduced from 62 MHz to 1 MHz. Then, the pulse was stretched to 800 ps by a fiber Bragg grating (FBG) stretcher. Through these fiber modules, the power of the pulse decreased. Therefore, three small Yb fiber pre-amplifiers were equipped. These pre-amplifications were needed to suppress amplified spontaneous emission (ASE) at the next amplifiers. After the three pre-amplifiers, the pulse was amplified up to several μJ by two Yb fiber amplifiers pumped by 10 W and 70 W LDs. Next amplifications are done by Yb:YAG lasers. A regenerative amplifier reduces repetition rate from 1 MHz to 50 Hz while amplifying the pulse. Finally, the pulse is amplified up to 10 J by

Copyright © 2013 CC-BY-3.0 and by the respective authors

the sequent Yb:YAG amplifiers. A grating pair and double prism pair are being considered as a compressor candidate. Whether the compressor is the grating pair or double prism pair, the pulse is compressed from 800 ps to 500 fs, and 500 fs pulse of 500 W average power at 50 Hz is generated by this Yb laser system.

PRESENT EXPERIMENTAL RESULTS

In this section, the experimental results and present laser status are described.

Yb Fiber Oscillator

The Yb fiber oscillator was mode-locked by nonlinear polarization rotation (NPR). Its structure was almost same as typical NPR mode-locked Yb fiber lasers [3]. However, the polarization beam splitter was not used as an output component because the output from it includes more ASE than that from other components in principle. In our oscillator, the reflected light from a grating was used for output. The power of it was 10 mW and the repetition rate was 62 MHz. The central wavelength was 1060 nm, and FWHM of the spectrum was 49 nm.

EO Fiber Module, FBG Stretcher and Preamplifiers

A part of the 62 MHz optical pulse was captured by a photodiode. The frequency of photodiode signal was reduced from 62 MHz to 1 MHz. The delay and voltage of 1 MHz signal was adequately adjusted for the EO module. Figure 2 describes the result of intensity modulation. The pulse was picked up from the pulse train as shown in Fig. 2. The SN ratio after the pre-amplifiers was about 100.

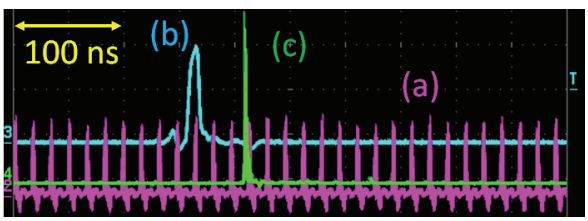


Figure 2: Intensity modulation result. (a) The pulse train from the oscillator, (b) The electric pulse applied on the EO module, (c) The pulse picked up by the EO module

A FBG has periodic refractive index in a fiber, and reflects light at designed wavelength. A FBG stretcher reflected light at different positions according to the wavelength, and gave the pulse positive dispersion. The pulse was stretched to 800 ps here.

The pulse was attenuated through the EO module and at the reflection of the stretcher. In order to suppress ASE at the Yb fiber amplifiers, one Yb fiber pre-amplifier was equipped after the EO module and two were after the stretcher, which were pumped by LDs of 150 mW, 150 mW and 200 mW respectively. By equipping these preamplifiers, the input power to the first Yb fiber amplifier was improved from 0.1 mW to 137 mW.

Yb Fiber Amplifiers

Two Yb fiber amplifiers amplified the pulse after the pre-amplification. The first amplifier consists of 10 W LD and 4 m long 10 μm-core Yb double cladding fiber. The second amplifier consists of 70 W LD and 2 m long 25 μm-core Yb double cladding fiber. The structure of them is described in Fig. 3. The edges of the fibers were cut at the angle of 8 degrees to reduce Fresnel reflection. The 70 W LD was so strong that the fiber chuck had heavy thermal load. For this reason, all-metal chucks were adopted for the both sides of the second amplifier. Additionally, the fiber chuck mounts were large, so they acted as good heat sink and reduced the thermal load of the fiber and fiber chucks.

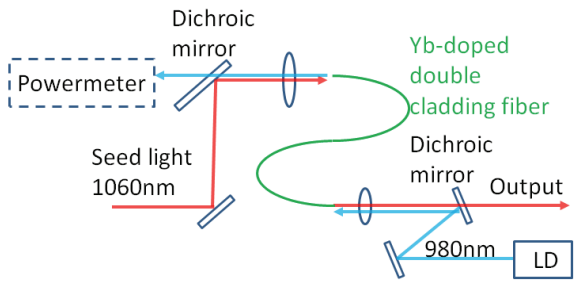


Figure 3: The structure of the Yb fiber laser amplifier.

Figure 4 shows the amplification result from the second amplifier. The 70 W LD was cooled by water, but the water temperature wasn't controled (was controled at room temperature). The maximum output power was 18.0 W then.

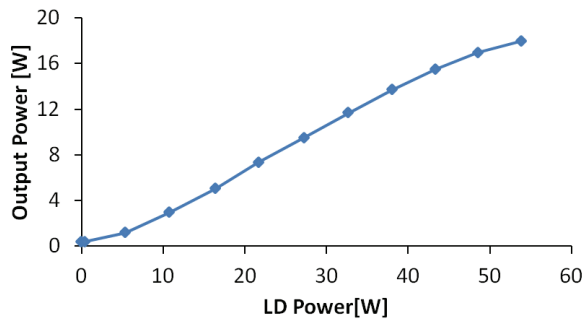


Figure 4: The output power from the second Yb fiber amplifier. The 70 W LD was cooled by water, but the water temperature wasn't controled.

The central wavelength of the LD was around 976 nm, but it depended on its temperature. Considering the narrow FWHM of Yb absobtion cross section around 976 nm, it was important to adjust the wavelength by controlling the cooling temperature. The experiment was done by measuring the LD power from the fiber at the seed laser injection side. The powermeter was set behind the dichroic mirror in Fig. 3. The measured power means the power not used for the amplification. Not all the power could be measured because of small diameter of the lens, but that was enough because the temperature to minimize the measured power was only the parameter we needed. From Fig. 5, Cooling

Copyright © 2013 CC-BY-3.0 and by the respective authors

temperature of 289 K was the best for over 50 W LD operation. The maximum output power was improved to 20.9 W at 289 K. The SN ratio was measured by a photodiode, and it was about 100. Additionally, the observation of this photodiode signal showed ASE was small. Therefore, the pulse energy could be calculated as 13 μJ when ASE was ignored.

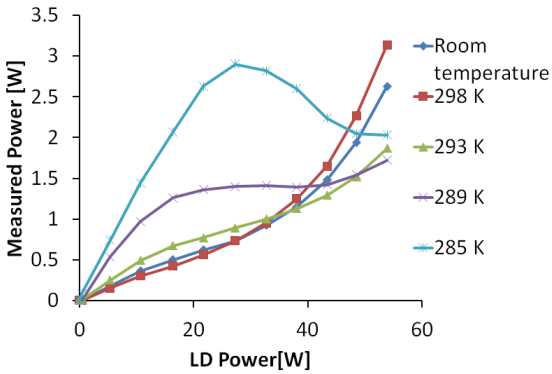


Figure 5: Power measurement experiment by changing cooling temperature.

Yb:YAG Solid Amplifiers

The first Yb:YAG amplifier is a regenerative amplifier. Here, the repetition rate will be reduced from 1 MHz to 50 Hz. The basic experiment was done to check whether a Pockels cell could pick up and dump the pulse. The result of this experiment showed the Pockels cell could pick up and dump it clearly. The SN ratio was over 150.

The final Yb:YAG amplifier is being designed now. Here, 50 pieces of Yb:YAG crystals are arranged symmetrically on the edge of a rotating disk. The seed pulse comes at 50 Hz, but each pulse injects on the different Yb:YAG crystals in 1 second. Therefore, the thermal load per one crystal decreases. The pulse energy will be amplified up to 10 J by 8 modules of 10 kW LD.

Compressor

Two ways to compress the pulse from 800 ps to 500 fs are now being considered. One is transmission grating pair. The other is double prism pair. The grating pair is often used for high intensity lasers. However, its cost is very high and a large vacuum chamber is required. Although the double prism pair cannot give large dispersion, its cost is relatively low and it may not need a vacuum chamber because the prism surface is very plane. To know the required distance for double prism compression, the dispersion was calculated based on Ref. [4]. In this calculation, the laser diameter was considered. The prism material was F2. The wavelength was 515 nm to make the dispersion large. The calculation result are shown in Fig. 6. From this calculation, it was shown that 32 times round trips between 3 m prism pair distance are needed to compress 800 ps pulse when the prism size is 50 mm and the FWHM of spectrum is 10 nm. Therefore, it will be difficult to cmpress the pulse by the double prism pair of 50 mm prisms.

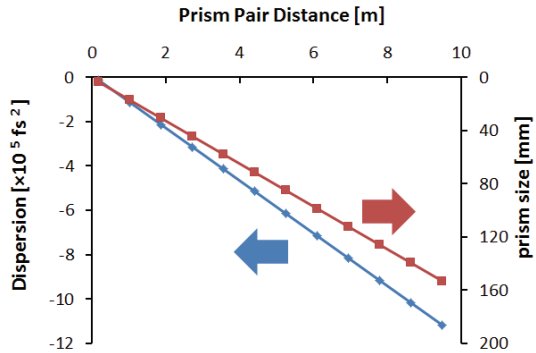


Figure 6: Dispesion and required prism size for the prism pair distance.

CONCLUSION

In this research, we reduced repetition reduction to 1 MHz, amplified the pulse up to 13 W average power without noise pulse, and achieved over 10 μJ pulse energy. The present laser parameters and the goal parameters are compared in Table 1. We will go to the stage of the Yb:YAG amplifiers. In the near future, the generation of 500 fs pulse of 500 W average power at 50 Hz will be achieved.

Table 1: Present Laser Parameters and Goal Parameters

	Present	Goal
Pulse energy	13 μJ	10 J
Repetition rate	1 MHz	50 Hz
Average power	13 W	500 W
Pulse duration	800 ps	500 fs

ACKNOWLEDGMENT

This work was partly supported by KAKENHI, Grants-in-Aid for Scientic Research(C)24510120.

REFERENCES

[1] K. Koyama, et al., "Designing Of Photonic Crystal Accelerator For Radiation Biology," IPAC2012, New Orleans, May 2012 , WEPPP019 , p. 2763, http://accelconf.web.cern.ch/AccelConf/IPAC2012/papers/weppp019.pdf

[2] E. L. Garwin, et al., "An Experimental Program To Build A Multimegawatt Lasertron For Super Linear Colliders," IEEE Transactions on Nuclear Science, Vol. NS-32, No. 5, Oct. 1985, http://epaper.kek.jp/p85/PDF/PAC1985_2906.PDF

[3] X. Zhou, et al., "Generation of 28-fs pulses from a mode-locked ytterbium fiber oscillator," OPTICS EXPRESS 16 (2008) 10.

[4] Z. Cheng, et al., "Compression of 2 mJ kilohertz laser pulses to 17.5 fs by pairing double-prism compressor: analysis and performance," Optics Communications 201 (2002) p.145-155.

Copyright © 2013 CC-BY-3.0 and by the respective authors

BELLA LASER AND OPERATIONS*

W.P. Leemans, J. Daniels, A. Deshmukh, A.J. Gonsalves, A. Magana, H.S. Mao, D.E. Mittelberger, K. Nakamura, J.R. Riley, D. Syversrud, C. Toth, N. Ybarrolaza, LBNL, Berkeley, CA 94720, USA

Abstract

The BELLA laser system is the first high repetition rate petawatt class laser in the world. The laser was acquired from THALES to allow laser plasma acceleration (LPA) experiments that aim at exploring the physics of linear and non-linear interactions of intense lasers with plasmas towards the development of a 10 GeV module. Here we present details of the operation of the BELLA laser and beam line systems, including the control and data acquisition system.

INTRODUCTION

Laser plasma accelerators (LPA) [1] have the potential to drastically cut the cost of doing science with accelerators due to their much reduced size compared to conventional accelerators of the same energy. While it could be decades before a laser plasma accelerator can match or exceed the capabilities of something like the proposed International Linear Collider—a 25 miles (40 kilometers) long machine that would produce electrons and positrons at extremely high energies (0.5 TeV center of mass), straw man designs [2] and more detailed physics studies are underway to explore the possibility of LPA technology towards a linear collider [3,4]. In recent years, LPAs have made significant progress towards producing high quality beams with ever higher energy. In 2004, three independent groups showed the first demonstration of relatively narrow energy spread electron beams at the ~ 100 MeV level from mm-scale devices [5-7]. In 2006 the first production was shown of GeV electron beams from a 3 cm long plasma channel guided LPA at LBNL [8] and in 2011 a novel method for controlling injection via longitudinal tailored density profiles was demonstrated [9]. In the 2006 experiments, the laser peak power was of the order of 40 TW and the operating plasma density was a factor of ~10 lower but extended over a ~10 times longer distance than in the 2004 experiments. Motivated by the success of these experiments, designs were developed at LBNL to achieve 10 GeV electron beams from meter-scale accelerator structures using a PW-class laser system, which led to the formal BELLA (BErkeley Lab Laser Accelerator) project proposal to the Department of Energy, Office of High Energy Physics in 2007. BELLA represents an essential step towards investigating how more powerful accelerators of the future might be more compact. The initial experiments with the BELLA laser system and facility are aimed at demonstrating that high quality 10 GeV electron beams can be generated using a laser powered plasma structure that is about 1 meter long. The research supported by BELLA will also investigate fundamental laser-plasma interaction physics that aims at optimizing the coupling efficiency of laser to electron beam energy, controlling both the energy spread and emittance of the electron beams, and staging multiple LPA modules together. The 10 GeV beams could also be used to study beam driven plasma wakefield acceleration, as well as positron production and subsequent acceleration in plasma based accelerators. Although its main purpose is accelerator research, the development of a compact 10 GeV accelerator has several potential applications. BELLA could be used to build a free-electron laser (FEL) operating in the soft x-ray window that produces few femtosecond radiation pulses that are intrinsically synchronized to laser pulses, to THz radiation pulses or directly to the electron beam. Such a device could be an extraordinarily valuable tool for biologists, chemists, materials scientists, and biomedical researchers, allowing them to observe ultrashort, nanoscale phenomena.

We will next discuss the performance of the BELLA laser. As the key physics in the LPA studies are primarily dependent on laser intensity, the key parameters are laser pulse energy, pulse duration, laser beam profile and their stability. From an operational point-of-view, pointing stability is also essential. We also will introduce the BELLA control system, which is used for both control of all experimental subsystems and data acquisition. Details will be presented elsewhere.

BELLA PROJECT

The project phase of BELLA consisted of the construction and commissioning of a PW-class laser that supports the research aimed at the development of 10 GeV LPA modules. The project was formally launched in October 2007 and funded in 2009. The scope of the BELLA project included the design and construction of the conventional facilities required to house and safely operate the BELLA laser, the acquisition of the BELLA laser system itself, design and construction of ancillary systems to support the laser operations, site and system integration, and performance verification of the BELLA laser system.

The BELLA facility has been fully designed to achieve all key performance parameters of the laser system and future experimental systems. This includes clean-room (class 10,000 and 1,000) areas for the laser and experimental areas, with gowning area, assembly area and tightly controlled environmental conditions to minimize temperature and humidity effects as well as low vibration

*Work supported by DOE, Office of High Energy Physics and NSF

Copyright © 2013 CC-BY-3.0 and by the respective authors

levels; a separate utility room that houses all power supplies and other heat producing equipment; a radiation shielded target area for all high power laser-plasma interaction experiments, including a beam dump to stop and absorb 10 GeV class electron beams; a control room equipped with computer hardware to allow remote operation of the laser system, equipment and personnel safety systems as well as experiments. Legacy infrastructure demolition in the BELLA building and subsequently construction of the new facility took place from October 2010 – March 2011 and March 2011-November 2011, respectively.

The BELLA laser was constructed by a commercial vendor (THALES) [10] and first built at the THALES factory from November 2009 through January 2012. Following factory acceptance testing in February 2012, the laser was shipped to Berkeley in April 2012 and installed at LBNL from April 2012 through July 2012. More than 80 crates arrived in April 2012 carrying well over 40 metric ton in equipment. The laser was first operated in July 2012 at which time a new world record was set: > 1 PW peak power at a repetition rate of 1 Hz [11].

Final acceptance testing took place in September 2012.

BELLA LASER PERFORMANCE

The overall layout of the BELLA facility is shown in Fig. 1. The laser system occupies a large optical table located in the BELLA laser bay. The power supplies for the laser are located in a separate utility room, which is located right above the laser bay. Following a sequence of amplifiers that increases the energy of initially stretched pulses from nanoJoules to tens of Joule, a grating based optical compressor generates sub-40 fs pulses with peak power up to 1.3 PW at 1 Hz. The beam transport system delivers and focuses (with an off-axis parabola) the high power laser pulses to a target region where the plasma source is located. An achromatic high power laser diagnostic telescope images the target region onto a dedicated suite of diagnostics system to analyze the laser beam properties at all power levels. The first optic in the telescope has a hole in the middle to allow the electron beam to pass through towards a monitoring phosphor screen, an integrating current transformer, the magnetic spectrometer system and the electron beam dump. The entire system is controlled remotely via a LabVIEW based control system. Details on the laser system, laser beam transport, laser diagnostics and control system are discussed next. Details on the magnetic spectrometer design and operation will be published elsewhere.

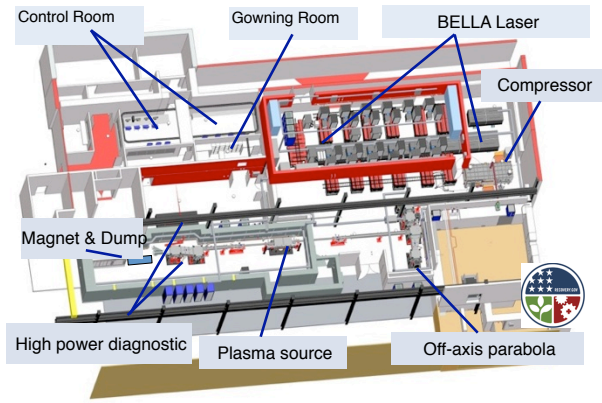


Figure 1: Layout of the BELLA facility. The laser beam is generated in the BELLA laser room. The Compressor is a grating based system for laser pulse compression. An off-axis parabola focuses the beam on the plasma source, which is located in a radiation shielded experimental area. The high power diagnostic is used to image the focused laser beam onto a broad suite of diagnostics. The magnet and beam dump are used to characterize the electron beams and safely stop them. The experiments are run remotely from a control room.

BELLA Laser System

The BELLA laser system is based on Ti:sapphire as gain medium. Pulses from a 75 MHz oscillator are first stretched, amplified in a regenerative amplifier, compressed and contrast improved in a cross-polarized wave (XPW) system. A booster amplifier and pre-amplifier followed by a first high-energy amplifier (AMP1) increase the energy to the 1.2-1.5 J level. A second high-energy amplifier (AMP2) brings the energy to about 20 J and a final amplifier (AMP3) increases this energy to as much as 65 J. The regenerative and booster amplifiers operate at 1 kHz, the preamplifier and AMP1 operate at up to 10 Hz, and AMP2 and AMP3 are operating at 1 Hz. The 1 Hz repetition rate is determined by the repetition rate of the twelve large aperture frequency doubled Nd:YAG pump lasers (GAIAs) that provide 15 J pulse energy each: four of them pump AMP2 and eight pump AMP3. The ultimate laser pulse energy in the main Ti:sapphire laser line can be adjusted with fine control from about 25 mJ to more than 40 J on target. The commissioned laser system is shown in Fig. 2.

Copyright © 2013 CC-BY-3.0 and by the respective authors

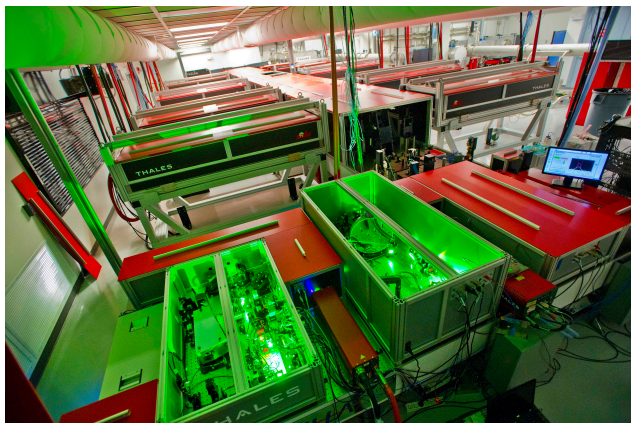


Figure 2: Picture of the BELLA laser system installed at LBNL. The green glow is from scattered light at 532 nm produced by the pump lasers in the front end of the laser. The high energy pump lasers (GAIA) are seen in the center part of the picture.

A plot of energy output vs. time is shown in Fig. 3. The best r.m.s. stability that has been obtained so far is of the order of 0.3%. The stability is affected by both vibrations causing beam motion and the stability of the pump laser systems.

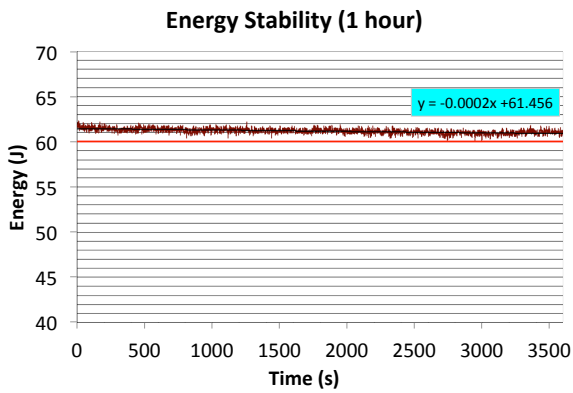


Figure 3: Example of BELLA laser energy stability vs. time.

Following amplification the wavefront of the beam can be adjusted and optimized using a commercial deformable mirror with 52 pistons. The deformable mirror (DM) has allowed focusing of the laser beam at full power onto the targets with a Strehl ratio in excess of 0.9. An example of the achieved mode profile at 32 J is shown in Fig. 5. Note that the mode was measured using an optic with hole in the middle (see below).

Following the DM, an all-reflective telescope magnifies the laser beam to ensure that the fluence is low enough to avoid damage on gratings of a four grating vacuum compressor. Pulse duration can be tuned by control of the separation of the gratings and pulse shape can be tuned using grating angles. To date, pulses as short as 35 fs have been produced at energies in excess of 42 J, i.e., providing >1 PW peak optical power in each pulse at a repetition rate of 1 Hz. The flexibility in pulse duration and energy tuning enable access to a broad range of pulse duration and peak power levels to carry out a large variety of studies of LPAs.

Laser Beam Transport System and Diagnostics

Following compression, the beam is sent to the target area using four routing mirrors, one of which is the final focusing off-axis paraboloid with a focal length of nominally 13.5 m. Each one of the routing mirrors is equipped with a beam pointing monitoring system and motorized controls to ensure correct pointing of the beam throughout the entire laser transport system. Leakage through one of the mirrors in the compressor is sent to a dedicated diagnostic bench where experiment relevant laser performance parameters are monitored. These include laser near- and far-field profiles, laser pulse shapes using a Frequency Resolved Optical Gating system (FROG/GRENOUILLE), laser pulse energy, laser pulse duration and beam wavefront using a Shack-Hartmann sensor. The wavefront sensor enables control of the DM to ensure high Strehl ratio beams at focus in the target chamber. An example of a GRENOUILLE trace and retrieved laser pulse shape are shown in Fig. 4. The shortest pulse duration obtained at the target location to date is about 35 fs (FWHM).

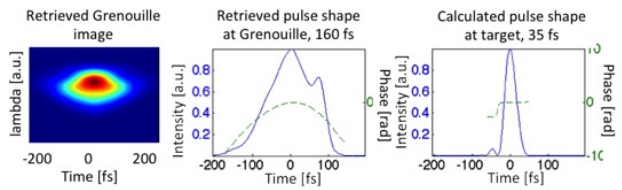


Figure 4: Example of a GRENOUILLE trace and a retrieved laser pulse shape obtained at ~ 40 J on target.

An example of the typical laser mode at medium energy is shown in Fig. 5. Similar or better quality modal shapes have been obtained at all energy levels. The Strehl ratio is typically in the range of 0.85-0.95.

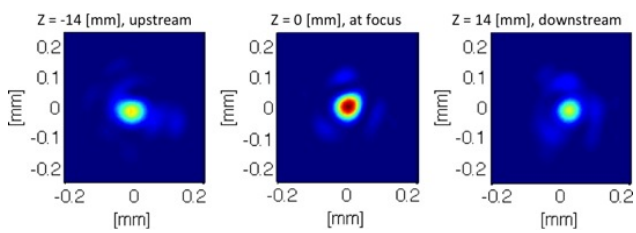


Figure 5: Example of the laser mode at ~32 J on target. The laser beam was imaged onto a 12 bit CCD camera using the high power diagnostic, including a wedge with hole. The hole contributes to the Airy pattern like fringes of the image and the actual focal quality of the beam is better as verified in separate measurements using a wedge without hole. The typical Strehl ratio of the beam at focus is higher than 0.85 and beams with 0.95 Strehl ratio have been obtained following extensive optimization with the deformable mirror.

Copyright © 2013 CC-BY-3.0 and by the respective authors

Significant attention has also been paid in the design and implementation of both the laser system and the beam line components. Due to the long focal length of the focusing system, tight tolerances on pointing stability are essential for experiments involving special capillary discharges. The floor of the BELLA facility was vibration tested and met tight specifications. Mirror mounts and supports were designed, constructed and tested/optimized to minimize vibrations. As a result, beam pointing stability at the focus (i.e., target chamber location) is measured to be better than 1.2 micro-rad. A beam monitoring system has been implemented to ensure also that on a day-to-day basis, the laser beam path is properly aligned.

CONTROL SYSTEM

The BELLA control system was developed in-house and incorporates requirements that had been developed during the BELLA project phase and are based on past and present experience with the development of laser plasma accelerators. The GEECS platform (Generalized Equipment and Experiment Control System) monitors and controls equipment distributed across a network, performs experiments by scanning input variables, and collects and stores various types of data synchronously from devices. Examples of devices include cameras, motors, and pressure gauges. GEECS is based upon LabView graphical object oriented programming (GOOP), allowing for a modular and scalable framework. Data is published for subscription of an arbitrary number of variables over TCP. A secondary framework allows easy development of graphical user interfaces for a combined control of any available devices on the control system without the need of programming knowledge. This allows for rapid integration of GEECS into a wide variety of systems. A database interface provides for device and process configuration while allowing the user to save large quantities of data to local or network drives.

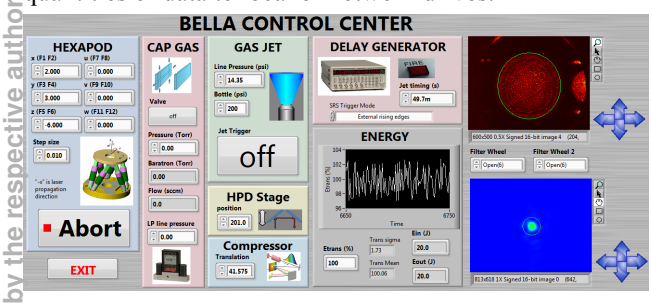


Figure 6: Graphical User Interfaces (GUI) such as this, containing data of different types, can be built in minutes with minimal programming knowledge using the GEECS framework.

ACKNOWLEDGMENT

This work was supported by the DOE, Office of High Energy Physics under contract DE-AC02-05CH11231. The BELLA Project was funded from the American Reinvestment and Recovery Act (ARRA). We would like to thank all present and past LOASIS members and collaborators for their contributions as well as DOE staff from the HEP office and the BSO office. Special thanks go to Ken Barat, Carlo Benedetti, Jeremy Coyne, Rob Duarte, Zak Eisentraut, Eric Esarey, Steve Fournier, Cameron Geddes, Steve Gourlay, Bob Gunnion, Mark Kirkpatrick, Doug Lockhart, Greg Mannino, Nicholas Matlis, George Sanen, Koen Schakenraad, Carl Schroeder, Ohmar Sowle, Suzanne Suskind, Jeroen van Tilborg, Jean-Luc Vay, Sue Walker-Lam, and Sergio Zimmermann for their contributions during the pre-planning and project phase of BELLA. We also want to acknowledge the THALES staff for their contributions.

REFERENCES

[1] E. Esarey, C. B. Schroeder, and W. P. Leemans, Rev. Mod. Phys. **81**, 1229-1285 (2009).
[2] W. P. Leemans and E. Esarey, Physics Today **62**, 44-49 (2009).
[3] C. B. Schroeder, E. Esarey, C. Geddes, C. Benedetti, and W. P. Leemans, Phys. Rev. ST-Accel. and Beams, **13**, 101301 (2010).
[4] C. B. Schroeder, E. Esarey, and W. P. Leemans, Phys. Rev. ST Accel. *Beams* **15** (2012).
[5] C. G. R. Geddes et al., Nature **431**, 538 (2004).
[6] S. P. D. Mangles et al., Nature **431**, 535 (2004).
[7] J. Faure et al., Nature **431**, 541 (2004).
[8] W. P. Leemans et al., Nature Physics **2**, 696 (2006).
[9] A. J. Gonsalves et al., Nature Physics **7**, 862-866 (2011).
[10] http://thales.nuxit.net/
[11]http://newscenter.lbl.gov/news-releases/2012/07/27/bella-laser-record-power/

Copyright © 2013 CC-BY-3.0 and by the respective authors

LATEST PLASMA WAKEFIELD ACCELERATION RESULTS FROM THE FACET PROJECT *

M. D. Litos†, E. Adli‡, C. I. Clarke, S. Corde, J. P. Delahaye, R. J. England, A. S. Fisher, J. Frederico, S. Gessner, M. J. Hogan, S. Li, D. Walz, G. White, Z. Wu, V. Yakimenko
SLAC National Accelerator Laboratory, Menlo Park, California 94025, USA
‡ Department of Physics, University of Oslo, 0316 Oslo, Norway

W. An, C. E. Clayton, C. Joshi, W. Lu, K. A. Marsh, W. B. Mori, N. Vafaei-Najafabadi
University of California Los Angeles, Los Angeles, CA 90095, USA

P. Muggli
Max Planck Institute for Physics, Munich, Germany

Abstract

SLAC's new Facility for Advanced Accelerator Experimental Tests (FACET) had its second user run in April–June, 2013. Several new milestones were reached during this run, including the achievement of beam driven plasma wakefield acceleration of a discrete witness bunch for the first time, and energy doubling in a noble gas plasma source. The FACET beam is a 20 GeV electron bunch with a charge of 3.2 nC that can be compressed and focused to a size of $20\,\mu\mathrm{m} \times 20\,\mu\mathrm{m} \times 20\,\mu\mathrm{m}$ rms. To create the two-bunch, drive/witness beam structure, a chirped and over-compressed beam was dispersed horizontally in a chicane and a bite was taken from its middle with a tantalum finger collimator, corresponding to a longitudinal notching of the beam due to the head-tail energy correlation. A new 10 terawatt Ti:Sapphire laser was commissioned and used during this run to pre-ionize the plasma source in order to increase the efficiency of energy transfer from the beam to the wake. Ultimately, a witness beam of hundreds of pC in charge was accelerated by a drive beam of similar charge in a preformed lithium plasma with a density of $5 \times 10^{16}\,\mathrm{cm}^{-3}$, experiencing gradients reaching several GV/m in magnitude.

INTRODUCTION

The field of plasma wakefield acceleration (PWFA) has long been motivated by a need for new technologies that can provide higher accelerating gradients than conventional microwave powered metallic structures in order to make multi-TeV energies and beyond accessible to future generations of linear colliders. A conceptual design was recently developed for a plasma wakefield powered linear collider with a center of mass energy of 1 TeV that is extendible to the multi-TeV regime [1]. The main linac consists of modular plasma accelerator stages into each of which a fresh electron beam is injected to drive a wake over a meter-scale plasma source to provide an energy gain of 25 GeV per stage to the primary collider beam. Besides the high average gradient of such a collider design, the wall-plug efficiency is another very attractive feature, estimated to be well over ten percent. Current research efforts in beam driven plasma wakefield acceleration are largely devoted to creating a single plasma accelerator stage akin to what would be used in a collider, first as a proof-of-concept, and then as a test bed for studying the complex dynamics involved in the beam-plasma interaction.

In order to achieve accelerating gradients on the order of 10 GV/m with a GeV-scale drive beam, plasma densities on the order of $10^{17}\,\mathrm{cm}^{-3}$ are required. This sets the plasma wavelength, and thus the scale of the longitudinal spacing between the drive and witness bunch, to distances on the order of 150 μm (=500 fs temporal spacing). The drive beam must have a density that is > 1.8 times the background plasma density in order to produce a nonlinear blowout [2], which sets the scale for the peak current to the kA scale with a transverse size on the order of a few tens of microns, which is ultimately focused down to several microns by the strong fields generated in the plasma. FACET is the only facility in the world that can meet these demanding beam requirements, as well as produce a witness beam of several hundred pC or more to sample the large magnitude fields.

Previous electron-beam-driven plasma wakefield acceleration experiments that were performed at SLAC's Final Focus Test Beam (FFTB) facility have shown that the PWFA mechanism can produce accelerating gradients in excess of 50 GV/m by observing the energy gain in the low charge tail of the wake-driving electron beam. The tail trailing behind the head of the beam sampled the accelerating phase of the plasma wake, finally doubling the energy of the 42 GeV electrons [3]. What remained to be demonstrated, however, was the acceleration of a coherent beam of electrons, rather than individual particles. FFTB lacked the capability to produce a distinct drive and witness electron beam with the required temporal spacing, on the order of 500 fs from center to center. Several years after the FFTB was decommissioned, FACET was designed and constructed with this goal in mind, leveraging the knowledge gained from the FFTB experiments and the linac infrastructure available at SLAC [4]. Now, FACET has finally been able to fulfill the experimental requirements needed to study the acceleration of actual beams via

* Work supported by DOE contracts DE-AC02-76SF00515, DE-AC02-7600515, DE-FG02-92-ER40727, and NSF contract PHY-0936266.
† litos@slac.stanford.edu

Copyright © 2013 CC-BY-3.0 and by the respective authors

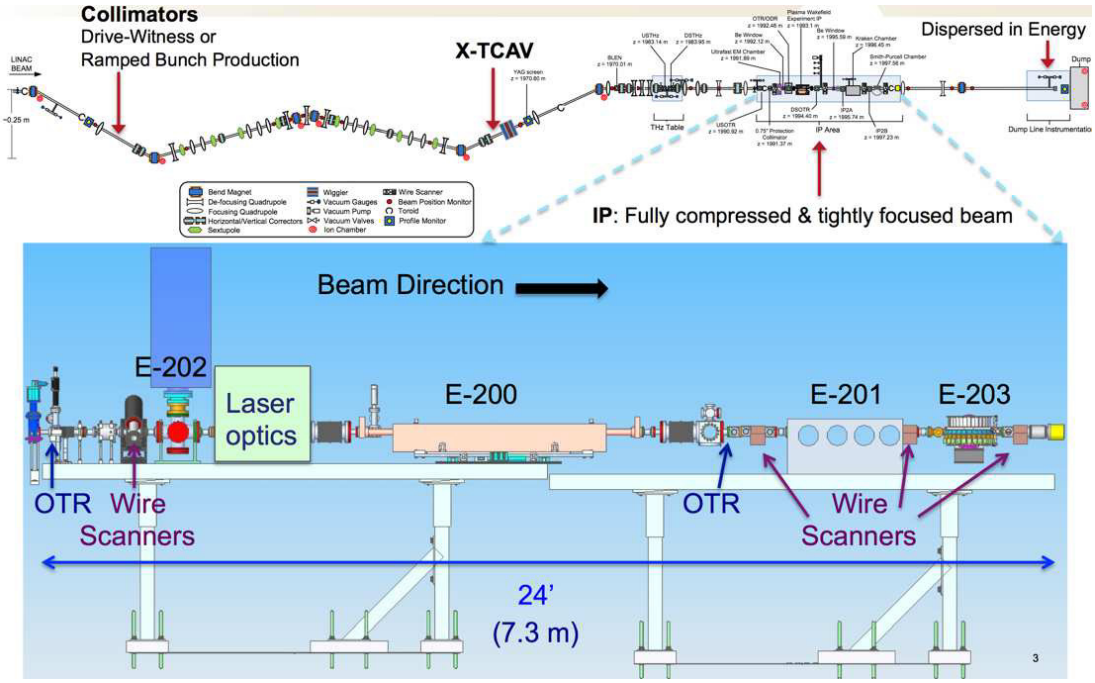


Figure 1: Top: The FACET beamline. Bottom: Detail of experimental area. The text "E200" marks the location of the plasma source.

beam-driven plasma wakefields, and has also continued to explore new dynamical regimes of plasma wakefield acceleration.

ELECTRON BEAM

The data presented here were taken by the E200 experiment from June 2013 during the second User Run of FACET. The first two kilometers of the main SLAC linac were used to provide a 20.35 GeV electron beam with a charge of up to 3.2 nC. In the final 100 m of the beamline a chicane provided the final compression of the beam, with a minimal bunch length of 20 μm rms, corresponding to a peak current of 20 kA. A final focusing section focused the beam down to the desired transverse dimensions at the entrance to the plasma source, approximately 20 μm $\times$ 20 μm Gaussian rms in x and y. An imaging spectrometer transported the beam from the exit of the plasma source to the final diagnostic area and ultimately to the beam dump. Figure 1 shows a schematic view of the final 100 m of the FACET beamline with a detail of the experimental area where the plasma source is located.

The two-bunch beam structure was generated by bisecting a linearly chirped, horizontally dispersed beam using a tantalum finger collimator. Jaw collimators were also employed to remove the spectral tails at the horizontal extrema, where the energy spread was uncorrelated with longitudinal position. The beam was then over-compressed in the chicane, placing one portion of the remaining beam in front of the other with the desired spacing optimized for PWFA experiments.

Two diagnostics were used to measure the longitudinal

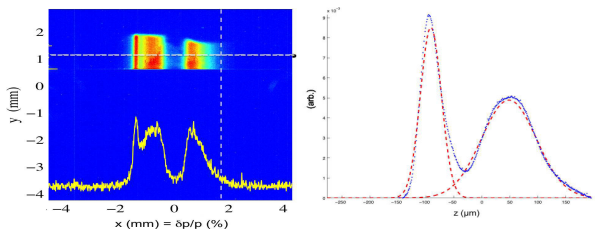


Figure 2: Specral profile of the elecron beam (left) and longidutinal profile of the electron beam (right) after notch collimation and before entering the plasma source.

phase space of the beam after collimation. The first was a wiggler spectrometer that measured the X-ray intensity profile generated by the beam in a low field triplet of wiggler magnets. The wiggler spectrometer is located at a point in the chicane with the same large magnitude of dispersion as the point where the beam is notched by the tantalum collimator further upstream, thus it provided direct feedback on how the beam is being notched in space and in energy on a shot-by-shot basis.

The second diagnostic used to measure the longitudinal phase space of the beam was an X-band transverse deflecting structure. This device streaked the beam itself onto an optical transition radiation screen located near the plasma source, roughly 25 m downstream. The streaking process precludes the beam from having an optimal profile for PWFA, however, so this method of measuring the longitudinal profile is limited to statistical studies of the beam profile used in the experiment. Figure 2 shows a typ-

Copyright © 2013 CC-BY-3.0 and by the respective authors

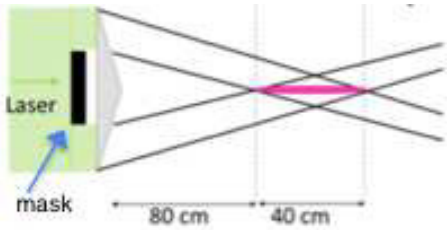


Figure 3: Schematic depiction of the axicon lens focusing the laser.

ical spectral and longitudinal measurement for a two-bunch beam prior to entering the plasma source for PWFA experiments.

PLASMA SOURCE

The plasma was generated by ionizing a lithium vapor, which was generated inside a heat pipe oven roughly 40 cm in length. A room temperature buffer gas of argon was used to contain the lithium vapor and also completely filled a parallel bypass line, which was able to be inserted into the beamline in lieu of the lithium oven for control measurements. The density and length of the lithium vapor can be controlled by adjusting the heat applied to the oven and the pressure of the buffer gas. The choice of a noble gas for the buffer is motivated by its high ionization threshold, which drastically reduces the likelihood of generating plasma outside of the lithium region.

A new 10 TW, 800 nm Ti:Sapphire laser system was installed and commissioned for the 2013 FACET User Run. The primary purpose of the laser system was to ionize the lithium vapor in the heat pipe oven, generating a wide column of plasma before the arrival of the electron beam. Though it has been shown that if the electron beam is dense enough, it can itself tunnel-ionize the outer shell electrons of a metal vapor and still subsequently drive a non-linear wake [5], using the laser to generate the plasma reduces the demand on the electron beam delivery somewhat. Preforming the plasma also leaves more energy available in the drive beam to be transferred to the plasma wake, which ultimately means a higher efficiency of energy transfer from the drive to the witness beam. Finally, a preformed plasma will also mitigate the head-erosion of the drive beam, allowing for much longer plasma interaction lengths [3, 6].

The laser was focused into the plasma using an axicon lens [7], which focuses the laser toward the central axis at the same convergent angle over all radii. Figure 3 shows a schematic demonstrating the axicon focusing method. This produces a radial intensity distribution that follows a Bessel function of the zeroth order and persists for over a meter of length before the laser diverges away from the axis in a ring shape and is dumped into an annular neutral density filter. A circular mask just before the axicon lens is used to control the start of the line focus, and the diameter of the laser beam determines the end of the line focus.

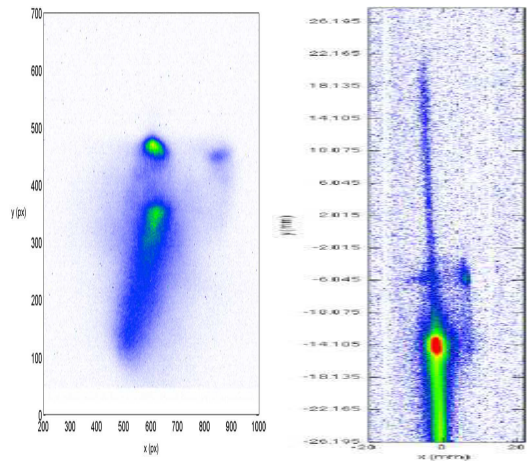


Figure 4: Left: Accelerated witness beam (top feature) with decelerated drive beam (bottom feature) produced in a preformed lithium plasma. Right: Energy doubled tail with decelerated beam core produced in self-ionized plasma generated in argon gas. In both plots energy increases with height.

ACCELERATION OF A WITNESS BEAM

An imaging spectrometer comprising a quadrupole doublet and a 1 m dipole was used to disperse the beam at the experimental dump table while imaging a plane at the exit of the plasma source. The imaging condition only holds for a given (adjustable) energy, however, so portions of the beam above and below the set energy are defocused. CCD cameras were used to image the Cherenkov light produced by the dispersed beam as it traveled through the air from the beam pipe exit window to the dump.

A drive beam with a peak current of 1.2 kA and a witness beam of several hundred pC trailing 126 μm (420 fs) behind it were sent into a pre-formed lithium plasma on the order of $\sim$40 cm in length with a density of 5.0×10^{16} cm^{-3}. The witness beam was accelerated by a few GeV over this distance, corresponding to average accelerating fields on the order of $\sim$5 GV/m. Portions of the drive beam were decelerated by as much as several GeV, and nearly all of the electrons in the drive beam lost at least some energy, an indication of efficient energy transfer to the wake. Figure 4 shows a typical shot of two-bunch PWFA, where the vertical axis corresponds to energy with higher energy toward the top.

ENERGY DOUBLING IN A NOBLE GAS

The FACET beamline can accommodate many different beam optics profiles, one of which is tailored to provide the highest possible compression of a single bunch. With this configuration in place, it was found that the density of the electron beam could reach values that were high enough to ionize the noble gas buffer medium in the oven bypass line. Further, the beam produced a strong wakefield in the plasma it generated, drastically decelerating the bulk of the

Copyright © 2013 CC-BY-3.0 and by the respective authors

beam and accelerating the rear tail of the beam to more than double its initial energy. Figure 4 shows the dispersed beam after driving a wake in argon gas over about 20 cm. The estimated longitudinal field strength inside the wake was on the order of $\sim 150\,\mathrm{GV/m}$.

The ability to drive a wake in a noble gas was due to a self-focusing process that the beam underwent as soon as it began to ionize even a small fraction of the argon gas. The wake produced in the low density plasma focused the beam transversely, and as the beam density increased, it ionized a larger fraction of the gas, which in turn led to a higher plasma density and larger focusing forces in the plasma wake. The process continued on in a positive feedback loop like this until eventually reaching a point where the beam could drive a non-linear wake in the blowout regime, after having nearly reached the matching condition for the plasma [8]. This description of the evolution of the beam was supported by simulations in the quasi-static 3D particle-in-cell code QuickPIC [9].

After focusing to its minimum size, on the order of a few microns, the beam could drive a fully non-linear wake, and experienced virtually no head erosion. Thus, it was able to continue to drive the wake over a very long distance, limited by the betatron function of the unfocused head of the beam that provided the ionized plasma medium. The avoidance of the head erosion limitation that is predicted in the literature [10] is particularly interesting because it may loosen the previously presumed high density requirement for an electron beam to drive a self-ionized plasma wake. In addition, a plasma stage made from a room temperature gas is far simpler and cheaper than an alkali metal vapor which must be maintained at hundereds of degrees Celcius. Further, a room temperature gas can have a perfectly flat longitudinal density profile throughout the stage, which is impossible with an alkali metal vapor inside a heat-pipe oven due to the density ramps near the oven boundaries.

SUMMARY AND OUTLOOK

FACET has succeeded in accelerating a distinct witness beam of electrons with multi-$\mathrm{GV/m}$ fields produced in a non-linear plasma wake produced by a high current drive beam in a pre-formed lithium plasma. This is the first experimental demonstration of acceleration of a high energy, high charge beam via beam-driven PWFA. FACET has also demonstrated that through the self-focusing mechanism, an under-dense beam can evolve through interaction with the plasma to achieve densities sufficient to drive a non-linear wake over long distances, even in media with high ionization potentials, such as noble gases. This result shows that head erosion is able to be suppressed without having to generate an over-dense, pre-matched drive beam before sending it into the plasma stage, which could open new possibilities for the design of a more optimal particle beam driver. It could also lead to the design of simpler, cheaper plasma stages, eschewing the heat pipe oven for a plain tube of gas.

The next FACET run will begin in late 2013 and will continue where the previous run left off by studying the effects of beam loading on the acceleration of the witness beam, as well as the ability to preserve the beam's emittance and minimize the final energy spread. Further, an upgrade in the ionization laser and a longer heat pipe oven will allow the plasma wake to be driven over much longer distance than in previous runs, which should lead to significantly higher net energy gain in the witness bunch. Improved diagnostics will also allow for better measurements of the beam before and after entering the plasma source, allowing for a deeper insight into the beam-plasma interaction in all of the PWFA experiments.

REFERENCES

[1] E. Adli, *et al.* arXiv (2013). 1308.1145v1.

[2] W. Lu, *et al.* Physics of Plasmas **13**, 5 056709 (2006).

[3] I. Blumenfeld, *et al.* Nature **445**, 7129 741 (2007).

[4] M. J. Hogan, *et al.* New Journal of Physics **12**, 5 055030 (2010).

[5] C. O'Connell, *et al.* Physical Review Special Topics - Accelerators and Beams **9**, 10 101301 (2006).

[6] N. Vafaei-Najafabadi. (submitted) (2013).

[7] J. H. MCLEOD. Journal of the Optical Society of America **44**, 8 592 (1954).

[8] K. A. Marsh, *et al.* PAC 2005 Proceedings pages 2702–2704 (2005).

[9] C. Huang, *et al.* Journal of Physics: Conference Series **46** 190 (2006).

[10] I. Blumenfeld. PhD Thesis, Stanford University pages 1–163 (2009).

Copyright © 2013 CC-BY-3.0 and by the respective authors

X-RAY RADIATION AND ELECTRON INJECTION FROM BEAM ENVELOPE OSCILLATIONS IN PLASMA WAKEFIELD ACCELERATOR EXPERIMENTS AT FACET

K. A. Marsh, W. An, C. E. Clayton, C. Joshi, W. B. Mori, N. Vafaei-Najafabadi (UCLA, Los Angeles, California, USA), P. Muggli (MPI, Munich, Germany), C. I. Clarke, S. Corde, J-P. Delahaye, R. J. England, A. S. Fisher, J. Frederico, S. J. Gessner, M. J. Hogan, S. Z. Li, M. D. Litos, D. Walz, Z. Wu (SLAC National Accelerator Laboratory, Menlo Park, California, USA), E. Adli (SLAC National Accelerator Laboratory, Menlo Park, California USA; University of Oslo, Oslo, Norway), Wei Lu (UCLA, Los Angeles, California, USA; Tsinghua University, Beijing, China)

Abstract

Plasma wakefield accelerator experiments at FACET at the SLAC National Accelerator Laboratory have shown a correlation between ionization-injected electrons and the betatron x-ray yield. Emittance spoiling foils were inserted into the beam and the x-ray yield, excess charge, and beam energy loss was measured. The excess charge and x-ray yield are attributed to the beam envelope oscillations where at the minima, the field of the beam is strong enough to create secondary ionization, and at the electron oscillation maxima, the beam electrons spontaneously radiate x-rays. Large amplitude beam oscillations are expected to yield more x-rays and create more excess charge, but the results show beam head erosion strongly limits the wakefield excitation.

INTRODUCTION

An important feature of any "blow out regime" plasma-based accelerator is the strong radial fields of the ion column, which creates electron betatron motion and x-ray radiation. This effect can be used to create MeV photons [1] and the x-ray characteristics can be used as a diagnostic of the electrons transverse motion. For example, matched beam propagation would be characterized by minimizing the x-ray radiation signal. Also, mismatched beams will collapse in size to where secondary ionization produces excess charge (i.e. dark current) [2]. Larger emittance beams have larger oscillation amplitudes and therefore they are expected to produce more x-rays and more excess charge. However, large emittance beams also have shorter head erosion lengths [3], which limits the distance over which x-rays and excess charge can be generated. In this paper we study experimentally which of these factors prevail.

SETUP

The experiments were performed at FACET at the SLAC National Accelerator Laboratory during the 2013 E200 PWFA experimental run. The 20.3 GeV electron bunch contained 2.0×10^{10} electrons with an rms bunch length of ~40 um. The x and y normalized emittances, ε_N, were designed to be 50 and 5 mm-mrad, respectively. Typically, the beam betas where 0.10 meter in x and 1.0 meter in y, giving a spot size at the plasma entrance of 11 μm in x and y. The beam was sent through a ~30 cm long rubidium heat pipe oven where the plasma was formed by the field of the beam via tunneling ionization. The Rb vapor was contained using argon as a buffer. The primary diagnostic measurements discussed here are: the x-ray radiation, beam charge, and beam energy. The x-ray yield was measured with a Lanex screen and CCD camera. A 1 mm thick Tungsten foil was placed in front of the screen, which gives a photon detection threshold of 200- 300 keV. SLAC toriods were used to measure the beam charge upstream and downstream of the plasma. The excess charge was measured using the difference between the toriod signals. The change in beam energy was measured with an imaging dipole spectrometer. To study emittance effects, emitttance spoiler foils were inserted into the beam 1 meter upstream of the plasma entrance. The foils and thickness used in the experiment were: Foil 1 Nicusil 3, 25.4 μm; Foil 2 25/75Au/Cu, 50.8 μm; and Foil 3 Nocoro, 80, 38 μm. The calculated rms scattering angles are 35, 58, and 64 μrad respectively. A figure showing the set up and the data analysis and methods can be can be found in [4, 5].

DENSITY RAMPS AND BEAM MATCHING

For a plasma with a sharp boundary, the beam matching condition is $\beta_{match} = 1/k_b$, where k_b is the plasma betatron wavenumber (Eqn. 2). For our experimental parameters, $\beta_{match} = 0.3$ cm. Beam matching on this scale is difficult to produce, but as shown in [1, 6] a density ramp can significantly reduce the oscillation amplitude of an unmatched beam, thereby reducing the expected x-ray yield. For the right beam parameters, the ramp can be used to produce matched beam propagation. A larger β can be used in proportion to the scale length of the ramp. For the plasma ramp at FACET, the matched β is 3.38 cm.

*The work at UCLA was supported by DOE grant DE-FG02-92-ER40727 and NSF grant PHY-0936266. Work at SLAC was supported in part by Department of Energy contract DE-AC02-7600515

Copyright © 2013 CC-BY-3.0 and by the respective authors

CALCULATION OF THE BEAM SIZE AND EMITTANCE WITH SPOILER FOIL INSERTED

When a foil is inserted, the new beam parameters at the plasma entrance can be calculated by propagating the no foil parameters from the beam waist back to the foil and then calculate the new beam parameter due to foil scattering θ. The new beam parameters at the foil are calculated using [7]

$$\varepsilon^2 = \varepsilon_0(\varepsilon_0 + \beta_0\theta^2)$$
$$\beta^2 = \beta_0^2\varepsilon_0 / (\varepsilon_0 + \beta_0\theta^2)$$
$$\alpha^2 = \alpha_0^2\varepsilon_0 / (\varepsilon_0 + \beta_0\theta^2) \quad (1)$$

After scattering, the new beam parameters can be propagated back to the oven entrance. The foils increase the beam emittance and the beam size at the plasma entrance, creating a greater mismatch. The beam envelope oscillation for a mono-energetic electron beam can be calculated using Eqn. 2 and is plotted in figures 1 and 2.

$$\frac{d^2\sigma}{dz^2} + k_b^2\sigma = \frac{\varepsilon_N^2}{\gamma^2\sigma^3} \qquad k_b = \frac{\omega_p}{c}\frac{1}{\sqrt{2\gamma}} \quad (2)$$

The figures illustrate how the beam envelope changes after inserting a foil. Figure 1 is plotted, using the experimental parameters in x, without the spoiler foil. Figure 2 shows the beam envelope with foil 1 inserted. With the foil inserted, the oscillation amplitude inside the plasma increases in proportion to the emittance ratio, $\varepsilon_{vacuum}/\varepsilon_{foil}$. Also, when the foil is inserted, the envelope minimum inside the plasma does not change. This is because, although β at the oscillation minimum is smaller, the emittance is proportionally larger and so σ_{min} is unchanged ($\sigma^2 = \beta\varepsilon$). Excess charge can be created when the drive beam pinches and the field exceeds the ionization threshold for secondary electrons from RbII and ArII. Injection of plasma electrons into the wake can limit the wake amplitude and reduce the accelerating gradient [4].

PARTICIPATING CHARGE AND, HEAD EROSION

If the head of the beam is not dense enough to ionize the Rb vapor, the beam electrons contained in that region will not participate in the wake formation. This causes a reduction in the bunch length, σ_z (but not necessarily the peak beam current).

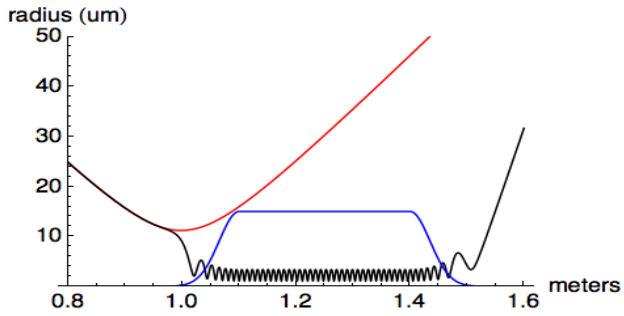


Figure 1: Plot of beam size envelope for 20.3 GeV and $2.7\text{x}10^{17}$ cm^{-3} plasma without spoiler foil (black). The beam envelope in vacuum (red). The plasma profile (blue).

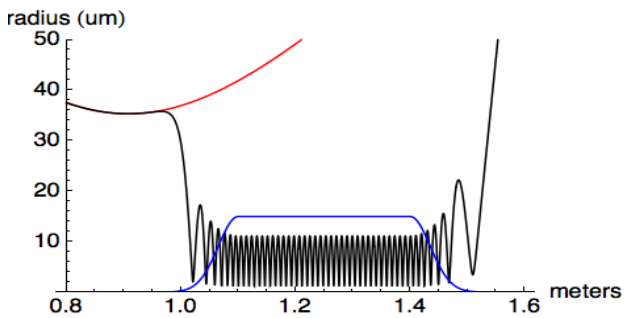


Figure 2: Same as figure 1 with spoiler foil inserted.

Head erosion is a physical effect that limits the length of the wake excitation [3]. It is due to the fact that the ionizing front of the beam is not in the blow out region and is not focused or guided by the ion channel. The unguided front of the beam expands, as it would do in vacuum, and the ionizing front moves back in the beam frame at a rate v_{etch} [3]. The head erosion length is given by $L_{he} \sim \sigma_z / v_{etch}$, where σ_z contains only the participating charge.

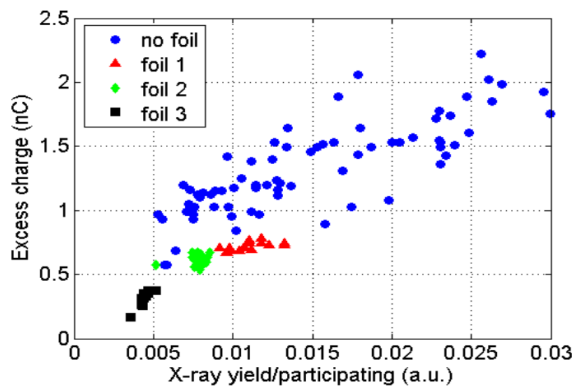


Figure 3: Experimental plot showing measured correlation of the excess charge verses x-ray yield.

Copyright © 2013 CC-BY-3.0 and by the respective authors

EXPERIMENTAL RESULTS

Figure 3, shows the correlation between the measured x-ray yield and the excess charge which takes into account the reduced participating charge. The measured participating charge is 90% for no foil, 70% with foil 1, 65% with foil 2, and 50%, with foil 3. The inferred σ_z is reduced 30 to 50% when the foils are inserted.

Both x-rays and excess charge are reduced as foils are added. Even accounting for the lower participating charge, the x-ray yield should increase with larger emittance since the oscillation amplitude increases with larger emittance. Figure 3 shows this expectation is not the case. This is because increasing emittance reduces L_{he} in three ways. First, the large beam size will reduce the participating charge causing a reduction in σ_z, second the etch rate is higher (v_{etch}~ε_N) and third, large beam mismatch causes emittance growth as the beam propagates. Head erosion theory [3] assumes matched beam propagation. However, for these experiments the beam was not matched. Simulations show mismatched beams have emittance growth and will erode faster than matched beams. Applying Eqn. 1, to foil 1, the emittance grows from 5 to 22.5 mm-mrad in y and from 50 to 165 mm-mrad in x, thus shortening the head erosion length by 3.3 to 4.5 times. As for the x-ray production, the effective length over which x-rays are produce is ~½ L_{he}. Emittance spoiling also showed a reduction in beam energy loss. Typical energy loss without foils was >12 GeV. This indicates the beam propagated approximately the entire length of the Rb vapor. The energy loss for with foil 1, 2 and 3 was approximately 7, 5, and 3 GeV, respectively. Although some of this reduction could be due to a smaller wake amplitude (resulting from reduced participating charge) simulations show, the main effect is the reduction in the length of wake excitation as emittance is increased. This implies the length of the wake formation was reduced as foils were inserted, further emphasizing the effect of head erosion on the experiments.

SUMMARY

While emittance spoiling would seem to increase the x-ray yield, the experiment shows a significant reduction in x-ray signal. Emittance spoiling also reduces the excess charge. The reduced energy loss indicates reduced wakefield excitation length. The entirety of the results, x-rays, excess charge and energy loss, imply severe beam head erosion when spoiler foils are used. With a preionized plasma head erosion is strongly mitigated. Recent results [8] with preionization show the participating charge is nearly 100%.

REFERENCES

[1] D. K. Johnson et al., Phys. Rev. Lett. 97 (2006) 175003.
[2] E. Oz et al., Phys. Rev. Lett. 98 (2007) 084801.
[3] I. Blumenfeld, Ph.D. thesis, Stanford University (2009).
[4] N. Vafaei-Najafabadi et. al. submitted.
[5] N. Vafaei-Najafabadi et. al. NA-PAC'13 Proceedings, MOPAC46.
[6] K.A. Marsh et al., Proceedings of the 2005 Particle Accelerator Conference (IEEE, Knoxville, Tennessee, 2005, p. 2702).
[7] J.R. Rosenzweig and P. Chen, Phys. Rev. D 39 (1989) 2039.
[8] M. Litos et. al. NA-PAC'13 Proceedings, THYAA2.

Copyright © 2013 CC-BY-3.0 and by the respective authors

EXPERIMENTAL PROGRESS ON STAGED LASER-PLASMA ACCELERATION*

S. Shiraishi†, T. Sokollik‡, C. Benedetti, A. J. Gonsalves, N. H. Matlis, K. Nakamura, B. H. Shaw, S. Steinke, J. van Tilborg, C. G. R. Geddes, C. B. Schroeder, Cs. Tóth, E. Esarey, and W. P. Leemans
LOASIS Program, LBNL, Berkeley, CA 94720, USA

Abstract

Recent progress on a staged laser-plasma accelerator (LPA) experiment is reported. The experiment utilizes a 40 TW class laser which is split into two pulses. The first laser drives the first LPA stage to produce an electron beam. The second laser drives the second LPA stage in a dark-current free regime and accelerates the electron beam from the first LPA. Injection from the first stage, triggering of plasma mirror and reflection of the second laser, and laser guiding in the second stage have been demonstrated. Optical spectral redshift of driving laser has been analyzed to estimate the wakefield amplitude and electron energy gain in the second stage.

INTRODUCTION

Laser-plasma accelerators (LPAs) have demonstrated accelerating gradients thousands of times greater than those of conventional accelerators [1]. Employing a capillary discharge waveguide, a high-quality GeV electron beam (e-beam) has been produced within a few centimeters, demonstrating that LPAs have great potential for reducing accelerator size and cost.

For applications such as high energy colliders, LPA designs will rely on sequencing multiple acceleration stages, each driven by its own laser [2, 3]. Limitations to the energy gain in a single stage include diffraction, dephasing, and pump depletion. Using a capillary waveguide to create a preformed plasma channel, laser pulses have been guided over many Rayleigh lengths ($z_{\rm R}$), minimizing diffraction and extending the accelerating length. If the laser is guided, and the e-beam dephasing controlled, energy gain is limited by depletion. To overcome pump depletion, staged acceleration is necessary to supply fresh laser pulses. Experiments performed so far utilize a single laser that drives the wakefield for both injection and acceleration. The on-going staging experiment at the LOASIS Program at Lawrence Berkeley National Laboratory will demonstrate driving of two modules with two independent laser pulses and coupling of the e-beam between them. Staged acceleration not only supplies fresh laser pulses to LPAs but it also allows independent control of electron injection and acceleration.

Experimental demonstration of staged LPAs requires understanding electron injection, performance of a plasma mirror (PM), and acceleration of externally injected e-beams. Controlled electron injection is an active area of research and various techniques such as self-trapping, density gradient, and ionization injections have been demonstrated [4, 5, 6, 7]. The PM is triggered when the leading edge of the pulse generates plasma on a solid target, reflecting the remainder of the pulse at the critical surface. The second laser pulse is coupled in to the acceleration beam line using the PM to keep the LPA compact [8]. Post-acceleration of e-beams requires understanding the amplitudes of wakefileds in the second stage. Laser spectra are analyzed as a diagnostic of plasma waves.

This paper reports the recent progress of the staged acceleration experiment at the LOASIS Program. Basic theory of laser propagation and redsfhit are presented to support the use of redshift as a wakefield diagnostic. Then, the experimental setup at the LOASIS Program is described. Initial results for electron injection, plasma mirror in-coupling and wake excitation performed independently of each other are presented in the results section followed by a concluding summary.

LASER PROPAGATION IN A PLASMA CHANNEL

Laser guiding is used to extend acceleration lengths in LPAs. However, accelerating fields, and hence redshifting of the laser, evolve differently depending on the guiding condition. In a capillary waveguide, the laser pulse transverse size can oscillate if the density profile is not matched to the laser spot size. The channel is characterized by a parabolic plasma density profile, $n(r) = n_0 + \Delta n r^2/r_{\rm m}^2$, where r is the radial position, n_0 is the on-axis density [9], and Δn is the channel depth at a matched spot size, $r_{\rm m}$ [10]. Such channels can provide guiding for a laser pulse with a Gaussian intensity profile, $|a|^2 = (a_0 r_0/r_{\rm s})^2 \exp(-2r^2/r_{\rm s}^2)$, where a_0 is the normalized laser vector potential given by $a_0^2 \simeq 7.3 \times 10^{-19}\ (\lambda[\mu{\rm m}])^2 I_0[{\rm Wcm}^{-2}]$, r_0 is the focal spot size, $r_{\rm s}$ is the spot size, and λ is the laser wavelength. Perfect guiding is achieved when $r_0 = r_{\rm m}$ and the laser is focused at the entrance of the channel ($r_{\rm i} = r_0$, ${\rm d}r_{\rm s}/{\rm d}z = 0$). Considering a low power pulse (without self-focusing), the laser pulse propagates in the channel according to

$$r_{\rm s}^2 = \frac{r_{\rm i}^2}{2}\left[1 + \frac{r_{\rm m}^4}{r_{\rm i}^4} + \left(1 - \frac{r_{\rm m}^4}{r_{\rm i}^4}\right)\cos\left(\frac{2\lambda z}{\pi r_{\rm m}^2}\right)\right], \quad (1)$$

where $r_{\rm i}$ is the spot size at the entrance of channel, and z is the propagation distance [10]. Examples of matched and mismatched guiding are shown in Fig. 1. The entrance of the capillary is set at $z = 0$, and the plasma channel is indicated with a cyan box. For matched guiding,

* Supported by DOE HEP, NSF and used the facilities at NERSC.
† Also at University of Chicago, Chicago, Illinois 60637, USA. Email: sshiraishi@lbl.gov
‡ Currently at Shanghai Jiao Tong University, Shanghai, China

Copyright © 2013 CC-BY-3.0 and by the respective authors

$r_i = r_m = 18\ \mu$m, the laser retains its spot size as it propagates through the channel. For mismatched guiding with r_i = 18 μm and r_m = 41 μm, the transverse spot size oscillates between r_i and r_m^2/r_i. The mismatched guiding leads to excitation of significant plasma waves only at localized regions of high intensity, creating an accelerating gradient that depends on the propagation distance. While

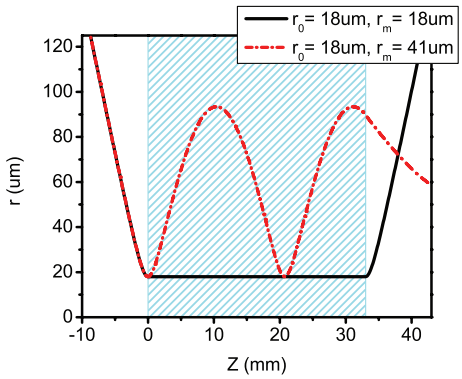


Figure 1: Laser spot size as a function of z.

matched guiding allows the most efficient coupling of laser energy to plasma waves, experimental conditions do not always allow the matched condition.

When the laser excites plasma waves, the laser energy is transferred to the wakefield and spectrally redshifts. In one-dimension, the evolution of the laser energy normalized to initial energy, ϵ, of a short laser pulse propagating in an underdense plasma is related to the amplitude of the wakefield as [11]:

$$\frac{\partial \epsilon}{\partial \omega_p t} = -\frac{k_p^2}{k_0^2}\left(\frac{E_{max}}{E_0}\right)^2, \qquad (2)$$

where k_p is the plasma wavenumber, k_0 is the central wavenumber of the input laser, ω_p is the plasma frequency, and E_{max}/E_0 is the maximum accelerating field normalized by the cold nonrelativistic wave breaking field. In addition, the mean wavenumber $\bar{k} = \varepsilon/A$ where A is the wave action, which is constant provided $\bar{k}/k_p \gg 1$. Therefore, E_{max} can be estimated through the redshift of optical spectra.

In experiments, the estimation of E_{max} is much more complex due to the transverse and longitudinal dynamics of the laser pulse. Particle-in-cell (PIC) simulations using INF&RNO were performed to study wake excitation and its relation to spectral redshifting [12]. INF&RNO is a two-dimensional cylindrical (r-z) code that adopts an envelope model for the laser pulse. Details are found in [12]. The laser pulse was focused 4.8 mm into the capillary with vacuum focus of r_0 = 18 μm and the channel was 33 mm long, r_m = 41 μm and $n_0 \sim 1.5 \times 10^{18}$cm^{-3}. Figure 2 shows simulated peak accelerating field E_{max} (solid black curve), normalized laser energy ε (dashed black curve) and mean wavenumber $\bar{k}$ (red dots) as functions of z. Since the guiding condition is mismatched, the laser intensity oscillates. There are two regions where the laser is strongly focused to excite a large plasma wave. The ε evolution shows that the majority of laser energy is deposited at locations of large wakefield and $\bar{k}$ tracks the ε. Even with mismatched guiding, one can gain insights into E_{max} by comparing simulated and measured spectra [13].

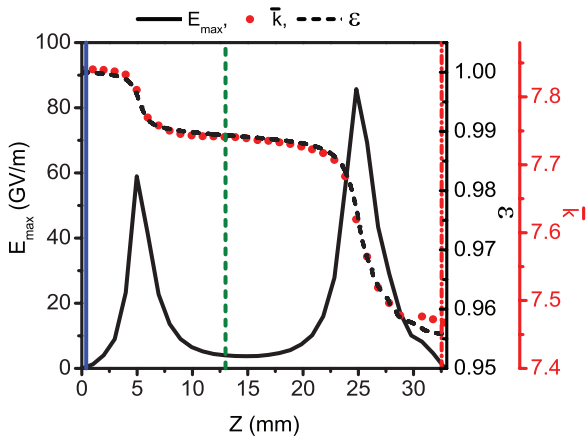


Figure 2: Simulated E_{max}, ε and $\bar{k}$ as a function of z.

EXPERIMENTAL SETUP

The staged acceleration experiment is on-going at the LOASIS Program and is performed using a 40 TW class Ti:sapphire laser system. A schematic of the experiment is shown in Fig. 3. A laser pulse is split into two pulses.

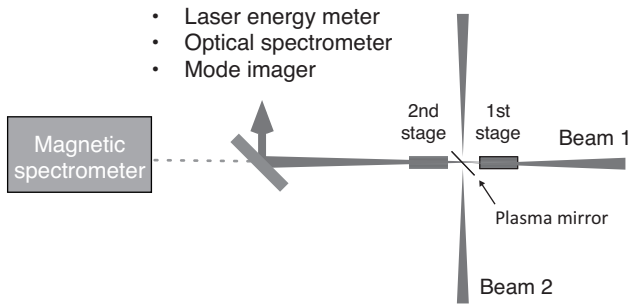


Figure 3: A schematic of the experiment.

Beam 1 drives the first stage to produce e-beams and Beam 2 reflects off the PM and drives the second stage for post-acceleration. Both laser pulses are focused on the entrance of capillary discharge waveguides [14, 15] by off-axis parabolic mirrors used at f/20. Focal spot sizes are $r_0 \simeq 20\ \mu$m. Injection in the first stage was performed with a pulse duration of 67 fs at full width at half maximum (FWHM), resulting in $a_0 \sim 0.9$. Beam 2 underwent a modulation in the splitting optic which lengthened the pulse duration to 130 fs for the initial experiments. Fluence of the Beam 2 impinging on PM was $\sim$ 500 J/cm^2 and excited plasma waves at $a_0 \sim 0.4$. The coupling distance between the two capillaries is $2-3$ cm. Preliminary experiments on electron injection, the plasma mirror reflectivity, and wake

Copyright © 2013 CC-BY-3.0 and by the respective authors

excitation performed independently of each other will be discussed.

Each LPA module used a capillary waveguide to guide the lasers. The capillaries were 33 mm long and 250 μm in diameter. For the injection experiment, various gases such as hydrogen, helium, and a mixture of nitrogen and helium were studied along with tailored plasma density. For the wake excitation experiment, hydrogen gas was used to optimize the guiding condition. A high voltage discharge ionized the gas and formed plasma $\sim$ 200 ns before the arrival of the laser. The plasma evolved from hydrodynamic motion and formed a plasma channel. The on-axis plasma densities for both experiments were $\sim 3 \times 10^{18}$ cm^3 and $r_{\rm m} \sim 35$ μm based on a scaling law derived from the simulation in [16]. Requirements for the plasma mirror were high reflectivity and good reflected mode [17]. The tape drive based plasma mirror was characterized, and the reflected laser was guided through the second stage.

RESULTS

For the injector study (1st stage), e-beams were produced by ionization of nitrogen atoms with tailored longitudinal plasma density channel. The averaged e-beam spectrum collected for 22 shots is shown in Fig. 4. The charge was 0.15 ± 0.13 pC, mean momentum 221 ± 22 MeV/c with $\sigma_p = 34 \pm 10$ MeV/c. The divergence was $\sigma_\theta = 1.4 \pm 0.2$ mrad. The fluctuation of the peak momentum was 14%. Optimizations to reduce the fluctuation in the e-beam peak energy are currently in progress.

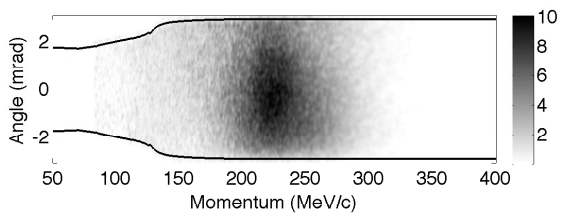


Figure 4: Averaged spectrum [nC/SR/(MeV/c)] of e-beams produced from the first stage.

The PM experiment showed fluence dependent reflective properties. When the fluence was lower than optimum, the PM triggered too late with respect to the arrival of the main pulse, transmitting a larger fraction of laser energy. When the fluence was higher than optimum, the plasma absorbed too much energy, resulting in a lower reflectivity as well as a poor surface quality. Optimum fluence of $\sim 300 - 500$ J/cm^2 resulted in 80% reflectivity and the reflected laser mode was as good as the input mode. This performance is believed to be sufficient for the experiment.

Laser beam 2 reflected off the PM and was coupled into the second stage. Optical spectra of the laser exiting the second stage is shown in Fig. 5 along with an input spectra. Based on a preliminary spectral analysis using simulations, the average accelerating field is $\sim$ 1 GV/m, and the energy gain of the e-beam would be $\sim 10 - 30$ MeV. Since the laser pulse duration was not optimized in the experiment shown here, various optimizations for wake excitation are in progress.

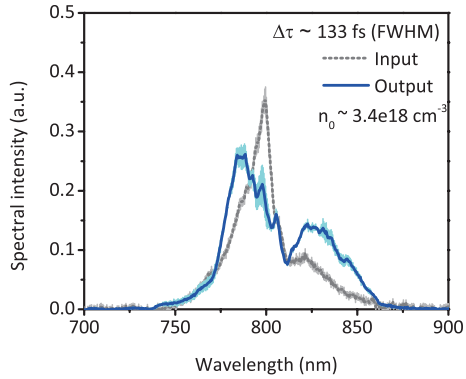


Figure 5: Input and output laser spectra guided through the second stage.

CONCLUSION

Recent progress of staged LPA was reported. Electron injection, plasma mirror in-coupling, and wake excitation in the acceleration stage were demonstrated independently of each other. Along with the experiments, the analysis of optical spectra to estimate energy gain from the acceleration stage was discussed. Optimizations to improve e-beam stability and efficiency of wakefield excitations are in progress.

REFERENCES

[1] E. Esarey, C. B. Schroeder, and W. P. Leemans, Rev. Mod. Phys. **81**, 1229 (2009).

[2] W. P. Leemans, and E. Esarey, Physics Today pp. 44–49 (2009).

[3] C. B. Schroeder, *et. al.*, Phys. Rev. ST Accel. Beams **13**, 101301 (2010).

[4] J. Faure, *et. al.*, Nature **444**, 737–739 (2006).

[5] A. Pak, *et. al.*, Phys. Rev. Lett. **104**, 025003 (2010).

[6] C. McGuffey, *et. al.*, Phys. Rev. Lett. **104**, 025004 (2010).

[7] A. J. Gonsalves, *et. al.*, Nature Physics **7**, 862–866 (2011).

[8] D. Panasenko, *et. al.*, J. Appl. Phys. **108**, 44913 (2010).

[9] P. Sprangle, J. Krall, and E. Esarey, Phys. Rev. Lett. **73**, 3544–3547 (1994).

[10] E. Esarey, and W. P. Leemans, Phys. Rev. E **59**, 1082 (1999).

[11] B. A. Shadwick, C. B. Schroeder, and E. Esarey, Phys. Plasmas **16** (2009).

[12] C. Benedetti, *et. al.*, AIP Conf. Proc. **1299**, 250 (2010).

[13] S. Shiraishi, *et. al.*, Phys. Plasmas **20**, 063103 (2013).

[14] D. J. Spence, and S. M. Hooker, Phys. Rev. E **63** (2000).

[15] A. J. Gonsalves, *et. al.*, Phys. Rev. Lett. **98** (2007).

[16] B. H. P. Broks, *et. al.*, J. Phys. D: Appl. Phys. **39**, 2377 (2006).

[17] T. Sokollik, *et.al.*, AIP Conf. Proc. **1299**, 233 (2010).

Copyright © 2013 CC-BY-3.0 and by the respective authors

GENETIC ALGORITHMS AND THEIR APPLICATIONS IN ACCELERATOR PHYSICS*

A.S. Hofler†, Thomas Jefferson National Accelerator Facility, Newport News, VA 23608, USA

Abstract

Multi-objective optimization techniques are widely used in an extremely broad range of fields. Genetic optimization for multi-objective optimization was introduced in the accelerator community in relatively recent times and quickly spread becoming a fundamental tool in multi-dimensional optimization problems. This discussion introduces the basics of the technique and reviews applications in accelerator problems.

GENETIC ALGORITHM OVERVIEW

Genetic and evolutionary algorithms (GAs and EAs, respectively) are examples of adapting models for processes observed in nature to create novel approaches to solving seemingly unrelated problems. These methods mimic biological reproduction, the theory of evolution, and the behavior of biological populations to solve mathematical optimization problems. Sets of solutions to an optimization problem are considered successively. The solutions from set i that more closely meet the optimization goal(s) are considered fitter, more inclined to survive, and are used to create the next $i+1$ set of solutions. As the selection and reproduction cycle repeats, the solutions produced are refined, and the defining characteristics for the best solutions coalesce to the optimal value(s). While not an immediately obvious method for optimization, GAs and EAs have proven to be highly effective in solving engineering and accelerator physics problems. Two recommended references on GAs, EAs, and optimization in general are [1, 2].

Optimization Problem Statements

Commonly, optimization problems are cast as minimizing or maximizing a cost function, and optionally, the independent variables may be subject to boundary constraints. Real world optimization problems tend to be multi-objective meaning there are multiple cost functions that must be minimized or maximized simultaneously subject to bounds and inequality constraints. Written generally, a multi-dimensional, multi-objective optimization (MOO) problem is

$$\begin{aligned} &\text{Optimize } f_j\left(x_1, x_2, ..., x_N\right) && j = 1, 2, ..., J, \\ &g_k\left(x_1, x_2, ..., x_N\right) \geq 0 && k = 1, 2, ..., K, \\ &x_{\min}^{(n)} \leq x_n \leq x_{\max}^{(n)} && n = 1, 2, ..., N, \end{aligned} \quad (1)$$

where Optimize can be either Minimize or Maximize for each objective function f_j, J is the number of objective functions to be simultaneously optimized, g_k are K inequality constraints, and x_n are the N independent variables to vary subject to a set of bounds constraints, $x_{\min}^{(n)}$ and $x_{\max}^{(n)}$. For a single-objective optimization (SOO), $J = 1$ and $K = 0$. GAs and EAs can be applied to both single- and multi-objective problems.

Solution existence and uniqueness is not guaranteed for SOO and MOO making them difficult to perform, but MOO has the additional complication that the objectives may conflict, meaning a set of independent variables that satisfies one objective goal causes another to move away from its optimal value. An example is minimizing two objective functions that inversely depend on the same independent variable, e.g. $f_1 = x_1$ and $f_2 = x_1^{-1} + x_2$ for $0.5 \leq x_1 \leq 1$ and $0 \leq x_2 \leq 1$. No single combination of x_1 and x_2 clearly minimizes both f_1 and f_2 simultaneously. In contrast, changing the problem to minimize one function and maximize the other creates two different optimization problems where the objectives do not conflict, and fortunately, both problems have unique solutions ($x_1 = 0.5$ and $x_2 = 1$ minimize f_1 to 0.5 and maximize f_2 to 3, while $x_1 = 1$ and $x_2 = 0$ maximize f_1 to 1 and minimize f_2 to 1).

For the simultaneous minimization problem, each possible x_1 value gives an equally valid solution to the minimization problem for $x_2 = 0$. Absent additional information about a preferred solution or system behavior, there is nothing to differentiate any particular solution from the rest in the x_1 interval. For instance, at $x_1 = 0.5$ and $x_2 = 0$, while $f_2 = 2$ is not its minimum value on the x_1 interval, f_1 is minimized to 0.5. This is the best solution for $x_1 = 0.5$ since $f_2 > 2$ for $x_2 > 0$. Similarly, $f_1 = 1$ and $f_2 = 1$ comprise the best solution for $x_1 = 1$. For the remaining values of the x_1 interval with $x_2 = 0$, neither f_1 nor f_2 attains its individual minimum value, but their values are the optimal ones for each fixed value of x_1. These solutions for $0.5 \leq x_1 \leq 1$ and $x_2 = 0$ are equivalent in terms of the optimization goals, and they form the set of solutions to this optimization problem. When objective functions conflict, a series of individual optimizations must be considered and solved, and the set of solutions is called the Pareto optimal front. The Pareto optimal front is important because it elucidates trade-offs between objectives.

Comparison to Standard Techniques

Historically, standard techniques used for multidimensional optimization problems are either iterative derivative-based methods or systematic parameter scans. GAs and

*Authored by JSA, LLC under U.S. DOE Contract DE-AC05-06OR23177. The U.S. Govt. retains a non-exclusive, paid-up, irrevocable, world-wide license to publish or reproduce this for U.S. Govt. purposes.

† hofler@jlab.org

Copyright © 2013 CC-BY-3.0 and by the respective authors

EAs are iterative but not derivative-based. They analyze a series of relatively large sets of solutions or populations to identify candidate solutions to produce new sets of solutions. Each new population is a generation and represents an iteration. Populations are composed of individuals, realizations of Eq. (1). A systematic parameter scan produces one very large exhaustive population in a single generation, and the data are analyzed at the end. GAs and EAs are smarter parameter scans because interleaving parameter space sampling and objective value analysis allows them to identify and concentrate on promising parameter space regions as they progress.

Genetic Algorithm Processing

The distinguishing characteristic of GAs and EAs is the simple but effective process by which the N-dimensional parameter space is sampled and the resulting objective values are analyzed. By way of caveat, there is great variability in algorithm designs, and this discussion may describe features and concepts that are not explicitly used or are omitted in a particular algorithm or application. The general process starts with an initial population created from a set of independent variable values that are randomly produced within the bounds constraints. This generation is a random sample of the N-dimensional parameter space. The objective values are ranked against the optimization goals, and a new population is generated from favorably ranked individuals. The cycle of ranking objectives and generating new populations repeats until the optimization goals are met within some specified tolerance or the maximum number of generations limit is reached.

Fitness is used to rank individuals in a population and indicates the relative strength of an individual. It is a function of the objectives and can include the constraints. Its exact form varies with algorithm and application. In the single objective case, the fitness function can be the objective value itself. Alternatively, fitness may be a measure of how well the objective values meet the optimization goals and adhere to the problem constraints [1, 3, 4]. Typically, stronger individuals have larger fitness values, but not always [3]. In some cases, the fitness concept is not explicitly invoked [5] but can be assumed to be the objective function value(s).

Some general fitness definitions for MOOs use the dominance concept [1] because it is suited to systems with conflicting objectives. An individual is said to dominate another if it is better in at least one objective and no worse in the others where the sense of "better" and "no worse" depends on the optimization goal for each objective. For an objective to be minimized, better means "$<$", and no worse means "$\leq$". In the minimization example above, $A = (x_1, x_2, f_1, f_2) = (0.5, 0, 0.5, 2)$ dominates $B = (0.5, 1, 0.5, 3)$ and $C = (1, 1, 1, 2)$ but not $D = (1, 0, 1, 1)$. Also, D dominates C but not A or B. B and C do not dominate each other, A, or D. If a dominance-based fitness function, for example, tallies for each individual the number of other individuals in a generation that dominate it, then the tally can be used to identify individuals that best approximate the Pareto optimal front because their tallies will be zero [3]. Applied to A, B, C, and D, the tallies are 0, 1, 2, and 0, respectively. A and D are the best estimates of the Pareto optimal front and are in fact on the Pareto optimal front. The individuals on the Pareto optimal front are said to be non-dominated with respect to each other and dominate at least one other individual in the generation.

With fitness values calculated, the selection and reproduction process starts. First, individuals are chosen to form the mating pool through a competition mechanism. For example, in tournament selection, individuals are picked at random, and a comparison of fitness values decides the winner. Only competition winners are placed in the mating pool, and only members of the mating pool are selected to reproduce. Thus it is possible to lose good individuals either through losing a competition or failing to be selected to participate. Elitist strategies counter this by giving the best individuals an advantage specific to the algorithm. Strength Pareto Evolutionary Algorithm 2 (SPEA2) [3] creates an archive of past and present best individuals, and only individuals from the archive are considered for the mating pool.

Next, individuals are chosen pair-wise from the mating pool to produce offspring through crossover, also known as recombination. GAs typically operate on binary encoded string representations of the independent variables, while EAs operate on vectors of decimal values. In the GA form, crossover mirrors the biological process. The two parent strings are split at the same randomly selected locations, and the substrings are exchanged to make the offspring. In the EA equivalent, the values of the two parents are directly exchanged to create the offspring, or linear combinations of the parent values are passed to the offspring. Offspring mutation follows. For the binary string, mutation is a randomly flipped bit ($0 \rightarrow 1$ or $1 \rightarrow 0$), and a randomly applied and generated offset for the EA version. Probability density functions (pdfs) determine the behavior of the EA crossover and mutation. The pdf configuration parameters can be tuned to affect the convergence behavior.

Differential Evolution (DE) [5] is often used for SOOs in accelerator applications while SPEA2 and Non-Dominated Sorting Genetic Algorithm II (NSGA-II) [4] are preferred for MOOs. SPEA2 and NSGA-II are elitist strategies, and now, an elitist DE is available for MOOs [6].

BEAMLINE COMPONENTS

Most beamline component GA- and EA-based design and optimization applications center on magnets and radio frequency (RF) and acceleration related devices. Early examples concentrate on magnet design and construction, and later ones are geared more toward acceleration systems.

Two magnet examples are wiggler and undulator magnet ordering and superconducting magnet design. Wiggler and undulator magnets are constructed from several smaller dipole magnets, and it is important to arrange the constituent magnets to minimize field errors. GAs and EAs

Copyright © 2013 CC-BY-3.0 and by the respective authors

can search through the many magnet order permutations and find the optimal arrangement [7], and GA-based magnet sorting and shimming continue to be integral to wiggler and undulator construction [8, 9, 10]. One of the earliest uses of Pareto optimality is a GA-based superconducting magnet design tool [11]. The tool identifies and creates multiple similar conceptual magnet designs meeting specified criteria that a magnet designer can then further evaluate with respect to manufacturing considerations. With this tool, a new magnet coil design was identified for use in the Large Hadron Collider.

The first application of GAs to RF devices was to optimize cavity designs based on higher order mode and resonance requirements [12]. With the renewed interest in GA and EA methods, the number of RF cavity optimizations has grown recently to include a variety of RF and superconducting RF (SRF) cavity designs: crab cavities [13], spoke cavities [14], choke-mode damped structures [15], microwave tubes [16], and klystron interaction structures [17]. Lastly, geometric dimension and relative dielectric permittivity optimizations for cylindrical and slab wakefield accelerators provide insights into the tradeoffs between transformer ratio and maximum accelerating wakefield electric field amplitude [18].

ACCELERATOR DESIGN

There are two modes of accelerator design using GAs and EAs. The first assumes a machine element layout where the field behavior of the magnets and accelerating devices is known, and the optimization searches for optimal set points, field amplitudes and phases, and element spacings to achieve specific beam quality and operating conditions. In other words, the optimization acts to tune the machine. The other mode builds on the first additionally varying physical features of beamline elements and systems to discern optimal designs or requirements for them; beamline element and operational set point optimizations are combined. Most applications fall in the first category, and with the growing appreciation for the power and flexibility of GAs and EAs in the accelerator field, the number of more holistic machine design applications is growing. Pareto optimality is especially important here because the front provides information about the many possible configurations and capabilities letting the designer choose the most suitable combination. In some cases, the front has even revealed unorthodox operating schemes that are comparable to or better than the standard solutions [19, 20, 21].

The ability to optimize a known machine layout is extremely useful. This form of optimization is well established, and only a fraction of the many examples will be highlighted here. The earliest application determines the quadrupole settings in injection and transfer lines for BESSY-II [22].

The tuning approach is used in mainly four ways. The most obvious use establishes the expected performance of a proposed or upgraded machine. A sample shows: positron momentum selection in a continuous wave positron source [23]; dynamic aperture optimization for a storage ring upgrade [24]; asymmetric distribution of longer insertion device straight sections in a storage ring light source [25]; a superconducting tape undulator-based light source [26]; a two-loop compact energy recovery linac (ERL) [27]; an electron linac for a gamma-ray source [28]; compression schemes for a free electron laser (FEL) [29]; and a bunch compressor for electron beam slicing [30].

Second, optimizing operational settings and relative element spacing can establish that a particular technology is suitable for a new or more demanding accelerator application. Most examples are direct current (DC) and RF gun injectors for FEL [31, 32, 33] and ERL light sources [34].

Third, accelerator physicists look for performance improvements for existing machines through alternative machine settings. Storage ring light sources benefit from this most to optimize brightness [20] and increase dynamic and momentum apertures [21, 35].

Lastly, this mode can identify tuning knobs or their settings to correct or avoid operational problems. Identification is needed for storage ring orbit bumps [36] and collider final focus optics tuners [37]. Finding knob settings is useful for controlling transport optics for muon experiments [38], restoring machine performance until failed components can be repaired [39], protecting equipment [40], and making machines insensitive to destructive beam instabilities such as beam break-up [41].

The second more encompassing accelerator design approach allows beam and beamline element performance to be considered together. This flips the model described above determining the suitability of a given technology or machine layout for an application. Instead the desired beam performance directly drives element design. Two advance examples of this approach are a preliminary spallation neutron source accumulator ring design study [42] and a muon solenoidal decay channel optimization [43].

The watershed accelerator physics applications showcasing the power of EAs, GAs, and Pareto optimality in general and this combined beam and element performance optimization are a laser profile and DC gun injector optimization for an ERL light source [19] and a damping ring optics evaluation tool that creates all viable optics layouts fitting in a given machine circumference [44]. They demonstrate that automating accelerator design is possible because GAs and EAs can manage the complexity of these problems and organize the results in a way to help the accelerator designer choose the best design among all possible designs meeting a set of criteria. The success and flexibility of these two optimizations led to the explosive growth in accelerator EA- and GA-based optimizations of all kinds. These two examples led to beam performance-based systems devoted to finding optimal: geometries for injector guns [45, 46] and accelerating elements [47, 48]; field profiles for storage ring dipoles [49] and fixed-field alternating gradient accelerator magnets [50]; undulator tapering profiles [51]; and an RF pulse time structure to compensate for beam loading

Copyright © 2013 CC-BY-3.0 and by the respective authors

in a linac [52].

REAL TIME AND DIAGNOSTIC APPLICATIONS

Two very successful real time applications of GAs are photocathode laser profile generation [53, 54] and phase space reconstruction [55]. Both examples configure several similar or identical elements. The shear number of permutations on the settings precludes enumerating and evaluating each setting in turn, so a GA is used to sample the available permutations and identify an optimal configuration. A third example extracts cavity parameters from pass band data for an SRF cavity installed in a multi-cavity assembly [56].

ACCELERATOR DESIGN TOOLS AND COMPUTATIONAL CONSIDERATIONS

Execution time is an important factor to consider when choosing GA and EA tools and the underlying computational structure. These population-based methods assume computations for individuals are independent and self-contained, so they are amenable to parallelization. The maximum time to calculate all results for a single individual determines the level of necessary parallelization. If an individual is modeled with a few finite polynomial expressions for example, serially processing individuals in a population is reasonable, and optimization extensions for Excel [57], MATLAB, and Mathematica are appropriate to use. Most problems in accelerator physics require simulation codes to model the underlying physical system and involve non-negligible execution times. For these situations, the results for individuals must be produced in parallel.

Several parallel frameworks are available affording various levels of flexibility and abstraction. The basic design has two main parts. The first is the GA or EA wrapped around a simulation job management system. The job management system handles communication between the optimization processing and the simulation code(s), and it dispatches simulations for individuals to available computer resources. Program and script based systems include: Alternate PISA (A Platform and Programming Language Independent Interface for Search Algorithms [58]) (APISA) [19, 45] and variations from TRIUMF [59] and Jefferson Lab [46], geneticOptimizer [60], and OPT-PILOT [61]. APISA and variants mainly use SPEA2, and the others use NSGA-II. Note OPT-PILOT has a Python-based graphical interface for viewing Pareto optimal fronts and associated decision variable values.

The parallel frameworks commonly assume access to a large number of compute nodes found in batch farm and high performance computer cluster configurations. Alternatively, idle desktop computers in an organization can be co-opted with APISA or Condor [17], a system that coordinates, monitors, and dispatches simulations to underutilized desktop computers. The advent of commercial cloud computing resources may provide on-demand high performance computer clusters to extend existing systems or obviate the need for local installations [62].

Some accelerator simulation systems include GAs and EAs in their optimization suite: TAO [63], COSY-GO [64], G-optimizer in TRACK [65], GeneticTRACY [62], elegant COGA [66], and a symbolic beam propagator [67]. Lastly, libraries are available such as PGAPack [68] and pikaia [69] to build custom systems.

CONCLUSION

The use of GAs and EAs is well established in accelerator physics as demonstrated by the variety of applications and tools presented here. The expanded capability of GAs and EAs to directly solve MOOs and identify inherent trade-offs has substantially increased their utility in the field and enables automated optimization of systems that are complex in terms of dynamics and the number of variables involved. The basics of GAs and EAs have been introduced to facilitate understanding of how these algorithms work and interpreting the results they produce.

REFERENCES

[1] K. Deb. John Wiley and Sons, Chichester, 2001.

[2] A. Konak et al. *Reliability Engineering and System Safety*, 91(9):992–1007, 2006.

[3] Eckart Zitzler et al. In *Evolutionary Methods for Design, Optimisation and Control with Application to Industrial Problems (EUROGEN 2001)*, pages 95–100, 2001.

[4] K. Deb et al. *IEEE Trans. Evolut. Comput.*, 6:182–197, 2002.

[5] R. Storn and K. Price. *J. Global Optimization*, 11:341–359, 1997.

[6] J. Qiang et al. IPAC 2013, Shanghai, China, May 2013, MOPWO062, pp. 1031-1033.

[7] R. Hajima et al. *Nucl. Instrum. Methods Phys. Res., Sect. A*, 318(1-3):822–824, 1992.

[8] F. Briquez et al. EPAC 2006, Edinburgh, Scotland, June 2006, THPLS118, pp. 3556-3558.

[9] J.-M. Ortega et al. IPAC 2012, New Orleans, LA, USA, May 2012, TUPPP048, pp. 1709-1711.

[10] S.C. Gottschalk et al. FEL 2012, Nara, Japan, August 2012, THPD11, pp. 567-570.

[11] S. Ramberger and S. Russenschuck. EPAC 1998, Stockholm, Sweden, June 1998, TUP10H, pp. 2014-2016 and TUP11H, pp. 2017-2019.

[12] A. Chincarini et al. *IEEE Transactions on Magnetics*, 31(3):1566–1569, 1995.

[13] C. Lingwood et al. IPAC 2010, Kyoto, Japan, May 2010, TUPEC056, pp. 1850-1852.

[14] M. Sawamura et al. SRF 2011, Chicago, IL, USA, July 2011, MOPO036, pp. 165-168.

[15] H. Zha et al. IPAC 2013, Shanghai, China, May 2013, TUPME026, pp. 1628-1630.

[16] S.G. Tantawi. FEL 2011, Shanghai, China, August 2011, TUOCI2_TALK.PDF.

Copyright © 2013 CC-BY-3.0 and by the respective authors

[17] J.D.A. Smith et al. PAC 2009, Vancouver, BC, Canada, May 2009, TH5PFP046, pp. 3303-3305.

[18] F. Lemery et al. IPAC 2011, Kursaal, San Sebastian, Spain, September 2011, WEPZ008, pp. 2781-2783.

[19] I.V. Bazarov and C.K. Sinclair. *Phys. Rev. ST AB*, 8(3):034202, 2005.

[20] L. Yang et al. EPAC 2008, Genoa, Italy, June 2008, THPC033, pp. 3050-3052.

[21] M. Borland et al. PAC 2009, Vancouver, BC, Canada, May 2009, TH6PFP062, pp. 3850-3852.

[22] D. Schirmer et al. PAC 1995, Dallas, TX, USA, May 1995, WAQ17, pp. 1879-1881.

[23] S. Golge et al. PAC 2007, Albuquerque, NM, USA, June 2007, THPMS067, pp. 3133-3135.

[24] C. Sun et al. PAC 2011, New York, NY, USA, March 2011, TUODN4, pp. 793-795.

[25] V. Sajaev et al. PAC 2011, New York, NY, USA, March 2011, THP125, pp. 2354-2356.

[26] D. Filippetto et al. FEL 2011, Shanghai, China, August 2011, MOPC14, pp. 129-132.

[27] M. Shimada et al. IPAC 2011, Kursaal, San Sebastian, Spain, September 2011, WEOAA03, pp. 1909-1911.

[28] D. Alesini et al. IPAC 2011, Kursaal, San Sebastian, Spain, September 2011, TUPO008, pp. 1461-1463.

[29] C.H. Yi et al. IPAC 2012, New Orleans, LA, USA, May 2012, TUPPC027, pp. 1224-1226.

[30] A. He et al. IPAC 2013, Shanghai, China, May 2013, WEPWA091, pp. 2307-2309.

[31] F. E. Hannon and C. Hernandez-Garcia. EPAC 2006, Edinburgh, Scotland, June 2006, THPLS115, pp. 3550-3552.

[32] A. Bacci et al. FEL 2006, Berlin, Germany, August 2006, MOPPH030, pp. 99-102.

[33] P.N. Ostroumov et al. LINAC 2008, Victoria, BC, Canada, September 2008, TUP117, pp. 676-678.

[34] C.X. Wang. PAC 2009, Vancouver, BC, Canada, May 2009, MO6RFP048, pp. 467-469.

[35] Z. Duan and Q. Qin. IPAC 2011, Kursaal, San Sebastian, Spain, September 2011, THPZ011, pp. 3705-3707.

[36] S.L. Smith et al. EPAC 2004, Lucerne, Switzerland, July 2004, THPKF067, pp. 2418-2420.

[37] J.K. Jones. EPAC 2006, Edinburgh, Scotland, June 2006, MOPLS117, pp. 837-839.

[38] M. Apollonio. PAC 2009, Vancouver, BC, Canada, May 2009, TH6PFP057, pp. 3835-3837.

[39] B. Sun et al. IPAC 2013, Shanghai, China, May 2013, TUPWA018, pp. 1760-1762.

[40] H. Hao et al. IPAC 2013, Shanghai, China, May 2013, TUPWO061, pp. 2006-2008.

[41] R. Nagai et al. PAC 2003, Portland, OR, USA, May 2003, FPAB078, pp. 3443-3445.

[42] J.D. Galambos et al. PAC 1997, Vancouver, BC, Canada, May 1997, 9W023, pp. 1018-1020.

[43] S.J. Brooks. EPAC 2004, Lucerne, Switzerland, July 2004, MOPLT104, pp. 776-778.

[44] L. Emery. PAC 2005, Knoxville, TN, USA, May 2005, RPPP047, pp. 2962-2964.

[45] I.V. Bazarov et al. *Phys. Rev. ST AB*, 14:072001, 2011.

[46] A. Hofler et al. *Phys. Rev. ST AB*, 16:010101, 2013.

[47] V.A. Goryashko. FEL 2010, Malmö, Sweden, August 2010, MOPB13, pp. 71-74.

[48] A.V. Samoshin et al. RUPAC 2012, St. Petersburg, Russia, September 2012, WEPPC009, pp. 461-463.

[49] C.-X. Wang et al. IPAC 2010, Kyoto, Japan, May 2010, THPE039, pp. 4605-4607.

[50] S.J. Brooks. PAC 2009, Vancouver, BC, Canada, May 2009, FR5PFP025, pp. 4357-4359.

[51] J. Wu et al. IPAC 2012, New Orleans, LA, USA, May 2012, TUPPP082, pp. 1780-1782.

[52] O. Kononenko et al. LINAC 2010, Tsukuba, Japan, September 2010, MOP021, pp. 94-96.

[53] C. Vicario et al. EPAC 2004, Lucerne, Switzerland, July 2004, TUPLT063, pp. 1300-1302 and PAC 2005, Knoxville, TN, USA, May 2005, MOPB008, pp. 642-644.

[54] H. Tomizawa et al. LINAC 2004, Lübeck, Germany, August 2004, MOP80, pp. 207-209 and FEL 2007, Novosibirsk, Russia, August 2007, WEBAU01, pp. 298-305.

[55] A. Bacci et al. SPARC/EBD-07/004 (2007); FEL 2007, Novosibirsk, Russia, August 2007, WEAAU02, pp. 284-289; and EPAC 2008, Genoa, Italy, June 2008, TUPC089, pp. 1263-1265.

[56] N. Yi et al. *Nucl. Instrum. Methods Phys. Res., Sect. A*, 462:356–363, 2001.

[57] B. Mukherjee. Cyclotrons 2001, East Lansing, MI, USA, May 2001, P1-08, pp. 21-23.

[58] S. Bleuler et al. In *Evolutionary Multi-Criterion Optimization (EMO 2003)*, pages 494–508. Springer, 2003.

[59] C. Gong and Y.-C. Chao. ICAP 2012, Rostock-Warnemünde, Germany, August 2012, TUABI1, pp. 67-71.

[60] M. Borland and H. Shang. Unpublished program (2007).

[61] A. Adelmann et al. ICAP 2012, Rostock-Warnemünde, Germany, August 2012, TUAAI2, pp. 62-66.

[62] C. Sun et al. PAC 2011, New York, NY, USA, March 2011, WEP151, pp. 1767-1769 and IPAC 2012, New Orleans, LA, USA, May 2012, MOPPC086, pp. 340-342.

[63] D. Sagan and J.C. Smith. PAC 2005, Knoxville, TN, USA, May 2005, FPAT085, pp. 4159-4161.

[64] K. Makino and M. Berz. ICAP 2006, Chamonix Mont-Blanc, France, October 2006, TUAPMP01_TALK.PDF.

[65] B. Mustapha and P.N. Ostroumov. ICAP 2009, San Francisco, CA, USA, August 2009, FR1IOPK01, pp. 245-250.

[66] M. Borland. APS LS-287, 2000.

[67] S.N. Andrianov et al. IPAC 2011, Kursaal, San Sebastian, Spain, September 2011, WEPC115, pp. 2280-2282.

[68] D. Levine. ANL-95/18 (1996).

[69] P. Charbonneau and B. Knapp. NCAR/TN-418+IA, National Center for Atmospheric Research, Boulder, Colorado, (1995) `http://www.hao.ucar.edu/modeling/pikaia/pikaia.php`

Copyright © 2013 CC-BY-3.0 and by the respective authors

A SPECIALIZED HIGH-POWER (50 kW) PROTON BEAMLINE FOR BNCT

Morgan P. Dehnel, Thomas M. Stewart, Tue Christensen, David E. Potkins, D-Pace, Inc.,
PO Box 201, Nelson, BC, Canada
Hirofumi Seki, Shinji Shibuya, Steve Domingo, Glenn James, Pat Creely, Steve Bucci, AccSys Technology, Inc., 1177 Quarry Lane, Pleasanton, CA 94566, USA

Abstract

D-Pace has developed a specialized high-power beamline for transporting a 20 mA, 2.5 MeV, CW proton beam for a Boron Neutron Capture Therapy (BNCT) application. The 2 m horizontal by 4 m vertical layout transports the space-charge dominated beam with less than 1% beam-spill using two sets of 10 T/m quadrupole doublets, DC XY steerer, 90 degree bending magnet, and AC XY magnets for raster-scanned, flat-topped, round or square intensity distributions deposited over targets with 40 – 100 mm maximum dimensions. Diagnostics include New Parametric Current Transformers (NPCT), graphite, water-cooled, electrically-isolated collimators with readbacks, and a low-power sapphire beam profile monitor for macro-pulsed beams (~100 micro-second wide pulses at low frequency). This paper describes the specialized: beam-optics, intensity distributions, and device designs.

INTRODUCTION

BNCT is a non-invasive therapeutic treatment of cancer (high-grade gliomas, cerebral metastases of melanoma; and head, neck, and liver cancer) [1] that involves two steps. First, tumour-localizing non-radioactive boron-10 delivery agents (such as boronophenylalanine i.e. BPA, or sodium borocaptate i.e. BSH) are injected into the patient [1]. Second, the patient is exposed to epithermal neutrons, which have a very high probability of reacting with the concentrated boron-10 residing in the cancer cells. This yields an energetic alpha particle, and a recoiling lithium nucleus which ionize a tremendous number of atoms and molecules within 5-9 microns (~size of cancer cell). This results in cancer cell death [1,2].

BNCT has a 50 year history at research nuclear reactors [3], and is established i.e. 16th International Congress on Neutron Capture Therapy, ICNCT (2014), is to be held in Helsinki. For widespread use of BNCT better delivery agents, improved dosimetry, and independence of nuclear reactors is required [3]. Barth [3], IAEA [4], Blue and Yanch [5] all emphasize the development of particle accelerators for BNCT. Strong growth in BNCT implementation in hospitals is anticipated since it can now be de-coupled from nuclear reactors through low energy (p,n) reactions provided by relatively inexpensive safe compact particle accelerator systems that can be turned off (as compared to a reactor) [6].

This paper describes the High Energy Beam Transport (HEBT) beamline developed for the BNCT treatment system utilizing an AccSys 2.5 MeV, 20 mA, CW proton Linac and the Li-7(p,n)Be-7 reaction.

HEBT BEAMLINE

The 10 rms RFQ beam was modeled thru HEBT (Figure 1) with 1st order Beamline Simulator [7] using acceptances greater than 3x the 10 rms emittances in both transverse phase-planes to define conservative apertures. TRACE-3D [7] simulations confirmed high beam transmission at 20 mA CW space-charge conditions. The finalized system in Figure 2 follows the principles [8-10].

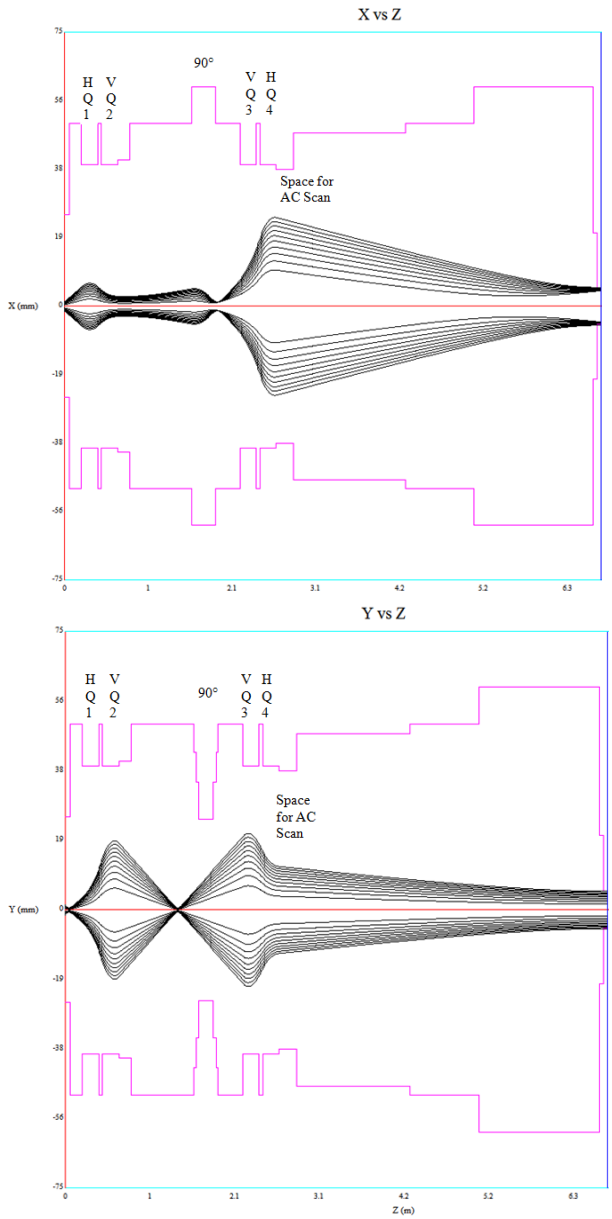


Figure 1: HEBT Horizontal & Vertical 1-10rms Beams.

Copyright © 2013 CC-BY-3.0 and by the respective authors

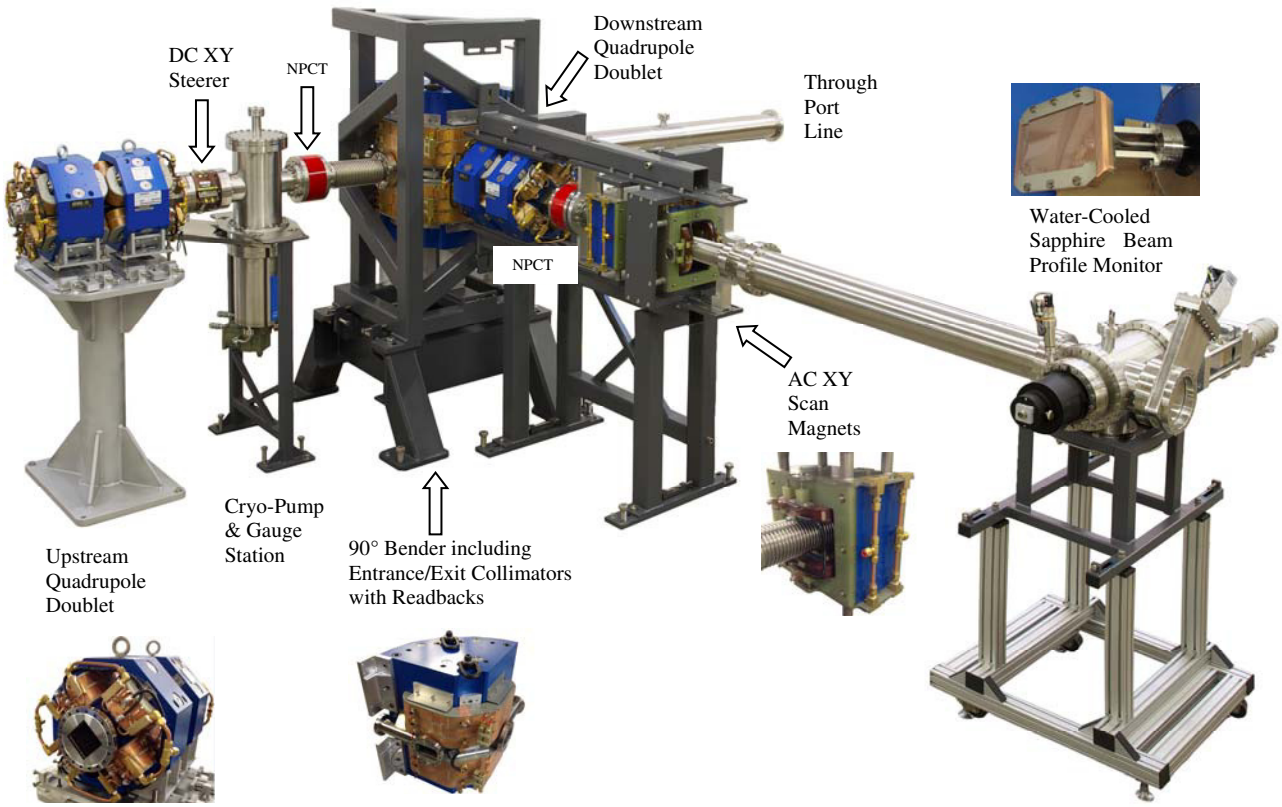


Figure 2: The HEBT system. The proton beam is injected into the HEBT from the RFQ at upper left, and the scanned beam exits at right (downstream of Beam Profile Monitor). The supports can be arranged in a horizontal format for factory testing as shown, or in a format where components downstream of the 90° Bender are in the vertical direction.

Ion-Optical Elements

The ion-optical elements are as follows: (1) Upstream Quadrupole Doublet {Bore = 82.3 mm, Effective Length (EL) = 202.3 mm, B_{Max} = 0.4 T}, (2) DC XY Steering Magnet {Iron Gap = 105 mm, EL = 184 mm, B_{Max} = 0.01 T}, (3) 90° Bender Magnet {Iron Gap = 52 mm, EL = 300 mm, B_{Max} = 1.3 T, Rogowski Pole Face Rotations = 0°}, (4) Downstream Quadrupole Doublet {Bore = 82.3 mm, EL = 202.3 mm, B_{Max} = 0.4 T}, and (5) AC XY Scan Magnet {Iron Gap = 97 mm, EL = 212 mm, B_{Max} = 0.0165 T, Frequency = 45 Hz}. All magnets designed with alignment fiducials for Ball Mounted Reflectors (BMR) used during final alignment with a laser tracker.

Upstream Horizontal Section Description

The Upstream Quadrupole Doublet is placed close to the RFQ (~200 mm space for a VAT™ gate valve, bellows, and flanging) since it serves to capture the diverging RFQ beam and to focus it through the 90° Bender which has a narrow gap resulting in reduced magnet cost, size, and power consumption. The transverse beam envelopes are largest through the Quadrupole Doublets and thus they are fitted with diamond-shaped beampipes that afford a larger acceptance than round beampipes for the very same magnet bore diameter (refer to lower left of Figure 2).

Immediately after the upstream doublet is the DC XY Steering Magnet which provides ± 8 mrad of steering capability. It is located downstream of the first doublet where a sensitivity analysis has shown it to be efficacious.

A cryo-pumping station with ports for gauges and leak testing are provided. The cryo-pump is separated from the beamline by a gate valve, so that it is not necessary to be purged to atmosphere if the HEBT is vented.

A Bergoz NPCT (96 mm diameter) provided by GMW measures the beam current in the upstream portion of the line. It comes with Conflat™ flanging as does all of the vacuum equipment. Experiments shall be undertaken to ensure H2+ is not affecting the proton beam current measurement [11].

A bellows is located immediately upstream of the 90° Bender Magnet. The bender magnet vacuum box is outfitted with electrically-isolated water-cooled 46 mm diameter graphite entrance and exit collimators with beamspill current readbacks to the control system. The device's handle greater than 2 kilo-watt beamspill power on average, but shall be used as a threshold interlock at 0.5% of total beam current for rapid "beam off" in the case of a component failure (i.e. power supply). The collimator ceramic insulators are protected by metal shrouds to prevent short-circuiting in the event of any migration of metal vapour from the targets. The bender vacuum box also has a thru port with gate valve and beampipe with pumping station port for DC beam experiments when the bender is off.

Copyright © 2013 CC-BY-3.0 and by the respective authors

Downstream Vertical Section Description

The Downstream Quadrupole Doublet captures the strongly diverging beam immediately downstream of the bender magnet. A Bergoz NPCT is next and provides a 2nd beam current measurement to establish transmission rates. The support structure can be used in both a horizontal and vertical configuration. A sapphire water-cooled low-power beamstop with a radhard MegaRAD3 Thermo CIDTEC camera for viewing low frequency macro-pulsed beams (~100 micro-second) is provided. The downstream vertical section is shielded to contain the neutron flux from the target.

D-Pace's standard <100 Hz AC XY Scan Magnet product can provide both generic raster and circular scanned beams as shown in Figures 3 and 4.

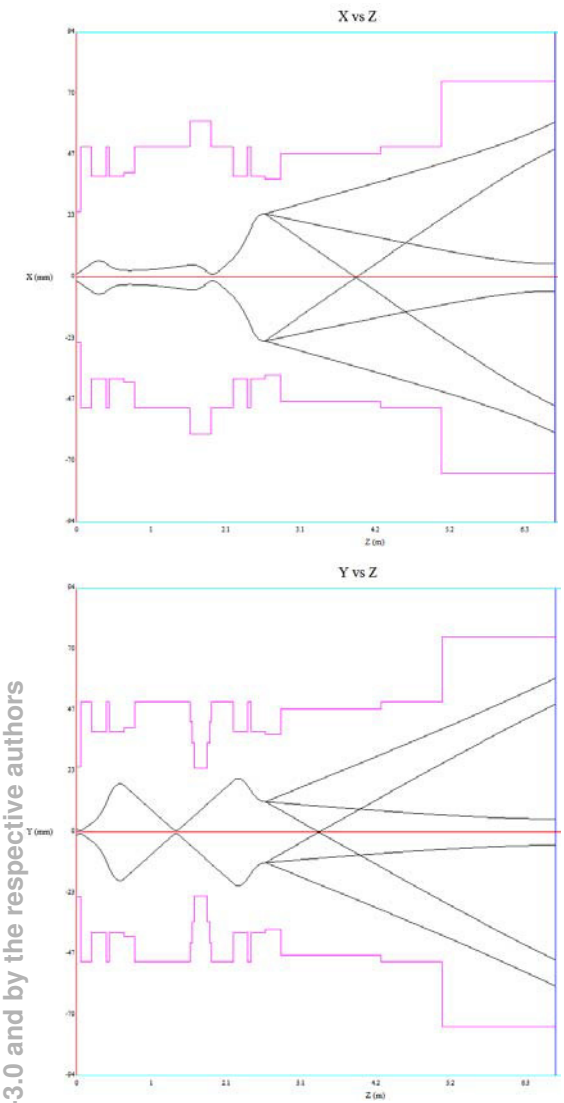


Figure 3: Horizontal and vertical 10 rms beam profile extents of AC Scanning (θ_{Max}= ±13.4 mrad) with 10 mm DC beam spot on target. Apertures confirmed.

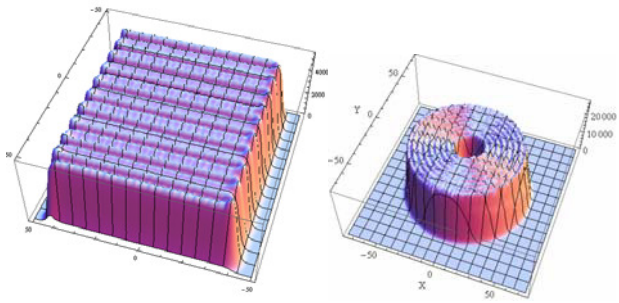


Figure 4: An example of generic square raster-scanned beam (left), and generic circular scanned beam (right) that D-Pace's standard product AC Scan Magnets can deliver. The customer shall tailor the undisclosed beam distributions on target according to their own proprietary algorithms through D-Pace's programmable two channel signal generator.

ACKNOWLEDGMENTS

We wish to gratefully acknowledge: the Canadian Government's R&D funding programme SRED; Buckley System's Ltd (BSL) for excellent development, manufacturing and testing work; Kurt J. Lesker, Bergoz, GMW, Thermo/CIDTEC & Testforce staff for wonderful support and equipment; and P. Schmor, B. Gyles, M. Stokely, J. Peeples, C. Humphries, J. Theroux and C. Hollinger for high-level technical consulting support.

REFERENCES

[1] R.F. Barth et al., "Boron Neutron Capture Therapy of Cancer : Current Status and Future Prospects", Clin. Cancer Res. (2005);11(11).

[2] Mohamed Alotiby, "Boron Neutron Capture Therapy for Cancer Treatments", Master of Science Thesis, Dept. Physics, University of Surrey (2012).

[3] R.F. Barth, "Boron Neutron Capture Therapy at the Crossroads: Challenges and Opportunities", Applied Radiation and Isotopes 67 (2009) S3-S6.

[4] IAEA-TECDOC-1223, (2001).

[5] T.E. Blue and J.C. Yanch, "Accelerator-based Epithermal Neutron Sources for Boron Neutron Capture Therapy of Brain Tumours", J Neurooncol. (2003);62(1-2):19-31.

[6] T.P. Wangler. J.E. Stovall, T.S. Bhatia, C.K. Wang, T.E. Blue, R.A. Gahbauer, "Conceptual Design of an RFQ Accelerator-Based Neutron Source for Boron Neutron-Capture Therapy", IEEE PAC, Vol. 1, pp. 678-680, (1989).

[7] Beamline Simulator, TRACE3D, www.ghga.com/accelsoft

[8] Morgan P. Dehnel et al, "The Design and Operation of an Industrial Beam Transport System for 15-30 MeV Protons", IEEE Trans. Ind. App's, Vol. 28, No. 6, pp. 1384-1391, (1992).

[9] Morgan P. Dehnel et al, "Beamline Developments in Commercial Cyclotron Facilities", CAARI2004, NIM B 241, pp. 655-659 (2005).

[10] Morgan P. Dehnel et al, "Industrial Beamline Design for Radioisotope Production", 17th Int'l Conf. on Cyclotrons, pp. 486-488 (2004).

[11] H. Deitinghoff, "Beam Dynamics Calculations for the Simultaneous Simultaneous Acceleration of Ions with Different Charge to Mass Ratios in a RFQ", EPAC96, pp.1218-1220, (1996).

Copyright © 2013 CC-BY-3.0 and by the respective authors

LARGE MOMENTUM ACCEPTANCE SUPERCONDUCTING NS-FFAG GANTRY FOR CARBON CANCER THERAPY*

Dejan Trbojevic, Brett Parker, BNL, Upton, New York, 11973, USA
Marco Pullia, CNAO, Pavia, Italy

Abstract

Carbon cancer radiation therapy has clear advantages with respect to the other radiation therapy treatments. Cost of the ion cancer facility is dominated by the delivery systems. New superconducting carbon ion gantry designs, based on the Non-Scaling FFAG (NS-FFAG) principle, are presented. The magnet size and weight is dramatically smaller with respect to existing gantries. The weight of the transport elements of the carbon isocentric gantry is estimated to be 1.5 tons to be compared to the 130 tons of the top-notch gantry in the Heidelberg ion therapy facility.

INTRODUCTION

A number of ion cancer therapy facilities are rapidly rising due to a clear advantage to any other radiation treatment of the cancerous tumors. This is due to a very localized energy deposition of ions at the "Bragg peak-as suggested by R. Wilson 1946 [1]. The ion cancer facility starts with an ion source, accelerator, and the delivery system (major cost). The Coulomb scattering and struggling define the final beam spot size–penumbra at the tumor. The best results in the cancer treatment are obtained by use of the spot size "pencil" beams with the transverse and longitudinal scanning technique. Usually the treatment time is of the order of couple of minutes. In proton cancer therapy the minimum beam volume size-voxel at the tumor (for the maximum distance of 27 cm in the patient) is ~715 mm^3, while for carbon ions it is ~14 mm^3. The transverse intrinsic spot for 206 MeV protons is ~11 mm, while for carbon ions is 2.9 mm. Carbon ions have advantage in the patient treatment, as they are more precise. Normal angle of ion arrival to the patient reduces the skin radiation. The Source to Axis Distance (SAD) parameter in the cancer treatment shows an optimum with SAD=∞ (beam arrives with normal angle of incidence to the patient skin).

A recommendation from the Workshop on Ion Therapy [1] in Bethesda MD (organized by Department of Energy (DOE), National Cancer Institute (NCI), National Institute of Health (NIH), and Department of Health & Human Services DHHS) was that the carbon or other ion therapy facility should include rotatable gantry, possibly made of superconducting magnets (to be able to reduce the size and cost) and with a large momentum acceptance.

This is a report on a large momentum acceptance superconducting NS-FFAG gantries. They have many advantages like: reduced size and weight, large momentum acceptance (200-400 MeV or 100-200 MeV/u etc.), fixed magnetic field, with the angle of incidence always normal to the patient (SAD=∞), and easy to operate, as the magnetic field is fixed during the treatment. We present two examples: the isocentric gantry and an eccentric gantry proposed, by Marco Pullia (CNAO-Italy). Both gantries have a large momentum acceptance – for one fixed magnetic field setting they can operate covering a large kinetic energy range (either between 200-400 MeV/u or 100-200 MeV/u). The normal angle of incidence is obtained by use of two scanning dual plane scanning magnets.

NS-FFAG PRINCIPLE

In recent years there has been a clear revival of the previous concept of the FFAG's, developed mostly in the 1950's. A concept of the NS-FFAG is based on strong focusing principle with a small dispersion function. The relationship: $\Delta x = D\ \delta p/p$ shows that the beam offset is small even for the large $\delta p/p$. Major differences between the NS-FFAG's with respect to the scaling FFAG's are variations of the tunes, time of flight, dispersion and amplitude functions with a momentum as shown in a gantry cell in Figure 1.

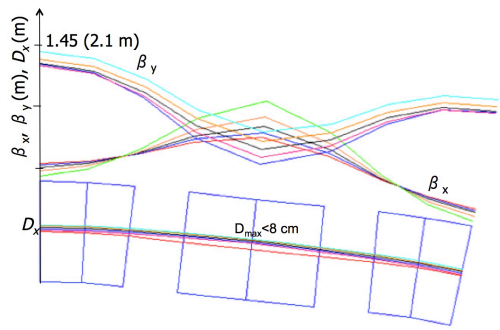


Figure 1: Betatron and dispersion functions in a gantry cell for the treatment energies.

BEAM DELIVERY - ION GANTRIES

The delivery system is the most expensive part of the ion cancer therapy facilities. Figure 2 shows the top-notch proton gantry at PSI in Switzerland. The scanning magnets are placed usually in front of the large 90°-bending magnet above the patient. This is to allow for the SAD=∞. To avoid the large magnet above the patient (for the proton gantries its weights is ~60 tons) a scanning system is placed above the patient. This solution (submitted to the Patent Office) not only removes the necessity of the large magnet but also always provides normal angle of incidence to the patient skin. A proton gantry design is shown in Figure 3.

* Work performed under Contract Number DE-AC02-98CH10886 with the auspices of the US Department of Energy

Copyright © 2013 CC-BY-3.0 and by the respective authors



Figure 2: The proton top-notch proton therapy facility at PSI, with the large bending magnet at the end.

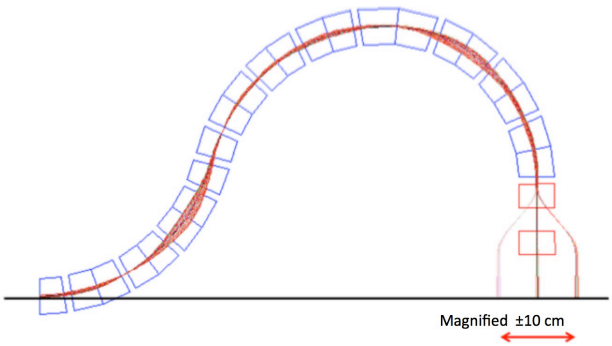


Figure 3: Our proton gantry design eliminates need for the large dipole and provides always 90° angle to the skin.

The carbon gantry operating at the Heidelberg ion cancer facility is of a large size as at the time when it was built and designed, relied on the existing safe warm magnet technology. The maximum kinetic energy of the carbon ions in Heidelberg is 430 MeV/u with a corresponding $B\rho$=6.624 Tm. For the magnetic field of 1.6 T produced by the warm magnet the radius of a curvature is R=4.1 m. To better perceive the size of this gantry in figure 4 a visitor is shown. The NS-FFAG superconducting gantry design is shown together with the Heidelberg gantry in Figure 6. A large number of small superconducting combined function magnets will reduce the size of the gantry. The number of magnets is 31, including the two scanning and the triplet magnets for defining the beam size. The superconducting magnets are made by superconducting wire wound directly onto the beam pipe, without using any iron. This reduces the weight. They have a small aperture r~3 cm. The dipole field in the defocusing magnet is B_{yD}= 4.55 T with gradient of G_d= −90 T/m, while the focusing magnet has opposite bending field of B_{yF}=-0.385 T with a gradient of G_F=150 T/m. The length of the focusing magnet is 20 cm while the defocusing one is 26 cm long. The bending angle of the defocusing magnet is θ_D=0.233 rad while the focusing combined function magnet has an angle of the opposite sign of θ_F=−0.152 rad. The magnetic field in the defocusing combined function magnet is equal to: $B_{DTOT} = B_D + (G_D * x)$, while for the focusing magnet it is: $B_{FTOT} = B_F + (G_F * x)$. The maximum magnetic field in the defocusing magnet is equal to B_{Dmax}=4.55 T at the lowest energy and B_{Dmax}=5.63 T at the highest energy (this is a combination of the bending field plus gradient multiplied by the orbit offsets for energies other than the central energy). The maximum field in the focusing combined function magnet is, for the lowest energy, B_{Fmax}=2.34 T, while for the highest energy it is B_{Fmax}=-3.4 T.



Figure 4: The Heidelberg gantry with a visitor. The large 45° magnet is shown above.

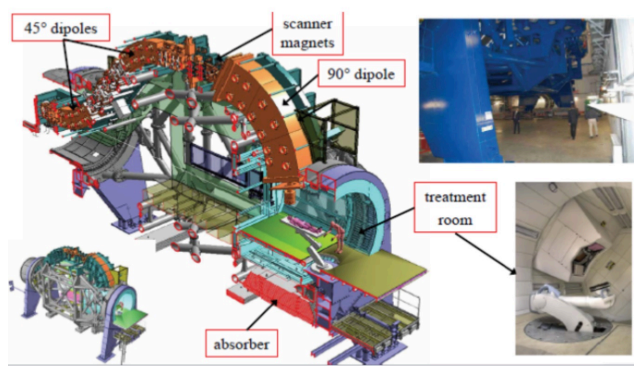


Figure 5: The whole structure of the Heidelberg carbon gantry with detail of the treatment room on the right side.

Copyright © 2013 CC-BY-3.0 and by the respective authors

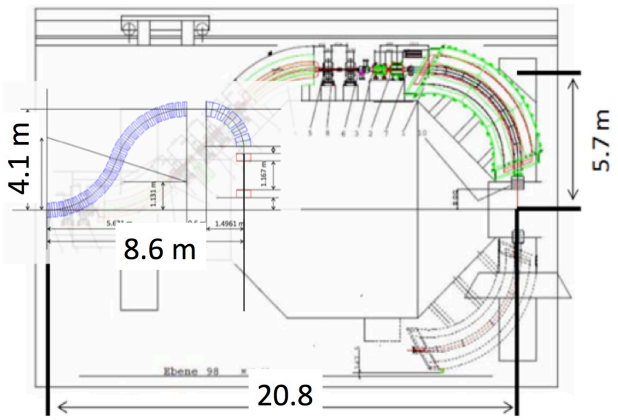


Figure 6: The carbon ion gantry with superconducting magnets is shown together with the Heidelberg gantry.

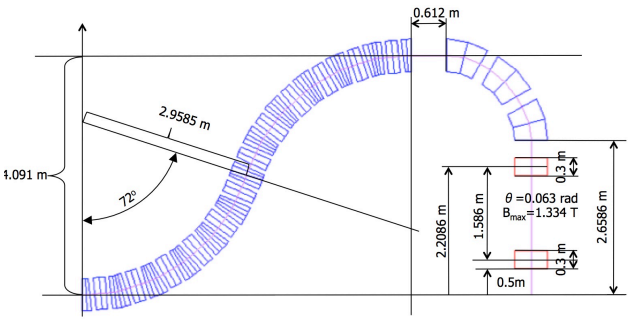


Figure 7: The carbon ion superconducting fixed field isocentric gantry layout. The scanning magnets are 30 cm long with a maximum required magnetic field of 1.35 T for the kinetic energy of 400 MeV/u (to be able to bend the beam ±10 cm at the patient (a distance between the two magnets is 1.566 m).

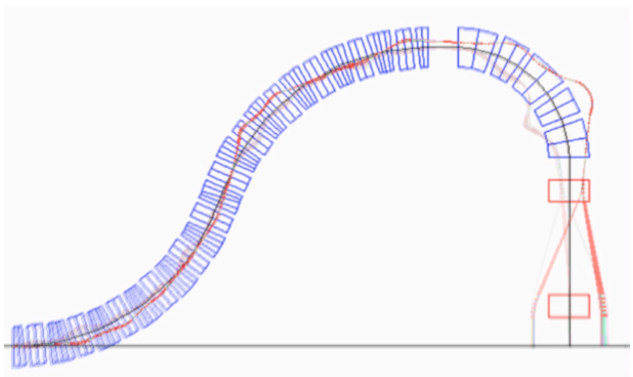


Figure 8: The fixed filed superconducting carbon isocentric gantry with beams of 202, 270, and 400 MeV/u. With the magnified (x10) scanning ±10 cm positions.

Two examples of the superconducting carbon ion gantries: the isocentric gantry (the same as in Fig. 6) and the eccentric one are shown in Figures 7&8, and Figures 9&10, respectively.

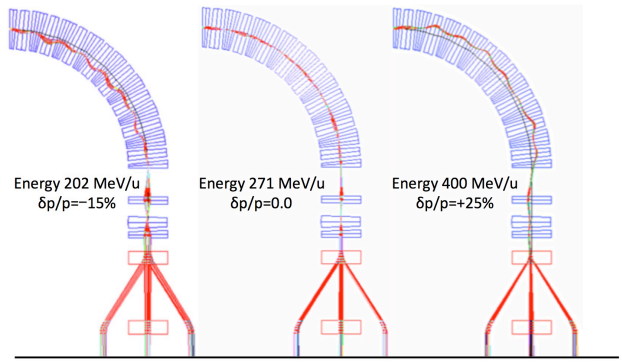


Figure 9: The 90°-superconducting gantry shown with carbon ions passing with three energies 202, 271, and 400 MeV/u under the fixed magnetic field, with scanning magnets. Positions of ±10 cm at the patient are magnified.

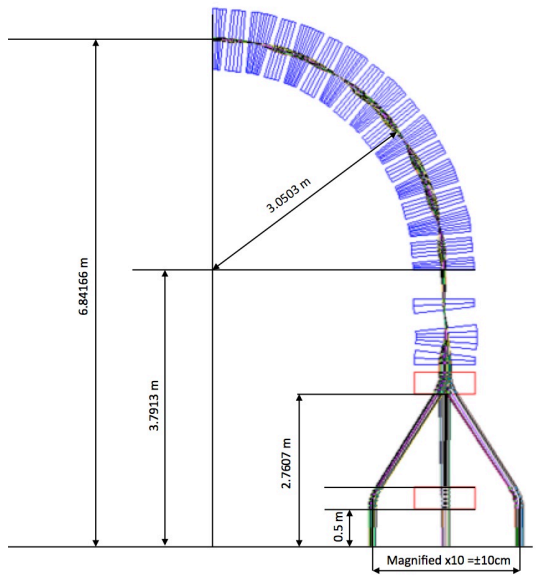


Figure 10: The layout of the 90° superconducting fixed field carbon gantry designed to fit to the CNAO eccentric gantry.

SUMMARY

The NS-FFAG superconducting gantries for carbon ion design with isocentric and eccentric case are presented. The gantry design fulfills a requirement of the very large momentum acceptance with a fixed magnetic field. Major advantages of the proposal are reduced size, weight, and easier operation as the magnetic field is fixed during the treatment time. New scanning system with SAD=∞ is presented. It reduces the size of the gantry, as it does not need the very large magnet at the end. The triplet magnets, placed above the scanning system, are used to define the beam size at the patient.

REFERENCES

[1] Robert Wilson, Radiology **47**, 487 (1946).
[2] Summary Report, Workshop on Ion Therapy, Bethesda, January 11-13, 2013.

Copyright © 2013 CC-BY-3.0 and by the respective authors

CYCLOTRON PRODUCTION OF POSITRON EMITTING RADIOMETALS

S. E. Lapi and T. Voller, Washington University in St. Louis, MO, 63110, USA

Abstract

The increase in use of Positron Emission Tomography (PET) for medical imaging has led to the development of numerous radiopharmaceuticals for use in preclinical and clinical research for oncology, cardiology and neurology [1]. While many of these biological processes can be investigated with probes radiolabeled with the more commonly used positron emitters, ^{18}F ($t_{1/2}$ = 110 min) and ^{11}C ($t_{1/2}$ = 20 min), imaging at longer timepoints requires radionuclides with longer half-lives. Thus, the production and purification of longer-lived position emitting radiometals has been explored to allow for imaging of peptides, antibodies and nanoparticles. This brief review will focus on the production and purification of ^{64}Cu ($t_{1/2}$ = 12.7 h) and ^{89}Zr ($t_{1/2}$ = 3.27 d).

INTRODUCTION

Positron Emission Tomography (PET), with its high sensitivity and resolution, is growing rapidly as an imaging technology for the diagnosis of many disease states. The success of this modality is reliant on the development of effective imaging compounds. Initially, research in this area was focused on the relatively short-lived PET isotopes ^{11}C and ^{18}F, but the short half-lives of these isotopes limit radiopharmaceutical development to those that probe rapid biological processes. To overcome these limitations, there has been a rise in alternative radionuclide tracer development in recent years. Below, in Table 1, are some examples of radiometals for use in nuclear imaging (all data from [2]).

Table 1: Examples of Positron Emitting Radiometals

Isotope	Production Route	Half-Life
^{64}Cu	^{64}Ni(p,n)	12.7 h
^{68}Ga	^{68}Ge Generator	68 min
^{86}Y	^{86}Sr(p,n)	14.7 h
^{89}Zr	^{Nat}Y(p,n)	3.27 d

While ^{68}Ga use has also increased recently, this short review will focus on the cyclotron produced isotopes, namely ^{64}Cu and ^{89}Zr.

Washington University in St. Louis has been producing and distributing longer-lived PET radionuclides to the research community for over 15 years. The radionuclides that have been produced include ^{64}Cu, $^{76/77}$Br, ^{66}Ga, ^{86}Y, ^{124}I, and ^{89}Zr. Presently, ^{64}Cu and ^{89}Zr are produced on a regular basis (weekly and biweekly respectively), while ^{86}Y and ^{76}Br are produced intermittently in lower quantities. The recent increase in production and shipping of ^{64}Cu to external institutions is illustrated in Figure 1 and is mainly due to the increase in clinical trials with this isotope.

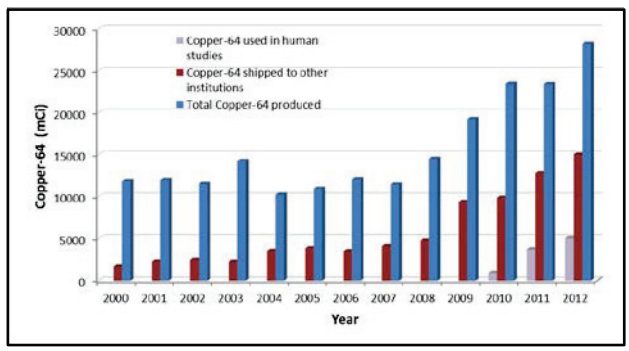


Figure 1: Production and Distribution of ^{64}Cu from Washington University in St. Louis.

TARGET PREPARATION AND BOMBARDMENT

Radiometal production starts with preparation of the target material on a suitable support for cyclotron bombardment. This may be an electroplated deposit, pressed powder pellet, or a foil placed in a suitable holder.

Preparation of ^{64}Ni Targets for Production of ^{64}Cu

Targets are prepared for ^{64}Cu production as per McCarthy *et al* [3]. Briefly ^{64}Ni metal is dissolved in 10 ml of 6.0 M nitric acid. The solution is then evaporated to dryness. The residue is dissolved in 1 ml of concentrated sulphuric acid and 5 mL deionized water and evaporated until slurry is formed. The resulting solution is diluted in 5 ml of deionized water. The pH was then adjusted to 9 with concentrated ammonium hydroxide (25%). Then 0.2 g of ammonium sulphate is added to the solution. This solution was transferred to an electrolytic cell with a graphite electrode as anode and a gold disc (target backing) as cathode. The cathode is cleaned with 6N HNO_3 to remove any metal residue on the surface. The cell is operated at 2.5 V with a starting current between 70-80 mA/cm^2. Final target weights are typically between 20 and 80 mg with a spot diameter of 5 mm.

The ^{64}Ni target is irradiated at a beam current of 20 µA for 60 to 80 µA-h with a Cyclotron Corporation CS-15 positive ion cyclotron, with a pneumatically-controlled cylinder sealing the back of the disc and providing cooling with recirculating chilled water. After irradiation,

*Work supported by the Department of Energy, Office of Science, Isotope Program under grant DESC0008657

Copyright © 2013 CC-BY-3.0 and by the respective authors

the cylinder is retracted, and the disk is ejected into a transfer line via pressurized nitrogen. The disc is brought up from the cyclotron vault to a shielded cell using vacuum. The target is then transferred manually to the processing hotcell.

Preparation of Y Foils for Production of ^{89}Zr

For the production of ^{89}Zr, a 0.64 mm thick ^{nat}Y disc is placed inside a niobium target holder. Nb was selected because of its high melting temperature (Tm = 2,468 °C) and high chemical inertness. Before each target holder was reused, it was scrubbed by hand using a cotton swab dipped in a slurry of Al_2O_3 powder and water. The target holder was placed in 6 M HCl for 1–4 h for cleaning and oven dried before mounting in the CS-15 cyclotron. During bombardment (typically 20 µA for 40 to 60 µA-h), the target holder assembly is cooled on the beam side by a He gas jet and on the reverse side by flowing chilled water. Following irradiation, the target remains in the solid target station for several hours to allow for the decay of short-lived contaminants, (^{89m}Zr) prior to processing as described below.

PURIFICATION

Following irradiation of the targets, the radionuclide of interest is separated from the target material by chemical processing.

Purification of ^{64}Cu

^{64}Cu is purified via an in-house automated system using a procedure adapted from the manual separation described in McCarthy *et al* [3] for use in a hotcell with remote operation [4].

The automated purification module consists of a series of PTFE or Kel-F based solenoid valves that direct liquid, gas, and vacuum flow. Processing of the irradiated enriched ^{64}Ni targets involves the dissolution of the nickel in 6M HCl in a custom made, heated PTFE vessel (30 min), active cooling of the dissolved nickel solution with a vortex tube (20 min), then recovery of the nickel via ion chromatography with 6M HCl, followed by an additional 6M HCl rinse of the dissolution vessel for higher recovery and removal of nickel from the resin, and elution of copper from the resin with 0.5M HCl. The entire chromatography process takes 40 minutes, and the liquid level is monitored via a camera to prevent the resin from drying out. The collected ^{64}Cu solution is then evaporated under argon (20 min) and reconstituted in 0.1M HCl. Another camera monitors the progress of the evaporation. Three radiation detectors are located by the dissolution vessel, column, and nickel recovery vial and provide real-time feedback on how well the process is proceeding. On average, the entire process takes about 2 hours from target introduction. The components required for these steps are located within the hot cell shown in Figure 2, while the control components and computer are located outside of the hot cell.



Figure 2: ^{64}Cu purification system.

The components are controlled using a USB digital input output (DIO) data acquisition unit and digital output modules. The in-house developed control program is easy to navigate and affords the operator flexibility during the synthesis. At the launching of the program, a series of dialog windows guide the operator in the preliminary preparation of the module. Once this procedure is fulfilled, the module is ready to start the synthesis. The operator also has the possibility to pause / abort the synthesis at any time during the sequence if a critical condition occurs. A diagnostic window is available to the operator for troubleshooting during synthesis, permitting the remote actuation of each step in the sequential procedure if adjustment is required due to a faulty condition.

Typical recoveries with this system are 96% or better of starting radioactivity and 98.6% of enriched ^{64}Ni target material.

Purification of ^{89}Zr

We have automated the ^{89}Zr purification method of Holland et al [5] on an in-house constructed system [6]. Using a custom software program made in LabVIEW, running on a laptop outside the hot cell 10 mL 2 M HCl is added to the dissolution vessel to dissolve the ^{nat}Y target. After waiting ~1 h for complete dissolution, the dissolved target is transferred to the separation column containing 100 mg of hydroxamate resin) through tubing using compressed air. Then, the Y is eluted from the column in 10 mL 2 M HCl and collected in a waste vial, leaving the ^{89}Zr bound on the column.

The column is rinsed with 10 mL water, which is collected in the same waste vial, and then ^{89}Zr is eluted in 1 mL 1 M oxalic acid and collected in a product vial as ^{89}Zr-oxalate. A schematic of the automated module for the separation of ^{89}Zr from the yttrium target material is shown in Figure 3.

Copyright © 2013 CC-BY-3.0 and by the respective authors

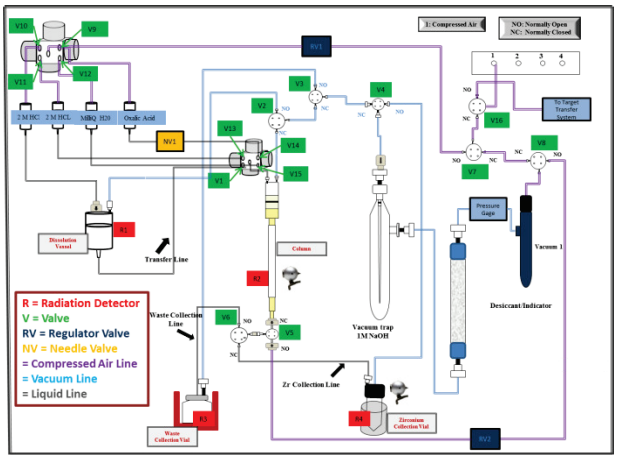


Figure 3: ^{89}Zr purification system.

QUALITY CONTROL

All isotopes undergo quality control procedures including radioisotopic purity and effective specific activity.

Radioisotope Purity

The radiochemical purities of the produced radioisotopes are assayed after end of purification via gamma spectroscopy with a high purity germanium well detector coupled to a multichannel analyzer. "Clean" ^{64}Cu spectra should show only the characteristic gamma ray at 1364 keV and the 511keV annihilation photon, while the ^{89}Zr spectra should display only the 909 keV characteristic gamma ray and the 511 keV annihilation photon. Figure 4 shows a typical high purity ^{89}Zr gamma ray spectrum.

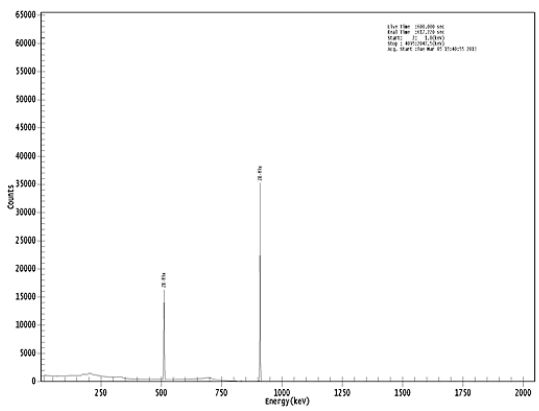


Figure 4: Gamma ray spectrum of ^{89}Zr.

Effective Specific Activity (ESA)

Effective Specific Activity (ESA) for radiometals can be defined as the amount of metals present that will bind to a suitable ligand per unit radioactivity. Determination of ESA involves titration with a suitable chelator. In this manner we can determine the amount of total metals that many interfere with the chemistry of each isotope. For example, below, in Fig. 5, is a titration curve for measurement of ^{64}Cu ESA with TETA.

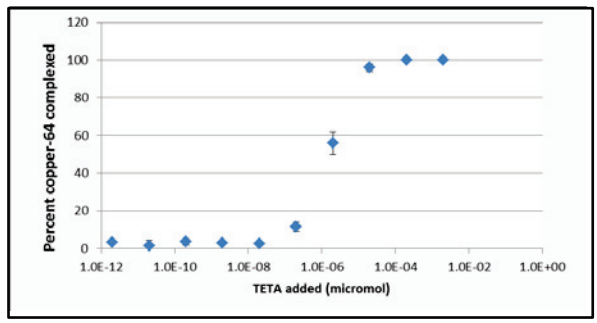


Figure 5: TETA titration for the determination of ESA for ^{64}Cu.

To determine the ESA, the point at which 50% of the radioactivity is complexed and doubled to determine the amount required to complex 100%. The total amount of transition metal complexed is determined and the users are supplied with an ESA in mCi/mmol total metal ions. Typical ESA varies from 7680 to 38400 mCi/µmol total binding metals from ^{64}Cu and from 45 to 1780 mCi/umol for ^{89}Zr.

CONCLUSION

Radiometal isotopes have enabled the investigation of various biological processes in the area of oncology, cardiology and neurology. Widespread use and clinical translation of these radionuclides requires robust optimized target preparation and purification methods for routine production.

ACKNOWLEDGMENTS

The authors would like to acknowledge Bill Margenau, Patricia Margenau, and David Ficke for operation of the CS15 cyclotron and Paul Eisenbeis, Evelyn Madrid and Efrem Mebrahtu for target preparation and isotope purification.

REFERENCES

[1] O. F. Ikotun and S.E. Lapi, Future Med. Chem. (2011) 3, 599-621.
[2] National Nuclear Data Center http://www.nndc.bnl.gov/
[3] D.W. McCarthy *et al.*, Nucl. Med. Biol. (1997) 24, 35-43.
[4] M. Kume *et al.*, Appl. Radiat. Isot. (2012) 70, 1803-6.
[5] J. P. Holland, Y. Sheh and J. S. Lewis, Nucl. Med. Biol. (2009) 36, 729-39.
[6] A. L. Wooten *et al.,* Applied Sciences. (2013) 3, 593-613.

Copyright © 2013 CC-BY-3.0 and by the respective authors

LOW ENERGY FUSION FOR A SAFE AND COMPACT NEUTRON SOURCE

S. Albright* and R. Seviour, IIAA, University of Huddersfield, UK, HD1 3DH

Abstract

Neutrons are primarily produced at large international facilities using either spallation reactions or nuclear fission. There is a demand for small scale neutron production for use at hospitals and borders for a variety of applications. Isolated fission sources and sealed tube deuterium-tritium fusors are able to provide a reliable neutron flux at small scale but are impractical due to the associated radioactivity. A beam of protons or deuterons accelerated onto a thin target will undergo a fusion reaction resulting in the emission of a quasi-monochromatic neutron beam. The total flux and energy spectrum of the neutrons produced through fusion is primarily dependent on target material, target thickness, beam energy and projectile. The use of neutrons for security screening at border crossings, ports and airports has the potential to drastically improve threat detection and contents verification. Monte Carlo code MCNPX is being used to investigate the most suitable target and beam characteristics for a neutron source for security applications.

INTRODUCTION

There are many areas of both science and industry which use neutron beams. There is growing interest in using neutrons for medical applications, such as Boron Neutron Capture Therapy (BNCT) [1], and for security applications, such as Pulsed Fast Neutron Analysis (PFNA) [2]. Medical and security applications in particular are not easily served by current neutron sources which tend to be either large and expensive or have radiotoxicology concerns.

For use in medical and security environments two important properties of a neutron source are that it be:

- Compact: Hospitals and airports in particular have limited space available.
- Clean: Radiotoxicity must be kept to a minimum to protect operators and reduce necessary safeguards.

Recently there has been an increased interest in using low energy accelerators (¡10MeV) to produce neutrons. There are sealed tube neutron sources on the market at present (such as the ING013 produced by the VNIIAA [3]) which use a Tritiated Titanium target bombarded by a deuteron beam to produce a high flux of quasi-monochromatic neutrons at $\approx$ 14MeV. Sealed tube sources are not practical for mass deployment due to both the radiotoxicology of Tritium and the legislative controls around their use and transport [4, 5].

In this paper we present simulated results showing that fusion reactions are capable of providing neutrons suitable for a range of industrial applications. Keeping the energy of the incident particles low enables the use of small accelerators and choosing the projectile/target combination correctly will prevent build up of any long lived radioisotopes.

Proton induced fusion reactions were simulated in the Monte Carlo code MCNPX [6] to show the effect of varying target and beam parameters on the neutron beam. The optimum parameters of the neutron beam depend upon the application. Fusion based neutron sources have been shown to satisfy the requirements of two very different applications. For PFNA the primary concern is that the neutron spectrum be both narrow and high energy. For BNCT the neutrons are moderated into the epithermal region therefore the spectrum from the source is unimportant and only the total flux and size of the source are of concern.

The nuclear inventory package EASY-II [7], which uses the fispact-II code [8], has been used to investigate the build up of isotopes in targets to ensure no long-lived radioisotopes are produced. EASY-II enables the build up, decay, and subsequent re-activation of isotopes to be simulated reducing the risk of potentially hazardous decay and transmutation chains being unidentified.

APPLICATIONS

A brief description of two valuable applications of a fusion based neutron source is given along with details of the optimum neutron beam properties for both applications. The two applications discussed are BNCT, a cancer treatment, and PFNA, a security technique.

BNCT uses a boronated drug, preferentially taken up by tumour tissue, and then bombarded by epithermal neutrons. The reaction ^{10}B + n $\rightarrow ^{7}$Li + α causes a massive dose of radiation to be delivered to the tumour whilst leaving surrounding tissue relatively untouched. As BNCT requires epithermal neutrons the beam must be moderated, the sourced neutron spectrum is therefore unimportant and instead maximising the flux whilst minimising the size of the source is the principle concern.

PFNA is a security technique which uses a high energy, monochromatic neutron beam to stimulate the emission of prompt gammas (γs) from material. The γs emitted in PFNA are unique to the element being interrogated allowing the precise content of cargo to be identified. By pulsing the source a volume can be broken into voxels giving a 3D breakdown of what is in a container and where it is located. For PFNA it is important that the neutron beam be; high energy, to maximise prompt gamma emission and minimise transmutation rates; and monochromatic, to minimise both voxel sizes and uncertainties in gamma emission rates.

* corresponding author: simon.albright@hud.ac.uk

Copyright © 2013 CC-BY-3.0 and by the respective authors

MONTE CARLO SIMULATION

Monte Carlo code MCNPX has been used to demonstrate the effect of changing beam and target parameters on neutron spectrum. The parameters which can be varied are target element, target thickness, beam energy and projectile. The two elements discussed are Magnesium and Beryllium as the results are representative of what most targets will produce.

The plots in Figure 1 and 2 show the change in neutron spectrum and flux with increasing beam energy. The very thin target used in these simulations (5μ m) meant that little energy was lost as protons travelled through the target. Since very little energy was lost the protons which reacted all had approximately the same energy.

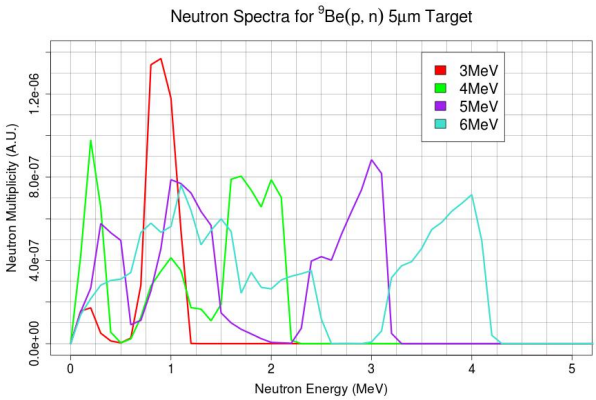


Figure 1: The neutron energy spectrum produced by a thin Beryllium target bombarded with protons with energy from 3-6 MeV.

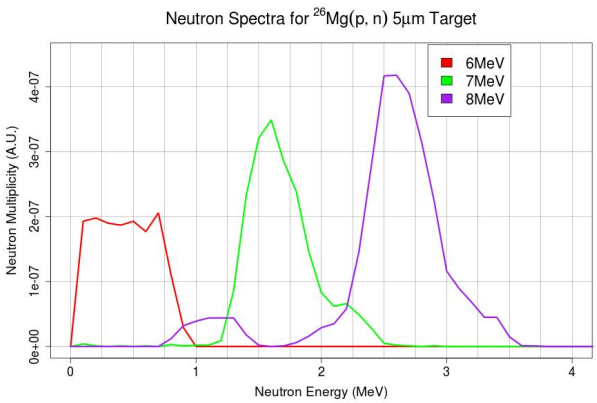


Figure 2: The neutron energy spectrum produced by a thin Magnesium target bombarded with protons with energy from 6-8 MeV.

The results in Figure 1 show that the ^{9}Be(p,n)^{9}B reaction very produces a broad spectrum of neutrons. Due to the spectral characteristics of a ^{9}Be target it would be most suited to an application like BNCT where the spectrum of the sourced neutrons is unimportant. The results in Figure 2 show that, for a thin target, the ^{26}Mg(p,n)^{26}Al reaction maintains a relatively narrow spectrum up to much higher beam energy and neutron energy than the ^{9}Be(p,n)^{9}B reaction. Due to the narrow spectrum the ^{26}Mg(p,n)^{26}Al reaction would be more suitable to an application like PFNA where spectral characteristics are the primary concern.

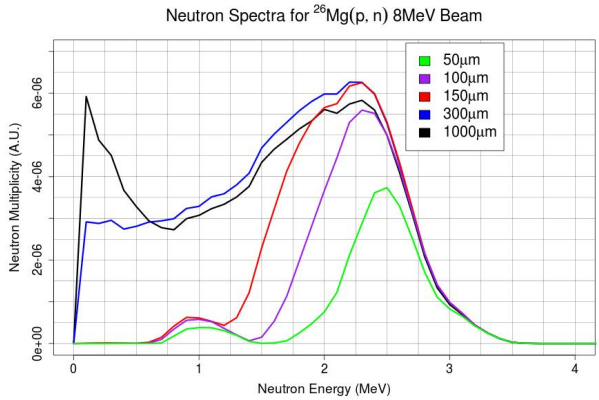


Figure 3: The neutron energy spectrum produced by a Magnesium target with thickness $50-1000\mu m$ bombarded by 8MeV protons.

The results plotted in Figure 3 show the impact of increasing target thickness on the neutron spectrum of the ^{26}Mg(p,n)^{26}Al reaction. The results in Figure 3 are characteristic of all accelerator based fusion reactions. As the thickness of the target increases the total flux and spectral width increase. Once the target is thick enough to slow incident projectiles below the fusion threshold energy the maximum neutron flux is reached ($\approx 300\mu$m in Figure 3), after this the only effect of increasing target thickness is increased neutron moderation.

ISOTOPE INVENTORY

As well as a thorough understanding of the neutron production properties of a target it is vital that the isotope production be well characterised. Under constant bombardment the target nuclei will transmute which may lead to a build up of radioactivity. Not only will the intended reaction occur (e.g. ^{26}Mg(p,n)^{26}Al) but other first generation reactions (e.g. ^{26}Mg(p,α)^{23}Na) and higher generation reactions (e.g. ^{26}Mg(p,n)^{26}Al(p,n)^{26}Si). The presence of additional decay channels and the production of higher generation isotopes poses a potential threat to the safety, and therefore applicability, of a fusion based neutron source.

Simulations were carried out in EASY-II to identify the isotopes produced in a selection of targets under proton bombardment. After 72 hours of continual 8 MeV proton bombardment on ^{9}Be and ^{26}Mg targets the isotopes shown in Table 1 were identified. The ^{9}Be target would be expected to have no latent activity, the initial fusion reaction and subsequent decays are:

$$^{9}\mathrm{Be} + \mathrm{p} \rightarrow ^{9}\mathrm{B} + \mathrm{n}$$

Copyright © 2013 CC-BY-3.0 and by the respective authors

$$^{9}\mathrm{B}(t_{\frac{1}{2}} \approx 8 \times 10^{-19}\mathrm{s}) \rightarrow ^{8}\mathrm{Be} + \mathrm{p}$$

$$^{8}\mathrm{Be}(t_{\frac{1}{2}} \approx 6 \times 10^{-17}\mathrm{s}) \rightarrow 2\alpha$$

The extremely short half lives of the products in the decay chain prevents any latent activity building up in the target. Table 1 shows that under proton bombardment ^{9}Be will also produce the radioisotope ^{7}Be($t_{\frac{1}{2}} \approx 53$d) through the interaction chain ^{9}Be(p,γ)^{10}B(p,α)^{7}Be.

Table 1: The Isotopes (Z>2) Produced after 72 Hours of 8 MeV Proton Bombardment of ^{9}Be and ^{26}Mg

^{9}Be	^{26}Mg
^{6}Li	^{16}O
^{7}Be($t_{\frac{1}{2}} \approx 53$ d)	^{20}Ne
^{10}B	^{23}Na
	^{24}Mg
	^{25}Mg
	^{26}Al($t_{\frac{1}{2}} \approx 7 \times 10^{5}$ y)
	^{26m}Al ($t_{\frac{1}{2}} \approx 6$ s)
	^{27}Al

As ^{9}B decays nearly instantaneously and ^{26}Al has a very long half life it would at first be assumed that ^{9}Be was a preferred target in terms of radiotoxicology. The 2nd generation isotope ^{7}Be is potentially more dangerous than ^{26}Al as, due to the differing decay rates, a larger amount of ^{26}Al would be required to take the activity above safe limits. In an industrial environment, be it medical, security or other, the residual activity of the target must not exceed safe limits but different applications may have different limits.

FUTURE WORK

At present there are no Monte Carlo codes able to accurately simulate low energy deuteron interactions and proton interactions can only be reliably simulated with nuclear data files. There is a loose trend for more energy being released (and therefore lower acceleration voltages needed) in deuteron induced reactions than proton induced reactions. Due to the higher energy release deuterons may be a better projectile for applications which require a high energy neutron beam.

Whilst cross-sections are known for most (d, n) reactions the energy spectra and angular distributions of the emitted neutrons remain mostly unpublished. Additional experimental data will broaden the range of projectile/target combinations which are understood and so enable neutron sources to be more effectively tuned to the application.

CONCLUSION

Two potential applications of low energy fusion based neutron sources have been discussed. For example in medicine neutron can be used for the cancer treatment BNCT, this requires an epithermal neutron beam which can be achieved by moderating a higher energy beam. For BNCT the sourced spectrum is unimportant so instead a high flux, low energy (and therefore compact) source can be used. The discussed ^{9}Be(p,n)^{9}B reaction would be suitable for this application as even at 3 MeV a fair neutron flux is achieved.

In security the neutron scanning technique PFNA requires a high energy, monochromatic beam. As the spectrum of the beam is most important for PFNA it would be acceptable to use a lower flux target which has better spectral properties. A target with characteristics similar to the ^{26}Mg(p,n)^{26}Al would be suitable for this application.

For either of these technologies to become a reality a low-cost compact source of neutrons need to be developed, and a key way in which both of these conditions can be achieved is through the use and development of neutron sources that utilise low energy reactions. A concern with any device based on nuclear interactions is the production of radioisotopes. Whilst radioisotopes are produced by both ^{9}Be and ^{26}Mg the level of activity may not be sufficient to pose a safety concern.

REFERENCES

[1] S. Green, Developments in Accelerator Based Boron Neutron Capture Therapy, J. Radiat. Phys. Chem. Volume 51, No. 4-6, 1998, pages 561-569.

[2] D. R. Brown, T. Gozani, Cargo Inspection Systen Based ob nPulsed Fast Neutron Analysis, J. Nuclear Instruments and Methods in Physics Research B, Volume 99, 1995, pages 753-756.

[3] website: http://vniia.ru/eng/ng/docs/ing_element_eng.pdf

[4] Ionising Radiations Regulations 1999
website: http://www.legislation.gov.uk/uksi/1999/3232/contents/made

[5] High-activity Sealed Radioactive Sources and Orphan Sources Regulations 2005
website: http://www.legislation.gov.uk/uksi/2005/2686/contents/made

[6] MCNP: Monte Carlo N-Particle Transport Code System Including MCNP6.1, MCNP5 1.60, MCNPX 2.70 and Data Libraries. Available from the Radiation Safety Information Computational Center (RSICC) at Oak Ridge National Laboratory as CCC-810.

[7] website: http://www.ccfe.ac.uk/EASY.aspx

[8] website: http://www.ccfe.ac.uk/assets/Documents/CCFE-R%2811%2911.pdf

Copyright © 2013 CC-BY-3.0 and by the respective authors

ACCELERATOR-BASED NEUTRON DAMAGE FACILITY USING LEDA*

N. Pogue, P. McIntyre, A. Sattarov, Texas A&M University, College Station, TX 77845, USA

Abstract

An accelerator based neutron damage facility (AND) is proposed to generate a high-dose fast neutron flux for testing of advanced reactor materials. The facility will be implemented in two stages. In AND-1, the 350 MHz LEDA RFQ will be re-commissioned to deliver 100 mA CW proton beam at 6.7 MeV. The beam will be targeted on a sheet-flow of Lithium to produce fast neutrons. Samples located at a target station behind the sheet flow will receive up to 10 dpa/year of neutron damage with a mean neutron energy of 2.37 MeV. In AND-2, the LEDA beam will be modulated to produce three 116 MHz bunch trains where they will be injected to three 100 MeV strong-focusing cyclotrons (SFC). The beams extracted from the three cyclotrons will be targeted 120 degrees apart onto sheet-flow Pb targets. Twenty one tensile samples located in the space between the three targets will receive up to 150 dpa/year of fast neutron damage with mean neutron energy ~8 MeV. AND-1 and AND-2 can provide the fast neutron flux needed for life-cycle damage studies for advance reactor technologies and for first-wall simulations for fusion systems.

INTRODUCTION

A design for an accelerator-based neutron damage (AND) facility has been devised to test advanced reactor materials. Since Three Mile Island there have been no new licenses issued for new construction in the US until just recently (2 reactors). Materials testing is one of the biggest hurdles and is of the utmost importance for two reasons: 1) The original lifetime for a nuclear power plant is 40 years and thus the current fleet has only remained operation due to lifetime extension every ten years, and 2) New reactor designs (Gen 4 and ADS systems) that are more efficient and clean require materials that remain unproven up to 200 dpa (displacement per atom). Currently, testing of materials to be used in advanced reactors is underway at facilities around the world such as HFIR and BOR60. However to reach 200 dpa within the sample takes over 15 years domestically and 10 years internationally. A decade long evaluation process enormously extends the selection process and material evolution.

As a consequence of this timeline, nuclear engineers have turned to the only method readily available, ions. Ions produce significantly more dpa per incident particle than neutrons. However, the mechanisms that ultimately dictate how the material swells and embrittles function differently for the two flavors of particles. Defect production, defect migration, defect annealing, production of interstitial clusters and loops, and H and He production, as well as how damage induced is effected by their presence, are all different for neutrons vs. ions. *Much has been learned about mechanisms that control damage from ion studies, but one cannot predict the damage a given neutron spectrum and dose will produce in a new material solely by experiments with ion damage.* Therefore, without a fast, high fluence neutron source, the ultimate lifetime and failure modes for materials to be used in advanced reactions cannot be ascertained.

Texas A&M Accelerator Research Lab (ARL) has devised an accelerator that can produce 200 dpa via neutron bombardment on several samples in less than 16 months, while also providing control of the temperature and chemical environment of the samples during exposure (problematic in reactors). The spectrum can be tuned to fully mimic conditions anticipated in future fission and fusion (currently not possible) reactors.

AND OVERVIEW

AND is comprised of two stages that utilizes several technologies developed by several groups. In the first stage the LEDA accelerator will be re-commissioned at ARL and send a 100 mA 6.7 MeV proton beam to a liquid Lithium sheet target similar to that developed by ANL. The second stage takes the proton beam from LEDA and accelerate 45 mA of the beam to 100 MeV using a set of 3 flux coupled Strong Focusing Cyclotrons (SFCs) developed at Texas A&M. The three beams are then directed to liquid Lead targets. The result of these two stages is a facility that can generate ~150 dpa/year using fast neutrons. An image of the facility is shown in Figure 1.

AND – PHASE 1

LEDA

The Low Energy Demonstration Accelerator, or LEDA, is one of the few RFQ accelerators that have achieved high current CW operation [1]. Initially built as the front end of the Accelerator Production of Tritium (APT), the accelerator was commissioned in 2003 and achieved in accelerating ~100 mA of beam to 6.7 MeV. In 2004, LEDA was decommissioned and remains in pristine condition within a high strength support structure, to maintain internal alignment among the cavity sections, while in storage (Figure 2). The current state of LEDA should assure that the time to re-commission at low power should be less than a year. Los Alamos National Lab (LANL) has agreed to make a 10-year loan of the LEDA system to Texas A&M University. ARL plans to move LEDA to Texas A&M along with pulsed RF power source, power supplies, transformers, and waveguides from LANL. The RF power loaned will be a pulsed system, but A&M has received commitment from CERN for two 1 MW 350 MHz CW power sources.

* Work supported by State of Texas and Mitchell Foundation
# npogue@physics.tamu.edu

Copyright © 2013 CC-BY-3.0 and by the respective authors

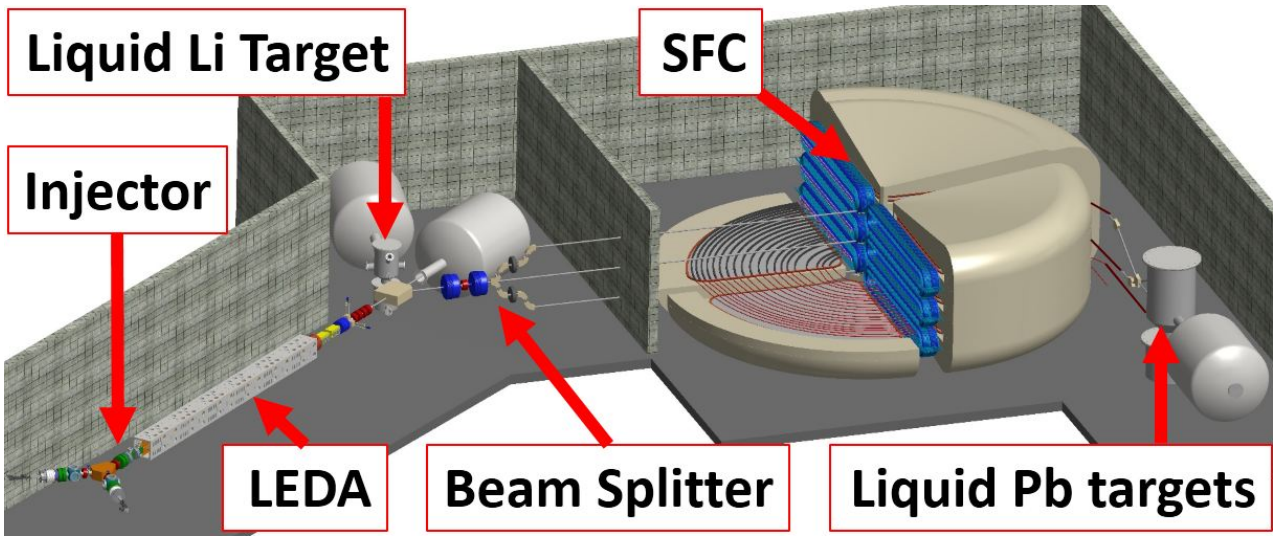


Figure 1: A diagram of the AND facility which identifies the critical system components. The LEDA and liquid Lithium target comprise Phase 1 and the SFC and Lead targets would be added to as Phase 2.

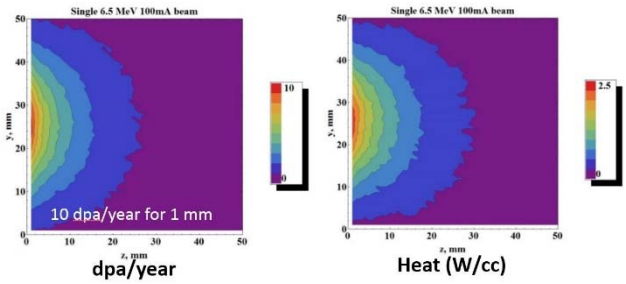


Figure 2: ~10 dpa/year is generated through a thickness of 1 mm. Such a rate is equivalent to current US capability.

Liquid Lithium Target

The 100 mA proton beam will be directed to a windowless liquid Li target to generate the neutrons for Phase 1. Li is used at this energy because the cross section is very large compared to other materials. The target must be molten so it can support the ~700 kW delivered by the beam. The Li is forced through a slit forming a flowing sheet of molten metal approximately 5 cm wide into a reservoir tank. The liquid in the tank is pumped through a heat exchanger and then pumped back to the slot iris. This approach has been developed at ANL and is planned to be used at facilities such as FRIB and RIKEN, but for stripping purposes. The AND system can produce at most 1.5 MW/cc. This power density is substantially lower than the 4.1 MW/cc electron beam used to test the device [2].

Neutron Damage – AND Phase 1

The Li window is ~2 mm thick and contains the Bragg peak of the protons and thus only neutrons bombard the sample. Dpa calculations were performed using a modified Kinchin and Pease model as is performed in the code SPECTER. The mean neutron energy for the AND-1 is 2.37 MeV and produces 10 dpa/year within the first 1 mm of the sample.

AND - PHASE 2

In Phase 2 the 350 MHz, 100 mA beam is split into 3 separate 116 MHz 15 mA beams. Each beam is then sent to TAMU100, a flux coupled stack of three strong focusing cyclotrons (SFCs). Using the SFC the beam is accelerated to 100 MeV and delivered to a molten Pb sheet flow target.

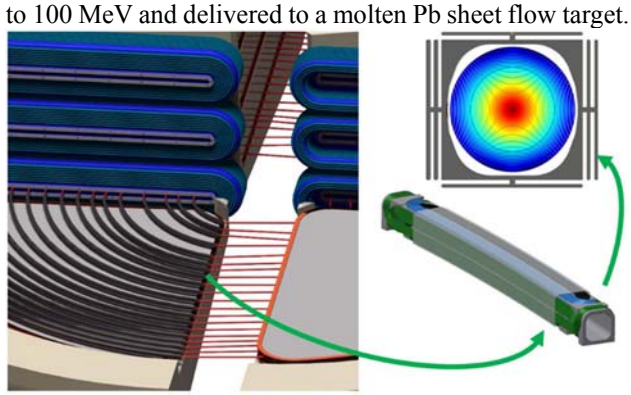


Figure 3: Left: SRF cavities (blue) and quadrupole channels are shown covering the proton projected orbits. Right: Detail of quad and the focusing field produced.

SFC – Strong Focusing Cyclotron

The SFC design incorporates three innovations (Figure 3) to bring the benefits of strong focusing to the cyclotron: 1) flux-coupled sector dipoles that permits one to stack multiple cyclotrons with a common footprint. 2) high-gradient superconducting RF cavities to increase the beam energy enough in each orbit (~2 MV/cavity) such that the succeeding orbits are fully separated; 3) As a consequence of the large separations, a set of beam transport channels are inserted in the aperture of the sector dipoles [3].

Each sector magnet has a pair of windings that each have a cold iron flux plate and generate ~1 Tesla. The sector dipoles of successive cyclotrons can thus be stacked upon one another and share a common warm-iron flux return. All magnet windings utilize MgB_2 superconductor, operating

Copyright © 2013 CC-BY-3.0 and by the respective authors

in the temperature range 15-20 K. The stack of flux plates is supported within a warm-iron flux return using low-heat-load tension supports in a magnetic design that cancels the Lorentz forces above and below each flux plate.

Each SRF cavity accelerates the 24 spiral orbits simultaneously, providing a minimum orbit separation of 5.6 cm for curved beam transport channels located in the aperture of each sector magnet. Each transport channel houses a pair of alternating-gradient Panofsky quadrupole lenses to provide an F-D strong-focusing doublet, and a window-frame dipole winding to facilitate correction of the dipole field for isochronicity. These winding also provides a built in septa for low-loss for injection and extraction.

The beam transport channels in the SFC are used to control beam size and achieve transport of larger beam current. Our simulations show that these innovations will provide reliable low-loss acceleration and transport of a 15 mA proton beam to 100 MeV in each SFC by using emittance management provided by the beam transport channels.

The beam is then extracted from each cyclotron and delivered to three molten Pb targets similar in nature to those described in the Lithium target section.

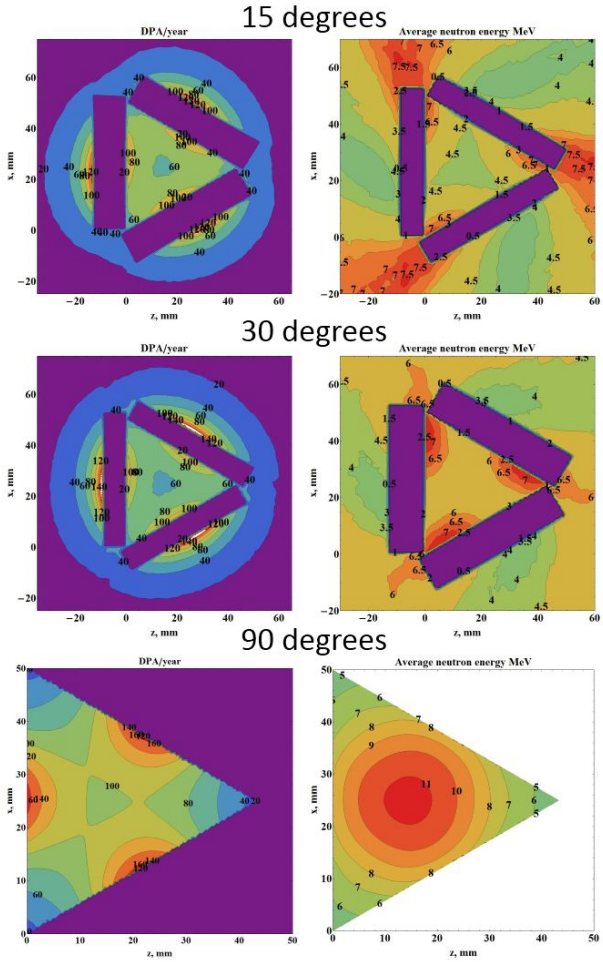


Figure 5: Angle dependence of damage and mean energy.

Neutron Damage – Phase 2

The angle at which the beam is brought to the Pb target has a dramatic effect on the mean energy and damage produced in the 21 tensile samples that are located within individually controlled environments (temperature and chemical). Three angles a re shown in Figure 5. The 15° version produced an average neutron energy of 4.5 MeV and a minimum of 50 dpa/year. The 30° had 5.5 MeV mean -60 dpa/year minimum, and the 90° case produced 8 MeV and a maximum of 160 dpa/year.

Comparing these results to the available user facilities, AND has higher fluence and average energy. If fact, AND would provide for the first time the capability to study neutron damage produced at the first wall of fusion reactors (14 MeV). AND out performs existing and designed (IFMIF) facilities at a fraction of the cost (Figure 4).

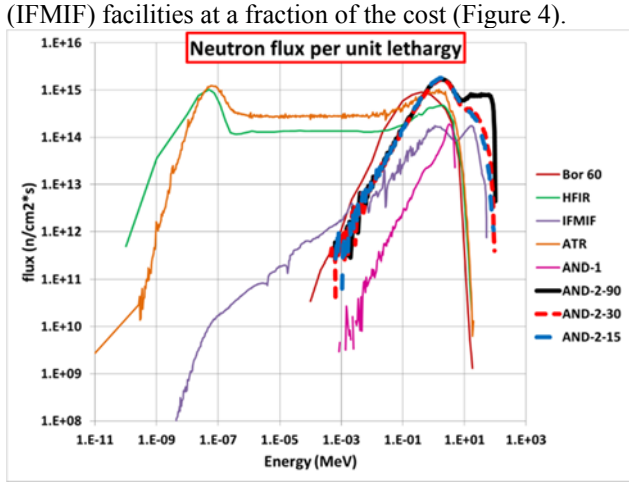


Figure 4: Comparison of AND 1&2 to other facilities around the world that are used for neutron irradiation.

SUMMARY

Ions are unable to predict damage type, ultimate lifetime, mechanical properties, and failure modes of candidate materials for advanced reactors. A high fluence fast neutron source is needed to provide critical data and reduce decade long experiments to ~1 year. ARL has devised such a facility using LEDA, SFCs, and liquid metal targetry. AND facility can provide over 150 dpa/year of damage (level needed for advanced reactors) on samples located with individually controlled environments that would uniquely support the advanced materials development for both fission and fusion.

ACKNOWLEDGMENT

Thanks to ANL, LANL, and CERN for their contributions as well as the Mitchell Foundation and the State of Texas for funding this work.

REFERENCES

[1] L.M. Young, Operations of the LEDA resonant RFQ', Proc. 2001 Particle Accelerator Conf., p.309 (2001),

[2] J. Nolen et al., "A High Power Beam-on-target Test of Liquid Li Target for RIA", Aug. 22, 2005, ANL-05/22

[3] P. McIntyre, Accelerator-Driven Subcritical Fission - How to Destroy the Transuranics in Spent Nuclear Fuel and Close the Nuclear Fuel Cycle, NA-PAC 2013, MOZAB1

Copyright © 2013 CC-BY-3.0 and by the respective authors

DEVELOPMENT OF LOW ENERGY ACCELERATOR-BASED PRODUCTION OF MEDICAL ISOTOPES

N. Ratcliffe*, R. Barlow, R. Cywinski, University of Huddersfield, Huddersfield, HD1 3BH, UK
P. Beasley, Siemens AG, Oxford, OX1 2EP, UK

Abstract

Here we present methods for production of new and existing isotopes for SPECT (Single Photon Emission Computed Tomography) and PET (Positron Emission Tomography) imaging using accelerator-based systems. Such isotopes are already widely used in medical diagnostics and research, and there is constant development of new drugs and isotopes. However the main production method for ^{99m}Tc, is currently in research reactors and is at risk due to scheduled and unscheduled shut downs. Therefore, a low cost an alternative accelerator-based system could provide many advantages. Various compact low energy proton machines are being proposed to enable cheap and accessible production: here we present a discussion of potential new SPECT isotopes and simulations of suitable targets for their manufacture.

INTRODUCTION

Currently the production of medical tracer isotopes for use in imaging techniques such as SPECT (Single Photon Emission Computed Tomography) and PET (Positron Emission Tomography) [1] relies principally upon an ageing fleet of nuclear reactors. For example the most common medical isotope ^{99m}Tc, used in over 80% of all radiopharmaceutical procedures, is currently produced, via its generator ^{99}Mo, by nuclear research reactors such as NRU-Canada and HFR-The Netherlands, which together produce over 60% of the worlds ^{99}Mo/^{99m}Tc supply. Both of these reactors are old (>50yrs) and close to decommissioning, and while several projects are looking at other production routes for this isotope, as yet there is no real replacement in place [2, 3]. As these reactors near their decommissioning, currently set at 2014-2016, there is considerable concern that we will soon be facing a similar situation to that of the 2010 isotope crisis, when both reactors were offline simultaneously resulting in a significant decrease in the supply of ^{99m}Tc and the postponing or cancelation of many vital radioisotope procedures [1–5]. Due to ^{99m}Tc monopolising the medical isotope market little work was done developing other isotopes and many potential isotopes fell by the wayside. The aim of this work is to resurrect some of these isotopes as alternatives to ^{99m}Tc as we head into another shortage in the hope of preventing another crisis. There are several short lived SPECT and PET isotopes that have the potential to take some of the workload from ^{99m}Tc.

* naomi.ratcliffe@hud.ac.uk

LOW ENERGY ISOTOPE PRODUCTION

We believe that the solution to this impending problem could lie in accelerator-based production methods, of both ^{99m}Tc and possible replacement isotopes. A collaboration with Siemens is focusing on the potential of a compact, low energy proton device for the generation of radioisotopes [6]. Such a machine could provide many more localised isotope production centres and allow for the use of isotopes with shorter halflives. A study of optimal target designs for such a system has been undertaken using GEANT4 simulations of low energy (<10MeV) proton induced reactions.

^{113M}INDIUM

^{113m}In is a metastable radioactive isotope that decays via a 392 keV γ into stable ^{113}In with a half life of 1.7hours [7]. In 1965 it was first proposed for use as an alternative medical tracer isotope to ^{99m}Tc for SPECT imaging in several applications such as brain and lung scanning. Trials of this isotope showed it to give results comparable to ^{99m}Tc images [7]. ^{113m}In showed several advantages over ^{99m}Tc such in terms of chemical properties. A successful generator production system for In was developed using ^{113}Sn [7, 8].

Generator Production

There are several advantages of a longer lived generator system, such as the Sn/In system. The longer gap between parent half life and daughter half life makes it easier to separate the two nuclei. It also increases the longevity of the system for example the Sn/In(parent half life approximately 118 days) system only needs replacing once every 6 months where as the Mo/Tc(parent half life approximately 3 days) system needs replacing weekly. However due the plentiful and cheap supply of Tc at the time very little serious work was carried forward with this isotope. The simplicity of the generator production system and the advantages available from such a system has prompted the exploration of a low energy method of production for this generator using the reaction:

^{113}In(p,n)^{113}Sn $\rightarrow$ ^{113m}In $\rightarrow$ ^{113}In

Preliminary simulation results from the TALYS data libraries show that such a reaction at 10 MeV gives a production cross section of 570mb. Further GEANT4 simulations have been used to study target designs and feasibility of this reaction using a <10MeV proton beam. In terms of daughter yield the most appropriate target thickness is that of just

Copyright © 2013 CC-BY-3.0 and by the respective authors

over the stopping distance, which from these simulations is given to be approximately 0.5mm. The generator and daughter activity for this reaction after a 30min irradiation of the target can be seen in Fig. 1.

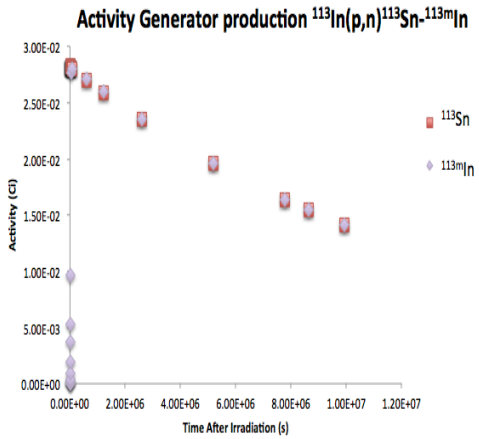


Figure 1: Activity of parent ^{113}Sn and daughter ^{133m}In produced from the generator reaction.

The lifetime of a typical Sn/In generator system is 3-6 months [9]. The activity for this time after irradiation can be seen in Fig. 1. Even after this time this small sample generator is producing an activity of 0.9 mCi which in comparison to a typical single dose of microcuries per gram [10], shows the potential of a low energy accelerator based system for the generator production of ^{113m}In.

Direct Production

Direct production of ^{113m}In appears to be less common due to the short halflife of the isotope and the lack of local facilities in which to produce it. However with the introduction of our proposed system it should be possible to make this a much more feasible production route. Both the TENDL and EXFOR libraries can be seen to agree that a cross section of just over 200mb can be obtained for the following reaction:

^{113}Cd(p,n)^{113m}In

for a proton beam between 9 and 10 MeV. The corresponding activity of In for a 0.5mm thick target after a 30min irradiation can be seen in Fig. 2.

The activity obtained for direct production is significantly larger than that of generator production. Such activity should be enough to service the needs for a local facility as is the proposed purpose of a low energy isotope production system.

^{87M}STRONTIUM

Strontium 87m is a metastable radioactive isotope that decays via a 388keV γ into stable ^{87}Sr with a half life of 2.8hours [11]. Several different strontium isotopes have an application in nuclear medicine as due to the similar

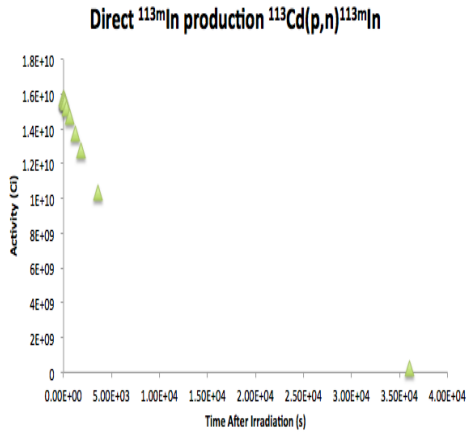


Figure 2: Activity of ^{113}In produced from the direct reaction.

chemistry to calcium it is readily taken up in bone. There are some isotopes such as ^{90}Sr which are undesirable for medial use as replace calcium in the bone and are toxic. Others however such as ^{87m}Sr can be used in both diagnostic and therapeutic techniques for various skeletal diseases [11–14].

Generator Production

^{87m}Sr is produced primarily using the ^{87}Y/^{87m}Sr generator. Literature shows many different possible methods of producing this generator. However these are all at higher energies ($>$20 MeV). This work is focusing on low energy techniques e.g. reactions such as

^{87}Sr(p,n)^{87}Y $\rightarrow$ ^{87m}Sr $\rightarrow$ ^{87}Sr

According to the TALYS/EXFOR libraries this reaction has a cross section of approximately 600mb at 10 MeV. Further study of target design were carried out using GEANT4 to obtain a suitable target that provides a viable yield for medical applications. The activity obtained from a 0.9mm thick metal target can be seen in Fig. 3.

Activity of the generator route from our simulations is of the order of curies whilst a diagnostic dose is of the order of millicurie. However from previous studied such as [11] it is apparent that this target is impractical and a compound target such as $SrCl_2$ would be more appropriate. This reduces the number of Sr nuclei within the target requiring a thicker compound target to keep the activity sufficient for the 2 week lifespan that is typical of this type of generator system.

Direct Production

It is also proposed that direct production of ^{87m}Sr is possible through the reaction:

^{87}Rb(p,n)^{87m}Sr

which according to the EXFOR libraries has a cross section of approximately 200mb in the energy range $<$10MeV. The TALYS libraries also gave a cross section of 240mb at

Copyright © 2013 CC-BY-3.0 and by the respective authors

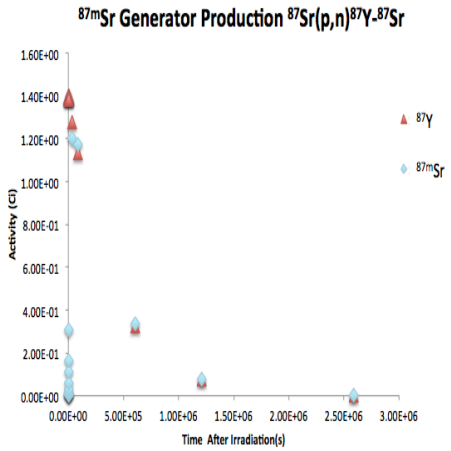


Figure 3: Activity of ^{87m}Sr produced using the ^{87}Y/^{87m}Sr generator.

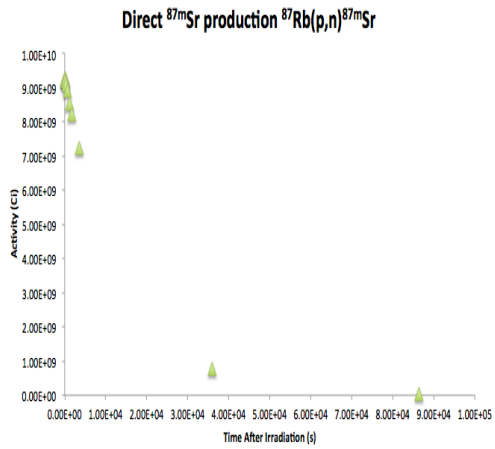


Figure 4: Activity of ^{87m}Sr produced using the direct reaction.

10MeV from which the activity of ^{87m}Sr that is produced after a 30min irradiation of a 0.5mm thick target can be seen in Fig. 4.

Even with such a simple, crude design such a large activity is obtained with this reaction. With more adjustment a suitable target could be configured so as to optimise the activity. An isotope with such a short half life is much more likely to be produced using the direct reaction on demand and so any effort to minimise the production time such as short irradiation time, from these initial results this time could be less than 30mins.

CONCLUSION

This work has shown a first test case of the feasibility and practicality of using a low energy proton accelerator system as a method of producing radioisotopes in quantities suitable for medical applications. This work will go on to optimise the low energy production routes for these isotopes in the hopes of minimising the reduction of SPECT isotopes in the predicated crisis. We will also go on to study the potential of using this system to manufacture potential isotopes to be introduced for both SPECT and PET.

ACKNOWLEDGMENT

N. Ratcliffe acknowledges the receipt of a joint EPSRC/Siemens CASE studentship.

REFERENCES

[1] M. Zakzouk, *The Medical Isotope Shortage: Cause, Effects and Options*, (Library of Parliament, Canada, 2009).

[2] *Cyclotron Produced Radionuclides: Principles and Practice*, IAEA, Technical Reports Series no.456, 2008.

[3] S. Zeisler, "Cyclotron Production of Technetium-99m," Workshop on Acclerator-driven Production of Medical Isotopes, Daresbury Laboratory, UK, 2011.

[4] *A Review of the Supply of Molybdenum-99, the Impact of Recent Shortages and the Implications for Nuclear Medicine Services in the UK*, Administration of Radioactive Substances Advisory Committee, 2010.

[5] J. Nolen, "Current and Possible New Methods for Acclerator-Based Production of Medical Isotopes," XXV International Linac Conference, 2010.

[6] P. Beasley and O. Heid, "Progress Towards a Novel Compact High Voltage Electrostatic Accelerator," PAC'11 New York, WEP207 (2011).

[7] J. Clements et al., "Indium 113m DIETHYLTRIAMINOPENTAXETIC Acid (DTPA): A New Radiopharmacutical For Brain Scanning," 1968.

[8] L. Colombetti et al., "Preparation and Testing of a Sterile Sn113-In113m Generator," 1969.

[9] N. Ramamoorthy et al., "Studies on the Preparation of ^{113}Sn-^{113m}In Generators," Isotopenpraxis Isotopes in Environmental and Health Studies, 2008.

[10] www.iem-inc.com/toolmed1.html

[11] J.F. Allen and J.J. Pinajian, "A ^{87m}Sr Generator for Medical Applications," International Journal of Applied Radiation and Isotopes, 1965.

[12] H.B.S. Kemp et al., "The Role of Fluorine-18 and Strontium-87m Scintigraphy in the Management of Infective Spondylitis," The Journal of Bone and Joint Surgery, 1973.

[13] M. Van Laere et al., "Strontium 87m Scannong of the Sacroiliac Joints in Ankylosing Spondylitis," Annals of the Rheumstic Diseases, 1972.

[14] R.L. Meckelnburg, "Clinical Value of Generator Produced 87-m Strontium," Journal of Nuclear Medicine, 1964.

[15] A.G.M. Janssen et al., "A Rapid and High-Yield Preparation Method for ^{87}/^{87m}Sr Generators Using the ^{88}Sr(p,2n) Reaction," Int. J. Radiat. Appl. Instrum. Part A, Appl. Radiat. Isot., 1986.

Copyright © 2013 CC-BY-3.0 and by the respective authors

AN OVERVIEW OF LIE METHODS FOR ACCELERATOR PHYSICS*

Alex J. Dragt, Department of Physics, University of Maryland, College Park, MD, USA

Abstract

We sketch how Hamiltonian mechanics can be formulated in Lie algebraic terms (indeed Poisson and Jacobi almost invented Lie algebras without knowing it), and how this formulation can be applied to the description and computation of particle orbits in accelerators in a way that both unifies linear and nonlinear theory and leads to explicit results for realistic machines [1–5].

WHAT IS A LIE ALGEBRA?

In grade school we learned how to add numbers to get other numbers, and how to multiply numbers to get other numbers. Mathematicians call an *algebra* any collection of entities for which addition-like and multiplication-like operations are defined.

The concept of numbers and their addition can be extended to the concept of vectors and vector addition. With vectors in mind, is it possible to define multiplication for vectors in such a way that multiplication of any two vectors again yields a vector? There are various possibilities. We will select one. Suppose, for the moment, we denote such multiplication by the symbol $\circ$. Thus, we denote the product of two vectors u and v by the symbols $u \circ v$.

Consider a multiplication rule that has the two properties

$$v \circ u = -u \circ v, \tag{1}$$

$$u \circ (v \circ w) + v \circ (w \circ u) + w \circ (u \circ v) = 0. \tag{2}$$

A multiplication rule with the two properties (1) and (2) is called a *Lie product* rule, and a vector space equipped with a Lie product rule is called a *Lie algebra*. We remark, for reasons which will become evident, that the condition (2) is called the *Jacobi* condition or identity.

IS THERE A LIE ALGEBRAIC STRUCTURE IN HAMILTONIAN MECHANICS?

Notation

Consider a $2n$-dimensional phase space with position coordinates $q_1 \cdots q_n$ and momentum coordinates $p_1 \cdots p_n$. Also, for convenience, introduce the notation

$$z = (q_1 \cdots q_n; p_1 \cdots p_n). \tag{3}$$

That is, z denotes a collection of $2n$ variables with the first n of them being the q's and the remaining n being the p's.

* Work supported in part by the University of Maryland and the U.S. Department of Energy Grant DE-FG02-96ER4DOE.

The Set of Phase-Space Functions Forms a Vector Space

Next let $f(z,t)$ be any function of z and possibly the time t. Evidently, since phase-space functions can be added together and the result is again a phase-space function, the set of all phase-space functions forms a vector space.

The Poisson Bracket Provides a Lie Product

Is there a way of "multiplying" phase-space functions that will satisfy the Lie product requirements (1) and (2)? There is. The *Poisson bracket*, denoted by the symbols $[f,g]$, of any two phase-space functions f and g is defined by the rule

$$[f,g] = \sum_{k=1}^{n} (\partial f/\partial q_k)(\partial g/\partial p_k) - (\partial f/\partial p_k)(\partial g/\partial q_k). \tag{4}$$

Then, it is obvious from its definition that the Poisson bracket has the property

$$[g,f] = -[f,g]. \tag{5}$$

What is not so obvious, and was observed by *Jacobi*, is that the Poisson bracket also has the property

$$[f,[g,h]] + [g,[h,f]] + [h,[f,g]] = 0. \tag{6}$$

Evidently (5) and (6) are analogs of the properties (1) and (2). Only the symbols for a product have been changed, with $\circ$ replaced by $[,]$. We conclude that the set of all phase-space functions with the Lie multiplication rule (4) constitutes a Lie algebra.

The Fundamental Poisson Brackets

Simple calculation shows that for the phase-space coordinates themselves there are the Poisson bracket results

$$[z_a, z_b] = J_{ab}, \ a,b = 1 \cdots 2n \tag{7}$$

where J is the $2n \times 2n$ matrix, called the Poisson matrix,

$$J = \begin{pmatrix} 0 & I \\ -I & 0 \end{pmatrix}. \tag{8}$$

Here 0 and I denote the $n \times n$ zero and identity matrices.

A RELATED LIE ALGEBRA IN HAMILTONIAN MECHANICS

Lie Operators

Given any phase-space function $f(z,t)$ there is a related differential operator, called a *Lie operator* and denoted by the symbols $:f:$, defined by the rule

$$:f: = \sum_{k=1}^{n} (\partial f/\partial q_k)(\partial/\partial p_k) - (\partial f/\partial p_k)(\partial/\partial q_k). \tag{9}$$

Copyright © 2013 CC-BY-3.0 and by the respective authors

Evidently, the action of $: f :$ on any function $g(z,t)$ is given by the relation

$$\begin{aligned} : f : g &= \sum_{k=1}^{n} (\partial f/\partial q_k)(\partial g/\partial p_k) - (\partial f/\partial p_k)(\partial g/\partial q_k) \\ &= [f,g]. \end{aligned} \tag{10}$$

We may view a Lie operator as a Poisson bracket waiting to happen.

Lie Operators Form a Lie Algebra

Since differential operators can be added and the result is again a differential operator, Lie operators form a vector space. Can the set of Lie operators also be given a Lie product rule? Let $\{: f :, : g :\}$ denote the *commutator* of the Lie operators $: f :$ and $: g :$,

$$\{: f :, : g :\} =: f :: g : - : f :: g : . \tag{11}$$

It is easily verified that the commutator satisfies requirements analogous to the Lie product requirements (1) and (2). Therefore one suspects that Lie operators might also form a Lie algebra with the Lie product symbol $\circ$ replaced by the symbols $\{,\}$. But is the commutator of two Lie operators again a Lie operator? It is. It can be shown from the Jacobi identity (6) that there is the beautiful relation

$$\{: f :, : g :\} =: [f,g] : . \tag{12}$$

Powers of Lie Operators

Based on the definition of a Lie operator, we can also define powers $: f :^{\ell}$ of Lie operators by the rules

$$: f :^{0} g = g, \tag{13}$$

$$: f :^{1} g =: f : g = [f,g], \tag{14}$$

$$: f :^{2} g = [f,[f,g]], \text{ etc.} \tag{15}$$

Lie Transformations

With powers of Lie operators defined, we can also define power series. A particularly important power series, called a *Lie transformation*, is that based on the Taylor coefficients of the exponential function and given by the rule

$$\exp(: f :) = \sum_{\ell=0}^{\infty} : f :^{\ell} /\ell!. \tag{16}$$

When applied to any function g, it follows that there is the result

$$\begin{aligned} \exp(: f :) g &= \sum_{\ell=0}^{\infty} : f :^{\ell} g/\ell! \\ &= g + [f,g] + [f,[f,g]]/2! + \cdots . \end{aligned} \tag{17}$$

INTEGRATING HAMILTON'S EQUATIONS OF MOTION AND SYMPLECTIC MAPS

Transfer Maps Arising from Hamiltonians

Suppose $H(z,t)$ is some Hamiltonian. Following Hamilton, it produces the set of first-order equations

$$\dot{q}_j = \partial H/\partial p_j, \tag{18}$$

$$\dot{p}_j = -\partial H/\partial q_j, \tag{19}$$

which can be written more compactly in the form

$$\dot{z}_a = - : H : z_a. \tag{20}$$

Let z^{in} denote a set of *initial* conditions at the initial time t^{in}, and suppose the equations of motion (20) are integrated to a *final* time t^{fin} to find final conditions z^{fin}. We may view the relation between z^{fin} and z^{in} as a *map* $\mathcal{M}$, often called a *transfer map*, that sends phase space into itself, and write

$$z^{fin} = \mathcal{M} z^{in}. \tag{21}$$

Effect of Small Changes in the Initial Conditions

Suppose we make small changes dz^{in} in the initial conditions. According to calculus, doing so will produce small changes dz^{fin} given by the relation

$$dz^{fin} = M(z^{in}) dz^{in} \tag{22}$$

where $M(z^{in})$ is the *Jacobian matrix* defined by

$$M(z^{in})_{ab} = \partial z_a^{fin}/\partial z_b^{in}. \tag{23}$$

The Symplectic Condition

If $\mathcal{M}$ arises from integrating Hamilton's equations of motion (20) for some Hamiltonian, as we have assumed, then it can be shown that $M(z^{in})$ must satisfy the (nonlinear) condition

$$M^T(z^{in}) J M(z^{in}) = J \tag{24}$$

for all z^{in} where M^T denotes the transpose of M. Matrices M that satisfy (24) are called *symplectic* matrices, and correspondingly maps $\mathcal{M}$ whose Jacobian matrices $M(z^{in})$ satisfy (24) for all z^{in} are called sympletic maps.

We have learned that integrating Hamilton's equations of motion produces symplectic maps. Conversely, it can be shown that every symplectic map arises from integrating Hamilton's equations of motion for some Hamiltonian. Thus, finding symplectic maps and solving Hamilton's equations of motion are equivalent tasks.

Taylor Representation of Transfer Map

Suppose some design orbit has been found, and now let the quantities z_a be *deviation* variables about the design orbit. In terms of these variables, $\mathcal{M}$ sends the origin into

Copyright © 2013 CC-BY-3.0 and by the respective authors

itself. Moreover, suppose the Hamiltonian is analytic in z so as to have a convergent Taylor expansion of the form

$$H(z,t) = \sum_{m=2}^{\infty} H_m(z,t) \tag{25}$$

where each $H_m(z,t)$ is a homogeneous polynomial (in the components of z) of degree m. Then the final and initial conditions will be related by Taylor expansions of the form

$$\begin{aligned} z_a^{fin} &= \sum_b R_{ab} z_b^{in} + \sum_{bc} T_{abc} z_b^{in} z_c^{in} \\ &+ \sum_{bcd} U_{abcd} z_b^{in} z_c^{in} z_d^{in} + \cdots . \end{aligned} \tag{26}$$

We note that the Taylor coefficients R_{ab}, T_{abc}, U_{abcd}, etc., occurring in (26) are not all independent, but rather are interrelated by the symplectic condition (24). The matrix R must be symplectic, and the entries in R, T, U, etc. are interrelated in a complicated way.

IS THE LIE ALGEBRAIC STRUCTURE OF HAMILTONIAN MECHANICS OF ANY USE?

Lie Representation of Transfer Map

Suppose $\mathcal{M}$ is a symplectic map that sends the origin into itself. It can be shown that any such map has the factorization

$$\mathcal{M} = \mathcal{R} \exp(: f_3 :) \exp(: f_4 :) \exp(: f_5 :) \cdots \tag{27}$$

where $\mathcal{R}$ is a linear symplectic map whose action is described by the symplectic matrix R and the f_m are homogeneous polynomials of degree m in the phase-space variables z^{in}. Moreover, unlike the Taylor representation (26), the homogeneous polynomials f_m are all independent. Any choice for the f_m produces a symplectic map, and every (origin preserving) symplectic map has a unique factorization of the form (27). Thus, in the case of accelerator physics, the effect of any beam-line element or collection of such elements, including the one-turn map for a circular machine, is characterized by a symplectic matrix R and a collection of polynomials f_m; and the symplectic condition is automatically built into the description. In particular, it can be shown that $\mathcal{R}$ describes linear behavior about the design orbit, f_3 describes second-order (such as might be caused by sextupoles) and yet higher-order effects, f_4 describes third-order (such as might be caused by octupoles) and yet higher-order effects, etc.

We also remark, in passing, that $\mathcal{R}$ can be written in terms of Lie transformations. In general there are two unique quadratic polynomials called f_2^c and f_2^a (where the superscripts c and a characterize the matrices associated with the polynomials as *commuting* or *anti-commuting* with J) such that there is the relation

$$\mathcal{R} = \exp(: f_2^c :) \exp(: f_2^a :). \tag{28}$$

In some important cases a single f_2 suffices, and its coefficients are related to phase advances and *Twiss* parameters.

Finally, in the case that $\mathcal{M}$ does not send the origin into itself, there is a first-degree polynomial f_1 such that $\mathcal{M}$ has the unique factorization

$$\mathcal{M} = \exp(: f_1 :) \mathcal{R} \exp(: f_3 :) \exp(: f_4 :) \cdots . \tag{29}$$

It can be verified that the Lie transformation $\exp(: f_1 :)$ produces translations in phase space, and describes the error effects of beam-line element misplacement or misalignment or (in the case of dipoles) mis-powering.

Lie Formulas for Multiplying/Concatenating Symplectic Maps

Given any two Lie transformations there are Lie algebraic rules for combining them. In particular there is a rule for manipulating exponents, called the *Baker-Campbell-Hausdorff* (BCH) theorem/series, that along with (12) leads to the result

$$\exp(: f :) \exp(: g :) = \exp(: h :) \tag{30}$$

with

$$\begin{aligned} h &= f + g + (1/2)[f,g] \\ &+ (1/12)\{[f,[f,g]] + [g,[g,f]]\} + \cdots . \end{aligned} \tag{31}$$

In the context of accelerator physics, suppose the transfer map for each beam-line element is known in the standard forms (27) or (29). Then the BCH theorem can be used to manipulate the various exponents appearing in the individual maps to again rewrite the product of the maps in standard form. That is, there are procedures for finding the net map for a full beam line, or any portion thereof, given the maps for the individual elements. In the case of case of a circular machine, one can combine all the maps for the individual beam-line elements together to find a full one-turn map, or even a several-turn map. Finally, the BCH theorem also provides a procedure for inverting symplectic maps.

Normal Form for a Symplectic Map

Suppose $\mathcal{M}$ is the one-turn map for a circular machine, and the machine tunes are not resonant. Then there is symplectic map $\mathcal{A}$, called the *transforming* or *normalizing* map, such that the map $\mathcal{N}$ given by

$$\mathcal{N} = \mathcal{A}\mathcal{M}\mathcal{A}^{-1} \tag{32}$$

has a particularly simple form, called a *normal* form. The normal-form process is the nonlinear analog of the concept of matrix diagonalization.

It can shown that $\mathcal{N}$ contains all information about tunes, anharmonicities, and chromaticities to any desired order; and $\mathcal{A}$ contains all information about linear and nonlinear lattice functions. The map $\mathcal{A}$ can also be used to construct nonlinear generalizations of the Courant-Snyder invariants, to analyze tracking data for the presence of KAM tori, and to generate matched beams including nonlinear effects.

Copyright © 2013 CC-BY-3.0 and by the respective authors

Computing Symplectic Maps $\mathcal{M}$

Given a Hamiltonian H, it can be shown that $\mathcal{M}$ obeys the equation of motion

$$\dot{\mathcal{M}} = \mathcal{M} : -H : . \tag{33}$$

Suppose H expanded in the form (25). How does one find the corresponding map $\mathcal{M}$ in the form (27)? We will first describe how R can be found, and then describe how the f_m can be found. Actually, it is computationally simpler to write $\mathcal{M}$ in the *reverse* factorized form

$$\mathcal{M} = \cdots \exp(: g_5 :) \exp(: g_4 :) \exp(: g_3 :) \mathcal{R}, \tag{34}$$

and then find the g_m. Once they are known the f_m can be found from the g_m by using concatenation formulas to bring (34) to the standard forward factorized form (27).

Finding R Since $H_2(z,t)$ is quadratic in the variables z, it can be written in the form

$$H_2(z,t) = (1/2) \sum_{ab} S_{ab}(t) z_a z_b \tag{35}$$

where $S(t)$ is a symmetric matrix. It can be shown that R is the solution to the matrix differential equation

$$\dot{R}(t) = JS(t)R(t) \tag{36}$$

with the initial condition

$$R(t^{in}) = I. \tag{37}$$

If S is time independent, (36) with the initial condition (37) can be integrated immediately to give the result

$$R(t) = \exp[(t - t^{in})JS]. \tag{38}$$

If S is time dependent, as will be the case if one wishes to include fringe-field effects (recall that here t plays the role of s, distance along the design orbit), then (36) must be integrated numerically.

Finding the g_m In general to find the g_m one must first transform the $H_m(z,t)$, with $m \geq 3$, to the *interaction picture* specified by $H_2(z,t)$ in a manner analogous to similar calculations in Quantum Mechanics. Define interaction picture Hamiltonian pieces $H_m^{int}(z,t)$ by the rule

$$H_m^{int}(z,t) = H_m(Rz,t) \text{ with } m \geq 3. \tag{39}$$

Then it can be shown that the g_m with $m \geq 3$ obey equations of motion of the form

$$\dot{g}_3 = -H_3^{int}, \tag{40}$$

$$\dot{g}_4 = -H_4^{int} + (: g_3 : /2)(-H_3^{int}), \text{ etc.} \tag{41}$$

with the initial conditions

$$g_m(z, t^{in}) = 0. \tag{42}$$

Presently explicit differential equations of this kind for the g_m have been worked out through $m = 8$.

In the approximation that $H_m(z,t)$ is t independent within each beam-line element, which amounts among other things to the neglect of fringe-field effects, there are a variety of ways for obtaining the g_m either analytically or numerically. If $H_m(z,t)$ is t dependent, as will be the case if fringe-field effects are to be taken into account, then the equations of the form (40), (41), etc. must be integrated numerically with the initial conditions (42).

Computing $\mathcal{M}$ for Realistic Beam-Line Elements: Use of Surface Methods

In this final subsection we will describe how to compute accurate transfer maps for realistic beam-line elements including all fringe-field and multipole effects. For simplicity we will limit our discussion to magnetic beam-line elements. Analogous treatments can be applied to the cases of electrostatic and RF electromagnetic fields.

In the previous subsection it was assumed that the $H_m(z,t)$ are given, which is equivalent, in the case of accelerator physics and the treatment of magnetic beam-line elements, to the assumption that the vector potential $\boldsymbol{A}$ for the the magnetic field $\boldsymbol{B}$ is known in analytic form so that a Taylor expansion can be performed to find the $H_m(z,t)$. That is, high-order spatial derivatives of $\boldsymbol{A}$ are needed about the design orbit.

However suppose, as is often the case, that only $\boldsymbol{B}$ is known, and moreover it is only known at a 3-D collection of grid points. For example, when iron is present, $\boldsymbol{B}$ can only be found numerically at a collection of grid points with the aid of some three-dimensional electromagnetic solver. What can be done then to find $\boldsymbol{A}$ and its high-order derivatives?

At first thought one might contemplate using numerical differentiation of grid-point data to determine $\boldsymbol{A}$ and its spatial derivatives. But it is well known to numerical analysts that numerical differentiation of grid-point data is intolerably sensitive to numerical noise in the data. Each differentiation operation amplifies noise. And it is high-order derivatives that are needed to compute $\mathcal{M}$ to high order.

This problem can be overcome, at least to reasonably high order, by the use of *surface methods*. By a theorem of *Neumann* the values of $\boldsymbol{B}$, and accordingly the associated values of $\boldsymbol{A}$, can be found within any volume V if the normal component of $\boldsymbol{B}$ is known on any surface S that bounds V. Moreover, it can be shown that the process of determining interior fields from fields on a surrounding surface is *smoothing*. That is, the interior field values are relatively insensitive to noise in the surface data. Finally, it can be shown that this smoothing overcomes the amplification of numerical noise associated with differentiation.

Straight beam-Line Elements There are two cases to be considered: straight (or essentially straight) beam-line elements, and curved beam-line elements with significant

Copyright © 2013 CC-BY-3.0 and by the respective authors

sagitta. In the case of straight beam-line elements it is possible to surround the design orbit by an imaginary cylinder. This cylinder can be conveniently assumed to have a circular, elliptical, or rectangular cross section. Circular cylinders are natural for the case of quadrupoles, sextuples, octupoles, etc. Cylinders with elliptical or rectangular cross sections may be more appropriate for elements for which the bore width is larger than the gap height. See Figure 1 for the case of a wiggler.

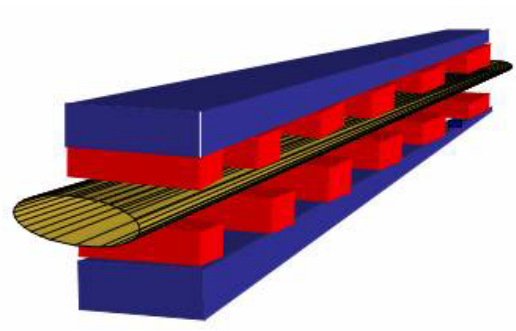


Figure 1: An elliptical cylinder, centered on the z-axis, fitting within the bore of a wiggler, and extending beyond the fringe-field regions at the ends of the wiggler.

For these cylindrical volumes V and their associated surfaces S it is possible to solve *Laplace's* equation by separation of variables. From these solutions it is possible to generate explicit formulas that determine $\boldsymbol{A}$ and its spatial derivatives at any interior point in terms of values of the normal component of $\boldsymbol{B}$ at selected grid points on S, and consequently the $H_m(z,t)$ can be found. The required surface values can be determined by extrapolation of the 3-D grid-point numerical values of $\boldsymbol{B}$ onto the selected grid points on S. Finally, the equations (36), (40), (41), $\cdots$ can be integrated to yield $\mathcal{M}$.

Curved beam-Line elements For curved beam-line elements with significant sagitta it is impossible to fit a straight cylinder within the bore of the element. In this case it is necessary to employ volumes V, and their associated surfaces S, that have a more complicated geometry. Figure 2 shows a convenient surface for the case of dipoles with significant sagitta, the surface of a bent box with straight end legs.

Unfortunately, for curved beam-line elements there are no geometries for which the Laplace equation is separable and therefore, while the results of Neumann still hold, there is no way to exploit them by explicit formulas. However, according to a theorem of *Helmholtz*, interior fields can also be computed from surface data providing *both* the normal component of $\boldsymbol{B}$ and the scalar potential ψ associated with $\boldsymbol{B}$ are known on the surface. Moreover, in this case the interior vector potential and its spatial derivatives can be found by multiplying the surface data by *known geometry-independent* kernels and then integrating the results over S.

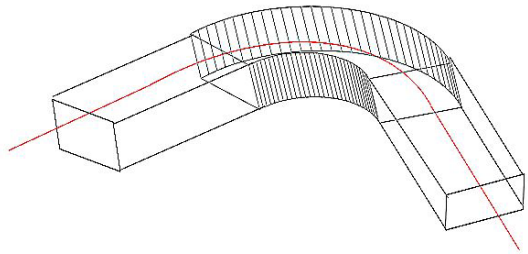


Figure 2: A bent box, fitting within a dipole, and having straight end legs that extend beyond the fringe-field regions at the entry and exit of the dipole.

Finally, this process is also smoothing: the interior values of $\boldsymbol{A}$ and its spatial derivatives so obtained are also relatively insensitive to noise in the surface data.

In practice, the procedure is as follows: First set up cubature points (specially selected grid points) on S, interpolate the numerical 3-D grid data for $\boldsymbol{B}$ onto the surface cubature points, and compute the normal component of $\boldsymbol{B}$ at these cubature points. In addition interpolate 3-D grid data for ψ, which can also be provided by 3-D electromagnetic solvers, onto the surface cubature points. Next multiply the surface data by the known kernels and integrate the results over the surface using cubature formulas. The result will be the interior vector potential and its spatial derivatives, and consequently the $H_m(z,t)$ can be found. Finally, the equations (36), (40), (41), $\cdots$ can be integrated to yield $\mathcal{M}$.

CONCLUSION

For both straight and curved beam-line elements, the use of Lie and surface methods makes it possible to compute, for the first time, accurate high-order transfer maps for realistic elements including all fringe-field and multipole error effects.

REFERENCES

[1] A. Dragt, *Lie Methods for Nonlinear Dynamics with Applications to Accelerator Physics*, (2013), available on the Web at http://www.physics.umd.edu/dsat/

[2] E. Forest, *Beam Dynamics: A New Attitude and Framework*, Harwood (1998).

[3] A. Chao, K. Mess, M. Tigner, and F. Zimmermann, Edit., *Handbook of Accelerator Physics and Engineering*, Second Edition, World Scientific (2013).

[4] A. Dragt, F. Neri, G. Rangarajan, D. Douglas, L. Healy, and R. Ryne, "Lie Algebraic Treatment of Linear and Nonlinear Beam Dynamics", *Ann. Rev. Nucl. Part. Sci.* **38**, pp. 455-496 (1988).

[5] C. Mitchell and A. Dragt, "Accurate transfer maps for realistic beam-line elements: Straight elements", *Phys. Rev. ST Accel. Beams* **13**, 064001 (2010).

Copyright © 2013 CC-BY-3.0 and by the respective authors

LONGITUDINAL EMITTANCE MEASUREMENT SYSTEM FOR THE ARIEL ELECTRON LINAC

A. Vrielink, Y.C. Chao, C. Gong, R. E. Laxdal, V. Zvyagintsev, TRIUMF, Vancouver, Canada

Abstract

As part of the ARIEL e-LINAC project at TRIUMF, a 1.3 GHz single-cell, room-temperature deflecting cavity has been developed to study the temporal distribution of an electron beam from a 300 kV thermionic gun. Beam bunches on the order of 100-200 ps long are produced from a biased grid with a 650 MHz RF voltage superimposed to periodically allow release of electrons. The RF deflector operates in a TM110-like mode, deflecting the electrons vertically with a magnitude dependent on their arrival phase. The cavity RF performance has been characterized through signal level and beam testing. The deflector is installed as part of a longitudinal emittance measurement system with beam collimation, a 90 degree analyzing magnet, the deflecting cavity and a final view screen. Initial beam bunch length measurements using this RF cavity, conducted in conjunction with the initial commissioning using a 100kV electron-gun and a 1.3GHz buncher, are presented. The beam bunch length was extracted by comparing data collected at a screen downstream of the deflector to an analytical model based on linear time-invariant system theory.

INTRODUCTION

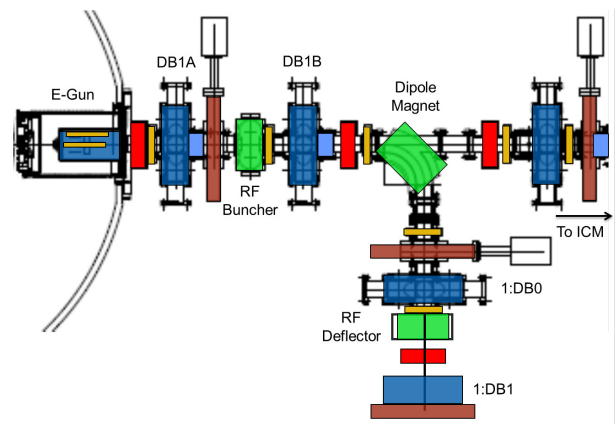


Figure 1: Low Energy Transport Line in the VECC Test Area.

The ARIEL project at TRIUMF is well under way, including a 50MeV linear accelerator using 1.3 GHz superconducting technology to accelerate a 10mA electron beam. TRIUMF is currently developing a 10MeV injection line for this electron linac in collaboration with the Variable Energy Cyclotron Center (VECC). A test area has been set up in the ISAC II building to commission various beamline components before installation in the ARIEL injection line and in Kolkata. The VECC Test Area consists of a 100kV (now 300kV) thermionic e-gun with an RF modulated gridded bias on the cathode at 650MHz, a low energy beam transport (LEBT), an injector cryomodule with a 1.3GHz superconducting 9 cell cavity, and a medium energy beam transport. Electron bunches ranging from 100-200ps long are emitted at a 1kHz repetition rate with a duty factor between 0.1% and 100%.

The LEBT section, pictured in Fig. 1, contains various beam diagnostics including linear profile monitors (LPMs), faraday cups, YAG screens and non intercepting beam profile monitors. The LPM consists of a vertical slit, horizontal slit and collimating hole which can be scanned across the beam to sweep the beam profile or inserted into the beam to select a beam profile.

THE LONGITUDINAL EMITTANCE MEASUREMENT SYSTEM

As part of the LEBT diagnostics, a longitudinal emittance measurement system was designed. It consists of an RF bunching cavity, dipole magnet, RF deflecting cavity in a 90° analyzing leg and downstream screen. The RF buncher manipulates the bunch length at a point downstream by accelerating late electrons in the bunch and decelerating early electrons. The dipole bends the beam into the analyzing leg, mapping the electron energy to the x axis through the dependence of the radius of curvature on electron energy, $\rho = \frac{\gamma\beta E_0}{qBc}$.

Circular apertures of 2mm diameter at the diagnostic boxes DB1A and DB1B (see figure 1) are used to limit the transverse emittance. The dipole magnet horizontal focusing is designed so an object at DB1B forms a dispersed focus at 1:DB0, such that a slit at 1:DB0 will select an energy slice of the beam.

In the analyzing leg, a 1.3GHz room temperature RF deflecting cavity maps the time spread of the beam to the vertical axis using E_y and B_x fields. A screen at 1:DB1 images the beam in the transverse plane. Using the deflector in conjunction with the dipole magnet, the beam energy and time spread can be extracted from the horizontal and vertical beam size, respectively. A solenoid upstream of 1:DB1 can be used to focus the beam at 1:DB1 with the RF devices off, producing a slight rotation of the $\Delta E/\Delta t$ (x/y) reference frame.

THE RF DEFLECTOR

The 1.3 GHz single cell deflecting cavity has been designed to analyze the temporal distribution of an electron

Copyright © 2013 CC-BY-3.0 and by the respective authors

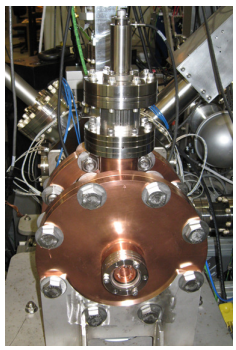


Figure 2: The deflecting cavity during installation.

beam bunch. The cavity is located in the analyzing leg of the injector line, as shown in figure 1. Pictured in Fig. 2, the cavity was designed after the Cornell deflector [1]. Similar in shape to a pillbox cavity, nose cones at the beam entrance and exit strengthen the on axis transverse fields. The cavity is operated in a TM_{110} like mode, resulting in a vertically deflected beam with the magnitude of deflection a sinusoidal function of the arrival phase of the electrons. Through CST simulations, for a β=1 particle the expected $\frac{R_\perp}{Q} = \frac{V_\perp^2}{\omega U}$ and transit time factor, T_0, were 930Ω and 0.51, respectively. $V_\perp$ is defined in equation 1, differing from a traditional potential to account for the effect of the magnetic fields on the beam.

$$V_\perp = \left| \int_{-\infty}^{\infty} c\beta B_x(z) e^{\frac{ikz}{\beta}} - iE_y(z) e^{\frac{ikz}{\beta}} \mathrm{d}z \right| \quad (1)$$

Signal Level Measurements

The deflector was manufactured at TRIUMF and after assembly and quality factor optimization, signal level measurements were conducted. While the quality factor of the cavity was 8800 before ultrasonic cleaning, close to the simulated value of $Q = 9766$, it is believed that soap residue has caused the current low quality factor of 5400.

The electromagnetic fields in the cavity were confirmed experimentally using the beadpull method. Magnetic fields on axis necessitated using both a dielectric and metallic bead. The dielectric bead only perturbs the electric field which can then be subtracted from the total perturbation with the metal bead to obtain the magnetic fields.

The results of the beadpull are shown in figure 3, normalized to emphasize the difference in field shape. Compared to simulation, the peaks of the experimentally determined fields are narrower. This is due to a slightly different nose cone length than in the CST model. As a result, the transit time factor of the cavity is increased and for $v = c$, T_0=0.56 ± 0.03. The effective shunt impedance of the cavity is smaller than expected though, with an $\frac{R_\perp}{Q}$ of 120 ± 10 Ω, 390 ± 20 Ω and 710 ± 30 Ω for a particle with a β of 0.51, 0.78, and 1 respectively.

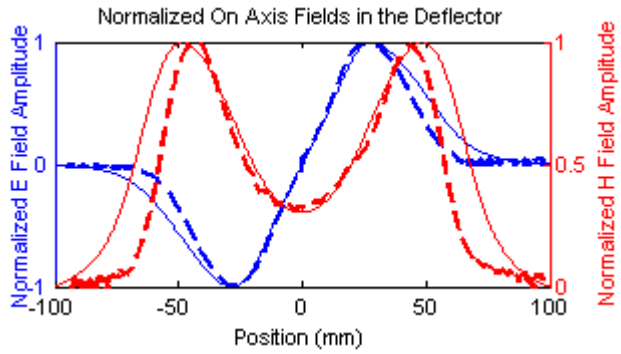


Figure 3: Fields along the beam axis of the deflector. The dashed line corresponds to the experimentally determined fields while the solid line corresponds to simulation.

Beam Loaded Measurements

Beam loaded commissioning of the cavity began in September, 2012, in conjunction with the commissioning of the LEBT section and 100keV e-gun [2]. The beam was bent into the analyzing leg using the dipole magnet, and images of the beam were taken using the screen at 1:DB1.

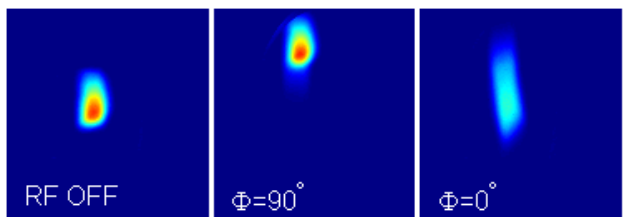


Figure 4: The effect of the deflector on the beam.

Turning on the deflector and scanning the RF phase produces a noticeable effect on the beam, even at low input powers. Figure 4 shows the effect of the deflector at an input power of 21W and RF phases of 90° (maximum centroid deflection) and 0° (diagnostic phase). The deflector imparts a vertical deflection to the beam given by $\frac{\Delta y}{\Delta z} = \frac{V_\perp}{\beta^2 E_T}$ where E_T is the total beam energy.

By measuring the maximum deflection at several deflector power levels, the deflector effective voltage can be obtained using the above equation. Figure 5 shows a plot of the deflecting voltage versus input power from which an effective shunt impedance of 0.71±0.05 MΩ was obtained. This agrees with the expected $R_\perp$ for a $\beta = 0.51$ electron of 0.65±0.03 MΩ from the beadpull.

INITIAL MEASUREMENTS

With the deflector commissioned, initial longitudinal emittance measurements have been conducted. By inserting the vertical LPM slit at DB1B, all particles have the same initial horizontal position. Their final position at the screen on 1:DB1 is thus, to first order, only a function of the particle energy and time of arrival at the deflecting cavity for a constant deflector power.

Copyright © 2013 CC-BY-3.0 and by the respective authors

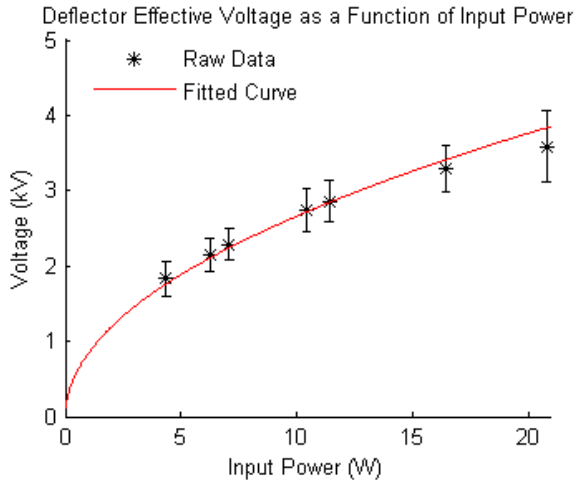


Figure 5: The effective voltage of the deflecting cavity.

The time spread is calibrated by sweeping the deflector from 0 to 360°. Comparing the maximum spread at the diagnostic phase (0°) with the maximum centroid deflection (±90°), the bunch length in RF degrees is obtained. The energy spread can be calibrated by sweeping the RF buncher from 0 to 360° or by scanning the e-gun voltage. Given the effective voltage of the buncher, the energy spread of the beam at 1:DB1 can be obtained by comparing the maximum horizontal spread at the bunching phase (0°) with the beam position at the accelerating phase (90°).

Since energy couples to x and time couples to y, the final image gives a representation of the longitudinal emittance. This is depicted in figure 6, where the RF deflector is on at constant power in the first three images and the indicated buncher power is increased to rotate the longitudinal phase space. For these images the focusing solenoid was on and the image is corrected for the rotated x-y frame. As expected from the Liouville theorem, longitudinally compressing the beam will inherently increase the bunch energy spread. Note that with the RF buncher and deflector off, the beam spot is much smaller than the perturbed images, indicating that the sampled longitudinal emittance is not significantly affected by the transverse emittance.

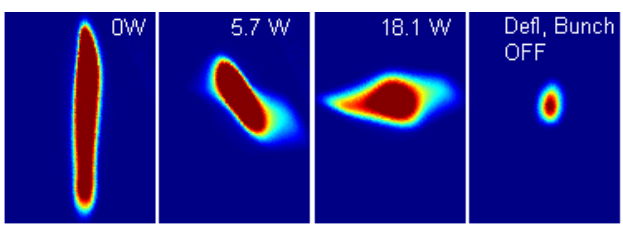


Figure 6: Rotation of the beam with the deflector on and the buncher power varied.

An alternative analysis method to determine the bunch length uses linear time invariant theory. For low space charge, the beam optics in the analyzing leg and the RF deflector can be considered a linear system and the maximum centroid deflection and maximum particle deflection over all arrival phases is time invariant. Such a system can be entirely characterized by its impulse response (i.e. the effect of the deflector on a single electron), which is well known. The output of the system will be the convolution of the input beam distribution with the impulse response function. For a uniform beam distribution of length Θ, measured in degrees RF, the centroid deflection over the maximum deflection is thus given by equation 2.

$$\frac{\Delta\bar{y}\,(\alpha)}{\Delta y_{max}} = (f * \Delta y_{\text{impulse}})(\alpha) \tag{2}$$

$$= \int_{-\infty}^{\infty} f\,(t)\, g\,(\alpha - t)\, dt \tag{3}$$

$$= \int_{-\infty}^{\infty} \text{Rect}\left(\frac{t - \theta/2}{\theta}\right) \sin\,(\alpha - t)\, dt \tag{4}$$

$$= \frac{\sin\,(\alpha) - \sin\,(\alpha - \theta)}{\theta} \tag{5}$$

Using this method, the bunch length can be determined by comparing the ratio of the maximum centroid deflection over the maximum particle deflection to theoretical predictions. Figure 7 shows an example of the maximum particle deflection as a function of phase offset for two different tests, highlighting the effect of bunch length in smoothing out the sinusoidal dependence. The ratio between centroid deflection and maximum particle deflection for the shorter and longer bunches is 0.9 and 0.6, respectively, corresponding to a 60° and 180° bunch length.

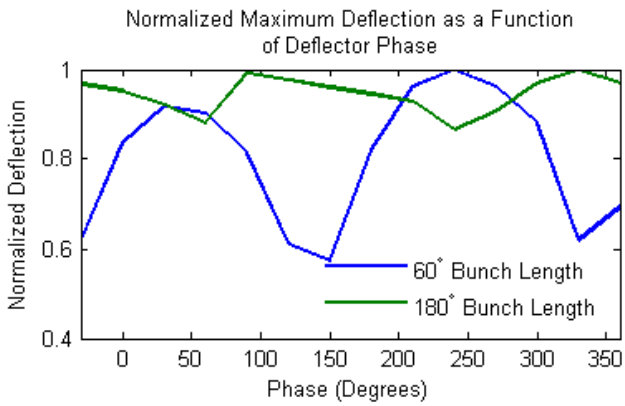


Figure 7: Maximum particle deflection as a function of RF phase for a short bunch (blue) and longer bunch (green). The phase is relative to the E-gun RF.

REFERENCES

[1] S.Belomestnykh et al., "Deflecting Cavity for Beam Diagnostics in ERL Injector," Proceedings of PAC'07, Alberquerque, 2007.

[2] Laxdal, R et al., "TRIUMF/VECC e-LINAC Injector Beam Test," Proceedings of LINCAC2012, Tel-Aviv, 2012.

Copyright © 2013 CC-BY-3.0 and by the respective authors

BEAM DUMP DESIGN FOR THE IN-FLIGHT FRAGMENT SEPARATOR USING HIGH-POWER BEAM*

J.Y. Kim, M. Kim, J.W. Kim#, Institute for Basic Science, Daejeon, Korea

Abstract

The beam dump is a critical component for the in-flight fragment separator using high-power primary beams at the rare isotope science project (RISP) in Korea. The maximum beam power is planned to be 400 kW, and a third of the primary beam power deposits at the isotope production target and the rest are dissipated at the beam dump. The beam dump is designed to be a rotating water drum, which is movable in the perpendicular direction to the beam to select the isotope beam of interest. The main primary ion beam is U, and its range at the energy of 200 MeV/u is only a couple of mm after passing through the shell structure of the drum. This short range requires its internal structure to confine water flow on the wall and to keep high-pressure. Some detailed thermo-mechanical and thermo-fluid analysis has been done using ANSYS and other codes.

INTRODUCTION

Rare isotope science project (RISP), which is to produce rare isotope beams by using both the in-flight fragment (IF) separation and isotope separation on-line (ISOL) methods is undergoing in Korea [1]. The main accelerator, which can provide a wide range of heavy ion beams, accelerating ^{238}U beam to 200MeV/u and proton to 600 MeV, is a superconducting linear accelerator for the IF separator. The IF separator uses a thin target to produce rare isotope beams and a beam dump is located after the first dipole magnet so as to remove unwanted primary beam.

The design of beam dump for in-flight separator using high power primary beam has been performed considering high power density deposited in beam dump. Approximately 30% of the primary beam power, which is used to produce RI beam, will be dissipated in a production target with typical thickness of d/R = 0.3, whereas the rest of primary beam that does not react with production target, will pass through magnetic system and be absorbed in beam dump. The maximum beam power deposited in the beam dump is up to about 300 kW for 200 MeV/u ^{238}U beams and the beam size on beam dump is expected to be around 10 mm in diameter.

Removal of high power primary beam in an IF separator is complicated due to different charge states in primary beam, short range in material and high power density at beam dump. Furthermore, if assuming the primary beam directly impacted on beam dump in the case of target malfunction, the beam dump should be capable of absorbing up to 400 kW during a short time. The cooling system, which can handle high power, is required to avoid structural breakdown and thermal runaway.

If wanted fragment beam is close to the primary beam in rigidity, the task of separation becomes more difficult. Trajectories of off-rigidity fragments and non-reacted beam can overlap with that of the isotope beam of interest at the beam dump. Beam dump system is required to intercept unwanted fragments and non-reacted primary beam minimizing the loss of wanted beam. For the purpose of intercepting the primary beam and off-rigidity fragments with different trajectories, it is necessary that the beam dump has two units and is movable.

A conceptual design of beam dump, and thermal analysis using ANSYS [2] and PHITS [3] are described.

DESIGN OF BEAM DUMP

Figure 1 shows a schematic layout of the separator, which has been designed to consists of two-stages. The purpose of the first stage, pre-separator is to produce RI beams and then to separate the primary and unwanted RI beams, while the second stage, main separator serves to identify the RI beam of interest. The momentum and angular acceptance of the separator have been designed to be ±5 % and ±50 mrad, respectively.

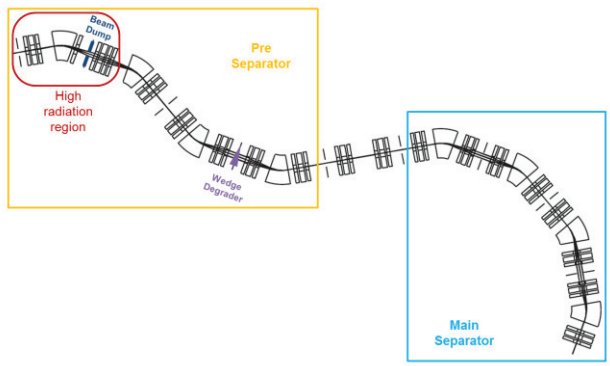


Figure 1: Schematic layout of the fragment separator.

As shown in Fig. 1, a dispersive focal plane is located after the first dipole magnet, and the beam dump is placed near the focal plane. The isotope beam of interest is separately by magnetic rigidity, but unwanted beam with the same Bρ is overlapped.

To remove the heat efficiently, we considered the beam dump consisting of two rotating water-filled cylinder as was adopted for FRIB [4]. A conceptual drawing of the beam dump system is shown in Fig. 2. The beam dump system will be located in a common vacuum space together with the dipole magnet and the production target. The beam dump rotates to prevent localized heating, and cooling water directly absorbs the beam power acting as a liquid beam dump. Titanium is chosen for the material of

* Work supported by Rare Isotope Science Project
#jwkim@ibs.re.kr

Copyright © 2013 CC-BY-3.0 and by the respective authors

the beam dump. The thickness of titanium shell is set to be 1 mm and the outside diameter is 60 cm. The depth of water chamber is 10 cm. The water flows into beam dump through the tube in the side plate, and flows along the helical blades, remove the heat deposited close to the drum surface and water itself.

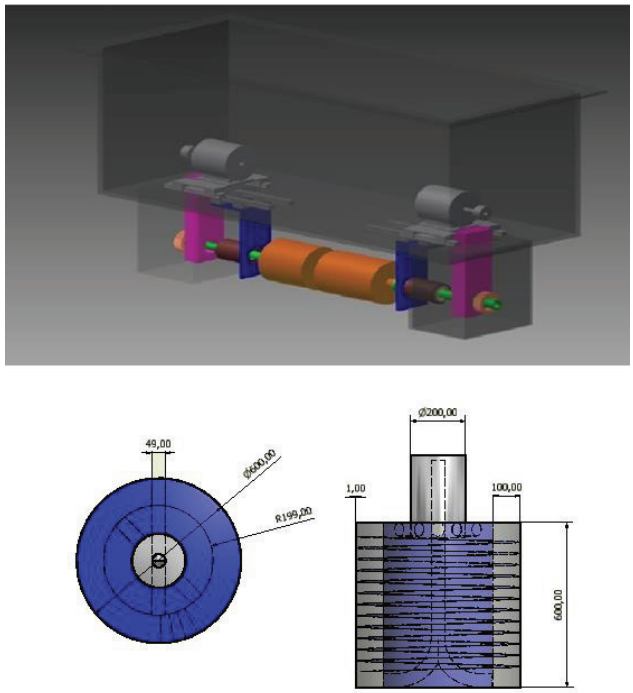


Figure 2: Schematic layout of the beam dump.

ENERGY LOSS AT THE BEAM DUMP

The non-reacted primary beam impacting the beam dump has a diameter of about 10 mm and a power of about 300 kW, which depend on chosen nuclear reaction and the thickness of the production target. Simulation using the codes LISE++ [5] and TRIM [6] was performed to study the energy loss at the beam dump assuming the target thickness corresponding to approximately 30% of the primary beam range.

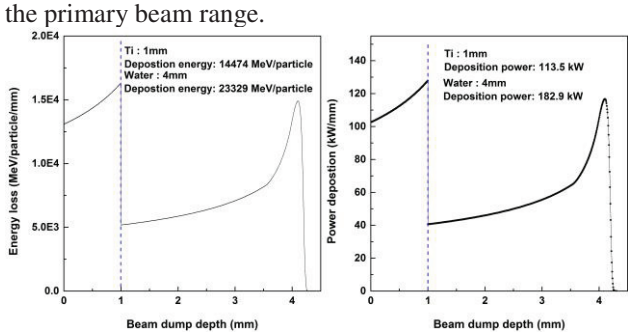


Figure 3: The energy loss (a) and the power deposition (b) of non-reacted ^{238}U beam at beam dump.

In the case of ^{238}U beam with 200 MeV/u, 400 kW, the energy and power of the non-reacted primary beam passing through the target are about 160 MeV/u, 300 kW. The energy loss and power deposition of ^{238}U beam at the beam dump are shown in Fig.3. When the ^{238}U beam hits the beam dump, about 40% of the ^{238}U beam power is lost in the 1-mm thick shell of beam dump and the rest is deposited in water. The energy loss and the range of charged particles depend on the incident particle and, its energy and on the material. The energy loss of different primary beams in the Table 1 assuming a full power beam hits the bam dump, which is an accident scenario.

Table 1: The energy loss and the power deposition assuming a 400 kW beam hitting the beam dump

Primary beam	Energy (MeV/u)	Intensity (pps)	Energy loss (MeV)		Power deposition (kW)	
			Ti	Water	Ti	Water
$^{238}U^{79+}$	200	5.17E+13	12453	35871	103.1	297
$^{124}Xe^{54+}$	235	8.58E+13	4053	25065	55.6	344.1
$^{112}Sn^{50+}$	242	9.22E+13	3412	23670	50.3	349.3
$^{40}Ar^{18+}$	268	2.33E+14	403	10307	15	384.6
$^{18}O^{8+}$	266	5.22E+14	79	4709	6.6	393.4

THE HEATING AND FLUX DISTRIBUTION IN THE BEAM DUMP

The radiation heating was estimated by using PHITS which simulate radiation transport. The beam dump was assumed to be a simple cylinder with 30 cm diameter and 60 cm high. The flux of unwanted fragments produced via in-flight fission of ^{238}U beam at 200 MeV/u, 400 kW, and the flux secondary particles which were produced by the reaction of ^{238}U beam and components of a beam dump is shown in Fig. 4. The flux is expressed in units of 1/cm^2/second, and the major flux of secondary particles is forward directed. The scattered in wide distribution in the outside of the beam dump, radiation is dominated by neutrons. Figure 4 (b) is the distribution of energy deposition due to absorb the primary beam and secondary particles in the beam dump.

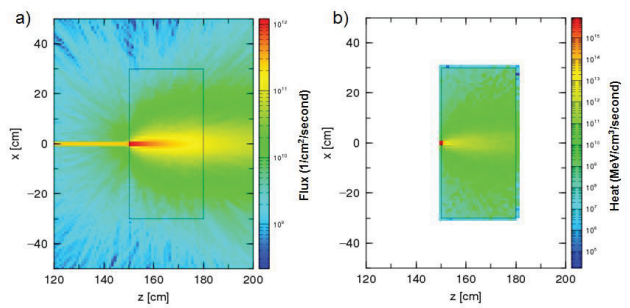


Figure 4: The distribution of the radiation flux (a) and the heat (b) on the beam dump.

Figure 5 shows, the flow velocity in the beam dump, which was calculated by using ANSYS in the same geometry as used PHITS calculation. We assumed that the deposited power is about 110 kW on titanium and about 290 kW on the water. The inlet temperature of cooling water was assumed 295 K. To cool beam dump considering margin of safety, the velocity of cooling

Copyright © 2013 CC-BY-3.0 and by the respective authors

water needs to be much higher than 5 m/s considering the melting point of Ti is about 1940 K. The energy deposition is highly concentrated on the titanium and the adjacent of the water.

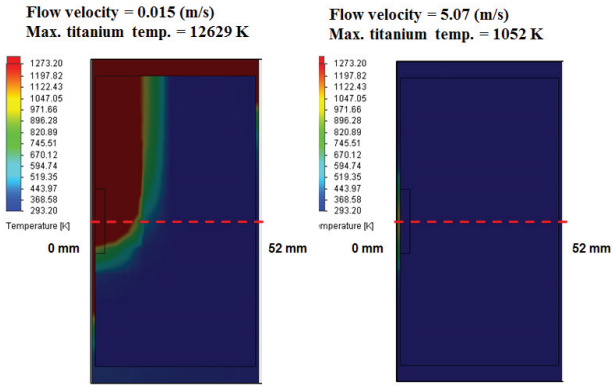


Figure 5: The temperature distribution in the beam dump due to absorption of 400 kW primary beams

The water is activated by nuclear reaction with the primary beam in the beam dump. The activity in water as function of cooling time is presented in Fig. 6. The activity calculation by using the PHIS was performed assuming 5600 h of irradiation with ^{238}U beam (200 MeV/u, 400 kW), which is an expected operation time of separator. With waiting time increasing, the activity of the tritium is dominant because the life time of tritium becomes relatively longer than others. Therefore, for the purpose of decreasing the activation level of the water used to cool the beam dump, there are essentially needed a filtering system to remove long-lived isotopes from water

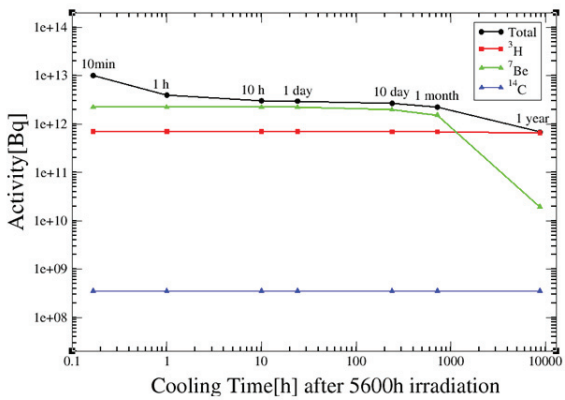


Figure 6: Activity of the beam dump as function of waiting time.

CONCLUSIONS

The designs of beam dump and water cooling loop in the IF separator for the RISP have been studied. As a first step, we calculate the power density deposited in beam dump, heat deposit distribution and cooling water flow. Considering the energy loss of a few different primary beams, it was decided that the path length inside the beam dump needs at least 150 mm to stop the primary beam. Based on this result, some mechanical design and thermo-fluid analysis on the beam dump system was performed. Since the activation of cooling water is significant, we will plans to filter some isotopes from activated water, which is included in the design of the water loop system.

ACKNOWLEDGMENT

This research was supported by the Rare Isotope Science Project of the Ministry of Science, ICT and Future Planning (MSIP) and by the National Research Foundation (NRF) of Korea.

REFERENCES

[1] J. W. Kim, "Status of the Rare Isotope Science Project in Korea" LINAC'12, Tel-Aviv, September 2012, TUPB028, p. 534(2012); http://www.JACoW.org

[2] ANSYS® Workbench, Release 14.5.

[3] H. Iwase et al., J. Nucl. Sci. Technol. 39 (2002) 114.

[4] R. Ronningen et al., "Materials under irradiation by heavy ions and perspectives for FRIB" HB2010, Morschach, Setember 2010, THO2C03, p. 662(2010).

[5] O.Tarasov and D.Bazin, Nucl. Instr. and Meth. B 266 4657 (2008).

[6] J. P. Biersack and L. Haggmark, Nucl. Instr. and Meth. 174 (1980), 257.

Copyright © 2013 CC-BY-3.0 and by the respective authors

BEAM POSITION ELECTRONICS BASED ON SYSTEM ON CHIP PLATFORM

M. Cargnelutti*, G. Jug, R. Hrovatin, Instrumentation Technologies#, Solkan, Slovenia

Abstract

With the advances in system-on-chip (SoC) technology, the CPU and FPGA are today enclosed in the same device. This enables high-speed processing, inherent fast communication and memory sharing between the two entities. However, dedicated tools for implementation are needed as the CPU and FPGA functionalities cannot easily be decoupled.

We used the advantages of the new architecture in the development of a booster BPM electronics. Its requirements are relaxed compared to up-to-now Libera beam position monitors. Proper design of the RF part of the instrument is still a challenge. Furthermore, with optimized FPGA design we target low overall power consumption so that the instrument can be cooled passively.

INTRODUCTION

Instrumentation used in particle accelerators is today one of the most demanding fields for electronic devices and of system integration. Required performances are usually at the cutting edge in terms of signal-to-noise ratio, computational power and data throughput. Even more impressive are the requirements in terms of reliability, long term stability and fault tolerance. As a consequence, instruments are usually a complex inter-connection of different boards that host RF circuits, field programmable gate arrays (FPGAs), communication buses and CPUs. Every logical component from hardware to software is optimized for the specific application.

On the other hand, not every accelerator, or at least not every part in it, needs a top-level device to work properly. A natural example here concerns beam position monitors (BPMs) used in synchrotrons boosters and injectors, compared to those used in the storage ring. Furthermore, a lot of applications have figures of merit such as low power consumption, no need for HW and SW maintenance, and user friendliness. This can be the case for a beam loss monitor (BLM), for example.

In this paper we introduce a compact platform that aims to host a wide range of applications, being able to cover all the points presented above. Details about the system design are presented in the third section. In order to give a real picture, we will consider the development of a BPM instrument for the European Synchrotron Radiation Facility (ESRF) booster [1] as an example.

* manuel.cargnelutti@i-tech.si
# www.i-tech.si

A NEW PLATFORM

Looking at the beam instrumentation used to monitor and stabilize an accelerator, every device suits a specific role, but it is possible to identify some key components that are always present:

- digital signal processing and elaboration units (e.g. FPGAs and CPUs)
- RF front-end and analogue signal processing chains
- internal communication buses
- power supply unit
- crate and cooling system (often is an active system with fans).

In this new development, we take advantage of the latest advances in SoC technology to introduce a compact platform that combines a high level of hardware integration with our knowledge regarding reconfigurable analogue signal processing.

HW and SW integration

Hardware and software are designed taking in account the balance between generality and optimization. It will be always possible to add specific features to customize it, opening at the same time the way for developing different applications, as shown in Fig. 1.

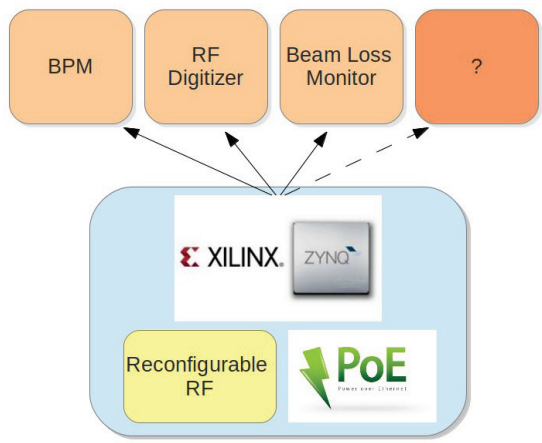


Figure 1: Platform concept based on SoC.

The core part is the SoC Xilinix Zynq 7020 [2] which combines the high-speed processing of the FPGA together with the flexibility of a CPU, all within the same chip. The inner communication between the two entities and the chance to share the same memory removes at the same time two of the biggest bottle-necks that still characterize separate-chip solutions:

- no communication protocols needed
- no data copy between FPGA and CPU.

Copyright © 2013 CC-BY-3.0 and by the respective authors

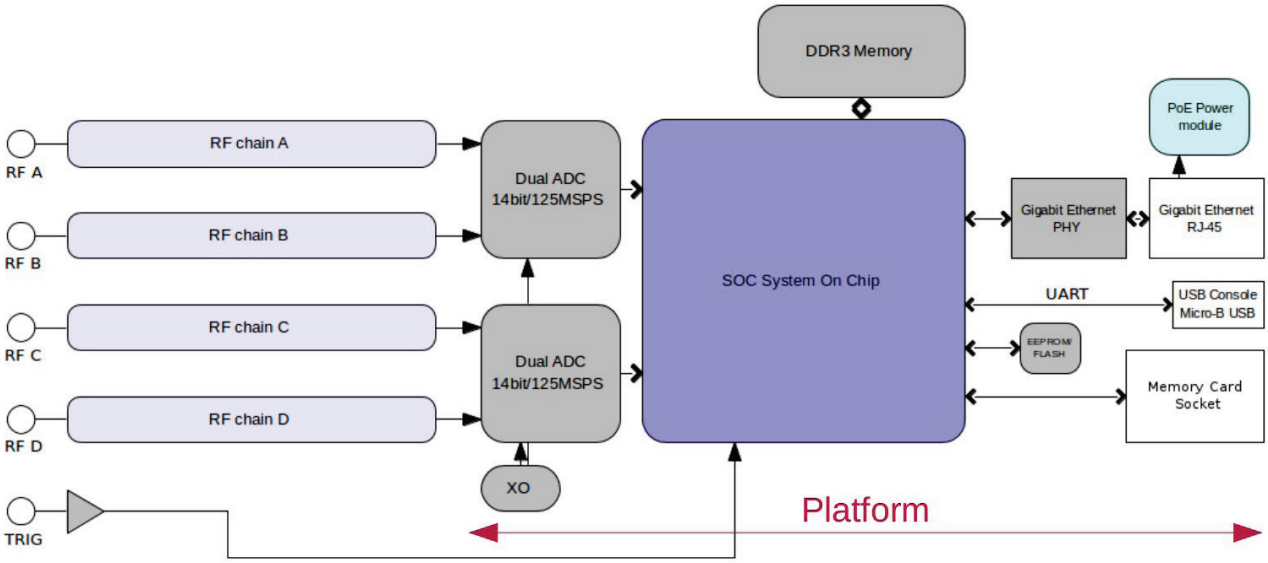


Figure 2: Basic HW architecture of the BPM instrument.

The specifics of the analogue front-end will cover the user requirements. Integrations with specific band-pass filters, phase-locked-loop and variable attenuators are possible if the application requires them. Figure 2 shows an example of the HW architecture of a BPM application.

Low power instrument

SoC requires less power than a multiple-board solution, and a proper selection of the RF components (amplifiers, analog-to-digital-converters (ADCs), etc.) reduces the amount of heat that the cooling system has to treat. This enables the way towards passive cooling with the integration of the heat sink in the crate. Consequently fans are no longer needed, and from the system point of view, the main advantages are:

- no moving parts means no maintenance required
- fans-induced noise is no longer present on the signals
- less space and less power required from the system.

With the low power requirement, precisely less than 15 Watt, the system can be powered over Ethernet according to the PoE standard IEEE802.3af.

In the case of accelerator applications, if the unit is powered over Ethernet, it is possible to put it closer to the machine (e.g. 5m), reducing at the same time the cost of cables and noise on the signal.

Easy SW maintenance

The unit software can be basically divided in the design that configures the FPGA and application and other interfaces supported by the operating system on the CPU side. The operating system running on Xilinx Zynq SoC is Linux OS.

In the presented platform, the software packages will not be installed in the device memory, but both FPGA and Linux code will be loaded from the same image when the unit is turned on. In more details two different boot procedures will be supported:

- ***memory card boot***: if a memory card is inserted in the device socket (see Fig. 2), then the Linux OS will boot from the image contained in the memory
- ***trivial File Transfer Protocol (TFTP) boot:*** if no memory is inserted, the boot procedure will start from the FLASH memory, and the software image will be downloaded from a configured TFTP server.

In both cases a software update can easily be realized replacing the software image in each unit, with no need to deal with packages and configuration files in the operating system. In particular for a complete set of units configured to use TFTP, only one image should be modified.

DESIGN CONCEPT FOR A BPM

The beam position monitor is the first application developed on this new platform, and 75 units will be installed in the ESRF booster ring [3].

Generally, the requirements for boosters are more relaxed compared with storage rings, and a resolution in the range of micrometers is more than enough. With a slight simplification of the measurement concept and the performances offered by this new platform, it is possible to match the requirements with an excellent price-to-performance ratio. Table 1 recaps part of the booster specifications that are important for the development.

Table 1: ESRF booster specifications

Parameter	**Value**
Circumference	300 m
Energy gap	200MeV – 6 GeV
RF frequency	352.2 MHz
Repetition rate	10 Hz
Required resolution	< 0.5 mm

Copyright © 2013 CC-BY-3.0 and by the respective authors

The RF front-end should deliver the signals to the ADCs, achieving both wide bandwidth and good signal quality. With the low power constraint, a clever design of each stage is necessary, and the use of filters and amplifiers should be limited to the strictly necessary. Obtained bandwidth ranges from 300 MHz to ~500 MHz, and special Surface Acoustic Wave (SAW) filters will be placed to enhance the signal quality at required frequency, in this case 352.2 MHz.

Sampling frequency is programmable in a range from 80 MHz to 125 MHz. Selected ADCs support such sampling frequency and output 14-bit data.
Data acquisition is started either providing an external trigger signal (see Fig. 2) or using the SW trigger functionality, with a 10 Hz maximum rate that meets the ESRF specifications. Samples acquired through ADCs are then processed in the FPGA through three different data paths and stored in different memory buffers, as shown in Fig. 3.

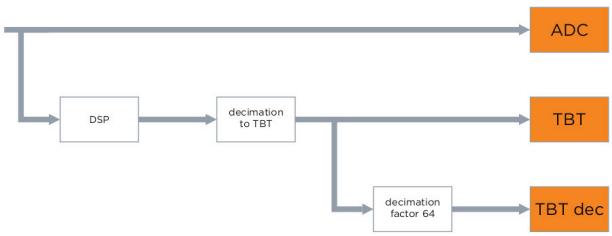


Figure 3: Data-paths and buffers overview.

- ***ADC raw data***: raw samples acquired at the sampling frequency, stored in a buffer with capacity 1 Msample.
- ***TBT data***: ADC samples regarding a whole turn in the ring are processed by a digital-down-conversion (DDC) algorithm using filters whose parameters are optimized for the machine physical dimensions and RF frequency. Data stored in the buffer are I and Q samples of each chain. Reducing the bandwidth, also the noise contribution is lower, and a better position resolution is then achieved. Its capacity is 256k samples.
- ***TBT-decimated data***: this buffer contains the data stored in the TBT buffer, after a decimation with factor 64. Its capacity is the same as the TBT buffer.

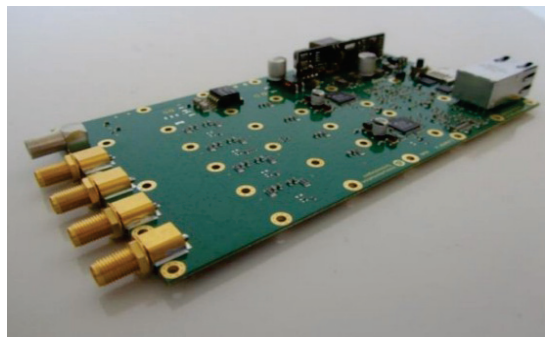
On the CPU side, data stored in the buffers can be further processed in order to deliver a more complete set of information to the user: from I and Q, also X and Y and sum signals are available. The position is computed using difference over sum formulas, and proper parameters can be tuned to remove offsets and adjust the gain.

The upper software layer provides the communication interface with the instrument. This is based on Standard Commands for Programmable Instruments (SCPI) specifications. Integration in the accelerator control system environment (EPICS, TANGO, etc.) can easily be done either implementing a specific server in the unit or using an external device server.

The development of the instrument is on the way with first prototype boards produced – see Fig. 4. First results of the measurements of the HW and ADC buffer part are within the specifications:

- crosstalk between RF channels is better than -60 dB
- expected position resolution at turn-by-turn frequency of 1 MHz is in the range below 10 micro-meters
- PoE functionality and boot options work properly.

Figure 4: BPM prototype board.



CONCLUSIONS

The development of a new compact electronics based on the SoC technology has been presented in this article. The introduced platform combines knowledge about reconfigurable RF front-ends with the advantages of a compact and passively cooled instrument that can be powered over Ethernet and booted from a server using only one SW image.

It is intended to be the base for several applications, but the BPM case is the first of these and is described in details. Many others such as RF digitizers, BLMs and beam current monitors will come in the future. FPGA and CPU software will be provided to the user in order to give the opportunity to extend and optimize the instrument's original functionalities.

As a first development, the BPM prototype is a promising application that shows very good performance, simple and straightforward architecture and an interesting price-to-performance ratio.

REFERENCES

[1] G. Jug, M. Cargnelutti, K. B. Scheidt, "Development of Compact Electronics Dedicated to Beam Position Monitors in Injectors and Boosters" IBIC'13, Oxford, September 2013, WEPC18.
[2] Xylinx Zynq-7000 web page: http://www.xilinx.com/content/xilinx/en/products/silicon-devices/soc/zynq-7000.html
[3] ESRF booster specifications: http://www.esrf.eu/Accelerators/Accelerators/Booster

Copyright © 2013 CC-BY-3.0 and by the respective authors

COMPARISON OF SIMULATIONS AND ANALYTICAL THEORY OF RADIATION HEATING ON THE ADVANCED PHOTON SOURCE SUPERCONDUCTING UNDULATOR*

Laura Boon†, Purdue University, West Lafayette, IN 47907, USA
Roger Dejus, Katherine C. Harkay and Mark Jaski, ANL, Argonne, IL 60439, USA

Abstract

Synchrotron radiation can potentially introduce large heat loads on the beam chamber of the superconducting undulator (SCU0) at the Advanced Photon Source (APS). With the photon absorber mask, a well-aligned centered beam in the upstream bending magnet allows only a small amount of radiation power, less than 1 W, to intercept the walls of the beam vacuum chamber in the cryostat, assuming no photon scattering. But beams with vertical orbit errors, especially, can deposit much higher heat loads on the beam chamber, above 100 W. An analysis was carried out to calculate the power on the vacuum chamber when the beam has an orbit error through the upstream bending magnet. This paper presents these analytical results compared to simulations that were performed using a 3D photon tracking code, Synrad3d.

INTRODUCTION

As part of the Advanced Photon Source Upgrade project [1], a test superconducting undulator (SCU0) was developed at Argonne National Laboratory [2]. The test SCU0 was installed in December 2012 [3]. To reduce heating on the superconducting coils, the beam chamber is thermally isolated from them. The cryo-coolers used to cool the beam chamber are able to handle up to 40 W of power (at 20 K) from transient and continuous wave sources. Radiation from the upstream dipole produces high amounts of power that can be incident on the beam chamber inside the SCU0 cryostat. SCU0 is in the downstream end of the straight section in sector 6, see Fig. 1. The upstream end of the straight section has a hybrid permanent magnet undulator (HPM). A photon absorber (PA) in the downstream end box of the HPM is used to shield the beam chamber outboard wall from direct, on-axis radiation.

CALCULATIONS

The power incident on the SCU0 beam chamber from primary photons can be calculated through ray tracings and analytically. Ray tracings are 2D projections of the dipole radiation fan on the 3D vacuum system layout. Ray tracings do not typically include the vertical distribution of the dipole radiation. So analytical calculations were performed to include the photon vertical distribution. Figure 2 shows the elliptical shape of the beam chamber in the SCU0 cryostat. The shape was taken into account for all the calculations and simulations shown in this paper. All calculations assume a beam current of 100 mA. Beam orbits are referenced to the dipole exit.

Ray Tracings

The layout of the radiation fan is seen in Fig. 1. By applying an off-axis electron beam orbit through the radiation source, the horizontal steering offset (x) and angle (x') limits can be determined. The steering limit is defined by when the radiation fan begins to intercept the outside edge of the beam chamber. The steering limit defined by ray tracings is shown in Fig. 3 (red dotted line). Due to the wide horizontal aperture of the beam chamber, only for very large steerings is there a concern about radiation heating. For positive offsets the photon absorber shields the beam chamber. The power incident on the beam chamber is calculated as follows. The APS main dipole magnet generates 6.65 kW of synchrotron radiation power per 100 mA. The horizontal fraction of energy that is incident on the SCU0 chamber is calculated using α/θ_{dipole} where $\theta_{dipole} = 77.54$ mrad is the full bending angle and α is the angle subtended by the SCU0 chamber. The power incident on the beam chamber is greatest for an electron beam that has a negative orbit offset. The power on the outside edge ranges from 0.3 W to 22.8 W. The power increases for larger negative offsets.

Analytical Calculations

The radiation heating load is calculated analytically using the method described in [4]. The following equation is integrated over the vertical opening angle in which the photon beam is incident on the beam chamber:

$$F = P_0 \frac{1}{(1+X^2)^{5/2}} \left[1 + \frac{5}{7}\frac{X^2}{1+X^2}\right]. \qquad (1)$$

In Eq. 1, P_0 is the fraction of total power produced by the dipole magnet that passes the photon absorber, and $X = \gamma\psi$, where γ is the relativistic factor, and ψ is the vertical opening angle between the radiation source and the SCU0 beam chamber.

Figure 3 is a contour plot of the power incident on the SCU0 chamber when the beam has a horizontal offset. The vertical photon distribution is included in the calculation. Radiation intercepts the top and bottom of the beam vacuum chamber and not just the outside edge. Again the contour plot shows that large negative offsets through the

* Work supported by U.S. Department of Energy, Office of Science, under Contract No. DE-AC02-06CH11357
† lboon@purdue.edu

Copyright © 2013 CC-BY-3.0 and by the respective authors

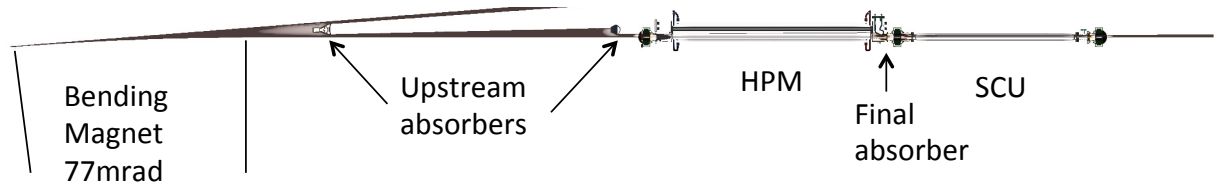


Figure 1: Top view schematic layout of the sector where the SCU0 is installed. The radiation is produced in the bending magnet, and photon absorbers are used to shield the SCU0 cryostat from direct radiation.

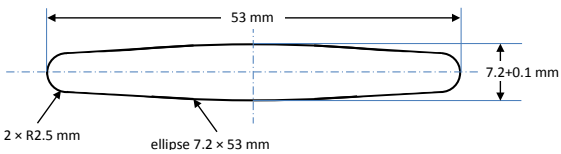


Figure 2: Elliptical shape of the beam chamber in the SCU0 cryostat.

dipole magnet produce the most power incident on the SCU0 beam chamber.

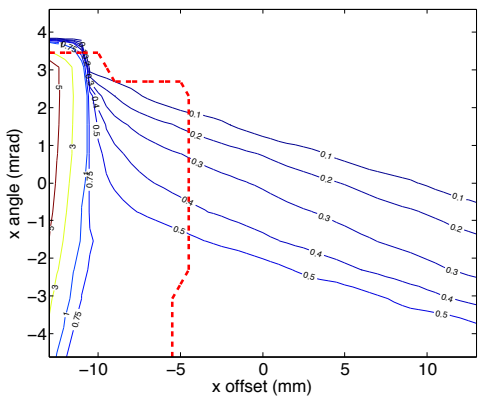


Figure 3: Comparison between ray tracings (dotted line) and analytical calculations (solid contours) of radiation power incident on the SCU0 beam chamber for a beam horizontally offset in the upstream bending magnet. To the left of the red dotted line is where radiation is incident on the outside edge of the SCU0 beam chamber. Power is shown in Watts. ($y = y' = 0$)

Figure 4 shows the power incident on the SCU0 chamber when the beam has a vertical steering error, offset (y) and angle (y') in the dipole magnet. Due to the small vertical aperture (7.2 mm) of the beam chamber, the incident power can reach over 100 W of power for relativity small vertical angles in the dipole. The vertical 'cut-off' of the heating on the SCU0 chamber is at 4 mm for two reasons. First, the upstream HPM has a vertical aperture comparable to that of the SCU0. This acts as a shield to the top and bottom of the SCU0 chamber. Second, the SCU0 chamber only has a vertical half aperture of 3.6 mm. Photons produced above that position will be absorbed in the taper before the SCU0 chamber.

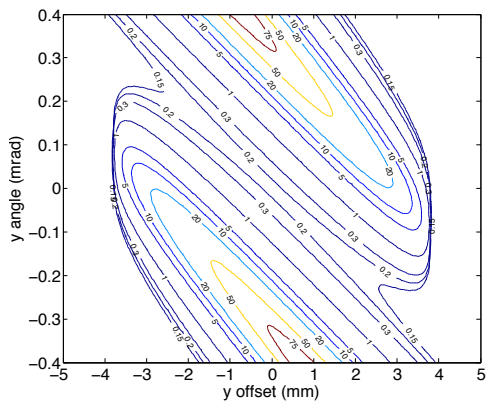


Figure 4: Power incident on the SCU0 cryostat for a beam that is off-axis vertically through the upstream bending magnet. Power is shown in Watts. ($x = x' = 0$)

The analytical results were compared with simulations in order to confirm our analytical model. Comparing Figs. 3 and 4, we note that vertical orbits in the dipole produce more heating on the beam chamber than comparable horizontal orbits. For this reason simulations were only done in the vertical plane.

SIMULATIONS

Synrad3d [5] was used to calculate the power of photons incident on the beam chamber. The total power on the beam chamber was calculated from the incident photon distribution and energy [6]. To simulate an off axis beam through the dipole magnet, an optimization of the correctors' strength was completed using BMAD [7]. The simulations included the electron beam trajectory through the entire sector. Coupling in the sector sextupoles creates a horizontal offset in the electron beam orbit for vertical steering. The horizontal offset was minimized through the choice of correctors and tolerance value in the optimization. For comparison with simulations, the analytical calculations account for the residual offset in x as well as the intended vertical offset or angle trajectory through the magnet. In the simulations, any photon reflections off the beam chamber were ignored because reflections are not included

Copyright © 2013 CC-BY-3.0 and by the respective authors

in the analytical model.

Figure 5 shows the comparison between the primary photon power calculated analytically and from the simulation. The incident power peaks at an offset of 2.8 mm. Then the power incident on the beam chamber drops to zero when the beam is offset more than 4 mm. The upstream undulator chamber shields the SCU0 beam chamber from the photon beam, similar to a photon absorber.

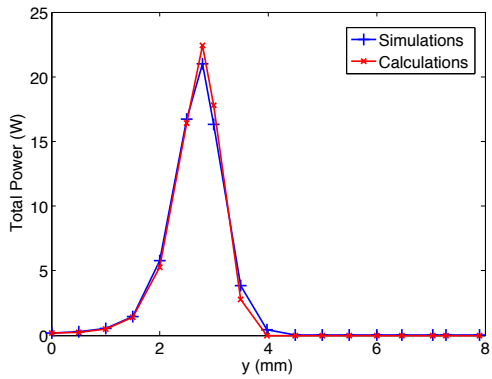


Figure 5: Analytical calculations and simulations of total synchrotron radiation power on the beam chamber wall for a vertical position offset in the upstream bending magnet.

Figure 6 is a comparison of analytical calculations and the corresponding simulations when an electron beam has a vertical angle through the upstream bending magnet. The incident power increases more slowly with just an angle offset in the electron beam. However, the maximum power is almost 4 times greater than an offset beam. The total power is greater for an angle because the highest-energy photons have the smallest opening angles from the electron beam trajectory. With an angle steering error the highest-energy photons intercept the beam chamber instead of passing though. Both sets of simulations have good agreement with the analytical values.

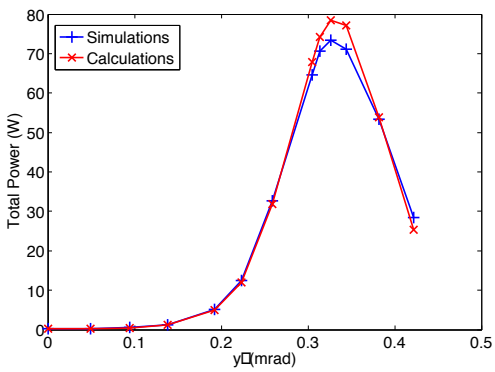


Figure 6: Analytical calculations and simulations of total synchrotron radiation power on the beam chamber wall for a vertical angle in the upstream bending magnet.

CONCLUSIONS

During user operation beam-position-limiting detectors are armed and limit the electron beam motion to ± 0.85 mm in x and ± 1.8 mm in y [8] at the exit of the bending magnet. According to the results shown here, the maximum power incident on the beam chamber is 25 W at these orbit limits, below the 40-W cooling capacity. Therefore, the greatest concern for radiation heating is during machine studies when the limits on beam motion are from the physical aperture of the beam chamber ($\pm 8 \times \pm 8.6$) mm [8]. Steering errors of this magnitude produce more radiation heating. To protect the SCU0 during machine studies, the current is turned off. Comparison of analytical calculations to simulations show that we have a good model for primary photon heating when the electron beam is off axis through the upstream bending magnet. In future work, photon scatting will be included in the analysis.

ACKNOWLEDGMENT

The authors would like to thank David Sagan and James Shanks for their guidance in running simulations in Synrad3d and BMAD.

REFERENCES

[1] APS Upgrade Preliminary Design Report, 2012.

[2] Y. Ivanyushenkov et al., IEEE Trans. on Applied Superconductivity, 21 (2011) 1717; Y. Ivanyushenkov et al., Proc. IPAC2012, MOPPP078, p. 744 (2012); journals.iucr.org/s/issues/2013/03/00/s130300aps.pdf

[3] K. Harkay et al., Proc. of NA-PAC 2013, WEOAA3.

[4] K. Kim, "Characteristics of synchrotron radiation", AIP Conf. Proc. 184, p.565 (1989).

[5] G. Dugan, D. Sagan, "Synrad3D Photon propagation and scattering simulation," Proc. ECLOUD10, Ithaca NY, (2010).

[6] L. Boon et al., THPC186, IPAC11, San Sebastian, Spain (2011).

[7] D. Sagan, "Bmad: A Relativistic Charged Particle Simulation Library," Nuc. Instrum. Methods A 558 p.356 (2006).

[8] Vadim Sajaev, private communication.

Copyright © 2013 CC-BY-3.0 and by the respective authors

THERMAL MODELING OF THE PROTOTYPE SUPERCONDUCTING UNDULATOR (SCU0)*

Y. Shiroyanagi, C. Doose, J. Fuerst, K. Harkay, Q. Hasse, Y. Ivanyushenkov, M. Kasa
Argonne National Laboratory, Argonne, IL 60439, USA

Abstract

A cryocooler-cooled superconducting undulator (SCU0) has been built, and cryogenic and magnetic tests have been completed. The device is currently installed in the Advanced Photon Source (APS) beamline. The device consists of a dual-core 42-pole magnet structure that is cooled to 4.2K with a system of four cryocoolers operating in a zero-boil-off configuration. In this paper, a thermal model of the beam chamber and its cooling circuit are presented. A temperature profile of the cooling circuit and heat load to cryocoolers are calculated based on steady-state temperatures. Comparison with cryogenic test results and future improvements will be discussed.

BACKGROUND

The superconducting undulator (SCU0) consists of a dual-core 42-pole magnetic structure that is cooled to 4.2K with a system of four cryocoolers operating in a zero-boil-off configuration. The design of the cryostat is based on a concept developed at the Budker Institute, Novosibirsk [1]. Figure 1 shows the overall cooling scheme of the cryostat. The beam chamber is cooled by the two bottom cryocoolers (Sumitomo RDK-408S) together with the inner thermal radiation shield, which is called the 20K circuit. The main and correction magnet leads and the thermal transitions of the beam chamber are connected to the first stages of all four cryocoolers through the outer thermal radiation shield, which is called the 60K circuit. The 4K circuit consists of the helium vessel, the magnetic structure, and the superconducting part of magnet leads. These are cooled by the 2nd stage of the top cryocoolers (Sumitomo RDK-415D). The magnet is cooled by circulating LHe, and it is thermally isolated from the beam chamber [2-4].

FEA MODEL

Finite element analysis (FEA) was conducted using ANSYS 14.5. Initially, heat loads at individual parts of the cryostat were calculated with fixed end temperatures. Thermal radiation heat was calculated in a separate model. Joule heating of the resistive parts of the current leads was also calculated separately. Then using these results, the 20K and 60K circuits were modeled including a simulated heat load imposed by the circulating electron beam. Temperatures and heat load at each cryocooler were calculated and compared with measured data. Table 1 is the calculated heat load of the individual parts of the cryostat based on the original design before the installation [1]. The 60K circuit heat loads are dominated by the magnet current leads. Static heat load through the main current leads are 47 W and through the correction current leads are 8.0 W. Main current lead heat increases to 63.85 W when they are energized to 650 A. The correction current lead heat increases to 12.2 W when they are energized to 70 A. Other sources include beam tube conduction and radiation from 295K to the outer shield. The 20K circuit heat loads are primarily the beam-induced heat load in the beam chamber that goes to the second stages of the bottom cryocoolers (408S) through the copper busbar and thermal links. The beam heat load is predicted to be 10 W at the 20K circuit and 6 W at the 60K circuit. The 4K circuit heat loads consist of the high-temperature superconducting (HTS) section of the magnet current leads, a very small portion of the beam heat through the beam chamber supports, heat through the cold mass supports made of Kevlar strings, and radiation from the inner shield to the cold mass.

In order to calculate the 20K and 60K circuit temperatures and heat, the magnet leads, the beam chamber, and the outer shield are modeled at steady state conditions. Figure 2 shows the overall temperatures of the 20K and 60K circuits as well as boundary conditions of this model. The outer shield is included in the calculation but not shown. Temperatures of the end flanges of the beam chamber and the top of the magnet leads are fixed at 295K. The coldest ends of the magnet leads are fixed at 3.42K, which is the measured temperature of the 2nd stage of the top cryocooler (415D). The load maps of the 1st stage top and 1st and 2nd stages of the bottom cryocoolers are implemented as temperature-dependent heat flow at each cold head.

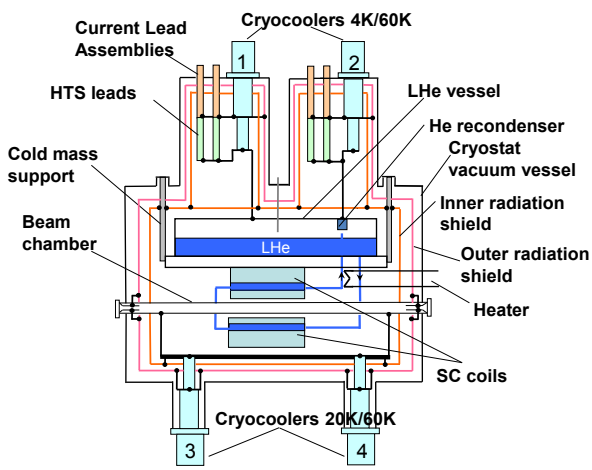


Figure 1: Cooling schematic.

*Work supported by the U.S. Department of Energy, Office of Science, under Contract No. DE-AC02-06CH11357
#yshiroyanagi@aps.anl.gov

Copyright © 2013 CC-BY-3.0 and by the respective authors

Table 1: Calculated Heat Loads of Individual Parts [W]

Heat Source	4K	20K	60K
Beam Induced Heat		10	6
Thermal Radiation	0.017	0.205	0.3
Beam Tube Bellows			4.8
Beam Tube Support@20K	0.08		
He Vent Bellows	0.0004	0.008	0.6
Cold Mass Supports	0.08		
Thermal Shield Supports		0.22	3.25
Correction Current leads (70 A)	0.064		8.02 (12.2)
Main Current Leads (650 A)	0.285		47 (63.85)
Total	0.526	10.43	69.97 (91)

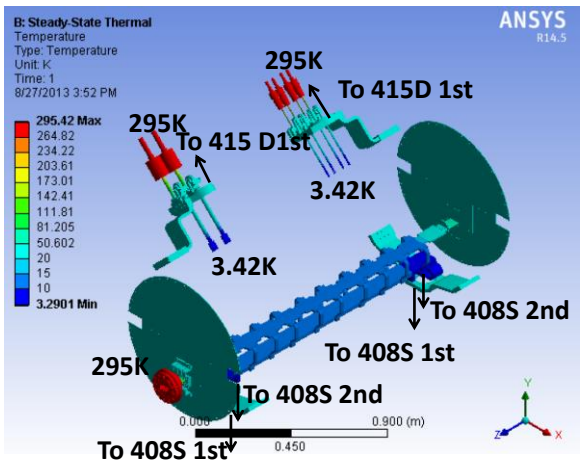


Figure 2: Calculated temperatures at the 20K and 60K circuits and their boundary conditions.

The cold head temperatures and heat loads at each cryocooler, except the top cryocooler 2nd stages, were calculated. The temperatures of the beam chamber were calculated based on the predicted beam-induced heat load [5,6]. The static heat load is calculated first, then the two dynamic heat loads. One is with beam on and the other is with both the beam and the magnet current on.

BEAM CHAMBER TEMPERATURES

Figure 3 shows the 20K circuit and the locations of temperature sensors. The sensors are numbered from the beam upstream to downstream. The main current leads are at the downstream side. Sensors 0 and 8 are on the stainless steel (SS) taper sections of the beam chamber while sensors 1 and 7 are on the stainless steel flat sections. These sections are linked to the outer shield and then to the 1st stages of the cryocoolers. The aluminum section is between the stainless-to-aluminum bi-metallic joints. Five sensors (2, 3, 4, 5, and 6) are on the aluminum section of the beam chamber and sensor 4 is near the center of the chamber. The aluminum section of the beam chamber is (thermally connected to the copper busbar through 20 copper links. The copper busbar is connected to the two bottom cryocooler 2nd stages (not shown).

Initially the beam heat was implemented in the model as a uniform heat flux in the beam chamber. However, the model calculated much lower temperatures at the stainless steel flat section than the measurement. So instead, the beam chamber inner surface is divided into three sections (aluminium, stainless steel flat, and stainless steel taper), and the heat load is applied based on S.H. Kim et al.'s beam-induced heat load calculation [5,6]. The SS taper heat load is 6.2 W, the SS flat heat load is 5.9 W, and the Al heat load is 4.7 W at 24-bunch mode and 100-mA beam current.

To reflect the circular beam shape, the beam chamber inner surfaces are divided into several strips and heat flux is distributed only on the center strips. The calculated temperatures are compared with the measurement by Harkay et al. in Fig. 4 [6]. For the static case, sensors 3 to 5 show ~7K. So the temperatures in the aluminum sections are uniform. Sensors 1 and 7 in the SS flat section are ~23K. When the beam current is on and the SCU magnet main current is at ~650 A, temperatures at sensors 2 and 6 rise above 20K since these are outside of the thermal links. Temperatures at 3, 4, and 5 rose to 13K. The SS flat sections 1 and 7 show as high as ~70K. Sensors 0 and 8 do not show the same temperatures in the measurement because the sensor positions are not known with sufficient accuracy. However, the average of these numbers agrees with the calculated values. So the calculated temperatures and measured temperatures have shown good agreement. Higher temperatures at sensors 1 and 7 suggest that more heat goes to the outer shield than originally designed [1]. An additional thermal link will be

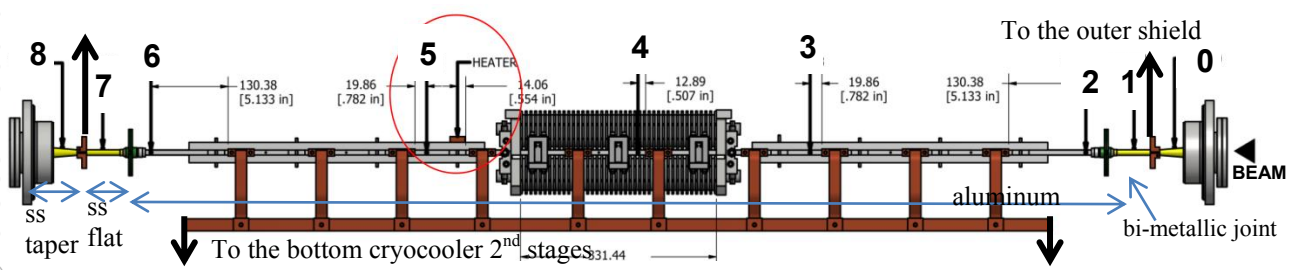


Figure 3: A schematic of the beam chamber, copper busbar, and locations of temperature sensors.

Copyright © 2013 CC-BY-3.0 and by the respective authors

attached to the end of the aluminum section of the beam chamber to lower the temperatures at sensor locations 1, 2 and 6, 7.

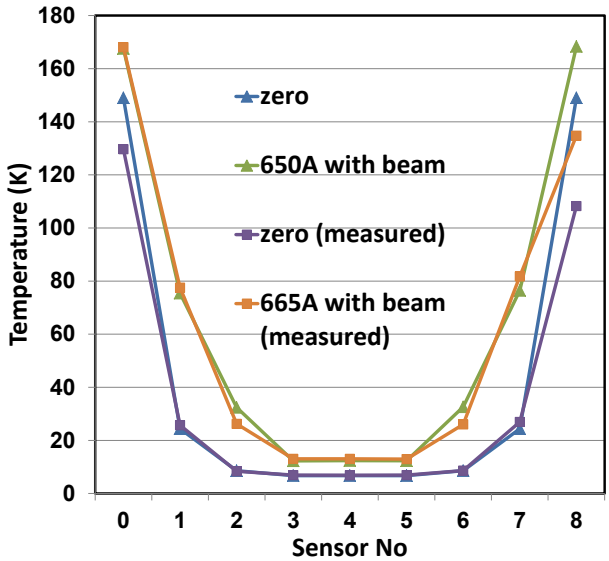


Figure 4: Calculated beam chamber temperatures are compared with measured temperatures.

COLD HEAD TEMPERATURES

Table 2 shows the calculated cold head temperatures based on the 20K and 60K circuit model and measured heat loads with 24-bunch mode beam and 665 A of SCU main current.

Table 2: Summary of Cold Head Temperatures [K]

	Static		Beam		Beam and current	
	Calc.	Meas.	Calc.	Meas.	Calc.	Meas.
TP1US	30.5	30.82	31.4	32.16	33.5	33.829
TP1DS	35.2	33.57	37.2	34.88	41.9	40.057
BT1US	30.0	30.18	30.9	32.16	32.7	33.736
BT1DS	31.1	30.83	32.3	34.88	34.7	35.116
BT2	6.75	6.715	10.38	10.09	10.40	10.335

In the actual system, the 20K circuit operates at ~10K and the 60K circuit at ~31K. The cold head temperatures show good agreement with measurement. Since measured heat is derived from the measured temperatures, the heat load at each cryocooler cold head agrees as well. A higher temperature at the top cryocooler downstream 1st stage (TP1DS) indicates the existence of a higher heat load from the main current leads. The bottom cryocooler downstream (BT1DS) also shows a slightly higher temperature than the upstream one (BT1US). However overall they are ~31K. So the magnet lead heat is well distributed to the 1st stage of all four cryocoolers as designed. A summary of heat loads is shown in Table 3. The 4K heat load is the sum of the heat loads of the individual parts from Table 1. The 20K and 60K heat loads are from the 20K and 60K circuit model. The calculated 60K static heat load was 63.66 W. The dynamic heat load with 650 A is 89.88 W. The measured static heat load is 63.01 W, and the dynamic heat load is 90.26 W. The calculated 20K heat load is 15.54 W due to the beam-induced heat. It agrees with the measured heat load of 15.09 W. Since the stainless steel flat sections show much higher temperature than expected, the beam heat going to the 60K circuit needs to be considered.

Table 3: Summary of Heat Loads [W]

	Static		Beam		Beam and current	
	Calc.	Meas.	Calc.	Meas.	Calc.	Meas.
4K	0.526	0.66	0.526	0.72	0.526	0.98
20K	0.188	-0.63	14.55	14.35	15.54	15.09
60K	63.66	63.01	68.13	68.0	89.88	90.26

DISCUSSION

The FEA calculated temperatures and heat loads show good agreement with the heat loads based on temperature measurements. The 4K heat load may include a larger error since the cryocooler load map does not have enough data points at this temperature range. The cryocooler cooling capacity is 3 W (1.5 W ea) at 4K, 40 W (20 W ea) at 20K, and 224 W (57 W ea for 415D and 55 W ea for 408S) at the 60K circuit. Thus, these heat loads are within the range. The 4K circuit model will be established in the next phase of this work. This FEA thermal model will be used for the future development of 1.1-m and 2-m devices (SCU1 and SCU2).

ACKNOWLEDGMENTS

We appreciate the useful discussions with L. Boon, R. Kustom, and S. H. Kim at the Advanced Photon Source. We also thank particularly Emil Trakhtenberg and Denise Skiadopoulos for the detailed design of the cryomodule.

REFERENCES

[1] Y. Ivanyushenkov et al., IEEE T Appl. Superconductivity 22(3), (2012) 4100804.
[2] D.C. Potratz et al., AIP Conf. Proc. 1434 (2012) 1191.
[3] Q. Hasse et al., "Fabrication and Assembly of A Superconducting Undulator for the APS," CEC-ICMC Proceedings (2013).
[4] J. Fuerst et al., "Cryogenic Performance of a Cryocooler-Cooled Superconducting Undulator," CEC-ICMC Proceedings (2013).
[5] S.H. Kim, APS Light Source Note ANL/APS/LS-329 (2012).
[6] K. Harkay et al., "Beam-Induced Heat Load Predictions and Measurements in the APS Superconducting Undulator," WEPSM06, NA-PAC'13.

Copyright © 2013 CC-BY-3.0 and by the respective authors

MODERNIZATION OF THE BERGOZ MULTIPLEXED BPM SYSTEM FOR THE APS UPGRADE*

X. Sun#, R. Lill, H. Bui, R. Keane, G. Decker, B. Yang, ANL, Argonne, IL 60439, USA

Abstract

The APS upgrade includes improvements to the Bergoz Multiplexed BPM system, which presently suffers from an aging data acquisition system. The upgrade leverages off the development of an eight-channel data acquisition system featuring modern FPGA flexibility that was designed for the monopulse BPM system. This upgrade also provides an external clock signal synchronized to the APS revolution clock that will eliminate the aliasing caused by the Bergoz asynchronous multiplexing interacting with different accelerator fill patterns. The upgrade will revitalize this system and demonstrate a cost-effective approach to improved beam stability, reliability, and enhanced postmortem capabilities. In this paper we will discuss the upgrade system specifications, design, and prototype test results.

INTRODUCTION

The Advanced Photon Source Upgrade (APS-U) project includes improvements to the commercial narrowband (Nb) Bergoz multiplexed Beam Position Monitor (BPM) systems [1], which were installed in 2000. The APS storage ring now makes use of 80 Bergoz modules that are connected to 10-mm buttons on a large-aperture, standard elliptical (42 mm by 85 mm) vacuum chamber. This NbBPM system presently suffers from an aging data acquisition system. The upgrade leverages off the development of an eight-channel data acquisition system featuring modern field-programmable gate array (FPGA) flexibility that was designed for the monopulse BPM system [2]. The new FPGA-based Beam Signal Processor (BSP100) will replace the old data acquisition system and controls for the existing Bergoz receivers located at P1s on the standard elliptical vacuum chambers.

The upgrade will revitalize this system and demonstrate a cost-effective approach to improved beam stability, reliability, and enhanced postmortem capabilities.

The noise floor, fill-pattern dependence, and intensity dependence of the prototype upgrade NbBPM system will be investigated.

UPGRADE SYSTEM SPECIFICATIONS

Beam stability improvement is an important part of the APS-U project, which will be supported by new and upgraded BPM electronic systems. Listed in Table 1 [3] are APS-U beam stability performance and goals for ID sources. To achieve these goals, the obsolete BPM electronics for the NbBPM, located at the standard elliptical vacuum chambers, will be replaced with a modern system providing improved resolution and drift characteristics.

Table 1: APS-U Beam Stability Performance and Goals

		AC rms motion 0.01-200 Hz		AC rms motion 0.01-1 k Hz		Long-term drift (One Week)	
		µm rms	µrad rms	µm rms	µrad rms	µm rms	µrad rms
Horizontal	Present	5.0	0.85	5.0-7.0*	NA	7.0	1.4
	Upgrade	3.0	0.53	6.0	1.14	5.0	1.0
Vertical	Present	1.6	0.80	3.7*	NA	5.0	2.5
	Upgrade	0.42	0.22	0.84	0.44	1.0	0.5

* Measurement up to 767 Hz

DESIGN

The BSP100 is a standalone Experimental Physics and Industrial Control System (EPICS) input/output controller (IOC), an FPGA-based (Altera Stratix® II), a C-sized VXI form factor, with eight high-speed 14-bit digitizers (Analog Device AD6645) running at 88 MSPS (one-fourth of the APS rf frequency) [2, 4]. The baseline design replaces the aging Bergoz data acquisition with the BSP100. The position signals from four Bergoz BPMs will be digitized with a single module. The BSP100's FPGA has five major blocks, the APS timing system receiver, the acquisition control block, the preliminary processing block, the continuous signal processing block, and the triggered processing block.

The turn-by-turn average from the preliminary processing block, which is same as that in the monopulse BPM system, is passed through a first-order low-pass filter with a cutoff frequency of about 1.4 kHz. Then it is converted to the engineering units and sent to several other blocks for processing, as shown in Figure 1.

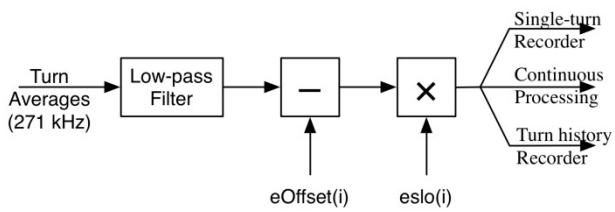


Figure 1: BSP100 Bergoz signal processing block diagram.

In the continuous processing block (shown in Figure 2), acquired data from the Bergoz BPMs will be available at EPICS rate and at a fast data stream. The BSP100

*Work supported by U.S. Department of Energy, Office of Science, under Contract No. DE-AC02-06CH11357.

#xiang@aps.anl.gov

Copyright © 2013 CC-BY-3.0 and by the respective authors

provides a 100-Mb/s TAXI-compatible link that carries data to the feedback system.

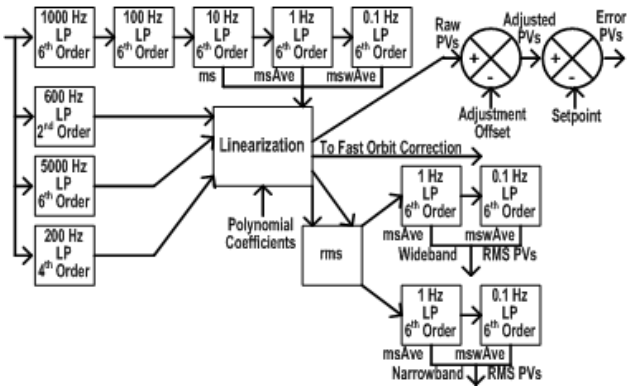


Figure 2: Continuous signal processing block diagram.

The BSP100 provides one second (262144 samples) turn-by-turn beam history, a virtual digital oscilloscope (4096 samples @ 88 MHz), single-turn acquisition, and slow beam history for machine studies and postmortems.

PROTOTYPE TEST RESULTS

The prototype of the NbBPM with BSP100 was installed at sector 38. The four 10-mm-diameter pickup electrodes were mounted on the standard elliptical vacuum chambers and connected to the 4-into-1-into-4 splitter with a variable attenuator between the four-way combiner/splitter, as shown in Figure 3. This setup minimized the physical noise from real beam motion, and only electronics noise was measured. Varying the attenuator simulated change in the intensity and noise.

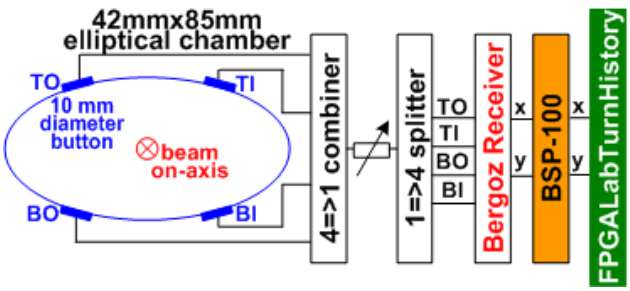


Figure 3: Measurements setup at Sector 38.

The signals from the 4-into-1-into-4 splitter combo went to the Bergoz receiver with BSP100 interface and simulated a beam on-axis. The FPGALabTurnHistory controlled the BSP100 module to clock the Bergoz BPM taking data using 324- or 24-singlet fills and eliminating aliasing lines caused by the Bergoz multiplexer beating against the fill pattern. The Bergoz receiver operated properly to an external frequency of 33.94 kHz, while varying an attenuator over the range 0 to 50 dB.

The sensitivities of 10-mm-diameter buttons in the standard elliptical chamber on horizontal and vertical planes are 0.058 mm^{-1} and 0.055 mm^{-1}, respectively [5]. The calibration factor formula of NbBPM is

$$d = \frac{1}{\text{Gain}} \frac{1}{\text{Sensitivity}}, \quad (1)$$

where d is the calibration factor, Gain is the Bergoz BPM module X/Y gain, and Sensitivity is the vacuum chamber sensitivity.

The gains of the Bergoz modules used in the measurement are $\text{Gain}_x = 0.148\text{V}/\%$ and $\text{Gain}_y = 0.161\text{V}/\%$.

The overall calibration factor of the NbBPM and the electronics system is 1.165 mm/V and 1.129 mm/V on horizontal and vertical planes, respectively. They were used in the following measurements.

The Fill Pattern Dependence

Figure 4 illustrated the root-mean-square (RMS) of the cumulative integral of the power spectral density (PSD) with 24- or 324-singlet fill patterns on the vertical plane. It shows the fill pattern dependence. The performance on the horizontal plane was similar.

The Intensity Dependence

Figures 5 and 6 represented the RMS of the cumulative integral of the PSD for various attenuations on the horizontal and vertical planes with 24- or 324-singlet fill patterns, respectively. They show the intensity dependence.

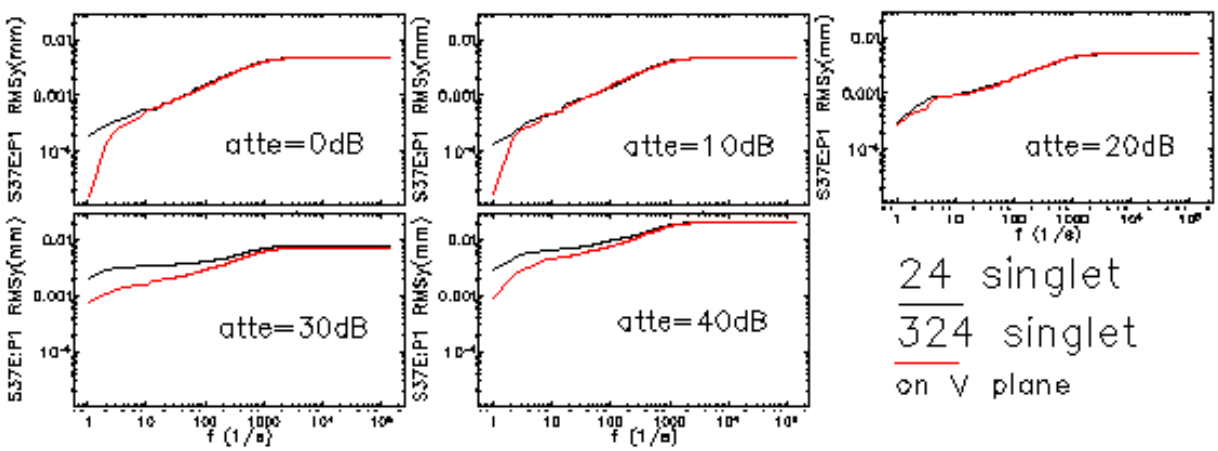


Figure 4: Cumulative RMS for different fill patterns on the vertical plane.

Copyright © 2013 CC-BY-3.0 and by the respective authors

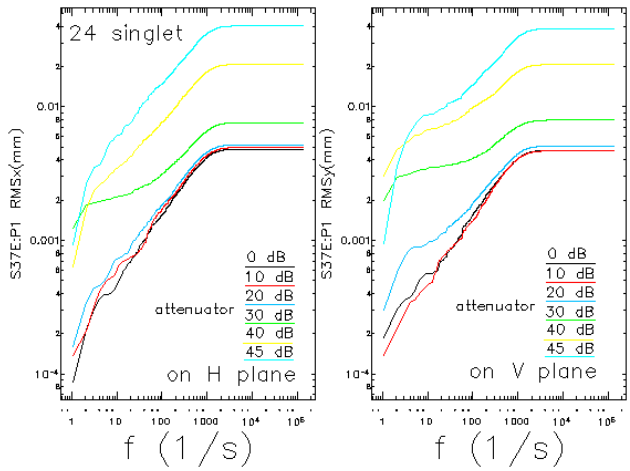


Figure 5: Cumulative RMS for different intensities with a 24-singlet fill.

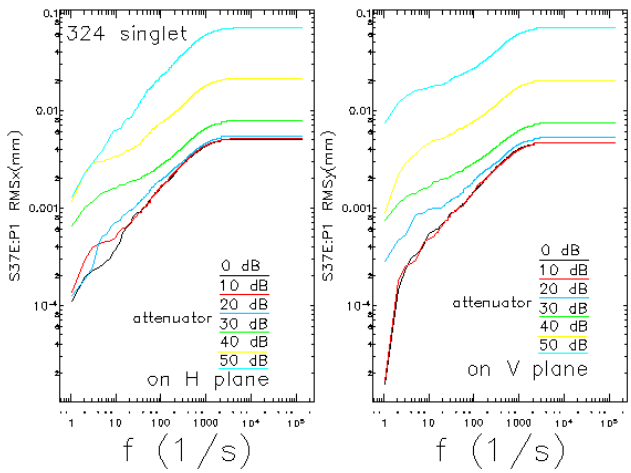


Figure 6: Cumulative RMS for different intensities with a 324-singlet fill.

The Synchronous and Asynchronous

Using the existing data acquisition system, aliasing spikes were observed in some P1 NbBPMs located at the standard elliptic vacuum chambers. The aliasing is caused by the beating of the Bergoz internal clocks with various other processing clocks residing within the NbBPM chassis and by different accelerator fill patterns, especially the hybrid fill pattern [6].

The upgrade prototype with BSP100 was provided an external clock signal synchronized to the APS revolution clock with the expectation of eliminating the aliasing. The noise data were taken with the 24-singlet fill pattern, shown in Figure 7.

There is no obvious difference on the vertical plane at sector 38 for the 24-singlet fill pattern with and without the external clock synchronized to the APS revolution clock. It may be because the aliasing appeared serious only in some sectors, especially for a hybrid fill.

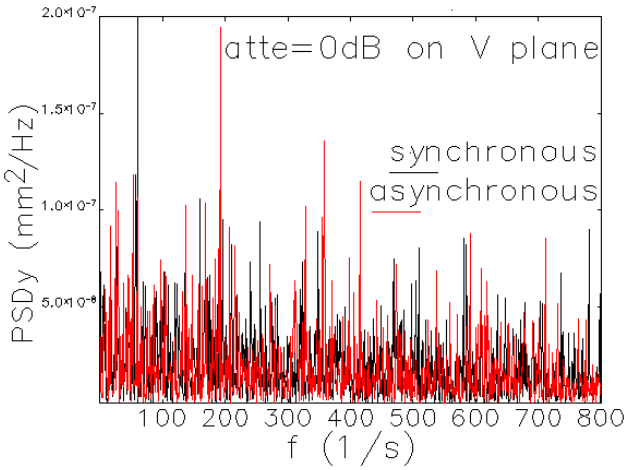


Figure 7: PSD for a 24-singlet fill on the vertical plane with and without the external clock synchronized to the APS revolution clock at sector 38.

SUMMARY

Using the 4-into-1-into-4 splitter with a variable attenuator between the four-way combiner/splitter, a prototype of an NbBPM with BSP100 was connected to the 10-mm-diameter buttons mounted on the standard elliptical chamber. A varying-intensity on-axis beam was simulated by changing the attenuator. The noise was measured with 24- and 324-singlet fill patterns. The intensity dependence and fill-pattern dependence were studied. More data for different fill patterns and off-axis beam will be conducted in the future.

REFERENCES

[1] R. Biscardi, J. Bittner, "Switched Detector for Beam Position Monitor," PAC'89, Chicago, Illinois, p. 1516 (1989); http://www.JACoW.org

[2] H. Bui et al., "Performance of FPGA-based Data Acquisition for the APS Broadband Beam Position Monitor System," BIW'08, Tahoe City, California, TUPTPF001, p. 80 (2008); http://www.JACoW.org

[3] G. Decker, private communication.

[4] E. Norum, private communication.

[5] S. Kim, "Four-Button BPM Coefficients in Cylindrical and Elliptic Beam Chambers," APS Light Source Note, ANL/APS/LS-274 (1999).

[6] X. Sun and O. Singh, "Tuning the Narrow-band Beam Position Monitor Sampling Clock to Remove the Aliasing Errors in APS Storage Ring Orbit Measurements," PAC'07, Albuquerque, New Mexico, FRPMN120, p. 4402 (2007); http://www.JACoW.org

Copyright © 2013 CC-BY-3.0 and by the respective authors

ULTRA-HIGH VACUUM SEAL FOR LONG CHAMBERS USING WIRE SEALS*

H. Fernandes#, P. Cappadoro, T. Corwin, D. Harder, P. He, C. A. Kitegi, W. Licciardi, M. Musardo, G. Rakowsky, J. Rank, C. Rhein, and T. Tanabe,
National Synchrotron Light Source II, Brookhaven National Laboratory, Upton, NY 11793, USA

Abstract

As the length of insertion devices (ID's) increase for synchrotron light sources, so does the need to have larger ultra high vacuum (UHV) sealed chambers, which in turn necessitates the use of creative ways of sealing these large chambers in the UHV range (10^{-11} torrs).The method specified below was used to seal a 4-meter test vacuum chamber successfully in the ultra high vacuum range. This method could be used for sealing ID chambers of lengths larger than 4 meters in the UHV range due to its simplicity and reduced cost advantage. This test chamber was also baked for 3 cycles to check for the integrity of the seals and final vacuum levels.

INTRODUCTION

The ultra high brightness NSLS-II storage ring is under construction at Brookhaven National Laboratory. It will have 3GeV, 500mA electron beam circulating in the 792m ring, with very low emittance (0.9nm.rad horizontal and 8pm.rad vertical). Significant increases in brightness requirements for the third generation ID has led to increased length of ID and hence increased length of vacuum chambers. The wire seal method outlined below depicts a way of sealing these long vacuum chambers in a cost efficient way. Other sealing methods for chambers such as Helicoflex ™ seals, metal gaskets, metal O-ring seals and differential pumping methods were studied as potential sources for sealing large vacuum chambers (>2.5 meters) [4]. Of these methods, only the wire seal made it to manufacturing, testing and optimization; the other methods were ruled out due to their high cost, difficulty in manufacturability by vendors due to low production quantities, or failure to meet UHV requirements in terms of operational efficiency and difficulty in installation. The wire seal was able to seal a 4-meter-long vacuum chamber in the UHV range and was also able to maintain the same vacuum specifications during and after baking. Here, we outline the procedure used to seal a 4 meter test vacuum chamber, specify the test results for this chamber, and mention possible methods to improve the wire seal.

TEST CHAMBER CONSTRUCTION SPECIFICATIONS

The seal was tested on a 4-meter test chamber that had a modular design. This design reduces the cost of the R&D chamber to a minimum, as it consists of mainly steel plates. The modular design of the vacuum chamber consists of a base plate as shown in Figure 1. A spacer plate has grooves cut for o-ring seals, which are placed between the front plate and the back plate. The distance between the front plate and the base plate is 0.75". This is maintained to a minimum in order to keep just enough room for bowing of the chamber inwards.

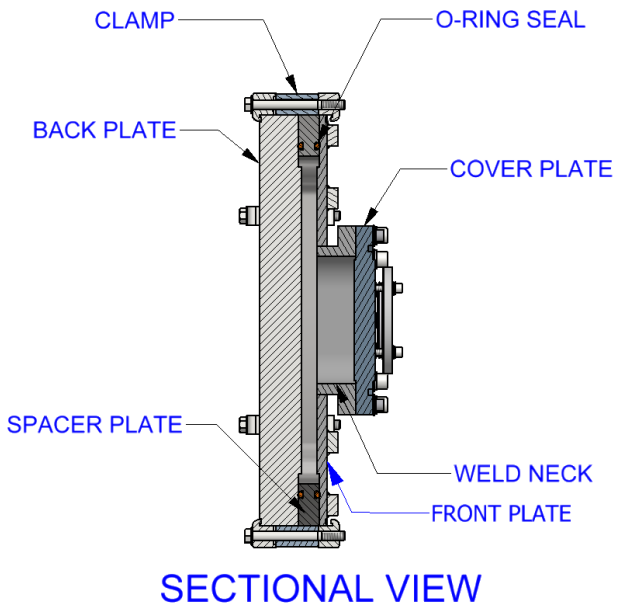


Figure 1: Construction details of test chamber.

O-ring seals were used on either side of the spacer plate to seal the spacer plate with the front plate and back plate. A weld neck was welded onto the front plate. During the first phase of the testing procedure, the top surface of the cover plate and the mating face of the weld neck were polished to 32 micro-inches surface finish because a wire seal would be placed and tested on this surface. During the second phase of the testing procedure, the two mating surfaces were polished to a 16 micro-inch surface finish. The length of the testing surface for the wire seal is approximately 3.6 meters. The entire vacuum chamber from end to end is 4 meters, as shown in Figure 2 below. Stiffening ribs were welded onto the surface of the front plate toward the cover plate. The main reason for the stiffening ribs was to have a chamber with adjustable stiffness which could be either increased or decreased by inserting stiffeners along the length of the stiffening ribs.

Copyright © 2013 CC-BY-3.0 and by the respective authors

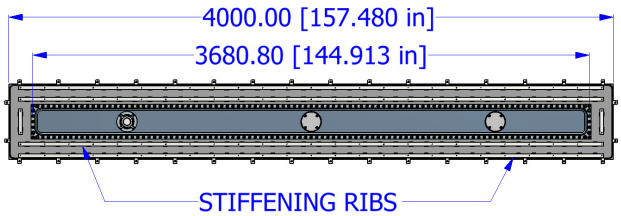


Figure 2: Construction details of test chamber.

In order to seal the face, it is essential to have a regular bolting pattern for the sealing face. 3/8 inch socket head cap screws along with washers were used with spacing between the bolts of 1.457 inches [2], as shown in Figure 3 below. At each of the corners of the cover plate, two set screws were used in order to prevent the cover plate from coming in contact with the wire during initial alignment. The set screws were loosened initially, so as to maintain a gap of more than 1 mm, which is the thickness of the wire.

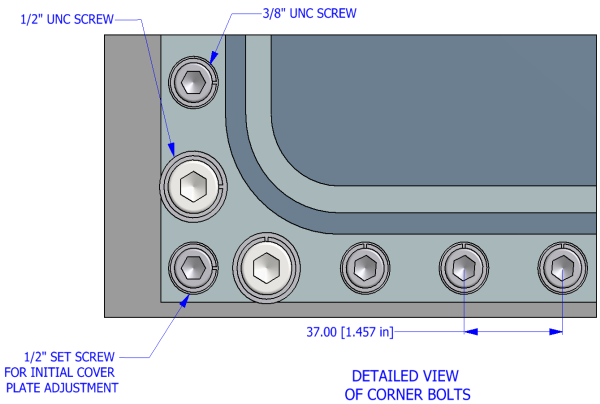


Figure 3: Corner bolt configuration.

Four wire seal adjusting fixtures are set at each end of the cover plate. The wire fixtures are designed such that the tension in the wire as well as the position with reference to the wire placed on the cover flange is adjustable using spring-held linkages, as shown in Figure 4. This design is a novel idea to adjust the tension in the wire seal, which in turn helps reduce sag in the wire, as well as positioning it as close as possible to the bolting pattern. This is a critical component in the installation and testing process, as the position of the wire has direct effects on the attainable vacuum pressure within the chamber.

Two annealed wire seals (aluminum) of different purity were tested on this chamber. Pure aluminium (99.95% pure and 1 mm thick), as well as pure aluminum (99.995% pure and 1 mm. thick, and much softer than the former) were tested.

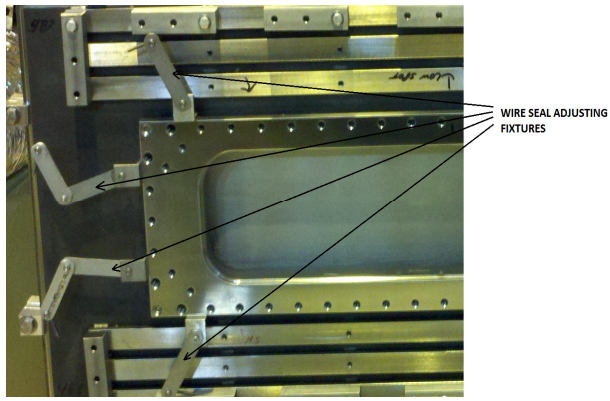


Figure 4: Wire seal adjusting fixtures.

TESTING PROCEDURE

The chamber was tested in the vertical position in order to replicate the actual ID chambers sealed while in operation. This also helps in determining the effect of sag of the wire, which is maximum at the center of the 3.6-meter sealing face.

The O-rings were placed in the spacer plate groove and the corresponding back plate and front plate were aligned with the spacer plate. Clamps were then installed to seal the back plate, spacer plate, and front plate. The cover plate was then aligned with the bolting pattern of the mating bolting pattern of the weld-neck flange. Wire seal adjusting fixtures were then installed with the wires and their position was adjusted with the linkages. It is critical to have the wire not more than 1/8 of an inch away from the edge of the center bolting hole.

Figure 5 illustrates the wire position with reference to the cross bolting hole pattern. Since the maximum sag in the wire is at the center, the wire would be further away from the edge of the center bolting hole. It is absolutely essential to adjust the tension and position in the wire, which in turn helps in keeping this distance to a minimum. Observations have shown that this is the critical position where vacuum leaks occur in the UHV range, if the wire seal is not aligned well during installation. The custom-designed dual linkage Wire Seal Adjusting Fixtures help in aligning and tensioning the wire to the correct tension and position.

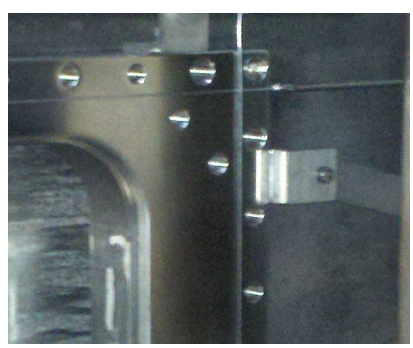


Figure 5: Cross wire configuration at the corner.

Copyright © 2013 CC-BY-3.0 and by the respective authors

At the cross point of the wire seal, as shown in Figure 5, ½-inch bolts were used to provide the required torque necessary to bolt the chamber at the cross point seal . A definite bolting pattern was followed, as mentioned by Savino [2]. The bolting sequence mentioned by Savino [2] helps in moving the crushed wire material away from the center and towards either end of the chamber. This is essential to maintain a uniform seal. The chamber was then pumped down to the UHV range through pump ports on the cover plate. A leak test was done to determine if the chamber was UHV compatible. This was followed by three baking cycle tests.

BAKING PROCEDURE

The chamber was then baked in an oven to 150 degrees C. This was done to replicate the actual baking procedure for all ID vacuum chambers at NSLS-II and study the effect of baking on the wire seal. During the baking process, the temperature was ramped to 150 degrees C in steps of 10 degrees per minute from a room temperature of 25 degrees C [1]. The pressure within the chamber was monitored during the entire baking process. The chamber was baked for a period of approximately 4 hours at 150 degrees C. The chamber was then left to cool down in the oven for a day. The vacuum chamber was then removed from the oven and tested for leaks. Three bake cycles were carried out on this chamber.

RESULTS AND CONCLUSION

Softer annealed aluminum wire seal which is 99.995% pure gave the same results as 99.95% pure wire. An important factor for UHV seals for large vacuum chambers was the surface flatness. The first test was conducted on a 32 micro-inch surface finish, which sealed the chamber. Chambers were leak tested to approx. 1.9×10^{-10} Torr Lit/sec. However, there were a few leaks observed at critical points, mainly around the center of the chamber where the sag in the wire was maximum, as well as around surface imperfection where the 32 micro-inch surface finishes were not maintained. These leaks were negotiated by increasing the torque on the bolts in this area and testing for leaks [5]. These leaks spots would seal if this process was used. However, on polishing the surface to 16 micro-inch, better results were obtained wherein the chamber was leak tested to 6.9×10^{-11}Torr Lit/sec, an improvement of ~ 64 %, compared to the 32 micro-inch surface finish.

It was also observed that the vacuum chamber pressure reduced from 2.15×10^{-5} Torr to 8.7×10^{-6} Torr, as seen in Figure 6, when the surface finish was reduced from 32 micro-inches to 16 micro-inches. This value is dependent on the elastomer O-ring seal. The position of the seal from the bolt edge also affects the seal. For optimal results, it was observed that the wire seal should not be placed any more than 1/8" away from the edge of the sealing bolt. Bolts used for sealing should have washers, and it is advisable to have bolts with maximum permissible torque (>250 inch-lb),; in case of a leak at certain spots, torquing down the bolts around the leak spots would mostly seal the leak. Vacuum levels of 10^{-6} torrs were obtained, as shown in Figure 6. After the first baking cycle, a few leaks were noticed at the edges; these were eliminated by progressively tightening the bolts in sequence. On doing so, vacuum level was maintained to the 10^{-6} torr range after the second and third baking cycle.

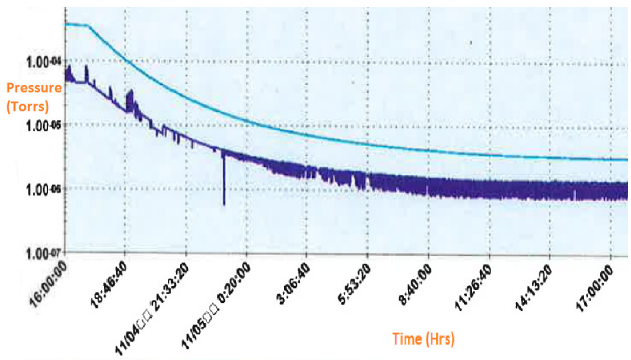


Figure 6: Pressure measurement.

ACKNOWLEDGMENT

The authors are grateful to key personnel at GNB, mainly Eric Raymond(Production Manager), Ken Harrison(President) and Larry Gilbert of Vacuum Solutions Group for manufacturing and conducting preliminary tests on the vacuum chamber as well as machining it to the specifications required by BSA.

The authors are also grateful to Jim Savino from CHESS for all the valuable support and feedback in designing and testing the vacuum seal test system.

The work at Brookhaven Nationals Laboratory was supported by the U.S. Department of Energy, Office of Science under contract 171565.

REFERENCES

[1] Michal Moraw et al., "Analysis of outgassing characteristics of metals", Pergamon Journals Ltd. Vol. 36, p. 523-525, 1986.

[2] J. Savino et al., "Inexpensive, reliable sealing of large UHV enclosures utilizing a progressively-deformed wire", MEDSI, 2010.

[3] J. Roth, "Vacuum Sealing Techniques".

[4] P.V.Head et al.,"Sealing techniques for large Ultra-high vacuum systems", Vacuum, Vol 32, p. 639-640, 1982.

[5] P.Lutkiewicz et al.,"Micro-damage propagation in Ultra-high vacuum seals"International Journal of Pressure Vessels and Piping, Vol 87, p. 187-196. April 2010.

Copyright © 2013 CC-BY-3.0 and by the respective authors

DESIGN AND TESTING OF FARADAY'S CUP FOR NSLS-II LINAC AND BOOSTER*

H. Fernandes#, B. Belkacem, W. Cheng, W. Guo, B. Kosciuk, J. Rank, S. Sharma, O. Singh, T. Tanabe and G. Wang
National Synchrotron Light Source II, Brookhaven National Laboratory, Upton, NY 11793, USA

Abstract

NSLS-II will provide 500 mA, 3 GeV beam of 1 nm emittance. It's planned to have top-off operation. To ensure bunch uniformity and constant current, the precise measurement of the charge becomes necessary. There are three Faraday Cup's at the end of the transport line in the Linac and Booster transport lines which serve this purpose. The details of the design consideration are presented in this paper. The Diagnostic group at NSLS-II, designed, prototyped and tested the Faraday Cup (FC). Power density calculations and FEA simulations were carried out for the three cases.

INTRODUCTION

At NSLS-II, the FC's serve as a beam dump and a charge measuring device, therefore we have three such devices at the end of each of the test beamlines. The beam energy in the Linac area is 200 MeV [1]. The beam size at FC1 and FC2 in the Linac transport line was found to be 0.2 mm horizontally and 0.5 mm vertically. Figure1 below indicates the location of FC1 and FC2 in the Linac area. Figure 2 indicates FC3 in the Booster area. The beam energy in the Booster area is 3 GeV with a beam size of 2.3 mm in the horizontal direction and 0.27 mm in the vertical direction.

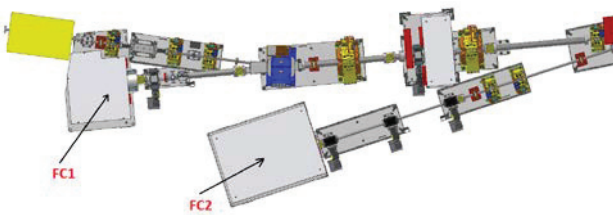


Figure 1: Location of Faraday's Cup in the linac area.

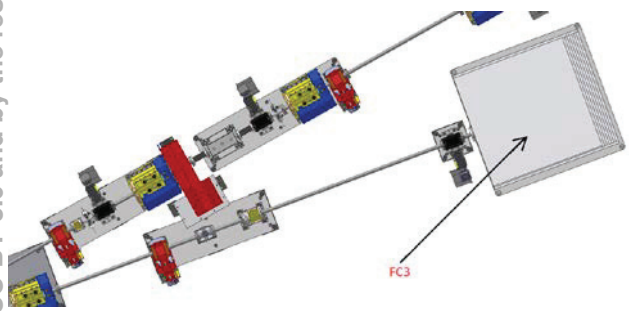


Figure 2: Location of the Faraday's Cup in booster area.

- Different devices are used to measure beam current. One way to measure the total charge of the beam in normal operation is by non intercepting devices such as current transformers (ICT, and DCCT). This non destructive method is independent of beam energy. These devices have to be calibrated to a device that will collect the totality of the electrons. For this reason an FC have to be installed close to the device to be calibrated (unknown losses between the two instruments introduce systematic errors).
- Another method to measure the charge is by using FCs. In this case, we need to stop and dump the electron beam for a certain period, preferably at full energy and bunch repetition rate. FCs are installed at the end of the transport lines. The beam will be sent to the FC during beam tune ups. Beam stops are used to absorb the entire beam.

MECHANICAL DESIGN

The designed Faraday Cup consists of a beam stop (graphite and copper pieces), which is essentially used to stop the beam. This is followed by a beam dump (stainless steel pieces). Details of this design are indicated in Figure 3.The radiation shower produced after stopping the beam must be absorbed. This is achieved by using layers of lead and borated polyethylene sheets. The third most critical component of the Faradays cup is its electrical circuit, which consists of an integrator followed by a digitizer. The ceramic brake isolates the beam dump from the rest of the assembly. The charge is measured by integrating the output voltage across the ceramic break. The beam dump consists of six plates which are one inch thick made of SS-304 and are bolted together. A knife-edge seal would ensure that the integrity of vacuum is maintained. This is machined on the first plate face of the SS-304 plate.

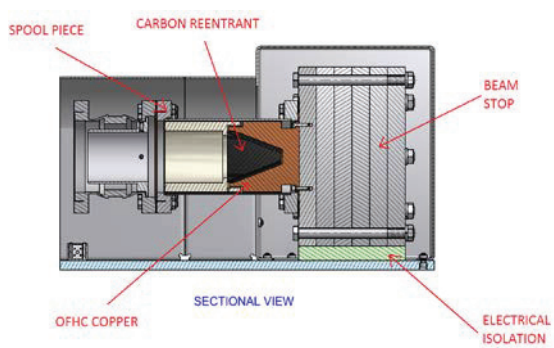


Figure 3: Construction details of FC.

Copyright © 2013 CC-BY-3.0 and by the respective authors

A carbon graphite cone is used mainly to reduce backscatter after beam stop shower. A spool piece is used to attach the components downstream of the beam stop. To prevent ozone generation, the front of the cup is in vacuum. Lead bricks are used for blocking the radiation and these bricks are surrounded by High Density Polyethylene (HDPE) sheets for shielding neutron radiation. The thickness of the lead and poly shields is based on the Linac and Booster beam parameters and was determined using Monte Carlo simulation. Typical lead and HDPE shielding configuration is shown in Figure 4. Shielding was provided in layers of lead and poly thickness to each of these dumps to block the radiation remaining from the steel plates, which is around 67.6KeV for FC3. The carbon re-entrant cone was machined at a cone angle of 30 degrees [2].

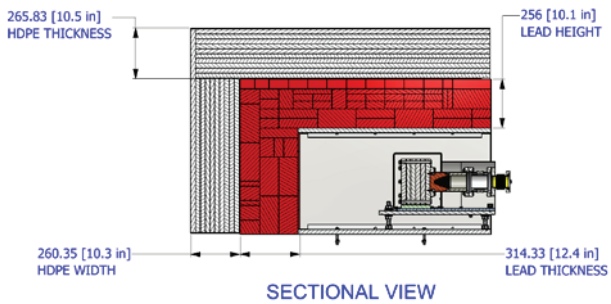


Figure 4: Shielding thickness for FC.

TESTING AND CALCULATION RESULTS

While penetrating the layers of the Faraday's Cup, the electrons interact with the material atoms both elastically and inelastically. For electrons with energy higher than tens of Mev, the energy loss is mostly through Bremsstrahlung, and can be well described by

$$E(x) = E_0 e^{-x/x_0} . \quad (1)$$

Where E0 is the initial energy and the radiation length

$$X_0 = \frac{716.4A}{Z(Z+1)\ln(287\sqrt{z})} g \cdot cm^{-2} . \quad (2)$$

With A as the atomic number and z the charge number.

The beam divergence, however, is mostly affected by the frequent Coulomb scattering with the nucleus. The angle growth rate is given by

$$\Delta\theta = \frac{13.6MeV}{\beta cp} z\sqrt{x/x_0}\,[1+0.038\ln(x/x_0)] . \quad (3)$$

To calculate the heat deposition and radiation issues, we consider FC3, which is subjected to most severe conditions. The initial beam size is calculated from the lattice functions, i.e., the emittance from the Booster is 40/4 nm in x/y; the relevant lattice functions at the entrance of the dump are $\beta_{x/y}$ =128.2/176.0, and $\gamma_{x/y}$=1.7/1.0. The subsequent angle and beam size were obtained by integrating Eq.(3). The beam property for FC3 is summarized in the following table.

Table 1: Beam Parameters through Materials for FC3

Material	L mm	X_0	ΣX_0	E_0 eV	σ_x mm	σ_y mm
start	0	0	0	3G	2.3	0.27
Graphite	76.8	0.45	0.45	1.9G	10	2.8
Copper	23.8	1.65	2.1	0.36G	44	23.4
Steel	151.2	8.6	10.7	67.6K	*	*

*The beam turns into a shower at the end of the steel plates. Beam size was also calculated based on the thicknesses and materials of each of these components. For the Linac FC, the beam size on the graphite surface was found to be an ellipse of 20 mm width and 24 mm height. The beam power is deposited on the surface as a conservative approximation. As can see in fig. 3, for a charge of 15 nC in the linac area, the maximum temperature was found on the graphite is 35 Degree C.

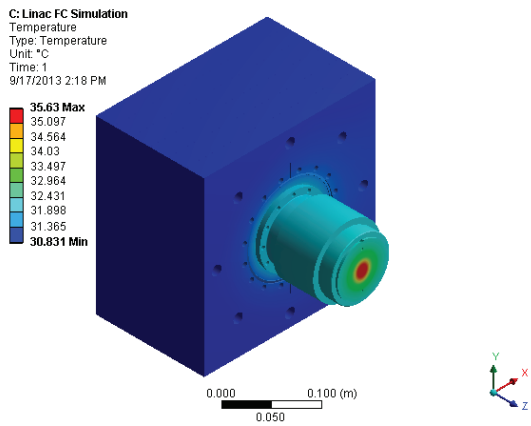


Figure 5: FEA simulation of linac transport line FC.

For the Booster FC, considering the charge of 10 nC, the total power was around 30 W, with maximum Temperature of around 196 Degree C.

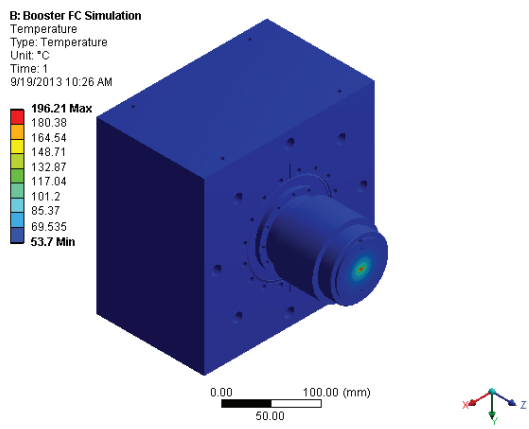


Figure 6: FEA simulation of booster transport line FC.

DESIGN OPTIMIZATION

Ensuring the accuracy of charge measurements require careful attention and accounting for all the error sources. In reality there are multiple reasons for electrons losses that must be considered during the design phases.

Copyright © 2013 CC-BY-3.0 and by the respective authors

- Penetration losses: Adequate size (radius and length) of the beam stop with a safety margin was calculated for preventing penetration losses. The design ensures that the width of the dump is 5 times the radiation length on both sides.
- Backscatter losses: The conical shape of the beam stopper reduced the electrons escape solid angle [3]. Graphite used has a low atomic number than the high Z value which helps the beam stop to slow the incoming beam and allow all the particles to flow to the conductive dump.
- Current leakage: Charge leakage due to insufficient impedance to ground may occur in the FC system: FC itself (support structure and enclosure), RF cables, integrator, or digitizer. The insulation is made of very high resistance material (G10 plate 0.75 inch thick). A known source was connected in parallel to the Faraday cup during integration tests, and leakage charge was found to be negligible (< 1pC).

BEAM MEASUREMENT

An RC network integrates the cup output voltage for measurement by a digitizer DC252 (4GS/channel, 2 GHz bandwidth, 10 bit resolution). The FC will be used to cross check the ICT's reading. To reduce signal loss, a low loss RF cable LMR900 is used to connect the FC to the digitizer. Figure 7 illustrates the bloc diagram of the FC system. The charge is calculated by integrating the voltage pulse area over a designated region of interest (ROI). $Q = \frac{1}{R}\int v.dt$, where R = digitizer input impedance. The digitizer output waveform is displayed in the control room from the appropriate CSS panel. Figure 8 is a screen shot of beam measured by the transport line FC2.

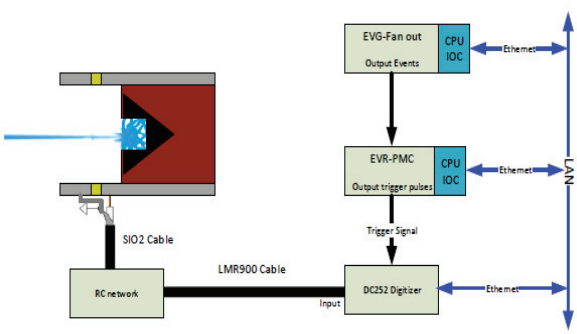


Figure 7: Block diagram of the FC measuring system.

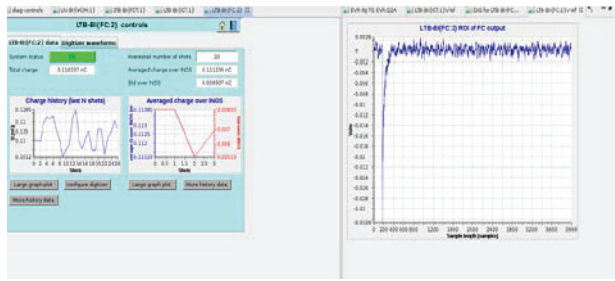


Figure 8: Transport line FC measured beam.



Figure 9: BINP FC VSWR measure- 20 GHz span.

CONCLUSION

During LINAC commissioning we have seen that FC1 does capture close to 100% of the beam seen at ICT1, while FC2 captures about 85% of the beam (FC1 closer from ICT1 than FC2). To measure the time structure of the beam FC1 will be replaced in the future by a wide bandwidth coaxial Faraday cup [3].

The heat simulation studies outlined above also indicate that the booster dump is much hotter than Linac dump but well within the melting point of graphite, hence a safe design.

REFERENCES

[1] R.P Filler et al., "NSLS-II Transport Line Progress", IPAC, 2012.
[2] Morgan, AFD et al., "Design of Faraday Cup at Diamond", DIPAC 2005, p.51.
[3] Jing Hu et al., "Faraday cup with nanosecond response and adjustable impedance for fast electron beam characterization", American Institute of Physics, July 2011.

Copyright © 2013 CC-BY-3.0 and by the respective authors

PREPARATION AND INVESTIGATION OF ANTIMONY THIN FILMS FOR MULTI-ALKALI PHOTOCATHODES

X. Liang, M. Ruiz-Osés, I. Ben-Zvi, Stony Brook University, Stony Brook, NY, 11794, USA
S. Schubert, E. Wang, Q. Wu, T. Rao, K. Attenkofer, J. Smedley, BNL, Upton, NY, 11793, USA
J. Wong, H. Padmore, LBNL, Berkeley, CA, 94720, USA
J. Jordan-Sweet. IBM T. J. Watson Research Center, Yorktown Heights, NY, 10598, USA

Abstract

Multialikali antimonide photocathodes exhibit high quantum efficiency in the visible light range, with low thermal emittance and are excellent candidate materials for high average current next generation ERLs or high repetition rate FELs. Although these materials have some excellent characteristics, control of the growth mode of the thin film and ultimately the surface roughness is difficult and will affect the emittance that can be obtained in high gradient fields. Being the first step in multi-alkali photocathode growth, the morphology of Sb films was investigated. X-ray diffraction pole figure (PF) measurement was used to determine the crystallinity of the Sb films. The measurements were complemented by atomic force microscopy (AFM) to determine the roughness and particle size. This study demonstrates how minor changes in deposition rate, thickness and substrate temperature can influence the Sb film properties.

INTRODUCTION

A.H. Sommer discovered that alkali metals such as Sodium (Na), Potassium (K), combined with antimony (Sb) result in photocathodes with high sensitivity and wide spectral response. Although methods for producing high QE films were established long ago, the remaining problems are mainly how to achieve good stoichiometric control so that long wavelength behaviour is reproducible and how to make very smooth films as required for high gradient photoinjectors. A collaboration of Stony Brook University, Brookhaven National Lab and Lawrence Berkeley National Laboratory aims to improve the performance of alkali antimonide photocathodes by using the tools of modern materials techniques such as X-ray diffraction (XRD), grazing incidence small angle X-ray scattering (GI-SAXS), X-ray reflectivity (XRR), AFM and X-ray photoelectron spectroscopy (XPS). [1-5]

This report will focus on recent progress in the analysis of the relationship between evaporation rates, film thickness and roughness.

EXPERIMENTALS

Ex-situ X-ray diffraction pole figure measurement was performed at the National Synchrotron Light Source (NSLS) X20A beam line at Brookhaven National Laboratory (BNL). For the PF measurement, the incident X-ray flux is approximately $8*10^{10}$ photons/second and the energy of the X-rays is 8.05KeV (λ = 1.5406Å). The size of the incident X-ray beam is 0.7 mm high and 0.7mm wide. The incident angle at the center of the linear detector was 20 degrees.

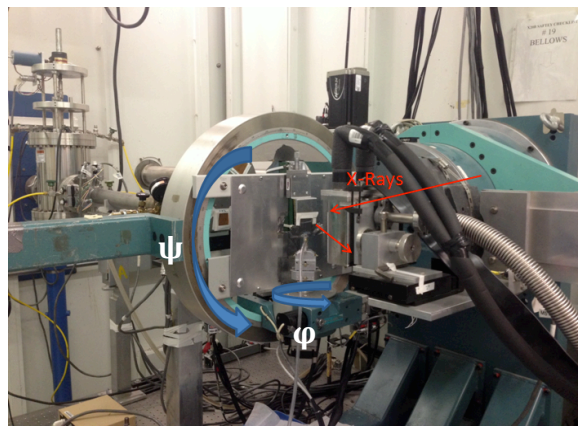


Figure 1: The experimental set up at the X20A beam line at NSLS. The beam line has a 4 circle Huber diffractometer, here just ψ and φ are moveable.

Si (100) wafers were used as the substrate, and all wafers were cleaned using hydrofluoric acid (HF), rinsed in deionized water and dried. The deposition was performed in a UHV chamber with a base pressure of 4×10^{-9} mbar; a Pfeiffer® Prisma QMG 200 residual gas analyzer (RGA) was used to monitored contaminants during growth. Values of H2O never exceeded 5.8×10^{-10} mbar, and CO/CO2 partial pressures were $< 1\times10^{-10}$ mbar during deposition. Deposition rates were monitored using an INFICON® quartz crystal film thickness monitor (FTM).

Surface topography was measured in air over a 1.5 × 1.5 micron area using a Nanosurf® Easyscan 2 AFM with a pyramidal Si (A-CLA mode) probe in BNL building 911 room 210A.

GROWTH PROCESS AND ANALYSIS

Ex-situ XRD PF measurement has been used to characterize the phases and texture changes of Sb thin films. The substrate size of 2cm ×1cm was used. Sb thin films were deposited on these in the UHV chamber by thermal evaporation, with the Sb being evaporated from

*Work supported by the United States Department of Energy through Contract numbers DE-AC02-98CH10886 and at Stony Brook University under Grant No. DE-SC0005713 with the U.S.DOE.
#liangx@bnl.gov

Copyright © 2013 CC-BY-3.0 and by the respective authors

PtSb beads. To cover a wide range of growth parameters, Sb films were deposited at different evaporation rates at 100C substrate temperature. For each evaporation rate, film thicknesses of 3nm and 10nm were produced; see table 1.

Table 1: Sb Thin Film Sample Preparation

Sample	Evaporation Rate	Thickness
a	0.2Å/s	3nm
b	0.2Å/s	10nm
c	0.4Å/s	3nm
d	0.4Å/s	10nm
e	1Å/s	3nm
f	1Å/s	10nm

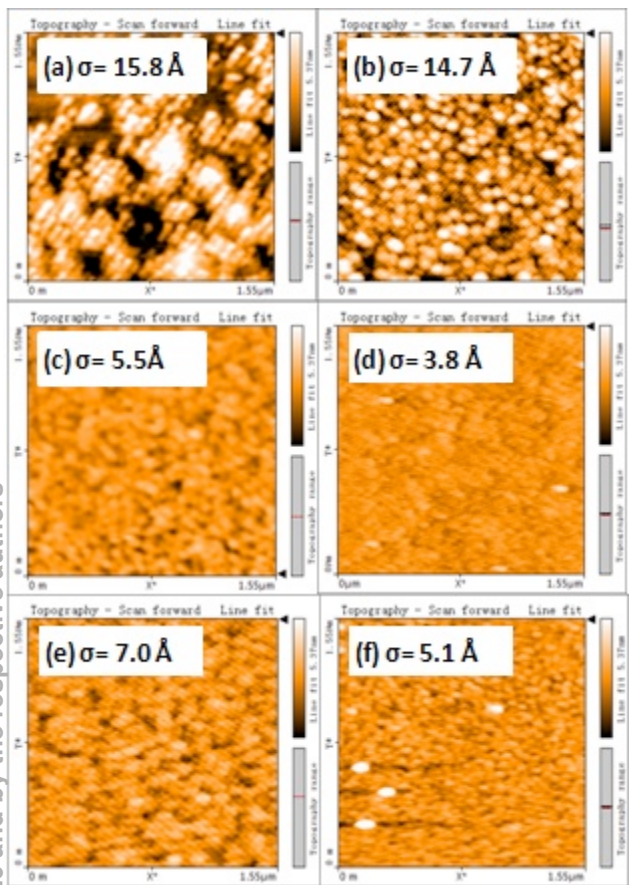


Figure 2: surface topography of six samples. (a) 0.2 Å/s, 3nm , σ=15.8Å;(b) 0.2 Å/s, 10nm, σ=14.6Å; (c) 0.4 Å/s, 3nm, σ=5.5Å; (d) 0.4 Å/s, 10nm, σ=3.8Å; (e) 1 Å/s, 3nm, σ=7.0Å; (f) 1 Å/s, 10nm, σ=5.1Å.

Figure 2 shows the topography and rms roughness of the sample. In general, the highest roughness values were measured for the lowest (0.2Å/s) evaporation rate samples. With the same evaporation rate, thicker films were smoother.

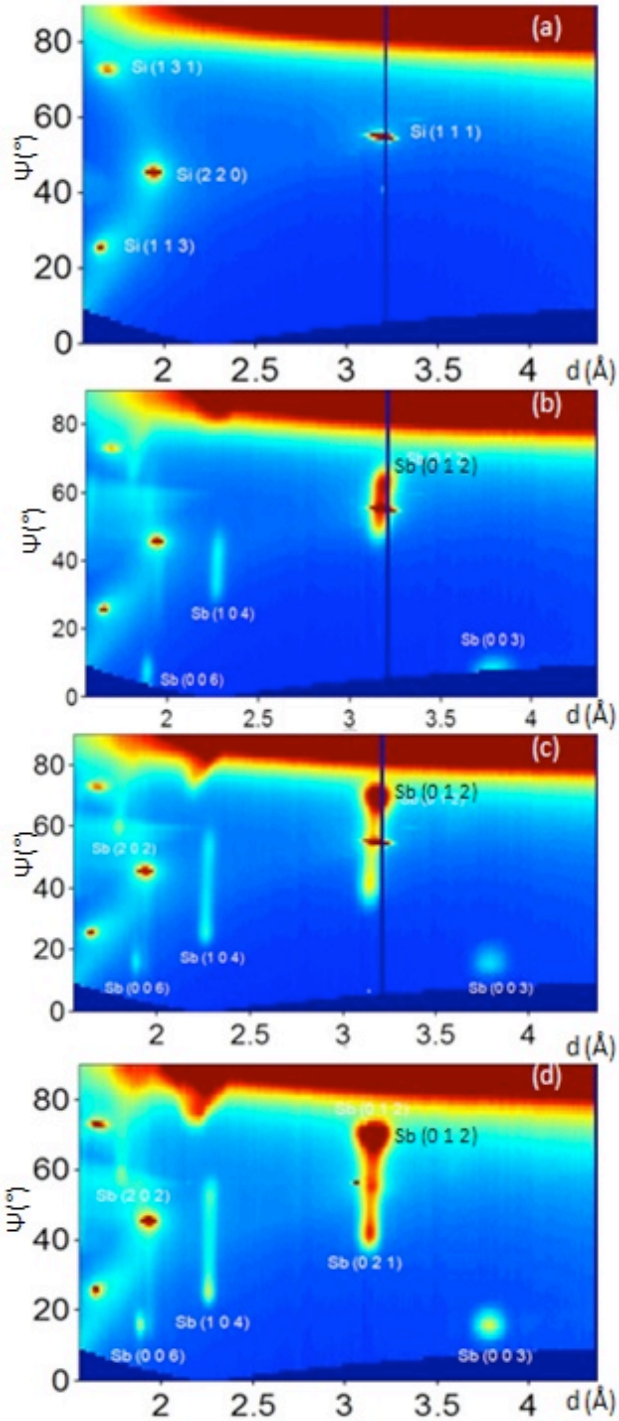


Figure 3: 2D reciprocal space maps; d is the spacing between the planes in the atomic lattice. (a) 0.2 Å/s, 3nm (b) 0.2 Å/s, 10nm; (c) 0.4 Å/s, 10nm; (d) 1 Å/s, 10nm.

The reciprocal space for the Sb films was acquired using radiation with λ=1.5406Å. In these measurements, the incidence angle ω=20° and 2θ=40°. Figure 3 shows the 2D reciprocal space maps. From these graphs, the crystal structure of the thin films can be identified. Figure 3 (a) shows an example of a 3nm Sb film. From this graph, strong Si diffraction peaks were detected. Si (131),

Copyright © 2013 CC-BY-3.0 and by the respective authors

(220), (113) and (111) planes can be identified. No Sb peaks were found from films of this thickness, as their thickness was less than the critical thickness for an amorphous to crystalline transition in this material. Figure 3(b) is for a 10 nm Sb film evaporated at 0.2Å /s corresponding to fig 2 (b); the diffraction peaks for the (012), (003), (006) and (104) planes are visible. (c) 10 nm Sb film evaporated at 0.4 Å /s corresponding to figure 2(d); this is the same as (b) but the (202) and (021) diffraction peaks are present. The intensity of other Sb peaks such as (012) (104) and (003) are increased. The strongest crystalline features are exhibited by the 10 nm Sb film evaporated at 1 Å /s, see figure 3(d); this figure is corresponds to figure 2(f). In figure 3(d), the diffraction intensity of plane Sb(0 12) is the highest.

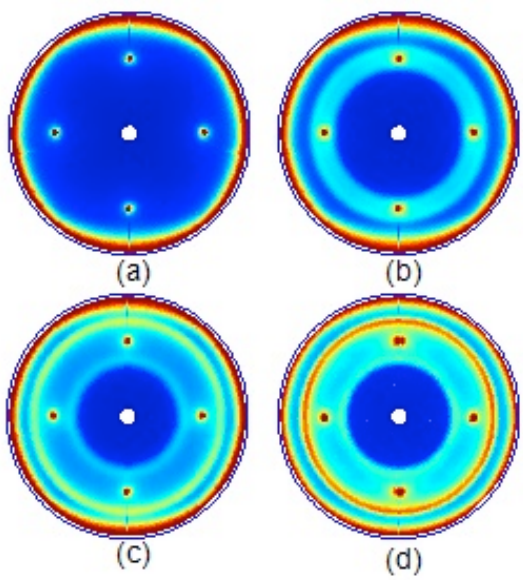


Figure 4: Pole figures of four samples with the same d-spacing. (a) 0.2 Å/s, 3nm; (b) 0.2 Å/s, 10nm; (c) 0.4 Å/s, 10nm; (d) 1 Å/s, 10nm.

Figure 4 presents the pole figure covering a range in d-spacing values from 3.0812 Å to 3.1435 Å. These values cover the Sb (012) peak. (a), (b), (c) and (d) respectively corresponding to figure 3 (a), (b), (c) and (d). The sharp spots in the image correspond to the Si (001) peak. As shown on (a), the background intensity observed is nearly flat and showed no Sb crystalline features. From (b) to (d), the ring structure due to polycrystalline Sb became narrower and sharper, perhaps due to the increase of particle size, though figure 3 makes it clear that there are two (012) orientations present in (c) and (d).

CONCLUDING REMARKS

The evolution of the crystalline structure and topography of Sb films with different evaporation rates and thicknesses at a substrate temperature of 100C has been investigated via X-ray diffraction pole figure and AFM measurements.

AFM measurements indicate the final surface roughness is mainly affected by the evaporation rate. The highest roughness values were measured at the lowest deposition rate of 0.2Å/s. Multi-alkali photocathodes are usually grown from Sb films. In order to avoid a high roughness surface, high deposition rates should be used.

Pole figure measurement shows that the deposition rate affects the crystallinity of the Sb film. The thickness also influences the final texture of the Sb film. When the Sb thickness is small, there is no fiber texture. When approaching a film thickness of 10nm, a significant fiber texture develops.

A wide parameter space still remains to be investigated, such as using different substrate temperatures and a wider range of deposition rates. The specific relationship between the initial Sb layer structure, roughness and the final performance of the cathodes also needs to be determined. Further to this, other sources of roughness will be measured, such as that which results from thin film strain on reaction with K and Cs.

ACKNOWLEDGMENTS

The authors are grateful to Christian Lavoie for his expert assistance. The analysis software used here were written by IBM. Research and experiments were carried out at the National synchrotron Light Source.

REFERENCES

[1] A. H. Sommer, Appl. Phys. Lett. 63, 3(4): p. 62-63.
[2] J. Smedley et al., IPAC 2011, 3206-3208 (2011).
[3] T. Vecchione et al., Appl. Phys. Lett. 99 (2011) 034103.
[4] S. G. Shubert, et al., APL Mater. 1, 032119 (2013).
[5] X. Liang et al., IPAC 2012, 670-672 (2012).

Copyright © 2013 CC-BY-3.0 and by the respective authors

SIMULATION AND OPTIMIZATION OF MULTI-SLIT BASED EMITTANCE MEASUREMENT FOR BNL ERL*

C. Liu†, D. Gassner, D. Kayran, M. Minty, P. Thieberger, BNL, Upton, NY 11973, USA

Abstract

A code for determining the beam emittance from a multi-slit image has been developed. To verify its validity, we simulated a beam distribution in 4D phase space at the multi-slit position and the resulting image at a downstream profile measurement device. We applied the algorithm to this image pattern to recover the beam emittance at the slit position. The dependence of the relative difference of the inferred emittance and the input emittance on the slit width and drift length are studied in detail and presented in this report.

INTRODUCTION

At the BNL ERL, a multi-slit device will be used for direct measurement of two dimensional beam phase space, which samples particles at discrete horizontal (or vertical) positions and projects the sampled beam on a downstream screen. The beam size and divergence of the sampled beam can be determined using the image acquired by the downstream profile device and the mask pattern dimensions. The emittance of the beamlets sampled by the multi-slit mask will be shown to be representative of the emittance of the beam incident on the mask. Here we will present the algorithm and its application using simulated data, and a study of geometry-dependent systematic errors in the inferred emittance.

ALGORITHM

The schematic for a multi-slit emittance measurement device is shown in Fig. 1. The incoming beam is sampled by a multi-slit mask. Beamlets formed by the mask project onto a profile measurement device and the resulting image is recorded. The beam size at the slits can be determined by the dimension of the slit pattern and the intensity of the beamlets. The beam divergence can be determined by the intensity distribution on the profiler.

The well accepted rules for multi-slit mask design [1, 2] are: the slit spacing is chosen such that beam is divided to 4-8 beamlets; the slit width is as narrow as possible as limited by current fabrication techniques; the drift length between mask and profiler is such that beamlets will spread out on the profiler until they overlap; the mask thickness is thick enough to stop most incoming particles; and the opening angle of the slit is comparable to the anticipated beam divergence.

Detailed formulas for slits emittance measurement can be found in Ref. [3]. The projection of the recorded image is usually treated as a multi-Gaussian distribution. The average divergence of each beamlet is calculated based on slit positions and peak positions. The rms divergence of the beamlets is calculated from the rms of the fitted Gaussian peaks. Suppose we get three arrays of parameters from multi-Gaussian fits of the projection, a, b and c, which are the intensity, peak position and sigma of the peaks. The slit positions are represented by an array x. The centroid of the beam at the mask is $< x >= \frac{1}{\sum_{i=1}^{n} a_i} \sum_{i=1}^{n} (a_i * x_i)$, here n is the number of beamlets. The rms size at the mask is

$$< x^2 >= \frac{1}{\sum_{i=1}^{n} a_i} \sum_{i=1}^{n} (a_i * (x_i - < x >)^2)$$

The average divergence of the beamlets is given by $x'_i = (b_i - x_i)/L$. The average divergence of the sampled beam is $< x' >= \frac{1}{\sum_{i=1}^{n} a_i} \sum_{i=1}^{n} (a_i * x'_i)$. The rms divergence of the beamlets is $\sigma'_i = c_i/L$. The rms divergence of the sampled beam at the mask is

$$< x'^2 >= \frac{1}{\sum_{i=1}^{n} a_i} \sum_{i=1}^{n} (a_i * \sigma_i'^2 + a_i * (\sigma'_i - < x' >)^2)$$

The position angle correlation term is

$$< xx' >= \frac{1}{\sum_{i=1}^{n} a_i} (\sum_{i=1}^{n} a_i * x_i * x'_i - \sum_{i=1}^{n} a_i < x >< x' >)$$

Then the emittance is calculated by

$$\epsilon = \sqrt{< x^2 >< x'^2 > - < xx' >^2}$$

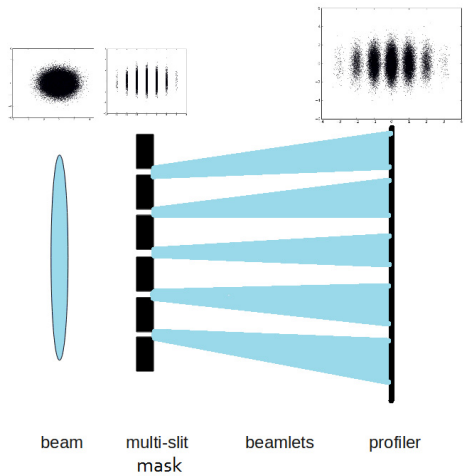


Figure 1: Schematic of a multi-slit emittance measurement device (not to scale).

* The work was performed under Contract No. DE-AC02-98CH10886 with the U.S. Department of Energy.

† cliu1@bnl.gov

Copyright © 2013 CC-BY-3.0 and by the respective authors

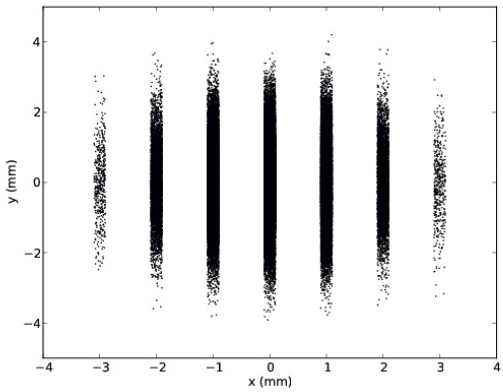


Figure 2: The intensity distribution of sampled beamlets at the mask.

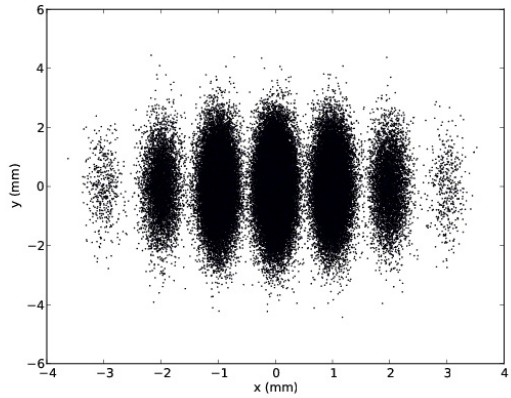


Figure 3: The intensity distribution of sampled beamlets at the profiler for a drift length of 0.15 m.

SIMULATION

It turns out to be difficult to implement cylindrically non-symmetrical masks in particle tracking code. Therefore, a standalone Python code has been developed to simulate a beam distribution in phase space and to track the distribution through a drift space. Space charge effects are not considered. The statistical error is minimized by generating and tracking 500,000 particles. The density distribution is set to be Gaussian in 4D phase space with standard deviation of 1 mm for position and 1 mrad for divergence for both planes (numbers are chosen according to the expected BNL ERL beam parameters). In the following, we will try to recover horizontal emittance with the algorithm presented in previous section.

The exact horizontal emittance of initial beam is 1.001 mm·mrad. The vertical multi-slit mask is designed with a slit width of 0.1 mm and a spacing between slits of 0.9 mm. One of the slits is set to be centered on the beam. The intensity distribution of the sampled beamlets at the mask is shown in Fig. 2. The horizontal emittance of the sampled beam is 0.998 mm·mrad. This shows that the sampled beam represents the real beam well in terms of emittance.

After propagation in a drift space (L =0.15 m), the beamlets project onto a profiler (YAG screen for the BNL ERL) with a 2D image shown in Fig. 3.

The projection of the 2D image at the profiler on the horizontal plane produces a 1D distribution of multiple quasi-Gaussian peaks. A Python program fits the distribution to multiple Gaussian peaks (a good approximation for our case with narrow slits). In the process, one finds the intensity of each beamlet, rms width and peak location. The Gaussian fits of the original distributions are shown in Fig. 4. The calculated emittance is 1.067 mm·mrad.

Slit Width Dependency

The Gaussian peak assumption and calculation of rms divergence of beamlets are possible due to the fact that the slit width is relatively small. Therefore, the finite slit width may introduce a systematic error in the final determined beam emittance; in principle, the narrower the slit, the closer the measured and real emittances will be. We studied the slit width dependency of the retrieved beam emittance with results shown in Table 1. In these simulations, the sum of slit width and slit spacing is kept constant at 1 mm so that total number of beamlets is always seven. Real emittance refers to the emittance of the initial beam, the sampled emittance is the emittance of the beam sampled by multi-slit mask, the simulated emittance is the emittance determined by the algorithm introduced. Deviation refers to the relative difference between simulated emittance and sampled emittance.

The slit width correction has been developed and will be presented in a separate note.

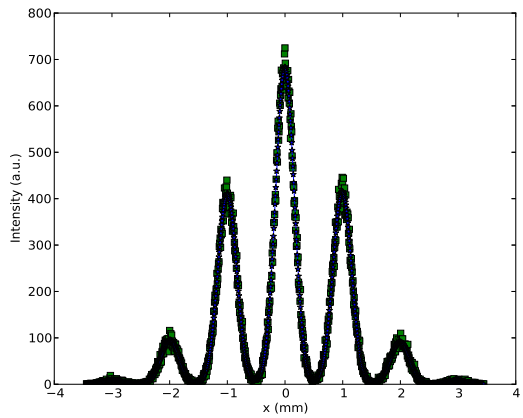


Figure 4: The horizontal projection of 2D image on the profiler and its multi-Gaussian fitting for a drift length of 0.15 m.

Drift Length Dependency

Slit widths smaller than 80 µm are difficult to produce due to mechanical fabrication limitations. For the BNL ERL, the slit width is designed to be 100 µm. One other parameter which has impact on the simulated emittance is the drift length. The well accepted criteria is that the drift length should be long enough until the beamlets overlap.

Copyright © 2013 CC-BY-3.0 and by the respective authors

Table 1: Slit Width Dependency of Simulated Emittance

Slit Width	Slit Spacing	Drift Length	Real Emittance	Sampled Emittance	Simulated Emittance	Deviation
0.05 mm	0.95 mm	150 mm	1.000 mm·mrad	0.993 mm·mrad	0.996 mm·mrad	0.3 %
0.08 mm	0.92 mm	150 mm	1.000 mm·mrad	0.995 mm·mrad	1.009 mm·mrad	1.4 %
0.10 mm	0.90 mm	150 mm	0.998 mm·mrad	0.991 mm·mrad	1.012 mm·mrad	2.1 %
0.12 mm	0.88 mm	150 mm	1.003 mm·mrad	1.006 mm·mrad	1.037 mm·mrad	3.1 %
0.15 mm	0.85 mm	150 mm	1.001 mm·mrad	0.993 mm·mrad	1.037 mm·mrad	4.4 %

Table 2: Drift Length Dependency of Simulated Emittance

Slit Width	Slit Spacing	Drift Length	Real Emittance	Sampled Emittance	Simulated Emittance	Deviation
0.10 mm	0.90 mm	100 mm	1.002 mm·mrad	1.005 mm·mrad	1.043 mm·mrad	3.8 %
0.10 mm	0.90 mm	120 mm	1.003 mm·mrad	0.997 mm·mrad	1.024 mm·mrad	2.7 %
0.10 mm	0.90 mm	150 mm	1.000 mm·mrad	0.997 mm·mrad	1.013 mm·mrad	1.6 %
0.10 mm	0.90 mm	180 mm	0.998 mm·mrad	0.990 mm·mrad	0.998 mm·mrad	0.8 %

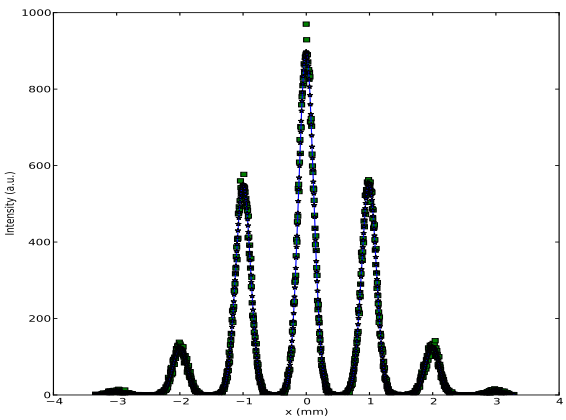


Figure 5: The horizontal projection and its multi-Gaussian fitting for drift length 100 mm case.

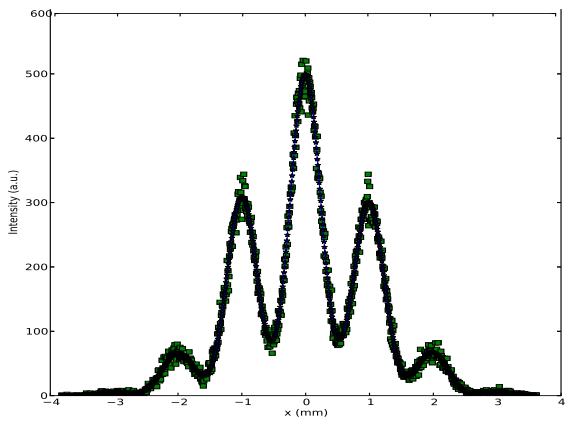


Figure 6: The horizontal projection and its multi-Gaussian fitting for drift length 230 mm case.

The following study explores the drift length dependency with results shown in Table 2.

The horizontal distribution and its multi-Gaussian fitting for 100 mm and 230 mm drift length are shown in Fig. 5 and 6. The beamlets overlap significantly with each other at a 230 mm drift length. We were able to determine a more accurate emittance from the fitting at 230 mm than at 100 mm. We believe this is due to the fact that the slit width contribution is less when the drift length is longer. Therefore, beamlet overlap is acceptable and desirable as long as reasonable fitting can be produced.

SUMMARY

We developed a program for analyzing a multi-slit image for emittance measurement. The functionality was verified in simulations. From these we conclude that the narrower the slit width the better precision of the emittance measurement and that beamlets overlap on the profile screen is to some extent desirable. In the future, we will include space charge effects in the simulation.

ACKNOWLEDGEMENTS

The author would like to thank Ilan Ben-Zvi for his support of the work.

REFERENCES

[1] P. Piot, J. Song, R. Li, GA Krafft, D. Kehne, K. Jordan, E. Feldl, and J.C. Denard. A multislit transverse-emittance diagnostic for space-charge-dominated electron beams. In *Particle Accelerator Conference, 1997. Proceedings of the 1997*, volume 2, pages 2204–2206. IEEE, 1997.

[2] Y. Li-Xin, D. Ying-Chao, X. Dao, L. Ren-Kai, Q. Hou-Jun, H. Wen-Hui, T. Chuan-Xiang, L. Yu-Zheng, and C. Jian-Ping. Multislit-based emittance measurement of electron beam from a photocathode radio-frequency gun. *Chinese Physics Letters*, 25:1640, 2008.

[3] M. Zhang. Emittance formula for slits and pepper-pot measurement. *Fermilab-TM-1988, October*, 1996.

Copyright © 2013 CC-BY-3.0 and by the respective authors

3D HALL PROBE CALIBRATION SYSTEM AT INSERTION DEVICE MAGNETIC MEASUREMENT FACILITY AT BNL *

M. Musardo#, T. Corwin, D. Harder, P. He, C. A. Kitegi, W. Licciardi, G. Rakowsky and T. Tanabe,
National Synchrotron Light Source II, Brookhaven National Laboratory, Upton, NY 11793, USA

Abstract

Hall probes are commonly used to measure local magnetic field, however they need to be calibrated. This paper describes the accurate 3D Hall probe calibration system developed by the NSLS-II Insertion devices group. The calibration system and the calibration curves are presented. An Arepoc 3D Hall probe used to characterize the Insertion Devices (IDs) has been calibrated. The probe contains three sensors oriented perpendicular to each other in order to measure three components of the magnetic field. The three Hall sensors are mounted on a circuit board and their active area dimensions are 0.05 mm x 0.05 mm with a linearity error up to 1 T less of 0.2%.

INTRODUCTION

The 3D Hall probe calibration system consists of a GMW dipole electromagnet, a precision magnet power supply system, a nuclear magnetic resonant teslameter (NMR) and a motorized probes supporting stage.

In order to perform an absolute and precise calibration, the Arepoc 3D Hall probe must be positioned in a known magnetic field. The coordinate frame of the probe is indicated in Fig. 2. Sensor 1 is perpendicular to z direction (longitudinal direction), sensor 2 is perpendicular to x direction (horizontal direction) and sensor 3 is perpendicular to y direction (vertical direction).

HALL PROBE CALIBRATION SYSTEM

GMW dipole electromagnet (see Fig. 1) and a low noise and high stability Danfysik System 8500 Power Supply are used to create a constant and uniform magnetic field in the region around the point midway between the coils. The maximum magnetic field obtained with a current of 140 A at pole gap of 30 mm is of about 2.148 T and the uniformity achieved is of 110 ppm in 10 mm^3. The magnet and the power supply are water cooled.

A Metrolab PT-2025 NMR Teslameter System (Fig. 1) precisely measures the absolute magnetic field produced by the GMW dipole magnet. It is based on the nuclear magnetic resonance effect and achieves 5-ppm absolute accuracy and 1mG resolution for measurements in the range from 430 G to 137 kG. A multiplexer with different NMR probes is used, because the magnetic field value could be in one of several probe's ranges. So the proper NMR probe needs to be chosen and positioned within the magnetic field in the right position. A motorized *NMR Probe Supporting Stage* (see Fig. 3) is used to manage the NMR probe and to position it in the center of the electromagnet.

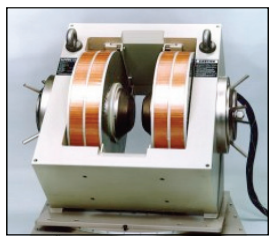




Figure 1: GMW dipole electromagnet and metrolab NMR teslameter.

An integrated digital multimeter is used to measure the Hall voltages of the sensor under calibration and a *Hall Probe Supporting Stage* (see Fig. 4), needed to move and rotate the probe during the calibration, provides precise controlled linear and angular motions in all required directions.

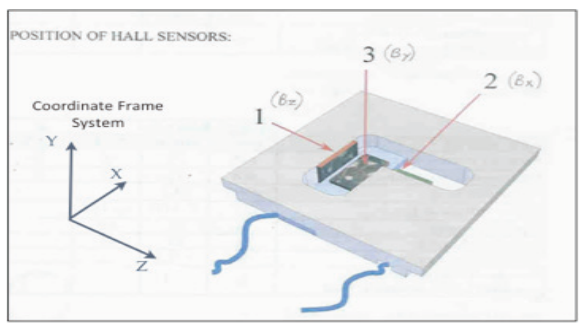


Figure 2: Coordinate frame system.

The control system written in LabView coordinates and automates the calibration measurements.

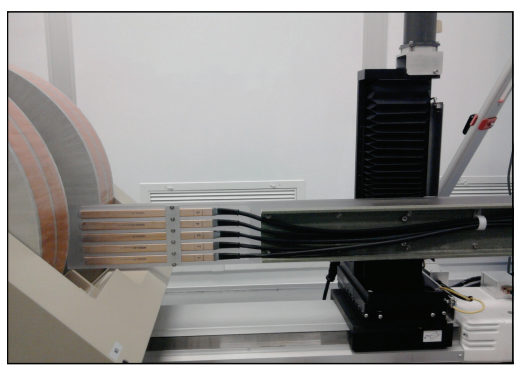


Figure 3: NMR probe supporting stage.

*Work supported by DOE contract DE-AC02-98CH10886
#musardo@bnl.gov

Copyright © 2013 CC-BY-3.0 and by the respective authors

The system is linked to a PC via GPIB for the NMR teslameter and a serial interface for the power supply and motion control system.

The control system synchronizes the readings of the sensor's voltage with the NMR probe signal and collects and processes the measurement data.

CALIBRATION PROCEDURE

Hall probe's output signal is a voltage that is proportional to the strength of the magnetic field in which the probe is placed. The calibration curve is a function that relates the Hall voltage to the strength of the field. For a 3D Hall probe is necessary to determine separate calibration curves for each of the three sensors. Knowing the calibration curve, you will be able to use the probe to measure the strength of an arbitrary magnetic field in the calibration range. The system calibration procedure includes the following steps: *System Setup*, *Alignment* and *Calibration.*

In the System Setup step the connections of all devices must be checked and powered on. After the setup, the system needs to be properly aligned before calibration scan can be executed. Alignment of the sensors into the electromagnet consists in three following steps:

- Align the NMR probes in the center of the electromagnet.
- Align the Hall probe in the rotating stage.
- Adjust the probes so that they are parallel to the electromagnet surfaces.

Imperfect alignment obviously leads to an underestimate of the field. Therefore is important to align the Hall probe as well as possible. Instead alignment is not an issue for the NMR probe, which measures the total magnetic field.

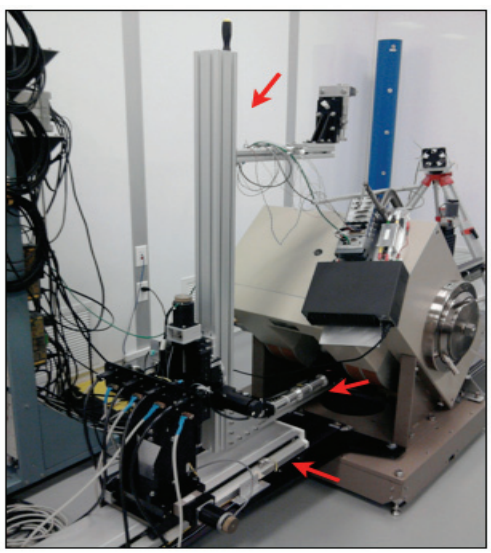


Figure 4: Hall probe supporting stage

The angular alignment of the Hall sensors with the transverse magnetic field of the electromagnet is made rotating the sensor around the z-axis and the y-axis until to maximize the reading of the multimeter (Hall probe voltage). In this way the deviation of the sensor from the perpendicular field direction can be reduced, because it is very sensitive to misalignment.

The calibration positions of the sensors along to the direction of the magnetic field of the electromagnet are obtained by rotating the probe of 90˚ around the axis of sensor. If the sensors are precisely perpendicular to the direction of magnetic field of the electromagnet then the maximum Hall voltage is measured. In this way for each sensor in the proper calibration position were determined the alignment angles.

A Hall sensor is not only sensitive to perpendicular magnetic field component $\mathbf{B}_{\perp}$, but also to the parallel component $\mathbf{B}_{\parallel}$. If magnetic field vector is not precisely orthogonal to the Hall probe, an additional voltage is added to the Normal Hall voltage (V_{NH}), due the field component in the plane of Hall sensor. This is known as Planar Effect (V_{PHE}) [1].

$$\begin{aligned} V_{NH} &= GR_H IB_{\perp} \\ V_{PHE} &\propto IB_{\parallel}^2 Sin(2\xi) \end{aligned} \qquad (1)$$

For low magnetic field (< 2T), the basic equation describing the relation between the local electric field **E,** the local current density **J** and the flux density **B** in a Hall sensor is given, neglecting the anisotropy effect, by

$$\mathbf{B} = \rho J - R_H(\mathbf{J}\times\mathbf{B}) - M\rho\mathbf{B}\times(\mathbf{B}\times\mathbf{J}) \qquad (2)$$

where ρ is the material resistivity, R_H is the Hall coefficient an M is the transversal magnetoresistance coefficient. The Hall voltage and the Planar effect are calculated from equation 2 and for materials with a low carrier mobility, the equation that describing the Planar Hall voltage may be written as [3]:

$$V_{PHE} = \frac{M\rho}{2t} IB^2 Sin^2\Theta Sin(2\xi) \qquad (3)$$

where t is the plate thickness, I is the applied current, Θ is the angle between B and axis perpendicular to the sensor and ξ is the angle between $\mathbf{B}_{\parallel}$ and the current.

To remove this error during the calibration, two configurations are considered: *Normal* and *Reverse* position. The *Reverse* position is obtained with a rotation of 180˚ around the orthogonal direction of the magnetic field of electromagnet. In *Reverse* position the polarity of the magnetic field and the Hall voltage changes sign, but does not change the planar Hall voltage, because is proportional to the square of the field. So the difference of the two voltages removes the Planar Effect:

$$\begin{aligned} V_{NH} &= \frac{V^{Norm} - V_H^{Rev}}{2} \\ V_{PNH} &= \frac{V^{Norm} + V_H^{Rev}}{2} \end{aligned} \qquad (4)$$

Copyright © 2013 CC-BY-3.0 and by the respective authors

The calibration step, for each sensor, can be described with the following operations:

1. Select the current on the Magnet Power Supplies System.
2. Choose the relevant probe according to the magnitude of the field.
3. Place the proper NMR probe at the center of the electromagnet.
4. Start the measurement scans with NMR teslameter in *Automatic Mode*: This mode sweeps the radio frequency over the whole range of the FINE potentiometer. This represents a variation of ± 5 % of the frequency actually selected by the COARSE potentiometer [2].
5. Read the NMR magnetic field locked.
6. Place the Hall sensor in the center of the electromagnet at alignment angles. Read the *Normal Hall Voltage.*
7. Rotate the sensor of 180º around the orthogonal direction of magnetic field in order to have the *Reverse* position.
8. Read the *Reverse Hall Voltage.*
9. Change the current of electromagnet and repeat the previous steps for whole calibration range.
10. Rotate the sensor of 90˚ respect to each other, in order to have the next calibration position and repeat previous steps.

The calibration was performed in the measurements range ± 1.9 T. The calibration at zero field was done using a zero-gauss chamber.

AREPOC CALIBRATION CURVE

The magnetic field from Hall probe voltage measurements can be written as: $B=f(V)$, where B is magnetic field, V is the voltage of Hall sensor and $f(V)$ is a nonlinear function: $f(V)=K_0+K_1V+...+K_nV^n$.

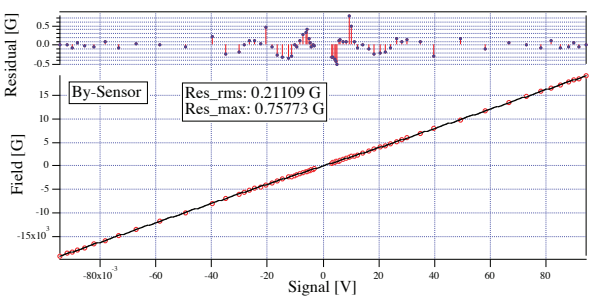


Figure 5: Calibration curve of By-sensor.

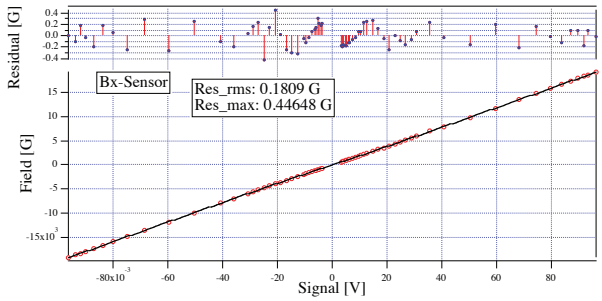


Figure 6: Calibration curve of Bx-sensor.

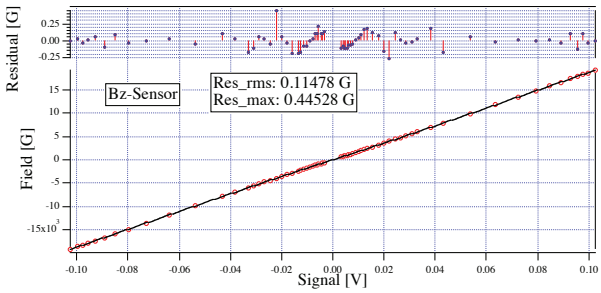


Figure 7: Calibration curve of Bz-sensor.

A polynomial fit of $B=f(V)$ was done to determine the coefficients (see Fig. 5, 6 and 7). Using the equation 4, the voltage due to the Planar Hall effect was cancelled. The best order of the polynomial fit is the minimum value that does not involve significant changes to the residual. The main nominal parameters of the probe (current 10 mA) are shown in table 1.

Table 1: Main Nominal Parameters

Sensors	Sensitivity [mV/T]	Offset Voltage [µV]
By-Sensor	63.3	< 60
Bx-Sensor	64.7	< 100
Bz-Sensor	66.9	< 20

CONCLUSION

The 3D Hall probe calibration system has been successfully used to calibrate an Arepoc 3D Hall probe. The system works very well and is capable of calibrating probes with high degree of accuracy.

REFERENCES

[1] C. Goldberg et al., *New galvanomagnetic effect*, Physical Review, Vol. 94, No. 5, pp. 1121 (1954).
[2] Metrolab Instruments SA, PT2025 NMR Teslameter, User's manual, V.2.0, (2003).
[3] R. S. Popovic, *Hall Effect Devices*, IOP Publishing, Bristol, England, (1991).

Copyright © 2013 CC-BY-3.0 and by the respective authors

NSLS-II MAGNETIC MEASUREMENT SYSTEM FACILITY*

M. Musardo#, T. Corwin, D. Harder, P. He, C. A. Kitegi,
W. Licciardi, G. Rakowsky, J. Rank, C. Rhein and T. Tanabe,
National Synchrotron Light Source II, Brookhaven National Laboratory, Upton, NY 11793, USA

Abstract

The National Synchrotron Light Source II at Brookhaven National Laboratory (BNL) is a storage ring of 3 GeV electron beam energy that will provide ultra high brightness and flux and exceptional beam stability using advanced insertion devices (IDs). The magnetic characterization of these devices is important to achieve these performances. In order to perform precise and accurate measurements of the NSLS-II IDs, several recent improvements on actual magnetic measurement system have been developed. The system includes a flipping coil bench to measure the first and second magnetic field integrals and a Hall probe bench to perform magnetic field measurements of different types of IDs.

The main features of the hardware system, control program and the recent improvements in the magnetic measurements system are presented.

INTRODUCTION

All insertion devices for NSLS-II have been bought from different vendors. It is planned to measure these devices at NSLS-II in order to confirm vendors. Our magnetic measurements are the final verification of the complex design and fabrication process, so that proper certification of device can be made. The magnetic measurement system facility at BNL consists in a Hall probe bench MMB-6500, built by Kugler, GmbH and an Integrated Field Measurement System (IFMS), provided by ADC [1].

HALL PROBE BENCH

The Hall probe mapping bench has an ultra-precision granite guide beam. There are nine conrolled axes. The air-ride Z axis has a travel distance of 6.5 meters. The trajectory deviation for the Z axis carriage is ± 7 µm and the positioning accuracy is ± 1 µm. The X and Y axes are high precision stages. Mounted to the Y stage carriage is a rotary stage. Mounted to the rotary stage is a small X-Y stage. Mounted to that is a pair of goniometers. Thus the extended Hall probe can be positioned in any orientation and then translated (see Fig. 1). The Z' axis is used as a follower stage for transporting the cables, so that cable loading does not affect the Z axis trajectory. Instrumentation is also carried on the follower stage (see Fig. 2).

The Z axis has two encoders. A linear scale encoder is used for the motion control and a laser interferometric encoder is used for generating triggers. A Delta Tau controller is used for motion control. A Senis 3D probe is used as the Hall sensor.

Each Hall sensor, arranged along X-axis, has been accurately calibrated to provide a calibration curve of its response to the strength of the magnetic field up 1.9 Tesla. The magnetic field sensitive volume for each sensor is 150x150x1 µm and the angular accuracy of axes with respect to the reference surface is about of ± 2°.

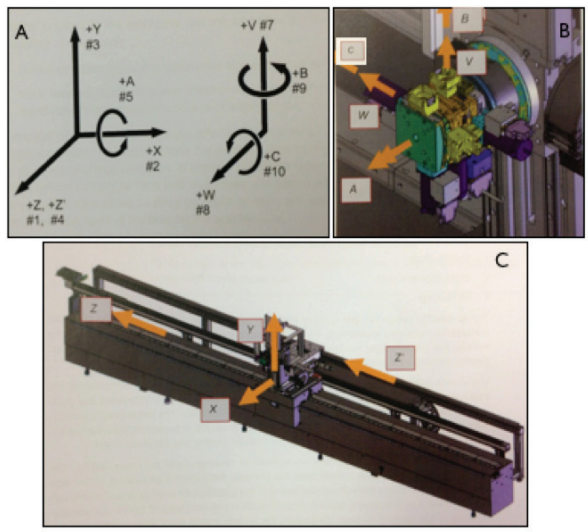


Figure 1: A: Machine coordinate system. Axis movements viewed from undulator towards granite. B: Arrangement of the goniometer head axes V, W, A, B and C. C: Arrangement of the three main linear axes X, Y, Z and auxiliary axis Z'.

In order to improve the accuracy and the repeatability of the Hall probe measurements, the electronics of the data acquisition have been upgraded. In particular a new time synchronization system has been developed in order to optimize the first integral repeatability and the precision of magnetic field measurements. Figure 3 shows the vertical field of a Damping Wiggler with period length of 100 mm at the minimum gap of 15 mm (blue line) and the field difference between two consecutive Hall scans (red line), which represents an absolute error of the magnetic field, measured with the initial triggering method. This error is a periodic and systematic curve with precise harmonic frequencies (see Fig. 4). The peak-to-peak amplitude is about of 30 G and occurs around the magnetic field gradient. It is a strong indication of a small jitter in the start trigger of the Hall probe measurements. This trigger jitter was reduced by changing from a motion controller generated trigger to a trigger generated by external Hardware, the parallel digital signal from the laser encoder is processed in external logic which feeds a trigger signal into an FPGA aboard a National Instruments CompactRIO real-time PAC. The

Copyright © 2013 CC-BY-3.0 and by the respective authors

CompacRIO also houses the digital-to-analog convertor which is used for data acquisition. In this fashion trigger latency for data capture is reduced to less the 1 μs.

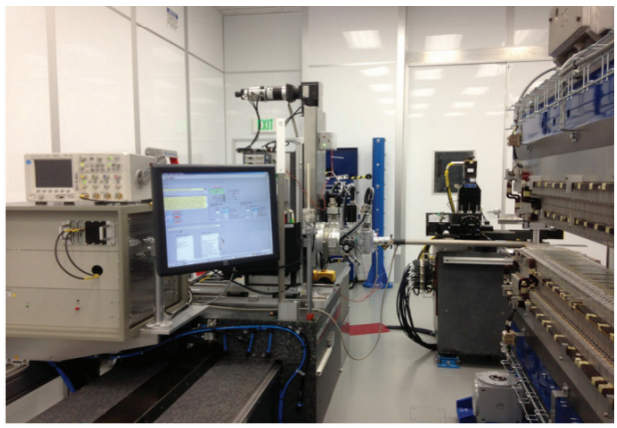


Figure 2: Hall probe measurement bench.

The magnetic measurements made with the new triggering system were carried out with a step of 1 mm and a scan speed of 24 mm/s.

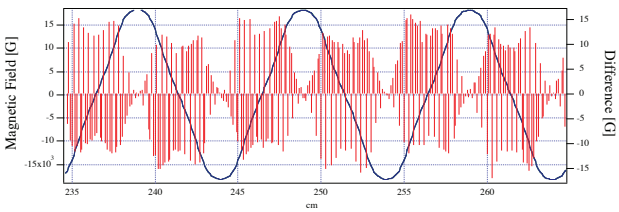


Figure 3: Magnetic field (blue line), difference of consecutive Hall measurements (red line).

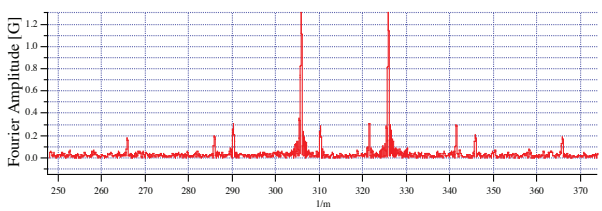


Figure 4: Spectral analysis of the difference.

Using this new system the error peak-to-peak is decreased to 5 G. (see Fig. 5), and also a improvement of the field integral repeatability was achieved.

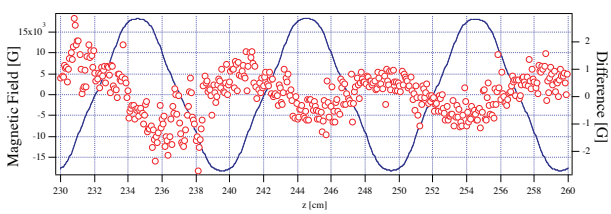


Figure 5: Magnetic field (blue line), the difference of consecutive Hall measurements (red dot).

The standard deviation for first field integral measurement of four consecutive scans is of 0.10 G m and for the second field integral is about 0.15 G m^2.

Figure 6 shows the horizontal electron trajectory of a Damping Wiggler obtained from four consecutive Hall probe measurements. The maximum absolute deviation is of few μm.

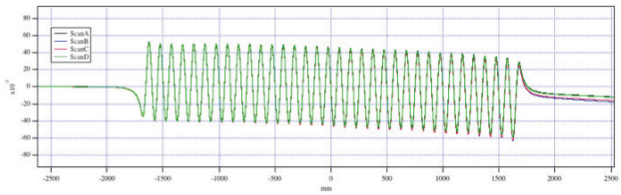


Figure 6: Horizontal electron trajectory of Damping Wiggler with period length of 100 mm at gap of 15 mm.

FLIPPING COIL BENCH

The flipping coil bench is typically used to characterise the integrated field of long insertion devices [2,3,4]. A long coil is stretched between the two ends of the device. The bench consists of two supports located at each end of an ID. The pedestals are made from granite with extremely flat ±10 μm tolerance on the top surface. Each pedestal has 3 leveling feet that also provide ±10 mm adjustment in the Z (longitudinal) and X (transverse) directions and 50 mm in the vertical direction. The six linear stages have Renishaw RELM linear encoder feedback with 0.1 μm resolution and ±1 μm accuracy. All axes have limit switches and a home limit switch that is used to tell the motion controller that it is near the home pulse located on the encoder. Two rotary direct drive servos are used to achieve 1 revolution per second with an angular accuracy of 40 arc-sec and encoder resolution of about 0.005 deg. These eight servomotors are controlled by a Delta Tau GeoBrick PMAC-2. A Keithley DVM 2701 integrator is used for data acquisition with a custom switching card to select the measurement source. A Stretched 38 AWG beryllium copper wire is used to support the flip coil given to it mechanical rigidity and to reduce its sag. Coil rigidity is desired to attenuate its vibrations, swings and curvature.

Some recent upgrades have been carried out to improve the accuracy and the repeatability of the field integrals at high measurement speed. In particular a new control software has been developed to perform "on-the-flight" measurements of both horizontal and vertical field integrals. The "on-the-fly" measurements are faster than the traditional "step-by-step" measurement, shortening significantly the measurement time of an ID. The measurement of the two field integral components in a range of 60 mm, with a measurement step of 1 mm and a scan speed of 55 mm/s is of 90 seconds against the 91 minutes using the old method "step-by-step".

Lot of measurements with different integration time and velocity were carried out in order to optimize the accuracy and the reproducibility of the field integral measurement. A maximum velocity of 55 mm/s and an integration time of 16.67 msec provide the best compromise between higher sensitivity (large step) and better spatial resolution (small step). These settings also ensure a good signal/noise ratio and a good repeatability.

Copyright © 2013 CC-BY-3.0 and by the respective authors

The integration time affects the amount of reading noise, as well as the reading rate of the instrument. So a digital filter has been used to stabilize noisy measurements. The digital filter places a specified number of A/D conversions into a memory stack. These A/D conversions occur consecutively within a selected reading window. The readings in the stack are then averaged to yield a single filtered reading. The stack has be filled using the "repeating average filters". To further reduce the high frequency electrical noise, created primarily from the several motors of the system, a capacitor of 1μF has been used (see Fig. 7, left).

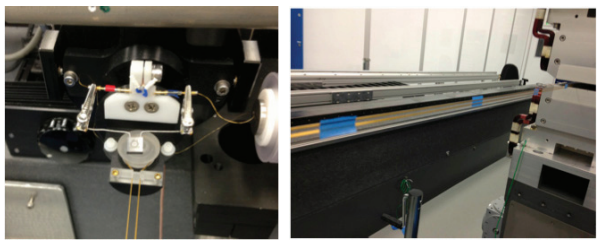


Figure 7: (Left) Electrical noise reduced by fitting a capacitor of 1 μF. (Right) Adhesive tape.

The function of the capacitor is to dampen random electrical noise, which causes small voltage fluctuation. In addition the capacitor helps to filter and remove the alternating currents caused by ripple voltage.

The disadvantage of an "on-the-fly" measurement is the vibration induced by the acceleration/deceleration at beginning and end of each movement. Electromechanical resonance was detected in the motors during the coil acceleration, causing small coil vibrations. To reduce this undesired effect, some pieces of adhesive tape were applied on the coil (see Fig. 7, right), it's a very simple and cheap solution, but efficient.

Figure 8 shows the horizontal (red line) and the vertical (blue line) field integrals as function of the transverse position. The standard deviation of five measurements is 7 G cm for the vertical field integral and of 3 G cm for the horizontal component. The repeatability of the measurement using just the coil rotation mode (Fig. 9) is 3.5 G cm for the vertical field integral and 2.5 G cm for the horizontal component.

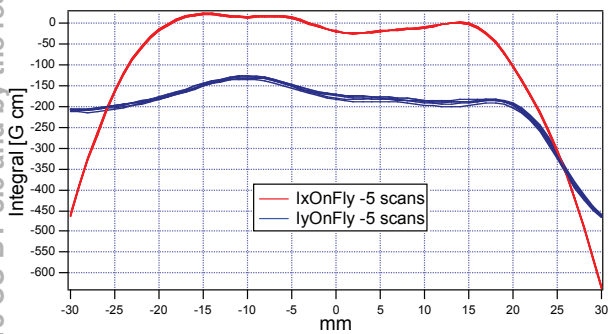


Figure 8: Horizontal field integral (red line), vertical field integral (blue line).

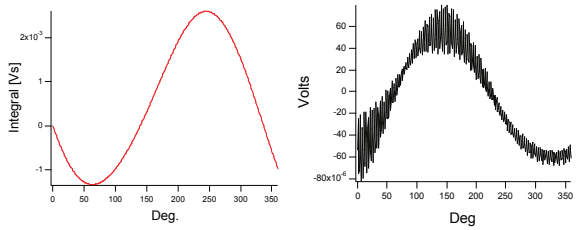


Figure 9: Voltage integrated (red line). Voltage readings (black line).

CONCLUSION

Replacing actual power supplies of the converter with DC batteries is an additional improvement of the Hall probe bench. The accuracy shall be increased as the use of DC batteries will eliminate time varying interference coupled into the converter via the power lines.

REFERENCES

[1] A. Deyhim et al., "Development of an integral field measurement system (IFMS) for NSLS-II," SRI'12, Lyon, France, 2012.

[2] I. Vasserman et al., "Insertion Devices: Magnetic Measurements and Tuning," ANL/APS/TB-53.

[3] Z. Wolf et al., "Undulator Long Coil Measurement System Tests," LCLS-TN-07-03.

[4] Z. Wolf et al., "Undulator Field Integral Measurements," LCLS-TN-05-22.

Copyright © 2013 CC-BY-3.0 and by the respective authors

UPGRADE OF BEAM INJECTION DIAGNOSTICS AT BNL NSLS

S. Seletskiy#, Y. Hidaka, B. Podobedov, X. Yang, BNL, Upton, NY 11973, USA

Abstract

In this paper we report the upgrade of the diagnostics of the beam injection system at BNL NSLS. Installation of commercially available turn-by-turn beam position monitors (BPMs) in the VUV and X-Ray rings allowed us to build the detailed injection models for each of the rings. In addition we built the tools for real time monitoring of and troubleshooting the beam injection into the rings.

INTRODUCTION

The NSLS accelerator complex consists of the 120 MeV linac, the booster accelerating the beam to 740 MeV and the two storage rings: 800 MeV VUV ring and 2.8 GeV X-Ray ring. Injection into each of the rings is performed at 740 MeV energy. The injection hardware in each of the rings consists of an injection septum (DC-magnet in case of the VUV ring and pulsed one for the X-Ray ring) and three fast multi-turn kickers. A single turn-by-turn (TBT) BPM was added to each ring for the purpose of injection monitoring. As a result a set of tools was created which are successfully used for troubleshooting injection problems. In this paper we discuss the operation of this diagnostics using the VUV ring as an example.

VUV RING INJECTION SETUP

The beam is injected into the VUV ring through the septum (BUISH) when the amplitudes of the three injection kickers (bumps BUIFB1, BUIFB2 and BUIFB3) are close to their peak values. Fig. 1 schematically shows the locations of the injection hardware and the fast kicker waveforms.

Since the duration of the kicker pulse is 1.3 us and the electron orbital period in the VUV ring is 170 ns the injected beam is affected by the kickers on multiple turns after the injection. This substantially complicates the injection process. At pick-up 5 (see Fig. 1) we installed a dedicated turn-by-turn BPM (Libera Electron [1]) to study and monitor the injection. The Libera unit is synchronized with the VUV ring orbital period and is triggered by the Booster extraction kicker trigger.

Since we can communicate to the machine from MATLAB through the "middle layer" software [2] and since the Libera settings and readings are easily accessible from MATLAB, Accelerator Toolbox (AT [3]) is a natural environment to model the ring injection. Thus we built the injection model by integrating the fast kickers into the AT model of the VUV ring.

The AT provides tools for beam tracking and calculation of lattice functions. Our AT model includes the linear ring lattice as well as kicks from sextupoles. It was calibrated with MATLAB-based LOCO [4].

#seletskiy@bnl.gov

BUILDING INJECTION MODEL

Since the kicker waveforms are nearly identical up to a scaling factor, we used the measured BUIFB2 waveform for each modelled bump. In simulations we only use half-wave of the sinusoid and ignore the residual kicker field. Each kicker's amplitude in the model is scalable, but the width of the waveform is kept constant.

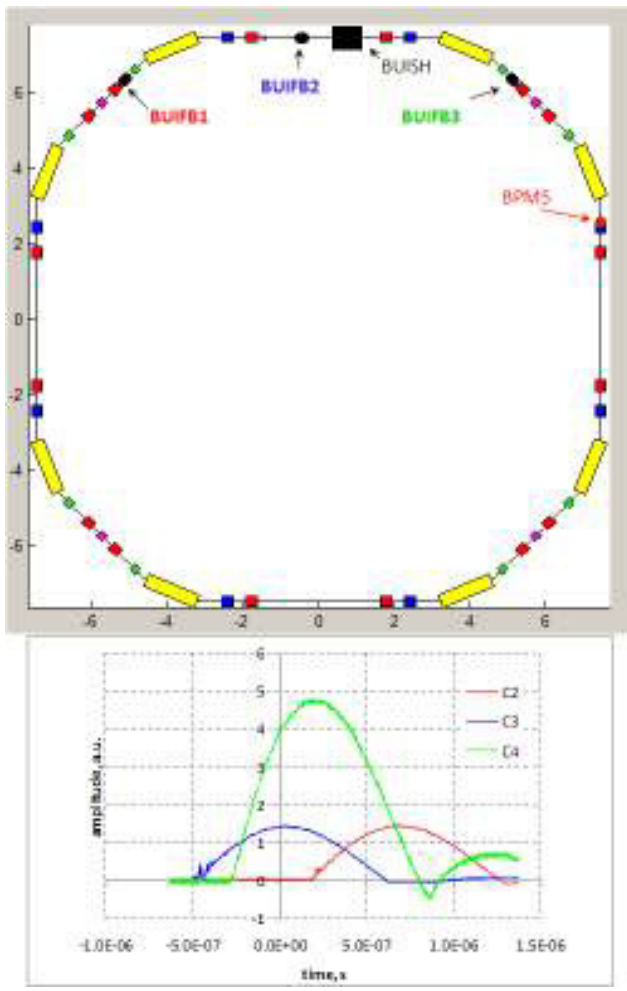


Figure 1: Locations of injection septum and fast injection kickers in the VUV ring (upper plot). The turn-by-turn diagnostics is connected to BPM5. Lower plot shows measured fast kicker waveforms in arbitrary units. Red line is BUIFB1, blue is BUIFB2 and green is BUIFB3.

Initial benchmarking of the model was performed with the stored single-bunch beam. Fig. 2 shows the readings of the TBT BPM over 20 turns versus the model predictions for the stored beam kicked with BUIFB1.

As one can see, there is a good agreement between the model predictions and the measured data. The same level of agreement was obtained for BUIFB2 and BUIFB3, as well as all three kickers turned on simultaneously. The benchmarking was performed both at the stored beam

Copyright © 2013 CC-BY-3.0 and by the respective authors

energy of 800 MeV and at injection energy of 740 MeV. Good agreement between the model and the measurements was also obtained at various beam currents, from a few milliamps typical for injected beam to more than hundred milliamps.

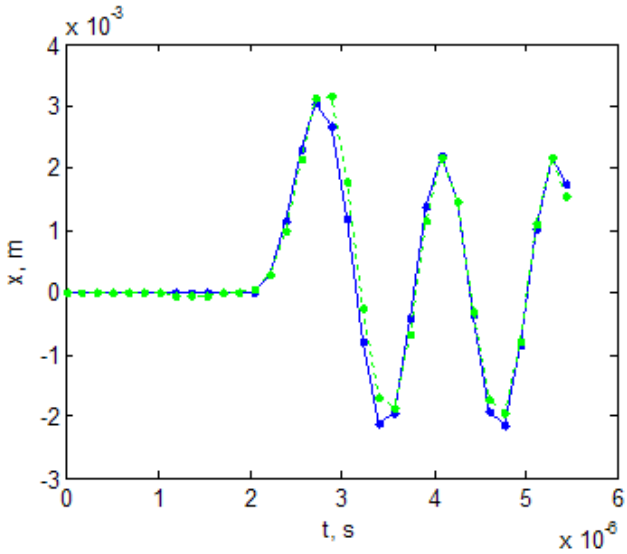


Figure 2: The oscillations of the stored beam kicked by BUIFB1 as read by TBT BPM #5 (green trace) and modelled (blue trace). Each dot represents BPM reading on a single turn.

Our next step was to measure the actual injection with the TBT BPM. We turned off the RF, to make sure that the beam is not accumulating in the ring. The obtained Libera readings are shown in Fig. 3.

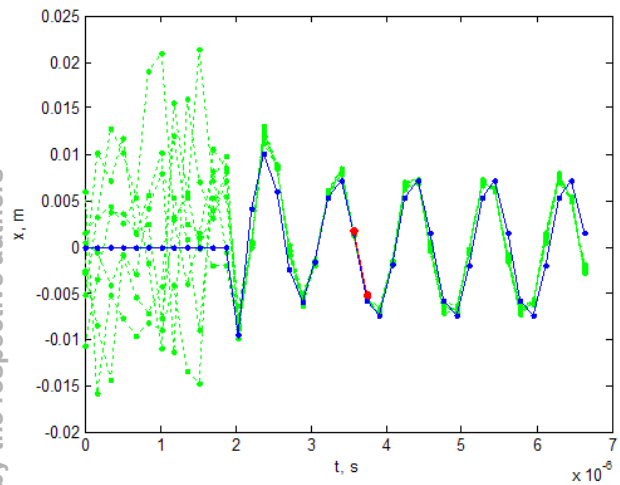


Figure 3: TBT BPM readings of the beam injected into the empty ring (green traces) taken over multiple injections. The noise up to the 12th turn (t≈2 μs) from beginning of the plot shows that there is no beam in the ring. Two red dots show the data we use to calculate the beam coordinates at injection point. The blue line shows the simulated trajectory of the beam injected with these initial coordinates.

As one can see, the injection readings are quite repeatable. The readings taken over multiple injections show that the beam is entering the ring on the 12th turn after the trigger comes to the Libera. This conclusion is confirmed by the sum signal from the TBT BPM buttons.

To find the initial horizontal coordinates (x, x') of the beam at the injection point we first determine x' at the BPM#5 location at the 21st turn (after Libera trigger) from the x-readings at the 21st and 22nd turn. Note, since the kickers are already off by this time we can use a simple single-turn matrix between the turns 21 and 22. Next, we find beam (x, x') at the exit of the injection septum on the 21st turn. Finally, we backtrack, taking into account the effects of the kickers, beam with found (x, -x') through the inversed ring lattice from turn #21 to turn #12 (from the Libera trigger). This gives us the initial beam coordinates at the moment of injection. We also use the found coordinates to simulate the trajectory of injected beam. As Fig. 3 demonstrates, the simulated readings of TBT BPM coincide with the experimental data quite well.

INJECTION MONITORING AND TROUBLESHOOTING

A dedicated software tool was created to monitor and to troubleshoot the injection. It is a MATLAB-based GUI that allows one to control the injection settings, take the readings of TBT BPM and analyze the obtained results by comparing them to the latest injection model. The user interface is shown in Fig. 4.

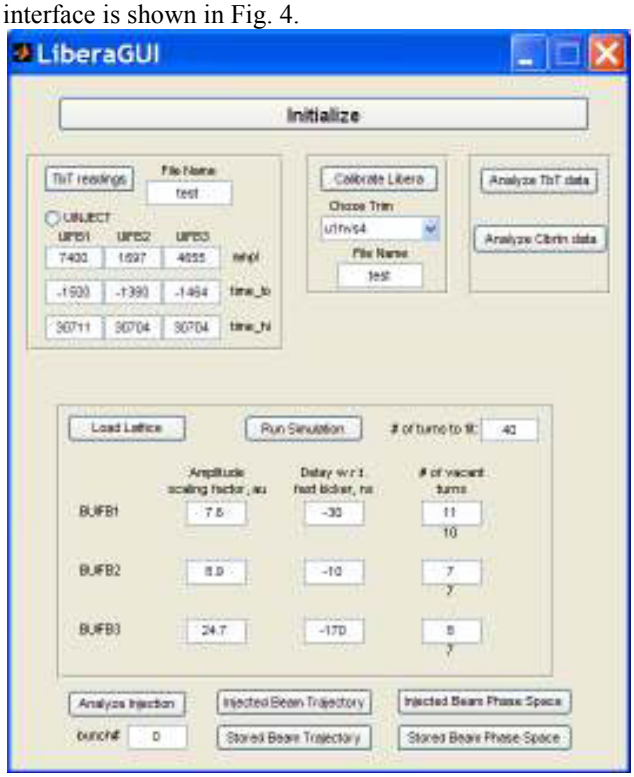


Figure 4: A GUI for the software tool to monitor, analyze and troubleshoot the injection process.

One of the most interesting examples demonstrating the power of the developed injection troubleshooting tools was during the failure of one of the kickers. As a result for some limited period of time we had to operate with two-bump injections, which is fairly unconventional.

Copyright © 2013 CC-BY-3.0 and by the respective authors

The failure of BUIFB1 caused a sharp decline in the injection rate. The measurements of the TBT BPM sum signal showed that a substantial part of the injected beam was lost on the 6th turn after the injection. The analysis of the measured injection data showed that on this turn the beam horizontal trajectory was deflected too much in the injection septum region, causing the beam loss (see Fig. 5).

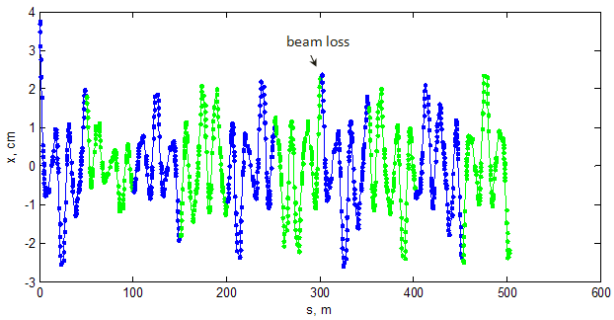


Figure 5: The betatron oscillations of injected beam obtained from the injection analysis. Only two kickers (BUIFB2 and BUIFB3) are operating at nominal settings. New turns start where the line colour changes. The initial s-coordinate corresponds to the injection septum exit on the first turn.

Scanning the kicker settings in our model with BUIFB1 off we found (Fig. 6) that increasing the nominal amplitude of BUIFB3 by a factor of ~1.7 significantly reduces the amplitude of the betatron oscillations of the injected beam.

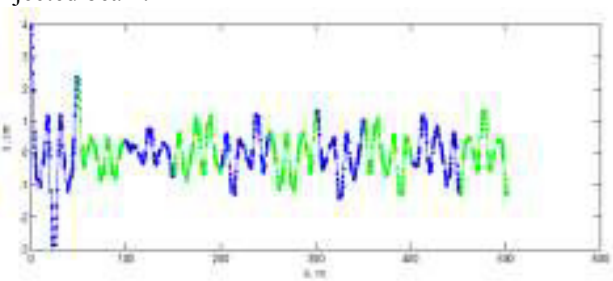


Figure 6: The projected betatron oscillations of the injected beam with only two kickers (BUIFB2 and BUIFB3) operating. BUIFB3 amplitude is set to its nominal value, while BUIFB2 amplitude is increased by factor of ~1.7. New turns start where the line colour changes. The initial s-coordinate corresponds to the injection septum exit on the first turn.

Indeed, when the kickers were set to the settings found in our simulations the beam loss disappeared and the injection rate increased significantly, as demonstrated in Fig. 7.

After BUIFB1 was repaired, as an additional test of our model, we simulated and performed a two-bump injection with BUIFB1 and BUIFB3. Our simulations showed that adjusting the BUIFB3 timing by -340 ns and increasing the amplitude of BUIFB3 by a factor of ~1.4 one can perform a two-bump injection with almost no loss. Measurements with found kickers' settings confirmed our analysis (see Fig. 7).

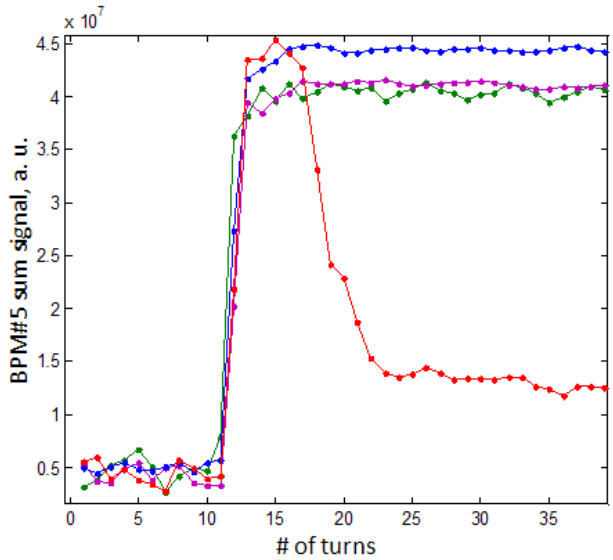


Figure 7: Sum signal of TBT BPM for the injected beam. Each point represents a BPM reading on a single turn. The injection is happening on the 12th turn. The green line represents the nominal 3-bump injection. Red line is two bump injection with BUIFB1 off. The magenta line is the modified two bump injection with increased BUIFB2 amplitude. The blue line is two bump injection with optimised settings of BUIFB1 and BUIFB3.

CONCLUSIONS

In this paper we presented the injection diagnostics tools based on the turn-by-turn beam position monitors installed at the NSLS storage rings. Using the example of the VUV ring we described the procedure of building the relevant injection model. We discussed the software that we developed for monitoring, analysis and troubleshooting of the injection process. As an ultimate demonstration of application of the developed tools we described our successful experience with optimizing a fairly unconventional two-bump injection, which was temporarily used during a kicker failure.

ACKNOWLEDGEMENTS

We are grateful for support from the NSLS. This work is supported in part by the U.S. Department of Energy (DOE) under contract No. DE-AC02-98CH1-886.

REFERENCES

[1] A. Kosicek, "Libera Electron beam position processor", Proceedings of PAC05, 2005.
[2] G. Portmann et al., "An accelerator control middle layer using MATLAB" Proceedings of PAC05, 2005.
[3] A. Terebilo, "Accelerator Toolbox for MATLAB" SLAC-PUB-8732, 2001.
[4] J. Safranek et al., "MATLAB-based LOCO", SLAC-PUB-9464, 2002.

Copyright © 2013 CC-BY-3.0 and by the respective authors

ALKALI ANTIMONIDE PHOTOCATHODES FOR EVERYONE

J. Smedley, K. Attenkofer, S. G. Schubert, BNL, Upton, NY 11973, USA
H. A. Padmore, J. Wong, LBNL, Berkeley, CA 94720, USA
J. Xie, ANL, Argonne, IL 60439, USA
M. Ruiz-Oses, I. Ben-Zvi, X. Liang, E. M. Muller, Stony Brook University, Stony Brook, NY 11794, USA
J. DeFazio, Photonis USA PA, Inc., Lancaster, PA, 17601, USA

Abstract

The next generation of x-ray light sources will need reliable, high quantum efficiency photocathodes. These cathodes will likely be from the alkali antimonide family, which currently holds the record for highest average current achieved from a photoinjector. In this work, we explore a new option for delivering these cathodes to a machine which requires them: use of sealed commercial vacuum tubes. Two sealed tubes have been introduced into a vacuum system and separated from their housing, exposing the active photocathode on a transport arm suitable for insertion into an injector. The separation was achieved without loss of QE in one case. These cathodes are compared to those grown via traditional methods, both in terms of QE and in terms of crystalline structure, and found to be similar.

INTRODUCTION

Alkali antimonide photocathodes have a long history in low-light photodetection, including image intensifiers. These needs have been met by commercial production; principally by RCA and its successors. The accelerator community also has great interest in alkali antimonide photocathodes – they are a prime candidate for use in high-brightness photoinjectors of free electron lasers and 4th generation light sources [1-3]. However, within the accelerator community, cathodes have traditionally been grown in dedicated vacuum systems tied to specific injectors. In some cases cathodes have been transferred from one system to multiple injectors, typically on a limited basis [2,4].

We have developed tools to understand the formation of these materials, both structurally and chemically, with the goal of altering the growth to produce cathodes with less roughness, better stoichometry, and larger crystal grains. The *in situ* techniques being used are x-ray diffraction (XRD), grazing incidence small angle x-ray scattering (GISAXS) and x-ray reflection (XRR). These tools enable determination of the crystal form of the cathode at each phase of growth, the film thickness and roughness, the texture and grain size of the film, and the presence of "imperfectly reacted" material. This work has been carried out at the National Synchrotron Light Source (NSLS) using beamline X21 and at the Cornell High Energy Synchrotron Source (CHESS) using beamline G3.

The goal of this work is to enable the large scale production of identical photocathodes, using recipes developed in the *in situ* analysis chamber, which will provide high QE while minimizing the surface roughness which can dominate the intrinsic emittance [5,6]. One aspect of this effort is collaboration with an industrial partner to produce photocathodes in sealed tubes which can be separated in vacuum.

Figure 1 shows a prototype photocathode in a sealed vacuum capsule. The substrate for growth is polycrystalline Molybdenum, which is brazed to the copper plug shown in the picture to the left. The capsule is sealed with a low temperature solder visible around the copper. A window on the isolated top electrode enables the QE of the device to be measured while the capsule is still sealed. The photocathode is visible as the blue area in the picture on the right, through this window.



Figure 1: Sealed photocathode.

EXPERIMENT

In the interest of space, the growth chamber with *in situ* x-ray analysis is described elsewhere [7]. This chamber has been used to measure both the capsule photocathodes, and to grow cathodes for comparison. The comparison cathodes are grown in a UHV chamber, with a typical operating pressure of 0.2 nTorr. Residual gas analysis confirms that the partial pressures of reactive gases (H_2O, CO) are better than 0.05 nTorr. Silicon [100] wafers 1x2 cm^2 are used as substrates; these are exposed to HF prior to installation, and baked to 500 C for an hour prior to growth. Once the substrate has cooled to 160 C, a further cleaning of the substrate is achieved by an initial potassium evaporation – XRR measurements confirm that this K does not remain resident on the surface, however the QE of cathodes grown is significantly improved by this initial step. Antimony is evaporated from PtSb beads; alkali-Bi sources from Alvatech are used to supply Potassium and Cesium. Deposition is sequential, with Sb evaporated, then K, then Cs, all at ~0.2 Å/s. The QE is observed during K and Cs evaporation, and the deposition is halted when the QE reaches a plateau. The "traditional" cathode is a multi-layer growth on a single substrate, with the first cathode "baked off" (substrate raised to 500 C for 10 min) prior to the growth of a second (recipe in Table 1).

Copyright © 2013 CC-BY-3.0 and by the respective authors

Table 1: Traditional Cathode Recipe

1st Layer	Temp	QE	2nd Layer	Temp	QE
15 nm Sb	100		15 nm Sb	125	
62 nm K	125	0.14	60 nm K	125	0.37
118 nm Cs	125	4.1	120 nm Cs	125	7.5

The Photonis photocathodes are also grown via sequential depositions, but on a Molybdenum substrate. The recipe used is similar to that used by the company for its transmission-mode cathodes (traditionally grown on glass substrates), and has yet to be optimized for this application. The spectral response of this cathode as delivered is shown in Figure 2.

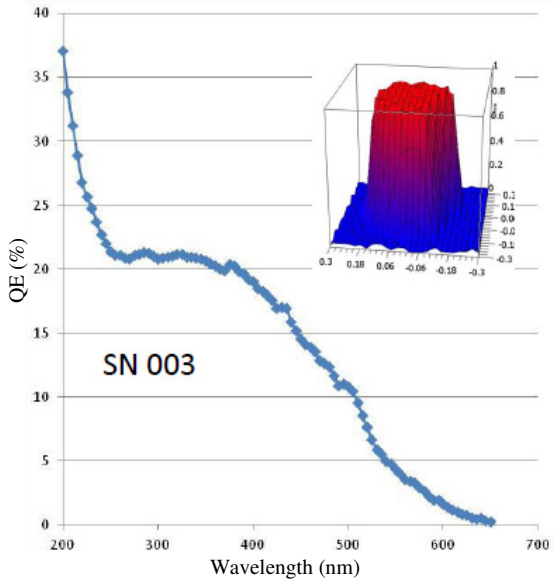


Figure 2: Spectral response of Photonis photocathode within the sealed tube. Inset shows spatial uniformity.

RESULTS

Transfer and Separation

The initial and final stages of the capsule loading and separation are shown in Figure 3. On the left is a capsule loaded onto the platen. On the right is the cathode ready to be transferred off the platen and into an injector. This design is compatible with the transfer system for the BNL 112 MHz Gun [8], and future iterations of this design will be tested in this gun (some design modifications are required to mask the solder joint from the gun).



Figure 3: Left – sealed cathode mounted on platen. Right – Cathode after cap is removed, still attached to platen.

The sequence of cap removal is shown in figure 4. First the platen with capsule is loaded onto the heater. Second, the platen temperature is increased slowly to ~100 C (the solder eutectic temperature is 72 C; thermal conduction from the platen to the solder joint as well as alloying of the solder with the base materials likely explains this difference). A manipulator is used to gently pry at the cap (bottom left), eventually resulting in the cap tipping away from the cathode (bottom right). The QE of the cathode is measured using a green (532 nm) laser immediately after the removal process (figure 5). The QE of the cathode initially decreases due to the rise in temperature (to 3.1% for cathode 1 and 1.8% for cathode 2); the first cathode recovered fully (actually slightly higher) once it cooled to room temperature. The second attempt resulted in a permanent degradation with a final QE of 3%, thought to be due to excessive overheating of the photocathode during the cap separation process.

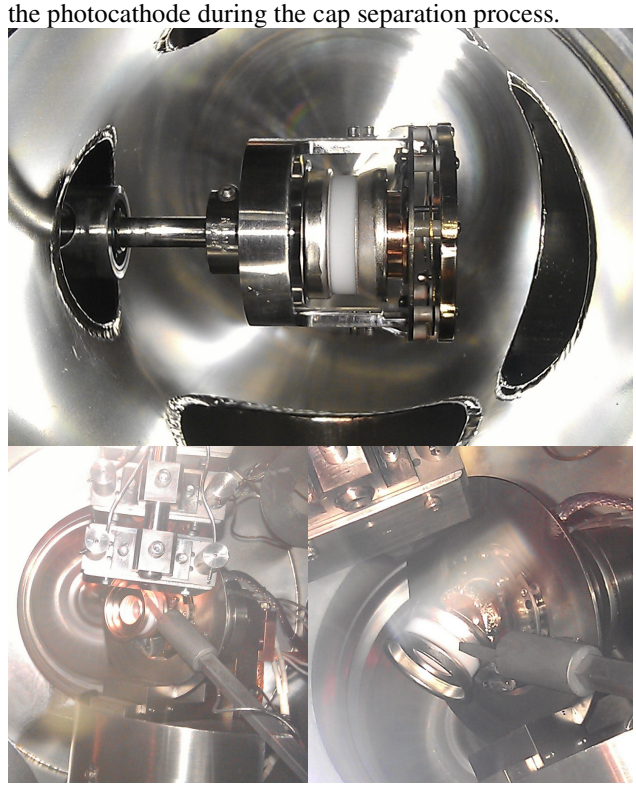


Figure 4: Top: Capsule loaded onto platen and mounted for insertion. Bottom Left: Finger positioned to remove cap. Bottom Right: Cap partially off.

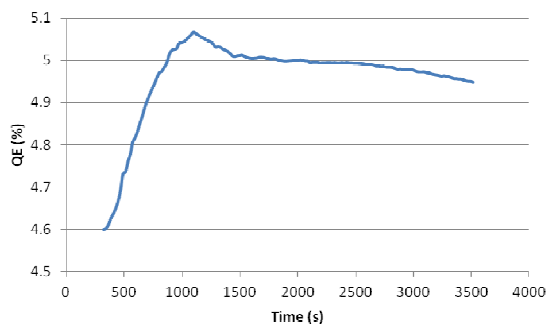


Figure 5: QE of cathode after cap removal. The QE rises due to the post-separation cooling of the substrate.

Copyright © 2013 CC-BY-3.0 and by the respective authors

X-ray Diffraction

Figure 6 shows the crystalline structure of both capsule cathodes, along with the "traditional" recipe cathode described above. For the traditional recipe, the cathode is cubic phase K_2CsSb with a mixed 222 and 220 surface textures. The grain size estimated from Scherrer analysis is 49.3±2.0 nm. No unreacted K_3Sb is observed in this cathode. The capsule cathodes are similar, except that they have a more pronounced 222 texture. The broader peak widths likely imply smaller grains (38.9±0.5 nm for cathode 1, 36.8±0.2 nm for cathode 2). The strong peak at 32.4 degrees is from the Molybdenum substrate.

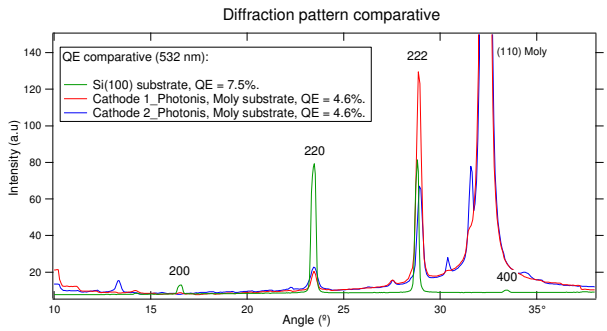


Figure 6: XRD results of two capsule cathodes after cap removal, along with a "traditional" recipe photocathode for comparison.

CONCLUSIONS

Sealed "Phototube like" photocathodes have been prepared to be separated in vacuum, allowing the photocathodes to emit electrons into a test system. The removal process can preserve the QE of the cathodes; 4.6% QE in the green was observed both before and after opening. While this QE is somewhat inferior to purpose-grown cathodes, the process has not yet been optimized and is expected to improve significantly. This technique has the potential to allow injector projects to purchase photocathodes that are produced commercially in batches, providing quality control and reproducibility, and dramatically reducing costs.

Further, the ability of these cathodes to be studied and compared to existing recipes using *in situ* materials diagnostic techniques will allow the evaluation and optimization of the cathode properties relevant to accelerator applications. These are somewhat different than traditional phototube attributes – in particular, the eventual ability to use GISAXS to evaluate surface roughness will provide insight into the expected intrinsic emittance of these cathodes. This was not possible on the current samples, as the growth substrate was "rough" polycrystalline Molybdenum. Samples grown on single crystal Molybdenum are already in production, and roughness measurements are part of the near-term future plan. In addition, other materials, such as Cs_3Sb and K_2NaSb, will soon be grown and evaluated in sealed-tube form. In the somewhat longer term, these cathodes will be tested in the BNL 112 MHz SRF injector.

This work was supported by the US DOE, under Contracts DE-AC02-05CH11231, DE-AC02-98CH10886, KC0407-ALSJNT-I0013, DE-FG02-12ER41837 and DE-SC0005713. Use of CHESS is supported by NSF award DMR-0936384.

REFERENCES

[1] L. Cultrera et al., Appl. Phys. Lett. 103 (2013) 103504.
[2] R. R. Mammei et al., Phys. Rev. ST - Accel. Beams 16 (2013) 033401.
[3] T. Vecchione et al., Appl. Phys. Lett. 99 (2011) 034103.
[4] http://wwwlasa.mi.infn.it/ttfcathodes/
[5] T. Vecchione et al., Proc. of IPAC2012, New Orleans, Louisiana, p. 655 (2012).
[6] S. G. Shubert et al., APL Mater. 1 (2013) 032119.
[7] J. Smedley et al., Proc. of IPAC2013, Shanghai, China, 464 (2013).
[8] T. Rao et al., Proc. of IPAC2013, Shanghai, China, 461 (2013).

Copyright © 2013 CC-BY-3.0 and by the respective authors

PROGRESS ON GROWING A MULTI-ALKALI PHOTOCATHODE FOR ERL AT BNL

E. Wang I. Ben-Zvi, S. Belomestnykh, T. Rao, J. Smedley, BNL, Upton, NY 11973, USA
X. Liang, M. Ruiz-Oses, Stony Brook University, Stony Brook, New York 11794, USA

Abstract

K_2CsSb is a robust photocathode capable of generating electron beams with high peak, high average current and low thermal emittance. During the last two years, a great improvement in the design and fabrication of a reliable deposition system suitable for K_2CsSb cathode growth and its insertion into BNL high current ERL SRF gun has been achieved. A standard procedure for the growth of multi-alkali cathodes combined with another procedure to transport these cathodes into the SRF gun was developed. The first cathode is planned to be grown on a copper insert and mounted into the 704 MHz gun. In this article, we will describe the progress of cathode growth and transport for ERL project. In particular, effect of excimer laser exposure and the cathode growth on Ta will be included.

INTRODUCTION

The multi-alkali photocathode is considered to be suitable for high current applications due to its high quantum efficiency at visible wavelengths. The photocathode of choice for BNL-ERL photo-injector is K_2CsSb due to its capability to generate high average current and low emittance electron beams. The 704 MHz SRF photoinjector is built for testing ERL concept up to 500 mA high average current. A multi-alkali photocathode deposition system for this gun was built by Advanced Energy Systems (AES) [1]. In last two years, we assembled entire system and grew several cathodes to find the optimal cathode preparation parameters. We also tested the transport cart and insertion of the cathode plug through the load-lock system. 0.2% QE was obtained from a K_2CsSb cathode grown on the copper substrate. Currently, the gun is being conditioned for CW SRF operation with a copper cathode plug and the vacuum in both the deposition chamber and the transport cart is maintained in low 10^{-10} torr range. The cathode will be deposited on this plug soon after the conditioning. The first cathode test in the gun is scheduled for November.

DESCRIPTION OF THE DEPOSITION SYSTEM

The K_2CsSb deposition system consists of a main deposition chamber and three source chambers attached to the main chamber but isolated from each other and the main chamber through gate valves. The main chamber is equipped with two view ports, an RGA, a quartz crystal monitor, anode, resistive heater and load-lock port. Ion pumps integrated with NEG pumps maintain the vacuum in low-10^{-10} torr scale. Each of the source chambers has one ion pump keeping the vacuum in mid-10^{-10} torr range. Bellows coupled manipulator can move the sources into the deposition chamber and locate them in front of the substrate. We use Alvatec Alkali metal source of type S and 99.999% purity pellets antimony source. The alkali sources are evaporated by resistive heating of the source container and the Sb is evaporated by heating a boat which holds the crucible containing Sb pellets. Each alkali arm contains two Cs or K sources to increase the evaporation area and cathode uniformity. To protect the sides of the cathode plug from being coated with the cathode material, an aperture is placed between the substrate and the source to limit the deposition area to a 0.75 inches diameter. The substrate can be heated or cooled by flowing dry N_2 gas through a pipe in contact with the stalk. With the same pipe, the stalk is maintained at LN_2 temperature when in the SRF gun. The stalk can be heated up to 200° C and maintained at optimal temperature for evaporation. To determine the initial quantum efficiency, the cathode is irradiated with a low power CW laser. Emitted electrons are collected at the anode in front of the cathode. The whole deposition system is placed in a class 10,000 clean room shown in Figure 1. The load lock connection port is inside a class 100 clean room to avoid accumulation of the particulates in section that comes in contact with the SRF gun.

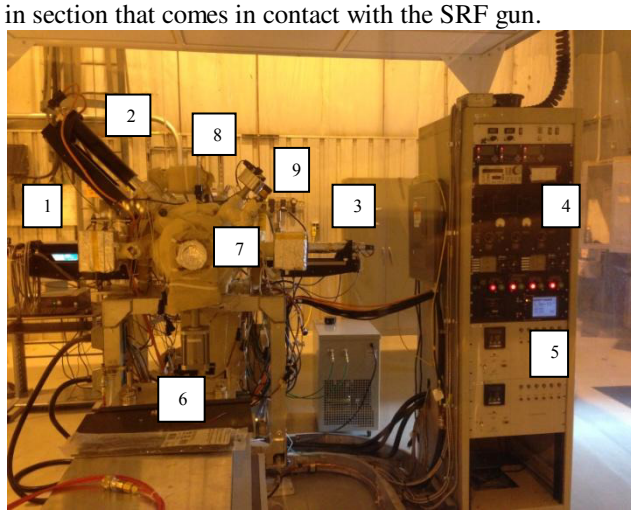


Figure 1: The picture of ERL-deposition system: 1 – K source; 2 – Sb source; 3 – Cs source; 4 – control system for valves and source; 5 – power supply for baking; 6 – table for supporting cathode transport cart; 7 – load lock port; 8 – heater; 9 – crystal monitor.

*Work supported by the United States Department of Energy through Contract numbers DE-AC02-98CH10886 and at Stony Brook University under Grant No. DE-SC0005713 with the U.S.DOE.
#wange@bnl.gov

Copyright © 2013 CC-BY-3.0 and by the respective authors

We use a specially designed transport cart to transfer the cathode between the deposition system and the SRF gun. The cathode substrate is an integral part of a grooved choke joint structure mounted inside the transport cart as shown on Figure 2c. The diameter of the copper stalk is 1 inch. The transport cart consists of a bellow manipulator and an intermediate section, which is connected to either the deposition system or the gun. The vacuum plenum of the cart is made up by two ion pumps and one TSP. During baking of the intermediate section prior to transferring the cathode, the cathode is protected from the gas load by a cold shield near the isolating valve. The QE of K_2CsSb cathode will be preserved for a few weeks in the low 10^{-10} torr vacuum achieved in the load-lock. Two identical transport carts have been fabricated to allow the gun to be tested with one cathode while the second is being prepared. The transport cart is shown in Figure 2a. Currently, the transport cart is attached to the gun for RF condition, see Figure 2b.

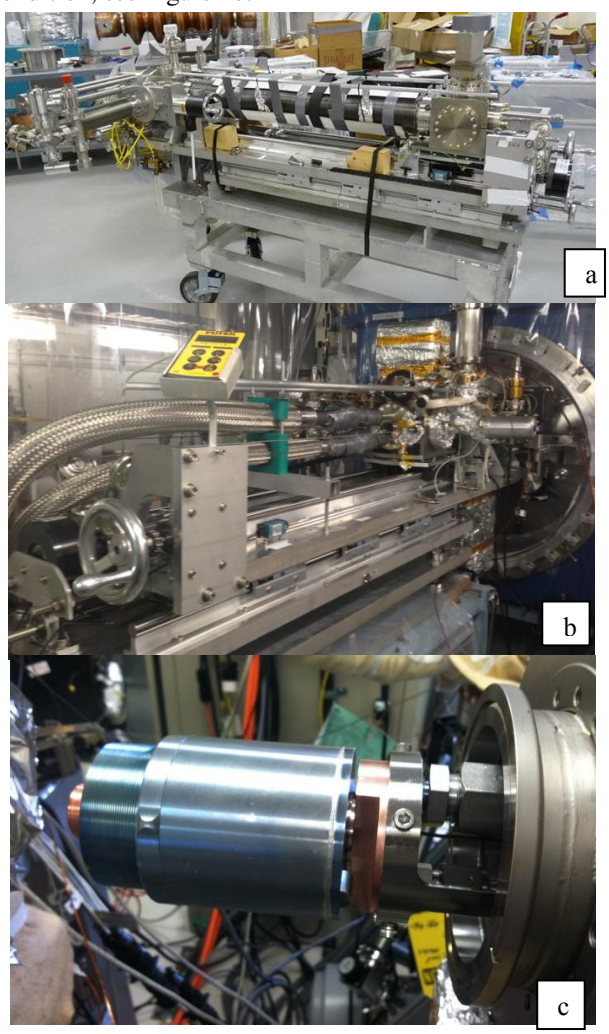


Figure 2: Photographs of the cathode and transport cart: a) The cathode transport cart; b) The transport cart attached to the gun and the cathode stalk inserted. Two line attached to the manipulator are for cooling the cathode in the gun. Same port will be used for heating the substrate during cathode preparation; c) The cathode stalk mounted on the transport cart.

STANDARD CATHODE GROWTH PROCEDURE

- Heat up the stalk to 100°C.
- Evaporate Sb layer to a thickness of 10 nm. The thickness is measured by a crystal monitor.
- Increase the substrate temperature to 140°C.
- Evaporate K layer to 20 nm while monitoring the photocurrent change. Stop evaporation when photocurrent reaches maximum amplitude.
- Decrease the temperature.
- Evaporate Cs when temperature goes to 130° C, while monitoring photocurrent. Cs evaporation is stopped when the QE plateaus.

SELECTION OF CATHODE SUBSTRATE

In the first gun tests with electron beam, we will use K_2CsSb photocathode grown on the copper stalk. Because copper atoms easily diffuse into K_2CsSb crystal, the QE of a single layer cathode is usually lower than pure K_2CsSb crystal. Typically, the QE of K_2CsSb on copper cathode would be around 0.1% to 0.2% following the standard growth procedure. We have grown a single K_2CsSb layer on the copper substrate in this deposition system several times. The best QE was 0.2%. Additional K_2CsSb layers reduce the probability of copper atoms diffusing into emission surface, thereby increasing the overall QE But the thicker layer may result in flaking of the cathode material, which is detrimental to SRF operation. It is shown that high QE K_2CsSb cathode can be grown on Si [2], however, the large dielectric loss of Si in CW SRF environment precludes its use in an SRF gun. To find the suitable metal substrate for the 704 MHz gun, we compared the performance of the cathode on two substrates, Mo and Ta, chosen for compatibility of their mechanical, thermal and electrical properties with the SRF gun. Both samples were from Goodfellow with better than 99.9% purity. The samples' thickness is 0.5 mm. The Mo sample has an optical quality surface finish. The Ta samples with different surface finishes were tested for QE. One Ta sample was polished by 9 um polishing compound with Metadi No 40-6543 diamond suspension from Beuhler. Another identical Ta sample was not polished. No *in situ* cleaning was performed on any of these samples and *ex situ* cleaning consists of only typical ultrasonic cleaning and rinsing with acetone prior to insertion in the vacuum chamber. We found the cathodes on polished and unpolished Ta substrates to have nearly the same spectral response. Also, QE of both cathodes is similar with a value of 2.53%. Then, with the same procedure, we obtained a 3% QE with Mo substrate. The operating life time of the cathodes on all these substrates, measured using a low power 532 nm laser beam was comparable. Therefore, both Mo and Ta are suitable substrates for growing K_2CsSb cathode. The next

Copyright © 2013 CC-BY-3.0 and by the respective authors

step was incorporating the substrate material in our pre-existing cathode stalk, to be inserted into SRF gun. We sputtered a Mo layer with different thicknesses onto a 1 inch diameter polished copper stalk. However, none of the Mo layers adhere to the copper well and easily flaked off raising concerns over its operation in SRF gun. Then, AES, Inc. brazed a 0.006" thick Ta foil on the copper stalk. The braze material is under the entire surface of the Ta foil. The Ta attached to the stalk well, as shown on the left hand side of Figure 3. We measured the particles generation and electrical contact for the Ta-Cu brazed sample before and after cooling down to LN_2 temperature. Four-point resistance measurement shows that the resistance between Ta and Cu did not change after the cool down cycle. In a class 100 clean room, we immersed a particulate free Ta-Cu brazed sample into LN_2 and after cooling cycle, we compared the particle count with another identical sample which did not undergo the thermal cycling. We found the particle counts of both samples are comparable. There was no fracture in either Ta or braze material after cooling cycle. Therefore, we chose the Ta-Cu brazed stalk for the 704 MHz SRF gun test. This stalk is currently under procurement.



Figure 3: Left – the dummy brazed Ta-Cu sample; Right – the polished copper cathode stalk with the choke joint section.

NON-THERMAL SUBSTRATE CLEANING AND CATHODE REMOVAL

While operating in an electron gun, the K_2CsSb cathodes have limited charge life time. Usually, new cathode layers are grown over the used layer. However, after a few evaporations, the collective layer becomes thick enough to flake and contaminate the gun environment. For an SRF gun, non superconducting material contaminations will lead to field quenching or field emission. Heating the substrate to 800˚C may remove the old layers but is not suitable for the 704 MHz gun stalk due to significant engineering problem associated with the design of the heavy cathode plug. We have demonstrated that 248 nm excimer laser can totally remove the K_2CsSb cathode and preserve the substrate roughness [3]. We grew a cathode following the standard procedure described above. The excimer laser beam size is 3.5 mm^2. A collinear green laser with spot size smaller than that of the UV laser was used to measure the change in QE. We found that with excimer laser energy density of 3.5 mJ/mm^2 and repetition rate higher than 30 Hz, the cathode photocurrent decreases to background within 10 seconds. Figure 4 shows the regions exposed to the excimer laser, appearing visibly different. We used EDX to measure the elements present on the surface. In the EDX spectrum, we found the Sb, K, Cs signals were completely eliminated in laser exposed areas.

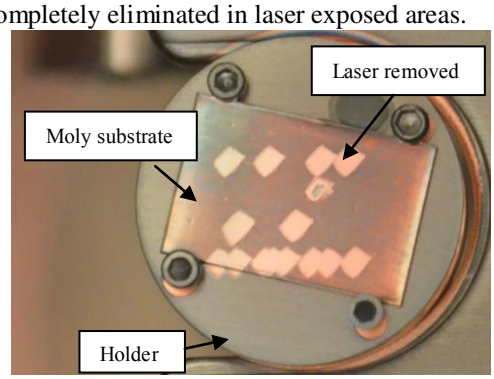


Figure 4: Excimer laser radiated K_2CsSb cathode sample. The rectangular regions are exposed to the laser. The cathode material in these regions is removed.

This technique can be used to address three issues associated with multi-alkali cathodes in high current photoinjectors. For instance, i) once the QE of the cathode decays below the design value, by irradiating it with the UV laser, we can clean substrate and remove the cathode simultaneously prior to fabricating the new cathode on the same substrate without any degradation of the UHV system. ii) Enhance the photoemission. We fabricated cathode with a stable 6% QE on a laser exposed Ta substrate. iii) In a photo-injector, by exposing the cathode to the UV laser, the cathode area could be exactly matched to the electron beam size, the halo electron beam generated either by the halo of the laser or the scattered laser beam can be completely eliminated, thereby improving the electron beam quality and reducing the beam loss induced pressure increase.

CONCLUSION

The cathode deposition system for the 704 MHz gun is ready for use. The photocathodes were grown on the copper cathode stalk a few times and a reasonable QE was obtained. The transport cart with the cathode stalk was pumped down to low 10^{-10} torr and tested in the SRF gun. We developed a new technique to remove the K_2CsSb cathode material by an excimer laser.

REFERENCE

[1] D. Pate, I. Ben-Zvi, T. Rao et.al R&D ERL: Photocathode Deposition and Transport System (2011).
[2] T. Vecchione, I. Ben-Zvi, et. al, Appl. Phys. Lett. **99**, 34103 (2011).
[3] E. Wang, T. Rao, and I. Ben-Zvi, to be published in Phys. Rev. ST Accel. Beams (to be published).

Copyright © 2013 CC-BY-3.0 and by the respective authors

TEMPERATURE DEPENDENCE OF PHOTOEMISSION FROM COPPER AND NIOBIUM*

J.R. Harris[1,#], A. Kara[2,3], C.W. Bennett[2], M. Galt[2],
A.D. Holmes[2], R.L. Swent[2], J.W. Lewellen[4], and J. Sears[5]

[1]Dept. of Electr. & Computer Engineering, Colorado State University, Fort Collins, CO 80523
[2]Department of Physics, Naval Postgraduate School, Monterey, CA 93943
[3]Lieutenant (Junior Grade), Turkish Navy
[4]Los Alamos National Laboratory, Los Alamos, NM 87545
[5]Laboratory for Elementary-Particle Physics, Cornell University, Ithaca, NY 14853

Abstract

Photocathodes remain the principal electron sources for many particle accelerators. With the increasing interest in the use of superconducting radiofrequency electron guns, it is important to understand how operation at cryogenic temperatures affects the performance of photocathodes. Here we report measurements of the quantum efficiency of copper and niobium under illumination with 266 nm light at temperatures between 85 K and 400 K. The quantum efficiency of copper was found to vary strongly over this range, while there was only a minimal change in the quantum efficiency of niobium.

INTRODUCTION

Superconducting radio-frequency (SRF) electron guns combine efficient CW operation with the excellent vacuum needed for high-quantum efficiency (QE) photocathodes and the high surface gradients needed to maintain the quality of high-charge bunches. However, they remain an immature technology, with a number of very different configurations currently being investigated [1]. One major concern has been how to best balance the tradeoffs associated with integrating photocathodes into these devices. As part of its research program on SRF guns [2,3,4,5], the Naval Postgraduate School has studied some of these issues, including the potential contamination from dispenser photocathodes [6,7] and cathode stalk cooling to mitigate thermal and RF losses [8]. Many SRF guns use a normal-conducting cathode which is mechanically isolated from the cavity to minimize heat leaks. But even without mechanical contact between the cavity and the cathode, the cathode will be radiatively cooled due to the surrounding 2 - 4 K environment. This raises the interesting question of how the cryogenic environment affects the performance of photocathodes. There have been many measurements of the QE of metal cathodes, including at cryogenic temperatures. However, comparing QE measurements from one experiment to the next is difficult because of differences in sample and testing conditions. Having a single experimental apparatus where the temperature of a cathode can be varied, while keeping other influences largely constant, aids in effectively isolating the dependence of QE on temperature. Accordingly, we modified the cathode stalk cooling experiment to serve as a temperature-controlled photoemission test stand, and used it to measure the QE of copper and niobium at temperatures from 85 K to 400 K with 266 nm light [9]. Our experimental apparatus and results are reported here.

EXPERIMENTAL APPARATUS

Figure 1 shows a schematic of the test stand. The cathode stalk (Fig. 2) was formed from a copper cylinder with a recess in the front surface to accept metal cathode samples, with the samples held in place by a copper retaining ring to provide good thermal and electrical contact between the samples and the stalk. Temperature control was provided by a liquid nitrogen line and a pair of resistive heaters in the back of the cylinder. The heaters were supplied from a variable autotransformer, while liquid nitrogen was supplied from a pressurized fill pot used for the experiments described in Ref. [8]. Temperature measurements were made with LakeShore DT-670-SD and DT-670-CU-HT diodes placed on the front and back faces of the cathode, respectively; these limited operation to temperatures at or below 400 K. The diodes were connected to a computer by a LakeShore 218 temperature monitor, and the data was recorded every 5 seconds by a LabView program.

The vacuum envelope was made from conventional UHV components, with an ion pump providing typical pressures of 3×10^{-8} - 4×10^{-7} Torr at room temperature during testing. In operation, the rate of cathode heating had to be limited to prevent vacuum pressure spikes. A ceramic break was placed around the cathode stalk, with the downstream end electrically isolated from the rest of the experiment to serve as the anode, and connected to a 10 kV Glassman high voltage supply. The floating end also contained a UV window and a small magnet to disperse the photoelectrons to prevent charging of the window. A Bergoz fast current transformer mounted outside the ceramic break provided a time-resolved measurement of the current flow on the stalk, and therefore served as a measure of emitted current.

*Work supported by the Office of Naval Research and the High Energy Laser Joint Technology Office.
#john.harris@colostate.edu

Copyright © 2013 CC-BY-3.0 and by the respective authors

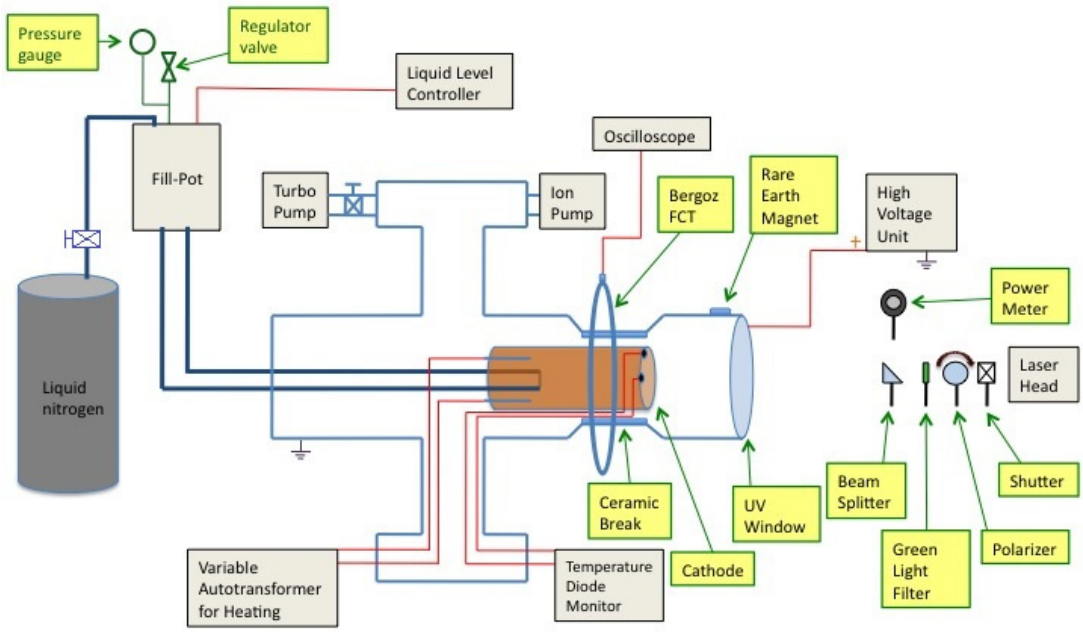


Figure 1: Schematic diagram of the temperature-controlled photoemission experiment [9].

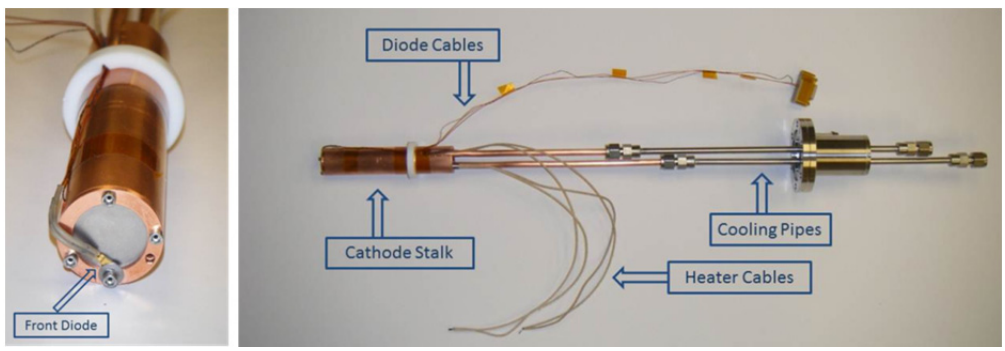


Figure 2: Photographs of the cathode stalk used in the temperature-controlled photoemission experiment, showing the niobium sample installed for testing [9].

Integrating under the transformer signal yielded the number of photoelectrons produced by each laser pulse.

This experiment used a frequency-quadrupled Continuum Minilite II Nd:YAG laser producing a 5 ns, 40 mW pulse of 266 nm light. A filter was used to block any light which was not fully converted to UV inside the laser, and a remote-controlled shutter and polarizer were used to control the laser power. Preliminary testing showed that at an anode voltage of 10 kV, the laser power on the cathode must be less than 4 mW to stay in an emission-limited, rather than space-charge-limited, regime. Conversely, our PM10 power meter required at least 5 mW to stay within its specified range and avoid a nonlinear response. To balance these requirements, 70% of the laser power was directed to the power meter using a beam splitter. The power meter measured the average power delivered to it by the laser; this was converted into the number of photons arriving at the cathode per shot using a conversion factor involving the measured UV window transmission coefficient, the nominal beam splitter power ratio, the laser repetition rate (10 Hz), and the energy per 266 nm photon.

RESULTS AND DISCUSSION

For this testing, a copper sample was machined from material already on hand, and a fine-grain niobium sample etched to 150 μm using buffered chemical polishing was provided by Cornell. Using the system described above, the sample temperatures were adjusted between 85 K and 400 K. At each temperature, the laser power was varied from the minimum power needed to avoid nonlinearity in the detector, to the maximum power that avoided the onset of space-charge-limited operation. The beam current data was integrated to determine the number of photoelectrons produced per laser pulse, and the power meter data was converted to find the number of photons arriving at the cathode per laser pulse. This data was plotted as shown in Fig. 3 and fit to a straight line, with the slope of that line giving the QE. Additional lines were used to conservatively bound the data, and the slopes of these lines set the upper and lower error estimates on the QE.

Copyright © 2013 CC-BY-3.0 and by the respective authors

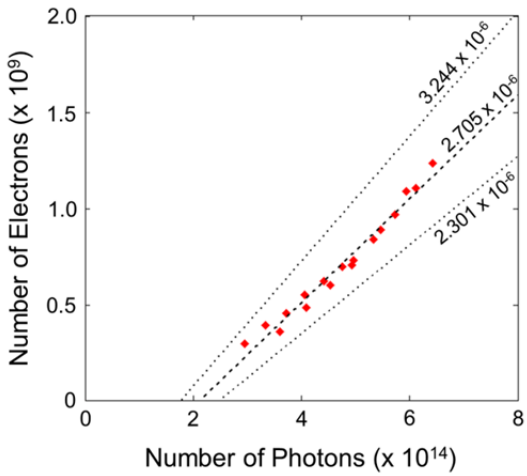


Figure 3: Data reduction for copper sample at 85 K, showing data, fitting line (dashed) and error bounding lines (dotted), with slopes (QE values) indicated.

Figure 4 summarizes the measured QE as a function of cathode temperature for the copper and niobium samples. Also shown are the measured vacuum pressures in the test stand at each temperature during the two sets of experiments. The measured QE of copper increased from 0.27 x 10^{-5} to 1.2 x 10^{-5} as the temperature increased from 85 K to 400 K. This represents a clear and statistically significant increase in QE by more than a factor of four. Over this range, the trend is well described by a quadratic fitting function (Fig. 5), except for the values at 200 K; the cause of this discrepancy is unknown. Vacuum pressure changed very little until the sample temperature exceeded about 350 K in these tests, suggesting that this does not explain the steady change in QE observed for copper.

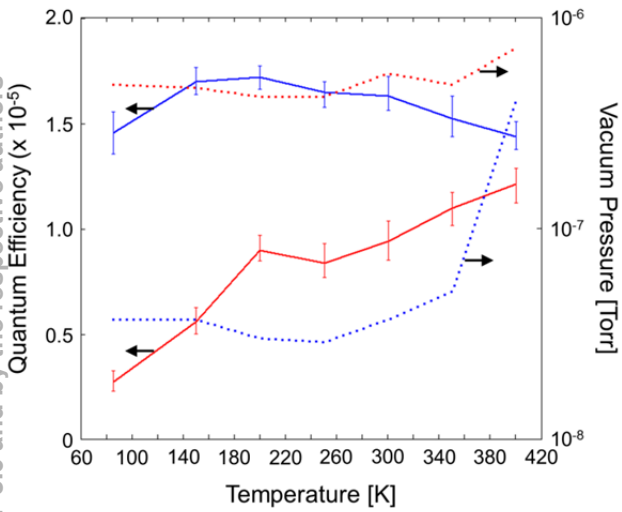


Figure 4: Measured QE (solid lines) and vacuum pressure (dotted lines) during experiments with copper (red) and niobium (blue) as a function of sample temperature.

By contrast, the observed dependence of QE on temperature for niobium is much weaker than for copper, with measured values varying from 1.4 to 1.7 x 10^{-5}.

This experiment found values of QE for copper and niobium that were generally in line with those reported in the literature [9], but the difference in the observed temperature dependence between copper and niobium is dramatic and unexplained. It is important to note that while the samples were handled and cleaned using standard vacuum procedures, the details of their surface conditions are unknown, and there was almost certainly some degree of oxidation present. However, this is representative of the likely surface conditions of these materials when used in actual accelerators.

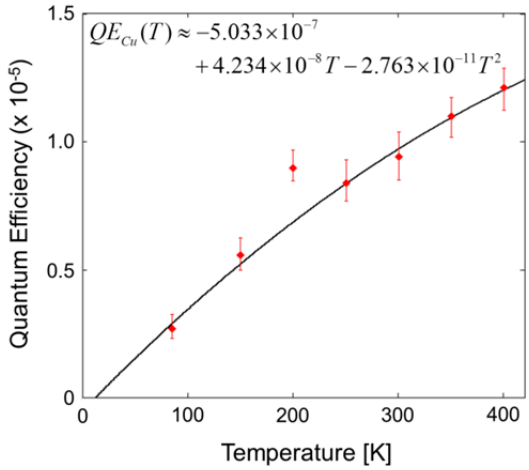


Figure 5: Measured QE of copper and fitting curve.

ACKNOWLEDGEMENTS

The authors would like to thank Brian Rusnak, Kevin Jensen, and Eric Montgomery for valuable assistance and discussions on experimental and theoretical issues associated with these tests.

REFERENCES

[1] A. Arnold and J. Teichert, Phys. Rev. ST Accel. Beams 14, 024801 (2011).
[2] S.P. Niles, et al., "NPS Prototype Superconducting 500 MHz Quarter-Wave Gun Update," in Proc. 2010 FEL Conference.
[3] J.R. Harris, et al., Phys. Rev. ST Accel. Beams 14, 053501 (2011).
[4] A.D. Holmes, et al., "Characterization of the First SRF Electron Beam Source at the Naval Postgraduate School," in Proc. 2012 International Particle Accelerator Conference.
[5] J.W. Lewellen, et al., submitted to the Journal of Directed Energy (2013).
[6] J.C. Jimenez, M.S. Thesis, Naval Postgraduate School (2010).
[7] E.J. Montgomery, et al., "Cesium Emission in Dispenser Photocathodes," Proc. 2010 FEL Conference.
[8] A.B. Baxter, M.S. Thesis, Naval Postgraduate School (2012).
[9] A. Kara, M.S. Thesis, Naval Postgraduate School (2013).

Copyright © 2013 CC-BY-3.0 and by the respective authors

BEAM POSITION AND PHASE MEASUREMENTS OF MICROAMPERE BEAMS AT THE MICHIGAN STATE UNIVERSITY REA3 FACILITY*

J. Crisp, D. Constan-Wahl, B. Durickovic, G. Kiupel, S. Krause, D. Leitner, S. Nash, J. A. Rodriguez#, T. Russo, R. Webber, W. Wittmer, NSCL/FRIB, MSU, East Lansing, MI 48824, USA
N. Eddy, C. Briegel, B. Fellenz, D. Slimmer, FNAL, Batavia, IL 60510, USA
M. Wendt, CERN, Geneva, Switzerland

Abstract

A high power CW, heavy ion linac will be the driver accelerator for the Facility for Rare Isotope Beams (FRIB) being designed at Michigan State University (MSU). The linac requires a Beam Position Monitoring (BPM) system with better than 100 micron resolution at 100 microamperes beam current. A low beam current test of the candidate technology, button pick-ups and direct digital down-conversion signal processing, was conducted in the ReA3 re-accelerated beam facility at Michigan State University. The test is described. Beam position and phase measurement results, demonstrating ~250 micron and ~1.5 degree resolution in a 45 kHz bandwidth for a 1.0 microampere beam current, are reported.

INTRODUCTION

The Facility for Rare Isotope Beams (FRIB) [1] will be a new accelerator-based user facility for research in nuclear physics. It will be located in the MSU campus and it is scheduled for completion in 2022. Its driver linac will accelerate ions as heavy as Uranium to energies higher than 200 MeV/u delivering up to 400 kW of beam power into a target. The desired Rare Isotope Beam (RIB) product of the reactions in the target will be transported to the different experimental areas after being selected in a fragment separator. Alternatively, the RIB can be thermalized, charge-bred and postaccelerated in the ReA re-accelerator [2] before being sent to an alternative experimental hall.

While the FRIB facility completion is scheduled for 2022, the first stage of the ReA re-accelerator was recently completed and connected to the Coupled Cyclotron facility (CCF) [2, 3]. During the measurements described in this paper, it has been used as a stand-alone accelerator to test the FRIB's prototype BPM system using a molecular Hydrogen beam produced by the off-line stable ion source.

DESCRIPTION OF REA3 AND THE BPMS

A Colutron-type ion source is used to produce several microamps of H_2^+ beam with an initial energy of 24 keV (defined by the 12 keV/u injection energy of the RFQ). The beam is then transported through an electrostatic transfer line and injected into a 4-rod 80.5 MHz RFQ after being bunched using a multiharmonic buncher. After the RFQ, the 600 keV/u beam is rebunched as it passes through a $\beta = 0.041$ SRF cavity operated at its zero-crossing phase (located in the first cryomodule (CM1) of the linac) and then accelerated to a few MeV/u when it passes through six more $\beta = 0.041$ SRF cavities located in the second cryomodule (CM2). Superconducting solenoids equipped with corrector coils inside the cryomodules are used to focus and steer the beam. During the tests, the two BPM sensors were installed in a drift space approximately 0.6 m down-stream of CM2 and separated by 2.08 m (Figure 1). Movable slits and Faraday cups in diagnostics stations before and after the BPMs were used to center and characterize the beam during the tests and beam attenuators and collimator slits were used to change the beam current.

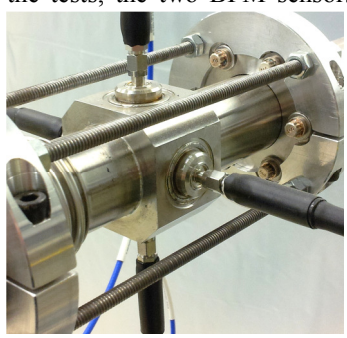


Figure 2: Prototype BPM as tested in ReA3.

The BPM system comprises two button-type BPM sensors (Figure 2, Table 1), signal amplifiers and digitizers that provide raw and processed data via EPICS channels to the control room. The button pickup has a design capacitance of 2 pF and impedance of 50 Ω. The

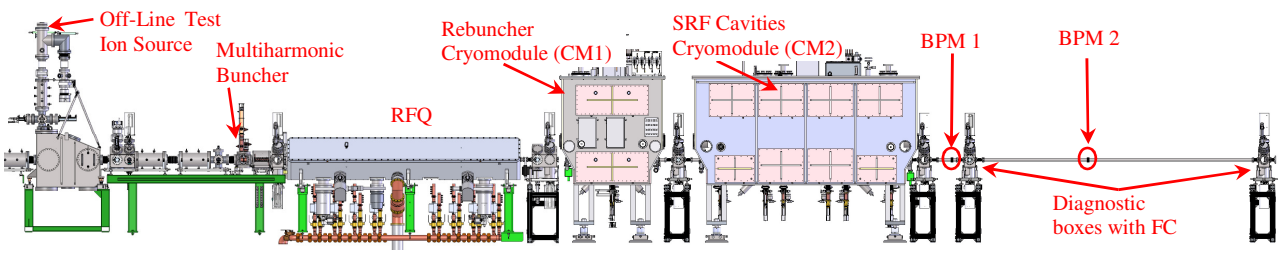


Figure 1: Layout of the ReA3 re-accelerator during the BPM tests.

* This material is based upon work supported by the U.S. Department of Energy Office of Science under Cooperative Agreement DE-SC0000661, the State of Michigan and Michigan State University, and the National Science Foundation, under Cooperative Agreement PHY-1102511.
#rodriguez@frib.msu.edu

Copyright © 2013 CC-BY-3.0 and by the respective authors

signals from the buttons are small (~ -80 dBm), requiring amplification before digitization. Each front-end channel has a low-noise amplifier with 80 dB gain and 14 MHz band width centered near the 2nd beam harmonic at 161MHz. The entire analog front-end is enclosed in a shielded box and connected to the bpm using solid copper shielded coax to further reduce noise from surrounding systems.

The signals are digitized and processed by an 8-channel digital receiver board developed at Fermilab. This board was initially used for the ATF damping ring BPMs [4]. The board consists of 125 MS/s 14 bit ADCs connected to a Cyclone III FPGA.

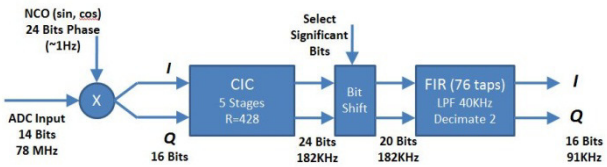


Figure 3: A block diagram of the DDC filter.

For the ReA3 system, an RF reference of 80.5 MHz is provided for the digitizer clock input. An internal PLL-based clock distribution chip sets the ADC clocks to operate at 32/33 of the RF clock. This undersamples the 161 MHz input signal producing an intermediate frequency (IF) of approximately 5 MHz. The IF signal is then processed by a Digital Down-Converter (DDC) circuit as shown in Figure 3. The output rate of the DDC is 91 kHz. The DDC yields the magnitude and relative phase of the input signal.

The 91 kHz output rate of the filter provides 2048 samples over a 22.5 ms window for each trigger. The beam pulse length was limited to approximately 25 ms for the tests. For each trigger, the front-end software reports the complete array of magnitude and phase data for the beam pulse as well as time-averaged values for positions, intensity and phase over the pulse.

Table 1: Characteristics of the BPMs

Parameter	Value
BPM aperture	1 3/8 in
Button diameter	20 mm
Signal frequency	161 MHz (2nd harmonic)
Trigger frequency	5 Hz

RESULTS OF THE TESTS

Several tests were conducted during 2012. The first tests confirmed the expected beam signal levels and uncovered an issue with electrical noise caused by the RFQ power amplifier. Electromagnetic shielding and filters were added to the BPM signal amplifiers in the following tests.

Beam Intensity Measurements

In an effort to understand the BPMs' performance at low currents and measure their response versus beam intensity changes, data were recorded while the beam current through the line was changed and measured in a Faraday cup located after the second BPM. The results of this measurement are shown in Figure 4 and demonstrate that the BPMs can be used with currents as low as 50 nA which is several orders of magnitude smaller than the anticipated 50 µA FRIB commissioning beam current. Their responses were linear over the range of available beam currents, which was limited by the ion source. The similarity in the results from the two BPMs indicates good reproducibility.

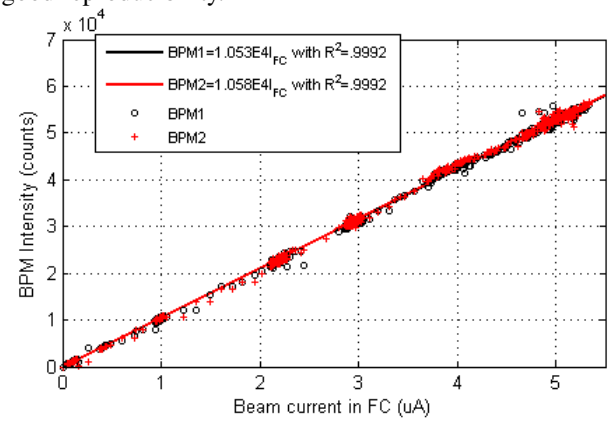


Figure 4: BPMs intensity signal vs. beam current. Currents as low as 50 nA could be measured.

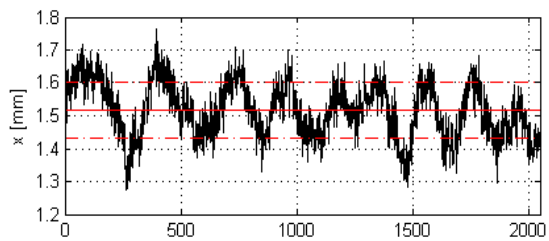


Figure 5: Typical measured beam position over 2048 consecutive samples (i.e. over 22.5 ms) for a 2 µA beam.

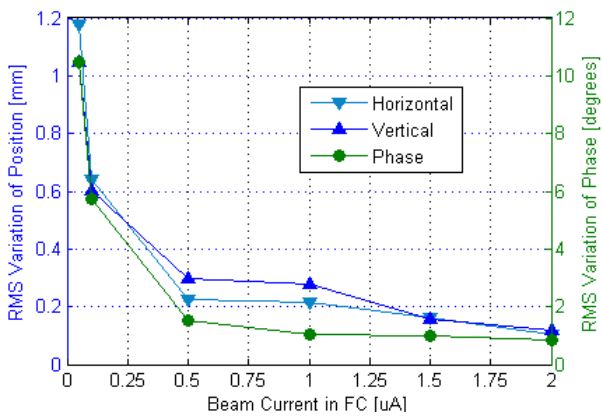


Figure 6: RMS variation of position and phase measurements as a function of beam current.

Variability of Position and Phase Measurements

Several experiments were conducted to characterize the resolution of the BPMs' position and phase measurements. Figure 5 shows the result of a typical

Copyright © 2013 CC-BY-3.0 and by the respective authors

measurement; Figure 6 shows a summary of the RMS distribution of position results as a function of current. Without an independent measurement of actual beam motion, this data merely sets an upper limit for the achieved measurement resolution.

The variability for currents lower than 0.5 µA seems to be defined by the BPM system itself; however, this may not be the case for higher currents. Figure 5 suggests that coherent beam motion might be dominant at the 2 µA current level. The resolution of the BPM system at currents between 1 and 2 µA might be a fraction of the ~100 µm shown in Figure 6.

Beam Position Measurements

To observe the BPM system response to changes in beam position, data was recorded while the beam was steered several millimetres horizontally and vertically using the last correctors in CM2. Inside the cryomodules, the corrector coils are embedded in the solenoids which explains the horizontal and vertical coupling apparent in Figure 7.

Currently the position and intensity is scaled linearly. A 3rd order two-dimensional polynomial is being implemented to linearize and decouple the positions and to correct the intensity. The polynomial compensates for non-linearity effects with good results over two thirds of the pickup aperture.

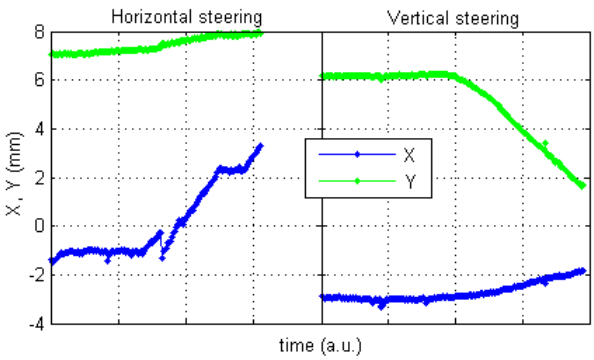


Figure 7: Beam position over time as it was steered horizontally (on the left) and vertically (on the right) during the test.

Phase Measurements

Simultaneous beam phase measurements enabled relative beam energy measurements by determining changes in time-of-flight. The beam phase at each of the two BPMs was observed as the beam energy was changed by scanning the RF phase of the last cavity in the second cryomodule.

Results show the expected sinusoidal-like phase variation between the two BPMs as a function of cavity phase setting (Figure 8). Measurement resolution was better than one degree of phase (17 picoseconds) in a 10 Hz bandwidth at 161 MHz for a 2 µA beam current.

The time-of-flight information provided by the BPMs has proven to be useful during the commissioning of the ReA3 linac. The time it takes to phase each cavity in the linac using the BPMs was reduced to a few minutes after automating the procedure, which is very important for FRIB given the number of cavities in the driver linac. More details on this procedure can be found in [5].

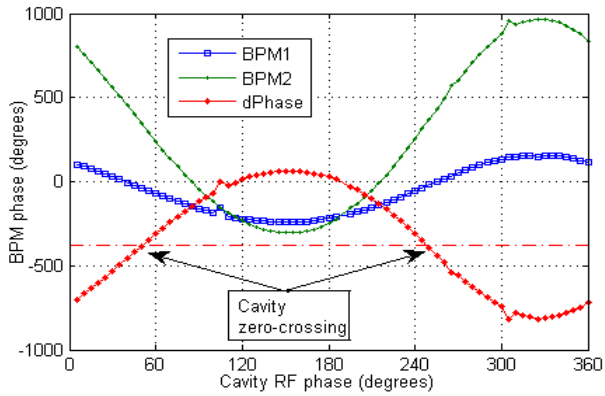


Figure 8: BPM phase measurements as the phase in the last cavity of CM2 is varied.

Signal to Noise Ratio Measurements

A spectrum analyser was used to measure noise with the amplifier located at the bpm and then at the digital receiver 18 m away. The noise power spectral density referenced to the amplifier input measured -167.4 dbm/Hz for both locations. No degradation in BPM signal quality was observed. This is relevant for FRIB because it is highly desirable that the amplifiers be located outside the tunnel to be shielded from ionizing radiation and accessible for maintenance.

CONCLUSION

The BPM experiments in the ReA3 facility have successfully demonstrated that high resolution for position and phase measurements with microampere beams can be achieved using button-type BPMs and 2nd harmonic signal processing. Scaling the ReA3 results to FRIB suggests a resolution 7 times better than the 100um at 100uAmp requirement. While work remains to assure this performance is achieved in the real FRIB accelerator environment, these tests provide a basis for proceeding with a FRIB BPM system design based on button-type pickups and a direct digital down conversion receiver.

REFERENCES

[1] J. Wei et al., “Progress towards the Facility for Rare Isotope Beams”, FRYBA3, NA-PAC'13 Proc.
[2] D. Leitner et al., “Status of the ReAccelerator Facility ReA for Rare Isotopes”, FRYBA4, NA-PAC'13 Proc.
[3] W. Wittmer et al., “Results from the Linac Commissioning of the Rare Isotope Reaccelerator - ReA”, MOPSM07, NA-PAC'13 Proc.
[4] N. Eddy et al., "High Resolution Bpm Upgrade for the ATF Damping Ring at KEK", DIPAC'11.
[5] B. Durickovic et al., “RF Cavity Phase Calibration using Electromagnetic Pickups”, THPHO14, NA-PAC'13 Proc.

Copyright © 2013 CC-BY-3.0 and by the respective authors

LIFETIME STUDY OF TUNGSTEN FILAMENTS IN AN H- SURFACE CONVERTER ION SOURCE*

I.N. Draganic#, J. F. O'Hara, and L. Rybarcyk, LANL, Los Alamos, NM 87545, USA

Abstract

The tungsten filaments are critical components that limit the lifetime of the H- surface converter ion source. Their finite lifetime has a huge impact on the maintenance schedules and overall availability of an accelerator facility. We present in this work a simple analytical filament lifetime model and 3D thermal simulation explaining basic phenomena of filament erosion and electrical resistance changes during a normal run of an H- production ion source at the Los Alamos Neutron Science Center (LANSCE). The calculation of filament longitudinal temperature profile takes into consideration the effects of ohmic heating, thermal conductivity and total emissivity for tungsten wires in high vacuum. The simulation includes the DC voltage operation of the filament with and without pulsed arc discharge current and gives the differential filament resistance changes, metal evaporation rates and theoretical electron emission currents. The results of the computation are compared with observed experimental data recorded using the EPICS control system during a normal LANSCE production cycle of 28 days with pulse repetition of 60 Hz and duty factor of 5%.

H- ION SOURCE LIFETIME

H- surface converter ion sources are well described elsewhere [1-4]. Three nearly-identical H- radial extraction converter ion sources (see Fig. 1A) have been utilized for proton beam production at LANSCE for more than 25 years. These H- sources deliver typical beam current up to 18 mA into an 80-kV electrostatic column and have operational lifetimes more than four weeks between accelerators maintains periods at a repetition rate of 60 Hz and duty factor of 5 %. Typical EPICS-recorded data of the extracted H- ion beams and an evolution of each filament's relative differential resistance during an entire cycle are presented in Figure 2. The negative-ion source consists of a filament driven arc discharge in a permanent-magnet, multi-cusp vacuum chamber for plasma confinement and a negatively biased converter electrode for H- beam production. The source uses two filaments made of high purity tungsten wires (99.99%), bent in a characteristic shape (see Figure 1B) with length of 297 mm, 1.6 mm thick diameter, weight of ~12 g and resistance of 7.8 mΩ at 295 K. Nominal filament currents of 100 to 106 A are driven by DC constant voltage power supplies (11 - 12V) bringing the wires to working temperature range of 2600 to 2700 K. The increase of filament temperature for higher electron output (plasma discharge) or more intense H- current is limited by the increasing of evaporation of filament material, which

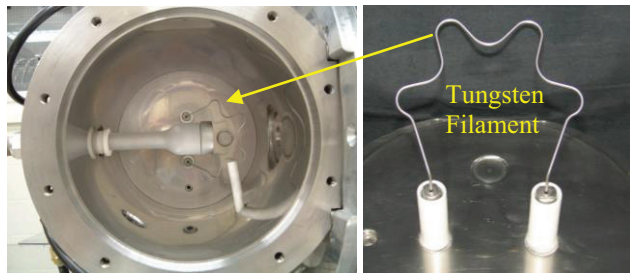


Figure 1: An internal side view of the LANSCE H- ion source is shown (A). New tungsten wire mounted on the water cooled ports (B).

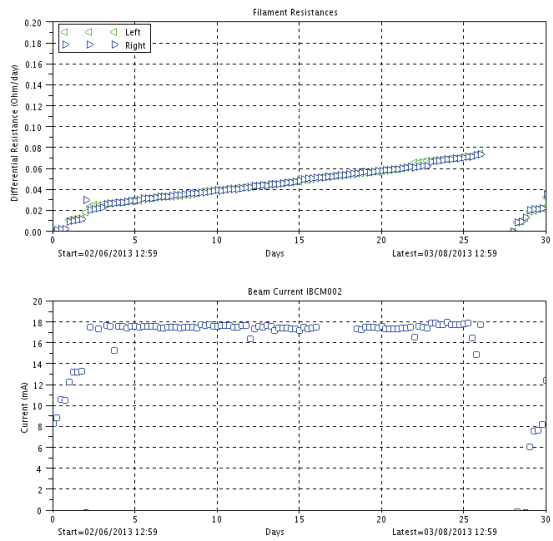


Figure 2: An EPICS application plots for operation monitoring purposes the filament relative differential resistances and the 80 keV extracted beam currents during a LANSCE beam production cycle (points every 6 hours).

decreases the lifetimes of the filaments, and ultimately limits the ion source operating period before replacement. The characteristics of tungsten filaments in vacuum at various high temperatures were studied in detail for incandescent lamps, radio tubes and in other scientific and engineering investigations [5-12]. There are two empirical criteria for critical differential resistance that predict the onset of filament failure: a) 12% of total increase in filament resistance or decrease in mass weight [5, 6] and b) 19 % of total increase in filament resistance or 10% of reduction in wire diameter [4, 8-12].

FILAMENT RELATIVE DIFFERENTIAL RESISTANCE

The LANSCE EPICS control system continuously records (a sample per minute) the filament currents and voltages, as well as the arc discharge peak currents and voltages. The filament resistances, based on U/I

*Work supported by the US Department of Energy under Contract Number DE-AC52-06NA25396

#draganic@lanl.gov

Copyright © 2013 CC-BY-3.0 and by the respective authors

measurements, change in the range from 100 to 115 mΩ (Figure 3A). The hot wire resistance increases over 140 times from the room temperature resistance. Differential resistance is calculated using a simple formula:

$$\frac{\Delta R}{R}=\frac{R_2-R_1}{R_1}=\frac{R_2}{R_1}-1=\frac{U_2 I_1}{U_1 I_2}-1 \quad (1)$$

where R_1 is the filament resistance at beginning of run (t_1=0) and R_2 is resistance recorded later during the cycle ($t_2 \neq t_1$). A characteristic relative differential resistance increase of 7.5% is shown in Figure 3B staying well below the 12% criteria. Digitized resistance data (40,000 points over 28 days) obtained using EPICS, enables easy data access and manipulation. The new filaments were weighed prior to installation and refurbishment to determine their mass, and later, after the production cycle and filament disassembly. The mass measurements are presented in Table 1. An average tungsten evaporation rate of 27 mg/day was observed. Measured relative mass changes were 2% less than the recorded differential resistances. Even after a correction for the inserted wire length into holder/ports, the discrepancy between mass and relative resistance measurements was considerable. Step-wise changes in both differential resistance graphs were observed during adjusting of the DC heating currents and source optimization. Systematic errors in differential resistances due to the long connection cables, shunts and voltage readings are being neglected.

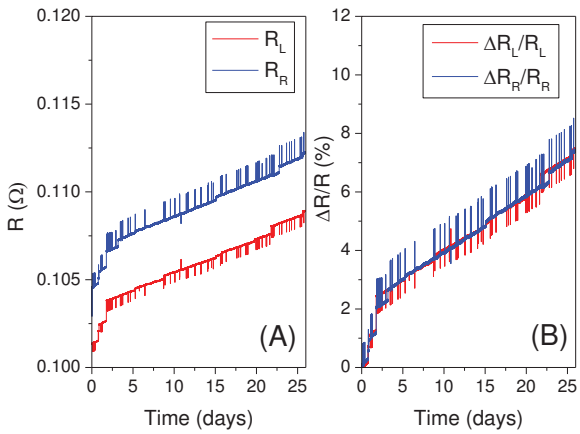


Figure 3: Characteristic filament resistances and relative differential resistances calculated using EPICS recorded U/I measurement data for both filaments.

Table 1: Mass Measurements and Recorded Differential Resistances from the EPICS Data are Listed. $\Delta M/\overset{*}{M}$ is a Length Corrected Evaporated Mass (k=1.072).

Filament	Left (#1)	Right (#1)
M1 (g) (before)	11.808	11.737
M1 (g) (after)	11.134	11.020
ΔM (g)	0.674	0.717
ΔM/M (%)	5.71	6.12
$\Delta M/M^*$ (%)	6.12	6.56
ΔR/R (%)	7.5	7.44

FILAMENT RESISTANCE MODEL

A simple analytical filament resistance model is needed to explain the wire erosion and recorded differential resistance behavior. The model has the following assumptions: a) an ideal wire is considered; it has a constant position/shape (no plastic deformation, sagging etc.), b) the filament temperature is constant across the wire length, c) thermal expansion is negligible, d) the mass evaporation is uniform over the wire surface and is a function of temperature, e) the total emissivity for tungsten wire varies only with temperature, f) the filament current is a sum of DC heating current and peak arc discharge current averaged by the duty factor, g) plasma sputtering is not taken into account, and h) microscopic effects like a recrystallization, grain growth, impurity content, electro-migration (Soret's effect) are not included [12]. The tungsten wire resistance is described using dimensional formula $R_i=\rho_i L_i/S_i$, for i=1(t_1=0), i=2 ($t_2 \neq t_1$); L and S are the wire length and cross section respectively. Because the filaments have very small thermal expansion differences ($L_1 \approx L_2$), equation (1) can be simplified:

$$\frac{\Delta R}{R}=\frac{\rho_1}{\rho_2}\frac{S_2}{S_1}\frac{L_1}{L_2}-1 \cong \frac{\rho_1}{\rho_2}\frac{S_2}{S_1}-1 \quad (2)$$

In our model, the specific electrical resistance is a linear function of temperature ($\rho_i=a+bT_i$). The time averaged mass evaporation is defined by the equation $\Gamma=\Delta M/A_e\Delta t$ or $\Gamma=(\rho_m L\Delta S)/(A_e\Delta t)$, where Γ(g/cm^3/s) is an evaporation rate [6. 11], A_e is the wire evaporation surface area, ΔM and Δt are evaporated mass and evaporation time, ΔS is a reduction in wire cross section and ρ_m is tungsten mass density (19.25 g/cm^3) [13]. Equation (2) can then be rewritten in the form:

$$\frac{\Delta R}{R}=\frac{b(T_2-T_1)}{\rho_1}+\frac{\Gamma(T_1)A_e\Delta t}{S_1\rho_m L}=\frac{b\Delta T}{\rho_1}+\frac{\Delta M}{M_1} \quad (3)$$

Equation (3) has two components. The first term takes into account material electrical characteristics and changes in filament temperature with filament current. This term represents "fast" processes and is independent of time, describes the tuning processes. The second term describes the "slow" processes including filament evaporation and steady state changes in filament mass and cross section. This time dependent term is a useful monitoring tool for the filament and source lifetime.

The filament temperature in our model is determined from the graphs presented in Ref. [6]. The temperature is defined by the heating current though filament, I, and the wire diameter d. For our model, we have created a two dimension polynomial fit to the data [6]: (surface function $T(K)=A_0+A_1 d+A_2 I+A_3 d^2+A_4 I^2+A_5 Id$).

The filament resistance model was applied to simulate the experimentally recoded data in Figure 2. Using estimated wire diameter after processing of H-source and recording total current for the left filament, calculation of the temperature was possible. Results of mass losses integrated over the run cycle and ΔR/R step changes are presented in Figure 4 and Table 2 showing a reasonable agreement with recorded data.

Copyright © 2013 CC-BY-3.0 and by the respective authors

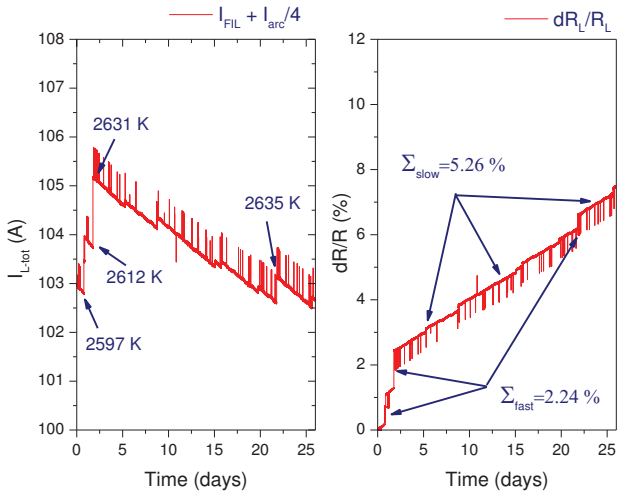


Figure 4: (A) Measured total left-filament current as a function of days during the run cycle. Also shown are associated changes in wire temperature after each source adjustment. (B) Measured left-filament differential resistance. Percent changes in differential resistances due "fast" and "slow" processes are shown.

Table 2: Measured Left Filament Differential Resistance Compared with Filament Model Calculation

Filament	Total (%)	Fast (%)	Slow (%)
EPICS data	7.50	2.24	5.26
Model	7.11	1.76	5.35

THERMAL FINITE ELEMENT ANALYSIS

A thermal finite element analysis was also performed to determine a steady state temperature profile. A 3D model of the tungsten filament was created. Included in the filament thermal simulations are the tungsten physical properties, ohmic heating, thermal conductivity and thermal emissivity in high vacuum [13]. A constant heating current of 103.5 A is applied to the filament. Arc current ranging from 0.75 A to zero is assumed to be decreasing linearly from one end of the filament to the other (discretized in 10 steps). Radiation and temperature boundary conditions across all wire segments are applied for 294 K at each end (due to water cooling loops). The total emissivity varies as a function of wire segment temperature. A peak filament temperature of 2684 K was calculated. The peak temperature moves from the center of the filament towards the higher-arc-current side (Fig. 5A). As the filament evaporates in a localized area close to the peak temperature location, the cross section of the filament decreases in that area. This decrease in cross sectional area causes an increase in resistance, which results in an even higher temperature for the same applied currents. This creates a runaway situation of decreasing wire cross section, increasing temperature and high evaporation rate that leads to creation of a localized hot spot that can cause catastrophic failure of the filament [7]. This typical filament failure mode is shown in Figure 5B.

We propose changing the polarity of the DC filament and arc voltages at least once per week in order to avoid hot spots created by this asymmetric ohmic heating.

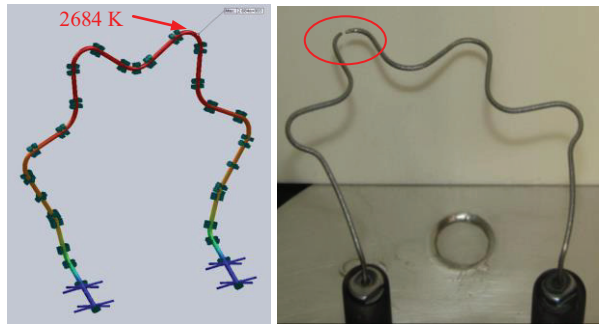


Figure 5: (A) 3D model of source filament and calculated temperature profile with the maximum-temperature location shown. (B) Photo showing a filament with a typical hot spot - breaking point failure.

ACKNOWLEDGEMENT

The authors are thankful to Jerry Paul and Nathan Okamoto for the filament mass measurements, production source processing stand data and source photos.

REFERENCES

[1] Bernhard Wolf, "Handbook of Ion Sources" (1995).
[2] Ian G. Brown, "The Physics and Technology of Ion Source" (2004).
[3] J. Sherman, et al. " Physical Insights and Test Stand Results for the LANSCE H^- Surface Converter Source", AIP Conf. Proc. **763**, AIP, Melville, NY, p.254 (2005).
[4] R. Keller, et al. "H^- Ion Source Development for the LANSCE Accelerator Systems", AIP Con. Proc. **1097**, AIP, Melville, NY, p. 161 (2009).
[5] G. Rouleau et al. "Tungsten Filament material and Cs dynamic equilibrium effects on a surface convertor ion source" Rev. Sci. Instrum. **79,** 02A514 (2008).
[6] M. Ardenne "Tabellen zur Angewandten Physik" (1963, Berlin) Band I and II.
[7] E. Chacon- Golcher, "Erosion and Failure of Tungsten Filament", LA-UR-08-5251 (2008).
[8] J. Röhrlich, et.al. "A Tandetron as proton injector for the eye tumor therapy in Beriln" Rev. Sci. Instrum. **83,** 02B903 (2012).
[9] A. Wilson, "Tungsten filament lifetime under constant-current heating", J. App. Phys, **40**, 1956, (1969).
[10] R. N. Bloomer, "High temperature properties of tungsten which influence filament temperatures, lives and thermionic-emission densities" Proc. IEEE, **B104**, 157, (1957).
[11] H.A. Jones and I. Langmuir, "The characteristics of Tungsten Filaments as Function of Temperature" General Electric Review, **30**, part I p 310, part II p 354, part III p408, (1927).
[12] R.P. Johnson, "Construction of Filament Surfaces", Phys. Rev., **54,** (1938) p459.
[13] "American Society of Materials - Metals Handbook" Edit by R. L. Stedfeld (1990) Vol. 2.

Copyright © 2013 CC-BY-3.0 and by the respective authors

PIN DIODE DETECTORS AT DARHT II*

Jeffrey B. Johnson, LANL, Los Alamos, NM 87544, USA

Abstract

PIN diode detectors are a useful diagnostic tool for accelerator operations. The DARHT Axis II electron beam accelerator utilizes an array of twelve PIN diodes to detect the location of high voltage column electron emissions during abnormal injector events. The PIN diodes are located outside the injector vacuum vessel and detect the x-rays that are produced when the -2 MeV column electrons strike the vacuum vessel wall. This paper describes the PIN diode selection, calibration and use on the accelerator.

INTRODUCTION

An array of twelve PIN diode detectors is used on the DARHT Axis II accelerator injector to monitor for abnormal high voltage events. The injector consists of a Marx bank pulse generator, high voltage column, thermionic cathode and a vacuum vessel as shown in Figure 1.

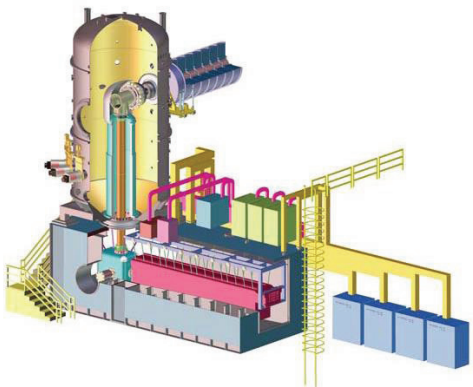


Figure 1: DARHT Axis II Injector.

During operation of the injector, abnormal events may occur. These include explosive electron emissions from the cathode and injector voltage droops from high voltage breakdowns of the cathode region or column. To help identify the precise location of such events, a PIN diode detector system was developed and installed on the injector. The PIN diodes detect the Bremsstrahlung radiation created when high energy electrons emitted during an abnormal event intercept the vacuum vessel wall. The array of twelve detectors is evenly spaced around the outside of the vacuum vessel.

PIN DIODE SELECTION

The sensitivity required for the PIN diodes was determined experimentally. A PIN diode detector assembly made by Emerge Semiconductors (100-PIN-250-HN-BG) was initially used as a single channel monitor for abnormal events. Data collected during a few abnormal events showed that this diode had the appropriate sensitivity to make the measurements. Unfortunately, the Emerge PIN diode assemblies are no longer available. An equivalent PIN diode assembly needed to be identified or built in order to construct the detector array. A market survey was conducted for a silicon PIN diode assembly similar to the Emerge detector and none could be found. This lead to the development a LANL designed detector assembly which uses a low cost commercial PIN diode chip and a custom made housing shown in Figure 2. The PIN diode chip selected was the OSI Optoelectronics PIN-RD-100. This chip has similar geometry (area and Si depth) compared to the Emerge diode. A steel housing was designed to hold the chip and provide some degree of collimation and shielding.

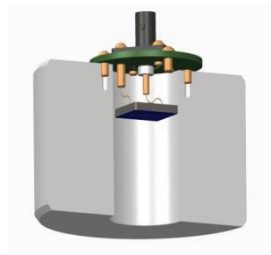


Figure 2: LANL PIN diode assembly.

CALIBRATION

The LANL PIN Diode detector assembly was calibrated against the Emerge detector using the DARHT Axis II accelerator Beam Clean up Zone (BCUZ) [1] as a radiation source. The BCUZ, shown in Figure 3, is an energy filter which absorbs beam energies below 3 MeV which occur during the rising and falling edges of the accelerator beam pulse.

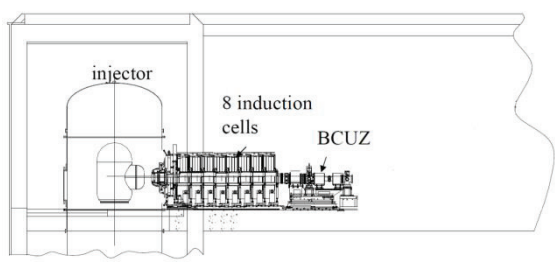


Figure 3: BCUZ region used for calibration.

The absorbed energy creates a pulse of broad band X-rays for the calibration. The central portion of the signal from the rising edge was used for the calibration. During calibration, the detectors were placed downstream from and just above the BCUZ. Detector reverse bias voltages

*Work supported by the U.S. Department of Energy under contract DE-AC52-06NA25396
johnsojb@lanl.gov

Copyright © 2013 CC-BY-3.0 and by the respective authors

were 1000 volts for the Emerge detector and 100 volts for the LANL detector. Calibration data in Figure 4 shows that the LANL detectors are more sensitive to the middle of the calibration pulse than the Emerge detector. The LANL detector response is not as fast due to the lower reverse bias voltage [2]. The sensitivity for the LANL detectors is 1.53×10^{-7} A/(R/s) for the lower dose rates from the BCUZ X-ray source.

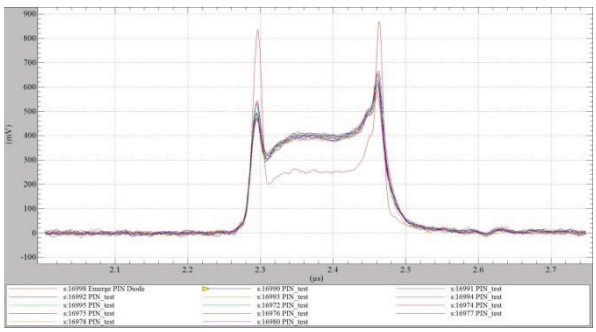


Figure 4: Calibration waveforms.

SYSTEM OPERATION

The PIN diode detectors must be operated with a reverse bias voltage applied across the P-I-N junction. To achieve this, a DC power supply is connected to the detector cable using a LANL designed bias tee as shown in Figure 5.

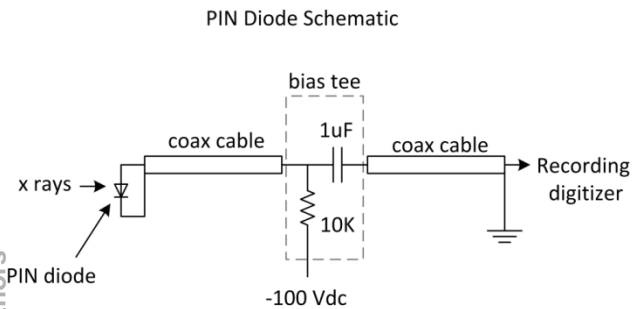


Figure 5: PIN diode schematic.

The bias tee can operate to 1000 VDC and has 1 microfarad of coupling capacitance. The large coupling capacitance provides extended low frequency response for slower signals produced during slower changing X-ray fluxes. There is one bias tee for each detector. A single DC power supply provides the bias voltage for all twelve detectors through a simple fan-out box. The detectors are operated with a 100 VDC reverse bias at DARHT to eliminate the electrical hazards associated with operation at greater voltage levels. Each detector output signal is recorded on its own high speed digitizer channel each time the injector is fired. The PIN diodes I layer is completely depleted at 80 volts reverse bias and the sensitivity will remain constant at any reverse bias greater than 80 volts as long as the output voltage stays less than half of the bias voltage. Increasing the reverse bias voltage increases the time response of the PIN diode.

RESULTS

On 9/25/2012, (shot 19274) an abnormal event occurred while operating the injector. The injector voltage pulse displayed a droop as shown in Figure 6. This occurred after the vacuum environment of cathode was accidently compromised which may have degraded the cathode surface leading to explosive electron emissions during pulsing. When this happens, it is likely that some of the emitted electrons do not enter the accelerator beam tube and instead impact the vacuum vessel wall.

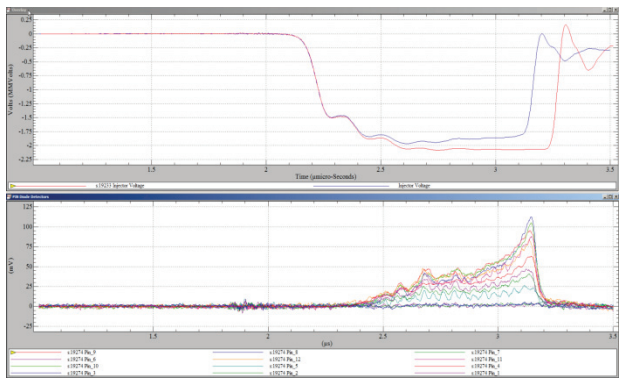


Figure 6: Injector voltage waveforms. Top waveform showing normal (red) and droop (blue) conditions. Bottom waveform shows PIN diode signals recorded during injector voltage droop.

A circular plot of the peak PIN diode signals shown in Figure 7 provides azimuthal information as to where electron emissions occurred inside the vacuum vessel.

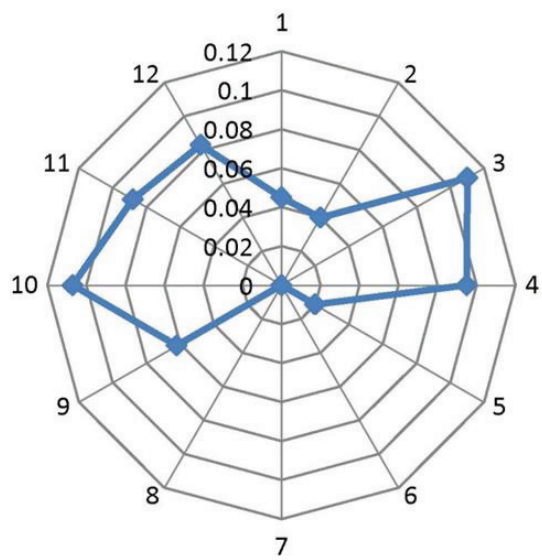


Figure 7: Circular plot of peak PIN diode signals during an abnormal injector event.

Copyright © 2013 CC-BY-3.0 and by the respective authors

CONCLUSIONS

A comparison of the PIN diode signal intensity shows that the LANL detectors are able to identify where electron emissions occur inside the vacuum vessel. The time response of detectors is limited by the low reverse bias voltage used with the system, but is adequate for the X-ray dose rates generated during abnormal injector events.

ACKNOWLEDGMENT

I would like to acknowledge C.Y. Tom of NS Tec for helping with the data collection during the calibration of the detectors.

REFERENCES

[1] C. Ekdahl, "Initial Electron-Beam Results From the DARHT-II Linear Induction Accelerator," IEEE Transactions on Plasma Science 33(2), (2005), 892.

[2] Robin L. Owen et al., "Determination of X-ray flux using silicon pin diodes," Journal of Synchrotron Radiation 16(pt2), (2009) 143.

Copyright © 2013 CC-BY-3.0 and by the respective authors

LANSCE-RM WIRE SCANNERS: SLIP-ENCODED SERIAL COMMUNICATION FOR MAINTENANCE DISPLAY AT THE INSTRUMENT*

J. Sedillo, J.D. Gilpatrick, LANL, Los Alamos 87545, USA

Abstract

The newest LANSCE-RM wire scanner control systems at Los Alamos National Laboratory's LANSCE particle accelerator facility utilize touch-panel displays for limited status and control at the instrument. Since the wire scanner control hardware utilizes a National Instruments CompactRIO embedded controller, no display may be interfaced to the CompactRIO via conventional means. Thus, in order to display information from the CompactRIO, a touch-panel display and computer combo unit has been added to each wire scanner control chassis with information being exchanged via a common, RS-232 interface. This paper describes the maintenance features available at the touch screen and the underlying SLIP communication scheme used for simple packetized transfer of data between the touch-panel display and the CompactRIO.

INTRODUCTION

The control system outlined in figure 1 represents the solution developed by LANSCE staff for wire scanner actuator control and data acquisition [1]. Among its assortment of features is the control system's chassis-mounted, touch-panel PC (TPC) for localized control and diagnostics of the wire scanner system.

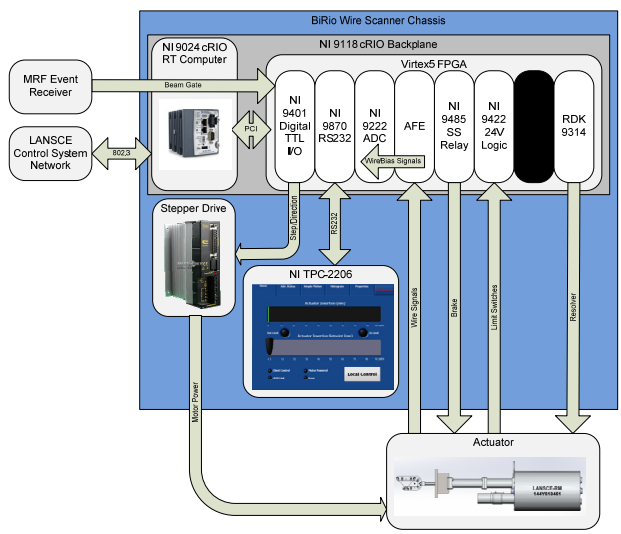


Figure 1: LANSCE-RM Wire Scanner Controller.

Although the touch panel PC offers a variety of high-bitrate interfaces (e.g. Ethernet and USB), the touch panel's RS-232, null-modem interface was chosen due to its ease of use and its common and direct interface to the compactRIO (cRIO) controller's FPGA (via the FPGA's NI 9870 RS-232 c-series module).

*Work supported by the U.S. Department of Energy.

MOTIVATION

RS-232 null-modem links offer a great deal of flexibility with how data is communicated since the hardware does not inherently provide the means to organize data meaningfully other than its FIFO approach. If context of the data may be derived from each individual byte communicated, then no expanded form of data encapsulation may be necessary. However, for more common situations where the data varies in content (e.g. varying data structures) and size (the size of the data structure in bytes), the implementation of a data encapsulation scheme will assist the receiver with making a clear determination of data boundaries by placing the data in "packets".

Data encapsulation schemes are fundamental to many familiar hardware communication systems, the most prevalent of which is 802.3 ethernet. Common encapsulation schemes leveraged on 802.3 networks include the familiar IP, TCP, UDP, etc. Given the successful standardization and implementation of these protocols, almost any one of them may be utilized for serial links implemented on hardware other than 802.3, depending on the application. Since the wire scanner's cRIO transmits a variety of data structures to the TPC and since the data can arrive in an unpredictable order, a data encapsulation method was required to assist both the TPC and cRIO to 1: understand the where a packetized data structure begins and ends, and 2: to determine how to direct the data to the proper methods for processing.

SLIP

IETF de-facto standard RFC1055, otherwise known as SLIP, was deemed the most suitable protocol for data encapsulation [3]. SLIP is an acronym for Serial-Line Internet Protocol and is a data-link layer protocol in the OSI conceptual model. SLIP was developed as a simple means of transmitting TCP/IP datagrams over serial lines when no standard yet existed and has since been replaced by PPP (Point-to-Point Protocol, RFC1661) in most applications. SLIP focuses only on packet framing, and therefore does not inherently provide a means for addressing, packet type identification, error detection/correction, or compression [2].

SLIP's simplicity made it an attractive choice for this application since encoding and decoding methods of more complex protocols would have been needlessly difficult to develop for the cRIO FPGA. Furthermore, the limitations of the SLIP protocol were of little concern since the wire scanner controller can operate without proper operation the TPC; and because the414-6541 link was short (<1 ft),

Copyright © 2013 CC-BY-3.0 and by the respective authors

low-speed (56kbps), and directly linked. These qualities ensure low probability of data corruption.

SLIP Encoding

The SLIP encoding method is generally simple to implement. Given a data structure that has been flattened into a 1-D array of bytes, the SLIP encoding method simply appends hexadecimal byte 0xC0 to the beginning and end of the array. These bytes encapsulate the data and form the boundaries of the SLIP packet (figure 2).

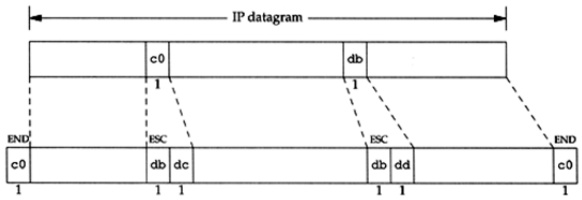


Figure 2: Slip packet layout [3].

If the 1-D array of data contains the value 0xC0, that value is replaced by 0xDBDC (two bytes). If 0xDB is encountered, it is replaced by 0xDBDD (two bytes). Through this method, special SLIP encapsulation characters and data cannot be mistaken by the SLIP decoder.

SLIP Decoding

SLIP decoding is slightly more complicated than encoding. In the ideal case, 0xC0 is the first byte a SLIP decoder encounters upon first receipt of SLIP-encoded serial data. The decoder must simply accumulate the bytes after the 0xC0 header until encountering 0xC0 again. In the not uncommon circumstance where the SLIP encoder utilized special byte patterns 0xDBDC and 0xDBDD, the SLIP decoder will replace 0xDBDC by 0xC0, and 0xDBDD by 0xDB. The data enclosed with the 0xC0 characters may then be passed to other routines for its appropriate use. In the event that a receiving system comes online after data transmission has progressed, the receiving system will simply disregard all data received until it encounters the next SLIP packet's 0xC0 header.

UTILIZATION

After implementing the SLIP encoding and decoding methods for the cRIO and TPC, a custom data encapsulation scheme was developed for incorporation within the SLIP packets. This was necessary to overcome SLIP's lack of a provision for identifying packet types.

Tag Length (1 byte)	Payload Length (2 bytes)	Tag (1-255 bytes)	Payload (1-65,535 bytes)

Figure 3: Custom packet structure.

The custom packet (Figure 3) specifies a 3-byte header and a variable-length payload. The first header byte represents a tag length in bytes. The remaining two header bytes represent the data payload length in bytes. The header is then followed by the tag and the data payload. The tag allows the receiving system to identify the data packet and direct its contents to the correct methods for proper use.

Three communication channels operate within the single, RS-232 link between the cRIO and TPC. The operational flow is shown in figure 4 and described in the sections that follow.

CompactRIO FPGA to TPC Channel

The wire scanner's CompactRIO FPGA sends wire scanner status information to the TPC. This status information includes: actuator position, limit status, sense wire continuity, remote operation status, the general error condition, network ID, beam gate, FPGA state, and the cRIO C-series module status.

The cRIO FPGA accumulates the data from its internal processes, encapsulates the data within "custom" packets with unique tags representative of the data, and then directs the custom packets through a SLIP encoding process. The SLIP packets that result are then directed to the RS-232 FIFO for transmission to the TPC. The FPGA has the least flexibility with regard to packet size since arrays dedicated to the transmission and reception of the packets must be of a fixed size prior to FPGA compilation. The corollary to this is that all packets transmitted to the FPGA from external systems must also fit within the FPGA's array size constraints.

TPC to CompactRIO FPGA Channel

The TPC sends commands to the cRIO FPGA for minimal control of the wire scanner actuator. Command information includes the actuator position setpoint and actuator operational envelope scan. These data allow for some localized control of the wire scanner actuator mechanism.

Data transmitted from the TPC to the cRIO FPGA occurs in a similar way to the "CompactRIO FPGA to TPC Channel" process. Although the TPC can dynamically allocate memory for substantially large SLIP packets, the size of the packets it transmits are of a size that are compatible with the maximum allocated array size of the cRIO FPGA's receive array.

CompactRIO RT to Touch Panel PC Channel

The cRIO RT system sends wire scanner configuration data to the TPC through the cRIO FPGA's RS-232 link. Configuration data includes:

- Actuator configuration: leadscrew pitch, stepper motor resolution, sense wire center positions, and mount angle.
- Motion control configuration: closed-loop control constants, position deadband, and stepper motor settings.
- Beam data acquisition configuration: AFE (Analog Front End) transimpedance values, ADC sampling rate, pre and post trigger samples, and macropulse waveform cumulative average count.

Copyright © 2013 CC-BY-3.0 and by the respective authors

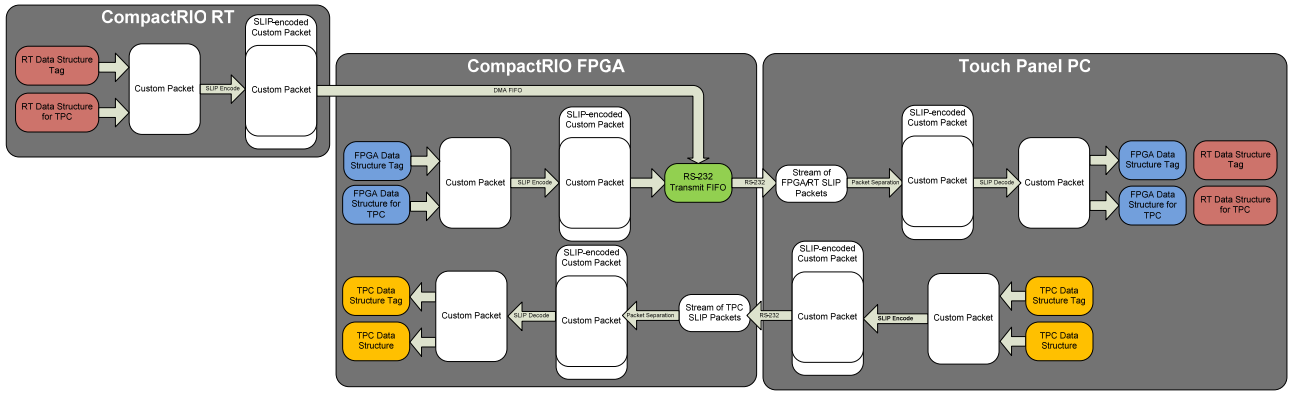


Figure 4: Overview of cRIO/TPC Communication flow.

The relatively large amount of data transmitted by the cRIO RT system to the TPC made it essential that data packets produced by the cRIO RT avoid the cRIO FPGA's bottlenecks. To do this, the cRIO RT encodes its data before transmitting the resulting data stream to a DMA FIFO read by the FPGA. Once the FPGA has completed sending its own packet stream to the TPC, it checks the DMA FIFO for data content. If data exists, the FPGA simply directs the data directly into the RS-232 FIFO for transmission to the TPC.

IMPROVEMENTS

SLIP is simply one of many methods for data encapsulation over serial streams. Again, SLIP does not inherently provide a means for addressing, packet type identification, error detection/correction, or compression. This work has compensated for SLIP's lack of packet type identification and required minimal error correction since a high-fidelity data link was utilized. More demanding applications may require more features from a SLIP implementation. In such cases, other protocols that possess the necessary features may be encapsulated within the SLIP packet or used outright, depending on the protocol and its compatibility with the application.

LANSCE-RM WIRE SCANNER PROJECT UPDATE

Six new LANSCE-RM wire scanner systems have been deployed throughout the LANSCE facility: two in the 201 DTL, Three in the 805 linac, and one in the switchyard. Integration of these systems is complete with all systems fully utilizable by LANSCE's central control room. Figure 5 shows a beam profile obtained by one of the wire scanners deployed in the 805 linac. Additional systems are planned for installation as resources become available.

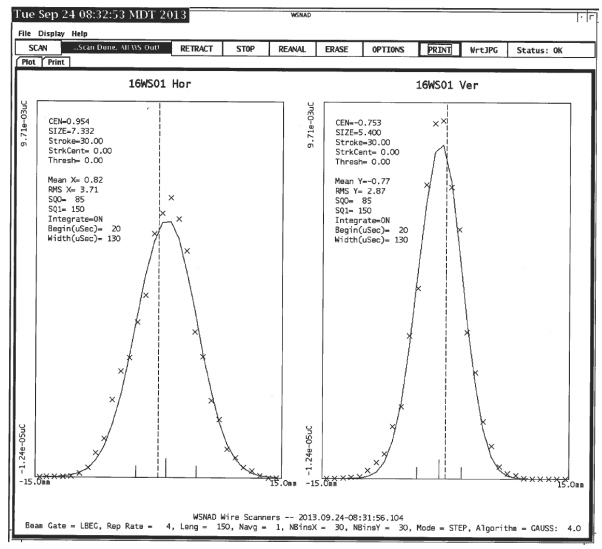


Figure 5: LANSCE Control Room view of wire scanner-acquired beam profiles.

REFERENCES

[1] J. Sedillo, et al. "First Test Results of the New LANSCE Wire Scanner." PAC '11, New York, March 2011 MOP236; http://www.JACoW.org

[2] J. Romkey, "A Nonstandard for Transmission of IP Datagrams Over Serial Lines: SLIP," RFC1055, http://www.ietf.org/rfc/rfc1055.txt

[3] http://recolog.blogspot.com/2012/10/serial-line-internet-protocol-slip.html

Copyright © 2013 CC-BY-3.0 and by the respective authors

ANALOG FRONT END DESIGN FOR HIGH SPEED DIGITIZING OF BEAM POSITION AND PHASE MEASUREMENTS AT LANSCE*

H. Watkins#, J.D. Gilpatrick, R. McCrady, LANL, Los Alamos, NM 87544, USA

Abstract

The Los Alamos Neutron Science Center (LANSCE) is currently developing beam position and phase measurements for its 805-MHz linac as part of the LANSCE risk mitigation project. Beam position and phase monitors (BPPMs) with four shorted strip lines have been installed throughout the linac. The BPPM electronics will sample each strip line at 240 MSPS and use a field programmable gate array (FPGA) to calculate position and phase of the beam relative to the linac reference. The beam micro-pulses from each electrode must be filtered and amplified to provide the correct frequency and amplitude level to the digitizer. This paper describes the signal conditioning required to interface LANSCE BPPMs to high speed digitizers, the diagnostic capabilities of the analog front end (AFE) module, digital control of the AFE module and design considerations to meet these objectives.

INTRODUCTION

Today's analog to digital converters (ADCs) are supporting higher sample rates and signal bandwidths allowing for direct sampling of RF signals that once required analog down conversion. The TI ADS62P49 14-bit ADC is being used at LANSCE to sample beam position and phase monitor (BPPM) signals. These signals are down converted digitally in a field programmable gate array (FPGA) to in-phase and quadrature-phase (I & Q) signals that are used to calculate position and phase of the beam centroid.

To take advantage of high speed digitizing and digital down conversion the micro-pulses from the BPPM's must be conditioned in frequency and amplitude to match the input range of the ADC. The analog front end (AFE) module was designed to interface between the BPPM and the digitizer to provide optimal signals for position and phase measurements.

This BPPM system is being developed as a replacement for LANSCE's legacy Δt system used for phase and amplitude adjustment of RF accelerating fields in the 805-MHz linac with the addition of measuring transverse beam position [1].

ARCHITECTURE

The hardware architecture for the system includes a 4-port BPPM, an AFE module, a 5-channel digitizer module and a Stratix 4 FPGA carrier board shown in Figure 1. The electronics system is housed in a VPX chassis that conforms to the ANSI/VITA 46.0-2007 standard [2].

The AFE module's printed circuit board design will conform to the VPX standard for size and backplane connections. Its power and control signals will come through the VPX backplane from the FPGA.

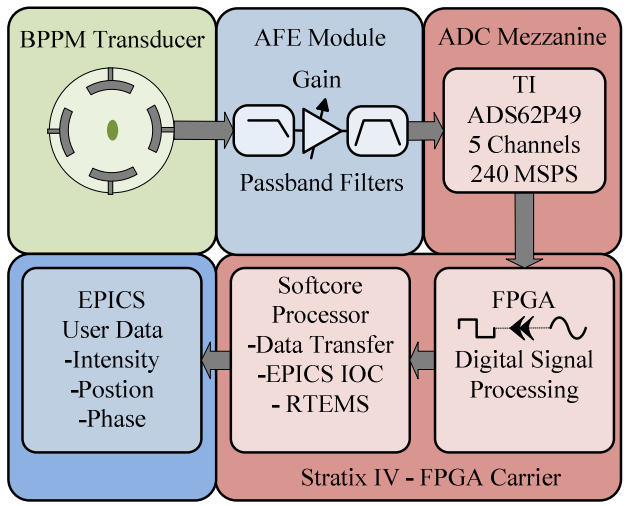


Figure 1: System Diagram

AFE DESIGN REQUIREMENTS

The following lists the design requirements for the AFE module to interface to the ADC. [1]

- Filter the micro-pulse signal to a fundamental frequency of 201.25MHz for sampling by the ADC while preserving pulse information.
- Increase the signal amplitude to match the dynamic range of the ADC without exceeding the 2Vp-p full scale range of the ADC.
- Provide a method of self calibration and signal integrity checks without beam present.
- Protect the digitizer from overdrive events.
- Provide conditioning for single micro-pulse position measurements.
- Provide remote control of the AFE gain and switching.

SIGNAL CONDITIONING

The AFE is designed to provide the filtering and gain to convert a micro-pulse from the BPPM to a sine wave that can be sampled by the ADC and analyzed by the FPGA.

Selectivity and Filtering

The beam doublets produced by the BPPM transducers are narrow micro-pulses occurring at the fundamental accelerating frequency (201.25MHz) with a pulse width of approximately one nanosecond. The ADC can only sample every four nanoseconds so the bandwidth of the pulse must be limited to provide a signal slow enough for the ADC to capture frequency and phase information.

*Work supported by the U.S. Department of Energy
#hwatkins@lanl.gov

Copyright © 2013 CC-BY-3.0 and by the respective authors

Harmonic amplitudes from the transducer can be equal or above the amplitude of the fundamental frequency and will cause interference with position and phase measurements. Figure 2 shows how the AFE module filters out higher order harmonics of the beam doublet and passes the fundamental frequency.

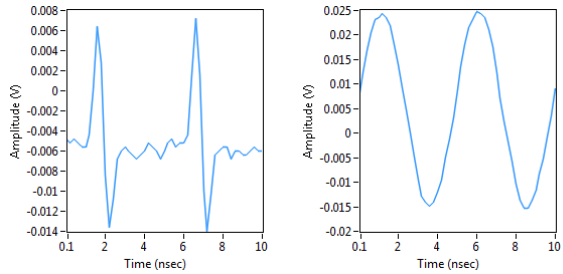


Figure 2: Transducer output and conditioned AFE signal

The harmonic selectivity requirement for the AFE is based on the ADC's spurious free dynamic range (SFDR) performance. The ADC's SFDR specification of -71dBFS [3] requires the AFE to provide rejection at least 10dB better (-81dB) at the harmonic frequencies.

The selectivity is provided by two filter stages in the AFE line-up. A low pass 5th order elliptical is used at the beginning of the line-up and a 3rd order band pass filter is used at the end to achieve the required selectivity.

The corner frequencies of the band-pass filter pass a 30MHz channel bandwidth. This channel bandwidth was selected based on the timing modulation of the beam. It is desirable for the system to analyze mini-pulses, short bursts of pulses (100nsec), at a 2.8MHz burst repetition rate. The bandwidth is intentionally larger than the repetition rate (10x) to maintain the pulse envelope for edge detection by the digital signal processor (DSP).

The low frequency corner of the band pass filter provides rejection of low frequency modulation components that occur from sources such as AC mains.

Gain and Noise

Due to space constraints in the accelerator, the BPPM transducers are shorter than a quarter wavelength of the fundamental frequency which results in reduced RF signal coupling. Two gain stages are added in the RF line-up to overcome losses from coupling, cabling and filtering.

The systems dynamic range requirement is 65dB minimum to provide optimal signal levels to the ADC over all beam conditions. This includes current settings, beam position, phase de-bunching and noise performance.

Measurements were done on BPPM's in the beam line to determine amplitude levels and a link budget analysis was performed to set the gain and noise figure of the line-up to levels that met the dynamic range requirement without exceeding the input range of the ADC. Table 1 shows the summary of the analysis.

Table 1: Link Budget Summary

RF Parameter	Link Budget	Requirement
Gain (dB)	20.2	20 typical
Noise Figure (dB)	11.8	23 maximum
Input Referred Noise (dBm)	-87.3	-76 maximum
Dynamic Range (dBFS)	77.1	65 minimum

The gain setting of the AFE is adjustable. Two fixed RF gain stages surround a digital step attenuator (DSA) which has 31dB of range in 1dB steps. A typical attenuator setting is 7dB to reach the typical gain setting but adjustment can be made to compensate for cable loss at different locations along the accelerator. The attenuator is digitally controlled by the FPGA. Support for automatic gain control by the FPGA is a future option.

SELF-DIAGNOSTIC

To support a method of self calibration and signal integrity checks the AFE module includes a switch matrix near the input connectors. The switch matrix allows the 201.25MHz reference to be injected upstream to the transducer or downstream through the AFE module for all four channels of the AFE. Figure 3 shows how the system can be tested in loopback mode for basic signal integrity or calibration mode to measure offsets in gain or phase internal to the AFE.

The switches selected are high-isolation terminated switches so the reference signal will not interfere with the desired signal during normal operation.

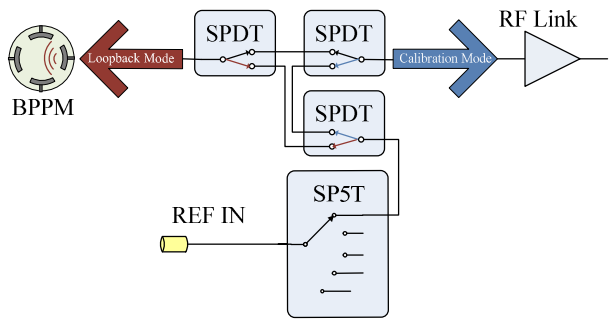


Figure 3: Single Channel Switch Matrix

Loopback mode

Injecting signals upstream of the AFE allows for loopback mode testing. This mode is intended for use when no beam is present. The reference signal can be injected from one channel of the AFE upstream to the transducer. Coupling occurs to the adjacent and opposite transducers in the BPPM. The coupled signal can then be analyzed by the three other channels of the AFE.

This mode allows the full system to be exercised. Problems with a particular signal path can be discovered by rotating the injection signal through all four paths of the BPPM. Imbalances in the signal paths can be analyzed and corrections applied to individual channels.

Copyright © 2013 CC-BY-3.0 and by the respective authors

Calibration Mode

Injecting signals downstream through the AFE line-up enables calibration mode. In this mode the AFE has injection points that are phase matched at the input to each channel. The 201.25MHz reference is switched into the AFE input and analyzed by the FPGA. This mode shows the amplitude and phase differences between each of the four RF line-ups. Corrections can be made in the FPGA to improve the phase and amplitude offsets of the AFE signal paths.

OVERDRIVE PROTECTION

It is desirable to operate the ADC to within 1dB of full scale to maximize dynamic range without clipping the ADC. However, the flexibility of having remote gain control also poses an overdrive hazard when transducer signals are at high amplitudes. The maximum voltage level specification for the ADC is 3.6V or +15dBm rms [3].

The ADC is protected from overdrive events by a limiter diode placed prior to the output connector. This diode forward conducts when a power level of +10dBm is reached. This clip point keeps the ADC from receiving power levels that would exceed full scale operation.

SINGLE PULSE MEASUREMENTS

Certain target areas at LANSCE receive very short beam pulses called micro-pulses (~1 nanosecond). These micro-pulses occur as single pulses during a machine cycle and repeat at slow repetition rates. One of the BPPM requirements is to make transverse position measurements of these pulses. The signal must be transformed into a waveform that can be passed by the AFE to the digitizer.

A set of RF switches in the line-up provide the ability to change from a low pass filter at the front of the AFE to a narrow band filter (5 MHz). The pulse energy rings this narrow filter at its resonant frequency creating a sine wave within the channel bandwidth of the AFE as shown in Figure 4. This signal is passed through the RF lineup to the digitizer and analyzed by the FPGA to calculate beam position of the micro-pulse. Narrow band filter technologies such a surface acoustical wave (SAW) and lumped element filters are being evaluated for this application.

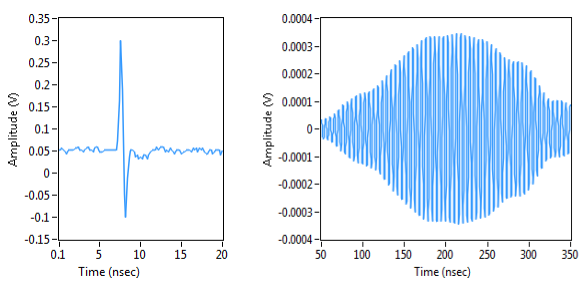


Figure 4: Single pulse to sine wave conversion

Measurements show that a trade-off exists between pulse length and amplitude level. Filters that ring for 200 nanoseconds have very small voltage level afterwards < 1 mV p-p. This low signal level will cause precision errors of up to 0.5mm for position measurements.

DIGITAL CONTROL

The AFE module has forty three digital control pins for selection of filters, gain and self diagnostic modes. The FPGA carrier card can only support eight lines of digital I/O since the majority of pins are assigned to the ADC channels. These control lines remain static the majority of the time making timing requirements fairly relaxed. In order to support the AFE module remotely through the FPGA a serial parallel interface (SPI) bus is used. The SPI bus requires four lines of communication (chip select, data in, data out and clock).

The SPI interface on the FPGA is connected to a general purpose I/O (GPIO) expander on the AFE module. Two GPIO expanders are used on the AFE module each supporting 28 pins of I/O. GPIO expanders can share data lines and clock but the chip select lines are separate to send instructions to each chip. This results in five digital control lines needed on the FPGA to support digital control of the AFE module.

CONCLUSION

The design phase is complete for the AFE module. Schematics have been created and the layout work for the printed circuit board is in process.

A two channel version of the system has been prototyped with evaluation boards so that the FPGA's DSP code could be evaluated. Final evaluation of the system and deployment are scheduled for 2014.

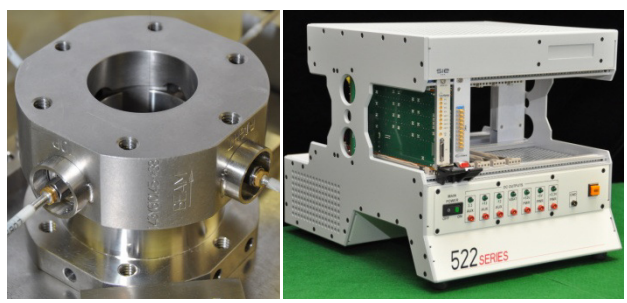


Figure 5: BPPM and VPX System

REFERENCES

[1] R. McCrady. "Requirements for measurements of beam position and phase in the LANSCE risk mitigation project" Private Communications, Sept. 2013.

[2] VITA, "VPX: Base Standard", *VITA*, ANSI/VITA 46.0-2007(R2013), 2007, Revised 2013.

[3] Texas Instruments, "Dual Channel 14-/12-Bit, 250-/210-MSPS ADC With DDR LVDS and Parallel CMOS Outputs", ADS62P49 datasheet, Apr. 2009 [Revised Jan. 2011].

Copyright © 2013 CC-BY-3.0 and by the respective authors

FABRICATION AND VALIDATION OF A NORMAL CONDUCTING RADIO FREQUENCY S-BAND DEFLECTING CAVITY FOR THE POHANG ACCELERATOR LABORATORY (PAL)

L. Faillace#, R. Agustsson, J. Hartzell, A. Murokh, S. Storms
RadiaBeam Technologies, 1717 Stewart St, Santa Monica CA, USA

Abstract

Radiabeam Technologies recently developed an S-Band normal-conducting Radio-Frequency (NCRF) deflecting cavity for the Pohang Accelerator Laboratory (PAL) in order to perform longitudinal characterization of the sub-picosecond ultra-relativistic electron beams. The device is optimized for the 135 MeV electron beam parameters. The 1m-long PAL deflector is designed to operate at 2.856 GHz and features short filling time and femtosecond resolution. RF design, fabrication, RF validation and tuning will be presented, as well as initial beam measurements.

INTRODUCTION

Some of the most compelling and demanding applications in high-energy electron beam-based physics, such as linear colliders [1], X-ray free-electron lasers [2], inverse Compton scattering (ICS) sources [3,4], and excitation of wakefields in plasma for future high energy physics accelerators [5,6] now require sub-picosecond pulses. Thus, improvement in resolution and capabilities of fast longitudinal diagnostics is needed.

RadiaBeam has recently developed and delivered an S-Band Traveling wave Deflecting mode cavity to be utilized for direct longitudinal phase space measurements of compressed electron beams at the Pohang Accelerator Laboratory X-ray SASE-FEL [7]. The PAL deflector takes advantage of the well-established cell machining in S-Band as well as our version of the SLAC-modified procedure for surface preparation for high RF power operation.

RF/THERMAL DESIGN

The initial 3D surface model used for RF simulations with HFSS [8] is shown in Figure 1. It is a disc-loaded traveling-wave (TW) structure operating in the TM_{110} mode at 2.856 GHz. Two coupler cells allow the input and output of the RF power provided by a standard WR284 metallic waveguide. The main deflecting cells, stacked in between the couplers, have a pillbox-like shape, each with holes located perpendicular to the deflection plane for the separation of the two dipole-mode field polarizations.

#faillace@radiabeam.com

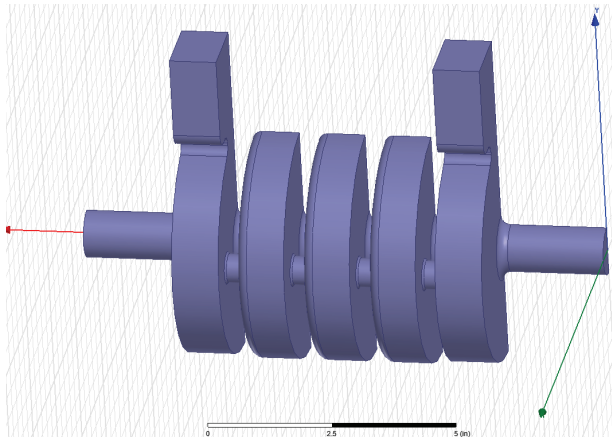


Figure 1: 3D surface model used for RF simulations in HFSS.

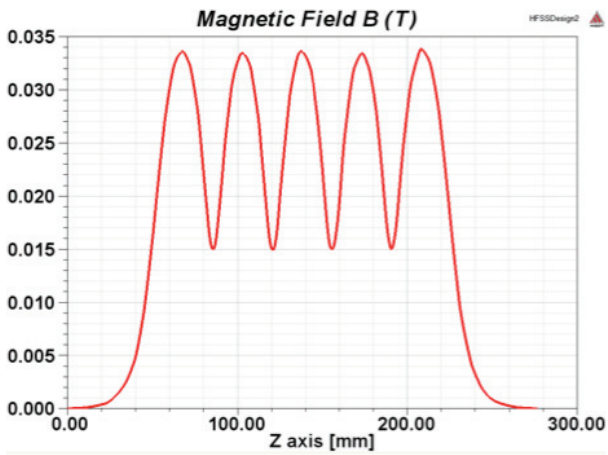


Figure 3: On-axis deflecting magnetic field profile.

The plot on the resulting on-axis deflecting magnetic field is given in Figure 2. The cell-to-cell phase shift is 120 degrees. The final full PAL deflector consists of an overall number (couplers plus main cells) of 28 cells. The main RF parameters for the L=1m long PAL deflector is listed in Table 1. The total deflecting voltage is equal to 8.5 MV, assuming an input RF power value of 10MW. Very good agreement was found between the simulated and the measured values.

Copyright © 2013 CC-BY-3.0 and by the respective authors

Table 1: PAL Deflector RF Parameters

RF Parameter	Value
2π/3-mode frequency f	2.856 GHz
Transverse Shunt Impedance r_T	28.7 MΩ/m
Unloaded Q	13,400
Attenuation α	0.15 m^{-1}
Group Velocity v_g	0.014 c
Kick/√Power	2.7 MeV/√MW
Length L	1 m

Thermal simulations were carried out with Ansys [9]. We only inserted a cooling channels system, very compact, for frequency/temperature stabilization. The result shown in Figure 3 refers to the case of an average RF power of 1kW. Due to the low temperature gradient (<3deg) across the structure, no internal channels were necessary.

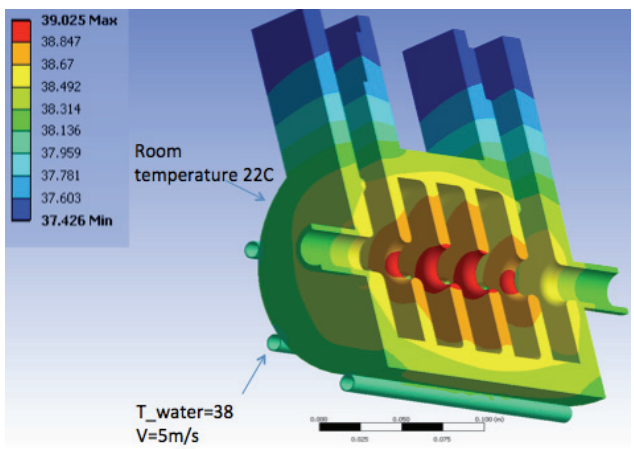


Figure 3: Thermal simulation of the PAL deflector model for 1kW average RF power.

THE PAL DEFLECTOR: TUNING AND INITIAL BEAM MEASUREMENTS



Figure 4: Picture of the PAL deflector after the final brazing and before installation.

The PAL deflector after final brazing and before installation is shown in Figure 4.

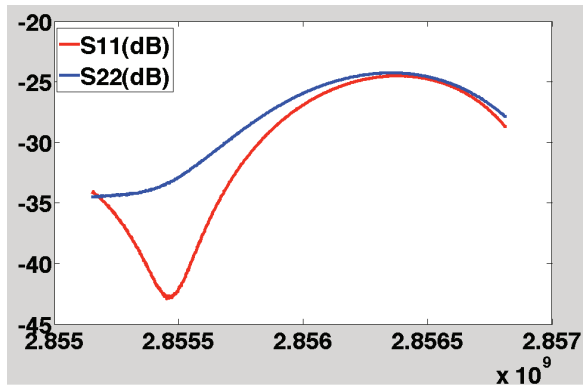


Figure 5: reflection coefficients at port1 and port2 (S11 and S22).

We measured the coupling coefficients at both ports, S11= -40dB (RF input port) and S22= -32dB with a SWR<1.05 for both ports.

The deflector cells were tuned to the spec (<±2°), at 22C and under nitrogen flow, by using the nodal shift procedure (plunger method).

From bead-pull measurements, we obtained the "flower"-like manifold that is plotted in Figure 6 showing a perfectly tuned 2π/3 operating mode.

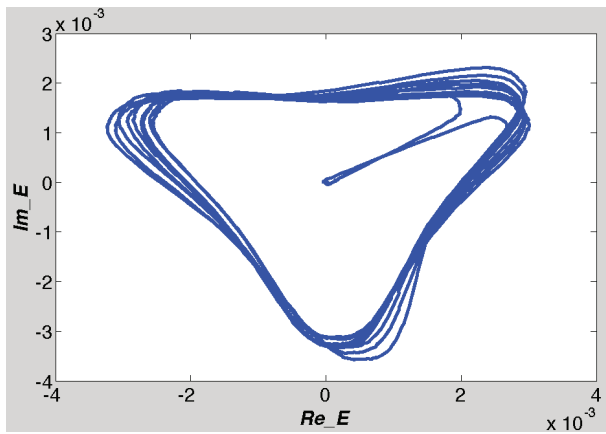


Figure 6: Polar plot of the on-axis electric field.

The bead-pull measurement (off-axis) of the electric field profile after final tuning is given in Figure 7.

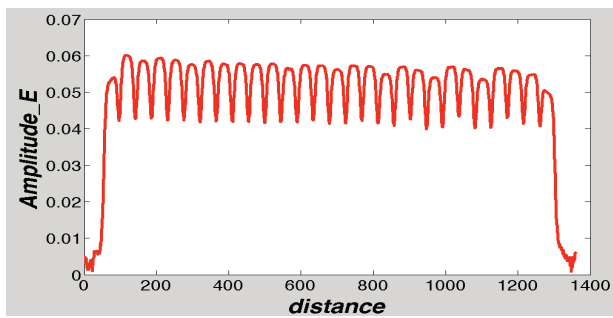
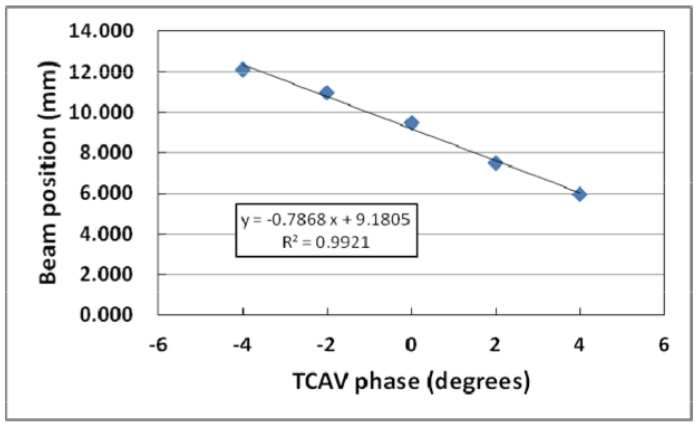
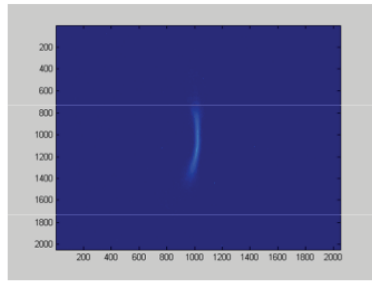


Figure 7: Off-axis electric field measurement (bead-pull).

Copyright © 2013 CC-BY-3.0 and by the respective authors



parameter	value
Laser inj. ph.	35 °
Beam energy	85.6 MeV
Beam charge	200 pC
TCAV RF power	0.137 MW



TCAV phase (degrees)	CM in Y (pixel)	beam position in Y (mm)	beam size in Y (μm)
4	716	5.943	1268.55
2	901.2	7.480	1267.40
0	1139.7	9.460	1238.08
-2	1317.9	10.939	1226.97
-4	1455.6	12.081	1262.24

(rms bunch length)
~ 1.53 ps
~ 0.456 mm
~ 1.57 degS

Figure 8: Low-power initial beam diagnostics at PAL by using the deflector delivered by RadiaBeam.

The S-Band deflector was delivered to PAL in May 2013. After RF conditioning, initial beam length measurements were performed in August (see Figure 8). Only a fraction of MW of RF power was required at the moment for the resolution of their 200pC, 85.6 MeV beam.

CONCLUSIONS

RadiaBeam Technologies has successfully completed design, fabrication, brazing and validation of an S-Band deflector for the Pohang Accelerator Laboratory (PAL) X-FEL. Upon delivery to PAL and EF conditioning, promising and satisfactory initial beam length measurements were carried out.

REFERENCES

[1] International Linear Collider Technical Review Committee Second Report, SLAC Technical Publications Department, Chapter 2, 15 (2003).
[2] Linac Coherent Light Source (LCLS) Conceptual Design Report, SLAC-R-593, Chapter 1, 9 (2002).
[3] I. V. Pogorelsky, et al., Phys. Rev. ST Accel. Beams 3, 090702 (2000).
[4] S.G. Anderson, et al., Velocity Bunching Of High-Brightness Electron Beams, submitted to Phys. Rev. ST AB.
[5] P. Muggli, et al., Phys. Rev. Lett. 93, 014802 (2004)
[6] J.B. Rosenzweig, N. Barov, M.C. Thompson, R.B. Yoder, Phys. Rev. ST AB 7, 061302 (2004).
[7] M. G. Kim, Design of the Pohang Accelerator Laboratory (PAL) X-ray Free Electron Laser (XFEL) Test Machine, Journal of the Korean Physical Society, Vol. 53, No. 6, December 2008, pp. 3741-3743.
[8] www.ansys.com
[9] www.ansys.com

Copyright © 2013 CC-BY-3.0 and by the respective authors

TRANSVERSE BEAM PROFILE DIAGNOSTIC USING FIBER OPTIC ARRAY*

S. Wu#, G. Andonian, T. Campese, A. Murokh, R. Agustsson,
RadiaBeam Technologies, Santa Monica, CA 90404, USA
R.K. Li, UCLA, Los Angeles, CA 90095, USA
M. Fedurin, R. Malone, K. Kusche, C. Swinson,
Brookhaven National Laboratory, NY 11961, USA

Abstract

The fiber-mesh diagnostic (FMD) is a transverse beam profile diagnostic based on the emission and detection of Cherenkov radiation produced as a relativistic electron beam traverses through an ordered bundle of fiber optics (SiO_2), arranged in a hexagonal close-pack configuration. Sub-10μm transverse beam profile resolution is attainable due to fiber optic core concentricity. Adequate SNR is achieved using a standard CCD sensor. A fiber optic taper input maximizes light collection efficiency by coupling each output channel to approximately single-pixel pitch. A v-groove holder and assembly process was developed to hold many fiber layers in the desired configuration. In this paper, we present results from a fully functional FMD prototype evaluated at the BNL ATF facility that demonstrates the efficacy of this diagnostic.

INTRODUCTION

The FMD was developed to address the need for higher resolution transverse profiling in low emittance electron beams. Standard techniques to measure the transverse extent of beams include fluorescent screens (such as YAG), observation of optical transition radiation, wire scanners and others. The resolution limit of these diagnostics hovers around >20μm. In the FMD, Cherenkov radiation is generated when a charged particle strikes a dielectric fiber that is placed at the Cherenkov angle. The device collects incoherent Cherenkov radiation, so the spatial profile is an accurate representation of the beam transverse charge distribution.

For a relativistic beam striking a dielectric, the Cherenkov angle, θ_C, is:

$$\theta_C = \cos^{-1}\frac{1}{n} \cong 46.5° \quad (1)$$

where n is refractive index of the fiber.

The approximate photons generated in each fiber are:

$$N_{photons} \approx \frac{2\alpha}{\sqrt{\pi}} N_e \left[\frac{d^2}{\lambda\sigma_x}\right]\left(\frac{\Delta\omega}{\omega}\right) NA \quad (2)$$

where α is the fine structure constant, d is the fiber core diameter, λ is the wavelength of light, N_e is the number of electrons, σ_x is electron beam RMS width, and Δω/ω is the fiber bandwidth.

A proof-of-concept experiment was executed at the UCLA Pegasus lab to demonstrate adequate photon yield for a single fiber [1]. The experiment results and theory were scaled for Brookhaven ATF parameters (Table 1). These results proved the feasibility to build a functioning prototype.

Table 1: Electron Beam Test Parameters

Facility	Energy (MeV)	Charge (pC)	Expected Photon Yield
UCLA Pegasus	2.5	25	10^4
Brookhaven ATF	57.6	100-1000	10^5-10^6

SYSTEM DESCRIPTION

The interaction point consists of an ordered array of single mode fiber optics (Fluorine-doped SiO_2, 6.8μm MFD, 245μm OD), which are also used at CERN for their radiation resistant qualities [2], to obtain multiple measurements in one instance. Cherenkov radiation is generated within the fibers, which also guide the radiation to an external CCD detector. Custom algorithms convert the multiple-fiber signals to a transverse profile charge distribution on a shot-to-shot basis.

The system consists of three key components:

(1) The fiber array at the interaction point
(2) The CCD acquires the Cherenkov signal
(3) DAQ logic converts signals to beam profile

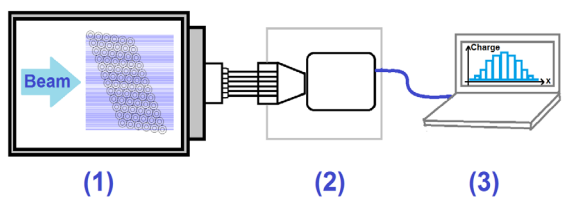


Figure 1: Diagram of System Design.

*Work is supported by U.S. D.O.E. Contract Number DE-SC0000870
#swu@radiabeam.com

Copyright © 2013 CC-BY-3.0 and by the respective authors

Fiber Holder Fabrication and Assembly

The fibers are bundled in a hexagonal configuration so that each core position is set. They are held together with a v-groove clamping method:

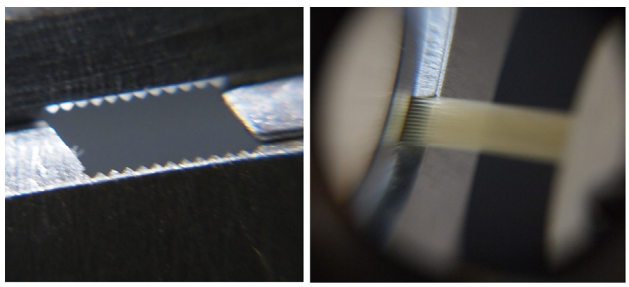


Figure 2: Photograph of fiber array. Fibers are clamped with v-grooves (Left). Fibers Assembled to holder (Right).

In order to correctly arrange fibers to the holder, fibers are initially bundled to single rows of 12. The first row settles into the v-grooves, and remaining bundles are laid onto the grooves of the previous layer. The tooling holds each layer taut during this process:

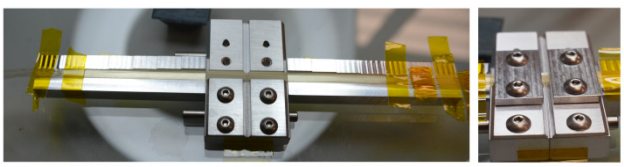


Figure 3: Tooling for holder assembly.

After the fibers are clamped to the holder, the holder arms are pulled apart, and fastened to the insertion rod:

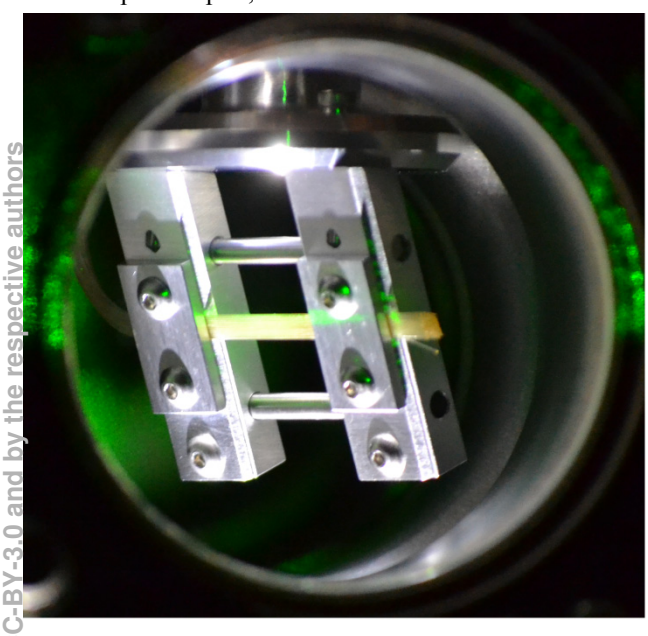


Figure 4: Fiber holder assembly in situ.

Camera Design

To maximize light collection efficiency, the fiber ends are mounted to a fiber optic taper input bonded directly to the CCD, providing a robust mounting surface. The result is focused light achieving almost single-pixel coupling, which optimizes the system's detection limit.

12-bit digital output is sent to the computer via Ethernet, enabling long distance data transmission needed from the experimental hall to the control room.

Data Acquisition

Prior to operation, fiber positions on the camera input are located by illuminating the fibers pointing to the camera. The sum of a 5x5 pixel region-of-interest for each location is ordered so that it represents the transverse position of each fiber core.

MATLAB interfaces with the camera. A TTL signal triggers the camera to capture an image, which is real-time processed to display the updated transverse profile. Background is subtracted from the profile, and the mean and RMS are calculated (See Fig. 5).

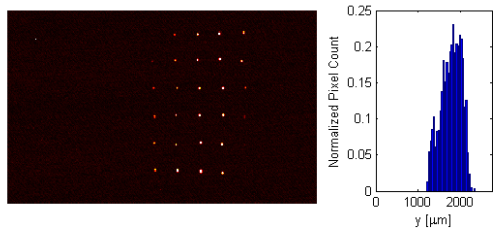


Figure 5: Raw image (Left), Single shot profile (Right).

RESULTS

The experiment was executed at Brookhaven ATF. YAG screens located on both sides of the FMD were used to benchmark the device under test.

Beam Width Measurements

YAG-based profile monitors along the beamline were used to tune the beam and for comparative studies with the FMD. A parabolic fit to the YAG-profile measurements was applied to calculate the expected beam width at the FMD location. Three beam widths were measured at 500pC and compared to the FMD measurements. The results are displayed in Figure 6, and shown in Table 2.

Table 2: Beam Width Comparisons at FMD Location

Calculated Width [μm] (YAG-profile monitors)	Measured Width [μm] (FMD)
171	139
341	365
448	449

Copyright © 2013 CC-BY-3.0 and by the respective authors

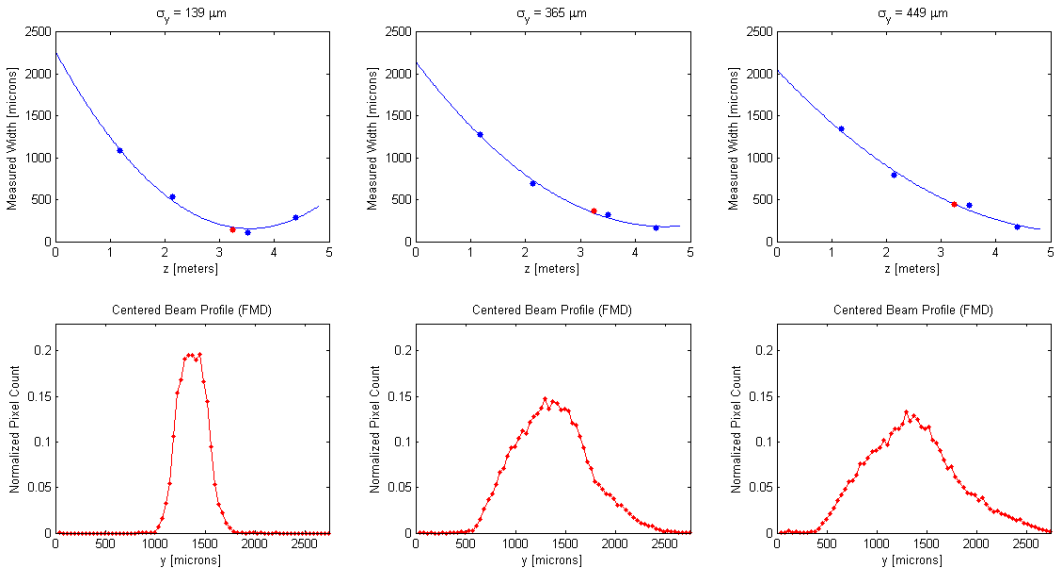


Figure 6: Top Row –Beam widths measured with YAG screens along the beamline (blue). Beam width measured with FMD plotted at the measured z- distance (red). Bottom Row – The averaged beam profile as measured with FMD.

The beam was also intentionally detuned to record a "non-Gaussian" profile with the FMD at 500pC (See Fig. 7) to observe profile features on the ~10μm scale.

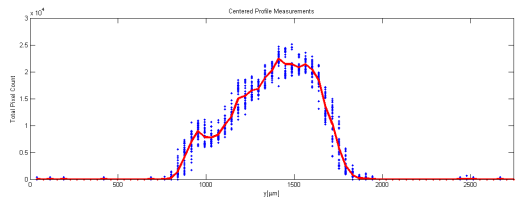


Figure 7: Each shot is centered (blue), and the averaged profile is calculated (red).

Quadrupole Scans

The current in an upstream quadrupole magnet was varied and the beam widths were recorded with FMD and a YAG-based profile monitor. The beam charge was 80pC. The emittance is calculated for both diagnostics and shows reasonable agreement (see Table 2).

Table 2: Comparison of Calculated Emittance

Diagnostic	Quad Distance [meters]	ϵ_n [mm-mrad]
YAG	2.58	4.2E-06
FMD	2.32	3.9E-06

CONCLUSION

The Fiber Mesh Diagnostic uses beam-generated Cherenkov radiation within a fiber optic array to characterize the beam transverse profile. The prototype was tested at the BNL ATF and its accuracy was compared to the YAG-profile monitors. The results were successful and demonstrated the viability of this diagnostic for high-precision transverse beam profile characterization. Future tests will address issues of fiber lifetime in high-radiation environments and an upgraded user-interface.

ACKNOWLEDGMENT

The authors would like to thank the staff at UCLA Pegasus and Brookhaven National labs for their expertise and the operation of their facilities. Work supported by DOE SBIR Grant No. DE- SC0000870.

REFERENCES

[1] R. Tikhoplav *et al.*, "Progress Report on Development of a High Resolution Transverse Diagnostic Based on Fiber Optics", *Proceed. IPAC 12,* MOPPRO090 (2012); http://www.JACoW.org

[2] "Fiber resists CERN's radiation to carry data," Newsdesk, May 2007, Historical Archive; http://www.optics.org/article/27855

Copyright © 2013 CC-BY-3.0 and by the respective authors

SCINTILLATOR DIAGNOSTICS FOR THE DETECTION OF LASER ACCELERATED ION BEAMS *

N. Cook†, R. Lefferts, Stony Brook University, Stony Brook, NY 11790 USA
O. Tresca, BNL, Upton, NY 11973, USA
V. Yakimenko, SLAC, Menlo Park, CA 94025, USA

Abstract

Radiation pressure acceleration with ultraintense laser pulses presents an exciting new scheme for accelerating ions. One of the advantages conferred by using a gaseous laser and target is the potential for a fast (several Hz) repetition rate. This requires diagnostics which are not only comprehensive for a single shot, but also capable of repeated use. We consider several scintillators as candidates for an imaging diagnostic for protons accelerated to MeV energies by a CO_2 laser focused on a gas jet target. We have measured the response of chromium-doped alumina (Chromox), CsI:Tl, and polyvinyl toluene (PVT) screens to protons in the $2-8$ MeV range using a CCD camera. We have calibrated the luminescent yield in terms of photons emitted per incident proton for each scintillator. We also discuss how light scattering and material properties affect detector resolution. Furthermore, we consider material damage and the presence of an afterglow under intense exposures. Our analysis reveals a near order of magnitude greater yield from Chromox in response to proton beams at >5 MeV energies, while scattering effects favor PVT at lower energies.

INTRODUCTION

Acceleration of protons by intense laser pulses has become an increasingly active area of study amongst nuclear, plasma, and accelerator physicists. Recent experiments with intense CO_2 laser pulses have produced collimated bunches of protons with energies greater than 1 MeV and narrow energy spread with the potential to do so at repetition rates on the order of $1-10$ Hz [1] [2]. The evolving nature of this field necessitates flexible diagnostic techniques suited to measure a myriad of experimental outputs.

Film and resin diagnostics offer single particle sensitivity but require weeks of analysis. MCPs offer a controlled gain curve and excellent resolution but are extremely delicate and ill-suited to high energy radiation. The use of scintillators has emerged as a flexible diagnostic as they may exhibit strong luminescence in response to an array of radiation types and energies; nonetheless their use necessitates precise calibration and their specific responses may vary by orders of magnitude [3]. The goal of these tests was to find a material which produces an adequate and consistent light yield under expected conditions (10^4-10^6 protons with energies $\sim 1-20$ MeV). The material should have sufficient resolution to determine bunch size, and should be relatively inexpensive and robust when exposed to high radiation flux at a repetition rate near 1 Hz.

EXPERIMENTAL METHOD

We narrowed our potential candidates to three scintillators: Chromox, CsI:Tl, and PVT. Chromox (Al_2O_3 : Cr_2O_3) is a ceramic phosphor designed to be durable under high radiation exposure and is responsive to ions in the MeV range [4] [5]. Chromox emits at ~693 nm. CsI:Tl is an inorganic crystal scintillator which emits at 550 nm. Though designed for photon detection, it's high-Z composition improves proton stopping power and makes it a high yield candidate. PVT is a low Z organic compound comprised of covalently bonded vinyl toluene chains, and as such it is easily damaged by high linear energy transfer (LET) radiation [6] [7]. BC-416 is the specific PVT variant tested, featuring added fluorophores as solvents to adjust the emission spectrum. It emits light through several channels, due to the presence of several solvents; the maximum of its emission spectrum occurs at 434nm, and its stated decay time is 4 ns.

We obtained a 1 inch diameter, 0.82 mm thick Chromox disc from Morgan Advanced Ceramics. We evaporated a 225 nm thick aluminium coating on the disc to diminish noise from electrons and X-rays. An uncoated 25 mm diameter by 1 mm thick CsI:Tl disc was purchased from Marketech International Ltd. The plastic scintillator is a 2" $\times$ 2" square, 1 mm thick, with a 50 μm Al coat, and has been used for previous proton experiments at the Accelerator Test Facility at BNL.

Experiments were performed at Stony Brook University using the Stony Brook Tandem Van de Graaff. Protons may be accelerated to total energies of $2-12$ MeV with 0.01% accuracy. Beam currents are flexible from 200 pA to 8.0 nA. Current regulation limits instantaneous uncertainties to no less than 10% regardless of beam parameters.

We used a Basler scA1400-17gm monochrome CCD camera to image the scintillator output. It features a 58% quantum efficiency at 545 nm, 12-bit image depth, and a 1392×1040 pixels sensor with 6.45μm $\times$ 6.45μm pixel size. The camera is paired with 75 mm $f\#/1.4$ tv-lens which corresponds to a maximum aperture of 0.414 sr.

RESULTS AND ANALYSIS

Captured images are analyzed following the European Machine Vision Association (EMVA) Model 1288 [8]. 300

* Work supported by Brookhaven Science Associates, LLC under Contract No. DE-AC02-98CH10886 with the U.S. Department of Energy.
† ncook@bnl.gov

Copyright © 2013 CC-BY-3.0 and by the respective authors

images were taken for each camera setting after specifying a 200x200 pixel A.O.I, from which an average background subtracted grey value was obtained, correlating the luminescence due to scintillation for given beam parameters. An average yield was then calculated using the EMVA Model given the optical parameters of our setup. A Lambertian falloff of light intensity versus the angle, θ, between the scintillator surface and the camera is assumed. This contributes a factor of $\cos\theta$ to the model. We define the yield according to

$$Y = \frac{\mu_\gamma}{f_\gamma N_p} \quad (1)$$

$$\text{and} \qquad f_\gamma = \frac{\Omega}{4\pi} T_w \cos\theta$$

where f_γ is the fraction of photons collected by the camera, which is a function of solid angle,Ω, weighted transparency of insertion devices, T_w, and θ. The yield Y then depends on $f\gamma$, N_p the number of protons, and μ_γ, the number of photons collected per pixel by the camera.

Table 1: Raw Photon Yields for Tests Done in Transmission for each Scintillator (All Uncertainties $\pm 5\%$)

Material	2 MeV	4 MeV	6 MeV	8 MeV
Chromox	75.5	216	393	728
PVT	51.9	80.3	174	256
CsI:Tl	0.812	2.32	3.15	4.75

Table 1 shows the measured yield-energy data accumulated during our tests. Tests were limited to 8 MeV due to proton penetration depth limitations. Uncertainties are dominated by current regulation instability on the order of $\pm$ 5%.

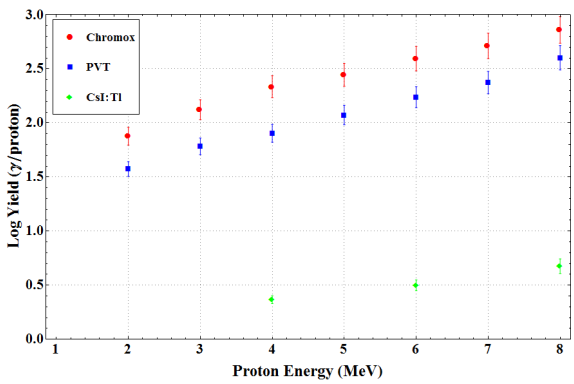


Figure 1: A comparison plot of $Log(Y(E))$ for each scintillator in transmission.

Chromox Transparency

Assuming a simple model of scintillation, light yield scales linearly with beam energy in absence of strong quenching. However, both Chromox and PVT yields do not correspond to a linear relationship. We consider the role of transparency in introducing nonlinearities in the yield. Chromox is constructed of granules of approximate size $w_g = 10 - 15\,\mu m$. Photons passing through the material may be scattered or reflected at each of the grain boundaries, such that the transmission coefficient through a granule is T_g. Assuming that $\frac{w_g}{w_c} \ll 1$ and $(1 - T_g) \ll 1$, we conclude that photon yield is a linear function of distance travelled through the material. Thus, we may use the range of protons in the scintillator, $r(E)$ as a linear transparency metric. We have

$$Y_A(E) = Y(E) * w_c(1 - r(E)) \quad (2)$$

where Y_A is the transparency-adjusted yield. Figure 2 demonstrates that Y_A scales linearly with proton energy. We then work backwards to make an "expected yield" fit.

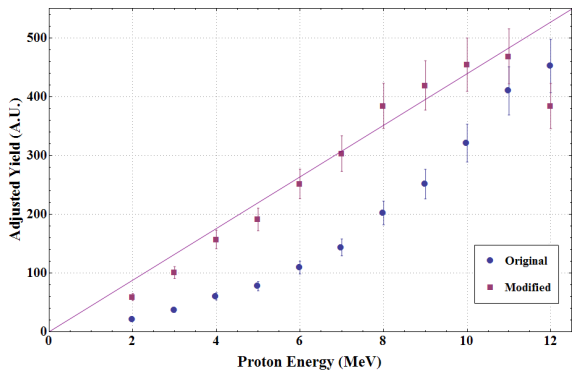


Figure 2: Chromox yield is shown with a penetration distance adjusment and corresponding linear fit. The raw yield is scaled down for comparison.

PVT Transparency and Damage

We performed a similar adjustment to the PVT yield, and after accounting for the Al coating, we achieve an improved fit. However, we observe a sharp discrepancy in the fit above 6 MeV. We believe this can be explained by non-radiative dissipation of deposited energy in the scintillator resulting in damage and a diminished yield for high incident flux [6]. To investigate, we placed the PVT under a continuous 8 MeV beam at 1 nA and examined the yield over time; we recorded a 31.6 % decline in mean intensity during 2 minutes of exposure. Afterwards, beam was blocked for 5 minutes, at which point the average yield was found to be consistent with the two minute value. As no significant afterglow was present, we conclude that there is a long term reduction in yield which corresponds to damage to the scintillator [9].

Resolution Analysis

For use in transmission, we performed comparative tests by imaging a pinhole with a 6 MeV CW beam. We imaged the output from each scintillator under these conditions, and the resulting images can be seen in figure 3. We then calculated the normalized intensity falloff from the edge of

Copyright © 2013 CC-BY-3.0 and by the respective authors

the pinhole along a fixed vertical axis, averaged over 300 images.

These tests demonstrate a significantly lower scattering in CsI:Tl, leading to a 20% falloff length of 0.31mm. For Chromox, we found a 0.79 mm falloff length, while PVT displayed the greatest scattering with a falloff length of 1.15 mm. We also observe greater fluctuations in the scattering properties of the PVT than the Chromox, suggesting further evidence of damage to the scintillator.

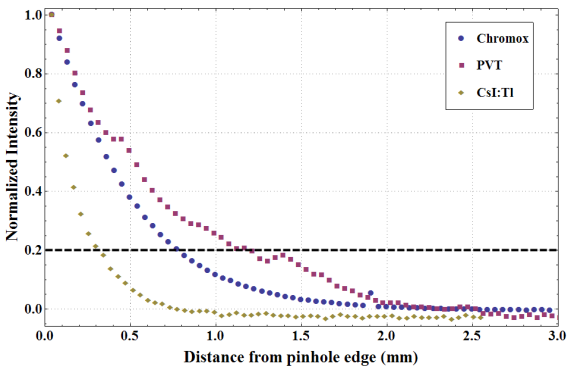


Figure 3: Intensity falloff from pinhole edge compared across three scintillator candidates.

Afterglow Analysis

Though boasting impressive scintillation response to ions and high $\frac{dE}{dx}$ particles, Chromox demonstrates an afterglow effect, only in part due to natural quenching. The granules introduces more lattice defects at grain boundaries, increasing the probability that photons are trapped away from an activator site thus enhancing afterglow. This effect has been measured in our Chromox sample both under continuous and pulsed beam conditions.

We generated a beam of 6 MeV protons at a current of 500 pA, and imaged the disc in reflection. The beam was shut off after an incidence period of several minutes, and the camera set to take pictures continuously at a 1 ms exposure time at approximately a 1 Hz rep rate. We found that there is significant afterglow for more than a minute after the beam is shut off. The sample exhibited a strong immediate afterglow, 28% of the value under beam exposure 1 s after beam shutoff. After 10 s, the afterglow intensity was less than 10% of the intensity under exposure. Even after 90 s, an afterglow of approximately 1.5% of the intensity under incidence was observed.

As laser acceleration produces sub-ns pulses, it is sensible to examine the afterglow under pulsed beam conditions as well. Though we cannot replicate experimental conditions with the tandem, pulsed beam was run at 3 Hz with 25 ms pulse lengths. A baseline response to the pulses was measured before blocking the beam to measure afterglow. Image intensity is plotted versus time in figure 4. It can be seen that in the case of pulsed beam, the light output falls much more quickly, reaching less than 3% of its nominal value after 0.1 s. Moreover, in this case, a stretched exponential of the form $e^{-(\frac{t}{\tau})^{\beta}}$ provides a strong fit candidate, with $\tau = 0.18$ms, and $\beta = 0.20$. This fit is characteristic of phosphorescence and suggests that Chromox is suitable for pulsed use at Hz-scale rep. rates.

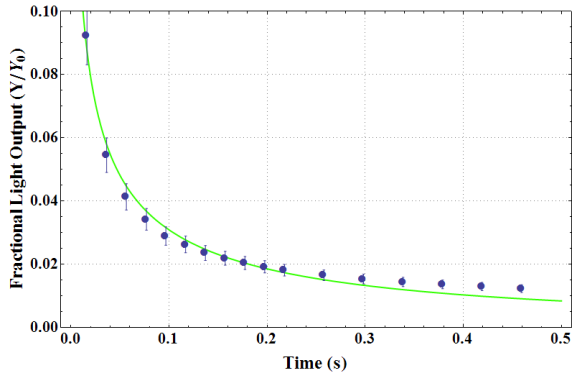


Figure 4: Chromox afterglow measured after a 5nA proton beam is pulsed for 25ms on, 325ms off.

CONCLUSION

We have measured the response of several candidate scintillators for use in a high rep rate laser acceleration experiment. Our findings suggest that Chromox has the strongest response to protons in the 2-10 MeV range. Resolution findings are worse than a single crystal scintillator like CsI:Tl, but acceptable for use with a Thomson spectrometer. Moreover, the afterglow in response to a pulsed beam is not significant on a 1s time scale, similar to the current maximum laser rep rate at ATF. Transparency remains a concern as it significantly reduces yield, depending on the geometry of the scintillator. Likewise, quenching remains a concern at high energies, but Chromox demonstrated the best radiation hardness among candidates. However, at low energies, photon scattering at grain boundaries reduces both yield and resolution for Chromox. Assuming comparable disc thickness, at energies < 4 MeV, a PVT based scintillator provides a superior response.

ACKNOWLEDGMENT

Many thanks are due to M. Babzien, A. Drees, K. Kusche, and A. Lipski for their contributions to this work.

REFERENCES

[1] C. Palmer et. al. Phys. Rev. Lett. 106 (2011) 014801.
[2] I. Pogorelsky et. al. NIM A. 620 (2010) 67-70.
[3] P. Forck et al. IEEE Trans. Nucl. Sci. 57 (2010) 1414-19.
[4] K.J. McCarthy et al. J. Appl. Phys. 92 (2002) 6541-45.
[5] K.J. McCarthy et al. J. Nucl. Mat. 321 (2003) 78-83.
[6] L. Torrisi et. al. NIM B. 166-67 (2000) 664-68.
[7] L. Zhao et. al. NIM A. 552 (2005) 449-55.
[8] European Machine Vision Association, "EMVA 1288 Standard for Characterization of Image Sensors and Cameras", 2010. http://www.emva.org/
[9] N. Cook, Dissertation, Stony Brook University. To Be Published.

Copyright © 2013 CC-BY-3.0 and by the respective authors

DIAMOND AMPLIFIER DESIGN AND PRELIMINARY TEST RESULTS

T. Xin#, [1, 2], S. Belomestnykh[1, 2], I. Ben-Zvi[1, 2], M. Gaowei[1, 2], E. Muller[1, 2], T. Rao[1], J. Skaritka[1]
J. Smedley[1], E. Wang[1], Q. Wu[1],

[1]Brookhaven National Laboratory, Upton NY 11973
[2]Stony Brook University, Stony Brook NY 11794

Abstract

Diamond as a large band gap material can be easily made to have negative electron affinity (NEA) surface. Using a few keV primary electrons as input and a few kV bias, the NEA diamond will emit cold electrons into vacuum with a large gain. We had tested and reported the performance of the diamond amplifier in our DC system. The best amplification achieved so far was above 170. Next step of the experiment is to test the diamond amplifier in a 112 MHz superconducting RF electron gun. In this report we describe the design of the amplifier containing a DC primary gun and light optics, to be tested in our SRF gun and relevant simulations. We also provide preliminary test results of the laser and electron beam transport.

INTRODUCTION

In previous papers, works on hydrogenation of CVD diamond and on measurements of secondary electron gain in a DC system at Brookhaven National Lab were reported [1-3]. The next step will be testing the diamond amplifier in a Superconducting RF (SRF) gun. For this purpose a specially designed cathode stalk is needed to work as a transporter/holder of a diamond in the gun. Besides that, we also designed a subsystem, which will be inserted into the cathode stalk and act as the DC stage of the amplifier.

DIAMOND AMPLIFIER

A basic diagram of a diamond amplifier is shown in Figure 1. A primary beam, with a few keV energy, hits the Pt coated back of the diamond and generates a cloud of electron/hole pairs inside the diamond. This entrance surface of the diamond is negatively biased hence the electrons separate from the cloud and drift across the bulk of diamond to the opposite, hydrogenated NEA emission surface. An anode is placed 200 μm away from the emission surface so that the electric field will extract the secondary electrons from the NEA surface of diamond into vacuum.

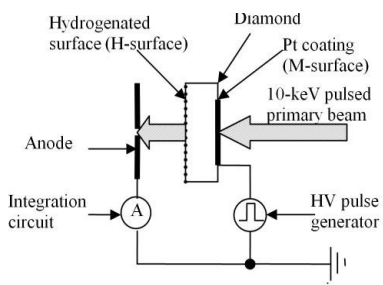


Figure 1: DC test of Diamond Amplifier (conceptual diagram) [1].

* This work was carried out at Brookhaven Science Associates, LLC under Contracts No. DE-AC02-98CH10886 and at Stony Brook University under grant DE-SC0005713 with the U.S. DOE.
#txin@bnl.gov

Design of Amplifier for SRF Gun Test

For the test of the Diamond Amplifier in an SRF gun, we need a special stalk to position the diamond in right location in the cavity and hold it there. The detailed description of the stalk can be found in previous papers [4, 5]. As for the source of primary electrons, we decided to use a newly designed DC assembly with a UV driven copper cathode. A CAD model and a photo of this system, which will hereby be called Amplifier, is shown in Figure 2.

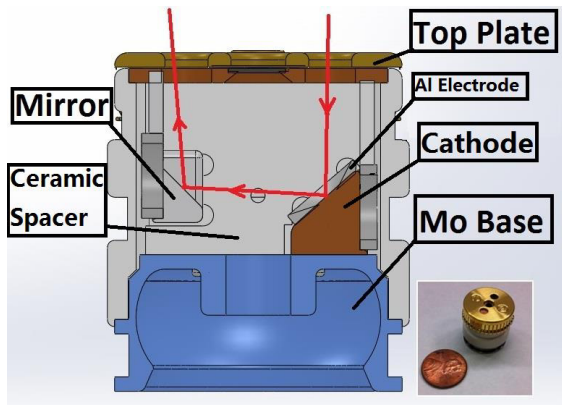


Figure 2: Section view of the Amplifier: red lines show the path of UV light. Smal insert is a photo of the first prototype Amplifier with a penny on the side as size reference.

This is the first prototype amplifier we made for SRF test. There are four major pieces. A gold plated copper top plate is used to hold the diamond and ground it to the cavity. A ceramic spacer serves as an insulator between the grounded top plate and biased molybdenum base. It also acts as a holder for the cathode and mirror and defines the crucial distance between the cathode and diamond. The third part is the cathode/mirror pair that will provide electron beam and guide the laser beam out of the cavity. The fourth part is the molybdenum base that works as the connection between the Amplifier and the transport arm.

Laser will come in through a hole in the top plate and illuminate the cathode. There is an aluminium electrode surrounding the cathode optimized for beam focusing. After the laser bounces off the mirror-finished cathode, it will hit a metal-coated mirror on the other side, which will redirect the laser out of the amplifier through an exit hole in the top plate. Figure 3 shows how the amplifier will be positioned in the stalk and cavity as well as depicts the paths of laser and electron beams. The angles of the cathode and mirror are chosen to meet two conditions. The first one allows the laser beam to escape the cavity with no obstacles. And the second condition is that the electron beam must hit the center of the diamond so that we do not

Copyright © 2013 CC-BY-3.0 and by the respective authors

have to worry about charging up of ceramic spacers. The cathode will be negatively biased by a DC power supply to -5 kV. The top plate will be grounded to the cavity though the gold plated fingers.

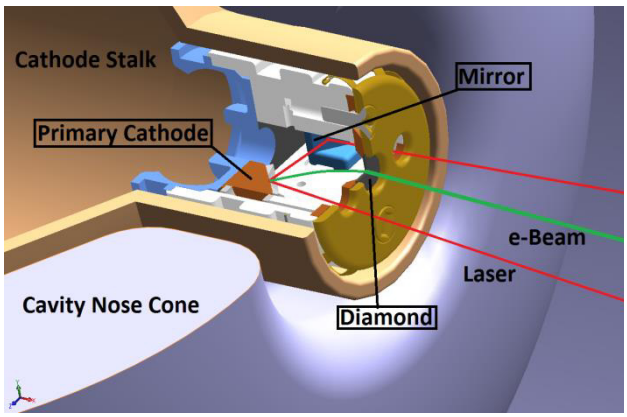


Figure 3: Diagram of laser and electron beam paths.

Simulation Result of Amplifier

In order to find the optimal orientation of the cathode, we used CST Particle Studio to simulate the trajectory of electron beam after it leaves the cathode. Table 1 shows parameters we used in the simulation.

Table 1: Parameters for simulation

Parameters	Value
High Voltage	-5 kV
Average Current	5 nA
Pulse width	1 nS
Repetition rate	80 kHz

After a few iterations the angle between the normal direction of cathode and axis of cavity is chosen to be 42 degrees. The distance between centers of the cathode and the diamond is optimized to 6.6 mm. Figure 4 shows the potential distribution inside the amplifier and the electron beam trajectory. We were able to guide the primary beam onto the center of Pt coating layer on back of the diamond. The distance between the center of the beam spot and the center of the diamond was eventually brought down to 180 μm. RF field leakage through the holes in top plate was taken into consideration and it was found that the field is low enough that there is no observable effect on the beam energy and position.

Prototype Testing Result

We built a prototype Amplifier this year and made some preliminary measurement on it to demonstrate the feasibility of our design in terms of laser and electron beam paths.

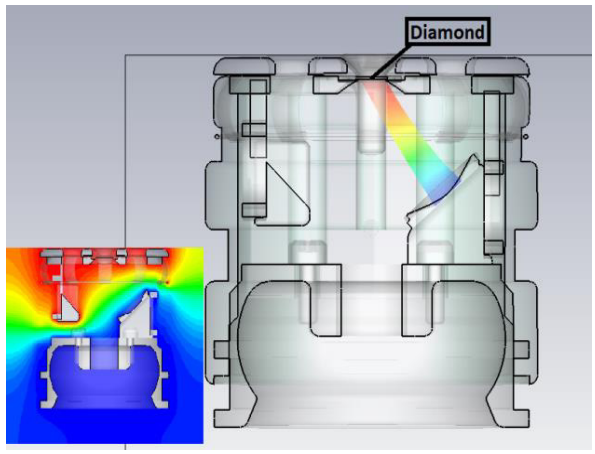


Figure 4: Trajectory of electron beam between primary cathode and diamond. Smaller picture shows the potential distribution inside the Amplifier.

Figure 5 shows the test with a green alignment laser. Incoming laser goes through the half pass Kapton film then illuminates the copper cathode. After two reflections it comes out of the exit hole on the other side of the top plate. The reflected laser beam was captured by the half pass film and indicated as a weaker spot.

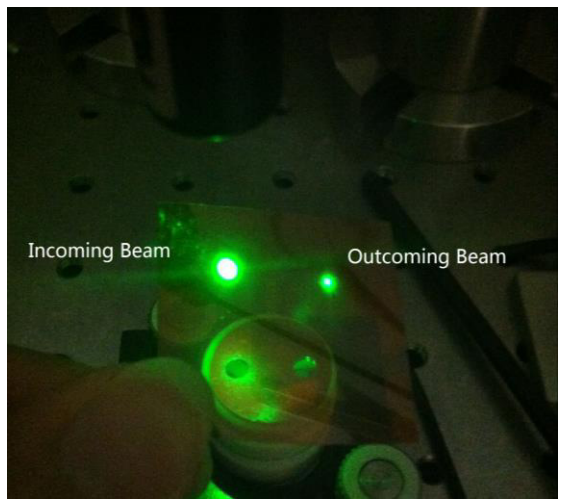


Figure 5: Demonstration of the laser beam passage.

We also measured the percentage of electrons that we were able to capture with a dummy electrode, which is acting in place of diamond. In this measurement we successfully applied -5 kV bias to the cathode. Then a 220 nm UV light was introduced to the amplifier. A deuterium lamp/monochromator system was used to generate the required UV light.

We recorded the current leaving the cathode and the current intercepted by an isolated dummy electrode under different bias voltages. The result of the measurement is shown in Figure 6.

Copyright © 2013 CC-BY-3.0 and by the respective authors

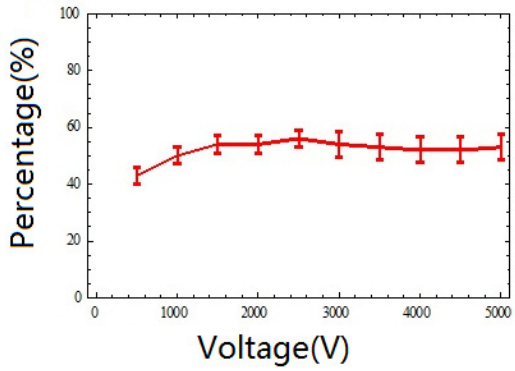


Figure 6: Percentage of electrons reaching dummy electrode over electrons leaving cathode.

One can see that about half of the electrons that left the primary cathode didn't make it to the dummy electrode. This can be result of stray light illuminating the cone shaped electrode sitting on top of the cathode. Since the spot size of UV light from lamp could not be reduced to exactly match the size of the copper cathode, we are expecting certain amount of electrons from the aluminium electrode. Figure 7 shows the effect of changing light spot size on the percentage of intercepted electrons.

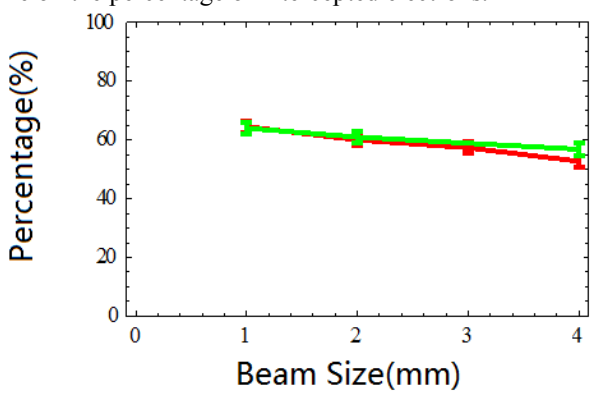
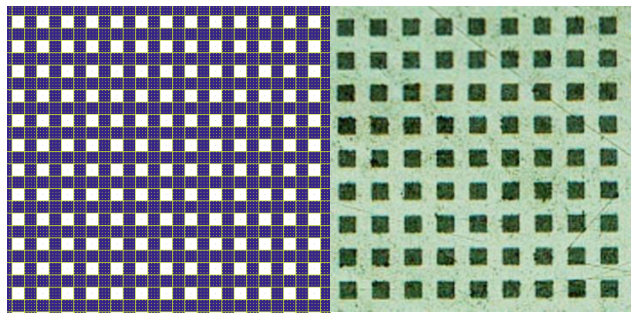


Figure 7: Percentage of electron intercepted by dummy electrode *vs.* UV light spot size.

Considering the total area of the electrode and the QE of the aluminium, it is possible that nearly half of the signal in the measurement of current leaving cathode was due to the photoemission from aluminium. In future tests the light source will be changed to a UV laser and the spot light will be sufficiently reduced to minimize the number of electrons caused by stray light.

Future Modification

We are planning to change the previous one hundred percent coverage metal coating to a lithographical patterned grid coating. Because the metal layer will reduce the energy of primary electrons, less coverage means larger effective impact energy from primary beam. Hence the total number of secondary electron product in each pulse will be increased according. The trade off is that the weaker electric field established by grid coating inside diamond will drag less secondary electrons to the emission surface. Figure 8 shows the pattern we are planning to use and the coating made from it.



a b

Figure 8: (a) Mask used for lithography; (b) Picture of back electrode made with patterned mask. The grid spacing is 50 μm.

CONCLUSION

For future tests of the Diamond Amplifier in a Superconducting RF gun, a DC subsystem was designed to provide primary electron beam inside the RF cavity. The system includes the following parts: a primary photocathode made of copper; an aluminium electrode for beam regulation; a metal-coated dielectric mirror to guide the laser out of the cavity; a holding mechanism to hold the diamond in position and ground it to the cavity; and a molybdenum base part to connect the amplifier to the transport arm. Simulation result from CST Particle Studio shows good aiming of electron beam onto the center of the diamond and acceptable DC field strength near the dangerous region. Experimental result verified the design of the optics for the laser beam and showed a reasonable capture ratio of electrons by the diamond. We are still working on improving the Amplifier in order to make it more compatible with our SRF electron gun.

REFERENCES

[1] X. Chang, et al, Electron beam emission from a Diamond-Amplifier Cathode, Phys. Rev. Lett. **105**, 164801 (2010).

[2] E. Wang, et al, Secondary-electron emission from hydrogen-terminated diamond: experiments and model, Phys. Rev. ST Accel. Beams **14**, 111301 (2011).

[3] E. Wang, et al, Systematic study of hydrogenation in a diamond amplifier, Phys. Rev. ST Accel. Beams **14**, 061302 (2011).

[4] T. Xin, et al, Design of the fundamental power coupler and photocathode inserts for the 112 MHz superconducting electron gun, Proceedings of SRF2011, Chicago, IL USA.

[5] T. Xin, et al, Simulations of multipacting in the cathode stalk and FPC of 112 MHz superconducting electron gun, Proceedings of IPAC2012, New Orleans, Louisiana, USA.

Copyright © 2013 CC-BY-3.0 and by the respective authors

MULTIPACTING STUDY OF 112 MHZ SRF ELECTRON GUN*

T. Xin#,1, S. Belomestnykh1,2, I. Ben-Zvi1,2, C. H. Boulware3, T. L. Grimm3, X. Liang1, T. Rao2, J. Skaritka2, E. Wang2, Q. Wu2
1) Stony Brook University, Stony Brook, NY 11794, U.S.A.
2) Brookhaven National Laboratory, Upton, NY 11973-5000, U.S.A.
3) Niowave, Inc., Lansing, MI 48906, U.S.A

Abstract

The 112 MHz quarter wave superconducting electron gun was designed and built as an injector for the coherent electron cooling experiment. Besides that, the gun is suitable for testing various types of photocathodes thanks to its specially designed cathode holder. In recent RF tests of the gun at 4 K, the accelerating voltage reached 0.9 MV CW and more than 1 MV in pulsed mode. During this testing, we observed several multipacting barriers at low electromagnetic field levels. Since the final setup of the gun will be different from the cool down test configuration, we want to understand the exact location of the multipacting sites. We used Track3P to simulate multipacting. The results show several resonant trajectories that might be responsible for the observed barriers, but fortunately no strong multipacting barriers have been found in the cavity.

INTRODUCTION

The fabrication of the 112 MHz SRF quarter wave cavity as well as the cryomodule has been finished and the cold test was successfully conducted early this year. The gap voltage had reached 0.9 MV in CW mode test and 1 MV in pulsed mode. Further increase in gap voltage was limited by radiation. During the conditioning process we encountered several multipacting barriers. The purpose of study shown in this paper is to investigate the relative strength of the known barriers to the ones that are predicted by the simulation under higher field level with different FPC and cathode stalk for future test so that the difficulty of future conditioning can be estimated.

EXPERIMENTAL ASPECTS

General Layout

The cavity and a new cryomodule were built and assembled at Niowave. The layout of the cavity, fundamental power coupler (FPC) and pickup antenna is shown in Figure 1. The FPC antenna was designed with an adjustment range allowing critical coupling at different levels of RF losses in the cavity. Special precaution was taken during the cool down to avoid the accumulation of residual gas on the outer conductor of the FPC. We suspected that changing of surface condition might explain multipacting in a previous cold test. Also a standing wave structure was introduced between the RF amplifier and the feed through of the FPC to further enhance the coupling in case stronger coupling is needed to condition a multipacting barrier. The design parameters of the 112 MHz electron gun are shown in Table 1.

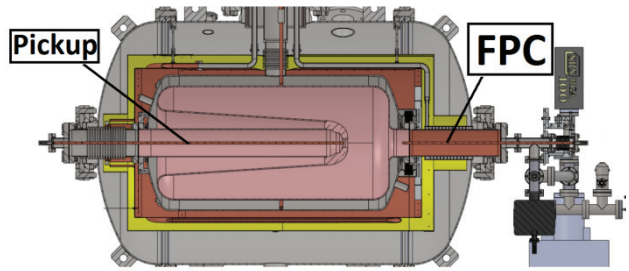


Figure 1: Layout of the 112 MHz SRF cavity horizontal test. The coaxial FPC approaches from the exit of the cavity and the pickup antenna goes through the nose cone part of the cavity and positioned 2 cm behind the entrance of the cavity.

Table 1: Design Parameters of the 112 MHz Electron Gun

Parameters	Value
Frequency	112 MHz
Charge per Bunch	1~3 nC
Repetition Rate	78 kHz
Acceleration Voltage	1~2 MV
Cavity Q_0	1.8e8
R/Q	122 Ω

Experimental Results

The cool down took about 4 hours to bring the cavity to superconducting status. To avoid condensation of residual gas on the FPC, the thermal shield was not cooled until later in the process.

Soon after the superconducting status was reached, the multipacting barriers were observed at relatively low field level. The corresponding gap voltage was estimated to be below 50 kV and the more accurate value was later confirmed to be in the range of 30 kV to 40 kV by Track3P simulation.

After overcoming the multipacting barriers, the cavity Q *vs.* accelerating voltage Vc was measured. Figure 2 shows the result of the measurement.

*This work was carried out at Brookhaven Science Associates, LLC under Contracts No. DE-AC02-98CH10886 and at Stony Brook University under grant DE-SC0005713 with the U.S. DOE.
#txin@bnl.gov

Copyright © 2013 CC-BY-3.0 and by the respective authors

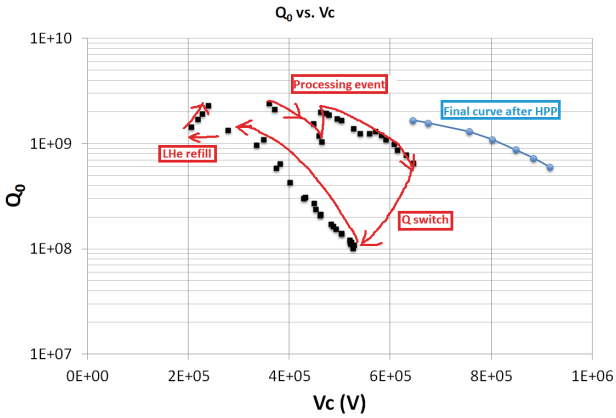


Figure 2: Q_0 *vs.* V_c during the 112 MHz SRF cavity cold test. The black squares show the process of conditioning and the blue dots show the final measurement after the high power pulse processing.

Black squares show the processing which includes the activation of emitter and the consequent Q switch. Blue dots show the final Q_0 *vs.* Vc curve after the high power pulse process. As we can see under CW mode the gap voltage reached 0.9 MV, only limited by the radiation concern at Niowave test facility.

MULTIPACTING SIMULATION

The multipacting barriers we encounter in this cold test were relatively easy to overcome as soon as we improved the FPC coupling. However, in a future test of the gun at Brookhaven National Lab, there will be a different fundamental power coupler. In addition, a cathode stalk, which is specially designed to transport and support the photocathode in the gun, will take the place of the pickup antenna [1, 2]. All these differences might introduce different multipacting barriers and we want to see the relative strength between the known one and the barriers predicted by simulations.

Secondary Electron Yield Curve

For the Secondary Electron Yield (SEY) curve, we chose Furman's model [3]. The SEY curves of the materials we encounter in our gun are shown in Figure 3. The parameters used to generate these curves are shown in Table 2. The formulae for three different type of secondary emission are shown bellow.

True secondary:

$$\delta_{ts} = \frac{s\times\frac{E_0}{E_{max}}}{s-1+\left(\frac{E_0}{E_{max}}\right)^s} \quad (1)$$

Elastic backscattering:

$$\delta_e = P_{1,e}(\infty) + \left(\hat{P}_{1,e} - P_{1,e}(\infty)\right) EXP\left[-\frac{\left(\frac{E_0}{W}\right)^p}{P}\right] \quad (2)$$

Rediffused electrons:

$$\delta_r = P_{1,r}(\infty)\left\{1 - EXP\left[-\left(\frac{E_0}{E_r}\right)^r\right]\right\} \quad (3)$$

Total SEY:

$$\delta = \delta_{ts} + \delta_e + \delta_r \quad (4)$$

The cavity and part of the beam pipe is made of niobium. For Niowave test, the center conductor of the FPC and pickup were copper.

Table 2: Parameters used to Generate SEY Curves

	Niobium	Copper
True secondary		
δ_{max}	1.36	1.88
E_{max}(eV)	300	276e
s	1.3	1.54
Elastic backscattering		
$P_{1,e}(\infty)$	0.001	0.02
$\hat{P}_{1,e}$	0.002	0.496
W	100	60.86
P	0.9	1
Rediffused		
$P_{1,r}(\infty)$	0.001	0.2
E_r	40	0.041
r	1	0.104

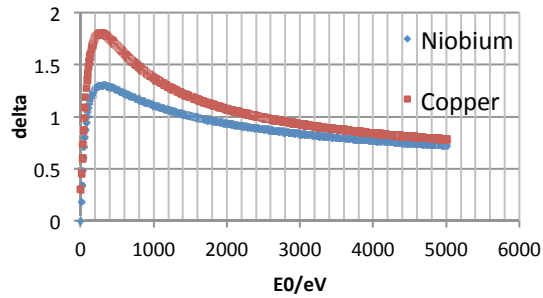


Figure 3: SEY curves of niobium (blue diamonds) and copper (red squares).

Simulation Result for Niowave Test

Figure 4 shows the electric field and magnetic field simulated by Omega3p. This field distribution was used as the input for Track3p simulation. The primary electrons were generated from the inner surface of the whole assembly near the vertical symmetry plane. Then the electrons would be tracked under the force exerted by the RF field. After each impact the phase of the field will be evaluated, if the direction of the field favours the emission of the secondary electron, the impact energy and the location of the electron will be recorded. If the field on impact phase doesn't allow the emission of secondary electron then the particle is removed from simulation. After 50 RF cycles, only the survived particle would be recorded and marked as resonance particle [4]. The total enhanced counter function of these particles will be calculated based on the impact energies and the SEY curve of the impact surface. By looking at the relative height and width of the Enhanced Counter Function peaks we can get the idea of the difficulties in overcoming those barriers.

Copyright © 2013 CC-BY-3.0 and by the respective authors

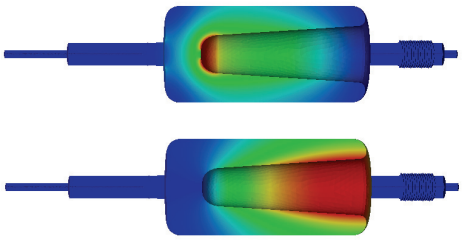


Figure 4: Electric (upper) and magnetic field (lower) simulated by Omega3p for the 112 MHz SRF cavity in the Niowave test configuration.

The simulation gives two potential bands of multipacting. Figure 5 shows the longitudinal location of resonance particles versus impact energy. Since the SEY curve of niobium surpass unity between 100 eV and 1300 eV, we only have to pay special attention to the particles that have impact energy fall into this range.

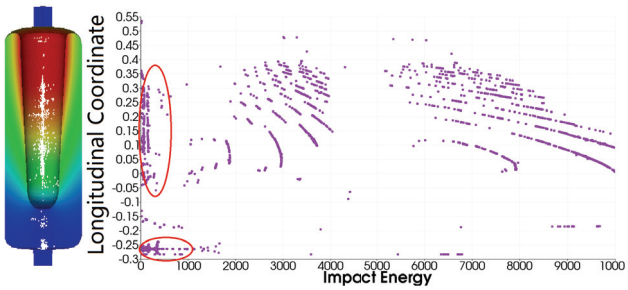


Figure 5: The diagram on the right hand side shows longitudinal location of potential multipacting sites. Picture on left hand side shows the locations (white dots) of those sites inside the cavity. The longitudinal Coordinate axis is mutually applicable to both pictures. The gap voltage was scanned between 100 V to 100 kV.

Post processing of Track3P data shows two multipacting barriers near 30 and 40 kV gap voltage, which is consistent with the observation during the Niowave cold test. Figure 6 shows the Enhanced Counter Function versus the gap voltage of the cavity. One site is located near the gap of the cavity and the other one is located near the high magnetic field region. Both of them survived 50 impacts in RF cycles.

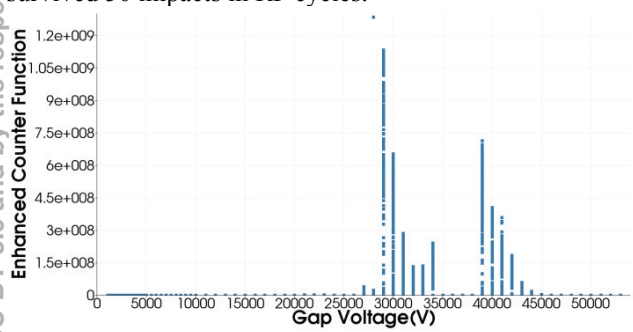


Figure 6: Enhanced Counter Function versus gap voltage of the cavity.

After identifying the field level of two multipacting barriers, we performed the single field mapping with Track3P and extracted two typical trajectories of the potential multipacting electrons. Figure 7 shows the trajectories of two suspicious multipactors. The one that is close to the gap of the cavity is a 1st order multipacting and the one located in the high magnetic field region is a 2nd order multipacting.

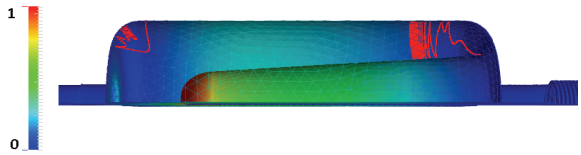


Figure 7: Trajectories of electrons at two multipacting sites (red lines). The left one is under 29 kV gap voltage and the right one appears at 40 kV gap voltage. The color scale indicates the relative strength of electric field.

CONCLUSION

The successful cold test at Niowave gave us a good opportunity to compare the experimental result with the simulation result of the multipacting barriers in the 112 MHz cavity. Two major sites of potential multipacting in the cavity were captured by the simulation of Track3p and also observed during the conditioning process. The multipacting barriers were relatively easy to overcome. This gives us more confidence in future test at BNL since the strength of the suspected multipacting barriers given by previous simulation in the FPC and cathode stalk are much lower than what we found from this run.

ACKNOWLEDGMENT

The authors wish to thank Dr. Ge from SLAC and Dr. Luo from LBNL for their help with Track3P issues.

This research used resources of the National Energy Research Scientific Computing Center, which is supported by the Office of Science of the U.S. Department of Energy under Contract No. DE-AC02-05CH11231.

REFERENCES

[1] T. Xin, et al, Design of the fundamental power coupler and photocathode inserts for the 112 MHz superconducting electron gun, Proceedings of SRF2011, Chicago, IL USA (2011).

[2] T. Xin, et al, Simulations of multipacting in the cathode stalk and FPC of 112 MHz superconducting electron gun, Proceedings of IPAC2012, New Orleans, Louisiana, USA (2012).

[3] M. A. Furman, et al, Probabilistic model for the simulation of secondary electron emission, Phys. Rev. ST Accel. Beams 5, 124404 (2002) 124404-1.

[4] L. Ge, et al. Multipacting simulation and analysis for the FRIB β = 0.085 quarter wave resonators using Track3p, Proceedings of IPAC2012, New Orleans, Louisiana, USA (2012).

Copyright © 2013 CC-BY-3.0 and by the respective authors

PROGRESS IN THE DEVELOPMENT OF TEXTURED DYSPROSIUM FOR UNDULATOR APPLICATIONS*

F. H. O'Shea†, R. Agustsson, Y.-C. Chen, T. Grandsaert II, A. Murokh and K. Woods
RadiaBeam Technologies, Santa Monica, CA 90404, USA
J.-H. Park, R. Stillwell, NHMFL, Tallahassee, FL 32310, USA

Abstract

RadiaBeam Technologies is in the process of developing bulk textured dysprosium as a potential replacement for CoFe steel as undulator poles. For cryogenic undulators that can be cooled below the ferromagnetic transition of dysprosium, textured dysprosium offers potential increase in the peak field of the undulator. Here we report on the progress of the project, including magnetization curves for the material.

INTRODUCTION

The operation of cryogenic permanent magnet undulators (CPMUs) at temperatures below the Curie transition of rare-earth metals offers the opportunity to develop new pole materials that take advantage of the existing cryogenic conditions to potentially produce higher peak field undulators. To this end, RadiaBeam Technologies has been investigating the use of dysprosium and gadolinium to replace the cobalt-iron (CoFe) typically used in high field hybrid undulators. CoFe is the pole material of choice for high field undulators because of its large saturation magnetization (2.35 T), very large initial permeability ($\mu_i \sim 10^4$) and small non-linear knee region which is the transition between the two regions. In single crystal form, dysprosium demonstrates much higher magnetic moment (>3 T [1]) at low applied field and cryogenic temperatures than CoFe [2]. However, single crystals of these materials are difficult and expensive to produce at the dimensions and scale required for undulator fabrication and polycrystalline versions of the materials are not useful for undulator applications because of low initial permeability.

A compromise between the single crystal and polycrystalline forms can be reached through a processing technique that generates so-called texture in the material. This technique takes advantage of a favorable energy difference between crystallographic orientations during a rolling and annealing cycle [3]. Briefly, the polycrystalline material is rolled out and then annealed near the melting point. For dysprosium, which has an *hcp* structure, grains within the foil that are oriented with the hardest axis within the plane of the foil are taken over by grains that have the hardest axis pointed normal to the plane of the foil in a process known as secondary re-crystallization. This process dramatically increases the permeability within the plane of the foil [1]. The foils can then be annealed together in stacks to produce a macroscopic piece for further machining.

MATERIAL DEVELOPMENT

We have previously reported the results of magnetic measurement of the textured dysprosium [2]. Those results showed that the textured dysprosium, made up of 100 μm thick foils, used in the initial 2-period prototype would not produce an improvement in peak field over CoFe poles. In that publication we suggested several changes that might increase the performance of the the textured dysprosium poles: operate the undulator at lower temperature, use thinner foils in the poles, and increase the complexity of the design of the undulator by installing backing magnets on the side of the poles opposite the magnetic gap. Because of those observations, all foils created subsequently have been 25 μm thick. Since that previous publication we have found evidence of another feature of the textured dysprosium that will influence future magnetic designs, namely that the direction of rolling affects the orientation of the easy axes of magnetization. Unfortunately, because cryogenic magnetic measurement techniques below 77 K require the use of liquid helium, we have had difficultly finding facilities willing to perform these measurements until recently.

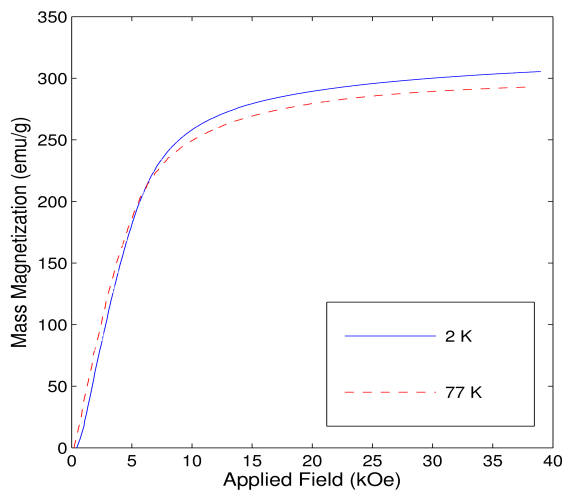


Figure 1: Comparison of the magnetic performance of textured dysprosium at 2 K and 77 K. The sample was cut such that the direction of measurement was within the rolling plane.

* Work supported by DOE under contracts DE-SC0006288 and NNSA SSAA DE-NA0001979
† oshea@radiabeam.com

Copyright © 2013 CC-BY-3.0 and by the respective authors

Temperature Effects

The first suggested solutions is to decrease the temperature of the device. A colder undulator would have both higher remanent magnetic field of the PrFeB magnets [4, 5] and higher initial permeability in the textured dysprosium poles. The former results in larger applied fields while the latter results in greater pole tip field per unit of applied field, both critical to attaining large on-axis magnetic fields [6]. Figure 1 shows a comparison between the magnetization of textured dysprosium at 2 K and 77 K. The two features of note are that above 5 kOe applied field, the colder textured dysprosium is more strongly magnetized and below 5 kOe, the warmer sample is more strongly magnetized. We would expect that as the material is cooled, it is more easily magnetized because the thermal energy that allows the individual dipoles to resist the torque of the applied field is reduced [7]. That appears to be the case at larger applied field (>10 kOe), but not lower applied field.

The shape of the measured sample in Fig. 1 was modified from the original shape to fit into the measurement device. The modification resulted in a large demagnetizing factor [8]. Because of this we hypothesize that the unexpected reversal of performance below 5 kOe can be explained by the effect of the large demagnetizing factor. At low applied field, we would expect that the actual applied field would be lower than the observed applied field, which is the abscissa of Fig. 1, in the case of stronger magnetization because the two are related as $H_{actual} = H_{observed} - NM$, where N is the demagnetizing factor and M is the magnetization of the sample.

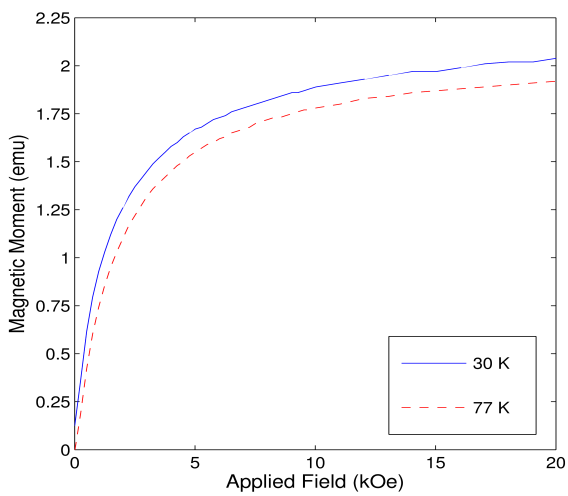


Figure 2: Comparison of the magnetic performance of textured dysprosium at 30 K and 77 K. The sample was cut such that the direction of measurement was within the rolling plane. Note the different ordinate as compared to Fig. 1.

To test this hypothesis, a different sample, manufactured identically and of smaller demagnetizing factor, was measured in a different measurement setup at a different location. The results of the measurements at 30 K and 77K, after correction for the demagnetizing factor, are shown in Fig. 2. It can be seen that the lower temperature magnetization curve always shows higher magnetization than the higher temperature curve, consistent with the hypothesis of a large demagnetizing factor in the measurement shown in Fig. 1 We chose to perform the second measurement at 30 K, instead of the previous 2 K, because that temperature can be maintained by a closed loop cold head, reducing future experimental complexity. 30 K is also the approximate temperature of maximum thermal conductivity of copper [9].

Orientation Effects

In previous simulation work, we have treated textured dysprosium as an anisotropic material with one hard axis, [0001], and two easy axes, $<10\bar{1}0>$ and $<11\bar{2}0>$. This is because the available simulation packages can only handle anisotropy of this 2+1 form [10]. The assumption is that there is an equal mixture of the two easy domains in the plane of the foil (the basal plane). However, the two easy axes are not equivalent, the $<10\bar{1}0>$ axis is actually harder than the $<11\bar{2}0>$ axis, even though both are much softer than the [0001] direction [11, 12]. Therefore, if the process that generates texture produces a preference for grain orientation, there will be a preferred direction for cutting the poles out of the bulk laminated material. The highest on-axis magnetic field will be obtained if the pole is manufactured such that the $<11\bar{2}0>$ axis is normal to the undulator mid-plane. This is, of course, a statement of the average direction in which each axis points.

Previous work studying textured dysprosium has observed that the texture develops such that the $<10\bar{1}0>$ axis is preferentially aligned with the direction of rolling [13]. We should, therefore, be able to detect this difference in measurements made on samples cut from the two different orientations. To measure the difference in magnetization, two samples were cut from the same piece of bulk laminated pole, called sample A and sample B. Sample A was measured along the direction of rolling and sample B was measured along the direction perpendicular to the rolling direction and the foil normal. As can be seen in Fig. 3, sample A is clearly magnetically harder than sample B, consistent with previous observations showing a preference for the texture to develop with the $<10\bar{1}0>$ axis along the direction of rolling. Both samples are more easily magnetized at lower temperature and the benefits of cooling the textured dysprosium to 30 K are almost entirely erased by non-optimal orientation of the texture relative to the undulator mid-plane.

Simulation has shown that, in a hybrid undulator design of 7-9 mm period length, the applied field at the pole tips is approximately 0.15 T. At this applied field, the remanent field of the textured dysprosium is 25% larger for a pole cooled to 30 K and cut such that the $<11\bar{2}0>$ axis is optimally oriented, as compared to a pole cooled to 77

Copyright © 2013 CC-BY-3.0 and by the respective authors

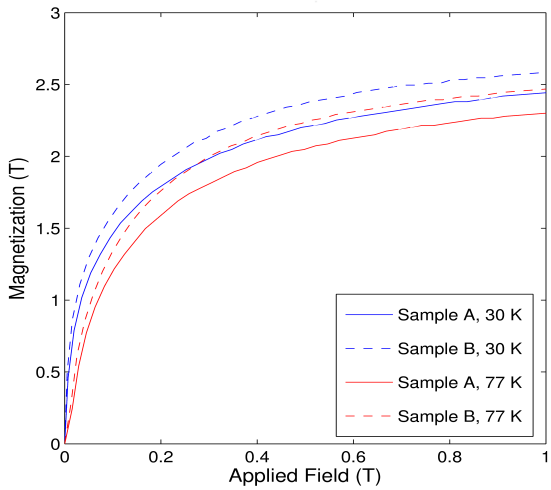


Figure 3: Comparison of the magnetic performance of textured dysprosium as a function of measurement along the two axes of the basal plane, $<10\bar{1}0>$ (sample A) and $<11\bar{2}0>$ (sample B), at two different temperatures.

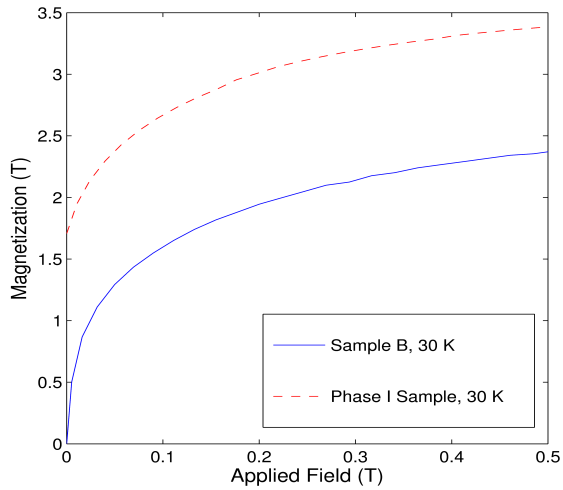


Figure 4: Comparison of the easy magnetization curves from the current sample B and the data presented in Ref. [2]. The decrease in magnetic performance is due to increased oxide formation in the updated procedure for making the bulk laminate.

K and cut such that the $<10\bar{1}0>$ axis is normal to the undulator mid-plane. In fact, this is a conservative estimate because the more easily magnetized material will apply a larger field at the pole tip.

Material Performance

It is clear from the preceding that the highest peak field will result from choosing sample B cooled to 30 K. By cutting the poles from the bulk laminate such that the $<11\bar{2}0>$ axis of the texture is oriented in the same direction as the dominant magnetic field. For example, in a vertically ($\hat{y}$) polarized planar undulator in which and electron in the mid-plane oscillates horizontally ($\hat{x}$) and the beam travels along the $\hat{z}$-direction, the texture of the dysprosium should be oriented such that ($\hat{x}$,$\hat{y}$,$\hat{z}$):([0001],$<11\bar{2}0>$,$<10\bar{1}0>$) for optimal performance. Previous simulation has shown that there is a small decrease in performance when the texture is oriented with the $\hat{x}$ and $\hat{z}$ directions switched, poles with this texture orientation are much easier to manufacture.

To more efficiently produce a large amount of bulk laminate textured dysprosium, we modified the processing technique that produced excellent magnetic results in earlier phases of the project. The principal modification was an intermediate annealing step during rolling to relieve strain from the rolling. Although x-ray 2θ scans of the material show good texture development [1], this additional step substantially increases the fraction of the bulk laminate that is made up of dysprosium oxide, reducing overall magnetic performance. This additional annealing step has been removed from the process and additional measurements are being performed at the time of publication.

ACKNOWLEDGMENT

We thank E. Mun and J. Betts at the National High Magnetic Field Laboratory at Los Alamos for the data used in Fig. 1 and T. Scrivnor for careful machining of the samples measured.

REFERENCES

[1] A. Murokh, *et al.*, submitted to NIM A.

[2] F. H. O'Shea, *et al.*, IPAC'13, Shanghai, China, WEPWA081, p. 2298, `http://www.JACoW.org`

[3] W. Swift, and M. Mathur, IEEE Trans Mag. 10, 308 (1974).

[4] K. Uestuener et al., 20th workshop on Rare Earth Permanent magnets, 2008, Crete, Greece.

[5] C. Benabderrahmane *et al.*, Nucl. Inst. Meth. A 669, 1 (2012).

[6] R. Dejus, M. Jaski and S. H. Kim, Argonne Nat. Lab. Rep. No. ANL/APS/LS-314.

[7] J.J. Rhyne and A.E. Clark, Journal of Applied Physics 38, 1379 (1967).

[8] J. A. Osborn, PHys. Rev. 67, 351 (1945).

[9] E. D. Marquardt, J. P. Le and R. Radebauch, 11^{th} International Cryocooler Conference (2000). `http://cryogenics.nist.gov/MPropsMAY/material properties.htm`

[10] O. Chubar, P. Elleaume and J. Chavanne, J. Synch. Rad. 5, 481- 484 (1998).

[11] D.R. Behrendt, S. Legvold and F.H. Spedding, Phys. Rev. 109, 1544 (1958).

[12] A.S. Chernyshov, *et al.*, Phys. Rev. B 71, 184410 (2005).

[13] R. H. Hopkins, Metal. Trans. 5, 1183 (1975).

Copyright © 2013 CC-BY-3.0 and by the respective authors

SURFACE PLASMON RESONANCE ENHANCED MULTIPHOTON EMISSION FROM METALLIC CATHODE*

H. To, R. Li, P. Musumeci, UCLA, Los Angeles, CA 90095, USA
G. Andonian, Radiabeam Technologies, Santa Monica, CA 90404, USA

Abstract

We investigate the use of surface plasmonic nanostructures in increasing the efficiency of copper photocathodes for high-brightness electron sources. A nanohole structure was fabricated, using focused ion beam milling, such that it exhibited a strong plasmonic response near 800 nm. The reflectivity of the nanostructured surface was significantly lower compared to that of a flat surface, due to plasmonic resonance effects. A previous experiment [1] demonstrated an increase in charge yield by over a factor of 100, using a slightly off-resonance structure. With this new near-resonant structure, the reflectivity is expected to be even lower and the charge yield enhancement factor even larger.

INTRODUCTION

Recently, progress has been made in using metal photocathodes to generate high brightness electron beams, as an alternative to using semiconductor cathodes [2]. Because of their prompt response, low vacuum requirements, robustness, and fabrication simplicity, metals are typically the preferred choice in high peak brightness photoguns [1]. However, metal cathodes are not without disadvantages, a significant one being that they are often highly reflective at optical and infrared wavelengths and in general offer lower QE than semiconductors [3].

We, at the UCLA Pegasus laboratory, have demonstrated the generation of electron beams through multiphoton emission using a copper photocathode with an 800 nm Ti:Sa incident laser [2]. At 800 nm, copper is ~95% reflective, and thus, most of the photons from the incident laser are wasted and do not participate in the multiphoton emission process [3]. To increase the efficiency of the cathode, an obvious solution would be to increase the absorptivity of copper at 800 nm. One way we propose to do this is to pattern a cathode surface with nanoscale features that take advantage of plasmonic effects.

THEORY

Recent advances in nano-plasmonics have enabled fine control of optical properties of metal surfaces by patterning them with sub-wavelength or nanoscale features [4]. Nanoscale features of the correct geometry can lead to surface plasmon resonance, or a resonant interaction between surface plasmons and incident photons [5]. This produces two major effects [4]: 1) significant reductions in metal reflectivity due to photons being absorbed by surface plasmons, and 2) large enhancements of local optical field intensity due to photon energy being stored in the surface plasmons. These nano-plasmonic phenomena could be applied to optimize the optical response of a cathode and obtain high efficiencies in photoemission charge yield.

Previously, we reported the first experimental results of the generation of relativistic electron beams from a nanostructured photocathode in a high gradient RF gun [2]. The aforementioned nanohole array structure exhibited a resonant response at ~810 nm. At 800 nm, the reflectivity of the nanopattern was ~60%, still producing a >100-fold enhancement in the multiphoton charge yield. With a nanopattern that is resonant closer to 800 nm, the charge yield can be expected to be greater.

SETUP

The geometry of the nanopatterns consist of rectangular arrays of nanoholes fabricated with focused ion beam (FIB) milling, as shown in Fig. 1. The patterns were milled onto a single crystal Cu(100) substrate to avoid pattern variation due to the random grain sizes and orientations associated with polycrystalline substrates.

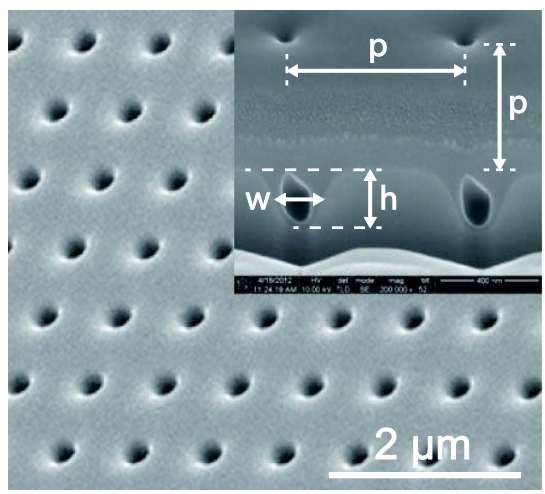


Figure 1 [1]: Scanning electron microscopy images of a nanohole array. Inset: Zoomed in profile view of nanoholes.

When using the nanohole array geometry, the resonant wavelength is much more sensitive to the spacing of the holes than to their depth, width, and even their shape [1]. Each nanohole has an approximately Gaussian profile, mainly due to the current density distribution of the milling ion beam. Finite Difference Time Domain (FDTD) simulations were performed to compare the

*Work supported by U.S. DOE Grants No. DE-FG02-92ER40693 and U.S. DOE SBIR Grant No. DE-SC0009656

Copyright © 2013 CC-BY-3.0 and by the respective authors

difference in resonant response between Gaussian-shaped holes and ideal rectangular holes, using the same depth, width, and spacing. We found that the resonant wavelength for these two profiles differed only by about 4 nm, as shown in Fig. 2. This finding is important in that it allows us to fine tune the resonant wavelength primarily by changing the hole spacing p, which is the most controllable and reproducible parameter in a FIB device.

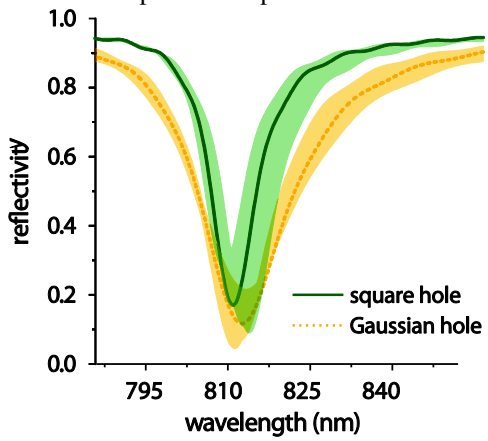


Figure 2 [1]: Simulated reflectivities at normal incidence of two types of nanohole pattern: square holes and Gaussian holes.

In this study, we fabricated nanopatterns with spacing p of 765 nm, shown in Fig. 3. The dimensions of the structure (spacing p, depth h, and FWHM width w of the holes) were optimized through finite difference time domain (FDTD) simulations. The values of h, w, and p are ~300 nm, ~200 nm, and ~765 nm respectively. The middle right pattern is the same as the top and middle left patterns, but rotated 90 degrees. This is to check the possibility of asymmetry in the nanoholes, i.e. the holes could be slightly elliptical rather than perfectly circular. Fig. 4 shows the reflectivity curves for the un-rotated and rotated patterns. When imaging the nanopattern at normal incidence using a 2 nm FWHM laser at the resonant wavelength, the incident light is strongly absorbed (Fig. 3).

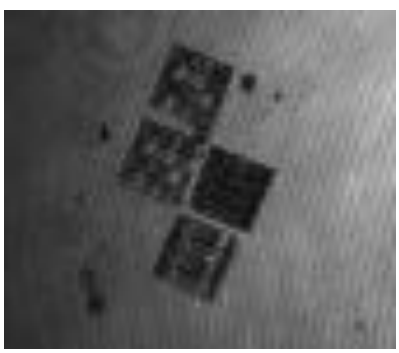


Figure 3: Nanopatterns with 200 nm FWHM width and 300 nm depth. Top left: 765 nm spacing. Middle left: 765 nm spacing. Middle right: 765 nm spacing, pattern rotated 90 degrees with respect to first two patterns. Bottom right: practice pattern. Pattern square sizes: ~ 100 μm by 100 μm.

When imaging the nanopattern at normal incidence using a 2 nm FWHM laser at the resonant wavelength, the incident light is strongly absorbed, as shown in Fig. 3. The measured resonant wavelength of this nanopattern is 795 nm with a bandwidth of 34 nm, and corresponds to a reflectivity of 12%. At 800 nm, the nanopattern exhibited a reflectivity of 23%.

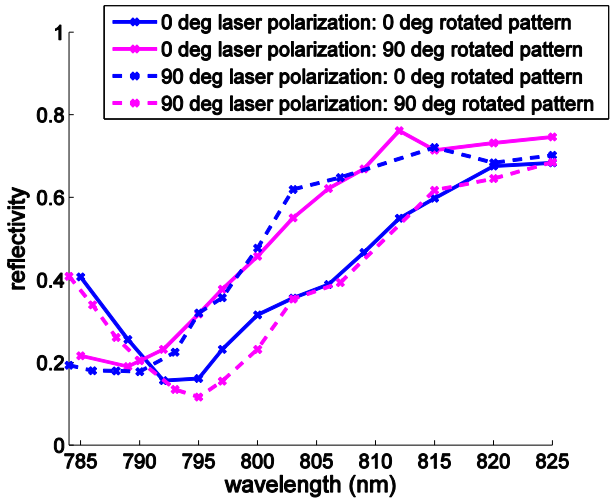


Figure 4: Reflectivity curves for most recent nanopatterns. Solid curves: 0 degree laser polarization. Dashed curves: 90 degree laser polarization. Blue curves: un-rotated pattern. Magenta curves: rotated pattern, 90 degrees with respect to un-rotated pattern.

ANALYSIS

The reflectivity curves in Fig. 4 indicate polarization dependence for the nanostructures. For a pattern, the un-rotated pattern for example, the resonant wavelength shifts when the laser polarization is changed by 90 degrees (blue curves). The rotated pattern exhibits the same behaviour, but in reverse (magenta curves). This suggests that the holes are indeed slightly elliptical in shape. The small shift (< 4 nm) in the plasmonic resonance peak can be explained due to some asymmetry in the FIB machine's focus in the x and y directions in agreement with the simulation prediction.

It is interesting to compare the potential increase in charge yield from the 795 nm resonance pattern to the previous 810 nm resonance pattern. In the previous experiment [1], IR laser pulses (150 fs FWHM) were focused to 120 μm rms and scanned around the nanopattern at near normal incidence (<1°) with a piezo-controlled mirror. The position of the laser spot on the cathode was monitored using a virtual cathode screen, and the generated beam charge was measured by a calibrated high efficiency beam profile camera. The maximum

Copyright © 2013 CC-BY-3.0 and by the respective authors

signal, obtained when the laser spot fully covered the nanopattern, was $Y_{exp} > 1.2 \times 10^2$ times greater than when the laser was hitting only a flat surface [1].

This large increase cannot by fully explained by just the change in IR reflectivity and absorption. The generalized Fowler-Dubridge theory [6] predicts an increase of $Y_{FD}=(1-R_p)^3/(1-R_f)^3=27$ times, where $R_p=64\%$ and $R_f=88\%$ are the measured reflectivities of the previous nanopattern and the flat cathode surface, respectively. The additional enhancement in charge emission can be attributed to the optical intensity enhancement due to surface plasmon resonance (Fig 5.).

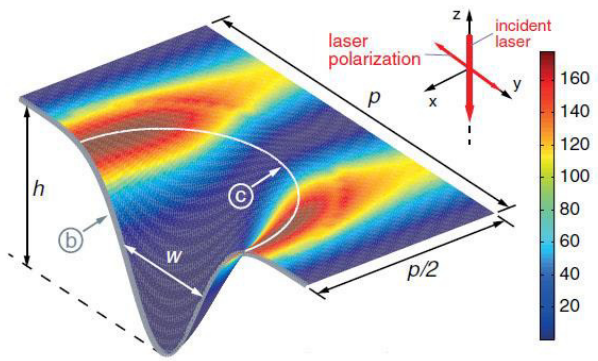


Figure 5 [1]: Intensity distribution on the nanohole surface.

It is estimated that a nanopatterned surface produces ~5 times more charge than a flat surface under equal absorbed intensity [1]. As mentioned, the more recent nanopattern exhibited a reflectivity of $R_p=23\%$. From a reflectivity standpoint alone, this corresponds to a charge enhancement factor of $Y_{FD}=(1-R_p)^3/(1-R_f)^3\sim250$ times. Taking into account the enhancement due to surface plasmon resonance, this suggests that the total enhancement factor could be at least 1000.

It is important to consider possible limitations to this large enhancement factor. It has been demonstrated that structural changes to a nanopatterned cathode surface occur when the absorbed fluence approaches 10 mJ/cm^2 [1]. The result is consistent with the 50 mJ/cm^2 limit reported for a flat copper surface [7] taking into account the ~5 times enhancement due to surface plasmonic effects. This sets an upper limit to incident laser power for nanopatterned surfaces that is lower than the limit for a flat surface, i.e. using an arbitrarily high laser power does not yield an arbitrarily high charge yield. In regards to an upper limit to charge yield, at present, it is unclear whether the localized emission of photoelectrons from a nanostructured cathode sets a different limit on the highest extractable charge density than a flat cathode case, but that should be an interesting topic for future studies.

CONCLUSION

In summary, this work demonstrated the potential to use plasmonic nanostructures to change the optical properties of a copper photocathode. In doing so, we were able to mitigate the inherent ~90% reflectivity of a flat copper surface. We showed a significant increase in charge yield from using a previous nanostructure that was 64% reflective at 800 nm, and thus, we can expect any even larger increase from the current nanostructure, which is 23% reflective. Our next steps include generating an electron beam with this nanostructured cathode and comparing its characteristics (charge yield, intrinsic emittance, and bunch length) to that of a beam from an ordinary flat cathode. We envision this work to be a promising step in a new direction of photocathode research.

ACKNOWLEDGMENT

We would like to thank Noah Bodzin (UCLA) for his technical support with the fabrication of the nanopatterns. This work is supported by U.S. DOE Grants No. DE-FG02-92ER40693 and U.S. DOE SBIR Grant No. DE-SC0009656.

REFERENCES

[1] R. Li et al., Phys. Rev. Lett. 110.7(2013), 074801.
[2] P. Musumeci et al., Phys. Rev. Lett. 104.8(2010), 084801.
[3] E. D. Palik, Handbook of Optical Constants of Solids, (New York: Academic Press, 1985).
[4] W. Barnes et al., Nature 424.6950(2003), 824-830.
[5] A. Polyakov et al., Phys. Rev. Lett. 110.7(2013), 074801.
[6] J. Bechtel et al., Phys. Rev. B 15.10(1977), 4557.
[7] S. Kirkwood et al., Appl. Phys. A 81.4(2005), 729-735.

Copyright © 2013 CC-BY-3.0 and by the respective authors

BEAM DYNAMICS DRIVEN REQUIREMENTS ON THE ARIEL E-LINAC SRF SEPARATOR CAVITY*

Douglas W Storey[1,2†], Yu-Chiu Chao[2], Lia Merminga[2],
[1]University of Victoria, Victoria, B.C, Canada, [2]TRIUMF, Vancouver, B.C, Canada

Abstract

A possible future extension to TRIUMF's ARIEL e-linac is the addition of a recirculation path for an Energy Recovery Linac (ERL), which will drive an Infrared or THz Free Electron Laser (FEL). The ERL electron beam will be interleaved with the single-pass beam bound for Rare Isotope Beam (RIB) production in the ARIEL facilities, allowing for simultaneous beam delivery to both FEL and RIB users. A superconducting RF separator will separate the beams at the exit of the linac at a frequency of 650 MHz in CW mode. After a second pass through the linac, the energy recovered ERL beam will pass through the separator cavity out of phase with the deflecting fields, and at a much lower energy, before continuing to a beam dump. Using the General Particle Tracer software, three-dimensional simulations of the beam dynamics of the passing beams have been performed to determine the requirements on the SRF separator's deflecting field uniformity. Operation of the FEL requires minimal emittance dilution of the ERL beam from the separator. This contribution describes the results of these studies and the requirements imposed on the SRF beam separator.

INTRODUCTION

The ARIEL e-linac will produce a 50 MeV, 10mA CW electron beam as the photo-fission driver for the production of neutron rich Rare Isotope Beams (RIB). This complementary RIB source will expand TRIUMF's existing ISAC experimental program. The electron beam is accelerated through an injector cryomodule to an energy up to 10 MeV, and two accelerating cryomodules (ACM) up to an energy of 50 MeV in cavities operating at 1.3 GHz [1].

A future phase will be the addition of a recirculation loop to return the electrons for a second pass through the main linac. This may be configured as a recirculated linac (RLA), accelerating the beam up to 75 MeV before continuing on for RIB production, or as an Energy Recovery Linac (ERL) with a Free Electron Laser operating in the back leg of the recirculation loop and interleaved with the RIB beam in the main linac.

Successful operation of the FEL depends on a low emittance beam, requiring minimal emittance dilution imparted during the separation of the beams at the exit to the main linac.

* Work supported by the Natural Sciences and Engineering Research Council of Canada.

† dstorey@uvic.ca

RF Separator Layout

Bunches bound for either RIB production or the ERL will have the same energy when reaching the separator section and will occupy alternating buckets of the 1.3 GHz accelerating RF. Separation of the bunches will then require RF separation at a frequency of 650 MHz at the exit of the main linac. Furthermore, the separator layout must also be compatible with the RLA operating mode, which will rely on the static magnetic separation of the two beams.

The basis of this separation scheme has been developed in [2] and comprises of an RF separator cavity imparting an initial differential transverse kick to the two beam types, followed by a steering dipole, a defocusing quadrupole to further enhance the separation, and finally a septum magnet to perform the final separation of the beams. This scheme is driven by rigid space constraints that require the full separation of the beams within a distance of about 3 m. The layout of the separation section of the e-linac is depicted in Fig. 1.

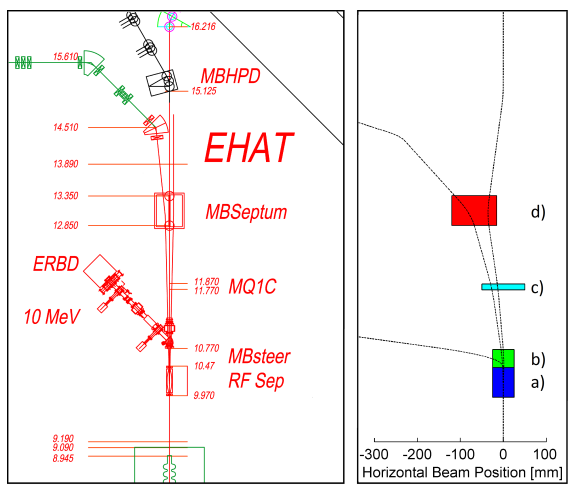


Figure 1: The layout of the ARIEL RF separator on the left with the beam deflections shown on the right. The elements shown are the a) RF separator cavity, b) dipole magnet, c) quadrupole, and d) septum.

In addition to the RIB and ERL beams, the decelerated beam after making its second pass through the ACM, will reach the RF separator with energy of 5 to 10 MeV and 90°out of phase with the cavities deflecting phase. It will therefore pass mostly unaffected through the separator cavity and receive a sharp deflection by the dipole magnet due to its low energy to be directed down a short transport line to a beam dump.

Copyright © 2013 CC-BY-3.0 and by the respective authors

An SRF cavity with RF Dipole geometry [3] is being considered for the RF separator. This cavity is compact in size and the transverse deflections are high with low peak electric and magnetic fields.

Beam Properties

The RF cavity will operate at 650 MHz to give opposing transverse momentum kicks to adjacent bunches from the main linac at $\pm 90°$. The required angular deflection imparted by the cavity is ± 4.5 mrad for beam energies of up to 66 MeV and currents up to 16 mA CW.

The incoming RIB and ERL beams will have normalized emittances of 5 mm-mrad in both x and y and the transverse RMS beam widths on entering the RF separator cavity are 0.68 mm and 0.42 mm respectively, as determined from the e-linac optics. The energy spread of the beam will be around 0.5%.

After deceleration in the main linac, the beam will have an energy of 5 to 10 MeV with a significant energy spread of about 5%. Additionally, the bunch length will be quite long, up to 6.5 mm RMS.

TRACKING SIMULATION

The simulations of the beam dynamics were performed using the General Particle Tracer (GPT) [4] to quantify the emittance growth of the beam primarily within the separator cavity. The fields in the separator cavity, as described in [5], were exported from the HFSS RF simulation tool on a grid with 1 mm spacing [6]. GPT in turn uses this field map in an 8-point bilinear interpolation to evaluate the field at a specific point in space.

Bunches of 100,000 macro-particles were initiated immediately before the RF cavity with Gaussian spatial distributions and divergences scaled to obtain 5 mm-mrad emittances. The macroparticles were given a uniform distribution of energy spread about the mean beam energy of 50 MeV for the ERL/RIB beams and 7 MeV for the decelerated beam.

The tracking simulation through the RF cavity was performed with varying incoming beam parameters, different momentum kick strengths, and different cavity geometries to determine the emittance growth imparted by the cavity.

RESULTS

For the nominal beam parameters, the emittance growth in the horizontal direction was found to be very minimal with well under a 1% increase. The emittance in the vertical direction was found to be mostly unaffected by the RF cavity within the parameter space studied.

Sensitivity Studies

To investigate the impact of the RF separator cavity under non-optimal beam properties, the transverse and longitudinal RMS sizes, energy spread, and transverse position of the beam were varied about their nominal values.

The horizontal emittance was found to be most sensitive to changes in the transverse beam sizes, particularly in x direction, as shown in Fig. 2. The emittance growth stays below 1% for beam widths under 2 mm but grows very quickly for larger beams.

The emittance showed very little dependence on both the energy spread of the beam and the transverse position.

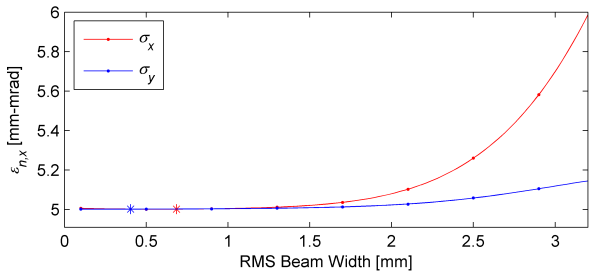


Figure 2: The normalized RMS transverse emittance, $\varepsilon_{n,x}$ at the exit to the RF separator cavity for different beam widths, for an RF voltage of 0.3 MV. The nominal beam widths are marked by the * symbol.

Increased Momentum Kick

Due to the limiting space within the TRIUMF E-Hall, a larger momentum kick imparted by the RF separator could achieve the separation of the beams in a shorter distance. This is desirable as it would loosen space requirements on the surrounding beam-line by allowing a shorter distance between the separator cavity and septum.

Increasing the transverse voltage of the RF cavity will amplify its effect on the emittance of the beam. This effect was studied with increasing deflecting voltages from the nominal 0.3 MV up to 1.7 MV for a 25 mrad angular deflection. This is nearing the upper limit of this cavity geometry with the peak fields approaching operational limits.

At the nominal beam parameters, minimal emittance growth is seen up to the maximum kick strengths studied, with the horizontal emittance increasing by less than 0.5%. Again, the emittance growth sees the largest correlation with the width in the x direction, as shown in Fig. 3. The emittance growth also shows a dependence on σ_y, bunch length, and shows a growing dependency on the y position of the beam.

Based on these results, the deflecting voltage of the cavity may be increased to approximately 0.7 MV, after which the emittance would become too sensitive to the beam width in the x direction. This corresponds to angular deflections after the separator cavity of up to around 10 mrad.

Field Uniformity

The main source of emittance dilution when passing through the separator cavity is the non-uniformity of the fields across the aperture, which causes beam particles to receive a different momentum depending on their transverse position. One way to achieve more uniform deflecting fields is to modify the geometry of the inner ridges of

Copyright © 2013 CC-BY-3.0 and by the respective authors

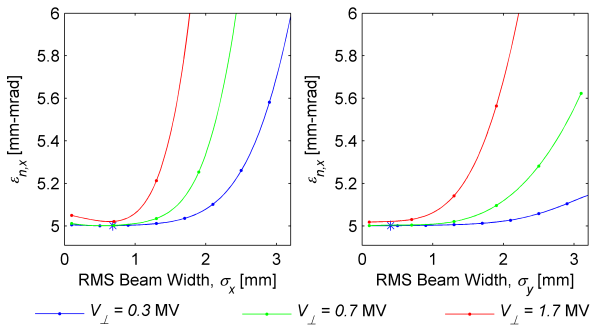


Figure 3: The normalized RMS transverse emittance, $\varepsilon_{n,x}$ at the exit to the RF separator cavity for different beam widths and varying momentum kick from 0.3 MV to 1.7 MV.

the RF dipole cavity to shape the fields in a more uniform way.

The cavity considered thus far has flat inner ridges, as shown in Fig. 4. By giving the inner ridges a slight outwards curvature, the field uniformity can be greatly increased with little effect on the RF properties of the cavity.

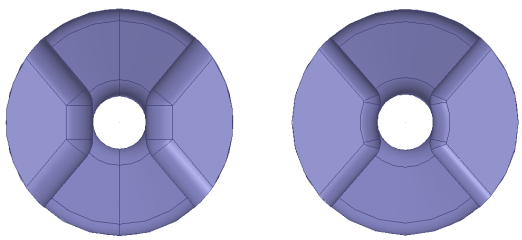


Figure 4: The cross section of the separator cavity with flat inner ridges on the left and curved ridges on the right.

In Fig. 5, the cavity with curved ridges contributes to the emittance growth similarly to the flat ridged cavity for RMS beam sizes less than 1.5mm, after which the curved ridge cavity results in lower emittance growths.

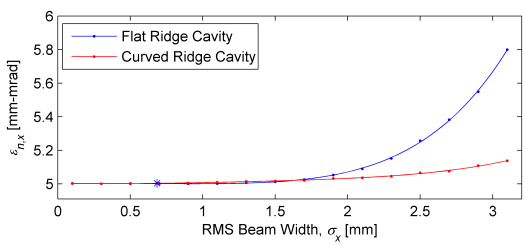


Figure 5: The normalized emittance, $\varepsilon_{n,x}$ at the exit to the RF separator cavity for the two different cavity geometries.

Decelerated ERL Beam

The decelerated beam passes through the RF separator cavity at the zero crossing, nominally with no deflections. However, as the bunch enters the cavity it sees the decreasing deflecting fields, imparting a small momentum to the bunch. While exiting, it sees the fields increasing again and receives an opposing kick. This results in a net zero angular deflection, but also a small horizontal deflection at the exit of the cavity. Additionally, since the bunch length of the decelerated beam is quite long, the head will see a small net angular deflection in the opposite direction as the tail, resulting in a small defocusing effect on the beam.

The scale of the horizontal deflection is approximately 0.5 mm for a 0.3 MV transverse deflecting voltage. This scales linearly with kick strength, resulting in a maximum offset of 2.5 mm for the highest kick strengths considered here, 1.7 MV. The defocusing effect was also found to be minimal.

Deflections of this size will not impede the safe passage of the decelerated beam through the separator cavity and dipole magnet without losing particles along the way. Quadrupoles located after the dipole along the dump beam line will ensure safe transport of the beam to the 10 MeV beam dump, located another 2 m past the separator cavity. The effect of the decelerated beam therefore does not impose any further requirements on the RF cavity.

CONCLUSION

These studies indicate that operating with nominal beam properties, the RF separator cavity will impart minimal emittance growth to the ERL and RIB bound beams. The beam width in the x direction contributes the largest to emittance dilution and for a cavity with flat inner ridges, RMS beam widths of under 2 mm will limit the emittance growth to less than 1%. Overall, the beam dynamics do not imply any stringent requirements on the RF separator cavity.

The upper limit to the deflecting voltage of the cavity is approximately 0.7 MV, after which with the emittance becomes very sensitive to the transverse beam width. This corresponds to a ± 10 mrad angular deflection by the RF cavity. This sensitivity may be decreased by using a cavity with better field uniformity such as one with curved inner ridges.

REFERENCES

[1] S. R. Koscielniak, "ARIEL Electron Linac," MOOBA1, NA-PAC'13.

[2] Y. Chao, S.R. Koscielniak, and C. Gong, "RF Separator and Septum Layout Concepts for Simultaneous Beams to RIB and FEL Users at ARIEL," IPAC'11, San Sebastian, Spain, September 2011, WEPC002, p. 1998 (2011).

[3] S.U. De Silva and J.R. Delayen, Phys. Rev. ST Accel. Beams 16 (2013) 012004.

[4] `http://www.pulsar.nl/gpt/`

[5] D.W. Storey et al., "Feasibility of an RF Dipole Cavity for the ARIEL e-linac SRF Separator," THPBA02, NA-PAC'13.

[6] `http://www.ansoft.com`

Copyright © 2013 CC-BY-3.0 and by the respective authors

FEASIBILITY OF AN RF DIPOLE CAVITY FOR THE ARIEL E-LINAC SRF SEPARATOR*

Douglas W. Storey[1,2†], Robert Edward Laxdal[2], Lia Merminga[2], Vladimir Zvyagintsev[2]
[1]University of Victoria, Victoria, B.C, Canada, [2]TRIUMF, Vancouver, BC, Canada

Abstract

A megawatt class CW e-linac is being designed and constructed at TRIUMF with the main goal of producing neutron rich isotopes for TRIUMF's Rare Isotope Beam (RIB) program. A possible extension of the beam-line will allow recirculation of the beam for an Energy Recovery Linac (ERL) to operate in tandem with the RIB user program. A superconducting cavity with RF dipole geometry is being considered for separation of the ERL and RIB beams at the end of the linac to provide simultaneous beams to both the ERL and RIB programs. This contribution describes optimization studies performed on the RF dipole design to determine if this geometry will meet the requirements of the ARIEL e-linac. The resulting 650 MHz structure has compact cavity dimensions, low peak fields, and high transverse shunt impedance. Due to the large aperture beam-line and stringent requirement on preserving beam quality, extensive focus has been placed on transverse uniformity of the deflecting fields.

INTRODUCTION

A future extension to the ARIEL e-linac [1] will be the addition of a recirculation path to the beam-line for an Energy Recovery Linac (ERL), the driver for an Infrared or THz Free Electron Laser (FEL). The ERL electron beam will be interleaved with the single-pass beam bound for Rare Isotope Beam (RIB) production in the ARIEL facilities, allowing for simultaneous beam delivery to both FEL and RIB users.

Bunches of electrons bound for either the ERL or RIB will occupy alternating buckets of the 1.3 GHz accelerating RF. The separation of the beams will take place at the exit of the main linac. The basis of this separation scheme is introduced in [2], which describes the layout and deflections required by each element in the separation complex: an RF separator, steering dipole, defocusing quadrupole, and septum magnet. This scheme is driven by the rigid space constraints that require the separation of the beams within a distance of about 3 m.

After energy recovery in its second pass through the accelerating modules, the recirculated ERL beam will reach the RF separator with beam energy of approximately 5 to 10 MeV, and 90°out of phase with the deflecting phase of the cavity. It will therefore pass mostly unaffected through the separator cavity and receive a sharp deflection in the dipole magnet and be directed down a short beam-line to a beam dump.

The initial separation will take place in an RF separator cavity operating at a frequency of 650 MHz, imparting opposing transverse momentum kicks to the ERL and RIB bound beams and deflecting them by ±4.5 mrad in the horizontal direction. This deflection will be amplified by the quadrupole magnet with the final separation of the beams reaching $\sim$ 35 mm by the time they reach the septum. At this point, the ERL beam will be directed around the recirculation loop and the RIB beam back towards the main linac axis.

Additionally, the layout of the separator section of the linac is compatible with a two pass Recirculating Linac in which the beam is directed around the recirculation loop after its first pass to be accelerated a second time in the main linac before continuing on for RIB production. This mode would not employ the RF separator cavity, but would rely on the static magnetic separation of the beams with different energies in the dipole.

The maximum beam energy at the exit of the main linac will be 66 MeV. This translates to a 0.3 MV transverse momentum kick imparted by the RF separator cavity and transverse deflecting field of $E_\perp = 1.3$ MV/m for a single deflecting cavity.

SRF SEPARATOR CAVITY

The RF dipole deflecting cavity is being considered for use in the ARIEL separator complex. This cavity is compact in size and the transverse deflections are high with low peak electric and magnetic fields. Extensive scaling studies have been performed on this geometry [3], however detailed optimization is required to fully access the suitability of this cavity design for the ARIEL e-linac separator.

The geometry of the RF dipole separator cavity is shown in Fig. 1. The inner ridge length of the cavity will be of order $\beta\lambda/2 = 230$ mm at 650 MHz, and the aperture 50 mm, the same as along the rest of the length of the e-linac.

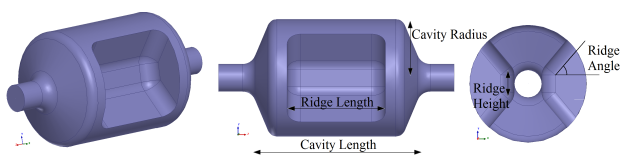


Figure 1: The RF dipole geometry showing the key parameters affecting the cavity performance.

* Work supported by the Natural Sciences and Engineering Research Council of Canada
† dstorey@uvic.ca

Copyright © 2013 CC-BY-3.0 and by the respective authors

In the deflecting mode, a transverse electric field is produced between the cavity ridges while the magnetic field circulates around them. The x component of the electric field provides the main contribution to the horizontal deflections while the y component of the magnetic field acts to decrease the deflection, by a relatively small amount. The deflecting mode of this cavity geometry is the lowest order mode of the cavity and the next higher order mode has a frequency far from the fundamental mode.

GEOMETRY STUDIES

The RF Dipole cavity behaviour has been studied using HFSS [4] to determine an optimal separator cavity geometry for the ARIEL separator specifications. The main goals of the optimization were to maximize the transverse shunt impedance while minimizing the peak electric and magnetic fields.

The parameters that have the most significant effect on the cavity behaviour are shown in Fig. 1. These are the height and length of the inner ridge, the angle of the ridge cut-out, and the length and radius of the cavity. For each change to the geometry, the cavity radius was adjusted such that the fundamental frequency of the cavity was held at 650 MHz.

The length of the inner ridge was varied, along with the cavity length, to determine the optimal ridge length. It was found that a ridge length of 0.6 times the cavity length consistently resulted in minimized electric fields, as seen in Fig. 2. The peak magnetic fields followed a similar trend. Increasing the overall cavity length also resulted in lower peak fields, and an increase in the transverse shunt impedance, $R_\perp$. For the remainder of the parameter search, the ridge length was set to 0.6 times the cavity length.

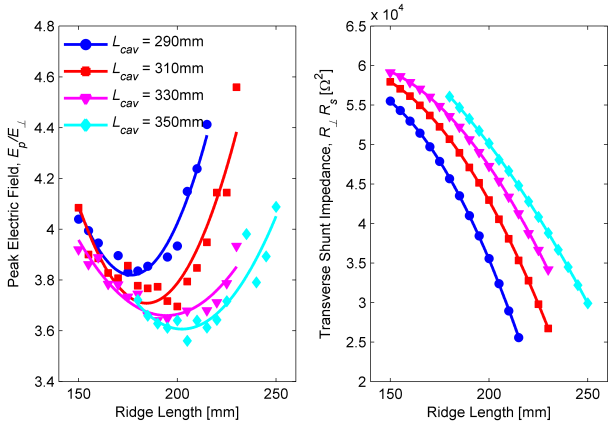


Figure 2: The peak electric fields on the left, and the transverse shunt impedance on the right for varying ridge and cavity lengths. For reference: $\beta\lambda/2 = 230$ mm at 650 MHz.

Next, the height and angle of the ridge were varied simultaneously for different cavity lengths. Again, the outer radius was adjusted to retain a cavity frequency of 650 MHz. The HFSS results show that the peak fields are lowest for larger ridge heights and larger ridge angles, as seen in Fig. 3. In each case, the electric field reaches a minimum value at a cavity length of approximately 380 mm. This corresponds to an inner ridge length of 230mm, precisely the value of $\beta\lambda/2$. The peak magnetic fields show a similar dependency on ridge length and angle.

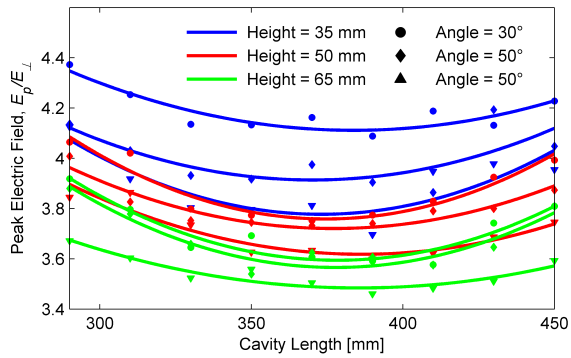


Figure 3: The peak electric fields for varying ridge height and angle and the cavity length. The colour of the line indicates the ridge height and the shape of the data point the angle of the ridge.

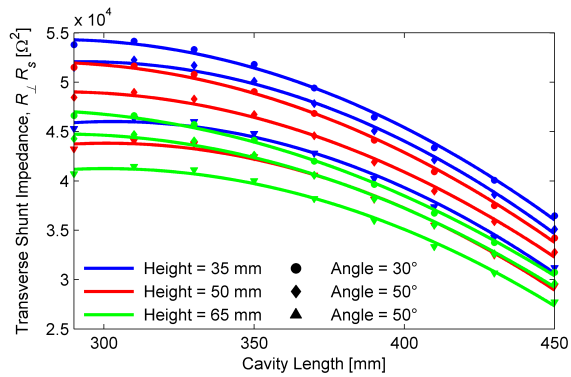


Figure 4: The transverse shunt impedance for varying ridge height and angle and the cavity length.

The transverse shunt impedance, Fig. 4, is seen to decrease with increasing cavity length as well as for larger ridge height and angle. This leads to conflict between the objective to minimize the peak fields while maximizing the shunt impedance.

A compromise of a ridge height of 50 mm and angle of 50°would provide reasonably high transverse shunt impedance while keeping the peak electric and magnetic fields below 5 MV/m and 10 mT for a transverse deflecting voltage of 0.3 MV. These are well below currently accepted upper limits for electric and magnetic fields in SRF cavities. Since the shunt impedance decreases with cavity length, a cavity length of $\sim$ 330 mm provides a compromise between minimizing the peak fields and maximizing the shunt impedance.

Copyright © 2013 CC-BY-3.0 and by the respective authors

Field Uniformity

Successful operation of an FEL requires a beam with low emittance, and therefore minimal emittance dilution of the ERL beam as it passes through the RF separator. Non-uniformity of the fields across the cavity aperture is one of the main sources of emittance growth.

A larger ridge height and angle results in the most uniform fields within the central portion of the cavity, leading to lower emittance growth. However, as noted in the previous section, a large ridge height and angle would also result in a lower shunt impedance.

Another way to achieve more uniform deflecting fields is to modify the shape of the inner ridge in such a way that forces the uniformity of the fields between the ridges. Giving the inner faces of the ridges a slight curvature allows the bars to come slightly closer together while maintaining the 50 mm diameter aperture, as well as shaping the fields in a more uniform way. This geometry is shown in Fig. 5, along with the cavity geometry with flat inner ridges.

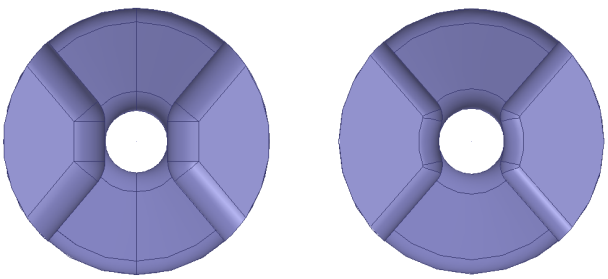


Figure 5: The cross section of the original RF dipole geometry, with flat inner ridges on the left and the modified separator cavity shape on the right, showing the curved faces of the inner ridge.

To quantify the field uniformity, the momentum gain in the x direction relative to the kick received by an on-axis particle was plotted across the aperture of the separator cavity, Fig. 6. The transverse radius within which the relative momentum kick is less than 2% of the on-axis kick strength was found to be 8.5 mm for the flat ridged cavity, compared to 12.5 mm for the curved ridge geometry. The shunt impedances of the two geometries are very similar and the peak electric and magnetic fields are slightly higher for the curved ridge cavity, but are still well below operational limits.

An in depth analysis of the beam dynamics has been performed to access the emittance growth of the ERL and RIB beams passing through the RF separator cavity [5]. It was found that under nominal beam conditions, the flat ridged cavity will contribute to acceptable emittance growth. For beams with larger RMS width or requiring stronger transverse momentum gain, the curved ridge may be useful to limit the emittance growth.

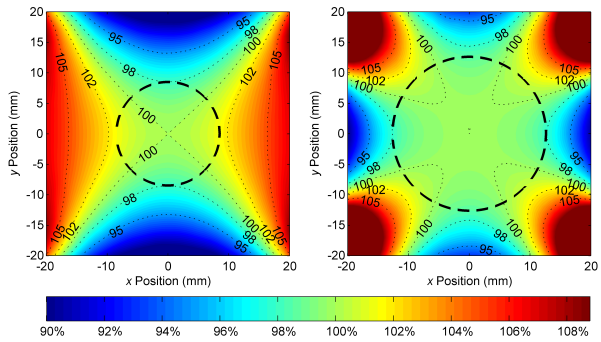


Figure 6: A comparison of the kick-uniformity for the RF dipole with flat ridge geometry on the left, and curved ridges on the right. The dashed circle shows the area in which the momentum kick is within 2% of the on axis kick strength.

CONCLUSION

The RF dipole cavity has been determined to be compatible with the requirements for the ARIEL e-linac RF separator. The main properties of the cavity with flat inner ridges are summarized in Table 1.

Table 1: Properties of the RF Dipole Separator Cavity Optimized for the ARIEL e-linac Requirements

Parameter	Value	Units
Frequency of the deflecting mode	650	MHz
Cavity length	330	mm
Cavity diameter	210	mm
Inner ridge length	198	mm
Transverse deflecting voltage, $V_\perp$	0.30	MV
Transverse deflecting field, $E_\perp$	1.30	MV/m
Geometry Factor, G	117	Ω
Transverse Shunt Impedance, $R_\perp/Q$	411	Ω
Peak electric field, E_p	4.5	MV/m
Peak magnetic field, B_p	7.8	mT

REFERENCES

[1] S. R. Koscielniak, "ARIEL Electron Linac," MOOBA1, NA-PAC'13.

[2] Y. Chao, S.R. Koscielniak, and C. Gong, "RF Separator and Septum Layout Concepts for Simultaneous Beams to RIB and FEL Users at ARIEL," IPAC'11, San Sebastian, Spain, September 2011, WEPC002, p. 1998 (2011).

[3] S.U. De Silva and J.R. Delayen, Phys. Rev. ST Accel. Beams 16 (2013) 012004.

[4] `http://www.ansoft.com`

[5] D.W. Storey, Y. Chao, and L. Merminga, "Beam Dynamics Driven Requirements on the ARIEL e-linac SRF Separator Cavity," THPBA01, NA-PAC'13.

Copyright © 2013 CC-BY-3.0 and by the respective authors

DESIGN, FABRICATION, MEASUREMENT, INSTALLATION AND ALIGNMENT OF 2 TYPES OF QUADRUPOLE-SEXTUPOLE COMBINED MAGNETS FOR THE UPGRADE OF THE 1.2 GEV BOOSTER SYNCHROTRON AT TOHOKU UNIVERSITY

W.Beeckman, S.Antoine, P.Bocher, F.Forest, P.Jehanno, P.Jivkov, M.J.Leray, L.Swinnen, S.Taillardat, , SIGMAPHI, Vannes, France
H.Hama, F.Hinode, Electron Light Science Centre, Tohoku University, Sendai, Japan

Abstract

The upgrade of the 1.2 GeV booster synchrotron is part of the recovery program from the March 11 2011, Great East Japan Earthquake. The replacement of standard quadrupoles by combined quadrupole-sextupole magnets will tame the head-tail instability by changing the chromaticity from the natural, negative, values to positive values, and prevent the unstable m=0 mode to develop.

In January 2012, Sigmaphi was awarded a contract for the design of 2 kinds of combined magnets and the fabrication of 8 magnets of each type, including rotating coil and Hall probe measurements of every unit. The contract also required disassembly of the old quadrupoles and installation of the new combined magnets, including disassembly/reassembly of the vacuum chambers and fitting with new UHV gaskets. Finally, all the booster magnets, namely 8 dipoles, 4 achromat quadrupoles and the 16 new combined function magnets were to be realigned within ±0.2 mm accuracy by mid-January 2013. The presentation outlines the main steps of the different operations and presents the achievements and results.

DESIGN

A general overview of the status of the project is given in [1] and we concentrate here on the magnets.

Table 1 presents the requirements for the new magnets.

Table 1: Magnet Requirements

Requirement	QSF	QSD
Quadrupole	k=2.01044 m^{-2}	k=2.21750 m^{-2}
Sextupole	2.4 times 4-pole m=4.825061 m^{-3}	3.8 times 4-pole m=8.426508 m^{-3}

Additional requirements are listed below

- Same geometry as old magnets including coil shape and electrical/water connections. Only the pole face may be changed.
- Magnetic centre at ±0.5 mm from mechanical centre in both transverse dimensions
- Alignment error may not be larger than ±0.2 mm
- 1 year from contract to end

All these requirements put together make a very demanding job with little freedom.

Many different designs of such combined magnets can be found in the literature. The extra function is added on top of the main multipole either through pole shaping [2][3], or by using extra coils that superimpose a second multipole [4][5]. By requirement, we must not only adopt the first scheme but we must also abide to the very strong constraint of keeping the magnetic circuit within the yoke shape of the existing magnets.

The pole profile [6] of such a combined function magnet is a superposition of the potentials, hence an equation $kxy+\frac{1}{6}m\left(3x^2y-y^3\right)=\frac{1}{2}kR^2+\frac{1}{6}mR^3$

The field components are summarized in table 2.

Table 2: Field Components

Field component	Bx	By
Quadrupole	ky	kx
Sextupole	mxy	$\frac{1}{2}m\left(x^2-y^2\right)$

Thus, the vertical component in the horizontal plane (y=0) is equal to $B_y = kx+\frac{1}{2}mx^2$

Starting from the above theoretical pole profile with a pole radius of 50 mm and maximum coil current of 700 A we can aim at designing a pole profile that satisfies the requirements. However, as shown below, incompatible symmetries generate differential saturations which prevent required fields to be achieved with the prescribed yoke thickness. The possible m/k ratio was redefined as m/k(QSF) ~ 1.0 (2.4) and m/k(QSD) ~ 1.8 (3.8)

The pink and green rectangles locate the 4 and 6-poles and the matching arrows the resulting field, adding on the right and subtracting on the left.

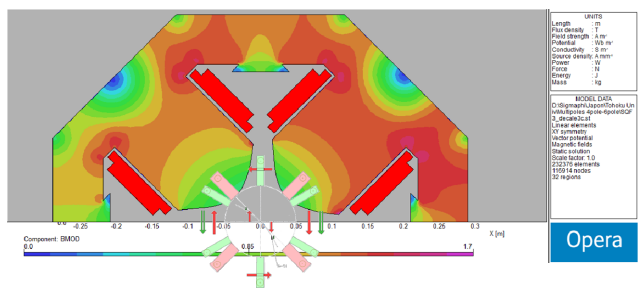


Figure 1: 2d cross-section of a combined magnet showing the strong differential yoke saturation.

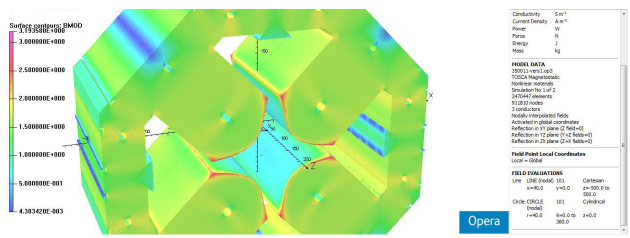


Figure 2: Opera3d model

Copyright © 2013 CC-BY-3.0 and by the respective authors

MEASUREMENTS

For pure multipoles, iso-modulus lines are concentric circles $|B^{(n)}| \propto r^{n-1}$ but for combined multipoles, the modulus $|B^{(2+3)}| = k^2 r^2 + \frac{1}{4} m^2 r^4 + \frac{1}{2} m x^3$ is not purely radial.

Hall probe measurements are therefore better suited than harmonic coils for some data.

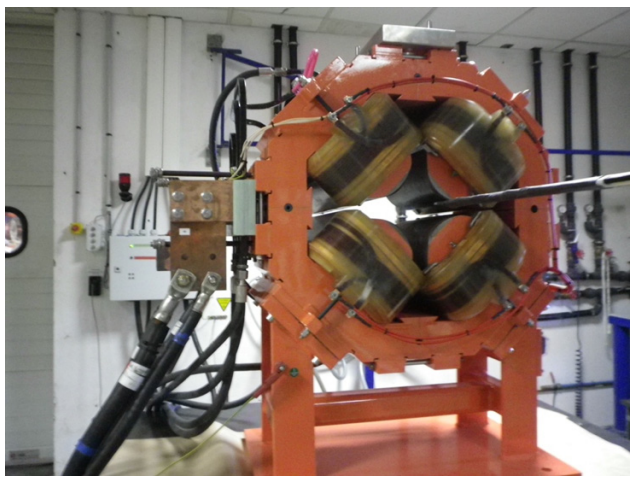


Figure 3: Hall probe median plane measurement.

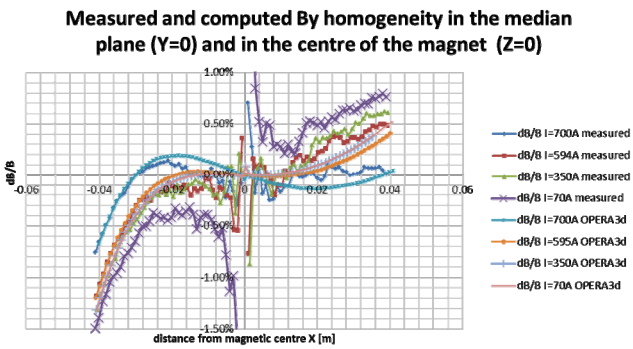


Figure 4: Homogeneity is computed from Hall probe data

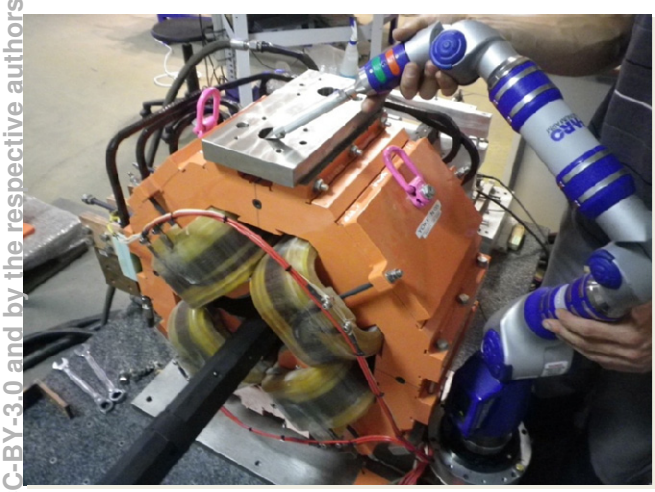


Figure 5: Faro arm fiducialization is performed on the harmonic coil measurement bench.

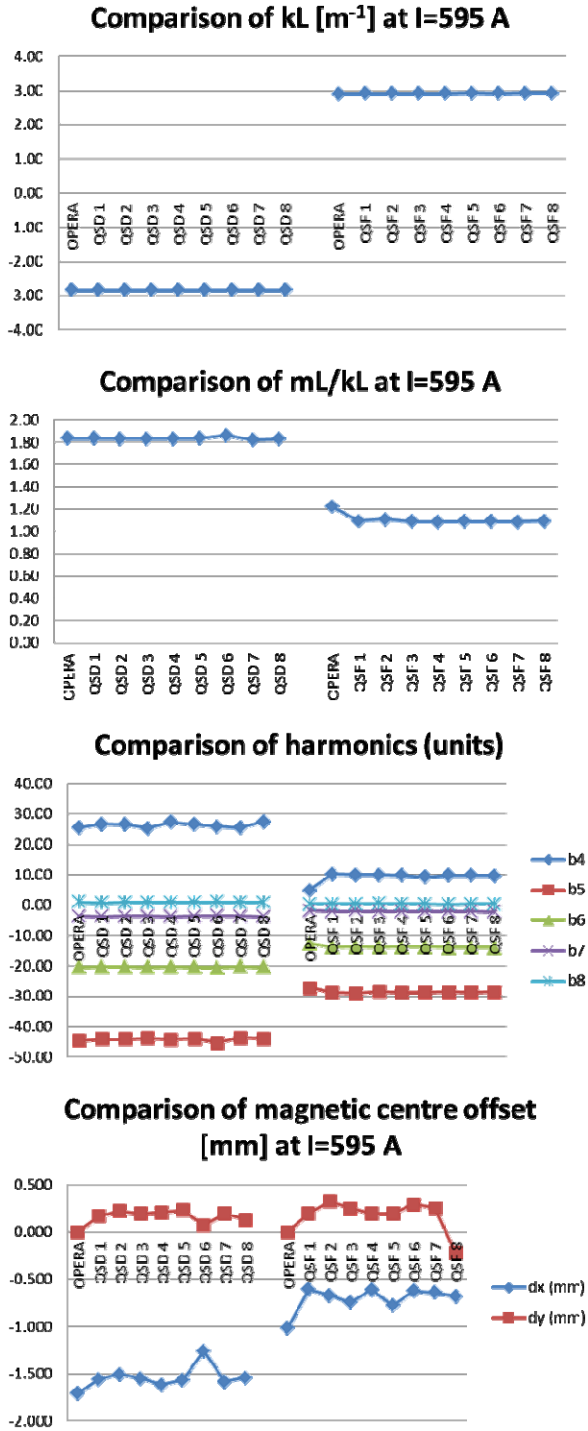


Figure 6: Some of the harmonic coil results showing a good reproducibility between magnets and a good agreement with the Opera3d models.

INSTALLATION AND ALIGNMENT

Replacing magnets in an existing facility is much more complex than installing new magnets in a newly built place since space is usually very crowded as shown in figures 7 below.

Disassembly and storage of the old magnets also required disassembly of the vacuum chambers and

Copyright © 2013 CC-BY-3.0 and by the respective authors

replacement of all UHV gaskets after installing the new magnets.

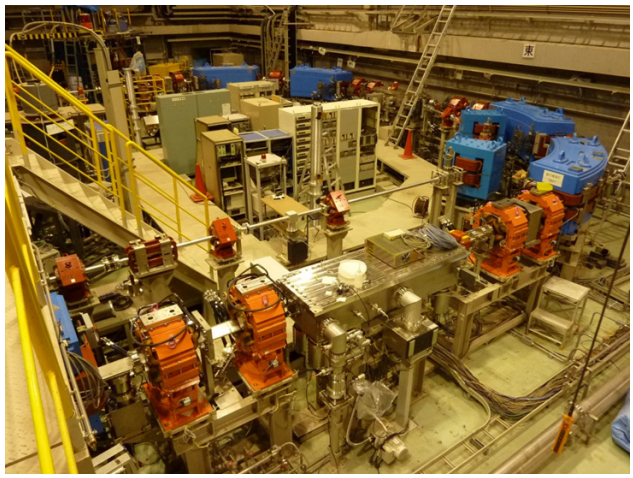


Figure 7: South and East sides with new magnets installed.

Alignment was performed using the following material.

- Tracker: Leica AT401
- Targets: Leica red-Ring Reflector 1.5”
- Monument holders: Hubbs 1.5 TSM M10
- Target holders: Hubbs 1.5 SMN 40mm 25mm outer diameter 46 mm.
- Software: Polyworks IMInspect Probing

Achieved accuracies are shown in figures 8 and 9.

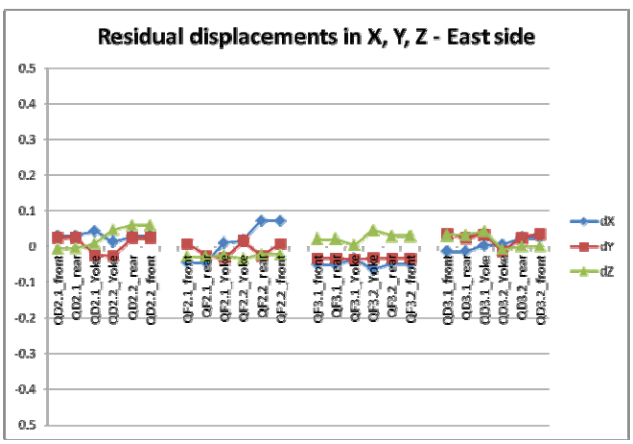


Figure 8: Alignment errors are much smaller than the required ±0.2 mm (East side).

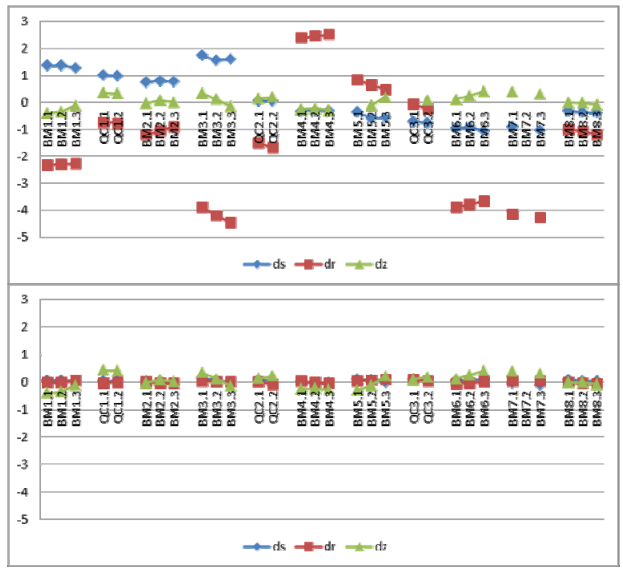


Figure 9: Dipoles and central quads positioning error before and after realignment (mm).

CONCLUSIONS

We have successfully designed, built, measured, installed and aligned 2 types of combined 4+6-poles.

All specifications were met but the integrated sextupole which is impossible to achieve with the prescribed geometry. A new set of possible m/k ratio was redefined.

Besides the 16 new magnets, the contract also included the removal of old quads, change of all UHV gaskets and realignment of all magnets including the 8 big dipoles.

Everything was finished by mid-January 2013, within the 1-year allotted time-schedule.

REFERENCES

[1] F. Hinode, S. Kashiwagi, T. Muto, I. Nagasawa, K. Nanbu, Y. Shibasaki, K. Takahashi, H. Hama, “Status of Upgrade Project of the 1.2 Gev Booster Synchrotron at Tohoku University”, IPAC2013, Shanghai.

[2] C.Y. Kuo, C.S. Hwang, C.H. Chang, “Development of Combined Function Magnets for the Taiwan Photon Source”, PAC2009, Vancouver.

[3] Xiangxue Zhao, Guangyao Feng, Shancai Zhang, Lin Wang, Hongliang Xu , Weimin Li, “Design Study of Combined Magnet with Combined Function”, PAC2009, Vancouver.

[4] Vanshree Thakur, R.K.Mishra, G.Singh, “2d-Simulation of Combined Function Quadrupole/Sextupole Magnet for Existing Booster Synchrotron”, PAC2009, Vancouver

[5] J. Yamazaki, M. Katoh, Y. Hori, M. Hosaka, A. Mochihashi, T. Kinoshita, K. Hayashi, Y. Takashima, S. Koda, “Development of Combined-Function Focussing Magnet”, UVSOR Act Rep (2002).

[6] H. Wiedemann “Particle Accelerator Physics Volume 1 “Basic principles and linear beam dynamics”, Springer Verlag 1992, pp88-100.

Copyright © 2013 CC-BY-3.0 and by the respective authors

DESIGN AND CONSTRUCTION OF THE PROTO-TYPE QUADRUPOLE MAGNTS FOR THE SUPERKEKB INTERACTION REGION

N. Ohuchi#, Y. Arimoto, H. Yamaoka, Z. Zong, M. Tawada, K. Tsuchiya, H. Koiso, Y. Ohnishi, A. Morita, H. Sugimoto, K. Oide, KEK, Tsukuba, Japan

Abstract

Construction of the SuperKEKB accelerator started from 2010. The final focusing system in SuperKEKB was designed, and it consisted of 8 superconducting quadrupole magnets. As part of the R&D of the final focusing system, two prototype magnets were designed and constructed. The magnets were cooled to 4 K, and they were excited over the design current and the field measurements were performed.

INTRODUCTION

SuperKEKB [1] is the upgraded machine of KEKB, and the design luminosity is $8\times10^{35}\mathrm{cm}^{-2}\mathrm{s}^{-1}$, which is 40 times higher than that achieved at KEKB. SuperKEKB has a single interaction point, IP, to collide the 7 GeV e- beam and the 4 GeV e+ beam with a finite crossing angle of 83 mrad. The colliding energy is planned to be increased to 12 GeV. The design concept of SuperKEKB is based on the Nano-Beam Scheme, originally proposed by P. Raimondi for SuperB [2]. In order to focus the beam at IP with the vertical beam size of about 50 nm, a pair of the quadrupole doublet system for LER and HER [3, 4], respectively, was designed with 8 superconducting magnets. As the R&D of the final focusing system, the QC1P and QC1E prototype magnets were constructed and cold tested at 4K. In this paper, the magnet designs, constructions and test results are reported.

DESIGNS OF QC1P/QC1E MAGNETS

The QC1P and QC1E magnets were designed for the e+ and e- beams, respectively, and they are located at the closest position to IP on each beam line [3].

QC1P Magnet Design

The QC1P is the collared quadrupole magnet without iron yokes in order to make the solenoid field profile required from beam optics. The magnet cross section is shown in Fig. 1, and the parameters are summarized in Table 1. The magnet consists of two layers of the superconducting coil, and the thickness of the two-layers is 5.425 mm. Because the separation between two beams at the front end of the QC1P magnet is only 61 mm, the outer radius of the magnet was designed to be 30.425 mm while the coil inner radius was 25 mm. The field gradient of the magnet was 76.17 T/m at the design current, I_d=1800 A, and the magnetic length was 0.3372 m. I_d was for the colliding energy of 12 GeV, and the magnet current for 11 GeV was 1624 A. For this magnet, the small Rutherford cable, which consisted of 10 strands, was developed. The cable size was 0.93 mm in mid-thickness × 2.5 mm in height, and the key stone angle of the cable was 2.09 degree because the coil inner radius was 25 mm. I_d is 60 % of the critical current of the cable, I_c, at 4.7 K. The cable parameters are listed in Table 2.

The magnetic field of the QC1P magnet was calculated with the magnet cross section model and with the whole magnet model including the lead end and the non-lead end. They are summarized in Table 3. The each coil was designed with three coil blocks, and b_6 and b_{10} of two layer coils were optimized to be 0.16 units and -0.02 units in the cross section, and -0.11 units and -0.05 units in the whole magnet, respectively, at the reference radius of R_{ref}=10mm.

QC1E Magnet Design

The QC1E magnet was located behind the QC1P magnet from the IP. The prototype magnet was designed with iron yokes, and the yoke outer radius was 70 mm. The magnet consisted of two layer coils, and the inner radius was 33 mm. The superconducting cable had same parameters as those for the QC1P magnet except for the cable keystone angle of 1.59 degree. The QC1E was designed to generate the field gradient of 91.73 T/m at I_d=2000 A, and the magnetic length was 0.3774m. The magnet current for 11 GeV was 1577 A. The magnet cross section was optimized with three coil blocks of each layer as same as the QC1P magnet, for b_6 and b_{10} to be -0.04 units and -0.08 units at R_{ref}=15mm, respectively. In the whole magnet, b_6 and b_{10} were optimized to be -0.17 units and -0.20 units, respectively.

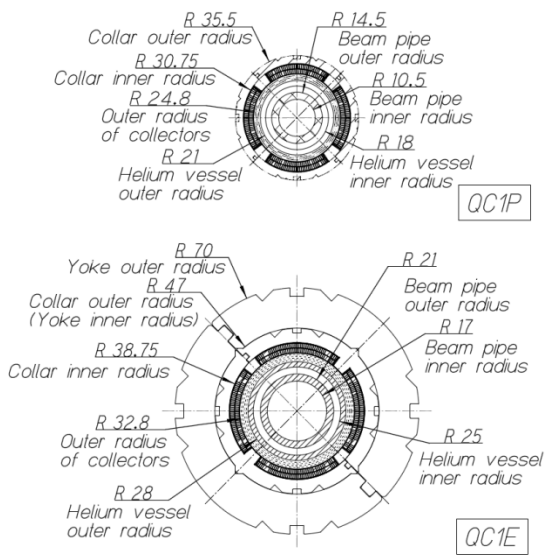


Figure 1: Cross sections of QC1P/1E prototypes.

#norihito.ohuchi@kek.jp

Copyright © 2013 CC-BY-3.0 and by the respective authors

Table 1: Magnet Parameters of Proto-types

	QC1P	QC1E
Magnet type	Non-yoke	Yoke
Coil inner/outer radius, mm	25.0/30.425	33.0/38.425
Collar or yoke outer radius, mm	35.5	70.0
Turn number per pole	25	34
Design current (I_d), A	1800	2000
Field gradient (G), T/m	76.17	91.73
Effective magnetic length (L_{eff}), m	0.3372	0.3774
Maximum field at I_d, T	2.61	4.17
I_d/I_c at 4.7 K, %	60	73

Table 2: Cable Parameters

	QC1P	QC1E
Cable type	Rutherford cable	
Cable size (mid-width × height), mm	0.93 × 2.50	
Keystone angle, degree	2.09	1.59
Number of strand	10	
Strand diameter, mm	0.498	
Cu/NbTi ratio	1.0	
Critical current at 5T, and 4.22 K	3165	3070
Critical current at 7T, and 4.22 K	1880	1830

Table 3: Design Error Field Components

		QC1P	QC1E
Field Gradient, T/m		76.17	91.73
R_{ref}, mm		10	15
Cross section	b_6, units	0.16	-0.04
	b_{10}, units	-0.02	-0.08
Whole magnet	b_6, units	-0.11	-0.17
	b_{10}, units	-0.05	-0.20

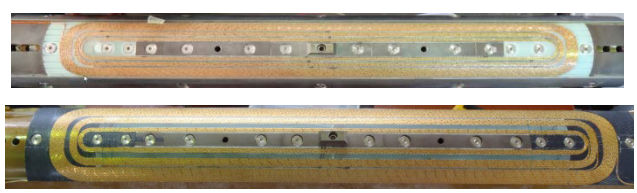


Figure 2: QC1P (upper) / QC1E (lower) coils.

CONSTRUCTION OF MAGNETS

The QC1P and QC1E prototype magnets were constructed in KEK. Since the cable was the small size of 0.93 mm × 2.5 mm, the cable tension during winding coil was carefully controlled. The tension was decreased from 130 N to 60 N as function of turn number. After winding coil, the coil was cured in the form block at the temperature of 130 degrees C. Figure 2 shows the cured coils of QC1P and QC1E. The average lengths of QC1P and QC1E coils were 384.14 mm and 430.31 mm to the design values of 384 mm and 430 mm, respectively.

The four coils were assembled together, surrounding a support bobbin in the vertical position. The coils were covered with multiple ground plane insulation layers. The 2-split High-Mn collars were assembled around the coils with 90 degree rotation every set of collars. Assembled collars were squeezed and keyed from the four directions at once with a hydraulic press. Until these assembly processes, the QC1P magnet was completed. Yoking process for the QC1E magnet was performed with the same collaring tool. The half–split iron yokes of 3 mm thickness were assembled around the collars with 90 degree rotation every set of yokes. Yokes were fitted to collars by the collaring press. Figures 3 and 4 show the completed QC1P and QC1E prototype magnets.

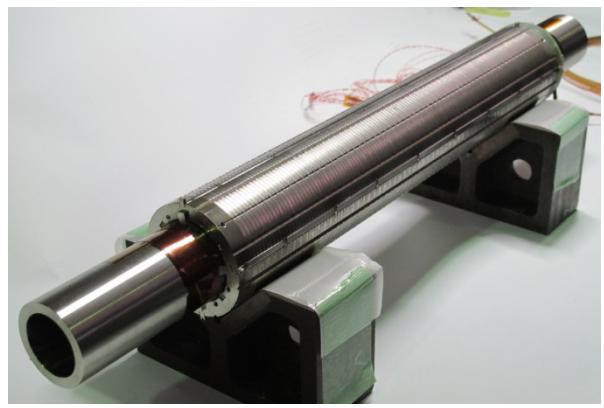


Figure 3: QC1P prototype magnet.

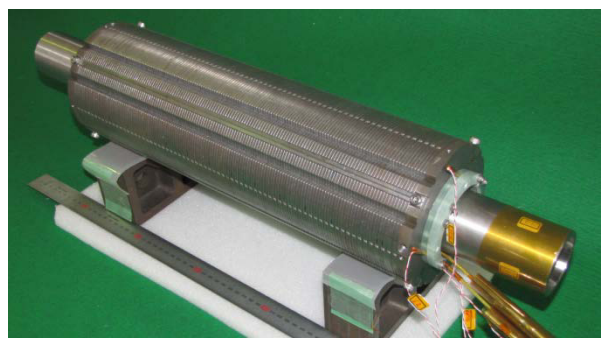


Figure 4: QC1E prototype magnet.

EXCITATION TESTS

Two magnets were installed into the vertical cryostat, individually, and they were cooled by liquid helium. The QC1P and QC1E prototype magnets were excited to 2100 A and 2157 A without quench, respectively. The maximum currents were limited by the power supply. The current of 2100 A of the QC1P magnet corresponded to 70 % of I_c on the load line at 4.7 K. The current of 2157 A of the QC1E magnet was 87 % of I_c.

Copyright © 2013 CC-BY-3.0 and by the respective authors

MAGNETIC FIELD MEASUREMENTS

Magnetic field measurements were performed with the harmonic coils. Two coils of 600 mm and 40 mm long were used for measuring the integral field and the field profile, respectively.

Integral Field Measurements

The integral field was measured with the 600 mm long harmonic coil. The coil radius was 9.55 mm. At the magnet currents of 1701.7 A for QC1P and 1561.7 A for QC1E, the measured integral field gradients were 24.32 T and 26.22 T, respectively. For comparison, the calculated integral field gradients of the QC1P and QC1E magnets at these currents are 24.28 T and 27.03 T, respectively.

The measured error field components at R=9.55 mm are shown in Table 4. From the result, the both magnets had large sextupole field components. The components can be converted at the reference radius of each magnet. a_3 and b_3 for QC1P are 2.95 units and 3.83 units at R_{ref}=10mm, and a_3 and b_3 for QC1E are 1.79 units and 8.64 units at R_{ref} =15mm, respectively. The beam optics simulation showed these sextupole components remarkably degraded the Touschek beam life time.

Table 4: Measured Error Field of Prototypes in Units

	QC1P		QC1E	
n	a_n	b_n	a_n	b_n
2	0	10000	0	10000
3	2.82	3.66	1.14	5.50
4	2.08	0.24	0.18	-0.28
5	0.35	0.23	0.06	-0.48
6	0.03	-0.56	-0.06	-0.31
7	0.07	0.13	-0.01	0.01
8	0.03	0.01	0.05	-0.00
9	-0.08	0.05	0.02	-0.00
10	0.02	0.01	-0.00	-0.02

Field Profile Measurements

The field profiles of the prototype magnets were measured with the 40 mm long harmonic coil. The coil radius was 9.74 mm. Figures 5 and 6 show the profiles of the field gradient, a_3 and b_3 along the axes of the QC1P and QC1E magnets, respectively.

From Fig. 5, a_3 and b_3 in the QC1P magnet straight section (-100mm<position<100mm) are in the range from -2 units to 2 units. On the other hand, in the QC1E magnet, b_3 is from 5 units to 8 units while a_3 is within plus or minus 1 unit.

For the QC1E magnet, the error field due to the coil deformation was calculated. The b_3 and a_3 components were produced by the dipole deformation of 4 quadrant coils. The coil movements in the radial direction by the measured b_3 component were calculated to be plus and minus 30 μm for the two coils in the left and right sides of the magnet cross section, respectively. For the QC1P magnet, the b_3 and a_3 of 3 units was produced by the dipole deformation of 10 μm.

As the results of the field measurements, the b_3 and a_3 correctors has been decided to be installed in the final focusing system in order to attain the acceptable Touschek beam life time of 600 seconds.

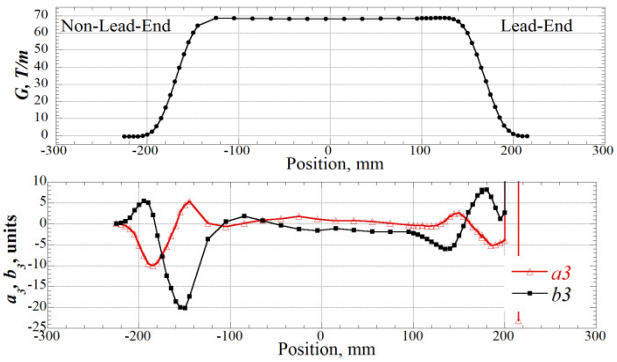


Figure 5: QC1P field profile measurement. I=1627 A.

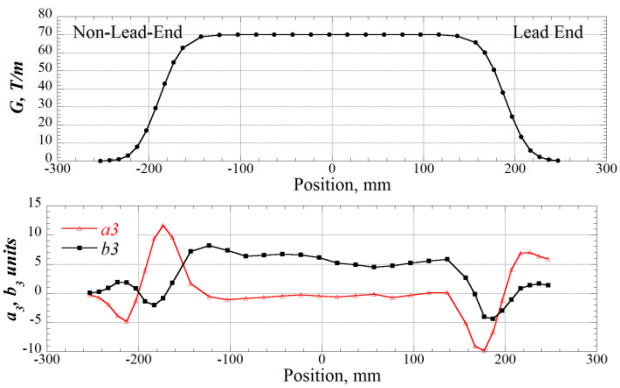


Figure 6: QC1E field profile measurement. I=1561 A.

SUMMARY

As the R&D of the SuperKEKB final focusing system, the prototype magnets of QC1P and QC1E were constructed and tested at 4K. The magnets were excited over the design current without any quenches. From the field measurements, the b_3 and a_3 correctors were decided to be installed in the final focusing superconducting magnet system.

REFERENCES

[1] K. Akai et al., "Design Progress and Construction Status of SuperKEKB," IPAC2012, New Orleans, May 2012, TUPPR006, p. 1822 (2012); http://www.JACoW.org

[2] P. Raimondi, 2nd SuperB Meeting, Frascati (2006).

[3] N. Ohuchi et al., "Design of the Superconducting Magnet System for The SuperKEKB Interaction Region," WEODA1, NA-PAC'13.

[4] B. Parker et al., "Superconducting Corrector IR Magnet Production for SuperKEKB," THPBA07, NA-PAC'13.

Copyright © 2013 CC-BY-3.0 and by the respective authors

MULTIPOLE MAGNETIC MEASUREMENTS USING A LOCK-IN AMPLIFIER TECHNIQUE*

C. Doose, M. Kasa, ANL, Argonne, IL 60439, USA

Abstract

Magnetic measurement systems for accelerator magnets typically use relatively complicated rigid rotating coils and digital integrators to capture the integrated coil signal as a function of angular position of the coil. This technique has proven to be reliable and accurate for measuring the field quality of conventional multipole magnets; however, the design and construction of the rotating coils ultimately determine the accuracy of the measurement system. A different concept and implementation of a simple stretched-wire rotating coil will be described. This system utilizes a single-turn radial coil continuously rotating at a fixed angular velocity. The coil signal and a reference pulse are sampled with a 24-bit ADC. A lock-in technique or an FFT can be used to determine the harmonic content of the signal and thus calculate the main field strength and angle, multipole coefficients, and magnetic center offsets. The main advantages of such a system are ease of coil manufacturing and simple mechanical system design.

INTRODUCTION

Motivation for this project was prompted by the need to quickly measure modified multipole magnets for the APS storage ring. Existing six-pole horizontal/vertical dipole corrector magnets were modified to become horizontal correctors and skew quadrupoles. A need to measure the multipole components and magnetic center of these new combination magnets prompted the design of a new, relatively simple multipole magnet measurement system.

The previous APS multipole magnetic measurement system used G-10 and ceramic Morgan coils that were supported in air bearings and driven by a DC motor. A 16-bit absolute encoder was used to trigger an integrator based on rotary position. This system had not been used in many years and the quality of the coil assemblies was questionable. We had recently completed magnetic measurements of a superconducting undulator (SCU) and had used a single-turn stretched coil to measure the integrated dipole components. Since we already had much of the hardware required, we decided to use a single-turn radial coil for harmonic field measurements of multipole magnets.

SYSTEM OVERVIEW

The following is a list of some of the features of the new multipole measurement system:

- Continuous coil rotation without slip rings
- Quasi-real-time measurements of individual multipole components using a lock-in amplifier (LIA)
- Measurement of the integrated magnetic field strength, multipole coefficients, magnetic-center offsets, and magnetic angle
- Automatic alignment of quadrupole and sextupole magnet positions relative to the center of rotation of the coil

The key components for the multipole measurement system were two Newport RGV100BL precision rotary stages. The precise control of position, velocity, and simultaneous timing allowed synchronous operation of both stages as if the coil wires were rigidly linked.

The system utilized a single-turn stretched coil in a radial configuration, as shown in Fig. 1. The coil-wire was 100-µm-diameter CuBe. The coil-wire ends were held in place with plastic fixtures connected to the rotary stages, as shown in Fig. 2. Coil fixtures can easily be made overnight on a 3D printer, so changing the radius of the coil would be a simple matter of changing the fixture radius. The coil was tensioned by moving the signal-end rotary stage in the longitudinal direction until the sag was minimized. The coil-wire sag was typically less than 200 µm when using a 1.5-m-long coil. Optical alignment telescopes were used to confirm the coil dimensions and alignment to approximately 50-µm accuracy.

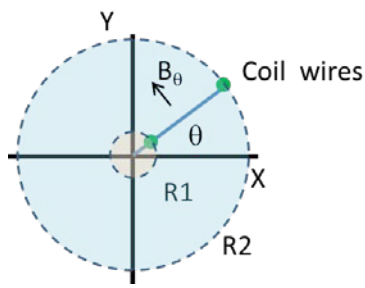


Figure 1: Radial coil configuration is sensitive to the radial component of the B field.

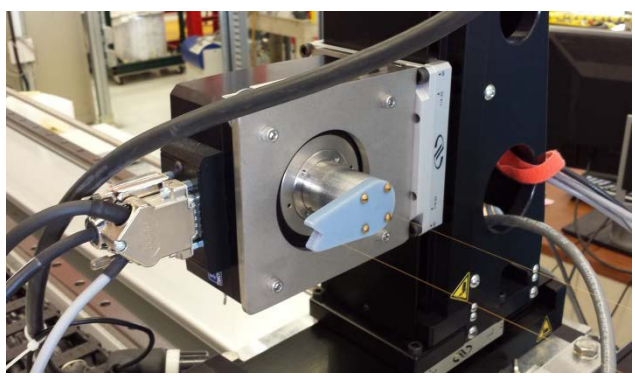


Figure 2: Signal-end rotary stage looking at the plastic coil positioning fixture.

*Work supported by the U.S. Department of Energy, Office of Science, under Contract No. DE-AC02-06CH11357

Copyright © 2013 CC-BY-3.0 and by the respective authors

The non-signal-end rotary stage was located at a fixed position; the signal-end rotary stage could be moved in all axes for alignment purposes. The signal-end rotary stage contained a sealed mercury-filled rotary connector from Mercotac. The rotary connector provided a means of coupling a low-noise signal from the rotating coil to the fixed signal cable. This rotary stage also utilized an opto-interrupter, which provided a trigger pulse for angular reference of the coil signal, as shown in Fig. 3.

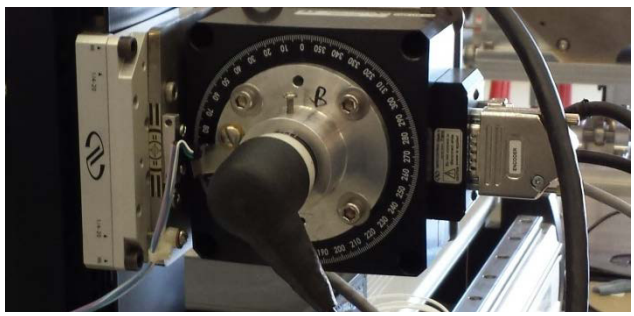


Figure 3: Signal-end rotary stage looking at the rotatable connector and opto-interrupter (left of stage scale), which provided a pulse for phase reference.

The two rotary stages were aligned to be co-linear, level, and parallel, and rotate in unison with a constant velocity of 1 rps. The coil signal could be amplified with gains of 10, 100, or 1000 before being digitized by a National Instruments dynamic signal analyzer (DSA) module.

LOCK-IN-AMPLIFIER

The integrated harmonic field components could each be separately measured using the rotating coil and a lock-in amplifier. Using National Instruments hardware and a LabVIEW software module downloaded from National Instruments, the LIA was easily implemented at very little cost. The software required two input signals, a reference and a measured signal, which were measured with the 24-bit analog-to-digital inputs of a PXI-4462 DSA module. The sampling rate of the DSA was 200 kHz and 25600 samples were recorded per coil revolution. This gave an angular resolution of 0.25 mRad between samples. The reference signal was provided by the opto-interrupter pulse, which occurred once per revolution.

The reference and measured signals were processed with LabVIEW software and the integrated field components were derived. The vertical and horizontal components were derived simultaneously and the individual harmonic number to be measured could be chosen through a user selectable software option. The software used the measured frequency and phase of the reference signal to create a new sine wave reference that was mixed with the measured signal [1]. The result of mixing the two signals was a DC signal and an AC signal with twice the reference frequency. The DC level was proportional to the measured signal at the reference frequency and was used to calculate the magnitude of the integrated field components. The LIA software also returned the phase of the measured signal relative to the reference signal.

The LIA measurement technique was convenient for initial magnet alignment or studying the effects of magnet coil current changes. The results can be observed in quasi-real time after a short settling time. The disadvantage of the LIA was that an individual measurement for each desired harmonic was required to fully characterize a particular magnet.

MULTIPOLE MEASUREMENTS

A multipole measurement (MM) technique was developed whereby ten rotations of the coil voltage signal were digitized and time averaged to create an averaged single-rotation time record. The time record harmonic content was then processed by a built-in LabVIEW FFT routine. The magnet main field strength, angle, and all harmonics were then calculated. Total time per measurement was approximately 15 seconds.

The rotating coil voltage waveforms of three different magnetic fields are shown in Fig. 4. The dipole and skew quad waveforms were generated by a six-pole combination dipole and skew quadrupole magnet. The SR quad waveform was from an APS 0.5-m storage ring quadrupole. The dipole and skew quadrupole signals had visibly large harmonic content. The skew octupole (a_4) is especially large at -344.3×10^{-4}. The relative normal and skew harmonic coefficients for each magnetic field from Fig. 4 are listed in Table 1. The b_2 and a_2 components represent the normal and skew quadrupole components, respectively. The components are relative to the main field for each case, and all are calculated at a specification radius of 10 mm.

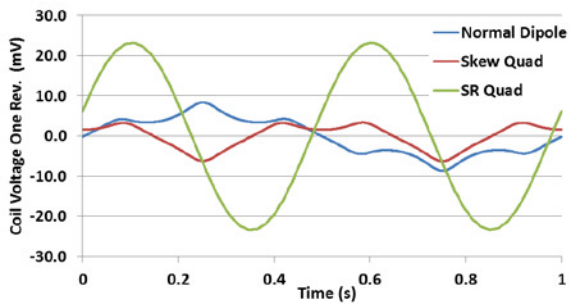


Figure 4: Digitized coil voltage waveforms for three different magnetic fields. “Normal Dipole” and “Skew Quad” are two configurations of the same six-pole magnet structure. The “SR Quad” is a 0.5-m-long APS storage ring quadrupole magnet.

Table 1: Relative Multipole Coefficients (10^{-4} units) at 10-mm Specification Radius (b_2, a_2 are quadrupole)

Harmonics	Normal Dipole	Skew Quadrupole	Normal Quadrupole
b_2, a_2	-7.4, -2.1	0, 10000	10000, 0
b_3, a3	2.8, 0.2	-16.9, 11.0	-1.0, -0.5
b_4, a_4	-0.5, -0.5	1.2, -344.3	-0.2, 0.1
b_5, a_5	-0.1, 0.3	-.1, 0.3	-0.004, 0.0

Copyright © 2013 CC-BY-3.0 and by the respective authors

Ambient Field and Magnet Alignment

The typical measurement sequence for a quadrupole magnet began with recording the ambient field with the magnet under test fully degaussed. The dipole components, due to the Earth's field, were then subtracted from subsequent measurement of the dipole components. This was most important for accurate measurement of the magnetic offset and alignment of quadrupole magnets since a quadrupole magnet is aligned to minimize the integrated dipole field. After the ambient measurement, the magnetic offsets and angle were measured and the magnet was aligned with a motorized magnet support table. Multipole measurements were then performed at the prescribed coil currents.

Measurement Repeatability and Resolution

A series of 16 measurements were performed over the course of 10 minutes using a storage ring 0.5-m quadrupole magnet. The results of the repeatability of the magnetic offsets and magnet angle are shown in Fig. 5. The coil radius for these measurements was 38.14 mm.

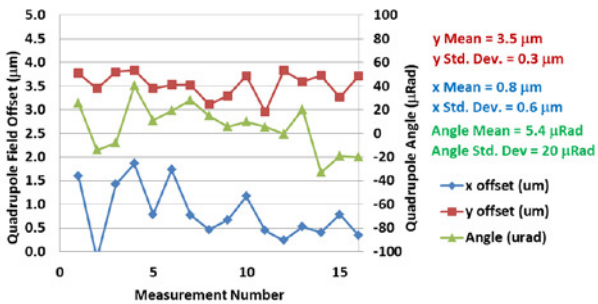


Figure 5: Plots of the measured magnetic offsets in x and y from the coil rotation center and the magnetic angle relative to gravity. The standard deviation of the offsets and angle were less than 1 µm and 25 µRad, respectively.

HARMONIC CALCULATIONS

The theory of harmonic magnetic measurements has been well known for many years [1], but can be confusing due to differences in notation and conventions. Two invaluable references used by the authors were by A. Jain [2] and L. Walckiers [3].

The instantaneous single-turn coil voltage can be described by:

$$V(t) = \sum_{n=1}^{\infty} K_n \left[C_n e^{-in(\omega t+\delta)}\right], \quad (1)$$

where

$$K_n = L\omega \left[\frac{R_2^n - R_1^n}{R_{spec}^{n-1}}\right]. \quad (2)$$

The complex Fourier components are

$$\mathbf{V_n} = K_n \mathbf{C_n} = K_n(B_n + iA_n), \quad (3)$$

where L is the magnet length; R_2 and R_1 are the coil major and minor radii, respectively; δ is the reference phase angle; R_{spec} is the specification radius; and B_n and A_n are the normal and skew integrated multipole coefficients, respectively. The relative multipole coefficients listed in Table 1—b_n and a_n—are B_n and A_n normalized to the main field components.

CONCLUSION

The implementation of a single-turn CuBe radial coil has proven to be an effective means to measure the harmonic content of accelerator magnets. By combining very accurately controlled rotary stages, a rotatable signal coupler, and a 24-bit DSA module, measurements of the main and harmonic field errors were possible with a simple radial coil design. Continuous measurements of an individual harmonic could be performed using the LIA technique, or when complete harmonic components were desired, the MM technique was chosen.

Repeatability, as shown in Fig. 5, was quite good. The absolute accuracy was dependent on how well the dimensions of the coil could be measured; typically it was on the order of 0.5% for a 38-mm coil radius. Presently the repeatability of the magnetic center measurements of the new system is approximately an order of magnitude better than the previous APS measurement system. Further testing of the system will be performed on calibration magnets and compared to previous APS multipole measurements performed over 20 years ago.

ACKNOWLEDGMENTS

The authors would like to thank S. H. Kim for his thoughtful insight with the details of the harmonic coefficient calculations. We also thank D. Pasholk for his quick modeling and printing of the coil-holding fixtures.

REFERENCES

[1] J. K. Cobb, J. J. Muray, "Magnetic Field Measurement and Spectroscopy in Multipole Fields," SLAC-39 UC-28, Particle Accelerators and High-Voltage Machines UC-34, Physics TID-4500 (37th ed.), February, 1965.

[2] A. Jain, "Harmonic Coils," CERN Academic Training Program, April 7-11, 2003.

[3] L. Walckiers, "Harmonic Coil Measurement Method," CERN Accelerator School on Magnets June 16-25, 2009.

Copyright © 2013 CC-BY-3.0 and by the respective authors

MAGNETIC MEASUREMENTS OF THE FIRST SUPERCONDUCTING UNDULATOR AT THE ADVANCED PHOTON SOURCE*

C. Doose, M. Kasa, ANL, Argonne, IL 60439, USA

Abstract

A superconducting (SC) undulator prototype designated SCU0 was installed in the APS storage ring in December, 2012, and is providing users with photons in the energy range of 80-100 keV. This device was assembled and tested during the majority of 2012. Detailed tests were performed related to cryogenics, vacuum, mechanical motion due to thermal contraction, and magnetic performance. Magnetic measurements have been performed using a horizontal measurement system, which utilizes Hall probes and an integral coil. The measurement system was configured without interfering with the cryogenic or vacuum systems of the SCU0 cryomodule. Some of the magnetic measurement results will be presented for local and integrated field measurements, integrated field uniformity, and integrated fields during a quench. The measured rms phase errors were typically less than two degrees. The measured change in the integrated field during an intentional quench was less than 35 G-cm. The magnetic performance of SCU0 has proven to be within design tolerance for field quality and quench characteristics. Beam-based integral measurements agree well with the magnetic measurements.

SCU0 BACKGROUND

SCU0 is a prototype superconducting undulator (SCU) that was installed in the APS storage ring during December 2012, and is presently operating successfully at the APS sector 6 beamline [1,2].

Table 1: SCU0 Magnetic Specifications

Period	16 mm
Magnetic gap	9.5 mm
Magnet length	331 mm
Design peak field	0.4 - 0.65 T
Design Current	200 - 500 A
Maximum achieved peak field	0.82 T
Maximum achieved current	740 A

Table 2: APS Undulator Error Tolerance

1st Vertical Field Integral	100 G*cm
1st Horizontal Field Integral	50 G*cm
1st Vert. Field Integral during quench	2100 G*cm
2nd Horz. And Vert. Integrals	1×10^{-5} G*cm^2
Normal and Skew Integrated Quadrupole	50 G

*Work supported by the U.S. Department of Energy, Office of Science, under Contract No. DE-AC02-06CH11357

The assembly of the SCU0 cryomodule began in January, 2012; the first magnetic measurements of the assembled device began in June 2012 and were completed in August. A second set of magnetic measurements was done in November and December of 2012. The first set of measurements was performed with the original pair of SC magnetic structures. From September to October, the SCU0 was disassembled to replace the Al beam chamber with a new design. In the process of disassembly one of the SC wires was possibly damaged. A spare magnet structure was available so it was installed rather than risk a failure of the suspect SC wire.

HALL PROBE MEASUREMENT RESULTS

The following section describes some of the typical measurement results while using a room temperature Hall probe to measure the local fields along the longitudinal axis (z). The measurement system utilizes a room-temperature Ti tubing, "warm-bore," as a guide tube for the carbon fiber Hall probe assembly. The Ti tubing is tensioned inside but isolated from the cold (~10 K) Al beam chamber. A similar concept is used by the Budker Institiute for SC wiggler magnetic measurements.

An overview of the measurement system is shown in Fig. 1. The 3.5-m-long stage is used to drive a carbon fiber Hall probe assembly through the Ti guide tube. Stages mounted to the ends of the SCU0 cryomodule provide support and tension for the Ti guide tube and horizontal transverse motion (x) for measuring up to ±10 mm from the central axis.



Figure 1: SCU horizontal magnetic measurement system with 3.5-m linear stage for Hall probe scans. SCU0 cryomodule is on the left.

1st and 2nd Field Integrals and Phase Errors

The measured 1st and 2nd vertical field (B_y) integrals from the measurements performed in August and December of 2012 are shown in Fig. 2 and Fig. 3. The final 1st integral values were +31 and -87 G*cm in August and December, respectively. The August measurements of

Copyright © 2013 CC-BY-3.0 and by the respective authors

the 1st integrals, with the original magnet structures, typically showed values below 35 G*cm when using the Hall probe system. With the replacement magnet structure, a current-dependent 1st integral was introduced. The current-dependent 1st field integrals from the December measurements are most likely due to stray fields from the configuration of the SC leads from the magnet structure to the terminals on the cryocoolers. The stray field appears to have been adversely affected after the replacement of the suspect magnet structure.

There is no provision for adjustment of the final 1st field integral value, but the 2nd integral is adjusted via end correction coils that are located on the ends of the magnet structures [3]. These end correction coils can be energized symmetrically or differentially with respect to each other. When adjusted differentially, a varying (along the length of the device) vertical dipole component is created, which affects the straightness of the 2nd field integral. Figure 3 depicts the 2nd field integrals with symmetrical and differential end-field correction currents measured in December and the original measurement in August. By adjusting the average and differential end correction currents, both the slope and straightness of the 2nd field integral (trajectory) can be optimized.

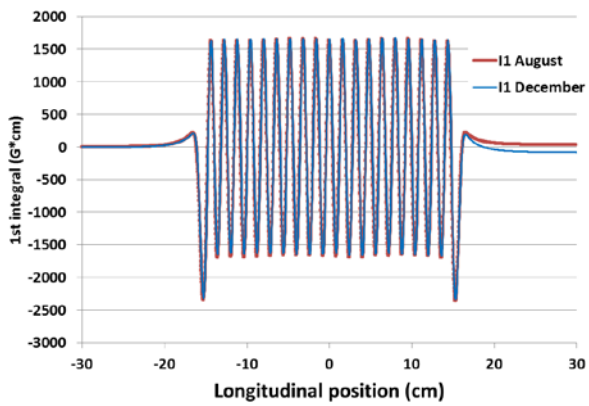


Figure 2: Plots of the SCU0 1st B_y field integrals at the design current of 500 A from August and December data. The final 1st integral values were +31 and -87 G*cm in August and December, respectively.

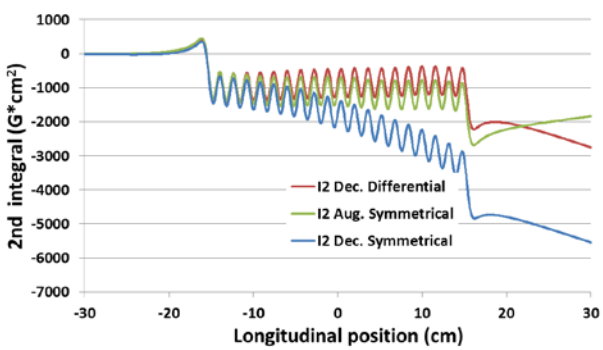


Figure 3: Plots of the SCU0 2nd B_y field integrals at the design current of 500 A from August and December data. The end correction coil currents were optimized using a 0.4% differential for the "Dec. Differential" case.

The measurements performed in August did not require any differential correction due to the fact that the 1st field integrals were naturally small and the 2nd field integrals were quite straight. Careful attention to SC lead dress was done during the initial assembly, but some compromises were made during the installation of the spare magnetic structure, which may have caused the increased stray field.

The data shown in this paper typically represents operation with optimized end correction coil currents set to minimize the 2nd field integrals using only symmetrical end correction currents. The measured K values from December and the phase errors from both the August and December measurements are depicted in Fig. 4.

The increased phase errors for the December measurements are due to a dipole component (from the SC stray field) that also affected the 1st field integrals, as shown in Fig. 2. If differential correction current was implemented, the phase errors during the December measurements could have been reduced to below 2 degrees and much closer to the August value of about 1 degree at 500 A.

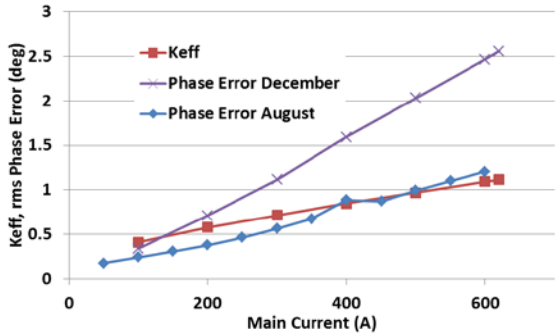


Figure 4: Plots of the SCU0 effective K value (K_{eff}) and phase errors as a function of current from the August and December Hall probe measurements.

INTEGRAL COIL RESULTS

A 4-mm-wide, 3.5-meter-long, single-turn stretched integral coil was used for measuring the static and dynamic 1st and 2nd field integrals as well as the multipole coefficients. The coil was rotated at 1 rps for the static field measurements and was fixed for measurements of the dynamic field integrals during a quench. The wire used for the coil was 100-μm-diameter CuBe stretched between two 4-mm-wide ceramic fixtures.

Static Integrated Field Measurements

The data in Fig. 5, labeled "I1 August" and "I1 December," were taken at fixed main coil currents. The data were recorded in the laboratory using the rotating coil system and using the storage ring with a beam-based integral measurement technique. The sign of the rotating coil field integral data was negated to agree with the beam-based data polarity. The data show that the change in the integrated field from 200 A to 500 A (the design operating range) was about 60 G*cm, which is within the APS tolerance of 100 G*cm.

Copyright © 2013 CC-BY-3.0 and by the respective authors

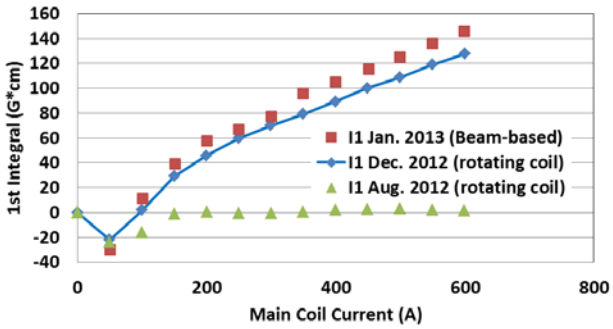


Figure 5: Plots of the SCU0 1st B_y field integrals as a function of current. These data were measured with a rotating coil in August and December, 2012, and using a beam-based technique with the APS storage ring in January, 2013.

Multipole Measurements

The rotating coil was also used to measure the integrated field uniformity over a horizontal range of ±4 mm. The curves in Fig. 6 show the integrated B_y (I1y) and B_x (I1x) along the x axis. It was discovered for the first time in August that a skew quadrupole component, which is larger than the APS undulator error tolerance, was present. It was decided to install the SCU0 as-is and use a feed-forward technique to adjust the beam coupling, if needed. This has proven successful in operation.

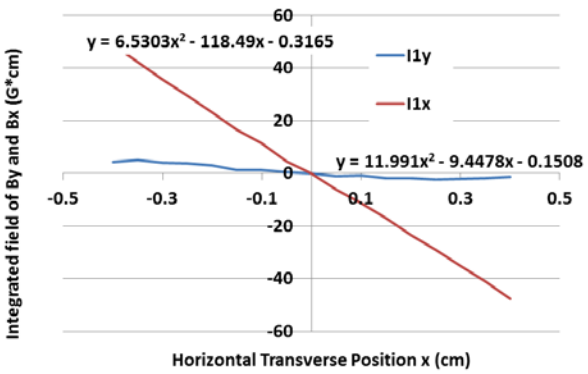


Figure 6: Plots of the SCU0 B_y (I1y) and B_x (I1x) 1st field integrals as a function of x position at a main coil current of 500 A. The normal and skew quadrupole components were -9.4 G and -118.5 G, respectively. The APS error tolerance is 50 G.

Dynamic Field Integral During a Quench

Measurements of the integrated field during quenches were done using a fixed coil. The data shown in Fig. 7 were taken during a forced heater-quench at 500 A. The 1st B_y integral curve was 35 G*cm p-p, which is 60 times less than the requirement of 2100 G*cm This low integral value is achieved by having the end correction coil currents slaved to the main current with an optimized look-up table. The look-up table was generated experimentally by optimizing the 2nd field integral (by adjusting the end correction current) at many fixed main coil currents.

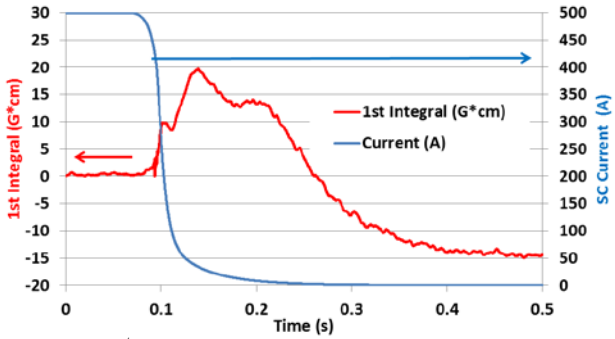


Figure 7: 1st B_y field integral and the main coil current as a function of time during a forced quench at 500 A.

CONCLUSIONS

The SCU0 magnetic measurements confirmed that all design parameters were within the APS error tolerances except for the integrated skew quadrupole component being slightly more than twice the 50-G tolerance. Measured phase errors were typically less than 2 degrees rms. The integrated field during a quench does not cause a beam dump; in fact it only causes a 60-µm beam motion. Comparing the August and December measurement results, it was found that initially the 1st field integral was very low and not current dependent, but after replacing one of the magnet structures, the 1st field integral was proportional to current but still within the error tolerance.

A new coil winding technique has been developed and will be implemented in the next SCU device. This new design was developed in order to minimize the skew quadrupole component, reduce machining cost, and improve the epoxy potting of the SC magnet structures.

The users in sector 6 have been routinely using the SCU0 at 685 A, 185 A above the design of 500 A.

ACKNOWLEDGMENTS

The authors would like to thank N. Mezentsev and V. Syrovatin from the Budker Institute for their collaboration with the "warm-bore" SCU measurement concept.

REFERENCES

[1] "The Advanced Photon Source First X-rays from the APS Superconducting Undulator," journals.iucr.org/s/issues/2013/03/00/s130300aps.pdf

[2] Y. Ivanyushenkov et al., "Status of the First Planar Superconducting Undulator for the Advanced Photon Source," Proceedings of IPAC2012, MOPPP078, p. 744 (2012); http://www.JACoW.org

[3] C.L. Doose, M. Kasa, S.H. Kim, "End-Field Analysis and Implementation of Correction Coils for a Short-Period NbTi Superconducting Undulator," Proceedings of PAC2011, New York, TUP241, p. 1280 (2011); http://www.JACoW.org

Copyright © 2013 CC-BY-3.0 and by the respective authors

SUPERCONDUCTING CORRECTOR IR MAGNET PRODUCTION FOR SUPERKEKB*

B. Parker#, M. Anerella, J. Escallier, A. Ghosh, H. Hocker, A. Jain, A. Marone, P. Wanderer
BNL, Upton, NY 11973, USA
Y. Arimoto, M. Iwasaki, N. Ohuchi, M. Tawada, K. Tsuchiya, H. Yamaoka, Z. Zong
KEK, Tsukuba, Ibaraki 305-0801 Japan

Abstract

SuperKEKB is an upgrade project underway at KEK, to increase the KEKB b-factory luminosity 40-fold by using nanobeam Interaction Region (IR) focusing optics [1] for which the production of new superconducting IR magnets and correctors is critical [2]. SuperKEKB corrector design and production is challenging since many different coils are needed for precise control of IR magnetic fields, in order to ensure good beam lifetime and there is very little space for them. SuperKEKB corrector production is about half completed and we report here on new techniques recently developed to address production challenges.

INTRODUCTION

The SuperKEKB IR magnet layout in the left-side and right-side cryostats is shown in Fig. 1. The SuperKEKB design has 83 mrad total crossing angle to separate the e^- (E) High Energy Ring (HER) and e^+ (P) Low Energy Ring (LER) beam lines in independent non-cryogenic vacuum apertures. A few millimetres of radial space is available for corrector coils atop support bobbins that serve as the inner cold mass containment wall and the main quadrupole coils' inner surface. The corrector requirements, presented in Table 1, evolved in response to results from optics optimization and tracking studies and differ from those available before production started [3].

Left-side corrector production commenced first using preliminary specifications provided before the right-side requirements were set. Later optics studies found that sextupole coils, b_3 and a_3, not in the original design, are needed; so these coils are added to the right-side layout. The majority of the corrector coils are located inside a main quadrupole coil; however, with insufficient space inside the first IR quadrupoles, QC1LP/RP, their b_4 correctors are wound on bobbins placed just outside the

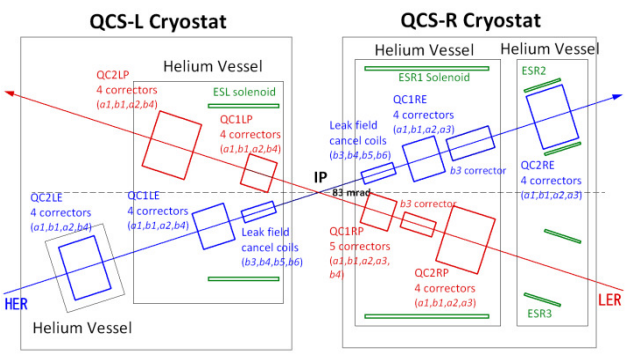


Figure 1: SuperKEKB IR magnet layout schematic.

Table 1: Corrector Integral Field Strength Requirements. Here R/L denote left- and right-side magnets and P/E denote the LER and HER beam lines. The right-side b_3 coils are placed between main magnets. The external field cancel coils for the HER are not included in this table.

Magnet	R_r	A_1	B_1	A_2	A_3	B_3	B_4
	mm	T•m	T•m	T	T/m	T/m	T/m^2
QC1RP	10	0.016	0.016	0.64	7.6	17.2	60
QC2RP	30	0.03	0.03	0.31	1.36		-
QC1RE	15	0.027	0.046	0.75	7	27	-
QC2RE	35	0.015	0.015	0.37	1.5		-
QC1LP	10	0.016	0.016	0.64	-	-	60
QC2LP	30	0.03	0.03	0.31	-	-	60
QC1LE	15	0.027	0.046	0.75	-	-	60
QC2LE	35	0.015	0.015	0.37	-	-	60

main coil (along with an a_3 corrector only for QC1RP). Because these first LER quadrupoles have insufficient space for magnetic flux return yokes between their coils and the nearby HER beam, there is significant external field leakage that must be dealt with so as not to adversely impact the HER optics. Requirements for these additional external field cancel coils for the HER are discussed later.

Both the corrector and cancel coils are attached to support bobbins via the BNL Direct Wind technique [4] using 0.35 mm diameter, single-strand superconducting round wire from Furukawa with a 1:1 Cu:NbTi ratio and critical current at 4.2K greater than 130 amps in a 5 T background field [5]. The wire is Kapton® overwrap insulated and adhesive coated to be compatible for use with BNL Direct Wind ultrasonic bonding technology.

CORRECTION COIL PRODUCTION

The SuperKEKB corrector requirements span a broad range of field harmonics and focusing strengths and are manufactured in many radius and length combinations. In order to make the best use of the available space attention to detail is needed regarding the careful nesting of coil layers. The QC2LE multi-layer arrangement shown in Fig. 2 offers an example of how lead management is an important consideration. At the bottom of the QC2LE coil stack is a single layer planar pattern [6] dipole winding over which skew dipole and then skew quadrupole planar coils are wound. The skew quadrupole is topmost because its ends, with fewer turns, are naturally shorter than those of the layers below and its four pole regions line up with

#parker@bnl.gov

Copyright © 2013 CC-BY-3.0 and by the respective authors

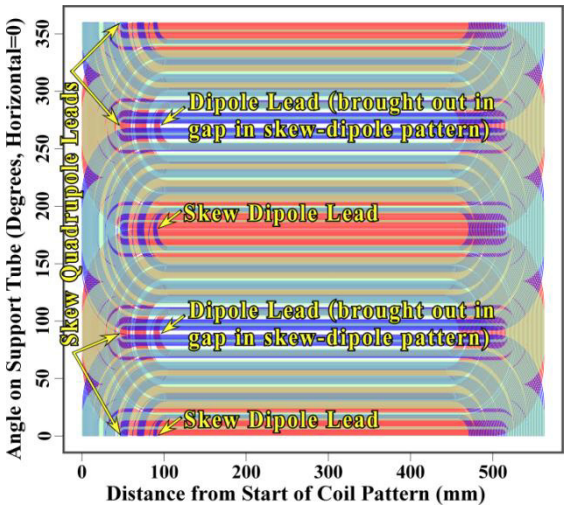


Figure 2: Multi-layer corrector coil winding example.

the lower pole regions. Thus it is possible to "see" the other current leads under the skew quadrupole pattern to bring them out over the top of the final coil package. But with this lead arrangement the dipole leads would be blocked by the skew dipole coil pack if we did not also open the mid-plane gap shown in the skew dipole pattern.

SuperKEKB beam lifetime is fairly sensitive to IR local field errors; so we use several field tuning spacers, in both the coil body and ends, to try to limit local field harmonic design errors to the level of a few gauss. For clarity a final b_4 coil winding is omitted from Fig. 2. The QC2LE b_4 integrated strength requirement is sufficiently small that we can use a short b_4 pattern that does not extend over the region of the previously wound coil leads

For some coils, such as the b_1, of QC1LE/RE, the current to reach the Table 1 value would be excessive with only a single coil layer. In this case we wind a_1 and a_2 layers first and move the b_1, coil out where we can use a shortened two-layer Serpentine style coil pattern [7] that does not block the a_1 and a_2 leads. The Serpentine pattern lets the b_1 leads exit cleanly even with a b_4 pattern of the same length wound on top of it [6].

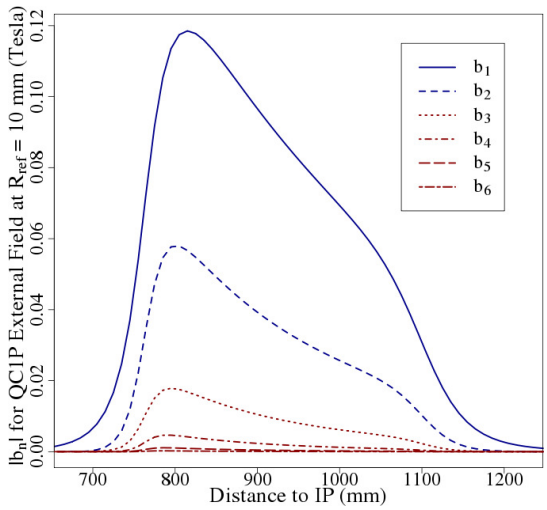


Figure 3: Decomposition into magnetic multipoles for QC1P external field plotted as a function of distance to the IP, for 10 mm reference radius, at the HER beam line.

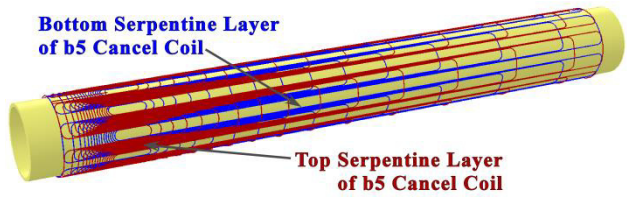


Figure 4: Final twisted b5 cancel coil winding used to generate the b5 and a5 fields shown in Fig.5. This pattern is a dual-layer Serpentine style coil winding with end turn spacing adjusted in both layers to achieve the desired field falloff with distance to the IP. Note that there are a large number of different sized coil end spacer gaps that must be filled with custom sized Nomex paper inserts.

CANCEL COIL PRODUCTION

External field leaking from the first LER quadrupoles, QC1LP\RP into the HER aperture, decomposed as a field multipole expansion, is plotted in Fig. 3. The linear, b_1, b_2, external field components are not of concern as they are easily included in the SuperKEKB IR optics; however, the non-linear fields shown in Fig. 3 would adversely impact HER beam lifetime. Via iterative adjustment of coil end turn spacing, four independent cancel coil windings, b_3, b_4, b_5 and b_6, are tailored to match the different external field profiles plotted in Fig. 3 that arise as the beam separation increases away from the IP.

We find that dual-layer Serpentine patterns, such as that shown in Fig. 4, are especially suited for use as cancel coils because they exhibit a simple, direct relationship between the straight section "body fields" and the end fields. At 10 mm reference radius the cancel coil's main harmonic dominates the total field until close to each coil end; so we developed fast codes that approximate the cancel coil field shape based on scanning at a single

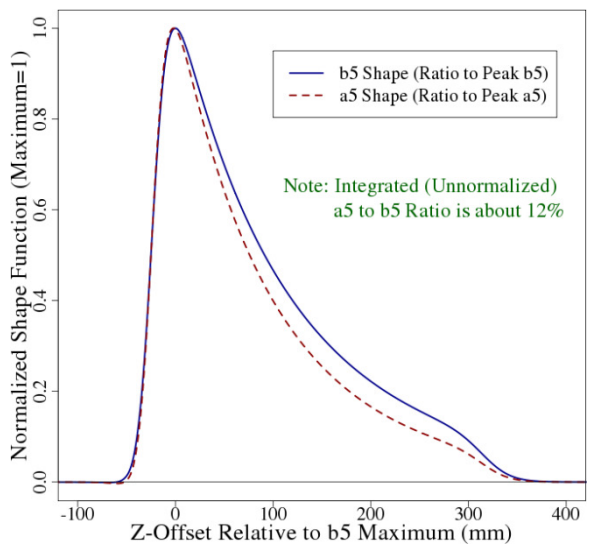


Figure 5: Normal and Skew Field Falloff Comparison. We plot b5 and a5 external field multipoles, with common peak normalization, to highlight their different shapes. A simple coil rotation cannot generate the correct a5 distribution from a pure b5; thus we must "twist" the coil pattern as a function of length along the coil support tube.

Copyright © 2013 CC-BY-3.0 and by the respective authors

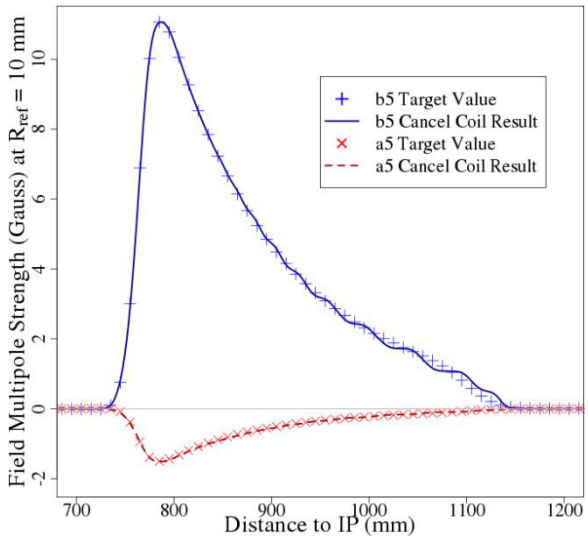


Figure 6: The b5 and a5 field multipole distributions generated by the b5 cancel coil with an applied twist transformation are compared here to the target goals set for perfect QC1P external field cancellation.

azimuthal angle rather than having to do a much more calculationally intensive full-angle range z-scan.

With an end turn spacing parameterization versus turn number that maps to specific shape features (e.g. regions of constant slope, a peak or a shoulder falloff), we can vary the end spacing in a smooth manner and after a few iterations come close to the desired external field target shape. With this candidate solution in hand we do a full harmonic z-scan to verify that unwanted higher-order end field harmonics are sufficiently small. A typical target normal-harmonic field shape curve, b_5, is plotted in Fig. 5. Note that in addition to b_5 there is a second a_5 curve shown that has a different falloff with distance from the IP. A similar shape difference between normal and skew occurs for all of the QC1P external field multipoles and this presented an unexpected design challenge.

The SuperKEKB quadrupoles experience a combined background field from the detector and compensation solenoids and are rotated in order to achieve the desired optics for the beam eigenplanes; the corrector magnets are rotated the same amount. A naive expectation was that the cancel coils could also be similarly rotated to provide the proper mix of normal and skew cancel fields; however, the SuperKEKB IR layout has some HER and LER quadrupoles at different vertical offsets to reduce needed corrector strengths. Unfortunately this combined rotation and offset results in our having to match different normal and skew external field target shape curves.

To alter the skew/normal field ratio we must rotate different sections of the coil pattern by different amounts, i.e. we have to twist the coil pattern. A uniform twisting of a pure b_5 coil pattern produces the required a_5 field profile as illustrated in Fig. 6. The most obvious field deviations from target values are the small constant field "shoulders" that result from the limited number of b_5 end turns available to optimize. The b_3 and b_4 cancel coils have more turns and smoother field profiles while the b_5 and b_6 coils, with fewer turns, have the largest relative tail deviations. Still the target b_5 and b_6 fields are already so small that these errors really do not matter.

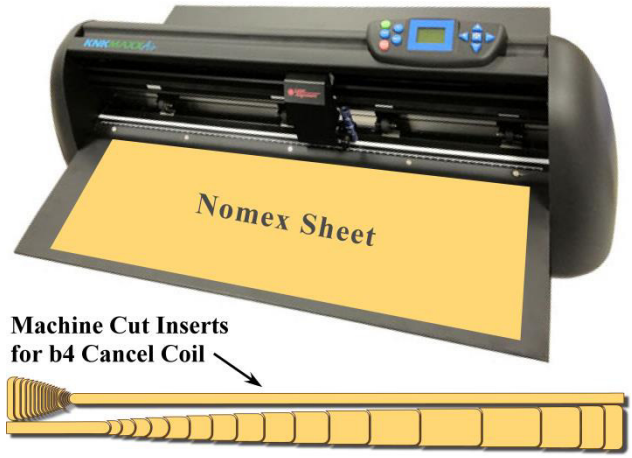


Figure 7: This machine automatically cuts coil end spacer inserts from Nomex sheets using information derived from a computer winding file. The pattern for a single b4 pole is also shown. The cut outs have tab connections to keep inserts in place until needed and avoid hand sorting.

While it is convenient for optimizing a magnetic design to use the large number of spacers shown in the patterns of Fig. 2 and Fig. 4, it is also a production nightmare to ask technicians to cut so many tiny fill pieces by hand. For SuperKEKB production we developed an automated procedure where the coordinates of the coil pattern are fed into Pro-Engineer software [7] that follows the coil path in 3 dimensions and then unwraps it to a flat pattern. To have a proper gap between the fill spacers and coil, this flattened path is thickened to simulate wire thickness and offset by a small amount. Additional processing removes extraneous lines and leaves only the shapes to be cut. That file is then read by the computer controlled flat pattern cutter shown in Fig. 7 that uses a small steel blade to cut the pattern from a sheet of Nomex [8].

REFERENCES

[1] H. Koiso, "Colliders for B-Factories," Proceedings of IPAC2011, WEZA02, pp. 1931-1935, 2011.
[2] N. Ohuchi, et al., "Design of the Superconducting Magnet System for the SuperKEKB IR," contribution WEODA1, NA-PAC'13.
[3] B. Parker et al., "Direct Wind Superconducting Corrector Magnets for the SuperKEKB IR," IPAC12, New Orleans, LA, WEEPPB013, p. 2191, 2012.
[4] B. Parker et al., "BNL Direct Wind Superconducting Magnets," contribution 4FO-6 to MT22, Marseille, France, September, 2011.
[5] Furukawa Electric Co., Ltd., Tokyo 100-8322, Japan.
[6] B. Parker and J. Escallier, "Serpentine Coil Topology for BNL Direct Wind Superconducting Magnets," PAC05, Knoxville, TN, TOAA010, p. 737, 2005.
[7] Now marketed as PTC Creo, see www.ptc.com.
[8] 24" Maxx Air from Klic-N-Kut, see knkusa.com.

Copyright © 2013 CC-BY-3.0 and by the respective authors

PARTIAL RETURN YOKE FOR MICE – ENGINEERING DESIGN*

H. Witte†, S. Plate, Brookhaven National Laboratory, Upton, NY, USA
J. Tarrant, STFC Rutherford Appleton Laboratory, Didcot, UK
A. Bross, Fermilab, Batavia, IL, USA

Abstract

MICE, which is an acronym for Muon Ionization Cooling Experiment, is a technology demonstration which is presently assembled at the Rutherford Appleton Laboratory in Didcot, UK. MICE aims to demonstrate ionization cooling experimentally, which is an essential technology for potential future accelerators such as a muon collider.

The MICE channel consists of up to 18 large bore superconducting solenoids, which produce a substantial stray field. This stray field can jeopardize the operation of electrical and electronic equipment in the MICE hall.

The concept of a partial flux return yoke has been developed, which reduces the stray field in the MICE hall to a safe level. This paper discusses the engineering design of the partial return yoke.

INTRODUCTION

MICE will be assembled in several steps [1]. At the time of writing it is aimed to finish construction of Step IV by summer/autumn 2014. MICE Step IV consists of 12 large bore superconducting solenoids (18 for Step VI). The MICE solenoids produce a substantial amount of stray field, which is a concern as some of the technical equipment in the MICE hall may not work.

This paper discusses the engineering aspects of a partial return yoke (PRY) for the MICE solenoids for Step IV; the partial enclosure is sufficient to reduce the stray fields to an acceptable level.

Details on the general design approach, the coil configuration of Step IV, expected shielding performance and effect on the performance of MICE are given in [2, 3].

ENGINEERING CONCEPT

The evolution of the PRY geometries is shown in Fig. 1. It is important to note that in general all shown geometries have a similar shielding performance. The vertical extensions (middle plot) have been found to further reduce the stray field behind the PRY by preventing flux leakage from the unshielded part. The final geometry, shown on the right, was chosen because of engineering considerations.

The MICE PRY will consist of in total eight shielding plates, each of which is about 4 m long and 1.5 m wide. The thickness of each shielding plate is 10 cm or 12 cm depending on the desired shielding performance. The weight

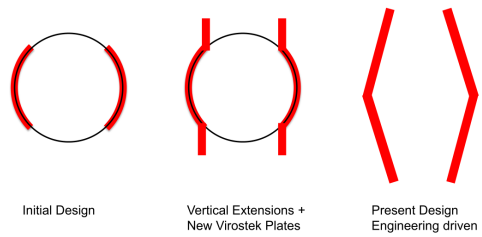


Figure 1: Evolution of the PRY geometry.

of a 10 cm thick shielding plate is about 4.8 tons, which is less than the limit of the lifting crane in the MICE hall.

To avoid field leakage (see section 'Vertical Gaps') two backing plates are installed on the inside and outside of the PRY covering the vertical joint. The thickness of each backing plate is half that of the PRY.

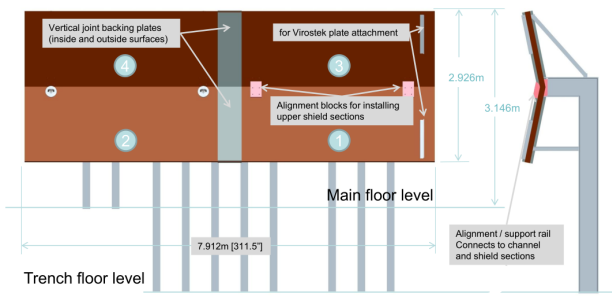


Figure 2: MICE partial return yoke.

SUPPORT STRUCTURE

The support structure has been designed to cope with the dead weight of the PRY as well as magnetic forces. The magnetic forces on the structure were evaluated using the Maxwell stress tensor. The forces were evaluated for each of the shielding plates separately. The main force component is in horizontal direction, directed such that the shielding plates want to move towards the MICE experiment. The maximum force is equivalent to 34 tons for half of the PRY (four shielding plates) and occurs for the 240 MeV flip mode. There is no net longitudinal or vertical magnetic force on the PRY due to symmetry reasons.

The support structure, as shown in Fig. 2, consists of several S-beams which are anchored in the floor of the MICE hall. An ANSYS study was carried out to evaluate peak stresses and deflections. While the stresses are not a concern (123 MPa) a maximum deflection of 5 mm was ob-

* Work supported by Brookhaven Science Associates, LLC under Contract No. DE-AC02-98CH10886 with the U.S. Department of Energy.
† hwitte@bnl.gov

Copyright © 2013 CC-BY-3.0 and by the respective authors

served at the top corner of the PRY. To avoid this eight horizontal support straps will be installed to transfer forces between the two PRY halfs. This reduces the deflection to 0.28 mm.

PENETRATIONS

Vertical Gaps

Vertical gaps in the PRY occur between two adjacent shielding panels. Initial investigations showed that vertical gaps in the PRY are detrimental for the shielding performance. Figure 3 shows the position of a vertical gap in the PRY near the tracker region. The simulation result of the stray magnetic flux behind the PRY at a radius of 1.5 m and beam height is shown in Fig. 4. The figure shows that depending on the width of the gap the stray field behind the PRY increases substantially.

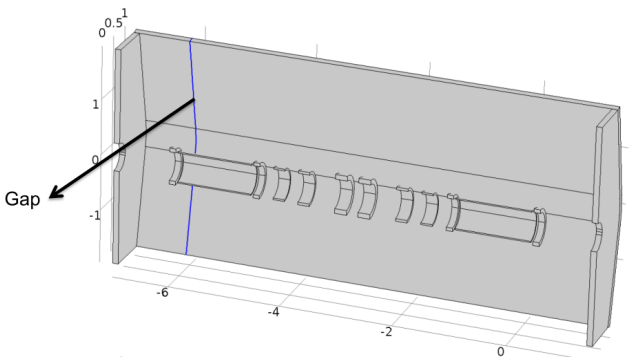


Figure 3: Geometry: Vertical gap in shield.

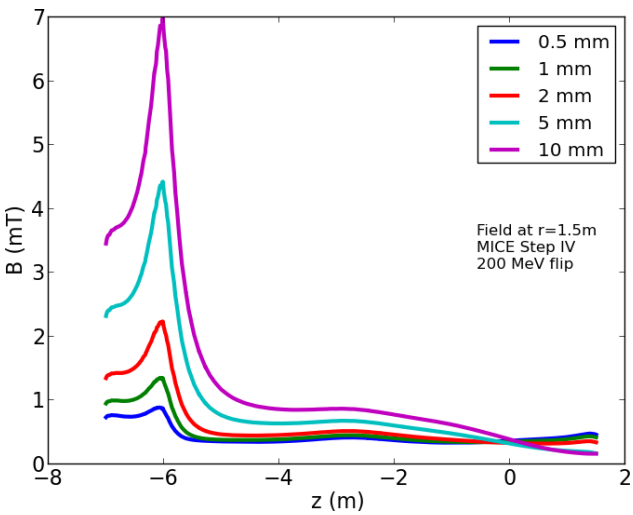


Figure 4: Modulus of the magnetic flux density at a radius of 1.5 m for 200 MeV flip mode assuming a vertical gap at $z = -6$ m.

To avoid performance impacts several potential solutions were studied. An adequate and easy to implement strategy is to double-up the PRY at the position of a vertical gap; Figure 5 illustrates the concept. Each of the two backing plates is required to be half the thickness of the shield. The width of each backing plate is 0.4 m. The backing plates work by forming a low magnetic reluctance joint between neighbouring PRY sections; at the joint the magnetic flux is redirected into the backing plates, thus avoiding the vertical gap.

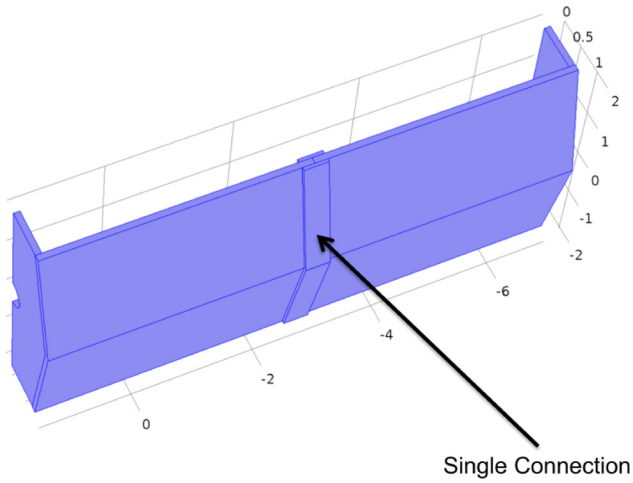


Figure 5: Concept of doubling up a vertical gap.

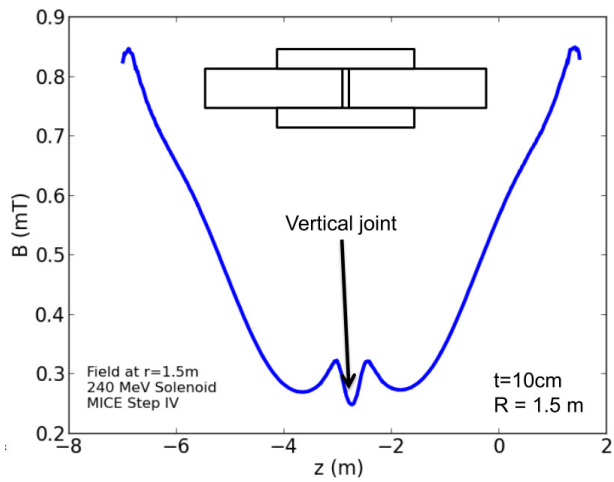


Figure 6: Modulus of the residual stray field at a radius of 1.5 m (beam height) for 200 MeV flip mode. The vertical gap is doubled up using to backing plates, each 40 cm long.

Horizontal Gaps

Horizontal gaps in the PRY were studied as well. Figure 7 shows simulation results for the 200 MeV flip mode. The figure shows that the stray field behind the PRY by comparison is far less sensitive to horizontal gaps. Even gaps of 20 cm width produce only an increase in stray field of about 1 mT.

MATERIAL CONSIDERATIONS

The PRY is planned to be made out of AISI 1010 steel, which is a cost efficient material for magnetic shielding.

Copyright © 2013 CC-BY-3.0 and by the respective authors

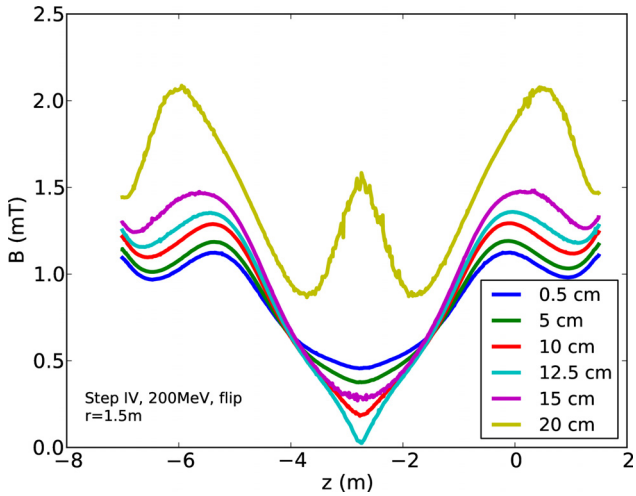


Figure 7: Modulus of the residual magnetic field at a radius of 1.5 m. The simulation assumes a horizontal gap in the PRY at beam height.

One of the disadvantages of AISI 1010 steel is the variation of the magnetic properties depending on the exact composition. In general the higher the iron content the better the magnetic properties. In order to estimate the shielding performance we use measured magnetization curves of 1010 steels which have been used in various HEP experiments [4]. For comparison three magnetization curves are chosen: one representing very good magnetic properties (labeled 'ARMCO Atlas'), one with intermediate magnetic properties (labeled 'St1010 Germany') and one with poorer magnetic performance (labelled 'St1010 ATLAS').

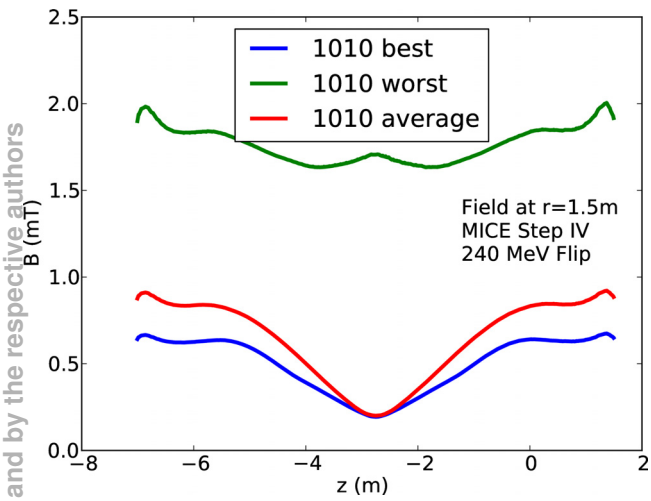


Figure 8: Stray magnetic field for different 1010 steels at a radius of 1.5 m (PRY finishes at a radius of about 1.35 m) and vertically at beam height.

The expected shielding performance can be seen in Fig. 8, which shows the residual stray magnetic field at a radius of 1.5 m or about 10 cm behind the PRY at beam height. The figure shows that the stray magnetic field (for 240 MeV flip configuration) varies between 0.6 and 2 mT. For average properties of 1010 steel a residual magnetic field of about 1 mT can be expected.

To limit the variability of the magnetic properties a better quality steel, for axample AISI 1008 or AISI 1006 can be chosen. In addition the PRY thickness can be increased which improves the shielding performance and hence the safety margin.

SCHEDULE

The PRY material procurement and fabrication is presently estimated to be completed in August 2014.

SUMMARY

This paper summarizes the engineering design of a partial return yoke for the Muon Ionization Cooling Experiment. A support structure was described which is capable of supporting the dead weight and magnetic forces on the PRY during operation. Both stresses and deflection are acceptable.

Penetrations of the PRY were studied and it was found that vertical gaps have a detrimental effect on the shielding performance. To avoid flux leakage vertical joints in the PRY are doubled up with two backing plates. Horizontal gaps are less critical and can be tolerated up to a width of several cm.

The designated material for the PRY is AISI 1010 steel. The magnetic properties of 1010 steel can vary significantly depending on the exact composition. Magnetization curves from literature of HEP physics experiments have been used to estimate the effect. It was found that the shielding performance for a 10 cm PRY varies from 0.6 mT up to 2 mT. To mitigate this a steel with a higher guaranteed Fe content can be chosen (for example AISI 1008 or 1006) and the PRY thickness can be increased to 12 cm.

REFERENCES

[1] M. Bogomilov et al., The MICE Muon Beam on ISIS and the beam-line instrumentation of the Muon Ionization Cooling Experiment, *Journal of Instrumentation*, 7(05):P05009, 2012.

[2] H. Witte and S. Plate, Partial Return Yoke for MICE, in *MAP-doc-4362, BNL-100819-2013-IR*, pages 1–39. Brookhaven National Laboratory, Upton, NY, 11713 (2013).

[3] H. Witte, S. Plate, J. Tarrant, and A. Bross, Partial Return Yoke for MICE – General Concept and Performance, in *Proceedings of NA-PAC13*, THPBA09 (2013).

[4] S. Sgobba, Physics and measurements of magnetic materials, (arXiv:1103.1069):25 p, Mar 2011. Comments: 25 pages, presented at the CERN Accelerator School CAS 2009: Specialised Course on Magnets, Bruges, 16-25 June 2009.

Copyright © 2013 CC-BY-3.0 and by the respective authors

PARTIAL RETURN YOKE FOR MICE – GENERAL CONCEPT AND PERFORMANCE*

H. Witte†, S. Plate, Brookhaven National Laboratory, Upton, NY, USA
J. Tarrant, STFC Rutherford Appleton Laboratory, Didcot, UK
A. Bross, Fermilab, Batavia, IL, USA

Abstract

MICE, which is an acronym for Muon Ionization Cooling Experiment, is a technology demonstration which is presently assembled at the Rutherford Appleton Laboratory in Didcot, UK. MICE aims to demonstrate ionization cooling experimentally, which is an essential technology for potential future accelerators such as a muon collider.

The MICE channel consists of up to 18 large bore superconducting solenoids, which produce a substantial stray field. This stray field can jeopardize the operation of electrical and electronic equipment in the MICE hall.

The concept of a partial flux return yoke has been developed, which reduces the stray field in the MICE hall to a safe level. This paper discusses the general concept and expected performance.

INTRODUCTION

Ionization cooling can be regarded as an essential technology for future HEP particle accelerators such as the muon collider, as it is the only known technology fast enough to reduce the emittance of a muon beam.

MICE, which aiming to demonstrate the concept [1], will be assembled in several steps. At the time of writing it is aimed to finish construction of Step IV by summer/autumn 2014. MICE Step IV consists of 12 large bore superconducting solenoids. The MICE solenoids produce a substantial amount of stray field (in excess of 50 mT), which is a concern as some of the technical equipment in the MICE hall may not work.

This paper discusses the design concept of a partial return yoke (PRY) for the MICE solenoids for Step IV. The engineering design is described in [2, 3].

METHODOLOGY

For the analysis of the problem and performance estimate two commercial finite element packages are employed: COMSOL Multiphysics (COMSOL AB, Tegnergatan 23, SE-111 40 Stockholm, Sweden) and Opera 3D from Cobham/Vectorfields (Cobham CTS Limited trading, 24 Bankside, Kidlington, Oxfordshire, OX5 1JE, UK).

The two software packages use different physics implementations, which allows to verify the obtained results. COMSOL solves for the magnetic vector potential:

$$\nabla \times \left(\mu^{-1}\nabla \times A\right) = J \ . \tag{1}$$

In this equation μ is the magnetic permeability, A the magnetic vector potential and J a current density. In contrast to this Opera 3D solves for the magnetic scalar potential ϕ:

$$\nabla\mu\nabla\phi - \nabla\mu\left(\int_{\Omega_J}\frac{J\times R}{|R^3|}\mathrm{d}\Omega_J\right) = 0 \ . \tag{2}$$

Contributions to the magnetic field from current carrying structures at a distance R are usually evaluated using Biot-Savart law and integrated over the domain Ω.

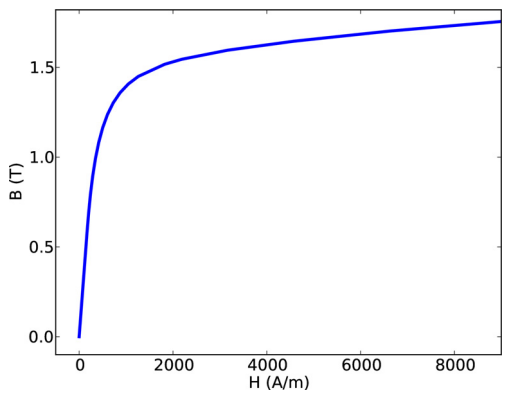


Figure 1: Magnetization curve of AISI 1010 steel.

For the simulations we assume that shielding iron will have the magnetic properties shown in Fig. 1. The magnetization curve was taken from Opera and is valid for AISI 1010 steel.

The coil geometries used in the simulation are summarized in Table 1.The MICE solenoids will be run in five different configurations. In two configurations the magnetic field flips in the centre of the MICE channel ('flip modes') whereas in three it does not ('solenoid modes'). The current densities for all cases are summarized in Table 2.

GENERAL CONCEPT

All MICE magnets are large diameter solenoids, which are relatively thin and short. From a shielding point of view an ideal solution is to encase the MICE magnets in a soft-iron cylinder. This is of course not practical; however, it is possible to achieve good shielding by only encasing MICE partially in this way. Fig. 2 shows the concept.

* Work supported by Brookhaven Science Associates, LLC under Contract No. DE-AC02-98CH10886 with the U.S. Department of Energy.
† hwitte@bnl.gov

Copyright © 2013 CC-BY-3.0 and by the respective authors

Table 1: Step IV, Coil Geometries

	z1 [m]	z2-z1 [m]	r1 [m]	r2 [m]
1	-6.0063	0.1106	0.258	0.324
2	-5.8582	1.3143	0.258	0.2793
3	-4.5063	0.1106	0.258	0.3176
4	-4.1508	0.1995	0.258	0.2878
5	-3.7116	0.2012	0.258	0.3027
6	-3.06	0.21	0.263	0.347
7	-2.65	0.21	0.263	0.347
8	-1.99	0.2012	0.258	0.3027
9	-1.549	0.1995	0.258	0.2878
10	-1.1104	0.1106	0.258	0.3176
11	-0.956	1.3143	0.258	0.2793
12	0.3967	0.1106	0.258	0.324

Table 2: Step IV, Current Densities in A/mm^2

Coil No.	Flip 1	Flip 2	Sol 1	Sol 2	Sol 5
1	-135	-135	135	135	135
2	-152	-152	152	152	152
3	-127	-127	127	127	127
4	-137	-151	55	66	16
5	-119	-142	62	71	44
6	-114	-137	60	71	113
7	114	137	60	71	113
8	119	142	62	71	44
9	137	151	55	66	16
10	127	127	127	127	127
11	152	152	152	152	152
12	135	135	135	135	135

As shown in the figure, the MICE PRY covers an azimuthal angle of about $\pm 60°$ just outside of the cryostats. The remaining parts are left unshielded because of spatial constraints. In practice the MICE PRY consists of eight 1.5 m wide and 4 m long iron plates. For the thickness we consider two cases: 10 cm, which is the nominal case, and 12 cm which offers a better shielding performance. Each shielding plate is tilted by $11.5°$ towards MICE to satisfy spatial restraints and to aid the shielding efficiency. In longitudinal direction the PRY is completed by additional shielding plates which connect the two side halves of the PRY (apart from a small opening with radius 250 mm for the beam).

PERFORMANCE

The magnetization in the PRY is equivalent to a magnetic field 1.1T for all operational modes of MICE Step IV. At this level the relative permeability of the shielding iron is about 1700–2000, which was found to be sufficient to suppress flux leakage.

Fig. 3 shows the stray magnetic field at a radius of 1.5 m at beam height, which is about 10 cm radially away from

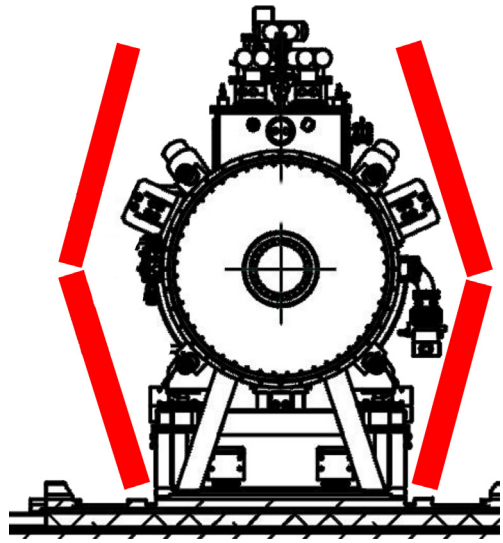


Figure 2: General Concept, frontal view. The partial return yoke is shown schematically in red.

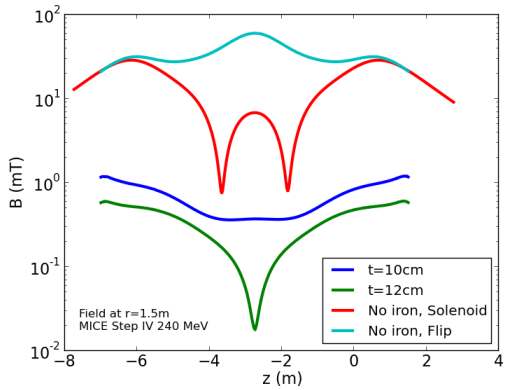


Figure 3: Modulus of the magnetic fringe field at a radius of 1.5 m at beam height.

the PRY. The figure shows a comparison between two unshielded cases (240 MeV flip and solenoid mode) and two shielded cases (solenoid mode). The two shielded cases differ in the thickness of the shield, which is 10 or 12 cm.

As shown in the figure, the PRY is effective in reducing the field level to 0.6–1.1 mT depending on the chosen thickness. This is a reduction by more than 50 to the unshielded case, where the stray fields are between 30–70 mT.

Fig. 4 visualizes the 5 Gauss line in 3D. The 5 Gauss line is important because of health and safety considerations. Shown is a comparison between the unshielded (left) and shielded case (right figure). The figure emphasizes that the fringe field extent is significantly reduced. In longitudinal direction the 5 Gauss line is reduced from about 13 to 8 m. In horizontal direction the 5 Gauss line finishes with the PRY, which is located at about 1.4 m. In vertical direction, which is not covered by the PRY, the 5 Gauss line is moved from 4.5 m to about 2 m.

Copyright © 2013 CC-BY-3.0 and by the respective authors

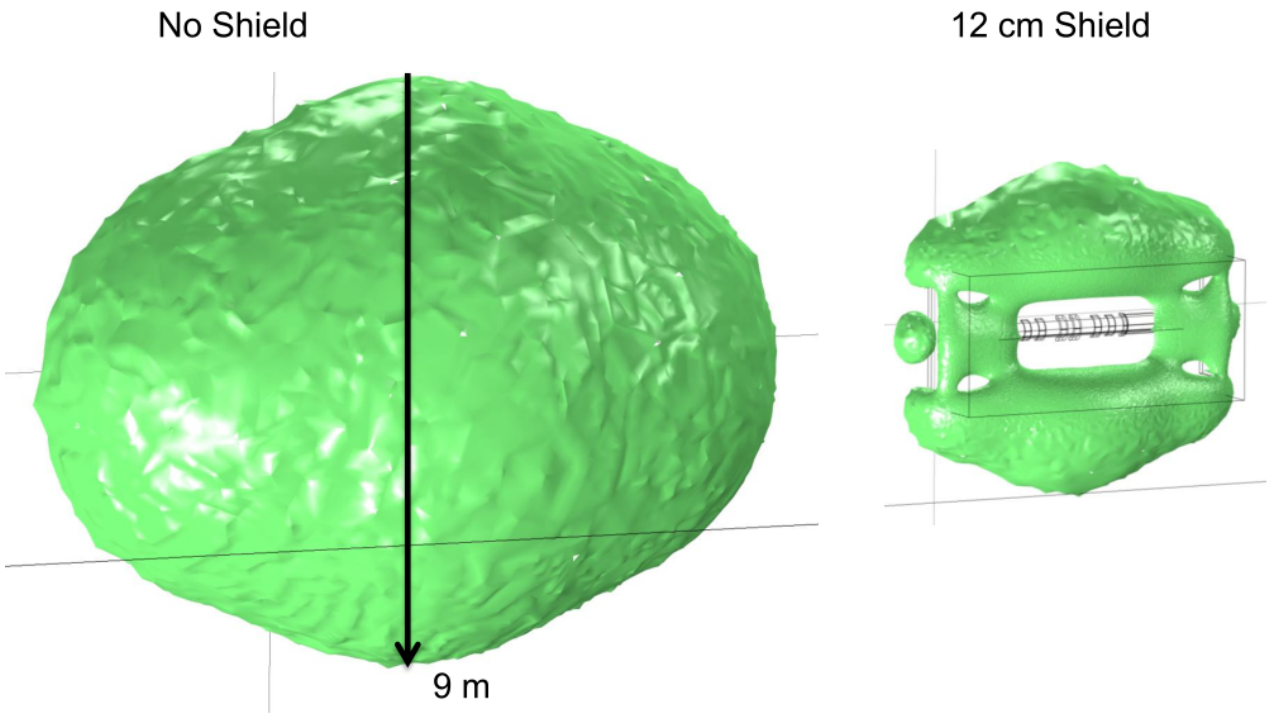


Figure 4: 5 Gauss iso-surface plot of MICE for the 200 MeV flip mode. The left figure shows the 5 Gauss surface for an unshielded scenario (no iron present) versus the case where the PRY is adopted.

EFFECT ON THE BEAM

The additional iron in close proximity to MICE changes the magnetic field in the channel. A particular concern is the asymmetry of the PRY due to the fact that in vertical direction MICE is unshielded. This leads to an asymmetric error field which can be detrimental for the performance of MICE. A particle tracking study using MAUS (MICE Analysis User Software) was carried out to address this [4].

The simulation consisted of 100,000 muons; simulated was the 200 MeV case (flip mode). It was found that due to the error field the mean beam position is shifted by about 100 μm, the beta function changes by about 10 mm and the discrepancy between emittances is about 1 μm.

The results indicate that the changes introduced by the MICE PRY have a barely measurable effect and therefore do not compromise the experiment.

SUMMARY

This paper outlines a shielding concept for the international Muon Ionization Cooling Experiment MICE, which is capable of reducing the stray fields in the MICE hall to a tolerable level. The MICE channel will not be encased fully due to spatial constraints, but the as shown the shielding performance is still sufficient to shield large parts of the MICE hall.

Two different shield thicknesses were studied; in comparison to a 10 cm thick PRY a 12 cm version reduces the stray magnetic field at a radius of 1.5 m by a factor of two or more and offers therefore more margin.

Simulation results suggest that the 5 Gauss line in the MICE hall in horizontal and longitudinal direction would be located just after the PRY. In vertical direction the distance to the 5 Gauss line is reduced by about a factor of 2.

The effect on the beam was studied using particle tracking simulations and it was found that the effect of the additional iron is negligible.

REFERENCES

[1] M Bogomilov, et al. The MICE muon beam on ISIS and the beam-line instrumentation of the muon ionization cooling experiment. *Journal of Instrumentation*, 7(05):P05009, 2012.

[2] Holger Witte, Stephen Plate, Jason Tarrant, and Alan Bross. Partial Return Yoke for MICE – Engineering Design. In *Proceedings of NA-PAC13*, 2013, THPBA08.

[3] Holger Witte and Stephen Plate. Partial Return Yoke for MICE. In *MAP-doc-4362, BNL-100819-2013-IR*, pages 1–39. Brookhaven National Laboratory, Upton, NY, 11713, USA, 2013.

[4] Chris Rogers and Holger Witte. Effect of iron partial return yoke on the mice beam. MICE Analaysis Meeting, January 2013. `http://micewww.pp.rl.ac.uk/issues/1161`.

Copyright © 2013 CC-BY-3.0 and by the respective authors

A STRIPLINE KICKER DRIVER FOR THE NEXT GENERATION LIGHT SOURCE*

N. Butler, F. Niell, J. Kinross-Wright, M. Gaudreau, M. Kempkes,
Diversified Technologies, Inc., Bedford, MA 01730, USA

Abstract

Diversified Technologies, Inc. (DTI) has designed and prototyped a novel high voltage pulse generator applicable to beam deflector applications. This work is funded by an SBIR grant from the U.S. Department of Energy in support of advanced accelerator development. The technical goals include 10 kV output into 50 Ω with 2 ns rise time and a repetition rate of 100 kHz. These challenging specifications were based on the original Next Generation Light Source (NGLS) fast deflectors (stripline kicker) required in the proposed beam switchyard. DTI believes the advanced pulse generator will have numerous applications requiring fast risetime and high repetition rate. This paper describes the current status of the project.

BACKGROUND

In Phase I of the project, DTI investigated several high-speed switching circuits, using a variety of emerging solid-state switch technologies, including GaN and SiC. After much experimentation, DTI has settled on an inductive adder circuit topology, using a two-step, silicon MOSFET Marx approach in each stage. The use of parallel FETs at each stage of the inductive adder allows a flexible design which can be adapted to new requirements. The Phase II prototyping efforts have validated the design approach. Figure 1 shows an operational prototype pulse generator.

Motivation

The NGLS facility concept uses a high bunch rate accelerator (1 MHz) to efficiently supply beam to 10 independent X-ray FEL beam lines. Each beam line receives pulses at 100 kHz, though the fields in the deflector must settle in less than 1 μs to avoid perturbation of un-deflected pulses in the bunch train from the accelerator.

It is envisioned that the deflection will be imparted by a symmetric pair of shaped parallel deflection electrodes, pulsed in opposition at 10 kV. Matching 50 Ω resistors terminate the deflector to avoid the creation of backward-traveling waves.

SYSTEM ARCHITECTURES

Various system designs were explored for producing the required pulse wave forms. The options included a direct series high voltage switch, solid-state Marx bank, inductive adder, or more conventional pulse transformers and transmission-line adders, several of which were considered in detail. The inductive adder was ultimately selected as the preferred development path for the remainder of the program. The favored embodiment of the overall pulse generator was based on measurements, multiple circuit test boards, extensive modeling, and practical considerations regarding component performance in the sub-nanosecond regime.

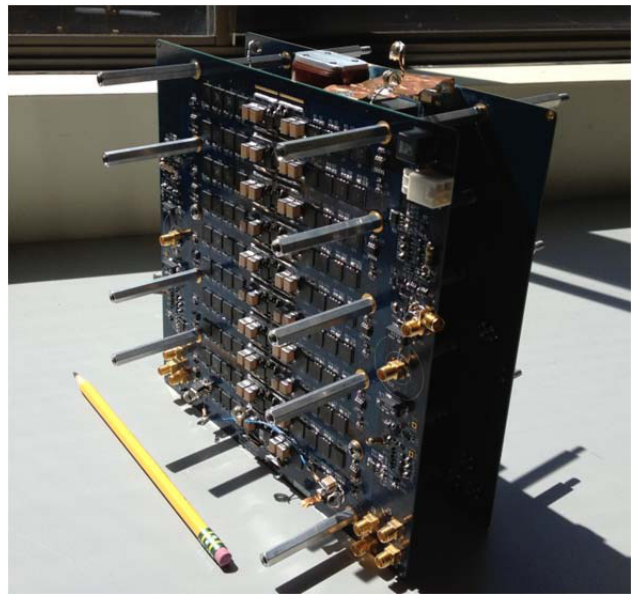


Figure 1: Prototype pulser hardware. In the center of the rectangle at the top is the output connection, and the two circuit boards on either side carry the pulse amplifiers and MOSFETs.

Pulse Generation

The overall pulse generation network is presented in Figure 2. This represents the principal schema, but variants on this approach have been developed as well. The key components exhibited in this figure include:

- Each stage is comprised of a pair of STMicroelectronics STL21N650 compensated silicon MOSFETs, capable of 2 nanosecond-class switching speed, along with extremely fast charge-pump driver circuitry to enable such fast switching. Note that the gate drivers must be referenced to the source pins in the diagram, meaning that one set of gate drivers must be floating – a key technological issue in this speed domain.
- A set of transformer cores, Tn, to couple the 1 kV pulses into a common tapered secondary structure. Matching the impedance of the output structure to

*Work supported by the Department of Energy

Copyright © 2013 CC-BY-3.0 and by the respective authors

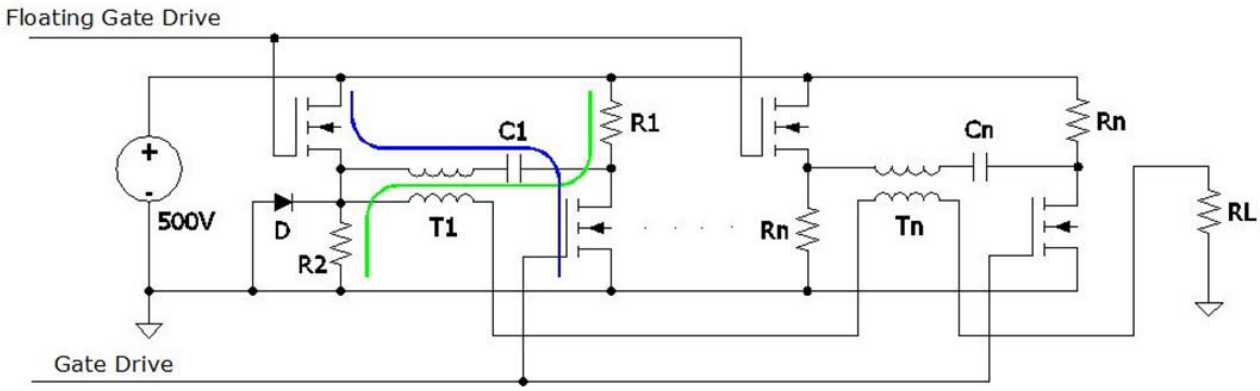


Figure 2: Basic inductive adder scheme, showing "n" stages. Note that the gate drives are shown all in parallel. This is due to DTI's innovative gate driver architecture which enables high voltage charge pump circuitry to drive multiple compensated-silicon MOSFETs with the speed required to achieve nanosecond-class switching. In this Marx arrangement, C1 is charged through resistors R1 and R2 (GREEN). The MOSFETs then discharge the capacitors through the transformers T1 through Tn, applying two times the charge voltage, or 1kV in the arrangement shown (BLUE). The secondaries of the transformers are a tapered stripline to match the output impedance of each stage to the load impedance RL. Diode D enables sharp turnoff to meet the stringent turnoff specification.

each stage's output impedance in a tapered fashion enables the fast leading edge required by the application.

Not shown is the gate driver circuitry or the circuit board itself. The pulse amplifier developed for driving the STL21N650 transistors was designed with minimum group delay and maximum gain to effectively utilize charge-pump drive techniques. This charge-pump design has been successful in prior work at DTI, and is ideally suited to this application. The circuit board itself is highly tuned for this pulse application—extreme care has been taken to achieve very low trace inductances. Plane-to-plane spacing was kept to 0.003 inch in order to achieve power traces under 300 pH. This was critical in order to switch 500 V and 50 A per transistor in roughly 3 nanoseconds. The small, low inductance parts allow for the fast switching speeds. This board technology was crucial and left the intrinsic inductance of the packaged parts as a limit to the achieved rise times.

In order to keep the overall size and parts count down, a 10-stage 1 kV-per-step approach was chosen. The Marx topology at each stage allows 1 kV to be applied to the transformer cores while still using the fast 650 V transistors. Four MOSFETs are used in parallel at each position to carry the current and keep the inductance down. Measured inductance of each stage comes to less than 8 nH, dominated by the leakage of the coupling transformer. Capacitors Cn are chosen to have low inductance and acceptable voltage ripple and recharge time. The pulse amplifiers used to drive the transistor gates are tailored specifically to pump the appropriate amount of charge required to turn the devices on, while still having a propagation delay in the 8 ns range and being driven by TTL signals. The amplifiers consist of four stages; first a FET stage for level shifting and inversion, then bipolar followers, and finally FET inverters backed by followers. Each was chosen specifically to utilize their respective strengths (FETs for fast turn on, bipolars for current, etc.). Additionally, the gate pulse amplifiers for the floating side of the Marx are floating, referenced to the source of those power FETs only. Blocking cores are used to stand off the pulsing and float the stages at AC, but still provide a DC charging path to ground.

In the absence of diode D in the circuit above, the core reset of T1 through Tn happens through recharging of the capacitors in the Marx stages. However, this process is lengthy and somewhat chaotic, so diode D shuts off the secondary current flow due to recharge, effectively damping the ringing at turnoff and removing any stray pulses allowing the output to settle to better than 1 V in less than 1 μs.

Current Results

An example waveform is shown in Figure 3. The purple trace shows the command pulse, the green shows a capacitively-coupled probe with an arbitrary scale, and the red trace shows the voltage into 50 Ω on a 2 kV/division scale. Note the turn-on of 10 ns, the turnoff of 10 ns and the flattop of 30 ns. The peak is 8 kV at 160 A, the power is 1.28 MW. At this power level, the system was run at 1 kHz repetition rate on the bench with anything but a fan for cooling of the FETs. The peak temperature of the FETs was 65 C. With more aggressive cooling, operation at 10 kHz repetition rate should be possible.

Figure 4 shows operation at 10 kV, 200 A into 50 Ω; a full 2 MW per pulse. The red trace is the command pulse and the gray trace is the output pulse at 2 kV/division. Note the 7 ns rise and 8 ns fall times with 20 ns flattop.

Current pulser hardware is capable of pulses as long as 70 ns without any additional electronics for core reset. Additional core reset circuitry has been explored, but is not necessary at this time to meet the requirements of the

Copyright © 2013 CC-BY-3.0 and by the respective authors

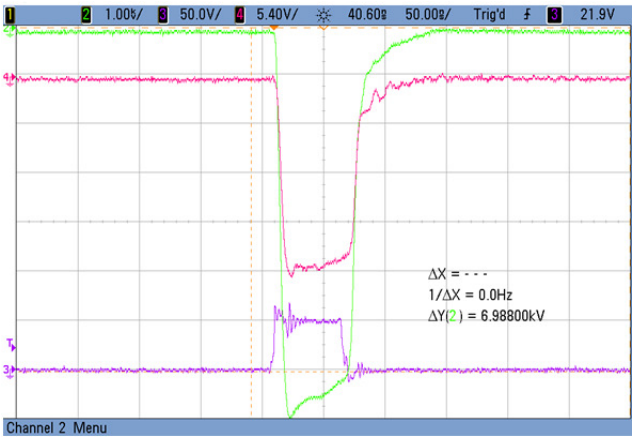


Figure 3: Performance at 8 kV into 50 ohms. Red trace is 2 kV/division. Note the 10 ns rise and 10 ns fall.

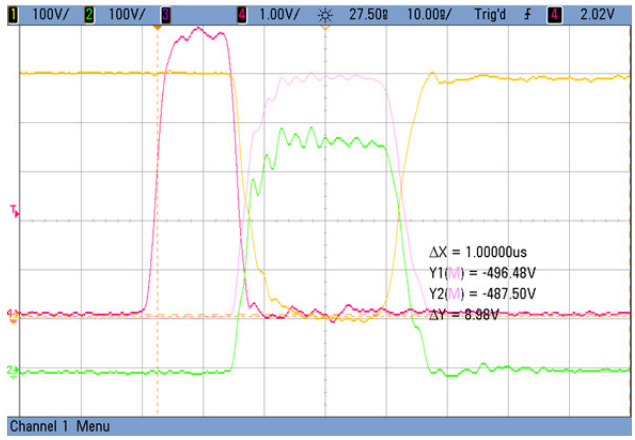


Figure 4: Operation at 10kV into 50 ohms. The faint gray trace is 2kV/division. At this higher power level, the transistors operate a touch faster, and the rise and fall times consequently are faster than at the 8 kV case.

NGLS kicker. Exploration of the current hardware limitations is underway, and it is likely that much higher currents are possible. The 200 A at 10 kV result was achieved with only 3 transistors at each location, and with the possibility of 4 transistors on the PCB. Perhaps 10 kV at 250 A may be in the future.

FUTURE PLANS

DTI is in the process of adapting this circuit architecture for other applications, including pulsed RF sources, pulsed plasma surface treatment systems and others. The remaining questions surround the maximum pulse rate and delivered power levels. Additionally, given the small size of the 2 MW pulser hardware, high voltage insulation and cooling are challenging. DTI will initially investigate immersion in oil bath, and later in phase-change cooling with refrigerants.

The current work is based on the C6 generation MOSFETs from STMicroelectronics. STMicroelectronics is currently shipping higher performance C7 generation devices, which will translate into faster pulses with more current capacity per device, or perhaps higher pulse repetition rates at the existing power levels. As these devices are available, we will be examining their performance in the current hardware.

Additionally, there are larger devices that are capable of as much as 125 A per device in single-state tests. This could project to a peak pulse of nearly 500 A at 10 kV, and testing is ongoing to explore the full performance envelope of the current architecture.

SUMMARY

The DTI team has designed and demonstrated the key elements of a solid-state kicker driver capable of meeting the NGLS requirements, and extension to a wide range of kicker driver applications. The MOSFET array switch itself is suitable for many accelerator systems with < 10 ns kicker requirements.

Copyright © 2013 CC-BY-3.0 and by the respective authors

PROGRESS ON THE MSU SUPERFERRIC CYCLOTRON GAS STOPPER MAGNET QUENCH PROTECTION AND COOLING SYSTEM

S. Chouhan, M. A. Green, G. Bollen, and A. F. Zeller, FRIB, Michigan State University, East Lansing MI 48824, USA; J. DeKamp, C. Magsig, D. Morrissey, J. Ottarson, and S. Schwarz, NSCL Michigan State University, East Lansing MI 48824, USA

Abstract

The MSU gas cyclotron stopper system is designed to decelerate rare isotope ions from energies from >50 MeV to energies in the 10 keV range. The ions are decelerated in low-pressure helium gas in vertical cyclotron magnet. The magnet and the system for decelerating the ions are mounted on a high voltage platform. The cyclotron gas stopper magnet is a warm iron superconducting cyclotron sector dipole. The maximum field in the gap (0.18 m) is 2.7 T. The outer diameter of magnet yoke is 3.8 m, with a pole radius of 1.1 m and Br = 1.8 T m. The desired field shape is obtained by the pole profile. Each coil of the two halves is in a separate cryostat and connected in series through a warm electrical connection. The entire magnet system will be mounted on a high voltage platform. The magnet coils have been fabricated and installed in their cryostats. The iron poles have been machined and assembled. This paper presents the progress on the magnet system fabrication and assembly.

INTRODUCTION

The fragmentation of fast heavy-ion particles enables fast, chemistry-independent production, separation and delivery of exotic isotope beams. The resulting beams of exotic nuclei have high energies (>50 MeV/u) and large emittances. The range of possible experiments with the fast beams can be extended by slowing down the fast ions. The ReA3 [1] re-accelerator under construction at MSU will re-accelerate the thermalized ions to provide low emittance exotic beams over a range of energies. The thermalization of the fast ions and their extraction using existing techniques are limited by space charge and other limitations.

A proposed solution to thermalize and extract light to medium mass ions and high intensity beams is to apply strong gradient-dipole magnetic field in a large magnetic gap (0.18 m) that forces the fast ion beams to follow spiral trajectory while slowing down in the gas. Concentrated thermalized ions near the central extraction port are then transported in to central extraction orifice via an RF-carpet. These extracted ions will be transformed into low energy beams using a differentially pumped ion-guide. The low energy ion beams can be transported directly to low-energy experiments or to other accelerators for reacceleration. The high performance and high field (2.7 T) super-ferric cyclotron gas stopper sector-magnet at National Superconducting Cyclotron Laboratory (NSCL), Michigan State University (MSU) will enable the capture of short-lived rare isotopes produced in nuclear reactions.

The cyclotron gas-stopper magnet design has evolved since its original design in 2007 [2]. A gradient dipole field is produced in a gap of 180 mm between sector cyclotron iron poles. The peak field in the gap is ~2.7 T. A pair of superconducting solenoid coils produce the field. The warm iron poles can be separated so that the deceleration system can be maintained. Each pole coil has its own helium cryostat and superconducting coil that operate at 4.3 K. The 300 K iron poles are physically connected through the magnet iron flux return path, but the superconducting coils are not physically connected. The forces on the magnet coils are transported to the iron return yoke through the cold mass supports. The magnet is oriented so that the common axis of the solenoid coils is horizontal. Thus the beam plane for the super-ferric cyclotron magnet is vertical. Each of the two magnet superconducting coils will be cooled using three PT-415 pulse-tube 4 K coolers with remote valves.

IRON POLES AND RETURN YOKE

The split iron poles and return yoke are shown in Fig. 1. One of the sector cyclotron pole pieces is shown in Fig. 2. Table 1 presents the parameters for the magnet [3].



Figure 1: The split magnet iron return path and poles.

*The material in this paper was supported in part by a grant for the National Science foundation under MSU grant number PHY-0958726.

Copyright © 2013 CC-BY-3.0 and by the respective authors



Figure 2: The machined sector cyclotron pole pieces on the 2.2-m diameter pole for the magnet. The coil cryostat is in the slot between the pole and the return iron yoke.

Table 1: Cyclotron Gas Stopper Magnet Parameters [3]

Parameter	Value
Number of Magnet Coils	2
Iron Pole Radius (m)	1.10
Iron Return Yoke Outer Radius (m)	~1.90
Average Induction in the Gap (T)	~2.0
Average Pole Half Gap (mm)	~90
Number of Coil Turns per Layer	31
Number of Layers per Coil	57
Coil Cross-section R / Z (mm)	80 / 80
Coil Peak Design Current (A)	200
Peak Coil Current Density (A mm^{-2})	54.9
Peak Magnetic Induction in Coil (T)	2.05
Magnet Self Inductance Assembled (H)	178
Magnet Peak Stored Energy (MJ)	3.56
Coil Cold Mass per Pole (kg)	~370
Magnet Cold Mass per Pole (kg)	~1240
Magnet Iron Mass (metric tons)	~167

MAGNET COILS AND QUENCH PROTECTION

The 1767 turn magnet coils were wet wound and molded to fit into the 80 mm by 80 mm final shape. A 22-turn non-inductive work hardened 6061-Al resistor with a resistance of 2.26 ohms was wound on the outside of the coil as part of the quench protection system [4]. When the magnet quenches, the diodes fire shunting the current into the resistor, which heats the coil from the outside. A quench, which fires the diodes, will cause the full current of the coils to flow in the resistor. It takes ~100 ms, for the outside of the coil to be heated to 10 K. The calculations show that both magnet coils will become fully normal in <4.3 s. At the start of the quench at full current 89 kW of heat will come from the resistor. This will boil the helium in the cryostat as well cause the coil to turn normal. Once the coil has turned normal, the coil rapidly discharges.

The coils were inserted in 304-stainless steel helium vessels so that there is space between the coil and the helium vessel to circulate helium in a thermal-siphon cooling loop used to cool and cool-down the magnet coils. The helium vessel is stiff to prevent deflection of the cold mass when the magnet sees unbalanced magnetic loads while in the iron. The helium vessel necks contain the quench protection [4] diodes (see Fig. 3), the LTS leads that connect of the bottom of the HTS leads through a vacuum tight feed-through between the helium vessel and the cryostat vacuum vessel, and 5 L of liquid helium out of the total of 7.4 L per coil. The LTS leads are designed so that their length is less than a minimum propagation zone length at the full design current of the magnet. In addition, the LTS leads within the helium vessel are designed to be cryogenically stable in helium gas.

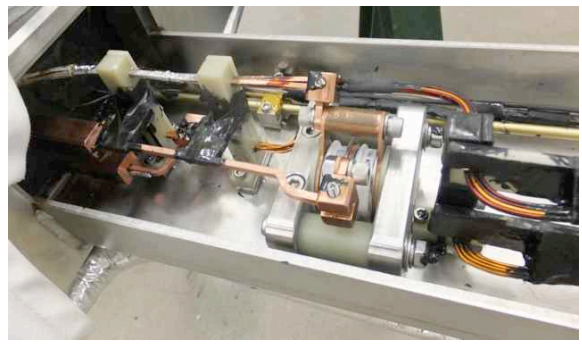


Figure 3: Quench Si diode assembly in the cryostat neck.

MAGNET COOLING SYSTEM

The tops of the HTS leads are connected thermally to the first stages of the coolers. Electrically the leads are insulated from the first-stages. The heat from 293 K to the top of the HTS leads at 45 to 50 K is conducted through the electrical insulation to the cooler first-stages at a temperature <40 K. The heat conducted down the leads to the cooler first-stages is ~20 W all other sources of heat to the cooler first stages amount to < 10 W. The projected cooler first-stage heat load is 10 W per cooler.

Each coil of the cyclotron gas stopper magnet is cooled and cooled-down using three PT-415 two-stage pulse tube coolers with remote rotary valves and ballast tanks. These coolers produce 1.35 W at 4.2 K while procucing 36 W at 40 K. The cooler cold heads mounted in the top of the turret are shown in Fig. 4.



Figure 4: The top of the coil 1 turret cryobox showing the cooler cold heads (labled A, B, and C), the current leads, the instrumentation plugs, and the safety vent tubes.

The cooler cold heads and the ballast tanks, which are mounted on the cryostat turret, are at a high voltage (up to 60 kV) with respect to ground. The rotary valves and the

Copyright © 2013 CC-BY-3.0 and by the respective authors

hoses to the compressors are at ground potential. The helium pipes between the rotary valves and the cooler cold heads are insulators that hold off up to 60 kV. Figure 5 shows a mockup of the coolers on the cryostat turret.

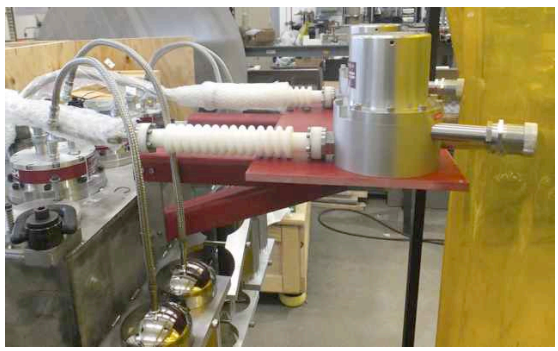


Figure 5: The coolers mounted on the coil turrent.

During a cool-down, the three coolers on each coil cryostat operate in parallel [5]. Helium gas from the magnet enters the three condenser heat exchangers from the top. The gas is cooled in the condenser boxes and is sent to the bottom of the magnet cryostat. Figure 6 shows two of the three condenser boxes. After entering the magnet cryostat, the cold helium goes up past the magnet coil along the inside and the outside of the coil. The helium leaving the top of the coil returns to the condenser boxes to be re-cooled. The thermal siphon circuit flow is by natural convection. The projected cool-down time for the magnet cold mass of 2480 kg from 293 K to 4.3 K is ~4 days using six coolers. The time to fill the helium vessels with 16 L of helium by liquefaction of 293 K gas is an additional day.



Figure 6: The condenser heat excahngers for two of the three coolers. Warm gas from the magnet enters the condenser from the top. Cold gas leaves from the condenser bottom.

CONCLUDING COMMENTS

Both magnet coil cryostats were leak checked and pumped out in preparation for the first test of the cryogenic system. Since the thermal siphon cryogenic cooling system only works when the axis of the magnet is horizontal (so that the condenser is ~3 meters higher than the bottom of the coil cryostat), the cooling-down and the testing of the cryogenic system can only be done with the magnet coil cryostats mounted on the iron poles. The magnet coils were mounted in the iron during September of 2013 in preparation for a magnet cool-down using all six of the PT-415 pulse tube coolers (see Fig. 7). During the fall of 2013, the magnet instrumentation will be connected and the high voltage system will be installed on the magnet. The first magnet cool-down using helium from gas bottles is expected in the winter of 2014. With luck, cryogenic testing and magnet coil training is expected to occur in the first half of 2014.



Figure 7: The magnet coil mounted in the cyclotron gas stopper magnet iron return yoke.

REFERENCES

[1] O. Kester, et al, "The MSU/NSCL Re-accelerator ReA3," *Proceedings of the SRF*, Berlin Germany, MOOCAU05, (2009).

[2] S. Chouhan, et al, "Design of a Superferric Magnet for the Cyclotron Gas-stopper Project at NSCL," *Proceedings of IEEE Particle Accelerator Conference* **PAC-07**, Albuquerque NM, USA, pp 524-526 (2007).

[3] S. S. Chouhan, et al, "The Superferric Cyclotron Gas Stopper Magnet Design and Fabrication," submitted to *IEEE Transactions on Applied Superconductivity* **23**, (2013).

[4] M. A. Green and S. S. Chouhan, "Cyclotron Gas-stopper Magnet Issues concerning Lead Stabilization, Magnet Quenching with Diodes and Resistors, and a Magnet Rapid Discharge System," FRIB Note M40201-CA-000106, 21 May 2013 (unpublished contact the first author at chouhan@frib.msu.edu.

[5] M. A. Green, S. S. Chouhan and A. F. Zeller, "Design Limitations on a Thermal Siphon 4 K Helium Loop for Cooling-down the Cyclotron Gas Stopper Magnet Coils," submitted to *Advances in Cryogenic Engineering* **59** (2014).

Copyright © 2013 CC-BY-3.0 and by the respective authors

MECHANICAL DESIGN OF THE CRYOGENIC SUB-SYSTEMS FOR ReA6 QUARTER WAVE RESONATOR CRYOMODULE*

M. Shuptar#, F. Casagrande, A. Fox, M. Johnson, M. Leitner, S. Miller, T. Nellis, M. Patil, T. Xu, Y. Xu, Facility for Rare Isotope Beams (FRIB), East Lansing, MI 48824, USA

Abstract

The driver linac for the Facility for Rare Isotope Beams (FRIB) consists of 49 cryomodules operated at 2 K utilizing 4 different types of superconducting resonators and 2 solenoid lengths which in turn requires 7 individual cryomodule configurations. The mechanical design requirements of the internal cryogenics of an FRIB cryomodule are determined by the piping and instrumentation diagram, which is discussed in the paper based on the FRIB quarter wave cryomodule type. In addition, heat load requirements and spatial constraints of other cryomodule sub-systems influence the cryomodule cryogenics design. The paper describes detailed design choices for the cryogenic headers and piping, a 2 K heat exchanger inside the cryomodule, solenoid current leads, and the bayonet connections to the cryogenic distribution system inside the accelerator tunnel. Different operating modes, which influence the cryogenic design, are summarized.

INTRODUCTION

FRIB is a US $700 million nuclear physics project to be built at the Michigan State University under a corporate agreement with the US Department of Energy (DOE) with a 7-year timetable [1]. According to the current FRIB baseline schedule fabrication and procurement of linac components will start mid-2014. Actual linac installation will begin end of 2016 after completion of conventional facilities and cryoplant construction [2].

Due to the heavy mass and correspondingly low velocity of the accelerated ions the FRIB driver linac [1] utilizes four different low-beta SRF resonator designs in cryomodules. Each cryomodule is equipped with niobium cavities which will operate at 2 K providing acceleration to the heavy ions. Due to the large number of cryomodules the FRIB project lends itself to a manufacturing mind-set that incorporates large scale production into the design of individual modules types. As a part of the manufacturing mind-set FRIB is currently developing a prototype cryomodule that will utilize 8 superconducting quarter-wave cavities, and is referred to as the ReA6 cryomodule. Upon completion the ReA6 cryomodule will test not only the general cryomodule design, but also the manufacturing methodology [3]. Even though ReA6 is a prototype module it will implement some design choices that differ from a typical FRIB cryomodule. The usefulness of the ReA6 module will not end with proof of concept of mechanical and manufacturing principals; after testing the module becomes a permanent part of FRIB's Re-Accelerator located in the experimental area of the facility.

* This material is based upon work supported by the U.S. Department of Energy Office of Science under Cooperative Agreement DE-SC0000661. Michigan State University designs and establishes FRIB as a DOE Office of Science National User Facility in support of the mission of the Office of Nuclear Physics.

shuptar@frib.msu.edu

BASIS OF REQUIREMENTS

Each cryomodule design starts by obtaining the system's requirements and then designing the specifications. For the cryogenics inside the ReA6 Quarter Wave Resonator (QWR) cryomodule the requirements are defined by; piping and instrumentation diagram (P&ID), heat load budget, cost and spatial constraints.

The ReA6 P&ID differs from an FRIB module because the operating constraints of the ReA6 are slightly different from an FRIB module. Since the ReA6 module will be built ahead of the FRIB cryoplant and will not be located in the tunnel its cryogenic layout specified on the P&ID includes a liquid nitrogen circuit not present in FRIB Cryomodules. ReA6 Resonators will also operate a 4.5 K compared to an FRIB module's resonators operating a 2 K [4].

Heat Load Budget

The heat load calculations outline the allowed heat load for each module. Constraining the heat load to each module budget ensures that the cryoplant is sized correctly. The heat load budget requirement for ReA6 cryomodule is shown in Table 1 [5].

Table 1: ReA6 β=0.085 Cryomodule Heat Loads

	Resonators (4.5 K)	**Focusing Magnets (4.5 K)**	**Thermal Shield (80 K)**
Static (W)	6.0	50.7	180.6
Dynamic (W)	80.0	1.3	23.2
Total (W)	**86**	**52**	**204**

The heat load budgets are also necessary to estimate the mass flow for three separate cryogenic loops. Calculation of the helium and nitrogen interfaces to the cryogenic distribution are given in (Table 2) [5]. To minimize vapour velocity and maximize helium capacity the headers needs to be sized effectively.

Copyright © 2013 CC-BY-3.0 and by the respective authors

Table 2: Flow Conditions for ReA6 Cryomodule

	T (K)	P (atm)	ṁ (g/s)
Nitrogen Supply	82	1.6 – 1.7	1.1
Helium Supply	4.5 – 5	3.0 – 3.5	8.5 – 9.9
Cavity Helium Return	4.5	1.286	4.6 – 5.4
Solenoid Helium Return	4.5	1.286	3.9 – 4.6
Megnet Leads Return	300	1.1	0.09
Nitrogen Return	82	1.6 – 1.7	1.1

Using Equation 1, the velocity vapour can be estimated.

$$\dot{m} = v\rho A. \quad (1)$$

Where ṁ is the mass flow rate, v is velocity of the vapour, ρ is the density of the gas and A is the minimal cross-sectional area needed to achieve the desired vapour velocity. The mass flow is taken from the heat budget and a vapour velocity limit of 7 m/s was imposed [6]. This limit prevents drag on the liquid within the header and also minimizes any vibratory disturbances. The calculation was done for each of the cryogenic circuits in the module.

The resonator circuit has a design contingency of facilitating 2 K helium. The header for resonators was calculated to need a minimum cross-sectional area of 18.08 cm^2 (or pipe with an inner diameter greater than 4.79 cm). The resonator header, magnet header and thermal radiation header have been sized with a 6" Schedule 5 and 4" Schedule 5 IPS pipe respectively. The benefit of a larger helium inventory inside the cryomodule will allow static pumping for 2 K operation given cryoplant and pumping limitations.

Spatial Constraints

The physical layout of the cryogenics within the cryomodule is constrained spatially by the other sub-systems; super-conducting resonators, thermal radiation shield, magnetic shield, alignment support structure and vacuum vessel as seen in figure 1.

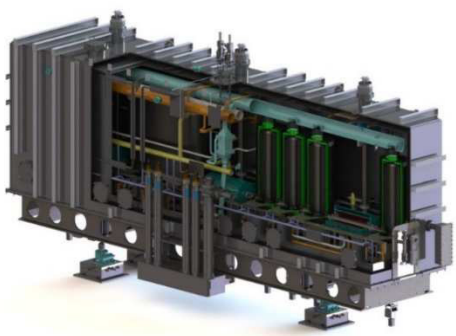


Figure 1: Cross-Section of ReA6 β=0.085 QWR Cryomodule.

Structurally the cryogenics will be supported from the vacuum vessel via G-10 plates and preloaded bellville spring washers to allow for thermal contraction. The cryogenic circuits are connected to the sub-systems using flexible couplings to minimize the transmission of micro-phonics.

CRYOGENIC CIRCUITS

The cryogenics of the ReA6 cryomodule is composed of three circuits: resonator, focusing magnet and thermal shield. The resonators and focusing magnets are placed on independent circuits so that they can be warmed and cooled independently which allows the resonators to be warmed above T_c and perform solenoid degaussing cycles [7]. Each circuit is based on a thermal siphon. The headers in the thermal siphon function as a liquid-gas phase separator; supplying liquid to the components and allowing gas from boil-off to be sent to the gas return. Each cryogenic circuit's temperature is dictated by the cryomodule's operating mode.

Resonator Helium Circuit

To reduce the number of components and simplify the fabrication, a single supply line supplies helium to the resonators and focusing/steering magnet circuits within the module. One circuit is used exclusively for cooling the resonators. For the resonators; the 4.5 – 5.0 K flow passes through a heat exchanger in series with a Joule Thomson (JT) valve to isenthalpically expand the helium. The heat exchanger for the ReA6 is sized for 10 g/s of flow. Even though ReA6 is designed to operate at 4 K but will have the ability to test at 2 K with batch pumping mode.

Focusing Magnet Helium Circuit

The focusing magnet helium circuit cools the focusing magnets (solenoids), magnet leads and thermally intercepting conductive components. The vapour cooled magnet leads will be purchased from a commercial vender. The circuit's other function is to minimize the heat loads to the resonators by thermally intercepting all components that provide a thermal heat load to the resonators. The helium from the 4.5 – 5.0 K supply passes through a JT valve to reduce its temperature before it enters a 4.5 K helium bath. To minimize the temperature of the liquid to each thermal intercept the circuit runs parallel flow to each intercept location. Intercepting components in parallel prevents excessive formation of large bubbles in the cryogen, reducing the effective heat transfer between the fluid and the thermally intercepted component.

Thermal Shield Nitrogen Circuit

The nitrogen circuit, which is unique to the ReA6 module, primary function is to reduce thermal radiation heat loads to the coldmass (the string 8 cavities and 3 solenoids within the module). The nitrogen circuit thermally intercepts all sub-systems between the room temperature vacuum vessel and the 4.5 K coldmass. The

Copyright © 2013 CC-BY-3.0 and by the respective authors

circuit also supplies nitrogen to the thermal shield which is responsible for minimizing the radiant heat loads.

BAYONET BOX

The nitrogen and helium are supplied to the cryomodule circuits by a bayonet box as shown in figure 2. The bayonet box is integrated into the cryomodule as its own sub-system. The modular box is utilized on the 49 cryomodules in the linac. This sub-system is geared toward a large scale manufacturing methodology. It is designed to be fabricated independently and then later mounted onto the cryomodule. From there the cryogenic circuits are welded to the bayonet box creating a permanent leak tight assembly. The bayonet box interfaces with the main cryodistribution by U-tube bayonets. The effective implementation of assembly line manufacturing is very important design for FRIB. ReA6 will be an important part of testing this manufacturing process.

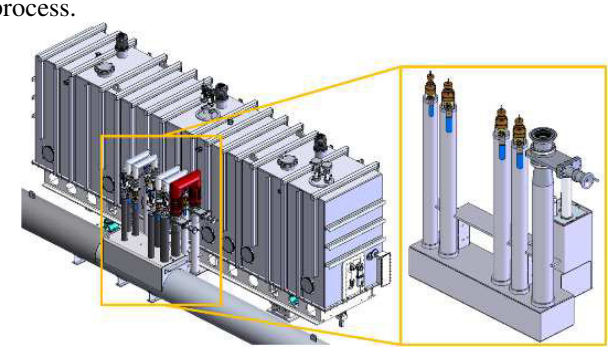


Figure 2: Cryomodule bayonet box interface to the helium distribution line.

CRYOGENIC PIPING & SAFETY

To design for manufacture, the cryogenic circuits were modelled after industrial piping systems. This approach reduces the number of custom made speciality parts without compromising quality and safety. Custom parts were minimized by using readily available industrial weldable components. Cryogenic piping was selected that adhere to the process piping code (ASME B31.3) and BVPC section VIII. Commercial piping selected adheres to the ASME Design by Rule and need for Design by Analysis was minimized. Commercially available formed bellows have been used which have been verified as per the ASME BPVC section VIII, Div. 2 code. Commercially available flexible metal hoses with welded end connection which are designed in accordance with ASME BPVC by the vendor have also been selected to couple the cryogenics circuits to the sub-systems. Welded bellows and the final system will be pressure tested in accordance with UG-99 (hydrostatic test) or UG-100 (pneumatic test).

Circuits have been equipped with lift-off plates and pressure relief valves to ensure that the cryogenic circuits do not produce pressures which would reach the yield stresses of the niobium resonators. The pressure relief valves are sized with a mass-flow rating for a failure mode during cryomodule cool down which would occur when there was a closed return valve and open supply valve. The lift-off disks operate for an operation failure mode. This failure mode would occur during accidental beamline or insulating vacuum loss with operating levels of liquid helium in the resonator and focusing magnet circuits [8].

REFERENCES

[1] J. Wei et al., “The FRIB Project - Accelerator Challenges and Progress”, Proc. of HIAT 2012, pp. 8–19.

[2] M. Leitner et al., “Status of the Linac SRF Acquisition for FRIB,” Proc. of LINAC 2012”, pp. 564–566.

[3] S. Miller et al., “Low-Beta Cryomodule Design Optimized For Large-Scale LINAC Installations, Proc. of SRF 2013”, pp. 1-2.

[4] M. Johnson, “ReA6 Cryodmodule P&ID”,MSU-FRIB T30602-MDE-0109-0000.

[5] Y. Xu et al., “ReA6 Cryomodule Analysis and Simulation Engineering Note”, MSU-FRIB T30602-TD-000495-R001, 2013 p. 8.

[6] U.Wagner, “Cryogenic Scheme, Pipes and Valve Dimensions”, Conceptual Review of SPL Short Cryomodule, CERN 2011” http://indico.cern.ch/materialDisplay.py?contribId=3&materialId=slides&confId=154284.

[7] M. Johnson et al., “Design Of The FRIB Cryomodule, Proc. of IPAC 2012”, pp. 2-3.

[8] Y. Xu et al., “Integrated Thermal Analysis Of the FRIB Cryomodule Design, Proc. of IPAC 2012”, p.3.

Copyright © 2013 CC-BY-3.0 and by the respective authors

IMPACT OF RADIATION ON THE MU2E PRODUCTION SOLENOID PERFORMANCE*

V.V. Kashikhin#, N. Dhanaraj, M.J. Lamm, N.V. Mokhov, V.S. Pronskikh,
FNAL, Batavia, IL 60510, USA

Abstract

The Muon-to-Electron conversion experiment (Mu2e) is under development at Fermilab to detect direct muon to electron conversion and provide evidence for processes violating muon and electron lepton number conservation not explained by the Standard Model of particle physics.

The Mu2e magnet system consists of three large superconducting solenoids. One of the magnets is Production Solenoid (PS) named after the pion production target installed in the magnet bore. The superconducting coils are protected from the secondary particle radiation by a massive Heat and Radiation Shield (HRS) made of bronze, which was optimized for the energy absorption and cost. This paper describes the impact of radiation on the magnet cooling, stability and quench.

INTRODUCTION

The Mu2e magnet system consists of three large superconducting solenoids [1]. PS is the first magnet in the chain [2], which collects and focuses pions and muons generated in interactions of an 8-GeV proton beam with a tilted high-Z target and directs them towards Transport Solenoid (TS), by supplying a peak axial field of 4.6-5.0 T and ~1 T/m gradient within a 1.5 m warm bore.

It is a challenging magnet because of the relatively high magnetic field and a harsh radiation environment. The PS coils are protected from radiation by 50-cm thick water-cooled HRS made of high-resistivity bronze, placed within the warm magnet bore. An extensive simulation effort has been carried out to optimize the shield parameters and get the radiation load below the tolerable levels with a sufficient safety margin [3].

The radiation heat reaching the coils must be extracted to the cryogenic system to maintain the necessary operating margin. It is achieved using a system of thermal bridges made of pure Al connected to the cooling tubes [4]. Electrical and thermal properties of the thermal bridges and the cable stabilizer are significantly degraded under the irradiation that impacts the cooling efficiency, magnet stability and quench performance.

RADIATION ANALYSIS

Simulations were performed with the MARS15 code [5] on the model shown in Fig. 1. The neutrons were propagated down to 0.001 eV. The full set of critical radiation quantities was calculated. The superconducting coil material was described using homogeneous approach (the material was represented as a mix of all elements with appropriate weight factors).

* This work was supported in part by Fermi Research Alliance under the U.S. Department of Energy Contract DE-AC02-07CH11359.
#vadim@fnal.gov

The peak calculated Displacement Per Atom (DPA), which characterizes the radiation damage in metals, was ~$2.5 \cdot 10^{-5}$ yr^{-1} and the peak power density was 12.6 μW/g [3]. Corresponding peak absorbed dose for the coil insulation is 240 kGy/yr; total dynamic heat load in the cold mass is 28 W. While the total dynamic heat load is relatively small, the power density distribution in the cold mass is strongly non-uniform, as shown in Fig. 2 that creates a localized hot spot in the middle of the first coil.

Taking conservative safety factors into account, the calculated DPA translates into the degradation of RRR in Al and Cu from the initial values of 600 and 80 to 100 and 50 respectively in about one year of experiment's operation [6]. These numbers are regarded as the minimum allowable values. The magnet will be equipped with RRR gauges that monitor the material property changes during the operation. Once the critical resistivity degradation is detected, the magnet will be thermo-cycled to the room temperature that restores the original resistivity in Al and ~87% of that in Cu [7]-[8].

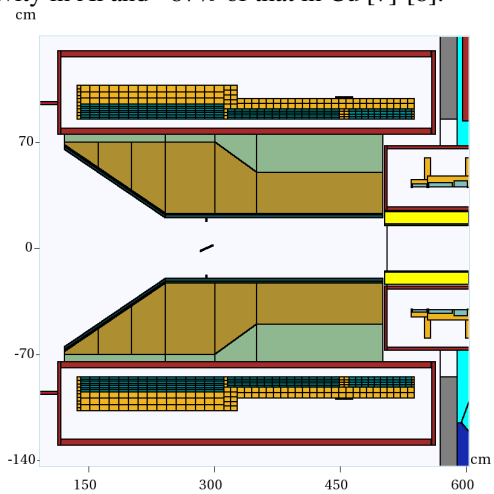


Figure 1: MARS model.

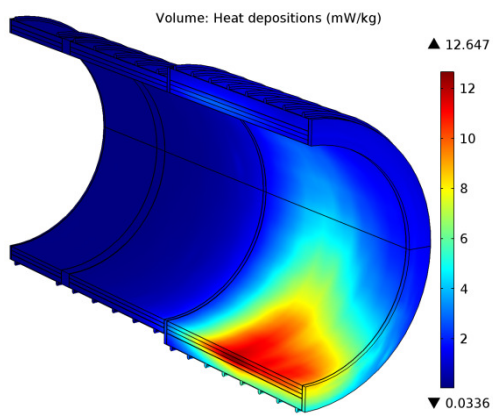


Figure 2: Radiation power distribution in the cold mass.

Copyright © 2013 CC-BY-3.0 and by the respective authors

THERMAL ANALYSIS

The 3D FEM model of the cold mass has been created using ANSYS code [9]. It contained all the relevant features, including the coil layers, interlayer and ground insulation, thermal bridges, structural support shells and the cooling tubes with the corresponding material properties. The cold mass is cooled using a thermo-siphon system that maintains the LHe temperature of 4.7 K.

The radiation heat is extracted from the coils using a system of thermal bridges made of pure (5N) Al attached to the inner and outer coil surfaces and connected to the cooling tubes on the outer cold mass surface [10]. The thermal bridge RRR will degrade under the irradiation.

Fig. 3 shows the temperature distribution in the coil when the material RRR is reduced to the minimum allowable values defined earlier. The local hot spot coincides with the magnet peak field location and therefore affects the operating margin.

The peak coil temperature shall not exceed 5.1 K in order to maintain the required thermal margin of 1.5 K with respect to the current-sharing temperature of 6.6 K at the peak field location. Fig. 4 shows the peak coil temperature as a function of Al RRR for the static (beam is off) and total (beam is on) heat loads. The peak coil temperature rises by ~200 mK after turning the beam on and gains another ~70 mK due to RRR degradation in the operating cycle that is accounted for in the magnet design.

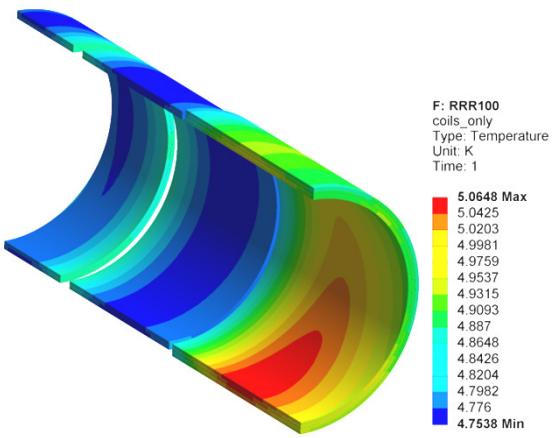


Figure 3: Temperature distribution in the coil.

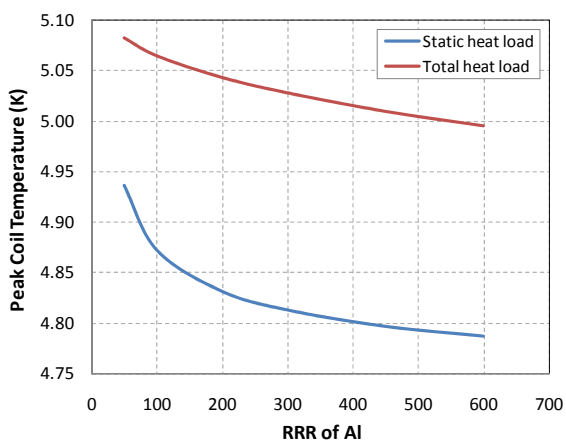


Figure 4: Peak coil temperature vs. RRR of Al.

MINIMUM QUENCH ENERGY

Stability of the superconducting state is characterized by the Minimum Quench Energy (MQE) that is the minimum energy released in the superconducting cable that triggers a quench. Both the electrical and thermal conductivities of the stabilizer material play an important role in the magnet stability.

MQE of the PS magnet has been analyzed using COMSOL Multiphysics code [11] for the stack of cables shown in Fig. 5, which included coupled thermal and electrical transient models. The analysis has been performed for the coil peak field location that has the smallest margin and consequently the lowest MQE.

The results of simulations are presented in Fig. 6. It is expected that most of the heat perturbations in the coils associated with cracks in the insulation and in the strand-stabilizer interface will occur during the commissioning without the beam. The relatively high initial MQE value of ~175 mJ, comparable to MQE in other large solenoids, will help to stabilize the magnet during that period.

The MQE degrades by ~25% due to coil temperature rise when the beam is on and gets progressively lower during the operation, reaching ~40 mJ at the end of the operating cycle. Thus the magnet becomes a factor of 4.4 less stable than during the commissioning, however, it is not expected to cause problems for DC operation.

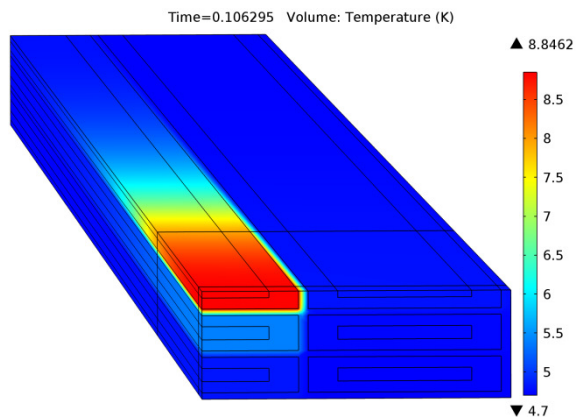


Figure 5: 1/8 of the cable stack model with the temperature distribution 0.1 s after the initial perturbation.

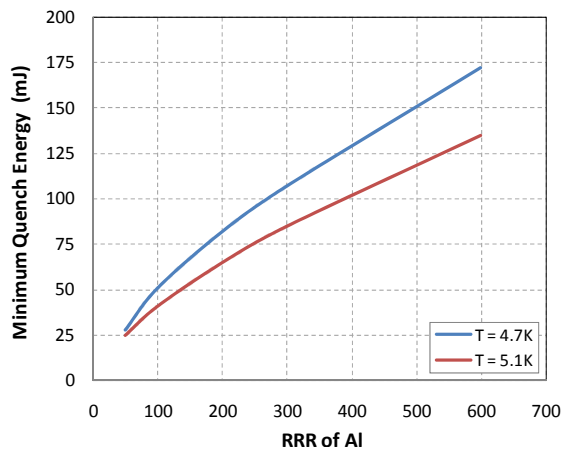


Figure 6: MQE vs. RRR of cable stabilizer.

Copyright © 2013 CC-BY-3.0 and by the respective authors

QUENCH PROTECTION

The purpose of the quench protection system (QPS) is to limit the peak coil temperature to 130 K and the peak coil to ground voltage to 600 V during any normally protected quench. It is achieved by detecting the resistive voltage rise associated with the quench development and extracting the stored energy to an external dump resistor.

The 3D FEM model of the PS magnet, created within the COMSOL Multiphysics code, contained all the relevant features, including the individual coil layers, interlayer and ground insulation, thermal bridges on the inner and outer surfaces of the coils, coil support structures, and the HRS. The energy dissipation due to eddy currents induced in the support shells and the HRS was also included. Extensive simulations of different normal and fault scenarios have been performed [12].

It was found that irrespective of the RRR, the highest coil temperatures during the normally protected quenches occur at the peak field quench location. Propagation of a quench originated at the peak field location is shown in Fig. 7 at the time when the multiple resistive zones are induced due to quench-back from the support structure. The peak coil temperature and the resistive voltage go up by ~23 K and ~510 V respectively as the result of RRR degradation in the operating cycle as shown in Fig. 8; however, they remain below the limits.

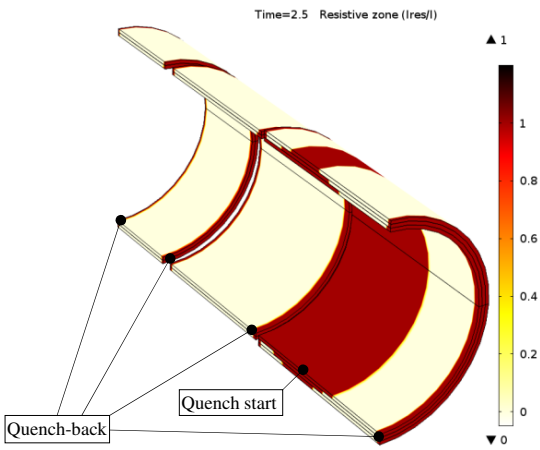


Figure 7: Resistive zone propagation (dark region).

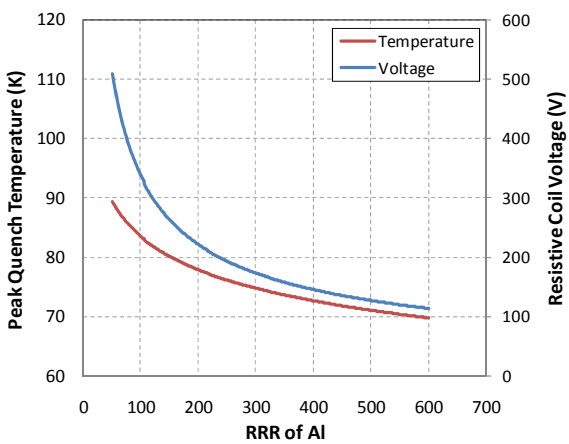


Figure 8: Quench temperature and voltage vs. RRR of Al.

Protection from the radiation has indirect structural effect on the magnet design due to field interaction with eddy currents induced in the HRS during quench. HRS is made from high-resistivity bronze to minimize the eddy currents; however because of the large HRS volume, the peak dynamic force on the cold mass is ~115 kN, which nearly equals to the cold mass weight. It is normally subtracted from the much larger PS-TS attractive force, but leads to force reversal when the TS is off. To address this issue, the cold mass has a 2-way axial support system designed to counteract the force in either direction [13].

SUMMARY

Radiation from the pion production target has a significant impact on the PS performance. In addition to the highly localized heat dissipation in the cold mass, the electrical and thermal properties of the stabilizer and the thermal bridges are considerably degraded, which is taken into account in the magnet design. Once the critical degradation is detected, the magnet will be thermo-cycled that will largely restore the original performance.

REFERENCES

[1] M.J. Lamm, et al., "Solenoid Magnet System for the Fermilab Mu2e Experiment," IEEE Trans. Appl. Supercond., Vol. 22, No. 3, June 2012, pp. 4100304.
[2] V.V. Kashikhin, et al., "Conceptual Design of the Mu2e Production Solenoid," IEEE Trans. Appl. Supercond., Vol. 23, No. 3, June 2013, pp. 4100604.
[3] V.S. Pronskikh, et al., "Optimization of Mu2e Production Solenoid Heat and Radiation Shield," Nuclear Phys. B Proc., to be published.
[4] V.V. Kashikhin et al., "Conceptual Design of the Mu2e Production Solenoid Cold Mass," Adv. in Cryo. Eng., AIP Conf. Proc., 1434, 893-900 (2012).
[5] N.V. Mokhov, http://www-ap.fnal.gov/MARS/
[6] V.S. Pronskikh and N.V. Mokhov, "Simulation of radiation quantities for accelerator-based experiments," Nuclear Data Sheets, to be published.
[7] J.A. Horak, T.H. Blewitt, "Isochronal recovery of fast neutron irradiated metals," Journal of Nuclear Materials, 49 (1973/74) 161-180.
[8] M. Yoshida, et al., "Low-temperature neutron irradiation tests of superconducting magnet materials using reactor neutrons at KUR," Adv. Cryo. Eng., AIP Conf. Proc. 1435, 167-173 (2012).
[9] http://www.ansys.com/
[10] N. Dhanaraj, et al., "Study of Thermosiphon Cooling Scheme for the Production Solenoid of the Mu2e Experiment at Fermilab," Adv. Cryo. Eng., AIP Conf. Proc., to be published.
[11] http://comsol.com/
[12] V.V. Kashikhin, et al., "Quench Protection Analysis of the Mu2e Production Solenoid," Adv. Cryo. Eng., AIP Conf. Proc., to be published.
[13] T.H. Nicol, et al., "Mu2e Production Solenoid Cryostat Conceptual Design," Adv. Cryo. Eng., AIP Conf. Proc., 1434, 885 (2012).

Copyright © 2013 CC-BY-3.0 and by the respective authors

A HIGHLY CONFIGURABLE AND SCRIPTABLE SOFTWARE SYSTEM FOR FULLY AUTOMATED TUNING OF ACCELERATOR CAVITIES *

J. M. Nogiec#, R. Carcagno, S. Kotelnikov, A. Makulski, R. Nehring, D. Orris, W. Schappert,
FNAL, Batavia, IL 60510, USA

Abstract

A software system has been developed to automate cavity tuning machines as part of a multi-laboratory collaboration. The system is based on a plugin framework containing a configurable set of components. Each component runs asynchronously and uses a framework for message based communication. Components run in either manual or automatic mode. In automatic mode, the system interprets a user-selected control script which executes a sequence of measurements, model calculations and tuning operations. A tuning script iterates until the prescribed tuning criteria are satisfied, or until aborted or paused by the user. In manual mode, the user controls the tuning process, deciding when and which component to run, and when tuning is complete. The software framework incorporates the blackboard architecture for sharing data and results between the various plugins. The results of the measurements and tuning are persisted in an XML-based data store, and components exist that retrieve and visualize the data. The software system is portable (Linux, Windows) and has been successfully deployed and used by Fermilab, DESY, and KEK.

INTRODUCTION

The Cavity Tuning Machine (CTM) is a result of collaborative efforts among DESY, KEK and Fermilab [1] [2], with the Fermilab team responsible for developing system electronics and software [3]. The goal for the project was to automate tuning of accelerator cavities with the intention to support high-throughput cavity fabrication for construction of large SRF-based projects.

The tuning process includes a sequence of measurements and model-based calculations to determine the required tuning parameters, followed by the actual tuning. This process is iterative and is continued until the π-mode frequency and field flatness as well as the cavity mechanical alignment are all within the required tolerances. Automating the tuning process shortens the time required to tune the cavity and ensures the repeatability and predictability of this process. In addition, trained operators can replace RF experts at performing cavity tuning.

The main building blocks of the CTM apparatus include the base frame with a positioning system that moves the cavity between various positions, the eccentricity measurement device to measure the shape of the cavity, the gate with actuators for tuning (mechanically deforming) the cavity cells, the bead-pull measurement system, the laser-based alignment setup, and various electronic components, such as motion controls, interlocks, a network analyser, DAQ boards, and a weather station [3].



Figure 1: The cavity tuning machine.

ARCHITECTURE

The software architecture of the CTM system is based on the concept of plug-ins, a solution built on the ability to dynamically load and execute specified components. The framework consists of a shell module and a set of plug-ins (see Fig. 2). The shell implements a queued state machine and provides the overall system control logic, data saving, control of plug-ins, and user interface integration. Each plug-in implements a separate measurement (e.g., eccentricity, field flatness) or functionality (e.g., positioning, model, assessment) and constitutes a complete module with its own user interface, logic and DAQ. A plug-in's front panel is integrated into the overall user interface. Plug-ins communicate via message queues.

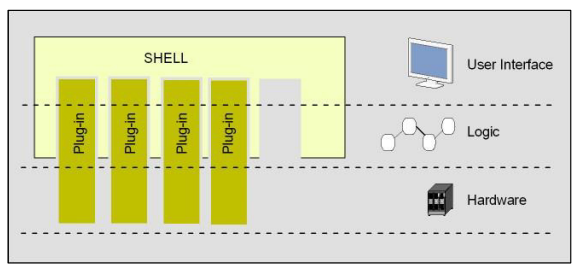


Figure 2: Plug-in architecture.

The system can operate in two modes: *manual* where the operator can use the controls available from the plug-in's front panel and *automatic* where the plug-in's front panel is disabled and the system controls the execution of plug-ins according to the logic specified in the script.

*Work supported by the U.S. Department of Energy under contract no. DE-AC02-07CH11359
#nogiec@fnal.gov

Copyright © 2013 CC-BY-3.0 and by the respective authors

This design, based on loosely coupled components, allows for separation of concerns and encapsulation and, therefore permits concurrent development of highly independent modules corresponding to the major measurements and functionalities defined in the system. The CTM framework utilizes a blackboard architectural model for implementing exchange of data between components, which aids in integrating the specialized modules and implementing diverse control strategies. Although functionally independent, plug-ins rely on a set of shared modules to uniformly implement common aspects such as logging, error handling, configuration and calibration data access, and data saving. Hardware access is also organized by a set of shared modules implementing logical devices.

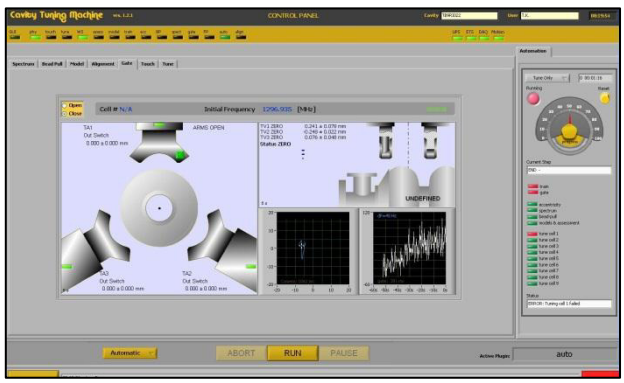


Figure 3: A plug-in executing in the automatic mode.

COMPONENTS

The CTM system has a number of plug-in components implementing its functionality. Each plug-in is designed as a state machine that executes a series of steps. This execution may be terminated (aborted) or temporarily paused. The user interfaces for each of the plug-in components are displayed inside a panel provided by the shell (see Fig. 3). The plug-ins' functionalities are as follows:

- The **train** plug-in is responsible for transporting the cavity along the base frame of the apparatus. It can move between predefined positions and also automatically position each cell inside the gate for tuning. When controlled manually it can move to any requested predefined position or move until stopped.
- The **eccentricity** plug-in performs calibration and measurement of cavity alignment by measuring the concentricity of individual cells to the cavity axis, the length of the cavity and the perpendicularity of its reference planes.
- The **spectrum** plug-in uses the network analyser to find all mode frequencies including the π-mode frequency.
- The **bead-pull** plug-in performs a field flatness measurement using a small metal bead that is moved along the cavity axis to perturb the electrical field. This perturbation results in a frequency shift measured by the network analyser. The component implements three variations of this measurement.
- The **tuning model** plug-in determines the change in the cell frequencies required to bring the π-mode frequency to the required target value with acceptable field flatness. This module has two models to be used depending on this how far the cavity is from being in tune.
- The **eccentricity model** plug-in calculates the differential deformation of the cavity cell walls required to straighten the cavity, and the expected deflection of the alignment laser as each cell is deformed. In addition, this plug-in examines the cell frequency changes required to tune the cavity, and calculates the amount by which the cells should be pre-detuned, if necessary.
- The **assessment** plug-in compares the results of the eccentricity tuning model's calculations and determines whether the cavity is acceptable for tuning or is already adequately tuned.
- The **alignment** monitoring plug-in tracks the cavity alignment using a laser and a camera attached at one end of the cavity, and a mirror at the opposite end. The camera detects the reflected laser beam spot and when the cavity bends, the laser spot shifts its position. This position is used by the machine to control and correct cavity alignment by moving the laser spot to the calculated desired position.
- The **gate** plug-in controls the tuning arms and jaws when closing and opening the cavity cells while following the pre-defined trajectory of movements. While operating arms and jaws, this component monitors both the frequency from the network analyser and the laser spot location.
- The **tuning** plug-in controls the three tuning jaws that squeeze or stretch the cavity cell according to the tuning plan calculated by the model plug-ins. During tuning both the alignment (laser spot position) and the frequency are monitored. The process is iterative and includes a sequence of adjustments followed by frequency measurements and continues until the resulting frequency is within an acceptance range.
- The **weather station** plug-in continuously acquires and records temperature, humidity and atmospheric pressure.
- The **automation** plug-in allows the user to run the automation scripts. Each script interacts with other plug-ins and performs a desired sequence of operations.
- The **interlock** plug-in ensures the safe operation of the machine. It enables the operator and scripts to examine and reset machine interlocks and prevents human access when the machine is in operation. It also monitors the internal statuses of various

Copyright © 2013 CC-BY-3.0 and by the respective authors

machine elements such as the motor controller, the UPS, instrumentation rack temperature, and the emergency trip system.

SCRIPTING

The automation plug-in executes automation scripts, which can perform all the measurements as well as cavity tuning, or just some select functionality such as calibration, cavity mounting or fine tuning. Users can supply their own scripts to further extend or customize the functionality of the machine. As with any other plug-in, the execution of a script can be suspended or aborted.

Automation scripts are sequences of instructions interpreted by the automation plug-in. The system uses a dedicated scripting language having 44 different instructions, which allow for communicating with plug-ins, controlling plug-in execution, controlling script flow, calling parameterized subroutines, handling exceptions, prompting the operator and accepting his responses, event logging and data saving, testing and resetting interlock status, manipulating indicators, obtaining the locality of the system, controlling tuning, switching between user interface panels, and sounding alert signals. In addition, automation scripts may have common sections which can be included inside several scripts, such as a set of subroutines that can be invoked from several scripts.

DATA HANDLING

The CTM software saves diverse data from all stages of the tuning process in files using the standardized XML format. This allows the use of a hierarchical structure for the output data and promotes self-describing data, where one can identify the values, names, and types of the data from the tags that describe them.

Each cavity has its own data file. Inside that file a sequence of sections represents the full history of measuring, evaluating and tuning of that cavity. The sections are chronologically ordered and represent outputs of various components. Each section is written immediately after the plug-in completes its action, thus allowing for restarting and continuation of an interrupted tuning process.

Since XML is a language used to represent data, and as such is not especially suited for human interpretation, a set of XSL transformations has been developed to aid in presenting cavity measurement and tuning results in a human-oriented form.

HARDWARE DEBUGGING

A separate program has been developed to facilitate testing, calibrating and adjusting hardware as well as debugging mechanical and electrical problems. It allows manual activation of all motors, and access and control of all connected instruments and peripherals, such as network analyser, weather station, DAQ boards or camera-based laser position system. Similar to the main tuning program, the maintenance program is configurable and can be extended by adding more test modules.

CONFIGURATION

The CTM system is highly configurable. A configuration consists of a list of components to be included in the system together with a set of their properties stored in an XML file. Each section of the file describes a set of parameters for a different plug-in component, such as eccentricity, bead-pull, train, arms, or jaws. A special program has been developed for examination and modification of these parameters. The program is extensible, and new sections can be easily added to support new plug-in components.

SUMMARY

The CTM system, a result of international collaborative efforts, has been successfully commissioned at DESY, Fermilab and KEK. Experience shows that the system has delivered on the promise to automate and shorten the tuning time of cavities.

The software developed to control and automate those machines is based on a plug-in architecture with loosely coupled components. The system is very modular, extensible and fully configurable. The blackboard-based design allows for integrating diverse specialized components and implementing various control strategies. The system's functionality can be extended or modified via scripting.

Data management, including measurement and tuning results as well as configurations and calibrations, is uniformly based on XML data format.

The system has been developed with a strong emphasis on operational safety and EU certification. It also has provisions for localization, with different behaviours specified for different laboratories. The CTM software system is portable and has been deployed on both Windows and Linux platforms.

ACKNOWLEDGMENT

The authors would like to thank their colleagues from DESY A. Goessel, J. Iversen, D. Klinke, G. Kreps, D. Proch, W.-D. Moeller, C. Mueller, and J.-H. Thie for their important contributions to the cavity tuning machine project, especially in the areas of mechanical design and fabrication and cavity tuning.

REFERENCES

[1] J.H. Thie et al., "Commissioning and Upgrade of Automatic Cavity Tuning Machines for the European XFEL," SRF 2011, Chicago, 2011.

[2] J.H. Thie et al., "Mechanical Design of Automatic Cavity Tuning Machines," Proceedings of SRF 2009, Berlin, Germany, 2009.

[3] R. Carcagno et al., "Control System Design for Automatic Cavity Tuning Machines," PAC09, Vancouver, Canada, 2009.

Copyright © 2013 CC-BY-3.0 and by the respective authors

A NEW FACILITY FOR TESTING SUPERCONDUCTING SOLENOID MAGNETS WITH LARGE FRINGE FIELDS AT FERMILAB

D. Orris, R. Carcagno, A.M. Makulski, J. Nogiec, R. Pilipenko, R. Rabehl, C. Sylvester, M. Tartaglia, Fermilab, Batavia, IL, USA

Abstract

Testing superconducting solenoid magnets with no iron flux return can be problematic for a magnet test facility due to the large magnetic fringe fields generated. These large external fields can interfere with the operation of equipment while precautions must be taken for personnel supporting the test. The magnetic forces between the solenoid under test and the external infrastructure must also be taken under consideration. A new test facility has been designed and built at Fermilab specifically for testing superconducting magnets with large external fringe fields. This paper discusses the test stand design, capabilities, and details of the instrumentation and controls with data from the first solenoid tested in this facility: the Muon Ionization Cooling Experiment (MICE) coupling coil.

INTRODUCTION

There has recently been a need to test solenoid magnets at Fermilab that have no iron flux return so the fringe magnetic fields could be relatively large. The Muon Ionization Cooling Experiment (MICE) Coupling Coil (CC) solenoid is the first such solenoid intended to be tested.

Since the existing dewars at Fermilab's Magnet Test Facility (MTF) are not large enough to test a MICE CC solenoid a new cryostat would be required. In addition, the large fringe field that would be produced by the solenoid would interfere with operations at MTF. At full operating current (210A) the 600 Gauss line would be at a radius of 3m and the 5 Gauss line would be at a radius of 15m. The 5 Gauss level is the limit for personnel with pacemakers and the 600 Gauss level impacts both personnel safety as well as the operation of equipment.

Several options were researched and the final decision was to build the solenoid test facility (SolTF) at the Fermilab Central Helium Liquefier (CHL) [1]. This location was selected because it had adequate space for the large test cryostat and the large fringe magnetic fields would not impact personnel and equipment operations: Personnel access could be managed to meet safety requirements. In addition, there was a sufficient source of liquid helium available to operate the new test facility.

SOLENOID TEST FACILITY

The new solenoid test facility (SolTF) would have to meet the cryogenic cooling, mechanical support, powering, quench protection, and data acquisition requirements for testing the MICE coupling coil at Fermilab. Table 1 lists some of the MICE CC specifications that SolTF must accommodate.

Table 1: MICE Coupling Coil Specifications for Testing

Parameter	Specification
Coil Design	96 Layers, 166 Turns in Series
Superconductor Strand	Cu/NbTi (MRI) 1.0 mm x 1.65 mm
Magnet Outer Structure Diameter	1860 mm
Magnet Weight	2.2 Tons
Cryogenic Cooling	Conduction Cooled
Helium Flow Rate	10 g/s
Cool Down Delta-T Limit	50 K Across the Magnet
Magnet Inductance	596 H
Maximum Current (4.5 K)	220 A
Stored Energy @220A	14.4 MJ
Peak Field (on axis)	2.6 T
Peak Field (on coil)	7.5 T
5G, 100 G, & 600 G Lines	15 m, 5m, 3m

Solenoid Test Cryostat

The cryostat used for the solenoid test facility was transferred to Fermilab from the National High Magnetic Field Laboratory (NHMFL) at Florida State University. The stainless steel vacuum vessel is 3.34m outer diameter, 3.32m inner diameter, and 2.7m high. The MICE CC coil would be tested in this cryostat using liquid helium conduction cooling.

The MICE CC solenoid is supported by a dished head assembly and four stainless steel rods each connected to a support bracket. The four support brackets are attached to the magnet with a G-10 block sandwiched between them to minimize heat conduction to the coil. G-10 rods between the support brackets and the cryostat wall prevent the magnet form moving horizontally. Although the cryostat was located as far as practical from the building's support columns and other fixed ferromagnetic material, tilt switches and displacement sensors were installed to monitor the magnet's vertical motion, if any, due to forces generated between the magnet and external magnetic material. Figure 1 is shows a 3-D model of the cryostat with the MICE CC solenoid.

Operated by Fermi Research Alliance, LLC under Contract No. De-AC02-07CH11359 with the United States Department of Energy

Copyright © 2013 CC-BY-3.0 and by the respective authors

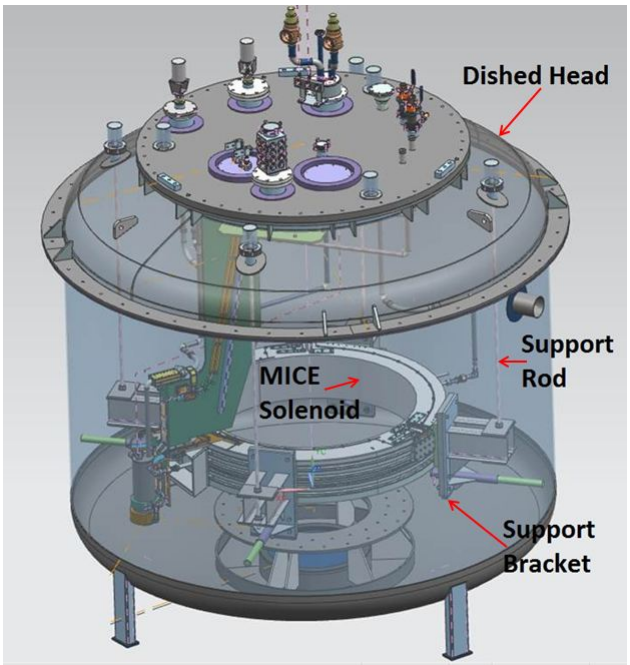


Figure 1: 3D model view of the SolTF Cryostat with the MICE Coupling Coil Supported from the Dished Head

Floor Layout

The solenoid test facility is located in the east annex of Fermilab's Central Helium Liquefier facility. The cryostat is located in the middle of the open floor space to optimize distance from magnetic materials, power panels, etc. A staging area with a support structure for the dished head is east of the cryostat for readying the solenoid for testing and the data acquisition and controls racks are located against the south wall where the maximum field is expected to be less than 20 Gauss.

The floor layout of the solenoid test facility is shown in Figure 2.

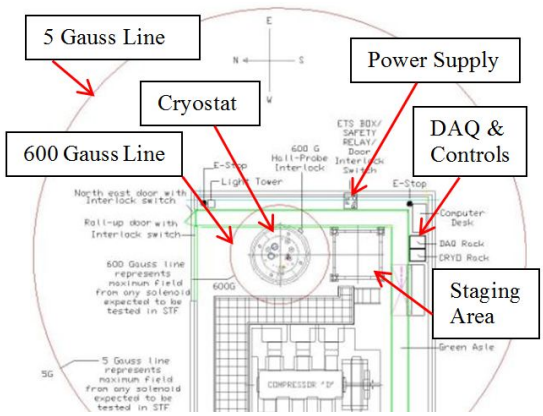


Figure 2: SolTF Floor Layout at CHL.

DATA ACQUISITION & CONTROLS

The DAQ and controls systems includes quench protection, fast and slow data logging for quench characterization, and cryo monitoring and controls. The quench protection and cryo controls are based on National Instrument's Compact-RIO (C-RIO), which uses a real-time operating system and FPGA. The data logging is based on National Instrument's PXI. The computer system consists of two operator stations, one devoted to managing the quench subsystem and another to monitoring and controlling of the cryogenic subsystem and the magnet. Each operator station is equipped with two monitors. Hardwired interlocks for equipment and personnel are also monitoring by this system.

Cryogenic Monitoring & Controls

The monitoring and control system is capable of both monitoring various process variables (temperatures, pressures, levels, flows, etc.) and controlling process variables (valves, levels, power, etc.) using PID regulators. The process interlock logic is a separate process that monitors vacuum, quench status and temperatures; it responds immediately to assigned events by closing or opening valves. The data archiver as well as all user interface programs resides in the top layer, the monitoring and control software resides in the real-time system layer, and the interlock logic and I/O in the FPGA part of the system [2]. Figure 3 shows the cryo monitoring and control display panel.

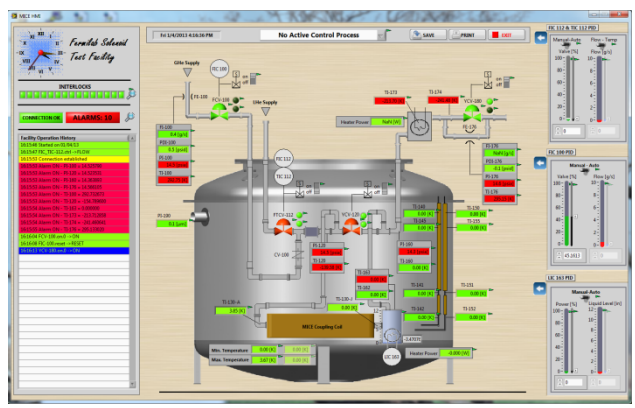


Figure 3: Cryo Monitoring and Control Display Panel. An Image of the cryostat with interactive parameters, such as temperature and pressure, are included in the Display.

Power System & Personnel Interlocks

The MICE power supply system was provided by Lawrence Berkeley National Laboratory (LBNL). This system includes a CryogenicLimited 240 Amp +10/-8.5 V power supply and energy absorber, and a circuit for disconnecting the power supply and enabling the passive diodes in the MICE solenoid. This system is also interfaced to the test stand quench detection system and hardwired personnel interlocks. A hardwired interlock "Electrical Trip System" (ETS) was built to enable or disable power to the bus based on several interlocks.

Copyright © 2013 CC-BY-3.0 and by the respective authors

These include the power supply access door, several "Emergency Off" buttons, etc. This system was installed in the power supply rack.

Quench Protection

The quench protection system uses an FPGA based digital quench detection (DQD) system [3]. Since the MICE CC magnet uses passive diodes for primary quench detection, the digital system provides redundant coil quench protection. The low temperature superconducting leads, however, are protected by the DQD for primary protection and an Analog Quench Detection (AQD) circuit for redundant protection. The quench detection system also provides the trigger to open the relays that connecting the power system to the magnet bus and ramps down the supply. A resistor in parallel with the output of the power system will generate enough voltage to turn on the cold diodes if the relays are opened at currents above ~25 A at 4.5K. Spot heaters were installed on the inner bore of the MICE CC to initiate a quench for verifying the operation of the quench protection system at low current. Figure 4 shows a heater induced quench at 46A while ramping at 0.010A/s.

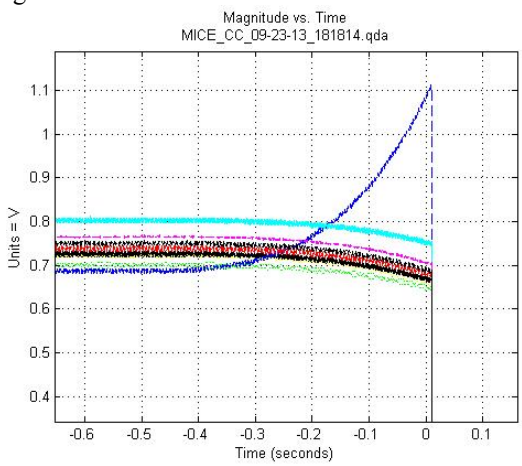


Figure 4: Heater Induced Quench of MICE CC at 46A. Coil 1, closest to the heater, quenched.

COOL DOWN AND TEST RESULTS

The MICE CC cool down is restricted to a 50K difference between the coldest and warmest coils. Since there are no temperature sensors on the coils, the resistance of the coils was monitored during cool down. This was accomplished by exciting the magnet with a trickle current of 10mA to 100mA while all eight coil voltages were monitored by the cryo monitoring scans. The calculated resistances were converted to temperatures based on resistance to temperature calculations provided by LBNL. Figure 5 shows all eighth coils transitioning to the superconducting state.

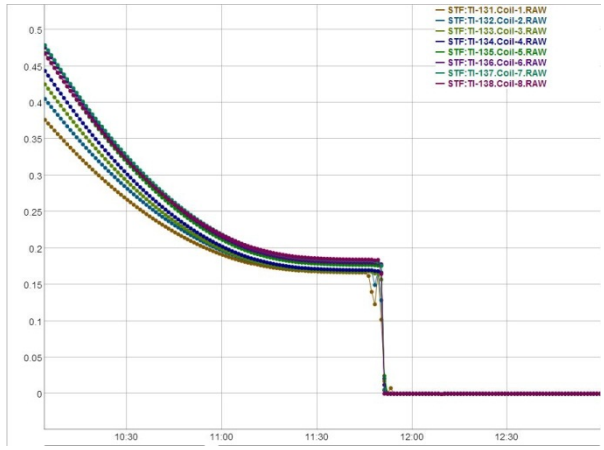


Figure 5: Plot of all MICE CC eighth coil voltages with 100mA current excitation during final cool down. The transition to the superconducting state is clearly seen.

The first ramp to quench occurred at 63A. Further analysis showed that the eighth coil #1 voltage signal rose to the threshold level in ~0.25ms. This was not a slow resistive growth but rather a voltage spike indicative of some coil motion.

SUMMARY

A new Solenoid Test Facility (SolTF) was built at Fermilab for testing conduction cooled superconducting magnets with large fringe magnetic fields. The facility was built in the Fermilab's Central Helium Liquefier (CHL) building since it had adequate space, liquid helium availability, and access to a crane for staging the magnets.

The Muon Ionization Cooling Experiment (MICE) Coupling Coil is the first magnet to be tested in this facility. The coil was recently cooled down and power tests have begun. A prototype capture solenoid coil built by Toshiba Corporation will be tested next. A mu2e prototype transport solenoid is expected to be tested next year.

REFERENCES

[1] R. Rabehl et al. To be published in Advances in Cryogenic Engineering, Volume 59.

[2] Jerzy Nogiec et al. "Software System for Monitoring and Control at the Solenoid Test Facility", submitted at the 14th International Conference on Accelerator & Large Experimental Physics Control Systems, ICALEPCS 2013, San Francisco, October 2013.

[3] R. Pilipenko et al., "An FPGA-Based Quench Detection and Continuous Logging System for Testing Superconducting Magnets", FERMILAB-PUB-12-546-TD, Oct 2012.

Copyright © 2013 CC-BY-3.0 and by the respective authors

STATUS OF PXIE 200 OHM MEBT KICKER DEVELOPMENT*

Gregory Warren Saewert#, Mohamed H. Awida, Brian Chase, Howard Pfeffer, Dan Wolff,
Fermilab, Batavia, IL 60510, USA
Daniil Frolov, Kuban State University, Krasnodar, Russia

Abstract

The proposed Project X machine at Fermilab must deliver a widely varying bunch pattern to provide beam to several experiments quasi-simultaneously. H- Beam is delivered to the 2.1 MeV Medium Energy Beam Transport (MEBT) section at 162.5 MHz continuous wave (CW) by a radio frequency quadrupole magnet (RFQ). Unnecessary beam bunches will be selectively chopped out in the MEBT by two identical choppers on a bunch-by-bunch basis and stopped by an absorber. The Project X Injector Experiment (PXIE) will be the test bed to demonstrate a chopper's ability to form an arbitrary bunch pattern. Presently two kicker system versions are under development. One proposed version is a 50 Ω structure driven by a ±250 V linear amplifier. The second proposed version is a 200 Ω helical, microstrip line structure driven by a 500 V bipolar switch. This paper describes the development status of the 200 Ω version and includes the design concept, comparison of 3D modelling work with prototype measurements, 200 Ω hardware description and progress with the driver.

SYSTEM REQUIREMENTS

The challenge for this application is the bandwidth requirement to chop beam continuously. Beam will be delivered to a number of experiments "at the same time", so kicking patterns would vary depending upon the needs of the experiments. Thus, the frequency at which bunches change from being kicked in and out will vary from 1 to 35 MHz average and 81.25 MHz peak for about 20 alternating bunches. This 200 Ω chopper offers a design solution by taking advantage of reduced power requirement and includes the development of a suitable driver.

Beam beta in the MEBT is .067 at 2.1 MeV, so the kicker can be a traveling wave structure (the "kicker") to slow down the propagating voltage pulse to match the beam velocity. The chopper consists of two 50 cm long traveling wave kickers parallel to each other on opposite sides of the beam. Applied voltage to the parallel kickers will always be of opposite polarity.

The MEBT's lattice allows for a chopper either to apply a voltage to only kick beam out to the absorber (the unipolar scheme), or to kick beam both in and out with opposite polarity voltages (the bipolar scheme). The unipolar scheme requires applying 0 V and 500 V and the bipolar scheme ±250 V. Voltage tolerance is ±25 V.

* Operated by Fermi Research Alliance, LLC, under Contract No. DE-AC02-07CH11359 with the United States Department of Energy
# saewert@fnal.gov

SYSTEM DESIGN

Component power dissipation is a big issue, and current flowing in the kicker does nothing to kick beam. These facts made it appealing to design a higher impedance system than 50 Ω. Power delivered to the load is a factor of four lower at 200 Ω, and the kicker structure's RF I^2R losses in the vacuum are lower by a factor of 16 (all other physical characteristics being the same). The downside is that all system components need to be developed. Figure 1 is the block diagram of intended system.

Helical Kicker

Meander line kickers have been implemented. However, limited power handling and evident pulse distortion suggested considering alternatives. Helical structures have also been built [1]. Constructing a cylindrically helical, 175 Ω microstrip line demonstrated promising results. Subsequent ~200 Ω versions with good mechanical uniformity resulted in good enough performance to proceed with the 200 Ω idea.

The helical wire is #13 flat magnet wire (.105" x .041") held above a copper ground tube by four ceramic spacers. This wire size was chosen to be stiff to hold its shape yet easy enough to wind tightly on a mandrel by hand. Electrodes, each 2-cm wide and .61 cm long, are attached to each turn of wire at the point closest to the beam. Beam aperture between the two facing helices is 16 mm. Figure 2a shows a photograph of a kicker prototype.

The single helix electrical characteristics and performance are affected when the two helices are positioned alongside each other, as in Fig. 2a, and driven with opposite polarities. The electrical effects are that impedance is lowered and propagation velocity reduced at the 3-5% level. Also, the helix microstrip line alone exhibits 900 MHz bandwidth but drops to about 600 MHz due to the second helix's proximity. Therefore, electrical measurements of a single helix are only valid when a zero voltage plane is installed to electrically mirror the missing helix. A metal surface positioned at beam-centre needs to extend the length of the helix, be parallel to the electrodes and grounded to the copper ground tube at both ends.

Magnetic coupling of the helical microstrip line geometry affects its characteristic impedance. The geometry for this 200 Ω helix would be 140 Ω line if laid out flat.

Estimated RF I^2R losses in the wire are about 6 W. However, the design requirements call for handling 40 W of inadvertent beam striking each helix. The ceramic spacers supporting the helix will conduct the heat to the copper ground tube. This nominal 1" diameter copper

Copyright © 2013 CC-BY-3.0 and by the respective authors

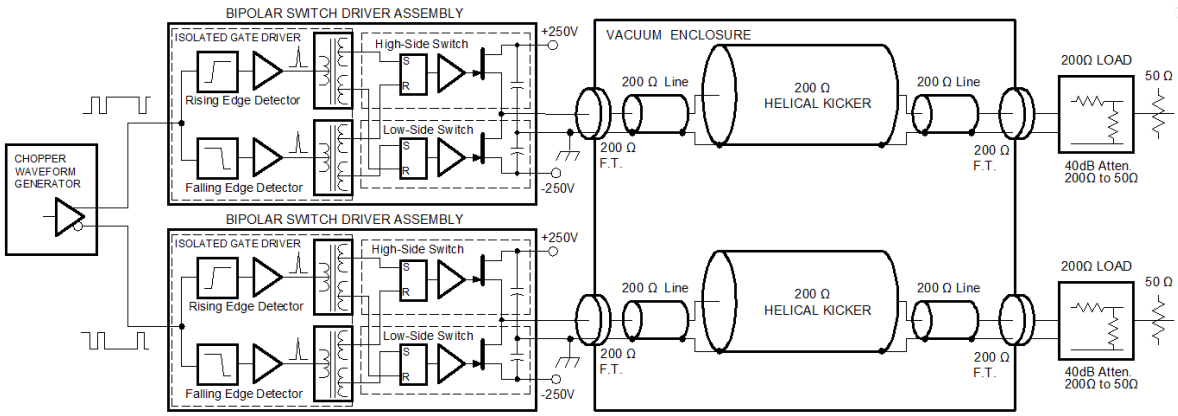


Figure 1: 200 Ω chopper electrical system block diagram. Two such systems are called for in the MEBT. Both driver and load are to be physically very close to the feed throughs.

tube is to be water cooled. The ceramic chosen is a type of machinable AlN having 50 W/m/K thermal conductivity available from Ceramic Products, Inc. Vacuum compatible epoxy is to be applied between all ceramic to copper surfaces to assist thermal conduction. The wire is estimated to rise <10°C but has yet to be confirmed by testing.

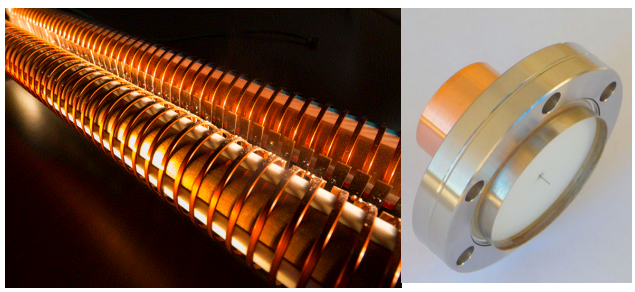


Figure 2: Hardware photos. a) Prototype kicker assembly. b) Cylindrical 200 Ω vacuum feed through.

The helix was modelled with 3D and 2D codes to determine wire height and helix pitch to achieve the desired characteristic impedance and traveling wave velocity. Agreements with a prototype helix were within 3-5%, but not quite good enough to provide precise dimensions. However, sensitivity data was obtained and then used to make adjustments to wire height and pitch of an existing prototype. A helix is in fabrication now with these adjustments.

Voltage tests revealed reflections from the far end of the helix in excessive of 10%, and TDR measurements revealed the characteristic impedance tapers down within the last turn or so at the ends to about 150 Ω. Modelling was used to evaluate optional solutions. The choice was to increase the impedance of the last turn by increasing the wire/ground spacing by 75%. This was done by decreasing the ground tube diameter under the last turn. Figure 4 shows the test result of applying this correction along with other minor adjustments achieving reflection level of ±3%.

Chopper Driver

The approach taking for the 200 Ω chopper driver was to develop a bipolar switch DC coupled to the helix. The required switching rates are those mentioned earlier, and rise/fall times need to be less than 2 ns, 5%-95%. Switching losses must be considered for the average rate of 35 MHz and are not trivial. A transistor's capacitive switching losses are CV^2f in a bipolar switch topology and amount to 3.5 W switching 100 V but 88 W switching 500 V having 10 pF Coss. The appeal to build a bipolar switch as a chopper driver was: (1) it has the DC coupled advantages; (2) designing a circuit from scratch for 200 Ω is easier than for 50 (at least in principle), and (3) the very low capacitance of available GaN FETs from Polyfet Devices, Inc. There is no single transistor available that can switch 500 V and handle its own capacitive switching losses at 35 MHz; but these FET losses come down with V^2 when connected in series to share voltage.

Current development effort is on a bipolar driver using cascode switches. Five FETs would be necessary per switch for 500 V with currently suitable and available FETs. The cascode switch is a modular design to allow for a variable number of common gate stages. A bipolar switch assembly is shown in Fig. 3 composed of 3-FET cascode switches.

Figure 1 shows the driver's major circuit blocks. The high-side switch floats with the load, so gate signal isolation must be designed for the maximum transient immunity of >250 kV/μs—well beyond commercial isolator ICs. (Low jitter fiber optic receivers are too physically large.) Narrow voltage pulses are generated at the ground-level from input rising and falling edges. These pulses set and reset latches on the cascode switches' control level that, in turn, reconstruct the ground-level chopper signal waveform and preserve timing information. Dead time is a settable parameter necessary to prevent shoot-through current. The cascode control board level includes a discrete GaN FET driver circuit, again. Not shown in any diagram is a 1 MHz, regulated AC voltage distribution system that delivers power to every isolated circuit board. Both high and low-

Copyright © 2013 CC-BY-3.0 and by the respective authors

side switches are totally isolated from power/ground. Thus, the driver can be biased with bipolar voltages or with a voltage offset from ground.

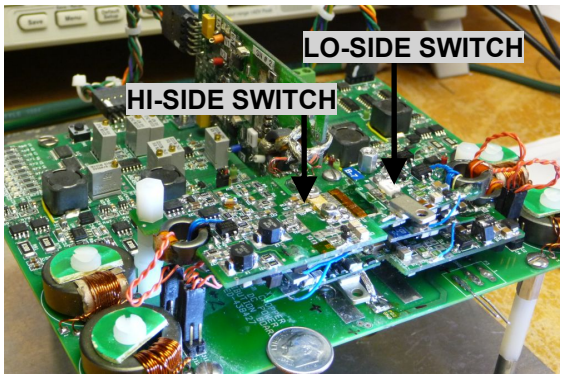


Figure 3: Bipolar switch composed of 3-FET cascode switches mounted to power distribution board.

200 Ω Lines, Feed Throughs and Load

This design is sensitive to reflections at impedance discontinuities particularly downstream of the helix. Reflections are re-reflected off the driver because of its very low impedance. Modelling verified a flat 200 Ω microstrip as the best line type to match to the helix. Feed throughs were custom made by MPC Products, Inc., and designed having isolated, cylindrical 200 Ω geometry; see Fig. 2b. Finally, the 200 Ω load was made by Elab, Inc. utilizing commercial attenuators but includes an input compensation network to minimize reflection.

PRELIMINARY RESULTS

Figure 4 is the through-voltage measurement observed at the 200 Ω load/attenuator output revealing the degree to which the 200 Ω transmission lines and load are matched to the helix. The major reflections are due to helix end effects that are not completely eliminated. Figure 5 shows the hardware included in this measurement. An assembly is currently being constructed that will include the feed throughs.

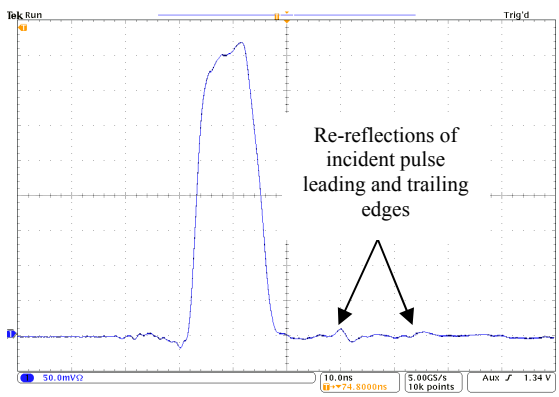


Figure 4: Through-voltage of incident pulse and all re-reflections. Reflection levels are ±3%.

Development efforts first investigated a cascode switch using 5 FETs and achieved 480 V but had issues. These were addressed and incorporated into the current design. A single stage bipolar switch was assembled to demonstrate switching to at least 100 V. This circuit (in Fig. 5) was successfully tested at 35 MHz CW and switches at 81 MHz easily for PXIE's 2 μs requirement. Current efforts are with 3-FET cascode switches in a bipolar assembly, but results are two preliminary to report.

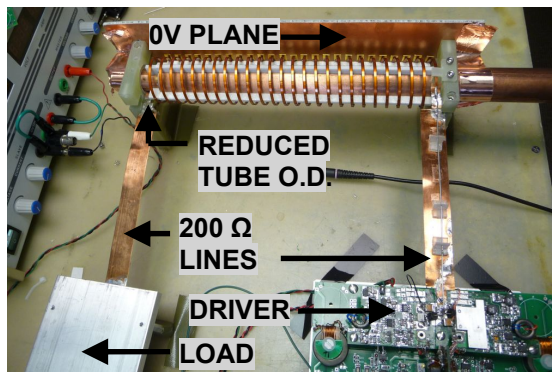


Figure 5: Reflection test setup. Helix is a 26 cm long prototype driven by 100 V (alt. ±50 V) bipolar switch.

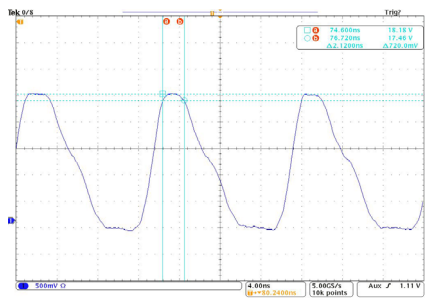


Figure 6: Helix through-voltage driven 0-100V, at 75 MHz. Bipolar switch driver is composed of 1-FET switches: <2 ns rise time (5-95%), fall time includes 2.4 ns dead time, 2.1 ns flattop.

SUMMARY

A 200 Ω microstrip line helix has been demonstrated to be a viable kicker option. Reflections are manageable. GaN FETs have been shown to be a good choice for a fast switch driver. A 100 volt single stage bipolar switch has been built and tested successfully for the continuous and burst mode operation requirement. A 300 volt 3-stage bipolar cascode switch is presently under development.

ACKNOWLEDGEMENTS

The authors acknowledge the contributions of Jeff Simmons for his technical craftsmanship.

REFERENCES

[1] J.S. Lunsford, el al., "Versatile H+ beam chopper system at LAMPF", IEEE Trans. on Nucl. Sci., Vol. NS-26, No. 3, June 1979.

Copyright © 2013 CC-BY-3.0 and by the respective authors

STORAGE RING AND INTERACTION REGION MAGNETS FOR A $\mu^+\mu^-$ HIGGS FACTORY*

A.V. Zlobin#, Y.I. Alexahin, V.V. Kapin, V.V. Kashikhin, N.V. Mokhov, S.I. Striganov, I.S. Tropin, FNAL, Batavia, IL 60510, USA

Abstract

A low-energy Muon Collider (MC) offers unique opportunities to study the recently found Higgs boson. However, due to a relatively large beam emittance with moderate cooling in this machine, large-aperture high-field superconducting (SC) magnets are required. The magnets need also an adequate margin to operate at a large radiation load from the muon decay showers. General specifications of the SC dipoles and quadrupoles for the 125 GeV c.o.m. Higgs Factory with an average luminosity of ~$2\cdot10^{31}$ $cm^{-2}s^{-1}$ are formulated. Magnet conceptual designs and parameters are reported. The impact of the magnet fringe fields on the beam dynamics as well as the IR and lattice magnet protection from radiation are also reported and discussed.

INTRODUCTION

The major advantage of a μ+μ- collider-based Higgs Factory (HF) [1] is the possibility of direct precise measurement of the Higgs boson mass and width. According to the general concept of such a machine [2], muons - in order to keep their longitudinal emittance and energy spread low - undergo only partial cooling leaving their transverse emittance relatively high (see Table 1). Therefore quite small values (a few cm) of the β-function at the Interaction Point (IP) are required resulting in a large beam size in the Final Focus (FF) quadrupoles.

Together with the necessity of magnets and detector protection from the muon decay showers, this leads to very large magnet apertures imposing challenging engineering constraints for magnet design and creating beam dynamics issues with magnet field quality and fringe fields.

Table 1: Higgs Factory Parameters

Parameter	Unit	Value
Circumference	m	300
Beam energy	GeV	62.5
Transverse emittance, $\varepsilon_{\perp N}$	(π)mm·rad	0.3
Longitudinal emittance, $\varepsilon_{\parallel N}$	(π)mm·rad	1.0
Beam energy spread	%	0.003
β^*	cm	2.5
Repetition rate	Hz	30
Muons/bunch	-	2×10^{12}
Average luminosity	$cm^{-2}s^{-1}$	2.5×10^{31}

Table 1 gives basic parameters of the HF Storage Ring (SR) preliminary design presented in [3]. The conceptual design and analysis of the Interaction Region (IR) large-aperture magnets has shown that the IR magnets with apertures ~500 mm and operation fields ~12 T are feasible using the Nb_3Sn technology.

This paper continues the design studies of the HF IR and SR magnets. The impact of the magnet field quality and fringe fields on the beam dynamics, the IR and lattice magnet protection from radiation are also discussed.

STORAGE RING LATTICE

The HF lattice layout and the beam sizes are shown in Fig. 1 for parameters given in Table 1. The IR includes FF quadruplet (with first quadrupole Q1 at 3.5 m from IP) and dipoles generating dispersion for subsequent 3-sextupole chromaticity correction [4]. The latter is necessary despite small energy spread to compensate the path length increase due to betatron oscillations. The matching section allows for β^* variation in wide range.

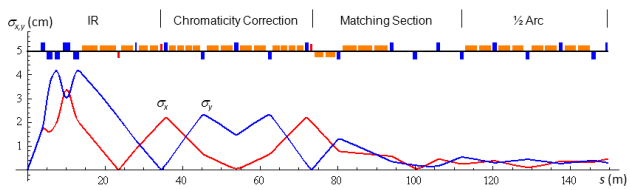


Figure 1: Layout and beam sizes in HF half-ring. Quadrupole magnets are shown in blue, dipoles in orange and sextupole correctors in red color.

MAGNET REQUIREMENTS

Table 2 shows the IR magnet parameters discussed in [3]. The orbit sagitta in IR dipoles is quite large – 8.1 cm. However, it does not affect the IR dipole bore diameter since it is determined by a large vertical beam size.

Table 2: IR Magnet Specifications

Parameter	Q1	Q2	Q3	Q4	B1
$10\sigma_{max}$ (mm)	234	411	339	415	405
G_{nom} (T/m)	74	-36	44	-25	0
B_{nom} (T)	0	2	0	2	8
L_{mag} (m)	1.00	1.40	2.05	1.70	4.10
Coil aperture (mm)	267	444	372	448	438
Quantity	1	2	1	1	2

Tables 3-4 present the maximum values of main parameters for the dipoles (B) and quadrupoles (Q) used in the chromaticity section (CS), the matching section (MS) and the arc (ARC). The most challenging magnets are the CS dipoles (B_{CS}), some MS dipoles (B_{MS}I) and the arc dipoles (B_{ARC}) which need high nominal operation field up to 10 T. This field level requires using the Nb_3Sn technology.

* Work supported by Fermi Research Alliance, LLC, under contract No. DE-AC02-07CH11359 with the U.S. Department of Energy and by the U.S. Department of Energy Muon Accelerator Program.
# zlobin@fnal.gov

Copyright © 2013 CC-BY-3.0 and by the respective authors

The magnet aperture outside the IR region reduces from 231 mm in CS quadrupoles to 92 mm in arc dipoles. Note, that the aperture size in the arc is defined by the arc dipoles due to a relatively large beam sagitta. To standardize the magnet designs in different sections it was decided to use for this study two different aperture sizes – large ~231 mm in CS and adjacent part of MS, and small ~130 mm in ARC and adjacent part of MS.

Table 3: SR Dipole Magnet Specifications

Parameter	B_{CS}	$B_{MS}I$	$B_{MS}II$	B_{ARC}
$10\sigma_{max}$ (mm)	225	222	127	92
B_{nom} (T)	10	10	6.4	10
L_{mag} (m)	1.8	2.4	3.6	3.0
Coil aperture (mm)	258	255	160	120
Quantity	13	2	3	8

Table 4: SR Quadrupole Magnet Specifications

Parameter	Q_{CS}	Q_{MS}	Q_{ARC}
$10\sigma_{max}$ (mm)	231	130	46
B_{nom} coil (T)	5.3	5.5	3.3
Length (m)	1.0	1.0	1.0
Coil aperture (mm)	264	163	79
Quantity	5	5	4.5

MAGNET DESIGNS AND PARAMETERS

The aperture of magnet coil in this study was defined as $10\sigma_{max}$ plus 30 mm for the beam pipe (BP) and absorber (ABS) plus 3 mm for BP insulation and helium channel. In the IR magnets the coil aperture was increased by ~50 mm with respect to this definition and limited by two sizes, 320 mm in Q1 and 500 mm in Q2-Q4 and B1-B2, to reserve extra space for IR magnet protection against radiation [3]. The coil aperture of CS and adjacent MS magnets was increased to 270 mm, and in ARC magnets and adjacent MS magnets to 160 mm. This allows using thicker inner absorbers in arc magnets if necessary.

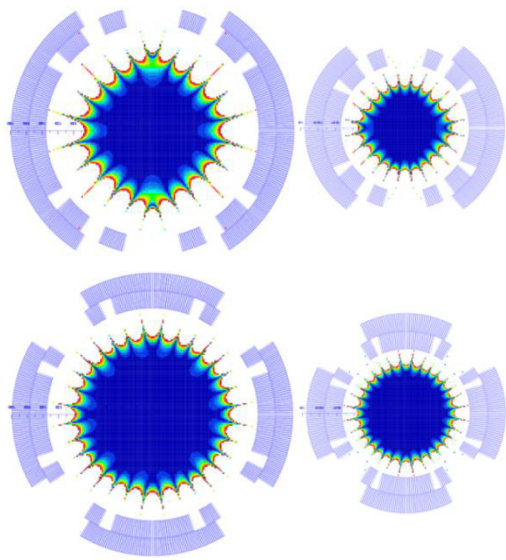


Figure 2: Coil cross-sections of HF SR dipoles (top) and quadrupoles (bottom) with 270 mm (left) and 160 mm (right) apertures.

The coil cross-sections were optimized with the ROXIE code [5] to achieve the required nominal operation field or gradient with margin and good field quality in the beam area of 8σ. As in our previous studies [3] the conceptual designs of the HF SR magnets are based on a 42-strand Rutherford cable, 21.6 mm wide and 1.85 mm thick, made of a 1 mm strand with Cu/nonCu ratio of 1.0. The cable is insulated with a 0.2 mm thick insulation.

All magnets are based on 2-layer, shell-type coils with remote iron yoke used mainly to reduce fringe fields. The optimized D and Q coil cross-sections for CS, MS and ARC sections are shown in Fig. 2.

The main magnet parameters at 4.5 K are reported in Table 5. Relatively low field level in CS, MS and ARC quadrupoles allows using the traditional NbTi technology. Therefore, the parameters of these magnets were calculated for both conductor options, NbTi and Nb_3Sn.

Table 5: Nominal Magnet Parameters at T_{op}=4.5 K

Parameter	Dipole		Quadrupole	
Coil ID (mm)	270	160	270	160
Max B_{op} (T)	10.0	10.0	-	-
B_{max} (T)	14.1	14.2	-	-
Max G_{op} (T/m)	-	-	33	36
G_{max} (T/m)	-	-	54.1*/96.6#	90.0*/160.8#
B_{max} coil (T)	15.8	15.6	8.7*/15.3#	8.3*/14.7#
Fraction of SSL	0.71	0.71	0.61*/0.34#	0.4*/0.22#
L (mH/m)	54.1	20.5	24.5	8.7
E_{op} (MJ/m)	4.33	1.84	0.59	0.12
F_{x_op} (MN/m)	9.25	5.98	0.89	0.25
F_{y_op} (MN/m)	-3.96	-2.66	-0.93	-0.28

* - NbTi; # - Nb_3Sn

The Nb_3Sn dipole magnets operate at 71% and the quadrupoles at 22-34% of their short sample limit (SSL) at 4.5 K. Using the same cable with NbTi strand in both quadrupoles reduces G_{max} to 54 and 90 T/m. However, the magnets still have quite large operation margin, they operate at 61% and 40% of the SSL for 270 mm and 160 mm quads respectively. The final choice of the superconductor for SR quadrupoles will depend on the results of radiation studies for these magnets.

Geometrical field harmonics at the corresponding R_{ref} are reported in Table 6. With optimized coil cross-sections the relative field errors in the area occupied by muon beams is ~10^{-4} (dark blue area in Fig. 2).

Table 6: Geometrical Harmonics (10^{-4}).

	ID, mm	R_{ref}, mm	b_3	b_5	b_6	b_7	b_9	b_{10}
D	270	90	-0.2	-0.1	-	0.2	1.2	-
	160	53	0.0	-0.1	-	0.5	1.1	-
Q	270	90	-	-	0.2	-	-	0.0
	160	53	-	-	0.1	-	-	0.0

The dynamic aperture (DA) on the plane of transverse particle positions at the IP and projection of the IR quad aperture onto this plane using linear optics functions is shown in Fig. 3. The DA analysis with MADX PTC code shows that field errors (after correction) reduce DA by a factor of 2 to a size of the magnet good field region.

Copyright © 2013 CC-BY-3.0 and by the respective authors

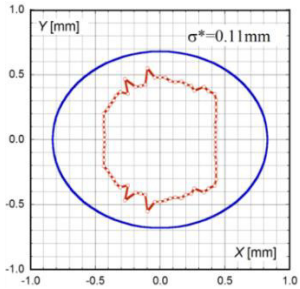


Figure 3: The dynamic aperture at IP and the projection of the IR quadrupole aperture (solid circle).

ENERGY DEPOSITION IN MAGNETS

Energy deposition and detector backgrounds induced by muon decays from both beams were simulated with MARS15 code [6] using our previous approach [7]. All the related details of geometry, materials and magnetic fields of the HF magnets in IR and SR were implemented in the 3D model along with a complete detector model, an optimized tungsten nozzle near IP and other components of the Machine-Detector Interface (Fig. 4).

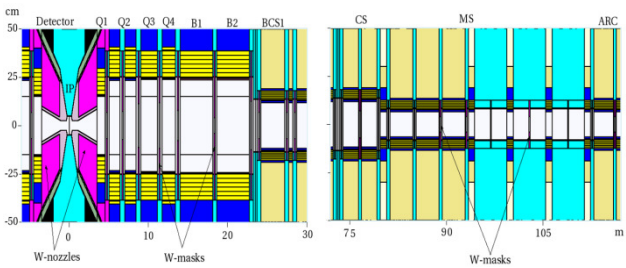


Figure 4: MARS model of HF MDI, IR and SR.

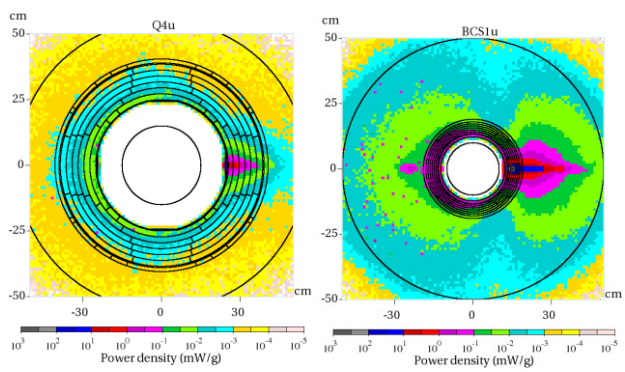


Figure 5: Power density (mW/g) in the IP ends of the Q4 quadrupole (left) and $B_{CS}1$ dipole (right).

To protect IR and SR magnets, 15 cm long, 10σ ID tungsten masks were installed in the magnet interconnect regions. Inner absorbers include up to 10-mm thick stainless steel liners inside each magnet with additional tungsten segments in both horizontal and vertical planes in some magnets along the ring.

Power density distributions were calculated for each collider ring magnet. The protection system performs adequately in the IR quadrupoles where the peak power density P_p is at or below the quench limit of ~5 mW/g for Nb_3Sn coils [3] (Fig. 5, left). However, it is ~10 times above the limit in B1 and B2 dipoles, and ~10^2 times above the limit for dipoles in CS, MS and ARC sections (Fig. 5, right). Additional tungsten inserts with the total radial thickness up to 5 cm, and a proper room for them in magnet apertures, are needed to reduce P_p below the limit.

Figure 6 shows the calculated dynamic heat load W_d in IR and SR magnets for both muon beams. The presented W_d values include both cold and potentially warm parts of magnet cross-section. The W_d in SR magnets is ~1 kW/m for the HF parameters of Table 1 except for the two dipoles at either end of the open section in MS and ARC, where it is ~2.5 kW/m. Note, that in spite of the low beam energy, the high number of decays in the HF keeps the level of W_d large as in the high energy machines [4], [7]. To reduce the W_d in the cold part of SR magnet system by ~100 times to the acceptable level of ~10 W/m, absorbers and masks have to be thermally insulated from the cold masses. It also requires extra space in magnet apertures.

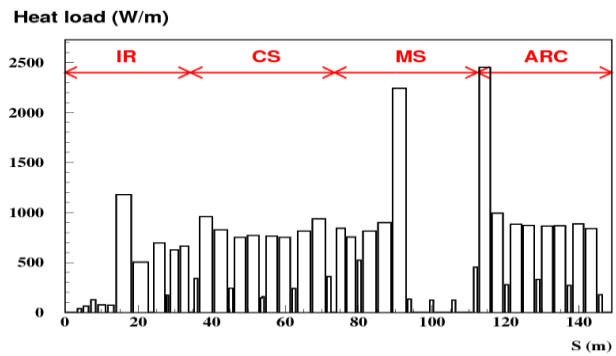


Figure 6: Dynamic heat load in IR and SR magnets.

SUMMARY

Preliminary design of HF based on the 125 GeV c.o.m. $\mu^+\mu^-$ collider including the IR and SR layout and the magnet system design concept was developed, and analysis of the beam dynamics and radiation issues was performed. It was found that protection of SR magnets from radiation and reduction of the dynamic heat load in the cold part of magnet cryostat present a serious problem and need further investigations and improvements including reiteration of the SR magnet system design.

REFERENCES

[1] Y. Alexahin et al., "A Muon Collider Higgs Factory for Snowmass 2013", arXiv:1308.2143v1 [hep-ph] 9 Aug 2013; Fermilab-Conf-13-245-T.
[2] D.V. Neuffer et al., "A Muon Collider as a Higgs Factory", Proc. of IPAC2013, Shanghai, China, May 2013, p. 1472.
[3] A.V. Zlobin et al., "Preliminary Design of a Higgs Factory $\mu^+\mu^-$ Storage Ring", ibid, p. 1487.
[4] Y.I. Alexahin et al., "Muon Collider Interaction Region Design", PRSTAB, 14, 061001 (2011).
[5] ROXIE, http://cern.ch/roxie/
[6] MARS15, http://www-ap.fnal.gov/MARS/
[7] N.V. Mokhov et al., "Muon Collider Interaction Region and Machine-Detector Interface Design", Proc. of PAC2011, NYC, March 2011, p. 82.

Copyright © 2013 CC-BY-3.0 and by the respective authors

HELICAL MUON BEAM COOLING CHANNEL ENGINEERING DESIGN *

G. Flanagan#, R. P. Johnson, S. Kahn, F. Marhauser, M. Neubauer
Muons, Inc., Batavia, 60510 IL, USA
M. L. Lopes, N. Andreev, R. Bossert, J. Tomkins, S. Krave, K. Yonehara
Fermilab, Batavia, 60510 IL, USA

Abstract

The Helical Cooling Channel (HCC), a novel technique for six-dimensional (6D) ionization cooling of muon beams, has shown considerable promise based on analytic and simulation studies. However, the implementation of this revolutionary method of muon cooling requires new techniques for the integration of hydrogen-pressurized, high-power RF cavities into the low-temperature superconducting magnets of the HCC. We present the progress toward a conceptual design for the integration of 805 MHz RF cavities into a 10 T Nb_3Sn based HCC test section. The concept we present includes a decoupling of the RF and magnetic channels and the pressure and thermal barriers needed within the cryostat to maintain operation of the magnet at 4.2 K while operating the RF and energy absorber at a higher temperature.

INTRODUCTION

A HCC consisting of a pressurized gas absorber imbedded in a magnetic channel that provides solenoid, helical dipole and helical quadrupole fields has shown considerable promise in providing six-dimensional cooling for muon beams. The energy lost by muons traversing the gas absorber needs to be replaced by inserting RF cavities into the lattice. Replacing the substantial muon energy losses using RF cavities with reasonable accelerating fields will require a significant fraction of the channel length be devoted to RF. However, to provide the maximum phase space cooling and minimal muon losses, the helical channel should have a short period and length. Demonstrating the technology of such a cooling channel would represent enormous progress toward the next energy frontier machine. We propose to design and build the 10 T, 805 MHz segment of a HCC. This corresponds to the second section of the HCC design discussed in [1].

KEY TECHNOLOGICAL BARRIERS

The key technological barriers include cooling of the helical solenoid coils made of the low temperature superconductor (LTS) in the presence of RF cavities embedded in the channel and operation of RF cavities in the presence of a magnetic field. Recent results [2,3] show pressurizing the RF cavities may solve the latter challenge. The first challenge, we believe, can be addressed by reducing the size of each RF cavity utilizing a low loss dielectric insert to ease physical constraints for a given frequency. This allows enough room between the cavities and the coils for the magnet coils, the magnet cryostat, the hydrogen pressure vessel, and the RF coaxial feeds to the individual cavities. Calculations show that the heat loads will be tolerable and RF breakdown of the inserts will be suppressed by the pressurized hydrogen gas. The work done on this problem is one of the key accomplishments of the project and has led to a solution to the engineering problem of feeding the RF power through the magnet cryostat.

The following sections describe more fully the dielectric cavity design concepts and the design concept for an integrated 10 T, 805 MHz HCC.

DIELECTRIC LOADED CAVITIES

We have reported progress on the design and testing of dielectric loaded cavities for a HCC in detail elsewhere [3,4]. Here we give a summary and then devote more time to the alternative technology of re-entrant cavities (see next section). The key idea behind using dielectric loaded cavities is the reduction of cavity radius and the associated easing of engineering demands that comes along with it. One can decouple the RF and magnetic channels.

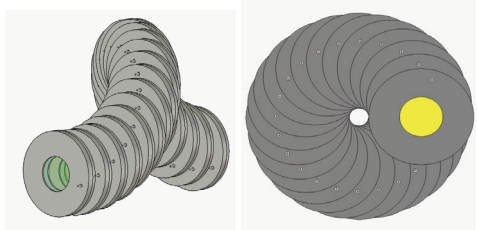


Figure 1: (Left) Illustration of RF cavities aligned to fit inside a HS magnet and cryostat. (Right) The end view shows the dielectric-filled region of the cavity (gray), where the yellow area corresponds to the region that the beam passes through. The small holes indicate the locations of the power feeds. Beryllium grids separate the cavities to make them RF pillboxes while not impeding oxygen-doped hydrogen flow. These are some of the building blocks of the integrated channel (see Figures 4 and 5).

RE-ENTRANT RF CAVITY ALTERNATIVE

As an alternative to using dielectric inserts for reducing the size of the RF cavities in order to fit them into a magnetic channel, we also consider a re-entrant RF structures. It is known that the cavity frequency can be lowered if one employs a half/quarter wave type upper torso. This increases the magnetic field at the perimeter.

*Work supported under U.S. DOE Grant Application Number DE-SC0006266
#flanagan@muonsinc.com

Copyright © 2013 CC-BY-3.0 and by the respective authors

Alternatively, one can argue this is a re-entrant structure with capacitive loading.

Both ways lower the frequency for a given radius. The benefits of this approach are:

- Reduced power requirements, even though some real estate length is lost due to smaller gap than cavity length.
- Reduced capital costs for cavities.
- Reduced operational costs for cavities.
- Reduced number of RF sources and cavities per helical period.
- Reduced costs for the RF system
- Required peak power in range of what can be done with magnetrons (< 1MW).
- Structure is easy to build, i.e. with the aforementioned idea of utilizing an outer pressure vessel (no pressure difference across cavities) we can use 3mm thin copper sheets and deep-draw cavity shape similar to SRF cavities, then EBW parts (full penetration welds). Tune and weld.
- High Q0, several factors higher than when using a ceramic.
- No triple joint junction and thus no associated field enhancement.
- Performance not limited by dielectric strength of the ceramic but RF breakdown limit in GH2.
- Mitigation of cross talk between cavities through gridded windows.
- The cavity design makes use of offset windows and re-entrant shapes to follow the helical path. Enough clearance for beam while minimizing Be-window radius. Field asymmetry along helical path is small as re-entrant shape (planar front) homogenized and concentrated field along gap and path of interest.
- More space for instrumentation etc.

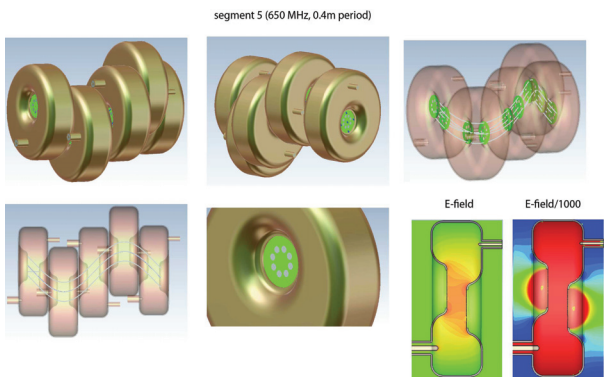


Figure 2. 3D conceptual design and initial simulations for the re-entrant cavities that could be used in mid-section of an HCC.

Currently we have explored two options for reducing the RF cavity sizes. Both options allow the cavities to be embedded in the helical magnetic/high pressure channel. The final technology choice will be made once the detailed simulation of the full cooling channel has been performed.

10 T Nb_3Sn HELICAL SOLENOID

Details of the magnet design effort to date have been reported elsewhere [4]. Here we give a summary for completeness. The invention of the Helical Solenoid (HS) magnet provides a simple configuration of coils to generate the solenoid, helical dipole, and helical quadrupole field components required for the HCC. The HS overcame the difficulty of very high coil currents required to produce the quadrupole field component in an ordinary magnet design. Note that the HS is not a bent solenoid. In a HS the coil planes are normal to the z axis, while a bent solenoid would have the coil planes normal to the equilibrium orbit.

Multi-coil HS magnet sections have been designed, constructed, and tested using NbTi [5] for the lowest field (5T, four coil) and YBCO for the highest field (15 T, 6 coil) HCC segments [6]. The coil design for the intermediate HCC section (10 T, continuous coil) is being made to provide a technology demonstration and develop practical experience with the construction and performance of a Nb_3Sn helical solenoid.



Figure 3: Conceptual drawing (left) and 3d printer version (right) of the Nb_3Sn HS spool and conductor that will be fabricated and tested in the Fermilab Vertical Magnet Test Facility. The test will use two layers of cable.

Additional studies are being performed with elliptical coil configurations. These are beyond the baseline studies designed to see if we can further ease overall engineering burden and improve performance (these studies are presented at this conference [7].

INTEGRATED HCC DESIGN

Figure 4 shows the essential features of a compact design of an HCC module where hydrogen-pressurized, dielectric-loaded RF cavities fit inside HS magnet coils. In this concept, the HS magnet and its 4 K cryostat are thermodynamically independent of the RF cavities and their power sources. Figure 4 shows a cut-away view of a module with 20 RF cavities that could be the first device to be built and tested. Figure 5 shows a three-dimensional view of the same module

Copyright © 2013 CC-BY-3.0 and by the respective authors

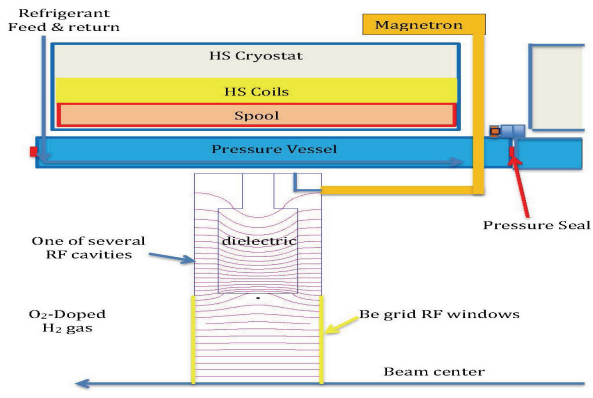


Figure 4: Conceptual diagram showing the features of a beam-cooling module with dielectric-loaded RF cavities, Be RF windows, pressure vessel, HS coil, and its cryostat.

The coax feed for each cavity comes from a magnetron power source fed through a break in the magnet structure where the magnet cryostats end [4]. The pressure vessel wall is refrigerated by circulating liquid or gas (water, LN2, or gaseous Helium), and could be machined to contain the coax power leads. Compared to earlier design concepts, this one has only one break between coils per module and no penetrations of the cryostat by RF feeds.

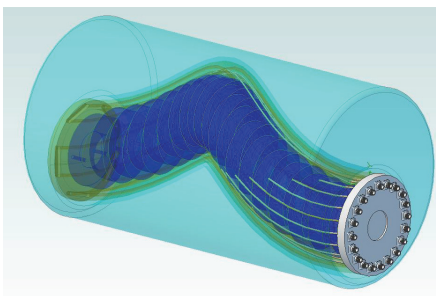


Figure 5: Three-dimensional visualization of Figure 4.

SIMULATION AND OPTIMIZATION

The design will be validated for muon cooling performance via G4Beamline [8] simulations. Of key importance will be the effect of the gaps between cryostats on the cooling performance. From the engineering design we will have detailed understanding of the fields within and between modules. The effect of the gap on the field will be propagated into G4Beamline and the effects studied. It is expected that any ill-effects of the gap can be overcome, at least in part, by having increased fields at the end of the modules. This study will be part of a larger study of field error tolerances.

The details of the dielectric cavities (and re-rentrant cavities) will also be ported to the simulation code. Additionally, all known details including RF coupling scheme will be taken into account in the simulation effort.

The G4beamline simulation will be used synergistically with the RF and magnet design tools to ensure the engineering design is able to provide a system optimized for cooling performance.

SUMMARY

Based on recent results we are moving toward combining several Muons, Inc. SBIR-STTR-developed inventions in an innovative practical engineering solution for a 10 T, 805 MHz muon-cooling channel suitable for a muon collider. The design will incorporate the HCC [9], a HS magnet [10], hydrogen-pressurized RF cavities [11], phase and frequency-locked magnetron power sources [12], emittance exchange using a continuous absorber [9], and be optimized using G4beamline Muon beam cooling simulations. The goal of the project is to optimize beam cooling for maximum collider luminosity while including all known engineering constraints, from material properties to affordable RF power sources and cryogenic loads, and to generate an engineering design of a segment of a channel as a prototype to build and test.

Demonstrating the technology of such a cooling channel would represent enormous progress toward the next energy frontier machine. We propose to design and build the 10 T, 805 MHz segment of a helical cooling channel.

REFERENCES

[1] S.A. Kahn et al., "Incorporating RF into a Muon Helical Cooling Channel," Proc. of IPAC'2010, Kyoto, Japan, p. 3509.
[2] K. Yonehara et al., "Summary of Dense Hydrogen Gas Filled RF Cavity Tests for Muon Acceleration," IPAC13, 2013.
[3] K, Yonehara et al., "High Power Tests of Alumina in High Pressure RF Cavities Muon Ionization Cooling Channels," IPAC13 Proceedings, 2013.
[4] R. P. Johnson et al., "Muon Beam Helical Cooling Channel Design," COOL13, 2013.
[5] N.Andreev et al., "Model NbTi Helical Solenoid Fabrication and Test Results," MT22, 2011.
[6] M. Yu et al., "Fabrication and Test of Short Helical Solenoid Model Based on YBCO Tape," Proc. of PAC'2011 p. 1118.
[7] S. Kahn et al., "Elliptical Muon Helical Cooling Channel Coils," NA-PAC 13, Pasadena.
[8] g4beamline.muonsinc.com
[9] Y. Derbenev and R. P. Johnson, PRSTAB 8, 041002 (2005).
[10] V. S. Kashikhin et al., "Design of Helical Solenoid Combined with RF Cavity," Proc. of IPAC'2010, p. 382.
[11] R.P. Johnson et al., in First International Workshop on Hydrogen in Materials and Vacuum Systems, AIP Conf. Proc. No. 671, pp. 328 – 335.
[12] G. Kazakevich et al., "Magnetron RF Source for the Project X Pulsed Linac," NA-PAC 13, Pasadena.

Copyright © 2013 CC-BY-3.0 and by the respective authors

DISPOSITION OF WEAPONS-GRADE PLUTONIUM WITH GEM*STAR

R.P. Johnson*, G. Flanagan, F. Marhauser, Muons, Inc., Batavia, IL, USA
C. D. Bowman, R. B. Vogelaar, ADNA Corp., Los Alamos, NM, USA

Abstract

An accelerator system like the SNS at ORNL can generate spallation neutrons to convert fertile elements like U238 in spent nuclear fuel (SNF) or Th232 into fissile isotopes to provide high temperature heat using technology developed at the ORNL Molten Salt Reactor Experiment. In the Green Energy Multiplier * Subcritical Technology Alternative Reactor (GEM*STAR) [1], the accelerator allows subcritical operation (no Chernobyls), the molten salt fuel allows volatiles to be continuously removed (no Fukushimas), and the SNF does not need to be enriched or reprocessed (to minimize weapons proliferation concerns). The molten salt fuel and the relaxed availability requirements of process heat applications imply that the required accelerator technology is available now. The accelerator can also be used to control the burning of fissile isotopes developed for weapons. A new opportunity is being considered by Russian and American scientists to use GEM*STAR to reduce the world inventory of weapons-grade plutonium leaving only remnants that are permanently unusable for nuclear weapons. This application could expedite the exploitation of this new accelerator-driven technology.

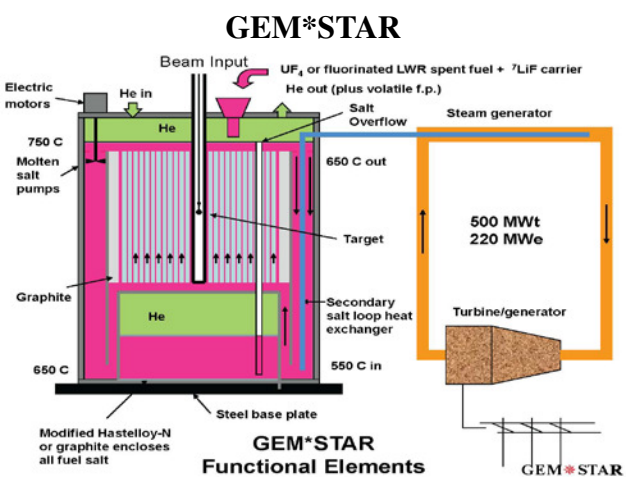


Figure 1: Conceptual arrangement of a GEM*STAR reactor unit configured to produce electricity. To produce diesel fuel, the secondary salt loop heats CH2 and H2O to produce CO and H2 for the Fischer-Tropsch process.

GEM*STAR is a graphite-moderated, thermal-spectrum, molten salt fueled reactor that is operated using an external accelerator to direct protons onto an internal spallation target. GEM*STAR can be operated with many fuels, without redesign, for process heat and/or for electricity generation. Figure 1 shows its basic components, where the active volume is 93% graphite (gray) and 7% molten salt made up of an appropriate eutectic mixture of lithium, uranium, plutonium, and/or thorium fluorides with a melting point above 500 C. Safety features of the design include the 500 MWt power output design limit, corresponding to not needing 1) a critical mass of fissile material for operation or 2) "defense in depth" measures for loss-of-coolant accidents since the heat generated by decays of fission products after the accelerator is turned off can be dissipated by passive external air cooling.

A helium flow over the hot core removes volatile radioactive isotopes and carries them to a relatively small underground tank where they are separated out cryogenically or with a centrifuge and then safely stored while they decay. This reduces the inventory of volatile isotopes in the reactor by a factor of a million compared to reactors used at Fukushima.

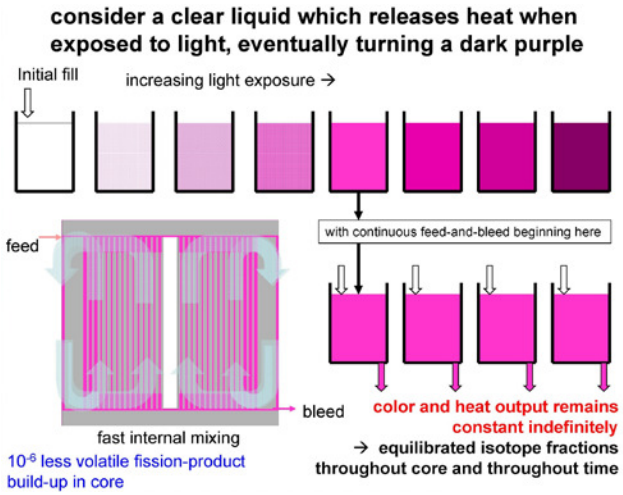


Figure 2: Concept of operating with equal fill and removal rates to maintain a constant reactor performance.

An essential feature of the design is the concept of feeding the reactor with a steady flow of fuel such that the concentration of fission products within the reactor stays constant for most of the 40-year reactor lifetime. As the fuel is fed into the reactor at a rate that maintains the 500 MWt output, an equal amount leaves the core through the salt overflow shown in figure 1 into a storage area under the core. Figure 2 shows an equivalent diagram of how the concentration of fission products reaches an equilibrium that can be maintained by this concept of adding molten salt fuel and removing it at the same rate.

Although the first approach to equilibrium takes some time (~5 years), a subsequent reactor can use the molten salt accumulated under the first reactor to start in an equilibrated state. Note that the heat from decaying reaction products will keep the overflow liquid from

* rol@muonsinc.com

Copyright © 2013 CC-BY-3.0 and by the respective authors

solidifying and that the radioactive fuel under the core can be moved to the next reactor using helium gas pressure.

We take the 1 MWb performance of the SNS SRF Linac at less than 10% duty factor as an existence proof that a CW Linac could make at least 10 MWb. Further, molten salt fuel for off-line process heat is an "end-run" around the reliability questions that have usually been raised regarding accelerator-driven reactors. The most stringent requirement has been the need to avoid accelerator trips of even a few seconds because of thermal stresses and consequent fatigue of solid pellets in fuel pins. This objection is not applicable to molten salt fuels. Longer-term interruptions that may affect electricity production are also not very important for off-line production of diesel fuel, which is our first objective.

One of the required safety aspects of GEM*STAR is the use of a proton accelerator to allow subcritical operation. Without a critical mass in the core, fission stops when the accelerator is turned off. In addition, GEM*STAR with accelerator, molten salt fuel, and graphite moderator allows the reactor itself to be simpler, less expensive, and intrinsically safe. Namely, GEM*STAR does not need mechanical control rods, a containment vessel to protect against escaping volatile radioactive elements, or a pressure vessel. Expensive chemical reprocessing is not needed for several fuel cycles such that it can be put off for 200 years.

In short, the complexity of modern nuclear reactors that many people are concerned by is shifted in GEM*STAR such that the complexity is in the accelerator, not the reactor or the fuel.

People sometimes cite problems with graphite reactors due to the Wigner Effect, wherein accumulated neutron-induced atomic displacements suddenly realign and cause an energy spike. In early days of graphite reactors, the temperature had to be periodically raised above 250 C to anneal the graphite to prevent this (see the Wikipedia articles on Wigner Effect and Windscale Fire). Annealing is not necessary in the GEM*STAR design, which operates above the annealing temperature.

Fast spectrum reactors or breeder reactors are often cited as a method to do what we want to do with GEM*STAR. The usual question is "why use an accelerator to do what can be done with a control rod?"

Here are some reasons. Compared to a thermal spectrum made possible by graphite moderator, the fission cross-sections for a fast reactor are many times smaller and the relative sensitivity to fission products is greater. This means you need many more neutrons (requiring more than 100 critical masses in the reactor), more responsive control rod feedback (the fraction of delayed neutrons is less than in a normal reactor), and the fuel has to be reprocessed to remove the fission products (chemically separated, which is a weapons proliferation concern, and an added expense).

WEAPONS GRADE PLUTONIUM (W-Pu)

The GEM*STAR design is appropriate for many fuels, especially to convert fertile material to fissile ones (U238 to Pu239 and Th232 to U233). Where the need is greatest depends on the country and situation. In the US, SNF is a growing issue that could be addressed with GEM*STAR, while in India, thorium is abundant and power needs are great.

However, with no change in design, GEM*STAR can provide neutrons to control reaction rates for fissile materials that were produced for weapons. As we will show, it destroys W-Pu so well that it is the most compelling first application. That it can turn a $50B expense into a profit for the US also adds to its attraction.

A plutonium bomb uses high explosives to compress Pu239 to form a critical mass. At just the right time in the compression, neutrons are injected into the mass to initiate the explosion. If enough Pu240, a neutron emitter, is in the mass, it can cause the explosion to start prematurely and reduce the effectiveness of the explosion. Weapons-grade plutonium, then, requires less than 7% Pu240. The US and Russia made many tonnes of W-Pu. According to the year 2000 U.S.-Russian Plutonium Management and Disposition Agreement [2], each country should each destroy at least 34 tonnes of it. The agreement specifies that each country must agree to how the other achieves this goal and that the two countries should destroy the W-Pu in lock step.

The present situation is that the US has decided to mix the W-Pu with uranium as oxides (MOX) to be placed in fuel rods to be burned in conventional light water reactors. Russia's plan is to use a fast breeder reactor.

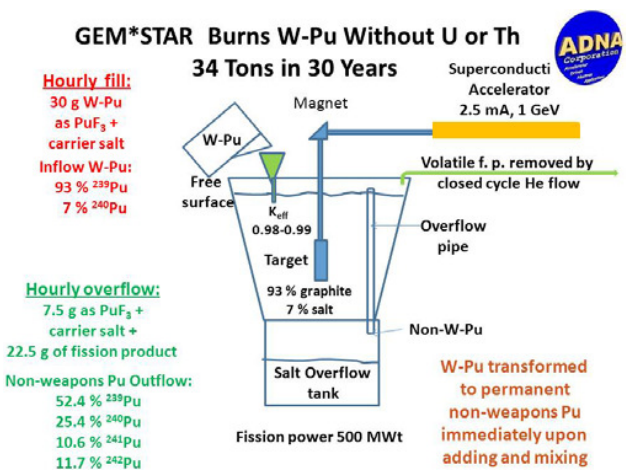


Figure 3: A GEM*STAR unit to generate heat by burning W-Pu while making remnants unusable for nuclear weapons. Four GEM*STAR units will treat 34 tonnes of W-Pu to provide 80 billion gallons of diesel fuel, which is about what the DOD needs for the next 30 years.

Figure 3 shows a conceptual picture of W-Pu utilization in GEM*STAR. A 2.5 MWb accelerator generates 500 MWt, reducing 30 g of W-Pu to 7.5 g per hour and adding the neutron generating isotopes Pu240 and Pu242. Figures 4 and 5 show the qualities of the W-Pu (back row-red) compared to the outputs of GEM*STAR (green), the

Copyright © 2013 CC-BY-3.0 and by the respective authors

Russian BN800 Fast Breeder (dark red), and the US MOX plan using Light Water Reactors (yellow). By passing the fuel through the reactor a second time, additional benefits can be seen. However, in the case of MOX, the fuel has to be reprocessed to remove fission products. GEM*STAR does not require reprocessing for a second pass.

Figure 4 is a comparison of the isotopes produced by the present plans of Russia and the US and by GEM*STAR. GEM*STAR does better because of the effectiveness of the thermal neutron spectrum both to produce Pu240 and Pu242, and to be less sensitive to fission products than MOX-LWR. Pu242 is even more effective than Pu240 to cause premature explosions in that it is a neutron emitter with a lifetime longer than Pu239.

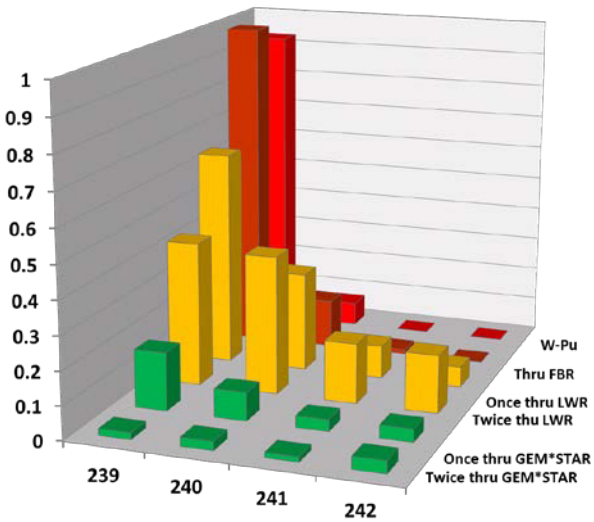


Figure 4: Isotopes remaining from the original W-Pu (red, 0.93 Pu239, 0.07 Pu240) after burning in the Russian FBR (dark red), once and twice in MOX-LWR (yellow), and once and twice in GEM*STAR (green).

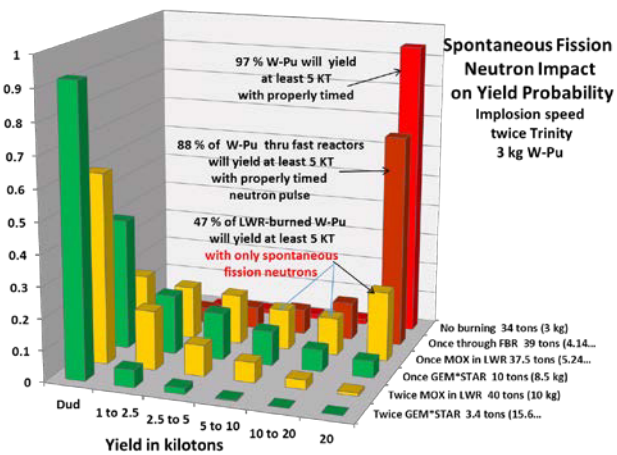


Figure 5: Yield probability of a nuclear weapon made from the output of the three reactors shown in Figure 4.

Figure 5 compares the yield probability for nuclear weapons material made from the output of the three reactors described in figure 4. The numbers have been scaled from calculations by J. Carson Mark [3]. Twice through GEM*STAR is clearly the best in that the amount of Pu239 is greatly reduced as is its utility for a weapon.

SUMMARY

The benefits of GEM*STAR for disposing of W-Pu can be summarized as follows:

- Burned W-Pu never useful for weapons
- Burned W-Pu never decays back to weapons useful material
- Conversion to non-W-Pu in minutes
- Pu isotopic mixture can be reduced from 34 tons to 0.2 tons if desired
- Also converts Commercial Pu (C-Pu) to-non-weapons-useful material
- Never requires a critical mass - no control rods
- No reprocessing or enrichment required
- No conversion to MOX; simple conversion of Pu metal and PuO_2 to PuF_3
- Fission energy converted to diesel and sold as green fuel to DOD
- No stored large volatile fission product inventory as in LWRs (Fukushima)
- Liquid fuel moved by He pressure; no radiation exposure to humans
- Operates at atmospheric pressure - No pressure vessel
- Passive recovery from a loss of coolant accident (LOCA)

The 2000 U.S.-Russian Plutonium Management and Disposition Agreement may be stalled because MOX plant costs at Savannah River have overrun, LWR sites in the US have not agreed to use the MOX fuel, and because the Russian breeder reactor solution lacks funding. The GEM*STAR design has been made to address many safety questions and to solve several problems. As discussed above, GEM*STAR can reduce weapons stockpiles more effectively than MOX or FBR and make a substantial profit doing it. We believe that following this approach in carrying out the US-Russian Agreement will demonstrate the unique features of GEM*STAR that will then lead to other successes in reducing SNF stockpiles and giving a jump-start to a new nuclear technology.

REFERENCES

[1] Charles D. Bowman, R. Bruce Vogelaar, Edward G. Bilpuch, Calvin R. Howell, Anton P. Tonchev, Werner Tornow, R.L. Walter, "GEM*STAR: The Alternative Reactor Technology Comprising Graphite, Molten Salt, and Accelerators," Handbook of Nuclear Engineering, Springer Science+Business Media LLC (2010).

[2] http://www.state.gov/r/pa/prs/ps/2010/04/140097.htm

[3] Science & Global Security, 1993, Volume 4, pp.111-128. Copyright 1993 Gordon and Breach Science Publishers S.A.

Copyright © 2013 CC-BY-3.0 and by the respective authors

A DIPOLE MAGNET FOR THE FRIB HIGH RADIATION ENVIRONMENT NUCLEAR FRAGMENT SEPARATOR*

S.A. Kahn#, A. Dudas, G. Flanagan, J. Nipper, Muons, Inc., Batavia, IL 60510, USA
M.D. Anerella, R.C. Gupta, J. Schmalzle, BNL, Upton, NY 11973, USA

Abstract

Magnets in the fragment separator region of the Facility for Rare Isotope Beams (FRIB) would be subjected to extremely high radiation and heat loads. Critical elements of FRIB are the dipole magnets which are used to select the desired isotopes. Since conventional NbTi and Nb_3Sn superconductors must operate at 4.5 K, the removal of the large heat load generated in these magnets would be difficult. High temperature superconductors (HTS) have been shown to be radiation resistant and can operate in the 40 K temperature range where heat removal is an order of magnitude more efficient than at 4.5 K. The coils of this magnet must accommodate the large curvature from the 30° bend that the magnet will subtend. This paper will describe the magnetic and conceptual design for these magnets.

INTRODUCTION

The FRIB facility at MSU will provide isotope beams for physics research with intensities not available elsewhere [1]. The facility will enable scientists to study the properties of nucleonic matter providing insight into the nuclear processes in stars as well as tests fundamental symmetries in nuclear physics. Large quantities of various isotopes are produced when a high power 400 kW linac beam hits the target. FRIB will have the ability to accommodate various primary beams from protons to uranium with energies up to 200 MeV/u. The beams will be incident on a carbon target to produce a variety of secondary nuclides with various ionic charge states. The fragment separator which follows the target consists of a series of three quadrupole magnets to provide focusing and two dipole bend magnets to select the desired nuclei. The beam enters the first dipole magnet with a spread of rigidities. The undesired nuclides are removed with a beam dump between the two dipole magnets.

As the production rate for a specific rare isotope can be very small, the magnets in the fragment separator will have large apertures and strong magnetic fields to maximize the collection of these rare isotopes. The radiation level in the fragment separator magnets is quite high and these magnets need to be radiation resistant. The radiation dose seen by the first quadrupole after the target is estimated to be 2.5×1015 neutrons/cm2 per year (10 MGy/year) [2] which corresponds to 10 kW/m of deposited power. The deposited power will drop by an order of magnitude before reaching the first bending dipole. The high radiation environment influences the magnet design and the choice of materials used. Although NiTi and Nb3Sn are robust conductor materials in radiation, they must operate at 4.5 K which is not practical, since the anticipated heat load would be difficult and expensive to remove at that temperature. HTS conductors are reasonably resistant against radiation and have a significant current density at 40 K where the heat capacity of the refrigerants is much larger and the Carnot efficiency is greater making heat removal easier.

Brookhaven National Laboratory has been involved in an R&D program to develop the quadrupole magnets for pre-fragment separator at FRIB [3,4,5,6] using HTS conductor. The design of the fragment separator dipole magnets will rely on the technology that was learned.

MAGNETIC DESIGN

The design parameters of the fragment separator dipole magnet are shown in Table I. There are two such magnets in the fragment separator which is used to select the desired nuclide. Each of these magnets bends the beam by 30º with a nominal field of 2 T. The magnet should have field uniformity better than 0.7% over the useful beam aperture for operating field between 0.5 and 2.0 T. We have chosen a superferric design for this magnet where HTS coils are used to magnetize the iron which provides the desired field. The coils surround the iron poles and are enclosed in their individual cryostat. The coil and cryostat package are recessed behind the iron pole to protect them from a direct exposure to the radiation from the beam. However, the main source of radiation is from neutrons that penetrate into the coils. Most of the radiation and associated heat will be deposited into the iron yoke which is at room temperature. It is estimated that ~1 kW will be deposited into coil cryostats. Figure 1 shows a sketch of the sector bend magnet where only one half of the upper half of the iron is shown. The upper and lower coils must each carry 256 kA-turns to produce the design 2 T field in the beam aperture.

Table I: Fragment Separator Dipole Magnet Design Parameters.

Parameter	Value
Bending Radius	4 m
Bend Angle	30º
Magnetic Length along Beam Path	2.094 m
Nominal Central Field	2.0 T
Operating Field Range	0 to 2.2 T
Field Uniformity in Good Field Region	<0.7 %
Good Field Width in Bend Plane	0.3 m
Good Field Height in Non-Bend Plane	0.2 m
Total Current Required in Each Coil	256 kA-turns
Operating Temperature	40 K

*Work supported by US DOE grants DE-SC-0006273 and DE-AC02-98CH10886
#kahn@muonsinc.com

Copyright © 2013 CC-BY-3.0 and by the respective authors

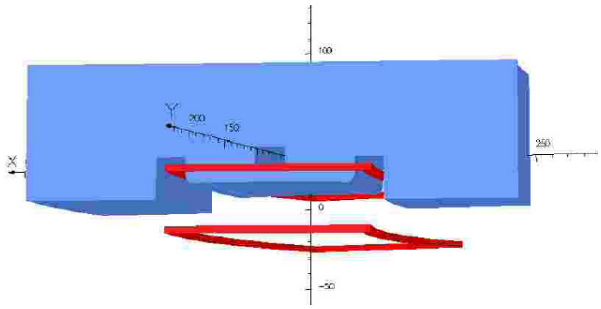


Figure 1: Model of the upper quarter of the magnet.

SUPERCONDUCTING COILS

We plan to wind the coils with YBCO conductor which will be operated at 40 K. The coils are located at a position where the field will be ~2.5 T with comparable radial and vertical components. As the critical current of YBCO conductor is sensitive to the local direction of the field we must design for the field component perpendicular to the conductor plane which has a lower critical current. To provide a safe margin against quenching the coils should be operated at two-thirds of the critical current at 40 K and in the $B_{\perp}$=2.5 T field. We expect that we can obtain 400 A using Super Power 12 mm (SCS 12050-AP) conductor under these conditions [7]. The coils will need 5.5 km of this conductor for the magnet.

An important consideration in the winding of the coils is that the field must preserve the transverse 2D profile. However the inner radius segment of the coil, which would be wound with negative curvature, is more difficult since the conductor will tend to spring back and unwind. Each turn must be constrained to avoid this from happening. A ¼ scale test coil with this configuration using the negative curvature segment was wound [8] and successfully tested. It was however necessary to use epoxy to hold the conductor turns together during the coil winding. We would like to minimize the use of epoxy on this magnet since organic materials can deteriorate in the radiation environment. It was decided to use a coil geometry where the inner radial segment was straight. The role of the coil in a superferric magnet is to magnetize the iron which determines the field quality. The configurations with straight and curved inner segments were compared using the Tosca 3-D EM finite element program. The fields of the two configurations differ by less than 1% in the good field region, which can be corrected by shaping the pole.

FIELD CALCULATIONS

The field error, ΔB/B, should be less than 0.7% for the operating field range from 0.7 to 2.0 T over the good field region defined in Table I. This is achieved by controlling the magnetization in the magnet yoke. Figure 2 shows the relative permeability in the iron. The iron on the smaller radius inner side shows more saturation than on the larger radius outer side. The rectangular hole in the hole is placed to effectively control the saturation. Figure 3 shows ΔB/B as a function of transverse position in the aperture for various field excitations. The field error is less than 0.7% for all values of B_0 in the region ±30 cm from the magnet center.

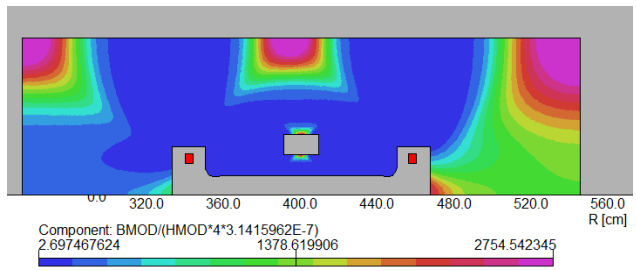


Figure 2: Relative permeability of the iron yoke is shown.

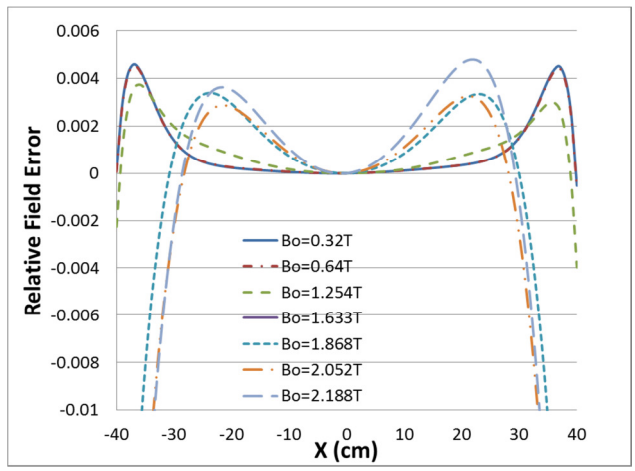


Figure 3: The relative field error, ΔB/B, as a function of position in the aperture. Curves are shown for different central fields ranging from 0.23 T to 2.188 T.

THERMAL AND STRUCTURAL ISSUES

The coils will feel substantial Lorentz forces when the magnet is fully energized. Table II shows the coil forces at the 2.0 T operating field and at the 2.2 T maximum design field. The large forces shown in Table II will require substantial mechanical support to minimize coil movement when the coils are powered. A preliminary study which attempts to constrain the coil forces with a support structure entirely within the cryostat produced coil deflections that were too large. External support that would penetrate into the cryostat and be anchored to the pole or flux return iron will be necessary. By using an external support the coil deflections are reduced significantly and the mechanical stress on the coil is reduced to 41 MPa which is acceptable. This approach will introduce some heat leaking into the cryostat. The design of the coil support will need to minimize the coil movement while also minimizing the heat generated.

Table II: Lorentz Forces per Unit Length on the Coil

Field	Coil	F_{radial}/Length	$F_{vertical}$/Length
Tesla		N/m	N/m
2.0	Outer	120735	105252
	Inner	-108828	108512
2.2	Outer	167079	112226
	Inner	-146093	117935

Copyright © 2013 CC-BY-3.0 and by the respective authors

Two approaches to cooling the cold mass are being considered. One approach described in the next section is to cool the coil by heat conduction from flowing helium in an aperture in the cold mass. The other approach is to cool by convection by flowing helium through the coil itself.

TEST COIL PROGRAM

A test coil is being constructed as part of an R&D effort for the magnet design. The test coil will be full sized, wound with YBCO conductor, however will have fewer turns to make it affordable with the resources available. The program will develop manufacturing techniques for winding and handling the large coils. It will also demonstrate that the coil can operate in a steady state condition with the anticipated heat load expected for the radiation environment in this magnet. In the test program we will develop the winding tooling and the cryogenic cold mass. The winding tooling shown in Fig. 4 is comprised of the winding bobbin which is attached to a back plate for support. As the winding bobbin is relatively thin it is attached to a back plate to support it during the winding and assembly process. The conductor tape is wound around the outer surface of the bobbin using 6.5 m of conductor for each turn. Stainless steel tape is used between each conductor turn as insulation. The coil and bobbin are wrapped with Nomax to insulate the coil. Two coils are wound on their respective bobbins and put together in a double coil assembly. The conductor on each of the two coils is wound with the opposite sense of rotation so that the coils can be connected in series at the inner conductor attachment slots. The coils wound in this manner will have the same current direction. Table III shows the parameters describing the bobbin. After the two coils are assembled together the back plates are removed.

Table III: Winding Bobbin and Cold Mass Parameters

Parameter	Value
Overall Length w/Coils	241.72 cm
Overall Width w/Coils	120.81 cm
Bobbin Depth	1.27 cm
Bobbin Thickness	3.5 cm
Orbit Curvature	4 m
Curvature of Outer Bobbin Surface	4.54 m
Pole Angle	30º
Distance between Coil and Iron Pole	3.9 cm

Additional tooling will be added to the wound two coil assembly for cooling of the coils and mechanical support. Figure 5 shows a view of the wound coils with the associated tooling. Outside the coils is a stainless steel support followed by a cooling section containing a hole for pressurized helium gas (referred to as outer pusher in the figure). The cooling channel will likely be made of stainless steel to match the expansion coefficient of the support structure. We have chosen stainless steel because of its superior strength and will gun drill the cooling aperture. Because of the size of the coil mass stucture it will likely be necessary to assemble shorter pieces that will be welded together. Heater strips will be inserted during the winding to simulate the heat load. The helium flow rate and pressure will be adjusted to maintain the coils at the operating temperature.

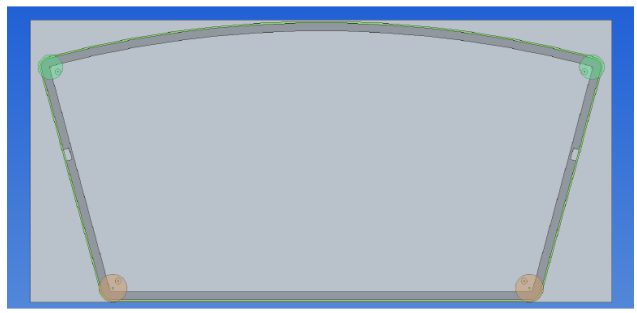


Figure 4: A sketch of the winding bobbin attached to the back plate support.

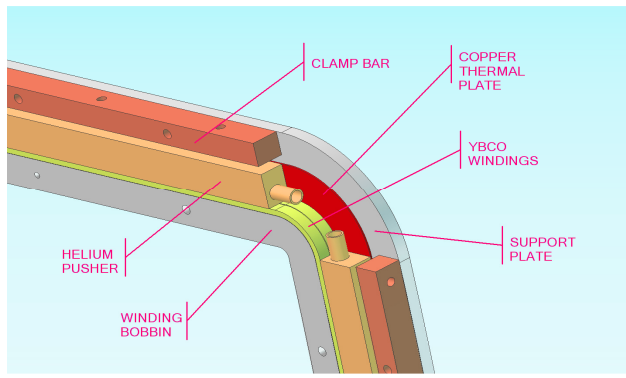


Figure 5: Open view of the double coil plus assembly structure with parts marked. Support plate on near side is removed to make inner parts visible.

REFERENCES

[1] The facility is described at http://www.frib.msu.edu
[2] A. F. Zeller, "Superconducting Magnets for RIA", *Adv. in Cryo. Eng*. **49A**, pp. 758-765, 2004.
[3] R. Gupta et al., "Radiation Resistant HTS Quadrupoles for RIA", *IEEE Trans. Appl. SuperCond*, **15,** pp 1252-1255, 2005.
[4] R. Gupta et al., "Design, Construction, and Test Results of a Warm Iron HTS Quadrupole for the Facility for Rare Isotope Beams", *IEEE Trans. Appl. Supercond.,* **18,** pp 236-239, 2008.
[5] S. Chouhan, D. Cole, J. DeKamp, C. Wilson, A. F. Zeller, "Radiation Resistant Superferric Quadrupole Magnets with Warm Iron", *IEEE Trans. Appl. SuperCond.,* **21,** pp 1813-1816, 2011.
[6] R. Gupta et al., "Second Generation HTS Quadrupole for FRIB", *IEEE Trans. Appl. SuperCond,* **21,** p 1888-1891, 2011.
[7] S. A. Kahn and R. C. Gupta, "High Radiation Environment Nuclear Fragment Separator Dipole Magnet", *Proceedings of IPAC12*. Pp 3605-3607, 2012.
[8] S. A. Kahn et al., "Fabrication and Testing of Curved Test Coil for FRIB Fragment Separator Dipole", *Proceedings of IPAC12,* pp 3611-3613, 2012.

Copyright © 2013 CC-BY-3.0 and by the respective authors

RADIATION TOLERANT MULTIPOLE CORRECTOR COILS FOR FRIB QUADRUPOLES*

S.A. Kahn#, Muons, Inc., Batavia, IL 60510, U.S.A.
R.C. Gupta, BNL, Upton, NY 11973, U.S.A.

Abstract

Multipole correction insert coils with significant field strength are required inside the large aperture superconducting quadrupole magnets in the fragment separator section of the Facility for Rare Isotope Beams (FRIB). Corrector coils made with copper can not create the required field and conventional low temperature superconductors are not practical in the fragment separator magnets which will operate at 40-50 K. The corrector coils for this application should be made of HTS as are the main quadrupole coils in this magnet. There is a significant advantage to using HTS in these coils as it can withstand the high radiation and heat load that will be present. This paper will describe the innovative design suitable for coils with the complex end geometry of cylindrical coils. We will look at the forces in the corrector coils from the main quadrupole fields and anticipate possible coil distortions.

INTRODUCTION

The FRIB facility will provide isotope beams for physics research with intensities not available elsewhere. Large quantities of various isotopes will be produced when a high power (400 kW) linac beam from protons to uranium hits the target. The magnets in the fragment separator region, which selects the rare nuclides from the multitude of secondary fragments, would be subject to extremely high radiation and high heat loads [1,2]. Figure 1 shows a sketch of the first part of the FRIB fragment separator. The first quadrupole magnet after the target will see a flux of 2.5×10^{15} neutrons/cm^2 corresponding to 10 MGy/year. Similar high heat loads are faced by other quadrupole and corrector magnets in the fragment separator region. The baseline fragment separator design for the first several quadrupoles is based on HTS magnet operating at 38-50 K as the removal of a heat load of this magnitude would be difficult and expensive for NbTi or Nb_3Sn superconductors since they are operated at 4.2 K. HTS on the other hand have a significant critical current density at 40 K where the Carnot efficiency is greater and the heat capacity of the refrigerants is significantly higher making heat removal easier.

Corrector magnet inserts, which will be placed between the beam tube and quadrupole coils would face the same challenging situation as the other magnets in the fragment separator region. As corrector magnet inserts made with copper coils do not generate enough field strength and because conventional superconductors would not be practical in this environment, HTS wound coils will be necessary for these corrector inserts.

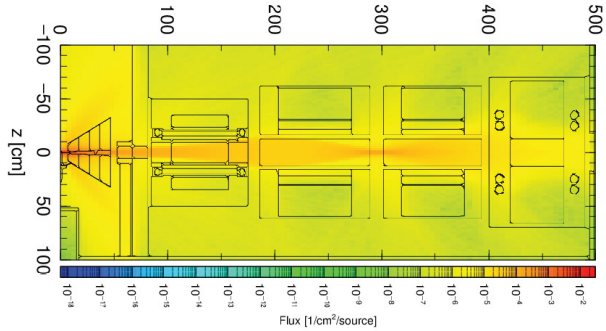


Figure 1: Proton flux seen in the first three quadrupoles of the fragment selector at FRIB. The figure is from ref [2].

CORRECTOR COIL DESCRIPTION

Seven quadrupole magnets in the fragment separator require multipole corrector inserts. Table 1 shows the beam line elements that follow the target. Table 2 shows the quadrupole, sextupole and octopole strengths for the quadrupole magnets that require multipole corrections [3]. The component strengths are evaluated at the reference radius shown in the table.

Table 1: Beam-line Elements in the Fragment Separator

Magnet	Half-gap (mm)	Field or Gradient	Length (m)	Element Position
Quad 1	100	-8,47 T/m	0.55	1.175
Quad 2	120	14.27 T/m	0.65	2.280
Quad 3	160	-11.67T/m	0.65	3.280
Octopole	130	163 T/m^3	0.50	4.570
Quad 4	140	6.53 T/m	0.55	5.350
Dipole 1	100 H, 150 V	2 T	1.75	6.900
Sextupole	100 H, 120 V	-42 T/m^2	0.40	9.320
Dipole 2	100 H, 200 V	-2 T	1.75	10.64
Quad 5	200	10 T/m	0.55	12.24
Quad 6	150	-4.95 T/m	1.357	13.54
Quad 7	160	4.2 T/m	1.357	15.51

The physical length of these inserts range from 0.6 to 0.7 m, with the effective length of the magnet being ~20% shorter. The inner radius of the octopole insert is between 75 and 110 mm adjusted to the various quadrupole apertures and the sextupole insert inner radius will be 5 mm larger than the corresponding octopole insert. The largest quadrupole pole tip field is 2.5 T, so the field at the insert coils is about 2 T. The design will assume that the sextupole and octopole fields at the insert coil radius are 0.25 T. The multipole coils should be shaped on a

*Work supported by DOE STTR grant DE-SC0006273.
#kahn@muonsinc.com

Copyright © 2013 CC-BY-3.0 and by the respective authors

cylinder to take up a minimum of radial space and the mounting tube needs to be radiation resistant and should have a minimum mass.

Table 2: Multipole components needed at the quadrupole elements. The component is shown at the reference radius.

Element	Ref. Radius	Quad. Field, T	Sextupole Field, T	Octopole Field, T
Quad 2	0.15 m	2.14	-0.06	-0.21
Quad 3	0.15 m	-1.75	-0.06	-0.12
Quad 4	0.15 m	0.98	0	0.1
Quad 5	0.20 m	2.00	0.21	0.04
Quad 6	0.20 m	-0.99	-0.12	0.09
Quad 7	0.20 m	0.84	-0.22	-0.13
Quad 8	0.20 m	-1.55	0.015	0.103

The BNL magnet division has made HTS R&D quadrupole magnets for the fragment separator region of FRIB [4, 5, 6]. These quadrupoles were super-ferric magnets where the coils magnetized the iron producing an iron dominated field. The magnet yoke is warm and is thermally isolated from the coils which are at cryogenic temperatures. This design minimizes the space for the coils and cryogenics, while allowing a wider pole region to improve magnetic efficiency. Figure 2 shows an Opera-3D representation the quadrupole magnet illustrating the coils and the upper half of the yoke.

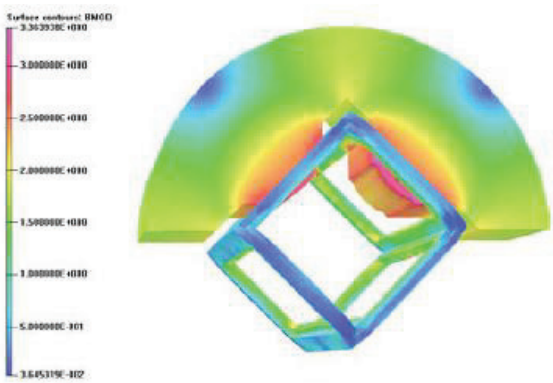


Figure 2: Opera 3D magnetic model of the FRIB fragment separator quadrupole. The sketch shows all of the coils and the upper half of the yoke.

Both YBCO and Bi-2212 are potential candidates to be used for these corrector coils. Both conductors can carry a reasonable current at 38-50 K and are radiation tolerant. In a study at the BLIP facility at BNL, a sample of YBCO conductor was irradiated and shown to withstand the cumulative effects of radiation over the anticipated lifetime of the facility [7]. In that study it was shown that the critical current, I_c, would be reduced by 20% for each dose of 10^{17} protons/cm^2. A similar study with Bi-2212 conductor showed that I_c was relatively unchanged for proton fluences up to 10^{17} protons/cm^2 [8].

The conductor for the corrector coils will be wound on a cylindrical mandrel. The Bi-2212 conductor is available as a round wire which is easier to wind on a cylinder. However Bi-2212 has the disadvantage that it has to be reacted at 890°C in pure oxygen after it has been wound. The YBCO conduct is available in tape form. YBCO conductors are formed by a continuous deposition of conductor and coatings onto a substrate that provides mechanical strength. The I_c of the YBCO conductors is sensitive to the orientation of the conductor in a magnetic field. This is an important consideration for the corrector coils since the dominant quadrupole field can be perpendicular to the conductor plane in various parts of the geometry. As such, YBCO available today, carries sufficient current to meet the requirement.

The end geometry of a coil wound on a cylinder with an YBCO tape conductor is more complicated than wound with a round Bi2212 wire. Since the tape does not want to bend in the "hard" direction, the tape conductor will tilt as it is wound around the ends on the cylindrical mandrel. The tilt angle will be slightly different for each turn. The ends will have to be supported to prevent movement in the small voids between turns caused by the varying tilt angles. Figure 3a and b show two views of the ends of a quadrupole test magnet wound with Nb_3Sn tape as an example.

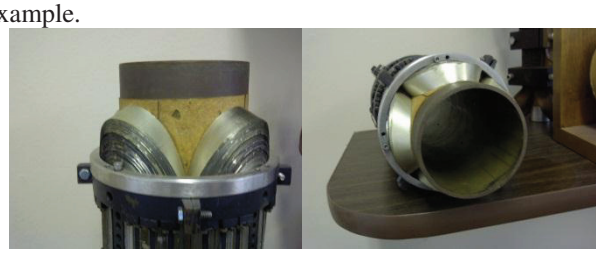


Figure 3: Photograph of coil ends of a test quadrupole wound with Nb_3Sn tape.

MAGNETIC SIMULATION

We have created an Opera2D [9] electromagnetic finite element model using of the correction coils inside the large aperture R&D quadrupole magnet built at BNL for FRIB. Figure 4 shows the sextupole coils inside the quadrupole magnet. (The quadrupole magnet should be rotated by 45° so that the quadrupole coils are on the x, y axes which is the normal orientation in an accelerator.) A similar model has been made for the octopole coils. Each half coil in each sextant (octant) will subtend 20° (15°) of the available 30° (22.5°). These angles are chosen to zero the contribution of the next largest allowed harmonic above the fundamental one. The allotted radial space for each corrector coil is 5 mm which must include the conductor plus its support structure. If YBCO conductor is used, a 3 mm wide tape such as Superpower SCS030 would be appropriate. Table 3 shows the engineering current density, J_E, in the coils required to produce 0.25 T at the multipole coils. Also shown is the conductor current and the corresponding critical current. The corrector coils carry current in the field of the quadrupole magnet. The radial and azimuthal forces in the central part of the magnet (away from the ends) are shown in

Copyright © 2013 CC-BY-3.0 and by the respective authors

Table 4 for the sextupole corrector coils and in Table 5 for the octopole coils. Since the corrector coils have a different symmetry from the dominant quadrupole coils the forces will be different on each individual coil. The correction coils could be deformed by these forces. The mechanical design of these corrector coils will need to be studied to minimize the effects of these forces.

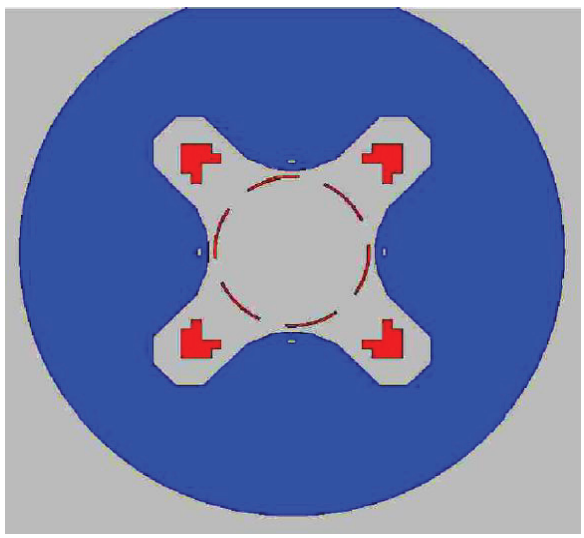


Figure 4: Sketch of the sextupole coils inserted into the BNL R&D quadrupole magnet.

Table 3: Current in the conductor for maximum field seen at the coils is shown along with the critical current of the conductor.

Coils	Field at Coils	J_E, amp/mm^2	I, amp	I_C(40 K)
Sextupole	0.25 T	110	58	96
Octopole	0.25 T	140	74	96
Main Quadrupole	2 T	125	211	400

Table 4: Forces on the sextupole coils from the quadrupole field.

Coil	Center Angle	<B>, T	F_r, nt/mm	F_ϕ, nt/mm
1	45°	1.8892	41.624	0
2	105°	1.9488	23.044	36.332
3	165°	1.6328	-19.272	32.345
4	225°	1.7555	-39.543	0
5	285°	1.8865	-20.073	-36.952
6	345°	2.1442	23.044	-36.332

Table 5: Forces on the octopole coils from the quadrupole field.

Coil	Center Angle	<B>, T	F_r, nt/mm	F_ϕ, nt/mm
1	45°	1.8666	32.696	0
2	90°	1.8770	0	33.068
3	135°	1.7688	-31.562	0
4	180°	2.4780	0	-40.441
5	225°	1.8666	32.696	0
6	270°	1.8770	0	33.068
7	315°	1.7688	-31.562	0
8	360°	2.4780	0	-40.441

REFERENCES

[1] A. Zeller et al., "Radiation Resistant Magnets for the RIA Fragment Separator", PAC'05, Knoxville, TN, USA.

[2] FRIB technical report, FRIB-T40204-CA-000104-R001 (1013).

[3] From the FRIB pre-separator optics spread sheet V2b dated 2010-07-15. As the FRIB CDR has not yet been published any numbers quoted are not necessarily reliable and are subject to change.

[4] R. Gupta et al., "Radiation Resistant HTS Quadrupoles for RIA," IEEE Trans on Appl. Superconductivity, **15** (2004) 1148.

[5] R. Gupta et al., "Design, Construction and Test Results of a Warm Iron HTS Quadrupole for the FRIB," IEEE Trans. on Appl. Superconductivity, **18** (2007) 236.

[6] R. Gupta et al., "Second Generation HTS Quadrupoles for FRIB," IEEE Trans. on Appl. Superconductivity, **21**, 1888.

[7] G.A. Greene et al., "The Effect of Proton Irradiation on the Critical Current of Commercially Produced YBCO Conductors," IEEE Trans. on Appl. Superconductivity, **19**(3), (2009) 3164.

[8] A.K. Ghosh and G.A. Greene, "Effect of Proton Radiation on the Critical Current and Critical Temperature of Bi-2212," submitted to 2011 Cryogenic Engineering Conference.

[9] Opera2D is an EM finite element program from Cobham Technical Service.

Copyright © 2013 CC-BY-3.0 and by the respective authors

ELLIPTICAL MUON HELICAL COOLING CHANNEL COILS*

S.A. Kahn#, G. Flanagan, Muons, Inc., Batavia, IL, 60510, USA
M.L. Lopes, K. Yonehara, FNAL, Batavia, IL 60510, USA

Abstract

A helical cooling channel (HCC) consisting of a pressurized gas absorber imbedded in a magnetic channel that provides solenoid, helical dipole and helical quadrupole fields has shown considerable promise in providing six-dimensional phase space reduction for muon beams. The most effective approach to implementing the desired magnetic field is a helical solenoid (HS) channel composed of short solenoid coils arranged in a helical pattern. The HS channel along with an external solenoid allows the B_z and B_ϕ components along the reference orbit to be set to any desired values. To set dB_ϕ/dr to the desired value for optimum focusing requires an additional variable to tune. We shall show that using elliptical shaped coils in the HS channel allows the flexibility to achieve the desired dB_ϕ/dr on the reference orbit without significant change to B_z and B_ϕ.

INTRODUCTION

A muon beam cooling technique, using a continuous gaseous hydrogen absorber inside a helical solenoid channel has shown promise to reduce muon phase space. This goal of this technique is to create bright muon beams with small emittance for use in particle accelerators and storage rings. Of particular interest is the development of a muon collider, which requires the reduction of the beam phase space by at least a factor of 10^6. Simulations have shown that the HCC can provide a significant phase space reduction [1]. The HCC is composed of a magnetic channel filled with pressurized H_2 gas absorber to reduce the particle energy. The lost energy is replaced in the longitudinal direction by RF. The desired field in the magnetic channel is comprised of helical dipole, helical quadrupole and solenoid components [2]:

Helical Dipole:

$$b_\phi = 2b_d I_1(k\rho)\cos(\phi - kz)/k\rho$$
$$b_\rho = 2b_d I_1'(k\rho)\sin(\phi - kz)$$
$$b_z = -k\rho b_\phi$$

Helical Quadrupole:

$$b_\phi = \frac{2b_q}{k^2\rho} I_2(2k\rho)\cos 2(\phi - kz - \phi_2)$$
$$b_\rho = \frac{2}{k} b_q I_2'(2k\rho)\sin 2(\phi - kz - \phi_2)$$
$$b_z = -k\rho b_\phi$$

where b_d and b_q are the dipole and quadrupole strengths, respectively, at $\rho = 0$. Implementing this channel with helical harmonic coils is difficult since $I_n(nk\rho)$ grows exponentially at large radius and the channel has large apertures. The HCC magnetic channel will be implemented with short solenoid coils arranged along the helical reference orbit. Figure 1 is a sketch of the helical solenoid (HS) channel [3]. This approach minimizes the magnetic field at the coils. To be effective the B_ϕ, B_z and dB_ϕ/dr of the HS at the reference orbit must match values from the theoretical formulae. B_ϕ and B_z can be set by HS coil current and adjusting an external solenoid field $B_{solenoid}$ (shown in Fig. 1). dB_ϕ/dr is important to control the beam focusing in the channel. To set this variable to an arbitrary value desired to optimize the channel requires an additional degree of freedom. In this paper we explore deforming the circular solenoids into elliptical rings to control the field gradient.

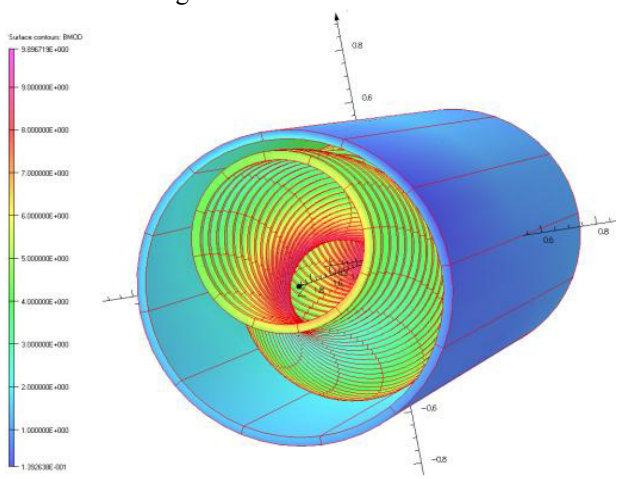


Figure 1: 3D layout of coils for the HCC channel. Note that the HS coils are placed in an external solenoid field.

Table 1: Field Properties of the Sections of the HCC Cooling Channel.

Section	λ	B_ϕ	dB_ϕ/dr	B_z	f
Units	m	T	T/m	T	MHz
1,2	1.0	1.29	-0.50	-4.25	325
3	0.9	1.43	-0.62	-4.73	325
4	0.8	1.61	-0.79	-5.32	325
5	0.5	2.58	-2.01	-8.51	650
6	0.4	3.22	-3.14	-10.63	650
7	0.3	4.30	-5.58	-14.18	650
8	0.3	4.30	-5.58	-14.18	1300

HCC CHANNEL DESIGN

The HCC channel that is proposed is divided into eight sections with each section providing a smaller final equilibrium emittance which requires progressively larger fields. The design field for each section is shown in

*Work supported by U.S. DOE STTR/SBIR grant DE-SC00006266
#kahn@muonsinc.com

Copyright © 2013 CC-BY-3.0 and by the respective authors

Table 1 [4]. The study concentrates on section 2 at the beginning and section 6 near the end of the channel. Near the end of the channel the coils need to be thick to provide the necessary current to achieve the fields required. Table 2 summarizes the variables to describe sections 2 and 6. The RF cavities are assumed to be filled with a dielectric or made with a re-entrant design to reduce the cavity radius. This permits the use of the smaller radius coils shown in the table.

Table 2: Parameters Describing the HCC Sections Used in the Study

Parameter	Unit	Section 2	Section 6
Helical Period	m	1.0	0.4
Helical Orbit Radius	cm	15.9	6.366
RF Cavity Radius	cm	19	9.4
Coil Inner Radius	cm	25	10.5
Coil Outer Radius	cm	30	20.5
Coil Current Density	Amp/mm^2	256	340
Coils per Period		20	16

A Biot-Savart integration was used to calculate the field from the elliptical coils. The field at each point was determined by integrating over the current from all coils that were within one helical period from that point. Because of the large dimensions of the coils, they were represented by 40-60 filaments distributed over the coil cross section.

ELLIPTICAL COILS

We describe the elliptical shape by its asymmetry, $A = (R_{major} - R_{minor})/(R_{major} + R_{minor})$. R_{major} is aligned with the radial direction, while is in the azimuthal direction. This definition permits R_{minor} to be larger than R_{major} when the ellipse is oblate.

Section 2:

Figure 2 shows the field profiles on the radial axis for the section 2 configuration with different A. The coil current is adjusted to give the desired B_ϕ from Table 1 on the reference orbit. Since the external solenoid field can be set independent of the B_ϕ, setting the external solenoid field $B_{solenoid}$=2.0 T produces the desired B_z. Figures 2a, b, c show B_ϕ, dB_ϕ/dr, and B_z, respectively. Figure 3 shows the value of these fields on the reference orbit as a function of the ellipse asymmetry. The field magnitude at the coils is 6.4 T which is within the range for using NbTi at 4.3 K.

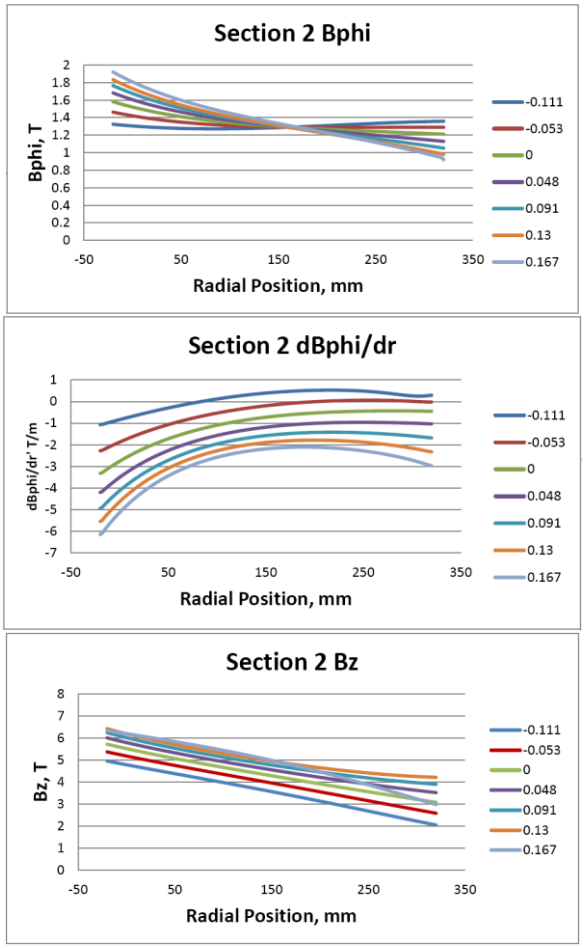


Figure 2: B_ϕ dB_ϕ/dr, and B_z vs. r for section 2. The different colors represent different ellipse asymmetries.

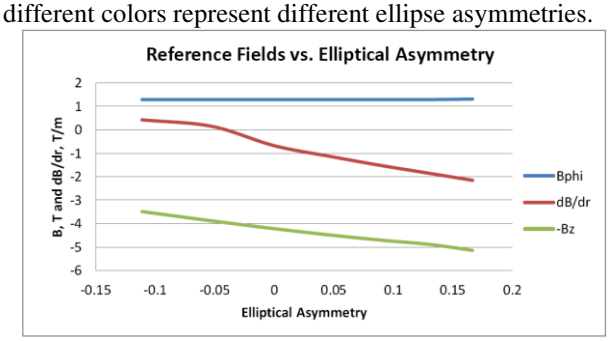


Figure 3: B_ϕ, and $-B_z$ in Tesla and dB_ϕ/dr in T/m on the reference orbit for different ellipse asymmetries.

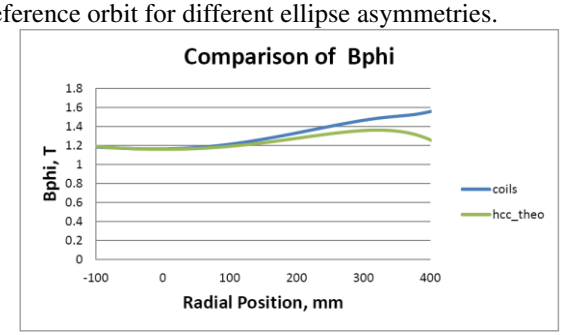


Figure 4: Comparison of the coil description of B_ϕ with the theoretical Bessel function description for section 2.

Copyright © 2013 CC-BY-3.0 and by the respective authors

Figure 4 compares the B_ϕ field from the HS description with the theoretical Bessel function description. The coil description does not yet correct for the sextupole which affects the field at large radius. For section 2, an oblate ellipse description with A=-0.14 produces a reasonable representation of the Bessel function field.

Section 6

Section 6 requires a large magnetic field and the coils must be fairly thick in order to produce that field. Figure 5 shows B_ϕ, dB_ϕ/dr and B_z for different elliptical asymmetries for section 6. Figure 6 shows B_ϕ, dB_ϕ/dr and B_z on the reference orbit as a function of elliptical asymmetry. Figure 7 compares the B_ϕ field calculated from the HS coils to the Bessel function description of the field for the case A=0.106 which approximates the theoretical description over most of the useful beam aperture. The external solenoid field is 14.2 T which can be made with Nb_3Sn conductor. The maximum field at the HS coils is 20 T which suggests that those coils could be wound with Bi-2212 conductor.

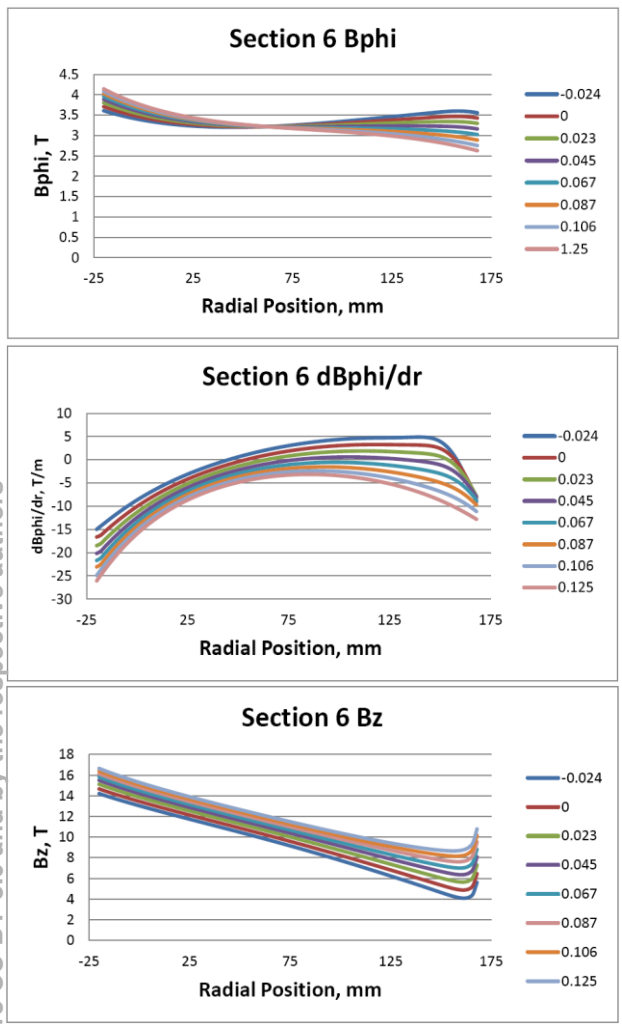


Figure 5: B_ϕ, dB_ϕ/dr, and B_z vs. r for section 2. The different colors represent different ellipse asymmetries.

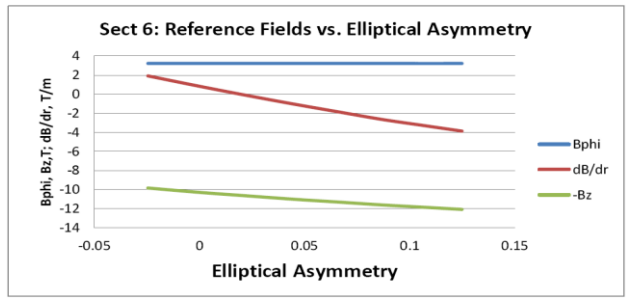


Figure 6: B_ϕ, dB_ϕ/dr, and $-B_z$ on the reference orbit as a function of elliptical asymmetry.

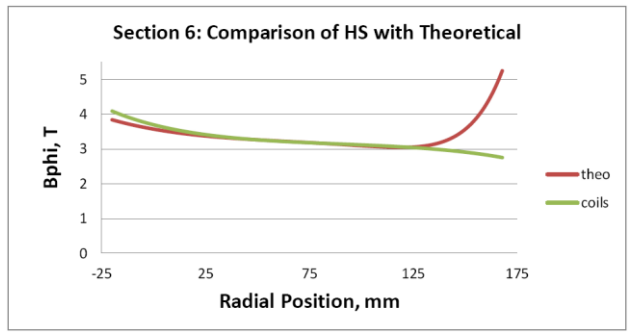


Figure 7: Comparison of B_ϕ calculated from the Bessel function description with that from HS coils.

CONCLUSIONS

Using elliptically shaped instead of circularly shaped coils provides an additional degree of freedom that can be used for matching the HS coils the Bessel function description of the field used for the HCC. Field maps made from the Biot-Savart integration of elliptical coils in the HCC can be used to describe the field for the muon cooling simulation program. This is a work in progress.

REFERENCES

[1] K. Yonehara et al., "Studies of a Gas-Filled Helical Muon Cooling Channel." Proceedings of EPAC'06, Edinburgh, p 2424.

[2] Y. Derbenev and R. Johnson, "Six-Dimensional Muon Beam Cooling Using a …", Phys. Rev. STAB. **8**, 041002 (2005).

[3] V.S. Kashikhin et al."Superconducting Magnet Systekm for Muon Beam Cooling", ASC'06, IEEE Trans. On Applied Superconductivity, **17,** no. 2, p 1055 (2007).

[4] K. Yonehara, R.P. Johnson, M. Neubauer, Y.S. Derbenev, "A helical cooling channel system for muon colliders", IPAC10, MOPD076.

Copyright © 2013 CC-BY-3.0 and by the respective authors

SIMULATION WORKSTATION

Thomas J. Roberts#, Muons, Inc., Batavia, IL 60510 USA

Abstract

The Simulation Workstation is a software toolkit that provides a universal Graphical User Interface to most particle simulation codes. This includes: constructing and displaying the simulated system graphically, running multiple simulation codes from a single system description, displaying particle tracks or histories with the objects of the system, flexibly generating plots and histograms, and comparing the results from multiple simulations. The workstation itself knows very little about particle simulations -- that knowledge is contained in the simulation codes themselves. As a consequence, the workstation can handle essentially any problem that any of the supported simulation codes can simulate. These include: beam optics calculations, ion source design, muon cooling channels, spacecraft radiation levels, nuclear reactors, complex shielding calculations, and accelerator driven subcritical reactors. The workstation offers interfaces to most CAD/CAE programs, enabling workflows that include multi-physics analysis by other programs. The Simulation Workstation will be portable among all major operating systems, will be freely available as open-source software, and will initially support these simulation codes: G4beamline [1], MCNP6 [2], and MAD-X [3]; additional codes can be added by users.

INTRODUCTION

When teaching beam dynamics and accelerator physics to students, user-friendly graphical tools are a big advantage, as they permit the construction and exploration of models with very little overhead. And for today's technology-driven students of the "Nintendo generation", graphical interfaces meet their expectations far better than text-based tools. Moreover, there are dozens of modeling codes available, so having a common user interface that can be used with multiple simulation codes will be a major advantage. Existing tools fall short of what is needed.

While the workstation has been designed with students in mind, accelerator physicists will also find it useful in dealing with the plethora of modeling tools and their different languages and data formats. The internal representation of the system is specifically designed to be useable as a text-based description of the system, and to make it easy for users to interface it to essentially any accelerator-modeling tool, regardless of its description language. In particular, this will make it straightforward to use fast but less realistic codes to design and optimize a system, and then use slower but more realistic codes to evaluate its performance. Graphical interfaces are emphasized, making it easy to construct the system graphically, display the system and its beam, and use on-screen controls to vary parameters and observe their effects immediately. Such exploration is essential to give students insight into how systems behave, and can be valuable to the experienced accelerator physicist, for tasks such as evaluating different techniques for tuning a system before it is built.

The user interface is centered around objects, which can be individual accelerator components, or arbitrarily complex collections of components with specified spatial relationships. Objects are stored in Libraries, which can easily be shared with other users. The use of URL-based component libraries will encourage collaboration among geographically diverse teams.

The Simulation Workstation provides the user with a single user interface to construct, design, optimize, analyze, and explore systems involving charged particle beams and other radiation. It is specifically designed to be interoperable with just about any existing simulation or beam optics code. This is possible for one simple reason: they necessarily have a common domain, with common concepts, common objects, and common operations. By abstracting these common elements into a new specification language, called *LinguaFranca*, a single GUI program can indeed interface to many simulation codes with relatively little effort. LinguaFranca has been specifically designed to make it easy to *instantiate* its description for other codes to read. Instantiation is not machine translation, which is known to be a difficult problem, but rather is performed by a sophisticated text-processing system that has been told by human developers how each LinguaFranca primitive is represented in the language of each simulation code.

The architecture of the Simulation Workstation is to be an overall control program that orchestrates the assembly of the various pieces required to prepare, perform, and analyze a simulation. Thus the user works with a single user interface to perform all related tasks. While it relies on interfaces to the simulation codes, the adaptation is always in the workstation, and no simulation code needs to be modified in order to work with it (some codes will benefit from modifications, especially on Windows).

The Simulation Workstation will be portable among the major operating systems (Windows, Linux, Mac OS X), and will be released as open-source software. This is the same overall commercialization model as for our highly successful program G4beamline [1]. The key to G4beamline's popularity is its excellent user interface; this project was inspired by that interface, and by what we perceived as ways to improve it. But rather than just improve this one code, we have chosen to design and develop a system that is customizable to improve the user experience for all related simulation codes.

tjrob@muonsinc.com

Copyright © 2013 CC-BY-3.0 and by the respective authors

THE SIMULATION WORKSTATION

The Simulation Workstation presents the user with a window ready to edit a simulation, as shown in Figure 1. The viewer is at the left, showing a 3-D image of the current system; the simulation shown is for the storage ring of a Very Low Energy Neutrino Factory [4]. The right-hand third of the window shows an edit panel at the top and a library panel at the bottom (showing a single row of three objects' icons, with scroll bar).

The 3-D Viewer

As a simple illustration of the viewer's flexibility, Figure 2 zooms in on the transition from straight to arc. This required the following simple user gestures:

1. Use the middle mouse button to pan the display to center the desired region.
2. Use the mouse scroll wheel to zoom in.
3. Use the viewer-control slider to set the solid opacity to 50%.
4. Use a viewer-control button to toggle the display of axes to on.
5. Use the left mouse button to select the last cell of the straight section (highlighted in red).

Total elapsed time: 3-5 seconds. The white line is the design coordinate axis, from the origin off the screen to the left, going once around the ring, and then right (+Z) to infinity. Design coordinates make it easy to lay out an accelerator or beamline by sequentially placing objects along the system centerline; bending magnets are accompanied by a bend in the centerline; they behave just like the implicit reference coordinates of beam optics programs like MAD-X.

The Edit Panel

The edit panel in the upper right is context sensitive, displaying appropriate information in response to user gestures.

The Library Panel

The library panel at lower right displays the objects currently in the library, sorted alphabetically. These can be simple parameterized components such as magnets and RF cavities, or they can be combinations of other objects, such as :Straight and :Arc (which define a cell for the corresponding region of the VLENF). In general there can be multiple Libraries (remote ones are configured via URLs), so library components are named LibraryName:name (no spaces). This is the default library whose name is empty, so the names simply begin with a colon. Objects can be dragged into the viewer and dropped in position; the edit panel can then be used to

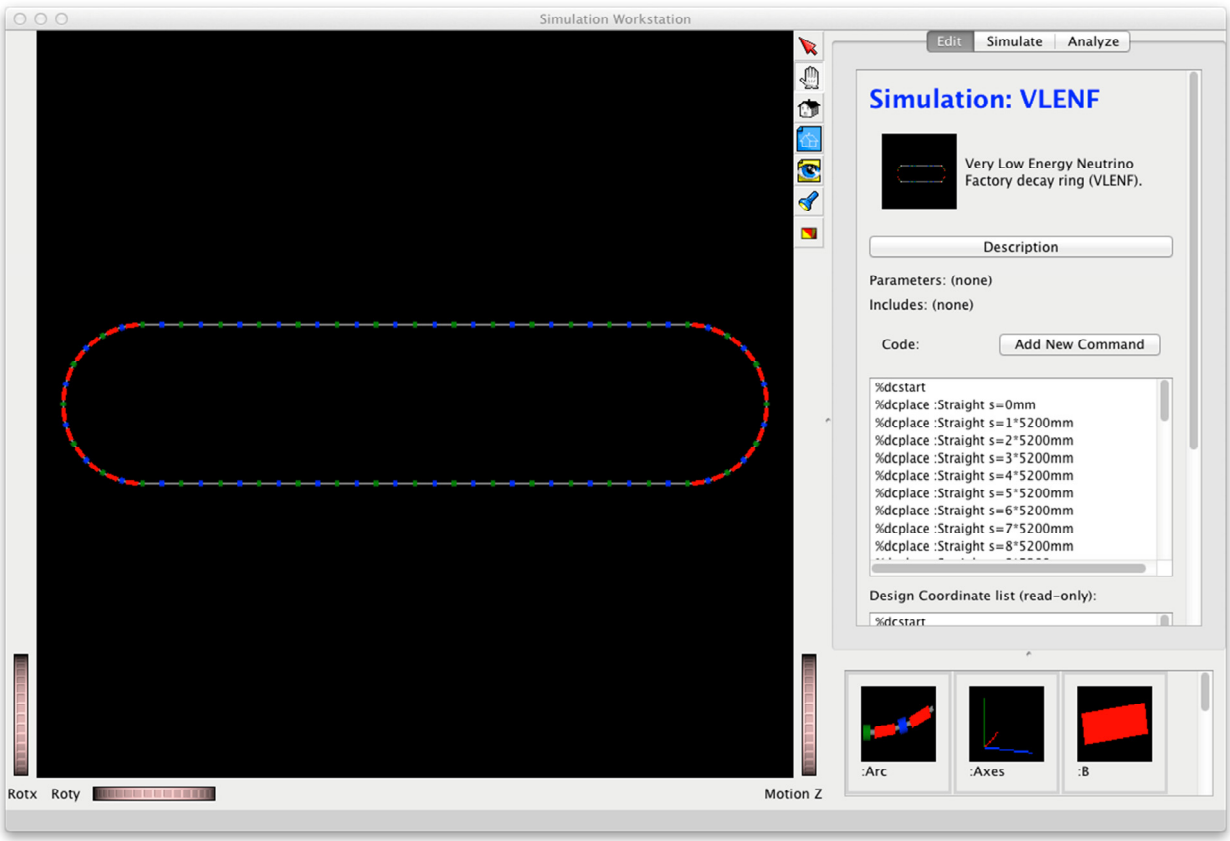


Figure 1: The Simulation Workstation Main Window, editing a VLENF simulation. Focusing and defocusing quads are green and blue, bending magnets are red, and beam pipes are gray. The 3-D viewer can be easily rotated, panned, and zoomed via the mouse, and individual objects can be selected and edited.

Copyright © 2013 CC-BY-3.0 and by the respective authors

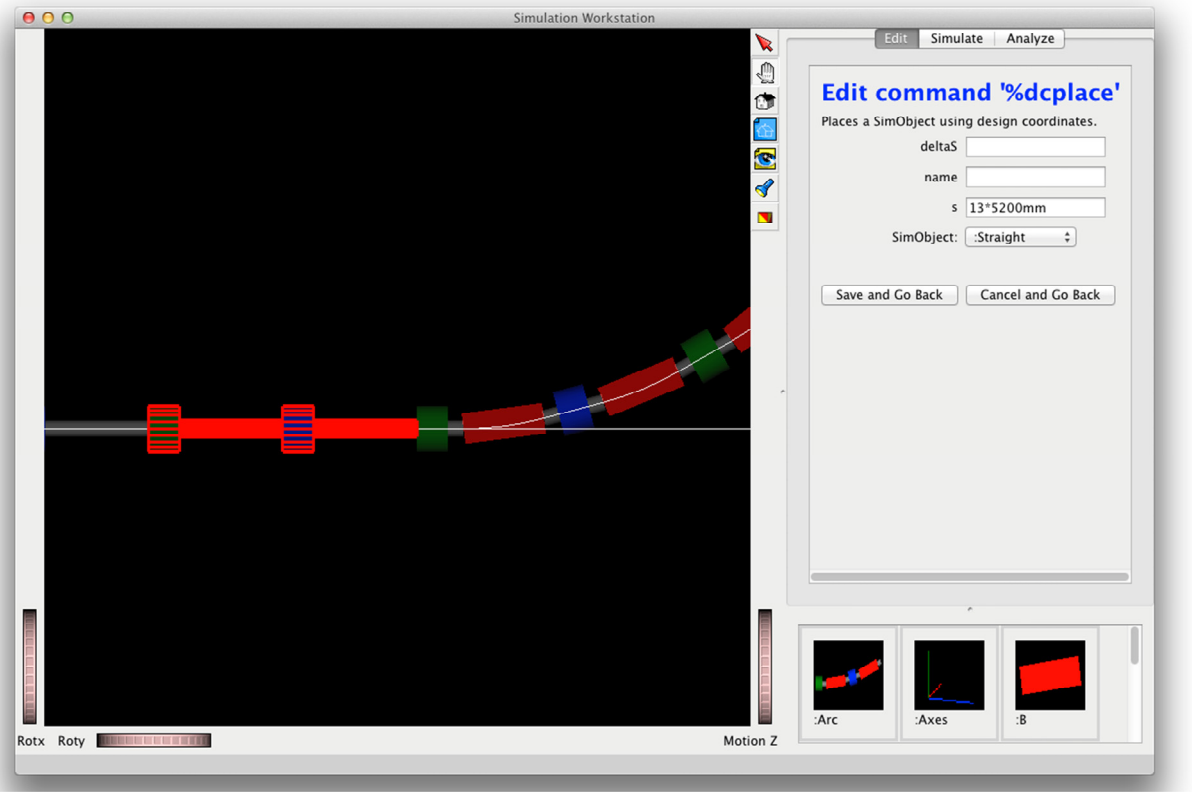


Figure 2: The system of Figure 1, but panned and zoomed, with the last Straight cell selected. Note the editing panel shows the command that put this cell into the simulation, placing the cell along the design coordinate axis.

tweak their position precisely. But for an accelerator system using Design coordinates, once the components are placed into the library they can simply be dragged into the edit panel and dropped – this places them sequentially along the design coordinate axis; The VLENF simulation has magnets and beam pipes placed sequentially into cells, and the cells placed sequentially into the simulation.

The Simulate Tab

The upper right panel has three tabs that change the entire mode of operation: Edit, Simulate, and Analyze. The Simulate tab provides an interface to manage the running of a simulation, using any configured simulation code. As a simulation runs, its output file(s) can be scanned as they are produced, and events displayed in sets of N (which defaults to 10 but is easily changed). A viewer-control slider permits the user to vary the opacity of solids, making it easy to see tracks inside them. Clicking on a track does two things: it hides any other events in the current set, and in the upper right it displays the track values at the point clicked and at track creation. By default tracks are colored by their charge, but the user can configure a color for each type of particle.

The Analyze Tab

The Analyze tab will make it easy for the user to create histograms and plots of quantities of interest. It will incorporate a complete Root [5] package, as well as an interface to simplify the creation of basic histograms and plots, with sliders to apply cuts (updating the plot in real time as the cuts are changed). The Analysis tab will incorporate feedback to the Simulate tab, permitting the user to identify interesting, unusual, or "outlier" events in a plot, and then re-simulate each event while viewing its tracks in the viewer. With G4beamline [1] this has proven to be a very powerful technique for understanding backgrounds and rare processes.

CONCLUSION

The Simulation Workstation is expected to become a useful addition to many students' and accelerator designers' toolkits. It has many innovative features not found in other programs that promise to improve users' productivity; its use of libraries should foster collaboration among geographically diverse teams.

REFERENCES

[1] G4beamline http://g4beamline.muonsinc.com
[2] MCNP6 http://mcnp.lanl.gov/
[3] MAD-X http://mad.web.cern.ch/mad/
[4] VLENF http://arxiv.org/abs/1206.0294
[5] ROOT http://root.cern.ch/

Copyright © 2013 CC-BY-3.0 and by the respective authors

STATUS OF SPALLATION NEUTRON SOURCE CRYOGENIC TEST FACILITY (CTF)*

M. Howell#, A. Coleman, B. DeGraff, S-H. Kim, T. Neustadt, J. Proulx, J. Saunders, W. Strong, D. Vandygriff, ORNL, Oak Ridge, TN 377831, USA
T. Xu, FRIB, East Lansing, MI 48824, USA

Abstract

The Spallation Neutron Source (SNS) is building Superconducting Radio Frequency (SRF) processing and testing facilities to support the reliability and sustainability goals of the enterprise. In addition, these facilities position the SNS superconducting linac (SCL) for improvement programs and future upgrades. Some of the testing facilities require cryogenic helium at both 4 K and 2 K. Currently, the Central Helium Liquefier (CHL) supplies 4 K helium to the linear accelerator and excess capacity is utilized to supply the test cave. As more facilities become available and testing is more frequent, it is essential to separate testing in the SRF facility from the operation of the accelerator. This paper describes the cryogenic system and the commissioning of that system at SNS to facilitate SRF testing needs. The initial phase of the project was to supply 4 K helium to a Vertical Test Area (VTA) and the test cave which is capable of housing either the Horizontal Test Apparatus (HTA) or a cryomodule. The scope of the initial phase of this project has been expanded. The system will be outfitted with warm pumping capability to produce 2 K helium in the testing systems. In addition, a liquid helium fill station will be incorporated to fill portable Dewars.

INTRODUCTION

The Spallation Neutron Source contains a superconducting linear accelerator which consists of eleven medium beta and twelve high beta cryomodules. The availability and reliability of the cryomodules has been high. However, the superconducting section of the linear accelerator has not met the energy specification of 1 GeV [1]. To increase the energy of the beam and meet future upgrade requirements, the performance of multiple cryomodules must be improved. To improve these cavities, there are two options. These cavities can be replaced which will involve removing, disassembling, and rebuilding cryomodules. This approach is cost prohibitive. A second option is to implement additional processing or conditioning of the superconducting cavities. SNS is currently installing and developing superconducting radiofrequency processing and test facilities to develop methodology in increasing beam energy and facilitating necessary repairs. The CTF refrigeration system will provide helium at both 4 K and 2 K to the SRF test facilities.

Multiple repairs of cryomodules have been performed at SNS by in house staff. These include tuner repairs, removal of HOM antennas, and repair of helium circuit, beam line vacuum and insulating vacuum leaks. In one case, a mild plasma processing was applied to a cryomodule to improve its performance [2]. After repair, the cryomodules have been qualified in the test cave using the CHL to supply helium. This couples the testing and qualification process to the actual operation of the linear accelerator. The implementation of the CTF decouples these two differing objectives.

DESIGN OVERVIEW

The original scope of the CTF refrigeration system was to provide 4 K helium to the test cave and the VTA [3]. This scope has been expanded to include adding 2 K capability through the use of a warm pumping system. Because the availability of liquid helium has been scarce, a liquid helium fill station to supply portable Dewars to the neutron instrument and sample environment areas has also been added to the scope. By having this subsystem, the liquid supply chain issues can be mitigated with the helium gas storage that is normally available in the CHL. A block flow diagram of the CTF system is included below in Fig. 1.

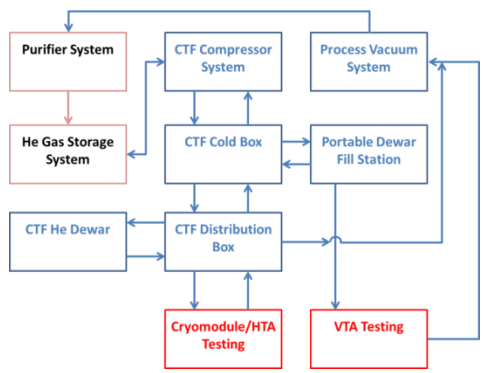


Figure 1: CTF Block Flow Diagram.

As system design has progressed and operational experience has increased, the cryogenic loads in the various testing modes have been further defined. Table 1 summarizes the estimated cryogenic loads of the various test modes. These loads are based on actual test results observed during operation of cryomodules in the test cave.

Table 1: Cryogenic Load Design Criteria

Test System	Nominal T_{bath}(K)	Primary Load (W)	Shield Load @4K (W)	Coupler Flow (g/s)
Cryomodule Test	4	400	200	< 0.5
	2	80	200	< 0.5
HTA Test (single cavity)	4	100	120	< 0.5
	2	20	120	< 0.5
VTA Test (CW)	4	600	None	NA
	2	150	None	NA

Copyright © 2013 CC-BY-3.0 and by the respective authors

The Linde LR280 was specified with a refrigeration capacity of 650 W at 4.4 K and liquefaction capacity of 240 L/hr. This system can operate in multiple operational configurations. The system cold box supplies helium through the distribution box and helium Dewar when servicing the test cave. However, the VTA and fill station are supplied from a second set of bayonets on the cold box.

To operate the test cave, the system will experience a combination of refrigeration and liquefaction loads. The cold box will supply sub-cooled supercritical helium through the distribution box to both the shield and primary circuits. The primary flow will return through the distribution box to the cold box and serve as a refrigeration load. However, the shield flow will return to the warm compressor system through an ambient heat exchanger. This will act as a liquefaction load on the machine along with the coupler flow.

For operation of the VTA or fill station, the CTF will be operated in liquefaction mode. The CTF will supply liquid helium to a 2000 L fixed Dewar within the fill station. This Dewar will be used as a reservoir to either fill the VTA Dewar or a portable Dewar. The detailed design of this subsystem is complete and fabrication is nearing completion. A model of the fill station system is included below in Fig. 2. The fill station is scheduled to be operational in the first half of FY 14.

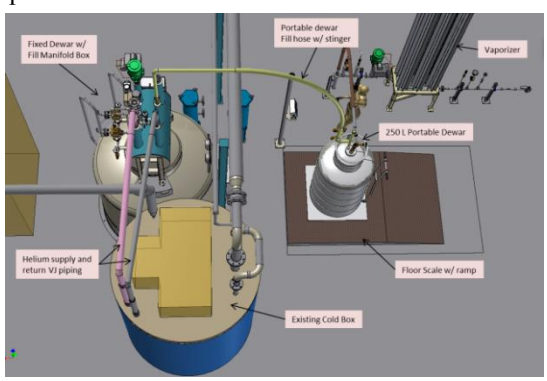


Figure 2: The model of fill station. [4]

The addition of a Kinney pumping skid will enable the system to operate at 2 K. SNS made use of the vast experience of personnel at Fermi National Laboratory in refurbishing this skid. This was a machine originally slated for operation at the SSC. It is a 10 g/s machine equipped with a blower, liquid ring vacuum pump, and oil pump. This portion of the system is scheduled to come on line in FY 14.

COMMISSIONING

The commissioning philosophy was to first start the warm part of the system including the compressor, gas management, and oil removal. This allowed any bugs to be worked out in the warm part of the system while being isolated from the cold box and turbines. The philosophy of this portion of the system was to make it as similar to the existing plant as possible to minimize operator training time, make use of existing control templates, and incorporate the Ganni Cycle [5] to use a floating discharge pressure system to match the load.

The primary goals of this portion of the commissioning were to test the operability, speed control, control functions and interlocks of the compressor, gas management, and oil removal system. Secondary goals were to gain valuable operator seat time and develop internal operating procedures. This test was completed at the end of January with a Linde representative present. The compressor screen shot is depicted below in Fig. 3.

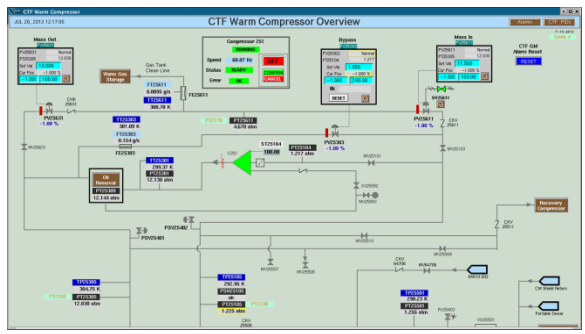


Figure 3: Warm compressor control screen.

After commissioning the warm system, a control logic review was conducted as a collaborative effort between SNS controls personnel and a Linde representative. During this review, the readiness of the controls was verified. The team verified that instrument loop checks, interlocks, operator controls, control algorithms, and initial loop tuning were properly implemented. The cold box PLC logic was reviewed thoroughly and a short action item list was generated and completed within a couple of weeks.

This positioned the team well to move to cold box commissioning. The cold box was operated integrated with the warm system and the helium Dewar. A simplified block flow diagram is included in Fig. 4. An example of the controls screens used during commissioning for this system is shown in Fig. 5. The goals of the cold box commissioning were:

1. Cool down cold box within specified time (< 6 hours)
2. Achieve specified capacities for refrigeration and liquefaction
3. Develop procedures and receive training
4. Demonstrate helium Dewar integrity and achieve specified boil off rate
5. Tune loops and refine control variables
6. Test interlocks and ensures system fails safe.

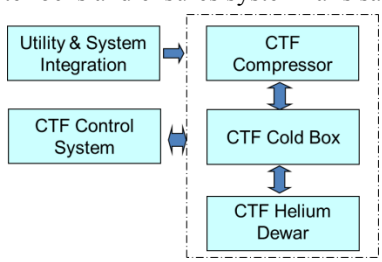


Figure 4: Cold box commissioning block flow diagram.

Copyright © 2013 CC-BY-3.0 and by the respective authors

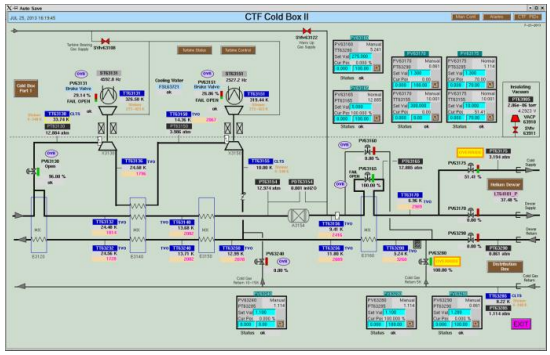


Figure 5: Cold box control screen II.

To commission the cold box in liquefaction mode, the cold box supplied helium to the helium Dewar and a small amount of vapour returned to the cold box. For commissioning, the distribution box was bypassed with three custom made u-tubes. The liquefaction rate was measured in two ways. The first was to observe how much the level increased in the helium Dewar over a specified amount of time. The second was to observe how quickly the helium gas storage pressure dropped in a specified amount of time and convert that to liquefaction rate. These two methods of calculation yielded results of 260 L/hr and 240 L/hr, respectively. Both met or exceeded the specified liquefaction rate. However, it is believed that the calculation method using helium gas storage tank pressure is more accurate than the method of using liquid level due to error introduced by level probe and helium Dewar geometry.

The cold box was commissioned in refrigeration mode by supplying helium to the Dewar and boiling it off with an electric heater. The maximum refrigeration capacity of the system was observed to be 750 W which is greater than the specified capacity. A screen shot of the helium Dewar with the input heater power of 759 W is included in Fig. 6. After the helium Dewar was filled, the system was shut down over night and the boil off rate was measured. It was found to be <0.75% per day as specified.

In addition to achieving the refrigeration and liquefaction capacities, interlocks were tested, internal operating procedures were developed, and loops were tuned. The commissioning gave opportunity to multiple operators to gain hands on experience with the system.

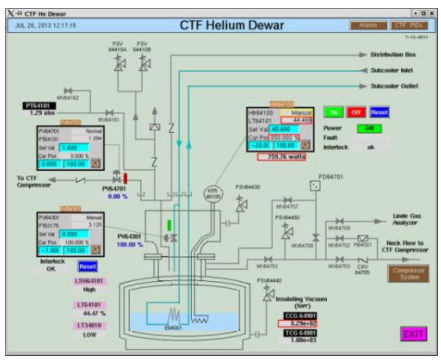


Figure 6: Helium Dewar control screen depicting refrigeration capacity.

LESSONS LEARNED

A few valuable lessons were learned during the design and commissioning of this system. One design change that was incorporated was to take the compressor bypass from after the second stage coalescer to minimize oil carry over. In the CHL system, oil accumulation is witnessed in the low and medium pressure headers. This change has eliminated this concern from the CTF system.

As controls personnel were performing check out of the gas management valves, it was discovered the Weka control valves required 5 atm instrument air pressure to operate [6]. The control valves in the CHL gas management system operate at 3atm air pressure. This required a change out of an air pressure regulator to accommodate operation of the CTF gas management control valves.

Another lesson learned involved bonding the cold box to ground. This was overlooked in the original installation of the system. The temperature sensors gave erroneous readings on both the TVO resistors and cryogenic linear temperature sensors (CLTS) [6]. This was corrected by connecting the box to ground.

This system was specified as a machine with frequent starts and stops that give ample opportunity to regenerate the 80 K and 20 K adsorbers. However in future systems, it may be advantageous to install isolation valves and a bypass. This can be used during warm up iterations and ensure that contamination does not enter other areas of the system.

ACKNOWLEDGMENT

We would like to thank all of the people that have made the fabrication, installation and commissioning of the CTF system possible. We recognize the dedication and hard work put forth by the SNS and Linde teams.

REFERENCES

[1] Kim, S-H., "SNS Superconducting Linac Operating Experience and Upgrade Path", LINAC'08, Victoria, Canada, September 2008.

[2] Kim, S-H., "R&D Status for In-Situ Plasma Surface Cleaning of SRF Cavities at Spallation Neutron Source", PAC2011, New York, New York, March 2011.

[3] Xu, T., "Status of Cryogenic System for Spallation Neutron Source's Superconducting Radiofrequency Test Facility at Oak Ridge National Lab", *Advances in Cryogenic Engineering 57*, edited by J.G. Weisend et al., Melville, New York, 2011, pp. 1085-1091.

[4] Willming, S., "Liquid Helium Filling Station", Presented at CTF Liquid Fill Station Preliminary Design Review, April 2013.

[5] Ganni, V., Design of Optimal Helium refrigeration and Liquefaction Systems, CEC-ICMC Short Course Symposium, 2007, Chapter 5.

[6] Strong, H. "CTF Readiness Review: Control System Overview", September 2013.

Copyright © 2013 CC-BY-3.0 and by the respective authors

RECENT IMPROVEMENTS IN PARTICLE SIMULATION SUPPORT IN ANALYST-MP*

J. F. DeFord, B. Held, A. Nichols, AWR Corporation, Mequon, WI 53092, USA

Abstract

Recent work on the Analyst product has simplified model development, improved result visualization, and added particle simulation functionality. The Analyst user interface has been updated with a new control layout, and support for automatic session recording, variables/expressions for all inputs, and units. For the study of multipacting and dark current phenomena a new volumetric particle source has been deployed, and changes to the way secondary generations are managed has simplified the identification of multipacting resonances.

INTRODUCTION

Analyst is a finite element-based tool used for design and optimization of three-dimensional structures in microwave engineering. In development of new particle accelerators, Analyst is used on a variety of components including RF modules, feed systems, deflectors, etc. When applied to the multipacting problem, driven RF or eigenmode calculations are performed to obtain field distributions, and these are then used in a separate particle simulation to search for particle resonances.

Recent work has improved the particle tracking algorithms and emission models [1]. The current version of the code employs a statistical secondary emission model that produces from an impact a set of zero or more electrons whose count and properties are obtained from samples of random variables that collectively enforce observed secondary emission behaviour [2]. The Analyst user interface has also been updated in response to user experience in the old system. Development on the particle simulation engine has focused on changes that make it easier to identify and interpret multipacting behaviour. These changes are discussed in the following sections.

VOLUMETRIC PARTICLE SOURCING

Previous versions of Analyst used a simple primary emission model for multipacting simulation. This model emitted one or more particles from each element face that lay on the model boundary. Particles were emitted at regular intervals during the first RF period, and subsequent particle motion and deterministic secondary generation were used to identify resonances. This technique is very efficient, but it does not necessarily require fewer emissions than a volumetric launch if one is to avoid missing resonances.

In addition to supporting primary emission from surfaces, Analyst now also allows initiation of particles in the volume by emitting a specified number from each mesh element (triangle or tetrahedron) during the first RF cycle. The position, direction vector, and emission time of each particle are all randomly chosen. The initial velocity of each particle is obtained by sampling a random variable, with the number of particles emitted per element controlled by a user input, and is typically of order 10^2.

As expected, the efficiency with which resonances are identified is a function of the choice of initial velocity distribution. Robust multipacting resonances involve low energy electrons because it is primarily low energy impacts (< 5 keV) that yield multiple secondary particles. Higher energy impacts can result in single reflected or re-diffused secondary particles, but do not contribute to gain in multipacting resonances. Consequently, initiating particles with high energy is usually of little utility in identifying resonances. In the low energy regime we studied the effects of using different velocity distribution functions, including a delta function (specified value), uniform over a range of values, and Boltzmann with a peak matching the secondary emission yield peak of surface material. We concluded that these functions were largely equivalent in initiating resonances in test structures, and the simplest approach of giving all of the particles the same initial energy (in the 100s of eV) is perfectly adequate. This value is an input parameter in the software, which defaults to the peak energy of the true secondary yield curve. Note that this choice does not imply that only particles with comparable energy exist in the simulation to initiate resonances. High-field regions will accelerate particles to high energies, and subsequent interaction with cavity walls will typically scatter some of these particles into low-field areas. However, with this approach the preponderance of particles in low field regions will be in an energy range to yield true secondaries on impact with common metals, increasing the odds that a resonance will be discovered if one is supported by the geometry/field-structure.

Volumetric sourcing produces an initial cloud of particles that rapidly dissipates, primarily due to collisions with cavity walls that produce no secondary particles. What remains after a few RF cycles is predominantly secondary particles that are in a resonance (Figure 1).

MULTIPROCESSING

Particle tracking is done by secondary generation, with each generation completed before the next one is started. Between generations secondary particles are redistributed across available processors to balance the computational load. Dependence of particle populations on processor count is undesirable, even when it does not lead to

*Work supported by DOE SBIR grant SC0002604.

Copyright © 2013 CC-BY-3.0 and by the respective authors

quantitative changes to the results of interest, and such dependencies are also problematic in automated regression testing systems. To make the results independent of processor count requires the creation of a particle index that does not depend on either processor count nor processor index. This index is formed on the basis of initial emission parameters and secondary history, and is composed of a small number of 64-bit integers (generally 3 or less). The index is unique for each particle, but simple interpretations of its values as integers are not evenly distributed in the set of integers, and as such it is not suitable for use in index-based load-balancing. So for this purpose an index hash (a single integer of a specified maximum size) is created based upon the index which is approximately evenly distributed, but is not generally unique. Load balancing is then performed on the basis of this hash, which has exhibited high-quality partitions in our testing.

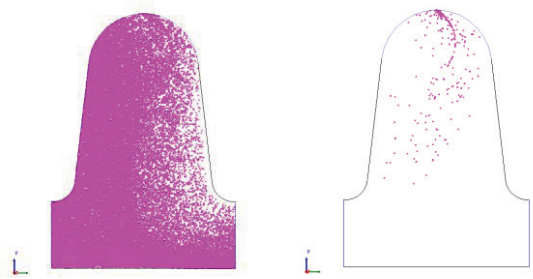


Figure 1: Particle cloud at 1 RF period (left), and after 2 RF periods (right) in 2-D RZ example. Ultimately a resonance is seen about cavity "equator" (top center of cavity).

SECONDARY DECIMATION

The number of secondary particles that are tracked at each generation is controlled via decimation. This is particularly important in highly resonant situations in which the particle growth is exponential. As with load balancing, an index hash is used for this purpose, and only particles with zero hash index are tracked. The existence of the untracked particles is accounted for in accumulated statistics, such as yield, but otherwise they are simply discarded.

MODEL CREATION AND RESULT PROCESSING

The Analyst user interface has been updated to simplify the creation and manipulation of complex geometry models. Changes include mouse-based solid construction, relative coordinate systems tied to geometric entities (for creating a solid at a location/orientation that is relative to another solid), and the aggregation of all model data in a property grid that allows rapid access and modification of model parameters (Figure 2).

Scripting is supported in the Analyst system, and is based upon the Python language. The new software automatically records the complete session in a script that can be replayed in order to reproduce the session. This recording can also be used as the basis for a user script.

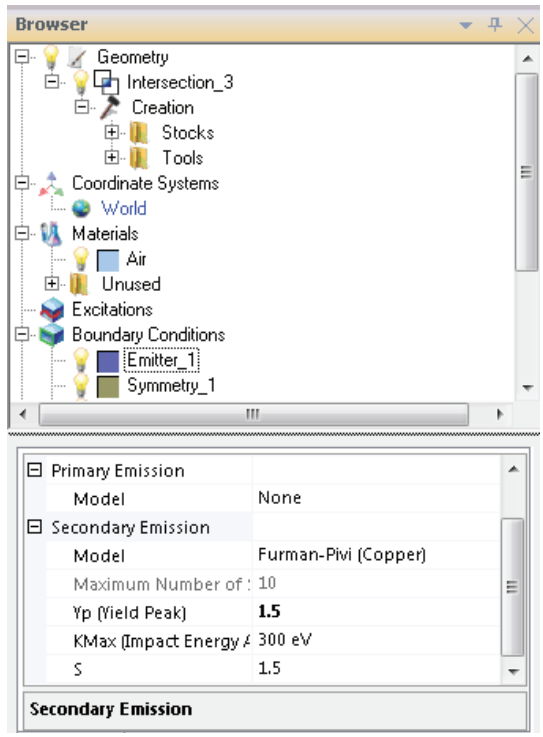


Figure 2: New model data browser in Analyst simplifies access to common elements.

Variables and expressions can now be entered in place of numeric values in all input fields. Variable definitions are collected in a single input panel for rapid access. Units are now comprehensively supported in the user-interface, and a variable has the unit of its associated expression. The expression parser observes rules associated with the use of quantities with units in expressions, so for example, it is not allowed to add a variable with unit of distance to another variable with unit of time. Moreover, values with the same unit but differing scales are handled automatically via conversion to a common scale, so for example, an expression of the form v=1m+1in is allowed and correctly evaluated.

Result visualization has been reorganized to allow simpler addition of filters to view elements (now called "annotations"). Annotations can now be created in advance of a simulation, allowing views that are updated as data become available. Previously in Analyst geometry visualization was done only in its own window, separate window from all result views. In the new system there is no distinction between the two, so geometry and result visualization can be rendered together in the same view.

As an example, we analysed an RF deflector cavity [3] (Figure 3). This structure uses a dipole mode resonant at 2.82 GHz, and the interest was to identify any multipacting bands below about 60 MV/m peak surface electric field. Figure 4 shows the mode electric field, which is a field annotation rendered together with an outline view of the original solid geometry.

Copyright © 2013 CC-BY-3.0 and by the respective authors

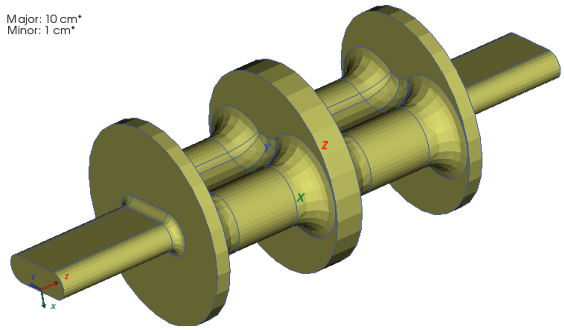


Figure 3: Deflector cavity geometry.

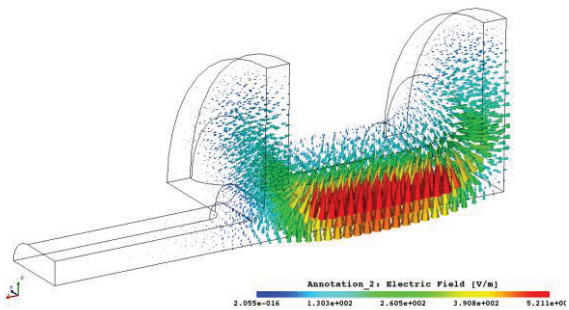


Figure 4: Electric field of mode in deflector cavity. Cavity is shown as modelled using 3 planes of symmetry. View is combination of structure and field annotations.

Running the problem at a single field level and dumping particles allows visualization of particular resonances. Particles can be rendered either as dots (their position at a particular instant in time), or as tracks that show the path of a particular particle or set of particles (Figure 5). In the deflector structure for the particular choice of secondary emission model there is a resonance near 50 MV/m in the vicinity of the connection between the beampipe and the cavity. Particles in this resonance return to the surface once every RF period as can be inferred from the individual particle statistics table that is output by Analyst.

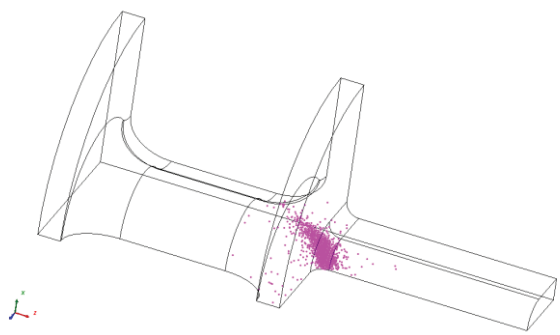


Figure 5: Particle distribution after 30 RF cycles in the multipacting band, showing accumulation of resonant particles near the fillet between cavity and beampipe.

Plots now contain one or more "measurements", which are data sources that can come from a simulation table or some other source. As with annotations, measurements are updated as data becomes available, so if a number of plots have been created and the simulation is rerun there is no need to recreate the plots as they will simply be updated with the new data when the simulation is finished. The enhanced counter function for the deflector cavity is shown in Figure 6. The particle count time history for a field level in the multipacting band is shown in Figure 7.

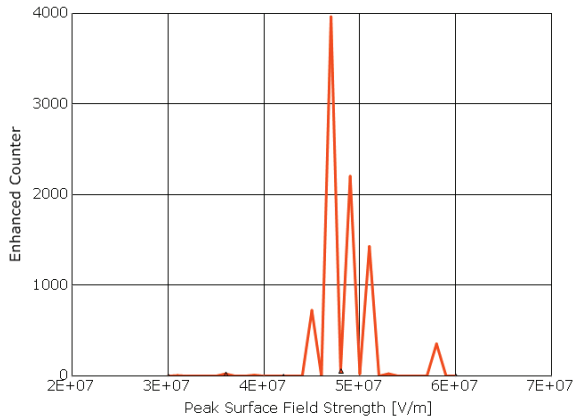


Figure 6: Enhanced counter function (number of particles surviving to 20 impacts including yield) as a function of peak surface electric field.

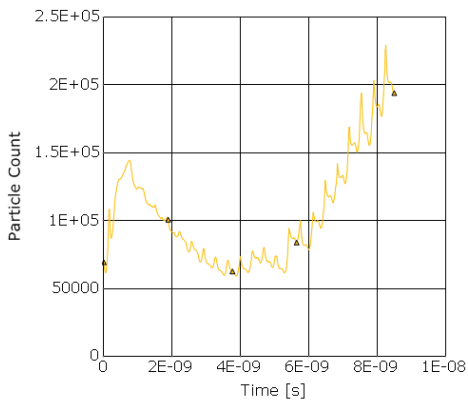


Figure 7: Particle count vs. time in deflector at 49 MV/m. Resonance is evident in late-time growth.

CONCLUSIONS

The Analyst finite-element software package has been updated, including improvements to the user-interface and particle simulation functionality. Changes in the way particles are sourced and secondary particles are managed now allows direct observation of particle count growth in resonant situations. Studies show expected multipacting resonances in test structures.

REFERENCES

[1] J. F. DeFord and B. Held, *14th Advanced Accelerator Concepts Workshop*. AIP Conference Proceedings, 1299, pp. 393-398 (2010).
[2] M. Furman, et al., LBNL-52807, June, 2003.
[3] I. Gonin, personal communication, June, 2013.

Copyright © 2013 CC-BY-3.0 and by the respective authors

PARAMETER OPTIMIZATION FOR MULTI-DIMENSIONAL LASER COOLING OF AN ION BEAM IN THE STORAGE RING S-LSR*

Z. He#, FRIB, Michigan State University, USA; Tsinghua University, China
J. Wei, FRIB, Michigan State University, USA
K. Osaki, H. Okamoto, Hiroshima University, Japan
A. Noda, M. Nakao, National Institute of Radiological Science, Japan
H. Souda, Gunma University Heavy Ion Medical Centre, Japan
Y. Yuri, TARRI, Japan Atomic Energy Agency, Japan
K. Jimbo, IAE, Kyoto University, Japan

Abstract

S-LSR is a compact ion cooler ring built in ICR, Kyoto University, aiming at creating ultra-low temperature ion beam by laser cooling. In order to approach lowest possible temperature at S-LSR in an experiment, parameters of laser cooling should be carefully chosen by simulation. This paper mainly concerns optimization of laser cooling parameters and prediction of possible low limit of beam temperature at S-LSR. Firstly, the adiabatic capture process of ion beam is introduced and studied. Then, different laser profile parameters are compared and an optimized value is chosen. After that, optimized solenoid field strength for 3-D coupling is proposed. At last, by choosing the parameters proposed, the lowest beam temperature achievable for S-LSR is predicted to be 10 K in transverse direction and 0.05 K in longitudinal direction.

INTRODUCTION

Cold beam, or low emittance beam, usually means less beam loss and smaller necessary beam aperture. Considerable effort towards ultra-cold beam was devoted in 1990's by two European teams (the TSR group at Max Planck Institute [1, 2] and the ASTRID group at Aarhus University [3, 4]). Both teams applied the laser cooling technique [5, 6] to various heavy ions and succeeded in reducing the longitudinal beam. However, the possible lowest emittance is limited by the linear coherent resonance crossing unavoidable in both TSR and ASTRID rings [4, 7, 8]. S-LSR [9], a compact ion cooler ring built in ICR, Kyoto University, has a potential to overcome the difficulties encountered by the European teams. For instance, we can reduce the betatron phase advance per single lattice period near or even below 90 degrees and avoid strong beam heating due to the linear resonance crossing. It is also possible to employ the resonant coupling method (RCM) [10, 11] and enables us to produce an ultimate ion beam that has a temperature near the absolute zero in all three dimensions [12, 13]. This paper mainly concerns optimization of laser cooling parameter and prediction of low limit of beam temperature at S-LSR.

* This work was supported by the U.S. National Science Foundation under Grant No. PHY-11-02511, Advanced Compact Accelerator Development project of MEXT, and Global COE program.
#hez@frib.msu.edu

BUNCHED-BEAM LASER COOLING

S-LSR is a compaction cooler ring with an electron cooling system and a laser cooling system. It has six-fold symmetric lattice and each lattice consists of a bending magnetic two quadruples and one 1.86 m long drift line, two of which are occupied by an electron cooler and a laser-beam interaction section as Fig. 1. A 40 keV Mg^+ beam is injected continuously into the ring and captured and bunched by a RF cavity. The laser is set co-propagating with the Mg^+ beam and is slightly tuned below the transmission frequency of the beam. With the synchrotron motion of bunched-beam, particles automatically falls into the cooling region of the laser, thus making bunched-beam cooling possible by single laser. [14]

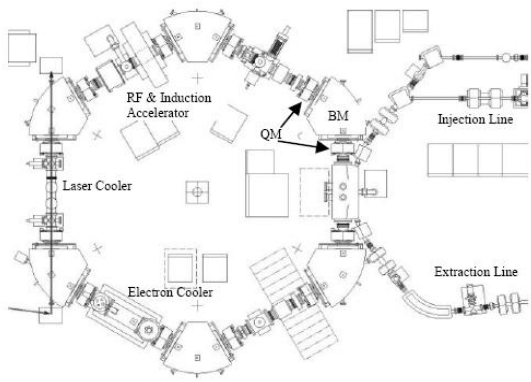


Figure 1: Layout of the ion storage ring [9].

In order to realize multi-dimensional laser cooling, the idea of RCM has been induced [10, 11]. In S-LSR, we adjust the working point around (ν_x, ν_y, ν_z) = (2.075, 1.120, 0.075) for 2-D cooling and working point around (2.075, 1.075, 0.075) for 3-D cooling. Longitudinal direction and horizontal direction are coupled by dispersion; horizontal direction and vertical direction are coupled by solenoid field.

Simulations are specially designed for this single laser bunched-beam cooling experiment at S-LSR. The parameters are all chosen according to the data or past experiment result of S-LSR. A molecular dynamic simulation code, CRYSTAL, developed for the laser-cooling and crystalline-beam study, was used [12].

Copyright © 2013 CC-BY-3.0 and by the respective authors

An ideal cooling method would cool all the particles to a certain low temperature. However, simulation shows that there are always particles not captured by laser in the longitudinal phase space, making a hot corona existing together with a cold beam core. See Fig. 2 for a typical longitudinal phase space distribution after laser cooling.

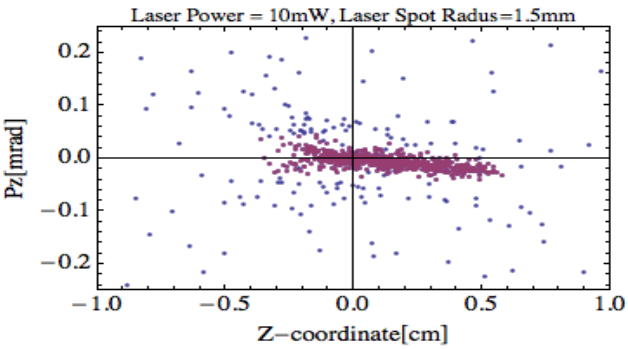


Figure 2: A typical phase-space plot after laser cooling. The magenta dots represent captured particles while blue dots shows hot beam corona.

COOLING PARAMETER OPTIMIZATION

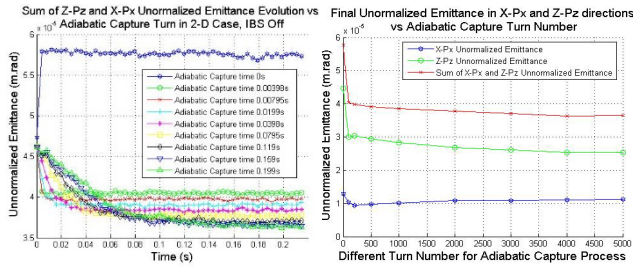
In order to maximize the cooling effect, various parameters should be optimized. Main experimental parameters are summarized in Table 1. Final detuning is chosen as minus half of the natural band width or $-\Gamma/2$, where the friction force is thought to be maximum. In our case, the frequency is 3.34 MHz or -1.1e-5 equivalent momentum spread. Laser scanning is applied in S-LSR to perform continuous laser cooling. Other parameters such as adiabatic capture time, laser spot size with saturation parameter, and solenoid field, should be carefully optimized by simulation. In this part, we assume that intra-beam scattering (IBS) effect is small enough and doesn't change the optimum value of each parameter, so we ignored the space-charge effect in the following simulations unless otherwise noted.

Table 1: Main S-LSR Parameters

Parameter	Value
Circumference	22.557 m
Average Radius	3.59 m
Ion Species	$^{24}Mg^{+}$
Kinetic Energy	40 keV
Frequency	25.145 kHz
Initial Momentum Spread	7.0e-4
Typical Laser Power	10 mW

Adiabatic Capture Process

At S-LSR, Mg^{+} beam is injected continuously in to the storage ring, forming a coasting beam circulating around the ring. To prevent emittance blowing up during the bunching, the adiabatic capture process is conducted in S-LSR. During the adiabatic capture process, the RF cavity voltage increases linearly from 0 to designed RF voltage decided by the synchrotron tune. So the only parameter needs to be optimized is the capture time. It can be easily seen from Fig. 3 that adiabatic capture process is a very effective procedure on preventing blowing up in emittance due to beam bunching process and even a very short period, would be far better than no adiabatic capture process. According to the result, an adiabatic capture time no less than 0.1s would be preferred by avoiding phase space dilution and strong emittance exchange.



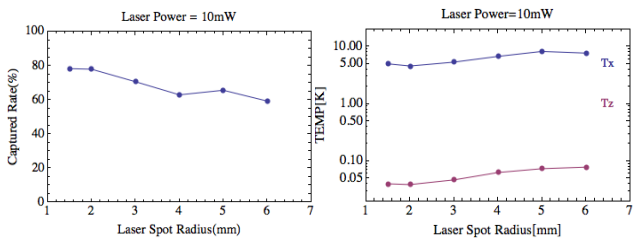
(a) (b)

Figure 3: (a) The sum of X-Px and Z-Pz un-normalized emittance evolution vs. different adiabatic capture time in 2-D case (b) Final un-normalized emittance in X-Px and Z-Pz directions vs. adiabatic capture turn number.

Laser Profile Parameter

The total output power of laser available at S-LSR has now become the main constraint. A maximum output laser power of no more than 15mW is now available. On the other side, by maintaining a certain laser power, the laser profile parameters, namely laser waist radius R and centre saturation parameter S are able to adjust where SR^2 is kept constant.

As a result, optimizing laser cooling effect by optimizing laser waist radius and centre saturation parameter is important. In our simulation, laser waist radius varies 1.5 mm to 6 mm. IBS is turned on. And laser is kept at 10 mW. Laser cooling was maintained for as long as 5s. 2-D cooling is applied in these simulations. The cooling result can be seen in Fig. 4.



(a) (b)

Figure 4: Laser profile parameter optimization of certain power of laser in 2-D laser cooling. (a) Capture rate of laser cooling using different vs. laser spot radius, (b) The final temperature of captured particles vs. laser spot radius, IBS on, number of particles simulated is 300.

From the result, we can see that the capture rate goes down while the final captured particle temperature goes up with laser radius going up, indicating smaller laser radius would be more effective in suppressing IBS effect in cold beam cores. If our goal is to get lowest possible captured beam temperature while maintaining a

Copyright © 2013 CC-BY-3.0 and by the respective authors

reasonable capture rate in real case, a smaller laser radius of 1.5 mm would be preferred.

Solenoid Field

In 3-D laser cooling process, solenoid field should be turned on to couple horizontal direction and vertical direction. However, an optimized solenoid field for S-LSR remains unknown. In this part, solenoid field is changed from 50 Gauss to 400 Gauss and 3-D laser cooling is put forward and the cooling effect is then checked. The result can be seen in Fig. 5.

According to the calculation, if our final target is to get a cold particle core instead of getting the lowest total emittance, we can find out that the best solenoid field would be around 100 Gauss. And no matter too big or too small solenoid field is not good for coupling condition. Low solenoid would reduce the coupling between vertical and horizontal direction and high solenoid field would break the coupling condition between longitudinal and transverse direction. So a suitable solenoid field should be chosen to attain good cooling effect.

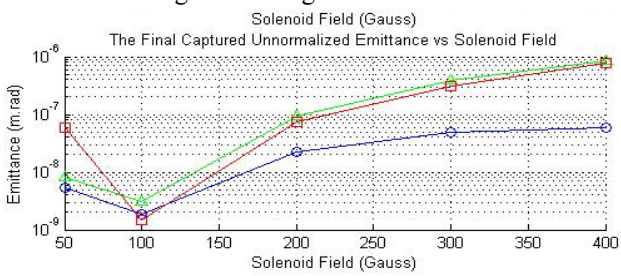
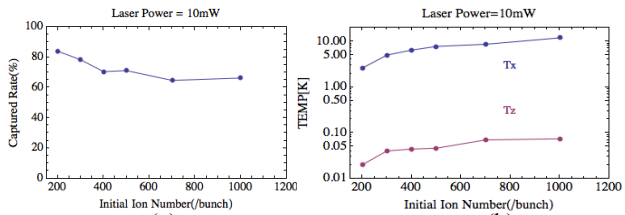


Figure 5: Result combination of cooling result vs. different solenoid field.

PREDICTION OF LOW- TEMPERATURE LIMIT AT S-LSR

Up to now, we have been talking about the optimum choices in bunched-beam laser cooling at S-LSR. Long term study shows that in order to achieve transverse laser cooling, differential resonance condition should be imposed. Laser scanning should also be imposed to increase particle capture. And it has also been suggested that in order to gain a more satisfactory cooling result, adiabatic capture process is needed. With very limited laser power, the laser profile should be adjusted and a small laser radius as 1.5 mm is preferable for compressing IBS heating effect. For 3-D laser cooling, a solenoid is opened to couple X and Y degree of freedom and the optimum solenoid field would be 100 Gauss.

To see how far we can actually go under this real situation, IBS effect is considered in the following simulations. The simulated number of particle is varied from 200 to 1000 to see the particle number dependence of IBS heating in S-LSR. According to the simulation result, capture rate drops, final rms beam radius, normalized cold beam core emittance and temperature goes up with the number of initial particles. This is because IBS effect gets enhanced by larger number of particles. Thus we prefer lower number of particles to reduce IBS heating effect. However, around 1000 particles per bunch are near the limit of detection. At that circumstance, we can achieve around 600 particles cooled. The final temperature of cold beam core would be around 10 K in transverse direction and 0.05 K in longitudinal direction, as shown in Fig. 6.



(a) (b)

Figure 6: S-LSR real situation laser cooling simulation with IBS on. Cool effect of different number of particles. (a) Final rms beam radius vs. number of particles; (b) Final transverse and longitudinal temperature vs. number of particles.

CONCLUSION

The power of the cooling laser currently available in S-LSR is quite limited. We then expect the achievable beam temperature to be much higher than the Doppler limit even with the RCM. Nevertheless, considering the high potential of S-LSR, according to the simulation study, even with this limitation in the laser system, it seems feasible to break the world record of lower limit of the beam temperature. This paper gives useful insights for the laser-cooling experiment under a practical situation. By carefully choosing laser cooling parameters, we can finally arrive in a cold ion beam with temperature around 10 K in transverse direction and 0.05 K in longitudinal direction. However, the result is a theoretical lower limit achievable by current S-LSR system and recent experiment results still arrive in higher temperature after cooling [15]. And we also expect that with an upgrade of the laser system in S-LSR in the future, a colder beam with an even lower temperature would be possible to be realized.

REFERENCES

[1] S. Schröder et al., Phys. Rev. Lett. 64, 2901 (1990).
[2] H-J. Miesner et al., Phys. Rev. Lett. 77, 623 (1996).
[3] J. S. Hangst et al., Phys. Rev. Lett. 67, 1238 (1991).
[4] N. Madsen et al., Phys. Rev. Lett. 83, 4301 (1999).
[5] D. J. Wineland et al. Phys. Soc. 20, 637 (1975).
[6] T. Hänsch, A. Schawlow, Opt. Com. 13, 68 (1975).
[7] J. Wei, Phys. Rev. Lett. 80, 2606 (1998).
[8] K. Okabe, H. Okamoto, JJAP, 42, 4584 (2003).
[9] T. Shirai, A. Noda, et al. Proc. EPAC 2004, WEPLT116, p. 2122 (2004).
[10] H. Okamoto, et al. Phys. Rev. Lett. 72, 3977 (1994).
[11] H. Okamoto. Phys. Rev. E 50, 4982 (1994).
[12] Y. Yuri et al. Phys. Rev. Lett. 93, 204801 (2004).
[13] M. Ikegami et al. PRST-AB 9, 124201 (2006).
[14] Hangst, J. S. et al. Phys. Rev. Lett. 74, 4432(1995)
[15] H. Souda, JJAP. 52, 030202(2013)

Copyright © 2013 CC-BY-3.0 and by the respective authors

APS FAST ORBIT FEEDBACK SYSTEM UPGRADE*

R. Lipa, N. Arnold, H. Bui, G. Decker, T. Fors, R. Laird, F. Lenkszus,
A. Scaminaci, N. Sereno, S. Shoaf, ANL, Argonne, IL 60439, USA

Abstract

A real-time feedback double-sector controller (RTFB DSC) for the APS Upgrade has been under design for the past year. Using the Xilinx Zynq-7000 All Programmable System on a Chip FPGA residing on the ZC706 board as the base platform, the upgrade path interfaces to the existing accelerator system and modernizes the beam position monitoring and feedback systems. The modernized system increases the RTFB system sample rate from 1.5 kHz to 22.6 kHz. We report the plan for sector-by-sector upgrades that will occur during system shutdowns and allow the upgraded sectors to operate with the existing sectors. The mapping of the RTFB DSC architecture is shown utilizing the targeted FPGA features. These features include the dual ARM Cortex™ A9 processors, multi-port DDR3 memory controllers, gigabit transceivers, and the programming logic interconnect for implementing advanced orbit feedback controller algorithms using floating-point DSP operations. The RTFB DSC FPGA architecture is revealed as well as subsequent progress on the chassis implementation.

INTRODUCTION

The RTFB DSC of the APS storage ring upgrade increases the processing power using modernized electronics to provide the functions, calculations, and interfaces of the present-day system and to improve the beam stability by increasing the sample rate to target a closed-loop bandwidth of at least 200 Hz. The network interface elements and functions on the RTFB DSC incorporate the EPICS software environment to control the process variables to configure and monitor the RTFB system. The RTFB DSC gigabit transceiver cores receive and transmit the global BPM error matrix over the real-time data highway (DH). The digital signal processing cores calculate the corrector drive vector using a response matrix multiplication and global BPM error vectors to obtain the local portion of the corrector drive vectors. The correction is then applied to the steering corrector power supplies located in that double sector. The RTFB DSC interfaces to a disparate and evolving set of equipment. The RTFB DSC advantageously uses the programmable FPGA features to attach to the various rates and protocols used by different equipment. The modern FPGA's integrated features, such as high-performance embedded processors, integrated DDR3 cores, numerous DSP and BRAM cores, gigabit Ethernet controllers, and gigabit transceiver blocks, along with the programmable fabric, allow decreasing the sample period and reducing the delay in correcting the electron orbit.

*Work supported by U.S. Department of Energy, Office of Science, under Contract No. DE-AC02-06CH11357

RTFB DSC SYSTEM ARCHITECTURE

The real-time feedback double-sector controller functions in the middle of the following existing [1] and proposed storage ring elements: monopulse rf beam position monitors (BPMs), Bergoz (i.e., narrowband) BPMs, existing x-ray BPMs, steering corrector power supplies, the Experimental Physics and Industrial Control System (EPICS), the timing and event systems, the low-level rf systems, and a machine (i.e., storage ring) protection system. The modernized RTFB DSC FPGA also provides the capability to interface to commercial BPMs (e.g., Libera Brilliance+ [2]) and to commercial x-ray data acquisition systems (e.g., Libera Photon [3]). Figure 1 is a block diagram of the system showing the RTFB DSC and the other storage ring elements and the interconnections. The upgrade design shows the mapping of the RTFB DSC architecture to a realizable modern implementation.

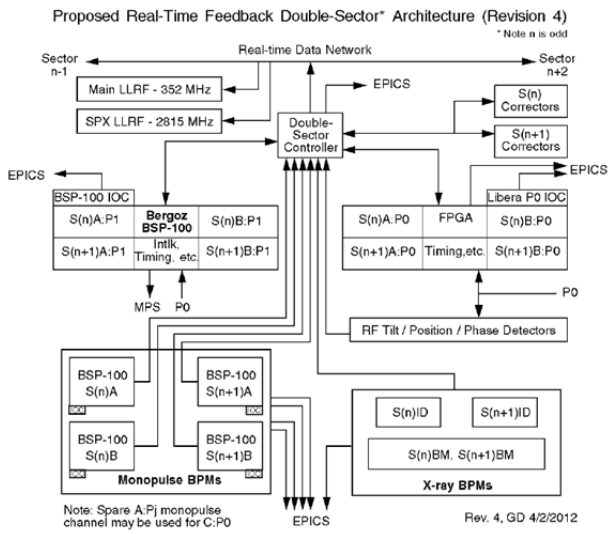


Figure 1: Real-time feedback double-sector controller architecture.

RTFB DSC IMPLEMENATION

The architecture maps into three functional chassis: 1) the APS2VME crate, which interfaces to the exiting reflective memory and EPICS networks; 2) the RTFB DSC chassis, which uses the ZC706 board [4] with its FPGA Mezzanine Connectors (FMC) for interfaces; and 3) the CMPSI-II chassis, which uses a KC705 board [5] and its FMC connectors interfaces as shown in Figure 2.

Copyright © 2013 CC-BY-3.0 and by the respective authors

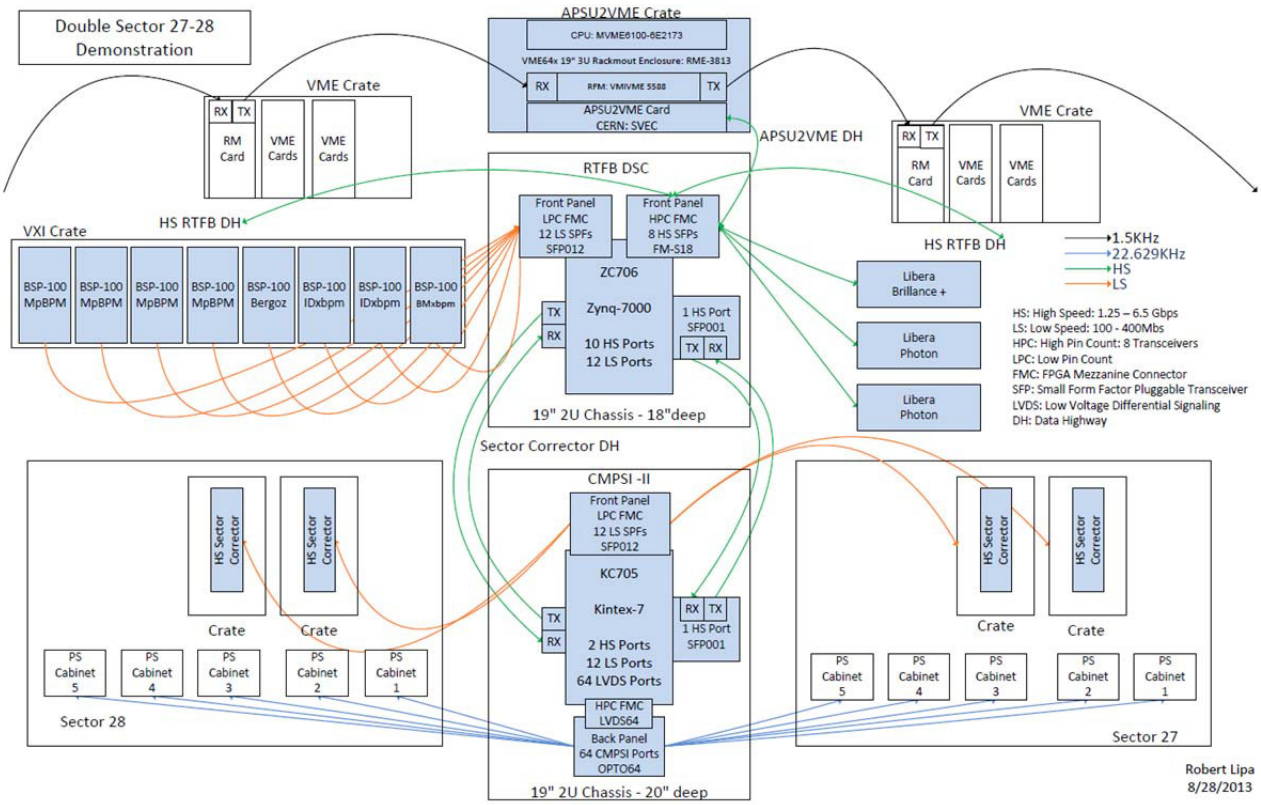


Figure 2: RTFB system architecture implementation using three chassis.

APSU2VME Crate

The APSU2VME crate is a rack-mountable chassis with 3U height accepting up to five horizontally mounted 6U cards. It contains three cards: a CPU, the Reflective Memory card, and the SVEC [6]. The SVEC is a versatile VME64x board with the features necessary to interface with both the existing 1.5-kHz sample network and the new 22.6-kHz sample network. Using the following SVEC features—VME64x backplane connector, front panel SFP module, DDR3 memories, and Spartan6 XC6SLX150T FPGA—the BPM error matrix can be transmitted and received between the two systems.

RTFB DSC Chassis

The RTFB DSC chassis is a custom low-cost 2U rack-mountable chassis interfacing to the BPMs, APSU2VME crate, commercial BPM, commercial x-ray data acquisition systems, and the Corrector Magnet Power Supply Interface—a second-generation (CMPSI-II) chassis. The RTFB DSC chassis contains the following components to be used to execute the RTFB algorithms on the various interfaces: a Xilinx ZC706 board, a Faster Technology FM-S18 FMC [7] with eight high-speed SFP channels, the SFP012, and the SFP001. The SFP012 is a custom 12-port SFP FMC accepting low-speed SFP modules. The SFP001 is a custom single-port SFP card holding one high-speed SFP module. Additionally the chassis contains a 12-V power supply, a fan controller, fans, and external connectors: LC, Ethernet, and USB.

CMPSI-II Chassis

The CMPSI-II chassis is also a custom low-cost 2U rack-mountable chassis. It interfaces to the RTFB DSC chassis, the CMPSI interfaces in the power supply (PS) cabinets, and a potential future high-speed sector corrector power supplies. The CMPSI-II chassis contains the following components to be used for applying the PS setpoints: a Xilinx KC705 board, the LVDS64, and the OPTO64. The LVDS64 is a custom LVDS FMC on the high pin count connector of the KC705. The OPTO64 is a custom board interfacing an LVDS cable to Harting connectors. The OPTO64 mounts an existing PS interface card. The ZC706 board and the KC705 board can communicate directly via the on-board SFP modules and the SFP001. The low pin count (LPC) connector could potentially communicate with a high-speed sector corrector using the currently defined LPC FMC pins.

SECTOR-BY-SECTOR UPGRADE

By replacing existing VME crates with two APSU2VME crates, one at each edge of the sectors being upgraded, and connecting the HS RTFB DHs of the RTFB DSCs with the upgraded sectors containing the RTFB DSCs between the two APSU2VME crates, the storage ring can be upgraded on a sector-by-sector basis during scheduled shutdowns. Thus the upgraded sectors can operate at the 22.6-kHz sample rate as the Sector 27 demonstration targets.

Copyright © 2013 CC-BY-3.0 and by the respective authors

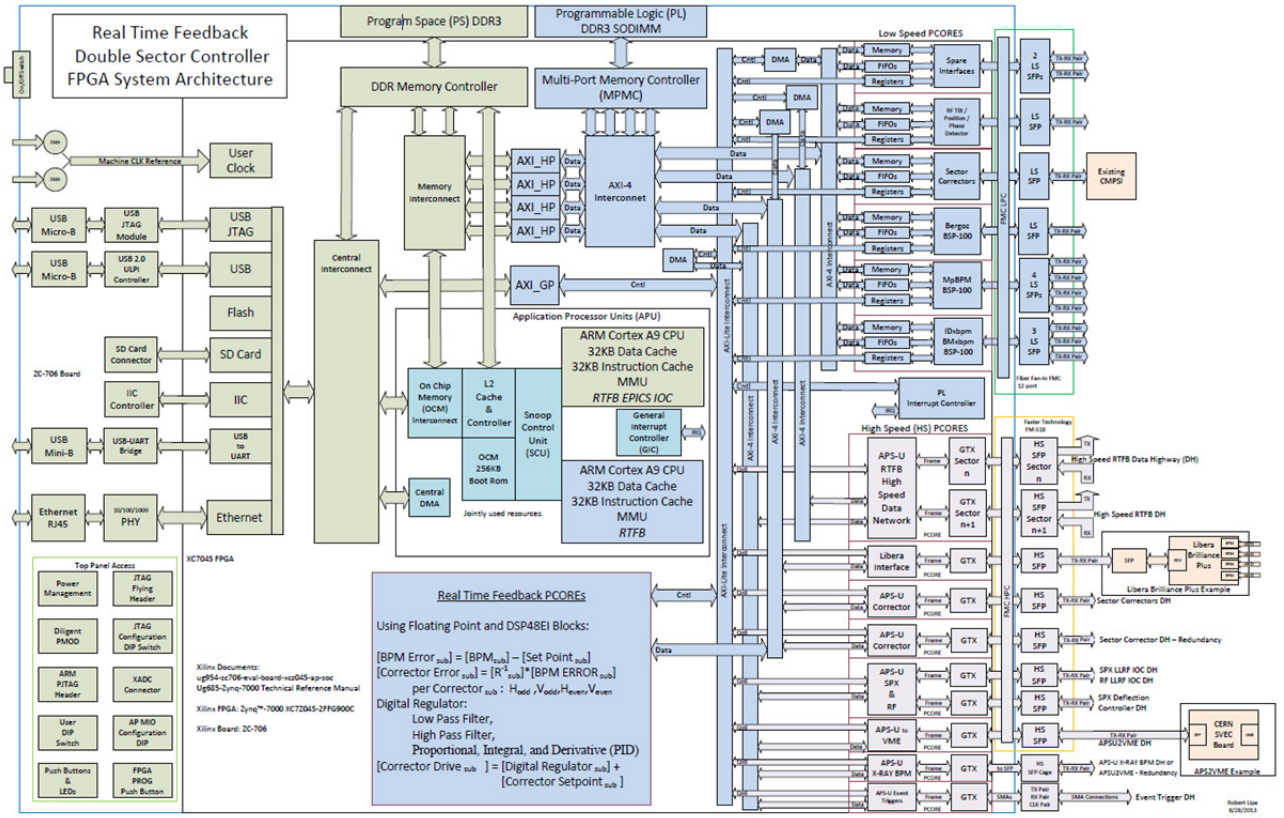


Figure 3: RTFB DSC FPGA architecture using Zynq-XC7Z045 FPGA.

RTFB DSC FPGA ARCHITECTURE

Using the Zynq-XC7Z045 FPGA features [8] and the features of the ZC706 board, the necessary function for the RTFB DSC maps can be realized. EPICS runs from Linux in the program space DDR3 memory on one of the ARM Cortex™ A9 CPUs. The RTFB algorithm runs on the other CPU with hardware assists from floating-point DSP cores in the programmable logic (PL) fabric. Figure 3 shows the FPGA architecture. With Vivado High-Level Synthesis [9] or System Generator, the RTFB algorithms can be implemented using floating-point DSP cores and exported as a PCORE. The PCOREs attach to the DDR3 controllers, GTX, and the CPUs via the AXI interconnect. The RTFB CPU coordinates the flow of the error and response matrix data between the RTFB PCOREs and the LS and HS interconnections via the AXI interconnect using the DMA controllers.

SUBSEQUENT PROGRESS

Routed versions of the SVEC FPGA with a (0) timing score have been created. The FPGA functions to interface to the existing system function and is created using the following FPGA features: VME64x core, VME-to-AXI DPR, 4-port RTFB DDR3 memory controller, Microblaze (MB) embedded processor with local memories and controllers, MB DDR3 memory, AXI interconnect, two AXI DMA controllers, and one GTP core.

CONCLUSION

The Fast Orbit Feedback System for the APS Upgrade utilizes the dual ARM Cortex™ A9 processors, multi-port DDR3 memory controllers, gigabit transceivers, and the programming logic interconnect to advance fast orbit feedback to a 22.6-kHz sample rate.

REFERENCES

[1] J. Carwardine, F. Lenkszus, “Real-Time Orbit Feedback at the APS,” AIP Conference Proceedings 451, pp. 125-144 (1998).
[2] Instrumentation Technologies, “Libera Brilliance+ Electron Beam Position Processor.”
[3] Instrumentation Technologies, “Libera Photon.”
[4] Xilinx, Inc.; http://www.xilinx.com/ZC706
[5] Xilinx, Inc.; http://www.xilinx.com/KC705
[6] Simple VME FMC Carrier (SVEC); http://www.ohwr.org/projects/svec/wiki
[7] Faster Technology, LLC; http://www.fastertechnology.com
[8] Xilinx Inc., “Zynq-7000 All Programmable SoC Technical Reference Manual,” June 2013.
[9] Daniele Bagni et al., “Zynq-7000 All Programmable SoC Accelerator for Floating Point Matrix Multiplication Using Vivado HLS,” XAPP1170, (v1.1), June 29, 2013.

Copyright © 2013 CC-BY-3.0 and by the respective authors

LINEAR ANALYSIS FOR SEVERAL 6-D IONIZATION COOLING LATTICES*

J. Scott Berg, Robert B. Palmer, Diktys Stratakis, BNL, Upton, NY, 11973, USA†

Abstract

In muon accelerators, ionization cooling is the only viable option for reducing the muon beam emittance to values necessary for a muon collider. An ionization cooling lattice requires a large momentum acceptance, small beta functions, an extremely large dynamic aperture, and a modest amount of dispersion to have good performance. The latter values are a function of beam momentum. One step in understanding the lattice performance is to determine these quantities for a lattice cell being studied. This is modestly more complex than usual since the lattice is generally highly coupled. We first review the general method for computing these quantities for a general lattice. Then we look at several lattices of interest, compute these quantities, and relate their values and momentum dependencies to the performance of the lattices.

ANALYSIS

To try to understand the behavior of cooling lattices, one can used standard techniques for analyzing accelerator lattices. These systems are highly coupled, and they are non-symplectic due to the presence of cooling. The symplecticity is further complicated by the use of kinetic momenta in most tracking codes. Use of canonical momenta would be challenging due to the strong transverse vector potentials that arise from the use of solenoids, but would arise in any case due to the use of short cells and large beam sizes. Symplecticity can be further compromised by use of a non-symplectic integrator with step sizes larger than needed for machine precision and magnetic field approximations that are not divergence-free.

Fixed Energy

At fixed energies, we find the closed orbit through a single cooling cell, then look at the linear map about that closed orbit. We then find the eigenvalues and eigenvectors of the linear map to get the tunes and the beta functions. More specifically, if M is the linear map about the closed orbit, then we find a matrix A such that $MA = AR$, where R is in the form

$$\begin{bmatrix} \lambda_1\cos\mu_1 & \lambda_1\sin\mu_1 & 0 & 0 \\ -\lambda_1\sin\mu_1 & \lambda_1\cos\mu_1 & 0 & 0 \\ 0 & 0 & \lambda_1\cos\mu_2 & \lambda_1\sin\mu_2 \\ 0 & 0 & -\lambda_1\sin\mu_2 & \lambda_1\cos\mu_2 \end{bmatrix} \quad (1)$$

Since M is not necessarily symplectic, we allow $\lambda_k \neq 1$.

We find the lattice parameters as a function of energy. We will not study energies for which the lattice does not have stable orbits in the sense that R is of the form (1).

The matrix A is not uniquely defined. There are three different degrees of freedom. First, one can exchange the first two columns of A with the last two columns, which corresponds to swapping the eigenvalues. Second, one can change the sign of one of the first two columns of A, which corresponds to changing the sign of μ_1 (similarly for the last two columns and the sign of μ_2). Finally, one can multiply A on the right by a matrix of the form (1) (but with different parameters than R). We will define A sufficiently to accomplish three goals: to resolve the sign ambiguity in μ_k in R; to be able to compute the beta functions; and to ensure that the two sets of eigenvalues and the beta functions are continuous functions of the energy (so that the 1 and 2 indices don't swap arbitrarily).

For a given energy, we scale both $\boldsymbol{a}_{2k-1}$ and $\boldsymbol{a}_{2k}$ ($\boldsymbol{a}_j$, $1 \leqslant j \leqslant 4$, is the jth column of A) by the same value, and possibly change the sign of $\boldsymbol{a}_{2k}$, so that $\boldsymbol{a}_{2k-1}^T J \boldsymbol{a}_{2k} = 1$, where

$$J = \begin{bmatrix} 0 & 1 & 0 & 0 \\ -1 & 0 & 0 & 0 \\ 0 & 0 & 0 & 1 \\ 0 & 0 & -1 & 0 \end{bmatrix} \quad (2)$$

and the order of coordinates is (x, p_x, y, p_y). If we change the sign of $\boldsymbol{a}_{2k}$, we also change the sign of μ_k. There is still an arbitrary rotation on the right side of A; we will insure that subsequent results are independent of that rotation.

Say we compute A_1 and A_2 for nearby energies. We would expect these matrices to be nearly the same, except for an arbitrary rotation on the right side of each one. If the columns of these matrices are $\boldsymbol{a}_{1;j}$ and $\boldsymbol{a}_{2;j}$, we compute the matrix S_{kl} with elements $s_{kl;ij} = \boldsymbol{a}_{2;2k-2+i}^T J \boldsymbol{a}_{1;2l-2+j}$. If $\det S_{11} > \det S_{12}$, then the columns of A_1 and A_2 refer to corresponding eigenvectors. If not, then the eigenvectors are in a different order in A_1 and A_2, and for one of the matrices the first pair of columns should be swapped with the second pair, and the eigenvalues should be swapped as well.

Each eigenvector pair describes a corresponding set of Courant-Snyder lattice functions. They relate the beam size and angular divergence to the area traced out by an ellipse. Since with coupling, oscillation is not in a fixed plane, the corresponding quantities must be independent of direction. They must also be independent of the arbitrary rotation on the right side of A. By analogy to the usual quantities, we can then define

$$\beta_k = a_{1,2k}^2 + a_{1,2k+1}^2 + a_{3,2k}^2 + a_{3,2k+1}^2 \quad (3)$$

* This manuscript has been authored by employees of Brookhaven Science Associates, LLC under Contract No. DE-AC02-98CH10886 with the U.S. Department of Energy. The United States Government retains a non-exclusive, paid-up, irrevocable, world-wide license to publish or reproduce the published form of this manuscript, or allow others to do so, for United States Government purposes.

† jsberg@bnl.gov

Copyright © 2013 CC-BY-3.0 and by the respective authors

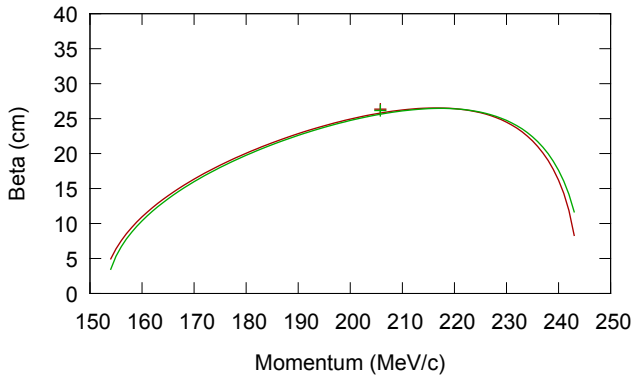


Figure 1: Beta functions vs. total momentum in stage 4 of the rectilinear FOFO (curves). The plus symbols are the beta functions and total momentum for the 6-D closed orbit.

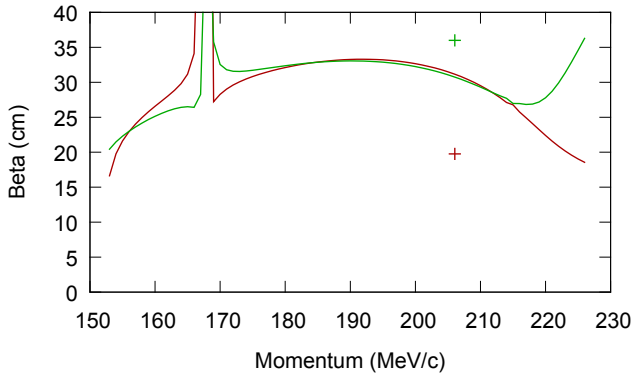


Figure 2: Like Fig. 1, but for the planar snake.

One could similarly define α_k and γ_k, though the usual relationships between these quantities do not necessarily hold since there are additional degrees of freedom due to coupling between the planes.

We calculate dynamic apertures as a function of energy by launching particles along the vector

$$\sqrt{2J_1}\boldsymbol{a}_1 + \sqrt{2J_2}\boldsymbol{a}_3 \tag{4}$$

and keeping track of the number of turns a particle survives as a function of J_1 and J_2.

6-D Fixed Point

We can also find the 6-D fixed point in the presence of acceleration and the average energy loss in the absorbers. All calculations are as for fixed energy but with 6-dimensional phase space vectors. Our additional variables are time and energy. The additional rows and columns of J may need a sign change or scaling factor depending on the exact implementation (blindly using energy and time, plus having momenta in eV/c, leads to a factor of $-c$ in J as used above). The eigenvalues will no longer have unit magnitude even for Maxwellian fields due to the presence of the absorber. Beta functions for the modes which are primarily transverse are computed according to (3).

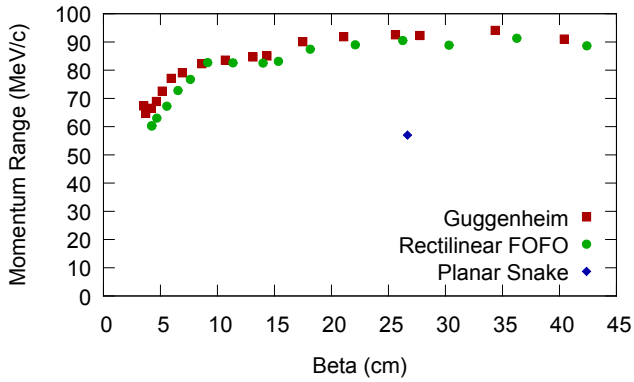


Figure 3: Momentum range vs. the geometric average of the beta functions at the 6-D fixed point.

One can calculate a "lossless" Q factor which arises solely from the average energy loss in the absorber and decays:

$$\frac{d\epsilon_6/\epsilon_6}{dN/N} = \frac{-2\ln|\lambda_1\lambda_2\lambda_3|(pc)\tau_\mu c}{L(m_\mu c^2)} \tag{5}$$

where ϵ_6 is the product of the emittances, N is the number of particles, λ_k are the eigenvalues of the one-cell map, p is the average total momentum for the closed orbit particle, τ_μ is the muon rest lifetime, m_μ is the muon rest mass, L is the cell length, and c is the speed of light. The Q value for the real lattice [1] is lower due to multiple scattering and energy straggling, which increase the emittances and cause particles to fall out of the dynamic aperture, dynamical losses of large amplitude particles, and emittance growth from mismatches and nonlinearities.

LATTICES

We study three cooling lattices. The first is a "Guggenheim" channel [2], where the beamline bends around in a circle while gradually moving perpendicular to the plane of the circle. A dipole field which is mostly in the vertical direction is generated by tilting the solenoid coils. In addition to generating bending, this creates dispersion (in position) at a wedge-shaped absorber. The solenoid field undergoes a single sinusoidal-like oscillation within the cell. The second is a rectilinear FOFO snake [3, 4], which has fields similar to the Guggenheim channel, but with smaller coil tilts and therefore a smaller dipole field, but where the beamline is straight. This requires vertical motion of the closed orbit to correct the bending from the dipole field. The third is a planar snake [5], which is a straight channel like the rectilinear FOFO. However, the solenoid field in one cell is opposite to the field in the next cell. In the presence of the dipole field generated from the tilts, this makes the period of this lattice two "cells" long. In addition, the direction of the tilts is chosen so that instead of dispersion in position at the absorber, there is dispersion in momentum. Thus a parallel-faced absorber can be used instead of a wedge.

Copyright © 2013 CC-BY-3.0 and by the respective authors

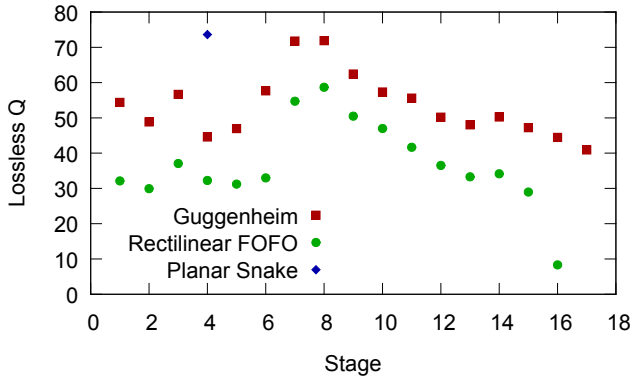


Figure 4: Lossless Q, vs. stage number. The planar snake has a beta function similar to stage 4 of either the Guggenheim or rectilinear FOFO.

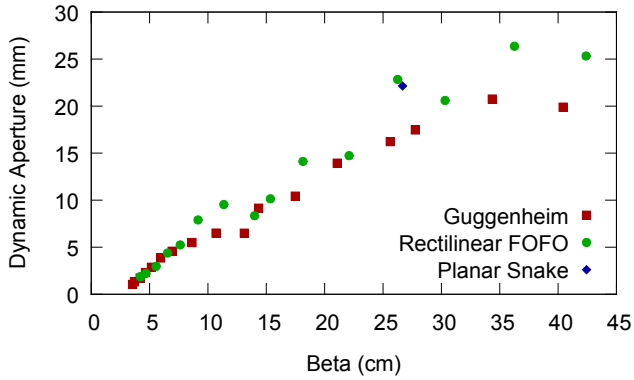


Figure 5: Dynamic aperture vs. the geometric average of the beta functions at the 6-D fixed point. Dynamic aperture is the average over the momentum passband of the smallest value of $J_x + J_y$ (normalized) beyond which there is at least one (J_x, J_y) pair which does not survive for 20 turns.

Calculations are performed using ICOOL [6] and computing linear maps via finite differences.

Figures 1 and 2 show the beta functions as a function of total momentum for a rectilinear FOFO (the Guggenheim is similar) and the planar snake. The rectilinear FOFO and Guggenheim operate in the passband between π and 2π phase advance. The planar snake operates similarly, except that the period is two cells, so what is shown in Fig. 2 is for a phase advance from 2π to 4π. There is thus a linear resonance (3π) near 168 MeV/c, which despite its weakness appears to be enough to truncate the operating passband. One also observes a strong change in the beta functions at the high energy end (there is a corresponding change in the closed orbit) arising from the approach to an integer tune. There are also indications of a coupling resonance near 213 MeV/c.

Figures 1 and 2 also show the beta functions at the 6-D fixed point. For the rectilinear FOFO and Guggenheim, the beta functions are close to what is found in the fixed energy calculation. For the planar snake, however, the beta functions are very different. At the fixed point, the two betatron tunes and the synchrotron tunes have the same fractional part (near 0.25), and one of the transverse eigenvectors and the longitudinal eigenvector have ellipse projections that have nearly equal areas in the transverse and longitudinal directions. Thus the planar snake appears to be operating on a synchro-betatron resonance, similarly to what is described in [7].

Energy acceptance of a lattice is important both to achieve good longitudinal cooling and acceptance as well as to limit losses from energy straggling. One can look at the momentum acceptance that can be achieved for a given beta function at the absorber. The result is shown in Fig. 3. The planar snake has a significantly reduced momentum acceptance compared to the other lattices. The rectilinear FOFO (at least as designed) does not perform quite as well as the Guggenheim for smaller beta functions.

Figure 4 shows the lossless Q for the lattices. Note that the lossless Q is significantly lower for the rectilinear FOFO than for the other lattices. Since this is mainly related to the energy lost or gained in each cell, and the RF gradients in the rectilinear FOFO are similar or larger than those used in the Guggenheim or planar snake, one would expect that the rectilinear FOFO could have improved performance, probably via some increase in the wedge thickness and subsequent tuning. This may explain the lower Q value found for the rectilinear FOFO (maximum of 9.5 [4]) compared to the Guggenheim (maximum of 11 [2]).

Figure 5 shows the dynamic aperture plotted against the beta function for the Guggenheim and rectilinear FOFO lattices. Note that the dynamic aperture is not proportional to the beta function for small beta (it is worse), which ultimately prevents achieving smaller emittances.

REFERENCES

[1] R. Palmer *et al.*, "Ionization cooling ring for muons," Phys. Rev. ST Accel. Beams **8**, 061003 (2005).

[2] D. Stratakis, R. C. Fernow, J. S. Berg, and R. B. Palmer, "Tapered channel for six-dimensional muon cooling toward micron-scale emittances," Phys. Rev. ST Accel. Beams **16**, 091001 (2013).

[3] V. Balbekov, "R_FOFO snake channel for 6D muon cooling," MAP-doc-4365 (2013). `http://map-docdb.fnal.gov/`

[4] D. Stratakis, J. S. Berg, R. B. Palmer, and V. I. Balbekov "A High-Performance Rectilinear FOFO Channel for Muon Cooling," to appear in the proceedings of the 2013 North American Particle Accelerator Conference (2013).

[5] R. B. Palmer, J. S. Berg, R. C. Fernow, and D. Stratakis, "A Planar Snake Muon Ionization Cooling Lattice," to appear in the proceedings of the 2013 North American Particle Accelerator Conference (2013).

[6] F. C. Fernow, "Recent Developments on the Muon-Facility Design-Code ICOOL," in *Proceedings of 2005 Particle Accelerator Conference, Knoxville, Tennessee* (IEEE, 2005) 2651.

[7] J. S. Berg, "Ionization cooling in all phase space planes with various absorber shapes, including parallel-faced absorbers," Nucl. Instrum. Methods A **569** (2006) 677.

Copyright © 2013 CC-BY-3.0 and by the respective authors

A PLANAR SNAKE MUON IONIZATION COOLING LATTICE *

Robert B. Palmer, J. Scott Berg, Diktys Stratakis, BNL, Upton, Long Island, New York, USA

Abstract

Muon Colliders require cooling in six dimensions (x, x',y, y', t, E). Several ionization 6D cooling lattices, using vacuum acceleration, are reviewed: RFOFO lattices, both curved [1] and rectilinear [2] cool one sign to low emittances; A Helical FOFO snake [3] cools both signs, but not to low emittances. A Planar Snake [4] lattice is proposed that cools both muon signs, and appears suitable for low emittances. The parameters and performance for an example suitable for the early stages of cooling is given.

INTRODUCTION

The Muon Accelerator Program (MAP) [5] is studying Muon Colliders with center of mass energies from 125 GeV to several TeV. All require 6 dimensional (x, x',y, y', E, t) cooling to transverse emittances of ≈ 0.31 mm, and longitudinal emittances ≈ 1.5 mm.

In transverse ionization cooling, in a low Z absorber (hydrogen or Lithium Hydride), both transverse and longitudinal momentum are lost. Radio-frequency (rf) cavities (only vacuum rf is considered in this paper) then restore the longitudinal momentum, leaving the reductions of the transverse components. Multiple scattering leads to a minimum (equilibrium) emittance that is proportional to the betatron $\beta_\perp$ divided by the relativistic β of the muon momentum.

For cooling in the longitudinal dimension, emittance exchange is required. Two methods are illustrated in Fig. 1a and b. In a), a wedge absorber is placed in a region with dispersion, so higher momentum muons have more energy loss than those lower. In b) a plane slab absorber is placed where there is angular dispersion. Emittance exchange can also be achieved in a Helical Cooling Channel [6] where absorbing material is everywhere while higher momenta have longer paths.

Periodic lattices allow lower transverse betatron lengths $\beta_\perp$, but introduce integer and half integer resonances defining the operating momentum range. Figure 2a, b, and c show three cases:

a) Simple lattices of equi-spaced solenoids operate above the single π resonance.

b) Bi-periodic lattices [7], with pairs of coils spaced by longer drifts operate between the 2π and π resonances and have an attractively level $\beta_\perp$ between these resonances.

c) Lattices with more complex coils sequences, such as the Helical FOFO Snake and Planar snake, which both operate between the 3π and 2π resonances.

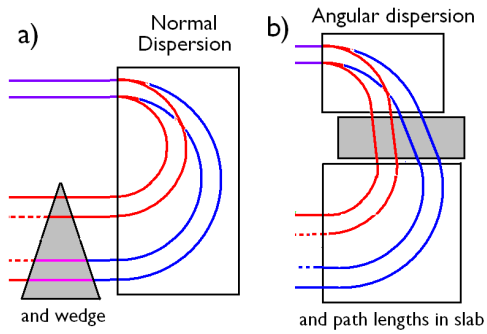


Figure 1: Emittance Exchange: a) using dispersion & wedge absorbers; b) using angular dispersion & slab absorbers.

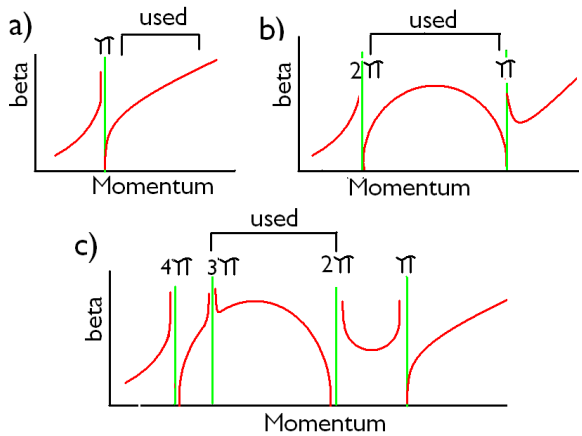


Figure 2: Lattice types: a) Simply periodic alternating solenoids; b) Bi-periodic alternating solenoids; c) Higher tune lattices (Helical Snake & Planar Snake).

GEOMETRIES

Figure 3 shows three lattice geometries. They could be curved, but we consider only straight geometries here.

RFOFO & RFOFO Rectilinear Lattices

Using alternating solenoids, Balbekov [2] has shown that the required dispersions can be generated by small tilts of the coils in either a simply periodic (FOFO) or bi-periodic (RFOFO) lattice. The tilts are small and alternate to generate periodic dipole fields (Fig. 3a). The performance of these lattices is essentially the same as with curved lattices [8], but with simpler engineering. Recent simulations [9, 10], have shown cooling from emittances close to those simulated from the initial phase rotation (15 mm transverse, 45 mm longitudinal) to that required in the baseline design (0.31 mm transverse and 1.5 mm longitudinal) with acceptable particle loss (of order 50%).

* Work supported by US Department of Energy under contract DE-AC02-98CH10886

Copyright © 2013 CC-BY-3.0 and by the respective authors

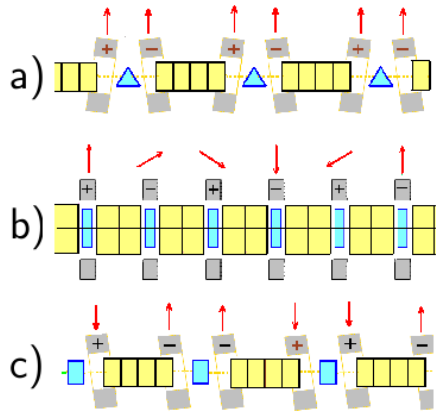


Figure 3: Geometries: a) Rectilinear RFOFO; b) Helical FOFO Snake; c) Planar Snake.

Despite the success of such simulations, there are reasons to seek alternatives. The current densities are high, in part because the coils on either side of the absorber are opposed; and for the same reason, the forces between them are outward, requiring supporting structures. The engineering of wedge shaped liquid hydrogen absorber will not be easy, and the fact that they only cool one sign is less than ideal.

Helical FOFO Snake

The Helical FOFO Snake [3] (Fig. 3b) is based on a periodic FOFO lattice with alternating focus solenoids, but the coil tilts are no longer in a single plane. Instead, the tilt directions rotate in azimuth giving closed orbits that perform an approximation to a helix. Because the lattice does not repeat for multiple sub-cells, there are more resonances, and the operating momenta are restricted to tunes between 3π and 2π - as in Fig.2c.

The lattice has two very attractive characteristics: 1) it uses absorbers with plane parallel windows that would be much easier to build than the wedges; and 2) it works for both signs simultaneously, possible because the lattice employs emittance exchange represented in Fig. 1b. Unfortunately the absorbers are located where the $\beta_\perp$s are at their maxima making it unsuitable for cooling to the smaller emittances.

Planar RFOFO Snake

This lattice[4] (see Fig. 3c) is, like the RFOFOs, based on bi-periodic focusing coils that give low betas at absorbers placed between the nearer pairs. But the polarities of the coils, instead of alternating, have the sequence $+|+-|-+|+$ etc., where the vertical bars indicate absorber locations. The number of field reversals is now only half that in an RFOFO, and the coils on either side of the absorber have the same polarity. Their fields no longer buck one another, and the magnet forces pull them together. A disadvantage is that the phase advances are doubled and the momentum acceptance, between 3π and 2π (see Fig. 2c) is reduced.

An attempt to find tilts that would give dispersions at the absorbers failed, but a solution was found, using very small tilts, giving large angular dispersions. The solution has tilts all in the same direction, resulting in dipole fields with the same pattern as the solenoids. This introduces a transverse resonance, at the tune 2π, at the high end of the momentum acceptance. This dispersion is highly non-linear: low over most of the momentum range, but very high near the 2π resonance, yet, at least for the example simulated, this was not a problem.

EARLY STAGE PLANAR RFOFO SNAKE

This example would be suitable for an early stage of 6D cooling for a Muon Collider. Parameters are given in Table 1. Figure 4 shows a cross section of one complete cell. The solenoid coils are tilted in the same direction alternatively by 7.3 and 17.9 mrad. The rf is at 201 MHz operating at 17 MV/m axial gradient, and a phase of approximately 30 degrees.

Figure 5 shows the betas as a function of length for a few cells. It is seen that, as in a normal RFOFO lattice, the betas are much lower at the absorbers than between them.

Figure 6 shows the dispersions as a function of length over a few cells. It is seen that, at the absorbers, the dispersion is not large, but the x dispersion at the absorber is changing rapidly as a function of length, corresponding to an angular dispersion of approximately 0.4.

Figure 7 shows the emittances and transmission. Cooling is good in both transverse and longitudinal emittance, with the rate of muon loss, after an initial miss-match, dominated by the inevitable decays. The quality factor $Q = (d\epsilon_6/\epsilon_6)/(dn/n)$ has a low initial value where matching losses dominate; a low value at the end as the emittances approach their equilibria; and a maximum value of over 9, which is approximately the same as that with a Rectilinear RFOFO lattice.

The results plotted in Fig. 7 and discussed above were obtained using a mode of ICOOL [11] simulation in which fields are defined along the axis, and the program derives the fields at other locations by a 5th order extrapolation. The lattice has since been simulated [12] with ICOOL using a field map, and also with G4BL [13] using the same map. The results are very similar or slightly better in these simulations.

CONCLUSION

Simulations of Rectilinear RFOFO 6 dimensional ionization cooling has given the required parameters, but there remain engineering challenges and two complete systems are needed for the two particle signs.

A Planar RFOFO Snake, using planar absorbers, can cool both signs simultaneously. An example lattice design of an early stage of cooling has been simulated and gives good performance. It uses coils on either side of the absorber, that have the same polarity, thus reducing the cur-

Copyright © 2013 CC-BY-3.0 and by the respective authors

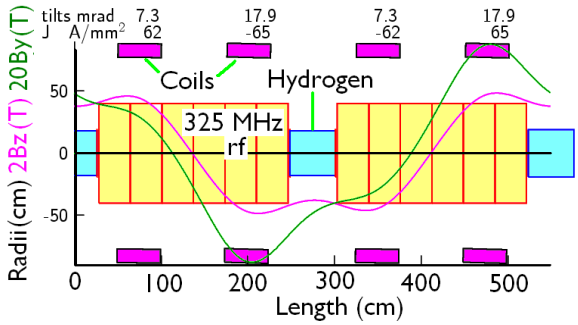


Figure 4: Section of an early stage of a Planar RFOFO Snake.

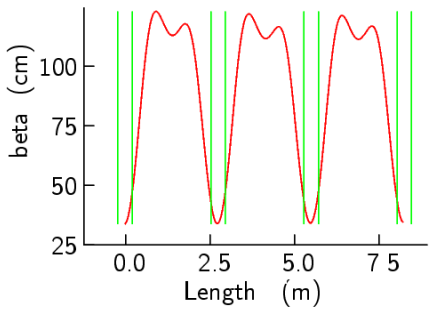


Figure 5: Beam betas as a function of length. The green lines define the location of the absorbers.

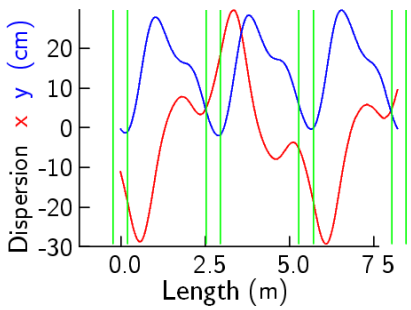


Figure 6: Dispersions as a function of length for the early stage lattice. The green lines define the location of the absorbers.

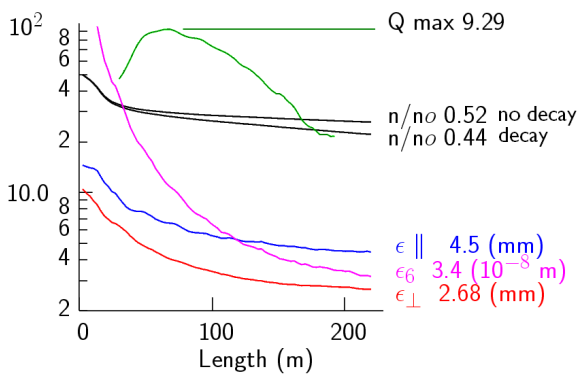


Figure 7: Emittances and transmission of early stage planar snake.

Table 1: Parameters of Early 6D Cooling Lattice

gap m	start m	dl m	rad m	dr m	tilt mrad	I/A A/mm^2
0.50	0.50	0.5	0.77	0.11	7.3	62.22
0.75	1.75	0.5	0.77	0.11	17.9	-65.45
0.50	3.25	0.5	0.77	0.11	7.3	-62.22
0.75	4.50	0.5	0.77	0.11	17.9	65.45

	material	length cm	radius cm
Half absorber	Liquid H_2	21.3	18
Absorber window	Aluminum	0.05	18
Gap	Vacuum	17.15	50
6 rf cavities	Vacuum	33	61
Gap	Vacuum	17.15	50
Absorber window	Aluminum	0.05	18
Half absorber	Liquid H_2	21.3	18

rent densities and forces. Non-linear angular dispersions are obtained with small tilts (0.5-1 deg.), enhanced by the 2π resonance at the high momentum end.

The concept is similar to that of a Helical FOFO Snake [3], but is here generated by alternating dipole fields in a single direction, conceptually giving planar snaking orbits, unlike the azimuthally rotating dipoles in the Helical Snake. The planar RFOFO snake allows betas at the absorbers to be much smaller than elsewhere. This result has been confirmed using field maps in both ICOOL and G4BeamLine. A design reaching the required final emittances has been tried, but its transmission is poor, and is not yet understood.

REFERENCES

[1] P. Snopok et al., IJMPA 24, p. 987 (2009).

[2] V. Balbekov, Proc. of PAC 2003, Portland, OR, p. 2017 (2003).

[3] Y. Alexahin, AIP Conf.Proc. 1222, p. 313 (2010).

[4] R.B. Palmer, 6D Cooling in Periodic Lattices, June 6, 2013, http://www.cap.bnl.gov/AAG/GroupMeetings/

[5] http://map.fnal.gov

[6] Y. Derbenev and R.P. Johnson, Phys. Rev. ST Accel. Beams 8, 041002(2005).

[7] A. Sessler, private communication (1999).

[8] D. Stratakis, et al., Phys. Rev. ST Accel. Beams 16, 091001 (2013).

[9] V. Balbekov , 6D Vacuum RF Mini-workshop (Batavia, IL, 2013), https://indico.fnal.gov/conferenceDisplay.py?confId=7402

[10] D. Stratakis et al. Proc. of NAPAC 2013, Pasadena, CA, THPHO12.

[11] R. C. Fernow, Proc. of PAC 2005, Knoxville, TN, p. 2651.

[12] D. Stratakis, MAP weekly Seminar, https://indico.fnal.gov/conferenceDisplay.py?confId=6959

[13] T. Roberts et al., Proc. of EPAC08, Genoa, Italy, WEPP120 (2008).

Copyright © 2013 CC-BY-3.0 and by the respective authors

SRF AND RF SYSTEMS FOR CeC PoP EXPERIMENT*

S. Belomestnykh#,1,2, I. Ben-Zvi1,2, C. H. Boulware3, J. C. Brutus1, T. L. Grimm3,Y. Huang1, D. Kayran1, X. Liang2, V. Litvinenko1,2, P. McIntosh4, A. Moss4, P. Orfin1, I. Pinayev1, T. Rao1, M. Ruiz Osés2, B. Sheehy1, J. Skaritka1, K. Smith1, R. Than1, J. Tuozzolo1, E. Wang1, A. Wheelhouse4, Q. Wu1, T. Xin2, Wencan Xu1, A. Zaltsman1
1) Brookhaven National Laboratory, Upton, NY 11973-5000, U.S.A.
2) Stony Brook University, Stony Brook, NY 11794, U.S.A.
3) Niowave, Inc., Lansing, MI 48906, U.S.A.
4) STFC/DL/ASTeC, Daresbury, Warrington, Cheshire, UK,WA4 4AD

Abstract

Efforts to experimentally prove the concept of coherent electron cooling are underway at BNL. A short 22 MeV linac will provide high charge, low repetition rate beam to cool a single ion bunch stored in RHIC. The linac will consist of a 112 MHz SRF gun, two 500 MHz normal conducting bunching cavities and a 704 MHz five-cell accelerating SRF cavity. The paper describes the SRF and RF systems, the linac layout, and discusses the project status, first test results and schedule.

INTRODUCTION

Coherent electron Cooling (CeC) is a technique promising significant luminosity improvement in high-energy hadron-hadron and electron-hadron colliders [1]. A Proof-of-Principle (PoP) experiment is under preparation at BNL to demonstrate its feasibility [2, 3]. This experiment aims to cool only one ion bunch stored in RHIC, requiring a high-bunch-charge (up to 5 nC), but low-repetition-rate electron beam. The bunch repetition frequency (78 kHz) is equal to the revolution frequency of ion bunches in RHIC. A short 22 MeV superconducting linac is being built to provide such beam [4]. The linac includes two superconducting RF (SRF) systems and one normal conducting RF system. The two SRF systems are a 112 MHz Quarter Wave Resonator (QWR) SRF photoemission electron gun [5] and a 704 MHz SRF booster cavity cryomodule. The normal conducting RF system comprises two copper bunching cavities [6] to provide velocity modulation for shortening the electron bunches between the two SRF cryomodules. The linac layout is shown in Figure 1. In this paper we describe the SRF and RF systems, report on the project status and test results, and discuss testing and commissioning plans.

112 MHz QWR SRF GUN

A superconducting 112 MHz quarter-wave resonator was developed by collaborative efforts of BNL and Niowave, Inc. [7, 8]. The gun operates at 4.5 K with liquid helium provided from a quiet helium source via the cryomodule cryogenic tower. We expect to achieve the

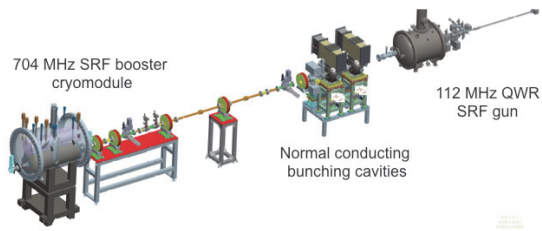


Figure 1: Layout of the CeC PoP linac.

cavity quality factor of 1.8×10^9. The QWR's center conductor geometry naturally accommodates a half-wavelength choke joint and allows mechanical decoupling of the cathode assembly from the niobium cavity [9]. A low-RF-loss photocathode stalk operates at room temperature. It is hollow, allowing inserting a small photocathode pack via a load lock system. We plan to use multi-alkali (CsK_2Sb or NaK_2Sb) photocathodes illuminated with a green (532 nm) light from a laser to generate the electron beam.

The 112 MHz gun is equipped with a dual-purpose fundamental RF power coupler / fine frequency tuning assembly [9]. The fine frequency tuning with a range of about 3 kHz will be used for remote frequency adjustment. It will complement a larger range (>78 kHz) tuner, which will be used only for an initial frequency set up. The mechanical design of the fundamental power coupler (FPC) is described elsewhere [10]. A focusing solenoid is placed on top of the FPC close to the cryomodule's beam exit flange.

After the first cryomodule cold test at Niowave in December of 2010 [7], the gun has undergone modifications. A new cryostat was designed and fabricated to be compatible with BNL's safety requirements and to have appropriate interfaces for installation in RHIC tunnel. The modified gun was cold tested again at Niowave in December of 2012 and February of 2013. During the tests we encountered multipacting zones at very low fields, which were processed only after we modified the RF input coupler to increase its coupling. Eventually, the gun reached an accelerating voltage of 0.92 MV, limited by an insufficient radiation shielding of the experimental set up. Figure 2 shows the gun cavity performance during the cold test.

*Work is supported by Brookhaven Science Associates, LLC under contract No. DE-AC02-98CH10886 with the US DOE.
#sbelomestnykh@bnl.gov

Copyright © 2013 CC-BY-3.0 and by the respective authors

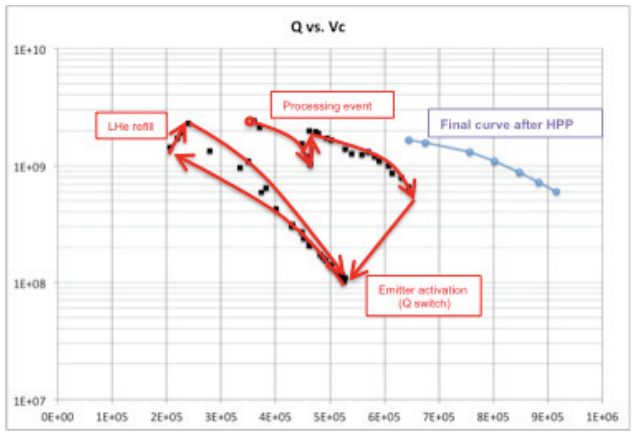


Figure 2: Q *vs.* V_c plot showing the gun cavity behavior during conditioning and the final curve.

After completion of the cold test, the gun was shipped to BNL and is currently installed in the RHIC tunnel. The commissioning will begin in early 2014.

500 MHz BUNCHING CAVITIES

Two single cell normal conducting cavities operating at 500 MHz will serve as bunching cavities, imprinting a velocity modulation along the electron bunch. The bunch will then shorten as they travel in the drift space between the two SRF cryomodules. The cavities are a contribution to the experiment from the Daresbury Laboratory, UK [6]. Formerly, they were installed in the now decommissioned SRS light source [11]. Figure 3 shows a cavity layout and Table 1 lists its parameters.

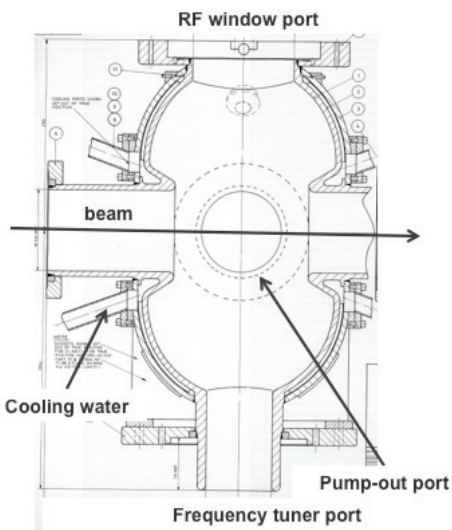


Figure 3: 500 MHz bunching cavity.

The fundamental power coupler is of a waveguide type coupled to the cavity via an aperture (port) at the cavity top, sealed with a disk ceramic window. The coupling is adjusted via moving a reflection plane in the waveguide. The original SRS configuration included a moveable waveguide short, which allowed adjusting coupling for different beam loading. As there will be very small beam loading in CeC PoP, we will adjust the short position for unity coupling only once – no need for a moveable short. The two cavities will be powered in parallel from an IOT-based RF power amplifier.

The cavities were delivered from Daresbury to BNL in early 2012. They have been particulate-free cleaned and refurbished, vacuum baked. The cavities are installed in the RHIC tunnel and being prepared for high power commissioning.

Table 1: Parameters of the 500 MHz Bunching Cavity

RF frequency	500 MHz
Accelerating voltage	0.3 MV
R/Q	178.5 Ohm
Geometry factor	38.2 Ohm
Cavity Q_0	31,000
Frequency tuning range	1.5 MHz
Cavity wall losses at 0.3 MV	16.3 W
Available RF power from IOT amplifier	50 kW

704 MHz BOOSTER CRYOMODULE

The 704 MHz booster cryomodule will house one 5-cell SRF cavity of the BNL3 shape [12-14]. The booster will deliver an energy gain up to 20 MeV. It will operate at 2 K with an internal superfluid heat exchanger to better isolate the cavity from microphonic noise originated in the cryogenic system. The mechanical design of the cold mass is described elsewhere [15]. A sectional view of the cryomodule is shown in Figure 4. A fundamental RF power coupler (FPC) will be of a coaxial antenna type and will be able to transmit power up to 20 kW CW. The cryomodule design is being finalized and its production will begin soon at Niowave, Inc. with the delivery to BNL scheduled for summer of 2014. Table 2 lists main parameters of the booster system.

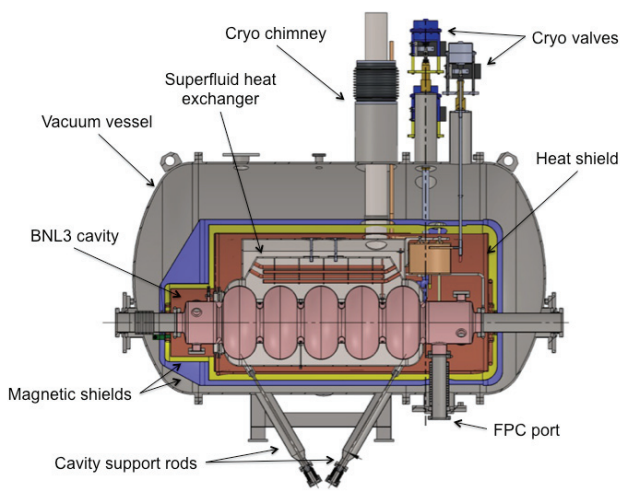


Figure 4: 704 MHz booster cryomodule for CeC PoP.

Copyright © 2013 CC-BY-3.0 and by the respective authors

Two cavities have been fabricated: BNL3-1 by AES, Inc. and BNL3-2 by Niowave, Inc (Figure 5). Both cavities have undergone standard preparation for vertical acceptance testing (bulk BCP, vacuum bake at 600ºC for 10 hours, light BCP, HPR). The tests will be performed in October/November of 2013.

Table 2: Parameters of the 704 MHz SRF Booster

RF frequency	704 MHz
Maximum energy gain	20 MeV
R/Q	506 Ohm
Geometry factor	283 Ohm
Cavity Q_0 at 4.5 K	2×10^{10}
Cavity RF losses at 2.0 MV	37 W
Frequency tuning range	78 kHz
Q_{ext} of FPC, min.	2.8×10^{7}
Available RF power from solid state amplifier	20 kW



Figure 5: BNL3-2 cavity at Niowave, Inc.

SUMMARY

A short 22 MeV linac for the CeC PoP experiment comprises two SRF systems and one normal conducting RF system. The 112 MHz SRF gun cryomodule has been fabricated and tested up to 0.92 MV, limited only by insufficient radiation shielding. It will be re-tested and conditioned to full voltage after installation in the RHIC tunnel is complete in January of 2014. This will be followed immediately by commissioning of the 2 MeV beam line. The beam line will include two single cell normal conducting bunching cavities operating at 500 MHz. The cavities were received from Daresbury in 2012, refurbished, vacuum baked and are currently installed in the RHIC tunnel. Two 704 MHz 5-cell cavities have been fabricated. One of the cavities will be chosen for integration into the booster cryomodule after both are tested in a vertical cryostat at BNL. The booster cryomodule design is being finalized and its fabrication will begin soon at Niowave. Its delivery to BNL is scheduled for summer of 2014. Installation of the booster cryomodule will complete the CeC PoP linac.

REFERENCES

[1] V. N. Litvinenko, Y. S. Derbenev, *Phys. Rev. Lett.* **102**, 114801 (2009).
[2] V. N. Litvinenko et al., "Proof-of-Principle Experiment for FEL-based Coherent electron Cooling," *Proc. PAC'2011*, p. 2064.
[3] I. Pinayev et al., "Progress with Coherent electron Cooling Proof-of-Principle Experiment," *Proc. IPAC'2013*, p. 1535.
[4] D. Kayran et al., "SRF Photoinjector for Proof-of-Principle Experiment of Coherent electron Cooling at RHIC," *Proc. IPAC'2012*, p. 622.
[5] S. Belomestnykh et al., "Superconducting 112 MHz QWR Electron Gun," *Proc. SRF'2011*, p. 223.
[6] D. M. Dykes and B. Taylor, "Development of a High Power RF System for the Daresbury SRS," *Proc. PAC'1983*, p. 3475.
[7] S. Belomestnykh et al., "Superconducting 112 MHz QWR Electron Gun," *Proc. SRF'2011*, p. 223.
[8] S. Belomestnykh et al., "Developing of Superconducting RF Guns at BNL," *Proc. LINAC'2012*, p. 324.
[9] T. Xin et al., "Design of the Fundamental Power Coupler and Photocathode Inserts for the 112 MHz Superconducting Electron Gun," *Proc. SRF'2011*, p. 83.
[10] J. C. Brutus et al., "Mechanical Design of 112 MHz SRF Gun FPC for CeC PoP Experiment," WEPAC07, NA-PAC'13.
[11] http://en.wikipedia.org/wiki/Synchrotron_Radiation_Source
[12] Wencan Xu, et al., "High current cavity design at BNL," *Nucl. Instr. and Meth. A* **622** (2010) 17-20.
[13] Wencan Xu, et al., "High Current SRF Cavity Design for SPL and eRHIC," *Proc. PAC'2011*, p. 2589.
[14] Wencan Xu et al., "Progress on the High-Current 704 MHz Superconducting RF Cavity at BNL," *Proc. IPAC'2012*, p. 2486.
[15] J. C. Brutus et al., "Mechanical Design of the 704 MHz 5-cell SRF Cavity Cold Mass for CeC PoP Experiment," WEPAC06, NA-PAC'13.

Copyright © 2013 CC-BY-3.0 and by the respective authors

NOVEL MECHANICAL DESIGN FOR RHIC TRANSVERSE STOCHASTIC COOLING KICKER

C.J. Liaw, J.M. Brennan, S. Bellavia, J. Tuozzolo, K. Mernick, M. Myers
Brookhaven National Laboratory, Upton, NY 11973, U.S.A.

Abstract

Based on the beam emittance measurement from the pickup, the RHIC Stochastic Cooling kicker uses sixteen narrowband high Q cavities (from 5 to 8 GHz) to kick (or to cool) the bunched beam on each of the two transverse planes in the two rings. The cavities are integrated to two pairs of cavity plates and installed in two UHV chambers. The new kicker features scissor like driving mechanism, frictionless flexure joints, water cooled cavity plates, small frequency shift (less than 0.05%) during the operation and maintenance free. Novel mechanical designs, including cavity plate, vacuum, cooling, driving mechanism, and support structure design, are presented. Structural and thermal analyses, using ANSYS, were performed to confirm chamber structural stability and to calculate the cavity plate deformation due to thermal and mechanical load. Good agreement between the calculated cavity plate deflection and the expected plate deformation from the cavity frequency shift measurements has been achieved. Three assemblies utilizing this design (1 for the vertical and 2 for the horizontal plane) were completed for the FY2012 run. Successful performance has been reported.

INTRODUCTION

RHIC has successfully employed the stochastic cooling technique to counteract the emittance growth in the high frequency bunched beam due to Intra Beam Scattering (IBS) in the past several runs [1]. Two essential components, a pickup (to measure the beam emittance in the transverse directions) and a kicker (to cool the beam transversely), are required for the transverse stochastic cooling. The new pickup design has been reported elsewhere [2]. This paper will focus on the mechanical design of the new transverse stochastic cooling kicker.

To minimize the input power, high Q resonant cavities were chosen as the new kicker in RHIC [3]. During the early stage kicker development, RHIC received a few stochastic cooling tanks from Fermilab as a gift, which were originally developed for the FNAL Tevatron. To take advantage of these tanks, the FNAL original vacuum chambers and the driving mechanisms [4] were used to accommodate those cavities and to drive them from the cooling position (with a smaller aperture) to the standby position (with a larger aperture for the injected beam). There are several disadvantages with these designs: (1) The cavity plate guide shafts could get stuck in vacuum, (2) The beryllium copper RF spring fingers could lose their contact with the beam pipe, (3) The actuator could deliver an excessive force to bend the shaft, (4) The vacuum space is too small for the application, and (5) The cavity frequencies are not repeatable.

The newly developed transverse stochastic cooling kicker has addressed all the mechanical problems described above. Novel mechanical designs for the system are described below. Structural and thermal analysis results are also presented.

*Work supported by Brookhaven Science Associates, LLC under Contract No. DE-AC02-98CH10886 with the U.S. Department of Energy

DESIGN REQUIREMENTS

The mechanical design requirements for the new transverse stochastic cooling kicker are: (1) To provide 16 high Q cavities, spanning the bandwidth of 5 to 8 GHz in 200 MHz intervals, for each kicker, (2) To split the cavities on the median plane and integrate them into two pairs of cavity plates, (3)To maintain repeatable cavity resonant frequencies, with a frequency shift of no more than 0.05% of their frequencies, (4) To provide a reliable actuator for the cavity plates, (5) To keep the cavity aperture at 20 mm, during the operation, and at no less than 124 mm, when not in use, (6) To provide a sufficient space in the vacuum chamber for an easy access and the installation of the cavity plates, (7) To provide adequate structural stability of the vacuum chambers and the support stands, and (8) To provide a bakable (up to 200°C) and maintenance free vacuum design.

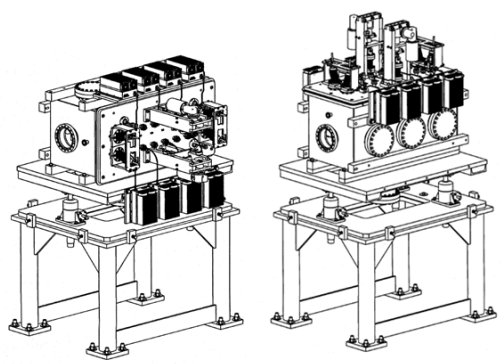


Fig. 1: One Half of a Horizontal and a Vertical Transverse Stochastic Cooling Kicker Assembly.

Copyright © 2013 CC-BY-3.0 and by the respective authors

TRANSVERSE KICKER ASSEMBLIES

The 16 cavities in each assembly are installed in two UHV chambers. Fig. 1 shows one half of a horizontal and a vertical transverse kicker assembly. One vertical and two horizontal kicker assemblies were completed for the FY2012 run.

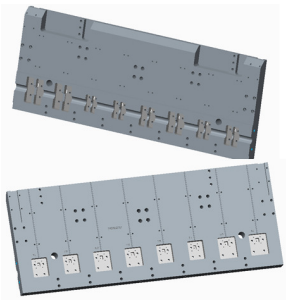


Fig. 2: A Typical Cavity Plate.

Unique Cavity Plate Design

Each 292 x 743 x 38 mm cavity plate is made of aluminum alloy 6061-T6 (Fig. 2), which is copper plated (25 microns thick) by Epner Technology. Flatness requirement on the split surface is within 13 microns along the plate length. Cavity shapes were accurately machined and fine cut by removing a small amount of material at a time to achieve the desired frequencies and the bandwidths. To obtain a repeatable cavity frequency, a closing force of ~ 13.6 kg (for the horizontal kicker) and of ~10 kg (for the vertical kicker), between two mating cavity plates, is required. Extension springs, by Lee Springs, were used on the side of each cavity to provide these forces (see Fig. 3). One cavity plate, with stiffer springs, serves as the hard stop to the mating plate, when the cavity plates are closing to each other.

The 50 ohms .14" (3.58 mm) OD semi-rigid shielded power cables, which were made by Advanced Technical Materials, are supported and cooled by the water cooled cavity plates (see Fig. 3 or Fig.4). Four ¼"-28 silver plated set screws, which are secured by four jammed set screws, are provided on each side of a cavity to tune the cavities (See Fig. 4).

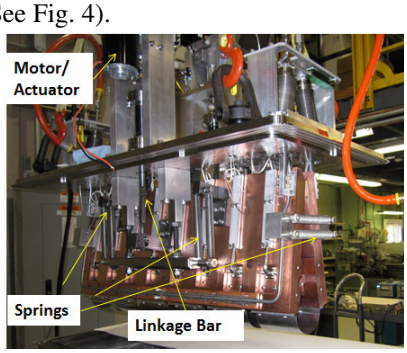


Fig. 3: Scissor Like Actuator.

Scissor Like Actuator

To take advantage of the commercially available frictionless pivot bearings, the scissor like actuators (Fig. 3) were chosen to drive the cavity plates. Each actuator includes a ball screw actuator (Motion Systems, 85151DUB) and a linkage bar, which are driven by a DC motor (Motion Systems, 73464-400 24V). The actuator could be disengaged from the motor at both ends of the 25 mm stroke. Each cavity plate is supported by a pair of frictionless pivot bearings (C-Flex Bearings, JD-20). The cavity plates are lifted and rotated, like a scissor, about their pivot bearings. With both cavity plates rotated an angle of ~ 8 degrees from the vertical median plane in the opposite direction, the required aperture of 124 mm is achieved. A mechanical stop is provided to keep the two cavity plates parallel to each other when they are at the closed position.

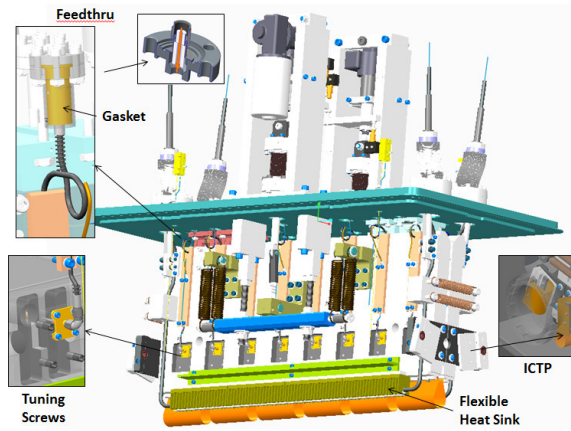


Fig. 4: Cavity Plate Assembly inside the UHV Chamber.

Custom Made Feedthru and Cable Strain Relief

To produce a reliable (high yield and bakable to 200°C) RF feedthru for the kicker, a custom designed RF feedthru was developed. The new 50 ohms SMA power connector is shown in Fig. 4, which has a stainless steel housing, a kovar center conductor, an alumina insulator and a Teflon insulator. The center conductor and the alumina insulator were silver brazed to provide the vacuum seal, which was fabricated by INTA Technologies. Ten custom made feedthrus were fabricated for testing, which were 100% leak tight and bakable to 200°C. To provide a strain relief to the unsupported cable, between the feedthru and the cavity plate, and to provide a vacuum seal to the feedthru, a novel dual purpose tubular shape copper gasket was also fabricated and installed (Fig. 4).

Stress Free Image Current Transition Piece

Image Current Transition Pieces (ICTP) are required to fill the gaps between the cavity plates and the neighboring beam pipes so that the excitation of high-order resonant modes could be avoided. Due to the scissor like motion of the cavity plates, the ICTP would fail easily with the

Copyright © 2013 CC-BY-3.0 and by the respective authors

repetitive and excessive bending and twisting stresses. A novel stress free transition piece has been successfully developed for the purpose (see Fig. 4), which installs a single end flex- hinge (SDP/SI S99FXS-075020) between the ICTP and the cavity plate to prevent the piece from rotating with the plate.

Low Thermal Noise Water Cooling Design

During operation, the power dissipation from each cavity and from each power cable are about 3 Wand 1 W respectively. With a water pipe rigidly attached the cavity plate (see Fig. 3), the calculated temperature gradient and the maximum thermal deformation on the cavities are 0.9°C and 160 microns respectively, which would result unacceptable frequency shifts in the cavities. Part of this deformation is caused by the different thermal expansions between the stainless steel pipe and the aluminum cavity plate. A novel flexible heat sink design (see Fig. 4) was developed to resolve the problem, which press fits the water pipe onto the fins of a convective heat sink (AAVID Thermalloy, Part no: 74925) so that the thermal contraction of the cooling pipe would not deform the cavity plate. Assuming that the water temperature was at 104°F (or 40°C), the thermal analysis result (using ANSYS) showed that the maximum temperature gradient would be ~ 1°C (see Fig. 5) and the maximum thermal deformation would be ~ 25 microns (.001") across the cavities, which is equivalent to a frequency shift of ~5 MHz. The predicted frequency shift agrees with the frequency measurements on the cavities. To meet the design requirement, the frequency shift can be further reduced to ~2 MHz by a proper tuning on each cavity.

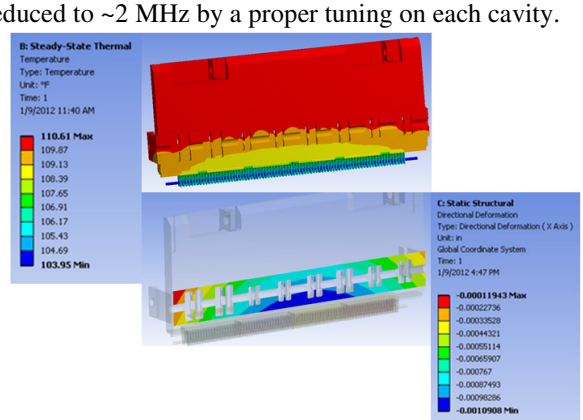


Fig. 5: Temperatures and Deflections on a Cavity Plate.

Large Rectangular Vacuum Chamber

Each UHV chamber has an interior dimension of 851 x 381 x 406 mm to allow install the cavity plates easily. Due to the rectangular opening and the long sealing length (~2565 mm long) on the top lid, no gaskets, including the Helicoflex metallic delta seal, could make a reliable UHV seal on top of the chamber. The solution was to weld the top lid onto the chamber and to protect the weld with a few stiffener bars around the chamber (see Fig. 1). Assuming that a 15 psi (0.1 MPa) external pressure is applied on the stainless steel chamber, the calculated maximum Von Mises stress along the weld is 21086 psi (0.145 GPa) (a safety factor of 1.4 to yielding strength) (Fig. 6) and the maximum deformation on the chamber is 0.3mm.

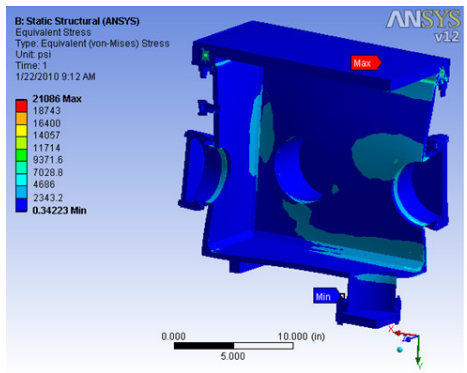


Fig. 6: Stresses on the vacuum Chamber.

CONCLUSIONS

We have developed a novel 5-8 GHz bandwidth bunched beam transverse stochastic cooling kicker, which uses scissor like actuators to drive the high Q cavity plates around the frictionless pivot bearings to obtain the required apertures. With a proper closing force applied on the cavity plates, using the flexible water cooled heat sink, and with some tuning, the cavity frequencies are repeatable within 0.05% of their frequencies during operation. By using the stress free Image Current Transition Pieces, eliminating wearable components, relieving strains on the power cables, silver plating or dicroniting stainless steel hardware, using only continuous water pipe, and venting all trapped vacuum volumes in the vacuum chamber, the vacuum components are virtually maintenance free. Three kicker assemblies were completed for the FY2012 run. Successful performance has been reported.

ACKNOWLEDGEMENT

The authors would like to thank Gary Miglionico and Vito De Monte for the design support.

REFERENCES

[1] J.M. Brennan, et al., "Stochastic cooling in RHIC", IPAC2012, New Orleans, LA.
[2] C.J. Liaw, et al., "Robust Mechanical Design for RHIC Transverse Stochastic Cooling Pickup", NA-Pac13.
[3] J.M. Brennan, et al., "Stochastic Cooling in RHIC', PAC 2009, Vancouver, Canada.
[4] P. Hurh et al., "The Mechanical Design of a Bunched Beam Stochastic Cooling Tank for the FNAL Tevatron", PAC1993.

Copyright © 2013 CC-BY-3.0 and by the respective authors

ROBUST MECHANICAL DESIGN FOR RHIC TRANSVERSE STOCHASTIC COOLING PICKUP

C.J. Liaw, J.M. Brennan, J. Tuozzolo, K. Mernick, V. De Monte, M. Myers
Brookhaven National Laboratory, Upton, NY 11973, USA

Abstract

The RHIC transverse Stochastic Cooling Pickup uses a pair of high resolution 4-8 GHz frequency band planar loop arrays to measure the Schottky signals from the bunched beams in the two transverse planes of the two rings. Precision alignment between the two 381 mm long array boards was achieved by surveying two specially designed alignment fixtures outside the vacuum chamber and using a pair of high resolution, motor controlled, and force balanced actuators. Robust mechanical design was achieved by excluding wearable mechanical joints and fragile electronics inside the vacuum chamber. Both mechanical designs and structural analysis results, for the vacuum chamber and for the array board supports, are presented. Two horizontal and two vertical plane pickups have been fabricated and installed in RHIC for the FY2012 run. Successful performance has been reported.

INTRODUCTION

The injected ion beams inside the two RHIC rings have a typical bunch rate of 10 MHz with 5 ns in length. The number of particles per bunch varies from 2 x 10^8 (for uranium) [1] to 1.5 x 10^9 (for gold) [2]. Due to intra-beam scattering (IBS), beam emittance would grow and reduce the intensity and the lifetime of the beam. RHIC has been successfully applying the stochastic cooling technique to correct this problem in the past 10 years. Based on the experience, a new transverse stochastic cooling system, which includes a broad band pickup and a kicker, has been developed recently. This paper will focus on the mechanical design of the new pickup.

McGinnis (1991) [3] developed a 4-8 GHz bandwidth bunched beam Stochastic Cooling Arrays for the Fermilab Tevatron. Due to the strong coherent frequency components presented in the high frequency bunched beam, the common mode Schottky signals from the two planar loop couplers must be subtracted before taking the measurement, which requires a high precision and repeatable mechanical alignment between the two arrays [3]. Hurh (1993) [4] designed a bunched beam Stochastic Cooling Tank for the FNAL Tevatron, which integrated the loop arrays into a vacuum chamber. The arrays were driven by two stepper motors through two guided plungers, which could provide different apertures for the changing beam size. Hurh's original design, however, has a few disadvantages, which include (1) The Teflon coated array board guiding shafts and the piezoelectric crystal inchworm motor could get stuck in vacuum, (2) The two pieces design BeCu image current transition assembly could buckle and reduce the aperture unexpectedly, and (3) The BeCu spring fingers on the image current transition assembly could lose their elastic strength and the contact forces on the beam pipe after the vacuum bake out.

Wei (2004) [5] applied the coasting beam theory and demonstrated that a 3-D stochastic cooling system with a 4-8 GHz bandwidth could effectively counteract IBS in RHIC. The 4-8 GHz Bunched Beam Stochastic Cooling Arrays, which were developed by McGinnis, were therefore adopted and retrofitted to become the sensor in the new pickup design. The newly developed transverse stochastic cooling pickup has addressed all the mechanical problems described above. Both mechanical designs and the supporting structural analysis results are presented below.

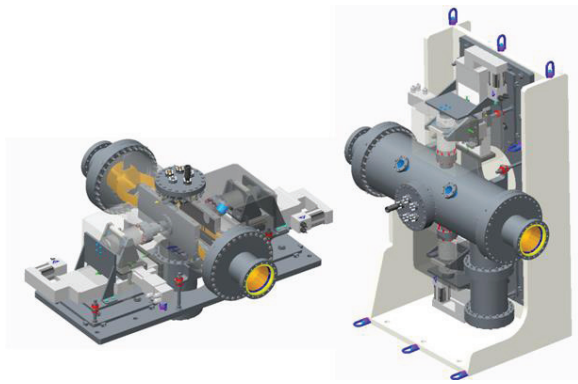


Figure 1: Horizontal and vertical stochastic cooling pickup.

MECHANICAL DESIGN OF THE TRANSVERSE STOCHASTIC PICKUP

The transverse stochastic cooling pickup could be installed either horizontally or vertically (see Fig. 1) to measure the Schottky signals from the RHIC bunched beam in the corresponding planes. The pickup integrates a pair of printed planar loop arrays, produced by Fermilab [3], with two aluminum backing boards being retrofitted into the newly designed UHV chamber. Two pickup leads and a proximity sensor (which is a pair of gold plated SST spring fingers, made by Lairtech) are provided on the two 381 mm x 152 mm x 17.5 mm array boards. Each array board is cantilever supported by a motor controlled precision linear stage, which is mounted on a four axes (X-Y-Z-theta) adjustable table. The linear stages provide a fine tuning on the relative alignment between two array boards in the X and the Z (or beam) direction. The alignment accuracy between the two array boards is required to be maintained within 50 microns

*Work supported by Brookhaven Science Associates, LLC under Contract No. DE-AC02-98CH10886 with the U.S. Department of Energy.

Copyright © 2013 CC-BY-3.0 and by the respective authors

during the operation. Apertures between the two pickup arrays are 0.7" (18 mm) and 3.5" (89 mm) for the operation and the standby positions respectively.

Precision Alignment between Array Boards

Precision alignment between two loop arrays was achieved by accurately monitoring the array positions, using the laser survey technology, and by using motor controlled high precision actuators to drive the array boards. To monitor loop array positions without breaking the vacuum, two special external alignment fixtures (Fig. 2) have been designed and installed on the mounting stages. Each fixture has four targets on the four corners. The distance between two targets was chosen to be the same as the plunger length so that one could measure the misalignment directly on the fixture. To position the array boards accurately, two high precision AeroTech Stages (AST150-100), with a stroke of 1.8" (46 mm), are used to drive the array boards perpendicularly to the beam direction through two rigid plungers (see Fig. 1). One of the AST150-100 stages is stacked with an AST100-050 stage, with a +/- 1 mm adjustment, to provide a longitudinal (or beam) direction adjustment. Both AST150-100 and AST100-050 have a resolution of 0.5 microns with a position accuracy of better than 5 microns. An alignment accuracy of ~15 microns is achievable between the two array boards. All the stages were custom retrofitted with a 'Home' position at the middle of the stroke. Two welded bellows (Standard Bellows SBC 300-200-3) were installed on both sides of each actuator stage to balance the vacuum forces on the stage.



Figure 2: External array board alignment fixtures.

Signal Feedthroughs and Cable Strain Relief

To seek for a more reliable RF feedthrough design, two types of signal feedthroughs were developed and tested on the pickup device for the comparison. One is a custom design and was fabricated by INTA Technologies, which provides the vacuum seal by brazing the alumina insulator onto a kovar center conductor (Fig. 3(A)). The other one is designed and made by SRI Hermetics (SRIVF102), which used the glass seal technology to seal a copper center conductor and a stainless steel housing (Fig. 3(B)). The former has a higher bake out temperature of 300°C and the latter gives a broader bandwidth. Both designs have a reasonable high yield.

To provide a strain relief to the unsupported cable, between the feedthrough and the array board, and to provide the vacuum seal, a dual purpose custom made copper gasket (made of 1/4 hard oxygen free copper) was also developed (Fig. 3(C)).

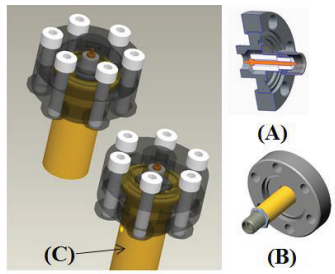


Figure 3: (A)INTA feedthru, (B) SRI feedthru, and (C) dual purpose copper gasket.

Long Lived Image Current Transition Piece

Image Current Transient Pieces (ICTP), which bridge the array boards and the beam pipes, are required to eliminate the excitation of the high-order resonant modes. To accommodate the aperture variations and to have a long service life, a special ICTP had been developed. Each ICTP includes a flexible 13 x 48 x 0.25 mm thick beryllium copper (C17200 Alloy 25) strip and a rigid copper plated 0.76 mm thick stainless steel structure (see Fig. 1), which has a rectangular opening on one end and a circular opening on the other end. Copper plated SST spring fingers are installed on the circular end, which are secured by a stainless steel spring ring, to provide a positive contact to the beam pipe. The stainless steel structure and the spring fingers are bakable to 300°C without losing their elastic strength. Fatigue test result, with repetitive bending between the minimum and the maximum aperture, demonstrated that the life time of the beryllium copper strip could exceed 10 k cycles without a failure, which is far beyond the application.

Maintenance Free Vacuum Design

Materials inside the vacuum chamber, which include stainless steel, copper, carbon coated polyimide, ferrite and aluminum are low outgassing. Vacuum components were cleaned and baked at 450°C for the stainless steel material and at 150°C for other materials before the installation. Venting holes were provided for all the trapped volumes. Stainless steel bolts were silver plated to avoid galling in vacuum. A vacuum pump (SAES Getters Model 4H0426) is installed underneath the vacuum chamber to maintain an UHV inside the chamber. There are no wearable components inside the vacuum chamber.

STRUCTURAL ANALYSES

Stage Linear Bearing Lifetime Analysis

The load distributions on the actuator stages were carefully planned and analyzed to increase the lifetime of the stage linear bearings. Figure 4 shows the actual stage loads vs. load capacities at the calculated CG locations and the expected travel life time for the stage bearings.

Copyright © 2013 CC-BY-3.0 and by the respective authors

The results show that the travel lifetime with the current design would be no less than 2.3 x 10^9 mm.

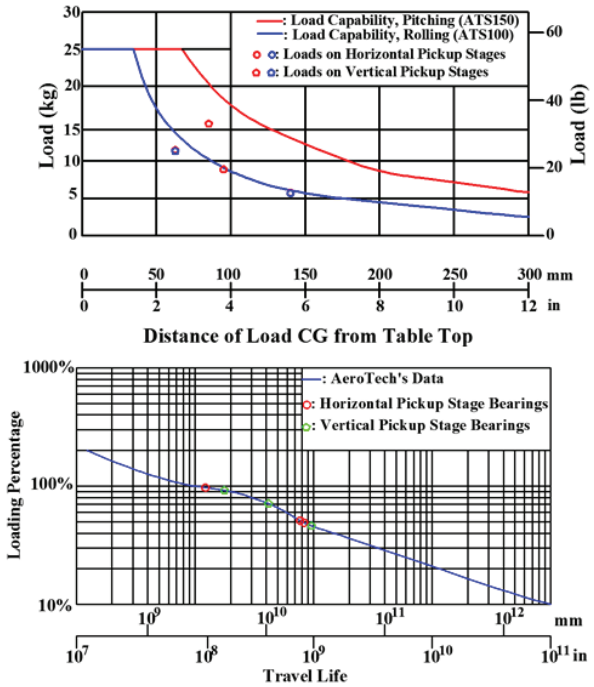


Figure 4: Actuator stage loads and stage bearing lifetime.

Support Structure Stress Analysis

The horizontal and the vertical stochastic cooling pickup assemblies have an overall weight of 193 kg and 315 kg respectively. When the chamber is in vacuum, a pressure load of 15 psi is applied on the surfaces of the chamber. All the components, except the pickup device and the supporting plates (which are made of aluminum), are made of 304 stainless steel. Stress analysis results, using ANSYS, showed that for the worst case when the pickup is supported vertically, the maximum stress and the maximum deformation on the support structure, due to the loads described above, are 6019 psi (41.5 MPa) (with a safety factor of 5 to yield) and .007" (0.18 mm) respectively (Fig. 5). The results have confirmed the structural stability of the pickup design.

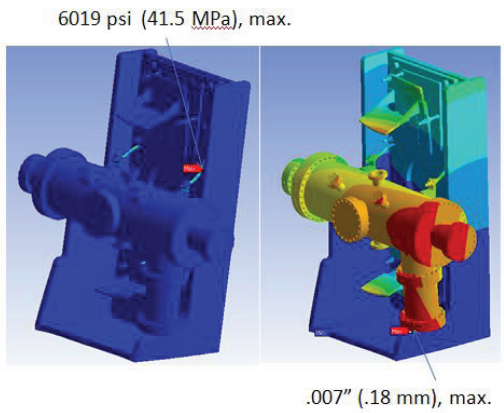


Figure 5: Structural analysis results using ANSYS.

CONCLUSIONS

We have developed a new mechanical design for the transverse stochastic cooling pickup, which can monitor and align the two 4-8 GHz bandwidth bunched beam Stochastic Cooling Arrays precisely without using any wearable mechanical guiding shafts or fragile electronics inside the vacuum chamber. The success of the custom designed image current transition piece, signal feedthrough, and cable strain relief has also improved the reliability of the vacuum components during operation. The pickup has been successfully operated since the 2011 run. The mechanical design has been proven to be robust.

REFERENCES

[1] J.M. Brennan, M. Blaskiewicz, K. Mernick, "Stochastic Cooling in RHIC," Proc. of IPAC 2012, New Orleans, LA, WEPPP082, p. 2900 (2012); http://www.JACoW.org

[2] M. Blaskiewicz, J.M. Brennan, R.C. Lee, K. Mernick, "Stochastic Cooling of a High Energy Collider," Proc. of IPAC 2011, San Sebastian, Spain, TUYA03, p. 913 (2011); http://www.JACoW.org

[3] D. McGinnis, J. Budlong, G. Jackson, J. Marriner, and D. Poll, "Design of 4-8 GHz Bunched Beam Stochastic Cooling Arrays for the Fermilab Tevatron," Proc. of PAC 1991, San Francisco, CA, p. 1389 (1991); http://www.JACoW.org

[4] P. Hurh, G. Jackson, "The Mechanical Design of a Bunched Beam Stochastic Cooling Tank for the FNAL Tevatron," Proc. of PAC 1993, Washington DC, p. 2148 (1993); http://www.JACoW.org

[5] J. Wei, M. Blaskiewicz, J. M. Brennan, "Stochastic Cooling Power Requirements," Proc. of EPAC 2004, MOPLT177, p. 941 (2004); http://www.JACoW.org

Copyright © 2013 CC-BY-3.0 and by the respective authors

HIGH INTENSITY RHIC LIMITATIONS DUE TO SIGNAL HEATING OF THE CRYOGENIC BPM CABLES *

P. Thieberger, C. Pai, K. Mernick, T. Miller, M. Minty, K. Hamdi, A. Ghosh and J. D'Ambra
Collider Accelerator Department, Brookhaven National Laboratory, Upton NY 11973, USA

Abstract

The signal cables from the beam position monitors (BPMs) in the cryogenic sections of the Relativistic Heavy Ion Collider (RHIC) need to satisfy somewhat conflicting requirements. On the one hand, the cryogenic load due to heat conduction along the cable needs to be small, which led to the use of stainless steel jacketed cables with Tefzel insulation. On the other hand, radio frequency losses need to be reasonably small to reduce heating due to dissipated signal power. As the beam intensity in RHIC increased over the years, and the bunches are becoming shorter, a point is being rapidly approached where these cables will soon become a performance limiting factor. Here we describe an extensive study of this problem including cable loss measurements as a function of temperature and frequency, characterization of the copper center conductor, and simulations using Particle Studio (PS) and ANSYS.

INTRODUCTION

The signal heating limitations of the RHIC cryogenic BPM cables were recognized and analyzed in 1995 [1, 2]. In particular, the Tefzel insulator has an operational temperature limit of 150 °C. Continuing RHIC upgrades to higher luminosities will hopefully lead next year [3] to the new goal of 111 bunches of 3E11 protons each with an RMS bunch length of 20 cm (henceforth the "upgraded beam"). The cable limit is expected to be approached, and more detailed estimates have now been performed to ensure safe and reliable operation.

CABLE LOSS MEASUREMENTS

Cable losses as a function of frequency were measured with a signal analyzer at eleven temperatures ranging from 4 K to the maximum operating temperature of the cable which is 423 K (150 °C). To perform these measurements at the various temperatures two different cryostats, an ice bath and an oven were used. A spare RHIC 125 cm long BPM cable was formed into a 10 cm diameter spiral and connected to two lead-in cables of the same type.

To take into account the temperature dependent losses in these lead-in cables, a short (8 cm long) "dummy" connection was used as shown in the Fig.1 inset, and the results shown in figure 1 were obtained by subtracting at each temperature the losses measured with the dummy from the ones measured with the sample under identical conditions. The frequency range up to 500 MHz contains over 95% of the signal power for 20 cm rms bunches.

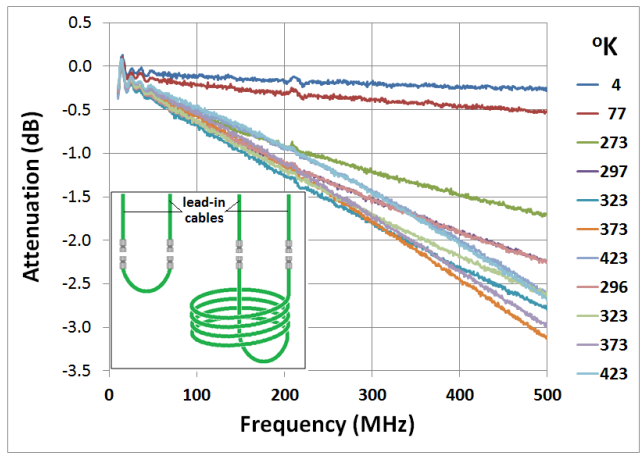


Figure 1: Cable attenuation as function of frequency measured at 11 temperatures ranging from 4 K to 423 K; the operating temperature limit for the cable.

From these curves, the losses per unit length are later calculated considering an effective cable length of 125 – 8 = 117 cm where 8 cm is the length of the "dummy" connection. The Fig. 1 data show that above ~180 MHz, some of the lower temperature losses are larger than losses at higher temperatures. This surprising behavior, which was confirmed by repeating the measurements with different signal analyzers, is probably due to peculiarities in the dielectric losses in the Tefzel insulator.

THERMAL CONDUCTIVITY

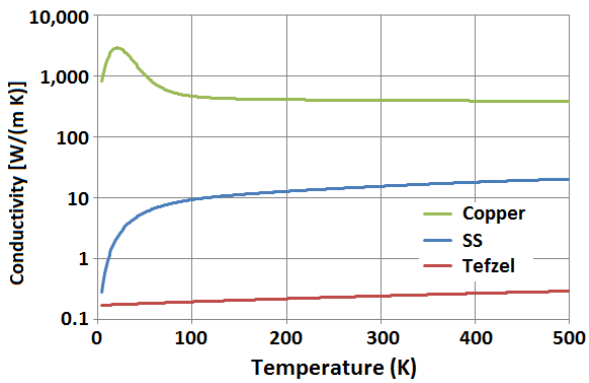


Figure 2: Thermal conductivities used for the simulations.

* Work supported by Brookhaven Science Associates, LLC under Contract No. DE-AC02-98CH10886 with the U.S. Department of Energy.

Copyright © 2013 CC-BY-3.0 and by the respective authors

The thermal conductivity of copper is a sensitive function of the impurity content and was determined by measuring a Residual Resistivity Ratio value of 131. Values of the thermal conductivity parameterized for various RRR values given by NIST [4] were used to calculate the thermal conductivity curve for copper through interpolation. The curve for Tefzel was generated from the room temperature value [7] adopting a slope similar to the one for Teflon. As shown in Fig. 2, this conductivity is so small that it isn't very significant.

SIGNAL AMPLITUDE AND FREQUENCY SPECTRA

The current pulse into 50 Ω generated by a BPM stripline is due to a superposition of charges induced directly by the beam and the ones reflected by the delay-line structure formed by the stripline and the rest of the BPM. In addition, that charge of course depends on the beam position. An extensive series of Particle Studio (PS) [5] simulations was performed to characterize these signals as a function of position for the three types of cryogenic BPMs present in RHIC (see Table 1).

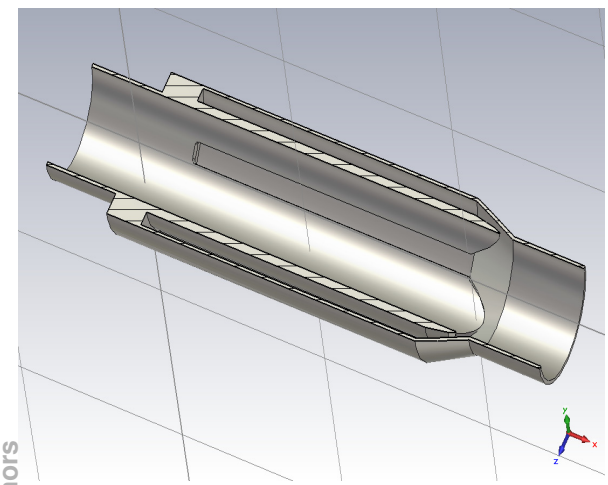


Figure 3: Cutaway view of the Type 2 BPM model used for the Particle Studio simulations.

Figure 3 is a cutaway view of one of the BPM PS models used for the simulations. The number of mesh-cells used was about 195,000. At the ends of the striplines, where in reality 50Ω feedthroughs are located, these feedthrough were simulated by 50 Ω resistors connected between the tip of the stripline and the vacuum housing. Figs. 4 and 5 show some of the results for a Type 2 BPM (see Table 1).

HEAT TRANSPORT SIMULATIONS

Power density inputs for the ANSYS heat transport simulations (Fig. 6) are calculated as if all the losses were dielectric. In reality resistive losses contribute too. The other extreme case of resistive losses only was also simulated with nearly identical results. The cable diameter is small enough to make it practically irrelevant where along the radius the energy is deposited.

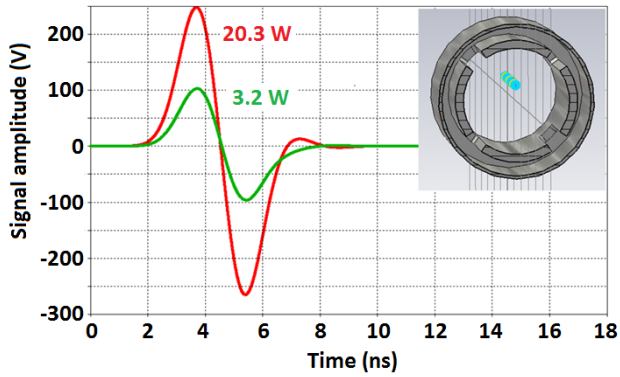


Figure 4: PS simulated signal amplitudes and powers from two opposite striplines induced by an upgraded beam displaced by 10 mm from the center line.

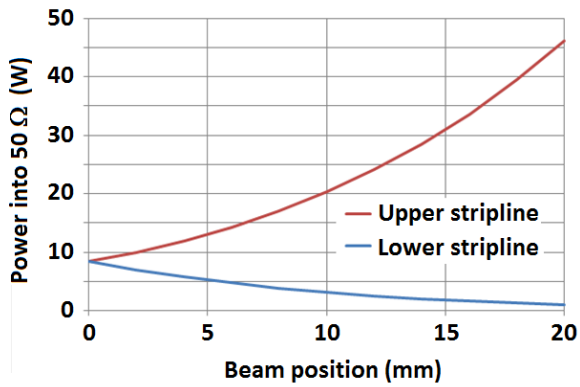


Figure 5: PS simulated signal power as function of beam position from two opposite Type 2 BPM striplines.

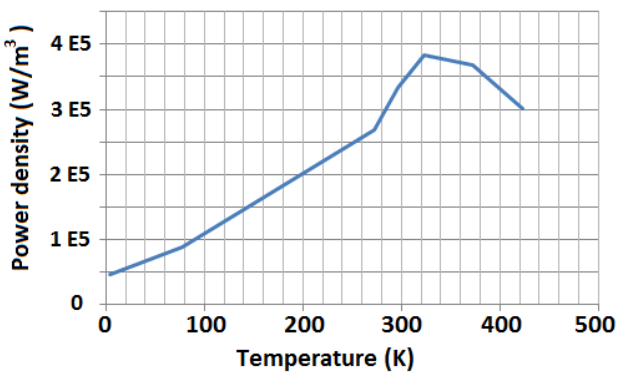


Figure 6: Power density in Tefzel as a function temperature calculated by convolving the cable frequency response with the signal frequency spectrum.

Copyright © 2013 CC-BY-3.0 and by the respective authors

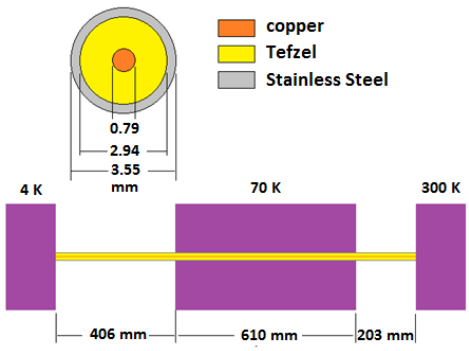


Figure 7: Schematic representation of the geometry used for the ANSYS heat transport simulations.

The geometry used for the ANSYS heat transport simulations is shown in Fig. 7. The curve labeled 1.00 in Fig. 8 shows the ANSYS simulated temperature profile along the cable for a type 2 BPM with a centered upgraded beam. The power or load factors labeling the other curves correspond to powers larger by the indicated factors.

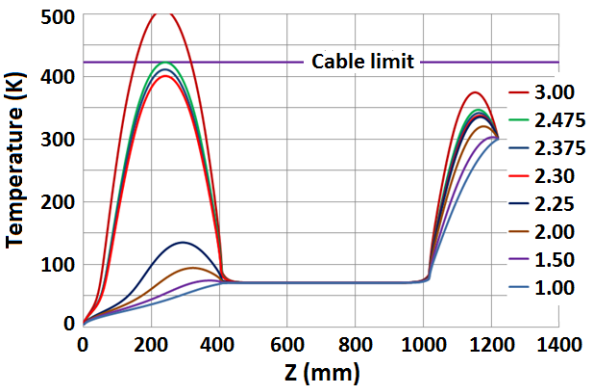


Figure 8: Cryogenic cable temperature profiles obtained from the ANSYS simulations. The curve labeled 1.00 corresponds to the upgraded beam centered in a type 2 BPM. The other labels indicate correspondingly higher power factors.

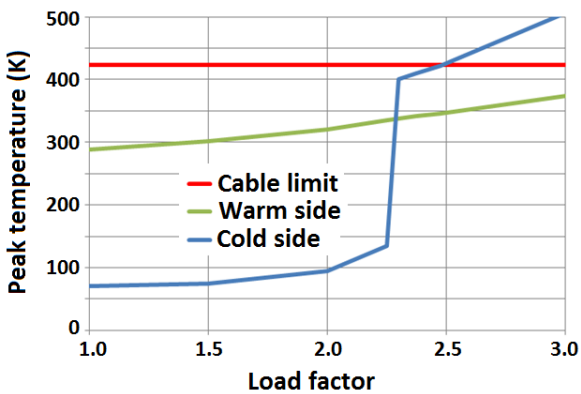


Figure 9: Peak temperatures as function of the load factor where 1.0 corresponds to the upgraded beam centered in a Type 2 BPM. The jump at the "cold" or BPM side of the cable indicates an incipient temperature runaway situation that must be avoided.

RESULTS AND CONCLUSIONS

The maximum allowable beam displacements to just avoid the incipient temperature runaway situation shown in Fig. 9 are shown in Fig.10 and Table 1.

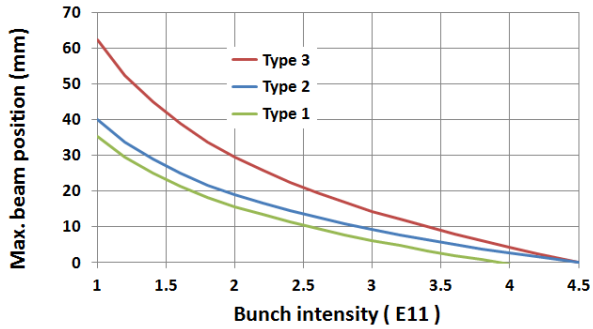


Figure 10: Maximum allowed beam displacements as function of bunch intensity of 111, 20 cm RMS bunches for the three types of BPMs.

Table 1: Maximum beam displacements to avoid cable damage with the upgraded beam for the 3 types of BPMs

BPM Type	#of planes	Location	Radius (mm)	Max. Δx (mm)
#1	1	Arcs	34.5	7.3
#2	2	Arcs	34.5	10.4
#3	2	Triplets	53.7	16.1

These results are more detailed than- but in general agreement with the ones obtained before [1, 2]. As shown in Fig. 10 and Table 1, operation with the upgraded beam should be possible provided excessive beam position excursions can be precluded by the use of beam abort interlocks. In practice, we note that there is some performance uncertainty due to crimping of the cable ends in the early days of RHIC [6]. In the future, we plan to verify the temperature rise predictions presented here with measurements using thermocouples

REFERENCES

[1] P. Cameron, et. al. 1995 PAC Proc., p. 2458.

[2] P. Cameron abd M. Morvillo, RHIC/AP/68, BNL, 1996.

[3] W. Fisher, et. al. STATUS OF HEAD-ON BEAM-BEAM COMPENSATION IN RHIC. ICFA Mini Workshop on Beam-Beam Effects in Hadron Colliders (BB2013); Geneva, Switzerland, 2013.

[4] http://cryogenics.nist.gov/MPropsMAY/OFHC%20Copper/OFHC_Copper_rev.htm

[5] Particle Studio, Computer Simulation Technology.

[6] C. J. Liaw, R. Sikora, R. Schroeder Proceedings of PAC07, MOPAS095, page 649.

[7] http://www2.dupont.com/Teflon_Industrial/en_US/assets/downloads/h96518.pdf

Copyright © 2013 CC-BY-3.0 and by the respective authors

UPGRADING THE RHIC BEAM DUMP FOR HIGHER INTENSITY*

C. Montag, S. Nayak, L. Ahrens, W. Fischer, H. Hahn, C.J. Liaw,
J. Mi, T. Roser, P. Thieberger, J. Tuozzolo, K. Yip, W. Zhang
BNL, Upton, NY 11973, USA

Abstract

Mechanical analysis of the RHIC beam dump window has shown that present heavy ion beam intensities are close to the tolerable limit, and will likely exceed that limit in future runs. Two approaches to upgrade the abort system for those projected higher intensities have been studied, namely replacing the existing window, and adding a vertical kicker that distributes the individual bunches more evenly across the window, thus reducing the heat load. We present the results of these studies and the present status of the upgrade project.

INTRODUCTION

The RHIC beam is aborted by a set of five kickers that deflect it horizontally into the dump. The dumped beam first passes through a 50 cm long C-C carbon block that dilutes its emittance before it exits the RHIC vacuum enclosure through a pair of 17-7 PH steel windows. Outside the beam vacuum, the aborted beam is diluted further by a second carbon block before it is absorbed by a massive steel block.

The RHIC beam dump system was originally designed for a 100 GeV/nucleon gold bunch intensity of $1 \cdot 10^9$ Au ions/bunch in 56 bunches. During the 13 years of RHIC operation, the actual beam intensity has been increased by more than a factor 2, to $1.3 \cdot 10^9$ Au bunches in 111 bunches. In addition, stochastic cooling [1] now results in much smaller emittances than originally envisioned during the RHIC design phase [2]. These developments led to a re-evaluation of the integrity of the vacuum window.

NUCLEAR INTERACTION AND MULTIPLE SCATTERING IN THE C-C CARBON BLOCK

Due to stochastic cooling the Au beam emittance in RHIC depends strongly on the bunch intensity. A simple scaling law can be derived from the fact that cooling rate and intrabeam scattering (IBS) growth rate counterbalance each other in the equilibrium.

With the cooling rate scaling with the bunch intensity as

$$\tau_{\mathrm{cool}}^{-1} \propto \frac{1}{N} \tag{1}$$

and the IBS emittance growth rate scaling as

$$\tau_{\mathrm{IBS}}^{-1} \propto \frac{N}{\epsilon_\perp^2 \epsilon_{\mathrm{L}}}, \tag{2}$$

* Work supported by Brookhaven Science Associates, LLC under Contract No. DE-AC02-98CH10886 with the U.S. Department of Energy.

Table 1: Double-Gaussian Fit Parameters for the Energy Deposition for Two Different Beam Emittances

emittance [πmm mrad]	4	8
bunch intensity 10^9	0.7	1.6
A_1 [MeV/cm^3]	$43.0 \cdot 10^{13}$	$66.8 \cdot 10^{13}$
σ_1 [mm]	0.51	0.62
A_2 [MeV/cm^3]	$0.77 \cdot 10^{13}$	$1.74 \cdot 10^{13}$
σ_2 [mm]	5.25	5.26

where $\epsilon_\perp$ and ϵ_{L} are the transverse and longitudinal emittances, respectively, the transverse emittance is therefore proportional to the bunch intensity [3]

$$\epsilon_\perp \propto N \tag{3}$$

for a constant longitudinal emittance ϵ_{L}. This scaling rule agrees well with simulation results that show a transverse equilibrium normalized 95 percent emittance of 4πmm mrad for $0.7 \cdot 10^9$ Au ions/bunch, and 8πmm mrad for $1.6 \cdot 10^9$ Au ions/bunch [3].

The interaction of a single incoming bunch with the C-C carbon block and the resulting energy deposition is simulated using the code MCNPX [4]. Nuclear interaction and multiple scattering in the C-C carbon block widens the distribution and reduces the peak intensity of the round Gaussian beam, while at the same time producing significant non-Gaussian tails. The resulting distribution is described by a double-Gaussian fit as

$$\rho(r) = A_1 \exp\left(-\frac{r^2}{2\sigma_1^2}\right) + A_2 \exp\left(-\frac{r^2}{2\sigma_2^2}\right), \tag{4}$$

where r is the radial particle coordinate, and A_1, A_2 and σ_1, σ_2 are the normalized amplitudes and RMS widths of the double-Gaussian distribution. Table 1 lists the double-Gaussian fit parameters for two different emittances. Together with the abort kicker pulse shape, the spatial energy distribution on the abort kicker window for the entire 111 bunches can then be calculated.

MECHANICAL AND THERMAL STRESS IN THE WINDOW

The RHIC beam dump system aborts the beam by applying a horizontal kick. The pulse shape of these abort kickers is designed such that after an initial fast rise that kicks the first bunch across the septum, the remaining bunches are spread out in a straight line by an oscillatory behavior of the kick, as shown in Figure 1.

Copyright © 2013 CC-BY-3.0 and by the respective authors

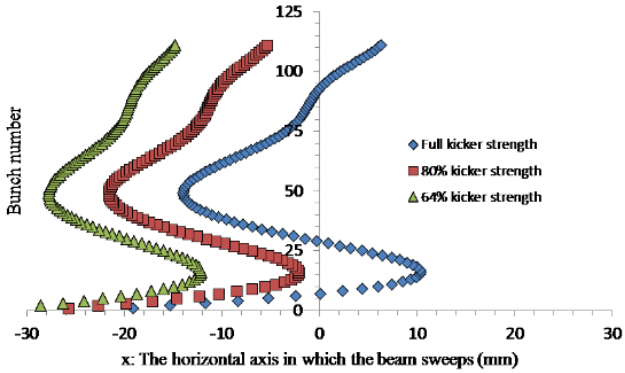


Figure 1: Kicker pulses for full kicker strength, and reduced strengths of 80 and 64 percent.

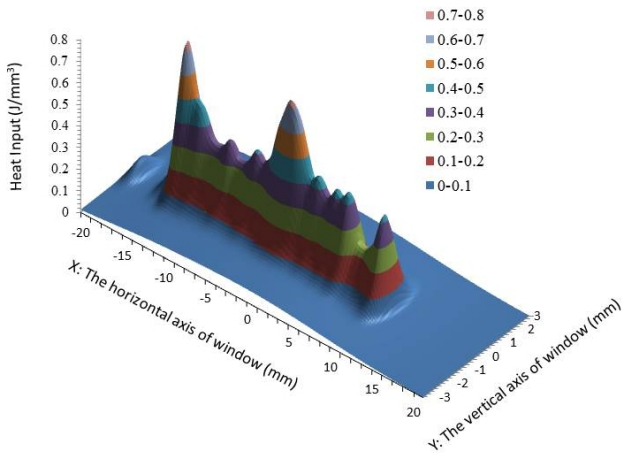


Figure 2: Heat input of 111 bunches of $0.7 \cdot 10^9$ Au ions on the beam dump window, assuming a 95 percent normalized emittance of 4π mm mrad.

This oscillating kick results in several distinct hot spots on the window surface where bunches are dumped in close vicinity due to the near-zero slope of the kicker pulse at its minima and maxima. Figure 2 shows the heat input for 111 gold bunches with a bunch intensity of $0.7 \cdot 10^9$ Au ions/bunch and a 95 percent normalized emittance of 4π mm mrad on the existing steel dump window. Table 2 lists the material properties for the 17-7 PH steel used for the RHIC abort window.

In the numerical analysis of the mechanical and thermal stress in the window we require a safety factor of two. An analysis of the heat deposition in the window reveals that at a 95 percent normalized emittance of 4π mm mrad a maximum bunch intensity of $0.7 \cdot 10^9$ gold ions per bunch is allowable. In this case, the maximum stress reaches half the yield stress of the present 17-7 PH steel window [5]. The success of the stochastic cooling effort results in emittances of 8π mm mrad at bunch intensities of $1.6 \cdot 10^9$. This will shrink the safety margin for the window below an acceptable level, so the beam dump system needs to be upgraded in the near future.

Table 2: Material Properties of 17-7 PH Stainless Steel and of Titanium 6242 Alloy

	steel 17-7 PH	Ti 6242
elastic modulus [GPa]	197	115
Poisson's ratio	0.29	0.32
yield stress [MPa]	940	960
ultimate stress [MPa]	1289	1016
therm. cond. $[\mathrm{W/m \cdot K}]$ (100°C)	16.4	7.1
therm. cond. $[\mathrm{W/m \cdot K}]$ (500°C)	21.8	
therm. exp. coeff. $[\mu\mathrm{m}/(\mathrm{m \cdot K})]$	12	8.1
specific heat $[\mathrm{J}/(\mathrm{kg \cdot K})]$	460	460
melting point [°C]	1400	1700
density $\mathrm{kg/m^3}$	7800	4540

UPGRADE SCENARIOS

To increase the allowable beam intensity at the reduced emittances, two possible upgrade scenarios are being considered. The first scenario involves replacing the 17-7 PH steel window with a different material, while in the second scenario a vertical kicker would be added to increase the spacing between individual bunches in the hot spots on the window surface. Both scenarios have been evaluated for two consistent combinations of intensities and emittances, namely $0.7 \cdot 10^9$ Au ions/bunch at a normalized 95 percent emittance of 4π mm mrad, and $1.6 \cdot 10^9$ Au ions/bunch at 8π mm mrad.

Window Replacement

Replacing the existing window with a high strength titanium 6242 alloy (see Table 2) raises the safety factor from 1.35 to 2.65 for a bunch intensity of $1.6 \cdot 10^9$ Au ions/bunch and the associated normalized emittance of 8π mm mrad, while at a low intensity of $0.7 \cdot 10^9$ Au ions/bunch and an emittance of 4π mm mrad the safety factor of two is exceeded even with the existing window, as listed in Table 3. Based on these results, the safety factor is expected to remain greater than two for intensities up to $2.1 \cdot 10^9$ Au ions/bunch with a corresponding normalized emittance of 10π mm mrad,

Vertical Kicker

To dilute the hot spots on the window, a vertical kicker may be added. The pulse waveform of this kicker needs to be chosen such that the vertical kicker pulse has its greatest slope at times when the slope of the horizontal kickers is near zero. A larger vertical kick amplitude results in a greater spread of the individual bunches on the window and therefore a lower heat load, which increases the safety factor for a given intensity and emittance. However, bunches that experience kicks near the minima and maxima of the sinusoidal vertical kicker pulse hit the window at a different vertical position, but their distance relative to each other is unchanged. The dependence of the resulting safety factor on the amplitude of the vertical kicker pulse is therefore

Copyright © 2013 CC-BY-3.0 and by the respective authors

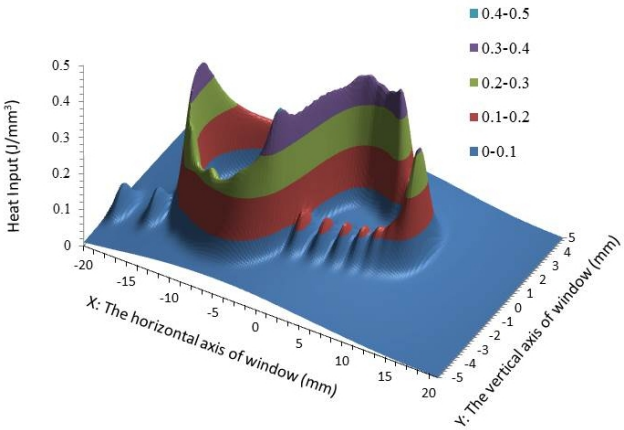


Figure 3: Heat input of 111 bunches of $0.7 \cdot 10^9$ Au ions with an emittance of 4π mm mrad on the beam dump window, with an additional vertical kicker.

Table 3: Safety Factor for the Various Abort System Configurations, for Two Different Beam Intensities. A minimum safety factor of 2 is required for safe operation of the RHIC abort system.

emittance [πmm mrad]	intensity [10^9]	steel 17-7 PH	Ti 6242	steel 17-7 PH and vertical kicker
8	1.6	1.35	2.65	2.47
4	0.7	2.80	5.11	4.88

nonlinear, and the gain increase is reduced at larger amplitudes. At the same time, achieving large kicker amplitudes is costly due to the required high kicker currents and voltages. For these reasons, the maximum vertical kick angle is chosen as $164\,\mu$rad, which corresponds to an orbit amplitude of 3 mm at the window. Table 4 shows lists the design paramters of such a kicker.

Simulations show that the lowest peak heat deposition is achieved by adding a vertical kicker with a cosine-like pulse shape of $8\,\mu$sec period, delayed by $2.64\,\mu$sec w.r.t. the horizontal kicker pulse. Figure 3 shows the resulting heat input distribution for a $4\,\pi$ mm mrad beam with $0.7 \cdot 10^9$ Au ions per bunch in 111 bunches. In this case, the safety factor for the 17-7 PH steel window is significantly raised, Table 3, and a bunch intensity of $2.0 \cdot 10^9$ Au ions/bunch in 111 bunches at a corresponding emittance of $10\,\pi$ mm mrad becomes feasible.

Table 4: Parameters of the Vertical Kicker Assembly

Total length [m]	1.83
Number of modules	3
Deflection angle peak-to-peak [mrad]	0.328
Au beam energy [GeV/n]	100
Integrated field [Tm]	0.28
Magnetic field strength [T]	0.152
Magnet current peak-to-peak [A]	6161
Voltage [kV]	5
Sine wave period [μsec]	8.0
Beam duration [μsec]	11.7

SUMMARY

We have investigated two scenarios to upgrade the RHIC beam dump system for higher heavy ion beam intensities, which is currently limited by mechanical and thermal stress in the stainless steel exit window. Replacing the existing window with a titanium alloy window would allow maximum bunch intensities of $2.1 \cdot 10^9$ Au ions per bunch in 111 bunches.

Alternatively, additional abort kickers could be installed that spread the aborted beam in the vertical direction, thus reducing the peak energy deposition in the window. A preliminary design of this kicker has been developed, which would allow for a maximum bunch intensity of $2.0 \cdot 10^9$ Au ions per bunch in 111 bunches.

While both scenarios result in very similar improvements of the RHIC beam dump system, replacing the exit window is significantly cheaper than adding a vertical kicker, though also very labor intensive. As an additional advantage, a window upgrade is inherently more fail-safe than an additonal vertical kicker since it is a passive system.

Based on these studies and considerations it has therefore been decided to replace the exit window with a titanium alloy one. A vertical kicker can then still be added in the future should the need arise.

REFERENCES

[1] M. Blaskiewicz et al., Phys.Rev.Lett. 105 (2010) 094801

[2] Y. Luo et al., "RHIC Performance for FY2012 Heavy Ion Run", TUPFI082, NA-PAC'13, to be published.

[3] M. Blaskiewicz, private communication

[4] http://mcnpx.lanl.gov/

[5] S. Nayak et al., C-A/AP/456

Copyright © 2013 CC-BY-3.0 and by the respective authors

OPTIMIZATION OF THE CAPTURE SECTION OF A STAGED NEUTRINO FACTORY*

H.K. Sayed,† H.G. Kirk, Brookhaven National Laboratory, Upton, NY 11973, USA
K.T. McDonald, Princeton University, Princeton, NJ 08544, USA

Abstract

A proposed staged Neutrino Factory, producing lower muon intensity of 10^{20} muons per year and 10-14 GeV muon beam energy, initially requires target station for 1 MW proton beam power with a proton beam energy of 3 GeV, which could be upgraded to the full power of 4 MW at 8-GeV beam energy. The optimization of the initial Target Station and the following Decay Channel and Buncher/Phase Rotator are discussed.

INTRODUCTION

In the baseline Neutrino Factory / Muon Collider design [1], sketched in Fig. 1, the muon beam is produced from pion decay by bombarding a liquid-mercury-jet target with a 4-MW pulsed proton beam, which delivers an intense muon beam of 10^{14} muons/sec from the incident beam of 10^{15} proton/s. In the proposed staged Neutrino Factory [2] with a 1-MW proton beam of 3-GeV energy, the Target Station uses a solid graphite target and produces a muon intensity of 10^{20} per year The target is embedded in a 15 (or 20) T solenoid magnet for the pion collection, shown in Fig. 2, which is followed by a lower field Decay Channel. The baseline design of the Target Station/Decay Channel will be retained during later stages of the Neutrino Factory to save the cost at the time of upgrade to the full 4-MW scenario.

The target and proton beam sizes and their tilt angles in the initial 3-GeV configuration are given in Table 1, which configuration produces 0.42 muons/protons at the end of the Target System.

Table 1: Proton Beam and Graphite Target Parameters for the Staged Neutrino Factory

Carbon rod target	Proton beam
Length 0.72 [m]	$\sigma_t = 2$ [nsec]
Diameter 0.692 [cm]	$\sigma_{x,y} = 0.0865$ [cm]
Angle to solenoid axis 42 mrad	42 mrad

The adiabatic variation in solenoid field strength along the beam near the target performs an emittance exchange affects the performance of the downstream Buncher, Phase Rotator, and Cooling Channel [3]. An optimization was performed using the MARS15 (2012) [4] and ICOOL [5] codes in which the rate of change of the field along the pion beam near the target was varied to maximize the number of muons that falls within the acceptance of the downstream accelerator chain (muons within 201.25 MHz RF bunches with momentum in the range 100300 MeV/c, transverse amplitude squared less than 0.03 m and longitudinal amplitude squared less than 0.15 m [3]).

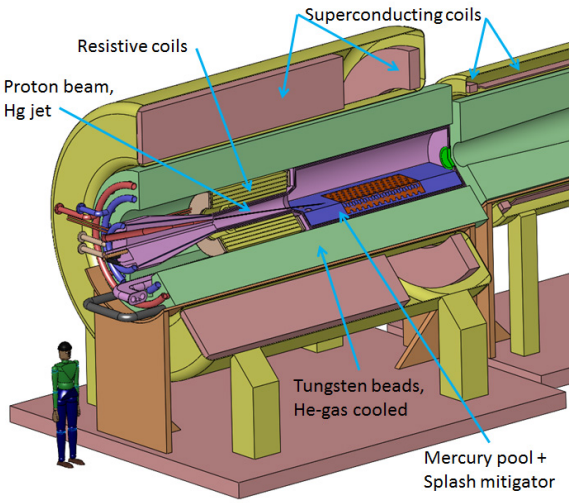


Figure 2: Neutrino Factory/Muon Collider target system.

The Target System utilizes a magnetic-field profile that peaks at $B_i = 15$ T at the target and tapers down to $B_f = 2.5$ T over a distance of $L_{\rm taper}$. In this study we optimized the length of this tapering solenoid $L_{\rm taper}$. The effect of solenoid-field profile on the captured-particle count and their phase-space distribution was studied by simulating the particles captured at the target and transported through the rest of the Front End. Various axial-field profiles were considered, based on an inverse-cubic form [6], from which the off-axis fields were calculated using Maxwellian series expansions. A sample of the axial-field profiles studied is shown in Fig. 3.

PION PRODUCTION AND CAPTURE AT THE TARGET

The MARS15 code [4] was used to simulate the particle production off the graphite target, using an incident 3-GeV proton beam with delta-function time distribution.

* Work supported by the US DOE Contract No. DE-AC02-98CHI10886.
† hsayed@bnl.gov

Copyright © 2013 CC-BY-3.0 and by the respective authors

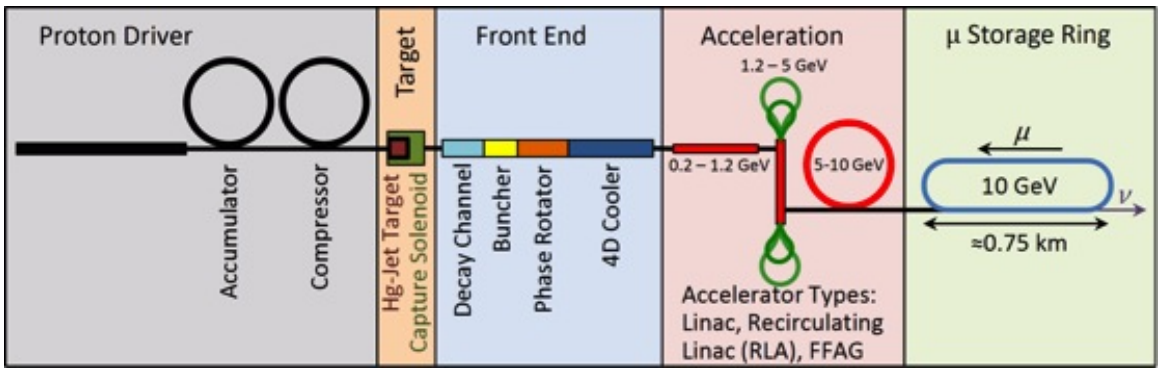


Figure 1: Neutrino Factory/Muon Collider Target System.

The kinematic parameters of the secondary pions, Kaons and muons at end of the graphite target were used as input for an ICOOL [5, 7] simulation through the tapered solenoid field and on to the end of the Cooling Channel. The transverse-momentum distribution of secondary pions at the downstream end of the graphite target is shown in Fig. 4. The beam-pipe geometry was simplified to have a constant 30-cm radius.

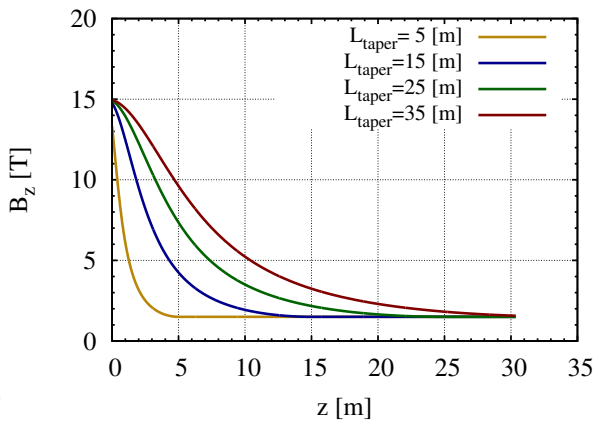


Figure 3: On-axis magnetic field profiles for the Target System.

THE FRONT END

The major systems of the Front End [3] of a Neutrino Factory are: Target System, Decay Channel, Buncher, Phase Rotator, and the Cooling Channel, as shown in Fig. 1. In this study, a constant solenoid field of 2.5 T was used to confined the muon beam throughout the Decay Channel, Buncher, and Phase Rotator, which ends some 150 m from the target, after which the beam was matched into the Ionization Cooling Channel [8] with ±2.8-T axial field in the alternating solenoid magnets.

The pions collected off the target are transport by the capture solenoid to the decay channel of 50-m length where most of the pions decay into muons. The muon beam is then bunched using a sequence of RF cavities with frequencies varying from 320 to 230 MHz over ≈ 33 m, while the bunching-cavity RF voltage increases linearly along the channel from 3.42 to 9.01 MV/m. In the 42-m-long Phase Rotator, lower-energy muons are accelerated and higher-energy ones are decelerated, until at the end of the Rotator and the original 15-m-long bunch of muons of both signs has been formed into a 48-m-long train with 33 bunches of μ^+ interleaved with 33 bunches of μ^-.

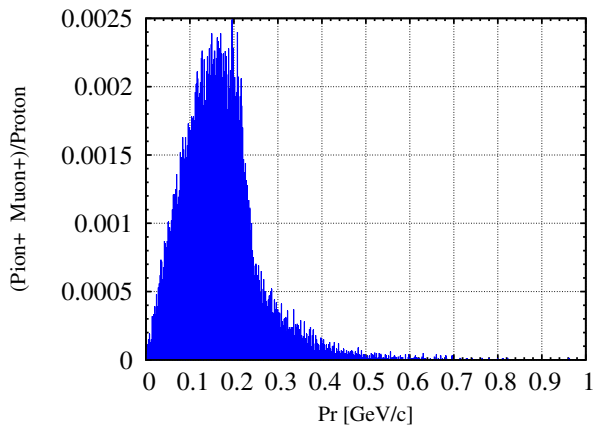


Figure 4: Pion transverse momentum at the end of the graphite target.

The transverse phase volume of the muon beam at the end of the Phase Rotator significantly larger than the acceptance of the later muon accelerator, but this volume is reduced by the Ionization Cooling section. The number of muons with the accelerator acceptances increases nearly linearly in the Cooler from $z = 150$ to 300 m as shown in Fig. 5.

OPTIMIZING THE TAPER LENGTH

The figure of merit for the optimization was taken to be the number of positive muons per incident proton within the subsequent muon-accelerator momentum acceptance [9], $100 < p_z < 300$ MeV/c, and acceptances in longitudinal and transverse phase space, $A_z < 150$ mm and $A_r < 30$ mm. The solenoid-taper length has a distinct in-

Copyright © 2013 CC-BY-3.0 and by the respective authors

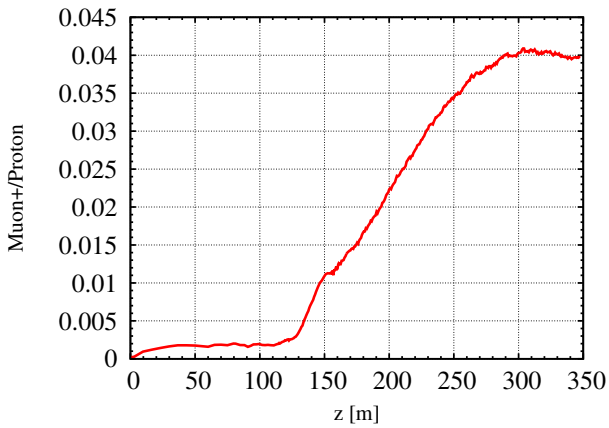


Figure 5: Number of muons within the accelerator-chain acceptance at various distances along the Front End.

fluence on the number of the transported muons to the end of cooling channel. Varying the length of the Taper resulted in higher muons yields, for $L_{\rm taper} \approx$ 3-4 m, as shown in blue in Fig. 6.

As we varied the taper length the longitudinal phase space changed accordingly, requiring RF-phase optimization, which increased the yield by $\approx$ 16-40 See the black curve in Fig. 6.

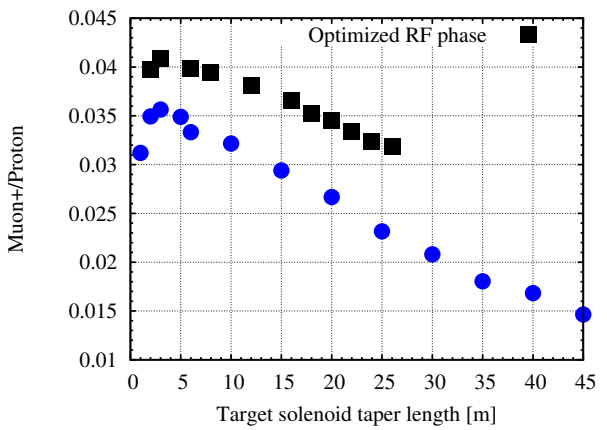


Figure 6: Muon yield from the Front End, within the acceptance of the accelerator chain *vs.* the solenoid taper length. The RF optimization (black curve) increased the Front End performance by $\approx$ 16-40%.

CONCLUSION

An optimization study of the capture section of the Front End of a staged Neutrino Factory was presented. The study was performed on a graphite target bombarded by a 3-GeV proton beam. The figure of merit of the optimization was the number of muons within the acceptance of the accelerator chains that follows the Front End. The target-solenoid field profile used in this study had an initial on-axis field $B_i = 15.0$ T, and final on-axis field $B_f = 2.5$ T, with the taper length $L_{\rm taper}$ being optimized for maximum yield of muons from the Front End (*i.e.*, at the beginning of the Muon Accelerator). Then, an optimization of the RF phase of the Buncher/Phase Rotator RF cavities was carried out. The best performance of the Front End was found to be $0.042\mu^+/p$. The optimum taper length was found to be 3-4 m, which is shorter than the optimum taper length when using an 8- GeV proton beam by 1-2 m.

ACKNOWLEDGMENT

The authors are grateful to X. Ding, R.B. Palmer, D. Neuffer and S.J. Berg for useful discussions.

REFERENCES

[1] M.M. Alsharo'a *et al.*, Recent Progress In Neutrino Factory And Muon Collider Research Within The Muon Collaboration, Phys. Rev. ST Accel. Beams **6**, 081001 (2003).

[2] M.A. Palmer *et al.*, Muon Accelerators for the Next Generation of High Energy Physics Experiments, Proc. IPAC13, TUPFI057.

[3] C.T. Rogers *et al.*, Muon front end for the neutrino factory, Phys. Rev. ST Accel. Beams **16**, 040104 (2013).

[4] N.V. Mokhov, The MARS Code System User's Guide, Fermilab-FN-628 (1995); N.V. Mokhov and S.I. Striganov, MARS15 Overview, AIP Conf. Proc. **896**, 50 (2007), http://www-ap.fnal.gov/MARS/

[5] R.C. Fernow, Ionization Cooling Code, https://pubweb.bnl.gov/~fernow/icool/

[6] K.T. McDonald, Analytic Forms for an Adiabatic Tapered Solenoid Gaussian Approximation to the Field Near $z = 0$, http://www.hep.princeton.edu/~mcdonald/mumu/target/taper.pdf

[7] R.C. Fernow, Physics analysis performed by ECALC9 (Sep. 30, 2003), http://nfmcc-docdb.fnal.gov/cgi-bin/ShowDocument?docid=280

[8] J. Gallardo *et al.*, An Ionization Cooling Channel for Muon Beams Based on Alternating Solenoids, Proc. PAC99, THP35.

[9] J.S. Berg *et al.*, Muon front end for the neutrino factory, Phys. Rev. ST Accel. Beams **9**, 011001 (2006).

Copyright © 2013 CC-BY-3.0 and by the respective authors

A HIGH-PERFORMANCE RECTILINEAR FOFO CHANNEL FOR MUON COOLING*

D. Stratakis#, J. S. Berg, R. B. Palmer, Brookhaven National Laboratory, Upton NY, USA
V. I. Balbekov, Fermi National Accelerator Laboratory, Batavia IL, USA

Abstract

An ionization cooling channel is a tightly spaced lattice containing absorbers for reducing the momentum of the muon beam, rf cavities for restoring the longitudinal momentum and solenoids for focusing the beam. Such a lattice is an essential step for a Muon Collider. Here, we explore a new scheme for designing ionization cooling channels for muon related applications. In this scheme, emittance reduction is achieved within a rectilinear channel with wedge absorbers for cooling and tilted solenoids for emittance exchange. Such configuration addresses several of the engineering challenges of a conventional helical channel. We numerically examine the performance of our proposed channel and compare it against conventional designs. We also review the conductor current densities requirements for all of the simulated scenarios.

INTRODUCTION

A key technical challenge in the development of a Muon Collider is that the phase space of the beam that comes from pion decay greatly exceeds the acceptance of downstream accelerators system. Therefore, a cooling channel is required. Given the short life time of a muon particle, ionization cooling is the only practical method that can be realized.

Over the past decade several progresses have been made in the design and simulation of 6D RFOFO cooling rings [1] based on emittance exchange. This is generally accomplished by using a wedge shaped absorber in a region with dispersion. Particles with higher energies will pass through more material than particles with lower energy as a result of dispersion, eventually leading to reduction of longitudinal emittance. Such rings have been shown to provide an impressive to two order magnitude reduction of the normalized 6D phase-space volume with a transmission well above 50%. In order to avoid the complexity arising from the required injection and extraction systems, those rings involved without loss in performance to a RFOFO helical channel [2], commonly known as the Guggenheim. A chief advantage of the Guggenheim is that avoids any issues related to absorber overheating.

Although a helical lattice can be advantageous in paper, still many questions remain. For instance, the beam can be intercepted by the fringe fields from the nearby solenoids. In addition, engineering constraints may arise at the last stages as the radius of curvature becomes less than 1.5 m. To further relax the aforementioned constraints we design and simulate here a rectilinear FOFO snake channel which has been proposed recently by one of the authors [3] and show that it can offer the same performance as the Guggenheim. In particular, we show that by applying a novel tapering scheme in which numerous parameters of the structure change from stage to stage based on the emittance reduction rate and transmission, we can achieve a good cooling efficiency that remains flat through the channel. This is because the beam emittance is always above the equilibrium emittance.

DESIGN PARAMETERS

The main issue with a channel of a fixed radius, cell length, and frequency is its gradual loss of cooling efficiency. Therefore, to keep the cooling process going we examine a tapered channel in which various parameters change in order to avoid reaching equilibrium. In this scheme, parameters such as cell length and radius of curvature progressively change from stage to stage based on the emittance reduction rate and transmission. Recent studies have shown [4] that such a concept improves performance substantially. In addition, with this approach the same emittance can be obtained in much shorter scale.

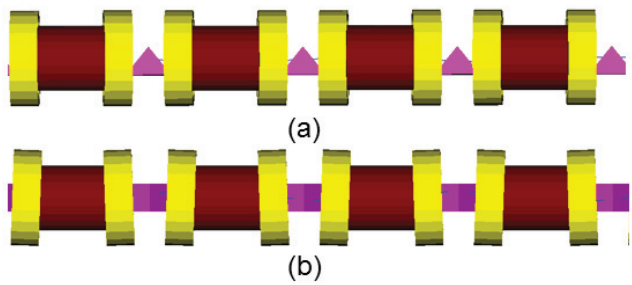


Figure 1: Conceptual design of our proposed rectilinear cooling channel: (a) Top view; (b) Side view. Note that the coils (yellow) are slightly tilted to generate dispersion.

At the first stage of the tapered channel the focusing will be relatively weak to avoid excessive angular divergence that can arise from the large transverse emittance of the initial muon beam. However, the weak focusing implies that the beta function and thus the equilibrium emittance are also relatively large, so the transverse cooling weakens as the limit is approached. To avoid this, this stage is terminated and we couple into the next stage that has a lower beta. This is achieved by simultaneously scaling down the cell dimensions and raising the strength of the on-axis solenoidal field. As a result this will produce a piecewise multi-stage shaped channel where each stage will consist of a series of

*Work supported by DE-AC02-98CH10886
#diktys@bnl.gov

Copyright © 2013 CC-BY-3.0 and by the respective authors

identical cells. A schematic of our proposed cooling system is shown in Fig.1. Note that the coils (yellow) are not evenly spaced; those on either side of the absorber are closer in order to increase the focusing at the wedge absorber (magenta). In order to produce dispersion, they are tilted by 1.1-1.3^0. The absorber is wedge shaped so that higher momentum particles go through the thicker part. Each lattice cell contains the same number of rf cavities (dark red) which, depending on the stage, can be 4, 5, or 6. The rf frequencies are either 325 MHz or 650 MHz. Those frequencies are chosen in order to match with the initial linac of Project X.

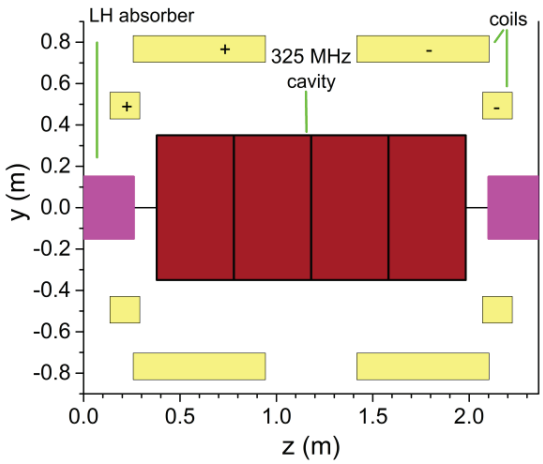


Figure 2: Close view of one cell at an early stage. Each cell has 4 coils and two of them are raped around the cavities. The tilt of the coils is not shown.

Figure 2 shows the side view of one cell at an early stage of the channel (Stage 2). This stage consists of a sequence of 14 identical 2.36 m cells, each containing four 0.4 m-long 325 MHz pillbox cavities, and a wedge-shaped liquid hydrogen absorber, with 28.6 cm central thickness and 100 deg. opening angle, to assure energy loss. Moreover, each cell contains four solenoid coils of opposite polarity, yielding an approximate sinusoidal variation of the magnetic field in the channel with a peak on axis value of 3.1 T and providing transverse focusing with a peak beta value of ~ 36 cm. In order to provide the required dispersion the coils are tilted by 1.1 deg vertically. The lattice transmits in a region from 155 to 248 MeV/c, with a central (reference) momentum of 204 MeV/c.

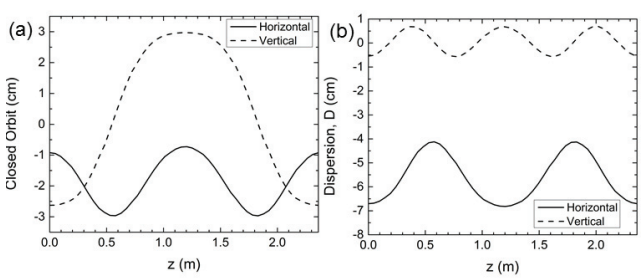


Figure 3: Closed orbit at the reference momentum of 204 MeV/c (left). Dispersion in the vertical and horizontal directions along the cell.

Deviation of the closed orbit along the cell for the reference momentum of 204 MeV/c is shown in Fig. 3(a). Notice that at the central momentum the vertical offset (dashed) from the center is ~ 2.6 cm at the entrance of the cell. Figure 3(b) displays the dispersion functions in x (solid) and y (dashed) along the cell. The dispersion at the absorber has the same sign in both directions and is mostly in the horizontal direction. Notice that the dispersion is maximum at the center of the absorber.

The beta function varies from 40.0 cm to 4.0 cm while the on-axis magnetic field increases progressively from 2.7 T to 13.1 T. It is important to emphasize that the maximum field on the coil at the last stage is 14.1 T with a current density of 196 A/mm^2. This value is below the critical published [5] limit for Nb_3Sn. The RF frequency is increased from 325 MHz to 650 MHz. Ideally, the cooling channel should be tapered with a continuously varying frequency. However, for practical implementation we keep the number of different frequencies as small as possible. As we will illustrate in the next section, 16 stages are enough to achieve the desired emittance for a Muon Collider. Detailed lattice parameters of our proposed channel can be found in Table 1.

SIMULATION DETAILS

Simulations of the channel performance where done using the ICOOL code with 100,000 particles. The simulation is initiated after the bunch merger. We generated 3D cylindrical field maps for each of the stages by superimposing the fields from all solenoids in the cell and its neighbour cells. The rf cavities were modelled using cylindrical pillboxes running in the TM010 mode. The cavities are enclosed with 100 μm metallic Beryllium windows. The wedge material was liquid hydrogen. The absorbers are enclosed in Al windows ranging from 500 μm (Stage 1) to 10 μm (Stage 16).

The lattice cooling efficiency is defined as the rate of change of the 6D emittance divided by the change of muons. It is often used to quantify the lattice performance and it is displayed in Fig. 4. One can see that for a rectilinear channel it remains relatively flat along the channel with a maximum near 9.5. The helical lattice appears to have a slight higher performance. Note that a more detailed comparison between the two schemes can be found elsewhere [6].

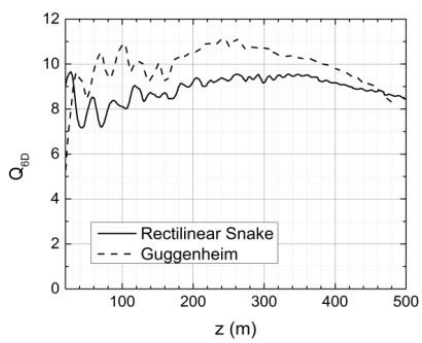


Figure 4: Cooling efficiency of the rectilinear channel (solid) and Guggenheim (dashed line).

Copyright © 2013 CC-BY-3.0 and by the respective authors

Table 1: Lattice Parameters of Our Proposed Tapered Rectilinear FOFO Channel

Stage	Cell length [m]	RF freq. [MHz]	RF grad. [MV/m]	Beta [cm]	B_o axis [T]	B_{max} coil [T]	Coil tilt [deg.]	Dispersion [cm]
1	2.75	325	17.5	40.0	2.7	7.1	1.1	6.6
2	2.36	325	17.5	35.8	3.1	5.5	1.1	6.8
3	2.02	325	18.5	28.6	3.6	7.8	1.1	7.5
4	1.73	325	17.5	25.1	4.1	5.6	1.2	3.4
5	1.49	325	19.5	21.1	4.9	7.9	1.3	5.0
6	1.38	325	18.0	17.4	5.4	8.5	1.1	3.8
7	1.27	325	20.5	14.6	6.0	9.4	1.2	5.4
8	1.15	325	20.5	13.5	6.5	10.2	1.1	4.4
9	0.995	650	24.0	10.8	7.7	10.4	1.1	2.9
10	0.806	650	27.0	8.7	9.5	12.9	1.1	2.3
11	0.806	650	26.0	7.1	10.3	12.7	1.1	1.8
12	0.806	650	27.0	6.1	11.0	13.0	1.1	1.7
13	0.806	650	27.0	5.2	11.6	13.5	1.1	1.6
14	0.806	650	26.0	4.3	12.6	14.1	1.1	1.4
15	0.806	650	26.0	4.0	13.1	14.2	0.5	0.6
16	0.806	650	26.0	4.0	13.1	14.2	0.5	0.6

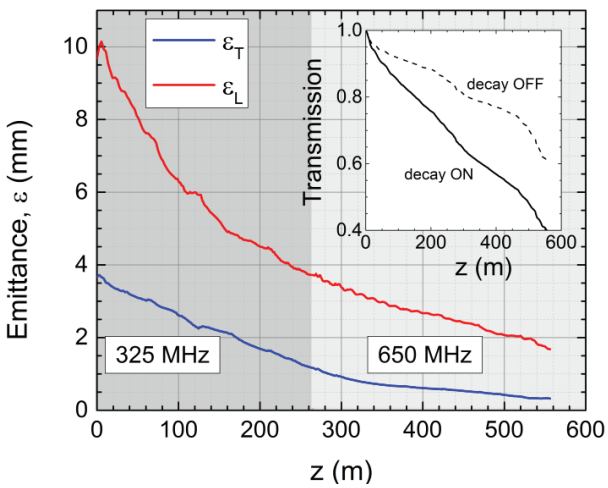


Figure 5: Longitudinal (red), transverse (blue) emittances and transmission as a function of distance along the channel. The final values of the emittances are also shown.

The transverse, longitudinal emittance and transmission including muon decays as a function of distance along stages 1 to 16 are shown in Fig. 5. The simulation produced a transverse emittance of 0.32 mm and a longitudinal emittance equal to 1.6 mm, which is close to the desired values for a Muon Collider. The transmission without decays is above 60%. If space-charge is included in the simulation an additional 10% of losses is predicted [7]. The quoted emittance values are normalized rms.

SUMMARY

Cooling large emittance muon beams is an essential step for a Muon Collider. A rectilinear FOFO snake channel may reduce the engineering challenges compared to conventional helical structures (like in a Guggenheim helix). As this study demonstrated, by performing tapering the desired emittances for a muon collider can be obtained with a transmission above 60% without decays and 40% with muon decays. The cooling rate remains relatively flat along the channel with a peak value of 9.5. Furthermore, the maximum field on the coil is 14 T which is within the published critical limit for Nb_3Sn. The next step would be to improve the matching between individual stages, which will aid in boosting the performance. The authors like to thank P. Snopok and R. Ryne for many fruitful discussions.

REFERENCES

[1] R. Palmer et al, *Phys. Rev. ST Accel. Beams* **8**, 081001 (2005).
[2] P. Snopok, et al., IJMPA 24, p. 987 (2009).
[3] V. Balbekov, MAP Document No. 4365 (2013).
[4] D. Stratakis et al., *Phys. Rev. ST Accel. Beams* **16**, 091001 (2013).
[5] http://fs.magnet.fsu.edu/~lee/plot/plot.htm
[6] J. S. Berg et al., Proc. of NAPAC 2013, Pasadena CA, THPHO04.
[7] D. P. Grote et al., Proc. of NAPAC 2013, Pasadena CA, THPHO13.

Copyright © 2013 CC-BY-3.0 and by the respective authors

SPACE-CHARGE LIMITATIONS ON THE FINAL STAGES OF A MUON COLLIDER COOLING CHANNEL*

D. P. Grote#, Lawrence Livermore National Laboratory, Livermore, CA, USA
D. Stratakis, R. B. Palmer, J. S. Berg, Brookhaven National Laboratory, Upton, NY, USA

Abstract

Muon Colliders use ionization cooling to reduce the emittance of the muon beam prior to acceleration. At the last stages of the cooling channel, the bunch has 4×10^{12} muons, an average momentum of 200 MeV/c, and an rms bunch of 2 cm. With this beam intensity and relatively low momentum, we expect space charge effects to have a significant impact on beam dynamics. Here, with the aid of the particle-in-cell code Warp, a 3D model is developed to examine space-charge for muon cooling lattices and some recent results are presented. The model includes 6D cooling with wedge shaped absorbers. We show that space-charge under certain conditions can cause a notable particle loss. Furthermore, we discuss some potential space-charge compensation mechanisms.

INTRODUCTION

A complete scheme for cooling a muon beam sufficiently for use in a muon collider has been previously described [1]. This scheme uses separate 6D ionization cooling channels for the two signs of the particle charge. In each, a channel first reduces the emittance of a train of muon bunches until they can be injected into a bunch-merging system. The single muon bunches, one of each sign, are then sent through a second tapered 6D cooling channel where the transverse emittance is reduced as much as possible and the longitudinal emittance is cooled to a value below that needed for the collider. The beam can then be recombined and sent through a final cooling channel using high-field solenoids that cools the transverse emittance to the required values for the collider. The baseline cooling requirement for cooling is shown in Fig. 1.

Theoretical estimates predict that at the last stages of the post-bunch-merge 6D cooling channel the rms bunch length is just 2 cm and contains $4\text{x}10^{12}$ muons. Thus, the peak current becomes ~4 kA at a ~200 MeV/c momentum. Due to this large current, space-charge forces can be present and thus, there is cause for concern that the existing 6D cooling lattice design may not work so well. Recent studies [2] with the Warp PIC code [3] confirmed this fact since it was shown that longitudinal space-charge can oppose cooling while simultaneously it causes severe particle losses. To reduce the space charge effects, the overall lattice was redesigned with a higher longitudinal emittance target, increased from 1.5 to 2.0. We note that those previous studies were assuming a matrix for longitudinal cooling and thus, the effect of a real absorber wedge was not taken into account. This paper will present results from recent studies on simulating full 3D space-charge effects on muon cooling lattices with more realistic wedge shaped absorbers.

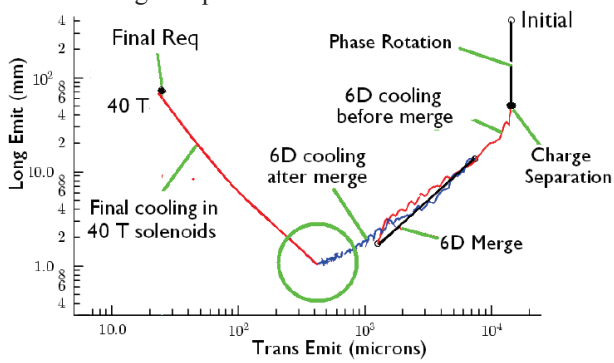


Figure 1: Baseline cooling requirement for the Muon Collider.

LATTICE DESIGN

In order to cool towards the micron scale emittances required for a Muon Collider a 16-stage tapering channel has been proposed. A detailed description of this lattice can be found elsewhere [4]. In this scheme, we apply the concept of tapering [5] where parameters such as cell length, focusing and radius of curvature progressively change from stage to stage based on the emittance reduction rate and transmission.

A segment of one stage of our proposed cooling system is shown in Fig. 2(a). Each stage consists of straight section with a number of identical cells like the one shown in Fig. 2(b) and Fig. 2(c). The coils (yellow) are

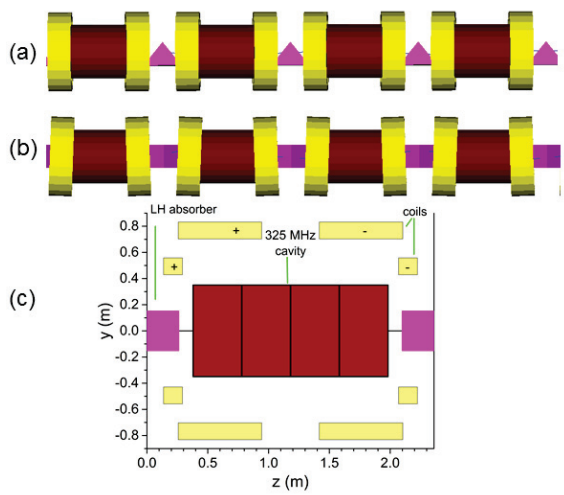


Figure 2: Cooling scheme for the Muon Collider. Fig. (c) depicts one lattice cell. The tilts of the magnets are not shown.

*Work supported by DE-AC02-98CH10886.
#dpgrote@lbl.gov

Copyright © 2013 CC-BY-3.0 and by the respective authors

not evenly spaced and in order to produce dispersion, they are tilted by 1.1-1.3^0. The liquid hydrogen absorber (magenta) is wedge shaped so that higher momentum particles go through the thicker part. Each lattice cell contains the same number of rf cavities (dark red) which, depending on the stage, can be 4, 5, or 6. We use only two sets of rf frequencies, namely 325 MHz and 650 MHz. The choice of 325 MHz is made in order to match with the initial linac of Project X. The cavity window material is Be.

SIMULATION RESULTS

The input beam in the simulations has a normalized transverse emittance of 3.63 mm and a normalized longitudinal emittance of 10.17 mm, while the average longitudinal momentum is 218 MeV/c. Note that those parameters closely resemble the baseline distribution of a muon beam before the final 6D cooling sequence of a Muon Collider [1]. We tracked 100,000 particles and included decay of muons. We generated 3D field maps for each of the stages by superimposing the fields from all the solenoids in the cell and its neighbour cells, including the solenoid tilts. The rf cavities were modelled using cylindrical pillboxes running in the TM010 mode.

Space-charge effects were studied by using the particle-in-cell code Warp. Warp was originally developed to simulate space-charge-dominated beam dynamics in induction accelerators for heavy-ion fusion (HIF). The code now has an international user base and is being applied to projects both within and far removed from the HIF community. A layer was added to Warp to read in and parse ICOOL input files allowing identical problem setup. Note though that Warp operates with time as the independent variable whereas ICOOL uses *s*, so there are small numerical differences in the calculations. During the calculation, Warp handles all operations except for the interaction with the material in the wedge absorber, which is handled by calls to the appropriate ICOOL routines.

The lattice as seen in the Warp simulation is shown in Fig. 3. This is a cell in the first stage of cooling. The simulation incorporates all aspects relevant to the beam motion, including the 3D solenoid field map, RF cavities with absorbing Be windows, and the wedge absorbers and windows. The wedges and RF cavity windows both act as perfectly conducting internal boundary conditions on the electrostatic potential. The beam macro-particles were generated with an initially Gaussian distribution in physical and velocity space.

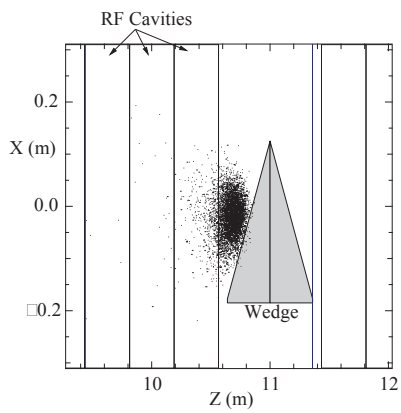


Figure 3: Lattice as known by the Warp simulation.

Before examining the effects of space charge, checks were carried out comparing ICOOL and Warp simulations without space-charge to check correctness of the models. The resulting emittance and particle numbers are shown in Fig. 4. Four cases are shown, ICOOL and Warp with and without muon decay. As can be seen, good agreement was obtained.

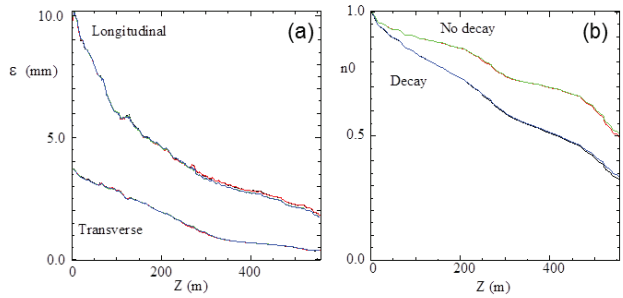


Figure 4: ICOOL and Warp cross-check without space charge (a) emittance, and (b) number of muons. Simulations are carried with and without muon decay using both codes.

In these initial simulations, the electrostatic self-field model was used. The resulting fields from the beam are significant, of order several MV/m, as can be seen Fig. 5. However, this is small compared to RF gradient, which is typically between 17 and 27 MV/m. Note the sharp cut off of the field at the RF cavity windows.

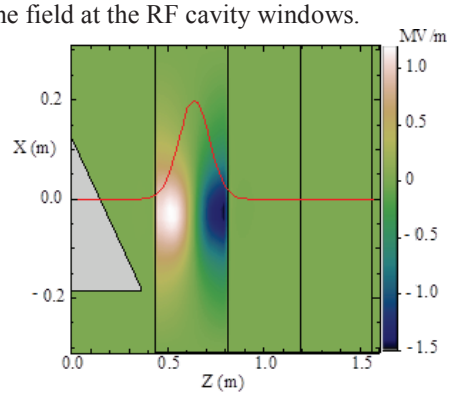


Figure 5: Longitudinal electric self-field. The red curve shows the scale current to show the location of the beam bunch.

The electrostatic potential was calculated on a 3D grid with an initially 2 cm transverse and 1 cm longitudinal cell sizes. As the simulation progresses and the lattice dimensions decreased, the grid cell sizes were correspondingly reduced. The simulations are significant, requiring on the order of a day of wall clock time, depending on the number of processors, because of the large number of time steps, > 500,000, to traverse the cooling channel. Note that the time step size is driven by the need to resolve the variations in the applied fields and not by the space-charge calculation.

Copyright © 2013 CC-BY-3.0 and by the respective authors

The results of the simulations with space charge are shown in Figs. 6, 7 and 8. The main effect of the space charge is to increase the particle loss. Little difference is seen in the emittances. There is a reduction in the longitudinal emittance, but it is associated with the increased particle loss. Most of the particle loss is longitudinal – the increase in the loss is not unexpected since the space charge increases the length of the pulse, pushing more particles out of the RF bucket. The increase in bunch length is shown in Fig. 8. The transverse size is unaffected.

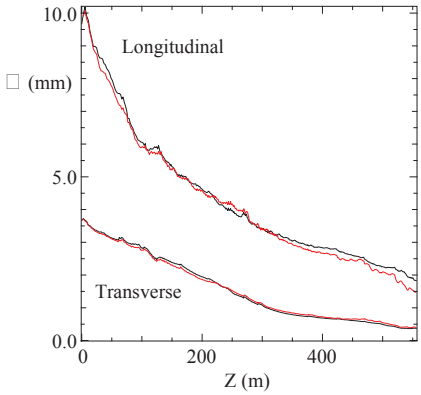


Figure 6: Beam normalized rms emittances along the channel with (red) and without (black) space-charge.

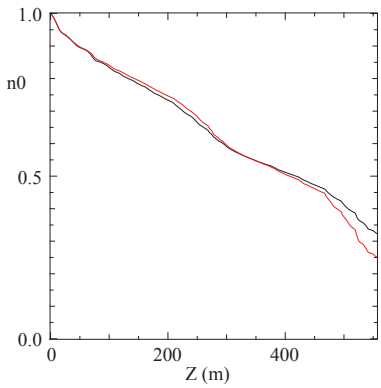


Figure 7: Fraction of beam remaining with (red) and without (black) space-charge.

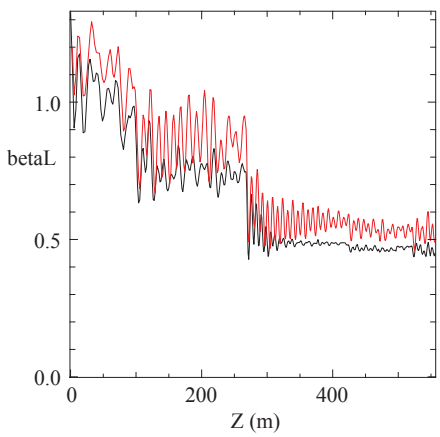


Figure 8: Longitudinal beta function with (red) and without (black) space-charge.

One possible method to reduce the particle loss is to increase the RF gradient, which increases the depth of the bucket. In the previous work [2], this was found to be effective. However, in the current lattice design, increasing the gradient was ineffective. Figure 9 shows the resulting emittances and particle losses with the gradient increased by steps of 1.5 MV/m in the last 8 stages. Note that the red line shows the default value of 26 MV/m while the yellow line corresponds to 46 MV/m which is the maximum gradient simulated. It is possible to obtain better performances if the beam is matched for each gradient accordingly. This will be investigated in more detail in a future study.

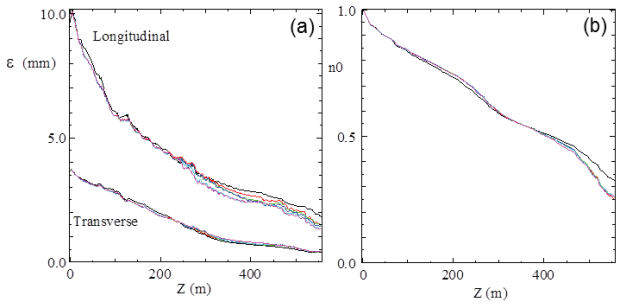


Figure 9: Emittances with varying RF gradients. The emittance is reduced with each 1.5 MV/m increment. The black curve, without space charge, is for reference. (b) Fraction of beam remaining for varying RF gradients. The black curve, without space charge, is for reference.

CONCLUSIONS

Towards the end of the cooling channel, the density of the muon bunch becomes significant enough that space charge effects can become important. A simulation campaign has been carried out, using the Warp code, to examine the effects. Warp uses a fully self-consistent PIC model to include space charge. The simulations show that there is little effect on the emittance, but an increase in the particle loss. Most of the particle loss is longitudinal, out the tail of the bunch. Unfortunately, the simple remediation of increasing the RF cavity gradient was not effective. Work examining other techniques to reduce particle loss will continue.

ACKNOWLEDGMENT

The authors like to thank R. Ryne and I. Haber for many fruitful discussions.

REFERENCES

[1] R. B. Palmer, Proc. of PAC 2007, Albuquerque NM, p. 1222 (2007).
[2] D. Stratakis et al., Proc. of IPAC 2013, Shanghai, China, p. 1553 (2013).
[3] J.-L. Vay, D. P. Grote, R. H. Cohen, A. Friedman, Comput. Sci. Disc. **5** (2012) 014019.
[4] D. Stratakis et al., Proc. of NA-PAC 2013, Pasadena CA, THPHO12.
[5] D. Stratakis et al., Phys. Rev. ST Accel. Beams **16**, (2013) 091001.

Copyright © 2013 CC-BY-3.0 and by the respective authors

RF CAVITY PHASE CALIBRATION USING ELECTROMAGNETIC PICKUPS*

B. Durickovic†, D. Constan-Wahl, J. Crisp, G. Kiupel, S. Krause, D. Leitner,
S. Nash, R. Rencsok, J.A. Rodriguez, R. Webber, W. Wittmer,
NSCL/FRIB, East Lansing, MI 48824, USA

Abstract

A method is presented using electromagnetic pickup probes for RF cavity phase calibration. (We used capacitive style pickup probes.) Pickup probes provide fast readings, and measurements of the phase difference between a pair of pickup probes provides enough information about the phase-energy curve to yield a fit for the zero-crossing phase. We present an overview of the algorithm and measurement results of an implementation on the ReA3 reaccelerator.

INTRODUCTION

The Facility for Rare Isotope Beams (FRIB) is a heavy ion fragmentation facility to produce rare isotopes far from stability for low energy nuclear science. The facility will utilize a high-intensity, superconducting heavy-ion driver linac to provide stable ion beams from protons to uranium at energies greater than $200\ \mathrm{MeV/u}$ and at a beam power of up to $400\ \mathrm{kW}$ [1]. The baseline design for the linac comprises over 300 accelerating superconducting cavities. A precondition for tuning the linac is calibrating the radio frequency (RF) phase of each of these cavities, which requires a phase scan combined with energy measurements. With such a large number of cavities as it is planned for FRIB, a need arises for an automated approach to calibrating cavity phase.

RF cavity phase calibration is the process of calibrating the cavity phase relative to the phase of the accelerated beam. For this purpose, the zero-crossing phase points (the phase points at which the cavity does not provide any acceleration) are determined. There are two such points in a full 360-degree phase range ($180°$ apart from each other), and we use the one on the bunching side of the phase slope as the reference. The value of the zero-crossing depends on the beam energy, thus the cavities need to be calibrated for every new energy tune. Therefore, cavity phase calibration is a necessary recurring task in operations.

We approached the concrete problem of calibrating the cavity phases on the ReA3 accelerator at Michigan State University [2], which is currently being commissioned. Prior to the installation of Beam Position Monitors (BPMs) in the ReA3 accelerator, the only method available for cavity phase calibration was energy measurements from silicon foil detectors. As these measurements are inherently slow, calibrating the six accelerating cavities currently installed in ReA3 could take up to several hours. Since capacitive style electromagnetic pickup probes provide fast readings, we explored the application of pickup probes for inferring the beam energy and thereby calibrating cavity phase. The capacitive style pickup probes we used were the two BPMs installed on the ReA3 beam line. The details of the BPMs in the ReA3 accelerator are presented in Rodriguez et al. [3]. The phase readouts were averaged over the four buttons for each BPM, so that for this purpose, the BPMs were effectively used only as electromagnetic pickup probes.

PRINCIPLE

The readouts from two pickup probes separated by a certain distance provide the phase difference of bunches at the two locations. It is important to keep in mind, though, that this is not the absolute phase difference, but its value modulo $360°$. In other words, the pickup probes do not provide information about the total number of bunches between the two locations, but only the fraction of the RF period that represents the "incomplete last bunch." The number of "complete bunches" between the two locations needs to be evaluated by other means. As will be shown, however, knowing this information exactly is not essential for the applicability of the method we are presenting.

The phase difference $\Delta\varphi$ between the pickup probes can be translated into the time of flight via

$$t(\Delta\varphi; n) = T_{RF}\left(n + \frac{\Delta\varphi}{360°}\right), \qquad (1)$$

where n is the truncated number of bunches between the pickup probes, T_{RF} is the RF period, and t is the time of flight. The integer n decreases with beam energy, and within energies attainable in the ReA3 accelerator (without deceleration), and with the BPMs separated by $2.08\ \mathrm{m}$, it ranges from 14 (for the beam energy after the RFQ of $600\ \mathrm{keV/u}$) to 8 (for the maximum beam energy after the linac of $1.9\ \mathrm{MeV/u}$). Translating the time of flight (1) into energy (non-relativistically), we obtain the dependence of energy per nucleon E/m on the phase difference $\Delta\varphi$:

$$\frac{E}{m}(\Delta\varphi; n) = \frac{1}{2}\left(\frac{Lf_{RF}}{n + \frac{\Delta\varphi}{360°}}\right)^2, \qquad (2)$$

where L is the distance between the pickup probes, and $f_{RF} = 1/T_{RF}$ is the RF frequency. Equation (2) can be in-

* Work supported by Michigan State University FRIB funds and by the U.S. Department of Energy Office of Science under Cooperative Agreement DE-SC0000661

† durickovic@frib.msu.edu

Copyright © 2013 CC-BY-3.0 and by the respective authors

verted eliminating the unknown number of bunches n into

$$\Delta\varphi(E) = \left(360^\circ L f_{RF}\sqrt{\frac{m}{2E}}\right) \mod 360^\circ. \quad (3)$$

This functional dependence, for the relevant range of energies, is shown in Figure 1, which is a graph we refer to as a *mod-360 hyperbola*.

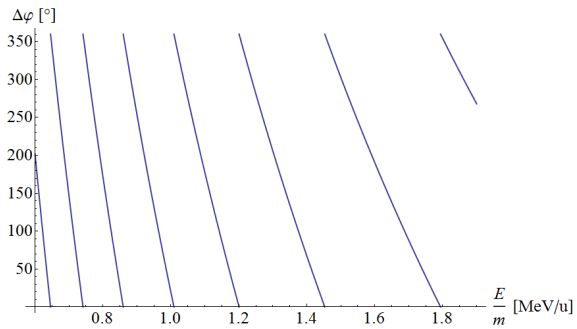


Figure 1: Bunch phase difference at pickup probes $\Delta\varphi$ as a function of beam energy per nucleon E/m. ($L = 2.08$ m)

In the method presented here, the beam energy is varied by changing the cavity phase

$$E(\Phi) = E_0 + QeV\sin(\Phi - \Phi_0)\,, \quad (4)$$

where Φ is the cavity phase, E_0 and Φ_0 are the zero-crossing energy and phase, respectively, Q is the beam charge state (an integer), and eV is the cavity amplitude. The dependence $\Delta\varphi(\Phi)$ of the measured phase difference on the cavity phase (the independent variable) is therefore obtained by composing the sine function $E(\Phi)$ (4) with the mod-360 hyperbola $\Delta\varphi(E)$ (3). Ideal measured data (pickup probes phase difference vs. cavity phase) should therefore be aligned along the curves shown in Figure 2. Note that this plot is not a broken sine function inasmuch as the mod-360 hyperbola $\Delta\varphi(E)$ (3) is not a broken line (cf. Figure 1).

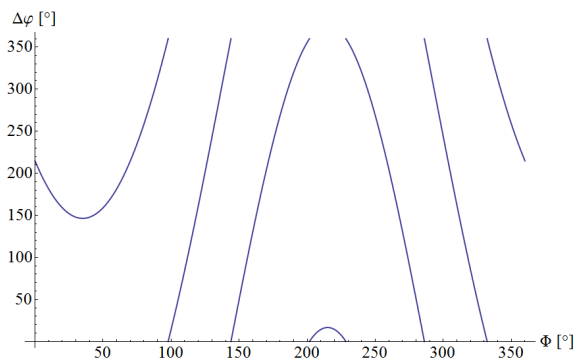


Figure 2: Ideal measured data: pickup probes phase difference $\Delta\varphi$ as a function of cavity phase Φ. ($E_0 = 600$ keV, $eV = 100$ keV, $\Phi_0 = 305^\circ$, $L = 2.08$ m)

Algorithm Outline

The first step in fitting for the sought parameter Φ_0 is to turn data in the form of $\Delta\varphi(\Phi)$ into a continuous-looking function, effectively a "reverse mod-360" operation. We refer to this process as *stitching*. Once the data are stitched, ordinate values are no longer restricted to a 360° window. Next, we eliminate the unknown parameter n from consideration by picking a reasonable estimate for it, and transforming the phase difference data into energy values. Then, we fit the sine curve $E(\Phi)$ (4), which yields three fitted parameters (E_0, eV, Φ_0) including the wanted zero-crossing phase Φ_0. An error in the estimate for n is mostly reflected in the error in E_0, while the effect on the fit in Φ_0 is negligible, as evidenced by numerical trials on measured data.

METHODS

The algorithm as outlined above was implemented in Python, with a curve fitting optimizer provided by the SciPy [4] *optimize* package and a graphical user interface (GUI) written using the *Traits* and *TraitsUI* packages, also included in the SciPy library. The EPICS [5] connection was established via PyEpics [6], which allowed the software to do a fully automated phase scan by setting cavity phase values, and reading cavity phase readbacks and BPM phase data, as well as any other EPICS channels that might be of interest (e.g. Faraday Cup readouts for beam intensity).

In order to be of practical use, in addition to the basic phase scan controls, data collecting, and fitting capabilities, the software also required data resampling functionality to produce meaningful fits. For various reasons, some measured data points need to be discarded. The most commonly observed cause of outliers in the ReA3 accelerator data was sparking between bender plates near the source, due to the fact that the source needs to operate in a high current mode in order for the pickup probes to provide a sufficient signal throughout the phase scan. Sparks would typically produce a single bad datapoint before the beam falls back into its trajectory. We were carrying out several measurements (typically 10, although in some instances 3 were sufficient) for each cavity phase, and such outliers were easily detectable due to a large deviation from the mean. However, other causes of error in the measurements lead to an entire set of measurements for a given cavity phase setpoint (referred to as a setpoint group) to be discarded, either because of a large rms, or as too far removed from the fitted curve. Therefore, the resampling was done at two levels: (1) within a setpoint group: removing single data points that are too far from the mean; (2) among setpoint groups: removing entire setpoint groups whose standard deviation is too large, or whose mean is too far from the fitted curve.

As far as the beam line configuration, we note that the locations where the BPMs were installed in the ReA3 accelerator were not chosen with this particular purpose in mind, and were less than ideal: they were about 0.6 m down-

Copyright © 2013 CC-BY-3.0 and by the respective authors

stream from the last accelerating cavity with no focusing or steering elements after the cavity, and separated by a distance of 2.08 m. These were the only two BPMs available, and so were used for all the cavities. The upstream cavities were therefore more challenging due to their greater distance from the BPMs.

RESULTS

Several test runs of the software were carried out on the ReA3 accelerator. The beam used in each case was molecular hydrogen H_2^+. The issue that made the calibration process slow at first was the tuning required to prepare the beam, which was not trivial due to the position of the BPMs and the lack of focusing and steering elements around them. Moreover, in order to obtain usable data, the beam must be tuned so as to provide a good signal from the BPMs throughout a full cavity scan. This is complicated by the fact that due to the design of the ReA3 superconducting RF cavities, they steer the beam as a function of phase setting [7]. Tuning was more challenging with the upstream cavities due to the greater distance to the BPMs and because of the effect of the cavity kicks is proportionately larger on the lower energy beam at the beginning of the linac. In the first runs, tuning was taking up to a few hours per cavity. As the tunes were developed, this time was significantly reduced, and in the last run tuning was taking an average of about 10 minutes per cavity.

We have empirically verified the claim presented above that the fit for the zero-crossing phase is not affected by an inaccurate estimate of the number n of bunches between the pickup probes. For all the measured data, varying n between extreme values attainable in ReA3, the resulting change in the fitted zero-crossing phase Φ_0 is less than $0.1°$, which is less than the estimated accuracy of the method.

In the last run, carried out in September 2013, we have developed a procedure to phase the linac sequentially, using the fitted zero-crossing phase value of the last cavity to set the cavity phase to nominal acceleration phase (in ReA3: $-20°$ off peak) before proceeding with the next one. The energy plot of the data for one cavity (after resampling), along with the fitted sine curve, is shown in Figure 3.

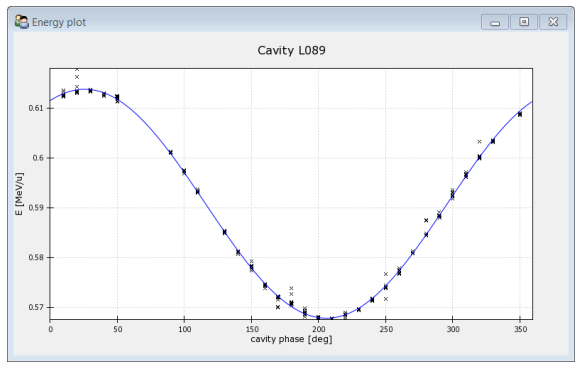


Figure 3: A screenshot of a window of the cavity phase calibration software that shows energy vs. cavity phase data (black) with the fitted sine curve (blue) for one of the accelerating cavities in the ReA3 linac.

CONCLUSION

A method for calibrating cavity phase using two capacitive style pickup probes by measuring the relative difference in phase between the two pickup probes was presented. No other measurements are necessary: the method does not require absolute energy measurements, since a reasonable estimate of the number n of bunches between the pickup probes is sufficient to yield an accurate fit for the zero-crossing phase Φ_0. The principle is based on simple equations: phase difference data are stitched together and transformed to the energy domain, where a sine function is fitted, and the abscissa offset represents the desired parameter Φ_0.

This algorithm was implemented and tested on the ReA3 accelerator. The implementation software had a direct connection with EPICS channels, automating the full cavity scan process, and it included data resampling features to deal with unacceptable levels of noise in the data. In the best case, a usable full cavity scan took only a couple of minutes, however this time is dominated by the time needed to tune the beam in order to prepare it for the scan. The latter time is strongly dependent on the position of the pickup probes relative to the cavity, and their separation distance, as well as the availability of tuning and focusing elements, and the reproducibility of previously developed tunes, all of which were less than ideal in our case. We still successfully calibrated the accelerating cavities in the ReA3 accelerator using BPMs as pickup probes.

REFERENCES

[1] J. Wei et al., "Progress towards the Facility for Rare Isotope Beams," FRYBA1, NA-PAC'13.

[2] D. Leitner et al., "Status of the ReAccelerator facility ReA for rare isotopes," FRYBA2, NA-PAC'13.

[3] J.A. Rodriguez et al., "Beam position and phase measurements of microampere beams at the Michigan State University ReA3 facility," THPAC20, NA-PAC'13.

[4] SciPy Python library for scientific computing, `http://www.scipy.org`

[5] Experimental Physics and Industrial Control System (EPICS), `http://www.aps.anl.gov/epics/`

[6] PyEpics Python interface for the Channel Access (CA) library of the EPICS Control System, `http://cars.uchicago.edu/software/python/pyepics3/`

[7] A. Facco and V. Zvyagintsev, "Beam steering in superconducting quarter-wave resonators: An analytical approach," Phys. Rev. ST Accel. Beams 14, 070101 (2011).

Copyright © 2013 CC-BY-3.0 and by the respective authors

MICE SPECTROMETER SOLENOID MAGNETIC FIELD MEASUREMENTS

M. Leonova# *on behalf of the MICE collaboration*
Fermilab, Batavia, IL 60510, USA

Abstract

The Muon Ionization Cooling Experiment (MICE) is designed to demonstrate ionization cooling in a muon beam. Its goal is to measure a 10% change in transverse emittance of a muon beam going through a prototype Neutrino Factory cooling channel section with an absolute measurement accuracy of 0.1%. To measure emittances, MICE uses two solenoidal spectrometers, with Solenoid magnets designed to have 4 T fields, uniform at 3 per mil level in the tracking volumes. Magnetic field measurements of the Spectrometer Solenoid magnet SS2, and analysis of coil parameters for input into magnet models will be discussed.

INTRODUCTION

The MICE experiment [1] located at Rutherford Appleton Laboratory consists of a dedicated beam line, which generates muons in a range of input momenta between 140 and 240 MeV/c and emittances between 2 and 10 π mm, and a cooling cell sandwiched between particle identification detectors (PID) and Spectrometer Solenoids (SS) equipped with scintillating fiber trackers, see Fig. 1. The cooling cell is designed to reduce the transverse emittance of a passing muon beam by about 10% using the ionization cooling principle.

Each spectrometer consists of a 4 T superconducting solenoid, and a tracker [2] composed of five planar scintillating-fibre stations, whose pacing has been chosen to optimize the performance of the reconstruction (track-finding efficiency and parameter resolution). Together, the spectrometers are required to determine the expected relative change of approximately 10% between the "before" and "after" beam transverse emittances with a precision of ±1% (i.e. 0.1% absolute measurement of the emittance). Therefore, the fields in the tracking volume should be known with high accuracy.

The MICE SSs were built at Wang NMR (Livermore, CA, USA). A schematic representation of the magnet (not drawn to scale) is shown in Fig. 2. The cryostat consists of a liquid helium vessel, an 80 K thermal shield, cold mass supports and a stainless steel vacuum vessel with 40-cm diameter bore. Each solenoid consists of five superconducting Nb-Ti coils wound on a single aluminum mandrel. Two Matching coils (M1, M2) match the muon beam in the SSs to the beam in the cooling cell. Two End coils (E1, E2) positioned around a Center coil (C) are designed to generate a uniform 4 T field over a 110-cm-long and 30-cm-diameter volume. The coil parameters

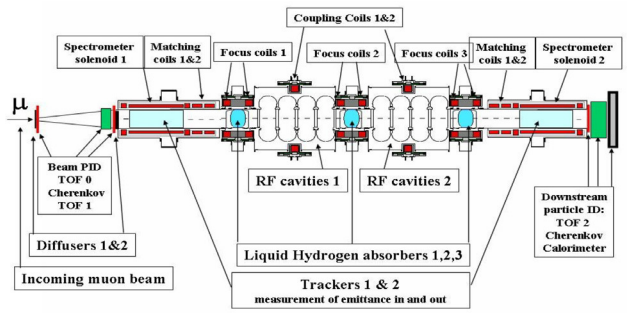


Figure 1: Layout of the MICE cooling cell. It is a prototype of a cooling channel section for use in a Neutrino Factory or a Muon Collider.

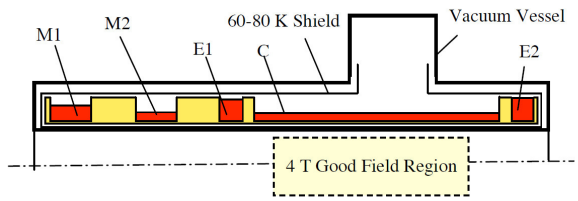


Figure 2: Top half of a schematic cross-section of one of the MICE SS.

	Match 1	Match 2	End 1	Center	End 2
Inner Coil Radius (mm)	258	258	258	258	258
Coil Thickness (mm)	46.165	30.925	60.905	22.125	67.783
Coil Length (mm)	201.268	199.492	110.642	1314.30	110.642
Current Center Axial Position* (mm)	124.00	564.00	964.00	1714.00	2464.00
Current Center Radial Position* (mm)	281.083	273.463	288.453	269.063	291.891
Coil Average J (A mm-2)	137.67	147.77	124.28	147.66	127.09
Number of Layers per Coil	42	28	56	20	62
Number of Turns per Layer	115	114	64	768	64
Total Number of Turns	4830	3192	3584	15360	3968
Design Current (A)**	264.83	285.60	233.68	275.52	240.21
Coil Self Inductance (H)^	12.0	5.0	9.0	40.0	11.3
Coil Stored Energy (MJ)**	0.42	0.20	0.26	1.55	0.32
Peak Field in Coil (T)**	5.30	4.32	5.68	4.24	5.86
Temperature Margin at 4.2 K (K)**	~1.6	~1.8	~1.5	~2.0	~1.5

* Based on Z = 0 is at the match coil end of the magnet cold mass (The center of MICE in these coordinates is at Z = -3487 mm) R = is the axis of the magnet (the MICE axis).
** This is at the maximum design current, which is based on the worst-case currents for the five coils.
^ The inductance of the two end coils and the center coil in series is about 74 H.

Figure 3: As built parameters of the second MICE SS.

given in Fig. 3 [3] are "as built", which are different from the original design and design by vendor. Each coil layer was thicker than anticipated with fewer turns per layer, thus, the currents in the coils were adjusted accordingly.

A model of the solenoids (together with other magnets, equipment and structures in the MICE experimental hall) will be used to simulate the fields for each momentum/emittance case for use in MICE data analysis. Thus, the magnetic field mapping is important to verify the coil geometry for the model and effects of magnetic material (detector shielding) on the field.

mleonova@fnal.gov
Work supported by US DOE under contract DE-AC02-07CH11359.

Copyright © 2013 CC-BY-3.0 and by the respective authors

HIGH PRECISION MAGNETIC FIELD MEASUREMENTS

CERN Detector Technologies Engineering and Mechanics group built a dedicated system for mapping MICE magnets [4]. The system includes: a 5-m long support system, the chariot containing a detachable service module for an NMR probe, disk with seven 3D Hall probes, and the Data Acquisition system. The setup of the magnet measurement device is shown in Fig. 4.

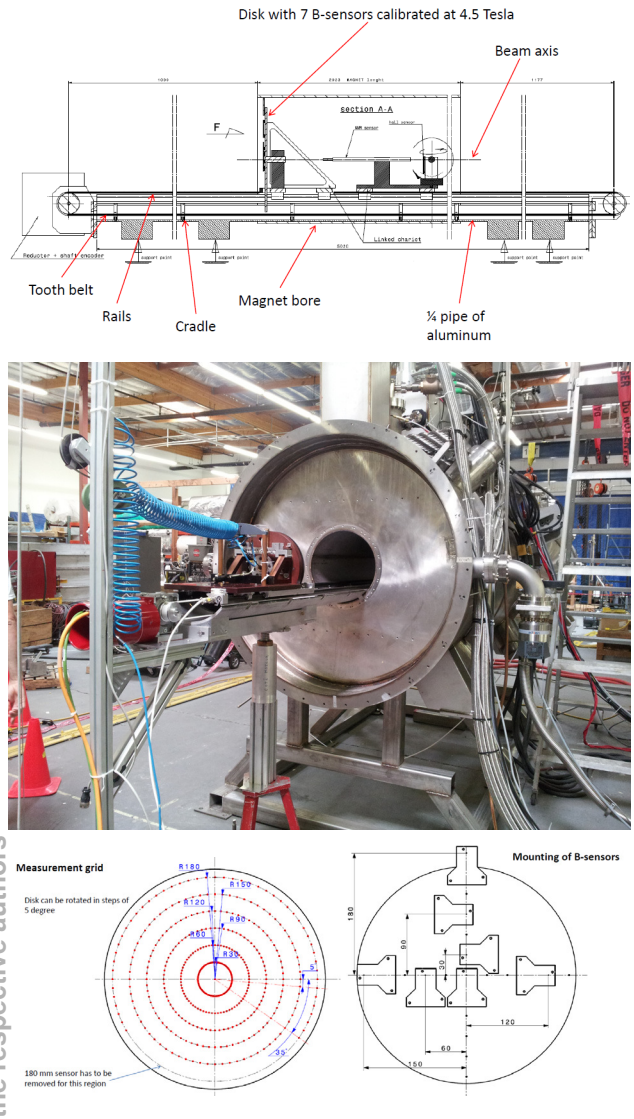


Figure 4: (Top) Magnet measurement device setup. (Center) Photo of the system in use for SS2 magnet. (Bottom left) Measurement grid of the device. (Bottom right) Mounting positions of the seven 3D Hall probe sensors on the disk.

The support is made of ¼" aluminum pipe. Other components of the device are made of non-conducting materials to avoid eddy currents. The chariot is moved by a motor with reduction gear box and encoder on the outgoing shaft. The disk with seven 3D Hall probes can be rotated in steps of 5°. The probe at 180 mm radius needs to be dismounted for rotation angles between 225° and 355° due to interference with the chariot.

The system is characterized by the following uncertainties: ± 0.5 mm probe radial position; ± 1 mrad disk rotation angle; < 0.5 mm longitudinal position; and ± 2 mT magnetic field measurement in 1 to 4 T region.

Magnetic measurements of MICE SS2 magnet were performed for two setups: without any magnetic material present near the solenoid, and with steel (US1010) plate and cage, mounted on the E2-coil side of the solenoid for shielding detectors present in MICE channel.

For each setup, a series of measurements were done for two coil current configurations: "Solenoid Mode" and "Flip Mode", corresponding to the two MICE cooling cell magnetic field configurations when operating with muons with an average momentum of 240 MeV/c and a β-function at the center of the absorbers of 420 mm. Figure 5 shows an example of one set of measurements; measurements for all 3D Hall probes at different radii are plotted (0 mm – 18 mm), thus, the scatter in the points.

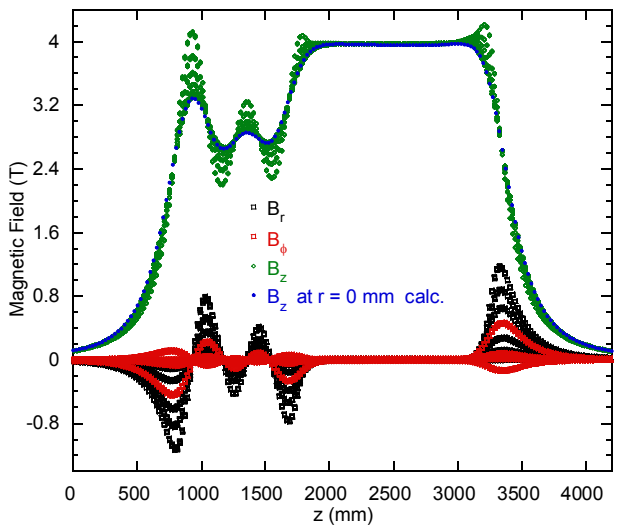


Figure 5: Measured field components for all probes, and a numerical calculation of the longitudinal field on magnetic axis using "as-built" coil parameters.

The typical measurement format was with 2 cm longitudinal steps and 20° disk rotation steps. There were additional faster measurement sets at currents adjusted to various percentage of a full current configuration to check linearity of field with current and study the hysteresis effect in the field (due to introduction of material in shielding plate). For these, the measurement format was with 5 cm longitudinal steps at only four disk rotation angles (0°, 40°, 180°, 220°). There were also additional studies to check for systematic uncertainties introduced by probes mounting on the disk (only 5 longitudinal positions, but with 5° disk rotation steps). We also measured coils powered at low current of 30 A: coils M1, M2, E1 and E2 individually, and coils E1-C-E2 together; the measurement format had varying longitudinal steps and 30° disk rotation steps.

Copyright © 2013 CC-BY-3.0 and by the respective authors

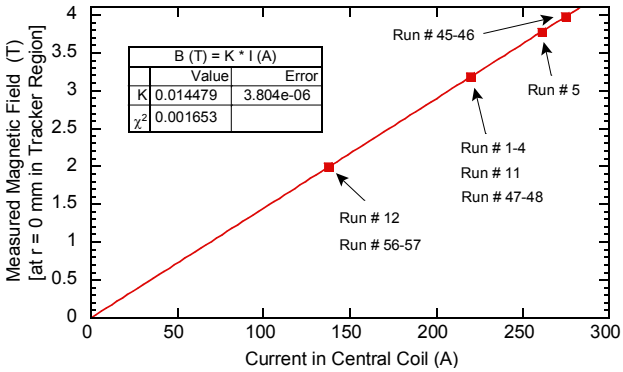


Figure 6: Magnetic field linearity study.

Figure 6 shows analysis of magnetic field linearity with current for a set of measurements without shielding plate, for "Solenoid Mode". There are several overlapping points at 80% current and 50% current, as indicated. The currents in coils were stable to ~0.05A (maximum variance) over ~2.5-hour measurement set, and set currents were reproducible to ~0.03A, as measured by the shunts installed to read coil currents directly [5]. The magnetic field is linear with current, with no indication of measurable offset at 0A.

Figure 7 shows zoom-in on the tracker region. Spread of the field measurements at each radial probe position comes from measurements at different disk rotation angles, and is due to shift of mapping device axis with respect to magnetic axis, as also indicated in Fig 8. An ~3% discrepancy between measurements and simulation was also observed in preliminary measurements [6], when we did not have a direct measurement of coil currents and precise survey of the mapping axis. These results together with the linearity

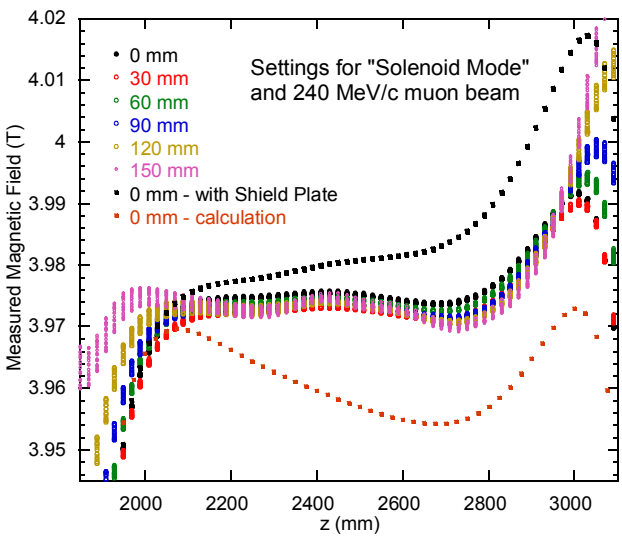


Figure 7: Longitudinal magnetic field component in the tracker region: measurements for 3D Hall probes at different radii for a case without shielding plate, measurements at 0 mm for a case with shielding plate, and a numerical calculation on axis (no shielding plate) using "as-built" coil parameters and measured coil currents.

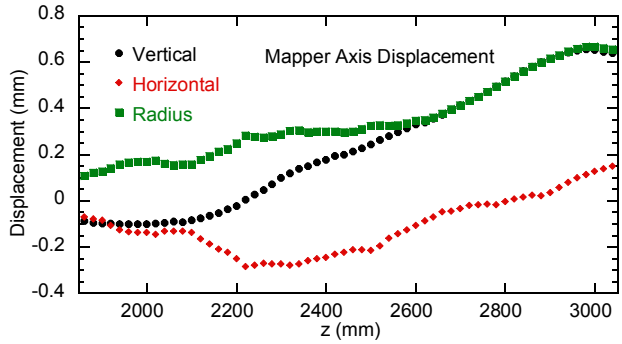


Figure 8: Survey of magnet measurement device axis (zoom-in on tracker region) in a coordinate system aligned to the cold mass axis.

studies indicate that this discrepancy does not come from control or measurement systems, but is due to the coils themselves. It is likely that the number of turns in coils E2, C, and possibly E1 are not as specified in [3], thus, the currents in the coils need to be adjusted to achieve the desired field configuration and uniformity.

The effect of shielding plate on magnetic field inside the solenoid agrees with the studies [7], indicating that reduction of current in the outer coil (E2) of ~2.5% is required to keep the desired magnetic field configuration. We plan to perform more field measurements around the shielding plate during the mapping of the MICE SS1.

ACKNOWLEDGEMENTS

We would like to thank the CERN Detector Technologies Engineering and Mechanics groups for magnetic measurement systems' design, fabrication and measuring and analysis support.

REFERENCES

[1] M. Bogomilov et al., JINST 7 (2012) P05009; MICE experiment web site http://mice.iit.edu

[2] M. Ellis et al., "The design, construction and performance of the MICE scintillating fibre trackers", Nuclear Instruments and Methods in Physics Research A 659 (2011) 136–153.

[3] M. A. Green and S. P. Virostek, "The Dimensions and Number of Turns for the Spectrometer Solenoids As-built compared to the Original Design", LBNL-899E, MICE Note 207, http://mice.iit.edu, (2008).

[4] F. Garnier, P-A. Giudici, F. Bergsma, "Magnet Measurement Device for MICE", CM30, http://www.physics.ox.ac.uk/MICECM30/index.asp, (2011).

[5] P. Hanlet et al., "Spectrometer Solenoid C&M Review" MICE Note 401, http://mice.iit.edu, (2013).

[6] M. Buehler et al., "Magnetic Measurements for a MICE Spectrometer Solenoid", MICE Note 397, http://mice.iit.edu, (2012).

[7] H. Witte and J. Cobb, "Effect of the magnetic shields on the magnetic field of the MICE channel", MICE Note 119, http://mice.iit.edu, (2005).

Copyright © 2013 CC-BY-3.0 and by the respective authors

STATUS OF THE MUON IONIZATION COOLING EXPERIMENT (MICE)*

Y. Torun, Illinois Institute of Technology, Chicago, IL 60616, USA†
M. Zisman, LBNL, Berkeley, CA 94720, USA
for the MICE Collaboration

Abstract

A muon collider and a muon-based neutrino factory are attractive options for particle physics. Their realization requires demonstration of muon ionization cooling, the only technique to rapidly reduce the emittance of the short lived tertiary muon beam. MICE, performed by a team from the U.S., Europe, and Asia at Rutherford Appleton Laboratory, will provide this demonstration. The experiment comprises one cell of a representative cooling channel, bracketed upstream and downstream by muon detection stations, each with a spectrometer solenoid (SS). Characterization of the RAL/ISIS muon beam line is complete. Fabrication of the two SS is nearly complete, with one having passed its acceptance tests, and the second nearly ready for testing. The first focus coil is presently being tested, with a second unit ready shortly. The cold mass for the coupling coil prototype is under test and its cryostat is in fabrication. Other required hardware, including RF cavities and liquid-H absorbers, is also being built. Their status and plans for carrying out the experiment are described.

CONCEPT AND STAGING

Ionization cooling of muons involves reducing the total momentum through energy loss while replenishing the component along the reference orbit with acceleration. MICE is a demonstration of muon cooling using a full cooling cell surrounded by tracking and particle identification detectors to measure each muon before and after it traverses the cell [1]. This way, a virtual beam can be constructed in software and its emittance measured with unprecedented precision. The goal is to measure a reduction of order 10% in normalized transverse emittance with a relative precision of 1% under different configurations of input beam and magnetic channel optics. Figure 1 shows the staging of the experiment. Step I, aimed at characterizing the beam using the particle identification detectors, is now complete. In addition, preliminary momentum reconstruction and emittance measurements were performed at this stage using the time-of-flight (TOF) detectors [2]. Reconstructed trace space distributions agree well with simulations for different combinations of momentum (140, 200 and 240 MeV/c) and normalized transverse emittance (3π, 6π and 10π mm). The first measurement of cooling with absorbers will take place in Step IV [3]. This will be followed by the final stage (Step VI) with the full cooling channel cell in place including RF acceleration [4].

* This work was supported by the Office of Science, U.S. Department of Energy under DOE contract number DE-AC02-05CH11231

† torun@iit.edu

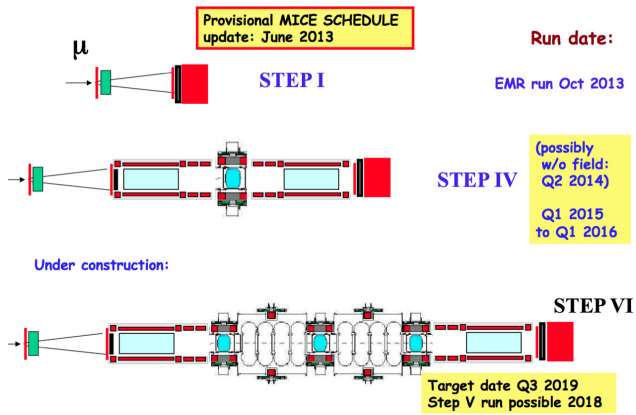


Figure 1: MICE staging and schedule.

BEAMLINE

A target system [5] utilizing a linear electromagnetic drive moves a Ti cylinder vertically toward the edge of the shrinking proton beam envelope just before extraction. In addition, a vertical closed orbit bump has been developed to steer the ISIS beam to meet the target at the correct phase and reduce losses in the machine induced by the MICE target [6]. Figure 2 shows the beamline elements and instrumentation. The pion beam from the target is captured by a quadrupole triplet (Q1-3) and momentum selected in a dipole (D1) before being directed into a decay solenoid (DS). A variable thickness proton absorber at the exit of the DS is used to remove protons from the beam. Momentum selection on the muons from pion decay is performed by

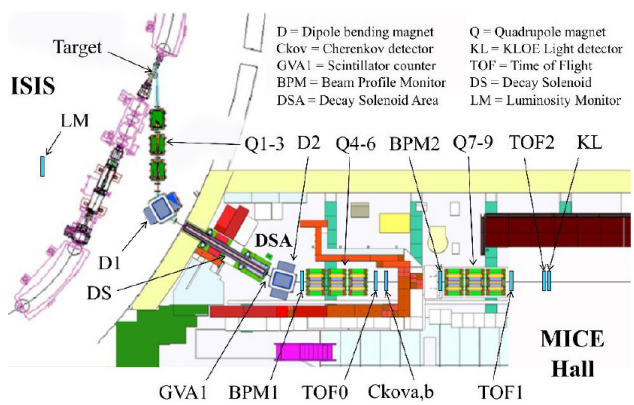


Figure 2: MICE beamline and instrumentation.

Copyright © 2013 CC-BY-3.0 and by the respective authors

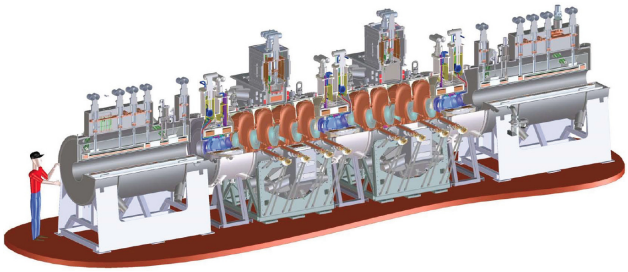


Figure 3: Partial cross section of the MICE channel showing, from the outside in: spectrometer solenoids; AFC modules with liquid hydrogen absorbers; RFCC modules with RF cavities, couplers and Be windows.

another dipole (D2). Two more quadrupole triplets (Q4-6, Q7-9) focus the muon beam. A variable thickness diffuser [7] is used to increase the emittance of the beam at the end of the beamline for some of the settings. The beamline settings have been successfully commissioned [8] and meet the experimental requirements [9].

COOLING CHANNEL HARDWARE

Figure 3 shows the layout of the final stage (step VI) of MICE. The cooling cell includes three AFC (Absorber-Focus Coil) and two RFCC (RF Cavity-Coupling Coil) modules.

AFC Modules

Liquid hydrogen absorber development is complete and the first absorber has been built and successfully tested [10]. Solid absorbers will also be tested in Step IV [11]. A cylindrical disc absorber has been built out of LiH and a wedge-shaped absorber has been designed [12]. Training and testing of the first AFC module magnet is complete and the second unit will be delivered to RAL shortly.

RFCC Modules

Ten RF cavity bodies have been built and most of the thin Be windows and ceramic vacuum windows are in hand [13]. One of the cavities was electropolished at LBNL [14] and is being assembled for operation in a vacuum vessel at the Fermilab MuCool Test Area (MTA) [15]. The tuning system for this cavity was built at Fermilab and LBNL and will be tested soon [16]. The first pair of RF power couplers is under fabrication at LBNL. A test stand at Daresbury Laboratory is being used to develop the RF amplifier chain that consists of four 2-MW systems. RF power and control system design is complete and installation is under way [17]. The first amplifier will be operated in the MICE hall soon. The cold mass for the first prototype coupling coil (CC) magnet is under test at a recently commissioned magnet test facility at Fermilab [18] and cryostat fabrication at LBNL is nearing completion. This CC magnet will be installed at the MTA in 2015. In the meantime, cavity tests will be carried out in the fringe field of a smaller magnet [19].

Spectrometer Solenoids

Assembly of both spectrometer solenoids is complete [20]. The first is on its way to RAL after successful final testing and magnetic field mapping [21]. Testing of the second is about to start.

DETECTORS

Two scintillating fiber trackers have been built [22] and successfully tested. The trackers will be installed inside the spectrometer solenoids and used to reconstruct muon position and momentum. The rest of the detectors are used for particle identification and most are labeled in Fig. 2. The two upstream TOF hodoscopes (TOF0, TOF1) [23], together with the Cherenkov counters (Ckova, b) [24] allow identification of incoming muons while the downstream calorimeter (KL) and electron-muon ranger (EMR) [25] next to it are used to reject muon decays and high energy pions [26]. The TOF counters also provide a measurement of the time coordinate for each muon. Assembly of the last detector, the EMR, was recently completed at the University of Geneva and a commissioning run will begin shortly to complete installation at RAL. The data acquisition system is complete and the software framework for Monte Carlo simulation, reconstruction and analysis of detector data is in place [27].

MAGNETIC SHIELDING

The MICE magnetic channel contains 18 large-bore superconducting coils over a length of about 15 m with no flux return. Steel walls have been installed at the edges of the MICE hall to shield the rest of the building (including the MICE and ISIS control rooms). However, detailed modeling has shown that the magnetic field within the hall would potentially interfere with operation of some components. This will be addressed by relocating some of the sensitive hardware and installing a partial return yoke (PRY) [28] around the magnetic channel to capture the flux. The conceptual design of the PRY is shown in Fig. 4 and detailed engineering is in progress.

OUTLOOK

The beamline has been operating successfully and all major cooling channel components are on track for delivery within the next few years. Commissioning of the last particle ID detector (EMR) is about to commence. Installation of the support infrastructure in the hall is well under way and a framework for controls and monitoring [29] is in place. Step IV of MICE will be ready early in 2015 for the first measurement of emittance reduction after a long ISIS shutdown. The latest version of the schedule can be obtained from the MICE website [30]. MICE is on track for demonstration of ionization cooling by the end of this decade which will pave the way for future muon based accelerator facilities [31].

Copyright © 2013 CC-BY-3.0 and by the respective authors

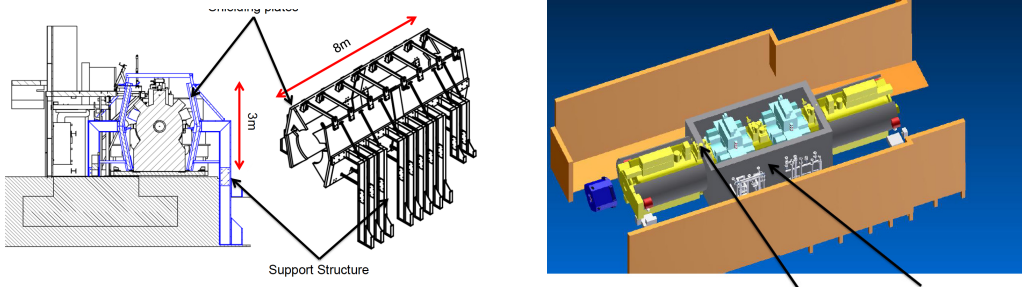


Figure 4: Partial return yoke concept for Step IV (left) and Step VI (right).

REFERENCES

[1] A. Blondel,"The MICE Experiment," IPAC2013, Shanghai, TUPFI046, p. 1454.

[2] L. Coney *et al.*, "MICE Step I: First Measurement of Emittance with Particle Physics Detectors," IPAC2011, San Sebastián, MOPZ016, p. 853.

[3] D. Rajaram and P. Snopok, "Muon Ionization Cooling Experiment Step IV," IPAC2013, Shanghai, TUPFI066.

[4] D. Rajaram and P. Snopok, "Muon Ionization Cooling Experiment Step VI," IPAC2013, Shanghai, TUPFI065.

[5] C. N. Booth *et al.*, "The design, construction and performance of the MICE target," J. Inst. 8 (2013) P03006.

[6] A. J. Dobbs *et al.*, "The MICE Muon Beam Line and Host Accelerator Beam Bump," IPAC2012, New Orleans, TUPPD001, p. 1404. A. Dobbs, L. Coney and D. Adey, "MICE Muon Beamline Particle Rate and Related Beam Loss in the ISIS Synchrotron," IPAC2011, San Sebastián, MOPZ035, p. 874.

[7] V. Blackmore *et al.*, "Particle Tracking and Beam Matching through the New Variable Thickness MICE Diffuser," PAC2011, New York, MOP023, p. 154.

[8] M. Bogomilov *et al.*, "The MICE Muon Beam on ISIS and the beam-line instrumentation of the Muon Ionization Cooling Experiment," J. Inst. 7 (2012) P05009.

[9] D. Adams *et al.*, "Characterisation of the muon beams for the Muon Ionisation Cooling Experiment," arXiv:1306.1509 [physics.acc-ph], to appear in Eur. Phys. J. C.

[10] S. Ishimoto *et al.*, "Liquid Hydrogen Absorber for MICE," IPAC'10, Kyoto, MOPEB065, p. 421.

[11] P. Snopok *et al.*, "Solid Absorber Program Status for MICE Step IV," IPAC2011, San Sebastián, MOPZ028, p. 859.

[12] C. T. Rogers *et al.*, "Wedge Absorber Design and Simulation for MICE Step IV," PAC2011, New York, MOP060, p. 220.

[13] D. Li *et al.*, "Progress of MICE RFCC Module," IPAC2012, New Orleans, THPPP093, p. 3954.

[14] T. Luo *et al.*, "Progress on the MICE 201 MHz RF Cavity at LBNL," IPAC2012, New Orleans, THPPC049, p. 3398.

[15] Y. Torun *et al.*, "Assembly and Testing of the First 201-MHz MICE Cavity at Fermilab," WEPMA16, NA-PAC'13.

[16] L. Somaschini *et al.*, "Tuner System Assembly and Tests for the 201-MHz MICE Cavity," WEPMA03, NA-PAC'13.

[17] K. Ronald *et al.*, "The RF System for the MICE Experiment," IPAC2013, Shanghai, WEPFI066, p. 2848.

[18] D. Orris, *et al.*, "A New Facility for Testing Superconducting Solenoid Magnets with Large Fringe Fields at Fermilab," THPBA16, NA-PAC'13.

[19] T. Luo *et al.*, "Multipacting Study for the RF Test of the MICE 201 MHz RF Cavity at MTA," WEPMA26, NA-PAC'13.

[20] S. Virostek *et al.*, "Final Assembly and Testing of the MICE Superconducting Spectrometer Solenoids," IPAC2012, New Orleans, THPPC035, p. 3362. S. Virostek *et al.*, "Assembly and Test of a Modified Spectrometer Solenoid for MICE," IPAC2013, Shanghai, THPPC048, p. 3621.

[21] M. Leonova, "MICE Spectrometer Solenoid Magnetic Measurements," IPAC2013, Shanghai, TUPFI054, p. 1468. M. Leonova, "Analysis of MICE Spectrometer Solenoid Magnetic Field Measurements," THPHO15, NA-PAC'13.

[22] M. Ellis *et al.*, "The Design, construction and performance of the MICE scintillating fibre trackers," Nucl. Instrum. Meth. A 659 (2011).

[23] R. Bertoni *et al.*, "The design and commissioning of the MICE upstream time-of-flight system," Nucl. Instrum. Meth. A 615 (2010) 14.

[24] L. Cremaldi *et al.*, "A Cherenkov Radiation Detector with High Density Aerogels," IEEE Trans. Nucl. Sci. 56 (2009).

[25] R. Asfandiyarov, "A totally active scintillator calorimeter for the Muon Ionization Cooling Experiment (MICE). Design and construction," to appear in Nucl. Instrum. Meth. A.

[26] M. Bonesini and Y. Karadzhov, "The Particle Identification System for the MICE Beamline Characterization," IPAC2011, San Sebastián, TUPC142, p. 1356.

[27] C. D. Tunnell and C. T. Rogers, "MAUS: MICE Analysis User Software," IPAC2011, San Sebastián, MOPZ013, p. 850.

[28] H. Witte *et al.*, "Partial Return Yoke for MICE – General Concept and Performance," THPBA08, NA-PAC'13. H. Witte *et al.*, "Partial Return Yoke for MICE – Engineering Design," THPBA09, NA-PAC'13.

[29] P. Hanlet and C. Booth, "Muon Ionization Cooling Experiment: Controls and Monitoring," IPAC2011, San Sebastián, MOPZ024, p. 856.

[30] `http://mice.iit.edu`

[31] M. A. Palmer, "The R&D Program for a Future Muon Collider," MOYAA2, NA-PAC'13.

Copyright © 2013 CC-BY-3.0 and by the respective authors

A CHARGE SEPARATION STUDY TO ENABLE THE DESIGN OF A COMPLETE MUON COOLING CHANNEL*

C. Yoshikawa#, C. Ankenbrandt, R. P. Johnson, Muons, Inc., Batavia, IL 60510, U.S.A.
Y. Derbenev, V. Morozov, JLAB, Newport News, VA 23606, U.S.A.
D. Neuffer, K. Yonehara, Fermilab, Batavia, IL 60510, U.S.A.

Abstract

The most promising designs for 6D muon cooling channels operate on a specific sign of electric charge. In particular, the Helical Cooling Channel (HCC) and Rectilinear RFOFO designs are the leading candidates to become the baseline 6D cooling channel in the Muon Accelerator Program (MAP). Time constraints prevented the design of a realistic charge separator, so a simplified study was performed to emulate the effects of charge separation on muons exiting the front end of a muon collider. The output of the study provides particle distributions that the competing designs will use as input into their cooling channels. We report here on the study of the charge separator that created the simulated particles.

INTRODUCTION

One of the most challenging components for a muon collider is the 6D cooling channel that must cool muons by six orders of magnitude in phase space before they decay (τ=2.2μs). The two most promising candidates are the Helical Cooling Channel [1,2] and Rectilinear RFOFO [3] designs. The Muon Accelerator Program (MAP) is a national effort headed at Fermilab that is charged with accessing the feasibility of building a muon collider and/or a neutrino factory based on a muon storage ring. A down-select competition between these contenders had been announced over the summer of 2013 with the expectation for each design to have results of simulations of all components in their channel by end of calendar 2013. Both concepts operate on a single sign of electric charge of the muon, but a charge separator had not been designed. The tight time constraint forbade the design of a realistic charge separator, so a study was performed to emulate the effects of a simplified charge separator on muons exiting the front end of a muon collider. The output of the study provides particle distributions that the competing designs will use as input into their cooling channels.

INITIAL STUDY

This study benefits from an earlier effort [4] that used bent solenoids to separate the opposite charges in the beam. Upon scrutiny of that study, we realized that it was possible to design a configuration that would separate the charges without the need to accelerate the muons above the momentum of 250 MeV/c expected from the front end of the system. A cartoon of the coil configurations that illustrate the basic layout of the charge separator is shown in Figure 1. There are two bent solenoids; the first "forward bend" (shown in white in Figure 1(a)) separates the charged beams vertically, while the second "reverse bend" (shown in red and blue in Figure 1) directs each beam back into the mid-plane. Each bend has three sectors: two "Norem matching" sectors [5] of half a Larmor oscillation length ($\lambda_L/2$) each and a mid-sector that has half the bending radius (and thus twice the vertical displacement angle) to adjust the vertical displacement at the end of the first bend. One of the beams will need to drift in a straight solenoid for a full λ_L in order to create separation between the two reverse bend sets of coils. For consistency with the earlier study, we chose the μ+ beam to traverse the longer path. Since there is no RF in the separator, the beam in the longer path is subject to larger longitudinal emittance growth, and that drives the performance of the charge separator. We will thus design to optimize the μ^+ beam and subsequently analyse the μ^- beam in the shorter channel.

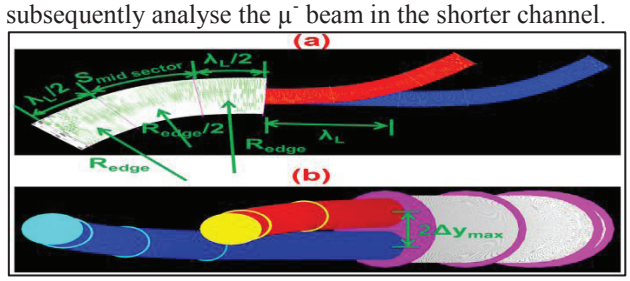


Figure 1: Cartoon of coil configuration illustrating the concept of a charge separator from a top view (a) and at the downstream end looking upstream (b).

A SIMPLIFIED CHARGE SEPARATOR

Designing a realistic charge separator will involve:

1. Dealing with fringe fields at the end of the forward bend and start of the two smaller solenoids.
2. Dealing with fringe fields between the two downstream solenoids.
3. Possibly tilting the coils in the downstream segments if the path difference introduced by the vertical displacement of the coils has a negative impact on performance.

The above complications and the time constraints motivated the need for a simulation setup that can extract the effects of a properly designed charge separator without having to design a realistic charge separator. Such a setup is illustrated in Figure 2 where the simple charge separator is introduced by way of two separate channels, one for each sign. Each channel incorporates large radii coils throughout both bends as well as in the

*Work supported in part by DOE STTR grant DE-SC0007634
#cary.yoshikawa@muonsinc.com

Copyright © 2013 CC-BY-3.0 and by the respective authors

middle straight in the case of the longer μ+ channel. All coils are confined to lie in the mid-plane as would be done for the forward bend in a realistic charge separator. The coil configurations produce magnetic fields that are well understood and produce expected particle trajectories. Collimators are introduced in the sections downstream of the forward bend to mimic the effect of coil apertures in a realistic charge separator.

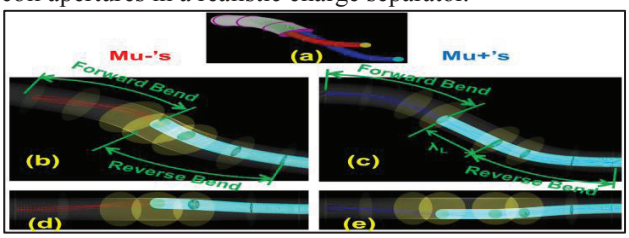


Figure 2: Association of a charge splitter coil concept in (a) to two separate simplified charge splitters (one for each sign) with transparent large radii coils. Yellow discs demarcate sectors. Oblique view of μ^-s in (b) and side view in (d) show vertical rise in forward bend and vertical drop in reverse bend. Oblique view of μ^+s in (c) and side view in (e) show vertical drop in forward bend and vertical rise in reverse bend.

OPTIMIZATION

The simple charge separator is utilized to optimize for maximum throughput and minimal longitudinal emittance growth, recalling there is no RF in the separator. As mentioned above, we will optimize for μ^+s which traverse the longer channel. Particles out of a 325 MHz version of the front end of a muon collider [6] were used as input, and since there is a roughly 20% loss of muons in the 4D cooler, we focused the optimization on particles exiting the phase rotator. Configurations considered in the optimization are given in Table 1, where each was designed to have the same vertical separation at the end of the first bend. Simulations were performed with G4beamline [7], and results of the optimization process are shown in Figure 3, where we have chosen the configuration with R_{edge}=6.32 m as the optimal based on transmission.

Table 1: Configurations in the Optimization

P=Pz	MeV/c	250						
B	T	2						
$\lambda_L=(2\pi P_z)/(B_\varphi c)$	m	2.62						
R_{edge}	m	3.21	4.25	5.28	6.32	7.36	8.39	9.43
α_{edge}(vert angle)	deg	7.4	5.6	4.5	3.8	3.2	2.8	2.5
$S_{mid\ sector}$	m	0	0.42	0.85	1.27	1.70	2.13	2.55
Δy_{max}	m	0.342						
$S_{Longer\ Channel}(\mu^+)$	m	7.86	8.71	9.56	10.41	11.26	12.11	12.96

LONGITUDINAL DISTORTION & ITS REMEDY

The μ^+s exiting the optimal charge separator configuration determined above will need to be caught into RF buckets immediately following the separator. Examination of the longitudinal phase space reveals distortion as shown in Fig. 4. Quantifying the particle losses and behaviour of ε_L in Fig. 5, a 9% loss and ε_L oscillation above the HCC acceptance is expected.

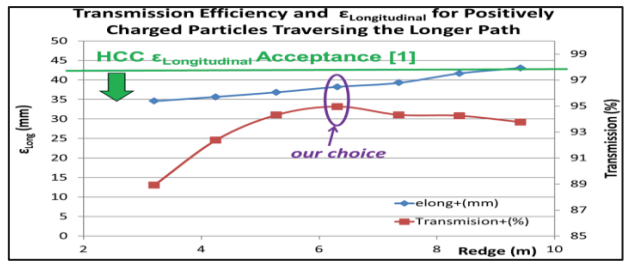


Figure 3: Results of optimization.

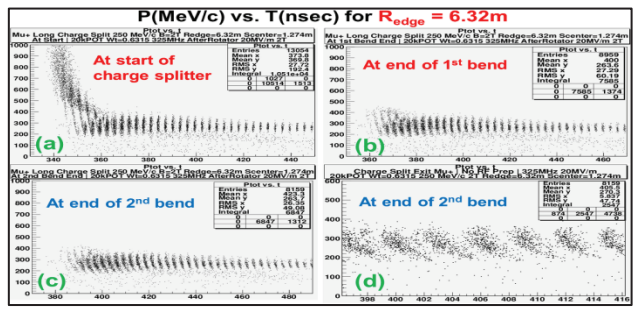


Figure 4: Longitudinal distortion at end of optimal configuration. P(MeV/c) vs. T(nsec) for μ+'s entering the charge separator are upright in (a) and begin to show some distortion at the end of the first bend in (b). Muons overlap neighboring bunches in (c), which is more easily seen in the zoomed-in view in (d).

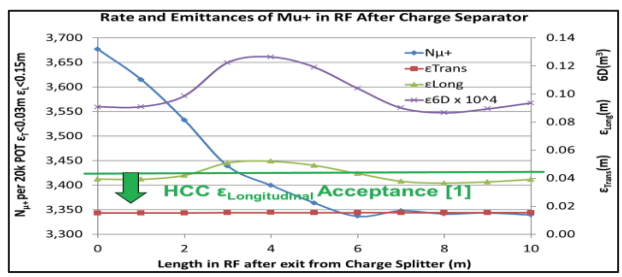


Figure 5: Rate and emittances of μ^+'s in RF after the charge separator.

A solution to counteract against this longitudinal distortion is to prepare the muon beam upstream of the charge separator as illustrated and explained in Figure 6, where RF gymnastics are applied to create a more upright ellipse in longitudinal phase space at the exit of the charge separator. Figure 7 shows the optimal configuration where particles exiting the phase rotator drift for 3 meters, followed by 4 m of RF (20 MV/m @ 325 MHz, same as upstream phase rotator) before traversing the charge separator and being caught and analysed in 10 m of RF of the same gradient and frequency. Figure 8 shows the longitudinal phase space of particles at the key locations described in Figure 6. While not perfectly upright, the particles that were subjected to the beam preparation in Figure 8(d) appear to have less distortion than those not having gone through the preparation in Figure 4(d).

Copyright © 2013 CC-BY-3.0 and by the respective authors

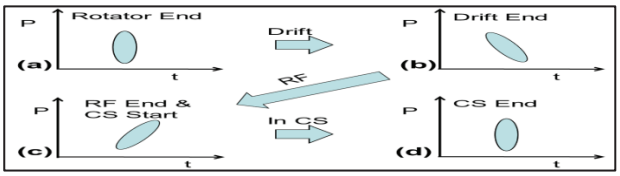


Figure 6: Longitudinal Phase Space Preparation Strategy. Longitudinal phase space of muons at the end of rotator in (a) are allowed to drift, resulting in (b) where RF is turned on to take advantage of the PvsT correlation. The rotated longitudinal phase space at end of the RF is shown in (c), which enters the charge separator and exits with an upright ellipse in (d).

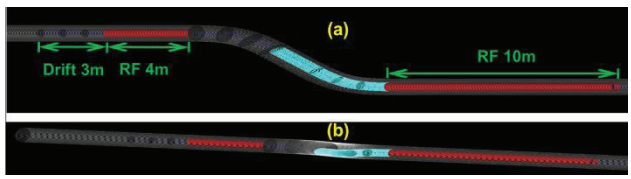


Figure 7: Oblique view in (a) of 3 m drift following phase rotator, followed by 4 m of RF (20 MV/m @ 325 MHz; same as rotator), followed by transit through the charge separator, followed by 10 m of RF to recapture the μ^+ beam. Side view is shown in (b).

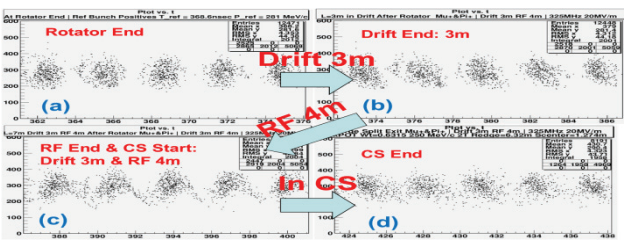


Figure 8: P(MeV/c) vs. T(nsec) for μ^+ through RF Preparation with 3 m of drift and 4 m of RF and traversed through the Charge Splitter. Panels a-d correspond to the same conditions as in Figure 6.

The improvement in rate of accepted muons and the reduction in the longitudinal emittance via the beam preparation are clearly seen in Figure **9** for μ^+s and Figure 10 for μ^-s. In the longer μ^+ channel, ε_L is lowered and remains within the HCC acceptance. The yield is also increased and remains flat in 10 m of RF, resulting in a net transmission increase of 14.6%. In the shorter μ^- channel, Figure 10 shows that while ε_L was within the HCC acceptance before the preparation, it is lowered further because of it. The increase in rate is not expected to be as dramatic, but is still significant at 10%. Final results are summarized in Table **2**.

SUMMARY

We presented a study to emulate the effects of a charge separator on muons exiting the front end of a muon collider to enable the design of a 6D cooling channel in absence of a realistic design of a charge separator. The output of this study provides particle distributions that the competing 6D cooling teams will use as input into their channels in the evaluation to be the baseline in MAP.

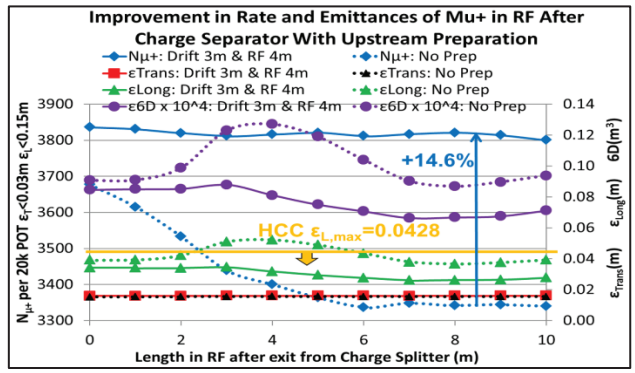


Figure 9: Improvement in Rate and Emittances of μ+'s in RF After Charge Separator with Upstream Preparation.

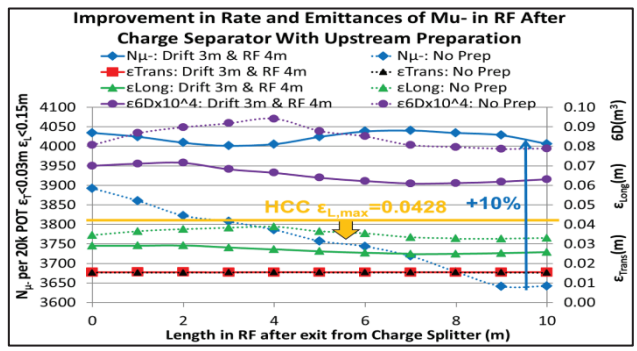


Figure 10: Improvement in Rate and Emittances of μ-'s in RF After Charge Separator with Upstream Preparation.

Table 2: Survival Rates and Emittances of Muons at 1 m Past a Charge Separator.

	ε_T		ε_L		ε_{6D}		$N_{survive}$	
units	mm-rad		mm		mm^3		per 20k POT	
Particle Species	μ^+	μ^-	μ^+	μ^-	μ^+	μ^-	μ^+	μ^-
At End of Rotator	15.66	15.54	30.06	27.71	7368	6690	4118	4221
R_{edge} = 6.32 m @ 1m Drift 3m; RF 4m	15.94	15.69	34.2	29.3	8519	7122	3831 (-7%)	4025 (-5%)
Acceptance of HCC	*20.4*		*42.8*		*12,900*			

REFERENCES

[1] K. Yonehara, R. P. Johnson, M. Neubauer, Y. S. Derbenev, "A helical cooling channel system for muon colliders", IPAC10, MOPD076, (2010).

[2] C. Yoshikawa, C. Ankenbrandt, R. P. Johnson, Y. S. Derbenev, V. Morozov, D. Neuffer, K. Yonehara "Complete Muon Cooling Channel Design and Simulations", IPAC13, TUPFI060 (2013).

[3] D. Stratakis et al., "A High-Performance Rectilinear FOFO Snake Channel for Muon Cooling", NA-PAC13, THPH012 (2013).

[4] R. Palmer and R. Fernow, "Charge Separation for Muon Collider Cooling", PAC11, MOP001 (2011).

[5] J. Norem, Phys. Rev. Spec. Top. – Acc. Beams 2, (1999) 054001.

[6] D. Neuffer and C. Yoshikawa, "Muon Capture for the Front End of a μ^+-μ^- Collider", PAC11, MOP030, (2011).

[7] G4beamline, T. Roberts, http://www.muonsinc.com

Copyright © 2013 CC-BY-3.0 and by the respective authors

MAGNETIC BUNCH COMPRESSION FOR A COMPACT INVERSE COMPTON SOURCE

B.R.P. Gamage[1*] and T. Satogata[1,2]
[1]Center for Accelerator Science, Old Dominion University, Norfolk VA, 23529, USA
[2]Thomas Jefferson National Accelerator Facility, Newport News VA, 23606, USA

Abstract

A compact electron accelerator suitable for inverse Compton source applications is in design at the Center for Accelerator Science (CAS) at Old Dominion University (ODU). Here we discuss two options for transverse magnetic bunch compression and final focus, each involving a 4-dipole s-chicane with M_{56} tunable over a range of 1.5-2.0m with independent tuning of the final focus to an interaction point β*=5mm. One design has no net bending, while the other has net bending of 90 degrees and is suitable for compact corner placement.

INTRODUCTION

There is significant interest in X-ray sources beyond those available at large third-generation, lab-based synchrotron light sources. Medical phase imaging, and industrial applications have been developed that have motivated development of compact light sources based on inverse Compton scattering (ICS) [1] that provide single beamline operation at a cost of about $10-15M. A compact ICS source is in design at the ODU CAS with an X-ray energy of up to 12 keV, flux of approximately 1.6×10^{14} photon/sec, and average brilliance of 1.5×10^{15} photon/$(\mathrm{s} \cdot \mathrm{mm}^2 \cdot \mathrm{mrad}^2 \cdot 0.1\%\mathrm{BW})$ [2].

This project consists of an optimized 500 MHz superconducting electron gun, 4K 500 MHz superconducting spoke cavity linac [3], and a bunch compressor to provide a short, high-brightness electron bunch to collide with an incoming laser beam to produce inverse Compton scattered photons. The electron beam requirements are shown in Table 1. The bunch length requirement of a few ps and energy spread requirement of 3×10^{-4} indicate the need for small longitudinal emittance (<7 eV-m) and well-corrected bunch compression. A practical system will also have tunable M_{56} to optimize the scattered photon beam.

Table 1: Electron Beam Parameters at Collision

Parameter	Value	Units
Energy	25	MeV
Bunch charge	10	pC
Repetition rate	100	MHz
Average current	1	mA
Normalized emittance	0.1	mm·mrad
$\alpha^*_{x,y}$, $\beta^*_{x,y}$	0, 5	-, mm
FWHM bunch length	3.0 (0.9)	psec (mm)
RMS energy spread	7.5	keV

DESIGN PHILOSOPHY

Traditionally dispersion-free chicanes are used for magnetic bunch compression, with $M_{56} < 0$ and $T_{566} > 0$[4]. However, these chicanes are not very compact and cancel dispersion only to odd orders. M_{56} tunability is also directly connected to the chicane transverse dimension, and so is limited.

For a compact design with tunable M_{56}, we have been investigating 4-dipole s-chicanes that alternate the bending directions of the center dipoles. A chicane of this type was investigated for the final bunch compressor of TTF-FEL [5]. S-shaped compressors are dispersion free to all orders, have greater M_{56} tunability, and can be wrapped in on themselves with large central bend angles to be made compact. As described in [5], M_{56} is tunable by adjusting the central dipole angle.

Initial designs considered combining quadrupoles in the compressor with quadrupoles outside the compressor to tune the final focus. However, the aggressiveness of the design final focusing to $\beta^* = 5$mm is best handled with a separate independent low-beta focus section. This sacrifices some small measure of compactness of the design, but greatly improves the orthogonality of tuning knobs for achromaticity, M_{56}, final focusing, and upstream matching. The linac design for this ICS suggests that a reasonable range for M_{56} tuning is 1.5-2.0m.

A typical s-shaped chicane compressor ensures achromaticity by having a net horizontal phase advance of 2π, with a pair of symmetrically-placed horizontal focusing quadrupoles to tune achromaticity and a vertical focusing quadrupole at the center symmetry point to control vertical betas. Here the compact design pushes us towards stronger focusing, and we investigate two designs: one with net 3π phase advance and a net 90° bend for corner use, and one with net 4π phase advance for larger dispersion and M_{56} lever arm. M_{56} is tunable for both designs by adjusting the center symmetric bend angles and rematching achromaticity and final focus.

DESIGNS AND RESULTS

We use elegant from the APS for lattice design, optimization, and particle tracking, including simulation of short quadrupole end effects as described in the next section. Each lattice has three quadrupoles in two symmetric families between the center dipoles. For a given central

* Author email: bgama002@odu.edu

Copyright © 2013 CC-BY-3.0 and by the respective authors

Table 2: 3π Bunch Compressor Parameters

Parameter	Value	Units
Final β_x,β_y	0.005	m
Final α_x,α_y	$< 10^{-8}$	-
Maximum β	≈ 85.8	m
M_{56}	1.498	m
Floor Dimensions	3×4	m
Dipole Lengths	0.8,1.0,0.8,1.0	m
Dipole Bend Angles	70,-115,-115,70	°
Max Quadrupole Gradient	≈ 9.5	T/m
Quadrupole Length	0.1	m

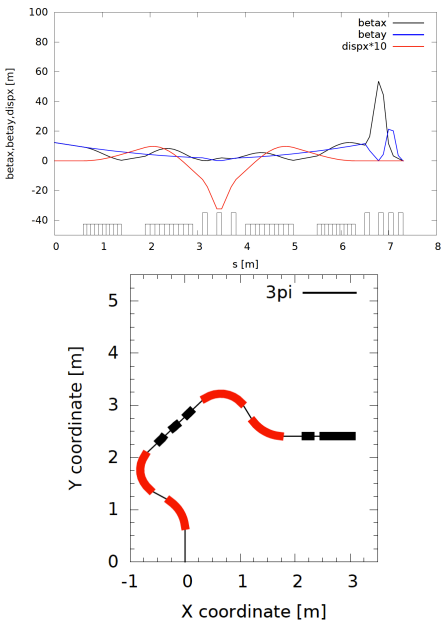


Figure 1: 3π bunch compressor optics and floor plan.

Table 3: 4π Bunch Compressor Parameters

Parameter	Value	Units
Final β_x,β_y	0.005	m
Final α_x,α_y	$< 10^{-8}$	-
Maximum β	$\approx$29.5	m
M_{56}	1.4	m
Floor Dimensions	2×4.3	m
Dipole Lengths	0.35,1.134,1.134,0.35	m
Dipole Bend Angles	40,-175,175,-40	°
Max Quadrupole Gradient	≈ 9.15	T/m
Quadrupole Length	0.1	m

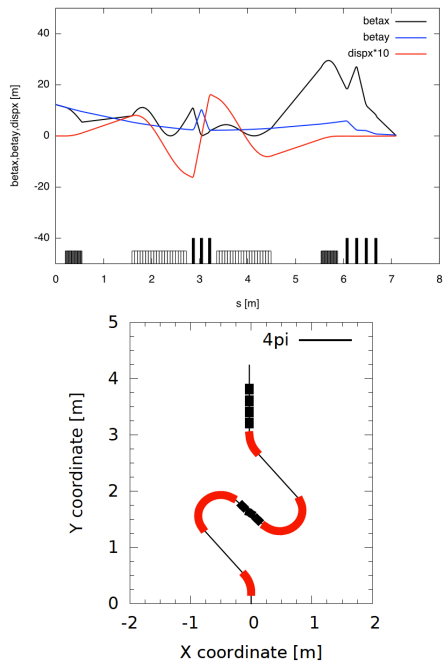


Figure 2: 4π bunch compressor optics and floor plan.

dipole bend angle (and hence M_{56}),

- The pair of symmetric quadrupoles are tuned to make the compressor achromatic.
- The center quadrupole is tuned to control vertical beam size entering the final focus section.
- The final focus is retuned to match collision IP conditions of $\beta^*_{x,y} = 5$mm and $\alpha^*_{x,y} = 0$.

In both designs, peak beam sizes are well-controlled, and chromatic effects of the final focus are minimal, indicating no need for nonlinear corrections that would otherwise distort the transverse phase space. Neither design includes sextupoles to control T_{566} as of present, though their inclusion should be straightforward at high dispersion locations in the bunch compressor to control longitudinal distribution linearity [9].

3π Compressor

The first compressor, denoted "3π", has a total dispersion phase advance of 3π and a net bending of 90°, making it suitable for a compact corner design. Four quadrupoles are used in the final focus. The floor layout and the transverse optics are shown in Fig. 1, and relevant parameters are shown in Table 2. The compressor fits in a 3.5×4m area, and in these conditions is tuned for $M_{56} = 1.498$m. Note that for this compressor, the first and fourth dipoles bend in the same direction to provide the dispersion cancellation and overall bend.

4π Compressor

The second compressor, denoted "4π", has a total dispersion phase advance of 4π and no net bending; it is more transversely compact than the 3π design. three quadrupoles are used in the final focus. The floor layout and the transverse optics are shown in Fig. 2 and relevant parameters are shown in Table 3. The compressor fits in a 2.0×4m area, and in these conditions is tuned for $M_{56} = 1.4$m. Additional quadrupoles may be added in the outside drifts for extra optics control.

Copyright © 2013 CC-BY-3.0 and by the respective authors

QUADRUPOLE CONSIDERATIONS

Fringe Fields

Since the quadrupoles in this design are comparatively short, we investigated the effect of inclusion of fringe fields on the transport and matching. Considering the fringe field to be symmetric on both ends, we used the single parameter Enge function [6] to calculate the required integrals for elegant to calculate the final beta functions with effects from the fringe fields from the quadrupoles. Elegant requires the normalized quadrupole fringe field $\tilde{k}(s)$ to be normalized [7], so using the field profile shown in Fig. 3 we found the Enge coefficient a_1=4.6.

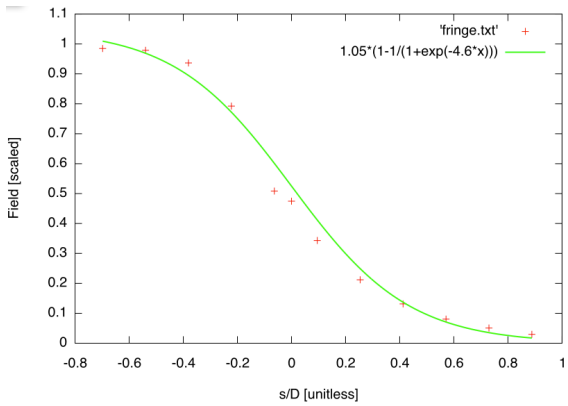


Figure 3: Fit of normalized fringe field for typical compressor quadrupole design.

Design Availability

The quadrupoles in both designs are typically 10 cm long with an exception of the focusing quartet of 4π compressor, which are 15 cm long, with a maximum field gradient of nearly 10 T/m. Some parameters for various quadrupoles used in these design are shown in Table 4.

With the design beam pipe diameter, these parameters match those of commercially available quadrupoles such as those from RadiaBeam. The air-cooled diamond quadrupole BEMQD-01-155-245 [8] is such a magnet which is close to the required dimensions while having a max gradient of 12 T/m.

Table 4: Quadrupole Data

Parameter	Value(range)	Units
Bore	0.04	m
Magnetic Field Gradient	2.5-9.7	T/m
Length	10	cm
Total Current (NI)	434-1684	A
Conductor cross-section (air-cooled)	4.3-16.84	cm^2
Conductor cross-section (water-cooled)	0.43-1.684	cm^2

Table 5: RadiaBeam Diamond Quadrupole

Parameter	Value	Units
Bore	0.0394	m
Max field gradient	12	T/m
Magnetic length	∼9.74	cm
Total current (NI)	1940.4	A-turns

FUTURE DIRECTIONS

Further optimization work on the bunch compressors will focus on tunability, chromatic compensation in the final focus, and T_{566} nonlinear longitudinal focusing to correct longitudinal bunch distortion from the linac. T_{566} should be straightforward to independently control to first order with the inclusion of sextupoles at high dispersion locations in the bunch compressor [9]. Beam dynamics will follow those in [10]. Plans of adding an upstream matching block between the linac and the compressor are in consideration

ACKNOWLEDGMENTS

Our thanks to K. Deitrick, J. Delayen, C. Hopper, G. Krafft, and R. Olave for their collaboration on the overall ODU CAS ICS design.

REFERENCES

[1] G. Krafft and G. Priebe, “Compton Sources of Electromagnetic Radiation”, Reviews of Accelerator Science and Technology Vol 3 Issue 1 (2010), pp. 147-163.

[2] T. Satogata, R. Gamage et al., “Compact Accelerator Design for a Compton Light Source”, Proc. of IPAC 2013, Shanghai, China (2013), WEPWA078.

[3] C. Hopper, K. Deitrick, and J. Delayen, “Geometry Effects on Multipole Components and Beam Emittance in High-velocity Multi-spoke Cavities”, Proc. of NA-PAC 2013, Pasadena, California (2013) WEPAC42.

[4] P. Piot, “State of the Art Electron Bunch Compression”, Proc. of LINAC 2004, Lübeck, Germany (2004), WE104.

[5] A. Loulergue and A. Mosnier, “A Simple S-Chicane for the Final Bunch Compressor of TTF-FEL”, Proc. of EPAC 2000, Vienna, Austria (2000), WEP4B01.

[6] R. Baartman and D. Kaltchev, “Short Quadrupole Parametrization”, Proc. of PAC 2007, Albuquerque, NM (2007), THPAN005.

[7] D. Zhou et al., “Explicit Maps for the Fringe Field of a Quadrupole”, Proc. of IPAC 2010, Kyoto, Japan (2010), THPD091.

[8] www.radiabeam.com, EMQD-01-155-245 specification sheet.

[9] R. J. England, “Longitudinal Shaping of Relativistic Bunches of Electrons Generated by an RF Photoinjector”, Ph.D. Thesis, UCLA (2003).

[10] C. R. Prokop, P. Piot, B. E. Carlsten, and M. Church, “Beam Dynamics Performances and Applications of a Low-Energy Electron-Beam Magnetic Bunch Compressor”, arXiv:1302.0726v1 (4 Feb 2013).

Copyright © 2013 CC-BY-3.0 and by the respective authors

IMPROVEMENT OF DIGITAL FILTER FOR THE FNAL BOOSTER TRANSVERSE DAMPERS

T. Zolkin*, The University of Chicago, Department of Physics, Chicago, IL 60637–1434, USA
N. Eddy†, V. Lebedev‡, FNAL, Batavia, IL 60510–5011, USA

Abstract

Fermilab Booster has two transverse dampers which independently suppress beam instabilities in the horizontal and vertical planes. A suppression of the common mode signal is achieved by digital notch filter which is based on subtracting beam positions for two consecutive turns. Such system operates well if the orbit position changes sufficiently slow. Unfortunately it is not the case for FNAL Booster where the entire accelerating cycle consists of about 20000 turns, and successful transition crossing requires the orbit drifts up to about 10 μm/turn, resulting in excessive power, power amplifier saturation and loss of stability. To suppress this effect we suggest an improvement of the digital filter which can take into account fast orbit changes by using bunch positions of a few previous turns. To take into account the orbit change up to N-th order polynomial in time the system requires $(N+3)$ turns of "prehistory". In the case of sufficiently small gain the damping rate and the optimal digital filter coefficients are obtained analytically. Numerical simulations verify analytical theory for the small gain and predict a system performance with gain increase.

INTRODUCTION

Consider a paraxial transverse motion of the particle with equilibrium energy in a circular accelerator. For further calculations we will be neglecting a coupling between transverse planes and consider only one of them for simplicity. Neglecting nonlinear effects, in an approximation of linear optics, the dynamics of a particle can be described by the "time" evolution of the betatron state-vector, $\tilde{\zeta}(s) = [q(s), p(s)]^{\mathrm{T}}$, where the variable s is the path length along the closed orbit and plays the role of time, q is the particle deviation in considered transverse direction with respect to the closed orbit, and $p = d\,q(s)/ds$ is canonically conjugated momentum.

The canonical transformation to the so-called normalized coordinates $(p, q) \to (\mathcal{P}, \eta)$:

$$\begin{aligned} \eta(s) &= q(s)/\sqrt{\beta(s)}, \\ \mathcal{P}(s) &= p(s)\sqrt{\beta(s)} + q(s)\,\frac{\alpha(s)}{\sqrt{\beta(s)}}, \end{aligned}$$

where $\beta(s)$ is a beta-function and $\alpha(s) = -\frac{1}{2}\,d\beta(s)/ds$, is performed in order to reduce the motion (from an initial position s_1 to a final one s_2) to the pure rotation of new normalized vector $\zeta(s) = [\eta(s), \mathcal{P}(s)]^{\mathrm{T}}$:

$$\begin{bmatrix} \eta(s_2) \\ \mathcal{P}(s_2) \end{bmatrix} = \begin{bmatrix} \cos\mu_{12} & \sin\mu_{12} \\ -\sin\mu_{12} & \cos\mu_{12} \end{bmatrix} \begin{bmatrix} \eta(s_1) \\ \mathcal{P}(s_1) \end{bmatrix},$$

where $\mu_{12} = \psi(s_2) - \psi(s_1)$ and $\psi(s)$ is a betatron phase advance

$$\psi(s) = \int_0^s \frac{d\bar{s}}{\beta(\bar{s})}.$$

Damper System

A general transverse damper is an active feedback system consisting of pickup station which measures the beam position, and a kicker which is located downstream and damps the betatron oscillations of the beam as a whole by applying an appropriate kick (see Fig. 1).

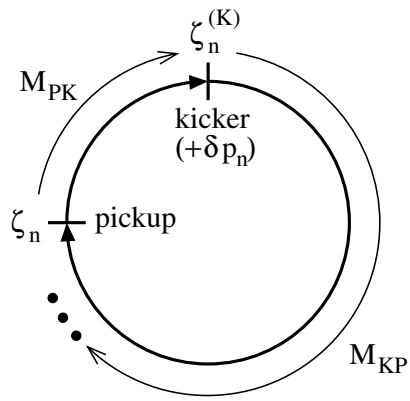


Figure 1: Schematic plot of the one turn transformation of the betatron state-vector in a lattice with damper.

For further considerations we will denote as ζ_n and $\zeta_n^{(\mathrm{K})}$ the normalized betatron-state vector on the n-th turn at the locations of the pickup and the kicker respectively, as $M_{\mathrm{PK}}(\mu_1)$ and $M_{\mathrm{KP}}(\mu_2)$ the transport matrices between pickup and kicker and between kicker and pickup, where $\mu_{1,2}$ are phase advances corresponding to those matrices, and as δp_n the change of particle momentum applied at the n-th turn by kicker. The above determines the betatron tune $\mu_0 = \mu_1 + \mu_2$.

Thereby, a one-turn map that recursively defines a new state-vector at the pickup location can be written as, [1]:

$$\zeta_{n+1} = M_{\mathrm{KP}}\,\zeta_n^{(\mathrm{K})} = M_{\mathrm{KP}}\left(M_{\mathrm{PK}}\,\zeta_n + \begin{bmatrix} 0 \\ \delta p_n \end{bmatrix}\right). \quad (1)$$

* zolkin@uchicago.edu
† eddy@fnal.gov
‡ val@fnal.gov

Copyright © 2013 CC-BY-3.0 and by the respective authors

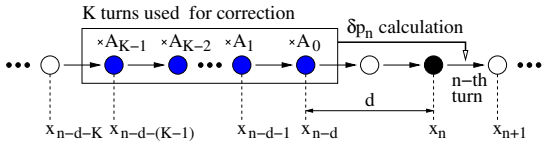


Figure 2: Schematic diagram representing the work of digital filter. Correction algorithm uses $\mathcal{K}$ turns of prehistory (blue circles) in order to calculate the change in momentum δp_n, which will be applied d turns later (for this diagram $d = 2$) after the current turn (n-th turn shown with a black filled circle).

DAMPING DYNAMICS FOR SMALL GAIN

In most general form the the angle correction algorithm which is based on $\mathcal{K}$ previous measurements is given by:

$$\delta p_n = \frac{g}{\sqrt{\beta_{\rm P}\beta_{\rm K}}} \sum_{k=0}^{\mathcal{K}-1} A_k \left(q_{n-d-k} + \delta q_{n-d-k}\right),$$

where g is the dimensionless gain, δq_i is an error of measurement introduced by pickup at i-th turn, A_i are the coefficients which define the properties of digital filer, d is an integer which determine the delay in turns after which the correction to be applied (typically $d = 0, 1, 2$ depending on the system), and, $\beta_{\rm P,K}$ denote a beta functions at the pickup and the kicker locations respectively. The schematic diagram of the algorithm is shown in Fig. 2.

For further simplification one can introduce a complex normalized variable $z = \eta - i\,\mathcal{P}$, which allow to rewrite matrix Eq. (1) as

$$z_{n+1} = e^{i\mu_2} \times \left[e^{i\mu_1} z_n - ig \sum_{k=0}^{\mathcal{K}-1} A_k \left(\Re\, z_{n-d-k} + \delta\eta_{n-d-k}\right)\right],$$

where $\delta\eta_i = \delta q_i/\sqrt{\beta_{\rm P}}$ is the renormalized error, and $\Re\, z$ is a real part of z. Below we will consider the beam dynamics in a presence of damper for the case of small gain.

Damping Rate

Temporarily omitting the heating term, $\delta\eta_i$, and taking into account that the contribution of the z^* term is averaged out for the case of small gain, the last equation can be solved by the use of the first-order perturbation theory. Looking for the solution in the form $z_n = z_0\, e^{i\mu n}$, where $\mu = \mu_0 + i g_d$ and g_d is a damping rate presumed to be small, finally gives

$$g_d = i\,\frac{g}{2}\, e^{-i(\mu_1+\mu_0 d)} \sum_{k=0}^{\mathcal{K}-1} A_k e^{-i\mu_0 k}. \qquad (2)$$

As one can see, the imaginary part of the damping rate should vanish in order to have critically damped system, i.e. $\Im\, g_d = 0$. This imposes an additional restriction on coefficients A_i.

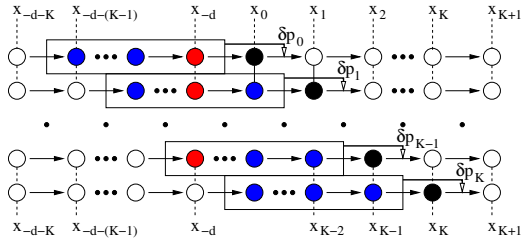


Figure 3: Schematic diagram representing the work of digital filter for $\mathcal{K}$ turns with single erroneous measurement ($(-d)$-th turn shown with a red circle).

Emittance Growth

To estimate the emittance growth excited by noise of the pickup measurements, we will keep only the heating term, while damping term will be omitted. If only one measurement is erroneous, let say $\delta\eta_0$, then summing the effect of $\mathcal{K}$ turns one obtains

$$z_{\mathcal{K}} = \left(z_0 - 2\, g_d\, \delta\eta_0\, e^{i\mu_0 d}\right) e^{i\mu_0 \mathcal{K}},$$

where Eq. (2) was used to find the sum. One can see that every single error $\delta\eta_i$ will contribute $\mathcal{K}$ turns multiplying the effect (see Fig. 3). That yields an increase of the emittance due to a single kick

$$\delta\epsilon = \frac{\overline{\langle \delta z \delta z^* \rangle}}{2} = 2\,\overline{\delta\eta^2}\left[(\Re\, g_d)^2 + (\Im\, g_d)^2\right] = 2\,|g_d|^2 \frac{\overline{\delta q^2}}{\beta_{\rm P}},$$

where in addition to the averaging over initial phases and amplitudes (operator $\langle \ldots \rangle$), we performed averaging over the kick amplitudes (operator $\overline{(\ldots)}$), and

$$\left(\overline{\delta q^2}\right)^{1/2} = \sqrt{\beta_{\rm P}}\, \left(\overline{\delta\eta^2}\right)^{1/2}$$

is the rms error of a single measurement. As one can see the emittance growth does not depends on the choice of coefficients A_i.

DESIGN OF THE DIGITAL FILTER

In general the digital filter should not be sensitive to the equilibrium orbit offset relative to the geometrical center of pickup. Otherwise, the system attempts to correct this offset which leads to increased voltage on the plates of the kicker and inefficiency of the algorithm. It is usually called a notch filter condition and it gives a constraint on coefficients A_i:

$$\sum_{k=0}^{\mathcal{K}-1} A_k = 0.$$

However, it is insufficient if the beam orbit is changing fast. For example, in FNAL Booster, successful transition crossing with high intensity beam requires fast change of equilibrium orbit in time. The present digital notch filter is not able to effectively suppress beam oscillations around transition.

Copyright © 2013 CC-BY-3.0 and by the respective authors

$$\begin{bmatrix} 1 & 1 & 1 & \cdots & (N+1)^0 & (N+2)^0 \\ 0 & 1 & 2 & \cdots & (N+1)^1 & (N+2)^1 \\ 0 & 1 & 4 & \cdots & (N+1)^2 & (N+2)^2 \\ \vdots & \vdots & \vdots & \ddots & \vdots & \vdots \\ 0 & 1 & 2^N & \cdots & (N+1)^N & (N+2)^N \\ \cos(\delta\mu) & \cos(\mu_0+\delta\mu) & \cos(2\mu_0+\delta\mu) & \cdots & \cos\left[(N+1)\mu_0+\delta\mu\right] & \cos\left[(N+2)\mu_0+\delta\mu\right] \end{bmatrix}. \quad (3)$$

The filter which would not be sensitive to the orbit change up to N-th order polynomial ($q_n^{\rm eq} \propto n^N$) requires at least $\mathcal{K} = (N+2)$ coefficients. It is easy to show, that they are related to the binomial coefficients and up to a common factor

$$A_k = (-1)^k C_k^{N+1}, \qquad k = 0, \ldots, N+1.$$

An additional constraint which optimizes the damping, $\Im\, g_d = 0$, gives

$$\sum_{k=0}^{\mathcal{K}-1} A_k \cos(\mu_0 k + \delta\mu) = 0,$$

where $\delta\mu = \mu_1 + \mu_0 d$. That increases the required number of turns to $\mathcal{K} = (N+3)$. If minimum possible number of coefficients is used, one can write matrix equation

$$\mathbf{M} \cdot [A_0, A_1, \ldots, A_{N+2}]^{\rm T} = 0$$

with the solution

$$A_k = (-1)^k \left[C_k^{N+1} \sin\left(\frac{N+3}{2}\mu_0 + \delta\mu + N\frac{\pi}{2}\right) + C_{k-1}^{N+1} \sin\left(\frac{N+1}{2}\mu_0 + \delta\mu + N\frac{\pi}{2}\right)\right],$$

where $k = 0, \ldots, N+2$, and matrix $\mathbf{M}$ is determined by Eq. 3. A common factor, ± 1, in front of all A_i must be added in order to have $\Re\, g_d > 0$.

Numerical Example for the FNAL Booster

The parameters of the Booster damper system are listed in Table 1. A numerical example of design of the digital filter which suppresses effect of orbit offset, and, its linear and quadratic changes with time is presented in Fig. 4. The real and imaginary part of the gain, g_d, as a function of particle frequency, ν, for horizontal and vertical degrees of freedom is shown in top figure. Optimal values of the coefficients for the digital filter, A_i, as a function of Booster betatron frequency, ν_0, for horizontal (middle figure) and vertical (bottom figure) degrees of freedom are presented as well. All calculations were performed for parameters listed in Table 1.

Table 1: Parameters of the FNAL Booster Damper System

	Horizontal	**Vertical**
Number of missing turns d	0	0
Betatron frequency ν_0	6.75	6.83
Fractional part of tune $\{\mu_0\} = \mu_0 - 6 \times 360°$	270°	298.8°
Pickup-kicker phase advance $\{\mu_1\} = \mu_1 - 6 \times 360°$	67.5°	288.5°

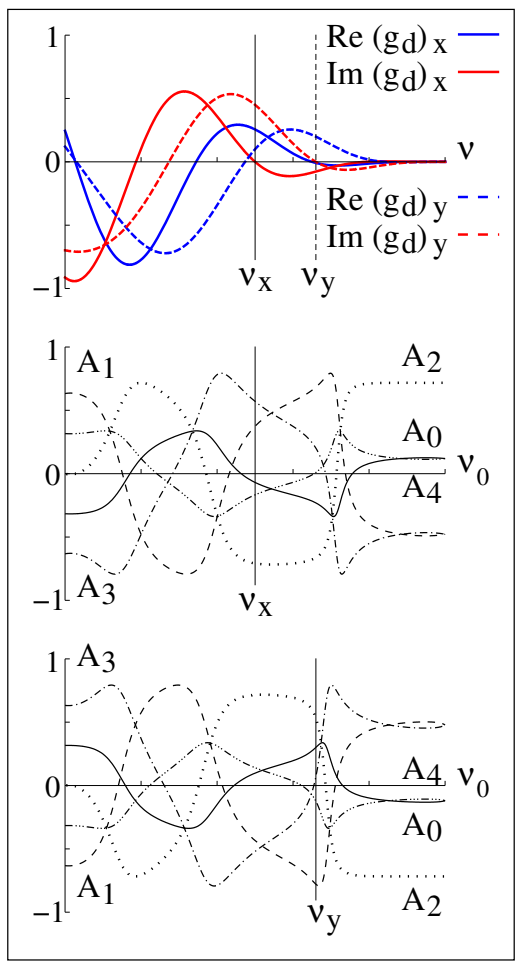


Figure 4: Numerical example of the digital filter design for FNAL Booster, $N = 2$. Both scales for ν and ν_0 are from 6.5 to 7.0.

REFERENCES

[1] R. De Maria, D. Valuch, G. Arduini, W. Höfle, G. Kotzian and V. A. Lebedev, "Suppression of Emittance Growth by Excited Magnet Noise with the Transverse Damper in LHC in Simulations and Experiment," Conf. Proc. C **110904**, 508 (2011).

Copyright © 2013 CC-BY-3.0 and by the respective authors

FAST FPGA BASED LOW-TRIGGER-JITTER WAVEFORM GENERATOR METHOD FOR BARRIER-BUCKET ELECTRONICS AT FAIR*

E. Bayer†, P. Zipf, University of Kassel, Kassel, Germany
H. Klingbeil, A. Klaus, GSI Helmholtz Centre, Darmstadt, Germany

Abstract

A new method for low trigger-jitter waveform generation is presented. The targeted application is the time-delayed, trigger synchronous waveform generation. The method can be implemented on a single FPGA, which drives an ADC. The phase-jitter between a trigger signal fed to the FPGA and the generated single sine waveform is σ= 40 ps and 275 ps peak-to-peak. The response time of the wave form generator is 50 ns. The amplitude and the offset of each sine wave can also be manipulated in real time. The waveform generator was designed for the use in the Barrier-Bucket system of the SIS100 synchrotron at the new Facility for Antiproton and Ion Research (FAIR) in Darmstadt, Germany.

INTRODUCTION

The GSI Helmholtz Centre for Heavy Ion Research in Darmstadt, Germany is an accelerator facility for High Energy Physics (HEP) research. In collaboration with 16 countries and physicists from all over the world, the Facility for Antiproton and Ion Research (FAIR) will be built as a major extension of the existing facility and will be one of the largest accelerator facilities in the world.

The presented waveform generator method is designed for the use in the pre-compression stage of the new SIS100 synchrotron. The existing SIS18 will be used as booster and will inject bunches of particles into 8 of 10 SIS100 buckets. After the particles have been accelerated to the final speed in the SIS100, they have to be compressed to a single bunch that takes 1/3 of the circumference. The preferred method to perform this task is called Barrier-Bucket. In this method, the amplitude of the bucket forming sine waves, which hold the bunches, is decreased adiabatically. After a certain time the bunches merge into a single long particle bunch in between the remaining sine waves. Now, to compress the beam without the loss of particles, one wave has to be moved towards the other adiabatically, means in steps less than 1 ns. Both sine waves have to be generated synchronously to the revolution trigger, coming from the Central Control System, which controls also the amplitude and the voltage offset of the sine waves. The BB-method is illustrated in Fig. 1. The constraints for the waveform generation system, listed in Table 1, are given by the physics of the accelerator and the desired bunch quality.

The task is therefore to gain control over the phase of the generated single sine waves in the sub nano-second region with a low response time. For this purpose a new waveform generation method was developed and implemented.

* Work supported by EU, EURONS contract No. 506065.
† e.bayer@gsi.de

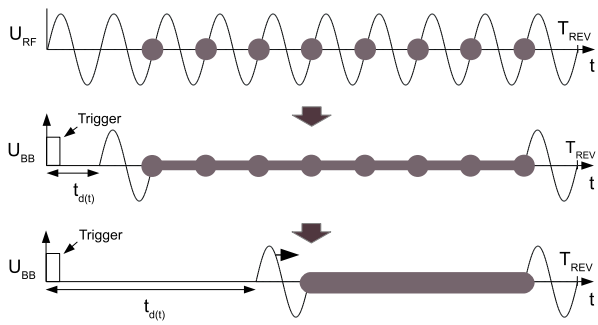


Figure 1: The procedure for beam pre-compression with the Barrier Bucket method (simplified).

Table 1: Specifications for the Barrier-Bucket Low-Level RF-System

Parameter	Value
Barrier Frequency f_b	1.5 ± 0.2 MHz
Revolution Period T_{REV} (= Trigger Period)	9.1 to 3.7 μs
Moving Time T_{MOV}	10 to 200 ms
Moving Step Resolution $\Delta t_{d(t)}$	$\leq$ 1ns
BB signal rise/fall time t_R and t_F	$\leq$ 10ns

We will introduce the new method in the next section. In the section "Design" the design structure and operation are explained. Subsequently, the measured performance of the system will be presented, followed by a conclusion.

WAVE GENERATION METHOD

In existing asynchronous triggered DDS methods, the incoming trigger signal is sampled with the internal system-clock frequency f_{sys}. As soon as a 0/1 transition is detected, a Digital-Analog-Converter (DAC) is driven by the system-clock and fed with the grid points of the desired waveform. The standard deviation of the resulting trigger-waveform jitter equals then $1/(f_{sys} \cdot \sqrt{12})$. To overcome this limitation, additional effort is necessary on both sides - on the input processing as well as on the signal synthesis part. The given task can therefore be divided into two subtasks. First, the relation of the incoming trigger-signal phase to the system-clock signal phase $\Delta\Phi$ has to be determined with a higher precision than simply by sampling the trigger signal and second, the generation of the phase accurate sine wave using this information. This procedure is illustrated in Fig. 2. In the following sections, the methods for a high precision phase measurement and for phase accurate signal generation are introduced.

Copyright © 2013 CC-BY-3.0 and by the respective authors

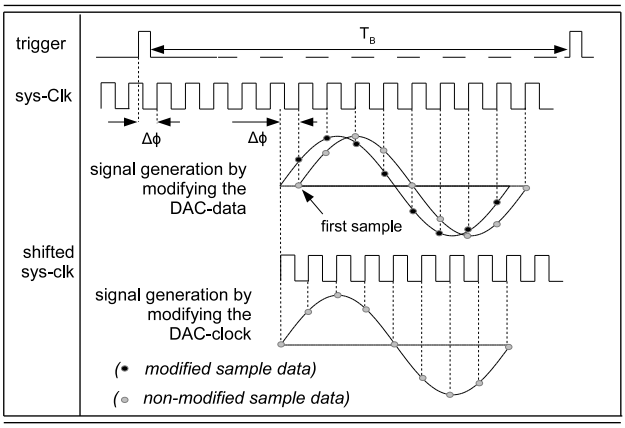


Figure 2: Principle of the phase accurate waveform generation by modifying the DAC data or, alternative, the DAC clock.

Phase Measurement

The first step in generating a low trigger-jitter waveform is the measurement of the phase relation between the trigger signal and the system clock, since the system clock is then used for the DDS algorithm. This corresponds to a time interval measurement. The accuracy has to be as good as possible, because the maximum phase deviation in the whole method is increased by the maximum deviation of the phase measurement. Therefore, to reduce the portion of the measurement inaccuracy, a high-precision FPGA time-to-digital (TDC) method was used for this purpose, which ensures a maximum deviation down to ∼30 ps [1]. The used TDC method is a tapped delay lines (TDL) technique with enhanced accuracy. The details of this TDC design can be found in [1].

Phase Accurate Waveform Generation

Generally, there are already methods for the generation of phase shifted waveforms. For example the CORDIC algorithm can be used to generate waveforms with the desired phase-offset by starting with a certain amplitude offset as is shown in Fig. 2. This approach works well for generation of continuous signals, when the waveform at the beginning and at the end of the waveform is of no interest. If a well shaped single sine wave has to be generated, one has to consider the phase-offset-cut artifacts on the edges of the waveform due to the variable phase offset, which results in large phase-jitter on the sine wave edges. A good alternative avoiding these effects is the shifting of the ADC driving clock instead of the ADC data as is shown in Fig. 2.

The common method to perform phase-shifts of the system clock in FPGA is using the build-in Phase-Locked-Loop (PLL) or a Delay Locked Loop (DLL). Here a phase-shift granularity of $(1/1024) \cdot T_{sys}$ is available [2]. The disadvantage of this approach is the relatively large reconfiguration time of the PLL that can take several microseconds [2]. These parameters exceeded the given constraints of our application. Therefore, a new method for the generation of a phase-shifted clock signal was implemented on a Virtex-4 FPGA. The implemented "phase-shifter" uses the routing resources of the FPGA as delay elements and produces delayed versions of the system clock. This is done by deploying the carry-chain MUX resources to access the clock signal. As the carry multiplexer are arranged in a column an evenly delayed signal can be produced in steps of 100 and 200 ps. The switching is performed within one clock cycle - means: down to 2 ns response time on the current FPGA families [3].

DESIGN

Structure

For the implementation of the waveform generator we take a phase-shifter, a high-precision TDC for phase-relation measurements, two secondary FPGA-TDC to measure phase-shifter delays and the DDS building block, which feeds a 14-bit ADC outside the FPGA. As the shifter delays measurements can be repeated, the secondary TDCs have a lower resolution and need less resources. We deploy the design from [4] for this purpose.

The implemented design makes extensive use of the temperature and voltage dependent gate delays in the FPGA. Therefore additional effort is needed to ensure a stable operation [4]. For this purpose a calibration and continuous recalibration functionality has been implemented on-chip for the phase-shifter delays as well as for the TDCs. The used calibration methodology can be found in [5]. The (re)calibration of these elements is scheduled within the idle phases of each element between the incoming trigger events. Since the trigger frequency may not be sufficient for using the trigger input for calibration, a controllable, system clock uncorrelated, internal pulser was implemented, which can be used as calibration signal.

The coarse structure of the system is shown in Figure 3. Its operation will be described in the next section.

Operation

The first task in the initialization phase of the system is the calibration of the TDCs. The inputs of the three TDCs are switched to the internal pulser and the 2^{16} events for the first calibration are collected. After the shifter TDCs are calibrated, the resulting delay of each shifter position is measured. Using this information the SD-LUT is constructed, which maps each possible needed delay within the system clock period (T_{SYS}) to a shifter position. After these steps the system is fully operational. Before each trigger event, the system receives three optical information streams - two streams containing the amplitude and amplitude offset information and one with the current phase-offset. When a trigger signal arrives, the time interval between the rising edge of the trigger and the following rising edge of the system clock is measured with the high-precision TDC. From this measurement and the current phase offset the required shifter delay is calculated in the event-phase-logic. A coarse counter is then loaded with the coarse portion of the phase-offset, which has a granularity

Copyright © 2013 CC-BY-3.0 and by the respective authors

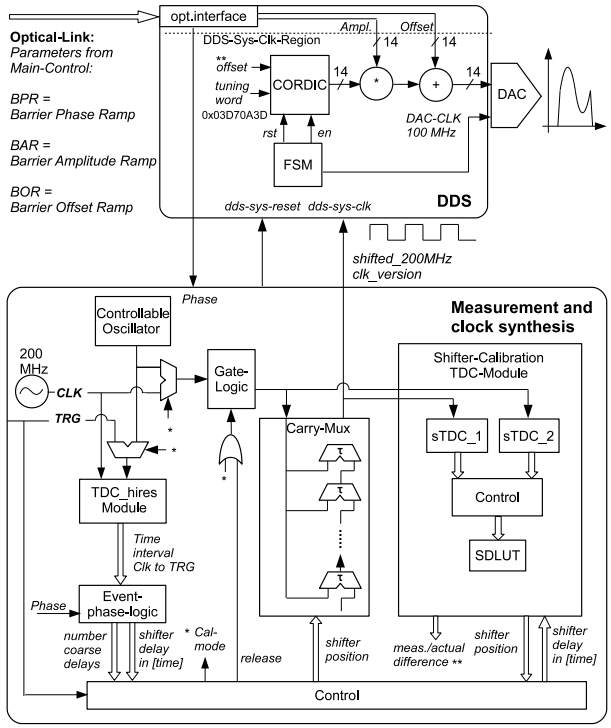


Figure 3: The block diagram of the system. The additional path for the combined mode is marked with (**).

of T_{SYS} and the phase-shifter is switched to the position corresponding to the fine shift value.

All these steps are done within a constant time window, which finishes with the release of the back-running coarse counter. As soon as the counter value reaches zero, the clock gate at the phase-shifter input is released and a defined number of shifted system clock pulses is generated. This pulse train is used as clock signal for the DDS part of the system. There, a finite state machine generates the DAC clock and the corresponding sine grid points by driving a CORDIC unit. At this point, the DAC data values can be manipulated, to adjust the needed sine amplitude and sine offset.

To further improve the jitter characteristics the combination of DAC data and DAC clock manipulation can be applied. For this purpose the difference between the actual delay of the set shifter position and the measurement value is sent to the DDS part of the system to adjust a corresponding offset in the DAC data.

MEASUREMENTS

Although the whole system can be implemented in a single FPGA connected to a DAC, the current setup is distributed between two FPGA boards, featuring together the needed interfaces. The clock pulse train is fed into the DDS-System by a single ended connection and is therefore exposed to the electromagnetic noise. For this reason the achieved performance was characterized by measuring the trigger-jitter of the generated pulse-train, the sine wave generated by DAC clock manipulation only and the sine wave generated by the combined method. The measured trigger-jitter of the pulse-train is σ = 58 ps and 350 ps peak-to-peak. The phase-jitter of the basic/combined method is σ= 63/35 ps standard deviation and 500/270 ps peak-to-peak deviation. Hence, the achievable performance for a single FPGA implementation is $\sigma = \sqrt{35^2 - (63^2 - 58^2)} \approx 25$ ps. The test readings of the sine wave for the combined method are presented in Fig. 4.

CONCLUSION

A new method for triggered waveform-generation was presented. The method of combined manipulation of the DAC-data and DAC-clock implementable in a single FPGA over-fulfills the requirements nearly by two orders of magnitude and outperforms the known instrumentation in means of trigger-jitter and device costs.

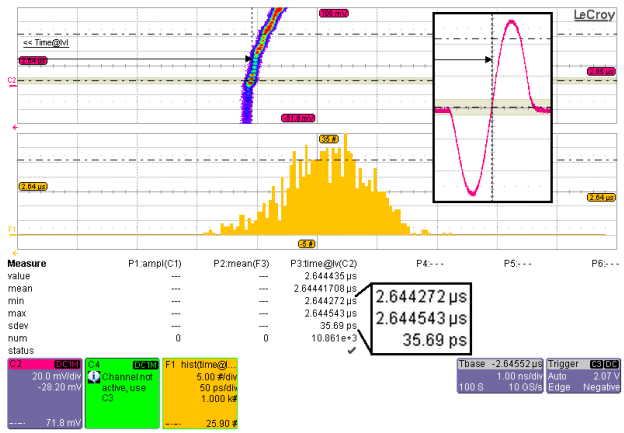


Figure 4: Jitter measurement between the trigger signal and the generated sine wave.

REFERENCES

[1] E. Bayer, P. Zipf and M. Traxler, "A multichannel high-resolution (<5 ps RMS between two channels) Time-to-Digital Converter (TDC) implemented in a field programmable gate array (FPGA)", IEEE NSS/MIC 2011, pp.876-879, 23-29 Oct. 2011.

[2] Xilinx: *Virtex-4 FPGA Configuration User Guide*, UG071 (v1.11) June 9, 2009, downloaded on: http://www.xilinx.com/ support/ documentation/ user_guides/ ug071.pdf.

[3] Xilinx: *Virtex-7 T and XT FPGAs Data Sheet: DC and AC Switching Characteristics*, DS183 (v1.12) March 7, 2013, downloaded on: http://www.xilinx.com/support/ documentation/ data_sheets/ ds183_Virtex_7_Data_Sheet.pdf

[4] E. Bayer, M. Traxler, "A High-Resolution (<10ps RMS) 48-Channel Time-to-Digital Converter (TDC) Implemented in a Field Programmable Gate Array (FPGA)", IEEE Trans. on Nuclear Science, vol.58, no.4, pp.1547-1552, Aug. 2011.

[5] J. Wu, "Several Key Issues on Implementing Delay Line Based TDCs Using FPGAs," , IEEE Trans. on Nuclear Science, vol.57, no.3, pp.1543,1548, June 2010.

Copyright © 2013 CC-BY-3.0 and by the respective authors

STUDY OF MICROPHONICS COMPENSATION FOR SRF CAVITY*

Z. Zheng[#,1,2], S. Zhao[1], Z. Liu[1], D. Morris[1], J. Wei[1], Y. Zhang[1]
[1]Facility for Rare Isotope Beams, Michigan State University, East Lansing, Michigan, USA
[2]Tsinghua University, Beijing, China

Abstract

Microphonics and Lorentz Force detune the resonance frequency of a SRF cavity, leading to perturbations of the amplitude and phase of its accelerating field. Although this disturbance could be compensated by a piezo-electric tuner or with additional RF power, these two methods have conflicts, which is observed as unstable RF fields in a recent experiment. These conflicts could be explained by a model. Further experiments on ReA3 [1] cryomodule validates a conflict suggested by the model. Overall optimization of control algorithm is still needed to effectively combine the two methods.

INTRODUCTION

Microphonics and Lorentz Force Detuning are major disturbances to the accelerating field of an SRF cavity. Usually, people can invest more RF power into the cavity to compensate these effects. However, RF power is expensive, especially for high gradient SRF cavities. An economical substitute is piezo-electric tuner, which sense and compensate the vibration with a fast feedback system. But the compensation is relatively rough, compared with the RF power method. It seems natural to combine the rough and cheap tuner with fine RF power to get an effective and affordable compensation. As we expect a stable accelerating field by simultaneously applying both tuners, we did observe strong interference between them. Section 1 describes these observations.

To understand the conflict in the combo control, we have developed a model in MATLAB. The model reveals a conflict that is resulted from a time delay of piezo tuner control response. When high frequency modulation is induced by RF power modulation, such a time delay corresponds to a large phase difference, which could amplify the unwanted oscillations rather than suppress them.

We added a low pass filter to verify our speculation. The phase fluctuation has been suppressed from ±7° to ±4°, but not completely eliminated. Although the combo control uses two compensation methods simultaneously, their control algorithms are in fact separate. Apparently we need an overall optimization for the combo control algorithm that includes piezo's time delay into consideration.

In this paper, we also compared performance of ADRC algorithm on the piezo tuner with the common PI algorithm. Although ADRC appears to be more efficient than PI in simulation [2], their experimental performance are comparable. Section 2 describes our observation.

CONFLICTS IN THE COMBO CONTROL

To compensate microphonics, a piezo tuner was installed on the quarter-wave resonator (QWR) in ReA3. However, it was only used to suppress helium pressure fluctuations (<1 Hz), not microphonics (>1 Hz). A major source of the microphonics is the vibration of the QWR, with a resonate frequency ~38 Hz. To test the

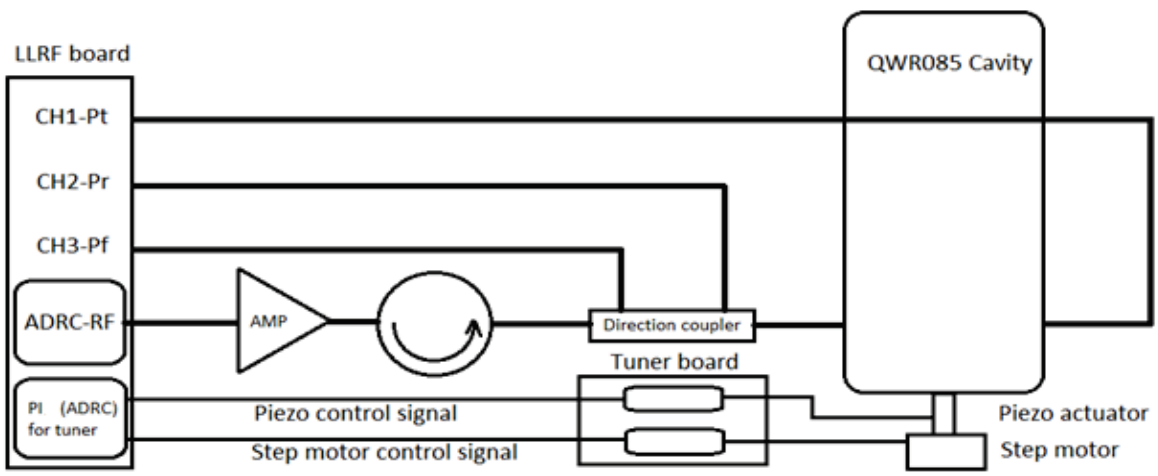


Figure 1: Test setup for a ReA3 cavity. CH1, CH2 and CH3 are three channels on the LLRF board receiving transmit (Pt), reflect (Pr) and forward power (Pf). RF power is controlled with ADRC. Piezo tuner is controlled by PI and later by ADRC.

*Work supported by the U.S. Department of Energy Office of Science under Cooperative Agreement DE-SC0000661.
#zhengw@frib.msu.edu

Copyright © 2013 CC-BY-3.0 and by the respective authors

performance of combo control, we arranged a test as shown in Figure 1. Cavity accelerating gradient was set to be1.3 MV/m.

Single Control by Piezo-electric Tuner

We first would like to observe the performance of single control, i.e., RF control is open loop and piezo tuner is controlled by PI algorithm. A slow tuner, the step motor in Figure 1, is triggered to move when the cavity is detuned out of the frequency range of piezo tuner. The PI controller has a proportional gain (K_p) of 3 and an integral gain (K_i) of 1×10^{-4}. Those parameters were tuned to achieve the most stable response. The performance of piezo tuner is shown in Fig. 2 with a large microphonics and in Fig. 3 with a small microphonics.

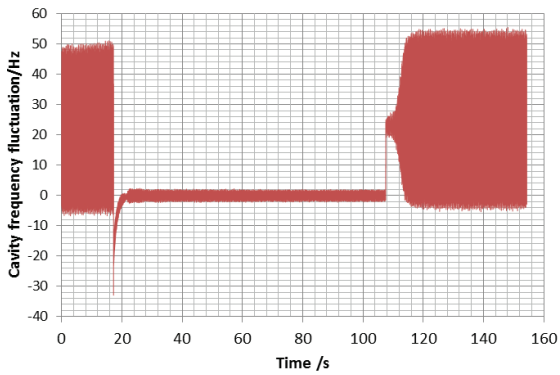


Figure 2: Performance of a piezo tuner with a large microphonics. The tuner was turned on at t=17 s and turned off at t=108 s.

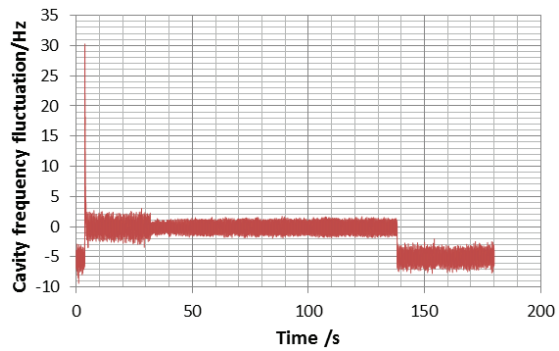


Figure 3: Performance of a piezo tuner with a small microphonics. Tuner was turned on at t=4 s with K_p=0 and $K_i=1\times10^{-4}$, K_p was changed to 3 at t=32 s, tuner was turned off at t=138 s.

It shows that a piezo tuner can reduce modulation of the cavity's resonance frequency to within ±2Hz for both large and small microphonics.

Performance of Combo Control

The motivation to use the combo control is to save the cost of RF power for compensation. But it turns out to be opposite result. Figure 4 shows the unstable phase of accelerating field with the combo control. It reveals conflicts between the RF power compensation and piezo tuner control, which drives a larger phase fluctuation.

To better understand the interference, we constructed a fundamental model, which should include fundamental parameters such as rise time of the piezo electric and basic components such as RF cavity, LLRF system, beam loading, microphonics and slow/fast tuner as Figure 1.

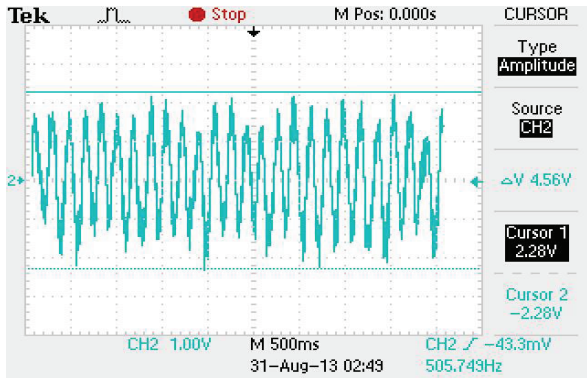


Figure 4: Unstable cavity phase with combo control. Phase fluctuation is up to ±41°.

Piezo tuner has a capacitance of ~36 uF, and an output resistance of 5 Ω. The rise time of charging T_{rc} thus is ~0.54ms (from 10% to 90%). In addition, piezo tuner also has a mechanical rise time. According to the data sheet provided by vendor, its mechanical resonant frequency (unloaded) is 5.5 kHz. Since the tuner is installed under the QWR bottom plate, which is weighed as ~2 kg compared with tuner's weight of 0.2 kg, the resonant frequency of the loaded case is

$$f = 5.5 * \sqrt{\frac{0.2}{2}} = 3 \text{ kHz}$$

The corresponding mechanical rise time is

$$T_{rm} = 1/(3f) = 0.1 \text{ ms}.$$

Since $T_{rm} < T_{rc}$, we use 0.54 ms in the model as the rise time, which is sufficiently fast considering the bandwidth of the ReA3 QWR (70 Hz).

With only rise time specified in the model, the combo control works well, as shown in Figure 5. It reduces the phase fluctuation to ±0.1°. But it is not the case we observed.

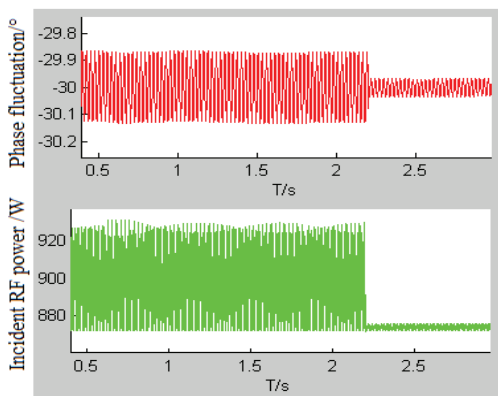


Figure 5: Simulation without piezo's time delay. RF control is on all the time, while piezo tuner is turned on at t=2.2 s.

Copyright © 2013 CC-BY-3.0 and by the respective authors

We adjust the model by including piezo's delay. The combo control becomes unstable when we add a time delay (≥0.16 ms) to the piezo, i.e., piezo tuner responses ≥0.16 ms later after receiving control signal. That delay could actually happen due to: 1) hysteresis and backlash of the piezo; 2) transport of mechanical wave; 3) loop delay of the electronic circuits, where hysteresis could be the most important contribution to the 0.16 ms delay.

Experiment Validation and Suppression

Delay of piezo tuner could cause an additional phase shift between tuner control and RF control. This phase shift is much larger for high frequency signal than low frequency, which enhances the high frequency fluctuation brought by RF compensation. To validate this concept of interference, we add a low pass filter before the tuner control. In simulation, it eliminates the unstable fluctuation when the delay is set to be 0.16 ms.

Experimentally, the low pass filter is added in the DSP code of the tuner control. The original microphonics is measured as ±7°.

To use the combo control, we closed the RF phase control loop and tuner control loop, while kept RF amplitude control loop open. When the low pass filter is bypassed, phase of the cavity acceleration field became unstable (±41°) as in Figure 4. After we applied the low pass filter as in the simulation, the phase fluctuation is reduced to ±4°, as shown in Figure 6.

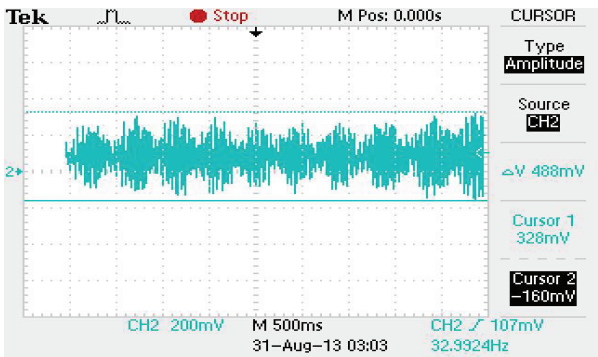


Figure 6: With low pass filter added before piezo tuner control, the phase fluctuation is reduced to ±4° for combo control.

Comparing with the background microphonics, the combo control reduces the phase fluctuations from ±7° to ±4°. The combo control works to some extent, but not as well as signal control. It did validate the conflict in the model, although a low pass filter cannot thoroughly mitigated the interference in the combo control. Since the cavity operated at a low gradient (1.3 MV/m) during experiment, no obvious reduction of RF power was observed in this experiment.

To optimize the performance of combo control, multi parameter optimization is needed for its control algorithm. There is no easy solution to use single parameter optimization approach in the combo control.

ADRC BASED PIEZO ELECTRIC TUNER

Besides the combo control test, we also applied ADRC algorithm on the piezo tuner to compare with PI controller. Different from what we expected in the simulation [2], the performance of ADRC (Fig. 7) is comparable with PI (Fig. 3), no obvious improvement. Both PI and ADRC performances are likely to be compromised by the hysteresis of the piezo tuner.

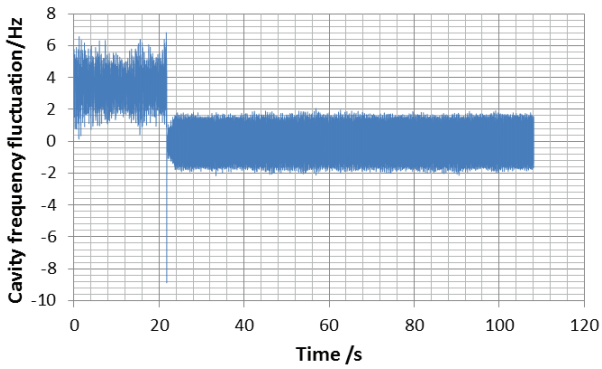


Figure 7: The performance of ADRC based piezo electric tuner. This is single control by piezo electric tuner. Tuner was turned on at t=22 s.

CONCLUSION

We did a series of experiments to benchmark the proposed combo control for microphonics compensation. It reveals that hysteresis induced time delay creates conflicts between piezo tuner and RF power control. A low pass filter before the piezo tuner control could suppress some interferences but not all of them. To achieve a good performance of combo control, a multi parameter control algorithm is needed.

We also compared ADRC and PI algorithms for the piezo tuner control, but found little difference.

REFERENCES

[1] Oliver Kester et al., "The MSU/NSCL Re-Accelerator ReA3," Proceeding of SRF2009, Berlin, Germany, MOOCAU05, p. 57 (2009).

[2] Z. Zheng et al., "ADRC control for beam loading and microphonics," Proc. of LINAC2012, Tel-Aviv, Israel, TUPB061, p. 615 (2012).

Copyright © 2013 CC-BY-3.0 and by the respective authors

NEXT GENERATION CW REFERENCE CLOCK TRANSFER SYSTEM WITH FEMTOSECOND STABILITY

P. Orel, S. Zorzut, P. Lemut, R. Hrovatin, Instrumentation Technologies, Solkan, Slovenia
S.G. Hunziker, V. Schlott, Paul Scherrer Institute, Villigen, Switzerland

Abstract

Present and future fourth generation light sources, such as the Swiss FEL, are placing strict requirements on current CW reference clock transfer systems. Both the added jitter and the long-term stability criteria need to be in the range of a few femtoseconds. In order to meet these requirements, the existing Libera Sync CW transfer system has been redesigned. All of the aspects of the system design have been revised and improved, from new measuring methods and better evaluation of components to careful pre-design testing and simulation. New fiber link topology, new approaches in thermal stabilization, improved power supply distribution and interconnection of carefully selected electrical and state-of-the-art optical components has led to a significant reduction in added jitter and excellent long-term stability of the system. Measurements repeatedly show the jitter performance to be below 6 fs_{rms}, integrated over the frequency range of 10 Hz to 10 MHz. Preliminary measurements of the long-term stability place the system in the range of a few tens of femtoseconds peak-to-peak of drift per day.

INTRODUCTION

Free Electron Lasers (FEL) require high performance synchronization throughout the entire machine; otherwise, its performance may be degraded or even fail. Typically, this high performance synchronization system is composed of two key subsystems. One is the source where a Reference Master Oscillator (RMO) is used. Its frequency range spans from a few 100 MHz to a few GHz. It has high close-in spectral purity and extremely stable frequency. The other extremely important element is the reference clock transfer system. Its goal is to deliver the reference signal to the users in either the optical or electrical domains while preserving initial reference clock signal purity and stability.

Typical requirements in terms of added jitter and long-term phase stability are below 10 fs for jitter and below 40 fs for phase stability per day [1]. For distances greater that 100m, the use of optical fibers as a transmission media is recommended since they exhibit low insertion loss, are insusceptible to EM interference and are reasonably inexpensive. Within the optical domain, two approaches are available.

The first is a pulsed-based system that uses the Michelson interferometer to detect optical path changes. The benefit of this approach is excellent long-term stability.

The other approach is based on a continuous wave (CW) modulation of an optical carrier in which phase detection and stabilization are done in the radio frequency (RF) domain. It offers the advantage of a system restart without re-tuning, high reliability and lower cost [2].

The Libera Sync 3 transfer system presented in this article is based on the CW modulation scheme.

THEORY OF OPERATION

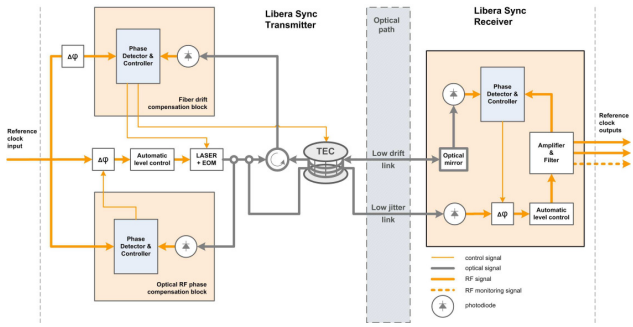


Figure 1: Block diagram of the system.

The figure above is a block diagram of the system that shows the basic principle of operation. The system is composed of a transmitter and a receiver units connected by two optical fiber links. The transmitter input signal is the CW RF reference clock signal coming from the RMO. This signal modulates the 1550 nm optical carrier through an electro-optical modulator. The optical signal is then split and fed into two separate paths. One of the signals along with the on-board control circuitry is used for link phase drift compensation and is partly reflected back at the receiver side. The other path is used for transfer of the low-added jitter signal. In the receiver, both incident optical signals are demodulated back into the RF domain.

In the transmitter unit, the fiber drift compensation is done by comparing the demodulated reflected signal phase with the phase of the input reference signal. The optical path compensation is provided using two principles. The slow changes are compensated by cooling or heating a fiber spool. The temperature of the fibers on the spool is changed in the opposite direction from the temperature change on the optical path between the transmitter and the receiver. Faster changes are compensated by changing the laser source temperature and thus the optical carrier wavelength. In this manner, the optical path is artificially extended or shrunk by taking advantage of the chromatic dispersion in the interconnection fiber.

To overcome optical limitations, two fibers are used, the first one for the transfer of a low-noise signal and the second one for the transfer of a low-drift reference signal.

Copyright © 2013 CC-BY-3.0 and by the respective authors

This combination yields ultra-low added jitter and low drift.

Design Approach and Implementation

In order to meet the tight performance requirements, a new development approach has been followed. Theoretical knowledge with simulations has been combined with prototyping and measurements of the individual components. Based on those results, a careful selection process has been commenced for both electrical and optical components.

Vital subsystems, such as the power supply distribution network, control system, temperature stabilization, mechanical layout and optics, have all been subject to prototyping, testing and tuning before being integrated into the final design.

The power supply subsystem proved to be as vital, and it has been specially developed to provide a low noise power rail for the RF circuitry especially the RF amplifiers.

The environmental conditions inside the box must be kept as constant as possible. In this context, a new temperature stabilization subsystem has been devised in which the temperature is kept stable to within 0.001°C.

The mechanical layout has been specifically designed to facilitate the environmental stabilization system inside the unit while simultaneously ensuring ease of manufacturing.

The RF amplifiers were tested and tuned in order to achieve low noise and low phase noise, respectively.

The layout of the fiber interconnections within the system is as symmetric as possible (temperature/humidity drift compensation). Using one single instead of two different fibers for drift stabilization guarantees independence from dispersion tolerances, as the laser's emission wavelength is varied to correct the link group delay. Rayleigh backscattering noise [3] increases the low-frequency phase noise as well as the phase noise floor in this bi-directional transmission. By reducing the coherence of the reflected light, the first effect can be minimized. To dispense with the added noise floor, a second uni-directional "low-noise" link, that is phase-locked to the first "low-drift" link and "cleaned", transmits the same signal but without backscattering noise. The stability of the "low-drift" link is further increased by operating photodiodes (out-of loop) in low AM-to-PM conversion operating points and by stabilizing the optical power. Furthermore, the optical power has been chosen to be sufficiently large so that the resulting shot noise limit enables achieving the envisaged phase noise floor.

Following that, all of the electronics have been integrated onto a single printed circuit board (PCB), thus allowing for better manageability and greater reproducibility.

Finally, the hardware platform is complemented with a software control system that monitors over 120 different parameters, from environmental data (temperature, humidity and pressure) to electronics and optics (phase detectors outputs, RF power levels, photodiode currents, laser temperature, etc.).

RESULTS

Jitter frequencies below 10 Hz are classified as wander and frequencies at or above 10 Hz as jitter [4]. Measuring these two parameters with a resolution of a few femtoseconds proved to be a challenge. Special measurement techniques along with specially developed equipment have been used.

Jitter Performance

In our case, the added jitter has been measured at offset frequencies ranging from 10 Hz to 10 MHz. The figure below shows the added jitter measurement of the Libera Sync 3 prototype.

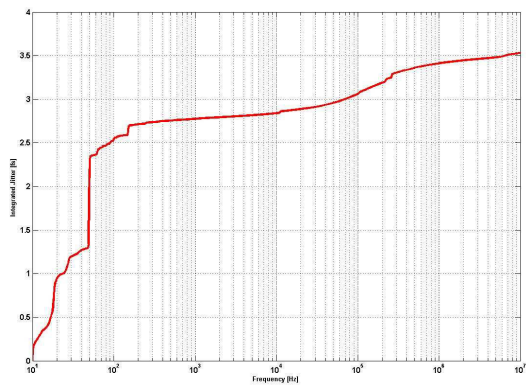


Figure 2: Integrated added jitter.

The majority of the jitter is concentrated in the lower frequency region between 10 Hz and 110 Hz. This has been attributed to mechanical vibrations and the coupling of the 50 Hz frequency component present in the environment at the time of the measurements. The total integrated jitter is slightly over 3.5 fs. This is a preliminary measurement and can be subject to change in the final implementation of the system. However, we do not expect a significant degradation.

Long-Term Phase Stability

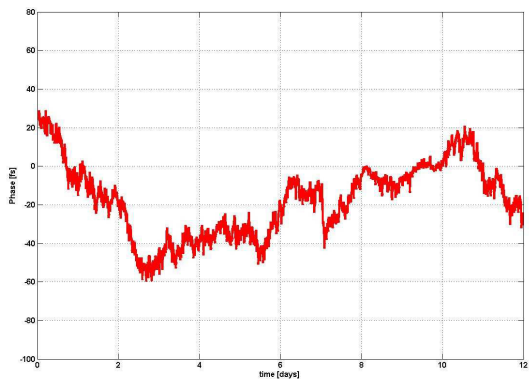


Figure 3: Phase drift.

Copyright © 2013 CC-BY-3.0 and by the respective authors

Phase drift, like jitter, is the undesired variation of the phase of an otherwise periodic signal. However, these variations happen at much lower frequencies and are regarded as a time variable phase offset in relation to an initial arbitrary phase. In our case, the measurement was done over a period of 12 days. The following figure shows phase drift stability of the Libera Sync 3 prototype in relation to a phase stable reference.

The maximum peak-to-peak phase drift has been measured at 88.7 fs while the average day-to-day phase drift has been calculated to be around 30 fs with a standard deviation of 8.9 fs.

Measurement Techniques

In order to measure added jitter in the femtosecond range, a differential technique (saturated mixer) has been used. In this case, the reference signal is split into two branches. One is used as the reference signal while the other contains the device under test (DUT). If the two signals are driven in a quadrature phase relation at the mixer input ports, the resulting baseband output difference signal is 0 V plus a small phase modulation of the carrier, which is regarded as the residual phase noise of the DUT. This residual phase noise is sampled and digitized by a signal source analyzer (SSA). The jitter is calculated by integrating the digitized phase noise spectrum over the offset frequency range and is normalized to the original carrier frequency. Despite limitations induced by non-symmetries and non-linearities of the mixer, the resolution of the measurement can be estimated to be on the order of 0.1 fs [5].

Phase drift measurements have been performed by using a phase detector unit specifically designed for this application. The detector unit has been built by following the same design steps and implementing the same technology that has been used for the Libera Sync 3 system itself. The phase drift measurement is based on the AD8302 integrated circuit (IC). When thermally stabilized and driven with proper RF power levels, this IC exhibits minimal phase drift. Combined with thermally stabilized splitters and special RF cables, the setup can reach an accuracy of about 10 fs of phase drift per day.

DISCUSSION

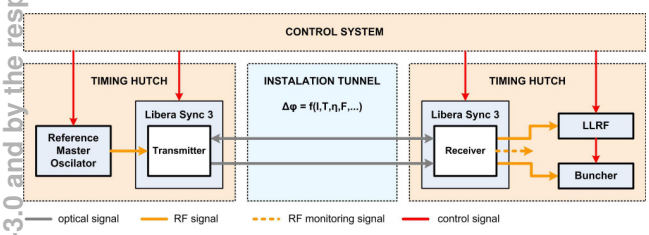


Figure 4: Example of use an accelerator environment.

Figure 4 shows an example of how the Libera Sync 3 transfer system can be integrated into an accelerator environment. The interconnecting RF cables from and to the transmitter and receiver units respectively as well as the fiber cables between them are also vital parts of this system, which require careful consideration.

The use of temperature-compensated RF cables with low temperature coefficients in the range of a few fs/mK is mandatory [6].

Phase drift in the optical fiber depends on link length, temperature and relative humidity variations, mechanical stress etc. Deviations of a few degrees in temperature and some tens of a percentage in relative humidity can contribute high phase drifts in the fiber link. The current Libera Sync 3 prototype provides a phase compensation range of approximately 360 ps. Therefore, if long distance operation is to be achieved, special care in selecting the fiber cable needs to be taken. Only loose type cabling preserves the temperature coefficient of the silica glass optical fiber in the range of 40 ps/kmK. In cases in which the estimated phase drift of the optical path exceeds the phase compensation range of the Libera Sync 3, the use of phase stable optical fibers is mandatory [7].

Finally, the Libera Sync 3 provides a user interface that can be operated manually or remotely. Manual operation is done by accessing the front panel controls along with the display, which is ideal for data examination and link tuning. Remote operation is done using SCPI commands over a standard 10/100 Mbit Ethernet connection, which is ideal for integration into the control system.

The current prototype works on a fixed frequency of approximately 3GHz. Future upgrades include extended operation range and support for other frequencies (6 GHz).

CONCLUSION

The new Libera Sync 3 transfer system integrates a novel approach with state-of-the-art technologies, ultimately providing outstanding performance, high reliability and reproducibility as well as ease of use.

REFERENCES

[1] V. Schlott et al., “Reference distribution system for SwissFEL”, Libera Workshop (2012).
[2] M. Vidmar et al., “Chasing Femtoseconds – How accelerators can benefit from economies of scale in other industries”, IPAC (2011).
[3] T.H. Wood, R.A, Linke, B.L. Kasper, and E.C. Carr, “Observation of coherent Rayleigh noise in single-source bidirectional optical fiber systems,” *J. Lightwave Technol.*, vol. 6, no. 2, pp. 346-352, Feb. 1988.
[4] ITU-T, “Recommendation G.810”, (August 1996)
[5] R. Boudot, E. Rubiola, “Phase noise RF and microwave amplifiers”, FEMTO-ST Institute (January 2012).
[6] K. Czuba, D. Sikora, “Temperature stability of coaxial cables”, ACTA Physica Polonica A (Vol. 119), (2011)
[7] M. Bousonville et al., “New phase stable optical fiber”, Proceedings of BIW, Newport News, Virginia, USA (2012).

Copyright © 2013 CC-BY-3.0 and by the respective authors

ENERGY DEPOSITION IN THE SECTOR 37 SCRAPER OF THE ADVANCED PHOTON SOURCE STORAGE RING*

J. C. Dooling†, M. Borland, Y. C. Chae, and R. Lindberg, ANL, Argonne, IL 60439, USA

Abstract

The horizontal scraper in the sector 37 straight section of the Advanced Photon Source storage ring serves as a diagnostic to probe both the edge of the beam as well as the physical aperture when the store is lost. Initially, the scraper was meant only to be a diagnostic; high-density, short-radiation-length material used in the device was intended to stop halo, not the full beam. Damage to this device was recently discovered, and as a result, we began an effort to model and improve the scraper. Modeling with `elegant` provides loss distributions for several scenarios such as muting one or both rf systems in combination with firing injection kickers. The loss distributions are used as input to a MARS model of the scraper. Beam dumps from 100 mA dissipate a total of 2600 J. Most of this energy is not deposited locally; however, depending on the geometry and physical make-up, sufficient power density exists to damage the device on beam-facing surfaces. Testing is currently planned to examine the suitability of different beam-facing materials. Because of non-local energy deposition, we are evaluating the secondary role for this scraper as a spoiler rather than a beam dump.

INITIAL DAMAGE AND TESTING

During the Spring 2011 APS shutdown, damage to the sector 37 (S37) scraper was observed, and the device was removed from the storage ring (SR). A photograph of the damaged region is presented in Figure 1; the view is looking downstream. The thickness of the W is 2.54 cm. The

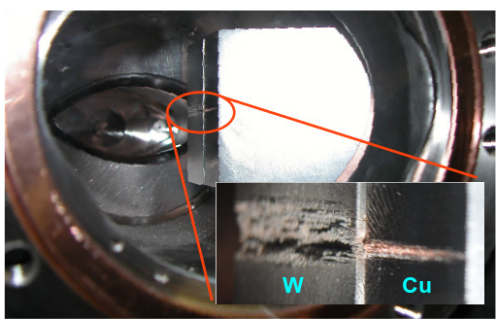


Figure 1: S37 scraper after removal from the SR in April 2011. View is looking downstream.

S37 scraper shown in Fig. 1 had been in use for seven years. The scraper was rebuilt using the same geometery and materials with the intention of employing the device only for diagnostics and collimation while a new design was considered. The rebuilt scaper was reinstalled in the SR in January 2012. Because of installation issues, the device was not used until the final day of the Spring 2012 run when beam dump studies were carried out. After shutdown the device was removed from the SR. During the study, beam was purposely dumped on the scraper using both 24-bunch and hybrid fill patterns. An image of the tungsten region damaged by 24-bunch beam dumps is presented in Figure 2.

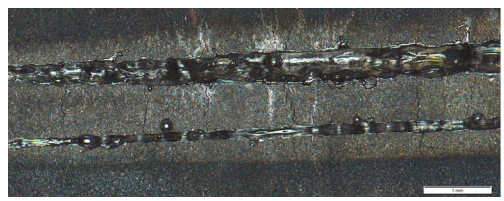
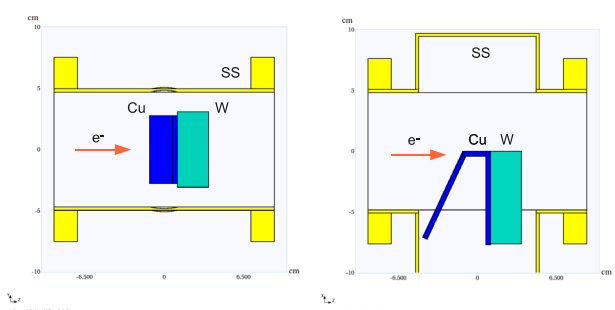


Figure 2: Tungsten region of the rebuilt S37 scraper after removal from the SR in May 2012. Beam motion: left to right.

SIMULATIONS

The particle-matter interaction program MARS [1] is used to estimate energy deposition within the scraper employing loss distributions generated with `elegant` [2]. The scraper components included in the MARS model that directly interact with the beam are shown in Figure 3; the beam travels from left to right. The tapered upstream portion is water-cooled copper. The downstream part is composed of scintered tungsten and is not directly water cooled.



(a) y-z view, x=-1.1 cm (b) x-z view, y=0 cm

Figure 3: Sector 37 baseline scraper geometry modeled in MARS; a) an elevation view at the edge of the scraper (x=-1.1 cm) and b) a plan view at beam elevation (y=0).

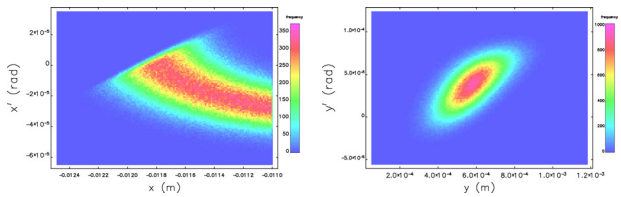
The loss distribution is generated by `elegant` for a hy-

* Work supported by the U.S. Department of Energy, Office of Science, under contract number DE-AC02-06CH11357.

† jcdooling@anl.gov

Copyright © 2013 CC-BY-3.0 and by the respective authors

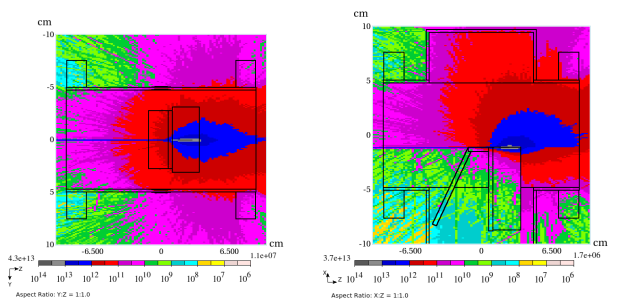
brid fill pattern; the distribution includes beam loading effects and quantum fluctuations [3]. These simulations allow us to test different beam loss scenarios, such as muting one or both rf systems or firing injection kickers after beam dump conditions have been detected. Phase-space loss distribution histograms are presented in Figure 4. The distribution represents the complete loss of 368 nC of circulating SR charge (100 mA) and is simulated with 10^5-10^6 trajectories.



(a) horizontal phase-space, x-x' (b) vertical phase-space, y-y'

Figure 4: Phase-space loss distributions on the S37 scraper generated by `elegant`. The pixel sizes are 10 μm and 1 μrad.

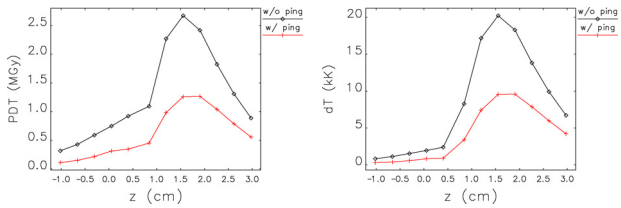
Electron/positron fluence distributions are shown in Figure 5 for the geometry presented in Fig. 3. To determine the



(a) y-z view, x=-1.1 cm (b) x-z view, y=0 cm

Figure 5: Electron/positron fluence in the Sector 37 baseline scraper geometry modeled in MARS. The two distributions overlay the geometry presented in Fig. 3.

stress on scraper material struck by the lost beam, we need to know the local energy deposition. For MARS simulations, the upstream copper portion of the scraper is divided into five equal-depth regions (Δz=0.357 cm). The tungsten is divided into seven regions, the first six with the same Δz and seventh with 1.1 mm added to make the total W-depth 2.54 cm. Peak dose and resultant temperature rise calculations are presented in Figure 6 assuming 100 mA (368 nC) are circulating in the SR in a hybrid-mode fill pattern. In Fig. 6, the change in temperature is calculated using Eq.(1) assuming all deposited energy appears instantaneously; this assumption ignores diffusion, which will be discussed below. Also, Fig. 6 shows the effect of firing one of the SR injection kickers after a dump has been detected. While firing kickers reduces the temperature increase significantly, it would not be sufficient to prevent melting.



(a) total deposited dose (PDT) (b) instantaneous temperature rise

Figure 6: Absorbed dose and instantaneous temperature excursions.

ANALYSIS

Energy deposition is provided by MARS dose distributions. The instantaneous temperature rise in a given volume element can be calculated from MARS dose distributions, assuming that no heat transfer occurs over the period of energy deposition. Temperature rise due to an absorbed dose D_{ab} is

$$\Delta T = \frac{D_{ab} A_w}{C_v}, \qquad (1)$$

where A_w is the atomic weight, and C_v is the molar heat capacity. According to the Law of Dulong and Petit, $C_v = \frac{\partial}{\partial T}(3k_B T N_A) = 3k_B N_A = 24.94$ J K^{-1}mole^{-1}, where k_B is Boltzmann's constant; most metals differ only slightly from this value. The actual values of C_v for Cu and W are 24.44 J K^{-1} mole^{-1} and 24.27 J K^{-1} mole^{-1}.

The temperature rise given by Eq.(1) assumes that the energy deposition given by MARS occurs at a single instant in time. In a real loss event, however, electrons are lost over several turns, and diffusive/dissipative mechanisms may play a role in reducing the temperature change ΔT. We have analytically estimated the effect of heat diffusion using the axially symmetric Green function solution to the diffusion equation. While this simplified model neglects other factors affecting heat transport, our primary goal was to determine if diffusion might dramatically change the temperature rise predicted in Fig. 6(b). According to our calculations, simple diffusion can reduce the temperature by 40%-60% in 24-bunch mode and between 60% and 80% in hybrid mode. Hence, while diffusion is not neglible, it does not appear to provide significant temperature reductions. Interestingly, scraper damage was more prominant for the 24-bunch-mode beam loss, which qualititively agrees with the diffusion mode predictions.

MATERIAL ASSESSMENT

Our purpose is to safely dump the circulating charge in the SR in case of a machine protection system (MPS) trip or some other sudden beam loss event. Presently, the preferred method is to passively absorb the beam in a scraper that also acts as a beam dump.

We address the choice of appropriate scraper material by considering the ratio of thermal stress to yield stress for a given heat load [4]. At the same time, we recognize that the

Copyright © 2013 CC-BY-3.0 and by the respective authors

heat load for a given irradiation also depends on the material chosen. Material properties affect heat loading because bremsstrahlung is the primary energy loss mechanism for high-energy electrons. The generation of bremsstrahlung radiation is roughly proportional to ρZ^2, where ρ and Z are the density and atomic number of the exposed material, respectively. In addition, our design must live within an allowable footprint in the existing SR.

Thermal stress may be expressed as

$$\sigma_T = E_Y \alpha \Delta T, \tag{2}$$

where E_Y is Young's Modulus of Elasticity, α is the thermal coefficient of expansion, and ΔT is the temperature rise defined in Eq.(1). We define the thermal stress parameter g as

$$g = \frac{E_Y \alpha \Delta T}{\sigma_y}, \tag{3}$$

where σ_y is the yield stress. The stress parameter can be written as

$$\begin{aligned} g &= \frac{E_Y \alpha E_T A_w}{\sigma_y C_{mol} \rho V} \\ &= \frac{E_Y \alpha A_w}{\sigma_y C_{mol}} k_B S_{pc} \frac{N_e}{\pi r_b^2}, \end{aligned} \tag{4}$$

where E_T is the total deposited energy, ρ is the density, V is the volume, k_B is Boltzmann's constant, S_{pc} is the collisional stopping power [5], and r_b is the radius of the beam. We assume the lost charge is uniformly distributed within r_b. In Eq.(4) we used the thin target approximation [6] $E_T \approx \frac{S_{pc}}{S_{pr}} N_e W_o \frac{\rho}{X_o} \Delta z$; also, $S_{pr} = \frac{W_o}{X_o}$, and $V = \pi r_b^2 \Delta z$. S_{pr} is the radiative stopping power, W_o is the electron energy, and X_o is the radiation length.

In Eq. (4), we have separated the material-related terms from the beam terms. S_{pc} is a function of both but varies slowly with atomic weight at 7 GeV. In Table 1, the g-ratio is calculated for several materials assuming $N_e = 2.3 \times 10^{12}$ and $r_b = 0.1$ mm.

Table 1: Material Properties and Thermal-to-Yield Stress Ratio. PG and PB represent pyrolytic graphite and polybutene 1300; both are assumed to be composed entirely of carbon.

Mat.	E_Y (GPa)	$\alpha \times 10^6$ (K^{-1})	C_{mol} $\left(\frac{J}{mole\text{-}K}\right)$	σ_y (MPa)	g
Be	248	12.4	16.44	345	11.6
PG	20.7	0.5	8.28	82.7	0.48
PB	6.9	4	10.08	37.9	2.30
Al	69	25	24.20	310	15.8
Ti	116	8.5	25.06	951	4.72
Cu	110	16.5	24.44	220	49.6
W	345	14.4	24.27	1510	49.6

Table 1 indicates only pyrolytic graphite exhibits a g-ratio less than 1; whereas, copper and tungsten show the largest g. The g-ratio for titanium, though relatively high, is still an order of magnitude lower than for copper. We note that based on the results in Table 1, one might conclude that copper and tungsten should suffer roughly equal damage; however, from direct observations, we know this not the case. In the actual scraper, the damage to the W block was much more severe than to the Cu one due in large part to the shorter radiation length and higher density in the W. Part of this difference may also be due to a horizontal offset in the tungsten that had its outboard surface 0.8 mm closer to the beam than that of the copper surface.

DISCUSSION

In the case of a 24-bunch beam dump, peak power densities are on the order of 10^{15}Wcm^{-2}. Fast beam loss diagnostics [7] indicate that shorter dumps usually found with 24-bunch fill patterns are more destructive. Using higher-melting-temperature, lower-Z materials while moving the beam with a kicker should increase the scraper damage threshold. Work is now underway to build a new scraper that will reduce both impedance and the generation of higher-order cavity modes. Of the 2600 J stored in the beam, only 760 J are deposited in the scraper after 1.24 X_o and 7.26 X_o of Cu and W, respectively. Reducing the scraper length in terms of X_o means the device will absorb even less energy and act more as a spoiler. Simulations of this approach show promise both in terms of survival of the spoiler and protection of downstream insertion devices.

ACKNOWLEDGMENT

Thanks to R. Soliday for assistance with data analysis scripts.

REFERENCES

[1] N.V. Mokhov, "The Mars Code System User's Guide," Fermilab-FN-628 (1995); http://www-ap.fnal.gov/MARS/; N.V. Mokhov, S.I. Striganov, "MARS15 Overview," AIP Conf. Proc. 896, pp. 50-60 (2007).

[2] M. Borland, Advanced Photon Source ANL/APS/LS-287 (2000).

[3] M. Borland, private communication, September 2011.

[4] D. Walz, private communication, June 2011.

[5] M. J. Berger et al., "Stopping powers for electrons and positrons," ICRU Report 37 ICRU, Washington, DC, 1984; http://physics.nist.gov/PhysRefData/Star/Text/intro.html

[6] R. H. Thomas et al., *Radiation Protection for Particle Accelerator Facilities*, NCRP Report 144, National Council on Radiation and Protection and Measurements, Bethesda, MD, 2003, p. 44 (2003).

[7] J. C. Dooling and M. Borland, "Simulation and Measurement of Beam Loss in the Narrow-Gap Undulator Straight Section of the Advanced Photon Source Storage Ring," IPAC'12, New Orleans, MOEPPB013, p. 107 (2012); http://www.JACoW.org

Copyright © 2013 CC-BY-3.0 and by the respective authors

ANDROID APPLICATION FOR ACCELERATOR PHYSICS AND ENGINEERING CALCULATIONS

M. Borland *

Abstract

Smartphones and tablets are increasingly capable computational devices, with fast processors and high-resolution displays. They are also nearly ubiquitous, suggesting that they can support the need of physicists and engineers to perform quick calculations in situations where using a full-blown simulation is not necessary or expedient. In this paper, we report on the design, features, and capabilities of an Android application inspired by these ideas. The application is called "TAPAs," which stands for Toolkit for Accelerator Physics on Androids. As the name—meant invoke the popular snacks of Spanish cuisine— suggests, the application provides a varied selection of calculations for electron storage rings, electron linear accelerators, electron guns, free-electron lasers, undulator design, synchrotron radiation, and engineering. The calculations are organized into separate sub-applications, which share input values to allow performing related calculations without re-entering data. The application is free of advertising and is available free of charge on the Google Play store.

INTRODUCTION

Physicists and engineers have long needed the ability to perform quick "back of the envelope" calculations. This need arises during discussions, meetings, and conferences, when running a simulation code is not possible or would take too long. It also arises in day-to-day work as one explores ideas at one's desk. The ability to perform a quick, reasonably accurate calculation can sometimes make all the difference between being productive and pursing a dead-end idea.

Such calculations may be performed mentally, with a pad and pencil, or with a hand-held calculator. Depending on one's ability to remember the appropriate equations, one might use a published handbook, memorized equations, or a "cheat sheet." In the not-to-distant past, it was not uncommon to have a programmable calculator that facilitated common calculations. At present, one is more likely to have a smartphone or tablet close by than a programmable calculator. Hence, it makes sense to develop smartphone or tablet "apps" to address the need for quick calculations.

Inspired by these ideas, we developed an Android application that performs a number of useful calculations of the sort that commonly come up in day-to-day work. The Android platform was chosen for its open-source nature and the low cost of entry for devices and development. Unlike other smartphone platforms, the Android Software Development Kit (SDK) is free and available for essentially all platforms, which allowed using Linux for development.

We used the Eclipse Integrated Development Environment (IDE), which is advantageous in that it helps one quickly learn both the Java language and the specific methods provided by Android. The web contains many resources, such as Android tutorials and user forums (e.g., StackExchange).

The application is called TAPAs, which stands for "Toolkit for Accelerator Physics for Androids" and also is meant to bring to mind the popular snacks of Spanish cuisine. The application is free of advertising and is available free of charge on the Google Play store.

SOFTWARE DESIGN

Those who are uninterested in software design may wish to skip this section, as it has little to do with how the application is used or what it can do. This section also assumes some familiarity with Android development.

The root activity of the application, MainActivity, is an extension of the ListActivity class, which presents a set of choices as a simple vertical list. In addition, MainActivity provides pop-up dialog using AlertDialog that acquaints users with recent changes. The SharedPreferences facility is used to remember the major and minor version of the last invocation, so that the pop-up dialog appears only on the first invocation of a new version. Finally, MainActivity loads a set of name/value pairs into a hash table, which provides default values for entries in the various calculations. As calculations are used, the values in the table are updated so that other applications have access to the new data. The hash table is part of a class that is implemented as a "static singleton," which means that there is only one instance of the class and it is shared by all methods that attempt to instantiate the class.

Below the main list are a series of sublists that are also instances of ListActivity. The activities in each sublist are implemented using an ActivityWithMenu class derived from the Activity class. As the name suggests, this new class provides an activity class with a predefined menu. This menu is used to control some basic settings of the application. The settings are saved between invocations and shared among activities using the SharedPreferences class. The widgets for each activity are embedded in a vertically-scrolled list, which helps in accommodating various screen sizes.

Individual calculation activities typically consist of a list of numerical entry and output widgets, in some cases accompanied by graphics. The numerical entry widgets use the EditNumber class, which extends EditText. This class provides two entry methods, one being a simple numerical

* michael.d.borland@gmail.com

Copyright © 2013 CC-BY-3.0 and by the respective authors

keypad and the other being a scientific calculator keypad. The latter provides the ability to perform calculations on quantities in the entry widgets, which can then be submitted as the new value for the entry widget used to invoke the calculator. EditNumber also includes a facility to limit the range of entries in order to prevent invalid calculations, as well as methods for setting, retrieving, and formatting numerical quantities. Values are stored to full precision even if they are displayed to partial precision, which helps preserve the consistency of displayed values, something that is not possible with the basic EditText class.

Calculation outputs are displayed using the NumberView class, which extends TextView. Like EditNumber, it provides storage, retrieval, and formatting of numerical values. The font size for the EditNumber and NumberView classes is under user control, which helps to accommodate screens of varying sizes and resolutions. We also extended the TextView and Button classes to make a ScaledTextView and ScaledButton classes, to provide the same control.

The structure of the code is such that it is straightforward to add new menus and calculations. The most time-consuming part is coding the XML file that specifies the graphical appearance of the screen.

FEATURES AND CAPABILITIES

Upon starting TAPAs, one is greeted by a simple list of topics. Clicking on one of these topics brings up a list of related calculations that are available for that topic. Often the calculations within a topic will share certain input values (e.g., the beam energy), so that changing it one calculation will change it in the others. In addition, *computed* values from one calculation are often shared with other calculations. This allows using the calculations in a coordinated fashion, which is why we used the word "toolkit" in the name.

Space does not permit a full account of the capabilities of TAPAs, which as of version 1.42 supports 40 different calculations. Instead, we will list the available calculations and highlight a few to give a flavor of what's available. In addition, space does not permit showing the equations used in the calculations or citing all of the original sources; we hope to do this in a future publication. Many of the calculations are based on formulae found in popular references [1, 2, 3, 4].

The **Electron Storage Rings** menu provides scaling of electron storage rings with size and energy; longitudinal dynamics, e.g., rf bucket parameters; harmonic number optimization; short-pulse x-rays with paired [5], or single crab cavities; tune resonance diagrams; top-up and swap-out calculations; gas scattering lifetime; and quantum lifetime.

The **Undulators** menu provides calculations of photon energy or wavelength from undulator parameters, and vice-versa; maximum field or K as a function of gap and period for hybrid permanent magnet and superconducting undulators; undulator optical effects; and undulator orbit effects. The **Synchrotron Radiation** menu provides energy, wavelength, power, and flux calculations for bending magnets, wigglers, and undulators.

The **Electron Linac** menu provides calculations of magnetic bunch compression; coherent synchrotron radiation effects in bending magnets [6, 7]; alpha magnets [8, 9]; charge, current, and beam power; and beam energy and rf power for SLAC-type linacs. The **Electron Guns** menu provides calculations of Richardson's Law, Child's Law, thermal emittance [10], and photocathode intrinsic emittance [11]. The **Free Electron Laser** (FEL) menu provides FEL calculations based on the one-dimensional equations [12] and Ming Xie's parametrization [13].

The **Electromagnetism** menu provides calculations of skin depth for nonmagnetic materials; cutoff frequency and attenuation for rectangular waveguide; and frequencies of pillbox cavity modes. The **Engineering** menu provides calculations for iron dominated magnet design; properties of dipole magnets and trajectories in dipoles; analysis of one-dimensional static heat flow; and estimates of temperature rise in cooling water.

The **Particle Passage Through Matter** menu provides calculations of radiation length, multiple Coulomb scattering, and brehmsstrahlung for electrons and protons in naturally-occurring elements [14].

The **APS-Specific Calculations** menu provides two calculations that are specific to the Advanced Photon Source (APS), namely, the single-bunch accumulation limit based on the impedance model [15] and the bunch length as a function of current based on a fit to measured data.

As a detailed example, Figure 1 shows the screen for one of the most-used calculations, namely, scaling of electron storage rings. This applies mostly well-known (e.g., [16]) scaling rules to allow quickly estimating equilibrium emittance, energy spread, energy loss per turn, etc., as a given light source storage ring design is scaled in number of cells and beam energy. One can use this application to quickly determine that scaling the 20-sector MAX-IV storage ring [17] ring to 40 sectors would give a ring size of APS which, at 7 GeV, would have an emittance of 222 pm. While most of the calculations are, as in this example, straightforward lists of inputs and outputs, some are more colorful, such as the resonance diagram shown in Figure 2.

Often the user may wish to perform additional calculations prior to entering a value, perhaps based on other values present in the interface. This is supported by an RPN-calculator-based entry dialog, shown in Figure 3. In many instances this dialog includes a menu that allows the pushing quantities from the interface onto the stack. Upon exiting the calculator interface, the top of the stack is placed into the entry box in question. To prevent invalid calculations, the calculator interface is sensitive to the valid return values for the quantity being entered, and will refuse to close if an invalid value (e.g., a non-positive value for the beam energy) is given.

CONCLUSIONS

The cost- and ad-free TAPAs application for Android devices provides a number of quick, convenient calculations

Copyright © 2013 CC-BY-3.0 and by the respective authors

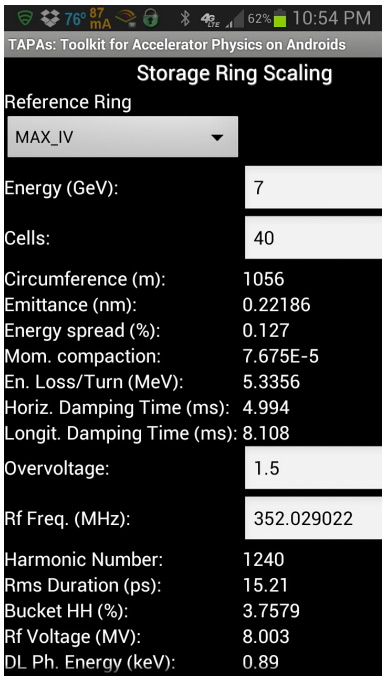


Figure 1: Electron storage ring scaling calculation.

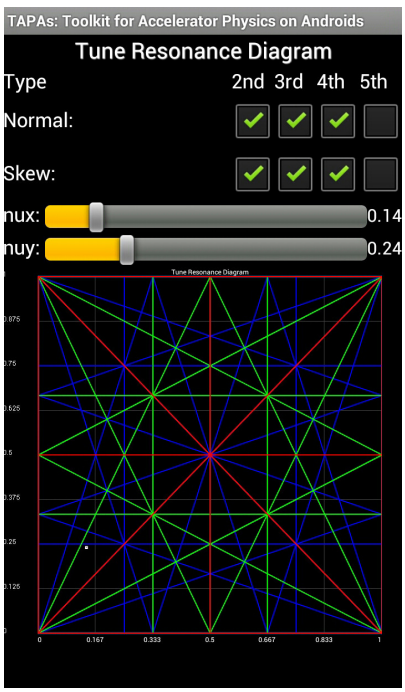


Figure 2: One of TAPAs' more colorful displays.

for use in back-of-the-envelope estimates and for analysis that would typically be performed with a handbook and calculator. The author hopes that it will prove useful and encourages users to send comments, suggestions, and bug reports to michael.d.borland@gmail.com.

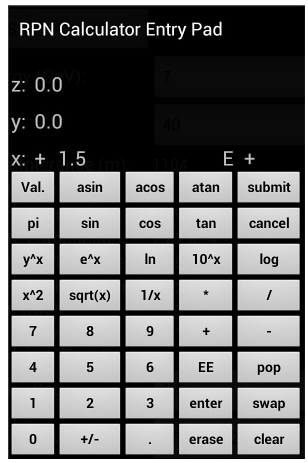


Figure 3: RPN-calculator based entry dialog.

Figure 4: QR code for obtaining TAPAs from the Google Play store.

REFERENCES

[1] A. W. Chao and M. Tigner, editors. Handbook of Accelerator Physics and Engineering.

[2] H. Wiedemann. Particle Accelerator Physics, 2nd ed., volume I. Springer, 1998.

[3] J. Murphy. Technical Report BNL-42333, (1989).

[4] A. Thompson et al. Technical Report LBNL/PUB-490, (2009).

[5] A. Zholents et al., NIM A, **425**, 385, (1999).

[6] E. L. Saldin et al., NIM A, **398**, 373, (1997).

[7] M. Borland, PRSTAB, **4**, 070701, (2001).

[8] H. A. Enge, Rev. Sci. Instr., **34**, 385, (1963).

[9] M. Borland. A High-Brightness Thermionic Microwave Electron Gun. PhD thesis, Stanford University, (1991). SLAC-402.

[10] J. Lawson. The physics of charged particle beams. 1988.

[11] W. Graves et al., PAC 2001, (2001).

[12] Z. Huang and K.-J. Kim, Phys. Rev. ST Accel. Beams, **10**, 034801, (2007).

[13] M. Xie, PAC 1995, 183 (1995).

[14] J. Beringer et al., Phys. Rev. D, **86**, 010001, (2012).

[15] Y.-C. Chae et al., PAC 2007, Albuquerque, NM, 4336-4338 (2007).

[16] H. Wiedemann. Particle Accelerator Physics II. Springer, Berlin, 1999.

[17] S. C. Leemann et al., Phys. Rev. ST Accel. Beams, , 120701, (2009).

Copyright © 2013 CC-BY-3.0 and by the respective authors

CRYOMODULE PERFORMANCE OF THE MAIN LINAC PROTOTYPE CAVITY FOR CORNELL'S ENERGY RECOVERY LINAC*

N. Valles†, R. Eichhorn, F. Furuta, M. Gi, D. Gonnella, D. Hall, Y. He, V. Ho, G. Hoffstaetter, M. Liepe, T. O'Connell, S. Posen, P. Quigley, J. Sears and V. Veshcherevich
Cornell University, CLASSE, Ithaca, NY 14853, USA

Abstract

Energy Recovery Linacs (ERLs) require strong damping of higher-order modes in main linac cavities to avoid beam loss from beam break-up effects. In addition, the cavities need to have very high intrinsic quality factors to minimize the size of cryogenic plants in CW cavity operation. We present world record results for a fully equipped multicell cavity in a cryomodule, reaching intrinsic quality factors at operating accelerating field of Q_0(E =16.2 MV/m, 1.8 K) $> 6.0 \times 10^{10}$ and Q_0(E =16.2 MV/m, 1.6 K) $= 1.0 \times 10^{11}$, corresponding to a residual surface resistance of 1.1 nΩ, which is more than three times better than the Q_0 design specification.

INTRODUCTION

Cornell University is developing a 5 GeV energy recovery linac (ERL). The SRF main linac of this ERL is designed to support high current beams, each at 100 mA with 77 pC bunch charge (one beam is accelerated and the returning beam is decelerated in the main linac), with small emittance.[1] These demanding beam requirements set tight constraints for electromagnetic and higher-order mode properties of the 1.3 GHz main-linac cavities.[2, 3] In addition to these RF properties of the cavity, the feasibility of operating a 5 GeV SRF linac in continuous wave mode requires the main-linac cavities to have 1.8 K quality factors of at least 2×10^{10} at E_{acc}=16.2 MV/m.[1]

Eventually, six 7-cell cavities along with other instrumentation will be commissioned within a prototype main linac cryomodule (MLC).[4] The precursor to the MLC is the horizontal test cryomodule (HTC) which can contain a single 7-cell cavity, two higher-order mode (HOM) absorbers and other experimental instrumentation.

The first prototype cavity has been fabricated,[5] and is being qualified in the HTC through several stages of hardware implementation. By performing measurements at various stages of implementation, the effects on the quality factor and higher-order mode spectrum can be characterized systematically, leading to tight control of the performance of the structure. In total, there are three verification stages, which have been discussed elsewhere.[6] The instrumentation effecting fundamental mode performance is summarized in Table 1.

Table 1: Key Elements Affecting the 7-cell's HOM Spectrum Incorporated in Each Iteration of the Horizontal Test Cryomodule Experiments. The fundamental mode couples to the on-axis input coupler with $Q_{ext} = 9 \times 10^{10}$ and the high-power coupler with $Q_{ext} = 5 \times 10^7$.

Stage	RF input method	HOM absorbers
HTC-1	On-axis coupler	none
HTC-2	High-power input coupler	none
HTC-3	High-power input coupler	2 SiC absorbers

Meeting gradient and quality factor specifications in each of these tests demonstrates the feasibility of the all the main systems needed for the MLC.

This paper details the final results of the three HTC experimental runs, focusing on the fundamental mode properties. Investigations of the higher-order mode spectrum are presented elsewhere.[7] We present quality factor measurements for all three tests and demonstrate that the cavity fabricated at Cornell exceeds design specifications.

METHODS

Cavity Preparation and Cryomodule Assembly

The construction[8] and preparation of the prototype main-linac 7-cell cavity, ERL 7.1, for HTC-1 has been described elsewhere.[5] An overview is presented here.

Following fabrication, ERL 7.1 received a 10 μm BCP, a 16 hour high-pressure rinse (HPR), was then cleanly assembled and baked at 120°C for 48 hours. The cavity was vertically tested, and found to exceed quality factor and gradient specifications. The cavity's Q vs E curve only showed mild medium field Q slope and reached 26 MV/m, limited by available RF power.

Following the successful vertical test, while maintaining a clean RF surface, the cavity was outfitted with a helium jacket, and installed in a horizontal test cryomodule for HTC-1. An axial RF coupler, (fundamental mode $Q_{ext} = 9 \times 10^{10}$) similar to the one used in the vertical test, was installed on the end of the cavity.

At the next stage of the tests, HTC-2, a high-power side mounted RF input coupler was added to the HTC-1 assembly. This antenna couples to the fundamental mode with $Q_{ext} = 4.5 \times 10^7$, so is strongly over coupled.

The final stage of the HTC tests, HTC-3, added beamline higher-order mode absorbers at each end of the cavity.

* Work supported by NSF Grants NSF DMR-0807731 and NSF PHY-1002467
† nrv5@cornell.edu

Copyright © 2013 CC-BY-3.0 and by the respective authors

To install these absorbers, HTC-2 had to be disassembled to allow removal of the axial coupler. After HTC-2, the cavity was reprocessed with a 5 μm BCP, 120°C bake, and an HF rinse to mitigate field emission in the HTC-2 experiment. HOM absorbers and the high-power RF coupler were installed and the cryomodule tested in its final configuration.

Experimental Procedure

The HTC cavity tests had three main goals: to measure the quality factor vs accelerating field (Q_0 vs E) of the cavity, to determine the quench field of the cavity, and to qualify each major stage of the assembly.

For each HTC experiment, the cavity was slowly cooled from 300 K to 1.8 K while maintaining a small temperature gradient (< 0.3 K) across the cavity in an attempt to prevent thermal-electric currents from trapping flux and degrading the quality factor of the cavity.[6] In HTC-1 the Q_0 vs E points were measured through standard RF methods–utilizing two RF probe ports[9]–and cryogenically by using the helium boil-off rate to determine the power dissipated from the cavity. Quality factor measurements in HTC-2 and HTC-3 required cryogenic methods to determine the performance of the structure, since the strongly over coupled high-power input coupler would not yield accurate Q_0 measurements.[5]

After measuring the cavity's quality factor at 1.6, 1.8 and 2.0 K, the quench field was determined and a Q_0 vs E curve was remeasured to determine whether quenching had a deleterious effect on the quality factor. Subsequently, to return the cavity to its original superconducting state, the cavity temperature was cycled to above its critical temperature, T_c, and the quality factor remeasured.

The BCS losses of the superconductor can be calculated with SRIMP, a code by J. Halbritter, which in turn can be used to determine material properties of the cavity from the temperature dependence of the quality factor.

RESULTS

HTC-1

Q_0 vs E measurements were performed after several thermal cycles.[6] RF and cryogenic measurements of Q_0 were in agreement. The quench field was 17.3 MV/m, and prior to quenching the cavity produced radiation at about 1 R/hr. After the 100 K cycle, the residual resistance of the cavity was ~5.8 nΩ.[5] Thermally cycling the structure led to a 50% increase in Q_0 at the operating temperature, and was maintained even after an intentionally fast cooldown.

After thermally cycling, the cavity exceeded the design specification of $Q(16.2\text{ MV/m}, 1.8\text{ K}) = 2 \times 10^{10}$ by 50%. The cavity set a world record for quality factor of a multicell cavity installed in a horizontal test cryomodule reaching $Q(5.0\text{ MV/m}, 1.6\text{ K}) = 6 \times 10^{10}$, as shown in Fig. 1.

HTC-2

In HTC-2, the quality factor was again measured over several rounds of thermal cycling, described in [6]. After the first 15 K thermal cycle the mid-field Q_0 improved ~50% at both 1.6 K and 1.8 K.[6] Administrative limits prevented quench field determination.

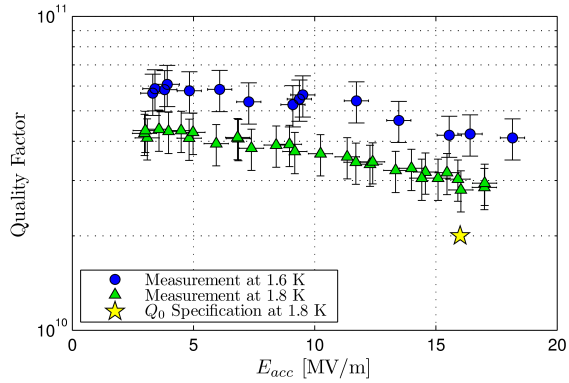


Figure 1: Q_0 vs E_{acc} measurement of ERL 7.1 in HTC-1.

Thermal cycles to 8.9 K and to room temperature did not increase Q_0 in HTC-2. This suggests that the most benefit for thermal cycles is obtained from peak temperatures in the region between 9.0 and 100 K.

In HTC-2, ERL 7.1's met the design specifications, but was limited by field emission coming from the end cell far from the high power coupler. The final Q_0 vs E plot is shown in Fig. 2

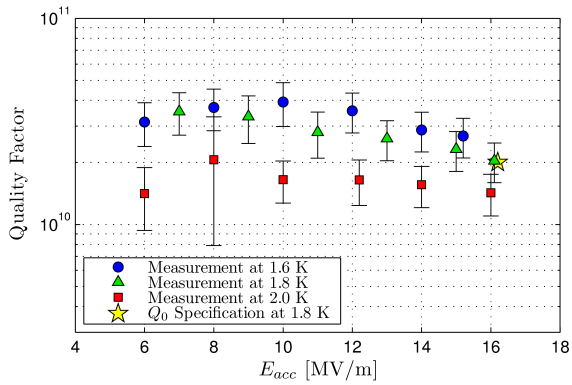


Figure 2: Q_0 vs E_{acc} measurement of ERL 7.1 in HTC-2.

HTC-3

The final stage of the HTC experiments included all the components and instrumentation that would be used in a full 6 cavity cryomodule for Cornell's Energy Recovery Linac. Initial measurements of cavity's quality factor were performed at 1.6, 1.8 and 2.0 K. Q_0 vs E measurements after the first cooldown exceeded the design specification,[6] but a thermal cycle was performed to determine whether or not additional improvement in Q_0 was possible. Fig. 3 shows the Q_0 vs E measurements post 10 K thermal cycle.

The prototype cavity ERL 7.1 was measured to have $Q_0(1.8\text{ K}) = 3.6 \times 10^{10}$, $Q_0(1.8\text{ K}) = 6.1 \times 10^{10}$ and $Q_0(1.6\text{ K}) = 1.0 \times 10^{11}$ at the operational gradient of

Copyright © 2013 CC-BY-3.0 and by the respective authors

16.2 MV/m, setting the world record Q_0 for a multicell cavity operating in a horizontal cryomodule.

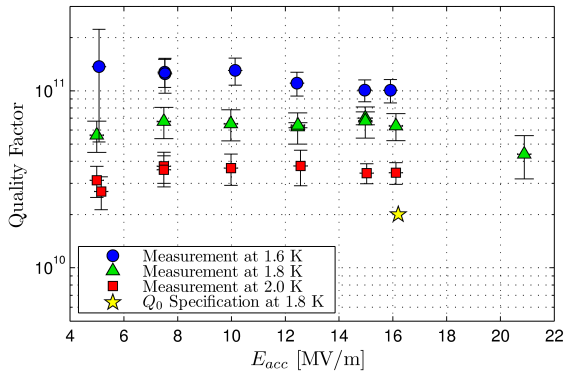


Figure 3: Final Q_0 vs E_{acc} measurement of ERL 7.1 in HTC-3. At the operating accelerating gradient and temperature, the cavity's Q_0 exceeds design specification by a factor of three, reaching 6×10^{10}. Accelerating gradients of 21 MV/m were achieved.

Finally, the superconducting parameters were characterized using SRIMP, finding that the residual resistance after thermal cycling was reduced from $\sim$3 nΩ to a very low value of just $\sim$1 nΩ.[6]

CONCLUSIONS

The main linac cavity exceeded design specifications in all three HTC experiments. Temperature cycling helped to improve the quality factor of the cavity by about 50%, with the most benefit being realized after thermally cycling to low temperatures above T_c.

Measurements of the prototype cavity outfitted with a high power coupler and two beamline HOM absorbers shows exceptional quality factor results at gradients up to 21 MV/m. At 1.8 K, the quality factor specification was exceeded by a factor of three. In addition, ERL 7.1 reached Q_0(16.2 MV/M, 1.6 K)=1.0×10^{11} in a fully outfitted cryomodule in HTC-3, breaking the world record that was set in HTC-1,[10] and demonstrating that very high Q_0 is achievable in horizontal cryomodules.

The HTC experiments demonstrate that extremely high quality factors can be preserved in a fully equipped cryomodule, and Q_0 does not necessarily have to degrade between vertical and horizontal testing.[6] This is clearly demonstrated by Fig. 4, which shows higher quality factors in the HTC-1 experiment than the vertical test, even though no surface treatment was performed between the tests.

Very high values of Q_0 in the HTC experiments are attributed to three factors: First, there are two layers of magnetic shielding in the cryomodule, compared with a single layer in the vertical dewar reducing the ambient magnetic flux in the cryomodule, which leads to a smaller residual resistance. Second, the tightly controlled cooling process of the cavity in the cryomodule minimizes both spatial and temporal gradients across the cavity, reducing flux pinning

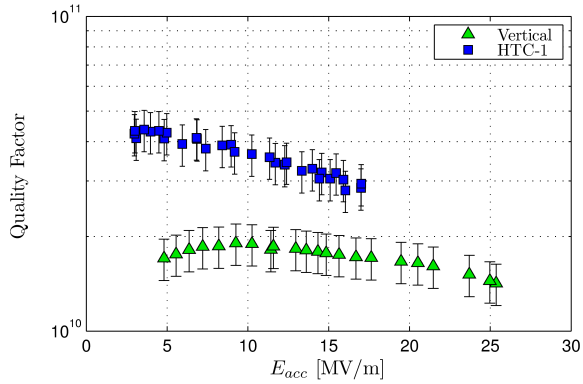


Figure 4: Comparison of Q_0 vs E measurements at 1.8 K of ERL 7.1 in the vertical test and HTC-1. HTC-1 exhibits much higher Q_0 than in the vertical case, though no surface processing was done between the two measurements.

in the superconductor. Third, the combination of HF rinse and a very uniform 120°C bake in a large furnace leads to surfaces having low BCS resistance.

Future work with this cavity will include beam tests in Cornell's Injector Cryomodule in the Fall of 2013. These measurements will use beam to measure the Q_0, R/Q and frequencies of higher-order modes in the HTC.

REFERENCES

[1] J. A. Crittenden, et al. Developments for Cornell's X-ray ERL. In *Proceedings of PAC 2009*.

[2] V. D. Shemelin. Suppression of HOMs in a multicell superconducting cavity for Cornell's ERL. In *SRF 2009*.

[3] N. Valles and M. Liepe. Seven-cell cavity optimization for Cornell's energy recovery linac. In *SRF 2009*.

[4] R. Eichhorn, et al. Design and construction of the main linac cryomodule for the energy recovery linac project at cornell. In *Proceedings of SRF 2013*.

[5] N. Valles, et al. Testing of the main-linac prototype cavity in a horizontal test cryomodule for the Cornell ERL. In *Proceedings of IPAC 2012*.

[6] N. Valles, et al. Record Quality Factor Performance of the Prototype Cornell ERL Main Linac Cavity in the Horizontal Test Cryomodule In *Proceedings of SRF 2013*.

[7] N. Valles, R. Eichhorn, G. H. Hoffstaetter, and M. Liepe. HOM Studies of the Cornell ERL Main Linac Cavity: HTC-1 through HTC-3. In *Proceedings of IPAC 2013*.

[8] V. Shemelin and P. Carriere. Frequency control in the process of a multicell superconducting cavity production. *Review of Scientific Instruments*, 83(4):043304, 2012.

[9] H. Padamsee, J. Knobloch, and T. Hays. *RF superconductivity for accelerators*. Wiley, New York, 1998.

[10] N. Valles, et al. The main linac cavity for cornell's energy recovery linac: Cavity design through horizontal cryomodule prototype test. *NIMPR-Section A*, (0):–, 2013.

Copyright © 2013 CC-BY-3.0 and by the respective authors

FERMILAB MUCOOL TEST AREA CAVITY CONDITIONING CONTROL USING LABVIEW

D.W. Peterson, Fermi National Accelerator Laboratory*, Batavia, IL 60510, USA
Y. Torun, Illinois Institute of Technology, Chicago, IL 60616, USA

Abstract

Automated RF cavity conditioning controls have been implemented in the Fermilab MuCool Test Area using National Instruments LabVIEW. Display of RF parameters, cavity gradient and diagnostic signals are provided for real-time monitoring. Oscilloscope traces and operating parameters are logged automatically. Gradient ramping and cavity breakdown detection allow unattended operation. Key parameters are made available to the Fermilab ACNET system for viewing by users.

SYSTEM OVERVIEW

The MuCool Test Area (MTA) consists of a beamline stub and experimental hall off of the 400 MeV H- section of the Fermilab LINAC [1]. The hall contains power supplies and cryogenics for a 5T superconducting solenoid as well as RF feeds for high power 201 MHz and 805 MHz. Cavity conditioning is currently performed at 805 MHz at up to 13 MW of RF power [2][3][4].

The computer test system consists of a Dell GX620 computer running National Instruments (NI) LabVIEW 2012[5]. Waveforms are acquired with the NI PCI-5105 60 MS/s, 12-Bit, 8-Channel Digitizer/Oscilloscope card. A GPIB bus communicates with the HP E4400B RF Signal Generator, LeCroy 625Zi oscilloscope, and Tektronix DPO7104 oscilloscope.

Triggering of acquisitions is by the RF gate TTL signal from a master timing distribution module. Additional signals into the PCI digitizer card are a diode detected sample of the cavity RF probe signal, a sample of the waveguide reflected power, and an optional signal from a cavity photo detector.

SOFTWARE DESIGN

The MuCool Cavity Test software has evolved over more than six years of activity [6][7]. LabVIEW has been used throughout the process. This latest version has implemented some important new features:

- A simplified user interface with multiple floating front panel windows.
- Cavity waveform analysis during each pulse, including cavity breakdown detection.
- A new cavity tuning algorithm.
- Gradient ramping and breakdown recovery.
- Verbose log files.
- Cavity waveforms are periodically saved to disk and can be viewed later.
- Breakdown events are recorded along with data from preceding and following pulses.
- A few key parameters are available on the ACNET control system.

User Interface

LabVIEW routines are called virtual instruments (VIs). Each VI has a front panel for user interaction and a block diagram that defines the program execution. In the cavity conditioning system the main front panel provides a general view of the cavity signals and pulse status. It also provides a launch point for the cavity conditioning control VIs, such as tuner control and cavity waveform analysis. Figure 1 shows the general flow of the program. Figure 2 shows the layering of various VI front panels. During any given user interaction, the panel of interest can be brought to the foreground or minimized as needed. Additional VIs are available for the user to set the data logging interval and to enter comments into the log file.

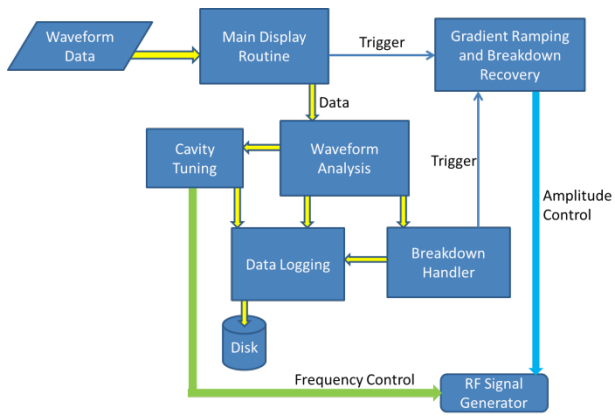


Figure 1: Simplified block diagram of the cavity conditioning program.

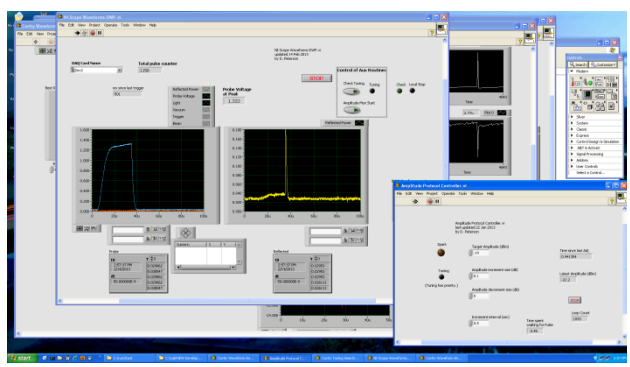


Figure 2: Screen capture of the overall user interface showing the layering of multiple VI front panels.

* Operated by Fermi Research Alliance, LLC, under Contract No. DE-AC02-07CH11359 with the United States Department of Energy

Copyright © 2013 CC-BY-3.0 and by the respective authors

Cavity Waveform Analysis

As the waveforms are acquired by the digitizer card they are passed to Cavity Waveform Analysis VI for all of the measurements, breakdown detection and triggering of the breakdown logging routines.

Measurements on the cavity probe waveform include peak voltage, rise time, fall time, exponential fits of filling time constant and decay time constant, and integrated values of cavity and reflected signals both inside and outside the RF gate time. Figure 2 shows the user waveform display of a normal cavity pulse with the RF gate signal and reflected power signal.

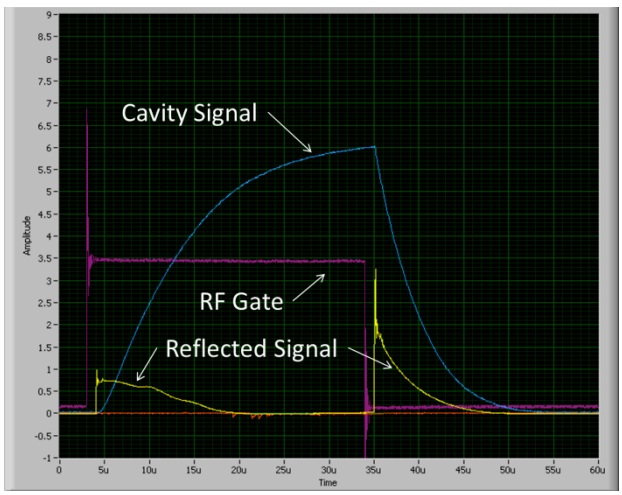


Figure 3: Typical main display showing cavity waveform, RF gate and reflected signal.

Cavity Breakdown Detection

The best way to detect cavity breakdown is to insert a fiber optic cable into the cavity and detect the flash of light when a spark occurs. Figure 4 shows the large light signal during a cavity breakdown event. Unfortunately, not all cavities have been outfitted with optics.

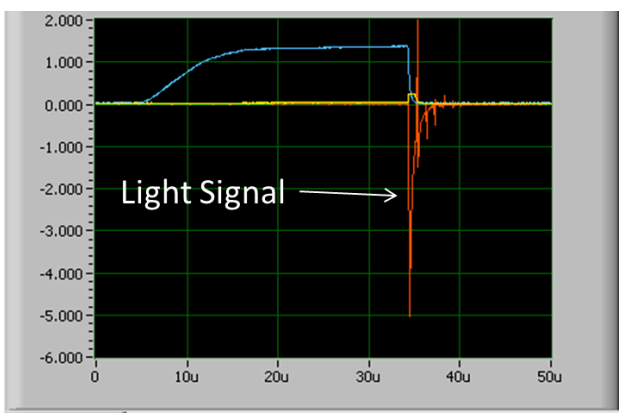


Figure 4: Auxiliary display showing pronounced light signal during a cavity breakdown event.

A reliable alternate method involves measuring the 90% to 10% fall time of the cavity probe waveform and triggering the breakdown capture VIs for any fall time shorter than a user settable trip value. Figure 5 shows a cavity breakdown event with the extremely steep cavity waveform falling edge. The reflected power spikes momentarily until an external high speed circuit detects the event and turns off the RF drive signal before the end of the RF gate. A typical 90% to 10% fall time in recent tests is approximately 12 µs for normal operation and less than 1 µs during breakdown.

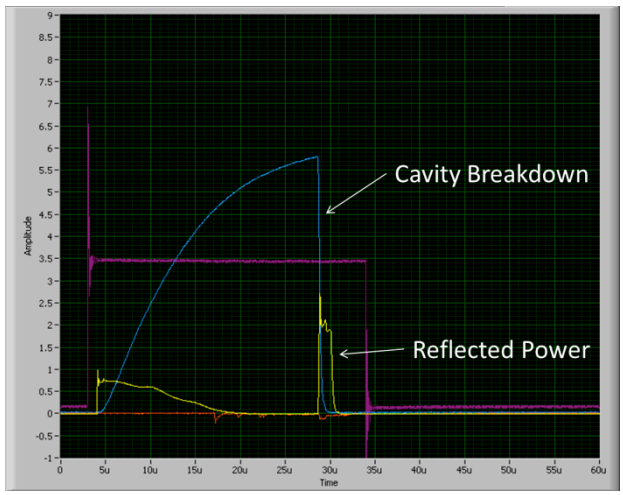


Figure 5: An example of a cavity breakdown event with the accompanying spike in the reflected power.

Cavity Tuning Algorithm

During normal cavity conditioning, enough power is dissipated in the walls of the cavity to raise the temperature and change the resonant frequency. Since the present test cavities do not have any means of compensating for this effect, the RF drive frequency must change to follow the cavity resonance. Previous versions of the software have used a gradient search to determine where the peak resonance occurs. Measurement noise when far off resonance often resulted in the algorithm taking many steps to converge or occasionally failing to converge.

The improved algorithm uses a sequence of n steps to move a predetermined distance, Δf, each side of the present center frequency while also recording either the cavity amplitude response or the ratio of integrated cavity probe signal vs. reflected signal inside the RF gate. The probe/reflected ratio has proven to be a very effective measurement of cavity performance. For efficiency, the step sequence takes the odd numbered steps going down in frequency and even numbers steps going up in frequency. For example, a complete step sequence using 5 steps each side of the center frequency, f_0, would be:

$f_0-\Delta f/n$, $f_0-3\Delta f/n$, $f_0-5\Delta f/n$, $f_0-4\Delta f/n$, $f_0-2\Delta f/n$, f_0, $f_0+2\Delta f/n$, $f_0+4\Delta f/n$, $f_0+5\Delta f/n$, $f_0+3\Delta f/n$, $f_0+\Delta f/n$, f_0.

After the steps are complete the signal vs. frequency array is passed to a Gaussian peak fitting routine which returns the least square fit to the measurements. The algorithm then moves the signal generator frequency by steps of $2\Delta f/n$ to the new calculated center frequency and the tuning cycle is complete. Typical search values in recent cavity testing have been $\Delta f = 10$ kHz and n=10.

Copyright © 2013 CC-BY-3.0 and by the respective authors

Gradient Ramping and Breakdown Recovery

An important part of cavity conditioning is the ability to push the cavity gradient to high field yet not cause serious damage to the cavity surface. The Amplitude Control routine has user settable parameters for amplitude increment step, step interval, and amplitude decrement if breakdown occurs. Amplitude increment occurs at the step interval except when cavity tuning is active. Amplitude decrement occurs immediately upon detection of a cavity breakdown event. Typical settings are an amplitude increment of 0.04 dB, a step interval of 10 seconds, and an amplitude decrement of 3.0 dB if a breakdown occurs.

Recording to Disk

When the LabVIEW program is started at the beginning of each cavity conditioning "Run", it increments the official run number and creates a file folder with the current date if one is not already present. A text log file is created with the date and run number in the file name. Digitizer waveforms are also stored in a file in the same folder. Due to the possibility of multiple runs in one day or one run spanning multiple days, it was decided to keep the log and waveform file sizes manageable by automatically creating a new folder at 00:00:00 each day of running and opening new files with the appropriate run number.

The log file includes time stamped data such as user comments, manual and automatic amplitude setting changes, periodic captures of cavity waveform parameters, and cavity waveform parameters during breakdown events.

Cavity waveform files are recorded periodically and at each breakdown event. A utility program has been written which provides quick viewing of waveforms in a movie format. The user has the option to single step though capture frames and to send the frame image to a graphic file in .png format or send the waveform data to a comma separated spreadsheet file.

The oscilloscopes trigger on every pulse and can also be commanded to write trace information to their internal hard drives periodically and at each breakdown event.

An additional background utility is constantly recording the digitizer waveform data in a circular buffer of 9 elements. When a breakdown event occurs, the buffer continues for 4 more pulses and then the entire buffer is written to a waveform file. This allows the user to view cavity waveforms surrounding the breakdown event.

Writing to ACNET

A background VI uses XML-RPC to write total cavity pulses, number of breakdown events, RF signal generator frequency and amplitude, cavity peak voltage and other parameters out to the Fermilab ACNET control system at a 1 Hz rate [8]. ACNET parameters are easily viewed on the internet and utilities are in place for automatic notification if values go out of user defined tolerances.

SUMMARY AND PLANS

The continued use of LabVIEW has enabled a rapid and efficient upgrade to the MuCool 805 MHz cavity conditioning controls. New measurement and control routines with automatic recording of cavity performance have permitted long conditioning runs over multiple days and will facilitate testing of other cavity designs [9].

Components are being installed to provide similar cavity conditioning capabilities in the 201 MHz RF systems. In addition to the features implemented in the 805 MHz system, the 201 MHz cavity conditioning system will have active resonance tuning control [10].

ACKNOWLEDGMENTS

The authors would like to thank the cavity conditioning teams not only for their long hours of vigilant service but also for their valuable suggestions for improvements in the software.

REFERENCES

[1] http://mice.iit.edu/mta/

[2] Y. Torun, "Vacuum RF Studies in the MuCool Test Area," All Experimenters Meeting, Fermilab, August, 2010 http://www.fnal.gov/directorate/program_planning/all_experimenters_meetings/special_reports/torun_aem81610.pdf

[3] Y. Torun et al., "Extended RF Testing of the 805-MHz Pillbox "All-Season" Cavity for Muon Cooling," WEPMA17, these proceedings.

[4] B. Freemire et al., "High Pressure Gas-Filled RF Cavities for Use in a Muon Cooling Channel," TUODA1, these proceedings.

[5] http://www.ni.com/labview/

[6] A. Kurup, "Automation of the 805MHz cavity conditioning procedure," MuCool Test Area RF Workshop, Fermilab, August 2007 http://mice.iit.edu/mta/mtarf1/mtarf1_kurup_805automation.ppt

[7] A. Kurup, "An Automated Conditioning System for the MuCool Experiments at Fermilab," IPAC2011, San Sebastián, Spain, September 2011, MOPZ011, p. 844 (2011); http://accelconf.web.cern.ch/AccelConf/IPAC2011/papers/mopz011.pdf

[8] K. Cahill, C. King, "Guide to the Data Acquisition Engine," Accelerator Controls Department, February 2002 http://www-bd.fnal.gov/controls/public/JavaControlsMoreLinks.htm

[9] D. Bowring et al., "RF Design and Characterization of a Modular Cavity for Muon Ionization Cooling R&D," WEPMA18, these proceedings.

[10] L. Somaschini et al., "Tuner System Assembly and Tests for the 201-MHz MICE Cavity," WEPMA03, these proceedings.

Copyright © 2013 CC-BY-3.0 and by the respective authors

SSR1 CRYOMODULE DESIGN FOR PXIE*

T. Nicol#, S. Cheban, M. Chen, M. Merio, Y. Orlov, D. Passarelli, T. Peterson, V. Poloubotko, O. Pronitchev, L. Ristori, I. Terechkine, Fermilab, Batavia, IL 60510, U.S.A,
P. Bhattacharyya, Variable Energy Cyclotron Centre, Kolkata, India

Abstract

Project X is a proposed proton accelerator complex intended to support Fermilab's role in intensity frontier research over the next several decades. It will replace the existing 40-year-old injector complex and add powerful new capabilities to support a large number of experiments in the energy range from 1 to 120 GeV.

Fermilab is planning a program of research and development aimed at testing of critical components. This program, known as the Project X Injector Experiment (PXIE), is being undertaken as a major element of the ongoing Project X R&D program.

PXIE contains two superconducting cavity cryomodules, one utilizing half-wave resonators (HWR), and the other, single spoke resonators (SSR). The first SSR cryomodule, known as SSR1 contains eight cavities and four solenoids in the following order: C–S–C–C–S–C–C–S–C–C–S–C, as well as active steering elements.

This paper describes the design of the SSR1 cryomodule and includes discussions of the system interfaces, vacuum vessel, magnetic and thermal shields, insulating and support systems, cavities, tuners, input couplers, focusing elements, and current leads.

INTRODUCTION

The SSR1 cryomodule will operate with continuous wave (CW) RF power and support peak currents of 5 mA chopped with varying patterns to yield an average beam current of 1 mA. The RF power per cavity at 1 mA average current and 2.2 MV accelerating voltage (β=0.22) should not exceed 4 KW with an overhead reserved for microphonics control.

The current beam optics design for Project X requires that the SSR1 cryomodule contains eight cavities and four solenoids in the following order: C–S–C–C–S–C–C–S–C–C–S–C. Horizontal and vertical dipole correctors are located inside each solenoid. A four-electrode beam position monitor (BPM) is located at each solenoid.

The intent is that this cryomodule has all external connections to the cryogenic, RF, and instrumentation systems made at removable junctions at the cryomodule itself. The only connection to the beamline is the beam pipe itself which will be terminated by "particle free" valves at both ends. Minimizing mean time between failure and repair and in-situ repair of some internal systems are important design considerations in the cryomodule design.

Figure 1 shows the linac layout including the location of the SSR1 cryomodule.

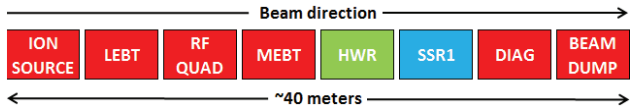


Figure 1: PXIE layout.

CRYOMODULE DESIGN

Eventually, Project X will require several different cryomodule designs for cavities operating at 162.5, 325, 650, and 1300 MHz. The SSR1 for PXIE is the first of these being developed at Fermilab. Details of individual cryomodule components are described below.

Cryogenic Systems and Vacuum Interfaces

There are two ways that cryogenic and vacuum systems are distributed to individual modules in superconducting magnets or cavity strings. Coarse segmentation refers to systems in which the cryogenic circuits and insulating vacuum inside individual cryostats are more or less continuous for long lengths, at least over the length of several cryomodules. Fine segmentation, refers to systems in which the insulating vacuum and the cryogenic circuits are confined to an individual cryomodule, the only connection between modules being the at beam tube. Fine segmentation is the configuration choice for Project X and PXIE cryomodules. Each individual vacuum vessel will be closed at both ends and the cryogenic circuits will be fed through bayonet connections at each cryomodule. Each cryomodule will have its own connection to the insulating vacuum pumping system. Also, each cryomodule will have its own 2 K heat exchanger and pressure relief line exiting near the middle of the module. This configuration provides flexibility in terms of cryomodule replacement and cooldown and warm-up times at the expense of requiring more individual cryogenic connections, cold-to-warm transitions at each end of each cryomodule, and extra space at each interconnect to close the beam tube.

Vacuum Vessel

The vacuum vessel serves to house all the cryomodule components in their as-installed positions, to provide a secure anchor to the tunnel floor, to insulate all cryogenic components in order to minimize heat load to 80 K, 4.5 K, and 2 K, as well as maintain the insulating vacuum. It is 1.219 m (48 inches) in diameter.

Magnetic Shield

Just inside the vacuum vessel, nearly in contact with the inner wall, is a magnetic shield to shield the cavities from the earth's field. Preliminary tests show that a 1.5 mm-thick mu-metal shield at room temperature reduces

* Supported by FRA under DOE Contract DE-AC02-07CH11359
# tnicol@fnal.gov

Copyright © 2013 CC-BY-3.0 and by the respective authors

the residual field inside the cryostat to less than 10 μT. It is likely that separate magnetic shields will be installed around individual magnetic elements to further reduce trapped fields in the superconducting cavities.

Thermal Shield and Multi-Layer Insulation

Each cryomodule will have a single thermal shield cooled with helium gas, nominally at 45-80 K. It is currently envisioned to be aluminum with cooling channels on both sides. Two 15-layer blankets of multi-layer insulation, between the vacuum vessel and thermal shield will reduce the radiation heat load from the room temperature vacuum vessel to approximately 1.5 W/m^2. A 5 K circuit will be available to intercept heat on the input couplers and current leads, but there is no plan to install a full 5 K thermal shield.

Support System

All of the cavities and solenoids will be mounted on individual support posts which are in turn mounted to a full-length strongback located between the vacuum vessel and thermal shield. This enables the entire cavity string to be assembled and aligned as a unit then inserted into the vacuum vessel during final assembly. Presently, the strongback is aluminum, but stainless steel is an option. Maintaining the strongback at room temperature helps minimize axial movement of the cold elements during cooldown, reducing displacement of couplers, current leads, and many other internal piping components.

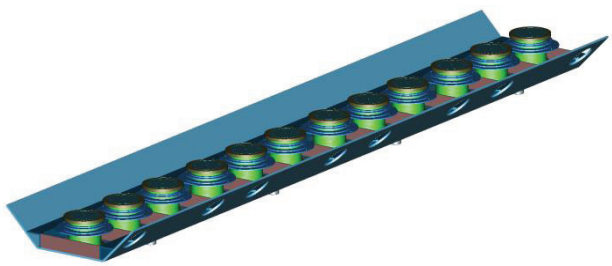


Figure 2: Strongback assembly.

The support posts are similar to supports utilized in SSC collider dipole magnets and ILC and XFEL 1.3 GHz cavity cryomodules. The main structural element is a glass and epoxy composite tube. The tube ends and the intermediate thermal intercepts are all assembled using a shrink-fit technique in which the composite tube is sandwiched between an outer metal ring and inner metal disk [1]. The strongback and support posts are shown in Fig. 2. All the cavities and solenoids are mounted to the support posts using adjustable positioning mechanisms.

Cavity and Tuner

The cryomodule contains eight single spoke, β=0.22, 325 MHz cavities operating in CW mode at 2 K in stainless steel helium vessels. Each has integral coarse and fine tuners that operate through a lever system and push on the cavity end wall. For ease of maintenance, tuner access covers are incorporated into the helium vessel design. The cavity and tuner system is shown in Fig. 3 and described more completely in [2].



Figure 3: Dressed cavity and tuner.

Input Coupler

The input coupler is a 105-ohm coaxial design that supplies approximately 2 kW CW to each cavity in PXIE and ultimately up to 18 kW CW in Project X. The coupler contains a single warm ceramic window. During cryomodule fabrication, the cold section is installed on the cavity in the cleanroom prior to assembly of the string. The warm section is installed from outside the vacuum vessel during final assembly. The inner conductor is solid copper with copper plated bellows to accommodate motion due to misalignment and thermal contraction. The cold end of the outer conductor is 316L-stainless steel. The warm end is copper with copper plated bellows. Heat load estimates don't suggest a significant penalty for not copper plating the outer conductor. A forced-air cooling tube is inserted into the inner conductor after assembly that supplies air to cool the coupler tip. Fig. 4 shows the current coupler design. The input coupler design is described more thoroughly in [3].

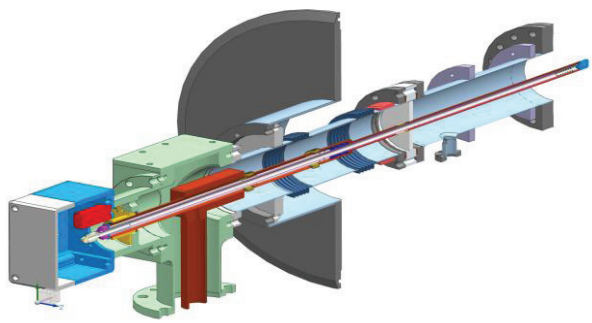


Figure 4: Input coupler assembly.

Current Leads

Each solenoid package contains three magnet coils, the main solenoid, operating nominally at 100 A and two steering correctors each operating nominally at 50 A. A conduction cooled current lead design modeled after similar leads installed in the LHC at CERN is being

Copyright © 2013 CC-BY-3.0 and by the respective authors

developed for use in PXIE [4]. Fig. 5 illustrates the conceptual design for the lead assembly. Thermal intercepts at 45-80 K and 5 K reduce the heat load to 2 K, nonetheless, these current leads represent a significant source of heat at the low temperature end. There will be one lead assembly for each magnetic element.

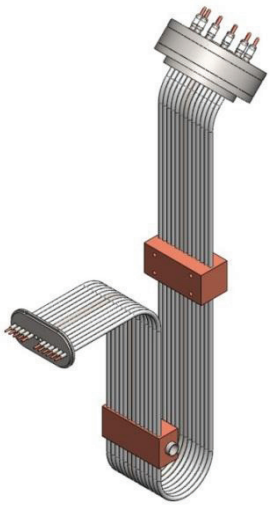


Figure 5: Conduction cooled current lead assembly.

Solenoid and Beam Position Monitor

The four magnet packages in the cryomodule each contain a focusing solenoid and two dipole correctors all operating in a helium bath at 2 K. The Project X lattice provides little room along the beamline for diagnostics either inside individual cryomodules or between adjacent modules. To conserve axial space along the beamline a button-type BPM has been chosen for installation in the SSR1 cryomodules. A total of four will be installed in the cryomodule and tested in PXIE, one at each solenoid. These devices are compact and lend themselves well to incorporation into the solenoid magnet package as shown below in Fig. 6. The bellows at either end of the beam tube allow independent adjustment of each magnet.

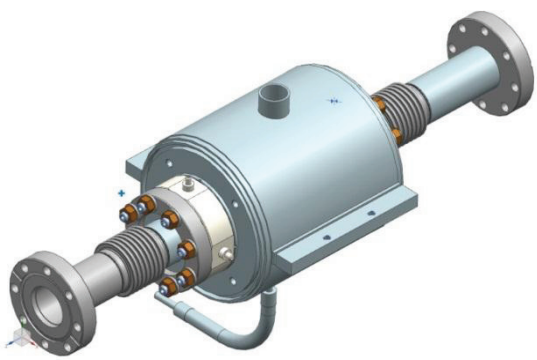


Figure 6: Focusing solenoid and BPM.

Final Assembly

The final assembly of the SSR1 cryomodule for PXIE is shown in Fig. 7.

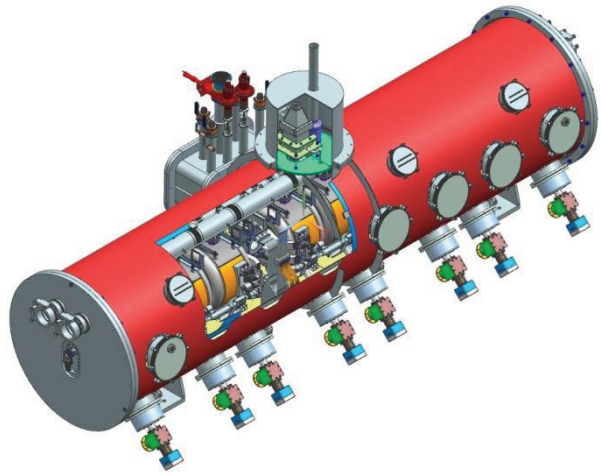


Figure 7: Final assembly.

HEAT LOAD ESTIMATE

Table 1 summarizes the estimated static and dynamic heat loads to each temperature level in the cryomodule assembly from the primary sources.

Table 1: Heat Load Summary for PXIE Cryomodule (W)

SSR1 (8 cav, 4 sol)	**70 K**	**4.5 K**	**2 K**
Input coupler static	42.88	22.56	4.00
Input coupler dynamic	0.00	0.00	2.00
Cavity dynamic load	0.00	0.00	14.24
Support post	33.12	4.32	0.60
Conduction lead assy	85.60	43.60	5.92
MLI (total 70 K + 2 K)	30.54	0.00	1.42
Cold to-warm transition	1.44	0.16	0.02
Total	**193.6**	**70.6**	**28.2**

SUMMARY

The design and modeling of the SSR1 cryomodule for PXIE is nearly complete and detailed drawings for the strongback, supports, and vacuum vessel are ready for procurement. In the coming months further details will be completed with the goal of beginning production of this first 325 MHz SSR1 cryomodule in FY14 [5].

REFERENCES

[1] T.H. Nicol, R.C. Niemann, and J.D. Gonczy, "Design and Analysis of the SSC Dipole Magnet Suspension System", Supercollider 1, p. 637 (1989).
[2] L. Ristori, et al, "Design of Single Spoke Resonators for PXIE", presented at IPAC 2012, paper ID: 2689-WEPPC057.
[3] S. Kazakov, et al, "Main Couplers Design for Project X", presented at IPAC 2012, paper ID: 2523-WEPPC050.
[4] A. Ballarino, "Conduction-Cooled 60 A Resistive Current Leads for LHC Dipole Correctors", LHC Project Report 691 (2004).
[5] S. Nagaitsev (ed.), "PXIE Design Handbook", Fermilab, January 2013.

Copyright © 2013 CC-BY-3.0 and by the respective authors

ENERGY DEPOSITION IN MAGNETS AND SHIELDING OF THE TARGET SYSTEM OF A STAGED NEUTRINO FACTORY*

P. Snopok,† Illinois Institute of Technology, Chicago, Illinois 60616, USA
N. Souchlas, Particle Beam Lasers, Northridge, CA 91324, USA
H.G. Kirk, Brookhaven National Laboratory, Upton, NY 11973, USA
K.T. McDonald, Princeton University, Princeton, NJ 08544, USA
C.T. Rogers, Rutherford Appleton Laboratory, Chilton, Didcot, Oxon, UK
X. Ding, UCLA, Los Angeles, CA 90095, USA

Abstract

In the Neutrino Factory and Muon Collider muons are produced by firing high energy protons onto a target to produce pions. The pions decay to muons which are then accelerated. This method of pion production results in significant background from protons and electrons, which may result in heat deposition on superconducting materials and activation of the machine preventing manual handling. In this paper we discuss the design of a secondary particle handling system. The system comprises a solenoidal chicane that filters high momentum particles, followed by a proton absorber that reduces the energy of all particles, resulting in the rejection of low energy protons that pass through the solenoid chicane. We detail the design and optimization of the system and energy deposition and shielding analysis in MARS15(2012).

INTRODUCTION

The baseline target concept for a Muon Collider or a Neutrino Factory [1] is a free jet of mercury impacted by a 4-MW, 8-GeV proton beam at 50 Hz within a 20-T magnetic field [2]. The magnetic field is produced by a coaxial array of cryogenically cooled superconducting (SC) coils and water-cooled resistive magnets. The superconducting coils are protected from secondary radiation from the target by internal shielding of He-gas-cooled tungsten beads.

The design proton beam energy and power will be approached in stages [2], beginning with a 1-MW, 3-GeV proton beam. A solid carbon target can be used in the initial stage, and replaced with a mercury target module at a later stage when higher beam power is utilized.

The 20-T field on the target is reduced to 1.5 T in a tapering field profile over $\approx$ 5 m, beyond which is an $\approx$ 60-m-long, 1.5-T solenoidal Decay Channel where secondary pions decay to form the muon beam. Roughly 10% of the proton beam power is transported into the Decay Channel [3, 4], mainly via soft protons from breakup of target nuclei, and energetic protons scattered from the beam. These protons would be transported by the Decay Channel into subsequent components of the Muon Collider/Neutrino Factory Front End [5], the Buncher, Phase Rotator, and Ionization Cooling sections. To minimize radiation damage to these components, and to keep their activation low enough that hands-on maintenance is feasible, the secondary protons should be removed from the Decay Channel. This is to be accomplished via a bent-solenoid chicane [6], sketched in Fig.1, in which most proton of energy above 500 MeV are deflected out of the Decay Channel, and by a 10-cm-thick Be absorber which removes most protons of lower energy.

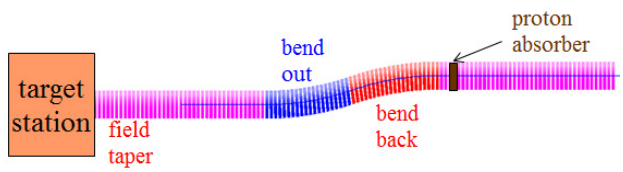


Figure 1: Sketch of the pion-production and Decay Channel, including a chicane to suppress energetic protons and an absorber for soft protons.

ENERGY DEPOSITION STUDIES

The higher-energy particles (mostly protons) which leave the beam in the chicane would pass through the coils of the bent solenoids unless the latter have adequate internal shielding. As for the superconducting coils of the target-system upstream of the chicane, we desire that the maximum energy deposition in the coils be less that 0.1 mW/g to permit an operational lifetime greater than 10 years of 10^7 s. This criterion is taken from studies [7] conducted for the ITER project.

To evaluate the amount of shielding required for the magnets of the Decay Channel chicane, we used a MARS15(2012) [8] simulation with field maps generated by G4beamline [9]. A preliminary version of these studies was reported in [10].

Given the complicated geometry of the chicane, adding tungsten shielding was not straightforward using only MARS extended geometry. However, a recently developed ROOT-based geometry framework [11] for MARS has made the task manageable with a wide variety of basic volumes provided by the ROOT TGeo module. The

*Work supported by the US DOE Contract No. DE-AC02-98CHI10886.
† psnopok@iit.edu

Copyright © 2013 CC-BY-3.0 and by the respective authors

TGeoCtub elementary volume (cut tubes with arbitrary entrance and exit angles) proved to be the most important for seamless shielding. The fact that the volume of each shielding or coil segment can be calculated precisely in ROOT removes the uncertainty intrinsic to MARS Monte-Carlo based volume calculation. Parts of the chicane as defined using ROOT are shown in Fig. 2.

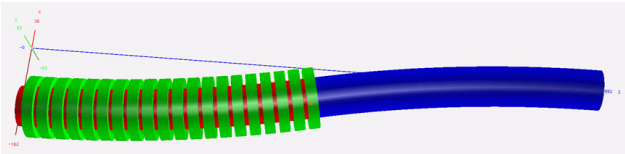


Figure 2: Chicane geometry as defined using ROOT. Red: shield, bend in; blue: shield, bend out; green: solenoidal coils of the bend-in.

In a straight solenoid with uniform field, particles move in helices about the (straight) trajectory of their "guiding center." The magnetic field of a bent solenoid, as in each half of the chicane, is toroidal, and the guiding center undergoes "curvature drift" perpendicular to the plane of the toroidal field [12]. For the 1.5-T field of the decay channel, whose beampipe has 30 cm radius, the curvature drift deforms the shape of the beam into an ellipse with semimajor axis of length 42 cm at the center of the chicane.

In a first study of possible shielding configuration for the chicane, the beampipe was assumed to have radius 42 cm, and the thickness of the tungsten-bead shielding was 35 cm. Figure 3 shows a "horizontal" section of the model of the chicane, together with contours of energy deposition as simulated by MARS15(2012).

The average power deposition in the superconducting coils of the chicane, averaged over azimuth, for the model of Fig. 3 is shown as the blue curve in Fig.4 as a function of position along the chicane, and is everywhere less than the "ITER" limit of 0.1 mW/g. To estimate the peak energy deposition in the coils, the MARS model was segmented azimuthally, leading to the results shown in the blue curve of Fig. 5, where the deposition in a few regions remains above the "ITER" limit.

In a second iteration of the study, only the central 4 m of the chicane was modeled with a beampipe of 40 cm radius, with the outer segments having a beampipe of 30 cm radius, as shown in Fig. 6. The thickness of the shielding in the central portion of the chicane was taken to have 40 cm thickness, while the thickness of the shielding was only 30 cm in the outer portions of the chicane. Contours of energy deposition in the midplane of the chicane are shown in Fig. 6, with the azimuthally averaged energy deposition, and the peak energy deposition, shown in red in Figs. 4 and 5, respectively. The thickness of the shielding downstream of the chicane was only 5 cm, which is not quite adequate, as shown in Fig. 5.

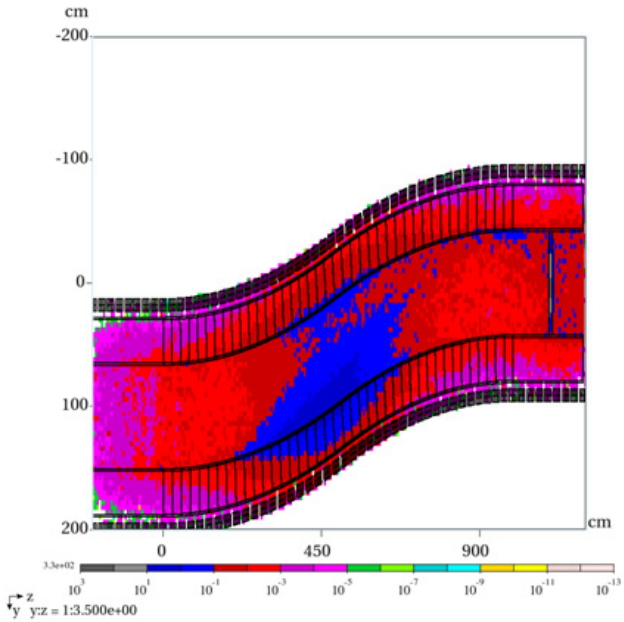


Figure 3: MARS15(2012) simulation of energy deposition in a model of the chicane with beampipe of 42 cm radius, surrounded by 35-cm-thick tungsten-bead shielding.

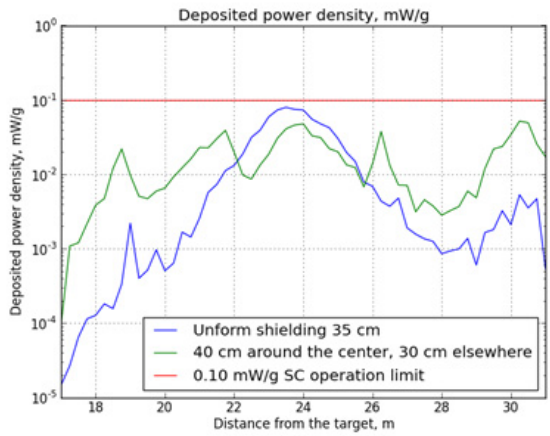


Figure 4: Simulated energy deposition in the superconducting coils of the chicane, average over azimuth.

SUMMARY

The models of shielding of the superconducting coils of the chicane investigated to date (based on MARS15(2012) simulations in the Default mode) appear to be close to providing sufficient protection against radiation damage for an operational lifetime in excess of 10 years. Simulations using MARS15 with MCNP data tables will be performed to evaluate better the energy deposition by low-energy neutrons, which may have been underestimated in the studies to date. Next steps in the studies are to introduce a beampipe which changes its cross section from circular to elliptical and back to circular along the chicane, along with shielding whose inner surface matches the beampipe

Copyright © 2013 CC-BY-3.0 and by the respective authors

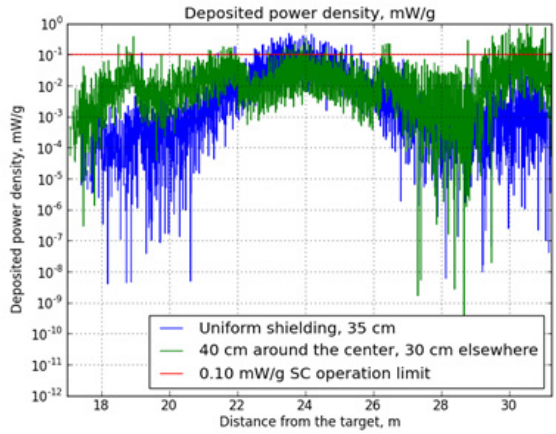


Figure 5: Simulated peak energy deposition in the superconducting coils of the chicane, based on an azimuthally segmented model.

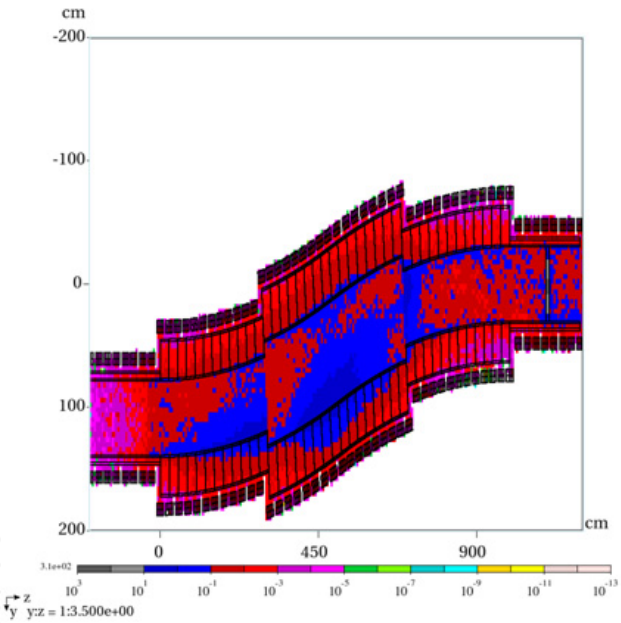


Figure 6: MARS15(2012) simulation of energy deposition in a model of the chicane with non-uniform beampipe of 42 cm radius around the central part of the chicane and 30 cm elsewhere, surrounded by 40 cm of tungsten-bead shielding around the central part of the chicane and 30 cm elsewhere.

and whose outer surface is circular, and with thickness that varies along the chicane.

REFERENCES

[1] M.A. Palmer *et al.*, Muon Accelerators for the Next Generation of High Energy Physics Experiments, Proc. IPAC13, TUPFI057.

[2] R.J. Weggel *et al.*, Design of Magnets for the Target and Decay Region of a Muon Collider/Neutrino Factory Target, Proc. IPAC13, TUPFI073.

[3] N. Souchlas *et al.*, Energy Flow and Deposition in a 4-MW Muon-Collider Target System, Proc. IPAC12, WEPPD036.

[4] J.J. Back *et al.*, Particle production and energy deposition studies for the neutrino factory target station, Phys. Rev. STAB **16**, 021001 (2013).

[5] C.T. Rogers *et al.*, Muon front end for the neutrino factory, Phys. Rev. ST Accel. Beams **16**, 040104 (2013).

[6] C.T. Rogers *et al.*, Control of Beam Losses in the Front End for the Neutrino Factory, Proc. IPAC12, MOPPC041.

[7] J.H. Schultz, Radiation Resistance of Fusion Magnet Materials, IEEE Symp. Fusion Eng., 403 (2003).

[8] N.V. Mokhov, The MARS Code System User's Guide, Fermilab-FN-628 (1995); N.V. Mokhov and S.I. Striganov, MARS15 Overview, AIP Conf. Proc. **896**, 50 (2007), http://www-ap.fnal.gov/MARS/

[9] T.J. Roberts *et al.*, G4beamline Particle Tracking in Matter Dominated Beam Lines, Proc. PAC11, MOP152.

[10] P. Snopok *et al.*, Energy Deposition and Shielding Study of the Front End for the Neutrino Factory, Proc. IPAC13, TUPFI067.

[11] ROOT Code Homepage: http://root.cern.ch/drupal/

[12] L. Spitzer, Jr, Equations of Motion for an Ideal Plasma, Ap. J. **116**, 299 (1952).

Copyright © 2013 CC-BY-3.0 and by the respective authors

OPTIMIZATION OF PARTICLE PRODUCTION FOR A STAGED NEUTRINO FACTORY*

X. Ding†, UCLA, Los Angeles, CA 90095, USA
H.G Kirk, Brookhaven National Laboratory, Upton, NY 11973, USA
K.T. McDonald, Princeton University, Princeton, NJ 08544, USA
J.J. Back, University of Warwick, Coventry CV4 7AL, UK

Abstract

A first stage of a Neutrino Factory based on muon beams might use a pulsed 3-GeV proton beam with 1-MW average power. We report on optimization of particle production by a carbon target inside a solenoid magnet for this scenario.

INTRODUCTION

The ultimate option for the final stage of a Neutrino Factory (NF) in the Muon Accelerator Program [1] is to use a 8-GeV (or more) proton beam of 4-MW average power interacting with a free-flowing mercury jet to create copious amounts of pions that are captured in a high-field solenoid magnet system. Two capture systems, referred to as IDS120h and IDS120j, as sketched in Fig. 1 have been used for the present study. Figure 2 shows that the axial magnetic field for both the IDS120h tapers adiabatically from 20 T and the IDS120j tapers from 15 T around the target to 1.5 T at the end of the target system. The inner radius of superconducting coils (SC) in the region surrounding the mercury jet target region is 120 cm to permit sufficient internal tungsten shielding for a 10-year operational lifetime of the SC coils against radiation damage [2].

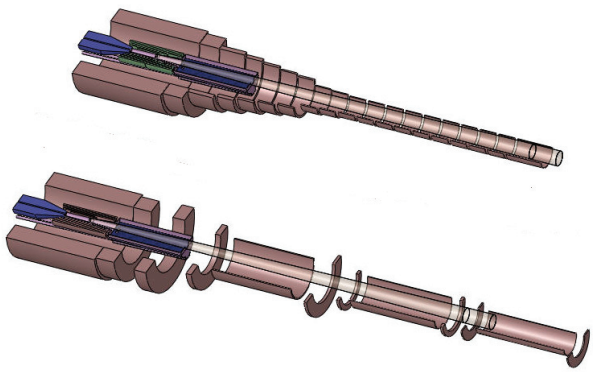


Figure 1: Lower half of the IDS120h (top) and IDS120j (bottom) target system.

A key feature in the staging scenarios [1] for a Neutrino Factory is initial operation of the proton driver at 3-GeV beam energy and 1-MW average beam power. As was noted in previous study, a radiation-cooled graphite target is a viable option for a 1-MW proton beam [3].

The particle production at the target depends on the target geometry as shown in Fig. 3, which illustrates the length and radius of the target, the radius of the proton beam, the orientation of the proton beam relative to the magnetic field, and the angle of the beam and target relative to each other (both of which lie in a vertical plane).

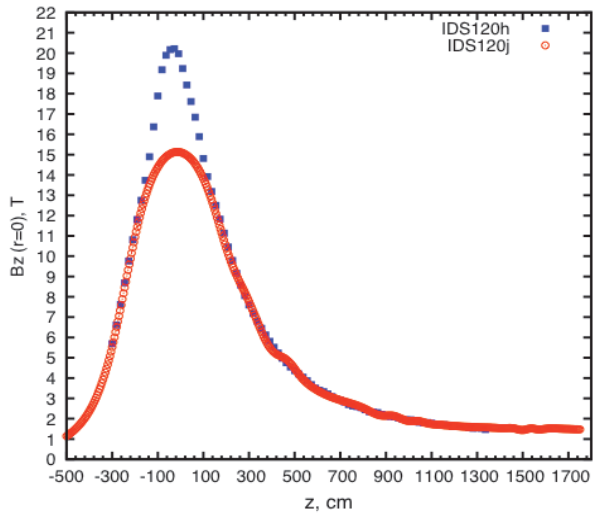


Figure 2: Longitudinal magnetic field along the solenoid axis of SC coils in the IDS120h (dashed line) and IDS120j (solid line) front-end channel.

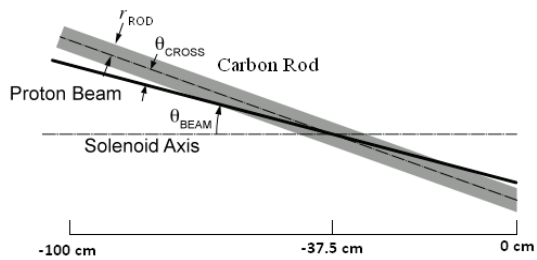


Figure 3: The carbon-target geometry. The proton beam and carbon target cross at z = -37.5 cm. The proton beam is launched at z = -100 cm.

In this paper, we report on the optimization of particle production (pion and muon yields) by a carbon target inside a solenoid magnet of IDS120h or IDS120j configuration. The pions and muons of interest for a Neutrino Factory are those with kinetic energies between 40 and 180 MeV, and we report rates of these at the transverse planes z = 0 m (downstream end of the beam/target interaction region) and z = 50 m.

We used four modes of the MARS15(2012) code [4] (denoted MARS15 below), as well as the FLUKA code [5]. The MARS15 modes used in this study were

*Work supported in part by US DOE Contract NO. DE-AC02-98CH110886.
†xding@bnl.gov

Copyright © 2013 CC-BY-3.0 and by the respective authors

Mode 1: MARS15 default mode (without either LAQGSM or the MCNP tables);

Mode 2: MARS15 with MCNPDATA (with the MCNP tables but without the LAQGSM mode);

Mode 3: MARS15 in LAQGSM mode (with the LAQGSM mode but without the MCNP tables);

Mode 4: MARS15 in LAQGSM mode with MCNPDATA (with both the LAQGSM mode and the MCNP tables).

OPTIMIZED TARGET PARAMETERS AND PARTICLE PRODUCTION OF IDS120H CONFIGURATION

Using the MARS15 default mode (Mode 1), our optimization started with a 3-GeV proton beam impinging on a carbon target with IDS120h configuration. The initial target radius was chosen as 0.75 cm and the target angle as 50 mrad to the solenoid axis of the SC coils [3]. The target and beam were tilted by the same angle with respect to the solenoid axis, while the beam radius (RMS spot size) was fixed to be either ¼, 1/3.5 or 1/2.5 of the target radius. Several runs were performed during each optimization cycle. In run 1 we varied the target length while keeping initial target radius, target angle fixed; in run 2 we varied the target radius using the new target length while keeping the target angle fixed; and in run 3 we varied the target angle with the new target radius. We repeated the above until convergence was achieved.

Figure 4 depicts the particle production as a function of target length, which shows that the target length corresponding to the peak of production is at 72 cm.

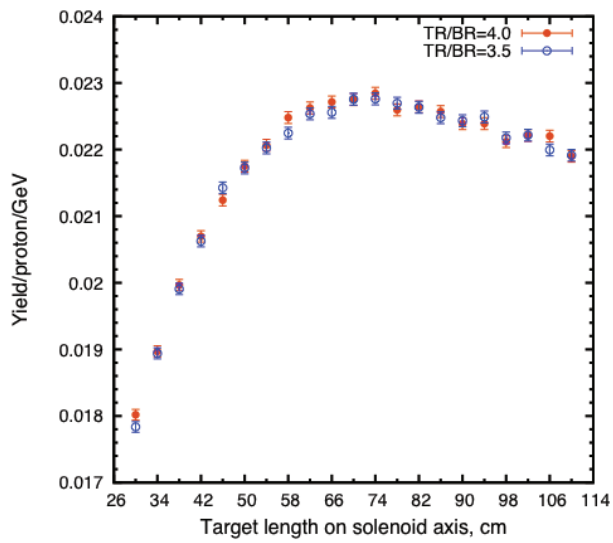


Figure 4: Particle production yields as a function of target length (TR/BR = target radius / beam radius).

Figure 5 shows the variation of particle production with target radius. The production is maximized when the target has a radius of 0.346 cm for a beam radius equal to 1/4 of this.

Figure 6 shows the particle production as a function of beam angle, with a peak around 42 mrad, when the beam radius is 0.0865 cm and the target has a length and radius of 72 cm and 0.346 cm, respectively. In comparison with the results of our initial setting in Fig. 4, the optimization has given a 15% increase in the peak of particle production (from 0.0228 to 0.0262 per proton per GeV).

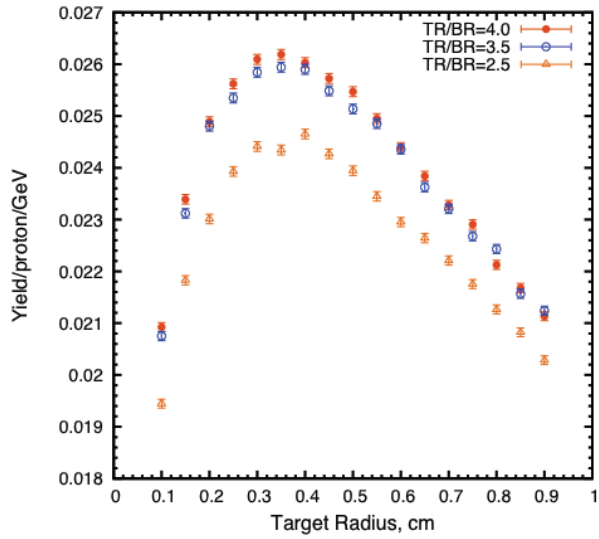


Figure 5: Particle production yields as a function of target radius.

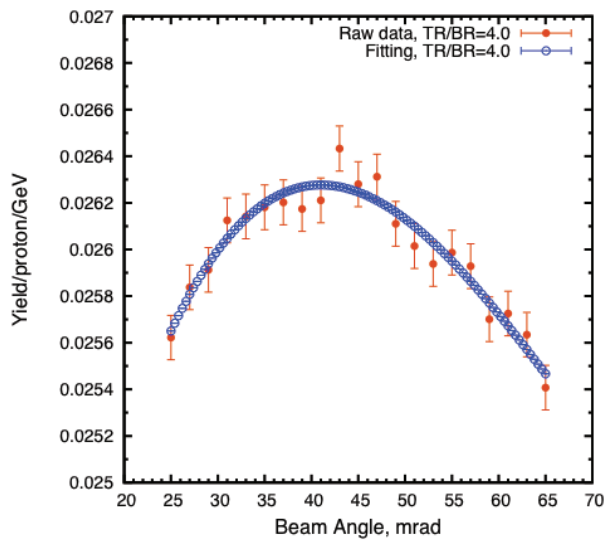


Figure 6: Particle production yields as a function of beam angle.

PARTICLE PRODUCTION AND ENERGY SPECTRA OF IDS120J CONFIGURATION

The above optimization of the carbon target in the IDS120h configuration for a 3 GeV proton beam was used as a starting point for studying particle production and energy spectra for the IDS120h configuration. Table 1 shows the particle production results using 10^5 incoming 3-GeV protons. The results using MARS 15 Modes 1 and 2 are similar, as are also those of Modes 3 and 4, which indicates that use of the optional MCNP mode in MARS15 does not play an important role in the particle production study.

Figures 7 and 8 show secondary-particle energy spectra from MARS15 Modes 1 and 4, respectively, and their

Copyright © 2013 CC-BY-3.0 and by the respective authors

comparison with FLUKA. A strange shape with both a peak and shoulder of soft pions at z = 0 m was observed using MARS15 Mode 1. However, this was not present when MARS15 was used in the LAQGSM mode, for which the results were more compatible with those from FLUKA.

Table 1: Particle Production Yields for the IDS120j Configuration using MARS15 and FLUKA

Running	Yield/proton/GeV z = 0 m	Yield/proton/GeV z = 50 m
MARS15 Mode 1	0.0341	0.0261
MARS15 Mode 2	0.0335	0.0254
MARS15 Mode 3	0.0299	0.0279
MARS15 Mode 4	0.0296	0.0273
FLUKA	0.0334	0.0298

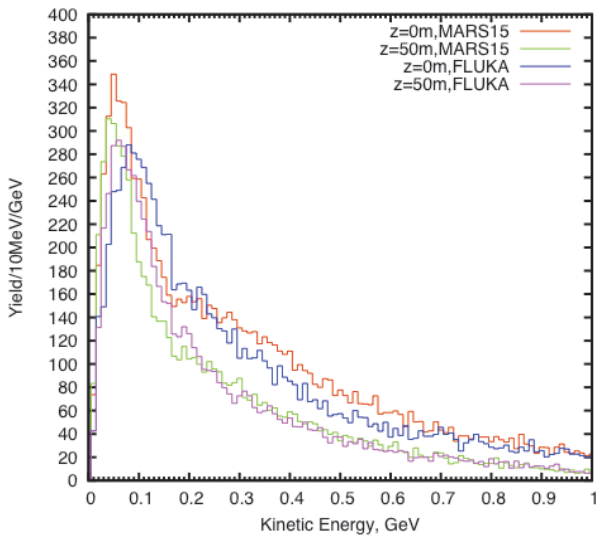


Figure 7: Energy spectra of all positive and negative pions and muons for 3 GeV protons at z = 0 m and z = 50 m for a carbon target from MARS15 Mode 1 and FLUKA.

CONCLUSIONS

With optimization of the geometric parameters for a carbon target impinged by a 3 GeV proton beam, particle production is around 0.0262 per proton per GeV when the target length is set at 72 cm, target radius at 0.346 cm, beam radius at 0.0865 cm and beam angle at 42 mrad for the IDS120h configuration. With these target parameters, we also studied four running modes of MARS15 for the IDS120j configuration and found energy spectra are comparable with those of FLUKA when the MARS15(2102) in LAQGSM mode with MCNPDATA was used. Production of negative pions from a carbon target with a 3-GeV proton beam is only about half that for positives in the energy range useful for a Neutrino Factory, which implies that there would be twice as many $\bar{\nu}_\mu$ (ν_e) as ν_μ($\bar{\nu}_e$) from a Neutrino Factory with these parameters.

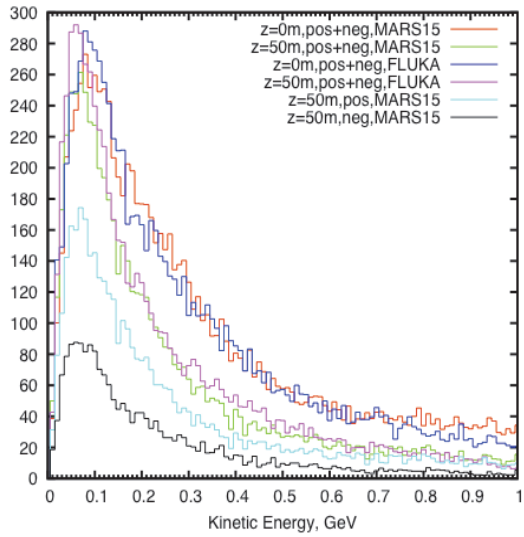


Figure 8: Energy spectra of all positive and negative pions and muons for 3 GeV protons at z = 0 m and z = 50 m for a carbon target from both MARS15 Mode 4 and FLUKA. Energy spectra of positive or negative pions and muons at z = 50 m from MARS15 Mode 4 are also shown.

ACKNOWLEDGMENT

We thank other colleagues from the Target Studies Collaboration for their help concerning this work.

REFERENCES

[1] M.A. Palmer *et al.*, Muon Accelerators for the Next Generation of High Energy Physics Experiments, Proc. IPAC13, TUPFI057.

[2] N. Souchlas *et al.*, A Pion Production and Capture System for a 4 MW Target Station, Proc. IPAC11, TUPS054.

[3] N.V. Mokhov, Particle production for a muon storage ring I. targetry and π/μ yield, Nucl. Instr. and Meth. A **472**, 546 (2001).

[4] N.V. Mokhov, The MARS Code System User's Guide, Fermilab-FN-628 (1995); N.V. Mokhov and S. I. Striganov, MARS15 Overview, AIP Conf. Proc. **896**, 50 (2007), http://www-ap.fnal.gov/MARS/

[5] G. Battistoni *et al.*, The FLUKA code: description and Benchmarking, AIP Conf. Proc. **896**, 31 (2007); A. Fasso *et al.*, FLUKA: A multi-particle transport code, CERN-2005-10, INFN/TC_05/11, SLAC-R-773, http://www.fluka.org/fluka.php

Copyright © 2013 CC-BY-3.0 and by the respective authors

A BUNCH LENGTH MONITOR FOR JLAB 12 GeV UPGRADE*

M. M. Ali, A. Freyberger, G. Krafft, J. Gubeli
Jefferson Lab, Newport News,VA 23606, USA

Abstract

A continuous non-invasive bunch length monitor for the 12 GeV upgrade of Jefferson Lab will be used to determine the bunch length of the beam. The measurement will be done at the fourth dipole of the injector chicane at 123 MeV using the coherent synchrotron light emitted from the dipole. The estimated bunch length is 333 fs. A vacuum chamber will be fabricated and a Radiabeam real time interferometer will be used. In this paper, background, the estimated calculations and the construction of the chamber will be discussed

INTRODUCTION

In recent days, many accelerators use short electron bunches. Measuring bunch length is important for operating and characterizing the accelerator. Bunch length measurement can be classified as invasive techniques such as zero-phasing [1] and deflecting cavity [2] or non-invasive techniques such as electro-optical sampling [3] and interferometers [4],[5]. In Jefferson Laboratory (JLab), we are going to measure the bunch length for the 12 Gev upgrade using the radiabeam Real time interferometer (RTI) [6]. The RTI is a solid state, compact and non-destructive. The experiment will be based on the Synchorotron light which will be emitted from the last bending magnet of the injector chicane. When the bunch length of the electron beam is shorter than the radiation wavelength, the electrons radiate in phase and the radiation power becomes proportional to the square of number of electrons per bunch (N^2) [7].

$$P_{total}(\lambda) = P(\lambda)[N + N(N-1)f(\lambda)] \quad (1)$$

where $P(\lambda)$ is the power radiated by single electron and $f(\lambda)$ is the form factor given by

$$f(\lambda) = |\int S(z) exp(\frac{-2\pi i z}{\lambda}) dz|^2 \quad (2)$$

where S(z) is the normalized longitudinal distribution function, z is the longitudinal position of the electrons and λ is the radiation wavelength. The form factor equals zero when the radiation is incoherent & equals one when the radiation is coherent.

COMPRESSION CALCULATION

In accelerator beam optics, the equation for an ellipse is normalized so ϵ the area of ellipse divided by π is on the right hand side. The general equation is given by

$$\gamma(\Delta\phi)^2 + 2\alpha(\Delta\phi)(\Delta E) + \beta(\Delta E)^2 = \epsilon \quad (3)$$

By compression, we desire to convert a horizontal upright ellipse to a tilted ellipse. The transformation array is given by

$$\begin{bmatrix} \Delta\phi' \\ \Delta E' \end{bmatrix} = \begin{bmatrix} M_{11} & M_{12} \\ M_{12} & M_{22} \end{bmatrix} \begin{bmatrix} \Delta\phi \\ \Delta E \end{bmatrix} \quad (4)$$

Equation(4) can be written as

$$\begin{bmatrix} \Delta\phi \\ \Delta E \end{bmatrix} = \begin{bmatrix} (M^{-1})_{11} & (M^{-1})_{12} \\ (M^{-1})_{12} & (M^{-1})_{22} \end{bmatrix} \begin{bmatrix} \Delta\phi' \\ \Delta E' \end{bmatrix} \quad (5)$$

Substituting by the values of it from eq.(5) into equation(3) and adding the terms of $(\Delta\phi')^2$, $(\Delta E')^2$ and $\Delta\phi'\Delta E'$, then the tilted ellipse twiss parameters will be

$$\gamma_1 = (M_{11}^{-1})^2\gamma_0 + 2(M_{11}^{-1})(M_{21}^{-1})\alpha_0 + (M_{21}^{-1})^2\beta_0 \quad (6)$$

$$\begin{aligned}\alpha_1 = {} & (M_{11}^{-1})(M_{12}^{-1})\gamma_0 \\ & + \left[(M_{11}^{-1})(M_{22}^{-1}) + (M_{12}^{-1})(M_{21}^{-1})\right]\alpha_0 \\ & + (M_{21}^{-1})(M_{22}^{-1})\beta_0 \end{aligned} \quad (7)$$

$$\beta_1 = (M_{12}^{-1})^2\gamma_0 + 2(M_{12}^{-1})(M_{22}^{-1})\alpha_0 + (M_{22}^{-1})^2\beta_0 \quad (8)$$

Assume that the longitudinal phase space distribution is a horizontal upright ellipse before compression with $\sigma_{\phi 0}$ and σ_{E0} as initial values for the bunch length and energy respectively. After the compression it will be $\sigma_{\phi,opt}$ and $\sigma_{E,opt}$ as shown in figure(1). let *M* be the magnification factor, so the bunch length will be compressed by a factor $\frac{1}{M}$ and to achieve the maximum minimum energy spread after compression, *M* must equal $\frac{\sigma_{\phi 0}}{\sigma_{\phi,opt}}$.

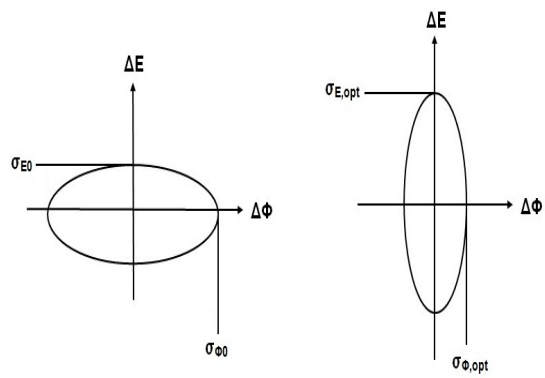


Figure 1: Phase space before & after compression.

* Work supported by the U.S. Department of energy under U.S. DOE Contract No. DE-AC05-06OR23177

Copyright © 2013 CC-BY-3.0 and by the respective authors

When there is a chirp, the horizontal upright ellipse will transform into a tilted ellipse and the transformation equation is given by

$$\begin{bmatrix} \Delta\phi_1 \\ \Delta E_1 \end{bmatrix} = \begin{bmatrix} 1 & 0 \\ -s & 1 \end{bmatrix} \begin{bmatrix} \Delta\phi_0 \\ \Delta E_0 \end{bmatrix} \quad (9)$$

Where $s = V \sin\phi$, V is the cavity offset voltage from the crest and ϕ is the offset phase from the crest in radians. Using the same technique as discussed before in equations [6,7 & 8] and notice that $\alpha_0 = 0$ when the ellipse was horizontal upright, then the new twiss parameters are

$$\gamma_1 = \gamma_0 + s^2\beta_0 \quad (10)$$

$$\alpha_1 = s\beta_0 \quad (11)$$

$$\beta_1 = \beta_0 \quad (12)$$

Since the amplification factor *M* is defined as "the new vertical distance divide by the old vertical distance" or "old horizontal distance divide by new horizontal distance", so $M = \sqrt{\frac{\gamma_1\epsilon}{\gamma_0\epsilon}}$.

Since $\epsilon = \sigma_{\phi 0}\sigma_{E0}$ $\quad \sigma_{\phi 0} = \sqrt{\beta_0\epsilon}$ $\quad \sigma_{E0} = \sqrt{\gamma_0\epsilon}$

$$\beta_0 = \frac{\sigma_{\phi 0}}{\sigma_{E0}} \quad (13)$$

$$\gamma_0 = \frac{\sigma_{E0}}{\sigma_{\phi 0}} \quad (14)$$

Square *M* and substitute by the previous values of γ_1, γ_0 and β_0

$$M^2 = 1 + s^2\frac{\beta_0}{\gamma_0} = 1 + s^2\frac{\sigma_{\phi 0}^2}{\sigma_{E0}^2} \quad (15)$$

The linear transfer matrix for the chicane is given by

$$\begin{bmatrix} \Delta\phi_2 \\ \Delta E_2 \end{bmatrix} = \begin{bmatrix} 1 & \frac{2\pi M_{56}}{\lambda E_{inj}} \\ 0 & 1 \end{bmatrix} \begin{bmatrix} \Delta\phi_1 \\ \Delta E_1 \end{bmatrix} \quad (16)$$

Where λ is the RF wavelength and E_{inj} is the energy at which the compression is done. Again using the same procedure as mentioned before, the final twiss parameters will be

$$\gamma_2 = \gamma_1 \quad (17)$$

$$\alpha_2 = -K\gamma_1 + \alpha_1 \quad (18)$$

$$\beta_2 = K^2\gamma_1 - 2K\alpha_1 + \beta_1 \quad (19)$$

Where $K = \frac{2\pi M_{56}}{\lambda E_{inj}}$. Since the ellipse transforms into a vertical upright ellipse, so $\alpha_2 = 0$, and from eq.(18) the maximum compression condition becomes

$$K = \frac{\alpha_1}{\gamma_1} = \frac{s\beta_0}{\gamma_0(1 + \frac{s^2\sigma_{\phi 0}^2}{\sigma_{E0}^2})} \quad (20)$$

$$M_{56} = \frac{\lambda E_{inj}}{2\pi} \times \frac{s\sigma_{\phi 0}^2}{\sigma_{E0}^2(1 + \frac{s^2\sigma_{\phi 0}^2}{\sigma_{E0}^2})} \quad (21)$$

From equation(15) $\quad M^2 - 1 = \frac{s^2\sigma_{\phi 0}}{\sigma_{E0}^2}$ $\quad$ and finally

$$M_{56} = \frac{\lambda E_{inj}}{2\pi s}\frac{M^2 - 1}{M^2} \quad (22)$$

CALCULATIONS

The Jlab injector chicane consists of nine quads and four dipole magnets with bending radius 3.125 m, the magnetic field is 1.3128 kG, the length of magnet is 30 cm and the bending angle is 5.5^0 as shown in figure(2). One would like

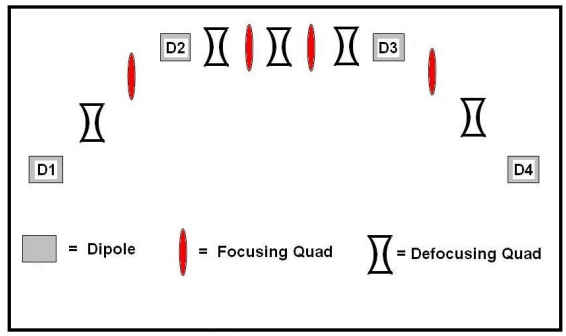


Figure 2: The Chicane.

to compare the bunch length at the third and fourth dipoles of the chicane in order to decide which place is better to do the experiment. Since the value of λ is 20 cm, E_{inj} is 67×10^6 keV and ϵ is 98.25 eV.rad then the bunch length will be calculated as follows.

For the fourth dipole, substituting with $M_{56} = 24$ cm in equation (21) and solving for s, one would find two values for s either 0.635×10^6 eV/rad or 8.256×10^6 eV/rad. Substituting from equations (10, 11 & 12) into equation (19), then

$$\beta_2 = K^2(\alpha_0 + s^2\beta_0) - 2Ks\beta_0 + \beta_0 \quad (23)$$

Substituting with s values, γ_0, β_0 and K value for $M_{56} = 24$ cm in equation (23), then β_2 is 0.031×10^{-6} rad/eV. Doing the same for $M_{56} = 12$ cm, then β_2 is 0.133×10^{-6} rad/eV. Substituting with the those values in $\sqrt{\epsilon\beta_2}$, the bunch length is 1.745×10^{-3} rad for ($M_{56} = 24$) and 3.6×10^{-3} rad for ($M_{56} = 12$). From these result, one can conclude that the bunch length will almost compress to its half value after the 3^{rd} dipole and compress fully after the 4^{th} dipole, then the best place to do the experiment is after the 4^{th} dipole.

A plane mirror will be used to deflect the synchorotron radiation to the RTI and it will confront a 3.25 degrees out of 5.5 degrees of the synchrotron radiation fan. The total energy per unit angular frequency emitted by a single electron moving on a circular orbit is given by [8]

$$\frac{dE}{d\omega} = \frac{9\sqrt{3}}{8\pi\omega_c}\frac{e^2\gamma^4}{3\rho\epsilon_0}y\int_y^\infty K_{5/3}(x)dx \quad (24)$$

where e is the electronic charge, γ is the relativistic factor, ρ is the bending radius, ϵ_0 is the free space permittivity, $K_{5/3}$ is the modified Bessel function and $y = \frac{\omega}{\omega_c}$, where $\omega_c = \frac{3}{2}\gamma^3\frac{c}{\rho}$ is the critical angular frequency. Since the radiation will be collected by a mirror at an angle $\Delta\theta = 3.25$ then

Copyright © 2013 CC-BY-3.0 and by the respective authors

the energy between two angular frequencies ω_1 and ω_2 is

$$E = \frac{3.25}{360}\frac{9\sqrt{3}}{8\pi}\frac{e^2\gamma^4}{3\rho\epsilon_0}\int_{y_1}^{y_2} y\int_{y}^{\infty} K_{5/3}(x)dxdy \qquad (25)$$

Since the repetition rate in JLAB is 500 MHz, power can be estimated by assuming the form factor is a Gaussian distribution, multiplying eq.(24) by $\frac{3.25}{360}$ and using equations (1), (2) then the estimated calculations for the power distribution as a function of wavelength for different bunch lengths is shown in fig (3).

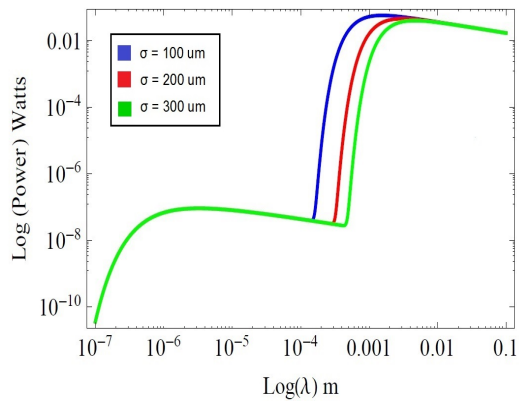


Figure 3: Power spectrum for different bunch lengths.

CONSTRUCTION OF THE CHAMBER

The old chamber and its component is shown in fig(4a) while the new one is shown in fig(4b). The new chamber is built with four additional ports, two of them are for the laser alignment assembly and the Synchorotron light (SL) assembly, while the other two is for the insertable mirror assembly. The difference between the new and old line is that the spool section is removed. The new chamber is made from 316 stainless steal with the same thickness as the old one so, it will have the same magnetic permeability. The chamber elastic limit is measured under vacuum and found to be 70 MPa which is much less than the elastic limit of the stainless steel.

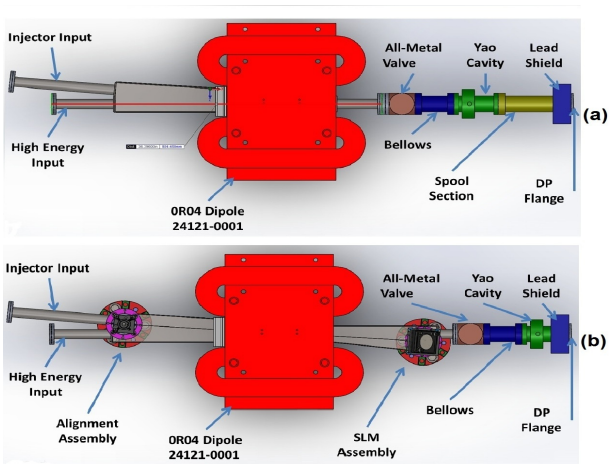


Figure 4: Old and new chamber.

The four assemblies are mounted on a rotatable flange with jacking screws to provide small angular correction as shown in fig(5). The alignment laser assembly has a cage

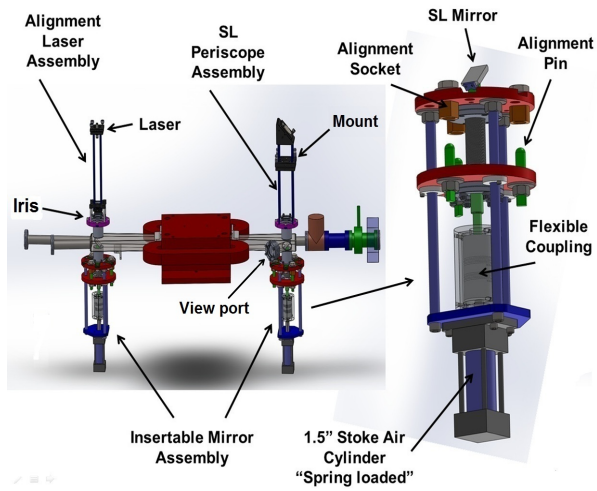


Figure 5: Chamber with laser & SL assembly.

system with a laser diode to help in the alignment. The insertable mirror assembly has a mirror in each one, one to help in the laser alignment while the other is to receive the synchorotron light and reflected upward to the RTI. Both assemblies are attached to stroke air cylinder which is a spring loaded to fail out in case losing air or electrical signals. Also, the chamber has a view port to make sure that the initial laser alignment is on the right spot.

CONCLUSION

The chamber will be installed by the end of the year and as the upgrade finishes, the RTI will be installed. The measurements will be taken in the second phase of the upgrade as JLAB will be operated for one cycle and the results will be compared to the zero-phasing technique used in the north linac.

REFERENCES

[1] D.Wang et.al., Physical Review E, vol.57, p.2283 (1998).

[2] R.Akre et.al., Proceedings of EPAC, 2002.

[3] G.Berden et.al., Physical Review Letters, vol.99, p.164801 (2007).

[4] B.Leissner et.al., Proceedings of PAC, 1999.

[5] P.Evtushenko et.al., Proceedings of AIP, 2006.

[6] J.Thangaraj et.al., Review of Scientific Instruments 83, p.043302 (2012).

[7] D.Wang et.al., Appl. Phys. Lett. 70 (4), 27 January 1997.

[8] David Jackson, Classical Electromagnetism, 3^{rd} edition.

Copyright © 2013 CC-BY-3.0 and by the respective authors

A HIGH-INTENSITY NEUTRON PRODUCTION SOURCE BASED ON ROTARY VALVING*

B. Rusnak, P. Fitsos, J. M. Hall, R. Souza, P. Peaslee, LLNL, Livermore, CA 94550

Abstract

As part of the effort to develop a fast neutron imaging capability at LLNL, a novel windowless deuterium gas target was developed for use with high-intensity pulse deuteron beams to generate neutrons via the $D(d,n)^3He$ reaction. The system was designed to create high-velocity, cross-flowing gas to minimize rarefaction due to beam heating in the target gas. The system also employs a unique gas beam stop to minimize knock-on neutrons from implanted deuterons over time. A prototype system employing rotary valving to generate and modulate gas flow, and a rotating aperture to minimize gas back streaming into the beamline vacuum system, was designed and built. Design details and supporting analyses of the gas dynamics of the system are presented.

INTRODUCTION

Investigating low-density features and materials that are heavily shielded within high-density materials is a challenge for x-ray techniques due to the attenuation of the x rays in the high-Z outer materials. Using the high penetrability of fast neutrons to create radiographic images is an alternative technique demonstrated to be very effective at creating cubic-millimeter-scale resolution images in heavily shielded low-Z test objects [1]. Technology development in the pursuit of creating a fast neutron imaging capability as a complimentary non-destructive evaluation (NDE) diagnostic to x rays has been on going at LLNL for the last decade [2].

Neutron Source Requirements

To achieve high penetrability in a variety of potential high Z materials, a 10-MeV neutron energy was chosen. In addition, this energy would not create short-lived activation products in air due to the $^{16}O(n,p)^{16}N$ reaction, which has a threshold above 10 MeV. The rapid decay of ^{16}N produces a background of high-energy gammas that are not only a radiological hazard but can degrade image resolution. To minimize image degradation due to an excess of scattered lower energy neutrons, the source neutrons also needed to be quasi-monoenergetic. For this application, having the energy width be approximately 10% was acceptable. To achieve nominal cubic-millimeter resolution, the source spot size needed to be at most 1.5 mm in diameter. These requirements placed significant constraints on the system and have strongly influenced the technology development path.

*This work performed under the auspices of the U. S. Department of Energy by Lawrence Livermore National Laboratory under contract DE-AC52-07NA27344.

Production Target Resolution Requirements

Production of quasi-monoenergetic high-energy neutrons can be readily achieved by impinging a deuteron ion beam onto a fixed length of high-pressure deuterium gas via the $D(d,n)^3He$ reaction. The maximum final neutron energy is determined by the incoming beam kinetic energy plus the Q value of the fusion reaction of 3.3 MeV, and the energy width of the neutron beam is directly related to the ion beam energy loss as the beam subtends the length gas cell. For this application, the deuterium gas cell is nominally 1.5 mm in diameter and 40 mm long. A deuteron beam of 7 MeV will be used to create ~10 MeV neutrons with a nominal 1 MeV energy width with 90% of the beam being in a forward directed.

Production Target Intensity Requirements

The neutron source intensity desired is 10^{11} n/sec/st at zero degrees. This was set by the goal of realizing a full 256-image computed tomographic (CT) reconstruction of a heavily shielded object in a nominal work shift. To achieve this intensity, 300 uA of average beam current will need to interact with nominally 3-bar deuterium gas at ambient temperature in the gas cell volume.

The small source spot size required for high-resolution imaging will create very high deposited power densities on any materials the beam interacts with, including any solid-material window typically used for making deuterium-gas neutron targets. This is due to the high energy loss of ion beams in solids at these low energies. Operating such a windowed source lends itself to DC accelerators as these provide the lowest possible average power for a given spot size in the window compared to pulsed beam structures. A great deal of experimentation over the years has shown that most windowed gas cells with millimeter-scale focal spots only achieve ~20–30 uA of average current before failure [3]. Given the factor of 10 higher beam currents needed to make the intensity requirements, an alternate approach to windowed gas cells was needed.

Another significant challenge due to the small spot size was stopping and disposing of the unreacted beam after the gas cell. For any solid high-Z stop, since the beam loses only 10% of its energy and does not appreciably enlarge when interacting with the deuterium gas, the beam stop needs to absorb 90% of the beam power over a stopping range of tens of microns. While grazing incident and rotating stop ideas were considered to prevent melting, there was concern that the density variations produced for the neutron beam would result in unwanted shadows on the radiographs, that the solid material would be damaged over time due to the pulsed nature of the

Copyright © 2013 CC-BY-3.0 and by the respective authors

beam and subsequent cyclic heating and cooling, and that the build-up of implanted deuterium over time would lead to "knock-on" neutrons that broaden and soften the desired fast-neutron spectrum and degrade the resolution; therefore, such a solid stop was not pursued.

The team evaluated the option of placing quadrupoles and dipoles downstream of the gas cell to defocus and then divert the expanded beam to a solid beam stop further down stream and out of the imaging flight line. This approach was rejected due to the need to have massive steel electromagnets in a high-neutron-flux region for extended periods where they would become activated and produce unwanted scattered neutrons that degrade resolution. Permanent magnets were not seen as viable due to a large bore needed downstream of the gas cell to capture the beam (at least 3–4" diameter) and concerns over their sensitivity to high fluxes of neutron radiation and the longer lived activation products that would be produced.

In response to these issues, an argon gas beam stop was developed to use in conjunction with the deuterium gas cell. Stopping the beam in a high-pressure gas will remove the three main issues related to solid stops.

The array of target challenges due to the small source spot size and beam current needed also precluded using the 14-MeV neutrons from the D(t,n)^{4}He reaction. DT tubes are easily capable of achieving some combination of small-source spot sizes, high intensity, and long lifetimes but not simultaneously and reliably as is needed for neutron imaging.

WINDOWLESS APERTURE

As an alternative to a physical window separating the deuterium gas cell from the beamline vacuum, a rotating aperture system was studied that would allow passage of a low-duty-factor, pulsed beam into the cell but would then restrict gas flow back up the beamline. The rotating aperture approach exploits the pulsed nature of commercial accelerators that operate at ~1–2% duty factor and can reduce the gas load and the associated differential pumping system size and cost significantly [4]. The effectiveness of the technology is maximized by achieving precision tolerances of less than 0.001-0.002" in the gaps between sealing surfaces when closed.

To achieve accurate timing of the rotating aperture with the ion beam, a series of vignetting equations were created that modeled the aperture opening behavior as a function of overall diameter, rotational speed, hole size, and beam diameter [5]. These equations allowed designing the system to accommodate the operational range of the pulsed accelerator system.

Hydrodynamic modeling done as part of the analysis effort that looked at gas flow into the vacuum with and without the beam interaction showed that the large peak powers in the beam macrobunch (~110 kW) would significant rarefy the gas in the cell due to rapid heating. The team concluded that the gas in the gas cell could not remain static, as that would lead to a roll-off of neutron intensity for peak currents above ~1 mA. Cross-flowing deuterium gas moving at a minimum of 400 m/s in front of the beam was effective at maintaining the required gas density [6]. To achieve such high cross-flow velocities, various concepts were explored using either venturis or pulsed valves opening against a large pressure differential. The approach pursued was to extend the rotating aperture technique to be a rotating valve as well. By using a valve to modulate the gas, a smaller gas compressor could be used to circulate gas in the system than would be needed for a simple venturi.

The rarefaction predicted in the deuterium section of the gas cell will be even greater in the argon beam stop section, as 90% of the beam power is deposited there, and the energy deposition of the beam in the stopping gas per unit length is a factor of 9.1 greater. Calculations show that achieving high cross-flow velocities with argon will be more difficult than deuterium due to the lower sound speed in the heavier gas. The goal is to realize flow velocities in the 300 m/s range.

ROTARY VALVING APPROACH

Straightforward modifications were made to the rotating aperture vignetting equations to adapt them for rotary valving. These equations were then used to calculate the effective opening areas of the rotating aperture and the rotary valve, which can be compared to the beam pulse, as shown in Figure 1.

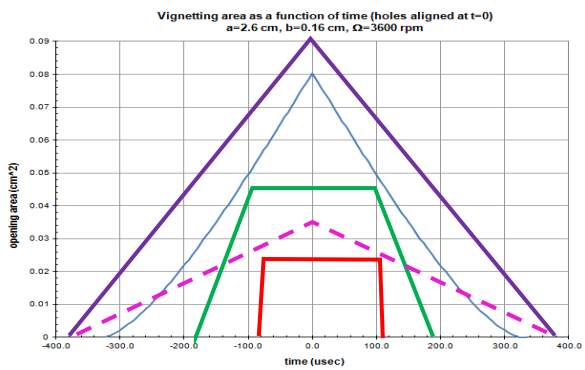


Figure 1: The plot shows the interrelation of the effective opening and the closing areas of the rotary valve gas inlet (purple), the aperture hole opening (light blue), the beam diameter opening (green), and representations of the gas pulse (purple dashed) and the deuteron beam (red).

Just as close tolerances were needed to reduce gas flow to the beamline when the aperture was closed, precision tolerances were also needed on the rotating valve portion of the assembly. The need to hold gap tolerances of less than 0.002" over the rotor length of nominally 14" drove many of the design choices. A system drawing is shown in Figure 2 and a finished system photo in Figure 3.

Copyright © 2013 CC-BY-3.0 and by the respective authors

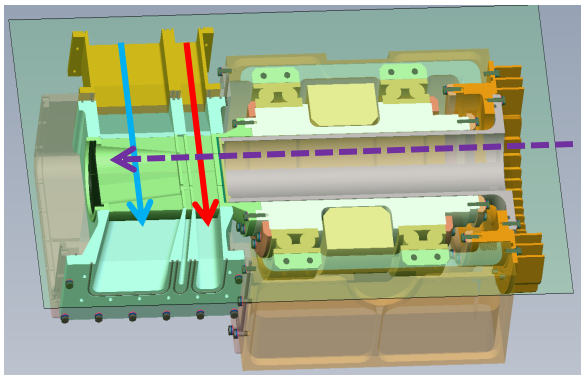


Figure 2: Cutaway of rotary valve system showing the ion beam (dashed) the cross-flowing deuterium gas (red), and the cross-flowing argon stopping gas (blue).

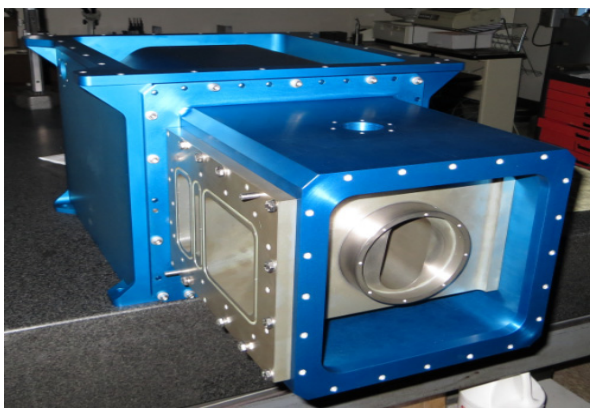


Figure 3: Photo of rotary valve being assembled, showing the central rotor inside the valve manifold (silver aluminium), and the outer aluminium case (blue anodized).

As the gas cell will ultimately need to operate in an intense neutron radiation field, design choices were made to improve reliability and ease disposal, including:

- Moving the motor ~12" away from the deuterium interaction point and being able to put in shielding
- Making as much of the assembly as possible out of 7075 aluminium to minimize longer lived activation products while maintaining good working strength and hardness
- Being able to use all metal seals on the assembly

GAS FLOW ANALYSIS

Extensive modeling allowed evaluation of the fluid flow of the gases in the cells. To simplify the studies and to better relate them to experiments, helium gas was used as a surrogate to deuterium, as it has comparable thermodynamic properties without the flammability hazard. Studies included:

- Helium (deuterium) cross-flow velocity and leakage with no beam
- Helium (deuterium) heating and density with beam energy present, shown in Figure 4
- Argon cross-flow velocity and leakage with no beam
- Argon heating and density with beam energy present
- Helium (deuterium) and argon intermixing with and without beam energy present
- Helium (deuterium) leakage down the beam line

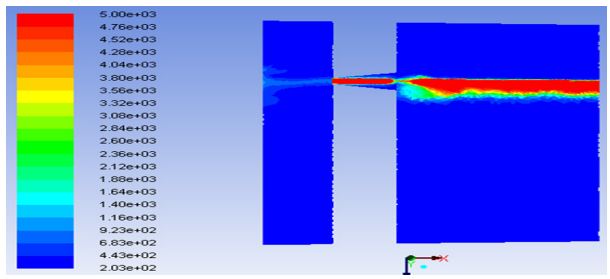


Figure 4: Temperature difference in Kelvin in the deuterium (left) and argon (right) streams due to variations in density and energy deposition with beam power present and the gases moving across the beam channel.

DESIGN DETAILS AND MACHINING

To sustain the tight tolerances needed to better seal the rotary aperture and valve sections, large-diameter bearing doublets were used successfully. To avoid the use of any type of rotary feed-through, which would be problematic at the 3600-rpm rotational speeds and the high radiation environment, a DC motor was installed in the chamber and attached to an aluminium heat sink. To reduce the risk of galling in the event the close-tolerance rotating surfaces contacted, those parts were coated with Ni-Lube, a nickel Teflon composite layer that significantly reduces friction.

ACKNOWLEDGEMENT

The authors would like to recognize the masterful machinist skills of Steve Reid and Peter Steinebrunner at the CHAMP Company, Campbell, CA, and their efforts to achieve the tight tolerances needed on this system.

REFERENCES

[1] J. M. Hall et al, "High-Energy Neutron Imaging Development at LLNL," Proc. of the 8th World Conf. on Neutron Radiography, Gaithersburg, MD, May 2007.
[2] B. Rusnak, J. M. Hall, S. Shen, "Rotating Aperture Deuterium Gas Cell Development for High Brightness Neutron Production," 2005 PAC, Knoxville, TN, May 2005.
[3] J. B. Marion, J. L. Fowler, Fast Neutron Physics, (New York: Interscience, 1960), Part I, 703.
[4] J. Guzek, "Elemental Radiography Using Fast Neutron Beams," doctoral thesis, March 1999.
[5] B. Rusnak, loc. cit.
[6] Loc. cit.

Copyright © 2013 CC-BY-3.0 and by the respective authors

ION-IRRADIATION RESPONSE OF GAFCHROMIC FILMS AND THEIR APPLICATION TO THE MEASUREMENT OF THE TRANSVERSE BEAM INTENSITY DISTRIBUTION

Yosuke Yuri, Tomohisa Ishizaka, Takahiro Yuyama, Ikuo Ishibori, and Susumu Okumura,
Takasaki Advanced Radiation Research Institute, Japan Atomic Energy Agency,
1233 Watanuki-machi, Takasaki, Gunma, Japan

Abstract

The response of radiochromic films, Gafchromic HD-810 and EBT2, was investigated using MeV/u-class proton and heavy-ion beams to apply the films to a measurement technique of the transverse beam intensity distribution at an azimuthally-varying-field cyclotron of Japan Atomic Energy Agency. The optical density of the irradiated films increased linearly with the particle fluence of the beam in a low-fluence region. The linear-response range of the fluence strongly depended on ion species as well as on the film type. By analyzing the film response to absorbed dose, it was found that the sensitivity of the film decreased for a beam with higher linear energy transfer. Based on the linear response of the Gafchromic film, we measured the relative intensity distribution of a large-area ion beam focused with multipole magnets. It was demonstrated that the present technique was useful for evaluation of the size and uniformity of the ion beam.

INTRODUCTION

Precise, handy evaluation of the transverse intensity distribution of a large-area ion beam with various ion species is required for materials and biological researches at the accelerator facility TIARA of Japan Atomic Energy Agency (JAEA). Radiochromic films, Gafchromic HD-810 and EBT2 (Ashland Inc.) [1], were, therefore, adopted as a possible measurement technique of the transverse beam intensity distribution. Various properties of the film, such as high spatial resolution (below 1 mm), large size (over 100 cm^2), thinness (for the penetration of a low-energy ion beam), and easy handling, are advantageous to the present purpose.

A beam irradiation experiment was carried out systematically in order to determine the applicability of Gafchromic films to various ion beams at the azimuthally-varying-field (AVF) cyclotron in TIARA [2]. Their response characteristics were investigated in a wide fluence range. Furthermore, the optical-density response of the films was analyzed in terms of linear energy transfer (LET) and dose [3]. Based on the linear-response characteristics of the films, we measured the relative intensity distribution of a large-area beam focused with multipole magnets [4] and evaluated the size and uniformity of the beam.

FLUENCE RESPONSE

HD-810 and EBT2 films were irradiated uniformly with 10-MeV ^{1}H, 13-MeV/u ^{40}Ar, and 3.5-MeV/u ^{129}Xe beams from the AVF cyclotron. The irradiated films were read at a resolution of 127 dpi with a general-purpose flat-bed scanner, LiDE50 (Canon Inc.), to digitize them into TIFF-formatted images with 16-bit RGB color intensity values. The film scanning was performed in more than one day after irradiation to prevent short-term color variation after irradiation. The optical density d_X in each color channel X (red, green, or blue) was determined from the equation: $d_X = \log_{10}((2^{16}\text{-}1)/I_X)$, where I_X is the 16-bit intensity value.

The response of HD-810 films irradiated with the ion beams is shown as a function of the fluence in Fig. 1. The increment of the optical density depends on the color channels for each ion species. The optical density obtained from the red channel is the largest at a given fluence in the linear-response region, while that from the blue channel is the least sensitive. This reflects that the film absorption sensitivity is higher in the longer wavelength region. Thus, the intensity distribution of the beam can be measured in a wide fluence range with a moderate signal-to-noise ratio by choosing an appropriate color channel of the scanned image. The range of the response curves shifted drastically toward a lower-fluence region for heavier-ion beams, as clearly seen in Fig. 1.

For EBT2, the optical density only of the green channel exhibited the linear response in a low-fluence range. The linear-response range is one order of magnitude lower than that of HD-810.

DOSE RESPONSE

The strong dependence of the film response on ion species, as shown in Fig. 1, is probably due to the difference of the LET in the active layer of the film. To see this, the particle fluence F is transformed into the dose D using the following relation: $D = c\,(LET/\rho)\,F$, where ρ is the density of the active layer of the film and c is a constant. The LETs of the beams at each layer of the films can be determined using SRIM code [5]. For example, the average LETs in the active layer (ρ = 1.08 g/cm^3) of HD-810 are 5.0×10^0, 1.2×10^3, and 1.1×10^4 keV/μm for the H, Ar, and Xe ion beams in the present case, respectively.

The response curves of the three ion species are replotted as a function of the average dose in the active layer of HD-810 in Fig. 2. For the proton beam, the linear response in Fig. 2(a) is similar to those observed in previous studies in spite of the differences in proton energy and scanners [6-8]. Although the linear-response dose range has been partially overlapped with the manufacturer's specifications (10~400 Gy) of the film in

Copyright © 2013 CC-BY-3.0 and by the respective authors

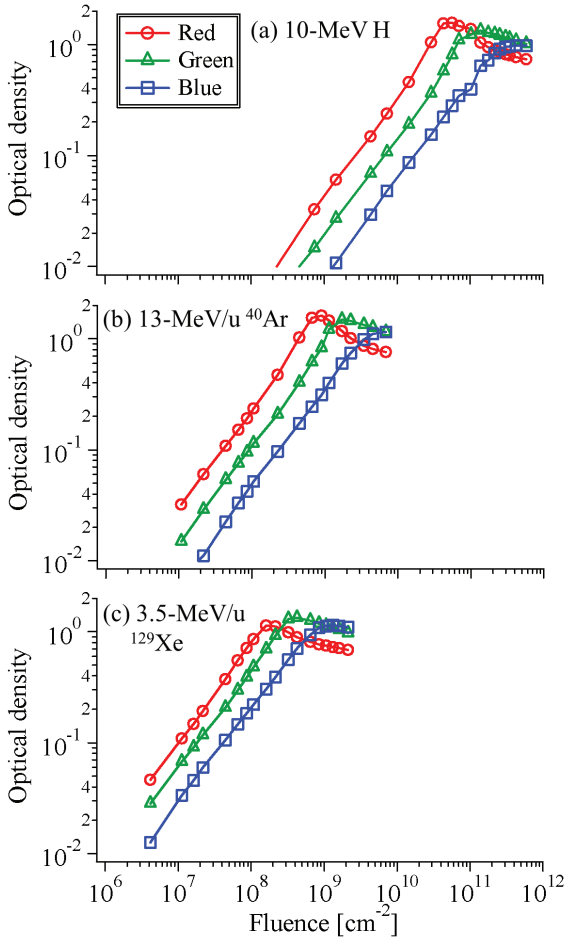


Figure 1: Response curves of the Gafchromic film HD-810 for three different ion beams as a function of the particle fluence.

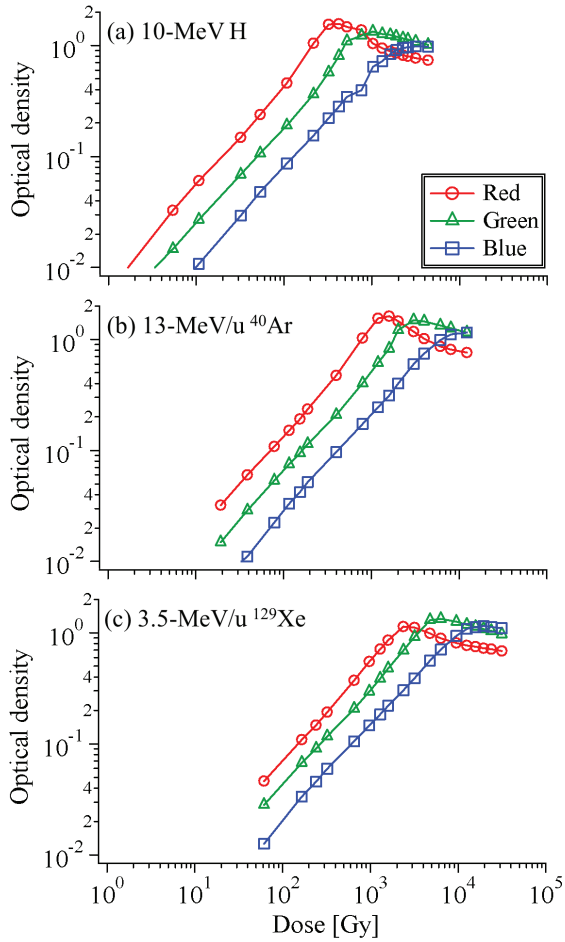


Figure 2: Response curves of the Gafchromic film HD-810 for three different ion beams as a function of the dose in the active layer of the film. The experimental data is the same as in Fig. 1.

all three ion species, the dose-response curves shift slightly to the right for heavier-ion beams and the film response seems still dependent on ion species. Therefore, the sensitivity of the film, defined here as a gradient of the linear-response region with respect to the dose, is evaluated for the three ion species and summarized as a function of LET in Fig. 3. The sensitivities of the EBT2 green channel for H and Ar beams are also plotted in Fig. 3. (The EBT2 film is not applicable to the 3.5-MeV/u Xe beam because the kinetic energy is too low for the beam to reach the active layer of the film.) It is clearly reconfirmed that the sensitivity is lower for heavier-ion beams and higher for EBT2. The sensitivity reduction for heavier-ion beams is probably because, for a heavy ion with a higher LET, the local dose along the ion's trajectory is very high and the coloration in the microscopic region becomes saturated: a large part of the deposited dose does not contribute to the film coloration. This tendency agrees well with previous studies [6, 9]. Similar sensitivity reduction of radiochromic films in a Bragg peak (where LET is large) is known as a quenching effect [10].

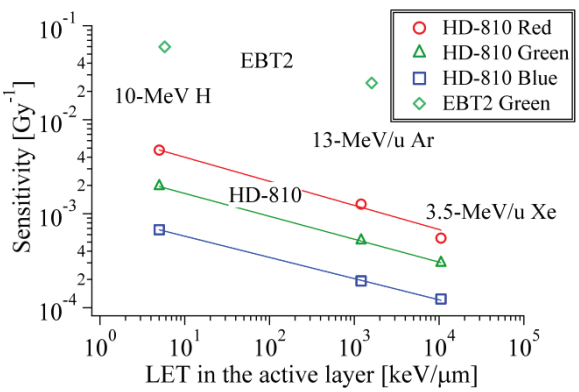


Figure 3: Sensitivity of the HD-810 and EBT2 films as a function of LET. For HD-810, the sensitivities of the red, green, and blue channels are fitted by power functions of $(\mathrm{LET})^{-0.26}$, $(\mathrm{LET})^{-0.24}$, and $(\mathrm{LET})^{-0.21}$ in the present case, respectively. For EBT2, the sensitivity of the green channel where the response is linear is plotted.

Copyright © 2013 CC-BY-3.0 and by the respective authors

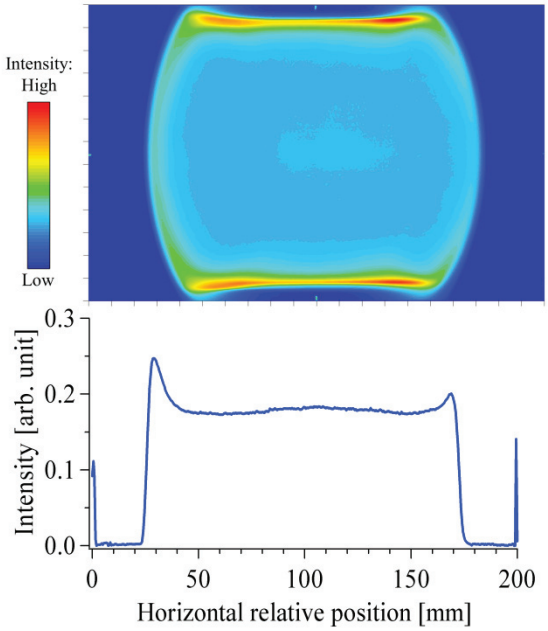


Figure 4: Relative transverse intensity distribution obtained from the optical density distribution of an HD-810 film. The film was irradiated with a 13-MeV/u Ar beam of 0.1 μA for 0.5 s, and scanned with the LiDE50 at a spatial resolution of 127 dpi. The 2D cross-sectional distribution is shown in the upper panel. In the lower panel, the 1D distribution is shown along the horizontal axis. The peaks appearing at both ends in the lower panel correspond to marks put on the film for indicating the central axial position.

INTENSITY DISTRIBUTION MEASUREMENT USING THE FILMS

As can be seen from Figs. 1 and 2, the response of the film is always linear in a low-fluence (low-dose) region where the optical density is well below unity. It is, thus, not always necessary to obtain the response curve in every experiment. This feature gives us a handy technique to measure the relative intensity distribution of the beam directly from the optical density. The relative distribution suffices for the evaluation of the size and uniformity.

Figure 4 shows the measurement result of the relative intensity distribution of a large-area ion beam, obtained from the optical density distribution of HD-810. As can be seen in the figure, the uniform intensity region is formed in the inner part of the profile. Such a beam was formed as follows: The ion beam from the cyclotron was first multiply-scattered with a thin foil to smooth the initial distribution into a Gaussian-like distribution and then focused by octupole magnets so that the intensity distribution could be made uniform on the target [11]. In this uniform-beam formation method, the intensity in the peripheral part of the beam can be very high due to overshooting the tail of the Gaussian-like beam focused by octupole magnets and thus the optical density of the high-intensity region may go beyond the available linear-response range of the Gafchromic film. Even in such a situation, the uniformity of the inner central region can be evaluated if the optical density in the uniform region is well below unity. In Fig. 4, the root-mean-square uniformity is evaluated as 7% in the 120-cm^2 flat-top region surrounded by a high-intensity peak. The uniformity is better (4%) in the inner 9-cm-square central region around the beam center, as predicted theoretically [4].

It is worthwhile to note that the beam uniformity, determined from the optical density of the Gafchromic film, is equal to that of the track-pore density distribution observed more microscopically through a track-etching technique [2, 12].

SUMMARY

The applicability of Gafchromic films HD-810 and EBT2 to proton and heavy-ion beams was investigated for the measurement and evaluation of large-area beam intensity distributions at the JAEA AVF cyclotron. The available fluence range was strongly dependent on ion species as well as on the film type. The sensitivity of the film was lower for a beam with higher LET.

Paying attention to the linear response of Gafchromic films, we developed a handy technique for obtaining the relative transverse intensity distribution of the beam. Using the technique, we confirmed that an ion beam with a uniform intensity distribution was formed by multipole magnets, and the size and uniformity of the beam was evaluated. Large-area proton and heavy-ion beams over 100 cm^2 can be realized at a uniformity of less than 10% and are applied to experiments for space [13] and materials science at TIARA.

REFERENCES

[1] http://gafchromic.com/
[2] Y. Yuri, T. Ishizaka, T. Yuyama, I. Ishibori, S. Okumura, A. Kitamura (Ogawa), T. Yamaki, and S. Sawada, Proc. 1st International Beam Instrumentation Conference, Tsukuba, Japan, 2012, p. 531.
[3] Y. Yuri, T. Ishizaka, T. Yuyama, I. Ishibori, and S. Okumura, Nucl. Instrum. Methods Phys. Res. Sect. A **727** (2013) 40.
[4] Y. Yuri, N. Miyawaki, T. Kamiya, W. Yokota, K. Arakawa, and M. Fukuda, Phys. Rev. ST Accel. Beams **10** (2007) 104001.
[5] http://www.srim.org/
[6] A. E. Buenfil et al., Nucl. Instrum. Methods Phys. Res. Sect. B **197** (2002) 317.
[7] D. S. Hey et al., Rev. Sci. Instrum. **79** (2008) 053501.
[8] F. Nürnberg et al., Rev. Sci. Instrum. **80** (2009) 033301.
[9] T. Kojima et al., Rad. Phys. Chem. **68** (2003) 975.
[10] D. Kirby et al., Phys. Med. Biol. **55** (2010) 417.
[11] Y. Yuri, T. Ishizaka, T. Yuyama, I. Ishibori, S. Okumura, and K. Yoshida, Nucl. Instrum. Methods Phys. Res. Sect. A **642** (2011) 10.
[12] A. Kitamura (Ogawa), T. Yamaki, Y. Yuri, S. Sawada, and T. Yuyama, to be published in Nucl. Instrum. Methods Phys. Res. Sect. B.
[13] M. Imaizumi, Y. Yuri, P. R. Bolton, S. Sato, and T. Ohshima, Proc. 38th IEEE Photovoltaic Specialists Conference (2012) 2831.

Copyright © 2013 CC-BY-3.0 and by the respective authors

SIMULATION OF X-BAND LINAC NEUTRON SOURCE

K. Tagi#, K. Dobashi, T. Fujiwara, and M. Uesaka, University of Tokyo, Tokyo, Japan
M. Yamamoto, Accuthera Inc., Kawasaki, Japan

Abstract

In Tokyo University, there is a plan of development of electron linac neutron source because the research reactor "Yayoi" was decommissioned and a new neutron source is required. This linac will be introduced in the core of the reactor, so measurement of nuclear fuel materials can be expected. The application of this research is to measure more accurate nuclear data of some atomic fuel materials. It is necessary for analysing debris in Fukushima 1st nuclear power plant.

30 MeV X-band linac is used and neutrons are generated by interactions between bremsstrahlung x-rays and materials. In this research, the thermal electron gun, the buncher and the target for the linac are optimized for generating as many neutrons as possible. Uranium can be used as target materials, so high neutron flux was gained from the calculation.

INTRODUCTION

Nuclear data, neutron cross section, is important because it can be applied to development of new reactor and analysis of debris in Fukushima 1st nuclear power plant. However, this data, especially the data of nuclear fuel materials, such as U, Pu, and Am, is not so correct. Figure 1 shows experimental data of total cross section of Pu-239 [1]. You can understand the accuracy of the peak at 1 eV is low. In addition, measurement of this data hasn't been done recently.

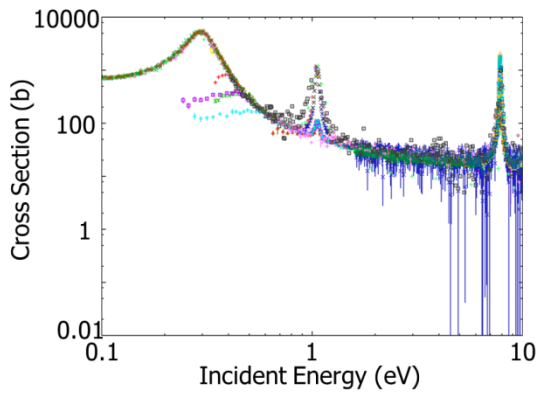


Figure 1: Experimental data of total cross section of Pu-239 [1].

Energy resolution is very important for the measurement of debris. The relation between time and energy is given by the equations

$$T[\mu s] = \frac{72.3L[\mathrm{m}]}{\sqrt{E[\mathrm{eV}]}}, \frac{\Delta E}{E} = -\frac{\Delta T}{T}. \quad (1)$$

For measuring data in 1% energy resolution, 1 μs is necessary when length of beam line is 5 m and beam energy is 10 eV, and 100 ns is necessary when length of beam line is 40 m and beam energy is 100 keV. So short pulse width is necessary for high energy resolution measurement. Pulse width of electron linac is much shorter than that of proton accelerator, so electron linac is suitable for our research.

PURPOSE

The purpose of my research is the development of electron linac driven neutron source for nuclear data measurement. Linac will be installed into the core of the "Yayoi" reactor which is now under decommissioning because in Yayoi, handling nuclear fuel materials are permitted. The reason why X-band linac is used for our neutron source is it enables us to set the accelerator in the core. But the klystron will be set out of the core.

COMPTON SCATTERING X-RAY SOURCE

For preliminary test of neutron source installation, 30 MeV X-band Linac has been tested. The Linac was originally designed for Compton scattering monochromatic X-ray source [2], shown in Figure 2. It is consisted of 3 MeV RF gun, alpha magnet, 30 MeV accelerator tube, and laser.

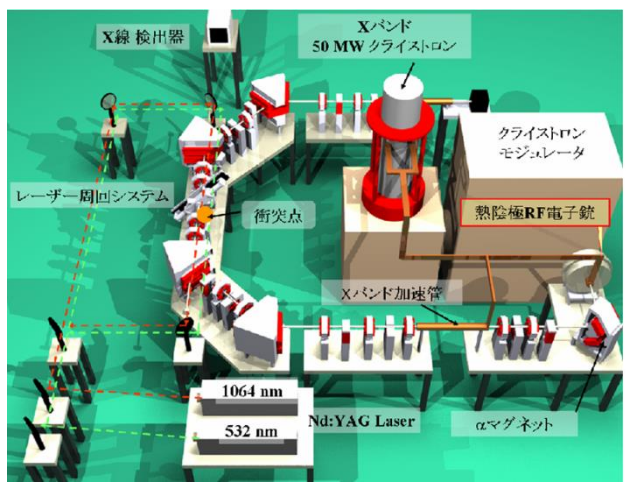


Figure 2: Compton scattering x-ray source.

In December 2012, the experiment of the RF electron gun was done. Figure 3 shows the current of it. The RF gun has is emittance, low current, and stability problem, so it is not suitable for neutron source.

Some part of this system, the RF source, the accelerator tube and the cooling system, will be used in the new neutron source. However, as I explained, RF gun is not suita-

Copyright © 2013 CC-BY-3.0 and by the respective authors

ble, so thermal DC gun and buncher is designed and will be installed. And neutron target is also designed.

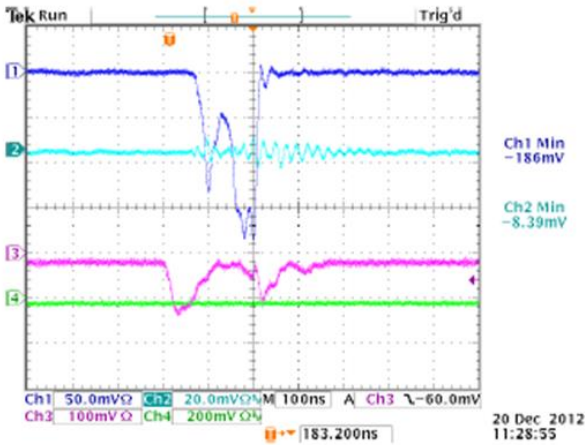


Figure 3: Current of thermal RF gun of Compton scattering x-ray source.

THERMAL ELECTRON GUN AND BUNCHER

Thermal Electron Gun

Stable current is expected to the thermal electron gun so it is suitable for our research. Electric field calculation by POISSON and beam transportation calculation by GPT was done [3-4]. The voltage of the gun was 20 kV. Figure 4 shows the result and Table 1 shows the gained parameters.

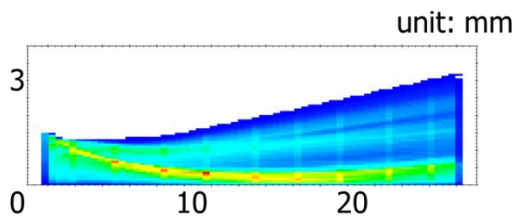


Figure 4: Simulation result of thermal electron gun.

Table 1: Parameters of Thermal Electron Gun

Parameter	Our Thermal Gun
Voltage	20 kV
Cathode Radius	1.5 mm
Beam size (σ) at z = 20 cm	0.224 mm
Emittance at z = 20 cm	0.674 mm-mrad

Buncher

The energy of thermal electron gun is 20 keV, so a buncher is necessary for smooth acceleration. The frequency is 11.424 GHz, the same as the accelerator tube of Compton scattering X-ray source and traveling wave mode is used. Electromagnetic field calculation by SUPERFISH and Beam transportation calculation by GPT was done.

Figure 5 shows the relation between the beam position and the internal diameter of the cavity to keep stable electric field. Figure 6 shows the relation between the electric field and the diameter at the gate of the cavity when the RF power was 5 MW. From this, we decided that the length of the buncher is 20 cm and accelerated energy is 4 MeV.

And from the electron gun and the buncher, the parameter shown in Table 2 can be expected.

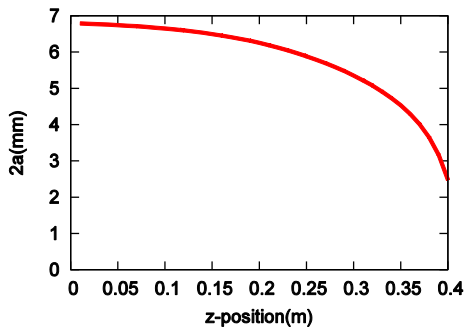


Figure 5: Relation between the beam position and the internal diameter of the cavity.

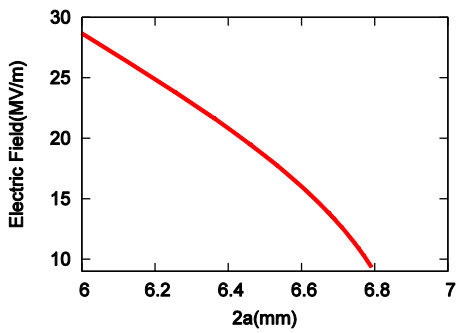


Figure 6: Relation between the electric field and the diameter at the gate of the cavity.

Table 2: Parameters of Electron Beam of Incident System

Parameter	Our Incident System
Energy	30 MeV
Max current	250 mA
Max pulse width	1 μsec
Intensity	50 pps
Max beam power	0.375 kW

NETURON TARGET

Electron linac neutron source has advantage of short pulse, but because of this, power of electron linac is lower than other neutron sources. Therefore, a high efficiency target should be developed for generating neutrons with high flux. Uranium target was simulated because it has photo fission effect and high flux can be expected [5].

Copyright © 2013 CC-BY-3.0 and by the respective authors

Linac will be set in the core of the plant, so nuclear fuel material can be used as the target. Figure 7 shows the neutron flux from various targets, calculated by PHITS, which was developed in JAEA [6]. The electron beam energy was 30 MeV. This shows that uranium target brings about twice as much flux as other target. And when beam energy was 30 MeV, beam power is 0.375 kW and uranium target was used, neutron flux of 3×10^{11} n/s was gained. However, way to treat fission product is important task.

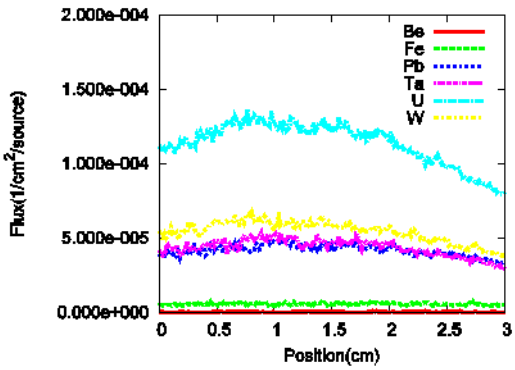


Figure 7: Comparison of neutron flux among several target materials.

CONCULUSION

Neutron source with 30 MeV X-band linac has been developed for measurement of neutron cross section. Thermal neutron gun and buncher were newly designed to combine with the existing accelerator tube. Various neutron target (including Uranium) was designed and neutron flux from target was calculated.In next years, electron beam and neutron beam is going to be measured.

REFERENCES

[1] M.B. Chadwick et al., "ENDF/B-VII.1 Nuclear Data for Science and Technology: Cross Sections, Covariances, Fission Product Yields and Decay Data," Nucl. Data Sheets, 112, (2011) 2887-2996.

[2] M. Uesaka et al., "Monochromatic tunable Compton scattering X-ray source using X-band multi-bunch linac and YAG laser circulation system," Nuclear Instruments and Methods in Physics Res. B 261 (2007) 867-870.

[3] K. Halbach and R. F. Holsinger, "SUPERFISH - A Computer Program for Evaluation of RF Cavities with Cylindrical Symmetry," Particle Accelerators 7 (1976) 213-222.

[4] M.J. de Loos et al. "General Particle Tracer: A new 3D code for accelerator and beamline design," Proceedings of EPAC, Sitges, Spain, p. 1241 (1996).

[5] V. Makarashvili et al., "Simulations of a LINAC-based photoneutron source," Nuclear Instruments and Methods in Physics Res. A 696 (2012) 136-140.

[6] K. Niita et al. "PHITS: Particle and Heavy Ion Transport code System, Version 2.23," JAEA-Data/Code 2010-022 (2010).

Copyright © 2013 CC-BY-3.0 and by the respective authors

DIRECT DIAGNOSTIC TECHNIQUE FOR A HIGH INTENSITY LASER BASED ON LASER COMPTON SCATTERING*

R. Sato†, Y. Yoshida, K. Nonomura, K. Sakaue, A. Endo, M. Washio
Waseda University, Tokyo, Japan

Abstract

In laser produced plasma (LPP) EUV source, high intensity pulse CO_2 laser is essential for plasma generation. To achieve high conversion efficiency and stable EUV power, we would like to measure laser profile in collision point and make feedback system. There is no way to directly measure a high intensity laser profile at the focus point. Therefore, we have been developing laser profiler based on laser Compton scattering. Laser profile can be measured by scanning focused electron beam while measuring Compton scattering signal. We use compact electron accelerator based on Cs-Te photocathode RF gun at Waseda university. Electron beam is focused by solenoid lens. We simulated beam size using GPT, obtained beam size of 10 μm rms. We measured beam size by Gafchromic film HD-810. We have succeeded in observing minimum beam size of about 20 μm rms. In this conference, we will report result of simulation, beam size measurements, and the present progress.

INTORODUCTION

Extreme ultraviolet lithography (EUVL) is the next generation lithography for integrated circuit fabrication at 22nm half pitch mode [1]. In EUVL, several 100W EUV light is based on Sn plasma produced by CO_2 laser. CO_2 laser is required more than 100 kHz repetition rate, 200 mJ, 100 μm spot size and 10 ns pulse duration. To achieve high conversion efficiency and stable EUV power, we would like to measure laser profile in collision point and make feedback system. However, there is no way to directly measure such high power laser profile.

We have been developing laser profiler based on laser Compton scattering (LCS). Laser profile can be measured by scanning focused electron beam while measuring Compton scattering signal. If both laser and electron beam have a gaussian distribution, the observed profile of Compton signal as a function of electron position is a gaussian distribution. Observed rms width can be written down as;

$$\sigma = \sqrt{\sigma_{\mathrm{laser}}^2 + \sigma_{\mathrm{electron}}^2} \qquad (1)$$

where σ_{laser} is the laser beam size, $\sigma_{\mathrm{electron}}$ is the electron beam size. If the electron beam size is much smaller than that of laser, the observed profile would be equivalent to the laser profile. To scan electron beam from various direction and reconstruct image used CT technique, we can obtain 2D laser profile.

Focused electron beam is a key issue of this method. The more electron beam is focused, the higher resolution laser profile we can obtain. To achieve small beam spot, we use low emittance electron accelerator and special design solenoid lens. In this paper, we discuss GPT simulation and results of beam size measurement by Gafchromic film.

ACCELERATOR SYSTEMS

A photocathode rf gun is one of the most high quality electron source. Because of high gradient electric field on the cathode, it can generate small emittance beam. At Waseda university, we have been performed the high quality electron beam generation and applied research experiments, such as laser Compton soft-Xray generation [2] and pulse radiolysis [3].

The cavity structure is based on the design of the BNL Type IV, which have 1.6 cell structure. The rf frequency is 2856 MHz. The cavity is able to produce low emittance beam with 5 MeV beam energy. We use Cs-Te photocathode which have a high quantum efficiency and achieve 1 nC / bunch. The seed laser is Nd:YLF mode lock oscillator with 119 MHz frequency. We use LN intensity modulator to pick pulse train, it chooses the number of pulses from 1 pulse to 100 pulses. The pulse trains are amplified by Yb fiber amplifier and LD pumped amplifier 4 pass system. After two amplifications, IR pulses are converted to UV pulses by two nonlinear doubling crystals.

The experiment set up is shown in Fig. 1. There are beam diagnostic instruments. A current transfer measure beam charge and pulse train stability. Alumina fluorescent plate (Demarquest Co.) beam profile monitor is located behind solenoid magnets. 45 degree bending magnet is used for energy measurement. Our accelerator system is characterized it's small structure, the total length is less than 3 m.

For this experiment, we designed new solenoid lens. The

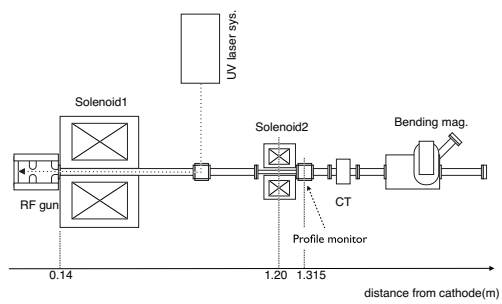


Figure 1: Schematic design of Waseda beam line.

* Work supported by NEDO(New Energy and Industrial Technology Development Organization).
† wase-nishicab61@akane.waseda.jp

Copyright © 2013 CC-BY-3.0 and by the respective authors

lens shape and magnetic field was studied POISSON simulation code. The magnetic field calculated by POISSON and measured is shown in Fig. 2. Position is axis of beam traveling direction. To focus 5 MeV electron beam, we designed to achieve that a maximum magnetic strength is 0.6 T.

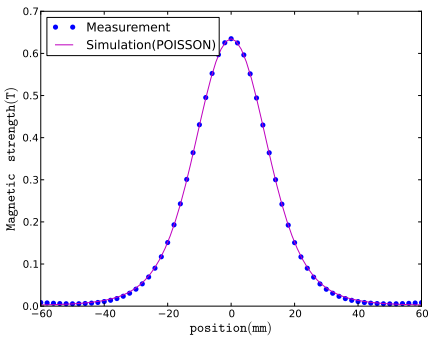


Figure 2: Magnetic field of Solenoid 2.

BEAM TRACKING BY GPT

We calculated focused electron beam by General Particle Tracer (GPT) [4]. The field of rf cavity and solenoid magnets were calculated by SUPERFISH and POISSON. Parameters of GPT are shown in Table 1. Number of particles seems very little, but there are no significant deference in results of beam size and emittance. Therefore, we used results of 1k data to optimize beam parameters and solenoid lens strength.

Figure 3 show beam size as a function of distance from cathode. The rf cavity accelerate the beam, and the emittance growth is controlled by Solenoid 1. The new solenoid lens, Solenoid 2, is placed 1.2 m downstream. It strongly focus the beam, Fig. 3 show the beam was focused to 15 μm at the position of 1.314 m.

Table 1: Parameters of GPT Simulation

Number of particles	1000
Space Charge	3D
Charge	50pC
Electric filed at cathode	100MV/m
Initial laser spot size	0.3 mm
Solenoid 1 strength	0.13 T
Solenoid 2 strength	0.5 T

Figure 4 show beam size at the focus point as a function of Solenoid 2 strength. The smaller beam spot is achieved as strong magnetic strength. On the other hand, a strong focusing make short focus distance and short focus spot. These characterization are obstacle to focus on the collision point.

Beam size and emittance versus beam charge is shown in Fig. 5. Smaller beam spot is also available by lower charge. 10 μm beam spot was achieved with 50 pC beam charge. In LCS, Compton signal flux depends on electron beam charge and laser intensity. Smaller beam spot and higher beam current are need, it is a contradictory demand. We plan to operate 50 $\sim$ 100 pC beam charge at LCS experiment. In this situation, calculated photon number is 8×10^4 photons / pulse, which is large enough for detecting LCS signal.

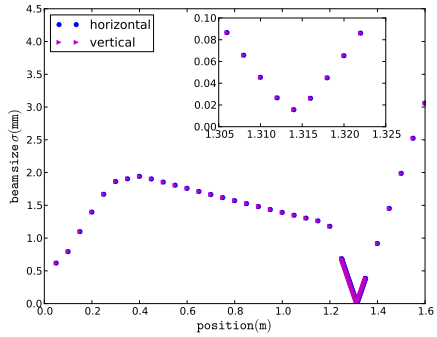


Figure 3: Beam size as a function of distance from cathode.

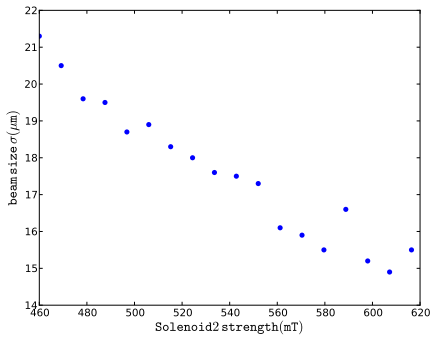


Figure 4: Beam size as a function of Solenoid 2 strength.

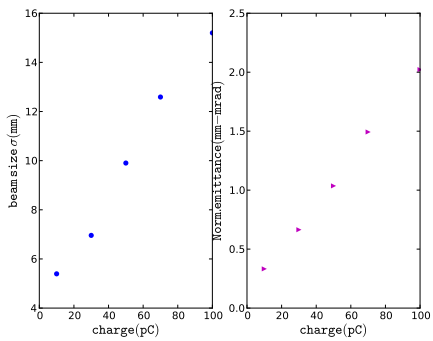


Figure 5: Beam size (left) and normalized eimttance (right) as a function of beam charge.

Copyright © 2013 CC-BY-3.0 and by the respective authors

BEAM SIZE MEASUREMENT

Gafchromic Film

Gafchromic radiochromic film [5] is used for measuring a beam intensity distribution. The film is discolored by ionizing beam irradiation. We choosed HD-810, this film is commonly used for the measurement of absorbed dose of high energy photons. First, we calculated divergence of electron beam in HD-810 by Monte Carlo simulation code EGS5. The results show the beam was't expanded in active layer (6.5 μm thickness).

Optical density (OD) of HD-810 was measured by a cold CCD camera. For the dose calibration, we irradiated electron beam with various irradiation time. Figure 6 show the result, and we used this calibration curve for beam size measurements.

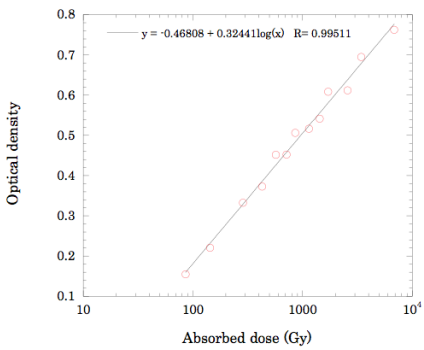


Figure 6: Calibration curve of HD-810 film.

Beam Size Measurement

We measured focused beam size by HD-810. The beam profile measured by HD-810 is shown in Fig. 7, focused beam size as a function of Solenoid 2 strength is shown in Fig. 8. The plots of Fig. 8 show average size of 3 measurements. In this experiment, the beam was 50 pC, 3.5 MeV and the irradiation time was 1 s. We achieved about 20 μm spot size. This results show our accelerator system fulfills the demand for high intensity laser profiler.

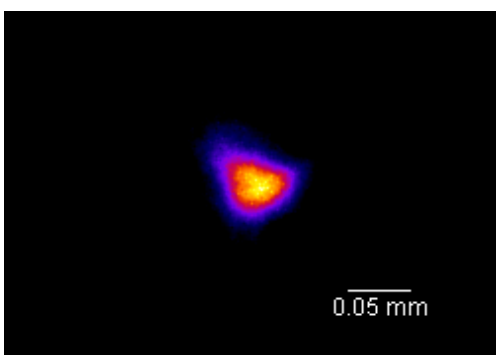


Figure 7: Beam profile measured by HD-810 film.

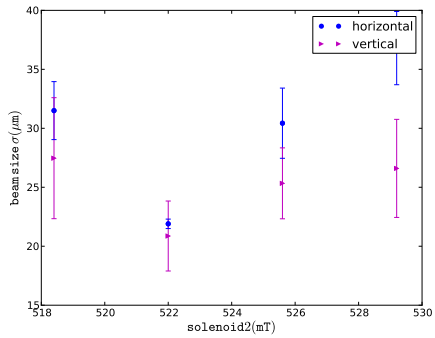


Figure 8: Beam size as a function of Solenoid 2 strength.

CONCLUSION

At Waseda university, we have been developing laser profiler based on LCS. Laser profile can be measured by scanning electron beam while measuring Compton scattering signal. Focused electron beam is a key issue of this method, so we designed new solenoid lens and measured beam size using HD-810. We achieved beam size of 20 μm, this is satisfactory beam size for laser profiler.

To produce small beam size, we have to operate with low beam charge. Therefore, we plan a multi bunch generation to 1 pulse of CO_2 laser. Our seed laser repetition rate is not satisfied this concept, so we will use optical delay line to change repetition rate. The UV pulse separate by PBS, and the pulse which is leaded to optical delay line return the initial line with 350 ps (2856 MHz) delay time.

We are preparing high repetition system, pulse CO_2 laser and the spectroscope to detect Compton scattering signal. In this winter, LCS experiments will be held to obtain CO_2 laser profile.

REFERENCES

[1] A. Endo, InTech (2012) DOI: 10.5772/38716

[2] K. Sakaue, et al., Radiat. Phys. Chem. 77 (2008) 1136-1141

[3] Y. Hosaka, et al., Radiat. Phys. Chem. 84 (2013) 10-13

[4] General Particle Tracer; `http://www.pulsar.nl/gpt/`

[5] Gafchromic film; `http://www.gafchromic.com/`

Copyright © 2013 CC-BY-3.0 and by the respective authors

CONCEPTUAL PHYSICS DESIGN FOR THE CHINA-ADS LINAC

J.Y. Tang*, P. Cheng, H.P. Geng, Z. Guo, Z.H. Li, C. Meng, H.F. Ouyang, S.L. Pei, B. Sun, J.L. Sun, F. Yan, C. Zhang, Z. Yang, IHEP, CAS, Beijing 100049, China
Y. He, Y. Yang, IMP, CAS, Lanzhou 730000, China

Abstract

The China-ADS project was launched in 2011 to pursue the R&D on key technologies towards a final demonstration facility on ADS with the capability of more than 1000 MW thermal power. The driver linac is defined to be 1.5 GeV in energy, 10 mA in current and in CW operation mode. It employs the superconducting structures except the RFQs. To meet the extremely high reliability and availability, the linac is designed with much installed margin and fault tolerance, including hot-spare injectors and local compensation method for key element failures. The accelerator complex consists of two parallel 10-MeV injectors, a joint medium-energy beam transport line, a main linac and a high-energy beam transport line. The conceptual physics design including beam dynamics studies with multiparticle simulations is presented here.

INTRODUCTION

The C-ADS (or China-ADS) project is a strategic plan to solve the nuclear waste problem and the resource problem for nuclear power plants in China. With its long-term planning, the project will be conducted in three or four major phases with the final goal to build a demo transmutation facility by 2032.

The C-ADS accelerator complex is a large CW proton linac consisting of several sections and uses superconducting (SC) acceleration structures except the RFQs, which is under developing in collaboration at IHEP and IMP. The main design specifications for the proton beam at the ultimate stage are shown in Table 1.

Table 1: Specifications for the C-ADS Linac

Particle	Proton	Unit
Energy	1.5	GeV
Current	10	mA
Beam power	15	MW
RF frequency	(162.5)/325/650	MHz
Duty factor	100	%
Beam Loss	<1	W/m
Beam trips/year[1]	<25000 <2500 <25	1s<t<10s 10s<t<5m t>5m

*tangjy@ihep.ac.cn

DESIGN CONSIDERATIONS

The C-ADS linac is designed to have very high beam power and very high reliability, which surpasses those of the existing proton linacs by far. However, several proposed CW proton/deuteron linac projects such as Project-X [1-2], EFIT or MYRRHA [3], IFMIF [4] and EURISOL [5], etc. are good models for the physics design and technical design of the accelerator. In addition, some pulsed high power proton linacs and some CW heavy ion linacs using SC cavities also serve as good reference examples. Although most of the design philosophy for the linac has been addressed by previous literatures, we still list the main principles here: 1) the whole linac consists of SC cavities except the RFQ which is room-temperature; 2) installed redundancy for all the parts of the accelerator will be applied; 3) as low as possible beam losses along the linac, with an upper limit of 1 W/m in warm sections and even lower in cold sections; 4) the acceleration efficiency and the number of cavity types will be balanced; 5) different transverse focusing structures are used to follow the acceleration structures and beam properties in different acceleration sections; 6) tune depression will be controlled to stay in the emittance dominated regime preferably; 7) the growths in both the rms emittance and halo emittance should be controlled strictly, and the ratio of acceptance and rms emittance should be kept large to avoid severe beam beams; 8) the phase advance per period is controlled below 90° to avoid parametric resonances.

DIFFERENT ACCELERATION SECTIONS

The linac consists of two injectors, a special medium-energy beam transfer line (MEBT2), and the main linac, as shown in Figure 1. Two identical injectors will be operated in the mode of one as the hot-spare of the other to provide quick switch in case of failure of the one in delivering beam to the main linac, which is considered crucial to achieve very high reliability of the whole accelerator. MEBT2 is to transport and match the beam from either of the two injectors to the main linac. However, in the early developing phase two different approaches of injector will be developed in parallel by two different teams. At a later phase, a decision based on the R&D development will be made about which injector scheme will be used in the future phase. The main linac section that consists of different acceleration sections will be developed in phases.

Copyright © 2013 CC-BY-3.0 and by the respective authors

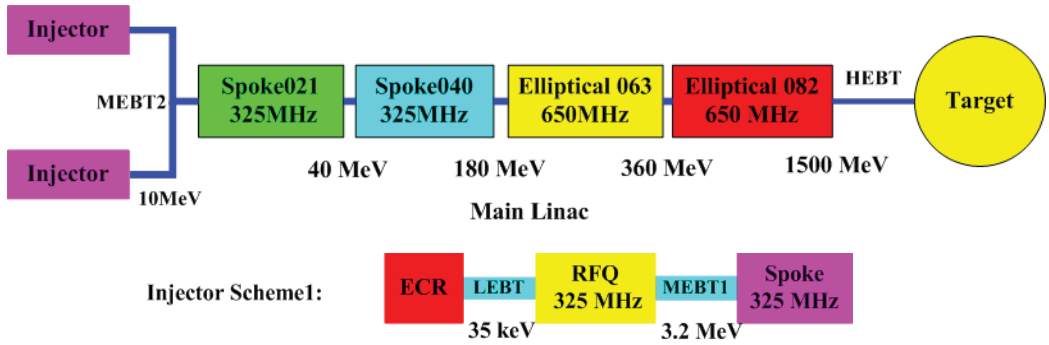


Figure 1: Layout of the C-ADS linac.

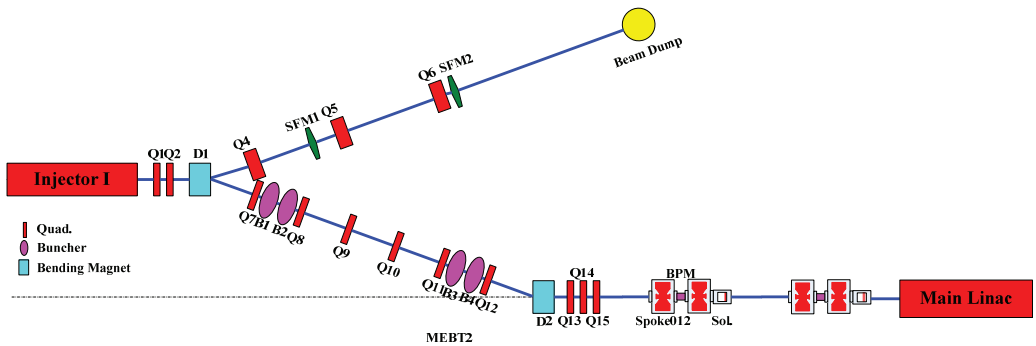


Figure 2: Schematic for MEBT2.

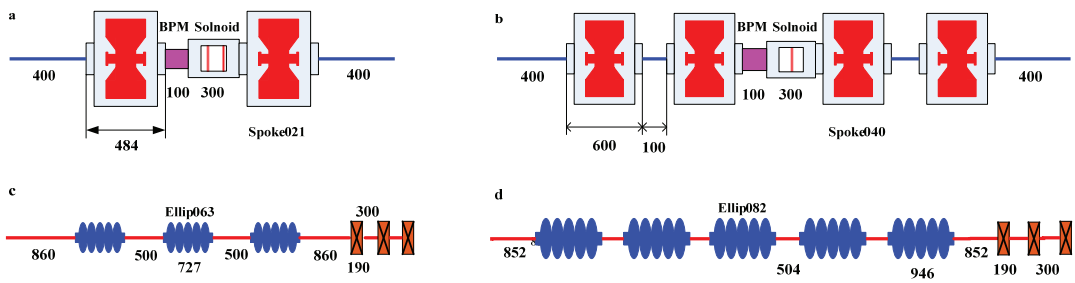


Figure 3: Lattice for the four sections in the main linac.

Injector

For the Injector-I scheme, a 325-MHz, 3.2-MeV, 4-Vane RFQ has been designed and a test stand is under fabrication. The inter-vane voltage is 55 kV, much smaller than the popular design, aiming to decrease the power density to a safe level. The injection energy of 35 kV is helpful in obtaining a relatively smaller output longitudinal emittance (0.16 mm.mrad in normalized rms), which is about 0.8 times the transverse one. The small longitudinal emittance is found very useful in designing the downstream SC sections. Then the MEBT1 [6] is to match the beam between the RFQ and the SC section of the injector. It is mainly composed of two bunchers, six quadrupoles and beam instrument devices.

The SC section of the injector has one long cryomodule (CM) of 8.5 m with twelve single spoke cavities [7] and eleven solenoids inside; it will accelerate the beam to 10 MeV. The geometry beta of the cavity is only 0.12 which is considered very small, and it increases the difficulty of developing the cavity. The compact lattice with short solenoid (150 mm) and larger absolute synchronous phase (-46 ~ -30°) is applied to improve the longitudinal beam dynamics.

MEBT2

It is a real challenge to design a merging beam line to connect the two injectors to the main linac, as this is a high-intensity beam requiring very strict control over beam loss and emittance growth. It is found difficult to control the emittance growths when a bending section is present, especially with the bunchers within the section. MEBT2 is also supposed to have a good collimation system to scrape the beam halo and non-trapped particles. The beam will be directed to a beam dump through an auxiliary beam line with a much reduced beam power when the injector is working in the hot-spare mode. The

Copyright © 2013 CC-BY-3.0 and by the respective authors

dump line is also used for the commissioning or beam setup of the injector.

As shown in Figure 2 [8], each of the mainstream lines of the MEBT2 consists of eight quadrupoles, two 20°-bending magnets and four 325-MHz single-gap normal conducting re-entrant type bunchers. In the common part, three quadrupoles, two Spoke012 cavities and two solenoids are used for the matching, while another two Spoke012 cavities serve as the back-ups.

Main Linac

To meet the strict requirement on stability and reliability, over-design, redundancy and fault tolerance strategies are implemented in the basic design. The fault tolerant design in the main linac is guaranteed by means of the local compensation and rematch method [9-10]. To cover the whole energy range from 10 MeV to 1.5 GeV in the main linac, at least four types of SC cavities are needed. We have chosen two single-spoke cavities working at 325 MHz with geometry β of 0.21 and 0.40, respectively, and two 5-cell elliptical cavities working at 650 MHz with geometry β of 0.63 and 0.82, respectively. For the nominal design, only 3/4 of the maximum available cavity voltage is used, whereas another 1/4 is reserved for the local compensation, and this redundancy is also beneficial to the cavity reliability.

There are four sections each consisting of one type of cavity, Spoke021 and Spoke040 for the lower energy part and Ellip063 and Ellip082 for the higher energy part. The lattice structures for each section are shown in Figure 3. The matching between two neighbouring sections is guaranteed by varying the parameters of the adjacent cavities and transverse focusing elements. With warm transitions between CMs, the replacement of failed CMs can be easily carried out; in addition, beam diagnostics and collimators can be arranged in the warm sections.

In total, thirty-eight Spoke021 cavities in seven CMs, sixty-four Spoke040 cavities in eight CMs, forty-two Ellip063 cavities in fourteen CMs and one hundred Ellip082 cavities in twenty CMs are used in the main linac. All the CMs have modest length of 5-10 m.

SOME SIMULATION RESULTS

End-to-end beam dynamics simulations are performed from the input of the RFQ to the end of the linac to verify the general beam dynamics and the matching between each part. The initial particle distribution at the entrance of the RFQ is assumed as 4D water-bag distribution with transverse rms emittance of 0.2 πmm mrad and the total particle numbers are 100000, and the optimized distributions at the RFQ exit are applied as the initial particle distributions for TraceWin.

The evolutions for both the rms emittances and halo emittance with different fractions are studied (see Figure 4). MEBT2 contributes to very important growth of the 100% emittance, almost 5 times in the transverse planes. It is expected that some halo particles can be collimated in MEBT2 with proper collimation schemes.

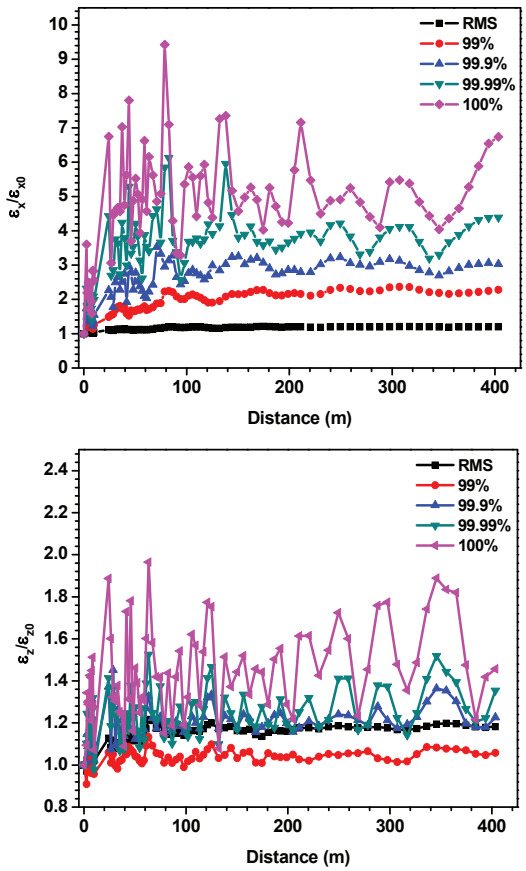


Figure 4: Halo development along the linac for different beam fractions.

ACKNOWLEDGMENT

The study is supported by the CAS Strategic Priority Research Program on ADS, and also by National Natural Science Foundation of China (Projects 11235012 and 10875099).

REFERENCES

[1] S. Nagaitsev, Proc. of 2011 PAC, New York, (2011) 2056.
[2] P.N. Ostroumov, New Journal Physics 8 (2006) 281.
[3] J-L. Biarrotte, F. Bouly, S. Bousson et al., Proc. of PAC09, Vancouver, Canada, (2009) 668.
[4] P.A.P. Nghiem, N. Chauvin, O. Delferriere et al., Proc. of HB2010, Morschach, Switzerland, (2010) 309.
[5] A. Facco, A. Balabin, R. Paparella et al., Proc. of Linac08, , Victoria, BC, Canada, (2008) 257.
[6] Jingyu Tang and Zhihui Li (ed.), Conceptual physics design of the C-ADS accelerators, IHEP-CADS-Report/2012-01E.
[7] C. Meng, Z.H. Li, J.Y. Tang, Error analysis and lattice improvement for the C-ADS Injector-I, in publishing in Chinese Physics C.
[8] Z. Guo, H.P. Geng, Z.H. Li, J.Y. Tang, Proc. of HB2012, Beijing, China, (2012).
[9] B. Sun et al., Proc. of HB2012, Beijing, China, (2012) 102.
[10] Z.H. Li, P. Cheng, H.P. Geng, et al., Phys. Rev. ST Accel. Beams 16, 080101 (2013).

Copyright © 2013 CC-BY-3.0 and by the respective authors

THZ BAND HORN ANTENNAS DESIGN

T.V. Bondarenko, S.M. Polozov, A.Yu. Smirnov,
National Research Nuclear University MEPhI, Moscow, Russia

Abstract

The report is concerned with the development of the irradiating antennas for THz radiation source. The THz radiation is irradiated by relativistic high brightness electron bunch traveling through the Cherenkov decelerating capillary channel [1]. Irradiation systems are built as horn antennas type with circular and rectangular cross-sections. Irradiating antennas are constructed directly to the open end of the capillary channel and are used for the THz radiation directivity enhancement after passing through the capillary output. The investigation of the horns directivities were performed using the far-field analysis of the emerging radiation. The antennas were also investigated to perform low values of the reflected power.

INTRODUCTION

High-power THz radiation source based on photoinjector and decelerating capillary channel is now one of the most discussable compact facilities providing monochromatic THz radiation of power high enough to be used for cargo introscopy [2].

Facility is based on two main parts: accelerating structure and decelerating radiating channel. Capillary is placed right after the accelerating structures and is made of copper with either dielectric coated inner surface or corrugated surface.

For effective irradiation of THz radiation from the capillary structure the high values of capillary RF matching with the open space and high directivity values are out to be fulfilled. Capillary that irradiates in the free space with its open end doesn't provide enough directivity that can be seen from the angular pattern shown in the Fig. 1. To enhance the directivity of the radiation the open end of the capillary must be attached to the irradiating antenna. As the capillary has a circular cross-section the optimal geometry of the horn is based on the horn antenna that is directly fitted to the metal parts of the capillary and is fabricated with it as a whole entity.

Main parameters of the antenna are the directivity, angle between the longitudinal axis and main lobe, main lobe angular width and horn power reflection coefficient. Angular width of the main lobe is the parameter defining the distance between two directions of the lobe with 3dB power decay between them. Important parameter is also bandwidth of the horn that is defined as frequency difference between horn working frequency (resonant frequency of the capillary) and the frequency of horn -20dB power reflection level.

There are several different types of horn designs. This article is concerned with the modelling of the horns with circular and rectangular cross sections. All antennas are discussed for the metal Cherenkov irradiating capillary with 300 μm aperture and 31 μm polytetrafluoroethylene coating on the metal surface. Resonant frequency of this type of capillary is 0.96 THz. Work band on the level of -3 dB of the maximal power transmission is 3.2%.

CIRCULAR HORN ANTENNA

Circular antenna is the most conventional type of antenna for such devices (Fig. 2). The model of the horn was built and calculated using the CST Microwave Studio [3]. To define the maximum effective horn parameters the electrodynamics characteristics were studied while varying the horn geometrical parameters. The opening angle was varied while the horn length was kept L=1 mm (fig. 3). After that with the angle equal 14.5 degrees (that corresponds to maximal directivity of the horn) length of the horn was varied (Fig. 3). The investigations were held in the frequency band of 0.7-1.1 THz.

The graphs in the Fig. 3 show that the increase of the horn opening angle decreases its directivity and bandwidth. Main lobe width is increased at the same time. Variation of the horn length leads to the enhancement of the directivity at the 4.8 mm length and then results in its reduction with higher values of the parameter. Inverse relationships are specific for main lobe direction and angular width.

Minimum of the reflection coefficient is defined at the 1 THz region for all discussed geometries. Opening angle enhancement leads to growth of the reflection on the resonant frequency value and bandwidth of the horn decreases. The frequency dependent values of the power reflection coefficients for varying geometrical sizes are depicted in the Fig. 4.

For more clearance the visualization of the horn directivity the directional diagrams are depicted in the Fig. 5. The diagrams are shown for the maximal directivity case of the horn antenna (length of the horn is 4.8 mm and 14.5 degrees opening angle). For maximal values of the mail lobe angular width the same graphs are shown in the Fig. 6. Antenna has corresponding parameters: 4.8 mm length and 57 degrees opening angle.

Characters of all dependences confirm the convention model of horn antennas modeling for lower frequency ranges.

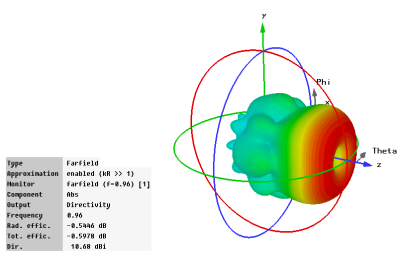


Figure 1: Directivity diagram of the open capillary end.

Copyright © 2013 CC-BY-3.0 and by the respective authors

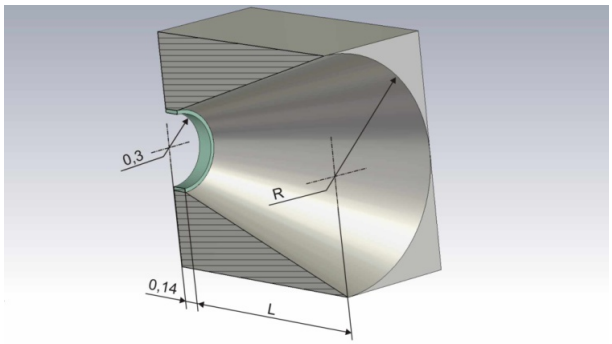


Figure 2: Circular horn antenna and the capillary.

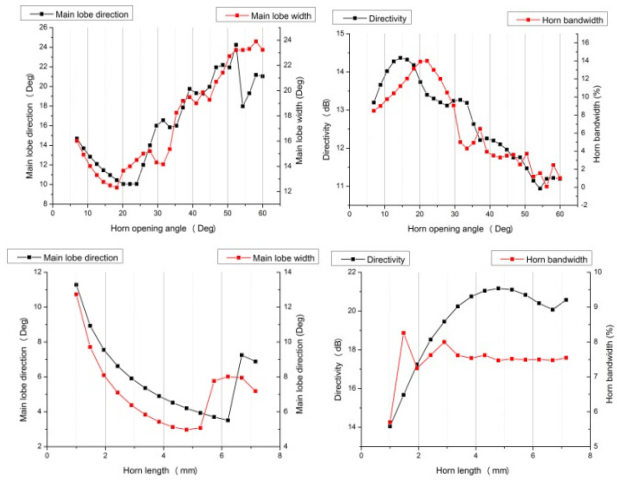


Figure 3: Dependences of electrodynamics characteristics vs. circular horn geometrical sizes.

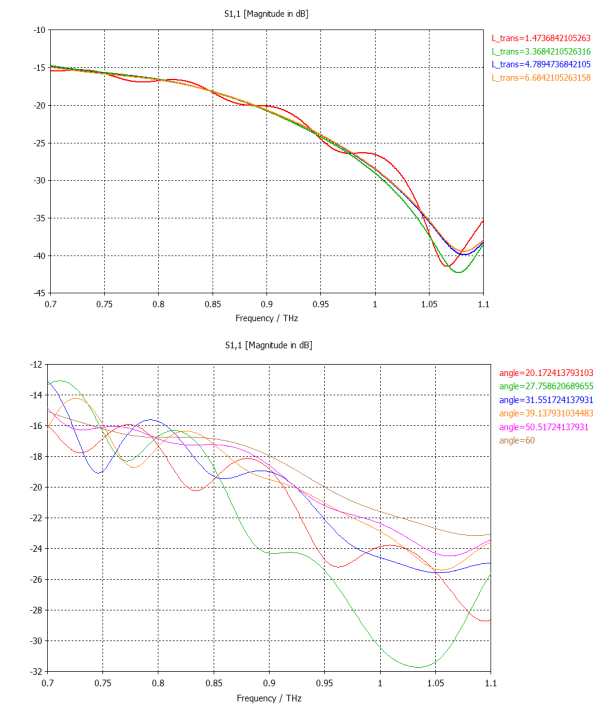


Figure 4: Reflection coefficients of the horn for different geometrical sizes of the horn.

At one definite point of horn opening it has maximal directivity and minimal value of main lobe angular width, minimal reflection coefficient and maximal bandwidth. Increasing of reducing of the angles leads to characteristics dramatic changing. Reduction of angular opening leads to unoptimized parameters levels and increasing – to enhanced values of phase distortions in its opening [3].

RECTANGULAR HORN ANTENNA

The second type of considered horns is the horn with variable cross-section (transition from circular to rectangular). The horn is attached directly to the coated capillary. The transition from circular to rectangular cross-section is done directly inside the opening (Fig. 7). To investigate the horn parameters the electrodynamics characteristics were tracked while changing the horn geometry.

The outstanding feature of this type horn vs. the circular horn is possibility to acquire the straightforward main lobe of the radiation. Dependences reveal the increase of horn directivity while opening angles reduction in both directions (Fig. 8). Increase of the openings in one of the planes leads to dramatic increase of the main lobe in this plane and a little less increase in another plane. Power reflecting coefficient of the horn increases if one of the opening angles equals zero. At even more increase of the parameter doesn't change. Horn bandwidth increases with opening increase and reaches the borders of investigated frequency region with the vertical opening angle equal 7.5 degrees [4].

For the case of maximal directivity of the horn (15 degrees opening angles in both planes) the length variation was held. The results of investigation consist in maximal directivity equal 22.5 dB with the horn length 2 mm. In whole band of 0.7-1.1 THz the reflection coefficient doesn't increased of -20 dB.

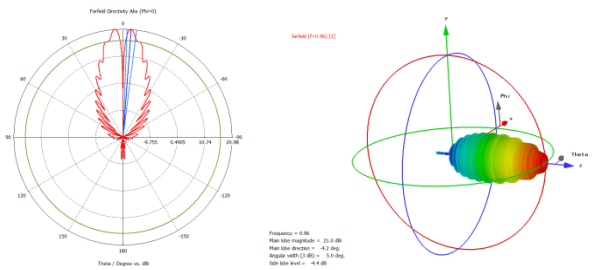


Figure 5: Circular pattern and 3D diagram for maximal directivity of circular antenna.

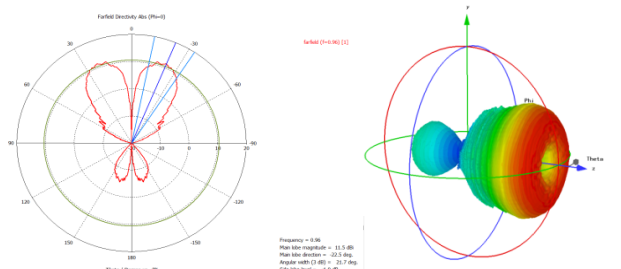


Figure 6: Circular pattern and 3D diagram for maximal main lobe angular width of circular antenna.

Copyright © 2013 CC-BY-3.0 and by the respective authors

For the horn with maximal directivity (2.71 mm length, opening angles 15 degrees) the circular patterns of the horizontal and vertical directions and 3D directivity diagram were acquired. The side lobes are practically absent and the main lobe is directed straight forward (Fig. 9). For the case of maximal main lobe angular width (7 mm length, 15 degrees vertical opening angle and 60 degrees horizontal one) the diagrams are represented in the Fig. 10.

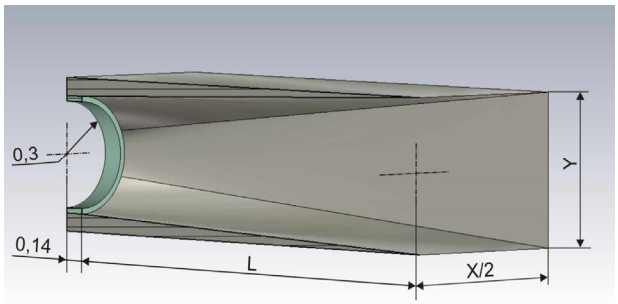


Figure 7: Horn antenna with circular to rectangular cross section transition and the capillary.

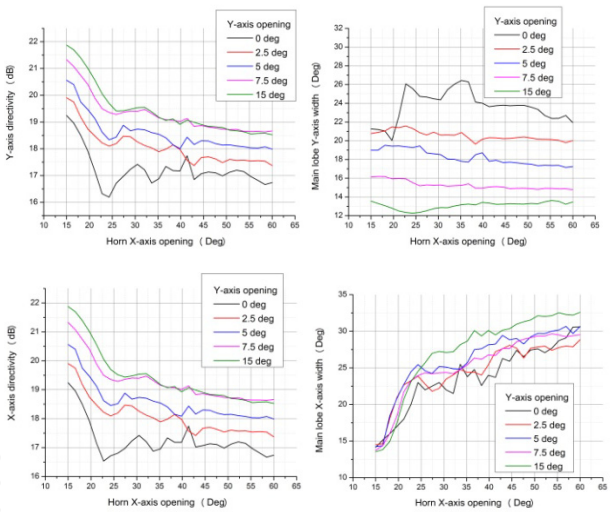


Figure 8: Dependences of electrodynamics characteristics vs. rectangular horn geometrical sizes.

CONCLUSION

By the means of the investigation results it turns out that to acquire high directivity of the THz radiation from the Cherenkov channel irradiating horn antenna can be effectively exploited. For the case when there is no need to irradiate the object placed directly on the axis of the channel the circular cross-section horn can be applied. If there is a demand for irradiation of the axis-aligned objects the rectangular cross section antenna can be used. Herein both types of the horns can be well-directed (~20 dB main lobe) after optimization and provide low levels of power reflection rates (<20 dB). Parameters and directivity diagrams of the both types of horns are declared for the cases of maximal directivity and for maximal main lobe angular widths.

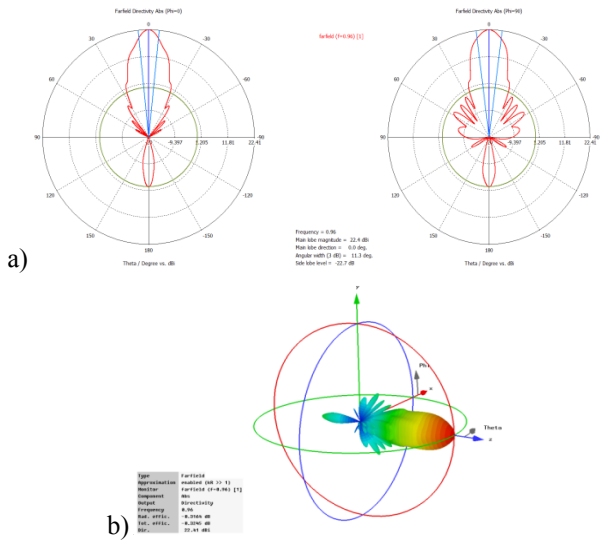


Figure 9: Circular pattern in horizontal plane (a - left), in vertical plane (a - right) and 3D directivity diagram for maximal directivity of rectangular antenna.

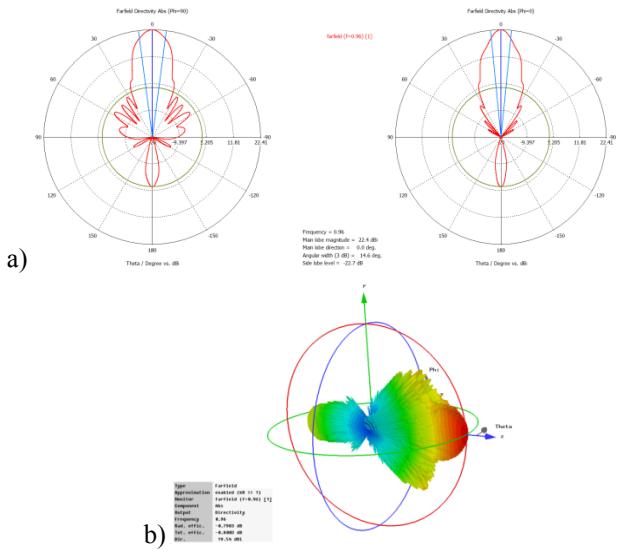


Figure 10: Circular pattern in horizontal plane (a - left), in vertical plane (a - right) and 3D directivity diagram for maximal main lobe angular width of rectangular antenna.

REFERENCES

[1] Bashmakov Yu.A., Bondarenko T.V., Polozov S.M., et al. RF photogun and Cherenkov decelerating system for a high power radiation source in sub-mm region / Problems of Atomic Science and Technology. Series: Nuclear Physics Investigations, 3 (79), 2012, p. 92-95.

[2] A.V. Smirnov, Nuclear Instruments and Methods in Physics Research A 480 (2002), 387–397.

[3] CST GmbH – Computer Simulation Technology, CST Microwave Studio 2006 user manual, 2006, http://www.cst.com

[4] Drabkin A.L., Zuzenko V.L., Kislov A.G., Antenna - feeder devices / M. “Sov. Radio”, 1974, 536 p. (in Russian).

Copyright © 2013 CC-BY-3.0 and by the respective authors

ANALYSIS OF PROPAGATED EFFECTS IN PROTON DEPTH-DOSE DISTRIBUTION CURVES DUE TO INITIAL BEAM ENERGY SPREAD

S. Zalel*, J.F. Piech, UROP students, Imperial College London
M. Aslaninejad, P. A. Posocco#, Imperial College London

Abstract

Proton therapy treatment planning uses depth-dose distribution curves of single initial beam energies to create Spread spread Out Bragg Peaks (SOBP). These are used to target specific regions in the body. However, the initial energy spread of the beams leads to an uncertainty in beam energy, affecting the dose distribution. In this paper, previous work (M. Aslaninejad et al., 2011: 189–196) on the depth-dose distribution of proton beams using inelastic-collision cross sections of liquid water is extended into use with chromatic beams. The effect of the initial energy spread on depth-dose distribution curves, the distal dose and the SOBP are discussed. Limits on beam energy spread are suggested.

INTRODUCTION

Proton therapy is advantageous over conventional radiation therapy as particles lose most of their energy at a particular location, depending on their initial energy. This effect is usually represented by means of depth-dose distribution curves. These are characterised by the Bragg Peak (BP) where the relative dose reaches a sharp maximum. As the range and shape of the BP depends on initial beam energy, the energy spread of protons within a beam distorts the theoretical BP and potentially compromises the effectiveness of the treatment. In this paper we extend previous work to account for the energy spread within a therapeutic proton beam.

Depth-dose distribution curves are a useful tool indicating which region will be most affected by incoming radiation. In the code developed in [1] depth-dose distribution curves in water are created by modelling proton beams using a combination of semi-empirical models and the Bethe-Bloch theory. At energies below 1 MeV the cross section is defined by a combination of semi-empirical models, such as the model of ionization processes by Rudd et al.. The stopping cross section gives information on the energy transferred per unit length as a function of particle energy. The total stopping cross section is the sum of the stopping cross sections of all interactions contributing to energy. Nuclear processes are disregarded.

The Bethe-Bloch formula is a good approximation for calculating energy lost per distance travelled for fast charged particles (i.e. with energies higher than 1MeV). Equation 1 shows the Bethe-Bloch formula according to Groom and Klein [2]:

$$\frac{1}{\rho}\frac{dE}{dx} = Kz^2\frac{Z}{A}\frac{1}{\beta^2}\left[\frac{1}{2}\ln\frac{2m_e c^2\beta^2\gamma^2 T_{max}}{I^2} - \beta^2 - \frac{\delta(\beta\gamma)}{2}\right], \quad (1)$$

where z it the charge of the incident particle, Z and A are the atomic number and the atomic mass of the absorber, respectively. I is the mean excitation energy, $\delta(\beta\gamma)$ is the density effect correction to ionisation energy loss and β and c are the usual relativistic factors. T_{max} is the maximum kinetic energy which can be imparted to a free electron in a single collision.

Other considerations that were taken into account in the code are:

- Straggling model: range travelled by individual protons is governed by a Gaussian distribution.
- Fragmentation: effectively reduced fluence attributed to proton decay.

These lead to the broad-beam depth-dose curve characterised by increased peak width and reduced peak height. Multiple scattering was also considered; this changes the shape of the depth-distribution by changing the ratio of peak to entrance dose.

EXTENSION TO CHROMATIC BEAMS

In the discussion above proton beams of single defined energies are used. However, real beams are characterised by an energy spread. This is due to individual characteristics of the accelerator, beam transport, and collimation system [3]. The width of the initial energy spectrum is expressed as a percentage error in the initial beam energy and is estimated in the order of magnitude of ±1% [4]. In this paper a superposition of Gaussian probability weighted monochromatic beams was used to simulate chromatic depth-dose distribution curves and values of up to 2% sigma have been used for several initial beam energies. This analytical method is a good approximation for the peak itself, however the shape of the tail is affected largely by other factors and may vary further from the model used [3].

The Effect of Energy Spread on the Bragg Peak

The depth dose distributions curves created for single proton Bragg peaks as function of the initial beam energy spread were used to study the effect of the chromatic beam on the treatment. The depth dose distributions of the proton beams were modelled along a 1-D axis being the path of the proton. Effects of 3-D scattering were not included.

Depth-dose distribution curves of varying initial energy spreads were produced for 70, 100, 150, 200 and 250 MeV to cover the entire range of energies used for treatment, with energy spreads of 0.1%, 0.2%, 0.5%, 1% and 2% sigma.

Figure 1 shows the effects of increasing energy spread on the BP for a 200 MeV proton beam. Due to the

*Supported by the Anglo Israel Association
#p.posocco@imperial.ac.uk

Copyright © 2013 CC-BY-3.0 and by the respective authors

superposition of the BPs of different energy and therefore slightly different range, we can observe that:

- The peak's height decreases,
- The peak's depth decreases and
- The peak's width increases.

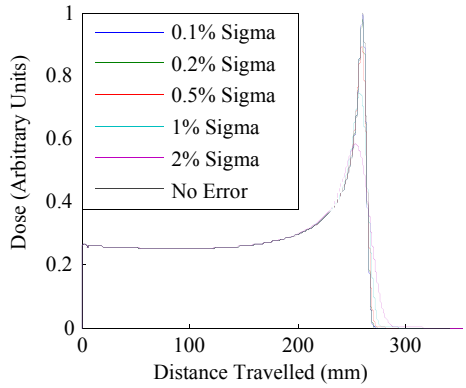


Figure 1: BPs (200 MeV) for different initial energy spread. Each BP has the same dose integral.

As the width of the Bragg Peak is of particular interest for the treatment, it was studied quantitatively. The peak width was defined as the distance from the peak's top to the distal point of a chosen percentage of peak's dose. Distal points of 95%, 50% and 5% of peak dose were used. Figure 2 shows the trend of 95% peak width for increasing energy spreads. As anticipated above, the distributed dose decreases less sharply for beams with a wider energy spread, meaning higher distal dose and more healthy irradiated tissue. While there is less of an effect in using lower energies, higher energy beams have a larger increase in peak width with increasing energy spread.

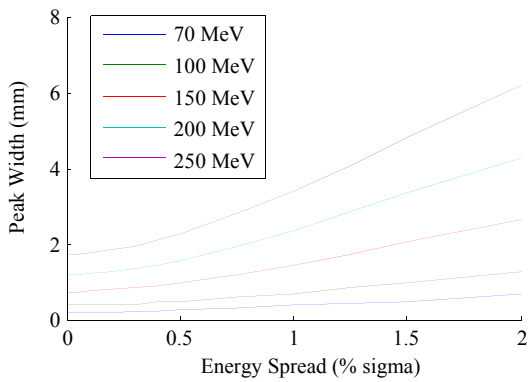


Figure 2: Peak width as distance between peak dose and distal 95%.

Investigations at all distal points found that the peak width is barely affected at energy spreads lower that 0.3% sigma. This is also the threshold point after which the distal dose rises significantly with energy spread. The distal dose encounters a 50% increase around 1% energy spread.

The Effect of Energy Spread on SOBPs

In clinical use, proton beams of initial energy between 70 to 250 MeV are superposed to create a plateau of uniform dose with the required width in order to treat a tumour effectively, depending on its shape, size and location. This is the Spread Out Bragg Peak (SOBP). The code was extended to produce this. As shown in Figure 3, the width of the plateau is called modulation width (from 90% proximal peak to 90% distal peak). The range is here defined as the distance from the entrance into the medium (zero distance travelled) to 90% distal peak.

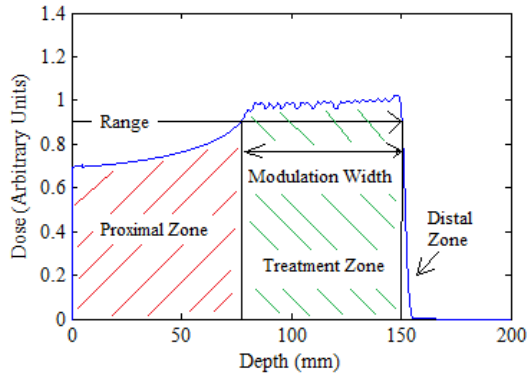


Figure 3: Sketch illustrating the different elements that were used to analyse the SOBP; proximal zone, treatment zone, modulation width, distal fall-off and range.

The shape (and uniformity) of the SOBP depends on the number of single peaks and their intensity. A common method in the literature [2, 4] uses a high intensity BP near the distal peak position and adding lower intensity peaks at regular intervals moving towards the proximal peak position. This creates a plateau characterised by a small peak at distal position and a sharp distal fall. Another method using different peak weighting produces a more uniform plateau but with a less sharp distal fall. The balance between the methods to create a smooth plateau with sharp distal fall is called distal-end optimization. Figure 4 shows an example of how to create a SOBP from its components: the most intense BP involved has most of the effect on the distal end.

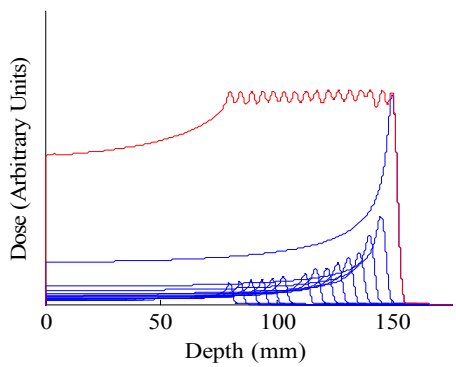


Figure 4: SOBP (80-150mm) using 15 BPs.

The chromatic beams were then used and their effect studied to learn to which extent the energy spread should be narrowed. The effect on the smoothness and uniformity of the peak were also studied.

Copyright © 2013 CC-BY-3.0 and by the respective authors

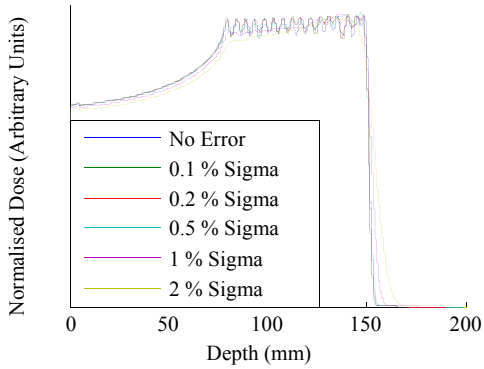


Figure 5: Same SOBP algorithm when using BPs of different initial energy spread (80-150 mm, 15 BPs).

Qualitatively, from investigating Figure 5 and similar SOBPs for different depths and widths, it was found that fewer single energy BPs were needed to create a smooth SOBP plateau when a higher energy spread was applied. Therefore a systematic study on the uniformity of the SOBP as function of the Energy Spread was launched varying the number of peaks for a SOBP 5 cm wide. The results plotted in Figure 6 show that above 0.5% sigma the reduction in the number of peaks needed for a given standard deviation is substantial. The drawback is that the distal falloff is less sharp, producing a higher distal dose.

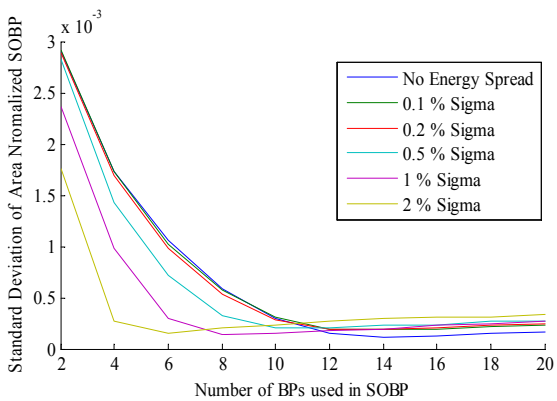


Figure 6: Standard deviation of the treatment zone as a function of BPs being used to create the SOBP. In this instance an SOBP between 10 and 15 cm was used.

Distal dose measurements were made at various modulation widths and depths. Figure 7 represents the results concisely. The distal dose is smaller for shallower and wider SOBPs because:

- For larger depths higher initial energies are needed making the distal BP wider (as shown previously in Figure 2).
- For smaller widths fewer BPs are needed and the contribution to the SOBP of the distal BP is higher, as there are a fewer components of lower energy BPs distal dose.

Below 0.5% sigma the energy spread has little influence (few percent) on the dose evaluated at 5 mm from the distal edge of the SOBP for low energy beams, whereas for higher energies the effect is significant.

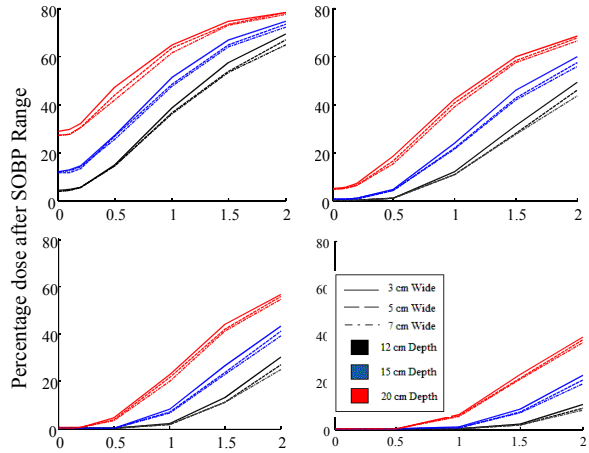


Figure 7: Graph showing the increasing distal dose at 3 mm, 5 mm, 7 mm and 10 mm (left to right, top to bottom) after the SOBP range. Different lines represent varying modulation widths while colours refer to differing ranges.

CONCLUSION

The energy spread of a proton beam causes a significant modification in shape of the Bragg Peak. This needs to be monitored and controlled in order to ensure the SOBP used in oncological treatments is modelled correctly so as to treat tumour efficiently and minimise damage to healthy tissue behind the tumour. Upper and lower limits on the beam energy spread are affected by considerations in the distal dose, the modulation width, the ratio between the zones and the shape of the resulting SOBP.

Taking into account the trade-off between the number of Bragg Peaks needed to ensure a uniform SOBP and the residual distal dose, from this work we can conclude that for beam energies:

- Lower than 100 MeV an energy spread greater than 0.5% sigma can be accepted.
- Greater than 150 MeV an energy spread lower than 0.5% sigma must be employed.

However, these considerations come from an over simplified 1-D geomet ry, where only water equivalent tissue is present, no interfaces between different tissues are simulated and a single-field treatment is applied. More work is needed to fill the gap between this study and the complex level of present-day treatment, however generalized, at a proton therapy centre.

REFERENCES

[1] M. Aslaninejad, C. Candela Juan, M. Crispin-Ortuzar, NIM-B 269 (2011) 189–196.
[2] D.E. Groom, S.R. Klein, Eur. Phys. J. C 15 (1-4) (2000) 163–173.R.
[3] T. Bortfeld, Medical Physics, Vol. 24, No. 12, Dec. 1997.
[4] F. Albertini, A dissertation submitted to ETH Zurich, 2011.
[5] Slopema, University of Florida, Proton Therapy Institute.

Copyright © 2013 CC-BY-3.0 and by the respective authors

A NOVEL SOLUTION FOR FFAG PROTON GANTRIES

J. Pasternak*, Imperial College London / RAL, STFC
P.R.N. Holland, G.W. Walton, UROP students, Imperial College London
M. Aslaninejad, Imperial College London
P. A. Posocco, Imperial College London / The Cockroft Institute / Gunnar Nilssons Cancerstiftelse

Abstract

In the recent years FFAG gantries have been studied for medical applications, but none has so far been realised. The FFAG solution would reduce the complexity of beam line set-up, its weight and therefore the cost of the rotating support, in particular for heavy ions. The Imperial College London is using the experience gained in the Pamela Project and in the design and commissioning of EMMA to work on a solution of a non-scaling FFAG gantry, which could potentially fulfil the full requirements for the spot scanning - parallel beam treatment technique, and provides an easy interface to the upstream accelerator. The preliminary results will be presented in this paper.

INTRODUCTION

The research on Fixed Field Alternating Gradient (FFAG) accelerators was restarted after long period of silence in recent years, which triggered the successful construction and operation of several scaling machines in Japan and the world's first linear Non-Scaling one - EMMA [1] in the UK. Following these vigorous progress it was proposed to apply the FFAG principle for next generation hadron therapy machines [2] aiming to reduce the cost of treatment by utilising the very strong focusing and high repetition rate offered by FFAGs to make the machine dimensions more compact and the treatment time shorter.

In modern hadron therapy applications it is preferred to use the gantry as the final beam transport system, which allows to precisely vary the beam angle at the patient in the large range simultaneously allowing to carefully control the beam spot size and position in the spot scanning. Although the existing gantry solutions (non-FFAG type) have been constructed and are in operation, they consist of room temperature iron magnet system with a very large weight and overall dimensions, which is a significant fraction of the total cost of the facility.

FFAG solutions for proton and carbon gantries have been proposed [2, 3], which allow to greatly reduce the size and weight of the gantry by using superconducting magnets. Stable particle orbits exist in such gantry for the broad momentum range eliminating a need for magnets' ramp or requiring to ramp only between small number of operational regimes, which offers an opportunity to reduce the treatment time. Thus FFAG gantries will contribute in decreasing the cost of modern hadron therapy facilities. It may be fed by any conventional medical accelerator including cyclotron or by a future medical FFAG.

* j.pasternak@imperial.ac.uk

FFAG gantries studied so far were based either on linear non-scaling magnets, scaling ones or such that break only partially the scaling law. This paper describes a novel gantry type using nonlinear non-scaling FFAG magnets, which explicitly violates the scaling law maintaining the zero-chromatic condition.

NONLINEAR NON-SCALING FFAG GANTRY DESIGN

Requirements and Assumptions

As the starting point of the study the classical shape of the gantry is assumed, in which the beam is firstly deflected outwards from the common incoming beam/patient axis, which also serves as gantry axis of rotation. Secondly the beam is deflected in opposite direction cancelling the initial negative angle and finally bending by the final 90° pointing at the patient. If this configuration is rotated using the incoming beam as the axis of rotation, it allows for the full flexibility in the choice of the treatment angle in a very broad angular range.

As the goal a gantry for proton therapy was chosen as it allows an easy comparison with other existing gantries and can be further extrapolated to a carbon case. It was also decided that the operation energy range of 100-200 MeV is potentially interesting especially for applications in paediatrics and is also quite ambitious at the start.

To simplify the orbit matching in the presence of rotation for different energies, zero dispersion condition is preferred at the input of the gantry. To avoid any correlations between the beam position and energy, zero dispersion at the patient is also required. The identity matrix is needed as the total betatron transfer map through the gantry, which will allow to set the particular condition required for treatment downstream the gantry in the non-rotating part and transparently reproduce it at the patient position simplifying the gantry operation.

Linear Optics Design

In order to minimize the orbit excursion in an FFAG many short cells are required with a very strong focusing. As the compromise between the orbit excursion, the maximum value of the magnetic field and space constraints in the magnet design, the design of the first bend consists of 8 identical FDF triplet cells, with the total deflection angle of -72°. As the preliminary studies showed that zero dispersion is preferred also at the end of the negative bend section as it minimises the orbit distortion downstream, the phase advance of $\pi/2$ rad per

Copyright © 2013 CC-BY-3.0 and by the respective authors

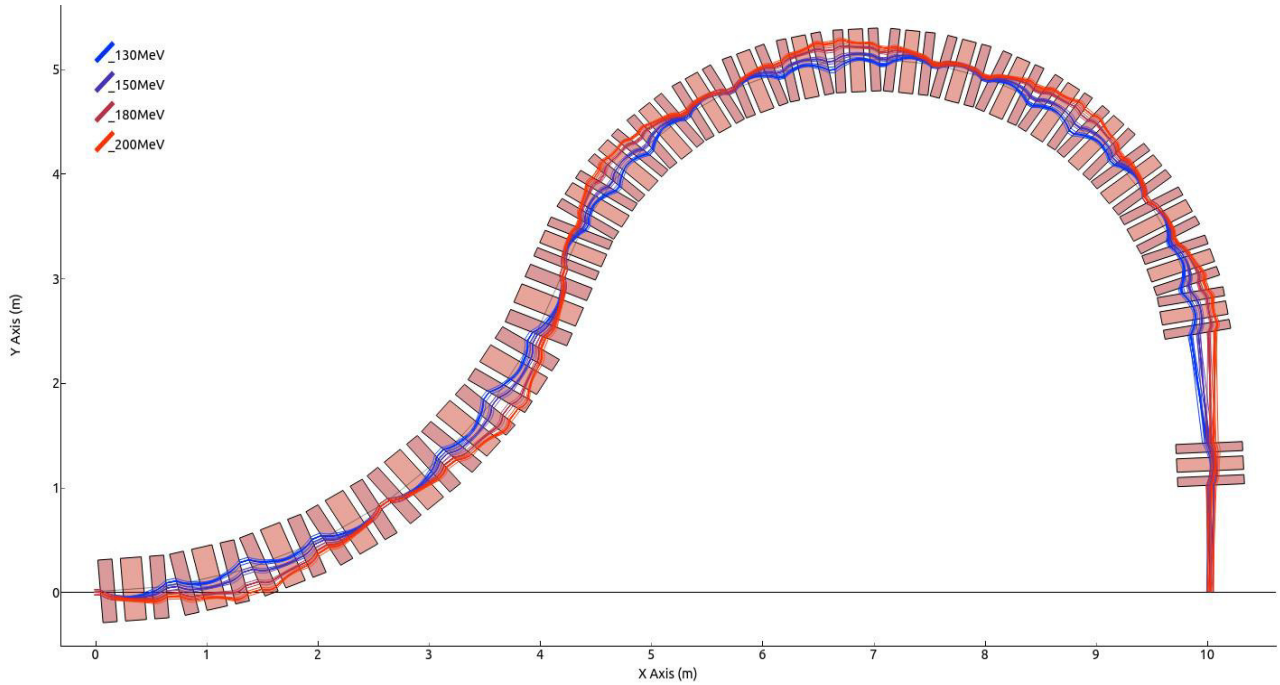


Figure 1: The layout of the novel FFAG gantry. The orbits for different energies and magnets have been 10 times enlarge for visibility. The zero dispersion condition can be clearly seen at the end of the first bending section and at the end.

cell was set in the bending plane to allow this condition; 3π/8 rad per cell was chosen in the non-bending one.

The next downstream bend section deflects the beam by 156.6° and consists of 17 identical FDF triplet cells. The value of deflection angle and the choice of the phase advances per cell (1.339 and 0.609 rad in bending and non-bending planes, respectively) have been adjusted to take into account the need to accommodate the final cell focusing the beam to the patient position, providing space to place scanning magnets and diagnostic tools, and allowing the magnetic field to practically decrease to zero at the patient position. The final cell is also of FDF triplet structure and it accommodates long straight sections of 1m in length. The additional constraints are such that the symmetric betatron functions and dispersion need to be the same as in the downstream section to assure the correct matching of the dispersion and the transparent character of the entire gantry. It sets the values of the phase advances in the final cell and together with the need for the total deflection of the gantry to be equal 90°, it fixes the value of the deflection in the final cell.

The layout of the gantry with all three cell types and long straight sections in the final cell are shown in Figure 1.

Nonlinear Optics Design

In order to avoid ramping the magnets optical conditions described in the previous section need to be preserved in a broad momentum range. In order to achieve it, the chromaticity correction is performed adjusting the phase advances in three points: at the central energy and two points close to the boundaries of the selected range (100-200 MeV) both in the bending and non-bending planes. In fact all 3 cell types are considered as periodic and the symmetry condition for the orbit is assumed. Multipole field components: dipole, quadrupole, sextupole and octupole ones are found numerically in the triplet magnets to fulfil the zero-chromatic condition in a broad momentum range. In addition the central orbit is controlled in two symmetric points to keep it centred in the vacuum chamber and to improve the stability of the numerical procedure. The resulting phase advances per cell are shown in Figure 2. The required total magnetic field obtained by summing all multipole components inside the transverse aperture, which was estimated to be about 6 cm is presented in Figure 3. The magnets assumed in the gantry would be of the superconducting type and rectangular in shape with the maximum field strength up to 4 T. Although the shortest magnet required would be only of 8.5 cm in length, it seems to be feasible. Table 1 shows the summary of the main parameters of the novel nonlinear non-scaling gantry.

Table 1: Main Gantry Parameters

Parameter	Value
Radius of the main arc [cm]	300
Proton energy range [MeV]	100-200
Max B field [T]	4
Betatron phase advance (H, V)	(12 π, 7 π)
Total number of magnets	78
Min magnet length [cm]	8.7
Magnet radius [cm]	~3

Copyright © 2013 CC-BY-3.0 and by the respective authors

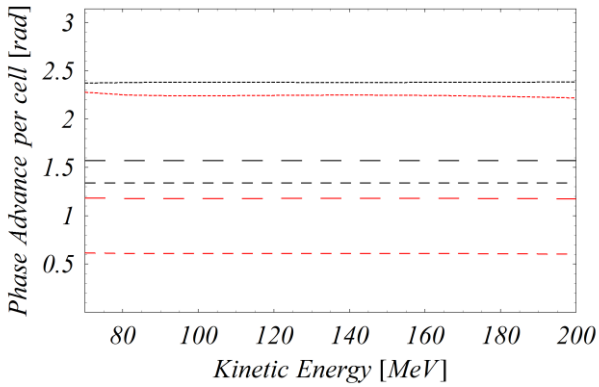


Figure 2: Phase advances per cell after correction for the first, middle and the final lattice cell types as a function of proton energy are shown using lines with decreasing order of dashing. The black and red lines correspond to bending and non-bending planes.

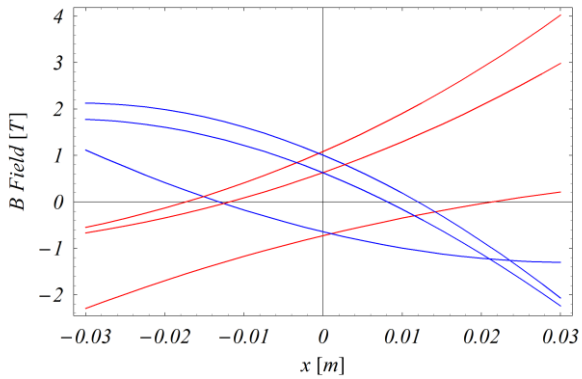


Figure 3: Total magnetic fields in all 3 lattice cell types (all 6 magnet types) within estimated aperture. Red and blue lines correspond to F and D magnets, respectively. The strongest field is required in the middle section, a bit weaker in the final cell. The different sign of deflection angle can also be seen in the magnets with the lowest fields. All magnets violate the scaling FFAG law.

TRACKING STUDIES

Tracking studies were performed in the designed gantry using Zgoubi [4, 5] and Elegant [6] codes. Results obtained with Zgoubi are presented in Figure 1, showing the orbits for different energy, while Figure 4 and 5 are showing the final phase spaces. The gaussian particle distribution with rms normalized emittance of 5π.mm.mrad was assumed. Some nonlinear distortions have been observed especially in the vertical plane, which are present only after beam passes the final cell, which may be due to a specific choice of the phase advance in that cell.

The results obtained using Elegant agreed on the middle momentum, however certain discrepancies have been observed for the off-momentum motion. It was identified for instance, that the current version of the code does not support octupole components in the combined function elements, while Zgoubi has this capability.

CONCLUSIONS

These results show that a nonlinear non-scaling FFAG gantry could be suitable for use in proton therapy. The principles of the design: the transparent beta propagation, zero dispersion and good beam transmission have been obtained. Further optimization to decrease the size and improve the final cell configuration will be performed. The gantry shown here would require superconducting magnets, which design needs still to be addressed.

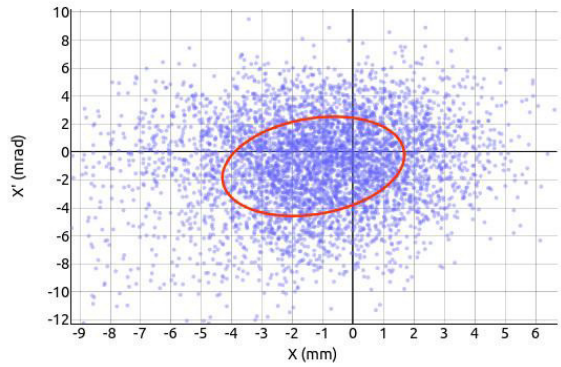


Figure 4: X-X' phase space at the end of the gantry obtained using Zgoubi at 150 MeV. Red ellipse corresponds to the rms geometrical emittance.

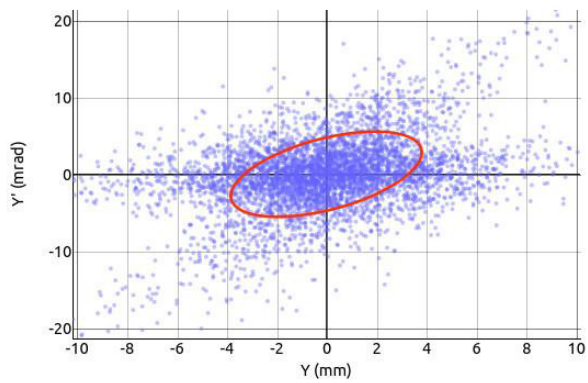


Figure 5: Y-Y' phase space at the end of the gantry obtained using Zgoubi at 150 MeV. Red ellipse corresponds to the rms geometrical emittance.

REFERENCES

[1] B. Muratori et al., TUPWO052, in proceedings of IPAC'13, Shanghai, China (2013).
[2] D. Trbojevic et al., THPMS092, in proceedings of PAC'07, Albuquerque, USA (2007).
[3] K.J. Peach et al., Phys. Rev. ST Accel. Beams 16, 030101 (2013).
[4] http://sourceforge.net/projects/zgoubi/
[5] http://www.hep.manchester.ac.uk/u/sam/pyzgoubi/
[6] http://www.aps.anl.gov/Accelerator_Systems_Division/Accelerator_Operations_Physics/elegant.html

Copyright © 2013 CC-BY-3.0 and by the respective authors

A READY-TO-USE APPLICATION OF LASER-PLASMA ACCELERATORS USING GABOR LENSES

R.M. Nichols*, UROP student, Imperial College London
M. Aslaninejad, N.P. Dover#, Z. Najmudin, J.K. Pozimski, Imperial College London
P. A. Posocco, Imperial College London / The Cockcroft Institute / Gunnar Nilssons Cancerstiftelse

Abstract

A realistic particle distribution for a proton beam generated by laser-plasma interaction is required in order to simulate its transport through a Gabor lens system intended for use in radiobiology experiments. A stack of radiochromic films were exposed to a laser-driven proton beam of 25 MeV at the Vulcan Petawatt Experiment at Rutherford Lab and subsequently analysed to find the energy deposited per film and therefore the energy spectrum of the beam. Combined with the information on the radial profile of the dose in the films, it was possible to generate an idealised particle distribution. This distribution was sampled and used as a realistic proton source in a simulation through the Gabor lens system published at IPAC'13, scaled down to 4 MeV to fit the radiobiology experiment requirements.

INTRODUCTION

An intense beam of ions is generated when a solid target, several microns thick, is irradiated by a high intensity laser pulse [eg. 1, 2]. In such a scheme, the laser ionises the surface of the target and accelerates electrons to high energies. These electrons travel through the target and upon exiting the target result in the generation of huge quasi-static electric fields, due to charge separation. This field accelerates the ions at the target surface, which are often protons, carbon and oxygen ions from the typical hydrocarbon layer on the target surface [3, 4].

Ion beams accelerated in this way have attracted interest in recent years due to their potential for use in radiotherapy and a number of other applications [5]. There has been considerable investment in recent years into hadron therapy, which can provide more targeted therapy for deep-seated tumours than conventional x-ray or electron radiotherapy. Current systems for proton therapy are extremely costly and laser-accelerated beams could offer in the long-term simple and compact treatment devices and therefore significantly reduce treatment costs. Meanwhile, while still requiring further development before being suitable for treatment, they are sufficient to allow biologists to study the effect particles produce in cells, and are already far more convenient than electrostatic accelerators commonly used for this purpose. Experimental radiobiology with particles is an area that has been only partially explored and with a strong impact on the modalities of particles delivery to patients and treatment outcomes.

We believe that laser-plasma accelerators of the current generation combined with a novel optical system based on Gabor lenses [6] is an ideal candidate for this application. If proven effective, Gabor lenses can be scaled to higher energies and thus easily applied to future laser-driven particle sources in a clinical environment.

THE PARTICLE DISTRIBUTION

The Vulcan Petawatt laser was focused to a focal spot of 4 μm (FWHM) at 45 angle of incidence onto a 100 μm thick Al target. The resultant accelerated proton beam was diagnosed using a film stack positioned 7.4 cm from the target. The stack itself is 0.66 cm thick and consisted of Al shielding followed by layers of RadioChromic Films, which darken when exposed to dose, alternated with spacers of either Fe or Al.

The set of RCFs (data taken in 2012) were scanned and the intensity value for each pixel was converted to dose by calibrating with pixel intensity values of images of RCFs exposed to known doses of radiation.

Calibration of the Films

Calibration images were obtained by scanning RCFs that had been exposed in three separate experiments when films were exposed to known doses of radiation using the Scanditronix MC 40 cyclotron at the University of Birmingham. In the area selected, the median pixel value is found for each of the colour channels of the image. A median is used rather than a mean as it will not be affected by outliers (caused by, for example, dust on the film). These values are then compared to the dose known to have irradiated the calibration films.

The results of the calibration are shown in Figure 1, in which the pixel intensity values are plotted as function of their known doses. The red channel is more sensitive than the green or blue channels and so it reaches its saturation point at a much lower dose. Therefore the red channel was used for the lower doses and the blue channel for the higher doses. The calibration switch point between the two channels was chosen at 200 Gy.

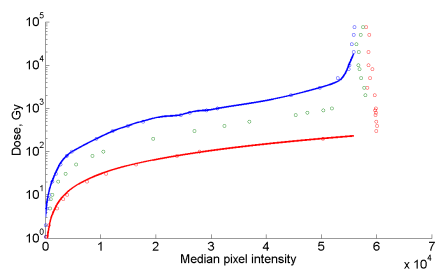


Figure 1: Calibration of how the red, green and blue channels of images of RCF respond to irradiation.

* Supported by the UK Engineering and Physics Research Council
# nicholas.dover08@imperial.ac.uk

Copyright © 2013 CC-BY-3.0 and by the respective authors

Image Conversion

For each processed image (an example in Figure 2), the image was disregarded if the mean intensity value over the entire film was less than twice the noise in the scanned image. Using this rule, only the first four RCF layers for this particular shot were used.

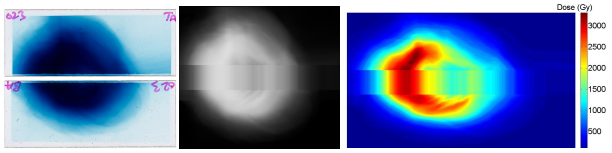


Figure 2: Scanned image of the first RCF (left), blue channel after processing (centre), dose map (right).

Reconstruction of the Energy Distribution

The dose deposited in each pixel of the scan of each RCF layer was calculated using the calibration. The mean dose in the layer was then converted to total energy deposited in the film's active layer, using the active layer density and thickness. For each of the four RCFs a profile of how much energy is deposited per proton in the active layer as a function of proton energy is generated using a series of TRIM Monte Carlo simulations [7].

The proton energy that dominates the energy deposition in each RCF is therefore found from the peak of the curves. To convert from energy deposited to the estimated proton number in the spectrum, the following initial assumptions were made:

- the area around the peak of the profile is selected using the 1/e width of the peak;
- inside this area protons of all energies deposit an equal amount of energy;
- protons with energies outside this area do not deposit any energy.

Therefore the energy deposited per proton is calculated by taking the average across this width. The number of protons in the beam depositing energy in each film is then given by the energy deposited in the film divided by the average energy deposited per proton in this peak. Hence the number of protons per MeV (dN/dE) is found by dividing the number of protons depositing energy by the width of the peaks in Figure 5. The number of protons at energies higher than 25 MeV, where the proton signal was below the noise, was set to zero.

Although the above assumptions give a good first estimate of the spectra, a large assumption is made by disregarding the dose deposited by the higher energy protons which could cause an overestimation of the particle numbers. Therefore, an iterative technique was used in which the initial spectral guess is convolved with the curve obtained with TRIM and the energy deposited in each film recalculated. The ratio of this new energy deposition value compared to the actual measured value is then found. The initial spectral guess is then modified by this ratio at each film layer, and this process is iterated until the energy deposited in each RCF calculated from the RCFs and the reconstructed energy spectrum was within 0.01%.

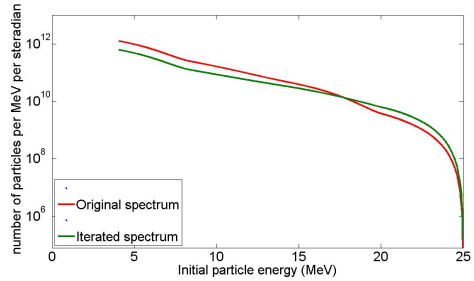


Figure 3: Comparison between the initial energy spectrum and the spectrum after iteration.

Reconstruction of the Transverse Distribution

The spreading of the beam in the direction transverse to the beam axis was assumed to be negligible over the depth of the stack (6.6 mm), as the distance between the films is less than 2% of the total distance travelled by the protons after the target. The mean transverse scattering within the stack was estimated from TRIM Monte Carlo simulations and was found to be $\sigma \approx 0.2$ mm for 35 MeV protons, negligible compared to the beam size.

The particle distribution was generated assuming that:

- the particles are emitted with cylindrical symmetry;
- the particles are emitted from a point like source;
- the particles are emitted at the same time, but with different energies;
- the particle distribution at each RCF is represented by a 2D Gaussian.

These assumptions reduce the 6D particle distribution to a 2D distribution (energy and radius). For each proton energy the particle number was first scaled with respect to the energy spectrum previously calculated. Then, a further modification depending on the spatial position was calculated by fitting a 2D Gaussian to the proton beam dose deposition profile (Figure 4). Below 5 MeV the distribution was given a spread similar to that of the first RCF in the stack.

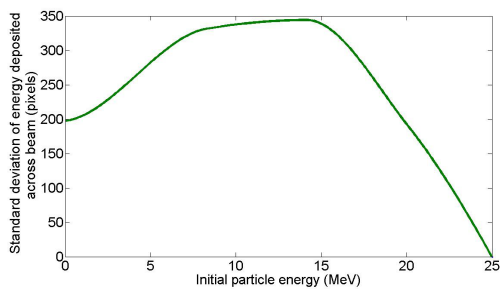


Figure 4: Spread of the dose distributed in the films as function of proton energy.

SIMULATION OF BEAM TRANSPORT

The particle distribution was converted into the GPT file format and used as input for the particle tracking simulations with GPT [8] using the lattice suggested in [6]. The preliminary results looked very unfavourable because the beam divergence is about 6 times larger than assumed and the number of particles above 10 MeV is too low for sufficient statistics (see Figure 5).

Copyright © 2013 CC-BY-3.0 and by the respective authors

Therefore a new Gabor lens with the radius of anode and cathode increased from ~20 to 35 mm was designed and the lattice setup updated (Figure 6), increasing the acceptance angle by a factor of 3. Only 200 particles are initially available for the original distribution (see Figure 5-E red scale) in the lowest energy bin considered for experiments (4 MeV) at twice the divergence angle (~240 mrad half cone angle) compared with the angular acceptance (~120 mrad) of the improved lattice: the transmission is therefore below 25% (~50 particles at start). In order to boost the statistical significance of the results an artifical particle distribution (120 mrad divergence angle and 2100 particles per energy bin) was used for comparison.

The beam trajectory behind the aperture shown in Figure 6 is well defined after energy selection. For the artificial distribution ~80% of the particles in this energy bin are transmitted. The distribution derived from experiment show similar characteristics, but the overall transmission is 7.5%, equivalent to a 33% transmission through the aperture. Both distributions (see Figure 7) show a sharp peak at the chosen energy of 4 MeV with a FWHM below the bin width of 93.8 keV, which should be fine for most applications.

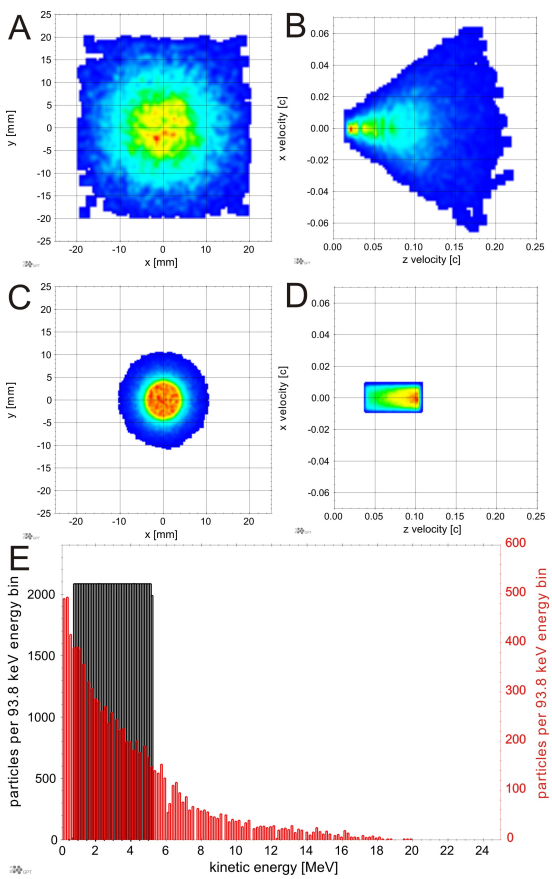


Figure 5: Graph A: transversal phase space (x,x') of the initial particle distribution and B the x-z velocity space both for the distribution generated experimentally; Graphs C and D: artificial distribution with reduced divergence angle and energy spread for comparison; Graph E: the particle number per energy bin for both distributions.

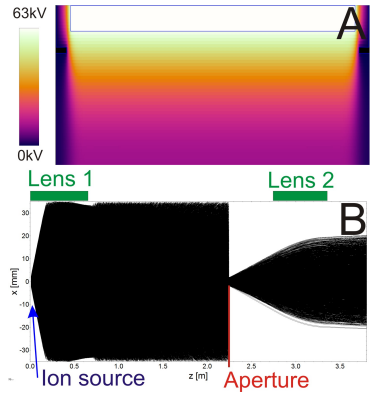


Figure 6: Lattice setup and a trajectory plot using a beam with ~120 mrad input divergence.

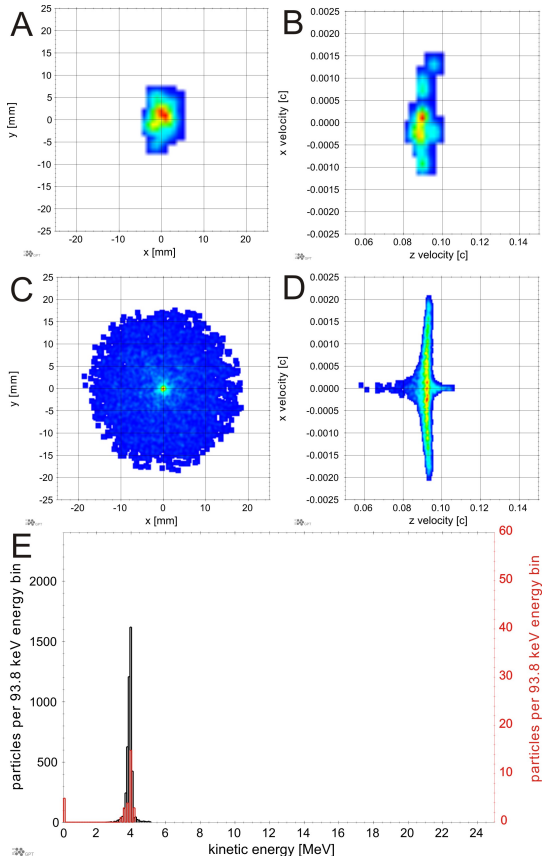


Figure 7: Graph A: transversal phase space (x,x') and B the x-z velocity space for the experimentally determined distribution after the aperture at 3.1 m; Graphs C and D: same plots for the artificial distribution.; Graph E: the particle number per energy bin for both distributions.

REFERENCES

[1] E. L. Clark, et al., Phys. Rev. Lett., 84, 2000.
[2] R. A. Snavely, et al., Phys. Rev. Lett., 85, 2000.
[3] A. Macchi, et al., Rev. Mod. Phys., 85, 2013.
[4] H. Daido, et al., Rep. Prog. Phys., 75, 2012.
[5] J. Fuchs, et al., Comptes Rendus Physique, 10, 2009.
[6] J. Pozimski and M. Aslaninejad. Laser and Particle Beams.
[7] J.F. Ziegler et al., "Stopping and range of ions in matter", 1985.
[8] 'General Particle Tracer', www.pulsar.nl/GPT/

Copyright © 2013 CC-BY-3.0 and by the respective authors

CHARACTERISATION OF NITROGEN CLUSTERS AND GAS JET TARGETS UNDER VARIED NOZZLE GEOMETRIES

C. Hughes, N.P. Dover*, Z. Najmudin, P.A. Posocco, Imperial College London

Abstract

Gas jets are widely used for targets in laser-plasma driven article acceleration experiments. Optimising the mechanism requires tailored gas jet density profiles. Therefore, high density gas profiles have been investigated and characterised using different types of nozzles: sonic, supersonic, slit and supersonic slit. Gas jet profile optimisation was examined using nozzles of different diameters while varying gas pressure between 0 and 100 bar and valve opening duration. Gas jets produced by the nozzles were characterised using an optical probe laser. The gas jet density profile was measured through interferometry which was captured using a CCD camera. A second camera was used to record the Rayleigh scattering from the laser to confirm the presence clustering in nitrogen at high pressures.

INTRODUCTION

Recent research into laser-plasma ion acceleration has demonstrated beams with various characteristics from a number of different target types. The use of solid targets presented two widely investigated mechanisms: target normal sheath acceleration (TNSA) and radiation pressure acceleration (RPA) [1]. For applications that require high energies and monoenergetic beams, RPA is seen as the more desirable mechanism for acceleration due to the characteristics of the accelerated beams, though has been difficult to achieve in experiments [2][3]. Solid targets can add complications to the ion source as they require very high laser contrast to avoid their destruction, create debris, result in multispecies beams, and may cause difficulty for high repetition rate systems for applications.

Gas jet targets have been seen to offer a solution to these issues. Gas jet targets have been widely used for laser wakefield electron acceleration [4], and some more recent studies for ion acceleration. For example, recent experiments have demonstrated monoenergetic proton beams from the interaction of a CO2 laser with gas jets [5], generated from the laser radiation pressure acting on a low density, but opaque, plasma. Interest in gas targets has led to the development and subsequent optimisation. The acceleration mechanism can be optimised via tailored gas jet density profiles through altering nozzle geometry (Figure 1).

Under high pressure and specific conditions a range of gases have been found to form small grouping of atoms which are loosely bound to each other through their Van der Waals forces. These are known as gas clusters. The formation of clustering in supersonic gas jets is a concept that has been observed for many years, along with their dependency on pressure and nozzle size [6]. Clustering gases are of interest in targetry mainly in relation to high intensity laser-plasma interaction as they provide very high absorption of laser energy [7]. It has also been shown that high pressure gas clustering can be utilised as targets in ion acceleration [8]. More recently, an experiment has been reported investigating a selection of nozzle geometries: sonic, supersonic, slit and supersonic slit (Figure 2).

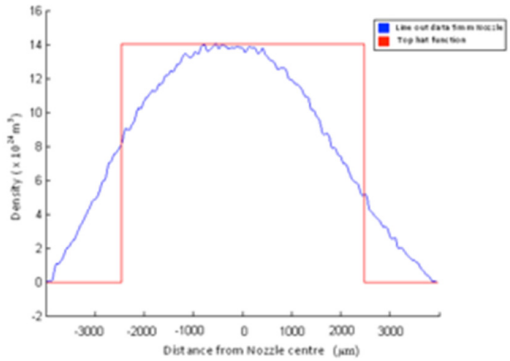


Figure 1: Ideal gas jet would possess a density profile that follows the shape of a top hat function. Actual jets do not produce such a steep density gradient.

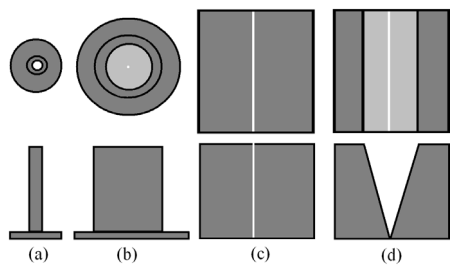


Figure 2: Examples of nozzle geometries for (a) sonic nozzle (b) conical nozzle (c) slit nozzle (d) supersonic slit nozzle.

EXPERIMENTAL SET-UP

Nozzles

A selection of nozzles was used to produce gas jets bearing different characteristics due to their geometries. Additionally, the effect of placing an insulator before the nozzles was investigated (Figure 3). These included a 10 mm diameter conical supersonic nozzle with an entrance aperture of 2 mm, a 2 mm diameter conical sonic nozzle and a slit nozzle. The slit nozzle was shaped with pliers from a 2 mm sonic nozzle to approximate the properties for this geometry. The slit dimensions were verified the CCD camera. This set up was found to be able to observe clusters in argon gas through a probing laser and the resulting Rayleigh scattering [9].

* nicholas.dover08@imperial.ac.uk

Copyright © 2013 CC-BY-3.0 and by the respective authors

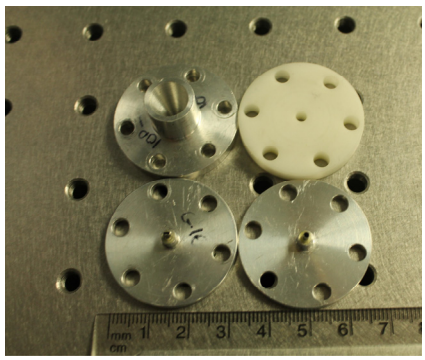


Figure 3: Nozzles used (diameters given). From left: (top) 10 mm conical nozzle, insulator (bottom) 2.5 mm by 1 mm slit nozzle, 2 mm conical nozzle.

The introduction of an insulator should reduce the likelihood of discharge onto the nozzle from the laser-plasma area. Discharge can lead to degradation of the nozzle or could obscure or completely obstruct the plasma feature that is being observed or, potentially, influence laser-plasma interactions differently.

Mach-Zehnder Interferometry and Rayleigh Scattering

High-pressured nitrogen gas was passed through nozzles inside a controlled vacuum chamber where the gas was then characterised using an optical probe laser. The laser used was a ~1 mW CW Helium-Neon 632.8 nm laser .The gas jet density profile was measured using a Mach-Zehnder interferometer (see Figure 4). After both paths were recombined, the fringe shift was captured using a high frame rate CCD camera, allowing measurement of the time evolution of the gas jet as well as the spatial properties. A second camera (Qimaging camera) was used to record the Rayleigh scattering from the laser to confirm the presence clustering.

For each of the nozzles, pressure, valve opening duration and gas jet-time evolution were investigated. Gas jet pressure was varied between 0 and 100 bar and valve opening duration between 6 ms and 150 ms with the fringe shift being taken at a time where the jet was deemed stable. The gas jet evolution to reaching this point of stability and after was also viewed.

Image Processing

Images produced through interferometry were analysed using a method earlier used to review gas jet density profiles of needle nozzles [10]. The processing script was written using Matlab.

Phase shift maps were compared with a reference (control) image to obtain the net phase shift experience under the gas evolution. Region containing shift - found above the nozzle - was then selected to reduce redundant processing and thus reduce computing time. The sampled region selected was Fourier filtered around the frequency space of the interferometry fringes to remove noise. This is then used to produce a 2D image of the phase shift as a function of space. Lastly, the geometrical conditions are applied resulting in a density profile that accounts for nozzle shape and symmetry. The Abel inversion was used for nozzles which possessed cylindrical symmetry (conical nozzles). Gaussian smoothing is also applied to remove noise and achieve main characteristic.

The area of interest from the density profiles was selected as 0.7-1 mm height above the nozzle exit, which is where the laser will be focussed on the high intensity laser experiments the gas targets, will be used for. This position is a chosen compromise between achieving the best density profile at the nozzle exit while avoiding any possibilities of ablating or melting of the nozzle caused by intense laser contact.

Scattered light from clusters will be visible in the images without any processing [9].

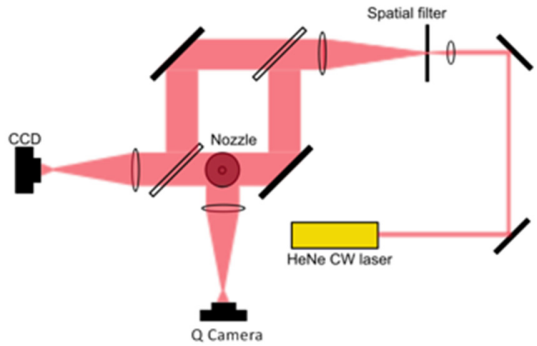


Figure 4: Experimental set up used. Combining Mach-Zehnder interferometry with an additional focussing lens and camera to image Rayleigh Scattering from the probing laser due to clusters within the gas medium.

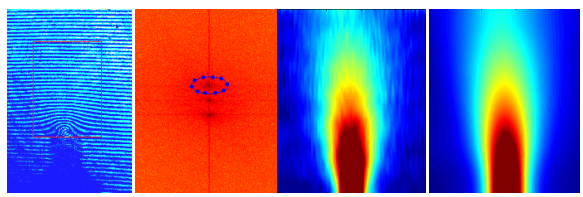


Figure 5: Interferometry image processing (from left): 1 showing region selected for transforming (red box), 2 showing Fourier transformed phase map with sample area highlighted (blue ring), 3 gas jet density profile, 4 smoothed density profile with geometric compensations.

CLUSTER FORMATION

From analysing the images taken by the Qimaging camera, Rayleigh scattering from the probing laser was not observed. This is believed to be resulting from: low camera resolution, light lost in path to camera and the intensity of the laser not being high enough to produce a measureable scatter when accounting for losses. The experimental set up will be amended to resolve these issues.

Density Profiles of Nozzles

Analysis of the phase maps indicates that both transverse (Figure 7) and parallel (Figure 8) of the slit nozzle have a different characteristic shape to that of the sonic nozzle (Figure 6) across the range of pressures. Throughout the phase line outs for the transverse slit, a

Copyright © 2013 CC-BY-3.0 and by the respective authors

plateau is visible around the region of highest phase shift, on the axis of the nozzle centre. This accounts for the wider diameter of the nozzle. A distinct, sharp peak is visible where the phase shift is at maximum for those when the slot nozzle is parallel to the probing laser (Figure 8). This was also expected due to its decreased diameter.

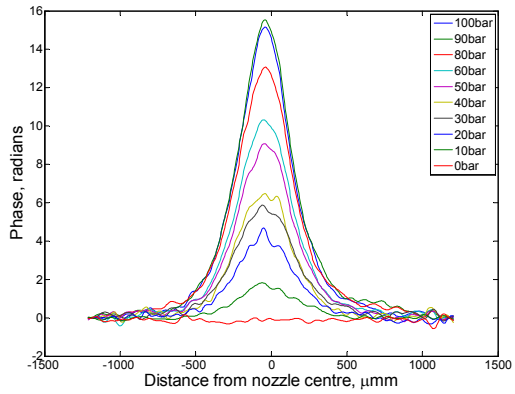


Figure 6: Phase line out 1 mm above nozzle normal to laser and gas jet for 2 mm diameter sonic nozzle.

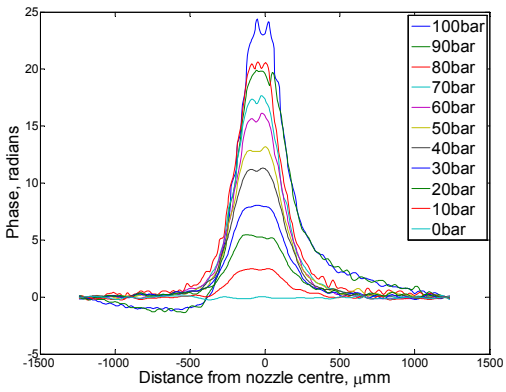


Figure 7: Phase line out 1 mm above nozzle normal to laser and gas jet for 2.5 mm x 1 mm slit nozzle at normal incidence.

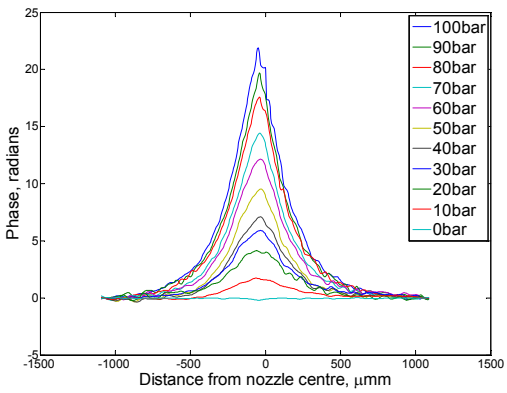


Figure 8: Phase line out 1 mm above nozzle normal to laser and gas jet for 2.5 mm x 1 mm slit nozzle at normal incidence.

Both orientations of the slit nozzle achieved higher phase shift than those achieved at the same pressures for sonic nozzle. This is a result of the decreased area at the exit of the nozzle.

The phase shift at the centre of the nozzle was found to be higher throughout the range of pressures when the slit was orientated normal to the laser. It was expected that greater phase shift would be observed when the slit of placed parallel as this would present a longer gas medium, more laser interaction and thus, greater phase shift. This could be a result of the experimental set up, i.e. slit on parallel to incidence or may suggest that the gas diverges differently from the slit nozzle to predictions.

CONTINUATION OF THE EXPERIMENT

A higher power laser will be incorporated in the set up. This should lead to a greater amount of Rayleigh scattering from the laser which should be detectable by the camera. An improved imaging system will be introduced to increase the scattering solid angle being captured by the imaging system. Coning and casing around the path between nozzle and camera may be added to reduce noise. Lastly, a lens will be placed before the nozzle to focus down the laser at the gas jet-laser interface.

New slit and supersonic slit nozzles have been designed (Figure 9) and these will be tested, following the same method and experimental set up as before.

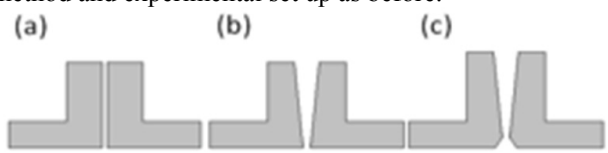


Figure 9: Supersonic slits: These are formed from two pieces as opposed to the single piece structure of the originals allowing the entrance aperture and nozzle diameter to be varied. Shown are the prism faces of each and all have a depth of 35 mm: (a) 15 mm x 15 mm (b) 15 mm x 15 mm with wall angle of 2° (c) 18 mm x 15 mm with wall angle 2° and lower of 65°.

ACKNOWLEDGEMENTS

This research was possible through the collaboration of Imperial College London and the Ogden Trust.

REFERENCES

[1] Daido, H. et al. , Rep. Prog. Phys 75, 2013.
[2] Kar, S. et al., PRL 18, 185006, 2012.
[3] Dollar, F. et al., PRL 17, 175005, 2012.
[4] Semushin, S et al., V, Rev. Sci. I. 72 2961, 2011.
[5] Palmer, C. A. J. et al., PRL, 106, 014801, 2011.
[6] Hagena, O.F. and Obert, W., 56, 1793, 1971.
[7] Snyder, E.M et al., PRL, 77, 3347 – 3350, 1996.
[8] Fukuda, Y. et al., PRL, 103, 165002, 2009.
[9] Guanglong, C., et al., AIP, 106, 053507, 2009.
[10] Cole, J., Characterisation of Gas Jets as Targets for Laser, Imperial College London, 2010.

Copyright © 2013 CC-BY-3.0 and by the respective authors

CONSTRUCTION AND TESTING OF THE DUAL SLOT RESONANCE LINAC*

N. Barov, D. Newsham, R.H. Miller, FAR-TECH, Inc., San Diego, CA 92121

Abstract

The dual slot resonance (DSR) linac is a novel method of providing enhanced coupling to a coupled cavity linac system, resulting in very strong coupling. For the 11-cell, 2856 MHz structure described here, the acceleration mode bandwidth is about 650 MHz, which is an order of magnitude greater than many traditional side-coupled and axis-coupled linacs. The strong coupling promotes phase and amplitude stabilization, and offers decreased sensitivity to fabrication errors. We describe the construction, tuning, and RF conditioning of the prototype structure.

INTRODUCTION

The basic concept of the DSR linac was reported in [1], and that article contains a more in-depth explanation of this linac type. FAR-TECH was granted a patent for this technology [2]. The geometry of a pair of linac cells is shown in Figure 1, which shows a half-geometry of the vacuum region inside the linac structure. A group of two resonant slots connect two adjacent linac cells through an intervening swept triangular volume which we refer to as a "void". The void region serves to provide RF coupling between the two slots. Each group of two slots has two collective resonant modes: a mode at around 1 GHz, and the working mode at the target operating frequency of 2.856 GHz. The mode split between these collective modes is so large that the pair of slots can effectively be considered a single oscillator at 2.856 GHz. The two slots serve the same purpose as a coupling cell in a side coupled linac. The advantages of the DSR linac include: a very large coupling with about 22% bandwidth, a compact geometry, no additional radial space required for the coupling cells, and shunt impedance competitive with a side-coupled linac. Simulations with HFSS [3] and with Omega3P [4] predict a shunt impedance ZT^2 of 85 $\mathrm{M\Omega/m}$. This is competitive with other linac designs featuring large coupling such as the PWT design [5], and is slightly less efficient than an equivalent side-coupled linac, which might have about 8-10% higher ZT^2 with the same basic cavity and nose cone shape. The linac is designed for the UCLA Pegasus laboratory to aid in ultra-short electron bunch experiments [6] by boosting the beam energy by a design 10 MeV. The linac can also be operated in bunching phase, which will further shorten the bunch length and enable better resolution for experiments such as electron diffraction studies. It is hoped that the DSR linac design will also find uses in industrial and medical applications.

* Work supported by DOE Office of High Energy Physics, DOE-SBIR #DE-FG02-08ER85034

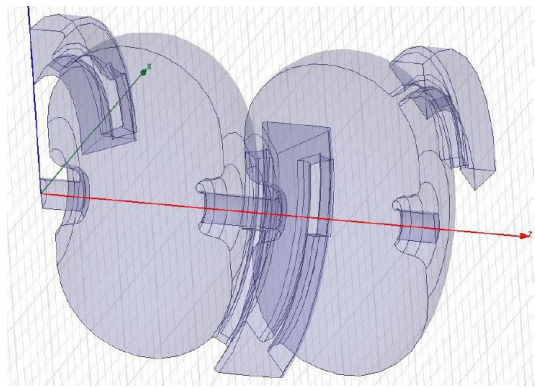


Figure 1: HFSS geometry used to model two cells of the DSR linac.

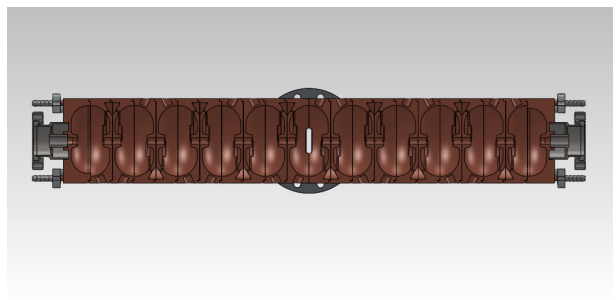


Figure 2: A cross section view of the 11-cell DSR linac.

DESIGN AND CONSTRUCTION

Design

An 11-cell DSR linac was designed with HFSS and Omega3P, as shown in Figure 2. End cells were transversely displaced in order to limit dipole kicks, and the central coupling cell shape was designed to minimize the mode pull due to the RF coupler. The linac is cooled with four cooling tubes running the length of the structure. The RF connection is via a WR284 waveguide and Skarpaas flange, and vacuum connections to the beamline are made with 2.75 inch ConFlat flanges. The beam clear aperture diameter is 8 mm. The band surrounding the accelerating mode extends from 2.513 to 3.153 GHz, making the frequency spacing from the accelerating mode to the closest nearby modes 45 MHz in our 11-cell structure. In a linac with $\pi/2$ phase advance per cell, the dispersion curve should be closed by tuning the even and odd oscillators to the proper frequency. The tolerance for the amount of closure depends on the overall bandwidth, and we have estimated that a residual stop band of as much as 3 MHz will not harm the electrical properties of the structure. Time

Copyright © 2013 CC-BY-3.0 and by the respective authors



Figure 3: A finished half-cavity copper part.

dependent studies simulating the RF fill transient, as well as steady-state field balance sensitivity studies, reveal that a larger stop band, beyond 10 MHz, does indeed start to affect performance.

Construction

The copper components for a half cell were made with a combination of lathe and 5-axis milling processes, which is more complicated than what is required for other linac types. We estimate that components for this linac type are 50-100% more expensive to machine than for conventional linac types, but this added cost is only a small fraction of the overall cost of producing the structure, and is offset by the simplified tuning method discussed below. Figure 3 shows a finished half-cavity part. The full linac was brazed with Au/Cu alloy in a dry hydrogen atmosphere using three braze steps.

TUNING AND BEAD PULL

The purpose of bead pull and structure tuning is to close the dispersion curve, achieve the correct operating frequency, and properly balance the field gradient in each cell. Tuning steps were interspersed with bead pull measurements and data fitting to a matrix model. A matrix description used one oscillator for each linac cell and one oscillator representing the collective mode of a pair of slots. The full eigenvalue equation has the form:

$$\mathbf{M}\mathbf{V} = \frac{1}{f^2}\mathbf{V} \qquad (1)$$

with $\mathbf{V}$ describing the voltage in each oscillator, and $\mathbf{M}$ for an example five-oscillator system is given by:

$$\mathbf{M} = \begin{bmatrix} \frac{1}{f_1^2} & \frac{k_{ac}}{2f_1^2} & \frac{k_{aa}}{2f_1^2} & & \\ \frac{k_{ac}}{2f_2^2} & \frac{1}{f_2^2} & \frac{k_{aa}}{2f_2^2} & \frac{k_{cc}}{2f_2^2} & \\ \frac{k_{aa}}{2f_3^2} & \frac{k_{ac}}{2f_3^2} & \frac{1}{f_3^2} & \frac{k_{ac}}{2f_3^2} & \frac{k_{aa}}{2f_3^2} \\ & \frac{k_{cc}}{2f_4^2} & \frac{k_{ac}}{2f_4^2} & \frac{1}{f_4^2} & \frac{k_{ac}}{2f_4^2} \\ & & \frac{k_{aa}}{2f_5^2} & \frac{k_{ac}}{2f_5^2} & \frac{1}{f_5^2} \end{bmatrix}, \qquad (2)$$

where the matrix for the full 21-oscillator system follows the same pattern, f_i is the natural frequency of the i^{th} oscillator, k_{ac} is the coupling coefficient from the cell to the coupling slots, and the remaining coupling terms are the next nearest neighbor coupling terms from one accelerating cell to another (k_{aa}) and from one set of coupling slots to another (k_{cc}).

The tuning procedure is significantly different for the DSR structure than for a conventional side-coupled structure. Adjustments made to a single slot in a two slot system are capable of adjusting the field balance of the structure, and these adjustments can be performed after the final braze. The effect of such tuning is shown in Figure 4, which shows the slope of the before and after plots to be mostly consistent, except between cells 7 and 8 where the adjustment was made. Adjustments to both slots also have an effect on the resonant frequency of the surrounding cells, and can be used to tune the structure frequency as a whole, as long as the dispersion curve tolerance is adhered to. Although the structure was built with dimple tuners in each cell and deformable wall push-pull tuners at the end cells, these did not have to be used to arrive at the final tune, and all tuning was performed entirely by slot adjustments. The tuning method consisted of tightening a two-piece aluminum collar around the linac while monitoring the mode frequencies. In the final field balance measurement, all cells were within $\pm 1.9\%$ of the average. The dispersion curve was closed to within 400 kHz, much better than the initial goal.

We believe this tuning method, together with relaxed tolerances afforded by the large bandwidth, can simplify the production of a DSR linac structure. RF measurements of the as-machined half cell components were consistent enough that we believe it may be possible to machine the components to their net final shape in one machining pass with no additional tuning cuts. It may also be possible to eliminate any stack-up and bead pull tests performed ahead of the brazing operation. In this scenario, the only difficult stage would be the final tuning, which can be guided by a computer model.

POWER DISTRIBUTION

For the installation at the Pegasus laboratory, we have acquired or built the major waveguide components to distribute the power to the linac, including a high-power phase shifter, directional coupler, power divider, and several adapters between different flange types. The power divider, shown in Figure 5, was designed and built by FAR-TECH following the idea of the variable tap-off (VTO) device developed for ILC [7]. The device has four waveguide ports including an input port, an isolated port, and two output ports. In order to change the power split, the fastening bolts must be loosened and the central cartridge rotated to the new position. The device was designed for infrequent changes to the power ration, as the adjustment also de-pressurizes the SF_6-filled waveguide. A challenge for the power divider RF design was to optimize the RF

Copyright © 2013 CC-BY-3.0 and by the respective authors

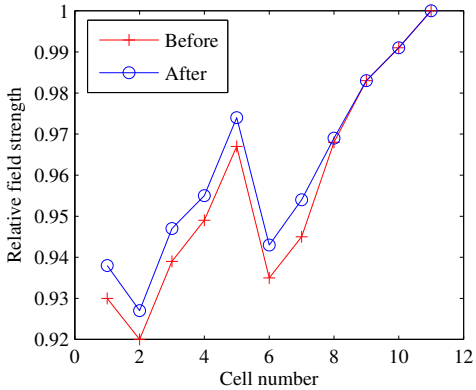


Figure 4: Effect of tuning slots balance between cells seven and eight.

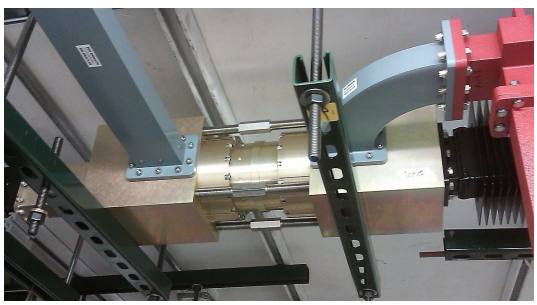


Figure 5: The waveguide variable power divider.

parameters (return loss, isolation, range of power split adjustment) while keeping the device as compact as possible, at just over 22 inches in length. The device was optimized with a computer-based minimization procedure, which resulted in a measured isolation and return loss of better than 24 dB for any power split setting, and adjustment of the power split between 0% and >98% from the input to the #2 port. The power divider was able to transmit the full klystron output of 12 MW under 1 atm of SF_6 pressure.

RF CONDITIONING AND TESTING

The linac was brought to the UCLA Pegasus laboratory for conditioning. After two days of conditioning, the input power was consistent with a 9.3 MeV energy gain through the structure using the calculated shunt impedance. The cavity field estimate should be considered imprecise because the lack of a flat top on the input RF pulse had the effect of the system never reaching steady-state, and the number was obtained by averaging the net input power over the last half of the pulse. Figure 6 shows the linac installed in the Pegasus beamline, just ahead of the spectrometer magnet. The testing of the linac with beam is reported by R. Li [8]. In actual operation, the linac reached 7.5-8.0 MeV energy gain with 1.8 MW power input. The energy gain was limited by the power divider setting, and with more power as well as slightly better vacuum ($< 3 \times 10^{-8}$ Torr), the full design energy gain of 10 MeV would likely be realized. The linac is used to boost the energy of the Pegasus laboratory gun, as well as to perform bunch compression through velocity bunching. This has allowed the facility to achieve < 100 fs electron pulses which are needed for ultrafast electron diffraction experiments.

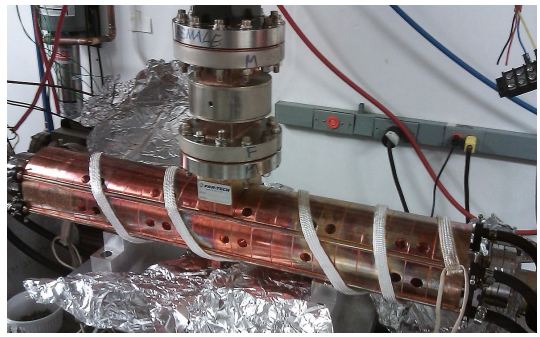


Figure 6: The DSR linac as installed in the Pegasus beamline at UCLA.

CONCLUSIONS

We have conceptually developed, built, and tested a linac structure based on dual slot resonance coupling. The linac was installed at the Pegasus laboratory at UCLA, where it is used to boost the beam energy and perform velocity bunching to achieve < 100 fs bunch length for ultrafast electron diffraction microscopy applications. The new linac design is more compact than a side-coupled structure and the large bandwidth, combined with the unique properties of the structure, results in simplified manufacturing.

ACKNOWLEDGMENT

We thank R. Li, H. To, and P. Musumeci of UCLA for their collaboration.

REFERENCES

[1] D. Newsham, N. Barov, R.H. Miller, Proc. of the 2011 Particle Accelerator Conference, p. 1897, (2011).

[2] N. Barov, and R.H. Miller, "Dual Slot Resonance Coupling For Accelerators", U.S. Patent #8232749

[3] HFSS Manual, v13.0, Ansoft Corp.

[4] C. Ng, et al., "State of the Art in EM Field Computation", Proc. of the 2006 EPAC Conference, (2006).

[5] D. Yu, et. al, "A Plane-Wave-Transformer Photoelectron Linac", Proc. of the 1997 Particle Accelerators Conference, (1998).

[6] P. Musumeci, M.S. Gutierrez, J.T. Moody, C.M. Scoby, "Time Resolved Relativistic Electron Diffraction", Proc. of the 2009 Particle Accelerators Conference, (2009).

[7] C.D. Nantista et al., "An RF Waveguide Distribution System for the ILC Test Accelerator at Fermilab's NML", Proc. 2007 Particle Accelerators Conference (2007).

[8] R. Li, et al., NA-PAC'13, to be published.

Copyright © 2013 CC-BY-3.0 and by the respective authors

DESIGN OF A COMPACT X-BAND LINAC STRUCTURE FOR KAERI-RTX-ISU MEDICAL CYBERKNIFE PROJECT

C. Eckman[1*], P. Buaphad[1], Y. Kim[1,2], T. Downer[1], A. Andrews[1], B. N. Lee[3], B. C. Lee[3], S. Y. Ryoo[4]
[1]Department of Physics, Idaho State University, Pocatello, ID 83209, USA
[2]Thomas Jefferson National Accelerator Facility, Newport News, VA 23606, USA
[3]Korea Atomic Energy Research Institute, Daejeon 305-353, Korea
[4]Radiation Technology eXcellence, Daejeon 305-353, Korea

Abstract

Recently, the Advanced Accelerator and Ultrafast beam Lab (AAUL) at Idaho State University (ISU), has been developing an X-band linac for the medical CyberKnife project by collaborating with Korean Atomic Energy Research Institute (KAERI) and Radiation Technology eXcellence (RTX) [1–3]. The medical CyberKnife is essentially an X-band linac, which is attached to a robotic arm for precise cancer treatment. The X-band linac has considerable advantages in cancer treatment over C-band or other RF linacs, partly due to its compact size and light weight. These qualities make the X-band linac easier to attach to a robotic arm, thus making it more maneuverable. Other advantages include a higher accelerating gradient and a higher shunt impedance. Since high mobility is necessary for precise cancer treatment, the compact X-band RF linac was selected for the CyberKnife project. This paper describes detailed design processes of the X-band linac structure, which was done with 2D SUPERFISH and 3D CST MICROWAVE STUDIO (CST MWS) electromagnetic simulation programs.

INTRODUCTION

Recently, ISU AAUL, KAERI, and RTX have been developing an X-band Standing Wave (SW) RF linac for the CyberKnife robotic radiosurgery system. CyberKnife is a non-invasive cancer treatment technique, which can be used for a multitude of cancers or tumors in the human body [4]. By adjusting a robotic arm housing the X-band linac precisely, CyberKnife can target with pinpoint accuracy. The X-band linac is used to deliver high doses of radiation directly to the cancer or tumorous areas. This process is a major improvement over older and harsher cancer treatment techniques and has the potential to save thousands of lives. The expected parameters of the X-band linac for the CyberKnife project is summarized in Table 1. The X-band linac consists of a π-mode SW linac structure with 15 cells and a coupler as shown in Fig. 1. By using the π-mode, a higher shunt impedance and a higher gradient can be obtained [5]. For the RF power source of the linac, an X-band coaxial pulsed magnetron manufactured by L-3 Communications was selected [6]. Therefore, the linac was optimized to make an RF resonance at 9.3 GHz.

* cryptoscientia@gmail.com

Table 1: Parameters of an Optimized X-band Linac

Parameter	Value	Unit
length of the linac	0.25	m
initial beam energy from gun	20	keV
maximum beam energy at linac exit	6	MeV
RF frequency	9.3	GHz
maximum RF input power	2.36	MW
shunt impedance	78	MΩ/m
maximum energy gain per cell	400	keV
unloaded quality factor	8306	·
external quality factor	7099	·

By knowing the RF resonant frequency, the cell lengths and cell radii of the linac structure can be calculated in advance. The cell length l of the π-mode SW linac structure is given by

$$l = \beta \frac{\lambda_{RF}}{2}, \quad (1)$$

where β is the relativistic velocity of electrons, and λ_{RF} is the RF wavelength of the linac structure [1]. In our linac design, the bunching cells in the linac structure correspond to the cells where β is smaller than 0.95. All these initial conditions were used in 2D SUPERFISH simulation to find a basic geometry of the linac structure. A MATLAB program was developed to work in conjunction with the 2D SUPERFISH program to design basic geometries of each bunching cell and nominal accelerating cell. These individual cells are then combined in series to form a full linac structure with good electric field symmetry. Therefore, we can save our working time to find full geometry of the X-band linac structure with good electric field symmetry by using the homemade MATLAB and SUPERFISH combined program. Then, 3D CST MWS was used to optimize the linac structure and coupler by starting with the full geometry generated by the MATLAB and SUPERFISH combined program. Once the design is completed with CST MWS, it will serve as a blueprint for an actual working model.

2D SUPERFISH SIMULATION

SUPERFISH is a 2D electromagnetic field solver created and distributed by the Los Alamos National Laboratory to evaluate cylindrically symmetric RF accelerator cavities [7]. The cells in the X-band SW RF linac structure

Copyright © 2013 CC-BY-3.0 and by the respective authors

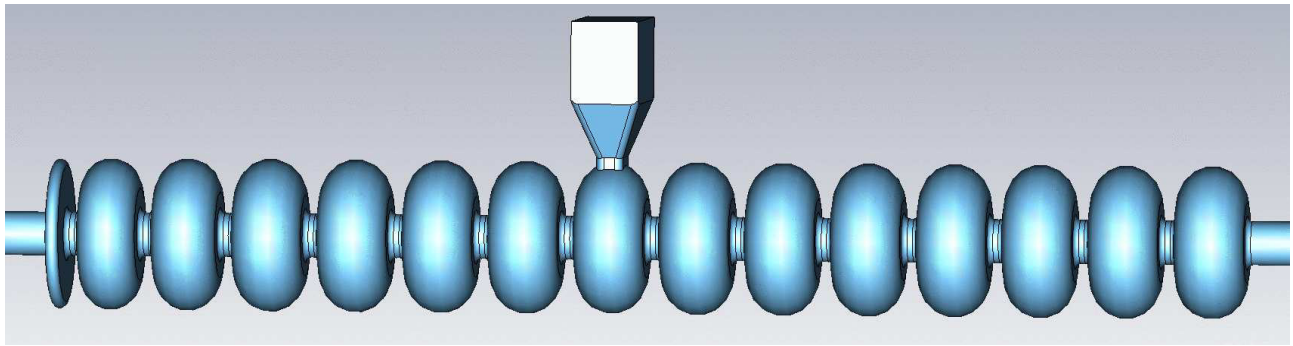


Figure 1: 3D CST MWS simulation result for an X-band linac structure with 15 cells summarized in Table 2.

were individually modeled using the SUPERFISH elliptical cavity tuning program ELLFISH. ELLFISH tunes an elliptical cell for explicit beam parameters and geometric constraints by making slight adjustments in the geometry of the cell. The geometric constraints are determined by the parameters of the electron beam. In this case, unbunched electron beam enters the linac structure with kinetic energy of 20 keV from the electron gun. Then, the bunching will be developed at bunching cells in the linac structure. The linac accelerates the electron beam through each cell in the structure and exits with a total energy of 6 MeV.

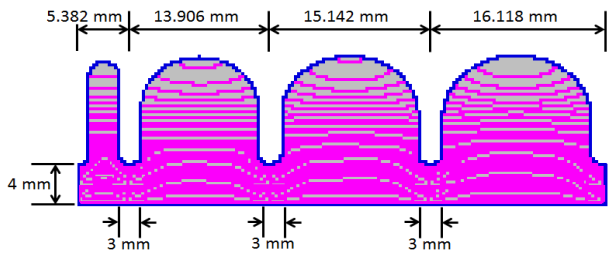


Figure 2: 2D SUPERFISH simulation result for a linac structure with four bunching cells.

The field symmetry along the linac cells is dependent upon the radius of the linac cells as summarized in Table 2. The semi-major and semi-minor ellipses of the elliptical cells can be calculated from the cell length, cell radius, and the desired septum thickness and iris radius. ISU AAUL has developed a MATLAB program to expedite the modeling of the linac structure with several bunching and nominal accelerating cells. The boundary constraints for the SW π-mode in the linac are hard coded into the program. The program allows for the user to input a desired frequency, the β values for the bunching cells and nominal cells with $\beta = 1$, and the desired iris radius. The program also offers an option to specify the mesh size and to add an extended beamline to the structure. The MATLAB program writes the geometrical parameters, calculated from the data input by the user, to several ELLFISH control files. ELLFISH executes each control file, optimizes the geometry for each cell, and writes the optimized geometries to a set of output files. The MATLAB program splices the individually optimized cell geometries, writes the multi-cell geometry to a single control file, and executes the control file in Autofish. Autofish performs an electromagnetic analysis of the multi-cell linac structure as shown in Fig. 2. WSFplot displays the longitudinal electric field. The shunt impedance, power dissipation, and transit-time factor are located in the PMI output files for the multi-cell linac structure.

Table 2: Detailed Geometry of the X-band Linac Cells

Cavity	Radius (mm)	Length (mm)
1^{st} bunching cell	13.680	5.382
2^{nd} bunching cell	13.850	13.906
3^{rd} bunching cell	13.906	15.142
4^{th} cell	13.949	16.118
5^{th} cell	13.950	16.118
6^{th} cell	13.950	16.118
7^{th} cell	13.951	16.118
8^{th} coupling cell	13.790	16.118
9^{th} cell	13.950	16.118
10^{th} cell	13.951	16.118
11^{th} cell	13.950	16.118
12^{th} cell	13.950	16.118
13^{th} cell	13.949	16.118
14^{th} cell	13.949	16.118
15^{th} cell	13.929	16.118

DESIGN OF RF COUPLER

The RF input is channeled through a WR-112 waveguide with an inside dimension of 28.4988 mm $\times$ 12.6238 mm with an allowable frequency range of 7.05 GHz to 10.0 GHz. Using these waveguide dimensions, the coupler design could be developed for the structure. Placing the coupler in the central location in the accelerating structure provides greater separation of modes [8]. The waveguide dimensions needed to be reduced to an appropriate size to couple with the X-band structure. This was accomplished by tapering the X-band waveguide to the RF power input window of the 8th coupling cell as shown in Fig. 1. The RF power input window to the coupling cell has the di-

Copyright © 2013 CC-BY-3.0 and by the respective authors

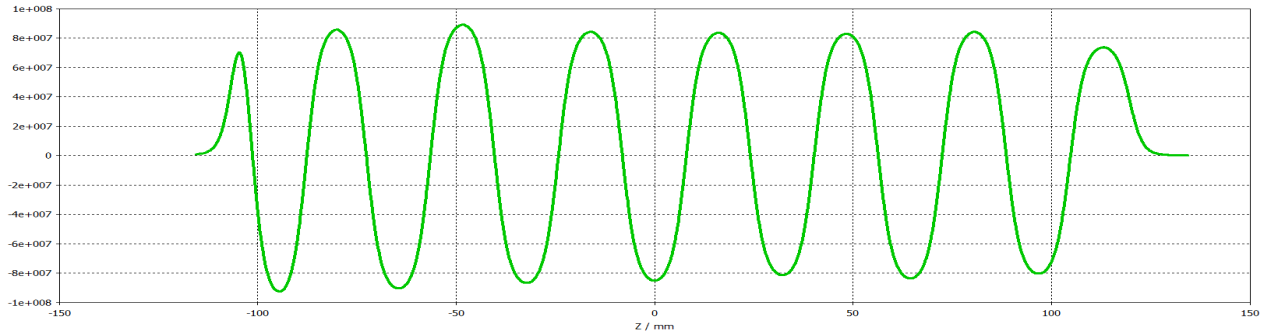


Figure 3: Electric field along the axis of the X-band linac structure summarized in Tables 1 and 2.

mensions of 10.7 mm $\times$ 5.0 mm and comes straight up out of the cell 1.0 mm. The waveguide, tapered area, coupler window and the coupling cell were tuned as a single cell, apart from the full structure. This single cell was given the proper boundary conditions in CST MWS as shown in Fig. 1. The dimensions of cell radius and coupler window have been tuned to obtain a coupler coefficient $\beta = 15$, which is the same as the total number of cells at the resonance frequency of 9.3 GHz. This coupling coefficient of $\beta = 15$ provides the maximum RF power coupling to each of the 15 cells in the full structure [8]. After this coupler is tuned individually, it is then placed into the full structure and tested once more. Experience shows that this coupler still will need an adjustment before it will work properly in the full linac structure.

3D CST MWS SIMULATION

CST MWS provides 3D manipulation and a more in-depth testing ground for the X-band structure [9]. To get a higher shunt impedance, generally, we may choose cell geometries with the nosecones. However, as shown in Figs. 1 and 2, all cells of the X-band linac structure have the bell shapes instead of the nosecone ones for easy fabrication. To obtain the symmetric electric field for the whole linac structure, the radius of each cell was individually modified by small increments [5]. These small increments were determined by the physical machining tolerances, which are ± 2 μm. Even small changes in the cell radius generate big impacts on the symmetry of the electric field. The cavity radius and the iris radius of each cell are inversely proportionally to the global frequency and the local electric field strength. Since the iris radius is directly related to the frequency separation between electromagnetic modes, we chose 4 mm for the iris radius of the linac structure to keep the mode separation larger than 5 MHz. Any shape made in CST MWS is carved from a default background of uniform conducting solid material and the carved shape is assumed to be vacuum. Once the cells, irises, and a coupler are connected into one solid structure, the electric fields can be optimized. The electric field was optimized for π-mode in CST MWS using the *Eigenmode Solver Parameters* tool to produce the desired field as shown in Fig. 3. This tool uses one of two solvers: the Advanced Krylov Subspace method (AKS) and the Jacobi-Davidson method (JDM). AKS measures modes with the lowest resonant frequencies, whereas the JDM measures modes at arbitrary positions specified by user input; this X-band structure used JDM [9]. The specifications of *Eigenmode Solver Parameters* tool were shown to be the first five modes above the frequency of 9.295 GHz. To help alleviate the calculation time, the *Boundary Conditions* toolbox has an option under the *Symmetry Planes* tab to cut the structure into symmetrical sections for calculation purposes. This process of optimizing the electric field was the most time consuming part of the X-band linac design.

SUMMARY

An X-band SW linac structure was successfully designed with SUPERFISH and CST MWS. The linac will be operated in π-mode to generate 6 MeV electron beam for the CyberKnife. The central RF coupler was designed and optimized to produce a symmetric electric field for the X-band structure as shown in Fig. 3. The final optimized geometry of the X-band linac structure is shown in Fig. 1 and its parameters are summarized in Tables 1 and 2. The next steps in the process are to simulate the X-band linac with a copper shell and design the heat dissipation method for the structure. Then it will be built and tested as an electron beam source for the medical CyberKnife project. Independently, we also have been optimizing a longer X-band linac structure with 25 cells.

REFERENCES

[1] http://www.isu.edu/~yjkim
[2] http://www.kaeri.re.kr
[3] http://www.irtx.co.kr
[4] www.cyberknife.com
[5] Yasser Nour *et al.*, in *Proc. IPAC2013*, Shanghai, China.
[6] http://www2.l-3com.com/edd/pdfs/EDDPM1110Xdatasheet.pdf
[7] http://laacg1.lanl.gov/laacg/services/download_sf.phtml
[8] D. Alesini *et al.*, Nucl. Instr. and Meth. A **554** (2005) 1.
[9] http://www.cst.com/

Copyright © 2013 CC-BY-3.0 and by the respective authors

COMPACT SCHEME FOR LASER-FREE THZ-SUB-THZ SOURCE*

A. V. Smirnov#, RadiaBeam Technologies Inc., Santa Monica, CA 90404, USA

Abstract

Undulator-free schemes based on resonant Cherenkov radiation in a small insertion device driven by a few MeV RF electron injector and alpha-magnet are considered. S- and C-band RF guns are compared to X-band multi-cell microlinac. Preference is given to planar radiator and wide quasi-flat sub-ps bunches that can be obtained with alpha magnet. It is shown that up to a milli-joule of sub-THz energy can be produced within a macropulse.

INTRODUCTION

Relatively insignificant number of facilities such as synchrotron radiation sources and free electron lasers (FELs) around the world are dedicated specifically to the THz range to deliver substantial power to users. Obviously, more facilities are needed to cover the rapidly growing demand in dedicated sources for THz science and technology [1]. However, conventional radiation facilities based on FELs, electron storage rings, and/or energy recovery linacs (ERLs) are too large, expensive, and not readily available for a broader community of researchers, investigators, scientists and commercial applicants to operate it on a flexibly customized, on-demand, independent base. For narrow bandwidth radiation generation, resonant Cherenkov resonant radiation is an attractive alternative to undulator radiation due to relative frequency independency from the beam energy (for relativistic beams) and due to the much higher equivalent shunt impedance. Coherence is provided by the Cherenkov synchronism between the microbunches and fundamental (or one of the lowest) eigenmode(s) along the interaction space hundreds of wavelengths long.

THE CONCEPT

This source concept illustrated in Fig. 1 can be utilized for container inspection, screening, safe imaging, cancer diagnostics, surface defectoscopy, and many other applications. Substantial average power can be provided by using thermionic, plasma [2], field [3] or secondary emission [4] that can be perfectly combined with RF cavity.

The THz radiation is generated by beam pre-bunching and chirping in the RF gun, followed by microbunching in a magnetic compressor and resonant Cherenkov radiation of an essentially flat beam in a robust, planar, structure with mm-sub-mm gap. The proof-of-principle has been successfully demonstrated recently on a 5 MeV beam driven by an L-band thermionic injector [5].

We calculate the energy radiated by a single microbunch using the modal energy loss found analytically with the eigenmode excitation theory applied in time domain [6] for matched outcoupling without trapped modes as follows:

$$W_{lb} \approx \frac{\omega}{4}\frac{rL}{Q}\frac{(q|\Phi|)^2}{|1-\beta_{gr}/\beta|}\left(\frac{1-\exp(-\alpha L)}{\alpha L}\right)^2, \qquad (1)$$

where $\omega = 2\pi f = h(\omega)v$ is the circular frequency of the resonant Cherenkov radiation, $h(\omega)$ is the wavenumber defined by the structure dispersion, q is the bunch charge, $r = E_z^2/dP/dz$ is the shunt impedance, $\beta = v/c$, Q is the Q-factor, $Q|\beta-\beta_{gr}|>>1$, $\alpha = \pi f/Qv_{gr}$ is the attenuation, and $\Phi = \exp\left(-(\omega\sigma_t)^2/2\right)$ is the formfactor for a Gaussian bunch having rms duration σ_t. Note Eq. (1) applied to, e.g., the 270 GHz setup [7], gives 9 μJ energy which is the same as measured [7].

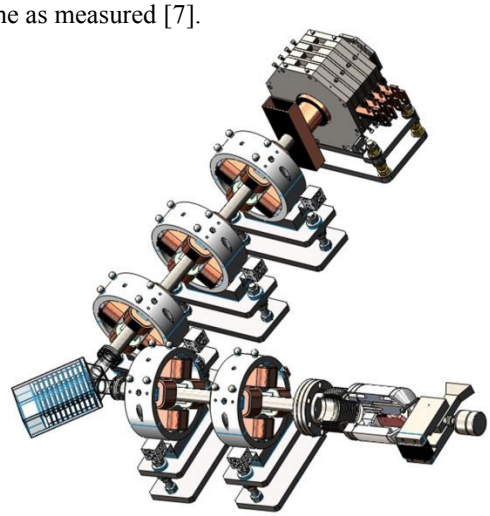


Figure 1: Schematics of the THz source beamline composed by quadrupoles, PM α-magnet, Cherenkov radiator, dipole magnet, and THz beam output.

Below we consider only briefly key features of beam dynamics, slow-wave structure, and general beamline design.

PLANAR CHERENKOV RADIATOR

Electromagnetic and mechanical engineering of a planar radiator [5,8,9] is used here as a prototype for a 0.67 THz radiator design shown in Fig. 2. The structure parameters are the following: r/Q=8 kΩ/m at 3 mm width of the grating, 0.6 mm interaction gap and 42 μm grove height; Q=1410, and 1" structure length.

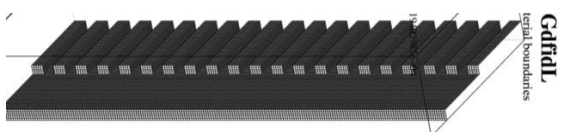


Figure 2: 20-period, bottom-half fragment of the planar radiator structure in GdfidL model (antenna horn is not shown).

*Work supported by US DoE Contract DE- SC-FOA-0000760
#asmirnov@radiabeam.com.

Copyright © 2013 CC-BY-3.0 and by the respective authors

Results of time domain GdfidL code [10] and analytical [6] simulations are in a good accordance and given in Figs 3-5 for 50 pC charge, 200 fs rms duration (60 μm rms length) bunch having ~0.7 formfactor Φ.

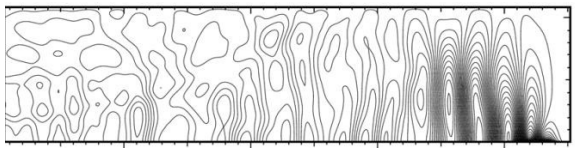


Figure 3: GdfidL contour plot in the median plane of the longitudinal electric field component of the wake induced in the 40-period SWS at t=15.2 ps.

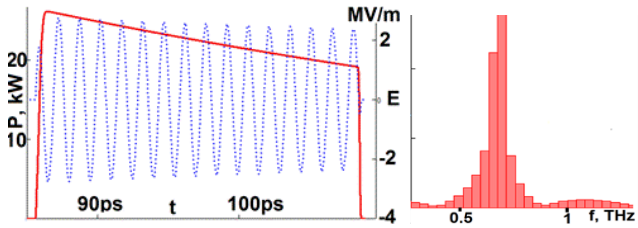


Figure 4: LEFT: Power (red) and field (blue) at the end of the structure vs. time. RIGHT: Field spectrum.

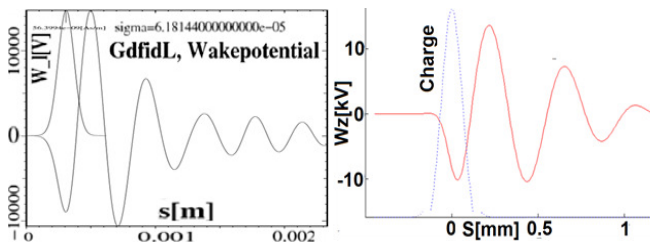


Figure 5: Wakepotential calculated numerically (left) and analytically (right) for 70 pC charge in the 40-period structure.

BEAM DYNAMICS SIMULATIONS

Performance features of the rugged, high group velocity, planar radiator imply forming of sub-mm long, sub-mm tall, and mm-cm wide bunches to efficiently utilize the low-energy beam having substantial emittance (compared to photoinjector not used here). We simulated with ASTRA code [11] 1.6 cell thermionic RF guns producing 1.8 MeV energy-modulated beam in S- and C-bands using BNL/UCLA/SLAC cavity shape. Field profiles used for S- and C-band RF gun simulations are shown in Fig. 6 to produce 1.8 MeV, 90 pC bunch with ~11μm normalized emittance. Cathode radius is 1 mm, for S-band and 0.5 mm for C- band (with cathode loading~17 and 86 A/cm2 respectively).

The beamline with the alpha-magnet have been optimized with ELEGANT for minimum vertical and longitudinal bunch dimensions in the radiator. The results are exemplified in Figs 7, 8 for C-band variant with 5 quadrupoles.

For X- band variant we considered here a biperiodic, 45-cell, tapered, side-coupled, 2 MeV microlinac designed and developed at RadiaBeam [12]. The microlinac structure was modified by using slightly longer regular cells to provide energy chirp simulated with PARMELA code [13] (see Fig. 9).

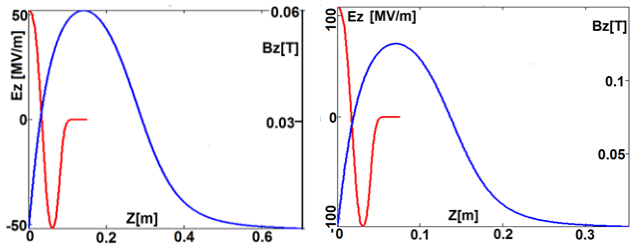


Figure 6: RF and magnetic field profiles used for 1.6-cell RF S-band (left) and C-band (right) gun ASTRA simulations.

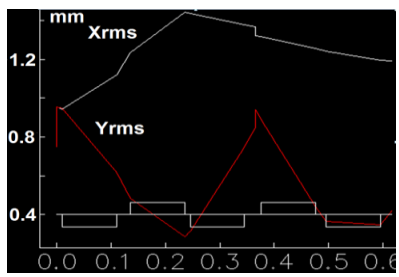


Figure 7. : Transverse RMS dimensions for 1.8 MeV 90pC bunch along 5-quad beamline optimized with ELEGANT together with α-magnet and energy filter (scraper) having 27% transmission.

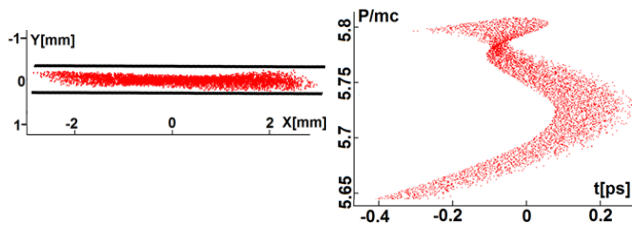


Figure 8: LEFT: Transverse beam profile in the 0.6mm interaction gap for C-band variant with 5 quadrupoles. RIGHT: Longitudinal phase space of the beam in the gap.

The beamline with 3 quadrupoles and α-magnet was optimized with ELEGANT code [14]. Benefit of energy filtering related to formfactor (see Eqn. (1)) is shown in Fig. 10. The ELEGANT results are compared to the GPT code [15] simulations with taking into account space charge in the beamline (see Fig. 11).

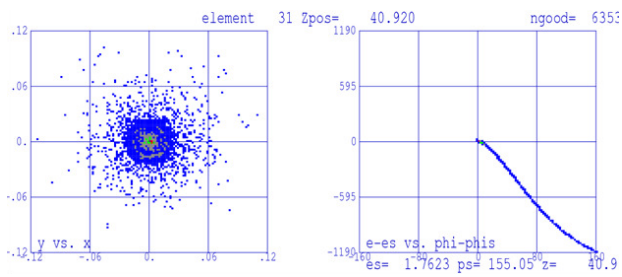


Figure 9: Transverse beam profile (left) and longitudinal phase space (right) for modified RadiaBeam biperiodic microlinac with side cells. Bunch charge 2 pC.

In Table 1 we summarized performance calculated for different beamlines with time domain model for 1" long

Copyright © 2013 CC-BY-3.0 and by the respective authors

planar radiator having 0.6×10 mm^2 interaction gap, 3.7 MΩ/m shunt impedance, β_{gr}=0.8 for 90 pC bunches produced from different RF injectors at 0.1% duty factor and 4 μs pulse length.

In Table 2 we characterize a low power 0.67 THz source driven by 2 MeV 9.4 GHz microlinac using 1" long, 0.6×3.2 mm^2 interaction gap planar radiator having 11.3 MΩ/m shunt impedance, β_{gr}=0.8 for 2 pC bunches having no losses in the radiator at 0.1% duty factor and 2.5 μs pulse length.

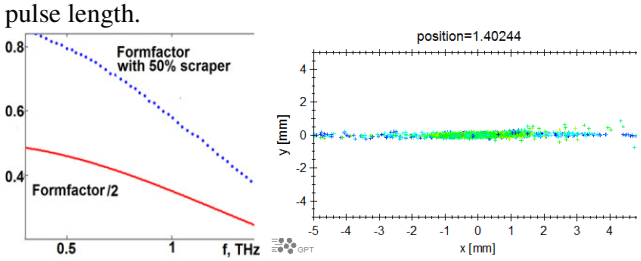


Figure 10: LEFT: Formfactor vs. frequency for the beam driven by RadiaBeam microlinac and microbunched in the beamline with and without energy filtering. RIGHT: Transverse beam profile simulated with GPT in the radiator having 0.6 mm vertical gap.

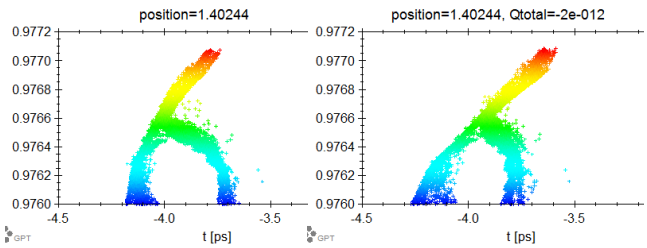


Figure 11: GPT simulations of longitudinal phase space without (left) space and including (right) charge in the beamline with 50% energy filtering.

Table 1: Simulated performance for the 0.67 THz source driven by S- and C- Band RF guns

Variant (RF band & # of quads)	Charge, pC	Trans-mission		Bunche σ, fs	Wmicro, nJ	Pmicro, kW	Wmacro, μJ	Pmacro, W
		Scraper, %	Radiator, %					
S-b 5q	13	15	94	105	46	2.2	524	131
S-b 3q	10	18	65	117	30	1.4	338	85
C-b 5q	25	28	100	130	165	7.8	3372	943
C-b 3q	17	27	68	105	78	3.7	1785	446

Table 2: Source performance with microlinac

Rep rate, Hz	Pulse t, μs	Charge, pC	σt, fs	Micropulse Energy, nJ	Peak THz power, W	Average THz power, mW	Macropulse THz power, W
40	2.5	2	132	2.4	23	2.3	23

CONCLUSION

Alpha magnet and quadrupoles can produce flat beams with a moderate aspect ratio ~10 making a good match to the gap of planar radiator. C-band RF gun is very promising configuration for the system and capable to produce a kW power within a macropulse.

ACKNOWLEDGMENT

The author is grateful to Bas van der Geer and Marieke de Loos for the GPT code simulations and Warner Bruns for the opportunity to use GdfidL code.

REFERENCES

[1] S. Chattopadhyay, S. T. Corneliussen, G. P. Williams, "Emerging Concepts, Technologies and Opportunities for Mezzo-Scale Terahertz and Infrared Facilities", THPKF084, EPAC'04, Lucerne, Switzerland p. 2454 (2004).

[2] G. Xia, M. Harvey, A. J. Murray, W. Bertsche, R. Appleby, S. Chattopadhyay. IPAC2013, Shanghai, China (2013) 452.

[3] V.N.Volkov et al., APAC'01, Beijing, China, p. 170 (2001).

[4] N.Y. Huang, H. Hama, IPAC'10, Kyoto, Japan, p. 4683 (2011).

[5] R. Agustsson, A. V. Smirnov et al. "Development of a Compact Insertion Device For Coherent Sub-Mm Generation", IPAC'13, WEPWA080, Shanghai, p. 2295 (2013).

[6] A.V. Smirnov, Nucl. Instrum. Methods Phys. Res., Sect. A 480 (2-3) 387 (2002).

[7] A.M. Cook et al. Phys. Rev. Lett. 103, 095003 (2009).

[8] A.V. Smirnov, "A Ps-Pulsed E-Gun Advanced to a T-Wave Source of MW-Level Peak Power", RUPAC'12, Saint-Petersburg, September 2012, TUPPB052, p. 430 (2012).

[9] A. Smirnov et al.,"Performance of Planar Radiator in the RadiaBeam-IAC Experiment",WEPBA18, these proceedings.

[10] W. Bruns, "The GdfidL Electromagnetic Field Simulator", http://www.gdfidl.de

[11] K. Floettmann, "ASTRA A Space Charge Tracking Algorithm", Version. 3, DESY, Hamburg, Germany (2011).

[12] S. Boucher, R. Agustsson, L. Faillace, J. Hartzell, A. Murokh, A. Smirnov, S. Storms, K. Woods. In Proceedings of IPAC2013, Shanghai, China, p. 3746 (2013).

[13] L. M. Young, "Parmela", Documentation by J. H. Billen, Los Alamos National Laboratory, LA-UR-96-1835, December 2005.

[14] M. Borland, "User's Manual for elegant", Program Version 25.0.2, Advanced Photon Source, March 2012.

[15] B. Geer, M. Loos, "The General Particle Tracer code", Pulsar Physics, the Netherlands, April 2001.

Copyright © 2013 CC-BY-3.0 and by the respective authors

ADAPTATION OF THE ISIS INDUCTION-CELL DRIVER TO A LOW-IMPEDANCE *X*-PINCH DRIVER

R.V. Shapovalov, W. Beezhold, V.I. Dimitrov (deceased), and R.B. Spielman
Idaho Accelerator Center, Pocatello, ID 83201, USA

Abstract

In this paper we summarize the work done to design a system to non-destructively convert the Idaho State Induction System (ISIS) induction cell driver (ICD) to a low impedance pulse power driver for *x*-pinch applications. The simulation results show that such a driver can supply about 300-kA peak current with about 70-ns rise time (10-90%). However, simulations also show that the negative reflective wave is formed, which can cause the destruction of the ISIS ICD's pulse forming line (PFL). Particular attention was taken to simulate the effect of misfire of one of the PFLs. To reduce the amplitude of this destructive wave, high power damping resistors should be placed after the output of each PFL. This would result in the maximum current achievable by this driver to be limited to about 200-kA peak value.

OVERVIEW

ISIS is a high-intensity, pulsed-power electron accelerator able to supply about 80 GW of power in a 35-nanosecond pulse [1]. It was donated to the Idaho State University by Titan Pulse Sciences, Inc. in 2002, and its primary purpose has been to serve as a radiation source for radiation effect testing in biological and semiconductor systems [2]. The power supply of ISIS [3] is composed from a Marx generator and five separate PFLs. Forty oil-filled, 77-ns-long cables connect the power supply to each acceleration unit (AU) of ISIS. The power supply of the ISIS is shown in Fig. 1. Each PFL produces a perfect 84-ns long, flat-topped 300-kV pulse which is directly used to accelerate electrons inside each AU.

In order to convert the ISIS power supply to a low-impedance *x*-pinch driver, an impedance transformer was designed [4]. The impedance transformer is the most important part of the *x*-pinch driver and serves to combine five, 300-kV outputs of the ISIS' induction cell driver (5 Ω each) into one, low-impedance (<1 Ω), 40-80 kV output to be fed to the *x*-pinch chamber. Analysis of the ISIS induction-cell driver showed that the most suitable spot for tapping its output pulse is at the end of the water-filled PFLs before the oil-filled connectors to the high-voltage cables [4].

We present the electrical circuit simulation results of proposed ISIS' based *x*-pinch driver. LTspice [5] simulations show that after directly connecting the output of each PFL to the impedance transformer and feeding the output pulse to *x*-pinch load, such a *x*-pinch driver can supply about 300-kA peak current with about 150-ns rise time (Fig. 3a). However, simulations also show, that the negative reflective wave is formed, which can cause the destruction of the ISIS PFL. Particular attention was taken to simulate the effect of misfire of one of the PFLs (Fig. 3b). To reduce the amplitude of this destructive wave, a high-power damping resistor should be placed after the output of each PFL. This would result in the maximum current achievable by this driver to be limited to about 200-kA peak value (Fig. 4a).

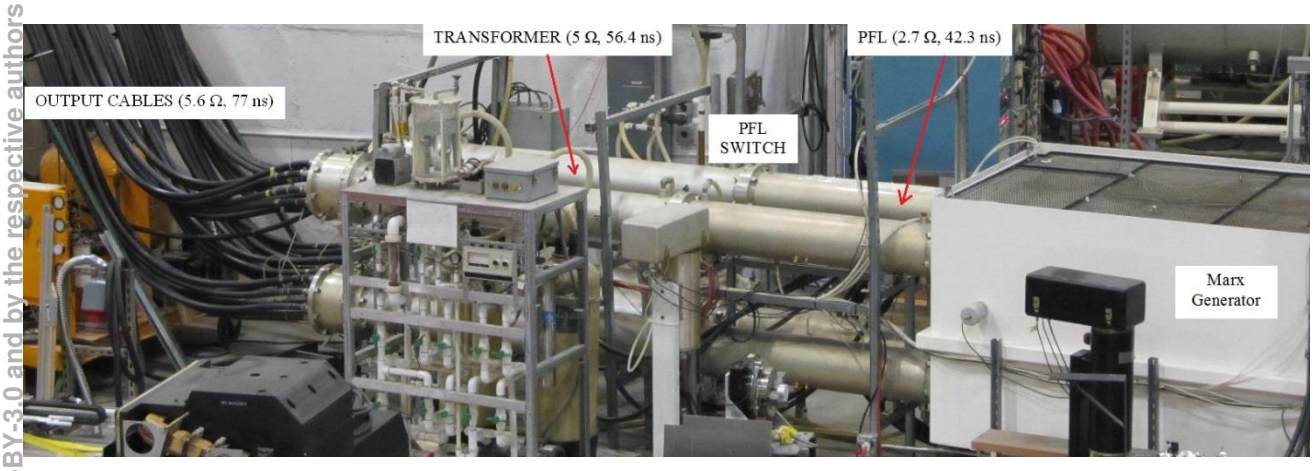


Figure 1: ISIS power supply.

Copyright © 2013 CC-BY-3.0 and by the respective authors

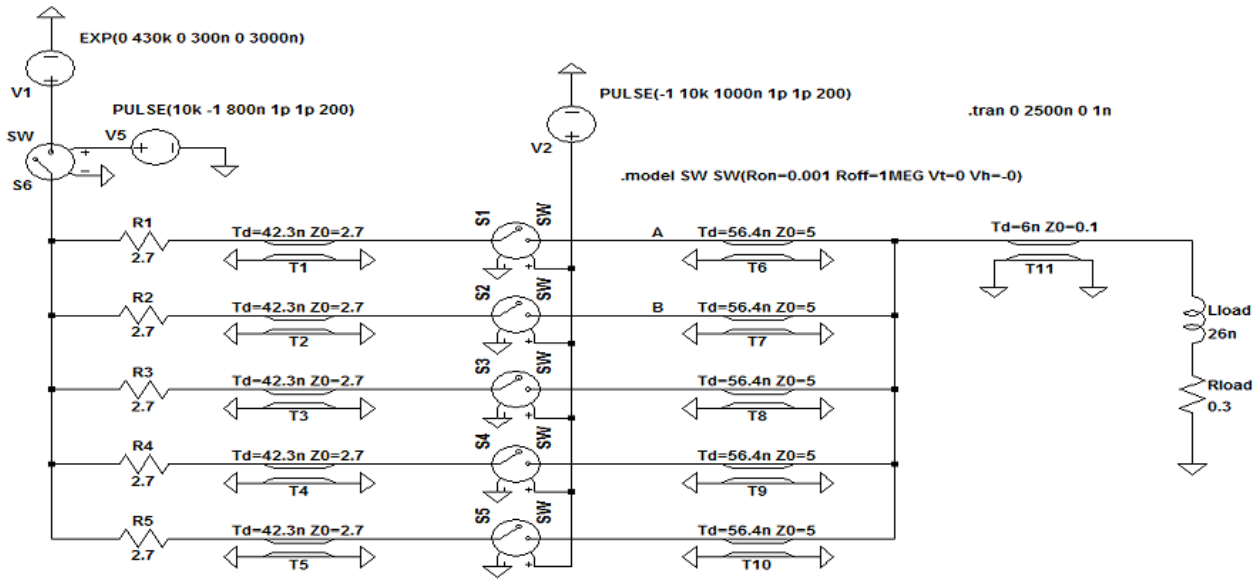


Figure 2: Electrical circuit of an ISIS-based *x*-pinch driver.

LTSPICE SIMULATIONS: 300-KA *X*-PINCH DRIVER

Figure 2 shows the electrical circuit of the ISIS' based *x*-pinch driver. The impedance transformer (represented by the transmission line element T11) is directly attached to the output of each PFL and the output of the impedance transformer is fed to the *x*-pinch load located in the middle of the vacuum chamber. The total inductance of the *x* pinch and all connection lines (header, lower feed, upper feed, etc.) can be roughly approximated to be equal to about 26 nH [6].

Simulation of current pulse as it propagates through the *x*-pinch load is shown in the Fig. 3a. After optimization of the impedance transformer parameters (6-ns long, 0.1 Ω), it was found that such a driver can supply about 320-kA peak current with 70-ns rise time (10-90 %).

Because the impedance transformer is necessary to transform down the impedance of PFLs by a factor of about 10, a reflective negative wave is formed traveling back to the PFL switch. This reflective wave will become even worse, if one or more PFL switches are not fired. Fig. 3b shows simulations of the voltage behaviour at the exit of PFL switch for two cases: the black line represents the scenario when all PFL switches are fired simultaneously (fire), and the red line represents the scenario when one PFL switch is not fired (misfire). As can be seen, the negative reflective wave with the maximum amplitude of about 150 kV is formed at the switch location for the normal regime of operation (fire). In the case of misfire of one of the switches, this reflective negative wave reaches the maximum amplitude of about 250 kV.

It is known [7], that such a high-voltage negative reflective pulse will probably destroy the PFL switch. Although the maximum current of about 320-kA peak value is achievable by this design, such a driver will probably not survive for a large number of shots due to possible damage to the PFL switches. As a result, a costly repairs would be necessary in the future.

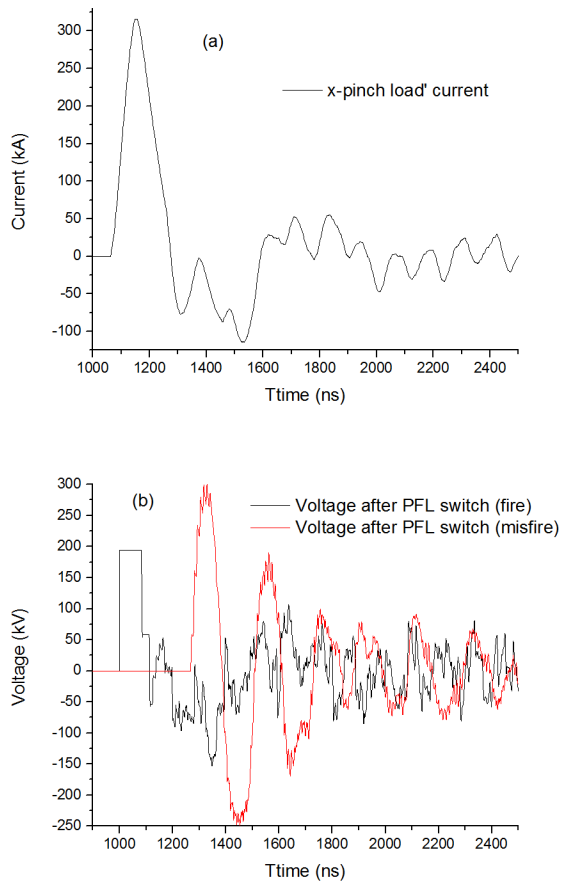


Figure 3: LTspice simulations of an ISIS-based *x*-pinch driver: (a) current measured at the *x*-pinch load (b) voltage measured after PFL switch.

Copyright © 2013 CC-BY-3.0 and by the respective authors

LTSPICE SIMULATIONS: 200-KA *X*-PINCH DRIVER WITH DAMPING RESISTORS

To reduce the amplitude of this destructive negative wave, high-power damping resistors (4.7 Ω) are placed after each PFL before the impedance transformer. This will reduce the amplitude of the reflective negative wave at the PFL switch location to the appropriate value, so the *x*-pinch driver can be safely operated.

As shown in Fig. 4a, such a modified *x*-pinch driver can supply about 200-kA peak current with 60-ns rise time (10-90%). The simulation results of the voltage behavior at the exit of the PFL switch for two cases, fire and misfire, as described above, are shown in Fig. 4b. In the normal regime of operation (fire), the amplitude of the negative reflective wave is almost reduced to the zero value. In the case of misfire of one of the switches, a negative reflective wave is still formed of maximum amplitude of about 25 kV, but the total duration of this wave is only about of 100 ns. This small negative reflective wave will probably not damage the PFL switches.

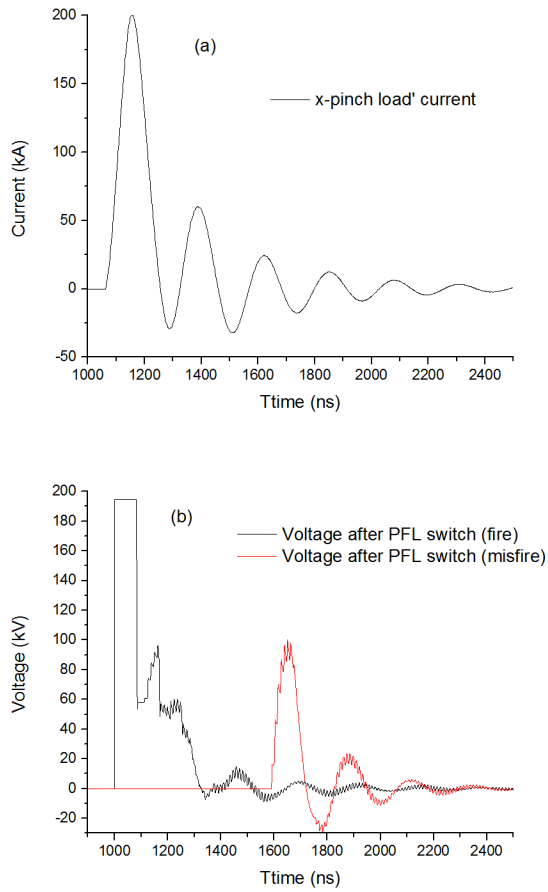


Figure 4: LTspice simulations of the ISIS-based *x*-pinch driver with a damping resistor placed after each PFL: (a) current measured on the *x*-pinch load (b) voltage measured after PFL switch.

CONCLUSION

In this report, we presented electrical circuit simulation results of a proposed ISIS-based *x*-pinch driver. LTspice simulations show, that after directly connecting the output of each PFL to the impedance transformer and feeding the output pulse to *x*-pinch load, such a *x*-pinch driver can supply about 300-kA peak current with about 70-ns rise time (10-90%). However, simulations also show, that the negative reflective wave is formed which can cause damage to the ISIS PFLs. Particular attention was taken to simulate the effect of misfire of one of the PFL switches, which causes the negative reflective wave to become even worse.

To reduce the amplitude of this destructive wave, a high-power damping resistor must be placed after the output of each PFL before the impedance transformer. This will to reduce the amplitude of the reflective negative wave at the PFL switch location to the appropriate value, so the *x*-pinch driver can be safely operated. But as a penalty, the maximum current achievable by this driver will be limited to about 200-kA peak value.

Taking into account these results and other considerations (time, effort and cost-needed to switch between the *x*-pinch operation mode and the normal operation mode of ISIS), the decision was made to design a new stand-alone, compact and portable pulse-power *x*-pinch generator [6].

ACKNOWLEDGMENT

This work was partially supported by DTRA grant HDTRA1-11-1-0035. Thanks a lot to Dr. V. Dimitrov for introducing me to pulsed power science and to Dr. W. Beezhold and Dr. R. B. Spielman for their helpful discussions and comments.

REFERENCES

[1] Titan Pulse Science Division, San Leandro, CA, "ISIS Manual," October 9 2004.

[2] V.I. Dimitrov, W. Beezhold, J. Ellis, V. Bailey, H. Lackner, and T. Webb "The ISIS Pulsed Power Accelerator Facility at ISU," 24 Annual HEART Conference, Santa Clara CA, March 2006.

[3] P. Corcoran, et al., "Experimental Test of the Power Supply and Prototype Cell for the 1.5 MeV SLIA Accelerator Unit," *1991 IEEE Particle Accelerator Conference*.

[4] V.I. Dimitrov "Progress Report for Grant DTRA1-11-1-0036," period May 19, 2011 – Sep. 1, 2012.

[5] LTspice IV Getting Started Guide, 2011 Linear Technology.

[6] R.V. Shapovalov "Design of a compact, portable plasma-radiation-source generator at the Idaho Accelerator Center," (to be published, 2013).

[7] Private communication with Dr. Vesselin I. Dimitrov. "The PFL switch is designed to hold the high-voltage positive pulse. The high-voltage negative reflective pulse will probably destroy this switch," Fall 2012.

Copyright © 2013 CC-BY-3.0 and by the respective authors

TRANSVERSE BEAM TRANSFER FUNCTIONS VIA THE VLASOV EQUATION*

M. Blaskiewicz†, V.H. Ranjbar
BNL Upton NY 11973 USA

Abstract

A semi-numerical method of integrating the Vlasov equation to obtain beam transfer functions directly as a function of frequency is presented. The results are compared with beam transfer functions calculated via particle tracking and excellent agreement is shown. The technique works well with both transverse wakes and detuning wakes from space charge.

INTRODUCTION AND THEORY

The stability and response properties of particle beams are encapsulated in beam transfer functions (BTFs) [1, 2, 3]. BTFs are relatively easy to measure making their accurate calculation of great practical interest. In this paper we will present two independent ways to calculate bunched beam transverse beam transfer functions, and show their agreement for some challenging parameters. To begin let θ denote azimthh, which increases by 2π each turn. Let t be clock time and let τ denote particle arrival time with respect to the synchronous particle so that $\theta = \omega_0(t-\tau)$, with ω_0 the synchronous angular revolution frequency. We use θ as the time-like variable and, to make a precise cross check possible, take linear rf so that

$$\frac{d\tau}{d\theta} = Q_s\epsilon \qquad \frac{d\epsilon}{d\theta} = -Q_s\tau, \tag{1}$$

where Q_s is the synchrotron tune and ϵ is the energy variable. with We consider a single transverse variable x and uniform focusing. Collective forces are taken in the continuum approximation with $dx/d\theta = p$ and

$$\begin{aligned}\frac{dp}{d\theta} &= -Q_\beta^2(\epsilon)x + F_e(\theta,\tau)\\ &+ 2Q_\beta\Delta Q_{sc}(\tau)[x-\bar{x}(\theta,\tau)]\\ &- \frac{q}{2\pi P_0\omega_0}\int_0^{2\tau_b} W_\perp(\tau_1)D(\theta,\tau-\tau_1)d\tau_1,\end{aligned} \tag{2}$$

where $Q_\beta(\epsilon) = Q_0 + Q_s\epsilon\omega_0\xi/\eta$ is the betatron tune, with chromaticity ξ and frequency slip factor η, $F_e(\theta,\tau)$ is the external driving force, $\Delta Q_{sc}(\tau)$ is the space charge tune shift as a function of longitudinal position in the bunch, and $\bar{x}(\theta,\tau)$ is the average beam offset. The wall induced forces are due the the transverse wake potential $W_\perp(\tau)$ and driven by the instantaneous dipole moment $D(\theta,\tau) = \bar{x}(\theta,\tau)I(\tau)$ with $I(\tau)$ the bunch current, q the particle charge, and P_0 the synchronous momentum. The force is limited to a single bunch of full length $2\tau_b$ but can be extended to uniformly filled rings.

To solve (1) and (2) using the Vlasov equation first introduce amplitude angle variables defined by $\tau = a\sin\psi$ $\epsilon = a\cos\psi$. Since all particle have constant a,

$$\frac{\partial F}{\partial\theta} + p\frac{\partial F}{\partial x} + \frac{dp}{d\theta}\frac{\partial F}{\partial p} + Q_s\frac{\partial F}{\partial\psi} = 0, \tag{3}$$

where $dp/d\theta$ is given by Eq (2). We normalise F so that $F dx dp a da d\psi$ is the number of particles in the phase space volume. To continue we define 3 transverse moments [4],

$$\{X(\psi,a,\theta),P,\Psi\} = \int dxdpF(x,p,a,\psi,\theta)\{x,p,1\}. \tag{4}$$

This gives

$$\frac{\partial X}{\partial\theta} + Q_s\frac{\partial X}{\partial\psi} = P(\psi,a,\theta), \tag{5}$$

$$\begin{aligned}\frac{\partial P}{\partial\theta} + Q_s\frac{\partial P}{\partial\psi} &= -Q_\beta^2(\epsilon)X + F_e(\theta,\tau)\Psi\\ &+2Q_\beta\kappa\left[X\int d\epsilon\Psi - \Psi\int d\epsilon X\right]\\ &-\frac{q\Psi}{2\pi P_0\omega_0}\int_0^\infty d\tau_1 W_\perp(\tau_1)q\int d\epsilon X(\epsilon,\tau-\tau_1)\end{aligned} \tag{6}$$

where $\Delta Q_{sc}(\tau) = \kappa\int d\epsilon\Psi$, $\bar{x}(\tau)\int d\epsilon\Psi = \int d\epsilon X$ and, for example,

$$\int d\epsilon X \equiv \int a_1 da_1 d\psi_1\delta(a\sin\psi - a_1\sin\psi_1)X(\psi_1,a_1,\theta),$$

and the occurences of τ and ϵ in (6) are understood to be shorthand for the amplitude angle representations. Next we substitute (5) in (6) and drop second partial derivatives with respect to ψ. We take $F_e(\theta,\tau) = F_0(\tau)\exp(-iQ\theta)$, and we take $X = X_1\exp(-iQ\theta - i\xi\omega_0\tau/\eta)$, with $Q = Q_0 + \Delta Q$. This yields

$$\left\{\Delta Q + iQ_s\frac{\partial}{\partial\psi} + \Delta Q_{sc}(a\sin\psi)\right\}X_1(\psi,a) = \tilde{F}(\tau)\Psi(a), \tag{7}$$

where

$$\begin{aligned}\tilde{F}(\tau) &= \frac{-e^{i\xi\omega_0\tau/\eta}F_0(\tau)}{2Q_0} + \kappa\int d\epsilon X_1\\ &+q^2\int_0^\infty d\tau_1\frac{W_\perp(\tau_1)e^{i\xi\omega_0\tau_1/\eta}}{4\pi Q_0 P_0\omega_0}\int d\epsilon X_1(\epsilon,\tau-\tau_1).\end{aligned} \tag{8}$$

* Work performed under the auspices of the United States Department of Energy
† blaskiewicz@bnl.gov

Copyright © 2013 CC-BY-3.0 and by the respective authors

The strategy is to solve (7) for $D_1 = q\int d\epsilon X_1$ resulting in a one dimensional integral equation for D_1 which will be solved numerically. To proceed let $\Delta Q_{sc}(a\sin\psi) = \lambda(a) + d\Lambda/d\psi$ where $\Lambda(a,\psi) = \Lambda(a,\psi+2\pi)$. Substitute $X_1 = X_2\exp(i\Lambda/Q_s)$ yielding

$$\left\{\Delta Q + iQ_s\frac{\partial}{\partial\psi} + \lambda(a)\right\}X_2 = e^{-i\Lambda/Q_s}\tilde{F}\Psi. \quad (9)$$

Multiply both sides by the integrating factor $\exp(-i\psi(\lambda+\Delta Q)/Q_s)$ and integrate from ψ to $\psi+2\pi$ employing the periodicity of X_2. Backsubstitute X_1 giving

$$X_1 = \frac{\Psi e^{iG(a,\psi)}}{Q_s R(a)}\int_{\psi}^{\psi+2\pi} d\psi_1\tilde{F}(a\sin\psi_1)e^{-iG(a,\psi_1)} \quad (10)$$

where $R(a) = 1-\exp(-2\pi i(\lambda+\Delta Q)/Q_s)$ and

$$G(\tau,\psi) = \int_0^{\psi} d\psi_1\frac{\Delta Q + \Delta Q_{sc}(a\sin\psi_1)}{Q_s}.$$

To proceed note that

$$D_1(\tau) = q\int adad\psi\delta(\tau - a\sin\psi)X_1(a,\psi)$$

yielding

$$D_1(\tau) = \int\hat{G}(\tau,\tau_1)q\tilde{F}(\tau_1)d\tau_1 \quad (11)$$

where

$$q\tilde{F}(\tau) = \frac{-e^{i\xi\omega_0\tau/\eta}qF_0(\tau)}{2Q_0} + \kappa D_1(\tau)$$
$$+\frac{q^2}{4\pi Q_0P_0\omega_0}\int_0^{\infty} d\tau_1 W_\perp(\tau_1)e^{i\xi\omega_0\tau_1/\eta}D_1(\tau-\tau_1) \quad (12)$$

and

$$\hat{G}(\tau,\tau_1) = \int_0^{\infty} ada\int_0^{2\pi} d\psi\delta(\tau - a\sin\psi)\Psi(a)e^{iG(a,\psi)}$$
$$K(a)\int_{\psi}^{\psi+2\pi} d\psi_1\delta(\tau_1 - a\sin\psi_1)e^{-iG(a,\psi_1)} \quad (13)$$

where $K = i\Psi/Q_sR$. To proceed assume $D_1(\tau)$ is defined at a set of equidistant points $\tau_k = k\Delta$ and that D varies linearly between these points. Then

$$q\tilde{F}(\tau) = \sum_{k=-N}^{N} a_k T(\tau - k\Delta),$$

where $T(x)$ is a triangle function of height 1 and half width at base Δ. For smooth bunches $D(\tau)$ is zero at the ends of the bunch so we take $\Delta = \tau_b/(N+1)$ where τ_b is the half bunch length. Next we do the integral over ψ in (13). For any smooth function $h(a,\psi)$,

$$\int_0^{2\pi}\delta(\tau - a\sin\psi)h(a,\psi)d\psi = \sum_{p=1,2}\frac{h(a,\psi_p)}{\sqrt{a^2-\tau^2}},$$

where the two angles satisfy $\sin\psi_{1,2} = \tau/a$ and the integral vanishes for $|\tau| > a$. Next we define a new radial variable u defined by $u^2 = a^2 - \tau^2$ so $udu = ada$. The dipole density is defined at the same set of lattice points as $\tilde{F}$ so

$$D_1(m\Delta) \equiv D_m = \sum_{n=-N}^{N} a_n M_{m,n}, \quad (14)$$

where

$$M_{m,n} = \int_0^{\sqrt{\tau_b^2-m^2\Delta^2}} duK(a)\sum_{p=1,2}e^{iG(a,\psi_p)}$$
$$\int_{\psi_p}^{\psi_p+2\pi} d\psi_1 T(n\Delta - a\sin\psi_1)e^{-iG(a,\psi_1)}. \quad (15)$$

In integral (15) $a = \sqrt{u^2+m^2\Delta^2}$ and $\sin\psi_p = m\Delta/a$. We have written a program which solves (14) with matrix element (15) and a_n from (12),

$$a_n = \frac{-e^{i\xi\omega_0 n\Delta/\eta}qF_0(n\Delta)}{2Q_0} + \kappa D_n$$
$$+\frac{q^2}{4\pi Q_0P_0\omega_0}\sum_{k=0}^{2N+1}\Delta W_\perp(k\Delta)e^{i\xi\omega_0 k\Delta/\eta}D_{n-k}. \quad (16)$$

SIMULATIONS

The solution of Equations (1) and (2) using particle tracking is straightforward [5, 6, 7, 8]. Before considering a sinusiodaly drive BTF we consider forces of the form $F_0(\tau,\theta) = f(\tau)\cos(Q\theta)\exp(gQ)\delta_p(\theta)$ where δ_p is the periodic delta function, Q is the real part of the drive tune, g is the imaginary part of the drive tune and $f(\tau)$ is nonzero only over the full bunch length, $2\tau_b$. Suppose $D_f(\theta,\tau)$ is the dipole response to a kick $f(\tau)$ given at $\theta = 0$. Then the response from all the kicks is

$$D(\theta,\tau) = \sum_{m=-\infty}^{\infty} D_f(\theta-2\pi m,\tau)\cos(2\pi mQ)\exp(2\pi gm). \quad (17)$$

To obtain a scalar we take the inner product

$$\hat{D}(\theta) = \int_{-\tau_b}^{\tau_b} d\tau f(\tau)D(\theta,\tau)$$
$$= \sum_{m=-\infty}^{\infty}\hat{D}_f(\theta-2\pi m)\cos(2\pi mQ)\exp(2\pi gm)$$

For a pickup at a fixed location one obtains the time series $\hat{D}(0), \hat{D}(2\pi), \hat{D}(4\pi), \ldots$, these values may be obtained with a single simulation. As long as $\hat{D}_f(\theta)$ does not grow more quickly than $\exp(g\theta)$ we will have

$$\hat{D}(2\pi k) = [A_Q\cos(2\pi kQ) + B_Q\sin(2\pi kQ)]\exp(2\pi gk)$$

Copyright © 2013 CC-BY-3.0 and by the respective authors

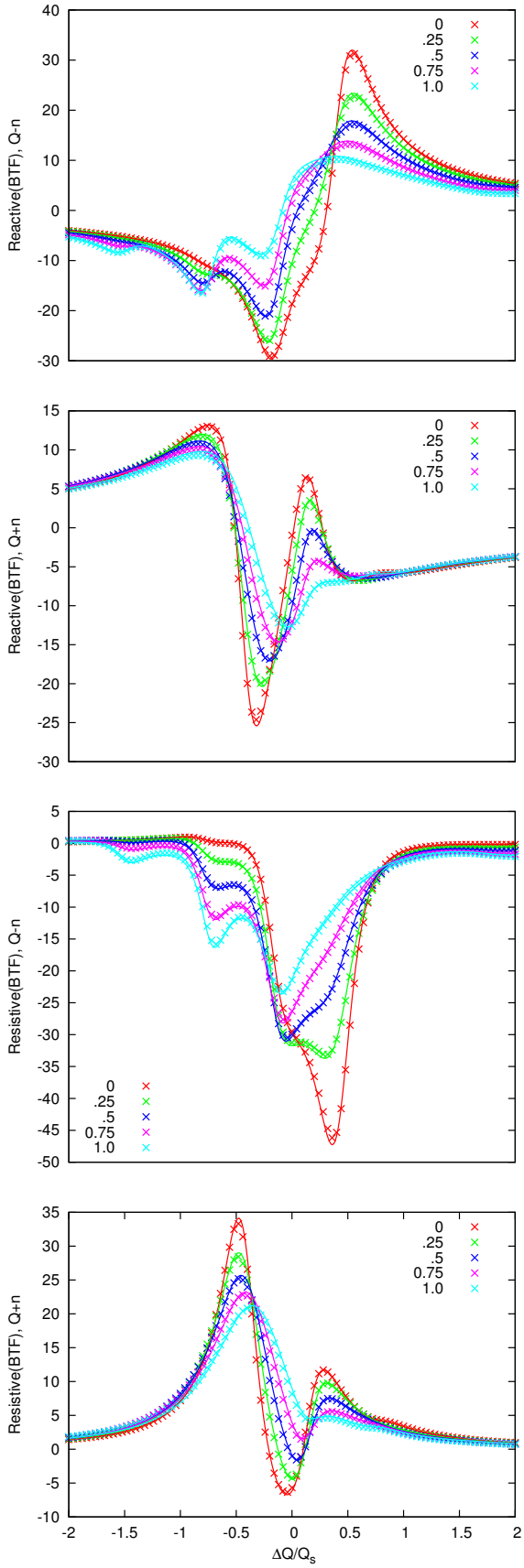


Figure 1: Simulated BTFs (solid lines) and those following from Eq (14) (crosses).

with

$$A_Q + jB_Q = \sum_{\ell=0}^{\infty} \hat{B}_f(2\pi\ell)\exp(2\pi\ell[jQ-g]) \qquad (18)$$

Hence, the entire BTF can be obtained with one simulation. For a real beam transfer function the force at the pickup is sinusiodal. We assume the frequency is $n\omega_0+\omega_1$ where n is an integer, $|\omega_1| \le \omega_0/2$. Then the driving force is given by

$$\begin{aligned} F_e(\theta,\tau) &= \delta_p(\theta)\cos[(n\omega_0+\omega_1)t], \\ &= \delta_p(\theta)\cos[(n\omega_0+\omega_1)(\tau+\theta/\omega_0)], \\ &\approx \delta_p(\theta)\cos(n\omega_0\tau)\cos(\omega_1 k(t)T_0) \\ &\quad -\delta_p(\theta)\sin(n\omega_0\tau)\sin(\omega_1 k(t)T_0) \end{aligned} \qquad (19)$$

where $T_0 = 2\pi/\omega_0$ and $k(t) = \mathrm{nint}(t/T_0)$. In a real BTF only the response at the drive frequency is measured so, with a sinusiodal kick one needs to run two simulations. One with a kick proportional to $\sin(n\omega_0\tau)$ and another with kick $\cos(n\omega_0\tau)$. During each simulation one takes inner products of the response with each sinusoid every turn. One finds

$$BTF(\omega_1) = \sum_{m=0}^{\infty}(C_m + jS_m)e^{-(j\omega_1+\epsilon)mT_0}$$

with

$$C_m = \int_{-\tau_b}^{\tau_b} d\tau D_{cos}(2\pi m,\tau)e^{-jn\omega_0\tau},$$

where $D_{cos}(\theta,\tau)$ is the response to a cosine kick at $\theta = 0$, and similarly for S_m. In these equations we have used the electrical engineering convention with $j = -i$ and allowed for an exponentially growing drive $\propto \exp(\epsilon t)$. The driving terms in the Vlasov approach are given by $F_0(\tau) = \exp(\pm jn\omega_0\tau)$ for the $Q \mp n$ sidebands, respectively. Figure 1 shows upper and lower sideband BTFs with $n\omega_0 = \pm\pi/2\tau_b$, varying chromaticity and a step function wake of size comparable to what is needed for a mode coupling instability. The peak space charge tune shift is 4 times the synchrotron tune. For more extreme parameters the disagreement increases and we continue to look for errors.

We would like to thank NERSC supported by the DOE under contract no. DE-AC02-05CH11231

REFERENCES

[1] D. Boussard, CERN 87-03, p. 416, 1987.

[2] R. Singh, et.al. PRSTAB **16** 034201 (2013).

[3] P. Görgen, in BB2013, 2013.

[4] F. Ruggerio, CERN-LEP-TH/84-21, 1984.

[5] R.H. Siemann, AIP conf 127, p. 368 (1983).

[6] K. Ohmi PRL **75**, 1526 (1995).

[7] M . Blaskiewicz PRSTAB **1** 044201 (1998).

[8] G. Rumolo, F. Zimmermannm CERN-SL-Note-2002-036 (2002).

Copyright © 2013 CC-BY-3.0 and by the respective authors

CONTROL OF INTRABUNCH DYNAMICS AT CERN SPS RING USING 3.2 GS/s DIGITAL FEEDBACK CHANNEL*

C. Rivetta†, J. D. Fox, J. M. Cesaratto, J. Dusatko, M. Pivi, K. Pollock, O.Turgut
SLAC National Accelerator Laboratory, Stanford, CA USA
H. Bartosik, W. Hofle, G. Kotzian, K. Li, CERN, Geneva, Switzerland

Abstract

The feedback control of intra-bunch instabilities driven by electron-cloud or strong head-tail interaction requires bandwidth sufficient to sense the vertical position and apply correction fields to multiple sections of a nanosecond-scale bunch. These requirements impose challenges and limits in the design of the feedback channel.

We present experimental measurements taken from the CERN SPS machine development studies with an intra-bunch feedback channel prototype. The performance of a 3.2 GS/s digital processing system is evaluated, quantifying the effect of noise and limits of the feedback channel in the bunch stability as well as transient and steady state motion of the bunch. The controllers implemented are general purpose 16 tap FIR filters and the impact on the bunch stability of controller parameters are analyzed and quantified. These studies, based on the limited feedback prototype, are crucial to validate reduced models of the system and macro-particle simulation codes, including the feedback channel. These models will allow us to predict the beam dynamics and controller limits when future wideband hardware is installed in the final prototype to stabilize multiple bunches.

INTRODUCTION

Intrabunch instabilities induced by electron-cloud (ECI) and strong head-tail interactions (TMCI) limiting factors to reach the maximum beam currents in the SPS and LHC rings [1]. Feedback techniques can stabilize bunch instabilities induced by electron cloud and strong head-tail interactions. The application of feedback control to stabilize the bunch is challenging because it requires large bandwidth to sense the transverse position and apply correcting fields to multiple sections of a nanosecond-scale bunch. These requirements impose technology challenges and limits in the design. The goal is to design a feedback control channel and to develop the hardware of a control system prototype to prove principles and evaluate the limitations of this technique by stabilizing a few bunches in the CERN SPS machine. This paper presents results from measurements conducted at SPS and validation studies of models of the feedback system using those measurements.

* Work supported by the U.S. Department of Energy under contract DE-AC02-76SF00515 and the US LHC Accelerator Research Program (LARP).

† rivetta@slac.stanford.edu

Copyright © 2013 CC-BY-3.0 and by the respective authors

FEEDBACK SYSTEM

A single bunch wideband digital feedback system has been developed to explore new technology and control techniques. The implementation of this system is based on a reconfigurable FPGA and ADC/DAC operating at 3.2 GS/s. The system is synchronized with the SPS RF clock and is able to perform diagnostic functions, set feedback parameters and record the bunch motion at selected intervals [2]. The present studies were conducted using an existing stripline device as a kicker with 160 MHz bandwidth. Future tests will be conducted using new wideband kickers, which are currently under development [3]. The four-electrode kicker is driven by 4- 90W amplifiers of 1GHz bandwidth. The pickup signal is equalized to compensate the frequency response of the device and the cables. The controller is implemented using a bank of simple FIR filters, processing each individual ADC samples across the bunch. The prototype is capable of setting 16-tap filters, and during the test 5-taps and 7-taps were used. Additionally, the filter parameters can be changed during the run, allowing to vary the controllers in the feedback system to process the bunch motion signals.

Feedback Model

The block diagram of the feedback system including noise sources and external signal perturbations is depicted in Fig. 1. The main blocks in this figure are modeled in both macro-particle simulation codes and tools where the bunch dynamics is represented by reduced order models to assess the stability margins of the system and study the bunch performance under the influence of noise and external perturbations. These models have to be validated

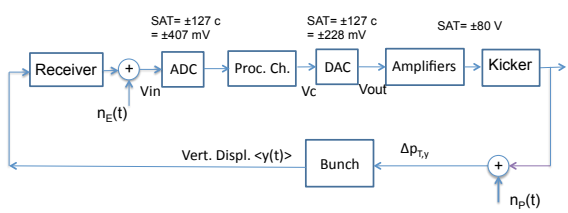


Figure 1: Block diagram feedback system.

with measurements in the SPS to be able to predict future operation conditions and evaluate the impact of limitations and non-linearities in the feedback hardware on the bunch stability and performance. The frequency response of the receiver and the RF power stage have been measured and appropriated models are included in the simulation tools [4].

ANALYSIS OF MD DATA

In January 2013, several machine developments (MDs) where conducted to test the 3.2 GS/s digital processing prototype. The feedback system was evaluated driving and stabilizing the transverse motion of a single bunch in the SPS ring. Multiple tests were performed changing main parameters of the beam and the controller. The main goal was to evaluate the performance of the new hardware - firmware and collect data to validate simulation models and explore the limits of the feedback technique in the stabilization of the intrabunch dynamics. It will allow to predict future tests and define new hardware-firmware for operation with multiple bunches.

To quantify the overall feedback loop gain tests were conducted using the feedback system to stabilize an unstable bunch. To generate the unstable bunch, the chromaticity was changed from positive to negative after injection. The beam becomes unstable in the vertical plane, mainly with mode 0 motion. The bunch with slight positive chromaticity is injected in the machine with the feedback system in open loop and 3500 turns after injection the chromaticity is set negative decreasing slightly as a function of the turn number. If the feedback system remains in open loop, the bunch becomes unstable. Figure 2 depicts the spectrogram of the vertical motion of the centroid showing the unstable motion and the shift in the fractional vertical tune due to lost of charge. Figure 3 shows the motion of a similar bunch when it is stabilized by the feedback system. In this case, the feedback loop is closed 2000 turns after injection and the beam is stabilized. This test was repeated for different loop gains, exhibiting stable motion for gains above a certain minimum value. Using the results of these tests with unstable beam and the feedback system operating in either open loop or closed loop, it is possible to characterize the overall loop gain of the system. It allows setting the gain of the different blocks in Fig. 1 combining additional information related to the transfer function of the feedback stages. To quantify the loop gain, the growth rate of the unstable motion of the bunch centroid was measured with the feedback system in open loop or in closed loop with low gain. The time interval to measure the growth rate was limited to make sure the measurement is conducted preserving the bunch charge. A summary of these measurements and the results of the growth rate estimation based on a simplified model of the feedback loop are shown in Fig. 4. Given the direct proportionally between the chromaticity and the number of turns, the growth time constant is plotted vs. the turn numbers or the chromaticity. The blue points depict the growth time constant measured when the feedback is in open loop and in closed loop with gains equal to 2 and 4 (unstable cases). The estimated time constants based on a simplified model for the damping are shown by the red circles. The green curve is a fitting to the growth time constant of the bunch vs. chromaticity if the feedback loop is open. The growth time constant (inverse of growth rate) decreases as a function of the number of turns because the chromaticity decreases slightly after switching from positive to negative. Assuming the simplified model for the damping bunch damping $\sigma_f(\xi) = 1/\tau_f(\xi) = 1/\tau_{OL}(\xi) - \sigma_D$, with ξ chromaticity, $\sigma_D = \sigma_1 G$ and G the controller gain, the constant is $\sigma_1 = 5.47 \times 10^{-4}$ turns^{-1}. This estimation defines the critical gain to stabilize the vertical mode 0 motion of the bunch. For example, to stabilize an unstable bunch with a growth rate $\sigma_{OL} = 0.01$ turns^{-1} ($\tau_{OL} = 100$) turns a gain $G > 17$ is necessary. More precise analysis of this motion was conducted via simulation using macro-particle simulation codes and a reduced models of the bunch dynamics. Using a reduced model of the bunch and representative model of the feedback system, the results depicted in Fig. 4 can be reproduced. For that case, motion of the bunch centroid was studied, with a 5-tap FIR filter and appropriated gains for the receiver and RF power stage. Figure 5 shows the results for the feedback system in open loop when the parameters of the bunch are set to define a growth time constant equal to $\tau_{OL} = 200$ turns. Figure 6 shows the unstable motion of the bunch centroid with the

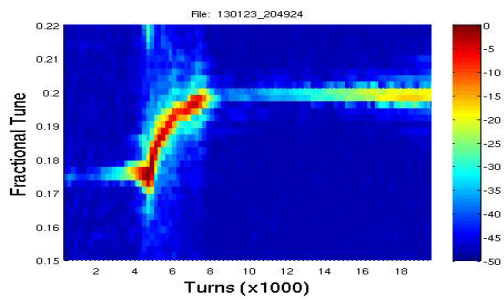


Figure 2: Spectrogram unstable bunch.

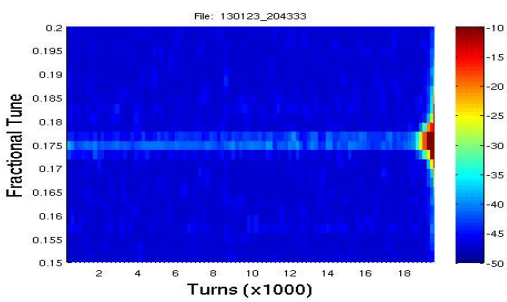


Figure 3: Spectrogram stable bunch.

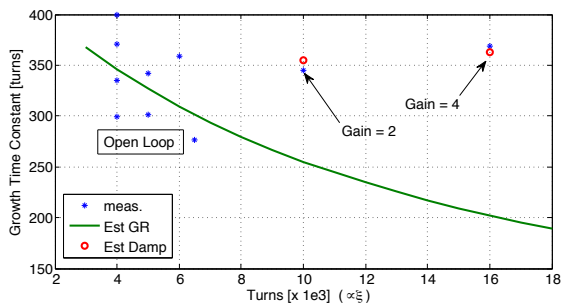


Figure 4: Growth time constant vs. chromaticity for open loop and closed loop G =2, 4.

Copyright © 2013 CC-BY-3.0 and by the respective authors

feedback gain $G = 4$, giving a $\tau_f = 360$ turns. Similar agreement of the final growth rate with the results depicted in Fig. 4 were obtained when the gain was set to $G = 2$.

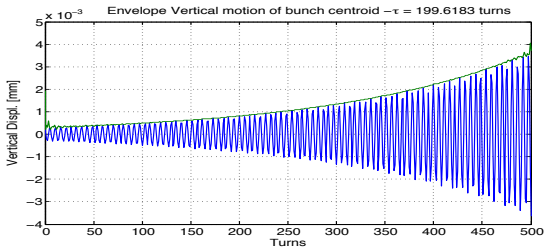


Figure 5: Unstable motion of the beam corresponding to $\tau_{OL} = 200$ turns in Fig. 4 - Open loop feedback - Reduced model simulation

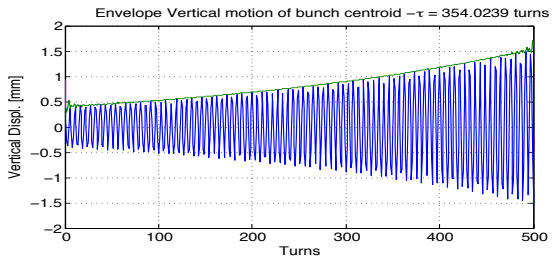


Figure 6: Unstable motion of the beam with feedback in closed loop and gain $G = 4$. - $\tau_f = 360$ turns in Fig. 4 - Reduced model simulation

Using macro-particle simulation codes and appropriated models for the receiver and RF power stages, the damping behavior can be reproduced as well.

Several parameters in the controller have been changed and the response of the bunch motion has been measured to quantify the robustness of the feedback system. Furthermore, this data displays how well the models are able to predict the effect of those variations in the stability and performance of the feedback system. The controller is parameterized by two variables, the gain G and the phase ϕ. Additionally, another important parameter in the feedback loop is the timing between the bunch position and both the ADC samples and the kicker signal. Other important parameters for the design of the overall system are the kicker-amplifier bandwidth and amplifier maximum power, and their impact in the feedback stability and performance are evaluated using simulations and reduced models for the system. In this paper, we show results of the impact on the stability of changes in the controller parameters G and ϕ. The nominal controller is set with a phase $\phi = 70^o$ giving a almost pure damping without changing the betatron tune. When the phase of the controller is set to $\phi = 30^o$ the tune frequency is changed for increasing gain. Figure 7 shows the fractional tune for different samples across the bunch when the feedback is in open loop around turns 0-2000, while Fig. 8 depicts the closed loop case with $G = 64$ and $\phi = 30^o$ for turns 4000-6000. It can be observed the tune shift from $f_\beta = 0.177$ to $f_\beta = 0.183$. Similarly, if the gain is set to $G = 16$ with $\phi = 30^o$ the fractional tune changes from $f_\beta = 0.177$ to $f_\beta = 0.178$. Figure 9 summarizes these measurements and compares them to the values of the complex dominant eigenvalues for the feedback system calculated from a simplified model of the bunch.

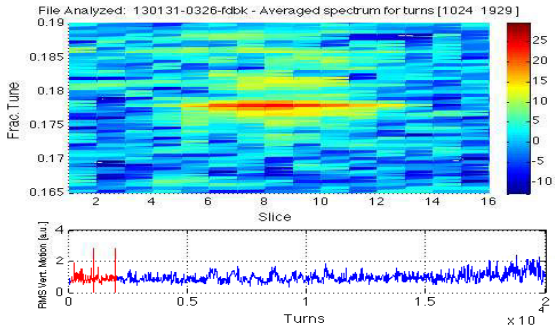


Figure 7: Fractional tune for multiple longitudinal samples of the bunches for feedback system in open loop.

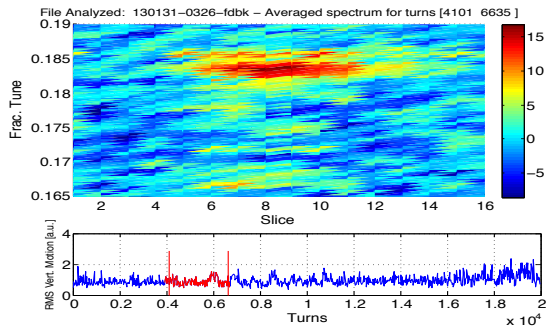


Figure 8: Fractional tune for multiple longitudinal samples of the bunches for feedback system in closed loop with $G = 64$ and $\phi = 30^o$.

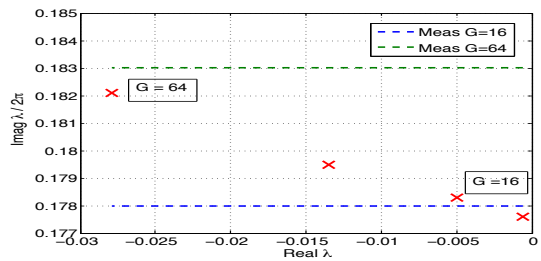


Figure 9: Location of dominant eigenvalues of the feedback system for $\phi = 30^o$ and increasing gain estimated from analytical model. Comparison with the measured fractional tune.

CONCLUSIONS

Several MDs were conducted at CERN SPS before the long shutdown. It allowed to commission and evaluate the performance of a 3.2 GS/s feedback channel prototype and collect data to validate macro-particle simulation

Copyright © 2013 CC-BY-3.0 and by the respective authors

codes and reduced models. We presented some results from these studies and the matching with the estimated parameters given by the simulation tools. Further analysis is in progress to analyze the bunch dynamics and quantify the models based on data collected when the bunch was driven by different excitations.

REFERENCES

[1] G. Rumolo et al., "Experimental Study of the Electron Cloud Instability in the CERN-SPS," EPAC'08, Genoa, Italy, pp. TUPP065 June 2008.

[2] J.D. Fox et. al., "A 4 GS/s Feedback Processing System for Control of Intra-Bunch Instabilities," , IBIC13, Oxford, UK Sept. 2013.

[3] J.M. Cesaratto et. al., "A Wideband Slotted Kicker Design for SPS Transverse Intra-Bunch Feedback ," , IPAC13, WEPME61, Shanghai, China May 2013.

[4] C. Rivetta., "Mathematical Models of Feedback Systems for Control of Intra-Bunch Instabilities Driven by Eclouds and TMCI," NA-PAC'11, New York, USA, pp. 1621-1623 (2011)

Copyright © 2013 CC-BY-3.0 and by the respective authors

SIMULATION STUDY ON TRANSVERSE LASER COOLING AND ORDERING OF HEAVY-ION BEAMS IN A STORAGE RING

Yosuke Yuri, Takasaki Advanced Radiation Research Institute, Japan Atomic Energy Agency,
1233 Watanuki-machi, Takasaki, Gunma, Japan

Abstract

The formation of three-dimensionally ultralow-temperature ion beams by means of laser cooling in a storage ring is studied with the molecular dynamics approach in which stochastic interaction between laser photons and ions is incorporated. The transverse motion of a coasting beam is cooled indirectly through horizontally-displaced lasers and resonant coupling at several different operating points. The indirect transverse cooling rate depends on the displacement and detuning of the lasers as well as on momentum dispersion. In the ultralow-temperature equilibrium state, a 3D ordered (but not crystalline) structure can be formed depending on laser-cooling conditions. The characteristics of the Coulomb-ordered beam are discussed in contrast to a 3D crystalline beam.

INTRODUCTION

Three-dimensional (3D) beam cooling is essential in order to generate an ultralow-emittance beam in a storage ring. It is expected that, at ultralow emittance, the beam is Coulomb-ordered where the relative particle configuration is arranged in order and, in the zero-emittance limit, Coulomb-crystallized where the betatron and synchrotron oscillations are fully suppressed [1]. A longitudinal, one-dimensional (1D) ordering phenomenon was already observed experimentally in ultralow-current (about 10^3 ions in the ring) ion beams using electron cooling [2-4]. It has been found, by theoretical studies, that ions in the ordered beam do not pass through each other longitudinally [5-7]. As to crystalline beams, however, even a 1D string crystal has not been realized up to now in spite of a laser-cooling experimental effort at a cooler storage ring S-LSR in Kyoto University [8]. It is actually very difficult to observe phase transition of a very low-intensity (about 10 ions per bunch) bunched beam clearly although the feasibility of 1D and 2D crystalline beams was predicted with a molecular dynamics (MD) simulation [9, 10].

We have recently demonstrated the feasibility of the three-dimensionally ordered state of an ion beam with 3D laser cooling for the first time [11]. In these proceedings, more detail MD simulation results are given on transverse laser cooling and the ordered state of heavy-ion beams. The stress is put on various characteristics of the Coulomb-ordered beam.

SIMULATION PARAMETERS

A dedicated MD simulation code CRYSTAL, in which stochastic interaction between laser photons and ions is incorporated, is employed for the present study [9]. An actual beam and lattice parameters of S-LSR (see Fig. 1) has been considered. The superperiodicity of the ring is six. The ring can fulfill the following requirements to reach an ultralow-temperature state of an ion beam [1, 12]: First, the storage ring must be operated below transition energy. Second, the bare betatron tune $\nu_{x,y}$ must be less than 0.35 per lattice period to avoid linear resonances at ultralow temperature. More desirably, it must be below 0.25 to avoid linear resonance crossing in the cooling process [13].

A coasting beam of 40-keV $^{24}Mg^{+}$ ions is assumed. The space-charge force is calculated efficiently by imposing a periodic boundary condition in the longitudinal direction. The initial transverse rms emittance and longitudinal rms momentum spread of the beam have been chosen from the recent experimental observation [8].

One co-propagating and one counter-propagating Gaussian cooling lasers with the waist radius of 5 mm are applied along one of the straight sections in the ring. The direct longitudinal laser-cooling force is extended to the horizontal direction through momentum dispersion by horizontally displacing the two Gaussian laser beams [14, 15, 10]. Moreover, the vertical direction is coupled with the horizontal one through a weakly-excited solenoid magnet by applying a resonant coupling scheme [16]. Three different operating points ($\nu_x = \nu_y = (\nu_0 =)$ 1.44, 1.60, and 1.90), which fulfil the above tune requirement, are chosen for comparison. To reduce the longitudinal momentum spread, the frequencies of the lasers are

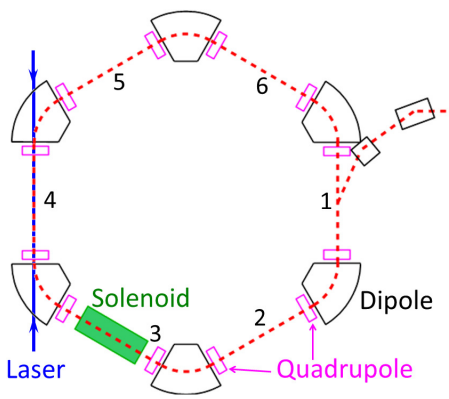


Figure 1: Schematic drawing of S-LSR. The circumference of the ring is 22.56 m. Six bending dipole and 12 quadrupole magnets have been excited so that the six-fold lattice superperiodicity can be realized. Numbers (1 to 6) in the figure express the number of straight sections for convenience. Two cooling lasers are injected along the fourth straight section. A solenoid magnet, installed in the middle of the third straight section, is excited for horizontal-vertical coupling.

Copyright © 2013 CC-BY-3.0 and by the respective authors

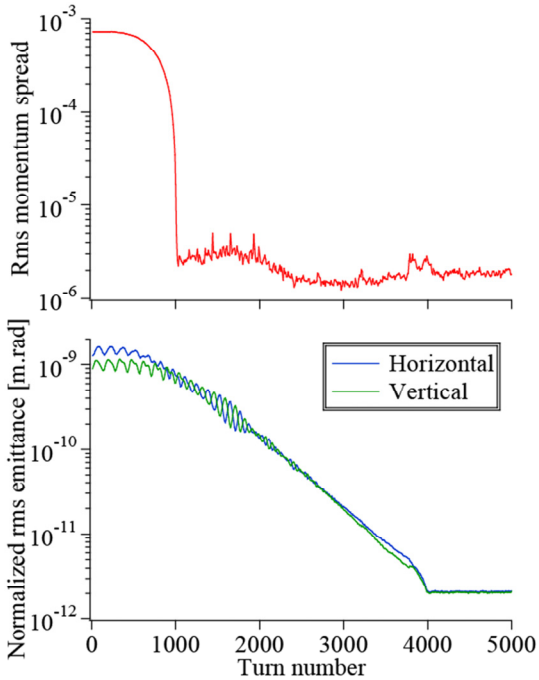


Figure 2: Time evolution of the longitudinal momentum spread and transverse emittance of the 40-keV $^{24}Mg^{+}$ ion beam during laser cooling. The bare betatron tune ν_0 is 1.44. The line density of the beam is 2.4×10^4 m^{-1}. The laser detuning is scanned in 1000 turns. The horizontal displacement and final detuning of the lasers are 3 mm and -81 MHz, respectively.

scanned from an initial detuning of -4.3 GHz to a final detuning on the order of -10 MHz in 1000 turns.

SIMULATION RESULTS

In the following, the result on ν_0 = 1.44 is mainly shown unless otherwise noted. A typical time evolution of the momentum spread and normalized rms emittance of the beam during laser cooling is shown in Fig. 2. The average dispersion function is 2.1 m in the laser cooling section for ν_0 = 1.44. The longitudinal momentum spread is decreased rapidly down to the order of 10^{-6} with the laser frequency scanning. The transverse emittance shrinks exponentially after the scanning is ended because the transverse cooling rate is higher at a smaller detuning. The 1/e cooling time is 20 ms after the laser scan in the present case. Similarly at the other higher tunes, beams with a line density on the order of 10^4 m^{-1} are laser-cooled down to the same order of the momentum spread and emittance. The cooling time is longer for higher tunes because of smaller dispersion. However, the dependence of the cooling rate does not always agree the linear theory that the transverse cooling rate is proportional to the dispersion [17].

Figure 3 shows the 3D ordered profile of the laser-cooled beam. Such ordered states of the laser-cooled beams can be generated also at ν_0 = 1.60 and 1.90, depending on the line density of the beam and the displacement and final detuning of the lasers. Although

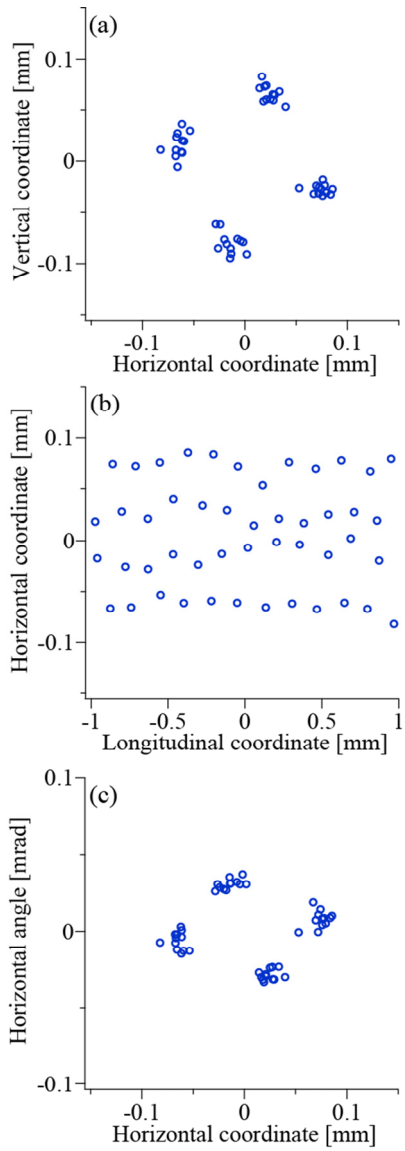


Figure 3: Real-space and phase-space configurations of the laser-cooled beam in Fig. 2. Each blue circle corresponds to a single $^{24}Mg^{+}$ ion.

the snapshot views of the real-space configuration in Figs. 3(a) and 3(b) are similar to those of a single-shell crystal, the phase-space profile is very different. According to Ref. [18], the transverse phase-space configuration in an ideal crystalline beam is always linear. On the other hand, the phase-space configuration of the ordered beam is not linear but square in the present case, as clearly seen from Fig. 3(c).

Another difference is the time evolution of the single-particle orbit and the cross-sectional profile. The transverse orbits of three ions arbitrarily picked out from the ordered beam are plotted in Fig. 4. Unlike a crystal, the orbits are not periodic with the six-fold superperiodicity of the ring, and the ions are still executing betatron oscillation, as shown in Fig. 4(a). The betatron tunes have been depressed from 1.44 to 1.20 in the equilibrium due to the space-charge effect. The trajectories of the ions in the beam cross-section are

Copyright © 2013 CC-BY-3.0 and by the respective authors

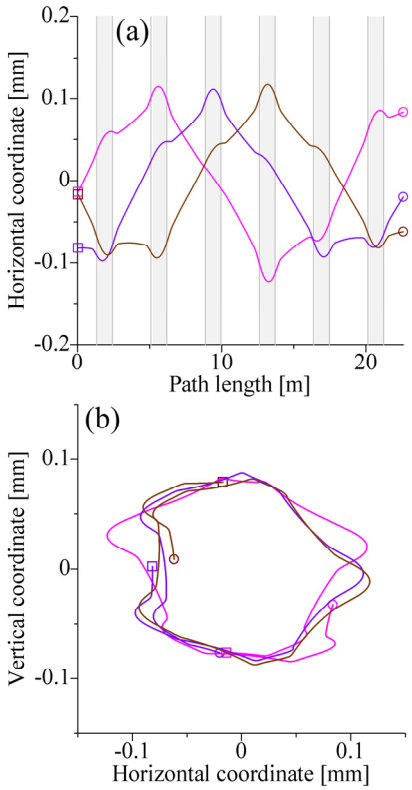


Figure 4: (a) Single-particle orbits of the beam in Fig. 3 while the beam circulates the storage ring once. The horizontal orbits of three ions arbitrarily picked out from the ordered beam are shown. The six gray shaded areas indicate the bending-magnet sections. (b) The trajectories of the three ions in the cross-sectional view are shown. In both panels, the square and circle symbols represent the initial and final coordinates of the ions during one turn, respectively.

shown in Fig. 4(b). It is obvious that the ions are rotating around the central axis. The rotation frequency while the beam goes around the ring once is 1.20, the same as the depressed betatron tune. Similarly, the ions rotate in both transverse phase planes. The dependence of the depressed tune and tune depression on the bare tune ν_0 is summarized in Fig. 5. It is worthy to note that an ordered beam is formed with a rather large tune depression at a high tune.

Since the longitudinal motion is almost frozen out by direct laser cooling, the longitudinal relative position does not change in the straight section. However, the relative position is changed due to the shear effect, depending on the horizontal coordinate in dipole bending magnets. In spite of this shear effect, the ordered configuration is stabilized: the shear effect is compensated because the horizontal coordinates of outer rotating ions are randomly changed every time the ions pass through the bending magnets.

The strength of the correlation in a beam can be estimated from a Coulomb coupling constant Γ [19]. The average temperature of the ordered beam in Fig. 3 is 3 mK in the longitudinal direction and 0.3 K in the

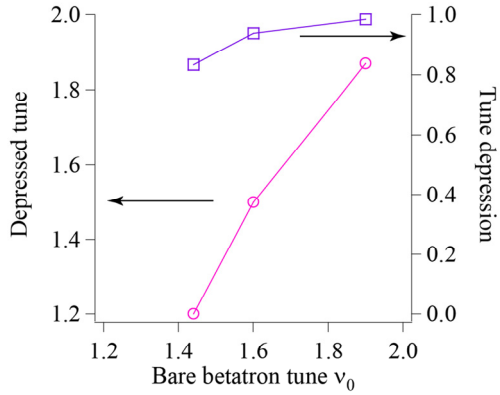


Figure 5: Depressed tune and the tune depression of 3D ordered beams formed at different operating points.

transverse direction. The longitudinal direction is sufficiently in a liquid phase ($\Gamma_{long} \sim 70$) while Γ of the transverse direction is relatively small ($\Gamma_{trans} \sim 0.7$) due to the rotation of ions.

SUMMARY

We studied 3D laser cooling of heavy-ion beams and the formation of the ordered structure in ultralow emittance with the MD simulation technique. The indirect transverse cooling worked well, depending on various laser and lattice parameters. The 3D ordered beams were formed by 3D laser cooling and exhibited unique characteristics such as the cross-sectional rotation unlike a crystalline beam. We have found that the 3D ordered beam is established in an excellent balance in spite of such anisotropy of the state.

REFERENCES

[1] J. Wei, X.-P. Li, and A. M. Sessler, Phys. Rev. Lett. **73** (1994) 3089.
[2] M. Steck et al., Phys. Rev. Lett. **77** (1996) 3803.
[3] H. Danared et al., Phys. Rev. Lett. **88** (2002) 174801.
[4] T. Shirai et al., Phys. Rev. Lett. **98** (2007) 204801.
[5] R. W. Hasse, Phys. Rev. Lett. **83** (1999) 3430.
[6] R. W. Hasse, Phys. Rev. Lett. **90** (2003) 204801.
[7] H. Okamoto et al., Phys. Rev. E **69** (2004) 066504.
[8] H. Souda et al., Jpn. J. Appl. Phys. **52** (2013) 030202.
[9] Y. Yuri and H. Okamoto, Phys. Rev. Lett, **93** (2004) 204801.
[10] Y. Yuri and H. Okamoto, Phys. Rev. ST Accel. Beams **8** (2005) 114201.
[11] Y. Yuri, to be published in J. Phys. Soc. Jpn.
[12] J. Wei, H. Okamoto, and A. M. Sessler, Phys. Rev. Lett. **80** (1998) 2606.
[13] K. Okabe and H. Okamoto, Jpn. J. Appl. Phys. **42** (2003) 4584.
[14] I. Lauer et al., Phys. Rev. Lett. **81** (1998) 2052.
[15] N. Kjærgaard and M. Drewsen, Phys. Lett. A **260** (1999) 507.
[16] H. Okamoto, Phys. Rev. E **50** (1994) 4982.
[17] H. Okamoto and J. Wei, Phys. Rev. E **58** (1998) 3817.
[18] H. Okamoto, Phys. Plasmas **9** (2002) 322.
[19] H. Okamoto, H. Sugimoto, and Y. Yuri, J. Plasma Fusion Res. SERIES **8** (2009) 950.

Copyright © 2013 CC-BY-3.0 and by the respective authors

ELECTRON CLOUD MEASUREMENTS USING A SHIELDED PICKUP IN A QUADRUPOLE AT CESRTA*

J.P. Sikora†, M.G. Billing, J.V. Conway, J.A. Crittenden
J.A. Lanzoni, Y. Li, CLASSE, Ithaca, New York 14853 USA

Abstract

We have recently constructed a shielded pickup in a quadrupole magnet for time-resolved detection of electron cloud. Cloud electrons pass into the detector through an array of small holes in the wall of the beam-pipe that shield the collecting electrode from the direct beam signal. There are two collectors, each aligned on a pole face: one near the longitudinal center of the quadrupole, the other in the fringe field. The signals from the collectors are recorded with a digital oscilloscope. We present a summary of the design, construction and commissioning of this device, as well as initial beam measurements. This work was performed at the Cornell Electron Storage Ring which has been reconfigured as a test accelerator (CESRTA) with positron or electron beam energies ranging from 2 GeV to 5 GeV.

INTRODUCTION

Investigation of electron cloud (EC) growth and decay is an important part of the CESRTA program. Shielded pickups (SPU) in two field free regions have been in use since 2009 and significant progress has been made in connecting simulations with data from these detectors [1]. Parameters used in simulation of the electron cloud are tuned to match the data, including modeling of the detectors . The introduction of dipole or quadrupole fields makes this connection more difficult, mostly in accurate modeling of the detectors rather than modeling of the electron cloud. There was an interest in constructing a simple device that would give time-resolved information about the EC density in a quadrupole field since there is some evidence and modeling that electron cloud could be trapped there [2, 3, 4].

The quadrupole shielded pickup (QSPU) is based on the successful design of the SPU. An important part of that design is the array of holes that connect the vacuum space to the detector. The 1:3 diameter to depth ratio of the holes provides significant attenuation of the direct beam signal [5]. This is important, since a typical direct beam signal will be tens of volts, while the largest (unamplified) electron cloud signals that we have seen are tens of millivolts. Even with this attenuation, some direct beam signal is visible in the detector output.

*This work is supported by the US National Science Foundation PHY-0734867, PHY-1002467 and the US Department of Energy DE-FC02-08ER41538, DE-SC0006505.

† jps13@cornell.edu

QSPU DETECTOR

The QSPU has two collectors, both aligned with a pole face as shown in Fig. 1: one in the longitudinal center of the quadrupole , the other is located in the fringe field. This paper contains data only from the centered detector.

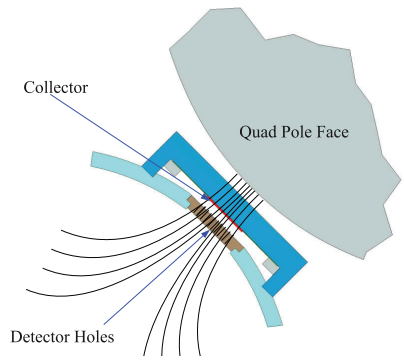


Figure 1: The QSPU detector is centered on one of the quadrupole pole faces. The rectangular collector is 10 x 100 mm copper on kapton centered longitudinally along the pole face behind an array of holes in the beam-pipe wall.

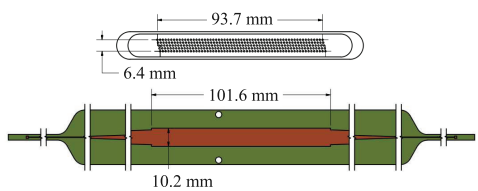


Figure 2: The 5 x 60 array of 0.79 mm diameter holes allow cloud electrons in the beam-pipe to enter the detector. The wall thickness is 2.4 mm. Electrons are collected on the copper flex circuit and the signal routed to feed-throughs at either end of the quadrupole chamber (not shown).

In the QSPU, the collector is an approximately 10 x 100 mm copper rectangle on a 0.13 mm thick kapton flex circuit with a ground plane shown in Fig. 2. Tapered striplines on the flex circuit couple the signal to SMA vacuum feed-throughs approximately 1 m apart at either end of the quadrupole chamber. For comparison, the collector in the field free SPU, is a 1.7 cm diameter button of the type used for beam position monitors.

Copyright © 2013 CC-BY-3.0 and by the respective authors

The collectors for both the QSPU and SPU and biased at +50 V to ensure the capture of incident electron current. The collector signals are AC coupled to a cable that is routed to two cascaded 20 dB amplifiers (ZFL-500 from Mini-Circuits) that give a total voltage gain of 100. The signals are digitized with an oscilloscope that uses a timing system trigger and provides signal averaging.

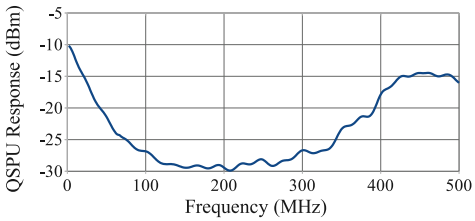


Figure 3: The response of the collector flex circuit was measured with a spectrum analyzer. There is a low-pass feature due to the collector capacitance with a -3 dB point at about 13 MHz and a high-pass feature above 300 MHz.

The QSPU collector has fairly high capacitance due to its construction on the thin kapton flex circuit. As shown in Fig. 3, it acts as a low-pass filter with a -3 dB rolloff at about 13 MHz. At frequencies above 300 MHz, the circuit has a high-pass characteristic that results in significant direct beam signal from the detector.

BEAM SIGNALS

Witness bunch measurements with the field free SPU have provided useful comparisons to simulations of EC density build-up using ECLOUD [1]. Most of these measurements have been carried out with pairs of bunches, where (roughly speaking) the first bunch generates a cloud and the second bunch accelerates this cloud into the detector. The revolution period at CESRTA is 2562 ns which is long compare to the expected EC decay time of about 100 ns. So with short trains of bunches, the EC density is taken to be zero with the arrival of the first bunch. The signal from the first bunch is dominated by photo-electrons and is much smaller than that of the second bunch, where electrons near the beam are accelerated to hundreds of electron volts into the detector.

Although the array of holes in the QSPU provides significant attenuation of the direct beam signal, it is still visible in the detector output. Figure 4 shows the output from a 20-bunch train of positrons with 14 ns spacing and a bunch population of 1.36×10^{11} (8.5 mA). The raw data is digitally filtered by convolving it with a 12 ns impulse response.

Figure 5 shows an overlay of witness bunch measurements with a field free SPU where a 10-bunch train of 5.3 GeV positrons is followed by a witness bunch with delays from 28 to 140 ns. All of the bunches have the same population of 1.36×10^{11} positrons/bunch. As witness bunches are placed at various distances after the bunch

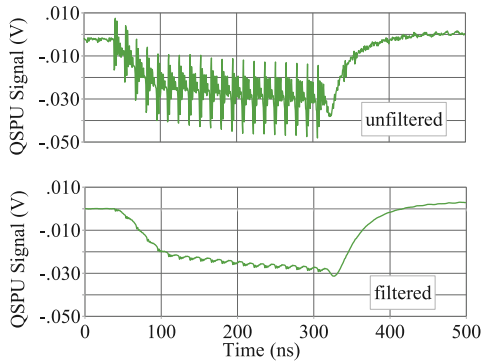


Figure 4: The signal from the QSPU with a 20-bunch train of 5.3 GeV positrons at 1.36×10^{11} positrons/bunch shows significant direct beam signal (upper). The data is filtered by convolving with a 12 ns impulse response (lower).

train, they map the decay of the cloud that the train produced. Also, the signal from the first bunch of the train is quite small, about 0.2 V or less, while the signal from the second bunch is roughly 1.7 V. This is consistent with EC density decaying to zero in the 2.5 μs beam revolution time.

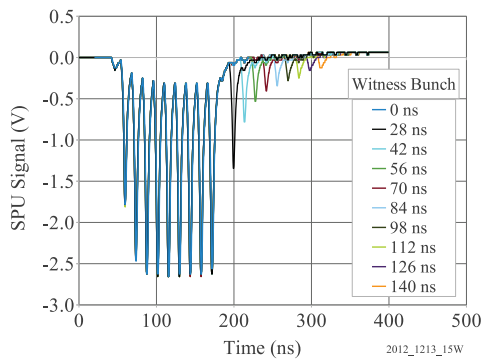


Figure 5: Signals from a field free SPU are overlaid, for a 10-bunch train that is followed by witness bunches at various spacings. The decreasing signals from the witness bunches show the decay of the cloud.

A similar measurement was made with the QSPU, where a 10-bunch train of 5.3 GeV positrons was followed by witness bunches from 28 to 84 ns. All bunches are at 8 mA (1.28×10^{11} positrons/bunch) and a 6 ns filter was applied to the data before plotting. The plots overlaid in Fig. 6 show a decrease in signal amplitude that is on a time scale similar to that of the field free SPU. An expanded detail in Fig. 7 shows the time delay between the direct beam signal and the peak in collection of electrons. This delay of about 18 ns is considerably longer than that observed in the field free region. The beam-pipe geometries are somewhat different – the field free SPU is in oval pipe with a height of 5 cm, whereas the quadrupole SPU is in round pipe that is 9 cm diameter. But it is likely that the presence of the

Copyright © 2013 CC-BY-3.0 and by the respective authors

7.4 T/m field is responsible for most of the time delay since the cloud electrons have more complicated trajectories.

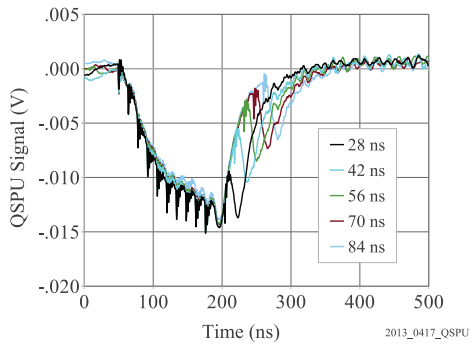


Figure 6: With the QSPU in a 7.4 T/m field, a 10-bunch train of positrons spaced by 14 ns is followed by a single bunch spaced at intervals from 28 to 84 ns. An overlay of these measurements shows a decrease in the witness bunch signal.

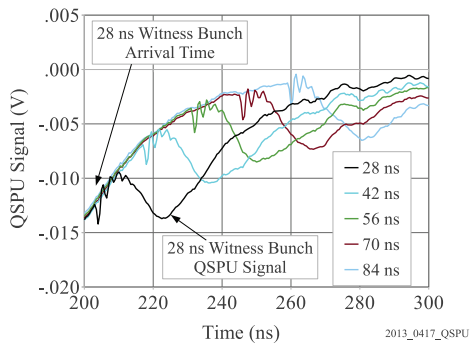


Figure 7: In this detail of the QSPU witness bunch signals, the direct beam signal is seen about 18 ns before the arrival of electrons in the detector.

Data was also taken with both the SPU and QSPU with a 20-bunch train of 14 ns spaced 5.3 GeV positrons. The bunch currents ranged from 4.3 to 10.4 mA/bunch which corresponds to 0.69×10^{11} to 1.67×10^{11} positrons/bunch. The overall shape of the signal from the field free SPU is an amplitude that increases quickly, then reaches an equilibrium value as can be seen in Fig. 8. The shape is similar over a range of bunch charges.

The overall shape of the QSPU signal with the same 20-bunch train (Fig. 9) changes with bunch charge. At higher bunch charge the signal never reaches an equilibrium value. There are also two slopes to the data: a rapid rise at the beginning followed by a more gradual increase out to the end of the bunch train.

CONCLUSIONS

We have constructed a device to make time-resolved measurements of electron cloud in a quadrupole. Witness bunch measurements after a train of ten bunches in the 7.4 T/m quadrupole field gives an electron cloud decay

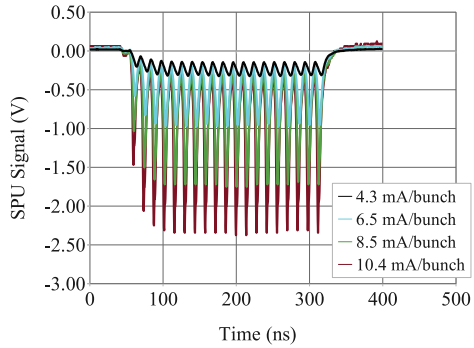


Figure 8: The SPU signal with a 20-bunch train of positrons at 5.3 GeV reaches an equilibrium value early in the train independent of bunch current.

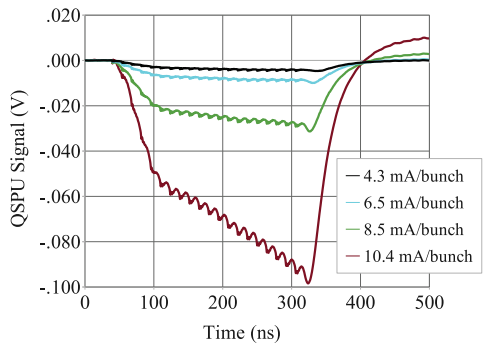


Figure 9: The QSPU signal with a 20-bunch train never reaches an equilibrium value and appears to have two slopes at the highest bunch charge of 10.4 mA/bunch (1.67×10^{11} positrons/bunch).

time that is similar to that obtained in a field free region. A 20-bunch train has a signal with a somewhat different character in the two types of detectors. The signal in the quadrupole does not reach equilibrium at the highest bunch currents. Further experiments and simulations are needed to better understand these initial measurements.

REFERENCES

[1] J.A. Crittenden and J. P. Sikora, "Electron Cloud Buildup Characterization Using Shielded Pickup Measurements and Custom Modeling Code at CESRTA", in Proc. of ECLOUD'12, La Biodola, Isola d'Elba, Italy, June 5-8 2012.

[2] L.F. Wang, H. Fukuma,S. Kurokawa, and K. Oide, Phys. Rev. E **66**, 036502 (2002).

[3] R.J. Macek *et al.*, "Electron Cloud Generation and Trapping in a Quadrupole Magnet at the Los Alamos Proton Storage Ring", Phys Rev ST-AB 1, 010101 (2008).

[4] J.R. Calvey *et al.*,Update on Electron Cloud Mitigation Studies at Cesr-TA, in Proc. of IPAC'11, San Sebastián, Spain, August 2011, TUPC170, pp. 796-798, (2011).

[5] M. Sands, "Energy Loss from Small Holes in the Vacuum Chamber,", PEP-253, Sept. 1977.

Copyright © 2013 CC-BY-3.0 and by the respective authors

EXPERIMENTAL STUDY OF HALO FORMATION IN SPACE CHARGE DOMINATED BEAM*

H. D. Zhang#, B. L. Beaudoin, R. A. Kishek,
University of Maryland, College Park, MD 20742, USA

Abstract

Beam halos are a group of particles with low density that are far away from the well-defined central beam core and have large transverse velocities. Beam losses from halos can require a larger aperture and impose restrictions on the beam current. Several theoretical techniques have been applied to analyze and understand halo formation, including the particle-core model, the free energy model as well as particle in cell (PIC) simulations. However, few experiments on beam halos have been carried out. Here, we describe an experimental study at the University of Maryland to understand and characterize space-charge induced halo formation. The experiments are conducted on the University of Maryland Electron Beam (UMER) and the results are compared with PIC simulations using WARP.

INTRODUCTION

Halo is generally understood as a population of particles that do, or will reach large transverse radii relative to a more intense, centralized beam core. It is associated with emittance growth, degradation of beam quality and particle loss [1]. Several analytic models such as the particle-core model [2] and the free energy model [3] are derived either to depict the process of halo formation or to describe the associated emittance growth. Many theoretical and simulation studies developed these ideas and discussed various mechanisms for halo formation. However, fewer experimental studies have been performed as it is hard to obtain a halo free beam, a crucial component to identify different mechanisms or sources for halo formation. The LEDA experiment [4] is an example for demonstrating agreement with the particle-core model. But its propagation length is limited and it is no longer operational. In this paper, we discuss a method to get a halo-free beam though envelope match and skewness correction. Based on the matched beam, we perform a mismatch experiment as well as a skewness test to verify the sources of halo formation in UMER. Then, we generate a pure breathing mode mismatch, and compare experiments with simulations to confirm this mode.

EXPERIMENT SETUP

UMER

UMER [5], is small compact electron ring with a low energy (10 keV) but relatively high beam current (0.6-100 mA). It is designed to study the physics of electron beams from the emittance dominated regime to space charge dominated regime. The results can be scaled to higher energy beams with higher mass. Fig. 1 shows a schematic of the UMER layout, and Table 1 lists its key parameters and Table 2 lists the beam parameters we will use in this discussion.

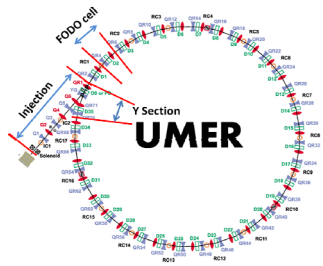


Figure 1: Diagram of UMER.

Table 1: UMER Design Parameters [5]

Parameter	Value
$\beta = v / c$	0.2
Pulse Length	20-120 ns
Beam Energy	10 keV
Current	0.6-100 mA
Ring Circumference	11.52 m
Lap Time	197 ns
Pulse Repetition Rate	10-60 Hz
FODO Period	0.32 m
Zero-current Phase Advance	0.760

Table 2: Beams in UMER [5]

Aperture#	r_0 (mm)	I (mA)	ε (μm)	χ
1	0.875	6	16.8	0.605
2	1.5	21	30.0	0.901

Image System

An imaging system was designed and dedicated for this work utilizing Ethernet cameras, in order to take and process images quickly. A system illustration is shown in Fig. 2. The cameras are connected to a control PC through a gigabyte Ethernet switch. The camera control PC can also control the magnets though the main control PC by sending an appropriate command. The whole system is integrated by a Matlab GUI code. It includes a camera control panel, Magnet control panel, image display and calculation panel, and the Auto picture scan panel. It allows one to change camera settings and take beam images, in order to calculate transverse beam parameters; such as centroid, size and rotation angle. This system can also be used for injection scan (empirical method discussed later) and phase space tomography.

*Work supported by the US Dept. of Energy, office of Science,
#haozhang@umd.edu

Copyright © 2013 CC-BY-3.0 and by the respective authors

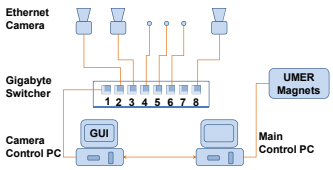


Figure 2: Illustration of imaging system.

ENVELOPE MATCH

Match Description and Fitting

We use a tracking code Trace3D to get a match solution. There are 3 different sections in UMER when we discuss beam envelope match, including injection, Y-section and ring section. Ring section contains 34 equivalent FODO cells, and the matched periodic envelope solution is defined by the emittance from Table 2 and the predefined lattice setting, specially the ring quadrupole strength. In UMER, the ring quadrupoles are setting to 659.0 G/m with positive and negative value alternating. Y-section contains a regular FODO cell, YQ and QR1, where the later two are pulsed Panofsky quadrupoles. Because the pipe for injection and recirculation go through YQ, the center line of YQ is off the ideal beam path by 10°, which results a slightly difference in peak gradient. We use Type 8 fitting procedure in Trace3D to find the quadrupoles setting for Y-section. Next step is to find appropriate injection quadrupole settings with the YQ and QR1 strength determined from last step. The lattice of injection starts from the aperture and ends at the entrance of a regular FODO cell. The final beam parameter is predefined by the ring FODO cell. Here, Q1 is usually small to avoid large ratio of two transverse sizes. The initial Twiss parameter at aperture is from Table 2. Using a Type 8 matching procedure in Trace3D, we will finally get a series of quadrupole setting either Q2-Q5 or Q3-Q6.

Empirical Matching

In practice, many factors, such as beam initial properties, lattices imperfection, vacuum condition and etc., will affect calculations and simulations, and make them deviate from experiments. The magnets strength obtained though calculation and simulation does not necessarily yield a good matching condition. A further empirical method will be used to achieve the final match. The idea here is to scan 4 injection quadrupoles and to take the envelope responses in more than 4 screens. The optimal solution can be obtained in a least square sense, i.e. $\Delta I = (R^{T}R)^{-1}R^{T}E$, where ΔI is the difference between current and updated quadrupole setting, R is response metrix, E is the envelope of current settings. An updated injection setting is given by I-ΔI. Details for this method can be referred to [6].

Correction for Skewness

Due to fringe field of solenoid and rotation error of injection quadrupoles, there is a beam rotation in each chamber inside the ring which also can be a source for halo formation. Here we use two skew quadrupoles in Q3 and Q6 to correct this rotation. The skew quadrupole is a type of UMER quadrupole with a normal pair of printed-circuits [6] and a 45-degree rotated pair as in Fig. 3. Each pair is powered by different current supplies, so the normal and skew components can be independently adjust. By scanning the skew quadrupoles and comparing the rotation angle of beam images in each chamber, we can minimize the rotation in least square sense similarly to the empirical matching.

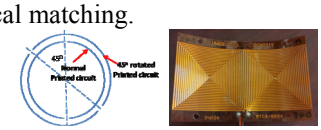


Figure 3: Schematic diagram of skew quadrupole (a) and piece of printed circuit (b).

Matching Result

After going through the process mention above, we obtain match beams of 6mA and 21 mA. The image of the beam for the first turn is shown in Fig. 4. The beam sizes in each chamber are plotted in Fig. 5. Note that, the screen is 28.6 mm ahead of ring chamber center and we also have a small difference of edge focusing in two transverse directions from dipole. Therefore, beam images in the screen are not round. Here, we calculate the average sizes are 3.55 mm, 2.79 mm for 6mA and 6.00 mm, 4.81 mm for 21mA and the standard derivations are 0.17 mm, 0.16 mm for 6mA and 0.30 mm, 0.17 mm for 21mA, which proof that we match the beam quite well. Meanwhile, the rotation angle is small, the average and standard derivation of which is only 0.4 degree and 8.3 degree for 6mA, and -1.4 degree and 7.7 degree for 6mA.

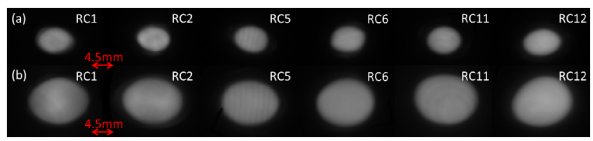


Figure 4: Matched beam images at different ring chamber: (a) 6mA; (b) 21mA.

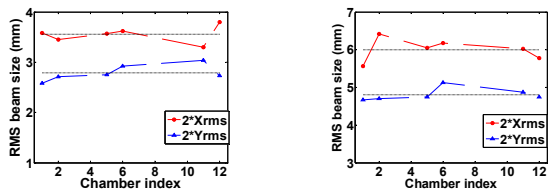


Figure 5: Plot of matched beam size 6mA (left); 21mA (right).

MISMATCH EXPERIMENT

Halo Related to Mismatch and Skewness

From the matched 6 mA beam, we mismatch the beam simple by reduce one of the quadrupole in the injection, e.g., Q5 by 20%, which is a huge error in realistic sense. We compared the beam images in RC5 between matched and mismatched case in Fig. 6. The phase space x-x' plot and y-y' plot is from phase space tomography. From the configuration space, it is clear that there are large amount of halo generated due to mismatch. From the phase space plot, there are also two hot spots in x-x' plot and large

Copyright © 2013 CC-BY-3.0 and by the respective authors

spikes in y-y' plot, which indicate an emittance growth related to that halo.

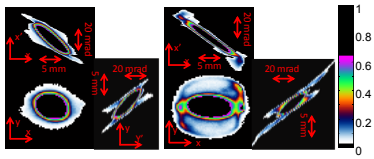


Figure 6: Comparison of matched (left) and mismatched (right) beam at RC5 in x-y, x-x', y-y' plots.

Beam rotation is also a driving source for halo formation. In order to see the halo generated in first turn, we intentionally introduce a 22.3° rotation in RC1 by setting the skew component of Q6 by 0.4 A (or 144.4 G/m peak gradient). The beam images are shown in Fig. 7. It is obvious from images in RC1 to RC5 that there is a wobbling mode related to beam rotation. When the beam finally gets close to equilibrium state (see in RC11 and RC12), the wobbling energy will be transfer to particles to form halo.

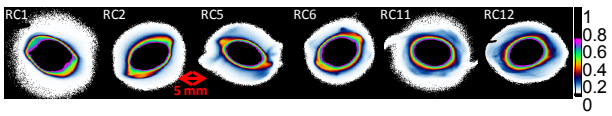


Figure 7: Halo generation from the rotation of the beam.

Pure Breathing Mode Generation

To generate quadrupole solutions that produce a pure breathing mode mismatch beam, we need to go back to the matched ellipse parameters at a little downstream of the screen in RC1, where two *beta functions* are equal. A breathing mode mismatch solution is obtained by scaling α_x, β_x, α_y and β_y there by a common factor μ^2, where μ is the mismatch parameter. From previous aperture condition and lattice settings in Trace3D, we change the setting of the final condition as the scaled twiss parameters, use a Type 8 matching procedure, and we can find the settings of quadrupole Q2-Q5, or Q3-Q6.

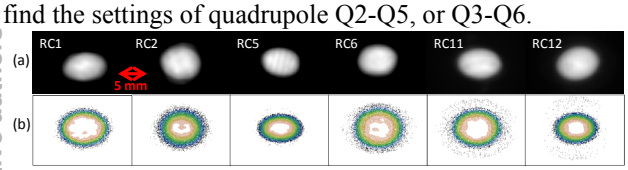


Figure 8: Breathing mode mismatch comparison between (a) experiment and (b) WARP simulation with mismatch parameter μ=1.3.

Here is an example of breathing mode mismatch using 6mA beam in Fig. 8 (a) where the mismatch parameter μ=1.3. Since the screen is offset from the center of each chamber, the breathing of beam envelope is not obvious from the images. To testify the mode we generate, we perform a PIC simulation using Warp [7]. The same emittance and current of 6mA beam are used and the breathing mismatch mode is generated the same way by scaling the α_x, β_x, α_y and β_y by a common factor μ^2 at the point when two *beta functions* are equal. The difference in simulation is we only use the ring section instead of starting from the aperture. The simulated images are shown in Fig. 8 (b). We plot the envelopes of this mismatched beam in Fig. 9 with dotted line from simulation and red dot representing the experimental data from each screen. From the plots, the experimental data lie on the simulation curve quite well which confirms a good agreement.

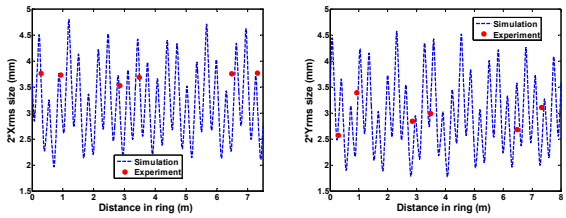


Figure 9: Envelope of the breathing mode mismatch: x (left) and y (right).

Next, we perform a FFT analysis to the envelope curves of breathing mode mismatch from simulation (see Fig. 10). We got a single strong peak for each direction with peak wave number 5.561 m^{-1} and 5.561 m^{-1} separately. This wave number is close to the result from analytic model 5.775 m^{-1}, which verifies that we generate a pure breathing mode.

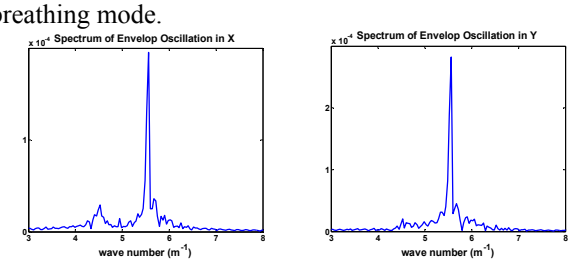


Figure 10: FFT analysis of the envelope for breathing mode mismatch: x (left) and y (right).

CONCLUSION

In this paper, we discussed a method in UMER for beam match which can be performed generally in any accelerator. We identified the sources for halo formation in UMER are from envelope mismatch and beam rotation. We generated a pure breathing mismatch mode in UMER and verified it. The pure mismatch mode has simpler dynamics, which will allow us study the halo formation related to mismatch quantitively. For near future, we will continue to study the breathing mode mismatch, especially compare beams in different space charge region.

REFERENCES

[1] A.V. Fedotov, et.al. *Proc. European Part. Acc. Conf.*, Vienna, p. 1289 (2000).
[2] R. Gluckstern. *Phys. Rev. Lett.*, 73 (1994).
[3] M. Reiser. *Journal of Applied Physics*, 70 (1991).
[4] C. K. Allen, et.al. *Phys. Rev. Lett.* 89, 214802 (2002).
[5] R.A. Kishek, et al., *R.A. Kishek, et al., Nuclear Instruments & Methods in Physics Research A,* in Press (2013).
[6] H. Li, Control and Transport of Intense Electron Beams, *Ph.D. Dissertation*, Univ. of Maryland, 2004.
[7] D.P. Grote, et al. *Nucl. Instr. and Meth. A*, vol. 415, p. 428 (1998).

Copyright © 2013 CC-BY-3.0 and by the respective authors

SNS PERFORMANCE AND THE NEXT GENERATION OF HIGH POWER ACCELERATORS*

J. Galambos#, on behalf of the SNS team, ORNL, Oak Ridge, TN 37830, USA

Abstract

The SNS accelerator at ORNL has been operating near the MW level for several years now. This presentation discusses the successes and challenges, new insight gained and lessons learned with regard to the operation of a modern high power accelerator. In particular, issues with the RFQ, the target and the superconducting RF linac are discussed. Also future high power proton accelerator plans and development needs are discussed.

RECENT SNS OPERATIONAL EXPERIENCE

The Spallation Neutron Source (SNS) accelerator reached the 1 MW operational power level in 2009. Over the past two years beam power has been run between 0.85 MW and 1 MW, as indicated in Fig. 1, with reduced power operation driven by considerations beyond accelerator components. For example the past year of operation, beam power was reduced to preserve target lifetime due to a target spare shortage. However, for the past few weeks, the operational power level has been increased up to 1.2 MW.

Extended running periods without power increase in 2010 – 2011 coincided with increased accelerator availability, as shown in Figure 2. After steady rises in operational hours and beam availability through 2011, the past 2 years show decreases in both these figures. These are due to target failures at the end of FY 2012, and the start of 2013 that severely reduced operational hours and negatively impacted the beam availability. The target issue is discussed in more detail below. Discounting the target failures, the accelerator availability for the years 2011-2013 was 92%, 94% and 89% (YTD) respectively.

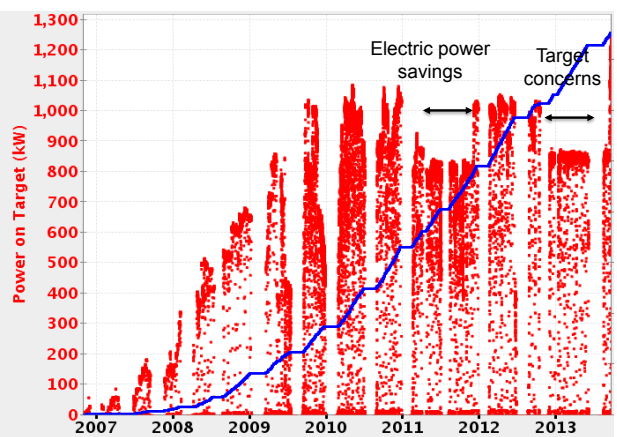


Figure 1: Power history of the SNS accelerator.

*This work was supported by SNS through UT-Battelle, LLC, under contract DE-AC05-00OR22725 for the U.S. DOE
jdg@ornl.gov

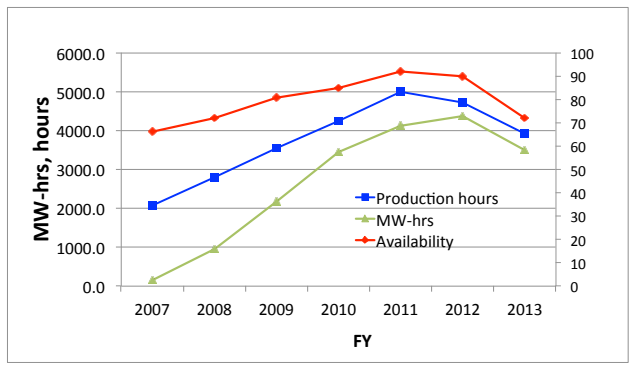


Figure 2: Operation hours and availability since initial operations in 2007.

RFQ Issues

The SNS RFQ experienced 2 detuning incidents in 2003 and 2009, which required retuning of the RFQ in order to operate. From the period mid-2011 through mid-2012 a reduction of beam current measured downstream of the RFQ was observed for all ion sources [1] (see Figure 3). This prompted a measurement of the field profile in the RFQ, and yet another perturbation was observed (see Figure 4). Interestingly, this field disturbance did not prevent operation of the RFQ, only a reduction in beam transmission. The first extended outage that allowed for retuning the field was summer of 2013. However, while there are suspected causes of the first two detuning incidents, this latest incident remains unexplained.

The field profile changes discussed above are likely specific issues related to the manufacturing of this RFQ. However, another perhaps more generic RFQ issue has been observed. This is the issue of discharge heating in the RFQ (in addition to the normal RF induced copper hearting [2]. The discharge related heating can be significant (~ 10% of total heat load) and is not constant, but rather dependent on the gas load history into the RFQ. Also it can change suddenly, complicating the cooling system and resonance control, which is designed for slower heat load changes. To accommodate this complication the low level RF control has been modified to provide fast modulation of the RFQ pulse length to help control the resonance error. However the additional pulse length margin used for this function is becoming limited as we reach the design pulse length of the machine (1 ms), and a new mitigation technique is being sought.

Copyright © 2013 CC-BY-3.0 and by the respective authors

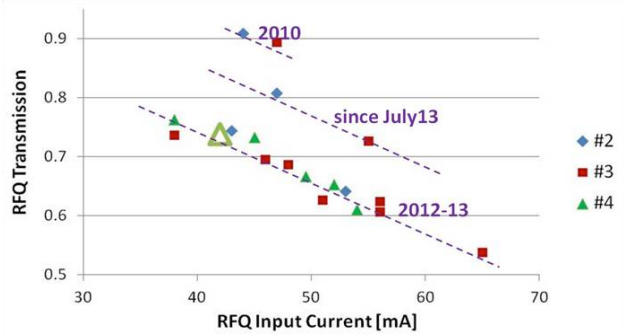


Figure 3: RFQ beam transmission as a function of input beam current indicating reduced transmission during the 2012-2013 detuned RFQ operation.

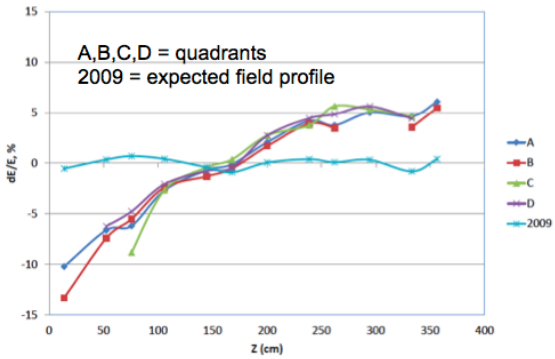


Figure 4: Field distribution along the SNS RFQ in 2012-2013 run.

Errant Beam

Machine protection has always been a major concern for high power operation at the SNS accelerator. Beam shut-off times were prescribed to protect the machine from prompt damage. Generally a 10-20 μs beam shut-off time has been accepted (damage can occur faster at lower beam energies where the stopping length is shorter). However, we have learned that the superconducting RF linac (SCL) cavities can be susceptible to performance degradation with beam loss periods lower than that required to actually approach melting temperatures [3]. In particular, beam trips caused by anomalies upstream of the SCL result in beam loss in the SCL, until the machine protection shuts off the beam. We refer to the beam lost in the SCL during these trips as "errant beam". Even if each individual errant beam pulse does not harm the SCL, we have noticed degraded cavity performance after prolonged exposure to repeated errant beam pulses. A suspicion for the degradation cause is that the slight local heating (a few K) caused by errant beam pulses may initiate the migration of trapped gas in the cavity surface, to a more vulnerable region of the cavity. Figure 5 shows the history of the operational beam energy. Following an beam energy increase in 2009 resulting from cryomodule equipment fixes, during 2009-2011 operation, a slow energy degradation occurred, raising concern about errant beam.

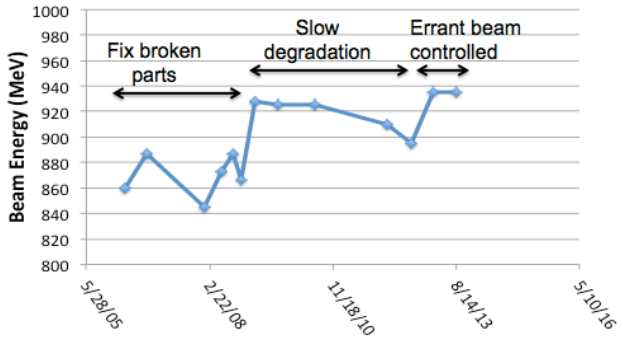


Figure 5: Operational linac output beam energy, indicating a period of performance degradation in 2009-early 2011.

An effort was initiated to identify and rectify causes of errant beam pulses. Two primary causes were identified: 1) pulses formed in the ion source with non-standard waveform shapes, and 2) pulses with premature upstream warm linac RF truncation. The first class constitutes < 10% of the trips and are caused by arcs in the source and electrostatic LEBT. Over 90% of the trips were caused by the RF faults, and the majority of effort was focused on these. We note that while the RF faults were damaging SCL performance, the actual down-time caused by the RF faults themselves was small (~ 30 trips per day each lasting < 1 minute).

One weakness identified, that contributed to increased RF fault rates, was insufficient attention to the vacuum quality which increased the frequency of arcs (hence RF trips). A more rigorous approach to vacuum maintenance improved this situation. Another reduction in fault frequency was reducing the number of trips allowed per second before requiring operator intervention from 2 to 1. Finally we also addressed a shortcoming the beam shutoff response time of the machine protection system. Namely, filters introduced to mitigate noise induced false machine trips also cased delays in the response time (up to > 300 µs in some cases). Even though electrical noise sources had been mitigated, the filters had not been removed. Eliminating these reduced the beam shut-off time to the design level of 10-20 µs and additional fast differential current systems are being deployed [4]. With these implementations the RF fault frequency was greatly reduced as shown in Figure 6. Also, the linac output beam energy has stabilized since instituting these changes, as indicated in Figure 5.

Copyright © 2013 CC-BY-3.0 and by the respective authors

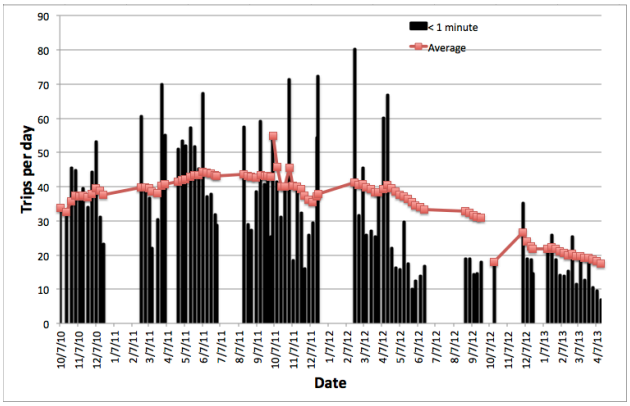


Figure 6: Short duration trip frequency (typical of warm linac RF faults) history at SNS.

Target Issues

High power accelerators require high power target systems. SNS uses a liquid mercury target system that has the advantage of combining the spallation material and coolant [5]. However the very short beam on target pulse (< 1 μs) introduces a complication of shock waves that cause cavitation damage. The target system includes a stainless steel vessel that contains the flowing mercury, and requires regularly scheduled replacement, using robotic, remotely controlled equipment. Until Sept. 2012, of the five target vessels used, there had been only one unplanned target replacement. However, in Sept. 2012 there were two target failures in rapid succession [6], which depleted the supply of spare targets, and resulted in the reduction of operating power (~850 kW) for almost one year, as seen in Figure 1. Investigation of the target failure mechanism resulted in identification of poor welds in a region of reduced stress that had not received adequate manufacturing oversight. Fabrication QA has subsequently been improved, but there is a time lag of ~ one year to manufacture these complicated, first of a kind structures, and replenish the target spare inventory.

In addition to the need to survive high power density, radiation damage effects, and intense pulsed stress levels the cavitation issue mentioned above introduces considerable uncertainty in target lifetime. Figure 7 shows a typical cavitation induced damage pattern, in sections of the upstream portion of the target vessel. There are 4 separate containment walls, and the inner-most bulk mercury facing wall is shown (this is the wall most subject to the cavitation damage). These cut-outs are part of an on-going target Post Irradiation Examination (PIE) effort. The cavitation pitting seen here is observed in a similar pattern as this on all targets. Especially pronounced is the narrow "cut-through" along the target mid-plane. The narrow line of cavitation damage is much more focused than the proton beam power distribution and is not well understood. Even if this layer is compromised, target operation is not limited. The following wall must also be compromised to produce a leak that halts operation, and to date this second wall does not show extensive damage. However PIE efforts are limited to date, we cannot see the entire second surface, and there is uncertainty in this area. New target designs include modified mercury flow patters to eliminate mercury stagnation near the region of observed pitting, and a removable outer shroud (outer vessel walls) to allow better PIE efforts. Targets with these changes are expected to be introduced into operation sometime in mid 2014.

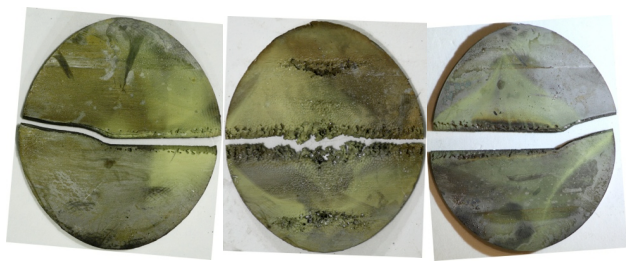


Figure 7: Three circular cross section cut-outs of the inner, front facing surface of target number 4 vessel – with a clear cavitation induced cut-through on the mid-plane.

A general lesson is that attention needs to be placed on the design and analysis of the target system, in addition to the accelerator. These systems are critical for operation of high power accelerators, and require development along side the accelerator components. Changes in this area require significant lead-time, and possibilities are limited due to the complete robotic maintenance approach that must be used.

NEXT GENERATION HIGH POWER PROTON ACCELERATORS

Recently the high power proton accelerator capabilities, planned upgrades and future facilities were surveyed [7], as part of the 2013 High Energy Physics Community Summer Study. Other facilities have high power proton accelerators in operations and in plans, and theses are summarized here. A more exhaustive facility list and explanation of R&D needs is explained in Ref. 7.

Existing Accelerators

There are many high power proton accelerators in operation today, in addition to SNS, as listed in Table 1. There are a number of different types of accelerators running at 100 kW or more today. Many of these involve rapid cycling synchrotrons (RCS) as part of the acceleration chain. Many of these operate, or have operated, as part of a higher energy collider chain. There are two accelerators that operate at the MW level: the PSI cyclotron chain and the SNS linac.

Copyright © 2013 CC-BY-3.0 and by the respective authors

Table 1:Parameters of Existing High Power Proton Accelerator Facilities

Facility	Max. Power (kW)	Energy (GeV)	Time Structure	Accelerator Type
TRIUMF	100	0.52	CW	cyclotron
LANSCE area A	80-120	0.8	120 Hz	linac
ISIS	200	0.8	40 Hz: TS1, 10 Hz: TS 2	linac + RCS
J-PARC MR (FX)	240	30	0.4 Hz x 5 us	3 GeV into RCS
J-PARC RCS	300	3	25 Hz x 1 us	181 MeV linac + RCS
FNAL MI	400	120	9.4 us every 2.2 s	Linac + RCS
CERN SPS	470	400	4.4 s cycle length	linac + 2 stage RCS
SNS	1,200	0.94	60 Hz	linac + accumulator
PSI	1,300	0.59	CW	2 stage cyclotron

Table 2: Parameters of Planned Upgrades for Existing Accelerator Facilities

Facility	Max. Power (kW)	Energy (GeV)	Time Structure	Accelerator Type
FNAL MI + ANU	700	120	9.4 us every 1.33 s	Linac + RCS
J-PARC MR (FX)	750	30	0.4 Hz x 5 us	3 GeV into RCS
CERN SPS	750	400	4.4 s cycle length	linac + 2 stage RCS
LANSCE area A	800	0.8	120 Hz x 625 us	linac
J-PARC RCS	1000	3	25 Hz x 1 us	181 MeV linac + RCS
SNS	2800	1.3	60 Hz	linac + accumulator

Table 3: Future High Power Proton Accelerators

Facility	Max. Power (kW)	Energy (GeV)	Time Structure	Accelerator Type
ESS	5	2.0	50 Hz x 2.5 ms	SRF linac + accumulator
CERN with SPL	4	5	50 Hz x 6 bunches	SRF linac + RCS
Project-X (stage 1+2)	3	3	CW linac /accumulator	CW SRF linac + accumulator
Project-X (stage 3)	2.3	60-120	10^{-5} duty factor	+ pulsed 8 GeV SRF linac + RCS
MYRHHA	2.4	0.6	CW	SRF linac
Daedalus	3	0.8	60 Hz	2 stage cyclotron

Planned Upgrades

Many of the existing accelerator facilities have plans for further power increases, and these are shown in Table 2. Here we consider upgrades being considered in the next 5-10 years with some active development effort. There are several MW class applications appearing, with the J-PARC upgrade, and several of the high-energy (> 10 GeV) RCS chains approaching the 1 MW level.

Future Facilities

Finally, future proton accelerators with at least 1 MW beam power and an on-going design or development effort are shown in Table 3. Interestingly, superconducting RF linacs play a prominent role in all cases, except Daedalus. Also, the beam energy in most cases is lower than those in Tables 1-2.

R&D Needs

Each specific high power project and application has unique development needs, but there are certain overarching common needs. A key consideration is management of beam loss to very low fractional levels when operating at or above 1 MW. The rule of thumb for hands-on maintenance (a necessary condition to make these accelerators affordable) is keeping beam loss below 1 W/m, which translates to < 1 part in 10^6 for 1 MW at full energy. Measuring beam profiles and emittance in the full 6-D phase space to this level is beyond present day capabilities. Improvements are needed in increased

Copyright © 2013 CC-BY-3.0 and by the respective authors

dynamic range for instrumentation and novel methods to measure the multi-dimensional phase space. Also, simulations cannot predict beam behaviour to this level. At present tuning for beam loss mitigation is largely an empirical exercise in high power facilities [8]. Significant advances in simulation are needed to directly use modelling tools for loss tuning (beyond machine design). As mentioned above, even low loss that does not introduce machine activation at SNS can cause equipment damage.

Another common area of concern for high power proton accelerators is designing a survivable target. Generally the targets are made as small as possible to provide an intense secondary beam, but this necessarily forces high hear loads, high radiation damage rates etc. As mentioned above for the pulsed SNS case there are cavitation issues. These high power targets require remote maintenance techniques for replacement and repair, and the possible activities are thus quite limited. In addition, construction and operation costs (e.g. spent target disposal) are considerable and need to be considered up front, along with the accelerator.

For the superconducting RF accelerators there are RF development needs. Generally the beam energy is quite low compared to linear collider applications, so the need to increase gradients to reduce the linac length is not as severe. However for the pulsed SRF applications, development of high power coupler and reduced cost high availability high peak power RF power sources are needed. For the CW applications, production of cavities with low Q is needed to minimize cryogenic loads.

For cases with ring injection, new charge exchange injection techniques need to e developed. Typically 10^{-4} of the beam is lost in an optimized foil stripping injection. As the beam powers increase, this localized beam loss may become intolerable. Also for cases with long injection times, the foil scattering in the circulating beam can cause intolerable emittance growth. Laser stripping [9] is an attractive alternative, but requires significant development.

Chopping beam gaps at low energy is needed for some multi-purpose accelerator applications to facilitate beam transfer to different targets / accelerator chains and to provide user desired timing characteristics. The chopping is planned for the micro-bunch time-scale at low energy for the Project-X case [10], and must be done at an extremely high efficiency to guarantee low loss at higher energy. These techniques remain to be proven.

Finally, for some applications high reliability is a major consideration. Traditional nuclear and high energy physics high power accelerator applications can tolerate short outages (hours – days), as they typically have single purposes with long collection periods (years). However the neutron scattering and accelerator driven systems (ADS) have more stringent reliability issues. Areas such as automatic recovery from failed RF stations and dual front-end systems are discussed, but remain to be demonstrated in operational conditions.

REFERENCES

[1] M.P. Stockli et al., Rev. Sci. Instrum. 85 (2014), to be published.

[2] S. Kim et al., "Stabilized operation of the Spallation Neutron Source radio-frequency quadrupole," Phys. Rev. ST Accel. Beams, 13, (2010), 7.

[3] S. Kim et al., "The Status of Superconducting Linac and SRF Activities at the SNS," to be published, Proceedings of the International Conference on RF Superconductivity, 2013, Paris France.

[4] W. Blokland and C. Peters, "A New differential and Errant Beam Current Monitor for the SNS Accelerator," submitted to International Beam Instrumentation Conference 2013 (IBIC'13), Oxford, England, September 2013.

[5] T.J. McManamy et al., "Overview of the SNS target system testing and initial beam operation experience," Journal of Nuclear Materials, Vol. 377, p. 1, Elsevier (2008).

[6] B. Riemer et al., "High Power Proton Accelerators and Spallation Targets," Proceedings of the 11th Meeting on Nuclear Applications of Accelerators, Bruges Be, to be published.

[7] J. Galambos, S. Nagaitsev, M. Bei, "High Intensity Secondary Beams Driven by Protons," http://arxiv.org/abs/1308.4719

[8] M. Plum et al., "Summary of the Working Group on Commissoning and Operation," Proceedings of HB2012, Beijing, China, 2012, http://accelconf.web.cern.ch/AccelConf/HB2012/papers/fro1b01.pdf

[9] See contributions of the 3rd Mini-workshop on laser stripping and accelerator applications, laser stripping workshop, https://indico.fnal.gov/conferenceDisplay.py?confId=6855

[10] S. Holmes et al., Project X Reference Design Report, http://projectx-docdb.fnal.gov/cgi-bin/ShowDocument?docid=776

Copyright © 2013 CC-BY-3.0 and by the respective authors

THE EUROPEAN SPALLATION SOURCE

Mats Lindroos*, Mohammad Eshraqi and David McGinnis, ESS AB, Lund, Sweden

Abstract

The European Spallation Neutron Source project includes a 5 MW superconducting linac, and aims for initial operation at 1.5 MW in 2019 with 5 MW capacity installed for 2023. Design considerations including the work done to find the minimum cost for preserved beam power will be discussed. This will include discussions on lessons learnt from SNS regarding e.g. superconducting RF performance and RF power sources. The design and construction plans and status will be described.

NEUTRON USAGE AND HISTORICAL BACKGROUND

The neutron beams are being used extensively in science and industry to investigate the properties of matter. The beams of neutrons are used to monitor the structure of the matter in atomic levels using scattering methods. These methods give a high precision information about matter and the high penetration property of neutron makes it the only probe for these measurements.

Most existing neutron sources in Europe are based on nuclear reactors. This approach has been taken to its limits set by both technical issues such as cooling but also by licensing which is non-trivial for any facility using fissile material. Compared to existing spallation sources ESS will be 30 times brighter and it will be the first spallation source with a time averaged flux of neutrons as high as the best research reactors. Europe has today over 5000 researchers who use neutrons and this community is asking for a new intense source of neutrons.

The need for the European Spallation Source (ESS) [1] was articulated 20 years ago but a decision to build it in Lund in Sweden was only taken in May 2009. A series of meetings organized in 1991 and 1992 by Forchungszentrum Jülich (FZ-J) and Rutherford Appleton Laboratory (RAL) explored the basis for an advanced accelerator driven pulsed spallation source, which later formed the basis for the specification for ESS [2]. The decision to site it in Lund was the final stage of a process initiated by the European Commission and steered by the European Strategy Forum on Research Infrastructures (ESFRI). ESFRI was created in 2002 and is a strategic instrument of EC to develop the scientific integration of Europe and to strengthen its international outreach [3].

* mats.lindroos@esss.se

THE ESS FACILITY

The spallation cross section for protons on heavy nuclei increases as a function of proton energy up to several tens of GeV [4]. Nonetheless it is generally agreed that a kinetic proton energy between 1-3 GeV is optimal for practical target and moderator designs, and in order to keep the shielding requirements reasonable.

The ESS accelerator design has gone through several evolutions. In 2002 a fully normal conducting design was proposed [5] in parallel to a pre-dominantly superconducting design derived from the CONCERT project [6]. In 2003 a new design was presented [2] with two front-ends consisting of ion-source, Radio Frequency Quadrupole (RFQ) and a Drift-Tube Linac (DTL) up to 20 MeV. The beams of the two front-ends were merged at 20 MeV and further accelerated in normal conducting structures up to 400 MeV and superconducting structures up to 1334 MeV. The facility had both a long pulse target station and a storage and accumulation ring for a short pulse target. To enable low loss injection into the accumulator ring H^- ions were proposed to be accelerated at a total beam power of 10 MW. In 2009, the competing ESS-Bilbao [7] team and the ESS-Scandinavia [8, 9] team both proposed a simplified 5 MW design with protons accelerated to 2.5 GeV by a mostly supercondcting linac with only one front-end to avoid the complex merging stage and higher beam energy to lower the required beam current. The requirement for a short pulse target station was also dropped to reduce cost. This makes it possible to accelerate H^+ ions, which should reduce losses due to intra-beam stripping of H^- ions and simplifies the ion source design.

The last design iteration was undertaken after cost objectives were set in autumn 2012. The main changes were: i) the implementation of energy staging to ease installation and commissioning, ii) the removal of cryomodules with RF systems and compensate by using operational experience from SNS and run the linac more aggressively, iii) the removal of additional cryomodules with RF systems and compensate by increasing the peak field in the cavities from 40 MV/m to 45 MV/m and iv) introducing new Multi Beam (MB) IOT technology for the high beta linac RF system in the baseline. For the staged commissioning the plan is to start with 1.5 MW in 2019 and complete remaining installation of linac to 2.0 GeV to provide 5 MW of beam by 2022. The staging doesn't only leave more time for installation but it also creates more time for the development of MB-IOTs.

As a result of this series of optimization and iterations the ESS linac beam current is proposed to be 62.5 mA and the final energy is fixed to 2.0 GeV to provide 125 MW of

Copyright © 2013 CC-BY-3.0 and by the respective authors

peak power to the target. More than 95 % of acceleration is done in superconducting structures. The linac accelerates a 2.86 ms long pulse with a repetition rate of 14 Hz, resulting in a 4 % duty cycle and giving an average beam power of 5 MW with a high demand on availability of the facility (>95 %). The former two parameters are set by the experiments, instrument design and scientific performance of ESS.

The ESS has the ambitious goal of becoming a sustainable research facility with zero release of carbon dioxide. This will be achieved through a combination of actions, but with the linac being the most energy hungry part of ESS, the energy efficient design of the RF power sources, the cryogenics systems and high-Q cavities are important issues.

THE ESS LINAC

The configuration of the current baseline linac is shown schematically in Fig. 1, and selected linac parameters are listed in Tab. 1 [10].

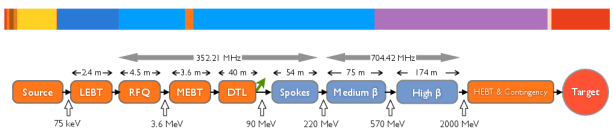


Figure 1: Top: Scaled Layout of ESS. The normal conducting structures are indicated by warm colors and the blue themes sectors indicate the superconducting structures. From left: Ion source, LEBT, RFQ, MEBT, DTL, Spoke, Medium β, High β, and HEBT (consisting of Contingency and beam transport, Dogleg, and Expander). Bottom: blob layout of the ESS linac.

The warm linac design has been done in a collaboration consisting of ESS, INFN Catania, CEA Saclay, ESS-Bilbao and INFN Legnaro, the superconducting cavities and their cryomodules are developed at IPN Orsay and CEA Saclay, and the HEBT is designed by ISA in Aarhus.

A proton beam of less than 80 mA is produced in a pulsed microwave-discharge source on a platform at 75 kV. A low-energy beam transport, LEBT, with two solenoid magnets as focusing elements brings the beam to the entrance of the RFQ. The LEBT has a chopper that cuts away the beam while the proton pulses from the ion source stabilize, preventing a beam with off-nominal parameters from being accelerated in the RFQ and lost at high energy. The 4-vane RFQ accelerates the beam to 3.6 MeV with small losses and a minimal emittance growth. It is designed specifically for ESS but it is based on the IPHI RFQ at Saclay. The RF frequency of the RFQ and the warm linac is 352.21 MHz. After the RFQ there is a medium-energy beam transport, MEBT, with three buncher cavities and 11 quadrupole magnets. The MEBT has several different functions: it has optics to match and steer the beam from the RFQ into the drift-tube linac, it has a comprehensive set of beam-instrumentation devices, it has a chopper which acts faster than the LEBT chopper since space-charge neutralization is not an issue in the MEBT, and it allows collimation of the transverse particle distribution. A drift-tube linac, DTL, with five tanks which each are $\leq$8.0 m long takes the beam from 3.6 MeV to 90 MeV. It has a FODO structure with permanent-magnet quadrupoles. Every second drift tube is empty or used for steering magnets and beam-position monitors.

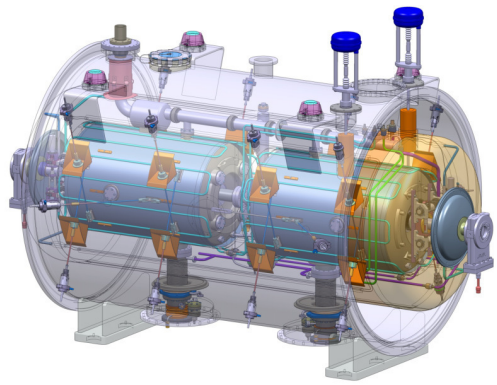


Figure 2: Spoke cavity cryomdoule for ESS

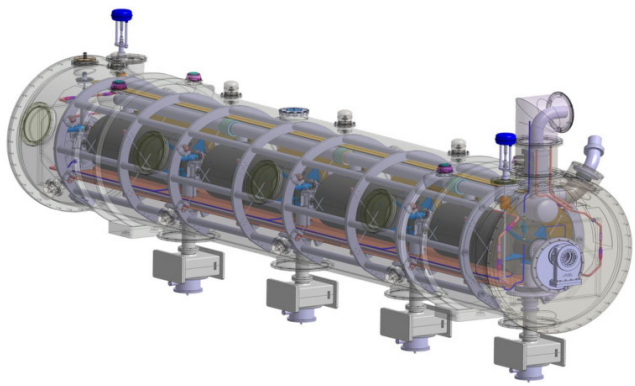


Figure 3: Elliptical cavity cryomdoule for ESS

The superconducting linac has three types of cavities: double-spoke resonators, six-cell medium-beta elliptical cavities and five-cell high-beta elliptical cavities. The linac has 13 spoke cryomodules (see Fig. 2) with two double-spoke resonators in each, and between the cryomodules there are warm quadrupole doublets. The spoke resonators operate at 352.21 MHz like the warm linac, but then there is a frequency doubling to the 704.42 MHz at the elliptical cavities. There are a total of 30 elliptical cavity cryomodules (see Fig. 2) with 9 medium-beta cryomodules with four cavities in each and 21 high-beta cryomodules with four cavities in each. There are quadrupole doublets between every cryomodule. The period length in the medium-beta and high-beta section is exactly the same to allow swapping the cryomodules in case of low performing medium-beta cavities.

Copyright © 2013 CC-BY-3.0 and by the respective authors

Table 1: ESS Linac Parameters

	Energy (MeV)	No.$_{modules}$	No.$_{cavities}$	β_G	T (K)	L$_{Period}$ (m)
Source	0.075	1	0	–	$\sim$ 300	–
LEBT	0.075	–	0	–	$\sim$ 300	–
RFQ	3.6	1	1	–	$\sim$ 300	Not fixed
MEBT	3.6	–	3	–	$\sim$ 300	Not fixed
DTL	90	5	5	–	$\sim$ 300	Not fixed
Spoke	220	13	26	0.50*	$\sim$ 2	4.14
Medium β	570	9	36	0.67	$\sim$ 2	8.28
High β	2000	21	84	0.86	$\sim$ 2	8.28
HEBT	2000	–	0	–	$\sim$ 300	Not fixed

* β_{opt}

All accelerating structures will be powered by klystrons or IOTs, except the spoke resonators where tetrodes might be used. The possibility of using Solid State Amplifiers is still under study. With one klystron per elliptical cavity plus a few for the warm linac, there will be more than 120 large tubes and more than 60 modulators depending on how many tube each modulator is feeding. A tube could be a klystron, an IOT or a tetrode. The density of components in the klystron building would become too high if these were to be positioned linearly. Instead they will be located in groups of eight klystrons and four modulators across the klystron building Fig. 4.

After the last cryomodule there is the contingency and upgrade section where additional cryomodules can be installed to compensate for a shortfall in linac performance and/or a power upgrade of the facility. The additional tunnel would also make it possible to bend the beam out for a second target station.

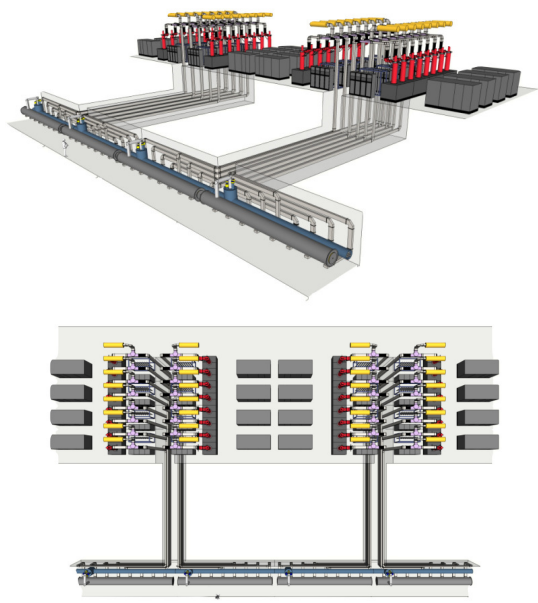


Figure 4: The ESS RF sources in and the RF waveguide stub lay-out. The 3D view on top and the view from top on bottom.

Then the beam is brought from the tunnel to the spallation target at the surface through two vertical bends and an expansion section. A raster scanning system is used to blow the beam up onto the desired profile of the proton-beam window and the target window.

RF SOURCES

The vast majority of structures in the ESS linac are superconducting cavities, therefore the dominant feature of the ESS RF system is the number of RF stations. The enormous gradients in the superconducting cavities is strong enough to deform the 4 mm thick niobium cavities by exerting a significant radiation pressure. This deformation is called Lorentz detuning and must be compensated, otherwise the deformed cavity will resonate at a different frequency which will destroy beam quality and induce losses. To handle variations in cavity coupling and Lorentz detuning there is one RF power amplifier per superconducting resonator; totaling 146 individual RF stations for the superconducting cavities. The core of each RF station is an RF power amplifier which is typically a klystron. For the high beta section of the linac consisting of 84 stations, the peak power required for the cavities is 1100 kW, Fig. 5.

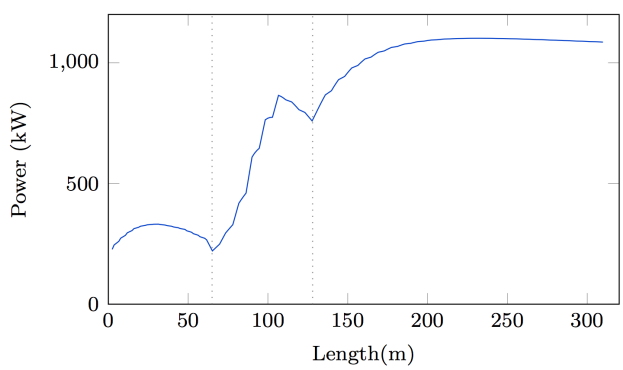


Figure 5: Power profile in the superconducting linac of the ESS, the three section divided by vertical dotted lines are the spoke, medium beta and high beta section.

Copyright © 2013 CC-BY-3.0 and by the respective authors

Even though the loaded Q of the cavities is quite low (7×10^5) to compensate for heavy beam loading, the Lorentz detuning for ESS can be quite severe. Without any Lorentz-detuning compensation, the resonant frequency of the cavities could shift up to 400 Hz. The bandwidth of the cavity in the absence of the beam, the unloaded cavity bandwidth, is 0.07 Hz, and the bandwidth in the presence of beam is almost 1 kHz. Comparing to the number of oscillation of the RF wave during the 2.86 ms of pulse length one can calculate that even this small difference in frequency can shift the RF wave with respect to bunches by more than one whole RF period. In addition, the beam pulse for the ESS linac is very long and is about a factor of three longer than the mechanical response time of the cavity to the Lorentz detuning. Other methods like predetuning of the cavity as done in the SNS linac is not sufficient in the case of ESS. To save on RF power overhead and maintain the beam quality, all superconducting cavities will be equipped with fast piezo-electric tuners to negate the Lorentz detuning of the cavities.

The klystrons are operated 30 % below the maximum saturated power so that variations in the RF system such as modulator droop, cavity coupling, residual Lorentz detuning, and power loss in the waveguide distribution system can be compensated. Also part of the overhead is used for stable regulation of the feedback loop. The target efficiency of the klystrons at maximum saturated power is 60 % which will give an operational efficiency of about 45 %. The required maximum saturated power for the klystrons is 1.5 MW. For stability, reliability and economic reasons, the klystrons will be powered in the pulsed cathode configuration.

The klystrons are energized using modulators. The modulators must supply a 3.5 ms long pulse at a rate of 14 Hz. The cathode voltage for each klystron is about 100 kV with a peak current of about 20 Amperes. For a modulator efficiency of 90 % and a power factor of 0.9, 120 kVA will be required for each klystron. For economical and space reasons, it has been decided to power two klystrons per modulator which limits the required power per modulator to 240 kVA. To handle the long pulse length of 3.5 ms, the modulators will implement solid-state switches at relatively moderate voltages and the output voltage pulse will be stepped up by a pulse transformer or equivalent technology.

The regulation of each RF system will be done independently with the low level RF system. Using modern digital technology, most of the regulation will be done with adaptive feed-forward algorithms. Feedback regulation will play a secondary role to the adaptive feed-forward so the required power overhead can be minimized.

With the large number of RF systems, it will be uneconomical for the high power waveguide of each RF system to have its own penetration to the tunnel. ESS will use a "stub" concept for distributing 16 RF systems into the tunnel as shown in Fig. 4. The stubs will provide access to additional conventional services such as water and power as well. In addition, the radiation shielding issues are best handled with the stub concept.

ESS is also considering the use of Inductive Output Tubes (IOTs) in place of klystrons for the high beta section of the linac. IOT shows the promise of high efficiency and much lower capital cost. IOTs can be thought of as a cross between klystrons and tetrodes. As in tetrodes, IOTs employ a grid to control electron flow from cathode to collector. These grids are very robust with the advent of pyrolithic carbon technology. Since IOTs are gridded tubes, no pulsed modulation system is needed to energize the cathode. This eliminates costly high voltages switches in the power supply for the IOT. Also a gridded tube can be run in deep class C that can produce very high efficiencies (less than 70 %). Also IOTs do not exhibit the severe saturation effect of klystrons. This permits the operation of IOTs at the maximum rated power in feedback loops which increases the efficiency of the RF system significantly. It is estimated that 3-4 MW of power consumption can be saved if klystrons are replaced by IOTs. Like klystrons, IOTs use a resonant output cavity to efficiently couple power from the electron beam at high frequencies. However the gain of an IOT is much lower than a klystron because an IOT uses a single output cavity while a klystron may employ 4-5 stages of cavities. With the advent of low cost solid stage RF amplifiers as pre-drivers, the high gain provided by multi-cavity klystrons is not required. Because of this low gain, IOTs require cathode voltages on the order of 35 kV as compared to 100 kV for high gain klystrons. The lower cathode voltage also reduces the cost of the power supply that energizes the IOT. Current estimates for a power supply for an IOT is 60 % the cost of a klystron modulator of comparable power. Currently there are no commercially available IOTs for the ESS power range. However there has been very good progress made in higher order mode multi-beam IOTs in which power levels of 1 MW have been achieved [11]. For a more detailed discussion on the ESS RF system and the potential of IOTs we refer to [12, 13].

SUMMARY

The European Spallation Source to be built in Lund will be the most powerful linac worldwide. Design and construction of ESS is done through an international collaboration and benefits from the experiences of the similar facilities. The construction of the ESS will start in 2014 and the accelerator will be operational in 2019. The beam power will be increased after the start up and will reach its nominal value of 5 MW by 2025 and scientists will be welcomed to perform experiments at the facility.

REFERENCES

[1] J. M. Perlado, M. Piera, and J. Sanz, "Option for spallation neutron sources," *Journal of Fusion Energy*, vol. 8, no. 3-4, pp. 181–192, 1989.

[2] F. H. Bohn, K. Bongardt, F. Carsughi, A. Claver, K. Klausen, C. Desailly, P. Fabi, I. Gardner, C. Hake, Laclare, J.-L., S. Palanque, D. Richter, and H. Tietze-Jaensch,

Copyright © 2013 CC-BY-3.0 and by the respective authors

eds., *The ESS Project, Vol III, Technical Report*. ESS Council, 2002. http://ess-scandinavia.eu/documents/VolIII.pdf

[3] ESFRI, "Strategy report on research infrastructures - roadmap 2010," 2011. http://ec.europa.eu/research/esfri

[4] K. van der Meer, M. B. Goldberg, E. H. Lehmann, H. A. Abderrahim, D. Bar, D. Berkovits, M. Daum, S. Dekelver, Y. Foucher, J. Gerber, F. van Gestel, W. Hajdas, Linder, H.-P., E. Malambu, I. Mardor, J. Oeyen, D. Saphier, A. Shor, M. Willekens, and Y. Yariv, "Spallation yields of neutrons produced in thick lead/bismuth targets by protons at incident energies of 420 and 590 mev," *Nuclear Instruments and Methods in Physics Research Section B*, vol. 217, no. 2, pp. 202 – 220, 2004.

[5] I. S. K. Gardner and *et.al.*, "The ESS 280/560 MHz acceleration system," tech. rep., ESS report, April 2002.

[6] B. Aune, A. Curtoni, M. Desmons, G. Devanz, Laclare, J.-L., Lagniel, J.-M., M. Luong, A. Mosnier, N. Pichoff, H. Safa, C. Travier, D. Uriot, K. Bongardt, R. Maier, and S. Martin, "SC proton linac for the concert multi-users facility," in *Proc. Particle Accelerator Conference*, (Chicago, USA), June 2001.

[7] F. J. Bermejo, J. Lucas, and I. Bustinduy, "Baseline design for the ESS-Bilbao superconducting proton linac," in *Proc. Particle Accelerator Conference*, (Vancouver, Canada), May 2009.

[8] S. Peggs, R. Calaga, R. Duperrier, M. Eshraqi, A. Jansson, M. Lindroos, G. Papotti, F. Plewinski, and J. Stovall, "Conceptual design of the ESS-Scandinavia accelerator and target," in *Proc. Particle Accelerator Conference*, (Vancouver, Canada), May 2009.

[9] M. Lindroos, S. Peggs, and C. Oyon, "The ESS superconducting linear accelerator," in *Proc. Conference on RF Superconductivity*, (Berlin, Germany), September 2009.

[10] M. Eshraqi, H. Danared, and D. McGinnis, "Design Options of the ESS Linac," in *Proc. International Particle Accelerator Conference*, (Shanghai, China), May 2013.

[11] E. L. Wright and H. Bohlen, "Progress in CPI Microwave Tube Development," *AIP Conference Proceedings*, vol. 807, p. 145, 2006.

[12] D. McGinnis, "The european spallation source," in *Proc. International Vacuum Electronics Conference*, (Paris, France), May 2013.

[13] M. R. F. Jensen, R. Garoby, F. Gerigk, M. Lindroos, D. McGinnis, E. Montesinos, and A. Sunesson, "Applications of high power induction output tubes in high intensity superconducting proton linacs," in *Proc. International Vacuum Electronics Conference*, (Paris, France), May 2013.

Copyright © 2013 CC-BY-3.0 and by the respective authors

PROGRESS TOWARDS THE FACILITY FOR RARE ISOTOPE BEAMS*

J. Wei[#1], D. Arenius[2], N. Bultman[1], F. Casagrande[1], C. Compton[1], K. Davidson[1], J. DeKamp[1], B. Drewyor[1], K. Elliott[1], A. Facco[1,4], V. Ganni[2], P. Gibson[1], T. Glasmacher[1], K. Holland[1], M. Johnson[1], S. Jones[1], R.E. Laxdal[5], D. Leitner[1], M. Leitner[1], G. Machicoane[1], F. Marti[1], D. Morris[1], J. Nolen[1,3], J. Ozelis[1], S. Peng[1], J. Popielarski[1], L. Popielarski[1], E. Pozdeyev[1], T. Russo[1], K. Saito[1], J. Savino[1], R. Webber[1], M. Williams[1], T. Xu[1], Y. Yamazaki[1], A. Zeller[1], Y. Zhang[1], Q. Zhao[1]
[1] Facility for Rare Isotope Beams, Michigan State University, East Lansing, MI 48824 USA
[2] Thomas Jefferson National Laboratory, Newport News, VA 23606, USA
[3] Physics Division, Argonne National Laboratory, Argonne, IL 60439, USA
[4] INFN - Laboratori Nazionali di Legnaro, Legnaro (Padova), Italy
[5] TRIUMF, Vancouver, Canada

Abstract

The Facility for Rare Isotope Beams (FRIB) is based on a continuous-wave superconducting heavy ion linac to accelerate all the stable isotopes to above 200 MeV/u with a beam power of up to 400 kW. At an average beam power approximately two-to-three orders-of-magnitude higher than those of operating heavy-ion facilities, FRIB stands at the power frontier of the accelerator family - the first time for heavy-ion accelerators. To realize this innovative performance, superconducting RF cavities are used starting at the very low energy of 500 keV/u, and beams with multiple charge states are accelerated simultaneously. Many technological challenges specific for this linac have been tackled by the FRIB team and collaborators. Furthermore, the distinct differences from the other types of linacs at the power front must be clearly understood to make the FRIB successful. This report summarizes the technical progress made in the past years to meet these challenges.

INTRODUCTION

During the past decade, facilities like the Spallation Neutron Source (SNS), the Japan Proton Accelerator Research Complex (J-PARC) and the PSI accelerator advanced the frontier of proton beam power by an order of magnitude to 1 MW level (Fig. 1) [1]. On the other hand, facilities for heavy ions has been at the 1 kW level of average beam power. FRIB currently designed and ready for civil construction at the Michigan State University will advance the frontier of heavy-ion beam power by two-to-three orders-of-magnitude to 400 kW.

On August 1, 2013, the Department of Energy's Office of Science approved Critical Decision-2 (CD-2), Approve Performance Baseline, and Critical Decision-3a (CD-3a), Approve Start of Civil Construction and Long Lead Procurements, for the FRIB construction project. The Total Project Cost for FRIB is $730M, of which $635.5M will be provided by DOE and $94.5M will be provided by Michigan State University. The project will be completed by 2022. "When completed, FRIB will provide access to completely uncharted territory at the limits of nuclear stability, revolutionizing our understanding of the structure of nuclei as well as the origin of the elements and related astrophysical processes."

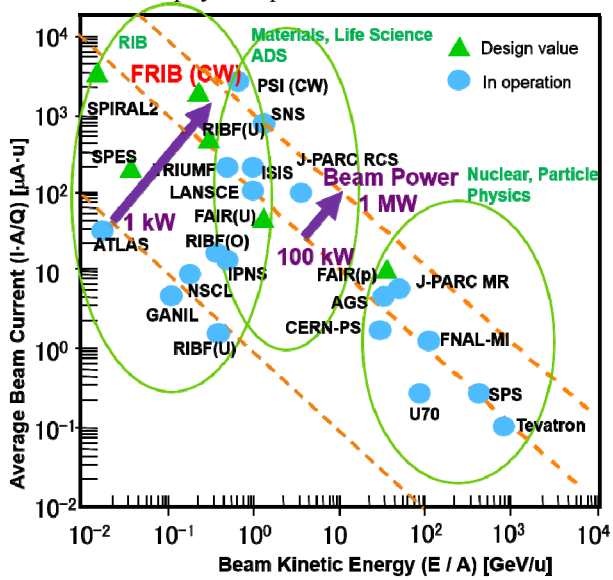


Figure 1: Average beam power as a function of the kinetic beam energy for various operating and proposed proton and heavy-ion accelerator projects.

The FRIB driver accelerator is designed to accelerate all stable ions to energies > 200 MeV/u with beam power on the target up to 400 kW (Table 1) [2]. As shown in Fig. 2, the driver accelerator consists of Electron Cyclotron Resonance (ECR) ion sources; a low energy beam transport containing a pre-buncher and electrostatic deflectors for machine protection; a Radiofrequency Quadrupole (RFQ) linac; linac segment 1 (with Quarter-wave Resonators (QWR) of β_0=0.041 and 0.085) accelerating the beam up to 20 MeV/u where the beam is stripped to higher charge states; linac segments 2 and 3 (with Half-wave Resonators (HWR) of β_0=0.29 and 0.53) accelerating the beam > 200 MeV/u; folding segments to confine the footprint and facilitate beam collimation; and a beam delivery system to transport to the target a tightly

*Work supported by the U.S. Department of Energy Office of Science under Cooperative Agreement DE-SC0000661
#wei@frib.msu.edu

Copyright © 2013 CC-BY-3.0 and by the respective authors

focused beam. The reaccelerator (ReA) consists of similar β_0=0.041 and 0.085 accelerating structures [3].

Table 1: FRIB Accelerator Primary Parameters

Parameter	Value	Unit
Primary beam ion species	H to ^{238}U	
Beam kinetic energy on target	> 200	MeV/u
Maximum beam power on target	400	kW
Macropulse duty factor	100	%
Beam current on target (^{238}U)	0.7	mA
Beam radius on target (90%)	0.5	mm
Driver linac beam-path length	517	m
Average uncontrolled beam loss	< 1	W/m

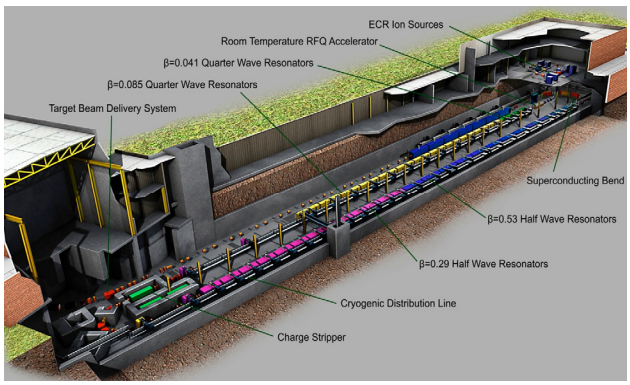


Figure 2: Layout of the FRIB driver accelerator.

DESIGN PHILOSOPHY

Full-energy linac technology is chosen to deliver primary beam that can meet the FRIB requirements of rare-isotope productivity and separation accuracy. Up to 400 kW of beams are focused to a diameter of 1 mm (90%), energy spread of 1% (95% peak-to-peak), and bunch length of < 3 ns (95%) on the target.

Superconducting (SC) technology is the energy-efficient choice for the CW linac. SC acceleration of heavy-ion beams is feasible from low energy (500 keV/u) with practically sized cavity bores by housing both the cavities and solenoids in a cryomodule. A two-gap scheme is chosen throughout the entire linac providing both efficient acceleration and focusing. Developments of digital low-level RF control and solid-state RF amplifier technologies have made individual cavity powering and control reliable and cost efficient.

Furthermore, high availability, maintainability, reliability, tunability, and upgradability are especially required for the FRIB accelerator to operate as a national scientific user facility.

- Availability: The accelerator is designed with high beam-on-target availability accommodating normal, alternative, and fault scenarios. In the normal scenario, a liquid lithium stripper is used to raise the average charge state of ^{238}U beam to 78+ for efficient acceleration. Alternatively, helium gas confined by plasma windows with differential pumping can be used to strip the ^{238}U beam to a lower average charge state of 71+. Fault scenarios include the situation when superconducting (SC) cavities underperform by up to 20% of the design gradients. Furthermore, key components and subsystems are implemented with spares and design redundancies.
- Maintainability: The average uncontrolled beam loss is limited to below 1 W/m level for all ion species from proton to uranium, to facilitate hands-on maintenance. For a proton beam at high energy, this level corresponds to an average activation of about 1 mSv/h measured at a distance of 30 cm from the beam chamber surface, 4 hours after operations shutdown. For heavy ions like uranium at low energies, activation and radiation shielding is of less concern; the 1 W/m limit addresses concerns in damage on superconducting cavity surfaces and in cryogenic heat load. To facilitate maintenance of individual cryomodules, warm interconnect sections are used between cryomodules, and U-tubes with bayonet connections are used for cryogenic distribution. Furthermore, identical, interchangeable cryomodules are used for each β type of the cavities.
- Reliability: A Machine Protection System (MPS) minimizes component damage and operational interruption caused by both acute (fast) and chronic (slow) beam losses. Upon acute beam loss, the MPS response time is 35 μs (including diagnostics, signal processing, and residual beam dumping). MPS responding to slow beam loss is complicated by low sensitivity of conventional ion chamber loss detection to low-energy heavy ions and beam-loss signal background from adjacent linac segments with which beam energies are significantly different. Beam-halo-monitor rings in the warm interconnect sections and possible thermal sensors at cold regions are planned for more sensitive loss detection [4].
- Tunability: The accelerator is designed to be easily tunable during both beam commissioning and operations. In linac segment 1, where beam transverse-phase advance is large, cold beam-position monitors (BPM) are implemented in the cryomodules. Efforts are made in establishing beam-tuning strategies based on virtual accelerators and on-line models under normal and fault conditions.
- Upgradeability: Space is reserved in linac segment 3 to house another 12 cryomodules to readily increase the energy of ^{238}U beam > 300 MeV/u. If cavities with 35% higher accelerating gradient are used in linac segments 2 and 3, the beam-on-target energy can be raised > 400 MeV/u for ^{238}U. The linac tunnel allows future expansion so that a dedicated light-ion injector can be added supporting rare isotope production using the isotope separation on-line (ISOL) method [2]. Using an RF deflector cavity and a Lambertson septum magnet, ^{3}He^{+} beam supplying protons to the ISOL target can share cycle with the

Copyright © 2013 CC-BY-3.0 and by the respective authors

^{238}U beam feeding the fragmentation target; thus simultaneous users are supported. Furthermore, space is reserved to house instrumentations including non-destructive diagnostics and sub-harmonic buncher that are compatible with future user demands of experiments.

ACCELERATOR PHYSICS CHALLENGES

The FRIB accelerator design combines the complexity of heavy ion accelerators with the engineering challenges of high-power accelerators. Due to the low charge-to-mass ratio, heavy ion acceleration is often not efficient. Uncontrolled beam loss, which usually is not an issue for low-power heavy ion machines, is of primary concern for the FRIB accelerator. Comparing with high-power proton machines like the SNS linac where apertures of the elliptical SC cavities are large and beam amplitude reaches maxima in the warm locations of the focusing quadrupole magnets, the apertures of the FRIB QWR and HWR accelerating structures are small and beam amplitude reaches maxima in the cold solenoid locations inside cryomodules. Requirements on beam halo prevention, detection and mitigation are stringent.

To maximize beam intensity on the target, beams of multiple charge states are accelerated simultaneously (2 charge states of 33+ and 34+ before stripping, and 5 charge states of 76+ to 80+ after stripping for ^{238}U). Bends of second-order achromatic optics are used to fold the beams, and cavity phases are adjusted so that beams are longitudinally overlapping at the charge stripper.

Conventional charge strippers like solid carbon foils are not sustainable at the power of a ^{238}U beam at 17 MeV/u during normal operations. FRIB accelerator lattice needs to accommodate beam acceleration of different charge states resulting from various stripping methods including liquid lithium and helium gas (average charge state from 63+ to 78+ for ^{238}U). Buncher cavities of fundamental (80.5 MHz and 322 MHz) and double (161 MHz) linac RF frequencies are strategically placed in the folding segments to preserve beam quality.

Due to the short stopping distance in surrounding materials, uncontrolled beam loss of the low-energy heavy ions can cause damage to the surface of accelerating structures much more easily than a proton beam. On the other hand, due to the low level of radio-activation, losses of low-energy heavy-ion beams are difficult to detect [4]. Beam-loss detection and machine protection often rely on beam scraping. On the other hand, scraping of partially stripped ions may lead to higher ionization further complicating beam collimation and machine protection.

Due to requirements of frequent transverse focusing in the superconducting acceleration structure, solenoids are placed inside cryomodules adjacent to cavities. Alignment tolerance of these solenoids is ±1 mm under cryogenic conditions. Horizontal and vertical steerers are needed to thread the beam and correct the beam orbit.

Stringent beam-on-target requirements demand tight optical control, error control, and advanced beam diagnostics. The primary beam of 400 kW needs to be focused into a diameter of 1 mm with below ±5 mrad transverse angular spread. The desired range of beam power variation on target is 8 orders of magnitude. Orbit stability needs to be controlled at 0.1 mm level.

TECHNOLOGY CHALLENGES

Charge Stripper

The FRIB baseline design of charge stripping is a liquid lithium film moving in front of the beam at high speed of about 50 m/s. During the last couple of years the stability of a thin liquid film with the correct thickness for the FRIB stripper was achieved at ANL. Tests with a proton beam produced by the LANL LEDA source were conducted in 2013 demonstrating that power depositions similar to the FRIB uranium beams could be achieved without destroying the liquid film (Fig. 3) [5].

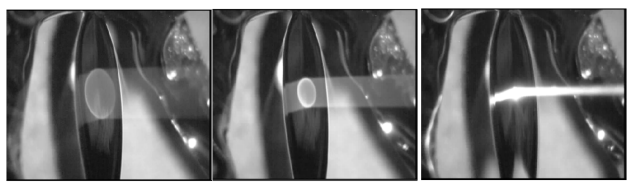


Figure 3: Liquid lithium film flowing at high speed (~ 50 m/s) intercepting a proton beam of about 60 kV at ANL. The test produced power deposition densities similar to the FRIB uranium beams.

An alternative option for the stripper consisting of a helium gas cell enclosed by plasma windows was considered. The BNL work has demonstrated that a conductance reduction of about 10 can be obtained with an aperture of 6 mm diameter [6].

Superconducting RF

FRIB driver linac is the first full-size SC linac using a large number (340) of low-β cavities. Cavity design is optimized not only for optimum performance but also for low production cost. This requirement guided the choice of the cavity geometries, materials and mechanical solutions, avoiding complicated shapes, minimizing the amount of electron beam welds, eliminating bellows, optimizing construction and surface treatment procedures. All FRIB cavities work with superfluid helium at 2 K. This innovative choice in a low-β linac allows operation of cavities in stable pressure conditions with high safety margin on the maximum surface fields.

After several years of development, the 2nd generation QWR prototypes are used in the ReA3 (7 of β_0=0.041 in operation and 8 of β_0=0.085 in construction). This cavity type underwent modifications including the displacement of the RF coupler from the bottom plate to the resonator side and an increased distance between the tuning plate and the inner conductor tip to remove a critical thermal problem in the design. The new tuning plate includes slots and undulations to increase its maximum elastic

Copyright © 2013 CC-BY-3.0 and by the respective authors

displacement and thus its tuning range, and a "puck" whose length can be adjusted for cavity tuning before final welding [7]. The 11 2nd generation prototypes of β_0=0.085 QWR have been tested in vertical dewars at 2 K exceeding FRIB design specifications (Fig. 4a).

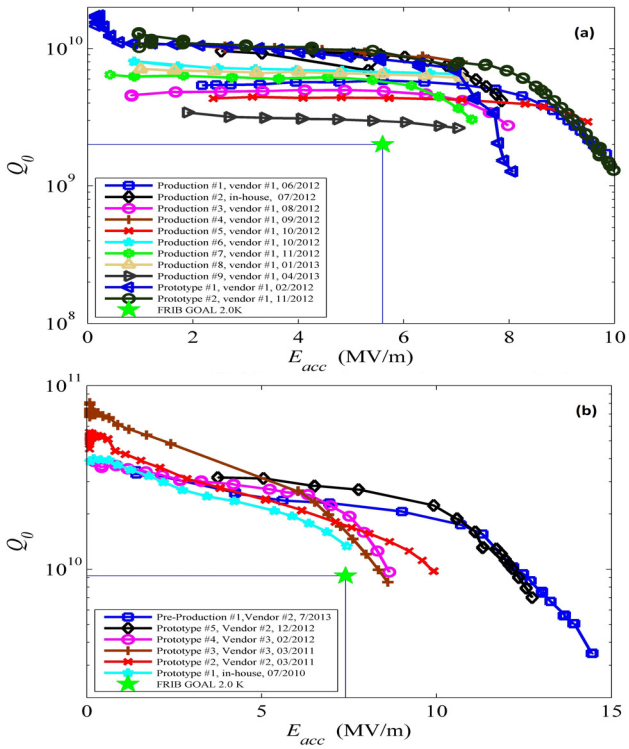


Figure 4: Q_0 vs. E_{acc} performance tested at 2 K for (a) β_0=0.085 QWR prototypes used in the ReA3, and (b) the prototype and pre-production β_0=0.53 HWR.

After testing 5 units of 2nd generation HWR prototype, the first production-design, 3rd generation β_0=0.53 HWR fabricated by an industrial supplier was tested in vertical dewars at 2 K exceeding FRIB design specifications (Fig. 4b). The 3rd-generation design optimization resulted in significant improvement of peak fields E_p/E_{acc}, B_p/E_{acc} and shunt impedance R_{sh}, with consequent reduction of the overall linac cost and operational risk. E_p and B_p in operation are below the safe values of 35 MV/m and 70 mT in all cavities. The apertures of all QWRs were enlarged from 30 to 36 mm, and their bottom rings were modified for efficient tuning-plate cooling using a low-cost design. In all cavities, the helium vessel is made of titanium to avoid brazed Nb-to-stainless-steel interface.

A "Technology Demonstration Cryomodule" was developed consisting of 2 β_0=0.53 HWRs operating at 2 K and a 9 T solenoid operating at 4.5 K arranged in a "top-down" configuration. The cryomodule was demonstrated excellent cryogenic and LLRF control stabilities. Local magnetic shielding was verified and adopted [8].

The FRIB cryomodule design has evolved significantly from the "top-down" ReA3 style to a "bottom-up" design (Fig. 5) [9]. An "Engineering Technology Cryomodule" containing the rail and support, vacuum, cryogenics for liquid nitrogen cooling and wire-position monitor was fabricated and successfully validated alignment requirements. Presently, the full-scale "bottom-up" prototype (ReA6 cryomodule) is under development starting with 2 production-design β_0=0.085 QWRs, a solenoid, 2 K cryogenics and full shieldings.

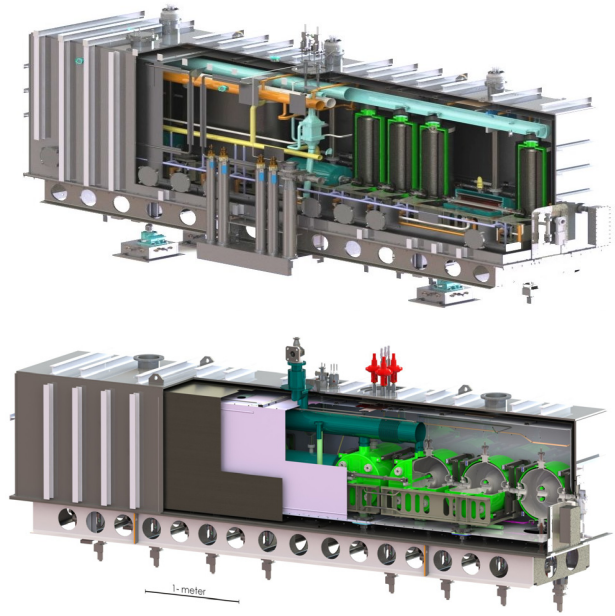


Figure 5: FRIB "bottom-up" cryomodule designs. The top cryomodule contains 8 β_0=0.085 QWRs, 3 solenoids, and 3 cold beam position monitors; the bottom cryomodule contains 8 β_0=0.53 HWRs and a solenoid.

ACQUISITION

After project baseline, the FRIB project entered into its final design phase when detail-engineering designs are performed. While critical processing and assembly are to be performed in house, mass production by industrial providers is facilitated as much as feasible. The FRIB accelerator project plans to place more than 100 procurements valued at more than $50k each. A procurement strategy is implemented for the best value to the FRIB project:

- For most procurements multiple providers are identified and competitions encouraged through strategic Request for Information/Proposal processes.
- FRIB evaluates how the project fits into the supplier's total capabilities and long-term business plans to gauge supplier management's commitment meeting production challenges. We develop long-term supplier relationships for mass production. Phasing of procurements from prototypes to production sensitizes vendors to be able to successfully produce the unique components at reasonable prices.
- Both FRIB technical and business staff works directly with the vendors' understanding their individual risk concerns and proposing mitigations. Weekly teleconferences and frequent site visits are maintained for most active procurements.

Copyright © 2013 CC-BY-3.0 and by the respective authors

So far, we have implemented this strategy to some major procurements including all the SRF material [8], the production of 174 β_0=0.53 HRWs [9], part of the liquid helium refrigerator [10], and the RFQ [11].

COLLABORATION & PARTNERSHIP

FRIB accelerator systems design has been assisted under work-for-others agreements by many national laboratories including ANL, BNL, FNAL, JLab, LANL, LBNL, ORNL, and SLAC, and in collaboration with many institutes including BINP, KEK, IMP, INFN, INR, RIKEN, TRIUMF, and Tsinghua University.

The cryogenics system is designed in collaboration with the JLab cryogenics team. The refrigeration process incorporates the cumulative experience from both JLab and SNS cryogenic systems. The recent experience gained from the JLab 12 GeV cryogenic system design is utilized for both the refrigerator cold box and the compression system designs. The Floating Pressure Process – Ganni Cycle is to be implemented to provide efficient adaptation to the actual loads.

The charge stripping system is under development in collaboration with the ANL Physics Division. We borrowed the LEDA ion source and LEBT from LANL to modify the optics to obtain a 3 mm diameter beam spot on the liquid-lithium film at MSU. Once the new optics is checked on a new platform that is matched to the ANL lithium loop, the device will be moved to ANL for the integrated test. BNL collaborated on the development of the alternative helium gas stripper.

The SRF development benefited greatly from the expertise of the low-β SRF community. FRIB is collaborating with ANL on the coupler and tuner developments, and assisted by JLAB on cavity processing and cryomodule developments.

FUTURE PERSPECTIVES

The FRIB accelerator design is advanced towards beginning technical construction in 2014. Early procurements before 2014 is strategically planned to establish the front end test stand to demonstrate critical components of the ECR ion source and the fully powered RFQ, to contract on long lead-time cryogenic refrigeration subcomponents, and to acquire SRF components to be assembled in the pre-production cryomodules. Upon fabrication, installation, and integrated tests, early beam commissioning will be staged from 2018 to 2020. The facility is scheduled to meet key performance parameters supporting user operations before 2022. We plan to reach full design capability in 4 years after the beginning of operations. Science driven upgrade options may be pursued at any stage of the project.

ACKNOWLEDGMENTS

We thank the Accelerator Systems Advisory Committee chaired by S. Ozaki for their valuable advice and guidance, P. Kneisel, and A.C. Crawford for their participation in the FRIB weekly teleconference, colleagues who participated in FRIB accelerator peer reviews including A. Aleksandrov, G. Ambrosio, W. Barletta, G. Bauer, G. Biallas, J. Bisognano, S. Bousson, S. Caspi, M. Champion, M. Crofford, R. Cutler, B. Dalesio, G. Decker, J. Delayen, N. Eddy, H. Edwards, J. Error, J. Fuerst, K. Kurukawa, J. Galambos, J. Galayda, J. Gilpatrick, S. Gourlay, M. Harrison, S. Henderson, L. Hoff, G. Hoffstaetter, J. Hogan, R. Kersevan, N. Holtkamp, H. Horiike, K. Hosoyama, C. Hovater, D. Hseuh, M. Ikegami, H. Imao, R. Janssens, R. Keller, J. Kelley, P. Kelley, M. Kelly, J. Kerby, A. Klebaner, J. Knobloch, R. Lambiase, C. LoCocq, K. Mahoney, J. Mammosser, T. Mann, W. Meng, N. Mokhov, Y. Momozaki, G. Murdoch, H. Okuno, P. Ostroumov, R. Pardo, S. Peggs, T. Peterson, C. Piller, J. Power, T. Powers, J. Preble, D. Raparia, T. Roser, R. Ruland, J. Sandberg, W.J. Schneider, D. Schrage, I. Silverman, J. Sondericker, W. Soyars, C. Spencer, R. Stanek, M. Stettler, J. Stovall, Y. Than, J. Theilacker, J. Tuozzolo, V. Verzilov, P. Wanderer, M. Wiseman, P. Wright, L. Young, and A. Zaltsman, and colleagues who advised and collaborated with the FRIB team including A. Burrill, K. Davis, X. Guan, W. Hartung, A. Hutton, S.H. Kim, K. Macha, G. Maler, E.A. McEwen, J. Qiang, T. Reilly, R. Talman, J. Vincent, X.W. Wang, Q.Z. Xing. At Michigan State University, the FRIB accelerator design is executed by a dedicated team of the FRIB Accelerator Systems Division with close collaboration with the Experimental Systems Division headed by G. Bollen, the Conventional Facility Division headed by B. Bull, the Chief Engineer's team headed by D. Stout, and supported by the project controls, procurements, ES&H of the FRIB Project, by the NSCL, and by the MSU.

REFERENCES

[1] J. Wei, Rev. Mod. Phys., **75**, 1383 (2003)
[2] J. Wei et al, HIAT'12, Chicago, p. 8 (2012).
[3] D. Leitner et al, FRYBA2, NA-PAC 2013.
[4] Z. Liu, et al, IPAC'12, New Orleans, p. 969 (2012).
[5] J. Nolen et al, FRIB Report FRIB-T30705-TD-000450 (2013).
[6] A. Hershcovitch and P. Thieberger, private communications.
[7] A. Facco et al, SRF'13, THIOD02, Paris (2013).
[8] K. Saito et al, SRF'13, MOP013, Paris (2013).
[9] M. Leitner et al, SRF'13, MOIOA01, Paris (2013).
[10] V. Ganni et al, CEC-ICMC, **59** (in press, 2013).
[11] E. Pozdeyev et al, WEOAB1, NA-PAC 2013.

Copyright © 2013 CC-BY-3.0 and by the respective authors

STATUS OF THE RARE ISOTOPE REACCELERATOR FACILITY REA*

D. Leitner[1,2], D. Alt[2], T. M.Baumann[2], C. Benatti[2], K. Cooper[2], B. Durickovich[1], K. Kittimanapun[2], S. Krause[2], A. Lapierre[2], L. Ling-Ying[2], F. Montes[2], D. Morrissey[2], S. Nash[2], R. Rencsok[2], A. J. Rodriguez[1], C. Sumithrarachchi[2], S. Schwarz[2], M. Steiner[2], M. Syphers[2], S. Williams[2], W. Wittmer[1], X. Wu[1]

[1]Facility for Rare Isotope Beams, Michigan State University, East Lansing, MI 48824 USA
[2]NSCL, Michigan State University, East Lansing, MI 48824, USA

Abstract

The Facility for Rare Isotope Beams (FRIB) is currently in the preliminary design phase at Michigan State University (MSU) [1]. FRIB consists of a driver linac for the acceleration of heavy ion beams, followed by a fragmentation target station and a ReAccelerating facility (ReA). While FRIB is expected to start commissioning in 2018, the first stage of ReA called ReA3 is already under commissioning [2, 3]. ReA was connected to the Coupled Cyclotron Facility at MSU in 2012 and has delivered its first radioactive ion beam to the experimental hall in 2013. An overview of the facility will be discussed. In addition, this paper focuses on the technical progress and first commissioning results with radioactive ion beams.

INTRODUCTION

Nuclear science research requires reaccelerated radioactive isotope ion beams in a range of kinetic energies from thermal energies to near 20 MeV/nucleon. Isotope Separation On-line (ISOL) and Projectile Fragmentation (PF) are the two most common methods used to produce high quality radioactive ions beams (RIBs) for the various nuclear science experiments. In the ISOL technique the RIBs are produced in a thick target from which they have to diffuse out before they can be ionized and used as radioactive beams. While this technique offers unmatched yields for a number of isotopes, chemically reactive isotope are more difficult and slow to extract.

Projectile fragmentation on the other hand can be used for a broad range of interesting nuclei, since the reaction products recoil out of the target in forward direction, which makes the production method chemically indifferent. In order to separate the desired isotope from the bulk of the other reaction products, in-flight fragmentation facilities are often combined with a high acceptance fragment separator [4]. This combination offers a versatile method to develop a wide range of isotopes in a short time. As an example, in the 10 years of operation of Coupled Cyclotron Facility at Michigan State University more than 1000 rare isotope beams have been produced and more than 870 have been delivered to users for experiments [5]. The energy however of those radioactive beams are close to the primary driver beam energy (80-150MeV/nucleon) which can be too high for some nuclear physics experiments.

The physics reach can be further enriched if such a facility is combined with a gas stopper and a re-accelerator. Then in addition to the fast RIBs of 50 to a few 100MeV/u, high quality beams can be provided from the lowest energies of a few 10s of keV/nucleon (for trapping and spectroscopy experiments) to an energy range between a few 100 keV/nucleon and 20

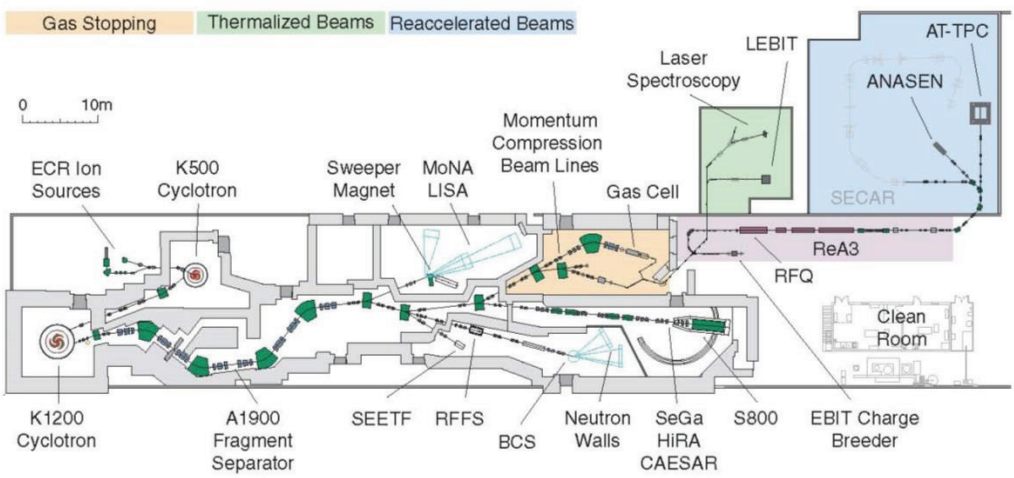


Figure 1: Facility layout of the National Superconducting Cyclotron Laboratory with the Coupled Cyclotron Facility and the newly commissioned gas stopping area and reaccelerated radioactive ion beam capabilities[5].

Copyright © 2013 CC-BY-3.0 and by the respective authors

MeV/nucleon. The recently commissioned re-accelerator facility ReA is the first rare isotope post accelerator coupled to a projectile fragmentation facility. An overview of the Coupled Cyclotron Facility and the ReAccelerator Facility is shown in Figure 1 and a detail layout of ReA is shown in Figure 2.

FACILITY OVERVIEW AND STATUS

The first stage of the re-accelerator facility ReA3 consists of a rare isotope beam stopping area, a transport section, a charge breeder, a compact SC-linac and a beam distribution system. In the stopping area, the rare isotopes are thermalized by using a combination of solid degraders with a linear gas cell [6]. After extraction, a low energy beam line [7] transports the 1+ or 2+ ions or molecules to the trapping areas and laser spectroscopy experiments, or to an Electron Beam Ion Trap (EBIT) [8, 9] for charge breeding and subsequent acceleration. The linac consists of a second off-line stable ion beam injector, a multi harmonic buncher, a room temperature RFQ, a buncher cryomodule (CM) and two low beta cryomodules with a total of fifteen superconducting cavities [2]. The last of the three cryomodules, designed for a beta equal to 0.085, is currently being assembled and is expected to be installed in July of 2014, after which phase 1 (ReA3) will be completed.

ReA3 is nominally capable of accelerating ions with a charge-to-mass ratio Q/A=0.25 from 300 keV/u to 3 MeV/u and for Q/A=0.5 from 300 keV/u to 6 MeV/u. In its final configuration ReA will consist of three buncher cryomodules, one β_o=0.041 and four β_o=0.085 accelerating CMs with a total of 41 superconducting quarter wave cavities (funding proposal submitted). In this configuration, ReA will nominally provide heavy ion beams from 0.3 MeV/u to 12 MeV/u for the heaviest ions and energies from 0.3 MeV/u up to 20 MeV/u for light ions. Figure 3 shows the nominal energy range of the facility in the first phase, and the high energy upgrades with the three additional beta=0.085 cryomodules. The first of the three high energy cryomodules is currently under design (see section below) and is expected to be completed in 2015.

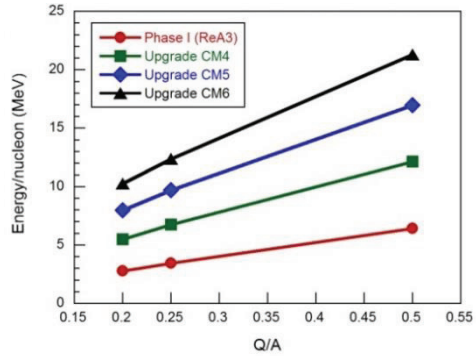


Figure 3: Energy range of the ReAccelerator facility [4].

The current facility was commissioned using stable beams between 2011-2012 [2, 3]. The linear gas stopper and low energy beam transport lines were commissioned with rare isotopes and stable beams in 2013[7]. The first of the three transport lines into the low energy beam hall was commissioned in summer of 2013 [3] and the first radioactive ion beam was delivered to users in August of 2013 (see below). The remaining two beam lines are under construction and are expected to be completed by December of 2013.

PILOT BEAM DEVELOPMENT

One of the challenges of radioactive post accelerators is the wide dynamic range that the beam diagnostics need to cover [10, 11]. Due to the low rate of the injected radioactive ions (10-10^6 pps), the front end and the linac must be phased and pre-tuned using stable (pilot) beams (10^9pps or more). Therefore in preparation for the radioactive ion beam commissioning experiment, stable pilot beams from the off-line injector ion source (H_2 and He)

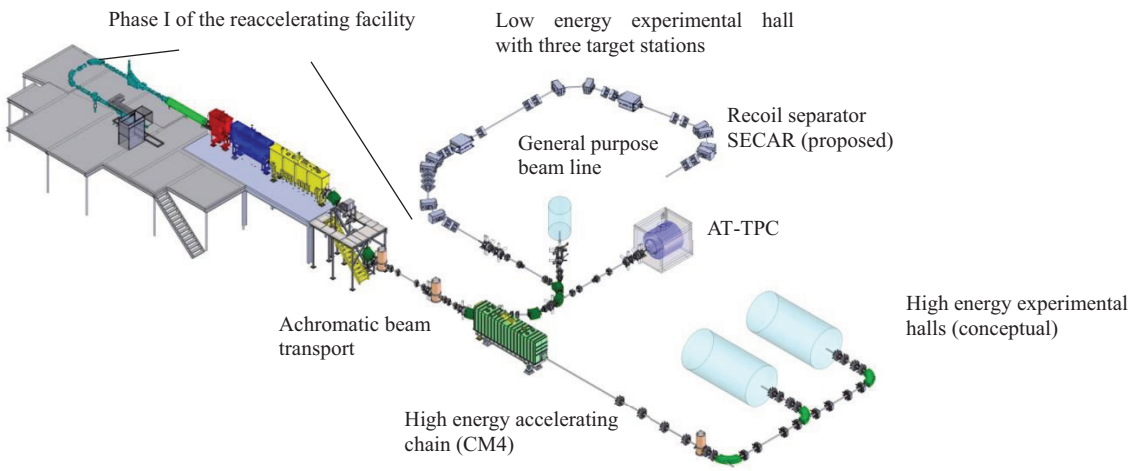


Figure 2: Layout of the ReAccelerator facility and the transport lines into the low energy experimental hall. In addition, the first cryomodule of the high energy section of the linac is shown.

Copyright © 2013 CC-BY-3.0 and by the respective authors

and heavy ion beams pilot beam from the EBIT were established. In order to scale from one A/Q to the next the injection voltage into the RFQ must be well matched to ensure efficient acceleration. For this purpose the energy acceptance of the RFQ was measured by varying the injection energy of the EBIT beam. Figure 4 shows the results of the calibration. An absolute energy acceptance of ±250V FWHM or ±0.75% relative was measured. This value is slightly lower than the simulated RFQ energy acceptance of ±2% for a 1.4nsec (±20 degree) long beam bunch [12] which will be further investigated.

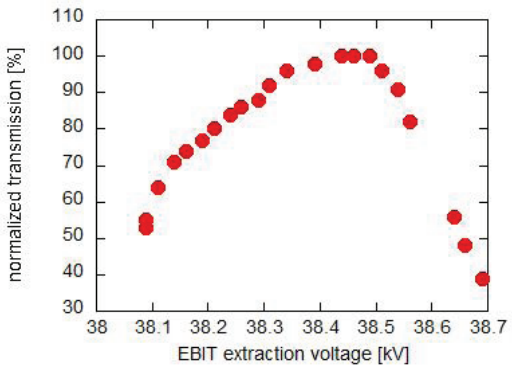


Figure 4: RFQ energy acceptance in dependence of the EBIT extraction voltage for a $^{16}O^{5+}$ beam.

In addition, the full acceleration scheme for radioactive ions was tested by injecting 1+ ^{85,87}Rb ions from the gas stopping area into the EBIT, charge breeding the rubidium ions to high charge states and subsequently accelerating $^{85}Rb^{27+}$ as well as $^{87}Rb^{28+}$with the linac. Figure 5 shows the superposition of four spectra measured with a scattering-gold foil silicon detector mounted at 30 degrees [10]. The first peak is recorded when the detector is retracted from the beam line and depicts the energy spectra of ^{241}Am α-calibration source (5.486 MeV). The second, third and fourth peaks are recorded as the beam line, the RFQ injection voltage, and RFQ vane voltage were scaled from the $^{16}O^{5+}$ pilot beam settings to the $^{40}Ar^{13+}$ beam (third peak) and finally to the $^{87}Rb^{28+}$beam (fourth peak). As the maximum A/Q scaling was only 4%, the linac settings were kept unchanged for this test. For the radioactive ion beam online experiment the linac was scaled using fixed velocity beam energy profiles in order to achieve the desired beam parameters and energy on target.

RADIOACTIVE ION BEAM COMMISSIONING

^{37}K Beam Production

To produce ^{37}K ($T_{1/2}$=1.23s), a primary beam of ^{40}Ca was extracted from the Coupled Cyclotron Facility at an energy of 140 MeV/nucleon, fragmented in a thin beryllium target, and separated in the A1900 fragment separator[5]. The ^{37}K was then transported to the beam stopping area, which consists of a high energy beam momentum compression beamline, a degrader and wedge

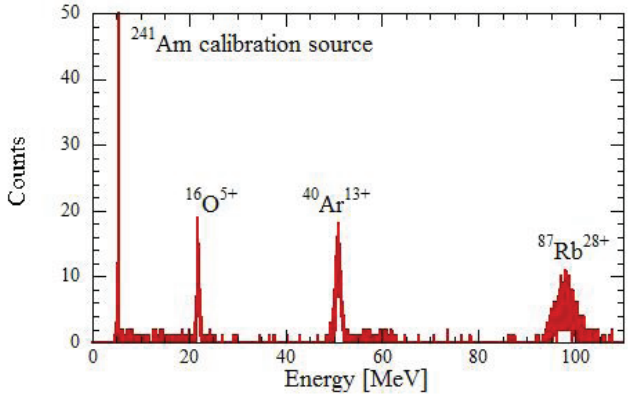


Figure 5: Energy spectra obtained using the scattering-foil silicon detector for three heavy ion tunes.

section, and a 1.2 m long linear gas cell operated at about 100Torr [6].

After the fragments are slowed down to less than one eV in the helium gas of the gas cell, they are extracted as singly or doubly charged ions and singly or doubly charged molecular ions, mass-analyzed and transported to the EBIT charge breeder.

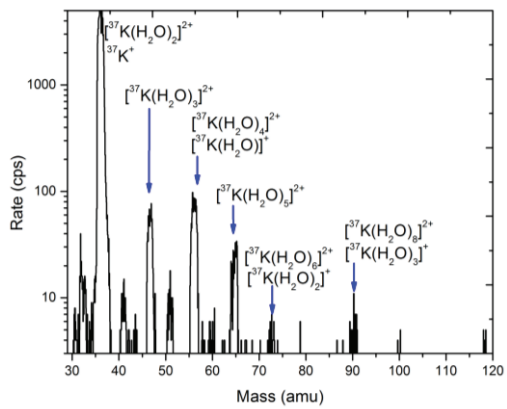


Figure 6: Scan of the extracted beam from the gas cell after the analyzing magnet in the low energy beam line.

As an example, Figure 6 [11] shows the mass (activity) scan of the beam extracted from the gas cell using a β-decay counter/Faraday cup assembly after the analyzing magnet in the low energy RIB injection line [11]. For potassium, the low energy beam consists mostly of ^{37}K ions (≈ 94%) and a few small peaks of weakly bound molecular 1+ and 2+ ions which are formed with one to a few water ligands from residual contaminates in the gas cell. In the preliminary commissioning tests this summer, ion beams with intensities of up to 10^5 particles per second have been thermalized and total extraction efficiencies of up to 14% have been achieved. Further increases of the efficiency are expected once the vacuum is improved in the cell. After mass analysis, the RIBs are injected into the EBIT charge breeder and charge bred to $^{37}K^{17+}$.

Copyright © 2013 CC-BY-3.0 and by the respective authors

Post-Acceleration

An important design choice for the ReA accelerator was the selection of an EBIT as charge breeder. With the expected rates of radioactive ions from the reaccelerator of 10 to 10^6 ions per second, minimizing the stable ion beam contamination from residual gas ions is an important factor. The ReA EBIT has a cryogenic ion trapping structure [9] to minimize the beam contamination from residual ions. As expected, the intensity levels for beam other than the typical residual gas ions such as nitrogen, helium, and oxygen are very low. As an example, Figure 7a shows the charge state spectrum of background ions from the EBIT where the positions of various ^{37}K charge states are indicated. Due to the energy required by the experiment of 2.4 MeV/nucleon, charge state of 15+ and higher were needed for the linac. Figure 7b shows a high resolution Q/A scan of the 16+ to 19+ region.

In addition to possible beam contaminations the charge breeding efficiency was considered as well when $^{37}K^{17+}$ (helium like ion) was selected as the best choice for the experiment. During off-line charge breeding tests, an efficiency of 4 to 5% into K^{17+} using stable potassium 1+ ions was achieved [9]. A similar efficiency was measured with radioactive ions with a repetition rate of 6Hz (≈167 ms charge breeding time). The efficiency was slightly lower (≈2%) when the repetition rate was increased to 20 Hz due to the shorter breeding time.

After the beam was extracted from the EBIT and mass analyzed, it was subsequently accelerated with the RFQ and the superconducting linac to an energy of 2.4 MeV/u using the first two cryomodules during the 80 hours of beam delivery. In order to achieve the required energy for the experiment several cavities were operated at twice the original specified gradients and all of them well beyond specification. Overall the cavity amplitudes were set at 170% of the nominal values and ran stable without any issues throughout the experiment. The overall transport efficiency from the EBIT through the linac was about 60% during the experiments (close to the maximum expected transmission through the MHB and the RFQ of about 70%). The linac and injection lines were pre-tuned using a $^{16}O^{7+}$ beam, and then scaled to $^{15}N^{7+}$ while maintaining a fixed velocity tune in the linac. Finally during the $^{37}K^{17+}$ delivery the linac and the injection line were scaled for the remaining 1.5%. Only minor corrections were necessary after scaling to deliver the beam to the experimental station [3]. Several decay counters along the beam line were installed to monitor the activity during the tuning process and optimize the transmission. Beam impurities were analyzed using in-beam silicon detectors and the ionization chamber mounted in the experimental station. In addition to the $^{37}K^{17+}$ ions, about 1000 ions/sec $^{13}C^{6+}$ and about 100 ions/ sec of $^{37}Cl^{17+}$ were identified as impurities in the accelerated beam.

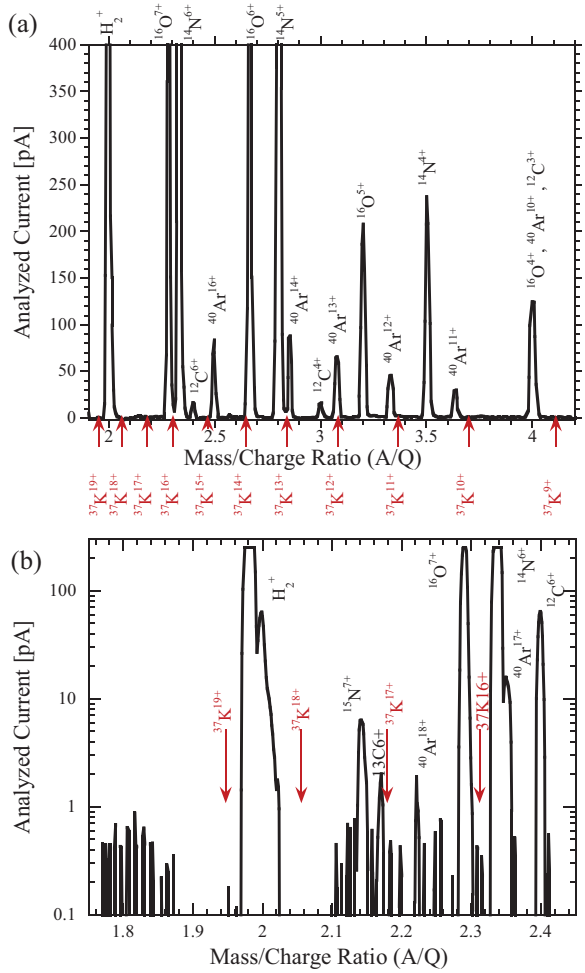


Figure 7: (a) Charge state distribution of the residual ion beam from the EBIT where the position of various $^{37}K^{n+}$ ions are indicated. (b) High resolution, high sensitivity A/Q scan, charge states for $^{37}K^{16+\ -\ 19+}$ ions are indicated.

Figure 8 shows two dimensional PID (particle identification) plots of the energy in the first segment (partial beam energy loss, delta-E) versus total energy (total beam energy loss) in all segments of the ionization chamber, in arbitrary units. This figure is provided courtesy of the ANASEN collaboration. The top panel shows the particle identification without injection of the ^{37}K into the EBIT, and the bottom panel with injection. The separation of mass 13 from 37 is evident, and it was for this reason that $^{37}K^{17+}$ was chosen for transport to the experiment. The small background rate of ^{37}Cl was relatively low and separated from the ^{37}K.

Copyright © 2013 CC-BY-3.0 and by the respective authors

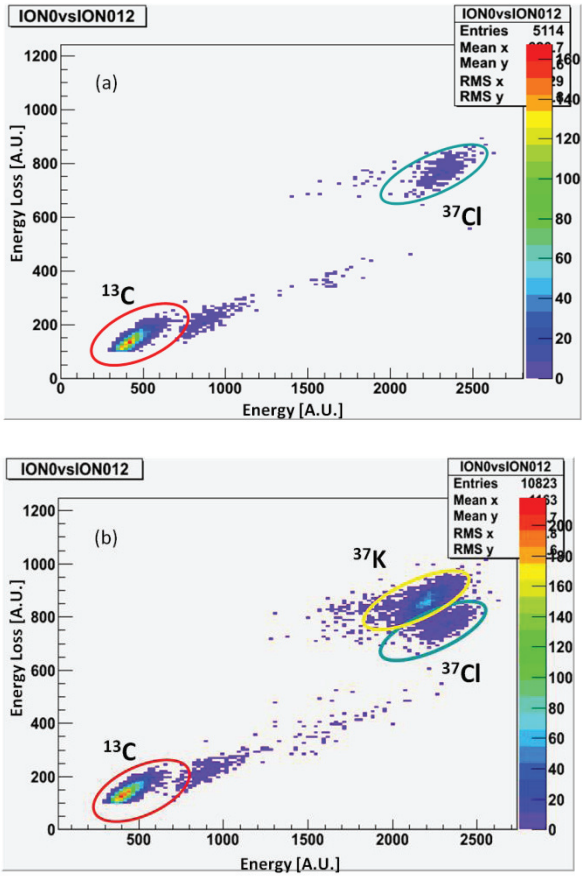


Figure 8: Particle identification (PID) obtained with the ANASEN ionization chamber. (a) PID without injection radioactive ^{37}K into the EBIT (b) PID when radioactive ^{37}K is injected into the EBIT.

FUTURE DEVELOPMENTS

The third cryomodule with a design β=0.085 is currently in its final assembly stage. It consists of eight quarter - wave SRF cavities and three superconducting solenoids for focusing. Once it is installed in the beam line it will add nominally 8.4 MV acceleration voltage to the accelerating chain. Eleven cavities have been successfully tested, all of which achieved a performance well above the nominal required accelerator gradient and Q-value (see figure 9) [2, 13]. A detailed description of the cavity design and its development can be found elsewhere [13]. Figure 9 shows the final acceptance test of the eight cavities mounted in the cryomodule.

In parallel the first cryomodule of the high energy accelerator chain is under development. It will consist of additional eight cavities and three solenoids, providing a nominal total accelerating voltage of 14.24 MV. Additionally one cold beam position monitor will be mounted after each solenoid. Contrary to the top-down cryomodule design of the first three cryomodules, where the coldmass is mounted on a strongback and supported from the top flange of the cryomodule, the new cryomodule is based on a modular bottom-supported design, which is optimized for mass-production and efficient precision assembly [14]. This cryomodule serves also as prototype cryomodule for the eleven FRIB β=0.085 cryomodules of linac section 1 [1].

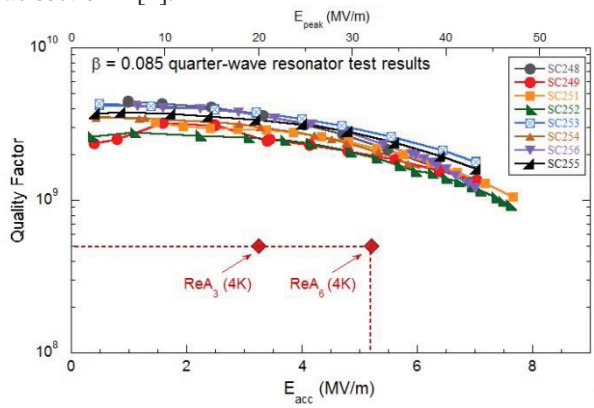


Figure 9: Q_0 vs. E_{acc} ($V_a/\beta\lambda$) curves measured during vertical acceptance tests of the β=0.085 ReA3 cavities at a temperature of 4.2 K.

ACKNOWLEDGMENT

The authors would like to thank the NSCL operations department and the excellent support from the technical departments. This work was supported by the National Science Foundation, under Cooperative Agreement PHY-1102511 and Michigan State University.

REFERENCES

[1] J. Wei, D. Arenius, N. Bultman, et al., NA-PAC'2013, Pasadena, CA, USA, 2013, http://www.jacow.org
[2] D. Leitner, D. Morris, S. Nash, et al., SRF'2011, Chicago, U.S.A., 2011, http://www.jacow.org/
[3] W. Wittmer, D. Alt, T. Baumann, et al., NA-PAC'2013, Pasadena, CA, USA, 2013, http://www.jacow.org
[4] D. Leitner, Nuclear Instruments and Methods in Physics Research Section B: Beam Interactions with Materials and Atoms in press, available online (2013).
[5] A. Stolz, G. Bollen, A. Lapierre, et al., Cyclotrons'2013, Vancouver, Canada, 2013, http://www.jacow.org
[6] W. Trimble, G. Savard, B. Blank, et al., Nuclear Physics A **746** (2004) 415.
[7] J.A. Rodriguez, S. Chouhan, A. Lapierre, et al., NA-PAC'2013, Pasadena, CA, USA, 2013, http://www.jacow.org
[8] S. Schwarz, G. Bollen, J. R. C. Lopez-Urrutia, et al., Review of Scientific Instruments **83** (2012) 02A908.
[9] A. Lapierre, S. Schwarz, T. M. Baumann, et al., RSI submitted (2014).
[10] G. Perdikakis, D. Bazin, J. Browne, et al., BIW'2012, Newport News, Virginia, 2012, http://www.jacow.org/
[11] S. J. Williams, T. M. Baumann, K. Cooper, et al., IBIC'2013, Oxford, England, 2013, http://www.jacow.org
[12] Q. Zhao, V. Andreev, F. Marti, et al., PAC07, Albuquerque, New Mexico, USA, 2007, http://www.jacow.org/, TUPAS054.
[13] A. Facco, E.C. Bernard, J. Binkowski, et al., IPAC'2012, New Orleans, Louisiana, 2012, http://www.jacow.org/
[14] S. Miller, N. Bultman, A. Fox, et al., SRF'2013, Paris, France, 2013, http://www.jacow.org/

Copyright © 2013 CC-BY-3.0 and by the respective authors

SUPERCONDUCTING GANTRY AND OTHER DEVELOPMENTS AT HIMAC

Y. Iwata*, K. Noda, T. Shirai, T. Murakami, T. Fujita, T. Furukawa, K. Mizushima, Y. Hara, S. Suzuki, S. Sato, and K. Shouda, NIRS, 4-9-1 Anagawa, Inage, Chiba 263-8555, Japan
T. Fujimoto, and H. Arai, AEC, 3-8-5 Konakadai, Inage, Chiba 263-0043, Japan
T. Ogitsu, KEK, 1-1 Oho, Tsukuba, Ibaraki 305-0801, Japan
T. Obana, NIFS, 322-6 Oroshi-cho, Toki-city 509-5292, Japan
N. Amemiya, Kyoto Univ., Kyoto-Daigaku-Katsura, Nishikyo, Kyoto 615-8510, Japan
T. Orikasa, S. Takayama, Y. Nagamoto, and T. Yazawa, Toshiba Corp., 1-1-1 Shibaura, Minatoku, Tokyo 105-8001, Japan

Abstract

New developments at HIMAC include a superconducting carbon gantry, a new therapy area with three new treatment rooms, and substantial enhancements to the synchrotron extraction system to enable energy-variation through multiple flattops within a synchrotron cycle to match characteristics of the gantry and three-dimensional raster scanning. The carbon gantry consists of ten combined-function superconducting magnets, allowing a very compact geometry – the length and the radius of the gantry are approximately 13 and 5.5 m, respectively, comparable to the dimensions of existing proton gantries. Further, these superconducting magnets are designed for fast slewing of the magnetic field to follow the multiple flattop operation of the synchrotron. In this paper, the recent developments of HIMAC are presented.

INTRODUCTION

Heavy-ion cancer-therapy using the Heavy-Ion Medical Accelerator in Chiba (HIMAC) has been carried out since June 1994. The successful cancer treatments have led us to construct a new treatment facility [1]. The new treatment facility equips with three treatment rooms; two of them have both horizontal and vertical fixed-irradiation-ports, and the other is a rotating gantry port as schematically shown in Fig. 1. For all the ports, the three-dimensional raster-scanning irradiation method with pencil beam will be employed [2].

In raster-scanning irradiation, a target is directly irradiated with high-energy carbon-ions, after being accelerated by a synchrotron ring. Since the position of the focused beam on a target is controlled by the fast horizontal and vertical scanning-magnets, the lateral dose distribution is determined by these scanning magnets. On the other hand, the depth dose-distribution is determined by beam energy. To control the depth dose-distribution, it is preferable to change the beam energy directly by the accelerators, instead of using energy degraders, since energy degraders may broaden the spot size of the beam on a target, and concurrently produce secondary fragments, which could adversely affect the depth dose-distribution.

To quickly change the energy of the beam, as provided by the synchrotron ring, we developed a multiple-energy operation with extended flattops [3]. The proposed operation enables us to provide carbon ions having various energies in a single synchrotron cycle; namely, the beam energy would be successively changed within a single synchrotron pulse. With this operation, the beam range could be controlled without using any energy degraders.

To further obtain precise dose distributions, we developed an isocentric superconducting rotating-gantry for carbon therapy [4]. This rotating gantry is designed to transport carbon ions having 430 MeV/u to an isocenter with irradiation angles of over ±180 degrees, and is further capable of performing the fast raster-scanning irradiation. The combined-function superconducting magnets will be employed for the rotating gantry. Use of the superconducting magnets with optimized beam optics allow a compact gantry design with a large scan size at the isocenter; the length and the radius of the gantry will be approximately 13 and 5.5 m, respectively, which are comparable to those for the existing proton gantries. This rotating gantry is currently under construction, and will be installed in the room G of the new treatment facility.

We report the recent developments of the multiple flattop operation as well as the superconducting rotating-gantry.

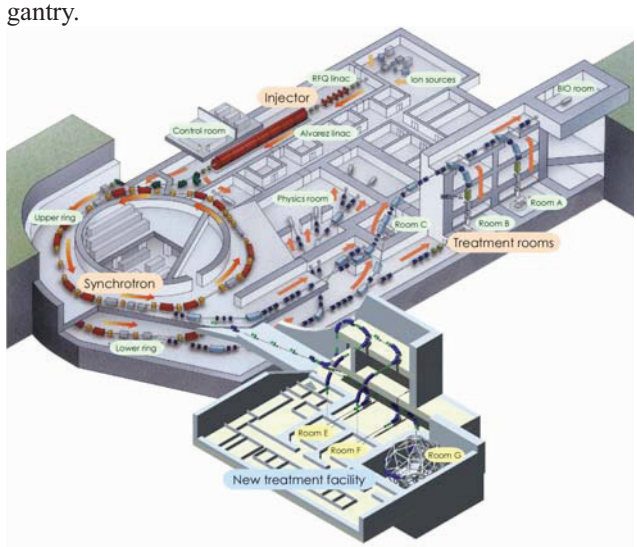


Figure 1: Layout of the HIMAC complex.

*corresponding author. E-mail: y_iwata@nirs.go.jp (Y. Iwata)

Copyright © 2013 CC-BY-3.0 and by the respective authors

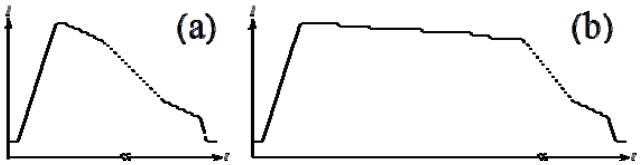


Figure 2: (a) Schematic drawing of synchrotron pattern for multiple-energy operation. (b) The same pattern as (a), but with the extended flattops. The beam is extracted from the synchrotron ring during these extended flattops.

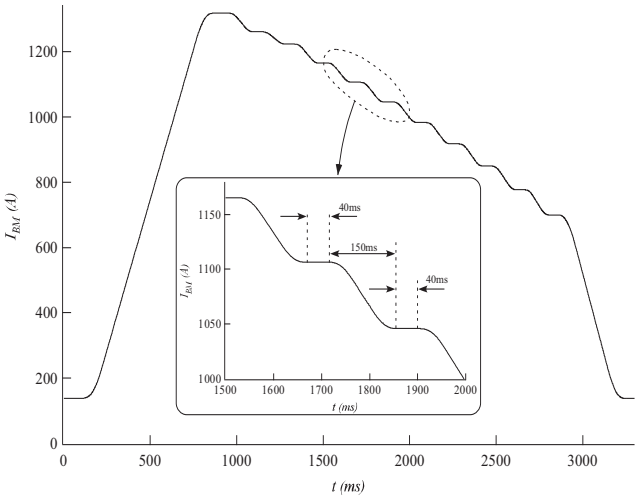


Figure 3: A current pattern for the main-bending magnets in the ring as a function of time. The currents of the 11 flattops correspond to the beam energies of 430, 400, 380, 350, 320, 290, 260, 230, 200, 170, and 140 MeV/u.

MULTIPLE FLATTOP OPERATION

The multiple-energy operation employs operation patterns having a stepwise flattop, as schematically shown in Fig. 2(a). With these operation patterns, the carbon ions injected in the ring are initially accelerated to the maximum energy, and then successively decelerated to lower energies. Although the stepwise pattern only has short flattops, where the beam can be extracted from the ring, we can extend the flattop and extract the beam during the extended flattop.

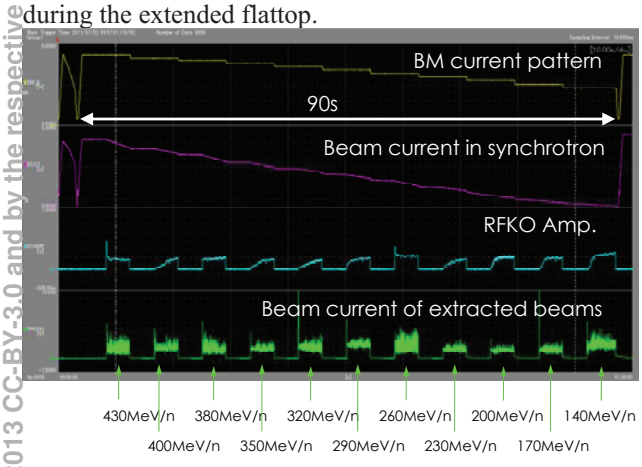


Figure 4: Current patterns for the main bending magnets, beam current in the synchrotron ring, RFKO amplitude, and the beam current of the extracted beam.

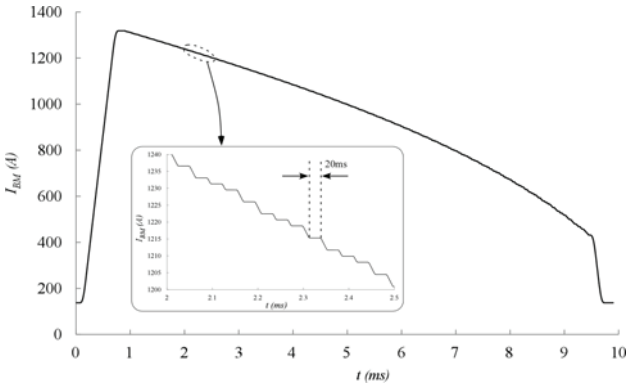


Figure 5: A current pattern for the main-bending magnets in the ring. This pattern has 201 flattops.

Having consecutively extended the flattops, as illustrated in Fig. 2(b), the beams having various energies can be extracted from the ring within a single synchrotron cycle, and hence the total irradiation time can be considerably reduced.

11-flattop pattern

To prove the principle of multiple-energy operation with extended flattops, we have performed beam acceleration and extraction tests using the stepwise operation pattern. In the tests, a current pattern for the main bending magnet having 11 short flattops, corresponding to 11 beam energies, was prepared as shown in Fig. 3. Further, similar patterns were prepared for other devices, such as the main quadrupole, sextupole magnets, the RF-acceleration cavity, and the beam-extraction devices in the extraction channel. By using the prepared operation patterns, the beam will be initially accelerated to 430 MeV/u, and then consecutively decelerated down to 140 MeV/u at an energy step of 20 MeV/u or 30 MeV/u. Results of the beam test are shown in Fig. 4. As can be seen in the figure, beams having 11 different energies were successively extracted from the synchrotron ring. The multiple-energy operation using this pattern was successfully commissioned, and has been used for scanning treatments since FY 2012.

Full energy-scan with 201-flattop pattern

The final goal of this project is to control the depth dose-distribution by varying the beam energy from the accelerators, namely, *full energy scanning*. To accomplish

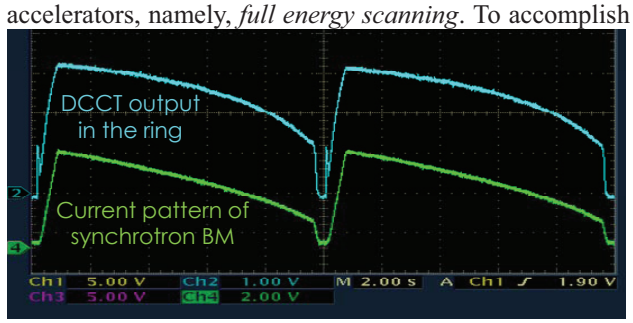


Figure 6: Current patterns for the main bending magnets, DCCT output in the synchrotron ring during beam acceleration tests using the 201-flattop pattern.

Copyright © 2013 CC-BY-3.0 and by the respective authors

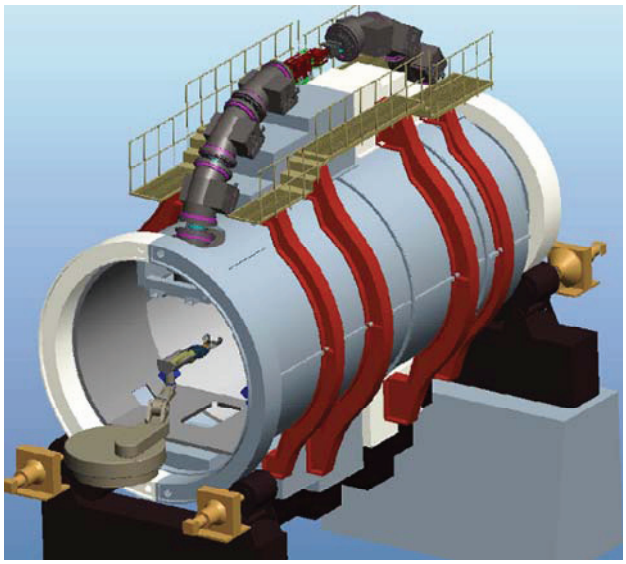


Figure 7: Three-dimensional image of the superconducting rotating gantry for carbon therapy.

this, it is required to change, the beam energy successively by an energy step corresponding to the water range of 1 or 2 mm. Since the maximum and minimum energies, as used in the raster-scanning irradiation, are 430 and 56 MeV/u, respectively, the synchrotron patterns having the 201 flattops will be needed to cover the entire energy range. Fig. 5 shows a current pattern of the main bending magnets having the 201 flattops.

Beam acceleration and extraction tests using the 201-flattop patterns were successfully made as shown in Fig. 6. In the test, we found that any of the 201 flattops can be extended, and that the beam can be extracted during the extended flattop. Hence, with this operation pattern having the 201 flattops - *the universal pattern*, the depth dose-distribution could be controlled without using any energy degrader.

SUPERCONDUCTING ROTATING-GANTRY

A three-dimensional image of the isocentric rotating gantry for the new treatment facility is presented in Fig. 7. This rotating gantry has a cylindrical structure with two large rings at both ends. The end rings support the total weight of the entire structure, and are placed on turning rollers so as to rotate the beam line on the rotating gantry along the central axis over ±180 degrees. Carbon beams, provided by the HIMAC, are transported with ten sector-bending magnets, mounted on the gantry structure through each of their supporting structures; they are directed on a target located at the isocenter. In the treatment room, a tumour in a patient is precisely positioned to the isocenter by using a robotic couch.

Layout and beam optics

A layout of the compact rotating-gantry is presented in Fig. 8. The rotating gantry has ten superconducting magnets (BM01-10), a pair of the scanning magnets (SCM-X and SCM-Y), and two pairs of beam profile-monitor and steering magnets (ST01-02 and PRN01-02). A total length and radius of the rotating gantry is 13 m and 5.45 m, respectively. All of these devices are installed and mounted on the cylindrical structure. Since beam focusing can be made only with the combined-function

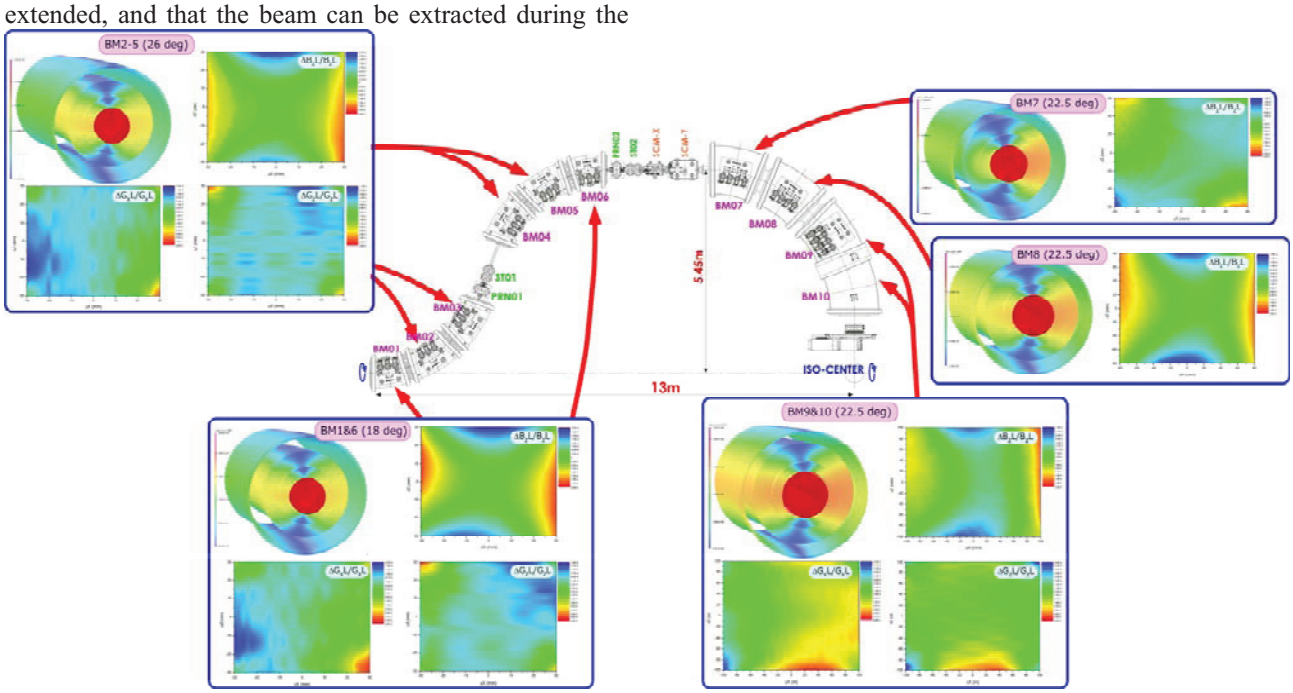


Figure 8: Layout of the superconducting rotating gantry. The gantry consists of ten combined-function superconducting magnets (BM01-10), a pair of the scanning magnets (SCM-X and SCM-Y), and two pairs of beam profile-monitor and steering magnets (ST01-02 and PRN01-02). Representative results of 3D magnetic field calculations for the five kinds of the superconducting magnets are also shown.

Copyright © 2013 CC-BY-3.0 and by the respective authors

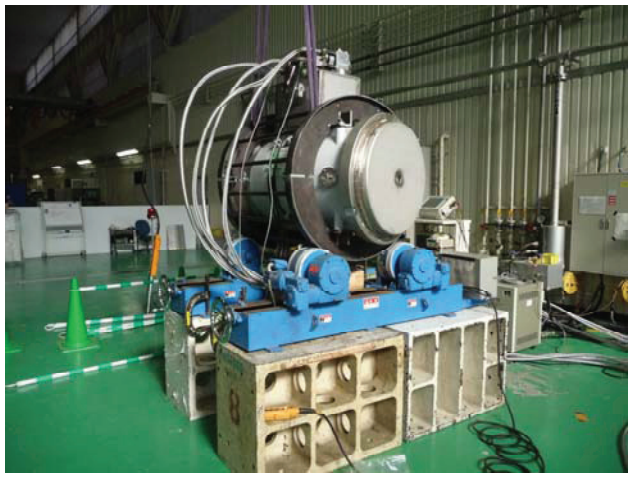


Figure 9: Picture of the test bench during rotation tests of the model superconducting-magnet.

superconducting magnets, no quadrupole magnets are needed to install in the rotating gantry, and thus we could design the compact rotating gantry. Details of the beam optics are provided in Ref. [4].

Field calculations

Based on the design of the beam optics, specification of the superconducting magnets was determined. According to their apertures, the magnets are categorized into five kinds. All the magnets have the surface-winding coil structure, and were designed by using a 3D electro-magnetic field-solver, the Opera-3d code [5]. In the code, the curved superconducting coils, having typically a few thousand turns per pole, as well as the cold yoke and vacuum chamber were precisely modelled, and a three-dimensional magnetic field was calculated. Representative results of the calculations are shown in Fig. 8. Having optimized the conductor position, we obtained the required uniformity of the calculated field.

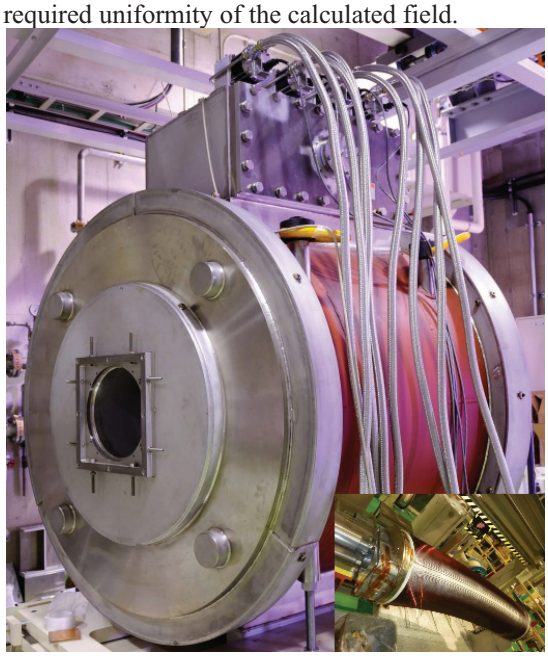


Figure 10: Picture of BM10 and its superconducting coil.

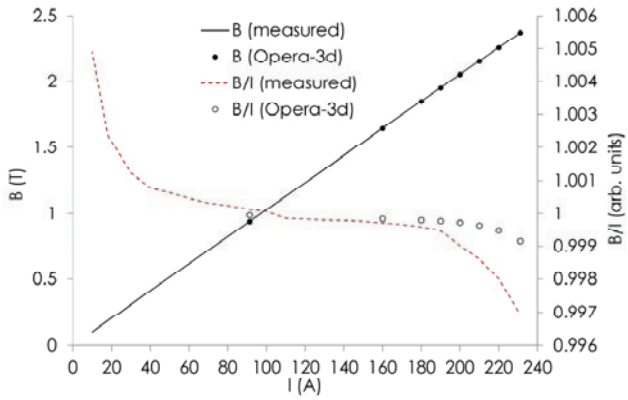


Figure 11: Measured magnetic field, *B*, and magnetic field as divided by coil current, *B/I*, as functions of coil current, *I*, for BM10. For comparison, calculated magnetic field is shown by the filled and open dots.

Rotation tests

Since the superconducting magnets on the rotating gantry are to be rotated over ±180 degrees during treatments, an unexpected quench of the superconducting magnets, as caused by rotations, is a concern. To verify this, a model superconducting magnet was developed and tested by Toshiba Corporation. This model magnet has a similar magnet structure as that of BM01-06, although this model magnet only has a dipole coil. Fig. 9 shows a picture of a test bench during rotation tests. Prior to the tests, the coil of the model magnet was cooled down to below 4K by cryocoolers, installed on the magnet. While exciting the superconducting coil with the maximum current, the model magnet was rotated by ±180 degrees, and the coil temperatures in the magnets were monitored. As a result, no unexpected temperature increase, which may cause quench problems, was observed.

Magnetic field measurements

The five superconducting magnets of BM01-BM04 and BM10 (Fig. 10) were constructed, and the rest of the five will be constructed within a year. Firstly, we measured central magnetic field by using an NMR probe. The NMR probe was installed in the middle of the magnet, and current of between *I*=10-240 A was applied for the dipole

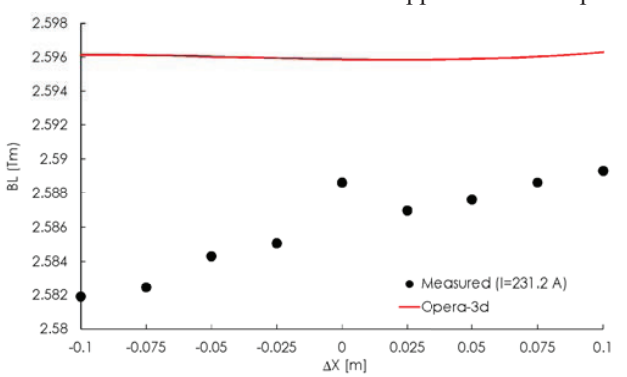


Figure 12: Measured BL products as a function of ΔX. Current for the dipole coil is *I*=231.2A. The solid curve show calculated result with the Opera-3d code.

Copyright © 2013 CC-BY-3.0 and by the respective authors

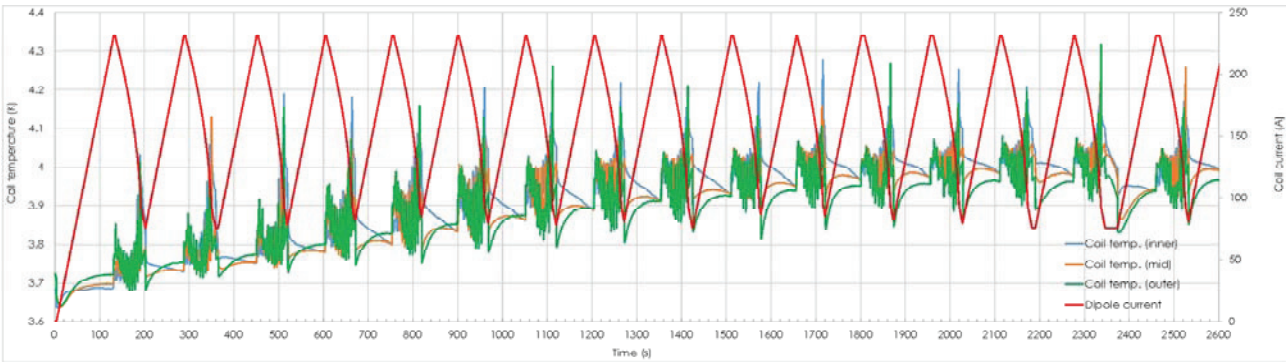


Figure 13: Results of the fast slewing tests for BM10. Average coil temperatures were converged below 4K.

coil of BM10. The measured magnetic field, B, and magnetic field as divided by the coil current, B/I, are shown by the solid and dashed curves in Fig. 11, respectively. For comparison, calculated results of B and B/I using the Opera-3d code are also plotted by the filled and open dots in Fig. 11, respectively. We found that the measured and calculated magnetic field agreed with each other, although the measured B/I curve at the maximum current slightly differs with the calculated curve. This discrepancy might be attributed to a difference in estimation of a packing factor for the laminated cold yoke.

Secondarily, measurements of magnetic field distributions along beam trajectories were performed. Measured-magnetic field distributions along the central beam trajectory were measured and integrated over the beam trajectories to determine a BL product and an effective length. The same analysis was made for the calculated distribution with the Opera-3d code. Fig. 12 shows the BL products of various beam trajectories, as shifted horizontally by ΔX, for the dipole current of I=231.2A. Here, the values of the BL products are normalized, so as to have the same effective length of $L=\rho\theta$=2.8m×22.5° for all the trajectories. Corresponding results, as calculated by the Opera-3d code, are also shown by the solid curves in the figures. The absolute values of the measured BL agreed with the calculated values within accuracy of a few times 10^{-3}; however we clearly see the quadrupole component of approximately GL~3.8×10^{-2} T for the measured field in Fig. 12. We presume that this unexpected quadrupole component might be attributed to an alignment error between the superconducting coil and cold yoke. However, since this magnet has the quadrupole coil, this quadrupole component can be corrected by adding or reducing current for the quadrupole coil by approximately ΔI=5 A from the applied quadrupole current of I~200 A.

Fast slewing tests

To simulate the multiple flattop operation, fast slewing tests were made. In the tests, currents of both the dipole and quadrupole coils were maximized to initialize the magnet, and then were decreased by 201 steps. In each step, coil currents were kept for 0.3 s, where carbon beams would be extracted from accelerators and transported through a beam-transport line including the rotating-gantry during this constant-current region. Further, the coil temperatures were measured with resistance temperature sensors, installed in the inner, middle and outer sides of the coil. A representative result for BM10 is provided in Fig. 13. Although the coil temperature gradually increases, we found that the average coil temperatures were converged around 4 K, while the critical temperature is approximately 6.8 K.

SUMMARY AND FUTURE PLAN

Recent developments of the HIMAC accelerator complex are reported. To take advantage of the fast raster-scanning irradiation, the multiple energy operation was developed. This operation using 11-flattop pattern was successfully commissioned, and is presently used in scanning-treatment operations. Furthermore, we successfully made beam acceleration and extraction tests with 201-flattop pattern, which enables us to perform the full energy scanning; this operation will be used for treatment operation in near future.

A compact superconducting rotating-gantry for carbon therapy is being developed. Having optimized the layout using the combined-function superconducting magnets, we could design the compact rotating-gantry. The design study as well as major tests of the superconducting magnets was completed, and the construction of the superconducting rotating-gantry is in progress. The rotating-gantry will be completed at the end of FY2014, and be commissioned in FY2015.

ACKNOWLEDGMENT

This work is supported by Ministry of Education, Culture, Sports, Science and Technology (MEXT), Japan.

REFERENCES

[1] K. Noda, *et al.*, Nucl. Instrum. and Meth. in Phys. Res. B 266 (2008) 2182.
[2] T. Furukawa, *et al.*, Med. Phys. 37 (2010) 5672.
[3] Y. Iwata, *et al.*, Nucl. Instrum. and Meth. in Phys. Res. A 624 (2010) 33.
[4] Y. Iwata, *et al.*, Phys, Rev. ST Accel. Beams 15 (2012) 044701.
[5] Opera Version 16, http://www.cobham.com/.

Copyright © 2013 CC-BY-3.0 and by the respective authors

ADVANCES IN SUPERCONDUCTING UNDULATORS *

Y. Ivanyushenkov#, Advanced Photon Source, ANL, Argonne, IL 60439, USA

Abstract

Superconducting technology could be employed for building undulators with enhanced parameters for synchrotron light sources and free-electron lasers. Expected and measured performance of superconducting undulators will be presented. Although superconducting technology is already working in superconducting wigglers, the development of superconducting undulators was slowed down by a variety of challenges that will be discussed. Possible solutions with examples will be presented. Finally, an overview of recent developments in superconducting undulators is presented in this paper.

INTRODUCTION

Insertion devices (IDs) are essential parts of modern and future light sources. The trends for IDs of future light sources are reviewed in [1]. Until now most IDs have been built using permanent magnets as a source of magnetic flux. At the same time, there is a growing interest in electromagnetic devices that use superconducting windings. As a matter of fact, superconducting wigglers are a well-established technology; such IDs are being used in many synchrotron light sources [1]. In comparison, the development of superconducting undulators is lagging behind the progress being made with superconducting wigglers.

This paper follows the review of developments in superconducting insertion devices given in [2] and concentrates on superconducting undulators (SCUs). The motivation of developing SCUs is first discussed, followed by a list of challenges. Examples of recent developments towards finding the solutions are then given. Finally, an overview of activities in superconducting undulators is presented.

SCU MOTIVATION

Interest in SCUs is stimulated by the fact that the SCUs can reach, for the same vacuum gap and period length, higher field events with respect to cryogenic permanent magnet undulators (CPMUs)—the state-of-the-art of permanent-magnet-based undulators. The undulator peak field for both technologies is compared in Table 1 [3]. In this table, NbTi-APC refers to a NbTi-superconductor with artificial pinning centers (APC).

A similar comparison is given in [4]. A careful analysis of CPMU and SCU technologies concludes that above the period length of 10 mm SCUs produce the highest fields. For the smaller period lengths, CPMUs can compete with NbTi SCUs, whereas Nb_3Sn or NbTi-APC devices are still superior.

*Work supported by by U.S. Department of Energy, Office of Science, under Contract No. DE-AC02-06CH11357.

#yury@aps.anl.gov

Table 1: CPMU and SCU Comparison [3]

	CPMU PrFeB	SCU NbTi	SCU NbTi-APC
Undulator period, mm	15	15	15
Magnetic gap, mm	5.2	6	6
Undulator peak field B, T	1.0	1.18	1.46
Undulator parameter K	1.40	1.65	2.05

SCU CHALLANGES

Development of SCUs is progressing relatively slowly due to several challenges. The first one concerns the requirement of high quality field from an undulator magnet. The second one is operating the SCU magnet coils at high current densities and providing adequate cooling in the presence of beam heating.

The first and second field integrals should be kept at a minimum to avoid electron beam position deviation by the undulator magnetic field. To achieve the highest performance of an undulator at higher harmonics, the phase error should also be kept at a level of a few degrees RMS. Those requirements are not easily achievable for multipole magnetic structures.

Cooling complex multi-coil superconducting magnetic structures of SCUs in the presence of heating by an electron beam is another challenging task. The possible solutions are discussed below.

SCU MAGNET

Magnet Design

A planar SCU generates a periodic magnetic field in a plane. For this, a set of linear currents is required as a minimum [5]. For practical reasons, a set of small racetrack coils (with dimensions of few a cm in height by a few cm in length) is used forming a multi-coil structure supported by a magnet former. The coils are usually vertically oriented due to a relatively short (15-30 mm) period length in the undulators. One undulator period contains two coils with the currents going in opposite directions. A magnet former, or a core, can be made of magnetic or non-magnetic material. A complete SCU magnetic structure is then made of two such magnets separated by a magnetic gap where a beam vacuum chamber can be located [6].

Such a magnetic design is adopted in the SCUs for the National Synchrotron Radiation Research Center (NSRRC), Taiwan [7], Advanced Photon Source (APS), USA [8], Diamond Light Source (DLS), UK [9], and Shanghai Synchrotron Radiation Facility (SSRF), China [10]. In the SCU for ANKA there is no beam vacuum

Copyright © 2013 CC-BY-3.0 and by the respective authors

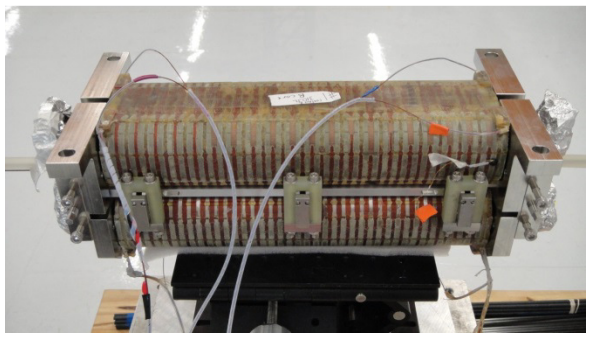


Figure 1: Magnetic structure of the test superconducting undulator SCU0 at the APS [8].

chamber, but a thin liner is used to shield SCU coils from the electron beam [11].

The above scheme is suited for winding SCU coils with the low-temperature superconductor (LTS) wires although the exact designs could vary. Both NbTi and Nb_3Sn superconductors were successfully used for making SCU magnet prototypes, but NbTi has been used so far in the completed devices.

There also have been attempts to use high-temperature superconductors (HTSs) for SCU magnets. The idea of making a zigzag-like pattern on the HTS YBCO ($YBa_2Cu_3O_7$) tape is suggested in [12]. An SCU magnet could then be built as a stack of such tapes. The expected field of this undulator could exceed 1 T for a period length of 7 mm and beam aperture of 2 mm. An undulator with such a small pole gap is targeted primarily at free electron lasers.

A prototype of an HTS magnet was built and tested by the ANKA group and Babcock Noell GmbH [13]. The achieved field was lower than the field of a NbTi-based magnet. This is due to a very low packing factor in a winding made of the HTS tapes, where a superconductor layer is very thin and occupies only about 1% of the tape overall thickness.

Magnetic Shimming

Magnetic and mechanical shimming is usually used to tune conventional undulators to achieve the required field integrals and phase errors. It is a common perception therefore that magnetic shimming should also be employed for SCUs. In the case of superconducting devices where a magnetic structure is enclosed in a cryostat, such an approach requires development of new shimming techniques.

One possibility for planar SCUs is to add extra iron pieces to a magnetic pole as described in [14]. The measured maximum field compensation is 2.43% for a shimming piece of height 25 mm in a 130-pole undulator magnet with period length of 15 mm and a 5.6-mm pole gap. An additional magnetic flux could be injected into a pole when a trim coil is mounted directly on the outer faces of the iron pole with a trim iron piece [15].

A concept of passive shimming, based on Faraday's law of induction, was suggested [16] and experimentally tested [17]. The induction-shimming system consists of a set of overlapping closed high-temperature superconductor (HTS) loops attached to the surface of the superconducting undulators. Each HTS loop covers two adjacent undulators' magnet poles. The undulators' field errors induce currents in the HTS loops and, as a result, the magnetic field generated by these induction currents minimizes the field errors. The compensation effect at a level of 6 mT was measured at a distance of 7.15 mm from the SCU test magnet having a period length of 14 mm. The estimated correction field would be about 17 mT for an undulator with a period length of 15 mm and a pole gap of 5 mm with a peak field of 1.5 T [17].

Superconducting switches are also suggested for use in SCU shimming as described in [18]. This concept utilizes a single current source and a set of superconducting switches to control the current direction in the trim coils.

At the same time, the experience of the APS group demonstrates that magnetic shimming is not required for a relatively short (300-mm-long) undulator magnet. The magnet former was machined with a precision of about 10 μm, and the winding was done accurately on a computer-controlled winding machine. As a result, a phase error below 2° RMS was measured. The required field integrals were also achieved without any magnetic shimming. Such tight mechanical tolerances are practically impossible for longer magnets; therefore, theoretical work was started in order to simulate possible geometrical errors in superconducting magnet windings and calculate their effect on the field quality [19]. It was found that for a given field error range, the phase error scales with the square root of the undulator length. This work needs to be continued to better understand the sources of the field errors in SCU magnets.

SCU COOLING

Heat Loads

Design of an SCU cooling circuit requires reliable prediction of expected heat load in a superconducting undulator. Since an SCU is a superconducting magnet, all the heat loads that are typical for a superconducting magnet system are also present in an SCU. These are conduction heat leaks through current leads and cold mass supports, and radiation heat load from the vacuum vessel at room temperature to a cold mass at liquid helium temperature. Those heat loads could be calculated with good precision.

Another source of heat in the SCU is the electron beam itself. There is a variety of ways for electron beam to generate heat in a beam chamber, but the largest contribution at a level of tens of Watts per a meter of chamber length is due to resistive wall wakefields.

In addition, the SCU could be heated by any uncollimated synchrotron radiation from the upstream bending magnet. This can be mitigated by placing an absorber upfront of the SCU and by making the SCU beam chamber bore wide enough for the bending magnet synchrotron radiation to pass through.

Copyright © 2013 CC-BY-3.0 and by the respective authors

Cooling Schemes

The task of an SCU cooling circuit is to keep the SCU magnet coil cool in the presence of static heat leaks in the cryostat and beam heating.

One possibility is to place the SCU magnet into a liquid helium bath as in superconducting wigglers [20]. The drawback of this approach is that the beam heat goes directly into the coolant and requires substantial cooling power at 4 K. This cooling power could be provided by cryocoolers or by a cryogenic plant. Taking into account that a modern cryocooler delivers only 1.5 W of cooling at 4 K, this approach is limited to a modest heat load at 4 K. The usage of a cryoplant is likely to be cost effective when a long string of superconducting undulators needs to be built, like in free electron lasers. This scheme could be modified by placing a thermal screen, a liner, into a beam chamber bore. This liner could then be cooled by a separate circuit and take most of the heat from the electron beam.

It should be noted that the electron beam heats the SCU magnet when the beam chamber is in thermal contact with the SCU coils. This situation could be avoided by thermally insulating the SCU magnet from the beam chamber. A vacuum gap can simply be used as a thermal insulator. Such an approach is adopted in the SCU for the APS [21]. In this undulator the SCU coils are indirectly cooled by LHe passing through the channels in the magnet cores. The LHe is kept in a tank inside the cryostat and, together with the magnet and piping, makes a closed system. The He vapor in this system is re-liquefied by a recondenser that is located inside the tank and cooled by a cryocooler. An electrical heater is used to trigger a thermosyphon effect for circulating LHe through the magnet cores.

A group in the UK is going to employ a similar cooling scheme for their SCU but will decrease the operating temperature to 1.8 K to gain a safety margin and to achieve the required critical current [9]. A Joule-Thomson expansion valve will be added to a cryogenic circuit, and a pressure of 16 mbar will be required on the effluent side of the helium expansion. A special scroll pump will be used for circulating He through the undulator magnet.

Cryogen-free systems are also possible. The SCU coils are conduction cooled by cryocoolers as in the SCU that is currently being built by the ANKA group and Babcock Noell GmbH [22].

MAGNETIC MEASUREMENTS

Measurement of magnetic performance of an SCU is another challenging task as it requires building a dedicated magnetic measurement facility. The measurement techniques employed for conventional undulators could not be directly applied for SCUs as in these devices the magnetic structure is located inside a cryostat and operated at cryogenic temperature.

It is a common practice that undulator coils are tested in a vertical liquid helium cryostat. Such a system usually contains a single or several Hall sensors mounted on a vertical stage. An example of such a system is CASPER-I (Characterization Setup for Phase Error Reduction) developed at ANKA [23]. Similar systems were built at Brookhaven National Laboratory [24] and the APS.

Recently a more advanced measurement facility called CASPER-II has been built by the ANKA group [25]. This system is targeted at characterization of conduction cooled SCU magnets. It is based on a horizontal, cryogen-free cryostat with easy access to a test coil. The system is equipped with a Hall probe for local field measurements and a stretched wire for measuring the field integrals.

The APS group in collaboration with a team from Budker Institute, Novosibirsk, Russia, has designed and built a horizontal measurement system [26]. This system utilizes a warm guiding tube approach. In this scheme, a Hall probe is guided through a thin-wall warm tube that is stretched inside the cold bore of the SCU beam chamber. The bore of the guiding tube is open at the ends thus giving easy access to the Hall probes and measurement coils. The system has been successfully operated for parameterization of the first superconducting undulator at the APS [27].

The superconducting undulators for free electron lasers are likely to have a smaller pole gap than the SCUs for synchrotron light sources. A technique for magnetic measurements of small-gap SCUs needs to be developed. One promising approach is a pulsed wire technique that can be used for direct measurements of the first and second field integrals. The possibility of using this method for accurate trajectory and phase error measurements is demonstrated in [28].

EXPERIENCE WITH SCU OPERATION

A number of SCU prototypes have been built in various institutions around the world, but a quantity of completed devices is substantially smaller. Therefore any experience of operating a superconducting undulator on a light source is extremely valuable.

Superconducting undulator SCU14 was in operation at ANKA light source for several years after installation in 2005 [29]. This was a 100-period device with a period length of 14 mm and variable gap of 8-25 mm built by ACCEL Instruments GmbH. The magnet was conduction cooled by three cryocoolers. The measured photon spectra of SCU14 agreed very well with the calculations. Initial studies of the SCU heating by the electron beam concluded that the dominant heat source was the synchrotron radiation produced in the upstream bending magnets: 1 W per 100 mA stored current at a beam energy of 2.5 GeV and an undulator gap of 8 mm [30]. The heat load produced by the image current was found to be negligible. In the following years a nonlinear beam chamber vacuum pressure rise with the electron beam current was observed. The large variation of the beam heat load was also measured for different gaps—between 1.6 and 3 Watts for an 8-mm gap with 120-mA average beam current [31]. This was attributed to electron multipacting as the main beam heat source at ANKA for normal user operation [32].

Copyright © 2013 CC-BY-3.0 and by the respective authors

The first superconducting test undulator, SCU0, was built and installed on the APS storage ring in December 2012. After commissioning in January 2013, the undulator is in user operation [33]. The SCU0 contains a relatively short magnet (330-mm length) in a 2-m-long cryostat [8]. The SCU0 magnet has a period length of 16 mm and a pole gap of 9.5 mm. It was designed to operate at a current of 500 A, but it routinely operates at a current of 650 A, delivering a magnetic field of about 0.8 T. The measured heat load on the SCU0 beam chamber is 16 W, which agrees very well with a calculated value of 14 W. For the eight-month period since commissioning, the device has demonstrated a LHe loss-free behavior. It is also observed that an SCU0 quench does not trigger an electron beam dump since the electron trajectory is deviated by only about 50 μm. On the contrary, an unintentional beam dump causes undulator quench. It takes about 20 minutes for the temperatures in the SCU0 to stabilize after quench. The device was characterized in terms of photon flux. As measured, the SCU0 produces about 40% higher photon flux at the photon energy of 85 keV as compared to a 2.4-m-long Undulator A, the most common hybrid undulator at the APS.

RECENT DEVELOPMENTS IN SCUs

A list of SCUs that have recently been built or are in the development stages (to the best of the author's knowledge) is given in Table 2. In this table SC stands for superconductor.

Table 2: SCUs Recently Built or Under Development

Light Source/ Institution	Period (mm)	Pole gap (mm)	K	No. of periods	SC	Status
NSRRC	15	5.6	1.96	≈132	NbTi	Proto-type
SSRF	16	9.5	0.9	10	NbTi	Proto-type
ANKA	15	5-16	2.1 max	100.5	NbTi	Being built
DLS	15.5	7.4	1.83	≈129	NbTi	Proto-type
NGLS/ LBNL	~20	TBD	TBD	~3000	Nb_3Sn	Proto-type
APS	16	9.5	1.2	20.5	NbTi	Built
	18	9.5	1.64	59.5	NbTi	Being built

CONCLUSION AND DISCLAIMER

Superconducting undulators continue to attract the interest of the light source community due to its promise of delivering high magnetic fields and therefore higher photon fluxes, especially at high photon energies.

In recent years a number of SCU prototypes have been manufactured and tested, and more undulators are currently being built. Various solutions are being suggested and implemented to overcome SCU challenges.

Experience gained in operating superconducting undulators confirms that such devices could successfully be operated in synchrotron light sources.

It is inevitable with an overview like this that some excellent work that has made valuable contributions to the development of superconducting undulators has been overlooked, but it was not intentional.

ACKNOWLEDGMENT

The author thanks S. Casalbuoni, J. Clarke, C.-S. Hwang and Z. Zhang for providing valuable information for this paper.

REFERENCES

[1] C.-S. Hwang et al., "Development trends for insertion devices of future synchrotron light sources," Phys. Rev. ST Accel. Beams 14 (2011) 044801.

[2] E.R. Moog and Y. Ivanyushenkov, "Developments in Superconducting Insertion Devices," Proc. of PAC2011, New York, THOBS1, p. 2077 (2011); http://www.JACoW.org

[3] S. Casalbuoni et al., "Test of short mockups for optimization of superconducting undulators coils," Proc. of MT23, Boston, USA, 3OrBC-03 (2013).

[4] J. Bahrdt and Y. Ivanyushenkov, "Short Period Undulators for Storage Rings and Free Electron Lasers," Journal of Physics: Conference Series 425 (2013) 032001.

[5] H.O. Moser and C.Z. Diao, "Finite-length field error and its compensation in superconducting miniundulators," Nucl. Instrum. Methods A535 (2004) 606.

[6] Y. Ivanyushenkov et al., "Status of R&D on a Superconducting Undulator for the APS," Proc. of PAC'09, Vancouver, Canada, MO6PFP078, p. 313 (2009); http://www.JACoW.org

[7] C.S. Hwang et al., "Mini-pole Superconducting Undulator for X-ray Synchrotron Light Source," IEEE Trans. Appl. Supercond. 16(2), (June 2006) 1855.

[8] Y. Ivanyushenkov et al., "A Design Concept for a Planar Superconducting Undulator for the APS," IEEE Trans. Appl. Supercond. 21(3), (June 2011) 1717.

[9] J.A. Clarke et al., "Status of the UK Superconducting Planar Undulator Project," Proc. of IPAC2013, Shanghai, China, WEPWA062, p. 2259 (2013); http://www.JACoW.org

[10] Z.C. Zhang et al., "Design of a Superconducting Undulator Magnet Prototype for SSRF," Proc. of IPAC2013, Shanghai, China, WEPWA035, p. 2205 (2013); http://www.JACoW.org

[11] C. Boffo et al., "A New Superconducting Undulator for the ANKA Synchrotron Light Source," Proc. of PAC2009, Vancouver, Canada, WE5RFP064, p. 2410 (2010); http://www.JACoW.org

Copyright © 2013 CC-BY-3.0 and by the respective authors

[12] S. Prestemon et al., "High Performance Short-Period Undulators Using High Temperature Superconducting Tapes," Proc. of PAC09, Vancouver, Canada, WE5RFP075, p. 2438 (2010); http://www.JACoW.org
[13] C. Boffo et al., "Industrial Experience on Superconducting Undulators," Workshop on Superconducting Undulators and Other New ID Sources, SRI2010, Argonne National Laboratory (2010); http://sri2010.aps.anl.gov/program/workshop-3/presentations/mon/Boffo.pdf
[14] J.C. Jan et al., "Magnetic-Field Shimming and Field Measurement Issue of the 130-Pole Superconducting Undulator," IEEE Trans. Appl. Supercond. 21(3), (June 2011) 1705.
[15] J.C. Jan et al., "Field Trimming by Iron Pieces and Coils in a Superconducting Undulator," IEEE Trans. Appl. Supercond. 19(3), (June 2009) 1332.
[16] D. Wollmann et al., "A new concept for reducing phase errors in superconducting undulators: Induction-shimming," Proc. of EPAC08, Genoa, Italy, WEPC135, p. 2323 (2008); www.JACoW.org
[17] D. Wollmann et al., "Experimental demonstration of the induction shimming concept in superconducting undulators," Proc. of PAC09, Vancouver, Canada, WE5RFP087, p. 2474 (2010); www.JACoW.org
[18] A. Madur et al., "Superconducting switch concept applied to superconducting undulator phase error correction," AIP Conf. Proc. 1234 (2010) 552.
[19] J. Bahrdt and Y. Ivanyushenkov, "Effect of Geometrical Errors on the Field Quality in a Planar Superconducting Undulator," Proc. of IPAC2012, New Orleans, LA, MOPPP065, p. 708 (2012); http://www.JACoW.org
[20] S.V. Khruschev et al., "Superconducting 63-pole 2 T Wiggler for Canadian Light Source," Nucl. Instrum. Methods A575 (2007) 38.
[21] E.R. Moog et al., "Development Status of a Superconducting Undulator for the Advanced Photon Source (APS)," Proc. of IPAC2010, Kyoto, Japan, WEPD047, p. 3198 (2010); http://www.JACoW.org
[22] C. Boffo et al., "Fabrication of the New Superconducting Undulator for the ANKA Synchrotron Light Source," Proc. of IPAC2010, Kyoto, Japan, WEPD021, p. 3135 (2010); http://www.JACoW.org
[23] E. Mashkina et al., "CASPER—A magnetic measurement facility for superconducting undulators," Journal of Physics: Conference Series 97 (2008) 012020.
[24] D. Harder et al., "Magnetic Measurement System for the NSLS Superconducting Undulator Vertical Test Facility," Proc. of PAC2005, Knoxville, TN, MPPT021, p. 1730 (2005); http://www.JACoW.org
[25] A. Grau et al., "In-Vacuum, Cryogen-Free Field Measurement System for Superconducting Undulator Coils," Proc. of IPAC2012, New Orleans, LA, MOPPP067, p. 714 (2012); http://www.JACoW.org
[26] Y. Ivanyushenkov et al., "Development Status of a Magnetic Measurement System for the APS Superconducting Undulator," Proc. of PAC2011, New York, TUP243, p. 1286 (2011); http://www.JACoW.org
[27] C. Doose and M. Kasa, "Magnetic Measurements of the First Superconducting Undulator at the Advanced Photon Source," THPBA06, these proceedings.
[28] D. Arbelaez et al., "A dispersion and pulse width correction algorithm for the pulsed wire method," Nucl. Instrum. Methods A716 (2013) 62.
[29] R. Rossmanith et al., "A Year's Experience with a Superconducting Undulator in the Storage Ring ANKA," Proc. of EPAC2006, Edinburgh, Scotland, THPLS123, p. 3571 (2006); http://www.JACoW.org
[30] S. Casalbuoni et al., "Investigations of the Thermal Beam Load of a Superconducting In-Vacuum Undulator," Proc. of EPAC2006, Edinburgh, Scotland, THPLS122, p. 3568 (2006); http://www.JACoW.org
[31] S. Casalbuoni et al., "Beam Heat Load and Pressure in the Superconducting Undulator Installed at ANKA," Proc. of IPAC2012, New Orleans, LA, MOPPP068, p. 717 (2012); http://www.JACoW.org
[32] S. Casalbuoni et al., "Beam heat load and pressure rise in a cold vacuum chamber," Phys. Rev. ST Accel. Beams 10 (2007) 093202.
[33] K. Harkay et al., "Superconducting Undulator Beam Commissioning Results," WEOAA3, NA-PAC'13

Copyright © 2013 CC-BY-3.0 and by the respective authors

DEVELOPMENT AND OPERATION OF THE SNS FAST CHOPPER SYSTEMS*

R. Saethre, D. Anderson, C. Deibele, V. Peplov, M. Stockli
ORNL, Oak Ridge, TN 37831, USA

Abstract

The Spallation Neutron Source (SNS) at Oak Ridge National Laboratory requires fast chopper systems to create a series of mini-pulses of H^- ions in the Linear Accelerator (LINAC) for injection into the accumulation ring. The fast chopper systems are in the front end of the accelerator with one chopper in the Low Energy Beam Transport (LEBT), immediately upstream of the Radio Frequency Quadrupole (RFQ), and another chopper in the Medium Energy Beam Transport (MEBT), downstream of the RFQ, where the beam energy is approximately 2.5 MeV. Clean bunching requires fast rise and fall time and low jitter to minimize the amount of charge in the ring extraction gap. The chopper systems operate at a burst frequency of 1 MHz and a burst width of greater than 1 ms and burst frequency of 60 Hz. The choppers have had historical reliability issues, especially in the LEBT system. This paper describes the development of reliable LEBT and MEBT choppers and the operational performance since SNS commissioning in 2006.

INTRODUCTION

A layout of the Spallation Neutron Source (SNS) at Oak Ridge National Laboratory is shown in Figure 1. The SNS consists of a Linear Accelerator (LINAC) which injects H^- beam pulses into a proton accumulation ring where they are extracted and transported to a liquid mercury target to generate neutrons for studying neutron sciences. The ion source in the front end system [1] produces an H^- beam that is chopped into mini-pulses for injection into the LINAC. The beam is accelerated through the LINAC and transported through the high energy beam transport (HEBT) section where it is injected into the accumulation ring. More than 1000 turns can be accumulated before the beam is extracted from the ring for transport to the mercury target. Four bipolar high voltage pulse generators in the Low Energy Beam Transport (LEBT) [2-4] section and two unipolar high voltage pulse generators in the Medium Energy Beam Transport (MEBT) [5-8] section create the beam mini-pulses.

The pulse generators and the structures they drive have had many reliability issues which have required extensive research and development to rectify. This paper summarizes the LEBT and MEBT chopper systems function, failure history, and development of reliable modules. It is focused on the reliability of the LEBT high voltage pulse generators used to apply pulses to the lens segments. Detailed descriptions of the LEBT and MEBT structure improvements can be found in the references.

*Work performed at Oak Ridge National Laboratory, which is managed by UT-Battelle, LLC, under contract DE-AC05-00OR22725 for the U.S. Department of Energy.

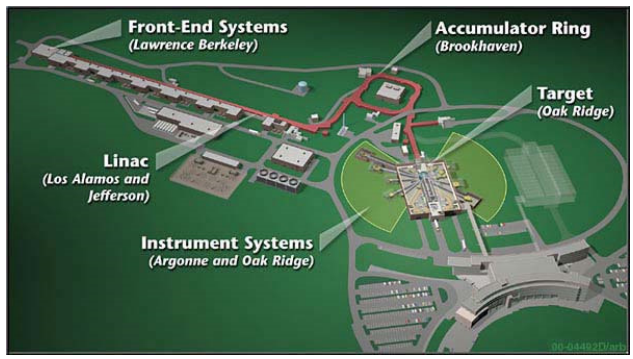


Figure 1: Layout of the Spallation Neutron Source in Oak Ridge, TN.

CHOPPER TIMING REQUIREMENTS FOR BEAM EXTRACTION

The choppers operate by generating fast rise/fall time high voltage pulses interspersed with periods of no high voltage, effectively deflecting the beam from the beamline to a target to generate gaps in the beam. The extraction kicker rise time sets the minimum gap required for the high voltage pulse generators used for chopping in the LEBT and MEBT. The beam gap in the accumulation ring must be clean and wide enough for the extraction kickers to fully turn on. If the head and tail of the beam in the ring are not sharp or the gap is not free of protons, the extraction kickers will partially deflect the beam during kicker turn on, causing activation of the extraction septum magnet.

The extraction kicker system consists of fourteen pulse forming networks (PFNs) located in the Ring Service Building, driving fourteen kicker magnets in the Ring Tunnel. Due to the design of the PFN, the rise time is fixed at approximately 200 ns. Figure 2 is a graph of the rise time of the extraction kicker magnet current.

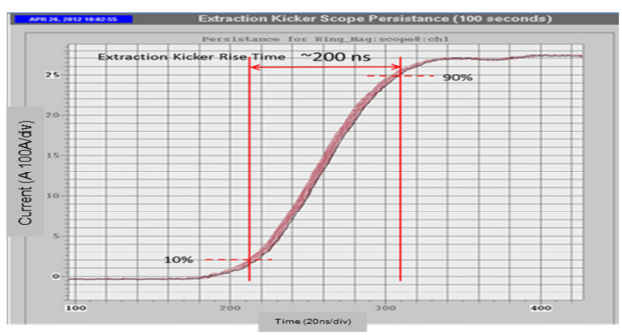


Figure 2: Extraction kicker rise time.

Copyright © 2013 CC-BY-3.0 and by the respective authors

The LEBT chopper structure is an electrostatic einzel lens split into four quadrants to deflect the beam to a diagnostic plate for a minimum of 200 ns to a maximum of 1000 ns, depending on the percentage of ring fill desired. [3] The chopping pattern rotates the beam around the diagnostic plate to limit heating. Figure 3 shows the timing sequence used to move the beam from one segment to another during either beam on or off time.

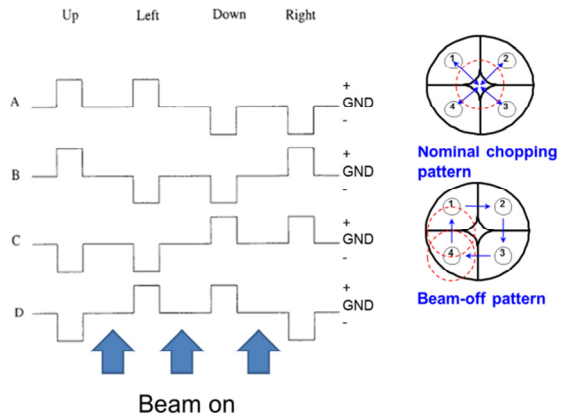


Figure 3: Four phase timing of LEBT chopper.

The LEBT chopper specifications require +/- 3 kV pulses with rise and fall times of < 50 ns and pulse widths varying from 200 ns to 1000 ns. The variable pulse widths provide for the ability to change the beam fill in the ring, beam ramping at the beginning of the macro-pulse and permits accelerator physics studies. See reference [4] for a discussion of the timing limitations of the LEBT high voltage pulse generators.

The MEBT chopper system consists of two high voltage pulse generators of opposite polarities to deflect the beam vertically. MEBT rise and fall times are specified to be less than 10 ns. The MEBT high voltage pulse generators [7-10] are used for sharpening the edges of the pulse and to clean the gap to minimize losses during extraction.

LEBT CHOPPER

The LEBT chopper system consists of four high voltage pulse generators each driving a segment of the einzel lens to deflect the beam. The lens is biased at near -50k Vdc for focusing and each segment is independently offset by another fraction of a 3 kVdc supply for steering. Figure 4 is a simplified block diagram showing the connections within the LEBT chopper system. Capacitive coupling is used to isolate the ground referenced pulse generators from the bias and steering voltage. A 20k Ohm resistor and the inductance of the cabling are used to isolate the bias and steering power supplies from the pulsed high voltage. A relay is used to disconnect the high voltage pulse generator from the structure.

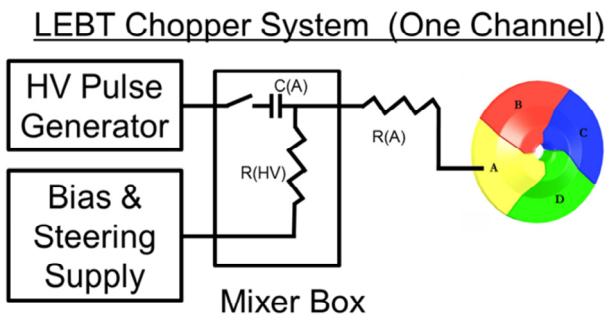


Figure 4: Block diagram of one channel of the LEBT chopper system

LEBT Structure

After very high arc rates in early 2007, the lens was redesigned with glue-free joints and 32 intersegment spark gaps to limit intersegment voltages to about 10 kV and to divert the energy away from the intersegment insulators [11]. In addition, the operational arc rate was reduced with high voltage conditioning and the addition of an automatic disconnect when more than 5 arc events occur in a 6 minute period.

LEBT High Voltage Pulse Generators

The LEBT high voltage pulse generators are a ¾-H bridge design where the capacitive load of the LEBT lens segment is either switched to the positive 3 kV rail, ground, or the negative 3 kV rail. The design uses eight high voltage metal oxide semiconductor field effect transistors (MOSFETs) stacked in series to create a single high voltage switch with enough voltage hold off to permit reliable operation during normal switching operation.

LEBT High Voltage Pulse Generator Failure Analysis

The high voltage pulse generators have experienced high failure rates since commissioning in 2006 with over 180 failures after 30,000 arc events since recording started in 2007.

Normally, a segment of the second lens arcs to ground, which is followed by intersegment arcs. Improvements to the LEBT structure reduced the number of arc events from approximately 8000 to 1000 per ~20 week long accelerator run cycle. The initial high voltage pulse generator failure count was 80 failures per run cycle. Failures of pulse generators only occurred when accompanied by an arc. Figure 5 is a chart of the LEBT high voltage pulse generator failures and arc event counts per run cycle. The rise in 2009 was likely caused by the aggressive increase in duty factor and beam current.

Copyright © 2013 CC-BY-3.0 and by the respective authors

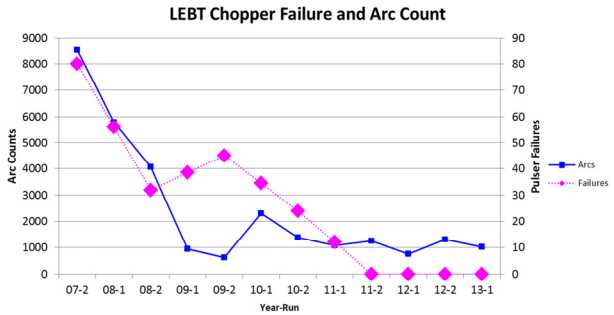


Figure 5: LEBT high voltage pulse generator MOSFET failures and arc events verses run cycle.

SNS has only six of these custom pulse generators in stock and four are used during operations. The two spares were enough to keep SNS running but repeated repairs of the MOSFETS and supporting components has irreparably damaged the printed circuit boards. The replacement time for a failed pulse generator is, at best, 1 hour when the failure occurs during normal business hours and up to 4 hours if it occurs when personnel are not already on-site.

LEBT Chopper Improvements

Multiple improvements to the high voltage pulse generators were tried up to 2011: the existing MOSFET snubber circuits were improved, transorbs on the output node and MOVs in the mixer box were added, and the series resistance was increased to limit the current. All of these resulted in limited improvements as seen in the failure rate in Figure 5.

Changes made during the summer shutdown of 2011 essentially eliminated failures. There have been three failures since 2011. None of these were for high voltage MOSFET failures: a diode isolation board had underrated parts installed, a timing logic board had a bad 1/4W resistor and a control voltage power supply failed after a lightning strike near the facility.

Failure Mode Analysis

MOSFETs can fail by two principle methods: over voltage or over current (thermal overheating). Our HV MOSFETs usually failed as a short. This implies that over voltage or punch through of the wafer was occurring. If the device failed from over current, it would fail as an open circuit when the wire bonds from the leads of the drain or source or the bulk semiconductor fuse open. Over voltage can be caused by the amplitude of the coupled arc voltage exceeding the individual MOSFET's high voltage hold-off rating.

An oscilloscope was added to capture and store every arc event. After more than 300 arc events a pulse generator failed. The oscilloscope traces in Figure a are examples where all high voltage pulse generators survived and Figure b where one did not. There is no significant difference between an event that caused a failure and one that did not. The amplitude, frequency, and shape of the arc voltage appearing at the pulse generator were similar.

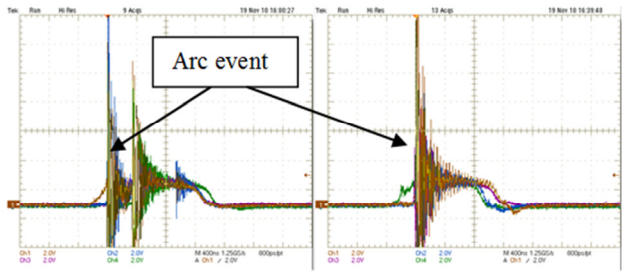


Figure 6: Examples of an arc event which did not result in a failure (Figure 6a) and one that did (Figure 6b).

The output voltage traces for all four pulse generators are shown overlaid to demonstrate the similar amplitude, duration and shape of an arc event. A detailed analysis of the energy transfer during an arc event is given in [5] and summarized here. Figure is a simplified schematic for analysis of the arc event equivalent circuit.

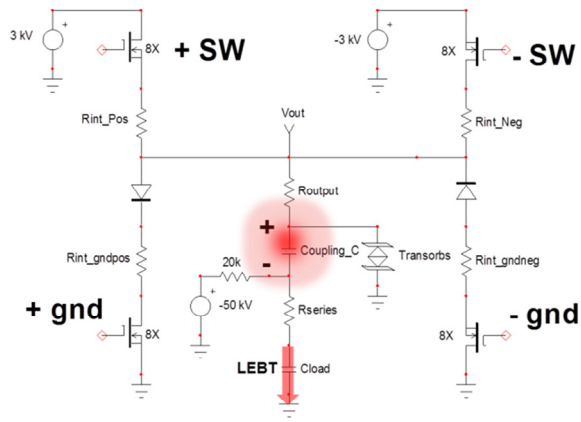


Figure 7: Simplified Schematic demonstrating an arc in the LEBT Structure and voltage reversal on the Coupling Capacitor.

The high voltage pulse generator 3kV power supplies do not supply enough voltage to exceed the 8kV rating of the stack and are therefore not a source of overvoltage failure. The 50 kV bias supply, however, could.

The coupling capacitor (Coupling_C) in the Mixer Box is charged to the dc bias voltage through the impedance of the pulse generator's high voltage circuit. LEBT structure arcing causes the load capacitance (Cload) to short, pulling the series resistor (Rseries) to ground. This causes the coupling capacitor's voltage to appear at the output of the pulser. The Transorbs and MOVs were sufficient to limit the voltage seen by the MOSFETs. Arc event simulations with a spark gap used in place of the LEBT structure showed that the voltage across the stack did not exceed the rating.

Gate Drive Latching

Another discovery was the realization that the fault could be in the gate drive circuit. The gate is turned on with a pulse through an isolation transformer and held on with a diode (D1) as shown in the schematic in Figure .

Copyright © 2013 CC-BY-3.0 and by the respective authors

This circuit is identical for all MOSFETs in each of the four legs of the ¾-H bridge. Another short pulse of negative polarity is sent to turn OFF the gate. The diode does not latch OFF the gate so the voltage decays back to zero after a few microseconds due the RC time constant of the gate capacitance and the series resistance.

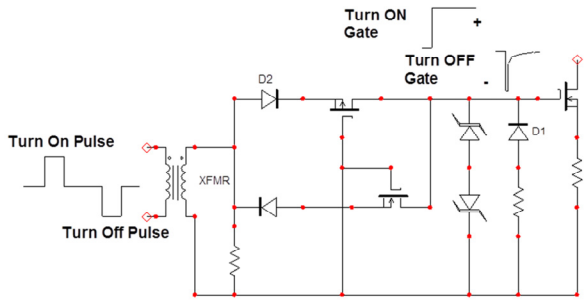


Figure 8: Gate drive schematic.

An arc event can cause a noise pulse in the low level drivers which results in a ringing pulse on the gate of each MOSFET. This places the switches in the high voltage legs at risk. One possibility is that a noise pulse turns ON all eight MOSFETs creating a shoot through condition where both the positive and negative MOSFETs are turned ON, resulting in high currents. This is not suspected as the cause of the failures because analysis of the failed devices determined the root cause to be due to over voltage not over current.

Another possibility is that the noise spike could latch ON only a few of the MOSFETs in a leg and leave OFF the others. This would force the remaining MOSFETs in the stack to hold off a higher voltage. During the normal operation each 1000 V rated MOSFET sees less than 750 V when the power supplies are charged to 3 kV. If two or more gates are latched ON the rest will have to hold off greater than the MOSFET's rating and fail. Transorbs were installed across the drain and source of the MOSFETs in the original design but the parasitic inductance of these devices likely made them ineffective snubbers for these fast transient events.

To simulate an arc event, a spark gap was used in place of the LEBT structure and triggered on command for multiple measurements. Measurements of the gate drive voltages during a simulated arc event showed many oscillations of the gate drive signal.

The oscillations could turn ON and OFF the device until they decayed lower than the gate threshold. If the last oscillation was above threshold for turn ON but lower than the turn OFF threshold the device would stay ON. In the summer of 2011 the diode was reversed in only the high voltage legs of the ¾-H bridge to latch OFF instead of ON. The decay rate was limited so as to exceed the maximum pulse width required for normal operation.

Rise/Fall Time Improvement

When the series resistance was increased during attempts to reduce failures, the rise and fall times on the LEBT structure increased to >100 ns, more than double the initial specification. By implementing the previously stated improvements, the series resistance of the circuit could be reduced, thereby decreasing the RC time constant. [6] The measured rise and fall times were reduced to less than 50 ns when measured on a simulated LEBT structure load as shown in Figure .

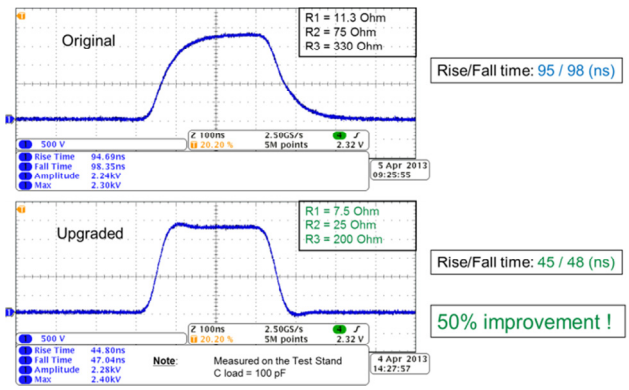


Figure 9: LEBT high voltage pulse generator rise/ fall time improvement chart.

The system with the reduced series resistance was installed during the summer 2013 maintenance period.

MEBT CHOPPER

The MEBT chopper system shown in Figure consists of two high voltage pulse generators of opposite polarities driving a transmission line structure into a 50 ohm load. The MEBT high voltage pulse generators were intended [7-10] to be used for both sharpening the edges of the pulse and to reduce the beam in the gap to minimize losses during extraction. The LEBT choppers were found to be more effective than anticipated so the MEBT choppers are primarily used for cleaning the gap.

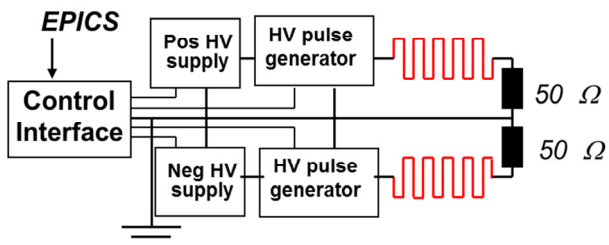


Figure 10: Block diagram of MEBT chopper system.

MEBT Structure

The MEBT rise and fall times were specified to be 10 ns. The pulse generators did achieve these from the start but the system was not impedance matched. The mechanical design of the structure [8] suffered failures due to water leaks, insufficient high voltage clearances and thermal performance issues.

In 2007 the structure was redesigned to eliminate these issues. [11] The new structure changed from the meander line design to a parallel plate transmission line type shown in Figure . The structure and HV pulse generators were impedance matched to reduce reflections of the fast HV edges from the pulse generators.

Copyright © 2013 CC-BY-3.0 and by the respective authors

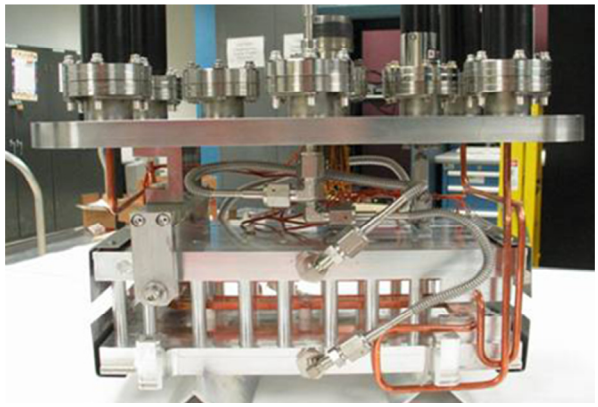


Figure 11: New MEBT structure design.

MEBT High Voltage Pulse Generators

The MEBT high voltage pulse generators are a two MOSFET series-switch design where the output resistive (50 ohm) load is either pulled to the high voltage rail or to ground. There is a positive pulse generator and a negative pulse generator that operate synchronously to assist the LEBT pulse generators in extraction gap formation.

Each high voltage pulse generator design uses five high-speed 1kV rated MOSFETs stacked in series for each leg to provide voltage hold off during normal operation. Improvements to the MEBT HV pulse generators include: matching the output impedance to 50 ohms by a custom cut copper bus (shown in Figure 12) upgrading the water cooled heat sinks and applying the LEBT gate drive latch technique described above.

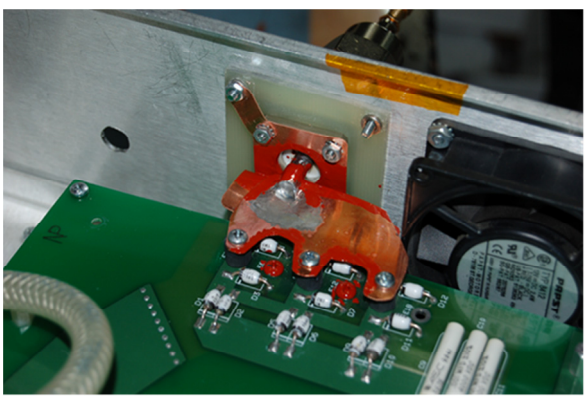


Figure 12: Matching 50 Ohm output impedance.

The pulse timing was changed so that the pulse generators were not ON during the pre-beam and beam OFF times to limit power dissipation in the MOSFETs.

SUMMARY

Continued development of and modifications made to the LEBT and MEBT fast chopper systems have greatly improved their reliability and therefore the availability of the SNS. The LEBT structure modifications and administrative controls to reduce arcing along with MOSFET triggering modifications have virtually eliminated high voltage pulse generator failures. This has permitted reducing the LEBT series resistance to values that meet the original rise and fall time specifications.

The improvements in the MEBT structure and impedance matching improved reliability of the structure. Additional development of the high voltage pulse generator cooling is still required.

ACKNOWLEDGMENT

The authors acknowledge the efforts of Sasha Aleksandrov, Doug Curry, Jeff Patterson and Charles Peters in the development and operation of the SNS fast choppers. In addition, we would like to thank the technicians Joshua Singleton and Jim Hicks for having the patience and skill to consistently repair and keep the choppers operational for years.

REFERENCES

[1] J. Staples, et al., "The SNS Front-end Accelerator Systems," Proceedings of the XIX International Linac Conference, 1998, Chicago, IL, USA, p 177.

[2] S. Nath, et al., "Beam Behavior through the SNS Chopper System," Proceedings of LINAC2002, 2002, Gyeongju, Korea, p. 130.

[3] J. Staples, et al., "The SNS Four-Phase LEBT Chopper," Proceedings of the 1999 Particle Accelerator Conference, 1999, New York, NY, p. 1961.

[4] V.V. Peplov, R. B. Saethre, "SNS LEBT Chopper Pulse Width Limitation", International Power Modulator and High Voltage Workshop, 2012 , San Diego, CA, USA p. 700.

[5] R. B. Saethre, V. V. Peplov, "SNS LEBT Chopper Improvements", in Proc. of the 2012 IEEE International Power Modulator and High Voltage Conference, San Diego, 2012, p.704.

[6] V.V. Peplov, R. B. Saethre, "Rise/Fall Time Enhancement of the Spallation Neutron Source LINAC LEBT Chopper System", International Pulsed Power Conference, 2013 , San Francisco, CA, USA p. awaiting publication.

[7] R. Hardekopf, et al., "Design, Construction, and Initial Operation of the SNS MEBT System," Proceedings of EPAC, 2004, Lucerne, Switzerland, p. 150.

[8] J. Staples, et al., "Design of the SNS MEBT," XX International Linac Conference, 1999, Monterey, CA, USA, p. 250.

[9] A. Aleksandrov, et al., "New Design of the SNS MEBT Chopper Deflector," Proceedings of PAC07, Albuquerque, NM, USA, p 1817.

[10] D. Oshatz, et al., "Mechanical Design of the SNS MEBT," Proceedings of the 2001 Particle Accelerator Conference, Chicago, IL, USA, p 1574.

[11] M.P. Stockli, et al., "Ramping Up the SNS Beam Power with the LBNL Baseline H- Source", CP1097, American Institute of Physics, Melville, NY, 2009, p. 223.

Copyright © 2013 CC-BY-3.0 and by the respective authors

Copyright © 2013 CC-BY-3.0 and by the respective authors

List of Authors

Bold papercodes indicate primary authors

— A —

Abeyratne, S. *MOPBA13*
Abliz, M. WEPSM09, WEPSM10, WEPSM11
Adli, E. *MOYBA1*, MOPAC02, MOPAC30, MOPAC38, MOPAC46, THYAA2, THOCA1
Adolphsen, C. WEOAA1, WEOBA1, WEPHO10, WEPMA10
Agladze, N.I. TUOBA1
Agustsson, R.B. TUOAB2, TUPSM27, *WEOCA2*, WEPBA17, WEPBA18, THOAA2, THPAC29, THPAC32, THPAC36
Ahrens, L. MOPBA04, TUPAC10, THPHO1
Akroh, A. MOZBA1
Al Marzouk, A.A. *MOPBA14*
Albert, F. *MOPAC21*, TUPMA10
Albright, S.C.P. *THODA1*
Alcorta, M. MOPSM02
Aleksandrov, A.V. *TUYBA1*, WEPBA15, WEPBA16
Alexahin, Y.I. THPBA19
Ali, M.M. *THPMA13*
Allezy, A.P. WEOAA1
Alt, D.M. MOPSM07, FRYBA2
Altinbas, Z. TUOCA2, TUPHO01
Amemiya, N. FRXB1
An, W. MOPAC38, MOPAC46, MOPAC47, THYAA2, THOCA1
An, Y.W. TUPBA03
Andersen, K.H. MOPMA04
Anderson, D.E. FRYBB2
Anderson, G.G. MOPAC43, TUPMA10
Anderson, J.E. WEZB1
Anderson, S.G. MOPAC43, TUPMA10
Andonian, G. MOOCB2, MOPBA17, MOPHO23, THPAC32, THPAC37
Andreev, N. THPBA22
Andrews, A. *TUPSM14*, MOPHO20, THPSM13
Anerella, M. TUOCA2, WEODA1, WEODA2, THPBA07, THPBA24
Ang, Z.T. WEPHO01
Ankenbrandt, C.M. TUPBA20, MOPAC26, MOPBA12, MOPMA21, THPHO19
Antipov, S.P. MOPAC24, MOPAC12, *MOPHO13*, *TUPMA08*, *THYBA1*
Antoine, S. THPBA03
Arai, H. FRXB1
Araki, S. TUPMA01
Arbelaez, D. WEOAA1
Arenius, D. WEOAA1, FRYBA1
Arimoto, Y. THPBA04, THPBA07
Arkan, T.T. *WEPAC29*
Arnold, N.D. THPHO03
Aronson, J.N. TUPHO01
Arsenyev, S. MOPAC25, WEPAC33, *WEPAC34*
Aryshev, A.S. TUPMA01
Aschenauer, E.C. TUPBA15
Aslaninejad, M. MOPMA05, THPSM10, THPSM11, THPSM12
Assadi, S. MOZAB1, *TUPAC26*, THODA2
Atoian, G. MOOBA2
Attenkofer, K. THPAC12, THPAC17
Avrakhov, P.V. *WEPAC14*
Awida, M.H. WEPAC21, WEPAC25, WEPAC29, *WEPAC32*, THPBA17

— B —

Baartman, R.A. *WEZBB1*
Baca, D. WEPHO14
Bacha, B. MOPHO17
Bachimanchi, R. TUPMA19
Back, B. MOPSM02
Back, J.J. THPMA11
Badakov, H. TUPSM27
Bai, M. TUPAC12, TUPBA04, *WETB1*, WEPBA05
Bai, S. TUPBA03
Bailey, B.J. TUOCB2
Baily, S.A. MOPMA18
Balbekov, V. THPHO12
Ball, M. TUPSM13
Bane, K.L.F. MOPAC30, *TUYB1*, WEOAA1, WEPAC46, *WEPBA19*
Banfi, D. TUPBA21
Baptiste, K.M. WEYA1
Barcikowski, A. WEOAB2
Barkley, W.C. WEPHO14
Barlow, D.B. TUPAC19
Barlow, R.J. THOBB2
Barov, N. WEPHO13, *THPSM14*
Barranco, J. TUPBA21
Bartnik, A.C. TUOBA1, WEOAA4
Bartolini, R. *MOOAB2*
Bartosik, H. FROAA3
Barty, C.P.J. TUPMA10
Bashkirov, V.A. WEOCB1
Bassi, G. *MOPBA03*
Baturin, S. MOPHO19
Batygin, Y.K. MOPMA14, MOPMA17, MOPSM05, TUPSM16, TUPSM17, TUPSM18
Baumann, T. FRYBA2
Bayer, E. *THPMA01*
Bazarov, I.V. MOPBA21, TUOBA1, TUOAB1, TUPMA15, WEOAA4
Beasley, P. THOBB2
Beaudoin, B.L. TUPAC31, TUPAC32, TUPAC33, FROAA1, FROAA6

Beebe, E.N. TUPHO01
Beeckman, W. *THPBA03*
Beezhold, W. THPSM21
Belkacem, B. THPAC10
Bell, G.I. *TUPHO02*
Bellavia, S. THPHO07
Bellodi, G. MOZBA1
Belomestnykh, S.A. TUOAA1, WEPAC06, WEPAC07, THPAC18, THPAC34, THPAC35, *THPHO06*
Ben-Zvi, I. MOPBA21, TUOAA1, TUPSM06, TUPSM07, TUPSM08, WEPAC06, THPAC18, THPAC34, THPAC35, THPHO06, THPAC12, THPAC17
Benatti, C. MOPSM07, FRYBA2
Benedetti, C. THOCA2
Benedetto, E. TUODB3
Bennett, C.W. THPAC19
Benson, S.V. WEPSM17
Bentley, P. MOPMA04
Berg, J.S. TUPBA10, TUPBA11, TUPBA13, WEODA2, *THPHO04*, THPHO05, THPHO12, THPHO13
Berg, K. TUOCB2
Bergstrom, J.C. MOPBA19
Berkaev, D.E. MOOAA2
Berls, B.L. MOPHO20, TUPSM14
Bernal, S. *TUPAC31*, FROAA1
Berrutti, P. *WEPAC21*, *WEPAC22*, *WEPAC23*, WEPAC29, WEPAC32
Berz, M. MOPBA11
Betts, S.M. MOPAC43
Bhattacharyya, P. THPMA09
Biedron, S. TUPSM09, WEPHO10, WEPMA01, WEPSM17
Billing, M.G. FROAA5
Biocca, A. TUOCB2
Bisognano, J. MOPHO26, *TUPMA19*
Bissen, M.J. TUPMA19
Björklund, E. MOPMA15
Black, A.T. TUOCB2
Blaskiewicz, M. MOZAA2, TUOAA1, TUXA1, TUPBA06, *FROAA2*
Blednykh, A. MOPBA03, MOPHO17, *WEPBA01*, *WEPBA07*
Blomberg, B.R. TUPSM24
Bluem, H. TUPSM04
Blum, E.B. MOPHO17
Bocher, P. THPBA03
Bogacz, S.A. TUPBA20
Bollen, G. THPBA12
Bonatto, A. *MOPAC01*
Bonatto, C. MOPAC01
Bondarenko, T.V. *THPSM08*
Boon, L.E. WEOAA3, WEPSM06, WEPSM07, *THPAC06*
Borden, T. MOPMA08
Borissov, E. WEPAC25, WEPAC29
Borland, M. MOYAB1, *MOPHO06*, *MOPHO07*, MOPHO10, MOPHO13, TUOBB2, TUPMA03, TUPMA04, WEOAA3, WEPSM06, WEPSM07, WEPSM12, WEPSM13, THPMA05, *TUPSM26*, *THPMA06*
Bosch, R.A. *MOPHO26*, TUPMA19, *TUPMA20*
Bossert, R. THPBA22
Boucher, S. TUOAB2, TUPSM28, WEOCB1, WEPBA18, *THOAA2*
Boulet, L.E. TUOAB1
Boulware, C.H. WEPAC33, THPAC35, THPHO06
Bowman, C. THPBA23
Bowring, D.L. WEPMA12, WEPMA16
Boyden, D. MOPAC17
Brandon, J.F. MOPMA20
Bratton, R.E. WEPHO14
Brau, C.A. TUPSM24
Brennan, J.M. MOZAA2, TUXA1, WEPMA25, THPHO07, THPHO08
Brice, S. TUPBA20
Briegel, C.I. THPAC20
Brindza, P.D. TUPAC28
Brooks, S.J. TUPBA13
Bross, A.D. *TUODB4*, TUPBA18, TUPBA20, THPBA08, THPBA09
Brouwer, L.N. *WEPBA12*
Brown, M. TUOAB1
Bruce, R. TUOCA1
Brüning, O.S. TUZAA2
Bruhwiler, D.L. *MOOCB2*, MOPBA17
Bruno, D. TUOCA2, *WEPHO05*
Brutus, J.C. *WEPAC06*, *WEPAC07*, THPHO06
Buaphad, P. MOPHO20, TUPSM14, THPSM16
Bucci, S. THOAB1
Bui, H. THPAC08, THPHO03
Bullock, B. WEPAC13
Bultman, N.K. MOPMA08, TUPSM20, WEOAB1, FRYBA1
Burkhardt, E. WEPAC05
Burrill, A. WEZAA2
Butler, N. WEOCA1, *THPBA11*
Byer, R.L. MOOBB2, MOPAC32
Bylinskii, I.V. WEPHO01
Byrd, J.M. WEOAA1

— C —

Calabretta, L. MOPBA05
Calanna, A. MOPBA05
Calic, S. WEPHO01
Campese, T.J. MOPHO25, THPAC32
Cancelo, G.I. TUODB2
Cappadoro, P.L. THPAC09
Carcagno, R.H. THPBA15, THPBA16

Cardona, J.F. WEPBA01
Cargnelutti, M. *THPAC04*
Carli, C. TUODB3
Carlsten, B.E. MOOAB1, TUPAC18, TUPAC21
Carneiro, J.-P. MOPMA13
Casagrande, F. THPBA13, FRYBA1
Casey, P.W. TUOCB2
Caspi, S. WEPBA12
Castilla, A. *WEPAC39*
Catelani, G. WEPAC12
Cesar, D.B. *MOPAC27*
Cesaratto, J.M. TUPAC25, FROAA3
Chae, Y.-C. TUOBB2, WEPSM06, THPMA05
Champion, M.S. WEPMA22, WEPMA23
Chang, X. *WEPHO13*, WEPMA11
Chao, Y.-C. THPAC01, THPBA01
Chase, B. TUODB2, WEPHO15, THPBA17
Cheban, S. THPMA09
Cheblakov, P.B. MOPHO17
Chen, A.Z. *TUPSM10*
Chen, C. TUOCB2
Chen, H.B. *WEYB4*
Chen, H.C. TUPBA09
Chen, J.F. MOPMA03
Chen, M. THPMA09
Chen, P. TUODB1
Chen, S.-H. MOOCB1
Chen, Y.C. THPAC36
Cheng, G. *WEPAC47*
Cheng, P. THPSM04
Cheng, W.X. MOPHO17, WEPBA06, THPAC10
Chiang, T.-C. MOPHO26
Chin, Y.H. *MOYBB1*
Choi, B.K. TUPSM24
Choi, J. MOPHO17
Choi, Y. MOPBA21, *TUPMA15*, TUPSM30
Chouhan, S. MOPMA07, THPBA12
Christensen, T. THOAB1
Chubar, O.V. TUPBA13
Chung, M. MOPBA06, *TUOBB1*, TUODA1, TUPAC15, WEPMA12
Church, M.D. TUPAC21, TUPSM12
Cianciosi, F. TUPSM27
Clarke, C.I. MOPAC38, MOPAC46, THYAA2, THOCA1
Clasby, B. WEPAC13
Clayton, C.E. MOPAC21, *MOPAC38*, MOPAC46, THYAA2, THOCA1
Clayton, J.E. WEPMA09
Colby, E.R. MOOBB2, TUOBA2
Coleman, A. THPBA28
Coleman, J.E. *TUPAC17*
Collins, C. MOZAB1
Collins, G. WEPHO08, WEPHO09
Collura, M.G. TUODA1
Colomb, D. TUOCB2
Comblin, J.F. MOZBA1
Comeaux, J. MOZAB1
Compton, C. WEPAC17, FRYBA1
Conde, M.E. TUPSM05, WEPMA08
Constan-Wahl, D. THPAC20, THPHO14
Conway, J.V. FROAA5
Conway, Z.A. WEOAB2, WEPAC05
Cook, A.M. MOPSM06
Cook, N.M. *MOPAC34*, *WEPMA25*, *THPAC33*
Cooper, C.A. WEZB1
Cooper, K. FRYBA2
Corde, S. MOPAC38, MOPAC46, THYAA2, THOCA1
Cork, C.W. WEYA1
Corlett, J.N. *TUZB1*, *WEOAA1*, WEYA1
Cormier-Michel, E. MOOCB2
Cornacchia, M. TUPAC31, FROAA1
Corwin, T.M. THPAC09, THPAC14, THPAC15
Costanzo, M.R. TUOCA2
Cousineau, S.M. WEODB2
Cowan, E.E. *TUPAC13*
Craievich, P. TUPSM27
Crawford, M.T. TUPAC17
Creely, P. THOAB1
Crisp, J.L. *THPAC20*, THPHO14
Crittenden, J.A. WEPBA09, FROAA5
Cultrera, L. TUOAB1
Current, M.I. WEYB2
Cywinski, R. THOBB2
Czajkowski, J. TUPSM13

— D —

D'Ambra, J.A. THPHO09
D'Elia, A. *TUPAC07*
Dal Forno, M. WEPMA01
Dale, D. WEPHO01
Dalesio, L.R. MOPHO17
Dallin, L.O. WEPSM05
Damborsky, K.C. MOZAB1
Daniels, C.S. WEOAA1
Daniels, J. THYAA1
Danilov, V.V. MOODB1, *WEPBA16*
Dash, R. *TUPAC02*
Davidsaver, M.A. MOPHO17
Davidson, A.W. *MOPAC39*
Davidson, K.D. FRYBA1
Davidson, R.C. TUPAC24
Davis, J. WEPHO14
Davydenko, V.I. MOOBA2
Dawson, W.C. TUOCA2, WEPBA05
Dayton, E.T. TUPMA10
De Long, J.H. MOPHO17
De Monte, V. THPHO08
De Santis, S. WEOAA1, WEYA1
De Silva, S.U. *WEPAC40*, WEPAC41, WEPAC43
Decker, F.-J. MOPAC30

Decker, G. MOPHO08, WEOAA3, WEPSM04, THPAC08, THPHO03
Decyk, V.K. MOPAC47
DeFazio, J. THPAC17
DeFord, J.F. *THPBA29*
DeGraff, B. THPBA28
Dehnel, M.P. *THOAB1*
Deibele, C. FRYBB2
Deitrick, K.E. WEPAC42
Dejus, R.J. WEOAA3, WEPSM06, WEPSM08, WEPSM09, WEPSM10, THPAC06
DeKamp, J. FRYBA1, THPBA12
Delahaye, J.-P. MOPAC38, MOPAC46, *TUPBA20*, THYAA2, THOCA1
Delayen, J.R. WEPAC39, WEPAC40, WEPAC41, WEPAC42, WEPAC43
Delgiusto, P. WEPMA02
Delp, W.W. WEOAA1
DeMello, A.J. WEPMA03, WEPMA16, WEPMA19, WEPMA21, WEPMA26
Denes, P. WEOAA1
Denisov, D.S. TUPBA20
Densham, C.J. TUYAA2
Derbenev, A.A. MOPHO17
Derbenev, Y.S. TUPAC28, THPHO19
Deriy, B. WEPSM08, WEPSM09, WEPSM11
Deshmukh, A. THYAA1
Dhakal, P. WEPAC01
Dhanaraj, N. THPBA14
Di Lieto, A. WEPHO05
Dimitrov, D.A. *MOPBA21*, TUPMA15, TUPSM30
Dimitrov, V.I. THPSM21
Dimov, V.A. MOZBA1
Ding, X.P. *THPMA10*, *THPMA11*
Ding, Y. WEOAA1
Dobashi, K. THPSM02
Dobbins, J. TUOBA1
Domingo, S. THOAB1
Donahue, R.J. WEOAA1
Donley, L. TUPMA03
Dooling, J.C. WEOAA3, WEPSM06, *THPMA05*
Doolittle, L.R. WEOAA1, WEYA1
Doose, C.L. WEOAA3, WEPSM06, THPAC07, *THPBA05*, *THPBA06*
Doran, D.S. WEPMA08
Dover, N. MOPAC34, THPSM12, THPSM13
Downer, T. THPSM16
Downey, J.S. WEPSM14
Doyle, J.A. WEYA1
Draganić, I. MOPMA14, MOPMA17, MOPSM03, *TUPSM16*, TUPSM18, *THPAC23*
Dragt, A. J. *THAP1*
Drees, K.A. TUOCA2, TUPAC11, TUPBA06, TUPBA08
Drewyor, B. FRYBA1
Drury, M.A. WEZAA2
Duan, Z. *WEPBA13*
Dudas, A. WEPBA15, WEPHO16, WEPHO17, WEPHO18, THPBA24
Dudnikov, V.G. *MOPAC26*, *TUPSM22*, *WEPBA15*
Duffy, L.D. MOOAB1
Duggins, D.O. WEPBA09
Dunham, B.M. TUOBA1, TUOAB1, WEOAA4
Dunning, M.P. WEOBA1
Durickovic, B. THPAC20, *THPHO14*, FRYBA2
Duris, J.P. TUPAC29, *TUPMA16*
Dusatko, J.E. TUPAC25
Dutheil, Y. *MOPBA04*, MOPBA05, *TUPAC10*

— E —

Eaton, D.W. TUPSM11
Eckman, C.F. *THPSM16*, MOPHO20, TUPSM14
Eddy, N. THPAC20, THPHO23
Edelen, J.P. *TUPSM09*
Edwards, R.L. MOPAC25
Efremov, M.Y. TUPMA19
Eichhorn, R.G. *WEPAC11*, *WEPAC13*, THPMA07
Eichten, E. TUPBA20
Eisen, E.L. WEPHO08
Eisert, D. TUPMA19
Ekdahl, C. TUPAC17
Eliasson, B. MOOCB1
Elliott, K. FRYBA1, *WEPAC18*
Ellison, J.S. MOPBA09
Elson, S. MOPAC25
Emery, L. MOPHO08, *MOPHO09*, TUOBB2, TUPMA03, WEOAA3, WEPSM06, WEPSM07, WEPSM12
Emma, P. MOPHO12, MOPHO15, WEOAA1
Endo, A. THPSM03
England, R.J. MOOBB2, *MOPAC28*, MOPAC31, MOPAC32, MOPAC33, MOPAC38, MOPAC46, THYAA2, THOCA1
Ent, R. TUPAC28
Erdelyi, B. MOPBA13, MOPBA15, MOPBA14, MOPBA16
Erickson, N. TUOAB1
Eriksson, M. MOPHO05
Erokhin, A.I. MOPHO17
Esarey, E. THOCA2
Escallier, J. WEODA1, THPBA07
Eshraqi, M. FRYAA2
Evtushenko, P.E. *WEZAA1*, WEPSM17

— F —

Fabris, A. WEPMA01, *WEPMA02*
Facco, A. WEPAC03, FRYBA1
Faillace, L. TUOAB2, *TUPSM27*, TUPSM28, THOAA2, *THPAC29*
Fang, Y. MOPAC02, *MOPAC49*
Farkas, Z.D. MOPAC30
Fathy, A.E. WEPMA22, WEPMA23

Fedotov, A.V. *TUOAA1*, *WEPBA08*
Fedurin, M.G. MOPAC24, MOPHO19, MOPHO25, TUPMA08, THPAC32
Felch, S.B. *WEYB2*
Feldman, D.W. FROAA1
Fellenz, B.J. THPAC20
Ferguson, P. WEPHO09, *WEPMA09*
Fernandes, H.C. *THPAC09*, *THPAC10*
Ferracin, P. *FRYAB1*
Filippetto, D. WEOAA1, WEYA1
Fiorito, R.B. WEPBA20, FROAA1
Firebaugh, J.D. TUPSM13
Fischer, W. TUXA1, TUOCA2, TUPBA06, TUPBA07, TUPHO01, THPHO10
Fisher, A.S. MOPAC38, MOPAC46, THYAA2, THOCA1
Fisher, M.V. TUPMA19
Fisher, S.E. MOPAC43, TUPMA10
Fite, J.M. MOOBA2
Fitsos, P. THPMA14
Flanagan, G. WEPMA12, *THPBA22*, THPBA23, THPBA24, THPBA26
Flanz, J. *THOBB1*
Fliller, R.P. MOPHO17, TUPMA07
Floyd, J.G. WEOAA1
Foley, M.H. WEPAC25
Folkman, K. MOPHO20, TUPSM14
Fonseca, R.A. MOPAC39, MOPAC47
Forest, F. THPBA03
Fors, T. THPHO03
Fortgang, C.M. MOPMA14, MOPMA17, MOPSM05, TUPSM16, *TUPSM17*, *TUPSM18*
Fox, A.D. WEPAC20, THPBA13
Fox, J.D. TUPAC25, FROAA3
Frak, B. TUOCA2
Frazee, R. MOPMA08
Frederico, J.T. MOPAC38, MOPAC46, THYAA2, THOCA1
Freemire, B.T. *TUODA1*, WEPMA12
Freyberger, A. THPMA13
Frigola, P. MOPHO25, TUPSM27
Frisch, J.C. *FRTB1*
Frolov, D. THPBA17
Fu, S. *MOZBA2*, TUODB1
Fuerst, J.D. WEPAC01, THPAC07
Fujimoto, T. FRXB1
Fujita, T.F. FRXB1
Fujiwara, T. THPSM02
Fukasawa, A. TUPSM27
Fukuda, M.K. *TUPMA01*
Full, S.J. *TUOBA1*
Furukawa, T. FRXB1
Furuta, F. THPMA07

— G —

Gabella, W.E. TUPSM24
Gabriel, G. TUOAB1
Gagliano, J. WEOAA3
Gai, W. MOPHO19, TUPMA08, TUPSM05, WEPMA08
Galambos, J. WEPBA16, *FRYAA1*
Galt, M.D. THPAC19
Gamage, B.R.P. THPHO21
Ganetis, G. WEPHO05
Ganni, V. FRYBA1
Gao, J. TUPBA03
Gaowei, M. THPAC34
Garcia-Bonilla, A.C. *WEPBA01*
Garnett, R.W. *MOPMA14*, MOPMA17, MOPSM05, TUPSM16, TUPSM17, TUPSM18
Gassner, D.M. TUOAA1, TUOCA2, TUPHO01, TUPSM06, TUPSM08, THPAC13
Gaudreau, M.P.J. WEOCA1, WEPHO11, WEPHO12, THPBA11
Ge, G.M. *WEPAC09*, *WEPAC10*, WEPAC11, THPMA07
Ge, L. MOPBA18
Geddes, C.G.R. THOCA2
Gee, A.J. *MOPBA15*
Gelmetti, F. WEPMA02
Geng, H. TUPBA03, THPSM04
George, G. MOPHO17
Gerbick, S.M. WEOAB2
Gessner, S.J. MOPAC02, *MOPAC30*, MOPAC38, MOPAC46, THYAA2, THOCA1
Ghosh, A.K. THPBA07, THPHO09
Gibson, D.J. MOPAC43, TUPMA10
Gibson, P.E. FRYBA1
Gilardoni, S.S. TUPAC06
Gilpatrick, J.D. THPAC25, THPAC26
Gilson, E.P. TUPAC24
Ginsburg, C.M. WEOAA1, WEPAC29
Gioia, J.G. TUPSM16
Glasmacher, T . FRYBA1
Gluskin, E. WEOAA3, WEPSM08, WEPSM09
Gong, C. THPAC01
Gong, C. *MOPAC41*
Gonin, I.V. *WEPAC25*
Gonnella, D. THPMA07
Gonsalves, A.J. THYAA1, THOCA2
Gorlov, T.V. WEPBA16
Grabenhofer, A.F. TUPSM11
Grandsaert, T.J. THPAC36
Granemann Souza, E. MOZBA1
Grassellino, A. *WEZAA3*, *THAP3*
Green, M.A. *THPBA12*
Green, M.A. MOPHO26, TUPMA19
Greenway, W.G. MOPAC19
Grender, I. TUPSM20
Grimm, C.J. WEPAC25, WEPAC29
Grimm, T.L. *WEYB1*, WEPAC06, WEPAC33, THPAC35, THPHO06

Grimmer, J.H. WEPSM10
Grisham, L. TUPAC24
Grote, D.P. THPHO13
Gu, X. *TUOCA2*, *TUPHO01*
Gubeli, J.G. THPMA13
Gulliford, C.M. *WEOAA4*
Gunion, R.F. TUOCB2
Guo, J. WEPHO17
Guo, W. MOPHO17, THPAC10
Guo, Y.Y. TUPBA03
Guo, Z. THPSM04
Gupta, R.C. THPBA24, THPBA25
Gurov, S.M. *MOPBA01*, MOPHO17

— H —

Ha, K. MOPHO17
Haber, I. TUPAC32, FROAA1
Haeuser, J. MOPMA14, MOPMA17
Hahn, H. THPHO10
Haj Tahar, M. *MOPBA05*
Hall, D.L. THPMA07
Hall, M. THPMA14
Hall, M.J. MOPMA15
Hama, H. THPBA03
Hamdi, K. TUOCA2, TUPHO01, THPHO09
Hamm, R.W. *FRZAP1*
Hammond, N.P. MOOAB2
Hanlet, P.M. TUODA1, WEPMA03, WEPMA16
Hao, Y. TUPBA13
Hara, Y. FRXB1
Harder, D.A. THPAC09, THPAC14, THPAC15
Harkay, K.C. *WEOAA3*, *WEPSM06*, *WEPSM07*, THPAC06, THPAC07
Harkins, J.P. WEOAA1
Harms, E.R. WEPAC29
Harris, G.L. WEYA1
Harris, J.R. MOPAC07, TUPSM09, WEPSM17, *THPAC19*
Harrison, M.A. MOPBA17, *MOPHO25*
Hartemann, F.V. TUPMA10
Hartzell, J.J. *TUOAB2*, WEOCA2, WEPBA18, THOAA2, THPAC29
Harwood, L. *MOZAA1*, WEZAA2
Hasse, Q.B. WEOAA3, THPAC07
Hast, C. WEOBA1
Haynes, W.B. WEPAC33
He, P. THPAC09, THPAC14, THPAC15
He, Y. WEPAC11, THPMA07
He, Y. THPSM04
He, Z.Q. *TUPAC14*, WEPAC03, *THPHO01*
Heath, C.E. MOPAC25
Heese, R. TUPMA07
Hegelich, B.M. WEOCB1
Held, B.L. THPBA29
Henderson, S. *MOXAP1*, MOPAC16, WEZB1
Henry, J. WEPAC47
Henry, P.F. MOPMA04
Hertlein, M.P. MOPHO22
Hettel, R.O. *MOYAB1*
Hidaka, Y. THPAC16
Hidding, B. MOOCB2
Higashi, N. WEODA1
Higo, T. TUPAC07
Hinode, F. THPBA03
Hirshfield, J.L. WEPHO19, WEPMA28
Ho, K.M.V. THPMA07
Ho, L.V. *TUPAC29*
Hock, J. TUOCA2, TUPHO01
Hocker, A. WEPAC29
Hocker, H.M. THPBA07
Höfle, W. FROAA3
Hoff, L.T. TUOCA2, TUPHO01
Hoff, M.D. *WEPMA19*, WEPMA20, WEPMA21
Hoffstaetter, G.H. *WEOAA2*, WEPAC09, WEPAC10, WEPAC11, THPMA07
Hofler, A.S. *THTB1*
Hogan, J. *WEZAA2*
Hogan, M.J. MOPAC02, MOPAC38, MOPAC46, THYAA2, THOCA1, *THAP2*
Holland, K. FRYBA1
Holland, P.R.N. THPSM11
Holm, A.I.S. MOPMA04
Holmes, A.D. THPAC19
Holmes, J.A. *WEODB2*
Holmes, S.D. *MOPMA09*, TUYAA1
Holzbauer, J.P. WEPAC01
Honda, Y. TUPMA01
Hopper, C.S. *WEPAC42*
Hovater, C. *TUZBA1*, TUPMA19, WEZAA2
Howell, M.P. *THPBA28*
Hrovatin, R. THPAC04, THPMA04
Hseuh, H.-C. MOPHO17
Hu, Y. MOPHO17
Huang, C. *MOPAC23*, *TUPAC18*, TUPMA13
Huang, G. WEOAA1, WEYA1
Huang, H. MOPBA04, TUOAA2, TUPAC10
Huang, R. WEYA1
Huang, T. TUODB1
Huang, W.-H. TUPSM03
Huang, Y. WEPAC06, WEPAC07, THPHO06
Huang, Z. MOPAC28, WEOAA1
Hubbard, W.A. TUOAB2
Huber, P. TUPBA20
Hughes, C. *THPSM13*
Hulsart, R.L. TUPBA08
Hummelt, J.S. WEPBA13, WEPBA14
Hunziker, S. THPMA04
Hurh, P. MOPAC16
Hyde, C. TUPAC28

— I —

Insepov, Z. WEPMA07

Ishibori, I. THPSM01
Ishizaka, T. THPSM01
Ivanov, A.A. MOOBA2
Ivanov, B.L. TUPSM24
Ivanov, E.V. WEPHO03, WEPHO04
Ivanyushenkov, Y. WEOAA3, WEPSM06, THPAC07, *FRYBB1*
Ives, L.R. *WEPHO08*, WEPHO09, WEPMA09
Iwasaki, M. THPBA07
Iwata, Y. *FRXB1*

— J —

Jackson, R.H. WEPHO09
Jacobs, K. MOPHO26, TUPMA19
Jacobson, B.T. TUOBB4
Jain, A.K. TUOCA2, WEODA1, THPBA07
James, G. THOAB1
Jamilkowski, J.P. TUOCA2
Jana, M.R. TUODA1, *WEPMA12*
Jarvis, J.D. TUPSM24
Jaski, M.S. WEPSM06, *WEPSM08*, *WEPSM09*, WEPSM10, WEPSM11, THPAC06
Jaski, Y. WEPSM14
Jecks, R. WEPAC06
Jehanno, P. THPBA03
Ji, Q. WEOBB2
Jiang, H. *TUODB1*
Jiang, Y. *WEPMA28*
Jimbo, K. *WEPBA02*, THPHO01
Jin, J. TUOCB2
Jing, C.-J. TUPSM05, WEPMA08, MOPAC12, MOPHO19, TUPMA08
Jing, Y.C. TUPBA14, TUPBA15
Jivkov, P. THPBA03
Jobe, R.K. MOPAC30, WEOBA1
Johnson, D.E. MOPMA13, TUYAA1
Johnson, J.B. *THPAC24*
Johnson, M.J. WEPAC20, THPBA13, FRYBA1, *TUPSM20*
Johnson, R.P. MOPAC26, TUODA1, TUPSM22, WEPHO15, THPBA22, *THPBA23*, THPHO19
Jones, R.M. TUPAC07
Jones, S. FRYBA1
Jongen, Y. *THYBB1*
Jordan-Sweet, J. THPAC12
Joshi, C. MOPAC02, MOPAC21, MOPAC38, MOPAC39, MOPAC41, MOPAC44, MOPAC45, MOPAC46, THYAA2, THOCA1
Joung, M.J. *WEPAC04*
Jug, G. THPAC04
Jung, J.-Y. WEOAA1

— K —

Kaducak, M. MOPMA09, TUYAA1
Kadyrov, R.A. MOPHO17
Kahn, S.A. THPBA22, *THPBA24*, *THPBA25*, *THPBA26*
Kaluzny, J.A. WEPAC01
Kanareykin, A. MOPAC12, MOPHO19, TUPMA08, WEPAC14
Kang, H.-S. *TUZB2*
Kang, Y.W. WEPMA22, WEPMA23
Kankiya, P. TUPHO01
Kapin, V.V. THPBA19
Kaplan, D.M. TUPBA20
Kara, A. THPAC19
Karimov, R. WEPHO08
Karkare, S.S. *TUOAB1*, MOPBA21, TUPMA15
Karnaev, S.E. MOPHO17
Kasa, M. WEOAA3, WEPSM06, THPAC07, THPBA05, THPBA06
Kasaev, A.S. MOOAA2
Kashikhin, V.S. WEPMA14
Kashikhin, V.V. *THPBA14*, THPBA19
Kasley, P.A. TUPSM13
Katsouleas, T.C. MOPAC10, MOPAC30
Kaufman, J.J. WEPAC13
Kay, J. MOOAB2
Kayran, D. TUOAA1, THPAC13, THPHO06
Kazakevich, G.M. *WEPHO15*
Kazakov, S. WEPHO19
Keane, R.T. THPAC08
Kedzie, M. WEOAB2
Keil, R.G. TUPMA19
Kellams, J.N. MOZAB1
Kelly, M.P. WEOAB2, WEPAC05
Kempkes, M.K. WEOCA1, THPBA11
Kephart, R.D. MOPMA09, TUYAA1, WEOAA1, *WEZB1*
Kewisch, J. TUPSM07, WEPBA05
Khabiboulline, T.N. WEPAC21, WEPAC22, WEPAC23, WEPAC25, WEPAC29, WEPAC32
Khalil, N.Z. *TUPBA26*
Khan, V.F. TUPAC07
Kharkov, Y. MOODB2
Kilpatrick, B.M. WEPAC13
Kim, A. TUOAB1
Kim, D.G. TUPAC04
Kim, E.H. TUPAC04
Kim, H.J. WEPAC04
Kim, J.-W. TUPAC04, THPAC03
Kim, J.Y. *TUPAC04*, *THPAC03*
Kim, K.-J. *THAP4*
Kim, M. TUPAC04, THPAC03
Kim, M. TUPAC04
Kim, S.-H. THPBA28
Kim, S.H. WEPSM06
Kim, S.H. WEOAB2, *WEPAC05*
Kim, Y. *MOPHO20*, TUPSM14, WEPBA18, THPSM16

Kimura, T. WEPHO08
Kinross-Wright, J. *WEPHO11*, THPBA11
Kirk, H.G. TUPBA09, TUPBA10, TUPBA11, TUPBA20, THPHO11, THPMA10, THPMA11
Kirz, J. MOPHO22
Kiselev, V.A. MOPBA01
Kishek, R.A. WEPBA20, *FROAA1*, FROAA6
Kitegi, C.A. THPAC09, THPAC14, THPAC15
Kittimanapun, K. FRYBA2
Kiupel, G. THPAC20, THPHO14
Klaus, A. THPMA01
Klebaner, A.L. WEOAA1
Klein, M. TUZAA2
Klein, M. MOPBA19
Kleman, K.J. TUPMA19
Klenov, V.S. MOOBA2
Kling, N.A. TUXA1
Klingbeil, H. THPMA01
Ko, C. MOPBA18
Koeth, T.W. TUPAC32, FROAA1
Koiso, H. WEODA1, THPBA04
Kolmogorov, A. MOOBA2
Kolski, J.S. *MOPMA15*, *TUPAC19*, *TUPAC20*
Koop, I. MOOAA2, WEPBA04
Koscielniak, S.R. *MOOBA1*, WEPHO01
Kosciuk, B.N. THPAC10
Koshiba, Y. WEOBA2
Kostin, R.A. WEPAC14
Kotelnikov, S. THPBA15
Kotzian, G. FROAA3
Kourbanis, I. MOPAC16, MOPMA09
Kovach, P. WEODA2
Koyama, K. THOBA4
Krafft, G.A. THPMA13
Kramasz, T.D. WEYA1
Krasnov, A.A. WEPHO03, WEPHO04
Krasnykh, A. WEPHO18
Krause, S.W. MOPSM07, THPAC20, THPHO14, FRYBA2
Krave, S. THPBA22
Krinsky, S. MOPBA03, WEPBA06, WEPBA07
Kruy, T.L. WEPSM14
Kubo, K. TUPBA25
Kürzeder, T. WEPAC13
Kunz, J.D. MOPBA10
Kurennoy, S.S. MOPMA14, *MOPMA16*, MOPMA17, MOPSM05, TUPSM16, TUPSM17, WEPAC33
Kuroda, R. WEOBA2, *WEOBB1*
Kusche, K. THPAC32
Kustom, R. WEPSM06, WEPSM07
Kutsaev, S.V. WEOAB2, WEPMA05
Kuzikov, S.V. *WEPSM02*, *WEPSM04*
Kwan, T.J. MOPAC23, TUPAC18, TUPMA13
Kwiatkowski, S. TUPMA09, WEYA1
Kyrpotin, A.N. MOOAA2

— L —

Laird, R. THPHO03
Lallement, J.-B. *MOZBA1*
Lambert, A.R. WEPMA19, *WEPMA20*, WEPMA21
Lambiase, R.F. TUOCA2, TUPHO01, WEPHO05
Lamm, M.J. THPBA14
Lang, J.C. WEOAA3
Lanzoni, J.A. FROAA5
Lapi, S.E. *THYBB2*
Lapierre, A. MOPMA07, MOPSM07, FRYBA2
Larose, H. WEOCB2
Latina, A. TUPAC07
Lawler, J.E. MOPHO26
Lawton, D. THPBA12
Laxdal, R.E. WEPHO01, THPAC01, THPBA02, FRYBA1
Lebedev, V.A. MOPAC16, MOPMA09, TUYAA1, *TUODA2*, TUPSM10, THPHO23
Lebrun, P. MOPBA24
Lee, C. MOPAC28
Lee, H.-J. TUPAC15
Lee, S.-H. WEPSM14
Lee, S.-Y. TUPBA18, TUPBA04
Leemann, S.C. *MOPHO05*, TUPMA02, *WEPSM05*
Leemans, W. *THYAA1*, THOCA2
Lefferts, R.S. THPAC33
Legg, R.A. TUPMA19, TUPMA20
Leitner, D. THPAC20, THPHO14, FRYBA1, MOPMA07, MOPSM07, *FRYBA2*
Leitner, M. MOPMA08, TUPSM20, WEPAC20, THPBA13, FRYBA1
Lellinger, R.E. WEYA1
Lemut, P.L. *THPMA04*
Lenkszus, F. TUPMA03, THPHO03
Leonova, M.A. TUODA1, WEPMA12, WEPMA16, *THPHO15*
Leray, M.J. THPBA03
Letchford, A.P. MOPMA05
Lettry, J. MOZBA1
Leveling, A.F. MOPMA21
Lewellen, J.W. *MOOAB1*, TUPSM09, THPAC19
Lewis, S.M. WEPBA14
Li, D. TUYAA1, WEOAA1, WEPMA03, WEPMA16, WEPMA19, WEPMA20, WEPMA21, WEPMA26
Li, F. TUODB1
Li, H. WEOBA1
Li, K.S.B. FROAA3
Li, N. TUOCB2
Li, P. TUODB1
Li, R.K. TUOBB4, TUPAC29, TUPMA16, TUPSM03, *THOAA1*, THPAC32, THPAC37
Li, S.Z. MOPAC02, MOPAC38, MOPAC46,

THYAA2, THOCA1
Li, Y. TUOBA1, WEPBA09, FROAA5
Li, Z. MOPBA18, WEPAC40, WEPAC43, WEPAC44
Li, Z. THPSM04
Liang, X. *THPAC12*, THPAC35, THPAC18, THPHO06, THPAC17
Liaw, C.J. *THPHO07*, *THPHO08*, THPHO10
Licciardi, W. THPAC09, THPAC14, THPAC15
Lidia, S.M. MOPAC19
Liepe, M. WEZBA1, WEPAC11, WEPAC12, THOBA2, THPMA07
Lill, R.M. THPAC08
Lillard, B. TUOAB1
Limborg-Deprey, C. *WEOBA1*
Lin, A. *MOXBP1*
Lin, F. *TUPAC28*
Lin, L.Y. MOPSM07, FRYBA2
Lindberg, R.R. THPMA05
Lindroos, M. *FRYAA2*
Lipa, R. *THPHO03*
Lipton, R.J. TUPBA20
Litos, M.D. MOPAC02, MOPAC30, MOPAC38, MOPAC46, *THYAA2*, THOCA1
Litvinenko, V. TUOAA1, TUPBA13, TUPBA15, WEPAC06, WEPAC07, THPHO06
Liu, A. *TUPBA18*
Liu, C. *TUPBA05*, *TUPBA06*, TUPBA08, TUPBA13, *THPAC13*
Liu, C.-S. MOOCB1
Liu, H.C. TUODB1
Liu, T.-C. *MOOCB1*
Liu, W. TUPSM05
Liu, X. TUOBA1, WEPBA09
Liu, Y. WEPBA16
Liu, Z. TUPAC14, WEPAC03, THPMA02
Lizon, D. C. MOPAC25, WEPAC33
Lombardi, A.M. MOZBA1
Lopes, M.L. WEODA2, THPBA22, THPBA26
Lopes, N.C. MOPAC02
Lopes, S.R. MOPAC01
Loseth, B.T. MOPBA11
Lou, T.P. WEOAA1
Louie, W. MOPHO17, WEPHO05
Lu, F. MOZAB1
Lu, W. MOPAC38, MOPAC46, MOPAC47, THOCA1, MOPAC39, THYAA2
Lu, X.H. *TUPSM03*
Ludewigt, B.A. WEOBB2
Luo, T.H. WEOAA1, WEPMA16, *WEPMA26*
Luo, Y. *TUXA1*, TUOCA2, TUPBA04, *TUPBA07*, TUPBA14, TUPBA15, TUPHO01
Luo, Y. *MOPSM01*
Lyles, J.T.M. *WEPHO14*
Lysenko, A.P. MOOAA2

— M —

Macek, R.J. TUPAC19, TUPAC20
Machicoane, G. WEOAB1, FRYBA1
Macridin, A. *MOYBB2*
Madrak, R.L. *WEPMA13*, *WEPMA14*
Madur, A. TUOCB2
Magana, A. THYAA1
Maggipinto, M.A. MOPHO17
Magsig, C. THPBA12
Maharjan, C. MOPAC34
Mahler, G.J. WEPAC07
Makarov, A.V. WEPMA14
Makdisi, Y. WEPBA05
Makino, K. MOPBA11
Makulski, A. THPBA15
Malhotra, S. TUYAA1
Malloch, I.M. *WEPAC17*, WEPAC18
Malone, R. THPAC32
Malyzhenkov, A. TUOBB3
Mammarella, F. WEPHO01
Mammosser, J.D. WEPAC01, WEPAC47
Mann, T.L. MOZAB1
Mao, H.S. THYAA1
Mapes, M. TUOCA2, TUPHO01
Marcus, G. WEOAA1
Marcus, M. MOPHO22
Marhauser, F. THPBA23, THPBA22
Marín, E. *TUPBA25*
Marks, S. TUOCB2
Marksteiner, Q.R. MOOAB1
Marone, A. TUOCA2, WEODA1, THPBA07
Marr, G.J. TUOAA2
Marsden, D. WEPHO08, WEPHO09, WEPMA09
Marsh, K.A. MOPAC02, MOPAC21, MOPAC38, MOPAC45, MOPAC46, THYAA2, *THOCA1*
Marsh, R.A. *TUPMA10*
Marti, F. FRYBA1
Martin, B. TUOAA1
Martinez, M.P. MOPMA15
Martins, J.L. MOPAC39
Marusic, A. TUOAA2, TUPBA04, TUPBA05, TUPBA06, TUPBA08
Matlis, N.H. THOCA2
Matsumura, Y. *THOBA4*
Maxwell, T.J. WEOBA1
Mayes, C.E. *TUTB1*, WEOAA2
McCormick, D.J. WEOBA1
McCrady, R.C. MOPMA14, MOPMA17, *MOPSM05*, TUPSM16, TUPSM18, THPAC26
McCuistian, B.T. TUPAC17
McDonald, K.T. TUPBA09, TUPBA10, TUPBA11, THPHO11, THPMA10, THPMA11
McGinnis, D.P. FRYAA2
McGuinness, C. MOOBB2

McIntosh, P.A. THPHO06
McIntyre, P.M. *MOZAB1*, TUPAC26, THODA2
McNeur, J.C. MOOBB2
Mead, J. MOPHO17
Melconian, K.E. MOZAB1, TUPAC26
Mendenhall, M.H. TUPSM24
Meng, C. TUODB1, THPSM04
Meng, M. TUODB1
Meng, W. TUOAA1, TUPBA13, TUPSM08
Méot, F. MOPBA04, MOPBA05, TUPAC10, TUPBA13
Merio, M. WEPAC25, THPMA09
Merminga, L. THPBA01, THPBA02
Mernick, K. *MOZAA2*, TUXA1, THPHO07, THPHO08, THPHO09
Mi, C. TUOCA2, WEPHO05
Mi, J.-L. TUPHO01, THPHO10
Michnoff, R.J. TUOCA2, TUPBA08
Midttun, O. MOZBA1
Mihalcea, D. TUPSM24
Mikulec, B. TUODB3, TUPAC06
Miller, R.H. THPSM14
Miller, S.J. WEPAC20, THPBA13
Miller, T.A. TUOCA2, TUPHO01, THPHO09
Miller, T.J. MOPHO26
Milloch, M.M. WEPMA02
Milocco, A. WEPMA02
Milton, S.V. MOPAC07, TUPSM09, WEPHO10, WEPMA10, WEPSM17
Minty, M.G. TUOCA2, TUPBA05, TUPBA06, *TUPBA08*, THPAC13, THPHO09
Mishakin, S. WEPSM04
Mishra, C.S. MOPMA09, TUYAA1
Mishra, S. MOPMA05
Mitchell, C.E. *WEPSM18*
Mitra, A.K. *WEPHO01*
Mittal, K.C. TUPAC02
Mittelberger, D.E. THYAA1
Miyamoto, A. *MOPHO04*, WEPSM01
Mizugaki, M. *WEOBA2*
Mizushima, K. FRXB1
Mo, Y. FROAA1
Møller, S.P. MOPMA04
Moens, V. TUOCA1, TUPAC15
Moir, D.C. TUPAC17
Mokhov, N.V. MOPMA21, THPBA14, THPBA15
Mondal, J. TUPAC02
Monroy, M.T. WEOAA1
Montag, C. *TUOAA2*, TUOCA2, *TUPAC11*, TUPHO01, *THPHO10*
Montazeri, B. MOOBB2, MOPAC28
Montes, F. MOPSM07, FRYBA2
Moody, J.T. *MOPAC43*
Moog, E.R. WEPSM08, WEPSM09, *WEPSM10*
Moore, T.P. TUOBA1, TUOAB1
Moretti, A. TUODA1, WEPMA03, WEPMA07, WEPMA12, WEPMA16
Morgan, G. TUPSM20, WEOAB1
Morgan, J.P. MOPMA21
Mori, W.B. MOPAC02, MOPAC10, MOPAC38, MOPAC39, MOPAC46, MOPAC47, MOPAC49, THYAA2, THOCA1
Morita, A. WEODA1, THPBA04
Moroz, V. WEYA1
Morozov, I.A. MOODB2
Morozov, V.S. TUPAC28, THPHO19
Morris, D. MOPMA20, THPMA02, FRYBA1
Morrissey, D.J. THPBA12, FRYBA2
Moss, A.J. THPHO06
Mu, Z.C. TUODB1
Muggli, P. *MOOBB1*, *MOPAC02*, MOPAC38, MOPAC46, MOPAC49, THYAA2, THOCA1
Muller, E.M. THPAC34, THPAC17
Munroe, B.J. MOPSM06, WEPBA14, *THOBA1*
Murakami, T.M. FRXB1
Murokh, A.Y. MOPHO25, TUOAB2, WEPBA17, THOAA2, THPAC29, THPAC32, THPAC36
Murphy, K. MOPAC19
Murphy, R.C. WEOAB2
Musardo, M.M. THPAC09, *THPAC14*, *THPAC15*
Mustapha, B. MOPMA06, *MOPSM02*, WEOAB2, *WEPMA05*
Musumeci, P. MOPAC27, MOPAC43, TUOBB4, TUPAC29, TUPMA16, TUPSM03, TUPSM28, THOAA1, THPAC37
Myers, M. THPHO07, THPHO08

— N —

Nadel-Turonski, P. TUPAC28
Nagaitsev, S. MOODB1, MOODB2, MOPAC16, MOPMA09, *TUYAA1*, WEPBA16, WEPBA17
Nagamoto, Y. FRXB1
Najmudin, Z. MOPAC34, THPSM12, THPSM13
Nakamura, K. THYAA1, THOCA2
Nakao, M. WEPBA02, THPHO01
Nantista, C.D. WEOAA1
Naranjo, A.C. WEPHO14
Nash, S. MOPSM07, THPAC20, THPHO14
Nassiri, A. WEPAC01, WEPAC02, WEPAC44
Nayak, S.K. THPHO10
Nehring, R. THPBA15
Neil, G. WEOAA1, WEPSM17
Nellis, T. THPBA13
Nemesure, S. TUOCA2, TUPHO01
Nesmiyan, I. TUPAC07
Neubauer, M.L. *WEPHO16*, *WEPHO17*, *WEPHO18*, THPBA22
Neuffer, D.V. MOPMA21, TUPBA11, TUPBA18, TUPBA20, THPHO19

Neustadt, T.S. THPBA28
Newsham, D.J. WEPHO13, *WEPMA11*, THPSM04
Ng, C.-K. *MOPAC31*, *MOPBA18*, WEOAA1, *WEPAC44*, *WEPAC46*
Ng, W. TUOCA2
Nguyen, C. TUOAB1
Nguyen, P. MOPMA08
Nichols, A.A. THPBA29
Nichols, R.M. THPSM12
Nicol, T.H. *THPMA09*
Niell, F.M. WEPHO11, THPBA11
Nieter, C. MOPBA21, TUPMA15, *TUPSM3*
Nikolskiy, K.I. WEPHO03, WEPHO04
Nipper, J.H. THPBA24
Nishimura, H. MOPHO23, TUOCB2, WEOAA1
Nishimura, Y. TUPSM01
Nishiyama, M. TUPSM01
Noble, R.J. MOPAC28, MOPAC31, MOPAC3
Noda, A. WEPBA02, THPHO01
Noda, K. FRXB1
Nogiec, J.M. *THPBA15*, THPBA16
Nolen, J.A. FRYBA1
Nonomura, K. THPSM03
Norem, J. *WEPMA07*
Norum, W.E. WEYA1
Novokhatski, A. WEPBA08
Nuhn, H.-D. WEOAA1
Nunes, R.P. MOPAC01
Nurkenov, S. WEPMA07

— O —

O'Connel, T. WEPAC11
O'Connell, T.I. THPMA07
O'Hara, J.F. MOPMA14, MOPSM05, TUPSM0, WEPAC33, THPAC23
O'Neill, C. MOPHO20, TUPSM14
O'Shea, F.H. MOPHO25, *WEPBA17*, *THPAC3*
Obana, T. FRXB1
Oddo, P. *WEPBA05*
Oganesyan, K.B. *MOPHO01*, *MOPHO02*, *MOPHO2*
Ogitsu, T. FRXB1
Ohnishi, Y. WEODA1, THPBA04
Ohuchi, N. *WEODA1*, *THPBA04*, THPBA07
Oide, K. WEODA1, THPBA04
Okamoto, H. THPHO01
Okamura, M. TUPHO01
Okugi, T. TUPBA25
Okumura, S. THPSM01
Olave, R.G. *WEPAC43*
Olivas, E.R. MOPMA16, MOPSM05, WEPAC3
Olivas, P.D. WEPHO14
Olsen, R.H. TUPHO01
Olsson, T. *TUPMA02*
Orel, P. THPMA04
Orfin, P. THPHO06
Orikasa, T. FRXB1
Orlov, Y.O. WEPAC29, THPMA09
Orris, D.F. THPBA15, *THPBA16*
Osaki, K. THPHO01
Ostiguy, J.-F. MOPMA10, MOPMA13
Ostroumov, P.N. MOPMA06, MOPSM02, TUYAA1, *WEOAB2*, WEPAC05, WEPMA05
Ottarson, J. THPBA12
Ouyang, H.F. TUODB1, THPSM04
Ovalle, E. MOZBA1
Ozelis, J.P. FRYBA1

— P —

Padmore, H.A. WEOAA1, THPAC12, THPAC17
Padrazo, D. MOPHO17
Pai, C. WEPBA05, THPHO09
Pak, A.E. MOPAC21
Pakter, R. MOPAC01
Palmer, M.A. *MOYAA2*, TUPBA20
Palmer, R.B. TUPBA11, TUPBA20, THPHO04, *THPHO05*, THPHO12, THPHO13
Pan, P. WEPMA26
Pande, M.M. TUYAA1
Pang, X. *MOPMA18*, TUPSM19
Panuganti, H. TUPSM24, *TUPSM25*
Papadopoulos, C. F. TUPMA09, WEOAA1, WEYA1
Papotti, G. *MOYAA1*
Pappas, G.C. TUOCB2, WEOAA1
Pardo, R.C. MOPSM01, WEOAB2
Paret, S. *TUPBA23*, WEOAA1
Paret, Z. TUPMA09
Park, H. WEPAC40, *WEPAC41*
Park, J. THPAC36
Park, J.H. *TUPSM04*
Parker, B. TUPBA13, TUPBA15, WEODA1, THOAB2, *THPBA07*
Paskvan, D.R. WEOAB2
Pasquinelli, R.J. WEPHO15, WEPMA03, WEPMA16
Passarelli, D. WEPAC21, THPMA09
Pasternak, J. *THPSM11*
Patil, M.S. THPBA13
Peaslee, P. THPMA14
Peggs, S. WEPMA25
Pei, S. THPSM04
Pellegrini, C. *FRZBP1*
Peng, J. TUODB1
Peng, S. FRYBA1
Penn, G. WEOAA1
Pennisi, T.R. TUPSM22
Peplov, V.V. FRYBB2
Peralta, E.A. *MOOBB2*, MOPAC28, MOPAC32, MOPAC33
Perdikakis, G. MOPMA07
Perevedentsev, E. MOOAA2, WEPBA04
Perry, A. *MOPMA06*
Petermann, K.V. TUOCB2
Peterson, D.W. WEPMA03, WEPMA16, *THPMA08*

Peterson, T.J. WEOAA1, WEPAC29, THPMA09
Pfeffer, H. THPBA17
Phillips, D. TUOCA2
Phillips, R.A. *WEPHO12*
Piech, J.F. THPSM10
Pieloni, T. TUPBA21
Pigeon, J.J. MOPAC41, *MOPAC44*
Pikin, A.I. TUOCA2, TUPHO01, TUPSM06
Pile, P.H. WEPBA05
Pilipenko, R.V. WEPAC29
Piller, C. TUPSM22
Pinayev, I. TUOAA1, WEPAC06, WEPAC07, WEPBA08, THPHO06
Piot, P. *MOZBB1*, TUPAC21, *TUPSM24*, TUPSM25, MOPAC15
Pischalnikov, Y.M. WEPAC25, WEPAC29
Pitcher, E.J. MOPMA04, *TUYAA2*
Placidi, M. WEOAA1
Plate, S.R. TUOCA2, THPBA08, THPBA09
Plawski, T. E. TUPMA19
Podobedov, B. *WEODB1*, THPAC16
Pogorelov, I.V. TUPHO02
Pogorelsky, I. MOPAC34
Pogue, N. MOZAB1, *THODA2*
Polikhov, S.A. WEPHO03, WEPHO04
Pollock, B.B. MOPAC21
Pollock, K.M. TUPAC25, FROAA3
Poloubotko, V. THPMA09
Polozov, S.M. THPSM08
Polyanskiy, M.N. MOPAC34
Poole, B.R. *MOPAC07*
Poor Řežaei, K. *WEPBA20*, FROAA1
Popielarski, J. FRYBA1
Popielarski, L. WEPAC17, WEPAC18, FRYBA1
Portillo, M. MOPMA07
Portmann, G.J. MOPHO22, TUOCB2, WEYA1
Posen, S. *WEZBA1*, *WEPAC12*, WEPAC13, *THOBA2*, THPMA07
Posocco, P.A. MOPMA05, *WEOCB2*, *THPSM10*, THPSM11, THPSM12, THPSM13
Potkins, D.E. THOAB1
Potts, R.E. WEODB2
Power, J.G. MOPAC12, TUPSM05, *WEPMA08*
Powers, T. TUPMA19, WEOAA1
Pozdeyev, E. *WEOAB1*, FRYBA1
Pozimski, J.K. MOPMA05, *THPSM12*
Preble, J.P. WEOAA1
Premo, K.S. WEPAC29
Prestemon, S. TUOCB2, WEOAA1
Previtali, V. TUOCA1
Pribaz, F. WEPMA02
Prieto, P.S. TUPSM13
Prokop, C.R. *TUPAC21*, TUPSM25
Pronitchev, O.V. THPMA09
Pronskikh, V.S. THPBA14
Prosnitz, D. WEOAA1
Prost, L.R. TUOBB1
Prosvetov, V.P. MOOAA2
Proulx, J.A. THPBA28
Ptitsyn, V. TUPBA13, TUPBA15, TUPBA26
Pulampong, T. MOOAB2
Pullia, M. THOAB2
Putnam, N. WEPAC18

— Q —

Qi, M. MOPAC28, MOPAC33
Qian, H.J. *TUPMA09*, WEOAA1, WEYA1
Qiang, J. TUPBA11, TUPBA23, WEOAA1, WEPSM18
Qiao, S. WEPSM01
Qin, Q. TUPBA03
Quigley, P. WEPAC11, THPMA07

— R —

Rabehl, R. THPBA16
Raginel, V. *TUODB3*, *TUPAC06*
Rahman, O.H. *TUPSM06*, TUPSM08
Raich, U. MOZBA1
Rakowsky, G. THPAC09, THPAC14, THPAC15
Ralph, J. MOPHO20, TUPSM14
Ralph, J.E. MOPAC21
Ramanathan, M. WEPSM14
Ranjbar, V.H. FROAA2
Rank, J. THPAC09, THPAC10, THPAC15
Rao, T. MOPBA21, TUPSM06, TUPSM08, THPAC12, THPAC18, THPAC34, THPAC35, THPHO06
Rao, X. WEOAB1
Raparia, D. MOOBA2, TUPHO01
Ratcliffe, N. *THOBB2*
Rathke, J. TUPSM04
Ratti, A. WEOAA1
Raubenheimer, T.O. MOPHO12, MOPHO15, WEOBA1, WEPBA19
Rawlins, A.W. TUOCB2
Read, M.E. WEPHO08, *WEPHO09*, WEPMA09
Redaelli, S. TUOCA1
Reece, C.E. WEZAA2
Rees, D. WEPHO14
Regan, C. TUOAB2
Reid, T. WEOAB2
Reimann, O. MOPAC02
Reinsch, M.W. WEOAA1
Rencsok, R. MOPSM07, THPHO14, FRYBA2
Řežanov, I. WEPHO03, WEPHO04
Rhein, C. THPAC09, THPAC15
Rice, S.A. *WEPAC35*
Riddone, G. TUPAC07
Riehn, E.J. TUPSM06, TUPSM08
Riley, J.R. THYAA1
Rimmer, R.A. WEPAC44, WEPAC47, WEPHO16, WEPHO17

Ristori, L. WEPAC21, WEPAC22, WEPAC23, WEPAC25, WEPAC29, *THOBA3*, THPMA09
Ritter, J. MOOBA2
Rivetta, C.H. TUPAC25, WEOAA1, *FROAA3*
Rizzato, F.B. MOPAC01, TUPAC01
Robak, S. MOPAC17
Robert-Demolaize, G. TUOAA2, *TUPAC12*, TUPBA04
Roberts, K.G. *TUOBB4*, TUPSM03
Roberts, T.J. MOPBA09, MOPBA12, *THPBA27*
Robin, D. MOPHO22, MOPHO23, TUOCB3, WEOAA1, WEPBA12, *THYAB2*
Robinson, D. WEOAA3
Rodriguez, J.A. *MOPMA07*, MOPSM07, THPAC23, THPHO14, FRYBA2
Rogers, C.T. THPMA10
Rogers, G.C. TUPMA19
Rogovsky, Yu. A. MOOAA2
Romanov, A.L. *MOOAA2*, *WEPBA04*
Romanov, G.V. WEPAC23
Romero, W.P. MOPAC25
Roncarolo, F. MOZBA1
Rong, L.Y. TUODB1
Rosas, P.J. TUOCA2, TUPHO01
Rose, J. MOPBA03, TUPMA07
Rosenzweig, J.B. MOOCB2, TUPSM27
Roser, T. TUXA1, TUPBA13, WEPBA05, THPHO10
Ross, M.C. MOPAC30
Rossi, A. TUOCA1
Rossi, C. MOZBA1
Rossi, S.L. TUOCB2
Roth, I. *WEOCA1*
Rouleau, G. TUPSM16
Rowe, A.M. WEPAC04
Roybal, R.J. MOPMA14
Ruelas, M. MOPHO25
Ruisard, K.J. FROAA1
Ruiz-Osés, M. THPAC12, THPAC17, THPAC18, THPHO06
Rusnak, B. *THPMA14*
Russell, S.J. MOOAB1
Russo, T. MOPMA08, THPAC20, FRYBA1
Rybarcyk, L. MOPMA14, MOPMA16, *MOPMA17*, MOPMA18, MOPSM05, TUPSM16, TUPSM17, TUPSM18, *TUPSM19*, THPAC23
Ryne, R.D. MOPBA06, TUPBA11, TUPBA28

— S —

Sabbagh, P. MOPMA04
Sabharwal, S. *WEYB3*
Sabol, D.M. WEPAC11
Saethre, R.B. *FRYBB2*
Saewert, G.W. *THPBA17*
Safranek, J.A. TUOCB1
Sahai, A. A. *MOPAC10*, MOPAC30
Saini, A. *MOPMA10*, *MOPMA12*, *MOPMA13*, WEPAC32
Saito, K. WEPAC20, FRYBA1
Sajaev, V. MOPHO06, MOPHO07, *MOPHO08*, MOPHO09, *TUOBB2*, TUPAC08, WEOAA3, WEPSM06, WEPSM07, WEPSM12
Sakaue, K. TUPMA01, TUPSM01, WEOBA2, THPSM03
Salvachua, B. TUOCA1
Samms, T. WEPHO05
Sampson, P. TUOCA2
Samulyak, V. *MOPBA06*, *TUPBA09*
Sanchez Alvarez, J.L. MOZBA1
Sandberg, J. TUOCA2, TUPHO01, WEPHO05
Sandoval, Jr., G. M. WEPHO14
Sannibale, F. TUPMA09, WEOAA1, *WEYA1*
Santana, M. TUPSM22
Sasaki, S. MOPHO04, *WEPSM01*
Sato, R. *THPSM03*
Sato, S. FRXB1
Satogata, T. *THPHO21*
Sattarov, A. MOZAB1, THODA2
Saunders, J. THPBA28
Savage, P. *MOPMA05*
Savard, G. MOPSM01
Savilov, A.V. WEPSM02
Savino, J.J. TUOBA1, FRYBA1
Sayed, H. K. *TUPBA10*, *TUPBA11*, *THPHO11*
Scaminaci, A.J. THPHO03
Scarvie, T. TUOCB2
Schächter, L. MOPAC28
Schaff, W.J. MOPBA21, TUOAB1
Schappert, W. WEPAC29, THPBA15
Schaumburg, H.D. *MOPBA16*
Schempp, A. MOPMA14, MOPMA17
Schenkel, T. *MOPAC19*, *WEOBB2*
Schlott, V. THPMA04
Schlueter, D. TUOCB2
Schmalzle, J. THPBA24
Schmidt, C.W. WEZB1
Schmidt, F. MOPBA12
Schoefer, V. MOPBA04, TUOAA2, TUPAC10
Schoenlein, R.W. WEOAA1
Schoessow, P. *MOPAC12*, MOPHO19, TUPMA08
Schreiber, G. THPMA01
Schrock, K. WEPHO11
Schroeder, C.B. THOCA2
Schroeder, K.M. WEOAA3
Schubert, S.G. THPAC12, THPAC17
Schulte, D. TUZAA2
Schulte, R.W. WEOCB1
Schultheiss, T. TUPSM04
Schultz, R.P. WEPMA16
Schwartz, B.T. TUPHO02

Schwarz, S. MOPMA07, THPBA12, FRYBA2
Schwarz, T.A. TUODA1
Scrivens, R. MOZBA1
Sears, J. WEPAC11, WEPAC13, THPAC15, THPMA07
Sedillo, J.D. *THPAC25*
Seki, H. THOAB1
Seletskiy, S. *TUPBA12*, *THPAC16*
Senchenko, A.I. MOOAA2
Sereno, N. WEOAA3, THPHO03
Serpico, C. *WEPMA01*, WEPMA02
Serrano, C. WEOAA1
Sethna, J.P. WEPAC12
Seung, S. *MOPBA17*, THOAA2
Severson, M.C. TUPMA19
Seviour, R. THODA1
Shaftan, T.V. MOPBA17, MOPHO17, *TUPMA07*
Shao, X. MOOCB1
Shapiro, M.A. MOPSM06, WEPBA13, *WEPBA14*, THOBA1
Shapovalov, R.V. *THPSM21*
Sharamentov, S.I. MOPSM01, WEOAB2
Sharkov, G.B. WEPHO03, WEPHO04
Sharma, A.S. TUPAC02
Sharma, S.K. THPAC10
Shatilov, D.N. MOODB1, TUPBA21
Shatunov, P.Yu. MOOAA2
Shatunov, Y.M. MOOAA2
Shaw, B. THOCA2
Shaw, J.L. MOPAC21, *MOPAC45*
Shchegolkov, D.Y. MOPAC23, *MOPAC24*, TUPMA13, WEPAC33
Shchelkunov, S.V. *WEPHO19*
Shea, T.J. *MOPMA04*
Sheehy, B. TUOAA1, TUPSM06, THPHO06
Shelley, F.E. MOPMA15
Shemelin, V.D. WEPAC13
Shemyakin, A.V. TUYAA1, TUPSM10
Shen, G. MOPHO17
Shen, X. TUPAC12, *TUPBA04*
Shibuya, S. THOAB1
Shiltsev, V.D. *MOOAA1*, *MOPAC15*, *MOPAC16*, MOPAC18, TUOBB1
Shin, K.R. *WEPMA22*, *WEPMA23*
Shin, Y.-M. *MOPAC17*, *TUPSM11*, *TUPSM12*, *MOPAC18*
Shirai, T. WEPBA02, FRXB1
Shiraishi, S. *THOCA2*
Shiroyanagi, Y. WEOAA3, WEPSM06, WEPSM07, *THPAC07*
Shishlo, A.P. *TUYB2*, WEODB2, WEPBA16
Shkolnikov, P. MOPAC34
Shoaf, S.E. THPHO03
Shoda, K. FRXB1
Shrey, T.C. TUOAA2
Shroff, K. MOPHO17
Shuptar, M. *THPBA13*
Shwartz, D.B. MOOAA2, WEPBA04
Sikora, J.P. *WEPBA09*, *FROAA5*
Silva, L.O. MOPAC02, MOPAC39, MOPAC47
Simakov, E.I. MOPAC23, MOPAC24, *MOPAC25*, *TUPMA13*, *WEPAC33*, WEPAC34
Simeoni, W. *TUPAC01*
Simonov, E.A. MOPHO17
Simpson, B.E. WEPHO11, WEPHO12
Singh, O. MOPHO17, THPAC10
Singh, P. TUYAA1
Sinyatkin, S.V. MOPBA01, MOPHO17
Sipahi, N. *WEPHO10*, WEPMA10
Sipahi, T. WEPHO10, *WEPMA10*
Skaritka, J. TUPSM06, TUPSM08, WEPAC06, WEPAC07, THPAC34, THPAC35, THPHO06
Skiadopoulos, D. WEOAA3
Skrinsky, A.N. MOOAA2
Slimmer, D. THPAC20
Smaluk, V.V. MOPHO17
Smedley, J. MOPBA21, THPAC12, *THPAC17*, THPAC18, THPAC34
Smirnov, A.V. MOPHO20, TUOAB2, TUPSM28, *WEPBA18*, THOAA2, *THPSM19*
Smirnov, A.Yu. THPSM08, *WEPHO03*, *WEPHO04*
Smith, E.N. WEPAC11
Smith, K.S. THPHO06
Smith, M.L. WEOAA3, WEPSM11
Smith, T.L. WEPAC02
Smolenski, K.W. TUOBA1, TUOAB1
Snopok, P. TUPBA20, *MOPBA10*, THPMA10, *MOPBA09*, *MOPBA11*
Snydstrup, L. TUOCA2, WEPAC06, WEPAC07
Sodomaco, N. WEPMA02
Sokollik, T. THOCA2
Solyak, N. MOPMA09, MOPMA10, MOPMA12, MOPMA13, TUYAA1, TUODB2, TUPBA12, WEPAC14, WEPAC22, WEPHO19
Somaschini, L. *WEPMA03*, WEPMA16
Sonnad, K.G. TUPAC13
Sooby, E. MOZAB1
Soong, K. MOOBB2, *MOPAC32*, MOPAC28, MOPAC33
Souchlas, N. THPMA10
Souda, H. WEPBA02, THPHO01
Souza, R. THPMA14
Spencer, J.E. MOPAC28, MOPAC31
Spentzouris, L.K. TUPSM05
Spickermann, T. TUPAC19, TUPAC20
Spielman, R.B. THPSM21
Spranza, E. WEPBA17
Stabile, P. *TUPSM13*
Stancari, G. *TUOCA1*, *TUPAC15*
Stanek, R.P. TUYAA1

Staples, J.W. TUPMA09, WEOAA1, WEYA1, WEPMA19, WEPMA20, WEPMA21
Steier, C. MOPHO22, MOPHO23, *TUOCB2*, WEOAA1
Steiner, M. MOPMA07
Steinke, S. THOCA2
Stem, W.D. *TUPAC32*, FROAA1
Stepanov, A.D. *TUPAC24*
Steski, D. MOOBA2
Stewart, T.M. THOAB1
Still, D.A. MOPAC18
Stillwell, R.L. THPAC36
Stockli, M.P. TUPSM22, FRYBB2
Stoltz, P. MOPBA24
Storey, D.W. *THPBA01*, *THPBA02*
Storms, S. WEOCA2, WEPBA18, THOAA2, THPAC29
Stout, D. *MOPMA08*
Stratakis, D. TUPBA11, THPHO04, THPHO05, *THPHO12*, *THPHO13*
Striganov, S.I. MOPMA21, THPBA19
Strong, W.H. THPBA28
Stupakov, G.V. WEOAA1, WEODB1
Sugimoto, H. WEODA1, THPBA04
Sukhanov, A.I. WEOAA1, WEPAC23
Sullivan, G. TUPAC17
Sullivan, M.K. TUPAC28
Sumithrarachchi, C. MOPMA07, FRYBA2
Summers, D.J. WEPMA26
Summers, R.D. WEPHO14
Sun, B. TUODB1, THPSM04
Sun, C. *MOPHO22*, MOPHO23, TUOCB2, WEOAA1
Sun, J.L. THPSM04
Sun, X. WEPSM06, *THPAC08*
Sun, Y. MOPHO07, *MOPHO10*, *MOPHO11*, *MOPHO12*, *MOPHO13*, *MOPHO14*, *MOPHO15*
Sutter, D.F. TUPAC31, *TUPAC33*, FROAA1
Suvorova, N.A. WEPAC33
Suzuki, S.S. FRXB1
Swent, R. THPAC19
Swinnen, L. THPBA03
Swinson, C. MOPAC24, MOPHO19, THPAC32
Sylvester, C. THPBA16
Syphers, M.J. MOPSM07, FRYBA2
Syversrud, D. L. THYAA1

— T —

Tagi, K. *THPSM02*
Taillardat, S. THPBA03
Tajima, T. WEPAC33
Takahashi, T. *TUPSM01*
Takatomi, T. TUPSM01, WEOBA2
Takayama, S. FRXB1
Takibayev, A. MOPMA04
Talman, R.M. TUPAC14
Tan, Y. TUOCA2, TUPHO01
Tanabe, T. THPAC09, THPAC10, THPAC14, THPAC15
Tang, C.-X. TUPSM03
Tang, J.Y. MOPMA03, *TUPBA03*, *THPSM04*
Tanke, E. MOPMA08, MOPSM07
Tarawneh, H. *MOPHO23*, TUOCB2
Tarrant, J.S. THPBA08, THPBA09
Tartaglia, M.A. THPBA16
Tauchi, T. TUPBA25
Tawada, M. WEODA1, THPBA04, THPBA07
Taylor, M.C. WEYB2
Temkin, R.J. MOPSM06, WEPBA13, WEPBA14, THOBA1
Tepikian, S. TUOAA1, TUOAA2
Terechkine, I. THPMA09
Terunuma, N. TUPMA01
Teryaev, V.E. WEPHO19
Than, R. TUOCA2, WEPAC06, WEPAC07, THPHO06
Theisen, C. TUOCA2, TUPHO01
Thieberger, P. TUOCA2, TUPBA08, TUPHO01, THPAC13, *THPHO09*, THPHO10
Thompson, J.R. WEPMA11
Thomsen, H.D. MOPMA04
Threlkeld, E.W. TUPMA16, *TUPSM28*
Thronson, C. MOPMA08
Tian, J.M. TUODB1
Tian, K. *TUOCB1*
Tian, Y. MOPHO17
To, H.L. TUPSM03, *THPAC37*
Tochitsky, S. MOPAC41, MOPAC44
Todd, A.M.M. TUPSM04
Tokpanov, Y. TUODA2
Tollestrup, A.V. MOPBA06, TUODA1, WEPMA12
Tomás, R. TUPBA04, TUPBA25
Tompkins, J.C. THPBA22
Tongu, H. WEPBA02
Torun, Y. TUODA1, WEPMA03, THPMA08, WEPMA12, *THPHO18*, *WEPMA16*
Tóth, C. THYAA1, THOCA2
Trakhtenberg, E. WEOAA3
Transtrum, M.K. WEPAC12
Trbojevic, D. *TUPBA13*, *TUPBA14*, *TUPBA15*, *THOAB2*
Tremaine, A.M. MOPAC43
Tresca, O. MOPAC34, THPAC33
Tropin, I.S. THPBA19
Trovò, M. TUPSM27
Tsang, S.H. WEOCB2
Tschirhart, R.S. MOPMA09
Tsoupas, N. MOPBA05, TUPBA13
Tsuchiya, K. WEODA1, THPBA04, THPBA07
Tsung, F.S. MOPAC10, MOPAC47
Tsvetkov, P.V. MOZAB1, THODA2

Tuozzolo, J.E. TUOAA1, TUOCA2, TUPHO01, WEPAC06, WEPAC07, THPHO05, THPHO07, THPHO08, THPHO10
Turgut, O. *TUPAC25*, FROAA3
Turvey, M.W. TUPSM22

— U —

Uesaka, M. THOBA4, THPSM02
Umer, R. WEPMA02
Urakawa, J. TUPBA25, TUPMA01, TUPSM01, WEOBA2

— V —

Vafaei-Najafabadi, N. MOPAC02, MOPAC38, MOPAC45, *MOPAC46*, THYAA2, THOCA1
Valerio, C.A. MOZBA1
Valishev, A. *MOODB1*, TUOCA1, TUPAC15, *TUPBA21*, WEPBA17
Valles, N.R.A. *THPMA07*
Valloni, A. *TUZAA2*
van Tilborg, J. THOCA2
Vandygriff, D.M. THPBA28
Varghese, P. TUODB2
Vasserman, I. WEPSM08, WEPSM09, WEPSM11
Vay, J.-L. *THAP5*
Veitzer, S.A. *MOPBA24*, TUPAC13
Veljak, L. WEPMA02
Venturini, M. WEOAA1
Verboncoeur, J.P. WEPAC35
Verma, A. TUPSM27
Veshcherevich, V. WEPAC11, THPMA07
Vetter, K. MOPHO17
Vieira, J. MOPAC02, MOPAC47
Vikharev, A.A. WEPSM02, WEPSM04
Vinco, M. WEYA1
Virostek, S.P. WEPMA03, WEPMA16, WEPMA19, WEPMA20, *WEPMA21*, WEPMA26
Vivoli, A. *TUODB2*
Vogelaar, R.B. THPBA23
Volk, J.T. WEPMA16
Voller, T. THYBB2
Vondrasek, R.C. MOPSM01
Vorobiev, L.G. MOPAC26, *MOPBA12*
Vretenar, M. MOZBA1
Vrielink, A.R. *THPAC01*

— W —

Waldron, W.L. MOPAC19, WEOAA1, WEOBB2
Waldschmidt, G.J. WEPAC02, WEPAC44
Walker, R.P. MOOAB2
Walton, G.W. THPSM11
Walz, D.R. MOPAC38, MOPAC46, THYAA2, THOCA1
Wan, W. MOPHO23, TUOCB2, WEOAA1, WEPBA12
Wanderer, P. TUOCA2, WEODA1, THPBA07
Wang, B. TUODB1
Wang, D. TUPBA03
Wang, E. TUPSM06, *TUPSM07*, *TUPSM08*, THPAC12, *THPAC18*, THPAC34, THPAC35, THPHO06
Wang, G. TUOAA1
Wang, G.M. *MOPHO17*, TUPMA07, THPAC10
Wang, H. WEPAC01, WEPAC02, WEPAC44, WEPAC47, WEPHO16
Wang, H. TUOAB1
Wang, J. WEPSM08
Wang, J. MOOCB1
Wang, N. TUPBA03
Wang, S. TUPBA03
Wang, S.C. TUODB1
Wang, Y. TUPBA03
Wangler, T.P. MOPMA17
Warnock, R.L. *MOPBA19*, *MOPBA20*
Warwick, T. WEOAA1
Washio, M. TUPMA01, TUPSM01, WEOBA2, THPSM03
Watkins, H.A. *THPAC26*
Weathersby, S.P. WEOBA1
Webber, R.C. THPAC20, THPHO14, FRYBA1
Wehlitz, R. MOPHO26
Wei, J. TUPAC14, WEPAC03, THPHO01, THPMA02, *FRYBA1*
Weis, C.D. MOPAC19
Wells, R.P. TUPMA09, WEOAA1, WEYA1
Welton, R.F. TUPSM22
Wen, Y.M. TUOCB2
Wendt, M. THPAC20
Weng, W.-T. TUPBA13
Westferro, F. WEPSM14
Wheelhouse, A.E. THPHO06
White, G.R. *TUXA2*, TUPBA25, THYAA2
White, S.M. TUPBA04, TUPBA07
Wilcox, R.B. WEOAA1
Wildman, D. WEPMA13, WEPMA14
Willeke, F.J. MOPHO17, TUPMA07
Williams, E.C. TUOCB2
Williams, J.E. *WEPSM17*
Williams, M. FRYBA1
Williams, R.S. WEPHO17
Williams, S. FRYBA2
Williams, S.J. MOPMA07
Wiseman, M. WEZAA2, WEPAC47
Wisniewski, E.E. *TUPSM05*, WEPMA08
Witte, H. *WEODA2*, *THPBA08*, *THPBA09*
Wittmer, W. MOPMA07, THPAC20, *MOPSM07*, THPHO14, FRYBA2
Wolff, D. THPBA17
Wong, J.J. THPAC12, THPAC17
Wong, M. WEPAC04
Woodley, M. TUPBA25

Woods, K.E. *WEOCB1*, THOAA2, THPAC36
Wu, D. WEPHO13
Wu, G. WEPAC01, WEPAC02, WEPAC44
Wu, J. MOPHO15
Wu, J. TUOCB2
Wu, Q. TUPSM06, WEPAC07, THPAC12, THPAC34, THPAC35, THPHO06
Wu, S. MOPBA17, *THPAC32*
Wu, S.S.Q. MOPAC43, TUPMA10
Wu, X. FRYBA2, MOPMA07, MOPSM07
Wu, Z. MOOBB2, MOPAC28, MOPAC32, *MOPAC33*, MOPAC38, MOPAC48, THYAA2, THOCA1

— X —

Xi, Y. MOOCB2
Xiao, A. MOPHO09, *TUPAC08*, WEOAA3, WEPSM07, WEPSM08, WEPSM09, *WEPSM11*, *WEPSM12*, *WEPSM13*
Xiao, L. MOPBA18, WEPAC44
Xiao, M. TUPBA03
Xie, J. THPAC17
Xin, T. WEPAC07, *THPAC34*, *THPAC35*, THPHO06
Xin, W.Q. TUODB1
Xu, G. TUPBA03
Xu, H. MOPHO17
Xu, J.Z. WEPSM11
Xu, S.Y. TUPBA03
Xu, T. THPBA13, THPBA28, FRYBA1
Xu, T. MOPAC18
Xu, T.G. TUODB1
Xu, W. WEPAC06, THPHO06
Xu, X.L. MOPAC47
Xu, Y. WEPAC03, *WEPAC20*, THPBA13

— Y —

Yair, O. TUPSM20
Yakimenko, V. TUPMA08, THYAA2, THPAC33
Yakovlev, V.P. MOPMA10, MOPMA12, MOPMA13, TUYAA1, WEPAC14, WEPAC21, WEPAC22, WEPAC23, WEPAC24, WEPAC29, WEPAC32, WEPHO15, WEPHO19
Yakub, A. TUPSM27
Yamamoto, M. THPSM02
Yamaoka, H. WEODA1, THPBA04, THPBA07
Yamazaki, Y. MOPMA20, FRYBA1
Yampolsky, N.A. MOOAB1, *TUOBB3*
Yan, F. THPSM04
Yan, Y.T. TUOCB1
Yancey, J.A. WEPAC06
Yang, B.X. TUPMA03, TUPMA04, *WEPSM12*, THPAC08
Yang, L. MOPHO17
Yang, S. WEPAC47
Yang, X. MOPHO17, THPAC16
Yang, Y. THPSM04
Yang, Y. WEYB4, *WEPAC01*, *WEPAC02*
Yang, Z. THPSM04
Yao, C. *TUPMA03*, *TUPMA04*, WEPSM13
Yarmohammadi Satri, M. MOZBA1
Yavuz, D. MOPHO26, TUPMA19
Yazawa, T. FRXB1
Ybarrolaza, N. THYAA1
Yin, L. TUOCB2
Yip, K. THPHO10
Yonehara, K. MOPBA06, TUODA1, WEPMA12, THPBA22, THPBA26, THPHO19
York, R.C. MOPHO26
Yoshida, M. THOBA4
Yoshida, Y. THPSM03
Yoshikawa, C.Y. *MOPMA21*, *THPHO19*
Yu, K. MOPBA06
Yu, P. *MOPAC47*
Yue, Y. TUPBA03
Yun, C.C. TUPAC04
Yuri, Y. WEPBA02, THPHO01, *THPSM01*, *FROAA4*
Yusof, Z.M. TUPSM05
Yuyama, T. THPSM01

— Z —

Zalel, S. THPSM10
Zaltsman, A. THPHO06
Zelenski, A. *MOOBA2*
Zeller, A. THPBA12, FRYBA1
Zemlyansky, I.M. MOOAA2
Zeng, L. TUODB1
Zeng, M. MOPAC39
Zeno, K. TUOAA2
Zhai, J.Y. TUPBA03
Zhang, C. TUPBA03, THPSM04
Zhang, H. MOPBA11, TUPHO02, *TUPHO04*
Zhang, H.D. FROAA1, *FROAA6*
Zhang, J.D. TUOCB2
Zhang, J.X. *MOPSM06*
Zhang, S. WEPSM17
Zhang, W. TUOCA2, TUPHO01, THPHO10
Zhang, Y. *TUZAA1*, TUPAC28, TUPHO02, TUPHO04
Zhang, Y. TUPAC14, WEPAC03, THPMA02, FRYBA1
Zhao, F.X. TUODB1
Zhao, Q. TUPSM20, WEOAB1, FRYBA1, *MOPMA20*
Zhao, S. THPMA02
Zhao, Z.T. *WEXA1*
Zharinov, Yu.M. MOOAA2
Zheng, Z. *WEPAC03*, *THPMA02*
Zholents, A. MOPAC12, MOPHO19, TUPMA08, WEOAA3

Zhou, Q.G. TUOCB2
Zhou, X. THOBA4
Zhukov, A.P. *WEYA2*
Zimmermann, F. TUZAA2
Zimmermann, S. WEOAA1
Zinkann, G.P. WEOAB2
Zipf, P. THPMA01
Zisman, M.S. WEPMA26, THPHO18, *TUOBA2*
Zlobin, A.V. *THPBA19*
Zolkin, T.V. *MOODB2*, *THPHO23*
Zolotorev, M.S. TUODA2, WEOAA1, WEYA1
Zong, Z.G. WEODA1, THPBA04, THPBA07
Zorzut, S. THPMA04
Zou, Y. *MOPMA03*
Zubets, V. MOOBA2
Zuchnik, T.J. TUPSM13
Zuo, S.S. MOPAC12
Zvyagintsev, V. THPAC01, THPBA02

Institutes List

AccSys
Pleasanton, California, USA
- Bucci, S.
- Creely, P.
- Domingo, S.
- James, G.
- Seki, H.
- Shibuya, S.

Accuthera Inc.
Kawasaki, Kanagawa, Japan
- Yamamoto, M.

ADNA
Los Alamos, New Mexico, USA
- Bowman, C.
- Vogelaar, R.B.

AEC
Chiba, Japan
- Arai, H.
- Fujimoto, T.

AES
Princeton, New Jersey, USA
- Bluem, H.
- Park, J.H.
- Rathke, J.
- Schultheiss, T.
- Todd, A.M.M.

AIST
Tsukuba, Ibaraki, Japan
- Kuroda, R.

ANL
Argonne, USA
- Abliz, M.
- Alcorta, M.
- Antipov, S.P.
- Arnold, N.D.
- Back, B.
- Barcikowski, A.
- Boon, L.E.
- Borland, M.
- Bui, H.
- Chae, Y.-C.
- Conde, M.E.
- Conway, Z.A.
- Decker, G.
- Dejus, R.J.
- Deriy, B.
- Donley, L.
- Dooling, J.C.
- Doose, C.L.
- Doran, D.S.
- Downey, J.S.
- Emery, L.
- Erdelyi, B.
- Fors, T.
- Fuerst, J.D.
- Gagliano, J.
- Gai, W.
- Gerbick, S.M.
- Gluskin, E.
- Grimmer, J.H.
- Harkay, K.C.
- Hasse, Q.B.
- Holzbauer, J.P.
- Ivanyushenkov, Y.
- Jaski, M.S.
- Jaski, Y.
- Jing, C.-J.
- Kaluzny, J.A.
- Kasa, M.
- Keane, R.T.
- Kedzie, M.
- Kelly, M.P.
- Kim, K.-J.
- Kim, S.H.
- Kruy, T.L.
- Kustom, R.
- Kutsaev, S.V.
- Laird, R.
- Lang, J.C.
- Lee, S.-H.
- Lenkszus, F.
- Lill, R.M.
- Lindberg, R.R.
- Lipa, R.
- Liu, W.
- Luo, Y.
- Moog, E.R.
- Murphy, R.C.
- Mustapha, B.
- Nassiri, A.
- Nolen, J.A.
- Norem, J.
- Ostroumov, P.N.
- Pardo, R.C.
- Paskvan, D.R.
- Perry, A.
- Power, J.G.
- Ramanathan, M.
- Reid, T.
- Robinson, D.
- Sajaev, V.
- Savard, G.
- Scaminaci, A.J.
- Schroeder, K.M.
- Sereno, N.
- Sharamentov, S.I.
- Shiroyanagi, Y.

- Shoaf, S.E.
- Skiadopoulos, D.
- Smith, M.L.
- Smith, T.L.
- Sun, X.
- Sun, Y.
- Trakhtenberg, E.
- Vasserman, I.
- Vondrasek, R.C.
- Waldschmidt, G.J.
- Wang, J.
- Westferro, F.
- Wisniewski, E.E.
- Wu, G.
- Xiao, A.
- Xie, J.
- Xu, J.Z.
- Yang, B.X.
- Yang, Y.
- Yao, C.
- Zholents, A.
- Zinkann, G.P.

ANSL
Yerevan, Armenia
- Oganesyan, K.B.

BARC
Mumbai, India
- Malhotra, S.
- Mittal, K.C.
- Mondal, J.
- Pande, M.M.
- Sharma, A.S.
- Singh, P.

BINP SB RAS
Novosibirsk, Russia
- Berkaev, D.E.
- Cheblakov, P.B.
- Davydenko, V.I.
- Derbenev, A.A.
- Erokhin, A.I.
- Gurov, S.M.
- Ivanov, A.A.
- Kadyrov, R.A.
- Karnaev, S.E.
- Kasaev, A.S.
- Kharkov, Y.
- Kiselev, V.A.
- Kolmogorov, A.
- Koop, I.
- Kyrpotin, A.N.
- Lysenko, A.P.
- Morozov, I.A.
- Perevedentsev, E.
- Prosvetov, V.P.
- Rogovsky, Yu. A.
- Romanov, A.L.
- Senchenko, A.I.
- Shatilov, D.N.
- Shatunov, P.Yu.
- Shatunov, Y.M.
- Shwartz, D.B.
- Simonov, E.A.
- Sinyatkin, S.V.
- Skrinsky, A.N.
- Smaluk, V.V.
- Teryaev, V.E.
- Zemlyansky, I.M.
- Zharinov, Yu.M.

BNL
Upton, Long Island, New York, USA
- Ahrens, L.
- Altinbas, Z.
- Anerella, M.
- Aronson, J.N.
- Aschenauer, E.C.
- Atoian, G.
- Attenkofer, K.
- Bacha, B.
- Bai, M.
- Bassi, G.
- Beebe, E.N.
- Belkacem, B.
- Bellavia, S.
- Belomestnykh, S.A.
- Ben-Zvi, I.
- Berg, J.S.
- Blaskiewicz, M.
- Blednykh, A.
- Blum, E.B.
- Brennan, J.M.
- Brooks, S.J.
- Bruno, D.
- Brutus, J.C.
- Cappadoro, P.L.
- Cheng, W.X.
- Choi, J.
- Chubar, O.V.
- Corwin, T.M.
- Costanzo, M.R.
- D'Ambra, J.A.
- Dalesio, L.R.
- Davidsaver, M.A.
- Dawson, W.C.
- De Long, J.H.
- De Monte, V.
- Di Lieto, A.
- Drees, K.A.
- Dutheil, Y.
- Escallier, J.
- Fedotov, A.V.
- Fedurin, M.G.
- Fernandes, H.C.
- Fischer, W.
- Fite, J.M.
- Fliller, R.P.
- Frak, B.

- Ganetis, G.
- Gassner, D.M.
- George, G.
- Ghosh, A.K.
- Gu, X.
- Guo, W.
- Gupta, R.C.
- Ha, K.
- Hahn, H.
- Haj Tahar, M.
- Hamdi, K.
- Hao, Y.
- Harder, D.A.
- He, P.
- Heese, R.
- Hidaka, Y.
- Hock, J.
- Hocker, H.M.
- Hoff, L.T.
- Hseuh, H.-C.
- Hu, Y.
- Huang, H.
- Huang, Y.
- Hulsart, R.L.
- Jain, A.K.
- Jamilkowski, J.P.
- Jing, Y.C.
- Kankiya, P.
- Kayran, D.
- Kewisch, J.
- Kirk, H.G.
- Kitegi, C.A.
- Kling, N.A.
- Kosciuk, B.N.
- Kovach, P.
- Krinsky, S.
- Kusche, K.
- Lambiase, R.F.
- Liang, X.
- Liaw, C.J.
- Licciardi, W.
- Litvinenko, V.
- Liu, C.
- Louie, W.
- Luo, Y.
- Maggipinto, M.A.
- Mahler, G.J.
- Makdisi, Y.
- Malone, R.
- Mapes, M.
- Marone, A.
- Marr, G.J.
- Martin, B.
- Marusic, A.
- Mead, J.
- Meng, W.
- Méot, F.
- Mernick, K.
- Mi, C.
- Mi, J.-L.
- Michnoff, R.J.
- Miller, T.A.
- Minty, M.G.
- Montag, C.
- Musardo, M.M.
- Myers, M.
- Nayak, S.K.
- Nemesure, S.
- Ng, W.
- Oddo, P.
- Okamura, M.
- Olsen, R.H.
- Orfin, P.
- Padrazo, D.
- Pai, C.
- Palmer, R.B.
- Parker, B.
- Peggs, S.
- Phillips, D.
- Pikin, A.I.
- Pile, P.H.
- Pinayev, I.
- Plate, S.R.
- Podobedov, B.
- Pogorelsky, I.
- Polyanskiy, M.N.
- Ptitsyn, V.
- Rahman, O.H.
- Rakowsky, G.
- Ranjbar, V.H.
- Rank, J.
- Rao, T.
- Raparia, D.
- Rhein, C.
- Riehn, E.J.
- Ritter, J.
- Robert-Demolaize, G.
- Rosas, P.J.
- Rose, J.
- Roser, T.
- Samms, T.
- Sampson, P.
- Samulyak, V.
- Sandberg, J.
- Sayed, H. K.
- Schmalzle, J.
- Schoefer, V.
- Schubert, S.G.
- Seletskiy, S.
- Shaftan, T.V.
- Sharma, S.K.
- Sheehy, B.
- Shen, G.
- Shrey, T.C.
- Shroff, K.
- Singh, O.
- Skaritka, J.
- Smedley, J.
- Smith, K.S.
- Snydstrup, L.
- Steski, D.
- Stratakis, D.

- Swinson, C.
- Tan, Y.
- Tanabe, T.
- Tepikian, S.
- Than, R.
- Theisen, C.
- Thieberger, P.
- Tian, Y.
- Trbojevic, D.
- Tresca, O.
- Tsoupas, N.
- Tuozzolo, J.E.
- Vetter, K.
- Wanderer, P.
- Wang, E.
- Wang, G.M.
- Wang, G.
- Weng, W.-T.
- White, S.M.
- Willeke, F.J.
- Witte, H.
- Wu, Q.
- Xin, T.
- Xu, H.
- Xu, W.
- Yang, L.
- Yang, X.
- Yip, K.
- Zaltsman, A.
- Zelenski, A.
- Zeno, K.
- Zhang, W.

CCR
San Mateo, California, USA
- Collins, G.
- Ferguson, P.
- Ives, L.R.
- Jackson, R.H.
- Karimov, R.
- Marsden, D.
- Read, M.E.

CERN
Geneva, Switzerland
- Adli, E.
- Akroh, A.
- Bartosik, H.
- Bellodi, G.
- Benedetto, E.
- Bruce, R.
- Brüning, O.S.
- Carli, C.
- Comblin, J.F.
- Dimov, V.A.
- Ferracin, P.
- Gilardoni, S.S.
- Granemann Souza, E.
- Höfle, W.
- Khan, V.F.
- Klein, M.
- Kotzian, G.
- Lallement, J.-B.
- Latina, A.
- Lettry, J.
- Li, K.S.B.
- Lombardi, A.M.
- Midttun, O.
- Mikulec, B.
- Ovalle, E.
- Papotti, G.
- Pieloni, T.
- Raginel, V.
- Raich, U.
- Redaelli, S.
- Riddone, G.
- Roncarolo, F.
- Rossi, A.
- Rossi, C.
- Salvachua, B.
- Sanchez Alvarez, J.L.
- Schmidt, F.
- Schulte, D.
- Scrivens, R.
- Tomás, R.
- Valerio, C.A.
- Valloni, A.
- Vretenar, M.
- Wendt, M.
- Yarmohammadi Satri, M.
- Zimmermann, F.

CIPS
Boulder, Colorado, USA
- Bruhwiler, D.L.

CLS
Saskatoon, Saskatchewan, Canada
- Bergstrom, J.C.
- Dallin, L.O.

CNAO Foundation
Milan, Italy
- Pullia, M.

Compa Industries, Inc.
Los Alamos, USA
- Baca, D.
- Bratton, R.E.
- Summers, R.D.

Cornell University (CLASSE), Cornell Laboratory for Accelerator-Based Sciences and Education
Ithaca, New York, USA
- Agladze, N.I.
- Bartnik, A.C.
- Bazarov, I.V.

- Billing, M.G.
- Boulet, L.E.
- Brown, M.
- Bullock, B.
- Clasby, B.
- Conway, J.V.
- Crittenden, J.A.
- Cultrera, L.
- Dobbins, J.
- Duggins, D.O.
- Dunham, B.M.
- Eichhorn, R.G.
- Erickson, N.
- Full, S.J.
- Furuta, F.
- Gabriel, G.
- Ge, G.M.
- Gonnella, D.
- Gulliford, C.M.
- Hall, D.L.
- He, Y.
- Ho, K.M.V.
- Hoffstaetter, G.H.
- Karkare, S.S.
- Kaufman, J.J.
- Kilpatrick, B.M.
- Kim, A.
- Lanzoni, J.A.
- Li, Y.
- Liepe, M.
- Lillard, B.
- Liu, X.
- Mayes, C.E.
- Moore, T.P.
- Nguyen, C.
- O'Connel, T.
- O'Connell, T.I.
- Posen, S.
- Quigley, P.
- Sabol, D.M.
- Savino, J.J.
- Schaff, W.J.
- Sears, J.
- Shemelin, V.D.
- Sikora, J.P.
- Smith, E.N.
- Smolenski, K.W.
- Sonnad, K.G.
- Talman, R.M.
- Valles, N.R.A.
- Veshcherevich, V.
- Wang, H.

Cornell University
Ithaca, New York, USA
- Karkare, S.S.
- Sethna, J.P.

CPI
Palo Alto, California, USA
- Eisen, E.L.
- Kimura, T.

Cryomagnetics, Inc.
Tennessee, USA
- Burkhardt, E.

CSFNSM
Catania, Italy
- Calanna, A.

CSU
Fort Collins, Colorado, USA
- Biedron, S.
- Edelen, J.P.
- Harris, J.R.
- Milton, S.V.
- Sipahi, N.
- Sipahi, T.
- Williams, J.E.

Current Scientific
San Jose, USA
- Current, M.I.

D-Pace
Nelson, British Columbia, Canada
- Christensen, T.
- Dehnel, M.P.
- Potkins, D.E.
- Stewart, T.M.

DCI-UG
León, Mexico
- Castilla, A.

Diamond
Oxfordshire, United Kingdom
- Bartolini, R.
- Hammond, N.P.
- Kay, J.
- Walker, R.P.

Diversified Technologies, Inc.
Bedford, Massachusetts, USA
- Butler, N.
- Gaudreau, M.P.J.
- Kempkes, M.K.
- Kinross-Wright, J.
- Niell, F.M.
- Phillips, R.A.
- Roth, I.
- Schrock, K.
- Simpson, B.E.

Duke ECE
Durham, North Carolina, USA
- Katsouleas, T.C.
- Sahai, A. A.

Elettra-Sincrotrone Trieste S.C.p.A.
Basovizza, Italy
- Cianciosi, F.
- Craievich, P.
- Dal Forno, M.
- Delgiusto, P.
- Fabris, A.
- Gelmetti, F.
- Milloch, M.M.
- Milocco, A.
- Pribaz, F.
- Serpico, C.
- Sodomaco, N.
- Trovò, M.
- Umer, R.
- Veljak, L.

EPFL
Lausanne, Switzerland
- Banfi, D.
- Barranco, J.
- Moens, V.

ESS
Lund, Sweden
- Andersen, K.H.
- Bentley, P.
- Eshraqi, M.
- Henry, P.F.
- Lindroos, M.
- McGinnis, D.P.
- Pitcher, E.J.
- Sabbagh, P.
- Shea, T.J.
- Takibayev, A.

Euclid TechLabs, LLC
Solon, Ohio, USA
- Antipov, S.P.
- Avrakhov, P.V.
- Jing, C.-J.
- Kanareykin, A.
- Kostin, R.A.
- Schoessow, P.
- Zuo, S.S.

Far-Tech, Inc.
San Diego, California, USA
- Barov, N.
- Chang, X.
- Miller, R.H.
- Newsham, D.J.
- Thompson, J.R.
- Wu, D.

Fermilab
Batavia, USA
- Alexahin, Y.I.
- Anderson, J.E.
- Andreev, N.
- Ankenbrandt, C.M.
- Arkan, T.T.
- Awida, M.H.
- Balbekov, V.
- Ball, M.
- Berrutti, P.
- Borissov, E.
- Bossert, R.
- Brice, S.
- Briegel, C.I.
- Bross, A.D.
- Cancelo, G.I.
- Carcagno, R.H.
- Carneiro, J.-P.
- Chase, B.
- Cheban, S.
- Chen, A.Z.
- Chen, M.
- Chung, M.
- Church, M.D.
- Cooper, C.A.
- Czajkowski, J.
- Denisov, D.S.
- Dhanaraj, N.
- Eddy, N.
- Eichten, E.
- Fellenz, B.J.
- Firebaugh, J.D.
- Foley, M.H.
- Ginsburg, C.M.
- Gonin, I.V.
- Grassellino, A.
- Grimm, C.J.
- Harms, E.R.
- Henderson, S.
- Hocker, A.
- Holmes, S.D.
- Huang, Y.
- Hurh, P.
- Jana, M.R.
- Johnson, D.E.
- Kaducak, M.
- Kapin, V.V.
- Kashikhin, V.S.
- Kashikhin, V.V.
- Kasley, P.A.
- Kazakov, S.
- Kephart, R.D.
- Khabiboulline, T.N.
- Klebaner, A.L.
- Kotelnikov, S.
- Kourbanis, I.
- Krave, S.

- Lamm, M.J.
- Lebedev, V.A.
- Lebrun, P.
- Leonova, M.A.
- Leveling, A.F.
- Lipton, R.J.
- Liu, A.
- Lopes, M.L.
- Macridin, A.
- Madrak, R.L.
- Makarov, A.V.
- Makulski, A.
- Merio, M.
- Mishra, C.S.
- Mokhov, N.V.
- Moretti, A.
- Morgan, J.P.
- Nagaitsev, S.
- Nehring, R.
- Neuffer, D.V.
- Nicol, T.H.
- Nogiec, J.M.
- Orlov, Y.O.
- Orris, D.F.
- Ostiguy, J.-F.
- Palmer, M.A.
- Pasquinelli, R.J.
- Passarelli, D.
- Peterson, D.W.
- Peterson, T.J.
- Pfeffer, H.
- Pilipenko, R.V.
- Piot, P.
- Pischalnikov, Y.M.
- Poloubotko, V.
- Premo, K.S.
- Previtali, V.
- Prieto, P.S.
- Pronitchev, O.V.
- Pronskikh, V.S.
- Prost, L.R.
- Rabehl, R.
- Ristori, L.
- Romanov, G.V.
- Rowe, A.M.
- Saewert, G.W.
- Saini, A.
- Schappert, W.
- Schmidt, C.W.
- Schultz, R.P.
- Schwarz, T.A.
- Shemyakin, A.V.
- Shiltsev, V.D.
- Shin, Y.-M.
- Slimmer, D.
- Snopok, P.
- Solyak, N.
- Stabile, P.
- Stancari, G.
- Stanek, R.P.
- Still, D.A.
- Striganov, S.I.
- Sukhanov, A.I.
- Sylvester, C.
- Tartaglia, M.A.
- Terechkine, I.
- Tokpanov, Y.
- Tollestrup, A.V.
- Tompkins, J.C.
- Torun, Y.
- Tropin, I.S.
- Tschirhart, R.S.
- Valishev, A.
- Varghese, P.
- Vivoli, A.
- Volk, J.T.
- Wildman, D.
- Wolff, D.
- Wong, M.
- Yakovlev, V.P.
- Yonehara, K.
- Zlobin, A.V.
- Zuchnik, T.J.

Forschungszentrum Jülich, Peter Gruenberg Institut (PGI-2)
Jülich, Germany
- Catelani, G.

FRIB
East Lansing, Michigan, USA
- Bollen, G.
- Borden, T.
- Bultman, N.K.
- Casagrande, F.
- Chouhan, S.
- Compton, C.
- Crisp, J.L.
- Davidson, K.D.
- DeKamp, J.
- Drewyor, B.
- Durickovic, B.
- Elliott, K.
- Facco, A.
- Fox, A.D.
- Frazee, R.
- Gibson, P.E.
- Glasmacher, T .
- Green, M.A.
- Grender, I.
- He, Z.Q.
- Holland, K.
- Johnson, M.J.
- Jones, S.
- Kiupel, G.
- Leitner, D.
- Leitner, M.
- Lin, L.Y.
- Liu, Z.
- Machicoane, G.
- Malloch, I.M.

- Marti, F.
- Miller, S.J.
- Morgan, G.
- Morris, D.
- Nellis, T.
- Nguyen, P.
- Nolen, J.A.
- Ozelis, J.P.
- Patil, M.S.
- Peng, S.
- Popielarski, J.
- Popielarski, L.
- Pozdeyev, E.
- Putnam, N.
- Rao, X.
- Rodriguez, J.A.
- Russo, T.
- Saito, K.
- Savino, J.J.
- Shuptar, M.
- Stout, D.
- Tanke, E.
- Thronson, C.
- Webber, R.C.
- Wei, J.
- Williams, M.
- Wittmer, W.
- Wu, X.
- Xu, T.
- Xu, Y.
- Yair, O.
- Yamazaki, Y.
- York, R.C.
- Zeller, A.
- Zhang, Y.
- Zhao, Q.
- Zhao, S.
- Zheng, Z.

GSI
Darmstadt, Germany
- Klaus, A.
- Klingbeil, H.
- Schreiber, G.

Gunma University, Heavy-Ion Medical Research Center
Maebashi-Gunma, Japan
- Souda, H.

Homi Bhbha National Institute (HBNI), DAE
Mumbai, India
- Dash, R.

HSRC
Higashi-Hiroshima, Japan
- Miyamoto, A.
- Sasaki, S.

HU/AdSM
Higashi-Hiroshima, Japan
- Okamoto, H.
- Osaki, K.

HZB
Berlin, Germany
- Burrill, A.

I-Tech
Solkan, Slovenia
- Cargnelutti, M.
- Hrovatin, R.
- Jug, G.
- Lemut, P.L.
- Orel, P.
- Zorzut, S.

IAC
Pocatello, IDAHO, USA
- Andrews, A.
- Beezhold, W.
- Berls, B.L.
- Dimitrov, V.I.
- Downer, T.
- Eckman, C.F.
- Folkman, K.
- Kim, Y.
- O'Neill, C.
- Ralph, J.
- Shapovalov, R.V.
- Spielman, R.B.

IAEA
Vienna, Austria
- Sabharwal, S.

IAMS
Taipei, Taiwan
- Wang, J.

IAP/RAS
Nizhny Novgorod, Russia
- Kuzikov, S.V.
- Mishakin, S.
- Savilov, A.V.
- Vikharev, A.A.

IAP
Frankfurt am Main, Germany
- Schempp, A.

IBA
Louvain-la-Neuve, Belgium
- Jongen, Y.

IBM T. J. Watson Center
Yorktown Heights, New York, USA
- Jordan-Sweet, J.

IBS
Daejeon, Republic of Korea
- Joung, M.J.
- Kim, D.G.
- Kim, E.H.
- Kim, H.J.
- Kim, J.-W.
- Kim, J.Y.
- Kim, M.
- Yun, C.C.

IF-UFRGS
Porto Alegre, Brazil
- Bonatto, A.
- Pakter, R.
- Rizzato, F.B.
- Simeoni, W.

IHEP
Beijing, People's Republic of China
- An, Y.W.
- Bai, S.
- Chen, J.F.
- Chen, P.
- Cheng, P.
- Fu, S.
- Gao, J.
- Geng, H.
- Guo, Y.Y.
- Guo, Z.
- Huang, T.
- Jiang, H.
- Li, F.
- Li, P.
- Li, Z.
- Liu, H.C.
- Meng, C.
- Meng, M.
- Mu, Z.C.
- Ouyang, H.F.
- Pei, S.
- Peng, J.
- Qin, Q.
- Rong, L.Y.
- Sun, B.
- Sun, J.L.
- Tang, J.Y.
- Tian, J.M.
- Wang, B.
- Wang, D.
- Wang, N.
- Wang, S.C.
- Wang, S.
- Wang, Y.
- Xiao, M.
- Xin, W.Q.
- Xu, G.
- Xu, S.Y.
- Xu, T.G.
- Yan, F.
- Yang, Z.
- Yue, Y.
- Zeng, L.
- Zhai, J.Y.
- Zhang, C.
- Zhao, F.X.
- Zou, Y.

IIT
Chicago, USA
- Ellison, J.S.
- Freemire, B.T.
- Hanlet, P.M.
- Kunz, J.D.
- Perry, A.
- Snopok, P.
- Torun, Y.

Illinois Institute of Technology
Chicago, Illinois, USA
- Kaplan, D.M.
- Snopok, P.
- Spentzouris, L.K.
- Torun, Y.
- Wisniewski, E.E.
- Yusof, Z.M.

Imperial College of Science and Technology, Department of Physics
London, United Kingdom
- Aslaninejad, M.
- Dover, N.
- Holland, P.R.N.
- Hughes, C.
- Najmudin, Z.
- Nichols, R.M.
- Pasternak, J.
- Piech, J.F.
- Posocco, P.A.
- Pozimski, J.K.
- Savage, P.
- Tsang, S.H.
- Walton, G.W.
- Zalel, S.

Imperial College of Science and Technology
London, United Kingdom
- Mishra, S.

IMP
Lanzhou, People's Republic of China
- He, Y.
- Yang, Y.

Indiana University
Bloomington, Indiana, USA
- Lee, S.-Y.
- Shen, X.

INFN-Pisa
Pisa, Italy
- Somaschini, L.

INFN/LNL
Legnaro (PD), Italy
- Facco, A.

INFN/LNS
Catania, Italy
- Calabretta, L.

Instituto Superior Tecnico
Lisbon, Portugal
- Fonseca, R.A.
- Lopes, N.C.
- Martins, J.L.
- Silva, L.O.
- Vieira, J.

IPM
Tehran, Iran
- Yarmohammadi Satri, M.

ISA
Aarhus, Denmark
- Holm, A.I.S.
- Møller, S.P.
- Thomsen, H.D.

ISU
Pocatello, Idaho, USA
- Andrews, A.
- Buaphad, P.
- Eckman, C.F.
- Kim, Y.

IUCEEM
Bloomington, Indiana, USA
- Lee, S.-Y.
- Shen, X.

JAEA/TARRI
Gunma-ken, Japan
- Ishibori, I.
- Ishizaka, T.
- Okumura, S.
- Yuri, Y.
- Yuyama, T.

JAI
Oxford, United Kingdom
- Pulampong, T.

JLAB
Newport News, Virginia, USA
- Ali, M.M.
- Arenius, D.
- Bachimanchi, R.
- Benson, S.V.
- Bogacz, S.A.
- Brindza, P.D.
- Castilla, A.
- Cheng, G.
- De Silva, S.U.
- Delayen, J.R.
- Derbenev, Y.S.
- Dhakal, P.
- Drury, M.A.
- Ent, R.
- Evtushenko, P.E.
- Freyberger, A.
- Ganni, V.
- Gubeli, J.G.
- Guo, J.
- Harwood, L.
- Henry, J.
- Hofler, A.S.
- Hogan, J.
- Hovater, C.
- Krafft, G.A.
- Legg, R.A.
- Lin, F.
- Mammosser, J.D.
- Morozov, V.S.
- Nadel-Turonski, P.
- Neil, G.
- Park, H.
- Plawski, T. E.
- Powers, T.
- Preble, J.P.

JLab
Newport News, Virginia, USA
- Reece, C.E.

JLAB
Newport News, Virginia, USA
- Rimmer, R.A.
- Satogata, T.
- Wang, H.
- Williams, R.S.
- Wiseman, M.
- Yang, S.
- Zhang, H.
- Zhang, S.
- Zhang, Y.

KEK
Ibaraki, Japan
- Araki, S.
- Arimoto, Y.
- Aryshev, A.S.
- Chin, Y.H.
- Fukuda, M.K.
- Higashi, N.
- Higo, T.
- Honda, Y.
- Iwasaki, M.
- Koiso, H.
- Kubo, K.
- Morita, A.
- Ogitsu, T.
- Ohnishi, Y.
- Ohuchi, N.
- Oide, K.
- Okugi, T.
- Sugimoto, H.
- Takatomi, T.
- Tauchi, T.
- Tawada, M.
- Terunuma, N.
- Tsuchiya, K.
- Urakawa, J.
- Yamaoka, H.
- Yoshida, M.
- Zhou, X.
- Zong, Z.G.

Kress GmbH
Biebergemuend, Germany
- Haeuser, J.

Kuban State University
Krasnodar, Russia
- Frolov, D.

Kyoto ICR
Uji, Kyoto, Japan
- Tongu, H.

Kyoto University, Institute for Advanced Energy
Kyoto, Japan
- Jimbo, K.

Kyoto University
Kyoto, Japan
- Amemiya, N.
- Jimbo, K.

LANL
Los Alamos, New Mexico, USA
- Arsenyev, S.
- Baily, S.A.
- Barkley, W.C.
- Barlow, D.B.
- Batygin, Y.K.
- Björklund, E.
- Carlsten, B.E.
- Coleman, J.E.
- Crawford, M.T.
- Davis, J.
- Draganić, I.
- Duffy, L.D.
- Edwards, R.L.
- Ekdahl, C.
- Elson, S.
- Fortgang, C.M.
- Garnett, R.W.
- Gilpatrick, J.D.
- Gioia, J.G.
- Hall, M.J.
- Haynes, W.B.
- Heath, C.E.
- Huang, C.
- Johnson, J.B.
- Kolski, J.S.
- Kurennoy, S.S.
- Kwan, T.J.
- Lewellen, J.W.
- Lizon, D. C.
- Lyles, J.T.M.
- Macek, R.J.
- Malyzhenkov, A.
- Marksteiner, Q.R.
- Martinez, M.P.
- McCrady, R.C.
- McCuistian, B.T.
- Moir, D.C.
- Naranjo, A.C.
- O'Hara, J.F.
- Olivas, E.R.
- Olivas, P.D.
- Pang, X.
- Rees, D.
- Romero, W.P.
- Rouleau, G.
- Roybal, R.J.
- Russell, S.J.
- Rybarcyk, L.
- Sandoval, Jr., G. M.
- Sedillo, J.D.
- Shchegolkov, D.Y.
- Shelley, F.E.
- Simakov, E.I.
- Spickermann, T.
- Sullivan, G.
- Suvorova, N.A.
- Tajima, T.
- Wangler, T.P.
- Watkins, H.A.
- Yampolsky, N.A.

LBNL
Berkeley, California, USA
- Allezy, A.P.

- Arbelaez, D.
- Bailey, B.J.
- Baptiste, K.M.
- Benedetti, C.
- Berg, K.
- Biocca, A.
- Black, A.T.
- Bowring, D.L.
- Brouwer, L.N.
- Byrd, J.M.
- Casey, P.W.
- Caspi, S.
- Colomb, D.
- Cork, C.W.
- Corlett, J.N.
- Daniels, C.S.
- Daniels, J.
- De Santis, S.
- Delp, W.W.
- DeMello, A.J.
- Denes, P.
- Deshmukh, A.
- Donahue, R.J.
- Doolittle, L.R.
- Doyle, J.A.
- Emma, P.
- Esarey, E.
- Filippetto, D.
- Floyd, J.G.
- Geddes, C.G.R.
- Gonsalves, A.J.
- Greenway, W.G.
- Gunion, R.F.
- Harkins, J.P.
- Harris, G.L.
- Hertlein, M.P.
- Hoff, M.D.
- Huang, G.
- Huang, R.
- Ji, Q.
- Jung, J.-Y.
- Kirz, J.
- Kramasz, T.D.
- Kwiatkowski, S.
- Lambert, A.R.
- Leemans, W.
- Lellinger, R.E.
- Li, D.
- Li, N.
- Lidia, S.M.
- Lou, T.P.
- Ludewigt, B.A.
- Luo, T.H.
- Madur, A.
- Magana, A.
- Mao, H.S.
- Marcus, G.
- Marcus, M.
- Marks, S.
- Matlis, N.H.
- Mitchell, C.E.
- Mittelberger, D.E.
- Monroy, M.T.
- Moroz, V.
- Murphy, K.
- Nakamura, K.
- Nishimura, H.
- Norum, W.E.
- Padmore, H.A.
- Pan, P.
- Papadopoulos, C. F.
- Pappas, G.C.
- Paret, S.
- Paret, Z.
- Penn, G.
- Petermann, K.V.
- Placidi, M.
- Portmann, G.J.
- Prestemon, S.
- Prosnitz, D.
- Qian, H.J.
- Qiang, J.
- Ratti, A.
- Rawlins, A.W.
- Reinsch, M.W.
- Riley, J.R.
- Robin, D.
- Rossi, S.L.
- Ryne, R.D.
- Sannibale, F.
- Scarvie, T.
- Schenkel, T.
- Schlueter, D.
- Schoenlein, R.W.
- Schroeder, C.B.
- Serrano, C.
- Shaw, B.
- Shiraishi, S.
- Sokollik, T.
- Staples, J.W.
- Steier, C.
- Steinke, S.
- Sun, C.
- Syversrud, D. L.
- Tarawneh, H.
- Tóth, C.
- van Tilborg, J.
- Vay, J.-L.
- Venturini, M.
- Vinco, M.
- Virostek, S.P.
- Waldron, W.L.
- Wan, W.
- Warwick, T.
- Weis, C.D.
- Wells, R.P.
- Wilcox, R.B.
- Williams, E.C.
- Wong, J.J.
- Ybarrolaza, N.
- Zimmermann, S.
- Zisman, M.S.

- Zolotorev, M.S.

LETI
Saint-Petersburg, Russia
- Baturin, S.

LLNL
Livermore, California, USA
- Albert, F.
- Anderson, G.G.
- Anderson, S.G.
- Barty, C.P.J.
- Betts, S.M.
- Dayton, E.T.
- Fisher, S.E.
- Fitsos, P.
- Gibson, D.J.
- Grote, D.P.
- Hall, M.
- Hartemann, F.V.
- Marsh, R.A.
- Pak, A.E.
- Peaslee, P.
- Pollock, B.B.
- Poole, B.R.
- Ralph, J.E.
- Rusnak, B.
- Souza, R.
- Tremaine, A.M.
- Wu, S.S.Q.

LLU/MC
Loma Linda, California, USA
- Bashkirov, V.A.
- Schulte, R.W.

Lund University
Lund, Sweden
- Seviour, R.

M.D.A.C.C.
Houston, Texas, USA
- Transtrum, M.K.

MAX-lab
Lund, Sweden
- Eriksson, M.
- Leemann, S.C.
- Olsson, T.

MEPhI
Moscow, Russia
- Bondarenko, T.V.
- Polozov, S.M.
- Smirnov, A.Yu.

MGH-FHBPTC
Boston, Massachusetts, USA
- Flanz, J.

Michigan State University
East Lansing, USA
- Rice, S.A.
- Verboncoeur, J.P.

MIT/PSFC
Cambridge, Massachusetts, USA
- Arsenyev, S.
- Cook, A.M.
- Duan, Z.
- Hummelt, J.S.
- Munroe, B.J.
- Shapiro, M.A.
- Temkin, R.J.
- Zhang, J.X.

MIT
Cambridge, Massachusetts, USA
- Lewis, S.M.

MPI-P
München, Germany
- Reimann, O.

MPI
Muenchen, Germany
- Muggli, P.

MSU
East Lansing, Michigan, USA
- Berz, M.
- Loseth, B.T.
- Makino, K.

Muons, Inc
Illinois, USA
- Ankenbrandt, C.M.
- Dudas, A.
- Dudnikov, V.G.
- Flanagan, G.
- Johnson, R.P.
- Kahn, S.A.
- Kazakevich, G.M.
- Marhauser, F.
- Neubauer, M.L.
- Nipper, J.H.
- Roberts, T.J.
- Vorobiev, L.G.
- Yoshikawa, C.Y.

MuPlus, Inc.
Newport News, USA
- Marhauser, F.

Nano Synergy, Inc.
Downers Grove, USA
- Insepov, Z.
- Nurkenov, S.

National Institute of Radiological Sciences
Chiba, Japan
- Fujita, T.F.

NCU
Chung Li, Taiwan
- Chen, S.-H.

NHMFL
Tallahassee, Florida, USA
- Park, J.
- Stillwell, R.L.

NIFS
Gifu, Japan
- Obana, T.

Niowave, Inc.
Lansing, Michigan, USA
- Boulware, C.H.
- Grimm, T.L.
- Jecks, R.
- Yancey, J.A.

NIRS
Chiba-shi, Japan
- Furukawa, T.
- Hara, Y.
- Iwata, Y.
- Mizushima, K.
- Murakami, T.M.
- Nakao, M.
- Noda, A.
- Noda, K.
- Sato, S.
- Shirai, T.
- Shoda, K.
- Suzuki, S.S.

Northern Illinois University
DeKalb, Illinois, USA
- Abeyratne, S.
- Al Marzouk, A.A.
- Blomberg, B.R.
- Boyden, D.
- Erdelyi, B.
- Gee, A.J.
- Grabenhofer, A.F.
- Mihalcea, D.
- Panuganti, H.
- Piot, P.
- Prokop, C.R.
- Robak, S.
- Schaumburg, H.D.
- Shin, Y.-M.
- Xu, T.

NPS
Monterey, California, USA
- Bennett, C.W.
- Galt, M.D.
- Holmes, A.D.
- Kara, A.
- Swent, R.

NSCL
East Lansing, Michigan, USA
- Alt, D.M.
- Baumann, T.
- Benatti, C.
- Brandon, J.F.
- Chouhan, S.
- Constan-Wahl, D.
- Cooper, K.
- DeKamp, J.
- Durickovic, B.
- Elliott, K.
- Johnson, M.J.
- Kittimanapun, K.
- Krause, S.W.
- Lapierre, A.
- Lawton, D.
- Leitner, D.
- Lin, L.Y.
- Magsig, C.
- Montes, F.
- Morrissey, D.J.
- Nash, S.
- Ottarson, J.
- Perdikakis, G.
- Portillo, M.
- Rencsok, R.
- Rodriguez, J.A.
- Schwarz, S.
- Steiner, M.
- Sumithrarachchi, C.
- Syphers, M.J.
- Williams, S.J.
- Williams, S.
- Wittmer, W.
- Wu, X.
- Zhao, Q.

ODU
Norfolk, Virginia, USA
- Castilla, A.
- De Silva, S.U.
- Deitrick, K.E.
- Delayen, J.R.
- Gamage, B.R.P.

- Hopper, C.S.
- Olave, R.G.
- Park, H.
- Satogata, T.

OHEP/DOE
Germantown, MD, USA
- Colby, E.R.

Old Dominion University
Norfolk, Virginia, USA
- Hyde, C.

Omega-P, Inc.
New Haven, USA
- Hirshfield, J.L.

ORNL RAD
Oak Ridge, Tennessee, USA
- DeGraff, B.
- Neustadt, T.S.
- Proulx, J.A.
- Saethre, R.B.
- Saunders, J.
- Shin, K.R.
- Vandygriff, D.M.

ORNL
Oak Ridge, Tennessee, USA
- Aleksandrov, A.V.
- Anderson, D.E.
- Champion, M.S.
- Coleman, A.
- Cousineau, S.M.
- Danilov, V.V.
- Deibele, C.
- Galambos, J.
- Gorlov, T.V.
- Holmes, J.A.
- Howell, M.P.
- Kang, Y.W.
- Kim, S.-H.
- Liu, Y.
- Pennisi, T.R.
- Peplov, V.V.
- Piller, C.
- Santana, M.
- Shishlo, A.P.
- Stockli, M.P.
- Strong, W.H.
- Welton, R.F.
- Zhukov, A.P.

PAL
Pohang, Kyungbuk, Republic of Korea
- Kang, H.-S.

Particle Beam Lasers, Inc.
Northridge, California, USA
- Souchlas, N.

PHOTONIS USA PENNSYLVANIA, INC.
Lancaster, USA
- DeFazio, J.

Politecnico di Torino
Torino, Italy
- Collura, M.G.

PPPL
Princeton, New Jersey, USA
- Davidson, R.C.
- Gilson, E.P.
- Grisham, L.
- Stepanov, A.D.

Private Address
Westmont, USA
- Borland, M.

PSI
Villigen PSI, Switzerland
- Hunziker, S.
- Schlott, V.

Purdue University
West Lafayette, Indiana, USA
- Boon, L.E.
- Qi, M.

Pusan National University
Pusan, Republic of Korea
- Lee, H.-J.

PU
Princeton, New Jersey, USA
- McDonald, K.T.

R&M Technical Enterprises
Pleasanton, California, USA
- Hamm, R.W.

RadiaBeam
Santa Monica, USA
- Agustsson, R.B.
- Andonian, G.
- Badakov, H.
- Boucher, S.
- Campese, T.J.
- Chen, Y.C.
- Faillace, L.

- Frigola, P.
- Grandsaert, T.J.
- Harrison, M.A.
- Hartzell, J.J.
- Jacobson, B.T.
- Murokh, A.Y.
- O'Shea, F.H.
- Ruelas, M.
- Seung, S.
- Smirnov, A.V.
- Spranza, E.
- Storms, S.
- Verma, A.
- Woods, K.E.
- Wu, S.

RAS/INR
Moscow, Russia
- Klenov, V.S.
- Zubets, V.

RISE
Tokyo, Japan
- Sakaue, K.
- Washio, M.

Ruhr-Universität Bochum
Bochum, Germany
- Eliasson, B.

SBUNSL
Stony Brook, New York, USA
- Lefferts, R.S.

SBU
Stony Brook, USA
- Chen, H.C.
- Gaowei, M.
- Khalil, N.Z.
- Liang, X.
- Maharjan, C.
- Muller, E.M.
- Yu, K.

Scandinova Systems AB
Uppsala, Sweden
- Eaton, D.W.

Siemens AG, Healthcare Technology and Concepts
Erlangen, Germany
- Beasley, P.

Siemens LLC
Moscow, Russia
- Sharkov, G.B.

Siemens Research Center
Moscow„ Russia
- Ivanov, E.V.
- Krasnov, A.A.
- Nikolskiy, K.I.
- Polikhov, S.A.
- Řežanov, I.
- Smirnov, A.Yu.

Sigmaphi Japan
Tokyo, Japan
- Swinnen, L.

Sigmaphi
Vannes, France
- Antoine, S.
- Beeckman, W.
- Bocher, P.
- Forest, F.
- Jehanno, P.
- Jivkov, P.
- Leray, M.J.
- Taillardat, S.

SIMIT
Shanghai, People's Republic of China
- Qiao, S.

SINAP
Shanghai, People's Republic of China
- Chen, C.
- Jin, J.
- Wen, Y.M.
- Wu, J.
- Yin, L.
- Zhang, J.D.
- Zhao, Z.T.
- Zhou, Q.G.

SLAC
Menlo Park, California, USA
- Adli, E.
- Adolphsen, C.
- Bane, K.L.F.
- Cesaratto, J.M.
- Clarke, C.I.
- Corde, S.
- Decker, F.-J.
- Delahaye, J.-P.
- Ding, Y.
- Dunning, M.P.
- Dusatko, J.E.
- England, R.J.
- Farkas, Z.D.
- Fisher, A.S.
- Fox, J.D.
- Frederico, J.T.
- Frisch, J.C.

- Ge, L.
- Gessner, S.J.
- Hast, C.
- Hettel, R.O.
- Hogan, M.J.
- Huang, Z.
- Jobe, R.K.
- Ko, C.
- Krasnykh, A.
- Lee, C.
- Li, H.
- Li, S.Z.
- Li, Z.
- Limborg-Deprey, C.
- Litos, M.D.
- Marín, E.
- Maxwell, T.J.
- McCormick, D.J.
- Montazeri, B.
- Nantista, C.D.
- Ng, C.-K.
- Noble, R.J.
- Novokhatski, A.
- Nuhn, H.-D.
- Pellegrini, C.
- Pollock, K.M.
- Raubenheimer, T.O.
- Rivetta, C.H.
- Ross, M.C.
- Safranek, J.A.
- Soong, K.
- Spencer, J.E.
- Stupakov, G.V.
- Sullivan, M.K.
- Tian, K.
- Turgut, O.
- Walz, D.R.
- Warnock, R.L.
- Weathersby, S.P.
- White, G.R.
- Woodley, M.
- Wu, J.
- Wu, Z.
- Xiao, L.
- Yakimenko, V.
- Yan, Y.T.

SOLEIL
Gif-sur-Yvette, France
- Klein, M.

Soreq NRC
Yavne, Israel
- Perry, A.

STAAR/AWR Corporation
Mequon, USA
- DeFord, J.F.
- Held, B.L.
- Nichols, A.A.

Stanford University
Stanford, California, USA
- Byer, R.L.
- McGuinness, C.
- Montazeri, B.
- Peralta, E.A.
- Soong, K.

STFC/DL/ASTeC
Daresbury, Warrington, Cheshire, United Kingdom
- McIntosh, P.A.
- Moss, A.J.
- Wheelhouse, A.E.

STFC/RAL/ASTeC
Chilton, Didcot, Oxon, United Kingdom
- Rogers, C.T.

STFC/RAL
Chilton, Didcot, Oxon, United Kingdom
- Densham, C.J.
- Letchford, A.P.
- Pozimski, J.K.
- Tarrant, J.S.

Stony Brook University
Stony Brook, USA
- Belomestnykh, S.A.
- Ben-Zvi, I.
- Cook, N.M.
- Liang, X.
- Litvinenko, V.
- Muller, E.M.
- Ruiz-Osés, M.
- Shkolnikov, P.
- Xin, T.

Susan Felch Consulting
Los Altos Hills, California, USA
- Felch, S.B.

Syracuse University
Syracuse, USA
- Cowan, E.E.

Taylor Consulting
USA
- Taylor, M.C.

Tech-X
Boulder, Colorado, USA
- Bell, G.I.
- Choi, Y.
- Cormier-Michel, E.

- Dimitrov, D.A.
- Nieter, C.
- Pogorelov, I.V.
- Schwartz, B.T.
- Stoltz, P.
- Veitzer, S.A.

Technion
Haifa, Israel
- Schächter, L.

Texas A&M University
College Station, Texas, USA
- Assadi, S.
- Collins, C.
- Comeaux, J.
- Damborsky, K.C.
- Kellams, J.N.
- Lu, F.
- Mann, T.L.
- McIntyre, P.M.
- Melconian, K.E.
- Pogue, N.
- Sattarov, A.
- Sooby, E.
- Tsvetkov, P.V.

The Imperial College of Science, Technology and Medicine
London, United Kingdom
- Larose, H.

The University of Texas at Austin
Austin, Texas, USA
- Hegelich, B.M.

The University of Tokyo, Nuclear Professional School
Ibaraki-ken, Japan
- Dobashi, K.
- Fujiwara, T.
- Uesaka, M.

Tohoku University, Research Center for Electron Photon Science
Sendai, Japan
- Hama, H.
- Hinode, F.

Toshiba
Tokyo, Japan
- Nagamoto, Y.
- Orikasa, T.
- Takayama, S.
- Yazawa, T.

TRIUMF, Canada's National Laboratory for Particle and Nuclear Physics
Vancouver, Canada
- Ang, Z.T.
- Baartman, R.A.
- Bylinskii, I.V.
- Calic, S.
- Chao, Y.-C.
- Dale, D.
- Gong, C.
- Koscielniak, S.R.
- Laxdal, R.E.
- Mammarella, F.
- Merminga, L.
- Mitra, A.K.
- Vrielink, A.R.
- Zvyagintsev, V.

Tsinghua University
Beijing, People's Republic of China
- Zeng, M.

TU Darmstadt
Darmstadt, Germany
- Kürzeder, T.

TUB
Beijing, People's Republic of China
- Chen, H.B.
- He, Z.Q.
- Huang, W.-H.
- Lu, W.
- Lu, X.H.
- Tang, C.-X.
- Xu, X.L.
- Yang, Y.
- Zheng, Z.

UCLA
Los Angeles, California, USA
- An, W.
- Andonian, G.
- Cesar, D.B.
- Clayton, C.E.
- Davidson, A.W.
- Decyk, V.K.
- Ding, X.P.
- Duris, J.P.
- Fukasawa, A.
- Gong, C.
- Ho, L.V.
- Hubbard, W.A.
- Joshi, C.
- Li, R.K.
- Lu, W.
- Marsh, K.A.
- McNeur, J.C.
- Moody, J.T.
- Mori, W.B.
- Musumeci, P.

- O'Shea, F.H.
- Pellegrini, C.
- Pigeon, J.J.
- Regan, C.
- Roberts, K.G.
- Rosenzweig, J.B.
- Shaw, J.L.
- Threlkeld, E.W.
- To, H.L.
- Tochitsky, S.
- Tsung, F.S.
- Vafaei-Najafabadi, N.
- Xi, Y.
- Yakub, A.
- Yu, P.

UFPel
Pelotas, Brazil
- Bonatto, C.

UFPR
Curitiba, Brazil
- Bonatto, A.
- Lopes, S.R.

UFRGS
Porto Alegre, Brazil
- Nunes, R.P.

UMAN
Manchester, United Kingdom
- D'Elia, A.
- Jones, R.M.
- Nesmiyan, I.

UMD
College Park, Maryland, USA
- Beaudoin, B.L.
- Bernal, S.
- Cornacchia, M.
- Dragt, A. J.
- Feldman, D.W.
- Fiorito, R.B.
- Haber, I.
- Kishek, R.A.
- Koeth, T.W.
- Liu, C.-S.
- Liu, T.-C.
- Mo, Y.
- Poor Řežaei, K.
- Ruisard, K.J.
- Shao, X.
- Stem, W.D.
- Sutter, D.F.
- Zhang, H.D.

UMiss
University, Mississippi, USA
- Luo, T.H.
- Summers, D.J.

UNAL
Bogota D.C, Colombia
- Cardona, J.F.
- Garcia-Bonilla, A.C.

Uni HH
Hamburg, Germany
- Hidding, B.

University of Chicago
Chicago, Illinois, USA
- Zolkin, T.V.

University of Florida
Gainesville, Florida, USA
- Turvey, M.W.

University of Huddersfield
Huddersfield, United Kingdom
- Albright, S.C.P.
- Barlow, R.J.
- Cywinski, R.
- Ratcliffe, N.
- Seviour, R.

University of Illinois
Urbana, USA
- Chiang, T.-C.
- Miller, T.J.

University of Kassel
Kassel, Germany
- Bayer, E.
- Zipf, P.

University of Oslo
Oslo, Norway
- Adli, E.

University of Pennsylvania School of Medicine, Perelman Center for Advanced Medicine
Philadelphia, USA
- Lin, A.

University of Tennessee
Knoxville, Tennessee, USA
- Fathy, A.E.

University of Tokyo
Tokyo, Japan
- Koyama, K.
- Matsumura, Y.
- Tagi, K.

University of Warwick
Coventry, United Kingdom
- Back, J.J.

US DOE
Washington, USA
- Zisman, M.S.

USC
Los Angeles, California, USA
- Fang, Y.
- Muggli, P.

USTC/NSRL
Hefei, Anhui, People's Republic of China
- Huang, R.

UTK
Knoxville, Tennessee, USA
- Potts, R.E.

UW-Madison/PD
Madison, Wisconsin, USA
- Lawler, J.E.
- Yavuz, D.

UW-Madison/SRC
Madison, Wisconsin, USA
- Bisognano, J.
- Bissen, M.J.
- Bosch, R.A.
- Efremov, M.Y.
- Eisert, D.
- Fisher, M.V.
- Green, M.A.
- Jacobs, K.
- Keil, R.G.
- Kleman, K.J.
- Rogers, G.C.
- Severson, M.C.
- Wehlitz, R.
- Yavuz, D.

Vanderbilt University, W.M. Keck Foundation Free-Electron Laser Center
Nashville, USA
- Gabella, W.E.

Vanderbilt University
Nashville, TN, USA
- Brau, C.A.
- Choi, B.K.
- Ivanov, B.L.
- Jarvis, J.D.
- Mendenhall, M.H.

Varian Medical Systems, Oncology Systems
Palo Alto, USA
- Clayton, J.E.

VECC
Kolkata, India
- Bhattacharyya, P.

Victoria University
Victoria, B.C., Canada
- Storey, D.W.

Virginia Polytechnic Institute and State University
Blacksburg, USA
- Huber, P.

Waseda University
Tokyo, Japan
- Endo, A.
- Koshiba, Y.
- Mizugaki, M.
- Nishimura, Y.
- Nishiyama, M.
- Nonomura, K.
- Sakaue, K.
- Sato, R.
- Takahashi, T.
- Washio, M.
- Yoshida, Y.

Washington University in St. Louis
St. Louis, USA
- Voller, T.

Washington University Medical School
St. Louis, USA
- Lapi, S.E.

Yale University, Beam Physics Laboratory
New Haven, Connecticut, USA
- Jiang, Y.
- Shchelkunov, S.V.

Yale University, Physics Department
New Haven, CT, USA
- Hirshfield, J.L.

Participants List